Head and Neck Imaging

Fourth Edition

Peter M. Som ▪ Hugh D. Curtin

VOLUMES ONE & TWO

SINONASAL CAVITIES

ORBIT AND VISUAL PATHWAYS

CENTRAL SKULL BASE

JAWS AND TEMPOROMANDIBULAR JOINTS

Mosby

VISIT…

Head and Neck Imaging

Copyright © 2003, Mosby, Inc. All rights reserved.

Copyright © 2003, Mosby, Inc. All rights reserved.

Head and Neck Imaging

FOURTH EDITION

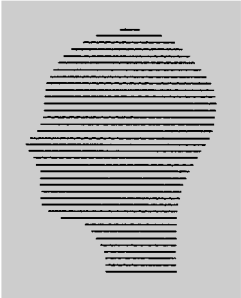

EDITED BY

Peter M. Som, M.D.
Professor of Radiology and Otolaryngology
Mount Sinai School of Medicine of New York University;
Chief of Head and Neck Radiology
Mount Sinai Hospital
New York, New York

Hugh D. Curtin, M.D.
Professor of Radiology
Harvard Medical School;
Chief of Radiology
Department of Radiology
Massachusetts Eye and Ear Infirmary
Boston, Massachusetts

Mosby

Copyright © 2003, Mosby, Inc. All rights reserved.

Mosby
An Affiliate of Elsevier Science

11830 Westline Industrial Drive
St. Louis, Missouri 63146

HEAD AND NECK IMAGING
Set ISBN:0-323-00942-5
Volume 1: 9997626044

FOURTH EDITION
Copyright © 2003, 1996, 1991, 1984 by Mosby, Inc.

All rights reserved. No part of this publication may be reproduced or transmitted in any form or by any means, electronic or mechanical, including photocopy, recording, or any information storage and retrieval system, without permission in writing from the publisher.

Permission to photocopy or reproduce solely for internal or personal use is permitted for libraries or other users registered with the Copyright Clearance Center, provided that the base fee of $4.00 per chapter plus $.10 per page is paid directly to the Copyright Clearance Center, 222 Rosewood Drive, Danvers, Massachusetts 01923. This consent does not extend to other kinds of copying, such as copying for general distribution, for advertising or promotional purposes, for creating new collected works, or for resale.

Library of Congress Cataloging-in-Publication Data

Head and neck imaging/[edited by] Peter M. Som, Hugh D. Curtin—4th ed.
p. ; cm.
Includes bibliographical references and index.
ISBN 0-323-00942-5
1. Head—Imaging. 2. Neck—Imaging. I. Som, Peter M. II. Curtin, Hugh D.
[DNLM: 1. Head—radiography. 2. Magnetic Resonance Imaging. 3. Neck—radiography. 4. Tomography, X-Ray Computed. WE 705 H43031 2003]
RC936 .H43 2003
617.5′10754—dc21

2002075146

Acquisitions Editor: Janice Gaillard
Developmental Editor: Hazel Hacker, Heather Krehling

GW/MVY

Printed in the United States of America

Last digit is the print number: 9 8 7 6 5 4 3 2 1

Copyright © 2003, Mosby, Inc. All rights reserved.

To Judy and Carole,

As we worked the long hours on this edition, the two of you gave us encouragement, support, love, and showed exceptional tolerance. We truly appreciate all that you did for us and the time that you allowed us to have in order to make this fourth edition possible. It is with our love and thanks that we dedicate Head and Neck Imaging *to you.*

P.M.S. and H.D.C.

Copyright © 2003, Mosby, Inc. All rights reserved.

Copyright © 2003, Mosby, Inc. All rights reserved.

Preface

When we embarked on the fourth edition of *Head and Neck Imaging,* every attempt was made to address the constructive comments we received from readers and reviewers of the third edition. Thus, the organization of this book has been modified and because many readers wanted *Head and Neck Imaging* to serve as a single definitive reference, the fourth edition has been expanded. *Head and Neck Imaging* is now more encyclopedic and detailed, presents more pathology, contains more images, and covers new imaging technologies. Although space limitations and a publishing date never allow a text to be truly all-encompassing, we have attempted to comply as thoroughly as possible with these requests.

The table of contents reflects a re-organization of the book. Compared to the third edition, this edition not only contains several new atlases of normal anatomy, but in many areas there are more detailed discussions of the anatomy. Pertinent physiology is now more thoroughly discussed to allow a better understanding of the function of the specific anatomic units. The pathology sections throughout the book have been enlarged to not only be more inclusive, but also to provide updated and more complete nomenclature and references for each disease. These enlarged sections also discuss pertinent statistics, new genetic concepts relating to a disease, epidemiological data, and contain a more detailed description of the pathology. As pathology is ever more becoming the final arbiter of disease, we believe that *Head and Neck Imaging* should serve, as much as possible, as a resource for this information.

Toward the pursuit of a more complete understanding of the field of head and neck imaging, a chapter discussing the current concepts of the genetics of tumor development and metastasis has been included. This chapter was added because we believe that in the near future, genetic-based imaging, a field now in its infancy, will become a considerably more important technology.

Being an imaging book, many new images have been included and unique older images have been upgraded. In addition, there is now a long overdue new chapter on ultrasound. The inclusion of this chapter fills a deficiency in the prior editions of *Head and Neck Imaging.* There is also a chapter dealing with the use of newer imaging modalities such as PET, MR-spectroscopy, and Thallium-201 imaging. The inclusion of these new sections better rounds out the scope of modalities that are currently being utilized in the field. There are also new chapters on swallowing studies, the trachea, skin and soft tissue lesions, and neural tumor spread. The paranasal sinus plain film section of the third edition was retained, as the growth of emergency room medicine has resulted in a resurgence of the use of these films.

The quality of any book is dependent on the excellence of the contributors' chapters. We were especially fortunate that our contributors submitted thorough, current, and detailed chapters accompanied by high quality images. As editors, it is always a pleasure to work with such wonderful material. In addition to asking some contributors from previous editions to again help us, there are many new contributors to the fourth edition. We are especially pleased with the enthusiastic contributions made by these new contributors, as these radiologists represent the future of the field.

Last, but far from least, the editors want to thank all of the editorial people at Saunders/Mosby, without whose guidance, patience, and knowledgeable advice this edition could not have been made. It was through their efforts that a new fresh format for the book was created. This includes more reference charts and tables, and a ''new look'' that we believe will make the fourth edition more accessible to our readers.

It is our hope that our readers will utilize the fourth edition of *Head and Neck Imaging* to not only help them in the diagnosis of head and neck imaging cases, but as a resource for the knowledge that is necessary to attain a well informed understanding of this fascinating and rewarding field.

Sincerely,

P.M.S.
H.D.C.

Copyright © 2003, Mosby, Inc. All rights reserved.

Copyright © 2003, Mosby, Inc. All rights reserved.

Contributors

Nadir G. Abdelrahman, M.D.
Post-Doctoral Fellow,
Massachusetts General Hospital,
Boston, Massachusetts

James J. Abrahams, M.D.
Professor of Diagnostic Radiology (Neuroradiology) and Surgery (Otolaryngology),
Director of Medical Studies,
Yale University School of Medicine,
New Haven, Connecticut

Sait Albayram, M.D.
Assistant Professor, Radiology,
Cerrahpasa Medical School,
Department of Radiology,
Kocamustafapasa Istanbul, Turkey

Suzanne Aquino, M.D.
Associate Radiologist,
Massachusetts General Hospital,
Assistant Professor of Radiology,
Harvard Medical School,
Boston, Massachusetts

Derek C. Armstrong
Staff, Division of Neuroradiology,
The Hospital for Sick Children,
Assistant Professor,
University of Toronto,
Toronto, Canada

Armand Balboni, M.Phil
Center for Anatomy and Functional Morphology,
The Lillian and Henry M. Stratton-Hans Popper Department of Pathology,
Mount Sinai School of Medicine,
New York University,
New York, New York

Mark A. Augustyn, M.D.
Ohio State University,
Columbus, Ohio

Shahid Aziz, D.M.D., M.D.
Assistant Professor,
University of Medicine and Dentistry of New Jersey,
New Jersey Dental School,
Newark, New Jersey

Bruce S. Bauer, M.D., F.A.C.S.
Chief, Division of Plastic Surgery,
The Children's Memorial Hospital,
Associate Professor of Surgery,
The Feinberg School of Medicine,
Northwestern University,
Chicago, Illinois

Mark L. Benson, M.D.
President, Radiology Associates, Inc.
Wheeling Hospital,
Wheeling, West Virginia

Larissa T. Bilaniuk, M.D.
Staff Neuroradiologist,
Children's Hospital of Philadelphia,
Professor of Radiology,
University of Pennsylvania School of Medicine,
Philadelphia, Pennsylvania

Susan I. Blaser, M.D.
Staff Neuroradiologist,
Division of Neuroradiology,
The Hospital for Sick Children
Associate Professor,
Medical Imaging,
University of Toronto,
Toronto, Canada

Margaret S. Brandwein, M.D.
Associate Professor of Pathology and Otolaryngology,
Mount Sinai School of Medicine,
New York, New York

Jan W. Casselman, M.D., Ph.D.
Director of MRI and Head and Neck Radiology,
Department of Medical Imaging—MRI
A.Z. Sint-Jan Brugge A.V., Bruges
A.Z. Sint-Augustinus, Antwerp, Belgium

J.A. Castelijns
Professor Doctor,
VU Medical Centre,
Amsterdam, The Netherlands

Copyright © 2003, Mosby, Inc. All rights reserved.

Donald W. Chakeres, M.D.
Professor of Radiology,
Department of Radiology,
Head of Neuroradiology and MRI Research,
Ohio State University,
Columbus, Ohio

Hugh D. Curtin, M.D.
Chief of Radiology,
Massachusetts Eye and Ear Infirmary,
Department of Radiology,
Boston, Massachusetts

Bradley N. Delman, M.D.
Assistant Attending Radiologist,
Mount Sinai Medical Center,
Assistant Professor of Radiology,
Mount Sinai School of Medicine of New York University,
New York, New York

Nancy J. Fischbein, M.D.
Assistant Professor of Radiology,
University of California at San Francisco,
San Francisco, California

Lawrence E. Ginsberg, M.D.
Associate Professor, Radiology and Head and Neck Surgery,
University of Texas,
M.D. Anderson Cancer Center,
Houston, Texas

Tessa Goldsmith, M.A., C.C.C./S.L.P
Clinical Specialist-Speech Language Pathologist,
Massachusetts General Hospital,
Boston, Massachusetts

Anton N. Hasso, M.D.
Professor, Department of Radiological Sciences,
Director, Neuroimaging Research and Development,
College of Medicine,
Professor of Radiological Science,
Professor of Otolaryngology,
Head and Neck Surgery,
University of California at Irvine,
Orange, California

Roy A. Holliday, M.D.
Director of Radiology,
The New York Eye and Ear Infirmary,
Professor of Clinical Radiology,
Albert Einstein College of Medicine,
New York, New York

Michael W. Hayt, M.D., D.M.D.
Director of Neuroradiology,
Center for Diagnostic Radiology,
Winter Park, Florida

Patricia A. Hudgins, M.D.
Professor of Radiology/Neuroradiology,
Director of Neuroradiology Fellowship Program,
Emory University School of Medicine/Hospital,
Atlanta, Georgia

Edward M. Johnson, Ph.D.
Vice-Chairman for Research,
Department of Pathology,
Associate Director for Shared Resources,
D.H. Ruttenberg Cancer Center,
Professor,
Pathology, Molecular Biology, and Cancer Biology,
Mount Sinai School of Medicine,
New York, New York

Takashi Kaneda, D.D.S., Ph.D.
Chief and Professor of Radiology,
Department of Radiology,
Nihon University School of Dentistry at Matsudo,
Japan

Edward E. Kassel, D.D.S., M.D., F.R.C.P.C., F.A.C.R
Neuroradiologist,
Mount Sinai Hospital and University Health Network,
Associate Professor,
Departments of Medical Imaging, Otolaryngology, and Ophthalmology,
University of Toronto,
Toronto, Canada

Todd T. Kingdom, M.D.
Director, Rhinology and Sinus Surgery,
Associate Professor,
Department of Otolaryngology,
University of Colorado Health Sciences Center,
Denver, Colorado

Ilhami Kovanlikaya, M.D.
Research Director,
Cedars-Sinai Medical Center,
Los Angeles, California

Jeffrey T. Laitman, Ph.D.
Distinguished Professor,
Professor and Director of Anatomy and Functional Morphology,
Professor of Otolaryngology,
Director of Gross Anatomy,
Mount Sinai School of Medicine,
New York, New York

Copyright © 2003, Mosby, Inc. All rights reserved.

J.S. Lameris, M.D., Ph.D.
Professor of Radiology,
University of Amsterdam,
Academic Medical Center,
Amsterdam, The Netherlands

William Lawson, M.D.
Professor, Vice-Chairman,
Department of Otolaryngology,
Mount Sinai Medical Center,
New York, New York

Michael H. Lev, M.D.
Director, Emergency Neuroradiology
and Neurovascular Laboratory,
Massachessetts General Hospital,
Staff Radiologist,
Massachessetts Eye and Ear Infirmary,
Assistant Professor of Radiology,
Harvard Medical School,
Boston, Massachusetts

William W.M. Lo, M.D.
Section Chief, Neurology,
St. Vincent Medical Center,
Clinical Professor of Radiology,
University of Southern California,
Los Angeles, California

Laurie A. Loevner, M.D.
Associate Professor of Radiology and
Otorhionlaryngology: Head and Neck Surgery,
University of Pennsylvania Medical System,
University of Pennsylvania School of Medicine,
Philadelphia, Pennsylvania

Mahmood F. Mafee, M.D.
Head, Department of Radiology,
Professor of Radiology,
University of Illinois at Chicago

M. Marcel Maya, M.D.
Neuroradiologist,
Department of Imaging,
Cedars Sinai Medical Center,
Los Angeles, California

David G. McLone
Department of Neurosurgery,
Childrens Memorial Hospital,
Chicago, Illinois

Suresh K. Mukherji, M.D.
Chief of Neuroradiology and Head and Neck Radiology,
University of Michigan,
Department of Radiology,
Ann Arbor, Michigan

Thomas P. Naidich, M.D., F.A.C.R.
Vice Chairman for Academic Affairs,
Professor of Radiology,
Professor of Neurosurgery,
Professor of Anatomy and Functional Pathology,
Mount Sinai Medical Center,
New York, New York

William R. Nemzek, M.D.
Medford Radiological Group,
Medford, Oregon

Tomohiro Okano, D.D.S., Ph.D.
Professor,
Department of Radiology,
Showa University School of Dentistry,
Tokyo, Japan

Patrick J. Oliverio, M.D.
Neuroradiologist,
Fairfax Radiological Consultants,
Inova Fairfax Hospital,
Fairfax, Virginia

James Rabinov, M.D.
Interventional Neuroradiology,
Massachusetts General Hospital,
Instructor in Radiology,
Harvard University,
Boston, Massachusetts

Deborah L. Reede, M.D.
Associate Professor,
New York University,
New York, New York

Joy S. Reidenberg, Ph.D.
Associate Professor,
Mount Sinai School of Medicine,
New York, New York

Caroline D. Robson, M.D.
Assistant Professor, Division of Radiology,
Children's Hospital,
Assistant Professor of Radiology,
Harvard Medical School,
Boston, Massachusetts

Copyright © 2003, Mosby, Inc. All rights reserved.

Reuben Rock, D.D.S., M.D.
Staff Radiologist,
Hartford Hospital,
Hartford, Connecticut

Laura V. Romo, M.D.
Assistant in Radiology,
Harvard Medical School,
Massachusetts Eye and Ear Infirmary,
Boston, Massachusetts

Osamu Sakai, M.D., Ph.D.
Research Fellow,
Department of Radiology,
Massachusetts Eye and Ear Infirmary,
Harvard Medical School,
Boston, Massachusetts
Assistant Professor,
Department of Radiology,
Jichi Medical School,
Tochigi, Japan

Pina C. Sanelli, M.D.
Clinical Assistant Attending,
New York Presbyterian Hospital,
Cornell Campus,
Assistant Professor of Radiology,
Weill Medical College of Cornell University,
New York, New York

Tsukasa Sano, D.D.S., Ph.D.
Assistant Professor,
Department of Radiology,
Showa University School of Dentistry,
Tokyo, Japan

J. Pierre Sasson, M.D.
Director of MRI Services,
Associate Director of Radiology Residency,
Mount Auburn Hospital,
Cambridge, Massachusetts
Clinical Instructor,
Harvard Medical School,
Boston, Massachusetts

Peter J. Savino, M.D.
Director, The Neuro-Ophthalmology Service,
Wills Eye Hospital,
Chairman, Department of Ophthalmology,
The Graduate Hospital,
Philadelphia, Pennsylvania

Charles J. Schatz, M.D., F.A.C.R.
Director of Head and Neck Imaging,
Tower Radiology,
Beverly Hills, California
Clinical Professor of Radiology,
Clinical Professor of Otolaryngology,
University of Southern California School of Medicine,
Los Angeles, California

Steven J. Scrivani, M.D., D.D.S., D.S.C.
Director,
The Center for Oral, Facial, and Head Pain,
The Pain Management Center,
New York Presbyterian Hospital,
Columbia Presbyterian Medical Center,
Edward V. Zegarelli Assistant Professor,
Oral and Maxillofacial Surgery,
Columbia University,
Columbia-Presbyterian Medical Center,
New York, New York

Joel M.A. Shugar, M.D.
Attending Physician,
Mount Sinai Hospital,
Associate Clinical Professor of Otolaryngology
Mount Sinai School of Medicine,
New York, New York

Peter M. Som, M.D.
Chief of Head and Neck Imaging,
Mount Sinai Hospital and Medical Center,
Professor of Radiology, Otolaryngology, and Anatomy and Functional Morphology,
Mount Sinai Medical School,
New York University,
New York, New York

Wendy R.K. Smoker, M.D.
Professor of Radiology,
Director of Neuroradiology,
Department of Radiology,
University of Iowa Hospitals and Clinicals,
Iowa City, Iowa

Joel D. Swartz, M.D.
President,
Germantown Imaging Associates,
Gladwyne, Pennsylvania,
Medical Director,
National Medical Imaging,
Philadelphia, Pennsylvania

Mark L. Urken, M.D.
Professor and Chairman,
Department of Otolaryngology,
Mount Sinai School of Medicine of New York University,
New York, New York

Copyright © 2003, Mosby, Inc. All rights reserved.

Michiel W.M. van den Brekel, M.D., Ph.D.
Head and Neck Surgeon,
Netherlands Cancer Institute,
Antoni van Leenwenhoek Hospital,
Assistant Professor,
Department of Otolaryngology,
Academic Medical Center,
University of Amsterdam,
Amsterdam, The Netherlands

Alfred L. Weber, M.D.
Chief of Radiology (Emeritus),
Department of Radiology,
Massachusetts Eye and Ear Infirmary,
Boston, Massachusetts
Professor of Radiology,
Harvard Medical School,
Cambridge, Massachusetts

Jane L. Weissman, M.D., F.A.C.R.
Director of Head and Neck Imaging,
Professor of Radiology and Otolaryngology,
Oregon Health and Science University.
Portland, Oregon

P.L. Westesson, M.D., Ph.D., D.D.S.
Chief of Diagnostic and Interventional Neuroradiology,
University of Rochester Medical Center,
Professor of Radiology and Professor
of Clinical Dentistry,
University of Rochester,
Rochester, New York,
Professor of Oral Diagnostic Science,
State University of New York at Buffalo,
Buffalo, New York,
Associate Professor of Oral Radiology,
University of Lund,
Lund, Sweden

Mika Yamamoto, D.D.S.
Research Fellow,
Department of Radiology,
Massachusetts Eye and Ear Infirmary,
Boston, Masssachusetts,
Instructor,
Department of Radiology,
Showa University School of Dentistry,
Tokyo, Japan

Robert A. Zimmerman, M.D.
Vice-Chairman of Radiology,
Chief, Division of Radiology,
Children's Hospital of Philadelphia,
Professor of Radiology and Professor of Radiology
in Neurosurgery,
University of Pennsylvania School of Medicine,
Philadelphia, Pennsylvania

S. James Zinreich, M.D.
Department of Neuroradiology,
Johns Hopkins Hospital,
Baltimore, Maryland

Copyright © 2003, Mosby, Inc. All rights reserved.

Copyright © 2003, Mosby, Inc. All rights reserved.

Contents

Section I

Sinonasal Cavities **1**

1 **Embryology and Congenital Lesions of the Midface** **3**
Thomas P. Naidich, Susan I. Blaser, Bruce S. Bauer, Derek C. Armstrong, David G. McLone, Robert A. Zimmerman

2 **Anatomy and Physiology** **87**
Peter M. Som, Joel M. A. Shugar, Margaret S. Brandwein

3 **The Ostiomeatal Complex and Functional Endoscopic Surgery** **149**
S. James Zinreich, Sait Albayram, Mark L. Benson, Patrick J. Oliverio

4 **Postoperative Complications of Functional Endoscopic Sinus Surgery** **175**
Patricia A. Hudgins, Todd T. Kingdom

5 **Inflammatory Diseases** **193**
Peter M. Som, Margaret S. Brandwein

6 **Tumors and Tumor-Like Conditions** **261**
Peter M. Som, Margaret S. Brandwein

7 **Facial Fractures and Postoperative Findings** **374**
Peter M. Som, Margaret S. Brandwein

Section II

Orbit and Visual Pathways **439**

8 **The Eye** **441**
Mahmood F. Mafee

9 **Orbit: Embryology, Anatomy, and Pathology** **529**
Mahmood F. Mafee

10 **Lacrimal Apparatus** **655**
Edward E. Kassel, Charles J. Schatz

11 **Visual Pathways** **735**
Robert A. Zimmerman, Larissa T. Bilaniuk, Peter J. Savino

Section III

Central Skull Base **783**

12 **Skull Base: Embryology, Anatomy, and Pathology** **785**
Hugh D. Curtin, James Rabinov, Peter M. Som

13 **Imaging of Perineural Tumor Spread in Head and Neck Cancer** **865**
Lawrence E. Ginsberg

Section IV

Jaws and Temporomandibular Joints **887**

14 **Embryology and Anatomy of the Jaw and Dentition** **889**
James J. Abrahams, Reuben Rock, Michael W. Hayt

15 **Dental CT Reformatting Programs and Dental Imaging** **907**
James J. Abrahams, Michael W. Hayt, Reuben Rock

16 **Dental Implants and Related Pathology** **919**
James J. Abrahams

17 **Cysts, Tumors, and Nontumorous Lesions of the Jaw** **930**
Alfred L. Weber, Takashi Kaneda, Steven J. Scrivani, Shahid Aziz

18 **Temporomandibular Joint** **995**
P.L. Westesson, Mika Yamamoto, Tsukasa Seno, Tomohiro Okano

Copyright © 2003, Mosby, Inc. All rights reserved.

Section V
Temporal Bone 1055

19 **Temporal Bone: Embryology and Anatomy** **1057**
Hugh D. Curtin, Pina C. Sanelli, Peter M. Som

20 **Temporal Bone: Imaging** **1093**
Donald W. Chakeres, Mark A. Augustyn

21 **Temporal Bone: Congenital Anomalies** **1109**
Laura V. Romo, Jan W. Casselman, Caroline D. Robson

22 **Temporal Bone: Inflammatory Disease** **1173**
William R. Nemzek, Joel D. Swartz

23 **Temporal Bone: Trauma** **1230**
Joel D. Swartz, Hugh D. Curtin

24 **Temporal Bone: Otosclerosis and Dysplasias** **1245**
Osamu Sakai, Hugh D. Curtin, Anton N. Hasso, Joel D. Swartz

25 **Temporal Bone: Tumors and Cerebellopontine Angle Lesions** **1275**
M. Marcel Maya, William W.M. Lo, Ilhami Kouvanlikaya

26 **Temporal Bone: Vascular Tinnitus** **1361**
William W.M. Lo, M. Marcel Maya

Section VI
Upper Aerodigestive Tract 1375

27 **The Oral Cavity** **1377**
Wendy R.K. Smoker

28 **Pharynx** **1465**
Suresh K. Mukherji

29 **Pediatric Airway Disease** **1521**
Caroline D. Robson, Patricia A. Hudgins

30 **The Larynx** **1595**
Hugh D. Curtin

31 **Trachea: Anatomy and Pathology** **1700**
J. Pierre Sasson, Nadir Abdelrahman, Suzanne Aquino, Michael H. Lev

32 **Videofluoroscopic Evaluation of Oropharyngeal Swallowing** **1727**
Tessa Goldsmith

Section VII
Neck 1755

33 **Embryology and Anatomy of the Neck** **1757**
Peter M. Som, Wendy R.K. Smoker, Armand Balboni, Joy S. Reidenberg, Patricia A. Hudgins, Jane L. Weissman, Jeffrey T. Laitman

34 **Fascia and Spaces of the Neck** **1805**
Peter M. Som, Hugh D. Curtin
Color plate follows page 1822

35 **Congenital Lesions** **1828**
Peter M. Som, Wendy R.K. Smoker, Hugh D. Curtin, Joy S. Reidenberg, Jeffrey T. Laitman

36 **Lymph Nodes** **1865**
Peter M. Som, Margaret S. Brandwein

37 **Ultrasound of the Neck** **1935**
J.A. Castelijns, Michiel W.M. van den Brekel, Suresh K. Mukherji, J.S. Lameris

38 **Parapharyngeal and Masticator Space Lesions** **1954**
Peter M. Som, Hugh D. Curtin

39 **Salivary Glands: Anatomy and Pathology** **2005**
Peter M. Som, Margaret S. Brandwein

40 **Thyroid and Parathyroid Glands: Anatomy and Pathology** **2134**
Laurie A. Loevner

41 **Skin and Soft–Tissue Lesions** **2173**
Bradley N. Delman, Jane L. Weissman, Peter M. Som

42 **Brachial Plexus** **2216**
Deborah L. Reede, Roy A. Holliday

43 **The Posttreatment Neck: Clinical and Imaging Considerations** **2239**
Peter M. Som, William Lawson, Mark L. Urken

44 **Genetics of Tumor Development and Metastasis** **2273**
Edward M. Johnson
Color plate follows page 2286

45 **New Imaging Techniques** **2294**
Suresh K. Mukherji, Nancy J. Fischbein, J.A. Castelijns

Index **I1**

Copyright © 2003, Mosby, Inc. All rights reserved.

Section I

Sinonasal Cavities

Copyright © 2003, Mosby, Inc. All rights reserved.

Copyright © 2003, Mosby, Inc. All rights reserved.

1

Embryology and Congenital Lesions of the Midface

Thomas P. Naidich, Susan I. Blaser, Bruce S. Bauer, Derek C. Armstrong, David G. McLone, and Robert A. Zimmerman

INTRODUCTION

EMBRYOLOGY OF THE FACE AND SKULL
- Development of the Face and Jaws
- Molecular Signaling and Tissue Patterning in the Face
- Development of the Palate
- Development of the Nasal Cavities and Septum
- The Facial Skeleton

TORI PALATINUS, MAXILLARIS, AND MANDIBULARIS

FACIAL CLEFTS
- Common Cleft Lip and/or Cleft Palate
  - Pathogenesis of Cleft Lip/Cleft Palate and of Cleft Palate
  - Genes and Heritability
  - Clinical Features
  - Facial Deformities
    - ***Lip***
    - ***Maxilla***
    - ***Nose***
      - *Unilateral Cleft*
      - *Bilateral Cleft*
  - Concurrent Malformations
  - Subtle Deformities in Parents of Patients with Common Clefts
- Midline Cleft Lip and Median Cleft Face Syndromes
  - Group A
  - Group B
  - Molecular Genetics
  - Concurrent Malformations
- Transverse Facial Clefts
- Clefts of the Lower Lip and Mandible
- Syndrome of Amniotic Bands

NASAL DERMAL SINUSES, CYSTS, HETEROTOPIAS, AND CEPHALOCELES
- Dermoids and Dermal Sinuses
  - Dermoids of the Skull
  - Nasal Dermal Sinuses
  - Nasal Dermoids and Epidermoids
- Heterotopic Brain Tissue
  - Nasal Heterotopias (Gliomas)
  - Nonnasal Heterotopias
    - ***Epignathus Teratoma***
    - ***Epulis***
- Cephaloceles
  - Sincipital Cephaloceles
    - ***Interfrontal Cephalocele***
    - ***Frontoethmoidal Cephaloceles***
      - *Frontonasal Subtype*
      - *Nasoethmoidal Subtype*
      - *Nasoorbital Subtype*
  - Basal Cephaloceles
    - ***Sphenoorbital Cephaloceles***
    - ***Sphenomaxillary Cephaloceles***
    - ***Sphenopharyngeal Cephaloceles***
    - ***Rarer Basal Cephaloceles***

DACRYOCYSTOCELES

HOLOPROSENCEPHALY
- Holoprosencephaly Facies
  - Cyclopia
  - Ethmocephaly
  - Cebocephaly
  - Absent Intermaxillary Segment with Central Defect and Hypotelorism
  - Intermaxillary Rudiment with Hypotelorism
- Brain Malformations
- Correlations Between Facies and Holoprosencephaly

Copyright © 2003, Mosby, Inc. All rights reserved.

FACIAL AND BRANCHIAL ARCH SYNDROMES
Pathogenesis
Hemifacial Microsomia (Goldenhar Syndrome, OAV Complex)
Face
Mouth
Ears
External Ear
Middle Ear
Inner Ear
Eyes
Central Nervous System
Plagiocephaly
Mandibulofacial Dysostosis (Treacher Collins Syndrome, Franceschetti-Zwalen-Klein Syndrome)
Branchio-Oto-Renal Syndrome (Ear Pits-Deafness Syndrome)
Nager Acrofacial Dysostosis Syndrome (AFD Nager)
Pierre Robin Sequence
PREMATURE CRANIAL SYNOSTOSES
Skull Shape
Scaphocephaly (Dolichocephaly, Canoe Head)
Trigonocephaly (Ax Head, Keel-Shaped Deformity)
Brachycephaly (Broad Head)
Oxycephaly (Turricephaly, Tower Head)
Plagiocephaly (Skew Head, Asymmetric Head)
Kleeblattschädel (Cloverleaf Skull)
Nonsyndromic Primary Craniosynostoses
Premature Sagittal Synostosis
Premature Unilateral Coronal Synostosis
Premature Metopic Synostosis
Syndromic Craniosynostosis (Craniofacial Dysostosis)
Molecular Genetics
Fibroblast Growth Factor Receptors
FGFR1
FGFR2
FGFR3
Other Signaling Systems
GL13
TWIST
MSX2
Relationship of Cranial Suture Morphogenesis and Craniosynostosis
FGF1, 2, and 3
Eponymous Craniosynostoses
Crouzon Syndrome
Apert Syndrome
Saethre-Chotzen Syndrome
Pfeiffer Syndrome
Jackson-Weiss Syndrome
Boston (Type 2) Craniosynostosis
Muenke Syndrome
Baere-Stevenson Cutis Gyrata Syndrome
CONCLUSION

INTRODUCTION

Traditionally, congenital malformations have been defined by their effect on gross anatomy and classified by phenotypic similarities.[1] Clinically valid constellations of pathology have been called syndromes and named for the authors who reported them. Recent work has begun to elucidate the molecular bases for the phenotypes observed to provide an improved method for defining disease entities.[2–25] This chapter reviews selected congenital malformations of the midface, both classically and as examples of the evolving classification by molecular genetics. Limitations in the information available make this approach uneven, but still useful.

Craniofacial malformations result from misregulation of normal tissue patterning.[2] In utero, signal transduction pathways normally relay information from outside the cell, through the plasma membrane and cytoplasm, into the nucleus in order to regulate and coordinate the expression of target genes (Fig. 1-1). From the nucleus, related information then passes outward to alter cytoplasmic structures, to modulate the cell response to incoming signals, and to coordinate activities of other cells, nearby or distant.[2] The signals employed often take the form of *ligands*, which may be diffusable (e.g., growth factors) or stationary (e.g., extracellular matrix–associated proteins). The ligands bind to molecules designated transmembrane receptors.[2] These transmembrane receptors present an extracellular domain, which can interact with external signals; a transmembrane domain, which spans the cell membrane; and an intracellular domain, which effects changes within the cell.[2] Binding of the ligand to the extracellular domain of the receptor alters receptor conformation and initiates changes that propagate along the molecule to alter enzymatic activity or regulatory properties within the intracellular domain. Receptors such as fibroblast growth factor receptors (FGFRs) and bone mophogenic protein (BMP) receptor are often kinases that catalyze the transfer of a phosphate group from adenosine triphosphate (ATP) to the side chains of amino acids within other proteins (the substrates).[2] The substrates may themselves be kinases. Therefore, binding of ligand to the extracellular domain of the receptor may cause phosphorylation of the intracellular domain of the receptor, leading to phosphorylation of intracellular substrates and altered

Copyright © 2003, Mosby, Inc. All rights reserved.

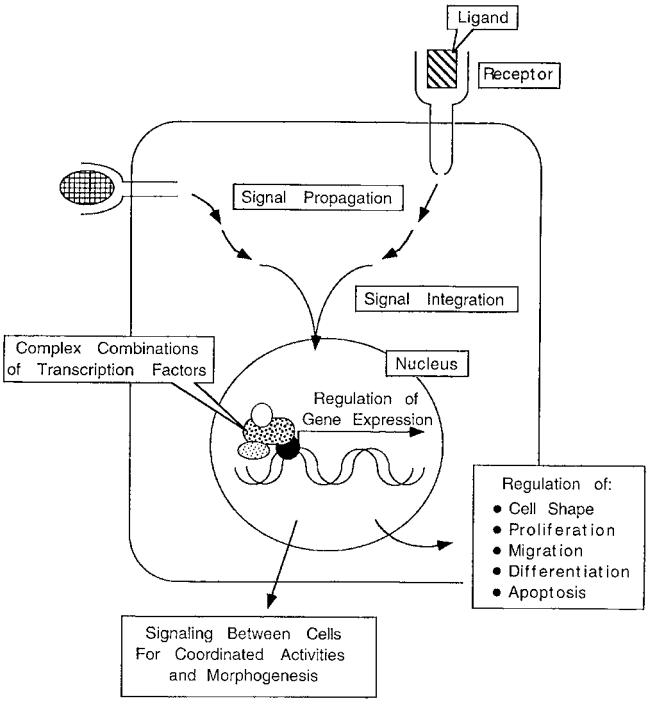

VIEW IMAGE

FIGURE 1-1 Cell signaling and signal transduction. Diagramatic representation. The outer square represents the cell surface. Ligand binding to the extracellular domain of the transmembrane receptor conveys information to the nucleus, where it affects gene regulation and transcription, alterations in cell shape, proliferation, migration, differentiation, apoptosis, and coordination of cell populations for further embryogenesis. (From Nuckolls GH, Shum L, Slavkin HC. Progress toward understanding craniofacial malformations. Cleft Palate-Craniofac J 1999;36:12– 26.)

activity of other intracellular proteins. In like fashion, interactions among proteins to form a complex can alter their conformation and activity, either subtly or substantially.[2] Complexes of proteins designated transcription factors associate with DNA to increase or decrease transcription of specific genes and to modify protein synthesis qualitatively and/ or quantitatively. Through these changes in protein activity, signals are propagated and integrated into circuits or networks that regulate gene expression and control cell proliferation, migration, differentiation, bilateral symmetry, and even death (apoptosis).[2] The coordinated control of cell populations is fundamental to the formation of complex structures such as the human face during embryonic development.[1–25] Derangements in this coordinated signaling lead to the malformations observed. Figures 1-2 and 1-3 depict the developing forebrain and its relationships to the developing face.[5–7]

EMBRYOLOGY OF THE FACE AND SKULL

Development of the Face and Jaws

The tissue that gives rise to the face and jaws derives from three major sources (Figs. 1-2 and 1-3):

1. The *ectoderm* provides the surface cover, and by ectodermal–mesenchymal interactions helps to pattern the developing structures.[3, 4, 20, 21]
2. *Neural crest cells* provide most of the facial mesenchyme.[3, 4, 7, 17, 23]
3. The *paraxial and prechordal mesoderm* contribute tissue that evolves into the myoblasts of the voluntary craniofacial muscles.[4]

The first sign of the future face is a surface depression, the stomodeum, situated just below the developing brain (Fig. 1-4). The ectoderm that overlies the early forebrain extends into the stomodeum, where it lies adjacent to the developing foregut. The junction between the surface ectoderm and the subjacent endoderm is called the oropharyngeal membrane. The line of attachment of the oropharyngeal membrane corresponds to Waldeyer's ring. Dissolution of the oropharyngeal membrane by the end of

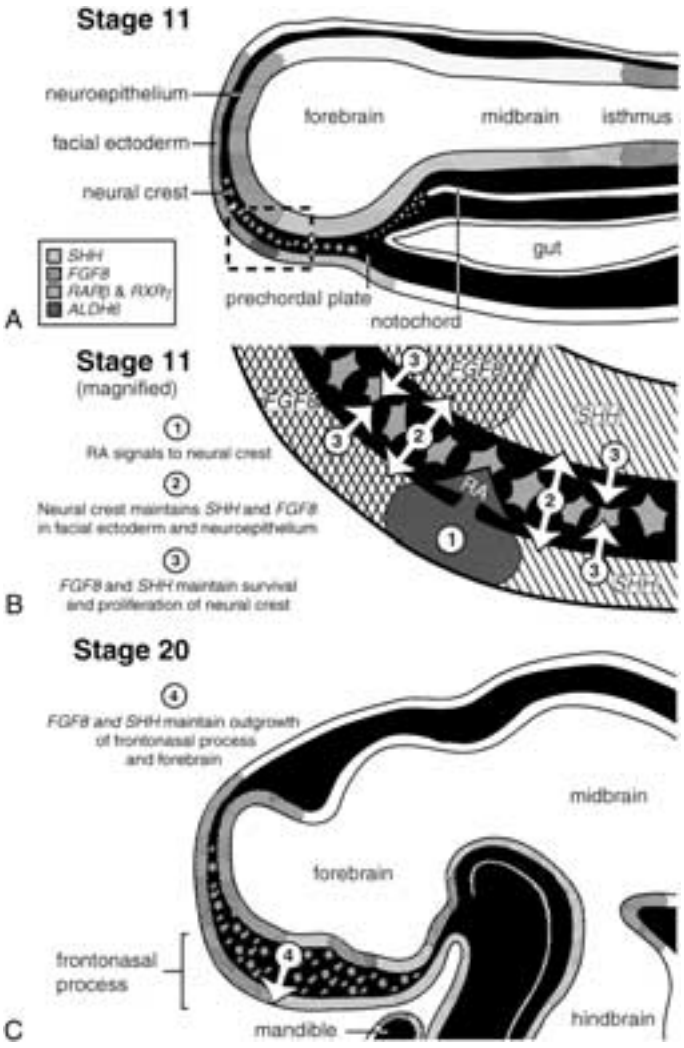

VIEW IMAGE

FIGURE 1-2 Establishing the forebrain. **A** to **C**, Patterning the forebrain and the frontonasal process in relation to the prechordal plate, anterior to the notochord. Roles of Sonic Hedgehog (*SHH*), fibroblast growth factor 8 (*FGF8*), retinoic acid (RA), retinoic acid receptor beta (RARβ), retinoic acid ''X'' receptor gamma (RXRγ), and aldehyde dehydrogenase 6 (ALDH6) in maintaining the outgrowth of the forebrain and the neural crest to establish the frontonasal process. In this and all future sagittal (lateral) images, anterior is displayed to the reader's left. (From Schneider RA et al. Local retinoid signaling coordinates forebrain and facial morphogenesis by maintaining *FGF8* and *SHH*. Development 2001;128:2755–2767.)

Copyright © 2003, Mosby, Inc. All rights reserved.

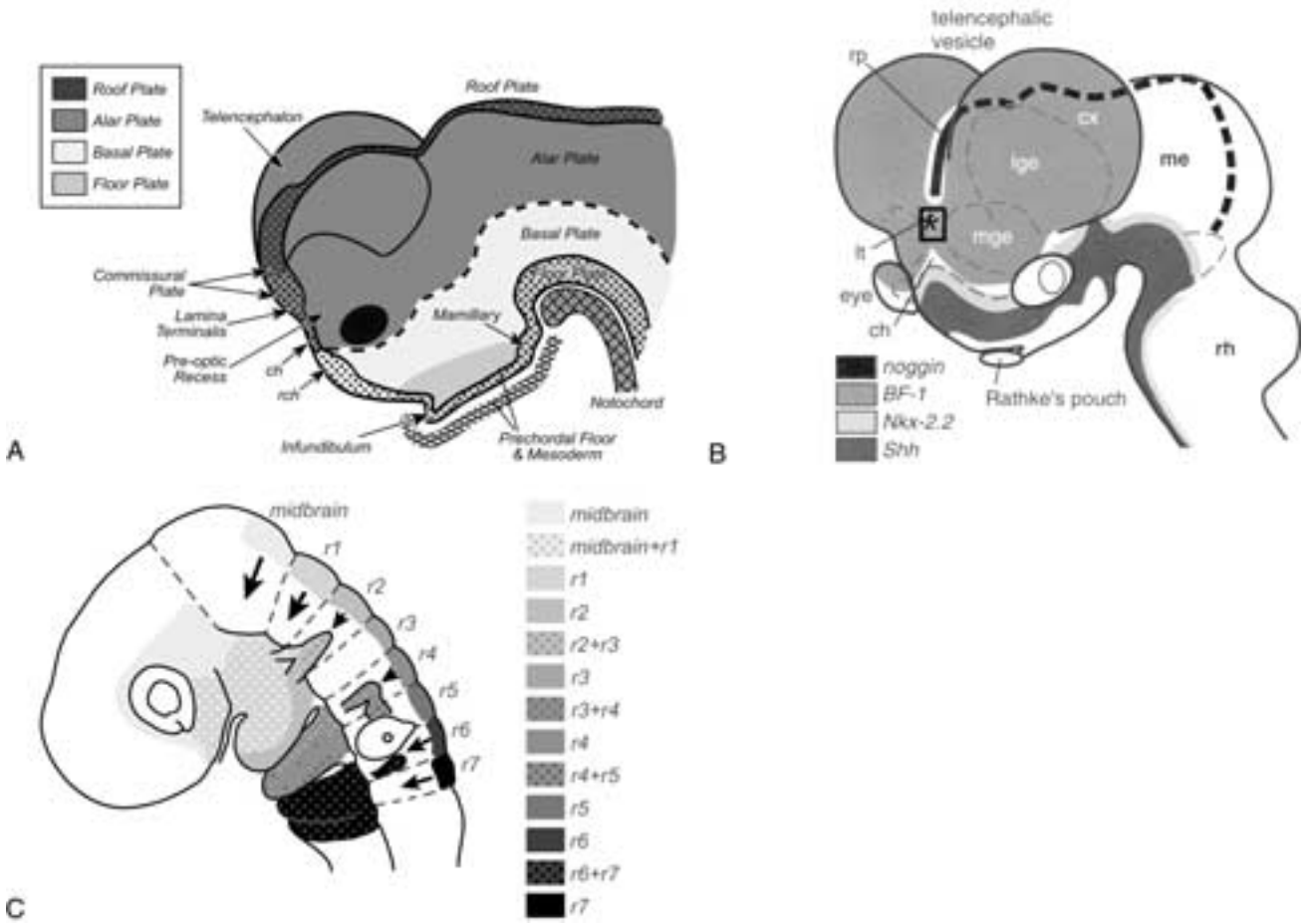

VIEW IMAGE

FIGURE 1-3 **A**, Schematic representation of the longitudinal organization of the forebrain. The optic stalk appears as a black oval. Black lines indicate the boundary of the telencephalic vesicle and the contours of the medial and lateral ganglionic eminences within it. Note the relationships among the alar-basal junction, the optic stalk, the chiasmatic plate anlage (*ch*), and the retrochiasmatic (rch) (anterobasal region) of the basal plate, and the relationships among the notochord, floor plate, prechordal floor, and infundibulum. **B**, Molecular designation of topography. Compare the topographc distribution of Sonic Hedgehog (*Shh*), *Nkx-2.2*, *BF-1*, and *noggin* with the anatomic locations shown in **A**. *Shh* is a gene that encodes a diffusable protein implicated in specifying the notochord and floor plate of the neural tube. It helps to regulate *Nkx-2.2*. *Nkx-2.2* is a homeobox gene first detectable at the 1-somite stage in a median rostral region of the neural plate just anterior to the rostral tip of the notochoral plate. *Shh* and *Nkx-2.2* define adjacent and nonoverlapping longitudinal neuroepithelial zones that extend along the entire central nervous system (CNS) and end anteriorly, where they cross the midline in the optochiasmatic region. Brain factor 1 (BF-1) may be regarded as an alar plate marker of the prosencephalon. It is expressed in most of the telencephalon, the preoptic region, the adjoining one half of the optic stalk, and one half of the optic cup. It is reciprocal to the expression of BF-2 in the other halves of the optic stalk and cup. *noggin* is a gene that encodes a secreted polypeptide with neural-inducing properties. It is expresssed in the roof plate along the entire neural axis. Its anterior end approximates the anterior extent of the prosencephalic vesicle and does not enter the lamina terminalis. *Rh*, rhombencephalon; *me*, mesencephalon; *cx*, embryonic cerebral cortex; *lge*, lateral ganglionic eminence; *mge*, medial ganglionic eminence. The anterior-medial alar region of the neural plate maps to the lamina terminalis of the brain (square with asterisk). *Shh* present in the mge is not shown for simplicity. **C**, Neural crest migration. Chick embryo model. The facial mesenchyme derives from cohorts of neural crest cells that migrate to specified regions within the developing face and branchial arches from defined segments of the forebrain, midbrain, and hindbrain rhombomeres r1 to r7. Note the relationships of the pathways of migration to the optic vesicle, the otic placode, and the developing cranial nerves 5, 7/8, and 9/10. Clonal variations and mutations in specific cohorts of neural crest cells can lead to malformations restricted to subsets of cells in specific topographies. In mammals, r2, r4, and r6 send streams of neural crest cells into branchial arches 1, 2, and 3, respectively. The streams of neural crest cells that arise in r3 and r5 turn sharply to join the streams from adjacent rhombomeres. (**A** and **B** from Shimamura K et al. Longitudinal organization of the anterior neural plate and neural tube. Development 1995;121:3923–3933. **C** from Köntges G, Lumsden A. Rhombencephalic neural crest segmentation is preserved throughout craniofacial ontogeny. Development 1996;122:3229–3242.)

Copyright © 2003, Mosby, Inc. All rights reserved.

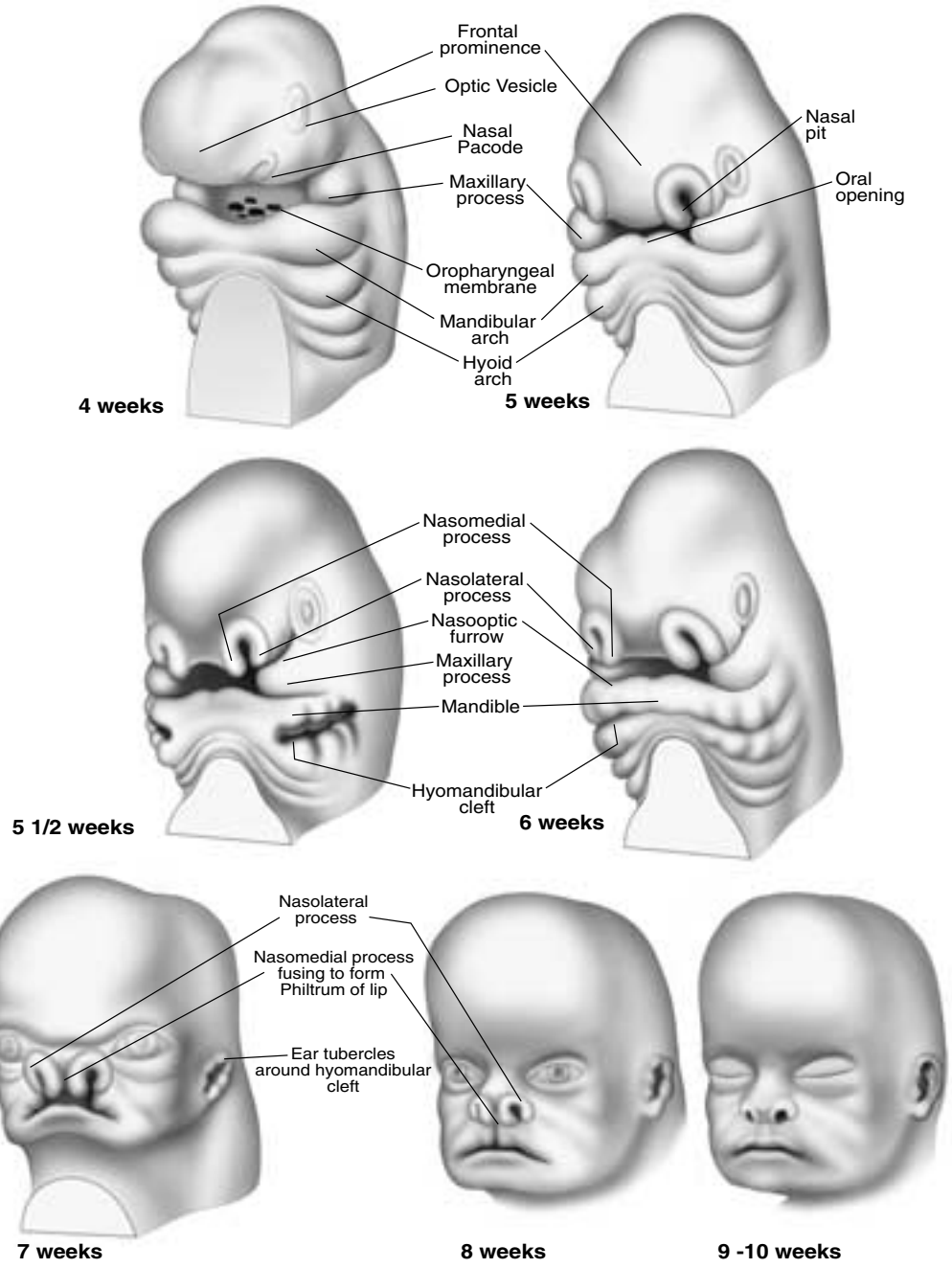

VIEW IMAGE

FIGURE 1-4 Embryogenesis of the face from 4 to 10 wg. See text. (Modified from Carlson BM. Human Embryology and Developmental Biology, 2nd ed. St. Louis: CV Mosby, 1999.)

the fourth week of gestation (wg) permits communication between the mouth and the foregut.[3] Waldeyer's ring connects the nasopharyngeal adenoids, the palatine tonsils, and the lingual tonsils.[14] The depth of Waldeyer's ring within the mouth of the newborn indicates the extent to which facial development results from thickening of the surface tissue external to the original ectodermal level.[14]

During the fourth week of gestation (wg), neural crest cells migrate to the developing face from the lower forebrain, the midbrain, and rhombomeres 1 and 2 of the upper hindbrain (Fig. 1-3C). Neural crest cells also migrate to other pharyngeal arches from the lower rhombomeres.[3, 6, 7] These migratory neural crest cells are the predominant source of facial connective tissue, including cartilage, bone, and ligaments. Since the neural crest cells migrate to the face as cohorts of cells from different portions of the brain, they carry with them different developmental programs. Mutations arising in the premigratory or early migratory neural crest cells may affect one specific clone of cells, which then carries that mutation to a predestined site in the face.

At 4 wg, five identifiable primordia surround the stomodeum (Fig. 1-4). The single, unpaired frontonasal prominence lies in the midline just superior to the

Copyright © 2003, Mosby, Inc. All rights reserved.

stomodeum. Embryologically, this prominence is related to the forebrain. Paired maxillary prominences lie on each side of the stomodeum superiorly, and paired mandibular prominences lie on each side of the stomodeum inferiorly. These processes originate from the first branchial (pharyngeal) arch.[3, 11] During the fourth to eighth wg, the frontonasal prominence gives rise to the median facial structures, and the paired maxillary and mandibular prominences give rise to the lateral facial structures.[3] Since the medial and lateral structures derive from different tissues, malformations of the face tend to affect either the median or the lateral structures separately, or their lines of junction.

By the end of the fourth wg, even before the neural folds close, paired thickenings of ectoderm appear on the surface of the frontonasal prominence just superolateral to the stomodeum.[3] These oval nasal placodes, located at 1 and 11 o'clock, give rise to the future nose and nasal cavities. Development of the nasal placodes (and the lens placodes) requires the paired box gene *Pax 6*.[3] In the absence of *Pax 6*, neither the nasal nor the lens placode develops.[3] During the fifth wg, mesenchyme in the margins of the nasal placodes proliferates to form horseshoe-shaped elevations (Fig. 1-4). The medial limbs of the horseshoes are designated the nasomedial processes. The lateral limbs of the horseshoes are designated the nasolateral processes. The nasomedial processes are longer than the nasolateral processes.[4] The tissue surrounding the placodes thickens and elevates, so the nasal placodes appear to become recessed within depressions in the surrounding tissue. The depressions are then designated nasal pits. The nasal pits are the primordia of the anterior nares (the future nostrils) and the nasal cavities.[4]

From 4 to 5 wg, the mandibular processes enlarge on both sides. From 5½ to 8 wg, their medial components merge in the midline, forming the point of the lower jaw (mentum) (Fig. 1-4).[3] Incomplete fusion at the mentum leaves the common midline chin dimple.[4] From 4 to 6 wg, the paired maxillary processes grow toward each other and toward the paired nasomedial processes.[3] The maxillary processes will ultimately give rise to the lateral two thirds of the upper jaw, the upper teeth (except for the incisors), and the palatal shelves that contribute to the hard palate. By the end of the sixth wg, the nasolateral processes begin to merge with the maxillary processes to form the ala nasi and the lateral border of the nostril on both sides (Fig. 1-4).[3] Along the junctions between the maxillary and nasolateral processes on both sides, nasolacrimal grooves still extend between the developing nose and eyes. The ectoderm along the floor of these grooves thickens to form solid epithelial cords, which detach from the grooves and then canalize to form the nasolacrimal ducts and lacrimal sacs. By the late fetal period, the nasolacrimal ducts extend from the medial corners of the eyes to the inferior meatuses in the lateral walls of the nasal cavity.[4] These ducts usually become completely patent only after birth. The nasomedial processes on both sides remain unfused.

From the sixth to the eighth wg, the cheeks and the corners of the mouth form by the merging of the maxillary and mandibular processes. The upper lip is completed during the seventh and eighth wg (Fig. 1-4).[3] The expanding nasomedial processes merge with the superficial regions of the maxillary processes on both sides along epithelial seams (fusion lines) designated nasal fins.[3] Mesenchyme penetrates the nasal fins, forms a continuous union between the nasomedial and the maxillary processes, and completes much of the upper lip and upper jaw on both sides. The two nasomedial processes then merge with each other across the midline to form the intermaxillary segment. The fusion of the two nasomedial processes displaces the frontonasal prominence posteriorly. Therefore, the frontonasal prominence does not contribute significantly to the definitive upper lip, jaw, or nasal tip, even though it formed a prominent portion of the stomodeal border at 4 to 5 wg.[3] The intermaxillary segment formed by the nasomedial processes is the precursor for the medial portion of the upper lip (the prolabium), the premaxillary component of the upper jaw containing the four upper incisors (the gnathogingival segment), and a triangular midline anterior wedge of palate (the primary palate) (Fig. 1-5).[3] The primary palate will later become continuous with the most rostral portion of the nasal septum. Fusion of the paired nasomedial processes also forms the tip and the crest of the nose and a portion of the nasal septum.[3]

From the sixth wg, the primordia of the auricles of the external ear begin to develop (Fig. 1-4). By the seventh wg, six mesenchymal swellings designated auricular hillocks form around the first pharyngeal groove on each side: three from the first branchial arch and three from the second branchial arch[3] (see the section on Hemifacial Microsomia). The auricular hillocks will merge with each other to form the

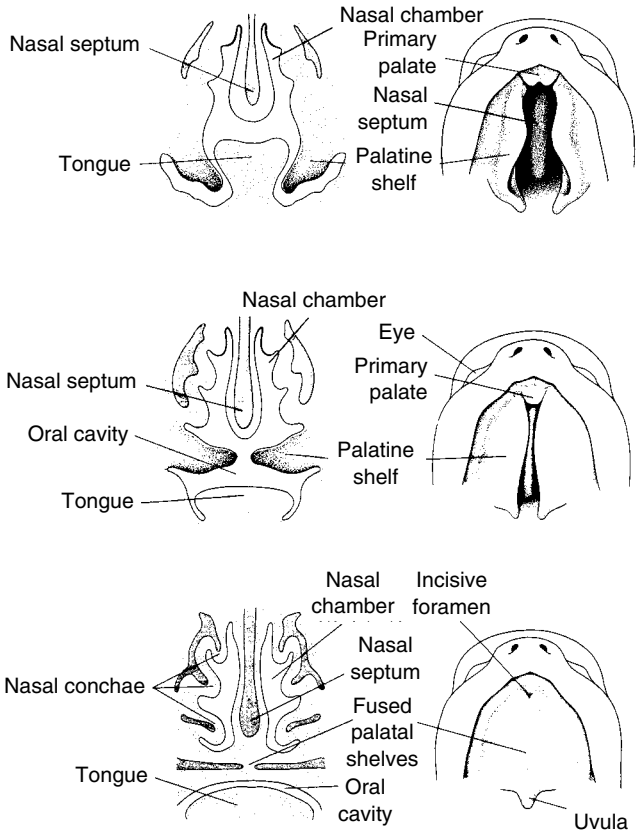

FIGURE 1-5 Embryogenesis of the palate from 6½ to 10 wg. (From Langman J. Medical Embryology: Human Development, Normal and Abnormal, 2nd ed. Baltimore: Williams & Wilkins, 1969.)

VIEW IMAGE

Copyright © 2003, Mosby, Inc. All rights reserved.

auricle. The groove between them will form the external auditory meatus.[3] Initially, the external ears are located inferomedially in the neck. As the mandible develops, the ears ascend laterally to the sides of the head at the level of the eyes.[4] During this time, descent of the nose and medial migration of the orbits above the nose are also observed.

Until the end of the sixth wg, the primitive jaws are composed of masses of mesenchyme.[4] A linear thickening of ectoderm, designated the labiogingival lamina, then begins to grow into the underlying mesenchyme. This lamina ''carves out'' a labiogingival groove, creating the separate lips and gingiva. It then degenerates, except in the midline, leaving the labiogingival groove between the lips and the gingivae, and a midline frenulum for the upper lip.[3, 4] Separation of the lips from the gingivae occurs only after the mesenchyme within the individual facial processes merge to form the upper lip, and is not found in regions where the facial processes fail to merge successfully (e.g., such a sulcus is deficient in patients with complete cleft lips).

Once the basic facial structures take shape, they are invaded by mesodermal cells associated with the first and second pharyngeal arches. These cells form (1) the muscles of mastication (first arch derivatives innervated by cranial nerve 5) and (2) the muscles of facial expression (second arch derivatives innervated by cranial nerve 7).[3] The relative proportions of the facial structures change during life. The midface remains underdeveloped during embryogenesis and early postnatal life and grows to full size later.[3] The mandible is initially small and shows later ''catch-up'' growth.

Molecular Signaling and Tissue Patterning in the Face

The facial primordia are analogous to limb buds and depend on highly similar molecular signaling for patterning and elongation. In both the face and limbs, for example, (1) mesenchymal–ectodermal interactions pattern the tissue, (2) sonic hedgehog, fibroblast growth factor (FGF), and retinoic acid signaling are critical for growth, (3) aristaless-like homeobox genes (*Prx1, Prx2, Alx3, Alx4*) serve as upstream regulators of sonic hedgehog, and (4) the homeobox gene *Msx1* is expressed in the rapidly proliferating mesenchyme near to the leading edge of the process.[3, 5, 11, 12] In the face, sonic hedgehog may be the morphogenic organizer, while fibroblast growth factors may serve as the stimuli for mesenchymal outgrowth.[3]

Facial and limb malformations are known to result from deficiency or excess of molecular signaling. Similar phenotypes, such as clefting, may result from either deficiency of the appropriate midline tissue or such excess of other midline tissue that the appropriate processes cannot meet to fuse in the midline. In experimental animals, *reduced* retinoic acid signaling diminishes expression of sonic hedgehog and fibroblast growth factor 8 (FGF8) in the mesenchyme, increases apoptosis (programmed cell death) locally, and decreases proliferation of tissue in the forebrain and frontonasal processes. These animals show holoprosencephalic phenotypes with hypoplastic forebrain, fused eyes, and absence of structures derived from the frontonasal process. Timely replacement of retinoic acid prevents this malformation.[5] Conversely, excess sonic hedgehog stimulates frontonasal growth and widens the frontonasal process (an average of 48%), so that (1) the developing palatal shelves fail to abut, leaving a cleft palate, and (2) more severe phenotypes show ectopic midfacial structures with duplication of the nasal bone.[12, 15]

Development of the Palate

The palate is formed from the seventh to the tenth wg from three primordia: an unpaired median palatine process and paired lateral palatine processes (Fig. 1-5).[6, 8, 9] The newly merged nasomedial processes form the median palatine process. This grows posteriorly to form a triangular bony structure designated the primary palate. In adult life, this portion is called the premaxillary component of the maxilla and gives origin to the four upper incisors.[3] The incisive foramen marks the posterior midline extent of the premaxilla. The lateral palatine processes first appear during the sixth wg and grow vertically downward on both sides of the tongue.[3] The growth of the palatal shelves also resembles the growth of the limb bud. It involves both ectodermal–mesenchymal interaction and growth factors like epidermal growth factor (EGF) and transforming growth factor alpha (TGF-alpha). The growing palatal processes may even display an apical ectodermal thickening similar to the apical ectodermal ridge of the limb bud.[3] During the seventh wg, hydration of hyaluronic acid within the palatal processes generates an intrinsic shelf-elevating force that elevates the palatal shelves from their early vertical position alongside the tongue into a definitive horizontal position above the dorsum of the tongue.[11] The epithelial cells along the medial edge of each palatal shelf contact each other and fuse together along an epithelial seam.[11] The two palatal shelves also fuse with the triangular primary palate anteromedially to form the Y-shaped fusion line (Fig 1-5). The success or failure of palatal fusion is strongly influenced by genetics and by physical constraints of the space available within the dividing nasooral cavity.

Following fusion of the palatal shelves, the seam cells migrate, orally and nasally, into epithelial triangles and subsequently into the oral and nasal epithelia.[23] Developmental programs for epithelial–mesenchymal interactions promote regionally specific palatal epithelial differentiation into nasal pseudostratified ciliated columnar cells and oral stratified squamous cells.[11] Growth factors localized within the developing palate appear to underlie the epithelial–mesenchymal interactions. Fibroblast growth factor 7 (FGF7), for example, is synthesized by the mesenchymal cells, while its receptor is synthesized in the overlying epithelia, establishing an integrated signaling system.[2]

Development of the Nasal Cavities and Septum

From 5 wg, the nasal pits deepen toward the oral cavity, forming substantial depressions. By 6½ wg, only a thin oronasal membrane separates the oral cavity from the nasal

Copyright © 2003, Mosby, Inc. All rights reserved.

cavities.[3] This oronasal membrane then breaks down, so that the oral cavity can communicate with the nasal cavities through openings posterior to the primary palate.[3] These openings are designated the nasal choanae. Fusion of the two palatal shelves then lengthens the nasal cavity and carries the communication posteriorly to the upper pharynx.[3] The nasal septum grows down from the frontonasal prominence to reach the level of the palatal shelves when the shelves fuse to form the definitive secondary palate. Anteriorly, the septum is continuous with the primary palate.[11] The actual fusion of the palate begins posterior to (not at) the incisive foramen and extends from there, both anteriorly and posteriorly, to complete the formation of the palate. The point of fusion of the secondary palatal shelves with the primary palate is marked by the incisive foramen.[11]

The Facial Skeleton

The cartilage of the nasal capsule is the foundation of the upper part of the face (Figs. 1-6 and 1-7).[24] The bony elements of the facial skeleton appear around it and replace it in part. The lateral masses of the ethmoid form by enchondral ossification of the nasal capsule. The frontal processes of the maxillary bones, the premaxillary bone, the nasal bones, the lacrimal bones, and the palatine bones all form in membrane in close relationship with the roof and lateral walls of the cartilaginous nasal capsule.[24] The vomer develops in membrane in relation to the perichondrium of the septal process.[24] Eventually, nearly all of the nasal capsule becomes ossified or atrophied. All that remains of the cartilage of the nasal capsule in adults is the anterior part of the nasal septum and the alar cartilages that surround the nostrils.

Specifically, the midline septal cartilage is directly continuous with the cartilaginous skull base. At birth, the skull base has three major ossification centers: the *basiocipital* center, the *basisphenoidal* center, and the *presphenoidal* center. The septal cartilage has not yet ossified. The lateral masses of the ethmoid have ossified, forming paired paramedian bones, but the cribriform plate is still cartilaginous or fibrous.[24] At birth, therefore, the entire midline of the face may be a lucent strip of cartilage situated between the paired ossifications in the lateral masses of the ethmoids. This lucent midline can simulate a midline cleft on imaging studies. The septal cartilage extends along the midline from the nares to the presphenoid bone.[24] Anteriorly and inferiorly, the septal cartilage attaches to the premaxillary bone by fibrous tissue.[24] Posteriorly, the septal cartilage is continuous with the cartilage of the cranial base. Inferiorly, the lower edge of the septal cartilage is slotted into a U- or V-shaped groove that runs along the entire upper edge of the vomer (Figs. 1-7 to 1-9).[24] This groove is designated the vomerine groove. It should not be mistaken for a midline cleft in the septum.

At about the time of birth or during the first year of life, a fourth center, the *mesethmoidal* center, appears in the septal cartilage anterior to the cranial base. This center will form the perpendicular plate of the ethmoid.[24] The residual portion of still unossified septal cartilage that extends posterosuperiorly toward the cranial base between the perpendicular plate of the ethmoid and the vomer is designated the sphenoidal tail of the septal cartilage.[24] Initially, the ossifying perpendicular plate is separated from the rest of the facial skeleton by (1) the unossified cartilage or fibrous tissue of the cribriform plates and (2) the sphenoidal tail (Figs. 1-7 to 1-9). At about the third to sixth year, the lateral masses of the ethmoid and the perpendicular plate of the ethmoid become united across the roof of the nasal cavity by ossification of the cribriform plate.[24, 25]

Somewhat later, the perpendicular plate unites with the vomer below.[24] As the two bones approach, the vomerine

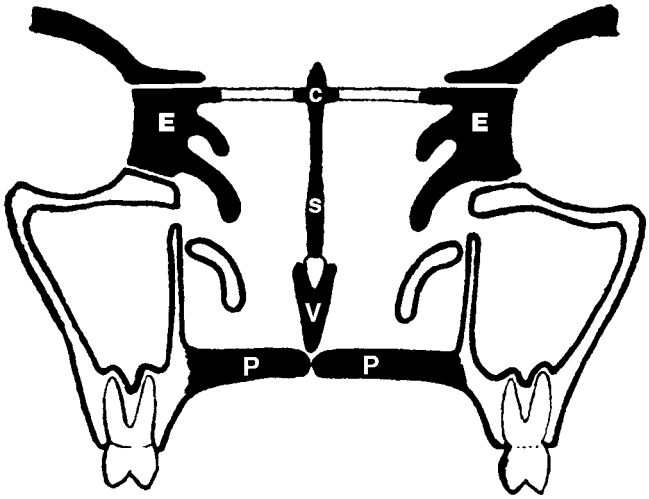

FIGURE 1-7 Diagram of the pattern of ossification around the nasal cavity. The ossified crista (*C*) and septal cartilage (*S*) form a ''cristal'' cross that is isolated from the lateral ethmoid centers (*E*) by the unossified cribriform plates and from the vomer (*V*) by the sphenoidal tail. Although the maxillae are ossified, only the palatal shelves (*P*) have been inked in to emphasize their relationships to the vomer. (Modified from Scott JH. The cartilage of the nasal septum (a contribution to the study of facial growth). Br Dent J 1953;95:37.)

VIEW IMAGE

FIGURE 1-6 Coronal cryomicrotome section through the nasal cavity of a full-term stillborn infant at the level of the optic globes. The lateral ethmoid centers (*E*), the midline vomer (*V*), and the palatal shelves (*P*) of the maxillae are well ossified. The unossified septal cartilage (*S*) slots into the vomerine groove in the upper surface of the Y-shaped vomer. The crista galli (*arrow*) is beginning to ossify, forming a pointed ''cap.'' The cribriform plates have not ossified. Note the normal position of the floor of the anterior fossa with respect to the two orbits and optic globes. *T*, Unerupted teeth.

VIEW IMAGE

Copyright © 2003, Mosby, Inc. All rights reserved.

VIEW IMAGE

FIGURE 1-8 Normal patterns of ossification of the nasal capsule, as shown by direct coronal CT in progressively older patients**. A** and **B**, Four-month-old girl. The lateral ethmoid centers and a small segment of vomer are ossified. The midline septal cartilage is entirely unossified. **C** and **D**, Five-month-old boy. The lateral ethmoid centers, the palatal shelves, the vomer, and the tip (*white arrow)* of the crista galli are ossified. The widened midportion of the septum (*white arrowhead* in **C**) is designated the septal diamond. The two sides of the vomerine groove give the posterior septum a bilaminar appearance (*white arrowhead* in **D**).

Illustration continued on following page

groove may become converted into a vomerine tunnel. This should not be mistaken for a bony canal around a dermal sinus or cephalocele. Growth of the septal cartilage continues for a short period after craniofacial union is complete. This may explain the common deflection of the nasal septum away from the midline.[24]

Because the appearance of the nasal septum varies with the patient's age, one must interpret imaging ''evidence'' of midline defects and sinus tracts carefully. Review of the CT appearance of the midline anterior fossa and nasal septum in 100 children aged 2 days to 18 years revealed the following normal patterns (Figs. 1-7 to 1-9):[1, 26]

1. The lateral ethmoid centers are ossified in all patients.
2. No *midline* ossifications of the anterior fossa or septum are present in 14% of patients less than 1 year of age.
3. The cribriform plate is not ossified in patients less than 2 months of age. It can be ossified from 2 to 8 months of age. It is fused across the midline from 8 months on.
4. The tip of the crista can be ossified from 2 days on. It is invariably ossified from 2½ years on.
5. The crista plus the cribriform plate forms a _/_ os-

Copyright © 2003, Mosby, Inc. All rights reserved.

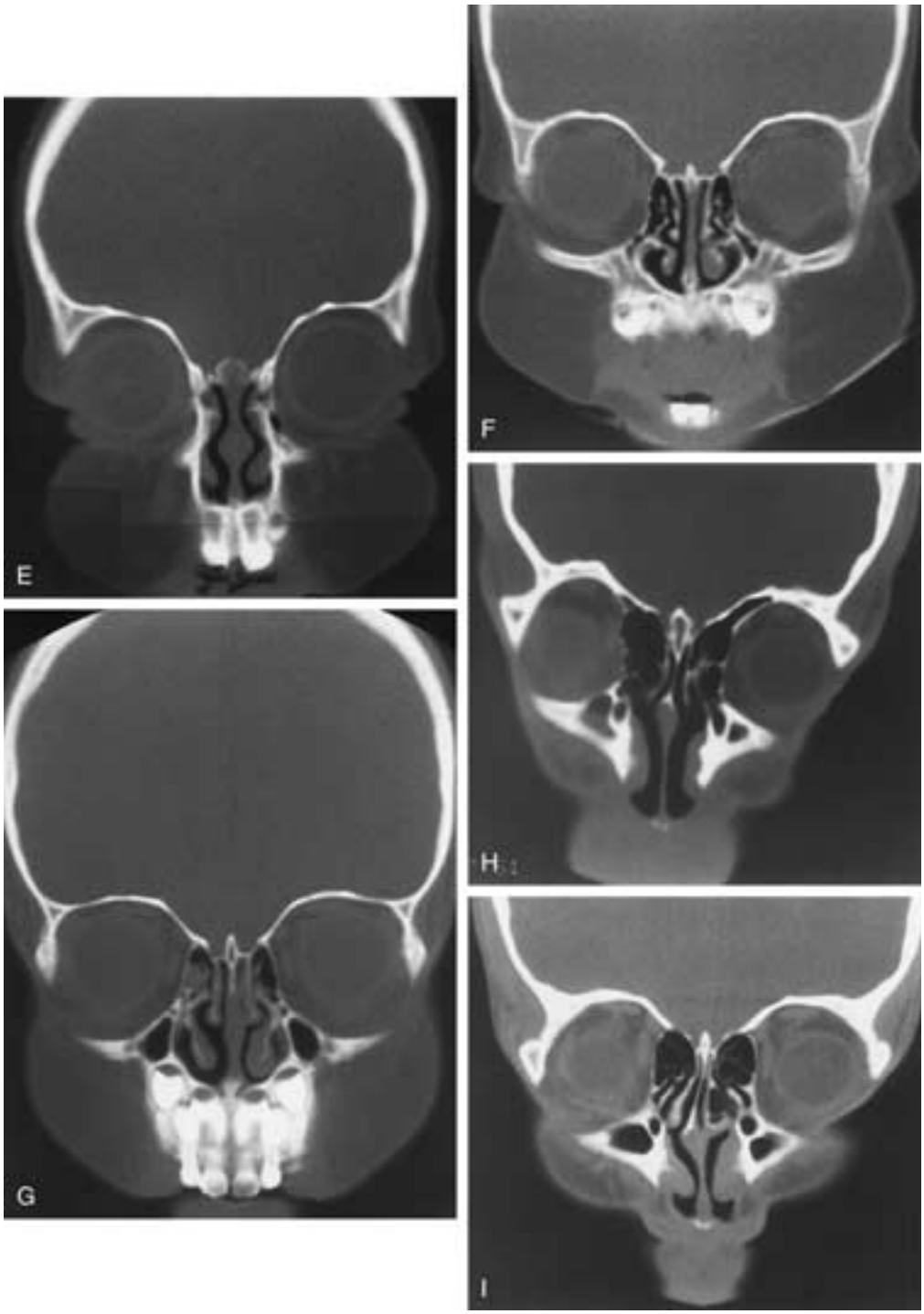

FIGURE 1-8 *Continued.* **E**, Eight-month-old boy. Anteriorly, the crista galli is incompletely ossified, forming a hollow cap. **F**, Further posteriorly, the crista and the cribriform plates have ossified together, roofing over the nasal cavity. The perpendicular plate of ethmoid is beginning to ossify as a bilaminar plate. The Y-shaped vomer is larger. **G**, Nine-month-old girl. The ossified perpendicular plate has enlarged and extended inferiorly toward the septal diamond. The ossified crista resembles a hollow diamond. **H**, Seventeen-year-old boy. The ossified perpendicular plate reaches the top of the septal diamond, where it may widen into a knob or fork. **I**, Eleven-month-old boy. The nasal septum frequently buckles at the septal diamond.

VIEW IMAGE

Copyright © 2003, Mosby, Inc. All rights reserved.

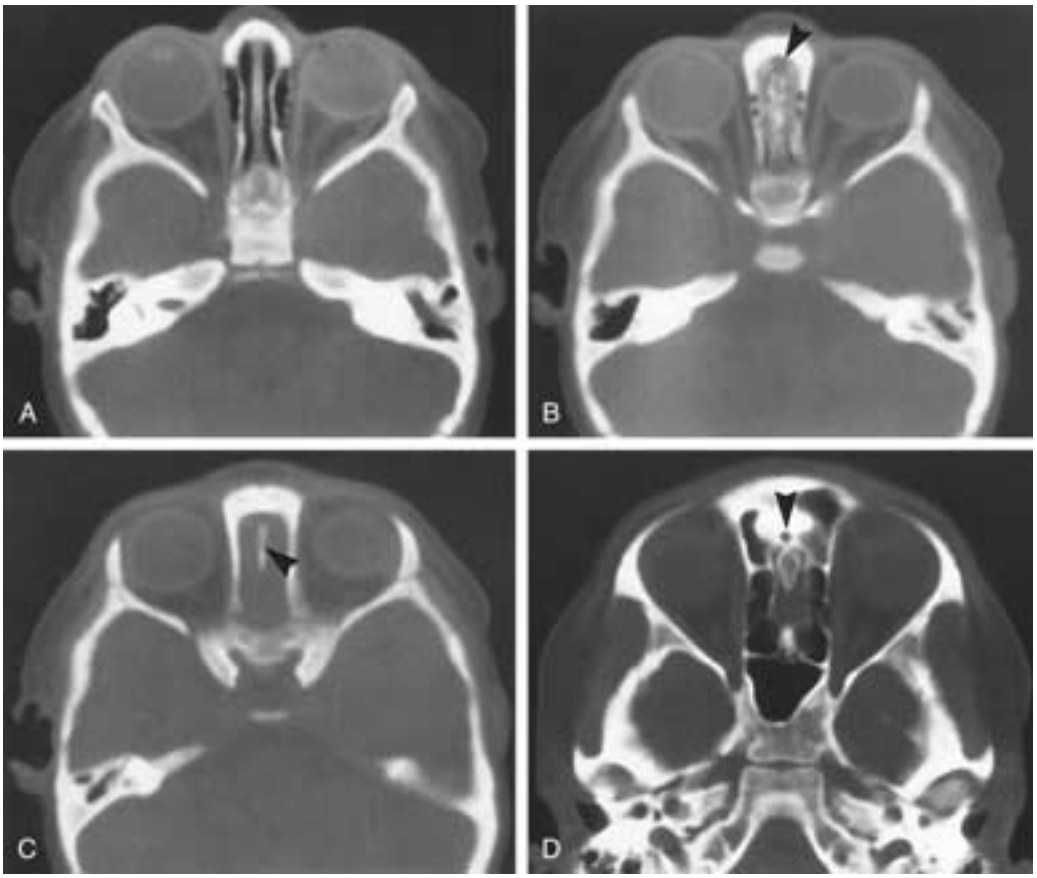

VIEW IMAGE

FIGURE 1-9 Normal pattern of ossification as shown on axial noncontrast CT. In the 11-month-old girl shown in **A** to **C**, serial axial images display the following: (**A**) The normal, thin nasal septum with faint parallel ossifications representing the vomer, (**B**) the normal midline defect (*black arrowhead*) anterior to the normal parallel ossification within the closing cribriform plates and crista, and (**C**) the upper portion of the crista (*arrowhead*) with a small fossa anterior to it. Comparing these images with the coronal sections in Figures 1-6 through 1-8 aids understanding of how the parallel ossifications arise. **D**, Twelve-year-old boy. The foramen cecum (*black arrowhead*) is a well-defined ostium situated just anterior to the diamond shaped ossified crista galli.

sification, with *no* ossification of the perpendicular plate, in patients 2 months to 5 months of age.

6. The ossified crista, cribriform plate, and perpendicular plate can form a bony ''cristal cross'' from 4 months on. These ossifications invariably form a cross from 11 months on.
7. A zone of *un*ossified tissue is seen within the crista in 60% of patients with a cristal cross. Such ostia can be present at any age from 4 months on.
8. The perpendicular plate of the ethmoid can be ossified as a single plate in patients aged 11 months to 18 years. It is ossified in the vast majority of patients older than 2 years.
9. The perpendicular plate is ossified as two parallel laminae in 15% of patients.
10. The nasal septum is widest at the midpoint of its vertical height in nearly all patients of all ages. This widening is designated the septal diamond.
11. The perpendicular plate widens inferiorly or splits to form an inverted Y at the septal diamond in 30% of patients, all older than 6 years of age.
12. The perpendicular plate reaches as far inferiorly as the septal diamond in 32% of all patients, 92% after age 6 years and 100% after age 13 years.

The ossified vomer exhibits a V- or Y-shaped superior border in 80% of patients at any age. The vomerine ossification appears as a single point anteriorly and as a V or Y posteriorly in 21% of patients. In 8% it is seen only as a single point.

In the *normal* patient then, one may expect to see no ossification in the midline of children under 1 year of age, an unossified zone within 60% of the cristal crosses, a ''bilaminar'' perpendicular plate of ethmoid in 15%, and a V- or Y-shaped upper surface of the vomer in at least 80% of patients (Figs. 1-6 and 1-7). These should not be overinterpreted as pathology.

The development of the ethmoid labyrinth is often asymmetric in contour and position.[27] As a consequence, 48% of normal patients show contour asymmetry of the fovea ethmoidalis with flattening of the ethmoid roof on one side, and 9.5% show an asymmetric position of the fovea ethmoidalis.[27] Of those with positional asymmetry, the

Copyright © 2003, Mosby, Inc. All rights reserved.

fovea is lower on the right in 63% and lower on the left in 37%.[27] This normal variation must not be misinterpreted as pathology.

TORI PALATINUS, MAXILLARIS, AND MANDIBULARIS

Torus palatinus is a benign thickening of normal cortical and medullary bone on the oral surface of the hard palate (Fig. 1-10).[28–35] It is covered by a thin, pale mucosa. The torus typically aligns along the median intermaxillary-interpalatine suture, protrudes downward from the apex of the palatal arch, and extends to both sides, approximately symmetrically. The regions of the palatal rugae and the greater palatine foramina are usually spared, so the tori have a ''faceted,'' triangular/diamond configuration.[32] The nasal aspect of the hard palate is never affected by simple torus palatinus.[31] *Torus maxillaris* signifies one or multiple unilateral or bilateral hyperostoses arising from the alveolar portion of the maxilla, usually in the molar region. Torus maxillaris internus arises along the lingual surface of the dental arch opposite the roots of the molars and may coalesce into lobular or irregular masses. Torus maxillaris externus appears as broader, sausage-shaped, or alate expansion(s) of the buccal aspect of the superior alveolar ridge.[28–32] *Torus mandibularis* signifies unilateral or bilateral hyperostoses arising along the lingual surface of the mandible between the alveolar border and the mylohyoid line (Fig. 1-11). They usually are found in relation to the apex of the second premolar[33] opposite the mental foramen.[29–32] *Multiple tori* may occur together. Tori maxillaris and mandibularis are found more commonly in skulls with torus palatinus (Figs. 1-10 and 1-11). Buccal hyperostoses of the maxilla and mandible commonly occur together in both sexes.[22] Torus palatinus and torus mandibularis may both be associated with a thick posterior wall of the glenoid fossa (tympanic plate).[37]

Torus palatinus is found in 19% to 60% of diverse ethnic

FIGURE 1-10 Torus palatinus. **A**, Open-mouth view. Large lobular torus palatinus in a 78-year-old woman. **B** to **D**, Coronal CT. **B**, Small, symmetric torus palatinus in a 30-year-old man. **C**, Large lobular asymmetric, pedunculated torus palatinus with bilateral tori mandibulares. **D**, Lobular pedunculated torus palatinus in a 45-year-old woman. (**A** and **D** from Naidich TP, Valente M, Abrams K, Spreitzer JJ, Doundoulakis SH. Torus palatinus. Int J Neuroradiol 1997;3:229–243.)

VIEW IMAGE

Copyright © 2003, Mosby, Inc. All rights reserved.

FIGURE 1-11 Torus mandibularis. **A**, Open-mouth view. A 30-year-old woman with bilateral tori mandibulares (*arrowheads*). **B**, A 39-year-old man. On axial CT, the tori manifest as marked denticulate cortical thickenings along the inner aspects of the mandibular arch. **C**, A 33-year-old woman. On coronal CT the tori manifest as marked cortical exostoses with minimal encroachment on the medullary cavity. (From Naidich TP. Pits, patches and protuberances. Hyperostosis mandibularis. Int J Neurol 1997;3:224–228.)

VIEW IMAGE

populations and in 20.9% of 2478 dental subjects of mixed heritage in the United States.[35, 37, 38] Tori have a distinct tendency toward heritability, with Oriental and Amerindian populations showing a particularly high incidence (44% to 60%).[30] In one study of approximately 150 Japanese families, Suzuki and Sakai showed that the incidence of torus palatinus in parents of Japanese children was 87.7% if the child had a torus but only 23.8% if the child had no torus.[33] Further, the larger the torus in the parent, the greater the incidence of tori in the children, the earlier their appearance, and the larger their size in the offspring.[19]

Tori are found in approximately 2% of newborns and increase in incidence with age.[34, 39, 40] After the newborn period, torus palatinus is approximately twice as common in females as in males.[35, 38–42] Tori grow as the patients grow, until maturity at 20 to 30 years of age, and then stabilize.[30, 33, 42] Unusual tori continue to increase in size in later decades of life.[30] Woo found no sex difference in the size or shape of the tori palatini in 2348 skulls.[30]

Torus palatinus is classified by shape into four major categories[34, 35]:

1. *Flat torus* is a smooth, bilaterally symmetric, broad-based exostosis that is mildly elevated, slightly convex, and oriented along the midline intermaxillary-interpalatine suture of the palate.
2. *Spindle torus* is a midline palatine ridge (the cresta palatina), which may contain a prominent median groove, signifying bilateral origin.
3. *Nodular torus* is a more bulbous hyperostosis formed from close juxtaposition of paired bilateral hemitori or from multiple smooth, discrete, bony protuberances.
4. *Lobular torus* is a large, pedunculated, mushroom-like mass that typically arises from a single base to form multiple secondary lobules separated by variably deep grooves.

Overall, flat and spindle-shaped tori palatini are the most common (86% combined). The larger nodular and lobular forms are seen in only 6% to 8% of patients.[21]

Most tori palatini are small, clinically insignificant, incidental findings on imaging studies. Only 22% are more than 2 cm in length.[42] Very rarely, large tori may restrict motion of the tongue, distort the oral air cavity, and cause speech disturbance. Substantial tori may have to be resected before a patient can be fitted with dental prostheses.

FACIAL CLEFTS

Deranged development of the frontonasal process and/or failure of adjacent processes to merge successfully results in

Copyright © 2003, Mosby, Inc. All rights reserved.

VIEW IMAGE

FIGURE 1-12 Facial clefting. **A**, Absence of the intermaxillary segment with *hypo*telorism. The maxillary processes form the normal lateral thirds of the upper lips. The midline rectangular defect indicates the site of the deficient intermaxillary segment with absent prolabium, incisors, and primary palate. There was consequent clefting of the secondary palate. Absent intermaxillary segment with hypotelorism signifies a high likelihood of holoprosencephaly. **B**, True midline cleft of the upper lip and philtrum with *hyper*telorism. The nose is normal. A 7-month-old girl with transethmoidal cephalocele and left optic nerve dysplasia (morning glory syndrome). True midline cleft lip signifies the high likelikhood of midline craniofaciocerebral and optic dysraphysm. **C** and **D**, Midline cleft lip is also found in association with Mohr syndrome (orofacial digital syndrome II [OFD II]). The presence of reduplicated great toes bilaterally helps to identify OFD II and to distinguish it from OFD I.

a coherent series of malformations. Insufficiency of the frontonasal and nasomedial processes may result in hypoplasia or absence of the nose and intermaxillary segment, with a roughly rectangular defect in the middle one third of the upper lip, absence of the incisors, absence of the primary palate with a cleft in the secondary palate, and *hypo*telorism. This is one common manifestation of holoprosencephaly[1, 6, 43, 44] (Fig. 1-12A). Failure of the two nasomedial processes to merge in the midline produces the rarer, true midline cleft lip and palate with *hyper*telorism. This is typically associated with cleft primary palate, diastasis of the medial incisors, double frenulum of the upper lip, dehiscence of the skull base, and basal encephaloceles (Fig. 1-12B). True midline cleft is also a feature of Mohr syndrome (Fig. 1-12D). Failure of the nasomedial processes to merge with the maxillary processes on one or both sides produces the typical unilateral or bilateral common cleft lip and/or cleft palate (Fig. 1-13). Discordant growth of the two divided processes may then result in offset of the premaxillary segment from the maxillary segment, a

Copyright © 2003, Mosby, Inc. All rights reserved.

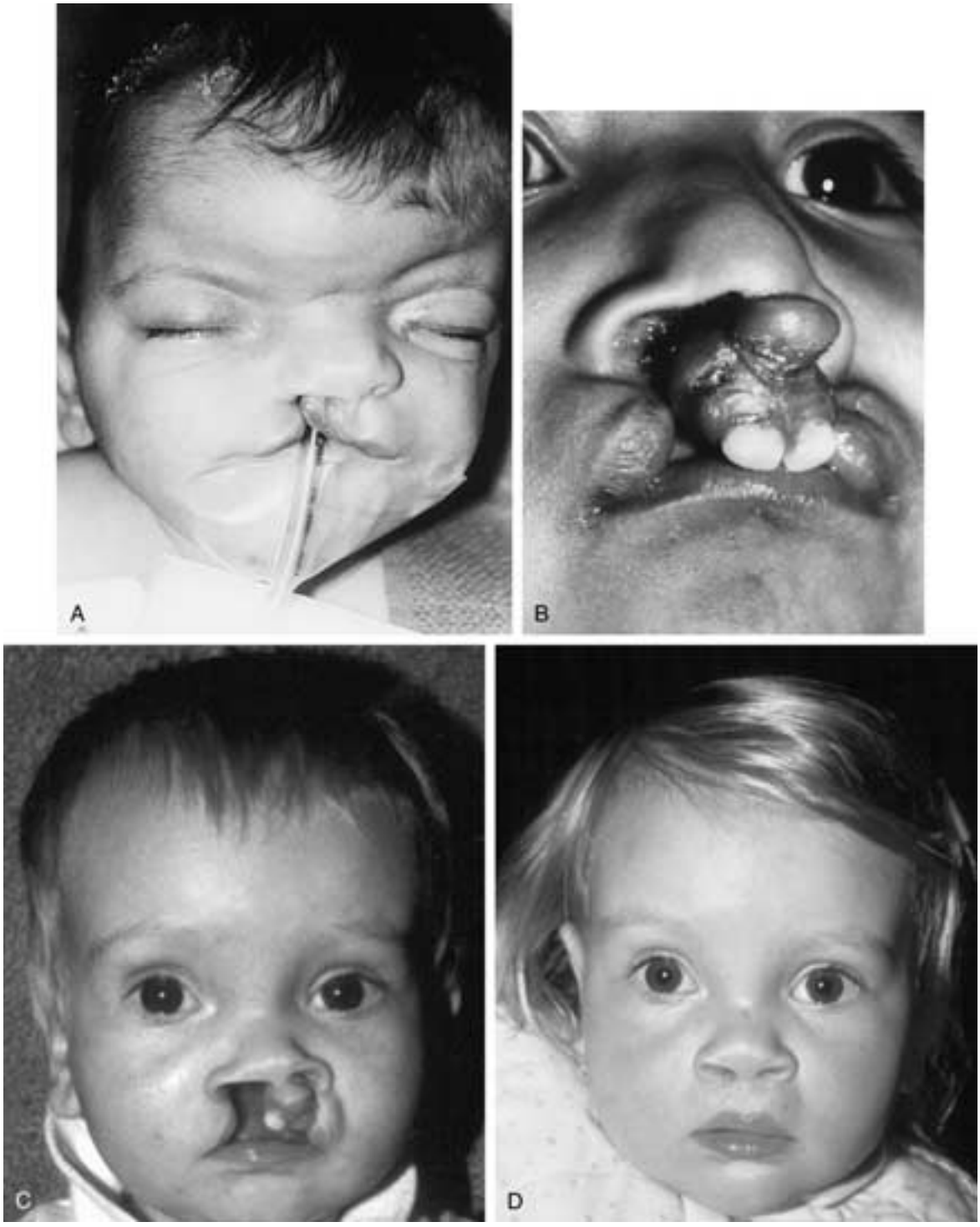

FIGURE 1-13 Facial clefting. **A**, Right unilateral common cleft lip and palate in a 4-day-old girl. The cleft extends into the base of a widened nostril. The intermaxillary segment is distorted. **B**, Bilateral common cleft lip and cleft palate with discordant forward growth of the intermaxillary segment in a 4-year-old boy. The normal canthi, alae nasi, and lateral thirds of the lip and jaw indicate normal formation and merging of the maxillary and nasolateral processes. The abortive prolabium, premaxillary segment, and central incisors attach to the vomer and project well anterior to their expected position, because failure to merge the facial processes led to discordant growth of the maxillary and intermaxillary segments. **C** and **D**, Bilateral common cleft lip and palate prior to (**C**) and following (**D**) surgical repair. There is near-symmetric restoration of the nose and upper lip, with some residual distortion caused by scar.

VIEW IMAGE

Copyright © 2003, Mosby, Inc. All rights reserved.

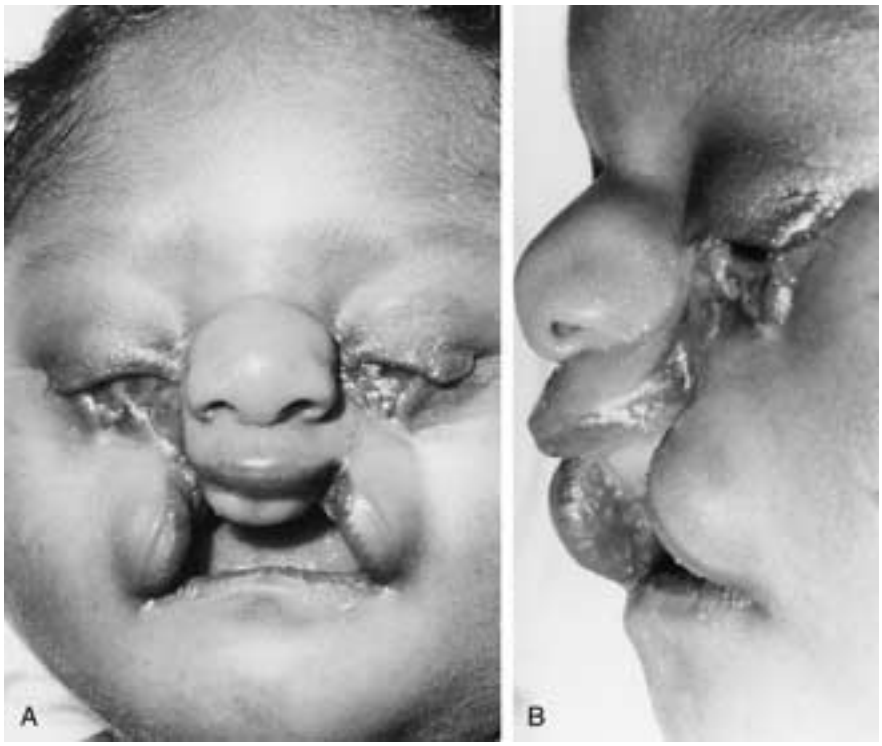

VIEW IMAGE

FIGURE 1-14 Facial clefting. Bilateral oblique oroocular clefts with bilateral common cleft lip. **A**, Frontal view. **B**, Lateral view.

widened nostril, a depressed ala nasi, and an anomalous nasal septum.[4] Failure to merge the nasolateral process with the maxillary process results in an oblique facial cleft extending from the inner canthus of the eye into the nose (Fig. 1-14). This cleft may occur in association with bilateral common cleft lip and/or palate. Failure to merge the maxillary with the mandibular process, unilaterally or bilaterally, results in a transverse facial cleft, also designated ''wolf mouth'' or macrostomia[45] (Fig. 1-15). The transverse cleft may occur in isolation or as part of syndromes such as hemifacial microsomia (see the section on Hemifacial Microsomia). Clefts that do not align along known lines of embryonic fusion likely represent the syndrome of amniotic bands (see the section on Syndrome of Amniotic Bands) (Fig. 1-16). The relative incidences of the facial clefts are given in Table 1-1.[30]

VIEW IMAGE

FIGURE 1-15 Facial clefting. Unilateral transverse facial cleft and macrostomia in an infant girl. (From Bauer BS, Wilkes GH, Kernahan DA. Incorporation of the W-plasty in repair of macrostomia. Plast Reconstr Surg 1982;70:752–757.)

Common Cleft Lip and/or Cleft Palate

Common clefts of the lip and/or palate account for 98.8% of all facial clefts.[46] They may involve the lip only, the lip and palate, or the palate only, unilaterally or bilaterally. Approximately 50% to 70% of all cases of cleft lip/palate are nonsyndromic.[13] The rest are divided among more than 300 presently recognized entities.[13] Cleft lip (with or without cleft palate) should be recognized as an entity distinct from cleft palate only, but the two conditions are usually considered together in series of facial clefting.[47]

The nature and incidence of clefting vary among populations. Caucasians show nonsyndromic clefting of the lip and/or palate in 1 per 700 to 1000 live births.[48] Clefting of the palate alone (cleft palate only) occurs less fequently: 6.5 per 10,000 births.[48] In 460 patients with oral clefts in France, the lesion was an isolated cleft lip in 19.1%, combined cleft lip plus cleft palate in 37.2%, and cleft palate only in 43.7%.[49] Of the 171 infants with complete cleft lip and palate, the clefts were unilateral in 58.5% and bilateral in 41.5%.[49] Study of 1669 consecutive *surgically treated* cleft lips and cleft palates in Iran found that, in that group, isolated cleft lips were slightly more common in women

Copyright © 2003, Mosby, Inc. All rights reserved.

VIEW IMAGE

FIGURE 1-16 Facial clefting. Nonanatomic clefts in a 12-year-old mentally retarded girl with the syndrome of amnionic bands. Lateral view. A long, thin band-like scar extends across the scalp and face from the temporoparietal region through the cheek and the corner of the mouth to the lower lip. The large posterior zone of atrophic skin, absent hair, tissue bulging, and inferior displacement of the ear indicate the site of an associated temporoparietal encephalocele. Imaging studies showed notching and separation of teeth where the band crossed the alveolar ridge.

(1.16:1) and that combined cleft lip/cleft palate was significantly more common in men (2.2:1).[50] Cleft palate only was very slightly more common in women (1.1:1).[50] The combination of cleft lip plus cleft palate is more common than either isolated cleft lip or isolated cleft palate.[50] Both isolated cleft lip and combined cleft lip/cleft palate are more often unilateral than bilateral and affect the left side more than the right (Table 1-2).[50] Unilateral left-sided clefting, unilateral right-sided clefting, and bilateral clefting occur in a ratio of 6:2:3 (Table 1-2).[50] Table 1-3 summarizes a 50-year experience with 2297 clefting patients in Denmark.[47]

Table 1-1
INCIDENCE OF FACIAL CLEFTS (*N* = 3988)

Cleft Type	Number	Percent
Common cleft lip/cleft palate	3940	98.8
True midline cleft lip	8	0.20
True midline cleft lip (part of the oro-facial-digital syndrome)	3	0.08
Pseudo-median cleft lip (holoprosencephaly)	7	0.18
Midline cleft nose	8	0.20
True bifid cleft nose	4	—
Unilateral and bilateral cleft ala nasi	4	—
Transverse facial cleft (macrostomia)	12	0.30
Oblique oro-orbital clefts	3	0.08
Cleft scalp	7	0.18
Total	3988	100

From Fogh-Andersen P. Rare clefts of the face. Acta Chir Scand 1965;129: 275–281.

Pathogenesis of Cleft Lip/Cleft Palate and of Cleft Palate

Both genetics and environment have been implicated in facial clefting. The risk of a child's being born with a cleft lip and palate is 4% if one parent *or* one sibling is affected but 17% if both one parent *and* one sibling are affected.[51] This indicates a heritable component. Dietary supplementation with vitamins B_6 and folic acid during the first trimester markedly decreases the risk of recurrence in women who had previously borne children with cleft lip and palate.[48] This indicates a potential role for teratogens (or deficiencies). Teratogens linked to facial clefting include cortisone, anticonvulsants such as phenytoin, salicylates, aminopterin, organic solvents, maternal alcohol ingestion, maternal diabetes mellitus, maternal rubella, and the season of gestation. Increased maternal and paternal age may also play a role.[48] Maternal smoking during early pregnancy is a clear risk factor for cleft lip/palate. Study of 2207 pregnancies leading to cleft lip/palate showed a definite increase in the incidence of cleft lip/palate in children of mothers who smoked during pregnancy and an increasing risk of cleft lip/palate with increasing amounts of smoking.[52] The odds ratio for clefting increases from 1.32 for women who smoke 1 to 10 cigarettes daily to 1.69 for those who smoke 21 or more cigarettes daily.[52] Smoking seems to synergize with uncommon polymorphisms in the TGF-alpha gene at chromosome 2p13 to increase the risk of cleft palate sixfold.[2] Statistically significant elevations in lactate dehydrogenase and creatine phosphokinase have been reported in the amnionic fluid of human fetuses with cleft lip/cleft palate (vs. control normal fetuses).[53]

Genes and Heritability

Families of patients with cleft lip (with or without cleft palate) rarely include individuals with isolated cleft palate, and vice versa, probably because the primary and secondary palates form independently.[48] Nonsyndromic orofacial clefting (OFC) (cleft lip with or without cleft palate) has been mapped to genes designated *OFC1* at chromosome 6p23, *OFC2* at 2p13, interactions between *OFC1* and *OFC2*, and *OFC3* at 19q13.2.[48] Patients with OFC constitute a heterogeneous group, with some clefts inherited by autosomal dominance, others as a multifactorial threshhold trait, and still others by oligogenic inheritance.[48]

The gene products related to cleft lip and cleft palate have been characterized as TGF-alpha (2p13), retinoic acid receptor alpha (RARA) (17q21.1), MSX1 (4p16.1), and BCL3 (19q13.2).[48] In animals the gene *endothelin-1* lies in the OFC1 region at chromosome 6p23-24.[48] ''Knockout'' mice deficient in OFC1 show craniofacial malformations including cleft palate.[48] Mice deficient in endothelin converting enzyme-1 or in endothelin-A receptor show nearly identical malformations. END1, the transcription factor dHAND, and the gene *MSX1* (*Hox 7*) may form a signal cascade that regulates the development of neural crest–derived branchial arch mesenchyme.[48, 54, 55]

Nonsyndromic cleft palate only (CPO) has uncertain inheritance but may arise as a recessive single major locus

Copyright © 2003, Mosby, Inc. All rights reserved.

Table 1-2
CLASSIFICATION OF CLEFTS BY TYPE AND SIDE (*N* = 1669 CONSECUTIVE SURGICALLY TREATED CLEFTS IN IRAN)

Type of Cleft	Unilateral Right	Unilateral Left	Bilateral	Total
Cleft lip	121 (24.1%)	297 (59.3%)	83 (16.6%)	501 (30%)
Cleft lip and palate	128 (16.5%)	373 (48%)	276 (35.5%)	777 (46.5%)
Cleft lip (not classified)				42 (2.6%)
Cleft lip and palate (not classified)				60 (3.6%)
Cleft palate				289 (17.3%)
Total	249 (14.9%)	670 (40.1%)	359 (21.5%)	1669 (100%)

From Rajabian MH, Sherkat M. An epidemiological study of oral clefts in Iran: analysis of 1669 cases. Cleft Palate-Craniofac J 2000;37:191–196.

with low penetrance.[48] *TGF-β3* is a major candidate gene for mutation in human isolated cleft palate.[22] It is localized in a temporally and spatially restricted fashion in the medial edge epithelia of the fusing palate. Culture of palatal shelves in the presence of neutralizing antibody to *TGF-β3* or anti-sense oligonucleotides to *TGF-β3* prevents fusion of the palatal shelves.[56] *TGF-β3* knockout mice show isolated cleft palates extending from the posterior soft palate into the hard palate for a variable distance.[11] Cleft secondary palates are seen in knockout mice with deficiency of the GABA-producing enzyme glutamic acid decarboxylase and deficiency of the β-3 subunit of the $GABA_A$ receptor genes.[48] A different lesion would appear to explain the rare human X-linked cleft palate.[11]

Clinical Features

Children with cleft lip and palate face aesthetic and functional problems (Fig. 1-13). The extent of these difficulties depends on the type of cleft and its severity. Functionally, the cleft in the *palate* is most significant, because the palate is critical to achieving adequate intraoral suction for early feeding and to closing the nasopharynx (velopharyngeal valve) for later speech. Aesthetically, children with cleft lip with or without cleft primary palate face potential postoperative asymmetries of the lip and nose, visible scars, and either tissue deficiencies or excess. Functionally, they face potential dental and orthodontic problems related to the effect of the cleft on the alveolar-maxillary position and on dental development. Those with complete cleft lip and palate and those with isolated clefts of the secondary palate face problems with speech and language, including limitation of the phonemic repertoire, poor intelligibility, and delayed development of expressive and receptive language skills. The degree of delay is directly related to the adequacy and timing of palate repair.

Further problems relate to the growth of the midface, dental occlusion, and the effect of the clefting on eustachian tube function. The degree of later midface deformity depends on the initial distortion in facial development, the timing and type of surgical repair, and the integration of cleft care for all aspects of cleft palate management. Clefting causes concurrent abnormalities in development and orientation of the palatal muscles (particularly the levator palatini and tensor veli palatini). Abnormality in these muscles directly affects the function of the eustachian tube, the child's ability to aerate the middle ear, and the incidence of otitis media. Special attention must be directed to the potential for loss of hearing secondary to infection and to any additional impact that this complication would have on speech development.

Facial Deformities

Physical examination and imaging reveal structural changes in most areas of the face.

Lip

The clefts of the lip may be complete, incomplete, unilateral, or bilateral. Incomplete clefting, whether unilateral or bilateral, can occur in isolation or in combination with a complete clefting of the opposite side of the lip. The distortions in the soft tissues of the lip vary with the cleft and its severity. *Complete unilateral clefts* of the lip extend from the floor of the nostril, through the lip, to a point below the nostril (Fig. 1-17). The lip is shortened on both sides of the cleft, usually asymmetrically, with greater shortening on the medial side. The normal landmarks of the vermillion-

Table 1-3
POINT PREVALENCE OF CLEFT PALATE AT BIRTH IN DENMARK (1936–1987) (*N* = 2297 PATIENTS)

Datum	Total Number of Live Births	Type of Cleft and Number with That Type of Cleft						Total
Cleft type		CPH	CPS	CPSM	$CPSM_C$	CP (?)	CPAA	
Males	1,951,353	362	244	231	152	38	177	1052
Females	1,841,710	563	268	198	149	44	172	1245
Gender ratio (M:F)	1.06	0.64	0.91	1.17	1.02	0.86	1.03	0.84
Totals	3,793,063	925	512	429	301	82	349	2297
Incidence per 10,000 live births		2.44	1.35	1.13	0.79	0.22	0.92	6.06

Abbreviations: *CPH*, Overt, isolated cleft palate involving the hard and soft palates; *CPS*, Overt isolated cleft of the soft palate only; *CPSM*, submucous isolated cleft palate; $CPSM_C$, the subgroup of CPSM that fulfills the Calnan criteria and were operated on for *CPSM* (this is a subgroup of the prior column); *CP* (?), isolated cleft palate, type unknown; *CPAA*, syndromic isolated cleft palate; isolated cleft palate and clefts associated with anomalies, syndromes, and mental disabilities. All cleft types are included.

Christensen K, Fogh-Andersen P. Etiological subgroups in non-syndromic isolated cleft palate. A genetic-epidemiological study of 52 Danish cohorts. Clin Genet 1994;46:329–335.

Copyright © 2003, Mosby, Inc. All rights reserved.

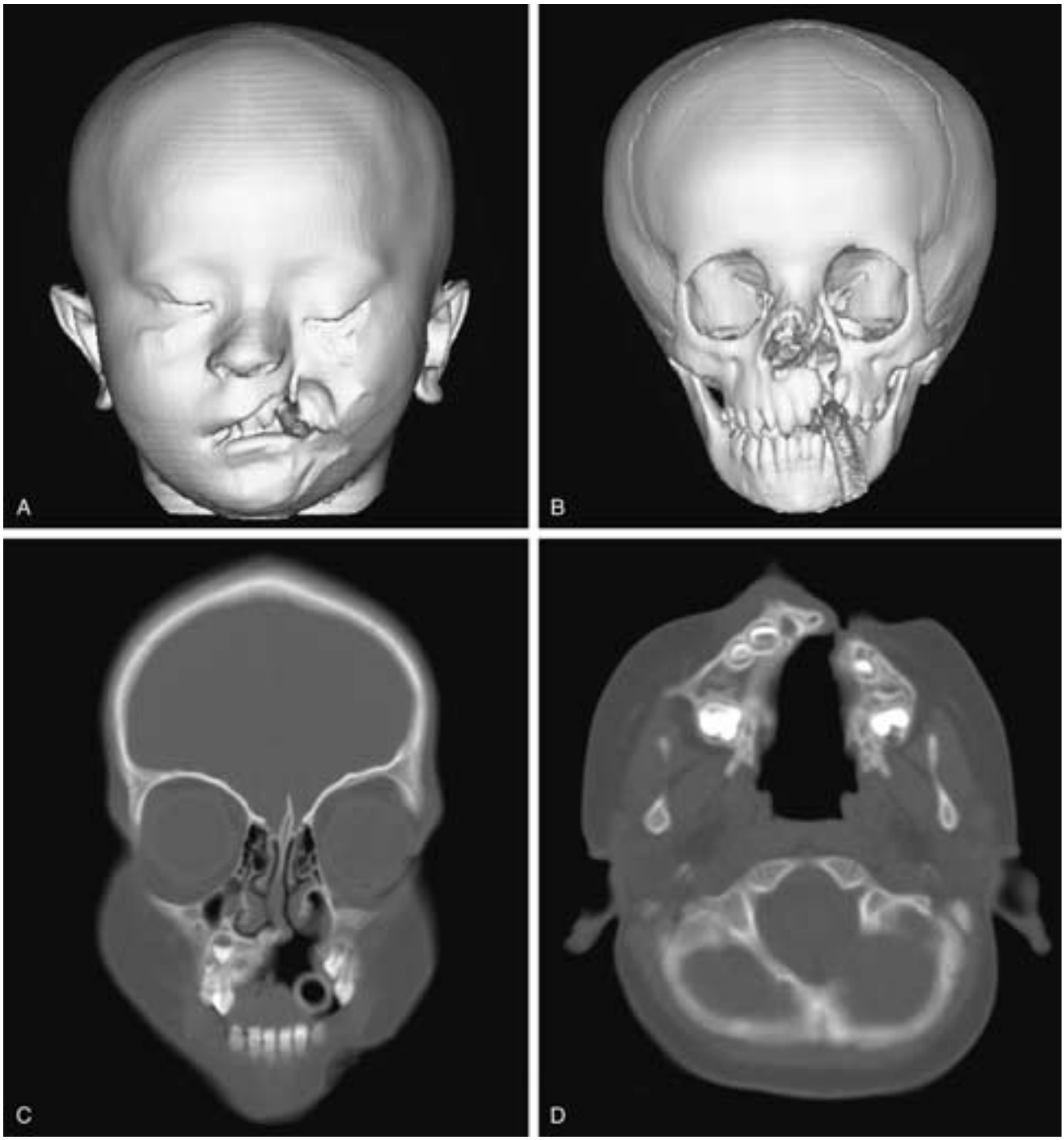

VIEW IMAGE

FIGURE 1-17 Unilateral cleft lip and palate in a 2-year-old boy. **A**, Three-dimensional CT of the skin surface. **B**, Three-dimensional CT of bone surface. **C**, Coronal CT. **D**, Axial CT. The unilateral cleft extends through the lip, the alveolar ridge, and the palate on the left. In this patient, the soft-tissue cleft lies lateral to the deformed ala nasi and extends toward the lacrimal sac fossa.

cutaneous junction and the vermillion-mucosal junction are distorted. The vermillion tapers upward along the cleft toward the nostril sill. There is a deficiency of vermillion on the medial side. The underlying muscle of the upper lip does not decussate in the midline of the lip, but streams parallel to the border of the cleft and inserts at the alar base. This altered course, failure of decussation, and concurrent distortion of the levator labii superioris create a ''fullness'' in the segment of the lip lateral to the cleft termed the orbicularis bulge. Patients with *incomplete unilateral cleft lips* show lesser degrees of vertical lip deficiency and muscle distortion proportional to the completeness of the cleft. There may be a small coloboma in the *lower* portion of the lip, a groove in the skin overlying the cleft, and absence of hair and sweat glands in the skin overlying the cleft.[57] Patients with *complete bilateral cleft lip* show similar disorganization of structure on both sides (Fig. 1-18). The central lip segment (prolabium) develops no underlying

Copyright © 2003, Mosby, Inc. All rights reserved.

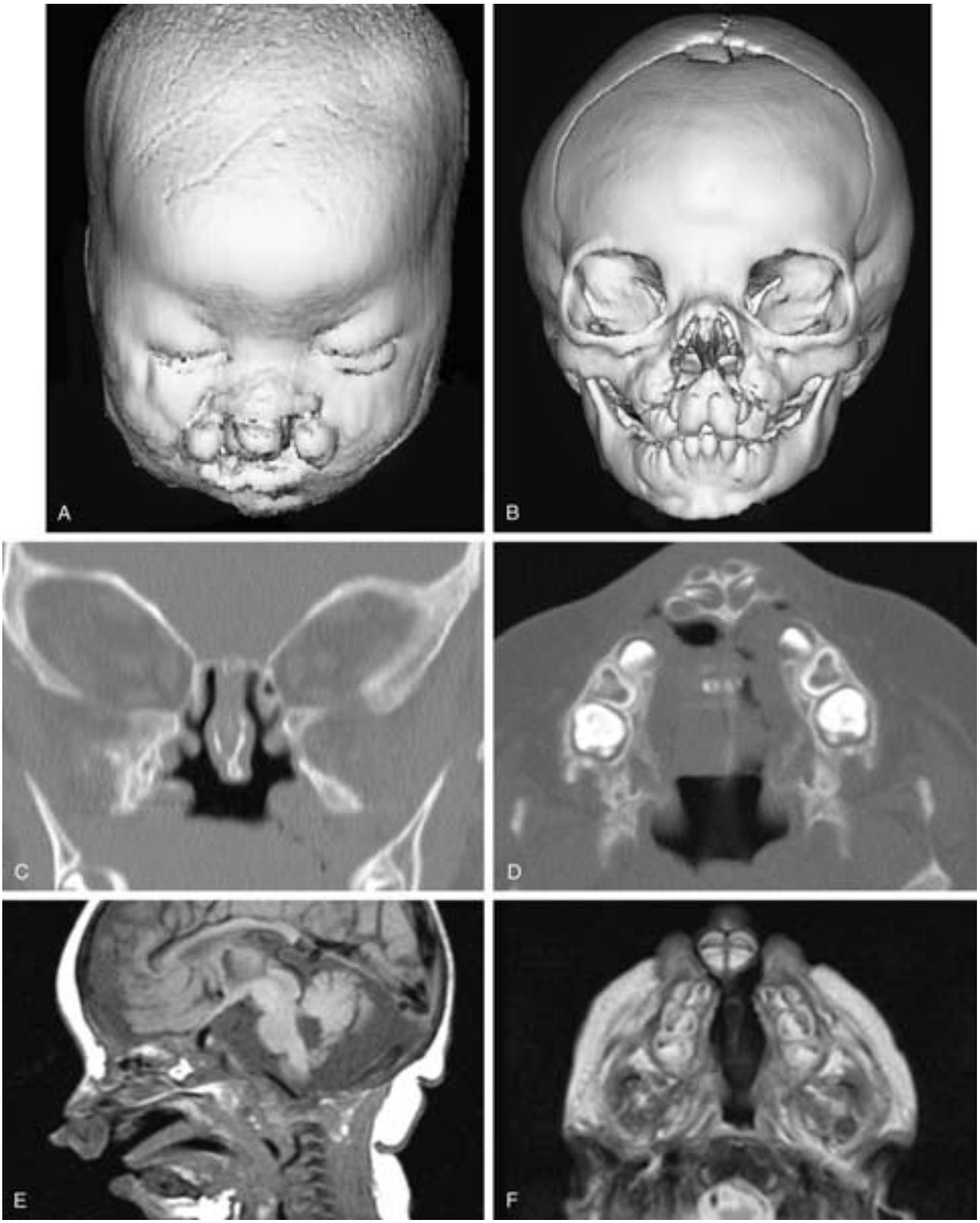

VIEW IMAGE

FIGURE 1-18 Bilateral cleft lip and palate in a 2-month-old boy. **A**, Three-dimensional CT of the skin surface. **B**, Three-dimensional CT of bone surface. **C**, Coronal CT. **D**, Axial CT. **E**, Saggital T1 MRI. **F**, Axial T2 MRI. The symmetric clefts extend through the lips, the bases of the nostrils, the alveolar ridges, and the palate, leaving a distorted premaxillary segment with the central prolabium isolated from the paired maxillary processes. The prominent central incisors and smaller lateral incisors are positioned far anterior to the maxillary arches. The clefts course obliquely from anterolateral to posteromedial between the primary and secondary palates (cf. Fig. 1-5) before continuing directly posteriorly between the two maxillary palatal shelves to either side of the ununited septum.

Copyright © 2003, Mosby, Inc. All rights reserved.

muscle, only connective tissue. The degree of deficiency of prolabial tissue varies in width and vertical extent. Minimal vermillion is present. The labial sulcus is absent. The underlying premaxilla varies in position and may project forward or remain in reasonable alignment. The position of the premaxilla significantly affects the appearance and position of the prolabial segment of the lip.

Maxilla

In comparison to persons with normal palates, those with cleft palates show consistent but variable degrees of midfacial hypoplasia. The anterior hemimaxilla shows a narrowed curvature on the side of the cleft (''arch collapse'') and upward tilting of the premaxillary segment.[58, 59] The palatal (inferior) end of the nasal septum nearly always lies on the side of the cleft, while the anterior nasal spine of the maxilla nearly always lies on the noncleft side.[58, 59] This asymmetry probably arises as the tongue pushes into the cleft, and the divided lip and cheek muscles pull asymmetrically on the anterior nasal spine. The posterior maxillary arch is widened in patients with unilateral cleft lip and palate, but the vertical development of the posterior maxilla is normal.[58–62]

Nose

Unilateral Cleft On the cleft side, the angle between the medial and lateral crura is obtuse, the ala is caudally displaced, the alar-facial groove is absent, and the alar-facial attachment is at an obtuse angle. There is real or apparent bony deficiency of the maxilla. The circumference of the naris is greater. The naris is retrodisplaced. The columella is shorter in the anteroposterior dimension, and the medial crus is displaced.The nasal septum is typically deflected toward the cleft side, both superiorly and posteriorly, then deflects back toward the noncleft side, with the caudal septum presenting in the normal nostril. The bony pyramid is also deflected toward the cleft side, with varying deficiencies of the skeletal support for the nose due to the deficiency of the maxillary segment on the side of the cleft.

Bilateral Cleft The most visible feature of the bilateral cleft nose is shortening and deficiency of the columella centrally, with splaying and caudal displacement of the alar cartilages to both sides. These distortions create the typical blunted flat nose, widened nostrils, and displaced alar bases. The nasal septum may be midline or variably deflected, depending on whether the cleft is incomplete or asymmetric. Similarly, variations in the position of the smaller segments of the lips and the underlying hemimaxillae affect the degree of nasal widening and flattening.[57]

Concurrent Malformations

Malformations of other body parts occur in 7.73% (Iranian series) to 36.8% (French series) of patients with cleft lip and/or cleft palate.[49, 50, 63] Malformations are more common with isolated cleft palate (46.7%) than with combined cleft lip plus cleft palate (36.8%) or isolated cleft lip (13.6%).[49] An American series of 3804 cases confirmed that concurrent malformations were more common with isolated cleft palate (51.7%) than with cleft lip plus cleft palate (26.2%).[63] In the French series, infants with clefting showed concurrent chromosomal syndromes (7.8%), recognized nonchromosomal syndromes (3.3%), facial anomalies (11.1%), eye anomalies (2.6%), ear anomalies (1.1%), and diverse malformations of the central nervous system (8.5%), skeletal system (7.8%), urogenital system (6.3%), cardiovascular system (4.6%), digestive system (3.3%), abdominal wall (1.3%), skin (0.43%), and other regions (2.6%).[49]

Subtle Deformities in Parents of Patients with Common Clefts

Parents of children with cleft lip and palate show an increased incidence of facial asymmetry, wider bizygomatic distance and wider tragus-subnasal distance than do controls, and an increased incidence of nasal deformity and microform cleft lip.[51] However, parents of children with clefts show no divergence from the normal population in their occlusion or dentition.[57] Compared to parents of normal children, parents of children with unilateral clefts show no asymmetry in tooth size and no difference in the incisor relationship, overjet, overbite, and intercanine widths.[57] Parents of children with unilateral and bilateral clefts display equal tooth number, tooth width, and intercanine widths.[57]

Midline Cleft Lip and Median Cleft Face Syndromes

Median cleft lip is a rare anomaly related to midline craniofacial-cerebral dysraphism.[46] In Fogh-Andersen's series of 3988 craniofacial clefts collected over 30 years (Table 1-1), median clefts of the upper lip were observed in only 15 cases (0.38).[46] Five (0.13%) were true median cleft lips (as considered here) (Fig. 1-12B), three more (0.08%) were true medial cleft lips occurring as part of the orofacial digital syndrome (Fig. 1-12C,D), and seven (0.17%) were pseudomedian cleft lips. An additional four (0.10%) were cases of median cleft nose. Nearly all cases of median cleft face syndrome occur sporadically.[64, 65] Only a few familial cases have been reported.[44, 66–68] An unexpectedly high 12% to 18% of patients with median cleft face syndrome are the products of twin gestation,[44, 66, 67] but the other twin is usually normal. Focal neurologic deficits are not reported with median cleft face syndrome[66, 67, 69–78] and do not appear to form part of the disease. These patients have variable intellectual development. Patient IQ does not appear to be related to the severity of facial clefting.

The midline craniofacial dysraphisms fall naturally into two groups: (A) an inferior group in which the clefting primarily involves the upper lip (with or without the nose) and (B) a superior group in which the clefting primarily affects the nose (with or without the forehead and upper lip). Group A is associated with basal encephaloceles, callosal agenesis (rarely lipoma), and optic nerve dysplasias such as optic pits, colobomas, megalopapilla, persistent hyperplastic primary vitreous with hyaloid artery, and morning glory syndrome (Figs. 1-19 and 1-20). Group B consists of patients with the median cleft face syndrome. This group is characterized by hypertelorism, a broad nasal root, and a median cleft nose (with or without median cleft upper lip, median cleft premaxilla, and cranium bifidum occultum frontalis).[66, 69] Group B patients manifest an increased incidence of

Copyright © 2003, Mosby, Inc. All rights reserved.

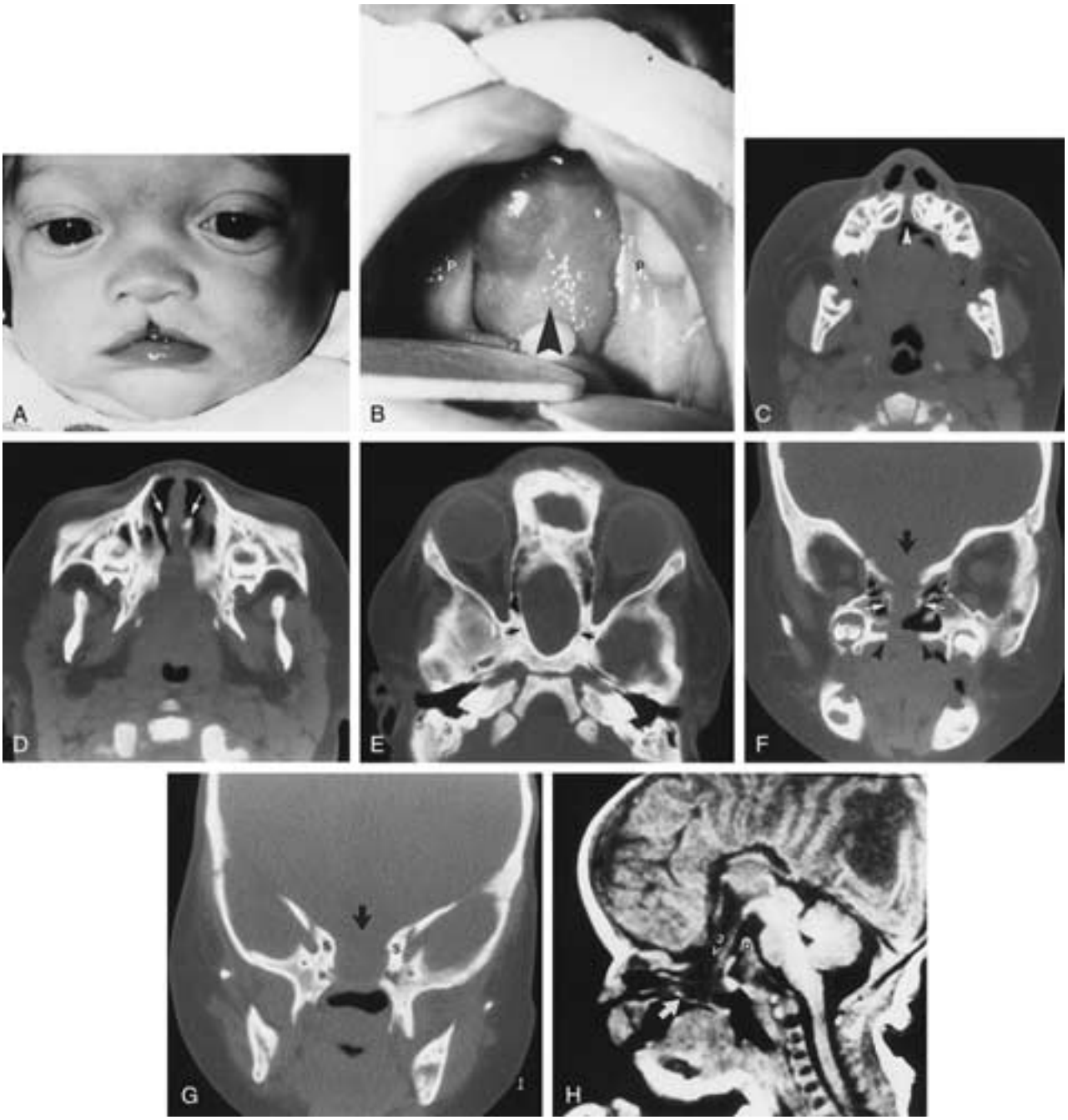

VIEW IMAGE

FIGURE 1-19 Craniofacial cerebral dysraphism. True midline cleft vermillion and philtrum with *hyper*telorism in a 4-month-old boy with progressive compromise of the airway. **A**, Facial clefting. **B**, View through the open mouth toward the palate demonstrates cleft palate with wide separation of the palatal shelves (*P*) and downward protrusion of a soft-tissue mass (*arrowhead*) into the oral cavity. CT in the axial (**C** to **E**) and coronal (**F** and **G**) planes demonstrates midline clefting in the superior alveolar ridge (*arrowhead* in **C**), abnormally wide nasal septum with cleft ethmoids (*white arrows* in **D** and **F**), cleft palate (*black arrowheads* in **F**), and a soft-tissue mass (*black arrow* in **F** and **G**) that bulges inferiorly through the sharply marginated ovoid canal (*black arrows* in **E**) in the cleft sphenoid (*S*) and ethmoid bones. **H**, Sagittal T1-weighted MR image demonstrates callosal agenesis and a transsphenoidal-ethmoidal cephalocele (*white arrows*) containing the third ventricle (*3V*), hypothalamus, and portions of the frontal lobes. The cephalocele extends downward into the oral cavity through the cleft sphenoid just anterior to the dorsum sellae (*D*). (Courtesy of Dr. Sharon Byrd, Chicago.)

frontonasal and intraorbital encephaloceles, anophthalmos/microphthalmos, and callosal lipomas (less frequently, callosal agenesis). Group B has only a weak association with basal encephaloceles or with optic nerve dysplasia (Fig. 1-21).[44]

Group A

True clefting of the *upper* lip is typically associated with *hyper*telorism and is a clear stigma of the likely concurrence of basal encephalocele, callosal agenesis or lipoma, and any of the diverse forms of optic nerve

Copyright © 2003, Mosby, Inc. All rights reserved.

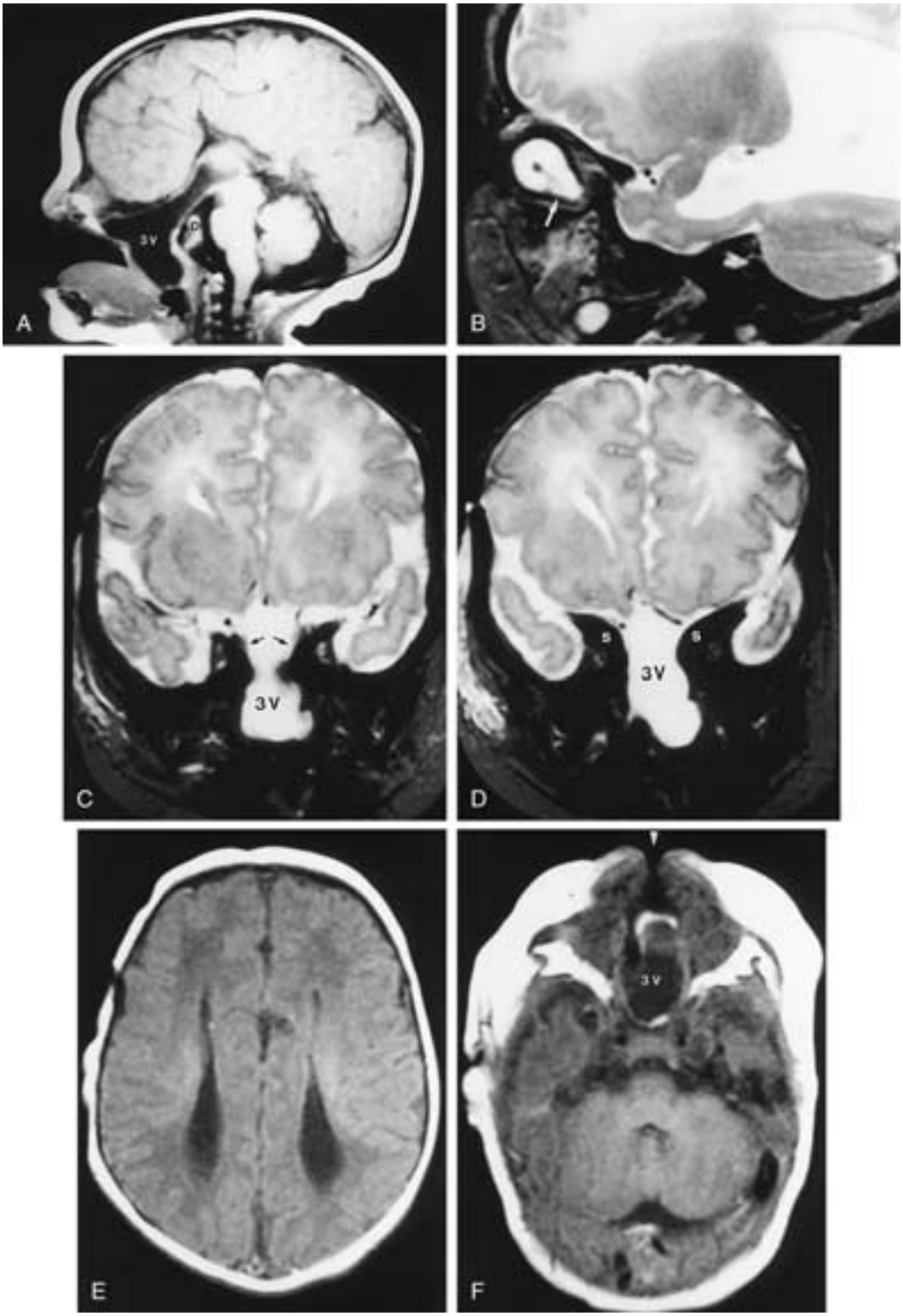

VIEW IMAGE

FIGURE 1-20 Craniofacial-cerebral dysraphism. True midline cleft upper lip. **A**, Midsagittal T1-weighted MR image shows a transsphenoidal-ethmoidal cephalocele, with the third ventricle (*3V*) and optic apparatus protruding downward through the defect in the sphenoid bone immediately anterior to the dorsum sellae (*D*) to rest on the tongue. The corpus callosum is absent. **B**, Sagittal T2-weighted MR image through the ocular globe demonstrates microphthalmia with coloboma (*arrow*). **C** and **D,** Coronal T2-weighted images through the cleft in the sphenoid (*S*). The cavernous sinuses (*arrows*) form the lateral walls of the hernia ostium. **E** and **F**, Axial T1-weighted images display the callosal agenesis **(E)**, the ovoid contour of the third ventricle (*3V*) within the midline defect in the sphenoid, and the midline cleft upper lip (*arrowhead*) (**F**).

Copyright © 2003, Mosby, Inc. All rights reserved.

VIEW IMAGE

FIGURE 1-21 Median cleft face syndrome, typical facies. **A**, Sedano facies type A in 3-month-old boy. **B**, Sedano facies type B in 4-day-old boy. **C**, Sedano facies type C in a young boy after repair of concurrent bilateral common cleft lip and palate. **D**, Sedano facies type D in a 3½- year-old boy. (**A**, **B**, and **D** from Naidich TP, Osborn RE, Bauer B, et al. Median cleft face syndrome: MR and CT data from 11 children. J Comput Assist Tomogr 1988;12:57.)

dysplasia (Figs. 1-12B, 1-19, and 1-20). The labial defect observed varies from a small notch, to a vertical linear cleft, to a small triangular deficiency of the midline upper lip vermillion (with or without philtrum), with absence of the labial tubercle. This defect is designated *true midline cleft upper lip*. Rarely, this defect may also occur as an isolated finding or as part of the orofacial digital syndromes I and II (Fig. 1-12C,D).[79–81]

Patients with median cleft upper lip may show basal encephaloceles, rare anomalies estimated to constitute

Copyright © 2003, Mosby, Inc. All rights reserved.

1.2% of all encephaloceles (Figs. 1-12B, 1-19, and 1-20).[82, 101–104] Table 1-4 summarizes the findings in a total of 30 cases collected from the literature and personal material.[43, 66, 83–100] In this series, 50% manifested midline cleft lip (but not nose), an additional 13% manifested agenesis, and 40% manifested optic nerve dysplasia (i.e., any of the spectrum of optic pit, optic/perioptic coloboma, morning glory disc, and/or megalopapilla). Since the reports are incomplete in many cases, the true concurrence of these anomalies is likely to be even higher.

To date, no report details the true incidence of encephalocele, callosal agenesis, and facial clefting in patients with optic nerve dysplasias.[90–93, 105–109] However, Beyer et al.[110] found one sphenoidal encephalocele in eight patients with 10 morning glory discs, a single-series incidence of 10% to 15%. Lipoma of the corpus callosum is observed in approximately 0.06% of all patients in both in vivo and necropsy studies.[111] Agenesis of the corpus callosum is present in 35% to 50% of such cases.[111] Midline interhemispheric lipoma may be associated with midline subcutaneous lipomas, cranium bifidum, and frontonasal encephaloceles.[66, 112, 113]

Group B

Median cleft face syndrome (frontonasal dysplasia) is a rare form of dysraphism that affects the midface (Figs. 1-21 and 1-22). The characteristic physical findings in median cleft face syndrome include hypertelorism, cranium bifidum occultum frontalis, widow's peak hairline, and midline clefting of the nose (with or without cleft upper lip, premaxilla, and palate).[44, 66, 69, 114–116] There may also be common clefts of the upper lip and palate, primary telecanthus, ocular colobomas, microphthalmia, and notching of the alae nasae. Hypertelorism is present in all cases of median cleft face syndrome and is the one *obligatory* finding.[69] The next most constant finding is true midline bony clefting of the nose. The other facial deformities may be present or absent in varying degree.

The types of facial clefting seen in this syndrome have been classified differently by different authors.[64, 66, 69] DeMyer classified the median cleft face syndrome into four classical facies, which represent the most frequently encountered combinations of the major and minor defects of median cleft face syndrome (Table 1-5).[64, 66] Sedano et al.[69] proposed an alternative classification of median cleft face syndrome (Table 1-6). These systems differ, in part, in the importance attributed to notching of the alae nasae (Table 1-7). In our opinion, the Sedano et al. classification appears to correlate best with the intracranial pathology and is the most useful system.

Molecular Genetics

In mice, severe nasal clefting results from defects in the aristaless-related genes (*Alx3* and *Alx4*), which are upstream regulators of *sonic hedgehog*.[117] Mice with the compound null mutation *Alx3/Alx4* show severe midline clefts of the nose with malformation, truncation, or absence of most of the facial bones, skull base, and other elements derived from neural crest.[117] There is significantly increased apoptosis localized to the outgrowing frontonasal process at (mouse) embryonic day (ED) 10.0, leading to an abnormal position of the nasal processes when they appear at ED 10.5.[117] Thereafter, failure of the medial nasal processes to fuse in the midline leaves defects ranging in severity from partial splitting of the nasal tip to wide separation and anterior truncation of the lateral halves of the nose.[117] The nasal capsule may form as two separate halves, each closed by a

Table 1-4
ANOMALIES ASSOCIATED WITH 30 BASAL ENCEPHALOCELES*

Anomaly	Manifestation	Number	%
Encephalocele site†	Sphenoidal	18	60.0
	Sphenoethmoidal	10	33.3
	Ethmoidal	2	0.7
	Hypothalamus, third ventricle or pituitary in cephalocele	15	50.0
Endocrine dysfunction	Hypothalmic/pituitary	6	20.0
	Diabetes insipdus with normal anterior pituitary	1	0.3
Corpus callosum	Agenesis	12 (+1?)	40.0 (43.0?)
	Median cleft lip but not nose	15	50.0
	Median cleft lip and median cleft nose	4	13.3
	''Fissure lip''‡	1	0.3
	''Harelip''‡	1	0.3
	Cleft palate‡ (of any type)	14	47.0
Eye anomalies	Hypertelorism	22	73.0
	Optic nerve dysplasia§	12	40.0
	Persistent fetal ocular vasculature	1	0.3
	Microphthalmos	2	0.7
Other pathology	Absent optic chiasm	1	0.3
	Absent chiasm and tracts	1	0.3
	Polymicrogyria	1	0.3
	Preauricular skin tags	1	0.3
	Hypospadias, chordee, lumbar dimple plus hemangioma	1	0.3

*Includes data from references 67 (patient 13), 123, 24 (case 1), 25, 26 (case 3), 131, 133 (cases 1 and 2), 134, 135 (cases 1 and 2), 132 (case 7), 136, 138, 141, 142, 143, 145, 146, 152, 149 (cases 1 through 5), 153, 154, 155, and 345.
†In many cases this is the best guess from the limited data available.
‡In these cases the exact nature of the cleft is uncertain.
§Any of the spectrum: optic pit, optic coloboma, megalopapilla, morning glory disc.

Copyright © 2003, Mosby, Inc. All rights reserved.

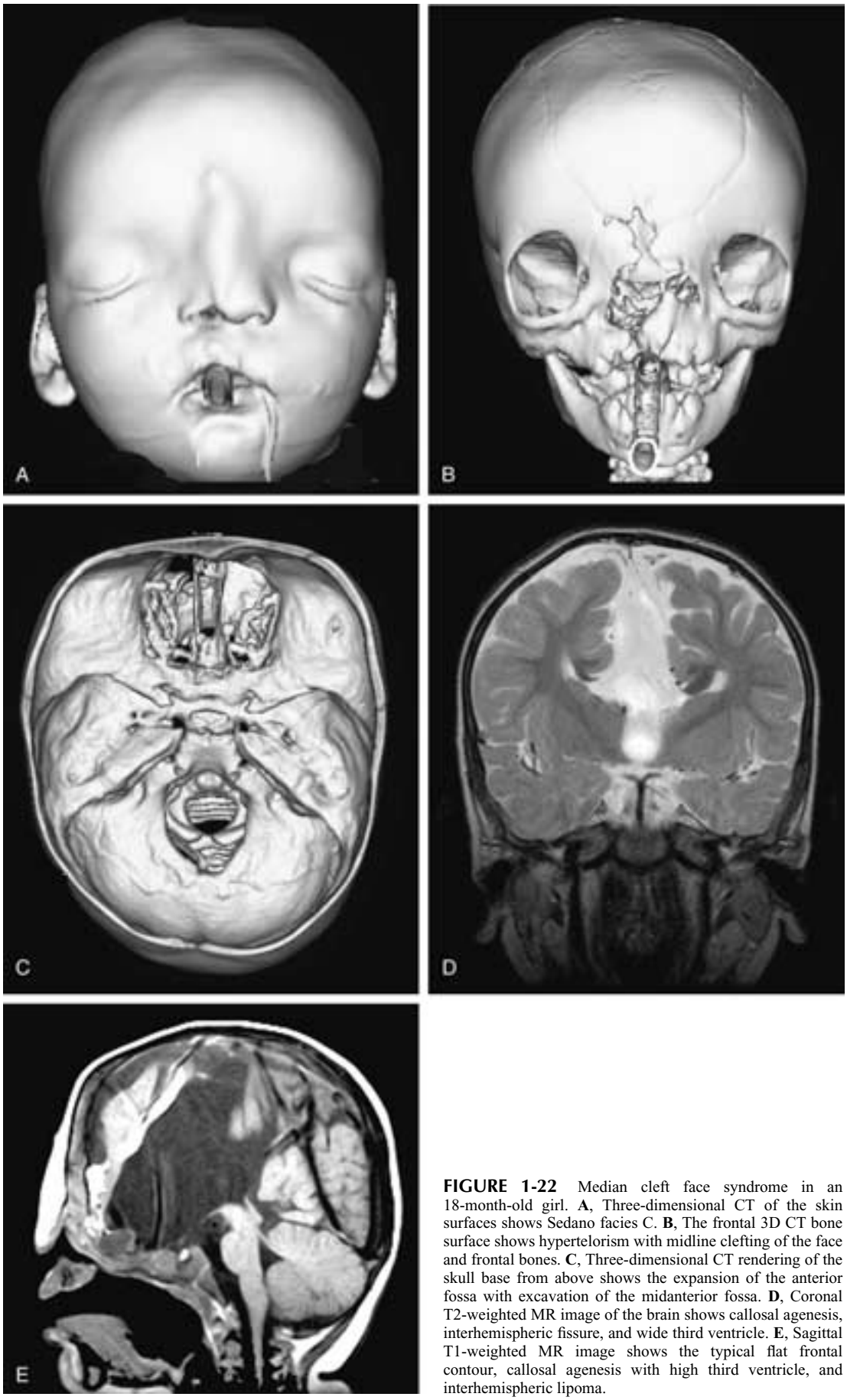

FIGURE 1-22 Median cleft face syndrome in an 18-month-old girl. **A**, Three-dimensional CT of the skin surfaces shows Sedano facies C. **B**, The frontal 3D CT bone surface shows hypertelorism with midline clefting of the face and frontal bones. **C**, Three-dimensional CT rendering of the skull base from above shows the expansion of the anterior fossa with excavation of the midanterior fossa. **D**, Coronal T2-weighted MR image of the brain shows callosal agenesis, interhemispheric fissure, and wide third ventricle. **E**, Sagittal T1-weighted MR image shows the typical flat frontal contour, callosal agenesis with high third ventricle, and interhemispheric lipoma.

VIEW IMAGE

Copyright © 2003, Mosby, Inc. All rights reserved.

Table 1-5
DeMYER CLASSIFICATION OF MEDIAN CLEFT FACE SYNDROME

Facies	Characteristics
I	Hypertelorism Median complete cleft nose Absence, hypoplasia, or median clefting of upper lip and premaxilla Cranium bifidum
II	Hypertelorism Median cleft nose A. Nose completely cleft B. Cleft nose with divided nasal septum C. Slight hypertelorism No median cleft of upper lip, premaxilla or palate Cranium bifidum present or not
III	Hypertelorism Median cleft nose and upper lip with or without median cleft premaxilla No median cleft palate No cranium bifidum
IV	Hypertelorism Median cleft nose No median cleft of upper lip, premaxilla or palate No cranium bifidum

From DeMyer W. The median cleft face syndrome: differential diagnosis of cranium bifidum occultum, hypertelorism, and median cleft nose, lip and palate. Neurology 1967;17:961–971.

remnant of the nasal septum, while a median nasal septum is absent.[117] The nasal labyrinth and anterior part of the nasal capsule are severely malformed and curved.[117] The premaxilla and maxilla are strongly affected and positioned laterally.[117] The palatine bones are cleft.[117] Portions of the skull base that derive from neural crest (the basipresphenoid and pterygoid processes) are severely malformed and broadened, whereas posterior elements of the skull base, derived from cephalic and somitic mesoderm, are normal.[117]

Table 1-6
SEDANO CLASSIFICATION OF FRONTONASAL DYSPLASIA*

Facies	Characteristics
A	Hypertelorism Broad nasal root Median nasal groove with absence of nasal tip No true clefting of the facial midline Anterior cranium bifidum present or not
B	Hypertelorism Broad nasal root Deep medial facial groove or true cleft of the nose or nose and the upper lip Cleft palate present or not Anterior cranium bifidum present or not
C	Hypertelorism Broad nasal root Nasal alar notching (unilateral or bilateral) Anterior cranium bifidum present or not
D	B and C

*Anterior cranium bifidum may be present or not in all four facies, A through D.
Sedano HO, Cohen MM Jr, Jirasek J, et al. Frontonasal dysplasia. J Pediatr 1970;76:906–913.

Table 1-7
CORRELATION OF SEDANO AND DeMYER CLASSIFICATIONS

Sedano Classification	Corresponding DeMyer Classification (Per Sedano)	Corresponding DeMyer Classification (Observed in this Series)
Type A	IV	IIB, IV
Type B	IA,* IIB, III	I, IIA, IIB
Type C	IIC	—
Type D	IA,* IB, IIA	I, IIA, IIC

*Patients who would be classified into DeMyer's Group IA may be classified as either Sedano facies type B or Sedano facies type D.
Modified from Sedano HO, Cohen MM Jr, Jirasek J, et al. Frontonasal dysplasia. J Pediatr 1970;76:906–913.

Compound null *Alx3/Alx4* mice also show severe reduction in the frontal and parietal bones, with widened fontanelles.[117]

Concurrent Malformations

Median cleft face syndrome has been found to coexist with many other syndromes.[44, 67, 68, 70–78, 113, 114, 118–125] One review of 11 cases of median cleft face syndrome found 3 type A facies, 4 type B, 4 type D, and no type C. Hypertelorism and a broad nasal root were found in 100% (by definition), true midline bony cleft of the nose in 8 of 11 (all cases except type A facies), median cleft upper lip in 3 of 11, common cleft lip in 3 of 11, common cleft palate in 3 of 11, cranium bifidum in 6 of 11, calcified falx in 6 of 11, interhemispheric lipoma in 5 of 11, Gorlin-Goldenhar syndrome in 2 of 11, and twinning in 2 of 11 patients.[44] We have also seen one patient with concurrent Kallmann syndrome, midline facial cleft, and hypotelorism.[126, 127]

The imaging features of median cleft face syndrome include hypertelorism, cranium bifidum, facial clefting, and intracranial calcifications related to interhemispheric lipoma and/or calcification of the anterior aspect of the falx (Fig. 1-22).[44, 123, 126, 127] The calcification of the falx produces a thick frontal crest that is most commonly found when a lipoma is present, but may be present without associated lipoma.[114]

Transverse Facial Clefts

Transverse facial clefts represent failure of the maxillary and mandibular processes to form the corner of the mouth and the cheek (Fig. 1–15).[45] (These are discussed in greater detail in the section on Hemifacial Microsomia.)

Clefts of the Lower Lip and Mandible

Median clefts of the lower lip and the mandible are rare in humans. They vary widely from a simple notch of the vermillion to a complete cleft of the lower lip involving the tongue, the chin, the mandible, the supporting structures of the median of the neck, the hyoid, and the manubrium sterni.[128] The anterior tongue is often bifid (rarely absent). It may be bound to the divided mandible (ankyloglos-

Copyright © 2003, Mosby, Inc. All rights reserved.

sia).[128, 129] The hyoid bone may be cleft or absent.[128] The clefting of the neck may be accompanied by cysts, chords, contractures, and even midline dermoids of the neck.[128, 129] These lower midline clefts may also be associated with midline clefting of the upper lip and nose.[129]

Cleft lower lip, mandible, and neck may result from mutations in upstream regulators of *sonic hedgehog* (e.g., the aristless-like homeobox genes *Prx1* and *Prx2*) that control cell proliferation during morphogenesis. *Prx1* and *Prx2* mutant mice show reduced size or absence of the midline mandible, an absent or single mandibular incisor, and reduction in their limbs. The mandibular features are consistent with reduced lateral expansion of the medial elements of the jaw. Treatment with the plant alkaloid jervine inhibits end organ response to sonic hedgehog and produces very similar phenotypes in the treated mice.[15, 117]

Syndrome of Amniotic Bands

Rupture of the amnion can precipitate a cascade of secondary events collectively designated the *amniotic band disruption complex*.[130] In this complex, bands of amnion may interrupt normal morphogenesis, crowd fetal parts, or actually disrupt previously formed parts.[130] Facial clefts may then result from a strand of amnion situated between and preventing the expected fusion of two facial processes, or from a strand of amnion that cleaves through a region not normally formed by fusion, leading to nonanatomic facial clefts and encephaloceles (Fig. 1-16).[130] The frequency and extent of such malformations are greater when the disruption occurs earlier in pregnancy.[130] In 33 cases of this syndrome wherein the timing of the amniotic rupture could be estimated, facial clefts were found in 96% of cases when the rupture occurred prior to 45 days' gestation but in no case in which the rupture occurred after 45 days.[130] Severe defects in the central nervous system and the calvarium such as anencephaly, cephalocele, and hydrocephalus were also common (88%) when the amnion ruptured before 45 days' gestation and were not seen thereafter.[130]

NASAL DERMAL SINUSES, CYSTS, HETEROTOPIAS, AND CEPHALOCELES

In the early embryo, the developing frontal bones are separated from the developing nasal bones by a small fontanelle called the fonticulus frontonasalis.[131–133] The nasal bones are separated from the subjacent cartilaginous nasal capsule by the prenasal space (Figs. 1-23 and 1-24). This space extends from the base of the brain to the nasal tip.[132] Midline diverticula of dura normally project *anteriorly* into the fonticulus frontonasalis and *anteroinferiorly* into the prenasal space. These diverticula touch the ectoderm. Normally, the diverticula regress prior to the closure of the bone plates of the anterior skull base. Normally, the fonticulus frontonasalis is closed by union of the nasal bones with the nasal processes of the frontal bone to make the frontonasal suture.[134] The prenasal space becomes obliterated as the cartilaginous nasal capsule develops into the upper lateral nasal cartilages and the

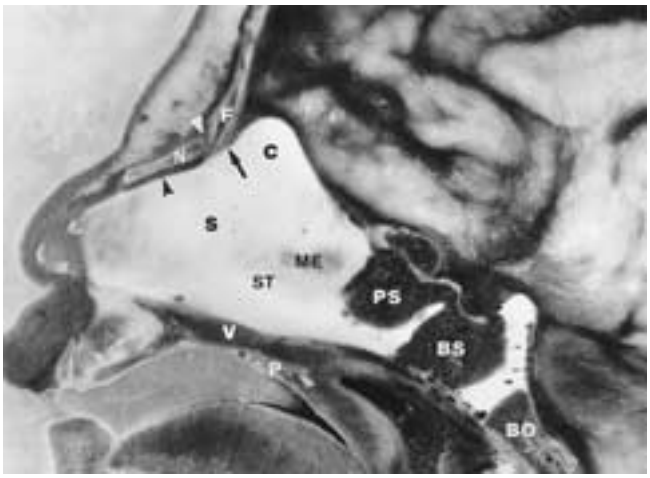

FIGURE 1-23 Midsagittal cryomicrotome section of a full-term newborn demonstrates the normal relationships at birth among the ossified frontal bone (*F*), the ossified nasal bone (*N*), the frontonasal suture (*white arrowhead*), and the cartilaginous nasal capsule (*large white structure*) that forms the still-unossified nasal septum (*S*) and crista galli (*C*). The ossified hard palate (*P*) and ossified vomer (*V*) lie below the septal cartilage. Note the direct line from the prenasal space (*black arrowhead*) through the foramen cecum (*black arrow*) to the normal depression or ''fossa'' just anterior to the crista galli. The midline septal cartilage is directly continuous with the cartilaginous skull base. The basioccipital (*BO*), basisphenoidal (*BS*), and presphenoidal (*PS*) ossification centers are well formed. The mesethmoidal (*ME*) ossification center is just beginning to form. When the vomer and mesethmoid enlarge, the residual cartilage between them is designated the sphenoidal tail (*ST*).

VIEW IMAGE

ethmoid bone including the crista galli, cribriform plates, and perpendicular plate of the septum.[132] The two leaves of the falx normally insert into the crista galli, one leaf passing to each side of the crista. At the skull base, the frontal and ethmoid bones close together around a strand of dura, leaving a small ostium designated the foramen cecum. Normally, this transmits a small vein. This foramen is easily

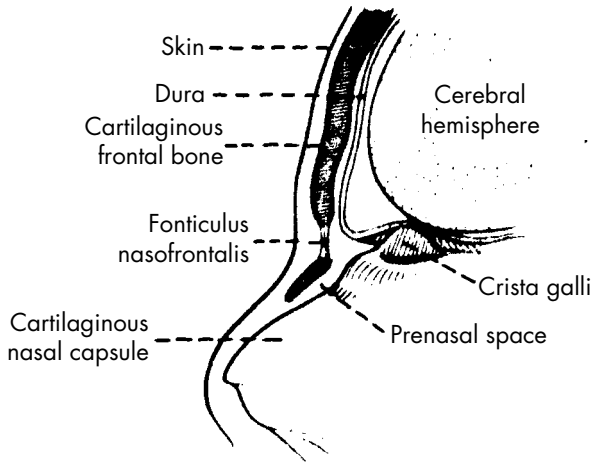

FIGURE 1-24 Diagram of the normal embryonic relationships among the dura, fonticulus frontonasalis, prenasal space, and surrounding structures. (From Gorenstein A, Kern EB, Facer GW, et al. Nasal gliomas. Arch Otolaryngol 1980;106:536.)

VIEW IMAGE

Copyright © 2003, Mosby, Inc. All rights reserved.

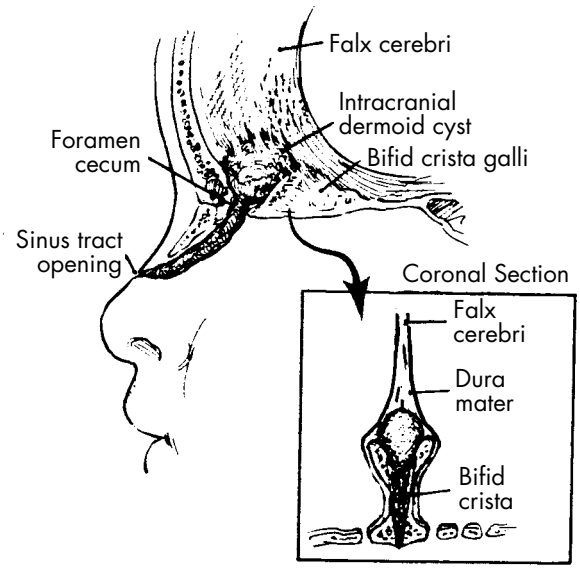

VIEW IMAGE

FIGURE 1-25 Diagram of a typical nasal dermal sinus and cyst traversing the prenasal space and the enlarged foramen cecum to form a mass anterior to and within a groove in the anterior concavity of the crista galli. *Inset*: The anatomic relationships of the leaves of the falx to the sides of the crista galli direct upward extension of the mass into the interdural space between the leaves of the falx. (From Gorenstein A, Kern EB, Facer GW, et al. Nasal gliomas. Arch Otolaryngol 1980;106:536.)

seen at the bottom of a small depression that lies just in front of the crista galli. It is not certain whether the foramen is situated exactly at the frontoethmoidal junction or between the nasal processes of the frontal bones.[132]

If the embryonic diverticula of dura become adherent to the superficial ectoderm, they may not regress normally. Instead, they may pull ectoderm with them as they retreat, creating an (ecto)dermal tract that extends from the glabella through a canal at the frontonasal suture to the crista galli or beyond the crista to the interdural space between the two leaves of the falx.[131, 132, 135] A similar persistent tract may pass from the external surface of the nose, under or through the nasal bones, and ascend through the prenasal space to enter the cranial cavity at the foramen cecum just anterior to the crista galli (Fig. 1-25). Such a tract would be associated with a widened foramen cecum, distortion and grooving of the crista galli, and extension into the interdural space between the two leaves of the falx. Depending on the precise histology of the portions of the tract that persist, these tracts could develop into superficial glabellar and nasal pits, fully patent glabellar and nasal dermal sinuses, and/or one or several (epi)dermoid cysts and/or fibrous cords. Rarely, the sinus tracts, cysts, and cords may extend into or become adherent to the brain itself.[136] Nasal cephaloceles and gliomas may arise by an analogous mechanism. Indeed, there are no valid *histologic* criteria to differentiate between the two entities.[137] If the dural diverticulum persists as a patent communication that contains leptomeninges, CSF and neural tissue, that state would constitute a glabellar or nasal meningoencephalocele (Fig. 1-26). If the developing structure becomes ''pinched off'' and (nearly) isolated from the cranial cavity by subsequent constriction of the dura and bone, it constitutes a heterotopic focus of meninges and neural tissue at the glabella and nose. Such a benign, nonneoplastic glial heterotopia is given the dreadful misnomer glabellar and nasal glioma (Fig. 1-27).

Dermoids and Dermal Sinuses

Dermoids of the Skull

Dermoids of the skull occur at sites related to the closure of the neural tube, the diverticulation of the cerebral hemispheres, and the lines of closure of the cranial sutures (Fig. 1-28). Pannell et al.[138] classified 94 dermoids of the skull into three groups: A. *Midline dermoids* (43%) affect the anterior fontanelle (25), glabella (1), nasion (2), vertex (1), and the occipital/suboccipital region (11). B. *Frontotemporal dermoids* (45%) affect the sphenofrontal (15), frontozygomatic (16), and sphenosquamosal (11) sutures. C. *Parietal dermoids* (13%) affect the squamosal (8), coronal (1), lambdoid (1), and parietomastoid (2) sutures. Bartlett et al.[139] categorized 84 orbitofacial dermoids into three slightly different groups. In this classification: A. *Frontotemporal dermoids* (64%) are single, slowly growing, asymptomatic lesions ranging from a few millimeters to several centimeters in size. They cluster about the eyebrows, are equally frequent on the left and right sides,

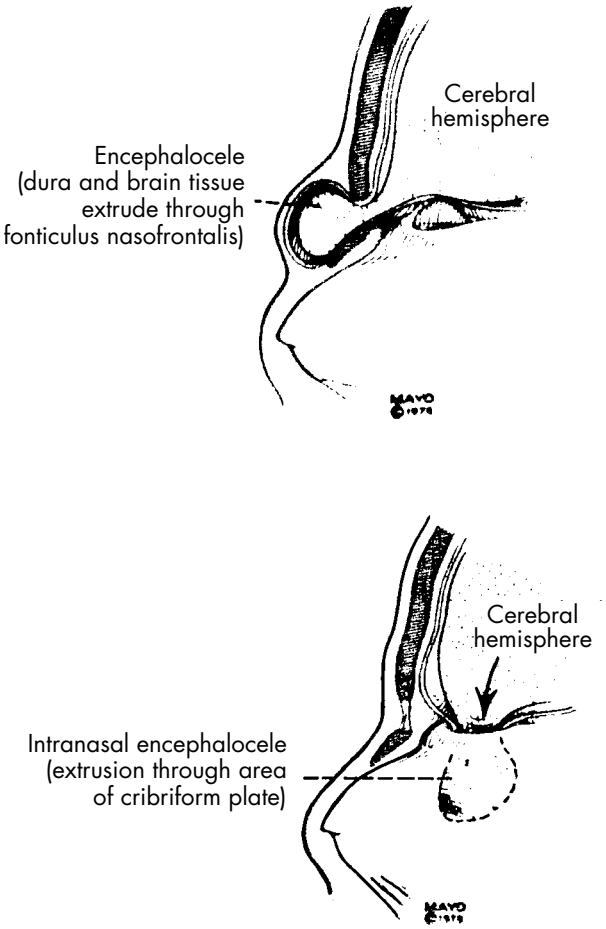

FIGURE 1-26 Schematic representation of the origin of (**A**) extranasal (glabellar) cephaloceles and (**B**) intranasal transethmoidal cephaloceles. (From Gorenstein A, Kern EB, Facer GW, et al. Nasal gliomas. Arch Otolaryngol 1980;106:536.)

VIEW IMAGE

Copyright © 2003, Mosby, Inc. All rights reserved.

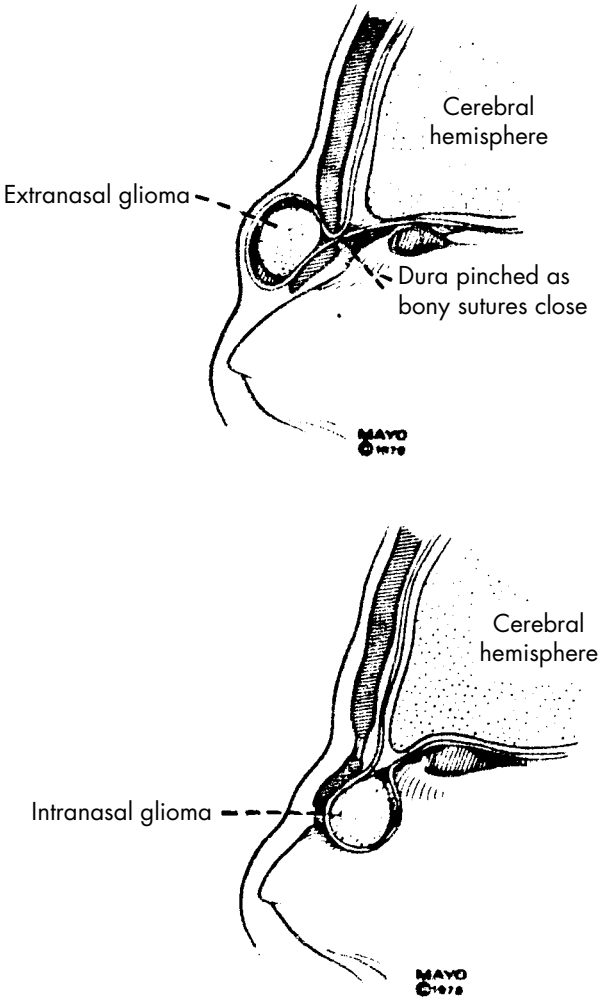

VIEW IMAGE

FIGURE 1-27 Schematic representation of the origin of (**A**) extranasal gliomas and (**B**) nasal gliomas. (From Gorenstein A, Kern EB, Facer GW, et al. Nasal gliomas. Arch Otolaryngol 1980;106:536.)

and show a slight female preponderance. None extends intracranially. B. *Orbital dermoids* (25%) are single lesions of variable size, are equally frequent on the left and right sides, and are more common lateral to the midaxis of the globe (two thirds) than medial to the midaxis of the globe (one third). Thirty percent of the orbital dermoids adhere to the orbital wall: 20% at the frontozygomatic suture laterally or the confluence of the sutures medially, and 10% away from the sutures. Females predominate in this group (2:1). C. *Nasoglabellar dermoids* (11%) are equally frequent on the left and right sides and equally frequent in males and females.[139]

Nasal Dermal Sinuses

Nasal dermal sinuses are thin (1-3 mm) epithelium-lined tubes[140] that (1) arise at external ostia situated along the midline of the nose and (2) extend deeply for a variable distance, sometimes reaching the intradural intracranial space. *Nasal dermoid and epidermoid cysts* are midline epithelium-lined cysts that arise along the expected course of the dermal sinus. They may coexist with dermal sinuses or present as isolated masses (Table 1-8[142]; Figs. 1-29 and 1-30). Nasal dermal cysts and sinuses constitute 3.7% to 12.6% of all dermal cysts of the head and neck and 1.1% of all such cysts throughout the body.[131, 140] There is no sex predilection.[131, 141–143] They may occur in isolation, as one of a small number of concurrent malformations, or as part of well-known syndromes, including hemifacial microsomia, frontonasal dysplasia, oro-facial-digital syndrome type I, and the *v*ertebral defects, imperforate *a*nus, *t*racheo*e*sophageal fistula, and *r*adial and *r*enal dysplasia (VATER) association.[144] Familial cases are known but rare.[144–146]

Nasal Dermoids and Epidermoids

Nasal dermoids and epidermoids cluster in three areas: the midline just superior to the nasal tip, the junction of the upper and lower lateral cartilages, and near the medial canthus. Glabellar cysts external to the frontal bone

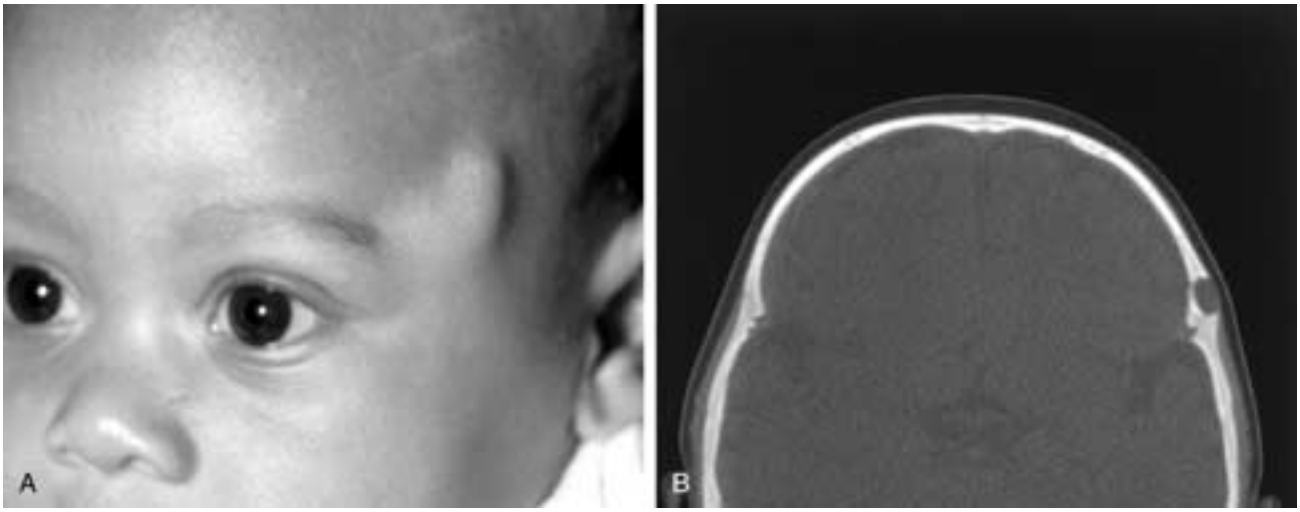

VIEW IMAGE

FIGURE 1-28 Left frontotemporal dermoid. Two patients. **A**, Infant boy with a soft-tissue ''bump'' close to the pterion. **B**, Noncontrast axial bone algorithm CT displays a sharply marginated, slightly expansile dermoid abutting onto the coronal suture.

Copyright © 2003, Mosby, Inc. All rights reserved.

Table 1-8
PRESENTING FEATURES OF NASAL DERMAL SINUS/CYST (*N* = 32)

Patient Presentation	Number of Patients	Superficial Infection	Behavior Change from Frontal Abscess	Recurrent Meningitis	Osteomyelitis
Sinus ostia	14	2	2	1	—
Midline cyst	18	1	1	1	1
Combined	32	3 (9%)	3 (9%)	2 (6%)	1 (3%)

From Pensler JM, Bauer BS, Naidich TP. Craniofacial dermoids. Plast Reconstr Surg 1988;82:953–958.

are less common (Figs. 1-31 and 1-32). True epidermoids occur as often as true dermoids, but epidermoids are more common at the glabella-nasion, whereas dermoids are more common along the bridge of the nose (Figs. 1-33 and 1-34).[141] On occasion, multiple sinus ostia are present or sinuses and cysts coexist at both the glabella and the nasal bridge.[131, 147]

Nasal dermal sinuses and cysts are usually detected early in life (mean age, 3 years) as midline nasal cysts (56%) or midline pits (44%), which may contain sparse wiry hairs (Table 1-8) (Figs. 1-35 and 1-36).[142, 148, 149] There may be intermittent discharge of sebaceous material and/or pus; intermittent inflammation; increasing size of the mass with variable degrees of broadening of the nasal root and bridge; intermittent episodes of meningitis; or behavioral change secondary to a frontal lobe abscess (Table 1-8).[142] The sinus ostium may be ''pinpoint'' and undetectable until pressure is applied against the nose to express cheesy material.[131] Nasal dermal cysts may be soft and discrete or indurated. They may erode through the overlying skin to form secondary sinus pits. True epidermoids are seven times more likely than dermoids to become infected.[141] Together, nasal dermal sinuses and cysts account for approximately 5% of the intracranial abscesses found in relation to all types of nasal, sinus, and orbital infections.[150]

Nasal dermal sinuses open at any site from the glabella downward along the bridge (dorsum) of the nose to the base of the columella.[151] In one family of identical triplets, each child had a nasal dermal sinus, but the ostia lay at three different sites (nasion, bridge, and tip).[144] Overall, the

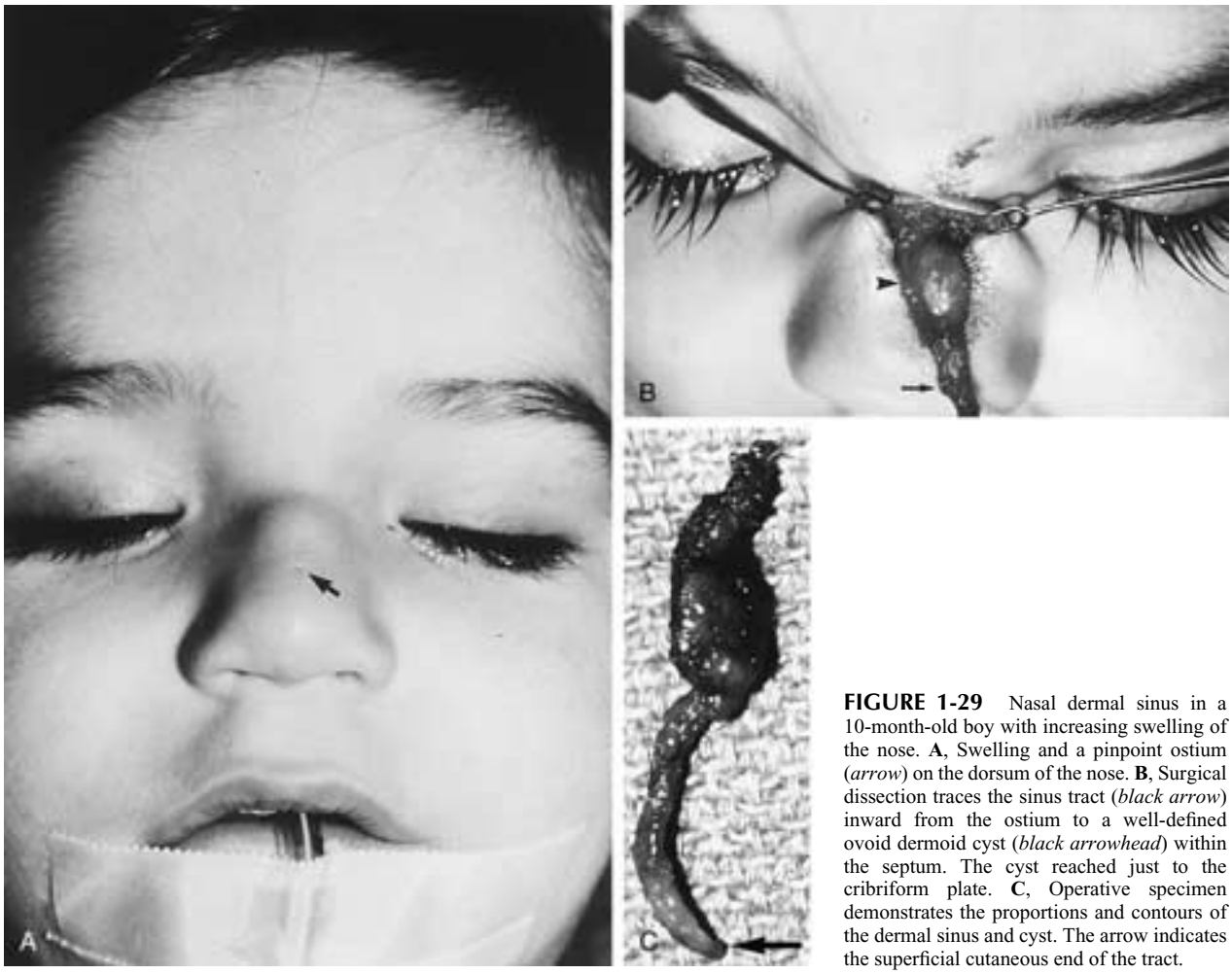

FIGURE 1-29 Nasal dermal sinus in a 10-month-old boy with increasing swelling of the nose. **A**, Swelling and a pinpoint ostium (*arrow*) on the dorsum of the nose. **B**, Surgical dissection traces the sinus tract (*black arrow*) inward from the ostium to a well-defined ovoid dermoid cyst (*black arrowhead*) within the septum. The cyst reached just to the cribriform plate. **C**, Operative specimen demonstrates the proportions and contours of the dermal sinus and cyst. The arrow indicates the superficial cutaneous end of the tract.

VIEW IMAGE

Copyright © 2003, Mosby, Inc. All rights reserved.

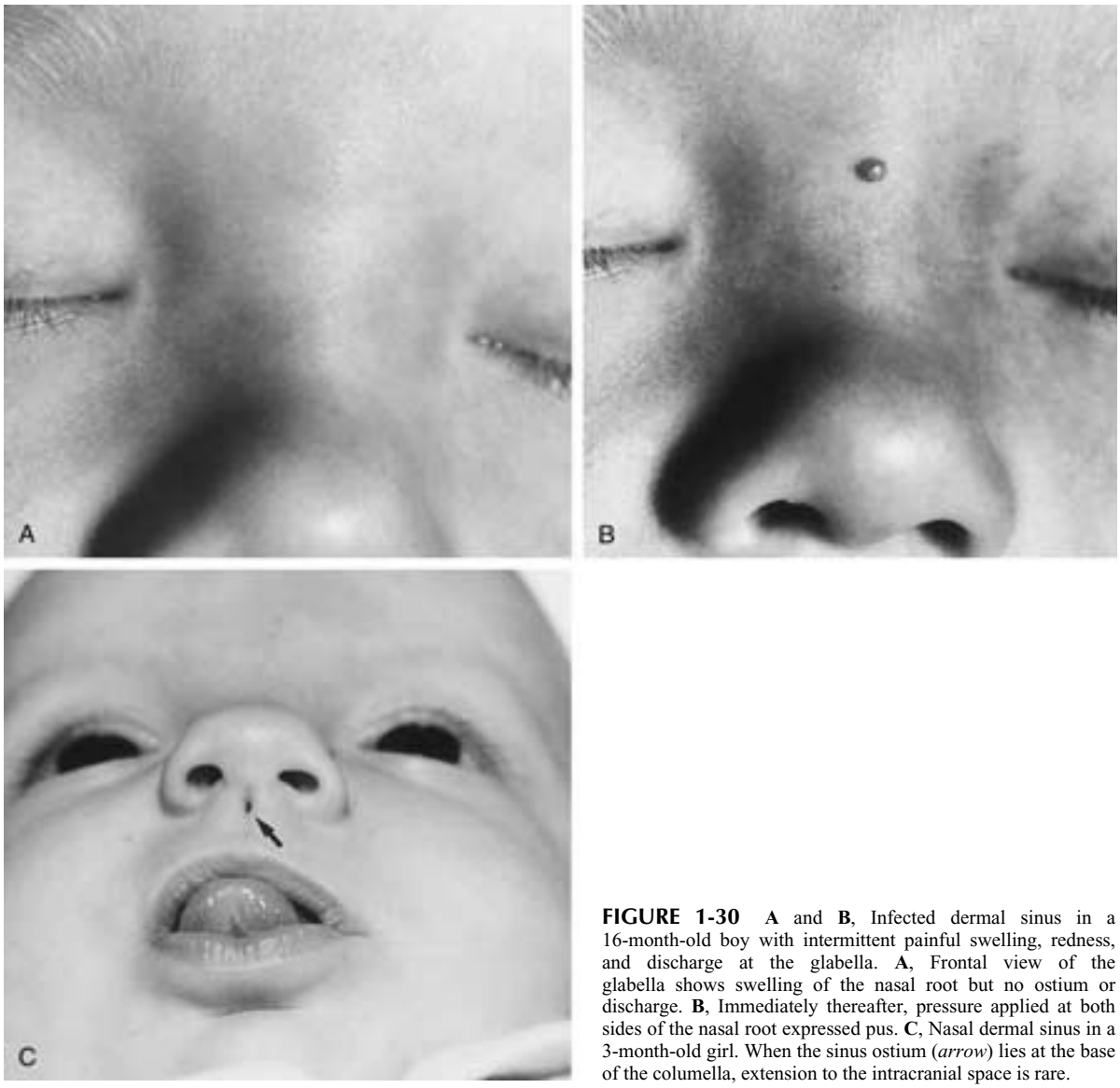

FIGURE 1-30 **A** and **B**, Infected dermal sinus in a 16-month-old boy with intermittent painful swelling, redness, and discharge at the glabella. **A**, Frontal view of the glabella shows swelling of the nasal root but no ostium or discharge. **B**, Immediately thereafter, pressure applied at both sides of the nasal root expressed pus. **C**, Nasal dermal sinus in a 3-month-old girl. When the sinus ostium (*arrow*) lies at the base of the columella, extension to the intracranial space is rare.

VIEW IMAGE

external ostium of the sinus is found at the glabella-nasion in 25%, the bridge of the nose in 31%, the nasal tip in 19%, and the base of the columella in 25% (Table 1-9).[148]

The depth to which nasal dermal sinuses and cysts extend is highly variable. The lesions can be shallow pits that end blindly in the superficial tissue (Fig. 1-30C) or long tubes that wander extensively extra- and intracranially (Figs. 1-36 and 1-37).[131] In Bradley's review of 67 children with nasal dermoids, the lesion was confined to the skin in 61% and extended deeply to invade the nasal bones in 10%. The lesion extended into the septal cartilage in 10%, the nasal bones and cartilage in 6%, and the cribriform plate in 12%.[141] Rare sinuses may traverse the entire anteroposterior extent of the nasal septum to end at the basisphenoid, where they attach to the dura just anterior to the sella.[131] Intracranial extension of the dermal sinus is more frequent in patients with multiple anomaly syndromes (67%) than in those with isolated nasal dermal sinuses (31%).[144] The location of the sinus ostium does *not* predict whether there is any intracranial extension. Intracranial extension can be associated with cysts and sinuses at *nearly* any site, but the frequency of such extension does change with sinus location (Table 1-9).[142] In Pensler et al.'s series,[142] each of four sinuses situated at the base of the columella passed directly to the nasal spine of the maxilla, with no intracranial extension. However, Muhlbauer and Dittmar[145] report a similar sinus that ascended to end in the ethmoid air cells; it did not enter the cranial cavity.

The intracranial end of (epi)dermoids usually affects the anterior epidural space near the crista galli, and from there may pass deeper, between the two leaves of the falx, as an *inter*dural mass.[142, 144] Rare lesions also extend into the brain.[136] In approximately 31% of cases with intracranial extension, the tissue extending inward is a fibrous cord devoid of (epi)dermal elements. At present, intracranial extension of a fibrous cord is not considered significant and has not been associated with sequelae on follow-up examination.[142]

Nasal dermal sinuses are resected for three major reasons: for cosmesis, to avoid/treat complications of local

Copyright © 2003, Mosby, Inc. All rights reserved.

infection, and to avoid/treat secondary meningitis and cerebral abscess (Fig. 1-38).[151] Late development of squamous cell carcinoma has not been observed with *nasal* dermal sinuses to date.

Imaging studies successfully display the course of sinus tracts and any sequelae of infection. The ostium and tract usually appear as isodense fibrous channels or as lucent dermoid channels that extend inward for a variable distance. Bony canals indicate the course of the sinus through the nasal bones, ossified nasal septum, and skull base (Fig.

FIGURE 1-31 Dermal cyst at the nasal tip in an 11-month-old boy. **A** and **B**, Lateral (**A**) and inferior (**B**) view of the nose shows a focal ''elfin'' expansion and upturning of the cartilaginous nose. **C** and **D**, Corresponding T2-weighted MR images in the sagittal (**C**) and coronal (**D**) planes show a focal mass and a signal change corresponding to the dermal cyst.

VIEW IMAGE

Copyright © 2003, Mosby, Inc. All rights reserved.

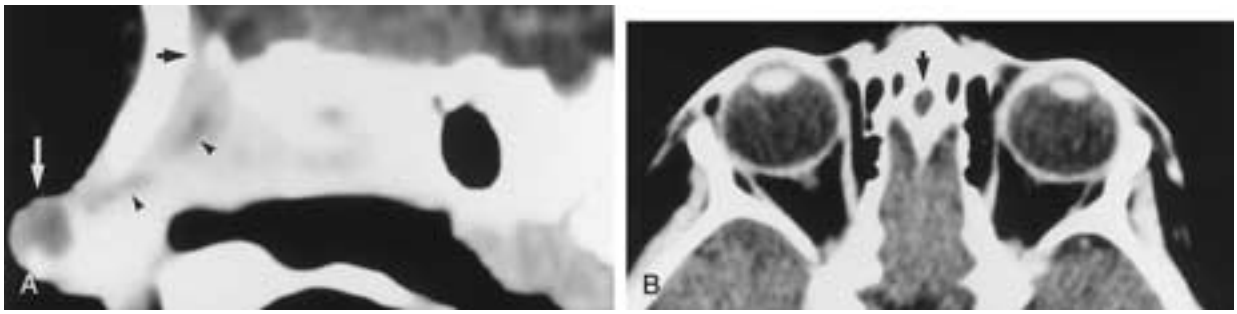

VIEW IMAGE

FIGURE 1-32 Dermal cyst the nasal tip. **A**, Sagittal reformatted CT. The lucent dermoid cyst (*white arrow*) at the nasal tip connects via a lucent track (*black arrowheads*) to an expanded foramen cecum (*black arrow*). **B**, Axial CT confirms the expansion of the foramen cecum (*arrowhead*).

1-32). An uncomplicated dermoid cyst appears as a well-defined lucency/signal with a sharply marginated capsule (Figs. 1-31 to 1-33). Swelling and edema around the cyst suggest secondary inflammation (Fig. 1-34).[152] The intracranial ends of dermoid cysts typically lie in a hollowed-out gully along the anterior surface of a thickened, enlarged crista.[131] This hollow gives a false impression of a *bifid* crista.[131] The intracranial portion of the dermoid may be lucent or dense. Unfortunately, the only proof of intracranial extension is actual demonstration of an intracranial mass. Imaging demonstration of an enlarged foramen cecum and distorted crista galli only *suggests* such extension; it does not prove it. Foraminal enlargement and distortion of the crista seem to form part of the malformation and may be present (1) with intracranial extension, (2) without intracranial extension, or (3) with intracranial extension of a *fibrous* cord rather than a dermoid.[142] In our own series of 32 cases,[142] the foramen cecum was wide and the crista was grooved anteriorly (bifid) in 6 of 6 cases (100%) with intracranial extension. However, the foramen

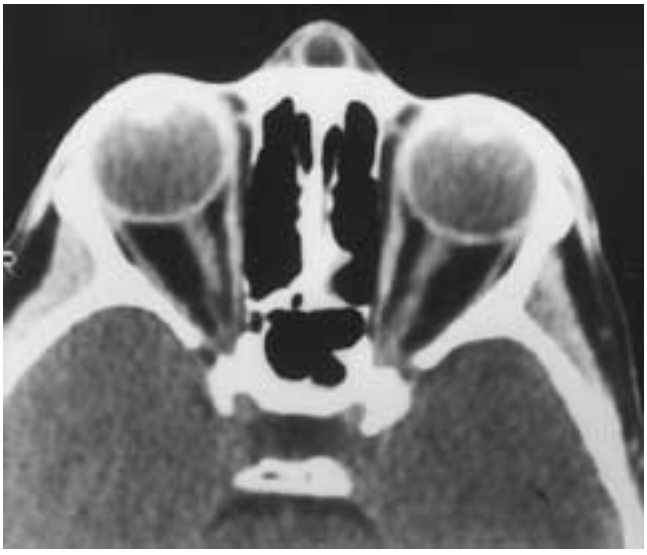

VIEW IMAGE

FIGURE 1-33 Extranasal epidermoid cyst with no infection. Axial noncontrast CT in a 4-year-old boy. The well-defined isodense cyst wall and lucent center are clearly separable from the adjoining soft tissues. The nasal bones are flattened. No intracranial component was present.

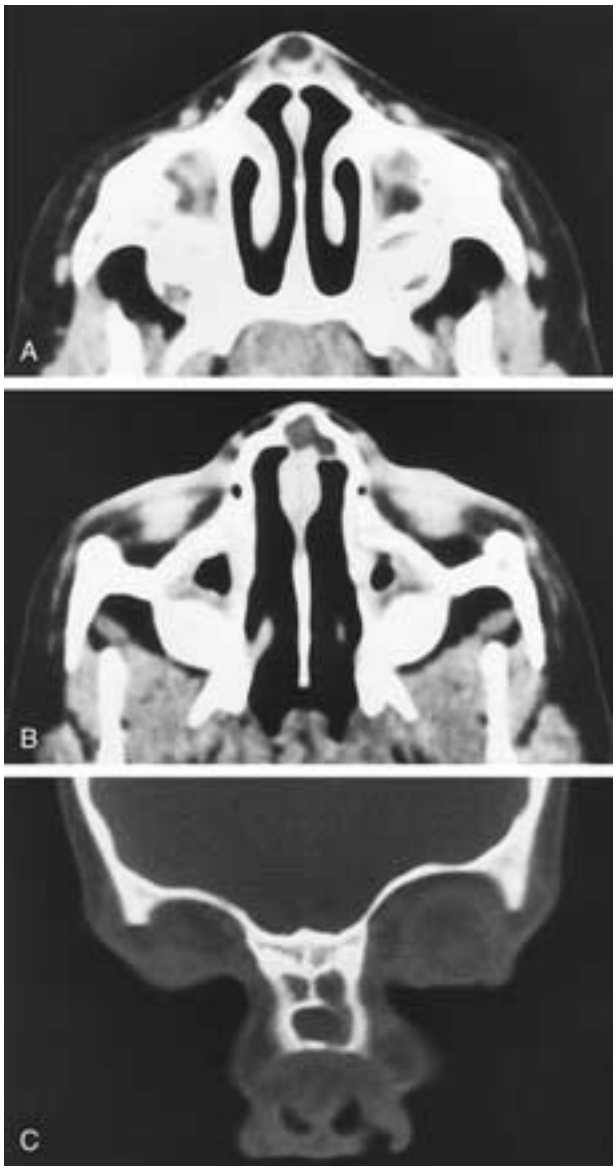

FIGURE 1-34 Mixed extranasal-intranasal dermoid with infection. **A** and **B**, Axial noncontrast CT demonstrates an extranasal (**A**) and an intranasal (**B**) mass, scalloped erosion of the nasal bones, and edema of the fat planes surrounding the cyst. **C**, Direct coronal CT shows the broadening and erosion of the nasal bridge.

VIEW IMAGE

Copyright © 2003, Mosby, Inc. All rights reserved.

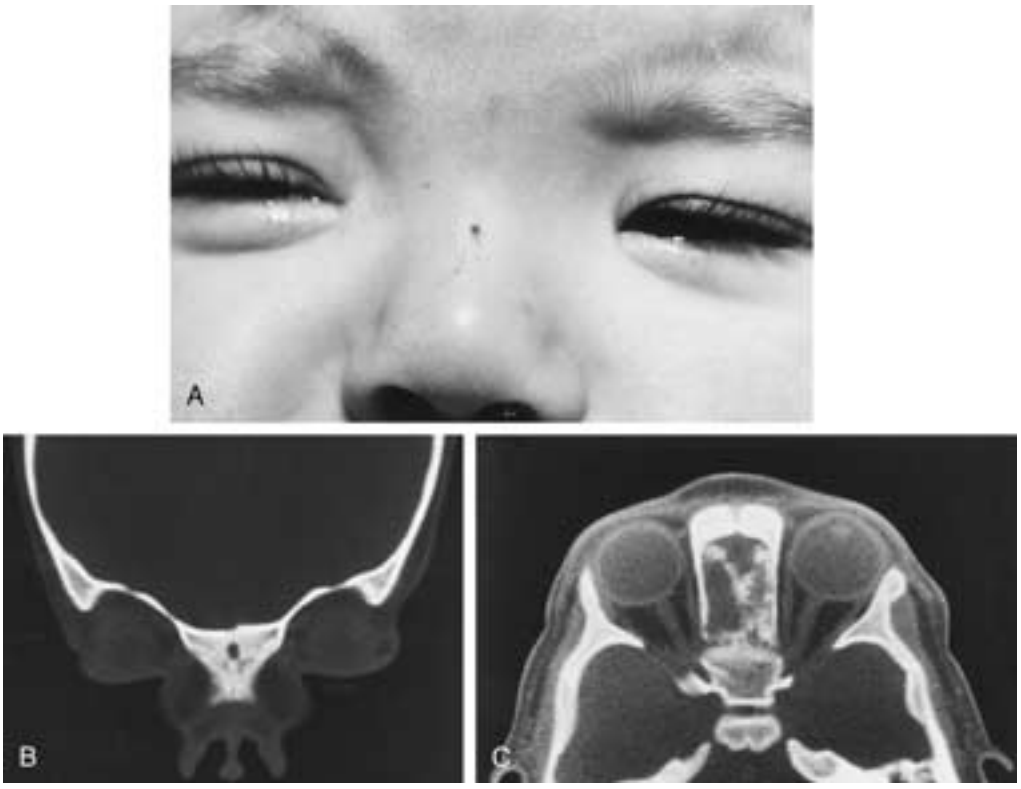

VIEW IMAGE

FIGURE 1-35 Nasal dermal sinus with intracranial extension. **A**, Frontal view of a 1-year-old girl shows a small tuft of hairs protruding from a midline dermal sinus on the dorsum of the nose. **B**, Direct coronal CT. A well-marginated canal penetrates between the nasal processes of the frontal bones. **C**, Axial CT scan reveals a large foramen cecum with anterior grooving of the crista galli. At surgery the dermal sinus tract and extranasal dermoid were traced upward through the foramen cecum into a 2 to 3 cm intracranial dermoid. This extended intradurally but did not attach to brain. A second ''arm'' of the intranasal dermoid passed posteriorly toward the sphenoid bone.

cecum was also wide in 10 of 26 cases (38%) with no intracranial extension, and the crista was grooved anteriorly in 7 of those 10 cases. To avoid unnecessary craniotomies, therefore, surgical studies suggest that the best approach is to dissect the extracranial portion of the tract along its entire length from the superficial ostium to the *extra*cranial surface of the enlarged foramen cecum, to sever the tract at the extracranial end of the foramen cecum, and then to send the severed end for pathologic examination. If the specimen shows (epi)dermal elements at the foramen cecum, the dissection is extended intracranially. If no (epi)dermal elements are found at the foramen cecum and if no mass is shown by imaging studies, the procedure is concluded without intracranial exploration.[131, 142]

Heterotopic Brain Tissue

Nasal Heterotopias (Gliomas)

Nasal gliomas are congenital masses of glial tissue that occur intranasally and/or extranasally at or near the root of the nose. They may or may not be connected to the brain by a pedicle of glial tissue. By definition, they do not contain any CSF-filled space that is connected with either the ventricles or the subarachnoid space of the head.[153]

Nasal gliomas and cephaloceles form a spectrum of related diseases (Figs. 1-23 to 1-27). Characteristic encephaloceles contain ependyma-lined ventricles filled with CSF. Prototypical nasal gliomas consist of solid masses of glial tissue that are entirely separate from the brain.[153] Transitional forms include solid lesions with *microscopic* ependyma-lined canals, solid lesions intimately attached to the brain by glial pedicles with no ependyma-lined spaces, and solid lesions attached to the dura by fibrous bands with no glial pedicles.[153] Analysis of cases reveals that the presence or absence of a pedicle and the presence or absence of *thin* ependyma-lined channels are not helpful in making surgically and radiologically useful distinctions among these lesions. Thus the medically significant differential diagnosis between nasal gliomas and encephaloceles depends on the presence (encephalocele) or absence (nasal glioma) of communication between the intracranial CSF and any fluid spaces within or surrounding the mass.[154, 155] Indeed, nasal gliomas remain connected with intracranial structures in 15% of cases, usually through a defect in or near the cribriform plate.[132]

Nasal gliomas are uncommon, accounting for only 4.5% of congenital nasal masses.[131, 156] They occur sporadically, with no familial tendency.[132] They usually affect both genders equally,[132] although a 3:1 male preponderance has been reported.[156] Up to 15% of patients with nasal heterotopias also manifest multiple cerebral heterotopias.[137] Other congenital malformations of the brain or body are

Copyright © 2003, Mosby, Inc. All rights reserved.

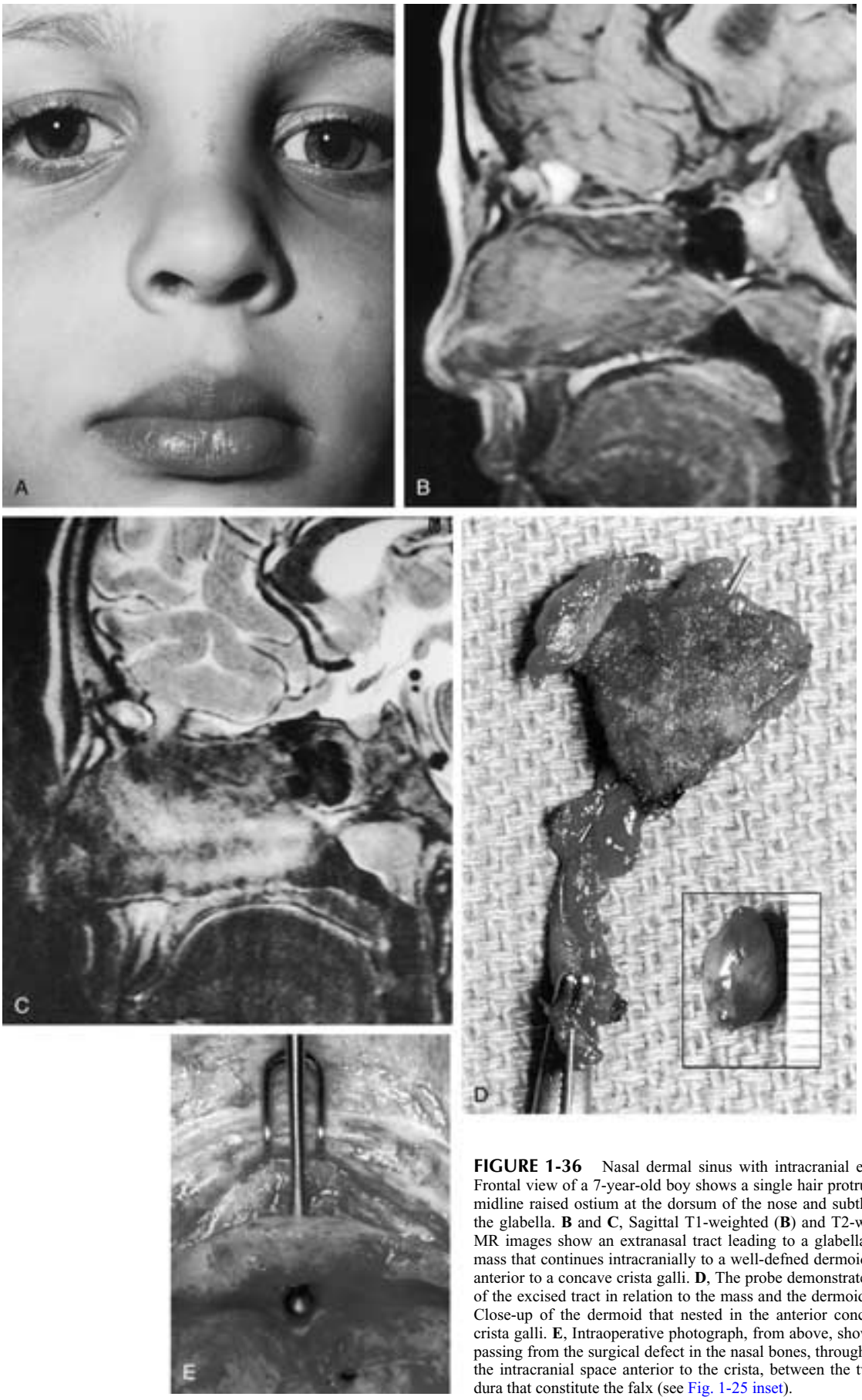

FIGURE 1-36 Nasal dermal sinus with intracranial extension. **A**, Frontal view of a 7-year-old boy shows a single hair protruding from a midline raised ostium at the dorsum of the nose and subtle fullness at the glabella. **B** and **C**, Sagittal T1-weighted (**B**) and T2-weighted (**C**) MR images show an extranasal tract leading to a glabellar soft-tissue mass that continues intracranially to a well-defned dermoid cyst seated anterior to a concave crista galli. **D**, The probe demonstrates the course of the excised tract in relation to the mass and the dermoid. *Inset in* **D**, Close-up of the dermoid that nested in the anterior concavity of the crista galli. **E**, Intraoperative photograph, from above, shows the probe passing from the surgical defect in the nasal bones, through the tract, to the intracranial space anterior to the crista, between the two layers of dura that constitute the falx (see Fig. 1-25 inset).

VIEW IMAGE

Copyright © 2003, Mosby, Inc. All rights reserved.

Table 1-9
NASAL DERMAL SINUSES: LOCATION OF OSTIUM VERSUS INTRACRANIAL EXTENSION (*N* = 16)

Location of Sinus Ostium	Number of Patients	Number (%) with Intracranial Extension
Glabella	4	2 (50%)
Nasal bridge	5	4 (80%)
Nasal tip	3	1 (33%)
Base of columella	4	0 (rare)

From Paller AS, Pensler JM, Tadinori T. Nasal midline masses in infants and children: dermoids, encephaloceles, and gliomas. Arch Derm 1991;127:362–366.

rare. Nasal gliomas are subclassified into extranasal, intranasal, and mixed forms (Fig. 1-27).[132, 157]

Extranasal gliomas (60%) lie external to the nasal bones and nasal cavities.[137, 157] They typically occur at the bridge of the nose, to the left or right of the midline, but, curiously, not in the midline itself. Extranasal gliomas may also be found close to the inner canthus, at the junction of the bony and cartilaginous portions of the nose, or between the frontal, nasal, ethmoid, and lacrimal bones. They may extend into the maxillary antrum between the lateral edge of the nasal bone and the nasal cartilage.[158] Clinically, extranasal gliomas present in early infancy or childhood as

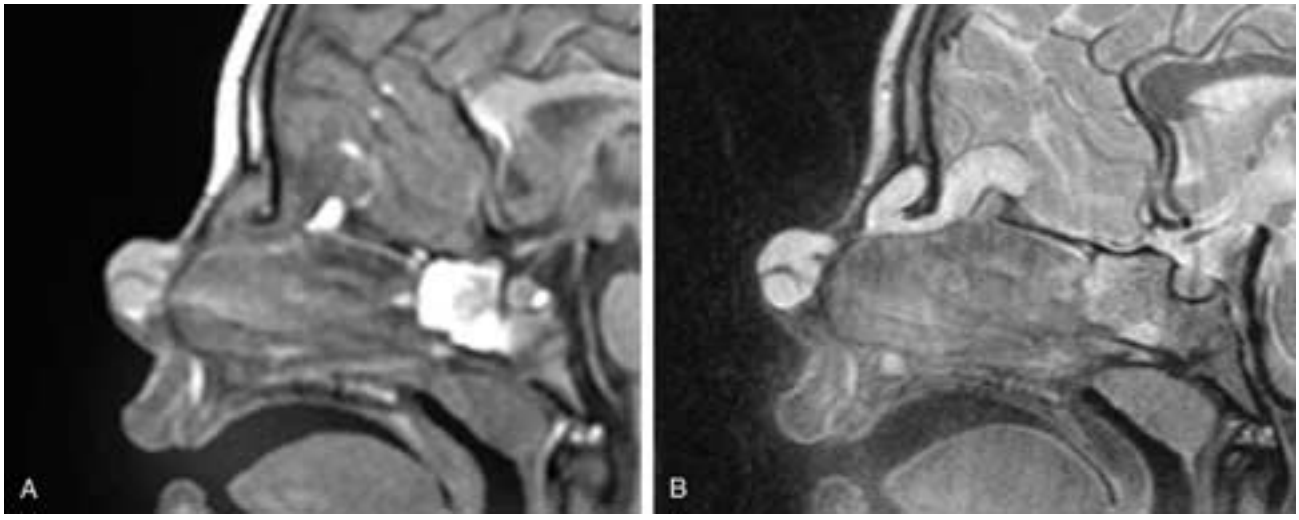

VIEW IMAGE

FIGURE 1-37 Nasal dermoid with intracranial extension. **A** and **B**, Sagittal T1-weighted (**A**) and T2-weighted (**B**) MR images in a 2-year-old girl with a bulbous nasal tip. The lesion expands the nasal tip and continues via a narrow tract to the glabella, where it forms a confluent transcranial mass at the glabella, the expanded prenasal space, the expanded foramen cecum, and the midline interdural space between the two leaves of the falx.

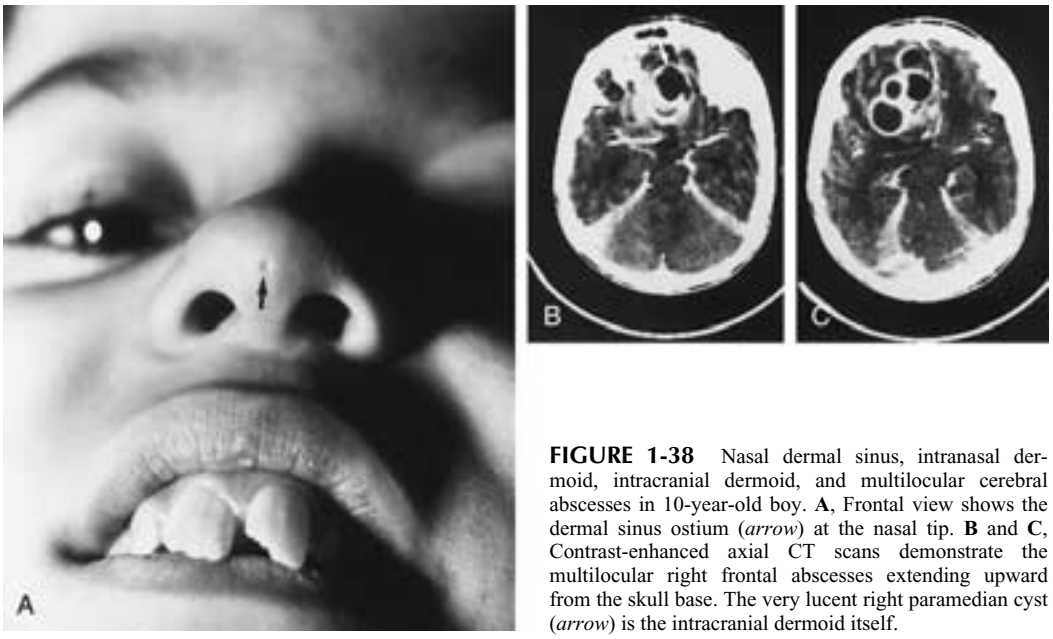

VIEW IMAGE

FIGURE 1-38 Nasal dermal sinus, intranasal dermoid, intracranial dermoid, and multilocular cerebral abscesses in 10-year-old boy. **A**, Frontal view shows the dermal sinus ostium (*arrow*) at the nasal tip. **B** and **C**, Contrast-enhanced axial CT scans demonstrate the multilocular right frontal abscesses extending upward from the skull base. The very lucent right paramedian cyst (*arrow*) is the intracranial dermoid itself.

Copyright © 2003, Mosby, Inc. All rights reserved.

firm, slightly elastic, reddish to bluish, skin-covered masses. Capillary telangiectasias may cover the lesion. They are typically unilateral, most frequently on the right, and are rarely bilateral.[156] Nasal gliomas exhibit no pulsations, do not increase in size with the Valsalva maneuver (crying), and do not pulsate or swell following compression of the ipsilateral jugular vein (negative Fürstenburg sign).[132, 149, 155, 159–161] These lesions usually grow slowly in proportion to adjacent tissue but may grow more or less rapidly.[132] They can cause severe deformity by displacing the nasal skeleton, the adjoining maxilla, and the orbital walls, potentially causing hypertelorism.[132]

Intranasal gliomas (14% to 30%) lie within the nasal or nasopharyngeal cavities (Figs. 1-29, 1-39).[137, 157] Intranasal gliomas usually present as large, firm, polypoid, submucosal masses that may extend inferiorly toward or nearly to the nostril.[132, 160] They may protrude through the nostril secondarily.[159] They usually attach to the turbinates and come to lie medial to the middle turbinate, between the middle turbinate and the nasal septum.[132] Rarely, they attach to the septum itself. They expand the nasal fossa, widen the nasal bridge, and deviate the septum contralaterally. Obstruction of the nasal passage may lead to respiratory distress, especially in infants. Blockage of the nasolacrimal duct may cause epiphora on the affected side. CSF rhinorrhea, meningitis, and epistaxis may be the presenting complaints. Intranasal gliomas are commonly confused with inflammatory polyps. However, nasal gliomas usually have a firmer consistency and appear less translucent than inflammatory polyps.[127, 153] Intranasal gliomas typically lie medial to the middle turbinate, whereas inflammatory polyps typically lie inferolateral to the middle turbinate. Only posterior ethmoid polyps project into the same space as the nasal glioma. As an additional criterion, nasal gliomas

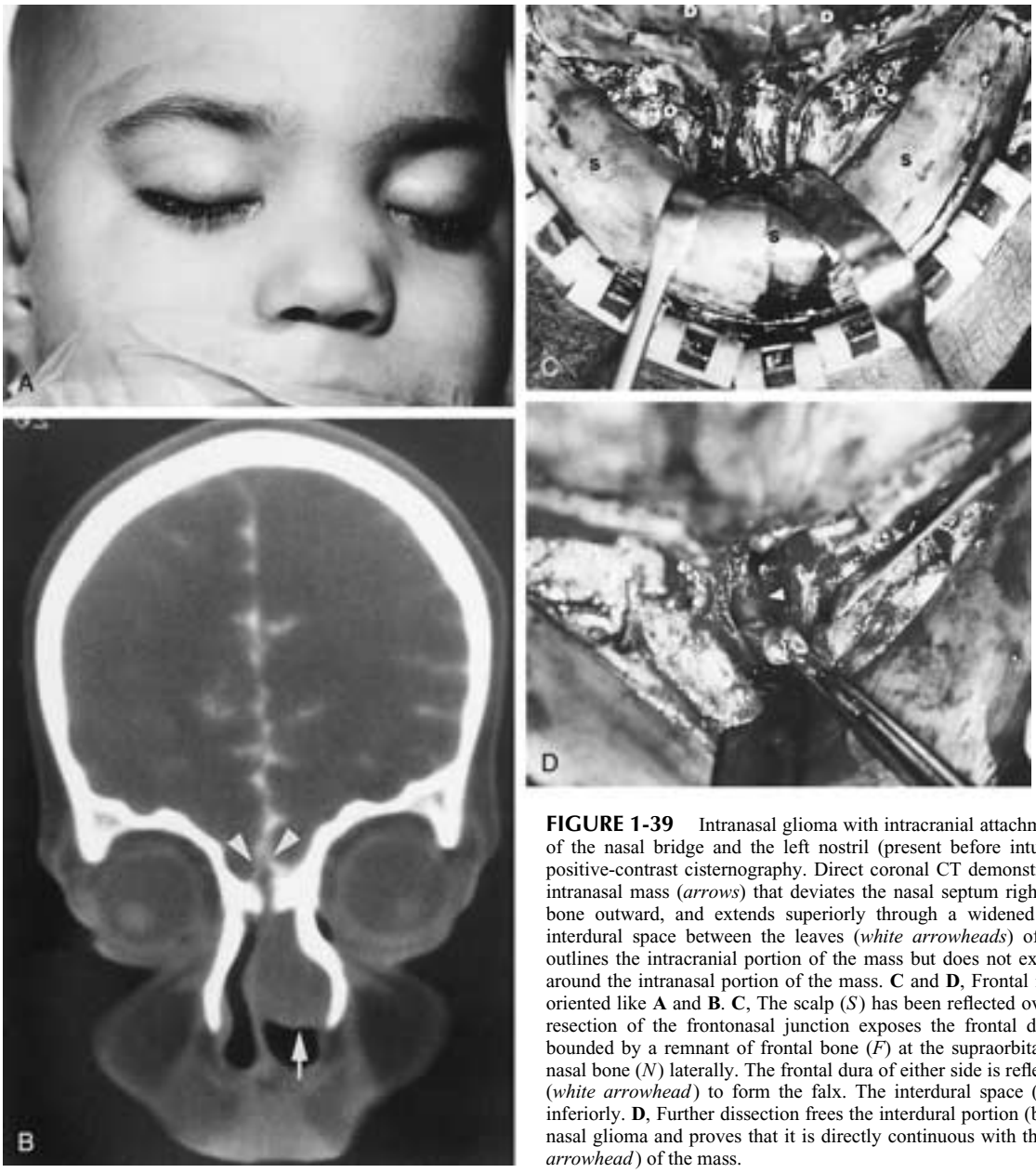

FIGURE 1-39 Intranasal glioma with intracranial attachments. **A**, Facies. Widening of the nasal bridge and the left nostril (present before intubation). **B**, Water-soluble positive-contrast cisternography. Direct coronal CT demonstrates a large left unilateral intranasal mass (*arrows*) that deviates the nasal septum rightward, bows the left nasal bone outward, and extends superiorly through a widened foramen cecum into the interdural space between the leaves (*white arrowheads*) of the falx. Opacified CSF outlines the intracranial portion of the mass but does not extend extracranially into or around the intranasal portion of the mass. **C** and **D**, Frontal intraoperative photographs oriented like **A** and **B**. **C**, The scalp (*S*) has been reflected over the orbits (*O*). Keyhole resection of the frontonasal junction exposes the frontal dura (*D*) and nasal cavity, bounded by a remnant of frontal bone (*F*) at the supraorbital ridges and a remnant of nasal bone (*N*) laterally. The frontal dura of either side is reflected inward in the midline (*white arrowhead*) to form the falx. The interdural space (*white arrows*) is widened inferiorly. **D**, Further dissection frees the interdural portion (between the forceps) of the nasal glioma and proves that it is directly continuous with the intranasal portion (*white arrowhead*) of the mass.

VIEW IMAGE

Copyright © 2003, Mosby, Inc. All rights reserved.

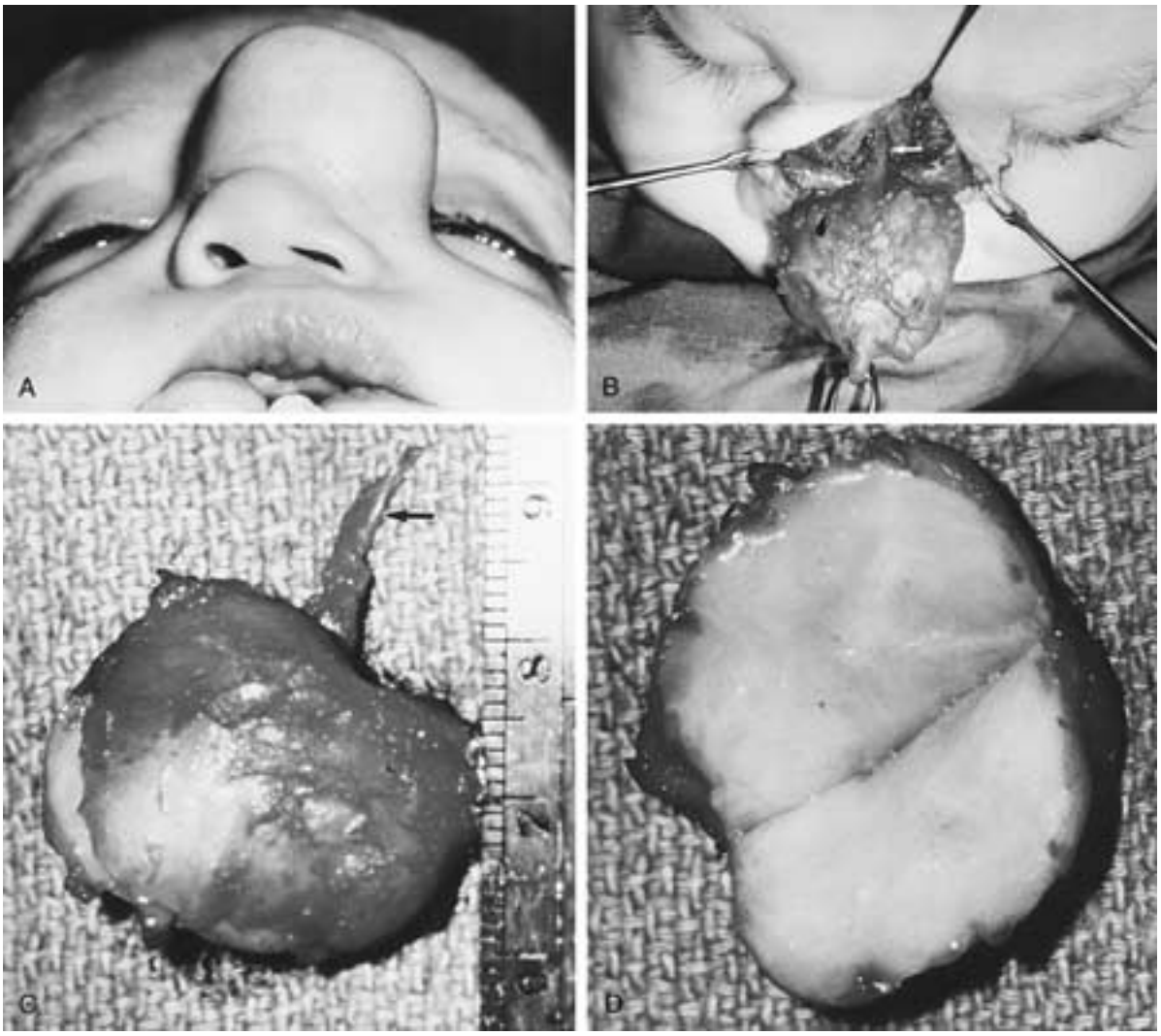

VIEW IMAGE

FIGURE 1-40 Mixed extranasal-intranasal glioma in an 8-month-old boy with a nasal mass that was present at birth and grew in proportion to the child. **A**, View of the face demonstrates a 3 by 3 by 3 cm firm left paramedian subcutaneous mass that displaces the septal and alar cartilage, narrowing the nostril. The mass did not pulsate or change size with crying. **B** and **C**, At surgery the mass was not bound to the subcutaneous tissue. It lay almost entirely external to the nasal bones, to the left of midline. A narrow stalk (*arrows*) passed directly through the left nasal bone and extended upward to the left cribriform plate. **D**, Bisecting the specimen revealed a homogeneous mass of smooth grayish-white shiny tissue. Histologic examination revealed brain and fibrous tissue consistent with nasal glioma.

typically present in infancy, whereas ordinary nasal polyps are exceptionally rare under 5 years of age.[161]

Mixed nasal gliomas (10% to 14%) consist of extranasal and intranasal components that communicate via a defect in the nasal bones or around the lateral edges of the nasal bones (Figs. 1-40 to 1-42).[137, 157] Rarely, these two portions communicate through defects in the orbital plate of the frontal bone or the frontal sinus. When *extra*nasal gliomas lie on *both* sides of the nasal bridge, the two components communicate with each other via a defect in the nasal bones, constituting a mixed nasal glioma.[155]

Histologically, nasal gliomas resemble reactive gliosis rather than neoplasia.[161] They consist of large aggregates or small islands of glial tissue with evenly spaced fibrous or gemistocytic astrocytes within vascularized fibrous tissue.[137, 158] The astrocytes may be multinuclear, but they exhibit no mitotic figures and no bizarre nuclear forms.[160] Fibrous connective tissue enwraps the blood vessels and extends outward to form collagenous septa that partially subdivide the mass.[160] Prominent zones of granulation tissue may be present.[160] The lesion is usually not encapsulated, but astrocytic processes, fibroblasts, and collagen may form a loose or dense connective tissue capsule.[132, 160, 162] *Extra*nasal gliomas are surrounded by dermis with dermal appendages.[132] *Intra*nasal gliomas are surrounded by minor salivary glands, fibrovascular tissue, and nasal mucosa.[132] Only 10% of reported nasal gliomas contain neurons.[160] Occasional lesions show distinct laminated ''cortical'' architecture, with an external acellular zone resembling the molecular layer of the cortex and an inner, more cellular zone.[137] Still other lesions have zones suggesting a pial layer around the glial tissue.[137] Calcification is rare.[153] Invasion

Copyright © 2003, Mosby, Inc. All rights reserved.

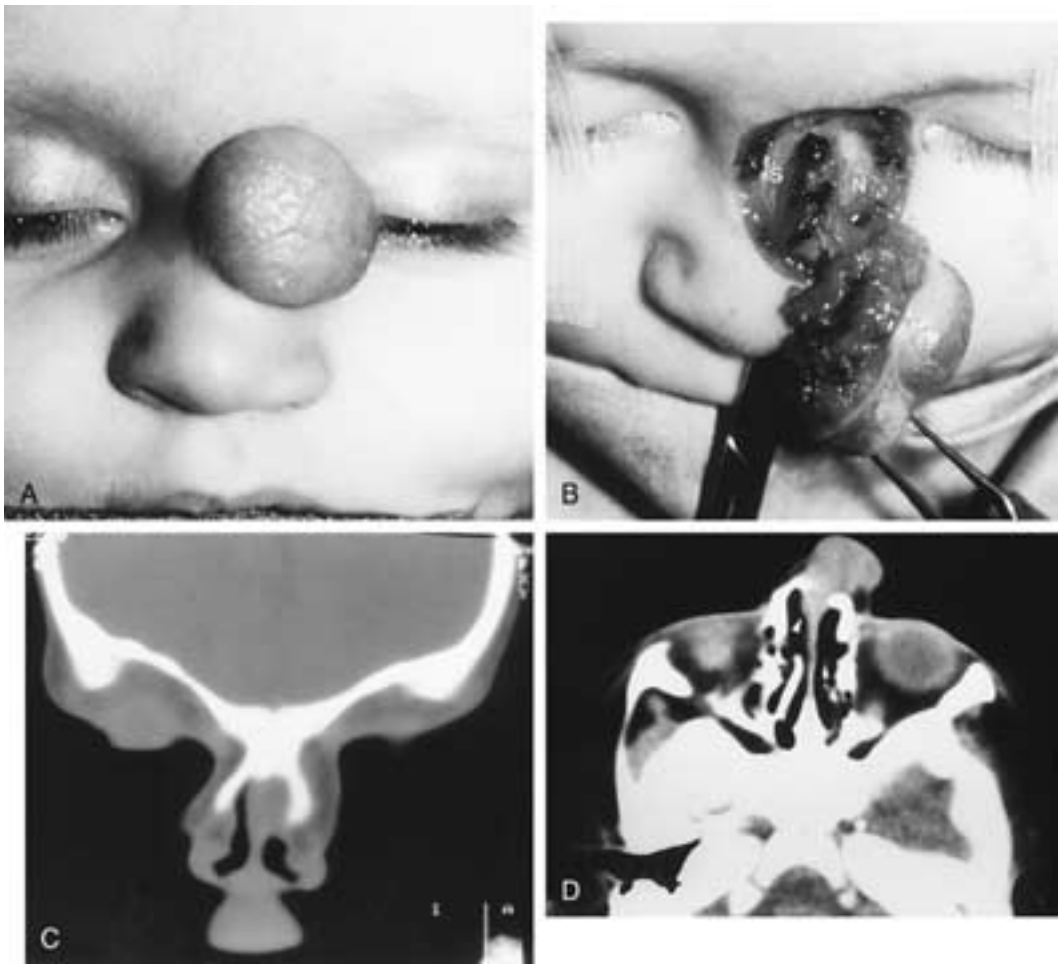

VIEW IMAGE

FIGURE 1-41 Mixed extranasal-intranasal glioma in a 6-month-old boy. **A**, Facies. The globular mass overlies the dorsum of the nose on the left. **B**, At surgery the lesion was found to have extended through the left nasal bones, bowed the septum (*S*) rightward, and bowed the residual left nasal bones (*N*) leftward. It was attached by a pedicle to the foramen cecum. **C** and **D**, Coronal and axial CT scans show that the mass extends through the resultant defect into the thickened nasal septum (*white arrowhead* in **D**). The crista galli and brain were normal. (Courtesy of Dr. Sharon Byrd, Chicago.)

of surrounding tissue has never been observed, and no metastases have been reported.[162] Thus, these lesions are classified as glial heterotopias, not neoplasias.[161, 163]

Nonnasal Heterotopias

Heterotopic brain tissue has also been identified at numerous nonnasal sites, including the orbit, hard palate, soft palate, nasopharynx, pterygopalatine fossa, tongue, upper lip, neck, and even lung.[164–170] These heterotopias may be grouped with the nasal gliomas but are probably better considered separately. Both nasal gliomas and nonnasal heterotopias contain glial cells within a fibrous matrix, but the nonnasal brain heterotopias typically show more advanced maturation and differentiation into neural components such as choroid plexus, ependyma-like epithelium, Nissl substance, and rare ganglion cells.[170] Nonnasal heterotopias are usually benign lesions. Solid lesions typically grow in proportion to the body. Cystic lesions may enlarge disproportionately rapidly, especially if they contain functioning choroid plexus.[170–172] Rarely, tumors have been reported in association with nonnasal heterotopias. Bossen and Hudson[173] reported a small oligodendroglioma arising within heterotopic brain tissue in the soft palate and nasopharynx. Lee et al.[174] reported a melanotic neuroectodermal tumor (melanotic progonoma) within an oropharyngeal mass of brain tissue.

Cleft palates have been reported in 6 of 17 patients (35%) with nasopharyngeal brain heterotopias.[175] Other nasopharyngeal lesions such as teratoid tumors, epignathi, dermoids, hairy polyps, and lipomas have also been associated with clefting of the soft palate.[176] It is unclear whether these concurrences reflect mechanical impediments to the formation of the palate or a midline ''clefting/twinning'' derangement of molecular signaling.

Epignathus Teratoma

Epignathus teratomas are congenital teratomas of the oropharynx found in 1 per 35,000 (up to 1 per 800,000) live births.[177] They occur sporadically, are more frequent in girls (female : male ratio = 3 : 1), and are more frequent in children of younger mothers.[177] Fetal history may disclose an elevated alpha-fetoprotein level and polyhydramnios due to

Copyright © 2003, Mosby, Inc. All rights reserved.

fetal difficulty with swallowing in utero.[177] These tumors are typically single masses attached to the skull base in the midline of the posterior nasopharynx, close to Rathke's pouch and the craniopharyngeal canal.[177] Infrequently, they may be multiple and/or may arise laterally.[177] Small epignathus teratomas are frequently pediculated and vary in position. Large tumors may extend intracranially via the craniopharyngeal canal, extend inferiorly to involve the hard palate, fill the oral cavity, deform the maxilla, and even protrude from the oral cavity.[177] Epignathus lesions are regarded as mature teratomas that do not recur after complete resection.[177] Malignant degeneration has not been described, but intracranial extension is often fatal.[177] Six percent of epignathus teratomas are associated with other malformations, most frequently cleft palate of mechanical origin.[177] Other concurrent malformations include duplicate pituitary glands, bifid noses, bifid tongues, and glossoptosis.[177] In the literature, five of seven patients with duplicate pituitary glands (71%) had concurrent epignathus teratomas, with or without callosal agenesis.[177]

Epulis

Congenital epulis is a rare tumor that affects the gingiva of infants.[178] The lesions may be single or multiple, are eight times more common in girls than in boys, and are three times more common in the maxilla than in the mandible.[178, 179] Epulides are usually not associated with malformations of the teeth, but hypoplasia or absence of the underlying tooth is seen occasionally.[178] Pathologically, the lesion is composed of large cells with eosinophilic granular cytoplasm within a vascular fibrous connective tissue.[178, 180] Electron microscopy shows that the tumor cells are filled with autophagosomes containing collagen precursors. Immunohistochemical stains are positive for vimentin and neuron specific enolase. These features suggest that epulis may arise from early mesodermal cells that express pericytic and myofibroblastic features, and which undergo cytoplasmic autophagocytosis.[180] Epulis may resolve spontaneously or require resection.[181] The lesions do not recur after resection and show no malignant potential.[178, 182]

Cephaloceles

Cephaloceles are congenital herniations of intracranial contents through a cranial defect.[183] When the herniation contains only meninges, it is designated a *cranial meningocele*. If the herniation also contains brain, it is called a *meningoencephalocele*. Cephaloceles are classified by the site of the cranial defect through which the brain and meninges protrude.[183, 190]

Sincipital Cephaloceles

Sincipital cephaloceles are cephaloceles situated in the anterior part of the skull.[161, 184–191] These include both interfrontal cephaloceles (Fig. 1-43) and frontoethmoidal cephaloceles (Figs. 1-44 to 1-49).[161] Sincipital cephaloceles

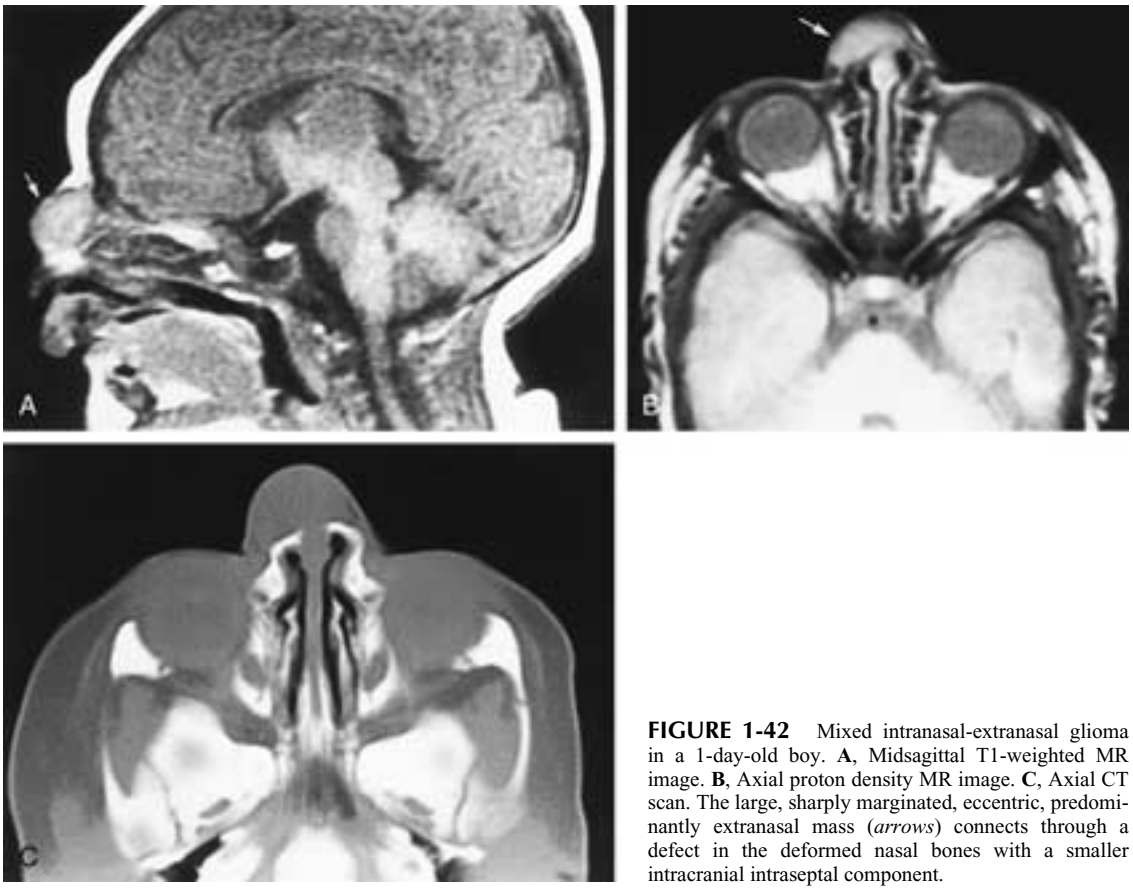

FIGURE 1-42 Mixed intranasal-extranasal glioma in a 1-day-old boy. **A**, Midsagittal T1-weighted MR image. **B**, Axial proton density MR image. **C**, Axial CT scan. The large, sharply marginated, eccentric, predominantly extranasal mass (*arrows*) connects through a defect in the deformed nasal bones with a smaller intracranial intraseptal component.

VIEW IMAGE

Copyright © 2003, Mosby, Inc. All rights reserved.

SUMMARY BOX 1-1

CLASSIFICATION OF CEPHALOCELES

I. Occipital cephaloceles
   A. Cervico-occipital (continuous with cervical rachischisis)
   B. Low occipital (involving foramen magnum)
   C. High occipital (above intact rim of foramen magnum)
II. Cephaloceles of the cranial vault
   A. Temporal
   B. Posterior fontanelle
   C. Interparietal
   D. Anterior fontanelle
   E. Interfrontal
III. Sincipital cephaloceles
   A. Interfrontal
   B. Frontoethmoidal
      1. Frontonasal
      2. Nasoethmoidal
      3. Nasoorbital
IV. Basal cephaloceles
   A. Transethmoidal
   B. Sphenoethmoidal
   C. Transsphenoidal
   D. Frontosphenoidal
V. Cephaloceles associated with cranioschisis
   A. Cranial-upper facial cleft
   B. Basal-lower facial cleft
   C. Acrania and anencephaly

Modified from Suwanwela C, Suwanwela N. A morphological classification of sincipital encephalomeningoceles. J Neurosurg 1972;36:201–211.

always present as external masses along the nose, orbital margin, or forehead.

Cephaloceles are common lesions, occurring in 1 per 4000 live births.[192, 193] The specific cephaloceles observed vary widely in different populations (Table 1-10). Sincipital cephaloceles are found in 1 in 35,000 live births in North America and Europe but in 1 per 5000 to 6000 live births in Southeast Asia.[194–196] Among Caucasians, occipital cephaloceles are most frequent (67% to 80%), while sincipital cephaloceles (2% to 15%) and basal cephaloceles (10%) are infrequent.[183, 190] Among Australian aborigines, Malaysians, and select Southeast Asian groups, sincipital cephaloceles are the most frequent form encountered. Occipital cephaloceles are closely linked with neural tube defects such as myelomeningocele and show a female preponderance (female : male ratio = 2.4 : 1).[197] Sincipital cephaloceles show no linkage to neural tube defects and no gender predominance.[190, 197]

Interfrontal Cephalocele

The interfrontal cephalocele presents anteriorly as a midline mass situated above the frontonasal suture. In this form, the cranial defect lies between the two frontal bones (Fig. 1-43).

Frontoethmoidal Cephaloceles

Frontoethmoidal cephaloceles are defined as cephaloceles that pass outward from the skull through a defect at the junction of the frontal and ethmoid bones, immediately anterior to the crista galli.[161, 185, 198, 199] Frontoethmoidal cephaloceles are then subclassified into nasofrontal, nasoethmoidal, and nasoorbital subtypes by the point at which the skull defect and hernia emerge *externally* (Fig. 1-44).[185, 196] In 120 Thai patients with frontoethmoidal cephalocele seen from 1992 to 1996, Boonvisut et al.[200] found that the internal ostium was a single opening centered at the foramen cecum anterior to the crista galli in 117 cases (97.5%), and paired, bilateral openings occurred at either side of the crista galli in 3 cases (2.5%). The external ostia of the frontoethmoidal cephaloceles were single or multiple and variable in position.[200] In all cases, the crista galli was intact, and the edge of the defect flared outward like a funnel.

Boonvisut et al.[200] classified the external ostia into type I (a single external opening between two adjacent bones) and type II (multiple external openings clustered in the same region). They then used the term *limited* to mean restricted to the territories within or between two adjacent bones and *extended* to signify extension of the bone defect to adjacent bones beyond the confines of the two bones affected primarily. For simplicity, they considered the narrow frontal processes of the maxilla to be nasal bones when classifying lesion ostia into limited or extended types.[200] In their system, type IA signifies a single ostium situated between or within a single pair of bones (e.g., limited to the frontonasal suture). Type IIA signifies multiple external ostia, each of which is limited to two adjacent bones, and type IIB signifies multiple external ostia, at least one of which is of the extended type. In their 120 cases, 106 (88.3%) of the external ostia were type I (85 type IA and 21 type IB). Fourteen (11.7%) of the external ostia were type II (10 type IIA and 4 type IIB).[200] The individual variations are tabulated in their paper.[200]

The relative frequencies of the individual subtypes of frontoethmoidal cephaloceles may vary with the population. In 120 cases of frontoethmoidal cephalocele from Southeast Asia, 39% were frontonasal, 42% were nasoethmoidal, and 18% were nasoorbital (Table 1-11).[196] In 30 cases from India, however, only 6.7% were frontonasal, 87% were nasoethmoidal, and 6.7% were nasoorbital.[195]

Frontonasal subtype In the frontonasal form of frontoethmoidal cephalocele, the cephalocele emerges from the bony canal between the frontal and nasal bones. The frontal bones are displaced superiorly. The nasal bones, frontal processes of maxillae, and nasal cartilage are all displaced inferiorly, away from the frontal bone, but retain their normal relationship to each other. The ethmoid bone is displaced inferiorly, so that the anterior end of the cribriform plate is depressed, the midline portion of the anterior fossa is very deep, and the crista projects into the defect from its inferior rim. The anterior portions of the medial orbital walls are displaced laterally. In this subtype, the bone canal is short, because the intracranial (frontoethmoidal) and extracranial (frontonasal) ends of the defect lie close together.[185]

Copyright © 2003, Mosby, Inc. All rights reserved.

In patients with the frontonasal subtype, the associated soft-tissue mass usually lies at the glabella or nasal root, between deformed orbits (Fig. 1-45).[184, 185] The mass may be small (1 to 2 cm) or larger than the infant's head. Large masses stretch and thin the skin (partially), obscure vision, and may block the airway.[201, 202] Large masses may also cause pressure deformities of the adjacent soft tissue and bone at the forehead, nose, and orbits and thereby cause telecanthus or true bony hypertelorism. Inferior displacement or lengthening on the medial orbital wall may cause an

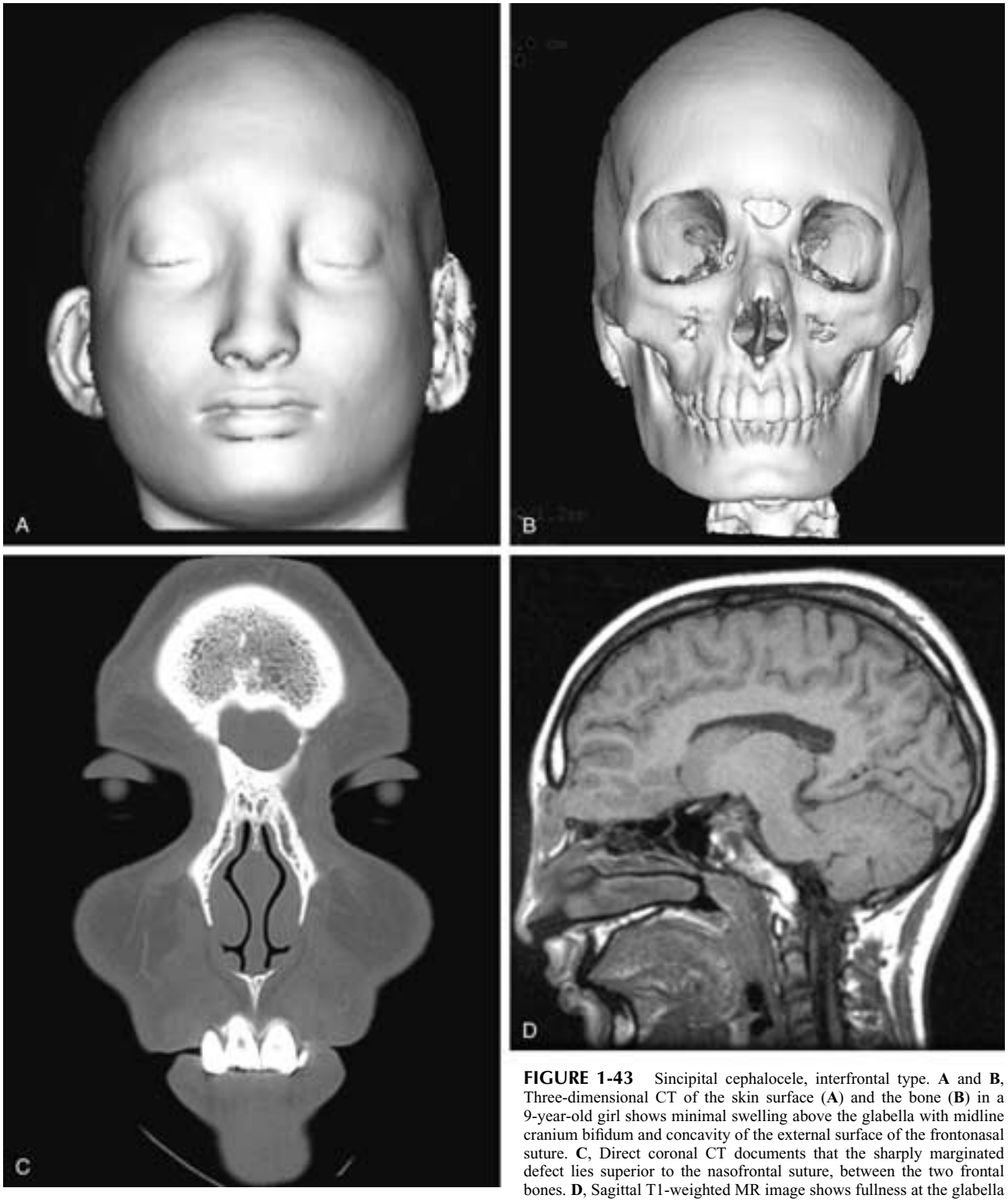

FIGURE 1-43 Sincipital cephalocele, interfrontal type. **A** and **B**, Three-dimensional CT of the skin surface (**A**) and the bone (**B**) in a 9-year-old girl shows minimal swelling above the glabella with midline cranium bifidum and concavity of the external surface of the frontonasal suture. **C**, Direct coronal CT documents that the sharply marginated defect lies superior to the nasofrontal suture, between the two frontal bones. **D**, Sagittal T1-weighted MR image shows fullness at the glabella and herniation of intracranial content through the cranial defect above and external to the nasal bones and nasal capsule.

VIEW IMAGE

Copyright © 2003, Mosby, Inc. All rights reserved.

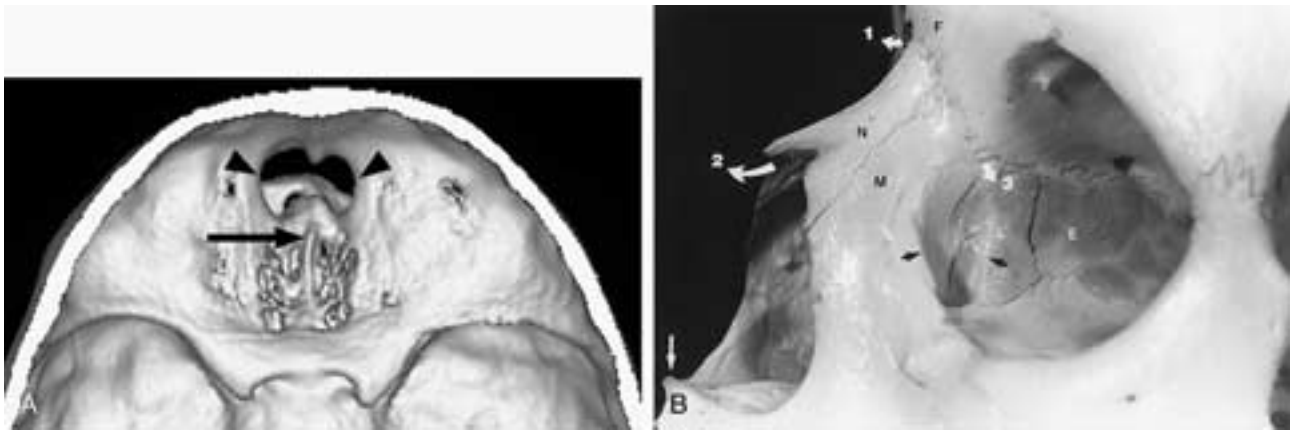

VIEW IMAGE

FIGURE 1-44 **A**, Three-dimensional bone CT of the internal aspect of the skull base shows the internal ostium of a frontoethmoidal cephalocele. All frontoethmoidal cephaloceles exit the skull via a single defect (97.5%) (*arrowheads*) or paired paramedian defects (2.5%) in the anterior fossa just anterior to the crista galli (*arrow*). **B**, Sites of the anterior ostia of frontoethmoidal cephaloceles. Dried adult skull displays the contours and relationships of the individual bones of the skull and face and the intervening sutures. Ethmoid bone or lamina papyracea (*E*), frontal bone (*F*), lacrimal bone (*L*), frontal process of the maxilla (*M*), and nasal bones (*N*). Note the interfrontal, internasal, frontonasal, and frontomaxillary sutures; the nasal spines (*arrow*) of the maxillae; and the lacrimal sac fossa (between the *black arrows*). The anterior crest of the lacrimal sac fossa is formed by the frontal process of the maxilla. The posterior crest is formed by the lacrimal bone. Cartilaginous structures are not displayed. The sites through which the three subtypes of the frontoethmoidal cephaloceles protrude are indicated by the numbered arrows. *1*, Frontonasal cephalocele. The frontonasal forms emerge at the frontonasal junction. The frontal bones form the superior margin of the defect. The nasal bones, frontal processes of the maxillae, and nasal cartilage form the inferior margin of the defect. *2*, Nasoethmoidal cephalocele. The nasoethmoidal forms emerge beneath the nasal bones superior to the cartilaginous nasal capsule. The nasal bones and the frontal processes of the maxillae form the superior margin of the defect. The nasal cartilage and nasal septum form the inferior margin of the defect. *3*, Nasoorbital cephalocele. The nasoorbital forms emerge along the medial wall of the orbit between the frontal processes of the maxilla and the lacrimal-ethmoid bones. The frontal process of the maxilla forms the anterior margin of the defect. The lacrimal bone and lamina papyracea of the ethmoid form the posterior wall of the defect.

Table 1-10
GEOGRAPHIC INCIDENCE OF CEPHALOCELE TYPES

Cephalocele Location	Boston[186] *N* = 265 (%)	Indiana[187] *N* = 67 (%)	Europe[188] *N* = 68 (%)	Japan[189] *N* = 40 (%)	Australia[190] *N* = 74 (%)
Cervico-occipital			11 (16%)		2 (3%)
Occipital	196 (74%)	55 (82%)	34 (50%)	14 (35%)	34 (46%)
Parieto-occipital				4 (10%)	
Parietal	34 (13%)	3 (4%)	6 (9%)	15 (38%)	13 (18%)
Lateral			1 (1%)		
Sicipital	31 (12%)	8 (12%)	16 (24%)	3 (7%)	25 (34%)
Nasopharyngeal	4 (2%)	1 (1%)		4 (10%)	

Modified from Naidich TP, Altman NR, Braffman BH, et al. Cephaloceles and related malformations. AJNR 1992;13:655–690.

Table 1-11
SITE OF MASS OR MASSES IN FRONTOETHMOIDAL CEPHALOCELES (*N* = 120)

Subtype of Frontoethmoidal Cephalocele	Total Number (Percent)	Number Presenting at Each Site
I. Frontonasal subype	47 (39%)	
Glabella		30
Middle of root of nose (between the eyes)		17
II. Nasoethmoidal subtype	50 (42%)	
Middle of root of nose (between the eyes)		29
Both sides of the base of the nose		9
Lower bridge of the nose		7
Widened bridge of the nose		5
III. Nasoorbital subtype	22 (18%)	
Inner canthus on one side		14
Both sides of the nose		6
Widened base of nose with one eye absent		2
IV. Multiple sites	1 (0.8%)	

From Charoonsmith T, Suwanwela C. Frontoethmoidal encephalomeningocele with special reference to plastic reconstruction. Clin Plast Surg 1974;1:27-47.

Copyright © 2003, Mosby, Inc. All rights reserved.

VIEW IMAGE

FIGURE 1-45 **A** and **B**, Facies. Frontonasal form of a frontoethmoidal cephalocele in 1-week-old girl. The lobulated 3 by 3 by 3 cm skin-covered mass protrudes between the orbits to overlie the nasal bones and nasal cartilage.

antimongoloid slant of the eyes.[202] The size of the soft-tissue mass tends to be proportional to the intracranial pressure, not the size of the internal ostium.[200]

Most frontonasal cephaloceles are firm, solid masses that exhibit no transmitted pulsations. Some are cystic, compressible, and pulsatile and increase in size with the Valsalva maneuver (crying). The mass usually grows as the child grows. Cystic masses may increase in size disproportionately rapidly as CSF pools within the sac. The cephalocele may be covered by intact skin, thin skin that ruptures to leak CSF, or no skin at all, exposing the meninges and brain to the environment. The falx frequently extends into the sac, partially subdividing it. The herniated brain may be well preserved, with recognizable gyri and sulci that converge toward the hernia ostium, or the herniated brain may be reduced to a mass of distorted gliotic tissue. Typically, the brain is not adherent to the base of the sac at the ostium but may be adherent to the meninges at the dome of the sac (60%).[201] The tips of the frontal lobes usually protrude into the defect symmetrically or asymmetrically (Figs. 1-46 and 1-47). The olfactory bulbs may herniate with the brain. The olfactory tracts are stretched. The optic nerves enter the skull normally, but may then recurve sharply anteriorly toward the hernia orifice. The internal carotid arteries course with the optic nerves. The anterior communicating artery may lie near the ostium. Concurrent anomalies such as holoprosencephaly and hydrocephalus may be present.[201]

Nasoethmoidal subtype In the nasoethmoidal form of frontoethmoidal cephalocele, the cephalocele emerges from the bony canal between the nasal bones and the nasal cartilage.The nasal bones and the frontal processes of the maxillae remain attached to the frontal bones above the sac, forming the anterosuperior wall of the canal. The nasal cartilage, nasal septum, and ethmoid bone are displaced posteroinferiorly, forming the posterior-inferior wall of the canal. The crista projects upward into the canal from the depths of the floor. The medial walls of the orbit form the lateral borders of the defect. These can be bony or membranous. In this group, the canal is long, because the intracranial (frontoethmoid) and extracranial (nasoethmoid) ends of the defect lie far apart. In the nasoethmoidal form, the bone defect is usually circular and is situated between the orbits, increasing the interorbital distance. The nasal bones remain attached to the frontal bones along the upper margins of the ostium. The cribriform plate lies at a normal height with respect to the orbits. The soft-tissue mass lies to one side of the midline, beside the nasal cartilage. It may be bilateral.[203] In patients with nasoethmoidal cephaloceles, the soft-tissue mass usually presents below the glabella, along a widened dorsum of the nose.
present on both sides of the nose and may extend to the inner canthus. Hydrocephalus is common. In Suwanwela's series, one of three patients had concurrent agenesis of the corpus callosum with an interhemispheric cyst.[185]

Nasoorbital subtype In the nasoorbital form of frontoethmoidal cephalocele, the cephalocele emerges from the bony canal at the medial wall of the orbit between the maxilla and the lacrimal/ethmoid bones (Figs. 1-48 and 1-49). The abnormal frontal process of the maxilla is displaced anteromedially to form the anterior margin of the defect. The lacrimal bone and lamina papyracea of the ethmoid are displaced posterolaterally to form the posterior edge of the defect.[161] The frontal bones, nasal bones, and nasal cartilage retain their normal relationship to each other. In this subtype, the canal is very long, because the intracranial (frontoethmoidal) and extracranial (medial orbital) ends of the defect are widely separated. Patients with nasoorbital cephaloceles commonly present with cystic soft-tissue masses at the nasolabial folds between the nose and the lower eyelid. These contain nubbins of brain.[185]

Frontoethmoidal cephaloceles induce secondary deformities in the facial skeleton. They impede development of the frontal sinuses, and increase the interorbital and intercanthal distances in most cases. The bitemporal widths and the angles between the lateral orbital walls are usually normal (97.5%), except in cases with microphthalmia or anopia (in which they are slightly decreased).[200] Displacement of the crista galli, the cribriform plate, and the perpendicular plate of the ethmoid bone may lead to maxillary hypoplasia.[204] In all cases, the faces of the patients appear longer than normal and the nasal cartilages are misshapen. The pyriform aperture is shorter and broader than normal and is displaced inferiorly.

Concurrent malformations found in 25 patients with

Copyright © 2003, Mosby, Inc. All rights reserved.

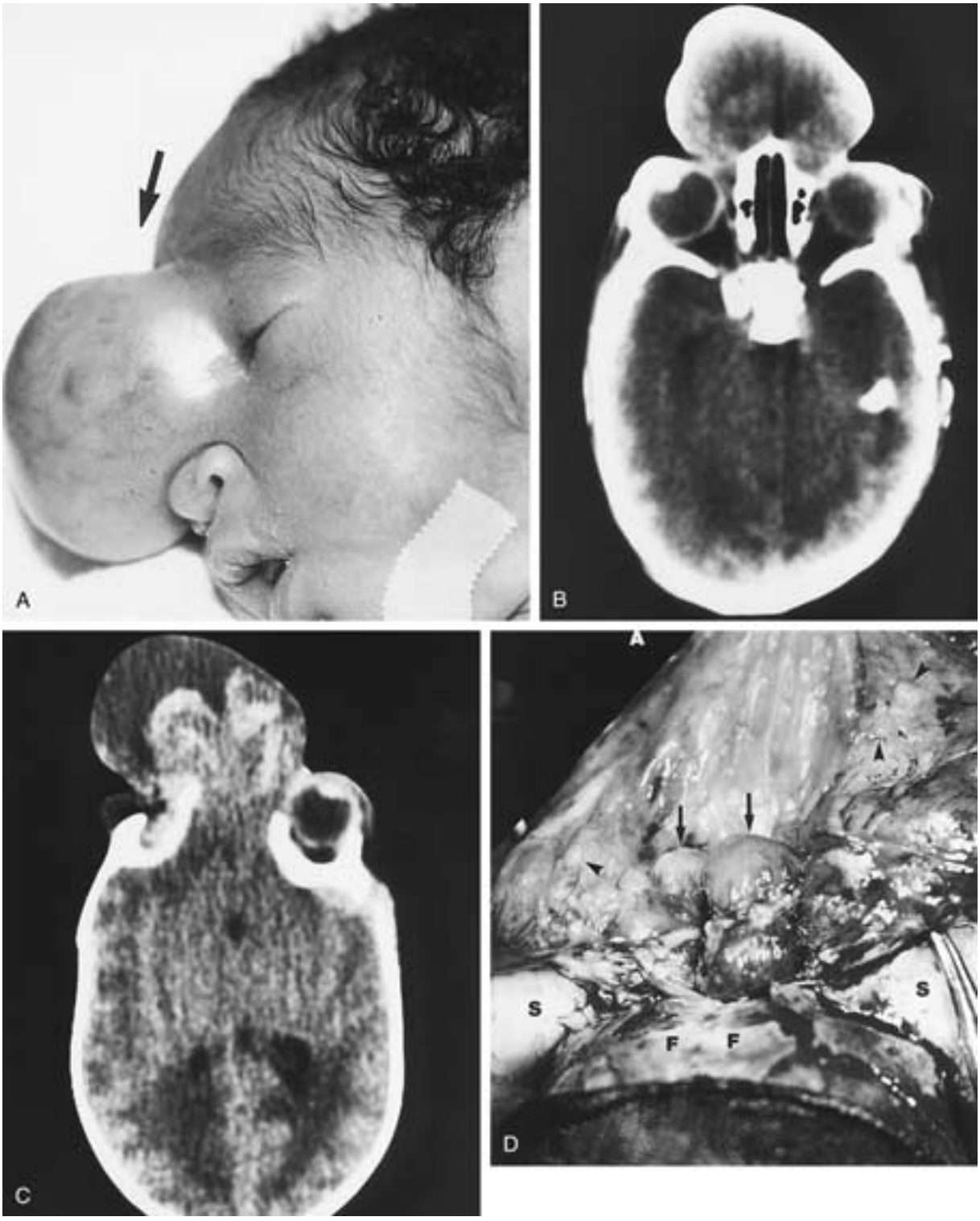

FIGURE 1-46 Frontonasal form of a frontoethmoidal cephalocele in a newborn girl. **A**, Lateral view of the face. A large skin-covered midline mass protrudes between the two orbits, overlies the nasal bones and nasal cartilage, and compresses the nostrils. The arrow indicates the angle of observation for the surgical photograph. Noncontrast CT (**B**) and contrast-enhanced CT (**C**) on 2 different days, oriented as in **D**, the surgical specimen. The ostium of the cephalocele lies above the ethmoid and nasal bones but below the frontal bones, so the lesion is a frontonasal type of frontoethmoidal cephalocele. The mass is predominantly cystic. The inferior portions of both frontal lobes protrude directly into the sac to different degrees, greater on the left. **D**, Surgical photograph. Anterior (*A*) view of the frontal bone (*F*) after reflection of the scalp (*S*) anteriorly and opening of the upper wall of the cephalocele to expose its contents. Most of the sac was filled by CSF. Portions of both frontal lobes (*arrows*) protrude into the sac, separated by the interhemispheric fissure. Multiple glial nodules (*black arrowheads*) stud the meninges that form the inner lining of the sac.

VIEW IMAGE

Copyright © 2003, Mosby, Inc. All rights reserved.

frontoethmoidal cephaloceles include microcephaly (24%), unilateral or bilateral microphthalmos (16%), hydrocephalus (12%), and seizures (4%).[161] Mental retardation was present in 43% of those old enough to test. CSF leakage and continuous bleeding from the exposed brain were major problems in those cephaloceles that lacked a skin cover or in which the thin skin cover ruptured. Rappoport et al.[201] found significant associated congenital anomalies such as microphthalmos, mental retardation, and syndactyly with appendicular constriction bands in 33% of these patients. In one patient with a large frontoethmoidal cephalocele, an arachnoid cyst overlying the right frontal lobe communicated with the external sac. Mahapatra et al.'s 30 cases of frontoethmoidal cephalocele from India showed hypertelorism (83%), enlarged head (from hydrocephalus) (16%), and microcephaly.[195]

The etiologies of frontoethmoidal cephaloceles have not been established satisfactorily. Clear variations in cephalocle incidence with geographic location and population suggest the possibility of a genetic basis for the lesions. David et al.[204] corrrelated advanced paternal age with frontoethmoidal cephaloceles and suggested an autosomal dominant inheritance pattern. Alternatively, Richards[205] noted an increased incidence of frontoethmoidal cephaloceles in impoverished rice farmers of Cambodia but a reduced incidence of encephaloceles in infants conceived in winter months, leading him to propose that aflatoxins, notably ochratoxin A, may represent a teratogenic cause of frontoethmoidal cephaloceles. Approximately 60% to 85% of frontoethmoidal cephaloceles have a good outcome unless there are concurrent severe anomalies.[191] In Brown and Sheridan-Pereira's series,[206] severe mental, motor, and/or visual handicaps were seen in only 30% and mild motor/visual handicaps in another 10%. The size of the fluid spaces does not determine the patient's prognosis. Imaging of these cephaloceles displays the bony defect, the nature of the herniating tissue, the effect on the adjacent tissue, and any concurrent intracranial ear, nose, and throat malformations.[126, 127, 207, 208]

Basal Cephaloceles

Basal cephaloceles are cephaloceles that protrude through the skull base. They include the sphenoorbital, sphenomaxillary, and sphenopharyngeal cephaloceles.[154, 191]

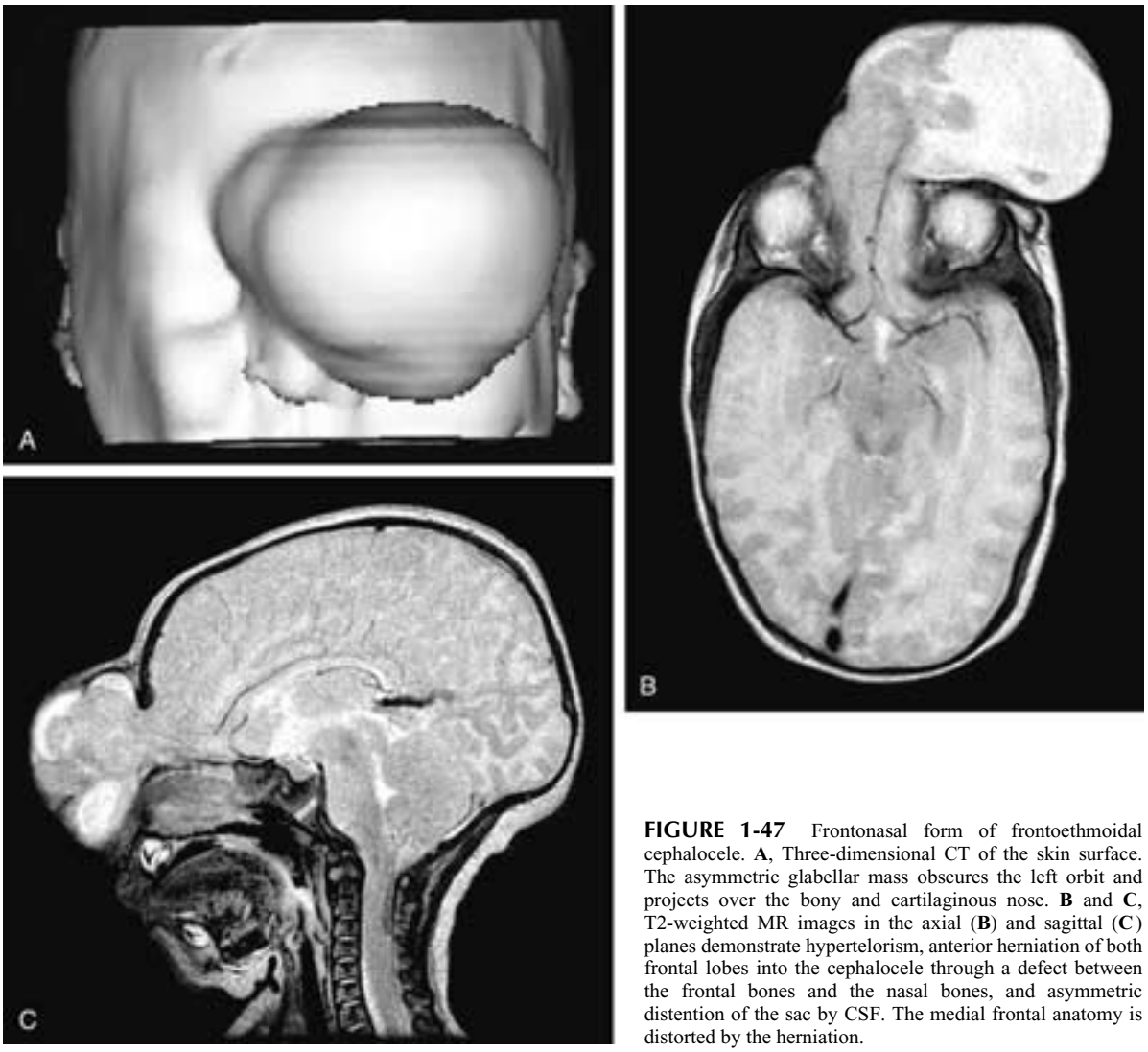

FIGURE 1-47 Frontonasal form of frontoethmoidal cephalocele. **A**, Three-dimensional CT of the skin surface. The asymmetric glabellar mass obscures the left orbit and projects over the bony and cartilaginous nose. **B** and **C**, T2-weighted MR images in the axial (**B**) and sagittal (**C**) planes demonstrate hypertelorism, anterior herniation of both frontal lobes into the cephalocele through a defect between the frontal bones and the nasal bones, and asymmetric distention of the sac by CSF. The medial frontal anatomy is distorted by the herniation.

VIEW IMAGE

Copyright © 2003, Mosby, Inc. All rights reserved.

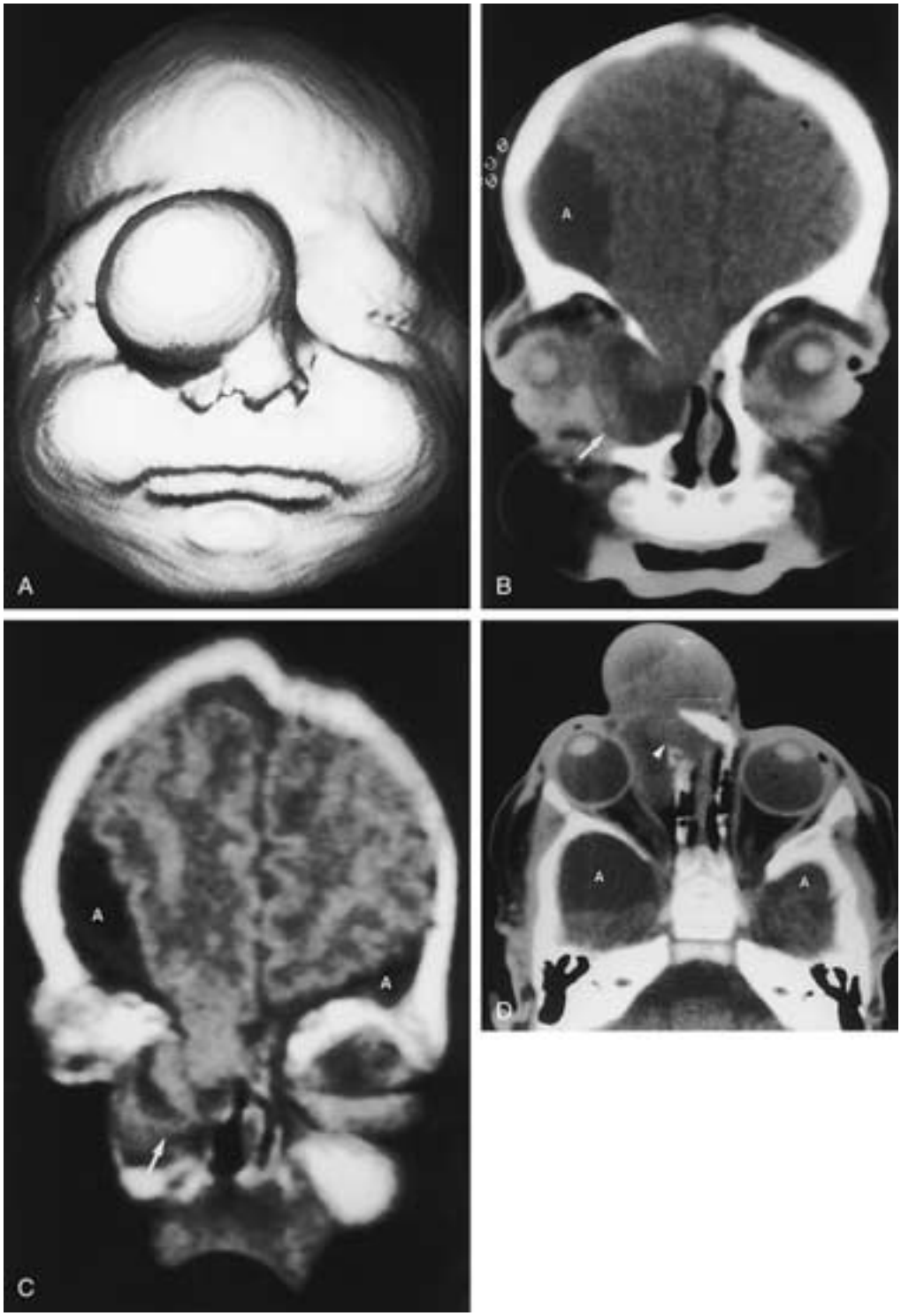

FIGURE 1-48 Unilateral nasoorbital cephalocele. **A**, Three-dimensional CT of the skin surface shows a large, eccentric, skin-covered mass at the medial right canthus. The cartilaginous nose is deviated inferiorly and leftward. Coronal CT (**B**) and coronal T1-weighted MR image (**C**) show lateral deviation of the right globe and muscle cone by inferior protrusion of a unilateral cephalocele (*white arrows*) containing brain and meninges. The cephalocele displaces the nasal mucosa medially and the orbital contents laterally. Bilateral anterior temporal fossa CSF spaces suggest concurrent arachnoid cysts (*A*). **D**, Axial CT demonstrates the defect (*arrowhead*) in the medial wall of the right orbit, the characteristic displacement of the muscle cone, and the narrowing of the ipsilateral nasal passage.

VIEW IMAGE

Copyright © 2003, Mosby, Inc. All rights reserved.

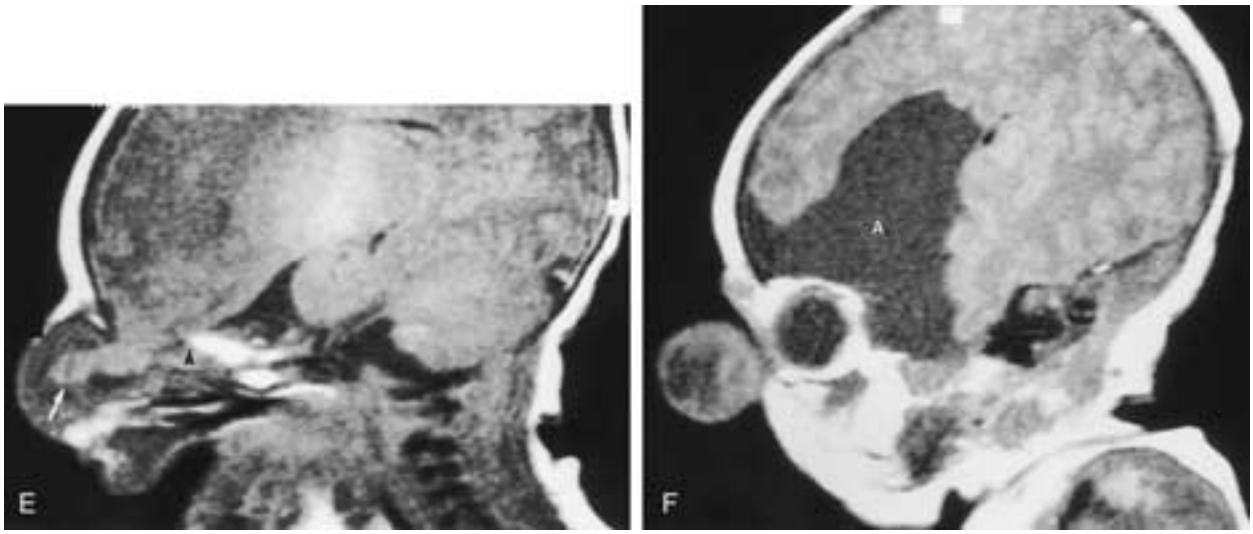

VIEW IMAGE

FIGURE 1-48 *Continued.* **E** and **F**, Sagittal T1-weighted MR images. The paramedian section (**E**) demonstrates the intracranial end (*black arrowhead*) of the osseous canal and direct extension of brain tissue (*white arrow*) into the medial orbit. The lateral section (**F**) demonstrates the prominent arachnoid cyst commonly found in these lesions.

Basal cephaloceles are not visible externally unless they grow large enough to protrude secondarily through the nostril or mouth.[25] They are classified by their point of exit from the skull as sphenoorbital, sphenomaxillary, and sphenopharyngeal.[154] In combined data on 20 basal cephaloceles, 1 (5%) was sphenoorbital, none was sphenomaxillary, and 19 (95%) were sphenopharyngeal.[197, 209]

Sphenoorbital Cephaloceles

Sphenoorbital cephaloceles exit the skull via the superior orbital fissure and come to lie in the orbit posterior to the globe.

Sphenomaxillary Cephaloceles

Sphenomaxillary cephaloceles exit the skull via the superior orbital fissure to enter the orbit, but then pass further inferiorly via the inferior orbital fissure to reach the pterygopalatine space. From there they may extend further into the infratemporal fossa.[210]

Sphenopharyngeal Cephaloceles

Sphenopharyngeal cephaloceles exit from the skull through or between the sphenoid and ethmoid bones. This group is then subclassified (from anterior to posterior) as purely transethmoidal, sphenoethmoidal, or purely transsphenoidal. In the same combined series of 20 cephaloceles, the subtypes of the 19 sphenopharyngeal cephaloceles were transsphenoidal (5 of 19, 26%), sphenoethmoidal (2 of 19, 11%), and transethmoidal (12 of 19, 63%).[158, 197]

Transethmoidal cephaloceles (63%) extend downward anteriorly, through a defect in the midline or along the cribriform plate, and do not involve the sella turcica.[197, 204, 209, 210] The hernia sac extends inferiorly into the sinuses or the nasal cavity[211] and typically contains portions of the frontal lobes and olfactory apparatus. *Transsphenoidal cephaloceles* (26%) extend downward posteriorly, through a defect in the floor of the sella turcica, to reach the nasal cavity (Figs. 1-19 and 1-20).[197, 209] If the palate is cleft, they may also extend further inferiorly into the oral cavity. The posterior margin of these defects is always the dorsum sellae. The lateral walls are the cavernous sinuses and the widely separated halves of the sphenoid bone. The anterior extent is very variable. The defect may involve the sella only or the sella plus the planum sphenoidale. *Sphenoethmoidal cephaloceles* (11%) extend downward through a combined sphenoidal and ethmoidal defect.[197, 204] In our experience, these are nearly always especially large transsphenoidal cephaloceles that extend unusually far anteriorly to involve the ethmoid bone.

As a group, the transethmoidal, transsphenoidal, and sphenoethmoidal cephaloceles are associated with hypertelorism, midline facial clefting, ocular clefting/colobomas, optic nerve dysplasia, and midline cerebral defects. They may be considered together as a craniofacial-cerebral dysraphic complex (Table 1-4). Blustajn et al.[217] noted dysgenesis of the internal carotid artery in two patients with transsphenoidal cephaloceles, hypopituitarism, hypertelorism, and optic nerve coloboma and suggested that all aspects of the syndrome might represent a disorder of neural crest migration. The transethmoidal group tends to have minor facial anomalies (two of three hypertelorism, two of three cleft lip/cleft palate), so they present later in life.[209] The transsphenoidal cephaloceles typically show more severe hypertelorism and facial clefting. The cephalocele sac contains the pituitary gland and the hypothalamus, the anterior recesses of the third ventricle, and the optic apparatus. Symptoms vary. In neonates and infants, the intranasal/pharyngeal soft-tissue mass usually causes a runny nose, nasal obstruction, mouth breathing, or snoring. Frequently, these symptoms are ignored.[218] If they are noted, the intranasal lesions then discovered may be mistaken for nasal polyps, as is true of nasal gliomas.[134] If the early signs are not appreciated, the basal cephaloceles may not be detected until adulthood, when they tend to

Copyright © 2003, Mosby, Inc. All rights reserved.

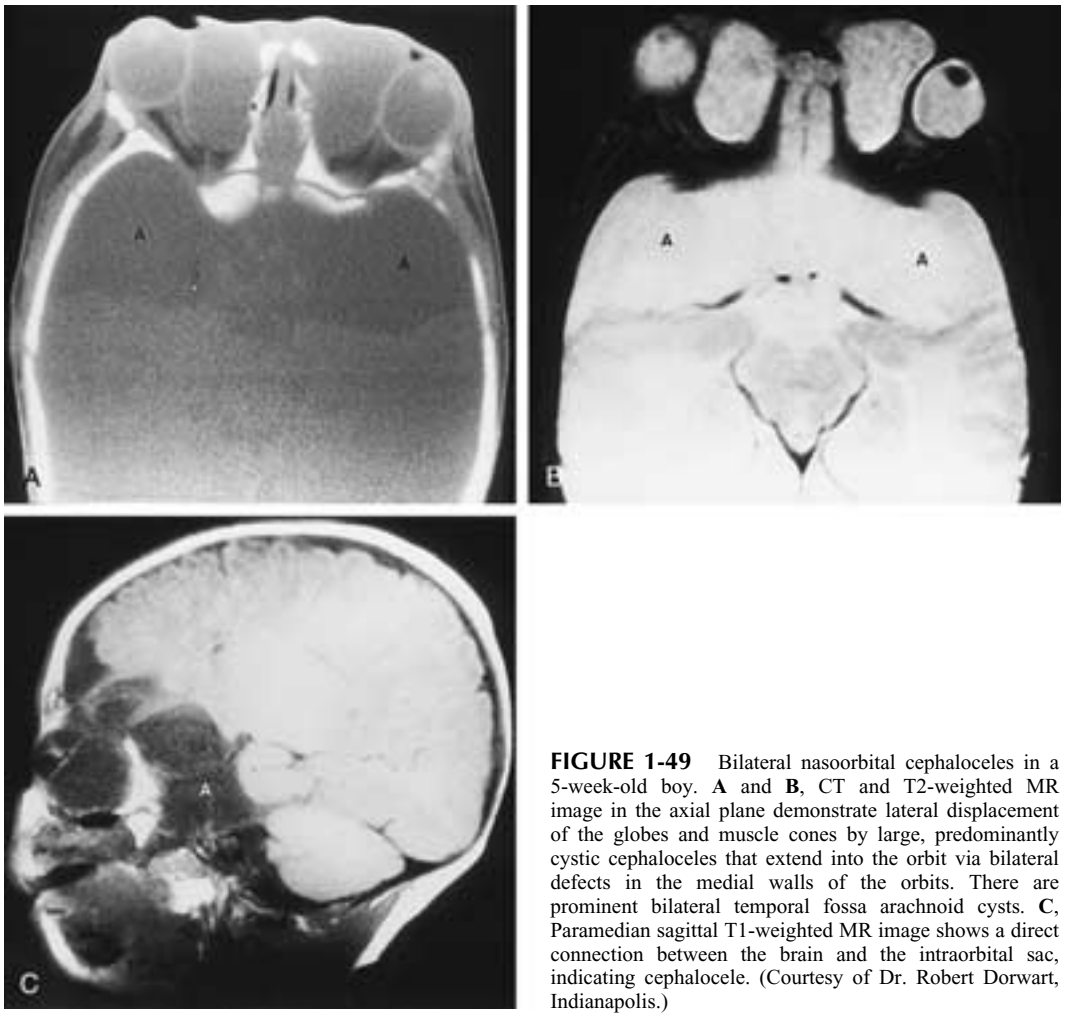

FIGURE 1-49 Bilateral nasoorbital cephaloceles in a 5-week-old boy. **A** and **B**, CT and T2-weighted MR image in the axial plane demonstrate lateral displacement of the globes and muscle cones by large, predominantly cystic cephaloceles that extend into the orbit via bilateral defects in the medial walls of the orbits. There are prominent bilateral temporal fossa arachnoid cysts. **C**, Paramedian sagittal T1-weighted MR image shows a direct connection between the brain and the intraorbital sac, indicating cephalocele. (Courtesy of Dr. Robert Dorwart, Indianapolis.)

VIEW IMAGE

present with visual disturbance, pituitary-hypothalamic dysfunction, or CSF rhinorrhea.[218] Basal cephaloceles, particularly transsphenoidal cephaloceles, carry a high operative mortality rate (50%) and a high risk of chronic severe neuroendocrine handicaps (70%).[191]

Rarer Basal Cephaloceles

Other forms of basal cephalocele are seen very infrequently. Losken et al.[210] identified a group of cephaloceles that entered the orbit directly by downward extension between the ethmoid bone medially and the orbital plate of the frontal bone laterally, *not* via the cribriform plate and *not* via the superior orbital fissure.[210] These authors designated this new group anterior ethmoidal cephaloceles (if the ostium lay close to the anterior ethmiodal foramen) and posterior ethmoidal cephaloceles (if the ostium lay close to the posterior ethmoidal foramen). Elster and Branch[219] and Soyer et al.[220] each reported a transalar form of sphenoidal cephalocele that extended downward through the greater wing of the sphenoid into the pterygoid fossa. Raftopoulos et al.[221] described a variation in which the cephalocele appears to have extended inferiorly through the sphenopetral fissure via the anterior foramen lacerum, displacing the foramen ovale anterolaterally.

DACRYOCYSTOCELES

Dacryocystoceles are the distended nasolacrimal ducts/sacs that result from imperforation of the lacrimal system in the newborn period and shortly thereafter.[222, 223] They are the second most common cause of neonatal nasal obstruction, after choanal atresia, and may require prompt therapy.[208] Dacryocystoceles commonly present as 5 to 12 mm round, tense blue to blue-gray masses situated just inferior to the medial canthi (Fig. 1-50).[222] In the newborn, therefore, dacryocystoceles may be confused with cephaloceles, especially the nasoorbital form of frontoethmoidal cephalocele.

Dacryocystoceles are usually unilateral, in either eye, but may be bilateral in 13% to 65% of cases.[223–226] Males and females are affected equally.[225–228] Nearly all cases are sporadic. The lacrimal *production* system is mature at birth, so full-term infants make tears from the first day of life on.[229] The volume of tears does not correlate with birth weight, placental weight, Apgar score, or maturity of the placenta.[229] However, the distal end of the nasolacrimal duct remains imperforate in many full-term newborns, estimated variably at 6% to 84%.[230–232] The incidence is known to be higher in premature and stillborn infants, perhaps because

Copyright © 2003, Mosby, Inc. All rights reserved.

stretching of the mucosa by breathing and crying helps to open the inferior end of the nasolacrimal duct.[233] Most neonatal dacryostenoses resolve spontaneously. In two series of uncomplicated congenital dacryostenoses, 90% of obstructed tear ducts opened spontaneously at 1 to 13 months of age.[227] Eleven percent required probing to open the duct.[223] Some of those with spontaneous opening of the obstruction re-present in adulthood with renewed stenosis and/or infection.

In 2% of patients with imperforate *distal* nasolacrimal ducts, concurrent obstruction of the *proximal* ducts creates a distended lacrimal sac cyst designated a lacrimal sac mucocele, amniocele, or dacryocystocele.[233, 234] Dacryocystoceles are sterile at birth and asymptomatic. They manifest as excessively large tear menisci along the lower lid margins, crusting of dried mucoid material along the lashes, and epiphora. Secondary dacryocystitis occurs in 0.5% to 6% of these patients and infrequently (2%) leads to a dacryopyocele (lacrimal sac abscess).[225] Periorbital cellulitis and septicemia may ensue.[232]

In approximately 11% to 24% of patients with dacryocystoceles, the distal intranasal end of the nasolacrimal duct distends to form an endonasal cyst (the nasolacrimal mucocele), which may cause partial or complete airway obstruction (Fig. 1-51).[231, 235, 236] These cysts are bilateral in about half of the patients (43% to 48%). Unilateral or partial bilateral obstruction presents as noisy breathing, increased inspiratory effort, restless sleep, and poor sucking. Because 80% of neonates show normal cyclic vasocongestion of the nasal mucosa on alternating sides, patients with unilateral endonasal cysts or partial bilateral obstruction may suffer cycles of respiratory distress when normal nasal engorgement reduces the residual airway. Because neonates breathe predominantly through the nose and will not open their mouths spontaneously to breathe, significant bilateral endonasal obstruction becomes an acute airway emergency, relieved suddenly when crying or mechanical devices open the mouth. Patients with an endonasal component of the dacryocystocele suffer dacryocystitis more frequently.[237, 238]

HOLOPROSENCEPHALY

The term *holoprosencephaly* was coined by DeMyer and Zeman[239] to include a group of cerebral malformations characterized by ''the tendency for the prosencephalon to remain as a whole, as a simple vesicle incompletely transformed into a complex di- and telencephalon with lobes and hemispheres'' (Fig. 1-52). It is characterized by hypoplasia or aplasia of the rostral brain and of the premaxillary segment of the face. Holoprosencephaly is the most common congenital brain malformation in humans.[240] It is found in 1 per 250 concepti but shows very high intrauterine lethality.[240–242] For that reason, the *clinical* incidence of holoprosencephaly is estimated to be 1 in 13,000 to 18,000 live births.[243] There is a female predominance.[244] Surviving patients with severe holoprosencephaly suffer developmental delay, failure to thrive, seizures, poor temperature control, and spastic quadriparesis.[245] Individuals with less severe forms of holoprosencephaly may survive past infancy, with developmental delay. They may even appear to be normal, only to be discovered later to have holoprosencephaly. Those with the least severe forms may show only mental retardation.

Approximately 50% of patients with holoprosencephaly show alteration in the number or structure of their chromosomes,[232] especially chromosomes 13 and 18.

FIGURE 1-50 Dacryocystocele. **A**, Frontal view of a 13-day-old girl with a tense bluish mass inferior to the medial canthus on the left. A far smaller lesion of the same type on the right had just subsided. **B**, Direct coronal CT demonstrates the large, tense left cyst (*arrow*) and a smaller right cyst (*arrow).* (**A** from Naidich TP, Heier LA, Osborn RE, Castillo M, Bozorgmanesh A, Altman N. Facies to remember number 6. Congenital dacryocystocele. Int J Neurol 1996;2:389–396.)

VIEW IMAGE

Copyright © 2003, Mosby, Inc. All rights reserved.

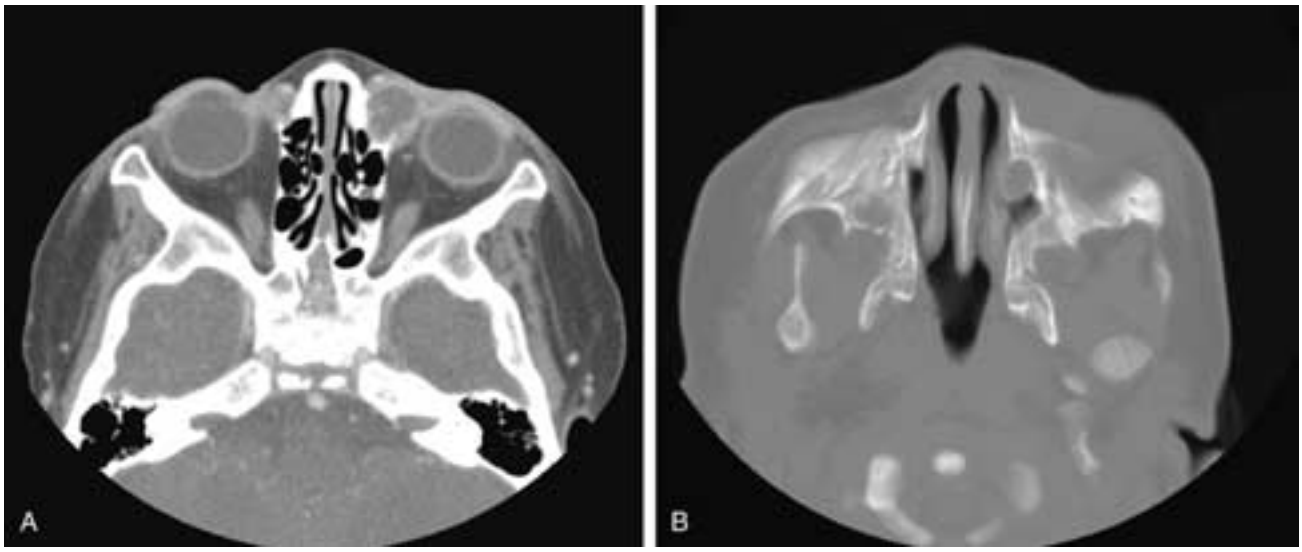

FIGURE 1-51 Dacryocystocele. **A** and **B**, Axial CT images of a 2-day-old girl with complex cardiac anomalies and asymmetric periorbital edema show asymmetric widening of the left nasolacrimal sac fossa by a tense dacryocystocele. The distended inferior end of the dacryocystocele protrudes into the nasal cavity, causing partial obstruction.

VIEW IMAGE

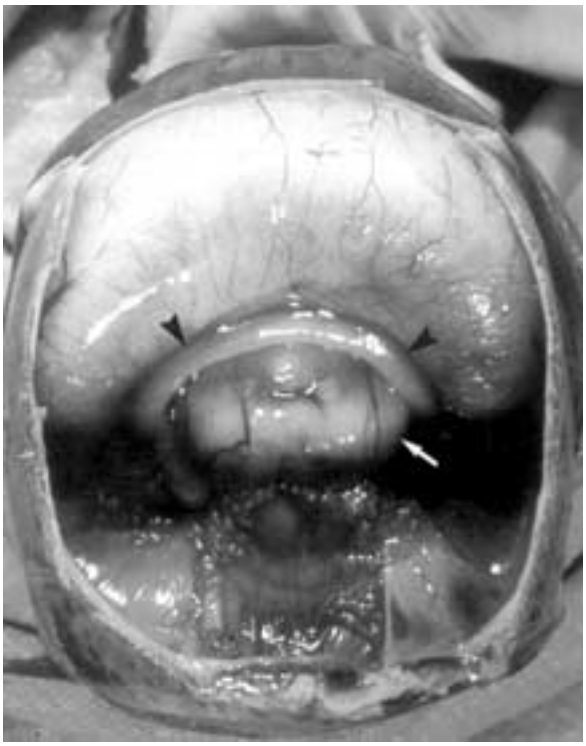

VIEW IMAGE

FIGURE 1-52 Alobar holoprosencephaly with dorsal cyst in a 1-month-old patient with cebocephaly. Gross pathology in situ. View from above at postmortem examination discloses the lissencephalic shield-shaped holoprosencephalon displaced anteriorly against the frontal bones by the large dorsal cyst. The cyst leads directly into the monoventricle deep to an everted hippocampal ridge (*arrowheads*). The holoprosencephalon shows no division into lobes. The diencephalon (*white arrow*) is similarly undivided. There is no falx cerebri. (From Smith MM, Thompson JE, Naidich TP, Castillo M, Thomas D, Mukherji SK. Facies to remember. Cebocephaly with single midline proboscis. Alobar prosencephaly. Int J Neuroradiol 1996;2:251–263.)

Approximately 70% of patients with trisomy 13 have holoprosencephaly.[243] Only 2.1% of patients with trisomy 18 have holoprosencephaly (but holoprosencephalic patients often show trisomy 18).[246] There is a definite association with the Meckel, Kallman, and hydrolethalis syndromes.[247] Recently, holoprosencephaly has been related to deletions and translocations in at least 12 chromosomal regions[248] (Table 1-12).

SIX3 is a transcription factor related to the *Drosophila* sine oculis/optix family of master regulatory genes that can lead to ectopic eye formation. The gene *Sonic Hedgehog* produces an extremely powerful secreted signaling protein (sonic hedgehog) that organizes adjacent tissues, including the notochord, the floor plate of the neural tube, the zone of polarizing activity of the limb bud, the ectodermal tips of the facial proceses, and the apical ectoderm of the second pharyngeal arch.[3] To act, hedgehog protein normally undergoes autoproteolytic cleavage and interacts with cholesterol to create an active, cholesterol-modified amino-terminal segment that remains associated with the membrane and initiates signal transduction.[2, 3, 10, 249] *TGIF* is transforming growth-interacting factor, a modulator of transforming growth factor-alpha. *ZIC2* is a zinc-finger transcription factor gene. The *PATCHED* gene (ptc) codes for a transmembrane receptor that downregulates expression of certain growth factors. *PATCHED* functions in a regulatory feedback pathway with sonic hedgehog, GLI, and Wnt1 (see also the section on Syndromic Craniosynostosis). The hedgehog proteins upregulate several genes, including *PATCHED*. Patched protein then builds up until it interrupts transmission of the hedgehog signal from the cell membrane to the nucleus. Mutations in the *PATCHED* gene cause Gorlin's basal cell nevus syndrome and some sporadic basal cell carcinomas.[250]

Other groups of genes may also play a role in at least some forms of holoprosencephaly. The genes *Otx1* (chro-

Copyright © 2003, Mosby, Inc. All rights reserved.

mosome 2p13), *Otx2* (chromosome 14q21-q22), *Emx1* (chromosome 2p14-p13), and *Emx2* (chromosome 10q26.1) are intimately involved with patterning large portions of the cerebrum, including the medial cerebral wall.[251–254] Recent work on the role of fibroblast growth factor 8 (fgf8) in modulating the expression of *Otx2* and *Emx2* suggest that this factor could also be related to holoprosencephaly.[255]

In humans, holoprosencephaly may be inherited as an autosomal dominant trait that causes haploinsufficiency for sonic hedgehog. At least 27 different mutations of the *Sonic Hedgehog* gene are known to cause a wide range of holoprosencephalic phenotypes.[240, 248, 256, 257] Translocations that mutate upstream regulators of *Sonic Hedgehog* are associated with mild phenotypes of holoprosencephaly.[258]

Classically, holoprosencephaly has been related to maternal diabetes and in utero exposure to radiation, alcohol, cocaine, *Toxoplasma gondii*, and syphilis.[259] Many teratogens that cause holoprosencephaly are now known to affect *Sonic Hedgehog*. The plant alkaloid jervine, for example, causes holoprosencephaly by inhibiting the tissue response to Sonic Hedgehog.[12] Severe cholesterol deficiency prevents formation of the active signaling moiety of *Sonic Hedgehog* and is the basis for the holoprosencephaly seen in 5% of the RSH/Smith-Lemli-Opitz syndrome.[2] Cleft palate and postaxial polydactyly are also part of this syndrome.[2, 10]

Holoprosencephaly Facies

Patients with severe forms of holoprosencephaly manifest a spectrum of orbital, ocular, nasal, and aural anomalies, including an elongated tube-like nasal analog termed the *proboscis*.[260] As a group, the facies of holoprosencephaly are characterized by hypotelorism (Fig. 1-12A). These facies must be carefully differentiated from the facies of the midline craniofacial-cerebral dysraphisms, in which *hyper*telorism is associated with true midline clefting of the nose and/or lip, cranium bifidum occultum, anophthalmos-microphthalmos, colobomas of the peripapillary retina, basal cephaloceles, dysgenesis of the corpus callosum, and intracranial lipomas. The holoprosencephalic facies are grouped into five major categories (Fig. 1-53).

Cyclopia

Cyclopia (Fig. 1-53A) is characterized by a single median bony orbit, which usually contains a variably well-formed eye. The ''eye'' may consist only of rudiments, may be a single globe with partial formation of one or two cornea(s), or may have partial or complete doubling of the globe(s) within the single orbit. The eyebrows may be absent, present only laterally, or united across the midline (synophrys). The nose may be absent or may consist of an elongated, fleshy, tube-like proboscis that arises from the glabella above the orbit and projects anteriorly. The proboscis has a single external ostium that leads to a blind-ending, mucous membrane–lined canal. No midline septum exists, but other septa, reminiscent of turbinates, may partition the channel. The mouth may be small or absent. The upper lip is present and uncleft, but the philtrum and labial tubercle are usually absent.

Table 1-12
GENES RELATED TO HOLOPROSENCEPHALY

Gene Name	Gene Product	Chromosome Location
HPE1	Product unknown	21q22.3
HPE2	SIX3	2p21
HPE3	Sonic hedgehog	7q36
HPE4	TGIF	18p11.3
HPE5	ZIC2	13q32
PATCHED	Patched protein	9q22.3

Data from Odent S. Attie-Bitach T, Blayau M, et al. Expression of the Sonic Hedgehog (*SHH*) gene during early human development and phenotypic expression of new mutations causing holoprosencephaly. Hum Mol Genet 1999;8:1683–1689.

Ethmocephaly

Ethmocephaly (Fig. 1-53B) is characterized by two separate hypotelorotic orbits, two separate eyes, and a median (or, rarely, a double) proboscis that projects anteriorly from a narrow attachment *between* the two eyes. There is no cleft lip or cleft palate. This facies is transitional between cyclopia and cebocephaly and is exceptionally rare.[261]

Cebocephaly

Cebocephaly (Fig. 1-53C) is characterized by two separate hypotelorotic orbits, two separate eyes, and a single tubular proboscis that attaches along the expected course of the nose and ''reclines on its side'' rather than projecting outward, as in cyclopia or ethmocephaly. The proboscis has a single midline ostium and a single blind-ending, mucous membrane–lined canal. There are no nasal bones or nasal septum; the presence of a nasal septum rules out cebocephaly. No olfactory epithelium or ganglia are present. The upper lip is typically present but may be hypoplastic. The philtrum may be partially formed, but there is usually no well-developed labial tubercle.

Absent Intermaxillary Segment with Central Defect and Hypotelorism

Absence of the intermaxillary segment (Fig. 1-53D) is characterized by two hypotelorotic orbits with two eyes, a flat or absent nasal bridge with hypoplastic alae nasi but no nasal septum, and a pseudomedian cleft of the upper lip (absent intermaxillary segment). The missing intermaxillary segment includes (1) the entire thickness of the middle third of the upper lip (prolabium) that normally forms the philtrum and the labial tubercle, (2) the premaxillary bone with the upper incisors, and (3) the primary palate. The secondary palate may be cleft or not.

Intermaxillary Rudiment with Hypotelorism

This facies (Fig. 1-53E) is characterized by bilateral lateral (common) cleft lip and a hypoplastic intermaxillary segment. The nasal bridge is flat or incompletely elevated but is better developed than in Facies 4 above. The nasal septum is present, but incomplete. The residual intermaxillary segment may be highly rudimentary or moderately well developed. These facies form a continuous spectrum with facies 4 (see above).

Major anomalies of the lower face may also be present in patients with alobar holoprosencephaly, including agnathia, microstomia, anostomia, and otocephaly (ear head).[262]

Copyright © 2003, Mosby, Inc. All rights reserved.

VIEW IMAGE

FIGURE 1-53 Typical facies associated with holoprosencephaly. Five types. **A**, Facies 1: cyclopia. (Courtesy of Dr. Fred Epstein, New York.) The complete upper lip, with a hint of a labial tubercle in the midline, could represent either fusion of the nasomedial processes independent of the frontonasal process or fusion of the two maxillary processes across the midline. **B**, Facies 2: ethmocephaly. (Courtesy of Dr. Michael Cohen, Halifax, Nova Scotia, Canada.) **C**, Facies 3: cebocephaly with synophrys (fusion of the two eyebrows across the midline). **D**, Facies 4: absent intermaxillary segment, flat nasal bridge, and rudimentary alae nasi (cf. Fig. 12A). Imaging disclosed alobar holoprosencephaly with dorsal cyst. **E**, Facies 5: hypotelorism with an intermaxillary rudiment (*white arrowhead*). Imaging disclosed lobar holoprosencephaly. (From Smith MM, Thompson JE, Naidich TP, Castillo M, Thomas D, Mukherji SK. Facies to remember. Cebocephaly with single midline proboscis. Alobar prosencephaly. Int J Neuroradiol 1996;2:251–263.)

Brain Malformations

Holoprosencephaly is regarded as a generalized reduction in the forebrain and the frontonasal prominence. As a consequence, the brain is typically microencephalic, weighing only 100 to 150 g at birth (vs. the normal 200 to 300 g).[263] The head is usually microcephalic but may manifest macrocrania when marked expansion of a dorsal cyst distends the intracranial space. Classically, the spectrum of brain anomalies seen with holoprosencephaly is divided into three groups: alobar, semilobar, and lobar forms. In the most severe *alobar form*, the supratentorial brain shows no differentiation into hemispheres or lobes (Fig. 1-52). There is no falx, no interhemispheric fissure, and no superior or inferior sagittal sinus. The deep gray nuclei including the thalami form a single deep gray mass with no (or a rudimentary) third ventricle. The holoprosencephalon contains an undivided monoventricle with no septum pellucidum and no differentiation into lateral ventricles or horns. This monoventricle frequently continues posteriorly into a large dorsal cyst, which displaces the holoprosencephalon anteriorly, close to the frontal bones (Fig. 1-52). The intermediate *semilobar form* is the one most frequently seen in clinical practice. Semilobar holoprosencephaly shows partial development of the interhemispheric fissure, falx, and sagittal sinuses, especially posteriorly. The monoventricle

Copyright © 2003, Mosby, Inc. All rights reserved.

shows partial differentiation into posterior and temporal horns in a ''batwing'' configuration, but no septum pellucidum. A small, partly formed third ventricle partially subdivides the deep gray matter into paired, partially united thalami. A dorsal cyst may be present or absent. The least severe form, *lobar holoprosencephaly*, is characterized by variably complete formation of the interhemispheric fissure, falx, and dural sinuses and at least partial formation of the lobes of the prosencephalon, the horns of the lateral ventricles, and the third ventricle. The development of the brain is most nearly normal posteriorly and substantially less advanced anteriorly. By definition, however, all forms of holoprosencephaly exhibit continuity of the frontal cortex across the midline, where normally the two frontal lobes would be separate.

Correlations Between Facies and Holoprosencephaly

Patients with *alobar* holoprosencephaly show facial abnormalities in 83% to 90% of cases.[239, 264] These abnormalities may be any of the five major categories of facies but often are facies 1 to 3. Therefore, detection of cyclopia, ethmocephaly, or cebocephaly strongly suggests the presence of alobar holoprosencephaly. However, 10% to 17% of patients with alobar holoprosencephaly have milder atypical facial changes or normal facies.[265] Patients with *semilobar* holoprosencephaly show facial anomalies less often, in 30% of cases in some series.[265] These usually are the milder facies 4 and 5 (Fig. 1-54). Facies 3—cebocephaly—can be seen with semilobar holoprosencephaly. Patients with *lobar* holoprosencephaly usually have normal facies but may also show facies 4 or 5 or subtle findings such as a single central incisor.[244]

Osaka and Matsumoto[265] correlated the presence of facial anomalies with the type of holoprosencephaly. In this review, facial anomalies were considered to be clefting of the lip and palate, not milder forms. These authors found an imperfect correlation: facial anomalies were seen in 47 of the 100 cases (47%). In these cases the holoprosencephaly was alobar in 80%, semilobar in 10%, lobar in 0%, ''abortive'' in 0%, and unclassified in 9%. Facial anomalies

FIGURE 1-54 Normal facies with semilobar holoprosencephaly. **A**, Frontal view. This normal-appearing child was evaluated for the small bulge at the upper medial right orbit. **B**, Direct coronal noncontrast CT documents that the orbital lesion (*arrowhead*) is a small dermoid. Absence of the interhemispheric fissure led to MR imaging. **C**, Axial T2-weighted MR image shows semilobar holoprosencephaly with absence of the interhemispheric fissure and falx anteriorly, partial subdivision of a monoventricle into temporal and occipital horns posteriorly (batwing configuration), incomplete third ventricle (*3*), partial separation of the thalami (*arrows*) with union of the deep gray matter (*arrowhead*) anteriorly, and a dorsal cyst (*C*). (From Smith MM, Thompson JE, Naidich TP, Castillo M, Thomas D, Mukherji SK. Facies to remember. Cebocephaly with single midline proboscis. Alobar prosencephaly. Int J Neuroradiol 1996;2:251–263.)

VIEW IMAGE

Copyright © 2003, Mosby, Inc. All rights reserved.

were absent in 53 of the 100 cases (53%). In those patients with no facial anomalies, the holoprosencephaly was alobar in 8%, semilobar in 20%, lobar in 50%, ''abortive'' in 20%, and unclassified in 0%. In at least one study, four patients with concurrent Dandy-Walker cyst and holoprosencephaly had normal facies.[264]

FACIAL AND BRANCHIAL ARCH SYNDROMES

The syndromes of the first and second branchial arches manifest as deficiencies of tissue and as hypoplasias of the maxillary and mandibular arches.

Pathogenesis

Differences among the dysplasias of the first and second branchial arch derivatives may reflect differences in the time of insult with respect to neural crest cell migration and differences in the cells targeted.[266] In mice, neural crest cells destined for the first and second visceral arches begin to migrate out of the neural folds when the embryo has five to nine somites.[266] Exposure to retinoic acid at and just prior to this time causes malformations of the visceral arches that appear to constitute the Goldenhar oculoauriculovertebral (OAV) spectrum (see the section on Hemifacial Microsomia).[266] Exposure to retinoic acid later, after the migration of neural crest cells into the first and second visceral arches is nearly complete, affects the formation of cells from the ectodermal placodes associated with the first and second visceral arches.[266] Excessive cell death initially involving placode-derived cells appears to underlie mandibulofacial dysostosis (MFD) (see the section on Mandibulofacial Dysostosis [Treacher Collins Syndrome]).[266] The normal ganglia are composed entirely of neural crest cells. Placodal cells then migrate into the distal part of the ganglia, where they differentiate rapidly into neuroblasts, while the crest cells contribute to later-differentiating neurons, and supporting Schwann sheath cells and satellite cells.[266] MFD appears to be directly related to excessive and/or premature cell death in the cell populations derived from the first and second ectodermal placodes.[266] Subsequent deficiencies in the tissues that form the dorsal aspects of the maxillary and mandibular prominences of the first visceral arch and the dorsal aspect of the second visceral arch may result directly from localized tissue damage or secondarily from inadequate promotion of growth and/or cytodifferentiation.[266]

Hemifacial Microsomia (Goldenhar Syndrome, OAV Complex)

Concurrent auricular, ocular, and facial anomalies are found in a heterogeneous group of overlapping conditions. Goldenhar described the triad of (1) epibulbar choristomas, (2) preauricular skin appendages and pretragal blind-ending fistulae in association with (3) mandibular facial dysostosis, now called Goldenhar syndrome.[267–269] To these, Gorlin and colleagues added concurrent vertebral anomalies and renamed the complex oculo-auriculovertebral (OAV) *dysplasia*.[270] Rollnick and Kaye then added microtia and called the condition the OAV *complex*.[271] In similar fashion, unilateral hypoplasia of the face and transverse facial clefts, previously termed hemifacial microsomia (HFM), and bilateral, more nearly symmetrical bifacial microsomia (BFM), have also been incorporated into the expanded OAV complex.[272] Further work has linked the OAV complex with the VATER sequence.[272, 273]

HFM is the second most common facial birth defect after cleft lip and palate (Fig. 1-55).[274] Males are affected more frequently than females: (1.2 to 1.8) to 1. The OAV complex

VIEW IMAGE

FIGURE 1-55 Microtia and hemifacial microsomia in two patients. **A**, Microtia. The pinna is deformed. The face appears normal. **B**, Hemifacial microsomia. The line formed by the two palpebral fissures and the line formed by the mouth converge to the region of the deformed, hypoplastic pinna. The right orbit, right eye, and entire right side of the face are asymmetrically smaller. The skin tag falls along the line between the pinna and the mouth.

Copyright © 2003, Mosby, Inc. All rights reserved.

usually arises sporadically but may be familial in up to 21% of cases.[275] About 45% of patients have affected relatives, and 5% to 10% have affected sibs.[271] The specific mode of inheritance and the effect of environmental factors are hotly debated but may be autosomal or X-linked dominant in at least some cases.[276] Among 204 patients with malformations of the external ear (microtia), HFM constitutes 70.5%, isolated microtia 23.5%, Goldenhar syndrome alone 3%, and Goldenhar syndrome within the OAV complex 3% of cases.[275] Goldenhar syndrome accounts for approximately 19% of cases of HFM and 4% to 8% of all cases of OAV complex.[274, 277] The specific incidences of the OAV conditions are estimated at 1 per 3500 to 5600 births for Goldenhar syndrome and 1 per 45,000 live births for the OAV complex.[267]

The OAV spectrum is believed to develop during the first 4 wg, during the period of blastogenesis.[278] Its pathogenesis is unknown. Three theories have been offered[280]: 1. OAV could result from interference with the vascular supply to the region, notably the primordial stapedial artery, leading to local hemorrhage in the developing first and second branchial arches.[276, 279] 2. OAV could reflect impaired interaction between neural crest cells and the branchial arch mesenchyme.[276] 3. OAV could reflect mutations in the *Msx* genes. These genes are a class of homeobox genes expressed in cephalic neural crest cells prior to their migration to form the craniofacial mesenchyme and are critical for differentiation of first branchial arch ectoderm-mesenchyme.[276] Manipulation of the *Msx* genes in mice leads to major abnormalities in first branchial arch derivatives.[281, 282] Similar genes function throughout the body. At present, therefore, the *Msx* genes are candidate genes for the OAV complex and other craniofacial malformations.[276] Some similarity exists between bilateral OAV syndrome and hypoglycemia associated with diabetic embryopathy, but the children with hypoglycemia do not manifest the facial asymmetry typical of HFM-OAV complex.[283]

The stigmata of the OAV complex include anomalies of the face, ears, and eyes, with numerous concurrent malformations of the central nervous system (CNS) (15%), skeleton (41%), heart (26%), gut (12%), and lungs (9%).[284]

Face

Facial asymmetry is seen in about 65% of patients, is severe in 20%,[272] and progresses during childhood.[272] The asymmetry may *not* be appreciable in the infant, but it becomes evident by age 4 years in most cases.[285] The hypoplasia may be predominantly vertical or predominantly transverse, but most patients show mixed vertical-transverse hypoplasia, with the greatest hypoplasia along the oblique line from the (residual) ear to the corner of the mouth (Fig. 1-55). Most HFM is unilateral (up to 94% in some series), but the microsomia may be bilateral in 16% to 35%.[286] The right side of the face is affected far more often than the left. In the *upper face*, the zygoma and the lateral maxilla are most affected.[287–289] The orbits are approximately equal in size in 96%, but differ in their vertical position in two thirds and in their horizontal position in 15% of HFM patients.[290] The interorbital distance remains normal. The nose and columella deviate toward the hypoplastic side. In the *lower face*, the mandible is affected most severely, so *mandibular* hypoplasia accounts for most of the asymmetry seen in HFM (Fig. 1-56). The ramus of the mandible is more severely hypoplastic than the body, so the mandible acquires a steeper slope. These changes cause anteroinferomedial displacement of the temporomandibular joint, lateral rotation of the lower jaw, and posterior displacement of the mandibular angle.[287–289]

The muscles of mastication show reduced volume that is ipsilateral to the side of HFM and roughly proportional to the degree of mandibular hypoplasia. Muscle mass is reduced about 50% in each of the masseter, temporalis, medial pterygoid, and lateral pterygoid muscles in grade 3 mandibular hypoplasia, but muscle mass is symmetrical and nearly normal in patients with only minimal manidibular hypoplasia.[291]

Sessile or pedunculated preauricular skin tags are found between the ear and the corner of the mouth in 20% to 88% of cases.[267] The skin tags are unilateral in 37% and bilateral in 25% of Goldenhar patients (Fig. 1-55). Skin tags may also arise at aberrant sites: retroauricular, nostril, nasal tip, and eyelids. They occasionally are seen in patients with apparently normal ears (4%). Preauricular and facial pits occur in 7% and preauricular sinuses in 6% to 29% of patients, with or without associated skin tags.

Mouth

The mouth may have a short transverse dimension (microstomia) or show marked elongation by unilateral or bilateral transverse facial clefts (Tessier No. 7) (macrostomia) (Figs. 1-15, 1-57). These clefts may appear as open clefts extending well lateral to the vermilion or as thickened fibrous bands on the buccal mucosa, Macrostomia is present in 17% to 62% of HFM patients. Cleft lip and/or cleft palate is common in the Goldenhar group (20%) and those with the full OAV complex (15% cleft palate, 7% cleft lip with or without cleft palate). The upper lip may have a shortened vertical height.[267] The palatal and tongue muscles may be hypoplastic, paralyzed, or both. The palate deviates to the affected side in 39% of HFM patients. Bifid tongue, bifid uvula, and double lingual frenulum have also been reported. About 35% of patients suffer velopharyngeal insufficiency secondary to asymmetric movement of the palate and the lateral pharyngeal wall. The ipsilateral parotid and other salivary glands may be normal, agenetic, or displaced. Ectopic salivary gland tissue may be present as a nasal mass in Goldenhar syndrome. There may be salivary fistulae.[267]

HFM often includes malocclusion and buccal crossbite on the affected side.[292] Dental maturation is asymmetric in half of these patients; however, the side of greater maturation may be either the affected or the unaffected side with equal frequency.[292] The teeth show defects in the primary enamel.[292] The distribution of these defects is concordant with the laterality of the craniofacial anomalies and is most pronounced on the maxillary incisors.[292]

Copyright © 2003, Mosby, Inc. All rights reserved.

Ears

External Ear

Microtia signifies an ear that is too small and/or malformed (Figs. 1-55 and 1-56).[286] Isolated nonsyndromal microtia is found in 0.016% of all newborns. Approximately 3.1% of microtia patients have Goldenhar syndrome, but microtia is found in up to 68% of Goldenhar patients. The microtia is typically unilateral (66%). Where it is bilateral, it is asymmetric in 65% to 90% of cases. The severity of the malformatiom in the external auditory canal parallels the change in the auricle. The external auditory canal is normal in 98% of those with a normal auricle and abnormal in 58% of grade 1, 100% of grade 2, and 86% of grade 3 microtia.[267]

Middle Ear

The severity of ossicular chain malformation parallels the severity of microtia and of mandibular hypoplasia. The ossicular chain is normal in 96% of those with normal auricles and abnormal in 52% of grade 1, 89% of grade 2, and 95% of grade 3 microtia. Radiologically, middle ear structures are abnormal in 70% of cases. Approximately one third of HFM patients have normal hearing. The rest show sensorineural hearing loss (6% to 16%), mixed conductive-

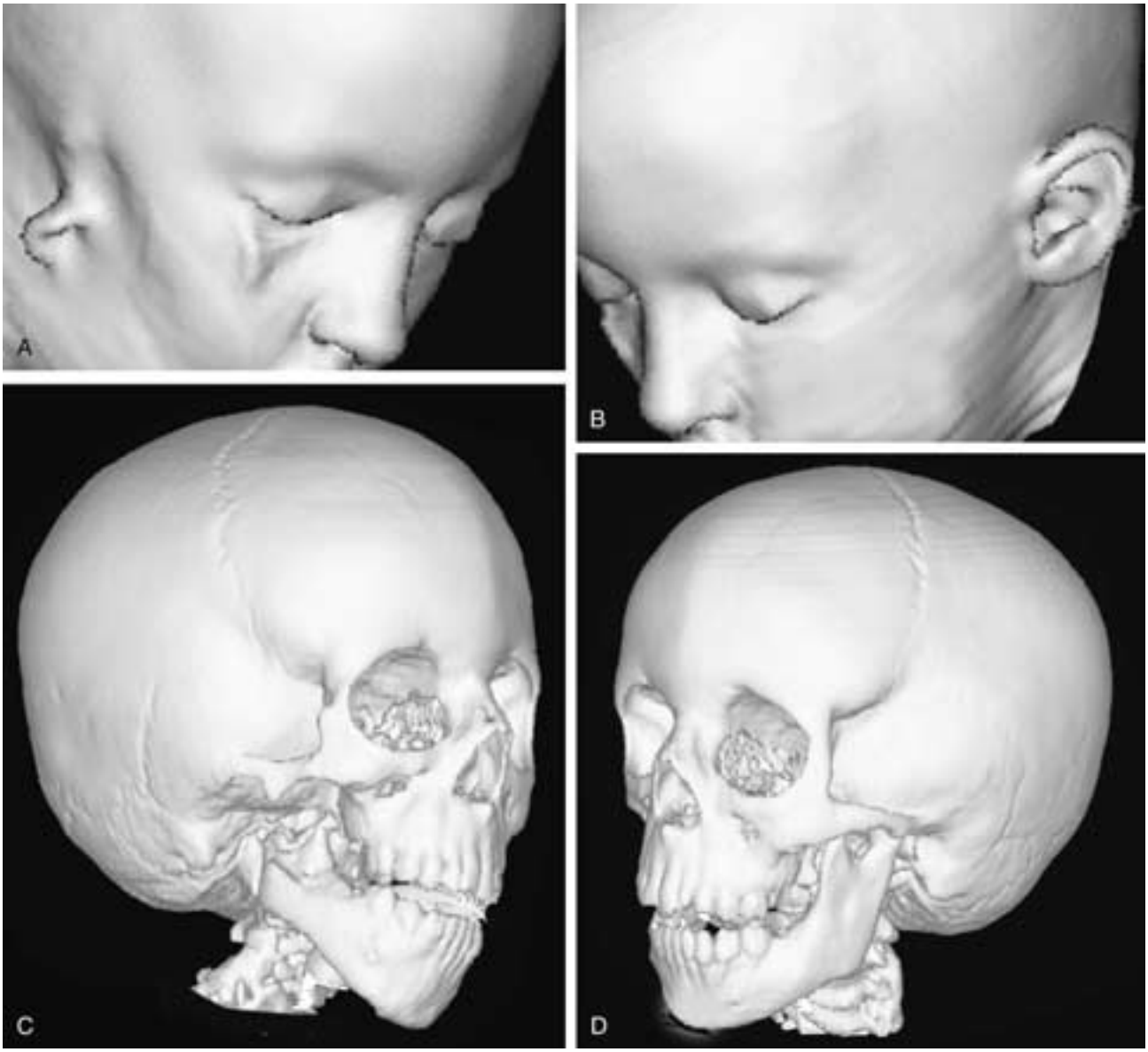

FIGURE 1-56 Goldenhar syndrome with vertebral malsegmentation. **A** to **D**, Three-dimensional CT surface renderings of the skin (**A** and **B**) and bone (**C** and **D**) of the two sides show right hemifacial microsomia with right microtia and hypoplasia of the right zygomatic arch, right maxilla, and right mandible, especially the angle and condylar process of the mandible. The lower right eyelid shows depression of the skin surface that corresponded to a coloboma.

VIEW IMAGE

Copyright © 2003, Mosby, Inc. All rights reserved.

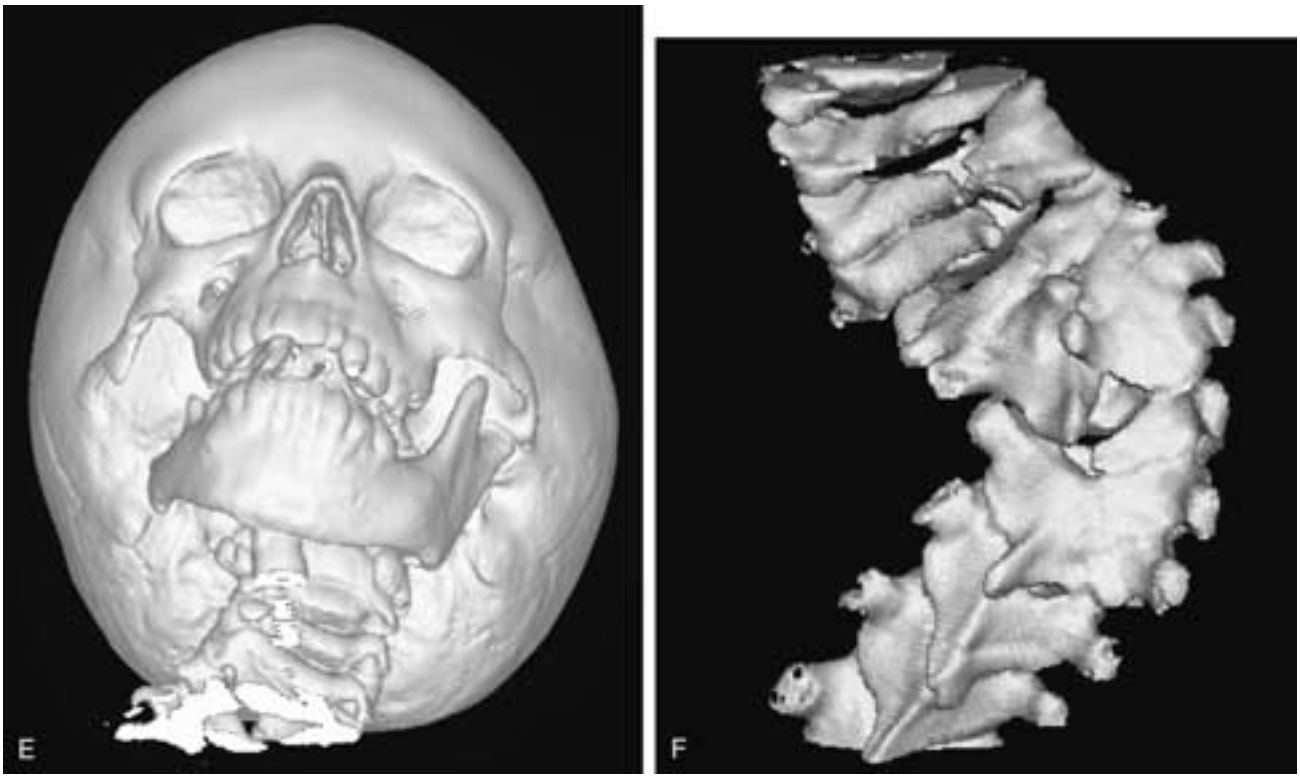

VIEW IMAGE

FIGURE 1-56 *Continued.* **E**, Frontal bone surface shows the marked deficiency of the right facial skeleton. **F**, The thoracolumbar spine shows malsegmentation and sharp-angle scoliosis.

sensorineural hearing loss (6%), or purely conductive hearing loss.[293]

Inner Ear

Inner ear anomalies are present in at least 6% of patients with Goldenhar and HFM syndromes (Fig. 1-57).[294, 295] Seventh nerve palsy is seen in 45% of HFM patients and correlates with the severity of the microtia. Radiologically, the facial nerve canal is abnormal in 83% of patients: 7% of grade 1 microtia, 38% of grade 2 microtia, and 63% of grade 3 microtia. The vestibules and semicircular canals may be dilated or small. The common crus may be absent.[296] The internal auditory canal can be asymmetrically smaller, shorter, and inclined upward. The cochlea and vestibule may be abnormal or absent.

Eyes

Characteristic ocular features of Goldenhar syndrome include epibulbar choristomas, colobomas of the upper lid, impaired ocular motility, and dacryostenosis (Fig. 1-58). Epibulbar choristomas are congenital, benign, nonproliferative masses of normal epidermal and connective tissue structures that are situated at abnormal sites. Their etiology is unknown. Choristomas are the most common epibulbar tumor in children.[269, 275, 297, 298] They are found in 4% to 32% of Goldenhar cases, 21% of HFM cases,[290] and 88% of OAV complex cases. Of 50 children with ocular ''dermoids,'' 46% had HFM. Half of these (22%) had signs of Goldenhar syndrome. Among 127 personal and published cases of Goldenhar, Feingold and Baum[269] found that 76% had dermoids (53% unilateral, 23% bilateral) and 47% had lipodermoids (28% unilateral, 19% bilateral). Most choristomas are subconjunctival (59%), often encroaching on the corneo-scleral limbus. A smaller number are limbal (41%). None are corneal.[275] A few arise on the eyelids.

Unilateral or bilateral colobomas of the *upper* lid are seen in 11% to 71% of Goldenhar cases, usually in the medial third or at the junction of the medial and middle thirds (Fig. 1-58).[275] *Lower*-lid colobomas may be seen in 6% of Goldenhar patients' eyes without concurrent upper-lid colobomas, but specific involvement of the lower lid suggests a diagnosis of MFD (Treacher Collins syndrome) rather than the Goldenhar-OAV complex.[293, 299] Other ocular features include ectropion (eversion of the lid margin) (25%), unilateral blepharostenosis (11%), blepharoptosis (2%), anophthalmia/cryptophthalmia/microphthalmia (2% to 12%), impaired ocular motility including esotropia, exotropia, and Duane's retraction syndrome (presumably secondary to hypoplasia of the oculomotor nerve or brain stem nuclei) (10% to 19%), and dacryostenosis (with or without lacrimal fistulae secondary to obstruction at the nasolacrimal duct or lower canaliculus) (11%).[275]

Copyright © 2003, Mosby, Inc. All rights reserved.

FIGURE 1-57 Hemifacial microsomia with some bilateral elements. **A** and **B**, This newborn girl shows bilateral preauricular skin tags (removed in **B**) and bilateral transverse facial clefts with macrostomia. She had malformed pinnae bilaterally, more severe on the right, and decreased hearing bilaterally, with an absent response on brainstem auditory-evoked potentials at 90 and 105 dB bilaterally. **C** to **E**, Serial coronal T2-weighted MR images, displayed from posterior to anterior, show hypoplasia of the external auditory canals bilaterally, large vestibules, and malformed lateal semicircular canals bilaterally. (**A** and **B** from Naidich TP, Smith MS, Castillo M, Thompson JE, Sloan GM, Jayakar P, Mukherji SK. Facies to remember. Number 7. Hemifacial microsomia. Goldenhar syndrome. OAV complex. Int J Neuroradiol 1996;2:437–449.)

VIEW IMAGE

Copyright © 2003, Mosby, Inc. All rights reserved.

VIEW IMAGE

FIGURE 1-58 Hemifacial microsomia. Goldenhar syndrome. This 4-month-old girl shows a large coloboma of the medial portion of the left upper lid (*between the curved white arrows*) and a whitish choristoma (*straight white arrow*) that straddles the corneoscleral limbus inferotemporally. There is a second, small coloboma of the lower lid medial to the choristoma. The caruncle is unusually prominent. (Case courtesy of Dr. Myron Tannenbaum, Miami, Florida.) (From Naidich TP, Smith MS, Castillo M, Thompson JE, Sloan GM, Jayakar P, Mukherji SK. Facies to remember. Number 7. Hemifacial microsomia. Goldenhar syndrome. OAV complex. Int J Neuroradiol 1996;2:437–449.)

Central Nervous System

Total or partial peripheral seventh nerve palsies have been seen in 12% of microtia patients and 22% to 45% of patients with HFM.[290] Seventh nerve palsies correlate well with both the severity of mandibular hypoplasia and the presence of sensorineural hearing loss. Facial paralysis is found in about 50% of grades 1 and 2 mandibular hypoplasia, increasing to almost 70% in grade 3. The trigeminal nuclei and nerve and other cranial nerves may also be deficient. Other CNS malformations, found in 5% to 15% of patients with the OAV complex, include hydrocephalus, absent septum pellucidum, absent corpus callosum, Arnold-Chiari and Dandy Walker malformations, microcephaly with partial anencephaly, anterior cephaloceles, posterior cervicooccipital cerebellocele with vermian agenesis, lipoma of the corpus callosum and vermis, frontal lobe hypoplasia, and unilateral arrhinencephaly ipsilateral to the side of the Goldenhar microtia and HFM.[267]

Plagiocephaly

Approximately 10% of patients with HFM show deformation of the frontal bone on the side of the predominant HFM.[300] The resultant HFM plagiocephaly phenotype mimics coronal synostosis, except that the affected ear is displaced anteroinferiorly, as expected for HFM, rather than posteroinferiorly, as expected for coronal synostosis. These plagiocephalic patients have orbital dystopia (86%), more severe microtia (57%), and a 43% incidence of parenchymal CNS anomalies such as callosal agenesis, encephalocele, and hydrocephalus. Goldenhar syndrome may be found in association with frontonasal dysplasia.[272]

Mandibulofacial Dysostosis (Treacher Collins Syndrome, Franceschetti-Zwalen-Klein Syndrome)

MFD is an autosomal dominant syndrome found in 1 per 50,000 live births. It is now linked to the *TCS* (*TCOF1*) gene at chromosome 5q31.3-q32 and shows variable expression within families.[10, 301] Approximately 60% of cases arise as new mutations. The mutation is thought to interfere with coding for a protein designated *treacle*, leading to haploinsufficiency for this protein.[301] Multiple different mutations within this gene may give rise to the Treacher Collins syndrome.[10] Allelic mutations in the *TCS* gene could explain the partial clinical overlap of the Treacher Collins syndrome with Goldenhar syndrome and Nager acrofacial dysostosis (see the section on Nager Acrofacial Dysostosis Syndrome), but this mechanism has not been proved.[301]

The obligatory features of MFD are marked hypoplasia of the malar bone, with or without malar clefts, hypoplasia of the mandibular ramus and condyle, marked antimongoloid slant of the palpebral fissures, obliteration of the frontonasal angle, colobomas of the lateral third of the *lower* lid with or without those of the upper lid, and/or malformations of the eyelashes (Fig. 1-59).[266, 293, 299, 302] Other stigmata include inferior extension of the hairline onto the cheeks, malformed auricles, deformity or absence of the external auditory canal, malformed middle ear and ossicles with conductive hearing loss, blind fistulae and/or skin tags situated between the auricle and the corner of the mouth, microstomia or macrostomia, abnormal dentition with malocclusion, and antegonial notching of the mandible.[266, 293, 299, 300] Orbital hypoplasia, microphthalmos, lacrimal duct atresia, craniosynostoses, and skeletal malformations have also been reported. Miscarriage or early death is common.[302] One tries to differentiate MFD from the Goldenhar-HFM-OAV complex by observing that MFD mandibles are symmetric bilaterally, with little variation among patients. Patients with MFD show far greater frequency of *lower*-lid colobomas, *marked* antimongoloid slant of the palpebral fissures, and infrequent choristomas, skin tags, and upper-lid colobomas. Facial asymmetry, phenotypic characteristics, and lack of inheritance patterns distinguish bifacial microsomia from MFD.[267]

Branchio-Oto-Renal Syndrome (Ear Pits-Deafness Syndrome)

Branchio-oto-renal syndrome (BORS) is characterized clinically by ear anomalies, hearing loss, preauricular pits, branchial fistulae, lacrimal duct stenoses, and renal dysplasia. There is variable expression within families; first-degree relatives may show varying features of HFM or BORS, but hemifacial microsomia is not a component of BORS itself. The syndrome is inherited as an autosomal dominant trait with high penetrance and variable expressivity. Patients with BORS show multiple different mutations and deletions in the *EYA1* gene at 8q13.3.[10] The gene affected is analogous to the *Drosophila eyes absent* gene.[10]

Copyright © 2003, Mosby, Inc. All rights reserved.

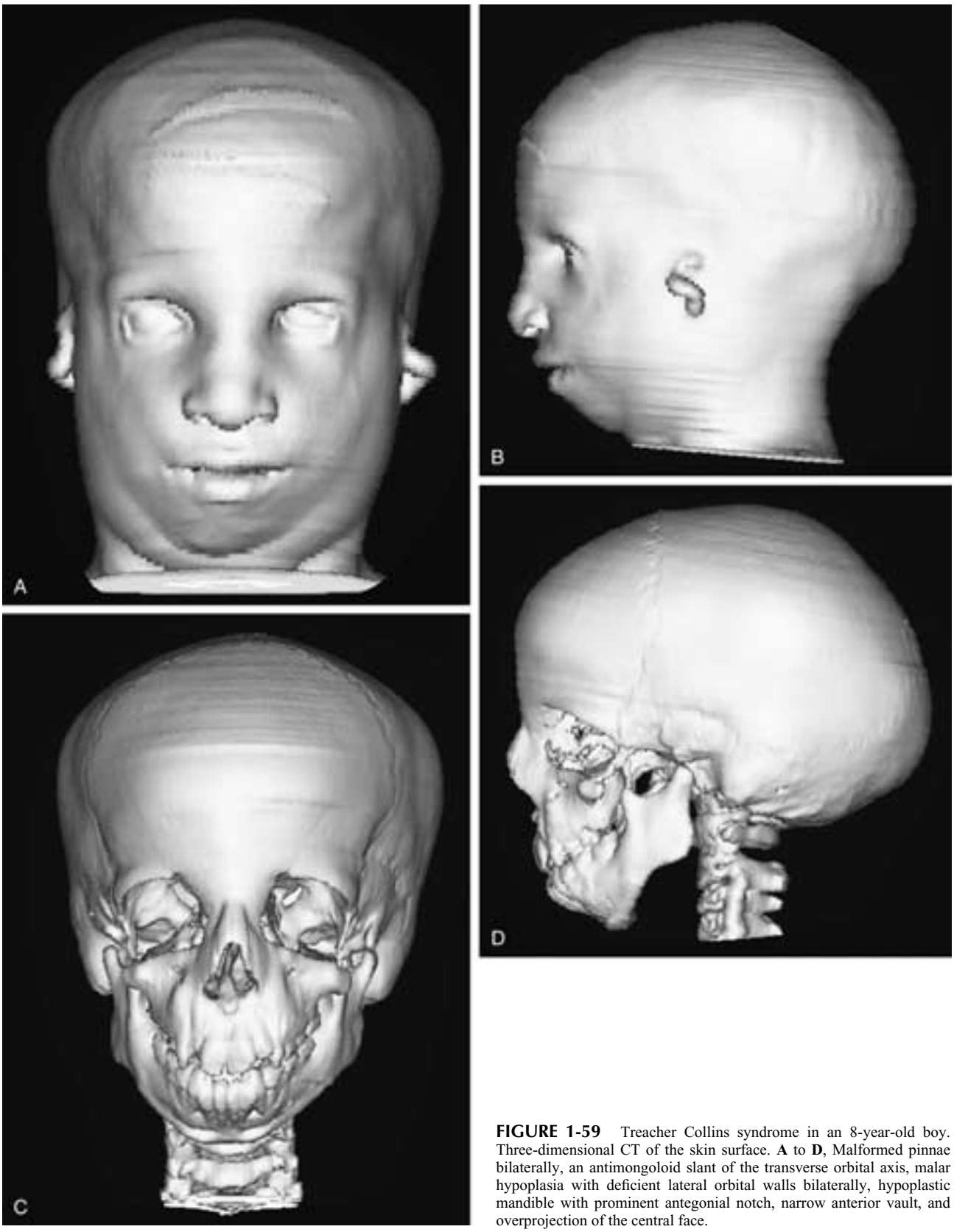

FIGURE 1-59 Treacher Collins syndrome in an 8-year-old boy. Three-dimensional CT of the skin surface. **A** to **D**, Malformed pinnae bilaterally, an antimongoloid slant of the transverse orbital axis, malar hypoplasia with deficient lateral orbital walls bilaterally, hypoplastic mandible with prominent antegonial notch, narrow anterior vault, and overprojection of the central face.

VIEW IMAGE

Copyright © 2003, Mosby, Inc. All rights reserved.

Nager Acrofacial Dysostosis Syndrome (AFD Nager)

AFD Nager is a form of MFD associated with radial defects. The condition may be sporadic or familial.[303] Craniofacial features include mandibular and malar hypoplasia, dysplastic ears with defects of the external auditory canal, conductive deafness, downward slanting of the palpebral fissures, absent eyelashes in the medial one third of the lower lids, microstomia, cleft palate, and a tongue-shaped extension of hair onto the upper cheek. The radial defects range from thumb hypoplasia to absent radial ray. Some patients with Goldenhar syndrome and radial defects appear to overlap with those with AFD Nager.[303]

Pierre Robin Sequence

The Pierre Robin sequence is characterized by micrognathia, glossoptosis, and cleft palate (Fig. 1-60). Girls are affected more than boys (female : male ratio = 3 : 2).[304] The sequence presents clinically as difficulty breathing, difficulty swallowing, and recurrent attacks of cyanosis.[304] Pierre Robin patients typically have palatal cleft-

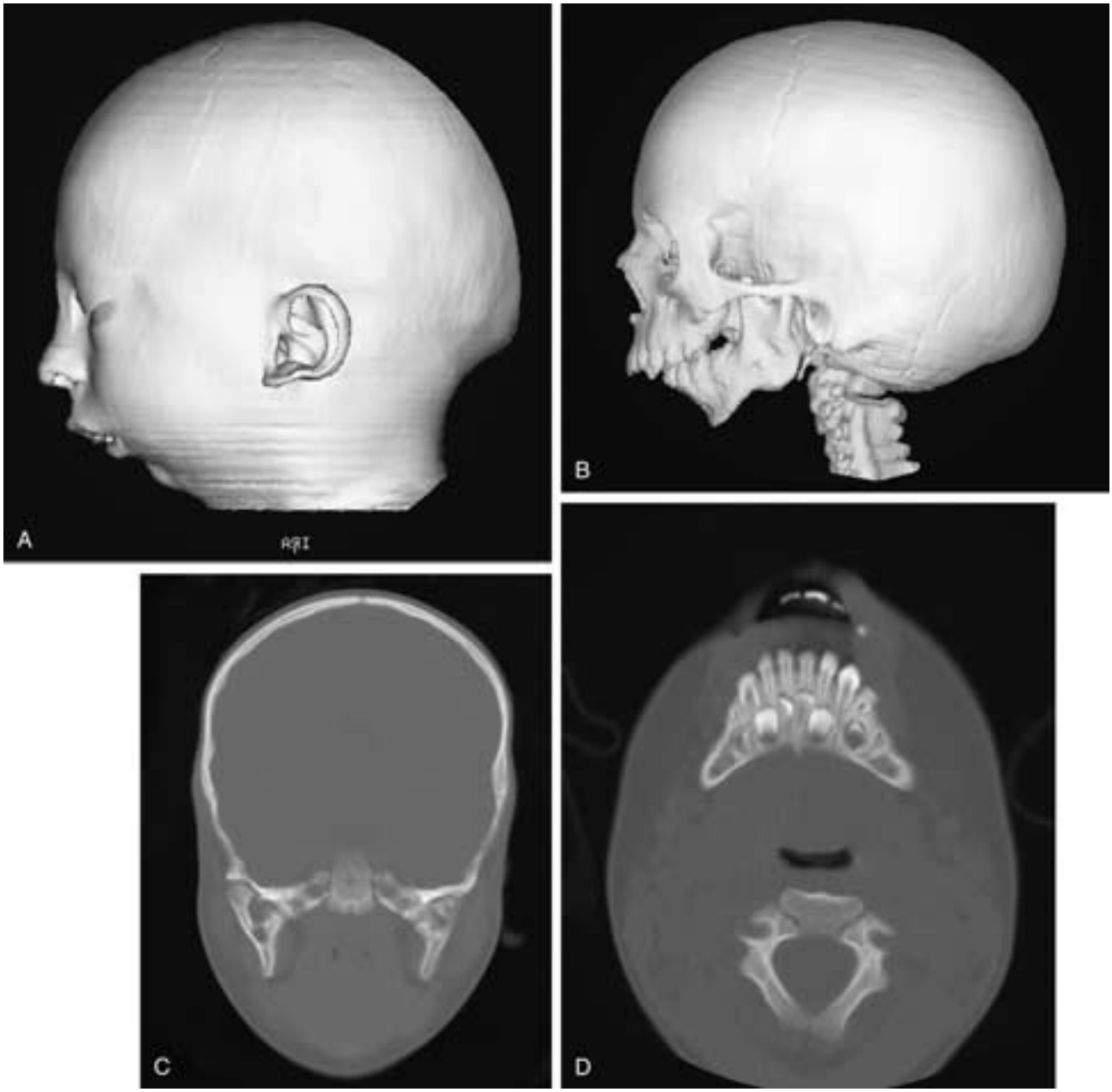

VIEW IMAGE

FIGURE 1-60 Pierre Robin sequence in a 2½-year-old boy with no catch-up growth of the mandible. **A** and **B**, Lateral 3D CT of the skin surface (**A**) and facial skeleton (**B**) show severe retrognathia and micrognathia. **C**, Coronal bone CT shows marked butressing of the mandibular condyle. **D**, Axial CT section shows a vertical orientation of the maxillary incisors but a horizontal course of the mandibular dentition.

Copyright © 2003, Mosby, Inc. All rights reserved.

Table 1-13
RELATIVE FREQUENCIES OF SYNDROMIC AND NONSYNDROMIC PRIMARY CRANIOSYNOSTOSES (1976–1999) (*N* = 2137)

Nonsyndromic Synostoses	Number	Percent	Syndromic Synostoses	Number	Percent
Scaphocephaly	870	40.7	Apert syndrome	88	4.1
Trigonocephaly	334	15.6	Crouzon syndrome	98	4.6
Lambdoid synostosis	18	0.8	Pfeiffer syndrome	30	1.4
Plagiocephaly	252	11.8	Saethre-Chotzen syndrome	54	2.5
Brachycephaly	107	5.0	Craniofrontonasal syndrome	22	10
Oxycephaly	147	6.9	Other syndromes	36	1.7
Complex	81	3.8	—		
Subtotal	1809	84.7%	Subtotal	328	15.3%

From Renier D et al. Management of craniosynostosis. Childs Nerv Syst 2000;16:645–658.

ing that may involve both the hard and soft palates or the soft palate only.[304] In 36 Brazilian children with isolated Pierre Robin sequence, all patients showed palatal clefting. The clefts were U-shaped in 27 (75%) (26 complete, 1 incomplete), and V-shaped in 9 (25%). The family history was positive for cleft lip/cleft palate in 27.7% of cases.[304] Thus, ''the primary event occurring in isolated Robin sequence may be cleft palate and not micrognathia. . . .''[304] The Pierre Robin sequence may be observed as an isolated sequence, as one of multiple nonsyndromal defects, or as one component of Stickler syndrome, velo-cardio-facial syndrome (22q11 deficiency), or other named syndromes.[304] Marques et al.[304] suggest that a multifactorial polygenic inheritance best accounts for the features of the Pierre Robin sequence.

PREMATURE CRANIAL SYNOSTOSES

Premature cranial suture synostosis signifies premature closure of one or more of the cranial sutures from any cause.[305, 306] Primary cranial synostoses occur in the absence of underlying brain or metabolic disease. Secondary cranial synostoses occur as the indirect consequence of reduced intracranial volume, often after shunting of hydrocephalus or a cerebral insult. Metabolic cranial synostoses arise from underlying disorders such as vitamin D–related rickets, familial hypophosphatasia, hyperthyroidism, and idiopathic hypercalcemia.[306, 307] Primary synostoses may occur as isolated phenomena (nonsyndromic synostosis, 85%) or as one part of multimalformation syndromes (syndromic synostosis, 15%).[308] Table 1-13 summarizes the distribution of 2137 primary craniosynostoses.[308]

Normally, the sutures become narrower and the fontanelles become smaller as the skull matures (Fig. 1-61). Closure of the suture does not occur along the whole length simultaneously, nor does it necessarily involve the entire depth.[309] The inner endosteal aspect of a suture appears to fuse in a more orderly fashion, whereas the outer ectocranial serrated surface shows greater variation.[309] The fontanelles normally close early: the posterior fontanelle by 8 weeks, the anterolateral fontanelle by 3 months, the anterior fontanelle by 15 to 18 months, and the posterolateral fontanelle by 2 years.[310] The mendosal suture closes first, at several weeks after birth. The metopic suture begins to close during the second year and is completely closed during the third year.[310] The sagittal, coronal, and lambdoid sutures normally close much later, in early to midadulthood.[309] The sagittal suture begins to close at 22 years, the coronal suture at 24 years, and the lambdoid suture at 26 years.[309] These sutures may become fully closed only at 35, 41, and 47 years, respectively.[309] On plain X-rays, the sagittal suture is frequently closed after 35 to 40 years and is usually closed after 50 years.[309] The coronal and lambdoid sutures are frequently closed, at least in part, after 50 years.[309] The sutures bordering the squamous portion of temporal bone never close completely, even in the elderly.[309] However, in analyzing cases of craniosynostosis, it is important to bear in mind that functional closure of the sutures usually occurs at about the time the fontanelles close, well before true bony synostosis develops.

Early descriptions of premature craniosynostosis were based on the physical appearance of the patient.[305, 311–314] Such descriptions of head shape and patient appearance, however, are not specific and do not necessarily predict whether specific sutures will be fused on imaging studies. Terms in common use will now be discussed.

Skull Shape

Scaphocephaly (Dolichocephaly, Canoe Head)

This signifies elongation of the calvarium in the anteroposterior (AP) direction, with narrowing in the transverse dimension (Fig. 1-62A). It usually results from premature closure of the sagittal suture but may reflect, instead, prior deformation of the head due to prematurity, soft bones, poor head control, and prolonged decubitus position of the premature infant's head in the intensive care unit.[311]

Trigonocephaly (Ax Head, Keel-Shaped Deformity)

This signifies sharp, anteriorly directed ridging of the midline frontal contour, usually from metopic synostosis (Fig. 1-62B).[314]

Brachycephaly (Broad Head)

This signifies abnormal widening of the transverse diameter of the calvarium, with a shortened AP dimension.

Copyright © 2003, Mosby, Inc. All rights reserved.

It typically results from coronal or lambdoidal synostoses that limit growth in the AP direction (Fig. 1-62C).

Oxycephaly (Turricephaly, Tower Head)

This signifies superior elongation of the calvarium. It is usually associated with bilateral coronal or bilateral lambdoid synostoses, which redirect brain growth anteriorly toward the anterior fontanelle-metopic suture complex or posteriorly toward the posterior fontanelle and lambdoid sutures.

Plagiocephaly (Skew Head, Asymmetric Head)

This signifies asymmetric contour of the calvarium from (1) positional deformation of the skull, (2) unilateral suture synostosis (usually unilateral coronal synostosis), or (3) asynchronous asymmetric synostoses of multiple sutures

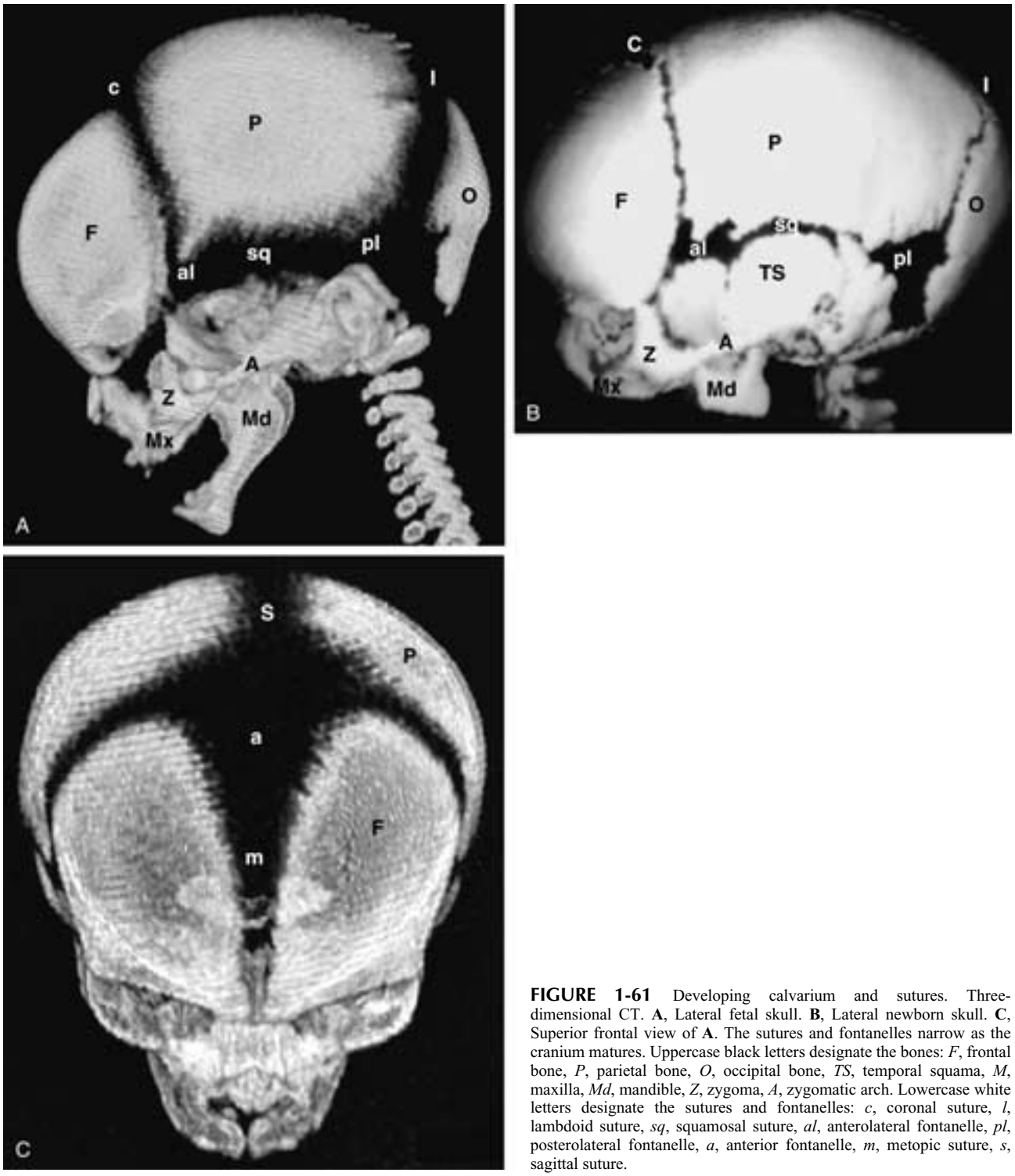

FIGURE 1-61 Developing calvarium and sutures. Three-dimensional CT. **A**, Lateral fetal skull. **B**, Lateral newborn skull. **C**, Superior frontal view of **A**. The sutures and fontanelles narrow as the cranium matures. Uppercase black letters designate the bones: *F*, frontal bone, *P*, parietal bone, *O*, occipital bone, *TS*, temporal squama, *M*, maxilla, *Md*, mandible, *Z*, zygoma, *A*, zygomatic arch. Lowercase white letters designate the sutures and fontanelles: *c*, coronal suture, *l*, lambdoid suture, *sq*, squamosal suture, *al*, anterolateral fontanelle, *pl*, posterolateral fontanelle, *a*, anterior fontanelle, *m*, metopic suture, *s*, sagittal suture.

VIEW IMAGE

Copyright © 2003, Mosby, Inc. All rights reserved.

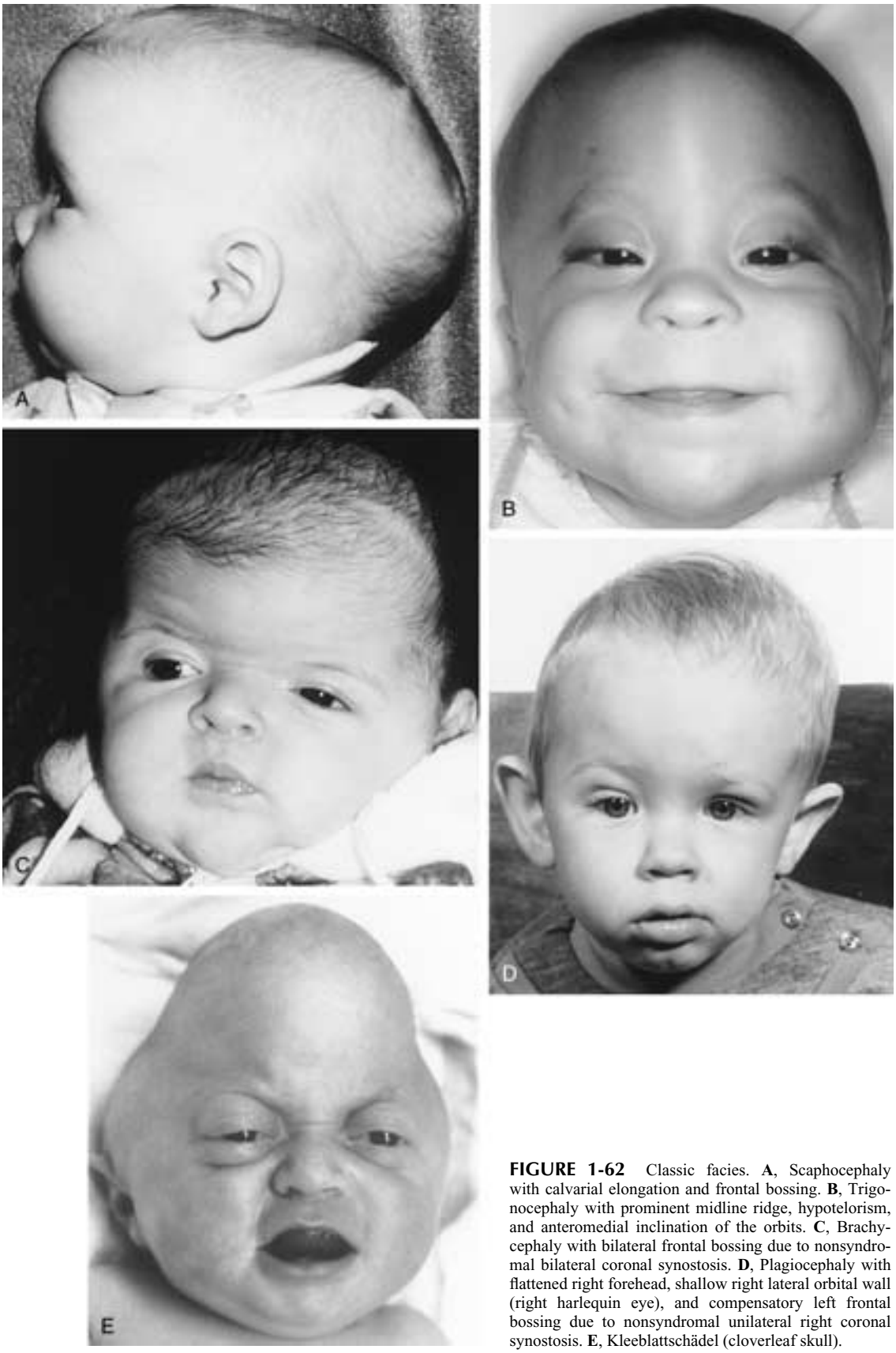

FIGURE 1-62 Classic facies. **A**, Scaphocephaly with calvarial elongation and frontal bossing. **B**, Trigonocephaly with prominent midline ridge, hypotelorism, and anteromedial inclination of the orbits. **C**, Brachycephaly with bilateral frontal bossing due to nonsyndromal bilateral coronal synostosis. **D**, Plagiocephaly with flattened right forehead, shallow right lateral orbital wall (right harlequin eye), and compensatory left frontal bossing due to nonsyndromal unilateral right coronal synostosis. **E**, Kleeblattschädel (cloverleaf skull).

VIEW IMAGE

Copyright © 2003, Mosby, Inc. All rights reserved.

bilaterally (Fig. 1-62D**)**. At present, the most common cause of cranial asymmetry is a positional deformation of the posterior aspect of the head designated posterior positional plagiocephaly. At present, therefore, the most common referral for possible synostosis is a benign, remediable positional deformation of the skull, not a true premature suture synostosis.[307–313]

Kleeblattschädel (Cloverleaf Skull)

This signifies a trefoil deformity of the calvarium related to severe constriction of calvarial growth at the coronal, lambdoid, and/or squamosal sutures bilaterally. In this condition, remarkable expansion of the temporal fossae inferolateral to the orbits creates the lateral lobes of the cloverleaf, while redirection of growth toward the sagittal suture and fontanelles raises the midline superior lobe (Fig. 1-62E). Exorbitism is often marked. Kleeblattschädel is found most frequently in the syndromal forms of craniosynostosis.

Nonsyndromic Primary Craniosynostoses

Nonsyndromic synostoses constitute 85% of all primary craniosynostoses (Table 1-13). Premature sagittal, coronal, and metopic synostoses are the most frequent forms. Lambdoid synostosis is least common (1% to 3%), affects the midface only incidentally, and will not be discussed specifically.

Premature Sagittal Synostosis

Premature sagittal synostosis is found in 2 to 10 per 10,000 live births and accounts for 40% to 70% of all nonsyndromal craniosynostoses.[306, 313] From 6% to 10% of cases are familial, with autosomal dominant inheritance and 38% penetrance. There is a male predominance (70% to 85% of cases).[313] The abnormal suture is often closed at birth. This restricts transverse growth of the skull, so the patients show scaphocephaly. A palpable ridge or indentation may mark the site of closure. Compensatory growth at the adjacent coronal and lambdoid sutures may lead to frontal bossing, occipital bossing, or both.[313] The anterior fontanelle is often closed. The sphenoid wings and orbits are not affected. As a result, these patients show very prominent foreheads that project far anterior to the orbits but remarkably little facial asymmetry. In contrast to other synostoses, concurrent intracranial abnormalities are exceptionally rare.

Premature Unilateral Coronal Synostosis

Premature unilateral coronal synostosis occurs in 0.7 to 4.8 per 10,000 births and accounts for 14% to 55% of synostoses.[313] Most cases are sporadic. Only 6.6% to 14.4% of cases are familial, with 60% penetrance. There is a slight female predominance (57% to 68%). The curvature of the coronal suture normally extends into the skull base along the adjoining sphenozygomatic, sphenofrontal, and sphenoethmoidal sutures. Unilateral coronal synostosis typically causes growth restriction along much of this arc unilaterally, leading to flattening of the forehead, zygoma, and orbit on the affected side (Figs. 1-62D and 1-63).[313] The eye and eyebrow appear to be displaced up and back (harlequin eye). Compensatory contralateral frontal bossing displaces the contralateral eye inferolaterally. These patients commonly show mild exorbitism, vertical strabismus, horizontal strabismus, and amblyopia.[313] Bone thickening at and surrounding the closed suture may cause a palpable coronal ridge and temporal prominence, but such thickening is far less apparent than is the midsagittal ridging associated with scaphocephaly. The ipsilateral anterior fossa is small. The ipsilateral temporal fossa is rotated toward the midline. The root of the nose is drawn ipsilaterally unless concurrent involvement of the frontosphenoid suture deviates the nose to the opposite side. The ipsilateral maxilla may show vertical hypoplasia. The ipsilateral ear (tragus) is pulled antroinferiorly. The anterior fontanelle deviates to the opposite side. Torticollis is found in about one quarter of these cases.[313]

Premature Metopic Synostosis

Premature metopic synostosis occurs in 1 to 10 per 70,000 births and accounts for 5% to 20% of all cranial synostoses. It is characteristically sporadic, with only 2% to 6% of cases showing familial inheritance, either as an autosomal recessive trait or as an autosomal dominant trait, with very low penetrance.[313] Closure of the metopic suture restricts expansion of the frontal midline, so these patients manifest symmetric lateral sloping of the forehead, short anterior fossa, forward bowing of the coronal sutures, orbital hypotelorism, and ethmoid hypoplasia (Figs. 1-62B and 1-64). The crista galli remains intact. The nasal septum and facial midline are usually straight. The medial walls of the orbits are thickened and rise unusually high. Therefore, the superomedial corners form the highest points of the orbital roofs, and the lateral orbits fall away inferiorly. The degree of orbital deformity correlates with the wedging of the forehead. The frontal lobes, frontal sulci, and ventricles are usually compressed. There may be callosal dysgenesis, hydrocephalus, or other intracranial anomalies.

Syndromic Craniosynostosis (Craniofacial Dysostosis)

The term *craniofacial dysostosis*[2, 10, 307, 315–344] identifies a group of syndromes that exhibit premature synostoses of cranial sutures as one prominent feature. More than 100 such syndromes are recognized.[3] Together they account for 15% of all primary craniosynostoses.[308] Traditionally, craniofacial dysostoses have been classified by their characteristic phenotypes and named by author or place as Crouzon, Apert, Saethre-Chotzen, Pfeiffer, Jackson-Weiss, Boston, and Muenke (Adelaide) syndromes (Fig. 1-65).[321] Recent work shows that such phenotypic classification is imprecise. Mutations of different genes involved in the same pathway create similar phenotypes. Identical mutations in fibroblast growth factor receptor 2 (FGFR2) have been found in patients classified phenotypically as having Pfeiffer and Crouzon syndromes, and in patients classified phenotypically as having Jackson-Weiss and Crouzon syndromes.[10] Therefore, the eponymous craniosynostotic syndromes should now be regarded as phenotypic extremes of FGFR and other mutations, not as nosologic entities. With the

Copyright © 2003, Mosby, Inc. All rights reserved.

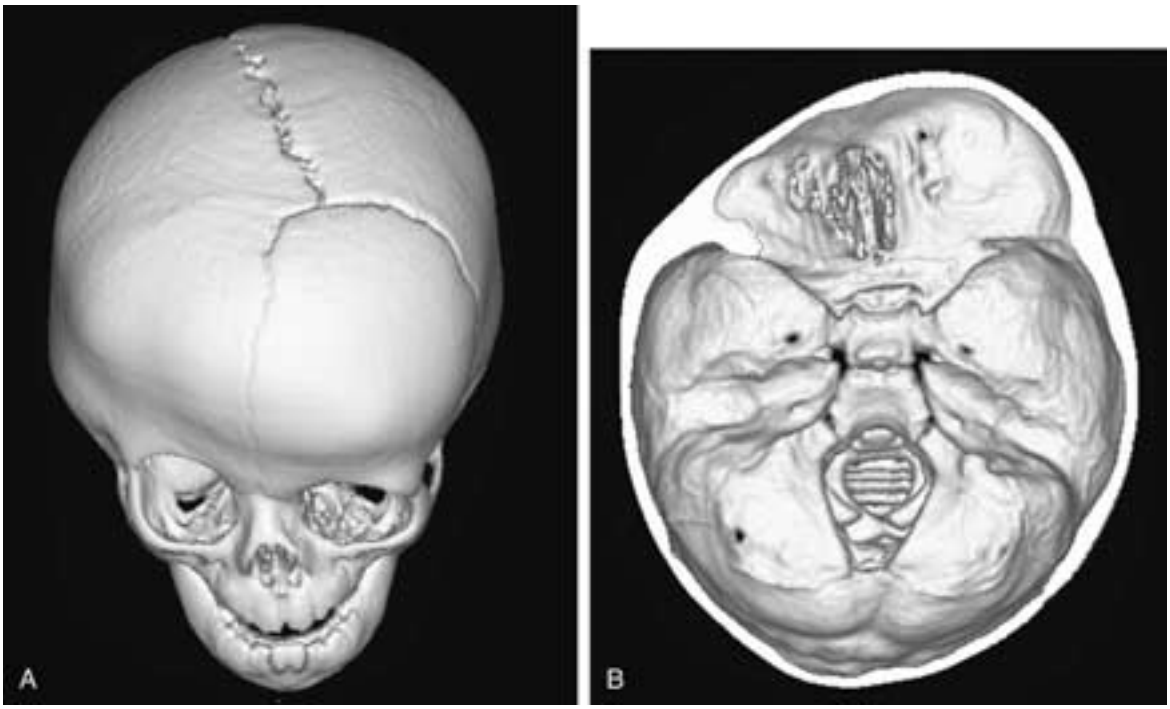

VIEW IMAGE

FIGURE 1-63 Nonsyndromal unilateral right coronal synostosis in a 7-month-old girl. **A** and **B**, Three-dimensional CT of the cranial surface (**A**) and a view of the skull base from within (**B**). The right coronal suture and anterior fontanelle are closed. The sagittal and left coronal sutures are patent. The metopic suture is faintly visualized. Asymmetric closure of the right coronal suture restricts growth of the ipsilateral anterior fossa and orbit, causing plagiocephaly, harlequin right eye, short right anterior fossa, high position of the right sphenoid wing-pterion, compensatory bossing of the left frontal contour, and inferior displacement of the left orbit.

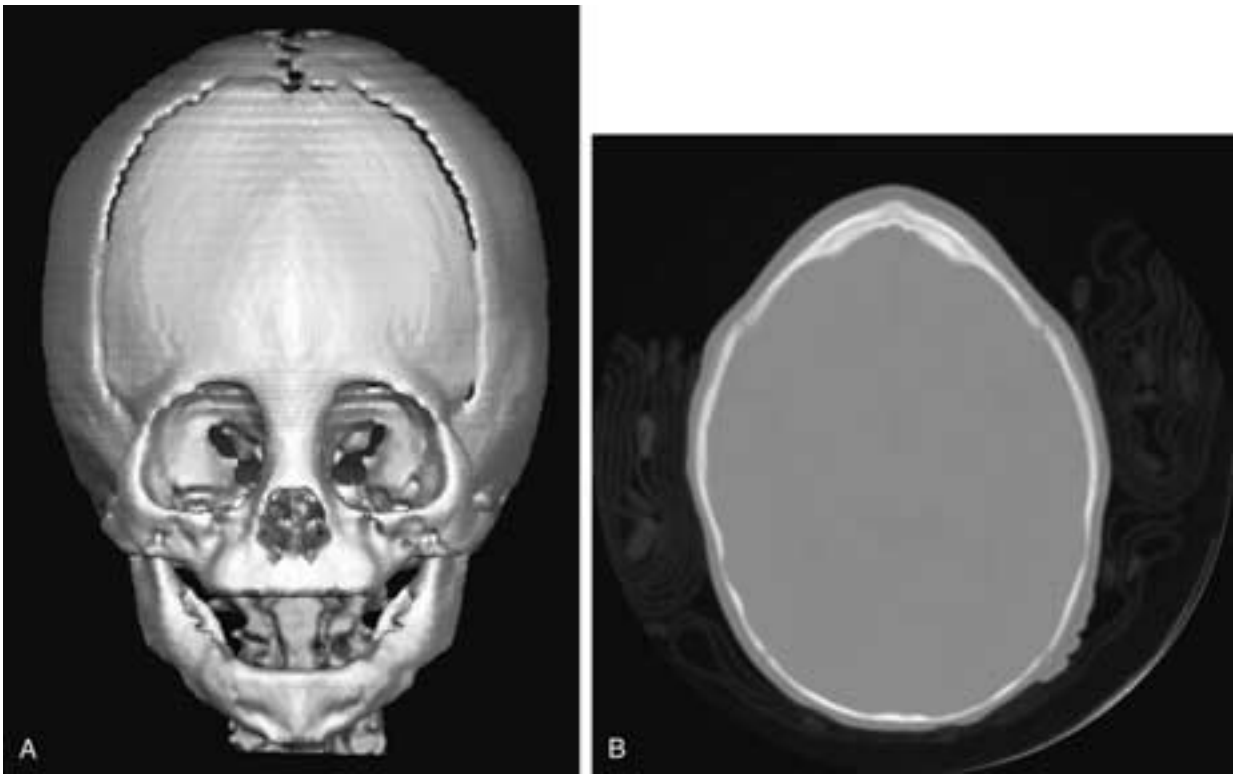

VIEW IMAGE

FIGURE 1-64 Trigonocephaly in a 3-month-old girl. **A**, Three-dimensional CT of the facial skeleton. **B**, Axial bone CT through the metopic suture. Premature closure of the metopic suture leads to hypotelorism, upward medial pointing of the orbital contours (''quizzical orbits'') and a keel-shaped brow.

Copyright © 2003, Mosby, Inc. All rights reserved.

exception of Apert syndrome (which does show consistent genetics), the clinical phenotypic classifications should be abandoned and replaced with molecular classifications of these syndromes.[326]

Molecular Genetics

Understanding the craniofacial dysostoses requires a background in the cell signaling mechanisms that control suture maturation. The next sections review these mechanisms preparatory to adressing the eponymous craniosynostosis syndromes.

Fibroblast Growth Factor Receptors

Four unlinked genes, *FGFR1* to *FGFR4*, constitute a family of genes that produce high-affinity receptors for the fibroblast growth factors (FGFs 1 to 9).[2] Of these, FGFR1, FGFR2, and FGFR3 are related to suture closure. The chromosomal locations of the FGF genes are: FGF1, 5q31-q33; FGF2, 4q26-q27; and FGF3, 11q13. FGFR genes 1 to 3 are located as follows: FGFR1, 8p11.2-11.1; FGFR2, 10q26; FGFR3, 4p16[326] (Table 1-14).

The FGFR genes encode a group of structurally related tyrosine kinase receptors of the subclass IV type. These FGFRs are situated at the cell membrane and share a three-part structure (Fig. 1-66; see also Fig. 1-1): (1) an *extracellular domain* composed of a variable number of immunoglobulin-like domains (Ig loops), (2) a *transmembrane domain* that bridges the cell wall, and (3) an *intracellular cytoplasmic domain* containing both a tyrosine kinase region responsible for tyrosine kinase activity and an

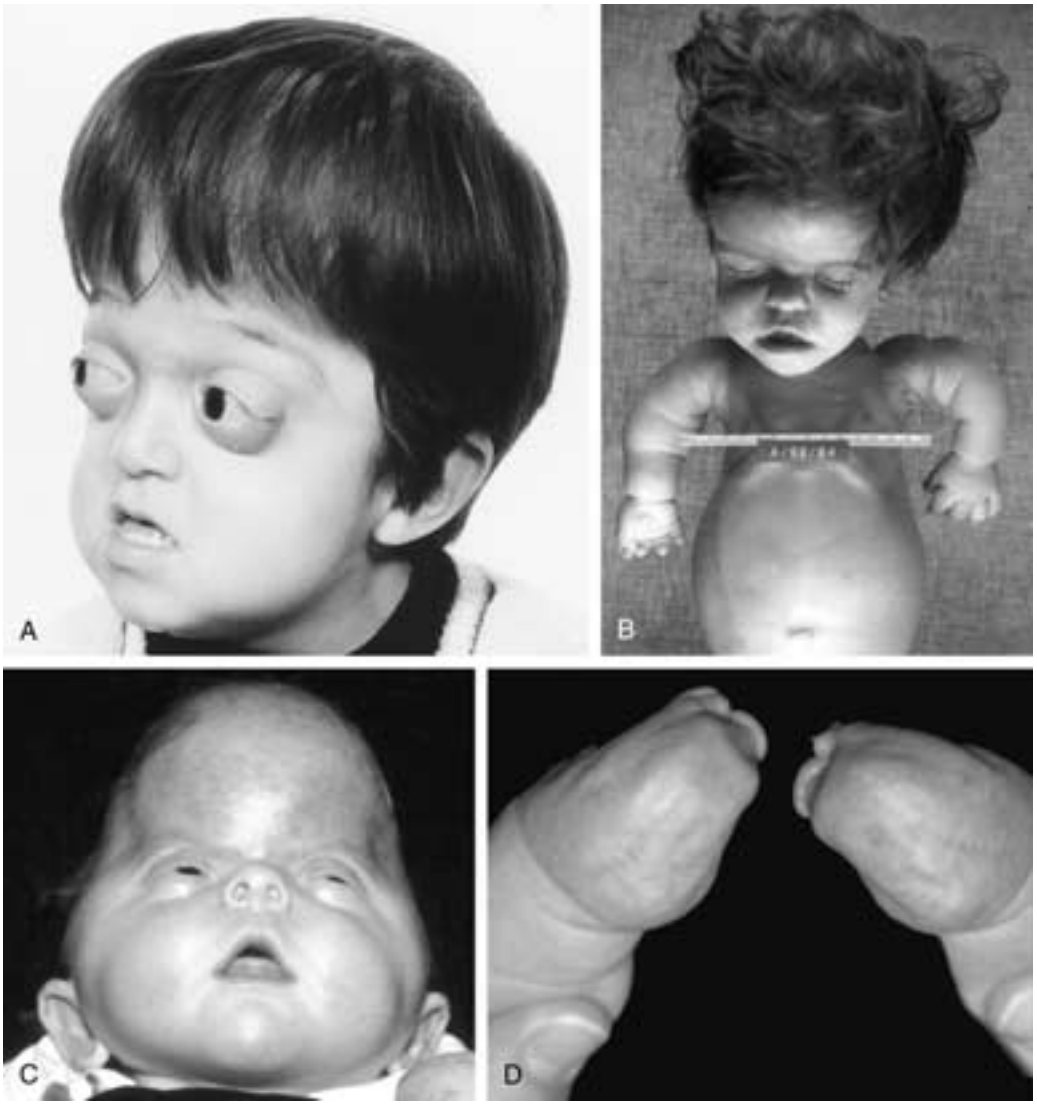

FIGURE 1-65 Facies of craniofacial dysostoses and achondroplasia. Four patients. **A**, Crouzon syndrome. Oblique view shows turricephaly, midface hypoplasia, hypertelorism, shallow bony orbits, marked bilateral exorbitism, and partial surgical closure of the eyelids to protect the globe. **B**, Homozygous achondroplasia in a 33-month-old girl with defective cartilage formation leading to a narrow skull base, secondary enlargement of the vault by hydrocephalus, and rhizomelic dwarfism. **C** and **D**, Apert syndrome (acrocephalosyndactylism type I). **C**, Frontal view shows brachycephaly, orbital hypertelorism, shallow orbits with bilateral exorbitism, maxillary hypoplasia and down-turned mouth. **D**, The hands show bilateral syndactylism involving all digits (type 3).

Illustration continued on following page

VIEW IMAGE

Copyright © 2003, Mosby, Inc. All rights reserved.

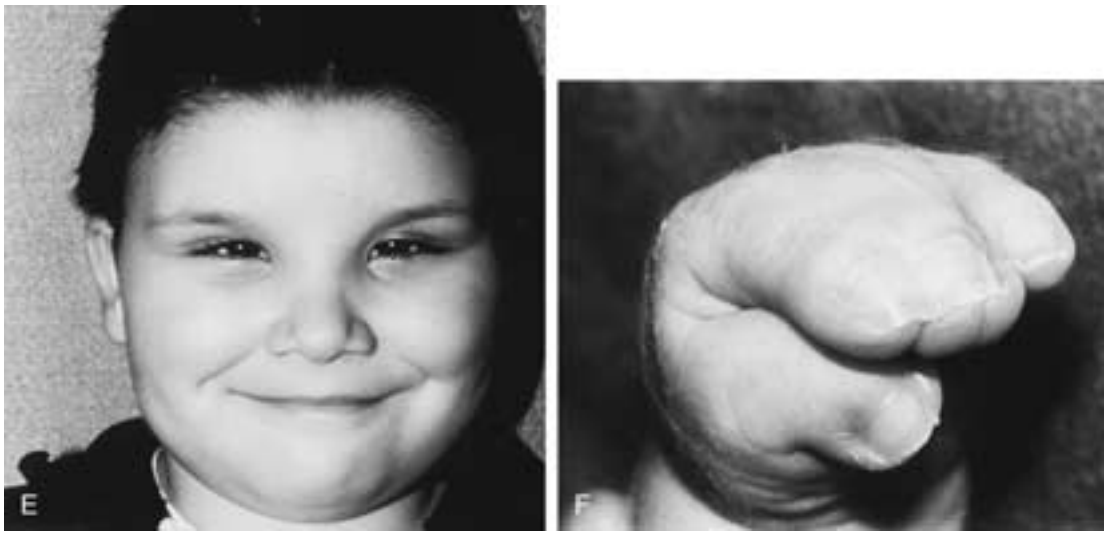

VIEW IMAGE

FIGURE 1-65 *Continued.* **E** and **F**, Saethre-Chotzen syndrome (acrocephalosyndactylism type III). **E**, Frontal view shows relatively mild facial asymmetry, mild midface hypoplasia, and ptosis of the eyelids. **F**, The hand shows cutaneous syndactyly of the central fingers with broadening of the other digits. (**B**, From Pauli RM, Conroy MM, Langer LO Jr, et al. Homozygous achondroplasia with survival beyond infancy. Am J Med Genet 1983;16:459–473.)

interkinase region.[10] The immunoglobulin-like domains Ig II and Ig III are necessary for ligand binding.[326] The FGFRs are normally activated (and controlled) by the presence of ligands, which serve as ''on'' signals to initiate phosphorylation. The binding of a ligand to the receptor in the *extracellular* domain normally promotes receptor dimerization. This initiates a sequence of cross-phosphorylation of the *cytoplasmic* domains, provision of binding sites for downstream signaling molecules, conformational changes, and increased kinase activity.[2]

In the craniofacial dysostoses, mutations in the FGFR genes create mutant proteins that allow the receptors to function independently of their normal ligand signals. The mutant receptor proteins form constitutive dimers, which activate the kinase domain and downstream signaling events, even in the absence of ligand.[2] That is, the mutated genes are always ''on,'' a ''gain-of-function'' mutation. Since FGFRs and FGF signaling guide development of multiple different organ systems, including the cranio-facial-oral-dental complex, the group of FGFR malformations exhibits a coherent set of multisystem anomalies affecting the skeleton, the central nervous system, the skin, and the auditory system.[2] The mutations that cause the craniofacial dysostoses cluster in the third Ig loop and in the linker region between Ig loops II and III. FGFRs 1, 2, and 3 each contain an analogous proline in the linker region between Ig loops II and III. Replacement of this proline with an arginine in any of these receptors causes craniosynostosis, with or without other skeletal malformations.[2] In FGFR1, this substitution causes the Pfeiffer syndrome. In *FGFR2*, the equivalent substitution causes Apert syndrome, and in *FGFR3* it causes Muenke nonsyndromic coronal craniosynostosis.[2] By receptor:

FGFR1 In FGFR1, replacement of the proline with an arginine at codon 252 (Pro252Arg) causes Pfeiffer syndrome.[2] Other proline substitutions at position 252 (Pro252) are seen with other nonspecific craniosynostoses.[10]

FGFR2 The FGFR2 gene is involved in most craniofacial dysostoses. Nearly all cases of Apert syndrome show one of two specific missense mutations at codons 252 and 253, which encode the linker region between the Ig II and Ig III domains of the extracellular domain.[10] These Apert-specific mutations consist of substitutions of tryptophan for serine at nucleotide 252 (Ser252Trp) or of arginine for proline at nucleotide 253 (Pro253Arg).[10] The Ser252Trp mutation accounts for 65% of Apert cases and, more commonly, causes concurrent cleft palate. The Pro253Arg mutation accounts for 35% of Apert cases and has a greater association with syndactyly.[327] A mild form of Apert syndrome has also been related to a different FGFR2 mutation, predicted to substitute phenylalanine for serine at position 252 (Ser252Phen-predicted). A study of 57 Apert

Table 1-14
CHROMOSOMAL LOCATIONS OF THE GENES FOR FIBROBLAST GROWTH FACTORS AND THEIR RECEPTORS

Fibroblast Growth Factors (FGF)	Chromosomal Location
FGF1	5q31-q33
FGF2	4q26-q27
FGF3	11q13
FGF8	10q25-q26
Fibroblast Growth Factor Receptors (FGFR)	**Chromosomal Location**
FGFR1	8p11.2-11.1
FGFR2	10q26
FGFR3	4p16

Data from Cohen MM Jr. Fibroblast growth factor receptor mechanisms. In: Cohen MM Jr, MacLean RE, eds. Craniosynostosis. Diagnosis, Evaluation and Management, 2nd ed. New York: Oxford University Press, 2000;77-94; Müller U et al. Molecular genetics of craniosynostotic syndromes. Arch Clin Exp Ophthalmol 1997;235: 545–550.

Copyright © 2003, Mosby, Inc. All rights reserved.

patients has shown an exclusively paternal origin of the mutation, which is thought to be related to advanced paternal age.[328]

Other FGFR2 mutations also cause craniofacial dysostoses. Substitution of leucine for serine at position 252 (Ser252Leu) or of serine for proline at position 253 (Pro253Ser) causes Crouzon-like and Pfeiffer-like phenotypes with only mild craniosynostosis.[10, 326] Mutation in the Ig IIIc portion of the extracellular domain of FGFR2 may produce the Jackson-Weiss syndrome.[329]

FGFR3 FGFR3 is the site of a spectrum of mutations that cause disorders of the axial and appendicular skeleton. These include achondroplasia, hypochondroplasia, and thanatophoric dysplasia II, as well as skin disorders. Achondroplasia is associated with a point mutation in the transmembrane domain of FGFR3 (Fig. 1-65B). A study of 10 achondroplasia patients showed an exclusively paternal origin of the mutation, which is thought to be related to advanced paternal age.[317] Hypochondroplasia is associated with a mutation in the intracellular tyrosine kinase domain of FGFR3. The form of thanatophoric dysplasia with cloverleaf skull is associated with mutation of the *extra*cellular domain of FGFR3, whereas the form of thanatophoric dysplasia without cloverleaf skull is associated with a mutation of the *intra*cellular domain of FGFR3.[10] Crouzon patients with concurrent acanthosis nigricans and Chiari I malformation show a specific mutation in the transmembrane domain of FGFR3 (Ala391Glu) at 4p16.3, just 11 amino acids away from the mutation site of achondroplasia.[10] In FGFR3, substitution of arginine for proline at codon 250 (Pro250Arg) is associated with Pfeiffer syndrome. Other proline substitutions at this site have been observed with nonspecific craniosynostoses.

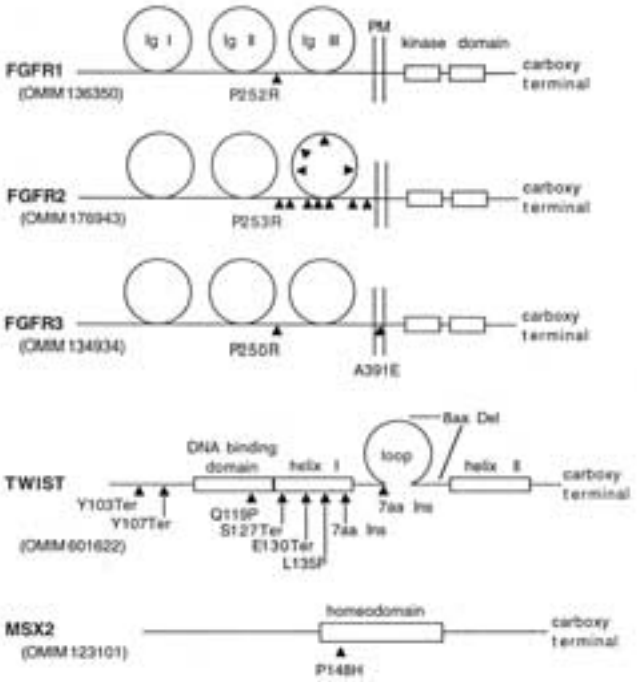

FIGURE 1-66 Molecular genetics of craniosynostoses. The craniofacial dysostoses reflect underlying derangements in signal transduction (see also Fig. 1-1). Diagrammatic representations of FGFRs 1 to 3, the basic helix-loop-helix transcription factor TWIST, and the homeodomain transcription factor *MSX2*. Each molecule is oriented horizontally, with the amino terminal to the left and the carboxy terminal to the right. FGFR 1 to 3. These receptor tyrosine kinases show a similar structure with (1) an extracellular domain composed of three Ig-like loops (Ig I to Ig III) and interposed linker regions between the loops, (2) a transmembrane domain that spans the plasma membrane (PM), and (3) an intracellular kinase domain. By convention, amino acid substitutions are designated by citing from left to right: the normal amino acid, the position at which that amino acid normally resides (counting from the amino terminal of the protein), and last, the new amino acid that has replaced the normal original. Each FGFR has a highly conserved proline at a slightly different position within the linker region between Ig II and Ig III. Amino acid substitutions at that site lead to craniofacial dysostoses. Illustrated here are substitutions of arginine (R) for proline (P) in FGFR1 (P252R), in FGFR2 (P253R), and in FGFR3 (P250R). Numerous other mutations in FGFR2 (*arrowheads*) also produce craniosynostoses. **TWIST**. Multiple mutations along the *TWIST* gene cause Saethre-Chotzen syndrome. ***MSX2***. A single point mutation in the homeodomain of *MSX2* can cause Boston-type craniosynostosis. *S*, serine; *P*, proline; *R*, arginine; *Y*, tyrosine; *L*, leucine; *Q*, glutamine; *H*, histidine; *A*, alanine; *E*, glutamic acid; *aa*, amino acid; *T*, termination, stop codon; *Del*, deletion; *Ins*, insertion. Additional mutations are discussed in the text. (From Nuckolls GH, Shum L, Slavkin HC. Progress toward understanding craniofacial malformations. Cleft Palate-Craniofac J 1999;36:12–26.)

VIEW IMAGE

Other Signaling Systems

Derangements of other genes and transcription factors may also be responsible for craniosynostoses.

GLI3 GLI3 is one of three members of a vertebrate family of zinc finger transcription factor proteins designated GLI (because they may be found in gliomas).[2] GLI interacts with hedgehog to affect expression of hedgehog responsive genes. In the absence of hedgehog, GLI is cleaved to a short form that represses hedgehog target genes. The presence of hedgehog preserves the full-length, active form of GLI and thereby allows hedgehog-responsive genes to be expressed.[18, 325] Known homology to the cubitus interruptus (*Ci*) gene in *Drosophila* predicts several functional domains for *GLI3*, including a DNA-binding zinc finger domain and a microtubule-binding domain.[2] Mutations in *GLI3* causes three distinct clinical disorders, two of which result in craniofacial dysmorphogenesis:

1. *Greig cephalopolysyndactyly* (GCPS) is an autosomal disorder defined predominantly by postaxial polydactyly of the hands and preaxial polydactyly of the feet with syndactyly. The craniofacial features of this disorder include macrocephaly with broad forehead, hypertelorism, broad nasal root, and occasional craniosynostosis. Mutations in *GLI3* associated with GCPS cause truncation of the molecule within the centrally located zinc finger domain and probably result in functional haploinsufficiency.[2]
2. *Pallister-Hall syndrome* (PHS) is caused by a frameshift in the *GLI3* sequence just downstream of the zinc finger domains, resulting in a differently truncated protein, which potentially retains partial function and DNA binding. PHS patients exhibit hypothalamic hamartomas, craniofacial anomalies, and polydactyly of the hands, usually central or preaxial. They do not display the hypertelorism or broad forehead seen with GCPS. Imperforate anus and laryngeal clefts have been reported in PHS.[2, 10]
3. *Postaxial polydactyly A* (PAP-A). The third *GLI3* mutation causes PAP-A. This mutation lies further

Copyright © 2003, Mosby, Inc. All rights reserved.

downstream in the gene and causes truncation of the molecule after the microtubule-binding domain but before several hundred carboxy-terminal amino acids.[2]

TWIST TWIST is a basic helix-loop-helix type of nuclear transcription factor that is homologous to the *Drosophila* gene *twist*. In *Drosophila*, *twist* is involved with dorsoventral patterning and muscle differentiation. Both *twist* and FGFR are coexpressed in early mesoderm in *Drosophila*. TWIST appears to regulate the expression and activity of the FGFRs.[2] The Saethre-Chotzen syndrome is caused by missense, nonsense, and insertion-type mutations in the human TWIST gene. It may also arise, less often, by mutations in FGFR2 and FGFR3.[2] Mice with TWIST defects show the same craniofacial features as humans, plus reduplication of the first digit, an infrequent feature of Saethre-Chotzen syndrome in humans.[10]

MSX2 *MSX2* (muscle segment homeobox gene 2) is a homeotic gene situated at chromosome 5q34-q35. *MSX2* normally interacts with a transcription factor, TFIIF, which acts on DNA to promote transcription of other genes. In the normal person, this binding occurs over a limited period of time, leading to a finite amount of ''product.'' [326] In patients with Boston (type II) craniosynostosis and limb malformations, an autosomal dominant mutation substitutes histidine for a highly conserved proline (Pro148His) within the homeodomain of *MSX2* (Fig. 1-66). This substitution impedes proteolysis of the *MSX2* protein and affects the dissociation of (transcription-promoting) *MSX2* from DNA.[326] Reduced dissociation of *MSX2* from DNA leads to increased time of binding, increased production of the gene product, and the clinical syndrome. In mice, *MSX2* is expressed in the embryo, both in the calvarial sutures and in the distal portion of the limb bud during skeletal patterning. Transgenic mice that overexpress the wild-type molecule exhibit the same craniosynostosis as mice expressing the mutant form of *MSX2*.[2]

Relationship of Cranial Suture Morphogenesis and Craniosynostosis

In humans, cranial neural crest cells differentiate into primary and secondary cartilage, enchondral bone, and membranous bone and give rise to most of the skeletal tissues of the skull.[330] In the vault, mineralization proceeds outward from several ossification centers from about 13 wg on. At about 18 wg the mineralizing bone fronts meet, and sutures are induced along the lines of approximation. The skull subsequently enlarges by appositional growth at the suture, with deposition of unmineralized bone matrix (osteoid) along the suture margins.[328]

The suture is anatomically simple. Two plates of bone are separated by a narrow space that contains immature, rapidly dividing osteogenic stem cells. One portion of these stem cells is recruited to differentiate into osteoblasts and make new bone. The remainder resist differentiation into osteoblasts, continue to proliferate, and maintain the suture.[328] These events are partially controlled by *Fgfr1*, *Fgfr2*, *Fgfr3*, *MSX2*, and TGF-beta, which are expressed in the sutures. Premature fusion at one suture prevents further growth at that suture. Excessive growth at other sutures then leads to skull distortion.[328]

FGF 1, 2, and 3

FGF2 is a known survival factor for neural crest cells. Low concentrations of FGF2 cause concentration-dependent *proliferation* of osteogenic stem cells. High concentrations of FGF2 induce *osteoblastic skeletogenic differentiation* of these cells. Through an autoregulatory loop, high concentrations of FGF2 normally downregulate fgf2 to modulate the FGF2 concentration. FGF1 and FGF3 also play a role.[328, 330–332] The normal suture is maintained by a gradient of FGF2 that balances these signals, allowing osteogenic stem cells to proliferate in the center of the suture (where the concentrations of FGF2 are low) and to differentiate into osteoblasts at the margins of the sutures (i.e., at the edges of the growing calvarial plates), where the concentrations of FGF2 are higher (Fig. 1-67).

In mice, *Fgfr2* is expressed only in proliferating osteoprogenitor cells. Downregulation of *Fgfr2* and upregulation of *Fgfr1* signal the onset of differentiation into osteoblasts. Osteopontin, a marker of osteoblast differentiation, then appears, following which *Fgfr1* (plus osteonectin and alkaline phosphatase) become downregulated. *Fgfr3* is expressed both in osteogenic cells and in cranial cartilage, including a plate of cartilage that underlies the coronal suture.[331]

In mice, implantation of FGF2-soaked beads in the subcutaneous tissue over the coronal suture disrupts the normal suture and leads to synostosis. The local increase in the concentration of FGF2 causes three effects: (3) ectopic expression of *Fgfr1* and osteopontin (i.e., osteoblastic differentiation) in the sutural mesenchyme beneath the bead, (2) downregulation of *Fgfr2* locally (where the concentration of FGF2 is high), and (3) ectopic upregulation of *Fgfr2* in a ring surrounding the bead (where the concentration of FGF2 has fallen to a critical level around the circumference of the bead).[331] Since *low* levels of FGF2 maintain the proliferating population of osteogenic stem cells at the suture, and *high* levels of FGF2 stimulate osteoblastic differentiation, the *excessive* (constitutive ''on'') *FGFR2* signaling due to FGF mutations causes osteogenic differentiation and premature cranial synostosis.[328, 332]

The role of *MSX2* and TWIST, and their interaction with the FGFRs, is poorly understood. *MSX2* expression is associated with apoptosis in several cell types during development. Therefore, the craniosynostosis seen in *MSX2* patients could be due to abnormalities in the programmed death of connective tissue cells at the suture site. *MSX2* may participate in the FGFR signaling pathway, since it is coexpressed with FGFRs at the apical epidermal ridge of developing limbs and at the periphery of membranous calvarial bones. BMP signaling also regulates MSX expression, suggesting that this transcription factor may serve as a focal point for integrating multiple pathways that regulate skeletal development.[2]

In other species, *twist* is known to be a critical gene for mesoderm induction and to function later as a myogenic switch. Expression of specific fibroblast growth receptors depends on *twist.* Null mutants for such receptors show abnormal directions of cell migration and defective muscle formation.[328] Mesodermal expression of the *msh* gene is turned on later in myogenesis and is abolished in *twist* mutants. Similar effects could contribute to the abnormal suture development seen in TWIST mutants.[328]

Copyright © 2003, Mosby, Inc. All rights reserved.

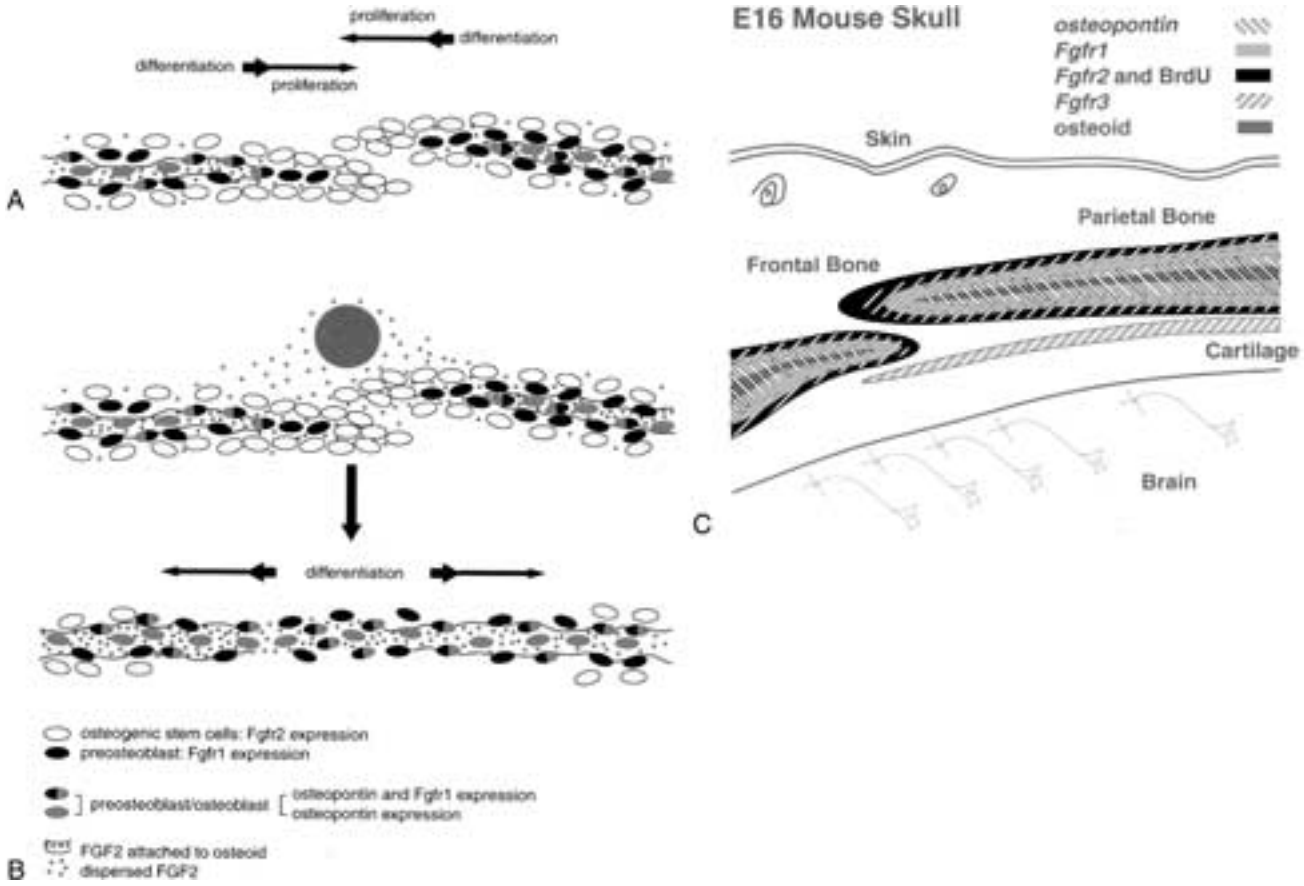

FIGURE 1-67 Molecular control of suture formation. **A** and **B**, Proposed model for the role of the FGFs and the FGFRs in balancing the proliferation and differentiation of osteogenic stem cells in the early fetal coronal suture of the mouse. **A**, Normal sutural growth. FGF2 is secreted by the osteoblasts. It is absorbed onto the unmineralized bone matrix. Lower levels of FGF2 diffuse into the extracellular environment of the sutural stem cells. These low levels of FGF2 stimulate the osteogenic stem cells to proliferate. These proliferating stem cells express *Fgfr2*. As new matrix is secreted by the differentiating cells, FGF2 levels rise in the environment of those osteogenic stem cells closest to the new matrix. The high levels of FGF2 stimulate these cells to differentiate into preosteoblasts. The process of differentiation involves downregulation of *Fgfr2*,exit from the cell cycle of proliferation, and subsequent upregulation of *Fgfr1*. Slightly later, there is upregulation of osteogenesis-related genes, including *osteopontin*. The preosteoblasts begin to secrete matrix and are then designated osteoblasts. *Fgfr1* is downregulated when differentiation is complete. **B**, Addition of ectopic FGF2 (*black circle* representing an FGF2-soaked bead) to the environment of the osteogenic stem cells raises the concentration of FGF2 locally and accelerates the process of differentiation, so the proliferating cell population is lost for the duration of the increased signal. This local increase in FGF2 mimics the effect of the gain-of-function, ''constitutively on'' mutations of FGFR1, FGFR2, and FGFR3 associated with the craniofacial dysostoses. **C**, Diagrammatic representation of the coronal suture of the fetal mouse. Summary of the expression patterns of the FGFR genes (*Fgfr 1, Fgfr2, and Fgfr3*) and of the osteogenesis-related gene *osteopontin*, a marker of osteoblast differentiation. *Fgfr2* is expressed only in proliferating osteogenic stem cells (osteoprogenitor cells). *Fgfr1* expression is associated with cell differentiation into osteoblasts. *Fgfr3* is expressed in both the osteogenic and chondrogenic portions of the skeletogenic membrane. The onset of differentiation toward osteoblasts is preceded by downregulation of *Fgfr2*, upregulation of *Fgrf1*, and upregulation of osteopontin. (From Iseki S, Wilkie AOM, Morriss-Kay GM. *Fgfr1* and *Fgfr2* have distinct differentiation- and proliferation-related roles in the developing mouse skull vault. Development 1999;126:5611–5620.)

VIEW IMAGE

Eponymous Craniosynostoses

Crouzon Syndrome

Crouzon syndrome (acrocephalosyndactyly type II) is the most frequent craniofacial dysostosis (1 per 25,000 births) (Figs. 1-65A, 1-68, and 1-69). It results from an autosomal dominant trait with variable expressivity. About 45% to 65% of cases are familial; the rest are sporadic.[308, 333] Clinically, Crouzon syndrome is characterized by bilateral coronal synostosis with a brachycephalic or oxycephalic vault. The sagittal and lambdoid sutures may also be affected. Typically, the sutures are not fused at birth but show progressive synostosis from about 1 year on.[308] Crouzon patients show maxillary hypoplasia with shallow orbits, bilateral exorbitism, and orbital hypertelorism. The nasal passages are partially obstructed, causing mouth breathing. *The hands and feet are spared*. Concurrent intracranial anomalies are common, including jugular venous obstruction with anomalous venous drainage (63%) and hydrocephalus. The hydrocephalus is more frequently progressive in Crouzon syndrome than in Apert syn-

Copyright © 2003, Mosby, Inc. All rights reserved.

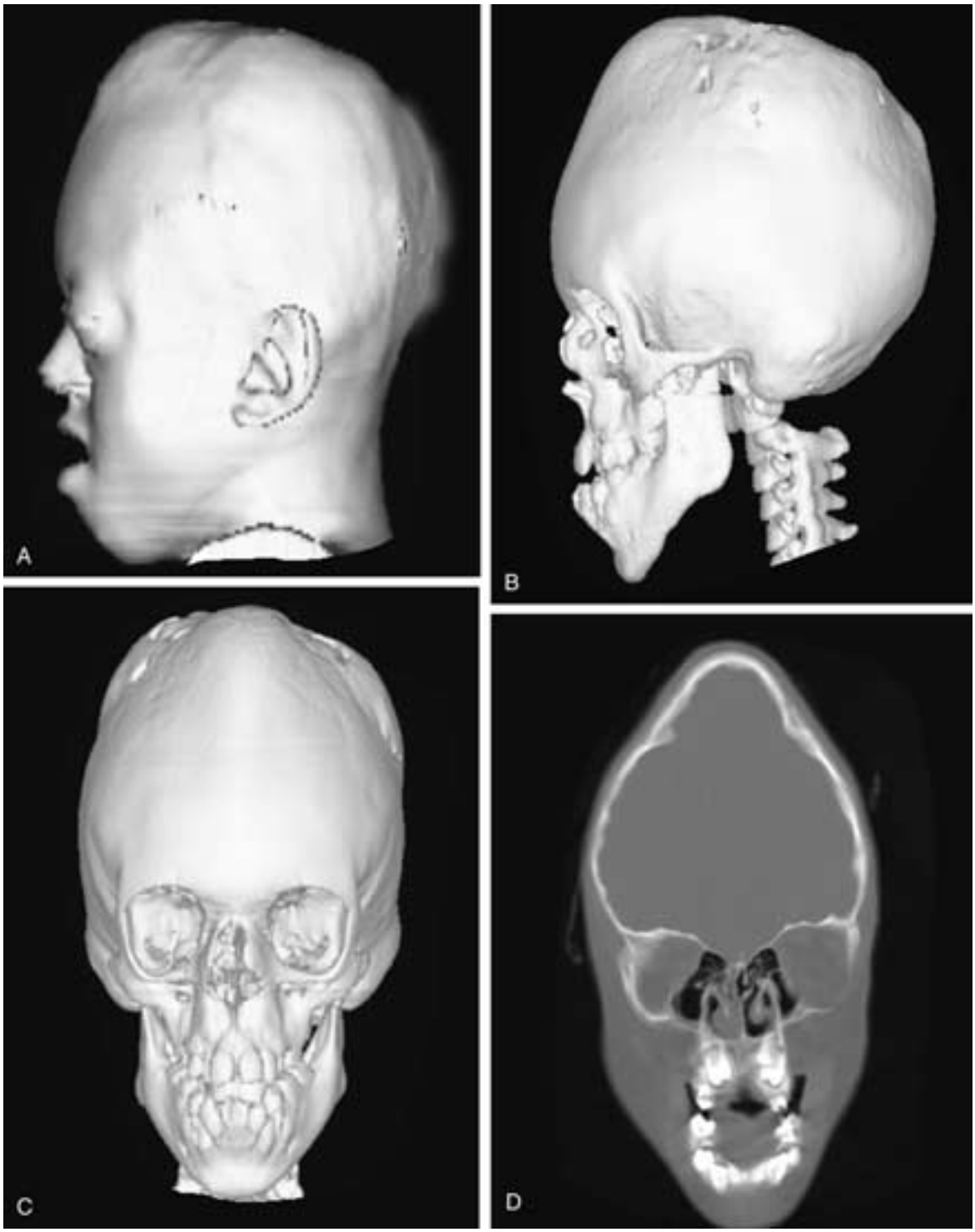

VIEW IMAGE

FIGURE 1-68 Crouzon syndrome in a 9-year-old girl. **A** to **C**, Three-dimensional CT of the lateral skin surface (**A**), the lateral facial skeleton (**B**), and the frontal facial skeleton (**C**). **D**, Direct coronal CT. The patient shows oxycephaly, shallow orbits with exorbitism, hypoplasia of the midface with narrow, partially obstructed nasal passages, relative prognathism, and an everted lower lip.

drome.[208, 334] Chiari I malformation is seen in 71.4% of Cruzon patients.[208] Other features reported in Crouzon patients include calcification of the stylohyoid ligament (50% of patients older than 4 years), cervical spine anomalies, especially fusions of C2-C5 (up to 40%), elbow malformations (18%), minor hand deformities (10%), and visceral anomalies (7%).[208] Of all craniofacial dysostoses, the Cruzon patients with the FGFR3 mutation have the highest incidence of jugular venous stenosis or atresia and enlarged emissary veins. This phenomenon could reflect a relationship to the FGFR3 achondroplasia spectrum, which classically displays such venous stenoses and hydrocephalus.[335]

Copyright © 2003, Mosby, Inc. All rights reserved.

Apert Syndrome

Apert syndrome (acrocephalosyndactyly type I) is an autosomal dominant craniofacial dysostosis. Most cases arise sporadically as new mutations, but the disorder may be transmitted through families with complete penetrance. Apert syndrome occurs in 1 per 50,000 to 100,000 births, so it is less common than Crouzon syndrome. Clinically, Apert syndrome is characterized by severe symmetric syndactylism of the hands and feet. This is subclassified by the digits affected as type I (affecting digits 2, 3, and 4), type II (affecting digits 2, 3, 4, and 5), and type III (affecting all five digits).[308] Apert patients show bilateral coronal synostoses with brachycephaly, a midline defect due to widened metopic and sagittal sutures, orbital hypertelorism, shallow orbits with bilateral exorbitism, exotropia, maxillary hypoplasia with downturned mouth, high-arched palate, class III malocclusion, and anterior open bite (Figs. 1-65C,D and 1-70).[333] In Apert syndrome, the cranial changes appear to be more severe than those in Crouzon syndrome. The midface hypoplasia is present from birth. There is more severe redirection of the anterior cranial base and orbits, with greater brain compression and more prominent bulging of the eyes.

Cleft palate is present in 30% to 42% of Apert patients.[308] Choanal stenosis is common, but atresia is rare. Hypoplasia of the posterior choanae may compromise the nasopharyngeal and oropharyngeal airways, increasing the risk of respiratory distress, sleep apnea, cor pulmonale, and sudden death.[208] Eustachian tube dysfunction, otitis media, and conductive hearing loss are common. Sensorineural hearing loss is rare.[208] Apert patients show an increased incidence of callosal agenesis, megalencephaly, and gyral anomalies. Hydrocephalus may require shunt decompression before craniofacial surgery is performed. Most patients have normal intelligence but display specific learning difficulties. Up to one third suffer mental retardation. Approximately 70% show fusion of the cervical vertebrae, usually C5 and C6.[333] Rhizomelic shortening of the lower limbs reduces the stature by 5% to 50%.[307] There may be ankylosis of the elbows, hips, and shoulders. Concurrent problems with the cardiovascular (10%), genitourinary (9.6%), gastrointes-

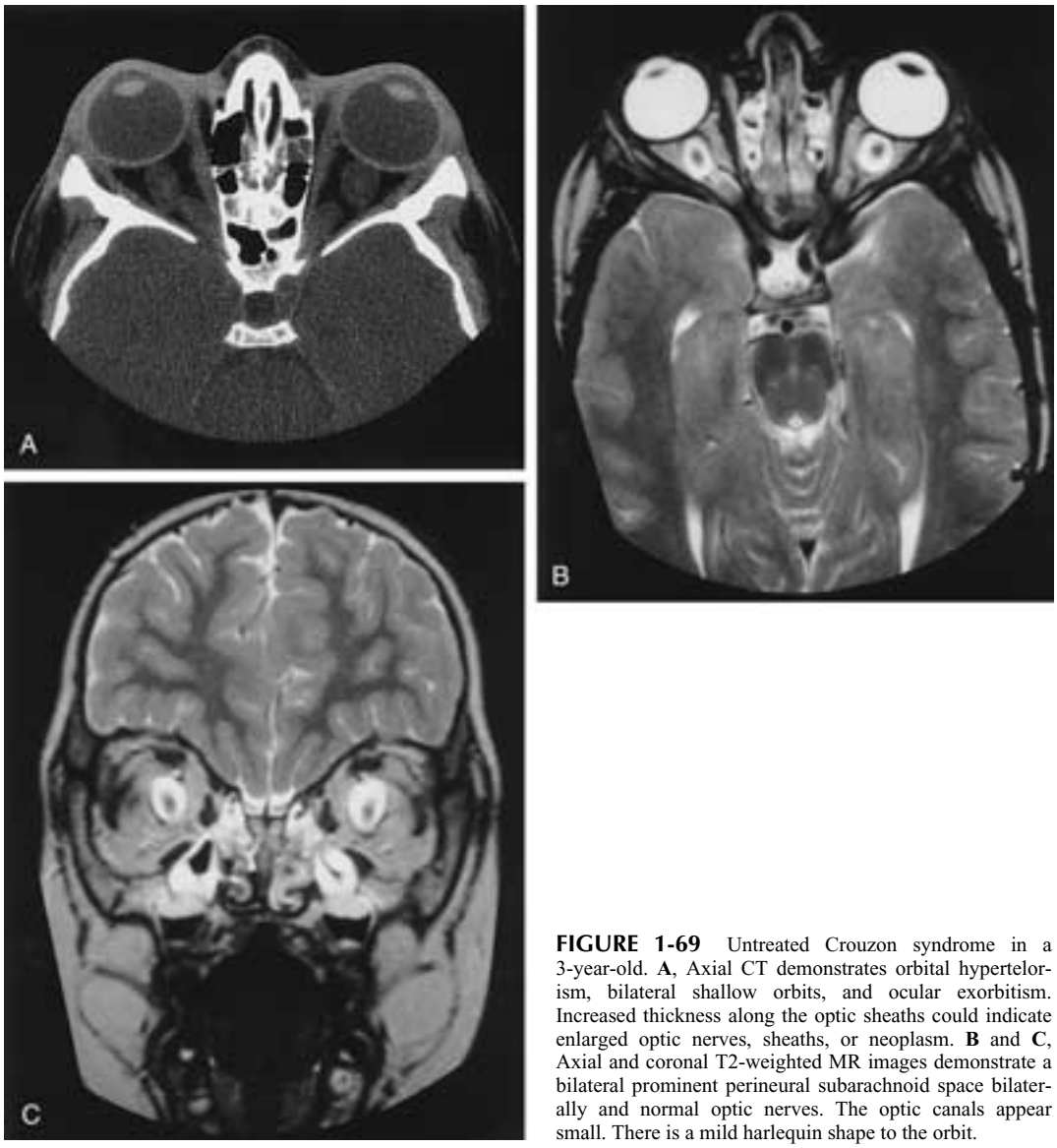

FIGURE 1-69 Untreated Crouzon syndrome in a 3-year-old. **A**, Axial CT demonstrates orbital hypertelorism, bilateral shallow orbits, and ocular exorbitism. Increased thickness along the optic sheaths could indicate enlarged optic nerves, sheaths, or neoplasm. **B** and **C**, Axial and coronal T2-weighted MR images demonstrate a bilateral prominent perineural subarachnoid space bilaterally and normal optic nerves. The optic canals appear small. There is a mild harlequin shape to the orbit.

VIEW IMAGE

Copyright © 2003, Mosby, Inc. All rights reserved.

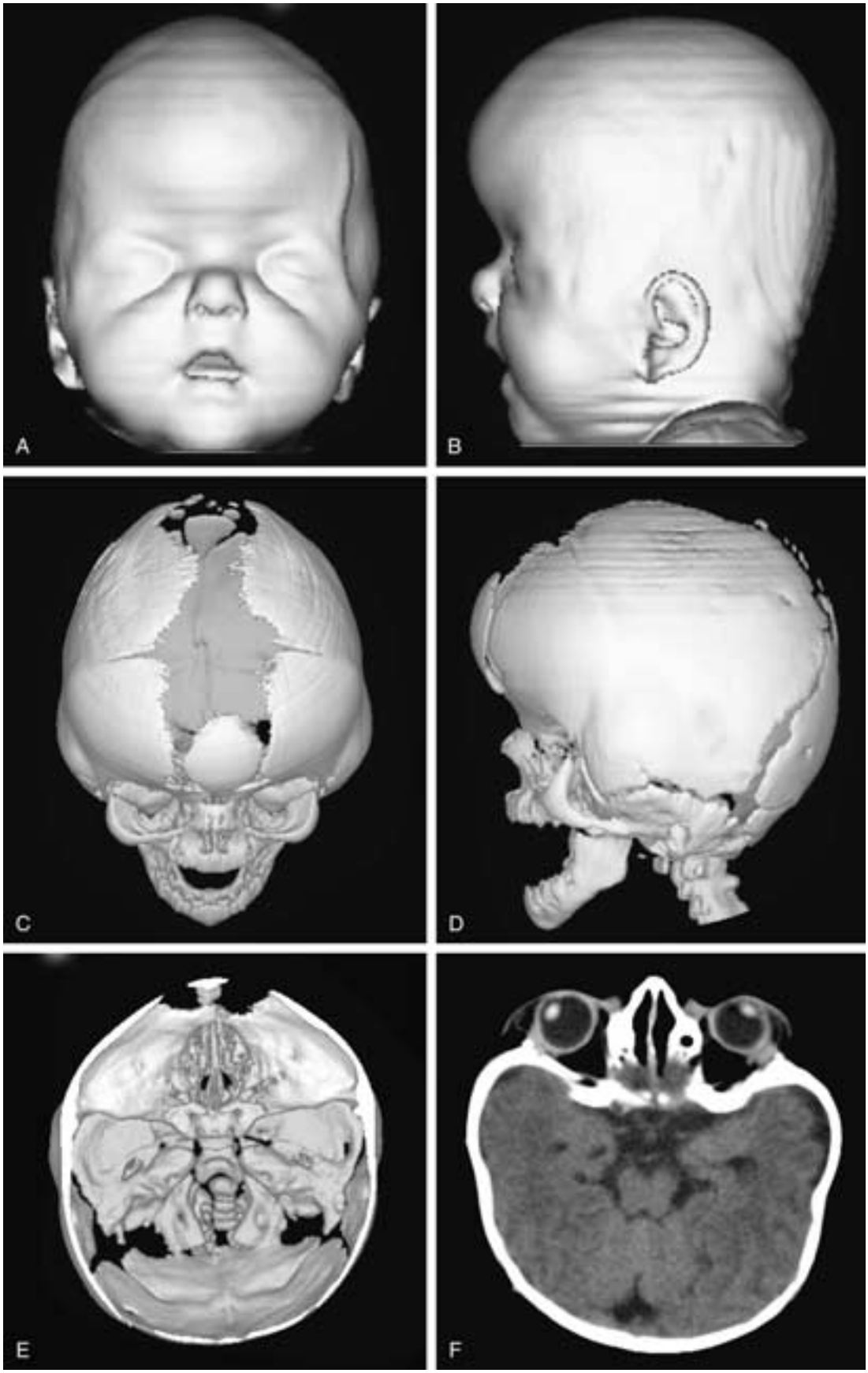

FIGURE 1-70 Apert syndrome in an infant boy. **A** to **D**, Three-dimensional CT displays of the frontal (**A**) and lateral (**B**) skin surfaces, and the corresponding frontal (**C**) and lateral (**D**) facial skeletons. **E** and **F**, Three-dimensional CT of the skull base (**E**) and an axial CT section through the orbits (**F**). The patient shows brachycephaly with fused coronal sutures bilaterally, wide patency of the sagittal suture, metopic suture and anterior fontanelle with an intrasutural bone, consequent hypertelorism, shallow symmetric anterior fossa, and midface hypoplasia with marked exorbitism.

VIEW IMAGE

Copyright © 2003, Mosby, Inc. All rights reserved.

tinal (1.5%), and respiratory (1.5%) systems contribute to patient morbidity.[208] The stylohyoid ligament may calcify in 38% to 88% of Apert patients.[208]

Saethre-Chotzen Syndrome

Saethre-Chotzen syndrome (acrocephalosyndactyly type III) is one of the more common craniofacial dysostoses, with an incidence of 1 per 50,000 to 1 per 100,000.[336] It is an autosomal dominant trait with complete penetrance (but variable phenotype) caused by mutations in TWIST, FGFR2, and FGFR3.[2] Saethre-Chotzen syndrome is characterized clinically by multiple suture synostoses with brachycephaly, hypertelorism with shallow orbits, maxillary hypoplasia, facial asymmetry, blepharoptosis, ear anomalies with prominent antihelical crura (crux cymbae), brachydactyly, and cutaneous syndactyly involving the second and third fingers (Fig. 1-65D,E).[326] Antimongoloid slant of the palpebral fissures, beaked nose, and a low-set frontal hairline are frequent. Increased intracranial pressure and mental retardation are infrequent.[326] The corresponding homozygous mutation causes cephalic neural tube defects and fetal lethality.

Pfeiffer Syndrome

Pfeiffer syndrome (acrocephalosyndactyly type V) is an autosomal dominant craniosynostosis with complete penetrance. It occurs in about 1 per 200,000 live births.[336] About 40% of the cases are familial, and 60% are sporadic.[308] Pfeiffer patients present clinically with soft-tissue syndactyly, broad great toes, broad thumbs, and radial deviation of the phalanges of the fingers (varus deformity). The head displays brachycephaly, short anterior fossa, receding lower forehead, supraorbital bar, hypertelorism, antimongoloid slant of the eyes, and flat nasal bridge.[307] The jaw is prognathic.[288, 326, 337] The clinical outcome of Pfeiffer patients varies widely, leading Cohen[338] to subclassify the disorder into three types. Type I is classic Pfeiffer syndrome, with a good clinical outcome. Type II shows severe concurrent CNS malformations with Kleeblattschädel and a poor prognosis. Type III shows severe CNS malformations without Kleeblattschädel, but still with a poor prognosis. Pfeiffer cases with Kleeblattschädel appear to map to FGFR2, while those with milder phenotypes generally map to FGFR1.[339]

Jackson-Weiss Syndrome

Jackson-Weiss syndrome is a clinically distinct autosomal dominant condition with craniosynostoses and concurrent foot anomalies.[333, 340, 341] The skull shape varies widely from brachycephaly to acrocephaly. Frontal prominence, hypertelorism, and strabismus have been noted. Intelligence is usually normal. The most consistent and distinctive feature of Jackson-Weiss syndrome is abnormality of the feet, with broad great toes, medial deviation of the toes, and tarsal-metatarsal coalitions. Hand anomalies are rare. There is great variability within families but high penetrance, so that some members have only foot deformities with no craniosynostosis.

Boston (Type 2) Craniosynostosis

Boston syndrome is an autosomal dominant condition localized to chromosome 5qter. It has a variable phenotype, including forehead retrusion, frontal bossing, turricephaly, and Kleeblattschädel. All affected individuals have recession in the supraorbital region in relation to the superior surface of the cornea. Most exhibit myopia or hyperopia.[326]

Muenke Syndrome

Muenke syndrome (Adelaide craniosynostosis) is an autosomal condition. Patients may show bicoronal synostosis (70%), unilateral coronal synostosis (30%), or simple macrocephaly.[333, 341] Muenke patients show midface hypoplasia (60%), downward slanting of the palpebral fissures (50%), strabismus and facial asymmetry (frequent), and sensorineural hearing loss (30%).[339] Broad halluces are seen clinically in 25%. Radiographs show short, broad middle phalanges in the hands but hypoplastic to absent middle phalanges in the toes.[339] Cone epiphyses are frequent in both hands and feet. Carpal and/or tarsal fusions are present in about 50%. Syndactyly and deviation of the great toes are not part of the syndrome.[339] A minority of Muenke patients show developmental delay.

Baere-Stevenson Cutis Gyrata Syndrome

The Baere-Stevenson syndrome is an extremely rare autosomal dominant form of craniosynostosis that leads to early death. Patients show Kleeblattschädel and severe dermatologic anomalies including corrugated skin furrows (cutis gyrata), extensive acanthosis nigricans, cutaneous or mucosal tags, and small nails. Other features include choanal atresia, bifid scrotum, and an enlarged umbilical stump. The mutation affects FGFR2, either in the transmembrane domain or in the extracellular domain at the linker region between the third Ig-like loop and the transmembrane domain.[339]

CONCLUSION

The broad spectrum of craniofacial malformations illustrates the differing ways in which basic embryologic mechanisms may deviate from the expected program.[342–344] Analysis of those malformations by molecular genetics is now providing increased understanding of the nature of those programs. Ultimately, it may be hoped that knowledge of the underlying mechanisms will allow us to tailor diets to meet the specific needs of each expectant mother to prevent these malformations and, at need, to call on the armamentarium of the body to effect scarless, seamless repair of any malformations that do occur.

REFERENCES

1. Naidich TP, Zimmerman RA, Bauer BS, Altman NR, Bilaniuk LT. Midface: embryology and congenital lesions. In: Som PS, Curtin HD, eds. Head and Neck Imaging, Vol. 1. St. Louis: CV Mosby, 1996;3–60.
2. Nuckolls GH, Shum L, Slavkin HC. Progress toward understanding craniofacial malformations. Cleft Palate-Craniofac J 1999;36:12–26.
3. Carlson BM. Human Embryology and Developmental Biology, 2nd ed. St. Louis: CV Mosby, 1999.
4. Moore KL, Persaud TVN. The Developing Human. Clinically Oriented Embryology, 6th ed. Philadelphia: WB Saunders, 1998.

Copyright © 2003, Mosby, Inc. All rights reserved.

5. Schneider RA et al. Local retinoid signaling coordinates forebrain and facial morphogenesis by maintaining *FGF8* and *SHH*. Development 2001;128:2755–2767.
6. Shimamura K, Hartigan DJ, Martinez S, et al. Longitudinal organization of the anterior neural plate and neural tube. Development 1995;121:3923–3933.
7. Köntges G, Lumsden A. Rhombencephalic neural crest segmentation is preserved throughout craniofacial ontogeny. Development 1996; 122:3229–3242.
8. Patten BM. The normal development of the facial region. In: Pruzansky S, ed. Congenital Anomalies of the Face and Associated Structures. Springfield, Ill: Thomas, 1985.
9. Langman J. Medical Embryology: Human Development, Normal and Abnormal, 2nd ed. Baltimore: Williams & Wilkins, 1969.
10. Elmslie FV, Reardon W. Craniofacial developmental abnormalities. Curr Opin Neurol 1998;11:103–108.
11. Ferguson MWJ. Development of the face and palate. Cleft Palate-Craniofac J 1995;32:522–524.
12. Hu D, Helms JA. The role of Sonic hedgehog in normal and abnormal craniofacial morphogenesis. Development 1999;126: 4873–4884.
13. Murray JC. Invited editorial. Face facts: Genes, environment, and clefts. Am J Hum Genet 1995;57:227–232.
14. Davies J. Embryology and anatomy of the head, neck, face, palate, nose and paranasal sinuses. In: Paparella MM, Shumrick DA, eds. Otolaryngology, Vol. 1. Philadelphia: WB Saunders, 1980;63–123.
15. ten Berge D, Brouwer A, Korving J, et al. *Prx1* and *Prx2* are upstream regulators of sonic hedgehog and control proliferation during mandibular arch morphogenesis. Development 2001;128: 2929–2938.
16. Lu M-F, Cheng H-T, Kern MJ, et al. *Prx-1* functions cooperatively with another paired-related homeobox gene, *prx-2*, to maintain cell fates within the craniofacial mesenchyme. Development 1999;126: 495–504.
17. Borchers A, David R, Wedlich D. *Xenopus cadeherin-11* restrains cranial neural crest migration and influences neural crest specification. Development 2001;128:3049–3060.
18. Brivanlou AH, Darnell JE Jr. Signal transduction and the control of gene expression. Science 2002;295:813–818.
19. Schilling TF. Genetic analysis of craniofacial development in the vertebrate embryo. BioEssays 1997;19:459–468.
20. Wedden SE. Epithelial–mesenchymal interactions in the development of chick facial primordia and the target of retinoid action. Development 1987;90:341–351.
21. Richman JM, Tickle C. Epithelial–mesenchymal interactions in the outgrowth of limb buds and facial primordia in chick embryos. Dev Biol 1992;154:299–308.
22. Proetzel G, Paulowski S, Wiles MV, et al. Transforming growth factor β3 is required for secondary palate fusion. Nat Genet 1995;11:409–414.
23. Carette MJM, Ferguson MWJ. The fate of medial edge epithelial cells during palatal fusion in vitro: an analysis by Dil labelling and confocal microscopy. Development 1992;114:379–388.
24. Scott JH. The cartilage of the nasal septum (a contribution to the study of facial growth). Br Dent J 1953;95:37–43.
25. Mood GF. Congenital anterior herniations of brain. Ann Otol Rhinol Laryngol 1938;47:391–401.
26. Naidich TP, Takahashi S, Towbin RB. Normal patterns of ossification of the skull base: ages 0-16 years. Paper presented at the 71st scientific assembly and annual meeting of the Radiological Society of North America, Chicago, November 19, 1985.
27. Lebowitz RA, Terk A, Jacobs JB, Holliday RA, et al. Asymmetry of the ethmoid roof: analysis using coronal computed tomography. Laryngoscope 2001;111:2122–2124.
28. Naidich TP, Valente M, Abrams K, Spreitzer JJ, Doundoulakis SH. Torus palatinus. Int J Neuroradiol 1997;3:229–243.
29. Naidich TP. Pits, patches and protuberances. Hyperostosis mandibularis interna. Int J Neurol 1997;3:224–228.
30. Woo J-K. Torus palatinus. Am J Phys Anthropol 1950;8:81–112.
31. van den Broek AJP. On exostoses in the human skull. Acta Neirland Morph 1943;5:95–118.
32. Thoma KH. Tumors of the Jaw. Oral Pathology, 3rd ed. St. Louis: CV Mosby, 1950;1336–1344.
33. Suzuki M, Sakai T. A familial study of torus palatinus and torus mandibularis. Am Phys Anthropol 1960;18:264–272.
34. Thoma KH. Torus palatinus. Int J Orthodont Oral Surg 1937;23: 194–202.
35. Kolas S, Halperin V, Jefferis K, Huddleston S, Robinson HBG. The occurrence of torus palatinus and torus mandibularis in 2,478 dental patients. Oral Surg Oral Med Oral Pathol 1953;6:1134–1141.
36. Lasker GW. Penetrance estimated by the frequency of unilateral occurrences and by discordance in monozygotic twins. Hum Biol 1957;19:217–230.
37. Hooton EA. On certain Eskimoid characters in Icelandic skulls. Am J Phys Anthropol 1918;1:53–76.
38. Lasker GW. Genetic analysis of racial traits of the teeth. Cold Spring Harbor Symp Quant Biol 1950;15:191–203.
39. Miller SC, Roth H. Torus palatinus: a statistical study. J Am Dent Assoc 1940;27:1950–1957.
40. Koemer O. Der torus palatinus. Z Ohrenh Krankh Luft 1910;61: 24–27.
41. Lachmann H. Torus palatinus bei Degenerieten, f. d. ges. Neurol Psychiatr 1927;111:616.
42. King DR, Moore GE. An analysis of torus palatinus in a transatlantic study. J Oral Med 1976;31:44–46.
43. Naidich TP, et al. Midline craniofacial dysraphism: midline cleft upper lip, basal encephalocele, callosal agenesis, and optic nerve dysplasia. Concepts Pediatr Neurosurg 1977;4:186.
44. Naidich TP, Osborn RE, Bauer B, et al. Median cleft face syndrome: MR and CT data from 11 children. J Comput Assist Tomogr 1988;12:57–64.
45. Bauer BS, Wilkes GH, Kernahan DA. Incorporation of the W-plasty in repair of macrostomia. Plast Reconstr Surg 1982;70:752–757.
46. Fogh-Andersen P. Rare clefts of the face. Acta Chir Scand 1965;129:275–281.
47. Christensen K, Fogh-Andersen P. Etiological subgroups in non-syndromic isolated cleft palate. A genetic-epidemiological study of 52 Danish birth cohorts. Clin Genet 1994;46:329–335.
48. Carinci F, Pezzetti F, Scapoli L, Martinelli M, Carinci P, Tognon M. Genetics of nonsyndromic cleft lip and palate: a review of international studies and data regarding the Italian population. Cleft Lip-Craniofac J 2000;37:33–40.
49. Stoll C, Alembik Y, Dott B, Roth MP. Associated malformations in cases with oral clefts. Cleft Palate-Craniofac J 2000;37:41–47.
50. Rajabian MH, Sherkat M. An epidemiological study of oral clefts in Iran: analysis of 1669 cases. Cleft Palate-Craniofac J 2000;37:191–196.
51. Sigler A, Ontiveros DS. Nasal deformity and microform cleft lip in parents of patients with cleft lip. Cleft Palate-Craniofac J 1999;36:139–143.
52. Raposio E, Panarese P, Santi P-L. Fetal unilateral cleft lip and palate: detection of enzymatic anomalies in the amniotic fluid. Plastic Reconstr Surg 1999;103:391–394.
53. Chung KC, Kowalski CP, Kim HM, Buchman SR. Maternal cigarette smoking during pregnancy and the risk of having a child with cleft lip/palate. Plast Reconstr Surg 2000;105:485–491.
54. Thomas T, Kurihara H, Yamagishi H, Kurihara Y, Yazaki Y, Olson EN, Srivastava D. A signaling cascade involving *endothelin-1*, dHAND and *Msx 1* regulates development of neural-crest-derived branchial arch mesenchyme. Development 1998;125:3005–3014.
55. Robert B, Sassoon D, Jacq B, Gehring W, Buckingham M, et al. *Hox-7*, a mouse homeobox gene with a novel pattern of expression during embryogenesis. EMBO J 1989;8(1):91–100.
56. Brunet CL, Sharpe PM, Ferguson MWJ. Inhibition of TGFβ 3, but not TGFβ 1 or TGFβ 2 activity, prevents normal mouse embryonic palate fusion. Int J Dev Biol 1995;39:345–355.
57. Haria S, Noar JH, Sanders R. An investigation of the dentition of parents of children with cleft lip and palate. Cleft Palate-Craniofac J 2000;37:395–405.
58. Laspos CP, Kyrkanides S, Tallents RH, Moss ME, Subtelny JD. Mandibular and maxillary asymmetry in individuals with unilateral cleft lip and palate. Cleft Palate-Craniofac J 1997;34:232–239.
59. Laspos CP, Kyrkanides S, Tallents RH, Moss ME, Subtelny JD. Mandibular asymmetry in noncleft and unilateral cleft lip and palate individuals. Cleft Palate-Craniofac J 1997;34:410–416.
60. Ross RB. Commentary on Laspos et al. Cleft Palate-Craniofac J 1997;34:232–239.
61. Kyrkanides S, Bellohusen R, Subtelny JD. Skeletal asymmetries of the nasomaxillary complex in noncleft and postsurgical unilateral cleft lip and palate individuals. Cleft Palate-Craniofac J 1995;32: 428–433.

Copyright © 2003, Mosby, Inc. All rights reserved.

62. Kyrkanides S, Klambani M, Subtelny JD. Cranial base and facial skeleton asymmetries in individuals with unilateral cleft lip and palate. Cleft Palate-Craniofac J 2000;37:556–561.
63. Croen LA, Shaw GM, Wasserman CR, Tolarova MM. Racial and ethnic variations in the prevalence of orofacial clefts in California, 1983-1992. Am J Med Genet 1998;79:42–47.
64. DeMyer W. Median facial malformations and their implications for brain malformations. Birth Defects (Orig Article Ser) 1975;11: 155.
65. Johnston MC, Hassell JR, Brown KS. The embryology of cleft lip and cleft palate. Clin Plast Surg 1975;2:195–203.
66. DeMyer W. The median cleft face syndrome: differential diagnosis of cranium bifidum occultum, hypertelorism, and median cleft nose, lip and palate. Neurology 1967;17:961–971.
67. Cohen MM et al. Frontonasal dysplasia (median cleft face syndrome): comments on etiology and pathogenesis. Birth Defects 1971;7:117.
68. Warkany J, Bofinger MK, Benton C. Median facial cleft syndrome in half-sisters: dilemmas in genetic counseling. Teratology 1973;8:273–285.
69. Sedano HO, Cohen MM Jr, Jirasek J, et al. Frontonasal dysplasia. J Pediatr 1970;76:906–913.
70. Bakken AF, Aabyholm G. Frontonasal dysplasia: possible hereditary connection with other congenital defects. Clin Genet 1976;10:214–217.
71. Fontaine G, Walbaum R, Poupard B, et al. La dysplasie frontonasale. J Genet Hum 1983;31:351–365.
72. Fragoso R, Cid-Garcia A, Hernandez A, et al. Frontonasal dysplasia in the Klippel-Feil syndrome: a new associated malformation. Clin Genet 1982;22:270–273.
73. Francois J, Eggermont E, Evens L, et al. Agenesis of the corpus callosum in the median facial cleft syndrome and associated ocular malformations. Am J Ophthalmol 1973;76:241–245.
74. Fuenmayor HM. The spectrum of frontonasal dysplasia in an inbred pedigree. Clin Genet 1980;17:137.
75. Hori A. A brain with two hypophyses in median cleft face syndrome. Acta Neuropathol 1983;59:150–154.
76. Ide CH, Holt JE. Median cleft face syndrome associated with orbital hypertelorism and polysyndactyly. Eye Ear Nose Throat Monthly 1975;54:150–151.
77. Kinsey JA, Streeten BW. Ocular abnormalities in the median cleft face syndrome. Am J Ophthalmol 1977;83:261–266.
78. Roizenblatt J, Wajntal A, Diament AJ. Median cleft face syndrome or frontonasal dysplasia: a case report with associated kidney malformation. J Pediatr Ophthalmol Strabis 1979; 16:16.
79. Gorlin RJ, Anderson VE, Scott CR. Hypertrophied frenuli, oligophrenia, familial trembling and anomalies of the hand: report of four cases in one family and a forme fruste in another. N Engl J Med 1961;264:486–489.
80. Townes PL, Wood BP, McDonald JV. Further heterogeneity of the oral-facial-digital syndromes. Am J Dis Child 1976;130: 548–554.
81. Starck WJ, Epker BN. Surgical repair of a median cleft of the upper lip. J Oral Maxillofac Surg 1994;52:1217–1219.
82. Ingraham RD, Matson DD. Spina bifida and cranium bifidum. IV. An unusual nasopharyngeal encephalocele. N Engl J Med 1943;228:815–820.
83. Avanzini G, Crivelli G. A case of sphenopharyngeal encephalocele. Acta Neurochir 1970;22:205–212.
84. Baraton J, Ernest C, Poree C, et al. The neuroradiological examination of endocrine disorders of central origin in the child (precocious puberty, hypopituitarism). Pediatr Radiol 1976;4: 69–78.
85. Byrd SE, Harwood-Nash DC, Fitz CR, et al. Computed tomography in the evaluation of encephaloceles in infants and children. J Comput Assist Tomogr 1978;2:81–87.
86. Corbett JJ, Savino PJ, Schatz NJ, et al. Cavitary developmental defects of the optic disc: visual loss associated with optic pits and colobomas. Arch Neurol 1980;37:210–213.
87. Danoff D, Serbu J, French LA. Encephalocele extending into the sphenoid sinus. J Neurosurg 1966;24:684–686.
88. Ellyin F, Khatir AH, Singh SP. Hypothalamic-pituitary functions in patients with transsphenoidal encephalocele and midfacial anomalies. J Clin Endocrinol Metab 1980;51:854–856.
89. Exner A. Uber basale Cephalocelen. Dt Z Chir 1907;908:23–41.
90. Goldhammer Y, Smith JL. Optic nerve anomalies in basal encephalocele. Arch Ophthalmol 1975;93:115–118.
91. Jacob JB. Les Meningoencephaloceles anterieures de la base du crane. Maroc Med 1961;40:73–104.
92. Koenig SB, Naidich TP, Lissner G. The morning glory syndrome associated with sphenoidal encephalocele. Ophthalmology 1982;89: 1368–1373.
93. Larsen JL, Bassoe HH. Transsphenoidal meningocele with hypothalamic insufficiency. Neuroradiology 1979;18:205–209.
94. Lewin ML, Shuster MM. Transpalatal correction of basilar meningocele with cleft palate. Arch Surg 1965;90:687–693.
95. Lichtenberg G. Congenital tumour of the mouth involving the brain and connected with other malformations. Trans Lond Soc Pathol 1867;18:250.
96. Manelfe C, Starling-Jardin D, Toubi S, et al. Transsphenoidal encephalocele associated with agenesis of corpus callosum: value of metrizamide computed cisternography. J Comput Assist Tomogr 1978;2:356.
97. Modesti LM, Glasauer FE, Terplan KL. Sphenoethmoidal encephalocele: a case report with review of the literature. Childs Brain 1977;3:140–153.
98. Oldfield MC. An encephalocele associated with hypertelorism and cleft palate. Br J Surg 1938;25:757–764.
99. Pinto RS, George AE, Koslow M, et al. Neuroradiology basal anterior fossa (transethmoidal) encephaloceles. Radiology 1975;117: 79–85.
100. Pollock JA, Newton TH, Hoyt WF. Transsphenoidal and transethmoidal encephaloceles: a review of clinical and roentgen features in 8 cases. Radiology 1968;90:442–453.
101. Sadeh M, Goldhammer Y, Shacked I, et al. Basal encephalocele associated with suprasellar epidermoid cyst. Arch Neurol 1982;39: 250–252.
102. Sakoda K, Ishikawa S, Uozumil T, et al. Sphenoethmoidal meningoencephalocele associated with agenesis of corpus callosum and median cleft lip and palate: case report. J Neurosurg 1979;51:397–401.
103. Van Nouhuys JM, Bruyn GW. Nasopharyngeal transsphenoidal encephalocele, crater-like hole in the optic disc and agenesis of the corpus callosum: pneumoencephalographic visualization in a case. Psychiatr Neurol Neurochir 1964;67:243–258.
104. Weise GM, Kempe LG, Hammon WM. Transsphenoidal meningohydroencephalocele: case report. J Neurosurg 1972;37:475.
105. Kindler P. Morning glory syndrome: unusual congenital optic disk anomaly. Am J Ophthalmol 1970;69:376–384.
106. Krause U. Three cases of the morning glory syndrome. Acta Ophthalmol 1972;50:188.
107. Malbran JL, Maria-Roveda J. Megalopapila. Archos Oftal B Aires 1951;26:331–335.
108. Itakura T, Miyamoto K, Uematsu Y, et al. Bilateral morning glory syndrome associated with sphenoid encephalocele: case report. J Neurosurg 1992;77:949–951.
109. Wexler MR, Benmeir P, Umansky F, et al. Midline cleft syndrome with sphenoethmoidal encephalocele: a case report. J Craniofac Surg 1991;2:38–41.
110. Beyer WB, Quencer RM, Osher RH. Morning glory syndrome: a functional analysis including fluorescein angiography, ultrasonography, and computerized tomography. Ophthalmology 1982;89:1362–1367.
111. Yock DH Jr. Choroid plexus lipomas associated with lipoma of the corpus callosum. J Comput Assist Tomogr 1980;4:678–682.
112. Suemitsu T, Nakajima SI, Kuwajimak, et al. Lipoma of the corpus callosum: report of a case and review of the literature. Childs Brain 1979;5:476–483.
113. Zee CS, McComb JG, Segall HD, et al. Lipomas of the corpus callosum associated with frontal dysraphism. J Comput Assist Tomogr 1981;5:201–205.
114. Pascual-Castroviejo I, Pascual-Pascual SI, Perez-Higueras A. Frontonasal dysplasia and lipoma of the corpus callosum. Eur J Pediatr 1985;144:66–71.
115. Tessier P. Anatomical classification of facial, craniofacial, and lateral facial clefts. J Maxillofac Surg 1976;4:69–92.
116. Roarty JD, Pron GE, Siegel-Bartelt J, et al. Ocular manifestations of frontonasal dysplasia. Plast Reconstr Surg 1994;93:25–30.
117. Beverdam A, Brouwer A, Reijnen M, Korving J, Meijlink F. Severe nasal clefting and abnormal embryonic apoptosis in *Alx3/Alx4* double mutant mice. Development 2001;128:3975–3986.

Copyright © 2003, Mosby, Inc. All rights reserved.

118. Aleksic S, et al. Intracranial lipomas, hydrocephalus, and other CNS anomalies in oculoaricularvertebral dysplasia (Goldenhar-Gorlin syndrome). Childs Brain 1984;11:285–297.
119. Shokeir MHK. The Goldenhar syndrome: a natural history. Birth Defects 1977;13:67–83.
120. Ryals BD, Brown DC, Levin SW. Duplication of the pituitary gland as shown by MR. AJNR 1993;14:137–139.
121. Chapman S, Goldin JH, Hendel RG, et al. The median cleft face syndrome with associated cleft mandible, bifid odontoid peg and agenesis of the anterior arch of atlas. Br J Oral Maxillofac Surg 1991;29:279–281.
122. Kurlander GJ, DeMyer W, Campbell JA. Roentgenology of the median cleft face syndrome. Radiology 1967;88:473–478.
123. de Villiers JC, Cluver PF, Peter JC. Lipoma of the corpus callosum associated with frontal and facial anomalies. Acta Neurochir Suppl (Wien) 1991;53:1–6.
124. Aleksic S, Budzilovich G, Reuben R, et al. Unilateral arhinencephaly in Goldenhar-Gorlin syndrome. Dev Med Child Neurol 1975;17:498–504.
125. Aleksic S, Budzilovich G, Greco MA, Epstein F, Feigin I, Pearson J. Encephalocele (cerebellocele) in the Goldenhar-Gorlin syndrome. Eur J Pediatr 1983;40:137–138.
126. Castillo M, Mukherji SK. Facies to remember. Number 2. Median cleft face syndrome with Sedano facies type D, callosal agenesis, interhemispheric lipoma, and dermoid. Int J Neuroradiol 1995;2:154–160.
127. Castillo M. Congenital abnormalities of the nose: CT and MR findings. Am J Roentgenol I994;162:1211–1217.
128. Oostrom CAM, Vermeij-Keers C, Gilbert PM, van der Meulen JC. Median cleft of the lower lip and mandible: case reports, a new embryological hypothesis and subdivision. Plast Reconstr Surg 1996;97:313–320.
129. Surendran N, Varghese B. Midline cleft of the lower lip with cleft of the mandible and midline dermoid in the neck. J Pediatr Surg 1991;26:1387–1388.
130. Higginbottom MC, Jones KL, Hall BD, Smith DW. The amniotic band disruption complex: timing of amniotic rupture and variable spectra of consequent defects. J Pediatr 1979;95:544–549.
131. Sessions RB. Nasal dermal sinuses—new concepts and explanations. II. Laryngoscope 1982;92 (suppl 29):1–28.
132. Gorenstein A, Kern EB, Facer GW, et al. Nasal gliomas. Arch Otolaryngol 1980;106:536–540.
133. McQuown SA, Smith JD, Gallo AE Jr. Intracranial extension of nasal dermoids. Neurosurgery 1983;12:531–535.
134. Choudhury AR, Ladapo F, Mordi VP, et al. Congenital inclusion cyst of the subgaleal space. J Neurosurg 1982;56:540–544.
135. Choudhury AR, Taylor JC. Primary intranasal encephalocele: report of four cases. J Neurosurg 1982;57:552–555.
136. Card GG. Dermoid cyst of nose with intracranial extension. Arch Otolaryngol 1978;104:301–302.
137. Yeoh GPS, Bale PM, de Silva M. Nasal cerebral heterotopia: the so-called nasal glioma or sequestered encephalocele and its variants. Pediatr Pathol 1989;9:531–549.
138. Pannell BW, Hendrick EG, Hoffman JH, et al. Dermoid cysts of the anterior fontanelle. Neurosurgery 1982;10:317–323.
139. Bartlett SP, Lin KY, Grossmank R, Katowitz J. The surgical management of orbitofacial dermoids in the pediatric patient. Plast Reconstr Surg 1993;91:1208–1215.
140. Nocini PF, Barbaglio A, Dolci M, Salgarelli A. Dermoid cyst of the nose: a case report and review of the literature. J Oral Maxillofac Surg 1996;54:357–362.
141. Bradley PK. Nasal dermoids in children. Int J Pediatr Otorhinolaryngol 1981;3:63.
142. Pensler JM, Bauer BS, Naidich TP. Craniofacial dermoids. Plast Reconstr Surg 1988;82:953–958.
143. Griffith BH. Frontonasal tumors: their diagnosis and management. Plast Reconstr Surg 1976;57:692–699.
144. Wardinski TD, Pagon RA, Kropp RJ, Hayden PW, Clarren SK. Nasal dermoid sinus cysts: association with intracranial extension and multiple malformations. Cleft Palatal-Craniofac J 1991;28: 87–95.
145. Muhlbauer WD, Dittmar W. Hereditary median dermoid cysts of the nose. Br J Plast Surg 1976;29:334–340.
146. Plewes JL, Jacobson I. Familial frontonasal dermoid cysts: report of four cases. J Neurosurg 1971;34:683–686.
147. Hacker DC, Freeman JL. Intracranial extension of a nasal dermoid sinus cyst in a 56-year-old man. Head Neck 1994;16:366–371.
148. Paller AS, Pensler JM, Tadinori T. Nasal midline masses in infants and children: dermoids, encephaloceles, and gliomas Arch Dermatol 1991;127:362–366.
149. Barkovich AJ, Vandermarck P, Edwards MSB, et al. Congenital nasal masses: CT and MR imaging features in 16 cases. AJNR 1991;12:105–116.
150. Maniglia AJ, Goodwin J, Arnold JE, Ganz E. Intracranial abscesses secondary to nasal, sinus, and orbital infections in adults and children. Arch Otolaryngol 1989;115:1424–1429.
151. Rohrich RJ, Lowe JB, Schwartz MR. The role of open rhinoplasty in the management of nasal dermoid cysts. Plast Reconstr Surg 1999;104:1459–1471.
152. Johnson GF, Weisman PA. Radiological features of dermoid cysts of the nose. Radiology 1964;82:1016–1021.
153. Black BK, Smith DE. Nasal glioma: two cases with recurrence. Arch Neurol Psychiatr 1950;64:614–630.
154. Harley EH. Pediatric congenital nasal masses. Ear Nose Throat J 1991;70:28–32.
155. Walker EA Jr, Resler DR. Nasal glioma. Laryngoscope 1963;73:93–107.
156. Puppala B, Mangurten HH, McFadden J, Lygizos N, Taxy J, Pellettiere E. Nasal glioma presenting as neonatal respiratory distress. Clin Pediatr 1990;29:49–52.
157. Morgan DW, Evans JNG. Developmental nasal anomalies. J Laryngol Otol 1990;104:394–403.
158. Choudhury AR, Bandey SA, Haleem A, Sharif H. Glial heterotopias of the nose. A report of two cases. Childs Nerv Syst 1996;12:43–47.
159. Braun M, Boman F, Hascoet JM, et al. Brain tissue heterotopia in the nasopharynx: contribution of MRI to assessment of extension. J Neuroradiol 1992;19:68–74.
160. Smith KR Jr, Schwartz HG, Luse SA, et al. Nasal gliomas: a report of five cases with electron microscopy of one. J Neurosurg 1963;20: 968–982.
161. Suwanwela C, Hongsaprabhas C. Frontoethmoidal encephalomeningocele. J Neurosurg 1966;25:172–182.
162. Heacock GL, Taqi F, Biedlingmaler J. Pathology quiz case 1. Nasal glioma. Arch Otolaryngol 1992;118:548–550.
163. Kurzer A, Arbelaez N, Cassiano G. Gliomas of the face: case report. Plast Reconstr Surg 1982;69:678–682.
164. Scheiner AJ, Frayer WC, Rorke LB, Heher K. Ectopic brain tissue in the orbit. Eye 1999;13:251–254.
165. Ibekwe AO, Ikerionwu SE. Heterotopic brain tissue in the palate. J Laryngol Otol 1982;96:1155–1158.
166. Leclerc JE. Cerebral tissue heterotopia in the soft palate. J Otolaryngol 1997;26:327–329.
167. Anand VK, Melvin FM, Reed JM, Parent AD. Nasopharyngeal gliomas: diagnostic and treatment considerations. Otolaryngol Head Neck Surg 1993;109:534–539.
168. Kallman JE, Loevner LA, Yousem DM, et al. Heterotopic brain in the pterygopalatine fossa. Am J Neuroradiol 1997;18:176–179.
169. Pasyk KA, Argenta LC, Marks MW, Friedman RJ. Heterotopic brain presenting as a lip lesion. Cleft Palate J 1988;25:48–52.
170. Hendrickson M, Faye-Peterson O, Johnson DG. Cystic and solid heterotopic brain in the face and neck: a review and report of an unusual case. J Pediatr Surg 1990;25:766–768.
171. Lasjaunias P, Ginisty D, Comoy J, Landrieu P. Ectopic secreting choroid plexus in the oropharynx. Pediatr Neurosci 1985–1986;12: 205–207.
172. Wismer GL, Wilkinson AH, Goldstein JD, et al. Cystic temporofacial brain heterotopia. AJNR 1989;10:S32–S33.
173. Bossen EH, Hudson WR. Oligodendroglioma arising in heterotopic brain tissue of the soft palate and nasopharynx. Am J Surg Pathol 1987;11:571–574.
174. Lee SC, Henry MM, Gonzalez-Crussi F. Simultaneous occurrence of melanotic neuroectodermal tumor and brain heterotopia in the oropharynx. Cancer 1976;38:249–253.
175. Uemura T, Yoshikawa A, Onizuka T, Hayashi T. Heterotopic nasopharyngeal brain tissue associated with cleft palate. Cleft Palate-Craniofac J 1999;36:248–251.
176. Mahabir RC, Mohammad JA, Courtemanche DJ. Lipoma on the cleft soft palate: a case report of a rare congenital anomaly. Cleft Palate-Craniofac J 2000;37:503–505.

Copyright © 2003, Mosby, Inc. All rights reserved.

177. Vandenhaute B, Leteurtre E, Lecomte-Houcke M, et al. Epignathus teratoma: report of three cases with a review of the literature. Cleft Palate-Craniofac J 2000;37:83–91.
178. Koch BL, Myer C III, Egelhoff JC. Congenital epulis. AJNR 1997;18:739–741.
179. Fuhr AH, Krogh PHJ. Congenital epulis of the newborn: centennial review of the literature and a report of a case. Oral Surg 1972;30:30–35.
180. Damm DD, Cibull ML, Geissler RH, et al. Investigation into the histogenesis of congenital epulis of the newborn. Oral Surg Oral Med Oral Pathol 1993;76:205–212.
181. Jenkins HR, Hill CM. Spontaneous regression of congenital epulis of the newborn. Arch Dis Child 1989;64:145–147.
182. Brito JA, Ragoowansi RH, Sommoerlad BC. Double tongue, intraoral anomalies, and cleft palate—case reports and a discussion of developmental pathology. Cleft Palate-Craniofac J 2000;37: 410–415.
183. Naidich TP, Altman NR, Braffman BH, et al. Cephaloceles and related malformations. AJNR 1992;13:655–690.
184. Finerman WB, Pick EI. Intranasal encephalomeningocele. Ann Otol Rhinol Laryngol 1953;62:114–120.
185. Suwanwela C, Suwanwela N. A morphological classification of sincipital encephalomeningoceles. J Neurosurg 1972;36:201–211.
186. Matson DD. Neurosurgery in Infancy and Childhood, 2nd ed. Springfield, Ill: Thomas, 1969;61–75.
187. Mealey J Jr, Dzenitis AJ, Hockey AA. The prognosis of cephaloceles. J Neurosurg 1970;32:209–218.
188. Fisher RG, Uiklein A, Kaith HM. Spina bifida and cranium bifidum: study of 530 cases. Mayo Clin Proc 1952;27:33–38.
189. Yokota A, Kajiwara H, Kochi M, Fuwa I, Wada H. Parietal cephalocele: clinical importance of its atretic form and associated malformations. J Neurosurg 1988;69:545–551.
190. Simpson DA, David DJ, White J. Cephaloceles: treatment, outcome and antenatal diagnosis. Neurosurgery 1984;15:14–21.
191. Peter JC, Fieggen G. Congenital malformations of the brain—a neurosurgical perspective at the close of the twentieth century. Childs Nerv Syst 1999;15:635–645.
192. Blumenfeld R, Skolnik EM. Intranasal encephaloceles. Arch Otolaryngol 1965;82:527–531.
193. Kennedy EM, Gruber DP, Billmire DA, Crone KR. Transpalatal approach for the extracranial surgical repair of transsphenoidal cephaloceles in children. J Neurosurg 1997;87:677–681.
194. Hoving EW. Nasal encephaloceles. Childs Nerv Syst 2000;16:702–706.
195. Mahapatra AK, Tandon PN, Dhawan IK, Khazanchi RK. Anterior encephaloceles: a report of 30 cases. Childs Nerv Syst 1994;10:501–504.
196. Charoonsmith T, Suwanwela C. Frontoethmoidal encephalomeningocele with special reference to plastic reconstruction. Clin Plast Surg 1974;1:27–47.
197. Czech T, Reinprecht A, Matula CH, Svoboda H, Vorkapic P. Cephaloceles—experience with 42 patients. Acta Neurochir (Wien) 1995;134:125–129.
198. Jacob OJ, Rosenfeld JV, Watters DA. The repair of frontal encephaloceles in Papua New Guinea. Aust N Z J Surg 1994;64:8568–8600.
199. Smit CS, Zeeman BJ, Smith RM, et al. Frontoethmoidal meningoencephaloceles: a review of 14 consecutive patients. J Craniofac Surg 1993;4:210–214.
200. Boonvisut S, Ladpli S, Sujatanond M, et al. Morphologic study of 120 skull base defects in frontoethmoidal encephalomeningoceles. Plast Reconstr Surg 1998;101:1784–1795.
201. Rappoport RL II, Dunn RC, Alhady F. Anterior encephalocele. J Neurosurg 1981;54:213.
202. Sargent LA, Seyfer AE, Gunby EN. Nasal encephaloceles: definitive one-stage reconstruction. J Neurosurg 1988;68:571–575.
203. Blumenfeld R, Skolnick EM. Intranasal encephaloceles. Arch Otolaryngol 1965;82:527–531.
204. David DJ, Sheffield L, Simpson D, White J. Frontoethmoidal meningoencephaloceles: morphology and treatment. Br J Plast Surg 1984;37:271–284.
205. Richards CGM. Frontoethmoidal meningoencephalocele: a common and severe congenital abnormality in South East Asia. Arch Dis Child 1992;67:717–719.
206. Brown MS, Sheridan-Pereira M. Outlook for the child with a cephalocele. Pediatrics 1992;90:914–919.
207. Zinreich SJ, Borders JC, Eisele DW, Mattox DE, Long DM, Kennedy DW. The utility of magnetic resonance imaging in the diagnosis of intranasal meningoencephaloceles. Arch Otolaryngol Head Neck Surg 1992;118:1253–1256.
208. Lowe LH, Booth TN, Joglar JM, Rollins NK. Midface anomalies in children. RadioGraphics 2000;20:907–922.
209. Moore MH, Lodge ML, David DJ. Basal cephalocele: imaging and exposing the hernia. Br J Plast Surg 1993;46:497–502.
210. Losken HW, Morris WMM, Earle JW. Unilateral exophthalmos caused by an anterior ethmoidal meningoencephalocele. Plast Reconstr Surg 1992;89:742–745.
211. Hao S-P, Wang H-S, Lui T-N. Transnasal endoscopic management of basal encephalocele-craniotomy is no longer mandatory. Am J Otolaryngol 1995;16:196–199.
212. Pollock JA, Newton TH, Hoyt WF. Transsphenoidal and transethmoidal encephaloceles: a review of clinical and roentgen features in 8 cases. Radiology 1968;90:442–453.
213. Sadeh M, Goldhammer Y, Shacked I, et al. Basal encephalocele associated with suprasellar epidermoid cyst. Arch Neurol 1982;39: 250–252.
214. Sakoda K, Ishikawa S, Uozumil T, et al. Sphenoethmoidal meningoencephalocele associated with agenesis of corpus callosum and median cleft lip and palate: case report. J Neurosurg 1979;51:397–401.
215. Van Nouhuys JM, Bruyn GW. Nasopharyngeal transsphenoidal encephalocele, crater-like hole in the optic disc and agenesis of the corpus callosum: pneumoencephalographic visualization in a case. Psychiatr Neurol Neurochir 1964;67:243–258.
216. Weise GM, Kempe LG, Hammon WM. Transsphenoidal meningohydroencephalocele: case report. J Neurosurg 1972;37:475.
217. Blustajn J, Netchine I, Fredy D, et al. Dysgenesis of the internal carotid artery associated with transsphenoidal encephalocele: a neural crest syndrome? AJNR 1999;20:1154–1157.
218. Yokota A, Matsukado Y, Fuwa I, et al. Anterior basal encephalocele of the neonatal and infantile period. Neurosurgery 1986;19:468–478.
219. Elster AD, Branch CL. Transalar sphenoidal encephaloceles: clinical and radiologic findings. Radiology 1989;170:245–247.
220. Soyer PH, Dobbelaere P, Benoit S. Case report: transalar sphenoidal encephalocele. Uncommon clinical and radiological findings. Clin Radiol 1991;43:65–67.
221. Raftopoulos C, David P, Allard S, Ickx B, Baleriaux D. Endoscopic treatment of an oral cephalocele. J Neurosurg 1994;81:308–312.
222. Naidich TP, Heier LA, Osborn RE, Castillo M, Bozorgmanesh A, Altman N. Facies to remember number 6. Congenital dacryocystocele. Int J Neurol 1996;2:389–396.
223. Mansour A, Cheng K, Mumma J, et al. Congenital dacryocele: a collaborative review. Ophthalmology 1991;98:1744–1751.
224. Broggi R. The treatment of congenital dacryostenosis. Arch Ophthalmol 1959;61:30–36.
225. Ffooks O. Dacryocystitis in infancy. Br J Ophthalmol 1962;46:422–434.
226. Noda S, Hayasaka S, Setogawa T. Congenital nasolacrimal duct obstruction in Japanese infants: its incidence and treatment with massage. J Pediatr Ophthalmol Strabismus 1991;28:20–22.
227. Petersen R, Robb R. The natural course of congenital obstruction of the nasolacrimal duct. J Pediatr Ophthalmol Strabismus 1978;15: 246–250.
228. Nordlow W, Vennerholm I. Congenital atresiae of the lacrimal passages: their occurrence and treatment. Acta Ophthalmol 1953;31: 367–371.
229. Patrick R. Lacrimal secretion in full-term and premature babies. Trans Ophthalmol Soc UK 1974;94:283–290.
230. Cibis G, Spurney R, Waeltermann J. Radiographic visualization of congenital lacrimal sac mucoceles. Ann Ophthalmol 1986;18: 68–69.
231. Menestrina L, Osborn R. Congenital dacryocystocele with intranasal extension: correlation of computed tomography and magnetic resonance imaging. J Am Osteopathol Assoc 1990;90:264–268.
232. Meyer J, Quint D, Holmes J, Witrak B. Infected congenital mucocele of the nasolacrimal duct. AJNR 1993;14:1008–1010.
233. Rand P, Ball WJ, Kulwin D. Congenital nasolacrimal mucoceles: CT evaluation. Radiology 1989;173:691–694.

Copyright © 2003, Mosby, Inc. All rights reserved.

234. Divine R, Anderson R, Bumsted R. Bilateral congenital lacrimal sac mucoceles with nasal extension and drainage. Arch Ophthalmol 1983;10:246–248.
235. Edmond J, Keech RV. Congenital nasolacrimal sac mucocele associated with respiratory distress. J Pediatr Ophthalmol Strabismus 1991;28:287–289.
236. Castillo M, Merten D, Weissler M. Bilateral nasolacrimal duct mucocele, a rare cause of respiratory distress: CT findings in two newborns. AJNR 1993;14:1011–1013.
237. Yee S, Siebert RW, Bower C, Glasier C. Congenital nasolacrimal duct mucocele: a cause of respiratory distress. Int J Pediatr Otorhinolaryngol 1994;29:151–158.
238. Peloquin L, Arcand P, Abela A. Endonasal dacryocystocele of the newborn. J Otolaryngol 1995;24:84–86.
239. DeMyer W. Holoprosencephaly. In: Vinken PJ, Bruyn GW, eds. Handbook of Clinical Neurology. Amsterdam: North Holland, 1977; 431–478.
240. Roessler E, Muenke M. The molecular genetics of holoprosencephaly: a model of brain development for the next century. Childs Nerv Syst 1999;15:646–651.
241. Nishimura H, Tanimura T, Semba R, Uwabe C. Normal development of early embryos: observation of 90 specimens at Carnegie stages 7 to 13. Teratology 1974;10:1–5.
242. Matsunaga E, Shiota K. Holoprosencephaly in human embryos: epidemiologic studies of 150 cases. Teratology 1977;16:261–272.
243. Urioste M, Valcarcel E, Gomez MA, Pinel I, Garcia de Leon R, Diaz de Bustamante A, Tebar R, Martinez-Frias ML. Holoprosencephaly and trisomy 21 in a child born to a nondiabetic mother. Am J Med Genet 1988;30:925–928.
244. Manelfe C, Sevely A. Etude neuroradiologique des holoprosencephalies (Neuroradiological study of holoprosencephalies). J Neuroradiol 1982;9:15–45.
245. Pauli RM, Pettersen JC, Arya S, Gilbert EF. Familial agnathiaholoprosencephaly. Am J Med Genet 1983;14:677–698.
246. Cohen MM Jr. Perspectives on holoprosencephaly: part I. Epidemiology, genetics, and syndromology. Teratology 1989;40:211–235.
247. Bachman H, Clark RD, Salahi W. Holoprosencephaly and polydactyly: a possible expression of the hydrolethalus syndrome. J Med Genet 1990;27:50–52.
248. Odent S, Attie-Bitach T, Blayau M, et al. Expression of the *Sonic Hedgehog* (*SHH*) gene during early human development and phenotypic expression of new mutations causing holoprosencephaly. Hum Mol Genet 1999;8:1683–1689.
249. Porter JA, Young KE, Beachy PA. Cholesterol modification of *Hedgehog* signaling proteins in animal development. Science 1996;274:255–259.
250. Pennisi E. Gene linkd to commonest cancer. Science 1996;272:1583–1584.
251. Kastury K, Druck T, Huebner K, et al. Chromosome locations of human *EMX* and *OTX* genes. Genomics 1994;22:41–45.
252. Simeone A, Acampora D, Gulisano M, Stornaiuolo A, Boncinelli E. Nested expression domains of four homeobox genes in developing rostral brain. Nature 1992;358:687–690.
253. Simeone A, Gulisano M, Acampora D, Stornaiuolo A, Rambaldi M, Boncinelli E. Two vertebrate homeobox genes related to the *Drosophila* empty spiracles gene are expressed in the embryonic cerebral cortex. EMBO J 1992;11:2541–2550.
254. Yoshida M, Suda Y, Matsuo I, Miyamoto N, Takeda N, Kuratani S, Aizawa S. *Emx 1* and *Emx 2* functions in development of dorsal telencephalon. Development 1997;124:101–111.
255. Rakic P. Neurocreationism—making new cortical maps. Science 2001;294:1011–1012.
256. Oliver G, Mailhos A, Wehr R, et al. *Six3*, a murine homologue of the sine oculis gene, demarcates the most anterior border of the developing neural plate and is expressed during eye development. Development 1995;121:4045–4055.
257. Roessler E, Belloni E, Gaudenz K, et al. Mutations in the human *Sonic Hedgehog* gene cause holoprosencephaly. Nature Genet 1996;14:357–360.
258. Meisler M. Mutation watch. Mammalian Genome 1997;8:305–306.
259. Castillo M, Mukherji SK. Disorders of ventral induction: holoprosencephalies. In: Castillo M, Mukherji SK, eds. Imaging of the Pediatric Head, Neck, and Spine. Philadelphia: Lippincott-Raven, 1996;33–36.
260. Smith MM, Thompson JE, Naidich TP, Castillo M, Thomas D, Mukherji SK. Facies to remember. Cebocephaly with single midline proboscis. Alobar holoprosencephaly. Int J Neurol 1996;3: 251–263.
261. Probst FP, Brun A. Structural organization of holospheric brains. In: Probst FP, ed. The Prosencephalies. Berlin: Springer-Verlag, 1979; 35–43.
262. Porteous ME, Wright C, Smith D, Burn J. Agnathia-holoprosencephaly: a new recessive syndrome? Clin Dysmorphol 1993;2:161–164.
263. Friede RL. Developmental Neuropathology, 2nd ed. Berlin: Springer-Verlag, 1989.
264. Kurokawa Y, Tsuchita H, Sohma T, Kitami K, Takeda T, Hattori S. Holoprosencephaly with Dandy-Walker cyst: rare coexistence of two major malformations. Childs Nerv Syst 1990;6:51–53.
265. Osaka K, Matsumoto S. Holoprosencephaly in neurosurgical practice. Neurosurgery 1978;48:787–803.
266. Sulik KK, Johnston MC, Smiley SJ, Speight HS, Jarvis BE. Mandibulofacial dysostosis (Treacher Collins syndrome): a new proposal for its pathogenesis. Am J Med Genet 1987;27:359–372.
267. Naidich TP, Smith MS, Castillo M, Thompson JE, Sloan GM, Jayakar P, Mukherji SK. Facies to remember. Number 7. Hemifacial microsomia. Goldenhar syndrome. OAV complex. Int J Neuroradiol 1996;2:437–449.
268. Goldenhar M. Associations malformatives de l'oeil et de l'oreille, en particulier le syndrome dermoide epibulbaire-appendices auriculares-fistula auris congenita et ses relations avec la dysostose mandibulofaciale. J Genet Hum 1952;1:243–282.
269. Feingold M, Baum J. Goldenhar's syndrome. Am J Dis Child 1978;132:136–138.
270. Gorlin RJ, Jue KL, Jacobsen U, Goldschmidt E. Oculoauriculovertebral dysplasia. J Pediatr 1963;63:991–999.
271. Rollnick BR, Kaye CI. Hemifacial microsomia and variants: pedigree data. Am J Med Genet 1983;15:233–253.
272. Cohen MM Jr, Rollnick BR, Kaye CI. Oculoauriculovertebral spectrum: an updated critique. Cleft Palate J 1989;26:276–286.
273. Beals RK, Robbins JR, Rolfe B. Anomalies associated with vertebral malformations. Spine 1993;18:1329–1332.
274. David DJ, Mahatumarat C, Cooter RD. Hemifacial microsomia: a multisystem classification. Plast Reconstr Surg 1987;80:525–535.
275. Mansour AM, Wang F, Henkind P, Goldberg R, Shprintzen R. Ocular findings in the facioauriculovertebral sequence (Goldenhar-Gorlin syndrome). Am J Ophthalmol 1985;100:555–559.
276. Stoll C, Viville B, Treisser A, et al. A family with dominant oculoauriculovertebral spectrum. Am J Med Genet 1998;78: 345–349.
277. Gosain AK, McCarthy JG, Pinto RS. Cervicovertebral anomalies and basilar impression in Goldenhar syndrome. Plast Reconstr Surg 1994;93:498–506.
278. Zelante L, Gasparini P, Scanderbeg AC, et al. Goldenhar complex: a further case with uncommon associated anomalies. Am J Med Genet 1997;69:418–421.
279. Figueroa AA, Friede H. Craniovertebral malformations in hemifacial microsomia. J Craniofac Genet Dev Biol Suppl 1985;l:167–178.
280. Cousley RRJ, Wilson DJ. Hemifacial micosomia: developmental consequence of perturbation of the auriculofacial cartilage model? Am J Med Genet 1992;42:461–466.
281. Foerst-Potts L, Sadler TW. Disruption of *Msx-1* and *Msx-2* reveals roles for these genes in craniofacial, eye, and axial development. Dev Dyn 1997;209:70–84.
282. Satokata I, Maas R. *Msx1* deficient mice exhibit cleft palate and abnormalities of craniofacial and tooth development. Nat Genet 1994;6:348–356.
283. Sadler LS, Robinson LK, Msall ME. Diabetic embryopathy: possible pathogenesis. Am J Med Genet 1995;55:363–366.
284. Horgan JE, Padwa BL, LaBrie RA, Mulliken JB. OMENS-plus: analysis of craniofacial and extracraniofacial anomalies in hemifacial microsomia. Cleft Palate-Craniofac J 1995;32:405–412.
285. Kearns GJ, Dent B, Padwa BL, et al. Progression of facial asymmetry in hemifacial microsomia. Plast Reconstr Surg 2000;105: 492–498.
286. Rollnick BR, Kaye CI, Nagatoshi K, Hauck W, Martin AO. Oculoauriculovertebral dysplasia and variants: phenotypic characteristics of 294 patients. Am J Med Genet 1987;26:361–375.

Copyright © 2003, Mosby, Inc. All rights reserved.

287. Smahel Z, Horak I. Craniofacial changes in unilateral microtia: I. An anthropometric study. J Craniofac Genet Dev BioI 1984;4: 7–16.
288. Smahel Z. Craniofacial changes in unilateral microtia: II. An x-ray study. J Craniofac Genet Dev Biol 1984;4:17–31.
289. Smahel Z. Craniofacial changes in hemifacial microsomia. J Craniofac Genet Dev Biol 1986;6:151–170.
290. Vento AR, LaBrie RA, Mulliken JB. The O.M.E.N.S. classification of hemifacial microsomia. Cleft Palate-Craniofac J 1991;28: 68–77.
291. Marsh JL, Baca D, Vannier MW. Facial musculoskeletal asymmetry in hemifacial microsomia. Cleft Palate J 1989;26:292–302.
292. Johnsen DC, Weissman BM, Murray GS, et al. Enamel defects: a developmental marker for hemifacial microsomia. Am J Med Genet 1990;36:444–448.
293. Caldarelli DD, Hutchinson JG Jr, Pruzansky S, Valvassori GE. A comparison of microtia and temporal bone anomalies in hemifacial microsomia and mandibulofacial dysostosis. Cleft Palate J 1980;17: 103–110.
294. Bassila MK, Goldberg R. The association of facial palsy and/or sensorineural hearing loss in patients with hemifacial microsomia. Cleft Palate J 1989;26:287–291.
295. Kirkham TH. Goldenhar's syndrome with inner ear defects. J Laryngol Otol 1970;84:855–856.
296. Manfré L, Genuardi P, Tortorici M, Legalla R. Absence of the common crus in Goldenhar syndrome. AJNR 1997;18:773–775.
297. Baum JL, Feingold M. Ocular aspects of Goldenhar's syndrome. Am J Ophthalmol 1973;75:250–257.
298. Elsas FJ, Green WR. Epibulbar tumors in childhood. Am J Ophthalmol 1975;79:1001–1007.
299. Caldarelli DD, Hutchinson JC Jr, Gould HJ. Hemifacial microsomia: priorities and sequence of comprehensive otologic management. Cleft Palate J 1980;17:111–115.
300. Padwa BL, Bruneteau RJ, Mulliken JB. Association between ''plagiocephaly'' and hemifacial microsomia. Am J Med Genet 1993;47:1202–1207.
301. Edwards SJ et al. Am J Hum Genet 1997;60:515–524.
302. Rune B, Sarnas KV, Aberg M, et al. Mandibulofacial dysostosis—variability in facial morphology and growth: a long-term profile roentgenographic and roentgen stereometric analysis of three patients. Cleft Palate-Craniofac J 1999;36:110–122.
303. Halal F, Herrmann J, Pallister PD, Opitz JM, Desgranges M-F, Grenier G. Differential diagnosis of Nager acrofacial dysostosis syndrome: report of four patients with Nager syndrome and discussion of related syndromes. Am J Med Genet 1983;14: 209–224.
304. Marques IL, Barbieri MA, Bettiol H. Etiopathogenesis of isolated Robin sequence. Cleft Palate-Craniofac J 1998;35:517–525.
305. Fernbach SK, Naidich TP. Radiological evaluation of craniosynostosis. In: Cohen MM Jr, ed. Craniosynostosis. Diagnosis, Evaluation and Management. New York: Raven Press, 1986;191–214.
306. Cohen MM Jr, MacLean RE. Craniosynostosis. Diagnosis, Evaluation, and Management, 2nd ed. New York: Oxford University Press, 2000.
307. Zimmerman RA. Skull development and abnormalities. In: Zimmerman RA, Gibby WA, Carmody RF, eds. Neuroimaging. Clinical and Physical Principles. New York: Springer, 2000;457–489.
308. Renier D, Lajeunie E, Arnaud E, Marchac D, et al. Management of craniosynostosis. Childs Nerv Syst 2000;16:645–658.
309. Hodges FJ III. Alterations in the skull with aging. In: Newton TH, Potts DG, eds. Radiology of the Skull and Brain, Vol. One, Book One, The Skull. St. Louis: CV Mosby, 1971;132–153.
310. Gooding CA. Cranial sutures and fontanelles. In: Newton TH, Potts DG, eds. Radiology of the Skull and Brain, Vol. One, Book One, The Skull. St. Louis: CV Mosby, 1971;216–237.
311. Huang MH, Mouradian WE, Cohen SR, Gruss JS, et al. The differential diagnosis of abnormal head shapes: separating craniosynostosis from positional deformities and normal variants. Cleft Palate-Craniofac J 1998;35:204–211.
312. Smits M, Wilmink JT. Synostotic and positional plagiocephaly. Two types of skull deformity studied with three-dimensional computed tomography. Int J Neurol 1998;4:405–411.
313. Park TS, Robinson S. Nonsyndromic craniosynostosis. In: McLone DG, ed-in-chief. Pediatric Neurosurgery: Surgery of the Developing Nervous System, 4th ed. Philadelphia: WB Saunders, 2001;345–361.
314. Posnick JC, Lin KY, Chen P, et al. Metopic synostosis: quantitative assessment of presenting deformity and surgical results based on CT scans. Plast Reconstr Surg 1994;93:16–24.
315. Reardon W, Winter RM, Rutland P, et al. Mutations in the fibroblast growth receptor 2 gene cause Crouzon syndrome. Nature Genet 1994;8:98–103.
316. Muenke M, Schell U, Hehr A, et al. A common mutation in the fibroblast growth factor receptor 1 gene in Pfeiffer syndrome. Nature Genet 1994;8:269–274.
317. Wilkie AOM, Slaney SF, Oldridge M, et al. Apert syndrome results from localized mutations of *FGFR2* and is allelic with Crouzon syndrome. Nature Genet 1995;9:165–172.
318. Preston RA, Post JC, Keats BJ, et al: A gene for Crouzon craniofacial dysostosis maps to the long arm of chromosome 10. Nature Genet 1994;7:149–153.
319. Shiang R, Thompson LM, Zhu YZ, et al. Mutations in the transmembrane domain of *FGFR3* cause the most common genetic form of dwarfism, achondroplasia. Cell 1994;78:335–342.
320. Rousseau F, Bonaventure J, Legeai-Mallet L, et al. Mutations in the gene encoding fibroblast growth factor receptor-3 in achondroplasia. Nature 1994;371:252–254.
321. Pauli RM, Conroy MM, Langer LO Jr, et al. Homozygous achondroplasia with survival beyond infancy. Am J Med Genet 1983;16:459–473.
322. Brueton LA, van Herwerden L, Chotai KA, et al. The mapping of a gene for craniosynostosis: evidence for linkage of the Saethre-Chotzen syndrome to distal chromosome 7p. J Med Genet 1992;29:681–685.
323. Vortkamp A, Gessler M, Grzeschik KH. *GLI3* zinc-finger gene interrupted by translocations in Greig syndrome families. Nature 1991;352:539–540.
324. Hui CC, Joyner AL. A mouse model of Greig cephalopolysyndactyly syndrome: the extra-toes mutation contains an intragenic deletion of the *Gli3* gene. Nature Genet 1993;3:241–246.
325. Mo R, Freer AM, Zinyk DL, et al. Specific and redundant functions of *Gli2* and *Gli3* zinc finger genes in skeletal patterning and development. Development 1997;124:113–123.
326. Müller U et al. Molecular genetics of craniosynostotic syndromes Arch Clin Exp Ophthalmol 1997;235:545–550.
327. Gorlin RJ. Fibroblast growth factors, their receptors and receptor disorders. Am J Cranio-Maxillofac Surg 1997;25:69–79.
328. Wilkie AOM. Craniosynostosis: genes and mechanisms. Human Mol Genet 1997;6:1647–1656.
329. Lejeunie E et al. Craniosynostosis: from a clinical description to an understanding of bone formation of the skull. Childs Nerv Syst 1999;15:676–680.
330. Sarkar S et al. FGF2 promotes skeletogenic differentiation of cranial neural crest cells. Development 2001;128:2143–2152.
331. Iseki S, Wilkie AOM, Morriss-Kay GM. *Fgfr1* and *Fgfr2* have distinct differentiation- and proliferation-related roles in the developing mouse skull vault. Development 1999;126:5611–5620.
332. Iseki S, Wilkie AOM, Heath JK, et al. *Fgfr2* and *osteopontin* domains in the developing skull vault are mutually exclusive and can be altered by locally applied FGF2. Development 1997;124:3375–3384.
333. Ackerman A et al. Skeletal malformations linked to fibroblast growth factor receptors. Int J Neuroradiol 1999;5:252–260.
334. Rollins N et al. MR venography in children with complex craniosynostosis. Pediatr Neurosurg 2000;32:308–315.
335. Robson et al. Prominent basal emissary foramina in syndromic craniosynostosis: correlation with phenotypic and molecular diagnoses. AJNR 2000;21:1707–1717.
336. Di Rocco C, Velardi F. Syndromic craniofacial malformations. In: McLone DG, ed.-in-chief. Pediatric Neurosurgery: Surgery of the Developing Nervous System, 4th ed. Philadelphia: WB Saunders, 2001;378–395.
337. Pfeiffer RA et al. Further delineation and review of the literature. Am J Med Genet 1964;90:301–320.
338. Cohen MM Jr. Pfeiffer syndrome update: clinical subtypes and guidelines for differential diagnosis. Am J Med Genet 1993;45:300–307.
339. Gorlin RJ. Fibroblast growth factors, their receptors and receptor disorders. Am J Cranio-Maxillofac Surg 1997;25:69–79.

Copyright © 2003, Mosby, Inc. All rights reserved.

340. Jackson CE, Weiss L, Reynolds WA, et al. Craniosynostosis, midface hypoplasia, and foot abnormalities: an autosomal dominant phenotype in a large Amish kindred. J Pediatr 1976;88:963–968.
341. Muenke M, Gripp KW, McDonald-McGinn D, et al. A unique point mutation in the *FGFR3* gene defines a new craniosynostosis syndrome. Am J Hum Genet 1997;60:555–564.
342. Couly GF, Coltey PM, Le Douarin NM. The triple origin of skull in higher vertebrates: a study in quail-chick chimeras. Development 1993;117:409–429.
343. Kawamoto HK Jr. The kaleidoscopic world of rare craniofacial clefts: order out of chaos (Tessier classification). Clin Plast Surg 1976;3:529.
344. Goodman RM, Gorlin RJ. Atlas of the Face in Genetic Disorders, 2nd ed. St. Louis: CV Mosby, 1977.
345. Derkay CS, Tunnessen WW Jr. Pictures of the month case 1 nasal glioma. Arch Pediatr Adolesc Med 1994;148:953–954.

Copyright © 2003, Mosby, Inc. All rights reserved.

2

Anatomy and Physiology

Peter M. Som, Joel M.A. Shugar, and Margaret S. Brandwein

INTRODUCTION TO THE SINONASAL CAVITIES
ANATOMY AND PHYSIOLOGY
- The Nose and Nasal Fossae
- Physiology
- Vascular Supply
- Nerve Supply

THE PARANASAL SINUSES
- Ethmoid Sinus
- Frontal Sinus
- Sphenoid Sinus
- Maxillary Sinus

PLAIN FILMS
PLAIN FILM VIEWS
- Horizontal Beam 5° Off-Lateral View
- Modified Caldwell View
- Modified Waters View
- Modified Base (Submentovertical or Submentovertex) View
- Rhese or Oblique View
- Nasal Bone Lateral View
- Nasal Bone Axial View

IMAGING ANATOMY
PLAIN FILM ANATOMY
- The Frontal Sinuses
- The Ethmoid Sinuses
- The Maxillary Sinuses
- The Sphenoid Sinuses
- Associated Structures Surrounding the Paranasal Sinuses

SECTIONAL IMAGING TECHNIQUES
- Computed Tomography
- Magnetic Resonance Imaging

SECTIONAL IMAGING ANATOMY
- The Nasal/Palatal Region
- The Pterygopalatine Fossa
- The Pterygoid Plates
- The Nasal Septum
- The Olfactory Recesses and Nasal Atrium
- The Margins of the Orbit
- The Lacrimal Fossa and Nasolacrimal Duct
- The Sphenoid Sinus Septum
- The Maxillary Sinus Walls

THE INTEGUMENT OF THE FACE AND SCALP
- The Facial Muscles
- Scalp and Forehead
- Orbit
- Cheek and Lips (Mouth)
- Cutaneous Innervation of the Face
- Arterial Supply of the Face and Scalp
- Venous Drainage of the Face and Scalp

INTRODUCTION TO THE SINONASAL CAVITIES

For most physicians, the ubiquitous nature of the allergic and infectious diseases that affect the paranasal sinuses and nasal cavities (sinonasal cavities) renders them the most often imaged and therefore the best known areas of the head and neck. In addition, facial fractures are common and range from the broken nose to the more severe complex fractures. Lastly, the disfiguring tumors of the sinonasal cavities have earned their fearsome reputation because of their poor prognosis and the facial carnage they wreak. It thus seems reasonable to start the discussion of head and neck imaging with the sinonasal region.

Copyright © 2003, Mosby, Inc. All rights reserved.

ANATOMY AND PHYSIOLOGY

The Nose and Nasal Fossae

The term *nose* usually refers to the external nose that projects ventral to the rest of the face, while the terms *nasal fossae* or *nasal cavities* refer to the internal nasal airways. Topographically the nose can be divided into subunits that have practical importance in reconstructive surgery.[1–6] These subunits consist of the nasal dorsum, nasal sidewalls, nasal tip and columella, alar lobule, and supraalar facets. The nasion is the junction of the root of the nose with the forehead, while the lower or caudal free margin of the nose is formed by the alar rim, columella, and tip. On either side, the lateral lower margin of the nose has an expanded, rounded area referred to as the alar lobule, which consists of skin and soft tissue posterior and inferior to the lateral crus of the lower lateral cartilage. The dorsum of the nose consists of the dorsum of the nasal bones superiorly and the dorsal border of the quadrangular cartilage with the medial attachments of the upper lateral cartilages inferiorly (Fig. 2-1). The bony-cartilaginous junction is called the rhinion. The junction of the alae with the face is known as the alar-facial junction.

The nose has an overall pyramidal shape. Superiorly on either side of the nose, the sidewall of the pyramid consists of the nasal bone and the ascending process of the maxilla with which it articulates. The nasal bones are narrower and thicker cranially where they articulate with the nasal process of the frontal bones. The posterior surface of the nasal bones in the midline articulates with the perpendicular plate of the ethmoid bone superiorly and the quadrangular cartilage of the nasal septum inferiorly. Caudally the nasal bones become wider and thinner. Inferiorly the nasal bones attach to and overlap the cephalic portion of the upper lateral cartilages. The bony pyramid thus stabilizes the upper lateral cartilages that form the inferior sidewall of the nasal cartilaginous pyramid.[1] Rarely, the nasal bones are fused in the midline or are absent and replaced by an elongated frontal process of the maxilla. The nasal bones are very infrequently multiple.

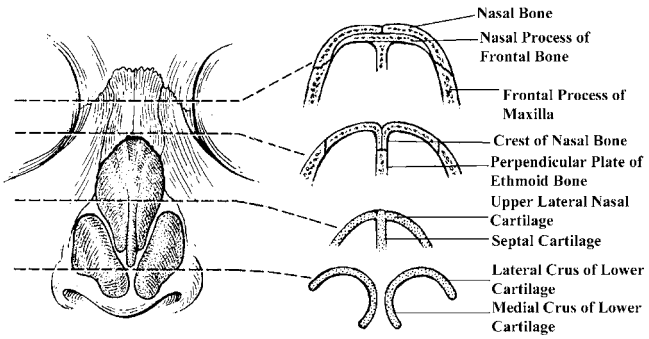

FIGURE 2-2 Frontal view of the nose with cross-sectional diagrams at various levels illustrating the support structure of the nasal pyramid. (Modified from Hollinshead H. Anatomy for Surgeons. The Head and Neck. Vol 1. New York, NY: Hoeber-Harper, 1954.)

VIEW IMAGE

The medial borders of the upper lateral cartilages are attached to the dorsum of the quadrangular cartilage of the septum and to each other. Laterally the upper lateral cartilages attach to the margin of the pyriform aperture (the osseous opening of the nasal cavity in the facial skeleton) by dense fibroareolar tissue. It is not uncommon to find accessory sesamoid cartilages in this area. The inferior border of the upper lateral cartilages are not attached and thus are mobile (Figs. 2-2 and 2-3).[2–5, 7]

On entering the nasal cavity, inspired air traverses the nasal valve. This is a circular area encompassed by the nasal septum, upper lateral cartilage, tip of the inferior turbinate, and floor of the nose. The total area encompassed by this valve provides the most important resistance to air flow in the nasal cavity.[8] Of slightly lesser importance is the angle formed by the meeting of the quadrangular cartilage of the nasal septum and the inferior border of the upper lateral cartilages, which is known as the nasal valve angle. Due to

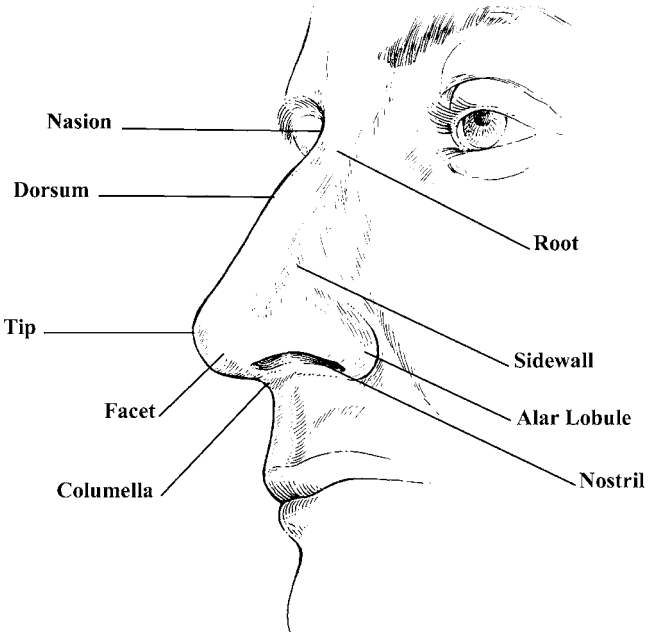

FIGURE 2-1 The surface anatomy of the nose illustrated in a left anterior oblique view.

VIEW IMAGE

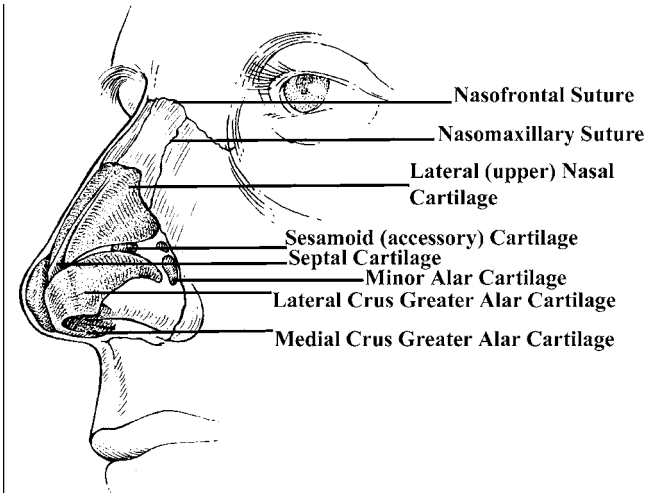

FIGURE 2-3 Left anterior oblique view of the nasal skeleton indicating the osseous and cartilagenous anatomy.

VIEW IMAGE

Copyright © 2003, Mosby, Inc. All rights reserved.

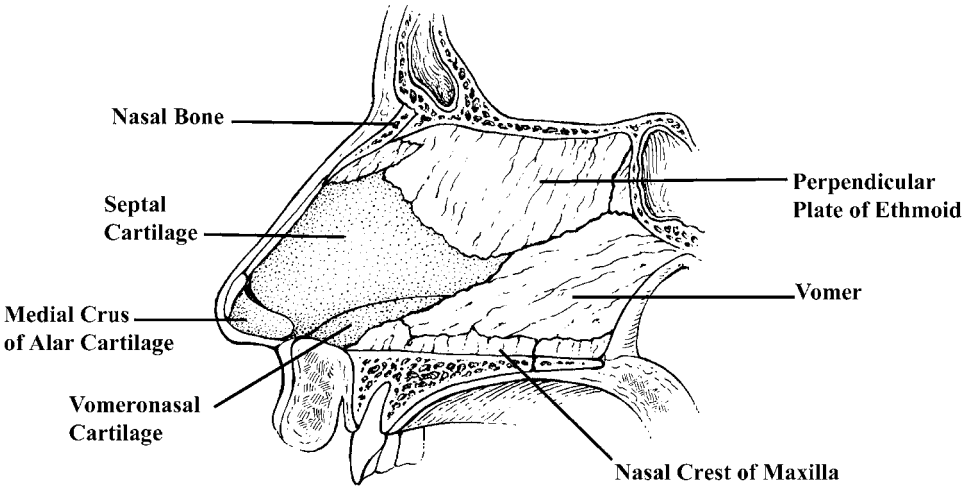

VIEW IMAGE

FIGURE 2-4 Diagram of a sagittal view of the nasal septum and hard palate.

its mobile nature, it is a dynamic structure that narrows and widens with the phases of respiration. It is thus a critical factor in determining airflow through the nasal cavity, and surgery in this area must preserve its integrity.

The lower paired lateral cartilages give the shape to the tip of the nose and base of the pyramid. Each lower lateral cartilage consists of medial crura and lateral crura. The point at which they meet dorsally is called the dome. The medial crura lie adjacent to the caudal end of the septum and attach to each other by loose connective tissue. At the dome, the lateral crura on either side extend superiorly and obliquely posteriorly toward the pyriform aperture, where they are attached by fibrous tissue. Sesamoid cartilages are also frequently found in this area of attachment. As each lateral crus extends superiorly, so does its lower border. The lower border thus does not parallel the alar rim. The soft tissue of the nose immediately below this area is devoid of cartilaginous support and is known as the alar lobule. The superior border of the lateral crus overlaps the distal ends of the upper lateral cartilages for a variable distance and is attached only by connective tissue. The skin covering the nose drapes across the angle formed at the junction of the medial and lateral crura, forming a triangular area called the facet (Figs. 2-2 and 2-3).

The nasal cavity on either side is separated by the nasal septum. The septum also helps support the bony and cartilaginous vault and the nasal tip. The main components of the nasal septum are the vomer, the perpendicular plate of the ethmoid, the quadrangular cartilage, the membranous septum, and the columella. Nasal bony crests from the upper surfaces of the palatine processes of the maxillae and the horizontal plates of the palatine bones also contribute to the inferior nasal septum (Fig. 2-4). The vomer may be bilaminar, due to its embryologic origin, and it and the perpendicular plate of the ethmoid bone are at times pneumatized. The perpendicular plate of the ethmoid fuses with the cribriform plate superiorly, and nasal septal surgery can cause a fracture of the cribriform plate, with a resultant cerebrospinal fluid leak. The vomer articulates superiorly with the perpendicular plate of the ethmoid and the crest of the sphenoid, anteriorly with the quadrangular cartilage, and inferiorly with the palatine bone and nasal crest of the maxilla. The vomer and quadrangular cartilage have a tongue-in-groove relationship with the thin edge of the cartilage, fitting into a groove of the vomer. The posterior border of the vomer is free and divides the posterior choanae (Fig. 2-4).

The quadrangular cartilage is the most important surgical component of the septum due to its supportive function, and it is that portion of the septum anterior to the pyriform aperture that is the most significant in this role.[1] Thus the portion of the septum that provides the principal support to the nose lies anterior to a line drawn from the rhinion to the nasal spine, and injury to this region can result in a saddle nose deformity. The septal cartilage has an unusually mobile articulation with the surrounding bones, with only connective tissue stabilizing this junction. This relationship allows mobility that minimizes the chance of fracture or dislocation.

The membranous septum is that portion of the septum that lies between the caudal end of the cartilaginous septum and the columella. It is comprised only of a core of subcutaneous tissue lined on either side by vestibular skin. The columella is the most inferior part of the septum, and it has as its central support the medial crus of the right and left lower lateral cartilages. The inferior border of the columella and the lower margin of the nasal alae form the boundaries of the nostrils or nares, which are the external openings of the nose and which provide entrance into the nasal fossae.

The nasal muscles are the procerus, nasalis (compressor naris including both transverse and alar parts), levator labii superioris alaeque nasi (part of the quadratus labii), depressor septi, and the anterior and posterior dilator naris. The procerus and the forehead muscles elevate the skin over the dorsum of the nose. The nasalis (both the transverse and the alar portions) compresses the nares, and the dilators and the levator superioris alaeque nasi dilate the nostrils (Fig. 2-5). The depressor septi draws the nasal tip downward. The importance of the nasal muscles can be demonstrated in seventh nerve paralysis, in which the resultant alar collapse leads to nasal obstruction (Table 2-1).

The nasal cavities, or nasal fossae, are separated in the midline by the nasal septum. Each cavity is roughly pear-shaped, being narrow above (cranially) and wide below (caudally). The roof is formed by the thin cribriform plate of the ethmoid, which is only 5 mm across at its widest

Copyright © 2003, Mosby, Inc. All rights reserved.

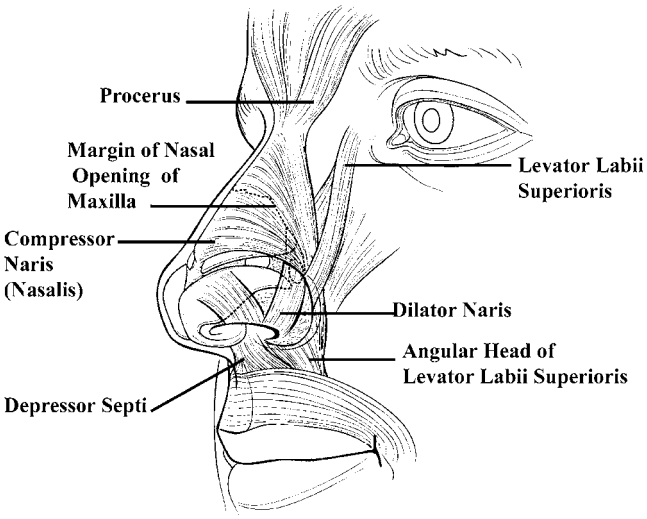

FIGURE 2-5 Left anterior oblique view of the nose illustrating the nasal musculature.

VIEW IMAGE

posterior margin. The floor of the nasal cavity is formed by the hard palate. The anterior two thirds of the hard palate is formed by the palatine processes of the maxillae, while the posterior one third is formed by the horizontal portions of the palatine bones.

The anterior portion of the nasal fossa that corresponds to the alar region of the nose is called the *vestibule*. It is lined with hair-bearing skin and sebaceous glands. Along the nasal septum there is no demarcation between the vestibule and the remaining nasal fossa. However, along the lateral wall there is a ridge, the limen vestibuli, that corresponds to the lower margin of the lateral crus of the cartilage, which marks the line of change from the skin of the vestibule into the mucous membrane of the remaining nasal fossa (Fig. 2-6).

The lateral wall of the nose is more intricate than the medial septal wall. Projecting from the lateral wall are three or four turbinates or conchae (Figs. 2-6 and 2-7). These conchae are scroll-like projections of bone that become smaller as they ascend the nasal cavity and that

Table 2-1
MUSCLES OF THE FACE

Muscle	Origin	Insertion	Innervation	Action
Procerus (pyramidalis nasi)	Fascia over lower nasal bone and upper lateral nasal cartilages	Skin between and above eyebrow	Facial nerve (VII) [T, lower Z, B]	Draws down medial angle of eyebrows Produces transverse wrinkles over bridge of nose
Compressor naris (nasalis)	Canine eminence near maxillary incisive fossa	Aponeurosis on nasal cartilages	Facial nerve (VII) [lower Z, B]	Draws ala of nose toward septum Compressor of nostrils
Depressor septi (depressor alae nasi)	Incisive fossa of maxilla	Septum and back of ala of nose	Facial nerve (VII) [Lower Z, B]	Narrows nostril, draws septum down
Dilator naris (anterior and posterior)	Margin of nasal notch of maxilla and lesser alar cartilage	Skin near margin of nostril	Facial nerve (VII) [Z, B]	Enlarges nasal aperture
Levator labii superioris (infraorbital head) and levator labii superioris alaeque nasi (angular head) zygomaticus minor (zygomatic head)	*Angular head* from upper frontal process of maxilla *Infra-orbital head* from margin of orbit near infraorbital foramen *Zygomatic head* from alar surface of zygoma	*Angular head* to greater alar cartilage, skin of nose, and lateral upper lip *Infraorbital head* into muscles of upper lip between angular head and caninus *Zygomatic head* into skin of nasolabial groove and upper lip	Facial nerve (VII) [Z, B]	*Angular head* elevates upper lip and dilates nostril *Infraorbital head* raises angle of mouth *Zygomatic head* elevates upper lip laterally
Zygomaticus (major)	Zygomatic portion of zygomatic arch	Angle of mouth and orbicularis oris, depressor anguli oris, and caninus	Facial nerve (VII) [Z, B]	Draws angle of mouth upward and backward (laughing)
Levator anguli oris (caninus)	Canine fossa of maxilla below infraorbital foramen	Into angle of mouth and muscles of orbicularis oris, depressor anguli oris, and zygomaticus	Facial nerve (VII) [Z, B]	Elevates angle of mouth
Risorius	Fascia over masseter superficial to platysma	Skin at angle of mandible	Facial nerve (VII) [Z, B]	Retracts angle of mouth (grinning)
Depressor labii inferioris (quadratus labii inferioris)	Lateral surface of mandible between symphysis and mental foramen	Skin of lower lip and orbicularis oris	Facial nerve (VII) [M, B]	Depresses lower lip and draws it laterally (irony)
Depressor anguli oris (triangularis) (in 50% of people) transverse menti part of triangularis	Continuous with platysma on oblique line of mandible	Angle of mouth into orbicularis oris and skin	Facial nerve (VII) [M, B]	Depresses angle of mouth, associated with grief

Table continued on following page

Copyright © 2003, Mosby, Inc. All rights reserved.

Table 2-1
MUSCLES OF THE FACE *Continued*

Muscle	Origin	Insertion	Innervation	Action
Mentalis	Incisive fossa of mandible	Skin of chin	Facial nerve (VII) [M]	Raises and protrudes lower lip, wrinkles skin, expresses doubt or disdain
Buccinator	Alveolar process of mandible opposite molar teeth and anterior border of the pterygomandibular raphe	Fibers converge toward angle of mouth where they blend with fibers of orbicularis oris muscle	Facial nerve (VII) [B]	Compresses cheeks, expels air from mouth, aids in chewing
Orbicularis oris	Sphincter muscle formed by contributions from various muscles and its own fibers Fibers from buccinator, levator anguli oris, depressor anguli oris, levator labii superioris, zygomaticus, depressor labii inferioris	Attaches to upper lip and lower lip, intermingles with fibers of origin, muscles, nasal septum	Facial nerve (VII) [lower Z, B, M]	Compression, contraction, and protrusion of lips. Involved in facial expression
Levator palpebrae superioris	Roof of orbit in front of optic foramen	Deep surface of upper eyelid, upper margin of superior tarsus, and superior fornix of conjunctiva	Cranial nerve III	Elevates eyelid voluntarily; attachment to superior tarsus acts involuntarily
Corrugater (supercilii)	Medial supraorbital	Skin of medial half of eyebrow	Facial nerve (VII) [Z, T]	Draws eyebrows downward and medially, produces wrinkles in frowning. Principal muscle in expression of suffering
Platysma	Fascia and skin over the upper part of the pectoralis and deltoid muscles	Lower border of the mandible and muscles of the lip	Facial nerve (VII) [C]	Produces a slight wrinkling of the skin surface of the neck, in an oblique direction, when entire muscle is brought into action. Anterior portion depresses the lower jaw and draws the lower lip and angles of the mouth down on each side
Oricularis oculi	*Orbital part* from medial orbital margin *Palpebral part* from palpebral ligament *Lacrimal part* from lacrimal bone	*Orbital fiber* arch around upper lid to lower lid and return to palpebral ligament *Palpebral fibers* go to *lacrimal fibers* to medial portion of upper and lower eyelids	Facial nerve (VII) [T, Z]	Sphincter of eyelids. The palpebral part is involuntary
Epicranius (occipitofrontalis)	Occipital bellies from lateral two thirds of superior nuchal line and mastoid process. Frontal bellies from epicranial aponeurosis at coronal suture	Skin of occipital region, skin of frontal region, and galea aponeurotica	Facial nerve (VII) [T, PA]	Moves scalp backward and forward, raises eyebrows (surprise)
Temporoparietalis	Temporal fascia above and anterior to the ear	Lateral border of the galea aponeurotica	Facial nerve (VII) [T]	Tightens scalp, draws back skin of temples
Auriculares (anterior, superior, posterior)	*Anterior:* temporal fascia and epicranial aponeurosis. *Superior:* epicranial aponeurosis and temporal fascia *Posterior:* mastoid process	*Anterior:* anterior and medial helix *Superior:* upper medial surface of auricle *Posterior:* Lower cranial surface of auricle	Facial nerve (VII) [T, PA]	Retracts and elevates ear

Branches of the facial nerve: B = buccal, C = cervical, M = mandibular, PA = posterior auricular, T = temporal, Z = zygomatic, lower Z = lower zygomatic.

are named respectively from inferiorly as the inferior, middle, superior, and supreme turbinates. The supreme turbinate is present in only 60% of cases. The air space beneath and lateral to each concha is called the meatus. The paranasal sinuses drain into the nose via these meati. The anatomy of the lateral nasal wall is discussed further in Chapter 3.

Physiology

There are three main physiologic functions of the nose: respiration, defense, and olfaction. In addition, a discussion of the physiology of the nose would not be complete without mention of the nasosystemic reflexes.

The nose plays an important role in respiration by

Copyright © 2003, Mosby, Inc. All rights reserved.

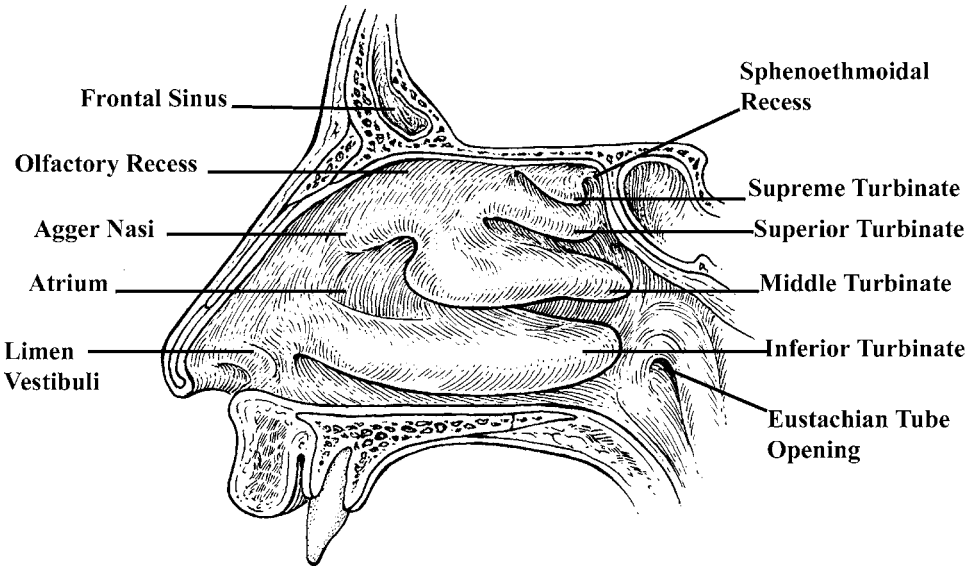

FIGURE 2-6 Diagram of a sagittal view of the lateral nasal fossa wall. The midline nasal septum has been removed.

VIEW IMAGE

effecting the nasal resistance and hence the airflow. The other effects of the nose on respiration are the humidification and warming of the inspired air.[8] In normal individuals with a tidal volume of <35 L/min, most respiratory airflow is nasal. Oral respiration is not physiologic and is a learned act that occurs during times of increased ventilatory demand.[9] This is well demonstrated in the case of newborns with bilateral choanal atresia, who, if not treated, would suffocate because they have not yet learned to breathe through their mouths.

Air enters the nares at an angle of 60° from the horizontal to reach the nasal valve, which has an area of only 0.32 cm^2. This is the most important factor contributing to nasal resistance and the resulting average airflow of 6.5 m/sec.[10] Once this point of resistance is passed, the nasal cross-sectional area increases with a decrease in airflow that results in turbulence. This turbulence is an important feature, as it allows increased contact of the air with the nasal mucosa. Once past the nasal valve area, the major airflow passes through the middle meatus. A lesser amount passes along the floor of the nose, and the least airflow is superiorly in the olfactory area.

Another modifier of nasal resistance is the dilator nasis muscle. This muscle dilates the nares, with a resultant decrease in resistance.[8] This becomes an important factor when increased ventilatory demand results in flaring of the nostrils.

Maintaining nasal resistance within certain limits is required for efficient pulmonary ventilation and gas exchange.[9] It should not be surprising that among the different factors affecting nasal resistance, two of the most important are hypoxia and hypercarbia, which decrease nasal resistance.[8]

The effect of gravity on the pooling of blood in the excessively vascular tissues over the turbinates leads to increased nasal resistance. This is commonly demonstrated by the observation in many patients that when they lie on one side, the dependent nasal chamber becomes progres-

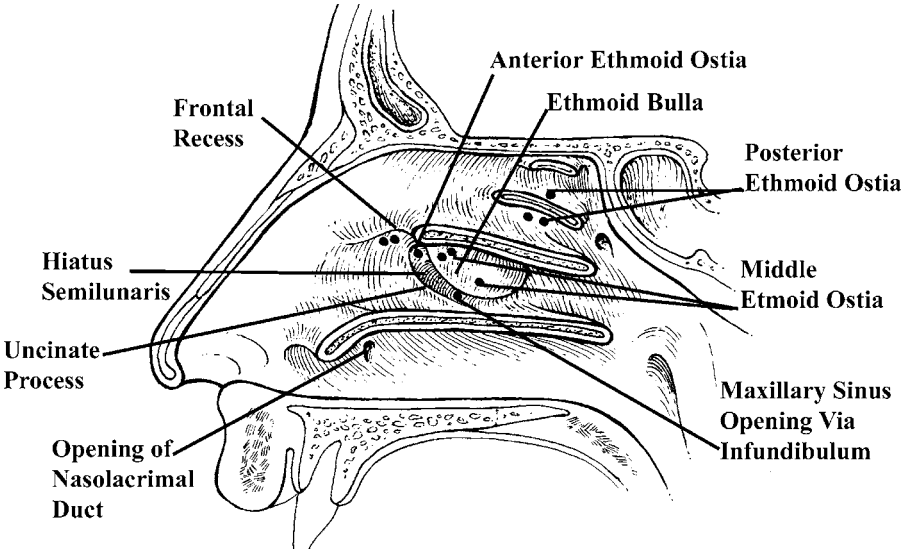

FIGURE 2-7 Diagram of a sagittal view of the lateral nasal fossa wall with the turbinates removed. The most common locations of the sinus ostia are indicated.

VIEW IMAGE

Copyright © 2003, Mosby, Inc. All rights reserved.

sively obstructed over a 15- to 20-minute period. When these patients turn to the opposite side, the clogged nasal fossa opens, and the dependent chamber becomes congested within 10 to 15 minutes.[7]

There are many other internal and external stimuli that affect nasal resistance by affecting the congestion of the nasal mucosa.[8] Some examples are vasomotor and allergic rhinitis, hormonal changes in pregnancy, thyroid dysfunction, and various medications. One phenomenon that affects nasal resistance is the nasal cycle. This occurs in 80% of individuals and results in one side of the nasal cavity being congested, with a decrease in serous and mucinous secretions, while the other side is decongested, with an increase in secretions.[8] The airflow through the nose is thus almost entirely through the patent side, and this alternates between the sides in a cyclical fashion every 1–4 hours. The function of the cycle is unclear; however, it can be documented on sectional imaging.[7] The appearance of the nasal cycle on imaging should not be confused with pathologic conditions.

Nasal resistance must be within certain limits; otherwise, the individual will have a subjective feeling of obstruction.[10] Thus the individual with a wide patent airway due to atrophic rhinitis or aggressive surgery will complain of nasal obstruction. When evaluating the cause of the patient's complaint, the clinician and radiologist should also be aware of the entity called paradoxical nasal obstruction. This situation occurs in patients who have learned to adapt to a long standing unilateral nasal obstruction.[8] The paradox exists because the patient complains of obstruction on the normal side when it becomes obstructed by congestion for various reasons, the most common being positional (with the normal side dependent), the nasal cycle, allergic rhinitis, or vasomotor rhinitis. The problem is corrected by directing treatment at the initially obstructed side.

Modification of the inspired air by humidification and warming are the other two main respiratory functions of the nose. The turbulent flow mentioned earlier allows the inspired air to interact over a large surface area.[10] Between 1 and 2 L of serous, watery secretions are produced daily by the serous glands of the nasal fossae, half of which is used to humidify inspired air.[11] The resultant nasal humidity is raised to 85%, which prevents drying of the lower airway and also enhances alveolar gas exchange.[8] Air entering the nose is efficiently warmed before reaching the lungs, and the average air temperature before entering the pharynx is 31 to 37° C . To perform this function, the average nose has about 160 cm^2 of mucous membrane, and the rich submucosal vasculature of the sidewalls of the nose makes an ideal surface for the conduction of heat to the air.[12]

The regulation of resistance, humidification, and temperature is performed by the specialized submucosal vascular network supplied by the autonomic nervous system.[13] There is a superficial capillary network that effects temperature change on the surface. At a deeper level there are venous lakes and sinuses that can produce changes in the thickness of the mucosa. Stimulation of the sympathetic nerves causes vasoconstriction, while stimulation of the parasympathetic system causes vasodilatation and nasal engorgement, with increased glandular secretions. The superficial mucosal vascular plexus works independently of the deep erectile vascular zone so that the surface temperature can vary independently of the patency or resistance of the airway. There are thus four major responses that the nasal tissue can give, depending on the nature of the inspired air: (1) hyperemia of surface vessels and filling of the erectile cavernous tissue in response to cold, dry air, (2) ischemia of the surface vessels and shrinkage of the erectile cavernous tissue in response to warm, moist air, (3) ischemia of the surface vessels and filling of the erectile cavernous tissue in response to warm air of average relative humidity, and (4) hyperemia of the surface vessels and shrinkage of the erectile cavernous tissue in response to superficial irritation.[3]

The second main function of the nose is one of defense. The mucosa of the nasal fossa is a vascular, pseudostratified columnar ciliated epithelium that contains both serous and mucinous glands. The term *Schneiderian membrane* is given to this mucosa, which is derived embryologically from the invaginating ectodermal nasal placodes. The mucosa lining the paranasal sinuses is very similar to that of the nasal mucosa except that it is less vascular, thinner, and more loosely attached to the bone. The mucosal surface is covered with a mucoid blanket that is serous around the cilia and mucoid on the remaining surface. This sticky layer is ideal for trapping particulate matter.[8] This surface film of mucus traps more than 95% of particulate matter larger than 4.5 μm. Thus the cilia beat in the lower viscosity layer, while the upper layer is transported by the motion of the tips of the cilia.[10] The coordinated ciliary action of the nasal mucosa prevents infection by propelling the mucus backward and downward into the nasopharynx at the rate of about 6.7 to 10 mm/min. The cilia beat at a rate of 160 to 1500 beats/min. The cilia function normally under most circumstances unless the mucous blanket is removed and drying occurs. Other factors can interfere with ciliary function, such as viral infection and topical decongestants. In these circumstances, cilial function is impaired.[12] The absence of ciliary movement leads to a stagnation of mucus, with the resultant necessity to frequently blow the nose and achieve postnasal clearing.[14] This movement of mucus is also affected by gravity and the traction that results from swallowing. It has been estimated that three fourths of the bacteria entering the nose are trapped by the mucus and that this nasal mucous blanket is renewed about every 10 to 20 minutes.[11] The normal nasal mucosa resists infection because the mucous blanket removes bacteria and some viruses before they can penetrate the mucosa. The mucus also contains antibacterial and antiviral substances such as lysozyme, interferon, and immunoglobulins (IgA, IgE, IgG) that are important defense mechanisms.

Olfaction occurs in the upper recesses of the nasal fossa. This region is bounded laterally by the superior nasal concha and the lateral nasal wall above this level, superiorly by the cribriform plate, and medially by a portion of the nasal septum. This olfactory epithelium is thicker (60 to 70 μm) than the surrounding respiratory epithelium (20 to 30 μm), and it covers an area approximately 1 cm^2 on each side. The epithelium is pseudostratified columnar and rests on a vascular lamina propria with no submucosa. There are four cell types in the olfactory mucosa.[2–5, 8] The first is the olfactory bipolar neuron which detects odors. The peripheral processes of these cells extend to the surface of the epithelium forming a tuft of olfactory hairs. The central

Copyright © 2003, Mosby, Inc. All rights reserved.

processes extend through the basal lamella to form a submucosal plexus that unites to form the 20 olfactory filia that pass through the cribriform plate. The bipolar neurons are replenished over a 7-week cycle. This is believed to be the only place in the body where special sensory cells are replaced after they die.[12] The remaining cells are microvillar cells whose function is still uncertain, supporting sustentacular cells, and basal cells that serve to replenish the bipolar cells. This mucosa has no ciliary action, and it is covered by a ''mucus'' that is derived from serous Bowman's glands deep in the lamina propria and from adjacent respiratory mucosal goblet cells. This mucous material spreads evenly over the surface of the olfactory epithelium, keeping it moist.

Although diffusion of odorants can provide access to the olfactory mucosa, the transport is facilitated by normal inhalation, and the most efficient transport of an odorant to the olfactory recess is accomplished by sniffing. Flavor, which is a combination of taste and smell, is thus affected if expired air does not reach the olfactory area.[14] The olfactory mucosa presents odorant molecules with certain constraints of absorption, solubility, and chemical reactivity.[12] Thus molecules may be perceived as being odorless for at least three reasons: (1) Their absorption by the mucus-lined respiratory nasal mucosal passages may be so high that all of the odorant is absorbed before it reaches the olfactory mucosa. (2) The molecules are not absorbed by the olfactory mucous secretions covering the olfactory mucosa and receptor cells. (3) A dried olfactory mucosa does not allow absorption, and thus there is no perception of smell.[3]

Once the odorant molecule reaches the receptor cell membrane, this molecule must alter the membrane potential of the olfactory receptor cell. The exact manner in which this is accomplished is not fully understood.[12] There are a number of theories of olfaction.[8] The molecular theory suggests that there are stereospecific receptors on the bipolar neurons. The temporal spatial theory suggests that the odor molecules are separated out in a manner that stimulates a specific area. Another theory claims that the odor molecules undergo some chemical reaction that depolarizes the bipolar cell. Regardless of which theory is correct, the ultimate event is depolarization of the bipolar cell, which results in a generator potential that leads to an action potential that travels along the first cranial nerve.

From the neuroepithelial receptor cells, fibers pass through the cribriform plate to terminate in the glomeruli of the olfactory bulb synapsing with the mitral and tufted cells that send their axons into the olfactory tract. The microcircuitry of these bulbs serves to narrow the spatial pattern of the glomerular inputs elicited by an odorant or a mixture of odorants.[12] From these bulbs, fibers then pass via the olfactory stria to medial and lateral septal nuclei situated just anterior and inferior to the rostrum of the corpus callosum. Then, from these septal nuclei, fibers pass into the limbic system, the uncus, the hippocampus, the parahippocampal region, the septum pellucidum, the fornices, the amygdala, and the gyrus rectus areas.[15] It has been noted that with orbitofrontal or medial thalamic lesions, odor discrimination and recognition are usually affected. However, in some cases, damage to these regions results in either no effect or an increased sensitivity to odor. It has also been noted that the recognition, interpretation, and memory of odors are located in the uncus and hippocampus, whereas the emotional response to odors is related to the entire limbic system.[15]

The maxillary division of the trigeminal nerve also plays a role in olfaction.[8] These nerve endings are sensitive to noxious stimuli such as ammonia. This can be used as a test for the malingering patient who feigns anosmia. The truly anosmic patient will respond to stimulation with ammonia, whereas the malingerer will deny it.

Olfaction is affected by the central processing of the messages from the olfactory area.[8] Clinically, olfactory cognition appears to develop between the ages of 3 and 5 years. Somewhere between the ages of 2 and 7 years, odor preferences are identified, and these are similar to those of adults living in the same area. That is, odors appear to be appreciated based upon individual experience and cultural restraints. It also appears that once an odor association is established, it is very difficult to erase it from memory and such an association may last for at least 1 year.[12] In humans, tests have shown that females have a better olfactory ability than males, both in threshold and in identification tasks.[12] In addition, olfaction is influenced by the menstrual cycle, being best at ovulation and poorest during menstruation. However, this effect is not simply hormonally related. Adaptation to odor also occurs so that the perception of an odor will fade if one is constantly exposed to it. This adaptation usually occurs within 5 minutes for chemical stimuli.

Abnormalities of the sense of smell include anosmia, which is the loss of the sense of smell; parosmia, which is a distortion or alteration of odors; and phantosmia, which is the usually constant perception of foul-smelling odors. Over 200 conditions have been associated with changes in olfaction, and these have been grouped into several categories.[12] The major categories associated with anosmia and the various percentages of occurrence from four major series are: (20% to 33%) obstructive nasal and sinus diseases (primarily nasal polyposis and chronic rhinitis), (15% to 32%) upper respiratory infection (URI) (persistent anosmia after the symptoms of the URI have resolved), and (9% to 32%) after head trauma (overall in adults, anosmia occurs in 5% to 10% of trauma cases, while in children transient anosmia occurs in 3.2% and permanent anosmia in 1.2%). Although frontal trauma most frequently causes anosmia, total anosmia is five times more likely after occipital trauma that results in a contra-coup shearing of the olfactory fibers) (0% to 8%) and with aging (More than half of the people 65 to 80 years old have a major decline in olfaction. This is also associated with Alzheimer's and Parkinson's diseases.), (0% to 8%) congenital (primarily familial anosmia and Kallmann's syndrome), (0% to 11%) toxic exposure (most toxins are either gases or aerosols), (8% to 16%) neoplasms (both sinonasal and intracranial tumors [25% of temporal lobe tumors are associated with olfactory disturbances]), (8% to 16%) psychiatric disorders (olfactory reference syndrome, Marcel Proust syndrome, etc.), parosmia and phantosmia (due to many causes, often associated with temporal lobe tumors or seizures), (0% to 26%) medications, (0% to 26%) surgery, and (0% to 26%) idiopathic causes (Table 2-2).[12]

The nasopulmonary and nasocardiac reflexes deserve mention.[8] The afferent pathway is via the maxillary division

Copyright © 2003, Mosby, Inc. All rights reserved.

Table 2-2
MAJOR CATEGORIES OF ABNORMALITIES ASSOCIATED WITH ANOSMIA

Obstructive nasal and sinus diseases
Upper respiratory infection
Head trauma
Aging
Congenital
Toxic exposure
Neoplasms
Psychiatric disorders
Medications
Surgery
Idiopathic

of the trigeminal nerve. After central processing, the efferent pathway is via the vagus nerve to the various end organs including the heart, lungs, and vascular system. The effects include apnea, hyponea, bradycardia, cardiac arrhythmias, and a decrease in peripheral vascular resistance. These reflexes are responsible for those cases of hypoxia that can occur with posterior nasal packing. The high-risk patient should thus be closely monitored. Sneezing is also a reflex mediated via the trigeminal nerve. The resultant forceful expulsion of air is believed to be a basic protective mechanism.

Vascular Supply

The vascular supply of the nasal fossa involves both external and internal carotid arterial supplies. Of the five arteries that supply the nasal cavity, the sphenopalatine artery is the most important.[16] This artery originates from the third segment of the internal maxillary artery. It then exits the superomedial aspect of the pterygopalatine fossa by way of the sphenopalatine foramen. The sphenopalatine artery then enters the nasal fossa behind and slightly above the posterior end of the middle concha.

The sphenopalatine artery has two major branches, the posterior lateral nasal branches and the posterior septal branches. The posterior lateral nasal arteries ramify over the nasal conchae, first giving off branches that supply the inferior turbinate and then giving rise to superior branches that supply the middle and superior turbinates. These lateral nasal branches also assist in supplying the maxillary, ethmoid, and sphenoid sinuses.

After giving origin to the posterolateral nasal branches, the main trunk of the sphenopalatine artery continues medially across the face of the sphenoid sinus. When it reaches the nasal septum, the sphenopalatine artery gives off its medial branches, the posterior septal arteries. These branches course anteriorly along the nasal septum. The most inferior of these branches becomes the nasopalatine artery. This vessel runs through the incisive canal to anastomose with the greater palatine artery (Fig. 2-8).

The anterior and posterior ethmoidal arteries originate from the ophthalmic artery, which is a branch of the internal carotid. They enter the nasal cavity at the level of the cribriform plate (frontoethmoidal suture line via the anterior and posterior ethmoidal canals) to anastomose with nasal branches of the sphenopalatine artery. They are the only arteries in the body that run lateral to medial. This rich anastomotic network provides an important potential collateral pathway between the internal and external carotid circulations.

There are two other arteries that also provide some blood supply to the nasal fossa. The terminal branch of the greater palatine artery enters the incisive foramen, where it anastomoses with the nasopalatine artery (a septal branch of the sphenopalatine artery). The final artery supplying the nasal fossa is the septal branch of the superior labial artery. It originates from the facial artery and supplies the medial wall of the nasal vestibule (Table 2-3).

Little's, or Kiesselbach's, area is a localized region of the anteroinferior nasal septum (Fig. 2-8). It is supplied by branches of the facial, sphenopalatine, and greater palatine arteries. This is often referred to as Kiesselbach's plexus and is the site of 90% of the cases of epistaxis (Table 2-4).[4]

The venous drainage of the nose is via the anterior facial vein, the sphenopalatine vein, and the ethmoid veins. The anterior facial vein and ethmoid veins communicate with the ophthalmic veins, which drain directly into the cavernous sinus. The sphenopalatine vein enters the pterygoid plexus, which ultimately drains into the cavernous sinus. Thus intracranial complications such as meningitis, abscess, and cavernous sinus thrombosis can result from nasal and sinus infections.[13]

VIEW IMAGE

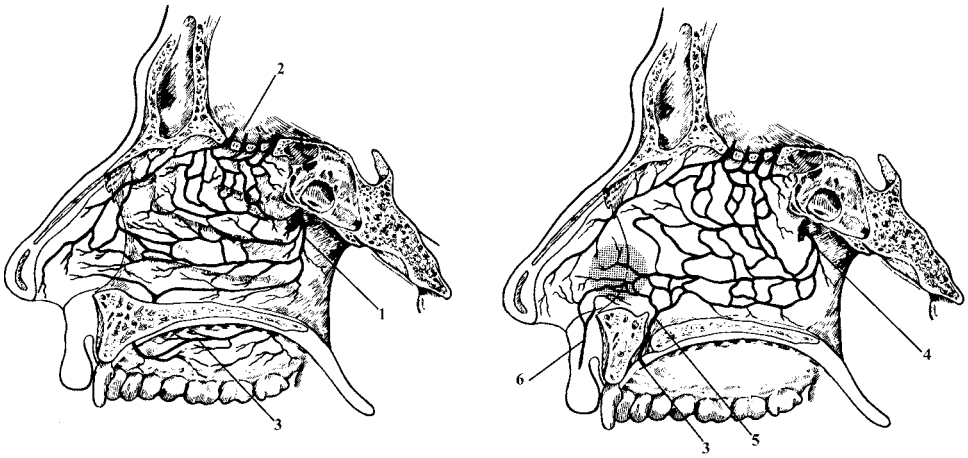

FIGURE 2-8 Diagrams of a sagittal view of the vascular supply of the (**A**) lateral nasal wall and (**B**) the nasal septum. 1, The posterior lateral nasal branches of the sphenopalatine artery; 2, the anterior and posterior ethmoidal arteries; 3, the greater palatine artery; 4, the posterior septal branches of the sphenopalatine artery; 5, the nasopalatine artery; and 6, the septal branch of the superior labial artery. The area of Kiesselbach's plexus is in dots on B. (From Osborn AG. The nasal arteries. AJR 1978; 130:89-97. Copyright 1978, American Roentgen Ray Society.)

Copyright © 2003, Mosby, Inc. All rights reserved.

Table 2-3
ARTERIAL SUPPLY OF THE SINONASAL CAVITIES

External carotid artery ↓ Internal maxillary artery ↓ Sphenopalatine artery ↓ Posterior lateral nasal branches Posterior septal branches (anastomose with ethmoidal arteries) ↓ Nasopalatine artery (anastomoses with the greater palatine artery via incisive foramen)
Internal carotid artery ↓ Ophthalmic artery ↓ Anterior and posterior ethmoidal arteries (anastomose with nasal branches of the sphenopalatine artery)
External carotid artery ↓ Greater palatine artery enters the incisive foramen (anastomoses with the nasopalatine artery)
External carotid artery ↓ Facial artery ↓ Septal branch of the superior labial artery facial artery

↓ = artery gives off the following branch

The lymphatic drainage follows the veins rather than the arteries. The lymphatics of the anterior half of the nose drain across the face to enter the level IB nodes. The lymphatics of the posterior half of the nose and nasopharynx drain into the retropharyngeal nodes and levels II, III, IV, and V nodes.

Nerve Supply

The motor supply to the nasal respiratory muscles (the procerus, the nasalis, and the depressor septi nasi) is mediated through the seventh cranial nerve. The integration of their contraction with the respiratory cycle is with the tenth cranial nerve. The physiologically important control of the circulation and secretomotor function to the normal airway is mediated by the autonomic system, primarily via the sphenopalatine ganglion. Sympathetic stimulation results in a pale, dry, shrunken mucosa, and parasympathetic stimulation causes a hypersecreting, hyperemic, swollen mucosa. Pain, temperature, and touch are mediated by branches of the first and second divisions of the fifth cranial nerve.[11, 12, 17]

The sensory innervation of the nasal mucosa is by branches of the maxillary and ophthalmic division of the trigeminal nerve. In the pterygopalatine fossa, the maxillary nerve gives branches to the sphenopalatine ganglion. These sensory nerves traverse the ganglion without synapsing. The nasal branch of the sphenopalatine ganglion enters the nasal cavity through the sphenopalatine foramen and then divides into the lateral posterior superior and medial posterior superior branches. The lateral posterior superior branch supplies the superior and middle turbinates. The medial posterior superior branch crosses the face of the sphenoid to reach the nasal septum as the nasopalatine nerve. Anteriorly, this nerve extends through the incisive canal to supply the gingiva and mucosa posterior to the incisor teeth.[12] The lower part of the nasal cavity is supplied by the greater palatine branch of the sphenopalatine ganglion. In the greater palatine canal this nerve gives off branches that pass through the perpendicular plate of the palatine bone to reach the nasal wall and supply the inferior turbinate and adjacent inferior and middle meatus. The anterior portion of the nasal cavity is supplied by the ophthalmic division of V_2. After the ophthalmic division of the trigeminal nerve (V_1) enters the orbit, it gives off branches, among which is the nasociliary nerve. This nerve runs in the medial orbit and gives off the anterior and posterior ethmoidal nerves, which then exit the orbit through the anterior and posterior ethmoidal canals, where they innervate the ethmoid mucosa, the dura in the anterior cranial fossa, and the roof of the nasal cavity. The posterior ethmoidal nerve supplies a small area of mucosa near the superior concha on both the medial and lateral nasal walls. The anterior ethmoidal nerve supplies both the medial and lateral nasal fossa walls via its lateral and medial internal nasal branches.

Table 2-4
ARTERIAL SUPPLY TO KISSELBACH'S PLEXUS

Kiesselbach's plexus is supplied by branches of: The Facial artery The Sphenopalatine artery The Greater palatine artery

The autonomic innervation of the nasal fossa comes via the pterygopalatine (sphenopalatine) ganglion. Secretomotor (parasympathetic and motor) neural fibers originate in the brainstem at the nervous intermedius. These fibers run with the facial nerve to the geniculate ganglion, where they leave the facial nerve as the greater superficial petrosal nerve. This nerve runs along the anterior face of the petrous portion of the temporal bone to the cavernous sinus, where it receives sympathetic fibers from the deep petrosal nerve (originating from the cavernous portion of the internal carotid artery). The combined nerve then enters the vidian (pterygoid) canal as the vidian nerve, which goes to the pterygopalatine ganglion. The parasympathetic fibers synapse with postganglionic fibers in this ganglion and follow the branches of the trigeminal nerve to supply the nasal fossae and palatal region. The sympathetic fibers are already postganglionic, and thus they do not have synaptic connections in the sphenopalatine ganglion. They follow the blood vessels to supply the nasal fossae and palatal areas.[4, 6]

THE PARANASAL SINUSES

All of the paranasal sinuses originate as evaginations from the nasal fossae.[18] As such, they are lined by a mucosa that is similar to that found in the nasal cavity, which is a pseudostratified columnar ciliated epithelium that contains both mucinous (goblet cells) and serous glands. The nasal septum, by contrast, is lined by squamous mucosa with a paucity of minor salivary glands and a thinner, tightly tethered lamina propria. Because the mucosa of the paranasal sinuses is attached directly to the bone, it is frequently referred to as mucoperiosteum.[19] Although the mucoperiosteum of the sinuses is slightly thinner than the nasal mucosa, it is continuous with the nasal mucosa at the various sinus ostia.

The functional reason for the presence of the paranasal sinuses has been debated since the sinuses were first described in 1800. The paranasal sinuses have been thought

Copyright © 2003, Mosby, Inc. All rights reserved.

to contribute resonance to the voice, humidify and warm the inspired air, increase the olfactory membrane area, absorb shock to the face and head, provide thermal insulation for the brain, contribute to facial growth, represent vestigial structures, and lighten the skull and facial bones. Of these, the only documented reason appears to be that the paranasal sinuses form a collapsible framework that helps protect the brain from blunt trauma.[19] Also not understood are the reasons that cause some sinuses to be well developed, while others are hypoplastic. A question related to sinus growth is why some sinuses are routinely asymmetric.

Ethmoid Sinus

The ethmoid sinuses are divided into groups of cells by bony basal lamellae that extend laterally to the laminae papyracea and superiorly to the fovea ethmoidalis.[20] These lamellae serve as attachments for the turbinates. There are thus five lamellae, one for each of the primary turbinates (middle, superior, and occasionally the supreme) and one for each of the secondary turbinates (bullae ethmoidalis and uncinate process). In the adult, the lamella is not a straight bony partition. Instead, it is almost inseparable from the other ethmoid septa due to the lamella's being pushed and distorted from its original straight configuration in the fetal ethmoid bone by the other ethmoid air cells.[21] The basal lamella of the middle turbinate is the most important, as it divides the ethmoid into anterior and posterior groups of cells that drain into the middle and superior meati, respectively. In addition, the basal lamella only extends from the posterior portion of the middle turbinate, where it is attached to the lateral nasal wall. No basal lamella is present along the anterior portion of the middle turbinate.[22] Instead, it is replaced by a medial lamella that attaches to the lateral cribriform plate. The anterior ethmoid cells are more numerous and smaller, whereas the posterior cells are larger and fewer.[21] The adult ethmoid has 3 to 18 cells. The lamellae of the remaining turbinates further subdivide the anterior and posterior groups of cells.[20] Each group of cells drains into grooves that appear at intervals running diagonally posteriorly to inferiorly and parallel to the lamella. The classification of the cells is therefore based on the drainage site of their ostium. Thus the anterior ethmoid is subdivided into frontal recess cells draining into the frontal recess, infundibular cells draining into the infundibulum and hiatus semilunaris, and bullar cells draining into a groove on the bullae ethmoidalis called the *superior hiatus*. The posterior ethmoid is subdivided into posterior and postreme cells draining into the posterior and postreme meati, respectively. This drainage pattern is of clinical significance because one would expect all cells draining into one groove to be similarly infected. The ostia of the ethmoid sinuses are the smallest of all of the paranasal sinuses, measuring only 1 to 2 mm in diameter. Of these ostia, those of the anterior ethmoid cells are smaller than those of the posterior cells, a factor probably contributing to the higher incidence of anterior ethmoid mucoceles.[21]

The ethmoid sinuses begin to form in the third to fifth fetal months, when numerous separate evaginations arise from the nasal cavity. The anterior cells are the first to so form as evaginations in the lateral nasal wall in the region of the middle meatus. Posterior cell development follows as evaginations in the superior meatal area. The ethmoid sinuses expand at their own expense and at the expense of the other sinuses until puberty or until the sinus walls reach a layer of compact bone. The lamellae prevent one group of cells from intermingling with another, but they do not prevent intramural expansion of one group into another. A concha bullosa results when posterior ethmoid cells extend intramurally to pneumatize the middle turbinate. This can result in a large obstructing turbinate or a focus of infection. There can also be extramural expansion of ethmoid cells outside the ethmoid to invade the frontal, maxillary, and sphenoid sinuses as well as the ascending process of the maxilla and lacrimal bone. Encroaching cells are the rule, and one can find any pattern of intramural and extramural expansion, which should be considered normal variations and not anomalies.[20]

There are some specific patterns of extramural spread that are of clinical significance (see also the discussion in Chapter 3). Anterior ethmoid cells can pneumatize the frontal process of the maxilla adjacent to the anterior attachment of the middle turbinate to the ethmoid crest of the ascending process of the maxilla. These are known as the aggar nasi cells, and they are located in relationship to the lacrimal bone. When present, they are the most accessible part of the ethmoid intranasally.[23] Anterior ethmoid cells can also pneumatize the roof of the orbit as supraorbital ethmoid cells. Failure to recognize disease in such cells may lead to failure of operations on the frontal sinus. On coronal images, if a bony septum is seen separating the ethmoid complex from the recess in the roof of the orbit, then the recess comes from the frontal sinus and not from the supraorbital ethmoid cells (see atlas axial and coronal Fig. 2-1B). A posterior ethmoid cell can invade the medial floor of the orbit, resulting in a Haller cell. These cells can be a source of persistent infection if overlooked.[22] A posterior ethmoid cell can also invade the sphenoid bone. Such an extension is usually superior and lateral and is known as an Onodi cell if it is related to the optic nerve.[20] A posterior ethmoid cell can invade the maxilla. When it does, the extension is posterior to the maxillary sinus, causing a double antrum.[24] This must be recognized so that the posterior wall of the maxillary sinus is opened to gain access to infection in that cell.

At birth the anterior ethmoid complex is about 5 mm high, 2 mm long, and 2 mm wide. The posterior cell group is 5 mm high, 4 mm long, and 2 mm wide. The sinuses have virtually reached their adult size by age 12 years. In the adult the ethmoid labyrinth is pyramidal in shape, with its base directed posteriorly. The average dimensions are 4 to 5 cm long, 2.5 to 3 cm high, 0.5 cm wide anteriorly, and 1.5 cm wide posteriorly.[23] Less commonly, the ethmoid can attain a flat, thin form in which the anterior and posterior dimensions are the same. This is important to recognize since the operating space will not increase as you go posteriorly.

The ethmoid bone resembles a cross in coronal section.[21] The horizontal part is represented by the cribriform plate. The vertical portion above the cribriform consists of the cristae galli. Below the cribriform plate the vertical portion consists of the perpendicular plate of the ethmoid, which contributes to the nasal septum. Attached to the lateral end of each cribriform plate is the actual ethmoid labyrinth.

Copyright © 2003, Mosby, Inc. All rights reserved.

From an anatomic standpoint, it is best to look at the ethmoid labyrinth as a box.[21] The superior surface, or roof, of the ethmoid is related to the anterior cranial fossa. Mosher calls this the tragedy surface because in inexperienced hands the ethmoid operation is one of the easiest operations with which to kill a patient.[23] The roof of the ethmoid is actually formed by the orbital process of the frontal bone. The underlying ethmoid cells bulge into this, producing a pitted surface called the fovea ethmoidalis. The fovea ethmoidalis descends 15° as it extends posteriorly. Thus, anteriorly the fovea ethmoidalis can be as much as 4 to 7 mm higher than the cribriform plate to which it is attached. This results in a thin ascending lamella of bone joining the lateral border of the olfactory fissure to the fovea ethmoidalis. This bone is extremely thin and is more commonly the site of surgical injury than is the cribrifrom plate.

The lateral wall of the ethmoid is related to the orbit. The posterior two thirds of this surface is formed by the lamina papyracea that covers the posterior ethmoid cells. These cells are related to the orbital contents, optic nerve, and medial rectus muscle. The lamina papyracea articulates with the frontal bone superiorly, the maxilla inferiorly, and the lesser wing of the sphenoid posteriorly. The anterior and posterior ethmoid foramina lie along the frontoethmoidal suture line that is just below the dural line. Thus, if during an external ethmoidectomy a surgeon remains below a line connecting these foramina, the anterior cranial fossa should not be entered. The ethmoidal vessels and nerves pass into the ethmoid complex via these foramina. Dehiscences can occur in the lamina papyracea, and mild degrees of hypoplasia can result in a lateral concavity to the lamina papyracea. This also occasionally results in a wide beveled opening in the lamina papyracea where the anterior and posterior ethmoidal canals are located. The anterior one third of the lateral wall of the ethmoid is formed by the lacrimal bone that covers the anterior ethmoid cells. These cells are thus related to the lacrimal apparatus and orbital contents. The lacrimal bone is thus the major landmark to the anterior ethmoid cells when approached externally.[23] The posterior surface of the ethmoid is formed by the lateral two thirds of the anterior face of the sphenoid sinus. This will be discussed further in the section on the sphenoid sinus. The medial wall of each ethmoid labyrinth is the turbinate surface from which project the middle, superior, and (when present) supreme turbinates. As discussed earlier, the support for the turbinates is the basal lamella. The attachment of the basal lamella of the middle and superior turbinates to the lamina papyracea and fovea ethmoidalis marks the entrance of the anterior and posterior ethmoid arteries into the ethmoid sinuses.[21] The middle turbinate is of paramount importance in intranasal surgery. It attaches anteriorly to the ethmoid crest of the ascending process of the maxilla and posteriorly to the ethmoid crest of the palatine bone (which is just anterior to the sphenopalatine foramen). The posterior half of the middle turbinate is loosely attached to the body of the ethmoid bone by the basal lamella, and only the posterior tip is firmly attached to the lateral nasal wall at the ethmoid crest of the palatine bone.[22]

The anterior half of the middle turbinate is more complex. Mosher divides it into an upper part called the superior overhang and a lower part called the inferior overhang.[23] The division point is a line drawn forward from the upper end of the superior meatus. The inferior overhang is also known as the tip of the middle turbinate and is at a lower level than the anterior insertion of the middle turbinate. The portion of the lateral wall of the nose between the anterior insertion and the tip of the middle turbinate is known as the atrium. The medial or nasal surface of the superior overhang consists of a medial lamella that inserts into the skull base at the lateral margin of the cribriform plate.[22] It conducts olfactory fibers and is thus part of the olfactory area. In addition, it serves as a major surgical landmark to the cribriform plate and should always be preserved as a landmark during operations on the ethmoid. The middle turbinate covers two elevations on the medial wall of the ethmoid. The more prominent elevation is the bulla ethmoidalis, which is more posterior and superior. It is an accessory turbinate pneumatized by anterior bulla air cells. The more anterior inferior elevation is the uncinate process. It is also an accessory turbinate and originates from the anterior point of attachment of the middle turbinate. It then runs parallel to the bulla ethmoidalis in an inferior posterior direction. The anterior insertion of the uncinate process overlaps the lacrimal bone and nasolacrimal duct and is a useful guide to the location of the nasolacrimal duct. This explains how the nasolacrimal duct can be injured by coming too far anteriorly when one is performing an infundibulotomy or middle meatal antrotomy.

The groove formed between the bulla ethmoidalis and the uncinate process is called the hiatus semilunaris. The hiatus semilunaris extends laterally to open into the infundibulum, which is lateral to the uncinate process. The depth of the infundibulum is thus dictated by the height of the uncinate process.[25] Anterior infundibular cells and occasionally the frontal sinus open into the anterior portion of the infundibulum, whereas the maxillary sinus opens into the posterior portion of the infundibulum. The lacrimal bone sits on the lacrimal process of the inferior turbinate and articulates superiorly with the frontal bone. Its anterior half covers the nasolacrimal duct, whereas its posterior half is related to the anterior ethmoid cells. It is frequently pneumatized in series with the aggar nasi cells and serves as a landmark to the nasofrontal duct.

The superior turbinate lies above and posterior to the middle turbinate. Since it lies behind the basal lamella of the middle turbinate, it marks the medial wall of the posterior ethmoid cells. Its posterior end abuts the face of the sphenoid. Occasionally there is a supreme turbinate that lies above the superior turbinate and, when present, marks the most posterior ethmoid cells.

The inferior surface of the ethmoid is related to the medial portion of the roof of the maxillary antrum below. The hiatus semilunaris marks the inferior extent of the ethmoid intranasally.[23] Thus the superior half of the lateral wall of the nose is formed by the ethmoid and the inferior half by the medial wall of the maxillary sinus.

The anterior end of the ethmoid is related to the posterior surface of the ascending process of the maxilla. It is the only solid boundary of the labyrinth.[23] This is an important landmark, as it defines the location of the nasofrontal duct and nasolacrimal duct. Intranasally it is defined by a line joining the insertion of the middle turbinate to the insertion of the inferior turbinate. The lacrimal bone lies between this

Copyright © 2003, Mosby, Inc. All rights reserved.

ascending process of the maxilla and the anterior ethmoid cells.

The ethmoid sinuses receive their blood supply from nasal branches of the sphenopalatine artery and from the anterior and posterior ethmoidal arteries, which are branches of the ophthalmic artery. Thus the ethmoid sinuses receive blood from both the internal and external carotid arteries. The venous drainage is into the nose via the nasal veins or via the ethmoidal veins, which drain into the ophthalmic veins. This latter pathway is responsible for cavernous sinus thrombosis after ethmoid sinusitis. The sensory innervation of the ethmoid mucosa is via the ophthalmic and maxillary divisions of the trigeminal nerve. The nasociliary branch of the ophthalmic division supplies the anterior cells via the anterior ethmoidal nerve. The posterior ethmoid cells are supplied by the posterior ethmoidal nerve from the ophthalmic division and the posterolateral nasal branches of the sphenopalatine nerve from the maxillary division of the trigeminal nerve. The lymphatics drain into the submandibular lymph nodes (Level I nodes).[21, 26] The proximity of the posterior ethmoid cells to the orbital apex, optic canal, and optic nerve can lead to loss of vision as a complication of benign or malignant disease or surgery on these sinuses.

Frontal Sinus

The frontal sinuses arise from one of several outgrowths originating in the region of the frontal recess of the nose. Their site of origin can be identified on the mucosa as early as 3 to 4 months in utero. Less commonly, the frontal sinus develops from anterior ethmoid cells of the infundibulum. The frontal sinuses are in effect displaced anterior ethmoid cells, and because they develop from a variable site, their drainage will be either via an ostium into the frontal recess or via a nasofrontal duct into the anterior infundibulum.[18, 20] In any instance, the opening or duct can be distorted by expansion of adjacent ethmoid cells. As noted earlier, the location of the nasofrontal duct is marked intranasally by the insertion of the middle turbinate or aggar nasi cells if present. Dissection in this area will lead to the ascending process of the maxilla, which will lead to the nasofrontal duct. From an external approach, the lacrimal bone is the preferred landmark to the nasofrontal duct.[23] Once the lacrimal bone is entered, the dissection proceeds anteriorly to the ascending process of the maxilla and hence to the nasofrontal duct.

Because on the average the frontal sinuses do not reach up into the frontal bone until about the age of 6 years, these sinuses are essentially the only paranasal sinuses that are absent at birth. Their development is quite variable but effectively appears to start only after the second year of life.[27] In otherwise normal individuals, both frontal sinuses fail to develop in 4% of the population. If there is persistence of a metopic suture, the frontal sinuses are small or absent. On the average, by the age of 4 years, the cranial extent of the frontal sinus reaches half the height of the orbit, extending just above the top of the most anterior ethmoid cells. By the age of 8 years the top of the frontal sinuses is at the level of the orbital roof, and by the age of 10 years the sinuses extend into the vertical portion of the frontal bone. The final adult proportions are reached only after puberty.[4, 27]

Based on a study of 100 normal frontal sinuses, the area of a patient's frontal sinuses correlates well with two lines that can be drawn on either a plain film or a coronal CT scan. One line extends vertically from the level of the highest point of the orbital roof to the most cranial margin of the sinus. The other line extends from the base of the crista galli obliquely to the most lateral margin of the sinus. On a Franklin-type head unit or on CT, the maximum length of each line is 63 and 74.5 mm, respectively. If either of these lengths is exceeded, the sinus is larger than the 99th percentile of the normal population and is considered abnormally enlarged.[28] The average frontal sinus has been described as being 28 mm high, 24 mm wide, and 20 mm deep. However, there is a wide range in frontal sinus size, and the frontal pneumatization may involve the vertical plate (squamosal portion) of the frontal bone, the horizontal plate (orbital roof) of the frontal bone, or both of these areas. Recognition of an orbital recess to the frontal sinus is particularly important if frontal sinus obliterative surgery is to be performed. If only the vertical portion of the sinus is obliterated because an orbital recess was not identified preoperatively, a mucocele eventually develops in the obstructed orbital recess.

Because the frontal sinus develops from a variable site, in approximately 40% of cases it drains into the ethmoidal infundibulum. In this case, the ethmoidal infundibulum can act as a channel for carrying the secretions (and infection) from the frontal sinus to anterior ethmoid cells and the maxillary sinus or vice versa. It is primarily in the patient whose nasofrontal duct opens directly in the frontal recess or above the infundibulum (85% of cases) that the frontal sinus is accessible to intranasal cannulation. The natural frontal sinus ostium is usually located in the posteromedial floor of the sinus.

As mentioned, the factors responsible for determining the extent of frontal sinus growth are poorly understood. One of the factors implicated in influencing frontal sinus size is a relationship between the cessation of frontal lobe growth and the development of the frontal sinus. Frontal lobe expansion normally ceases its anterior growth by 7 years of age, at which time the inner table of the frontal bone stops its forward migration. Any further development of the frontal bone occurs secondary to anterior growth of the outer frontal table and sinus pneumatization. The ipsilateral frontal sinus is abnormally enlarged in patients with the Dyke-Davidoff-Masson syndrome with an underdeveloped hemicerebrum and in cases of early childhood damage to the frontal lobe.[29, 30] In addition, a direct relationship between the mechanical stresses of mastication and frontal sinus enlargement has been demonstrated, as has a direct relationship with growth hormone, as seen in acromegaly.[5, 30]

In some patients a frontal bulla develops. This is an upward displacement of the frontal sinus floor caused either by encroachment from the opposite frontal sinus or, more frequently, by an underlying ethmoid cell. This bulla may influence frontal sinus drainage, and it has been implicated as a cause of chronic frontal sinusitis in some patients.[4]

Each frontal sinus is a single cavity, although rare duplication of a sinus has been reported.[4] Usually the frontal sinuses are asymmetric in size. Often the larger sinus

Copyright © 2003, Mosby, Inc. All rights reserved.

extends across the midsagittal plane, so that a midline incision may inadvertently enter this sinus rather than the intended opposite smaller sinus. The normal sinus contour tends to be slightly scalloped, and intrasinus septa may extend into the sinus from one-half to one-third the height of the sinus cavity. Such septations can create recesses of the sinus that can be overlooked at surgery if preoperative imaging was not performed.

The larger the sinus cavity, the better the septations are developed. Conversely, in a hypoplastic frontal sinus, the sinus is usually a single, smoothly contoured cavity devoid of septations. As mentioned, the frontal sinus can pneumatize both the vertical and the horizontal (orbital) plates of the frontal bone. The deepest area of the vertical portion of the sinus is near the midline at the level of the supraorbital ridge, and the medial sinus floor and the caudal anterior sinus wall are thinnest in this area. As a result, the sinus is best approached for a trephination at this level. This thin anterior wall also permits the controlled fracture that is necessary in creating an osteoplastic flap of the frontal sinus.[21]

The intersinus septum is in reality the remaining frontal bone between the two frontal sinuses. It is usually in the midline at its base or lower portion; however, it may then deviate far to one side, depending on the differential growth rates of the frontal sinuses. Although the septum is almost always complete, focal areas of acquired or congenital dehiscence do occur, allowing intercommunication between the two frontal sinuses or herniation of the mucosa of one sinus into the contralateral sinus.[18] The normal well-developed frontal sinus abuts the superomedial orbital margin, but it does not encroach on the orbit and remodel it. Any flattening of this orbital margin should suggest the presence of an expanding frontal sinus process (mucocele, pneumocele, etc.).

Occasionally a central frontal sinus cavity is encountered, in the midline, just above the level of the nasion. This presumably is the result of a displaced ethmoid cell.

There is a rich sinus venous plexus (Breschet's canals) that communicates with both the diploic veins and the dural spaces. The main arterial supply to the frontal sinus is via the supraorbital and supratrochlear arteries derived from the ophthalmic artery. The venous drainage is primarily through the superior ophthalmic vein, and the sinus lymphatics drain across the face to the submandibular lymph nodes (level IB). The sensory innervation of the sinus mucosa is via the supraorbital and supratrochlear branches of the frontal nerve, which is a branch of the first division of the trigeminal nerve.

Sphenoid Sinus

The sphenoid sinuses emerge in the fourth fetal month as evaginations from the posterior nasal capsule into the sphenoid bone. This occurs just above small crescent-shaped ridges of bone, the sphenoidal conchae, that projects from the undersurface of the body of the sphenoid bone. These conchae grow forward, fusing with the posterior ethmoid labyrinth. Complete absence of the sphenoid sinus is rare. The degree of pneumatization, however, varies considerably. The sinus starts its major growth in the third to fifth year of life, and by age 7 years the sinus usually has extended posteriorly to the level of the anterior sella turcica wall. By the age of 10 to12 years the sinus usually has obtained its adult configuration.[20] The lack of any sinus pneumatization of the sphenoid bone by the age of 10 years should suggest the possibility of ''occult'' sphenoid bone pathology.[31] This is most commonly seen in diseases that require a large marrow demand to compensate for chronic anemia. Thus it is found in young patients with thalassemia and with chronic renal failure.

The average adult sphenoid sinus is 20 mm high, 23 mm long, and 17 mm wide. The posterior sinus development is variable. Depending on the degree of pneumatization, the sinus is classified as nonpneumatized, presellar, or sellar. In 60% of pneumatized sinuses, the sinus cavity extends posteriorly to the anterior sella turcica wall and lies under the sella floor (sellar). In 40% of sinuses, the sinus cavity extends only to the anterior wall of the sella turcica (presellar). In fewer than 1% of cases, the sphenoid sinuses do not develop posteriorly enough to reach the anterior sella wall (nonpneumatized). In this latter group of patients the thick, bony posterior sinus wall is a contraindication to transsphenoidal hypophysectomy.[32]

In 48% of people there are lateral recesses from the main sphenoid sinus cavity that extend into the greater sphenoid wing, where it forms the floor of the middle cranial fossa and the posterior orbital wall, the lesser sphenoid wing, or the pterygoid process. The pterygoid process is pneumatized in 25% of patients and is extensively pneumatized in 8% of patients.[33] It should be noted that there is considerable variation in the degree of pneumatization on the left and right sides of the sphenoid sinus. As a result of sphenoid pneumatization, the foramen rotundum may either be completely outside the sinus or bulge into the lower lateral sinus wall. Similarly, the vidian canal may either be within the sphenoid bone proper or elevated on a septum within the sinus cavity.

As mentioned earlier, the posterior ethmoid surface shares a common wall with the anterior face of the sphenoid sinus. The perpendicular attachment of the superior turbinate divides the face of the sphenoid into thirds.[23] The lateral two thirds form the common party wall with the posterior ethmoid cells. The medial one third of the sphenoid sinus's anterior wall is the free intranasal surface that is bounded by the superior turbinate laterally, the septum medially, the cribriform plate superiorly, and the upper surface of the posterior choanae inferiorly. The area bounded by the intranasal face of the sphenoid and the superior turbinate is called the sphenoethmoidal recess.[25] The ostia of the sinus is 2 to 3 mm in diameter and 2 to 5 mm from the midline and lies in the upper portion of the intranasal surface, 1.5 cm above the floor of the sinus. The normal drainage of each sphenoid sinus in the erect posture thus relies entirely on ciliary action. The ostium of the sphenoid can be located by passing a beaded probe 7 cm posterior to the anterior nasal spine upward at an angle of 30° to the floor of the nose.[34] The posterior wall of the sinus can lie up to 9 cm from the anterior nasal spine. If the probe goes beyond 9 cm, one must be concerned that the probe is intracranial. The sphenopalatine artery crosses the face of the sphenoid below the ostium. This must be cauterized or reflected inferiorly when approaching the sphenoid sinus.

The sphenoid sinus septum is usually in the midline ante-

Copyright © 2003, Mosby, Inc. All rights reserved.

riorly, aligned with the nasal septum. However, from this point it can deviate far to one side and even be twisted, creating two unequal sinus cavities. With the exception of the sinus roof, the other sinus walls are of variable thickness, depending on the degree of pneumatization. However, even in poorly developed sinuses the roof is thin, often measuring only 1 mm (planum sphenoidale). This wall is thus consistently vulnerable to perforation during surgery.

When the sphenoid sinuses are well developed, neighboring structures can be identified by their indentation into the sinus cavity. Thus, in addition to the already mentioned vidian or pterygoid canal and the foramen rotundum (maxillary nerve [V_2]), the optic nerve, the internal carotid artery, and the sphenopalatine ganglion all can be seen projecting toward the sinus cavity. Not only is knowledge of the anatomic relationships of the sphenoid sinus important because surgical complications may be avoided, but such knowledge can help explain unusual symptoms that arise from sphenoid sinus disease. Thus, from anteriorly to posteriorly, the sinus roof is related to the floor of the anterior cranial fossa, the optic chiasm, and the sella turcica. The lateral wall is related to the orbital apex, the optic canal, the optic nerve, the cavernous sinus, and the internal carotid artery. Situated posteriorly are the clivus, prepontine cistern, pons, and basilar artery. The sinus floor is the roof of the nasopharynx, and the anterior sinus wall is the back of the nasal fossa medially and the posterior ethmoid laterally. These anatomic relationships can present potential surgical hazards because fracture and removal of any sinus septations or indentations can lead to damage of the adjacent vessel or nerves. In addition, surgery in the sphenoid sinus can easily perforate the sinus walls and regions of the sphenoid sinus wall may be dehiscent.[35, 36] This is especially so with regard to the planum sphenoidale, the lateral sinus wall, and the medial roof of a lateral sinus recess into the greater sphenoid wing or pterygoid process. The latter area is frequently the site of spontaneous CSF leak into the sphenoid sinus, and in such cases this area should be carefully scrutinized.

There is a reciprocal relationship between the size of the sphenoid and the posterior ethmoid cells. When the posterior ethmoid invades the sphenoid it is usually in a posterior and superior direction, which will bring it into relationship with the optic nerve. It is thus important not to go further posteriorly than the face of the sphenoid when performing an ethmoidectomy. This can be accomplished by identifying the face of the sphenoid prior to performing the ethmoidectomy. The roof and lateral wall of the sphenoid sinus are continuous with the fovea ethmoidalis and laminae papyracea, respectively. Thus the sphenoid sinus is also an excellent surgical landmark from which to commence an intranasal ethmoidectomy.

The arterial supply of the sphenoid sinus is from branches of both the internal and external carotid arteries. The posterior ethmoidal branch of the ophthalmic artery may contribute vessels to the roof of the sphenoid sinus, and the floor of the sinus receives blood from the sphenopalatine branch of the maxillary artery. The venous drainage flows into the maxillary vein and the pterygoid venous plexus.

The sphenoid sinus is innervated from both the second and third divisions of the trigeminal nerve. The posterior ethmoid nerve from the nasociliary branch of the ophthalmic division supplies the roof of the sinus, and the sphenopalatine branches of the maxillary division supply the sinus floor.[36] The lymphatics drain into the retropharyngeal lymph nodes.[3]

Maxillary Sinus

The maxillary sinus is the first of the paranasal sinuses to form. At approximately the seventieth day of gestation, after each nasal fossa and its turbinates are established, a small ridge develops just above the inferior turbinate, marking the future uncinate process. Shortly after this, an evagination just above this ridge, the uncibullous groove, is seen, which then proceeds to enlarge laterally from the nasal cavity. This is the site of the original maxillary sinus bud. By birth a rudimentary sinus, measuring up to $7 \times 4 \times 4$ mm or, on the average, about 6 to 8 cm^3 is present, with its longest dimension in the anteroposterior axis.[21] The developing maxillary sinus initially lies medial to the orbit. The annual growth rate of the maxillary sinus is estimated to be 2 mm vertically and 3 mm anteroposteriorly.[37] By the end of the first year, the lateral margin of the sinus extends under the medial portion of the orbit. The sinus reaches the infraorbital canal by the second year and passes inferolaterally to it during the third and fourth years. By the ninth year the lateral sinus margin extends to the malar bone. Lateral growth ceases by the fifteenth year.

In infancy the maxillary sinus floor lies at the level of the middle meatus. By the eighth to ninth year the sinus floor is near the level of the nasal fossa floor.[38] From this point there is considerable variation in the further growth of the lower recess of the sinus. If the sinus continues to grow downward, it reaches the actual plane of the hard palate by age 12 years. The final descent of the sinus, signaling the cessation of sinus growth, is not complete until the third molar has erupted. In 20% of adults the most dependent portion of the maxillary sinus is above the nasal cavity floor. It lies at the same level as the nasal floor in 15% of adults and below this level in 65% of adults.[38] The mean dimensions of the adult maxillary sinus are 34 mm deep, 33 mm high, and 25 mm wide. The average volume of the adult maxillary sinus is 14.75 ml.

For the most part the maxillary sinuses develop symmetrically, with only minor common variations. Unilateral hypoplasia and bilateral hypoplasia occur in 1.7% and 7.2% of people, respectively.[39, 40] Hypoplasia of the maxilla results from trauma, infection, surgical intervention, or irradiation to the maxillary that occurs during the development of this bone. These conditions can damage the maxillary growth center, producing a small maxilla and thus a ''hypoplastic'' sinus. Underdevelopment also occurs in first and second branchial arch anomalies such as Treacher Collins syndrome, mandibulofacial dysostosis, and thalassemia major when the demand for marrow prohibits sinus pneumatization.

The maxillary sinus lies within the body of the maxillary bone. Behind the inferior orbital rim, each sinus roof, or orbital floor, slants obliquely upward so that the highest point of the sinus is in the posteromedial portion, lying directly beneath the orbital apex. The groove and canal for the maxillary nerve lie in the middle third of the sinus roof. About 1 cm behind the inferior orbital rim, the canal dives

Copyright © 2003, Mosby, Inc. All rights reserved.

downward to exit on the anterior face of the maxilla via the infraorbital foramen, which is about 1 cm below the inferior orbital rim. The medial antral wall is the inferolateral wall of the nasal cavity. The curved posterolateral wall separates the sinus from the infratemporal fossa. Each sinus has four recesses: the zygomatic recess, extending into the malar eminence or body of the zygoma; the palatine recess, which is usually small and variable, extending into the hard palate; the tuberosity recess, extending downward above and behind the third upper molar; and the alveolar recess, extending into the alveolar process of the maxilla. As discussed earlier, a posterior ethmoid cell can extend into the posterior maxilla and compartmentalize portions of the maxillary sinus. These uncommon septa usually divide the antrum into anterior and posterior sections, each of which may drain via accessory ostia into the nasal fossa. Rarely, a horizontal septum can divide the antrum into superior and inferior, or medial and lateral, portions.

The floor of the sinus is lowest near the second premolar and first molar teeth and usually lies 3 to 5 mm below the nasal floor. The roots of the three molar teeth often form conical elevations that project into the sinus floor. Less often the roots of the premolar and, even more rarely, the canine teeth project into the antrum. Occasionally there is dehiscent bone over the tooth roots, so that only sinus mucosa covers these roots and separates them from the main sinus cavity.[21] The lower expansion of the antrum is intimately related to dentition; when a tooth erupts, the vacated space becomes pneumatized, thus expanding the sinus lumen.

In the adult disarticulated skull the medial wall of the maxillary bone has a large hole, the maxillary hiatus, that exposes the interior of the maxillary sinus. However, in life, or in an articulated skull, this hole is partially covered by portions of four bones.[24] In addition to the portions of the ethmoid bone (to be discussed further), the perpendicular plate of the palatine bone covers part of the posterior maxillary hiatus, while the lacrimal bone covers the anterior and superior regions.

The inferior turbinate covers the inferior portion of the maxillary hiatus. It attaches anteriorly to the conchal crest of the ascending process of the maxilla and posteriorly to the conchal crest of the palatine bone. It has a thin maxillary process that articulates with the inferior rim of the maxillary hiatus. When performing an inferior meatal antrostomy, it is thus easier to enter the maxillary sinus through this thin bone in the upper part of the inferior meatus rather than through the thick bone of the maxilla in the lower part of the meatus. When performing an inferior meatal antrostomy, it is important to remember that the nasolacrimal duct terminates in the anterior superior portion of the inferior meatus.

The ethmoid bone is the last bone to help close the maxillary hiatus, as it rests above the line of attachment of the inferior turbinate as the uncinate process and ethmoid labyrinth. Below the uncinate process, the medial maxillary hiatus is covered by the opposing nasal and sinus mucosa. This membranous area is called the fontanelle. It is divided into a posterior and an anterior fontanelle by the ethmoidal process of the inferior turbinate, which extends superiorly to contact the uncinate process. This membranous area can break down secondary to infection, with the resultant formation of accessory ostia. In addition, this area of the middle meatus can be safely penetrated when the natural maxillary ostium cannot be clinically cannulated because of a large uncinate process or when it is believed that the orbit is at risk.[21] Above the uncinate process is the hiatus semilunaris and the remainder of the ethmoid labyrinth. The ostium of the maxillary sinus is on the highest part of the medial sinus wall and can be up to 4 mm in diameter. It does not open directly into the nasal fossa but rather into the posterior portion of the ethmoidal infundibulum, which, via the hiatus semilunaris, opens into the nasal cavity. The channel of the infundibulum is approximately 5 mm long and is directed upward and medially into the nasal fossa. The sinus ostial location dictates that sinus drainage in the erect position is accomplished by intact ciliary action. Thus a narrow infundibulum can interfere further with sinus drainage.

The location of the sinus ostium can be variable. When high, it lies just below the orbital floor. The ostium can also open further anteriorly in the infundibulum, bringing it even closer to the orbit. Thus, depending on the situation, the surgeon may elect to enter the maxillary sinus at a lower level such as the membranous fontanelle, as discussed earlier.

The maxillary sinus is vascularized via branches of the maxillary artery, and the supply is essentially topographic. Thus the infraorbital, greater palatine, posterosuperior alveolar, and anterosuperior alveolar arteries all contribute a blood supply. In addition, there are lateral nasal branches of the sphenopalatine artery and a small contribution from the facial artery. The venous drainage is anteriorly via the anterior facial vein and posteriorly via the maxillary vein. The maxillary vein joins the superficial temporal vein to form the retromandibular (posterior facial) vein, which drains into the jugular vein. However, the maxillary vein also communicates with the pterygoid venous plexus, which anastomoses with the dural sinuses through the skull base. It is through this latter pathway that maxillary sinusitis can lead to meningitis.[36]

The nerve supply to the antrum is via branches of the second division of the trigeminal nerve, namely, the branches of the superior alveolar nerves (posterior, middle, anterior), the anterior palatine nerve, and the infraorbital nerve. Of these, the posterior superior alveolar nerve pierces the posterior antral wall and runs forward and downward in a small canal to supply the molar teeth. The lymphatics of the main sinus drain into the lateral retropharyngeal and internal jugular nodes (levels II, III, and IV), and those of the lateral portion of the antrum drain into the submandibular nodes (level IB).

PLAIN FILMS

In the present-day environment of emergency room medicine, there has been a resurgence of the use of plain film radiographs of the paranasal sinuses. In part this reflects their comparatively low cost, low radiation dose, and ready availability. These plain film studies are either the initial and only imaging study or, if clinically indicated, they may be followed by computed tomographic (CT) and/or magnetic resonance (MR) imaging studies. There are a number of plain film radiographic views available for evaluating the paranasal sinuses; however, only four of these projections

Copyright © 2003, Mosby, Inc. All rights reserved.

are routinely employed. These consist of two frontal projections—the Caldwell and the Waters views—a base (submentovertex) view, and a lateral view. The most popular of the additional views include the oblique projection (Rhese view), other craniocaudal angulations of the frontal projection (transorbital, posteroanterior projections), the Towne view, the Granger view, and the modified Waters view.[27, 41]

If possible, the plain film examination should be performed with the patient sitting or standing erect so that any air-fluid levels can be clearly identified. If the patient cannot tolerate erect positioning, a cross-table lateral film with a horizontal beam should be obtained to visualize any potential air-fluid levels. If neither of these approaches can be used, on either supine or prone films any free sinus fluid will layer on the dependent sinus wall, and the sinus will

PLAIN FILM VIEWS

Horizontal Beam 5° Off-Lateral View

To achieve the horizontal beam 5° off-lateral view, the patient's head is positioned laterally relative to the cassette, and the nose is then rotated 5° toward the cassette from the true lateral position. If the patient is seated, the cassette is usually placed in the vertical position. If the patient is lying down in either the semiprone or the prone position, the cassette is positioned horizontally. The central ray enters perpendicular to the cassette and is centered at the outer canthus of the eye in the middle of the film. The orbitomeatal line is parallel to the base of the film (Fig. 2-9). The purpose of using the 5° off-lateral view rather than the true lateral view is to rotate the posterior walls of the maxillary antra slightly so that they do not superimpose on one another. This permits individual evaluation of the integrity of the posterior antral bony margins.

Modified Caldwell View

For the modified Caldwell view, the patient is positioned directly facing the cassette in either the sitting or the prone position. The midsagittal plane is perpendicular to the film. The orbitomeatal line is perpendicular to the cassette, and the central ray is angled 15° caudally as it enters the posterior skull. The central ray also serves as the centering point of the skull on the cassette. If the patient is properly positioned, this view projects the petrous pyramids in the lower third of the orbits (Fig. 2-10). The Caldwell view is the best projection for examining the frontal and ethmoid sinuses in the frontal projection.

Modified Waters View

For the modified Waters view, the patient is positioned facing the cassette in either the erect or the prone position. The orbitomeatal line is angled 37° to the plane of the cassette. The central ray is centered on the film perpendicu-

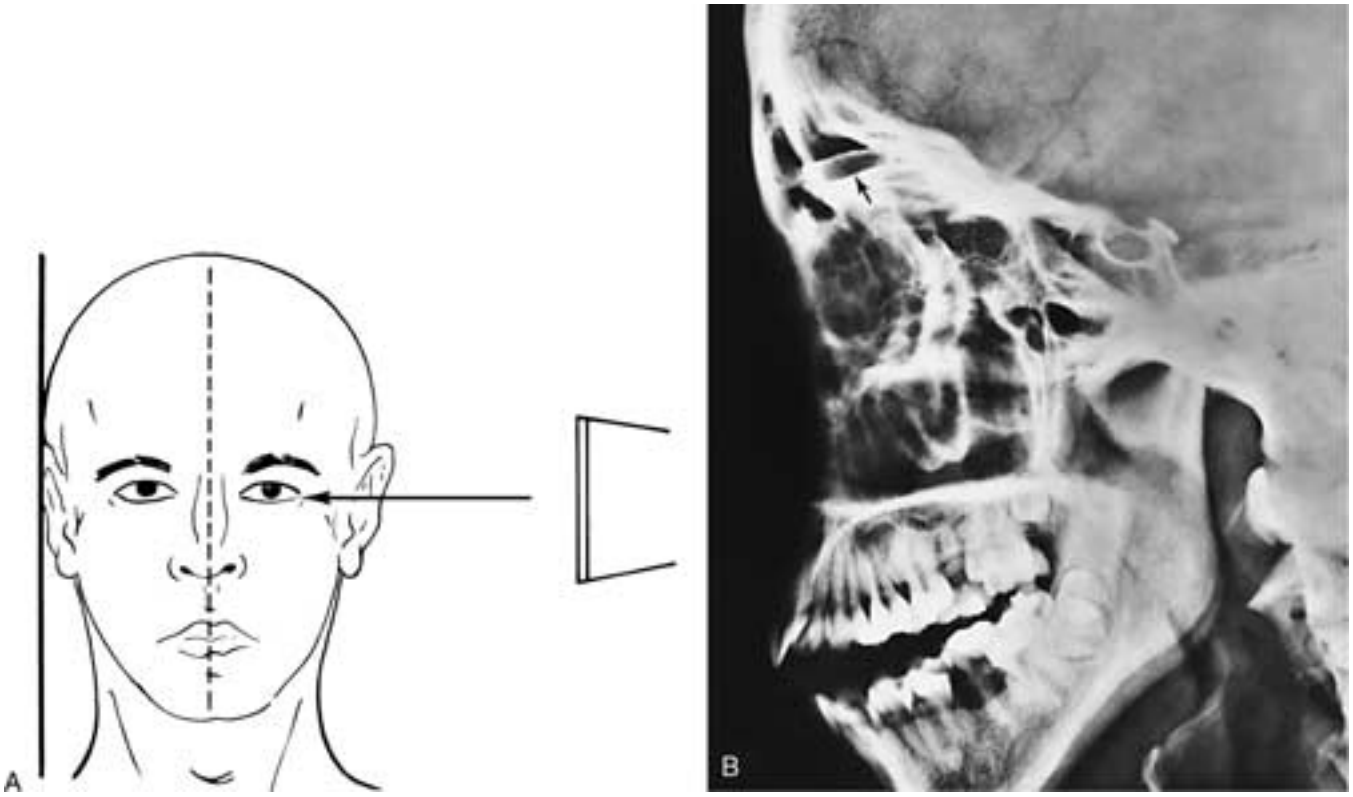

FIGURE 2-9 Lateral view. **A**, Positioning diagram. **B**, Sample radiograph. Note the extension of the frontal sinus into the orbital roof (*arrow*).

VIEW IMAGE

Copyright © 2003, Mosby, Inc. All rights reserved.

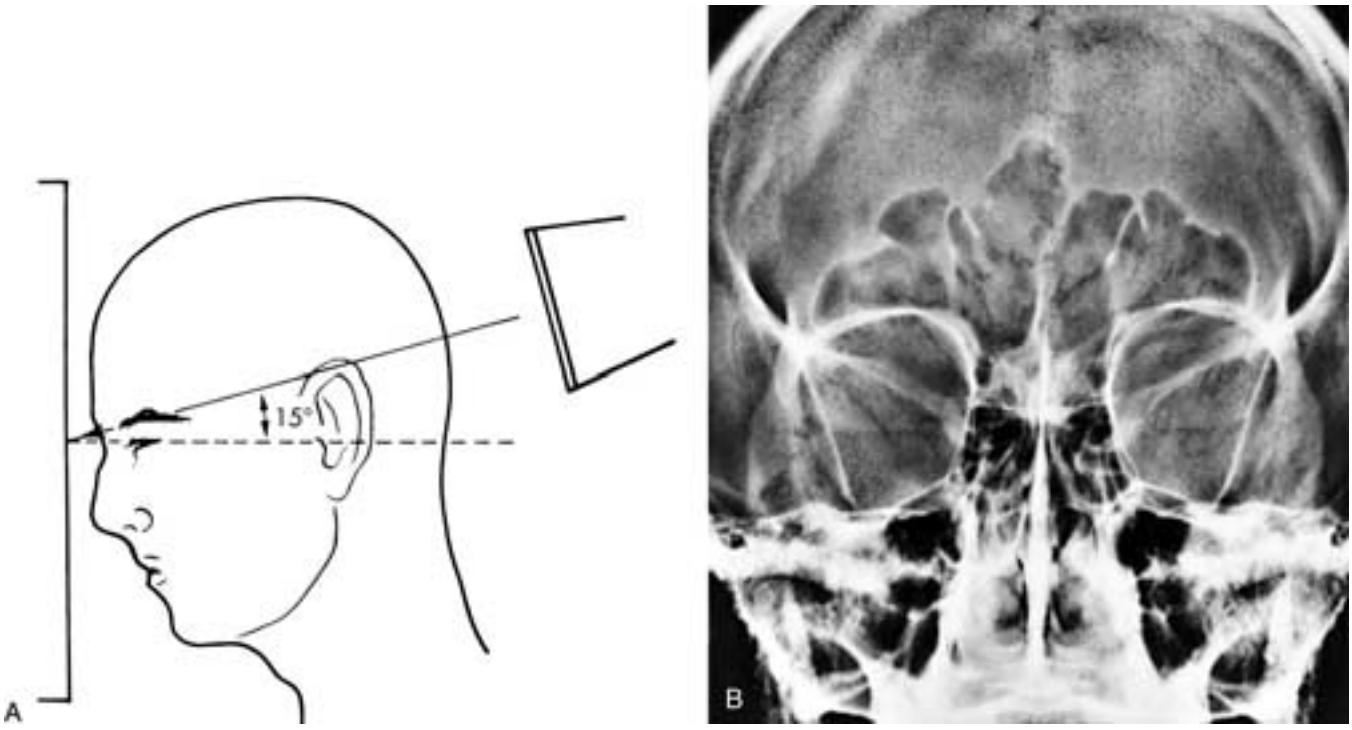

FIGURE 2-10 Modified Caldwell view. **A**, Positioning diagram. **B**, Sample radiograph.

VIEW IMAGE

lar to the cassette, emerging at the anterior nasal spine of the patient (Fig. 2-11A,B).

Variations in the positioning angle may be required to give the ''perfect'' Waters view. On the one hand, if the head is not sufficiently extended, the petrous pyramids are projected over the maxillary sinuses, thereby obscuring sinus detail. On the other hand, if the head is hyperextended, the maxillary sinuses become distorted and foreshortened, thus obscuring sinus disease. The ''perfect'' Waters view has the petrous pyramids projected just below the floor of the sinus cavities. This is the best single view for the evaluation of the maxillary antra in the frontal projection. Another variation is to use the Mahoney modification with the mouth open.[41] The open-mouth Waters view normally allows good visualization of the lower posterior sphenoid sinus margins (Fig. 2-11C).

Modified Base (Submentovertical or Submentovertex) View

The modified base view was described by Schuller and Pfeiffer.[41] The reference line used is the infraorbital line, which runs from the infraorbital margin to the center of the external auditory meatus. The goal of the positioning is to have the infraorbitomeatal line parallel to the film plane. This projection is considerably easier to obtain with the patient in either the sitting (erect) or the prone position. Patients with cervical or thoracic degenerative disease, those with a short neck, or those who are obese have difficulty extending the head sufficiently if the examination is attempted with the patient supine. The central ray is directed perpendicular to the infraorbitomeatal line and centered 1 inch anteriorly to the plane of the external auditory meatus (Fig. 2-12). A modification, with the centering 1½ inches in front of the external auditory meatus, has also been suggested.

A variation of the traditional submentovertex view is the Welin, or overangulated base, view. This view results in an average angle of 120° open posteriorly between the infraorbitomeatal line and the cassette. This overangulation is accomplished by tilting the top of the cassette toward the patient while the patient's head is fully extended, as in the modified base projection. The central ray is directed to the level of the frontal sinus. This position provides a useful adjunct view for evaluation of the anterior and posterior walls of the frontal sinuses (Fig. 2-13). It is also a good view for evaluating the lateral and, to a lesser extent, the medial walls of the maxillary antra. The sphenoid and ethmoid sinuses, with the nasal cavity superimposed, are thrown into relief with this projection.

Rhese or Oblique View

The Rhese view is excellent for studying the posterior ethmoid air cells, which are otherwise obscured by superimposition of the anterior cells in the frontal views. Superimposition of the anterior right and left ethmoid cells in the Rhese view, however, tends to limit its usefulness in paranasal sinus examination. Correct positioning places the optic canal just off the midorbit in the lower outer quadrant. Each side is imaged separately, and then the images are compared. The patient is placed in either the seated erect

Copyright © 2003, Mosby, Inc. All rights reserved.

position or the prone position. Then the median sagittal plane of the body is centered with the midline of the cassette. With the orbit centered in the portion of the cassette to be used, the flexion of the head is adjusted so that the canthomeatal line is perpendicular to the film. The patient's head is rotated so that the median sagittal plane forms an angle of 53° with the plane of the film. The central ray enters the skull posteriorly at an angle of 15° with the canthomeatal line and emerges at the midorbit (Fig. 2-14).[41] Short of sectional imaging, the oblique views coupled with a Caldwell view provide the least obscured images of the ethmoid cells.

Nasal Bone Lateral View

To achieve the nasal bone lateral view, the patient is usually placed in a semiprone position, with the body rotated so that the median sagittal plane of the head is horizontal and parallel to the plane of the tabletop. The interpupillary line is also perpendicular to this plane. The flexion of the head ought to be such that the orbitomeatal line is parallel with the transverse axis at the tabletop. The jaw should be supported with a sandbag to prevent rotation. The film is placed under the frontonasal region and centered at the nasion. The focal-film distance should be 36 inches (Fig. 2-15).

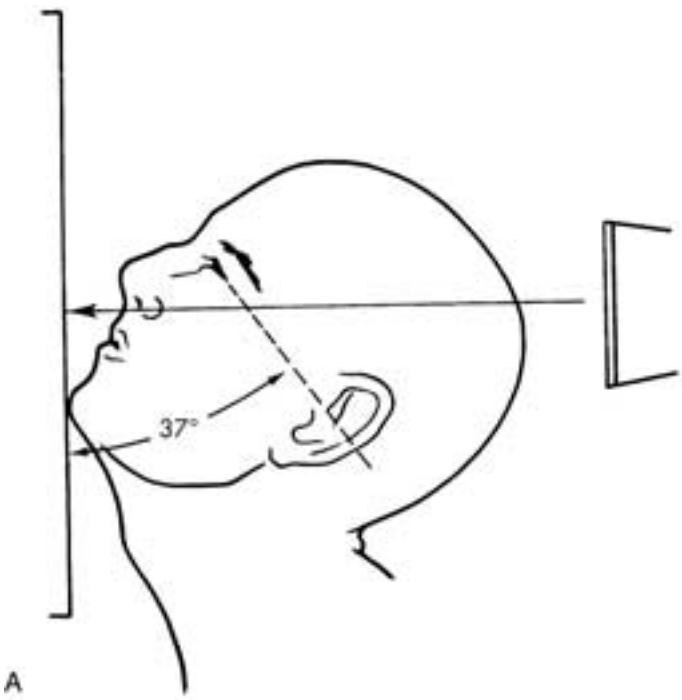

FIGURE 2-11 Modified Waters view. **A**, Positioning diagram. **B**, Sample closed-mouth radiograph. **C**, Sample open-mouth radiograph.

VIEW IMAGE

Copyright © 2003, Mosby, Inc. All rights reserved.

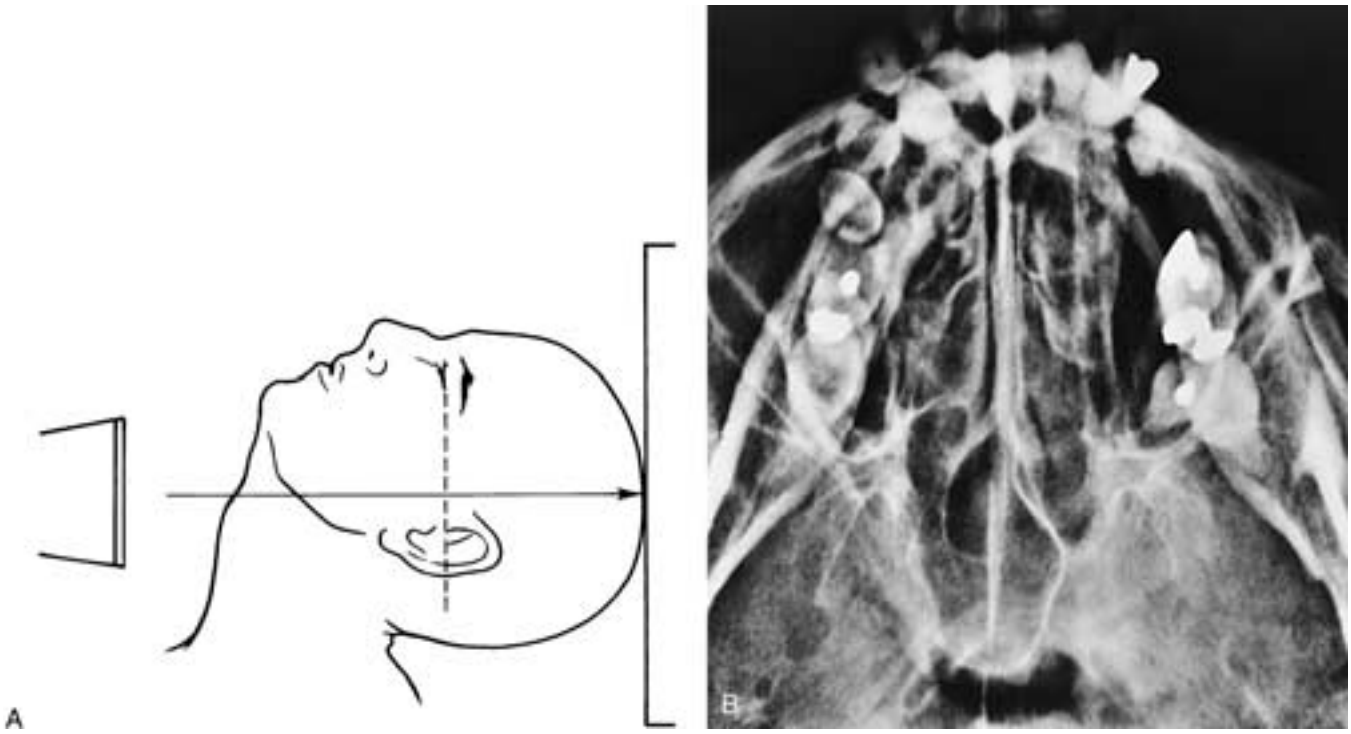

VIEW IMAGE

FIGURE 2-12 Modified base view. **A**, Positioning diagram. **B**, Sample radiograph.

Nasal Bone Axial View

The success of the nasal bone axial projection depends on either having the patient hold the occlusal film correctly between the front teeth or placing the larger film cassette under the patient's chin so that the plane of the film is at right angles to the glabelloalveolar line. The central ray should be directed along this line at right angles to the plane of the film (Fig. 2-16).

IMAGING ANATOMY

Despite the most meticulous attention to technical detail, plain film examinations have substantial limitations. That is, even if interpreted by a knowledgeable radiologist, the full degree of both soft-tissue and bone disease may be consistently underestimated. In response to this limitation, in the recent decade and a half it has become popular to perform limited, low-cost, low-dose, coronal CT studies as

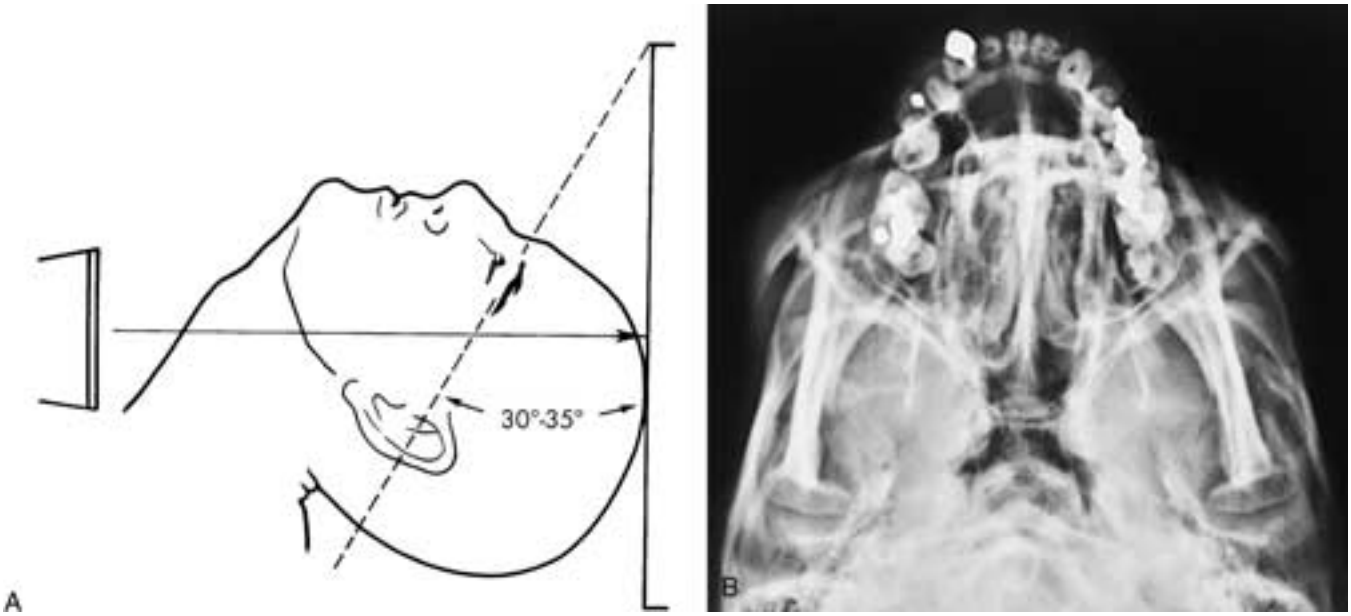

VIEW IMAGE

FIGURE 2-13 Overangulated base view. **A**, Positioning diagram. **B**, Sample radiograph.

Copyright © 2003, Mosby, Inc. All rights reserved.

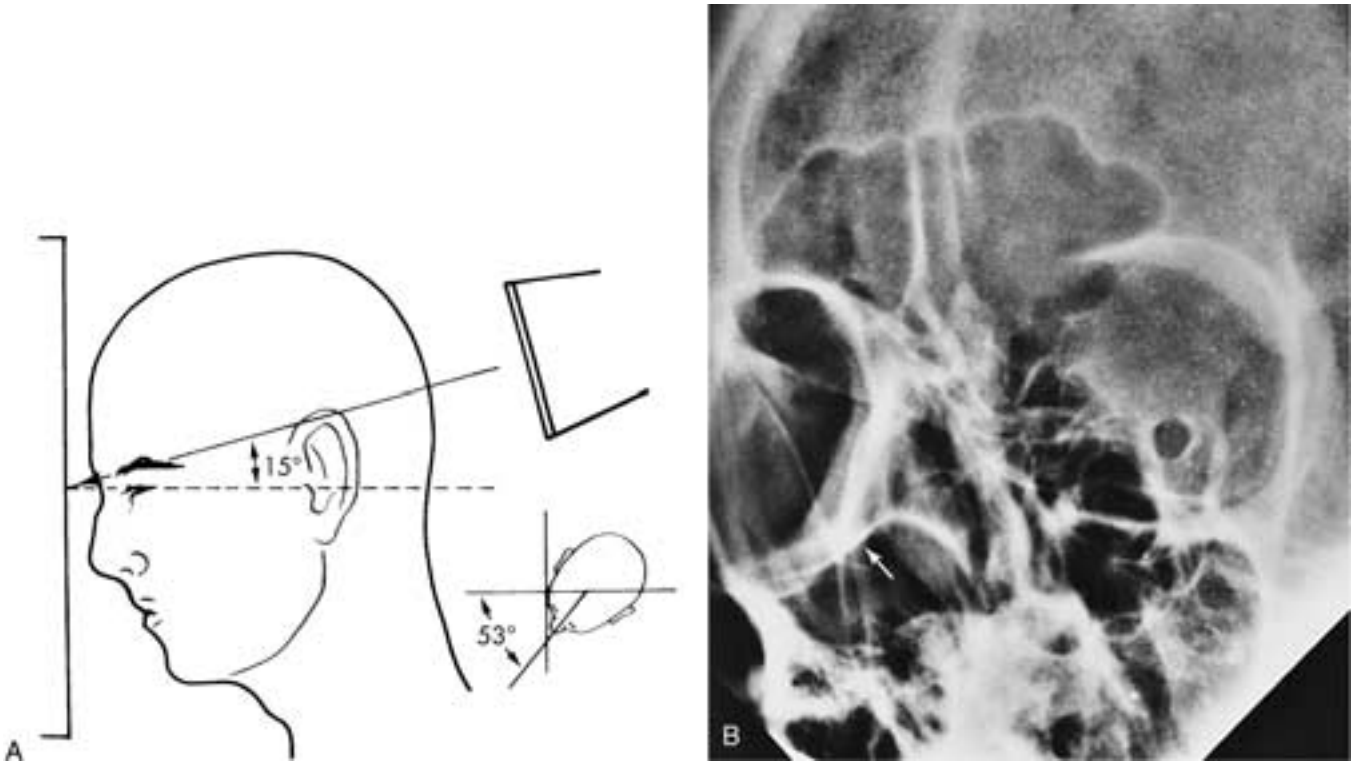

VIEW IMAGE

FIGURE 2-14 Rhese (oblique) view. **A**, Positioning diagram. **B**, Sample radiograph. Note the visualization of the right orbital floor (*arrow*).

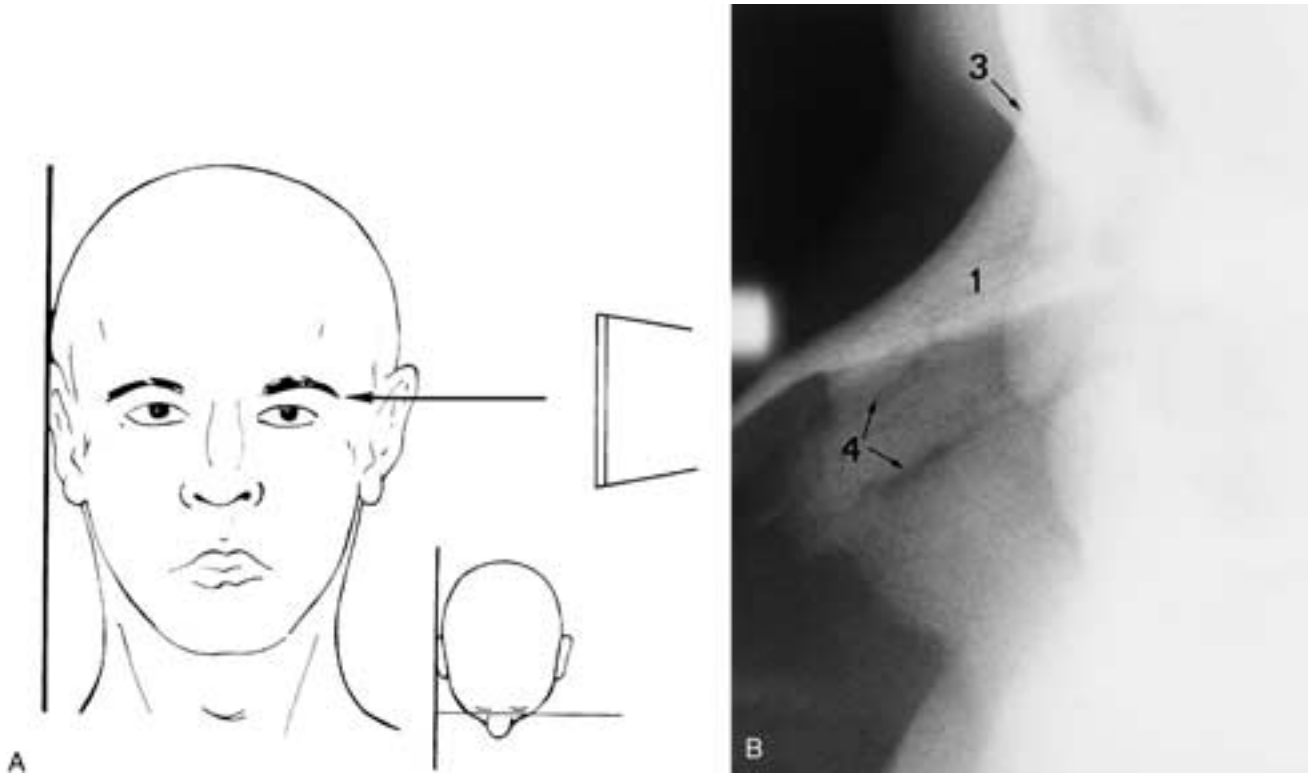

VIEW IMAGE

FIGURE 2-15 Lateral nasal bone view. **A**, Positioning diagram. **B**, Sample radiograph.

Copyright © 2003, Mosby, Inc. All rights reserved.

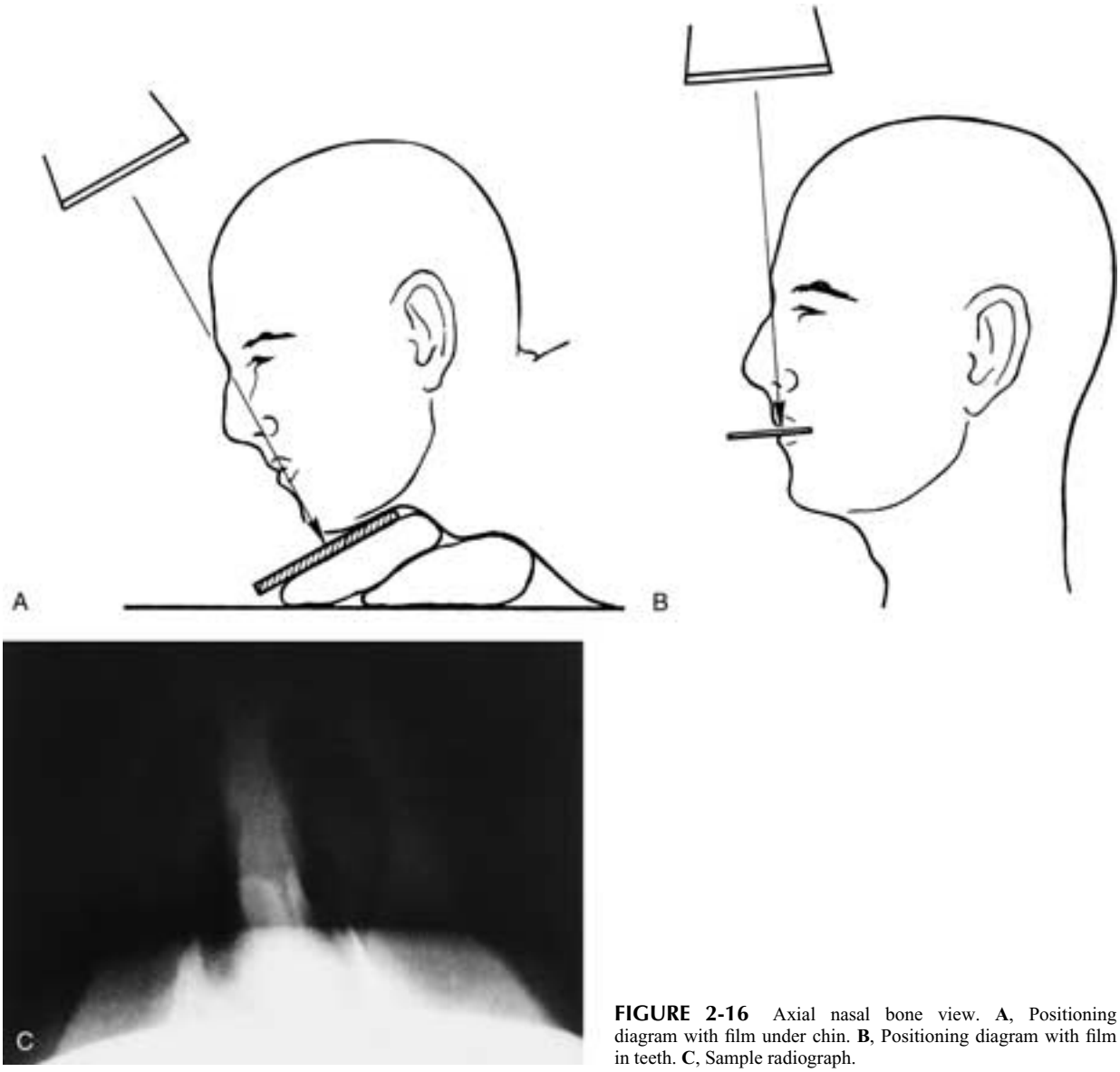

FIGURE 2-16 Axial nasal bone view. **A**, Positioning diagram with film under chin. **B**, Positioning diagram with film in teeth. **C**, Sample radiograph.

VIEW IMAGE

an alternative to the plain film examination. Although the radiation dose of these limited CT studies is lower than that of the routine CT examination, it usually is higher than that of a plain film series. This radiation dose and the frequency of these examinations represent a net radiation risk to the population. Thus the clinical setting for these studies should be carefully monitored so that patient dose and examination cost are balanced by the radiologist's choice of the best study to provide the information needed by the clinician determining the patient's management.

Patients who have signs and symptoms of acute sinonasal disease usually do not require any radiologic study, as most often they respond to conservative medical management. If the clinician is concerned that obstruction to sinus emptying has occurred, an erect plain film study will provide good visualization of any air-fluid level. The plain film examination also provides a gross assessment of sinus disease, usually all the information that is needed by the clinician at this initial stage of assessment. However, if the patient has associated signs or symptoms that suggest extension of disease outside the boundaries of the sinonasal cavities, a more detailed examination such as either a contrast-enhanced CT scan or an MR imaging study should be performed to provide better disease mapping. Signs or symptoms that should signal CT or MR imaging include headache, retro-orbital pain, orbital pain, suboccipital pain, facial swelling, orbital inflammatory disease, and proptosis.

It is estimated that between one third and one half of patients with acute sinonasal inflammatory disease will progress to chronic disease. In these cases, it is probable that some type of surgical intervention will be a part of further treatment, and a preoperative CT scan should be obtained. Not only is disease mapping more complete on CT scans than on plain films, but normal anatomic variants can be identified that may influence surgery or aid the surgeon in avoiding an operative complication. That is, if sinus surgery is planned, a plain film examination can not only be avoided, but it should be considered inadequate as a preoperative study.

Copyright © 2003, Mosby, Inc. All rights reserved.

In the patient with signs and symptoms of sinonasal inflammatory disease, CT, not MR imaging, is the suggested initial examination because the details of the bone/soft tissue/air interface are better seen on CT and the CT examination costs less than an MR imaging study. In addition, on MR imaging, because air, desiccated secretions, calcifications, and ossifications all give signal voids, they may be indistinguishable from one another. However, with CT, such differentiation is routine. Lastly, if there are no symptoms to suggest the intracranial spread of inflammatory disease, contrast is not necessary for the CT study. Thus, for most patients with sinonasal inflammatory disease, a noncontrast CT study provides the most detailed information at the lowest cost.

However, if the clinician suspects that a sinonasal tumor is present, the examination of choice is MR imaging due to its better differentiation of soft tissues. Thus, compared to CT, MR imaging can distinguish better between tumor and adjacent obstructed secretions or inflammatory disease.

To identify the early manifestations of sinonasal disease, it behooves the radiologist to become fluent in sinonasal anatomy as it appears on plain films, CT, and MR imaging. That is, before mastery in the analysis of pathologic cases is possible, the radiologist must be able to move confidently through the visual thicket of normal radiographic anatomy and its variants. The important role of the radiologist in evaluating disease in the sinonasal cavities is better appreciated when it is considered that the clinician can directly observe only a small portion of the volume of interest. Clearly, imaging provides the most thorough noninvasive evaluation of the nasal cavities and paranasal sinuses.

The following section addresses the normal sinonasal anatomy as seen on plain films, CT scans, and MR images. The common denominator leading to the successful interpretation of these examinations is the anatomy itself, and once this is learned, its depiction as rendered by any specific modality will be clearly and easily approached. Thus, technology per se is irrelevant as long as it meets the final test of delineation of structure. There are 22 bones in the facial area and calvarium that are routinely seen on images or films through the facial region: 1 frontal, 2 parietal, 1 occipital, 2 temporal, 1 sphenoid, 2 zygoma, 2 maxilla, 2 palatine, 1 ethmoid, 2 lacrimal, 2 nasal, 2 inferior turbinates, 1 vomer, and 1 mandible.

The normal sinonasal anatomy is presented in two sections. The first section discusses the normal anatomy as seen on plain films and contains a presentation of anatomic variants and potential problems that are created by overlying soft-tissue structures and bones.[32, 42–46] The second section presents sectional anatomy and is illustrated with CT images in the axial, coronal, and sagittal projections.[47–51] Further discussion of the paranasal sinus anatomy is presented in Chapter 3.

PLAIN FILM ANATOMY

The Frontal Sinuses

The main or vertical portion of the frontal sinuses is best visualized in the Caldwell and Waters projections (Figs. 2-10B and 2-11B). On occasion the Rhese view can better display some of the sinus contours, particularly in the smaller sinuses (Fig. 2-14B). The anterior and posterior sinus walls are best evaluated in the lateral and base (submentovertex) views (Figs. 2-9B and 2-17). However, in these projections, only those portions of the sinus walls that are parallel to the incident beam (perpendicular to the film plane) are visualized. The adjacent curvilinear surfaces are obliquely oriented to the incident x-ray beam and only contribute to the perceived density of the adjacent calvarium. Thus, on the lateral view, only the midsagittal anterior and posterior frontal sinus tables are visualized, and on the base view (depending on the angulation and the particular curvature of the skull), it is usually the caudal portions of the sinus walls that are identified. It is important to remember that only these limited areas of the frontal sinus anterior and posterior walls are seen routinely on these projections. One may not assume that the entire sinus table is normal simply because it appears intact on the lateral or base views. This is especially true in suspected fractures of the posterior table or if an erosion of this bone is in question. Sectional imaging clarifies this issue.

The horizontal portion of the frontal sinus is best seen in Caldwell (Fig. 2-18) and lateral (Fig. 2-9B) views. The depth of this recess can be best assessed by evaluating the posterior extent of pneumatization in the bony roof of the orbit, as shown on these projections.

Because the frontal sinuses develop independently from anterior ethmoid cells, asymmetry is the rule. Differential sinus growth is responsible for displacement of the intersinus septum to one side. However, this septum is usually near the midline at its caudal extreme, near the level of the glabella (Fig. 2-19). If the intersinus septum is displaced far to one side at this lower margin, an expansile process such as a mucocele within a frontal sinus should be suspected.

Unilateral or bilateral sinus aplasia or hypoplasia can occur. The smaller sinuses usually consist of a single, centrally concave recess (Fig. 2-20). Because of their small

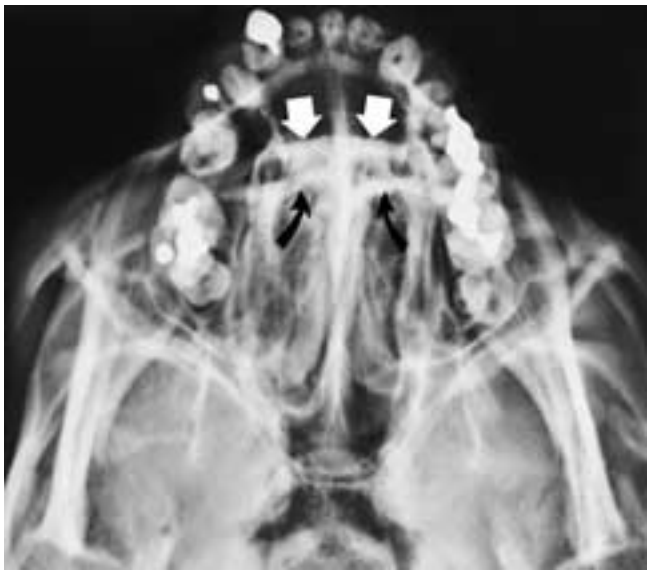

FIGURE 2-17 Overangulated base view with the anterior table of the frontal sinus (*large arrows*) and the posterior table (*curved arrows*) projected over the midpalate and nasal structures.

VIEW IMAGE

Copyright © 2003, Mosby, Inc. All rights reserved.

FIGURE 2-18 Caldwell view shows well-developed frontal sinuses. On the right side, the sinus pneumatizes the roof of the orbit. This is seen as air (*x*) contained within a thin white sinus margin (*arrow*) that is projected through the orbit.

FIGURE 2-19 Caldwell view shows a well-developed frontal sinus. Note the scalloped contour and the thin white mucoperiosteal line. Normal septations project into the sinus cavity (*white arrows*). The intersinus septum is to the right of the midline cranially but is near the midline caudally (*black arrows*). Despite the large size of the frontal sinuses, the orbital contours remain normal and are not encroached upon.

FIGURE 2-20 Caldwell view shows an aplastic right frontal sinus and a hypoplastic left frontal sinus. Note the smooth contour of the hypoplastic sinus.

size, there is little sinus air compared with the amount of overlying bone, and these sinuses almost always appear somewhat ''clouded'' on plain films, even if they are disease free. As such, they are difficult to evaluate. Rhese and Waters views may help to evaluate these small sinuses (Fig. 2-21).

The normally developed frontal sinus is always less dense than the adjacent frontal bone. The frontal bone, as part of the calvarium, is composed of cortical bone (forming both its inner and outer tables) and medullary bone (middle table, or diploic space) interposed between the two cortices.

FIGURE 2-21 Waters view shows hypoplastic frontal sinuses and a small central sinus cell, a not uncommon finding. This view complements the Caldwell projection for evaluating the frontal sinuses.

Copyright © 2003, Mosby, Inc. All rights reserved.

VIEW IMAGE

FIGURE 2-22 Caldwell view shows a moderately well-developed left frontal sinus. The right frontal sinus is aplastic. The perisutural sclerosis of the lambdoid suture is projected over the right frontal area and may mimic a clouded sinus contour. The ''linea nominata'' (*arrows*) is seen bilaterally. This line is formed by the greater wing of the sphenoid as it forms the calvarium in the anterior-most temporal fossa.

The diploic space is made up of a bony latticework that is less dense than cortical bone but osseous nonetheless. Frontal sinus development proceeds by invagination of an air-containing mucosal sac into the diploic space, thus replacing the osseous latticework of the medullary bone. Because the air-containing sinus cavity is less dense than medullary bone, the sinuses invariably appear less dense than the adjacent frontal bone. In general, the density of the normal frontal sinus is comparable to that of the superior orbital fissure as seen on the Caldwell view.

The larger sinuses normally have scalloped margins with septations that can project well into the sinus cavity (Figs. 2-18 and 2-19). If these scallops and septations are not seen and instead a smooth sinus contour is present, the diagnosis of a mucocele should be considered. The mucocele creates the smooth contour by progressively eroding the septations and remodeling the sinus shape.

Normally the frontal sinuses never violate the orbital contour, no matter how large they become (Fig. 2-19). If there is a downward and lateral flattening of the superomedial orbital rim, a mucocele should be suspected.

The normal superomedial orbital margin often appears unsharp on Caldwell and Waters views. This is because this area curves not only from medially to laterally in the orbital rim, but also from vertically to horizontally as the bone of the forehead region merges into the bone of the orbital roof. Usually a repeat Caldwell view at a slightly different angulation or a Rhese view allows this orbital margin to be visualized intact so that erosion is not erroneously diagnosed.

The margins of each frontal sinus are outlined by a thin (1 mm), dense rim, the mucoperiosteal (white) line, that separates the sinus from the adjacent frontal bone. If this line is not visualized, it could be the result of active infection, which is common, or bone destruction from tumor, which is rare. In the case of active inflammatory disease, there is increased mucosal vascularity that results in increased mobilization of the calcium in the surrounding bone, and this results in a loss of the mucoperiosteal white line. In chronic infection the thin, sharp white line is replaced by an unsharp, thick zone of sclerosis or reactive bone. This thickened white zone indicates only that the frontal sinus was exposed to previous chronic infection and does not necessarily imply that there is currently active sinus infection.

In the Caldwell view, the lambdoidal perisutural sclerosis of the occiput, a normal finding, can be projected over the region of the frontal sinus and can mimic a chronically thickened reactive margin of an opacified sinus (Fig. 2-22). Comparison of the Caldwell view to Waters or Rhese view permits correct interpretation.

On occasion, it is difficult to distinguish between a completely clouded (opacified) frontal sinus and an absent (aplastic) sinus. With good-quality films, some frontal sinus margin can almost always be identified, albeit poorly, on at least one of the plain films in the sinus series. If no such margin is seen, an aplastic sinus is the probable diagnosis. Sectional imaging will resolve any remaining issue.

On the lateral view a bone density area is usually seen at the base of the frontal sinuses anteriorly, near the nasion (Fig. 2-23). This represents the overlapping lower bony sinus walls and the superomedial orbital margins. The

FIGURE 2-23 Lateral view shows normal bone density near the anterior base of the frontal sinuses (*arrow*). This ''pseudo-osteoma'' is not seen on either the Caldwell or Waters view.

VIEW IMAGE

Copyright © 2003, Mosby, Inc. All rights reserved.

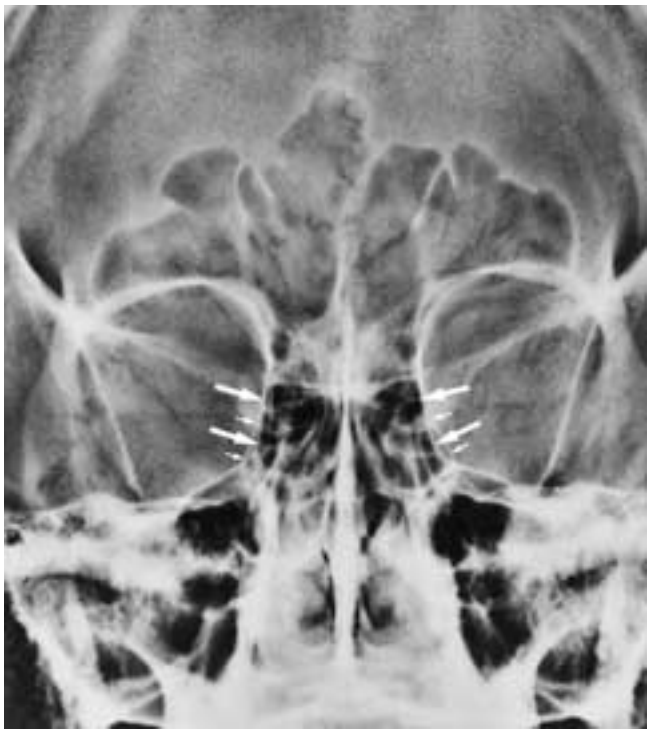

VIEW IMAGE

FIGURE 2-24 Caldwell view shows that the posterior ethmoid lamina papyracea (*small arrows*) is lateral to the more anterior lamina papyracea (*large arrows*). The medial orbital wall extends obliquely between them, reflecting the conical shape of the orbit. Also note the horizontally oriented normal ethmoid septa.

nasofrontal suture is usually situated just anteriorly. The dense bony area should not be confused with an osteoma. When seen from the front (Caldwell and Waters views), no osteoma is visualized and the bone in this region appears normal. Occasionally on the lateral view, small, bony ridges also are seen projecting from the anterior or posterior sinus walls. These are the sinus septa seen from the side.

The Ethmoid Sinuses

The ethmoid sinuses are best evaluated on the Caldwell view. However, in every plain film projection, some ethmoid cells are superimposed on others. This reflects the fact that the ethmoid sinuses are not a single sinus cavity, as are the other paranasal sinuses, but rather are formed by 3 to 18 cells that are packed into the ethmoid bone. This superimposition can lead to confusion on the plain film examination when the patient has symptoms referable to these cells, and yet the ethmoid sinuses appear normal. This situation arises because an isolated group of cells can be totally opacified, while all of the adjacent cells remain normally aerated. The air in these normal cells nullifies the plain film ''clouding'' of the infected cells, and the net result is often a very unimpressive plain film appearance. In this clinical circumstance, sectional imaging identifies any localized ethmoid disease.

On the Caldwell view, the normal density of the ethmoid sinuses can be judged by comparing it with the air density around the inferior turbinate of the nasal fossae. This reflects the fact that the ethmoid sinuses and the nasal fossae are of approximately the same anteroposterior depth, and thus the density of the air volume is about the same.

The thin lamina papyracea forms the lateral boundary of the ethmoid bone, separating it from the orbit. This medial orbital wall is oriented obliquely to an anteroposterior incident beam. Thus the majority of this oblique, thin, bony plate is not visualized on routine plain film studies. The straight or slightly concave lateral line that appears to form the medial orbital wall on a Caldwell view is in reality only the posterior ethmoid margin near the sphenoid bone. The anterior margin abutting the lacrimal bone is more medially placed and often is poorly seen (Fig. 2-24). It can be best localized by following the outline of the orbital rim from the superior aspect around to the superomedial margin and then caudally to the medial contour.

On the Waters view, only the most anterior ethmoid cells can be visualized, with the lacrimal bone separating them from the orbit (Fig. 2-25). The middle and posterior ethmoid cells are hidden from view by the nasal fossae structures. Similarly, the lateral and base views have so many overlapping structures that only gross localization of an ethmoid process can be achieved. On the base view the palate, nasal septum, turbinates, and anterior calvarium overlay the ethmoids, and on the lateral view the lateral orbital margins and even the frontal processes of the maxilla may project as vague dense zones overlying the ethmoid cells (Figs. 2-17 and 2-23). These should not be misinterpreted as sites of pathology. Although some isolation of the posterior ethmoid cells can be obtained on a Rhese view, some overlapping of ethmoid cells still occurs. Sectional imaging is indicated for proper mapping.

On the Caldwell view a small indentation, or groove, is often seen along the upper medial orbital wall. This is the anterior ethmoidal canal, and it transmits the vessels of the

FIGURE 2-25 Waters view isolates the anterior ethmoid cells and the overlying lacrimal bones (*arrows*).

VIEW IMAGE

Copyright © 2003, Mosby, Inc. All rights reserved.

same name along with the nasociliary nerve (Fig. 2-26). Because the canal is formed from the ethmoid bone below and the frontal bone above, it represents the level of the floor of the anterior cranial fossa. Less often seen on plain films are the posterior ethmoidal canals, which transmit the posterior ethmoidal nerve and vessels.

The ethmoidomaxillary plate is the posteroinferior boundary between the ethmoid and maxillary bones. It is best seen in the Caldwell view and is a useful plain film landmark for localizing the spread of tumors (Fig. 2-27).

Supraorbital ethmoid cells are ethmoid sinus extensions into the orbital plate of the frontal bone. Unlike the frontal sinuses, the supraorbital ethmoid cells tend to be symmetric. If such a cell is present on one side, it should be present on the opposite side. If one of these supraorbital cells is not seen, opacification or destruction should be suspected. Sectional imaging performed in the coronal plane resolves any questionable case. On the Caldwell view the supraorbital ethmoid cells appear as slightly curvilinear lucent zones in the superomedial orbital roof (Fig. 2-28). Their posterior extent is best evaluated on either a Waters or a lateral view. It is clinically important to ascertain whether a pathologic process is in a supraorbital ethmoid sinus or in the frontal sinus because the surgical approaches to these sinuses differ.

FIGURE 2-27 Caldwell view shows the ethmoidomaxillary plate (*curved arrow*). This is the boundary between the posteroinferior ethmoid bone and the maxillary bone.

VIEW IMAGE

The Maxillary Sinuses

The maxillary sinuses are best evaluated by the Waters view. Unlike the frontal and sphenoid sinuses, the maxillary sinuses tend to be symmetric in size and configuration, with only minor variations being common. When some degree of hypoplasia is present, the roof of the smaller antrum has a greater downward slant on its lateral margin than does the larger sinus (Fig. 2-29). On plain films this may simulate a blowout-type orbital floor fracture. However, in the hypoplastic sinus, there usually is an identifiably thicker lateral bony sinus wall that results from the poorer than normal pneumatization of the maxilla. Although this may be misdiagnosed as thickened sinus mucosa, this confusion is not likely to be made by the radiologist who is aware of the appearance of a hypoplastic antrum.

A small sinus can also result from diseases of the sinus wall that cause bone expansion, with resultant encroachment into the antral cavity. Such diseases include fibrous dysplasia, ''brown'' tumors of hyperparathyroidism, Paget's disease, and rare giant cell tumors. In these cases, at least one dimension of the original sinus may be identified as being fully developed, and the ''bony changes'' can be

FIGURE 2-26 Caldwell view demonstrates medial indentations in the lamina papyracea (*arrows*) that represent the anterior ethmoidal canals. These canals mark the level of the floor of the anterior cranial fossa.

VIEW IMAGE

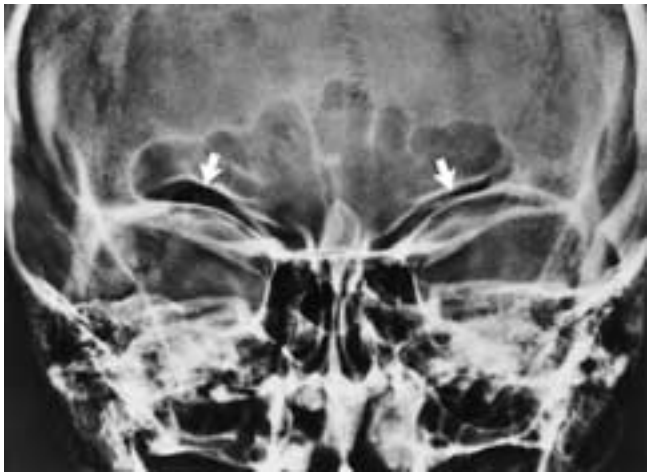

FIGURE 2-28 Caldwell view shows a curvilinear collection of air (*arrows*) just above each orbital margin. These areas appear darker than the frontal sinuses because the air in these supraorbital ethmoid cells is projected over the air in the frontal sinuses.

VIEW IMAGE

Copyright © 2003, Mosby, Inc. All rights reserved.

VIEW IMAGE

FIGURE 2-29 Waters view shows that the right maxillary sinus is smaller than the left. This hypoplasia is noted by the thicker lateral bony sinus wall and the more exaggerated downward slant of the sinus roof when compared with the left side. Also note that there is a suggestion of mucosal thickening in this normal hypoplastic right antrum due to its smaller sinus cavity and its thicker sinus walls when compared with the left side.

visualized bulging into the sinus, as well as being formed by abnormally textured bone. These changes differentiate these conditions from a simple hypoplastic antrum. Often sectional imaging may be necessary to resolve difficult cases.

Similarly, conditions that arrest the growth of the maxilla result in a small ''hypoplastic'' antrum. These childhood conditions include severe infection, trauma, tumor, irradiation, and congenital first arch syndromes.

The most lateral extension of the maxillary sinus is the zygomatic recess. This portion of the sinus hollows out the body of the zygoma, and when compared with the main antral cavity, it has less air and more surrounding bone. Because of this, the recess usually appears ''clouded'' on a Waters view and is often misinterpreted as representing mucosal thickening (Fig. 2-11B,C). True mucosal changes are best seen extending along the adjacent lower lateral antral wall.

On the lateral view, the anterior and posterior walls of the zygomatic recesses are seen as two overlapping V's projected over the main maxillary sinuses. These should be evaluated routinely to assess the possibility of early bone destruction in these recesses (Fig. 2-30). Also seen on the lateral view is the cranial continuation of the posterior wall of the zygomatic recess, the most anterior margin of the temporal fossa, which also represents the portion of the greater sphenoid wing that forms the oblique orbital line on the Waters and Caldwell views (Figs. 2-22 and 2-31).

The infratemporal maxillary sinus wall is a sigmoid-shaped, curved posterolateral surface. It is poorly seen on the Caldwell and Waters views. The most lateral extent (the back of the zygomatic recess) and the most medial margin (the anterior wall of the pterygopalatine fossa) can be identified on the lateral view (Fig. 2-31). The base view provides the best visualization of the curved nature of this wall, as well as an en face projection of portions of the pterygopalatine fossa and pterygoid plates (Figs. 2-32 and 2-33).

The medial wall of the maxillary sinus is best seen on the Caldwell view. Unfortunately, the overlying nasal structures anteriorly and the sphenoid sinuses and skull base structures posteriorly obscure most detail. Only the inferior turbinates and the lower medial antral wall are identified consistently. The clinically important osteomeatal complex is well visualized only on coronal sectional imaging.

Slight asymmetry, minimal rotation, and the physiologic nasal cycle all contribute to making one nasal turbinate larger than the other. As long as some air can still be visualized around the contour of the turbinate, separating it from the lateral nasal fossa wall and the nasal septum, the turbinate is probably not pathologically enlarged. Asymmetry per se should not be overdiagnosed as pathology. On the lateral view, the posterior tips of the inferior conchae are often seen projecting over the posterior antra, and they should not be confused with a pathologic mass (Fig. 2-34). Also on the lateral view, air trapped under or above the inferior turbinate can produce a linear lucency that may mimic a fracture.

Little consistent detail about the middle turbinates is obtained from plain film studies, and sectional imaging is necessary to provide accurate information.

FIGURE 2-30 Lateral view with large arrows pointing to the zygomatic recess of one maxillary sinus and small arrows outlining the opposite zygomatic recess. These recesses are routinely seen on lateral views as overlapping Vs. The air around them is air in the main maxillary sinus cavities, which are located nearer the midline. The S is in the sphenoid sinus, with its posterior and superior limits clearly visible on this lateral film.

VIEW IMAGE

Copyright © 2003, Mosby, Inc. All rights reserved.

VIEW IMAGE

FIGURE 2-31 Lateral view with long arrows pointing to one posterior antral wall, which also forms the anterior margin of the pterygomaxillary fissure near the midline. The short arrow indicates the upward continuation of the posterior portion of one V that forms the zygomatic recess of one antrum (Fig. 2-30). The short arrow points to the bone just behind the orbit, which forms the anterior border of the temporal fossa. Open arrows indicate the upper, flat nasal fossa surface of the hard palate. The lower oral surface is slightly concave downward in configuration.

VIEW IMAGE

FIGURE 2-32 Base view with large arrows pointing to the curved anterior margin of the right middle cranial fossa (greater sphenoid wing). The small, straight arrows indicate the straighter posterior wall of the right orbit. The lateral margin is formed by the zygoma; the medial portion is formed by the greater sphenoid wing. The curved arrows outline the ''sigmoid-shaped'' posterior wall of the maxillary sinus. Each sphenoid sinus cavity (*S*) is seen well.

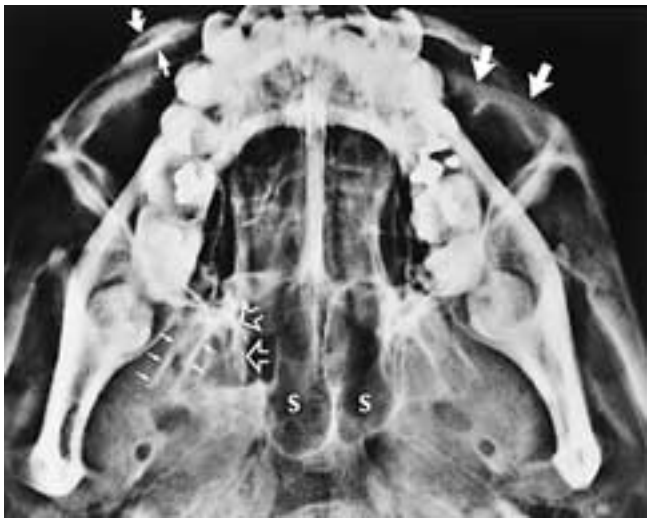

VIEW IMAGE

FIGURE 2-33 Base view with open arrows pointing to the medial pterygoid plate. Because the lateral pterygoid plate curves laterally as it descends from the skull base, the two small arrows point to the line of the lateral pterygoid plate near the skull base, and the three small arrows indicate the lateral pterygoid plate near the level of the hard palate. The large arrows point to the anterior wall of the left zygoma and maxilla. The frontal bone's anterior table (*curved arrow*) and posterior table (*small, straight arrow*) are also indicated on the right side. Each sphenoid sinus cavity (*S*) is seen well.

The anterior antral wall is not well seen on any view. Both the lateral and overangulated base views reveal only limited portions of this wall (Fig. 2-33).

The lateral view best delineates the inferior extension of the maxillary sinus and its relationship to the hard palate and teeth roots (Fig. 2-35). The sinus cortex of this alveolar recess can be elevated normally by unerupted molar teeth. Although this is well seen on the lateral view, its often broad upper surface can simulate an air-fluid level or a localized mass on a Waters view. This is especially notable in older children and teenagers.

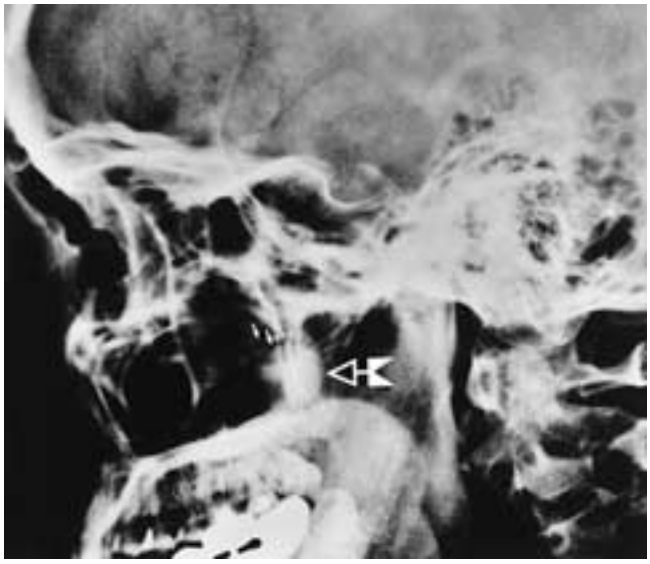

FIGURE 2-34 Lateral view with the large arrow pointing to the posterior tip of the normal inferior turbinate. Normal air just above the turbinates (*small arrows*) may mimic a fracture line.

VIEW IMAGE

Copyright © 2003, Mosby, Inc. All rights reserved.

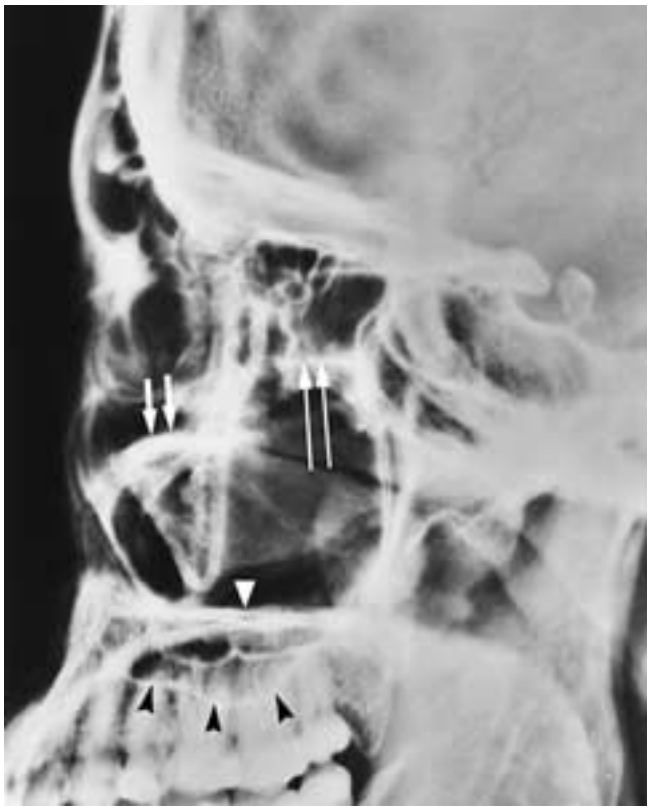

VIEW IMAGE

FIGURE 2-35 Lateral view demonstrates maxillary sinus extension (*black arrowheads*) below the level of the hard palate (*white arrowhead*). The shorter arrows point to the anterolateral and most inferior orbital floor on one side, and the longer arrows point to the posteromedial and most superior orbital floor near the orbital apex.

The antral roof, or orbital floor, is flattest and lowest anterolaterally. It is also highest and most angulated posteromedially. The majority of the midportion of the antral roof is seen almost tangentially on a Caldwell view, and thus this large surface is usually seen as a single line in this projection. On the Caldwell view a second, smaller, more slanted line is seen superomedially in the orbital floor. This line represents the orbital apex floor; a notch at the lateral aspect of this line identifies the site of the infraorbital groove (Fig. 2-36).

On the lateral view the orbital floor is usually seen as two separate lines; one anteriorly, near the level of the inferior orbital rim, represents the lowest, most lateral, and flattest area of the floor; the second, located higher and more posteriorly, represents the medial orbital apex region. The slanting floor joining these two areas is not normally seen on the lateral view (Fig. 2-35). However, on a nonconed Rhese view (or optic canal view), the contralateral orbital floor is often seen extending from the anterior orbital rim almost to the orbital apex.

The Waters projection gives a better view of the inferior orbital rim. However, much of the orbital floor is seen obliquely en face, and small fractures, depressions, or erosions may not be detected. Three roughly parallel lines are seen near the inferior orbital margin in the Waters view. The most superior of these is the soft-tissue skin margin overlying the inferior orbital rim. The middle line is the actual bony inferior orbital rim, and the lowest line is the roof of the antrum located about 1 cm behind the rim, the lowest point of the orbital floor. About 1 cm below the middle third of the inferior orbital rim, the infraorbital foramen is seen. It transmits the second division of the trigeminal nerve to the cheek and nasal region (Fig. 2-37).

On the Waters view a small lucency is occasionally seen in the lateral antral wall. This is the canal for the posterior superior alveolar nerve and should not be confused with a fracture (Fig. 2-38).

On the Caldwell view the foramen rotundum is projected through the superomedial portion of the antrum (Fig. 2-36).

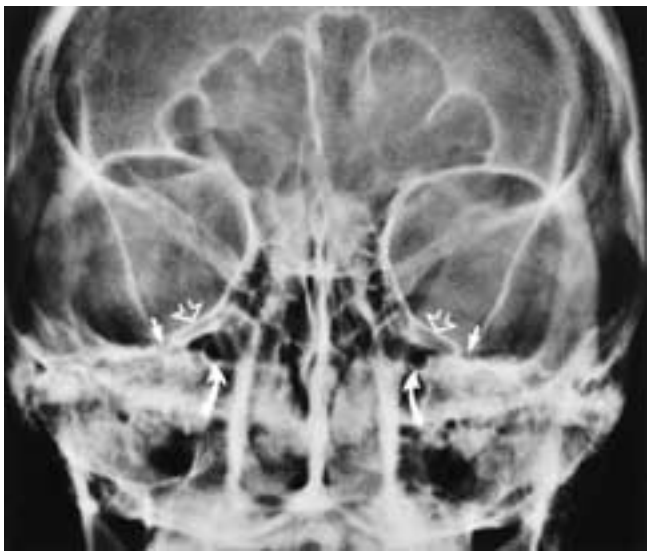

VIEW IMAGE

FIGURE 2-36 Caldwell view with open arrowheads indicating posteromedial orbital floors. The straight arrows point to the posterior margin of infraorbital canals. The curved arrows point to each foramen rotundum.

FIGURE 2-37 Waters view with curved arrow pointing to the infraorbital foramen. The open arrow indicates a soft-tissue line over the inferior orbital rim. The short arrow points to the bony inferior orbital rim, while the long arrow indicates the lowest point of the orbital floor, which is about 1 cm posterior to the orbital rim. The small arrows outline the margins of the superior orbital fissure projected through the right antrum.

VIEW IMAGE

Copyright © 2003, Mosby, Inc. All rights reserved.

VIEW IMAGE

FIGURE 2-38 Waters view with arrows indicating the canals for the posterior and superior alveolar nerves.

The superior orbital fissure is easily identified and normally has a slightly concave lateral appearance (Fig. 2-39). If the superior orbital fissure is followed inferiorly and slightly laterally, it points to the foramen rotundum. The maxillary nerve (V_2) runs through this foramen, crosses the pterygopalatine fossa and retromaxillary fissure, enters the infraorbital fissure, exits via the infraorbital canal, and supplies the cheek and nasal regions.

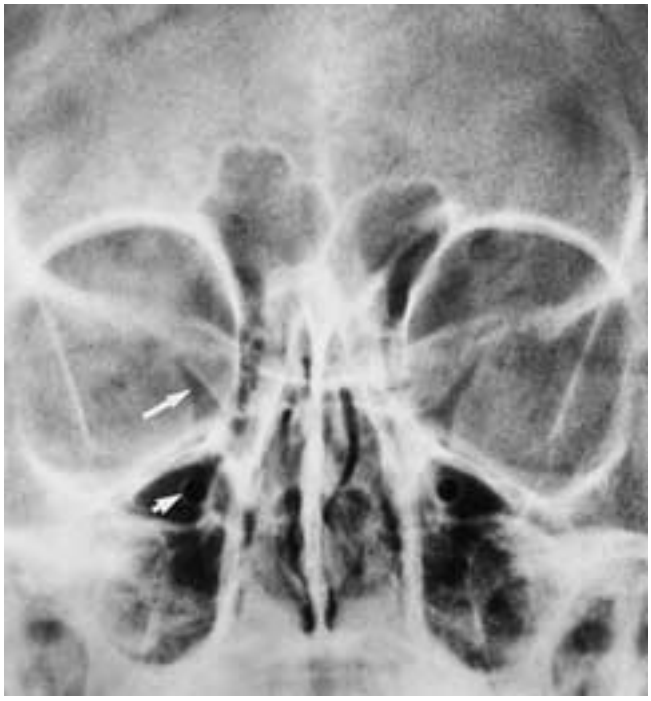

VIEW IMAGE

FIGURE 2-39 Caldwell view shows the superior orbital fissure (*large arrow*) and the foramen rotundum (*short arrow*), which is at the lower lateral margin of the superior orbital fissure.

The two foramina rotunda are usually symmetric in size and configuration. The superior orbital fissures, on the other hand, need not be as symmetric. The most important observation is that the bony cortical rims on either side of each fissure are thin and sharply defined. These fissures are narrower superolaterally and wider inferomedially. It is through this wider area that the veins and nerves traverse the fissure (Fig. 2-39). On the Waters view the lower portions of the superior orbital fissures are projected through the upper medial antra. These can simulate either a fracture of the inferior orbital rim or a septum of the antral roof (Fig. 2-37).

The infraorbital fissure can sometimes be seen on the Waters view as a pair of parallel thin cortical lines that are oriented anteroposteriorly. Their course is parallel, rather than divergent, and their configuration distinguishes them from the posteriorly located superior orbital fissure.

The inferior orbital fissure is poorly seen on the routine sinus views and can be best evaluated on the Towne view (Fig. 2-40).

The oblique orbital lines (linea innominata) are seen in both the Waters and Caldwell views. They represent the most anterior portions of the medial temporal fossa and usually are formed by the greater sphenoid wings. At the lower margin of each innominate line a sharp medial turn is seen, indicating the lower margin of the temporal fossa and the beginning of the infratemporal fossa. Occasionally

FIGURE 2-40 Towne view with arrows outlining the margins of the inferior orbital fissure. The superior line is formed by the sphenoid bone, and the inferior line is formed by the maxilla.

VIEW IMAGE

Copyright © 2003, Mosby, Inc. All rights reserved.

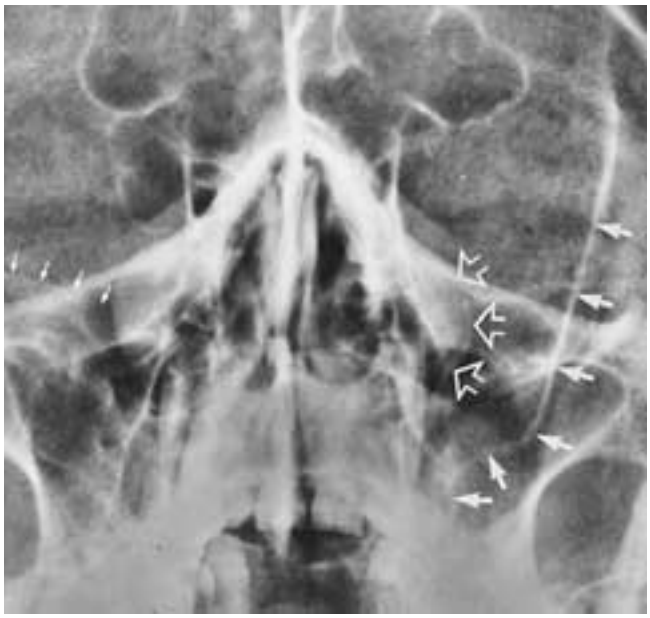

VIEW IMAGE

FIGURE 2-41 Waters view with arrows pointing to the left oblique orbital line. At its lower margin the line bends medially at the level of the infratemporal fossa. The line then bends downward at the level of the lateral pterygoid plate. The small white arrows point to the upper rim of the right middle cranial fossa. The open arrows indicate the left nasal margin, which can mimic a cyst or polyp in the medial antrum.

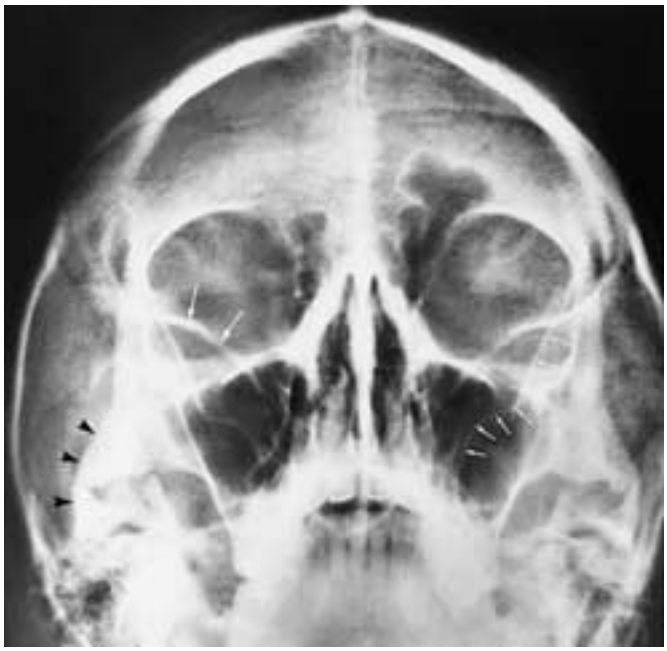

FIGURE 2-42 Waters view with smaller arrows outlining the left oblique orbital line, its inferior extension to the infratemporal fossa, and finally the lateral pterygoid plate. The larger arrows point to the upper anterior margin of the right middle cranial fossa. The arrowheads outline the right zygomatic arch.

VIEW IMAGE

this line is seen to continue medially and then bend downward, outlining the lateral pterygoid plate (Figs. 2-41 and 2-42).

The superior bony margin of the middle cranial fossa is a concave posterior ridge that is formed medially by the lesser sphenoid wing and laterally by the posterior edge of the orbital plate of the frontal bone. The curved margin can be seen projected through the orbit and upper antrum on the Waters view (Figs. 2-41 and 2-42).

The body of the zygoma and the zygomatic arches are well seen in the Waters and base views (Figs. 2-17 and 2-42). Alternate views for this arch are the underpenetrated base view and the ''jug handle,'' or oblique zygomatic projection. The posterior portions of the arch are best seen on a Towne view. The zygomaticotemporal suture in the zygomatic arch is an obliquely oriented line that is seen routinely and should not be confused with a fracture. Occasionally the zygomaticofacial canal can be seen in the lateral body of the zygoma. It transmits the zygomaticofacial nerve.

On the Waters view the soft-tissue shadow of the upper lip is often seen traversing the lower antrum (Fig. 2-43). This shadow usually extends laterally to the lower maxillary sinus margin. Similarly, a mustache also can produce such a shadow. These soft-tissue densities should not be confused with true retention cysts of the lower antrum, which unlike the shadows just described can be identified as cysts on a lateral view. Similarly, the nasal alae can mimic cysts of the medial antral wall in the Waters view (Fig. 2-41).

Soft-tissue swelling of the cheek can mimic ''clouding'' of the antrum on a Waters view. This usually can be identified by elevation of the superior skin line over the inferior orbital rim. However, sectional imaging may be necessary in some cases to isolate the maxillary sinus from the overlying swollen skin and subcutaneous tissues.

In the lateral view the coronoid processes of the mandible project over the inferoposterior maxillary sinuses. This is

FIGURE 2-43 Waters view with arrows outlining the shadow of the upper lip, which is projected over the lower maxillary sinus.

VIEW IMAGE

Copyright © 2003, Mosby, Inc. All rights reserved.

especially noted if the mouth is closed. If these coronoid processes are blunt or rounded, they may simulate retention cysts (Fig. 2-44). If the coronoid processes are sharply pointed, they may simulate a fractured bone segment or an unerupted tooth.

The Sphenoid Sinuses

The sphenoid sinuses are probably the most difficult sinuses to evaluate by routine films because they are buried deep in the skull base and are surrounded by the facial bones, nasal cavity structures, and occiput on the frontal views; the mastoids and lateral skull base structures on the lateral view; and the calvarium and pharynx on the base views. The sphenoid sinuses are extremely variable in their configuration. About one half of the population has only a central sinus cavity, and the other half has, in addition, lateral recesses. These recesses can extend into the greater wings of the sphenoid, lesser wings, and pterygoid processes.

The central, or main, sphenoid sinus cavity is best evaluated on the lateral, base, and open-mouth Waters views (Figs. 2-30 and 2-33). The sinus roof (planum sphenoidale), the sella floor (lamina dura), and the posterior development of the sinus cavity are all well seen on the lateral view; the floor and anterior sinus walls, however, are partially obscured by the overlapping lateral skull base. The base view provides a means of evaluating the sinus depth and lateral extension. The open-mouth Waters view allows evaluation of the lower posterior sinus wall as it is projected through the mouth.

VIEW IMAGE

FIGURE 2-44 Lateral view with arrows pointing to the coronoid process of the mandible, which is projected over the lower posterior antrum in this closed-mouth view.

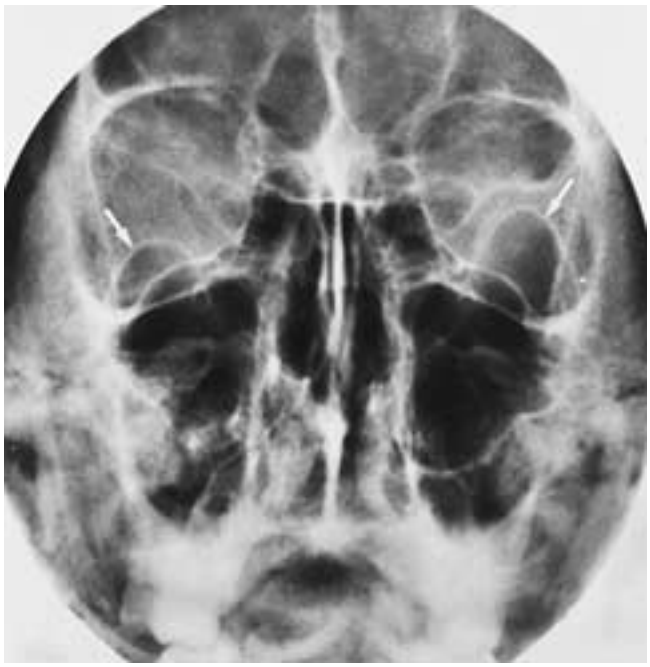

FIGURE 2-45 Caldwell view shows lateral sphenoid sinus pneumatization of the greater sphenoid wings as they form the posterior orbital walls (*arrows*). They are limited on all but their inferomedial margins (where they join the main sinus cavity) by the thin white mucoperiosteal line of the sinus margin.

VIEW IMAGE

The lateral sinus extensions into the greater wing of the sphenoid can go into the floor of the middle cranial fossa and up into the posterior orbital wall. These extensions are seen best on the Caldwell and Waters views. On the Caldwell view the ''orbital recess'' is seen as a ''lytic'' area in the lower lateral orbit. There is a thin cortical white line outlining its contour except in its lower, medial portion. It is at this margin that this sphenoid recess communicates with the main sinus cavity (Fig. 2-45). On the Waters view the lateral sphenoid sinus recesses in the floor of the middle cranial fossae are projected through the maxillary sinuses. They have a variable shape, depending on the configuration of the recess. They can appear as ''dog ears'' or can simulate compartments of the maxillary sinus (Fig. 2-46). Regardless of their shape, they always join the central sphenoid sinus medially and, when normal, are always rimmed by a thin white cortical line.

Pterygoid pneumatization results in a triangular lucency in the pterygoid plates in the lateral view and a round or oval lucency in the pterygoid process in the base view (Fig. 2-47). These recesses, when normal, are again outlined by a thin white cortical line.

The plain film appearances of all of these recesses are classic. Once they are mastered, the interpreter should not confuse them with pathologic processes.

In patients with a pituitary mass who may require a transsphenoidal surgical approach, special attention should be given to evaluating the posterior extent of the main sphenoid sinus cavity. If more than 1 or 2 mm of bone remains between the posterior margin of the pneumatized sinus and the anterior sella wall (less than 1% of the cases), most surgeons avoid a transsphenoidal hypophysectomy. This relationship is most easily seen in the lateral view.

Copyright © 2003, Mosby, Inc. All rights reserved.

VIEW IMAGE

FIGURE 2-46 Waters view shows lateral recesses of sphenoid sinuses extending into the greater sphenoid wings in the floor of the middle cranial fossa. The arrows outline the right ''dog-ear-shaped'' recess projected through the maxillary sinus. There is also a recess on the left side.

Associated Structures Surrounding the Paranasal Sinuses

There are a number of important structures that surround the paranasal sinuses and project over them on the plain film examinations.

On the lateral view, the anterior walls of the middle cranial fossa are seen as paired curvilinear lines that project over the sphenoid sinus cavities and merge posteroinferiorly with the bone density of the skull base. The planum sphenoidale is clearly identified as a straight, bony line. The cribriform plate is not as well seen as it continues anteriorly from the planum sphenoidale. However, a line drawn connecting the nasion and the anterior planum very closely approximates the level of the cribriform plate. The fovea ethmoidalis (ethmoid sinus roofs) lie just lateral to and above the cribriform plates. They usually are identified as slightly concave, downward thin, bony lines positioned just above the plane of the cribriform plates. The orbital roofs are situated higher and more laterally than the fovea ethmoidalis. Thus one can roughly localize a lytic process on a lateral film by evaluating which of these lines is eroded. The more superior the line, the more lateral the process (Fig. 2-48). The midline crista galli is best seen on the Caldwell view. This intracranial structure rests on the midline upper surface of cribriform plates.

The bony nasal septum is not seen optimally on any plain film projection, but it is best evaluated on the Caldwell view. Only gross deviation of the bony septum can be appreciated. The cartilaginous septum is poorly seen on plain films and is well visualized only on sectional imaging.

In the lateral view the anterior nasal spine usually has a sharply triangular appearance. The film must often be ''bright lighted'' to properly evaluate the spine. Destruction of the anterior nasal spine should raise the question of prior surgery or trauma. Midfacial anomalies, Hansen's disease (leprosy), other infectious processes, and carcinomas can also result in nonvisualization of this spine.

The hard palate is best evaluated in the lateral view. Its upper nasal surface is flat and usually has a clear cortical margin. The lower oral surface is slightly concave downward, and it also has a good cortical margin (Fig. 2-31).

In the base view, three paired lines are consistently seen. The most posterior of these is concave posteriorly and represents the greater wings of the sphenoid bone as they form the anterior margin of the middle cranial fossae. The second and most often the anterior pair of lines are relatively straight, being obliquely oriented to the midsagittal plane and open-faced anteriorly. Each line is composed medially by the sphenoid bone as it forms the posterior orbital wall and laterally by the orbital surface of the zygoma. The suture between these bones often can be identified clearly. Medially these two sets of paired lines (each primarily formed by the sphenoid bone) join at the pterygoid processes. The third pair of lines are sigmoid (S-shaped) and represent the infratemporal or posterolateral antral walls. Depending on the angulation used to make the base view, the sigmoid line can be anterior to, overlapping and crossing, or posterior to the orbital lines (Figs. 2-32 and 2-33).

In the base view the pterygoid fossa is seen as a V-shaped space with its apex placed anteriorly. The pterygoid plates are usually seen as three thin, bony lines. The medial pterygoid plate is seen as a single line. However, the lateral pterygoid plate is seen as two separate lines, a lateral line that represents the most caudal end of the lateral pterygoid plate at the level of the hard palate and a central or medial

FIGURE 2-47 Base view with large white arrows outlining the pneumatized pterygoid process. The small black arrows point to the foramen spinosum, and the large black arrow indicates the right foramen ovale. The small white arrows outline the posterior margin of the tongue.

VIEW IMAGE

Copyright © 2003, Mosby, Inc. All rights reserved.

VIEW IMAGE

FIGURE 2-48 Lateral view with small arrows pointing upward indicating the planum sphenoidale in the midline. The small arrows pointing downward outline the roof of the ethmoid sinuses (fovea ethmoidalis). The long arrows indicate the laterally positioned roofs of the orbit. The short arrows outline the curved anterior margins of the middle cranial fossa.

line that represents the lateral pterygoid plate near the skull base. The lateral pterygoid plate is seen as two lines because this plate has a curved, laterally tilted shape, which results in the main body of this plate being oblique to a craniocaudal incident beam. As a result, only the upper and lower bony margins are directly ''on end'' to the beam. Occasionally the hamulus of the medial pterygoid plate can be seen on the base view. The pterygoid fossa is thus the space, open posteriorly, between the medial and central pterygoid lines near the skull base and between the medial and lateral lines near the hard palate.

In the base view the frontal bone casts two transverse lines across the anterior portion of the ethmoid and maxillary sinuses. These lines correspond to the anterior and posterior cortices of the frontal bone. In addition, the anterior surface of the body of the zygoma and the anterior wall of the maxilla cast a transverse line across the anterolateral skull base. The relationship of the frontal table lines to the zygomaticomaxillary lines depends on the particular angulation used in the base view (Figs. 2-32, 2-33, and 2-49). In the more markedly angulated base view, the lacrimal canals can also be seen projected through the medial antral walls and hard palate.

The nasopharyngeal soft tissues should be carefully and routinely examined because disease can spread from this area into the sinonasal cavities and vice versa. This evaluation is best accomplished on the lateral view. The presence of a soft-tissue fullness in the roof and uppermost posterior wall of the nasopharynx may indicate adenoidal tissue, lymphoma, nasopharyngeal carcinoma, a Thornwalt cyst, or other lesions. If an ''adenoidal'' mass abuts on the upper surface of the soft palate, it may account for respiratory-related symptoms such as snoring or sleep apnea. Thus obliteration of the posterior nasal airway should always be noted in the radiologist's report.

On the base view the uvula, the posterior surface of the soft palate, and the back of the tongue all can cast transverse soft-tissue shadows across the skull base. In particular, the tongue base is often visualized extending transversely across the sphenoid sinuses. This should not be confused with sinus ''clouding'' and should be correlated with the lateral and open-mouth Waters views. The air in the nasopharynx and oropharynx is routinely seen as a low-density region projected over the central skull base. The degree of tube angulation and neck extension determines if this air shadow primarily represents the nasopharynx or the oropharynx. Thus a rectangular shadow with its greatest dimension extending from side to side suggests the nasopharynx, while a more square-shaped shadow suggests the oropharynx. On the routine base view, fullness in the region of the palatine tonsils can produce lateral soft-tissue

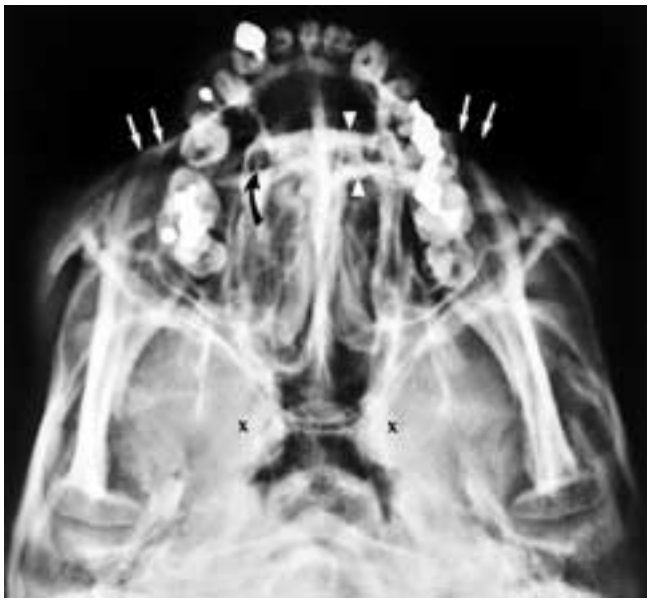

FIGURE 2-49 Base view with arrows indicating the anterior wall margin of the maxilla and the zygoma. The curved arrow points to the nasolacrimal duct, which in this film is projected over the frontal bone's anterior and posterior margins (*arrowheads*). The soft-tissue shadows of the palatine tonsils (*Xs*) can also be seen.

VIEW IMAGE

Copyright © 2003, Mosby, Inc. All rights reserved.

masses that overlie the posterior nasal fossae and pharyngeal airway (Fig. 2-49).

On the lateral view the pinna of the ear occasionally is projected over the sphenoid sinus and nasopharynx. This may simulate a mass and is usually seen on slightly underpenetrated films. It can be identified as an artifact by tracing out the entire ear lobe.

The nasal bones are best evaluated in the lateral view (Fig. 2-15B). The nasofrontal suture is identified easily at the level of the nasion. Also, the nasomaxillary sutures can often be seen. There are no normal sutures or bone segments that routinely traverse the midline nasal bones. However, several radiolucent lines are usually present in the lateral aspect of the nasal bones. These lines, which are the normal grooves for the nasociliary nerves and vessels, roughly parallel the plane of the midline nasal bones, and they should not be confused with fractures. As a general rule, there should be no lucent lines that extend across the midline nasal bones, and any such line or lines must suggest the diagnosis of a fracture. Medial depression of the nasal bones is best evaluated in the occlusal (axial) and Waters views. As mentioned, when evaluating the nasal bones, attention should also be paid to the anterior nasal spine.

In a patient with recent nasal trauma, clinical examination can usually determine whether a fracture is present. The examiner places the thumb and index finger on either side of the bridge of the nose and gently rocks the fingers from side to side. In cases of fracture the patient has exquisite local pain. By comparison, if there is only hemorrhage and edema (often markedly deforming the nasal contour) without fracture, the patient is only slightly tender. Thus, in such cases, strictly speaking the x-ray request for nasal films should read ''Nasal fracture, please evaluate for the number of fractures and any displacement'' rather than ''Rule out a nasal fracture.'' The radiologist's report should include a comment on the number and location of the fractures and whether there is depression or elevation of the fracture segments. These nasal fractures are usually best seen on sectional imaging.

SECTIONAL IMAGING TECHNIQUES

Computed Tomography

The mucosal surfaces and the bony framework of the sinonasal cavities are well suited for investigation by CT. Because the radiologist and the clinician are as interested in soft-tissue disease as they are in bony changes, it would be convenient if each scan could be viewed at an appropriate window and center level that optimizes both subtle soft-tissue differences in attenuation as well as fine bony detail. Unfortunately, there is no one combination of window and center (level) settings that optimally accomplishes both of these aims. The soft tissues are best shown at narrow windows that allow easy discrimination between the attenuation values of muscle, fat, and tumor, as well as some distinction between entrapped secretions and cellular soft tissues. In addition, narrow windows allow prompt detection of any enhancement differences on contrast-enhanced CT scans. Such soft tissue settings have window values in the range of 150 to 400 HU.

Conversely, bone detail is best shown at wide window settings in the range of 3000 to 4000 HU. In addition, these wide window settings allow the most accurate evaluation of the air soft-tissue interfaces. This reflects the fact that almost all commercial vendor algorithms have difficulty handling abrupt transitions in attenuation values from very low (air) to very high (bone) attenuation regions. Thus, when the same images are viewed side by side at both narrow and wide window settings, the air spaces and the bones always appear larger at the narrower settings but are more accurately seen at the wider window settings (Fig. 2-50).

The appearance at wide window settings correlates accurately with the true measurements of the air spaces and the thickness of both soft-tissue disease and bone. In addition, at narrow window settings, volume-averaging errors allow a small soft-tissue mass to be obscured by surrounding sinus air and a focal area of abnormal bone to be obscured by adjacent normal bone.

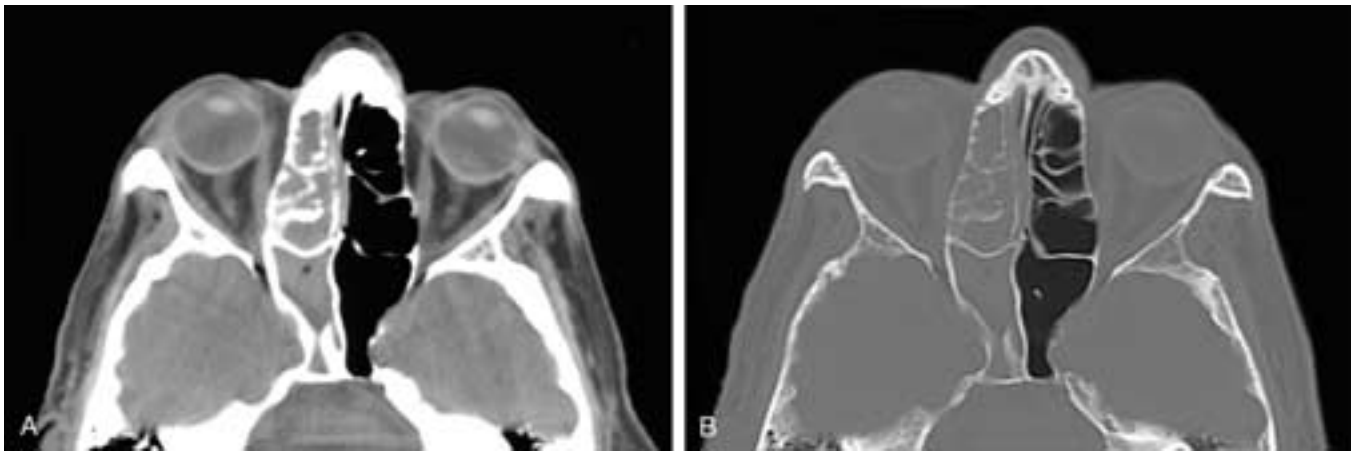

FIGURE 2-50 **A**, Axial CT scan through the ethmoid and sphenoid sinuses viewed at narrow ''soft-tissue'' window settings shows opacification of these sinuses, with apparent sclerosis and thickening of the surrounding bone and ethmoid septae. **B**, Same image viewed at wide ''bone'' window settings shows that the bones are not sclerotic and thickened. The wide window views of the bone most closely reflect the actual bony changes.

VIEW IMAGE

Copyright © 2003, Mosby, Inc. All rights reserved.

In summary, the most accurate assessment of mucosal soft-tissue disease and bone is accomplished at wide window settings. However, the best distinction of watery sinonasal secretions from more viscous or desiccated secretions or a tumor requires narrow window settings.

Because of the popularity of endoscopic sinus surgery and its focus on the osteomeatal complex, the limited coronal CT study has become the most requested imaging examination of the sinonasal cavities. These studies best show the osteomeatal unit and are designed to limit the patient's radiation dose. Such limited CT examinations also are comparable in price to a plain film study. Although this approach is adequate for most patients, there are some pitfalls in interpreting such limited studies. Specifically, the anterior and posterior walls of the frontal, maxillary, and sphenoid sinuses are not well seen in the coronal view, and any abnormality or violation of these walls is most often overlooked or underestimated if only coronal views are available. In addition, because of varying patient compliance with the degree of neck extension, the coronal scan angle varies from patient to patient and often from examination to examination on the same patient. This alters the appearance of some anatomic landmarks and may make precise localization of ethmoid disease difficult. Such variation may soon be eliminated with the greater use of the multidetector CT scanners that allow precise coronal plane reconstructions from axial scans.

The axial studies provide the best CT evaluation of the anterior and posterior sinus walls. Thus, while a limited coronal CT study may be an adequate examination for most patients with suspected inflammatory sinonasal disease, the interpretation of such a study must be viewed with a caveat in mind. Namely, whenever there is total opacification of the frontal, maxillary, or sphenoid sinuses, a complete axial and coronal CT examination should be performed. In addition, if the patient has a suspected neoplasm, a complete axial and coronal examination ought to be performed to provide the most detailed analysis of the sinonasal cavities and the adjacent skull base.[52–54]

The axial examination is most often performed with the patient supine, the hard palate perpendicular to the table top, and the scanning plane parallel to the inferior orbitomeatal (IOM) line. The IOM line is readily identified on a lateral scout view. In addition, the cranial and caudal limits of the average scan (a level just above the top of the frontal sinuses and the bottom of the maxillary teeth, respectively) can be easily localized off the lateral scout view. The routine study should be obtained as 3 mm contiguous scans throughout the scan volume. Narrower slice thicknesses are usually unnecessary unless there is a specific region of interest. Spiral CT can also be performed at 3 mm intervals and reconstructed at 1 to 3 mm intervals.

Just as volume averaging may cause diagnostic difficulties in the coronal view, there are three levels in the axial view that may cause interpretive difficulties. These levels correspond to three bony planes, all of which are nearly parallel to the axial scan plane: the floor of the anterior cranial fossa, portions of the orbital floor, and the hard palate. Because knowledge of extension of disease across these bony planes is critical for the surgeon in determining some surgical procedures (for example, an antral tumor growing into the orbit, or a nasoethmoid or sphenoid tumor extending into the anterior cranial fossa), a coronal study must also be obtained whenever imaging of these bony planes is essential.

Because most adult patients have dental amalgams or metal bridges that cause considerable artifact, direct 90° coronal CT scans (to the IOM plane) are usually of limited diagnostic value because the involved teeth lie immediately below the sinonasal areas of interest. In addition, many patients cannot sufficiently extend their necks (because of pain, vertigo, arthritis, etc.) in either the supine or prone position to obtain such 90° coronal studies. In general, a scan plane is chosen that extends from a caudad margin just anterior to the dental fillings to a cranial point just posterior to the area of greatest interest (osteomeatal unit, orbit, sphenoid, etc.). These coronal studies are routinely obtained as 3-mm-thick contiguous slices.[55, 56] Spiral CT is now a viable alternative technique to the conventional multislice approach. This may be especially pertinent in the coronal view, where the faster spiral CT minimizes patient motion. In addition, the newer multidetector CT scanners allow excellent coronal images to be created at any desired scan angle from images made in the axial plane.

The routine CT study performed to evaluate sinonasal inflammatory disease does not require intravenous contrast administration. However, if one needs to determine if a nasal mass extends into an adjacent sinus or simply obstructs the sinus, or if there is suspected intracranial extension of disease, contrast should be given. In such instances, contrast CT is usually performed because the patient cannot have an MR study, as MR better visualizes mass/secretion interfaces and intracranial disease. There are a variety of methods for administering the CT contrast, and today a power injector is commonly used. If multiple serial CT slices are obtained, a small volume (10 to 20 ml) may be given as a bolus to ''load'' the patient and then the remaining contrast given at a slower rate throughout the examination. If spiral CT is used, the rapid scanning time allows the delivery of a larger effective bolus throughout the examination.

Magnetic Resonance Imaging

As the era of MR imaging proceeds, new sequences and techniques are constantly being suggested. However, these approaches are primarily variations of facilitating the acquisition of basic T1-weighted and T2-weighted information. The advantage of imaging without ionizing radiation is occasionally outweighed by a claustrophobic patient's rejection of the procedure (about 10% of cases) or the presence of metal hardware, foreign bodies, or a pacemaker that abrogates the examination. Industry has responded to most of these problems by producing implantable nonmagnetic materials, nonparamagnetic support equipment for use with the more critically ill patient, and open MR units. Although bone is not directly imaged on MR, invasion of bone marrow and gross bone erosion can be easily identified.[57, 58] Fine bone alterations as well as focal calcifications are difficult, if not impossible, to see on MR imaging, and they are far better demonstrated on CT.

There stills remains some debate regarding the indications for the use of MR contrast material. Below the skull base, contrast enhancement occurs in most tumors and

Copyright © 2003, Mosby, Inc. All rights reserved.

inflammatory tissue, as well as in some normal mucosa. As a result, the region of enhancement may contain a variety of normal as well as pathologic tissues, and the actual pathology may appear larger than it actually is. Despite this, some authors have recommended the use of double- and even triple-dose MR contrast agents to better assess the pathology visually. However, no new pathology was identified in such high-dose studies, and today single contrast dosing is the rule.[59] Actually, in day-to-day practice, pathology is often better mapped on noncontrast T1-weighted and T2-weighted images than on enhanced studies. However, if the pathology has spread intracranially, contrast-enhanced MR is superior to noncontrast studies in demonstrating an intracranial tumor margin and dural disease, as well as any intracranial complications of sinusitis such as meningitis, cerebritis, intracranial abscess, and orbital complications.[59, 60] Some radiologists firmly believe that fat suppression offers better visualization of contrast-enhanced areas. This is especially true when there is orbital involvement. However, other radiologists believe that the use of fat suppression techniques introduces unwanted artifacts that complicate image interpretation. Although most studies are done with fat suppression, the final decision is based on the preference of the radiologist.

MR contrast may also help in differentiating between entrapped secretions and a solid mass, as there is peripheral enhancement of uniformly thick, inflamed mucosa around secretions, while there usually is enhancement of a tumor nodule either centrally or along the margin of a neoplasm.[61, 62] Lastly, an MR contrast-focused study of the skull base and cavernous sinuses is the best way to identify perineural tumor spread. This topic is discussed in detail in Chapter 13.

The basic MR examination usually includes axial and coronal images. The scan thickness should be 3 to 5 mm, and a narrow interslice distance (1 mm) is suggested. Basic or equivalent T1-weighted and T2-weighted information should be obtained, whether by conventional spin echo or fast scan imaging. Fat suppression can be used in selected cases but is rarely necessary unless contrast-enhanced sequences are also obtained. The best study for an individual patient is often the one that is most confidently read by the radiologist. Thus sagittal images, though not necessary in the routine case, may help, especially in evaluating the cribriform plate region or the orbital floor. Gradient echo or FLAIR-type images can also be obtained to confirm the presence of hemorrhage.

Because there is no uniformity in the literature regarding the optimal TR and TE, these parameters can be varied to some degree to limit the total duration of the MR study, alter the resolution, or produce more scan slices in a single scan sequence. The greatest challenge for the imager is to tailor the examination to each patient so that all of the necessary information is gathered without unduly lengthening the examination. An additional benefit of this approach is that more patients can be examined in a given work day.

SECTIONAL IMAGING ANATOMY

This section highlights the anatomy that can be seen on CT and MR imaging of the sinonasal cavities. The anatomy is divided into sections to help organize the anatomic detail. For specific anatomic descriptions of the sinuses, one should also review the previous sections dealing with plain film anatomy. Only the pertinent anatomic details are mentioned in the following sections. The reader is also referred to the images in the atlas section.

The Nasal/Palatal Region

Far anteriorly on coronal images, the nasal bones and frontal processes of the maxilla form the upper outer nasal contour.[47] The upper nasal septum is formed by the perpendicular plate of the ethmoid bone above and the septal cartilage below. Inferiorly, the premaxilla is seen; anteriorly, at the level of the hard palate, is the anterior nasal spine. Within the hard palate and about 1 cm behind the anterior premaxilla is the incisive foramen. This foramen extends cranially as two separate incisive canals that open on either side of the base of the nasal septum. Together these canals and the foramen form a Y shape on coronal images. These canals transmit the terminal branches of the sphenopalatine arteries and their anastomoses with the terminal branches of the greater palatine arteries. The canals also transmit the nasopalatine nerves.

On coronal images, the palatine spines are seen on the oral surface of the hard palate. Lateral to the spines are the palatine grooves in which run the palatine vessels and nerves. The greater palatine foramen is seen posteriorly at the lateral junction of the lateral hard palate and the maxillary alveolus. The anterior surface of this canal is formed by the maxillary bone, the posterior surface by the palatine bone. Extending upward from the greater palatine foramen toward the pterygopalatine fossa is the pterygopalatine canal. The canal transmits the anterior palatine nerve and the descending palatine artery. Occasionally the lesser palatine foramen may be identified. It also extends to the pterygopalatine fossa and opens just posterior to the greater palatine foramen. The lesser palatine foramen transmits the posterior palatine nerve.

The anterior two thirds of the hard palate on each side is formed by the palatine process of the maxilla, the posterior one third by the horizontal process of the palatine bone. The most posterior medial wall of the antrum is formed by the vertical portion of the palatine bone.

The Pterygopalatine Fossa

The pterygopalatine fossa is a small, thin rectangular space directly behind the perpendicular plate of the palatine bone and in front of the pterygoid process of the sphenoid bone. On axial images it appears that this space is directly posterior to the medial back wall of the maxillary sinus, this observation often leading to the false impression that the anterior wall of the pterygopalatine fossa is formed by the maxillary bone. In actuality, although the palatine bone cannot be separated on images from the maxillary bone, it is the ascending portion, or perpendicular plate of the palatine bone, that forms the anterior wall of the pterygopalatine fossa.

The pterygopalatine fossa communicates with five

Copyright © 2003, Mosby, Inc. All rights reserved.

anatomic areas: (1) the nasal fossa (via the sphenopalatine foramen), (2) the mouth (via the greater and lesser pterygopalatine canals, which open on the palate through the greater and lesser palatine foramina), (3) the infratemporal fossa (via the retromaxillary space or fissure), (4) the orbit (via the inferior orbital fissure), and (5) the intracranial compartment and skull base (via the pterygoid or Vidian canal and the foramen rotundum).

More specifically, the medial boundary of the fossa is formed by the sphenopalatine foramen, which is at the craniocaudal level of the posterior tip of the middle concha, about 1 cm dorsal to it. This foramen may be seen connecting the nasal fossa with the pterygopalatine fossa. Within the pterygopalatine fossa are the sphenopalatine ganglion, portions of the maxillary nerve, and the internal maxillary artery. It is actually the sphenopalatine artery (the terminal branch of the internal maxillary artery) that runs through this foramen. All of these structures are supported by fat, which fills the majority of the pterygopalatine fossa. The nasopalatine nerve (a branch of the sphenopalatine nerve, which is a branch of the maxillary nerve [V_2]), also passes through the sphenopalatine foramen.

Extending posteriorly into the middle cranial fossa via the skull base are two canals. The lower and more medial canal is the pterygoid or Vidian canal, while the upper and more lateral canal is the foramen rotundum/canal. The Vidian canal may be almost entirely within the sphenoid bone or sitting well within the sinus on a septum above the sinus floor. Similarly, the foramen rotundum may protrude into the lateral lower wall of the sphenoid sinus or may be completely lateral to the sinus. More posteriorly, the optic canal may protrude into the upper lateral sinus wall. These sphenoid sinus variations are discussed in detail in Chapter 3.[47]

The Pterygoid Plates

The medial pterygoid plate is almost vertically oriented. The lateral plate is tilted so that its lower end, at the level of the hard palate, is more lateral than its cranial margin at the skull base. The pterygoid fossa lies between these plates. These relationships are often best appreciated on coronal images. The medial or internal pterygoid muscle arises from the medial side of the lateral pterygoid plate within the pterygoid fossa, and the lateral or external pterygoid muscle arises from the lateral side of the lateral plate. The tendon of the tensor veli palatini muscle passes around the laterally concave-shaped hamulus of the lower medial pterygoid plate to form part of the soft palate.

The Nasal Septum

The nasal septum is formed anteriorly to posteriorly by the medial crura of the alar cartilages, the septal cartilage, the perpendicular plate of the ethmoid bone, and the vomer. Inferiorly, the nasal crests of the maxilla and palatine bones contribute to the base of the septum. The posterior edge of the vomer joins the undersurface of the sphenoid bone at the sphenoid rostrum, a prominent triangular ridge on the underbody of the sphenoid bone. In addition to deviations of the nasal septum, nasal spurs can occur on either side. These usually triangular bony excrescences occur at the level of the junction of the perpendicular plate of the ethmoid bone and the vomer.

The Olfactory Recesses and Nasal Atrium

The olfactory recess is the narrow channel-like region of the nasal cavity on either side of the upper nasal septum. These spaces continue up to the cribriform plate. On either side, the olfactory recess widens posteriorly into the sphenoethmoidal recess. This marks the junction between the ethmoid and sphenoid bones.

In the anterior lateral nasal cavity, just below and medial to the agger nasi cells, is the region referred to as the nasal atrium. This atrium region is continuous with the more posterior nasal fossa (see Chapter 3).

The Margins of the Orbit

On coronal images through the superior orbital rims, a localized notch, or foramen, can be seen along the medial orbital margin. This is the supraorbital notch (or foramen), and the supraorbital artery and nerve pass through it. Medial to the supraorbital notch is the frontal notch, which transmits the frontal artery and the frontal nerve. Although the orbital surface of the orbital roof is smooth, the intracranial margin of the orbital roof has bony ridges that, in a general way, reflect the impressions of the gyri of the base of the frontal lobes.

Along the medial orbital walls are the anterior ethmoidal canals, which are seen as medial indentations in the upper lamina papyracea. They transmit the anterior ethmoidal nerves and vessels. The lower margins of these canals are formed by the ethmoid bones, and the upper margins are formed by the frontal bones. More posteriorly are the similarly formed posterior ethmoidal canals, which transmit their respective vessels and nerves.

In the middle third of the orbital floor are the infraorbital foramen and canal. The canal extends from the inferior orbital fissure posteriorly to the anterior maxilla. This canal runs parallel to the orbital floor except in its most anterior portion, where, starting about 1 cm behind the inferior orbital rim, it turns downward to exit as the infraorbital foramen about 1 cm below the inferior orbital rim on the anterior face of the maxilla.

The inferior orbital fissure is about 2 cm long and is angled at about 45° (open anteriorly) with the midsagittal plane. This fissure is narrowest in its midportion and widens at both its medial and lateral margins. This fissure separates the lateral orbital wall from the orbital floor, and at the lateral posterior margin of the inferior orbital fissure the temporal fossa becomes the infratemporal fossa.

The circular configuration of the anterior orbit slowly changes to a more triangular shape in the posterior orbit. This change in shape occurs because the medial orbital floor elevates, and the lower lamina papyracea tilts laterally, as the larger posterior ethmoid cells are encountered.[47]

The thin lacrimal bone has a slightly concave lateral configuration, forms the anterior medial orbital wall, and overlies the anterior ethmoid cells. The ethmoid lamina

Copyright © 2003, Mosby, Inc. All rights reserved.

papyracea, which lies just behind the lacrimal bone, tends to be even thinner and has a straighter configuration than the lacrimal bone.

The Lacrimal Fossa and Nasolacrimal Duct

The fossa for the lacrimal gland is a shallow, smooth indentation in the frontal bone along the upper outer aspect of the orbital roof. The lacrimal groove is in the lower medial orbital wall and is related to the lacrimal sac of the nasolacrimal system. It is actually preseptal in location and not in the orbit, being anterior to the posterior lacrimal crest. The lacrimal groove is also anterior to the nasolacrimal canal, which lies in the medial antral wall. This reflects the anatomy of the nasolacrimal canal, which runs downward and posteriorly at about a 20° angle with the coronal plane. On imaging, the lacrimal groove creates a normal ''dehiscence'' in the medial orbital floor that should not be confused with a focal site of erosion. The caudal opening of the nasolacrimal canal is in the medial antral wall under the inferior turbinate (lateral wall of the inferior meatus). The medial wall of the nasolacrimal canal is formed superiorly by the lacrimal bone and inferiorly by the lacrimal process of the inferior turbinate. The lateral wall is formed entirely by the maxilla. See Chapter 10.

The Sphenoid Sinus Septum

The sphenoid intersinus septum is usually in the midline anteriorly, but posteriorly it may be angulated sharply to one side. This creates two unequally sized sinuses, and once the scan plane moves posterior to such an angled septum, it will appear as if there is only one sphenoid sinus cavity. In the floor of the sinus runs the Vidian canal. This canal may lie entirely within the sphenoid bone or may be elevated by a septum and lie within the lower sinus cavity. The foramen rotundum anteriorly and the optic canal posteriorly can also be partially within the lateral sinus wall. If any of these canals do project into the sinus cavity, or if there is dehiscence of the bony wall separating the canal from the sinus, injury to the nerve can occur during sinus surgery. This topic is discussed further in Chapter 3.

The Maxillary Sinus Walls

The medial wall of the maxillary sinus is partially bone and partially membrane. This membranous area forms a C shape, which is closed posteriorly and bridges the posterior attachment of the inferior turbinate. The anterior wall of the maxillary sinus has a slightly concave anterior configuration, with the concavity marking the site of the canine fossa. This fossa lies cranial to the lateral incisor and canine teeth and caudal to the infraorbital canal, and the caninus muscle arises in it. The posterior sinus wall is curved and sigmoid-shaped, and the infratemporal fossa fat abuts its posterior surface. Within the posterolateral antral wall there is a thin canal for the posterosuperior alveolar nerve. This canal should not be confused with a site of bone erosion or a fracture.

THE INTEGUMENT OF THE FACE AND SCALP

The facial bones, calvarium, and contained spaces receive the primary attention of the imager. However, in a limited way, the overlying skin, muscles, nerves, and vessels that supply them are also seen on images of the sinonasal cavities and head. The following sections briefly review the muscles, nerves, arteries, and veins that involve the face and scalp.[6]

The Facial Muscles

The facial muscles can be thought of as connecting bone and skin. These muscles are responsible for facial expression, and they create tension lines (Langer's cleavage lines) in the skin that are oriented at right angles to the plane of the muscle fibers. These tension lines, which deepen with age as the skin loses its elasticity, can be used to hide surgical incisions. These muscles are summarized in Table 2-1. The nasal muscles have already been discussed in the section on The Nose and Nasal Fossae[63, 64] under the heading of ''Anatomy and Physiology.''

An important concept to understand is that the mimetic muscles of the face, including the platysma, are interconnected by a fibrous aponeurosis called the superficial musculoaponeurotic system (SMAS). This system divides the subcutaneous fat into two layers and acts as a tensor of the facial muscles (see also Chapter 34).

Scalp and Forehead

On the scalp and forehead are the occipital and frontal bellies of the occipitofrontal (epicranius) muscle and the corrugator supercilii muscle. The occipital belly elevates the skin of the forehead, and the frontal belly pulls the skin toward the eyebrow. The corrugator supercilii draws the brow medially, creating frown lines near the glabella. There is the temporoparietalis muscle, which draws the skin back from the temple region and tightens the scalp. There are also small muscles (auriculares anterior, superior, and posterior) that are related to the ear and that retract and elevate the ear. The layers of the scalp include the skin, the superficial fascia or tela subcutanea (in which runs most of the blood vessels and cutaneous nerves), the epicranial aponeurosis or gala aponeurosis, loose connective tissue, and the cranial periosteum or pericranium.

Orbit

About the eye is the orbicularis oculi, which is composed of a series of concentric muscular rings. Closure of the eye is the result of coordinated contraction of the entire muscle. Blinking involves only the palpebral region of the muscle. This palpebral portion of the muscle attaches posterior to the medial palpebral ligament and aids in pumping tears from the lacrimal sac.

Copyright © 2003, Mosby, Inc. All rights reserved.

Cheek and Lips (Mouth)

In the region of the cheek and lips (mouth), the buccinator muscle serves to compress the cheeks, to help expel air, and to aid in mastication. As such, it is more a muscle of mastication than a muscle of facial expression. The orbicularis oris acts to compress, contract, and protrude the lips. Elevation of the upper lip is caused by the levator labii superioris and the levator labii superioris alaeque nasi muscles, while the levator anguli oris muscle elevates the angle of the lip. Similarly, the lower lip has the depressor labii inferioris (irony) muscle and the depressor anguli oris (grief) muscles. The lesser (minor) and greater (major) zygomaticus muscles elevate the angle of the mouth (laughing), and the lesser zygomaticus muscles help produce the nasolabial fold. The risorius muscle retracts the angle of the mouth (grinning). The mentalis muscle raises and protrudes the lower lip and wrinkles the skin (disdain). The transverse menti muscle is present in about 50% of people; it crosses the midline just under the chin. Lastly, the platsyma muscle assists in depressing the lower jaw and lip and tenses the skin of the neck. These facial muscles are summarized in Figure 2-51.

Cutaneous Innervation of the Face

On a lateral projection of the head and face, a line drawn from the vertex of the head to the tip of the chin defines a plane. The cutaneous innervation of the skin and head by the trigeminal nerve is anterior and above this plane; the cutaneous distribution of the cervical nerves is posterior and below this line. The trigeminal distribution follows the major branches of this nerve. Thus, the first division supplies the upper nose to its tip, around the medial, upper, and lateral orbits, and the upper scalp. The second division of the trigeminal nerve supplies the lateral nose, upper lip, and skin between the nose and mouth. It also supplies the skin over the malar eminence of the zygoma and a tapering triangle of skin along the anterior side of the scalp. The third division supplies the lower lip, chin, lateral face to the level of the lower mandibular border, and lateral scalp up to the line drawn from the vertex to the chin tip. The superficial cervical plexus supplies the ear, periauricular region, and anterior neck. The posterior divisions of the cervical nerves supply the posterior scalp and neck. These cutaneous nerves derive from the second, third, and fourth cervical nerves as they form the cervical plexus. The superficial cutaneous branches include the smaller occipital nerve (C2), the greater auricular nerve (C2 and C3), the cervical cutaneous nerve (C2 and C3), and the supraclavicular nerve (C3 and C4). These areas are summarized in Figure 2-52.

Arterial Supply of the Face and Scalp

The vascular supply of the face and head comes from branches of both the external and internal carotid arteries. The branches from the internal carotid artery are terminal branches of the ophthalmic artery, the supratrochlear and supraorbital arteries. They supply the upper periorbital region and immediate forehead. The major branches of the external carotid artery are the superficial temporal artery (supplies most of the forehead and scalp), the transverse facial artery (supplies the lateral face), the facial artery (supplies the central and lower portions of the face), the posterior auricular artery (supplies the back of the auricle or pinna and the periauricular region), and the occipital artery (supplies the posterior scalp, upper posterior neck, auricle, and a meningeal branch that enters the skull through the jugular foramen and supplies the dura of the posterior fossa).[63–65] These relationships are summarized in Figure 2-53.

Venous Drainage of the Face and Scalp

The drainage of the face is primarily via the facial vein and the retromandibular vein. The frontal vein begins in a venous plexus in the forehead that anastomoses with the superficial temporal vein. The frontal vein then descends to the root of the nose, where the nasal arch vein joins the parallel frontal vein of the opposite side. The supraorbital vein runs down the forehead and anastomoses with the frontal vein near the medial canthus to form the angular vein. The angular vein runs down the side of the nose in the nasolabial fold to the level of the lower orbit or bottom of the nose, where it becomes the anterior facial vein, which drains the blood from the nose and lips. It then follows the course of the facial artery down across the face, over the mandible, to join the common facial vein that drains into the internal jugular vein near the level of the hyoid bone. The anterior facial vein is joined by the superior and inferior palpebral veins, the superior and inferior labial veins, the buccinator vein, and the masseteric vein.

The superficial temporal vein starts in the scalp in a venous plexus that communicates with the frontal and supraorbital veins, the opposite superficial temporal vein, and the posterior auricular and occipital veins. Frontal and parietal veins join and then are in turn joined above the zygomatic arch by the middle temporal vein, which receives tributaries from orbital veins. This vein is then joined by the maxillary vein draining the infratemporal fossa. The pterygoid plexus drains the sphenopalatine, middle meningeal, deep temporal, pterygoid, masseteric, buccinator, alveolar, and some palatine veins and communicates via the inferior orbital fissure with the ophthalmic vein. It also communicates with the facial vein and cavernous sinus. Together the superficial temporal vein and the internal maxillary vein form the retromandibular vein, which receives tributaries from the parotid and auricular veins and from the transverse facial vein. At the lower margin of the parotid gland, the retromandibular vein joins the common facial vein and also anastomoses with the external jugular vein. The posterior auricular vein communicates with the superficial temporal and occipital veins and descends behind the auricle to join the posterior facial vein and form the external jugular vein. The occipital vein begins as a plexus at the back of the vertex of the scalp and as a single vein descends into the suboccipital triangle, where it is joined by the deep cervical and vertebral veins. It can join the internal jugular vein directly or join the posterior auricular vein. The occipital vein receives the parietal emissary vein, which communicates with the superior sagittal sinus and the mastoid emissary vein, which communicates with the transverse sinus. The veins of the forehead and upper lids drain into the orbit and the inferior and superior branches of the ophthalmic vein.[63–65] The relationships are summarized in Figure 2-53.

Copyright © 2003, Mosby, Inc. All rights reserved.

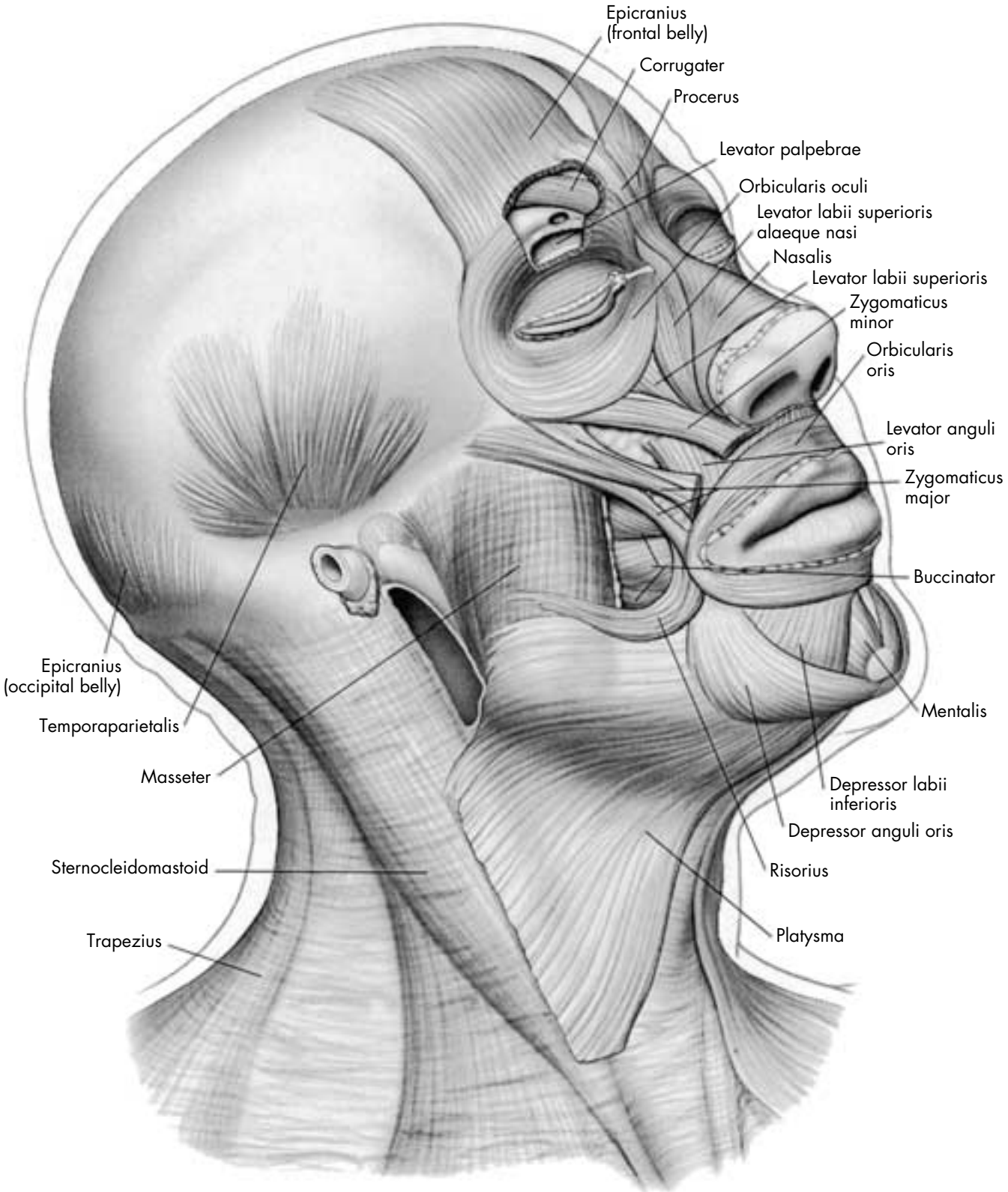

VIEW IMAGE

FIGURE 2-51 Drawing of the face and neck in the right lateral oblique view. The facial muscles and the superficial neck muscles are shown.

Copyright © 2003, Mosby, Inc. All rights reserved.

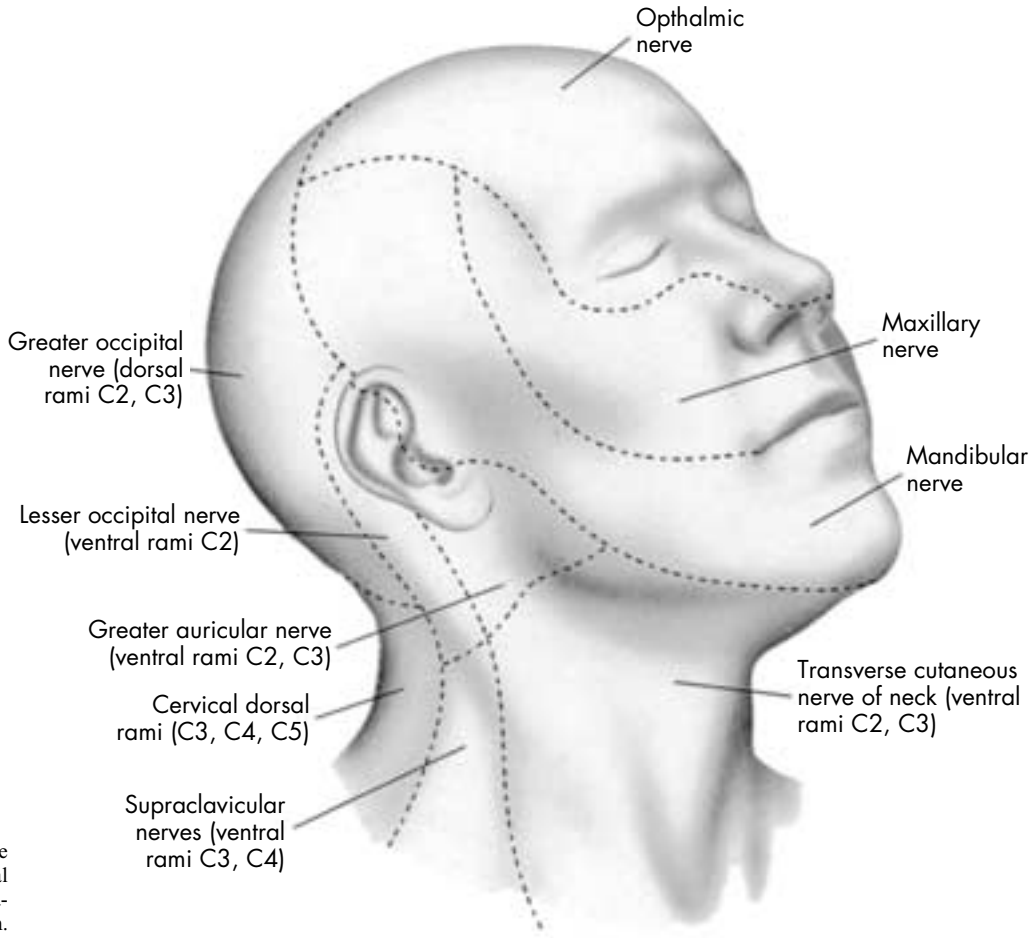

VIEW IMAGE

FIGURE 2-52 Drawing of the face and neck in the right lateral oblique view. The cutaneous innervation of the face and scalp is shown.

Copyright © 2003, Mosby, Inc. All rights reserved.

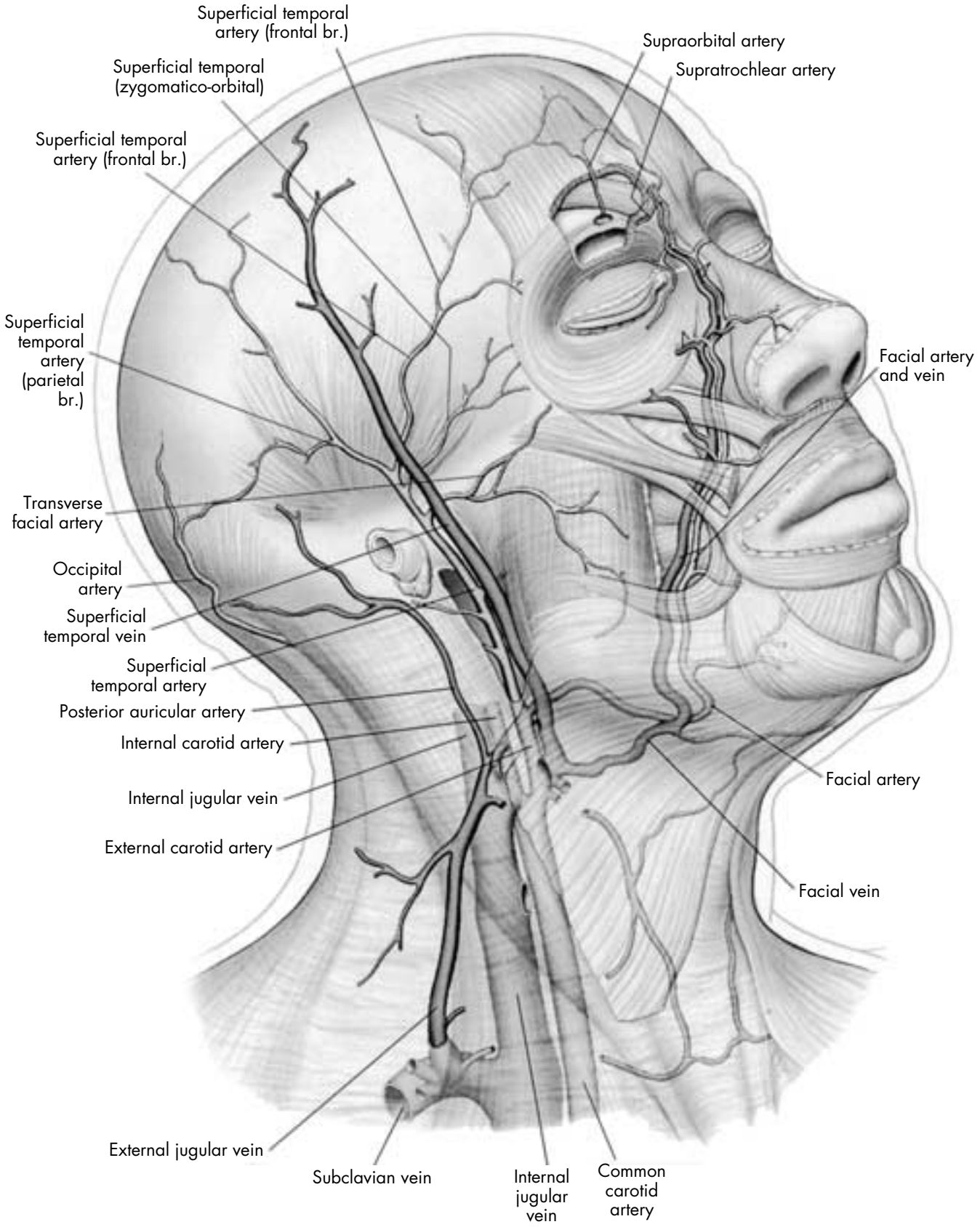

FIGURE 2-53 Drawing of the face and neck in the right lateral oblique view. The major arteries and veins of the face and upper neck are shown.

VIEW IMAGE

Copyright © 2003, Mosby, Inc. All rights reserved.

ATLAS OF NORMAL ANATOMY OF THE PARANASAL SINUSES

AEthCan	Anterior Ethmoidal Canal
Agger Nasi Cell	Agger Nasi Ethmoid Cell Deep to Lacrimal Bone
Alv Rec M	Alveolar Recess of Maxillary Sinus
Ant Clin Proc	Anterior Clinoid Process
AntCranFossa	Anterior Cranial Fossa
AntEth Can	Anterior Ethmoidal Canal
Ant Nas Spine	Anterior Nasal Spine
Att Inf Turb	Attachment of Inferior Turbinate
Basal Lam Mid Turb	Basal Lamella of the Middle Turbinate
Bas Nas Cav	Base of Nasal Cavity Above Hard Palate
Bas Nas Sep	Base of the Nasal Septum as it attaches to Hard Palate
Bulla	Bulla Ethmoidalis
Can	Canine Tooth
Car Can	Carotid Canal
Cen Inc	Central Incisor Tooth
CG	Crista Galli
Clivus	Clivus
Colum	Columella
Concha Bullos	Concha Bullosa Middle Turbinate
Cor Proc	Coronoid Process of Mandible
Cort Wt Line	Cortical Dense White Line Surrounding the Frontal Sinuses
Crib Plt	Cribriform Plate
Crista Galli	Crista Galli
DS	Dorsum Sellae
E	Ethmoid Sinus
F	Frontal Sinus
FB	Frontal Bone
Floor of Sella	Floor of Sella Turcica
For Lac	Foramen Lacerum
For Ovale	Foramen Ovale
For Rot	Foramen Rotundum
Fovea Eth	Fovea Ethmoidalis of Frontal Bone
F Proc Max	Frontal Process of Maxilla
FrontZyg Sut	Fronto-Zygomatic Suture
Fst Mol	First Molar Tooth
Fst Pre Mol	First Premolar Tooth
Gr Pal Can	Greater Palatine Canal
Great Wing Sph	Greater Wing of the Sphenoid Bone
Hamulus Med Pter Plt	Hamulus of the Medial Pterygoid Plate
Hard Pal	Hard Palate
Hor Plt Pal	Horizontal Plate of Palatine Bone
IC Lig	Interclinoid Ligament
Incis Can	Incisive Canal
Incis For	Incisive Foramen
Inf Meatus	Inferior Meatus
InfOrCan	Infraorbital Canal
InfOrFis	Inferior Orbital Fissure
InfOrFor	Infraorbital Foramen
InfTemFossa	Infratemporal Fossa
Inf Turb	Inferior Turbinate
Infra Or Canal	Infraorbital Canal
Infra Or For	Infraorbital Foramen
IOF	Inferior Orbital Fissure
Lac Bone	Lacrimal Bone
Lac Sac Fossa	Lacrimal Sac Fossa
Lam Dura Sella	Lamina Dura of Sella
LamPap	Lamina Papyracea of Ethmoid
Lat Inc	Lateral Incisor Tooth
Lat Pter Plt	Lateral Pterygoid Plate
Lat Rec S	Lateral Recess of Sphenoid Sinus
Lac Sac	Lacrimal Saccule
Les Pal Can	Lesser Palatine Canal
Less Wing Sph	Lesser Wing of the Sphenoid Bone
Limbus	Sphenoid Bone Limbus
LPap	Lamina Papyracea Ethmoid
M	Maxillary Sinus
Man Hd	Mandibular Head
Mand For and Can	Mandibular Foramen and Upper Canal
Mand Notch	Mandibular Notch
Max Alv	Maxillary Alveolus
Max Exost	Maxillary Exostosis
Max Pal Sut	Maxillary Palatine Suture
Max Teeth Rts	Maxillary Teeth Roots
MB	Maxillary Bone
Med Pter Plt	Medial Pterygoid Plate
Med Wall M	Medial Wall of Maxillary Sinus
MidCranFossa	Middle Cranial Fossa
Mid Meatus	Middle Meatus
Mid Sut Pal	Midline Suture Between Left and Right Halves of Hard Palate
Mid Turb	Middle Turbinate
MSept	Maxillary Sinus Septum
Nasal Cavity	Nasal Cavity Airway
Nasal Fossa	Nasal Fossa Air Space
Nasal Septum	Nasal Septum
NasoLac Duct	Nasolacrimal Duct
NasoFtl Sut	Nasofrontal Suture
NasoLac Can	Nasolacrimal Canal
NB	Nasal Bone
Nose	Nose Cartilages and Soft Tissues
Nostril	Nostril of Nose
NP	Nasopharynx
OC	Optic Canal
Olf Groove	Olfactory Groove
OlfRec	Olfactory Recess
Open Nasolac Duct	Opening of the Nasolacrimal Duct into the Middle Meatus
Opt Can	Optic Canal
Or	Orbit
Or Roof	Orbital Roof
Pal Proc Max	Palatine Process of Maxilla
Palatal Recesses Max	Palatal Recesses of the Maxillary Sinuses
PerpPlt Eth	Perpendicular Plate of the Ethmoid Bone
Pet Apex	Petrous Apex
PEthCan	Posterior Ethmoidal Canal
Plan Sphen	Planum Sphenoidale
Post Ant Cr Fossa	Posterior Edge of Anterior Cranial Fossa

Copyright © 2003, Mosby, Inc. All rights reserved.

PostEth Can	Posterior Ethmoidal Canal
PPF	Pterygopalatine Fossa
Pter Fossa	Pterygoid Fossa
Ptery Proc S	Pterygoid Process of Sphenoid
Pty Rec S	Pterygoid Recess of Sphenoid Sinus
Ramus Man	Ramus of Mandible
Rostrum Sphenoid	Rostrum of Sphenoid Bone
S	Sphenoid Sinus
SB	Sphenoid Bone
Sec Mol	Second Molar Tooth
Sec Pre Mol	Second Premolar Tooth
Sella	Sella Turcica
Septum	Septum Within a Sinus
SphenoEth Rec	Sphenoethmoidal Recess
Sph Sin Ostium	Sphenoid Sinus Ostium
SOF	Superior Orbital Fissure
S Sep	Sphenoid Sinus Septum
STSut	Sphenotemporal Suture
Styl Proc	Styloid Process
Supraor Can	Supraorbital Canal Tub
Supraor Grv	Supraorbital Groove
Sup Turb	Superior Turbinate
SZySut	Sphenozygomatic Suture
Thd Mol	Third Molar Tooth
Torus Pal	Torus Palatinus
Torus Tub	Torus Tubarius
Tub Sel	Tuberculum Sellae
Uncin Proc	Uncinate Process of Ethmoid
Vidian Can	Vidian Canal (Pterygoid Canal)
Vomer	Vomer
ZB	Zygomatic Bone
Zyg Arch	Zygomatic Arch
ZygoTemp Can	Zygomaticotemporal Canal

Within the axial anatomic atlas, Figures 10A, B, and C show variations in the size of the sphenoid sinuses with lateral and pterygoid recesses. Figure 21A shows an alveolar recess of the maxillary sinus, with the sinus extending caudal to the hard palate. Figures 21B and C show the incisive canals and the incisor foramen.

Within the coronal anatomic atlas, Figure 10 shows variations in the pneumatization of the lower maxillary sinus. Figure 10A shows palatal recesses. Figure 10B shows lack of pneumatization of the maxillary alveolus. Figure 10C shows pneumatization of the inferior turbinate. Figure 11 shows a typical example of a torus palatinus and maxillary exostoses. Axial Figure 16A and coronal Figure 11B show pneumatization of the inferior turbinate by the maxillary sinus. Figures 14-17 show variations in sphenoid sinus configuration and the location of the foramen rotundum and Vidian canals near and within the sinus. Axial and coronal Figures 1B show frontal sinus pneumatization of the orbital roofs. The presence of bone between the ethmoid complex and the recess differentiates these from supraorbital ethmoid cells.

Copyright © 2003, Mosby, Inc. All rights reserved.

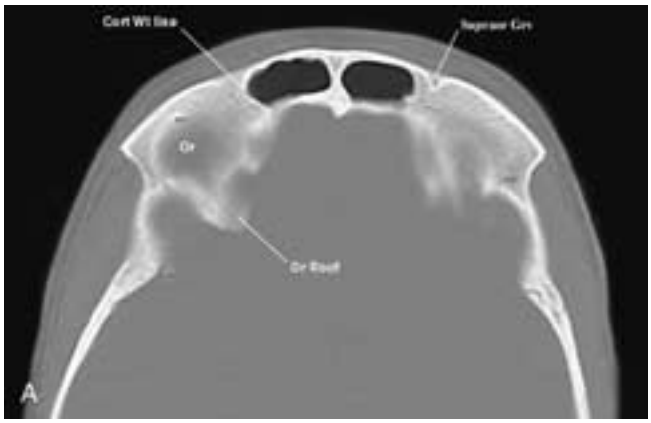

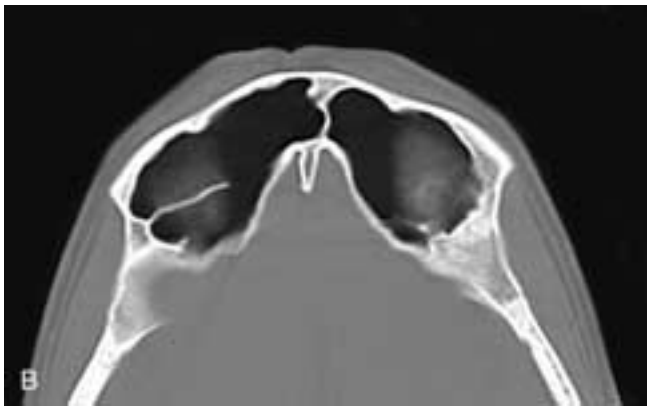

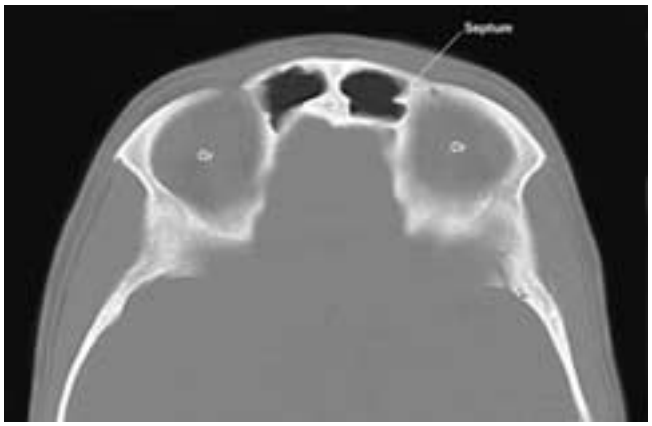

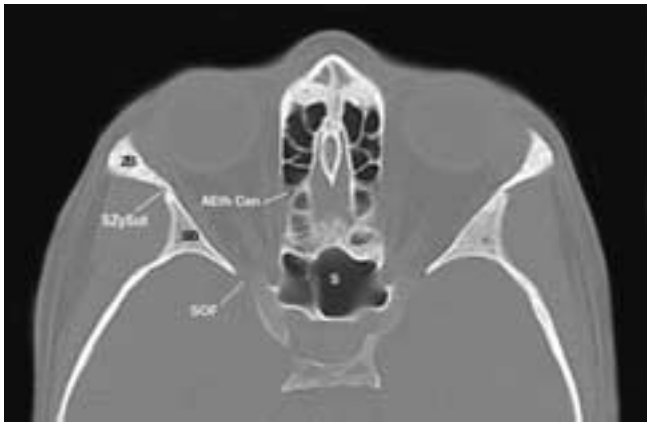

Copyright © 2003, Mosby, Inc. All rights reserved.

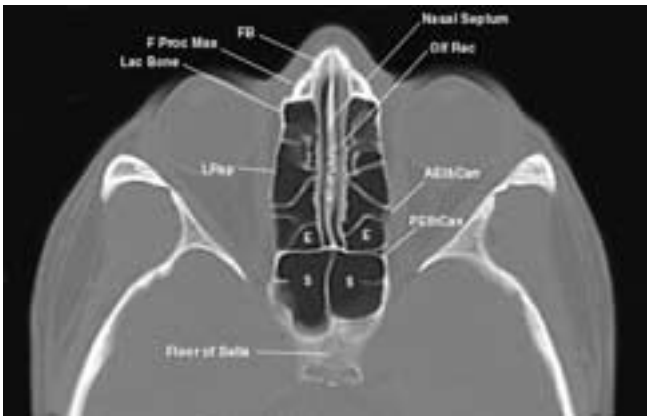

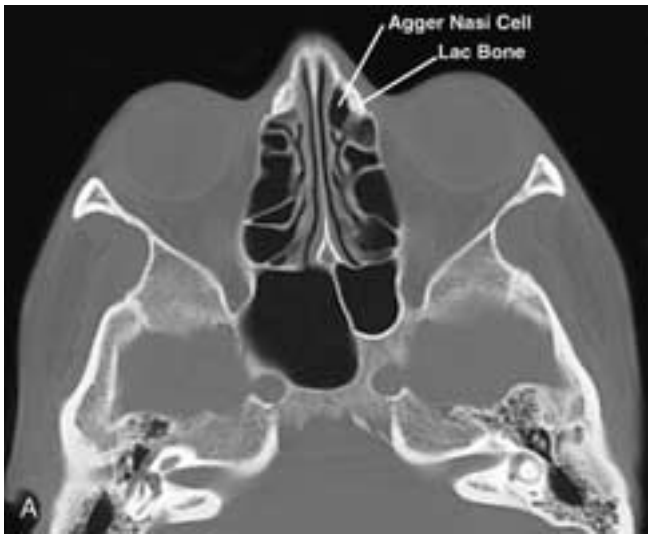

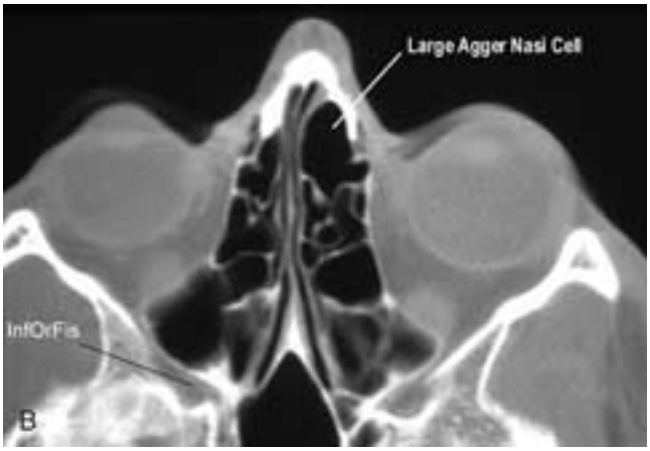

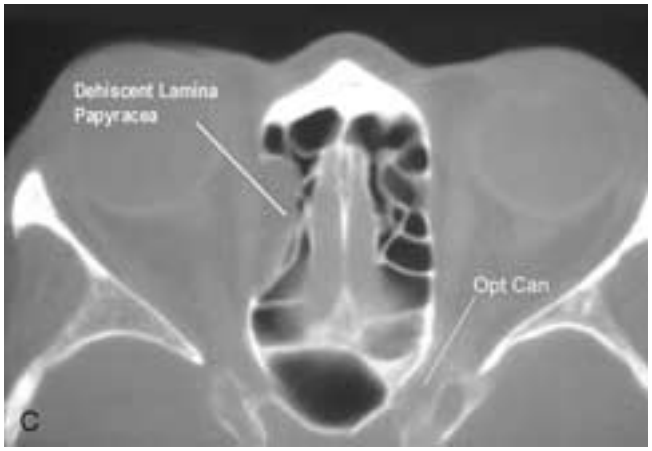

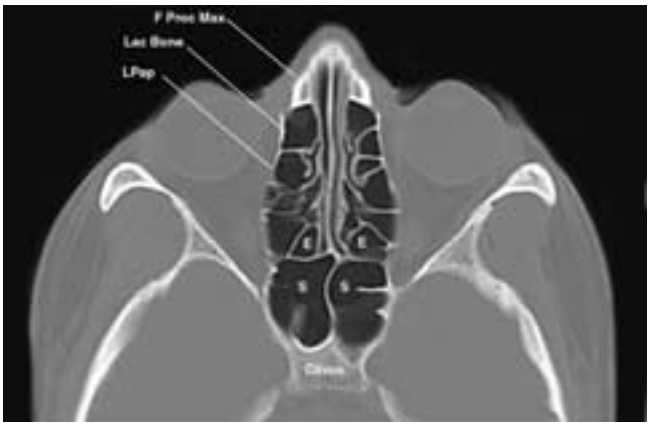

Copyright © 2003, Mosby, Inc. All rights reserved.

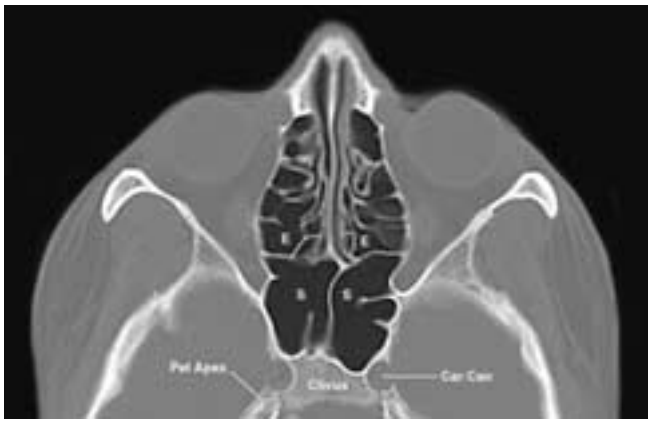

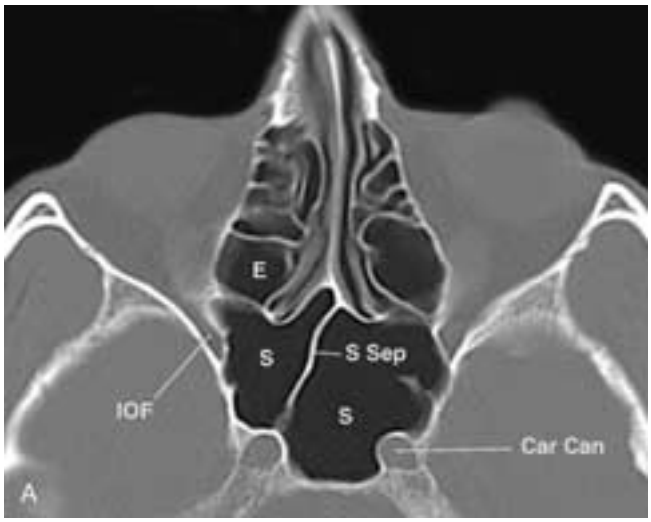

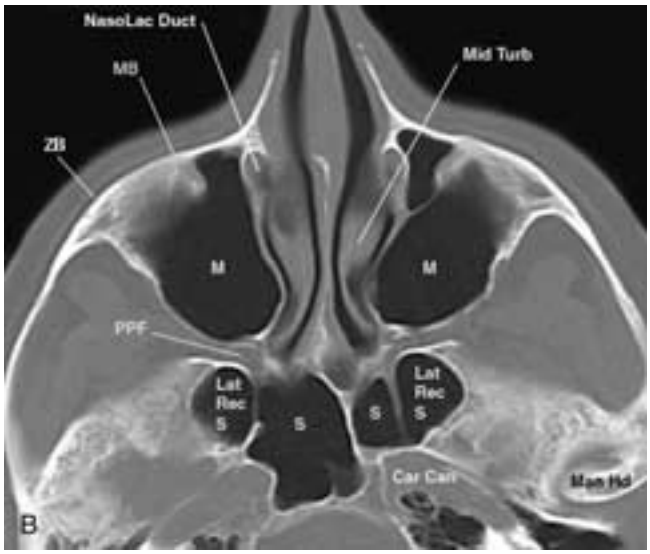

Copyright © 2003, Mosby, Inc. All rights reserved.

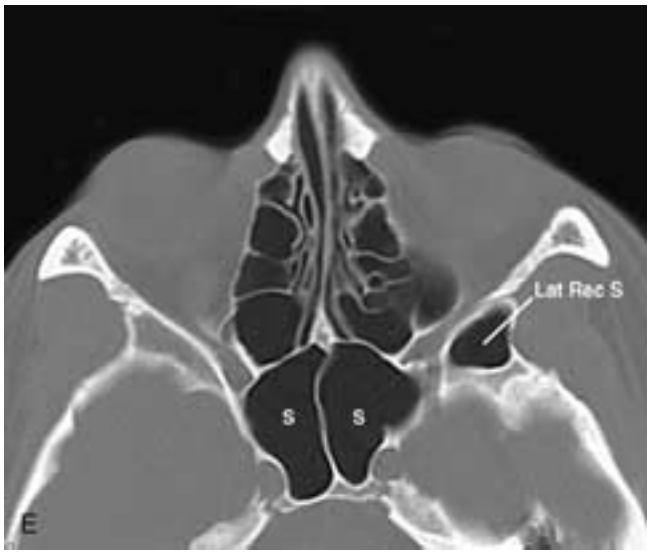

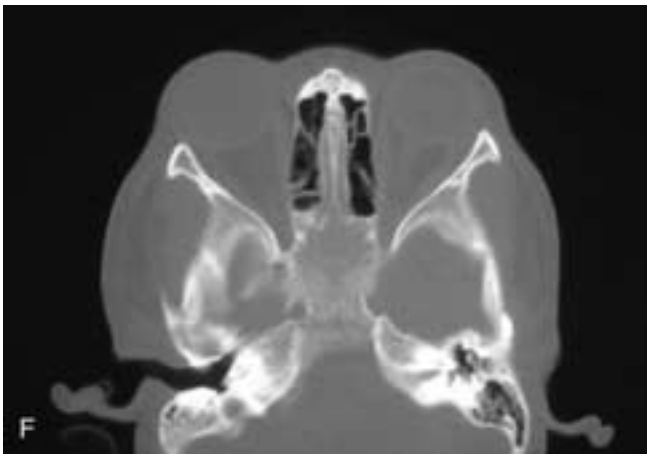

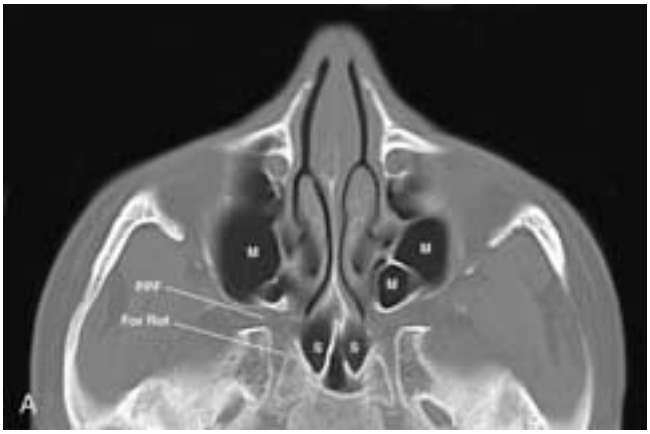

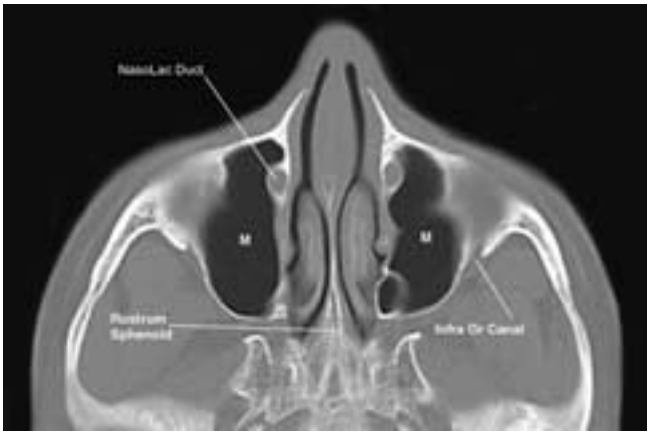

Copyright © 2003, Mosby, Inc. All rights reserved.

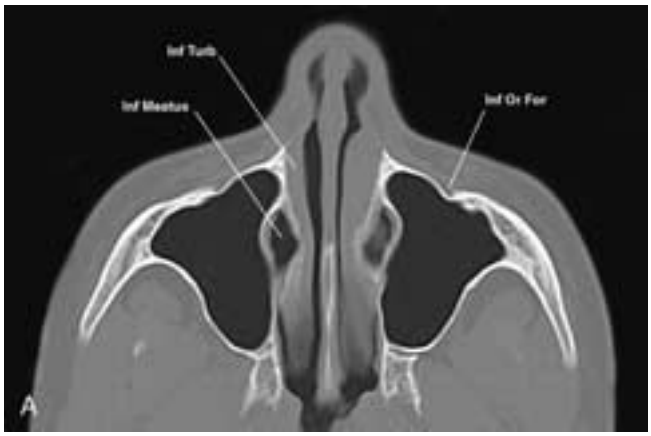

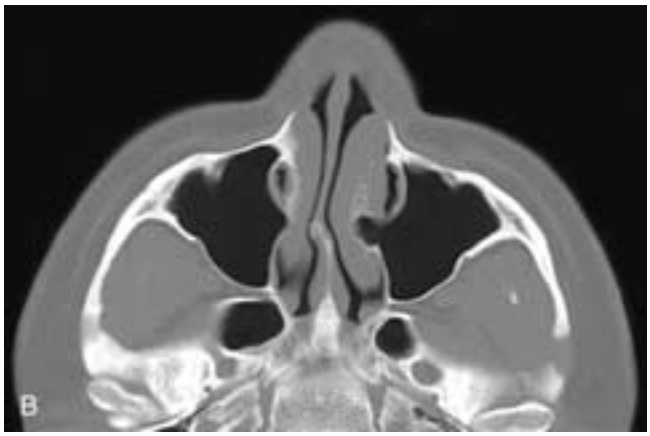

Copyright © 2003, Mosby, Inc. All rights reserved.

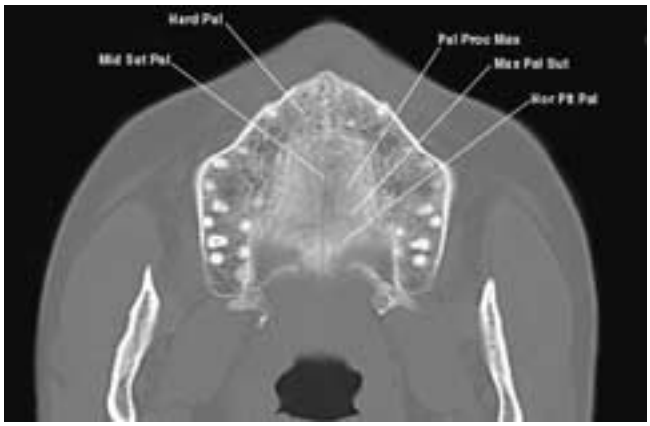

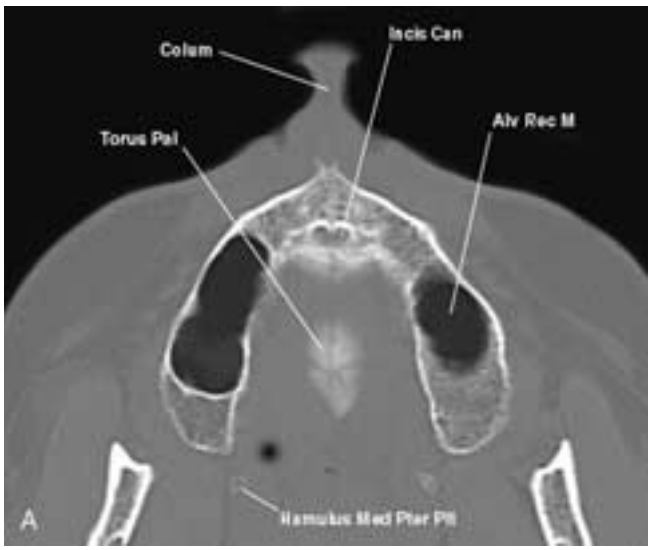

Copyright © 2003, Mosby, Inc. All rights reserved.

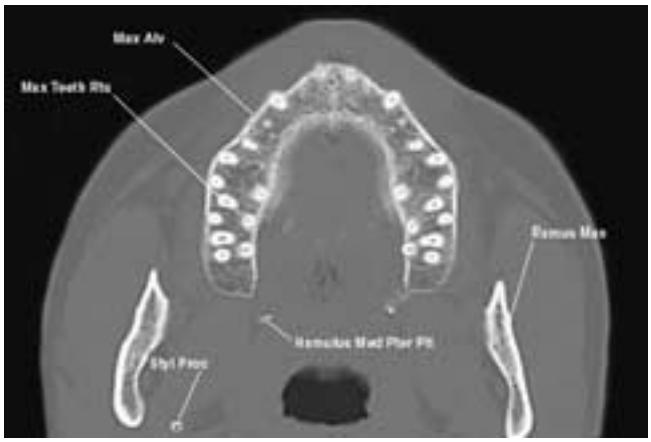

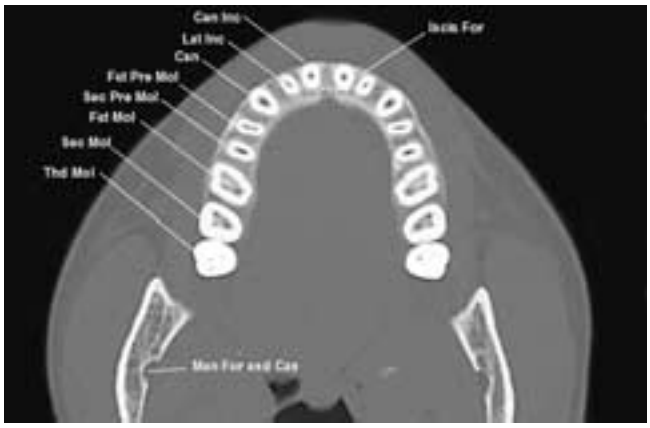

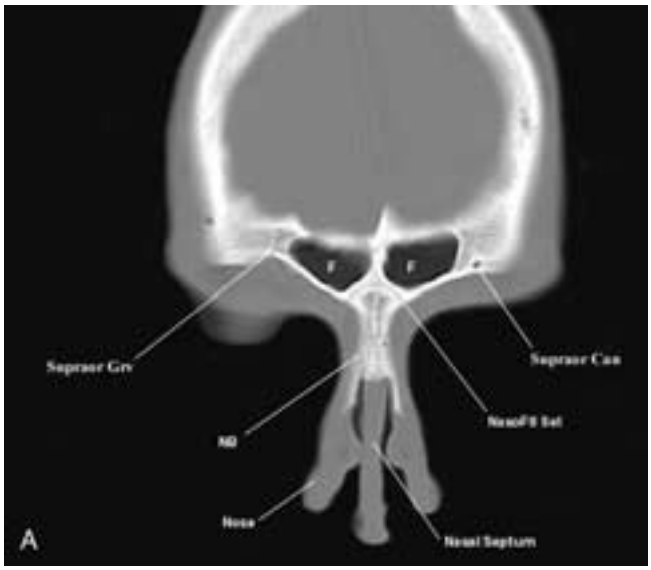

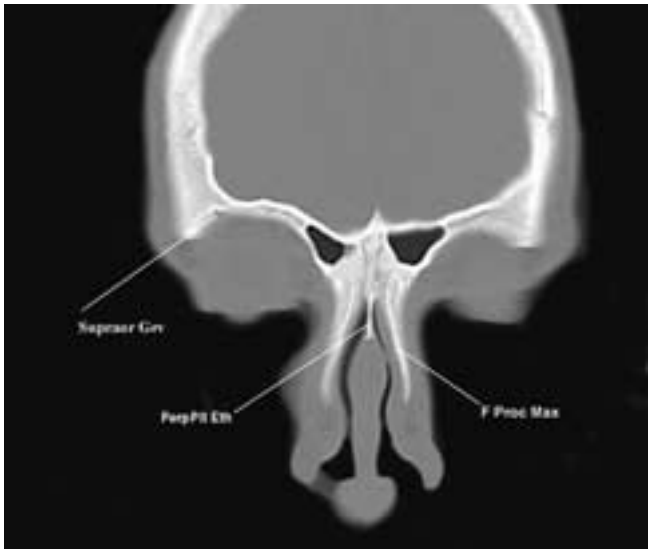

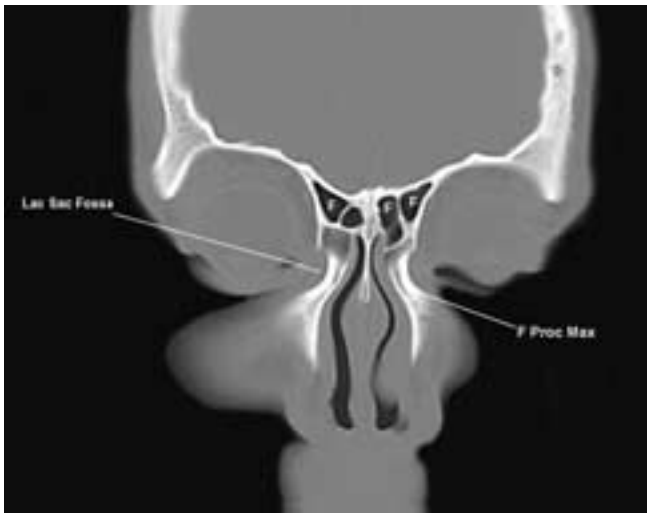

Copyright © 2003, Mosby, Inc. All rights reserved.

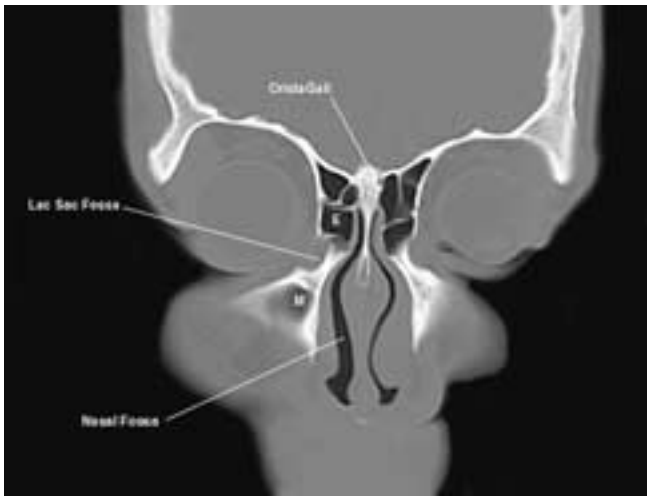

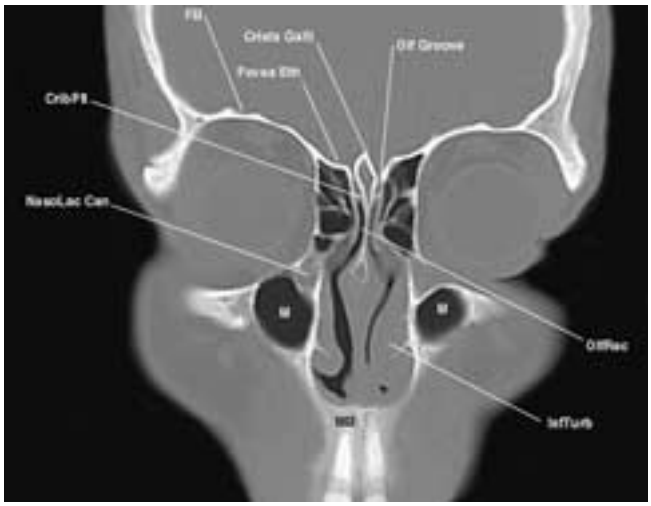

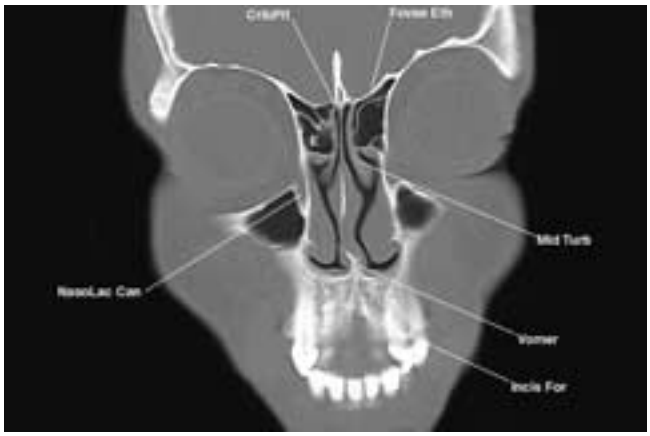

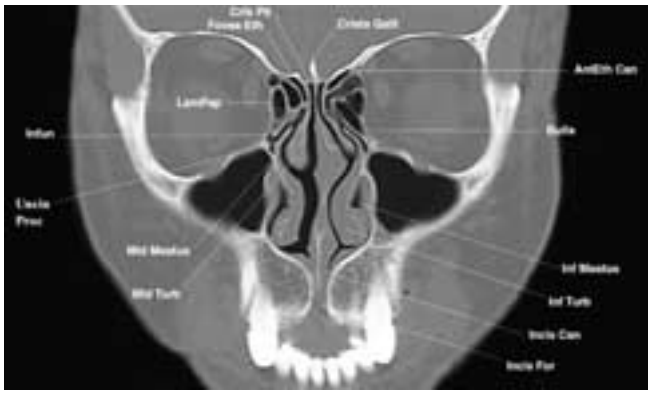

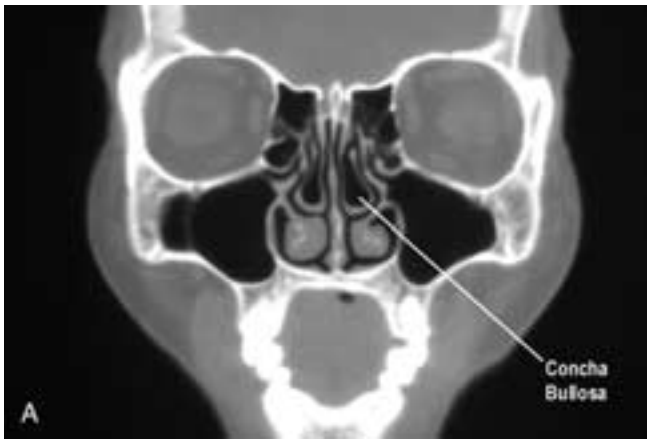

Copyright © 2003, Mosby, Inc. All rights reserved.

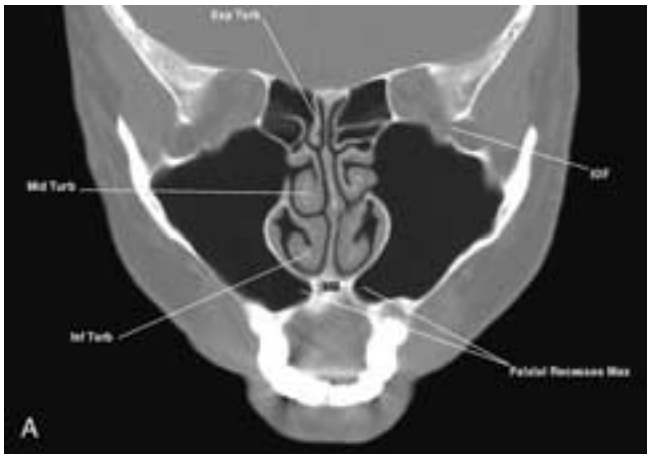

Copyright © 2003, Mosby, Inc. All rights reserved.

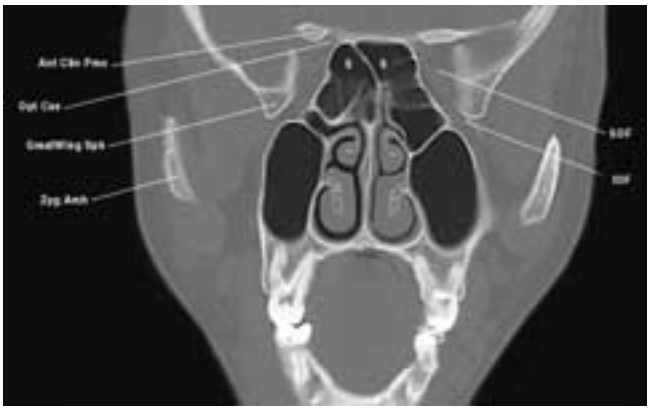

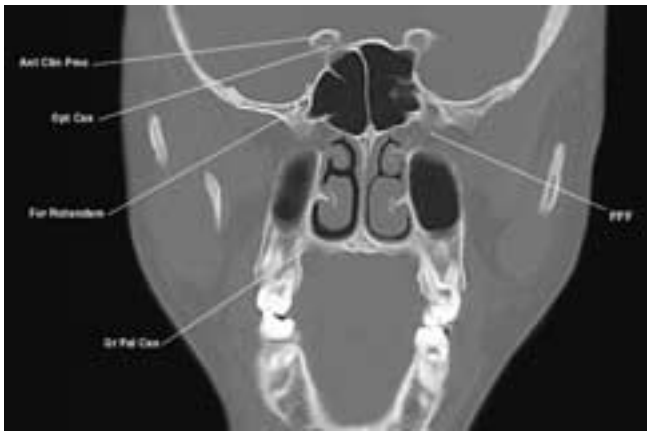

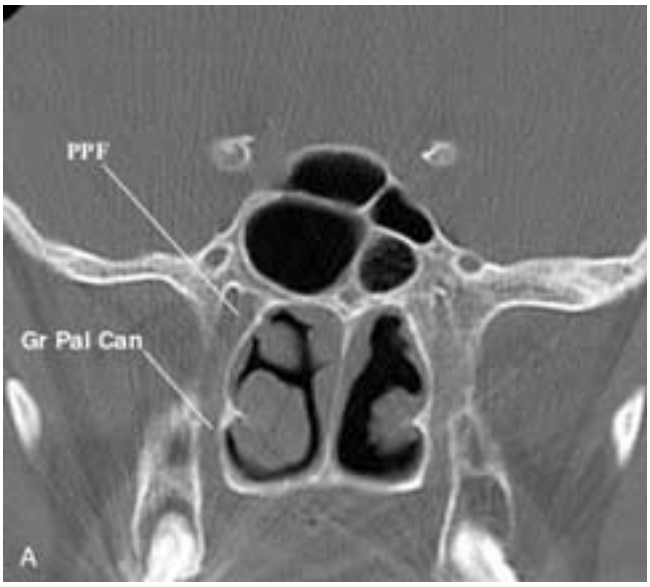

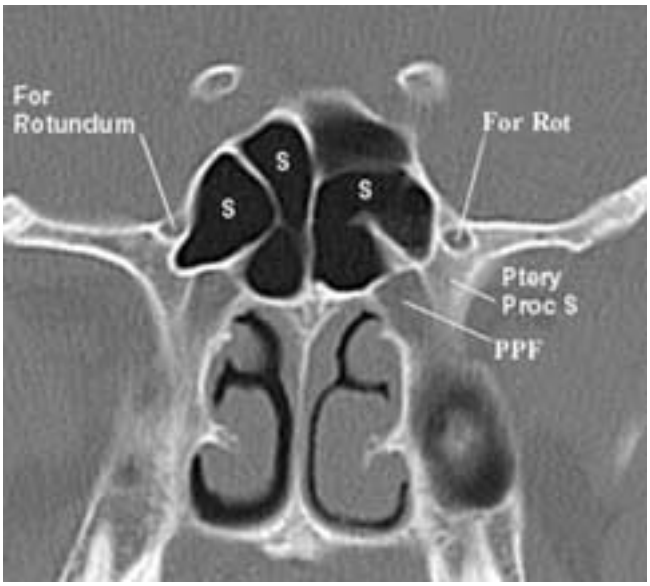

Copyright © 2003, Mosby, Inc. All rights reserved.

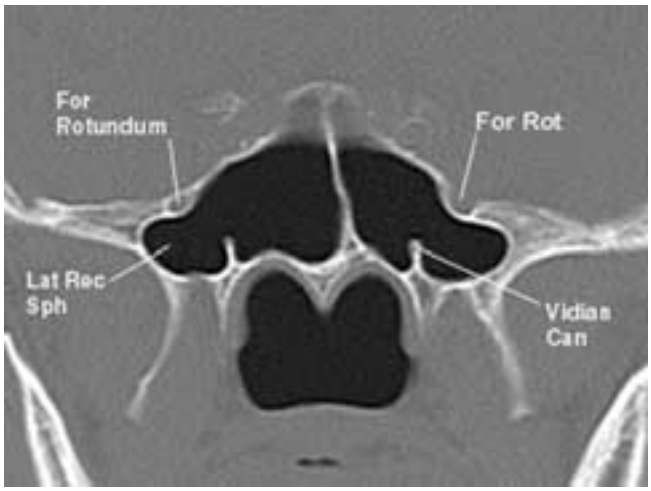

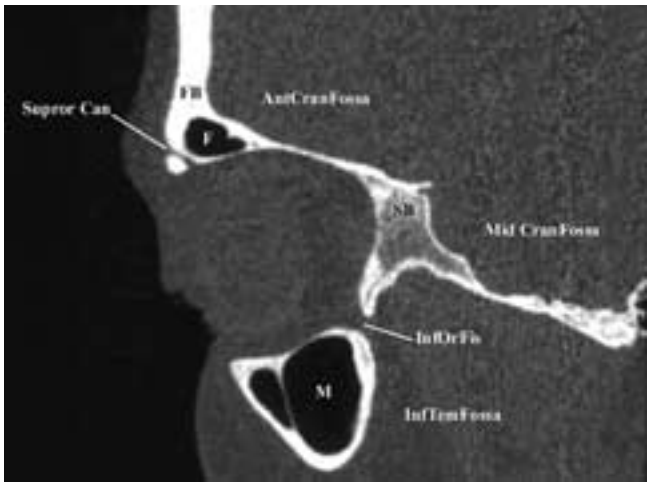

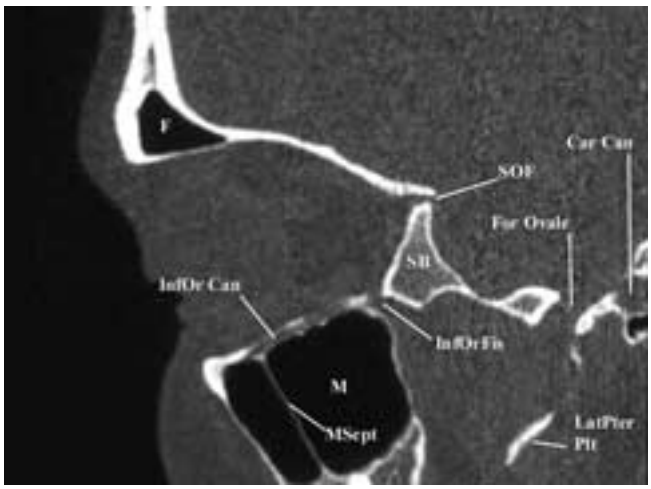

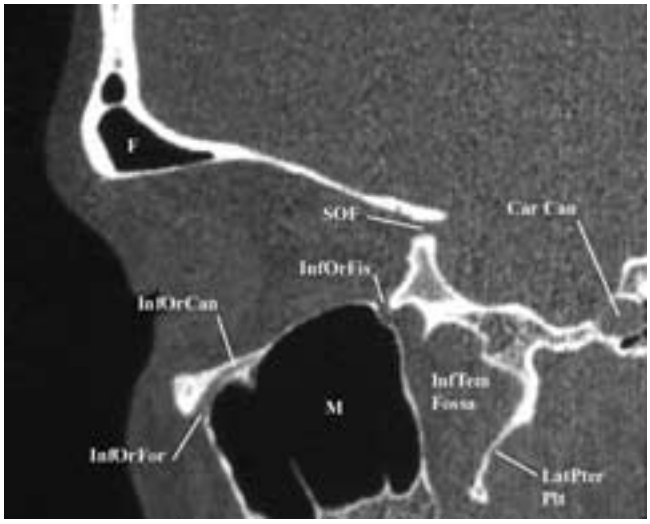

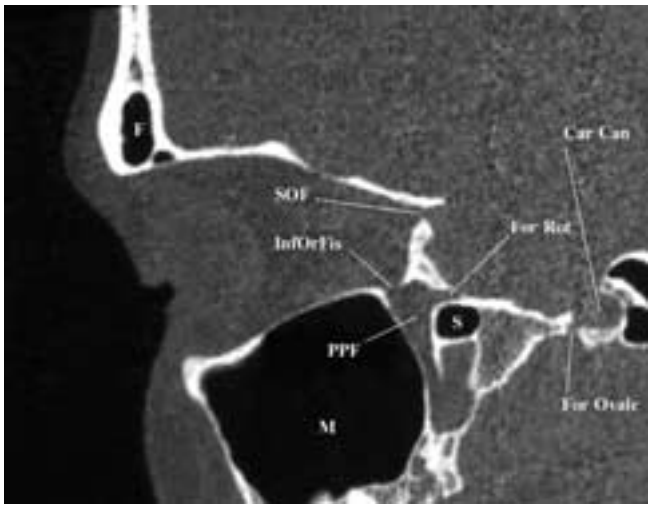

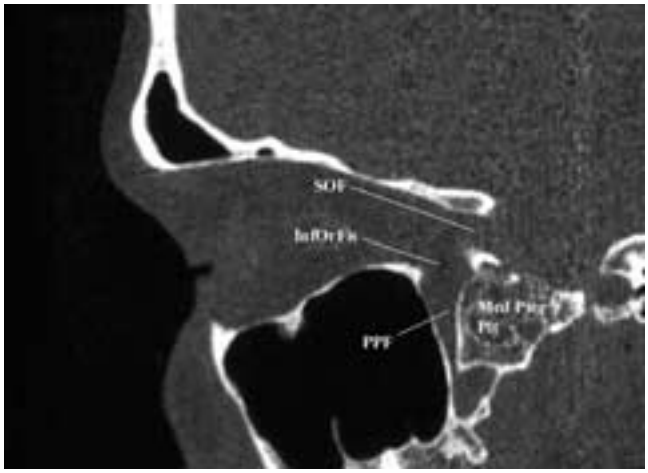

Copyright © 2003, Mosby, Inc. All rights reserved.

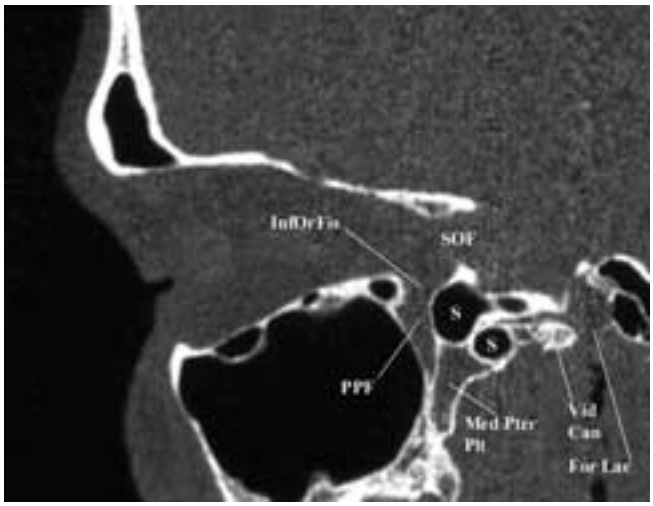

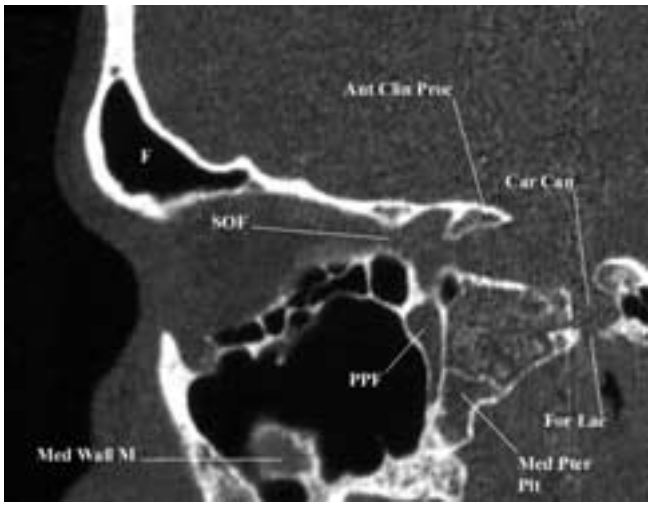

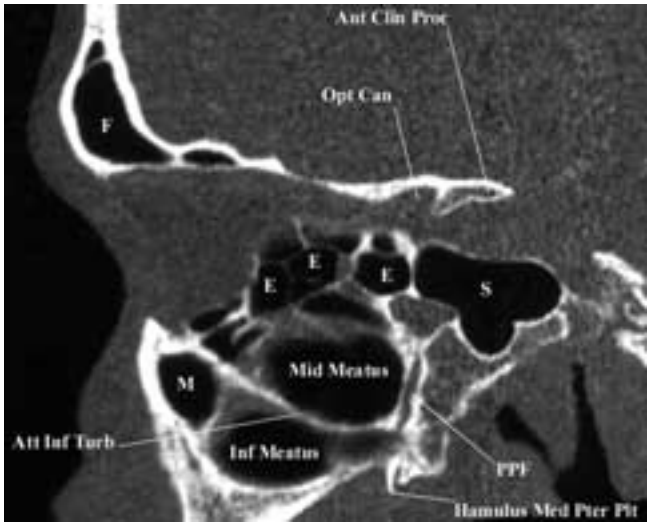

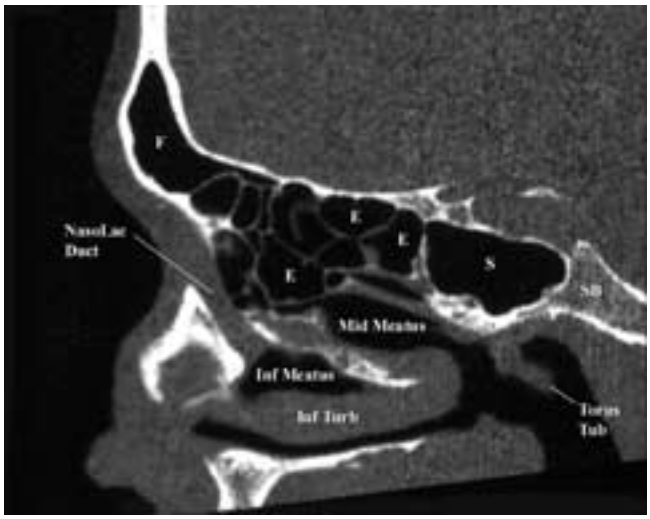

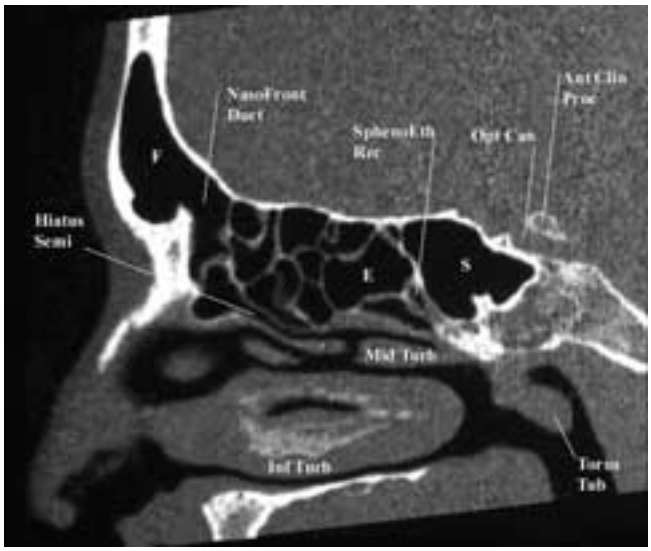

Copyright © 2003, Mosby, Inc. All rights reserved.

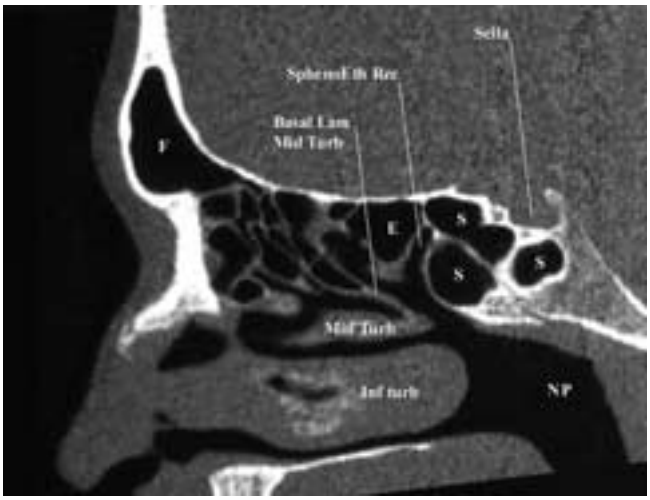

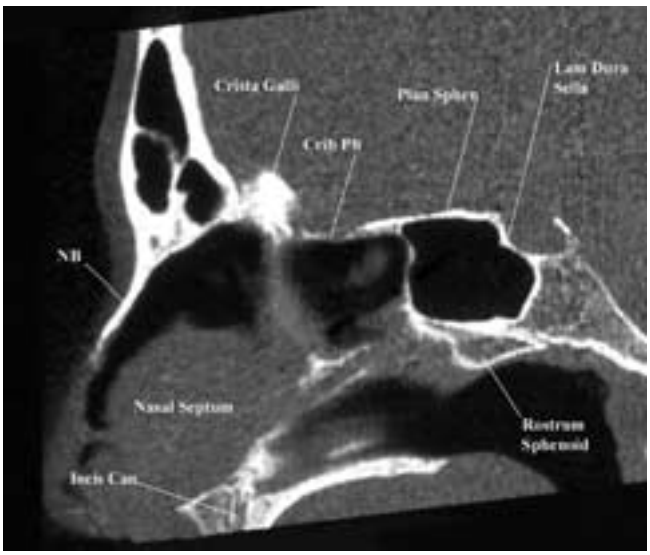

Copyright © 2003, Mosby, Inc. All rights reserved.

REFERENCES

1. Tardy M, ed. Surgical Anatomy of the Nose. New York, NY: Raven Press, 1990;1, 47, 65.
2. Williams H. Basic science and related disciplines. In: Paparella M, Shumrick D, eds. Otolaryngology. Vol. 1. Philadelphia, WB Saunders, 1973;329–346.
3. Last R, ed. Anatomy Regional and Applied. 6th ed. Edinburgh and London: Churchill Livingstone, 1978;398–406.
4. Hollinshead W. The nose and paranasal sinuses. In: Hollinshead W, ed. Anatomy for Surgeons. Vol. 1. New York: Hoeber-Harper, 1954; 229–281.
5. Goss C, ed. Gray's Anatomy of the Human Body. 27th ed. Philadelphia: Lea & Febiger, 1963.
6. Graney D, Baker S. Anatomy. In: Cummings C, Fredrickson J, Harker L, Krause C, Schuller D, eds. Otolaryngology: Head and Neck Surgery, Vol 1. 2nd ed. St. Louis: CV Mosby, 1993;627–639.
7. Zinreich SJ, Kennedy DW, Kumar AJ, et al. MR imaging of normal nasal cycle: comparison with sinus pathology. J Comput Assist Tomogr 1988;12:1014–1019.
8. Phillips P, McCaffrey T, Kern E. Physiology of the human nose. In: Blitzer A, Lawson W, Friedman W, eds. Surgery of the Paranasal Sinuses. Philadelphia: WB Saunders, 1991;25–40.
9. Meyerhoff W. Physiology of the nose and paranasal sinuses. In: Paparella M, Shumrick D, eds. Otolaryngology. Vol 1. 2nd ed. Philadelphia: WB Saunders, 1980;297–318.
10. Kimmelman C. The problem of nasal obstruction. In: Kimmelman C, ed. The Otolaryngologic Clinics of North America. Vol 22. Philadelphia: WB Saunders, 1989;253–264.
11. Paff G, ed. Anatomy of the Head and Neck. Philadelphia: WB Saunders, 1973;183–203.
12. Leopold D. Physiology of olfaction. In: Cummings C, Fredrickson J, Harker L, Krause C, Schuller D, eds. Otolaryngology—Head and Neck Surgery. Vol 1. 2nd ed. St. Louis: CV Mosby, 1993; 640–664.
13. Abramson M, Harker L. Physiology of the nose. In: Bernstein L, ed. The Otolaryngologic Clinics of North America. Vol 6. Philadelphia: WB Saunders, 1973;623–635.
14. Hilger J, Hilger P. Physiology of the nose and paranasal sinuses. In: Goldman J, ed. Principles and Practice of Rhinology. New York: Wiley, 1987;15–25.
15. Yousem DM, Geckle RJ, Bilker WB et al. Posttraumatic olfactory dysfunction: MR and clinical evaluation. AJNR 1996;17:1171–1179.
16. Osborn A. The nasal arteries. Am J Roentgenol 1978;130:89–97.
17. Fried R. The Hyperventilation Syndrome: Research and Clinical Treatment. Baltimore: Johns Hopkins University Press, 1987.
18. Schaeffer J, eds. The Embryology, Development and Anatomy of the Nose, Paranasal Sinuses, Nasolacrimal Passageways and Olfactory Organs in Man. Philadelphia: P. Blakiston's Son, 1920.
19. Graney D. Anatomy. In: Cummings C, Fredrickson J, Harker L, et al, eds. Otolaryngology: Head and Neck Surgery. Vol 1. St. Louis: CV Mosby, 1986;845–850.
20. Van Alyea O. Nasal Sinuses: Anatomic and Clinical Considerations. 2nd ed. Baltimore: Williams & Wilkins, 1951.
21. Ritter R. The Paranasal Sinuses: Anatomy and Surgical Technique. 2nd ed. St. Louis: CV Mosby, 1978.
22. Wigand M. Endoscopic Surgery of the Paranasal Sinuses and Anterior Skull Base. New York: Thieme, 1990.
23. Mosher H. Symposium on the ethmoid. The surgical anatomy of the ethmoid labyrinth. Trans Am Acad Ophthalmol Otolaryngol 1929: 376–410.
24. Hajek N, ed. Pathology and Treatment of the Inflammatory Diseases of the Nasal Accessory Sinuses. 5th ed. Vols. 1, 2. St. Louis: CV Mosby, 1926.
25. Hollingshead W, ed. Anatomy for Surgeons. 3rd ed. Vol. 1. Philadelphia: Harper & Row, 1982.
26. Zinreich SJ, Mattox DE, Kennedy DW, et al. Concha bullosa: CT evaluation. J Comput Assist Tomogr 1988;12:778–784.
27. Dodd G, Jing B. Radiology of the Nose, Paranasal Sinuses and Nasopharynx. Baltimore: Williams & Wilkins, 1977;59–65.
28. Urken M, Som P, Lawson W, et al. The abnormally large frontal sinus. Part I: a practical method for its determination based upon an analysis of 100 normal patients. Laryngoscope 1987;97:602–605.
29. Enlow D. Handbook of Facial Growth. Philadelphia: WB Saunders, 1975;120–121.
30. Shapiro R, Schorr S. A consideration of the systemic factors that influence frontal sinus pneumatization. Invest Radiol 1980;15: 191–202.
31. Fujioka M, Young L. The sphenoidal sinuses: radiographic pattern of normal development and abnormal findings in infants and children. Radiology 1978;129:133–136.
32. Yanagisawa E, Smith H. Normal radiographic anatomy of the paranasal sinuses. Otolaryngol Clin North Am 1973;6:429–457.
33. Etter L. Atlas of Roentgen Anatomy of the Skull. Springfield, IL: Charles C. Thomas, 1955.
34. Goldman J. Intranasal sphenoethmoidectomy and antrostomy. In: Goldman J, ed. The Principles and Practice of Rhinology. New York: Wiley, 1987;403–411.
35. Graney D. Anatomy. In: Cummings C, Fredrickson J, Harker L, et al., eds. Otolaryngology: Head and Neck Surgery. 2nd ed. Vol 1. St. Louis: CV Mosby, 1993;901–906.
36. Pandolfo I, Gaeta M, Blandino A, Longo M. The radiology of the pterygoid canal: normal and pathologic findings. AJNR 1987;8: 479–483.
37. Proetz A. Essays on the Applied Physiology of the Nose. St. Louis: Annals Publishing, 1953.
38. Alberti P. Applied surgical anatomy of the maxillary sinus. Otolaryngol Clin North Am 1976;9:3–20.
39. Karmody C, Carter B, Vincent M. Developmental anomalies of the maxillary sinus. Trans Am Acad Ophthalmol Otolaryngol 1977;84: 723–728.
40. Sperber G. Craniofacial Embryology. 4th ed. London: Wright, 1989;144–146.
41. Merril V, ed. Atlas of Roentgenographic Positions. 3rd ed. St. Louis: CV Mosby, 1967.
42. Yanagisawa E, Smith H. Radiographic anatomy of the paranasal sinuses IV: Caldwell view. Arch Otolaryngol 1968;87:311–322.
43. Yanagisawa E, Smith H, Merrell R. Radiographic anatomy of the paranasal sinuses III: submentovertical view. Arch Otolaryngol 1968;87:299–310.
44. Yanagisawa E, Smith H, Thaler S. Radiographic anatomy of the paranasal sinuses II: lateral view. Arch Otolaryngol 1968;87:196–209.
45. Yanagisawa E, Smith H. Radiology of the normal maxillary sinus and related structures. Otolaryngol Clin North Am 1976;9:55–81.
46. Zizmor J, Noyek A. Radiology of the nose and paranasal sinuses. In: Paparella M, Shumrick D, eds. Otolaryngology. Vol. 1. Philadelphia: WB Saunders, 1973;1043–1095.
47. Potter G, ed. Sectional Anatomy and Tomography of the Head. New York: Grune & Stratton, 1971.
48. Gambarelli J, Greinel G, Chevrot L, et al. Computerized Axial Tomography: An Anatomic Atlas of Serial Sections of the Human Body, Anatomy-Radiology-Scanner. Berlin: Springer-Verlag, 1977.
49. Ferner H, ed. Pernkopf Atlas of Topographical and Applied Human Anatomy. Vol. 1. Baltimore: Urban and Schwarzenberg, 1980.
50. Schatz C, Becker T. Normal and CT anatomy of the paranasal sinuses. Radiol Clin North Am 1984;22:107–118.
51. Terrier F, Weber W, Ruenfenacht D, et al. Anatomy of the ethmoid: CT endoscopic and macroscopic. AJNR 1985;6:77–84.
52. Mafee M. Preoperative imaging anatomy of nasal-ethmoid complex for functional endoscopic sinus surgery. Radiol Clin North Am 1993;31:1–30.
53. Mafee M, Chow J, Meyers R. Functional endoscopic sinus surgery: anatomy, CT screening, indications, and complications. AJR 1993; 160:735–744.
54. Hudgins P. Complications of endoscopic sinus surgery: role of the radiologist in prevention. Radiol Clin North Am 1993;31:21–32.
55. Som P. Paranasal sinuses and pterygopalatine fossa. In: Carter B, ed. Computed Tomography. New York: Churchill Livingstone, 1985; 101–130.
56. Mancuso A, Hanafee W, ed. Computed Tomography and Magnetic Resonance Imaging of the Head and Neck. Baltimore: Williams & Wilkins, 1985;1–19.
57. Brant-Zawadzki M, Norman D. Magnetic Resonance Imaging of the Central Nervous System. New York: Raven Press, 1987.
58. Lloyd G, Lund V, PD P, et al. Magnetic resonance imaging in the evaluation of nose and paranasal sinus disease. Br. J Radiol 1987;60:957–968.

Copyright © 2003, Mosby, Inc. All rights reserved.

59. Vogl T, Mack M, Juergens M, et al. MR Diagnosis of head and neck tumors: comparison of contrast enhancement with triple-dose gadodiamide and standard-dose gadopentetate dimeglumine in the same patient. AJR 1994;163:425–432.
60. Yousem D, Kennedy D, Rosenberg S. Ostiomeatal complex risk factors for sinusitis: CT evaluation. J Otolaryngol 1991;20: 419–424.
61. Yousem D. Imaging of sinonasal inflammatory disease. Radiology 1993;188:303–314.
62. Lanzieri C, Shah M, Krauss D, et al. Use of gadolinium-enhanced MR imaging for differentiating mucocele from neoplasm in the paranasal sinuses. Radiology 1991;178:425–428.
63. Graney D, Baker S. Anatomy. In: Cummings C, Fredrickson J, Harker L, et al., eds. Otolaryngology: Head and Neck Surgery. 2nd ed. Vol. 1. St. Louis: CV Mosby, 1993;305–314.
64. Quiring D, Warfel J. The Head, Neck, and Trunk Muscles and Motor Points. 2nd ed. Philadelphia: Lea & Febiger, 1960.
65. Gray S, Skandalakis J. Embryology for Surgeons: The Embryological Basis for the Treatment of Congenital Defects. Philadelphia: WB Saunders, 1972.

Copyright © 2003, Mosby, Inc. All rights reserved.

Copyright © 2003, Mosby, Inc. All rights reserved.

3

The Ostiomeatal Complex and Functional Endoscopic Surgery

S. James Zinreich, Sait Albayram, Mark L. Benson, and Patrick J. Oliverio

HISTORIC PERSPECTIVE
TECHNIQUES OF EVALUATION
- Plain Films
- Computed Tomography
  - Examination Protocol
  - Radiation Exposure
  - Image Display
- Magnetic Resonance Imaging

NASAL CYCLE
INTERPRETATION OF IMAGING STUDIES
NORMAL ANATOMY
- Mucociliary Clearance
- Normal Anatomy (Ostiomeatal Unit)
- Frontal Cells

ANATOMIC VARIATIONS AND CONGENITAL ABNORMALITIES
- Variations of the Middle Turbinate
  - Paradoxic Curvature
  - Concha Bullosa
  - Other Variations
- Nasal Septal Deviation
- Uncinate Process Variations
- Deviation
- Attachment
- Pneumatization
- Infraorbital Ethmoid Cells (Haller's Cells)
- Onodi Cells
- Ethmoid Bulla Variations
- Extensive Pneumatization of the Sphenoid Sinus
- Medial Deviation or Dehiscence of the Lamina Papyracea
- Aerated Crista Galli
- Cephalocele
- Posterior Nasal Septal Air Cell
- Asymmetry in Ethmoid Roof Height
- Anatomy Adjacent to the Sinonasal Cavities
- Systematic Radiographic Evaluation
  - Routine Report
    - *Step One*
    - *Step Two*
    - *Step Three*
- Radiographic Appearances of Inflammatory Sinus Disease
  - Acute Sinusitis
  - Chronic Sinusitis
  - Fungal Sinusitis
  - Allergic Sinusitis
  - Orbital Complications of Sinusitis

COMMON FESS TECHNIQUES
- Types of FESS

RADIOGRAPHIC EVALUATION FOLLOWING SINUS SURGERY
- Expected Findings

OPERATIVE COMPLICATIONS

HISTORIC PERSPECTIVE

Sinonasal inflammatory disease is a serious health problem that affects an estimated 30 to 50 million people in the United States.[1] Traditionally, plain films were the modality of choice in evaluation of sinus pathology. Clinical and radiographic emphasis was directed primarily to the maxillary and frontal sinuses. In recent years, it has become evident that sinusitis is primarily a clinical diagnosis. The role of imaging is to document the extent of disease, to answer questions regarding ambiguous cases, and to provide an accurate display of the anatomy of the sinonasal system.

Copyright © 2003, Mosby, Inc. All rights reserved.

Imaging now provides the surgeon with a detailed ''road map'' for guiding the functional endoscopic sinus surgery procedure. Today, computed tomography (CT) is the modality of choice for the imaging evaluation of the morphology in this area.

Although most patients with sinonasal inflammatory disease are initially treated medically, the disease often does not resolve. Patients with persistent disease usually require surgical intervention, and the surgical treatment of refractory inflammatory sinus disease has undergone revolutionary changes in the last 10 to 20 years. These advances are due to an improved understanding of the mucociliary clearance pathways in the nasal cavity and paranasal sinuses, improved endoscopes that afford direct access to nasal cavity and ethmoid sinus drainage portals, and the availability of high-resolution coronal CT images that provide an accurate display of the regional anatomy.

Functional endoscopic sinus surgery (FESS) was first described independently by both Messerklinger in the German literature and Wigand, Steiner, and Jaumann in the English literature in 1978.[2–4] FESS was introduced in the United States in 1984 by Kennedy et al., and subsequent evolution of the technique has occurred through innovations in both the surgical and radiologic fields.[5, 6]

This chapter will discuss the imaging modalities available for patients with surgically amenable inflammatory sinus disease and describe the pertinent imaging anatomy and anatomic variants of the paranasal sinuses and adjacent structures, review the radiographic appearance of inflammatory sinus disease and describe FESS procedures.

TECHNIQUES OF EVALUATION

Plain Films

The standard plain film sinus series usually consists of four views: lateral, Caldwell, Waters, and submentovertex. The anatomy displayed on each of these views is reviewed in Chapter 2.[7] Although the standard radiographs may be accurate in showing air-fluid levels, the degree of chronic inflammatory disease present is consistently and significantly underestimated. Furthermore, the superimposition of structures precludes the accurate evaluation of the anatomy of the ostiomeatal channels, with which the modern surgeon needs to be familiar.[6, 8–11]

Computed Tomography

CT is currently the modality of choice in the evaluation of the paranasal sinuses and adjacent structures.[6, 8–11] Its ability to optimally display bone, soft tissue, and air provides an accurate depiction of both the anatomy and the extent of disease in and around the paranasal sinuses.[6, 8–11] In contrast to standard radiographs, CT clearly shows the fine bony anatomy of the ostiomeatal channels.

Many authors stress the importance of performing the initial CT scan after a course of adequate medical therapy to eliminate or diminish reversible mucosal inflammation. Several authors also suggest routine pretreatment with a sympathomimetic nasal spray 15 minutes prior to scanning in order to reduce nasal congestion (mucosal edema) and thus improve the display of the fine bony architecture and any irreversible mucosal disease.[12]

The coronal plane best shows the ostiomeatal unit (OMU), shows the relationship of the brain to the ethmoid roof, and correlates closely with the surgical orientation. Thus, the coronal plane should be the primary imaging orientation for evaluation of the sinonasal tract in all patients with inflammatory sinus disease who are endoscopic surgical candidates.[6–8, 11] This can be accomplished by direct coronal scanning or by reformatting data acquired in the axial plane into coronal plane images.

If direct scanning is done, the coronal study optimally should be performed in the prone position so that any remaining sinus secretions do not obscure the OMU. In patients who cannot tolerate prone positioning (children, patients of advanced age, etc.), the hanging head technique can sometimes be utilized. In this technique, the patient is placed in the supine position and the neck is maximally extended. A pillow placed under the patient's shoulders facilitates positioning. The CT gantry is then angled to be perpendicular to the hard palate. However, it is not always possible to obtain true direct coronal images with this technique.

Patients who are intubated or have tracheostomy tubes usually cannot tolerate positioning for coronal scans. Similarly, young children, patients with severe cervical arthropathy, and patients who are otherwise debilitated often cannot tolerate direct coronal positioning. In such patients, spiral scanning or thin section, contiguous axial CT images with coronal reconstructions are performed.

Axial images complement the coronal study, particularly when there is severe disease (opacification) of any of the paranasal sinuses and surgical treatment is contemplated. The axial studies are needed, as the posterior walls of various sinuses are not well seen, if at all, in the coronal plane. Axial images are particularly important in visualizing the frontoethmoid junction and the sphenoethmoid recess.

Today spiral CT offers the advantage of speed and the ability to generate very thin images. With the use of double spiral scanners or multidetector technology, the slice thickness can be reduced to 0.5 mm or less. For the pediatric, elderly, and debilitated patients who may not be able to remain still for prolonged periods of time, this technique offers the best opportunity to acquire a motion-free, high-quality study. The patient may be positioned prone with the head hyperextended or supine with the head in neutral position on the scanning table. Given the ability of spiral CT to generate very thin images, the quality of reconstructed coronal and/or sagittal images is virtually indistinguishable from that of images obtained in the primary scan plane. In phantom studies performed with the parameters outlined in Box 3-1, a lens dose of 14 mGy was measured for scanning the paranasal sinuses in either the axial or coronal position.[13]

The recent introduction of multidetector CT scanners has allowed even more refined reconstructions in planes other than the primary scan plane. Motion and reconstruction artifacts may still create very minor image degradation, but this is offset by the lack of obscuration of important anatomy by ''spray'' artifact from dental restorations. Since the original data set is acquired in the axial plane, the important

Copyright © 2003, Mosby, Inc. All rights reserved.

VIEW IMAGE

FIGURE 3-1 CT lateral topogram shows the patient's position during the examination. Dotted lines represent the scanner gantry angulation, which should be as perpendicular as possible to the hard palate (*arrows*).

anatomy of the OMU is not imaged at the same time as the metallic restorations, so the artifact is projected well away from the crucial landmarks. This multidetector scanner most likely will become the scanner of choice for imaging the sinonasal cavities.

Examination Protocol

For direct coronal scanning, the patient is placed prone on the scanner table, with the chin hyperextended. The scanner gantry is angled perpendicular to the hard palate (Fig. 3-1). The angulation of the scan plane is very important, as Melhem et al. noted that variations in scan angulation greater than 10° from the plane perpendicular to the hard palate result in significant loss of anatomic detail of the structures of the OMU.[14]

Scanning is performed as contiguous 3-mm-thick images from the anterior wall of the frontal sinus through the posterior wall of the sphenoid sinus. Contiguous scans are essential to avoid loss of information through ''skipped'' areas.[14] The field of view should be adjusted to include only the areas of interest. This not only helps reduce artifact from the teeth and associated metallic restorations, but magnifies the small anatomic structures of the nasal cavity and adjacent paranasal sinuses.[9]

The original exposure settings for sinus CT were 125 kVp, 450 mAs, and 5-second scan time. However, Babbel et al. showed that there was no compromise of image quality when the milliampere-second (mAs) setting was reduced to 200 mAs (2-second scan time), and recent work by Melhem et al. showed no significant loss of diagnostic quality with mAs settings of 160 or even 80 mAs (2-second scan time).[12, 14] It is therefore recommended that the exposure settings be 125 kVp and 80 to 160 mAs. Box 3-1 summarizes the sinus CT examination protocol.[10]

SUMMARY BOX 3-1

Parameters for Sinus CT

Patient position	Prone
Angulation	Perpendicular to hard palate
Field of view	14 cm
Thickness	3 mm, contiguous
Exposure	125 kVp and 80–160 mAs

Radiation Exposure

To review briefly, the radiation exposure (dose) that a patient receives is known as the radiation-absorbed dose. This dose is a measure of the total radiation energy absorbed by the tissues, and it is expressed in an SI unit known as the *Gray* (Gy). One Gy is the amount of radiation needed to deposit the energy of 1 joule (J) in 1 kg of tissue (Gy = 1 J/kg). Formerly, the unit used to express the radiation-absorbed dose was the *rad* (1 rad = amount of radiation needed to deposit the energy of 100 ergs in 1 g tissue). The conversion of the rad to the Gy is: 1 Gy = 100 rad.[15, 16]

A more useful term is *radiation dose equivalent*, which takes into account the quality factor Q of the radiation (radiation dose equivalent = radiation dose absorbed × Q). This quality factor accounts for the varying biologic effectiveness of different forms of ionizing radiation. For x-rays, $Q = 1$; thus, the radiation-absorbed dose is equivalent to the radiation dose equivalent. Currently the SI unit of radiation dose equivalent is the *Sievert* (Sv); the former unit was the *rem*. Therefore, for diagnostic x-rays, 1 Gy = 1 Sv and 1 Sv = 100 rem.[15, 16]

The radiation dose equivalent is dependant on the kilovolt peak (kVp) and mAs. For a given kVp, the radiation dose equivalent varies linearly with the mAs. At 125 kVp the radiation dose equivalent for a CT slice is approximately 1.1 to 1.2 cSv/100 mAs (1.1 to 1.2 rem/100 mAs). The actual dose varies slightly from machine to machine. Table 3-1 shows that the radiation dose equivalent for a CT slice can be considerably reduced using a low mAs technique.[10]

In contiguous CT imaging, the dose delivered to a particular region scanned (for example, the paranasal sinuses) is approximately equal to the per-slice dose. The dose delivered to a region is less than the per-slice dose if

Table 3-1
RELATIVE RADIATION DOSE FOR SINUS CT (UTILIZING 125 kVp)

mAs	Radiation Dose Equivalent
450	4.95–5.40 cSv (4.95–5.40 rem)
240	2.64–2.88 cSv (2.64–2.88 rem)
160	1.76–1.92 cSv (1.76–1.92 rem)
80	0.88–0.96 cSv (0.88–0.96 rem)

Source: Zinreich S. Imaging of inflammatory sinus disease. Otolaryngol Clin North Am 1993;26(4):535–547.

Copyright © 2003, Mosby, Inc. All rights reserved.

Table 3-2
ESTIMATED EFFECTIVE DOSE EQUIVALENT OF COMMON EXAMINATIONS

Examination	Effective Dose Equivalent
Sinus series, four views	7.0 mrem
Chest, PA and lateral	7.2 mrem
Kidneys, ureters, bladder (KUB)	8.7 mrem
Lumbar spine, five views	125.1 mrem
CT, brain*	112.0 mrem
CT, sinus (160 mAs)†	51.2 mrem
CT, sinus (80 mAs)‡	25.6 mrem

*120 kVp, 240 mAs, 10-mm slice thickness, contiguous.
†125 kVp, 160 mAs, 3-mm slice thickness, contiguous.
‡125 kVp, 80 mAs, 3-mm slice thickness, contiguous.
Source: Zinreich S. Imaging of inflammatory sinus disease. Otolaryngol Clin North Am 1993;26(4):535–547 and Zinreich S, Abidin M, Kennedy D. Cross-sectional imaging of the nasal cavity and paranasal sinuses. Operative Techniques Otolaryngol Head Neck Surg 1990;1(2):93–99.

there is a gap between slices, and the delivered dose is higher if there is overlap between slices.

Image Display

The effective dose equivalent was developed as a way of representing the fraction of the total stochastic risk of fatal cancers and chromosomal abnormalities resulting from the irradiation of a particular organ or tissue when the body is uniformly irradiated.[15, 16] A system of weighting is used to take into account the individual sensitivity of the body's major tissues and organs.[15, 16] A full discussion of the effective dose is beyond the scope of this chapter. Suffice it to say that for a given examination, the effective dose to the patient is less than the dose (radiation dose equivalent) received by the area scanned. A list of effective dose equivalents for some common radiographic procedures is presented in Table 3-2.[15, 17]

Windows are chosen to highlight the air passages, the bony detail, and the soft tissues. Usually a window width of +2000 Houndsfield units (HU) and a level of −200 HU are good starting parameters. The window and level settings can then be manipulated manually to display optimally the anatomic detail of the uncinate process and ethmoid bulla. Once this is accomplished, these settings can be used to film the entire study.[6, 8–11]

Sagittal reconstructions can be obtained for a morphologic orientation, and various distances and angles can be measured to aid in the passage of instruments during surgery. If only coronal scans are obtained, axial reconstructions can help display the position of the internal carotid arteries and optic nerves with respect to the bony margins of the posterior ethmoid and sphenoid sinuses.

Magnetic Resonance Imaging

Although magnetic resonance (MR) imaging provides better visualization of soft tissue than CT, its disadvantage is its inability to display optimally the cortical bone–air interface.[9, 10] Because both cortical bone and air have signal voids, at times MR imaging is unable to discern the intricate anatomic relationships of the sinuses and their drainage portals. Thus, MR imaging cannot be reliably used as an operative road map to guide the surgeon during FESS.

NASAL CYCLE

There is a side-to-side cyclic variation in the thickness of the nasal mucosa known as the nasal cycle (see Chapter 2), and the signal intensity of the mucosal lining of the nasal cavity and the ethmoid sinuses varies in concert with the nasal cycle.[18, 19] Thus, during the edematous phase of the nasal cycle, the mucosal signal intensity on T2-weighted images is similar to the appearance of mucosal inflammation, limiting the usefulness of MR imaging in these patients (Fig. 3-2).[11, 12] Interestingly, there is no cyclic variation of the mucosal signal in the frontal, maxillary, or sphenoid sinuses, and increased mucosal thickness and increased signal on T2-weighted images in these sinuses are always abnormal.[18, 19] To date, with respect to the paranasal sinuses, MR imaging has proven most helpful in the evaluation of the regional and intracranial complications of inflammatory sinus disease, in identifying complications of its surgical treatment, and in mapping neoplastic diseases (see Chapters 5 to 7).[20–24]

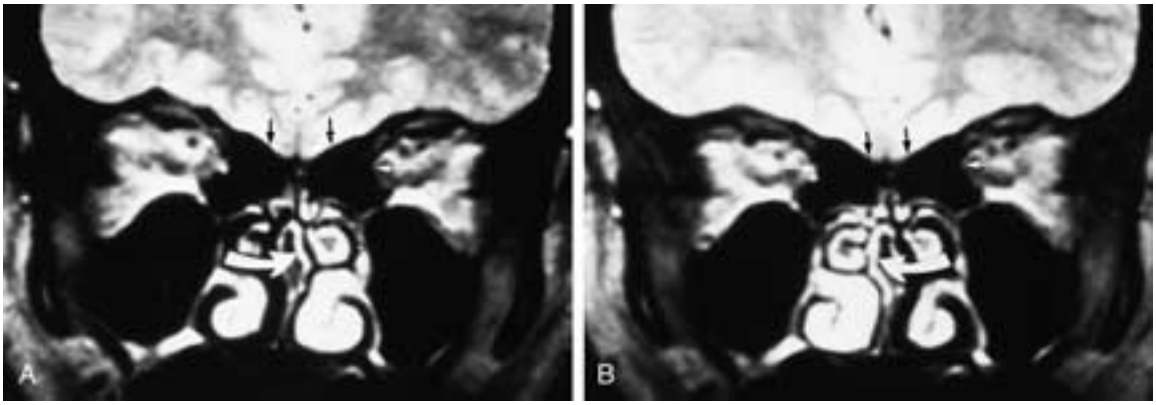

FIGURE 3-2 Nasal cycle on MR imaging. **A** and **B**, Coronal T2-weighted MR images of the anterior ethmoid sinuses show the changing edema of the nasal cavity (*curved arrow*), the ethmoid sinus mucosa, and the changing size of the turbinates. Note the lack of signal for definition of the ethmoid sinus roof and lamina papyracea (*arrows*).

VIEW IMAGE

Copyright © 2003, Mosby, Inc. All rights reserved.

INTERPRETATION OF IMAGING STUDIES

In any imaging study, the radiologist must use a variety of skills to provide consistent, accurate interpretations. With regard to the paranasal sinuses, these skills include the following:

1. Detailed knowledge of the anatomy of the paranasal sinuses
2. Systematic reading pattern
3. Detailed knowledge of the common pathologies affecting the region
4. Working knowledge of the available surgical options and their radiographic appearance
5. Awareness of common operative complications and their radiographic appearance

NORMAL ANATOMY

Mucociliary Clearance

An understanding of the regional anatomy and the importance of the anterior ethmoid sinus structures is critical if one is to understand the flow pattern of the mucous blanket coating the paranasal sinuses. The movement of this mucous blanket is referred to as mucociliary clearance. Further, one must be acquainted with the concept that inflammatory sinus disease results primarily from interference of mucociliary clearance due to compromise of the drainage portals (ostiomeatal channels) of the individual sinus cavities.

The mucosa of the paranasal sinuses and nasal fossae is made up of a ciliated cuboidal epithelium that secretes mucus. This mucus covers the epithelium and, as such, is referred to as a mucous blanket. The cilia are in constant motion and act in concert to propel the mucus in each sinus toward the sinus ostium and then, once in the nasal fossae, back toward the pharynx (see also Chapter 2). The pattern of flow is specific for each sinus and persists even if alternative openings are surgically created in the sinus.[25–27] One of the reasons that FESS has gained such wide acceptance is that its goal is to restore sinus drainage via the normal anatomic drainage pathways, thus allowing normal mucociliary clearance.

In the maxillary sinus, mucous flow originates in the antral floor and is then directed centripetally toward the primary ostium. The mucus is then transported through the infundibulum to the hiatus semilunaris, whence it passes into the middle meatus and ultimately into the nasopharynx. This pattern of mucus movement persists even after a nasal antrostomy is created.[25–27]

In the frontal sinus, the mucus flows up along the medial wall, laterally across the roof, and medially along the floor. As the flow approaches the medial aspect of the floor, some is directed into the primary ostium and the remainder is recirculated. The cleared mucus travels down the frontal recess and then into the middle meatus, where it joins the flow from the ipsilateral maxillary sinus.[25–27]

The posterior ethmoid and sphenoid sinuses clear their mucus into the sphenoethmoidal recess. The flow then enters the superior meatus and subsequently the nasopharynx.

Thus, there are two main ostiomeatal channels. The anterior OMU includes the frontal sinus ostium, frontal recess, maxillary sinus ostium, infundibulum, and middle meatus. These channels provide communication between the ipsilateral frontal, anterior ethmoid, and maxillary sinuses. The posterior OMU consists of the sphenoid sinus ostium, the sphenoethmoidal recess, and the superior meatus. The imaging investigation of these regions should be directed to optimally display these ostiomeatal channels.

Normal Anatomy (Ostiomeatal Unit)

Correct interpretation of sinonasal imaging studies requires an understanding of the anatomy of the lateral nasal wall and its relationship to adjacent structures (Fig. 3-3).[28, 29] The lateral nasal wall contains three bulbous projections: the superior, middle, and inferior turbinates (conchae). The turbinates divide the nasal cavity into three distinct air passages: the superior, middle, and inferior meati. Each respective meatus is lateral to its corresponding turbinate. The superior meatus drains the posterior ethmoid air cells and, more posteriorly, the sphenoid sinus (via the sphenoethmoidal recess). The middle meatus receives drainage from the frontal sinus (via the frontal recess), the maxillary sinus (via the maxillary ostium and subsequently the ethmoidal infundibulum), and the anterior ethmoid air cells (via the ethmoid cell ostia). The inferior meatus receives drainage from the nasolacrimal duct.

The imaging evaluation of the morphology of this area should focus on the anatomic structures surrounding three specific ‘‘tight spots.’’ Anteriorly, the first area comprises the structures surrounding the frontal recess. The second area consists of the structures surrounding the infundibulum and middle meatus. The third and most posterior area includes the anatomic structures surrounding the sphenoethmoid recess. Summary Boxes 3-2, 3-3, and 3-4 outline the individual anatomic structures found in each of these tight spots.

On CT scanning, the first coronal images display the outline of the frontal sinuses (Fig. 3-4). The frontal sinuses have an overall funnel shape, and their aeration varies from patient to patient and from side to side in individual patients. Some sinuses are small and occupy only the diploic space of the medial frontal bone, while other sinuses can be large enough to extend through the floor of the entire anterior cranial fossa. In general, a central septation separates the left and right sides; however, often there may be several septations. The floor of the frontal sinus slopes inferiorly toward the midline.

Close to the midline, the primary ostium is located in a depression in the floor. The frontal recess is an hourglass-like narrowing between the frontal sinus and the anterior middle meatus through which the frontal sinus drains (Figs. 3-5 to 3-7).[8] It is not a tubular structure, as the term *nasofrontal duct* might imply, and therefore the term *recess* is preferred.

Anterior, lateral, and inferior to the frontal recess is the agger nasi cell. This cell is a remnant ethmoturbinal and is present in nearly all patients. It is aerated and represents the most anterior ethmoid air cell, usually lying deep to the lacrimal bone. It usually borders the primary ostium or floor of the frontal sinus, and thus its size may directly influence

Copyright © 2003, Mosby, Inc. All rights reserved.

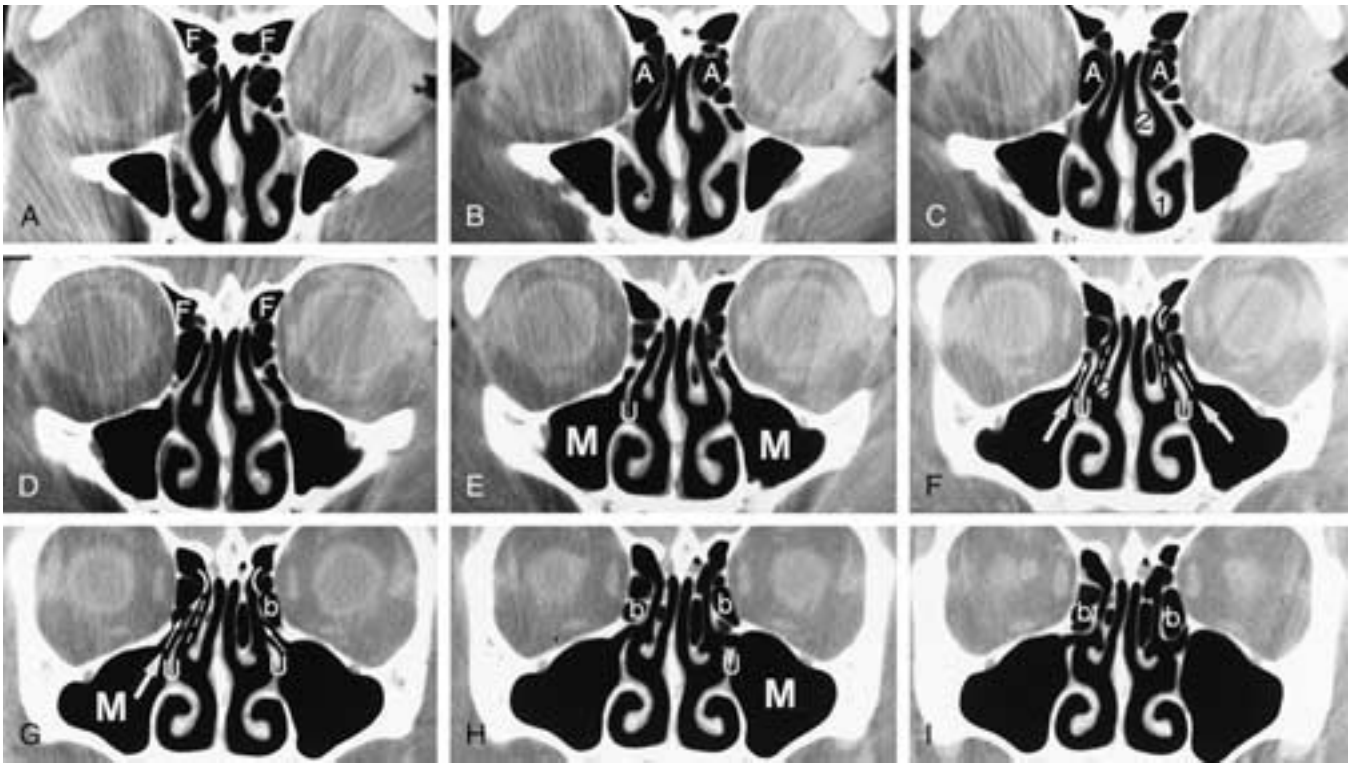

VIEW IMAGE

FIGURE 3-3 Coronal CT display of paranasal sinus anatomy. **A** to **I**, Thin section coronal CT images of a cadaver specimen. Frontal sinus (*F*), agger nasi cell (*A*), ethmoid bulla (*b*), maxillary sinus (*M*), basal lamella (*black arrow*), sphenoid sinus (*S*), inferior turbinate (*1*), middle turbinate (*2*), superior turbinate (*3*). The anterior ostiomeatal unit is displayed in images **F** through **H**. Frontal recess (*small curved lines*), middle meatus (*dashed lines*), infundibulum (*small arrows*), and primary ostium of the maxillary sinus (*large white arrows*).

the patency of the frontal recess and the anterior middle meatus. The frontal recesses are the narrowest anterior air channels and are common sites of inflammation. Their obstruction subsequently results in loss of ventilation and mucociliary clearance of the frontal sinus.

Frontal Cells

Frontal cells are invariably found in relation to the anterior ethmoid air cells and the agger nasi cell (Fig. 3-7). The recognition and subsequent definition of the appearance and etiology of frontal cells was initiated by J. Parson Schaeffer. During the course of his observations of the embryonic development of the sinuses, he discovered that it is possible, although infrequent, for one cell to aerate each half of the frontal bone, each with a separate communication to the frontal recess. Schaeffer coined the term *frontal cell* to describe this phenomenon.[30, 31] Van Alyea subsequently defined the frontal cell as a cell encroaching on the frontal recess or frontal sinus.[32–34] He considered supraorbital ethmoid, agger nasi, and intersinus septal cells, as well as cells limited to the frontal recess, as frontal cells. Bent et al.[35] defined frontal cells more specifically as belonging to one of four categories, detailed in Table 3-3. They also stated that all frontal cells derive from the anterior ethmoid sinus behind the agger nasi cell and pneumatize the frontal recess above the agger nasi cell. Each type of frontal cell may obstruct the nasofrontal communication or the frontal sinus itself.

SUMMARY BOX 3-2

Frontal Recess "Tight Spot" Anatomy

- Frontal sinus
- Frontal cell(s)
- Agger nasi
- Frontal recess
- Nasofrontal process
  *anterior bony beak
- Middle meatus

SUMMARY BOX 3-3

Infundibulum/Middle Meatus "Tight Spot" Anatomy

- Ethmoid bulla
- Uncinate process
- Infundibulum
- Maxillary sinus
- Primary ostium of maxillary sinus
- Middle turbinate
- Middle meatus
- Hiatus semilunaris
- Retrobullar recess
- Basal lamella

Copyright © 2003, Mosby, Inc. All rights reserved.

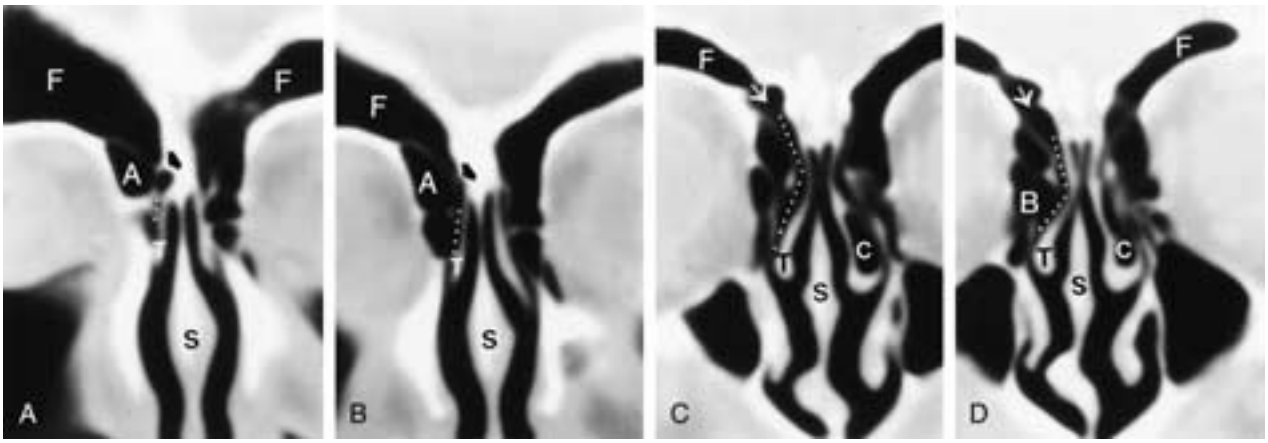

VIEW IMAGE

FIGURE 3-4 Anatomy of the frontal sinus. Coronal CT images of the frontal sinuses from anterior (**A**) to posterior (**D**) show the relationship between the frontal sinus (*F*) and the middle meatus (*dotted line*). Note that there is a bony strut (*heavy black arrow* in **A** and **B**) separating the frontal sinus and the anterior middle meatus. This separation is lost on the more posterior images (**C** and **D**) revealing the position of the frontal recess (*white arrow*). Note the position of the frontal cell (*A*) and its relationship to the frontal recess. Nasal septum (*S*), ethmoid bulla (*B*), middle turbinate (*T*), and concha bullosa (*C*).

The uncinate process is a superior extension of the lateral nasal wall (medial wall of the maxillary sinus).[8, 10] Anteriorly, the uncinate process fuses with the posteromedial wall of the agger nasi cell and the posteromedial wall of the nasolacrimal duct. The uncinate process has a ''free'' (unattached) superoposterior edge. Laterally this free edge delimits the infundibulum (Fig. 3-8). The infundibulum is the air passage that connects the maxillary sinus ostium to the middle meatus. Posterior to the uncinate process is the ethmoid bulla, usually the largest of the anterior ethmoid cells. The uncinate process usually courses medial and inferior to the ethmoid bulla. The ethmoid bulla is enclosed laterally by the lamina papyracea.

The gap between the ethmoid bulla and the free edge of the uncinate process defines the hiatus semilunaris. Medially, the hiatus semilunaris communicates with the middle meatus, the air space lateral to the middle turbinate.[8, 10] Laterally and inferiorly, the hiatus semilunaris communicates with the infundibulum, the air channel between the uncinate process (caudal border) and the inferomedial margin of the orbit (cranial border). The infundibulum serves as the primary drainage pathway from the maxillary sinus.[10, 11]

SUMMARY BOX 3-4

Sphenoethmoid Recess "Tight Spot" Anatomy

- Superior turbinate
- Posterior ethmoid sinus
- Primary ostium of sphenoid sinus
- Sphenoid sinus
- Optic nerve
- Carotid canal
- Foramen rotundum
- Vidian canal

The structure medial to the ethmoid bulla and the uncinate process is the middle turbinate. Anteriorly it attaches to the medial wall of the agger nasi cell and the superior edge of the uncinate process. Superiorly it adheres to the lateral edge of the cribriform plate. As it extends posteriorly, the middle turbinate emits a number of posterolaterally coursing bony structures. The first such ''laterally fanning'' attachment to the lamina papyracea is the basal lamella, which is posterior to the ethmoid bulla (Figs. 3-9, 3-10). This bony structure serves to separate the anterior and posterior ethmoid cells.

In most patients, the posterior wall of the ethmoid bulla is intact, and an air space is usually found between the basal lamella and the posterior ethmoid bulla. This air space, the sinus lateralis, may extend superior to the ethmoid bulla and

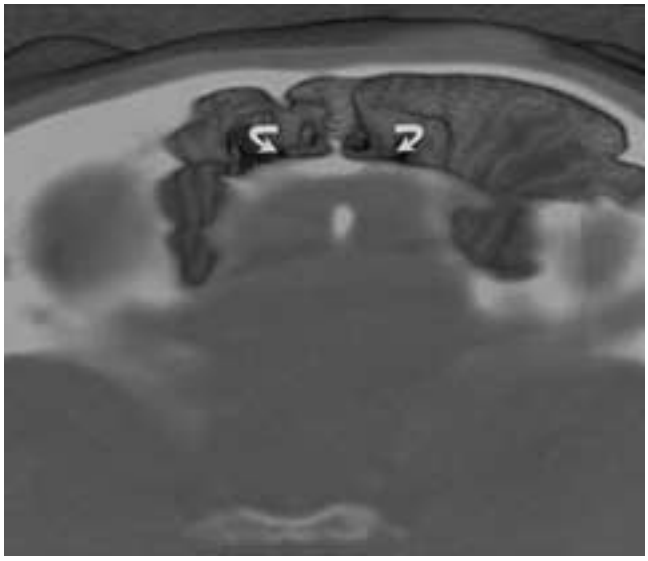

FIGURE 3-5 3D image of the floor of the frontal sinus. The roof of the frontal sinus is removed to demonstrate the floor of the frontal sinus, with emphasis on displaying the location of the frontal recess (*curved arrows*).

VIEW IMAGE

Copyright © 2003, Mosby, Inc. All rights reserved.

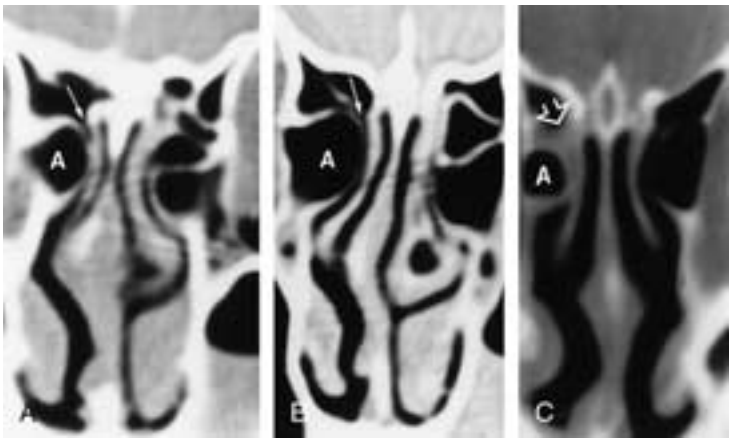

FIGURE 3-6 Anatomy of the frontal recess. **A** and **B**, Coronal CT images reveal a patent frontal recess (*white arrow*) despite the presence of a large agger nasi cell (*A*). **C**, Coronal CT image in a different patient with an obstructed right frontal recess and mucoperiosteal thickening in the right frontal sinus (*open arrow*). Agger nasi (*A*).

VIEW IMAGE

communicate with the frontal recess (Fig. 3-11). Recently, the sinus lateralis has been renamed by an international surgeon's group and is now called the retrobullar recess cell.[36] If it extends above the ethmoid bulla, this extension would be called the suprabullar recess cell. A dehiscence or total absence of the posterior wall of the ethmoid bulla is common and may provide communication between these two usually separated air spaces.

The posterior ethmoid sinus consists of air cells between the basal lamella and the sphenoid sinus. The number, shape, and size of these air cells vary significantly from person to person.[8, 9, 11, 37]

The sphenoid sinus is the most posterior sinus. It is usually embedded in the clivus and is bordered superoposteriorly by the sella turcica. Its ostium is located medially in the anterosuperior portion of the anterior sinus wall and communicates with the sphenoethmoidal recess and the posterior aspect of the superior meatus. The sphenoethmoidal recess lies just lateral to the nasal septum and can sometimes be seen on coronal images, but it is best displayed in the sagittal and axial planes (Figs. 3-12, 3-13).[8, 10]

The relationship between the aerated portion of the sphenoid sinus and the posterior ethmoid sinus must be accurately demonstrated so that the surgeon can avoid operative complications (Fig. 3-14). Usually in the paramedian sagittal plane, the sphenoid sinus is the most superior and posterior air space. Horizontally oriented structures within the sphenoid sinus are actually separations between the posterior ethmoid sinus (Fig. 3-15). All sphenoid sinus septations are vertically oriented. This relationship is well demonstrated on axial and sagittal images. The number and position of the septations in the sphenoid sinus are quite variable, and of particular importance are septations that adhere to the bony canal wall covering the internal carotid artery, which often projects into the posterolateral sphenoid sinus. Less often, the canal of the vidian nerve (pterygoid canal) and the canal of the second division of the trigeminal nerve can project into the floor of the sphenoid sinus.

Anatomically, the paranasal sinuses are in close proximity to the anterior cranial fossa, the cribriform plate, the internal carotid arteries, the cavernous sinuses, the orbits and their contents, and the optic nerves as they exit the orbits.[38–42] The surgeon must be especially cautious when maneuvering instruments directed cranially and dorsally in order to avoid inadvertent penetration and damage to these structures.[6, 11, 40, 41]

ANATOMIC VARIATIONS AND CONGENITAL ABNORMALITIES

Even though nasal anatomy varies significantly from patient to patient, there are some specific variations that occur repeatedly within the population. The prevalence of these variations, as reported by several groups of investigators, are outlined in Summary Box 3-5.[43–53] Certain anatomic variations are thought to be predisposing factors for the development of sinus disease or operative complications. Thus, it is necessary for the radiologist and surgeon to be cognizant of these variations, especially if the patient is a candidate for FESS.

Variations of the Middle Turbinate

Paradoxic Curvature

Normally, the convexity of the middle turbinate bone is directed medially, toward the nasal septum. When paradoxically curved, the convexity of the bone is directed laterally toward the lateral sinus wall(Fig. 3-16). The inferior edge of the middle turbinate may assume various shapes with exces-

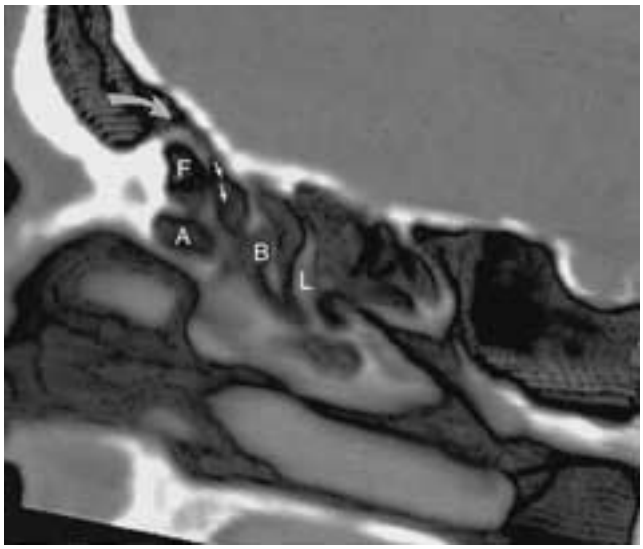

FIGURE 3-7 Saggital 3D image of the frontal recess and adjacent anatomy. This three-dimensional image of the lateral nasal wall reveals the agger nasi cell (*A*) and the frontal cell (*F*). Note the frontal recess behind these structures (*large curved arrow, small arrows*). Ethmoid bulla (*B*), basal lamella (*L*).

VIEW IMAGE

Copyright © 2003, Mosby, Inc. All rights reserved.

Table 3-3
FRONTAL CELL TYPES I–IV

TYPE I	Single frontal recess cell above agger nasi cell
TYPE II	Tier of cells in frontal recess above agger nasi cell
TYPE III	Single massive cell pneumatizing cephalad into frontal sinus
TYPE IV	Single isolated cell within the frontal sinus

sive curvature, which in turn may narrow and/or obstruct the nasal cavity, infundibulum, and middle meatus. Because of this potential narrowing or obstruction, most authors agree that paradoxic middle turbinates can be a contributing factor to sinusitis. Certain authors have, however, found no significant relationship between paradoxically curved middle turbinates and recurrent sinusitis: Lloyd reported no correlation between the variant and increased incidences of asymptomatic sinusitis, and Calhoun et al. found no statistical correlation between paradoxical curvature of the middle turbinate and symptomatic sinusitis.[44, 54]

Concha Bullosa

A concha bullosa is an aerated turbinate, most often the middle turbinate. Although it may be either unilateral or bilateral (Fig. 3-17), Lloyd et al. report it occurring bilaterally more frequently.[55] Less frequently, aeration of the superior turbinate may occur, and an aerated inferior turbinate is uncommon. Concha bullosae are classified according to the degree and portion of turbinate pneumatization. When the pneumatization involves the bulbous segment of the middle turbinate, the term *concha bullosa* applies. If only the attachment portion of the middle turbinate is pneumatized, and the pneumatization does not extend into the bulbous segment, it is known as a lamellar concha.

The reported prevalence of concha bullosa, or pneumatized middle turbinate, varies greatly. Two separate cadaveric studies found concha bullosa in 8% and 20% of specimens, respectively.[51] The reported prevalence of the radiographic appearance of concha bullosa on coronal CT scans ranges from 14% to 53%.[44, 53] The significant discrepancy in the reported prevalence of concha bullosa is due to several possible factors. Attempts to determine the general prevalence of this variation have been characterized by the use of diverse study populations, different criteria for pneumatization, and analytic methods. These varying features have undoubtedly affected the results of the investigations.

Although middle turbinate pneumatization has been suspected as a potential cause of middle meatal obstruction and resultant sinusitis, the definitive relationship between concha bullosa and sinusitis continues to be debated. A concha bullosa involving the middle turbinate may enlarge

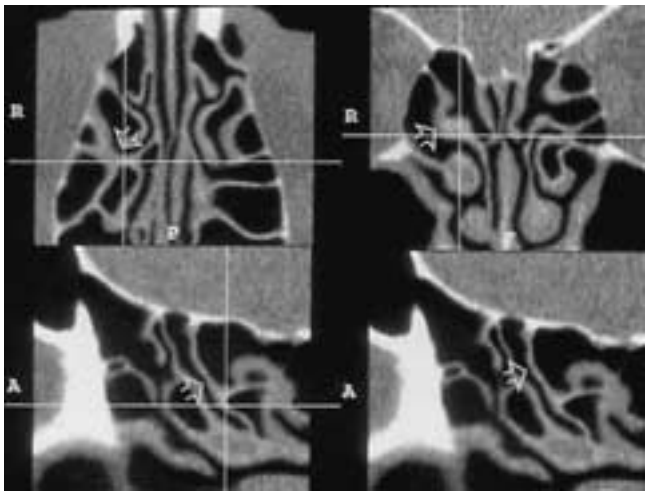

FIGURE 3-9 Triplanar display of the basal lamella (*open arrows*).

VIEW IMAGE

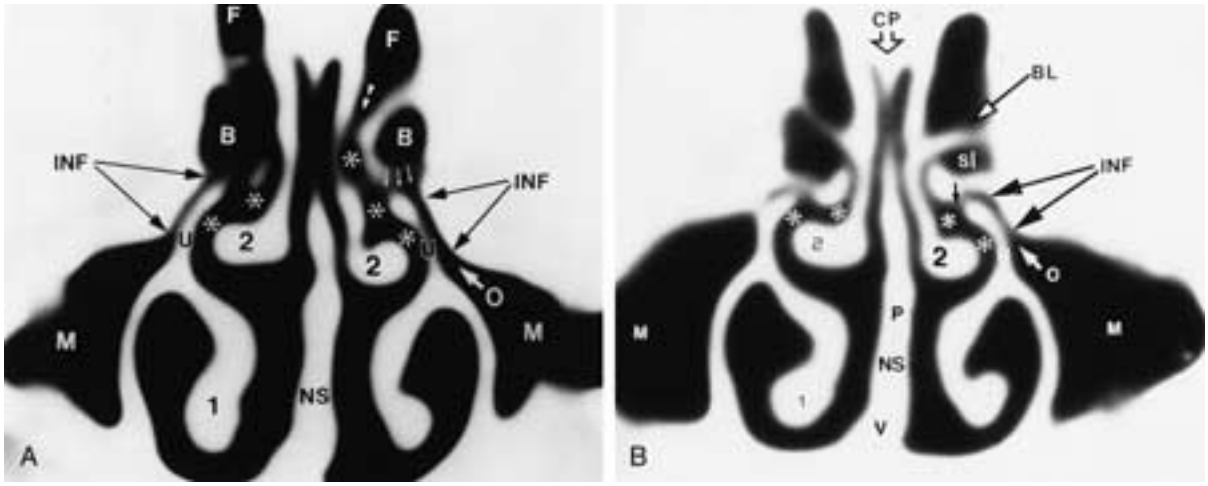

FIGURE 3-8 Anterior ostiomeatal channels. Coronal CT images through the anterior ethmoid sinuses show the air passages communicating with the frontal sinus (*F*), anterior ethmoid sinus, and maxillary sinus (*M*). The primary ostium (*O*) of the maxillary sinus communicates with the infundibulum (*INF*). The infundibulum is bordered medially by the uncinate process (*U*) and laterally by the orbit. In turn, the infundibulum communicates with the middle meatus (*asterisks*) through the hiatus semilunaris (*most medial white arrows in* **A**, *small black arrow in* **B**). The frontal recess (*white arrowheads*) is patent. The ethmoid bulla (*B*) is usually the largest air cell in the anterior ethmoid sinus. Note the vertical attachment of the middle turbinate (*2*) to the cribriform plate (*CP*) and its lateral attachment to the lamina papyracea, the basal lamella (*BL*). The air space between the basal lamella and the ethmoid bulla is the sinus lateralis (*sl*). Inferior turbinate (*1*), nasal septum (*NS*), vomer (*V*), and perpendicular plate of the ethmoid bone (*P*).

VIEW IMAGE

Copyright © 2003, Mosby, Inc. All rights reserved.

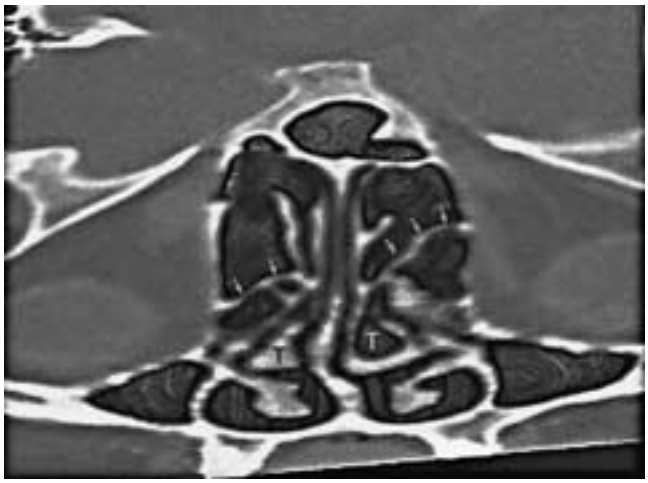

VIEW IMAGE

FIGURE 3-10 3D of the basal lamella. This three-dimensional image, viewed from superoanteriorly, reveals the anterior segment of the middle turbinates (*T*). Note the lateral attachment of the middle turbinate to the lamina papyracea—the basal lamella (*arrows*).

the turbinate, so that it obstructs the middle meatus or the infundibulum, and extensively pneumatized middle turbinates are associated with a higher prevalence of ipsilateral sinus disease.[43, 56] This is especially true when the concha bullosa exists in conjunction with another anatomic configuration that may obstruct the ostiomeatal complex, such as an extensively pneumatized ethmoid bulla.[51]

The air cavity in a concha bullosa is lined with the same epithelium as the rest of the sinonasal cavities. Thus these concha bullosa cells can experience the same inflammatory disorders that affect the paranasal sinuses, and obstruction of the drainage of a concha may also lead to mucocele formation (Fig. 3-18). Isolated or smaller conchae bullosae, or those in which pneumatization is confined to the anterior or inferior aspect of the middle turbinate (farther from the ethmoid infundibulum), are less frequently associated with symptoms of sinusitis.[51]

Other Variations

Additional variations of the middle turbinate can occur, including medial displacement, lateral displacement, lateral bending, L shape, and sagittal transverse clefts (Fig. 3-19). Medial displacement of the middle turbinate is the result of other middle meatal structures (i.e., polypoid disease, pneumatized uncinate process) encroaching upon the middle turbinate. Lateral displacement of the middle turbinate is usually due to the compression of the turbinate toward the lateral nasal wall by a septal spur or septal deviation. Either or these two variants may predispose to sinus disease.[51] L-shaped and lateral bending of the middle turbinate, as well as sagittal or transverse clefting, may also be observed; however, these variants are not associated with sinusitis.[51]

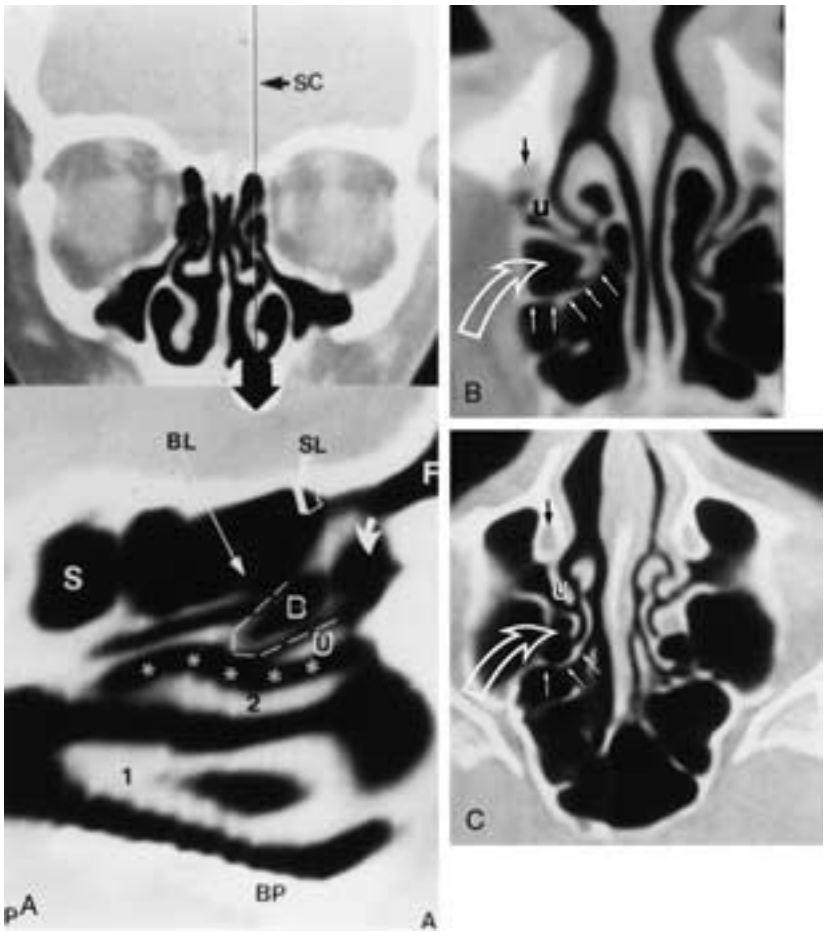

VIEW IMAGE

FIGURE 3-11 Anatomy of the basal lamella and sinus lateralis. **A**, Sagittal reconstructed plane (*SC*) from direct coronal CT data shows the outline of the basal lamella (*BL*) and the position of the sinus lateralis (*SL*) between the basal lamella and the ethmoid bulla (*B*). The position of the hiatus semilunaris (*dashed U-shaped line*), the frontal recess, and the anterior middle meatus (*curved arrow*) are noted. Frontal sinus (*F*), sphenoid sinus (*S*), uncinate process (*U*), middle meatus (*asterisks*), inferior turbinate (*1*), middle turbinate (*2*), bony palate (*BP*), anterior (*A*), and posterior (*P*). **B** and **C**, Axial CT images show the orientation of the uncinate process (*u*) and its association with nasolacrimal duct (*small black arrow*). Note the attachment of the basal lamella (*small white arrows*) to the lamina papyracea. The ethmoid bulla (*curved arrow*) is the air cell anterior to the basal lamella, and in both of these patients the posterior wall of the air cell is incomplete, providing direct communication between the ethmoid bulla and the sinus lateralis.

Copyright © 2003, Mosby, Inc. All rights reserved.

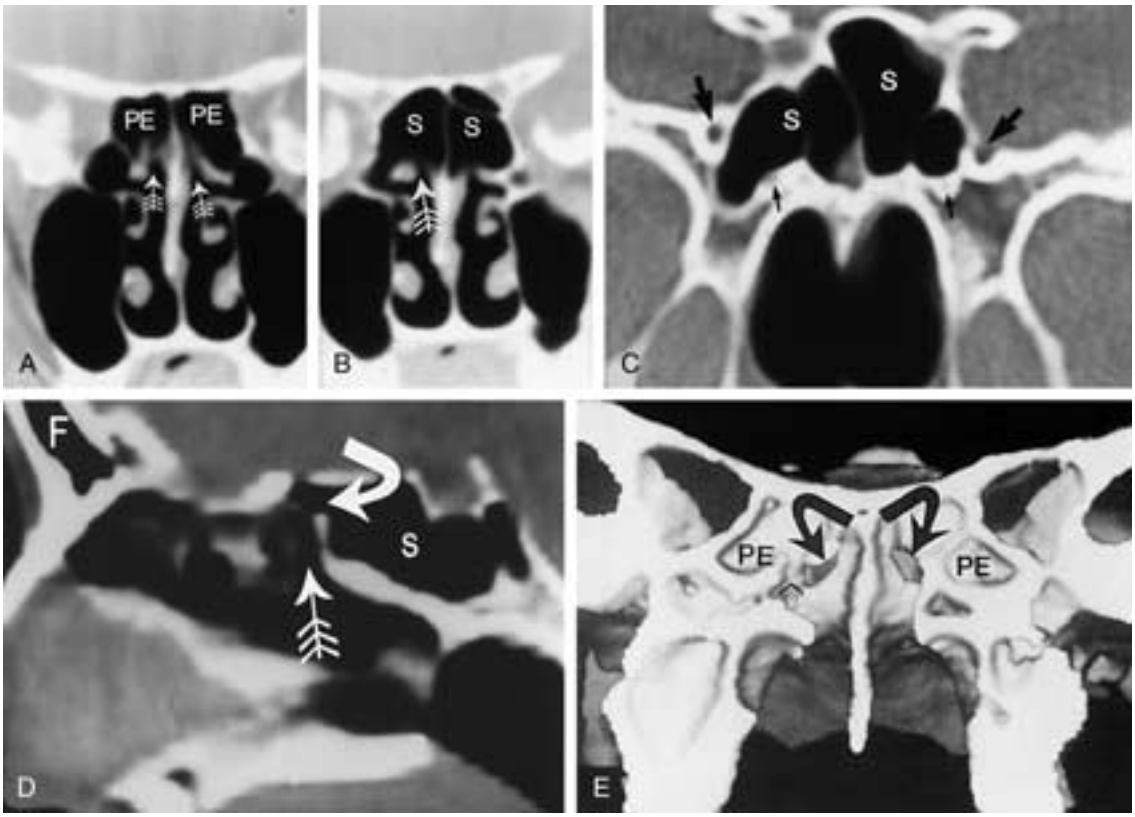

VIEW IMAGE

FIGURE 3-12 Sphenoid sinus anatomy. **A** and **B**, Coronal CT images show the boundary between the posterior ethmoid sinus (*PE*) and the sphenoid sinus (*S*). This boundary is best recognized by the position of the sphenoethmoidal recess (*feathered arrows*). It is relatively clear that the coronal image is through the anterior sphenoid sinus when only the inferior edge of the sphenoethmoidal recess is identified (**B**). **C**, Coronal CT image through the sphenoid sinus (*S*) shows the number and orientation of septations within the sinus, as well as the relationship to the foramen rotundum (*heavy black arrow*) and vidian canal (*fine black arrow*). **D**, Paramedial sagittal CT image shows the position of the sphenoid sinus ostium (*curved arrow*) and the sphenoethmoidal recess (*feathered arrows*). Frontal sinus (*F*), and sphenoid sinus (*S*). **E**, Three-dimensional CT image with a coronal cut–plane view through the posterior aspect of the posterior ethmoid sinus (*PE*) reveals the orientation of the sphenoethmoidal recess (*open arrow*) and position of the sphenoid sinus ostia (*curved arrows*).

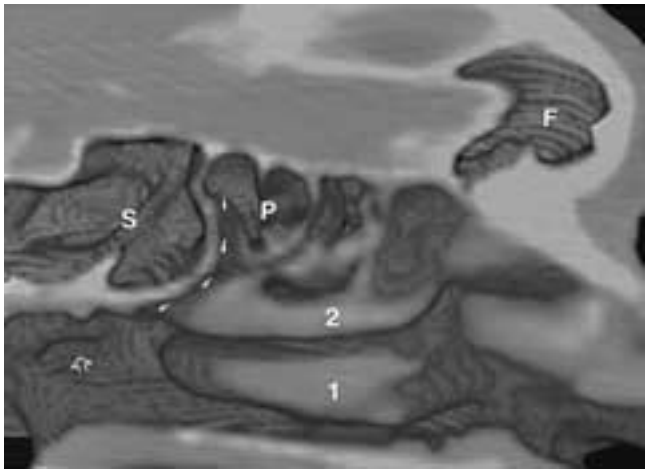

VIEW IMAGE

FIGURE 3-13 Saggital 3-D image of the sphenoethmoid recess. Three-dimensional image of the lateral nasal wall reveals the sphenoid sinus (*S*), the posterior ethmoid sinus (*P*), and the sphenoethmoid recess (*small arrows*). Inferior turbinate (*1*), middle turbinate (*2*), frontal sinus (*F*), fossa of Rosenmueller (*open arrow*).

Nasal Septal Deviation

The nasal septum is fundamental to the development of the nose and paranasal sinuses. Nasal septal deviation is usually congenital but may be posttraumatic in some patients. Malalignment of the components of the adult nasal septum (septal cartilage, perpendicular ethmoidal plate, and vomer) may cause deviation of the nasal septum, deformity of the chondrovomerine articulation, or a septal spur. Asymptomatic septal deviation is observed in 20% to 31% of the population; however, more significant deviation, especially at the level of the chondrovomerine articulation, may contribute to sinusitis symptoms.[46, 48] Severe asymmetric bowing of the nasal septum may compress the middle turbinate laterally, narrowing the middle meatus (Fig. 3-20), and the presence of associated bony spurs may further compromise the OMU. Obstruction, secondary inflammation, swollen membranes, and infection of the middle meatus have all been observed as a result of severe nasal septal deviation.[57]

Copyright © 2003, Mosby, Inc. All rights reserved.

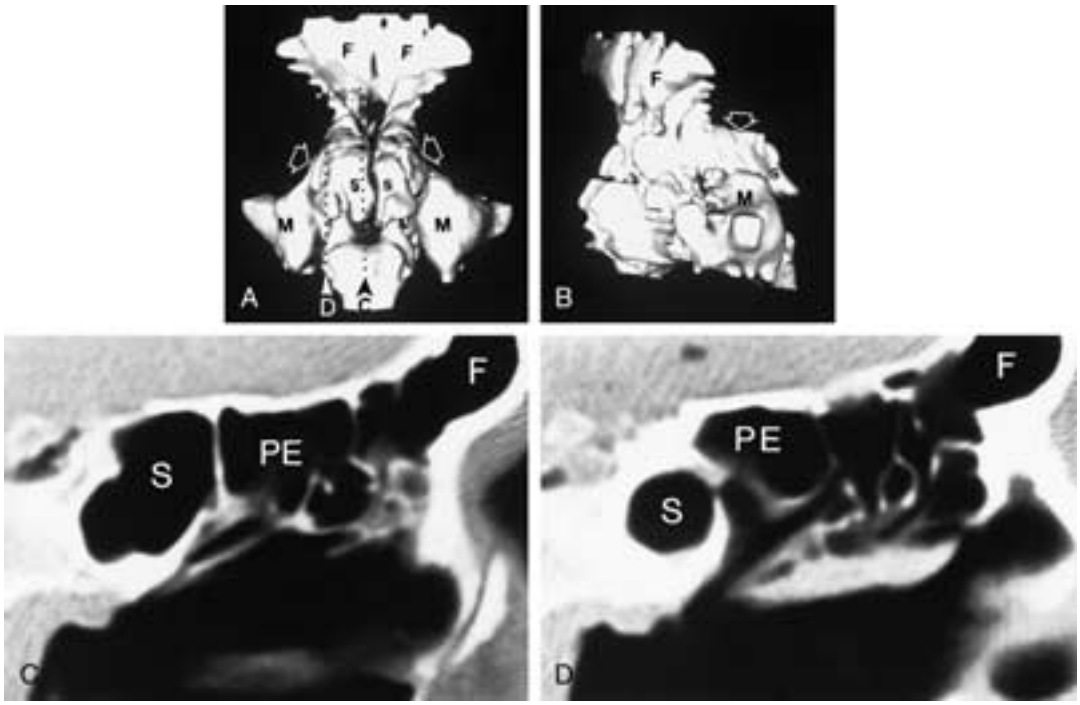

VIEW IMAGE

FIGURE 3-14 Anatomic relationship of the posterior ethmoid and sphenoid sinuses. **A** and **B**, Posterior (**A**) and anterolateral (**B**) views from three-dimensional CT images of a ''cast'' of the aerated nasal cavity, nasopharynx, and paranasal sinuses viewed from behind (**A**) and from the left side (**B**). Note that the posterior ethmoid sinus (*open arrows*) is wider and positioned more superiorly than the sphenoid sinus (*S*). The dotted lines denote the position of the sagittal planes displayed in **C** and **D**. Frontal sinus (*F*) and maxillary sinus (*M*). **C**, Paraseptal CT image of a cadaver head shows that the sphenoid sinus (*S*) is the most posterior and superior air space and that it is accessible from the posterior ethmoid sinus (*PE*). Frontal sinus (*F*). **D**, Sagittal CT image of a cadaver head performed approximately 1.5 cm lateral to the nasal septum shows that the sphenoid sinus (*S*) is inferior to the posterior ethmoid sinus (*PE*). Frontal sinus (*F*).

Uncinate Process Variations

Deviation

The uncinate process is one of the crucial bony structures of the wall of the lateral nasal cavity. Together with the ethmoid bulla, it forms the boundaries of the hiatus semilunaris and ethmoid infundibulum, the structures through which the frontal and maxillary sinuses drain. The course of the free edge of the uncinate process may be configured in a variety of ways. In most cases, it either extends slightly obliquely toward the nasal septum, with the free edge surrounding the inferoanterior surface of the ethmoid bulla, or it extends more medially to the medial surface of the ethmoid bulla. If the free edge of the uncinate is deviated in a more lateral direction, it may cause narrowing or obstruction of the hiatus semilunaris and infundibulum. Less frequently, a medial deviation or ''curling'' of the uncinate is encountered, which may result in the structure's contact and subsequent obstruction of the middle meatus (Fig. 3-21).

FIGURE 3-15 Relationship between the posterior ethmoid sinus and the sphenoid sinus. Coronal CT image through the middle sphenoid sinus reveals a horizontal bony membranous structure (*solid arrow*). This structure is not a septation; rather, it represents the separation from the sphenoid sinus inferiorly and the posterior ethmoid sinus superiorly. Septations (*open arrow*) are vertically oriented.

VIEW IMAGE

Attachment

Normally, the upper tip of the uncinate process attaches to the lateral nasal wall in the location where agger nasi cells are commonly found. Anatomic variations of this attach-

Copyright © 2003, Mosby, Inc. All rights reserved.

SUMMARY BOX 3-5

Reported Prevalences of Anatomic Variations

	Agger Nasi Cell	Enlarged Ethmoid Bulla	Haller Cells	Pneumatized Uncinate Process	Deviated Uncinate Process	Paradoxical Middle Turbinate	Concha Bullosa	Nasal Septal Deviation	Onodi Cells
Zinreich et al.	Nearly all	8%	10%	0.4%	3%	15%	36%	21%	
Bolger	98.5%		45.1%	2.5%		26.1%	53%	18.8%	
Lloyd	3%	17%	2%		16%	17%	14%		
Van Alyea	89%								98%
Messerklinger	10–15%								
Lebowitz	86%							31%	
Scribano et al.		4%	24%	18%: combination of pneumatization and deviation			67%		
Wanamaker			20%		45%		30%	20%	
Driben et al.									39%
Tonai & Baba	86.7%		36%			25.3%	28%		
Yousem			10–45%			Less than 10%	34–53%		
Joe Weinberger et al.					15%	3%	15%		14%
Perez-Pinas et al.	Nearly all	0%	3%	0%	4.5%	10%	73%	80%	11%

ment include attachment to the lamina papyracea, the lateral surface of the middle turbinate, or the fovea ethmoidalis in the floor of the anterior cranial fossa (Fig. 3-22). It is necessary for the surgeon to be cognizant of any of these variations in the patient undergoing FESS, especially when an uncinatectomy is contemplated. In particular, if the uncinate process attaches to the ethmoidal roof or middle turbinate, the surgeon must take special care not to put aggressive traction or torque on the upper tip of the structure during uncinatectomy, as this could inadvertently damage the ethmoid roof and result in CSF rhinorrhea or other intracranial complications.

Sometimes the free edge of the uncinate process adheres to the orbital floor, or inferior aspect of the lamina papyracea. This is referred to as an atelectatic uncinate process (Fig. 3-23) and is associated with a hypoplastic, and often opacified, ipsilateral maxillary sinus due to closure of the infundibulum. For surgical planning, it is important to note this variant, as the ipsilateral orbital floor is low-lying as a result of the hypoplastic maxillary sinus, increasing the risk of inadvertent penetration of the orbit during surgery.

An additional variant of the uncinate process configuration is its extension superiorly to the roof of the anterior ethmoid sinus, causing the superior infundibulum to end as a ''blind pouch.'' This continuation of the uncinate is referred to as the lamina terminalis. In these cases, the infundibulum drains via the posterior aspect of the middle meatus.

Pneumatization

Pneumatization of the uncinate process, also referred to as an uncinate bulla, has been suggested as a predisposing factor for impaired sinus ventilation, especially in the anterior ethmoid, frontal recess, and infundibular regions (Fig. 3-24).[58] Functionally, the pneumatized uncinate process resembles a concha bullosa or an enlarged ethmoid bulla. The pneumatization of the uncinate process is believed to be due to extension of the agger nasi cell within the anterosuperior portion of the uncinate process.[21] The reported incidence of this variant is relatively low, ranging from 0.4% to 2.5% to 18%.[11, 43]

Infraorbital Ethmoid Cells (Haller's Cells)

Infraorbital ethmoid cells are pneumatized ethmoid air cells that project along the medial roof of the maxillary sinus and the most inferior portion of the lamina papyracea, below the ethmoid bulla and lateral to the uncinate process (Fig. 3-25). These cells were first identified by Haller in 1765 and subsequently named after him; recently, however, the preferred term for these air cells has been changed to reflect both a growing trend that discourages the naming of structures after anatomists who first describe them, as well as the need for international standardization and descriptive nomenclature for anatomic terms.[36] Most often, infraorbital

Copyright © 2003, Mosby, Inc. All rights reserved.

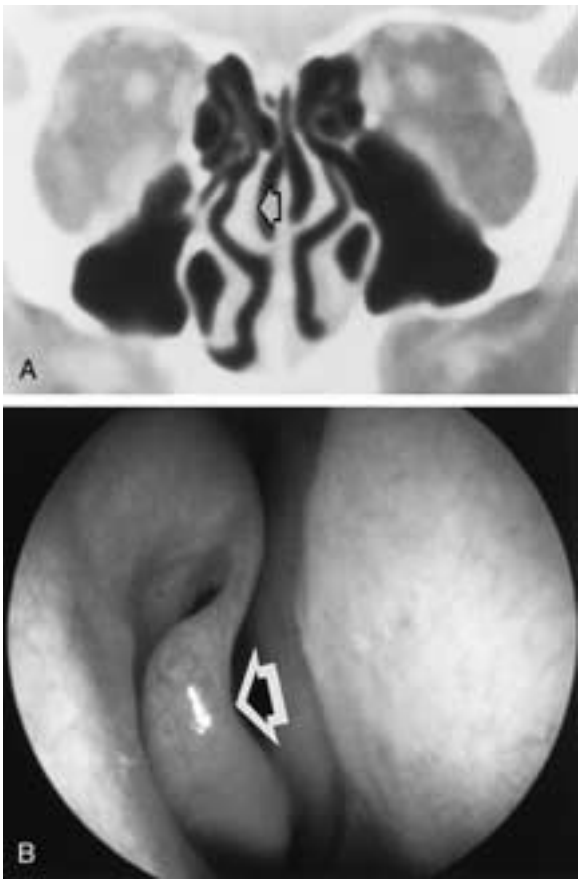

VIEW IMAGE

FIGURE 3-16 Paradoxic middle turbinate. **A**, Coronal CT image demonstrates bilateral paradoxic middle turbinates. The right side is highlighted (*solid arrow*). **B**, Endoscopic view correlates with the CT findings (*arrow*).

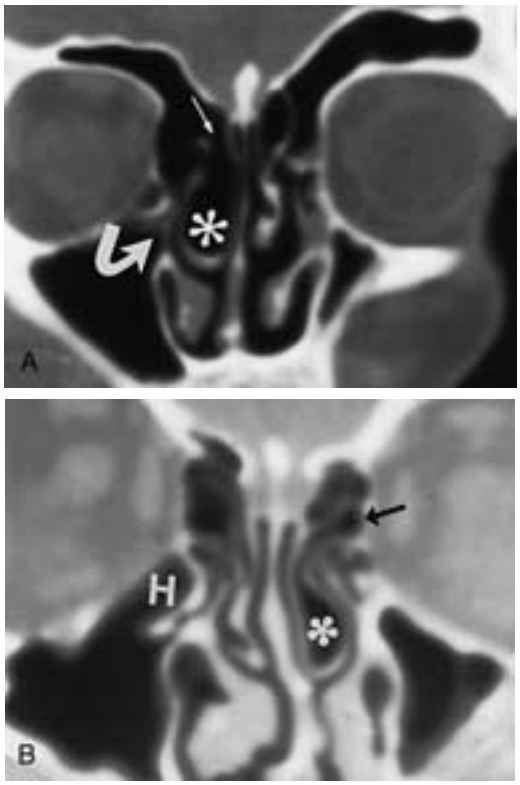

VIEW IMAGE

VIEW IMAGE

FIGURE 3-17 Concha bullosa in two different patients. **A**, Coronal CT image demonstrates a prominent right concha bullosa (*asterisk*) with communication to the frontal recess (*small arrow*). Note the obstruction of the right middle meatus (*curved arrow*). **B**, Coronal CT image demonstrates a left-sided concha bullosa (*asterisk*) with communication to the sinus lateralis (*small arrow*). Note the contralateral Haller (infraorbital ethmoid) cell (*H*).

ethmoid cells arise from the anterior ethmoid cells and are closely related to the infundibulum.[48] These cells contribute to the narrowing of the infundibulum and may also compromise the adjacent ostium of the maxillary sinuses. Consequently, many authors cite infraorbital ethmoid cells as a factor in recurrent maxillary sinusitis.[57, 58]

Some authors consider the existence of this variant a predisposing factor for recurrent maxillary sinusitis. However, Bolger et al. reported an incidence of 45%, and their study found no statistical difference between the prevalence of infraorbital ethmoid cells in patients presenting with recurrent maxillary sinusitis and asymptomatic patients. This led these investigators to suggest that the role of infraorbital ethmoid cells in disease should be evaluated on an individual basis, depending on the size, placement, and evidence of inflammation in the cell.[43]

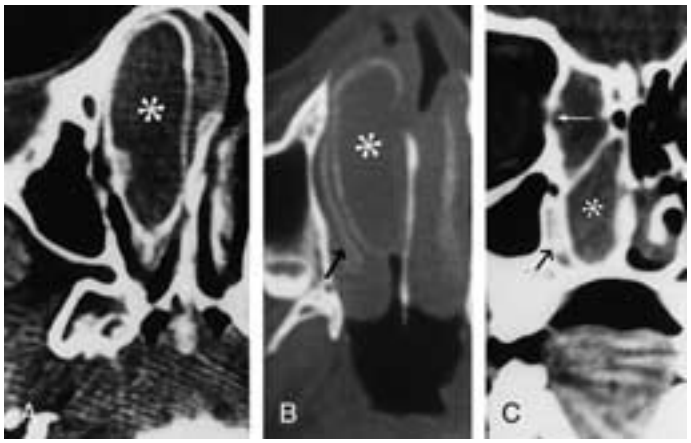

FIGURE 3-18 Mucocele within a concha bullosa. Axial (**A** and **B**) and coronal (**C**) CT images show a prominent soft-tissue mass (*asterisk*) well circumscribed by a bony perimeter (the bony framework of the concha bullosa). The inferior turbinate is compressed against the medial wall of the maxillary sinus (*black arrow*). In the coronal image, the extent of the obstruction of the nasal cavity is apparent, as is the presence of a more superior mucocele, which erodes the lamina papyracea (*white arrow*).

VIEW IMAGE

Copyright © 2003, Mosby, Inc. All rights reserved.

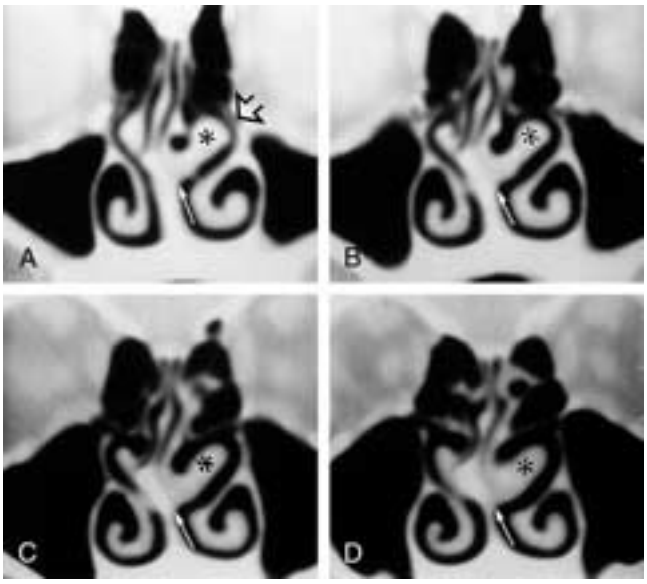

VIEW IMAGE

FIGURE 3-19 Coronal CT scans. **A** to **D**, The free edge of the middle turbinate may also assume some other shapes. Note its prominent lateral curvature in this case (*asterisk*). It obstructs the nasal passage (*fine white arrows*) and contributes to the position of the uncinate process and, therefore, the prominent narrowing of the infundibulum (*open arrow*).

Onodi Cells

Two primary definitions of Onodi cells have been presented in the literature. The first defines them as the most posterior ethmoid cells, being superolateral to the sphenoid sinus and closely associated with the optic nerve.[39, 59, 60] Another, more general description defines Onodi cells as posterior ethmoid cells extending into the sphenoid bone, situated either adjacent to or impinging upon the optic nerve.[36] The reported incidence of Onodi cells ranges from 3.4% to 51%.[52] This discrepancy is most likely due to the use of different criteria to define these cells. Onodi cells abut or may even surround the optic nerve, thereby placing this nerve at risk when surgical excision of these cells is performed.

Onodi cells are also a potential cause of incomplete sphenoidectomy. If a surgeon is operating in an Onodi cell, he or she may recognize landmarks traditionally associated with the sphenoid sinus (internal carotid artery, optic nerve) and thus mistakenly conclude that the sphenoid sinus has been entered.

Ethmoid Bulla Variations

The ethmoid bulla is usually the largest and most constant anterior ethmoid air cell. Its appearance varies considerably, based on the extent of pneumatization; extensive pneumatization may obstruct the ostiomeatal complex. Elongated ethmoid bullae are usually the result of pneumatization that extends in a superior to inferior direction rather than in an anterior to posterior direction. Because such pneumatization does not extend in an anterior or posterior direction, elongated ethmoid bullae are relatively unlikely to obstruct the ostiomeatal complex.

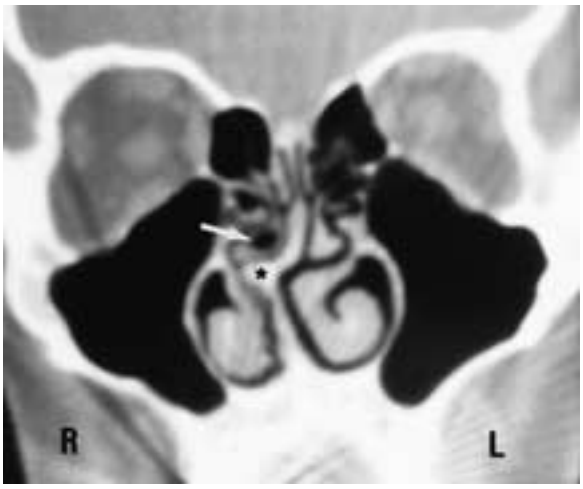

FIGURE 3-20 Nasal septal deviation with spurring. Coronal CT image demonstrates that there is deviation of the nasal septum toward the right side, with a right-sided cartilaginous nasal ''spur'' (*asterisk*). Note the ipsilateral concha bullosa (*arrow*). Both of these anatomic variants contribute to marked narrowing of the right nasal cavity and ethmoid passages.

VIEW IMAGE

Extensive Pneumatization of the Sphenoid Sinus

Although encountered infrequently, pneumatization of the sphenoid sinus that extends into the lesser wing and the anterior and posterior clinoid processes is important to note. A pneumatized anterior clinoid process is associated with Type 2 and Type 3 optic canal configurations (see below), making these nerves especially vulnerable to injury during FESS.[61] A more extensive description of the relationship between the posterior paranasal sinuses and the optic nerves, optic nerve configurations, and their reported incidence can be found in the sections discussing the systematic evaluation of paranasal sinus CT examinations (Fig. 3-26).

Medial Deviation or Dehiscence of the Lamina Papyracea

Medial deviation or dehiscence of the lamina papyracea may be either congenital or the result of prior facial trauma. In either case, if the surgeon does not know about this

FIGURE 3-21 Medially curved uncinate process. **A** and **B**, Coronal CT images through the ethmoid sinuses show a prominent right-sided deviation of the nasal septum (*straight open arrow*). Note the medially curved left uncinate process (*curved open arrow*), which is medially displacing the left middle turbinate (+) and obstructs the left middle meatus. A left-sided Haller (infraorbital ethmoid) cell is present (*small arrow*).

VIEW IMAGE

Copyright © 2003, Mosby, Inc. All rights reserved.

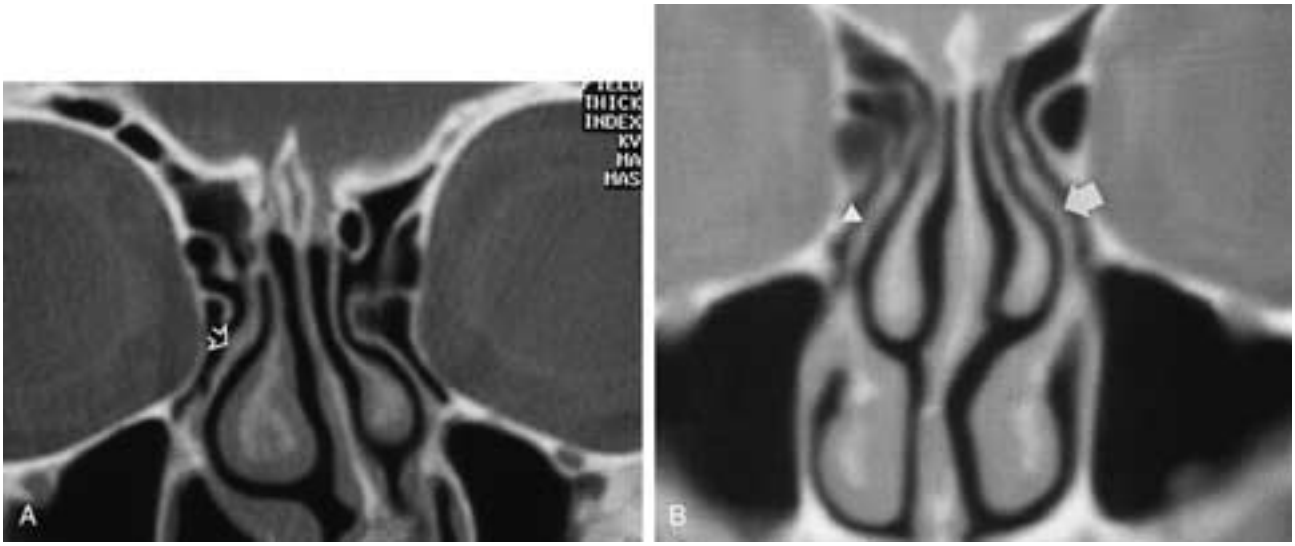

VIEW IMAGE

FIGURE 3-22 Variations in the superior attachment of the uncinate process. **A**, Coronal CT image obtained at the level of the frontal recess reveals that the right uncinate process (*open arrow*) attaches to the superior right middle turbinate. **B**, Coronal CT image reveals that the left uncinate process (*solid arrow*) attaches to the roof of the ethmoid sinus. On the right side, the uncinate (*arrowhead*) adheres to the medial agger nasi cell and frontal cell.

VIEW IMAGE

FIGURE 3-23 Atelectatic uncinate process. Coronal CT scan shows that the right uncinate process is apposed to the inferomedial aspect of the orbit (*arrows*). The resultant obstruction of the infundibulum is usually the cause of the prominent inflammatory process in the ipsilateral maxillary sinus (*small black M*). Note that, in this case, as is often seen, this is associated with hypoplasia of the ipsilateral maxillary sinus compared with its counterpart (*large white M*).

FIGURE 3-24 Uncinate bulla. Coronal CT image demonstrates an air cell within the right uncinate process (*asterisk*). The cell contributes to the narrowing of the right infundibulum and middle meatus.

VIEW IMAGE

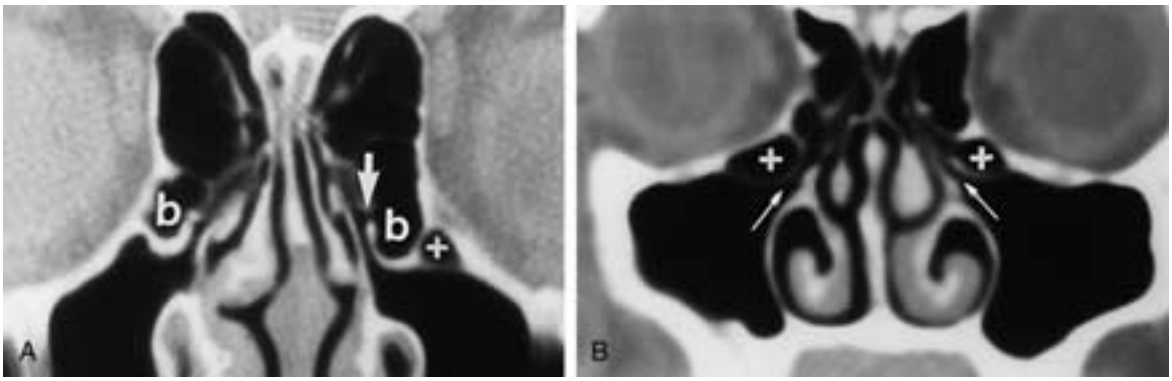

VIEW IMAGE

FIGURE 3-25 Haller (infraorbital ethmoid) cell. **A**, Note the left Haller (infraorbital ethmoid) cell (+) with the ethmoid bulla ostia located medially (*b*), opening into the infundibula (*arrow*). **B**, Bilateral Haller (infraorbital ethmoid) cells (+). Note their close proximity to the uncinate process and their influence on the infundibula (*small arrows*).

Copyright © 2003, Mosby, Inc. All rights reserved.

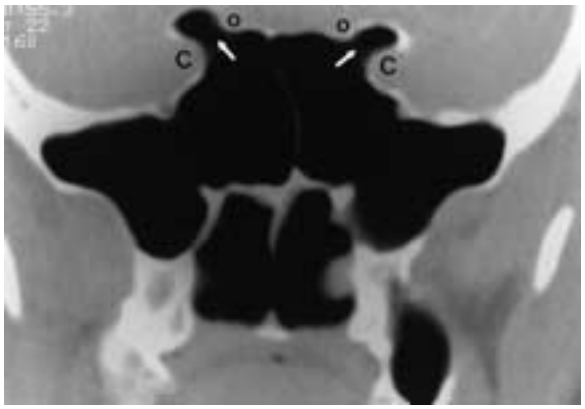

VIEW IMAGE

FIGURE 3-26 Extensive pneumatization of the sphenoid sinus. Coronal CT image shows pneumatization of both anterior clinoid processes (*arrows*) and their relationship to the optic nerves (*o*) and internal carotid arteries (*C*). The presence of anterior clinoid pneumatization is an important indicator of optic nerve vulnerability during FESS.

situation preoperatively, the orbital contents are placed at risk during surgery, as the surgeon will not know that there is a restricted ethmoid complex in which to operate (Fig. 3-27). Both excessive medial deviation and bony dehiscence of the lamina papyracea occur most often at the site of the insertion of the basal lamella into the lamina papyracea, thus rendering this portion of the lamina papyracea most delicate.

Aerated Crista Galli

When aeration of the normally bony crista galli occurs, the aerated cells may communicate with the frontal recess, and obstruction of this ostium can lead to chronic sinusitis and mucocele formation within the crista galli. To avoid unnecessary surgical extension into the anterior cranial vault, it is important to recognize an aerated crista galli and differentiate it from an ethmoid air cell prior to surgery.

Cephalocele

Cephaloceles involving the anterior cranial fossa floor may be congenital, occur spontaneously, or be the result of previous ethmoid or sphenoid sinus surgery. Preoperative coronal CT scanning is especially well suited to display the extent of any such areas of missing bone (Figs. 3-28, 3-29) (see also Chapters 1, 4, and 5).[62]

Posterior Nasal Septal Air Cell

Air cells are commonly found within the posterosuperior portion of the nasal septum and, when present, communicate with the sphenoid sinus. As a result, any inflammatory disease that occurs within the paranasal sinuses may also affect these cells (Fig. 3-30). Such disease may opacify this cell, causing it to resemble a cephalocele. CT and MR imaging usually define the involved pathology and resolve any differential diagnostic problems.

Asymmetry in Ethmoid Roof Height

It is important to note any asymmetry in the height of the ethmoid roof, as there is a higher incidence of intracranial penetration during FESS when this anatomic variation occurs. Intracranial penetration is more likely to occur on the side where the position of the roof is lower.[63]

Systematic Radiographic Evaluation

Routine Report

When interpreting sinus CT studies, it is helpful to use a systematic approach. In this regard, most radiologists progress from anterior to posterior when describing findings. As one reads the study, a mental checklist should be made of important structures for evaluation and comment. The reporting system normally includes three steps, which will now be described.

Step One

Identify and describe the important structures of the paranasal sinuses (there are 14 such structures). The dictated report should mention the status of these structures on both the right and left sides. The structures to identify are as follows:

- Frontal sinus
- Frontal recess
- Agger nasi cell and anterior ethmoid sinus
- Maxillary sinus
- Uncinate process
- Infundibulum
- Ethmoid roof
- Ethmoid bulla
- Basal lamella
- Sinus lateralis
- Posterior ethmoid sinus
- Sphenoid sinus
- Middle meatus
- Nasal septum and nasal turbinates

VIEW IMAGE

FIGURE 3-27 Medial deviation of the left lamina papyracea. Coronal CT images optimally demonstrate the outline of the lamina papyracea in relation to the anterior ostiomeatal channels. Medial deviation (*open arrow*), when present, should not be confused with an ethmoid bulla. Note that the medially deviated lamina papyracea lies in close proximity to the lateral attachment of the middle turbinate, the basal lamella (*white arrow*).

Copyright © 2003, Mosby, Inc. All rights reserved.

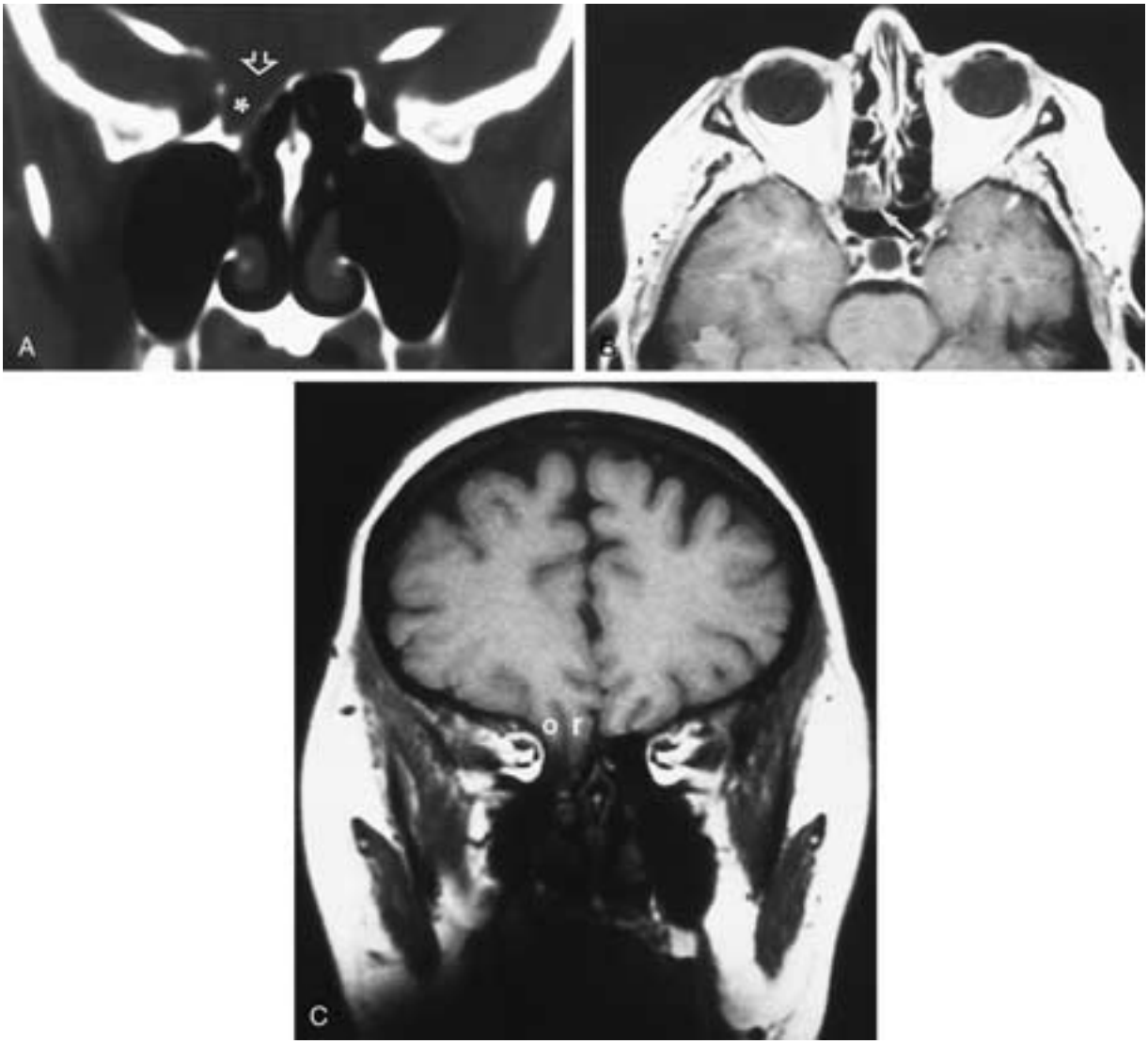

VIEW IMAGE

FIGURE 3-28 CT and MR imaging display of an encephalocele. Coronal CT image (**A**) through the posterior ethmoid sinus shows erosion of the roof of the posterior ethmoid sinus (*open arrow* and *asterisk*). Axial T1-weighted MR image (**B**) shows an isolated soft-tissue mass within the posterior ethmoid sinus (*arrow*), which on the coronal T1-weighted MR image (**C**) is confirmed to be an encephalocele. Gyrus rectus (*r*) and gyrus orbitales (*o*) are noted.

VIEW IMAGE

FIGURE 3-29 CT and MR imaging appearance of an encephalocele. **A**, Coronal CT image through the posterior ethmoid sinus shows a wide erosion of the ethmoid sinus roof (*open arrow*), with a soft-tissue mass penetrating into the ethmoid sinus (*asterisk*). Left (*L*), right (*R*). **B**, Sagittal T1-weighted sagittal MR image shows the outline of the brain tissue (*large arrows*), meninges, and cerebrospinal fluid (*small arrows*).

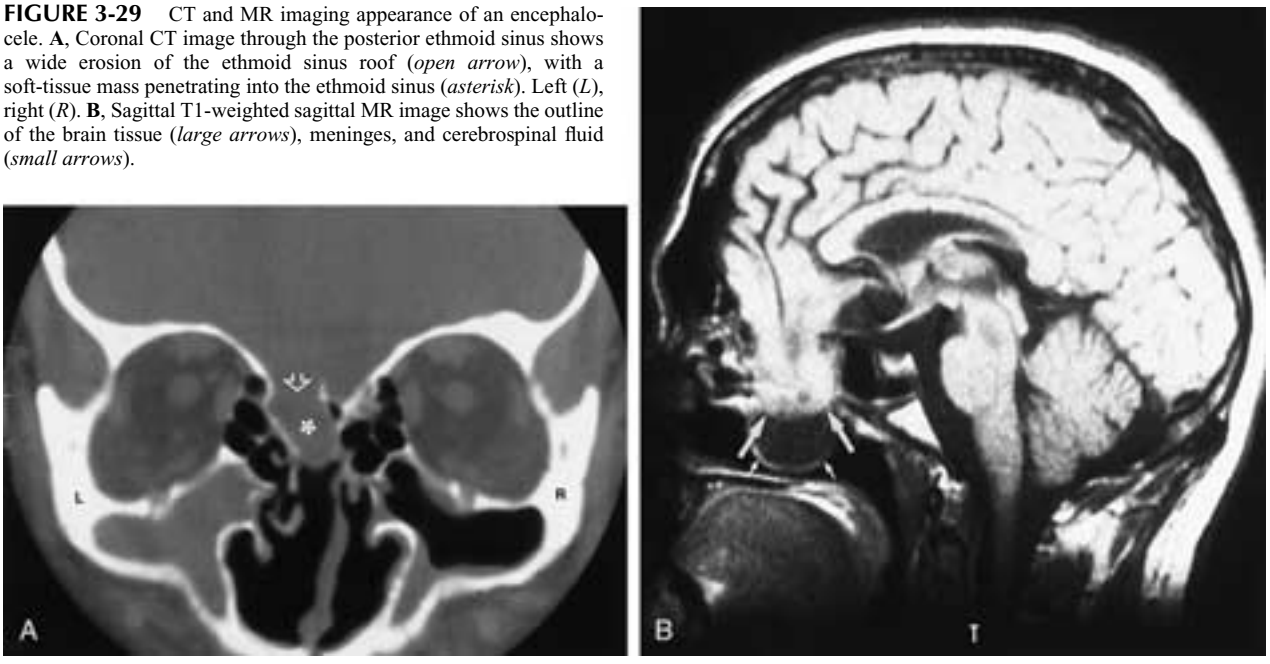

Copyright © 2003, Mosby, Inc. All rights reserved.

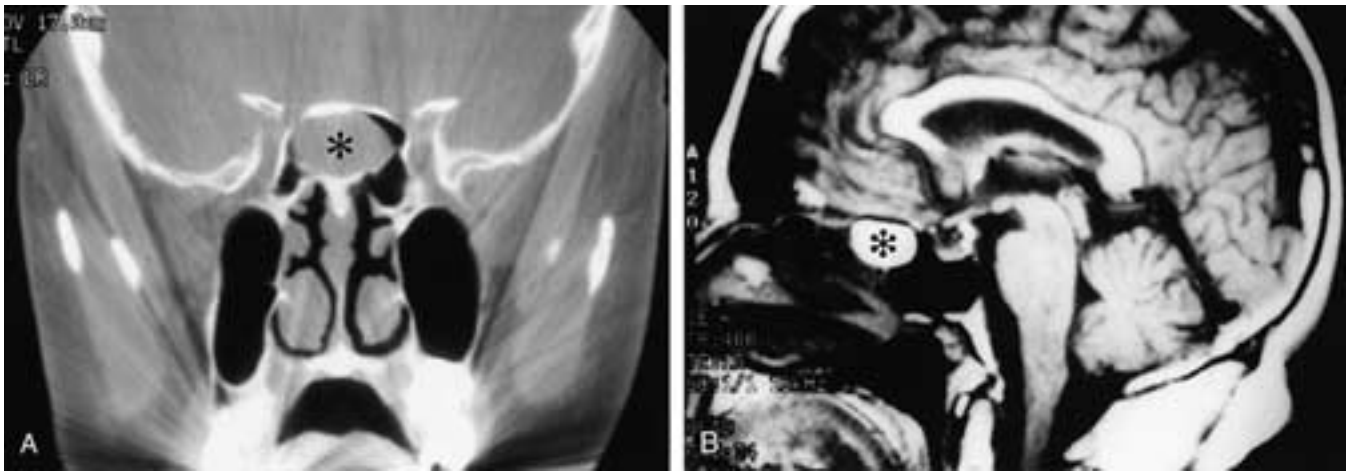

VIEW IMAGE

FIGURE 3-30 Nasal septal air cell. **A**, Coronal CT image demonstrates an expansile mass in the anterior sphenoid sinus (*asterisk*). **B**, Sagittal T1-weighted MR image displays the hyperintense inflammatory mass (*asterisk*), which is well separated from the intracranial compartment. This was proven to be a mucocele within a posterior nasal septal air cell.

Step Two

Evaluate the critical relationships. In addition to describing findings directly related to the diagnosis of inflammatory sinus disease, it is important for the radiologist to evaluate several critical areas that aid in surgical planning. The symmetry of the ethmoid roof should be noted. Careful attention should be paid to the status of the lamina papyracea, and any dehiscence or excessive medial deviation should be reported. The relationship of the sphenoid sinus and posterior ethmoid air cells with the internal carotid artery and optic nerves should be clearly mentioned. In particular, extensive expansion of the sinuses around the internal carotid artery or the optic nerve, as well as bony dehiscences adjacent to either structure, should be noted and reported to the referring surgeon (Fig. 3-31). The incidence of bony dehiscence around the presellar and juxtasellar portions of the internal carotid artery ranges from 12% to 22%.[61, 64, 65]

Frequently the carotid canal extends into the aerated portion of the sphenoid sinus, and in many such cases the sphenoid sinus septations adhere to the bony covering of the carotid canal. The surgeon must be made aware of this situation in order to prevent fracturing of the sphenoid sinus septum/carotid canal junction and puncturing of the carotid artery.

The relationship between the posterior paranasal sinuses and the optic nerves is crucial to note during the radiographic examination (Fig. 3-32). The optic nerves, carotid arteries, and vidian nerves develop prior to the paranasal sinuses, which accounts for their influence on congenital variations in the walls of the sphenoid sinus. Awareness of the intercommunication between the sphenoid sinus, posterior ethmoid cells, and optic nerves is paramount to avoid potentially devastating operative complications during FESS. Delano et al. described four discrete classifications of the various relationships that exist between the optic nerves and posterior paranasal sinuses.[61] Type 1 optic nerves include those that course immediately adjacent to the sphenoid sinus, without indentation of the wall or contact with the posterior ethmoid air cell. This is the most common type, occurring in 76% of patients. Type 2 nerves course adjacent to the sphenoid sinus, causing indentation of the sinus wall, without contact with the posterior ethmoid air cell. Type 3 nerves course through the sphenoid sinus, with at least 50% of the nerve surrounded by air. Type 4 nerves course immediately adjacent to the sphenoid sinus and posterior ethmoid sinus. The optic nerve is exposed without a complete bony margin in all cases where it travels through the sphenoid sinus (Type 3) and in 82% of cases where the nerve is impressed on the sphenoid sinus wall (Type 2).

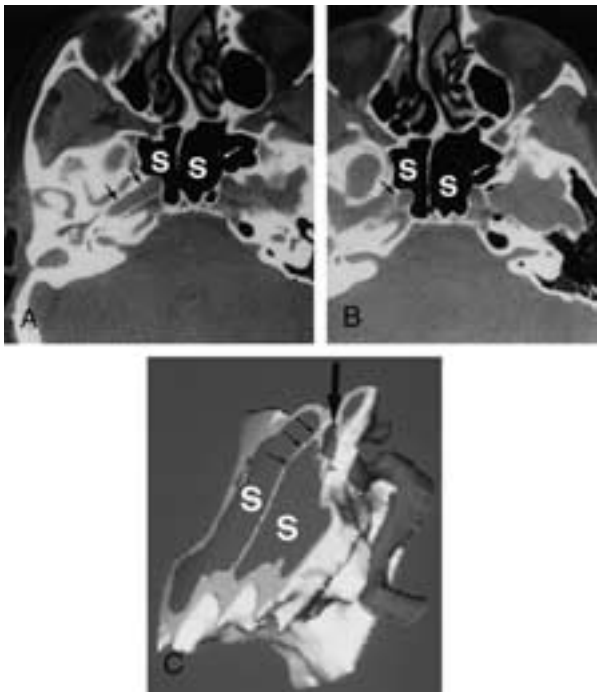

VIEW IMAGE

FIGURE 3-31 Relationship of the carotid canal to the sphenoid sinus. **A** and **B**, Axial CT images through the sphenoid and ethmoid sinuses show that the carotid canals (*small black arrows*) penetrate into the sphenoid sinus (*S*). An incomplete sphenoid sinus septum (*white arrow*) connects to the bony covering of the carotid canal. **C**, Three-dimensional images of the sphenoid sinus (*S*) and presellar and juxtasellar portions of the internal carotid artery (*black arrow*) graphically display the close relationship between the internal carotid artery and the sphenoid sinus septation (*small black arrows*).

Copyright © 2003, Mosby, Inc. All rights reserved.

VIEW IMAGE

FIGURE 3-32 Relationship of the optic nerves to the sphenoid sinus. Type 3 optic nerves (*black arrows*) course through the sphenoid sinus, with more than 50% of the nerves surrounded by air. Note that there is dehiscence of the bone covering the right optic nerve (*curved white arrow*). This increases the risk of optic nerve damage during FESS.

Delano et al. also found that 85% of optic nerves associated with a pneumatized anterior clinoid process were of the Type 2 or Type 3 configuration, and 77% were dehiscent. Therefore the presence of anterior clinoid pneumatization is an important indicator of optic nerve vulnerability during FESS because of the frequent association of this pneumatization with both bony dehiscence and Type 2 and 3 optic nerve configurations.[61]

Step Three

Lastly, but just as important as steps one and two, is the evaluation of the ''character'' of the bony framework of the nasal vault and paranasal sinuses. It has been noted that a prominent thickening of the bone about a paranasal sinus may occur, especially in patients who have had several surgical procedures and in patients with repeated exacerbations of chronic inflammation (Fig. 3-33). Similar changes have been noted in patients with Wegener's granulomatosis and in patients who suffer from a prolonged chronic inflammation and have had no previous surgery. Unfortunately, to date there is no good pathophysiologic explanation of this finding. However, it is believed that this change is directly related to the underlying inflammatory process and periosteal stimulation.

Bone may not be visualized on CT for several reasons. Bone may have been removed during a prior surgical procedure and, therefore, a defect is noted. Evidence of prior surgery should be sought on the CT examination and established through a proper medical history. Bone may not be seen because it is deossified secondary to chronic pressure from a mucocele or because the bone is invaded and destroyed by tumor. The associated mass will suggest the etiology, and MR imaging may afford a distinction between these two processes (see Chapter 6). Lastly, bony dehiscences may be developmental, and in the absence of prior surgery or associated pathology, this diagnostic possibility should be considered.

Radiographic Appearances of Inflammatory Sinus Disease

Acute Sinusitis

Acute sinusitis usually is due to bacterial infection of an obstructed paranasal sinus. The obstruction is often the result of apposition of edematous mucosal surfaces from an antecedent viral upper respiratory tract infection. The edematous mucosa disrupts the normal mucociliary drainage pattern of the sinus, and obstruction of the sinus ostium results. This, in turn, alters the oxygen tension within the obstructed sinus and predisposes the sinus to a bacterial superinfection.[24, 43, 66] Acute sinusitis usually involves only a single sinus, with the ethmoid sinus being the most common location.[57, 66] There is an increased risk of regional

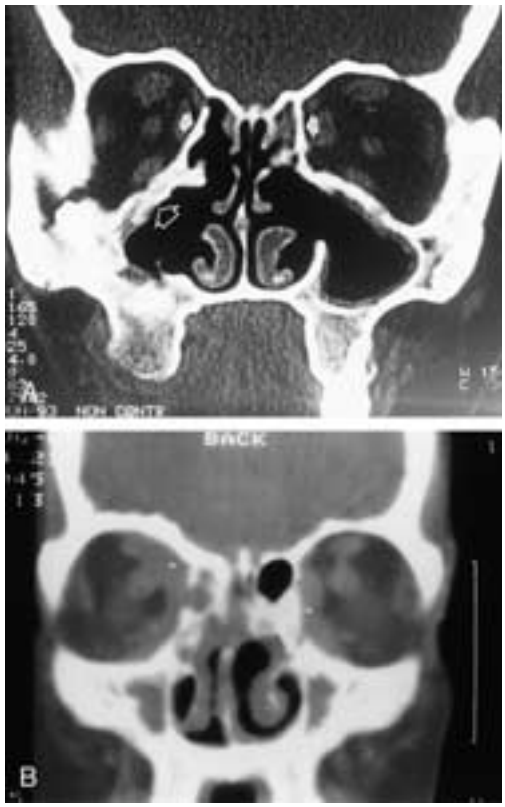

VIEW IMAGE

FIGURE 3-33 Osteitis of the paranasal sinus walls. **A**, Coronal CT image through the ethmoid sinus shows that the patient has had bilateral antrostomies, uncinectomies, and partial anterior ethmoidectomies. Note the pronounced thickening of the orbital floors bilaterally but more severely on the right side (*open arrow*). There is marked thickening of the lamina papyracea bilaterally (*solid arrows*). These changes are occasionally seen in patients who have undergone multiple surgical procedures in this area. **B**, Coronal CT image through the anterior ethmoid sinus in a patient with Wegener's granulomatosis. Note the diffuse, pronounced bony thickening of the perimeter of the maxillary sinuses and lamina papyracea, as well as the presence of soft-tissue masses (*asterisks*) within the orbits.

Copyright © 2003, Mosby, Inc. All rights reserved.

and intracranial complications, with involvement of the frontal, ethmoid, and sphenoid sinuses.[57] Acute sinusitis is rarely the result of a pure viral infection. A thorough discussion of sinusitis is presented in Chapter 5.

Chronic Sinusitis

Chronic sinusitis is diagnosed when the patient has repeated bouts of acute infection or persistent inflammation.[57, 66] Staphylococcus, streptococcus, corynebacteria, bacteroides, fusobacteria, and other anaerobes and anerobes are more commonly involved in chronic sinusitis than in acute sinusitis.[43, 57, 66] The radiographic findings are quite variable and are discussed in Chapter 5.[67] The sinuses most commonly involved with chronic sinusitis are the anterior ethmoid air cells.

Opacification of the OMU has been found to predispose patients to the development of sinusitis. Zinreich et al. found middle meatus opacification in 72% of patients with chronic sinusitis. In this study, 65% of these patients had mucoperiosteal thickening within the maxillary sinus, and all of the patients with frontal sinusitis had opacification of the frontoethmoidal recess.[6, 8, 9] Opacification of the OMU without frontal, maxillary, or anterior ethmoid sinus inflammatory disease was rare.[6, 8, 9] Yousem et al. found that when the middle meatus was opacified, there were associated inflammatory changes in the ethmoid sinuses in 82% of patients and in the maxillary sinuses in 84% of patients.[68] Bolger et al. found that when the ethmoid infundibulum was free of disease, the maxillary and frontal sinuses were clear in 77% of patients.[43]

Babbel et al. reviewed 500 patients with screening sinus CT scans and defined five recurring patterns of inflammatory sinonasal disease.[69] The five anatomic patterns were infundibular, OMU, sphenoethmoidal recess, sinonasal polyposis, and sporadic or unclassifiable. The infundibular pattern (26% of patients) referred to focal obstruction within the maxillary sinus ostium and ethmoid infundibulum, which was associated with maxillary sinus disease. The OMU pattern (25% of patients) referred to ipsilateral maxillary, frontal, and anterior ethmoid sinus disease (Fig. 3-34). This pattern was due to obstruction of the middle meatus. Sparing of the frontal sinus was sometimes seen as a result of the variable location of the nasofrontal duct insertion in the middle meatus. The sphenoethmoidal recess pattern (6% of patients) resulted in sphenoid or posterior ethmoid sinus inflammation caused by sphenoethmoidal recess obstruction. The sinonasal polyposis pattern (10% of patients) was due to diffuse nasal and paranasal sinus polyps. Associated radiographic findings included infundibular enlargement, convexity (bulging) of the ethmoid sinus walls, and thinning of the bony nasal septum and ethmoid trabeculae.[28, 69, 70]

Certain anatomic variants, as described above, have been implicated as causative factors in the presence of chronic inflammatory disease. Stammberger and Wolf and Lidov and Som found that a large concha bullosa produced signs and symptoms of sinusitis.[58, 71] However, Yousem et al. found that the presence of a concha bullosa did not increase the risk of sinusitis.[68] This was corroborated by Bolger et al., who found that the presence of a concha bullosa, paradoxic turbinates, Haller cells, and uncinate process pneumatization were not significantly more common in patients with chronic sinusitis than in asymptomatic patients.[43] Yousem et al. found that the presence of nasal septal deviation and a horizontally oriented uncinate process was more common in patients with inflammatory sinusitis.[68] Although the presence of these variants may not necessarily predispose to sinusitis, it appears that the size of a given anatomic variant and its relationship to adjacent structures plays an important role in the development of sinusitis.[37]

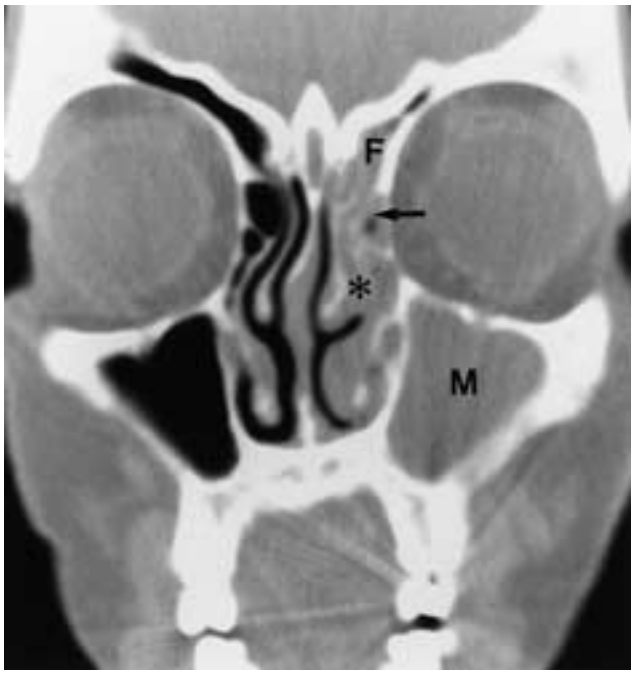

FIGURE 3-34 OMU pattern of sinusitis. Inflammatory changes obstruct the left middle meatus (*asterisk*), with resulting opacification of the left maxillary (*M*), frontal (*F*), and anterior ethmoid (*arrow*) sinuses.

VIEW IMAGE

Fungal Sinusitis

Fungal sinusitis may be suspected clinically when the patient fails to respond to standard antibiotic therapy.[37, 57, 68, 72, 73] According to Som and Curtin, two circumstances can be seen that suggest the presence of fungal infections: soft tissue changes in the sinus associated with thickened, reactive bone with localized areas of osteomyelitis, and the association of inflammatory sinus disease with involvement of the adjacent nasal fossa and the soft tissues of the cheek.[21, 22] These signs of aggressive infection are atypical of bacterial pathogens. This topic is described in detail in Chapter 5.

Allergic Sinusitis

Allergic sinusitis occurs in 10% of the population and typically produces a pansinusitis with symmetric involvement.[28, 69] CT often shows a nodular mucosal thickening with thickened turbinates; air-fluid levels are rare unless bacterial superinfection occurs.[28, 67] This topic is discussed in more detail in Chapter 5.

Orbital Complications of Sinusitis

About 3% of patients with sinusitis have some form of orbital involvement. These complications are more common in children than in adults, and the orbital manifestations may

Copyright © 2003, Mosby, Inc. All rights reserved.

be the initial clinical signs of sinus infection. Complicated sinusitis is the most common cause of orbital infection, accounting for 60% to 84% of cases.[38, 74–77] The origin of the infection most commonly is in the ethmoid sinuses. In decreasing order of frequency, the sources of the infection are the frontal, sphenoid, and maxillary sinuses. The ethmoid and maxillary sinuses are present at birth and therefore are the source in younger children. The topic of orbital infection is discussed in detail in Chapter 9.

COMMON FESS TECHNIQUES

For the surgical treatment of inflammatory sinonasal disease, FESS has largely replaced more traditional sinus surgery techniques. It is now believed that obstruction of the drainage portals of the sinuses, particularly the anterior ethmoids, is the primary cause of recurrent sinusitis. The rationale for FESS is that these techniques allow restoration of the flow of sinus secretions through their native drainage portals, allowing the inflamed sinus to return to a normal state, thus hopefully alleviating the patient's symptoms.[26, 78, 79]

Types of FESS

Panje and Anand have developed a classification system to standardize the type of FESS technique that is appropriate based on the preoperative extent of sinus disease as determined by CT imaging.[79] These authors outline the various types of FESS in the following manner:

Type I

Uncinatectomy with or without agger nasi cell exenteration.

Indications

1. Isolated OMU thickening of mucous membrane
2. Infundibular disease
3. Patent maxillary sinus ostia without maxillary sinus membrane thickening or cysts
4. Unsuccessful prior inferior maxillary sinus antrostomy or antrotomy with irrigation
5. Prior septoplasty or adenoidectomy with continued paranasal sinus symptoms

Type II

Uncinatectomy, bulla ethmoidectomy, removal of the sinus lateralis mucous membrane, and exposure of the frontal recess or frontal sinus.

Indications

1. OMU thickening of the mucous membrane
2. Evidence of anterior ethmoid sinus opacification, including obstruction of the infundibulum
3. Limited frontal recess disease
4. Unsuccessful prior inferior maxillary sinus antrostomy or antrotomy with irrigation
5. Prior septoplasty or adenoidectomy with continued paranasal sinus symptoms

Type III

Type II plus maxillary sinus antrostomy through the natural sinus ostium.

Indications

Same as for Type II, with the following:

1. Maxillary sinusitis, as evidenced by membrane thickening or sinus opacification
2. Stenotic or edematous maxillary sinus ostium

Type IV

Type III plus complete posterior ethmoidectomy.

Indications

Same as for Type III, with the following:

1. Total ethmoid involvement
2. Nasal polyposis with extensive ethmoidal and maxillary sinus disease
3. Prior Type I or Type II FESS without a response or with progression of sinus disease

Type V

Type IV plus sphenoidectomy and stripping of the mucous membrane.

Indications

Same as for Type IV, with the following:

1. Evidence of sphenoid sinusitis
2. Pansinusitis and rhinitis

In practice, Types II and III are the most commonly performed FESS techniques.

RADIOGRAPHIC EVALUATION OF PATIENTS FOLLOWING FUNCTIONAL ENDOSCOPIC SINUS SURGERY

Expected Findings

Evaluation of the postoperative patient is similar to that of the preoperative patient. Ideally, the CT scan should be performed in the coronal projection. Given the fact that a surgical procedure was performed, the type and extent of surgery must be established. Subsequently the emphasis is on the anatomy. The mental checklist should identify and mention the presence or absence of the 14 important structures discussed earlier in this chapter. A close look at the nasal cavity and paranasal sinus boundaries and the important relationships described previously should once again be observed and evaluated. Areas of bony thickening or dehiscence should be noted.

Areas that merit close scrutiny on follow-up (postoperative) CT scans are as follows:

1. *Frontal recess*. The frontal recess should be identified to determine its patency. Postoperatively, one often finds that recurrence of disease is due to persistent obstruction in this area. It is the narrowest channel within the anterior ethmoid complex, and it is a structure that is very difficult to access surgically. Therefore, the frontal recess is the area most likely to be affected by inflammatory disease in a patient with a previous paranasal sinus surgical procedure. To this

Copyright © 2003, Mosby, Inc. All rights reserved.

VIEW IMAGE

FIGURE 3-35 Anatomic landmarks to be evaluated in patients after FESS. **A**, Coronal CT image through the anterior ethmoid sinuses shows a prominent asymmetry in the position of the roof of the ethmoid sinuses (*solid arrowheads*). The intracranial penetrations (*fine black arrow*) are usually on the side where the roof is lower in position. **B**, Coronal CT image through the anterior ethmoid sinus in a patient after bilateral uncinatectomies and partial middle turbinectomies (*fine white arrows*). If there is an intraorbital complication during such a surgical procedure, it usually involves the lamina papyracea at the attachment of the basal lamella (*curved arrow*).

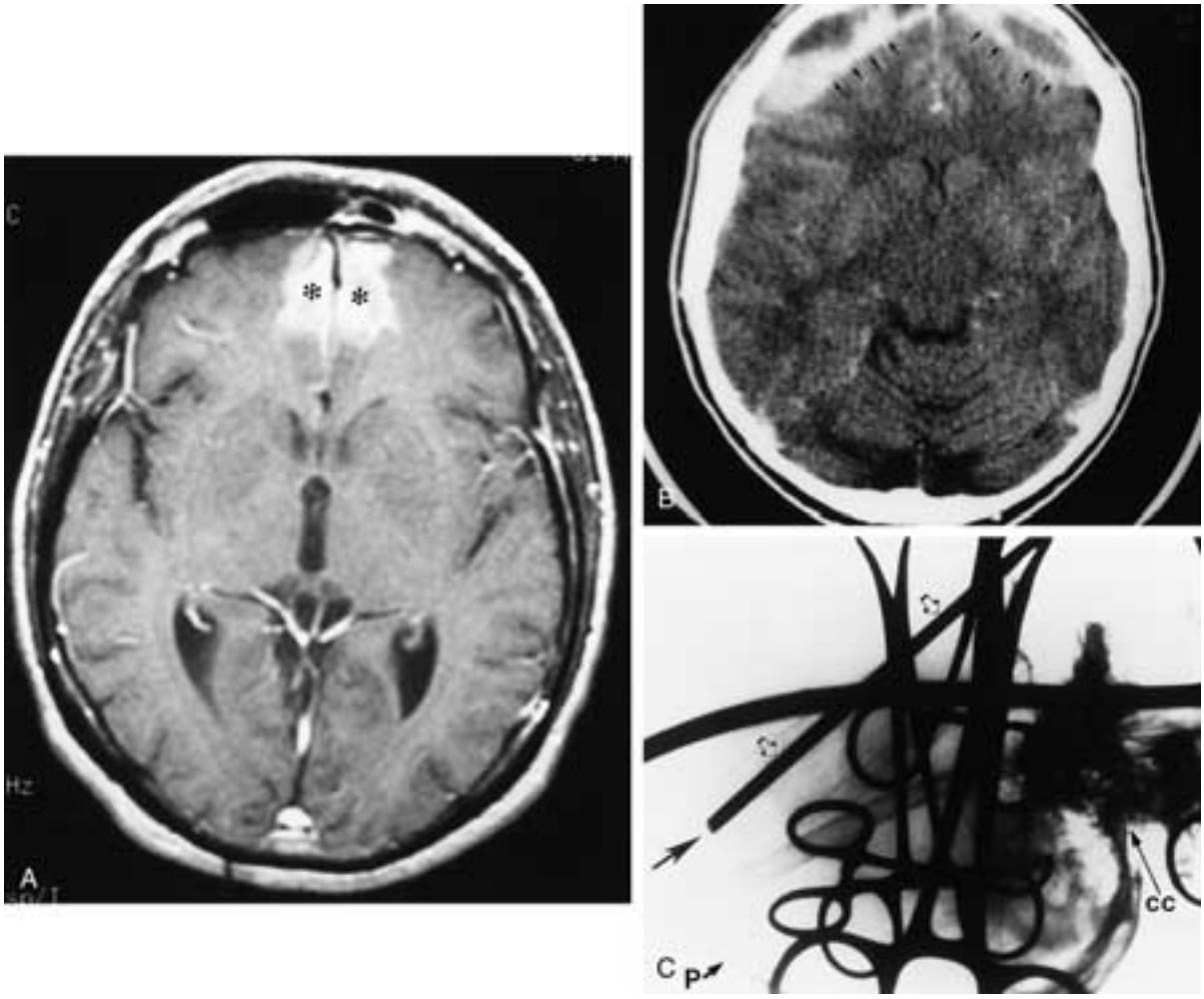

VIEW IMAGE

FIGURE 3-36 Intracranial complications from FESS. **A**, Axial T1-weighted MR image after gadolinium-DTPA administration shows abnormal bifrontal parenchymal enhancement (*asterisks*) caused by encephalitis from perforation through the cribriform plate. **B**, Axial CT image shows bilateral acute subdural hematomas (*arrows*) after FESS. **C**, Intraoperative cross-table lateral skull radiograph shows the intracranial extension of an endoscope (*open arrows*). Note the position of the endoscope in the deep portion of the posterior frontal lobe (*solid black arrow*). Overlying surgical instruments are noted. Craniocervical junction (*CC*) and parietal bone (*P*).

Copyright © 2003, Mosby, Inc. All rights reserved.

end, note should be made of the agger nasi cell (if it remains), because its persistence may continue to narrow the frontal recess.

2. *OMU*. Note should be made of the extent of the uncinatectomy and removal of the ethmoid bulla. The course of the infundibulum should be examined for persistent anatomic narrowing. The outline of the middle turbinate should be examined to determine whether a middle turbinectomy has been performed. If so, then careful attention should be paid to both the vertical attachment of the middle turbinate to the cribriform plate and the attachment of the basal lamella to the lamina papyracea. Traction applied on the vertical attachment and basal lamella of the middle turbinate during the course of a middle turbinectomy can cause a fracture of the lamina papyracea or the cribriform plate. These breaks in the continuity of the lamina papyracea and ethmoid roof are easily demonstrated on coronal images (Figs. 3-35, 3-36).
3. *Lamina papyracea*. Inspection of the entire course of the lamina papyracea should be carried out to evaluate the integrity of this structure. Postoperative dehiscences are commonly found just posterior to the nasolacrimal duct, and these may be caused by the uncinate resection (Figs. 3-13, 3-35).
4. *Ethmoid roof*. Asymmetry in the position of the roof (fovea ethmoidalis) of the ethmoid sinuses should be noted. Intracranial penetrations usually occur on the side where the position of the roof is lower. One should examine for a break in the continuity of this roof (Fig. 3-35).[63]
5. *Sphenoid sinus area*. The margins of the sphenoid sinus should be evaluated for bony dehiscence or cephalocele.

Operative Complications

The topic of operative complications is discussed in Chapter 4.

REFERENCES

1. Moss A, Parsons V. Current estimates from the National Health Interview Survey, United States, 1985. Hyattsville, Md: National Center for Health Statistics, 1986.
2. Messerklinger W. Endoscopy of the nose. Baltimore: Urban & Schwartzenberg, 1978.
3. Messerklinger W. Zur Endoskopietchnik des mittleren Nassenganges. Arch Otorhinolaryngol 1978;221:297–305.
4. Wigand ME, Steiner W, Jaumann MP. Endonasal sinus surgery with endoscopic control: from radical operation to rehabilitation of the mucosa. Endoscopy 1978;10:255–260.
5. Kennedy DW, Zinreich SJ, Rosenbaum AE, et al. Functional endoscopic surgery: theory and diagnostic evaluation. Arch Otolaryngol 1985;111:576–582.
6. Zinreich S, Kennedy D, Rosenbaum A, et al. Paranasal sinuses: CT imaging requirements for endoscopic surgery. Radiology 1987;163: 769–775.
7. Som P. Sinonasal cavity. In: Som P, Bergeron T, eds. Head and Neck Imaging. St. Louis, Mosby-Year Book, 1991;51–168.
8. Zinreich S. Paranasal sinus imaging. Otolaryngol Head Neck Surg 1990;103:863–868.
9. Zinreich S. Imaging of chronic sinusitis in adults: x-ray, computed tomography, and magnetic resonance imaging. J Allergy Clin Immunol 1992;90:445–451.
10. Zinreich S. Imaging of inflammatory sinus disease. Otolaryngol Clin North Am 1993;26:535–547.
11. Zinreich S, Abidin M, Kennedy D. Cross-sectional imaging of the nasal cavity and paranasal sinuses. Operative Techniques Otolaryngol Head Neck Surg 1990;1:93–99.
12. Babbel R, Harnsberger HR, Nelson B, et al. Optimatization of techniques in screening CT of the sinuses. Am J Roentgenol 1991;157:1093–1098.
13. Bernhardt TM, Rapp-Bernhardt U, Fessel A, Ludwig K, et al. CT scanning of the paranasal sinuses: axial helical CT with reconstruction in the coronal direction versus coronal helical CT. Br J Radiol 1998;71:846–851.
14. Melhem ER, Oliverio PJ, Benson ML, et al. Optimal CT screening for functional endoscopic sinus surgery. Am J Neuroradiol 1996;17: 181–188.
15. Beck, DSc T. Radiation Physicist, Dept. of Radiology, The Johns Hopkins Hospital, Baltimore. Personal communication.
16. Curry TS, Dowdey JE, Murry RC. Christensen's Physics of Diagnostic Radiology. 4th ed. Philadelphia: Lea & Febiger, 1990;372–391.
17. Jones DJ, Wall BF. Organ doses from medical x-ray examinations calculated using Monte Carlo techniques. NRPBR186. London: National Radiological Protection Board, 1985.
18. Zinreich SJ, Kennedy DW, Kumar A, et al. MR imaging of normal nasal cycle: comparison with sinus pathology. J Comput Assist Tomogr 1988;12:1014–1019.
19. Kennedy D, Zinreich S, Kumar A, et al. Physiologic mucosal changes within the nose and ethmoid sinus: imaging of the nasal cycle by MRI. Laryngoscope 1988;98:928–933.
20. Zinreich S, Kennedy D, Malat J, et al. Fungal sinusitis: diagnosis with CT and MR imaging. Radiology 1988;169:439–444.
21. Som P, Curtin H. Chronic inflammatory sinonasal diseases including fungal infections: the role of imaging. Radiol Clin North Am 1993;31:33–44.
22. Som P. Imaging of paranasal sinus fungal disease. Otolaryngol Clin North Am 1993;26:983–994.
23. Som P, Dillon W, Curtin H, et al. Hypointense paranasal sinus foci: differential diagnosis with MR imaging and relation to CT findings. Radiology 1990;176:777–781.
24. Weber A. Inflammatory diseases of the paranasal sinuses and mucoceles. Otolaryngol Clin North Am 1988;21:421–437.
25. Shankar L, Evans K, Hawke M, et al. An Atlas of Imaging of the Paranasal Sinuses. London: Martin Dunitz 1994;41–72.
26. Stammberger H. Functional Sinus Surgery. Philadelphia: B.C. Decker, 1991;273–282.
27. Kennedy DW, Zinreich SJ. The functional endoscopic approach to inflammatory sinus disease: current perspectives and technique modifications. Am J Rhinol 1988;2:89–93.
28. Harnsberger R. Imaging for the sinus and nose. In: Harnsberger R, ed. Head and Neck Imaging Handbook. St. Louis: Mosby-Year Book, 1990;387–419.
29. Hosemann W. Dissection of the lateral nasal wall in eight steps. In: Wigand ME, ed. Endoscopic Surgery of the Paranasal Sinuses and Anterior Skull Base. New York: Thieme Medical, 1990;36–41.
30. Schaeffer JP. The Nose, Paranasal Sinuses, Naso-lacrimal Passageways, and Olfactory Organs in Man. Philadelphia: P. Blakiston's Son & Co., 1920.
31. Schaeffer JP. The genesis, development, and adult anatomy of the nasofrontal region in man. Am J Anat 1916;20:125–146.
32. Van Alyea OE. Ethmoid labyrinth: anatomic study, with consideration of the clinical significance of its structural characteristics. Arch Otolaryngol 1939;29:881–902.
33. Van Alyea OE. Frontal cells: an anatomic study of these cells with consideration of their clinical significance. Arch Otolaryngol 1941;34: 11–23.
34. Van Alyea OE. Sphenoid sinus: anatomic study, with consideration of the clinical significance of the structural characteristics of the sphenoid sinus. Arch Otolaryngol 1941;34:225–253.
35. Bent JP, Cuilty-Siller C, Kuhn FA. The frontal cell as a cause of frontal sinus obstruction. Am J Rhinol 1994;8:185–191.
36. Stammberger HR, Kennedy DW, Bolger WE, et al. Paranasal sinuses: anatomic terminology and nomenclature. The Anatomic Terminology Group. Ann Otol Rhinol Laryngol Suppl 1995;167:7–16.

Copyright © 2003, Mosby, Inc. All rights reserved.

37. Yousem D. Imaging of sinonasal inflammatory disease. Radiology 1993;188:303–314.
38. Buus D, Tse D, Farris B. Ophthalmic complications of sinus surgery. Ophthalmology 1990;97:612–619.
39. Hudgins P. Complications of endoscopic sinus surgery: the role of the radiologist in prevention. Radiol Clin North Am 1993;31:21–31.
40. Hudgins P, Browning D, Gallups J. Endoscopic paranasal sinus surgery: radiographic evaluation of severe complications. Am J Neuroradiol 1992;13:1161–1167.
41. Maniglia A. Fatal and major complications secondary to nasal and sinus surgery. Laryngoscope 1989;99:276–283.
42. Maniglia A. Fatal and other major complications of endoscopic sinus surgery. Laryngoscope 1991;101:349–354.
43. Bolger W, Butzin C, Parsons D. Paranasal sinus bony anatomic variations and mucosal abnormalities: CT analysis for endoscopic sinus surgery. Laryngoscope 1991;101:56–64.
44. Lloyd GAS. CT of the paranasal sinuses: study of a control series in relation to endoscopic sinus surgery. J Laryngol Otol 1990;104: 477–481.
45. Messerklinger W. On the drainage of the normal frontal sinus of man. Acta Otolaryngol 1967;163:176–181.
46. Lebowitz RA, Brunner E, Jacobs JB. The agger nasi cell: radiological evaluation and endoscopic maagement in chronic frontal sinusitis. Operative Techniques Otolaryngol Head Neck Surg 1995;6:171–175.
47. Scribano E, Ascenti G, Loria G, et al. The role of the ostiomeatal unit anatomic variations in inflammatory disease of the maxillary sinuses. Eur J Radiol 1997;24:172–174.
48. Wanamaker HH. Role of Haller's cell in headache and sinus disease: a case report. Otolaryngol Head Neck Surg 1996;114:324–327.
49. Driben JS, Bolger WE, Robles HA, et al. The reliability of computerized tomographic detection of the Onodi (sphenoethmoid) cell. Am J Rhinol 1998;12:105–111.
50. Tonai A, Baba S. Anatomic variations of the bone in sinonasal CT. Acta Otolaryngol 1996;Suppl 525:9–13.
51. Joe JK, Ho SY, Yanagisawa E. Documentation of variations in sinonasal anatomy by intraoperative nasal endoscopy. Laryngoscope 2000;110:223–229.
52. Weinberger DG, Anand VK, Al-Rawi M, et al. Surgical anatomy and variations of the onodi cell. Am J Rhinol 1996;10:365–370.
53. Perez-Pinas I, Sabate J, Carmona A, et al. Anatomical variations in the human paranasal sinus regions studied by CT. J Anat 2000;197: 221–227.
54. Calhoun KH, Waggenspack GA, Simpson CB, et al. CT evaluation of the paranasal sinuses in symptomatic and asymptomatic populations. Otolaryngol Head Neck Surg 1991;104:480–483.
55. Lloyd GA, Lund VJ, Scadding GK. CT of the paranasal sinuses and functional endoscopic surgery: a critical analysis of 100 symptomatic patients. Laryngol Otol 1991;105:181–185.
56. Zinreich SJ, Mattox DE, Kennedy DW, et al. Concha bullosa: a CT evaluation. J Comput Assist Tomogr 1988;12:778–784.
57. Laine F, Smoker W. The ostiomeatal unit and endoscopic surgery: anatomy, variations, and imaging findings in inflammatory diseases. Am J Roentgenol 1992;159:849–857.
58. Stammberger H, Wolf G. Headaches and sinus disease: the endoscopic approach. Ann Otol Rhinol Laryngol Suppl 1988;134:323.
59. Kainz J, Stammberger H. Danger areas of the posterior rhinobasis. An endoscopic and anatomical-surgical study. Acta Otolaryngol 1992; 112:852–861.
60. Yeoh KH, Tan KK.The optic nerve in the posterior ethmoid in Asians. Acta Otolaryngol 1994;114:329–336.
61. Delano M, Fun FY, Zinreich SJ. Optic nerve relationship to the posterior paranasal sinuses: a CT anatomic study. Am J Neuroradiol 1996;17:669–675.
62. Laine FJ, Kuta AJ. Imaging the sphenoid bone and basiocciput: pathologic considerations. Semin Ultrasound CT MRI 1993;14: 160–177.
63. Dessi P, Moulin G, Triglia JM, et al. Difference in height of the right and left ethmoidal roofs: a possible risk factor for ethmoidal surgery: prospective study of 150 CT scans. Laryngol Otol 1994;108:261–262.
64. Johnson DW, Hopkins RJ, Hanafee WN, et al. The unprotected parasphenoidal carotid artery studied by high-resolution computed tomography. Radiology 1985;155:137–141.
65. Kennedy DW, Zinreich SJ, Hassab MH. The internal carotid artery as it related to endonasal sphenoethmoidectomy. Am J Roentgenol 1990;4:7–12.
66. Evans F, Sydnor J, Moore W, et al. Sinusitis of the maxillary antrum. N Engl J Med 1975;293:735–739.
67. Gullane P, Conley J. Carcinoma of the maxillary sinus: a correlation of the clinical course with orbital involvement, pterygoid erosion or pterygopalatine invasion and cervical metastases. J Otolaryngol 1983;12:141–145.
68. Yousem D, Kennedy D, Rosenberg S. Ostiomeatal complex risk factors for sinusitis: CT evaluation. J Otolaryngol 1991;20:419–424.
69. Babbel R, Harnsberger H, Sonkens J, et al. Recurring patterns of inflammatory sinonasal disease demonstrated on screening sinus CT. Am J Neuroradiol 1992;13:903–912.
70. Scuderi A, Babbel R, Harnsberger H, et al. The sporadic pattern of inflammatory sinonasal disease including postsurgical changes. Semin Ultrasound CT MR 1991;12:575–591.
71. Lidov M, Som P. Inflammatory disease involving a concha bullosa (enlarged pneumatized middle nasal turbinate): MR and CT appearance. Am J Neuroradiol 1990;11:999–1001.
72. Moloney J, Badham N, McRae A. The acute orbit, preseptal, periorbital cellulitis, subperiosteal abscess, and orbital cellulitis due to sinusitis. J Laryngol Otol 1987;12:1–18.
73. Centeno R, Bentson J, Mancuso A. CT scanning in rhinocerebral mucormycosis and aspergillosis. Radiology 1981;140:383–389.
74. Osguthorpe J, Hochman M. Inflammatory sinus diseases affecting the orbit. Otolaryngol Clin North Am 1993;26:657–671.
75. Walters E, Waller P, Hiles D, et al. Acute orbital cellulitis. Arch Ophthalmol 1976;94:785–788.
76. Weber A, Mikulis D. Inflammatory disorders of the paraorbital sinuses and their complications. Radiol Clin North Am 1987;25:615–631.
77. Patt B, Manning S. Blindness resulting from orbital complications of sinusitis. Otolaryngol Head Neck Surg 1991;104:789–795.
78. Vinning EM, Kennedy DW. Surgical management in adults: chronic sinusitis. Immunol Allergy Clin North Am 1994;14:97–112.
79. Panje WR, Anand VK. Endoscopic sinus surgery indications, diagnosis, and technique. In: Anand VK, Panje WR, eds. Practical Endoscopic Sinus Surgery. New York: McGraw-Hill, 1993;68–86.

Copyright © 2003, Mosby, Inc. All rights reserved.

4

Postoperative Complications of Functional Endoscopic Sinus Surgery

Patricia A. Hudgins and Todd T. Kingdom

SURGICAL COMPLICATIONS
- Major and Minor
  - Hemorrhage and Vascular Injury
  - Skull Base Injury, Including CSF Leak
  - Orbital Complications

ENDOSCOPIC SINUS SURGERY
- Theory and Treatment Options
- FESS Outcomes
- The FESS Procedure and Imaging Findings
  - Overview of the FESS Procedure
  - Postoperative Findings: Expected and Complications

SURGICAL COMPLICATIONS

Major and Minor

The paranasal sinuses are flanked on all sides by important structures. Thus, only the delicate lamina papyracea separates the ethmoid complex from the orbit, the roof of the ethmoids (fovea ethmoidalis) separates these cells from the anterior cranial fossa, the fenestrated cribriform plate separates the roof of the nasal cavity from the anterior cranial fossa, a thin bony carotid canal may separate the cavernous internal carotid artery from the mucosa of the sphenoid sinus, and the optic canal may be surrounded by the sphenoid sinus when there is a pneumatized anterior clinoid process. In addition, glistening, moist, diseased mucosa may look identical to periorbita or even dehiscent, inflamed meninges. As a result of this compact anatomy, when performing functional endoscopic sinus surgery (FESS), it is the endoscopist's experience and anatomic knowledge of the many potential structural variations that may occur in this region that help avoid surgical catastrophes.[1–3]

Preoperative sinus computed tomography (CT) is essential to understand the individual's anatomy and thereby avoid intraoperative complications. However, ultimately, most surgical complications from the endoscopic approach are probably sporadic and are not specifically the result of variant anatomy. Nonetheless, the standard of care is that anatomic variants believed to predispose to surgical complications should be mentioned by the radiologist in the preoperative CT interpretation (see Chapter 3).[4]

Surgical complications can be divided into major and minor events. Complications that require further surgical intervention, or blood transfusion, or that result in a new patient deficit or death, are considered major and include cerebrospinal fluid (CSF) leak, optic nerve injury, ocular motility deficits, injury to the nasolacrimal duct, permanent anosmia, and major intraoperative or perioperative hemorrhage. The incidence of major complications ranges from 0.5% to 9% and the complication rate increases with an inexperienced surgeon, severity of disease (extensive polyposis can hinder the surgeon's visibility), the extensive nature of the surgery, prior FESS, and unusual anatomic variants.[5–9]

Minor complications include periorbital swelling or orbital emphysema, small orbital hematomas, temporary olfactory dysfunction, bleeding that does not require reoperation or blood transfusion (minor epistaxis), and tooth pain. Synechiae and scar formation associated with recurrent symptoms following surgery are reported to occur in 4% to 8% of cases. Usually, the synechiae develop between the lateral nasal wall and the lateral aspect of the middle turbinate, in which case there will be a lateral deviation of the nasal septum. Formation of synechiae in this area can cause middle meatal stenosis and inadequate sinus drainage. Synechiae may also occur between the inferior turbinate and the nasal septum or within the frontal recess.

Approximately 18% of patients reportedly develop recurrent inflammatory disease after a FESS procedure. Although this is not considered a true complication, such recurrent disease is usually mentioned along with the other complications of FESS. The recurrent inflammatory disease

Copyright © 2003, Mosby, Inc. All rights reserved.

may be present because sinusitis is a complex disease that cannot be completely cured by surgery or because the recurrent disease reflects incomplete FESS that did not fully address the ostiomeatal obstruction. Failed FESS is probably underreported, and its exact incidence is not known.

Hemorrhage and Vascular Injury

Hemorrhage requiring transfusion or postoperative packing is a major complication and fortunately is unusual. Extensive disease, especially polyposis, prior FESS, and chronic steroid or aspirin use are risk factors for significant hemorrhage. Bleeding from the internal maxillary artery branches is likely if the turbinates or nasal septum are involved, and injury to the sphenopalatine, anterior, and posterior ethmoidal arteries is the most common reason for hemorrhage.[1]

Posterior bleeding may result from injury to the sphenopalatine artery at the anterior wall of the sphenoid sinus.[10] Injury to the internal carotid artery (ICA) is the most devastating and, fortunately, the rarest complication.[7, 8, 11] (Fig. 4-1). The ICA is vulnerable when surgery is performed in or around the posterior ethmoid air cells and the sphenoid sinus, as absence of the bony carotid wall in the posterior ethmoid or sphenoid sinus is not uncommon. An autopsy series found 71% of ICAs bulging into the sphenoid sinus, with bone only microns in thickness protecting the carotid artery in many cases.[12] In a large CT series, 31.4% of patients had at least one ICA at risk, with extremely thin, bony wall seen on CT about the ICA in 17% of patients and no bony covering found in 14.4%.[13] On the traditional CT window settings used for preoperative sinus imaging, and without intravenous contrast, at times only an estimate of the ICA location can be made. When there is extensive superolateral pneumatization of the posterior ethmoid cell, termed the *Onodi cell*, the ICA and optic nerve may bulge into the pneumatized cell. Pneumatization of the anterior clinoids should be noted, as both the optic nerve and the ICA are theoretically placed at risk. Finally, intrasphenoidal bony sinus septums that insert on or near the carotid canal should be described in the radiology report. Although these septums are variable, they usually arise from the posterior or posterolateral sphenoid sinus wall and are attached at the level of the ICA. If there is a surgical attempt to resect such a septum, the twisting and applied torque may fracture the bone at the level of the ICA and inadvertently injure the vessel.[4] In summary, the ICA is vulnerable during FESS at the lateral wall of the sphenoid sinus if there is a bony septum abutting the lateral wall near the ICA canal, if Onodi cells are present, and if there is a pneumatized anterior clinoid process.

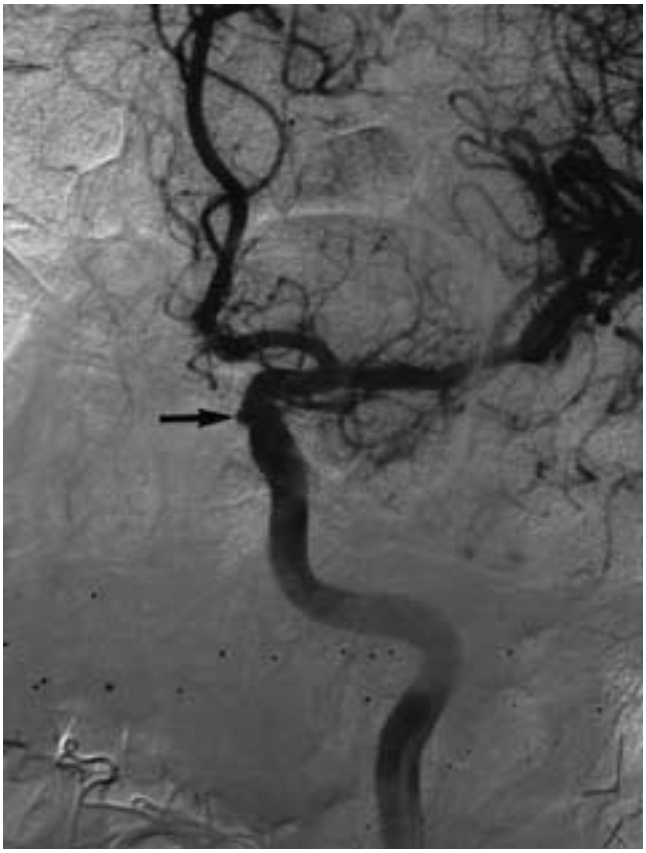

VIEW IMAGE

FIGURE 4-1 Intraoperative hemorrhage during posterior ethmoidectomy. Conventional angiogram, lateral view of a left ICA injection, obtained several hours after massive intraoperative hemorrhage, shows a small pseudoaneurysm (*arrow*) of the left ICA. The patient underwent a test balloon occlusion, developed no neurologic deficits, and had permanent balloon occlusion.

If intraoperative bleeding cannot be stopped with packing, immediate diagnostic conventional angiography is indicated. Perforation or pseudoaneurysm of the cavernous ICA can be assessed on diagnostic angiography, followed by transvascular treatment by the interventional neuroradiologist with endovascular balloon occlusion or coiling of the injured ICA. Temporary balloon occlusion is usually performed initially to determine whether there is an intact circle of Willis that will permit the patient to tolerate sacrifice of the ICA.

Skull Base Injury, Including CSF Leak

Anterior skull base injury results in pneumocephalus, subdural hematoma, intracranial hemorrhage or contusion, cerebritis, or an abcess. There also may be focal encephalomalacia of the gyrus rectus when there has been perforation of the cribriform plate. Factors associated with such injury include dehiscence of the cribriform plate, ethmoid roof, or sphenoid roof (Fig. 4-2). CSF fistula occurs rarely in FESS, but FESS is one of the most common causes of CSF leak.[14] Subsequent development of meningitis or intracranial abscess is unusual, as the defect is generally detected intraoperatively by the surgeon and repaired immediately.[14, 15]

The roof of the ethmoid air cells may be unusually low on one side, potentially placing this ethmoid complex at risk for inadvertent surgical penetration of the anterior cranial fossa. Any asymmetry (especially if marked) in the height of the ethmoid roof on either side should also be noted in the radiology report. Any thinning or dehiscence of the ethmoid roof, cribriform plates, or roof of the sphenoid sinus (whether posttraumatic, congenital, or from prior surgery) is important preoperative information for the surgeon. Therefore, the position, symmetry, and integrity of the roof of the ethmoids, cribriform plate, and planum sphenoidale are always assessed by the radiologist prior to FESS to help avoid a surgical complication (also see Chapter 3). This is

Copyright © 2003, Mosby, Inc. All rights reserved.

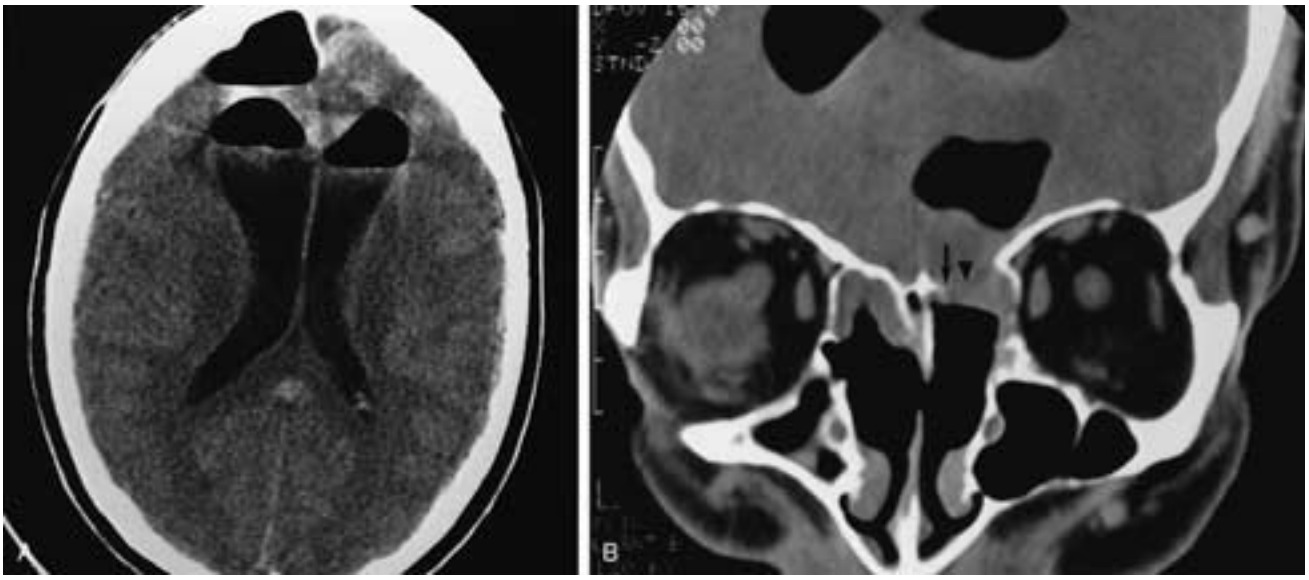

VIEW IMAGE

FIGURE 4-2 Anterior skull base defect with pneumocephalus. The patient presented with headaches immediately following FESS. A CT scan was obtained several days after FESS, revealing pneumocephalus and an anterior skull base defect. **A**, Axial CT scan shows massive intracranial air, including intraventricular air. This implies that the surgical instruments went through the bony anterior skull base. **B**, Direct coronal CT scan shows resection of the entire left middle turbinate, cribriform plate (*arrow*), and roof of the ethmoids (*arrowhead*).

especially important for revision FESS, as previous FESS remains the single most important risk factor for iatrogenic CSF leak.[14]

The anterior vertical insertion of the middle turbinate lies along the lateral edge of the cribriform plate. It is an important surgical landmark, as medial to it is the cribriform plate and lateral lies the roof of the ethmoids. The anterior ethmoid artery (AEA) enters the olfactory fossa at this location, making the lateral cribriform plate, or lateral lamella of the olfactory groove, the thinnest portion and the area most ''exposed'' to perforation.[2] Thus, during FESS, the endoscope must remain lateral to the vertical insertion of the middle turbinate. The olfactory nerve fibers pass through the cribriform plate, and surgical injury to the olfactory mucosa or torque applied to the middle turbinate may injure these fibers as well as create a CSF leak.[3] If the entire vertical insertion of the middle turbinate has been partially or completely resected during prior surgery, it should be noted that an important surgical landmark is missing. Disturbance of olfactory function occurs in about 20% of the patients who have a CSF leak or an anterior skull base defect as a result of FESS.[16]

The posterior ethmoid roof at the border between the posterior ethmoids and sphenoid sinus is an underrecognized location of CSF leak.[1] This area should be scrutinized by the radiologist, especially prior to revision FESS. The posterior ethmoid roof is especially vulnerable to injury because it may be inadvertently misinterpreted during FESS as the anterior aspect of the sphenoid sinus.

When postoperative CSF rhinorrhea is suspected, the nasal secretions should be tested to confirm that CSF is present. Although the glucose-oxidase test was formerly used for this purpose, its high incidence of false-positive results led to the use of the β2-transferrin test. This test is highly sensitive and capable of detecting CSF in only a few millimeters of nasal secretions. If the β2-transferrin test is positive, imaging examinations are indicated.[15, 16]

For the diagnosis and localization of CSF leak following FESS, the literature does not express a definitive bias toward the use of either MR cisternography, high-resolution CT, or CT cisternography. Each has distinct advantages and disadvantages. MR and CT cisternography can identify the actual site of CSF leakage within the nasal cavity or paranasal sinuses, provided that there is an active CSF leak. The MR study, however, does not provide adequate bony detail. Plain high-resolution CT does provide a detailed display of the bone at the site of the leak; however, it does not show the flow of CSF into the sinus. In difficult cases, it is recommended that both techniques be utilized for accurate diagnosis or that a CT cisternogram study be performed. However, since the radiation dose that results from high-resolution CT is significant, MR cisternography is usually the first technique employed. The reported sensitivity of MR cisternography in the diagnosis of CSF fistulae ranges from 87% to 100%. If this examination does not provide adequate information, then high-resolution CT may be utilized. The sensitivity of high-resolution CT reportedly ranges from 71% to 92%. However, in some cases these results may be misleading, as congenital or other bony abnormalities seen may not be associated with the CSF leak.

In many institutions, a radionuclide CSF study is utilized as the initial radiologic screening examination for patients with suspected CSF leaks. Before beginning the study, the otolaryngologist places absorbent pledgets in the nasal cavity. Usually, three to four are placed on each side, and note is made of their location within the nasal cavity. Next, 400 to 500 Ci of ^{111}Indium-labeled (^{111}In) DTPA is placed in the subarachnoid space by the radiologist via a cervical or lum-

Copyright © 2003, Mosby, Inc. All rights reserved.

bar puncture. The patient is imaged with a gamma camera at multiple intervals for up to 24 hours. Any position or activity known to provoke the leak is encouraged. Even if the images of the head and neck do not show evidence of a leak, indirect scanning evidence may confirm the presence of a leak by showing activity in the bowel. Such activity indicates that the patient is swallowing CSF as it leaks into the nasal cavity. At 24 hours, the nasal pledgets are removed and assayed. The results are compared with ^{111}In activity in a serum sample drawn at the same time. A ratio of pledget activity to serum activity is determined and expressed in terms of counts per gram. Pledgets showing activity 1.5 times greater than serum activity are considered positive. It is then possible to predict the general area of the leak based on which pledgets show increased activity. Even if none of the pledgets have increased activity, if there is increased activity over the abdomen the radionuclide test is considered positive.

The radiographic evaluation for CSF leak necessitates careful attention to technique and detail. On coronal CT imaging, CSF leak is suspected when there is a bony defect and a fluid level at the site of the defect. These two findings in the setting of a clinically suspected CSF leak strongly predict the presence of a leak. Because the defect may be only millimeters in size, thin-section CT in multiple planes is essential for small defects.

CT cisternography is useful to confirm the leak and can be performed on an outpatient basis. The study begins with a noncontrast thin-section 3-mm coronal CT scan of the sinuses and anterior skull base in the prone coronal position. In the axial plane, 5-mm-thick sections may be adequate. If there is a single bony defect, with or without sinus opacification, in conjunction with a strong clinical history, no further imaging is needed to direct the surgical repair. If no bony defect is seen, the level of clinical suspicion determines whether further imaging is necessary. If the clinical suspicion of a leak is low, the study is deemed normal.

However, if the clinical suspicion of a leak is high, cisternography with intrathecal contrast can be performed. Usually, about 5 ml of nonionic contrast material is placed in the lumbar subarachnoid space, the fluoroscopy table is tilted head down for 1 to 2 minutes, and cranial flow of contrast is confirmed using fluoroscopy. Any maneuvers that provoke CSF rhinorrhea, such as a Valsalva maneuver, should be performed by the patient prior to rescanning. CT scans in the prone coronal and supine axial planes are then repeated. Visualization of contrast within a bony defect or contrast material within a sinus, air cell, or nasal cavity indicates a leak (Fig. 4-3). In subtle cases, there may be no visual suggestion of contrast accumulation, but region of interest (ROI) measurements in a sinus may be increased compared to ROI measurements obtained on the precisternogram CT. Sinus wall sclerosis or osteitis is seen commonly in patients with failed FESS, and the sclerosis might be misinterpreted as contrast extravasation if the precisternogram scan is not carefully compared to the postcontrast scan (Fig. 4-4). Images are best viewed magnified on a workstation, with varied window and level settings to improve detection of contrast accumulation.

Nuclear medicine cisternography can be performed at the same time as CT cisternography. It is especially helpful if the leak is questionable or subtle or if bilateral defects are seen and the site of the leak is not clear.

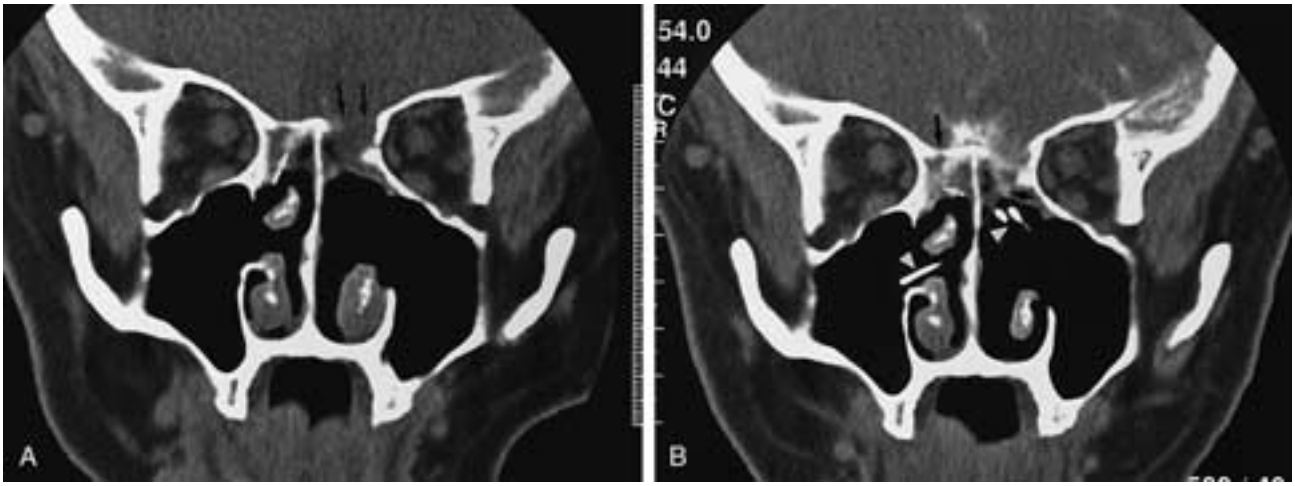

VIEW IMAGE

FIGURE 4-3 Persistent nasal discharge months after FESS. **A**, Precisternogram coronal CT scan, 3-mm slice thickness, intermediate window, shows obvious bony dehiscence at the posterior ethmoid roof on the left (*black arrows*). Postoperative findings include a thinned, straightened septum from prior septoplasty, widening of each maxillary sinus infundibulum including bilateral uncinectomies, complete resection of the left middle turbinate, and bilateral ethmoidectomies. There is high density within the right complex (*white arrow*), probably from osteitis. This bony sclerosis is often seen in chronic sinus inflammatory disease, especially following FESS. **B**, Postcisternogram coronal CT scan shows high-density nonionic contrast within the subarachnoid spaces. There is a collection of contrast within the soft tissue filling the left posterior ethmoid (*black arrow*) at the location of the bony dehiscence. Subtle contrast accumulation is also seen in the right ethmoid complex (*white arrow*) inferior to the osteitis. The smaller bony defect on the right (*long black arrow*) was not seen on the precisternogram portion of the study. Nasal pledgets, placed for the nuclear cisternogram, are seen bilaterally (*arrowheads*). These were removed at 24 hours to detect the presence of radiopharmaceutical. This additional portion of the study confirms the presence of a leak and is helpful in subtle cases. Also note that the window and level settings (window—500, level—40) are narrower than those used for screening sinus CT. The narrower settings improve visualization of contrast.

Copyright © 2003, Mosby, Inc. All rights reserved.

VIEW IMAGE

FIGURE 4-4 CSF rhinorrhea months following FESS. This precisternogram coronal CT scan shows the need for precontrast imaging. There is definite osteitis within the right posterior ethmoid complex, but the bony dehiscence is on the left. If only a postcisternogram CT scan had been obtained, the high density on the right might be misinterpreted as contrast accumulation, implying a right-sided leak.

Most iatrogenic skull base defects are detected intraoperatively at the time of injury, and 90% are successfully repaired during the FESS procedure at the first attempt.[14–16] A leak is suspected when there is pooling of clear fluid at the surgical site. A low dose of intrathecal fluorescein placed during or just prior to surgery, with subsequent visualization of the fluorescein at the suspected defect intraoperatively, confirms the leak.[17] A free patch repair involving fascia, mucoperiosteum from the turbinate or nasal septum, free fat, muscle, or fibrin glue may be used.[15] Endoscopic repair of CSF leak is the procedure of choice, with craniotomy reserved for the largest or most complicated defects.

CSF fluid leak, meningitis, or even meningoencephalocele, complications that are associated with FESS, present clinically days to years after surgery.[11, 18] Nonspecific symptoms of nasal obstruction, nasal discharge, or headaches may suggest recurrent sinus inflammatory disease; meningitis is rarely the presenting event. Because the symptoms of CSF leak and recurrent inflammatory disease are similar, careful radiographic assessment of the skull base is especially important in the patient with suspected FESS failure.

The rhinologist will suspect a skull base defect if there is pooling of clear fluid in the nasal cavity or if a frank intranasal mass is detected at nasal endoscopy. Cross-sectional imaging is essential to confirm the bony defect or leak (Fig. 4-2B), characterize the size and pinpoint the location of the bony defect, and determine if there is downward herniation of meninges or brain. The radiologic workup is complex, requiring more than one imaging procedure in subtle defects and MR imaging in large defects when pseudomeningocele (Fig. 4-5) or meningoencephalocele (Fig. 4-6) is suspected. A screening sinus CT scan alone is rarely enough to confirm and precisely characterize the defect.

Computer programs for intraoperative surgical guidance, now widely available, are useful in the workup of a CSF leak. These systems require preoperative CT imaging using a vendor-specific technique, which always includes extremely thin slice increments to allow high spatial resolution, multiplanar reformation capability. The CT data are loaded onto a computer system in the operating room, the data are registered to the patient using fixed fiducial markers, and the location of intranasal instruments is confirmed on the CT image by a system using either optical or electromagnetic detectors. When a CSF leak is strongly suspected, the surgeon may anticipate the need for CT surgical guidance, and the cisternogram can be performed using the required parameters. Thus, extremely thin axial CT sections, with multiplanar reformation capability, are used both for the diagnosis of a bony defect and for surgical guidance.[19] When a leak is detected, the multiplanar reformations allow precise defect localization and accurate measurement of both the depth and the width of the defect. In this regard, the thinner slices improve CSF leak detection.

When a soft-tissue mass is seen within the sinus, especially if it abuts the skull base, herniation of intracranial contents should be suspected. Meninges, CSF, or even the anteroinferior aspect of the frontal lobe can herniate downward through a skull base defect. MR imaging, including postgadolinium-enhanced images, is recommended to characterize the soft tissue within the sinus.[11]

Orbital Complications

Orbital complications are also considered mild or severe and can be secondary to trauma to the nasolacrimal duct, inadvertent penetration of the lamina papyracea, or direct injury to the optic nerve.

Epiphora, or tearing due to interruption of the nasolacrimal duct, and dacryocystitis can result from injury to the duct. Fortunately, most ductal injuries heal spontaneously or remit by spontaneous fistularization into the middle meatus. However, stenosis or total occlusion of the nasolacrimal duct can result from more severe injury. The injury can occur during anterior enlargement of the infundibulum, usually when a backbiter is used to resect the uncinate process, enlarging the communication between the infundibulum and the middle meatus. Injury can also occur distally when an anterior maxillary antrostomy is performed near the inferior meatus.[20] In experienced surgical hands, the reported incidence of post–middle meatal antrostomy epiphora due to nasolacrimal duct injury is between 0.3% and 0.7%. Cross-sectional CT imaging can be used to assess the duct but is not commonly requested, as the duct can be directly explored by the surgeon.[21] Dacryocystography is another method used to assess the lumen of the nasolacrimal duct (see Chapter 10). Ductal dilatation with balloon dacryocystoplasty may be performed or a surgical dacryocystoplasty may be performed to restore the patency of the stenosed ductal segment.[21]

Predisposing anatomic features and variations in both major and minor orbital complications include unnoticed lamina papyracea dehiscences, medially deviated segments of the lamina papyracea (usually above or below the insertion of the basal lamella), prominent deviation of the nasal septum and large concha bullosa (which cause additional spatial limitations during the FESS ethmoidectomy procedure), and an uncinate process that adheres to the

Copyright © 2003, Mosby, Inc. All rights reserved.

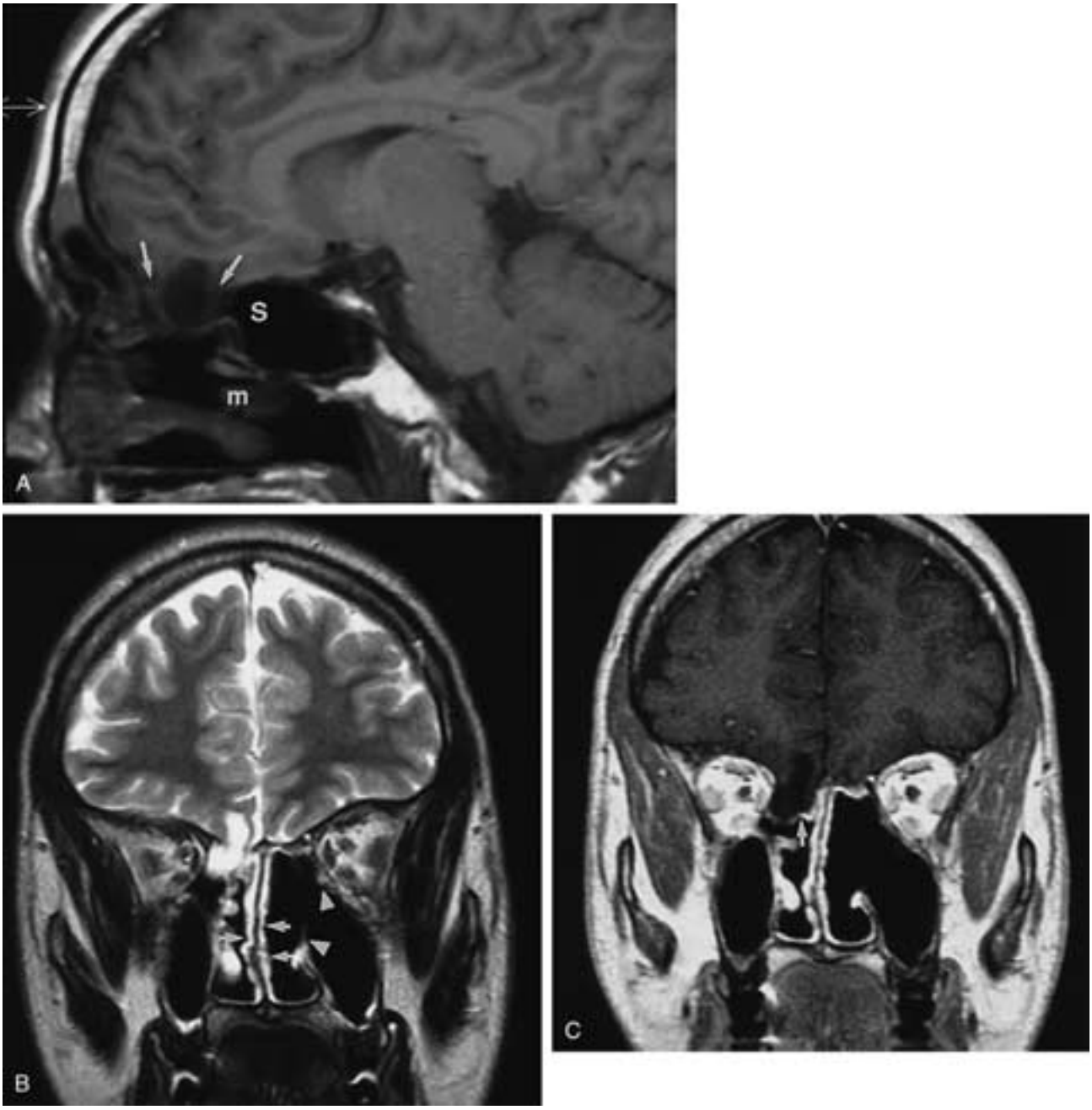

VIEW IMAGE

FIGURE 4-5 Pseudomeningocele, right. Persistent ''sinusitis'' with nasal discharge was noted 1 year following FESS. **A**, T1-weighted sagittal MR image shows a large anterior skull base defect in the posterior ethmoid complex (*arrows*), immediately anterior to the sphenoid sinus (*S*), with intranasal herniation of meninges and CSF. Note that the midportion of the middle turbinate has been resected. The residual posterior middle turbinate is denoted by *m*. **B**, On the T2-weighted coronal MR image, the right intranasal pseudomeningocele is noted, and is clearly contiguous with a region of encephalomalacia in the anterior frontal lobe. Postoperative changes include an irregular septal contour following a septoplasty (*arrows*), total left ethmoidectomy, marked widening of the left maxillary ostium and infundibulum (*arrowheads*), and complete resection of the left middle turbinate, including the vertical insertion. **C**, T1-weighted coronal contrast-enhanced MR images show subtle enhancement of the inferior aspect of the pseudomeningocele (*arrow*) and normal mucosal enhancement of the nasal cavity.

Copyright © 2003, Mosby, Inc. All rights reserved.

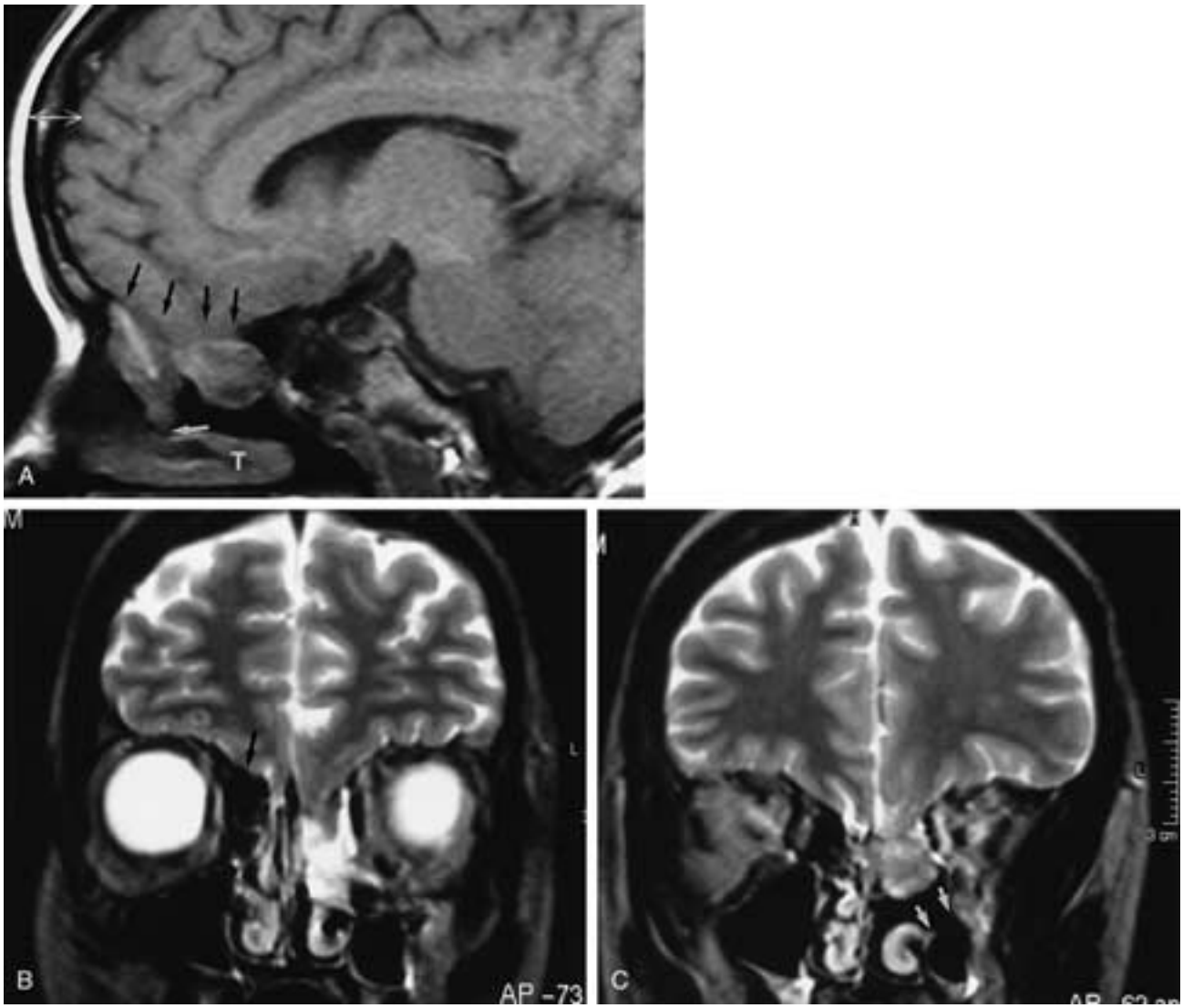

VIEW IMAGE

FIGURE 4-6 Postoperative meningoencephalocele, left. Nasal obstruction and persistent rhinorrhea was noted 6 months following FESS. **A**, On this T1-weighted sagittal MR image, note the defect in the anterior skull base (*black arrows*) and the complex large soft-tissue mass in the nasal cavity. The anterior portion of the mass abuts the inferior turbinate (*white arrow*). Inferior turbinate denoted by *T*. **B**, T2-weighted coronal MR image confirms that the mass is primarily fluid inferiorly, but there is intranasal herniation of the frontal lobe. The intact ethmoid roof on the right is denoted by the arrow. **C**, T2-weighted coronal MR image posterior to **B** shows that this portion of the meningoencephalocele is primarily brain tissue. Note the widened maxillary ostium and infundibulum on the left (*arrows*) following surgery and uncinectomy and resection of the left middle turbinate. No surgery had been performed on the right side.

inferior lateral orbit under the ethmoid bulla (atelectatic uncinate process).

When the lamina papyracea has been violated, mild complications may be periorbital ecchymosis, orbital emphysema, or a small orbital hematoma. For these minor injuries, treatment includes close observation for development of proptosis, orbital massage to decrease the intraocular pressure, and antibiotic treatment to prevent development of infection. Imaging is rarely required for these mild orbital FESS complications.

More severe orbital complications from medial orbital wall injury include a large orbital hematoma, edema and swelling of the orbital soft tissues, orbital abscess, injury to the superior or medial rectus muscle (Fig. 4-7), and injury to the optic nerve. The resulting symptoms include orbital pain, proptosis, diplopia, and vision loss.

Orbital hematoma occurs due to either rupture of the orbital ciliary veins or direct injury to the ethmoidal arteries.[21, 22] At the superior aspect of the lamina papyracea, near the level of the superior oblique and medial rectus muscles, the AEA runs within the anterior ethmoidal canal (AEC) and perforates the bony ethmoid wall (Fig. 4-8).[23] It is here that the vessel is most vulnerable. The AEC is often seen on screening sinus CT scans, especially if there is extensive pneumatization of supraorbital air cells. It may have a very thin or dehiscent bony canal, running exposed within the superior ethmoid complex (Fig. 4-9).[22] If the AEA is transected, it may retract into the orbit, the surgeon

Copyright © 2003, Mosby, Inc. All rights reserved.

VIEW IMAGE

FIGURE 4-7 Diplopia noted immediately after FESS. On this noncontrast axial CT scan, note the small bony fragment, from the lamina papyracea, within the medial rectus muscle on the right (*arrow*).

will lose control of the artery, and an orbital hematoma will result.

Less often there can be injury to the posterior ethmoidal artery, which runs through the posterior ethmoidal foramen approximately 10 to 12 mm posterior to the anterior ethmoidal foramen. Injury to the posterior ethmoidal artery can also cause intraorbital hematoma. However, this artery is relatively close to the optic nerve, and due to this proximity, even small posterior ethmoidal hematomas can cause serious nerve damage, with resultant blindness.

The anterior lamina papyracea may be violated during uncinectomy or surgery of the agger nasi cell. Additionally, incidental lamina papyracea dehiscence, either from prior surgery (Fig. 4-10) or from a previous fracture, likely predisposes to orbital injury during FESS. Congenital

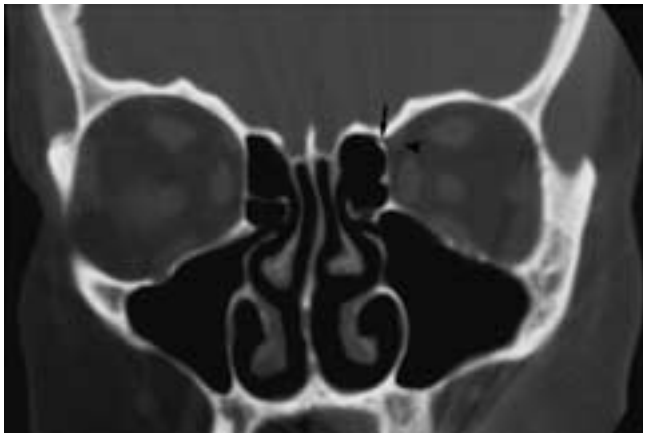

VIEW IMAGE

FIGURE 4-8 Anterior ethmoidal artery canal. Coronal CT scan. Note the narrow bony canal (*arrow*) on the left at the superior aspect of the medial orbital wall, just medial to the superior oblique muscle (*arrowhead*). Visualization of the canal is variable and was not seen on the contralateral side in this patient.

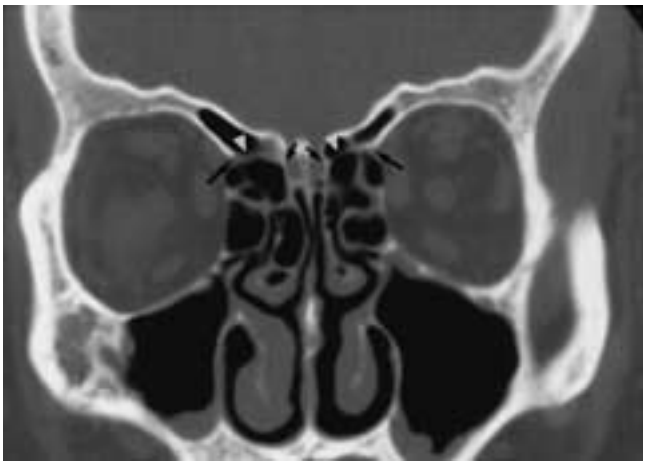

FIGURE 4-9 Coronal CT scan. ''Dehiscent'' anterior ethmoidal arteries bilaterally. When the supraorbital ethmoid cells are well pneumatized, the AEA and AEC are well seen. Note the medial (*small arrows*) and lateral (*large arrows*) portions of the canals. No bone is seen around either the right or left AEA (*white arrowheads*).

VIEW IMAGE

dehiscence of the lamina papyracea is rare but should be noted on a preoperative sinus CT report (Fig. 4-11).[24] Periorbital fat prolapsing through the defect into the ethmoid complex may be misinterpreted by the surgeon as hypertrophied or diseased mucosa or polypoid disease, and the forceps may tear the fat or injure the extraocular muscles.

Maxillary or ethmoid sinus hypoplasia and a laterally displaced uncinate process also predispose to orbital trauma during FESS. Normally, the medial wall of the orbit is in the same vertical plane as the maxillary ostium.[25] With ethmoid

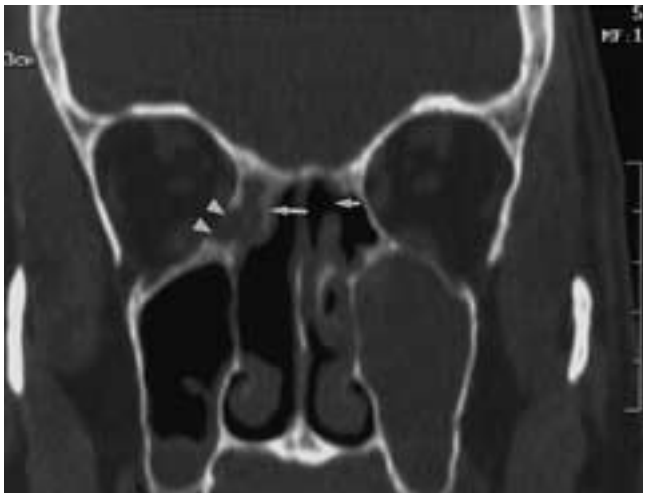

FIGURE 4-10 Recurrent sinusitis and lamina papyracea dehiscence on the right. Axial CT scan data were acquired at 1-mm slice thickness, and this coronal reformatting was performed. There has been a prior septoplasty, ethmoidectomy bilaterally, resection of the inferior portion of the right middle turbinate with a residual superior portion (*long arrow*), and resection of the insertion of the left middle turbinate (*short arrow*), and there is recurrent mucosal thickening in the right maxillary antrum and opacification of the right ethmoid and left maxillary sinuses. Note the lamina papyracea dehiscence on the right (*arrowheads*), increasing the potential risk of orbital injury during revision FESS.

VIEW IMAGE

Copyright © 2003, Mosby, Inc. All rights reserved.

VIEW IMAGE

FIGURE 4-11 Lamina papyracea dehiscence, left. On this axial sinus CT scan, dehiscence of the left lamina papyracea with herniation of extraconal fat (*arrows*) into the ethmoid complex is seen. There was no history of prior trauma or surgery.

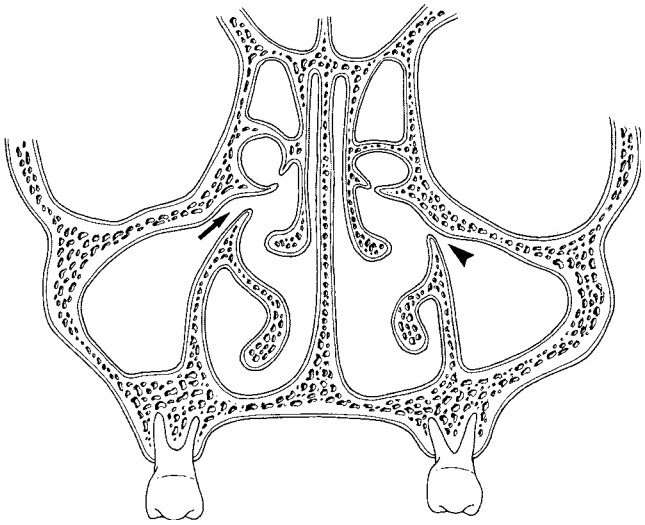

VIEW IMAGE

FIGURE 4-12 Maxillary sinus hypoplasia. Coronal diagram of the sinonasal cavity at the level of the osteomeatal unit. On the normal right side, the maxillary sinus opens into the infundibulum through the internal ostium (*arrow*). Note that the ostium is in the same vertical plane as the lamina papyracea. If the maxillary sinus is hypoplastic, as on the left, the medial antral wall is located laterally and the ostium (*arrowhead*) is lateral to the lamina papyracea. This variant predisposes to orbital penetration.

hypoplasia, the medial orbital wall is medial to the vertical plane of the maxillary ostium, presumably predisposing to orbital penetration during FESS.[4, 26] A similar anatomic relationship exists when there is a hypoplastic maxillary sinus; the medial orbital wall is located medially with respect to the maxillary ostium (Fig. 4-12). Uncinate process lateralization, hypoplasia, or even total absence is also associated with severe maxillary sinus hypoplasia.[27] Although most surgical injuries to the lamina papyracea are probably sporadic, the status of the bony orbital walls should be noted on the screening sinus CT report.

Postoperative orbital soft-tissue or osseous injury is best evaluated with direct coronal and axial CT imaging (or by using reformatted coronal images acquired from axial images using a multidetector scanner) with review of both soft-tissue and bone window settings. If orbital infection or abscess is suspected, the addition of intravenous contrast may facilitate the differentiation of phlegmon from frank abscess (Fig. 4-13). MR imaging is less sensitive in detecting small bony defects in the thin lamina papyracea, but it clearly delineates the orbital soft tissues, including the optic nerve.

Blindness from direct optic nerve injury is a rare but a devastating FESS complication. The optic nerve is vulnerable during dissection in the lateral recess of the sphenoid sinus and when there is a pneumatized superolateral recess of the sphenoid sinus. The sinus wall may be markedly thinned or even nonexistent, especially when the sphenoid sinus is excessively pneumatized.

As previously mentioned, pneumatization of the anterior clinoid process and resultant protrusion of the optic canal into the sphenoid sinus, which occurs in 8% of the population, is a potential risk factor and should be noted when seen on a preoperative sinus CT scan. The Onodi cell, a posterior ethmoid cell within the upper sphenoid sinus, occurs 3% to 15% of the time and may predispose to optic nerve injury when the FESS procedure involves the sphenoid sinus.[4] Surgical dissection in the sphenoid sinus is not commonly performed during most FESS procedures, but occurs when there is extensive polyposis or isolated sphenoid sinus disease. Optic nerve injury, therefore, is rare, and if the intraorbital optic nerve is injured, the anatomic surgical landmarks were not appreciated by the surgeon. Sporadic reports of intraorbital optic nerve transection are rare.[28]

Radiographic evaluation of the patient presenting with post-FESS symptoms suggesting orbital complications should include a thin-section CT scan performed in the

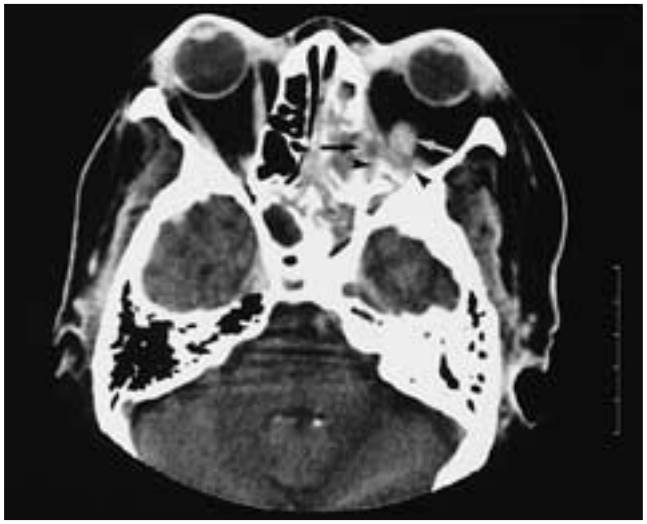

VIEW IMAGE

FIGURE 4-13 Orbital apex infection, left. Axial contrast-enhanced CT scan obtained 1 day following surgery. Proptosis, orbital pain, and decreased motility were noted. Note the bony defect in the lateral wall of the posterior ethmoid complex (*black arrow*), phlegmonous changes in the apex (*arrowheads*), and thickening of the inferior rectus muscle (*white arrow*). The diffuse sinus opacification may be seen immediately after surgery.

Copyright © 2003, Mosby, Inc. All rights reserved.

coronal and axial planes. On CT, penetration into the orbit through the lamina papyracea is indicated by proptosis, obliteration of orbital fat planes, orbital emphysema, retrobulbar hematoma, and distortion of the extraocular muscles or the optic nerve. Injury of the periorbital contents may be difficult to detect, but bony damage should be visible. The optic nerve should be traced in its entirety from the insertion at the posterior globe to the chiasm. The CT examination is usually diagnostic; however, if orbital and intracranial injury extent is unclear, MR imaging should also be performed.

ENDOSCOPIC SINUS SURGERY

Theory and Treatment Options

As discussed in Chapter 3, prior to the development of FESS, surgical sinus procedures were performed under the assumption that the sinus mucosa was the primary abnormality and that if the mucosa was stripped or resected, the chronic sinusitis would resolve. Poor outcomes necessitated reassessment of that theory. During the 1970s and 1980s, Messerklinger in Austria, Draf and Wigand in Germany, and Kennedy in the United States proposed that the mucosa was secondarily diseased and that a stenotic sinus ostium or a narrowed nasal cavity region obstructed the sinus, leading to hyperplastic, edematous mucosal changes.[29, 30] Stagnant sinus secretions then became infected, the mucosal changes became more severe, and the ostium was further obstructed. A cycle of mucosal swelling, sinus obstruction, infection, and worsening of mucosal swelling followed.[31] It has been shown that with improved sinus ventilation and drainage, the ciliated mucosal epithelium usually normalizes, with resolution of symptoms.[32]

Development of recurrent acute or chronic sinusitis is multifactorial, and ensuring ostial patency is only part of the treatment. Mucociliary function, transport, and clearance of secretions theoretically should normalize with the creation of a patent sinus ostium.[33] This concept likely oversimplifies treatment, as abnormal sinus ventilation, defective mucociliary function, and systemic conditions such as atopy, aspirin intolerance, and asthma also contribute to sinus inflammatory disease.

Disease or obstruction of the ethmoid sinuses is the primary event in chronic or recurrent acute sinusitis affecting the ethmoid complex, frontal sinuses, and maxillary sinuses.[34] Radiographic studies have shown that the ethmoids are the most common location for inflammatory disease. When the ethmoids are abnormal, the frontal and maxillary sinuses are more often abnormal; when the ethmoid complex is clear, the maxillary and frontal sinuses are generally normal.[31, 35–37]

Surgical procedures used in this region include widening of the ethmoid infundibulum and treating variants in the ostiomeatal complex. The most common procedure includes removal of the uncinate process and widening of the maxillary sinus ostium and infundibulum, resection of diseased mucosa in the frontal recess, unroofing the ethmoid bulla, and removing the bony septae in the anterior ethmoid complex. Total endoscopic sphenoethmoidectomy, a more extensive surgery often performed for sinonasal polyposis, involves exenteration of the ethmoid complex, opening the sphenoid sinus, and widening the ostiomeatal complex and the maxillary sinus infundibulum. Between these two procedures is a range of surgical treatments specific to each disease location (also see Chapter 3).

Endoscopic sinus surgery is individualized to each patient and to the specific sites of disease seen on nasal endoscopy and screening sinus CT. The procedure may be unilateral or bilateral and may be minimal, with only one or two sites treated (Fig. 4-14), or extensive, with multiple sites treated. In general, the trend with FESS is to operate conservatively and to do less surgery in order to preserve more mucosa.

FESS Outcomes

The success of FESS, defined as significant clinical improvement of preoperative symptoms, normalization of the mucosa and sinus ostia seen during endonasal examination, or resolution of abnormal CT findings, ranges from 78% to 95%.[8, 38–41] From 10% to 20% of patients, therefore, may report no benefit or are worse after FESS.[40, 42] There may be discordance between subjective patient-reported symptoms and the objective endonasal and/or CT examination. Alternatively, resolution or significant improvement in symptoms may be reported by the patient, with only small changes in abnormalities found at physical examination or CT imaging. In turn, the physical and CT examinations may return to normal but the patient may report continued symptoms. Subjective symptomatic relief is the primary end result, regardless of the objective examinations. The post-FESS sinus CT results, therefore, supplement the

FIGURE 4-14 Subtle post-FESS findings. On this coronal CT scan, note that the nasal septum is unusually straight, with loss of the normal mucosal contours. There has been minimal resection of the inferior turbinates. The surgery was performed to relieve symptoms of chronic nasal obstruction.

VIEW IMAGE

Copyright © 2003, Mosby, Inc. All rights reserved.

clinical data. Long-term outcome data on FESS have only recently become available. Most outcome data are short-term, with reexamination 3 months to 3–8 years after surgery. It is therefore difficult to report the efficacy of the procedure accurately, as it depends on which parameter is considered. Symptom reports are by definition subjective. The outcome depends on the degree of preoperative disease, the presence of polyposis, and which surgical procedure is performed. In summary, it is common for objective examinations to diverge from subjective patient reports, but FESS has been established as effective based on symptoms.

Recurrent acute sinusitis, chronic sinusitis, sinogenic headache, recurrent polyposis with infection or nasal obstruction, or nasal drainage are generally considered symptoms suggestive of surgical failure.[38] Sinogenic headache is defined as midface dull aching or pressure, often localized to the medial canthal region, which correlates with inflammatory disease in the ethmoid complex or ostiomeatal unit.[43] An abnormal nasal examination with mucopurulent rhinorrhea, erythema and edema of the mucosa, scarring at surgical sites, or recurrent or residual polyps, coupled with an abnormal sinus CT examination, are also considered surgical failures, especially when associated with patient symptoms.[39]

Indicators or predictors that suggest a higher likelihood of a poor outcome include smoking, allergy, asthma, aspirin intolerance, sinonasal polyps, cystic fibrosis and polyps, prior ''classic'' sinus surgery, and possibly gastroesophageal reflux disease.[40, 42, 44] Recurrent or residual sinonasal polyposis is common, occurring in about 30% to 40% of patients with polyps.[40, 42] In fact, recurrent or residual polyps are the most common endoscopic finding following FESS and one of the most common reasons patients return for revision surgery.[40, 45] As patients with polyposis, regardless of the etiology, represent a different population from patients without polyposis, outcome data for the two groups should be reported separately.

It is well established that the findings on preoperative CT images of the sinuses are not specific for sinonasal inflammatory disease, and there is no association between symptom severity and CT findings.[46, 47] The incidence of asymptomatic sinonasal mucosal thickening or opacification is high. The definition of sinusitis (adopted by the American Academy of Otolaryngology–Head and Neck Surgery, the American Academy of Otolaryngic Allergy, and the American Rhinologic Society) does not even include radiographic findings but relies solely on symptoms and physical examination findings.[48] Therefore, most surgeons would not operate on the basis of sinus CT abnormalities alone.

Sinus CT does appear to have prognostic significance for symptom resolution following FESS. The distribution and severity of disease on CT may predict the postoperative endoscopic appearance of the sinonasal region, the success of sinus surgery, and the likelihood of disease recurrence following FESS.[42, 49–51] Sinonasal polyposis with bilateral disease is the single best preoperative radiographic predictor of surgical failure.[51] Severe disease, as defined by bilateral ethmoid disease and involvement of one or two dependent sinus cavities, also is a strong predictor of FESS failure.[42]

Several objective staging systems for rhinosinusitis have been proposed and may be used to aid the patient and surgeon in making treatment decisions and predicting the surgical outcome.[42, 49, 50] The staging system at this time is an investigative tool used to quantify the degree of disease and to determine prospectively if the amount of disease correlates with surgical success. One system, termed the *Lund staging system for rhinosinusitis*, grades CT findings, anatomic variants, the surgical score, the symptom score, and the endoscopic appearance score.[52] With respect to the CT portion of the system, each sinus group is graded 0–2, with 0 indicating no abnormality, 1 partial opacification, and 2 total opacification. The ostiomeatal complex is graded 0 (not obstructed) or 2 (obstructed). Normal variants including absent frontal sinuses, concha bullosa, paradoxic middle turbinates, Haller cells, everted uncinate process or agger nasi cell pneumatization are graded 1 (present) or 0 (absent) (Table 4-1). Each side is considered separately. The CT outcome number is combined with the surgical and symptom scores for a total number to categorize the extent of rhinosinusitis and to aid the surgeon in objectively determining the need for surgery or revision FESS.

Table 4-1
LUND STAGING SYSTEM

Sinus
0—normal
1—partial opacification
2—total opacification
Ostiomeatal complex
0—no obstruction
2—obstructed
Normal variants
0—absent
1—present
Absent frontal sinuses
Concha bullosa
Paradoxical middle turbinates
Haller cells
Everted uncinate process
Agger nasi cell pneumatization

The FESS Procedure and Imaging Findings

Overview of the FESS Procedure

When assessing a postoperative sinus CT study, it is helpful to begin the interpretation with a thorough discussion of the anatomic changes that resulted from the surgery, including which structures were resected and which structures remain intact. This is especially important for the FESS procedure, as there is no routine surgery, since each operation is carefully individualized for the specific patient. After that task, the scan is assessed for residual or recurrent sinus disease. Revision FESS carries the same potential complications as initial surgery, so review of the integrity of the lamina papyracea, cribriform plate, roof of the ethmoids, and sphenoid sinus pneumatization is as important as the first preoperative sinus CT interpretation. Injury to the nasolacrimal duct occurs at a slightly higher rate with revision surgery, especially when a radical ethmoidectomy is performed.[53]

Copyright © 2003, Mosby, Inc. All rights reserved.

Understanding the FESS procedure facilitates recognition of surgical changes on the CT study. Septoplasty is an adjunctive procedure often performed during FESS to gain surgical access or treat nasal obstruction. The deviated septum can obstruct the nasal cavity, restricting endoscopic access to the ethmoid complex and ostiomeatal unit. By resecting the deviated septum or a bony septal spur, the surgeon can more easily move the endoscope posteriorly through the nasal cavity. Also, a severe septal deviation or spur can result in nasal obstructive symptoms or chronic sinusitis due to mass effect in the middle meatus, stenosing the ethmoid recess or maxillary sinus infundibulum.[54, 55]

The next step is infundibulotomy by resecting the uncinate process. A large concha bullosa or polyp is resected if it blocks access to the uncinate. Once the uncinate has been removed, the surgeon has visual and surgical access to the maxillary ostium, frontal recess, and anterior ethmoid complex. The ostium of the maxillary sinus is inspected, and obstructing polyps or hyperplastic mucosa are resected to restore normal drainage. After uncinectomy, the maxillary sinus ostium may be extended posteriorly and inferiorly, but only the minimal amount of bony resection is performed. If indicated, an ethmoidectomy is performed from anterior to posterior. The extent of this procedure is determined by the CT scan and direct visualization of disease. The ethmoid bulla is taken down as the first step in any ethmoid procedure, especially if the bulla is diseased, deviates the middle turbinate, or is so large as to obstruct the hiatus semilunaris.

If there is disease in the frontal sinus or recess, the natural ostium is identified and obstructing polyps or mucosa are resected. This is one of the most difficult areas to access and treat surgically. A large agger nasi cell may obstruct identification of the frontal recess. Other important variants here include frontal cells or superior orbital cells. The AEA must be identified prior to further dissection. The recess may be extremely narrow and obliquely angled. Generally, once the ostium is isolated, polyps or cysts can be removed, but disease located laterally is not resected. Occasionally, the bony ostium may be widened.

The ground lamella, or the posterior horizontal insertion of the middle turbinate to the lamina papyracea, separates the anterior from the posterior ethmoid cells. When significant disease is seen in the posterior ethmoid complex, the surgical dissection will be extended to treat these locations. The posterior ground lamella is carefully perforated, and the posterior ethmoid cells are entered. The roof of the ethmoid complex is identified prior to any additional surgery to avoid injury to the skull base. Careful removal of polyps, diseased mucosa, or inflammatory debris is then performed.

The usual approach to the sphenoid sinus, if necessary, is through the nasal cavity to the natural ostium at the sphenoethmoidal recess, medial to the turbinates. To gain access, it may be necessary to resect the posterior aspect of the middle turbinate.[33] A second approach is transethmoidal. In these cases, the surgeon relies on the screening preoperative sinus CT scan to be familiar with the individual anatomy in this region. It is essential that the optic nerve and internal carotid artery, and their relationship to the posterior ethmoid and sphenoid sinuses, are well understood prior to the surgical procedure.

Postoperative Findings: Expected and Complications

The postoperative CT scan reflects the surgical procedures that were performed. In the radiographic report, there should be a description of the surgical changes present and the presence of any recurrent soft tissue (likely related to scar and fibrosis), hyperplastic mucosal disease, or polyps. Radiographically, differentiation between scar, fibrosis, and diseased mucosa may not be possible.[56] One of the most common reasons for FESS failure is poor control of mucosal inflammation.[57] Recurrent symptoms following FESS are related to surgical undertreatment of a region, residual variants, restenosis from scar or adhesions, recurrent hyperplastic mucosa, or residual or recurrent polyposis. Two endoscopic findings that correlate best with a poor outcome are scarring of the ethmoids and scarring of the middle meatal antrostomy. The location of a scar or mucosal disease is particularly important to describe, especially if it occurs at a sinus ostium. Thus, significant mucosal thickening in a maxillary antrum may be secondary to recurrent stenosis at the maxillary sinus infundibulum due to a scar or a polyp. Given the theory of sinusitis, it is likely that mucosal thickening and outlet stenosis, although different in location, are causally related.

The most common CT finding in a patient with failed FESS is mucosal disease, with or without associated anatomic factors.[57] In descending order of frequency, recurrent mucosal disease is reported in the anterior ethmoid sinuses, the maxillary sinus, the posterior ethmoid sinuses, the frontal sinus, and the sphenoid sinus.[57, 58] Residual agger nasi cells, Haller cells, and ethmoid air cells are also seen in failed sinus surgery patients. Recurrent or residual polyps are commonly found, especially if polyposis was treated at the initial procedure.

The following is a location-specific description of the CT findings commonly seen when revision FESS for recurrent symptoms is being considered. These findings are summarized in Table 4-2. After septoplasty, the nasal septum on CT imaging appears straightened and the mucosa is thinned (Fig. 4-14). Bony spurs should no longer be seen. A complication of septoplasty is compromise of the septal arterial blood supply, which may lead to a septal perforation. Any bony septal interruption seen on CT should be reported by the radiologist.

The appearance of the middle turbinate is variable, depending on the extent of the surgical procedure. If a middle turbinate concha bullosa has been resected, this should be noted by the radiologist.

Table 4-2
ANATOMIC VARIABLES THAT MAY PREDISPOSE TO RECURRENT DISEASE AFTER FESS

Persistent septal deviation
Lateralized middle turbinate
Residual uncinate process
Residual ethmoid, frontal, or superior orbital cells
Scar at the maxillary infundibulum
Scar at the frontoethmoid infundibulum
Sinonasal polyposis
Residual variants—agger nasi cells, concha bullosa, Haller cells
Sinus wall osteitis

Copyright © 2003, Mosby, Inc. All rights reserved.

There is controversy in the surgical literature regarding whether middle turbinectomy is efficacious. Following partial middle turbinectomy, some authors report a lower incidence of recurrent frontal sinusitis, while others report a higher incidence.[59] Reasons not to resect the middle turbinate include its role in olfaction, the possible increased incidence of frontal sinusitis, and fear of mucociliary dysfunction. Most surgeons will not resect the entire middle turbinate, as the vertical insertion of the turbinate on the skull base is an important surgical landmark. As previously mentioned, a cardinal surgical rule is to stay lateral to the middle turbinate in order to avoid creating a CSF leak. If the entire turbinate is resected, this important surgical landmark is removed.

After partial turbinectomy, the middle turbinate may be intentionally opposed to the nasal septum (Fig. 4-15). Thus, the turbinate cannot narrow the middle meatus. This ''medialized middle turbinate'' contributes to maintaining a patent middle meatus and is a desired finding on postoperative CT or nasal examination. Lateralization of the middle turbinate, or scar formation between the turbinate and the lateral nasal wall, is associated with recurrent sinus inflammatory disease (Fig. 4-16).[57]

Widening of the maxillary sinus ostium and infundibulum is seen after uncinectomy, and different degrees of maxillary sinus opening are seen, depending on the extent of surgery. As described previously, only the uncinate process may be resected or there may have been a wider maxillary osteotomy. Subtotal resection of the uncinate process may be intentional, as total uncinectomy reportedly carries a risk of frontal recess scarring.[40] On the other hand, incomplete uncinectomy is a factor in recurrent sinus inflammatory disease. Any soft tissue at the maxillary ostium or infundibulum, or a residual total or partial uncinate process, should be noted by the radiologist. Synechiae or scar at the natural ostium are common postoperative findings (Figs. 4-15, 4-16).[40]

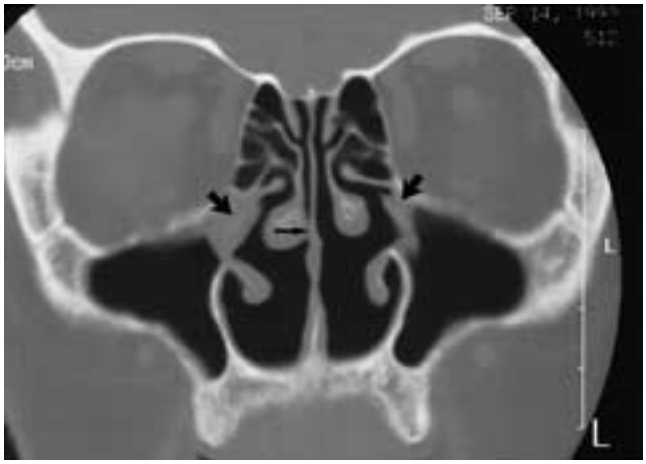

VIEW IMAGE

FIGURE 4-15 Recurrent symptoms, probably due to functional and flow changes after extensive FESS. Postoperative findings on this sinus coronal CT scan include a septoplasty, resection of most of the inferior turbinates, and a medialized right middle turbinate (*black arrows*). There is soft tissue in both maxillary sinus ostia (*thick arrows*). The soft tissue on the right is polypoid and probably represents recurrent polyps. On the left, it likely represents scar.

Middle meatal antrostomy is believed to contribute to the recirculation syndrome, which occurs when mucus that exits the natural maxillary sinus ostium enters the nasal cavity and reenters the maxillary sinus through a surgically created opening separate from the natural ostium (Fig. 4-17).[33, 40] The nasal antral window is an antrostomy surgically created immediately below the lateral insertion of the inferior turbinate and is not in continuity with the natural ostium. It was commonly performed in conjunction with the Caldwell-Luc procedure.[60] Widening or relieving obstruction of the natural ostium is currently preferred over the surgical creation of a new and separate opening in the medial wall of the maxillary sinus. Any medial maxillary sinus wall defect seen on the postoperative CT scan should be noted by the radiologist (Fig. 4-17B).

The most common CT appearance of the ethmoid complex after surgery is that of a common anterior ethmoid cavity with resection of multiple ethmoidal septations (Fig. 4-16). The ethmoidectomy may have been either partial or total, and the CT scan will reflect the procedure. Intact or residual ethmoid air cells, including the ethmoid bulla, should be reported by the radiologist, as residual cells are one of the major reasons for FESS failure (Fig. 4-18).[56] Scar formation at the ethmoid infundibulum, obstructing the sinus outflow, should be noted, as this finding is also

VIEW IMAGE

FIGURE 4-16 Recurrent sinusitis after FESS. Screening sinus coronal CT scan shows changes from septoplasty (straight septum with irregular mucosal contour), resection of the inferior aspect of both inferior and middle turbinates, total ethmoidectomy on the right, and partial ethmoidectomy on the left. There is soft-tissue scar or fibrosis at both maxillary sinus ostia (*arrowheads*), a lateralized left middle turbinate that is adherent to the lateral nasal wall (*white arrow*), and inflammatory changes in the left ethmoid complex. Minor mucosal thickening is seen in the alveolar recess of both maxillary sinuses, but the most important observation is soft tissue obliterating the anterior maxillary ostia (*arrowhead*) bilaterally. It is unclear whether this finding affects maxillary sinus clearance, but it should be mentioned by the radiologist. Incidental note is made of both anterior ethmoid arteries within anterior ethmoid canals (*black arrows*). Note the proximity of the lateral AECs near the superior oblique muscles.

Copyright © 2003, Mosby, Inc. All rights reserved.

associated with failed FESS.[40] Most commonly, residual cells are located in the roof of the ethmoid complex and far posteriorly near the sphenoid sinus. Many surgeons leave these extreme cells intact in order to avoid perforation into the floor of the anterior cranial fossa or injury to the optic nerve.

Early frontal recess stenosis may be asymptomatic but should be noted, as it likely predisposes to future mucocele formation (Fig. 4-19).[42, 61] Causes of frontal sinus obstruction after FESS include residual agger nasi cells, residual frontal cells, and bony or soft-tissue obstruction of the infundibulum. Persistent ethmoid sinus disease is also a significant cause of recurrent frontal sinus disease, and prior ethmoidectomy is reported to be associated with frontal sinus disease.[42] Some of these outcomes appear discordant, and clearly long-term follow-up is necessary to understand and clarify what appear to be contradictory outcomes.

Recurrent frontal sinus disease following FESS is a difficult clinical problem. Resistant frontal sinusitis has been traditionally treated by an osteoplastic flap procedure, an external surgical approach that obliterates the sinus cavity (see Chapter 7).[62] Alternative transnasal endoscopic approaches to the frontal sinus have been proposed, and early results appear promising.[61, 63, 64] The most commonly performed procedure, termed a *Draf-type drill out* or *modified intranasal Lothrop procedure*, involves resecting all anterior ethmoid air cells and the uncinate process near the frontal recess and performing an endoscopic frontal sinusotomy. On CT, the frontal recess will appear widened and resection of the structures described will be seen. A more extensive Draf procedure will include resection of the inferior interfrontal sinus septum, the superior nasal septum, and the frontal sinus floor to the level of the orbit. This procedure, generally reserved for the most recalcitrant disease, creates a large anatomic opening with the goal of preventing recurrent stenosis.

The worst outcome based on symptoms, clinical examination, and the post-FESS CT scan, occurs in patients with extensive sinonasal polyposis. The failure rate in this group, reportedly as high as 75%, is so high that most series report diffuse polyposis outcomes separately from those in patients without polyps or with only a few polyps (Fig. 4-20).[42] Aspirin intolerance, asthma, and atopy are often seen with polyposis, suggesting a systemic but poorly understood association.[65] It has been proposed that polyposis is a systemic disease, thereby explaining the higher rate of recurrence.[38] The common CT findings seen in this group of patients are recurrent severe mucosal thickening and polyps in both operated and nonoperated sinuses and in the nasal cavity. These patients with sinonasal polyposis, with or without fungal involvement, often undergo multiple endoscopic procedures, and as the surgical risk rises with each operation, the radiologist should be particularly vigilant in assessing the lamina papyracea and anterior bony skull base.

Dense sclerotic new bone in a previously operated cavity is a common finding in patients who have failed FESS (Fig. 4-21). Similar changes may be seen in the bone of the middle

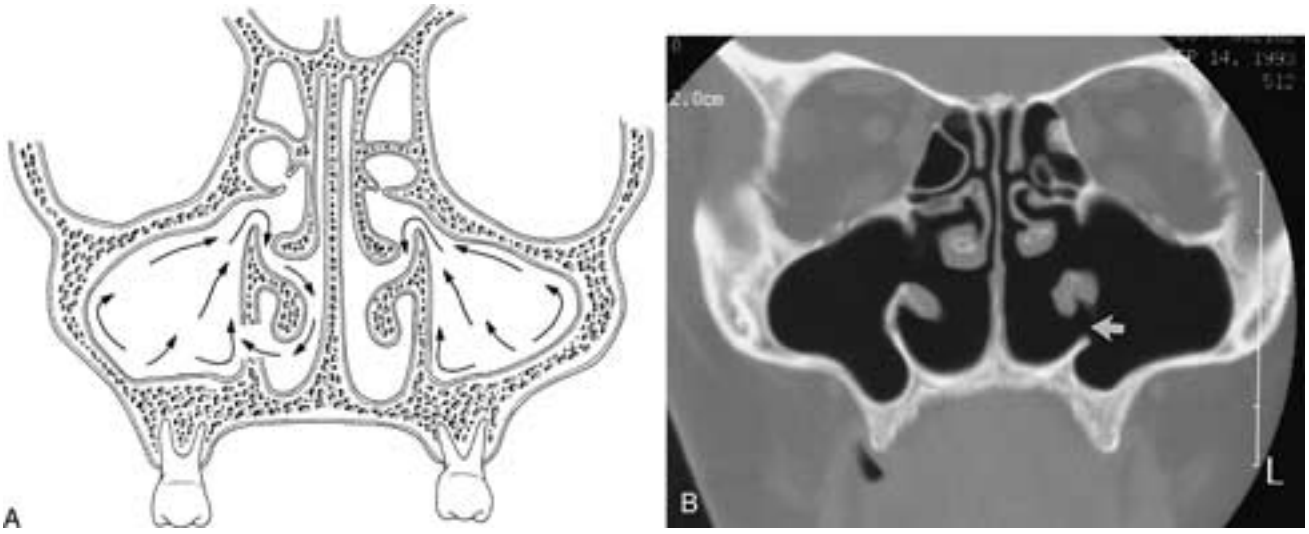

VIEW IMAGE

FIGURE 4-17 Recirculation syndrome. **A**, Coronal diagram of the sinonasal cavity at the level of the ostiomeatal unit. Middle meatal antrostomy is believed to contribute to the recirculation syndrome, which occurs when mucus that exits the natural maxillary sinus ostium enters the nasal cavity and reenters the maxillary sinus through a surgically created opening separate from the natural ostium (right side). The nasal antral window is an antrostomy surgically created immediately below the lateral insertion of the inferior turbinate and is not in continuity with the natural ostia. Any middle maxillary sinus wall defect seen on the postoperative CT scan should be noted. Note the normal mucociliary pattern on the left beating toward the natural ostium. **B**, Coronal CT scan. Note the patent middle meatal antrostomy on the left (*arrow*). There is also nearly complete resection of the inferior turbinates. No recurrent sinus inflammatory changes are noted. The meatal antrostomy, turbinate resection, and extensive loss of mucosa may contribute to abnormal sinus ventilation and function, resulting in nasal dryness and crusting simulating recurrent sinusitis.

Copyright © 2003, Mosby, Inc. All rights reserved.

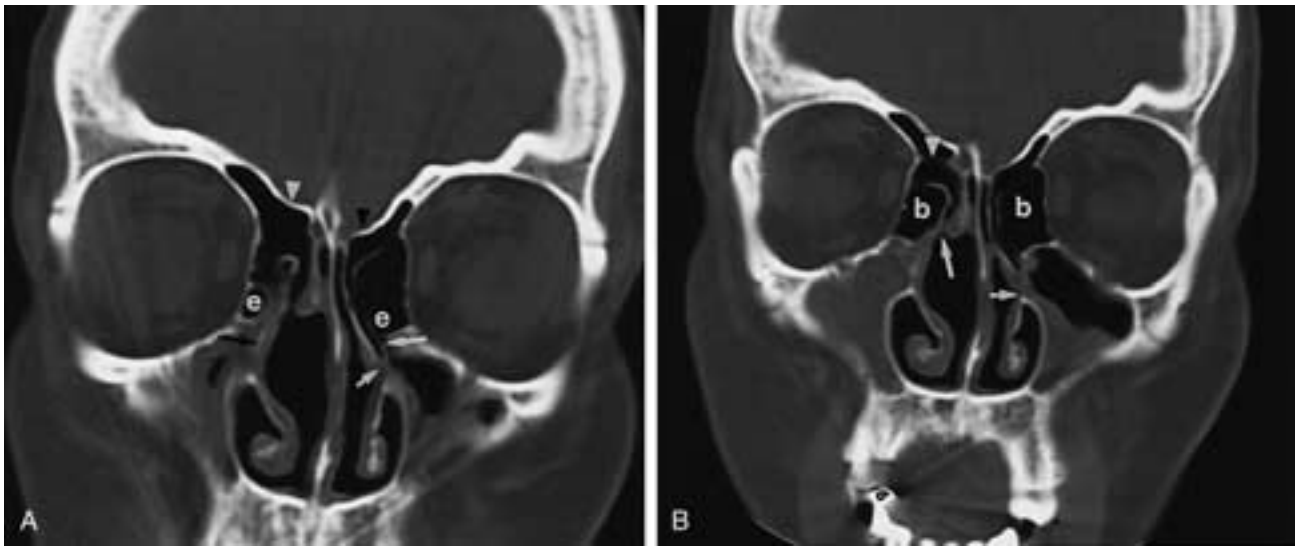

VIEW IMAGE

FIGURE 4-18 Recurrent sinusitis, preoperative scan prior to revision surgery. **A**, Coronal CT scan. On the right side, note the residual uncinate process (*black arrow*) and inflammatory hyperplastic mucosa in the maxillary sinus. Hyperplastic mucosa is seen along the uncinate process and the residual anterior ethmoid air cell (*e*), contributing to infundibular stenosis. On the left side, the inferior aspect of the middle turbinate (*short white arrow*) is lateralized and adherent to the residual uncinate process (*long white arrow*). Note the residual ethmoid air cell (*e*). There is asymmetry of the ethmoid roofs, with the left roof (*black arrowhead*) 8 mm lower than the right (*white arrowhead*). **B**, Coronal CT scan posterior to **A**. There are residual ethmoid bullar cells (*b*) bilaterally, and infundibular stenosis with adhesions between the middle turbinate and the lateral nasal wall on the left (*short arrow*) and the bulla and lateral nasal wall on the right (*long arrow*). Incidental note is made of an unprotected anterior ethmoid artery (*arrowhead*), without a bony canal, in the right ethmoid roof.

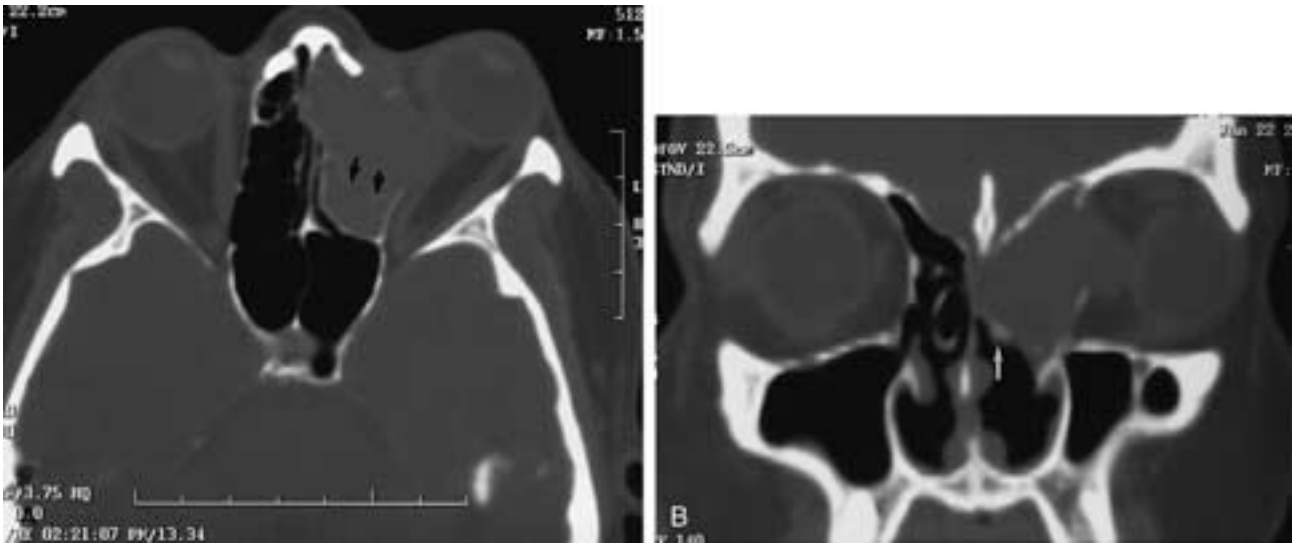

VIEW IMAGE

FIGURE 4-19 Post-FESS frontoethmoidal mucocele, likely due to postoperative frontal recess stenosis. **A**, On the axial CT scan, 1-mm slice thickness, the left ethmoid sinus is airless and expanded. Deossification of the medial orbital wall results in poor visualization of the bony wall, and there is intraorbital, extraconal extension of the mucocele. Note the posterior displacement of the anterior wall of the posterior ethmoid sinus (*arrows*). **B**, The high-resolution coronal reformation shows a prior septoplasty, resection of both inferior turbinates, with only the inferior aspect of the left middle turbinate remaining (*arrow*), and the large mucocele. Recurrent frontoethmoidal recess stenosis from synechiae or mucosal disease likely led to the mucocele. The patient complained only of proptosis.

Copyright © 2003, Mosby, Inc. All rights reserved.

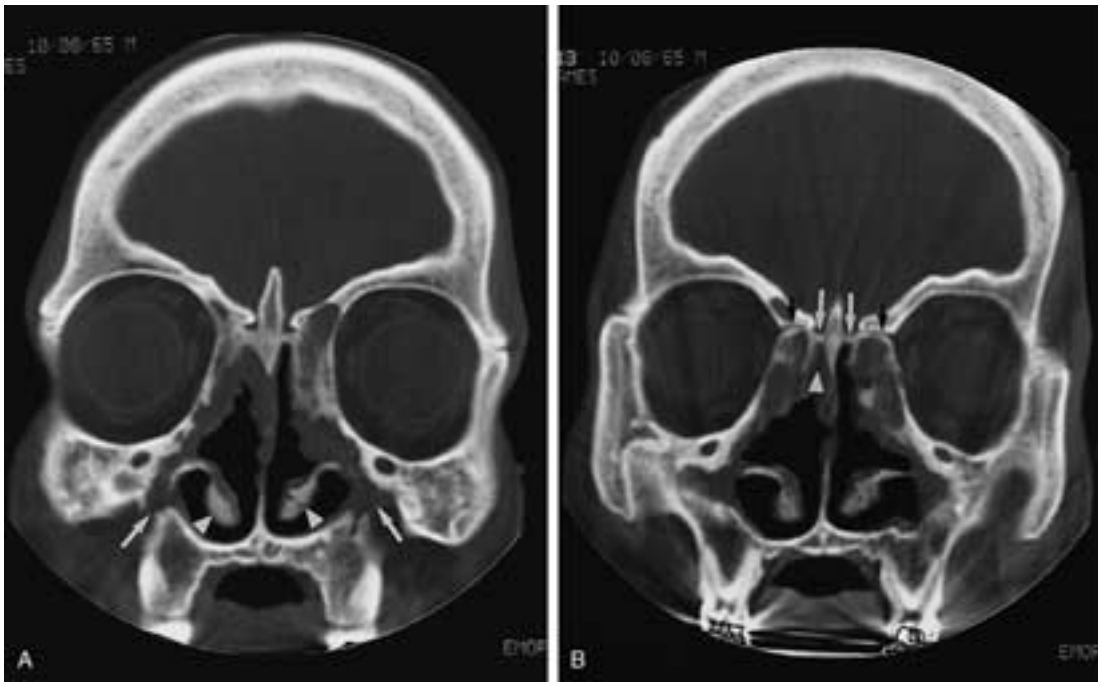

VIEW IMAGE

FIGURE 4-20 Recurrent polyposis. **A**, On this coronal CT scan, note the maxillary sinus hypoplasia, prior Caldwell-Luc defects (*arrows*), and diffuse recurrent mucosal thickening. There is extensive osteitis involving all the sinus cavity walls and even the bone of the inferior turbinates (*arrowheads*). **B**, Coronal CT scan posterior to **A**. Inflammatory mucosal changes are seen medial to the right middle turbinate (*arrowhead*). This area is almost never approached surgically, as injury to the perforated cribriform plate (*white arrows*) can result in CSF leak. The sinus walls are so dense and sclerotic that the anterior ethmoid artery canals (*black arrows*) are well seen.

turbinate.[66] Histopathologic study reveals an increase in bone physiology with bone resorption, neogenesis, and fibrosis, similar to chronic osteomyelitis.[67] Chronic inflammatory changes are seen even when the overlying mucosa is normal. It is not clear whether this is a response to chronic infection or surgery or whether it is causal in the continuing cycle of sinusitis. These poorly understood osseous changes should be noted on screening sinus CT because of their frequent coexistence with chronic sinusitis. The bony changes may be isolated to a portion of a sinus, may be present throughout the sinus walls, or may be strategically located at the sinus ostium. This is an area of active basic research because of the potential implications for long-term antibiotic treatment.[67]

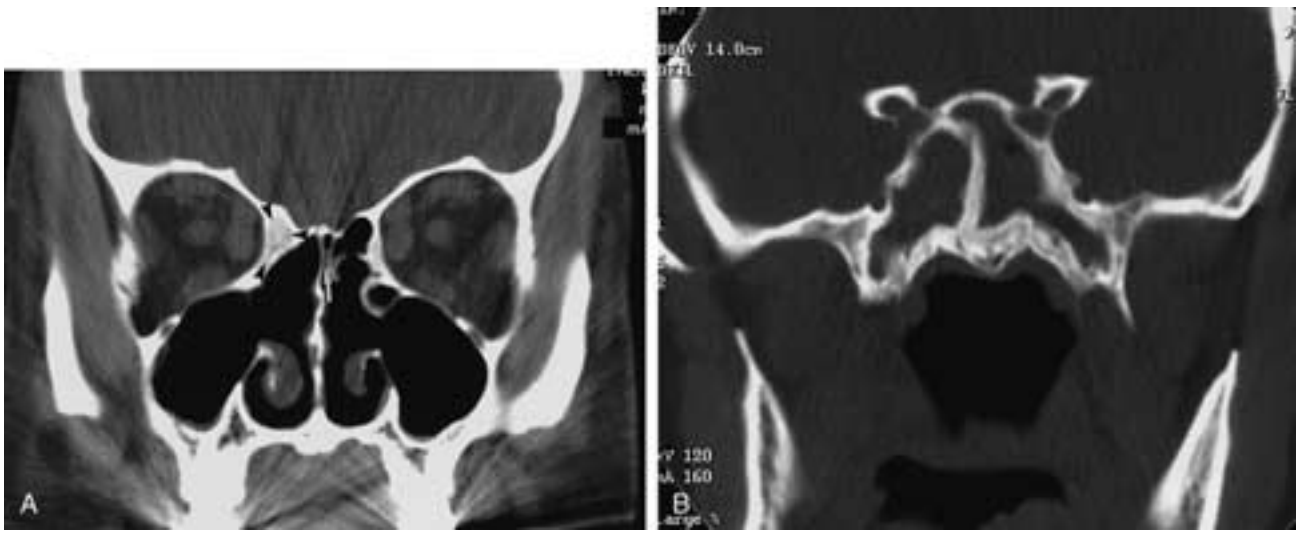

VIEW IMAGE

FIGURE 4-21 Failed FESS, two separate patients with osteitis. **A**, Coronal CT scan. At this level the maxillary ostia and infundibulum are widely patent, and the residual left middle turbinate is adherent to the nasal septum (*arrow*), a desired postoperative result, as the ethmoid infundibulum is patent. Note that at this level the entire right middle turbinate, even the vertical portion, has been resected. This observation should be reported in the dictation, as an important surgical landmark is gone. The dense sclerosis within the right ethmoid complex (*arrowheads*) is seen and represents a new finding. The significance of this physiologic bony change is not well understood, but it likely relates to chronic osteitis and inflammatory changes and is a common finding in patients with recurrent symptoms after FESS. **B**, Coronal CT scan. In this patient with recurrent sphenoid sinusitis after FESS, note the sclerosis of the sinus walls and the intersphenoidal septum.

Copyright © 2003, Mosby, Inc. All rights reserved.

REFERENCES

1. Stankiewicz JA. Complications of endoscopic intranasal ethmoidectomy. Laryngoscope 1987;97:1270–1273.
2. Stankiewicz JA. Complications in endoscopic intranasal ethmoidectomy: an update. Laryngoscope 1989;99:686–690.
3. Rontal M, Rontal E. Studying whole-mounted sections of the paranasal sinuses to understand the complications of endoscopic sinus surgery. Laryngoscope 1991;101:361–366.
4. Meyers RM, Valvassori G. Interpretation of anatomic variations of computed tomography scans of the sinuses: a surgeon's perspective. Laryngoscope 1998;108:422–425.
5. Maniglia AJ. Fatal and other major complications of endoscopic sinus surgery. Laryngoscope 1991;101:349–354.
6. Kinsella JB, Calhoun KH, Bradfield JJ, et al. Complications of endoscopic sinus surgery in a residency training program. Laryngoscope 1995;105:1029–1032.
7. Maniglia A. Fatal and major complications secondary to nasal and sinus surgery. Laryngoscope 1989;99:276–283.
8. Weber R, Draf W, Keerl R, et al. Endonasal microendoscopic pansinus operation in chronic sinusitis. II. Results and complications. Am J Otolaryngol 1997;18:247–253.
9. Keerl R, Stankiewicz J, Weber R, et al. Surgical experience and complications during endonasal sinus surgery. Laryngoscope 1999; 109:546–550.
10. May M, Levine HL, Mester SJ, Schaitkin B. Complications of endoscopic sinus surgery: analysis of 2108 patients—incidence and prevention. Laryngoscope 1994;104:1080–1083.
11. Hudgins PA, Browning DG, Gallups J, et al. Endoscopic paranasal sinus surgery: radiographic evaluation of severe complications. AJNR 1992;13:1161–1167.
12. Rhoton AL Jr, Renn WH, Harris FS. Microsurgical anatomy of the sellar region cavernous sinuses. In: Rand RW, ed. Microneurosurgery. 2nd ed. St. Louis: C.V. Mosby, 1978; •••.
13. Johnson DM, Hopkins, RJ, Hanafee WN, Fisk JD. The unprotected parasphenoidal carotid artery studied by high-resolution computed tomography. Radiology 1985;155:137–141.
14. Hegazy HM, Carrau RL, Snyderman CH, et al. Transnasal endoscopic repair of cerebrospinal fluid rhinorrhea: a meta-analysis. Laryngoscope 2000;110:1166–1172.
15. Senior BA, Jafri K, Benninger M. Safety and efficacy of endoscopic repair of CSF leaks and encephaloceles: a survey of the members of the American Rhinologic Society. Am J Rhinol 2001;15:21–25.
16. Weber R, Keerl R, Draf W, et al. Management of dural lesions occurring during endonasal sinus surgery. Arch Otolaryngol Head Neck Surg 1996;122:732–736.
17. Mattox DE, Kennedy DW. Endoscopic management of cerebrospinal fluid leaks and cephaloceles. Laryngoscope 1990;100:857–862.
18. Stankiewicz JA. Cerebrospinal fluid fistula and endoscopic sinus surgery. Laryngoscope 1991;101:250–256.
19. Caversaccio M, Bachler R, Ladrach K, et al. Frameless computer-aided surgery system for revision endoscopic sinus surgery. Otolaryngol Head Neck Surg 2000;122:808–813.
20. Lawson W. The intranasal ethmoidectomy: evolution and an assessment of the procedure. Laryngoscope 1994;104(Suppl 64):13–16.
21. Janssen AG, Mansour K, Bos JJ. Obstructed nasolacrimal duct system in epiphora: long-term results of dacryocystoplasty by means of balloon dilation. Radiology 1997;205:791–796.
22. Stankiewicz JA, Chow JM. Two faces of orbital hematoma in intranasal (endoscopic) sinus surgery. Otolaryngol Head Neck Surg 1999;120:841–847.
23. Chung S-K, Dhong HJ, Kim HY. Computed tomography anatomy of the anterior ethmoid canal. Am J Rhinol 2001;15:77–81.
24. Moulin G, Dessi P, Chagnaud C, et al. Dehiscence of the lamina papyracea of the ethmoid bone: CT findings. Am J Neuroradiol 1994;15:151–153.
25. May M, Sobol SM, Korzec K. The location of the maxillary os and its importance to the endoscopic sinus surgeon. Laryngoscope 1990;100: 1037–1042.
26. Driben JS, Bolger WE, Robles HA, et al. Maxillary sinus hypoplasia: classification and description of associated uncinate process hypoplasia. Otolaryngol Head Neck Surg 1990;103:759–765.
27. Bolger WE, Woodruff WW, Morehead J, Parsons DS. Maxillary sinus hypoplasia: classification and description of associated uncinate process hypoplasia. Otolaryngol Head Neck Surg 1990;103: 759–765.
28. Stammberger H. Results, problems, and complications. In: Stammberger H, ed. Functional Endoscopic Sinus Surgery. Philadelphia: B.C. Decker, 1991;459–477.
29. Messerklinger W. On the drainage of the normal frontal sinus of man. Acta Otolaryngol 1967;63:176–181.
30. Kennedy DW, Zinreich SJ. Functional endoscopic approach to inflammatory sinus disease: current perspectives and technique modifications. Am J Rhinol 1988;2:89–96.
31. Stammberger H. Endoscopic surgery—concepts in treatment of recurring rhinosinusitis. Part I. Anatomic and pathophysiologic considerations. Otolaryngol Head Neck Surg 1986;115:143–146.
32. Guo Y, Majima Y, Hattori M, et al. Effects of functional endoscopic sinus surgery on maxillary sinus mucosa. Arch Otolaryngol Head Neck Surg 1997;123:1097–1100.
33. Waguespack R. Mucociliary clearance patterns following endoscopic sinus surgery. Laryngoscope 1995;105(Suppl 71):1–40.
34. Lawson W. The intranasal ethmoidectomy: evolution and an assessment of the procedure. Laryngoscope 1994;104(Suppl 64):13–16.
35. Havas TE, Motbey JA, Gullane PJ. Prevalence of incidental abnormalities on computed tomographic scans of the paranasal sinuses. Arch Otolaryngol Head Neck Surg 1988;114:856–859.
36. Zinreich SJ, Kennedy DW, Rosenbaum AE, et al. Paranasal sinuses: CT imaging requirements for endoscopic surgery. Radiology 1987; 163:769–775.
37. Bolger WE, Butzin CA, Parsons DS. Paranasal sinus bony anatomic variations and mucosal abnormalities: CT analysis for endoscopic sinus surgery. Laryngoscope 1991;101:56–64.
38. Levine HL. Functional endoscopic sinus surgery: evaluation, surgery, and follow-up of 250 patients. Laryngoscope 1990;100:79–84.
39. Rice DH. Endoscopic sinus surgery: Results at 2-year followup. Otolaryngol Head Neck Surg 1989;101:476–479.
40. Chambers DW, Davis WE, Cook PR, et al. Long-term outcome analysis of functional endoscopic sinus surgery: correlation of symptoms with endoscopic examination findings and potential prognostic variables. Laryngoscope 1997;107:504–510.
41. Lazar RH, Younis RT, Long TE, Gross CW. Revision functional endonasal sinus surgery. Ear Nose Throat J 1992;71(3):131–133.
42. Kennedy DW. Prognostic factors, outcomes, and staging in ethmoid sinus surgery. Laryngoscope 1992;102(Suppl 57):1–18.
43. Stammberger H, Wolf G. Headaches and sinus disease: the endoscopic approach. Ann Otol Rhinol Laryngol Suppl 1988;134:3–23.
44. King JM, Caldarelli DD, Pigato JB. A review of revision functional endoscopic sinus surgery. Laryngoscope 1994;104:404–408.
45. Hosemann W, Kuhnel T, Held P, et al. Endonasal frontal sinusotomy in surgical management of chronic sinusitis: a critical evaluation. Am J Rhinol 1997;11:1–9.
46. Bhattacharyya T, Piccirillo J, Wippold FJ II. Relationship between patient-based descriptions of sinusitis and paranasal sinus computed tomographic findings. Arch Otolaryngol Head Neck Surg 1997;123: 1189–1192.
47. Stewart MG, Sicard MW, Piccirillo JF, Diaz-Marchan PJ. Severity staging in chronic sinusitis: are CT scan findings related to patient symptoms? Am J Rhinol 1999;13:161–167.
48. Lanza DC, Kennedy DW. Adult rhinosinusitis defined. Otolaryngol Head Neck Surg 1997;117:51–57.
49. Gaskins RE. A surgical staging system for chronic sinusitis. Am J Rhinol 1992;6:5–12.
50. Friedman WH, Katsantonis GP, Bumpous JM. Staging of chronic hyperplastic rhinosinusitis: treatment strategies. Otolaryngol Head Neck Surg 1995;112:210–214.
51. Stewart MG, Donovan DT, Parke RB, Bautista MH. Does the severity of sinus computed tomography findings predict outcome in chronic sinusitis? Otolaryngol Head Neck Surg 2000;123:81–84.
52. Lund VJ, Holmstrom M, Scadding GK. Functional endoscopic sinus surgery in the management of chronic rhinosinusitis. An objective assessment. J Laryngol Otol 1991;105:832–835.
53. Kerrebijn JDF, Drost HE, Spoelstra HAA, Knegt PP. If functional sinus surgery fails: a radical approach to sinus surgery. Otolaryngol Head Neck Surg 1996;114:745–747.
54. Matthews BL, Smith LE, Jones R, et al. Endoscopic sinus surgery: outcome in 155 cases. Otolaryngol Head Neck Surg 1991;104: 244–246.

Copyright © 2003, Mosby, Inc. All rights reserved.

55. Elahi MM, Frenkiel S. Septal deviation and chronic sinus disease. Am J Rhinol 2000;14:175–179.
56. Katsantonis GP, Friedman WH, Sivore MC. The role of computed tomography in revision sinus surgery. Laryngoscope 1990;100: 811–816.
57. Chu TC, Lebowitz RA, Jacobs JB. An analysis of sites of disease in revision endoscopic sinus surgery. Am J Rhinol 1997;11:287–291.
58. Vleming M, de Vries N. Endoscopic paranasal sinus surgery: results. Am J Rhinol 1990;4:13–17.
59. Fortune DS, Duncavage JA. Incidence of frontal sinusitis following partial middle turbinectomy. Ann Otol Rhinol Laryngol 1998;107: 447–453.
60. Alusi HA. A new approach to the surgical treatment of chronic maxillary sinusitis. J Laryngol 1980;94:1145–1149.
61. Kuhn FA, Javer AR, Nagpal K, Citardi MJ. The frontal sinus rescue procedure: early experience and three-year follow-up. Am J Rhinol 2000;14:211–216.
62. Weber R, Draf W, Keerl R, et al. Osteoplastic frontal sinus surgery with fat obliteration: technique and long-term results using magnetic resonance imaging in 82 operations. Laryngoscope 2000;110:1037–1044.
63. Gross WE, Gross CW, Becker D, et al. Modified transnasal endoscopic Lothrop procedure as an alternative to frontal sinus obliteration. Otolaryngol Head Neck Surg 1995;113:427–434.
64. Weber R, Draf W, Kratzsch B, et al. Modern concepts of frontal sinus surgery. Laryngoscope 2001;111:137–146.
65. Jantti-Alanko S, Holopainen E, Malmberg H. Recurrence of nasal polyps after surgical treatment. Rhinology 1989;Suppl 8:59–64.
66. Biedlingmaier JF, Whelan P, Zoarski G, Rothman M. Histopathology and CT analysis of partially resected middle turbinates. Laryngoscope 1996;106:102–104.
67. Kennedy DW, Senior BA, Gannon FH, et al. Histology and histomorphometry of ethmoid bone in chronic rhinosinusitis. Laryngoscope 1998;108:502–507.

Copyright © 2003, Mosby, Inc. All rights reserved.

5

Inflammatory Diseases

Peter M. Som and Margaret S. Brandwein

ACUTE RHINOSINUSITIS
AIR-FLUID LEVELS
CHRONIC SINUSITIS
- Allergic Sinusitis
- Vasomotor Rhinitis
- Fungal Sinusitis
  - Fungal Hyphal Diseases
  - Fungal Yeast Forms

CYSTS AND POLYPS
- The Pediatric Patient
- The HIV-Positive Patient

MUCOCELES
CORRELATION OF IMAGING AND CLINICAL FINDINGS
IMAGING "NORMAL" MUCOSA
MAGNETIC RESONANCE OF PROTEIN SOLUTIONS
IMAGING
- Benign Sinonasal Mucosal Disease
- Polyps and Cysts
- Mucoceles
- Fungal Diseases

INFECTIOUS DESTRUCTIVE AND GRANULOMATOUS SINONASAL DISEASES
- *Actinomyces* and *Nocardia*

NONINFECTIOUS DESTRUCTIVE SINONASAL DISEASE
- Imaging

CHOLESTEATOMAS
ENLARGED AERATED SINUSES
SMALL OR ABSENT AERATED SINUSES
COMPLICATIONS OF INFLAMMATORY PARANASAL SINUS DISEASE AFFECTING ADJACENT AREAS
THE NEED FOR PREOPERATIVE IMAGING
FOREIGN BODIES
ANOSMIA
SYNDROMES AND SINUSITIS
- Kartagener's Syndrome
- Primary Ciliary Dyskinesia Syndrome
- Young's Syndrome
- Sertoli-Cell-Only Syndrome
- Hyperimmunoglobulinemia E Syndrome
- Churg-Strauss Syndrome
- Nijmegen Paragraph Signbreakage Syndrome
- Croup
- Acquired Immune Deficiency Syndrome
- Aspirin Triad Syndrome
- Silent Sinus Syndrome
- Toxic Shock Syndrome
- Cyclic Vomiting Syndrome
- Yellow Nail Syndrome
- (P)FAPA Syndrome
- Ataxia Telangiectasia Syndrome
- Wiskott-Aldrich Syndrome

ACUTE RHINOSINUSITIS

Sinonasal inflammatory disease is a ubiquitous illness, and virtually everyone experiences multiple episodes of either a viral, bacterial, allergic, vasomotor-related, or reactive type of sinonasal inflammation. Of these, it is the common cold that is the most frequent infectious malady of the upper respiratory tract, and it is one of the major causes of absenteeism from work. The primary clinical manifestations of this viral infection are clear, watery, profuse nasal discharge and nasal stuffiness that usually persist for less than a week. The evoked inflammatory changes are completely reversible. The most common causative agents are rhinoviruses, parainfluenza and influenza viruses, adenoviruses, and respiratory syncytial virus.[1]

The typical cold is rarely imaged and it remains primarily a viral rhinitis with little significant sinusitis. If imaging is obtained, it usually shows thickening of the nasal fossae

Copyright © 2003, Mosby, Inc. All rights reserved.

mucosa, swelling of the turbinates, and little, if any, sinus mucosal disease.

If the clear nasal discharge becomes mucopurulent, a secondary bacterial infection has developed. This occurs when the swollen nasal or sinus mucosa causes obstruction of a sinus ostium. This causes the oxygen tension within the sinus to decrease and the normal bacterial flora becomes altered, resulting in a secondary-type acute bacterial sinusitis. Direct sinus puncture or open surgical biopsies yield the most accurate bacterial cultures for a sinusitis, as these procedures prevent contamination by the nasal flora.[2] The most commonly implicated pathogens from such studies are *Streptococcus pneumoniae* (pneumococcus), *Haemophilus influenzae*, and beta-hemolytic streptococcus. Rarely, *Staphylococcus aureus* and *Pseudomonas* infections occur.[3] Pathogenic anaerobes are rare in acute sinusitis. However, in cases of chronic sinusitis with persistently low intrasinus oxygen tensions, anaerobes predominate. These anaerobes include peptostreptococci, *Bacteroides sp. lanchnicus*, and fusobacteria.[4, 5] In the case of the maxillary sinus, it is estimated that 10% to 20% of the infections are secondary to dental infection or are the result of a complication of a tooth extraction.[6]

When imaging sinus mucosal inflammation from any cause, the inflamed mucosa enhances and there are variable amounts of submucosal edema and increased surface secretions (Fig. 5-1). There is no apparent prognostic relationship between the clinical response to the cause of the inflammation and the degree of submucosal edema or the amount of sinus secretions. An important point to note is that normal sinus secretions and submucosal fluid are each about 95% water. As these two fluids in varying amounts comprise the major response to sinonasal inflammation, inflammation is characterized by a water dominated response. This is important when MR imaging inflammation, where the signal intensities will be those of water.

If the sinus ostium is only transiently obstructed, with conservative treatment the bacterial sinusitis often resolves within 4 to 7 days. Sinusitis can cause pain over the affected sinus: cheek pain is associated with an antral infection, frontal pain may be caused by a frontal sinusitis, pain between the eyes may indicate an anterior ethmoid sinusitis, and suboccipital pain is often the result of a posterior ethmoid or sphenoid sinusitis. By comparison, a true headache is estimated to occur in only 3% of patients with sinusitis. Conversely, only 7% of headaches are the result of sinusitis.

Although a generalized headache can occur, it is unusual and may reflect intracranial spread of the sinonasal infection. Due to a rich venous emissary plexus between the posterior frontal sinus mucosa and the meninges, acute frontal sinusitis is most likely to spread intracranially, and clinical manifestations of this may be present in as few as 36 to 48 hours after initial presentation. Sphenoid and ethmoid sinusitis are the next most likely to progress to intracranial

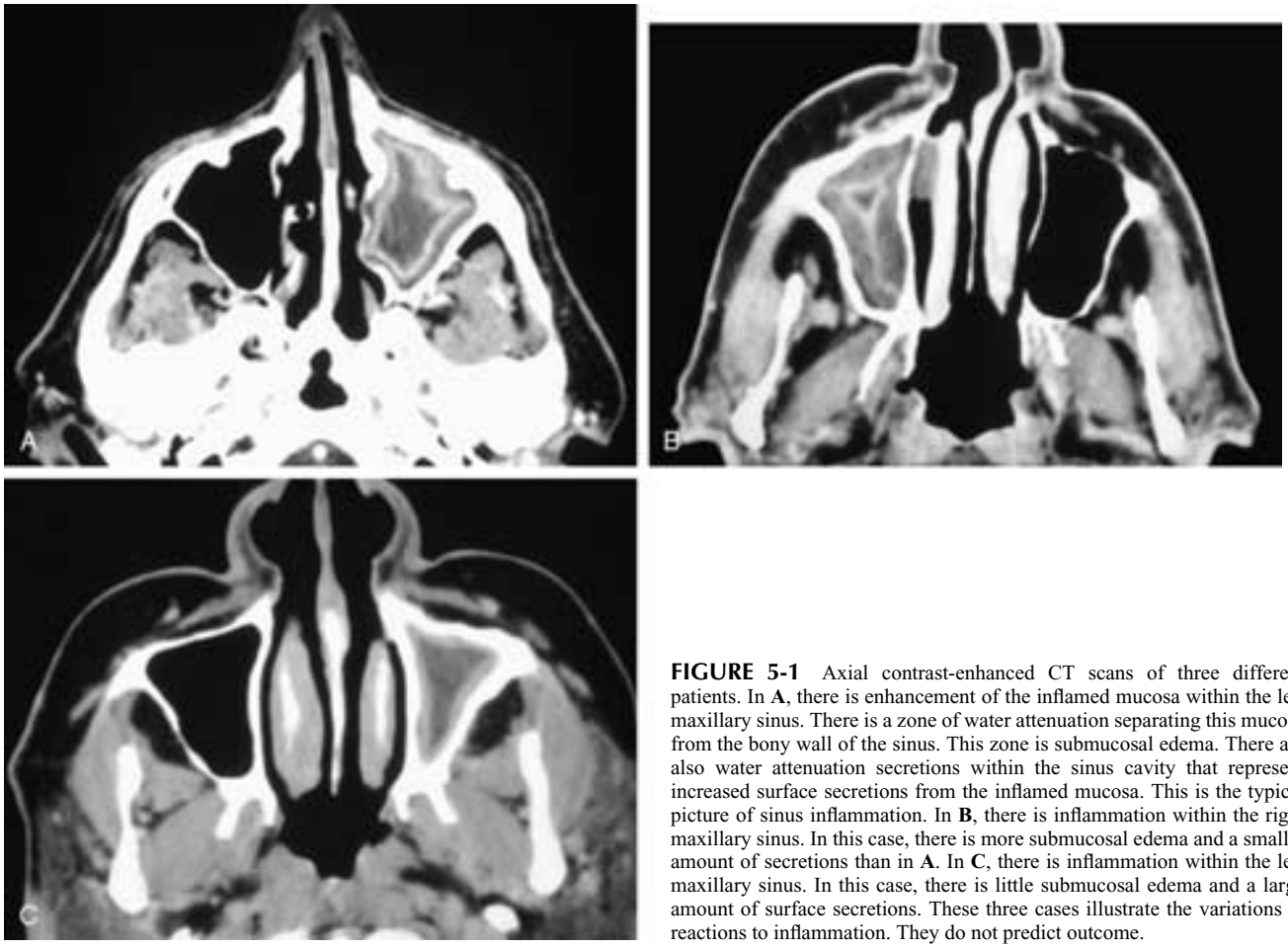

FIGURE 5-1 Axial contrast-enhanced CT scans of three different patients. In **A**, there is enhancement of the inflamed mucosa within the left maxillary sinus. There is a zone of water attenuation separating this mucosa from the bony wall of the sinus. This zone is submucosal edema. There are also water attenuation secretions within the sinus cavity that represent increased surface secretions from the inflamed mucosa. This is the typical picture of sinus inflammation. In **B**, there is inflammation within the right maxillary sinus. In this case, there is more submucosal edema and a smaller amount of secretions than in **A**. In **C**, there is inflammation within the left maxillary sinus. In this case, there is little submucosal edema and a large amount of surface secretions. These three cases illustrate the variations in reactions to inflammation. They do not predict outcome.

VIEW IMAGE

Copyright © 2003, Mosby, Inc. All rights reserved.

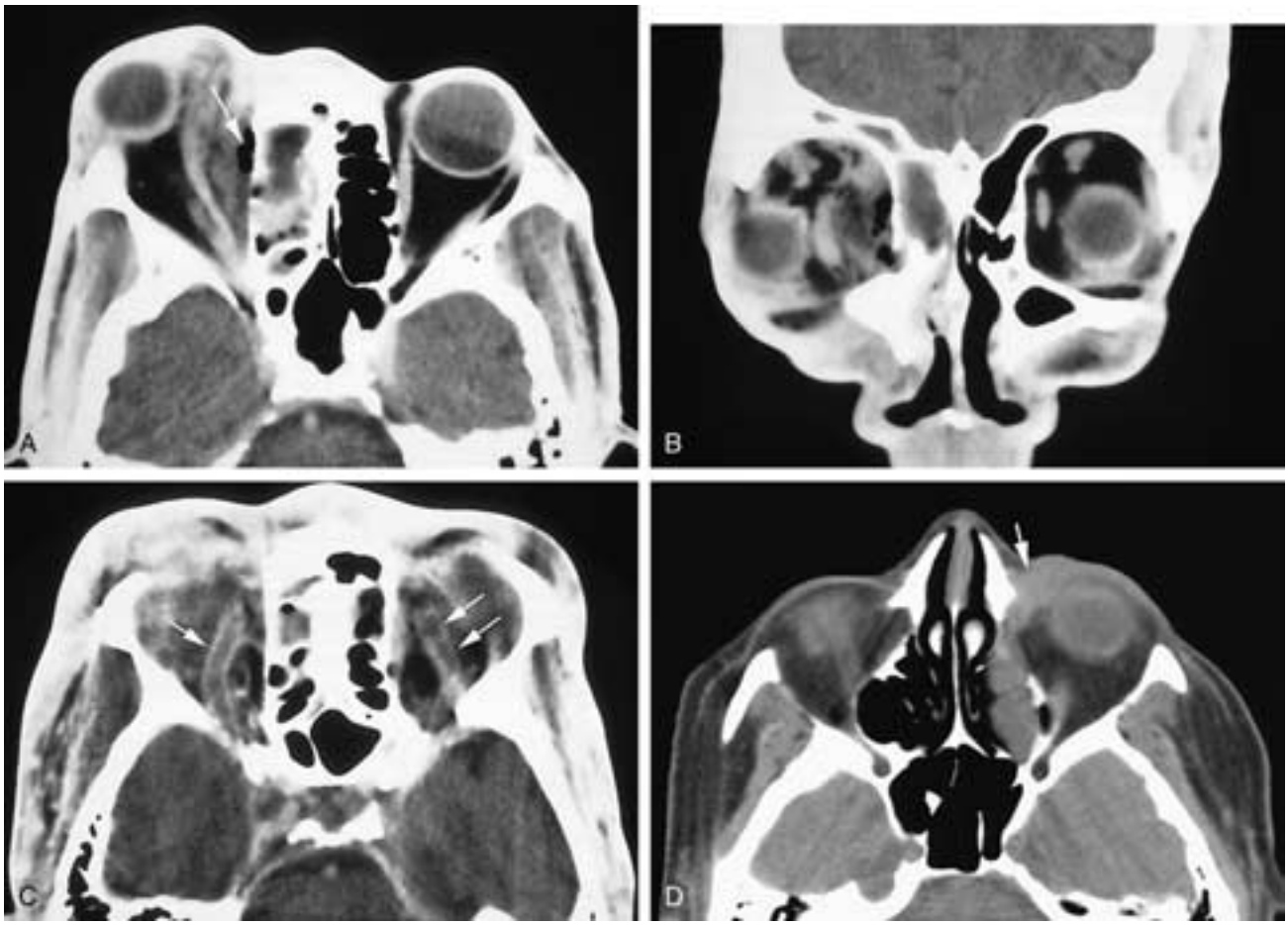

VIEW IMAGE

FIGURE 5-2 Axial (**A**) and coronal (**B**) contrast-enhanced CT scans on a patient with a right ethmoid sinusitis, a right orbital cellulitis, and air in an abscess (*arrow*). The globe is proptotic and laterally displaced. There is no gross defect in the right lamina papyracea. In **C**, a patient developed a right orbital cellulitis secondary to a right ethmoid sinusitis. The infection spread via the right superior ophthalmic vein (*arrow*) to the cavernous sinus, across the sella's vascular bed to the left cavernous sinus, and then retrograde into the left orbit via the left superior ophthalmic vein (*arrows*). In **D**, there is a left ethmoid sinusitis that spread through the lamina papyracea into the left lacrimal saccular area (*arrow*) and presented clinically as an acute dacryocystitis. This is a case of pseudodacryocystitis secondary to an ethmoid sinusitis.

infection. Intracranial extension from maxillary sinusitis rarely occurs.

Because headache may be the symptom most often suggesting intracranial extension of sinusitis, the causes of headache have been studied. In one study of 92 patients with headache, migraine was found to be the most frequent cause of headache. In decreasing order of occurrence, the other causes were tension-type headache, sinusitis, and epilepsy. The percentage of the findings relevant to headache on CT scans, MR studies, Waters' projections, and electroencephalograms were, respectively, 4.2%, 33.3%, 16%, and 25%. Observed imaging findings associated with headache included sinusitis, dilatation of the basal cistern, dilatation of the temporal horn of the lateral ventricle, pseudotumor cerebri, and mesiotemporal sclerosis. The conclusion of this study was that the most important points in evaluating these patients are taking a proper history of headache, obtaining a thorough physical and neurologic examination, and performing an MR imaging study.[7]

However, the cause of a headache may not be found on imaging studies. In another study on both HIV-seropositive and HIV-seronegative patients over a 2-year period, 50% of all subjects reported a headache. However, the frequency and characteristics of the headaches were not different between the two groups, and the headaches were neither more frequent nor different in HIV-seropositive individuals with advanced immunosuppression. There was no correlation between headache and abnormal CSF parameters, cranial MR imaging abnormalities, including the presence of sinusitis, or the use of zidovudine.[8]

Acute bacterial sinusitis is more likely to spread to the orbits than extend intracranially (Fig. 5-2A–C) (also see Chapter 9). The thin lamina papyracea and the absence of valves in the anterior and posterior ethmoidal veins allow unobstructed intraorbital spread of acute bacterial infection. Sphenoid and maxillary sinusitis are the next most likely to spread to the orbits, followed by frontal sinusitis. Older reports erroneously implicate frontal sinusitis as a major source of orbital infection. However, such cases are more likely the result of supraorbital ethmoid sinusitis. Of all orbital infections, nearly two-thirds arise secondary to sinusitis.

Copyright © 2003, Mosby, Inc. All rights reserved.

The contiguous spread of inflammation from infected ethmoid sinuses into the surrounding tissues of the lacrimal drainage system can produce symptoms easily confused with those of acute dacryocystitis (Fig. 5-2D) (also see Chapter 10). Cases of pseudodacryocystitis arising from anterior ethmoiditis have been reported, and the importance of differentiating these etiologies was noted, as the surgery of choice is an anterior ethmoidectomy rather than dacryocystorhinostomy when such pseudodacryocystitis proves unresponsive to antibiotic therapy.[9]

Acute bacterial sinusitis is the result of sinus ostial obstruction. Thus, bacterial sinusitis occurs as a sinus-by-sinus event rather than as a generalized systemic process. It is more common to find contiguous unilateral bacterial sinusitis than it is to encounter pansinusitis. Even with pansinusitis, one or more sinuses are usually more severely affected. Therefore, as a general rule, asymmetric sinusitis is a hallmark of bacterial disease. By comparison, diffuse, nonlocalized pansinusitis is more often found in allergic patients, presumably as a result of a systemic process rather than a localized obstruction.

With reference to acute maxillary sinus disease, periodontal disease is associated with a twofold increase in the risk of developing maxillary sinusitis. Recognition of this relationship is especially important in the clinical management of patients, particularly those planning to have implant surgery.[10]

Necrotizing fasciitis is a rare condition that usually affects the trunk, perineum, and limbs. Head and neck involvement is particularly rare, and in most cases it is secondary to orbital or dental infection. A case of craniofacial necrotizing fasciitis secondary to a maxillary sinusitis was reported. Although treated intensively and aggressively, the patient died 1 week after hospital admission. This report emphasizes the importance of early diagnosis and aggressive management in these cases.[11]

The relationship between acute sinusitis and ischemic stroke is also largely unexplored. However, the anatomic proximity of the paranasal sinuses and the internal carotid artery suggests that inflammation of the sinuses could easily extend to the intracranial vasculature. Four patients with acute ischemic stroke and extensive disease of the paranasal sinuses have been reported. All of these patients had strokes involving the cavernous internal carotid artery and all also had extensive sinus disease, especially involving the sphenoid sinus. This report suggests that, although rare, there may be a relationship between acute paranasal sinusitis, particularly sphenoid sinusitis, and ischemic stroke.[12]

Sphenoid sinusitis may also cause optic neuritis. Possible mechanisms of nerve damage include direct spread of infection, occlusive vasculitis, and bony deficiency in the wall of the sinus. Patients presenting with isolated optic neuritis and atypical headache should have a CT or MR study. An opaque sphenoid sinus in the context of decreased visual acuity should not be dismissed as coincidental, but considered as pathologic and the patient referred for drainage (Fig. 5-3).[13]

Evaluation of potential acute graft-versus-host disease (AGVHD) after bone marrow transplantation is becoming increasingly common. Imaging of the paranasal sinuses is part of the fever workup for these patients. In a retrospective case control study of 45 adults receiving allogeneic or matched bone marrow transplantation, AGVHD developed in 28 (62%). All patients had paranasal sinus imaging with either CT or plain films for evaluation of possible sinusitis, and no direct correlation was found.[14] On the other hand, another study showed that CT of the paranasal sinuses is advised in patients suffering hemoblastoses, with an increased risk of infectious complications during the transplantation phase, because pathologic findings can be expected in 21% of these patients. The authors emphasized that the diagnosis of and therapy for an acute sinusitis are especially important prior to allogenous bone marrow transplantation.[15]

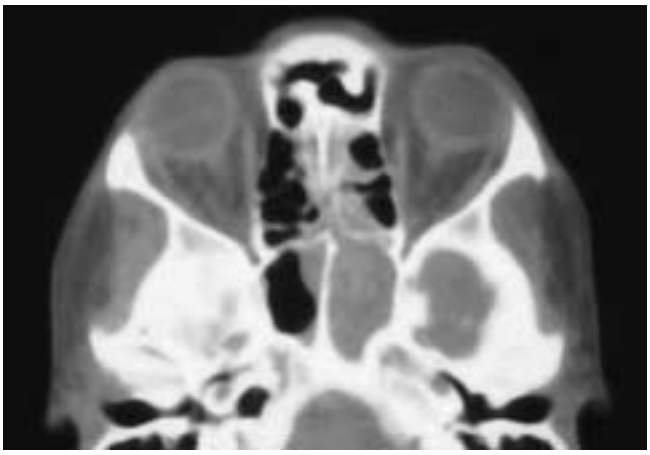

FIGURE 5-3 Axial CT scan of a patient with left optic neuritis and a chronic suboccipital headache. The brain was normal on CT and MR studies. There is opacification of the left sphenoid sinus, and minimal mucosal disease is present in the the right sphenoid sinus and in both ethmoid sinuses. The patient had no symptoms referable to the sinuses. Surgery revealed sinusitis, and in the immediately postoperative period the patient's headache and visual findings resolved. The walls of the sphenoid sinus were intact.

VIEW IMAGE

AIR-FLUID LEVELS

Air-fluid levels are most common in the maxillary sinuses and are the result of acute bacterial sinusitis with obstruction of the sinus ostium. The obstruction does not allow normal sinus drainage to occur, and the sinus secretions accumulate within the sinus cavity. Although bacterial sinusitis is the most common cause of a paranasal sinus air-fluid level, it probably occurs in only 25% to 50% of patients with this disease (Figs. 5-4 to 5-6). In prior decades, when antral lavage was a common therapy for acute obstructive bacterial sinusitis, air-fluid levels could be seen within the sinus for 2 to 4 days after the lavage, reflecting the presence of residual saline that was used in the lavage. If lavage is performed, follow-up films should be obtained at least 7 days after the lavage. A persistent air-fluid level after 7 days indicates renewed sinus obstruction.

Nasogastric tube placement is common in patients with loss of consciousness, severe trauma, or who are post operative. Prolonged supine positioning, and irritation and edema caused by the tube, interferes with normal sinus drainage, and within 24 hours air-fluid levels can be seen in

Copyright © 2003, Mosby, Inc. All rights reserved.

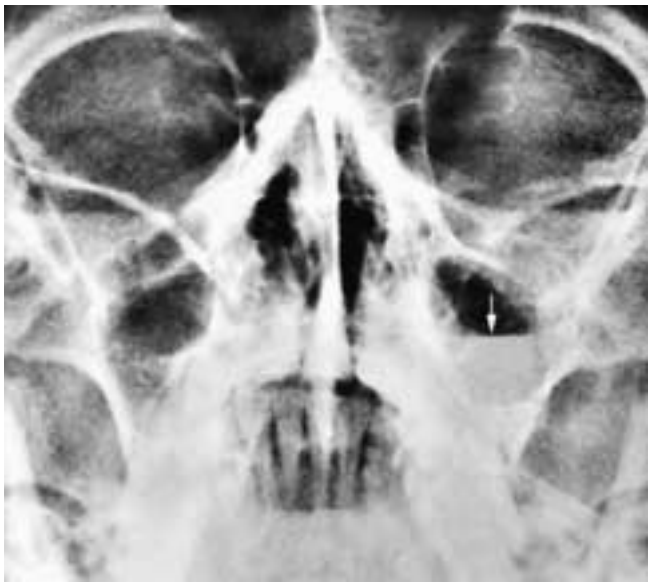

VIEW IMAGE

FIGURE 5-4 Waters view shows a left maxillary sinus air-fluid level (*arrow*) with minimal mucosal thickening within the sinus. The remaining sinuses are normal. This patient had acute bacterial sinusitis.

any or all of the paranasal sinuses.[16] After several days the sinuses may become completely opacified with secretions, and imaging will reveal an apparent pansinusitis. These sinus opacifications usually clear within a few days after the nasal tube is removed and the patient has started to vary head position.

A mucosal tear or rent can occur with physical trauma, regardless of whether a sinus wall fracture occurred. Often, such a tear occurs after blunt trauma, and an air-fluid (air-blood) level usually indicates the presence of a mucosal tear. However, a coincidental acute sinusitis in the affected sinus may cause clinical confusion, which can be avoided by performing a CT or MR study. On CT, intrasinus blood is

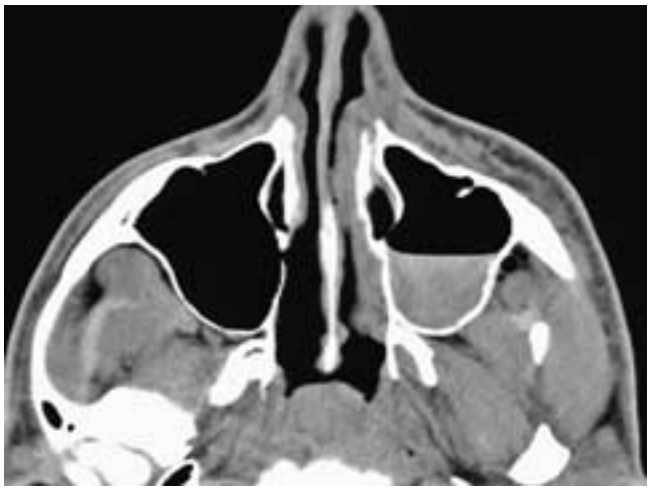

VIEW IMAGE

FIGURE 5-5 Axial CT scan shows an air-fluid level in the left antrum in this patient with a clinically acute sinusitis. The attenuation of the fluid is that of watery ''mucous secretions.'' Also note the slight cellulitis in the left facial soft tissues, as evidenced by thickening of the skin, subcutaneous fat, and facial musculature.

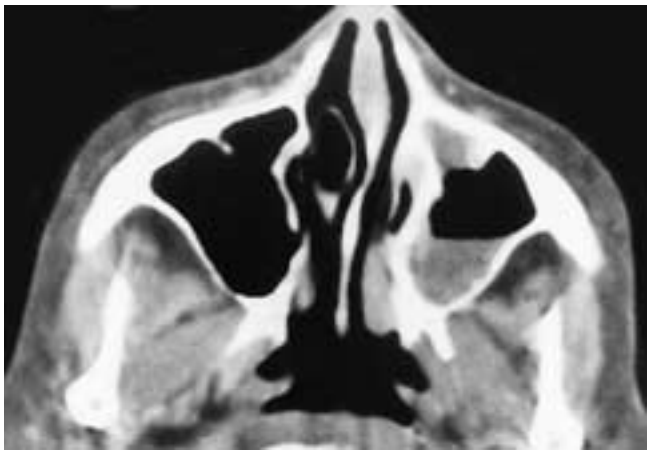

FIGURE 5-6 Axial CT scan shows a left maxillary sinus mucoid attenuation air-fluid level with minimal mucosal thickening. The right maxillary sinus is normal. Clinically this patient had acute bacterial sinusitis.

VIEW IMAGE

denser than normal mucosal edema and inflammatory secretions, and since this is an acute process, desiccated secretions within the sinus are not a consideration (Fig. 5-7). On MR T1-weighted images, intrasinus blood (after 24 to 48 hours) has a high signal intensity (Fig. 5-8). By comparison, acute inflammatory related tissues have a low T1-weighted signal intensity. Thus sectional imaging can resolve questionable cases of sinus hemorrhage.[17, 18]

Barotrauma is a disorder that affects aviators, parachutists, divers, and caisson workers. It most often is associated with an upper respiratory tract infection (34%) accompanied by swelling of the mucosa around the sinus ostium. In these patients, this anatomic substrate prevents rapid pressure equilibration across this ostium, which creates a negative intrasinus pressure that causes rupture of submucosal vessels and sinus hemorrhage. Mucosal and submucosal hemorrhage occurs, usually associated with pain over the involved sinus. Epistaxis is the second most common symptom. The frontal sinus is involved in 68% of cases, the

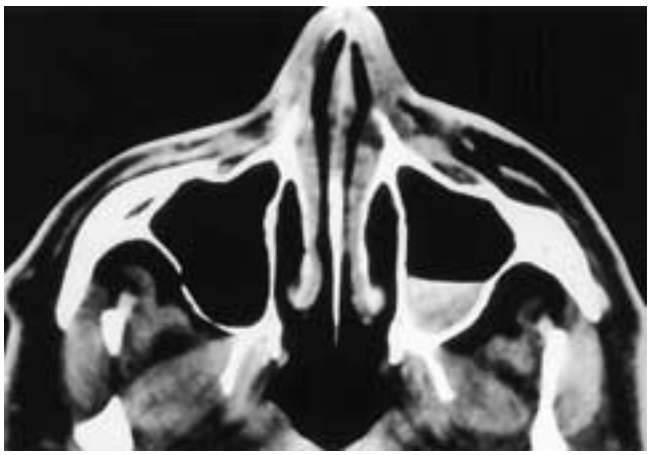

FIGURE 5-7 Axial CT scan shows an air-fluid level in the left maxillary sinus. The fluid is dense compared to water attenuation (see Figs. 5-5 and 5-6) in this patient, who had received blunt facial trauma. This patient had sinus hemorrhage.

VIEW IMAGE

Copyright © 2003, Mosby, Inc. All rights reserved.

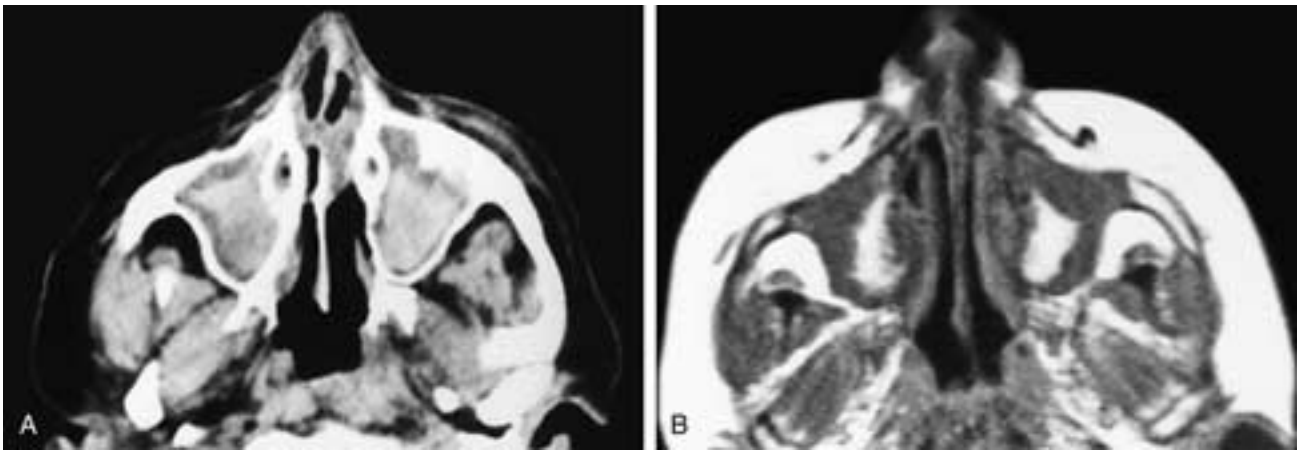

VIEW IMAGE

FIGURE 5-8 In **A**, an axial CT scan shows central areas of increased attenuation in both maxillary sinuses, separated from the sinus walls by a thin zone of mucoid attenuation. This picture is consistent with either chronic sinusitis with desiccated sinus secretions, fungal sinusitis with a mycetoma, or sinus hemorrhage. In **B**, a T1-weighted MR image, the central area of each maxillary sinus has high signal intensity consistent with hemorrhage. The surrounding low signal intensity material is mucosa and fresh secretions.

ethmoid sinus in 16%, and the maxillary sinus in 8%. On plain film studies, mucosal thickening can be detected in the frontal sinuses (24%), the ethmoid sinuses (15% to 19%), and the antrum (74% to 80%); however, an air-fluid level (present in 12% of cases) appears to only be seen in the maxillary sinus.[19]

Hemorrhage can also result from bleeding disorders such as von Willebrand's disease, in which bleeding tends to occur at mucosal surfaces, and possibly Oler Weber Rendu syndrome. Hemophilia, on the other hand, tends to involve internal bleeding and is not associated with a sinus air-fluid level. Coagulation disorders and acute leukemia may also produce air-fluid levels. Rarely, chemically induced sinusitis can produce an air-fluid level. Chromates and other industrial pollutants have been implicated in such cases. Despite the rhinitis and rhinorrhea associated with allergy, few air-fluid levels are seen.

The significance of an air-fluid level varies, depending on the paranasal sinus involved. In the frontal sinuses an air-fluid level usually means acute bacterial sinusitis (Fig. 5-9). As previously mentioned, intracranial complications can occur readily, often within 48 hours (Fig. 5-10).[20] The clinician should be alerted immediately regarding a frontal sinus air-fluid level, as these patients require prompt, vigorous treatment, often including intravenous antibiotics. Failure of a clinical response and the beginning of resolution of the air-fluid level within another 48 to 72 hours after the onset of treatment usually mandates sinus trephination. Such aggressive therapy usually avoids any intracranial complications.

An ethmoid sinus air-fluid level is rare and usually is not associated with either trauma or acute infection. However, if an ethmoid mucocele ruptures and partially drains into the nasal fossa, an air-fluid level may result in what is invariably a mucopyocele. This unusual occurrence is the most common cause of an ethmoid air-fluid level (Fig. 5-11A).

In the sphenoid sinus an air-fluid level may indicate the presence of acute sinusitis or nasal cavity obstruction. An air-fluid level in a supine and/or unconscious patient may only indicate poor sinus drainage. In a trauma patient, a sphenoid sinus air-fluid level may also signify the presence of either hemorrhage or CSF from a skull base fracture. Most often these fractures involve the floor of the anterior cranial fossa or the mastoid portion of the temporal bone, not the sphenoid sinus walls. In the case of anterior skull base fractures, because the dura is firmly attached to the bone, a fracture here is likely to cause a dural rent and resulting CSF rhinorrhea.[21] With the patient supine, the CSF drains back into the sphenoethmoidal recess and into the sphenoid sinus. In the case of a temporal bone fracture with an intact tympanic membrane, the CSF drains into the hypotympanum of the middle ear, escapes via the eustachian tube into the upper nasopharynx and nasal fossa, and then into the sphenoid sinus. Thus CSF rhinorrhea with or without a

FIGURE 5-9 Caldwell view shows soft-tissue clouding of both frontal sinuses and in the right ethmoid sinuses. There is also a right frontal sinus air-fluid level (*arrow*) in this patient with acute bacterial sinusitis.

VIEW IMAGE

Copyright © 2003, Mosby, Inc. All rights reserved.

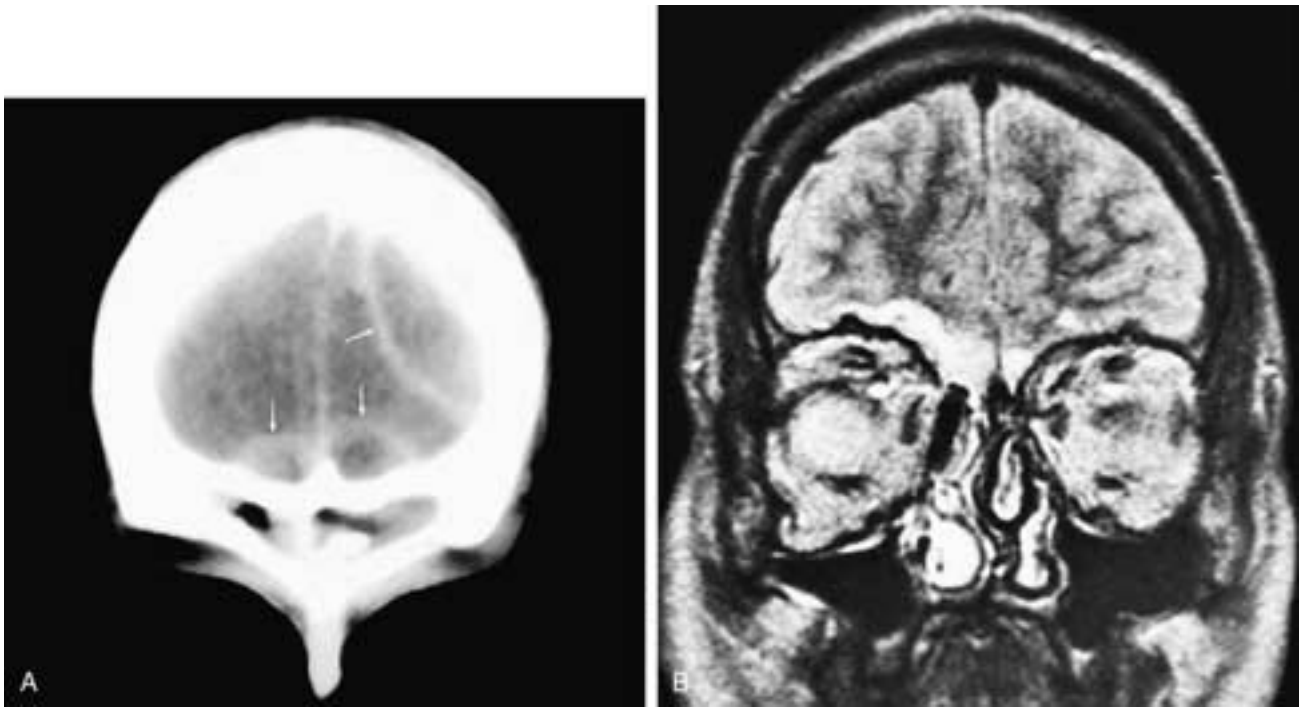

VIEW IMAGE

FIGURE 5-10 In **A**, a coronal CT scan, there is an osteoma obstructing the left frontal sinus and three epidural abscesses (*arrows*) that occurred within 48 hours of the initial frontal sinus symptoms. In **B**, a coronal T2-weighted MR image, there is an area of high signal intensity above the right orbit and in the base of the midline anterior cranial fossa. This patient had cerebritis secondary to frontal sinusitis.

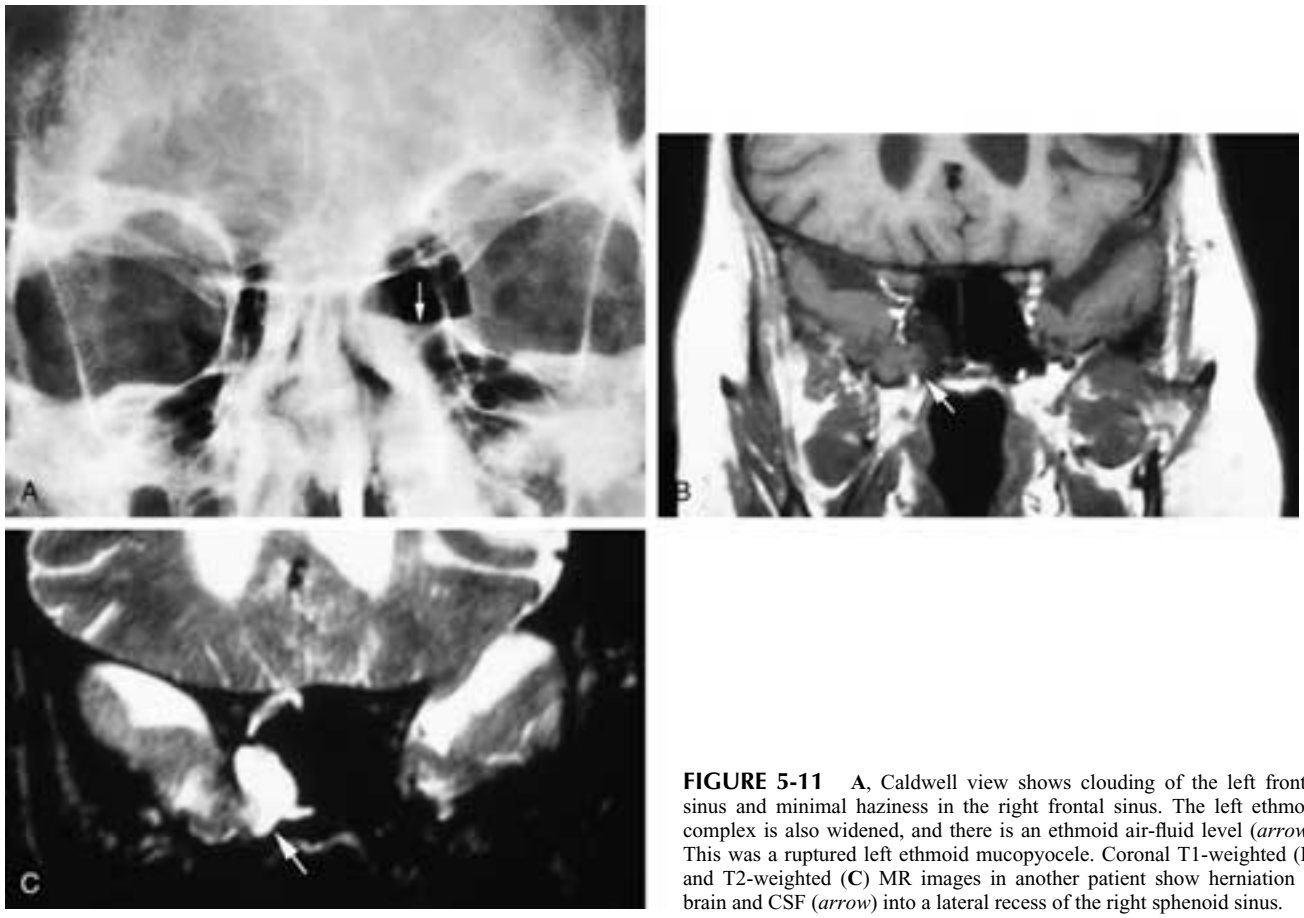

FIGURE 5-11 **A**, Caldwell view shows clouding of the left frontal sinus and minimal haziness in the right frontal sinus. The left ethmoid complex is also widened, and there is an ethmoid air-fluid level (*arrow*). This was a ruptured left ethmoid mucopyocele. Coronal T1-weighted (**B**) and T2-weighted (**C**) MR images in another patient show herniation of brain and CSF (*arrow*) into a lateral recess of the right sphenoid sinus.

VIEW IMAGE

Copyright © 2003, Mosby, Inc. All rights reserved.

sphenoid sinus air-fluid level may reflect a temporal bone fracture.

CSF fluid may also enter the sphenoid sinus spontaneously, usually through a dehiscence in the medial aspect of the roof of a lateral sinus recess (Fig. 5-11B,C). A CSF leak associated with a pituitary tumor or surgery is rare.

CHRONIC SINUSITIS

Chronic sinusitis results from either persistent acute inflammation or repeated episodes of acute or subacute sinusitis. It is estimated that up to one third of patients with acute sinusitis develop some evidence of chronic sinusitis. The chronic disease can result in an atrophic, sclerosing, or hypertrophic polypoid mucosa. These varied mucosal changes most often coexist with one another and with areas of acute inflammation of either an infectious or allergic etiology. Because chronically inflamed and scarred mucosa loses some of its ciliary function, it becomes less resistant to future infection so that a vicious cycle of infection and reinfection may occur in patients with chronic sinusitis. The bony sinus walls surrounding a chronically infected sinus usually become thickened and sclerotic with reactive new bone formation. This bony response is found with all chronic inflammations regardless of etiology and presumably is a response to both the increased local blood flow associated with inflammation and periosteal involvement. However, on CT, care must be taken when viewing a sinus with mucosal disease at narrow ''soft-tissue'' windows, as bone appears denser and wider than it truly is. This is a problem of the algorithms of all CT manufacturers, and the actual bone density and size are best seen on wide window settings (Fig. 5-12).

Epithelial hyperplasia and mucosal infiltration of leukocytes are common features of chronic rhinosinusitis. It has been shown that the epithelium can produce chemoattractant cytokines that may contribute to leukocyte infiltration in rhinosinusitis. Mucosal IL-8 expression is increased in patients with chronic rhinosinusitis, and the level of expression directly correlates with disease severity.[22]

Chronically obstructed sinus secretions can result in four possible outcomes: (1) the sinus obstruction can abate and the sinus will clear, (2) the obstructed secretions can remain indefinitely within the sinus as watery secretions, (3) the entrapped secretions can become desiccated, or (4) the secretions can progressively accumulate and a mucocele can develop. These entities will be described further in the section on Imaging.

Nasal polyps are uncommonly associated with chronic inflammation and when present are most often solitary. By comparison, multiple nasal polyps are common with allergic-type rhinosinusitis. Although mucosal thickening in the nasal fossae, sphenoid, ethmoid, and frontal sinuses is more common in patients with acute asthma than in control subjects, maxillary sinus mucosal thickening is no more common in asthmatic patients than in control subjects.[23]

Allergic Sinusitis

Nearly 10% of the population has allergic rhinosinusitis, which generally involves the sinuses symmetrically. The most common form is seasonal pollinosis, and the prevalent form in North America is ragweed allergy. Spores, molds, and mites are also important antigens.[24] Allergic reactions are manifestations of type I immunologic disorders, which reflect an IgE reagin-antibody reaction, with a resulting release of mediators that produce sneezing, nasal obstruction, and watery rhinorrhea. Profuse secretions associated with nasal obstruction can result in some retained secretions and eventual infection.[24] Thus the coexistence of bacterial and allergic sinusitis is not uncommon. The resulting hypertrophic, thickened, and redundant allergic sinus mucosa is often referred to as *hypertrophic polypoid mucosa*, which is less capable than normal mucosa of resisting subsequent infections. Rarely, in the maxillary sinus, hypertrophic mucosa can become so redundant that it prolapses into the nasal fossa, simulating an antrochoanal polyp.[25] The difference is that in these unusual cases the prolaped tissue is simply redundant mucosa rather than an actual polyp.

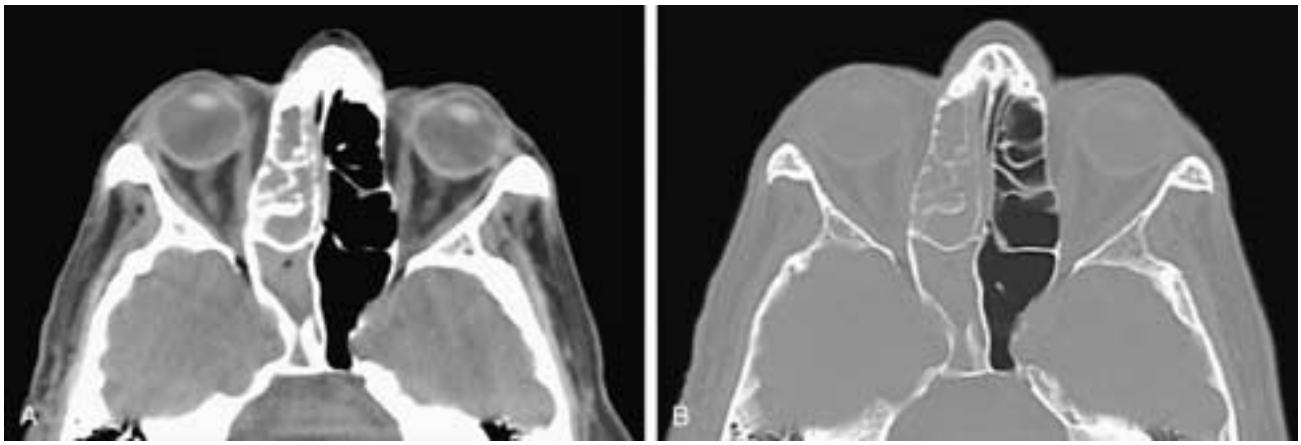

FIGURE 5-12 Axial CT scan (**A**) shows opacification of the right ethmoid and sphenoid sinuses. The ethmoid septae and the surrounding bone appear thickened and sclerotic on this narrow ''soft-tissue'' windowed image. This might imply a chronic process. However, in **B**, the same image viewed at wide ''bone'' window settings, the bone appears normal and similar to that on the left side. This is the more accurate assessment of the bone size and density in this patient with clinically acute sinusitis.

VIEW IMAGE

Copyright © 2003, Mosby, Inc. All rights reserved.

Tissue eosinophilia is a characteristic histologic feature of allergic sinusitis in children and adults, especially those with asthma. However, eosinophilia is not sensitive for allergic sinusitis and does not correlate with the severity of mucosal thickening, as seen on CT scans.[26]

As mentioned, infectious rhinosinusitis is caused by a variety of agents that produce both acute and chronic inflammation that may be associated with secondary polyp formation. These patients commonly have a secretory IgA deficiency.[27] There is evidence to suggest that fluctuating glucose levels occurring in concert with other factors (allergy, infection) may promote nasal polyps in patients with diabetes.[28] In general, nasal polyps in children are uncommon, and 29% of such cases are associated with cystic fibrosis. Between 10% and 20% of children with cystic fibrosis have nasal polyps. Thus, the presence of chronic sinusitis and nasal polyps in a child should prompt an investigation to rule out cystic fibrosis.[29, 30]

The triad (aspirin intolerance) of aspirin usage, nasal polyps (often highly destructive), and bronchial asthma is less commonly encountered, as the generalized use of acetaminophen products has replaced aspirin usage. This triad is associated with severe destructive-type nasal polyposis. In general, about 20% of patients with nasal polyps have asthma, and conversely, about 30% of asthmatic patients have polyps.[29–31] Nickel workers who have worked 10 years or more in nickel-refining facilities have a 4% incidence of inflammatory nasal polyps with squamous metaplasia and dysplasia. They are at increased risk of developing carcinomas in the lung, nasal fossa, and larynx.[32]

Vasomotor Rhinitis

Vasomotor rhinitis refers to the symptoms of nasal congestion, watery discharge, and nasal polyps occurring in the absence of obstruction, ciliary dysfunction, or allergy. These patients do not have evidence of IgE-mediated disease and do not have positive skin tests. Instability of the autonomic nervous system has been implicated as the underlying problem. Vasomotor rhinitis can be stimulated by emotional stress, endocrine imbalance, atmospheric pressure changes, irritants, and as a reaction to medications. Among conditions associated with vasomotor rhinitis in some reports are antihypertensive medications, abuse of nasal sprays and drops, birth control pills, pregnancy and ''premenstrual colds (estrogen related),'' hypothyroidism (2% to 3% of patients), emotional stress, poor environmental temperature control, irritants (dust, gases, chemicals, aerosol cosmetics, and air pollutants such as sulfur dioxide and tobacco), recumbent position, nasal airway exclusion (postlaryngectomy, choanal atresia, marked adenoidal hypertrophy), Horner's syndrome, and systemic disorders such as superior vena cava syndrome, cirrhosis, and uremia.[33] When considering causes of nasal obstruction, vasomotor rhinitis is often a diagnosis of exclusion. Although no consistent imaging findings have been reported in patients with vasomotor rhinitis, one could expect at most to see mild swelling of the turbinates, some increased nasal secretions, and mild mucosal thickening within the sinuses.

Fungal Sinusitis

A variety of fungal diseases involve the sinonasal cavities. These include aspergillosis, mucormycosis, candidiasis, histoplasmosis, cryptococcosis, coccidioidomycosis, North American blastomycosis, rhinosporidiosis, and myospherulosis.[34] There are four clinicopathologic classifications of mycotic sinonasal disease: (1) acute invasive fulminant disease, (2) chronic invasive infection, (3) noninvasive mycotic colonization (''fungus ball'' or mycetoma), and (4) allergic mycotic sinusitis. These four types of infection can be seen with any fungus but are most commonly a result of *Aspergillus* infection. Not infrequently, the pathologic diagnosis of mycotic disease requires heightened clinicopathologic suspicion. From a pathologic viewpoint, hyphae may be sparse in allergic mycotic sinusitis, being found only beneath the mucosal surface or only within the mucin. In early invasive sinusitis, hyphae may be confined to the vessels. A thick sinonasal mucus of unusual color (green, brown, or black) should raise the clinical suspicion of a mycotic infection. Hyphal fragments may be impossible to classify without culture confirmation, and pathologic correlation is always necessary to distinguish clinical infection from laboratory contamination. The sinonasal fungal diseases can be classified as being either fungal hyphal diseases or fungal yeast forms (also see the section on imaging).

Fungal Hyphal Diseases

Aspergillosis infection is caused by the fungus *Aspergillus*, a member of the Ascomycetes class. It is a ubiquitous organism frequently found in soil, decaying food, fruits, and plants. The spores are also common contaminants of the respiratory tract and the external auditory canal. *A. fumigatus* is the major human pathogen; however, *A. flavus* and *A. niger* can also cause human infections. Of the culture-confirmed cases of mycotic sinusitis, 87% contained some *Aspergillus* species as the sole pathogen or as a copathogen.[35]

Acute fulminant *Aspergillus* sinusitis occurs in the immunosuppressed, especially granulopenic patients with hematologic malignancies. Initial complaints are those of acute sinusitis such as nasal discharge, sinus pain, and/or periorbital swelling. Clinical examination of the nasal cavity and palate shows pale, ischemic tissue that may progress to gray and blackened, gangrenous tissue. The ability of *Aspergillus* to invade vessels is aided by its production of elastase and proteases. As the infection spreads through vascular and neuronal routes, orbital nerve invasion occurs, progressing to blindness. Treatment involves surgical debridement and antifungal agents. Treatment with antifungal medications usually includes itraconazole or one of the newer oral azoles (voriconazole).[36] The tissue at debridement is typically bloodless due to hyphal-related thrombosis. The prognosis for these patients is usually grave. *Aspergillus* sinusitis is not uncommon in immunocompromised patients and is unusual in immunocompetent patients.[37]

Chronic invasive *Aspergillus* sinusitis can be found in normal hosts living in highly endemic areas such as the Sudan or Saudia Arabia. Asymptomatic nasal colonization

Copyright © 2003, Mosby, Inc. All rights reserved.

has also been demonstrated. The Middle Eastern cases are quite distinctive in that they occur in immunologically normal patients, probably because of prolonged exposure to large inocula of spores. In the United States, chronic invasive sinusitis is most commonly seen in mildly immunosuppressed patients such as diabetics. Most patients respond to surgical debridement and antifungal therapy.[38–40]

A mycetoma is the benign fungal hyphal colonization of a cavity or space. In the sinonasal tract, a mycetoma may develop in response to changes in the local microenvironment such as occur after surgery, radiotherapy, and anecdotally, in association with smoking marijuana. Patients with mycetomas may complain of chronic sinusitis, or they may be entirely asymptomatic. Therapy is conservative curettage, but benign recolonization may occur.

Patients with allergic mycotic sinusitis have a history of allergic sinusitis, polyposis, and possibly allergic asthma. Serum eosinophilia, elevated IgE, cutaneous sensitivity to fungal antigens, and the presence of fungus-specific serum precipitins support the diagnosis of allergic mycotic sinusitis. Conservative curettage and systemic steroid therapy are the recommended treatments.[41] Histopathologically, hyphae are sparse and noninvasive, and they may be seen only after special stains are examined. Culture confirmation is necessary because the hyphal fragments do not allow definitive identification. Because of the environmental prevalence of *Aspergillus*, it is the assumed cause of most allergic fungal sinusitis cases. However, the dematiaceous fungi may also cause allergic sinusitis.

Rhinocerebral mucormycosis (also phycomycosis or zygomycosis) is a disease caused by several genera of the fungi of the class Zygomycetes (formerly Phycomycetes) and the family Mucoraceae. The genera, in order of decreasing frequency, are *Rhizopus*, *Mucor*, and *Absidia*. The members of the class Zygomycetes can be found in decaying fruit (especially those with a high sugar content), vegetables, soil, old bread, and manure. The zygomycetes have been isolated sporadically in some studies of indoor environments. Various spices, herbal teas, and birdseed harbor *Rhizopus* and *Absidia*. Iatrogenic subcutaneous wound infections by *Rhizopus* can be caused by Elasto-plastR brand bandages.

The Zygomycetes have a propensity for infecting uncontrolled diabetic patients as well as patients with hematologic malignancies (e.g., acute leukemia); chronic renal failure and acidosis; malnutrition; cancer; cirrhosis; and prolonged antibiotic, steroid, or cytotoxic drug therapy. *Rhizopus* grows favorably in an acidic, high-glucose environment, which relates to its elaboration of ketone reductase. The acidosis, in addition to providing a favorable growth environment, also further impairs polymorphonuclear leukocyte function.

Sinus mucormycosis occurs predominantly as an invasive rhinocerebral infection. The clinical course may be acute, invasive, and fulminant, just as in aspergillosis. The organism tends to spread rapidly from the nasal fossa to the paranasal sinuses and the fungus invades blood vessels, causing endothelial damage that initiates thrombosis, ischemic and hemorrhagic infarction, and purulent inflammation. Eventually the orbits and cavernous sinuses are invaded via the ophthalmic vessels. Invasion of the base of the brain is an end-stage event, and the entire progression of the disease can occur in only a few days. Perineural invasion can also occur, usually along the branches of the trigeminal nerve.[42]

Diabetic patients may develop a more chronic invasive sinusitis, which is amenable to debridement and antifungal therapy. In AIDS patients, whose neutrophil function is largely intact, mucormycosis is actually a rare infection.[43] Clinically, black, crusting, necrotic tissue is seen over the turbinates, septum, and palate. By comparison, in immunosuppressed patients, focal ischemic areas may be found instead of the more typical black crusts. In the cases occurring in nondiabetic patients, pulmonary and disseminated infections are more common. Among survivors there is a high incidence of blindness, cranial nerve palsies, and hemiparesis. The best therapy is adequate surgical debridement and systemic intravenous amphotericin B.[34]

Mucormycoses has been documented in nondiabetic, nonimmunosuppressed patients. A preexisting foreign body, marijuana use, or prior surgery or radiotherapy may be predisposing factors in these unusual cases.[44, 45]

Fungi from the order Entomophthorales, which are also Zygomycetes, may cause granulomatous rhinoentomophthoromycosis in normal hosts from tropical climates. Cases have been reported in U.S. inhabitants with no history of travel, and Entomorphthora species have been isolated from algae, ferns, insects, and reptiles (*Basidiobolus ranarum* and *B. haptosporus*). Entomophthorales infection begins as a submucosal nasal mass that slowly expands, causing enormous erosion, destruction, and deformity of the nasal and labial soft tissues. The rhinocerous-like midface expansion is similar to that seen in advanced cases of rhinoscleroma.

Pseudallescheria boydii (formerly called *Allescheria boydii*) is the current nomenclature for this fungus of the Ascomycetes family. It is a ubiquitous organism most commonly found in rural areas, and it is isolated from soil, poultry, cattle manure, and polluted waters. *P. boydii* sinusitis, which may be fulminant and lethal, has been reported in immunocompromised patients. It has also been described in normal patients and may resolve with adequate therapy. Like aspergillosis, this disease may be either saprophytic or invasive. *P. boydii* has been reported to involve the maxillary, ethmoid, and sphenoid sinuses. The present treatment of choice is miconazole, with surgical debridement if necessary.[46, 47]

Fungal Yeast Forms

The yeasts of the genus *Candida* are part of the normal mucocutaneous flora. However, under certain circumstances, *Candida* may produce either a minor or a life-threatening disease. Minor infections may result as overgrowths in patients on antibiotic therapy. The more severe *Candida* infections occur almost exclusively in patients with compromised immune systems. Today, candidiasis represents the most common and most lethal of the opportunistic fungal infections among immunocompromised patients.[34] Most infections are caused by *Candida albicans*, but *C. tropicalis*, *C. stellatoidea*, and *C. krusei* may also cause disease. When the paranasal sinuses are affected, it is usually in otherwise healthy patients who have been on broad-spectrum antibiotics. The maxillary sinuses are almost exclusively involved, and orbital and intracranial

Copyright © 2003, Mosby, Inc. All rights reserved.

complications are rare. Infections can also occur after maxillary trauma. The treatment of choice for the sinus disease is antral lavage with topical nystatin.[48]

Histoplasma capsulatum is present worldwide and is endemic in the midwestern, central, and southeastern regions of the United States. Exposure to *H. capsulatum* occurs through exposure to aerosolized bird or bat droppings and contaminated soil or fertilizers. As with most inhaled mycotic pathogens, the most common manifestation of histoplasmosis is a subclinical pulmonary infection, usually a function of a small exposure source and the state of patient immunity. Patients may develop acute pneumonia after massive inhalation. Chronic cavitating and fibrosing pulmonary infection, sclerosing mediastinitis, and disseminated infection with bone marrow and adrenal involvement (resulting in Addison's disease) are more serious sequelae of histoplasmosis.

Before the AIDS epidemic, disseminated histoplasmosis was rarely seen, and when it was encountered, it was usually in elderly patients or those immunosuppressed by chemotherapy or hematologic malignancy. Today, disseminated histoplasmosis and extrapulmonary histoplasmosis in the face of HIV seropositivity are included as one of the criteria for AIDS. Disseminated histoplasmosis presents with fever, septicemia, pneumonia, hepatic or renal failure, CNS infection, or skin lesions. It is thought to be due to reinfection from an endemic focus or, less frequently, reactivation of latent disease. Head and neck manifestations of disseminated disease in AIDS patients include cervical adenopathy, pharyngitis, tonsillitis, and ulcerating oral lesions. Non-AIDS patients may also develop histoplasmosis of the oral cavity and larynx. Rarely, there can be involvement of the nasal mucous membranes, resulting in edema and nasal obstruction. Even more rarely, pansinusitis can occur. The current treatment of choice is amphotericin B.[34, 49, 50]

Cryptococcus neoformans is a ubiquitous yeast of worldwide distribution. It is associated with pigeon excreta and pigeon nesting sites, and human infection results from inhalation of aerosolized droppings.[34] It may cause asymptomatic, localized pulmonary granulomata. Cryptococcal pneumonia or disseminated infection can develop in immunosuppressed patients. Cryptococcal meningitis occurring in the AIDS population is thought to follow respiratory infection, and the frontal and maxillary sinuses have been documented as primary sources of infection. Isolated sinonasal disease is uncommon but is identical to that of histoplasmosis, and the treatment is the same as for histoplasmosis.[51, 52]

Coccidioidomycosis is a disease caused by the dimorphic fungus *Coccidioides immitis*. The pathogenesis and clinical manifestations of the disease are almost identical to those of histoplasmosis. *C. immitis* is endemic in the southern United States and in northern Mexico, as well as a few sites in Central America and South America. It has been estimated that 20% of cases reported yearly are diagnosed outside the endemic areas, thus widening the relevance of this organism. *C. immitis* is extremely infectious. Illness ranges from subclinical infections to disseminated and often lethal infections, depending on the patient's immune status, infectious dose, nationality, and other factors such as pregnancy. Most of the head and neck disease affects the laryngotracheal axis, with or without concurrent pulmonary disease. Sinonasal involvement is rare.[53, 54]

Myospherulosis is not a fungal disease but rather an iatrogenic condition that is caused by the interaction of red blood cells with petrolatum, lanolin, or traumatized human adipose tissue.[34] Microscopically, large sporangium-like sacs filled with spherules are produced that can be mistaken for a fungus. The disease was first recognized as skin lesions in East Africans; however, in the United States the disease has involved the nose, paranasal sinuses, and middle ear. In these patients there was always prior surgery (i.e., the Caldwell-Luc procedure), and the surgical defect was packed with gauze impregnated with petrolatum. It is important to recognize this disease as an innocuous iatrogenic process so that it is not confused with a true fungal disease and given unwarranted therapy.

CYSTS AND POLYPS

The most frequent complications of inflammatory rhinosinusitis are polyps and cysts. The retention cyst is the most common, being found incidentally on routine plain film examinations in about 10% to 35% of patients. A mucous retention cyst results from the obstruction of a submucosal mucinous gland, and the cyst wall is the duct epithelium and capsule of the gland itself.[55, 56] Although by strict pathologic criteria a retention cyst can be called a *mucocele*, the radiographic and clinical findings of these two entities are sufficiently different to merit distinction (see the section on mucoceles). Mucous retention cysts can occur in any paranasal sinus, along any wall, but are most commonly found in the maxillary sinus. As mentioned, they usually are an incidental imaging finding.

Serous retention cysts result from the accumulation of serous fluid in the submucosal layer of the sinus mucosal lining. These cysts tend to occur in the base of the maxillary sinuses, and the lining of a serous retention cyst is the elevated sinus mucosa. By contrast, as mentioned, the lining of a mucous retention cyst is the actual obstructed ductal epithelium.

By comparison to serous retention cysts, polyps result from an expansion of fluids in the deeper lamina propria of the Schneiderian mucosa in the nasal fossa and paranasal sinuses. These polyps may result from allergy, atopy, infection, or vasomotor impairment.[57] Paranasal sinus and nasal polyps have an identical histology. Allergic polyps tend to have a significant population of eosinophils, more than what is usually seen in inflammatory polyps, and such polyps may be associated with allergic mucin, comprised of a sea of eosinophils in mucin and Charcot-Leydin crystals, which are the result of eosinophil degranulation. As mentioned, the associated allergic sinusitis tends to cause diffuse symmetric disease rather than localized disease. It has been suggested that there is an interaction between eosinophils and fibronectin that may play a role in edema formation, which contributes to the growth of nasal polyps.[58]

Inflammatory and allergic polyps rarely bleed and are not damaged by manipulation or compression. However, fibrosis and neovascularization of polyps (especially nasal polyps) can result in a vascularized polyp that pathologically mimics an angiofibroma. Anatomic and imaging

Copyright © 2003, Mosby, Inc. All rights reserved.

features that distinguish a vascularized polyp from an angiofibroma include the following: (1) the former is located in the nasal fossa rather than in the nasopharynx, (2) the polyp does not extend into the pterygopalatine fossa, and (3) the polyp is easily removed. These polyps are poorly vascularized, further distinguishing them from angiofibromas.[59]

As mentioned, nasal polyps are most often associated with allergy and, when found in this clinical setting, they are usually multiple. Histologically there are a number of secondary changes that can occur with these polyps: infarction, surface ulceration, mucoid liquefaction, stromal cell atypia, and metaplasia of the surface epithelium. Carcinoma arising from surface metaplasia is very rare and is almost always associated with an external carcinogenic promoter, either smoking or some occupationally related promoter. On the other hand, atypia of stromal cells may be misinterpreted as a malignancy because of its microscopic resemblance to rhabdomyosarcoma or myxoid sarcoma.[57, 60]

Polyps are the most common expansile lesions in the nasal cavity. Although they usually are small and cause little deformity, if left unattended in the presence of progression, they can become highly deforming. Eventually they may remodel, disrupt, and destroy the central facial region. They can destroy the medial antral walls, cause hypertelorism, and break through intracranially either via the roof of the nasal cavity and ethmoid complex or via the sphenoid sinus. This marked degree of destruction may be found among medically underserved patients with intractable allergic polyps (primarily aspirin intolerance) and patients with a high level of denial. Destruction secondary to polyposis is an indolent process, causing little if any pain. Although surgery is the treatment of choice for large polyps, in allergic patients desensitization has in some cases shown dramatic results in reducing the number and size of these polyps.[61] Etiologically, in addition to allergy, polyps have been associated with vasomotor rhinitis, infectious rhinosinusitis, diabetes mellitus, cystic fibrosis, aspirin intolerance, and nickel exposure.[61]

On occasion a maxillary sinus polyp may expand and prolapse through the sinus ostium, presenting as a nasal polyp. These are referred to as antrochoanal polyps, which represent 4% to 6% of all nasal polyps. Most are unilateral solitary lesions, but bilateral antral inflammatory disease is found in as many as 30% to 40% of cases. Almost 8% of these patients have additional nasal polyps, and 15% to 40% of patients have a history of allergy.[60–62] These latter statistics have prompted the suggestion that there is an etiologic relationship to allergy, but this theory has not been borne out. Most antrochoanal polyps occur in teenagers and young adults. If such polyps are surgically snared in the nasal fossa like routine nasal polyps, without regard to their antral stalk, 20% to 30% of them will recur, usually within 2 years.[61] The proper treatment is via a Caldwell-Luc or endoscopic intraantral approach.

Ethmoidochoanal and sphenochoanal polyps have also been described. The latter are rare. The etiology of these polyps appears to be similar to that of the antrochoanal polyp.[63]

The Pediatric Patient

In the pediatric patient, there is little correlation between active infection and sinus opacification and mucosal thickening. This is particularly true in children less than 4 years of age and especially in children less than 2 years of age, in whom tears, retained secretions, and normal redundant mucosa may account for these findings.[16, 64–67] In all such pediatric patients, identification of thickened sinus mucosa should be carefully evaluated in the clinical setting prior to making a diagnosis of active infection. Tissue eosinophilia is characteristic of chronic pediatric sinusitis, especially in children with asthma. However, the presence of allergy does not predict tissue eosinophilia, and the degree of tissue eosinophilia does not correlate with the severity of mucosal thickening as seen on CT scans.[68]

Persistent sinusitis in a pediatric patient may indicate the presence of cystic fibrosis. In these patients, persistent nasal obstruction and sinusitis often lead to hypoplasia of the frontal sinuses, presumably secondary to insufficient aeration. Additional conditions to consider in children with repeated episodes of sinusitis include immune deficiency syndromes, HIV infection, allergic sinusitis, unusual allergies such as aspirin intolerance, and immobile cilia syndrome. In ruling out the latter syndrome, it may be useful to recommend that the clinician submit a brush biopsy specimen from the lateral nasal wall for electron microscopy. Brush biopsy specimens submitted in glutaraldehyde are superior to routine forceps specimens for visualizing the ultrastructure of ciliated cells. Lastly, children under the age of 10 years rarely develop allergic nasal polyps. Thus the presentation of a nasal polyp in the first few years of life should raise the suspicion of an encephalocele, while the appearance of nasal polyposis should suggest the diagnosis of cystic fibrosis.[69, 70]

The HIV-Positive Patient

In recent decades, there has been considerable interest in the prevalence and type of paranasal sinus inflammatory disease in HIV-positive patients.[71] Minimal sinus inflammatory disease may be clinically significant for these patients, and early treatment should be initiated. HIV specifically affects T helper lymphocytes, as well as monocytes, macrophages, and other parenchymal cells. One of the many ripple effects of the loss of T helper cells is dysfunction of the B lymphocytes, which results in unusually severe bacterial infections. The B cells are unable to respond normally to antigenic stimulation due to the loss of lymphokine-induced stimulation. AIDS patients may develop sinusitis secondary to the usual bacterial agents (*H. influenzae*, *S. pneumoniae*, *S. viridans*, *Moraxella catarrhalis*, coagulase-negative staphylococci, *Staph. aureus*), plus other bacteria (*Pseudomonas aeruginosa* and *Legionella pneumophila*) that are considered opportunistic pathogens and rarely cause sinusitis in normal hosts.[72, 73]

MUCOCELES

A mucocele is the most common expansile lesion to develop in a paranasal sinus. Pathologically, it is defined as a collection of mucoid secretions surrounded by mucus-secreting respiratory epithelium. Although histopathologically both lesions consisit of mucous secretions surrounded by an epithelial lining, mucoceles and retention

Copyright © 2003, Mosby, Inc. All rights reserved.

cysts are distinguished by their clinical and imaging features.[74]

The retention cyst, as mentioned, is a spherical mucoid-filled cyst that develops when a mucous gland of the sinus mucosa becomes obstructed. The epithelium of the duct and gland capsule is the cyst wall. These cysts are common, usually incidental findings identified in at least 10% of people. They are within the sinus cavity, and almost always some surrounding sinus cavity air remains. Although these cysts can occur in any sinus, they are most common in the maxillary sinus and they rarely cause any remodeling of the sinus wall.

By comparison, a mucocele develops from the obstruction of a sinus ostium or a compartment of a septated sinus, and the wall of the mucocele is the sinus mucosa. The sinus is completely filled and airless, and the sinus cavity is expanded as the bony walls are remodeled outward. An expanded sinus cavity is critical to making the diagnosis of a mucocele, as without this finding, the sinus is properly referred to as an obstructed sinus. Mucoceles occur in all of the paranasal sinuses, with most developing in the frontal sinuses (60% to 65% of cases). Between 20% and 25% occur in the ethmoid sinuses, and 5% to 10% in each sinus occur in the maxillary and sphenoid sinuses.[75–77]

At first, the sinus cavity expansion results in remodeled, intact surrounding bone. However, at some point the sinus cavity may become so large that periosteal repair can no longer maintain sinus wall ossification and deossification occurs. On imaging these areas appear as absent bone, but they may be mistaken for areas of eroded bone.

Rarely, a retention cyst or polyp may become so large that it completely fills the antrum and widens the infundibular region, making distinction from an early mucocele impossible. However, this is of no clinical significance, as the surgical treatment of these lesions is the same.

The classic mucocele is a sterile lesion that presents with signs and symptoms resulting from the mass effect of the lesion. Thus, frontal sinus mucoceles are commonly associated with inferolateral proptosis, a superomedial orbit mass, frontal bossing, nasal obstruction (unilateral or bilateral), and nasal voice quality. Ethmoid mucoceles are associated with lateral proptosis, nasal stuffiness, and possibly a nasal quality to the voice. A supraorbital mucocele can cause downward proptosis, as these mucoceles arise in the mid-roof of the orbit. They also may cause a mass in the floor of the anterior cranial fossa. Maxillary mucoceles may present as a cheek mass, upward displacement of the eye, and nasal obstruction. Sphenoid mucoceles may present with decreased vision, suboccipital headache, and, rarely, fullness in the roof of the nasopharynx. Pain is uncommon and may indicate the presence of an infected mucocele or a pyocele (mucopyocele). Mucoceles have also been reported in an Onodi cell, a pneumatized anterior clinoid process, and a concha bullosa. The potential for vision loss in the two former cases must be noted.[78]

An atelectatic or silent sinus results in effects almost opposite to those of an antral mucocele. Clinically this entity is, as the name implies, asymptomatic, and is revealed only when the major ophthalmologic complication, enophthalmos, becomes evident. It is postulated that chronic sinusitis leads to ostial obstruction, which, in turn, leads to chronic negative pressure within the sinus. Eventually there is retraction of the maxillary sinus walls leading to collapse of the orbital floor and enophthalmia. The findings also include lateral bowing of the uncinate process and inward bowing of the posterior sinus wall. Awareness of this entity is important, as endoscopic osteal decompression of the sinus can avoid ophthalmologic complications.[79 80]

CORRELATION OF IMAGING AND CLINICAL FINDINGS

Occasionally, some patients may have symptoms of sinonasal inflammatory disease and normal CT and MR imaging studies. Conversely, some patients may have identifiable mucosal thickening on imaging studies and be asymptomatic. In most adult patients, there is a fairly good correlation between significant mucosal disease as seen on imaging and clinical presentation. However, for patients with treated acute sinonasal inflammatory disease, clinical improvement may occur well ahead of resolution of mucosal disease as seen on CT and MR studies. Thus, it is always treacherous for a radiologist to definitively imply that the presence of sinonasal mucosal thickening accounts for the patient's symptoms. Conversely, the radiologist should not imply that a normal sinus imaging study means that the patient does not have symptoms or is a malingerer. The radiologist's report should identify the sinuses involved and assess the degree of mucosal disease in each sinus, and reference to specific clinical symptoms should not, in general, be given.

This reference to the clinical presentation also applies to the terms *acute disease* and *chronic disease*. The presence of an air-fluid level in a patient with acute symptoms of sinonasal infection correlates well. However, many patients with acute sinusitis will not have air-fluid levels, and their imaging appearance may be indistinguishable from that of someone with subacute or chronic disease. Similarly, thickening and sclerosis of a sinus wall implies chronic, recurrent disease. It does not indicate whether any mucosal thickening in that sinus is due to acute or chronic change. Thus, without good clinical correlation, the terms *acute mucosal disease* and *chronic mucosal disease* should not be used by the radiologist. If thickened, sclerotic bone is seen, it merely indicates that there has been a chronic process in that sinus at some time. A dictation might include a statement such as ''Thickening and sclerosis of the sinus wall suggests some chronicity to the disease affecting that sinus.'' It should not qualify the acute or chronic nature of the mucosal disease presently identified within that sinus. In fact, such a sinus may contain scarred, thickened mucosa without any inflammation.

With regard to the nasal cavity, as long as, on imaging, some airway can be identified around the turbinates and the nasal septum, patients rarely complain of nasal obstruction. This imaging rule applies even in the presence of slightly enlarged turbinates and varying degrees of nasal septal deviation.

IMAGING "NORMAL" MUCOSA

The resolution of present-day CT and MR scanners is such that physiologic mucosal thickening from the nasal

Copyright © 2003, Mosby, Inc. All rights reserved.

cycle can be routinely seen. Thus, unilateral swelling of the middle and inferior turbinates, with minimal ipsilateral ethmoid and maxillary mucosal thickening, usually reflects this physiologic event (see Chapter 3). This is true provided that the opposite middle and inferior turbinates appear small and almost crenated, and a thin airway around the swollen turbinates remains. Usually, normal sinus mucosa is so thin that it is not seen routinely on CT and MR imaging, probably because it is volume averaged out at the sinus air/bone interface. When mucosal thickening is seen incidentally on MR studies in an asymptomatic patient, the mucosa probably is minimally inflamed or scarred.

Brain MR imaging studies have confirmed the lack of imaging specificity for sinus mucosa, as mucosal thickening of up to 3 mm may be present in clinically normal patients. In addition, clinically silent focal areas of ethmoid mucosal thickening were found in 66% of patients.[81] In another series of 263 patients, clinically silent areas of mucosal thickening were found in nearly 25%.[82]

Generally, normal sinuses contain air that directly abuts the bony walls of the sinus. Thus, whenever sinus mucosa is seen at the interface between air and bone, that mucosa is thickened, and, as such, it should be mentioned by the radiologist. However, mucosal inflammation, fibrosis, or physiologic engorgement cannot be confidently distinguished. The overall evaluation of the sinus mucosa is more easily and thoroughly performed on CT and MR imaging than it is on plain films.

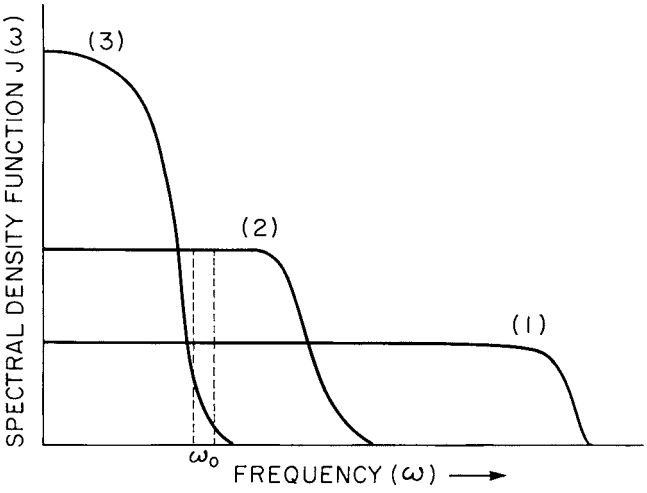

VIEW IMAGE

FIGURE 5-13 Diagram of a spectral distribution curve for physiologic solutions. The number of molecules at a specific frequency $J(\omega)$ is graphed against the range of frequencies (ω). Curve (1) is for water and illustrates that a wide range of frequencies is present, but there is no preponderance of molecules at any one frequency. Curve (2) shows what happens as macromolecular proteins are added to the water system. A more limited number of frequencies is present due to the large number of more slowly tumbling macromolecular proteins and because the water molecules of higher frequencies drop out as they are magnetically bound to the large proteins. Curve (3) illustrates that when a large number of macromolecular proteins are added to the systems, most of the molecules have a very limited range of slower frequencies. ω0, Lamor frequency.

MAGNETIC RESONANCE OF PROTEIN SOLUTIONS

For a specific solution, the concentration of macromolecular proteins affects the T1 and T2 relaxation times. The clinical relevance of this is that the T1-weighted and T2-weighted signal intensities of proteinaceous solutions may be quite varied for specific entities such as cysts, mucoceles, etc. Diagnostic problems in clinical interpretation can arise if this phenomenon is not understood and appreciated. Therefore, the following is a brief, simplified review of T1 and T2 relaxation times in macromolecular protein solutions.

The term *lattice* refers to the overall magnetic environment of the system being studied. A proton spin system can be excited by the addition of energy, and the most efficient way to transfer that energy to the protons is to choose an exciting pulse that is at the Larmor frequency. Once excited, the spin system tends to rid itself of the excess energy and return to an equilibrium state. The excess energy is absorbed by the lattice, and the time it takes for this process to occur is referred to as the spin-lattice or T1 relaxation time.

The most efficient transfer of this excess energy from the excited protons to the lattice occurs when the net molecular rotation of the lattice is at the Larmor frequency. Thus, if a system does not have many molecules rotating at the Larmor frequency, the energy absorption is inefficient and the T1 relaxation time is long. Conversely, if the system has most of its molecules rotating at or near the Larmor frequency, the T1 relaxation time is efficient and short. A study of the number of molecules in a system that are rotating at various frequencies yields a spectral distribution function that can be graphed as the number of molecules at a specific rotational frequency versus the range of frequencies (Fig. 5-13).

Analysis of pure water shows that these small molecules have a wide range of net rotational frequencies, but there is no preponderance of molecules at any one frequency, including the Larmor frequency. Thus pure water has a long T1 relaxation time. As large physiologic macromolecular proteins with relatively slow tumbling frequencies are added to pure water, for a variety of reasons the net rotational motion of the system slows. This effect continues as more macromolecular protein is added, until a protein concentration is reached at which there is a maximum number of molecules with a net rotation at the Larmor frequency. At this concentration the T1 relaxation time is the shortest for the system. As more macromolecular protein is added, the net rotational frequency of the system continues to slow and falls below the Larmor frequency. Consequently, for these more concentrated protein solutions, the T1 relaxation time is long. Thus, for such physiologic solutions, as one proceeds from low macromolecular protein concentrations to high concentrations, the T1 relaxation time goes from long to short to long (Fig. 5-14). This is reflected as the T1-weighted signal intensity goes from low to high to low.

With reference to the T2 relaxation time, initially, after the spin system has been excited, all of the protons can be considered as precessing at the same frequency. However, variations in the local magnetic environment of each proton cause the speed of precession to change by varying amounts, and the result of these magnetic inhomogeneities is that the

Copyright © 2003, Mosby, Inc. All rights reserved.

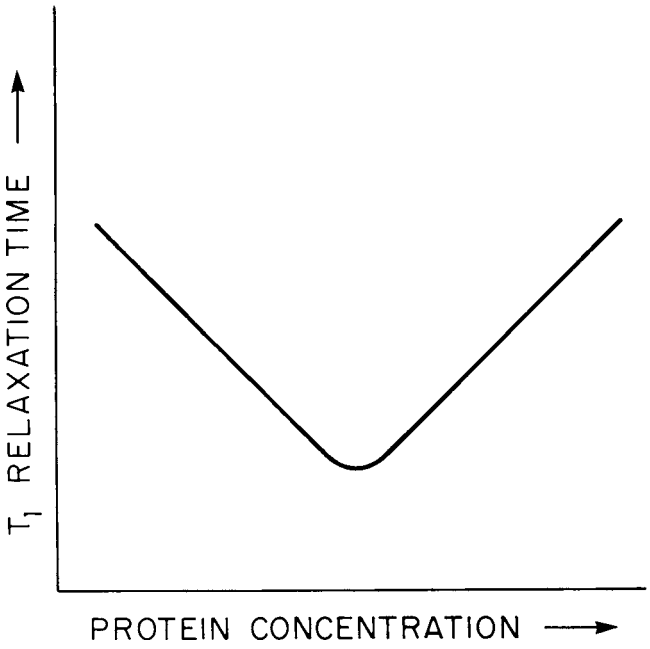

VIEW IMAGE

FIGURE 5-14 Graph of T1 relaxation time versus macromolecular protein concentration. As protein is added to a water system, the T1 relaxation slows until the net frequency of the lattice is that of the Lamor frequency. At that protein concentration the T1 relaxation time is the most efficient (shortest). As still more protein is added, the net frequency of the system slows below that of the Lamor frequency, and the T1 relaxation time again becomes less efficient.

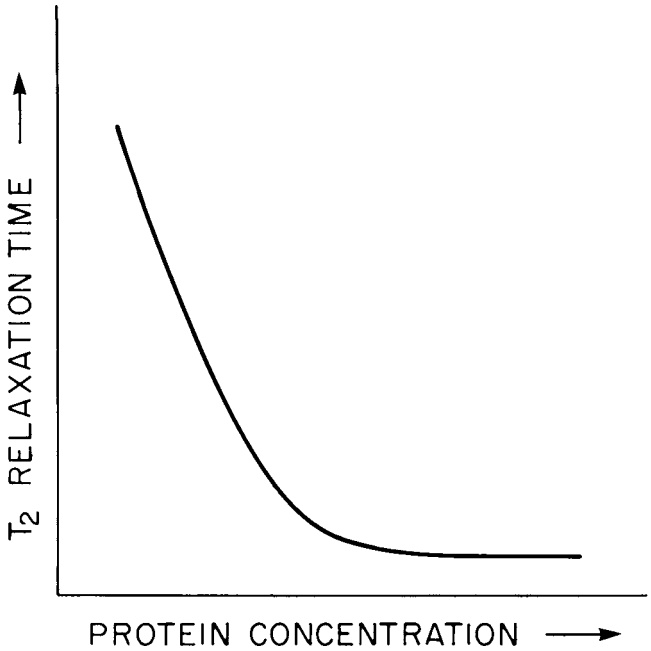

VIEW IMAGE

FIGURE 5-15 Graph of T2 relaxation time versus macromolecular protein concentration. The more protein added to the system, the lower (faster) the T2 relaxation time. This relationship holds until the system becomes a solid. In a solid, the T2 relaxation time is the fastest it can be, and it becomes a plateau.

protons start to precess at a wider and wider range of frequencies. This interaction is referred to as spin-spin relaxation or dipole-dipole dephasing, and the T2 relaxation time is a measure of this process. For pure water, all the molecules are the same, and they are moving so rapidly that they have little effect on the local magnetic fields of particular protons. Hence in pure water the excited protons precess in phase for a long time, and the T2 relaxation time is long. As macromolecular solute is added, the net frequencies slow so that there is more time for spin-spin interactions. In addition, more molecular inhomogeneity is introduced into the system. Thus, as the protein concentration increases, the T2 relaxation time decreases. However, in viscous solutions and solids, the T2 effects reach a maximum and the T2 relaxation time plateaus at its shortest time (Fig. 5-15). In fact, the T2 relaxation falls from the milliseconds range (thousandths of a second) for physiologic protein solutions to the microseconds range (millionths of a second) for solids. Such rapid dephasing does not allow any magnetic signal to be detected on MR imaging, and a signal void is observed. Lastly, when the T2 relaxation times are ultrashort in the microseconds range, this effect dominates any observed T1 relaxation, and signal voids are also observed on T1-weighted MR imaging. This phenomenon is often referred to as the *T2 effect on the T1 relaxation time*. With this simplified background, one can approach the MR signal intensities of sinonasal secretions (Fig. 5-16).

Normal sinonasal secretions form a complex solution that is in equilibrium with the interstitial fluids.[83] By weight, about 95% of these secretions is water and 5% is solids; virtually all of the solids are macromolecular proteins, predominantly (60%) mucous glycoproteins. Thus normal sinonasal secretions are predominantly water, and on MR

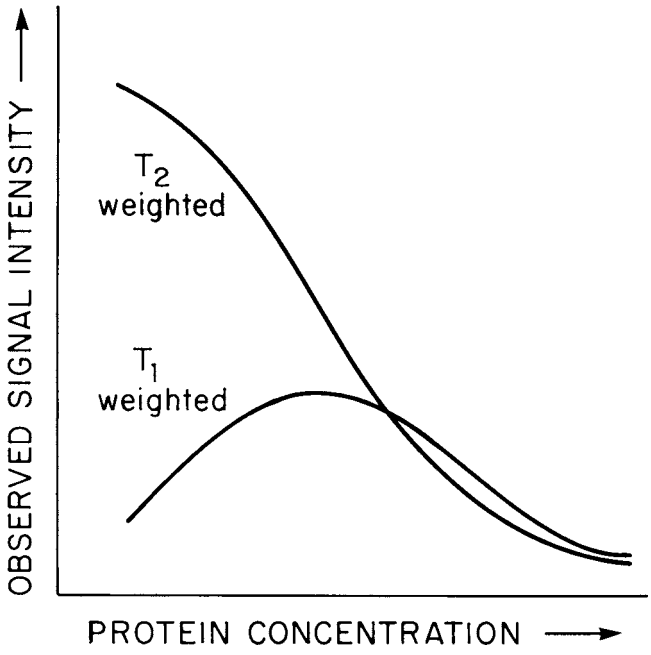

VIEW IMAGE

FIGURE 5-16 Graph of laboratory-observed T1-weighted and T2-weighted signal intensities versus macromolecular protein concentration. These curves reflect the relaxation times shown in Figures 5-14 and 5-15.

Copyright © 2003, Mosby, Inc. All rights reserved.

imaging they have long T1 and T2 relaxation times. These are observed as low T1-weighted and high T2-weighted signal intensities.

When normal sinonasal secretions become chronically obstructed, a number of predictable changes occur that alter the protein concentration, the amount of free water (that fraction of the water molecules that magnetically is independent of the effects of the macromolecular proteins), and the viscosity. These changes occur as a result of alterations in the composition and function of the obstructed sinus mucosa, which increases the number of goblet cells that are responsible for the production of the mucous glycoproteins. There is also decreased clearance of the mucous glycoproteins, and with time, the sinus mucosa also reabsorbs free water in the secretions. The result of these changes is an increase in the mucous protein concentration. The sinonasal secretions progressively change from primarily watery and serous to a thick mucus. Then they become a desiccated, stonelike mucous plug when the protein content is above about 35%.

These changes are predictable, but the rate of their evolution is highly variable, both between patients and within the various sinuses of a given patient. The protein concentration directly correlates with the T1-weighted and T2-weighted MR signal intensities of the secretions. This is shown by observing that the graphs of clinically observed T1-weighted and T2-weighted signal intensities reflect the laboratory signal intensities predicted in the prior discussion of the T1 and T2 relaxation times (Figs. 5-16 and 5-17).

As the protein content rises from 5% to about 25%, both the T1 and T2 relaxation times shorten as predicted. However, the T2 shortening is not seen on the MR images because the T2-weighted signal intensity remains high (white) throughout this range. The rise of the T1-weighted signal intensity is more easily observed on the clinical scans.

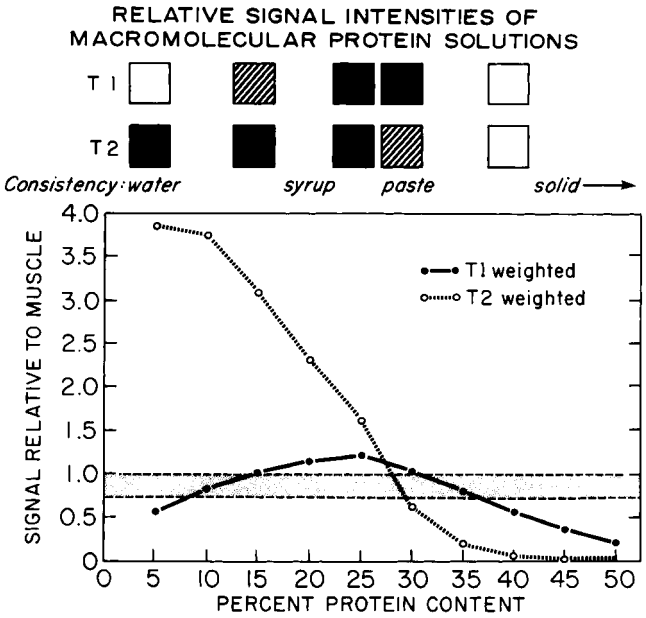

VIEW IMAGE

FIGURE 5-17 Graph of clinically observed T1-weighted and T2-weighted signal intensities versus macromolecular protein concentration. The horizontal zone of gray represents the intermediate range of signal intensity compared with that of the brain. The relationship of the relative physical consistency of the solutions to the signal intensities is shown at the top of the graph. These curves parallel those in Figure 5-16.

Protein crosslinks occur at a protein concentration of about 25% to 30%. This correlates with the increased viscosity observed clinically. Crosslinking also slows the macromolecular motion, which in turn allows dipole-dipole dephasing to become a more significant factor. As a result, the T2 relaxation time and signal intensity plummet. The T1-weighted signal intensity falls back to a low value between the protein content range of 25% to 40%. Above a concentration of 35% to 40%, virtually all of the free water has been eliminated from the secretions and direct macromolecular protein-protein binding occurs. This results in a sudden increase in the viscosity of the secretions. These semisolid and solid protein mixtures have ultrashort T2 relaxation times. These are noted first as low T2-weighted signal intensities and then as signal voids on both T1-weighted and T2-weighted MR images.

Thus, the chronically entrapped secretions become progressively thickened and concentrated, and the MR signal intensities vary with the protein concentration. This may result in anatomically similar collections having variable signal intensities. A high protein concentration can produce signal voids on both T1-weighted and T2-weighted MR images, and thus appear indistinguishable from a normal aerated sinus on MR images (Figs. 5-18 and 5-19). Although the etiology of the signal voids is different (ultrashort relaxation times for the former versus paucity of protons for the latter), the observed imaging blackness is the same. Thus the radiologist can easily underestimate the presence of such chronic desiccated secretions, and therefore the severity of the sinus disease, if MR is the only imaging examination used. CT can distinguish an aerated sinus from a chronically obstructed sinus, as dried secretions are dense (high attenuation), reflecting their high protein concentration, while air is black. CT can also diagnose chronic bone changes and differentiate some radiodensities such as calcification, ossification, or a tooth. Therefore, CT, not MR, is recommended as the first modality for patients with suspected chronic inflammatory disease.[83–85]

IMAGING

Benign Sinonasal Mucosal Disease

On plain films the earliest sign of thickened mucosa is often a hazy or vaguely ‘‘clouded’’ appearance of the involved sinus. In such cases, a thickened mucosal margin per se may not yet be identified. If this appearance is not the result of technical or extrinsic factors (the entire film looks hazy, there is overlying swelling of the soft tissues of the cheek, etc.), then this sinus is abnormal. Most commonly this appearance is the result of a combination of retained secretions and minimal mucosal thickening (Fig. 5-20). Once the mucosa is thick enough to be distinctly identifiable on plain films, the mucosa usually appears as a uniformly thick soft-tissue density zone that separates the sinus air from the bone (Fig. 5-21).

There are several situations that may falsely cause a hazy sinus appearance. For instance, haziness is often seen on plain films in the maxillary zygomatic recesses. These areas

Copyright © 2003, Mosby, Inc. All rights reserved.

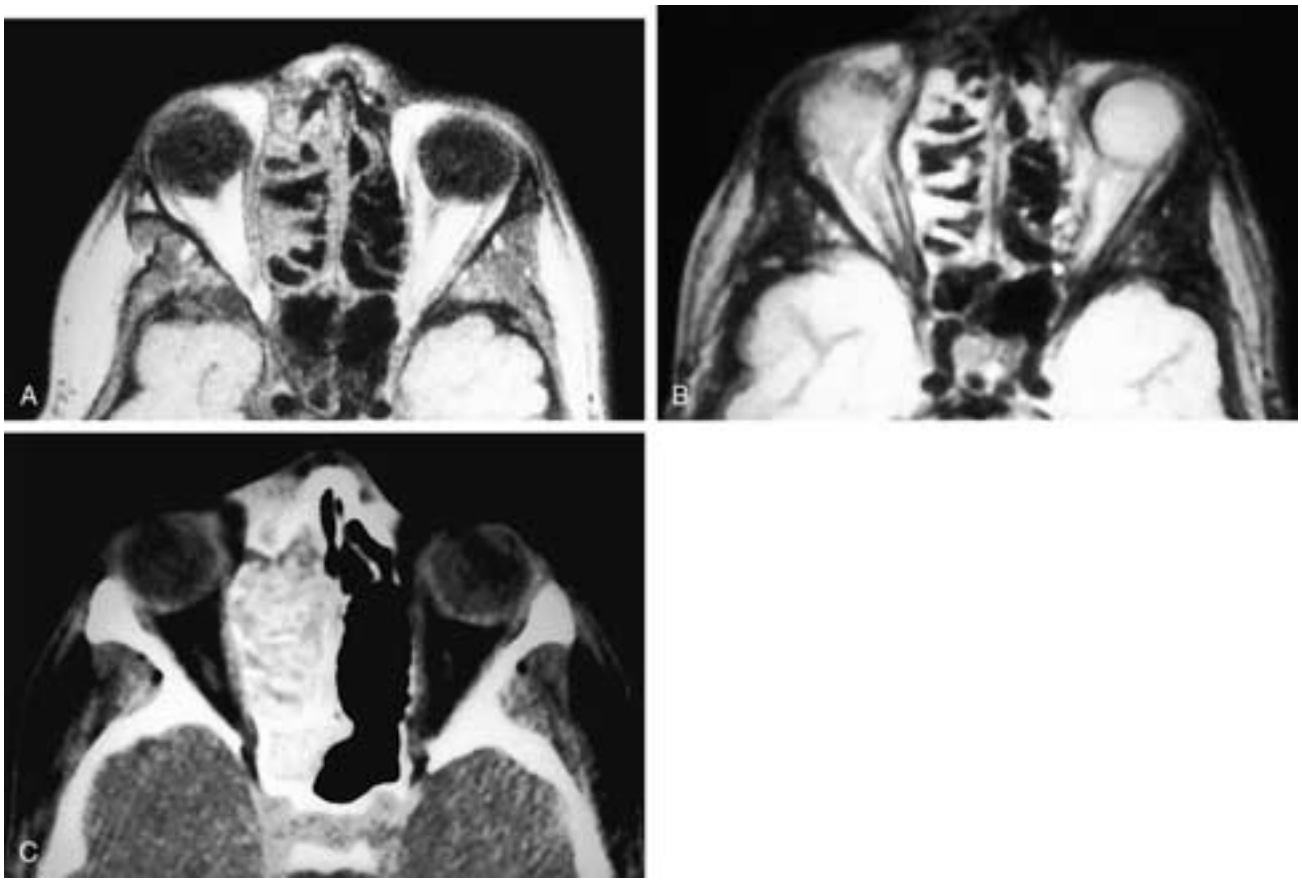

VIEW IMAGE

FIGURE 5-18 Axial T1-weighted (**A**) and T2-weighted (**B**) MR images show what appears to be moderate ethmoid sinusitis with residual aeration in scattered right ethmoid cells and in the right sphenoid sinus. In a CT scan (**C**) these sinuses are completely opacified, with desiccated secretions that are separated from the sinus walls by a thin zone of mucoid attenuation. This patient had chronic sinusitis.

of the antra have less air and thicker surrounding bone than the main sinus cavity and almost always appear slightly clouded when compared with the main body of the sinus.

Maxillary sinus hypoplasia is another cause of nonspecific sinus density on plain films. However, in most cases, the associated findings of a greater downward angulation of the lateral aspect of the orbital floor and a larger ipsilateral orbit (and often a larger superior orbital fissure) allow a diagnosis to be made. However, definitive evaluation of the mucosa within a hypoplastic sinus may be impossible without CT or MR imaging. In addition, axial sectional imaging clearly allows pathology in the soft tissues of the cheek to be separated from that in the maxillary bony wall or in the sinus mucosa.[86, 87]

The unique anatomy of the ethmoid complex can also lead to underdiagnosis of pathology, as resolution of the numerous closely packed ethmoid air cells is beyond the sensitivity of plain films. The increased density associated with mucosal thickening in an isolated group of ethmoidal cells may be almost completely nullified by air-containing surrounding cells and the adjacent sphenoid sinus.

The sensitivity of the plain film examination of the ethmoid sinuses may be increased by paying close attention to the appearance of the intrasinus septa. Poorly visualized septa may belie the presence of mucosal thickening or fluid (Fig. 5-22). However, definitive diagnosis of minimal or focal ethmoid cell disease requires sectional imaging. The lack of visualization of these ethmoid septa with no obvious soft-tissue mass may also result from pneumosinus dilatans, mucocele, or previous ethmoidectomy.

In the sphenoid sinuses, minimal mucosal thickening is usually not identifiable on plain films because these sinuses are partially obscured by many overlapping bone and soft-tissue structures. Air-fluid levels can be identified on films taken in the erect position, but CT or MR is required in most cases to accurately identify mucosal disease.

Sinus opacification can be the result of a combination of mucosal thickening, increased sinus secretions, and submucosal edema. The mucosal thickening can vary from a few millimeters to a thick, hypertrophic, redundant mucosa. In some cases, increased mucosal secretions dominate, while in others, submucosal edema is dominant (Fig. 5-1). However, there seems to be no correlation between the dominant type of reaction and the clinical outcome. Rather, these various components seem simply to reflect differences in the individual response to an inflammatory insult, as previously mentioned. With reference to MR imaging, inflammation will have an impact on the MR signal intensities, as it is associated with increased sinus secretions and submucosal edema, both of which are about 95% water. Thus the presence of inflammation will be associated with the signal

Copyright © 2003, Mosby, Inc. All rights reserved.

FIGURE 5-19 Axial T1-weighted (**A**) and T2-weighted (**B**) MR images show expansion of the ethmoid complexes, with apparently moderate mucosal thickening in the ethmoid sinuses. The sphenoid sinuses appear aerated. However, a CT scan (**C**) shows that the expanded ethmoid and sphenoid sinuses are totally opacified, with desiccated secretions. This patient had chronic sinusitis.

VIEW IMAGE

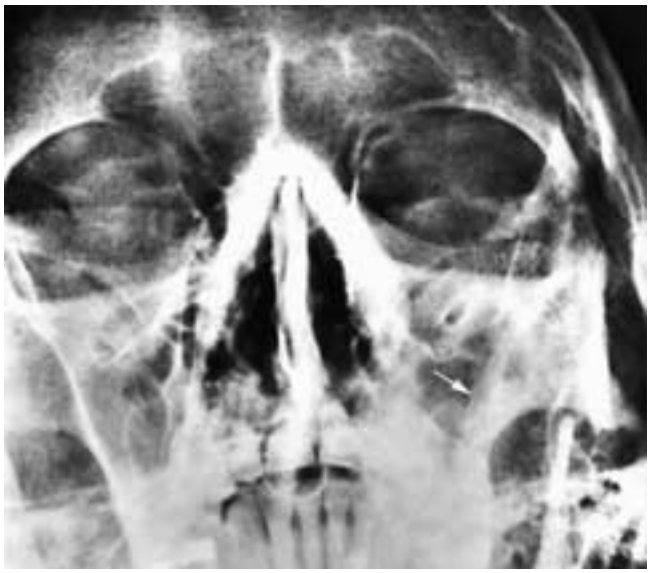

FIGURE 5-20 Waters view shows a clouded or hazy right maxillary sinus without any identifiable mucosal thickening. The left antrum is also hazy, but there is a definite area of mucosal thickening along the lateral sinus wall (*arrow*). This patient had acute sinusitis.

VIEW IMAGE

FIGURE 5-21 Waters view shows mucosal thickening (*arrows*) in the left antrum. As the mucosa becomes progressively thickened, it heaps up into polypoid masses. This patient had sinusitis.

VIEW IMAGE

Copyright © 2003, Mosby, Inc. All rights reserved.

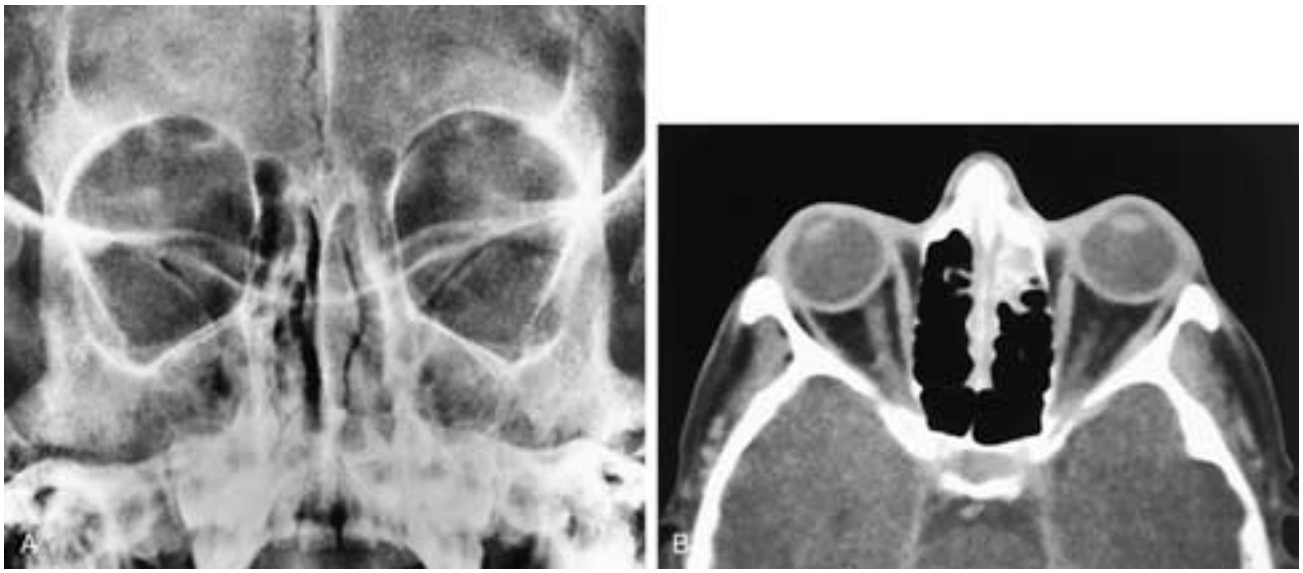

VIEW IMAGE

FIGURE 5-22 In a Waters view (**A**) there is opacification of a left hypoplastic frontal sinus, the left ethmoid sinuses, and both maxillary sinuses. An axial CT scan (**B**) on a different patient who had normal sinus plain films. There is localized inflammatory disease in the left anterior ethmoid cells. However, the left middle and posterior ethmoid cells and the left sphenoid sinus are well aerated. Because on a frontal film this air may negate the soft-tissue density of the anterior ethmoid disease, the frontal plain films may appear normal. Both of these patients had acute sinusitis.

intensities of water, namely, low T1-weighted and high T2-weighted signal intensities.

After several days of inflammation, increased calcium resorption from the sinus walls can be observed on plain films. The cause is unknown but may be the result of increased mucosal vascularity. Plain films show a ''washing out'' of the thin mucoperiosteal white line adjacent to each sinus cavity. This effect is most evident in the frontal and maxillary sinuses.

Conversely, when inflammation has been present for many months or years, the sinus walls become thickened by reactive bone (Fig. 5-23). In the maxillary sinus, this bone may become so thick as to decrease sinus cavity size, a finding confirmed on CT scans.

Chronic sphenoid sinusitis can also result in thickened, sclerotic surrounding bone. Often these patients complain of suboccipital pain or headaches (Fig. 5-24). Rarely, cavernous sinus thrombophlebitis and thrombosis can develop as a

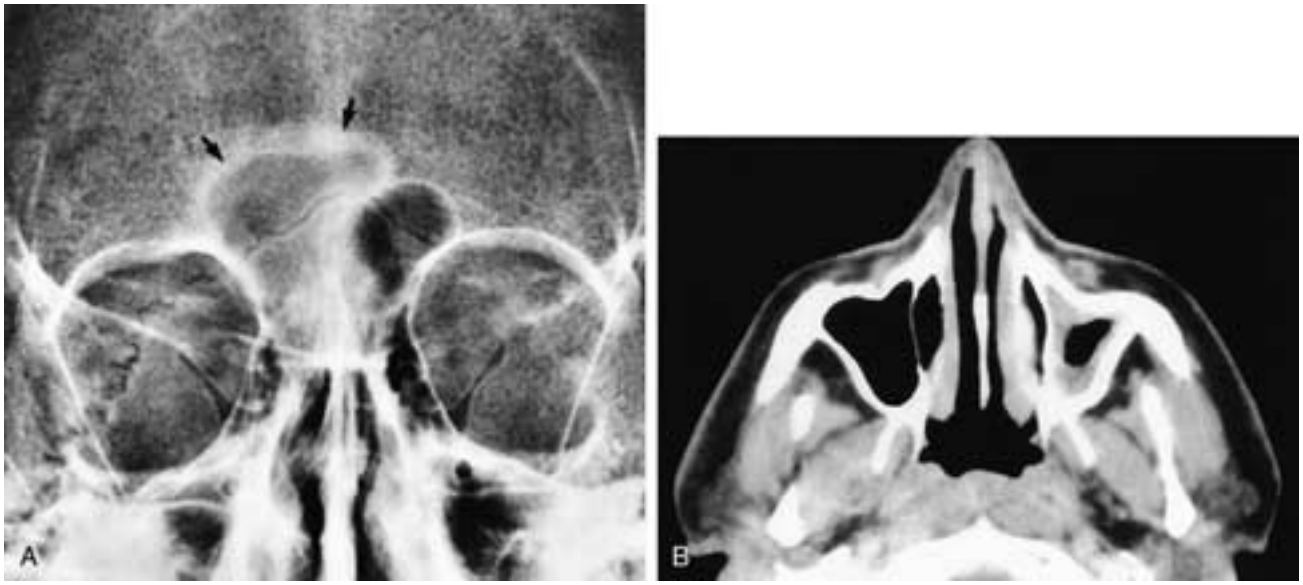

VIEW IMAGE

FIGURE 5-23 Caldwell view (**A**) shows a zone of reactive sclerosis around a clouded right frontal sinus (*arrows*). This suggests that there had been chronic disease in this sinus at one time. There also is minimal clouding of the right ethmoid sinuses. This patient had chronic sinusitis. In **B**, an axial CT scan shows thickening and sclerosis of the walls of the left maxillary sinus and mucosal thickening within this sinus. The mucosal disease may be acute sinusitis, noninfected edematous mucosa, or chronically scarred mucosa. The bone reaction indicates that there has been chronic inflammation in this sinus. This patient had chronic sinusitis.

Copyright © 2003, Mosby, Inc. All rights reserved.

VIEW IMAGE

FIGURE 5-24 Axial CT scan shows an opacified left sphenoid sinus surrounded by thickened, sclerotic bone. This patient had chronic suboccipital headaches and chronic sinusitis.

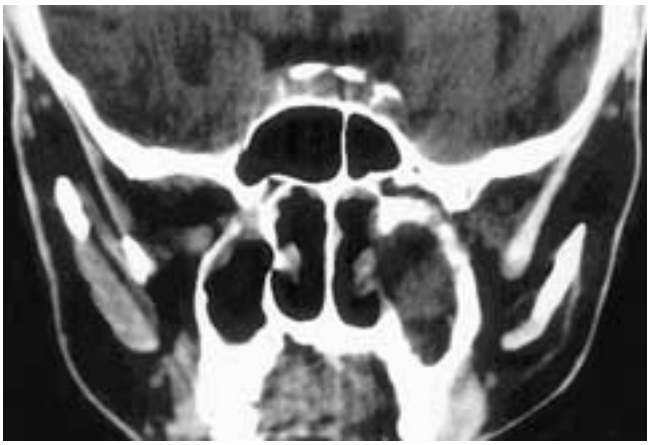

VIEW IMAGE

FIGURE 5-25 Coronal CT scan shows mucosal thickening in the left maxillary sinus associated with thickened, sclerotic bone in the sinus walls. However, unlike Figures 5-23 and 5-24, there are areas of rarefaction and early sequestrum formation along the upper antral wall. Minimal mucosal disease is also present in the right maxillary sinus. This patient had chronic sinusitis with osteomyelitis.

complication of sphenoid sinusitis that may lead to meningitis. Most patients with intracranial-type symptoms will initially have a CT or MR study. Such examinations should always include the skull base and paranasal sinuses to eliminate these as a source of the disease and symptoms.

Osteomyelitis of the bones of the face and paranasal sinuses is uncommon and is usually associated with localized pain. The involved bone has a mottled, irregular appearance on both plain films and CT. There may be sequestra, as well as areas of thickened and sclerotic bone (Fig. 5-25).

More commonly, osteomyelitis may be posttraumatic or iatrogenic. It is most often found following an osteoplastic flap procedure for frontal sinus inflammatory disease. A poorly vascularized and/or infected bone flap may result in osteomyelitis of the flap, a recognized complication of this procedure.

Postirradiation osteitis is rarely seen today in the facial bones because of megavoltage equipment and improved radiation treatment planning. Radiation osteitis is probably most commonly encountered in the mandible, usually in patients irradiated for carcinomas of the tongue and floor of the mouth. In patients irradiated for maxillary sinus carcinomas, the first manifestation of sinus osteomyelitis may be localized pain, swelling, and inflammation over the zygoma and maxilla, initially suggesting tumor recurrence. However, eventually a bone sequestrum is extruded, and symptoms temporarily improve. Multiple sequestra are usually extruded, and it is not uncommon for the osteitis to become clinically manifest up to 1 or 2 decades after irradiation. On CT the involved facial bones appear shattered, fragmented, and sclerotic (Fig. 5-26). Superficial sequestra should be specifically identified and localized to aid therapy.

When evaluating mucosal thickening on postcontrast CT scans, if the thickened mucosa does not enhance, it is probably not actively infected and usually is fibrotic and scarred. Active infection has a thin zone of mucosal enhancement with a variable zone of lower-attenuation submucosal edema (Fig. 5-1). If the sinus is opacified, the CT appearance shows roughly concentric rings or zones: an outer bony wall ‘‘ring,’’ a water or mucoid attenuation (10 to 18 HU) submucosal ring, a thin infected mucosal enhancing ring, and a central zone of entrapped mucoid secretions (Fig. 5-1). Although most minimal to moderate mucosal thickening is seen as a fairly uniformly thick soft-tissue zone on sectional imaging, thicker, more redundant mucosa can appear almost nodular or ‘‘wavelike.’’ In these instances, the disease tends to involve the sinus diffusely, unlike the focal nodularity often seen with tumors.

In all CT examinations, the sinuses should be viewed at wide window settings so that mucosal disease is not falsely interpreted as a hypoplastic or aplastic sinus (Fig. 5-27).

On MR imaging the thickened, inflamed mucosa typically has a low signal intensity on T1-weighted images, an intermediate intensity signal on proton density (PD) images, and a high signal intensity on the T2-weighted images (Figs. 5-18, 5-19, and 5-28). These changes reflect the high water content of the inflamed tissues. The high T2-weighted signal intensity is helpful in differentiating inflamed tissues from almost all sinonasal tumors. At most, such tumors tend to have an intermediate T2-weighted signal intensity. Dense scar or fibrosis has a low to intermediate signal intensity on all imaging sequences, a useful finding in differentiating it from inflammation and most tumors on the T2-weighted images. Unfortunately, both tumor and the vascularized scar tissue/granulation tissue that develops after surgery have similar signal intensities, and they cannot, at present, be confidently differentiated on MR imaging.

Unilateral swelling of the middle and inferior nasal turbinates, especially in the absence of concurrent paranasal sinus disease, probably reflects the normal nasal cycle. In these cases, a thin zone of air remains, separating the turbinates from the nasal septum and the lateral nasal wall. If this air space is not present, the turbinates probably are pathologically enlarged. Clinical correlation can help

Copyright © 2003, Mosby, Inc. All rights reserved.

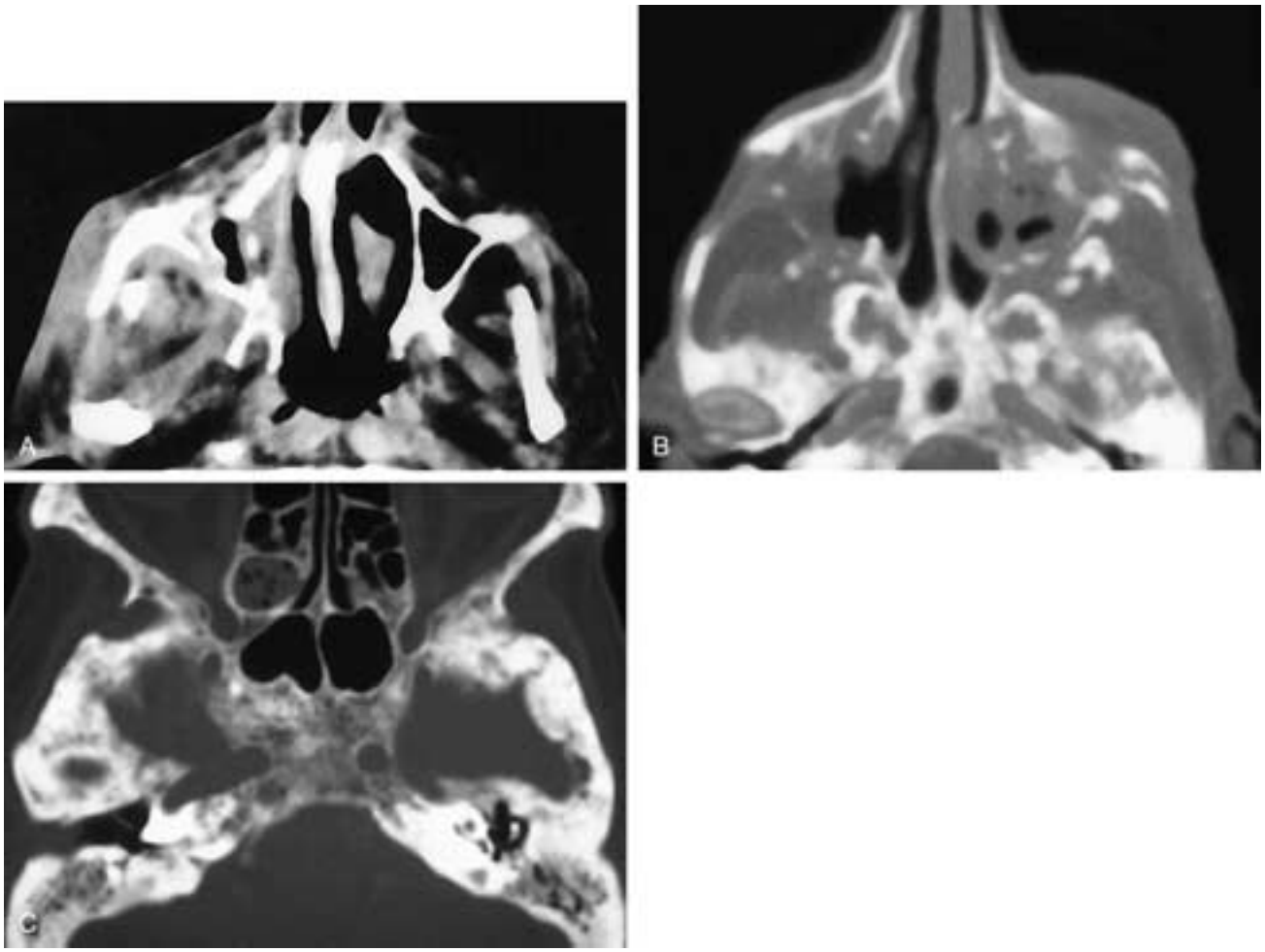

VIEW IMAGE

FIGURE 5-26 In **A**, an axial CT scan, there is fragmentation of the right maxillary sinus's bony walls, with sclerosis and thickening of the bone. Mucosal thickening is also present in the sinus. This patient had radiation osteitis and sinusitis. In **B**, an axial CT scan shows extensive sclerosis and fragmentation of the facial bones, with some of the osseous structures having been extruded as sequestra. This patient had radiation osteitis. In **C**, an axial CT scan shows areas of both dense bone and ''washed-out,'' permeated-appearing bone in the skull base and posterior ethmoid and sphenoid sinus margins. Some secretions are also present in the most posterior right ethmoid cells. This patient had radiation osteitis after radiation therapy for a nasopharyngeal carcinoma.

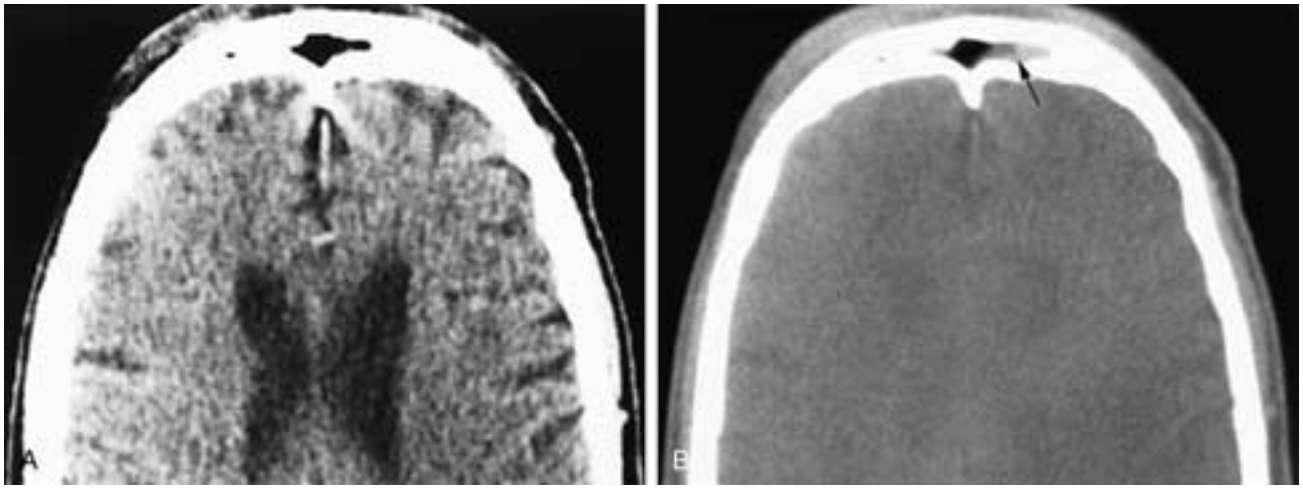

VIEW IMAGE

FIGURE 5-27 In **A**, an axial CT scan viewed at a ''soft-tissue'' window setting, the left frontal sinus appears well aerated. However, in **B**, inflammatory mucosal thickening in the left frontal sinus (*arrow*). This patient had a headache and acute sinusitis.

Copyright © 2003, Mosby, Inc. All rights reserved.

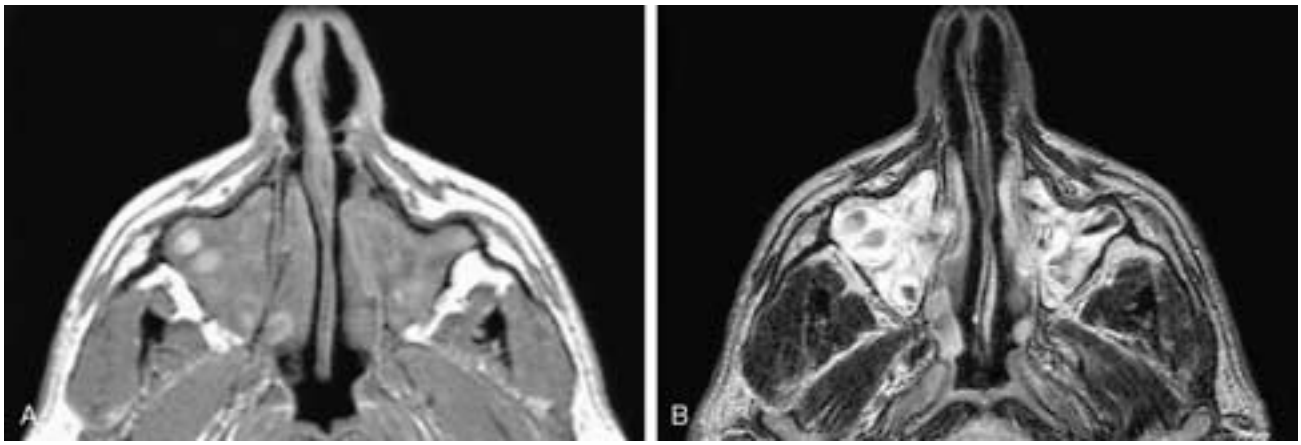

VIEW IMAGE

FIGURE 5-28 Axial T1-weighted (**A**) and T2-weighted (**B**) MR images show both maxillary sinuses filled with nonhomogeneous signal intensities. In **A**, the majority of the sinus content has a low to intermediate signal intensity, while in **B**, it has a high signal intensity. This represents heaped-up, inflamed mucosa and is the characteristic MR imaging appearance of inflammation. The areas of higher signal intensity in **A** and lower signal intensity in **B** are sites of desiccated secretions. This patient had chronic sinusitis.

resolve any issue.[88] On postcontrast CT and MR images, the turbinates will enhance whether enlarged physiologically or pathologically. On MR images they have low T1-weighted and high T2-weighted signal intensities (Fig. 5-29). Nasal turbinate swelling may also represent an allergy to contrast material on postcontrast CT scans. This is easily confirmed if the turbinates are normal on the initial noncontrast scan.[89]

Polyps and Cysts

The intrasinus polyp and the retention cyst cannot be differentiated on either plain films or sectional imaging. However, this is of little consequence, as both are common benign entities and any treatment is the same.

On all imaging, retention cysts and polyps are homogeneous soft-tissue masses with smooth, outwardly convex borders (Figs. 5-30 to 5-39). Multiple or single lesions may be present; most are small and clearly do not fill the entire sinus cavity. If a cyst or polyp occurs in the roof of the maxillary sinus in a patient with a history of recent trauma, the plain film examination may simulate a blowout fracture (Fig. 5-31). However, coronal CT or MR imaging will

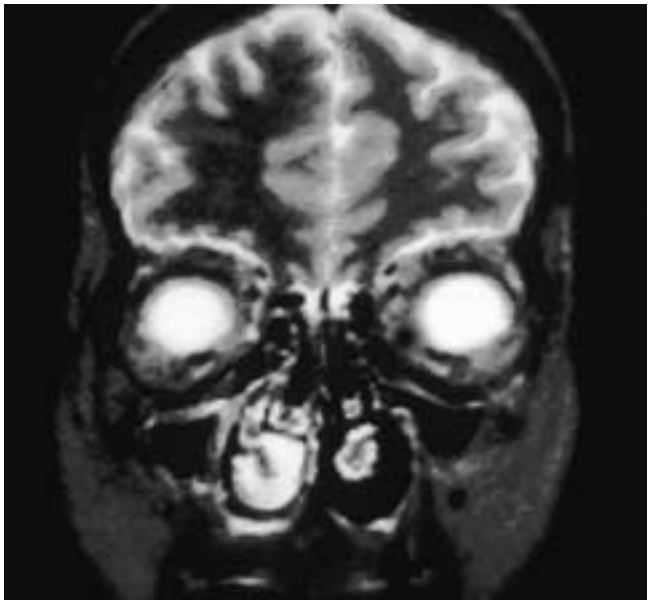

VIEW IMAGE

FIGURE 5-29 Coronal T2-weighted MR image shows swelling of the right inferior and middle turbinates, while the left turbinates have a shrucken appearance. In addition, there is some mucosal thickening in the right maxillary and ethmoid sinuses. This is an example of the normal nasal cycle in a symptomatic patient.

FIGURE 5-30 Waters view shows a solitary left antral retention cyst or polyp (*arrows*). This cyst typically has a smooth, outwardly convex contour. The remaining antrum and the other sinuses are normal.

VIEW IMAGE

Copyright © 2003, Mosby, Inc. All rights reserved.

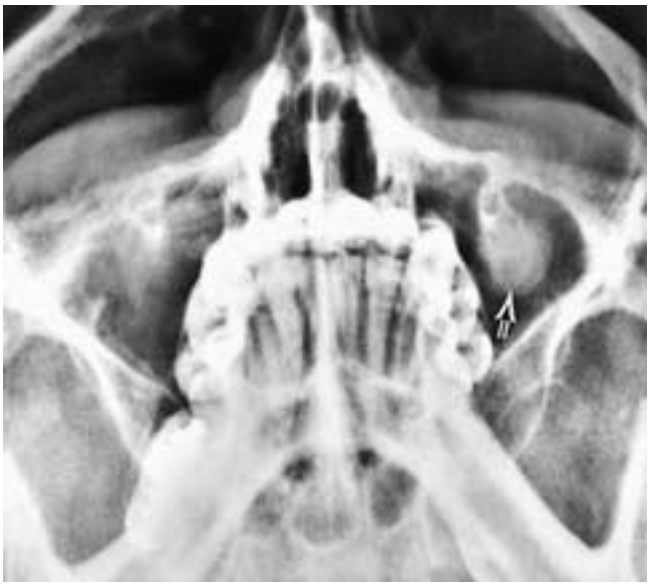

VIEW IMAGE

FIGURE 5-31 Waters view shows a retention cyst or polyp (*arrow*) in the roof of the left maxillary sinus. If there was a history of recent orbital trauma, this could be mistaken for part of a blow-out fracture. In this patient, coronal sectional images would have demonstrated an intact orbital floor.

demonstrate an intact orbital floor, with the cyst or polyp in the antral mucosa.

On the Waters view, a prominent infraorbital canal may mimic a cyst or polyp in the roof of the antrum. Similarly the nasal alae can simulate a medial wall antral cyst or polyp, and unerupted teeth, the lips, or a mustache can simulate a cyst or polyp on the floor of the maxillary sinus. The coronoid process of the mandible can simulate a cyst or polyp in the posterior floor of the antrum on a lateral plain film taken with the patient's mouth closed.

As a cyst or polyp enlarges to fill at least half of the antrum, it behaves like a water-filled thin balloon, the upper surface flattens out, and it resembles an air-fluid level (Fig. 5-40). A true air-fluid level is a fluid level throughout the entire involved sinus, with a concave upward meniscus at the margins of the fluid. Additionally the planar surface of the fluid will directly reflect gravity in every head position. On MR imaging these cysts or polyps usually have characteristics similar to those of mucosal inflammation, again reflecting the high water and low specific protein content. Thus, they tend to have low to intermediate T1-weighted and high T2-weighted signal intensities. If the protein content of the cyst or polyp fluid increases, either due to infection or the passage of time, the T1-weighted signal intensity may become high, reflecting the shortening of the T1 relaxation time.

Retention cysts and polyps are usually asymptomatic and are incidental radiographic findings. However, if they enlarge to fill the entire sinus, they may obstruct sinus drainage and become symptomatic. Rarely, these lesions can remodel the sinus walls and expand the sinus cavity. But in most cases on sectional imaging, small pockets of remaining sinus air can be identified overlying part of the convex margin of the lesion (Fig. 5-34). This distinguishes such a cyst or polyp from a mucocele, although when the lesion is large, the distinction is of more intellectual interest than clinical significance.

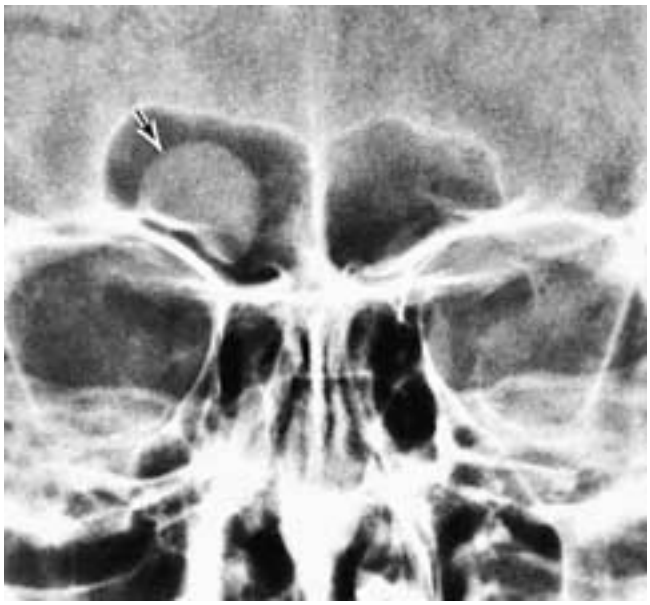

FIGURE 5-32 Caldwell view shows a retention cyst (*arrow*) in the right frontal sinus. Note that this sinus is otherwise normal.

VIEW IMAGE

On sectional imaging, a typical antrochoanal polyp appears as a soft-tissue polyp that completely fills a maxillary sinus. Usually the infundibular region is widened, and there is a slight extrusion of the antral mass into the middle meatus. Alternatively, the polyp can extend through a secondary sinus ostium. At this stage, such an antrochoanal polyp can be confused with hypertrophic polypoid antral mucosa that has also extended through the sinus ostium. However, as the polyp grows, it fills the ipsilateral nasal fossa and extends back into the nasopharynx (Figs. 5-41 to 5-44). It may become sufficiently large to hang down into the oropharynx. Although the medial antral wall may eventually be deossified or destroyed, the remaining antral walls are rarely remodeled. This can be a difficult

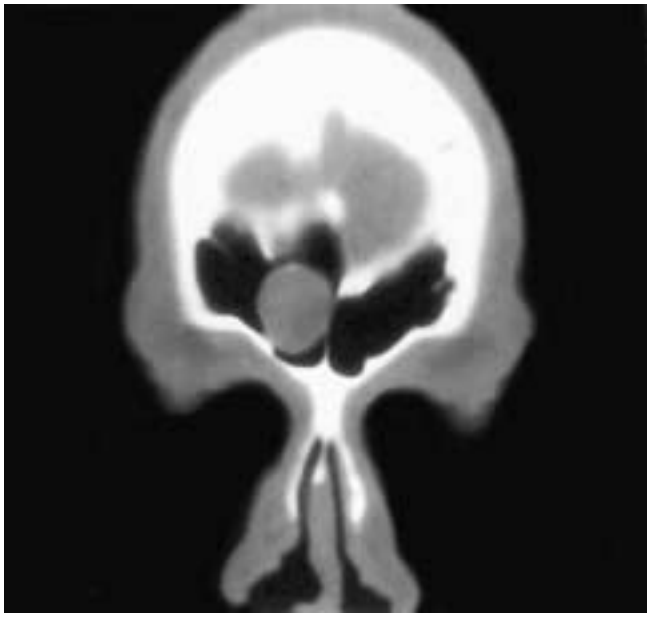

FIGURE 5-33 Coronal CT scan shows a solitary retention cyst or polyp in the right frontal sinus. The sinus is otherwise normal.

VIEW IMAGE

Copyright © 2003, Mosby, Inc. All rights reserved.

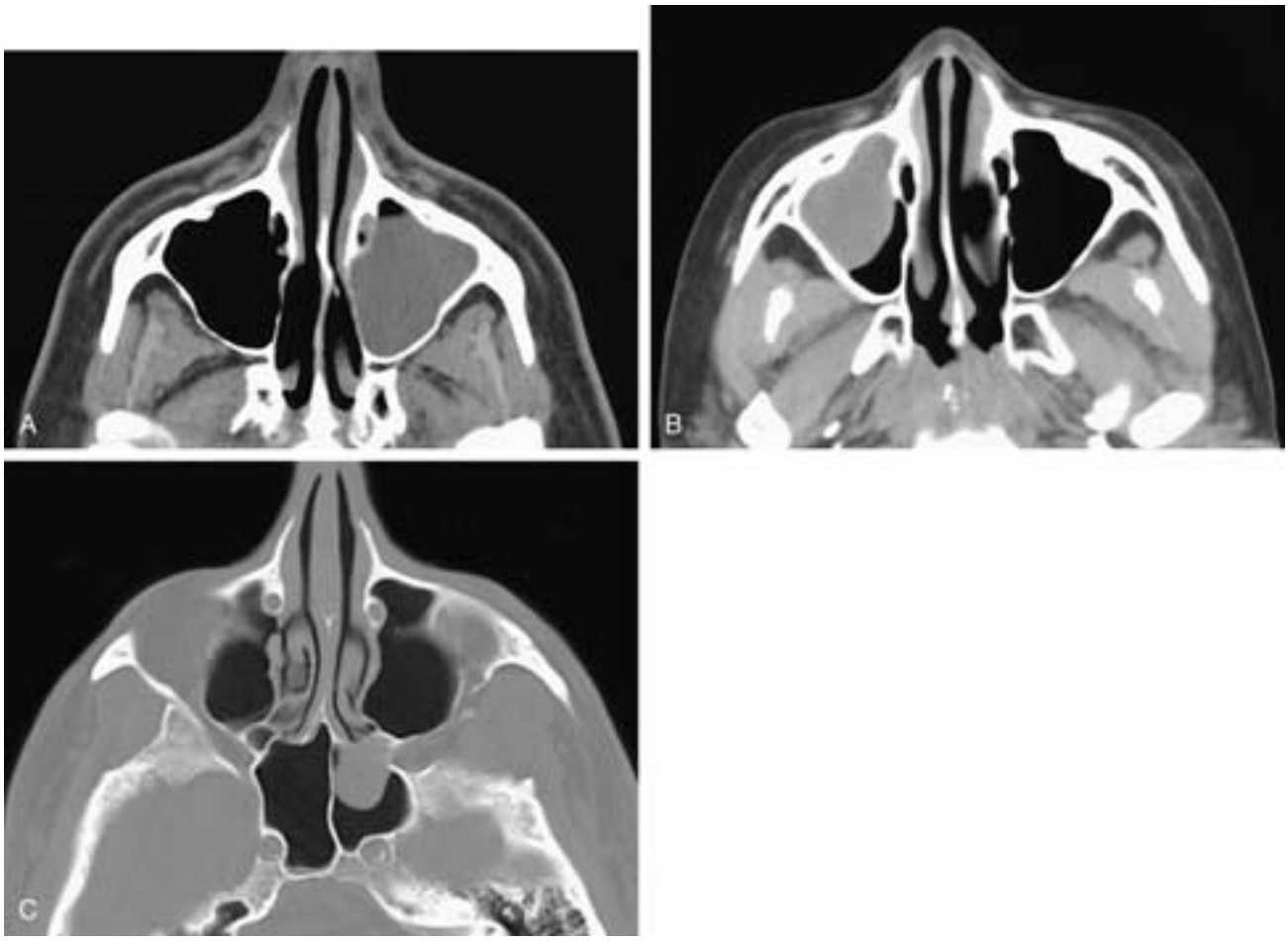

VIEW IMAGE

FIGURE 5-34 Axial CT scans. In **A**, there is a large retention cyst or polyp in the left maxillary sinus. A small amount of air is present over the upper surface of the lesion, and the sinus cavity is not enlarged. In **B**, there is a typical retention cyst or polyp in the right maxillary sinus. Note that the convex margin of the lesion is smooth and that the remaining sinus is normal. In **C**, there is a retention cyst or polyp in the left sphenoid sinus and minimal mucosal thickening in the right sphenoid sinus.

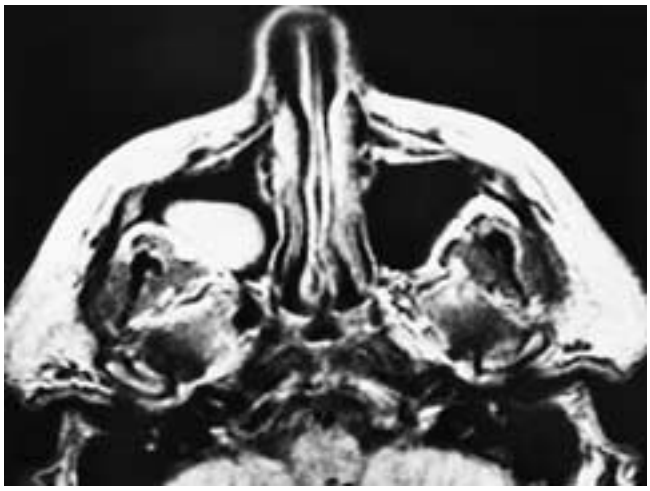

VIEW IMAGE

FIGURE 5-35 Axial proton density MR image shows a solitary retention cyst or polyp with a typically high signal intensity in the right antrum.

diagnosis on plain films, but it is rarely misdiagnosed on sectional imaging. Histologically, antrochoanal polyps differ from inflammatory polyps in that they are fibrotic, with minimal inflammation. The normal minor salivary tissue is obliterated. Of note, atypical fibroblasts may be seen within the lesion, mimicking a neoplastic process. Thus the radiologist may assist the pathologist in ruling out neoplasm by confirming a benign, slowly growing lesion.

On plain films, nasal polyps are often seen as a vague increased soft-tissue density within the nasal fossa. However, on sectional imaging they usually can be identified as discrete single or multiple broad-based soft-tissue masses (Figs. 5-45 to 5-59). On CT, more recent polyps tend to have a mucoid attenuation (10 to 18 HU), with mucosal enhancement occasionally seen at the polyp's surface. However, those polyps that have had sufficient time to develop stromal fibrosis plus desiccation of the secretions tend to have higher overall attenuation (20 to 35 HU). On MR imaging, typically the dominant feature is the high water and low protein content that gives the polyps low to intermediate T1-weighted and high T2-weighted signal intensities. When multiple polyps are present, often intermixed with mucoceles, the

Copyright © 2003, Mosby, Inc. All rights reserved.

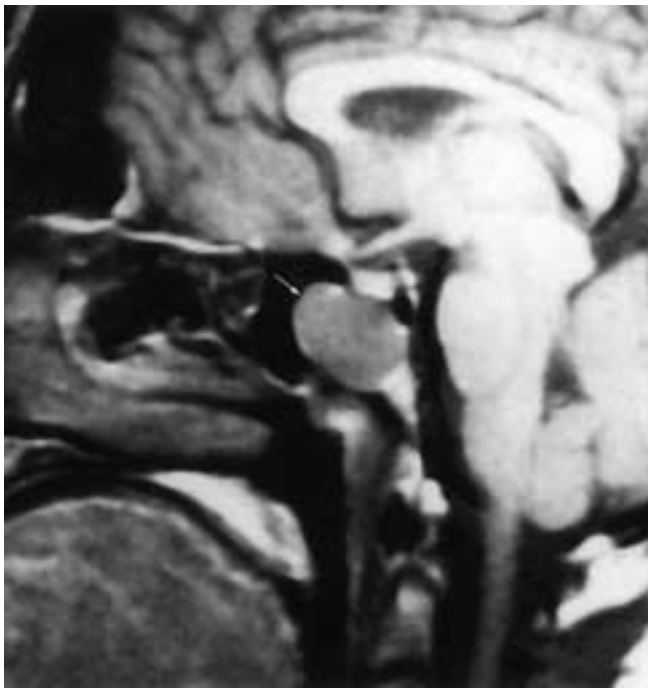

VIEW IMAGE

FIGURE 5-36 Sagittal T1-weighted MR image shows a solitary nonobstructing retention cyst or polyp (*arrow*) in the sphenoid sinus. This is the type of lesion that was formerly referred to as a *mucocele* in the older literature.

entrapped secretions usually have variable T1-weighted and T2-weighted signal intensities (Figs. 5-56 and 5-57). It is this variable imaging appearance that distinguishes such polypoid masses from tumors, which tend to have more homogeneous signal intensities.[83, 90, 91]

On CT, when there are multiple polyps crowded within the nasal vault, they can form an overall conglomerate mass that may be difficult if not impossible to distinguish from a tumor. This is especially true of bulky lesions such as inverting papillomas and lymphomas that tend to remodel the surrounding bone. However, two findings typical of sinonasal polyps can reliably establish their diagnosis on CT studies. First, an ethmoid polypoid mucocele that involves

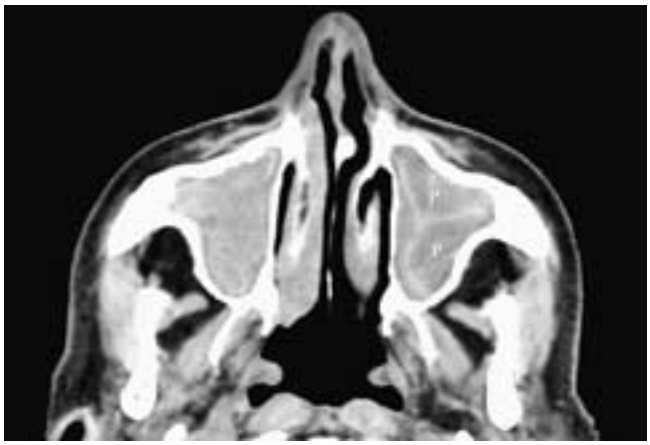

FIGURE 5-37 Axial CT scan shows both maxillary sinuses to be filled. On the right side, there is higher-attenuation material centrally within the sinus cavity representing desiccated secretions. However, on the left side, desiccated secretions form a thin curvilinear zone of higher attenuation, outlining the mucosal polyps (*P*) in this sinus.

VIEW IMAGE

the ethmoid labyrinth unilaterally or bilaterally is characterized by widening of the ethmoid complex, with little if any destruction of the delicate ethmoid septa.[74, 92] The individual ethmoid cells are filled with polypoid mucosa and entrapped mucoid secretions. The CT appearance of each sinus cavity is that of a central high-attenuation region (desiccated secretions) separated from the bony sinus wall by a thin zone of lower mucoid attenuation. By comparison, a solid mass (either a single polyp, a mucocele, or a tumor) will destroy these septa, and in this latter circumstance it is impossible to distinguish a benign lesion from a low-grade malignant process. The preservation of ethmoidal septa, as seen in polypoid mucoceles, unequivocally signifies the presence of benign disease (Figs. 5-52 and 5-53).

Secondly, the finding of a unilateral or bilateral expansile sinonasal mass with cascading, looping, or curvilinear areas of fairly high attenuation (desiccated secretions) in a background matrix of mucoid attenuation (10 to 18 HU) is specific on CT for the presence of a benign process. Usually, these polypoid masses are separated from the adjacent bones by a thin zone of mucoid material (Figs. 5-50 to 5-53). This

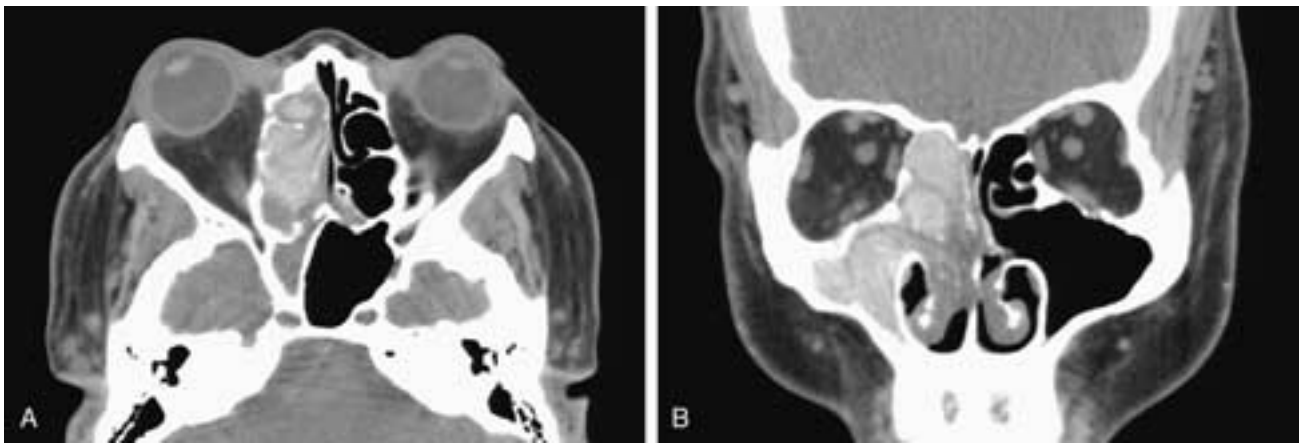

VIEW IMAGE

FIGURE 5-38 Axial (**A**) and coronal (**B**) CT scans show opacification of the right ethmoid, sphenoid, and maxillary sinuses. Within the ethmoid and maxillary sinuses are polypoid areas of higher attenuation representing desiccated secretions within chronic polyps. This patient had no history of allergies. Note that the left-sided sinuses are virtually normal.

Copyright © 2003, Mosby, Inc. All rights reserved.

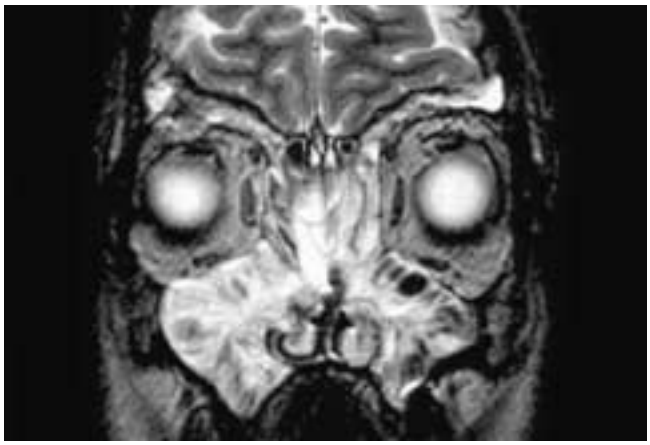

VIEW IMAGE

FIGURE 5-39 Coronal T2-weighted MR image shows soft tissues opacifiying the ethmoid and maxillary sinuses. Overall, the signal intensity is high. However, there are multiple areas of lower signal intensity that represent partially desiccated secretions within polyps. This was an allergic patient with extensive polyposis.

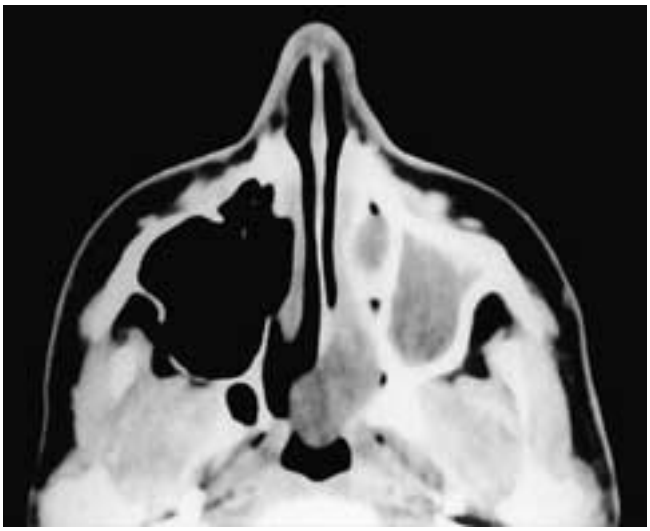

FIGURE 5-41 Axial CT scan shows a mucoid density mass filling the left maxillary sinus. It extended through the infundibulum into the left nasal fossa and nasopharynx. This patient had an antrochoanal polyp.

VIEW IMAGE

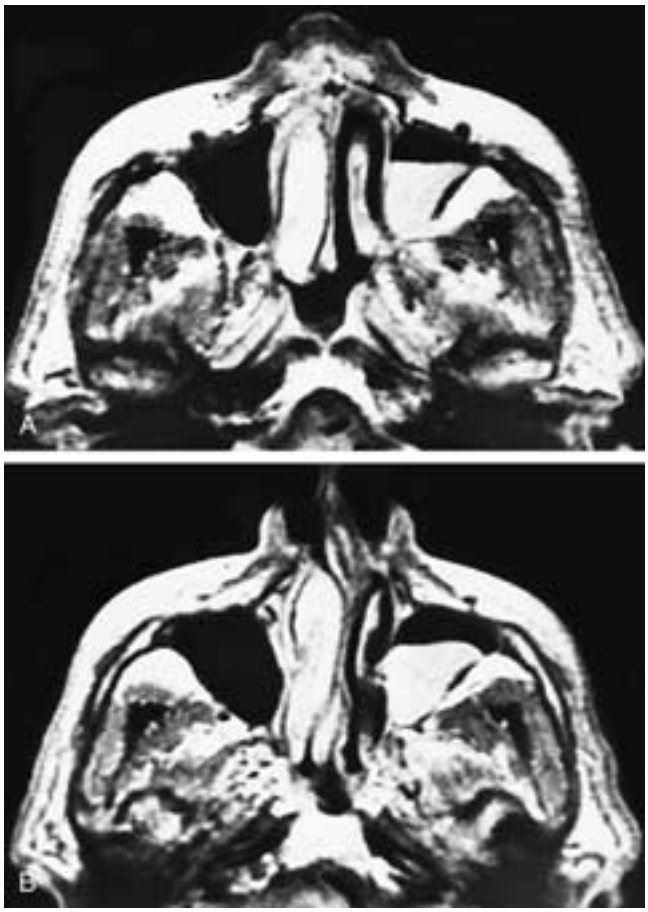

VIEW IMAGE

FIGURE 5-40 Axial proton density MR images. In **A**, the image is through the lower sinus and there is an apparent air-fluid level. However, in **B**, the image is through the midsinus, and a convex margin is seen identifying this high signal intensity retention cyst or polyp. Because large cysts or polyps are essentially fluid-filled bags, gravity can flatten portions of large lesions to simulate an air-fluid level.

unique CT appearance is seen in about 20% of patients with nasal polypoid masses.

On MR, the signal intensity is determined by the degree of desiccation of the secretions entrapped within the sinuses and between and within the polyps. The resulting variable appearance of signal intensities is diagnostic of inflammatory disease. The primary diagnostic problem arises when semisolid or completely desiccated secretions are present. These dried secretions give signal voids on T2-weighted images and, depending on the degree of desiccation, either low signal intensity or signal voids on T1-weighted images. Possible confusion with an aerated sinus can occur unless a CT study is available for comparison (Figs. 5-18 and 5-19).

Sinonasal mucosa adjacent to polyps will enhance on MR imaging, while secretions and fluid within and around the polyps will not enhance. This appearance is distinctive from that of a neoplasm, which enhances more uniformly.

The CT finding of a high-attenuation central region separated from the sinus wall by a thin zone of mucoid attenuation material can be seen in three distinct cases in order of likelihood: chronic inspissated (desiccated) secretions, a mycetoma (usually from aspergillosis), and intrasinus hemorrhage (Figs. 5-8A and 5-60).[93] Although a specific diagnosis may not always be possible on CT, this appearance reliably indicates that the soft-tissue mass is not a tumor.[57] The MR imaging finding of a central intrasinus region of signal void or low T1-weighted and T2-weighted signal intensity can represent either desiccated secretions in chronic sinusitis, a mycetoma in a patient with sinus fungal disease, a sinolith, or an intrasinus tooth (antrum) (Figs. 5-18, 5-19, and 5-61 to 5-66).

The mycetomas are semisolid and have paramagnetic ions, both contributing to their low signal intensity or signal voids on all imaging sequences. Any inflammatory reaction around the mycetoma will have the typical MR imaging characteristics of infections or polyps.[94]

Copyright © 2003, Mosby, Inc. All rights reserved.

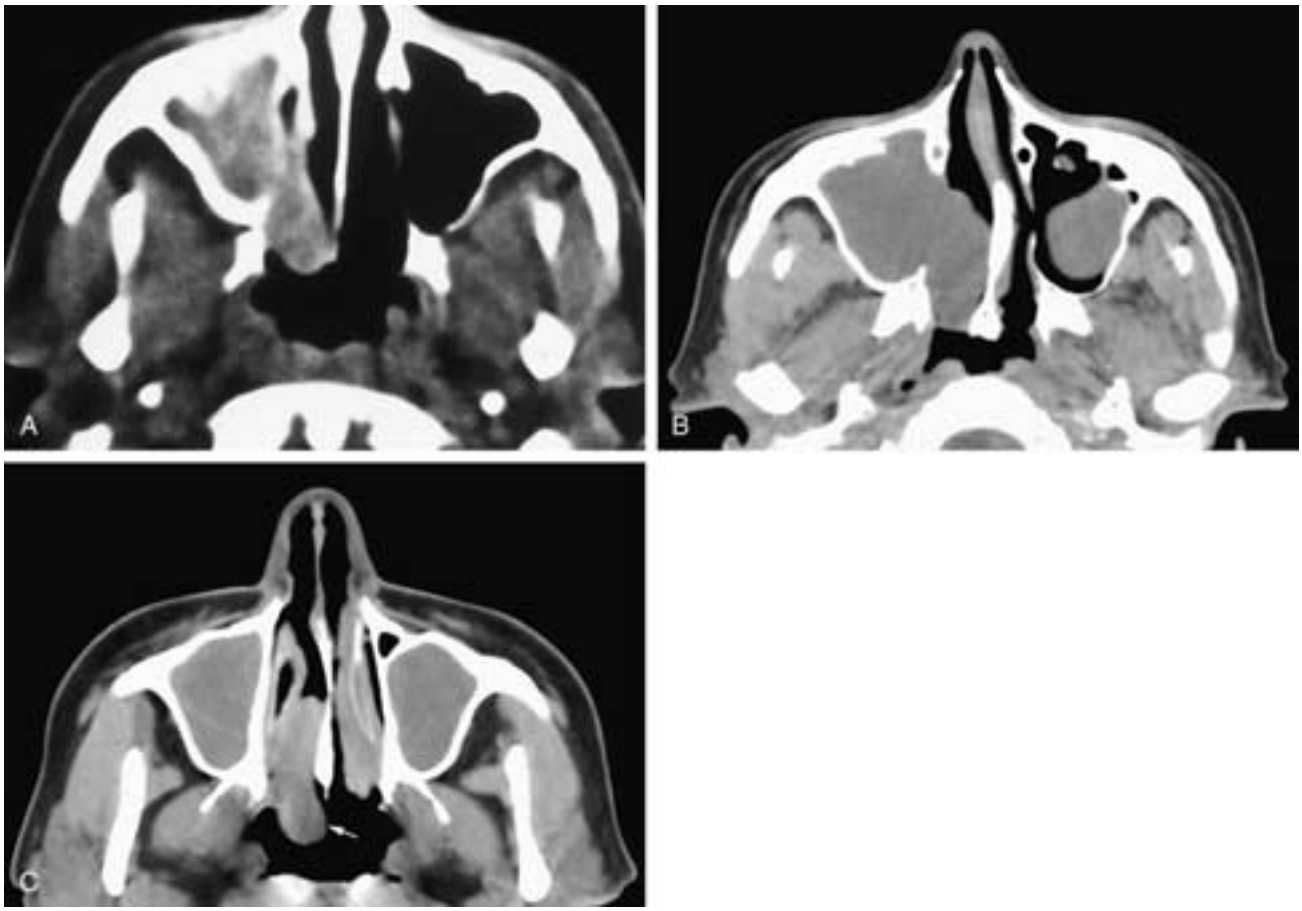

VIEW IMAGE

FIGURE 5-42 **A**, Axial CT scan shows a right maxillary sinus polypoid mass that has prolapsed into the posterior right nasal fossa. This patient had an antrochoanal polyp. Axial cranial (**B**) and caudal (**C**) CT scans on another patient show a polypoid mass in the right maxillary sinus that has extended into the right nasal fossa and prolapsed into the nasopharynx (*arrow*). This patient also had an antrochoanal polyp.

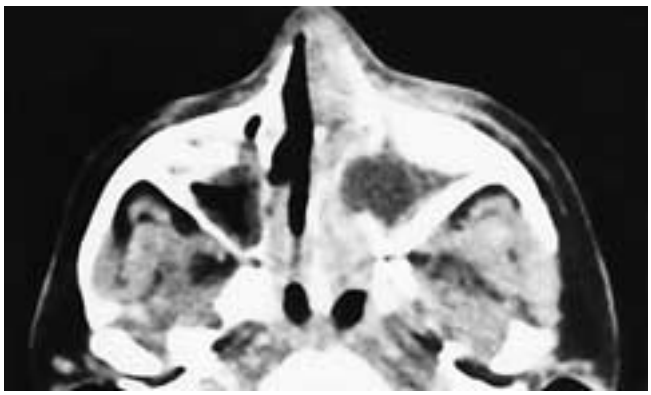

VIEW IMAGE

FIGURE 5-43 Axial contrast-enhanced CT scan shows a mucoid attenuation polypoid mass in the left maxillary sinus that bulges into the left nasal fossa. Inflammatory mucosal changes are seen in both nasal fossae, and there is enhancement of the mucosa around the polyp. This patient had an antrochoanal polyp.

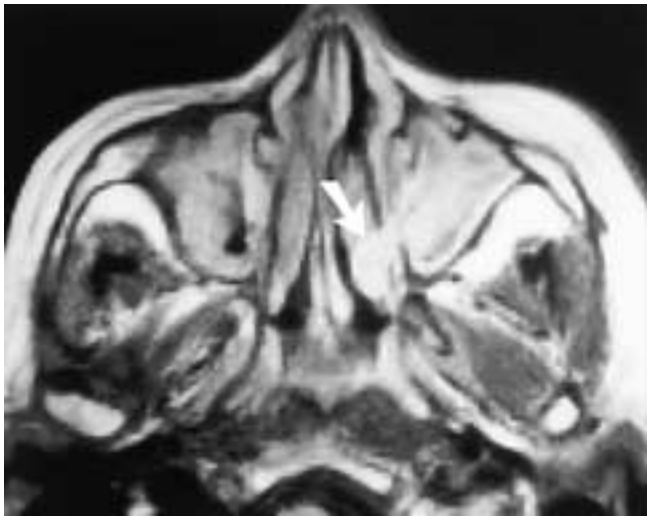

FIGURE 5-44 Axial proton density MR image shows inflammatory changes in both maxillary sinuses. On the left side, a polypoid mass fills the left maxillary sinus and extends into the nasal fossa (*arrow*). This patient had an antrochoanal polyp.

VIEW IMAGE

Copyright © 2003, Mosby, Inc. All rights reserved.

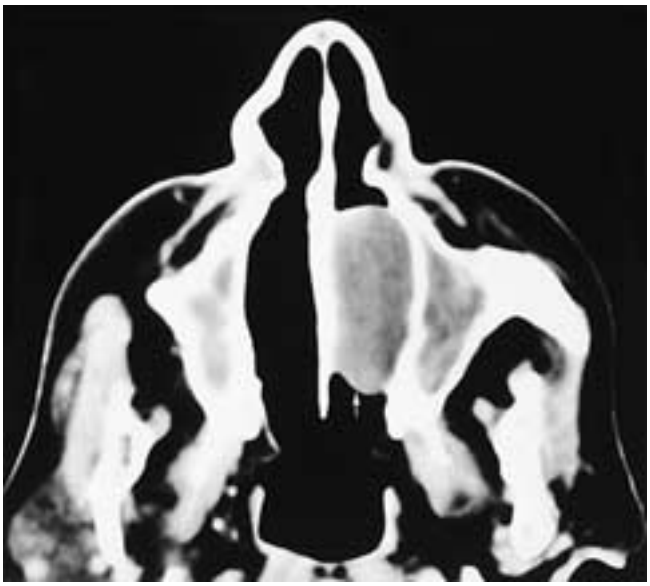

FIGURE 5-45 Axial CT scan shows a solitary mucoid attenuation left nasal mass (*arrow*). There are also secretions and inflammatory mucosal disease in both maxillary sinuses. This patient had a nasal polyp and sinusitis.

VIEW IMAGE

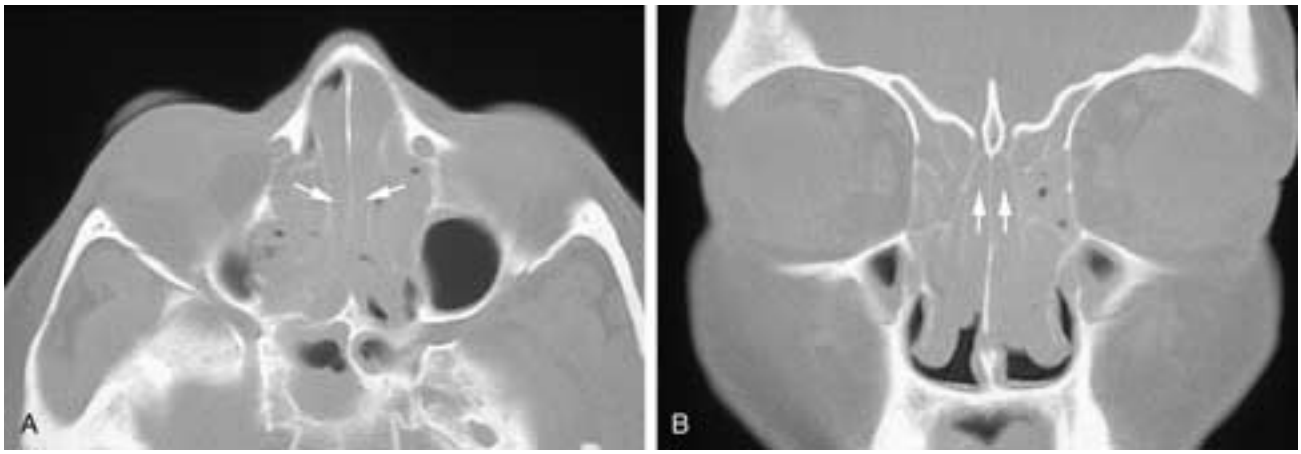

VIEW IMAGE

FIGURE 5-46 Axial (**A**) and coronal (**B**) CT scans show soft-tissue disease opacifying the ethmoid sinuses and inflammatory mucosal thickening in the sphenoid and maxillary sinuses. Polypoid soft tissues also fill both nasal fossae. Note that the normally thin olfactory recesses of the upper nasal fossae are widened (*arrows*). This suggests that the nasal masses are chronic nasal polyps.

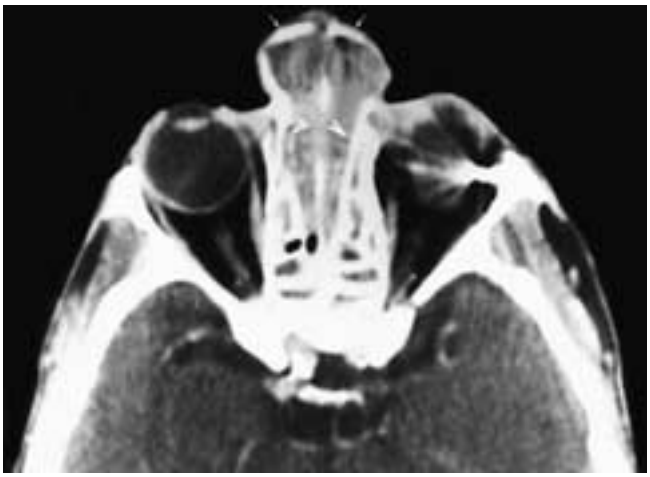

VIEW IMAGE

FIGURE 5-47 Axial contrast-enhanced CT scan shows bilateral nasal masses that have displaced the nasal bones anterolaterally (*small arrows*) and thinned part of the nasal septum. The upper nasal fossae are widened by the nasal masses, and the medial aspect of the each ethmoid complex has been displaced laterally (*arrowheads*). There are also secretions in both ethmoid sinuses. This patient had nasal polyposis and sinusitis.

FIGURE 5-48 Axial CT scan shows multiple bilateral nasal polyps, inflammatory mucosal thickening in the left maxillary sinus, and opacification of the right maxillary sinus. This patient had nasal polyposis and sinusitis.

VIEW IMAGE

Copyright © 2003, Mosby, Inc. All rights reserved.

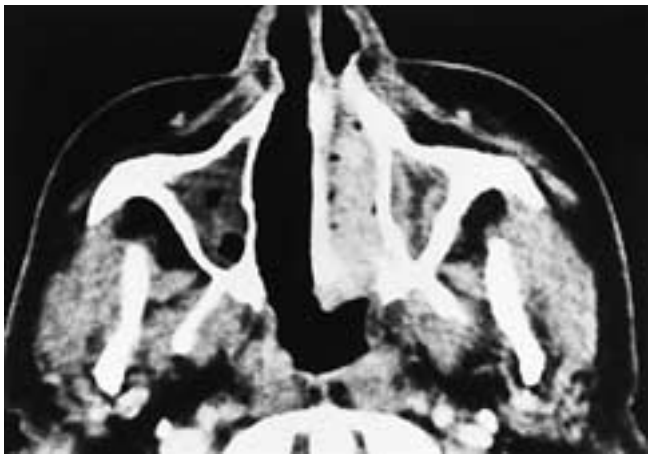

VIEW IMAGE

FIGURE 5-49 Axial contrast-enhanced CT scan shows an enhancing left nasal fossa polypoid mass. There are mucosal enhancement and secretions in the left maxillary sinus and mucoid secretions in the right maxillary sinus. This patient had nasal polyps and sinusitis.

An intrasinus hemorrhage initially has a low signal intensity on all imaging sequences. However, when the blood becomes oxidized to methemoglobin (by 24 to 48 hours after the trauma), it has a high T1-weighted and an intermediate T2-weighted signal intensity. Thus, with MR imaging, intrasinus hemorrhage can be distinguished in almost all cases from desiccated secretions and a mycetoma (Fig. 5-8).[17, 18] It should be noted that as long as some air remains in the sinus, it is rare to have any entrapped secretion desiccate enough to have high T1-weighted signal intensity.

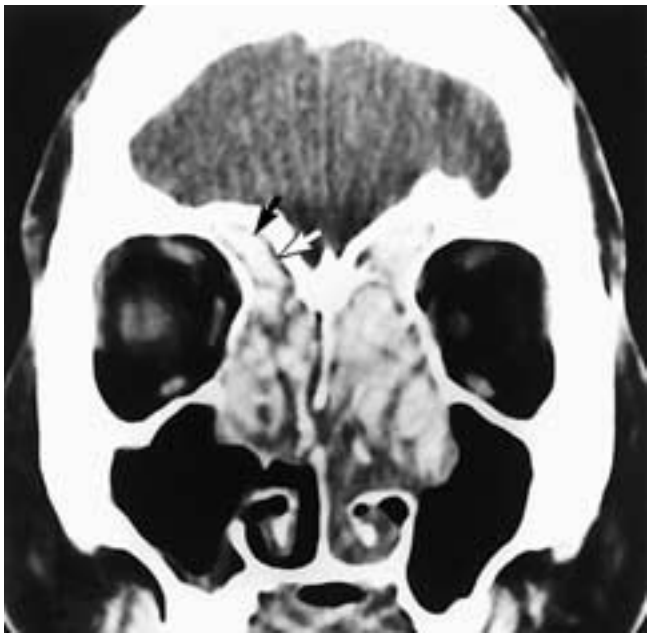

VIEW IMAGE

FIGURE 5-50 Coronal CT scan shows multiple high-attenuation soft-tissue masses extending from the ethmoid sinuses into the nasal fossae. Each polypoid mass is separated from the adjacent bone by a thin zone of mucoid attenuation material (*arrows*). The polyps are also embedded within a matrix of mucoid secretions. This patient had nasal and paranasal sinus polyposis.

Mucoceles

On plain films a frontal sinus mucocele first appears as a slightly clouded sinus with a smooth, ovoid, or rounded contour, in contrast to the normal frontal sinus, which has a scalloped contour with septation extending into the sinus and a density similar to that seen in the superior orbital fissure. The normal thin mucoperiosteal white line becomes hazy. If chronic sinusitis predates mucocele development, a zone of dense reactive bone may surround the sinus. As the

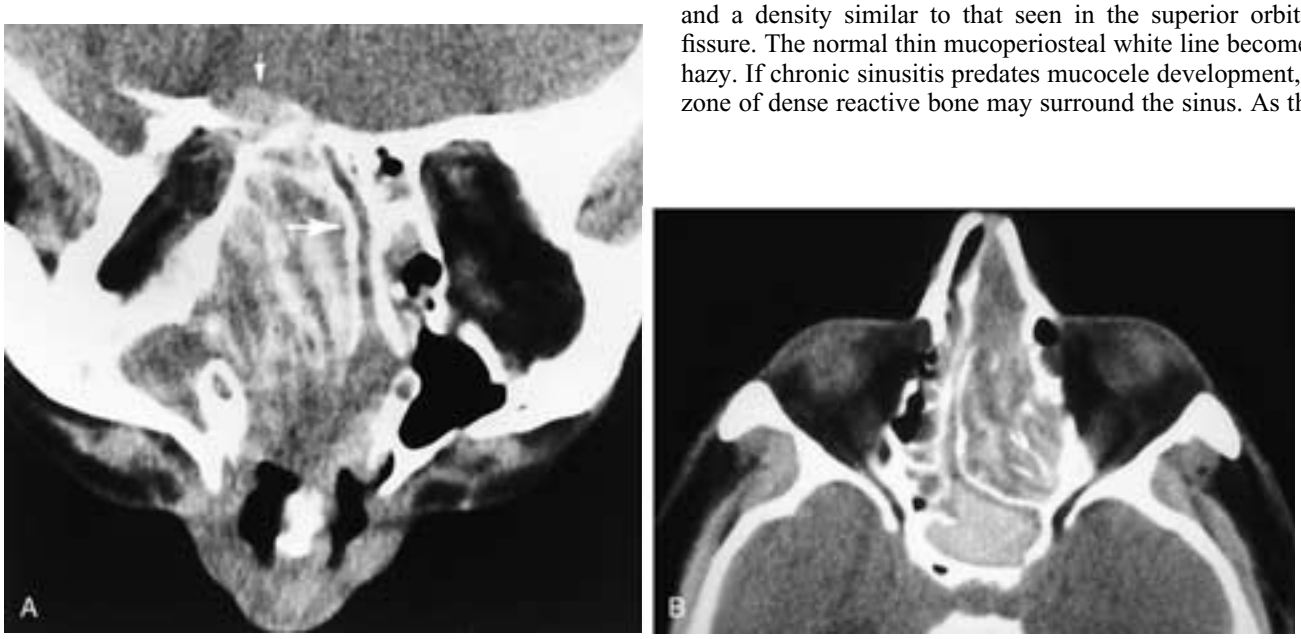

VIEW IMAGE

FIGURE 5-51 Coronal CT scan (**A**) shows an expansile right nasoethmoid mass that has displaced the nasal septum to the left (*large arrow*). The mass has also focally broken into the floor of the anterior cranial fossa (*small arrow*). Within the mass are discrete high-attenuation polypoid masses embedded within mucoid secretions. There are also inflammatory changes in the left ethmoid sinuses. This patient had polyposis. An axial CT scan (**B**) on another patient shows a high-attenuation soft-tissue mass in the sphenoid sinus that is separated from the sphenoid sinus's bony wall by a zone of mucoid attenuation. There also is an expansile left nasoethmoid mass that has discrete high-attenuation polypoid areas within mucoid secretions. This patient had polyposis and a sphenoid sinus polyp.

Copyright © 2003, Mosby, Inc. All rights reserved.

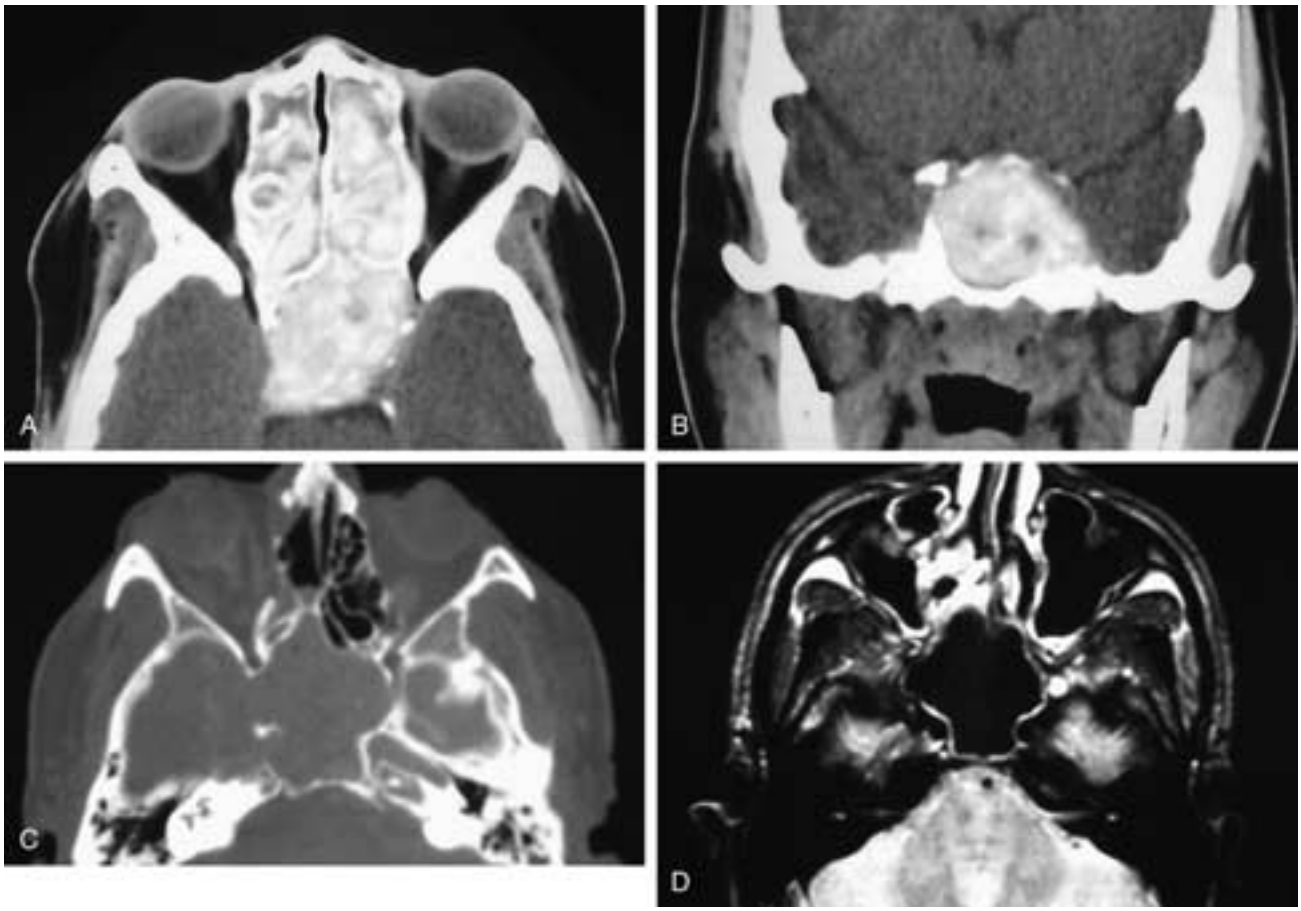

VIEW IMAGE

FIGURE 5-52 Axial (**A**) and coronal (**B**) CT scans show an expansile ethmoid complex mass that has remodeled the thin lamina papyracea laterally. The ethmoid sinuses are filled with high-attenuation material that is separated from the adjacent bone by a thin zone of mucoid attenuation. The sphenoid sinuses are also filled with dense material; however, the sphenoid sinus walls are deossified and appear destroyed. This patient had paranasal sinus polyposis. This case illustrates how the central facial bones can remodel in response to chronic pressure, while the central skull bones primarily deossify. **C**, Axial CT scan on another patient who had had a prior right external ethmoidectomy. Now the CT scan shows an opacified sphenoid sinus with apparent erosion of the skull base along the right side of the sinus. Axial T2-weighted MR image (**D**) shows high signal intensity in the inflammatory sphenoid sinus mucosa and no erosion of the adjacent skull base. This area of the skull base demonstrates pressure deossification from the mucocele. The dried sinus secretions seen in **C** have a signal void in **D** that could easily be overlooked if only MR was available.

mucocele erodes the sinus contour in the vertical plate of the frontal bone, it also slowly erodes the anterior and posterior frontal sinus tables. This results in a loss of bone density on frontal plain films that more than compensates for the soft-tissue density of the mucoid secretions. Thus a frontal sinus mucocele tends to maintain a radiodensity that is equal to or slightly less than that of the adjacent normal frontal bone. If one observes an expansile frontal sinus mass that is denser than the adjacent frontal bone, a fibroosseous lesion is a more likely diagnosis than a mucocele. As a frontal sinus mucocle enlarges, it tends to displace the superior-medial orbital margin downward and laterally, correspondingly displacing the eye (Figs. 5-67 to 5-70). A radiolucent frontal sinus mucocele is seen only when it becomes so large as to erode most of the sinus tables (Figs. 5-70 and 5-71).

A hypoplastic frontal sinus on plain films has a single, smooth, centrally concave border that may simulate a mucocele. The normally scalloped margins of larger sinuses are not present for assessment of possible erosion. However, regardless of the sinus capacity, the boundaries of a normal frontal sinus never violate the orbital contour. Any downward and outward displacement of the superomedial orbital rim (and a similar displacement of the eye) should be considered presumptive evidence of a frontal sinus mucocele until proved otherwise. Similarly the base of the frontal intersinus septum is normally in the midline, and any displacement of this portion of the septum to one side is also suggestive of a frontal sinus mucocele.

The midline segments of the anterior and posterior frontal sinus tables are seen on lateral plain films. Plain films are insensitive in detecting erosion of these tables off of the midline. It is important for the surgeon to know, prior to surgery, whether the posterior frontal sinus wall is intact. Sectional imaging of a suspected frontal sinus mucocele is then mandatory, and asymptomatic intracranial mucocele extention thus can be fortuitously discovered.

Mucoceles can extend posteriorly into the horizontal plate (orbital roof) of the frontal bone, as well as up into the vertical plate. Once in the orbital roof, a mucocele can extend both cranially into the floor of the anterior cranial

Copyright © 2003, Mosby, Inc. All rights reserved.

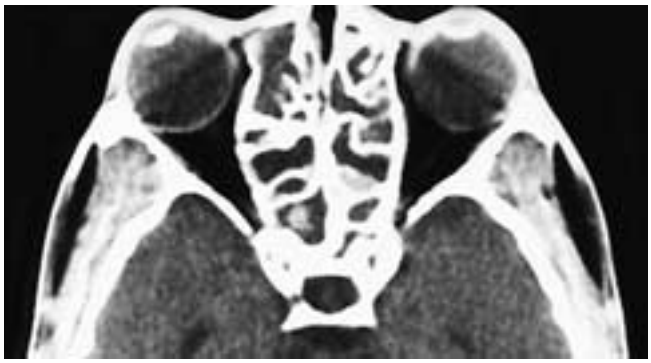

VIEW IMAGE

FIGURE 5-53 Axial CT scan shows opacification of the ethmoid sinuses with widening of the anterior and middle ethmoid complexes. The lamina papyracea remains intact. Several discrete high-attenuation polyps are seen within the mucoid secretions filling the ethmoid cells. The delicate intercellular septa are intact. This patient had a polypoid mucocele.

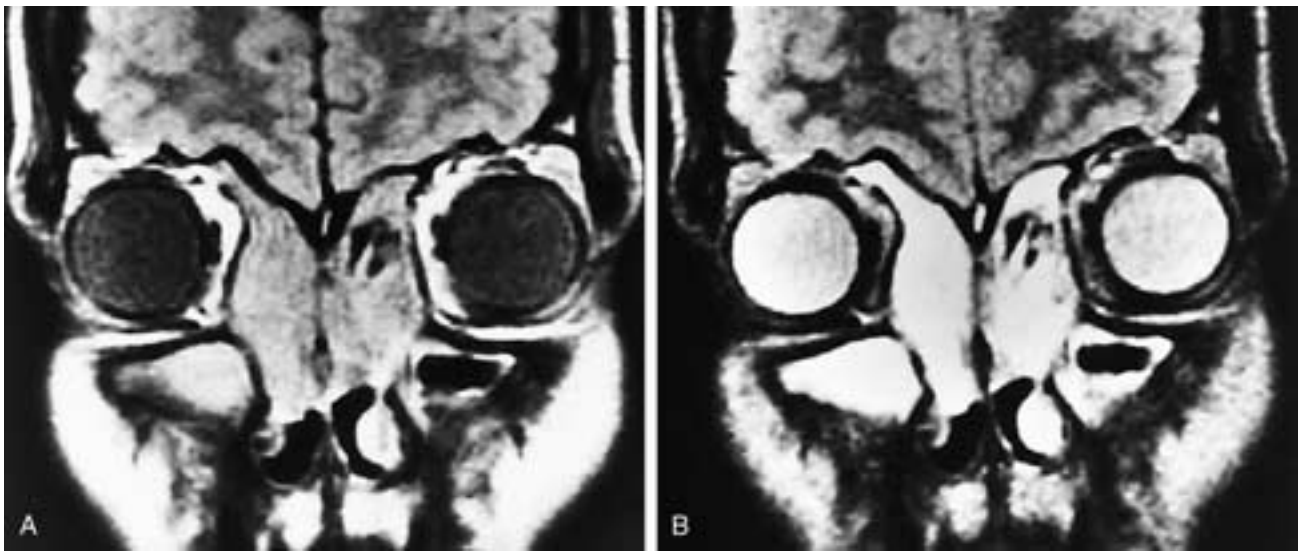

VIEW IMAGE

FIGURE 5-54 Coronal proton density (**A**) and T2-weighted (**B**) MR images show bilateral nasoethmoidal expansile masses causing some hypertelorism. These masses have the signal intensities of inflammatory tissue. This patient had polyposis and sinusitis.

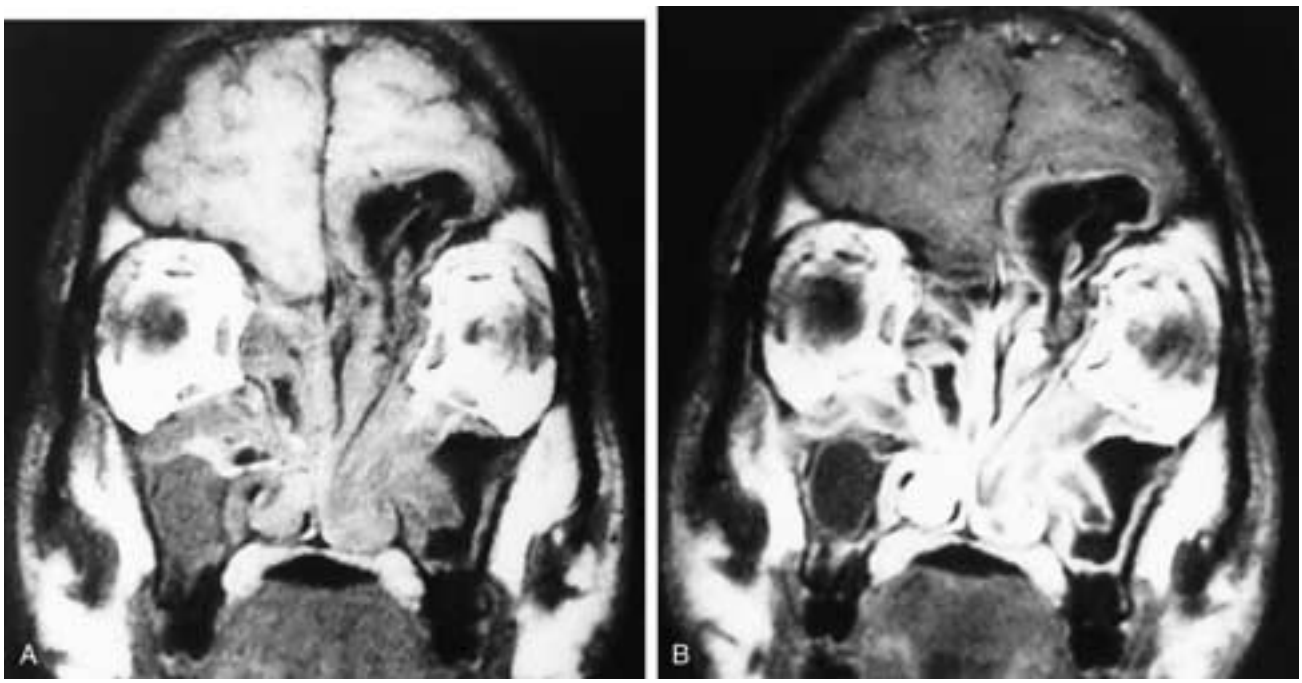

VIEW IMAGE

FIGURE 5-55 Coronal T1-weighted MR images without contrast (**A**) and with contrast (**B**). There are polypoid masses in the nasal fossae, the maxillary sinuses, and the ethmoid complexes. The disease has broken intracranially on the left side. There are areas of high, intermediate, and low signal intensity. In **B**, the mucosal surfaces of the polyps enhance. This patient had polyposis.

Copyright © 2003, Mosby, Inc. All rights reserved.

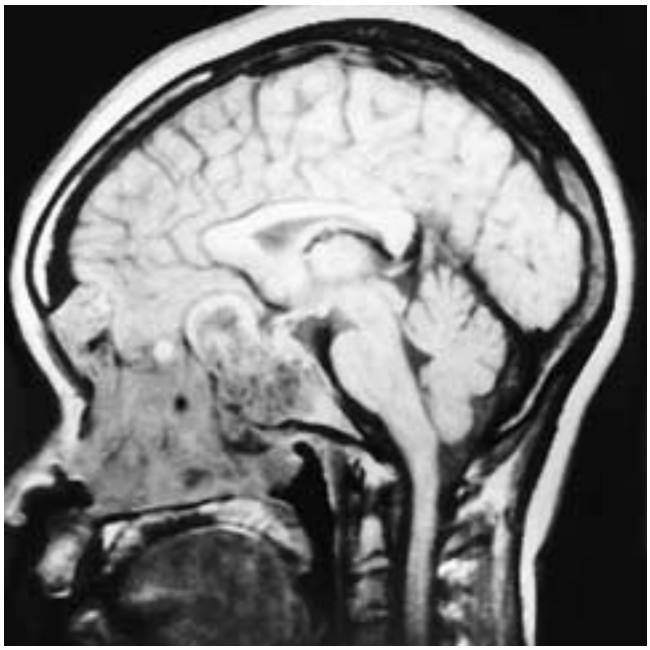

VIEW IMAGE

FIGURE 5-56 Sagittal T1-weighted MR image shows a nonhomogeneous signal intensity polypoid mass in the sphenoid and ethmoid sinuses, breaking intracranially. Increased soft tissues are also present in the nasal fossae. This patient has polyposis.

fossa and caudally. If this orbital roof extension is not appreciated at the time of surgery, which is usually performed extracranially for the more obvious vertical plate disease, complications from an orbital roof mucocele may require a second operation and an intracranial approach. In the event that frontal sinus surgery was performed without preoperative sectional imaging, and retrospectively the plain films suggest the presence of horizontal recess disease, then postoperative CT or MR imaging is necessary to resolve this issue and provide an important prospective baseline study.

Ethmoid mucoceles usually arise from the anterior rather than the posterior ethmoid cells, presumably because the anterior ethmoid ostia are the smallest of any in the paranasal sinuses.[95, 96] Mucous viscosity also promotes mucoceles, as ethmoid mucoceles are common in patients with cystic fibrosis.[97] Ethmoid mucoceles are typically expansile, thinning and remodeling the lamina papyracea and bowing it laterally into the orbit, resulting in a laterally displaced globe. This may be very difficult to diagnose on plain films despite clinical evidence of a mass. The obliquely oriented lamina papyracea is not well seen on frontal films, and the air density of normal ethmoid cells surrounding the mucocele can partially nullify the soft-tissue density of the mucocele. An air-fluid level in the ethmoid complex can indicate an ethmoid mucocele rupture, with partial drainage into the nasal cavity and adjacent ethmoids. In these cases, a mucopyocele is usually present at the time of discovery (Fig. 5-11).[98]

Mucoceles also can arise in supraorbital ethmoid cells; these are best demonstrated on Caldwell films or coronal images. Infection or a polyp in the lower portion of the supraorbital cell can be the cause of obstruction that leads to these mucoceles, which typically erode through the middle third of the orbital roof and displace the globe inferiorly.

Polypoid mucoceles may involve the entire ethmoid complex, either unilaterally or bilaterally. Characteristically, sectional imaging confirms that ethmoid septa are preserved within the opacified, expanded ethmoid complex. The plain film findings may be only diffuse opacification of the ethmoid complex.

The typical antral mucocele totally opacifies the maxillary sinus and expands the sinus cavity (Fig. 5-72). Unchecked antral mucoceles may eventually overtake the osteoblastic ability of the outer maxillary periostium, resulting in frank bone destruction, thus making the distinction from neoplasia difficult on plain films (Fig. 5-73). If the orbital floor is elevated, the patient may experience diplopia. Rarely, if the mucocele spontaneously collapses after thinning the orbital floor, the globe may descend, causing enophthalmos and diplopia. If the antrum has been compartmentalized by a septum, a mucocele may be limited to only one of these sinus sections. Obviously,

Text continued on page 228

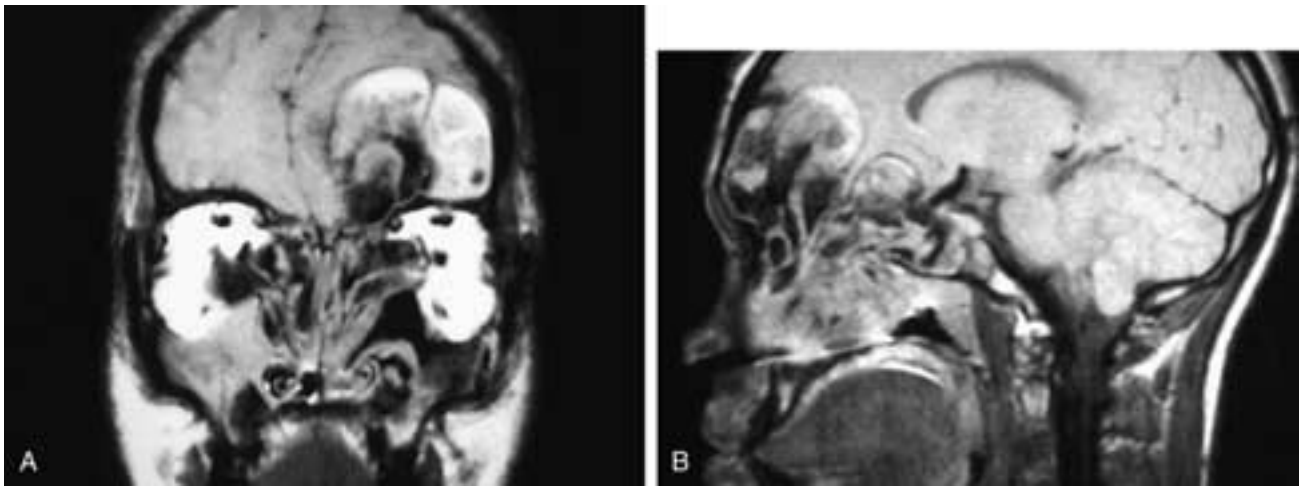

VIEW IMAGE

FIGURE 5-57 Coronal (**A**) and sagittal (**B**) T1-weighted MR images show multiple sinonasal polypoid masses that have extended into the medial aspect of each orbit, broken through intracranially, and obstructed the maxillary sinuses. These are areas of high, intermediate, and low signal intensity throughout the lesion, as well as areas of signal void. This patient had polyposis from aspirin intolerance.

Copyright © 2003, Mosby, Inc. All rights reserved.

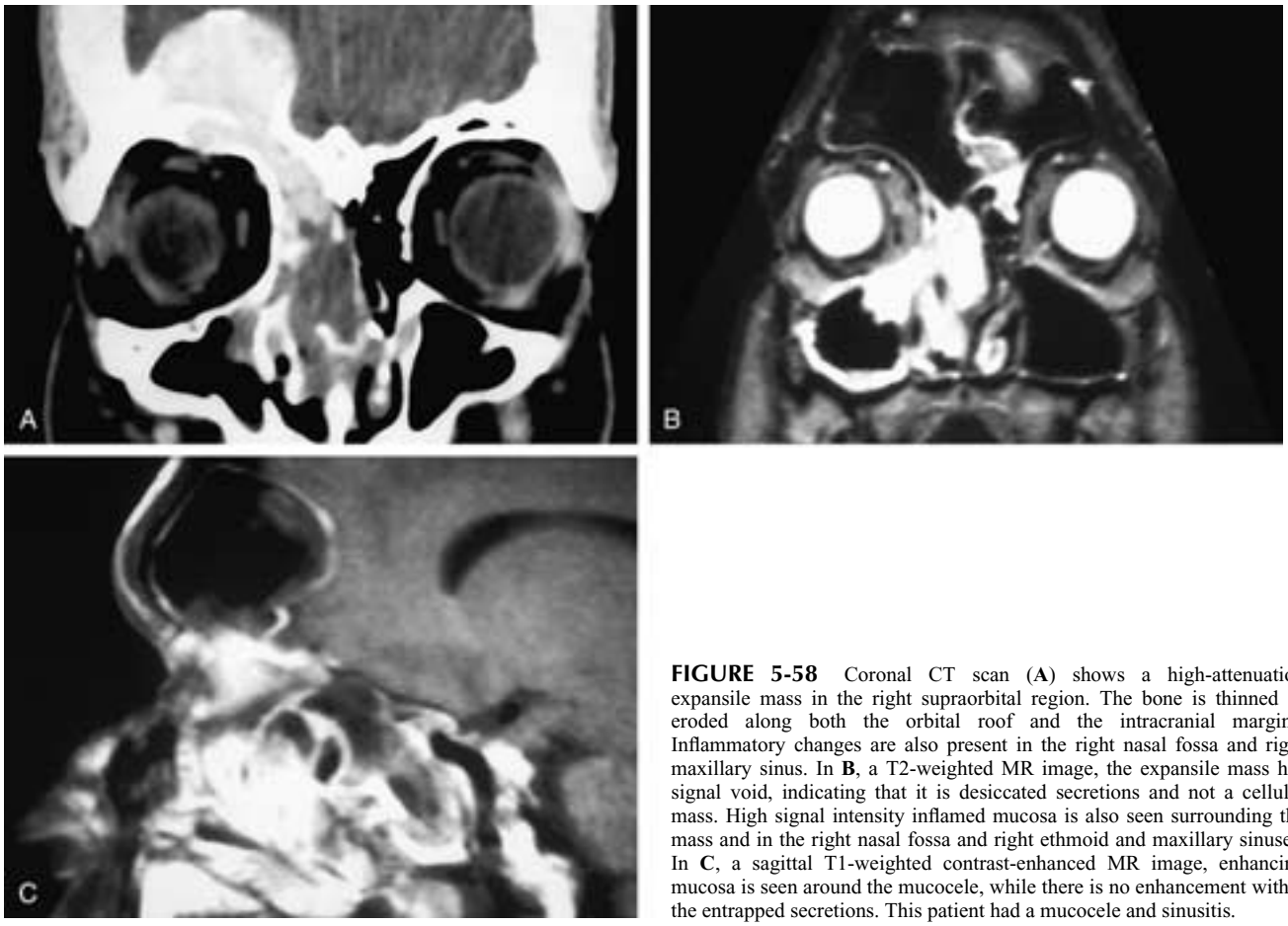

FIGURE 5-58 Coronal CT scan (**A**) shows a high-attenuation expansile mass in the right supraorbital region. The bone is thinned or eroded along both the orbital roof and the intracranial margins. Inflammatory changes are also present in the right nasal fossa and right maxillary sinus. In **B**, a T2-weighted MR image, the expansile mass has signal void, indicating that it is desiccated secretions and not a cellular mass. High signal intensity inflamed mucosa is also seen surrounding the mass and in the right nasal fossa and right ethmoid and maxillary sinuses. In **C**, a sagittal T1-weighted contrast-enhanced MR image, enhancing mucosa is seen around the mucocele, while there is no enhancement within the entrapped secretions. This patient had a mucocele and sinusitis.

VIEW IMAGE

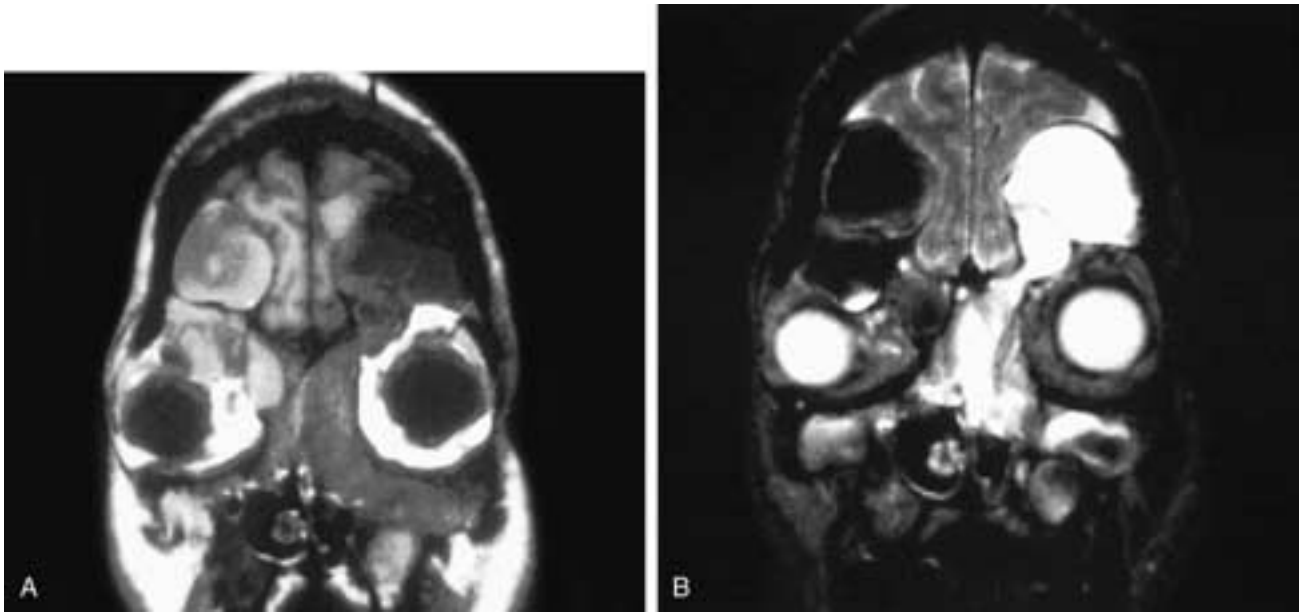

VIEW IMAGE

FIGURE 5-59 Coronal T1-weighted (**A**) and T2-weighted (**B**) MR images show bilateral sinonasal polypoid masses that have broken intracranially, into the left superomedial orbit from the left frontal sinus, and down into the right superior orbit from a right supraorbital ethmoid cell. The signal intensities of the left-sided lesions are those of classical inflammation. The right-sided lesions contain thicker inspissated secretions and have intermediate T1-weighted and low T2-weighted signal intensities. This patient has polyposis.

Copyright © 2003, Mosby, Inc. All rights reserved.

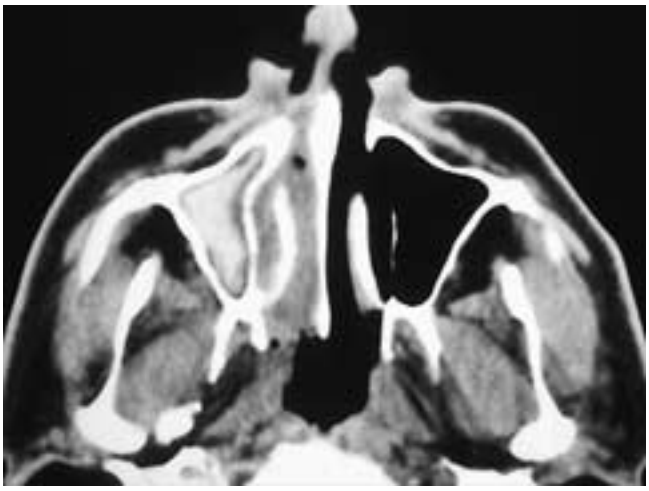

FIGURE 5-60 Axial CT scan shows high-attenuation material within the right maxillary sinus, separated from the sinus bony wall by a thin zone of water attenuation. The most common cause of this CT appearance is desiccated secretions. A mycetoma in fungal sinusitis and intrasinus hemorrhage also can have this appearance. This patient had chronic sinusitis.

VIEW IMAGE

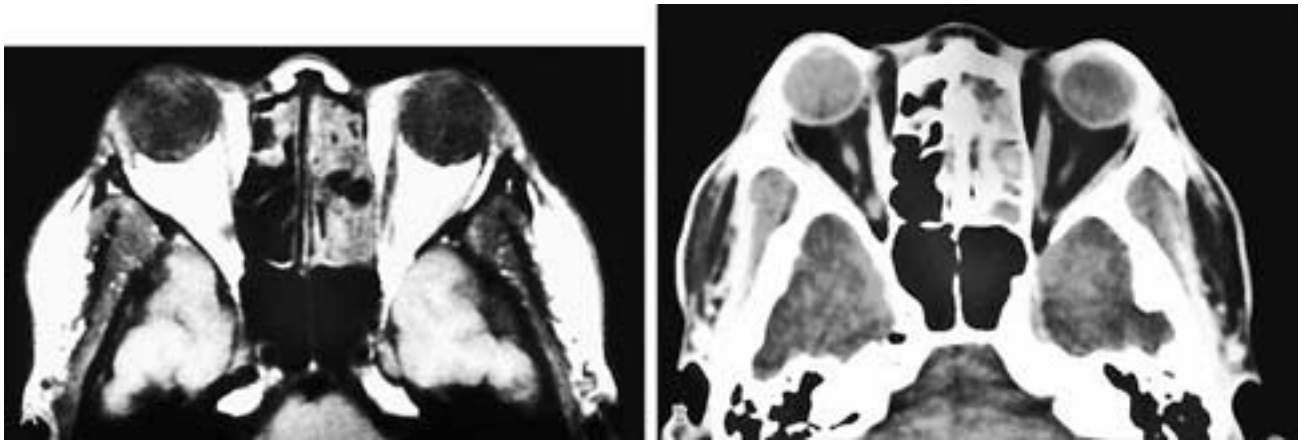

FIGURE 5-61 Axial T1-weighted MR image (**A**) shows presumed inflammatory disease in the left ethmoid complex with apparent aeration of some middle ethmoid cells. However, the axial CT scan (**B**) shows total opacification of the left ethmoid sinuses. At surgery, the middle ethmoid cells were found to contain aspergilloma. This patient has aspergillosis.

VIEW IMAGE

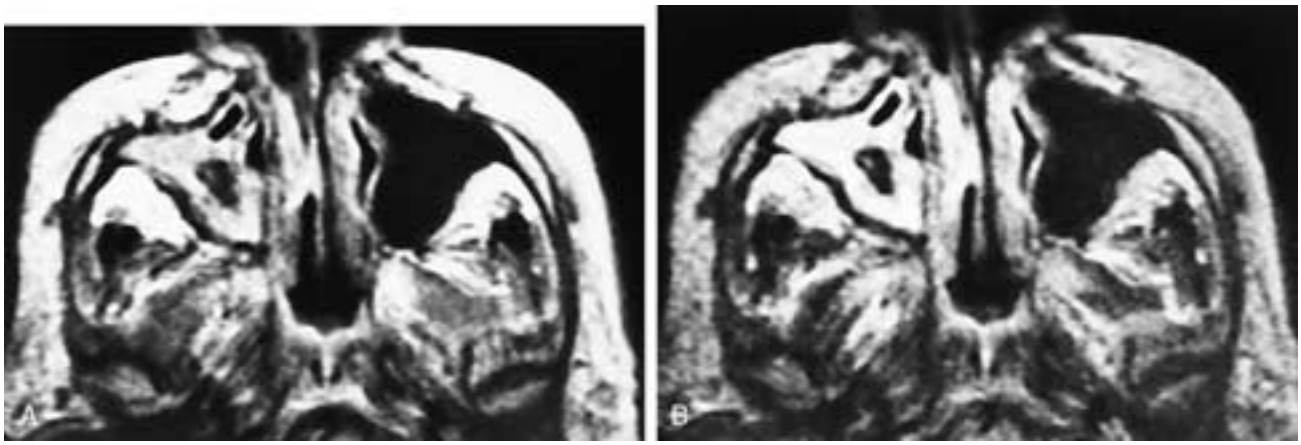

FIGURE 5-62 Axial proton density (**A**) and T2-weighted (**B**) images show inflammatory-type mucosal thickening in the right maxillary sinus. In the center of the sinus is an ovoid mass with low signal intensity. This is an aspergilloma with surrounding inflammation. This patient had aspergillosis.

VIEW IMAGE

Copyright © 2003, Mosby, Inc. All rights reserved.

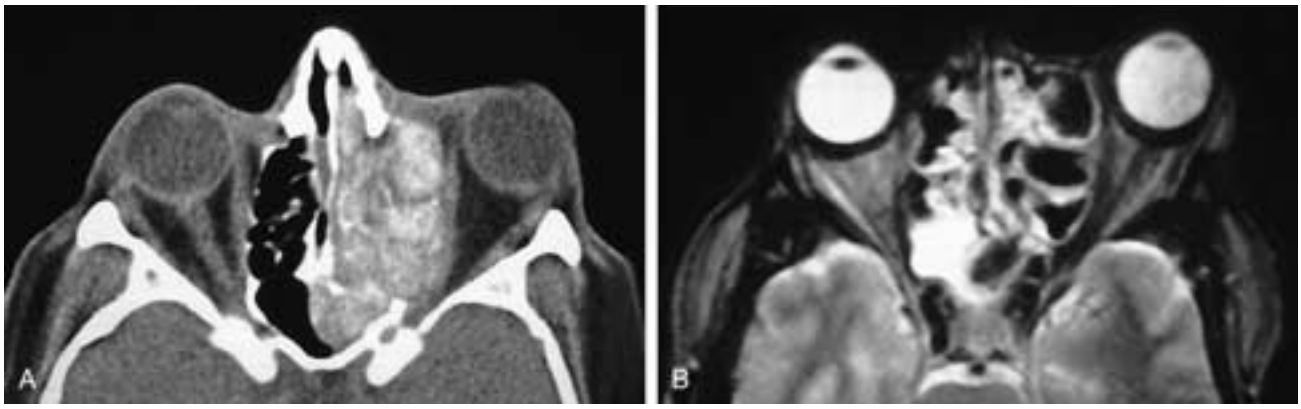

VIEW IMAGE

FIGURE 5-63 Axial CT scan (**A**) shows a mass in the left ethmoid and sphenoid sinuses that has broken out into the left orbit. There are discrete areas of high attenuation. The localized areas of high density on this non-contrast CT makes an inflammatory process likely, but not definite. However in **B**, a T2-weighted MR image, the areas of high attenuation in **A** have signal voids. This indicates that they are most likely either desiccated secretions or mycetomas. This patient had aspergillosis.

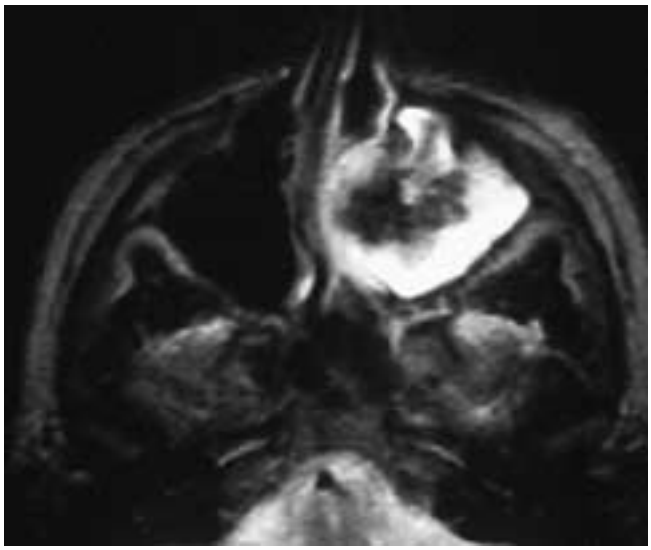

VIEW IMAGE

FIGURE 5-64 Axial T2-weighted MR image shows inflammatory disease with a high signal intensity in the left maxillary sinus. Centrally within the sinus is a region of both low signal intensity and signal void. This was an aspergilloma. This patient had aspergillosis.

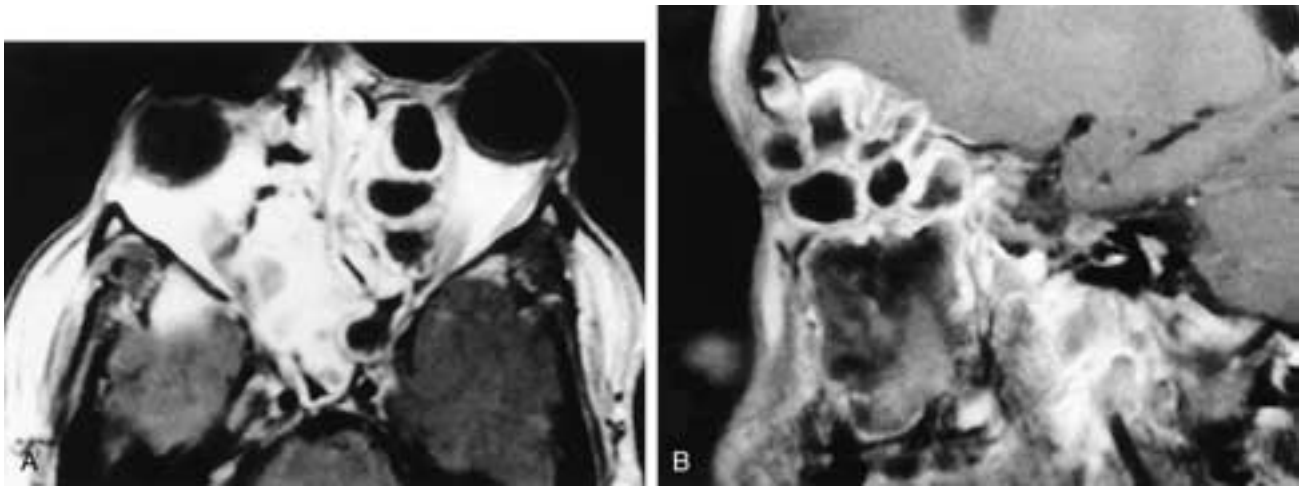

VIEW IMAGE

FIGURE 5-65 Axial (**A**) and sagittal (**B**) contrast-enhanced T1-weighted MR images show widening of the ethmoid complex by a mass that has also broken into the floor of the anterior cranial fossa and the left orbit. Enhancing mucosa is seen surrounding areas of signal void. The maxillary sinuses are also involved by the process. None of the sinuses were aerated on CT, and the areas of signal void were aspergillomas. This patient had aspergillosis.

Copyright © 2003, Mosby, Inc. All rights reserved.

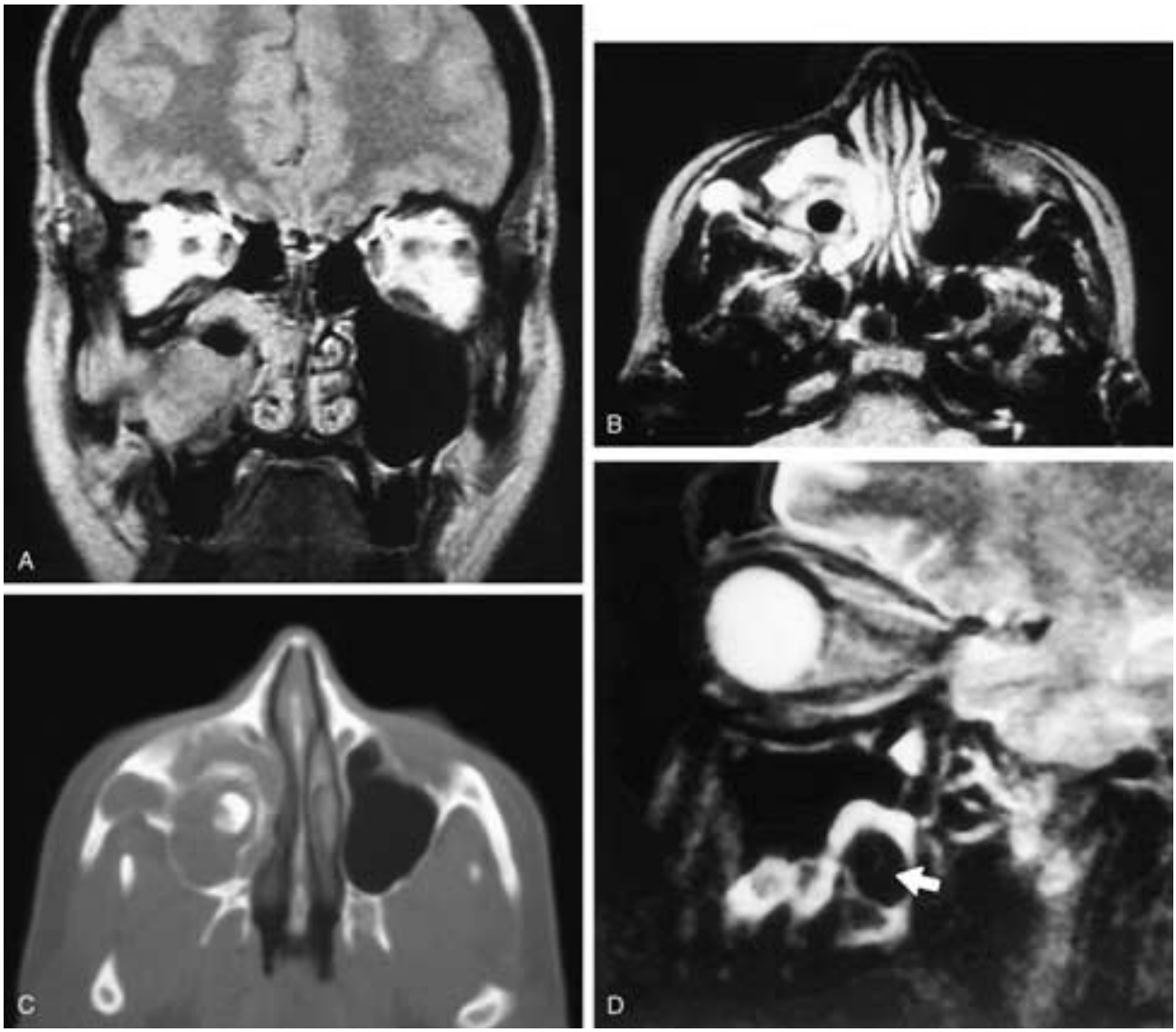

VIEW IMAGE

FIGURE 5-66 Coronal T1-weighted (**A**) and axial T2-weighted (**B**) MR images show a slightly expanded right maxillary sinus filled for the most part with inflammatory-type material. Within the sinus is an area of signal void. This could have been residual sinus air, desiccated secretions, a mycetoma, or a sinolith. An axial CT scan (**C**) shows that it was a tooth in a dentigerous cyst. A sagittal T2-weighted (**D**) image on another patient shows an area of signal void (*arrow*) just under the floor of the maxillary sinus. This patient had an undescended molar tooth.

there are significant clinical implications of an unexplored posterior compartmental mucocele. In such cases, the radiologist may be the only physician to detect this hidden mucocele and direct the surgeon to it (Fig. 5-74).[99]

Sphenoid sinus mucoceles have the highest incidence of surgical complication of all mucoceles. Due to their proximity to the optic nerve, blindness is the most serious major postoperative complication. Most sphenoid mucoceles expand anterolaterally into the posterior ethmoids and the orbital apex. Less commonly, expansion may occur upward into the sella turcica and cavernous sinuses or downward into the nasopharynx and posterior nares. In rare cases, intracranial extension can even result in areas of brain necrosis.[100, 101] Occasionally they may extend into the sphenoid sinus recesses in the greater wings and the pterygoid processes.[102] If sufficiently large, sphenoid sinus mucoceles may cause optic canal and orbital apex syndromes. The critical role of the radiologist is to accurately localize the relationship of the optic nerve to the mass, thereby guiding the surgeon during surgical decompression.

Multiple paranasal sinus mucoceles have been reported after facial fractures and in patients with severe allergies. Patients with aspirin intolerance seem to be particularly prone to develop multiple aggressive mucoceles that may extend intracranially.[103]

The finding on CT of an expanded, airless sinus cavity filled with fairly homogeneous mucoid attenuation (10 to 18 HU) secretions is diagnostic of a mucocle.[104] However, if the entrapped secretions are particularly viscid and proteinaceous, the attenuation can increase to 20 to 45 HU, similar to that of muscle. If the sinus is airless, filled with a mucoid density but not expanded, the diagnosis is that of an obstructed sinus, not a mucocele (Figs. 5-75 and 5-76). When a mucocele is present, the sinus walls are remodeled and may be of almost normal thickness, thinned, or partially eroded (Figs. 5-77 to 5-90). In the latter two cases, the sinus

Copyright © 2003, Mosby, Inc. All rights reserved.

VIEW IMAGE

FIGURE 5-67 Caldwell view shows clouding of the right frontal and ethmoid sinuses. There is thinning and downward displacement of the right superomedial orbital rim. This patient has sinusitis and right frontal sinus mucocele.

FIGURE 5-69 Caldwell view shows a loss of the normal left frontal sinus margin scalloping (*arrows*) and portions of the normal white mucoperiosteal line around the sinus and in the roof of the left orbit. This patient had a left frontal sinus mucocele.

VIEW IMAGE

mucosa and the sinus wall periostium are all that surround the mucous secretions. If a mucopyocele is present, the inflamed sinus mucosa is seen as a thin line of enhancement just inside the bony sinus walls, establishing the diagnosis of an infected mucocele (Fig. 5-91).[32]

Prior Caldwell-Luc procedures may result in a fibrous septum between the lateral margin of the anterior sinus wall surgical defect and the posterior sinus wall. Synechiae can form and organize into a solid fibrous wall. The resulting septum can obstruct the drainage from the lateral portion of the sinus, while the sinus cavity medial to the septum drains normally. Thus an expansile mass in the lateral maxillary sinus is diagnostic of this condition. As it enlarges, a lateral antral mucocele may extend into the body of the zygoma and present in the cheek as a soft-tissue mass or it may extend into the lateral, inferior orbit (Figs. 5-92 and 5-93).

On MR imaging, the signal intensities of a mucocele are determined by the protein content of the entrapped secretions. As previously discussed, secretions become more con-

VIEW IMAGE

FIGURE 5-68 Caldwell view shows slight haziness in the right frontal sinus, as well as flattening and downward displacement of the right superomedial orbital rim. The frontal intersinus septum is also displaced to the left side. This patient had a right frontal sinus mucocele.

FIGURE 5-70 Caldwell view shows a left hypoplastic frontal sinus that has lost the normal thin mucoperiosteal white line. Instead, there is a thick zone of surrounding sclerosis (*arrows*). There is also erosion of the left superomedial orbital rim. This patient had a left frontal sinus mucocele.

VIEW IMAGE

Copyright © 2003, Mosby, Inc. All rights reserved.

VIEW IMAGE

FIGURE 5-71 Caldwell view shows a smoothly contoured, enlarged frontal sinus. There is a surrounding zone of sclerosis, and only the most lateral portion of the left frontal sinus appears normal. There is erosion of the right superior and superomedial orbital rim, and a mound of soft tissue is seen above the mass (*arrows*). This patient had a frontal sinus mucocele that caused the forehead to bulge and resulted in right proptosis.

centrated and viscous over time and the T1-weighted and T2-weighted signal intensities vary. The relaxation-time shortening can be used to approximate the viscosity of the secretions, as shown in Figure 5-17 (Figs. 5-94 to 5-101).[83] On contrast-enhanced MR images, the sinus mucosa enhances and is seen as a uniformly thin zone surrounding the nonenhancing secretions. If a mucopyocele is present, the infection causes increased viscosity of the secretions, shorter relaxation times, and thickening of the mucosa.

If there is a mucoid collection in the antrum and a double bony wall is seen in the maxillary sinus, often at the most anterior or posterior margin of the sinus, it implies that the bony floor has been elevated by an odontogenic process (Fig. 5-102). This is important to recognize, as the surgical treatment of an odontogenic cyst differs from that of an antral mucocele.

VIEW IMAGE

FIGURE 5-72 Waters view shows opacification of the right maxillary sinus, with thinning of the lower lateral sinus wall (*arrow*) and some expansion of the sinus cavity. This patient had a right maxillary sinus mucocele.

VIEW IMAGE

FIGURE 5-73 Waters view shows an opacification of the right maxillary sinus, with apparent erosion of the lower lateral sinus wall (*arrows*). This looks like a carcinoma but is actually thinning of the bone secondary to a maxillary sinus mucocele.

VIEW IMAGE

FIGURE 5-74 Lateral view multidirectional tomogram shows an expanded compartment (*arrows*) in the posterior portion of the maxillary sinus. This patient had a mucocele in a posterior sinus compartment.

Copyright © 2003, Mosby, Inc. All rights reserved.

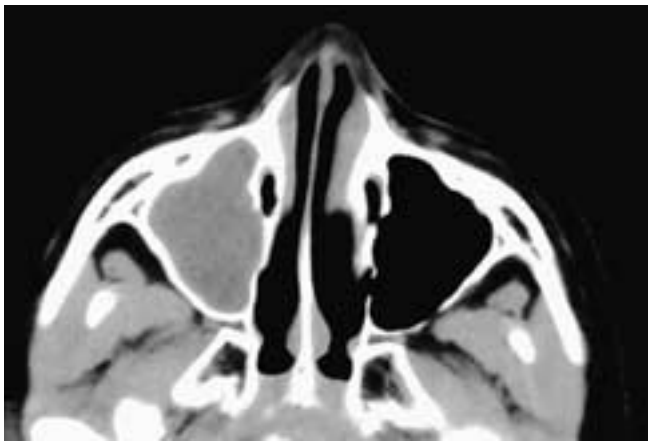

VIEW IMAGE

FIGURE 5-75 Axial CT scan shows an opacified right maxillary sinus. The attenuation of the material is approximately that of water. The sinus cavity is normal in size. This is an obstructed sinus, not a mucocele. In a mucocele, the sinus cavity must be enlarged.

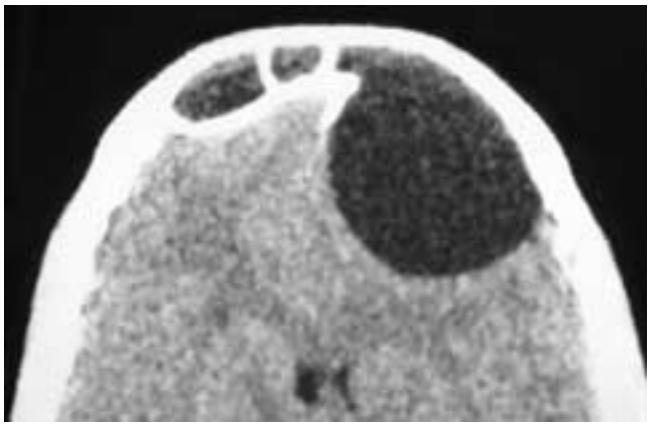

VIEW IMAGE

FIGURE 5-77 Axial CT scan shows a large, expansile mucoid attenuation mass in the left frontal sinus that has thinned the posterior sinus table and bulged intracranially. A smaller mucocele that extended down into the orbit is also present on the right side. The left mucocele contents are separated from the brain by sinus mucosa, deossified bone, and the meninges. This patient had bilateral frontal sinus mucoceles.

Fungal Diseases

Mycotic sinusitis has a highly variable appearance. During early infection, merely nonspecific mucosal inflammation in the nasal fossa or paranasal sinus(es) is seen.[105, 106] Most often either the maxillary sinus or ethmoid sinuses are involved. The sphenoid and frontal sinuses are only occasionally affected.[107] Air-fluid levels are uncommon and, when present, suggest a bacterial infection. The surrounding bone in mycotic sinusitis may be thickened and sclerotic, eroded, or remodeled. Most often it is the combination of these bone changes that suggests either an unusual infection or fungal disease.[108]

Soft-tissue disease is often found both in the nasal fossa and the paranasal sinuses. In antral mycotic sinusitis, the nasal disease may act as a bridge for extension of infection into the cheek. This finding suggests an aggressive infection or fungal disease, as antral bacterial sinusitis rarely

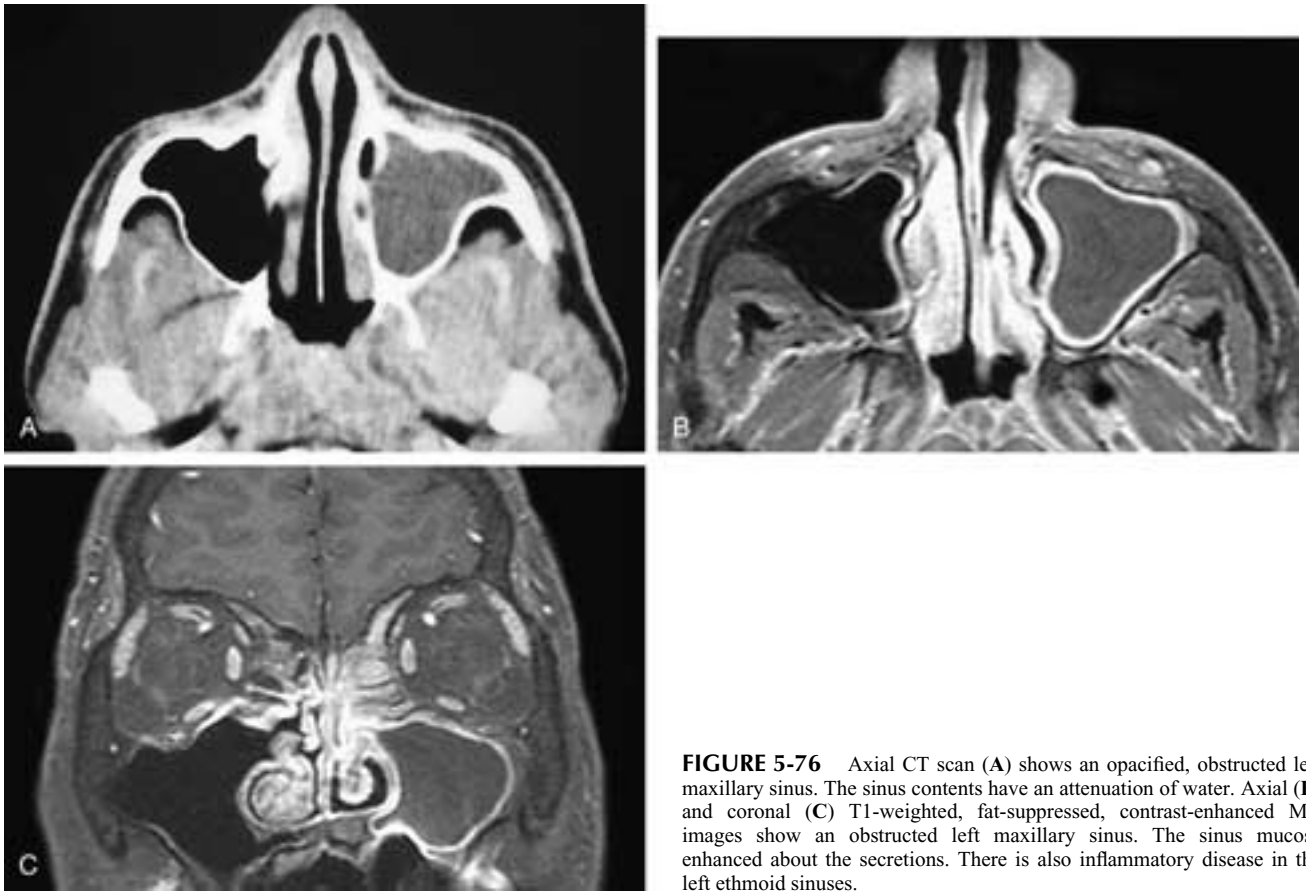

VIEW IMAGE

FIGURE 5-76 Axial CT scan (**A**) shows an opacified, obstructed left maxillary sinus. The sinus contents have an attenuation of water. Axial (**B**) and coronal (**C**) T1-weighted, fat-suppressed, contrast-enhanced MR images show an obstructed left maxillary sinus. The sinus mucosa enhanced about the secretions. There is also inflammatory disease in the left ethmoid sinuses.

Copyright © 2003, Mosby, Inc. All rights reserved.

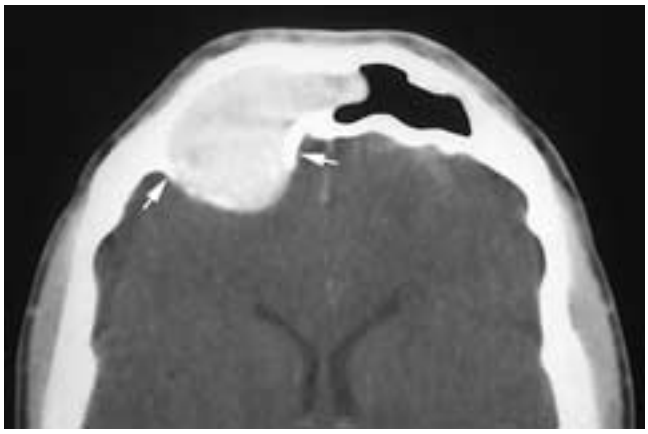

VIEW IMAGE

FIGURE 5-78 Axial CT scan shows a high-attenuation, expansile right frontal sinus mass that has remodeled the margins of the posterior sinus table (*arrows*). However, most of the posterior sinus wall is deossified. This patient had a right frontal sinus mucocele.

VIEW IMAGE

FIGURE 5-79 Axial CT scan shows an expansile left frontal sinus mass that is bulging into the upper left medial orbit. There is primarily bone remodeling rather than bone destruction. This patient had a left frontal sinus mucocele.

extends into the facial soft tissues.[109] Intrasinus concretions within a mycetoma can be seen occasionally on plain films and CT (Figs. 5-103 to 5-105).[110, 111] As previously discussed, the signal void and adjacent sinus inflammation of a mycetoma mimic the MR imaging appearance of nonspecific chronic infection with desiccated secretions (Figs. 5-61 to 5-65).

INFECTIOUS DESTRUCTIVE AND GRANULOMATOUS SINONASAL DISEASES

Actinomyces and *Nocardia*

Actinomycosis is a commensural organism of human and bovine hosts; unlike most true fungi, they have not been identified as environmental saprophobes. The human pathogen, *Actinomyces israelii* (and, less often, *A. eriksonii*) is normally present around teeth, especially carious teeth, and in tonsillar crypts. It is classified as a filamentous bacterium rather than a fungus because (1) it reproduces by fission rather than by sporulation (as do perfect fungi) or filamentous budding (as do imperfect fungi), and (2) muramic acid is present in its cell walls and mitochondria are absent, both of which are features of bacteria.

Actinomyces has limited pathologic potential in the normal host. Antecedent trauma or other precursors are necessary predisposing factors for invasive infection. There are three forms: cervicofacial, thoracic, and abdominal; the cervicofacial is the most common form of infection. Soft-tissue abscesses and draining cervical fistulae develop as a result of secondary *Actinomyces* infection of periapical abscesses. Actinomycosis can also present in the neck without the characteristic sinus tracts. These sinuses can occasionally have long tracts, communicating with the soft tissues of the back and chest. Aspiration of oral *Actinomycetes* from carious teeth may lead to pulmonary abscess formation and pneumonia. Rarely, *Actinomyces* may be the cause of sinonasal, laryngeal, or pharyngeal disease.

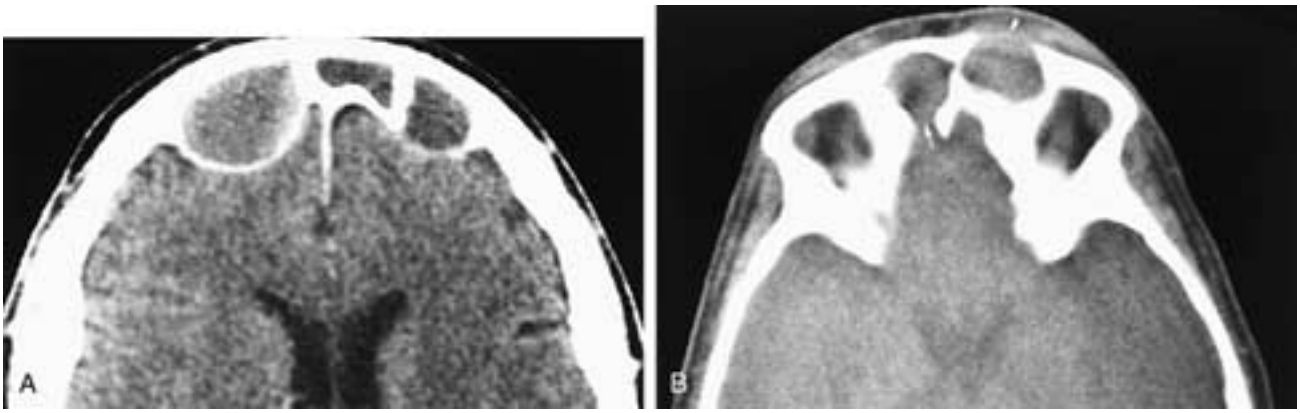

VIEW IMAGE

FIGURE 5-80 Axial CT scan (**A**) shows bilateral frontal sinus expansile masses. Each mass has thinned and remodeled the posterior sinus wall, and each mucocele bulges intracranially. On the plain film, the posterior sinus wall appeared intact. This patient had bilateral frontal sinus mucoceles. Axial CT scan (**B**) on another patient shows an expansile mass in each of the left and right frontal sinuses. The left-sided mass has broken through the anterior sinus wall (*arrowhead*), and the right-sided mass has broken through the posterior sinus wall (*arrow*). This patient had bilateral frontal sinus mucoceles.

Copyright © 2003, Mosby, Inc. All rights reserved.

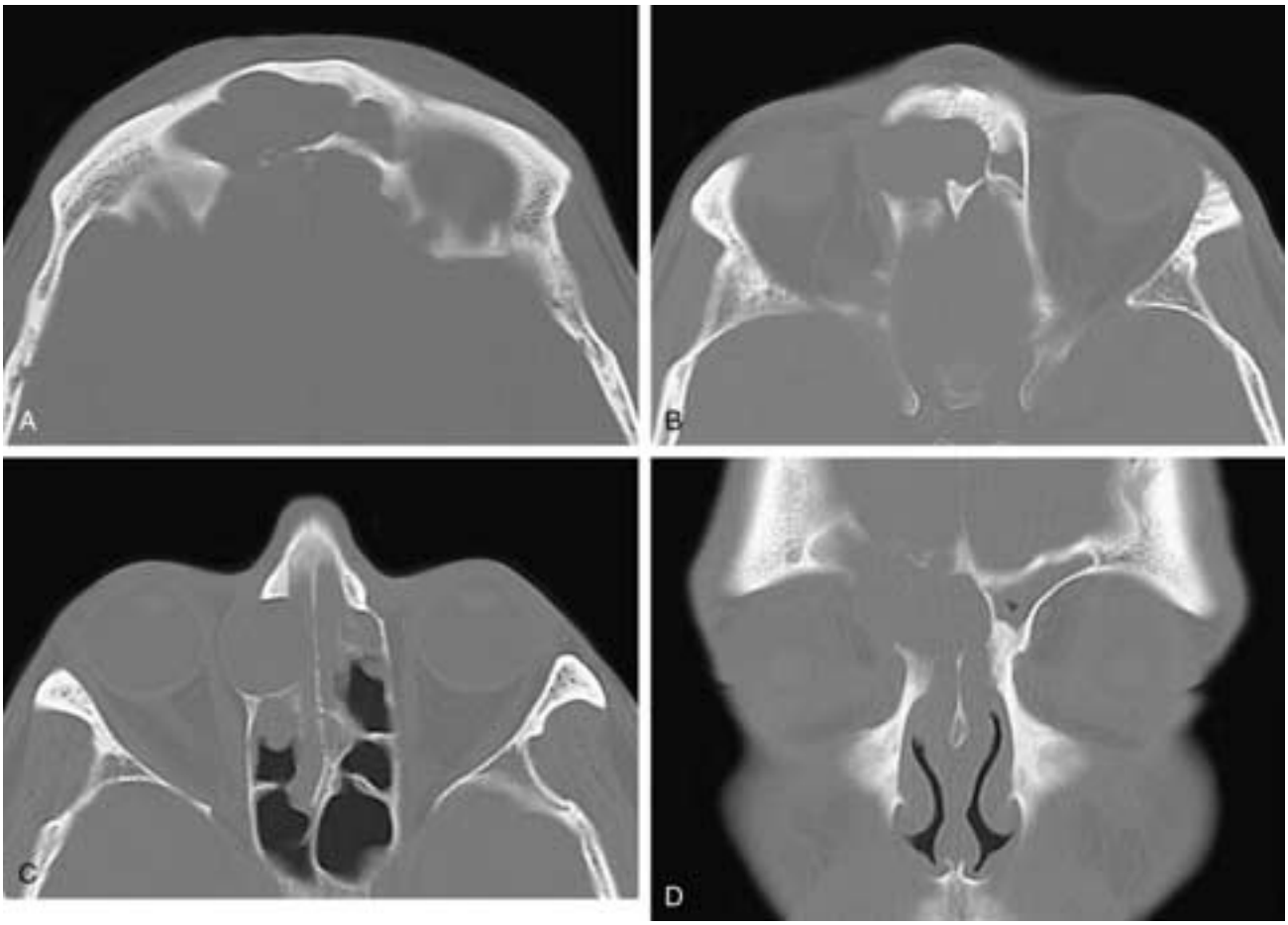

VIEW IMAGE

FIGURE 5-81 Serial axial CT scans from cranial (**A**) to caudal (**C**) and a coronal CT scan (**D**) show an expansile mass in the right frontal and ethmoid complex. There are areas of marked thinning of the surrounding bone. This patient had a right frontoethmoid mucocele.

The pale yellow ''sulfur granules'' or ''grains'' observed clinically are microcolonies of bacilli. On hematoxylin and eosin (H&E) stain, only blue amorphous masses are visible. The slender, filamentous nature of these bacilli is apparent on special stains. The filaments may mimic fungi in their tendency to branch. *Actinomycetes* are routinely not acid-fast, although occasionally they may be weakly acid-fast. This point can help distinguish *Actinomyces* on tissue sections from *Nocardia*. The latter filamentous

VIEW IMAGE

FIGURE 5-82 Coronal CT scan shows an expansile water attenuation mass in the superomedial left orbit. The globe is displaced downward and laterally. This is the typical direction of eye displacement from a frontal sinus mucocele.

FIGURE 5-83 Coronal CT scan shows a water attenuation mass in the roof of the left orbit displacing the globe downward. This is the typical direction of eye displacement from a supraorbitial ethmoid mucocle.

VIEW IMAGE

Copyright © 2003, Mosby, Inc. All rights reserved.

VIEW IMAGE

FIGURE 5-84 Coronal CT scan shows a high-attenuation mass in the left orbital roof displacing the globe downward. There is thinning of the bone in the roof of the orbit, and some inflammatory disease is seen more proximally in the left ethmoid sinuses. This patient had a left supraorbital ethmoid mucocle.

bacterium does not stain well with H&E but does stain well with a modified Ziehl-Neelson stain. The distinction between these two filamentous bacteria is important because their sensitivity to antibiotics differs; penicillin is the drug of choice for *Actinomyces*, but *Nocardia* (most human infection is caused by *N. asteroides*) is unresponsive to penicillin and can be treated with sulfa drugs. The diagnosis of actinomycosis is confirmed by an aerobic culture.[34, 112–114]

Tuberculosis (TB) is caused by *Mycobacterium tuberculosis* and *M. bovis*, aerobic bacilli with a thick, multilayered capsule of complex lipids and waxes, which accounts for their staining and immunogenic properties. Once stained, they are resistant to decolorization by acid alcohol and hence are acid-fast. The disease has a worldwide distribution. *M. tuberculosis* is spread through aerosolized respiratory droplets from patients with cavitary TB. *M. bovis* and probably *M. tuberculosis* can cause infection via oral ingestion, although mucosal breaks are probably required. A definite resurgence has been reported in the United States as a result of (1) immigrant populations from endemic countries, (2) reactivation of disease in the elderly population, and (3) the AIDS pandemic. More than 25,000 cases were reported in the United States in 1993 (10 cases per

VIEW IMAGE

FIGURE 5-85 Coronal CT scan (**A**) shows soft tissue attenuation material in both ethmoid sinuses and nasal fossae. In addition, there are ''mucoid'' density expanded areas in the roof of each orbit breaking both intracranially and intraorbitally. This patient had bilateral supraorbital ethmoid mucoceles and sinusitis. Coronal CT scans (**B** and **C**) on another patient show a water attenuation left frontal sinus mucocele (*black arrow*) and a higher-attenuation left supraorbital ethmoid mucocele (*white arrow*). It is important to identify both types of mucoceles, as the surgical approach for each is different.

Copyright © 2003, Mosby, Inc. All rights reserved.

VIEW IMAGE

FIGURE 5-86 Axial CT scan shows an expansile water attenuation left ethmoid sinus mass that has extended into the orbit and displaced the medial rectus muscle laterally (*arrow*). This patient had a left ethmoid sinus mucocele.

VIEW IMAGE

FIGURE 5-88 Coronal CT scan shows a water attenuation, expansile, right ethmoid sinus mass that bulges into the right orbit and displaces the eye laterally and slightly downward. This patient had a right ethmoid sinus mucocele.

100,000 people), a 14% increase over reported rates in 1985, which were at a nadir since national reporting began in 1953.[115] The common tuberculous pulmonary disease may be asymptomatic or cause fever, weight loss, and bloody sputum. Head and neck involvement in TB is rare and is thought to be the result of direct infection from expectorated sputum, as well as from hematogenous-lymphatic spread. The sinus disease may be nonspecific; however, when bone involvement occurs, the dominant symptom is pain. The treatment is prolonged antituberculous chemotherapy. Nasopharyngeal and sinonasal TB may clinically and histologically mimic Wegener's granulomatosis. This distinction has a grave consequence because administering the steroid and immunosuppressive agents indicated for active Wegener's granulomatosis may result in miliary progression of unrecognized TB. Also, nasopharyngeal TB can be accompanied by lymphadenopathy. This may clinically mimic nasopharyngeal carcinoma, especially in the Asian population at risk for this neoplasm.[116]

Syphilis is a worldwide disease that has been rising in incidence since the 1980s.[117] In 1977, the rate per 100,000 people in the United States was 10.4. The rate per 100,000 has been between 40 and 60 from 1988 to 1992, and more than 110,000 cases were reported in the United States in 1992. Changing patterns of sexual promiscuity and prostitution have led to the disease resurgence. Syphilis is caused by *Treponema pallidum*, which is usually transmitted through sexual relations, although it can also be transmitted through blood transfusions. By contrast, *T. pertenue* is transmitted through nonvenereal, direct contact.

Syphilis may be divided clinically into three distinct phases: primary, secondary, and tertiary. The first two stages may escape clinical notice. Primary acquired syphilis develops within 1 week to 3 months following exposure. A characteristic chancre develops at the site of infection. Chancres can also develop after orogenital contact. Oral sites include the lips, palate, gingiva, tongue, and tonsil. Chancre has also been reported in the nose.[34, 118] Secondary syphilis occurs weeks to months after the primary chancre and is the result of systemic infection. There is a macular-papular rash that coalesces into warm, moist areas to form hyperplastic lesions: condyloma lata or flat condylomata. Head and neck manifestations of secondary syphilis include condyloma lata, which may occur in the larynx, ears, and nasolabial folds. Tertiary syphilis is a late manifestation seen years to decades after primary infection.

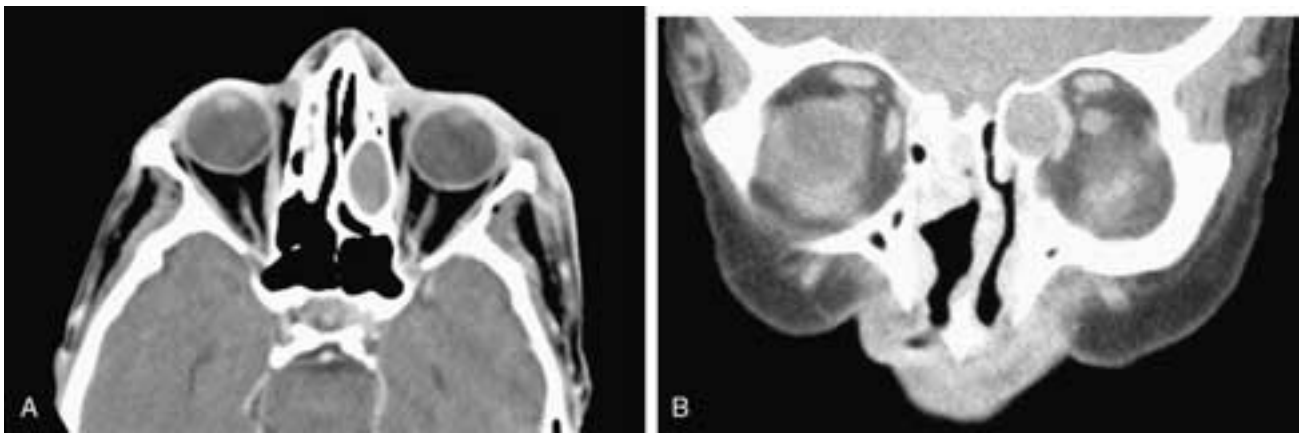

VIEW IMAGE

FIGURE 5-87 **A**, Axial CT scan shows an expansile, water attenuation, left ethmoid sinus mass that is minimally remodeling the lamina papyracea laterally. This patient had a left ethmoid mucocele. Coronal CT scan (**B**) on another patient shows an expansile right ethmoid sinus mucocele.

Copyright © 2003, Mosby, Inc. All rights reserved.

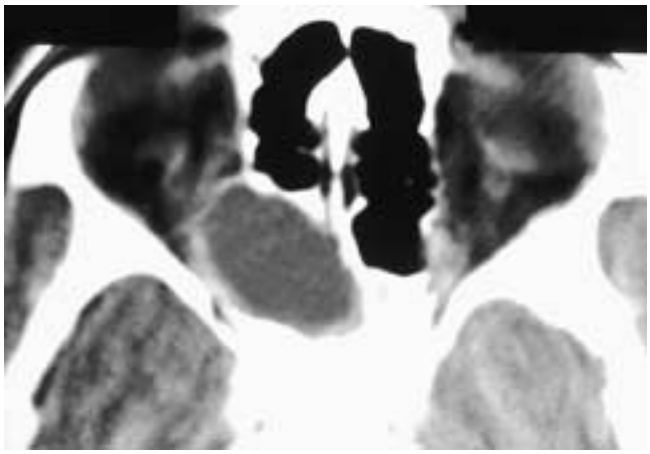

VIEW IMAGE

FIGURE 5-89 Axial CT scan shows a water attenuation, expansile mass in the right posterior ethmoid/sphenoid sinus area. The mass displaces the optic nerve and medial rectus muscle downward and laterally. This patient had a sphenoethmoidal mucocele. In these cases, the radiologist must carefully note the position of the optic nerve in relationship to the mass in order to help guide the surgeon away from intraoperative complications.

Ulcerated erosive gummas with indurated margins may develop. The gumma is a destructive, usually painless granulomatous process, which most likely represents a hypersensitivity reaction to *T. pallidum*, as well as progression of the disease to the tertiary phase. Gummas tend to develop in intramembranous bones such as those of the scalp, face, nose, nasal septum, and paranasal sinuses.[34, 118, 119] Without awareness of patient serology, the radiologist should be aware that syphilis can mimic Wegener's granulomatosis or sinonasal fungal disease. Mandibular resorption has been reported and may lead to spontaneous fracture. The treatment of choice remains penicillin.

Congenital syphilis may develop if transplacental infection occurs after the fourth fetal month (when immune competence develops) and within 2 years of the acquired maternal infection. The primary manifestations occur in the mucocutaneous tissues and bones; in the head and neck the

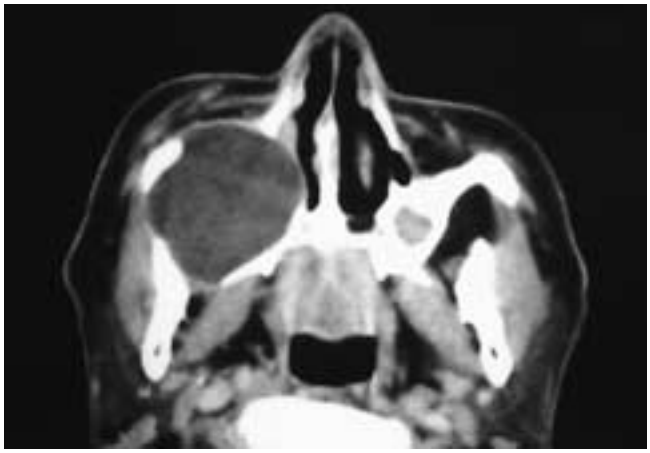

VIEW IMAGE

FIGURE 5-90 Axial CT scan shows a large, expansile mucoid attenuation right maxillary sinus mass. Portions of the bony wall are thinned. This patient had a right maxillary sinus mucocele.

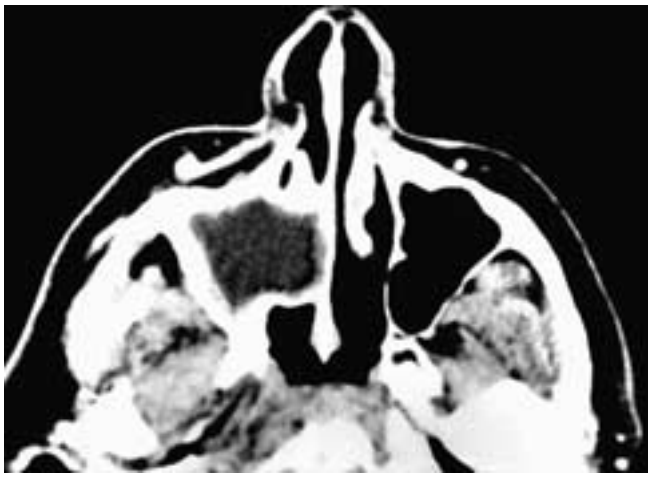

FIGURE 5-91 Axial contrast-enhanced CT scan shows an expansile right maxillary sinus mucoid attenuation mass that has a thin enhancing rim. This patient had a right maxillary sinus mucopyocele.

VIEW IMAGE

stigmata include frontal bossing (of Parrot), small maxilla, high palatal arch, Hutchinson's triad (Hutchinson incisors), interstitial keratitis, eighth nerve deafness, saddle nose, and mulberry molars.[34] The spirochete causes a periostitis that interferes with bone development.[120]

The differential diagnosis of syphilis includes yaws (*framboesia tropica*), a nonvenereally transmitted infection caused by *T. pertenue*, which occurs in children and young adults primarily in nongenital, unclothed areas. It is endemic in Central and West Africa and Southeast Asia. Uncommonly the late stages of the disease produce granulomas in the mucous membranes of the sinonasal cavities. These granulomas produce severe ulcerations of the nasal region (gangosa) and proliferative exostoses along the medial wall of the maxillary sinus (goundou). The treatment is penicillin. Histologically the spirochetes of *T. pertenue* tend to be more epidermotropic than those of *T. pallidum*, which can be present mainly at the dermal-epidermal junction and dermis. However, the clinical history is probably most helpful in distinguishing between syphilis and yaws.

Rhinoscleroma, which is caused by *Klebsiella rhinoscleromatis*, a gram-negative bacterium, is an infection that is endemic at tropical latitudes (Central America, Chile, and Central Africa), at subtropical latitudes (India, Indonesia, Egypt, Algeria, and Morroco), in temperate latitudes (Eastern and Central Europe), and in the Russian republics. *K. rhinoscleromatis* is an organism of low infectivity and is not a normal commensal organism. Human-to-human contact is assumed to be the only mode of transmission, and the infection results only after prolonged exposure.

Rhinoscleroma affects the nasal cavity and sinuses; however, it can involve the entire upper respiratory tract, so much so that the general name *scleroma* had been advocated. The natural course of this infection evolves through three stages. The early stage is the atrophic catarrhal stage; the involved mucosa is reddened and atrophic, with a foul purulent discharge and crusting. The clinical differential diagnosis in this early stage includes infection with *Klebsiella ozaenae*. The granulomatous stage may appear, months to years later, as waxy, ulcerating inflammatory masses that distend and deform the mucosal surfaces. The

Copyright © 2003, Mosby, Inc. All rights reserved.

VIEW IMAGE

FIGURE 5-92 Axial CT scan (**A**) on a patient who had had a right Caldwell-Luc procedure. There is an expansile mass (*arrowhead*) in the lateral portion of the sinus. The medial portion of the sinus (*small arrows*) is aerated. This patient had a right postoperative maxillary sinus mucocele. In **B**, a coronal CT scan on a different patient who had had a left Caldwell-Luc procedure, there is an expansile mass in the lateral portion of the left maxillary sinus that has broken into both the left orbit and the cheek (*arrows*). This patient had a left maxillary sinus postoperative mucocele.

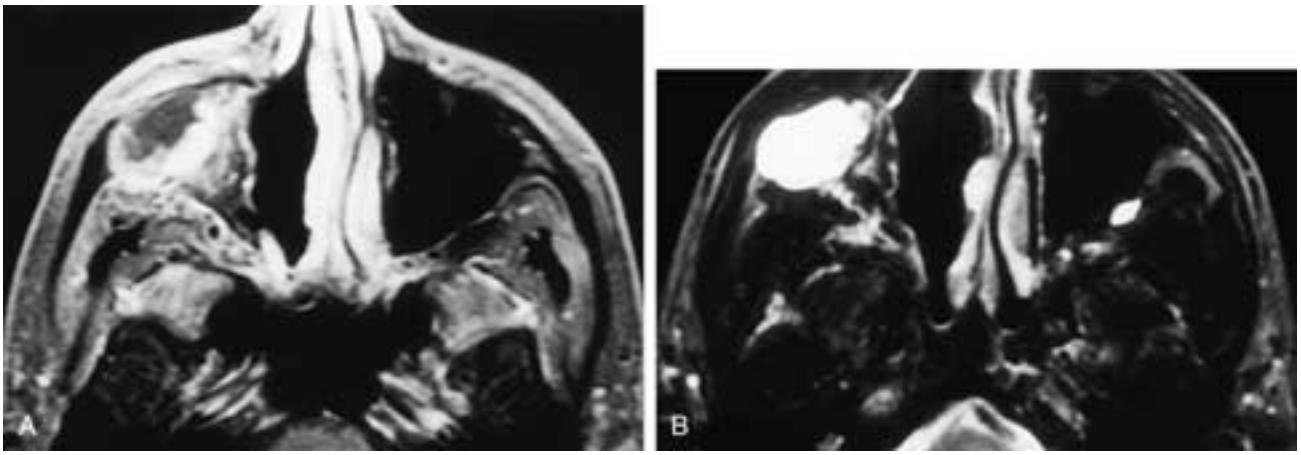

VIEW IMAGE

FIGURE 5-93 Axial T1-weighted (**A**) and T2-weighted (**B**) MR images on a patient who had a right medial maxillectomy. There is a nonhomogeneous inflammatory-type collection in the zygomatic region of the remaining sinus cavity. The medial portion of this cavity remains well aerated. This patient had a postoperative right maxillary sinus mucocele.

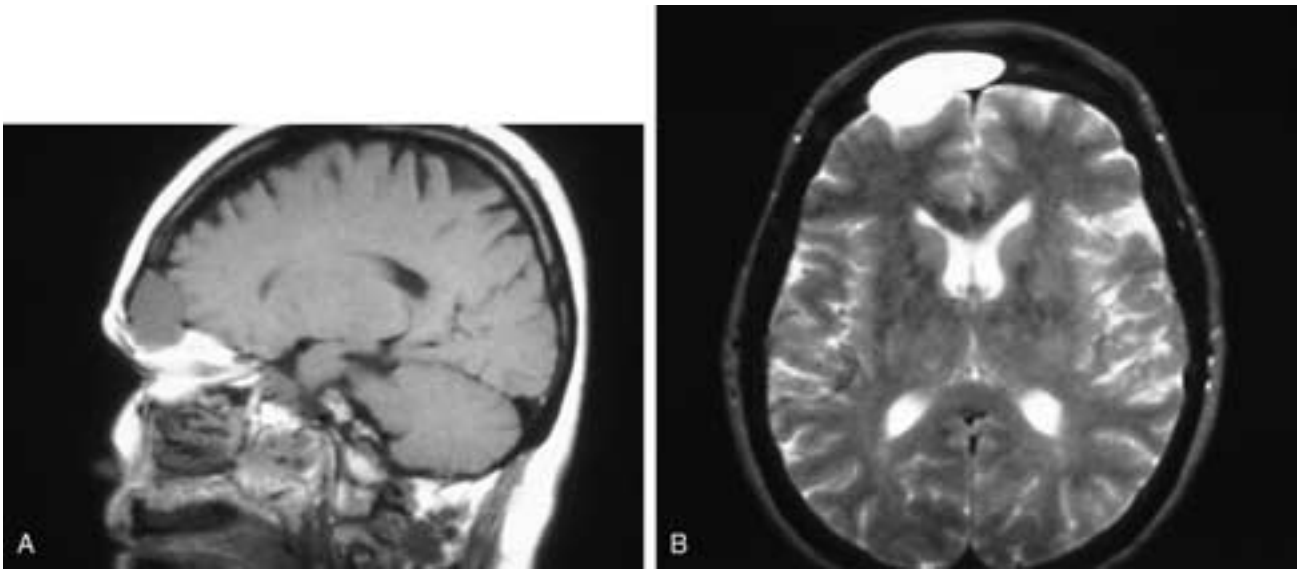

VIEW IMAGE

FIGURE 5-94 Sagittal T1-weighted (**A**) and axial T2-weighted (**B**) MR images show an expanded, airless frontal sinus filled with material that has a low T1-weighted and a high T2-weighted signal intensity. The mass extends down into the upper medial orbit. The posterior sinus wall appears eroded but is only deossified by the chronic pressure of this right frontal sinus mucocele.

Copyright © 2003, Mosby, Inc. All rights reserved.

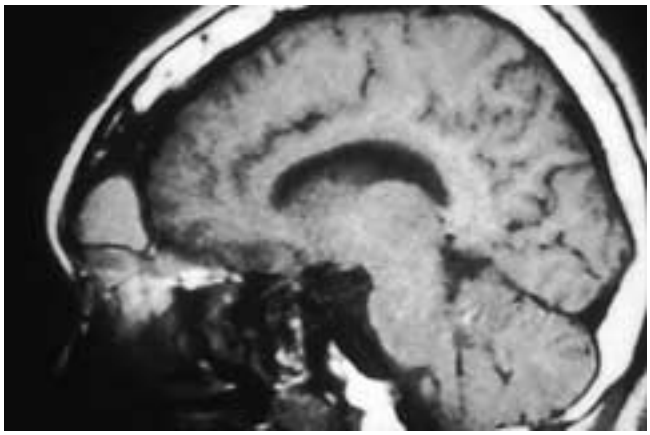

FIGURE 5-95 Sagittal T1-weighted MR image scan shows an expansile frontal sinus mass with an intermediate signal intensity. This mass had a high T2-weighted signal intensity. This patient had a frontal sinus mucocele.

VIEW IMAGE

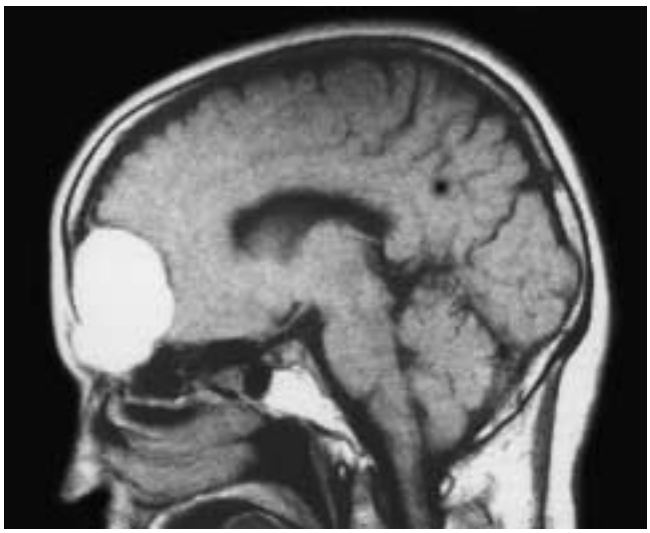

VIEW IMAGE

FIGURE 5-96 Sagittal T1-weighted MR image shows an expansile frontal sinus mass with high signal intensity. The mass has extended both down into the medial orbit and back into the anterior cranial fossa. The mass also had a high T2-weighted signal intensity. This patient had a frontal mucocele.

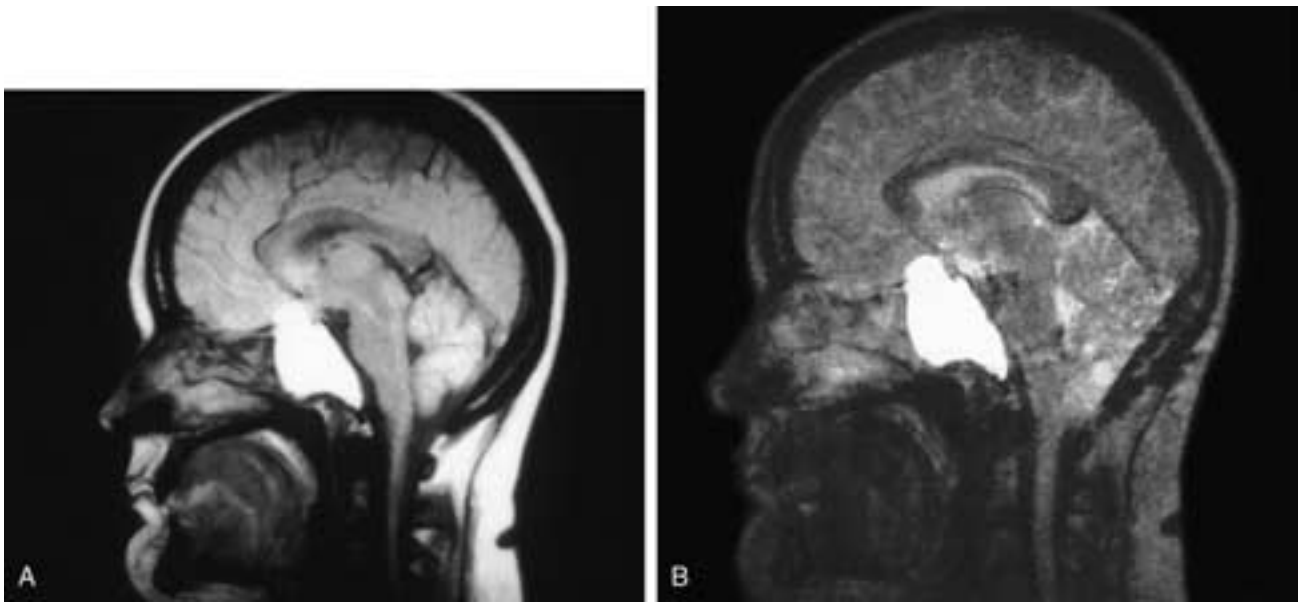

VIEW IMAGE

FIGURE 5-97 Sagittal T1-weighted (**A**) and T2-weighted (**B**) MR images show an expansile sphenoid sinus mass that has high signal intensity on both sequences. This patient had a sphenoid sinus mucocele.

Copyright © 2003, Mosby, Inc. All rights reserved.

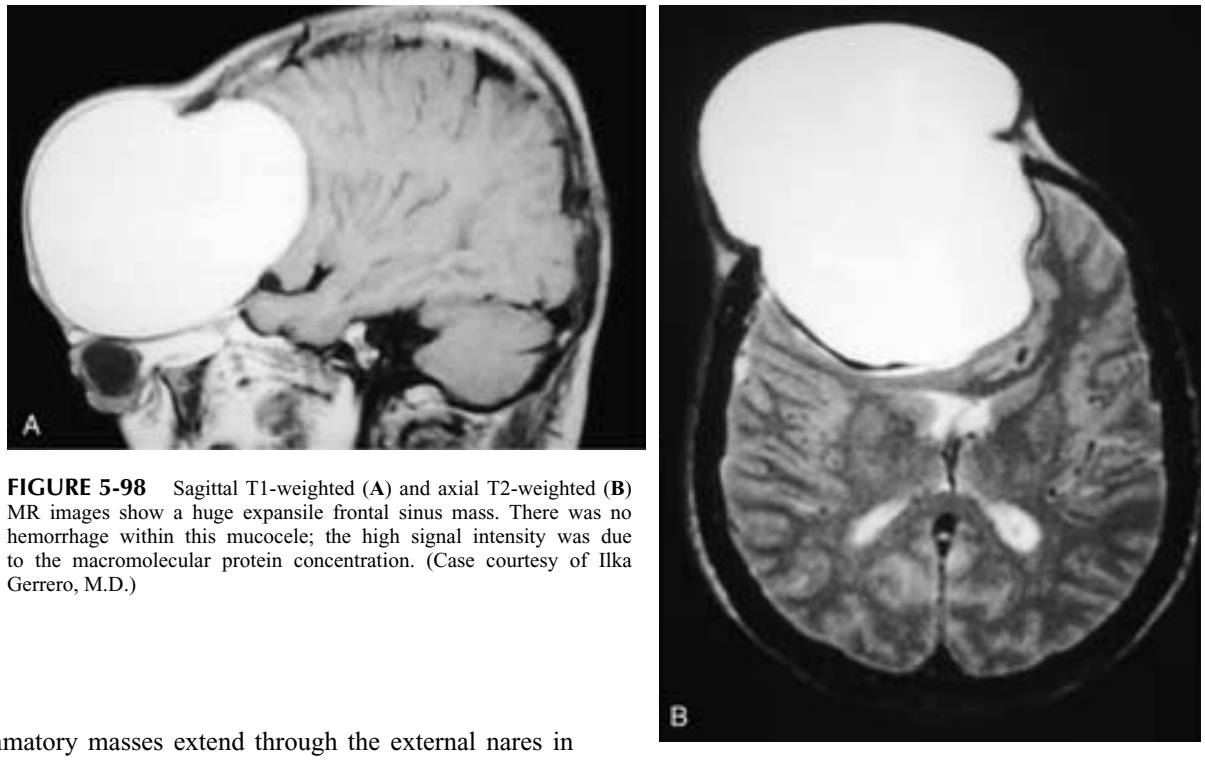

FIGURE 5-98 Sagittal T1-weighted (**A**) and axial T2-weighted (**B**) MR images show a huge expansile frontal sinus mass. There was no hemorrhage within this mucocele; the high signal intensity was due to the macromolecular protein concentration. (Case courtesy of Ilka Gerrero, M.D.)

inflammatory masses extend through the external nares in severe cases and may distort the soft tissues of the midface, resulting in a rhinoceros-like appearance. The clinical differential diagnosis includes leprosy and syphilis. The final sclerotic stage is characterized by fibrosis along with the inflammation, culminating in stenosis.[121]

Rhinosclerosis has been reported in AIDS patients, but the mucocutaneous infections do not appear to differ from those occurring in the usual hosts.[122] The treatment of choice is surgical excision to open the airway and long-term antibiotic therapy, usually with tetracycline.[34]

North American blastomycosis is caused by *Blastomyces dermatitidis*, and the disease is endemic in the Ohio and Mississippi River basins. The disease is not confined to North America and has been detected in South America and Africa. A noted increase in blastomycosis has been seen among avid bird watchers. Based on point source case studies, it appears that closeness between the individual's face and soil (e.g., picking up objects from the ground to examine them) makes one more vulnerable to infection.

Blastomyces may cause disease either through inhalation or through traumatic inoculation into skin. Clinically, blastomycosis may present as the acute onset of pneumonia with fever, productive cough, and myalgias. Patients with insidious infection have symptoms such as weight loss, malaise, anorexia, and a chronic cough that may clinically mimic tuberculosis. Most of the head and neck lesions involve the skin, but involvement of the larynx and nasal

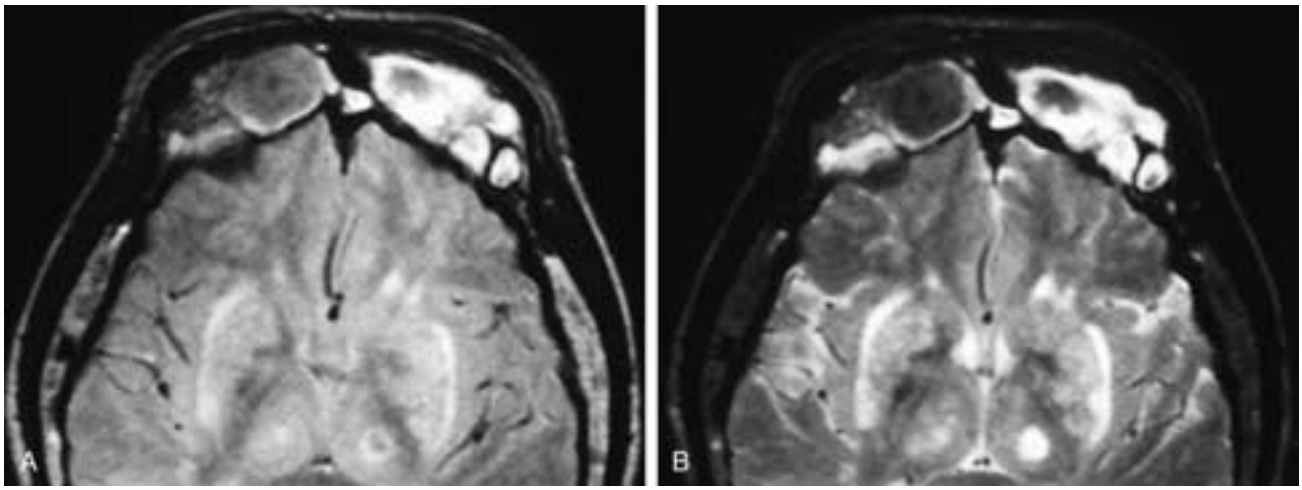

FIGURE 5-99 Axial T1-weighted (**A**) and T2-weighted (**B**) MR images show bilateral expansile, nonhomogeneous frontal sinus masses. On the right side, the mass has overall low to intermediate T1-weighted and low T2-weighted signal intensities. On the left side, the mass has an overall high signal intensity on both T1-weighted and T2-weighted images. This patient had bilateral frontal sinus mucoceles.

Copyright © 2003, Mosby, Inc. All rights reserved.

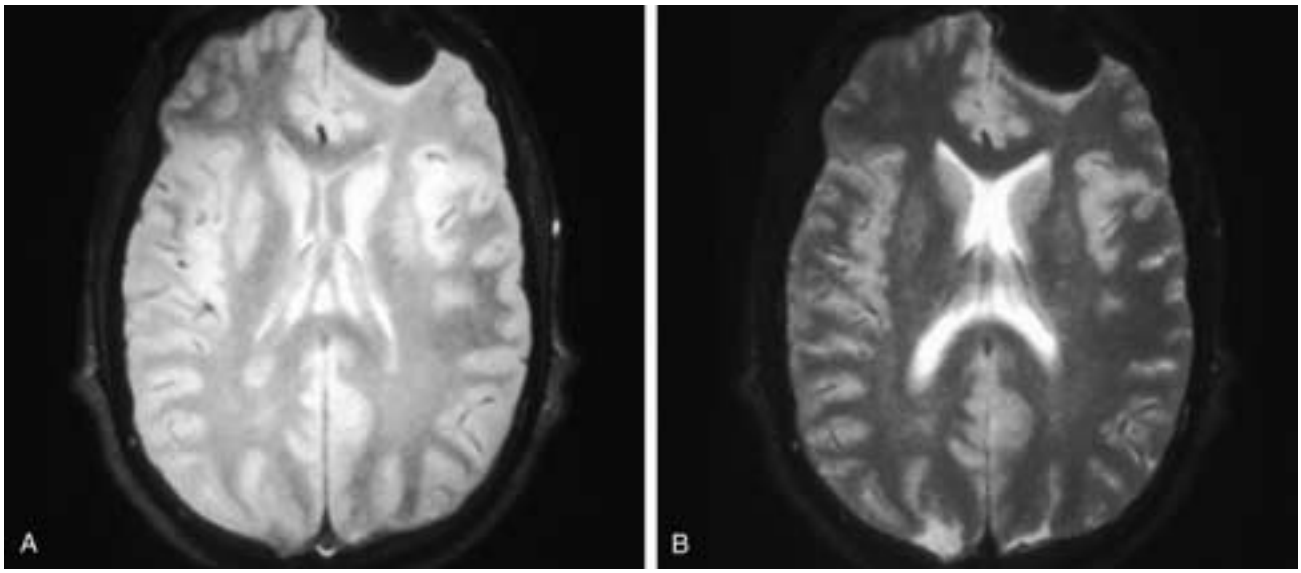

VIEW IMAGE

FIGURE 5-100 Axial proton density (**A**) and T2-weighted (**B**) MR images show an expansile mass in the left frontal sinus that has signal voids on both sequences. This was a frontal sinus mucocele with dried, desiccated secretions.

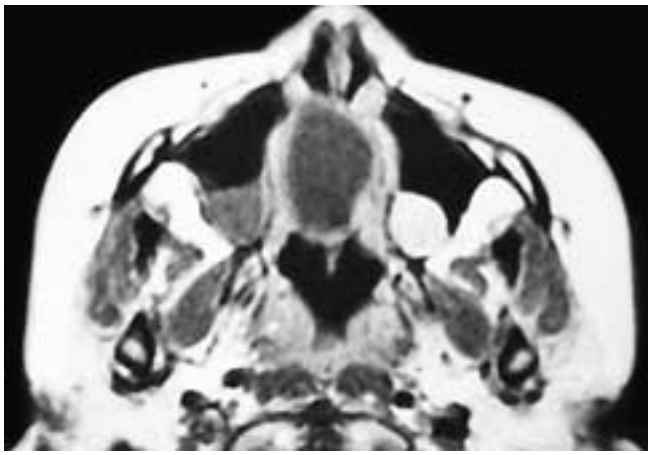

FIGURE 5-101 Axial T1-weighted MR image shows an expansile process that arose in a pneumatized middle turbinate (concha bullosa). This mucocele has a low T1-weighted signal intensity and had a high T2-weighted signal intensity. Also present is a small retention cyst in the posterior recess of each antrum. On the right side the cyst has low T1-weighted signal intensity, while on the left side the cyst has intermediate signal intensity. This patient had a mucocele of a concha bullosa.

VIEW IMAGE

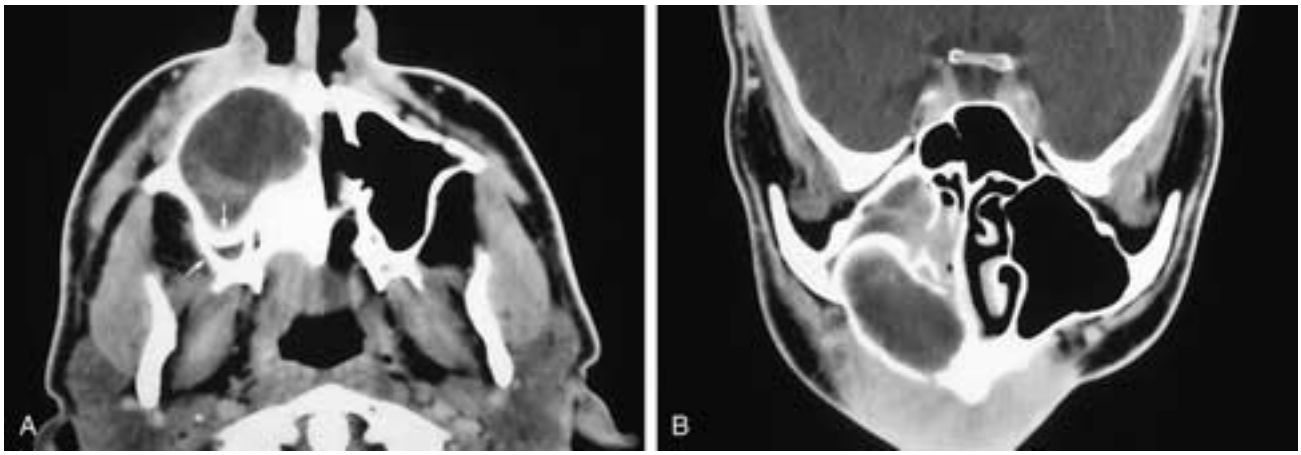

VIEW IMAGE

FIGURE 5-102 Axial (**A**) and coronal (**B**) CT scans show a water attenuation expansile mass in the lower right maxillary sinus. In **A**, there are two bony walls seen posteriorly (*arrows*). In **B**, they can be seen to be due to elevation of the sinus floor by a cystic mass arising below the sinus. Obstructed secretions are also present within the right maxillary sinus. This patient had a right radicular cyst and maxillary sinusitis.

Copyright © 2003, Mosby, Inc. All rights reserved.

VIEW IMAGE

FIGURE 5-103 Axial CT scan shows a high-attenuation region in the left maxillary sinus separated from the bony walls of the sinus by a thin zone of mucoid attenuation material. There is also some remodeling of the medial maxillary sinus wall. This patient had aspergillosis with an aspergilloma.

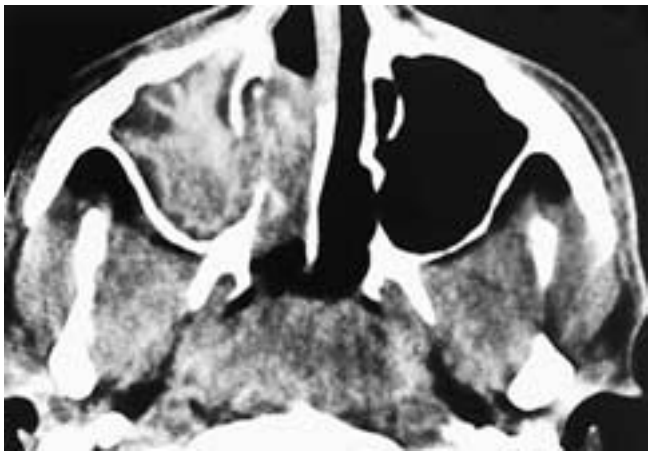

VIEW IMAGE

FIGURE 5-104 Axial CT scan shows a stellate high-attenuation soft-tissue mass in the right maxillary sinus and nasal fossa. The mass is separated from the bone by a thin zone of mucoid attenuation material. There is focal destruction of the medial antral wall. This patient had aspergillosis with an aspergilloma.

cavity has been reported. The laryngeal disease may appear clinically identical to carcinoma. Oral lesions may have associated draining sinuses, mimicking actinomycosis. The primary treatment of choice is amphotericin B.[34, 123]

South American blastomycosis (paracoccidioidomycosis) is caused by the dimorphic fungus *Blastomyces brasiliensis*. The disease is endemic to South America, especially Brazil, Colombia, Venezuela, Uruguay, and Argentina. As with coccidioidomycosis, a wide range of disease can be seen, from subclinical to clinical, in immunologically normal patients, patients who are immunosuppressed, and patients with AIDS. Aspiration with subsequent hematogenous dissemination is thought to be the mode of transmission because pulmonary involvement is common. It may produce painful, destructive granulomas of the alveolar process, gingiva, nasal cavity, and, rarely, the paranasal sinuses.[5, 123, 124] The primary treatment is amphotericin B, which cures more than 90% of the cases.[125]

Leprosy is caused by the pleomorphic acid-fast bacterium *Mycobacterium leprae*. The disease occurs in almost all tropical and warm temperate regions, including Latin America, South and Southeast Asia, Saharan Africa, the Mediterranean basin, and Northern Europe. In the United States, endemic states include Florida, Louisiana, Texas, California, and Hawaii. Leprosy affects more than 11 million people worldwide; the number of indigenous cases in the United States has remained stable (10 to 29 per year) over the last two decades. However, the number of imported cases reported in the United States has dramatically increased (up to 300 per year) since the late 1970s. This increase in imported cases did not lead to increased transmission among the U.S. population.

Leprosy is a disease of low infectivity transmitted through prolonged exposure either through nasal secretions or through injured skin. Immunologically, leprosy can be graded by the host response as tuberculoid leprosy (characterized by a robust immunologic response, with few bacilli and with the possibility of spontaneous cure), borderline leprosy, and lepromatous leprosy (characterized by anergy to the lepromin test and abundant bacilli). Clinically there is a widespread, symmetrical facial distribution of lesions lead-

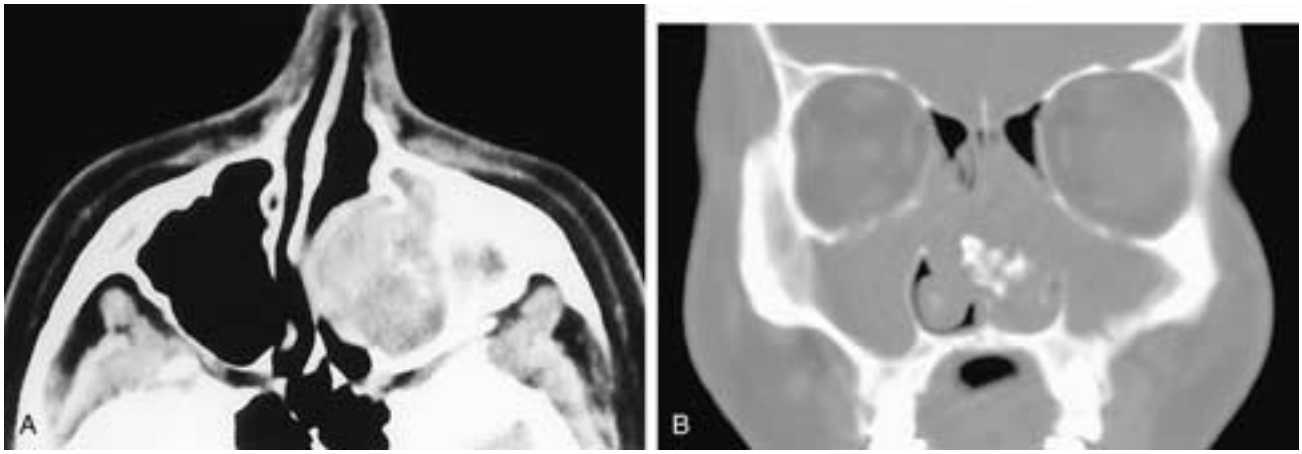

VIEW IMAGE

FIGURE 5-105 Axial CT scan (**A**) shows a soft-tissue mass in the left maxillary sinus that has thickened the posterior bony wall and thinned or destroyed the medial wall. Within the mass are several discrete calcifications. This patient had aspergillosis. Coronal CT scan (**B**) on a different patient shows soft-tissue disease in both ethmoid and maxillary sinuses and within both nasal fossae. In addition, there are calcifications in the nasal septum. This patient had aspergillosis.

Copyright © 2003, Mosby, Inc. All rights reserved.

VIEW IMAGE

FIGURE 5-106 Lateral plane film shows erosion of the anterior nasal spine (*arrow*). There is also soft-tissue disease in the maxillary sinuses and nasal fossa. This patient had no prior surgery or trauma to this region. This patient had leprosy.

ing to a coarsening of features. The earlobes and nose are especially enlarged and infiltrated. Intranasal and paranasal sinus involvement is common and occurs after cutaneous nasal involvement. The changes in the sinonasal cavities are those of nonspecific chronic sinusitis and rhinitis. Later changes resemble those of a chronic granulomatous disease. A characteristic finding is progressive erosion of the anterior nasal spine. If previous surgery, trauma, and congenital maxillonasal dysplasia are not applicable to the patient, this finding is pathognomonic of leprosy (Fig. 5-106). Retrograde laryngeal involvement usually follows nasal disease. The treatment of choice remains the long-term administration of sulfone derivatives (dapsone).[125]

Rhinosporidiosis is caused by the fungus yeast *Rhinosporidium seeberi*.[126] The disease has a worldwide distribution but is endemic in places like India, Sri Lanka, Malaysia, Brazil, and Argentina. In the United States, cases have been reported in the rural South and West. Preceding mucosal trauma (e.g., by digital contamination or dust storms) is considered necessary in establishing the infection.[127] Patients with rhinosporidiosis generally are otherwise healthy. *Rhinosporidium* most commonly infects the conjunctiva and nasal cavity, with resultant friable, lobulated polyps that may cause obstruction of the nasal fossae and may be confused with neoplasms, especially cylindrical cell papilloma.[34] The nasal polyps are sessile, soft, pinkish, usually unilateral, and they may diminish aeration in the paranasal sinuses. The treatment of choice is surgical excision or electrocautery.

Glanders, or farcy, is caused by the bacterium *Pseudomonas mallei*. It is contracted by contact with horses, mules, or donkeys. In humans the disease is characterized either by an acute fulminant febrile illness that may lead to death or by a chronic indolent granulomatous disease. *Farcy* refers to the nodular abscesses found in the skin, lymphatics, and subcutaneous tissues.[125] The nasal manifestations of glanders are nasal cellulitis and necrosis that produce septal perforations. The treatment is with sulfonamides.

Leishmaniasis causes mucocutaneous infection (*Leishmania tropica*, known as Oriental sore or ''Old World'' sore; *L. mexicana* or *L. brasiliensis*, known as espundia or ''New World'' sore). The disease is endemic to Central and South America. After the initial primary cutaneous sores appear, satellite lesions develop in the nose and mouth; these sores are painful, mutilating erosions that can secondarily involve the sinuses.[125, 128] Scarring may eventually constrict the nose or mouth, producing gross deformities that interfere with swallowing. The majority of the oronasal diseases are caused by *L. brasiliensis*, and the treatment of this established oronasal disease is with amphotericin B.

NONINFECTIOUS DESTRUCTIVE SINONASAL DISEASE

Wegener's granulomatosis is a necrotizing granulomatous vasculitis that usually affects the upper and lower respiratory tracts and causes a renal glomerulonephritis. A limited form of Wegener's granulomatosis may occur, with a more benign course in which only the sinonasal tract is affected. The initial disease may present as a chronic, nonspecific inflammatory process of the nose and sinuses and may remain as such for 1 to 2 years. Usually the nasal septum is first affected. The process becomes diffuse, and septal ulceration and perforations may result in a ''saddle nose'' deformity. Secondary bacterial infections complicate the clinical and imaging pictures.

The diagnosis of Wegener's granulomatosis may be difficult to establish early in the disease course or during periods of inactivity. The radiologist can suggest biopsy of the paranasal sinuses as opposed to the nasal cavity. Although this site is not as readily accessible as the nasal cavity, it has a greater yield of specific diagnostic features that aid the pathologist. Serum antineutrophil cytoplasmic antibodies (ANCA) are elevated during periods of active disease. In the absence of a specific diagnosis of Wegener's granulomatosis, it behooves the pathologist and the clinician to rule out other infectious and malignant causes of destructive sinonasal disease. Wegener's granulomatosis is probably autoimmune in origin, and the treatment of choice is cyclophosphamide, steroids, and possibly other cytotoxic drugs. Long-term remissions have been achieved; however, it is impossible to predict how long a remission will last.[125, 129]

Lethal midline granuloma, which was once classified as a granulomatous disease, was then reclassified as malignant midline reticulosis or polymorphic reticulosis.[129, 130] The disease is now classified as a lymphoma, and it is discussed in Chapter 6.

Sarcoidosis is a systemic, multisystem disease characterized by noncaseating epithelial granulomas.[131–133] An infectious etiology has been sought for these granulomas. Two decades ago, experimental data were presented suggesting the transmissibility of these granulomas, hence fulfilling one of Kock's postulates for an infectious etiology.

Copyright © 2003, Mosby, Inc. All rights reserved.

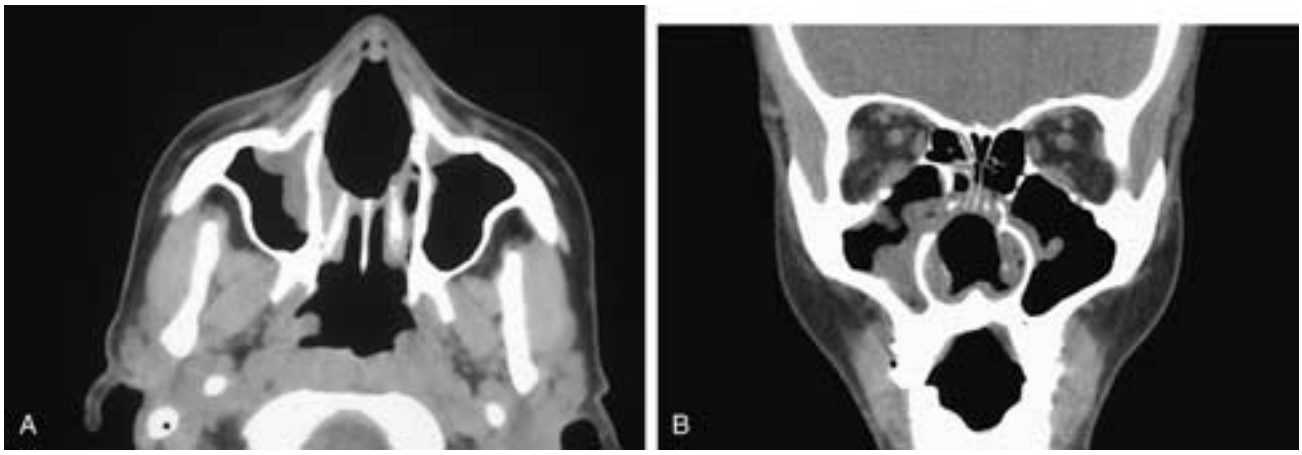

VIEW IMAGE

FIGURE 5-107 Axial (**A**) and coronal (**B**) CT scans show destruction of the nasal septum and portions of each medial maxillary sinus wall and the lower ethmoid complex. The distribution of disease suggests a granulomatous process. This patient was a chronic cocaine abuser.

Patients with sarcoidosis have elevated levels of antibodies to *Mycobacterium paratuberculosis*. However, direct inoculation of sarcoid tissue into a thymic mouse has failed to isolate an infectious agent, so at present no known agent has been directly implicated in the etiology of sarcoidosis.

Sarcoidosis has a predilection for the Scandinavian countries and for the rural southeastern United States. It is most common in African-American females with a median age of 25 years. Nasal sarcoidosis occurs in 3% to 20% of the patients with systemic sarcoidosis. When it occurs, there are multiple small granulomas of the nasal septum and turbinates. There may be nasal discharge, obstruction, and epistaxis. Polypoid degeneration of the nasal fossa mucosa may occur, but the paranasal sinuses are rarely affected. Sarcoidosis is not generally a destructive disease in the sinonasal tract; however, destruction of the nasal septum and turbinates can occur in unusual cases. Rarely, sharply defined lytic bone lesions may occur in the calvarium and facial skeleton. Steroid therapy may suppress the inflammatory reaction and provide symptomatic improvement, but fibrous organization of the granulomas may lead to organ dysfunction.[34, 134]

Exposure to beryllium may result in chronic granulomas of the nasal fossa. These granulomas may be indistinguishable from those of tuberculosis, leprosy, and sarcoidosis.[128] Chromate salts have been implicated as a cause of nonspecific granulomas of the nasal cavity; involvement of the paranasal sinuses is a late and unusual event. Cocaine abuse has become a major worldwide problem. Cocaine causes a necrotizing vasculitis and subsequent granuloma of the nasal septum, which with prolonged exposure usually results in septal erosion. Erosion of the nasal vault margins and the adjacent sinuses can occur in chronic abusers. A nonspecific mucosal inflammation may also occur in the nasal fossa. A mucosal reaction to the talc used to ''cut'' the cocaine can also occur.

Imaging

In general, the destructive granulomatous diseases result in variable sinonasal mucosal changes, ranging from nonspecific inflammation with mucosal thickening and nasal secretions to a localized soft-tissue mass. Nasal cavity involvement usually precedes paranasal cavity disease. The nasal septum may be focally thickened by a bulky soft-tissue mass or septal erosion may be present. When the paranasal sinuses are involved, the maxillary and ethmoid sinuses are most often affected. The sphenoid sinuses are uncommonly involved, and the frontal sinuses are almost always spared. When the sinuses are affected, there is usually nonspecific inflammatory mucosal thickening. Air-fluid levels are rare. The bones of the nasal vault and affected paranasal sinuses may be thickened and sclerotic, reflecting the chronic nature of the inflammatory reaction. Sinus obliteration by reactive bone may also occur.[135] Similarly there may be areas of bony erosion, reflecting either osteomyelitis or necrosis. If the nasal disease becomes a bulky soft-tissue mass, there may, in addition, be remodeling of the adjacent bones (Figs. 5-106 to 5-111).[122]

On MR imaging, these diseases may have low T1-weighted and high T2-weighted signal intensities suggestive of an inflammatory disease. They also may have low to inter-

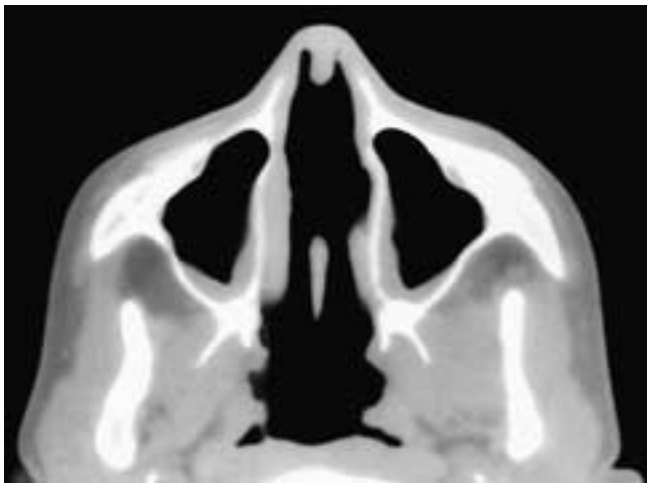

FIGURE 5-108 Axial CT scan shows a large erosion of the nasal septum and minimal mucosal thickening in the maxillary sinuses. This appearance suggests a granulomatous process. This patient was a chronic cocaine abuser.

VIEW IMAGE

Copyright © 2003, Mosby, Inc. All rights reserved.

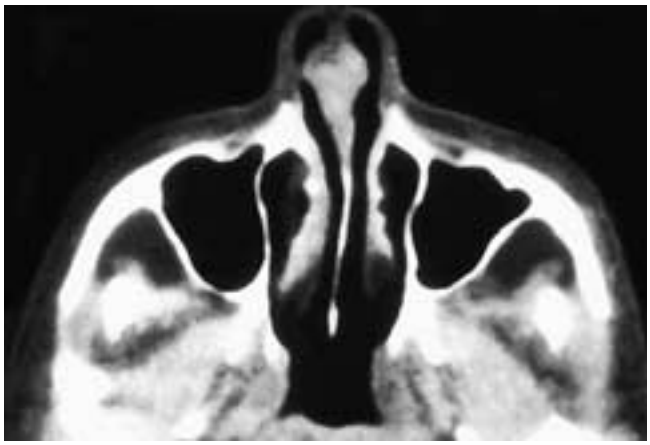

VIEW IMAGE

FIGURE 5-109 Axial CT scan shows localized soft-tissue thickening of the anterior nasal septum. This appearance suggests either granulomatous disease or a cartilaginous tumor. This patient had Wegener's granulomatosis.

mediate T1-weighted and T2-weighted signal intensities simulating malignancies. They all enhance with contrast.[136] However, not all septal masses represent granulomatous-type disease. In addition to chondroid tumors, a septal abscess can occur, usually following local trauma (Fig. 5-110B,C).

CHOLESTEATOMAS

Several entities in addition to mucoceles can cause sinus cavity enlargement. An epidermoid inclusion cyst (or cholesteatoma) is a cystic keratin-filled mass lined by stratified squamous epithelium. In the frontal bone, these cysts probably arise from a congenital inclusion rest or after traumatic implantation. They may develop either in the diplöe or, less frequently, in the outer table of the skull. On plain films they appear lucent when compared with the adjacent normal frontal bone. The margins may be slightly scalloped or smooth, and there is a thin, uniform white line that identifies the lesion's contour. These latter two findings help differentiate an epidermoid inclusion cyst from a mucocele (Fig. 5-112). Confusion with a mucocele may occur if an epidermoid inclusion cyst arises within or adjacent to the frontal sinus.[137, 138] These cysts may also rarely arise from other flat facial bones.[139]

In the antrum, invasion of buccal epithelium via an oroantral fistula has also been proposed as a possible etiology for an antral epidermoid inclusion cyst. A type of ''cholesteatoma'' or pseudocholesteatoma may develop within a chronically infected sinus after active infection has subsided. The breakdown products of the purulent exudate, as well as any blood, may contain cholesterol products that result in cholesteatomatous debris.[140–142]

An antral epidermoid inclusion cyst must also be differentiated from an odontogenic keratocyst. The latter is a benign cystic neoplasm arising from odontogenic rests that

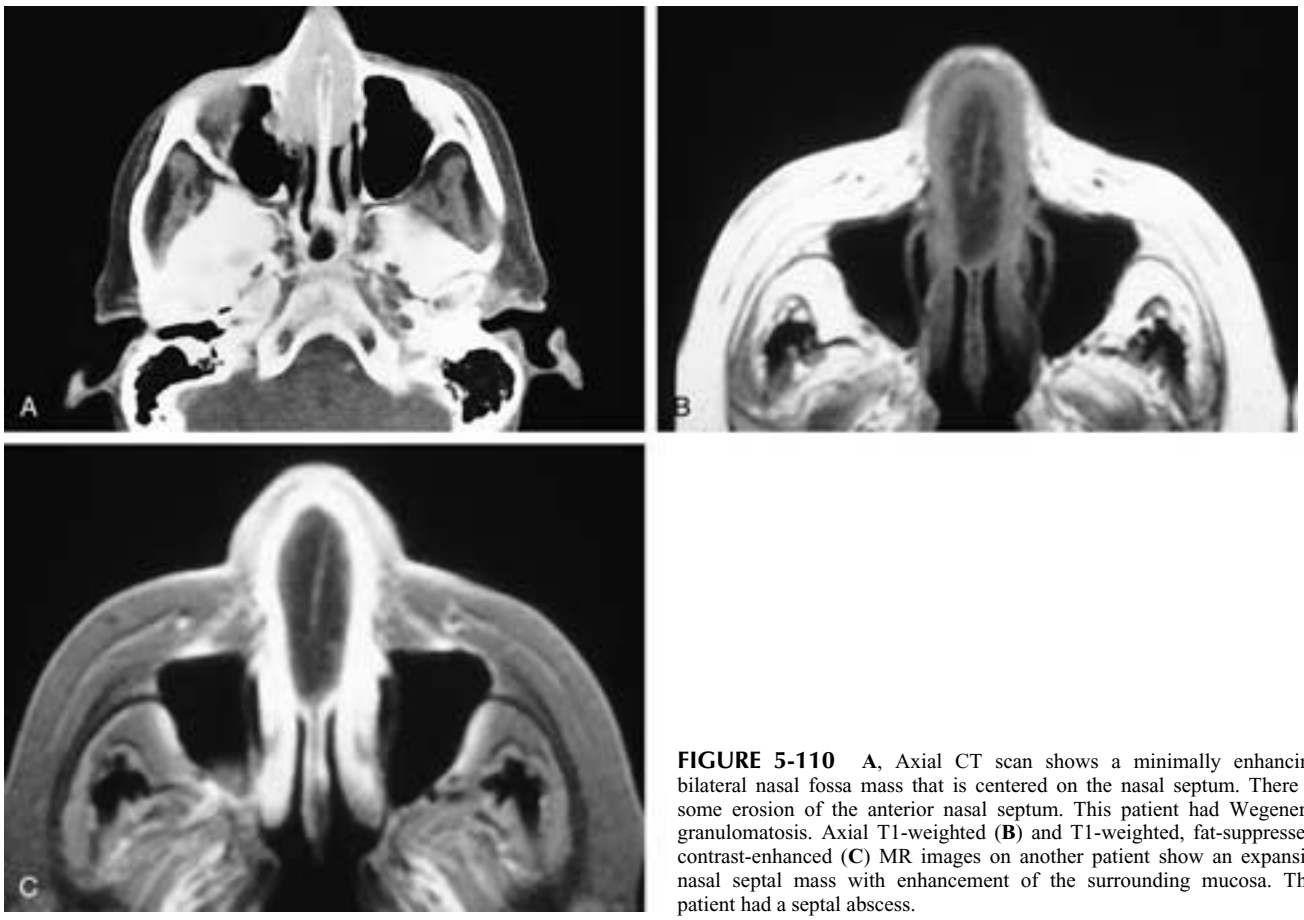

FIGURE 5-110 **A**, Axial CT scan shows a minimally enhancing bilateral nasal fossa mass that is centered on the nasal septum. There is some erosion of the anterior nasal septum. This patient had Wegener's granulomatosis. Axial T1-weighted (**B**) and T1-weighted, fat-suppressed, contrast-enhanced (**C**) MR images on another patient show an expansile nasal septal mass with enhancement of the surrounding mucosa. This patient had a septal abscess.

VIEW IMAGE

Copyright © 2003, Mosby, Inc. All rights reserved.

FIGURE 5-111 Axial CT scan (**A**) shows moderate degrees of inflammatory disease, with fluid levels in both maxillary sinuses. There is also some disease in both nasal fossae and erosion of a portion of the nasal septum. This pattern of disease suggests a granulomatous process. Coronal (**B**) and axial (**C**) CT scans on another patient show erosion of the nasal septum and portions of the turbinates. Inflammatory soft tissues are present in the ethmoid and maxillary sinuses. Both of these patients had sarcoidosis.

VIEW IMAGE

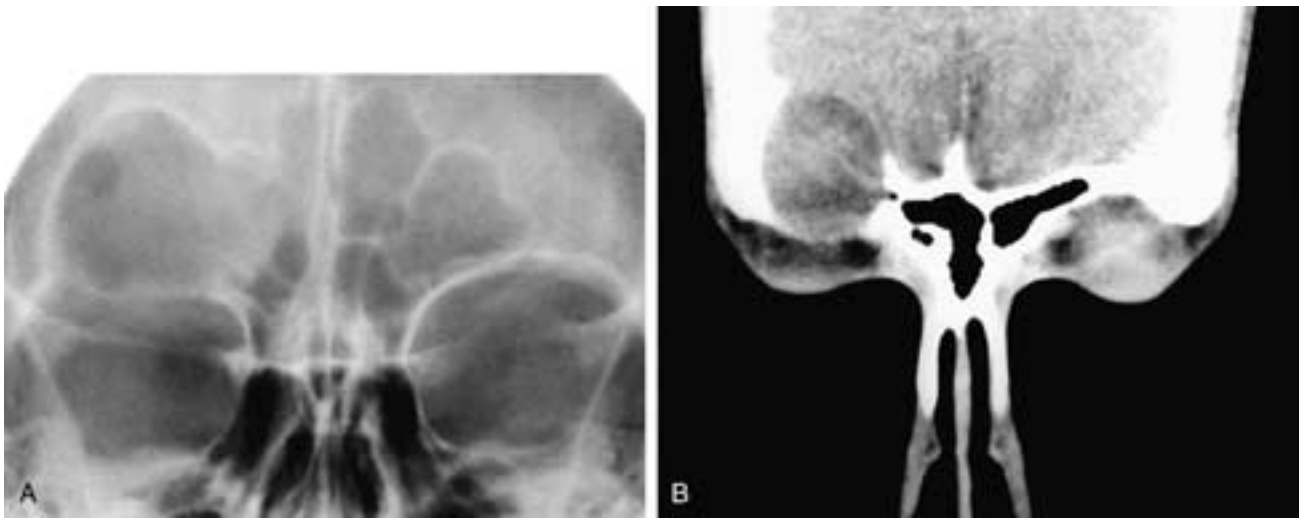

FIGURE 5-112 Caldwell view (**A**) shows a smoothly expansile lesion in the lateral right frontal bone, which is thinning and depressing the right orbital roof. A thin white mucoperiosteal line surrounds the mass. Coronal CT scan (**B**) shows the localized, expansile, homogeneously ''mucoid'' attenuation mass, which is depressing the right orbital roof. This patient has a cholesteatoma of the frontal bone.

VIEW IMAGE

Copyright © 2003, Mosby, Inc. All rights reserved.

may also remodel and expand the maxilla (see Chapters 6 and 17).

On CT, an epidermoid inclusion cyst or a cholesteatoma appears as an expansile lesion that has soft tissue, mucoid-like attenuation. If it occurs within a sinus cavity, it may be indistinguishable from a mucocele. On MR imaging, depending on the fatty components of the cholesterol, there can be an intermediate to high signal intensity on T1-weighted images and there usually is an intermediate to high signal intensity on T2-weighted images (Fig. 5-113).[143, 144]

ENLARGED AERATED SINUSES

When evaluating a large sinus, there are no definitive measurements that define abnormal enlargement. Part of the problem is lack of pathologically confirmed etiologies for these processes. In one study, a sinus was judged to be abnormally large if its size exceeded that of 99% of the normal population.[145, 146] Using that criterion and taking into account magnification factors for films taken on a Franklin head unit (3.4%) or a standard 40-inch focal-

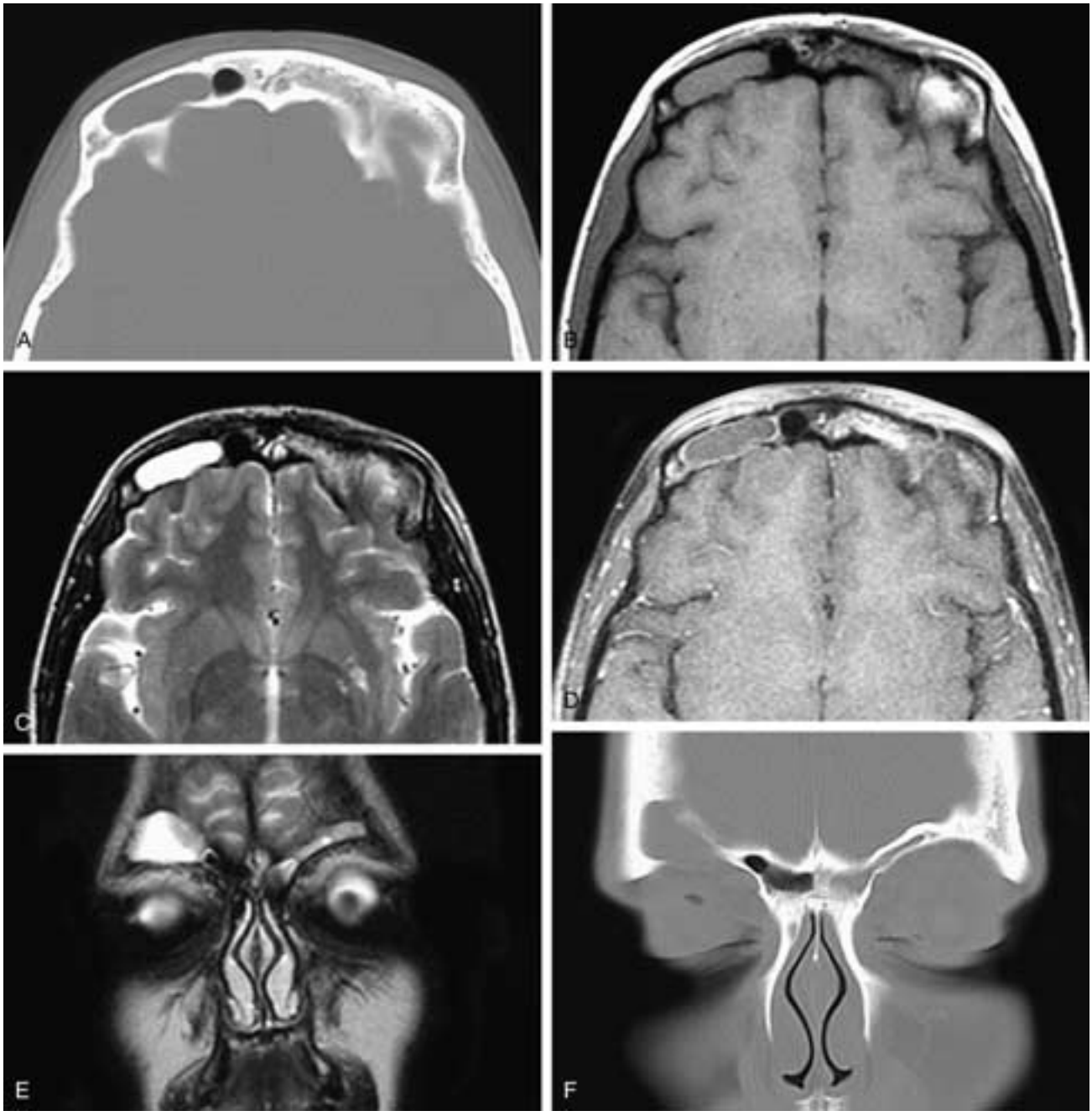

FIGURE 5-113 Axial CT scan (**A**) shows a smoothly marginated mass in the right frontal bone. The medial aspect of the mass abuts on the right side of the right frontal sinus. Axial T1-weighted (**B**) and T2-weighted (**C**) MR images show the mass to have an intermediate T1-weighted and high T2-weighted signal intensity. Axial T1-weighted, fat-suppressed, contrast-enhanced MR image (**D**) shows some enhancement around the margins of the mass. Coronal T2-weighted (**E**) MR image and coronal CT scan (**F**) show that the mass is adjacent to the right frontal sinus and has broken down into the roof of the right orbit. There is also some inflammatory disease in the left supraorbital sinus. This patient had a cholesteatoma of the right frontal bone.

VIEW IMAGE

Copyright © 2003, Mosby, Inc. All rights reserved.

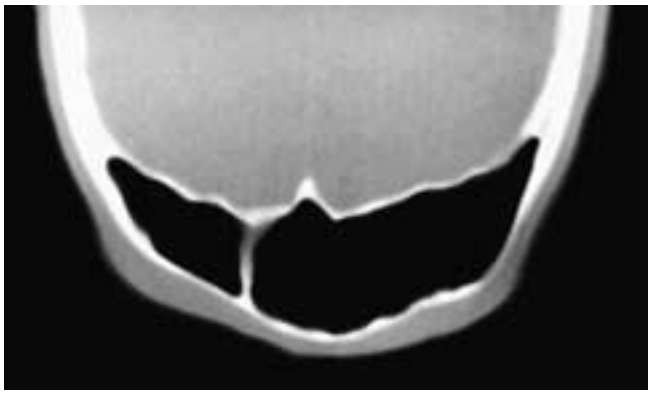

VIEW IMAGE

FIGURE 5-114 Coronal CT scan shows a very large, normally aerated frontal sinus. Despite its size, there was no bossing of the forehead or remodeling of the inner table. This patient had a hypersinus.

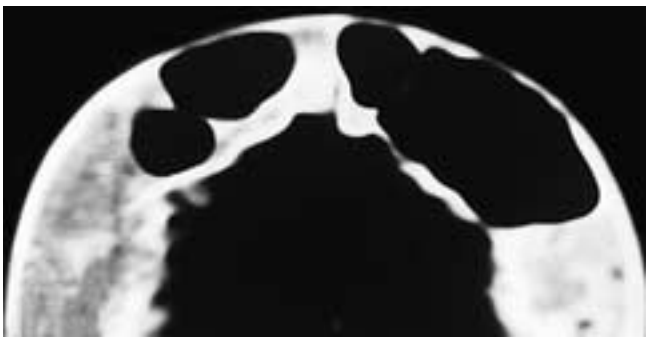

VIEW IMAGE

FIGURE 5-115 Axial CT scan shows large frontal sinuses in a patient with a dense cortical calvarium and hyperostosis interna. Despite the size of these sinuses, there was no deformity of the forehead or inner sinus table. This patient had hypersinuses.

distance Caldwell view (10.3%), if a line drawn from the base of the crista galli to a point of maximum distance along the perimeter of the sinus exceeds 74.4 mm (head unit) or 79.3 mm (posteroanterior skull film), the sinus is larger than 99% of normal frontal sinuses and may be referred to as a *hypersinus*. This term refers to an enlarged, aerated sinus that does not expand its normal bony contours (Figs. 5-114 and 5-115).

Pneumosinus dilatans refers to an aerated sinus that is abnormally expanded (either the entire sinus or a portion of the sinus). The sinus walls are intact and of normal thickness, but remodeled and outwardly displaced. Pneumosinus dilatans may result in frontal bossing, diplopia, or a nasal mass, depending on which portion of the sinus is expanded. Accordingly it is this extension of the sinus beyond the normal bony boundaries that differentiates pneumosinus dilatans from hypersinus. If the entire sinus is not involved, the remaining sinus dimensions are usually normal (Fig. 5-116).[147, 148]

Pneumocele refers to an aerated sinus with either focal or generalized sinus cavity enlargement and thinning of the bony sinus walls. It is the latter feature that differentiates pneumosinus dilatans from a pneumocele (Figs. 5-117 to 5-121). This distinction stems from the clinical literature, where the integrity, or lack of integrity, of the sinus wall was observed as a differentiating point. Although a ''valve'' theory has been suggested as an etiology for the delayed pressure equilibration that apparently occurs in pneumoceles, no such valve has been demonstrated physiologically.

At present there is no clear understanding of the factors that either influence the development of normal sinuses or signal the normal cessation of sinus growth. Consequently the etiology of excessive sinus aeration and growth that produces hypersinus, pneumosinus dilatans, and pneumocele is unclear.[146] The pneumocele's growth can be arrested by creating a surgical window (i.e., antrostomy, ethmoidectomy, sphenoid sinusotomy) to allow rapid pressure equilibration. The cosmetic deformity that may result from either a pneumosinus dilatans or a pneumocele can be dealt with surgically if necessary by collapsing the sinus.

In the sphenoid sinus, the planum sphenoidale may be bowed cranially by an overlying meningioma simulating pneumosinus dilatans on imaging.[149] However, a meningioma will bow primarily the sphenoid roof, sparing the other sinus walls. The intracranial component of the meningioma can then be confirmed on CT or MR imaging. The sphenoid bone is usually thickened and sclerotic adjacent to the neoplasm.

Enlarged, aerated frontal sinuses may also be seen in systemic conditions such as acromegaly, Dyke-Davidoff

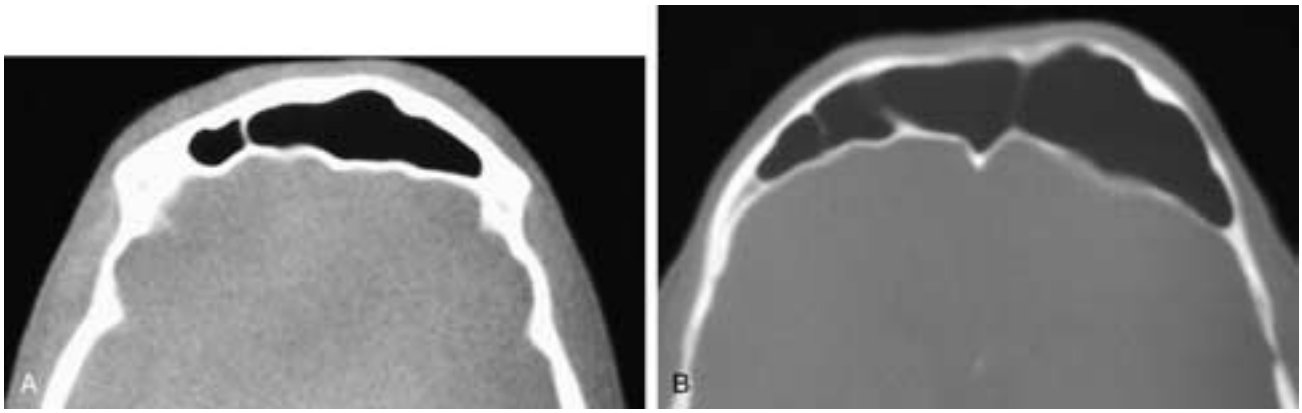

VIEW IMAGE

FIGURE 5-116 **A**, Axial CT scan shows an enlarged left frontal sinus that has not thinned the bone of either the anterior or posterior sinus walls. However, the anterior wall has been minimally bowed forward, causing a bulge in the forehead. This patient had a pneumosinus dilatans. **B**, Axial CT scan on another patient shows a very large frontal sinus with anterior bowing of the anterior sinus table. This patient also had pneumosinus dilatans.

Copyright © 2003, Mosby, Inc. All rights reserved.

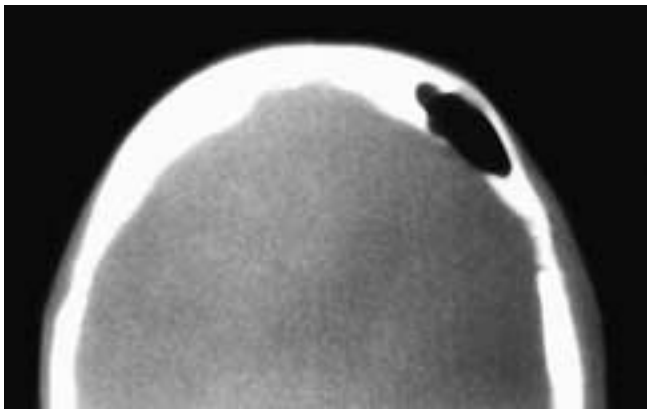

VIEW IMAGE

FIGURE 5-117 Axial CT scan shows the upper region of a large left frontal sinus with normal mucosa. A portion of the posterior sinus wall is thinned. This patient had a pneumocele.

Masson syndrome, Sturge-Weber syndrome, homocystinuria, lipodystrophy (lipoatrophic diabetes), Marfan's syndrome, myotonic dystrophy, and Turner's syndrome (Fig. 5-122).[150]

SMALL OR ABSENT AERATED SINUSES

Small or absent but aerated sinuses are associated with a variety of abnormalities. A hypoplastic small sinus may be the result of developmental failure or encroachment from expanding sinus wall bone. Hypoplastic sinuses are associated with syndromes such as Binder's syndrome (maxillonasal dyplasia or maxillovertebral syndrome), Cockayne's syndrome, Down's syndrome, otopalatodigital syndrome (type 1), Prader-Willi syndrome, Schwarz Lélek syndrome, and Treacher Collins syndrome. Hypoplastic sinuses may also be the result of developmental bone abnormalities such as

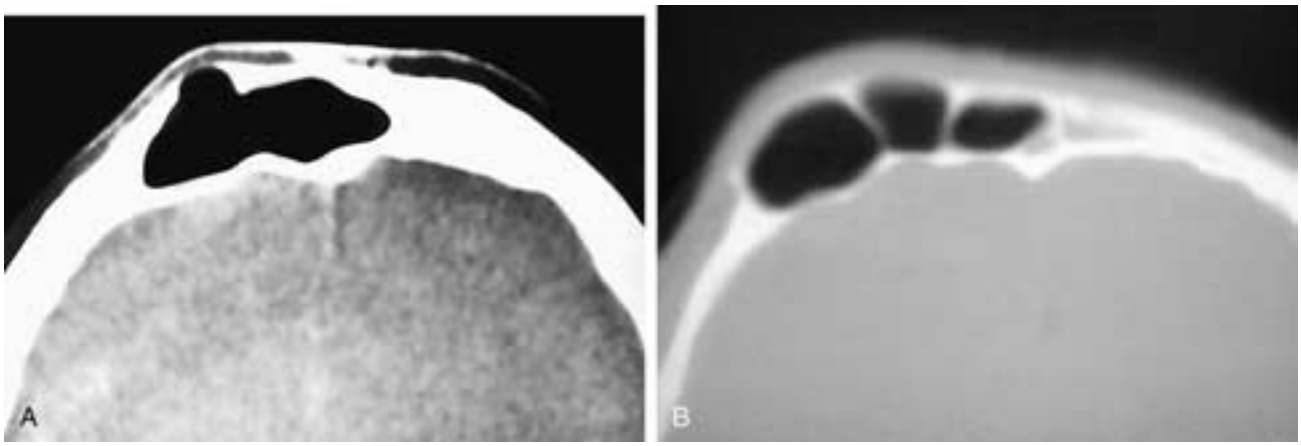

VIEW IMAGE

FIGURE 5-118 **A**, Axial CT scan shows a normal-sized right frontal sinus that has focally thinned the anterior sinus wall, causing a bulge in the forehead. This patient had a pneumocele. **B**, Axial CT scan on another patient shows a minimally expanded right frontal sinus with thinning of the anterior table. This patient also had a pneumocele.

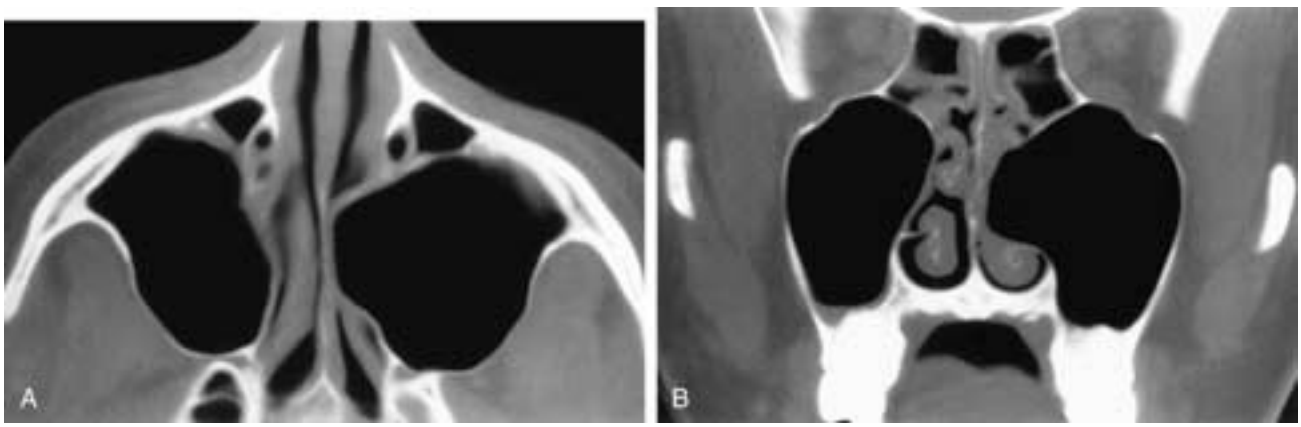

VIEW IMAGE

FIGURE 5-119 Axial (**A**) and coronal (**B**) CT scans show an aerated, expanded left maxillary sinus. The sinus walls are thinned. This patient had a pneumocele.

Copyright © 2003, Mosby, Inc. All rights reserved.

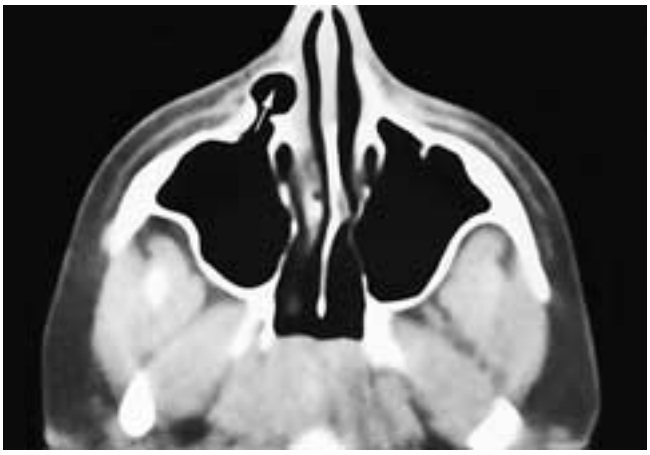

VIEW IMAGE

FIGURE 5-120 Axial CT scan shows a focal anterior enlargement of the right maxillary sinus (*arrow*) that has thinned the sinus wall and caused some cheek fullness. This patient had a pneumocele.

cleidocranial dysplasia, craniodiaphyseal dysplasia, craniometaphyseal dysplasia, fibrous dysplasia, frontometaphyseal dysplasia, frontonasal dysplasia, metaphyseal chondrodysplasia (Jansen type), osteodysplasty (Melnick needles), osteopathia striate with cranial sclerosis, osteopetrosis, pyknodysostosis, other conditions such as Paget's disease, and hematologic conditions that affect the marrow space such as sickle cell anemia and thalassemia. Hypoplastic sinuses may also be associated with endocrine diseases such as hypopituitarism and hypothyroidism.[150] Lastly, irradiation to a child's face can destroy the bony growth center and result in a hypoplastic bone. As a result of the small bone, the sinus cavity within the bone is small.

COMPLICATIONS OF INFLAMMATORY PARANASAL SINUS DISEASE AFFECTING ADJACENT AREAS

In the present antibiotic era, most acute paranasal sinus infections are successfully treated. It is only in a few cases

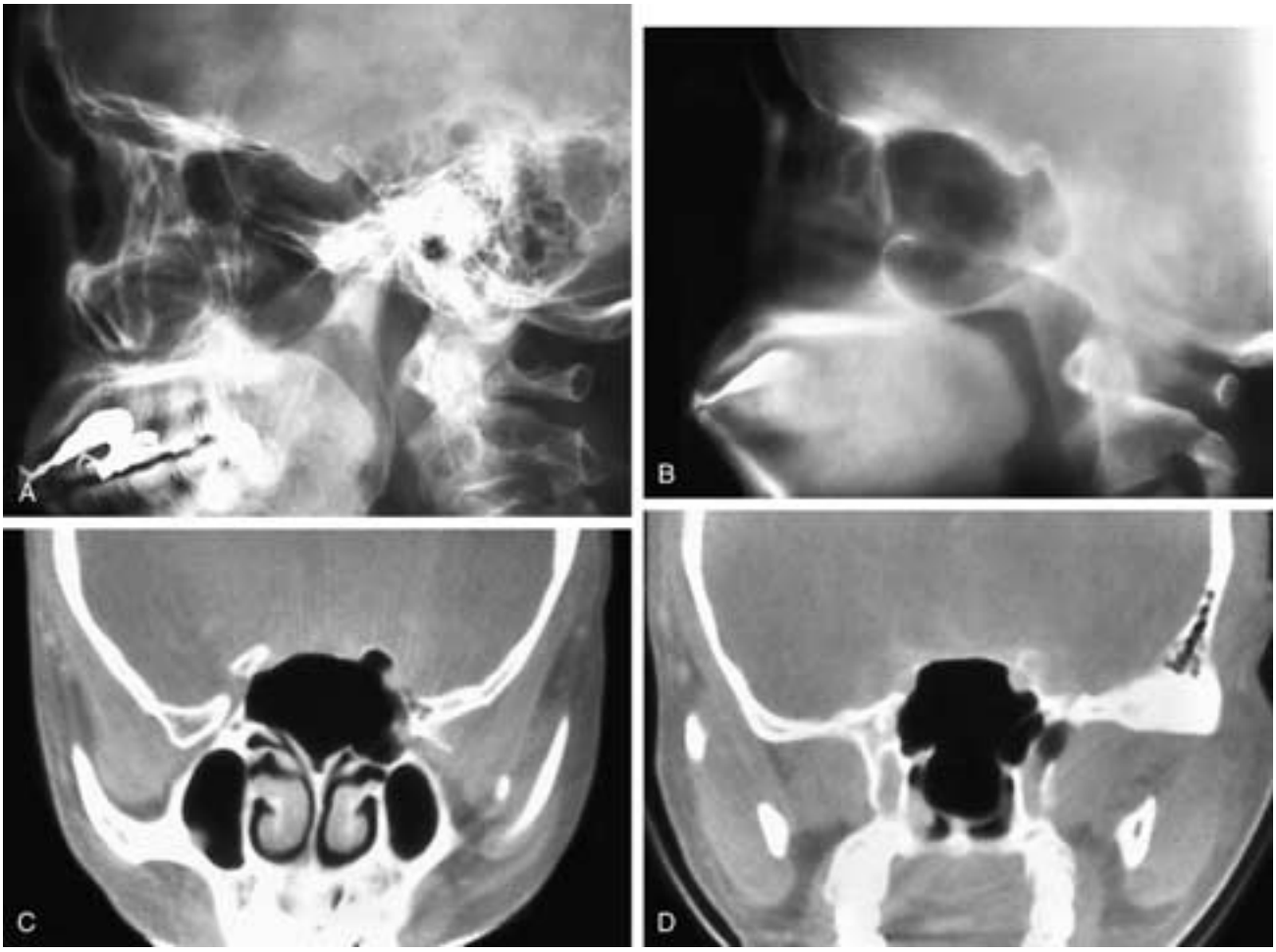

VIEW IMAGE

FIGURE 5-121 Lateral plane film **A** and multidirectional tomogram **B** show an expanded sphenoid sinus with thinned bony sinus walls. The sinus floor is displaced downward so that it rests atop the soft palate, the planum sphenoidale is elevated, and the posterior clivus is bowed backward. Coronal CT scans through the anterior **C** and the posterior **D** sphenoid sinus show the thinned bony walls and extension of the sinus into a pneumatized and expanded left anterior clinoid process. This patient had a pneumocele. When he traveled in an airplane, the sphenoid sinus expanded and compressed his left optic nerve, causing visual symptoms. He was cured by surgery.

Copyright © 2003, Mosby, Inc. All rights reserved.

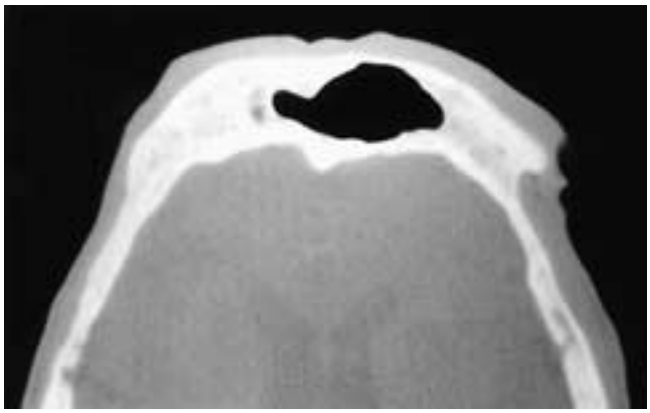

VIEW IMAGE

FIGURE 5-122 Axial CT scan shows an expanded left frontal sinus in a patient with a thick, cortical-type calvarium. The sinus mucosa is normal. This patient had acromegaly.

that surgical intervention is required to help control an acute infection. However, a delay in initiating proper treatment, organisms resistant to the chosen antibiotics, or incomplete treatment regimens all can allow an initially localized infection to spread to adjacent regions.[151, 152]

About 3% of patients with paranasal sinusitis experience some related orbital or preseptal inflammatory disease. These various complications include retention edema of the eyelids, preseptal cellulitis, preseptal abscess, orbital cellulitis, subperiosteal orbital abscess, orbital abscess, and cavernous sinus thrombosis.[151, 153] Such orbital complications are discussed in Chapter 9. In addition, 15% to 20% of the cases of retrobulbar neuritis are secondary to posterior ethmoid and sphenoid sinusitis, and in some of these cases the neuritis can apparently occur without other manifestations of orbital inflammatory disease.[76, 154]

The ethmoid sinuses are clearly most often implicated as the source of infection for orbital complications. The thin lamina papyracea and the anterior and posterior valveless ethmoidal veins allow rapid access of infection into the orbit.[155] Sinusitis of the sphenoid, maxillary, and frontal sinuses are, in descending order, less likely to cause orbital infection.

Inflammatory pseudotumor (IMF), also referred to as *inflammatory myofibroblastic tumor*, is a fibro-inflammatory space-occupying lesion or, most likely, a number of entities with overlapping histologic features, the true nature of which is only beginning to be elucidated. The lung, liver, and gastrointestinal tract (omentum and mesentery) are the most common sites for IMF. Orbital inflammatory pseudotumors are a broad category of idiopathic, nonspecific, nonneoplastic, chronic inflammatory processes without identifiable local or systemic causes. On rare occasions, mucosal thickening in the nasal fossae and paranasal sinuses is seen in patients with concurrent orbital pseudotumor. These mucosal changes may be noninfectious and consistent with pseudotumor.[156] The association of the orbital and sinonasal diseases may suggest this diagnosis; however, more commonly, orbital pseudotumor is either an isolated finding or is associated with routine, unrelated sinonasal inflammatory disease.

Maxillary sinus pseudotumor can also occur without associated orbital complications. Unlike its orbital counterpart, which rarely involves the adjacent bone, antral pseudotumor usually presents with areas of bone erosion, sclerosis, and remodeling, often mimicking the imaging appearance of an aggressive fungal infection or an antral malignancy (Figs. 5-123 and 5-124).[157] The differential diagnosis of such orbital and sinonasal disease must also include Wegener's granulomatosis.

Occasionally sinusitis can lead to intracranial complications such as meningitis, epidural abscess, subdural abscess, cerebritis, and cerebral abscess (Fig. 5-10).[158] Only 3% of intracranial abscesses are the result of sinusitis, most commonly frontal sinusitis, followed in descending order by sinusitis in the sphenoid, ethmoid, and maxillary sinuses. The propensity for frontal sinusitis to spread intracranially is due to the rich emissary network (Beçhet's plexus) connecting the posterior sinus mucosa with the meninges.[151]

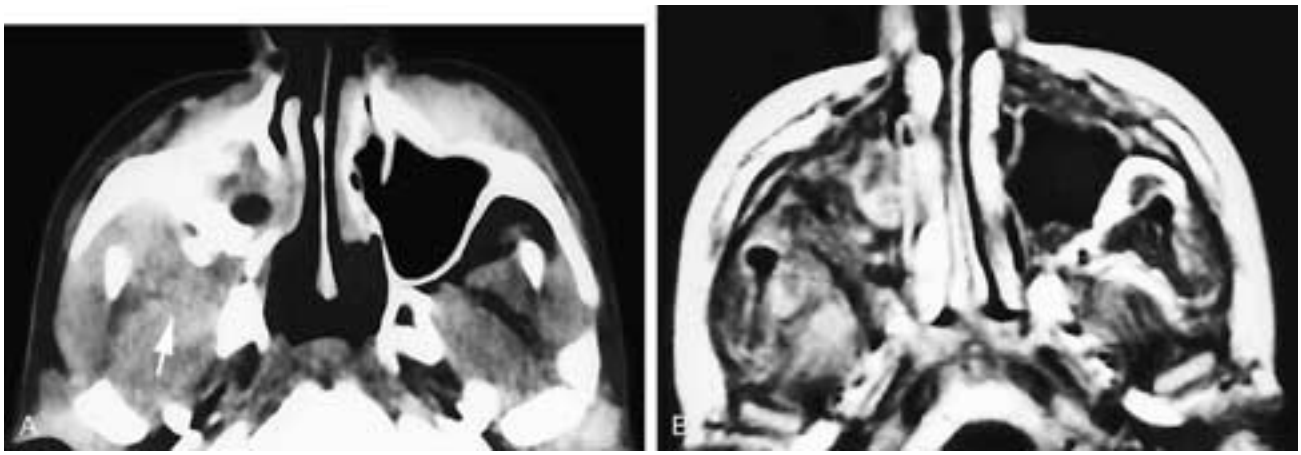

VIEW IMAGE

FIGURE 5-123 Axial CT scan **A** shows an infiltrating lesion in the right infratemporal fossa (*arrow*), thickening of the right maxillary sinus bony walls, and soft-tissue disease in this sinus. An axial T1-weighted MR image **B** shows the soft-tissue disease; however, the thickened, sclerotic bone is almost undetected. This patient had an antral pseudotumor.

Copyright © 2003, Mosby, Inc. All rights reserved.

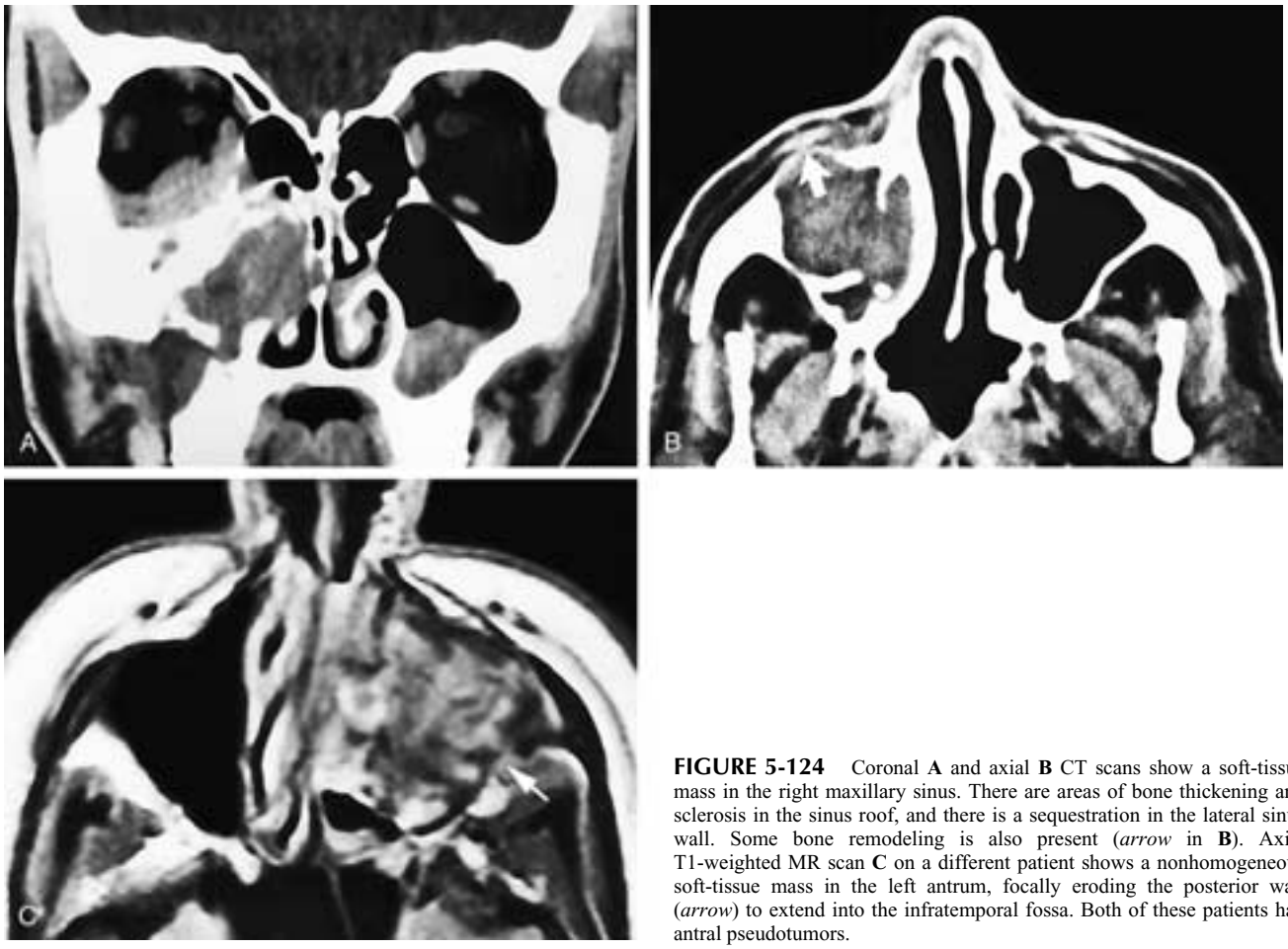

FIGURE 5-124 Coronal **A** and axial **B** CT scans show a soft-tissue mass in the right maxillary sinus. There are areas of bone thickening and sclerosis in the sinus roof, and there is a sequestration in the lateral sinus wall. Some bone remodeling is also present (*arrow* in **B**). Axial T1-weighted MR scan **C** on a different patient shows a nonhomogeneous soft-tissue mass in the left antrum, focally eroding the posterior wall (*arrow*) to extend into the infratemporal fossa. Both of these patients had antral pseudotumors.

VIEW IMAGE

Osteomyelitis can be a complication of chronic, smoldering bacterial or fungal sinusitis or sinusitis in patients with previous irradiation to the facial bones. The dominant clinical finding is persistent pain; the radiographic manifestations include focal rarefaction of bone, sequestrum formation, reactive thickening of the bone, bony sclerosis, and ultimately fragmentation of the bone.

Over the frontal sinus, a subgaleal abscess can form secondary to sinusitis. This occurs via osteothrombophlebitis and may or may not be associated with frank osteomyelitis. This subgaleal abscess is also called a Pott's puffy tumor.[159, 160]

Overall, intracranial and intraorbital complications are more likely seen with acute sinusitis, whereas osteomyelitis is more likely a complication of chronic sinusitis.

THE NEED FOR PREOPERATIVE IMAGING

Chapters 2 and 3 discussed numerous anatomic variations between and within individuals. Some of these are incidental findings. However, if the surgeon is unaware of these variations prior to surgery, operative complications may occur. In addition, if preoperative imaging is not performed, unknown pathology that may influence treatment decisions can be overlooked (Fig. 5-125). Thus it is strongly recommended that prior to any sinus surgery, an imaging study should be performed.

FOREIGN BODIES

A great variety of foreign bodies have been reported in the sinonasal cavities. Some are made of plastic materials (e.g., beads) or other nonradiopaque materials (e.g., gauze) that cannot be visualized on plain films, and others are radiodense (i.e., metallic) and can be localized easily on routine radiographic examinations (Fig. 5-126). If a foreign body is present for a sufficiently long time, it may act as a nidus and become encrusted with mineral salts. As such, these calcified masses are referred to as either rhinoliths or sinoliths, depending on whether they are located in the nasal fossa or a paranasal sinus, respectively (Figs. 5-127 to 5-129).[161, 162] If on CT a solitary calcification is seen within a sinus cavity, invariably it is the result of infection. Nearly 50% of the time that multiple discrete intrasinus calcifications are present, the cause is infection, often of a fungal etiology.[163] Tumors also account for about 50% of the cases of multiple sinonasal calcifications. The most likely lesions are olfactory neuroblastoms, inverted papilloma, or a chondroid tumor. Rarely, intrasinus ossification can occur, the implications being the same as those of calcifications.

ANOSMIA

The two most common causes of anosmia are of an idiopathic origin and secondary to sinonasal inflammatory

Copyright © 2003, Mosby, Inc. All rights reserved.

disease. Usually, imaging shows essentially normal sinuses or inflammatory mucosal thickening obliterating the nasal olfactory recess(es). Intracranial disease may also result in anosmia, for instance Kallman's syndrome, which consists of a primary eunuchoidism, secondary to hypogonatropic hypogonadism, and associated congenital anosmia, usually with absence of the olfactory bulbs and tracts. Coronal MR images best show the absence of these olfactory structures and allow differentiation of this syndrome from the other more common causes of anosmia (Fig. 5-130).[164–167]

SYNDROMES AND SINUSITIS

Sinusitis may be associated with numerous clinical syndromes, which are briefly reviewed in this section.

Kartagener's Syndrome

Kartagener's syndrome is an autosomal recessive inherited disease characterized by the clinical triad of bronchiectasis, sinusitis, and situs inversus. It is caused by an ultrastructural defect in the cilia that results in impaired mucociliary clearance. It is usually diagnosed during childhood, with only a small number of cases discovered in adults. Prompt, appropriate treatment of respiratory infections can minimize irreversible lung damage.[168]

Primary Ciliary Dyskinesia Syndrome

Primary ciliary dyskinesia, also known as immotile cilia syndrome and dyskinetic cilia syndrome, is the generic term for a heterogeneous group of inherited diseases with motility

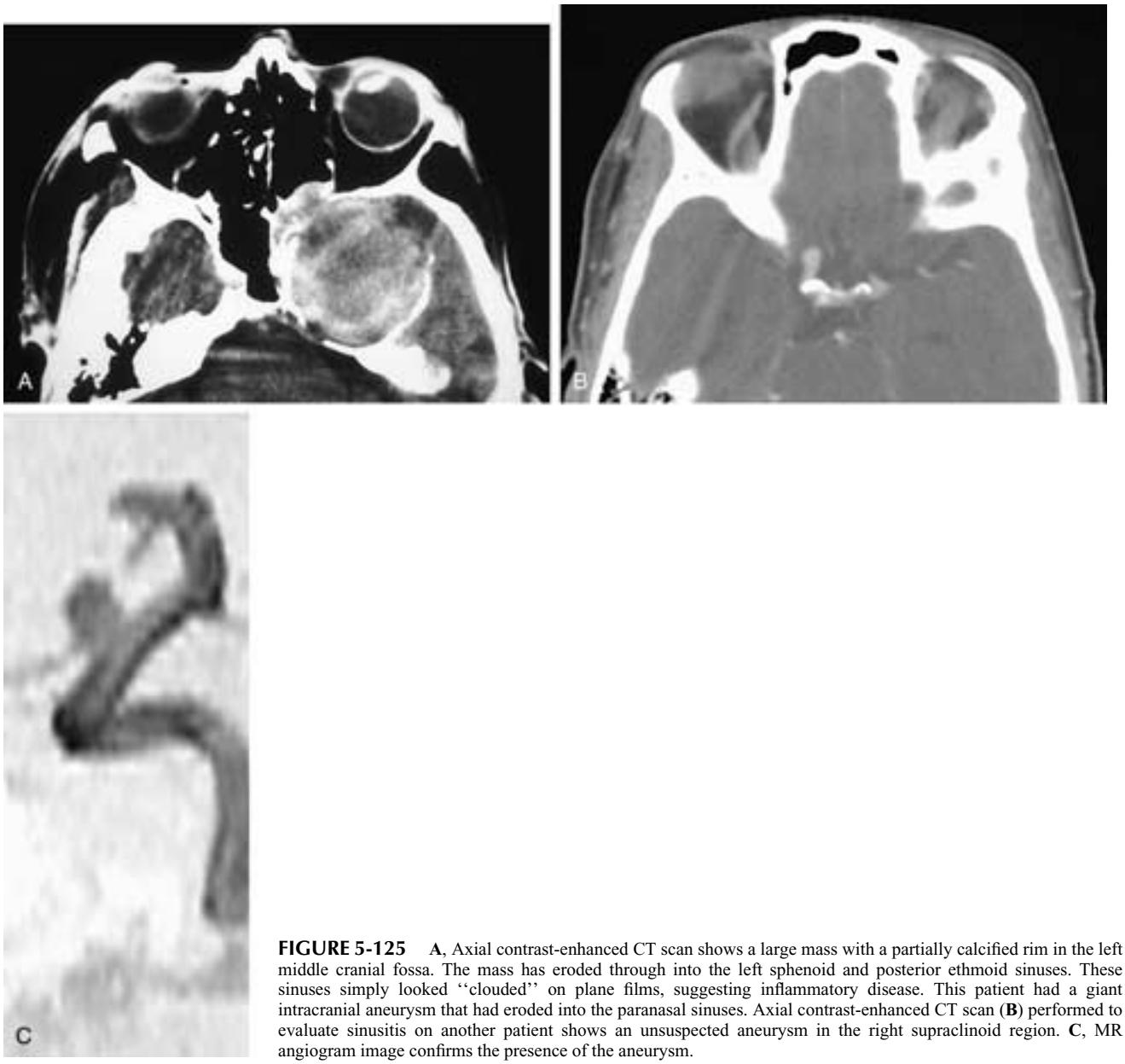

FIGURE 5-125 **A**, Axial contrast-enhanced CT scan shows a large mass with a partially calcified rim in the left middle cranial fossa. The mass has eroded through into the left sphenoid and posterior ethmoid sinuses. These sinuses simply looked ''clouded'' on plane films, suggesting inflammatory disease. This patient had a giant intracranial aneurysm that had eroded into the paranasal sinuses. Axial contrast-enhanced CT scan (**B**) performed to evaluate sinusitis on another patient shows an unsuspected aneurysm in the right supraclinoid region. **C**, MR angiogram image confirms the presence of the aneurysm.

VIEW IMAGE

Copyright © 2003, Mosby, Inc. All rights reserved.

disturbance resulting from defective ciliary ultrastructure. It is an autosomal recessive disorder with no sex predilection. Diagnostic criteria include chronic bronchitis, otitis, and childhood-onset sinusitis. Additionally, one or more of the following criteria must be present: Kartagener's syndrome, a dextrocardia situation, markedly reduced frequency in ciliary motility, or an essential ultrastructural deviation in more than 20% of the square cuts (e.g., reduced number of dynein arms). Vital microscopy and electron microscopy of the ciliated mucosa can distinguish primary and secondary ciliary dyskinesia and the rare case of primary ciliary dyskinesia without ultrastructural abnormalities. In special cases, establishing the cell tissue culture may allow for better ciliary evaluation and may be necessary for diagnosis.[169] Certain specific defects in the ciliary axoneme can be found, which are pathognomonic of the syndrome. The defects include missing dynein arms, abnormally short dynein arms, spokes with no central sheath, missing central microtubules, and displacement of one of the nine peripheral doublets. The most pronounced clinical manifestations are chronic paranasal sinusitis (52%) and chronic bronchiectasis (52%), followed by bronchopneumonia (26%), chronic bronchitis (21%), and nasal polyps (15%).[170, 171] Treatment with clarithromycin can be clinically useful in these patients.[172]

Young's Syndrome

Young's syndrome, also known as sinusitis infertility syndrome and Barry Perkins Young syndrome, is manifested by obstructive azoospermia and chronic sinopulmonary infection. Evaluation of nasal mucociliary transport reveals mucociliary stasis or decreased clearance. Ciliary ultrastructure is normal, but with decreased ciliary density, goblet cell hyperplasia, and low ciliary density. This is a chronic syndrome, which is less severe than syndromes with primary failure of mucociliary transport such as cystic fibrosis and primary ciliary dyskinesia. Young's syndrome should be considered in the differential diagnosis of patients suffering from chronic rhinosinusitis, particularly with cystic fibrosis and primary ciliary dyskinesia syndrome.[150, 173]

FIGURE 5-126 Lateral plane film shows a metallic snap foreign body in the nasal fossa (*arrow*).

VIEW IMAGE

FIGURE 5-127 Coronal CT scan shows mucosal thickening in both ethmoid and maxillary sinuses, in the upper nasal fossae, and in both concha bullosa. In addition, there is a calcified rhinolith (*arrow*) in the right nasal fossa. This patient had sinusitis and a rhinolith.

VIEW IMAGE

Sertoli-Cell-Only Syndrome

The association of repeated sinus-bronchial-pulmonary infection and male infertility is well known in the literature in association with conditions such as cystic fibrosis, immotile cilia syndrome, and Young's syndrome. It is rarely seen otherwise. However, a patient with sinusitis, bronchiectasis, and sterility due to Sertoli-cell-only syndrome has been reported. Testicular biopsy showed absence of spermatogones and other germ cells, and nonspecific alterations were found in nasal cilia axonemes in the presence of DNA branches. A sweat test was negative. Recent studies have shown an increase in the prevalence of Sertoli-cell-only syndrome.[174]

Hyperimmunoglobulinemia E Syndrome

Hyperimmunoglobulinemia E syndrome, also known as hyper IgE syndrome, Job's syndrome, Buckley's syndrome, and HIE syndrome, is an autosomal recessive disease characterized by eczematoid dermatitis, recurrent suppurative skin infections, chronic purulent sinusitis, otitis media, pneumonia, impaired neutrophil chemotaxis, and high levels of serum IgE. There are also depressed specific cell-

Copyright © 2003, Mosby, Inc. All rights reserved.

VIEW IMAGE

FIGURE 5-128 **A**, Coronal CT scan shows inflammatory mucosal thickening in the right maxillary sinus and nasal fossa. A calcified rhinolith or sinolith is also present in the infundibulum (*arrow*). This patient had sinusitis and a sinolith/rhinolith. **B**, Coronal CT scan on another patient shows an intrasinus maxillary sinus tooth. This situation can occur when there is a highly situated, unerupted maxillary molar tooth.

mediated immune responses and a deficient antibody response.[150]

Churg-Strauss Syndrome

The Churg-Strauss syndrome is a rare multisystem disease classified among the various vasculitides. It occurs primarily in adults and is rare in children. The initial symptoms are usually bronchial asthma and allergic rhinitis and sinusitis, which may progress to pulmonary, cardiac, and renal manifestations. Typical symptoms include fever, weight loss, sinusitis, myalgia and arthralgia, testicular pain, pulmonary infiltrations, asthma, pericardial effusion, peripheral neuropathy, seizure, and eosinophilia. Biopsies reveal necrotizing arteritis with eosinophilia.[175] The Churg-Strauss syndrome should be considered in the differential diagnosis if bronchial asthma and resistant sinusitis occur coincidentally. It is often difficult to establish the diagnosis, and frequently the syndrome is diagnosed only after several

VIEW IMAGE

FIGURE 5-129 Coronal (**A**) and axial (**B**) CT scans show extensive calcifications within the frontal sinuses. These were dystrophic calcifications in chronically obstructed sinuses, and they could be called sinoliths.

Copyright © 2003, Mosby, Inc. All rights reserved.

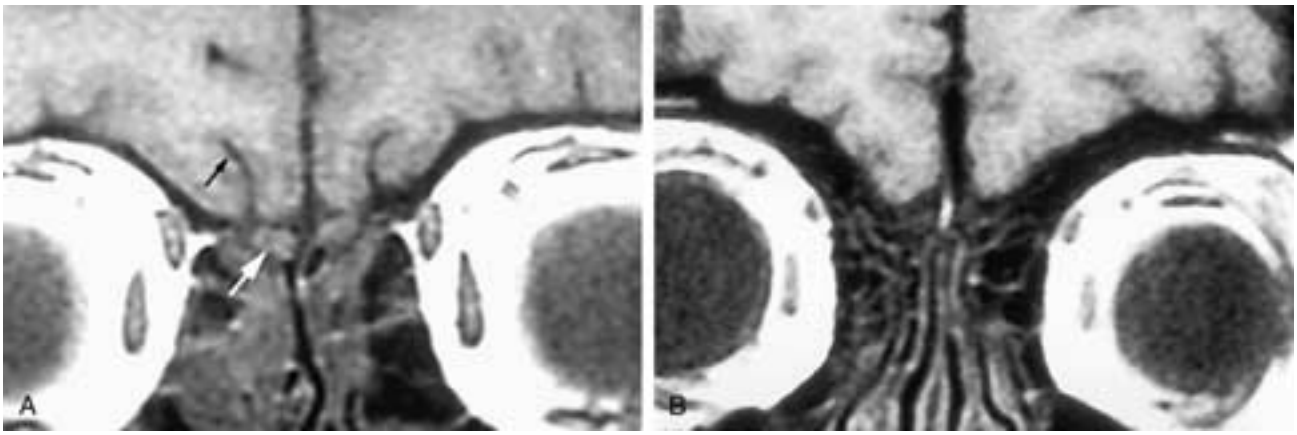

VIEW IMAGE

FIGURE 5-130 Coronal T1-weighted MR images. In **A**, a normal patient, the olfactory bulb (*white arrow*) and olfactory sulcus (*black arrow*) are well seen bilaterally. In **B**, a patient with anosmia, olfactory bulbs and sulci are absent in this patient with Kallman's syndrome. (Case courtesy of David Yousem, M.D.)

years. The therapy of choice is treatment with steroids, sometimes supplemented by cytotoxic drugs.[176] The long-term prognosis is good and does not differ from that of polyarteritis nodosa, although most patients need low doses of oral corticosteroids for persistent asthma even many years after clinical recovery from vasculitis.[177] However, the presence of severe gastrointestinal tract or myocardial involvement is significantly associated with a poor clinical outcome.

Nijmegen Paragraph Signbreakage Syndrome

Patients with nijmegen paragraph signbreakage syndrome (NBS) have microcephaly with decreased size of the frontal lobes and narrow frontal horns, agenesis of the posterior part of the corpus callosum with colpocephaly and temporal horn dilatation, callosal hypoplasia with abnormal CSF spaces and wide cerebral cortex, and pachygyria. The invariable sinusitis associated with NBS is a result of primary immunodeficiency. Like patients with ataxia telangiectasia and other breakage syndromes, those with NBS show an inherited susceptibility to malignancy and hypersensitivity to X and gamma radiation. CT is therefore contraindicated in these patients, and MR imaging should be the method of choice for diagnostic imaging.[178]

Croup

The etiology and clinical features of croup were studied in 132 children aged 3 months to 7 years. A diagnosis of laryngotracheobronchitis was made in 93.2%, and the pathogens identified included parainfluenza viruses, respiratory syncytial viruses, influenza A viruses, *Mycoplasma pneumoniae*, and adenoviruses. Bacterial tracheitis was present in 5.3% of cases, due to *S. viridans* and *Staph. aureus*. Fever of more than 3 days' duration was noted in 71% of children with bacterial tracheitis and in 28% of children with laryngotracheobronchitis. Among children with laryngotracheobronchitis, complications of pneumonia, acute otitis media, or sinusitis were more frequently observed when there was a fever for more than 3 days (40% versus 17% for those with fever of shorter duration). Thus children with fever of long duration and more severe manifestations of airway obstruction probably have bacterial croup syndrome or a complication thereof.[179]

Acquired Immune Deficiency Syndrome

Sinusitis is relatively rare among HIV-seropositive patients (3.3%) and may be clinically masked by other infections such as meningitis. Cure is difficult, relapses are frequent in spite of suitable treatment, and these are associated with a decline in immunocompetence.[180]

There is an amazing gamut of exotic agents that can cause sinusitis in seropositive patients, from algae to mushrooms. Bacterial sinusitis in patients with AIDS is caused by *P. aeruginosa* and *L. pneumophilia*, which are considered opportunistic bacterial pathogens that rarely cause sinusitis in normal hosts. Rare cases of *Microsporidium*-associated chronic sinusitis in HIV-seropositive patients have been reported, as have cases of *Septata intestinalis*–associated sinusitis. It appears that functional defects in local mucosal immunity may partially explain the acquisition of opportunistic mucosal infections in many HIV-seropositive patients.[181]

Aspirin Triad Syndrome

The aspirin triad syndrome is defined as aspirin sensitivity, asthma, and chronic sinusitis with polyposis. The sinusitis associated with this disease is often fulminant and difficult to treat. Surgical treatment may be necessary to control the sinusitis in the majority of these patients, and multiple procedures may be necessary for some patients. Controlling the sinusitis may alleviate the asthmatic symptoms and reduce the need for steroids. Long-term follow-up and aggressive medical management of chronic sinusitis will decrease the risk of orbital and other complications.[182, 183]

Copyright © 2003, Mosby, Inc. All rights reserved.

Silent Sinus Syndrome

Silent sinus syndrome was discussed earlier in this chapter. In response to chronic maxillary sinusitis, it is believed that a negative pressure develops within the obstructed sinus and, with time, the sinus walls collapse, allowing enophthalmus to occur.

Toxic Shock Syndrome

Toxic shock syndrome may occasionally be associated with sinusitis. A patient was described who presented with *S. pneumoniae* sinusitis, severe sepsis syndrome, and a desquamative rash.[184]

Cyclic Vomiting Syndrome

Although it remains a mysterious disorder since its description over a century ago, cyclic vomiting syndrome appears to be more prevalent than has been appreciated. Children are primarily affected, with vomiting that can range from an explosive, intermittent cyclic pattern to a low-grade, daily, chronic pattern. The etiologies causing a cyclic vomiting pattern include abdominal migraine, chronic sinusitis, intracranial neoplasm, anomalies of and mucosal injury to the gastrointestinal tract, urologic abnormalities, and metabolic and endocrine disorders. The cyclic pattern of vomiting is a symptom complex that can be induced by heterogeneous disorders that either cause or contribute to the vomiting. Once the cyclic vomiting pattern is identified, systematic diagnostic testing is warranted to look for these underlying disorders.[185, 186]

Yellow Nail Syndrome

Onset of the symptoms of yellow nail syndrome, also known as *yellow nails-bronchiectasis-lymphedema syndrome*, occurs in adults. It is characterized by thickened, smooth yellow- or green-colored nails with transverse ridging and excessive curvature, onycholysis, primary lymphedema due to lymphatic hypoplasia, chronic cough, pleural effusions, bronchiectasis, sinusitis, and a propensity to develop malignancies.[150, 187]

(P)FAPA Syndrome

The (P)FAPA syndrome (periodic fever, adenitis, pharyngitis, and aphthous stomatitis) was described in 1987. The etiology of this periodic syndrome remains unknown. In these children, this is an exclusionary diagnosis for a condition in which various treatments (antibiotics, antipyretics, nonsteroidal anti-inflammatory agents) have proved ineffective. The repetition of the periodic bouts of fever results in depressive disorders, absenteeism from school, and a drop in weight. In two of three patients there was chronic sinusitis, polyposis, and increased levels of immunoglobulin A. In all three patients, cimetidine was well tolerated and resulted in a disappearance of the periodic fever.[188]

Ataxia Telangiectasia Syndrome

Ataxia telangiectasia syndrome (Louis-Bar syndrome, Boder-Sedgwick syndrome, cephalo-oculocutaneous telangiectasis syndrome, sinopulmonary infectious syndrome) is either a familial (50%) or sporadically occurring autosomal recessive disease characterized by oculocutaneous telangiectasias, progressive cerebellar ataxia, and a defect in the cellular immunity of the immunoglobulin system. The last condition results in recurrent sinusitis and pulmonary infections. These patients have a predisposition to develop malignancies, endocrine disturbances, a high susceptibility to irradiation, and mental deficiency in one-third of cases. The onset of symptoms occurs in childhood.[150]

Wiskott-Aldrich Syndrome

Wiskott-Aldrich syndrome, also known as Wiskott-Aldrich-Huntley syndrome and eczema-thrombocytopenia syndrome, is as an X-linked recessive disorder that occurs in males. The onset of symptoms is in infancy or early childhood, and characteristically there is eczema, bloody diarrhea, recurrent infections (otitis, sinusitis, pneumonia), purpura, congenital thrombocytopenia, cellular and humoral immune deficiencies (without adenoidal development), anemia, and a predisposition to develop malignancies.[150]

REFERENCES

1. Potsic W, Wetmore R. Pediatric rhinology. In: Goldman J, ed. The Principles and Practice of Rhinology. New York: Wiley, 1987;801–845.
2. Carpenter J, Artenstein M. Use of diagnostic microbiologic facilities in the diagnosis of head and neck infections. Otolaryngol Clin North Am 1976;9:611–629.
3. Fried M, Relly J, Strome M. Pseudomonas rhinosinusitis. Laryngoscope 1984;94:192–196.
4. Evans F, Sydnor J, Moore W, et al. Sinusitis of the maxillary antrum. N Engl J Med 1976;293:735–739.
5. Frederick J, Braude A. Anaerobic infection of the paranasal sinuses. N Engl J Med 1974;290:135–137.
6. Van Alyea O. Nasal Sinuses: Anatomic and Clinical Considerations. 2nd ed. Baltimore: Williams & Wilkins, 1951.
7. Aysun S, Yetuk M. Clinical experience on headache in children: analysis of 92 cases. J Child Neurol 1998;13:202–210.
8. Berger JR, Stein N, Pall L. Headache and human immunodeficiency virus infection: a case control study, Eur Neurol 1996;36:229–233.
9. Remulla HD, Rubin PA, Shore JW, Cunningham MJ. Pseudodacryocystitis arising from anterior ethmoiditis. Ophthalmol Plast Reconstr Surg 1995;11:165–168.
10. Abrahams JJ, Glassberg RM. Dental disease: a frequently unrecognized cause of maxillary sinus abnormalities? AJR 1996;166:1219–1223.
11. Raboso E, Llavero MT, Rosell A, Martinez-Vidal A. Craniofacial necrotizing fasciitis secondary to sinusitis. J Laryngol Otol 1998;112:371–372.
12. Perez Barreto M, Sahai S, Ameriso S, Ahmadi J, Rice D, Fisher M. Sinusitis and carotid artery stroke. Ann Otol Rhinol Laryngol 2000;109:227–230.
13. Moorman CM, Anslow P, Elston JS. Is sphenoid sinus opacity significant in patients with optic neuritis? Eye 1999;13:76–82.
14. Deutsch JH, Hudgins PA, Siegel JL, et al. The paranasal sinuses of patients with acute graft-versus-host disease. AJNR 1995;16:1287–1291.

Copyright © 2003, Mosby, Inc. All rights reserved.

15. Oberholzer K, Kauczor HU, Heussel CP, Derigs G, Thelen M. [Clinical relevance of CT of paranasal sinuses prior to bone marrow transplantation]. Rofo Fortschr Geb Rontgenstr Neuen Bildgeb Verfahr 1997;166:493–497.
16. Odita J, Akamaguna A, Ogisi F, et al. Pneumatization of the maxillary sinus in normal and asymptomatic children. Pediatr Radiol 1986;16:365–367.
17. Zimmerman R, Bilaniuk L, Hackney D, Goldberg H, Grossman R. Paranasal sinus hemorrhage: evaluation with MR imaging. Radiology 1987;162:499–503.
18. Som P, Shugar J, Troy K, et al. The use of MR and CT in the management of a patient with intrasinus hemorrhage. Arch Otolaryngol 1988;114:200–202.
19. Fagan P, McKenzie B, Edmonds C. Sinus barotrauma in divers. Ann Otol Rhinol Laryngol 1976;85:61–64.
20. Remmier D, Boles R. Intracranial complications of frontal sinusitis. Laryngoscope 1980;90:1814–1824.
21. Tamakawa Y, Hanafee W. Cerebrospinal fluid rhinorrhea: significance of an air-fluid level in the sphenoid sinus. Radiology 1980;135:101–103.
22. Rhyoo C, Sanders SP, Leopold DA, Proud D. Sinus mucosal IL-8 gene expression in chronic rhinosinusitis. J Allergy Clin Immunol 1999;103:395–400.
23. Crater SE, Peters EJ, Phillips CD, Platts-Mills TA. Prospective analysis of CT of the sinuses in acute asthma. AJR 1999;173:127–131.
24. Stahl R. Allergic disorders of the nose and paranasal sinuses. Otolaryngol Clin North Am 1974;7:703–718.
25. Nino-Murcia M, Rao V, Mikaelian D, et al. Acute sinusitis mimicking antrochoanal polyp. AJNR 1986;7:513–516.
26. Baroody FM, Suh SH, Naclerio RM. Total IgE serum levels correlate with sinus mucosal thickness on computerized tomography scans. J Allergy Clin Immunol 1997;100:563–568.
27. Ballenger J, ed. Diseases of the Nose and Throat. Philadelphia: Lea & Febiger, 1977;105–114, 155–167.
28. Smith M. Dysfunction of carbohydrate metabolism as an element in the set of factors resulting in the polysaccharide nose and nasal polyps (the polysaccharide nose). Laryngoscope 1971;81:636–644.
29. Schramm VJ, Effron M. Nasal polyps in children. Laryngoscope 1980;90:1488–1495.
30. Jaffe B, Strome M, Khaw K, et al. Nasal polypectomy and sinus surgery for cystic fibrosis: a 10 year review. Otolaryngol Clin North Am 1977;10:81–90.
31. Moloney J. Nasal polyps, nasal polypectomy, asthma and aspirin sensitivity: their association in 445 cases of nasal polyps. J Laryngol Otol 1977;91:837–846.
32. Torjussen W. Rhinoscopical findings in nickel workers, with special emphasis on the influence of nickel exposure and smoking habits. Acta Otolaryngol (Stockh) 1979;88:279–288.
33. Fairbanks D, Raphael G. Nonallergic rhinitis and infection. In: Cummings C, Fredrickson J, Harker L, Krause C, Schuller D, eds. Otolaryngology Head and Neck Surgery. 2nd ed. Vol. 1. St. Louis: Mosby Year Book, 1993;775–785.
34. Myerowitz R, Guggenheimer J, Barnes L. Infectious diseases of the head and neck. In: Barnes L, ed. Surgical Pathology of the Head and Neck. Vol 2. New York: Marcel Dekker, 1987;1771–1822.
35. Waxman J, Spector J, Sale S, et al. Allergic aspergillus sinusitis: concepts in diagnosis and treatment of a new clinical entity. Laryngoscope 1987;97:261–266.
36. Swift AC, Denning DW. Skull base osteitis following fungal sinusitis. J Laryngol Otol 1998;112:92–97.
37. Moss RB, Beaudet LM, Wenig BM, et al. *Microsporidium*-associated sinusitis. Ear Nose Throat J 1997;76:95–101.
38. Daghistani K, Jamal T, Zaher S, et al. Allergic aspergillus sinusitis with proptosis. J Laryngol Otol 1992;106:799–803.
39. Milroy C, Blanshard J, Lucas S, et al. Aspergillosis of the nose and paranasal sinuses. J Clin Pathol 1989;42:123–127.
40. Kameswaran M, Al-Waddei A, Khurana P, et al. Rhinocerebral aspergillosis. J Laryngol Otol 1992;106:981–985.
41. Blitzer A, Lawson W. Fungal infection of the nose and paranasal sinuses. Part I. Otolaryngol Clin North Am 1993;26:1007–1035.
42. McLean FM, Ginsberg LE, Stanton CA. Perineural spread of rhinocerebral mucormycosis. AJNR 1996;17:114–116.
43. Blatt S, Lucey D, DeHoff D, et al. Rhinocerebral zygomycosis in a patient with AIDS. J Infect Dis 1991;164:215–216.
44. Tyson J, Gittelman P, Jacobs J, et al. Recurrent mucormycosis of the paranasal sinuses in an immunologically competant host. Otolaryngol Head Neck Surg 1992;107:115–119.
45. Pafrey N. Improved diagnosis and prognosis of mucormycosis: a clinicopathologic study of 33 cases. Medicine 1986;65:113–123.
46. Mader J, Ream R, Heath P. *Petriellidium boydii (Allescheria boydii*) sphenoidal sinusitis. JAMA 1978;239:2368–2369.
47. Travis L, Roberts G, Wilson W. Clinical significance of *Pseudallescheria boydii*: a review of 10 years experience. Mayo Clin Proc 1985;60:531–537.
48. Chapnick J, Bach M. Bacterial and fungal infections of the maxillary sinus. Otolaryngol Clin North Am 1976;9:43–54.
49. Wheat L, Conolly-Stringfield P, Baker R, et al. Disseminated histoplasmosis in AIDS: clinical findings, diagnosis and treatment, and review of the literature. Med 1990;69:361–374.
50. Oda D, McDougal L, Fitsche T, et al. Oral histoplasmosis as a presenting disease in AIDS. Oral Surg Oral Med Oral Pathol 1990;70:631–636.
51. Browning D, Schwartz D, Jurado R. Cryptococcosis of the larynx in a patient with AIDS: an unusual cause of fungal laryngitis. South Med J 1992;85:762–764.
52. Lynch D, Naftolin L. Oral *Cryptococcus neoformans* infection in AIDS. Oral Surg Oral Med Oral Pathol 1987;64:449–453.
53. Boyle J, Coulthard S, Mandel R. Laryngeal involvement in disseminated coccidioidomycosis. Arch Otolaryngol Head Neck Surg 1991;117:433–438.
54. Fish D, Ampel N, Galgiani J, et al. Coccidioidomycosis during HIV infection. A review of 77 patients. Medicine 1990;69:384–390.
55. Fascenelli F. Maxillary sinus abnormalities: radiographic evidence in an asymptomatic population. Arch Otol Laryngol 1969; 90:190–193.
56. Zizmor J, Noyek A. Inflammatory diseases of the paranasal sinuses. Otolaryngol Clin North Am 1973;6:459–485.
57. Som P, Sacher M, Lawson W, et al. CT appearance distinguishing benign nasal polyps from malignancies. J Comput Assist Tomogr 1987;11:129–133.
58. Nakagawa T, Yamane H, Shigeta T, Takashima T, Nakai Y. Interaction between fibronectin and eosinophils in the growth of nasal polyps. Laryngoscope 1999;109:557–561.
59. Som P, Cohen B, Sacher M. The angiomatous polyp and the angiofibroma: two different lesions. Radiology 1982;144:329–334.
60. Batsakis J. The pathology of head and neck tumors: nasal cavity and paranasal sinuses. Part 5. Head Neck Surg 1980;2:410–419.
61. Barnes L, Verbin R, Gnepp D. Diseases of the nose, paranasal sinuses and nasopharynx. In: Barnes L, ed. Surgical Pathology of the Head and Neck. Vol 1. New York: Marcel Dekker, 1985: 403–451.
62. Smith C, Echevarria R, McLelland C. Pseudosarcomatous changes in antrochoanal polyps. Arch Otolaryngol 1974;99:228–230.
63. Weissman J, Tabor E, Curtin H. Sphenochoanal polyps: evaluation with CT and MR imaging. Radiology 1991;178:145–148.
64. Towbin R, Bundar J. The paranasal sinuses in childhood. Radiographics 1982;2:253–279.
65. Glasier C, Ascher D, Williams K. Incidental paranasal sinus abnormalities on CT of children: clinical correlation. AJNR 1986;7: 861–864.
66. Glasier C, Mallory GJ, Steele R. Significance of opacification of maxillary and ethmoid sinuses in infants. J Pediatr 1989;114:45–50.
67. Kronemer KA, McAlister WH. Sinusitis and its imaging in the pediatric population. Pediatr Radiol 1997;27:837–846.
68. Baroody FM, Hughes CA, McDowell P, Hruban R, Zinreich SJ, Naclerio RM. Eosinophilia in chronic childhood sinusitis. Arch Otolaryngol Head Neck Surg 1995;121:1396–1402.
69. Shugar J. Embryology of the nose and paranasal sinuses and resultant deformities. In: Goldman J, ed. The Principles and Practice of Rhinology. New York: Wiley, 1987;113–131.
70. Johnson J. Infections. In: Cummings C, Fredrickson J, Harker L, Krause C, Schuller D, eds. Otolaryngology Head and Neck Surgery. Vol 1. St Louis: CV Mosby, 1986;887–900.
71. Chong W, Hall-Craggs M. Prevalence of paranasal sinus disease in HIV infection and AIDS on cranial MR imaging. Clin Radiol 1993:47:166–169.
72. O'Donnell J, Sorbello A, Condoluci I, et al. Sinusitis due to *Pseudomonas aeruginosa* in patients with HIV infection. Clin Infect Dis 1993;16:404–406.

Copyright © 2003, Mosby, Inc. All rights reserved.

73. Schlanger G, Lutwick LI, Kurzman M, Hoch B, Chandler FW. Sinusitis caused by *Legionella pneumophila* in a patient with the acquired immune deficiency syndrome. Am J Med 1984;77: 957–960.
74. Som P, Shugar J. The CT classification of ethmoid mucoceles. J. Comput Assist Tomogr 1980;4:199–203.
75. De Juan E, Green W, Iliff N. Allergic periorbital mycopyocele in children. Am J Ophthalmol 1983;96:299–303.
76. Finn D, Hudson N, Baylin G. Unilateral polyposis and mucoceles in children. Laryngoscope 1981;91:1444–1449.
77. Zizmor J, Noyek A. Cysts, benign tumors and malignant tumors of the paranasal sinuses. Otolaryngol Clin North Am 1973;6:487–508.
78. Lim CC, Dillon WP, McDermott MW. Mucocele involving the anterior clinoid process: MR and CT findings. AJNR 1999;20:287–290.
79. Hazan A, Le Roy A, Chevalier E, et al. [Atelectasis of the maxillary sinus. Analysis of progression stages. Apropos of 4 cases]. Ann Otolaryngol Chir Cervicofac 1998;115:367–372.
80. Gillman GS, Schaitkin BM, May M. Asymptomatic enophthalmos: the silent sinus syndrome. Am J Rhinol 1999;13:459–462.
81. Rak K, Newell JI, Yakes W, et al. Paranasal sinus on MR images of the brain: significance of mucosal thickening. AJR 1991;156:381–384.
82. Moser F, Panush D, Rubin J, et al. Incidental paranasal sinus abnormalities on MRI of the brain. Clin Radiol 1991;43:252–254.
83. Som P, Dillon W, Fullerton G, Zimmerman R, Rajagopalan B, Marom Z. Chronically obstructed sinonasal secretions: observations on T1 and T2 shortening. Radiology 1989;172:515–520.
84. Dillon W, Som P, Fullerton G. Hypointense MR signal in chronically inspissated sinonasal secretions. Radiology 1990;174:73–78.
85. Som P, Dillon W, Curtin H, et al. Hypointense paranasal sinus foci: differential diagnosis with MR imaging and relation to CT findings. Radiology 1990;176:777–781.
86. Bassoiouny A, Newlands W, Ali H, et al. Maxillary sinus hypoplasia and superior orbital fissure asymmetry. Laryngoscope 1982;92:441–448.
87. Modic M, Weinstein M, Berlin A, et al. Maxillary sinus hypoplasia visualized with computed tomography. Radiology 1980;135:383–385.
88. Kennedy D, Zinreich S, Kumar A, et al. Physiologic mucosal changes within the nose and ethmoid sinus: imaging of the nasal cycle by MRI. Laryngoscope 1988;98:928–933.
89. Brock J, Schabel S, Curry N. CT diagnosis of contrast reaction. J Comput Tomogr 1981;5:63–64.
90. Som P, Dillon W, Sze G, MW L, Biller H, Lawson W. Benign and malignant sinonasal lesions with intracranial extension: differentiation with MR imaging. Radiology 1989;172:763–766.
91. Som P, Curtin H. Chronic inflammatory sinonasal diseases including fungal infections: the role of imaging. Radiol Clin North Am 1993;31:33–44.
92. Jacobs M, Som P. The ethmoidal ''polypoid mucocele.'' J Comput Assist Tomogr 1982;6:721–724.
93. Naul L, Hise J, Ruff T. CT of inspissated mucus in chronic sinusitis. AJNR 1987;8:574–575.
94. Zinreich S, Kennedy D, Malat J, et al. Fungal sinusitis: diagnosis with CT and MR imaging. Radiology 1988;169:439–444.
95. Lloyd D, Bartram C, Stanley P. Ethmoid mucoceles. Br J Radiol 1974;47:646–651.
96. Ritter R. The Paranasal Sinuses: Anatomy and Surgical Technique. 2nd ed. St. Louis: CV Mosby, 1978.
97. Canalis R, Zajtchuck J, Jenkins H. Ethmoid mucoceles. Arch Otolaryngol 1978;104:286–291.
98. Zizmor J, Ganz AR. Mucoceles of paranasal sinuses. NY State J Med 1972 Jul 1; 72(13):1710–1715.
99. Som P, Sacher M, Lanzieri C, et al. The hidden antral compartment. Radiology 1984;152:463–464.
100. Close L, O'Connor W. Sphenoethmoidal mucoceles with intracranial extension. Otolaryngol Head Neck Surg 1983;91:350–357.
101. Osborn A, Johnson L, Roberts T. Sphenoidal mucoceles with intracranial extension. J Comput Assist Tomogr 1979;3:335–338.
102. Chui M, Briant T, Gray T, et al. Computed tomography of sphenoid sinus mucocele. J Otolaryngol 1983;12:263–269.
103. Price H, Batnitzky S, Karlin C, et al. Multiple paranasal sinus mucoceles. J Comput Assist Tomogr 1981;5:122–125.
104. Perugini S, Pasquini U, Menichelli F, et al. Mucoceles in the paranasal sinus involving the orbit: CT signs in 43 cases. Neuroradiology 1982;23:133–139.
105. Demaerel P, Brown P, Kendall B, et al. Case report: allergic aspergillosis of the sphenoid sinus: pitfall on MRI. Br J Radiol 1993;66:260–263.
106. Chang T, Teng M, Wang S, et al. Aspergillosis of the paranasal sinuses. Neuroradiology 1992;34:520–523.
107. Romett J, Newman R. Aspergillosis of the nose and paranasal sinuses. Laryngoscope 1982;92:764–766.
108. Centeno R, Bentson J, Mancuso A. CT scanning in rhinocerebral mucormycosis and aspergillosis. Radiology 1981;140:383–389.
109. Shugar J, Som P, Robbins A, et al. Maxillary sinusitis as a cause of cheek swelling. Arch Otolaryngol 1982;108:507–508.
110. Kopp W, Fotter R, Steiner H, et al. Aspergillosis of the Paranasal Sinuses. Radiology 1985;156:715–716.
111. Stammberger J, Jakse A, Beaufort F. Aspergillosis of the paranasal sinuses: x-ray diagnosis, histopathology and clinical aspects. Ann Otol Rhinol Laryngol 1984;93:251–256.
112. Richtsmeier WJ, Johns ME. Actinomycosis of the Head and Neck. CRC Crit Rev Clin Lab Sci 1979 Nov;11(2):175–202.
113. Bhatia P, Obafunwa J. Rare infections of the nose and paranasal sinuses. Trop Geograph Med 1990;42:289–293.
114. Kingdom T, Tami T. Actinomycosis of the nasal septum in a patient infected with HIV. Otolaryngol Head Neck Surg 1994;71:675–677.
115. MacGregor R. A year's experience with tuberculosis in a private urban teaching hospital in the post-sanatorium era. Am J Med 1975;58:221–228.
116. Bath A, O'Flynn P, Gibbin K. Nasopharyngeal tuberculosis. J Laryngol Otol 1992;106:1079–1080.
117. Control CFD. Annual summary. Morbid-Mort Weekly Rep 1981;19:3.
118. McNulty J, Fassett R. Syphilis: an otolaryngologic perspective. Laryngoscope 1981;91:889–905.
119. Olansky S. Syphilis Rediscovered. Chicago: Year Book Medical Publishers, 1967. Disease-a-month; 1–30.
120. Larsen S. Syphilis. Clin Lab Med 1989;9:545–557.
121. Andraca R, Edson R, Kern E. Rhinoscleroma: a growing concern in the US? Mayo Clin Proc 1993;68:1151–1157.
122. Becker T, Shum T, Waller T, et al. Radiological aspects of rhinoscleroma. Radiology 1981;141:433–438.
123. Lazow S, Seldin R, Soloman M. South American blastomycosis of the maxilla: report of a case. J Oral Maxillofac Surg 1990;48:68–71.
124. Sposto M, Scully C, Almeida O, et al. Paracoccidioidomycosis. A study of 36 South American patients. Oral Surg Oral Med Oral Pathol 1993;75:461–465.
125. Beeson P, McDermott W. Textbook of Medicine. 14th ed. Philadelphia: WB Saunders, 1975:164–539.
126. Lasser A, Smith H. Rhinosporidiosis. Arch Otolaryngol 1974; 102:308.
127. Thianprait M, Thagerngpol K. Rhinosporidiosis. Curr Top Med Mycol 1989;3:64–85.
128. Harrison T. Harrison's Principles of Internal Medicine. 9th ed. New York: McGraw-Hill, 1987.
129. Fauci A, Wolff S. Wegener's granulomatosis and related diseases. Dis Month 1977;23:1.
130. Harrison D. Midline destructive granuloma: fact or fiction? Laryngoscope 1987;97:1049–1053.
131. Gordon W, Cohn A, Greenberg S, et al. Nasal sarcoidosis. Arch Otolaryngol 1976;102:11–14.
132. Fredricks DN, Relman DA. Infectious agents and the etiology of chronic idiopathic diseases. Curr Clin Top Infect Dis 1998;18: 180–200.
133. Johns CJ, Michele TM. The clinical management of sarcoidosis. A 50-year experience at the Johns Hopkins Hospital. Medicine (Balt) 1999;78:65–111.
134. Mailland A, Geopfert H. Nasal and paranasal sarcoidosis. Arch Otolaryngol 1978;104:197–201.
135. Paling M, Roberts R, Fauci A. Paranasal sinus obliteration in Wegener's granulomatosis. Radiology 1982;144:539–543.
136. Le Hir P, Marsot-Dupuch K, Bigel P, et al. Rhinoscleroma with orbital extension: CT and MRI. Neuroradiology 1996;38:175–178.
137. Zizmor J, Noyek A. Radiology of the nose and paranasal sinuses. In: Paparella M, Shumrick D, eds. Otolaryngology. Vol 1. Philadelphia: WB Saunders, 1973;1043–1095.

Copyright © 2003, Mosby, Inc. All rights reserved.

138. Taveras J, Wood E. Diagnostic Neuroradiology. Baltimore: Williams & Wilkins, 1964;141–142.
139. Wax M, Briant T. Epidermoid cysts of the cranial bones. Head Neck 1992;14:293–296.
140. Dodd G, Jing B. Radiology of the nose, paranasal sinuses and nasopharynx. Baltimore: Williams & Wilkins, 1977:59–65.
141. Verbin R, Barnes L. Cysts and cyst-like lesions of the oral cavity, jaws and neck. In: Barnes L, ed. Surgical Pathology of the Head and Neck. Vol 2. New York: Marcel Dekker, 1985;1278–1281.
142. Kunt T, Ozturkcan S, Egilmez R. Cholesterol granuloma of the maxillary sinus: six cases from the same region. J Laryngol Otol 1998;112:65–68.
143. Koenig H, Lenz M, Sauter R. Temporal bone region: high resolution MR imaging using surface coils. Radiology 1986;159:191–194.
144. Latack J, Kartush J, Kemink J, et al. Epidermoidomas of the cerebellopontine angle and temporal bone: CT and MR aspects. Radiology 1985;157:361–366.
145. Urken M, Som P, Lawson W, Edelstein D, McAvay G, Biller H. The abnormally large frontal sinus. Part I: a practical method for its determination based upon an analysis of 100 normal patients. Laryngoscope 1987;97:602–605.
146. Urken M, Som P, Lawson W, et al. The abnormally large frontal sinuses II: nomenclature, pathology and symptoms. Laryngoscope 1987;97:606–611.
147. Dross P, Lally J, Bonier B. *Pneumosinus dilatans* and arachnoid cyst: a unique association. AJNR 1992;13:209–211.
148. Benedikt R, Brown D, Roth M, et al. Spontaneous drainage of an ethmoid mucocele: a possible cause of pneumosinus dilatans. AJNR 1991;12:729–731.
149. Lombardi G. Radiology in Neuro-Ophthalmology. Baltimore: Williams & Wilkins, 1967.
150. Taybi H. Metabolic disorders. In: Taybi H, Lachman R, eds. Radiology of Syndromes, Metabolic Disorders, and Skeletal Dysplasias. 4th ed. St. Louis: CV Mosby, 1996:635–637.
151. Kutnick S, Kerth J. Acute sinusitis and otitis: their complications and surgical treatment. Otolaryngol Clin North Am 1976;9:689–701.
152. Carter B, Bankoff M, Fisk J. Computed tomographic detection of sinusitis responsible for intracranial and extracranial infections. Radiology 1983;147:739–742.
153. Zimmerman R, Bilaniuk L. CT of orbital infection and its cerebral complications. Am J Roentgenol 1980;134:45–50.
154. Rothstein J, Maisel R, Berlinger N, et al. Relationship of optic neuritis to disease of the paranasal sinus. Laryngoscope 1984;94: 1501–1508.
155. Bilaniuk L, Zimmerman R. Computer assisted tomography: sinus lesions with orbital involvement. Head Neck Surg 1980;2:293–301.
156. Eshaghian J, Anderson R. Sinus involvement in inflammatory orbital pseudotumor. Arch Ophthalmol 1981;99:627–630.
157. Som P, Brandwein M, Maldjiian C. Inflammatory pseudotumor of the maxillary sinus: CT and MR ftndings in six cases. Am J Roentgenol 1994;163:689–692.
158. Kaufman D, Litman N, Miller M. Sinusitis: induced subdural empyema. Neurology 1983;33:123–132.
159. Williams H. Infections and granulomas of the nasal airways and paranasal sinuses. In: Shumrick D, ed. Otolaryngology. Vol 3. Head and Neck. Philadelphia: WB Saunders, 1973;27–32.
160. Babu RP, Todor R, Kasoff SS. Pott's puffy tumor: the forgotten entity. Case report. J Neurosurg 1996;84:110–112.
161. Price H, Batnitzky S, Karlin L, et al. Giant nasal rhinolith. AJNR 1981;2:271–273.
162. RSNA. Case of the day: case IV, rhinolith. Radiology 1983;146: 251–252.
163. Som P, Lidov M. The significance of sinonasal radiodensities: ossification, calcification, or residual bone? AJNR 1994;15:917–922.
164. Yousem D, Turner W, Snyder P, et al. Kallmann's syndrome: MR evaluation of olfactory system. AJNR 1993;14:839–843.
165. Knon J, Ragland R, Brown R, et al. Kallmann syndrome: MR findings. AJNR 1993;14:845–851.
166. Li C, Yousem D, Doty R, et al. Neuroimaging in patients with olfactory dysfunction. AJR 1994;162:411–418.
167. Yousem D, Geckle R, Bilker W, McKeown D, Doty R. MR evaluation of patients with congenital hyposmia or anosmia. AJR 1996;166:439–443.
168. Gomez de Terreros Caro FJ, Gomez-Stern Aguilar C, Alvarez-Sala Walther R, Prados Sanchez C, Garcia Rio F, Villamor Leon J. [Kartagener's syndrome. Diagnosis in a 75 year-old woman]. Arch Bronconeumol 1999;35:242–244.
169. Dombi VH, Walt H. [Primary ciliary dyskinesia, immotile cilia syndrome, and Kartagener syndrome: diagnostic criteria]. Schweiz Med Wochenschr 1996;126:421–433.
170. Min YG, Shin JS, Choi SH, Chi JG, Yoon CJ. Primary ciliary dyskinesia: ultrastructural defects and clinical features. Rhinology 1995;33:189–193.
171. Armengot M, Carda C, Basterra J. [Incomplete ciliary axonema: another cause of ciliary dysmotility syndrome?]. Acta Otorrinolaringol Esp 1998;49:57–59.
172. Nishi K, Mizuguchi M, Tachibana H, et al. [Effect of clarithromycin on symptoms and mucociliary transport in patients with sinobronchial syndrome]. Nihon Kyobu Shikkan Gakkai Zasshi 1995;33: 1392–1400.
173. Armengot M, Juan G, Carda C, Montalt J, Basterra J. Young's syndrome: a further cause of chronic rhinosinusitis. Rhinology 1996;34:35–37.
174. Carrion Valero F, Ferrer Gomez C, Pascual Izuel JM. [Sino-bronchial infections and male sterility. Presentation of a new variant]. Arch Bronconeumol 1998;34:405–408.
175. Louthrenoo W, Norasetthada A, Khunamornpong S, Sreshthaputra A, Sukitawut W. Childhood Churg-Strauss syndrome. J Rheumatol 1999;26:1387–1393.
176. Trittel C, Moller J, Euler HH, Werner JA. [Churg-Strauss syndrome. A differential diagnosis in chronic polypoid sinusitis]. Laryngorhinootologie 1995;74:577–580.
177. Guillevin L, Cohen P, Gayraud M, Lhote F, Jarrousse B, Casassus P. Churg-Strauss syndrome. Clinical study and long-term follow-up of 96 patients. Medicine (Balt) 1999;78:26–37.
178. Bekiesinska-Figatowska M, Chrzanowska KH, Sikorska J, et al. Cranial MRI in the Nijmegen breakage syndrome. Neuroradiology 2000;42:43–47.
179. Chiu TF, Huang LM, Chen JG, Lee CY, Lee PI. Group syndrome in children: five-year experience. Chung Hua Min Kuo Hsiao Erh Ko I Hsueh Hui Tsa Chih 1999;40:258–261.
180. Martinez-Subias J, Dominguez LJ. Urpegui A, Sancho E, Royo J, Valles H. [Sinus manifestations of the acquired immunodeficiency syndrome]. Rev Neurol 1997;25:1620–1623.
181. Moss RB, Scott TA, Goldrich M, et al. Nasal mucosal cells in human immunodeficiency virus type 1-seropositive patients with sinusitis. J Clin Lab Anal 1996;10:418–422.
182. McFadden EA, Woodson BT, Massaro BM, Toohill RJ. Orbital complications of sinusitis in the aspirin triad syndrome. Laryngoscope 1996;106:1103–1107.
183. McFadden EA, Woodson BT, Fink JN, Toohill RJ. Surgical treatment of aspirin triad sinusitis. Am J Rhinol 1997;11:263–270.
184. Friedstrom SR, Awad J. Toxic-shock-like-syndrome due to *Streptococcus pneumoniae* sinusitis. Scand J Infect Dis 1999;31:509–510.
185. Li BU. Cyclic vomiting: the pattern and syndrome paradigm. J Pediatr Gastroenterol Nutr 1995;21:S6–S10.
186. Li BUK, Murray RD, Heitlinger LA, Robbins JL, Hayes JR. Heterogeneity of diagnoses presenting as cyclic vomiting. Pediatrics 1998;102:583–587.
187. Luyten C, Andre J, Walraevens C, De Doncker P. Yellow nail syndrome and onychomycosis. Experience with itraconazole pulse therapy combined with vitamin E. Dermatology 1996;192:406–408.
188. Pillet P, Ansoborlo S, Carrere A, Perel Y, Guillard JM. [(P)FAPA syndrome: value of cimetidine]. Arch Pediatr 2000;7:54–57.

Copyright © 2003, Mosby, Inc. All rights reserved.

6

Tumors and Tumor-like Conditions

Peter M. Som and Margaret S. Brandwein

GENERAL CONSIDERATIONS
BENIGN AND MALIGNANT EPITHELIAL TUMORS
- Papilloma
- Squamous Cell Carcinoma
- Adenocarcinoma (Intestinal-Type Adenocarcinoma)
- Salivary Tumors
  - Adenoid Cystic Carcinoma
  - Mucoepidermoid Carcinoma
  - Pleomorphic Adenoma
  - Epithelial-Myoepithelial Carcinoma

BENIGN AND MALIGNANT NEUROECTODERMAL, NEURONAL, NERVE SHEATH, AND CENTRAL NERVOUS SYSTEM TUMORS
- Paraganglioma
- Olfactory Neuroblastoma
- Sinonasal Neuroendocrine Carcinoma and Sinonasal Undifferentiated Carcinoma
- Malignant Melanoma
- Melanotic Neuroectodermal Tumor of Infancy
- Primitive Neuroectodermal Tumor and Ewing's Sarcoma
- Peripheral Nerve Sheath Tumors
  - Schwannoma
  - Neurofibroma
  - Traumatic Neuroma
  - Malignant Peripheral Nerve Sheath Tumor
  - Granular Cell Tumor
- Meningioma and Craniopharyngioma
- Chordoma
- Choristoma
  - Nasal Glioma
  - Ectopic Pituitary

LYMPHOPROLIFERATIVE AND HEMATOPOIETIC DISORDERS
- Lymphoma
- Granulocytic Sarcoma
- Multiple Myeloma
- Extramedullary Plasmacytoma
- Langerhans' Cell Granulomatosis
- Rosai-Dorfman Disease
- Thalassemia

BENIGN AND MALIGNANT PRIMARY SOFT-TISSUE TUMORS
- Vascular
  - Angiofibroma
  - Angiomatous Polyp
  - Hemangioma
  - Angiosarcoma
  - Hemangiopericytoma
  - Kaposi's Sarcoma
- Muscle
  - Leiomyoma and Leiomyosarcoma
  - Rhabdomyoma
  - Rhabdomyosarcoma
- Lipoblastic
  - Lipoma and Lipoma-Like Lesions
  - Liposarcoma
- Fibroblastic
  - Fibrosarcoma (Including Desmoid Tumor)
  - Malignant Fibrous Histiocytoma
  - Benign Fibrous Histiocytoma
  - Inflammatory Myofibroblastic Tumor
  - Solitary Fibrous Tumor
  - Fibromyxoma and Myxoma

BENIGN AND MALIGNANT OSSEOUS LESIONS AND TUMORS (INCLUDING FIBROOSSEOUS LESIONS)
- Benign Tumors
  - Osteoma and Exostosis
  - Osteochondroma
  - Chondroma
  - Osteoid Osteoma and Osteoblastoma

Copyright © 2003, Mosby, Inc. All rights reserved.

Ossifying Fibroma (Cemento-Ossifying Fibroma)
Tumor-Like Conditions and Giant Cell–Rich Lesions
Fibrous Dysplasia
Cemento-Ossifying Dysplasia
Cherubism
True Giant Cell Tumor
Giant Cell (Reparative) Granuloma
Aneurysmal Bone Cyst
Paget's Disease
Sarcomas
Osteogenic Sarcoma and Chondrosarcoma
Mesenchymal Chondrosarcoma
ODONTOGENIC LESIONS AND TUMORS
Jaw Cysts
Follicular Cyst
Periodontal Cyst
Odontogenic Keratocyst
Calcifying Odontogenic Cyst
Fissural Cyst
Developmental Cyst
Odontogenic Tumors
Ameloblastoma (Including Unicystic Ameloblastoma)
Cementoblastoma
Odontoma
Calcifying Epithelial Odontogenic Tumor
HAMARTOMAS, TERATOMAS, AND TERATOCARCINOMAS
METASTATIC DISEASE TO THE SINONASAL CAVITIES

GENERAL CONSIDERATIONS

The sinonasal tract plays host to an enormous variety of neoplasms derived from a multitude of tissue types. Sinonasal neoplasias can be broadly classified as either epithelial or mesenchymal. Epithelial neoplasia may arise from the Schneiderian lining mucosa (e.g., papillomas, squamous carcinomas, intestinal-type adenocarcinoma), minor salivary tissue (which includes the whole array of benign and malignant minor salivary tumors), neuroendocrine tissue (e.g., sinonasal neuroendocrine carcinoma), or olfactory mucosa (olfactory neuroblastoma). Each of the mesenchymal tissues of the sinonasal tract can give rise to benign and malignant neoplastic counterparts. Thus one can expect an array of tumors with benign, malignant, or unknown biologic potential, recapitulating their tissue of derivation (bone, cartilage, fibroblasts, smooth and skeletal muscle, vessels, etc.).

By comparison to the ubiquitous nature of sinonasal inflammatory disease, neoplasms affecting the paranasal sinuses and nasal cavities are rare. Carcinomas are by far the most common neoplasm, yet they comprise only 0.2% to 0.8% of all malignancies and about 3% of all malignant tumors that arise in the head and neck.[1] In the SEER (surveillance, epidemiology, and end results) data of the National Institutes of Health, which followed more than 50,000 upper aerodigestive tract malignancies from 1973 to 1987, only 3.6% of these tumors occurred in the sinonasal tract.[2]

Despite their statistically low incidence, sinonasal malignancies are a clinically significant group of neoplasms with an overall grave outlook. They usually present at an advanced tumor stage, and often surgeons are reluctant to be appropriately aggressive for fear of creating either an undesirable cosmetic deformity, prolonged morbidity, or gross dysfunction. Furthermore the complex, compact anatomy of the region often limits the extent of surgical resection and contributes to serious radiotherapeutic complications.[3, 4] Although surgery remains the primary treatment modality, combined chemotherapy and radiation therapy now play a significant role for these patients, especially for those who present with advanced disease.

Sinonasal tumors can remain clinically silent until they reach an advanced stage. In addition, coexisting infection can overshadow the clinical presentation, further delaying diagnosis. Patients with antral and ethmoidal cancers have an average delay of 6 months between the onset of symptoms and the establishment of a final diagnosis.[3] Pain secondary to malignancy usually signifies an advanced tumor stage and possible perineural tumor invasion, especially with adenoid cystic carcinoma. Tooth or gum pain may indicate an antral tumor, whereas a headache may signify skull base invasion and intracranial extension. Inexplicably, pain is not often associated with the bone destruction that accompanies these tumors. Common complaints of patients with sinonasal tumors include diplopia, decreasing vision, proptosis, nasal stuffiness, anosmia, nasal-quality voice, epistaxis, and a facial mass. Maxillary sinus tumors cause trismus, epiphora, orbital pain, proptosis, or trigeminal or sphenopalatine ganglion–related deficits secondary to dorsal tumor spread. Ethmoid tumors usually cause nasal stuffiness, orbital complaints, and headache from intracranial tumor spread. Frontal sinus tumors may deform the face, spread intracranially, or extend into the orbits, while sphenoid sinus tumors can extend into the nasopharynx, intracranially (especially to the cavernous sinuses), and into the orbit.

With improved imaging technology, superior tumor mapping and staging are now available, and this accurate information permits more realistic treatment planning with regard to cure versus palliation.[5] Surgical techniques have also improved, and better tumor extirpation can be achieved with less morbidity and facial deformity. In addition, enhanced tumor mapping equates with more accurate

Copyright © 2003, Mosby, Inc. All rights reserved.

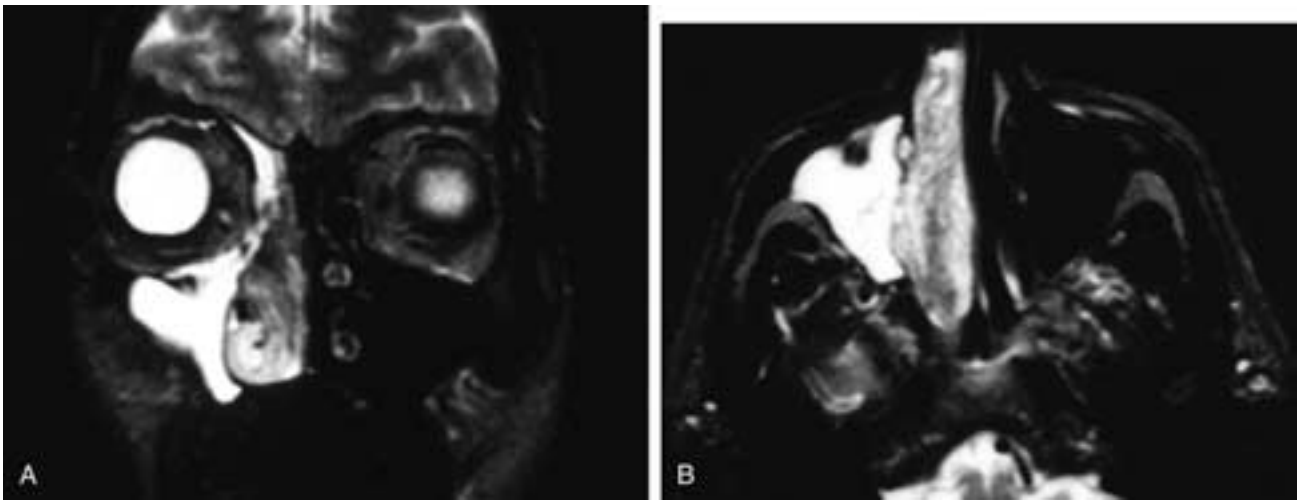

VIEW IMAGE

FIGURE 6-1 Coronal (**A**) and axial (**B**) T2-weighted MR images show a polypoid, nonhomogeneous right nasal fossa mass that has intermediate signal intensity. The right maxillary sinus, the right lateral ethmoid sinuses, and the lower nasal fossa have high signal intensity material that represents obstructed secretions. The tumor does not extend directly to the orbital margin. Such a high degree of tumor mapping was not possible on CT, where the secretions and tumor had similar attenuations. This patient had an inverted papilloma and obstructed secretions.

placement of radiation fields. To provide the tumor mapping necessary for decisions regarding resectability and curability, the radiologist must be aware of the critical areas of tumor extension that will alter a surgical or irradiation treatment plan. These areas include tumor extension into the floor of the anterior and middle cranial fossae, the pterygopalatine fossae, the orbits, and the palate.[6] The proximity of the paranasal sinuses and their structural communication via the nasal fossae allow tumor spread between sinuses. Thus the radiologist must describe in detail the sinus and the precise areas within each sinus that are apparently affected by neoplasm. Although primarily a communication tool with clinicians, gray scale and color 3D reconstructions allow the tumor to be visualized within the framework of the facial bones and skull base. Newer treatment-planning computers are now able to utilize the raw data of these images to help prepare treatment plans.[7]

Nodal metastasis from sinonasal carcinomas is one of the gravest prognostic signs. The retropharyngeal nodes are the primary lymph nodes draining the paranasal sinuses and nasal vault. However, these nodes or their lymphatic channels are frequently obliterated by repeated childhood infections. Accordingly, for adults, sinonasal malignancies often metastasize to the secondary nodes in levels I and II (see Chapter 36). Such nodal metastases occur in approximately 15% of patients and are associated with tumor extension to the skin, alveolar buccal sulcus, or pterygoid musculature, often as demonstrated on CT and MR studies.[4] Thus the radiologist should be thorough and precise in reporting tumor extension in these sites. The presence of cervical nodal disease is predictive of distant metastases, which have been found in 34% of autopsied patients.[6]

One of the major imaging problems of precise tumor mapping is distinguishing tumor from adjacent inflammatory disease. Basing this distinction on routine CT attenuation values is fraught with inaccuracies. Contrast-enhanced CT can improve the results; however, MR imaging is superior in making this distinction. Inflammatory secretions and tissues have high water content and thus have high T2-weighted signal intensities (see Chapter 5). By comparison, virtually all sinonasal tumors are highly cellular, with relatively little intracellular and intercellular water, and the majority of these tumors have an intermediate signal intensity on T2-weighted images (Figs. 6-1 and 6-2).[8, 9] Thus, the mainstay of the MR imaging distinction between tumor and adjacent inflammatory tissues is the T2-weighted MR sequence. It is rare for sinonasal tumors to have inherently high T2-weighted signal intensities, which may be seen with benign or low-grade minor salivary gland tumors, schwannomas, rare hemangiomatous lesions, and polypoid tumors such as inverted papillomas. Therefore these tumors may not be as amenable to accurate T2-weighted tumor mapping.

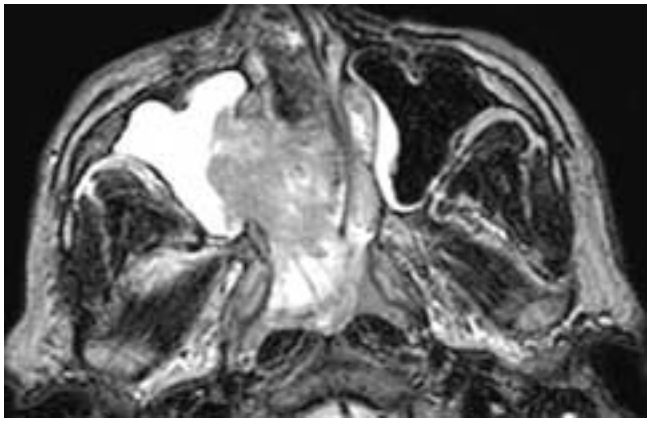

FIGURE 6-2 Axial T2-weighted MR image shows a large right-sided nasal fossa mass that has destroyed most of the medial wall of the right maxillary sinus and extends back into the nasopharynx. The mass has areas of high signal intensity that represent sites of necrosis. The right maxillary sinus is obstructed, and inflammatory mucosal thickening is seen in the left antrum. This patient had a squamous cell carcinoma and obstructed secretions.

VIEW IMAGE

Copyright © 2003, Mosby, Inc. All rights reserved.

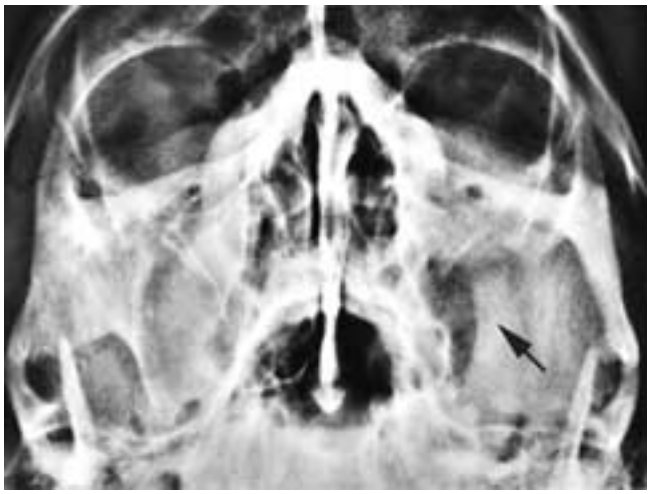

VIEW IMAGE

FIGURE 6-3 Waters view shows that the lateral wall of the left maxillary sinus is totally destroyed (*arrow*). The right lateral antral wall is intact. This is an example of aggressive bone destruction. This patient had a squamous cell carcinoma of the left antrum.

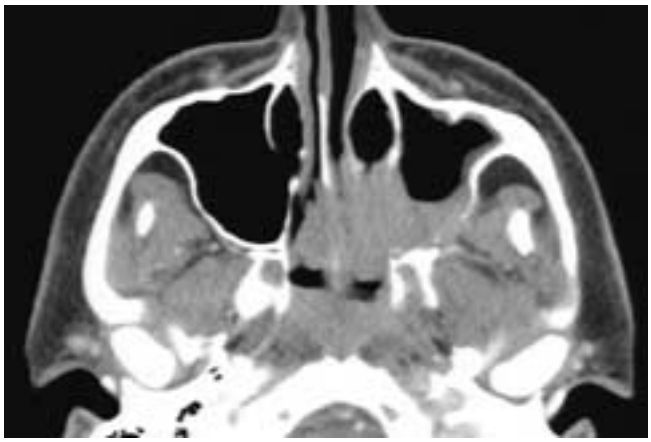

VIEW IMAGE

FIGURE 6-4 Axial CT scan shows a destructive mass in the left posterior nasal fossa that has destroyed portions of the medial and posterior left maxillary sinus walls. There is also some destruction of the left pterygoid process, and tumor extends into the left retromaxillary fat. This patient had a squamous cell carcinoma.

Small tumors may often elude clinical and radiologic detection. Unfortunately, it is at this early stage that tumors may be most curable.[4] Small sinonasal tumors often have MR characteristics indistinguishable from those of adjacent inflammation. In addition, radiologists are reluctant to diagnose a tumor in the absence of adjacent bone involvement. Thus, on imaging, many small tumors are often misdiagnosed as inflammatory polypoid disease. Bony changes are seen in larger tumors and allow for a more definitive imaging diagnosis of neoplasm. The pattern of bone involvement (either aggressive bone destruction or bone remodeling) can aid in generating a radiographic differential diagnosis.[10–12]

Squamous cell carcinoma is associated with aggressive bone erosion, usually with only small bony fragments remaining (Figs. 6-3 to 6-6). Metastatic carcinomas, as well as some sarcomas and lymphomas, can also cause aggressive bone destruction, but they are less often encountered. By comparison, most sinonasal mucoceles, polyps, inverted papillomas, and rarer lesions such as minor salivary gland tumors, schwannomas, extramedullary plasmacytomas, most lymphomas, olfactory neuroblastomas, most sarcomas, and hemangiopericytomas tend to primarily remodel rather than aggressively destroy bone (Fig. 6-7).

For most tumors, one of these patterns of bone involvement appears to be dominant. Although the bony pattern is not sufficiently specific to predict histology, the radiologist can still use the type of bone involvement to occasionally question some histologic diagnoses. Thus, if a patient has a unilateral polypoid nasal mass and a microscopic diagnosis of a ''large cell lymphoma,'' but the radiographic pattern of bone destruction is predominantly aggressive, the radiologist might question this diagnosis and recommend ancillary diagnostic tests such as immunohistochemistry. This might lead to a diagnosis such as ''sinonasal undifferentiated carcinoma'' (SNUC), which is in the pathologic differential diagnosis of large cell lymphoma. In fact, immunohistochemistry is routinely performed for all sinonasal ''round cell'' tumors to distinguish between SNUC, sinonasal neuroendocrine tumor (SNEC), olfactory neuroblastoma, malignant lymphoma, embryonal rhabdo-

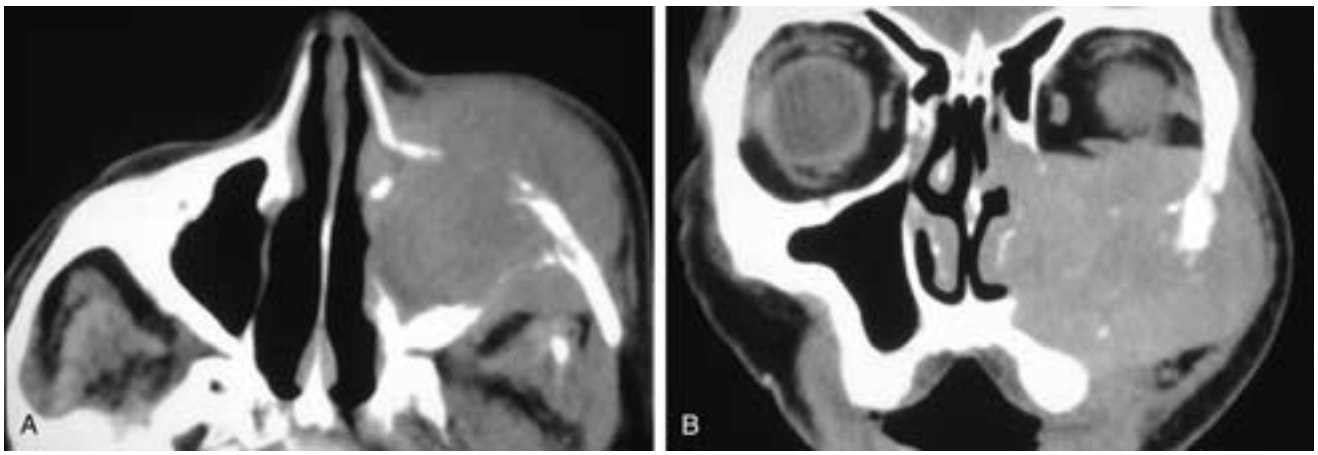

VIEW IMAGE

FIGURE 6-5 Axial (**A**) and coronal (**B**) CT scans show a large left maxillary sinus mass that has destroyed most of the sinus walls and the body of the zygoma. The tumor extends into the left lower ethmoid complex, the left orbit, and the left retromaxillary fat in the infratemporal fossa. This patient had a squamous cell carcinoma.

Copyright © 2003, Mosby, Inc. All rights reserved.

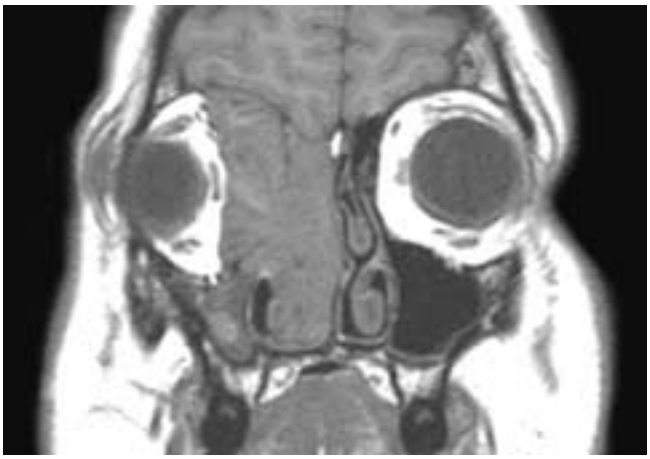

VIEW IMAGE

FIGURE 6-6 Coronal T1-weighted MR image shows a large intermediate signal intensity mass that fills the right ethmoid complex and nasal fossa. The tumor extends into the right orbit, and there is erosion of part of the roof and medial floor of the right orbit, the fovea ethmoidalis, and the right cribriform plate, as evidenced by the loss of the bone signal void in these areas. The right maxillary sinus is obstructed by the tumor. This patient had a squamous cell carcinoma.

myosarcoma, extramedullary plasmacytoma, olfactory neuroblastoma, and amelanotic melanoma. Immunohistochemistry may be performed on unstained slides from the original biopsy (Table 6-1).

Tumor biology and prognosis are multifaceted issues. Host immune surveillance may limit tumor growth for a variable period of time, sometimes for many years. Successive activation of tumoral oncogenes or additional loss of tumor suppressor genes correlates with tumor progression or the acquisition of aggressive features (see Chapter 44), but the lethal propensity of certain tumors is, unfortunately, poorly understood. In addition to tumor biology, the critical anatomic location of the neoplasm has prognostic significance. Thus a lesion confined to the antrum generally has a better prognosis than one located in the pterygopalatine fossa or central skull base. However, certain tumors are highly aggressive regardless of location and despite a noninfiltrating imaging appearance. For example, a nasal fossa melanoma usually has a benign polypoid imaging appearance, yet the 5-year survival prognosis is abysmal (Fig. 6-8). Thus, the invasive, or lack of invasive, margins of a tumor cannot always be used to predict biologic aggressiveness. Clearly, the pathologic diagnosis is more important in predicting prognosis than the imaging appearance of a tumor. Yet, the radiographic tumor mapping may also predict survival if critical anatomic areas are involved that are not readily amenable to treatment.

Sclerotic bone is usually not seen with neoplastic processes and is more commonly seen with bacterial inflammatory disease or more aggressive infection (e.g., fungal disease) or granulomatous disease. Frank sinonasal osteomyelitis usually appears as foci of bone rarefaction and sclerosis, often with sequestra. Radiation osteitis also can produce a similar bone reaction. Tumor invasion rarely causes osteoblastic bony sclerosis, but it can occur with

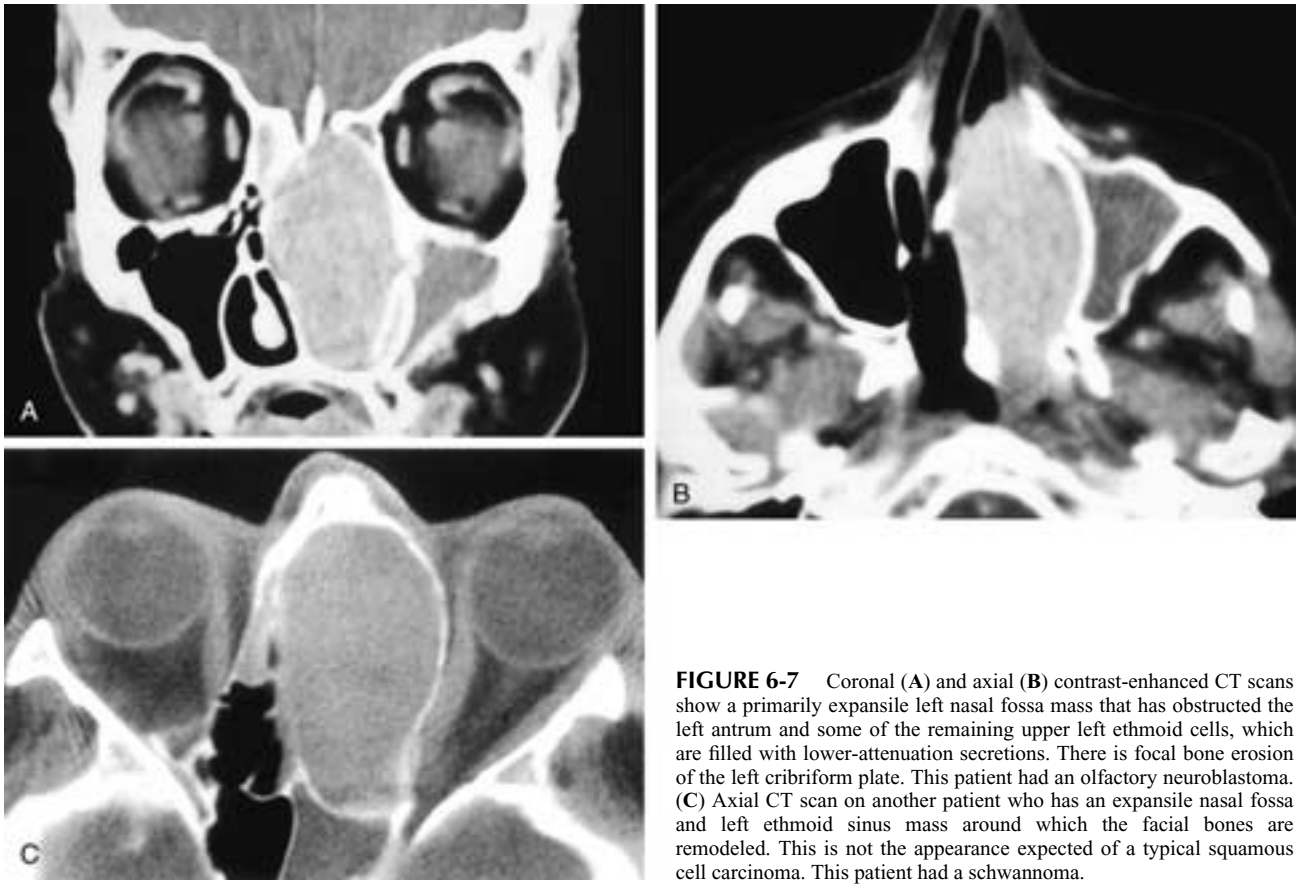

VIEW IMAGE

FIGURE 6-7 Coronal (**A**) and axial (**B**) contrast-enhanced CT scans show a primarily expansile left nasal fossa mass that has obstructed the left antrum and some of the remaining upper left ethmoid cells, which are filled with lower-attenuation secretions. There is focal bone erosion of the left cribriform plate. This patient had an olfactory neuroblastoma. (**C**) Axial CT scan on another patient who has an expansile nasal fossa and left ethmoid sinus mass around which the facial bones are remodeled. This is not the appearance expected of a typical squamous cell carcinoma. This patient had a schwannoma.

Copyright © 2003, Mosby, Inc. All rights reserved.

Table 6–1
IMMUNOHISTOCHEMICAL ANALYSIS OF ENT MALIGNANCIES

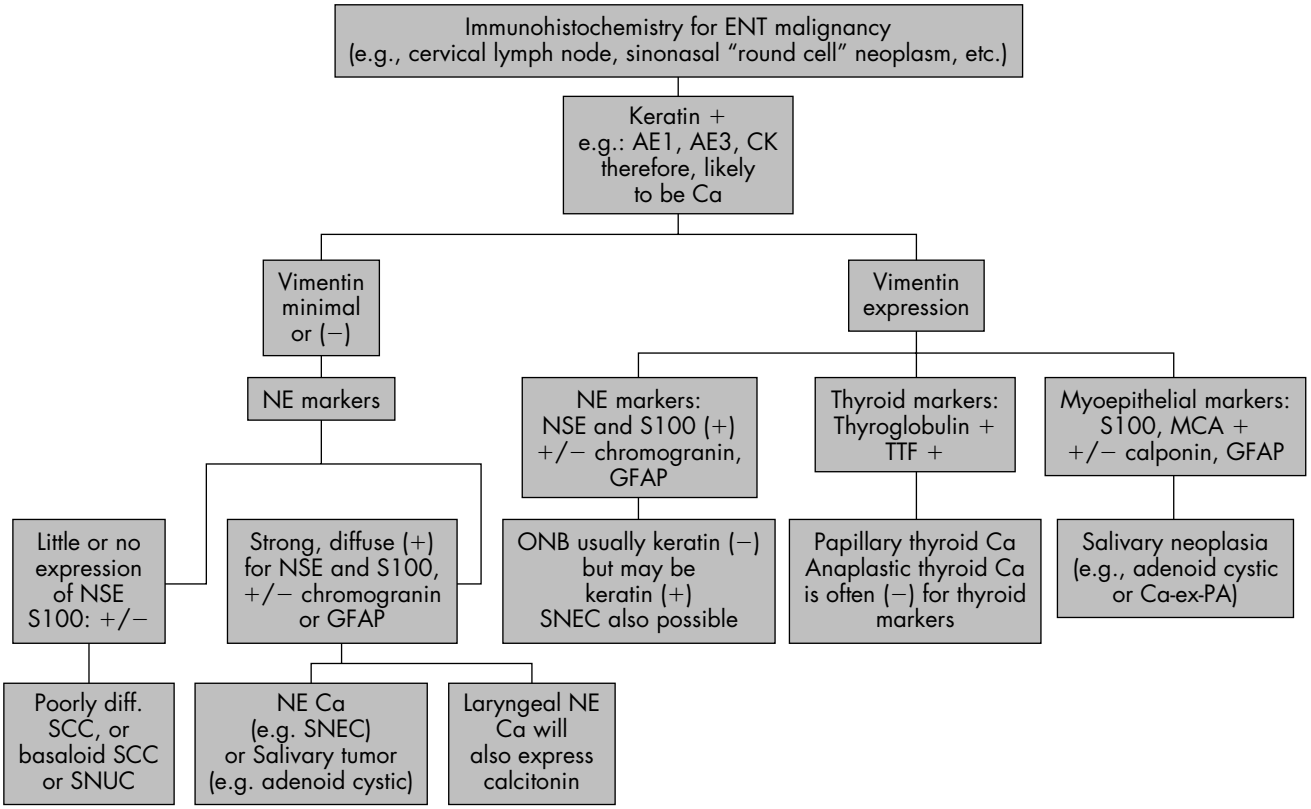

AE1, AE3, CK = low- and high-molecular weight keratins
Ca = carcinoma
Calponin = a marker of late smooth muscle differentiation
GFAP = glial fibrillary acidic protein
Keratin = a structural protein of epithelial differentiation
MCA = muscle cell actin
NE = neuroendocrine
NSE = neuron specific enolase
ONB = olfactory neuroendocrine carcinoma
S100 = a protein expressed in myriad neuronal and mesenchymal tissues
SCC = squamous cell carcinoma
SNUC = sinonasal undifferentiated carcinoma
SNEC = sinonoasal neuroendocrine carcinoma
TTF = thyroglobulin transcription factor
Vimentin = an intermediate filament

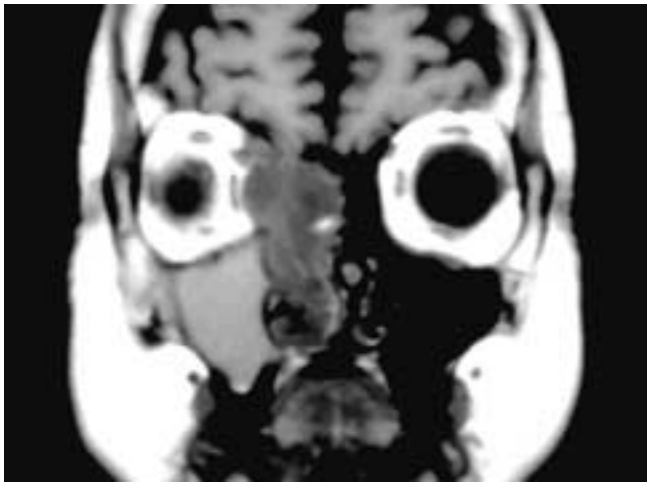

VIEW IMAGE

FIGURE 6-8 Coronal T1-weighted MR image shows a low signal intensity mass in the right ethmoid complex and nasal fossa. The tumor has broken into the right orbit, but the tumor interface with the orbital fat is smooth and not infiltrative. The right maxillary sinus is chronically obstructed with intermediate signal intensity secretions. This patient had a melanoma.

anaplastic carcinoma, nasopharyngeal carcinoma, and osteosarcoma. Fibrous dysplasia and ossifying fibroma both result in characteristic dense, expanded bone. The sclerotic facial bone changes of Paget's disease may be indistinguishable from those of osteoblastic metastatic prostate cancer, but the presence of associated pagetoid calvarial disease allows differentiation. Osteoblastic metastases from breast carcinoma can occur; however, such lesions are usually a mixed blastic and lytic process. Dense osteoblastic bone may also be found as a reaction to meningiomas.

Tumoral calcifications in the sinonasal cavities are uncommon. Discrete solitary or multiple calcifications within a mass usually signify a chronic inflammatory process, either bacterial or fungal. Such calcifications have also been reported with osteoblastomas, osteochondromas, chondromas, chondrosarcomas, and olfactory neuroblastomas. ''Calcifications'' can be seen in inverted papillomas; however, these radiodensities are actually foci of residual bone. Diffuse calcifications within a lesion with invasive margins auger a sarcoma rather than a carcinoma, usually either a chondrosarcoma, an osteosarcoma, or an undifferentiated sarcoma.

Copyright © 2003, Mosby, Inc. All rights reserved.

Despite the long list of diagnostic possibilities, a unilateral polypoid nasal mass with ''calcifications'' is most likely to be either an olfactory neuroblastoma or an inverted papilloma. A nasal septal mass with calcifications is most likely to be either a chondroid tumor or the result of fungal disease.

As mentioned, although the radiologist is constantly tempted to offer pathologic diagnoses, there are only rare instances in which the CT and MR imaging is specifically pathognomonic. Therefore, the primary radiographic contribution is accurate tumor mapping, with awareness of the critical anatomic sites that will influence treatment planning. Final treatment planning must await pathologic diagnosis.

BENIGN AND MALIGNANT EPITHELIAL TUMORS

Papilloma

The term *Schneiderian mucosa* refers to the ectodermally derived lining of the nasal cavity and paranasal sinuses, composed generally of stratified ciliated columnar cells, loose abundant lamina propria, and minor salivary glands and on their ducts. This unique mucosa may give rise to three distinct histomorphologic papillomas: fungiform, inverted, and oncocytic, collectively called Schneiderian papillomas.[1, 13] Schneiderian papillomas are uncommon, representing only 0.4% to 4.7% of all sinonasal tumors, which are 25 to 50 times less common than the pedestrian polyp.[13] These papillomas are not the result of allergy, chronic infection, smoking, or other noxious environmental agents, as they are almost invariably unilateral. It has been suggested that their rarity in children mitigates against a viral etiology.[14–16] However, many sensitive and specific viral studies confirm the association of fungiform and inverted papillomas with human papilloma virus.[17, 18]

Fungiform papillomas (septal, squamous, or exophytic) comprise 50% of Schneiderian papillomas. They usually occur in males between the ages of 20 to 50 years, and 95% arise on the nasal septum. They are solitary (75%) and unilateral (96%), have a warty or verrucous appearance, and are quite unlikely to undergo malignant transformation.[13, 14, 19] Histologically, fungiform papillomas have stratified keratinized squamous mucosa on fibrovascular stalks.

Inverted papillomas (endophytic papillomas) comprise 47% of Schneiderian papillomas and most commonly occur in males between the ages of 40 to 70 years. Characteristically, they arise from the lateral nasal wall near the middle turbinate and extend into the sinuses. This secondary extension involves the maxillary and ethmoidal sinuses, but extension into the sphenoid and frontal sinuses has been documented.[13, 14, 20] Rarely, an isolated inverted papilloma may arise within a sinus without any nasal involvement. Inverted papillomas rarely arise from the nasal septal wall, and fewer than 4% occur bilaterally.[13, 14] The most common presenting symptoms are nasal obstruction, epistaxis, and anosmia. Secondary sinusitis and tumor extension into the sinuses and orbits can cause pain, purulent nasal discharge, proptosis, diplopia, and a nasal vocal quality.

Macroscopically, inverted papillomas appear as hard white polyps with a wrinkled, prune-like surface. Microscopically, hyperplastic squamous epithelium can be seen replacing seromucinous ducts and glands, resulting in an endophytic growth pattern (Fig. 6-9). The surrounding mucosa usually reveals squamous metaplasia and hyperplasia, considered incipient changes. For this reason, mere polypectomy results in high recurrence rates that vary from 27% to 73%.[13] Lateral rhinotomy with en bloc resection of the lateral nasal wall and mucosa is the preferred procedure for all but the smallest localized lesions. This more extensive surgical approach has decreased recurrence rates to 0% to 14%, with most relapses occurring within 2 years.[13, 14] However, there has been a controversial trend over the last decade of more conservative endoscopic management, which is indicated only for the treatment of more limited lesions with planned surveillance. Thus, the radiologist may assist the surgeon in choosing the optimal surgical approach by not only mapping the lesion but noting its size.[21, 22]

Carcinoma-ex-inverted papilloma has been reported in 3% to 24% (average, 13%) of cases. Carcinoma may be concurrent with, or develop subsequent to, inverted papilloma. Most reported malignancies are squamous cell carcinomas, but verrucous carcinoma, mucoepidermoid carcinoma, spindle cell carcinoma, clear cell carcinoma, and adenocarcinomas may also occur.[13]

Oncocytic Schneiderian papillomas (cylindric cell papillomas) represent only 3% of the Schneiderian papillomas. They are similar to inverted papillomas in their affinity for the lateral nasal wall, age of onset, and predominance in males. On gross examination, they are beefy red and soft, mimicking malignancy. Microscopically, there are stratified, tall (cylindrical) oncocytic cells with numerous small intraepithelial cysts filled with mucin and neutrophils (Fig. 6-10). The cysts occasionally cause confusion with rhinosporidiosis, but slightly more than superficial perusal at high power can end this confusion.[13]

The imaging findings for all of these papillomas can vary from a small nasal polypoid mass to an expansile nasal mass that has remodeled the nasal vault and extended into the sinuses, causing secondary obstructive sinusitis[23] (Figs. 6-11 to 6-13). The MR and CT findings are nonspecific.[24, 25]

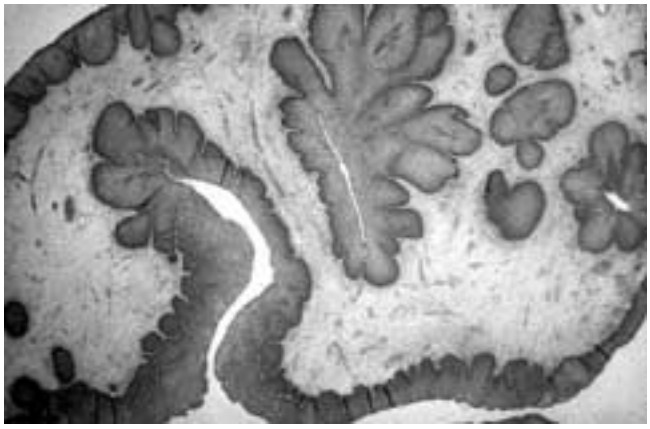

FIGURE 6-9 Inverted papilloma. Nonkeratinizing squamous epithelium proliferates within this loose stroma, forming ribbons and invaginating islands.

VIEW IMAGE

Copyright © 2003, Mosby, Inc. All rights reserved.

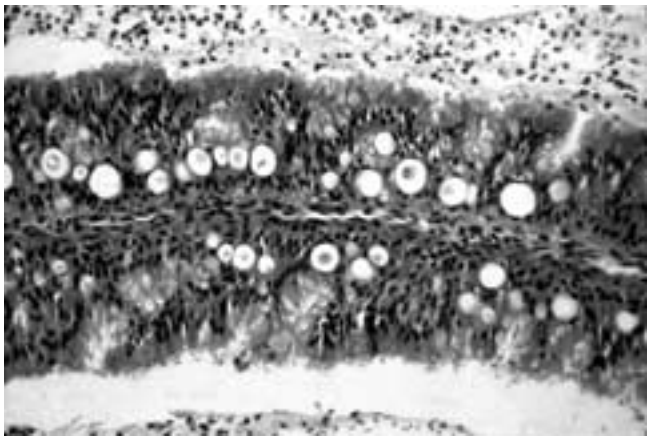

VIEW IMAGE

FIGURE 6-10 Oncocytic Schneiderian papilloma (cylindrical papilloma). This unusual form of Schneiderian papilloma is composed of tall oncocytes with a microglandular pattern. It can resemble, and may contain areas of, inverted papilloma.

Although apparent calcifications have been reported within the inverted papillomas, these radiodensities are in reality residual bone fragments.[21, 26] Nonetheless, the imaging differential diagnosis of a unilateral polypoid mass with apparent calcifications must include inverted papilloma (Fig. 6-14). The nasal septum usually remains intact, but it may be bowed to the opposite side by the mass. In patients with prior surgery including a medial antrectomy for an inverted papilloma, any polypoid mass that bridges the antral-nasal border on imaging must be considered a recurrence. A unilateral mass localized to the lateral nasal wall and the middle meatus region is predictive of inverted papilloma. A lobulated surface pattern, also typical, was noted in 19 of the 29 CT scans of cases.[27] Although a septal-based solitary polypoid mass could be any of these papillomas, the location most strongly suggests a fungiform papilloma. When an area of aggressive bone destruction is seen along the margin of an inverted papilloma, the radiologist must raise the possibility of an associated carcinoma.

Squamous Cell Carcinoma

Overall, cancer of the nasal cavity and paranasal sinuses is uncommon. In the United States, the incidence is reported to be 0.75 per 100,000 people.[28] From 25% to 58% of the sinonasal carcinomas arise in the antrum, 25% to 35% arise in the nasal cavity, 10% arise in the ethmoid complex, and only 1% arise in the sphenoid and frontal sinuses.[1, 13] Secondary extension to the maxillary sinus is common, occurring in 80% of patients with sinonasal carcinoma. A number of occupations have been epidemiologically linked to sinonasal malignancies. Workers exposed to nickel have a 40–250 times greater chance of developing squamous cell cancer.[29] Workers involved in the production of wood furniture, chromium, mustard gas, isopropyl alcohol, and radium are also at risk for developing carcinomas of the nasal cavity and paranasal sinuses. The latency period from onset of occupational exposure to tumor discovery may be up to three decades. Some 15% to 20% of the patients have a history of chronic sinusitis and polyposis; however, a causal relationship is doubtful.[13] Coexistent inverted and cylindric cell papillomas, previous irradiation, and immunosuppression (i.e., lack of immune surveillance) may increase the risk of developing sinonasal carcinoma.[13, 30] Metachronous or synchronous tumors are seen in 15% of patients with sinonasal carcinomas; 40% of the secondary tumors occur in the head and neck, and 60% occur below the clavicles in the lungs, gastrointestinal tract, and breasts.[13]

Histologically, squamous cell carcinoma (SCC) can be recognized as infiltrating broad bands, nested islands, or small clusters of malignant cells, which have a variable amount of eosinophilic cytoplasm. Keratin formation within cells, and between groups of cells (keratin pearls) belies the tumor's mucosal origins. Intercellular bridges may also be seen, appearing as fine hair-like connections between malignant cells (Fig. 6-15). Poorly differentiated or undifferentiated SCC produce little or no keratin by light microscopy. These cells can appear as oval malignant cells with little cytoplasm and large nucleoli, mimicking large cell lymphoma. They may be confirmed as

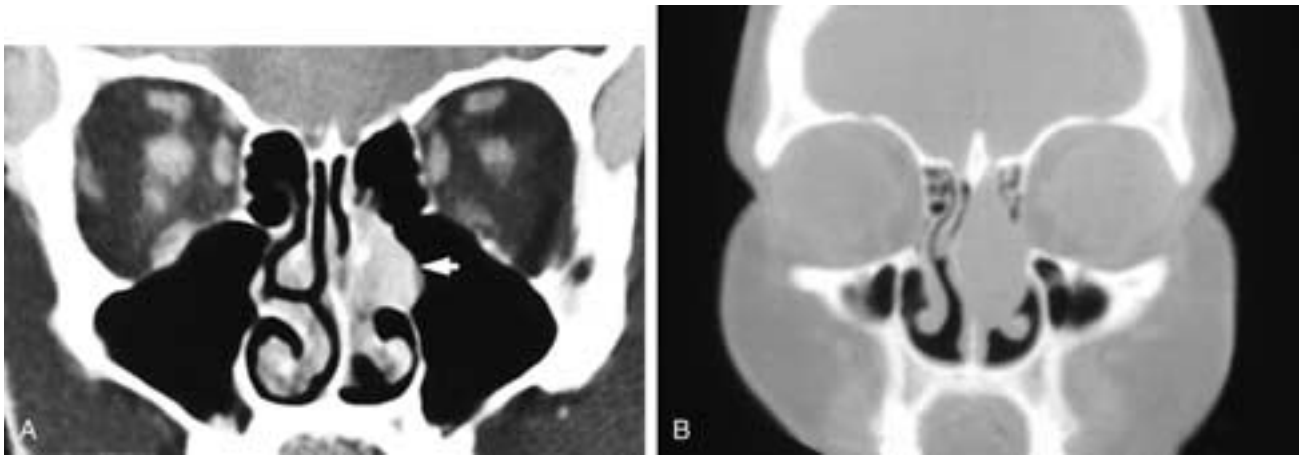

VIEW IMAGE

FIGURE 6-11 **A**, Coronal CT scan shows a small polypoid mass in the left nasal fossa (*arrow*) obliterating the middle meatus. There is no associated bone destruction. This patient had an inverted papilloma. **B**, Coronal CT scan on another patient shows an expansile left nasal fossa polypoid mass that bows the nasal septum to the right. There is no gross bone erosion. This patient had an inverted papilloma.

Copyright © 2003, Mosby, Inc. All rights reserved.

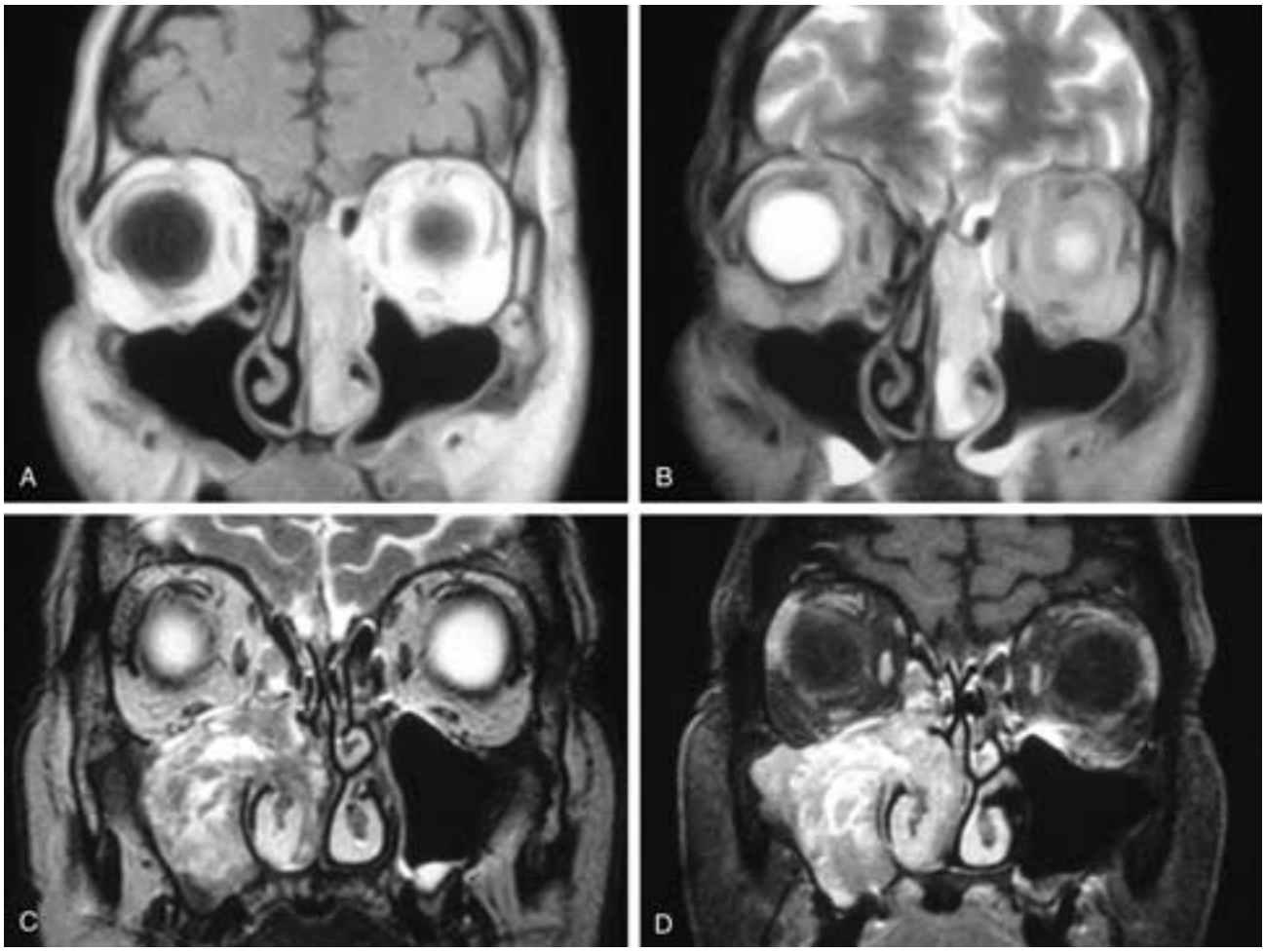

VIEW IMAGE

FIGURE 6-12 Coronal T1-weighted (**A**) and T2-weighted (**B**) MR images show a left nasal fossa and an ethmoid sinus mass. There is no gross infiltrative bone destruction, and there are obstructed secretions in the upper and most lateral left ethmoid cells. This patient had an inverted papilloma. Coronal T2-weighted (**C**) and T1-weighted (**D**), fat-suppressed, contrast-enhanced MR images show an expansile right maxillary sinus mass that extends into the right nasal fossa and ethmoid complex. The mass has highly irregular mixed signal intensity, possibly suggesting a disorganized-type tumor. This patient had an inverted papilloma and illustrates the poor correlation that often exists between the MR appearance of tumor organization and the actual pathology of the lesion.

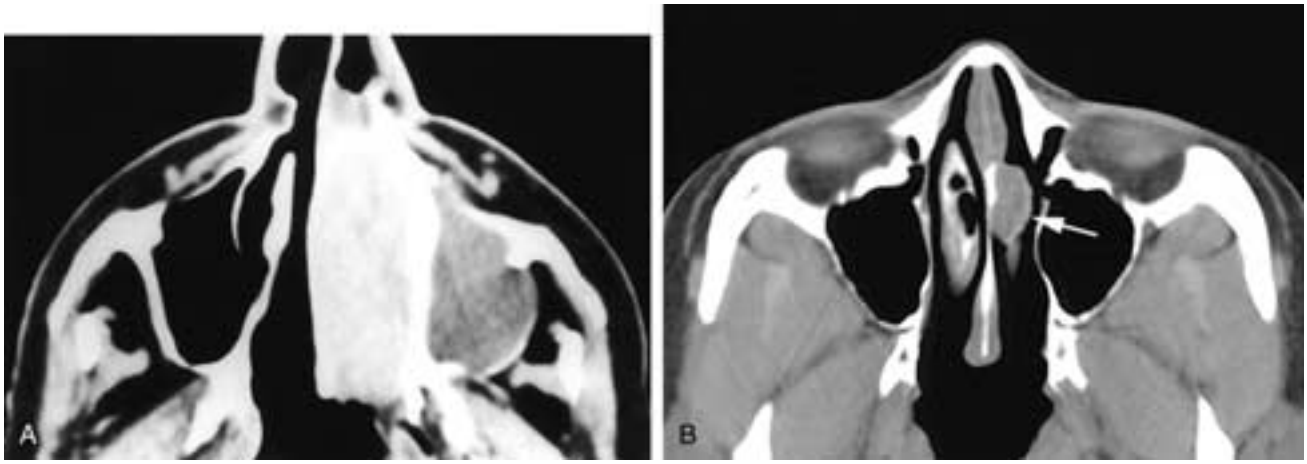

VIEW IMAGE

FIGURE 6-13 Axial CT scan (**A**) shows a large, expansile, enhancing mass in the left nasal fossa that has obstructed the left maxillary sinus, causing a mucocele to form, as noted by the modeled left antral wall. The nasal vault bones are intact. This patient had an inverted papilloma. Axial CT scan (**B**) on another patient shows a polypoid mass arising from the left side of the nasal septum (*arrow*). No erosion of the septum is seen. This patient had a fungiform papilloma.

Copyright © 2003, Mosby, Inc. All rights reserved.

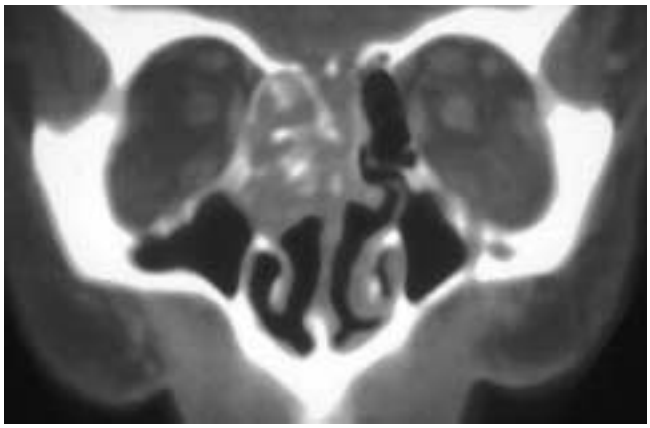

VIEW IMAGE

FIGURE 6-14 Coronal CT scan shows a right ethmoid sinus and an upper nasal fossa mass. The right lamina papyracea is intact, and there is thinning or erosion of the cribriform plate. There are also apparent calcifications within the tumor. This patient had an inverted papilloma. The radiodensities were pieces of residual bone and not tumoral calcifications.

SCC by immunohistochemistry, which reveals keratin expression.

Carcinomas of the nasal cavity tend to occur in males between 55 and 65 years of age. Most are low-grade tumors arising on the nasal septum near the mucocutaneous junction. The middle turbinate is also a common site. Patient prognosis relates to tumor stage rather than exact site within the nasal cavity.[30, 31] The treatment may be surgery, irradiation, or both. Local recurrences are found in 20% to 50% of the cases, and about 80% of these develop within the first year. Only 15% develop nodal metastases and only 10% have distant metastases. The overall 5-year survival rate is 62%.

Carcinoma of the maxillary sinus has been the most extensively studied of the sinonasal malignancies. The specific site of origin of antral carcinomas is thought to have prognostic significance and is important in planning therapy and in comparing the treatment results of various medical centers. Historically, the antrum was divided into an infrastructure and a suprastructure; however, this classification was soon modified into an infrastructure, a mesostructure, and a suprastructure, with the lines of division being

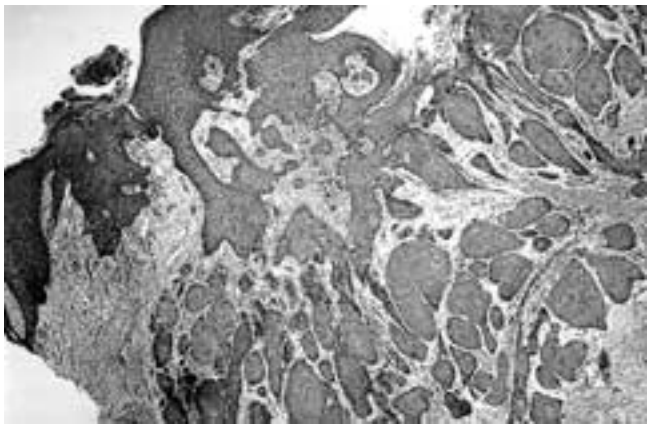

VIEW IMAGE

FIGURE 6-15 Squamous cell carcinoma: Irregularly shaped infiltrating islands of carcinoma are present below the surface mucosa. The eosinophilia of these islands indicates keratinization.

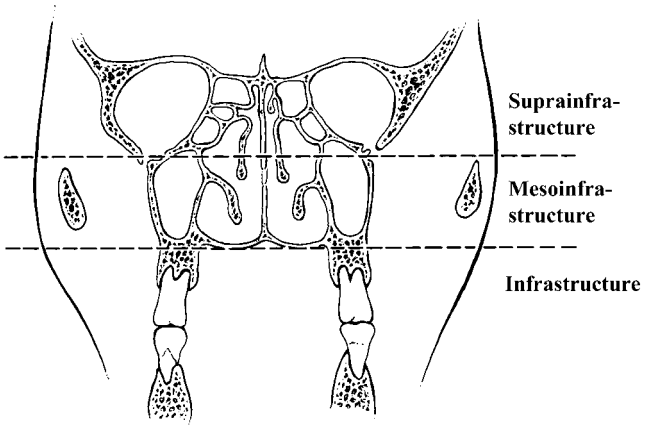

VIEW IMAGE

FIGURE 6-16 Diagram of a coronal view of the sinonasal cavities. The lines divide the maxillary sinuses into three zones: suprastructure, mesostructure, and infrastructure. Tumors limited to and below the mesostructure usually can be resected by a partial or total maxillectomy without an orbital exenteration. Tumors involving the suprastructure usually need an orbital exenteration to reduce the chance of tumor recurrence.

drawn on a coronal view of the sinuses through the antral floor and the antral roof (Fig. 6-16).[32] Using this system, tumors limited to the mesostructure and infrastructure require a partial or total maxillectomy, whereas tumors that involve the suprastructure require a total maxillectomy and possible orbital exenteration. Ohngren divided the antrum into posterosuperior and anteroinferior segments by drawing a line on a lateral view of the face from the medial canthus to the angle of the mandible (Fig. 6-17). He suggested that tumors limited to the anteroinferior segment had a better prognosis.[32] It was not until the early 1960s that the TNM

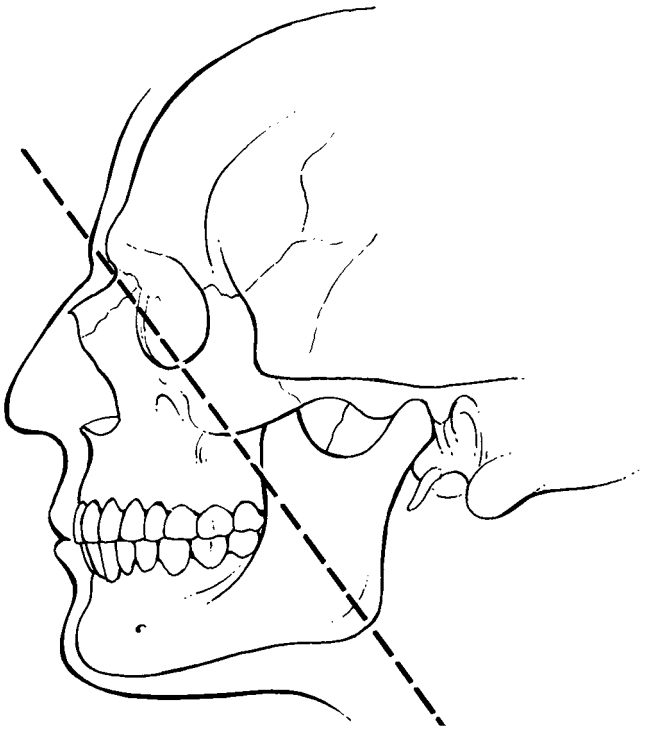

FIGURE 6-17 Diagram of the lateral view of a skull with Ohngren's line drawn. Tumors anterior to this line tend to have a better prognosis.

VIEW IMAGE

Copyright © 2003, Mosby, Inc. All rights reserved.

system was first applied to antral cancers, and in 1976 the American Joint Committee on Cancer (AJCC) developed a TNM system based on Ohngren's line.[32] Harrison has criticized this TNM classification because it does not correspond to the clinical experience with these tumors.[33] He suggested that T-1 tumors should be defined as those neoplasms that are limited to the antral mucosa, without bone erosion and without regard to Ohngren's line, because clinically it is often impossible to determine where this line occurs. A T-2 tumor has bone erosion but no extension beyond the bone, and a T-3 tumor has extension to the orbit, ethmoid complex, or facial skin. Finally, a T-4 tumor extends to the nasopharynx, sphenoidal sinus, cribriform plate, or pterygopalatine fossa. In 1997, the AJCC modified its staging definitions as follows: TX = the primary tumor cannot be assessed; T0 = no evidence of disease; Tis = carcinoma in situ; T1 = tumor limited to the antral mucosa, with no erosion or destruction of bone; T2 = tumor causing bone erosion or destruction, except for the posterior antral wall, including extension into the hard palate and/or the middle nasal meatus; T3 = tumor invasion of any of the following: bone of the posterior wall of the maxillary sinus, subcutaneous tissues, skin of the cheek, floor or medial wall of the orbit, infratemporal fossa, pterygoid plates, or ethmoid sinuses; T4 = tumor invasion of orbital contents beyond the floor or medial wall including any of the following: the orbital apex, cribriform plate, base of the skull, nasopharynx, sphenoid, or frontal sinuses.[34]

Antral carcinomas are almost twice as common in men as in women, and nearly 95% occur in patients over age 40 years.[13, 35] The radioactive contrast medium Thorotrast is clearly established as an etiologic factor in antral carcinoma.

When the tumors are small, they often are misdiagnosed as chronic sinusitis, nasal polyposis, lacrimal duct obstruction, tic douloureux, or cranial arteritis. At diagnosis, 40% and 60% of patients have facial asymmetry, a tumor bulge in the oral cavity, and tumor extension in the nasal cavity. At least one of these findings is present in almost 90% of cases.[36] Surgery plus adjuvant radiotherapy is the treatment of choice. Despite controversy in the literature, neoadjuvant radiation therapy provides no survival advantage compared to postoperative radiation therapy; the latter is associated with fewer complications.[13] Orbital exenteration is performed only if orbital periosteum is involved with tumor, as documented during surgery, either by gross examination or frozen section evaluation. Curative surgery generally is not attempted if there is central skull base destruction, tumor in the pterygopalatine fossa, tumor extension into the nasopharynx, regional or generalized metastases, advanced patient age, poor general patient health, or patient refusal to accept treatment.[13, 37] The 5-year survival rate varies from 20% to almost 40%, with mean figures ranging from 25% to 30%.[38] The main cause of failure is local recurrence, and 75% of these occur within 5 months of initial treatment.

Although more than 100 cases of primary frontal sinus carcinoma have been reported, it is still a rare entity. The presenting symptoms are similar to those of acute frontal sinusitis; patients have pain and swelling over the frontal sinus. However, in patients with frontal sinus carcinoma the frontal bone erodes rapidly, and few patients survive for more than 2 years.[4, 39]

Primary sphenoid sinus carcinoma is also rare. It is often difficult to distinguish primary sphenoid carcinoma from secondary extension from a posterior ethmoid or nasal fossa carcinoma. As with frontal sinus carcinomas, few of these patients survive longer than 1 or 2 years. Intracranial extension of squamous carcinoma is relatively common; however, an associated subarachnoid hemorrhage is rare.[40]

Poorly differentiated squamous cell carcinoma can be confused histologically with rhabdomyosarcoma, melanoma, large cell lymphoma, SNEC, and anaplastic plasmacytoma.[41] As mentioned, immunohistochemistry can confirm the diagnosis (Table 6-1).

On plain films, all patients with paranasal sinus carcinoma have a soft-tissue sinus mass, and 70% to 90% have evidence of bone destruction (Fig. 6-18).[35, 42] The primary reason to perform sectional imaging on these patients is to

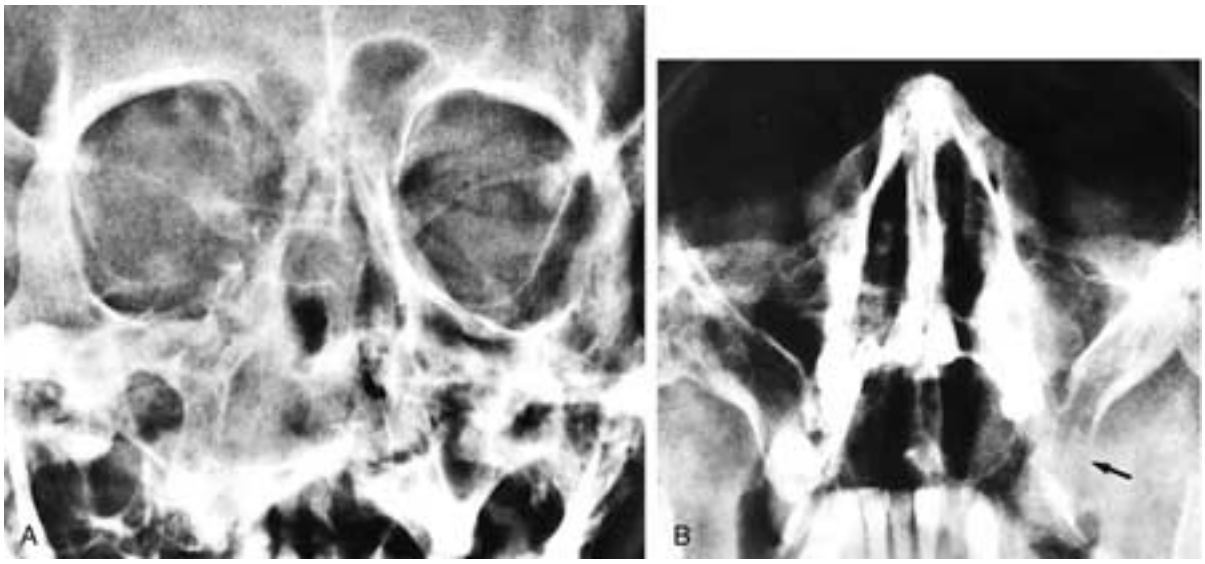

FIGURE 6-18 **A**, Caldwell view shows clouding of the right ethmoid and maxillary sinuses, with destruction of the right lamina papyracea and a portion of the floor of the right orbit. Squamous cell carcinoma. **B**, Waters view shows destruction of the lower lateral wall of the left maxillary sinus (*arrow*).

VIEW IMAGE

Copyright © 2003, Mosby, Inc. All rights reserved.

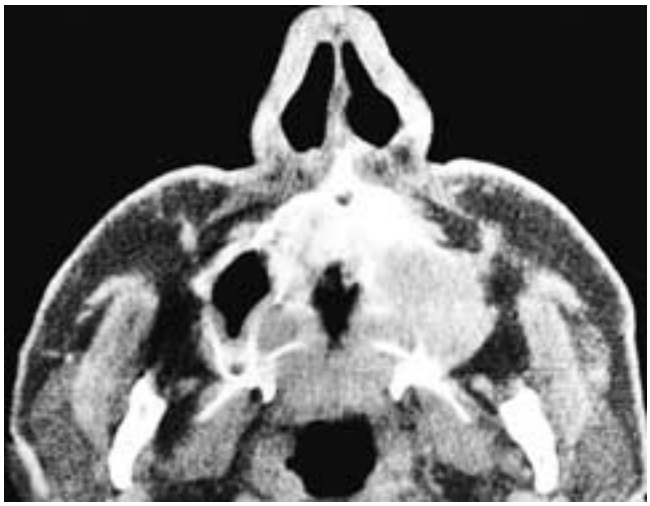

FIGURE 6-19 Axial CT scan shows an aggressively destructive lesion of the lower left antrum and palate. This patient had a squamous cell carcinoma.

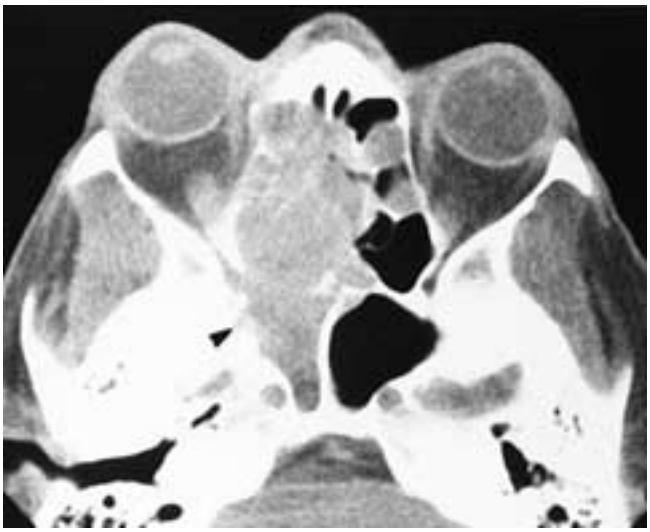

FIGURE 6-21 Axial CT scan shows a destructive lesion of the right ethmoid sinus that has extended into the nasal fossa and the sphenoid sinus. There is focal erosion of the skull base (*arrowhead*). This patient had a squamous cell carcinoma.

better visualize the extent of spread beyond the sinus cavity. On contrast-enhanced CT, carcinomas have a variable but slight enhancement. On MR imaging, these tumors have an intermediate T1-weighted and a slightly higher T2-weighted signal intensity. Carcinomas also enhance with contrast. Sinus carcinomas are fairly homogeneous; however, larger tumors may have areas of necrosis and hemorrhage (Figs. 6-5 and 6-19 to 6-37). The characteristic imaging feature of these carcinomas is their strong tendency to destroy bone aggressively, regardless of tumor differentiation. Bone remodeling is uncommon. Usually the area of bone destruction is substantial compared with the size of the soft-tissue tumor mass. However, the imaging findings are not specific.[43]

Basaloid squamous carcinoma refers to an aggressive, poorly differentiated variant of squamous carcinoma that may be confused with adenoid cystic carcinoma. We have seen a case in which there was CT and MR evidence of extensive bone destruction of the margins of the orbit, the floor of the middle cranial fossa, the right cavernous sinus, and much of the calvaria. There was considerable dural disease and tumor in the right orbit, paranasal sinuses, and scalp, as well as mucoceles of the left ethmoidal sinus with desiccated secretions (Fig. 6-36).[44]

Adenocarcinoma (Intestinal-Type Adenocarcinoma)

Approximately 10% of all sinonasal tumors are of glandular origin.[13] Sinonasal adenocarcinomas can be classified as either minor salivary gland tumors (e.g., adenoid cystic carcinomas, mucoepidermoid carcinomas, acinic cell carcinomas, and benign and malignant pleomor-

FIGURE 6-20 Coronal CT scan shows a destructive lesion of the left ethmoid sinus that has extended into the orbit. This patient had a squamous cell carcinoma.

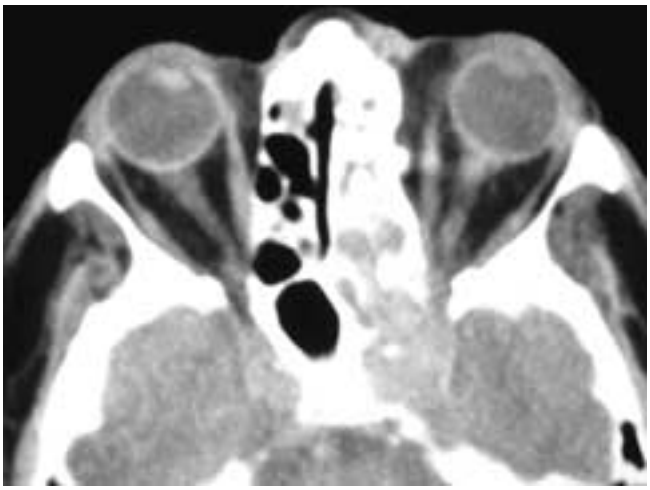

FIGURE 6-22 Axial contrast-enhanced CT scan shows a destructive mass in the sphenoid sinus and posterior ethmoid complex. The tumor erodes into the medial orbital apex and extends into the left cavernous sinus. This patient had a squamous cell carcinoma.

Copyright © 2003, Mosby, Inc. All rights reserved.

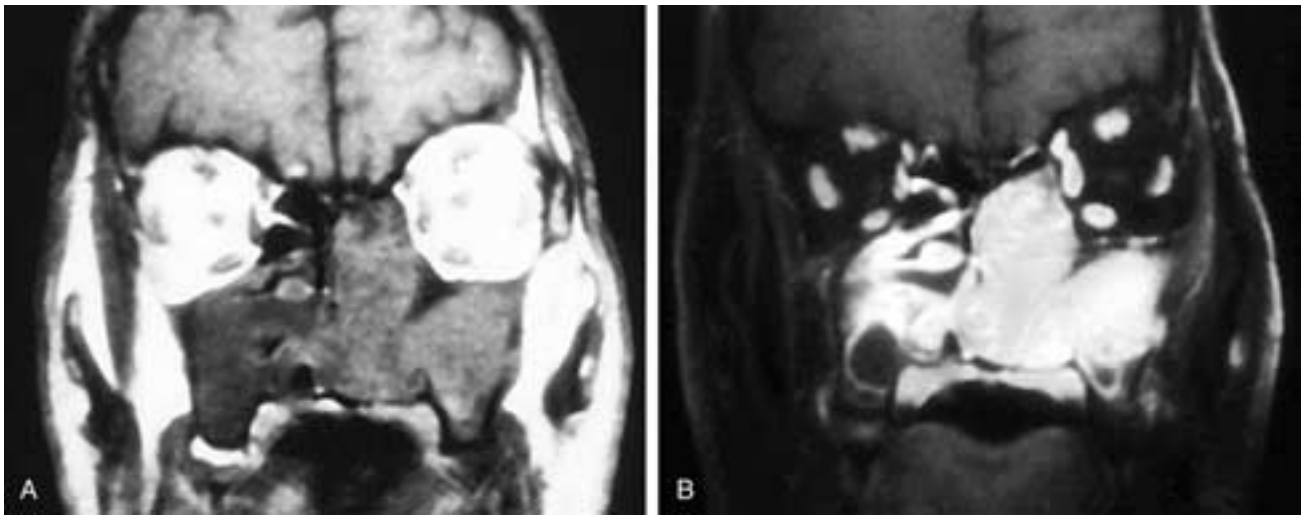

VIEW IMAGE

FIGURE 6-23 Coronal T1-weighted MR scans without contrast (**A**) and with contrast (**B**) show a mass in **A** of intermediate signal intensity that has destroyed some of the left antral walls and fills the left nasal fossa. Lower signal intensity material (secretions) fills the right antrum and nasal fossa. This appearance accurately reflected the findings at surgery. In **B**, the tumor enhances, the inflamed mucosa enhances, and some normal right ethmoid mucosa enhances. This presents a falsely large impression of the tumor size. This patient had a squamous cell carcinoma.

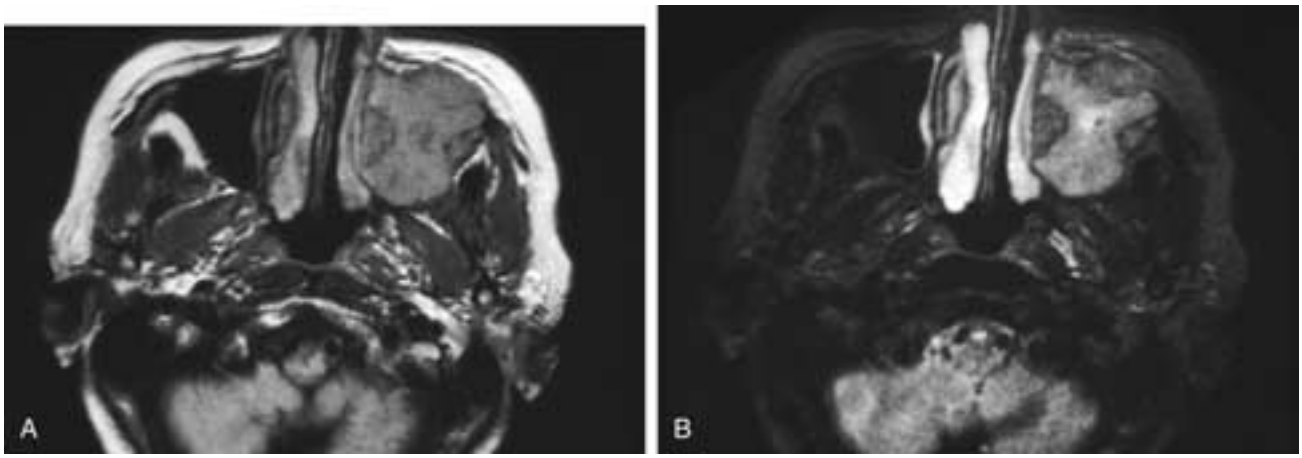

VIEW IMAGE

FIGURE 6-24 Axial T1-weighted (**A**) and T2-weighted (**B**) MR images show a destructive lesion in the left maxillary sinus that extends into the left infratemporal fossa and left cheek. The tumor has an intermediate signal intensity on both images but appears to brighten on the T2-weighted image. This is typical of most cellular tumors. Note that the tumor does not have as high a T2-weighted signal intensity as the turbinates or the inflamed mucosa along the medial wall of the right antrum. Such tumors almost never have a signal intensity that is lower on T2-weighted images than on T1-weighted images. This patient had a squamous cell carcinoma.

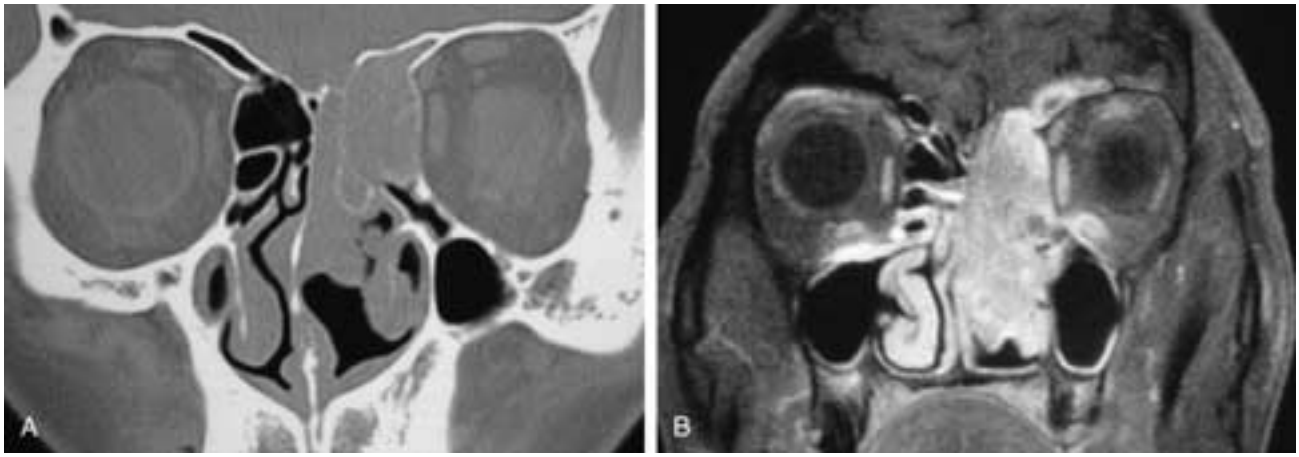

VIEW IMAGE

FIGURE 6-25 Coronal CT scan (**A**) shows a mass in the left ethmoid complex and upper nasal fossa. The bone in the region of the left cribriform plate and medial fovea ethmoidalis appears permeated but not completely destroyed. From this image, one might conclude that there is no intracranial disease. However, in **B**, a coronal T1-weighted, fat-suppressed, contrast-enhanced image, the enhancing tumor is seen to extend along the left floor of the anterior cranial fossa. This patient had a squamous cell carcinoma.

Copyright © 2003, Mosby, Inc. All rights reserved.

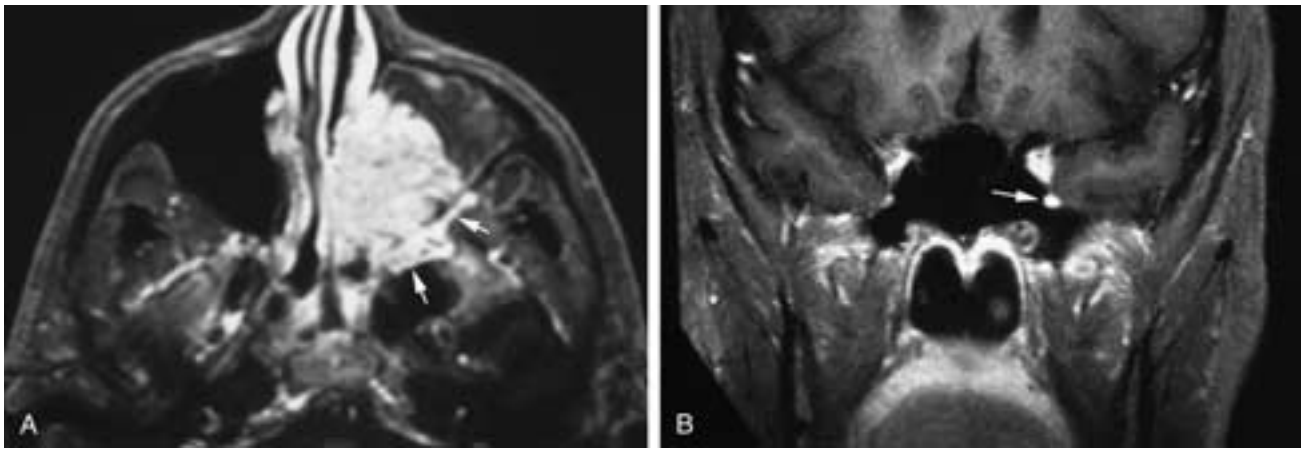

VIEW IMAGE

FIGURE 6-26 Axial (**A**) and coronal (**B**) T1-weighted, fat-suppressed, contrast-enhanced images. (**A**) A destructive mass in the left nasal fossa and maxillary sinus with tumor in the left pterygopalatine and infratemporal fossae (*arrows*). In **B** the left second division of the trigeminal nerve (*arrow*) is enlarged and enhanced, signifying perineural tumor extension. This patient had a squamous cell carcinoma.

phic adenomas), intestinal-type adenocarcinomas, or sinonasal neuroendrocrine carcinomas.

Sinonasal *intestinal-type adenocarcinoma* (ITAC) was so named because of its histologic resemblance to various intestinal tumors, ranging from the benign polyp to frank adenocarcinoma. These tumors occur primarily in males (75% to 90% of cases) between 55 and 60 years of age. These tumors were first recognized among workers in the

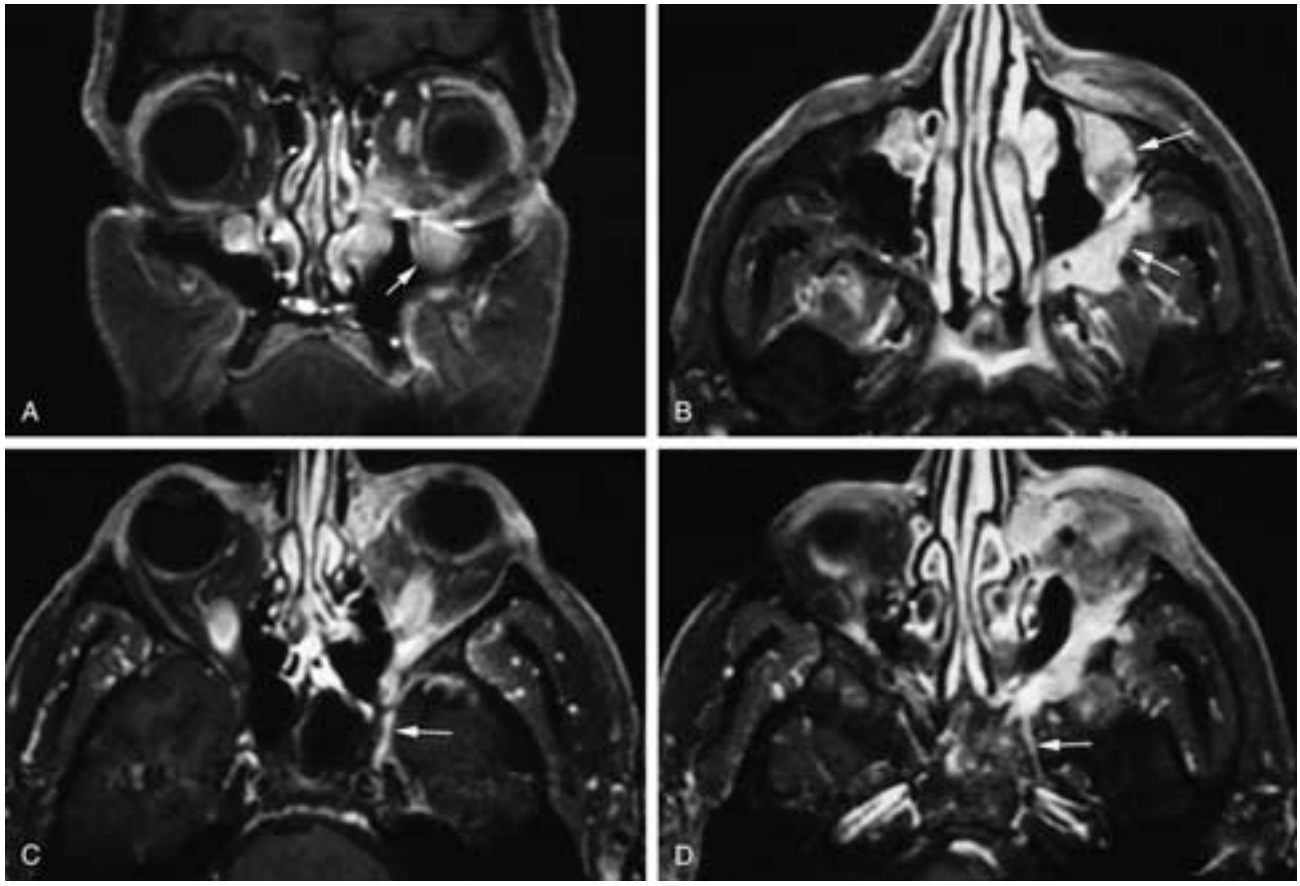

VIEW IMAGE

FIGURE 6-27 A series of T1-weighted, fat-suppressed, contrast-enhanced MR images. In a coronal view (**A**), a tumor mass is seen in the upper medial lower left maxillary sinus, the left ethmoid complex, and the orbit. Tumor also is seen in the infraorbital nerve (*arrow*). An unrelated inverted papilloma is also present in the upper medial right antrum. In an axial view (**B**) the tumor is seen extending along the course of V_2 (*arrows*). In an axial view (**C**) the tumor extends along V_2 in the left cavernous sinus (*arrow*). In an axial view (**D**) the tumor extends along the vidian nerve (*arrow*). This patient had a squamous cell carcinoma.

Copyright © 2003, Mosby, Inc. All rights reserved.

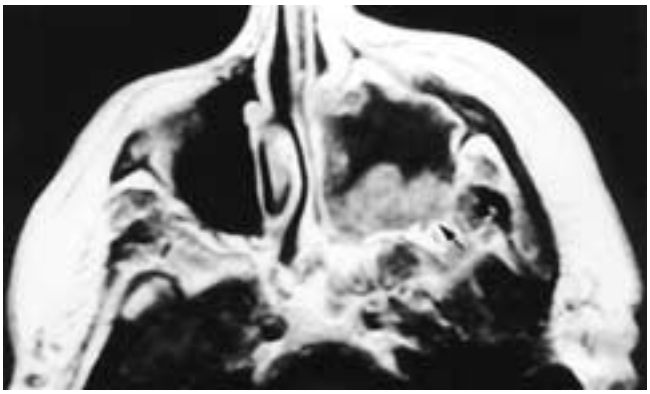

VIEW IMAGE

FIGURE 6-28 Axial T1-weighted, contrast-enhanced MR image shows a destructive lesion in the posterior left antrum. The tumor has extended into the infratemporal fossa (*arrow*). This patient had a squamous cell carcinoma.

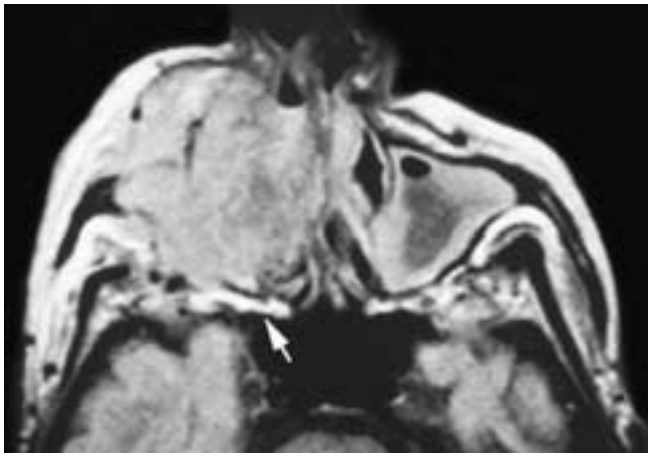

VIEW IMAGE

FIGURE 6-29 Axial proton density MR scan shows a large, destructive tumor in the right antrum. The zygoma and the soft tissues of the cheek have been invaded. However, the fat (*arrow*) in the pterygopalatine fossa remains intact. The lack of invasion of the central skull base greatly improves this patient's chance of cure. Incidentally noted are obstructed secretions in the left antrum. This patient had a squamous cell carcinoma.

VIEW IMAGE

FIGURE 6-30 Coronal T1-weighted (**A**) and sagittal (**B**) MR images show an intermediate signal intensity mass destroying the walls of the left maxillary sinus. There is minimal invasion of the orbital floor that was clinically silent. Incidental inflammatory mucosal thickening is present in the right antrum. This patient had a squamous cell carcinoma.

Copyright © 2003, Mosby, Inc. All rights reserved.

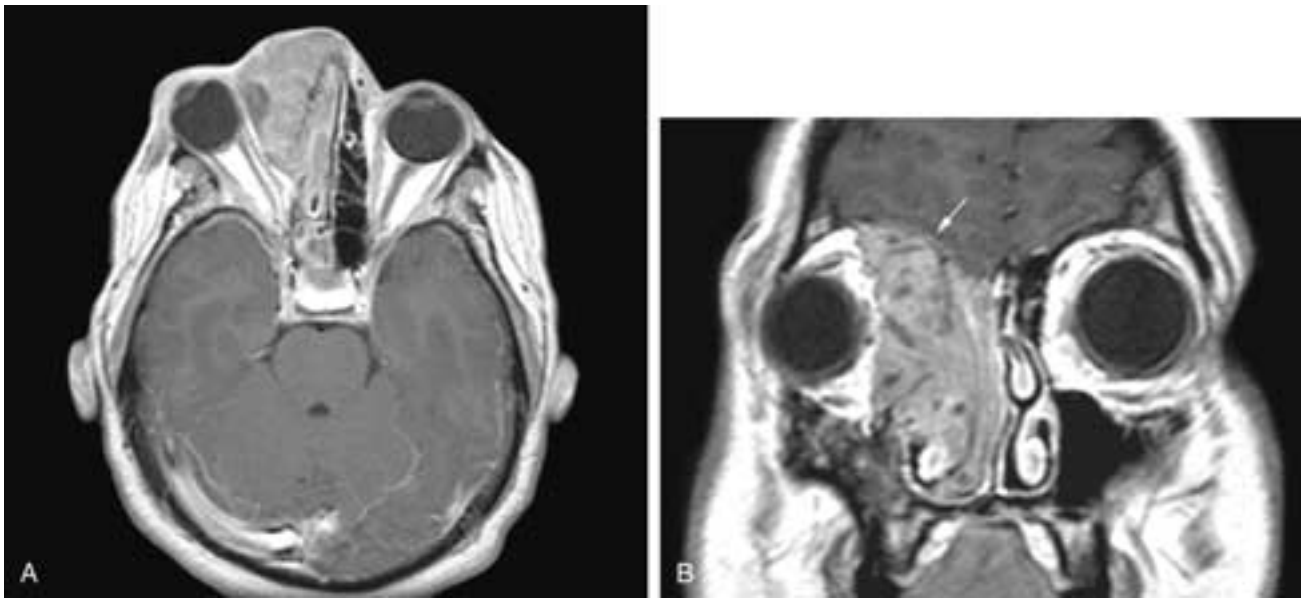

VIEW IMAGE

FIGURE 6-31 Axial (**A**) and coronal (**B**) T1-weighted, fat-suppressed, contrast-enhanced MR images show a large tumor in the right ethmoid complex with extension into the orbit. The medial rectus muscle has been invaded, and the globe is laterally displaced and flattened by the tumor. In addition, in **B**, dural enhancement is seen (*arrow*), indicating tumor invasion. This patient had a squamous cell carcinoma.

hardwood and shoe industries and in people who use certain carcinogenic snuffs, particularly Bantus.[45, 46] Workers exposed to wood dust have an almost 900 times greater relative risk of developing adenocarcinoma and a 20 times greater relative risk of developing squamous carcinoma.[47, 48] ITAC can be classified as either low-grade or high-grade tumors. The papillary variant is invariably associated with low-grade cytology (grade I) and has a distinctly favorable prognosis (Fig. 6-37). The high-grade colonic or signet cell types especially resemble colonic and gastric carcinomas. In these cases, it is wise to rule out metastases from these gastrointestinal sites. Such an event is rare; only 6% of all metastases to the sinonasal cavities are from primary gastrointestinal tract tumors (the most common tumors that metastasize to the head and neck are tumors of the kidney, lung, breast, testis, and gastrointestinal tract).[13, 49] Patients with sporadic ITAC tend to have shorter survival times than those with occupational exposure–related tumors. The reason for this is related to the initial tumor stage at the time of discovery. Sporadic tumors, not associated with inhaled promoters, are more likely to occur in the maxillary sinus. By contrast, occupational exposure–associated ITAC are more likely to occur in the nasal cavity and ethmoids. The maxillary sinus tumors are more likely to become symptomatic and to be diagnosed at an advanced stage, unlike the nasal cavity and ethmoid tumors, which may become symptomatic before they invade local structures.[47, 48]

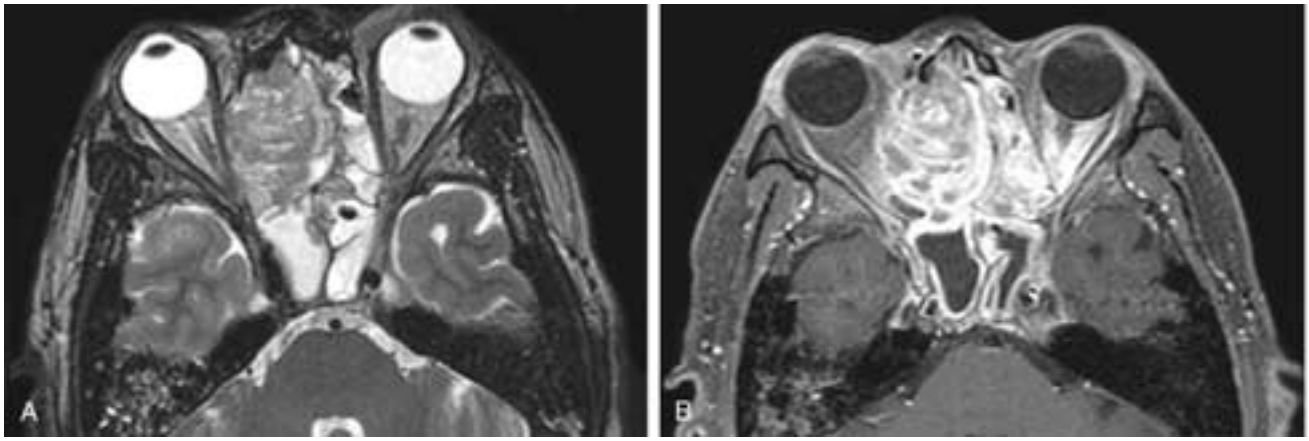

VIEW IMAGE

FIGURE 6-32 Axial T2-weighted (**A**) and T1-weighted, fat-suppressed, contrast-enhanced MR images show a destructive mass in the right ethmoid complex and right orbit. Tumor extends into the left ethmoid complex. In **B**, there is poor separation of the tumor and any obstructed secretions in the left ethmoid cells. However, in **A**, this distinction is clear. There was no invasion of the left orbit. The sphenoid sinuses were obstructed. This patient had a squamous cell carcinoma.

Copyright © 2003, Mosby, Inc. All rights reserved.

The imaging characteristics of these tumors are nonspecific and are indistinguishable from those of squamous cell carcinoma.

Salivary Tumors

Adenoid Cystic Carcinoma

Salivary gland tumors can arise anywhere within the sinonasal cavities, but most commonly arise in the palate and then extend into the nasal fossae and paranasal sinuses. The most common diagnoses, in order of decreasing frequency, include adenoid cystic carcinoma, pleomorphic adenoma, mucoepidermoid carcinoma, adenocarcinoma not otherwise specified (NOS), acinic cell carcinoma, carcinoma ex-pleomorphic adenoma, and oncocytoma.[50]

Adenoid cystic carcinomas (ACC) account for about 35% of minor salivary gland tumors.[51] Of the primary sinonasal lesions, 47% arise in the maxillary sinuses, 32% involve the nasal fossae, 7% reside in the ethmoidal sinuses, 3% occur in the sphenoidal sinuses, and 2% are found in the frontal sinuses.[13] ACC usually arise in Caucasians between 30 and 60 years of age, although these neoplasms have been reported in an age range of 4 days to 86 years. Symptoms last an average of 5 years and relate to the mass effect and neural involvement of the tumor. A dull pain signals

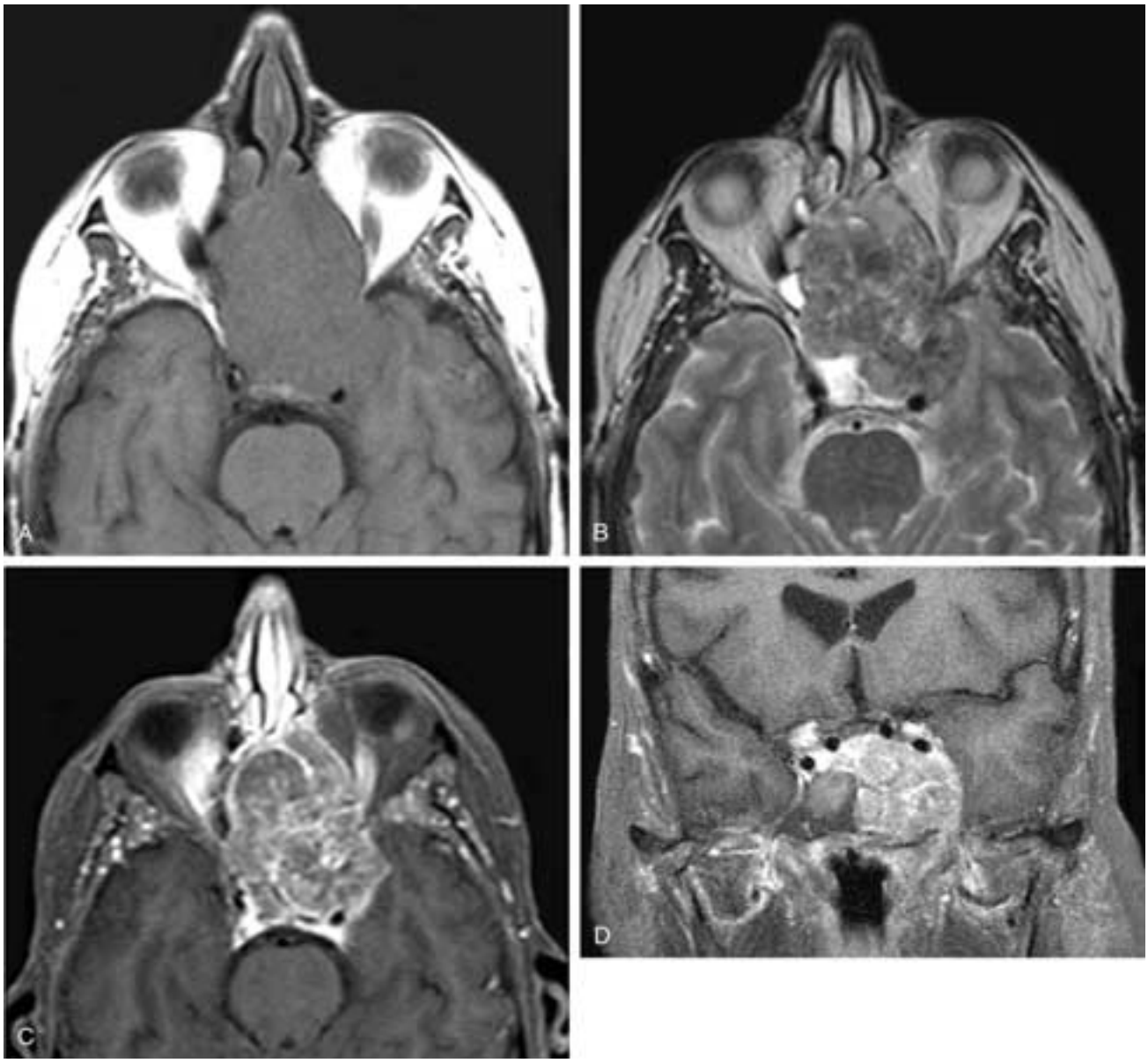

VIEW IMAGE

FIGURE 6-33 Axial T1-weighted (**A**), T2-weighted (**B**), and T1-weighted, fat-suppressed, contrast-enhanced (**C**) MR images show a destructive mass in the ethmoid sinuses, nasal fossae, and left cavernous sinus. The tumor has also broken into the left orbit. Note that in **B** there are obstructed secretions (high signal intensity) in the few remaining left ethmoid and sphenoid sinuses. In **C**, the tumor extension into the cavernous sinus and left temporal lobe is better seen. This is confirmed in **D**, a coronal T1-weighted, fat-suppressed, contrast-enhanced MR image. This patient had a squamous cell carcinoma.

Copyright © 2003, Mosby, Inc. All rights reserved.

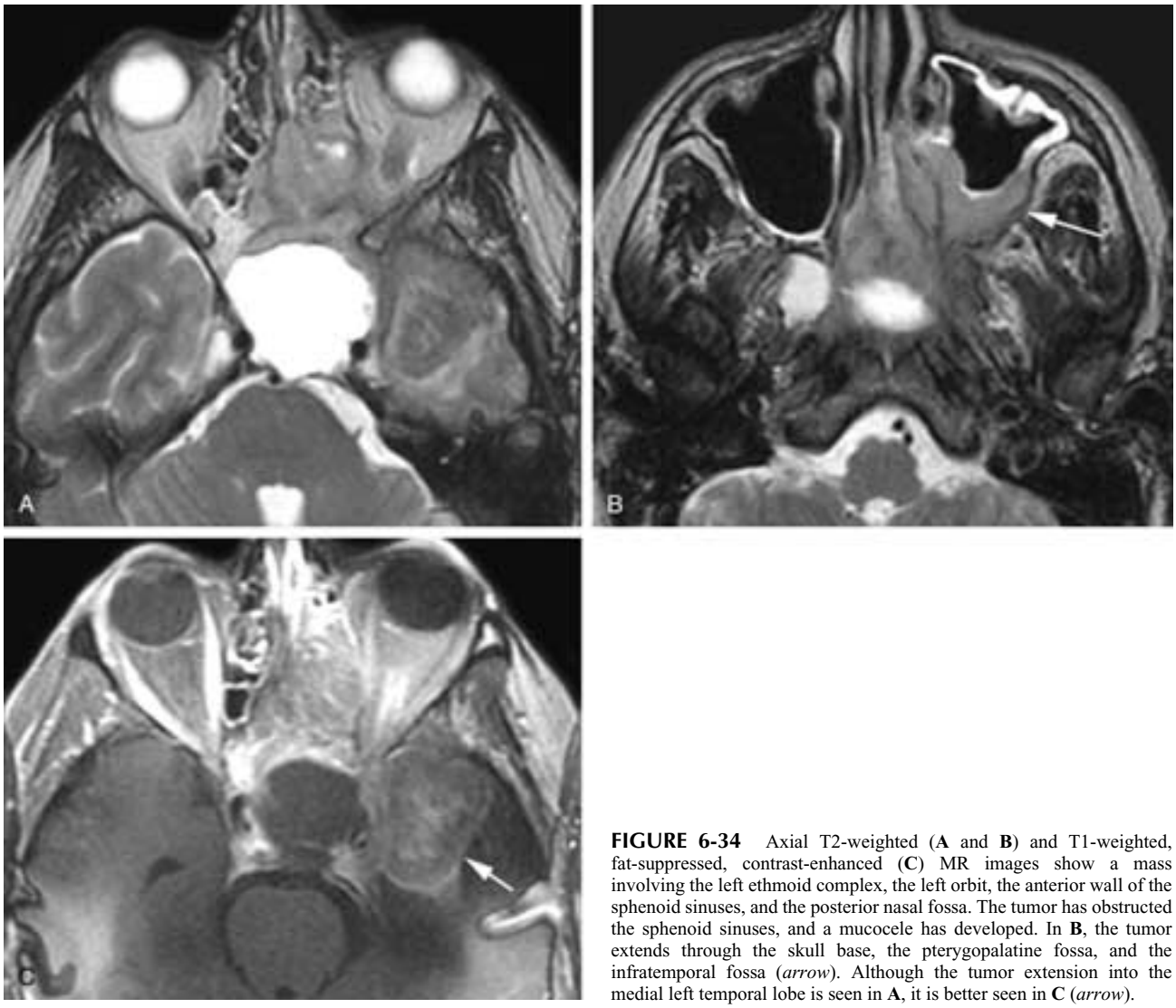

FIGURE 6-34 Axial T2-weighted (**A** and **B**) and T1-weighted, fat-suppressed, contrast-enhanced (**C**) MR images show a mass involving the left ethmoid complex, the left orbit, the anterior wall of the sphenoid sinuses, and the posterior nasal fossa. The tumor has obstructed the sphenoid sinuses, and a mucocele has developed. In **B**, the tumor extends through the skull base, the pterygopalatine fossa, and the infratemporal fossa (*arrow*). Although the tumor extension into the medial left temporal lobe is seen in **A**, it is better seen in **C** (*arrow*).

VIEW IMAGE

perineural tumor invasion, which is characteristic of this tumor (see Chapter 13).

Histologically, ACC is composed of basaloid epithelial cells and myoepithelial cells. ACC forms three different architectural patterns: tubular, cribriform, and solid, with elaboration of a basement membrane and a collagenous matrix (Fig. 6-38). ACC that is predominantly tubular is considered well differentiated. If 30% or more is composed of cribriform patterns, it is classified as moderately differentiated. A poorly differentiated ACC is composed of 30% or more of the solid pattern. A temporal progression of patterns (grades) may be observed.[52]

''Skip lesions'' within nerves are known to occur; thus, negative surgical margins have little prognostic significance. The local postsurgical recurrence rate is 62% within 1 year and 67% to 93% within 5 years.[13] The local recurrence rate for ACC is highest in the sinonasal tract (63%). While the rate of local recurrence is highest within the first 5 years, a significant number of patients develop locoregional recurrence after 10, 15, and 20 years. The 5-, 10-, and 15-year survival rates for 36 patients with sinonasal ACC (treated

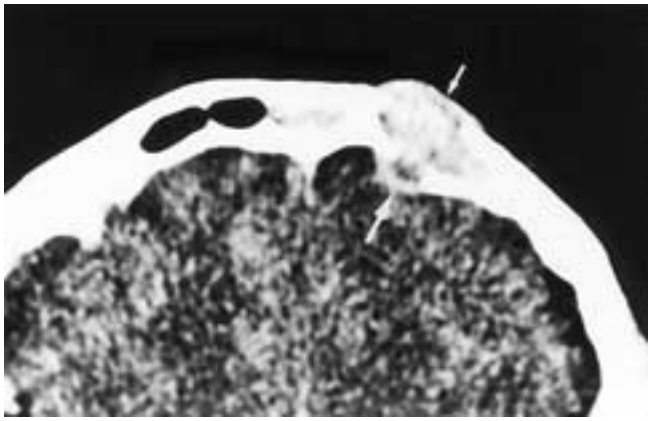

FIGURE 6-35 Axial CT scan shows an enhancing mass in the left frontal sinus that has eroded both the anterior (*small arrow*) and posterior (*large arrow*) sinus walls. This patient had a rare frontal sinus squamous cell carcinoma.

VIEW IMAGE

Copyright © 2003, Mosby, Inc. All rights reserved.

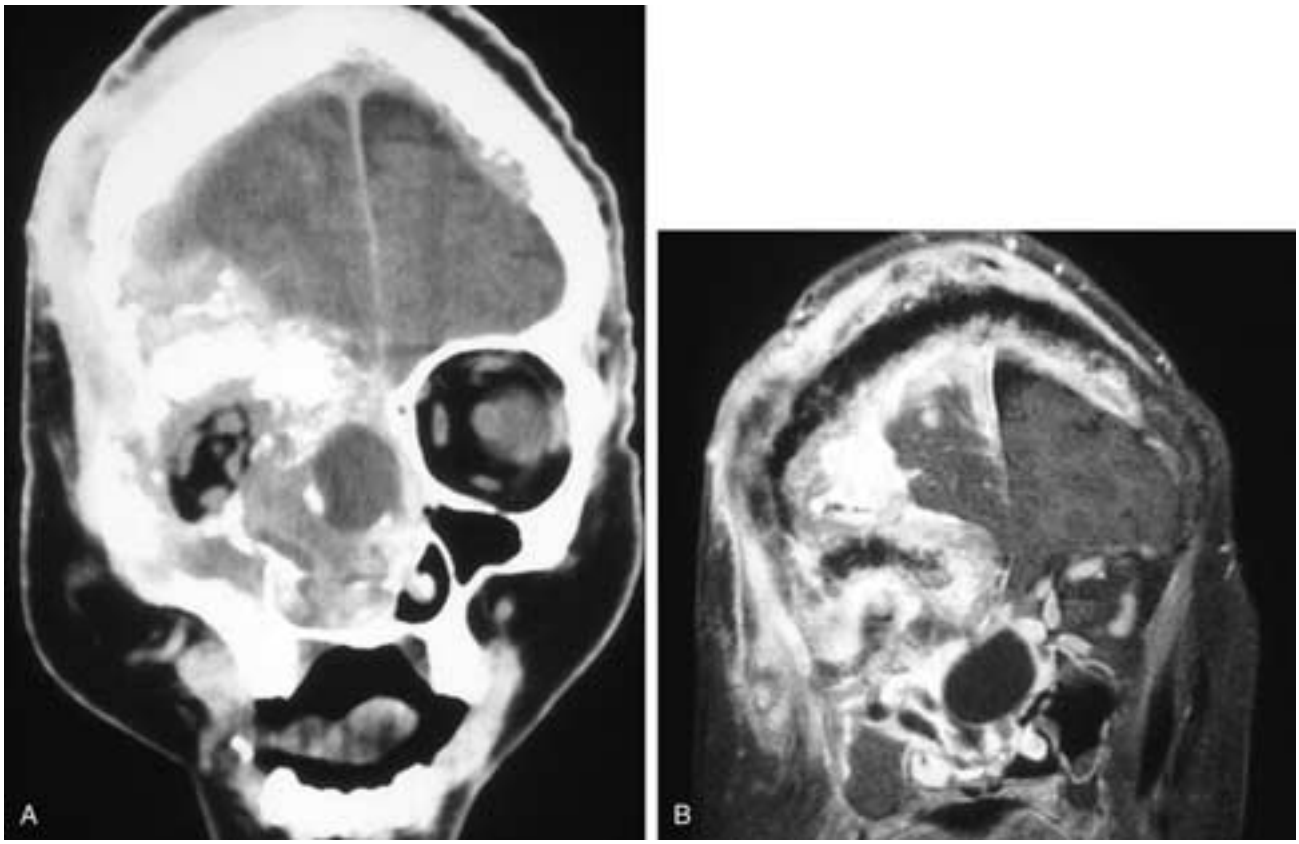

VIEW IMAGE

FIGURE 6-36 Coronal contrast-enhanced CT scan (**A**) and coronal T1-weighted, fat-suppressed, contrast-enhanced MR image (**B**) show a highly destructive tumor involving the nasal cavity, the right ethmoid and maxillary sinuses, the orbit, the right calvaria, dura, brain, and scalp. This highly aggressive tumor growth would be unusual for a typical squamous cell carcinoma. This patient had an adenosquamous carcinoma.

between 1962 and 1985) were 70%, 55%, and 55%.[53] Another report of 24 patients with sinonasal ACC (treated between 1962 and 1985) had similar survival rates at 5, 10, and 15 years (82%, 55%, and 43%).[54] As a result, 5-year survival data may give an erroneous indication of the absolute survival rate.[55] Some authorities have stated that no matter how long these patients have a disease-free interval, they will eventually die of ACC. A solid or basaloid pattern is associated with a poorer outcome. Antral tumors have the worst prognosis; 46% of patients are alive at 5 years, but only 15% are disease free.[13] About half of the sinonasal tumors have distant metastases, primarily to the lungs, brain, cervical lymph nodes, and bone.

Wide surgical excision is the treatment of choice. ACC

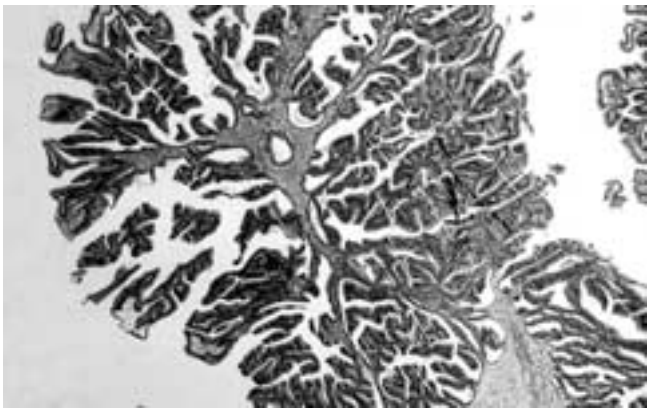

VIEW IMAGE

FIGURE 6-37 Intestinal-type adenocarcinoma (ITAC): This papillary tumor is composed of thin fronds lined by bland columnar epithelium. Although histologically bland, this low-grade ITAC is capable of local invasion.

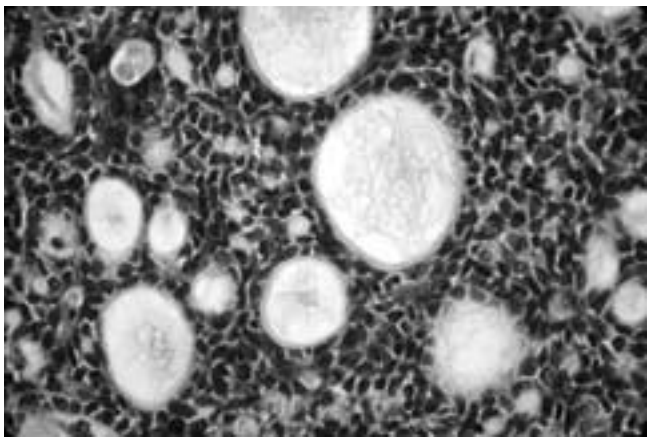

FIGURE 6-38 Adenoid cystic carcinoma (ACC): This high-power view shows a carcinoma composed of basaloid cells, here producing a cribriform (Swiss cheese) pattern.

VIEW IMAGE

Copyright © 2003, Mosby, Inc. All rights reserved.

are radiosensitive, but they are not curable with radiation therapy alone. Despite the fact that overall patient survival may not be affected by radiation treatment, better local tumor control may be achieved if postoperative irradiation is given.

Mucoepidermoid Carcinoma

Mucoepidermoid carcinomas (MEC) rank third in frequency among sinonasal malignancies of the minor salivary glands after ACC and adenocarcinomas NOS. Most of these tumors involve the antrum and nasal cavity. Almost all minor salivary gland MEC are of the high-grade or intermediate-grade variety.[50]

Histologically, MEC is composed of epidermoid cells (squamous, keratin-producing cells), intermediate cells (large, clear, non-mucin-producing cells), and goblet or mucinous cells. Grading of MEC is more predictive when histologic features of aggression are taken into account, rather than basing grading on the relative proportion of solid, epidermoid areas to cystic, mucinous components.

The biologic activity of these high-grade and intermediate-grade lesions resembles that of the adenocarcinomas. Surgical resection with negative margins is the treatment of choice for sinonasal MEC. Adjuvant radiotherapy should be considered for inadequately resected cases. Tumor grade is a very important prognosticator for MEC, and preoperative knowledge of the tumor grade can be helpful in planning for a lymphatic dissection. While inadequately resected tumors will recur, a fully low-grade tumor acts no differently than a benign tumor; its ability to metastasize appears almost nil. There is not much data available concerning survival of patients with sinonasal MEC.

Pleomorphic Adenoma

Benign mixed tumors of the sinonasal cavities are rare; most lesions occur within the nasal fossa. Usually they arise from the nasal septum, although one-fifth of the cases originate from the lateral nasal wall. The nasal septal location is curious because the septal submucosa is sparsely populated with minor salivary glands compared with the remainder of the sinonasal tract. A series of 41 cases of nasal cavity pleomorphic adenomas revealed that 90% of the cases originated from the septum and 10% (4 cases) arose in the lateral nasal wall.[56] The second most common site of origin is the maxillary sinus. Overall, pleomorphic adenoma is statistically the third most common minor salivary gland neoplasm.

Histologically, pleomorphic adenomas consist of epithelial and myoepithelial cells. The epithelial component produces ductal and glandular patterns, solid areas, and commonly undergoes squamous metaplasia. The myoepithelial component produces the abundant chondroid and myoid matrix so typical of these tumors (Fig. 6-39).

Intranasal and paranasal pleomorphic tumors are more cellular than their major salivary gland counterparts, and often the minor salivary gland lesions consist almost entirely of epithelial cells with little or no mesenchymal stroma.[55] Wide surgical excision usually prevents recurrences; however, recurrence of the tumor may be delayed well beyond the traditional 5-year period. Malignant change in a sinonasal pleomorphic adenoma is rare.[57] Benign metastasizing pleomorphic adenoma, or metastasizing pleomorphic adenoma, is an infrequent tumor that metastasizes, despite benign histology, usually to the lungs and soft tissues. A benign metastasizing nasal septal pleomorphic adenoma reportedly spread to an ipsilateral submandibular node.[56, 58]

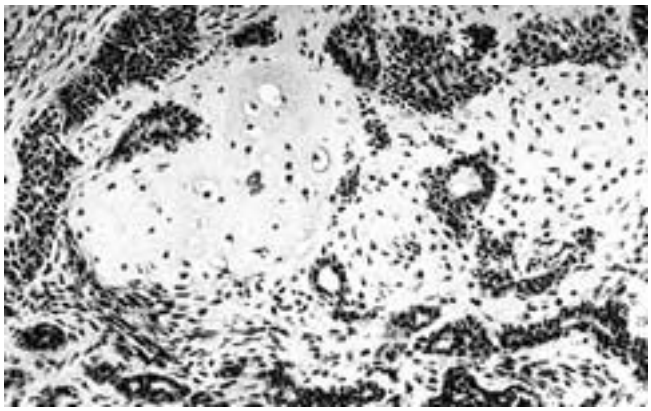

FIGURE 6-39 Pleomorphic adenoma: Glandular ductal elements are interspersed with a mesenchyme-like matrix produced by myoepithelial cells. In the center, a chondroid matrix is seen.

VIEW IMAGE

On imaging of salivary tumors, typically, pleomorphic adenomas remodel bone. Often, the nasal tumors develop as a spherical mass rather than the more typical polypoid lesion associated with most other tumors. When such a spherical configuration is seen, either a salivary gland tumor or a rare schwannoma should be considered in the imaging differential diagnosis. On CT, the less cellular salivary tumors may appear nonhomogeneous because of mesenchymal stroma, cystic degeneration, necrosis, or serous and mucous collections.[50] The highly cellular tumor tends to have a homogeneous appearance and may cause some bone erosion. On MR imaging, these tumors tend to have an intermediate signal intensity on T1-weighted images. The T2-weighted signal intensity depends on the cellularity of the neoplasm; highly cellular types usually have an intermediate signal intensity, while the stromal or less cellular variety have a high T2-weighted signal intensity (Figs. 6-40 to 6-53).[59]

The imaging characteristics of malignant pleomorphic tumors are nonspecific and are similar to those of SCC. Occasionally, they may have grossly less invasive margins on imaging than an SCC. Although this may allow an imaging diagnosis to be suggested, it is not a sufficiently reliable finding to truly differentiate these lesions.

Epithelial-Myoepithelial Carcinoma

Epithelial-myoepithelial carcinoma is an uncommon, low-grade epithelial neoplasm composed of variable proportions of ductal cells and large, clear-staining myoepithelial cells arranged around the periphery of the ducts. About 120 cases have been reported in the world literature, most of which were located in salivary glands, especially the parotid gland. A few cases have occurred in unusual locations such as the breast, lacrimal gland, nose, paranasal sinus, trachea, bronchus, and lung. A case was reported in the nasal cavity with extension to the nasopharynx. The recurrence and metastatic rates of epithelial-myoepithelial carcinoma varied from 35% to 50% and from 8.1% to 25%, respectively, for all sites.[60]

Copyright © 2003, Mosby, Inc. All rights reserved.

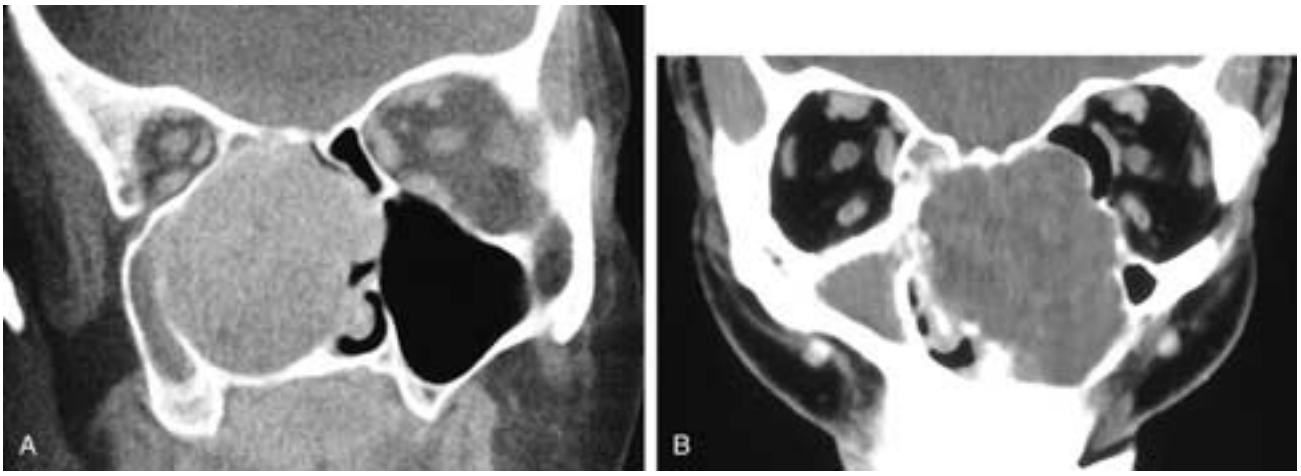

VIEW IMAGE

FIGURE 6-40 **A**, Coronal CT shows an expansile right nasal fossa mass that has remodeled most of the surrounding bone. It also has obstructed what remains of the right maxillary sinus. This patient had a low-grade mucoepidermoid carcinoma. **B**, Coronal CT scan on another patient shows a primarily expansile mass filling the nasal fossae and the left ethmoid and maxillary sinuses. The right antrum is obstructed by the mass. This patient had a low-grade mucoepidermoid carcinoma.

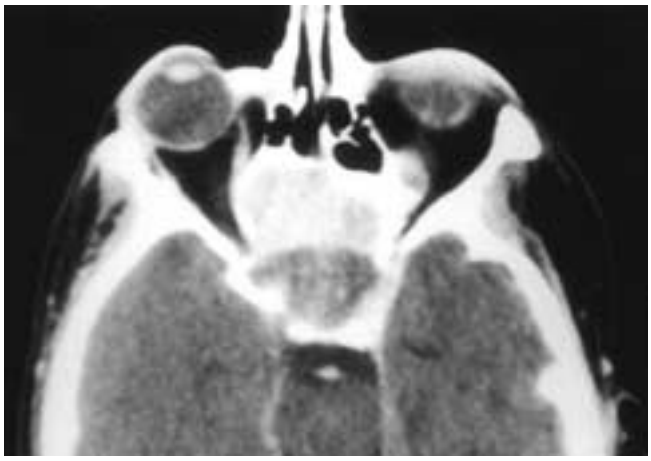

VIEW IMAGE

FIGURE 6-41 Axial CT scan shows an enhancing expansile mass in the posterior ethmoid sinuses. The sphenoid sinuses are obstructed with lower-attenuation secretions. Some bone remodeling is also present in the lamina papyracea. This patient had a mucoepidermoid carcinoma and a sphenoid mucocele.

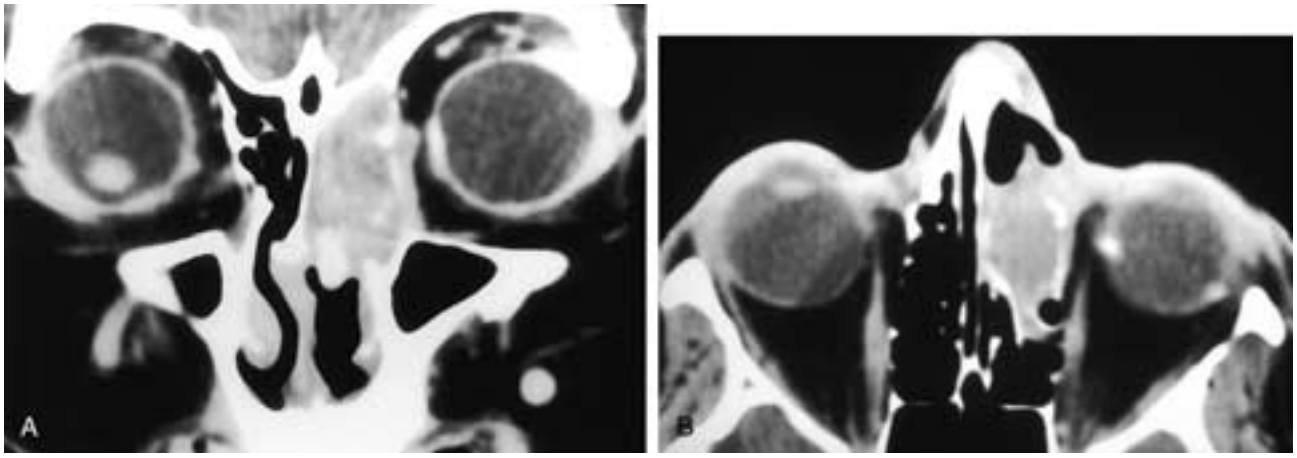

VIEW IMAGE

FIGURE 6-42 Coronal (**A**) and axial (**B**) CT scans show a slightly expansile mass in the left ethmoid sinuses. Although there is some destruction of the lamina papyracea with minimal invasion of the orbit, there is also an element of widening or remodeling of the ethmoid complex. This patient had a mucoepidermoid carcinoma.

Copyright © 2003, Mosby, Inc. All rights reserved.

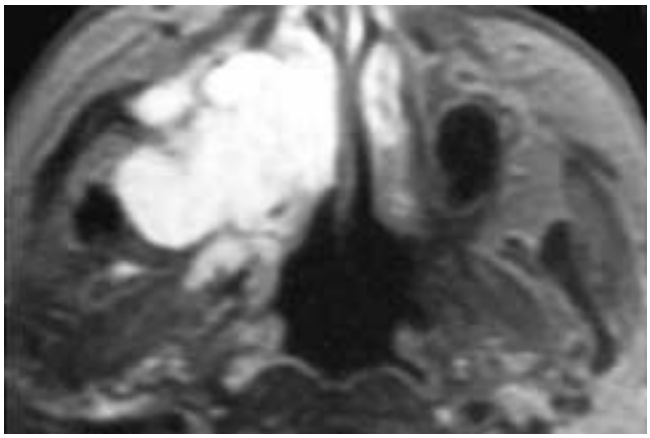

FIGURE 6-43 Axial T2-weighted MR image shows an expansile right maxillary sinus mass that extends into the infratemporal fossa. The tumor has high signal intensity, suggesting that it contains water-like products such as mucoid secretions. This patient had a mucoepidermoid carcinoma.

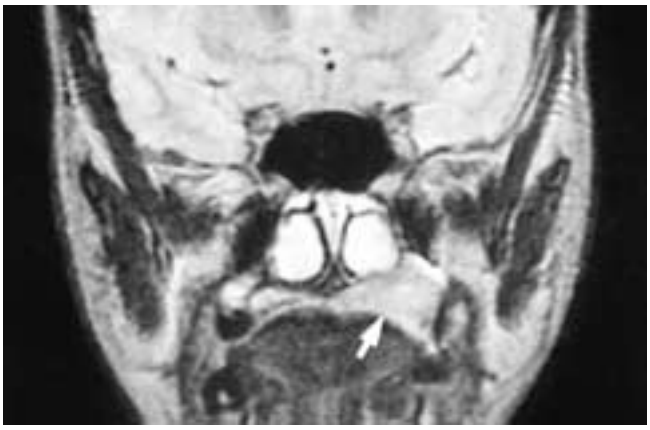

FIGURE 6-44 Coronal proton density MR image shows a mass (*arrow*) in the left palate with extension to the lower left antrum. This patient had a high-grade mucoepidermoid carcinoma.

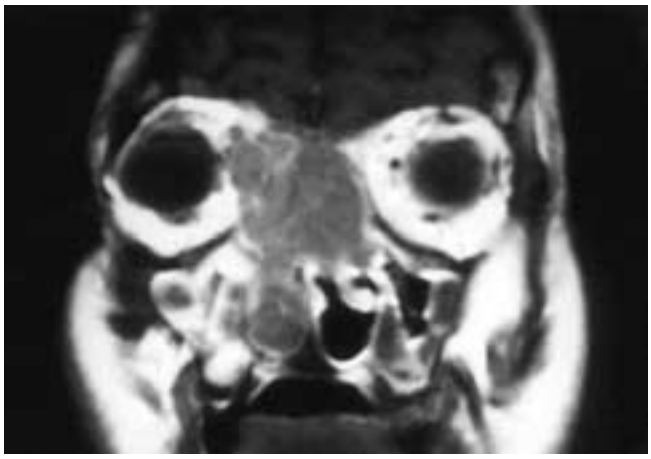

FIGURE 6-45 Coronal T1-weighted, contrast-enhanced MR image shows a nodular, destructive lesion in the nasal fossae and both ethmoid sinuses. The tumor has invaded the right orbit and skull base. Inflammatory disease is present in both antra. This patient had an adenocarcinoma.

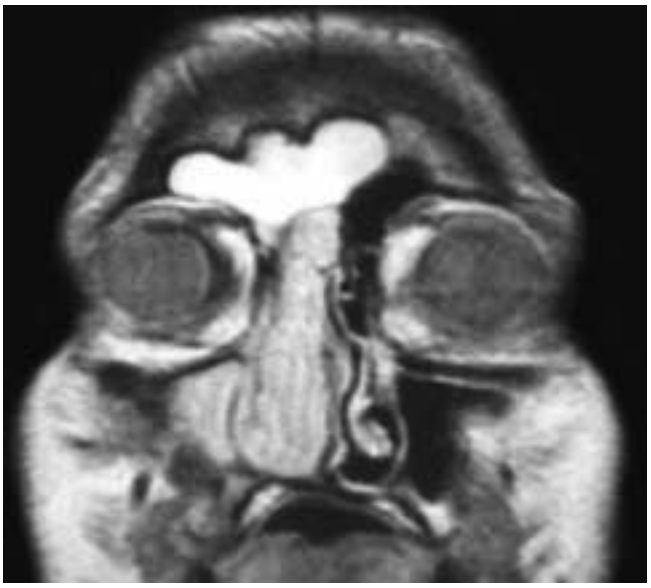

FIGURE 6-46 Coronal T2-weighted MR image shows an expansile right nasoethmoid mass that extends into the base of the right frontal sinus. The lesion obstructs the right frontal and right maxillary sinuses. This patient had an adenocarcinoma.

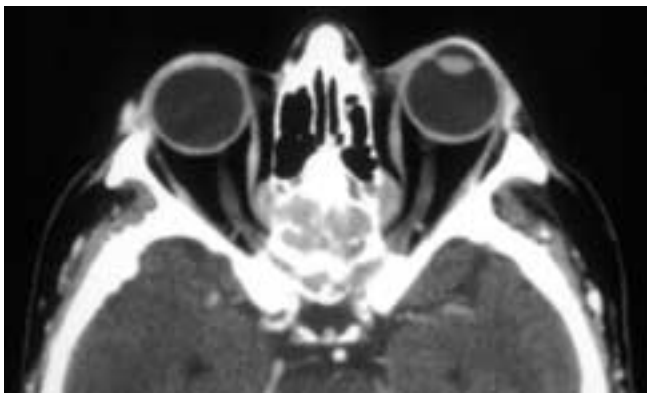

FIGURE 6-47 Axial contrast-enhanced CT scan shows a partially expansile and destructive mass in the posterior ethmoid complexes, nasal fossae, and anterior sphenoid sinuses. The tumor has broken into both orbits; however, the margins of the tumor with the orbital fat are not grossly invasive. This patient had an adenocarcinoma.

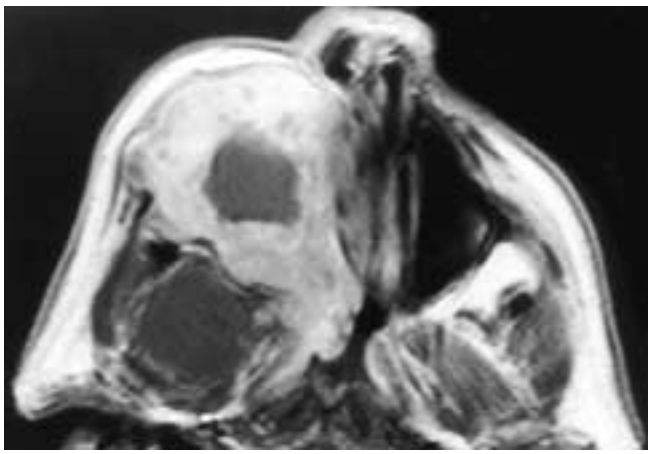

FIGURE 6-48 Axial T1-weighted, contrast-enhanced MR image shows a large, destructive tumor in the right maxillary sinus that has invaded the overlying skin, the nasal fossa, the infratemporal fossa, and the central skull base. This appearance is similar to that of a squamous cell carcinoma; however, this patient had an adenoidcystic carcinoma.

Copyright © 2003, Mosby, Inc. All rights reserved.

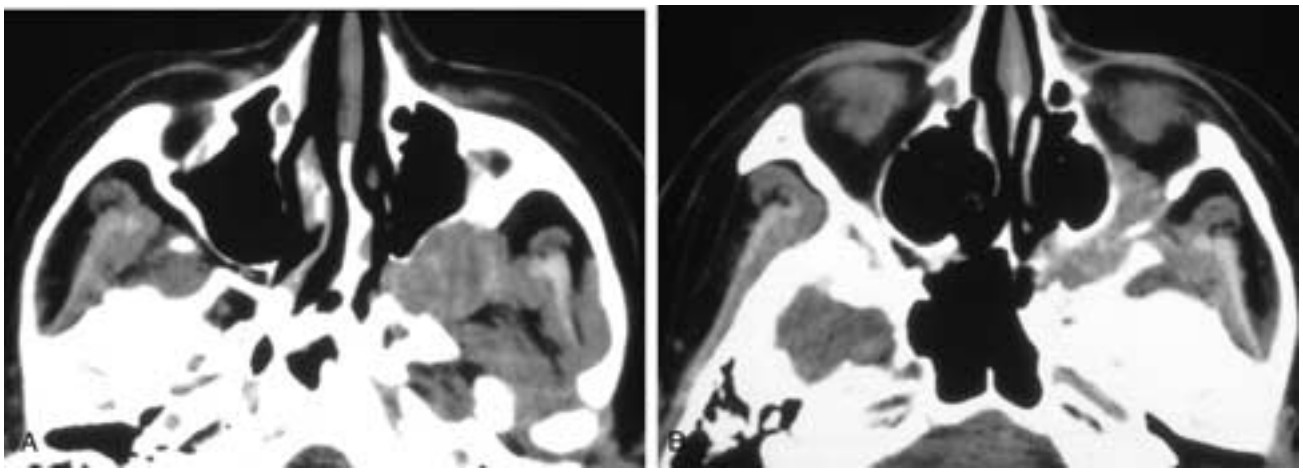

VIEW IMAGE

FIGURE 6-49 Axial CT scans show a mass in the left pterygopalatine and infratemporal fossae that has both thinned and remodeled the posterior antral wall (**A**). The tumor has extended up into the left orbital apex and the skull base (**B**). This patient had an adenoidcystic carcinoma.

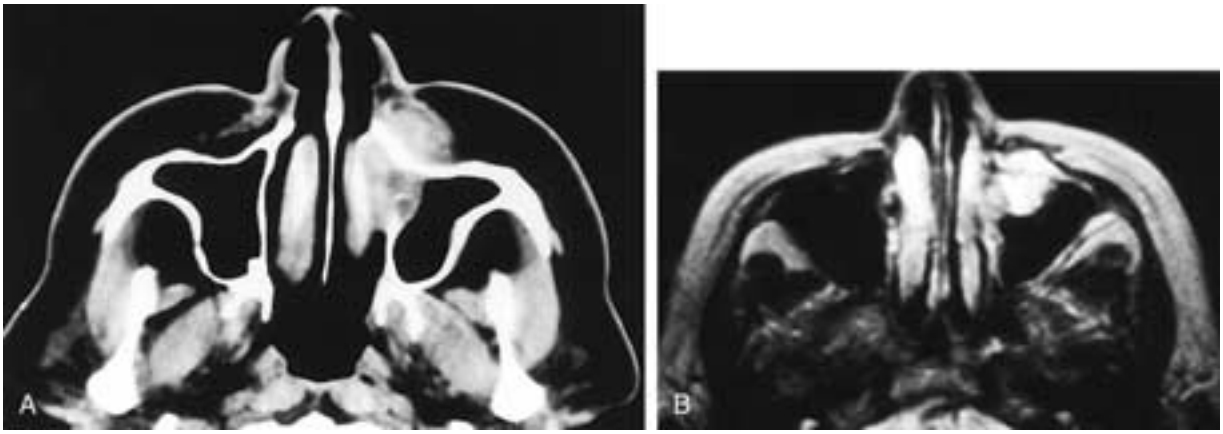

VIEW IMAGE

FIGURE 6-50 Axial CT scan (**A**) shows a mass in the anteromedial left maxillary sinus and the adjacent left cheek. There is some destruction of the medial antral wall. In **B**, a T2-weighted MR image, the mass has high signal intensity. This patient had an adenoidcystic carcinoma.

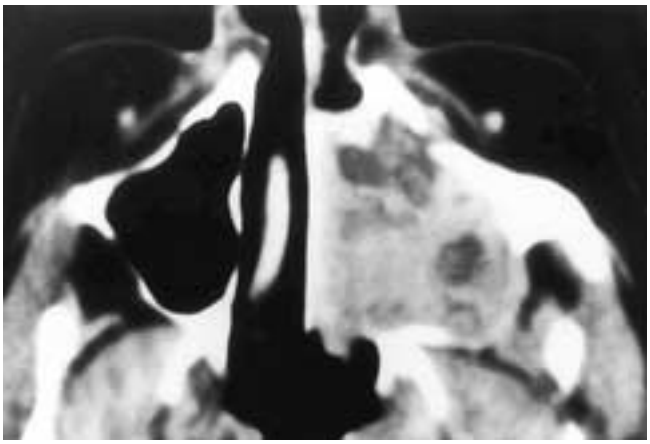

VIEW IMAGE

FIGURE 6-51 Axial CT scan shows a partially expansile, partially destructive, nonhomogeneous tumor in the left maxillary sinus. The lesion has extended into the nasal fossa and the infratemporal fossa. This patient had an adenoidcystic carcinoma.

BENIGN AND MALIGNANT NEUROECTODERMAL, NEURONAL, NERVE SHEATH, AND CENTRAL NERVOUS SYSTEM TUMORS

Paraganglioma

Primary paragangliomas in the sinonasal tract are extraordinarily rare. The diagnosis of a paraganglioma in this region almost always represents a large glomus jugulare tumor that has usually extended into the sphenoid and ethmoid sinuses (Fig. 6-54).[61, 62] However, at least two cases of sinonasal paraganglioma have been reported.[63, 64] Histologically, paragangliomas are composed of nests of epithelioid, neuroendrocrine cells ensheathed by Schwannian sustentacular cells.

Treatment may include surgery and radiotherapy. In one case, 22 years later the tumor recurred and showed rapid

Copyright © 2003, Mosby, Inc. All rights reserved.

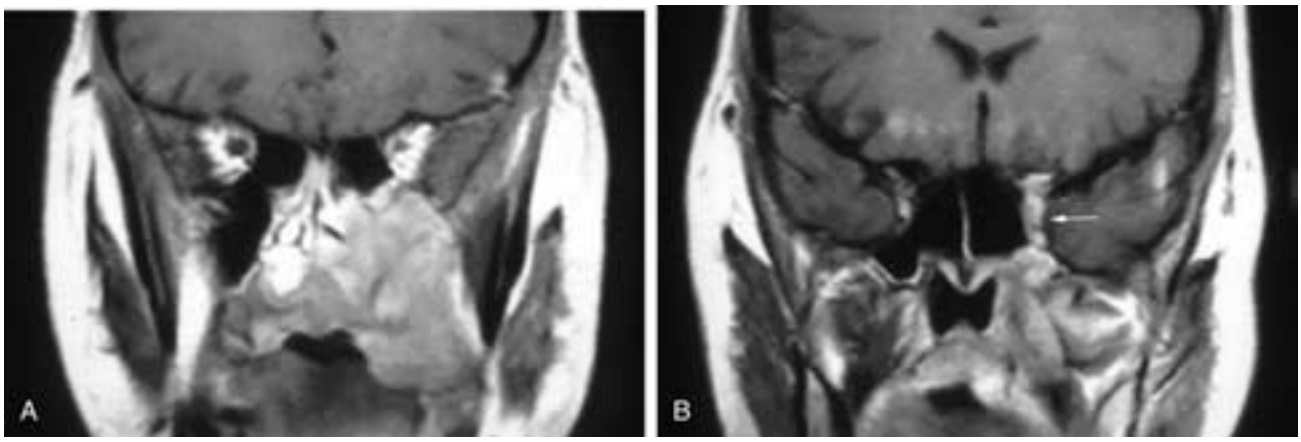

VIEW IMAGE

FIGURE 6-52 Coronal T1-weighted, fat-suppressed, contrast-enhanced MR ventral (**A**) and dorsal (**B**) images show a large mass in the left antrum, lower nasal fossa, and hard palate. The tumor has extended back through the pterygopalatine fossa and invades the left cavernous sinus (*arrow*). This patient had an adenoidcystic carcinoma.

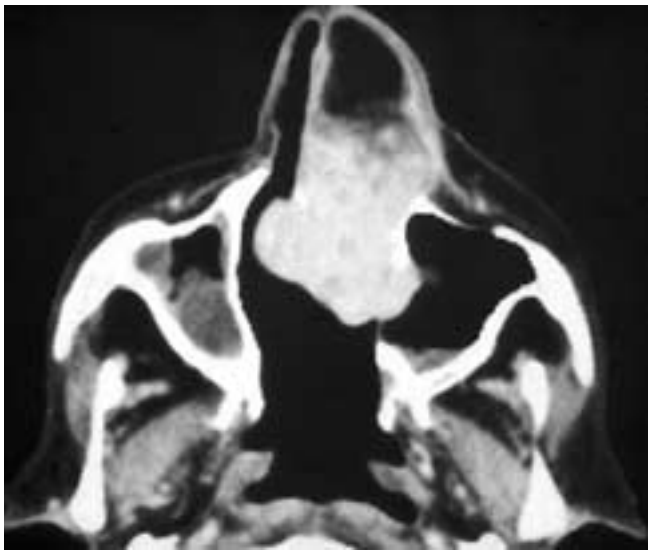

FIGURE 6-53 Axial CT scan shows a bulky nodular mass arising in the nasal septum and laterally displacing the left nose and medial antral wall. This patient had a pleomorphic adenoma.

VIEW IMAGE

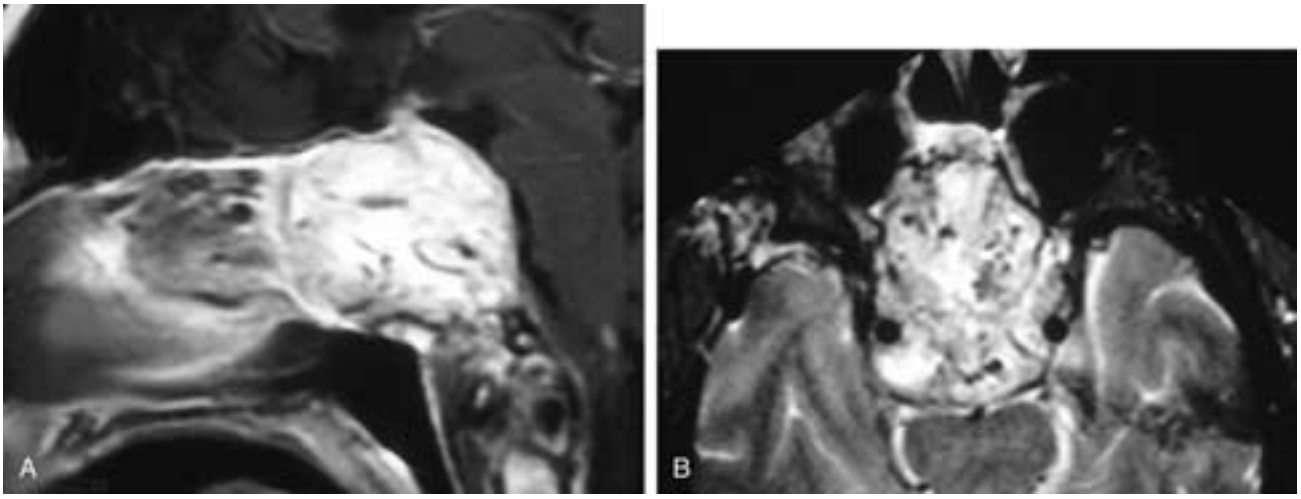

VIEW IMAGE

FIGURE 6-54 Sagittal (**A**) and axial (**B**) T1-weighted, fat-suppressed, contrast-enhanced MR images show an enhancing mass in the sphenoid sinus. There is invasion of the clivus, and there are flow voids within the tumor. This patient had a paraganglioma of the sphenoid sinus.

Copyright © 2003, Mosby, Inc. All rights reserved.

growth due to malignant transformation that may have been related to the radiotherapy.[63]

On imaging, these tumors are usually expansile, enhanced, and may have vascular signal voids on MR imaging. These lesions are discussed in more detail in Chapter 39. When a primary paraganglioma is encountered, it is more likely that the true diagnosis is a well-differentiated sinonasal neuroendocrine carcinoma.

Olfactory Neuroblastoma

Olfactory neuroblastoma (ONB) (historically referred to as esthesioneuroblastoma) is a neural crest–derived neoplasm arising from the olfactory mucosa in the superior nasal fossa. It occurs with a bimodal age distribution, peaking in the second and sixth decades, and representing 16.8% and 22.8% of all sinonasal tumors for these age groups, respectively. However, the age of these patients ranges from 3 to 88 years.[65, 66] ONB usually presents as a solitary soft-tissue nasal polyp that may bleed profusely on biopsy. It may also occur as a bilateral nasal mass; this usually happens in medically neglected patients.

Histologically, ONB is composed of small, relatively bland round malignant cells with scanty cytoplasm. A fibrillary background is characteristic of ONB, and ultrastructurally corresponds to neuronal processes formed by the most differentiated tumor cells. Groups of tumor cells that are centripetally aligned around tangles of neurofibrillary processes appear by light microscopy as Homer-Wright rosettes. An abundance of these rosettes indicates a well-differentiated tumor. Flexner-Wintersteiner rosettes represent evidence of true olfactory differentiation and are seen as gland-like structures formed by columnar or cuboidal tumor cells.

The term *ganglioneuroblastoma* refers to ganglionic maturation within a neuroblastoma. This may be seen at initial tumor presentation (referred to as differentiating neuroblastoma) and is associated with an improved prognosis. Ganglionic maturation may also be seen after a chemotherapeutic response of neuroblastoma. This type of de novo or secondary ganglionic differentiation is not seen in ONB. This may reflect inherent distinctions between olfactory neuroepithelium (a direct extension from CNS neurons) and the postsynaptic sympathetic neuroblasts that give rise to neuroblastomas.

Hyams introduced a four-tier grading system of ONB: grade I ONB represents the most differentiated tumor, with rosette formation and no pleomorphism, mitotic figures, or necrosis, while grade IV ONB reveals no histologic evidence of neuronal/neuroendocrine differentiation, and the findings of pleomorphism, mitotic activity, and necrosis are present. Hyams was able to correlate tumor grade with prognosis. More recently, the question has been raised if grade IV ONB tumors are actually not ONB, but better classified as sinonasal neuroendocrine carcinomas (see below). Additionally, the less differentiated an ONB appears to be, the greater the need to rule out other diagnoses such as undifferentiated carcinoma (sinonasal undifferentiated carcinoma), large cell lymphoma, melanoma, extramedullary plasmacytoma, and embryonal rhabdomyosarcoma. Immunohistochemistry has become the standard adjunctive test to resolve these issues.

The Kadish staging system is a clinically based staging system for sinonasal tumors. Those lesions confined to the nasal cavity are stage A, those with disease in the nasal cavity and one or more paranasal sinuses are stage B, and those with disease extending beyond the nasal cavity and paranasal sinuses are stage C.[67] Both the Hyams grading system and the Kadish staging system can be used as independent predictors of outcome.[68] In the Kadish staging system, the 5-year survival rates for patients with stage A, B, and C tumors are 75%, 68%, and 41.2% respectively.[66, 67] Craniofacial resection can be curative for up to 90% of patients, as this approach addresses microscopic disease at the cribriform plate and in the olfactory bulbs, which are below the detection threshold of current radiographic imaging.[69] By contrast, a recurrence rate of nearly 50% can be seen after an extended lateral rhinotomy for stage A and stage B patients. The 5-year survival rate for all patients is 69%.[70] A more recent report indicates 80.4% disease-free survival at 8 years.[71] When survival is stratified for tumor grade, the 5-year disease-free survival for patients with low-grade and high-grade tumors is 80% and 40%, respectively.[72] Locoregional and distant metastasis occurs in up to 38% of patients.[73] Late recurrences or metastatic disease can occur up to two decades after initial presentation. Negative prognostic factors include female sex, age over 50 years at presentation, tumor recurrence, metastasis, high tumor grade, and Kadish stage C at presentation.[72]

Preoperative imaging is crucial to tumor mapping and planning the extent of surgery. On CT, ONBs usually are homogeneous, enhancing masses that primarily remodel bone. They commonly extend into the ipsilateral ethmoid and maxillary sinuses and rarely involve the sphenoid sinuses. When large, they can extend to involve both sides of the nasal cavity and the paranasal sinuses. Gross calcifications can occur within the tumor mass, and they can also be seen histologically.[74] On MR imaging these tumors have an intermediate signal intensity on all imaging sequences, with the T2-weighted signal intensity being higher.[75] They also enhance with contrast (Figs. 6-55 to 6-61). When imaging these tumors, the radiologist must carefully evaluate the floor of the anterior cranial fossa for tumor extension into this region. If intracranial tumor extension is seen, the imager should attempt to distinguish between tumor that remains extraaxial (with only dural disease) and tumor that has invaded brain, as such a differentiation alters surgery. In some of the larger tumors that have intracranial extension, peripheral tumor cysts can occur at the margins of the intracranial mass. These cysts have their broadest base on the tumor, and when seen, they strongly suggest the imaging diagnosis of this tumor.[76]

Sinonasal Neuroendocrine Carcinoma and Sinonasal Undifferentiated Carcinoma

Sinonasal neuroendocrine carcinoma (SNEC) and sinonasal undifferentiated carcinoma (SNUC) were first described in the 1980s, but remarkably few series of either have been reported. SNEC and SNUC can be conceptualized

Copyright © 2003, Mosby, Inc. All rights reserved.

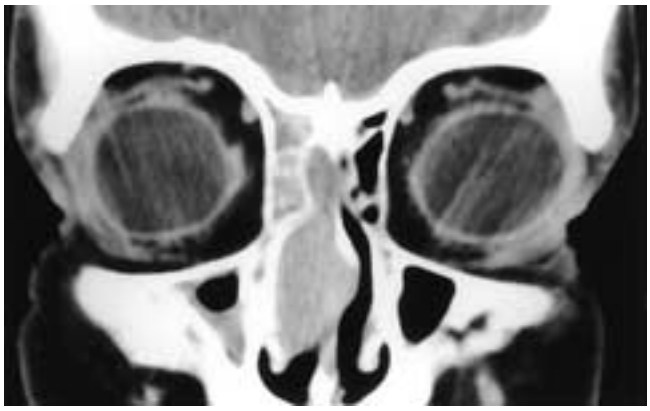

VIEW IMAGE

FIGURE 6-55 Coronal CT scan shows an expansile right nasal fossa mass obstructing the right ethmoid and maxillary sinuses. The lesion is limited to the sinonasal cavities. This patient had an olfactory neuroblastoma.

FIGURE 6-56 Coronal T2-weighted MR image shows a small right nasoethmoid mass (*arrow*) of intermediate signal intensity with inflammatory changes in the lateral right ethmoid complex and both maxillary sinuses (high signal intensity). The tumor extends through the cribriform plate. This patient had an olfactory neuroblastoma.

VIEW IMAGE

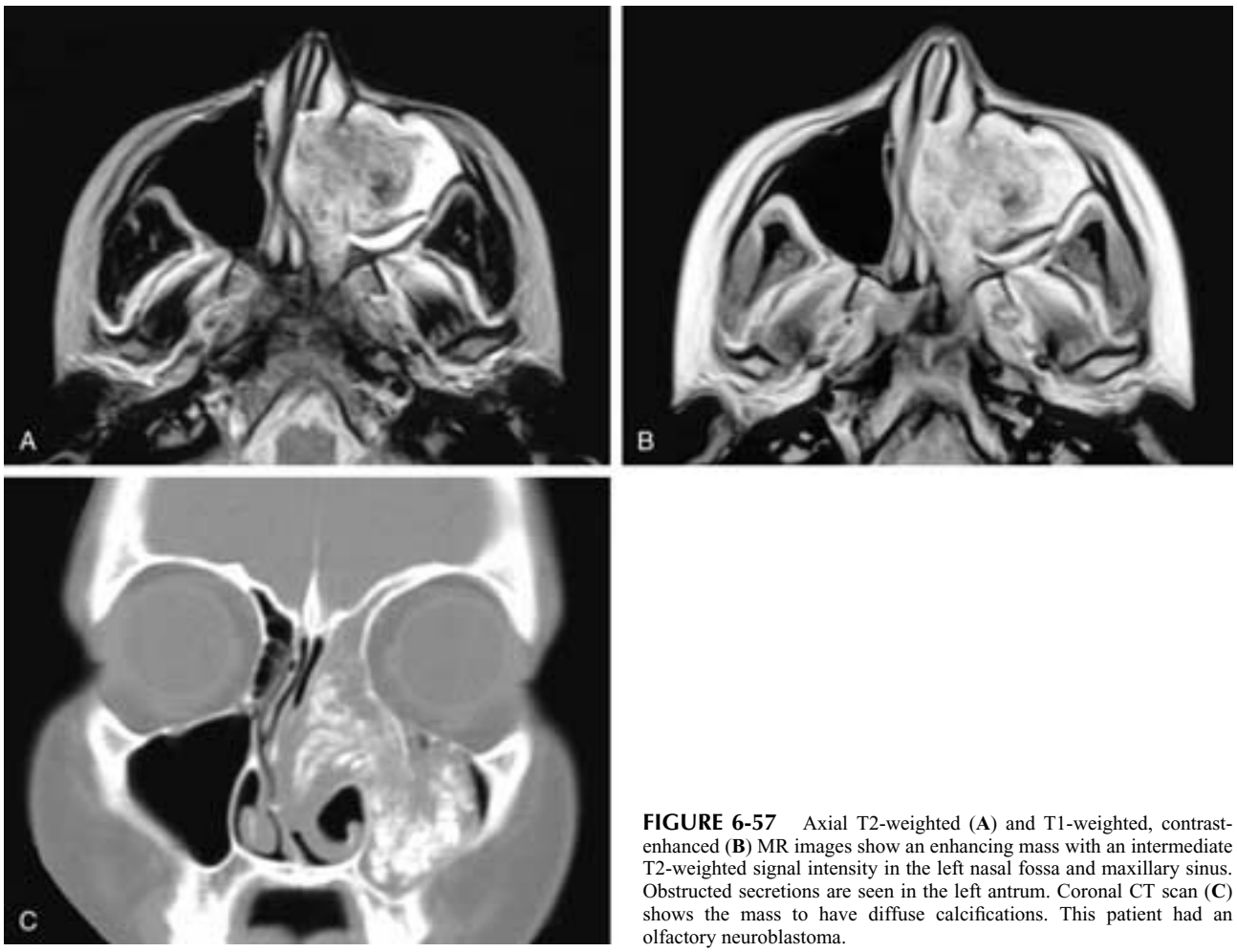

FIGURE 6-57 Axial T2-weighted (**A**) and T1-weighted, contrast-enhanced (**B**) MR images show an enhancing mass with an intermediate T2-weighted signal intensity in the left nasal fossa and maxillary sinus. Obstructed secretions are seen in the left antrum. Coronal CT scan (**C**) shows the mass to have diffuse calcifications. This patient had an olfactory neuroblastoma.

VIEW IMAGE

Copyright © 2003, Mosby, Inc. All rights reserved.

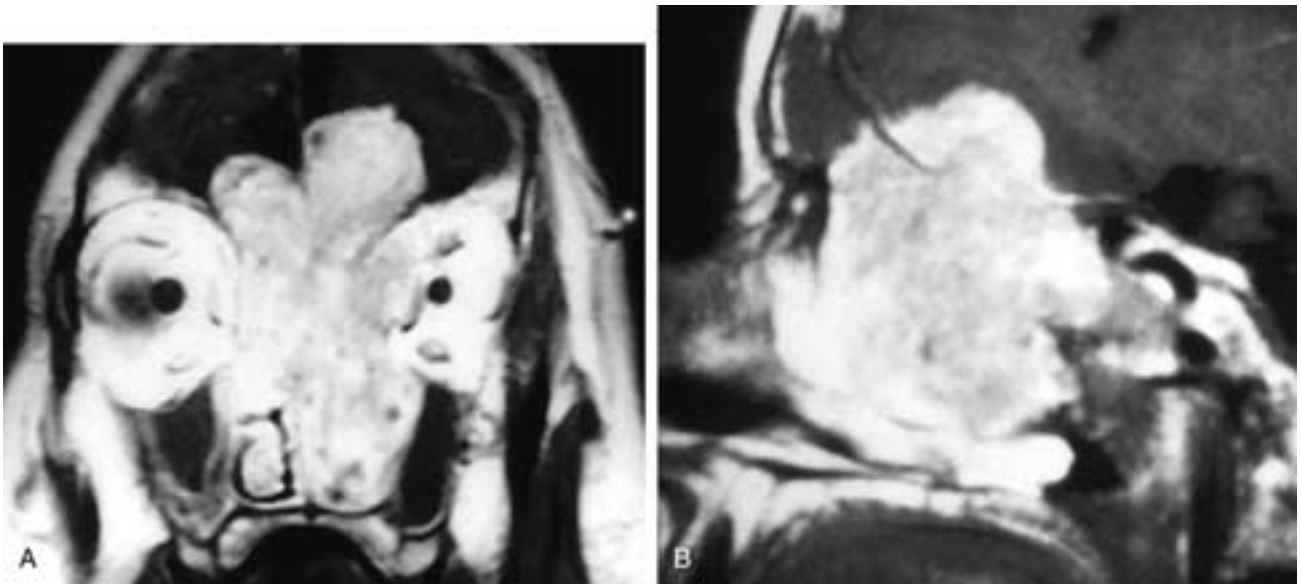

VIEW IMAGE

FIGURE 6-58 Coronal (**A**) and sagittal (**B**) T1-weighted, contrast-enhanced MR images show a large, enhancing nasal fossa mass that has broken through the floor of the anterior cranial fossa and displaced the frontal lobes upward. The tumor has also extended into each orbit and into the left maxillary sinus. This patient had an olfactory neuroblastoma.

as being part of a spectrum of neuroendocrine-type tumors, with ONB representing the most specialized and differentiated neuroendocrine tumors and SNUC having dubious or weak neuroendocrine qualities.

SNEC was first proposed in 1982, when it became clear that some tumors were less differentiated than ONB but still retained neuroendocrine features.[77] Many had been buried in the literature as oat cell carcinoma, atypical carcinoid, malignant paraganglioma, or anaplastic or undifferentiated carcinoma. SNEC is defined as a malignant neoplasm with evidence of neurosecretory granules. Lacking evidence of a neurofibrillary background by light microscopy, as is seen in ONB, it is less differentiated and more ''carcinomatous'' than ONB. The term *sinonasal undifferentiated carcinoma* was first coined by Frierson and colleagues to define a group of sinonasal tumors with no obvious differentiation that

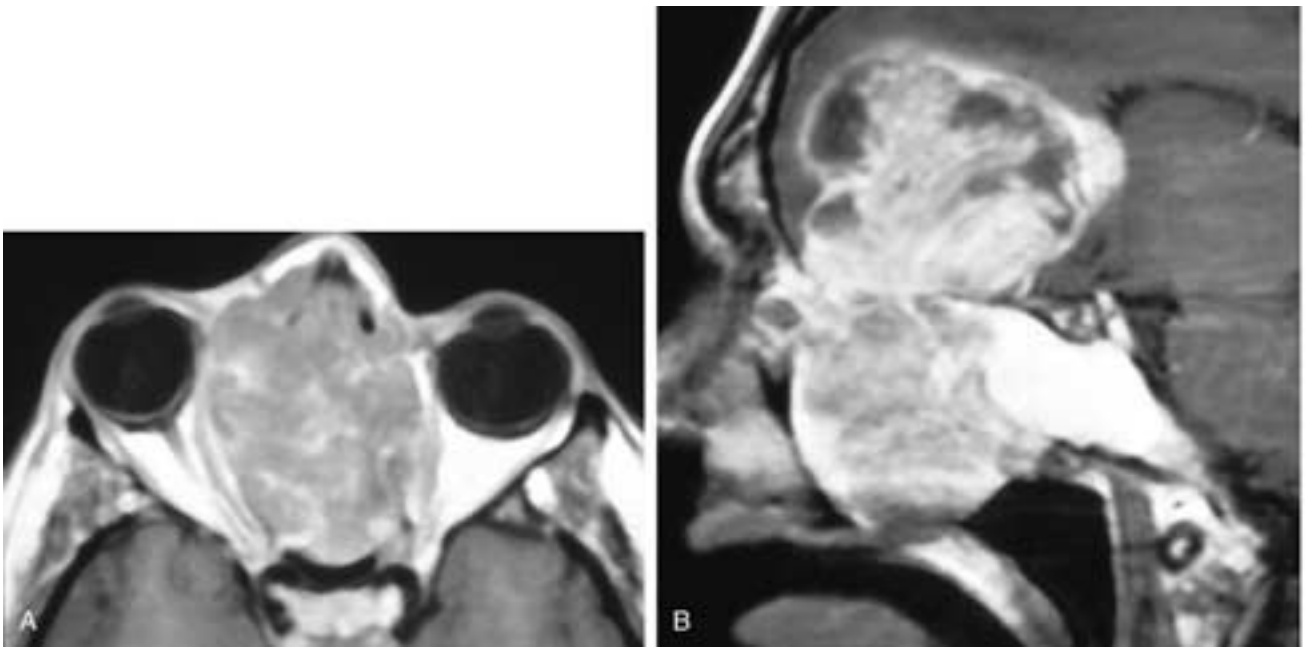

VIEW IMAGE

FIGURE 6-59 Axial (**A**) and sagittal (**B**) T1-weighted, contrast-enhanced MR images show an enhancing mass in the ethmoids and nasal fossa. The mass has extended into the anterior cranial fossa, and several small cystic areas are seen within the intracranial portion of the tumor. The mass has also extended into both orbits, and the sphenoid sinus is obstructed. This patient had an olfactory neuroblastoma.

Copyright © 2003, Mosby, Inc. All rights reserved.

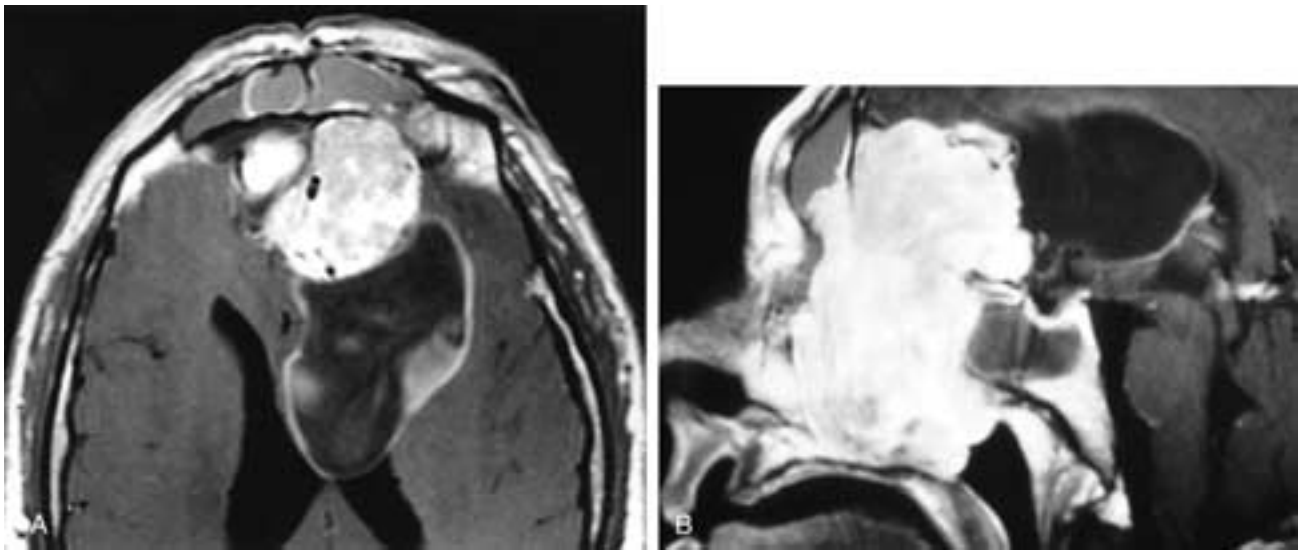

VIEW IMAGE

FIGURE 6-60 Axial (**A**) and sagittal (**B**) T1-weighted, fat-suppressed, contrast-enhanced MR images show a large, enhancing sinonasal mass that obstructs the frontal and sphenoid sinuses and extends intracranially. There is a large cyst at the intracranial margin of the tumor. This patient had an olfactory neuroblastoma.

were united by their obviously aggressive clinical course.[78] These tumors were previously diagnosed as ''anaplastic'' or ''undifferentiated.'' A possible etiologic relationship to heavy metal exposure, coal mining, the chemical industry, and shoemaking has been reported.[78, 79]

Few demographic or prognostic comparisons can be made between SNUC, SNEC, and ONB due to their rarity. In the group reported by Silva et al., 20 patients diagnosed with SNEC were compared with 9 patients with ONB.[77] The mean age of the patients with SNEC was 50, while that of the patients with ONB was 20. However, other studies of larger groups of ONB patients reflect the true bimodal age peak of ONB, with a median age of 49.[78] Gallo et al. found that the mean age of patients with SNUC was 56.7 for men and 68 for women.[79] Most cases of SNEC/SNUC occur in the same sites as ONB (superior nasal cavity, superior turbinates, ethmoids). Presenting symptoms relate to a sinonasal tumor: nasal obstruction, epistaxis, decreased visual acuity, diplopia, and pain.

The radiographic findings of SNEC and SNUC are usually indistinguishable from those of SCC: an aggressive soft-tissue mass that erodes and invades adjacent bone rather than remodeling it (Fig. 6-62). In contrast, the CT and MR imaging findings of ONB are usually those of an expansive mass. In smaller SNEC lesions, the mass is usually polypoid and confined to one nasal fossa, often with involvement of a surrounding ethmoid or medial maxillary sinus margin. Larger lesions may extend into adjacent structures such as the orbit and the cranium.

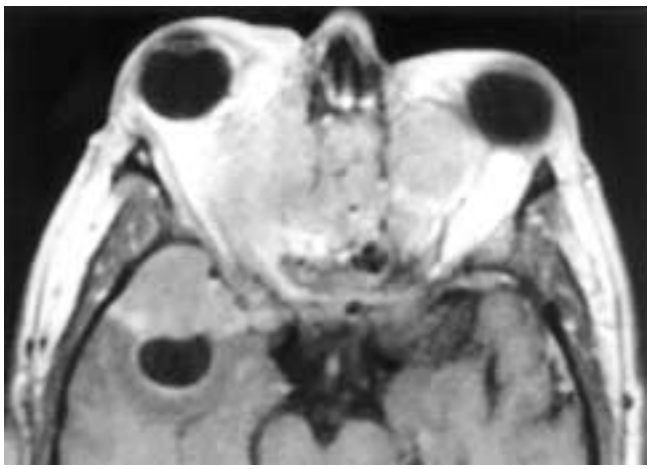

VIEW IMAGE

FIGURE 6-61 Axial T1-weighted, contrast-enhanced MR image on a patient who previously had a craniofacial resection for an olfactory neuroblastoma. There is a large enhancing recurrence extending into the orbits and the anterior cranial fossa. Note the small, broad-based cyst at the intracranial margin of the tumor. Such a cyst is highly suggestive of the diagnosis. This patient had an olfactory neuroblastoma.

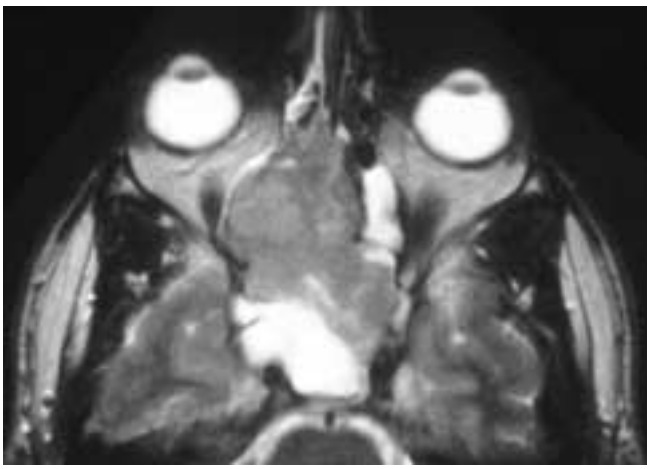

FIGURE 6-62 Axial T2-weighted MR image shows a destructive mass in the nasal fossae and both ethmoid complexes. The tumor has extended into the right orbit and the sphenoid sinus, which contains obstructed secretions. Both cavernous sinuses are also invaded. This patient had an olfactory carcinoma.

VIEW IMAGE

Copyright © 2003, Mosby, Inc. All rights reserved.

Histologically, SNEC is composed of cells with fine ''salt and pepper'' chromatin, with a variable amount of cytoplasm. Architecturally, classic neuroendocrine patterns can be seen: nesting, organoid, trabecular, and/or a ribboning pattern. Glandular-type differentiation may be seen. SNUC is composed of cells with little cytoplasm and large nuclei. No histologic tendency toward neuroendocrine architecture is seen. However, SNEC/SNUC and ONB may also appear quite similar histologically; immunohistochemistry is crucial for sorting out these entities.

In terms of clinical course, the prognosis of SNEC and SNUC seems to be related to the stage at the time of diagnosis. Silva et al. reported 5- and 7-year survival rates of 100% and 88%, respectively, for his cohort of 20 patients with SNEC but noted a propensity for early metastases and local recurrence. They reported evidence of metastases to lymph nodes, brain, and spine in all cases of theirs in which metastatic disease was present, except for one where the lungs and femur were involved.[77] Similarly, in our study, 7 of the 10 patients developed metastatic disease, either to cervical lymph nodes (2 cases), pelvis (2 cases), thoracic spine (1 case), brain (1 case), or skeletal bones (1 case). In our study, two patients with SNEC died of disease at 14 and 41 months. The other two patients in our series with SNEC were alive, with no evidence of disease, at 31 and 108 months. Outcomes for SNUC have been reported to be generally poor.

Malignant Melanoma

Melanocytes in the sinonasal tract migrate from the neural crest during embryonic development.[13] The etiology of sinonasal melanomas is unknown, but they represent less than 3.6% of sinonasal neoplasms. Less than 2.5% of all malignant melanomas occur in the sinonasal cavities. These melanomas are two or three times more common in the nose than in the sinuses and most frequently arise from the nasal septum.[80, 81] Occasionally, they develop around the inferior and middle turbinates. The antrum is involved in 80% of paranasal sinus cases, usually in conjunction with the nasal cavity. Rare cases develop in the ethmoid sinuses. The frontal and sphenoid sinuses are virtually never involved as primary sites.[13, 80–82] Sinonasal melanomas generally develop in patients 50 to 70 years of age. The most common complaints are nasal obstruction and epistaxis, with pain occurring as an initial complaint in only 7% to 16% of patients.[13, 80, 81] Satellite tumor nodules are common.

Wide local surgical excision with or without postoperative radiation therapy is the treatment of choice. Up to 40% of patients with sinonasal melanomas present with positive neck nodes.[83, 84] Up to 65% of patients with melanoma have a local recurrence or metastases within the first year after surgery. Metastatic disease usually follows local recurrence.

Metastases tend to affect the lungs, lymph nodes, brain, adrenal glands, liver, and skin. Treatment of recurrences yields surprisingly good results.[13] The median survival time is 18 to 34 months.[83, 84] Occasional cases may be mysteriously dormant for up to a decade before there is an explosive recurrence. Nasal cavity melanomas have a better prognosis than tumors originating in the paranasal sinuses; the average survival time of all of these patients is 2 to 3 years, and the 10-year survival rate is 0.5%. The differential diagnosis of melanoma includes undifferentiated carcinoma, lymphoma, embryonal rhabdomyosarcoma, ONB, and extramedullary plasmacytoma.[41]

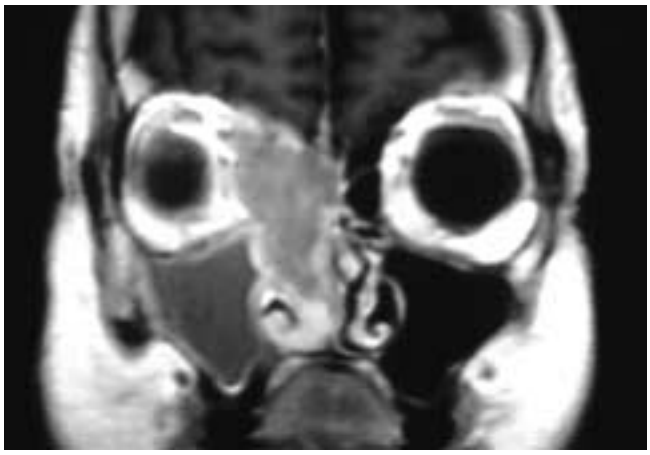

FIGURE 6-63 Coronal T1-weighted, contrast-enhanced MR image (on the same patient as in Fig. 6-8) shows an enhancing mass in the right ethmoid complex and nasal fossa. The tumor has broken into the right orbit but has a smooth interface with the orbital fat. The right antrum is obstructed by the mass. This patient had a melanoma.

VIEW IMAGE

Melanomas tend to remodel bone, although elements of frank bone erosion also may be present. Because of their rich vascular network, melanomas enhance well on contrast-enhanced CT and MR scans, and their MR imaging appearance is usually that of a homogeneous mass of intermediate signal intensity on all imaging sequences. However, some melanomas have high T1-weighted signal intensity primarily because of the presence of hemorrhage and, to a lesser degree, paramagnetic melanin (Figs. 6-8 and 6-63 to 6-67). These melanomas may have a deceptively noninvasive border on imaging, suggesting that they are low-grade lesions. Such lesions emphasize the lack of correlation between the imaging evidence of a noninvasive

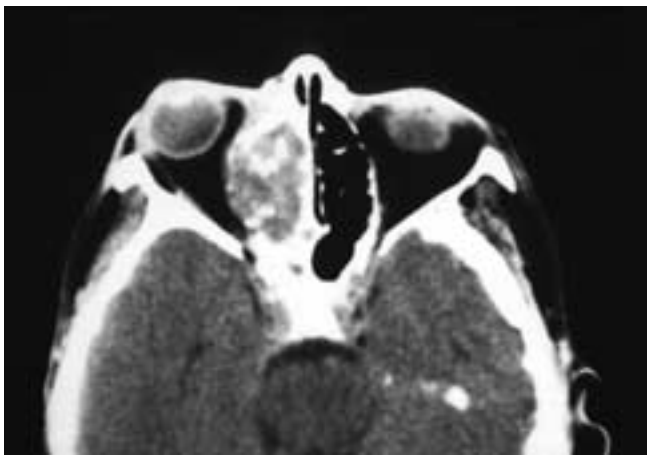

FIGURE 6-64 Axial CT scan shows an expansile mass in the right ethmoid complex that is bulging into the right orbit. Most of the lamina papyracea and ethmoid septations are destroyed or thinned. Radiodensities within the mass were residual pieces of bone. This patient had a melanoma.

VIEW IMAGE

Copyright © 2003, Mosby, Inc. All rights reserved.

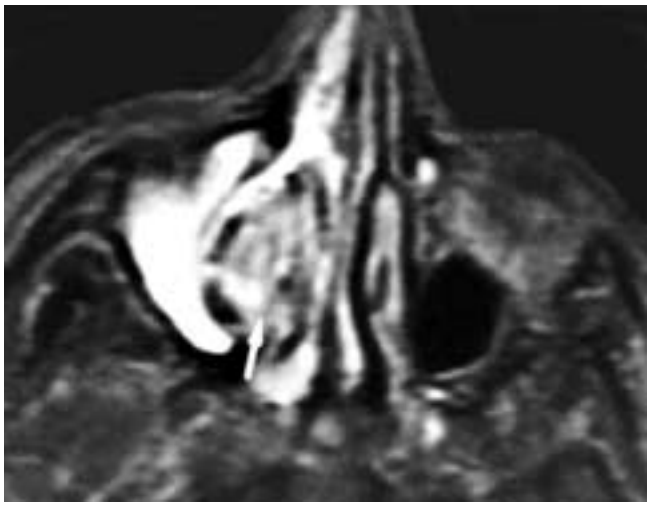

VIEW IMAGE

FIGURE 6-65 Axial T2-weighted MR image shows an expansile right nasal fossa mass (*arrow*) that obstructs the right antrum. The tumor has a low to intermediate signal intensity, and the obstructed secretions have a high signal intensity. This patient had a melanoma.

tumor margin and the biologic aggressiveness of the tumor. Most of these tumors occur in the nasal fossa. However, a rare case was reported to arise in the frontal sinus in a patient who presented with forehead swelling and progressive confusion.[85]

Pathologically, melanomas are known as the ''great mimickers,'' as they produce myriad patterns composed of varying cell types. Melanomas may be epithelioid, sarcomatoid, plasmacytoid, or clear cell. Pink nucleoli, intranuclear holes, and cytoplasmic melanin can be seen (Fig. 6-68). The diagnosis can be confirmed immunohistochemically by the expression of S100 and HMB-45.

Melanotic Neuroectodermal Tumor of Infancy

This is an extremely rare neuroectodermal tumor that occurs almost exclusively prior to the age of 1 year. It is a rapidly growing soft-tissue mass of either the upper or lower jaws, the CNS, or the orbit. The anterior maxilla is the most common site, accounting for 71% of all cases. Bone invasion may occur. Histologically, these tumors are distinctive, with tubular or alveolar formations of large melanin-containing cells around nests of smaller neuroblastic cells. A series of 20 cases has been reported by Kapadia and colleagues, 5 of 12 (45%) patients with follow-up developed recurrence within 4 months of diagnosis, but none metastasized.[87] Treatment is usually local excision. Only two or three malignant cases have been reported, with metastases to lymph nodes, liver, bones, adrenal glands, and soft tissues.[65, 86, 87]

Primitive Neuroectodermal Tumor and Ewing's Sarcoma

Ewing's sarcoma (ES) is a highly malignant small, round cell tumor that accounts for 5% to 10% of all primary bone malignancies. About 60% of cases occur in the lower extremities and pelvis.[88] Almost 90% of patients are between 5 and 30 years of age at diagnosis. Only 1% to 4% of all ES occur in the bone and soft tissue of the head and neck, most commonly the mandible, followed by the maxilla, calvaria, and cervical vertebrae.[89] ES rarely arises from the nasal cavity/paranasal sinuses and has been seen as a complication of radiation therapy for retinoblastoma.[90–92]

Primitive neuroectodermal tumor (PNET) is a malignancy of childhood and early adulthood that is closely related to ES. PNET occurs most commonly as a soft tumor of the lower truck or lower extremities. Association with a major nerve trunk has been seen in one third of the cases. PNET does occur in the head and neck, usually in the sinonasal cavities (Fig. 6-69) and has also been reported in patients who have survived retinoblastoma.[93–96] Patients with ES/PNET typically present with pain and localized swelling.

Radiographically with ES, a destructive soft-tissue lesion is seen with a typical ''onion skin'' type of periosteal reaction. Less often with both ES and PNET, a ''sunburst'' type of periosteal reaction can be seen.

Pathologically, ES and PNET appear as malignant ''small blue round cell tumors'' that are relatively bland in appearance. The distinction between these two neoplasms is based on immunophenotypic and ultrastructural findings. PNET shows some evidence of neuroendocrine differentiation, such as neurosecretory granules and cellular processes by electron microscopy (EM) and evidence of expression of two or more neuroendocrine markers (this neuroendocrine differentiation is quantitatively much less than that seen in ONB). ES, on the other hand, reveals no evidence of any kind of differentiation. Both tumors are associated with chromosomal translocation (11;22) (q24;q12) that forms the fusion protein EWS/FLI-1; EWS/ERG.

The treatment of choice for ES and PNET is local excision, with radiation therapy for the incompletely excised

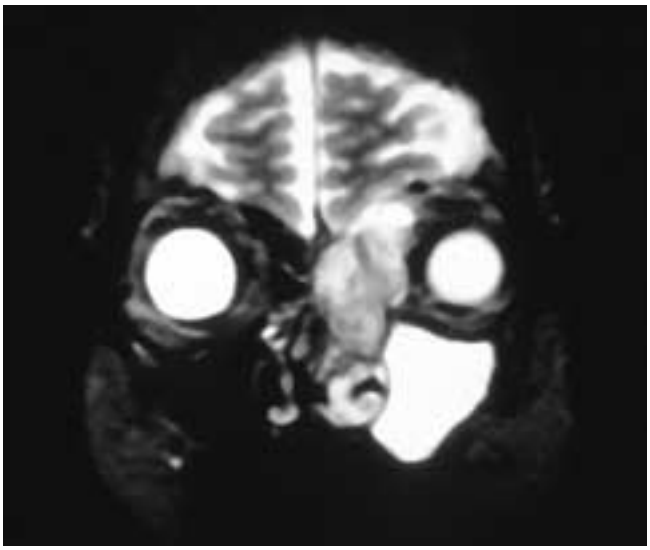

FIGURE 6-66 Coronal T2-weighted MR image shows a mass in the left ethmoid complex and nasal fossa. The tumor has extended into the left orbit and has a smooth interface with the orbital fat. The adjacent sinuses are obstructed. This patient had a melanoma.

VIEW IMAGE

Copyright © 2003, Mosby, Inc. All rights reserved.

FIGURE 6-67 Axial CT scan (**A**) shows an enhancing, expansile polypoid mass in the left nasal fossa. The left antrum is obstructed. There is virtually no bone destruction associated with this benign-appearing lesion. Axial CT scan (**B**) on another patient shows a primarily expansile right nasal fossa mass that obstructs the right antrum. There is a greater element of bone destruction than in **A**. Coronal CT scan (**C**) on a third patient shows a primarily destructive mass in the nasal fossae, ethmoid sinuses, and left maxillary sinus. The tumor has invaded the left orbit and the floor of the anterior cranial fossa. All of these patients had melanomas. These three cases illustrate the variation of the imaging appearance of this tumor.

VIEW IMAGE

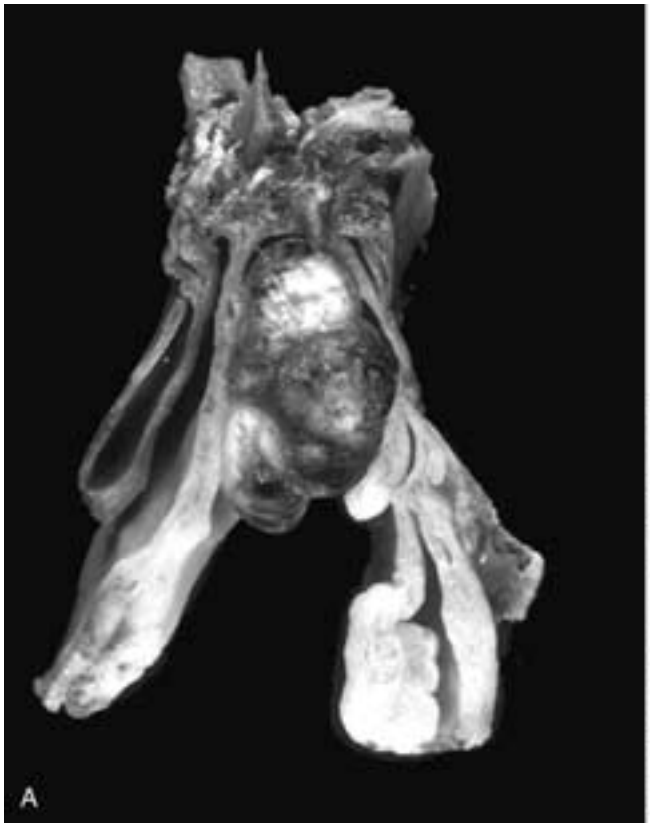

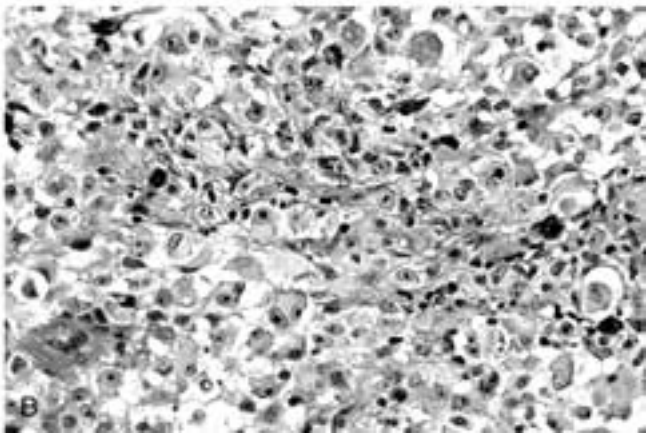

FIGURE 6-68 Melanoma: Gross specimen (**A**) shows a polypoid pigmented tumor of the superior nasal cavity. In **B**, brown melanin pigment is seen within these highly malignant cells.

VIEW IMAGE

Copyright © 2003, Mosby, Inc. All rights reserved.

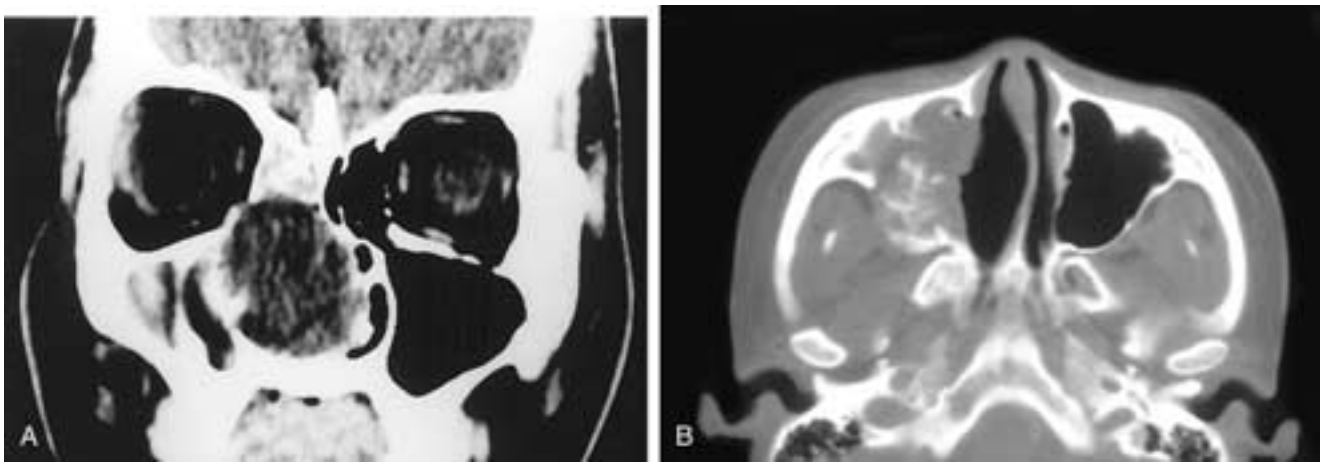

VIEW IMAGE

FIGURE 6-69 Coronal CT scan (**A**) shows a mucoid attenuation mass expanding the right nasal fossa. Bony thickening is present along the adjacent right nasal vault wall. Axial CT scan (**B**) taken after biopsy of the mass shows irregular tumoral bone within the right antrum bulging into the infratemporal fossa. This patient had a primitive neuroectodermal tumor.

lesions. Micrometastases, which are present in 15% to 30% of patients, are treated with chemotherapy. The 5-year survival rates have risen from less than 10% in the prechemotherapy era to the current 60% to 79%. ES recurs locally in 13% to 20% of patients (65% at postmortem), usually coinciding with the completion of chemotherapy. The tumors metastasize to the lungs (86%), skeleton (69%), pleural cavity (46%), lymph nodes (46%), dura and meninges (27%), and CNS (12%). Because of its rarity in the facial area, ES of the sinonasal cavities probably should be considered a metastasis from an infraclavicular primary tumor until proven otherwise. The significance of the distinction between ES and PNET is that PNET is somewhat more chemosensitive than ES and is associated with a longer mean survival after multimodality therapy.

Peripheral Nerve Sheath Tumors

Schwannoma

Peripheral nerve sheath tumors is the currently preferred term for benign and malignant neoplasms that arise from neuronal axons and/or their supporting cells (Schwann cells and fibroblasts). Confusing terminology has arisen in the literature, with many names representing the same lesion. One of the difficulties in discussing neurogenic neoplasms is that there is also controversy regarding whether nerve sheath tumors arise from Schwann cells or neuroectodermal perineural cells.[65] Today most investigators use the term *Schwann cell* to describe both of these cells. The terms *schwannoma, neurinoma, neurilemoma,* and *perineural fibroblastoma* all refer to the same tumor.[1] Peripheral nerve sheath tumors are common in the head and neck. Up to 40% of these tumors occur in head and neck sites. Only 4% of these tumors occur in the sinonasal cavities.[97–99]

A schwannoma is defined as a tumor composed entirely of nerve-supporting cells, without neuronal elements. It is a benign, encapsulated, slowly growing tumor that occurs in patients 30 to 60 years of age. It is two to four times more common in females than in males. The most common sites are the vagus nerve in the neck and the eighth cranial nerve. Only about 65 cases have been reported in the sinonasal cavities, and most of these occurred in the nasal fossa, maxillary sinuses, and ethmoidal sinuses.[1, 65, 100] In rare cases, a schwannoma can occur in the olfactory bulbs (Fig. 6-70). This is a distinctly different entity than ONB. The most common complaint is a painless mass.

Schwannomas rarely undergo malignant change. At surgery, the nerve of origin may occasionally be found to be stretched over the tumor. In these cases, the surgeon may be able to extirpate the lesion while preserving the nerve. By contrast, neurofibromas are defined as having neuronal elements as an integral part of the tumor. They appear as swellings arising directly from the nerve, and the nerve must be sacrificed to excise the lesion.[65]

Histologically, schwannomas have two major components: the Antoni A areas, characterized by a compact arrangement of elongated spindled cells, and the Antoni B areas, characterized by a loose myxoid stroma with few spindled cells. This variation is reflected in their CT appearance, which ranges from a variably enhancing homogeneous ovoid mass to a primarily cystic lesion.[101] On contrast-enhanced CT, about one third of the cases enhance more than muscle, one third have attenuation values similar to that of muscle, and one third are primarily cystic.[99] The enhancement on CT and MR images occurs presumably because of extravascular extravasation of the contrast into a poorly vascularized tumor matrix. The MR imaging characteristics of schwannomas are those of an intermediate T1-weighted and a variable T2-weighted signal intensity that reflect whether the lesion is highly cellular (intermediate signal intensity) or cystic and stromal (nonhomogeneously high signal intensity). All schwannomas are roughly ovoid shaped, noninfiltrating, bone-remodeling lesions, and any site of aggressive bone destruction should raise the possibility of a malignancy rather than a schwannoma (Figs. 6-71 to 6-74).

Copyright © 2003, Mosby, Inc. All rights reserved.

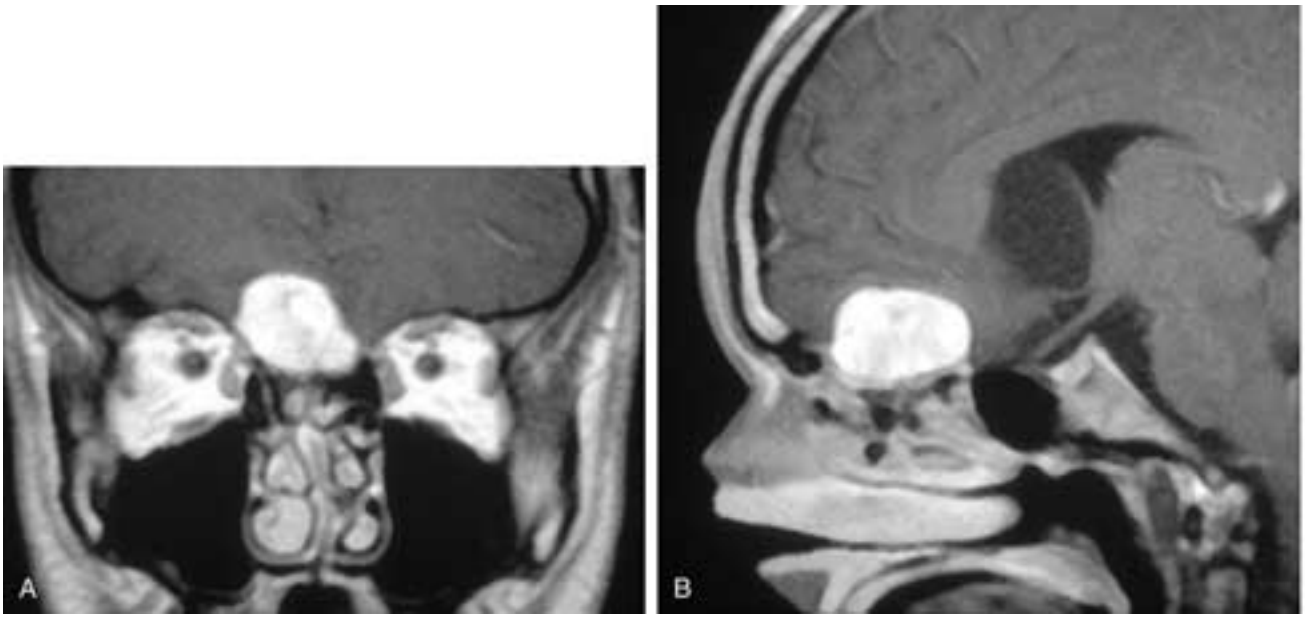

VIEW IMAGE

FIGURE 6-70 Coronal (**A**) and sagittal (**B**) T1-weighted, contrast-enhanced MR images show an ovoid mass sitting on the cribriform plate region and minimally displacing both the fovea ethmoidalis and the cribriform plate caudally. This was a rare schwannoma of the olfactory bulbs of the first cranial nerve. (Case courtesy of Dr. Geoffrey Parker.)

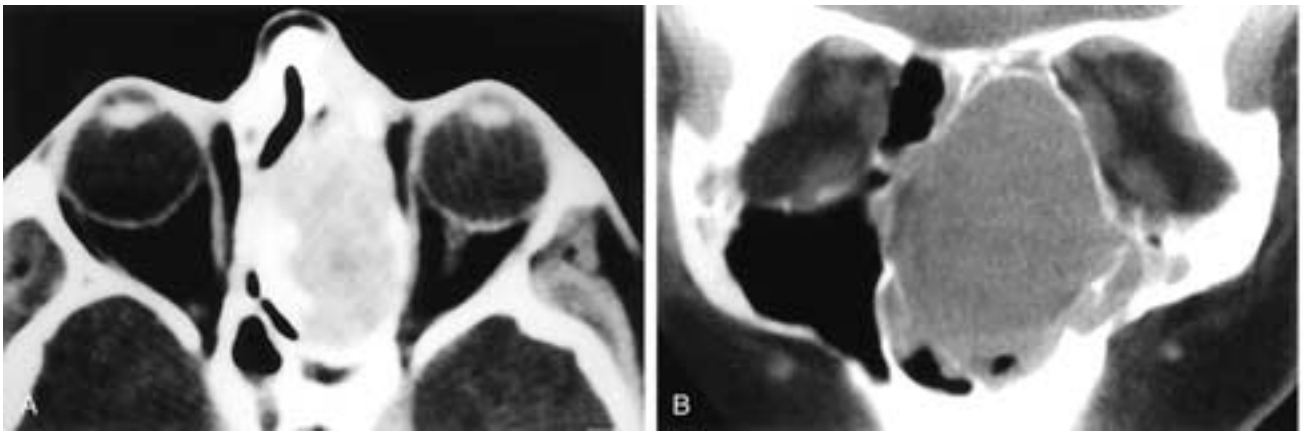

VIEW IMAGE

FIGURE 6-71 Axial CT scan (**A**) shows an expansile, homogeneous mass in the left ethmoid sinuses that has remodeled the surrounding bone. Coronal CT scan (**B**) on another patient shows a large, expansile mass in the left nasal fossa and ethmoid sinuses. The left antrum and right ethmoid sinuses are obstructed by the mass. The surrounding bone is remodeled rather than destroyed. Both of these patients had a schwannoma. Also see Fig. 6-7C.

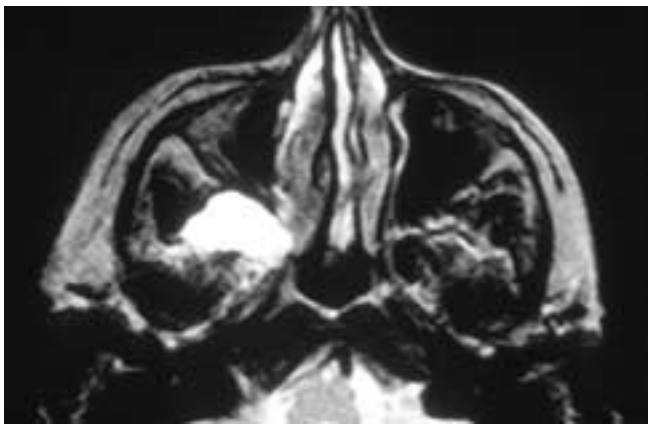

VIEW IMAGE

FIGURE 6-72 Axial T2-weighted MR image shows a high signal intensity mass in the right pterygopalatine and infratemporal fossae. The adjacent posterior antral wall has been remodeled anteriorly. This patient had a schwannoma.

Copyright © 2003, Mosby, Inc. All rights reserved.

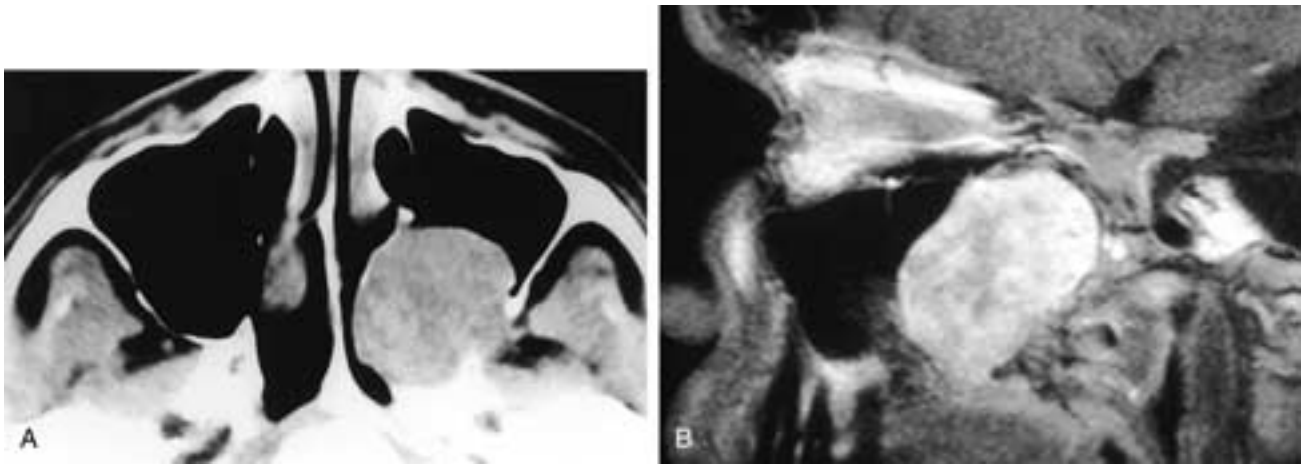

VIEW IMAGE

FIGURE 6-73 Axial CT scan (**A**) and sagittal T1-weighted, fat-suppressed, contrast-enhanced MR image (**B**) show an expansile mass in the pterygopalatine fossa that has remodeled the posterior maxillary sinus wall anteriorly. This patient had a schwannoma.

Neurofibroma

Neurofibroma is a benign, fairly well-circumscribed, but nonencapsulated nerve sheath tumor. Histologically, it is relatively uniform, composed of fibroblastic cells and neuronal elements within a collagenized matrix. Neurofibromas may occur as a solitary tumor or as multiple tumors. Neurofibromas, especially in a young patient, may herald the onset of other tumors with neurofibromatosis (von Recklinghausen's disease). This disease is transmitted as an autosomal dominant trait with variable penetrance. It is characterized by café au lait spots, multiple neurofibromas, and characteristic bone lesions.[102] Multiple neurofibromas are more likely to be associated with neurofibromatosis (Fig. 6-75).[99] Approximately 8% (5% to 15%) of these tumors may have malignant degeneration.[103, 104] The clinical appearance of a plexiform neurofibroma is considered pathognomonic of neurofibromatosis even in the absence of other signs. This tumor usually remains within the confines of the perineurium and resembles a ''giant nerve,'' a ''bag of worms,'' or a ''string of beads.''[65]

Neurofibromas can have a variable CT appearance, depending in part on the degree of cystic degeneration and fatty replacement present within the lesion. On contrast-enhanced CT, these tumors may enhance homogeneously, contain multiple cystic areas, or have predominantly fatty attenuation. The degree of fatty replacement within some neurofibromas is far more extensive than that ever seen in schwannomas and may at times cause the radiologist to suggest the diagnosis of lipoma. Neurofibromas remodel bone and do not cause aggressive bone destruction. They are roughly ovoid in shape and have noninvasive margins. If bone has been destroyed, the possibility of a malignant degeneration should be considered. On MR imaging they usually are nonhomogeneous tumors with overall intermediate T1-weighted and high T2-weighted signal intensities. The plexiform lesions in particular often have a fairly high T2-weighted signal intensity and have a ''bag of worms'' configuration rather than a solitary ovoid shape.

Traumatic Neuroma

Traumatic neuroma is not a true neoplasm but a reparative lesion that occurs after disruption of a peripheral nerve. If the proximal portion of the nerve cannot reestablish contact with the distal portion, the proliferating Schwann cells and axons grow haphazardly and form a traumatic neuroma. Excision with approximation of the nerve endings is the treatment of choice.[65]

Malignant Peripheral Nerve Sheath Tumor

Malignant peripheral nerve sheath tumor (MPNST), a term that has replaced *malignant schwannoma,* refers to a neuroectodermal sarcoma that is the malignant counterpart of a neurofibroma.[105] Up to half of MPNSTs occur in patients with neurofibromatosis (von Recklinghausen disease). The typical solitary MPNST occurs in adults, usually between the third and sixth decades of life. Only 9% to 14% of MPNSTs are found in the head and neck. The cranial nerves, large cervical nerves, sympathetic chain, and inferior alveolar nerve are the most commonly involved nerves. Symptoms include an enlarging mass, occasional pain, paresthesia, muscle weakness, and atrophy.[65]

Schwann cells are modified fibroblasts that produce collagen and have a spindled morphology. Some MPNSTs can then be confused histologically with fibrosarcomas.[65] Association with a nerve trunk, immunohistochemical expression of S-100, and ultrastructural evidence of redundant basement membrane and cellular processes aid in establishing the correct diagnosis. MPNSTs associated with neurofibromatosis behave more aggressively than isolated lesions. The 5-year survival rates are 15% to 30% with neurofibromatosis and 27% to 75% without it. Tumors that exceed 7 cm in size, have more than 6 mitoses per 10 high-power fields, and are located near the central body axis have a poorer prognosis. Local recurrences and hematogenous pulmonary metastases are common, whereas lymph node metastases are rare.[106] Their imaging characteristics may be similar to those of SCC (Fig. 6-63).

Copyright © 2003, Mosby, Inc. All rights reserved.

Granular Cell Tumor

Granular cell tumors (histologically referred to as myoblastomas) are uncommon benign tumors that are most commonly seen in the dermis and subcutis as single or multinodular lesions. In the head and neck, they occur as subcutaneous tumors of the skin of the nose, eyelids, forehead, scalp, and neck. They also may develop in the lips, floor of the mouth, lateral tongue, palate, pharynx, larynx, and trachea. Granular cell tumors rarely occur in the paranasal sinuses. Most occur in patients 35 to 40 years old. There is a general female predominance, and a disproportionate number of cases occur in African-American patients.

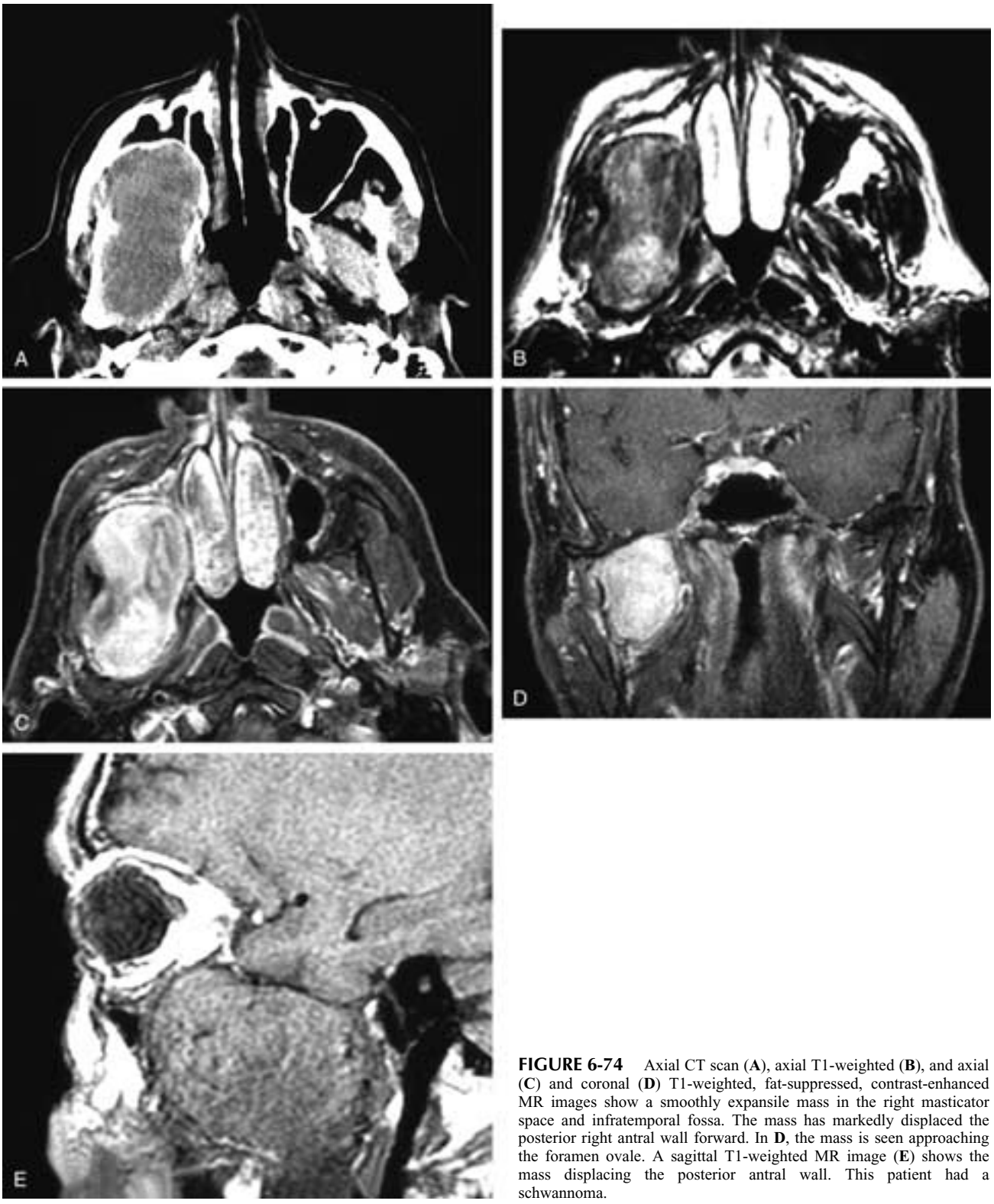

FIGURE 6-74 Axial CT scan (**A**), axial T1-weighted (**B**), and axial (**C**) and coronal (**D**) T1-weighted, fat-suppressed, contrast-enhanced MR images show a smoothly expansile mass in the right masticator space and infratemporal fossa. The mass has markedly displaced the posterior right antral wall forward. In **D**, the mass is seen approaching the foramen ovale. A sagittal T1-weighted MR image (**E**) shows the mass displacing the posterior antral wall. This patient had a schwannoma.

VIEW IMAGE

Copyright © 2003, Mosby, Inc. All rights reserved.

FIGURE 6-75 Axial cranial (**A**) and caudal (**B**) and coronal (**C**) T1-weighted, fat-suppressed, contrast-enhanced MR images show multiple well-delineated enhancing masses in the right orbit, paranasal sinuses, nasal fossa, and cavernous sinus. The left sphenoid sinus is obstructed. There are also bilateral acoustic neuromas. These were neurofibromas in a patient with neurofibromatosis.

VIEW IMAGE

However, in this latter group, laryngeal granular cell tumors do not occur.

Most granular cell tumors reach a size of 1 to 5 cm and are composed of polyhedral cells with eosinophilic granular cytoplasm and round to oval nuclei. Histologically, there are ''packettes'' of histiocyte-like cells with abundant eosinophilic granular cytoplasm and small round to oval nuclei (Fig. 6-77). If an association with a nerve can be seen, it indicates tumor origin rather than potential aggressiveness. Cellular pleomorphism, necrosis, or mitotic figures should

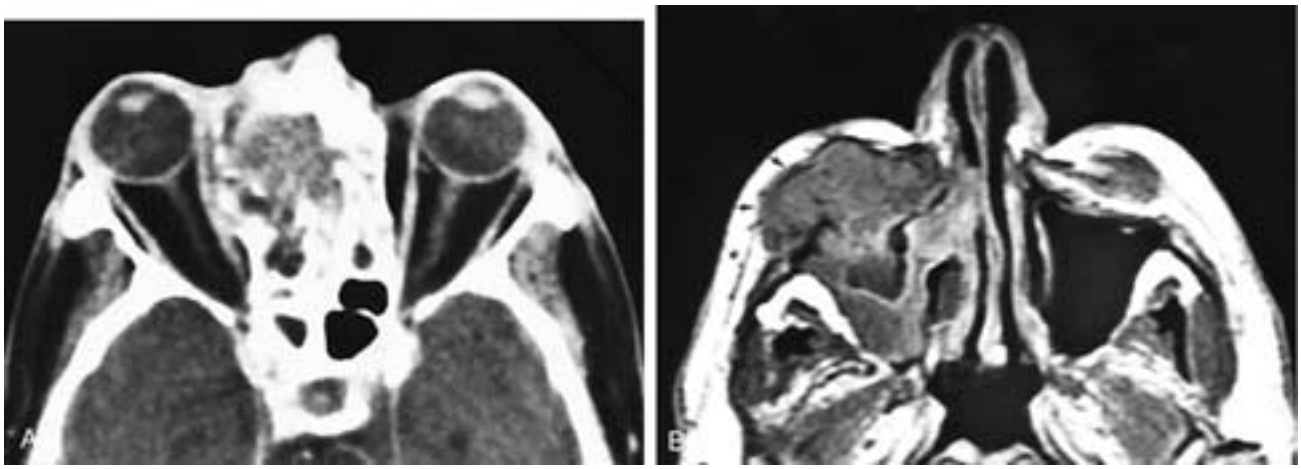

VIEW IMAGE

FIGURE 6-76 Axial CT scan (**A**) shows an expansile right anterior ethmoid mass that erodes the lamina papyracea and bulges into the right orbit. This patient had a malignant schwannoma. Axial T1-weighted MR image (**B**) on another patient shows a destructive lesion originating in the roof of the right maxillary sinus (*arrows*). The mass has a low T1-weighted signal intensity and an intermediate T2-weighted signal intensity. This patient had a malignant schwannoma of V_2.

Copyright © 2003, Mosby, Inc. All rights reserved.

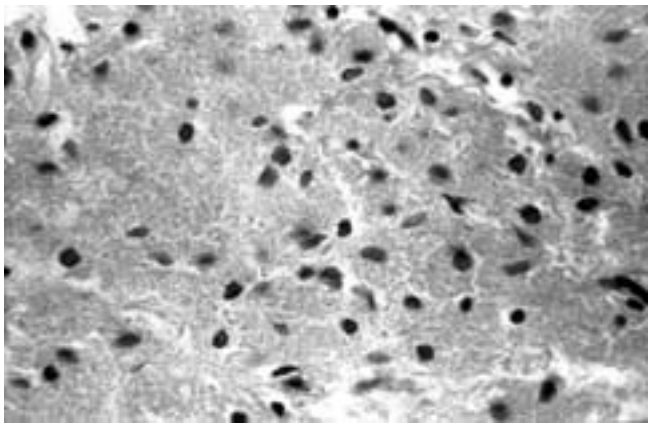

VIEW IMAGE

FIGURE 6-77 Granular cell tumor: This neoplasm is composed of bland cells with abundant granular cytoplasm and small nuclei. The granules correspond to lysosomes containing myelin.

not be present.[65] Ultrastructurally, cytoplasmic granules can be seen as autophagolysosomes containing myelin-like structures. This confirms the Schwannian lineage. Excision is curative, even for those tumors that may be incompletely excised. Rarely, malignant granular cell tumors may be encountered. Malignant granular cell tumors are either large yet histologically benign and metastatic, or they are histologically malignant and metastatic.[107] On imaging, they usually have slightly irregular margins and are located in the subcutaneous fat, deep to the skin line (Fig. 6-78).

Meningioma and Craniopharyngioma

Meningiomas are benign, slowly growing tumors arising from rests within the arachnoid villi, usually in relation to the major dural sinuses. They comprise 13% to 18% of all primary intracranial tumors and are two to four times more common in females than in males; their incidence peaks near 45 years of age.[65] These tumors can extend from or arise outside of the neuroaxis; however, this is uncommon. When meningiomas are encountered outside of the neuroaxis, about two thirds are actually direct extensions from an intracranial or intraspinous lesion.[108, 109] Primary extracranial meningiomas are quite rare, comprising less than 1% of cases.[110] Most of these extraneuroaxis meningiomas occur in the head and neck, and also have been reported in the calvarium, orbit, nose, paranasal sinuses, oral cavity, middle ear, skin of the scalp, and cervical soft tissues.[65, 111, 112] Very rarely, an extracranial meningioma might represent a metastasis from an intracranial meningioma.[113]

The imaging characteristics of these sinonasal meningiomas are those of an enhancing, expansile mass with bone remodeling. Most lesions lie in the nasal vault, and adjacent sclerotic, reactive bone may be a dominant feature. This reactive bone radiographically mimics fibrous dysplasia. If the tumor has spread extracranially, the skull base remodeling and the sinonasal tumor extension are best seen on coronal images. On MR imaging, these tumors have signal intensities similar to those of the brain on all imaging sequences. They enhance, and vascular flow voids are rarely observed (Figs. 6-79 to 6-81).

Craniopharyngioma is a rare, histologically benign, expansile intracranial neoplasm derived from retained embryonic odontogenic rests within Rathke's pouch. It occurs in children and adults as solid and cystic calcifying tumors. Histologically, these epithelial tumors resemble ameloblastomas. A case of craniopharyngioma invading the nasal cavities and paranasal sinuses was reported in a patient who presented with nasal obstruction. Imaging showed a destructive mass of the skull base with involvement of the sinonasal cavities.[114] In another report, a 7-year-old boy complained of intermittent epistaxis for several months. CT scans showed a mass in the left ethmoid sinus and

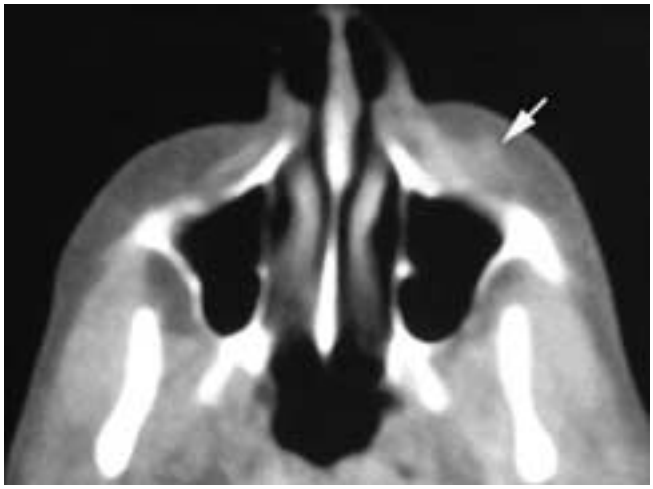

VIEW IMAGE

FIGURE 6-78 Axial CT scan shows a small soft tissue mass in the left cheek (*arrow*). The mass is within the subcutaneous tissues, adjacent to the anterior maxillary sinus wall. There was no bone erosion. This patient had a malignant granular cell tumor.

FIGURE 6-79 Sagittal T1-weighted MR image shows an enhancing anterior cranial fossa mass that extends caudally into the sinonasal cavities. The epicenter of this tumor is above the level of the cribriform plate, suggesting the intracranial origin of the lesion. This patient had a meningioma.

VIEW IMAGE

Copyright © 2003, Mosby, Inc. All rights reserved.

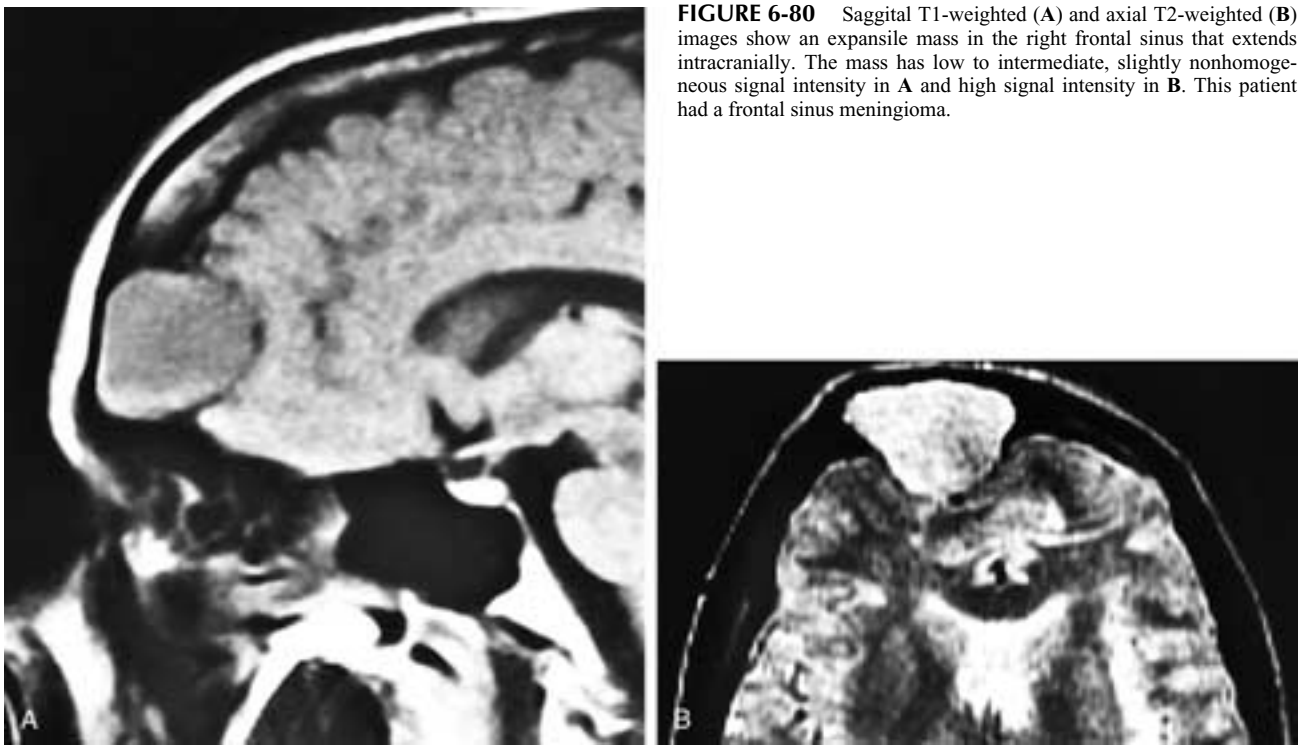

FIGURE 6-80 Saggital T1-weighted (**A**) and axial T2-weighted (**B**) images show an expansile mass in the right frontal sinus that extends intracranially. The mass has low to intermediate, slightly nonhomogeneous signal intensity in **A** and high signal intensity in **B**. This patient had a frontal sinus meningioma.

endoscopic sinus surgery removed the mass completely, which was a craniopharyngioma[115] (see also Chapter 12).

Chordoma

Chordomas are indolent, invasive tumors arising from embryonic notochord remnants representing about 1% of all primary malignant bone tumors.[116] The majority of tumors present either in the spheno-occipital (primarily clivus) area (30%) or in the sacrococcygeal area (51%). A smaller percentage may occur in other sites along the cervical or thoracic spine (19%). Rare chordomas have been reported in the ethmoid, maxilla, and mandible.[117, 118] In these cases, the tumor presumably arises in notochordal remnants that separated from the main notochord during the extreme mesodermal movements of the face that take place in early embryogenesis. These ectopic rests can be located in the paranasal sinuses.[117, 119]

There is a broad age range for chordomas of the head and neck, from the first through the eighth decades of life, with a broad peak incidence in the third to fifth decades. Presenting symptoms include visual changes, cranial nerve deficits, and headache, symptoms for the most part referable to a skull base mass.

Histologically, chordomas are composed of strands and islands of cleared epithelial cells, some of which have a characteristic ''soap bubble'' (physillifarous cells) appearance. These cells produce an abundant myxoid/chondroid-type matrix (Fig. 6-82). Therefore, the differential diagnosis

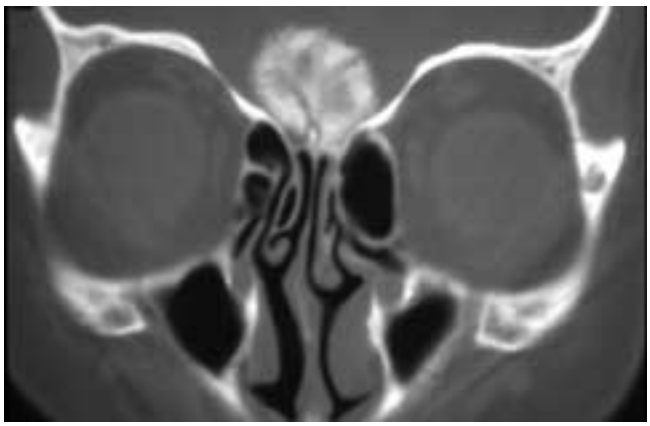

FIGURE 6-81 Coronal CT scan shows a heavily calcified ovoid mass in the anterior cranial fossa resting on the cribriform plate. This patient had an old ''burnt-out'' meningioma.

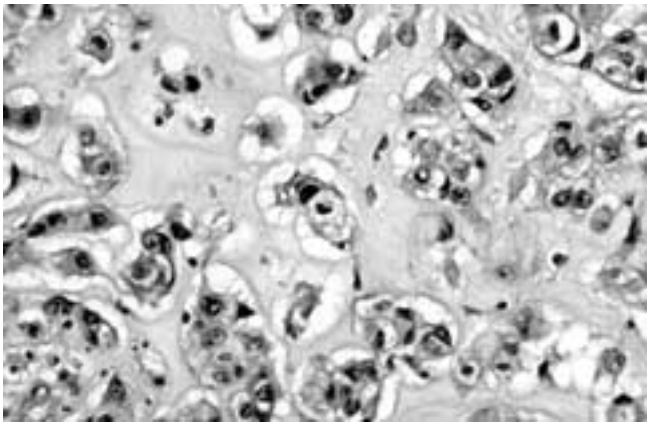

FIGURE 6-82 Chordoma: The ''physilliferous'' cells of chordoma contain bubble-like cytoplasmic vacuoles. Nests of tumor cells are present in lacunar spaces within a myxoid stroma.

Copyright © 2003, Mosby, Inc. All rights reserved.

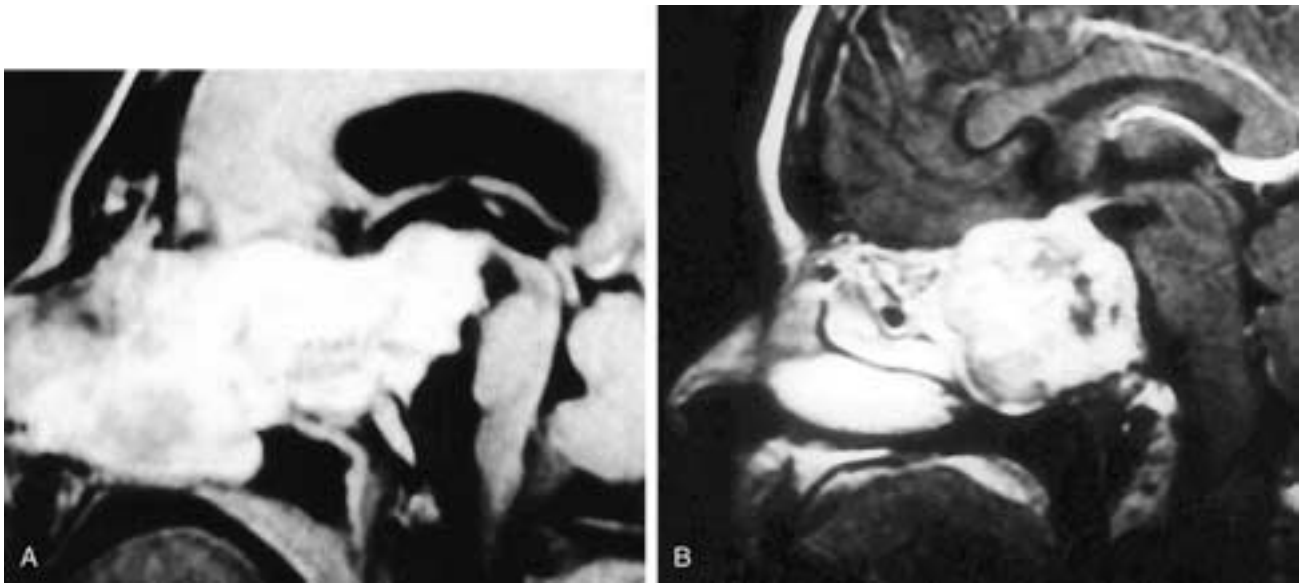

VIEW IMAGE

FIGURE 6-83 Sagittal T1-weighted, contrast-enhanced MR image (**A**) shows a large, enhancing mass that replaces almost the entire clivus and extends forward to fill the sinonasal cavities. There is also a large dorsal extension of this tumor. This is an unusually large chordoma with uncharacteristic exuberant ventral and dorsal growth. Sagittal T1-weighted, contrast-enhanced MR image (**B**) shows a bulky, nonhomogeneously enhancing mass in the clivus and sphenoid sinus. This is a more characteristic MR appearance of a chordoma than that shown in **A**.

of chordomas in the sinonasal tract includes chondroma, chondroblastic osteosarcoma, chondrosarcoma, and pleomorphic adenoma, all of which are fairly uncommon at this site.[120–122] Immunohistochemically, chordoma cells express cytokeratin, thus excluding tumors such as chondroma, chondroblastic osteosarcoma, and chondrosarcoma. As chordomas routinely express S-100, the differential diagnosis of a salivary tumor (namely, pleomorphic adenoma) is best excluded on light microscopy.

Chordomas have traditionally been treated by surgery plus adjuvant radiotherapy; however, recent data indicate an improved local control rate with higher-energy proton beam therapy.[123] Generally, patients with cranial chordomas have a lower metastatic rate (6.6%) than those with sacral tumors, but the former are obviously more likely to suffer morbidity/mortality due to the lack of tumor control.

On contrast-enhanced CT, the classic chordoma is a minimally enhancing, destructive lesion that has areas of dystrophic calcification and residual bone fragments. On MR imaging, chordomas are extremely variable in appearance, and they can have anywhere from low to high signal intensity on any sequence (Figs. 6-83 and 6-84).[124] Only rarely does a classic chordoma arising within the clivus grow sufficiently large to involve the posterior nasal vault and the paranasal sinuses. The only reported case in the maxillary sinus mimicked a mucocele (Fig. 6-85).[117] Recurrences of clival chordomas along the margins of the surgery have been reported to occur in the nasal soft tissues, the nasal septum, and the maxilla (Fig. 6-86)[125] (see also Chapter 12).

Choristoma

The term *choristoma* refers to histologically normal mature tissue present in an ectopic site, such as salivary tissue within the external auditory canal or thyroid tissue within the tongue base. Choristomas usually produce small incidental masses. Sinonasal or nasopharyngeal choristomas have been reported, albeit rarely.[126–128]

Nasal Glioma

A nasal glioma is also, by definition, a choristoma and not a true neoplasia, as the term *glioma* might imply. It presents

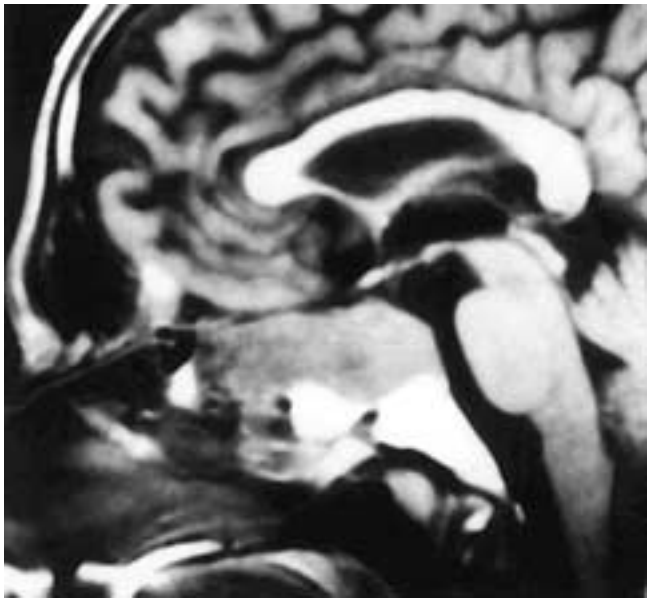

FIGURE 6-84 Sagittal T1-weighted MR image shows an intermediate signal intensity mass in the upper clivus, the sphenoid sinuses, and the ethmoid sinuses. There is little intracranial extension. This patient had a chordoma.

VIEW IMAGE

Copyright © 2003, Mosby, Inc. All rights reserved.

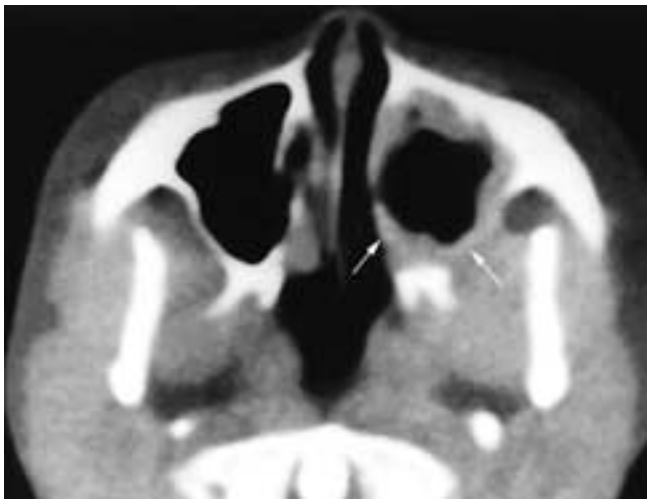

FIGURE 6-85 Axial CT scan performed after surgical drainage of a presumed mucocele shows thinning or destruction of the medial and posterior antral walls (*arrows*), with fairly uniform soft tissues lining the antrum. This patient had a rare chordoma of the maxillary sinus.

VIEW IMAGE

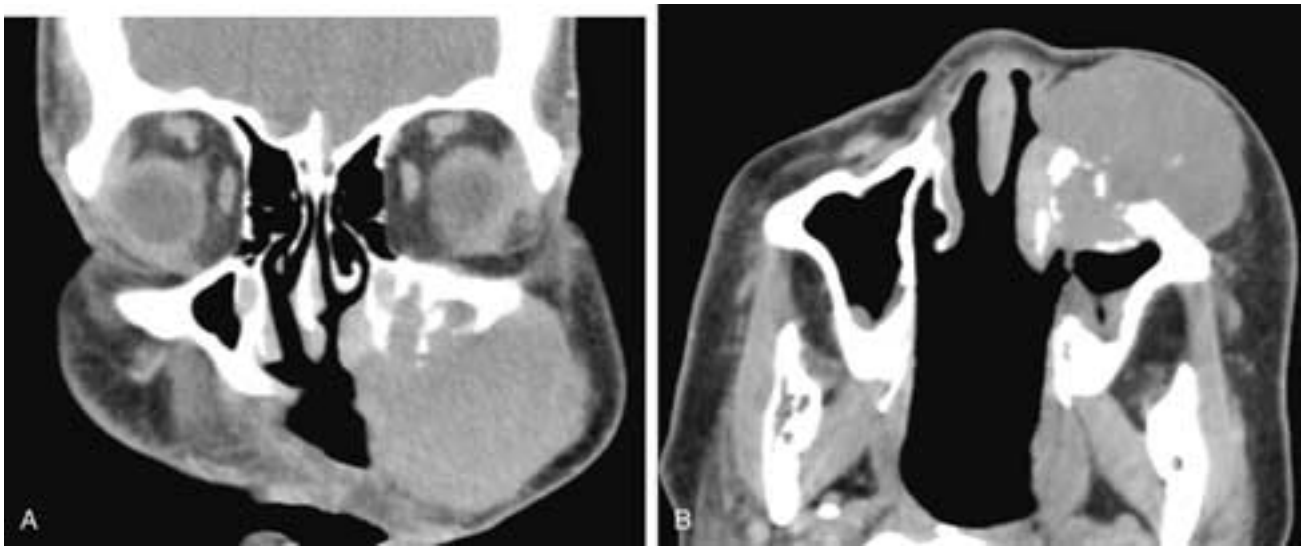

VIEW IMAGE

FIGURE 6-86 Coronal (**A**) and axial (**B**) CT scans through the paranasal sinuses show a destructive soft tissue mass in the left maxillary sinus. Part of the nasal septum had been removed at the time of prior surgery. This patient developed a recurrent chordoma along the course of the original operative procedure for a skull base chordoma.

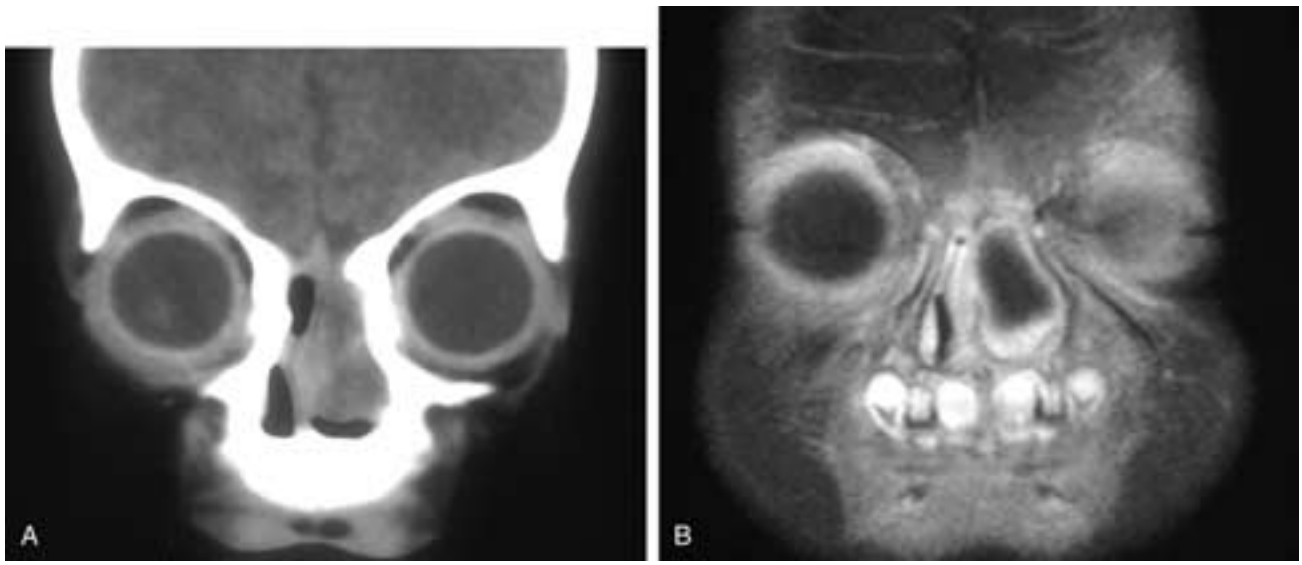

VIEW IMAGE

FIGURE 6-87 Coronal CT scan (**A**) and T1-weighted, fat-suppressed, contrast-enhanced MR image (**B**) on a newborn show a cystic, expansile mass in the left nasal cavity. No intracranial communication was demonstrated. The central floor of the anterior cranial fossa was intact. This region is not yet ossified in the newborn. This patient has a nasal glioma.

Copyright © 2003, Mosby, Inc. All rights reserved.

as a subcutaneous mass of the nasal bridge with intranasal extension (60%) or as a polyp confined to the nasal vault. Radiographically, an intracerebral extension or a cribriform plate defect needs to be ruled out. If an intracerebral communication, in particular a CSF communication, is found, this lesion is better classified as a cephalocele (Fig. 6-87) (see also Chapter 1). Histologically, a glioma is composed of disorganized glial and fibrous tissue.

Ectopic Pituitary

Nelson's syndrome is defined as the presence of an enlarging pituitary tumor, elevated fasting plasma ACTH, and hyperpigmentation after bilateral adrenalectomy in patients with Cushing's disease. Ectopic functioning pituitary tissue within the sphenoid sinus is a rare occurrence. The development of Nelson's syndrome presenting as a sphenoid mass was described in a young woman whose only functioning hypophyseal tissue was within the sphenoid sinus.[129]

LYMPHOPROLIFERATIVE AND HEMATOPOIETIC DISORDERS

Lymphoma

About half of all patients with malignant lymphoma clinically present with disease in the head and neck, most often as cervical lymphadenopathy. Only 10% of head and neck lymphomas are extranodal, usually involving the tonsils, sinonasal tract, and thyroid. The last usually develops in association with Hashimoto's thyroiditis.[130, 131]

Sinonasal lymphoma (SNL) is more common in Asian than in Western populations, where it represents the second most frequent group of extranodal lymphomas after gastrointestinal lymphomas. It has previously been referred to in the literature as lethal midline granuloma, malignant midline reticulosis, or polymorphic reticulosis. These are clinically inexact terms that imply a lack of definitive pathologic diagnosis. These terms have been replaced by microscopic and phenotypic classifications.[132] SNL can be classified as either B-cell, T-cell natural killer cell (T/NK-cell), or T-cell natural killer precursor cell (T/null-cell) phenotypes. The Revised European and American Lymphoma classification (REAL) is presented in Table 6-2, which includes SNL within the classification of extranodal lymphomas.

Some pertinent clinicopathologic distinctions can be made between B-cell and T-cell SNL.[133–137] B-cell phenotype SNL typically involves the paranasal sinuses, with a slight predominance in Western countries. Presenting symptoms relate to paranasal sinus involvement; patients may present late with pain, a facial or palatal mass, or ocular symptoms. These lymphomas are more likely to be associated with ocular symptoms and are more likely to have orbital extension than T/NK-cell phenotype SNL. T-cell SNL is most common in Asian and South American countries. The majority of T-cell SNLs have the natural killer T-cell phenotype T/NK-cell, however, a small percentage lack this phenotype and are classified as T/null-cell SNL. These tumors are typically located in the nasal cavity and have an aggressive, angioinvasive growth pattern that often results in necrosis and bony erosion. The term *angiocentric T-cell lymphoma* refers to those T-cell lymphomas that grow around and into vessels and are associated with necrosis. Patients with T-cell SNL are younger, with a lower male-to-female ratio than those with B-cell SNL. T-cell SNL is more commonly associated with the Epstein-Barr virus (EBV) than is B-cell SNL.[138–141] Typically, T-cell SNL, especially angiocentric

Table 6-2
REVISED EUROPEAN AND AMERICAN LYMPHOMA (REAL) CLASSIFICATION

B-Cell Neoplasms
I. Precursor B-cell neoplasm
  1. B-lymphoblastic leukemia/lymphoma
II. Peripheral B-cell neoplasms
  1. B-cell chronic lymphocytic leukemia/small lymphocytic lymphoma
  2. Lymphoplasmacytoid lymphoma/immunocytoma
  3. Mantle cell lymphoma
  4. Follicle center lymphoma, follicular
    - Provisional cytologic grades: small cell, mixed small and large cell, large cell
    - Provisional subtype: diffuse, predominantly small cell type
  5. Marginal zone B-cell lymphoma
    - Extranodal (MALT type +/– monocytoid B cells)
    - Nodal (+/– monocytoid B cells)
    - Splenic (+/– villous lymphocytes)
  6. Hairy cell leukemia
  7. Plasmacytoma/myeloma
  8. Diffuse large cell B-cell lymphoma
    - Subtype: primary mediastinal (thymic) B-cell lymphoma
  9. Burkitt's lymphoma
  10. Provisional category high-grade B-cell lymphoma, Burkitt's-like

T-Cell and Putative Natural Killer (NK) Cell Neoplasms
I. Precursor T-cell neoplasm
  1. T precursor lymphoblastic lymphoma/leukemia
II. Peripheral T-cell and NK-cell neoplasms
  1. T-cell chronic lymphocytic leukemia/prolymphocytic leukemia
  2. Large granular lymphoproliferative (LGL) disorder
    - T-cell type
    - NK-cell type
  3. Mycosis fungoides/Sézary's syndrome
  4. Peripheral T-cell lymphoma (small cell, mixed small and large cell, large cell)
    - Provisional subtype: lymphoepithelioid cell lymphoma
  5. Angioimmunoblastic T-cell lymphoma (AILD)
  6. Angiocentric lymphoma
  7. Intestinal T-cell lymphoma (+/– enteropathy associated)
  8. Adult T-cell lymphoma/leukemia (ATL/L)
  9. Anaplastic large cell lymphoma (ALCL), CD30+, T- and null-cell types

Hodgkin's Disease
1. Lymphocyte predominance
2. Nodular sclerosis
3. Mixed cellularity
4. Lymphocyte depletion
5. Provisional category: lymphocyte-rich classic Hodgkin's disease
6. Provisional category: anaplastic large cell lymphoma, Hodgkin's disease–like

Unclassifiable
1. B-cell lymphoma, unclassifiable (low grade/high grade)
2. T-cell lymphoma, unclassifiable (low grade/high grade)
3. Malignant lymphoma, unclassifiable

Copyright © 2003, Mosby, Inc. All rights reserved.

Table 6-3
COMPARISON OF THE DEMOGRAPHICS AND SURVIVAL OF SEVERAL RECENT SERIES OF B-CELL AND T-CELL SNL PATIENTS

Author	Year	Country	Total Cases	Med Age	B-Cell Cases
Ko	2000	Korea	48		
Quraishi	2000	UK	24	72	21/24 (87%)
Rodriguez	2000	USA	26	44	13
Aviles	2000	Mexico	108		
Lei	1999	Hong Kong	25 SNL 19 NPL		NSL: 4/16 (25%) NPL: 11/16 (69%)
Yang	1997	Taiwan	34	60	2/20 (10%)
Nakamura	1997	Japan	32		
Harabuchi	1996	Japan	18	18	
Davison	1996	USA	30	44.5	
Liang	1995	Hong Kong	100	50	8/45 (33%)
Abbondanzo	1995	USA	120	59	101/120 (84%)
Arber	1993	Peru	14		2 (14%)
Kojima	1992	Japan	20		9 (45%)

Abbreviations: AWD = alive with disease, DID = died of intercurrent disease, DOD = died of disease, EBV = Epstein-Barr virus, NED = no evidence of disease, NPL = nasopharyngeal lymphoma, SNL = sinonasal lymphoma, YR = years, YS = year survival.

References: Abbondanzo, SL, Wenig BM. Non-Hodgkin's lymphoma of the sinonasal tract. A clinicopathologic and immunophenotypic study of 120 cases. Cancer 1995;75:1281–1291.
Arber DA, Weiss LM, Albujar PF, Chen YY, et al. Nasal lymphomas in Peru. High incidence of T-cell immunophenotype and Epstein-Barr virus infections. AMJ Surg Pathol 1993;17:392–399.
Aviles A, Diaz NR, Neri N, et al. Angiocentric nasal T/natural killer cell lymphoma: a single centre study of prognostic factors in 108 patients Clin Lab Haematol 2000;22(4):215–220.
Davison SP, Habermann TM, Strickler JG, et al. Nasal and nasopharyngeal angiocentric T-cell lymphomas. Laryngoscope 1996; 106(2 Pt 1):139–143.
Harabuchi Y, Imai S, Wakashima J, et al. Nasal T-cell lymphoma causally associated with Epstein-Barr virus: clinicopathologic, phenotypic, and genotypic studies. Cancer 1996;77(10):2137–2149.
Ko YH, Ree HJ, Kim WS, et al. Clinicopathologic and genotypic study of extranodal nasal-type natural killer/T-cell lymphoma and natural killer precursor lymphoma among Koreans. Cancer 2000;89(10):2106–2116.

lymphomas, may present with, or progress to involve, numerous extranodal sites such as skin, liver, larynx, kidney, breast, testis, and prostate. In addition to the development of extranodal disease, T/NK-cell SNL may be associated with hemophagocytic syndrome, a fatal complication that may be associated etiologically with EBV reactivation.[142]

SNL is treated with a combination of local irradiation and chemotherapy with an anthracycline-based regimen. B-cell SNL is usually responsive, whereas in Asian studies, T/NK-cell SNL is less responsive and has a worse prognosis. Table 6-3 compares some recent series of B-cell and T-cell SNL patients regarding demographics and survival. Generally, survival is dependant upon tumor stage and grade rather than phenotype.

On CT and MR imaging, lymphomas in the sinonasal cavities tend to be bulky soft tissue masses that enhance to a moderate degree.[143, 144] These tumors also tend to remodel bone, although occasionally aggressive bone invasion is seen.[145–148] Most often the disease is located in the nasal fossae and maxillary sinuses.[149] Less often, lymphoma is found in the ethmoid sinuses, and only rarely is it found in the sphenoid and frontal sinuses. On MR imaging, it tends to have an intermediate intensity signal on all imaging sequences and it enhances after contrast administration (Figs. 6-88 to 6-93).

Granulocytic Sarcoma

Granulocytic sarcoma, or chloroma, is a rare complication of acute and chronic myeloid leukemia. It represents a soft-tissue infiltrate of immature myeloid elements that develops in 3% of patients with acute and chronic myeloid leukemia. The term chloroma describes the green hue seen when these tumors are sectioned. The color, caused by the cytoplasmic enzyme myeloperoxidase, fades after exposure to air. The mean patient age is 48 years, and most patients (85%) present with a solitary lesion. In the head and neck, osseous lesions have been reported in the skull, face, orbit,

Copyright © 2003, Mosby, Inc. All rights reserved.

Table 6-3 (*Continued*)

T-Cell Cases	Overall Survival	Notes
45, plus 3 NK precursor neoplasms	1 YS 41%	Strong association with EBV Progression to extranodal disease
3/24 (13%)	5 YS 40%, 10 YS 33%	
13	4 NED 1, 2, 3, 9 YR	Progression to extranodal disease
108 (100%)	8-year overall and disease-free survival ranged from 79% to 90%	
NSL: 12/16 (75%) NPL: 5/16 (31%)	Overall 5 YS (33% versus 82%) and disease-free 5 YS (36% versus 76%) and worse in NSL than NPL patients, correlating with age and bulky disease	
18/20 (90%)	Mean survival 84.2 months Overall 5 YS 63%	
32 (100%)	Overall 5 YS 49%	Strong association with EBV
18 (100%)	Median survival 6 months	Strong association with EBV Extranodal involvement
30 (100%)	10/30 (33%) NED 12/30 (40%) DOD 6/30 (20%) DID	Strong association with EBV
35/45 (77%)	Improved survival correlated with age (<60), stage I disease, and absence of clinical (B) symptoms	
19/120 (16%)	24/66 patients (36.4%) DOD 17/66 (25.7%) NED 13/66 (19.7%) AWD 12/66 (18.2%) DID or unknown	Extranodal involvement
11 (78%)		Strong association with EBV
9 (45%)	2 YS was poorer for T-cell than B-cell lymphomas Survival correlated with stage	

Kojima M, Hosomura Y, Kurabayashi Y, et al. Malignant lymphomas of the nasal cavity and paranasal sinuses. A clinicopathologic and immunohistochemical study. Acta Pathol Jpn 1992;42(5):333–338.

Lei KI, Suen JJ, Hui P, et al. Primary nasal and nasopharyngeal lymphomas: a comparative study of clinical presentation and treatment outcome. Clin Oncol (R Coll Radiol) 1999;11(6):379–387.

Liang R, Todd D, Chan TK, et al. Treatment outcome and prognostic factors for primary nasal lymphoma. J Clin Oncol 1995;13(3):666–670.

Nakamura S, Katoh E, Koshikawa T, et al. Clinicopathologic study of nasal T/NK-cell lymphoma among the Japanese. Pathol Int 1997;47(1):38–53.

Quraishi MS, Bessell EM, Clark D, et al. Non-Hodgkin's lymphoma of the sinonasal tract. Laryngoscope 2000;110(9):1489–1492.

Rodriguez J, Romaguera JE, Manning J, Ordonez N, et al. Nasal-type T/NK Lymphomas: a clinicopathologic study of 13 cases. Leuk Lymphoma 2000;39:139–144.

Yang Y, Gau JP, Chang SM, et al. Malignant lymphomas of sinonasal region, including cases of polymorphic reticulosis: a retrospective clinicopathologic analysis of 34 cases. Chung Hua I Hsueh Tsa Chih (Taipei) 1997;60(5):236–244.

and paranasal sinuses, whereas extramedullary tumors have been reported in the nasal cavity, paranasal sinuses, nasopharynx, tonsil, mouth, lacrimal gland, salivary glands, and thyroid gland.[150] An associated myeloproliferative disease is found in 48% of patients, and acute myeloid leukemia occurs in 22% of the cases. However, 30% of patients with granulocytic sarcoma have no hematologic disease at the time of initial diagnosis. The onset of granulocytic sarcoma may be a harbinger of the development of acute blast crisis within a few months of the diagnosis. The prognosis of patients with acute myeloid leukemia is not altered by the development of a chloroma; however, in patients with chronic myeloid leukemia and other myeloproliferative disorders, the granulocytic sarcoma is an ominous sign because it is associated with the acute or blastic phase of the disease.[150–152] On CT, chloromas are enhancing, homogeneous masses, usually with slightly infiltrative margins.[153] On MR imaging, they have intermediate to high signal intensities on all imaging sequences, and they enhance with contrast administration.

Multiple Myeloma

Multiple myeloma (MM) is the most common member of a group of diseases known collectively as plasma cell dyscrasias. These diseases, including Waldenstrom's macroglobulinemia, heavy chain disease, and primary amyloidosis, all have a malignant proliferation of plasma cells or lymphocytoid plasma cells with monoclonal immunoglobulin or immunoglobulin fragments in the patient's urine. The proliferation of neoplastic cells is associated with bone destruction and involves the bone marrow of the axial skeleton. However, the soft tissues can also be involved. MM usually affects patients over the age of 40 (mean age is 63) and has a roughly equal sex distribution. The most frequent complaints are bone pain (63%), weakness (23%), and weight loss (15%). Extraosseous plasmacytoma is the initial manifestation of MM in only 5% of patients.[150] In the head and neck, soft-tissue masses occur primarily in the nose, paranasal sinuses, nasopharynx, and tonsils. Patients may have oronasal

Copyright © 2003, Mosby, Inc. All rights reserved.

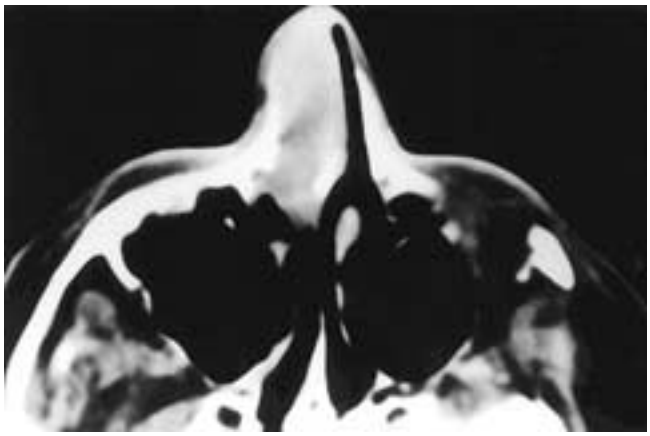

VIEW IMAGE

FIGURE 6-88 Axial CT scan shows a soft-tissue mass in the right nose and anterior nasal fossa. There is widening of the involved right side, and there is no bone erosion. This patient had a large cell lymphoma.

bleeding as a primary manifestation of hyperviscosity. Skeletal lytic lesions are found in 85% of patients, and a combination of lytic bone lesions, osteoporosis, and pathologic fractures is found in 63% of patients at disease onset.[148] Paraosseous tumor extension through destroyed cortical bone is found in 50% of patients at autopsy. In 10% to 12% of patients with MM, amyloidosis is present. Infection and renal failure are the primary causes of death. With the use of alkylating agents, steroids, and local irradiation, the median survival time is 20 months; 66% of patients are alive after 1 year, 32% after 3 years, and 18% after 5 years.[153] The imaging characteristics appear to be similar to those of lymphomas.

Extramedullary Plasmacytoma

Extramedullary plasmacytoma (EMP) is a rare soft-tissue malignancy composed of plasma cells. Eighty percent of these tumors occur in the head and neck, 28% occur in the nasal cavity, and 22% occur in the paranasal sinuses.[150]

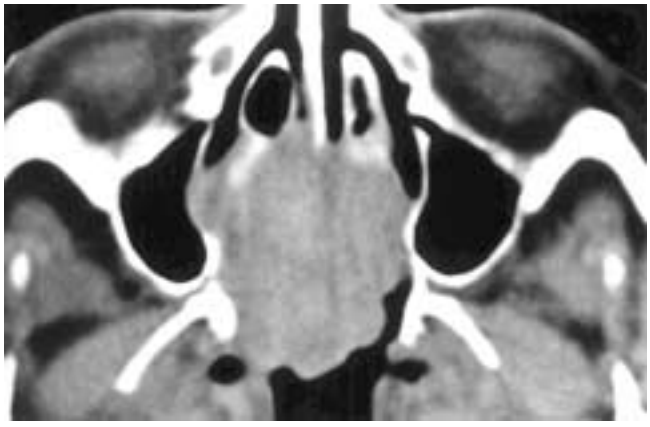

VIEW IMAGE

FIGURE 6-89 Axial CT scan shows a bulky, lobulated posterior nasal fossa mass centered on the nasal septum. There is minimal thinning of the medial right antral wall. The dominant finding is expansion of the nasal vault. This patient had a large cell lymphoma.

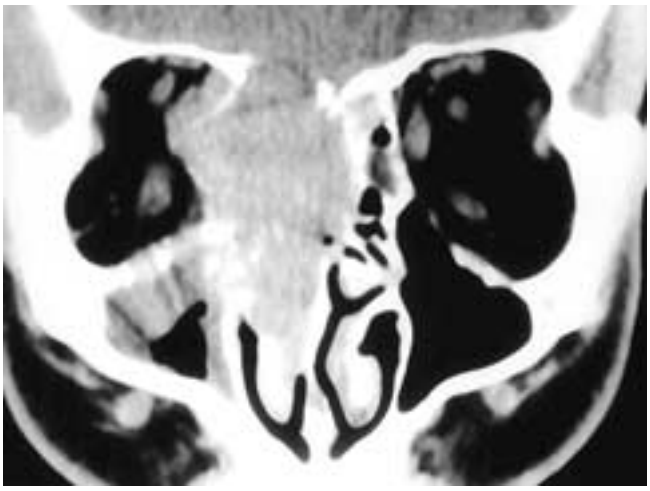

FIGURE 6-90 Coronal CT scan shows a bulky soft-tissue mass in the right ethmoid and nasal cavity. The tumor has invaded the right orbit and the floor of the anterior cranial fossa. There is also obstruction of the right antrum. This is a more aggressive appearance of a large cell lymphoma and, based on the imaging appearance, could be a carcinoma.

VIEW IMAGE

They represent 3% to 4% of all sinonasal cavity tumors.[154, 155] About 20% of head and neck EMPs are initially associated with MM. The tumors are four times more likely to occur in males than in females, and 90% of the patients are white; 95% of the tumors occur over the age of 40 years (mean is 59 years).[150] The most common presenting symptoms are a soft-tissue mass (80%), airway obstruction (35%), epistaxis (35%), local pain (20%), proptosis (15%), and nasal discharge (10%). The mean duration of symptoms is 4½ months.

Histologically, plasmacytomas range from well-differentiated cells indistinguishable from mature, benign

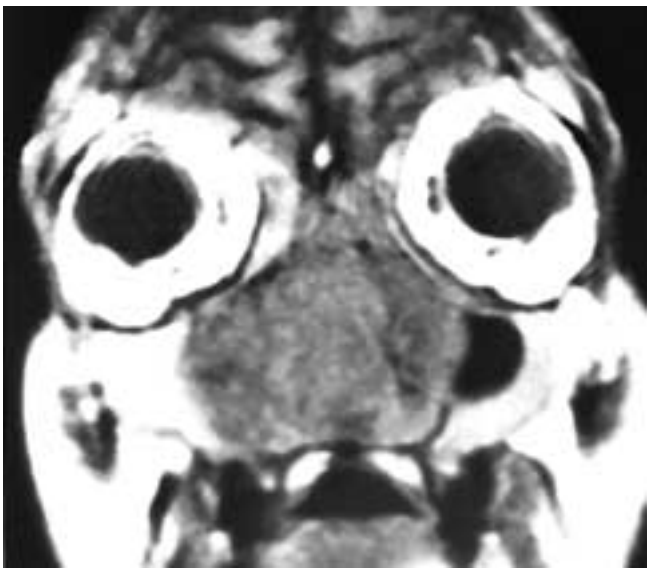

FIGURE 6-91 Coronal T1-weighted MR image shows an expansile bilateral nasal cavity mass that extends into the ethmoid and maxillary sinuses. The mass has a low to intermediate signal intensity and had a slightly higher T2-weighted signal intensity. This patient had a large cell lymphoma.

VIEW IMAGE

Copyright © 2003, Mosby, Inc. All rights reserved.

plasma cells to poorly differentiated tumor cells. The former can be distinguished from a benign plasma cell infiltrate by the demonstration of immunoglobulin clonality via immunohistochemistry. Poorly differentiated anaplastic plasmacytoma can also be distinguished from anaplastic carcinoma, ONB, melanoma, and large cell lymphoma by immunohistochemistry.[150, 156] Radiation therapy and surgery are the treatments of choice; alkylating agents and steroids help patients with painful bone lesions and patients with systemic disease. Eventually, 35% to 50% of patients with primary EMP develop MM. Local bone destruction and persistent primary tumors after radiation therapy are not necessarily poor prognostic indicators. Between 31% and 75% of patients are alive after 5 years; however, the median length of survival after the onset of MM is less than 2 years.[150]

On CT, EMPs of the sinonasal cavities are homogeneous, enhancing polypoid masses that remodel surrounding bone.[157, 158] On MR imaging they have an intermediate signal intensity on all imaging sequences, they enhance, and because they are highly vascular, they may have vascular flow voids (Figs. 6-94 to 6-97).

Langerhans' Cell Granulomatosis

Langerhans' cell granulomatosis (LCG or histiocytosis X) is the current term for a group of childhood diseases including eosinophilic granuloma (EG), Hand-Schuller-Christian (HSC) disease, and Letterer-Siwe (L-S) disease. EG is a more localized form of LCG, often manifesting as a solitary bone lesion, whereas HSC disease and L-S disease are multifocal or disseminated diseases that involve the lymph nodes, skin, liver, spleen, lung, head and neck, or gastrointestinal tract. The etiology is unknown; however, some researchers suggest that all forms of LCG are clonal.[159, 160] Others, however, believe LCG to be a benign, possibly reactive process.[161]

The head and neck are frequently involved in LCG, usually the flat bones of the skull or the jaws. Patients often present with otitis media and/or destructive temporal bone lesions. Sinonasal involvement is virtually unreported, but sphenoid involvement has been seen.[150, 163, 164]

The histology of LCG is distinctive, but immunohistochemical confirmation is important.[161, 165] LCG is characterized by a polymorphous cellular infiltrate of mononuclear

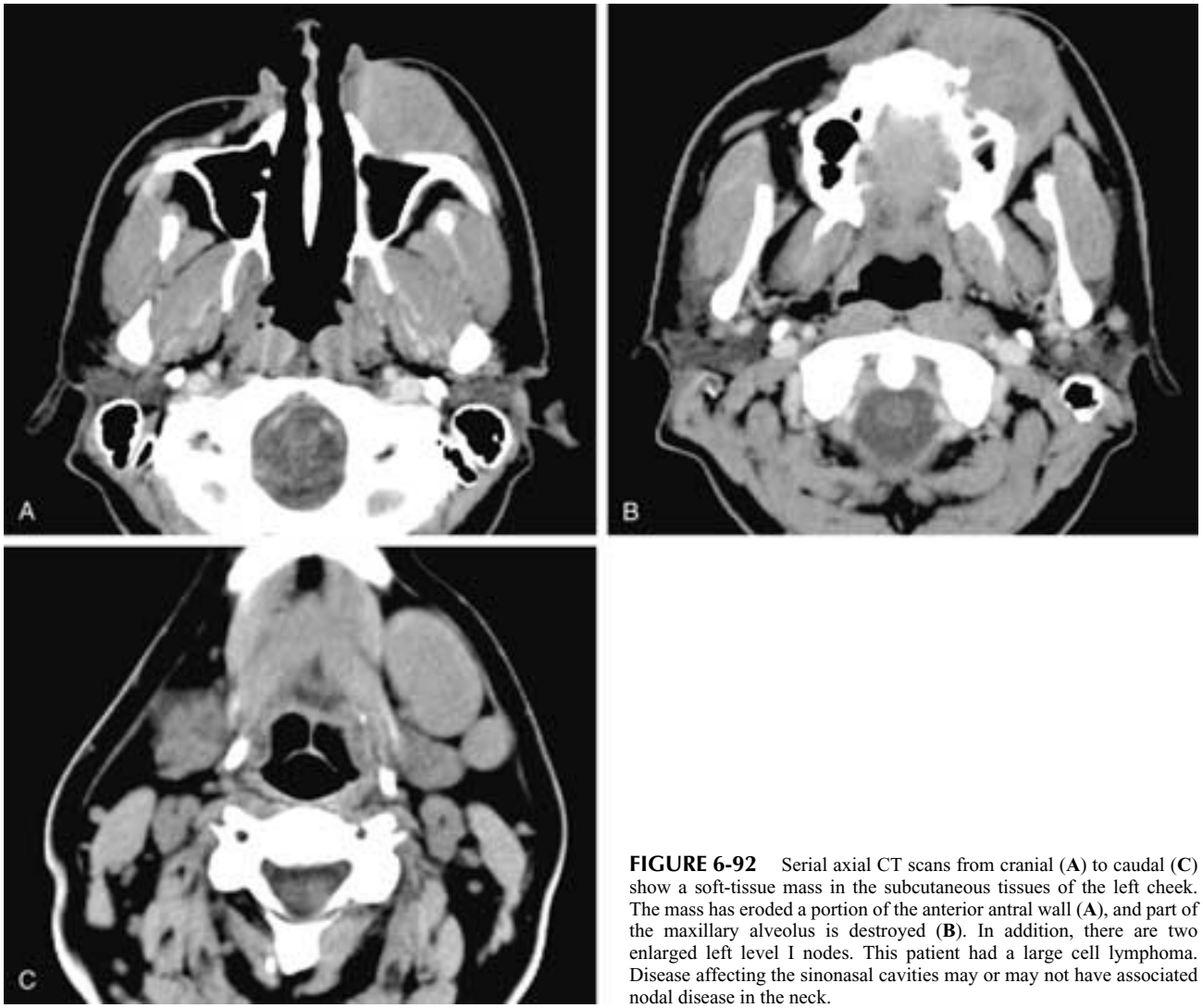

FIGURE 6-92 Serial axial CT scans from cranial (**A**) to caudal (**C**) show a soft-tissue mass in the subcutaneous tissues of the left cheek. The mass has eroded a portion of the anterior antral wall (**A**), and part of the maxillary alveolus is destroyed (**B**). In addition, there are two enlarged left level I nodes. This patient had a large cell lymphoma. Disease affecting the sinonasal cavities may or may not have associated nodal disease in the neck.

VIEW IMAGE

Copyright © 2003, Mosby, Inc. All rights reserved.

FIGURE 6-93 Coronal (**A**) and axial (**B**) T1-weighted and axial T2-weighted (**C**) MR images show a soft-tissue mass in the medial right cheek lying against the anterior antral wall (*arrow*). There may be thinning of the wall immediately adjacent to the mass. The mass has a low to intermediate T1-weighted signal intensity and a higher intermediate T2-weighted signal intensity. This patient had a large cell lymphoma.

VIEW IMAGE

or multinucleated histiocytes (Langerhans' cells), with lobated or grooved (clefted) nuclei, mixed with varying numbers of eosinophils, granulocytes, and lymphocytes.[161, 165] Immunohistochemically, Langerhans' cells are typically positive for S-100 protein and, more specifically, CD1a. Intracytoplasmic Birbeck granules are diagnostic of LCG cells on ultrastructural analysis.[166]

The mixed infiltrate of histiocytes and eosinophils, and the presence of phagocytosis in LCG, may be mistaken for reactive histiocytosis, Hodgkin's disease, and sinus histiocytosis with massive lymphadenopathy (SHML or

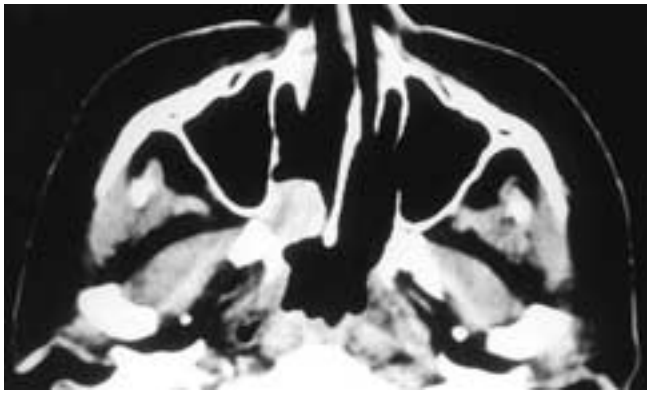

VIEW IMAGE

FIGURE 6-94 Axial CT scan shows a small polypoid mass along the right posterior lateral nasal wall. There is no associated bone erosion. This patient had an extraosseous plasmacytoma.

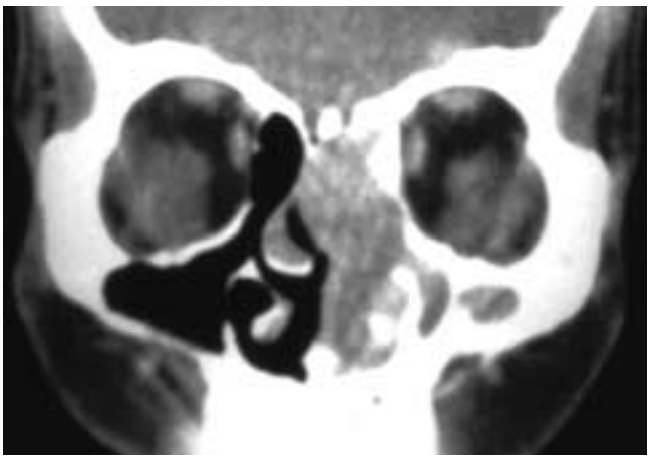

FIGURE 6-95 Coronal CT scan shows a soft-tissue mass filling the left nasal cavity and left ethmoid sinuses and obstructing the left antrum. There is focal erosion of the cribriform plate region; otherwise, the marginal bone about the mass is intact. This patient had an extramedullary plasmacytoma.

VIEW IMAGE

Copyright © 2003, Mosby, Inc. All rights reserved.

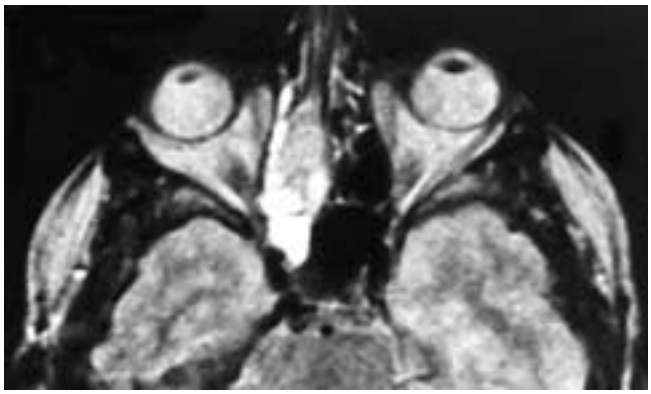

VIEW IMAGE

FIGURE 6-96 Axial proton density MR image shows a right ethmoid and nasal mass that has a low to intermediate signal intensity. Surrounding the mass are chronically obstructed secretions with high signal intensity. This is a nonspecific imaging appearance. This patient had an extramedullary plasmacytoma.

Rosai Dorfman disease). The characteristic feature of SHML is prominent lymphophagocytosis (emperipolesis). SHML cells lack the typical nuclear features of LCG cells and, furthermore, lack the characteristic intracytoplasmic Birbeck granules seen on ultrastructural analysis.[166]

Treatment of LCH is based on the degree of disease involvement.[161] Biopsy or curettage of osseous lesions and, at times, low-dose radiation therapy are the treatments of choice for localized LCG. Aggressive or refractory disease may require chemotherapy. Generally, the greater the degree of organ involvement, the worse the prognosis. Alessi and colleagues subclassified 28 children with LCG as having either type I (monostotic disease—7 children), type II (multiple sites without visceral involvement—15 children), or type III (presentation with disseminated disease including visceral involvement—6 children).[162] Patients with type I disease had an excellent prognosis after local curettage, whereas patients with type III disease all died despite chemotherapy. A poor prognosis was associated with polyostotic bone disease, additional soft-tissue lesions of the skin, lymph node involvement, hepatosplenomegaly, diabetes insipidus and hypothalamic dysfunction, and disseminated bone marrow involvement.

On CT, bone involvement can vary from a well-localized destructive process to an infiltrative mass. Enhancement after contrast administration is seen on CT and MR imaging. Soft-tissue involvement is nonspecific, and again can vary

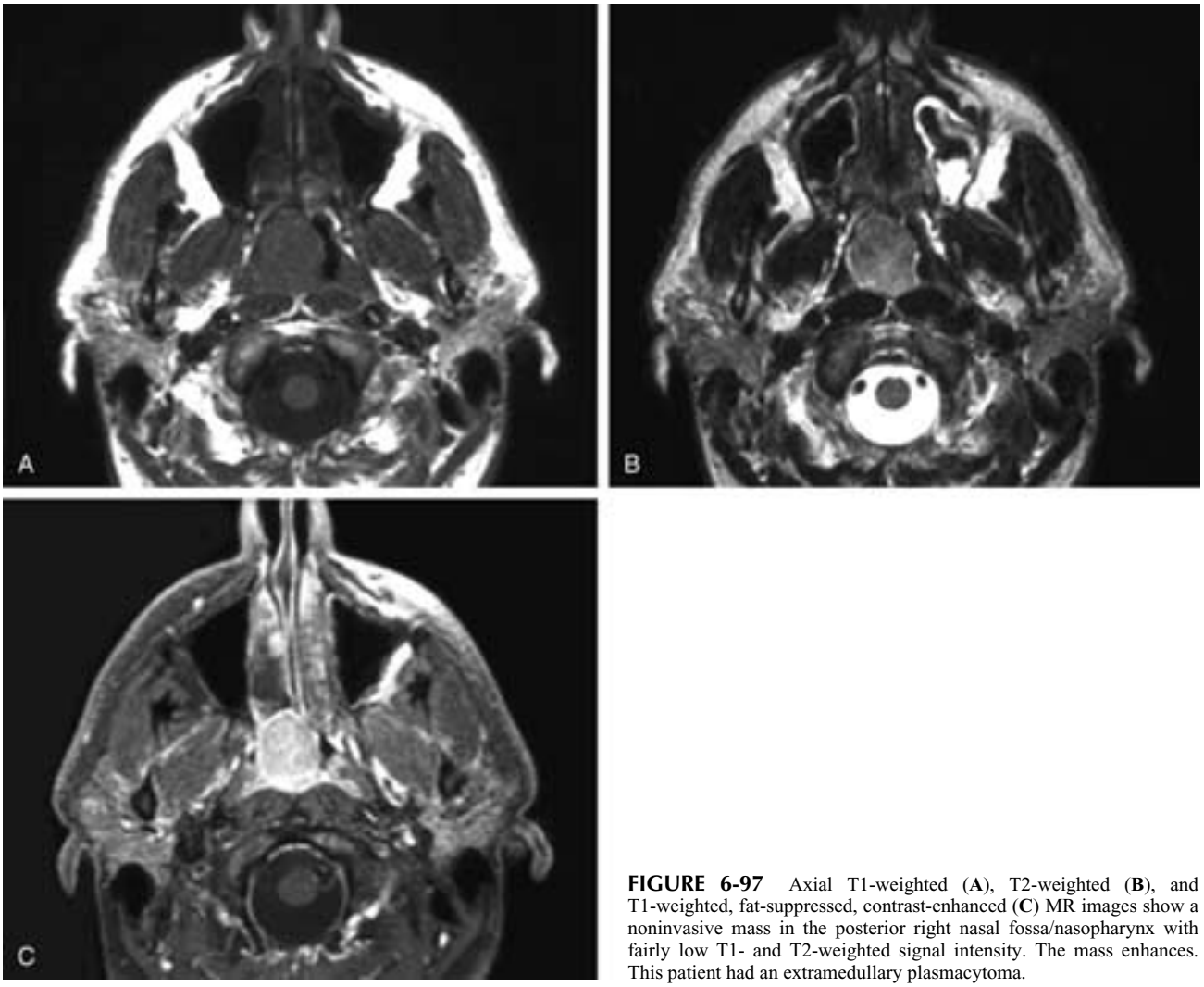

FIGURE 6-97 Axial T1-weighted (**A**), T2-weighted (**B**), and T1-weighted, fat-suppressed, contrast-enhanced (**C**) MR images show a noninvasive mass in the posterior right nasal fossa/nasopharynx with fairly low T1- and T2-weighted signal intensity. The mass enhances. This patient had an extramedullary plasmacytoma.

VIEW IMAGE

Copyright © 2003, Mosby, Inc. All rights reserved.

from a fairly well defined mass to one that has infiltrative margins. On MR imaging, there usually is an intermediate T1-weighted signal intensity and an intermediate to high T2-weighted signal intensity.[167] As mentioned, there is marked enhancement after contrast administration. Overall, MR imaging is usually better in assessing bone marrow invasion and any soft-tissue disease, while the actual bone disease is often better seen on CT.

Rosai-Dorfman Disease

Rosai-Dorfman disease (massive lymphadenopathy with sinus histiocytosis) is a rare idiopathic benign histiocytic proliferation usually seen in young patients. The massive lymphadenopathy most commonly involves the cervical lymph nodes, with a predominant infiltration of sinusoidal histiocytes. Nearly half of the patients have extranodal involvement, the majority of which (75%) occur in sites in the head and neck. Paranasal sinus involvement has been reported, usually in conjunction with cervical adenopathy and multifocal extranodal lesions.[168–171] On CT, the paranasal sinus disease was a bulky, homogeneous mass similiar in appearance to lymphoma.

The clinical presentation depends upon the involved site. Patients may present with nasal obstruction, stridor, proptosis, decreased visual acuity, facial pain or tenderness, cranial nerve deficits, mandibular tenderness, dermal infiltrates, and mass lesions.

Rosai-Dorfman disease can be self-limiting. In other cases, surgery for locoregional lesions can result in long-term disease control. Sinonasal disease can be managed by endoscopic resection, although refractory cases may require chemotherapy, radiotherapy, steroids, or more extensive surgery. The imaging findings are nonspecific.

Thalassemia

Thalassemia is a hereditary anemia characterized by defective hemoglobin synthesis and ineffective erythropoiesis caused by reduction and abnormalities in globin chain synthesis. Disease severity correlates with homozygosity and with the ensuing relative decrease in globin production and the stability of the residual globin chain excess. Patients with thalassemia minor syndromes are heterozygous and develop mild anemia and persistent microcytosis. Thalassemia intermedia is a homozygous state characterized by a moderate hemolytic anemia that presents during physiologic stressors such as infection, pregnancy, or surgery. Thalassemia major is a homozygous state that produces severe, life-threatening anemia; it can be classified as beta-thalassemia (diminished beta-globin chains) or alpha-thalassemia (decreased alpha-chain production).

Alpha-thalassemia major usually is incompatible with life and presents as hydrops fetalis. Beta-thalassemia is an autosomal recessive disorder that occurs primarily in patients of Mediterranean origin. The defect in β-globin synthesis results in imbalanced globin chain synthesis, delayed erythroid maturation, and severely decreased red cell survival.

Patients become symptomatic early in life, requiring chronic transfusion therapy. Iron overload, due to increased gastrointestinal absorption and blood transfusion, is the major cause of tissue damage, morbidity, and death.

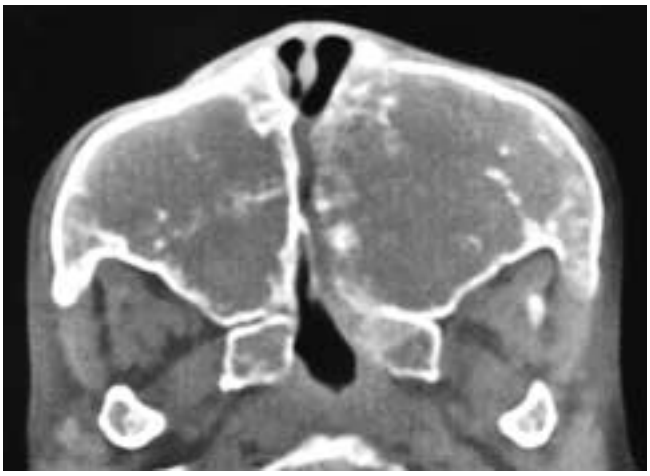

FIGURE 6-98 Axial CT scan at a wide window setting shows a markedly expanded maxilla with no development of the maxillary sinuses. The surrounding cortical bone is intact. The central portions of each maxilla are filled with expanded marrow. This patient had thalassemia.

VIEW IMAGE

The radiographic features of beta-thalassemia are due in large part to compensatory bone marrow expansion. A markedly expanded marrow space leads to various skeletal manifestations in the spine, skull, facial bones, ribs, etc. The classic radiographic changes of thalassemia in the skull include a thickened calvarium and a ''hair-on-end'' appearance. In the facial area, sinus pneumatization is delayed and the maxilla is expanded secondary to marrow expansion, which can result in both malocclusion and a cosmetic deformity. On CT, soft-tissue density material (marrow) is seen filling and expanding the maxillae, and this process may extend into the central skull base and mandible (Figs. 6-98 and 6-99).[172] Because sinus pneumatization only occurs in a bone once red marrow has converted to yellow marrow, often the frontal, sphenoid, and maxillary sinuses are poorly developed, and the only sinuses seen are the ethmoids.

Advances in the management of thalassemia major (bone marrow transplantation, iron-chelating therapy) have greatly improved the prognosis.[173, 174]

BENIGN AND MALIGNANT PRIMARY SOFT-TISSUE TUMORS

Vascular

Angiofibroma

The nasopharyngeal angiofibroma (juvenile angiofibroma) is an uncommon, highly vascular, nonencapsulated polypoid mass that is histologically benign but locally aggressive. It represents 0.05% of all head and neck neoplasms and occurs almost exclusively in males.[13] However, a few cases have been documented in females, and it has been suggested that when such a diagnosis is made, sex chromosome studies should be performed to investigate the possibility of genetic mosaicism.[175] The

Copyright © 2003, Mosby, Inc. All rights reserved.

typical patient is a male between 10 and 18 years of age, although the lesion may occasionally present in older patients.[13] The presenting symptoms include nasal obstruction, epistaxis, facial deformity, proptosis, nasal voice, sinusitis, nasal discharge, serous otitis media, headache, and anosmia. Almost all angiofibromas originate from the posterior choanal tissue near the pterygopalatine fossa and sphenopalatine foramen and fill the nasopharynx. Tumor growth is asymmetric, and one side is always the primary site of involvement. Extension into the pterygopalatine fossa occurs in 89% of the cases and results in widening of this fossa, with resultant anterior bowing of the posterior ipsilateral antral wall.[176] Although there are other slowly growing lesions that may also similarly widen the pterygopalatine fossa (e.g., lymphomas, lymphoepitheliomas, schwannomas, and fibrous histiocytomas), the vast majority of antral bowing is caused by nasopharyngeal angiofibromas.[177] The sphenoid sinus is involved by extension through the roof of the nasopharynx in 61% of cases. Angiofibromas also spread into the maxillary and ethmoid sinuses in 43% and 35% of cases, respectively.[175] Intracranial extension occurs in 5% to 20% of cases and

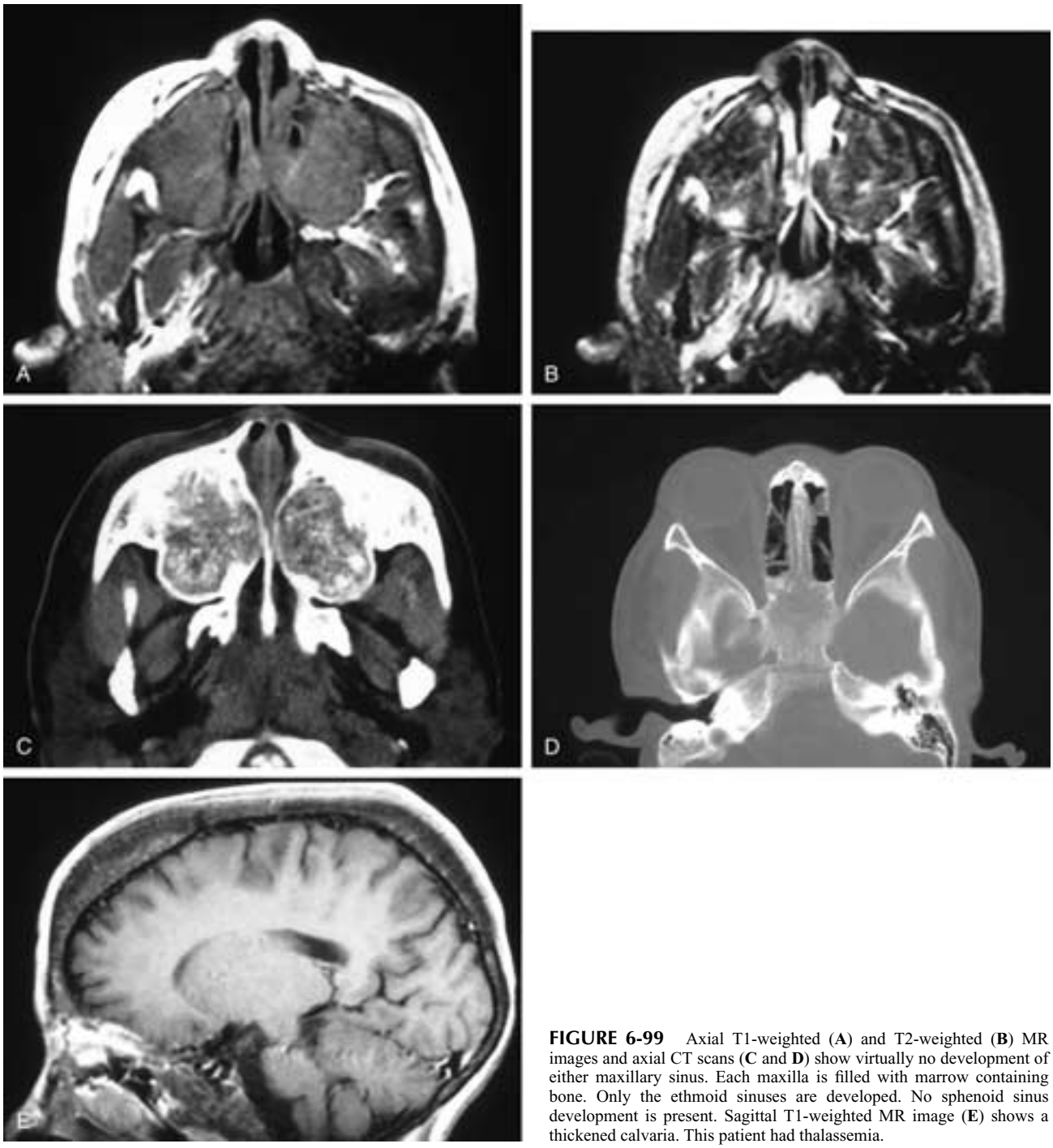

FIGURE 6-99 Axial T1-weighted (**A**) and T2-weighted (**B**) MR images and axial CT scans (**C** and **D**) show virtually no development of either maxillary sinus. Each maxilla is filled with marrow containing bone. Only the ethmoid sinuses are developed. No sphenoid sinus development is present. Sagittal T1-weighted MR image (**E**) shows a thickened calvaria. This patient had thalassemia.

VIEW IMAGE

Copyright © 2003, Mosby, Inc. All rights reserved.

VIEW IMAGE

FIGURE 6-100 Lateral view shows a large nasopharyngeal mass that has displaced the posterior antral wall anteriorly (*arrow*). The mass also extends into the sphenoid sinuses. This patient had an angiofibroma.

primarily involves the middle cranial fossa.[13] Most often this extension progresses from the pterygopalatine fossa into the orbit (through the inferior orbital fissure) and then intracranially through the superior orbital fissure. Direct intracranial extension from the sphenoid or ethmoid sinuses is uncommon. Biopsy should not be attempted in an outpatient or office facility because of tumor vascularity. Sectional imaging and angiography are sufficient to establish the diagnosis.[178] Histologically, thick-walled vessels are embedded in densely collagenized fibrous stroma. The differential diagnosis includes a fibrosed antrochoanal or nasal polyp and an angiomatous polyp.

Plain film findings of an angiofibroma include a soft-tissue nasopharyngeal mass, widening of the pterygopalatine fossa with anterior bowing of the ipsilateral posterior antral wall, and opacification of the sphenoid sinus (Fig. 6-100). A polypoid nasal mass may cloud the ipsilateral ethmoid and maxillary sinuses. If the superior orbital fissure is widened, intracranial extension will be present.

Contrast-enhanced CT shows an enhancing mass with the anatomic distribution described above (Figs. 6-101 and 6-102). Intraorbital or intracranial extension is much better visualized on CT than on plain films. On contrast-enhanced CT, the imaging must be done while contrast material is flowing freely. If scanning is delayed, the rich vascular tumor network will wash out the contrast medium. Dynamic scanning also identifies the highly vascular nature of these tumors.[179] MR imaging reveals a mass of intermediate signal intensity on T1-weighted and T2-weighted sequences, with multiple-flow voids that represent the major tumor vessels (Figs. 6-102 and 6-103). The primary imaging tasks are mapping the lesion for the surgeon and documenting any intracranial spread.[180–182] These tumors tend to deossify the adjacent skull base; however, the imaging may suggest aggressive erosion. Most often, the cavernous sinus is displaced rather than invaded, and current skull base surgical techniques usually allow such tumor extension to be resected.

Angiography demonstrates that the major feeding vessels are the internal maxillary artery and the ascending pharyngeal artery on the dominant side (Fig. 6-104). Cross-circulation from contralateral branches of the external carotid artery and occasional feeding branches from the internal carotid arteries are found. The latter are usually associated with intracranial tumor extension. Subselective angiography is usually necessary to identify all of the feeding vessels. Preoperative embolization of the external carotid artery's nutrient branches greatly reduces the blood loss at surgery.[13]

The treatment of choice is surgery. Unresectable intracranial disease, if present, can be irradiated. Control rates of 78% using a dose of 30 to 35 Gy have been reported, and an additional 15% of the cases can be controlled by a second course of radiotherapy.[183] Although the radiation affects tumor vascularity, the fibrous tumor component remains unchanged and a residual mass will be seen on imaging indefinitely. Experts disagree about the effect of estrogen therapy on angiofibromas. Although some cases of decreased tumor size and vascularity have been reported after estrogen therapy, this response is not achieved in most patients.[13] Similarly, the role of chemotherapy remains unclear.

Angiomatous Polyp

The angiomatous polyp is a fibrosed, vascularized nasal polyp, presumably the response to minor trauma.[184] A choanal polyp may become quite vascularized and is termed an *angiomatous polyp.* The significance of this lesion is that

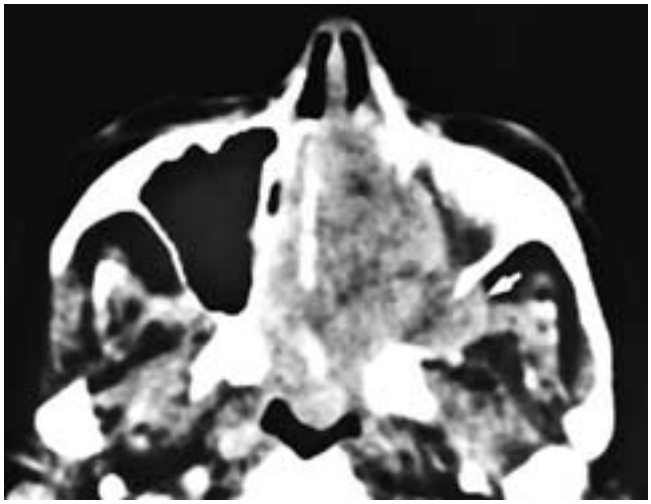

FIGURE 6-101 Axial contrast-enhanced CT scan shows a left nasopharyngeal and nasal fossa enhancing mass that has extended into the left antrum, widened the left pterygopalatine fossa, and extended into the left infratemporal fossa (*arrow*). There were only obstructed secretions in the right nasal fossa. This patient had an angiofibroma.

VIEW IMAGE

Copyright © 2003, Mosby, Inc. All rights reserved.

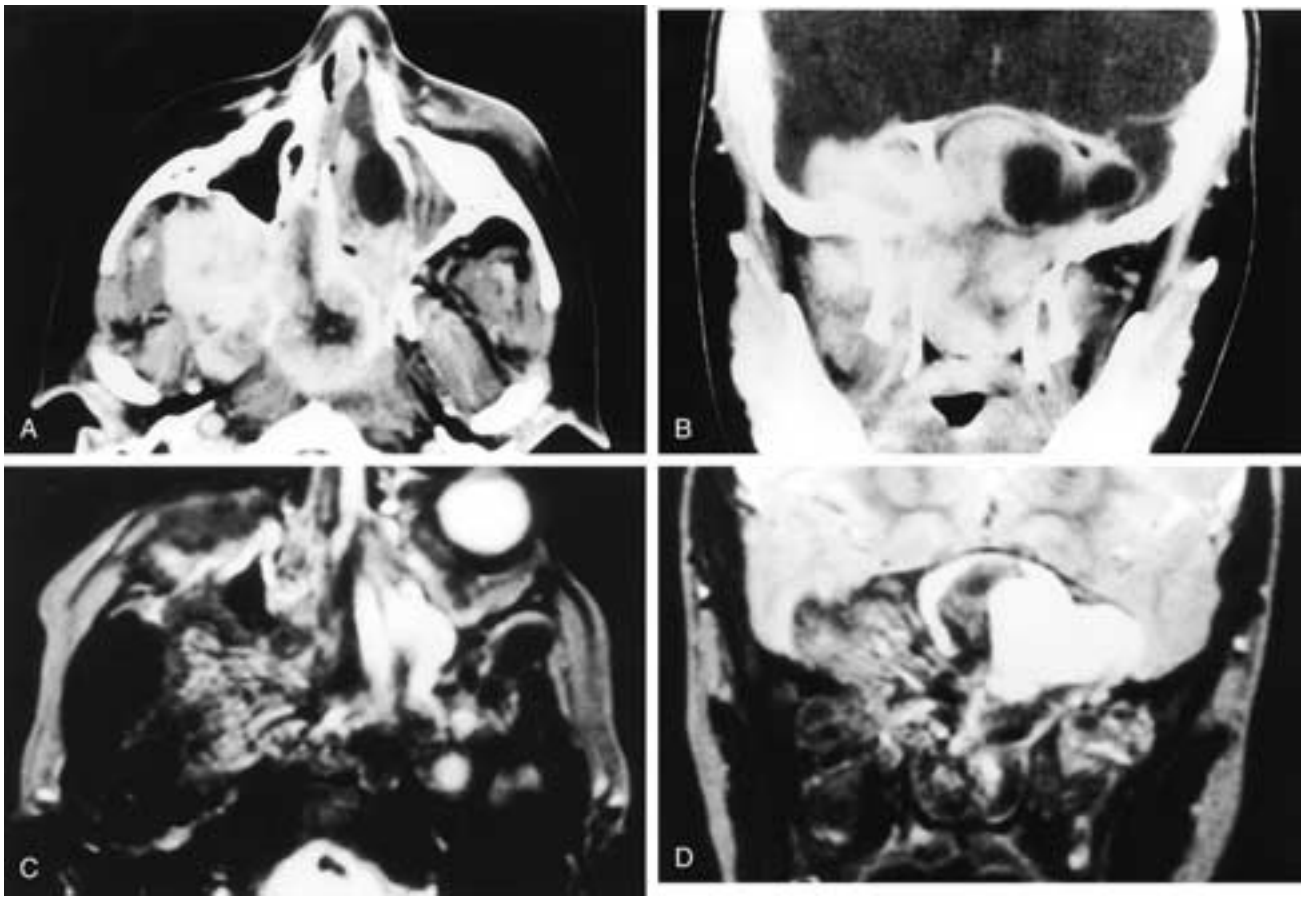

VIEW IMAGE

FIGURE 6-102 Axial **(A)** and coronal **(B)** CT scans show a large enhancing mass that fills the nasopharynx and nasal fossae, bows the posterior wall of the right maxillary sinus forward, and extends into the right infratemporal fossa. The tumor has also destroyed the floor of the sphenoid sinus and the right middle cranial fossa. There is a nonenhancing region in the vicinity of the left sphenoid sinus. Axial T2-weighted **(C)** and coronal **(D)** proton density MR images show that the mass is filled with serpiginous signal voids, reflecting its highly vascular nature. The left sphenoid sinus is filled with high T2-weighted fluid. This patient had a large angiofibroma with a left sphenoid sinus mucocele. The skull base was not destroyed, but only deossified from the chronic pressure of the tumor. Both cavernous sinuses were intact but were elevated by the mass.

histologically it can be confused with a nasopharyngeal angiofibroma.[176] Several points differentiate these two lesions: (1) the angiomatous polyp is located primarily in the nasal fossa and not in the nasopharynx; (2) the polyp does not extend into the pterygopalatine fossa and only rarely protrudes into the sphenoid sinuses. In these cases, the tumor enters the sinus through the anterior wall and not the sinus floor, as with angiofibromas; (3) these polyps do not extend intracranially; (4) on angiography the polyps have only a few demonstrable feeding vessels compared with the rich vascular supply of the angiofibroma; (5) on CT the angiomatous polyp does not enhance as well as the angiofibroma; (6) vascular flow voids are usually not seen on MR imaging, as they are in angiofibroma; (7) these polyps are easily ''shelled out'' surgically, as are routine nasal polyps, whereas the nasopharyngeal angiofibroma is difficult to remove from its primary attachment site; and (8) angiography and embolization are not necessary in patients with angiomatous polyps (Fig. 6-105).

The pathologic distinction between an angiomatous polyp and an angiofibroma may be difficult, and hence the pathologist may need to rely on the radiologist's impression in arriving at a correct diagnosis.

Hemangioma

Hemangiomas of the nasal cavity occur most commonly on the septum (65%), lateral wall (18%), and vestibule (16%). Most arise in the anterior septum near Kisselbach's plexus, and most are of the capillary type. Lesions arising on the lateral wall usually are of the cavernous type. Epistaxis and nasal obstruction are the most common patient complaints. Simple excision is generally curative for these lesions, which rarely exceed 2 cm in their greatest dimension. In the nasal cavity, hemangiomas also tend to develop in the inferior and middle turbinates. These lesions are diagnosed when small because they cause dramatically severe epistaxis. Rarely, intranasal hemangiomas may develop in the second trimester of pregnancy. Most of these lesions spontaneously regress within 4 to 8 weeks after delivery.[185] Hemangiomas of the paranasal sinuses are very rare; two have been described in the maxillary sinuses and two in the sphenoid

Copyright © 2003, Mosby, Inc. All rights reserved.

sinuses. The sphenoid sinus cases showed destruction of the skull base.[185]

On CT, these hemangiomas enhance, and in the nasal cavity they are usually inseparable from the middle or inferior turbinates. Hemangiomas have an intermediate signal intensity on all MR imaging sequences they enhance, and vascular flow voids occasionally may be present (Figs. 6-106 to 6-108).

Hemangiomas can also occur as solitary lesions in bone. These tumors account for only 0.7% of all primary bone tumors. In the head and neck, the most common sites are the skull (53%), mandible (10.7%), nasal bones (9%), and cervical vertebrae (6%). Although many patients have a history of local trauma, a causal relationship remains doubtful. The lesions occur twice as often in females as in males; the average age of onset is 31 years. Most commonly, patients experience a firm, nonpainful swelling that is associated with a pulsating sensation. Actual bruits are rarely heard. When hemangiomas involve the facial bones and mandible, angiograms have revealed that the blood supply is from the facial artery or the internal maxillary artery. The inadvertent surgical violation of an intraosseous hemangioma can be associated with exceptionally rapid blood loss, often as much as 3500 ml. Even so, surgery is the primary treatment of choice. Embolization may greatly reduce operative blood loss, provided that the operation is performed shortly after embolization, before a collateral circulation can develop.[116]

Radiographically these lesions have a ''sun ray,'' ''soap bubble,'' or ''honeycomb'' appearance and enhance on contrast-enhanced CT scans. On MR imaging, they have low to intermediate T1-weighted and high T2-weighted signal intensity. They also enhance (Fig. 6-109).

Angiosarcoma

Angiosarcoma refers to malignant neoplasia derived from vascular tissue. The term includes other vascular tumors, such as hemangioendothelioma, in which endothelial differentiation is more prominent, or lymphangiosarcoma, derived from lymphatic tissue. Angiosarcomas account for only 2% to 3% of all soft-tissue sarcomas. Approximately half of all angiosarcomas occur in the skin and subcutaneous tissues of the head and neck, particularly the scalp, legs, and trunk. A smaller percentage of angiosarcomas occur in the breast (particularly after radiotherapy for breast carcinoma), liver (particularly after Thorotrast exposure), bone, and spleen.[186, 187]

Cutaneous angiosarcomas occur over a wide age range but are most common in the seventh decade of life. There is a male predominance. Cutaneous and osseous angiosarcomas may present as raised or flat, spreading blue or red masses that can have a bruise-like appearance, causing dull local pain and swelling of the affected region.

Sinonasal and nasopharyngeal angiosarcomas are extremely uncommon, comprising 11% of head and neck angiosarcomas.[187–189] They present with epistaxis, nasal obstruction, headaches, and proptosis.[190] Angiosarcomas can also occur as primary intraosseous tumors and represent less than 1% of all primary bone malignancies. Head and neck angiosarcomas comprise 15% of solitary osseous angiosarcomas, arising most frequently in the mandible and skull.

FIGURE 6-104 Lateral subtraction angiogram shows the typical highly vascular tumor appearance of an angiofibroma.

VIEW IMAGE

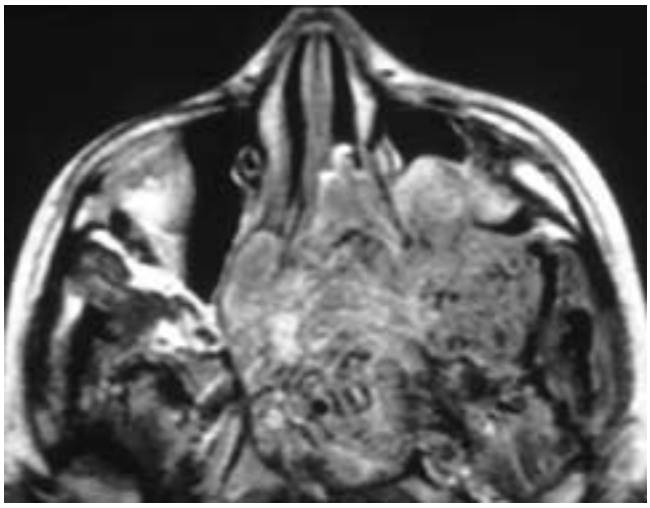

FIGURE 6-103 Axial T1-weighted MR image shows a large left nasopharyngeal and nasal fossa mass that extends into the left antrum. The mass also extends into the infratemporal fossa via the pterygopalatine fossa, which is widened and destroyed. The tumor further extends laterally to involve the left pterygoid muscles. There are multiple vascular-type flow voids within the mass. This patient had a large angiofibroma.

VIEW IMAGE

Copyright © 2003, Mosby, Inc. All rights reserved.

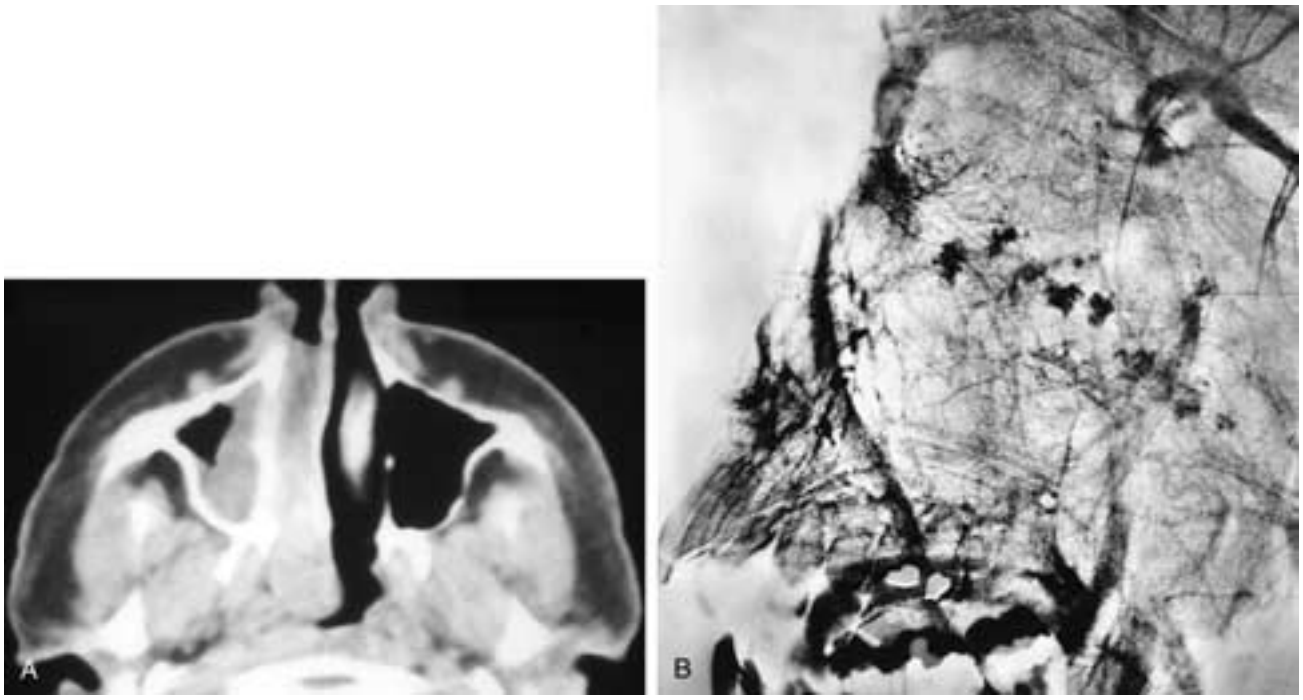

VIEW IMAGE

FIGURE 6-105 Axial CT scan (**A**) shows a right nasal fossa polypoid mass that extends back into the nasopharynx but does not arise there. The mass does not extend into the pterygopalatine fossa or the sphenoid sinus. A biopsy specimen was interpreted as an angiofibroma. **B**, A lateral subtraction angiogram shows only focal areas of increased vascularity, without the typical vascular appearance of an angiofibroma. This patient had an angiomatous polyp.

The histologic appearance of angiosarcoma varies dramatically with the tumor grade. Well-differentiated angiosarcoma (malignant hemangioendothelioma, hemangiosarcoma) produces obvious blood-filled vascular spaces. There is a combination of ''closed'' lumina, which are finite and delineated, as well as serpiginous ''open'' lumina, which are insidiously infiltrating interanastomosing spaces. Low-grade angiosarcomas produce abundant open vascular lumina, and have a minimal solid component and a low-grade cytology. High-grade angiosarcomas are densely cellular, infiltrative sarcomas. The amount of malignant vascular lumen formation varies and may be focal. Cytologically, these tumors are frankly malignant, with nuclear pleomorphism and atypical mitotic figures. Immunohistochemistry may be necessary to distinguish high-grade tumors from other sarcomas, namely the demonstration of Ulex, CD31 and CD34 expression.

Surgical resection is indicated as the primary treatment for angiosarcomas. However, the insidious infiltrating pattern of angiosarcoma may render complete resection impossible; therefore, adjuvant radiotherapy may be necessary. Local recurrences are common. The rate of cervical lymph node metastasis reported for cutaneous angiosarcomas varies from 10% to 41%, and the reported

VIEW IMAGE

FIGURE 6-106 Coronal CT scan shows a mass in the right nasal cavity, maxillary sinus, and ethmoid complex. Obstructed secretions are present in both the right antrum and ethmoid sinuses. Most of the bone around the margin of the tumor is intact. This patient had a hemangioma.

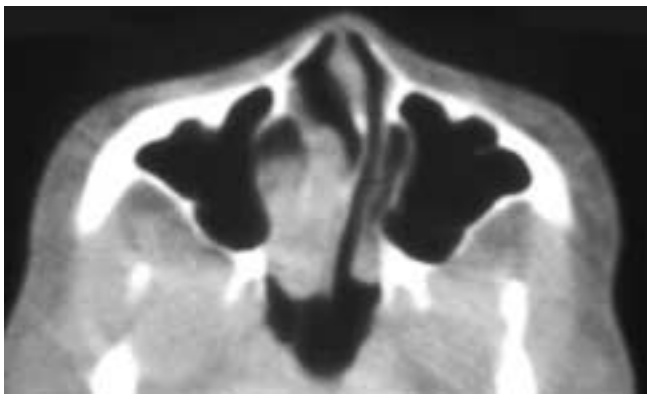

FIGURE 6-107 Axial CT scan shows a mass in the right inferior turbinate, with incidental bowing of the nasal septum convexity to the left. This patient had a hemangioma.

VIEW IMAGE

Copyright © 2003, Mosby, Inc. All rights reserved.

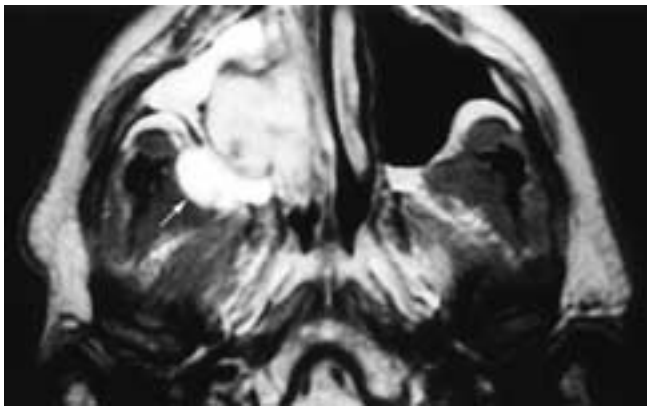

VIEW IMAGE

FIGURE 6-108 Axial T2-weighted MR image shows the tumor to have a high signal intensity, but not as high as the signal intensity of the obstructed secretions in the right antrum. The chronic antral obstruction has led to the development of a mucocele (*arrow*), which bulges into the right infratemporal fossa. This patient had a hemangioma.

rate of distant metastasis ranges from 33% to 63%.[191] The 5-year survival rate is poor, ranging from 41% to 18%.

The prognosis for intraosseous angiosarcomas varies with the tumor grade. Grade I lesions recur locally but do not metastasize, as do grade II and III lesions. For patients with solitary tumors, there is a 20% 5-year survival rate. The 5-year survival rate for patients with multifocal osseous tumors is 36%, reflecting the predominance of grade I tumors in this group. Inexplicably, sinonasal tumors appear to have a better prognosis than skin, soft-tissue, and osseous tumors, with a lower recurrence rate, a higher salvage rate, and a lower metastatic rate. Barnes reported that 6 of 10 patients with sinonasal angiosarcomas were recurrence free after 0.5 to 5 years (median, 29 months), and an additional patient was disease free at 12 years after one recurrence at 8 years.[188–191] On CT and MR imaging these tumors are aggressive, bone-destroying lesions with considerable enhancement.

Hemangiopericytoma

Hemangiopericytomas (HPCs) are uncommon vascular lesions that arise primarily in the lower extremities, retroperitoneum, and pelvis. However, 15% occur in the head and neck, and of these, 55% arise in the nasal cavity.[193] HPCs are thought to be derived from Zimmerman's pericytes, contractive cells that surround the outer aspect of small vessels. The lower extremities and the retroperitoneum-pelvis are the most common sites for HPCs. The head and neck is the third most common site; tumors occur in the neck, the perioral soft tissues, and, lastly, the sinonasal tract. Sinonasal hemangiopericytomas (SNHPCs) present as gray to tan, spongy, vascular, polypoid masses. Nasal obstruction and epistaxis are common presenting symptoms.[194, 195] Other presenting complaints include watery rhinorrhea, serous otitis media, proptosis, infraorbital anesthesia, and facial pain. SNHPCs generally involve the nasal cavity along with one or more sinuses. A review of the literature revealed an overall recurrence rate of 19% (22 of 115 cases). The majority of recurrences (19 of 22) were single (16%), and most (14 of 19) occurred within the first 5 years after resection. However, first recurrences after the first 10 years have occurred. Multiple recurrences were a rarer finding, seen in only 4 of 115 cases. Overall, three patients (2.6%) developed metastases (usually locoregional sites and local lymph nodes). Four patients (3.5%) ultimately died of disease (usually from a lack of local control). This confirms the general low-grade malignant potential of this neoplasm. It appears that no single feature of SNHPC can predict the course of this basically low-grade neoplasm. The prognosis of SNHPC most likely strongly depends on the tumor stage at initial presentation and on the completeness of primary resection. Features such as mitotic rate, necrosis, and nuclear pleomorphism are probably significant for high-stage or incompletely resected tumors.[196] The diagnosis of SNHPC remains one of histologic pattern recognition, and traditionally, immunohistochemistry has aided in excluding other diagnoses. Vimentin has been consistently expressed by the tumor spindle cells of HPC. However, recent studies have shown that factor XIIIa is also expressed by HPC (as well as by tumors of fibrohistiocytic

VIEW IMAGE

FIGURE 6-109 Axial CT scan (**A**) viewed at a wide window setting shows a 2.5 cm round lesion in from the left zygoma. The inner and outer cortices, although thinned, are preserved. The trabeculae radiate in a spoke wheel pattern. Axial T1-weighted, contrast-enhanced, fat-suppressed MR image (**B**) shows the enhancing, without evidence of large regional vessels. This patient had an intraosseous hemangioma.

Copyright © 2003, Mosby, Inc. All rights reserved.

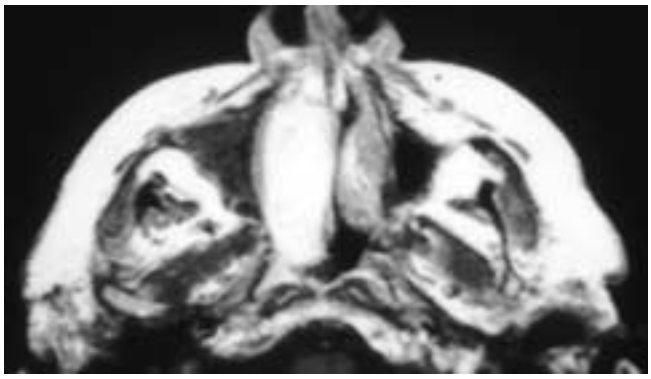

VIEW IMAGE

FIGURE 6-110 Axial T1-weighted MR image shows a high signal intensity expansile mass in the right nasal cavity. Obstructed inflammatory disease is present in the right antrum. This patient had a hemangiopericytoma.

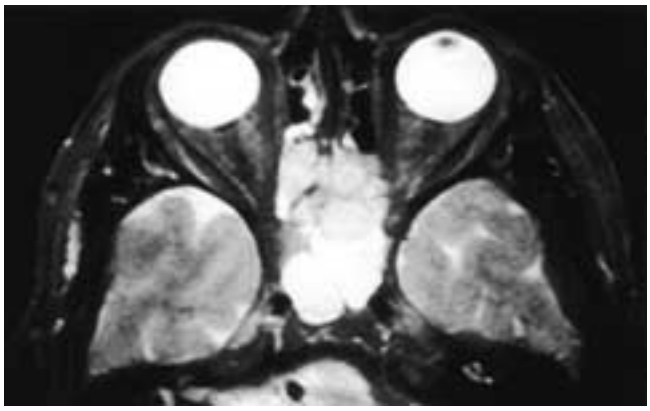

VIEW IMAGE

FIGURE 6-112 Axial T2-weighted MR image shows an intermediate signal intensity mass in the posterior ethmoid sinuses and anterior sphenoid sinuses. The remaining obstructed sphenoid sinuses are filled with high signal intensity secretions. This patient had a hemangiopericytoma.

differentiation) and hence may be yet another helpful positive marker in establishing an immunohistochemical profile. The role of chemotherapy is still evolving, but initial reports show promise.[185, 194, 197]

Microscopically, fusiform or spindle cells can be seen, forming short fascicles and bundles that become more dense around vessels. The abundant vessels have typical cuffs of perivascular hyalinization. Staghorn vessels may be rare. Nuclear pleomorphism is not normally present in SNHPCs.

On CT, HPCs are expansile, bone-remodeling lesions with a variably enhancing, fairly homogeneous appearance (Figs. 6-110 to 6-112). On MR imaging, they enhance and have low to intermediate T1-weighted and higher T2-weighted signal intensity. They tend to occur in the nasal fossa and in the maxillary sinus.[198]

Kaposi's Sarcoma

The classic form of Kaposi's sarcoma (KS) is an indolent tumor that occurs most commonly as soft red nodules on the lower limbs and, less commonly, on the upper limbs. Lesions may be multicentric and coalescent, but they rarely exceed 2 cm. Patients with classic KS are usually over the age of 50 at the time of tumor diagnosis, although 3% to 4% of the cases of the classic form are diagnosed in patients less than 15 years old. Patients with classic KS usually have long survival periods and die of something other than KS.

From the literature and the files of the Armed Forces Institute of Pathology (AFIP), Gnepp, Chandler, and Hyams compiled a total of 83 cases of classic KS, which affected the head and neck.[199] Of all the classic KS cases, 8% affected cutaneous sites on the head and neck, and only 2% affected the mucosal surfaces. Mucosal sites included the conjunctiva, palate, tongue, gingiva, and tonsil. Dermal sites included the eyelids, nose, ears, and face. By comparison, HIV-associated KS very commonly affects the skin of the head and neck (32%) and upper airway mucosal surfaces (19%). Common sites include the palate, gingiva, buccal mucosa, tongue, larynx, trachea, nasal cavity, and paranasal sinuses. These patients tend to be decades younger than patients with the classic cases (mean age, 38 years), though there is overlap among the two age groups.[199–204] The imaging findings are not diagnostic and usually show a noninfiltrating soft-tissue mass.

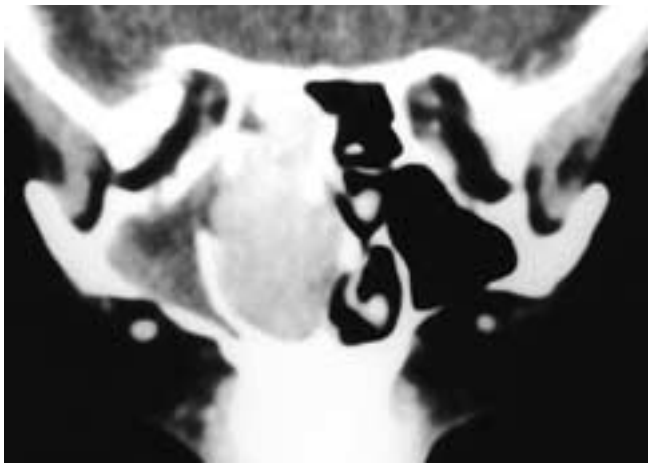

VIEW IMAGE

FIGURE 6-111 Coronal CT scan shows an enhancing right nasal fossa mass that extends into the right ethmoid sinuses. The right antrum is obstructed. There is primarily bone remodeling about the mass. This patient had a hemangiopericytoma.

Muscle

Malignant soft-tissue sarcomas (STSs) represent approximately 1% of all newly diagnosed malignancies in the United States.[205] The 1991 NCI (National Cancer Institute) SEER (Surveillance, Epidemiology, and End Results) data report that the U.S. incidence of reported new sarcomas for that year represented 5700 cases.[206] The majority of primary STSs originate within the extremities (59%), followed by the trunk (19%), retroperitoneum (13%), and head and neck (9%).[207] Sarcomas occur over a wide age range, starting in the first decade of life; however, the peak incidence occurs after the sixth decade of life.[208]

Leiomyoma and Leiomyosarcoma

Sinonasal smooth-muscle neoplasia are derived from the perivascular smooth-muscle tissue that is abundant in the

Copyright © 2003, Mosby, Inc. All rights reserved.

sinonasal tract. Both leiomyomas and leiomyosarcomas are rare occurrences. Fu and Perzin identified only two leiomyomas and six leiomyosarcomas from 256 nonepithelial sinonasal tumors.[209]

Leiomyomas have been reported to arise from the nasal septum, turbinates, vestibule, and choanae.[210–213] As the vascular component may be prominent, leiomyomas may present with epistaxis. Sinonasal leiomyosarcomas are rare, with fewer than 50 reports in the literature.[214, 215] On occasion, leiomyomas may present as more extensive lesions involving multiple sinuses.[216] The AFIP reported on nine cases of sinonasal tract leiomyosarcoma, which constitute the largest such series.[217] Either the nasal cavity alone or contiguous paranasal sinuses were involved. There is an equal sex distribution and an average age incidence of 50 years.[218] The sinonasal symptoms are nonspecific; patients complain of unilateral nasal obstruction, bleeding, and pain.

Leiomyomas are benign smooth-muscle tumors, the vast majority of which affect the female genital tract. In a compiled series of 257 head and neck leiomyomas, the most common sites of occurrence were the cervical esophagus (36%), subcutis (23%), and oral cavity (20%). The nasal cavity and sinuses were affected in only eight (3%) cases; the turbinate was a site of preference.[219] Five of these eight cases could be subclassified as angioleiomyomas; in all likelihood they were derived from the nasal erectile vasculature, which has thick vascular walls. Angioleiomyomas have been associated clinically with sharp knife-like pain, which probably relates to vascular constriction.

Histologically, leiomyomas are composed of bland whorls of spindled cells with blunt cigar-shaped nuclei. Immunohistochemistry confirms the expression of smooth muscle markers (actin, desmin). Angioleiomyomas have a prominent vascular component that may be compressed or thick-walled. The absence of nuclear pleomorphism, necrosis, and a prominent mitotic rate separates leiomyomas from leiomyosarcomas. Leiomyosarcomas are distinguished from leiomyomas by the presence of more than 10 mitoses per high-power field, atypia, and necrosis. The malignant cells of the epithelioid variant appear less spindled and more cuboidal. This variant is more likely to arise in the stomach or the mesentery but has been found in head and neck sites.[217]

On imaging, these tumors, like most sarcomas, tend to be homogeneous masses, often primarily expansile rather than invasively destructive (Fig. 6-113). They tend to have high

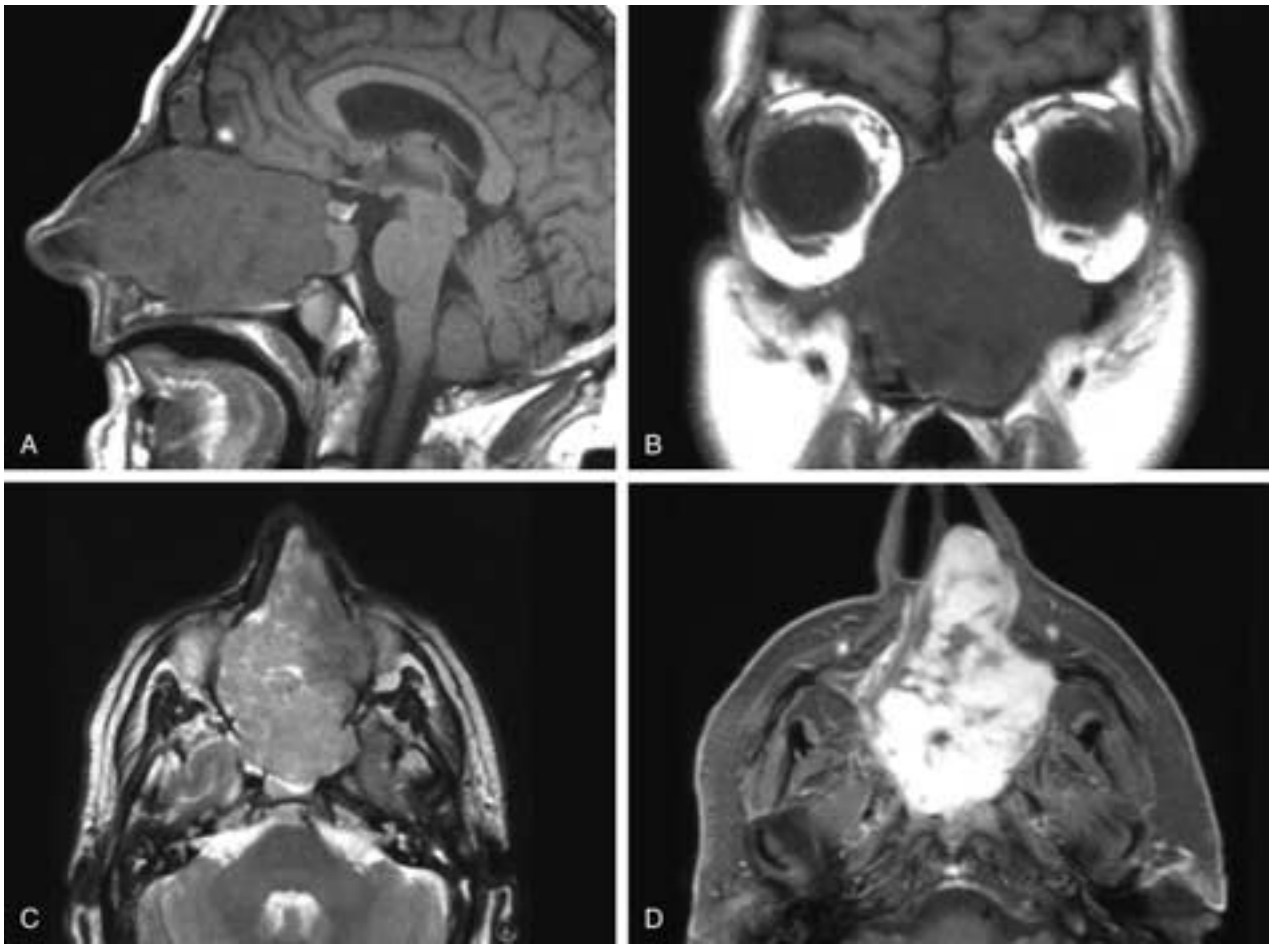

VIEW IMAGE

FIGURE 6-113 Sagittal (**A**) and coronal (**B**) T1-weighted MR images and axial T2-weighted (**C**) and T1-weighted, fat-suppressed, contrast-enhanced (**D**) MR images. In **A** and **B**, there is a fairly homogeneous, expansile nasal fossa mass that has elevated the floor of the anterior cranial fossa and bowed the lamina papyracea laterally. The medial floor of the left orbit is also elevated. There was no gross intracranial invasion or invasion of either orbit. The mass is nonhomogeneous on the T2-weighted and contrast-enhanced images. This patient had a leiomyosarcoma.

Copyright © 2003, Mosby, Inc. All rights reserved.

T2-weighted signal intensity, and they enhance after contrast administration.

Both leiomyomas and leiomyosarcomas are treated primarily by surgery. Resection can be conservative for leiomyomas, as these are curable. Sinonasal leiomyosarcomas require a wider surgical approach, as they are locally aggressive tumors. About 75% of patients have a local recurrence and 35% develop metastases. At least 50% of patients die of the disease, usually within 2 years of diagnosis.[218] Adjuvant radiotherapy or chemotherapy has no proven efficacy.[217] Tumor stage and distribution have been found to affect disease-free survival. Kuruvilla and colleagues found that of 30 patients with sinonasal leiomyosarcomata, 10 had tumors confined to the nasal cavity, none of which recurred.

Rhabdomyoma

Rhabdomyomas are rare benign tumors with skeletal muscle differentiation. They represent about 2% of all skeletal muscle tumors.[219] Clinically, rhabdomyomas can be classified as either cardiac or extracardiac.

Cardiac rhabdomyomas are most commonly associated with tuberosclerosis. Extracardiac rhabdomyomas are rare but have a tendency to affect head and neck sites such as soft tissues of the face and neck, the oral cavity, and the larynx. Histologically, rhabdomyomas can be classified as either fetal type (myxoid versus cellular types), adult type, or juvenile-intermediate type; histologically, the last type lies between the fetal and adult types. In a compiled series of 46 head and neck fetal rhabdomyomas, about half of the patients were in their second decade of life or older at diagnosis, and there was a male predisposition.[219] Five of these cases (11%) originated in the nasopharynx.[220, 221]

Rhabdomyosarcoma

Rhabdomyosarcoma (RMS) is a soft-tissue sarcoma of skeletal muscle derivation. It comprises 20% of all soft-tissue sarcomas, and it is the most common soft-tissue sarcoma in children (75%). It is the seventh most common pediatric malignancy following leukemia, CNS tumors, lymphoma, neuroblastoma, Wilms' tumor, and osteogenic sarcoma.[221] The majority of patients with RMS (78%) are under 12 years of age, and 43% of patients are under 5 years of age. Only 7% of cases occur in the second decade of life, and 2% to 4% of cases occur in each subsequent decade. In the head and neck, the most common sites for all RMSs are the orbit (36%), nasopharynx (15.4%), middle ear and mastoid (13.8%), sinonasal cavities (8.1%), face (4.5%), neck (4.1%), larynx (4.1%), and oral cavity. Sinonasal RMS may occur over a wide age range and commonly presents with nasal obstruction.[223–226]

Histologically, RMS can be classified as embryonal, botryoid (a variant of embryonal RMS), alveolar, and pleomorphic types based on the growth pattern, differentiation, and shape of tumor cells. The majority of head and neck RMSs can be classified as either the embryonal type or its botryoid variant, or alveolar. Embryonal RMS (ERMS) is composed of round cells with darkly staining hyperchromatic nuclei, scant cytoplasm, short, spindled cells with central elongated nuclei, tapered ends, and eosinophilic or amphophilic cytoplasm. Botryoid ERMS (5% of cases) is a noteworthy subtype that has a characteristic polypoid ''bunch of grapes'' clinical appearance. It is associated with the most favorable prognosis of all RMSs. Histologically, it grows as a polypoid tumor with a prominent myxoid stroma in which hypocellular and more cellular areas are seen with a subepithelial condensation of tumor cells, the *cambium layer*. Most RMSs arise from skeletal or cardiac muscle cells.

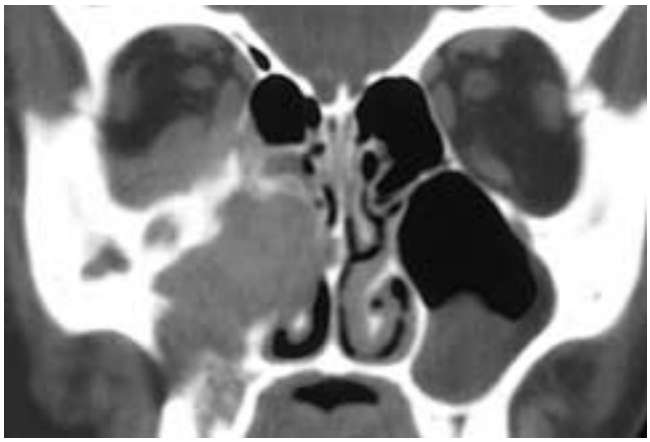

FIGURE 6-114 Coronal CT scan shows a soft-tissue mass in the right maxillary sinus. The medial sinus wall and portions of the antral roof are destroyed, and the tumor extends into the right orbit, ethmoid sinuses, and right nasal cavity. Despite these local areas of destruction, there are large areas where there is intact bone adjacent to the tumor. This patient had a rhabdomyosarcoma.

VIEW IMAGE

The general approach to RMS is resection plus adjuvant therapy. Regional lymph node sampling is appropriate; however, prophylactic lymph node dissection is not necessary. Resection followed by chemotherapy is the mainstay of therapy. Radiation therapy is not necessary after complete surgical resection with adequate margins.[227] Survival depends on the site (orbit better than parameningeal), histologic type (botryoid and embryonal better than alveolar), and stage. Tumors at nonorbital and nonparameningeal sites also have a favorable prognosis.

On imaging, RMSs usually have elements of both bone remodeling and bone destruction. On contrast-enhanced CT, these tumors enhance moderately and generally homogeneously. On MR imaging, they also tend to be remarkably homogeneous, they have intermediate signal intensities on all imaging sequences, and they enhance with contrast (Figs. 6-114 to 6-116). They can also appear on imaging as indistinguishable from SCC.

Lipoblastic

Lipoma and Lipoma-Like Lesions

These lesions, which include the ordinary lipoma, myxoid lipoma, angiolipoma, pleomorphic lipoma, spindle-cell lipoma, myelolipoma, hibernoma, and lipoblastoma, have various reported frequencies; however, they have not been reported to arise within the sinonasal cavities. The lipomas are discussed in Chapter 41.

Liposarcoma

Liposarcoma is one of the most common soft-tissue sarcomas of adulthood, usually occurring in the lower extremities and retroperitoneum. The head and neck region

Copyright © 2003, Mosby, Inc. All rights reserved.

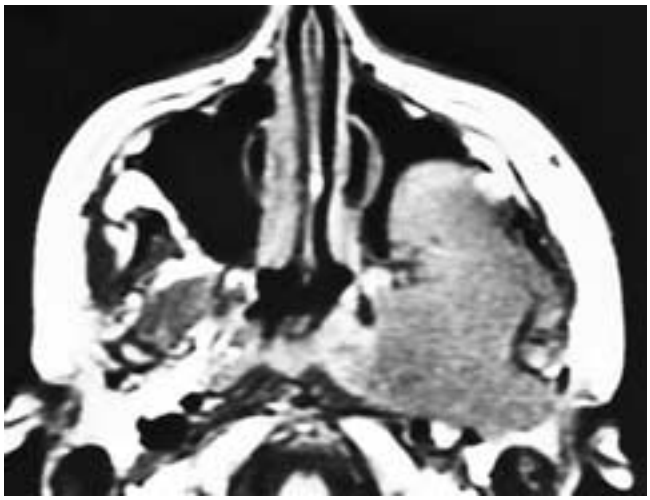

VIEW IMAGE

FIGURE 6-115 Axial T1-weighted MR image shows a homogeneous mass in the left infratemporal fossa extending into the left antrum and the skull base. The mass has an intermediate signal intensity. This patient had a rhabdomyosarcoma.

is involved in (5.6%) of liposarcomas.[186] The soft tissues of the neck, scalp, and face are the most common sites for liposarcomas above the clavicles, comprising 54% of head and neck cases.[228] Hypopharyngeal and laryngeal sites were affected in 38% of 76 cases of head and neck liposarcoma reviewed from the Royal Marsden Hospital over a 50-year period.[228] The sinonasal tract is an extremely rare site for either liposarcoma or lipoma.[185]

Liposarcomas can be polypoid pedunculated tumors that are soft and yellow/tan/gray upon sectioning. A spectrum of histology is seen, ranging from low-grade (lipoblastic liposarcoma, lipoma-like, sclerosing liposarcoma, or atypical lipoma) or intermediate to high-grade (myxoid liposarcoma, pleomorphic liposarcoma, round cell liposarcoma, dedifferentiated liposarcoma). Low-grade tumors are characterized by an abundance of mature, histologically benign adipose tissue coursed by collagenous fibrous tissue. Lipoblasts may be focal. They have characteristic ''chicken claw''–shaped nuclei that are indented by cytoplasmic fat globules. Their chromatin is usually dense and pyknotic, but enlarged nucleoli may be found. Myxoid liposarcoma is a common histologic pattern generally seen in soft-tissue liposarcoma. The stromal background is loose and myxoid, perforated by a fine ''chicken-wire'' meshwork of arborizing vessels. The lipoblasts appear as univacuolated signet ring cells and multivacuolated cells.

Generally, liposarcomas are properly treated by resection with adequate margins. Radical neck dissection is not usually warranted for low-grade tumors, but high-grade liposarcomas may develop locoregional metastases. The rarity of this tumor in the sinonasal tract precludes discussion of specific disease-free survival.

Based on the general experience with liposarcomas elsewhere in the body, on CT these lesions have an overall low (fatty) attenuation value (-65 to -110 HU), and irregular areas of soft-tissue density are seen within the lesion. The tumor margins may infiltrate adjacent soft tissues. MR imaging shows a nonhomogeneously high T1-weighted and an intermediate T2-weighted signal intensity.[229]

Fibroblastic

Fibrosarcoma (Including Desmoid Tumor)

Fibrosarcomas (desmoid tumors, aggressive fibromatoses) are infiltrative, nonmetastasizing, unencapsulated fibroblastic tumors that account for 12% to 19% of all soft-tissue sarcomas (STSs). They occur most often in the lower extremities and trunk; only 15% occur in the head and neck. Most head and neck tumors involve the sinonasal cavities (18.3%), larynx (14.8%), and neck (sternocleidomastoid) (6.1%). Fibromatoses (desmoid tumors, grade I fibrosarcomas) are more likely to occur in the pediatric population. Higher-grade fibrosarcomas (grades II/III) usually arise in patients between 20 and 60 years of age,[185] but may also occasionally occur in the pediatric population.[209, 230]

Grade II or III head and neck fibrosarcomas are more likely to present as bony jaw tumors than as STSs. Those occurring in the older population (30%) are usually the secondary jaw sarcomas, arising in previously irradiated or diseased bone such as bone with fibrous dysplasia, Paget's disease, giant cell tumors, bone infarcts, and osteomyelitis.

Fibromatoses (desmoid tumors) are histologically very bland and well differentiated, and appear as densely cellular spindle cell malignancies producing a collagenous matrix. The fascicles or bundles of tapered spindle cells grow in a variable intersecting pattern, seen on cross-section as ''herringbone'' areas. The diagnosis is firmly established on biopsy when the pathologist can identify the bland fibroblasts insidiously infiltrating host tissue. Examination during surgery shows that this white-tan scar-like tumor sends out innumerable tentacles, making complete extirpation virtually impossible. Positive resection margins are the rule. Nuclear pleomorphism, a significant mitotic rate, and necrosis are generally not seen, and, when present, indicate transformation to a higher grade (grade II or III fibrosarcoma).

Complete surgical excision with ample margins is the treatment of choice. Recurrences after resection are common, and in some series recurrence rates are as high as 90%.[208, 231] Progression to higher-grade fibrosarcoma may occur in occasional cases, usually after radiotherapy. Grade II and grade III fibrosarcomas develop local recurrences within 18 months of treatment and metastases within 2 years of recurrences.[185] The overall prognosis depends on the adequacy of the surgical resection, sarcoma grade, size, and location, male sex, and the presence of pain or cranial nerve symptoms. Of these parameters, sarcoma grade and resection margin status are probably the most important. Only 1% to 11% of patients develop positive regional lymph nodes; however, the 5-year survival rates are only 33% to 69%.[185]

Bony fibrosarcomas tend to spread more aggressively than their soft-tissue counterparts. Most grade II or grade III jaw fibrosarcomas have 5-year survival rates ranging from 27% to 40%. Metastases occur to the lungs and to other bones; only 3% spread to regional lymph nodes.[232] In addition, the younger the patient is when the tumor appears, the better is the prognosis. Although the local recurrence rate of pediatric fibrosarcoma is similar to that for adults (17% to

Copyright © 2003, Mosby, Inc. All rights reserved.

47%), younger patients have metastases in only up to 14% of cases, and they have a higher 5-year survival rate of 85%.[185] In a series of sinonasal fibromatoses, five patients (21%) (four adults and one child) developed single or multiple recurrences within 6 to 34 months.[155, 233]

The imaging findings are nonspecific. On CT, fibrosarcomas have a generally homogeneous, minimally enhancing appearance. They also tend to remodel bone (Fig. 6-117). On MR imaging, they have low to intermediate signal intensities on all imaging sequences and enhance minimally.

Malignant Fibrous Histiocytoma

Malignant fibrous histiocytoma (MFH) is one of the most common soft-tissue sarcomas below the clavicles. While it has been recognized that MFH has become a ''waste-basket'' category for some sarcomas, there is a group of sarcomas that truly reveal both fibroblastic and histiocytic phenotypes. Only about 3% occur in the head and neck, and most of these occur in the skin, orbit, or sinonasal cavities.[185, 234, 235]

A number of histologies, either uniform or a mixture of patterns, may be seen in MFH, which can be histologically classified as myxoid, angiomatoid, inflammatory, and giant cell type. Most MFHs have a storiform/pleomorphic pattern. Whorls and fascicles of malignant fibroblastic spindle cells forming a ''rush-mat'' or radiating ''star-like'' (storiform) pattern characterize MFH. The putative ''histiocytic'' component is composed of plump epithelioid cells and larger multinucleated giant cells that have bizarre nuclei. If a prominent myxoid background is present, these sarcomas

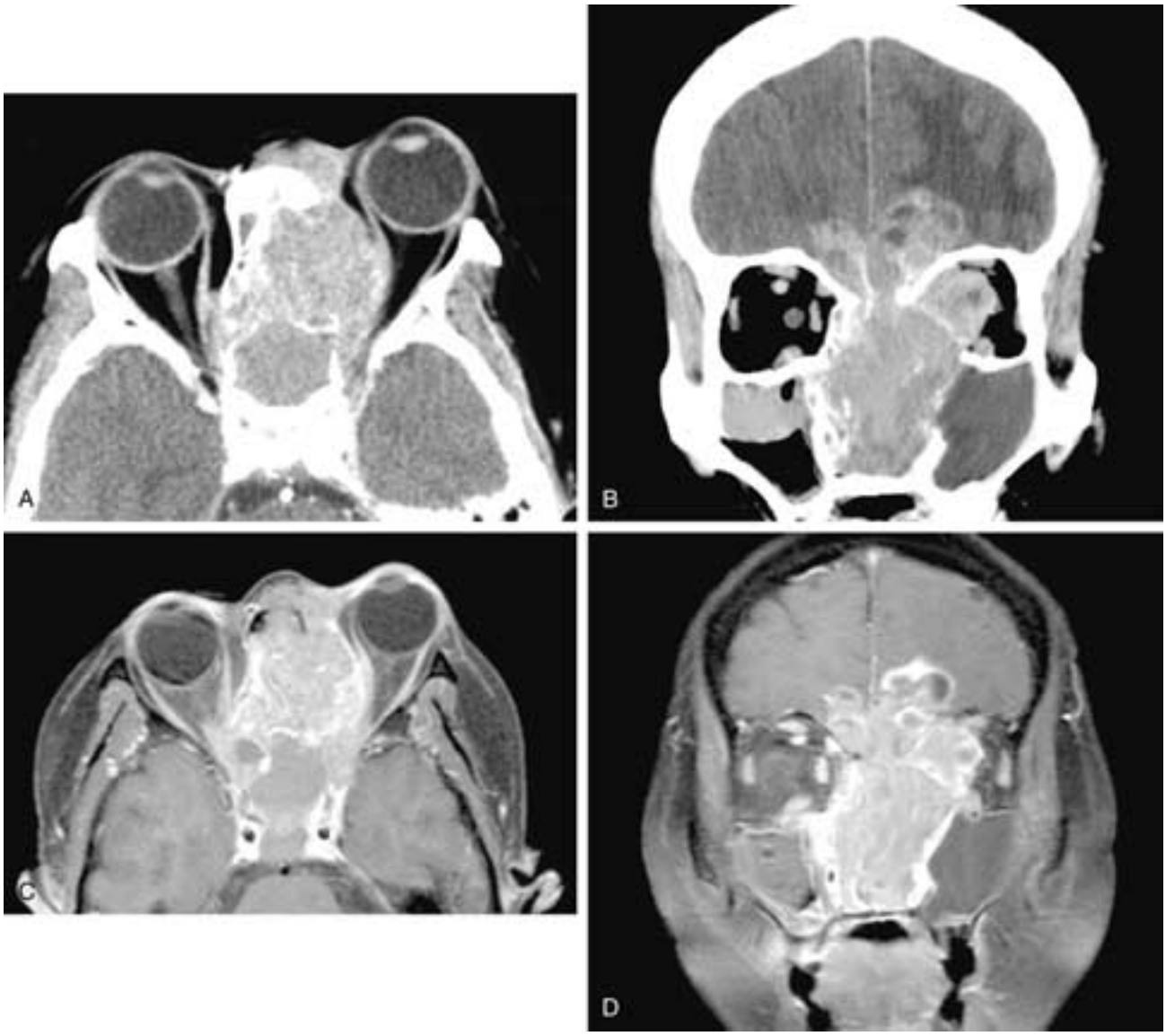

FIGURE 6-116 Axial (**A**) and coronal (**B**) contrast-enhanced CT scans show a destructive mass that has broken into the anterior cranial fossa and invaded the brain. The tumor also has extended into both orbits and obstructed the left antrum. Incidental inflammatory disease is present in the right maxillary sinus. Axial (**C**) and coronal (**D**) T1-weighted, contrast-enhanced MR images confirm the disease mapping and the presence of a sphenoid sinus mucocele. Statistically, in a 45-year-old male, this imaging appearance should suggest the diagnosis of squamous cell carcinoma. This patient had a rhabdomyosarcoma.

VIEW IMAGE

Copyright © 2003, Mosby, Inc. All rights reserved.

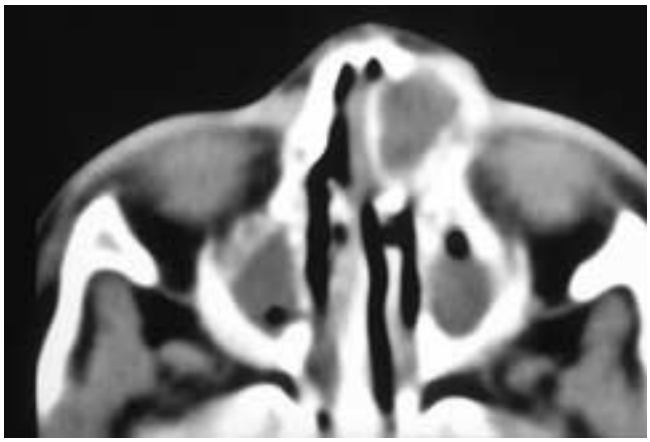

VIEW IMAGE

FIGURE 6-117 Axial CT scan shows a soft-tissue mass in the left lacrimal duct region bulging into the left nasal fossa. The bone has been remodeled around the lesion. Incidentally noted are inflammatory secretions in both maxillary sinuses. This patient had a low-grade fibrosarcoma.

can be classified as myxoid MFH. As with other sarcomas, focal metaplastic mesenchymal elements such as cartilaginous or osseous differentiation may be seen in MFH. A marked inflammatory infiltrate may be present, thus warranting the designation of *inflammatory MFH.*

MFHs express vimentin diffusely; other markers, such as desmin, may be seen focally. The immunohistochemical pattern of MFH also has many nonspecific markers: antibodies to lyzozyme, alpha-1 antitrypsin, and acid phosphatase mark some MFHs. Nemes and colleagues have shown that FXIIIa, a marker of histiocytes and pericytes, can be expressed in MFH and in HPC.[236] Therefore, strong, diffuse expression of FXIIIa in the right circumstances may support the diagnosis of MFH.[237]

The 2-year survival rate for all MFHs is 60%. Local recurrences develop in 27% of cases, 75% within 2 years of diagnosis. Cervical nodal metastases occur in 12% and distant metastases in 42% of cases. Of the eight nasopharyngeal carcinoma survivors with secondary sinonasal MFH, none were disease free at follow-up and six died of disease without distant metastasis within 30 months.[185]

On contrast CT, these tumors usually enhance moderately and either aggressive bone destruction or bone remodeling can occur, making the CT characteristics nonspecific (Fig. 6-118).[238, 239] On MR imaging, fibrous histiocytomas usually have intermediate signal intensities on all imaging sequences, and contrast enhancement may be nonhomogeneous.

Benign Fibrous Histiocytoma

Benign fibrous histiocytoma (dermatofibroma) is a histologically benign lesion with fibroblastic and histiocytic components that most commonly occurs in the dermis and subcutis. It has been reported anecdotally as a sinonasal lesion.[240] Histologically, fibrous histiocytomas are composed of whorls of benign fibroblastic cells with a radiating, storiform pattern admixed with multinucleated giant cells. They can be distinguished from MFH, as they are less cellular and lack nuclear pleomorphism, abnormal mitotic figures, and necrosis.

Inflammatory Myofibroblastic Tumor

Inflammatory myofibroblastic tumor (IMFT) (also referred to as inflammatory pseudotumor and plasma cell granuloma) is a poorly understood ''emerging'' entity that manifests as a space-occupying lesion composed of a benign lymphoplasmacytic and myofibroblastic infiltrate. In the head and neck, IMFT most often affects the periorbital and orbital soft tissue. It has also been described in the supraglottic larynx and the salivary glands. At least 17 cases have been reported involving the sinonasal tract, nasopharynx, pterygomaxillary space, and parapharyngeal space. These have occurred over a wide age range from childhood (3 years) to old age (the ninth decade). In the sinonasal tract, they present as polypoid masses causing nasal obstruction. Maxillary sinus involvement may result in a soft tissue mass with bony erosion and remodeling.

In the parapharyngeal and pterygomaxillary spaces, IMFT can cause trismus and pain. Systemic symptoms such as fever, weight loss, malaise, anemia, hypergammaglobulinemia, and elevated sedimentation rate may also be present. It is quite common for patients with IMFT to undergo multiple biopsy procedures in order to establish a diagnosis.[241–248]

On biopsy evaluation, IMFT appears to be a diagnosis of exclusion. Excised tumors have been described as fleshy, whorled, and firm or myxoid. The polymorphous appearance of IMFT may reflect its variable etiology or its shifting histology during disease course. Lymphocytes, plasma cells, histiocytes, fibroblasts, and myofibroblasts are the basic components of IMFT, with mutable proportions. Four basic histologic patterns have emerged: (1) a dominant lymphoplasmacytic infiltrate, (2) a dominant lymphohistiocytic infiltrate, (3) a predominantly ''young and active'' myofibroblastic process, and (4) and a predominantly collagenized process with a lymphoplasmacytic infiltrate. Lymphoplasmacytic IMFT consists of a mature lymphoid infiltrate with germinal centers and a rich plasma cell infiltrate—hence the name plasma cell granuloma. Lymphohistiocytic IMFT most closely resembles an infectious process, as foamy histiocytes are prominent. The ''young and active'' IMFT has a

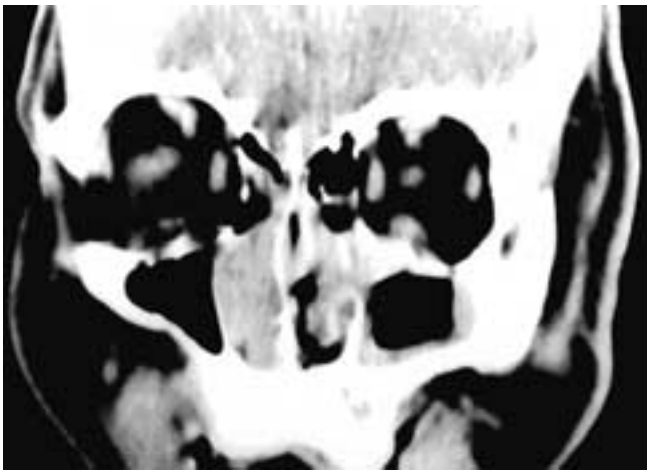

FIGURE 6-118 Coronal CT scan shows an expansile polypoid mass in the right nasal fossa (*arrowhead*). There is no bone erosion, and the nasal septum is intact. Inflammatory disease is present in the left antrum and nasal cavity. This patient had a fibrous histiocytoma.

VIEW IMAGE

Copyright © 2003, Mosby, Inc. All rights reserved.

densely cellular fascicular and storiform pattern resembling that of fibrous histiocytoma, except for the inflammatory infiltrate or nodular fasciitis (see Chapter 41 for a discussion of nodular fasciitis, which characteristically arises from superficial fascia and presents as a freely movable subcutaneous nodule). Overlapping histologic features between IMFT, nodular fasciitis, and fibrous histiocytoma corroborate the place of these entities in the pathologic spectrum between reactive and neoplastic processes. Collagenized IMFT is paucicellular and resembles a desmoid tumor, but with a prominent inflammatory infiltrate, and a zonation/maturation effect may be observed. Progression of patterns may also be seen in some long-standing cases necessitating multiple procedures.[241–248]

IMFTs of solid organs (e.g., lung, liver) are resected for diagnostic purposes and so effectively treated. Coffin et al. reported single or multiple recurrences in 25% of patients after initial excision; two cases progressed to sarcomatous transformation. However, the recurrent or transformed cases still showed a tendency to remain localized.[244] Recurrence was more often seen in patients with mesenteric or retroperitoneal tumors. In head and neck sites, including the sinonasal tract, most IMFTs do resolve/regress with excisional biopsy and steroid therapy; however, some IMFTs may persist and worsen, requiring more aggressive therapy such as radiotherapy.[241–248]

Solitary Fibrous Tumor

Solitary fibrous tumor (SFT) is an uncommon spindle-cell neoplasm derived from primitive mesenchymal or fibroblast-like cells. First recognized as a pleural neoplasm (fibrous mesothelioma), SFT has gained greater recognition and has been described in other soft tissues, including the head and neck.[249–251]

In the sinonasal tract, SFT presents as a firm, polypoid, well-circumscribed or encapsulated soft-tissue neoplasm. Histologically, SFT is composed of bland spindle cells arranged in a ''pattern-less pattern''; focally storiform or fascicular growth patterns or hemangiopericytoma-like vascular patterns are seen. Collagen deposition to the point of keloid-like hyalinization can be seen. Myxoid areas and rich vascularity are present, with hyalinized vessels. The tumor boundary may be circumscribed or infiltrative. Immunohistochemically, SFT expresses vimentin, CD34, and CD99. SFT is usually cured by resection; recurrences or progression to higher-grade tumors (mitotic figures, necrosis, pleomorphism, increased cellularity) are rare.

Fibromyxoma and Myxoma

A number of other benign or low-grade neoplasms can develop from pleuripotential mesenchymal cells, producing fibromyxoid and myxoid tumors. These tumors are related to fibroosseous lesions; however, they contain no osseous or odontogenic matrix. Fibromyxomas and myxomas tend to occur during the second and third decades of life.

Radiographically, fibromyxomas are soft-tissue, primarily expansile masses when they involve the sinuses, although focal areas of aggressive bone destruction may be present. These lesions usually have flecks or thin strands of calcification dispersed within the tumor substance (Figs. 6-119 and 6-120).

Histologically, one sees bland stellate fibroblastic cells producing myxoid stroma. A variable collagenizing component may be present. Sinonasal fibromyxomas can be locally aggressive, with a significant recurrence rate, especially if treated by curettage.[219] Therefore, complete surgical excision is the treatment of choice.

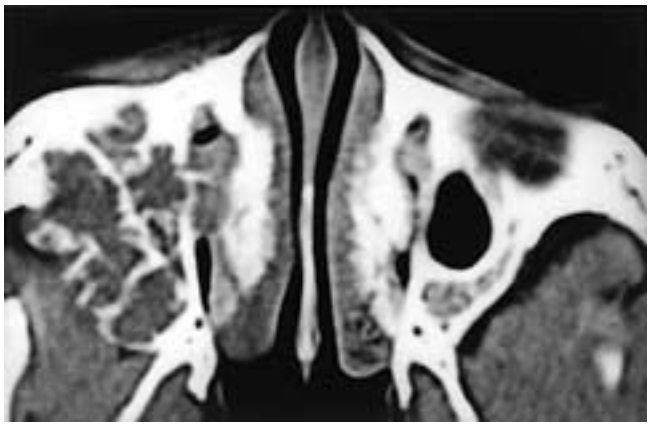

FIGURE 6-119 Axial CT scan shows a partially destructive and partially expansile mass in the right maxillary sinus. The lesion contains lacelike areas of calcification. This patient had a fibromyxoma.

VIEW IMAGE

A myxoma is a benign mesenchymal tumor composed of undifferentiated stellate cells producing a myxoid stroma. These tumors are generally uncommon and have been reported in the heart (atrial myxoma), subcutaneous tissues, bone, genitourinary tract, and skin. Head and neck myxomas are usually intraosseous; those of the jaws represent 40% to 50% of all head and neck myxomas. Mandibular myxomas have been presumed to arise from odontogenic tissue and hence are also called odontogenic myxomas. Those that arise from the maxillary bone may extend to the maxillary sinus and nasal cavity.[252] On CT they are cystic-appearing lesions that do not enhance (Fig. 6-121).[253]

BENIGN AND MALIGNANT OSSEOUS LESIONS AND TUMORS (INCLUDING FIBROOSSEOUS LESIONS)

Of the nonepithelial tumors that involve the sinonasal cavities, nearly 25% are osseous or fibroosseous lesions. These lesions and tumors can be categorized as lesions of abnormal bone development causing tumoral masses (Paget's disease, fibrous dysplasia, cemento-ossifying dysplasia, cherubism, giant cell reparative granuloma), benign osseous tumors (osteoma, osteochondroma, exostosis, osteoid osteoma, osteoblastoma, ossifying fibroma, chondroma, giant cell tumor), and malignant tumors (chondrosarcoma, osteogenic sarcoma).

Benign Tumors

Osteoma and Exostosis

Osteoma is a benign expansile proliferation of mature bone that occurs within bone. Exostosis is a benign, expansile proliferation of mature bone that occurs on the surface of bone. When an exostosis projects intracranially

Copyright © 2003, Mosby, Inc. All rights reserved.

from the calvarium, it is also referred to as an enostosis. Osteomas are found almost exclusively within the membranous bones of the skull and face, most commonly within the frontal sinuses, followed by the ethmoid sinuses. Maxillary and sphenoid sinus osteomas are rare. The high prevalence of frontal and ethmoid sinus osteomas may be related to the fact that these sites represent the junction of membranous and enchondral development of the frontal and ethmoid bones.[254]

Osteomas of the sinuses are not uncommon and may be seen in up to 1% of radiographs obtained for sinus symptoms. Sinus osteomas may be asymptomatic, or patients may complain of headache, sinus symptoms, or a frontal mass. They obstruct the frontal sinus in 17% of cases, resulting in the need for immediate surgery (Fig. 6-122).[209] They can also obstruct the lacrimal apparatus.[255] Almost all osteomas remain confined to the sinuses, often conforming to the contour of the sinus. However, osteomas are also the

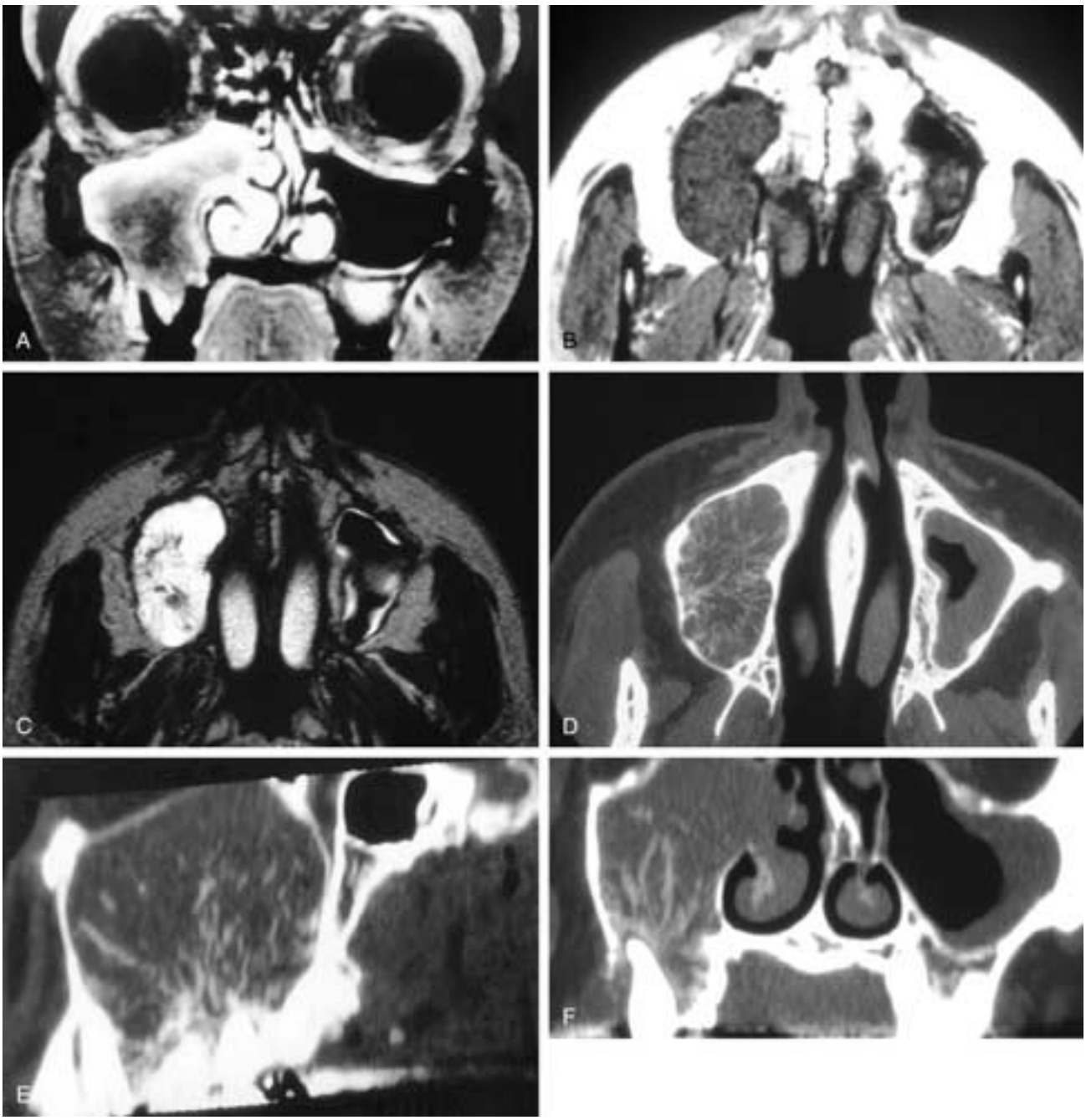

VIEW IMAGE

FIGURE 6-120 Coronal T1-weighted (**A**), axial T1-weighted (**B**), and T2-weighted (**C**) MR images, axial CT scan (**D**), and reformatted sagittal (**E**) and coronal (**F**) CT scans show an expansile low signal intensity mass filling the right maxillary sinus. Minimal nonhomogeneity is seen in **B**. Very fine lacelike signal voids are seen in **C**. Entrapped high signal intensity secretions are present around the lesion. The CT scans show that within the lower portion of the mass there are thin, lacelike calcifications. This patient had a fibromyxoma.

Copyright © 2003, Mosby, Inc. All rights reserved.

FIGURE 6-121 Coronal CT scan (**A**) shows an expansile mass in the left anterior maxilla (*arrow*). The surrounding bone is intact. This patient had a myxoma. Note the similarity to Figure 6-117, from a patient with fibromatosis. Axial T1-weighted (**B**), axial T2-weighted (**C**), and axial (**D**) and coronal (**E**) T1-weighted contrast-enhanced MR scans on a different patient show a large mass destroying part of the right maxillary alveolus and expanding and filling the left maxillary sinus, elevating and thinning the orbital floor. There is no infiltration of the orbit. The teeth roots are exposed by the tumor, and the tumor is fairly homogeneous in signal intensity. This patient had a myxoma.

VIEW IMAGE

most common benign paranasal sinus tumors associated with spontaneous CSF rhinorrhea, pneumocephalus, and tension pneumocephalus (Figs. 6-123 and 6-124).[256–258] Osteomas tend to grow slowly; the mean growth rate has been estimated at 1.61 mm/yr (range, 0.44 to 6.0 mm/yr) in a series of 13 patients with successive sinus radiographs.[259]

Multiple osteomas can be a manifestation of Gardner's syndrome, a very rare autosomal dominant transmitted disorder consisting of (1) intestinal polyposis with progression to intestinal adenocarcinoma, (2) benign skin and subcutaneous neoplasia, such as epidermoid inclusion cysts and desmoid tumors, and (3) multiple osteomas, with a proclivity for the mandible. These osteomas can arise within the second decade of life and precede intestinal polyps, which are usually diagnosed after the third decade of life (Figs. 6-125 and 6-126).

Exostoses occur in the external auditory canal (''swimmer's ear'') or on the palate or mandible (torus palatini or torus mandibularis). The latter usually presents as a painless bulging of the alveolus, possibly causing dentures to fit poorly (Fig. 6-127). Torus palatinus (Fig. 6-128) is seen in the hard palate, at the junction of the left and right horizontal plates of the palatine bones and the palatine processes of the maxilla.

Osteomas usually are small, incidental findings on plain films, where they have a variable bone density, ranging from very dense and sclerotic, for the ivory-type osteoma, to a progressively less dense and less ossified lesion for the

Copyright © 2003, Mosby, Inc. All rights reserved.

FIGURE 6-122 Coronal (**A**) and axial (**B**) CT scans show an osteoma in the right frontal sinus. This osteoma arises from the roof of the sinus. Axial CT scan (**C**) on another patient shows a large left frontal sinus osteoma that obstructs the sinus.

VIEW IMAGE

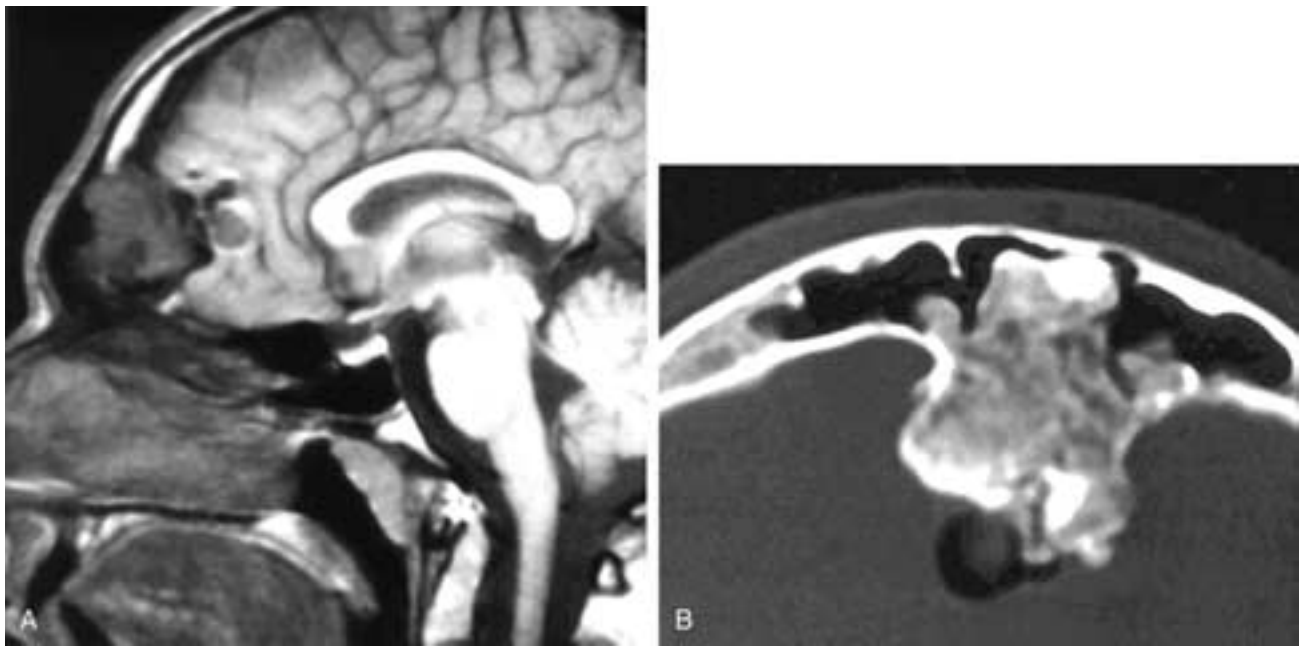

VIEW IMAGE

FIGURE 6-123 Sagittal T1-weighted MR image (**A**) and axial CT scan (**B**) show an osteoma arising from the posterior frontal sinus wall and extending intracranially. A small amount of air is seen in the adjacent frontal lobe region. Notice how much more clearly this diagnosis can be established on CT. In **A**, this could just as easily be a nonossified cellular tumor.

Copyright © 2003, Mosby, Inc. All rights reserved.

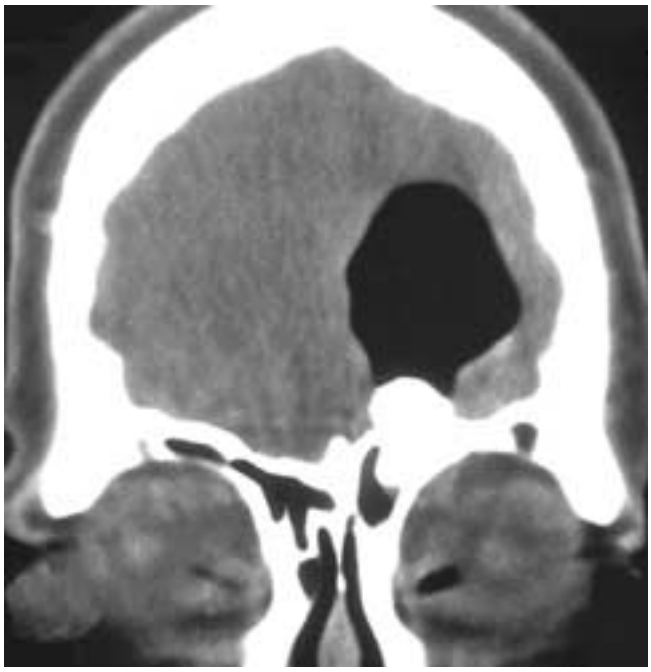

VIEW IMAGE

FIGURE 6-124 Coronal CT scan shows an osteoma in the roof of the left frontal sinus with a large collection of intracranial air.

FIGURE 6-125 Lateral view shows multiple osteomas of the facial bones, mandible, and calvaria. Gardner's syndrome.

VIEW IMAGE

VIEW IMAGE

FIGURE 6-126 Coronal CT scans (**A** and **B**) through the frontal sinuses show multiple osteomas in the right frontal sinus and supraorbital ethmoid sinuses. A supraorbital mucocele has developed in the most lateral aspect of this sinus. This patient had Gardner's syndrome.

Copyright © 2003, Mosby, Inc. All rights reserved.

VIEW IMAGE

FIGURE 6-127 Axial CT scans (**A** and **B**) show multiple exostoses along both the buccal and lingual cortices of the maxillary alveolus. This patient has maxillary exostoses. In **C**, an axial CT scan shows multiple mandibular exostoses along the lingual cortices. In **D**, an axial CT scan shows exuberant exostosis in this patient with mandibular exostoses. Axial (**E**) and coronal (**F**) CT scans show extensive mandibular exostoses. Notice how these exostoses narrow the volume of the floor of the mouth.

Copyright © 2003, Mosby, Inc. All rights reserved.

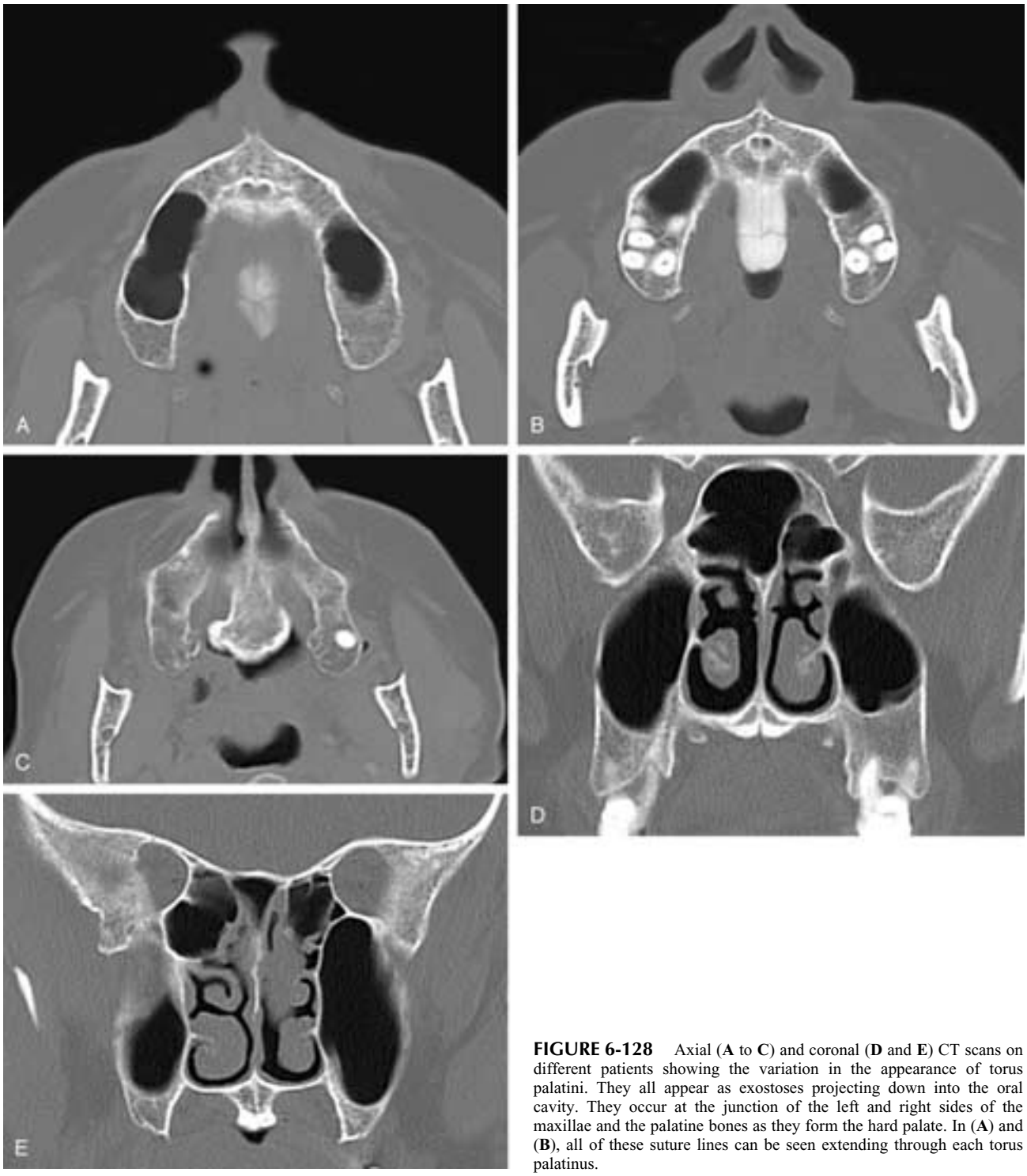

FIGURE 6-128 Axial (**A** to **C**) and coronal (**D** and **E**) CT scans on different patients showing the variation in the appearance of torus palatini. They all appear as exostoses projecting down into the oral cavity. They occur at the junction of the left and right sides of the maxillae and the palatine bones as they form the hard palate. In (**A**) and (**B**), all of these suture lines can be seen extending through each torus palatinus.

VIEW IMAGE

fibrous osteoma (Figs. 6-129 to 6-133). In fact, some fibrous osteomas may be confused on plain films with a retention cyst or polyp. On CT, osteomas arise from one of the sinus walls or the intersinus septum. The differences between the compact, cancellous, and fibrous types of osteoma correlate with the degree of bone matrix density seen within the lesion. On MR imaging these lesions give a nonhomogeneous, low to intermediate signal intensity on all imaging sequences. Based purely on MR imaging findings, their osseous nature may go undetected (Fig. 6-123).

Pathologically, osteomas are composed of dense, hard, mature bone, with only small amounts of fibrous tissue. The cancellous, or mature, osteoma has sparse intertrabecular spaces that may be empty or filled with fat, fibrous tissue or hematopoietic elements. Fibrous osteomas contain abundant mature lamellar bone, with greater amounts of intertrabecu-

Copyright © 2003, Mosby, Inc. All rights reserved.

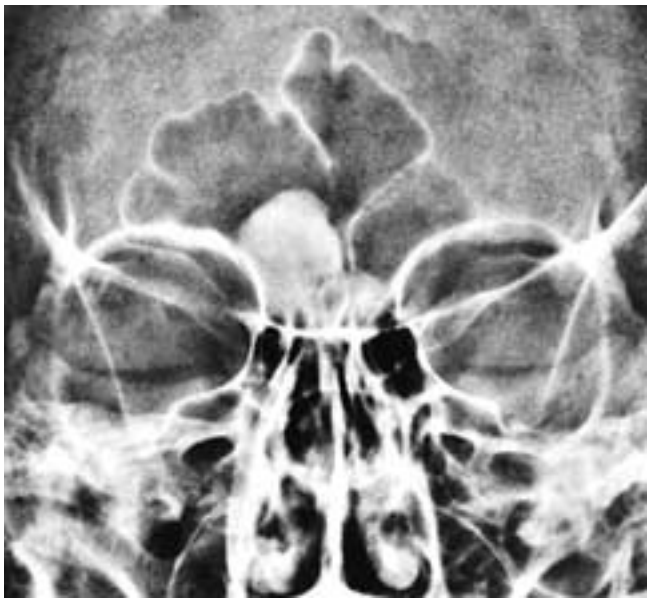

VIEW IMAGE

FIGURE 6-129 Caldwell view shows an ivory-type osteoma in the base of the right frontal sinus. The sinus is not obstructed.

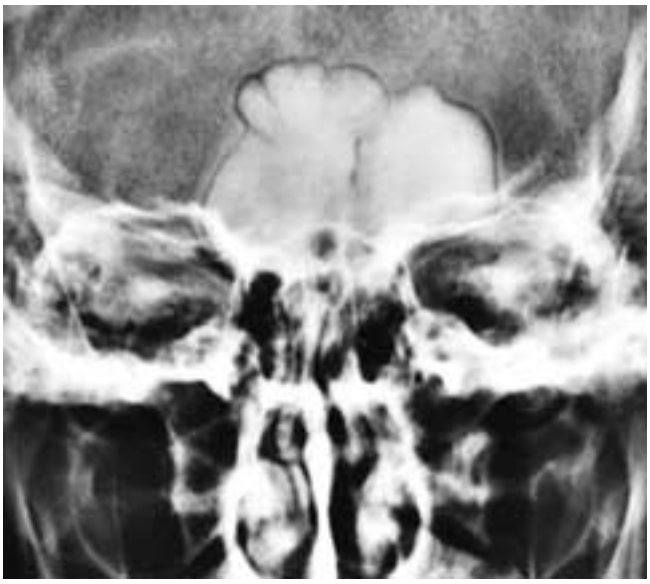

FIGURE 6-131 Caldwell view shows bilateral frontal sinus osteomas. Note that in this patient the osteomas have remained within the contour of the frontal sinuses, and a thin rim of air is seen outlining each osteoma.

VIEW IMAGE

lar fibrous tissue. Exostoses are seen as compact layers of dense cortical bone without a medullary component.

Osteochondroma

An osteochondroma is a benign cartilage-capped osseous growth arising from the surface of bone. They represent 35% to 50% of benign osseous lesions and 8% to 15% of all osseous tumors.[254] They are believed to represent a developmental abnormality rather than a neoplastic process. Osteochondromas arise from any bone developing via enchondral ossification. Because the craniofacial bones are membranous, sinonasal osteochondromas are rare. The mandible (coronoid process and condyle) was the most common site (52%) of 63 head and neck ''osseous'' osteochondromas reported in the literature.[254] They have also been reported rarely in the sphenoid bone, maxillary tuberosity, zygomatic arch, and nasal septum. Most osteochondromas have a limited growth potential; expansion ceases with axial skeletal maturation. However, some osteochondromas may continue to grow after skeletal maturation.

Radiographically, these tumors tend to have a pedunculated mushroom shape. The cartilaginous cap is often not visible and, when seen, may be focally calcified. On MR imaging, the tumors have a nonhomogeneous low to intermediate signal intensity on all imaging sequences (Figs. 6-134 and 6-135).

VIEW IMAGE

FIGURE 6-130 Caldwell view shows a left polypoid mass that is slightly denser than the adjacent frontal bone. This patient had a fibrous-type ''soft'' osteoma. PA view shows bilateral frontal osteomas. Note how the osteomas have conformed to the sinus contour.

FIGURE 6-132 Caldwell view shows an osteoma in the left ethmoid complex.

VIEW IMAGE

Copyright © 2003, Mosby, Inc. All rights reserved.

VIEW IMAGE

FIGURE 6-133 Lateral view shows an osteoma in the sphenoid sinuses.

Pathologically, cortical and cancellous bone, with a cartilaginous ''cap,'' are seen. This ''cap'' may become atrophic with time. Simple resection is the treatment of choice, and only 1% to 2% of lesions recur. Similarly, only 1% to 2% of solitary osteochondromas undergo malignant change, usually to chondrosarcomas.

Chondroma

Chondromas are completely benign cartilaginous tumors. The definition of chondromas may vary with the tumor site, and there may be no absolute criteria distinguishing chondromas from grade I chondrosarcomas in some confined areas, such as the larynx. However, no diagnosis of ''chondroma'' should be accompanied by radiologic evidence of destruction or histologic evidence of pleomorphism. It is well appreciated that lack of pleomorphism on a limited biopsy does not rule out the possibility of a grade I or higher chondrosarcoma. The majority of head and neck chondromas (70%) have been reported in the nasal cavity and ethmoids. Others may occur in the maxilla, sphenoid sinuses, palate, and nasopharynx. There is no sex predilection, and about 60% occur in patients less than 50 years of age.[254] Wide surgical excision with negative margins is the treatment of choice.[260, 261]

On CT, calcifications within the tumor matrix are not always seen. These lesions tend to be expansile, remodel bone, and have an attenuation less than that of muscle but greater than that of fat.[262, 263] They do not provoke sclerotic bone at their margins. On MR imaging, they usually have low T1-weighted and high T2-weighted signal intensities, and they enhance. The imaging findings are not specific.

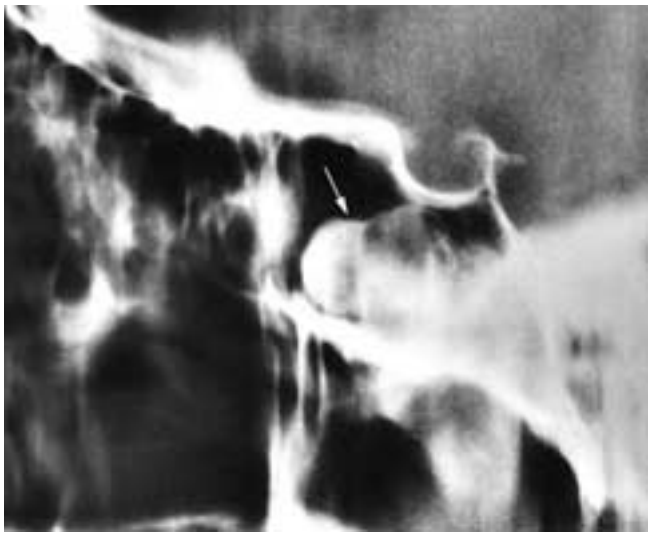

VIEW IMAGE

FIGURE 6-134 Lateral multidirectional tomogram shows a partially ossified, pedunculated mass in the sphenoid sinus (*arrow*). This patient had an osteochondroma.

Osteoid Osteoma and Osteoblastoma

Osteoid osteoma is a benign expansile neoplasm characteristically associated with nocturnal pain. It represents 11% of benign bone neoplasms, with a male-to-female ratio of 2:1. The majority of patients are diagnosed between 5 and 25 years of age, and the femur and tibia are the most commonly affected bones. In 26 culled literature cases of the head and neck, the mandible and cervical vertebrae were the most common sites.[254] Osteoid osteomas have been rarely reported in the frontal, ethmoid, and maxillary bones. Patients describe a dull pain that usually worsens at night, intensifies with activity, and is relieved by rest and aspirin.

On plain films and CT, the classic lesion is a dense cortical ovoid mass with a 1 to 2 mm low-density nidus. However, the nidus also may be dense and difficult to identify radiographically.[254] Histologically, the nidus is recognized as a tangled array of new osteoid bony trabecula surrounded by reactive bone. The intertrabecular tissue is vascular and fibrotic. Simple excision or curettage is curative.

Osteoblastoma (giant osteoid osteoma) is a benign expansile lesion representing only 3% of all benign bone tumors. There is a peak incidence in the second decade of life, with a male-to-female ratio of 2:1. The most common

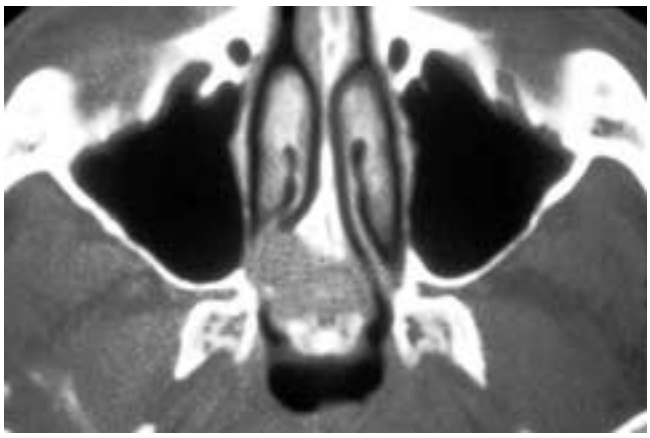

FIGURE 6-135 Axial CT scan shows an expansile, partially calcified mass in the posterior nasal septum. This patient had an osteochondroma.

VIEW IMAGE

Copyright © 2003, Mosby, Inc. All rights reserved.

sites of occurrence are the vertebral column (34%) and the long bones of the appendicular skeleton (30%). However, osteoblastomas are more likely to involve the head and neck (15% of 364 cases) than are osteoid osteomas.[264] The mandible is the most common site (usually the mandibular body), followed by the cranium and maxilla. Ethmoid and sphenoethmoid osteoblastomas have also been reported.[254] Patients present with a painful mass; however, the pain does not have the consistent pattern encountered with osteoid osteoma (nocturnal and relieved with aspirin).

Radiographically, osteoblastomas tend to be expansile and remodel adjacent bone. They range from 2 to 10 cm in diameter; in contrast, the nidus of osteoid osteomas is invariably less than 1 cm. Osteoblastomas have a variable radiographic appearance; some lesions have large, discrete areas of organized bone density, and others have a mixed osseous and fibrous appearance. The latter tends to be more nodular and more coarsely organized than most ossifying fibromas and some fibrous dysplasias (Figs. 6-136 and 6-137).[256, 265, 266]

Pathologically, osteoblastomas are virtually identical to osteoid osteoma. Histologically, one sees interconnecting trabeculae of osteoid or woven immature bone. The term *aggressive osteoblastoma* (juvenile aggressive osteoblastoma) is reserved for recurrent tumors or those with histologic atypia. Histologically, these lesions have a denser population of epithelioid osteoblasts, with prominent mitotic activity and multifocality.[267] At times, the distinction between aggressive osteoblastoma and a well-differentiated osteogenic sarcoma may be difficult. Conservative surgery, consisting of local excision or curettage, cures 80% to 90% of the cases of benign osteoblastoma. Aggressive osteoblastomas recur locally but do not metastasize.[254]

Ossifying Fibroma (Cemento-Ossifying Fibroma)

Ossifying fibroma (OF) is a benign expansile tumor occurring most commonly in tooth-bearing regions in the second or third decade of life, with a female predominance. OF arises from the periodontic ligament, most commonly in the molar or premolar regions of the mandible, followed by the maxilla.[254] Many synonyms exist for this tumor (cemento-ossifying fibroma, fibroosseous lesion, psammomatoid ossifying fibroma, etc.), reflecting its ability to produce a variable matrix. Patients present with a painless, solitary expansile mass.

OF can also arise in the nasal cavity, usually from the lateral nasal wall or ethmoid complex. If it is sufficiently large, OF can affect the frontal, sphenoid, and maxillary sinuses.

Radiographically, OF appears as an expansile, circumscribed tumor with well-defined borders. The surrounding bone appears normal. The internal organization of OF reveals discrete zones of either variable osseous or fibrous tissue. CT usually reveals large, nonossified areas of fibrous tissue density, in contrast to fibrous dysplasia (FD).[255] Ideally, FD can be distinguished from OF by its noncircumscribed nature, as it ''blends'' into relatively abnormal bone, and its propensity for multiostotic involvement. However, some cases of OF may be indistinguishable from FD on CT imaging. The MR imaging appearance of OF can be quite variable, depending on the composition of this lesion.[268]

Pathologically, OF is composed of densely cellular, well-circumscribed fibrous tumor. Ossification, or cementoossification, commences at the periphery. The ossification is composed of immature woven bone that matures into lamellar bone. This is unlike FD, in which bony trabeculae are produced throughout the lesion but are highly atypical, without maturation or normalization. Cementum formation is seen as acellular coalescing spherical calcifications that have distinctive basophilic perimeters.

OF is optimally treated by conservative surgical excision, although larger tumors may require more aggressive resection. Compared with the clinical behavior of FD, which can remain stable, OF has a greater tendency to behave aggressively (grows faster and recurs more quickly after surgery) and to expand internally toward the orbits, nasal fossae, and sinus cavities rather than to deform the outer surface bones (Figs. 6-138 to 6-141).[269] Tension pneu-

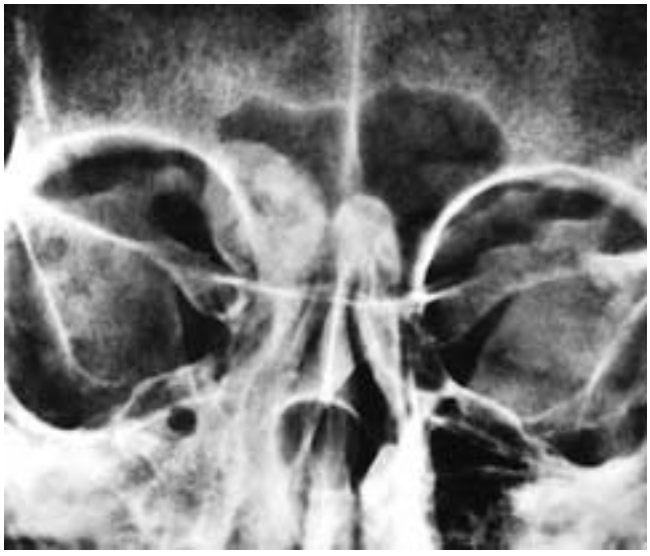

VIEW IMAGE

FIGURE 6-136 Caldwell view shows bone density masses in the ethmoid sinuses that project into the anterior cranial fossa. There is also disease-increased density in both ethmoid sinuses. This patient had a benign osteoblastoma.

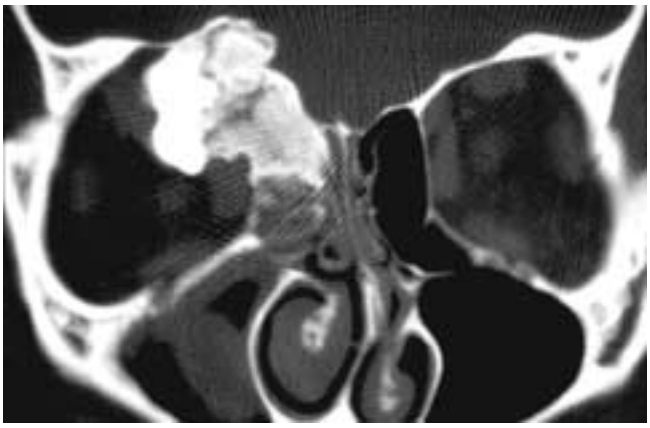

VIEW IMAGE

FIGURE 6-137 Coronal CT scan shows a bone-density lesion in the right frontal and ethmoid bones. The bone is expanded, and the cortices are intact. Part of the lesion has a ''ground glass'' appearance; however, the lateral portion of the mass has very dense bone production. This patient had a benign osteoblastoma.

Copyright © 2003, Mosby, Inc. All rights reserved.

VIEW IMAGE

FIGURE 6-138 Waters view shows an expansile bony mass in the lateral wall of the right maxillary sinus. The mass has displaced the lateral sinus wall toward the midline (*arrows*). This patient had an ossifying fibroma.

mocephalus has been reported as an uncommon complication of an OF.[270]

Tumor-Like Conditions and Giant Cell–Rich Lesions

Fibrous Dysplasia

Fibrous dysplasia (FD) is an idiopathic skeletal disorder in which medullary bone is replaced by poorly organized, structurally unsound fibroosseous tissue. Most patients are under 30 years of age at diagnosis.[271] The majority of cases (75% to 80%) are limited to the monostotic form (MFD), which most often involves the ribs or femur. The craniofacial bones may be involved in monostotic FD in up to 25% of cases; most commonly affected are the maxilla and mandible.[272] Polyostotic FD (PFD) comprises 20% to 25% of all cases. Usually there is unilateral bone involvement, but in severe cases bilateral disease can occur. The

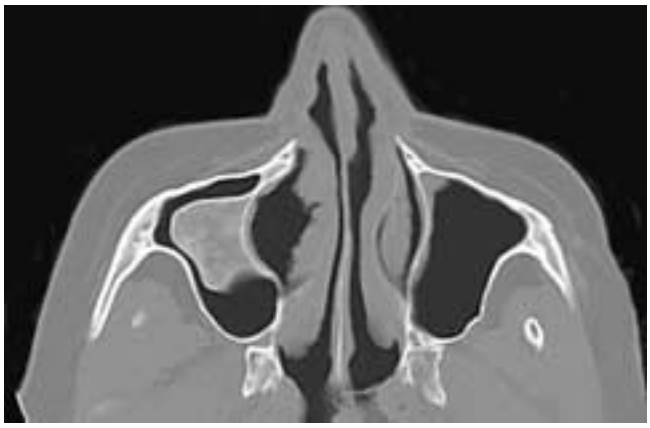

VIEW IMAGE

FIGURE 6-139 Axial CT scan shows a ''ground glass'' bony mass projecting into the right maxillary sinus cavity. There is a surrounding cortex. This patient had an ossifying fibroma.

craniofacial bones are more often (40% to 50%) involved in PFD.[271, 272]

Albright's syndrome consists of PFD plus pigmented skin macules and sexual precocity. This syndrome is relatively rare. It is 40 times less common than MFD, and it occurs almost exclusively in females. The skin pigmentations have irregular margins (''coast of Maine''), as opposed to the smoother-bordered pigmentations (''coast of California'') of neurofibromatosis.

Patients with craniofacial FD involvement usually present with asymmetric cheek swelling.

Encroachment into the paranasal sinuses, nasal fossae, orbit, or neurovascular canals can lead to nasal obstruction, headaches, and visual disturbances. Recently, it has been appreciated that involvement of the frontal and sphenoid sinuses by FD can result in mucoceles. Extensive maxillary involvement results in facial distortion, referred to as leontiasis ossea (''lion face'').

New FD lesions usually do not develop after the growth plates have fused. Some lesions, however, continue to grow after skeletal maturation.

Histologically, FD appears as irregular, disformed bony trabeculae of immature woven bone, which are thinned, C-

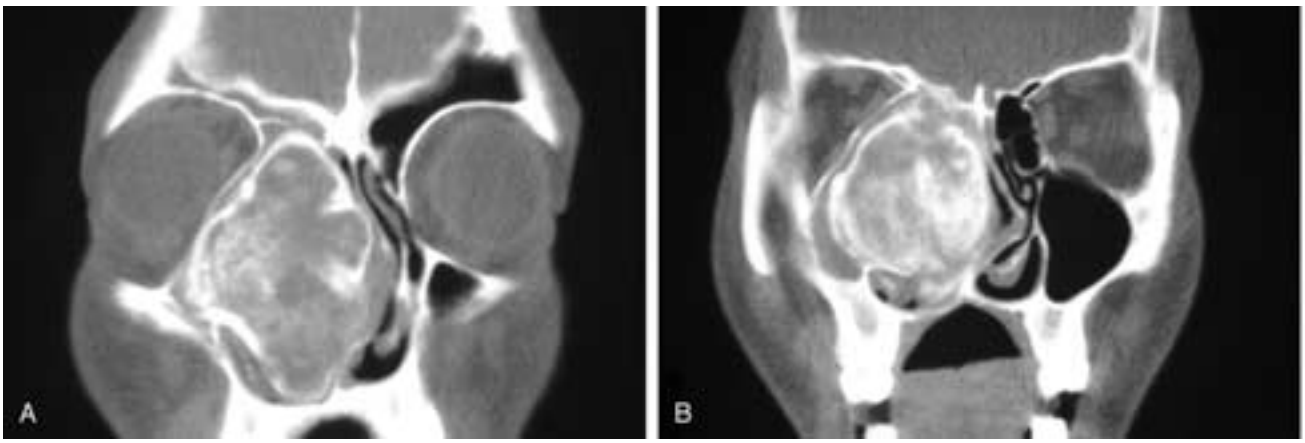

VIEW IMAGE

FIGURE 6-140 Coronal CT scans (**A** and **B**) show an ovoid expansile mass projecting into the right nasal fossa and the right ethmoid and maxillary sinuses. Obstructed secretions are present in the remaining right antrum. Surrounding the partially ossified mass is a cortex. This patient had an ossifying fibroma.

Copyright © 2003, Mosby, Inc. All rights reserved.

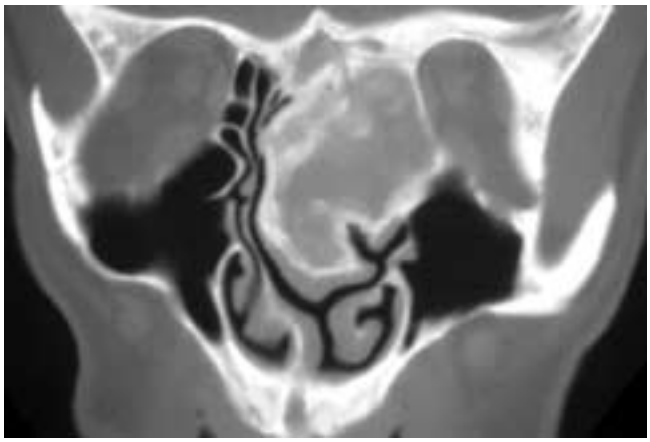

VIEW IMAGE

FIGURE 6-141 Coronal CT scan shows a mass in the left ethmoid complex and nasal fossa. There is a cortex surrounding a primarily nonossified mass. This patient had an ossifying fibroma.

FIGURE 6-142 Caldwell view shows a mixed ''lytic'' and ''blastic'' expansile lesion in the left frontal bone (*arrows*) that has depressed the superior orbital margin. This patient had fibrous dysplasia.

VIEW IMAGE

or S-shaped, and referred to as *Chinese characters.* The trabeculae are embedded in, and blend into, vascularized fibrous tissue lacking the osteoblastic rimming of normal bone. Serial biopsies over time do not reveal maturation of this woven bone into lamellar bone.[271] Surgery is used only to correct deformities, relieve pain, correct functional problems, decompress a mucocele, or resect sarcomas. FD recurs in 20% to 30% of cases, usually within 2 to 3 years of initial therapy.[271]

Malignant transformation of bone with FD is very rare (less than 1% of cases). In a review of 83 sarcomas complicating FD, 57% of the patients had MFD and 43% had PFD. The craniofacial bones are most commonly involved, and irradiation may promote malignant transformation. The average latency period from diagnosis of FD to development of malignancy is 13½ years. The majority of these tumors are osteogenic sarcomas, followed by fibrosarcomas and chondrosarcomas.[271]

The radiologic appearance varies according to the degree of fibrous tissue present. Thus, the bone texture can range from a nonhomogeneous mixture of bone and fibrous tissues to a predominantly fine, bony ''ground glass'' appearance. The disease expands the diploic or medullary space and widens the bone. A thin, intact rim of cortical bone is often seen over the margins of the involved bone. MR imaging usually shows a low to intermediate signal intensity on all imaging sequences, and often the cortical bone overlying the medullary disease can be identified as a zone of low signal intensity. There usually is intense enhancement with contrast. If areas of high T2-weighted signal intensity are present within an obstructed or involved sinus, the presence of a mucocele should be considered (Figs. 6-142 to 6-153).[273, 274] Because there is often an overlap in the imaging appearance of FD and ossifying fibroma, the term *benign fibroosseous lesion* has been suggested to describe the imaging findings of both lesions.[275]

Cemento-Ossifying Dysplasia

There are a number of cementum-containing lesions that may affect the jaws. Periapical fibrous dysplasia (periapical cemental dysplasia) produces lytic and then blastic expansile periapical lesions, usually affecting the lower anterior jaw. The etiology is unknown. It is usually seen in patients more than 20 years of age and is more prevalent in African Americans.[271] The lesions are usually smaller than 1 cm. Radiographically, early lesions appear as periapical radiolucencies. As cementum or osteoid is produced, central calcification is seen radiographically, which becomes more

FIGURE 6-143 Caldwell view shows a dense expansile lesion of the left frontal and zygomatic bones that has encroached on the left orbit. This patient had fibrous dysplasia.

VIEW IMAGE

Copyright © 2003, Mosby, Inc. All rights reserved.

dense and uniform as the lesion matures. Focal cemento-osseous dysplasia is characterized by the formation of an expansile cystic lesion, which usually occurs in the posterior mandible. It may occur in dentulous or edentulous bone.

There is a pronounced female predominance, with a peak incidence in the fourth and fifth decades. Radiographically, one sees an expansile cystic lesion that may or may not be associated with a tooth and can be either lucent, opaque, or mixed density, possibly with a sclerotic rim.

Florid cemento-osseous dysplasia appears to be a diffuse form of periapical cemental dysplasia. It is characterized by the development of multiple expansile jaw tumors containing cementum or osteoid. These lesions affect the lower jaw more commonly than the upper jaw and may be symmetric. Black middle-aged women are most commonly affected. Radiographically, the lesions are cystic, mixed lytic/blastic.

Cherubism

Cherubism (familial multilocular cystic disease of the jaw, hereditary fibrous dysplasia) is a nonneoplastic disease limited to the jaws and characterized by bilateral, painless jaw enlargements that are said to give the patient a cherubic appearance. Cherubism may appear sporadically or be familially transmitted. It is inherited in an autosomal dominant fashion, with high (nearly 100%) penetrance in males and variable (50% to 75%) penetrance in females. The disease appears between the ages of 6 months and 7 years and is characterized by bilateral fullness of the jaws. The eyes appear to look up as the lower sclera are exposed. The disease often develops rapidly until age 7 years and then gradually regresses. The mandible is involved first, followed by the maxilla in about two thirds of the cases. Most of the radiographic changes occur in the mandible, where expansile cystic masses are seen in the angles and ramus. As the disease progresses to the maxilla, the sinus opacifies and the orbital floor may be bulged upward. The latter finding is one of the causes of the upward-looking eye of cherubism.[276] Pathologically, one sees proliferating fibrous connective tissue with numerous multinucleated giant cells indistinguishable from those of giant cell reparative granuloma. The disease is self-limited and is usually diagnosed after the age of 2 years. Treatment is usually not necessary, but if embarked on for cosmetic or other reasons, it will not provoke regrowth of lesional tissue.[277–279]

FIGURE 6-145 Coronal CT scan show a ''ground glass'' density expansile bony process that has encroached on the orbits and obliterated the frontal, ethmoid, and maxillary sinuses and portions of the nasal fossae. This patient had fibrous dysplasia.

VIEW IMAGE

FIGURE 6-144 Coronal CT scan shows that the medullary bone of the left frontal and ethmoid bones is expanded; however, the cortices are intact. The medulary space has a ''ground glass'' appearance. This patient had fibrous dysplasia.

VIEW IMAGE

True Giant Cell Tumor

Giant cell tumor (GCT) of bone (previously referred to as osteoclastoma) is an uncommon, benign, yet potentially locally aggressive tumor that comprises up to 5% of all primary bone neoplasia. More than 75% of these tumors are located in the epiphyseal region of long bones, half of them occurring about the knee. There is a female predisposition, and the majority of affected patients are beyond the second decade of life. GCT of the head and neck is extraordinarily rare.[271, 280] Huvos identified 3 GCTs of the cranium and maxilla out of 265 GCTs treated at the Memorial Sloan-Kettering Cancer Center.[280] Kujas and colleagues identified only seven cases of true GCT of the skull and cervical vertebrae after reviewing neuropathology specimens collected over 50 years.[281] An association

Copyright © 2003, Mosby, Inc. All rights reserved.

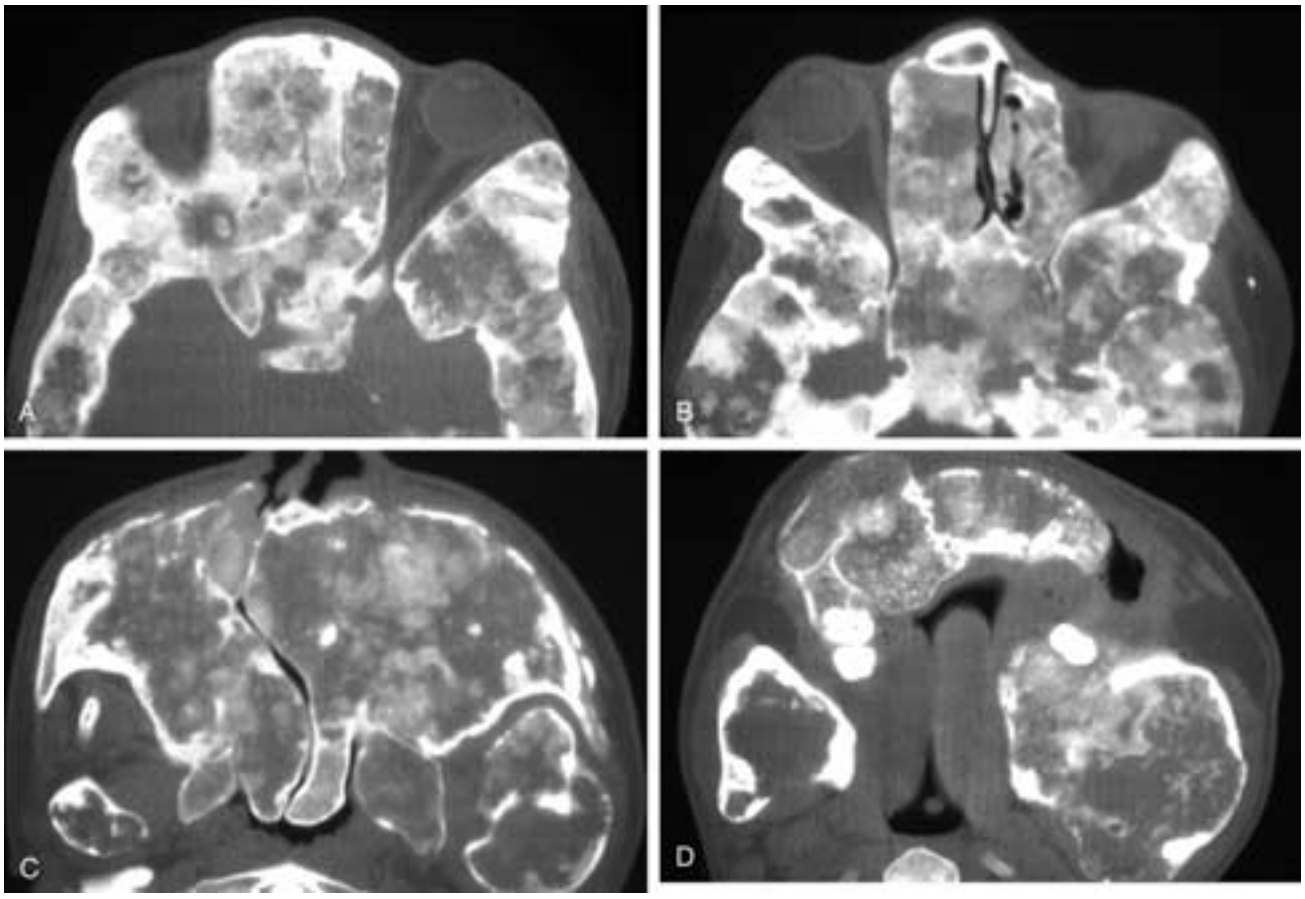

VIEW IMAGE

FIGURE 6-146 Axial serial CT scans (**A** through **D**) through the facial region show that all of the facial and skull base bones are greatly expanded, with intact cortices. Their medullary spaces are filled with ossified and nonossified regions. The skull base foramina, orbital apices, and paranasal sinuses are all obliterated. The mandible is also affected. This patient had fibrous dysplasia.

between GCT of the jaws and Paget's disease has also been noted.[280]

Histologically, GCTs are characterized by a diffuse population of osteoclastic giant cells spread across a background of short spindled cells with nuclei identical to those within the giant cells. This latter point allows for distinction between GCT and the myriad other osteoclastic giant cell–rich lesions that may affect bone. There may be dozens to hundreds of nuclei within the osteoclastic giant cells. Identification of these gargantuan benign giant cells also aids in establishing the diagnosis. Hemorrhage and hemosiderin deposition are not prominent features of GCTs. Reactive bone may be seen in the periphery of the tumor, as the ossified cartilage may undergo some remodeling. The differential diagnosis of GCT of the head and neck includes central giant cell reparative granuloma (CGCRG), ''brown tumor'' of hyperparathyroidism, or, more rarely, giant cell–rich osteogenic sarcoma. The distinctions between these entities may be impossible to make on a biopsy without radiographic and clinical correlation (Fig. 6-154).

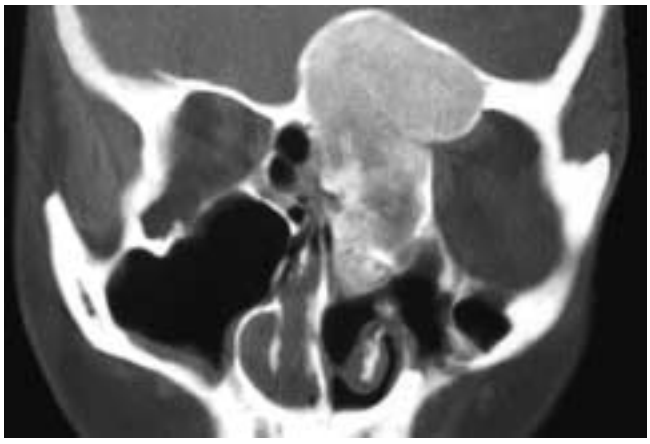

VIEW IMAGE

FIGURE 6-147 Coronal CT scan shows a localized region of expanded bone in the left frontal and ethmoid bone. The medullary space has a ''ground glass'' appearance, and the cortices are intact. This patient had fibrous dysplasia.

There is considerable demographic (age of diagnosis) and histologic overlap between GCT and CGCRG, so that these two entities may represent a spectrum of a single disease process that is modified by patient age and site of occurrence.[282, 283]

The treatment of choice is complete surgical excision or curettage. The recurrence rate for GCT at all sites is 30% to 50% after curettage. Most local failures occur within 2 years of initial therapy.[284] Approximately 10% to

Copyright © 2003, Mosby, Inc. All rights reserved.

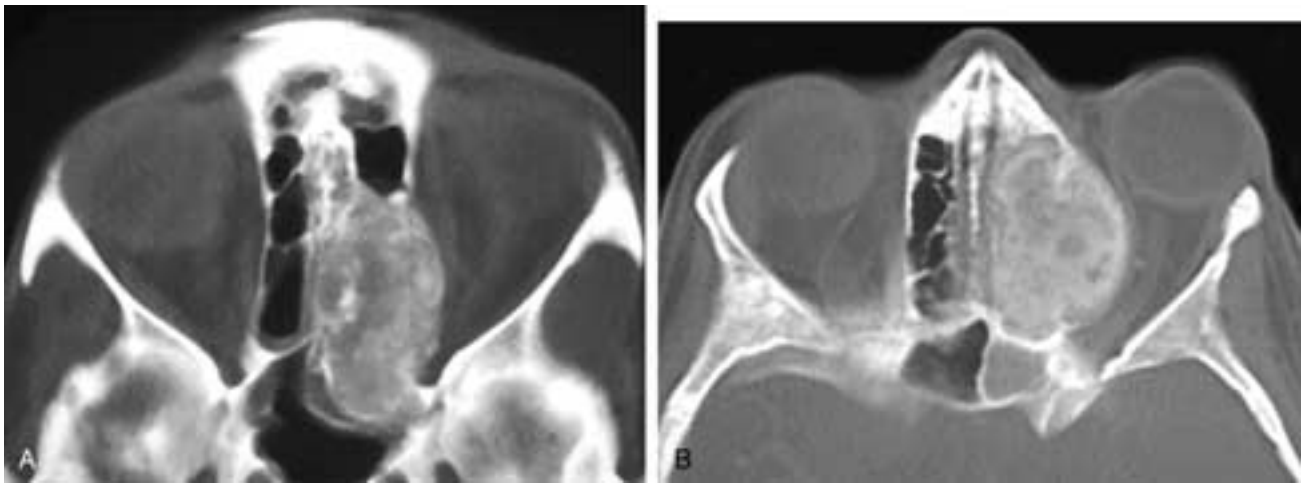

VIEW IMAGE

FIGURE 6-148 Axial CT scan (**A**) shows a ''ground glass''-appearing bony process in the left ethmoid and sphenoid bones. There is encroachment into the left orbit. This patient had fibrous dysplasia. Axial CT scan (**B**) shows an expansile ''ground glass''-appearing bony process in the left ethmoid complex. The left sphenoid sinus is obstructed by the process. Notice the similarity to **A**. This patient had an intraosseous meningioma.

15% of GCTs show clinical or histologic evidence of malignancy. Malignancy can occur de novo or as secondary transformation. Almost all secondary malignant transformations have been previously irradiated. Radiation therapy should be reserved for surgically inaccessible tumors, as GCTs are generally not radiosensitive and as radiation therapy is accompanied by the threat of malignant transformation.

On CT the tumors enhance moderately, and they tend to destroy and remodel bone.[285, 286] On MR they usually have fairly low signal intensity on all sequences, and they enhance.

Giant Cell (Reparative) Granuloma

Giant cell (reparative) granuloma (GCG) is an entity of uncertain etiology that may affect either the jaw bones

FIGURE 6-149 Axial CT scans (**A** and **B**) and coronal CT scan (**C**) show an expansile ''ground glass''-appearing process in the right maxilla. The lesion affects the maxillary alveolus as well as the sinus walls. The sinus cavity is reduced by the encroachment of the bony process. This patient had fibrous dysplasia.

VIEW IMAGE

Copyright © 2003, Mosby, Inc. All rights reserved.

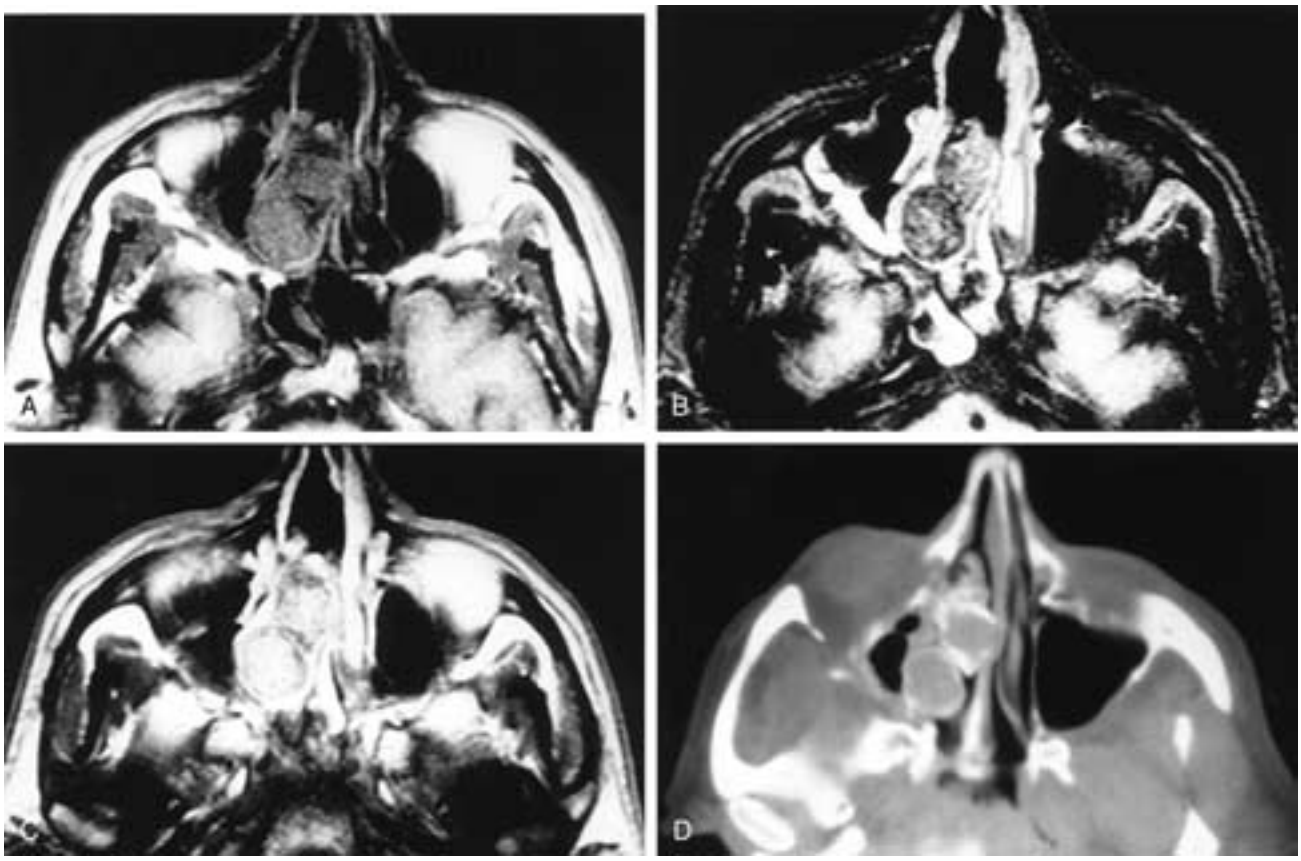

VIEW IMAGE

FIGURE 6-150 Axial T1-weighted (**A**), T2-weighted (**B**), and T1-weighted, contrast-enhanced MR images (**C**) and an axial CT scan (**D**) show a polypoid right posterior nasal cavity mass that has low T1-weighted and intermediate T2-weighted signal intensity and diffusely enhances. The CT scan shows the lesion to have an intact bony cortex and nonossified central regions. This patient had fibrous dysplasia.

(central giant cell granuloma [CGCG]) or the intraoral soft tissues (peripheral giant cell granuloma [PGCG]). The term *reparative* was originally introduced by Jaffe, but recently this modifier has been dropped from the name, as there is no evidence to support this function. PGCG is four times more common than CGCG. PGCG presents as an expansile mass of the gingiva or alveolar mucosa that rarely extends to the underlying bone. It occurs over a broad age range, with a peak incidence in the fourth decade of life. PGCG may occur after tooth extraction or with ill-fitting dentures and therefore may be related to trauma. There is a female predisposition, which implies hormonal sensitivity.

CGCG presents as an expansile, destructive intraosseous jaw mass. There is also a female predisposition, but the majority of patients present prior to the fourth decade of life. There is no association with prior trauma.

Radiographically, PGCG rarely is clearly visualized. However, CGCG typically appears as a multiloculated, expansile lytic lesion on plain film (Fig. 6-155).[185, 285–288] On CT, CGCG is bulky and enhancing and can be seen to aggressively erode the maxillary sinus walls or to have an expansile, remodeling apearance. On MR imaging, CGCG has an intermediate signal intensity on both T1-weighted and T2-weighted images. As such, the MR appearance may mimic that of SCC.[241]

Pathologically, GCG characteristically has a hemorrhagic, fibroblastic background with innumerable osteoclastic giant cells. This background is helpful in distinguishing GCRG from GCT. The latter lacks the diffuse hemorrhage, hemosiderin, and fibroblasts, and the background cells are identical to the nuclei of the osteoclastic giant cells. The giant cells of GCT are diffusely and evenly dispersed throughout the tumor. In contrast, the brown tumor of hyperparathyroidism has uneven clumps of osteoclasts, perivascular hemorrhage, and hemosiderin deposition.

It is useful to know the serum calcium and parathyroid hormone levels when dealing with any giant cell lesion. In hyperparathyroidism the calcium level is elevated unless the patient is already severely calcium depleted. Serum parathyroid homone (PTH) is elevated with a brown tumor of hyperparathyroidism and is normal with other GCTs. PTH is also normal in tumor-induced osteomalacia, which radiologically can mimic severe hyperparathyroidism.[289] Giant cell granuloma arising in the skull base is discussed in Chapter 12.

Aneurysmal Bone Cyst

An aneurysmal bone cyst (ABC) is neither an aneurysm nor a true cyst, but it does occur in bone. Rather, it is a benign, nonneoplastic, expansile osseous lesion. ABC occurs mainly in females over the age of 20 years and represents only 1% to 2% of all primary bone tumors. It can

Copyright © 2003, Mosby, Inc. All rights reserved.

present as a slowly or rapidly enlarging mass with nonthrobbing pain. ABCs may occur de novo; however, they may be ''engrafted upon'' (occur in conjunction with) another primary osseous tumor. This process may be pathologically identified in as many as one third of ABCs; the most common findings are GCT, unicameral bone cyst, or nonossifying fibroma.[284] Between 3% and 12% of ABCs occur in the head and neck, and they have also been reported in the maxilla, orbit, ethmoid, and frontal bones.[290] In a review of 64 reported cases of jaw ABC, the ratio of mandibular to maxillary cases was 2.4:1, with a predisposition for the posterior mandible. There was a wide age range, with a median age of 17 years.[291] Primary paranasal sinus/nasal cavity ABC has rarely been described and has been seen in conjunction with preexisting primary bone pathology.[292, 293]

Histologically, ABCs are composed of large, variably sized, blood-filled cystic and sinusoidal nonendothelium-lined spaces traversed by fibroblastic cells. New bone formation is evident; osteoid formation, osteoclast giant cells, and plump background spindle cells are seen. Hemorrhage and hemosiderin deposits are present. Surgical resection or curettage is the treatment of choice; in the jaws,

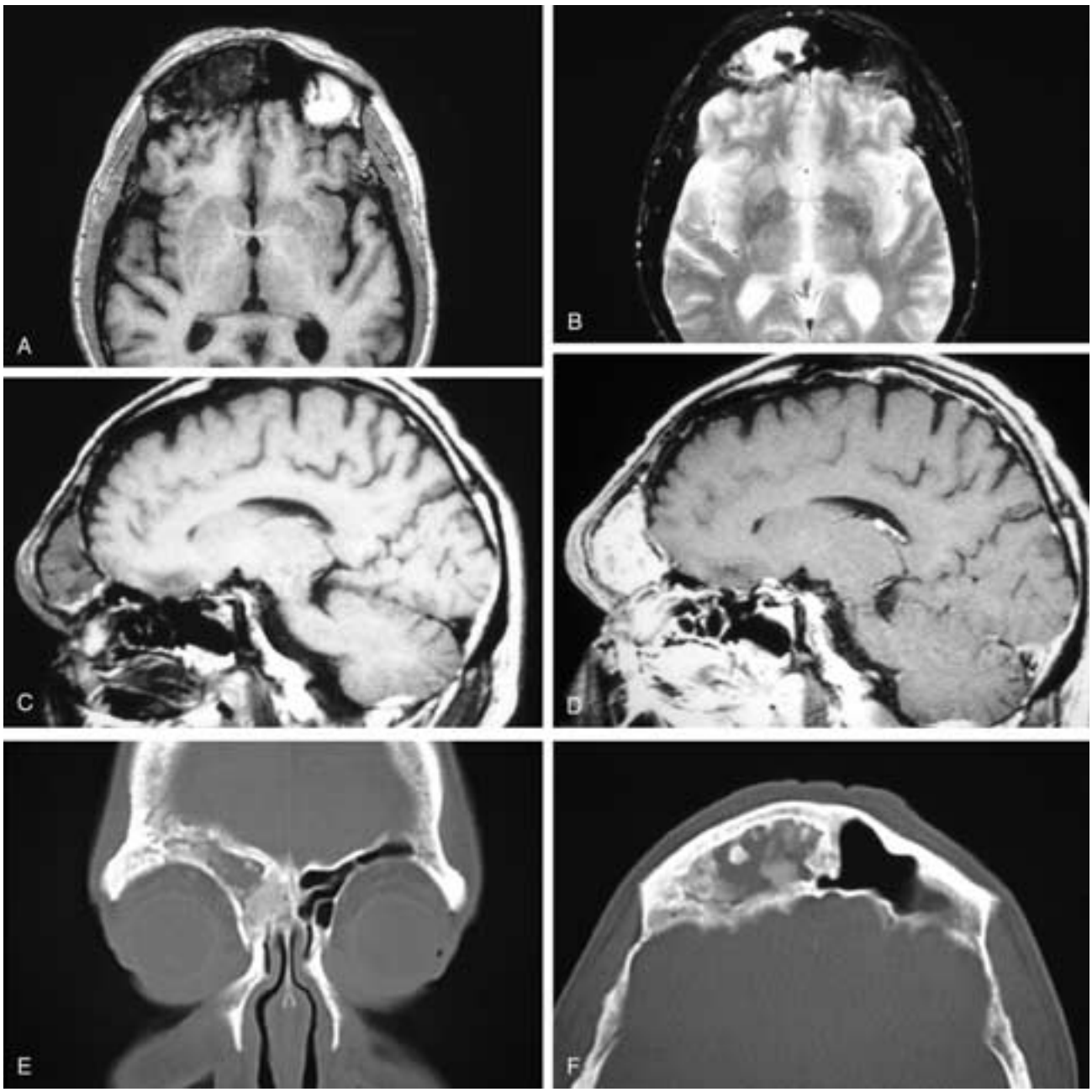

VIEW IMAGE

FIGURE 6-151 Axial T1-weighted (**A**), T2-weighted (**B**), sagittal T1-weighted (**C**), and T1-weighted, contrast-enhanced (**D**) MR images and coronal (**E**) and axial (**F**) CT scans show a nonhomogeneous right frontal sinus mass that has low signal intensity in **A**, high signal intensity in **B**, and diffusely enhances in **D**. The CT scans show the bone to be expanded, with intact cortices and a medullary space filled with ossified and nonossified regions. This patient had fibrous dysplasia.

Copyright © 2003, Mosby, Inc. All rights reserved.

currettage has a somewhat higher recurrence rate (20% to 38%) than resection (11% to 25%).[284]

Radiographically, this lesion may be unilocular or may demonstrate a multilocular ''soap bubble'' or ''honeycomb'' radiolucency (Fig. 6-156). Kaffe and colleagues found that the majority of cases were radiolucent (87%), mixed (11%), or radiopaque (2%); the radiographic appearance was less common.[291] Fifty-three percent were multilocular, 43% were unilocular, and 3% were not loculated. The peripheral bone margins were defined but not corticated in 39%, well defined in 33%, and diffuse in 28%. Bony remodeling and destruction can be seen (Fig. 6-157). On MR imaging, the classic findings are those of multiple cysts with fluid-fluid levels (Figs. 6-158 and 6-159).

Paget's Disease

Paget's disease (osteitis deformans) is a bone disorder of unknown etiology. Increased osteoclastic and osteoblastic activity results in the disorderly production of abnormally dense yet mechanically fragile bone. The disease usually occurs in patients over 50 years old, and its incidence increases with age, ranging from 3% to 5% of people older than 40 years to 11% of those older than 80 years.[294] There is a male predominance and some familial predisposition. The disease is usually (90%) polyostotic and involves the vertebrae (76%), calvaria (65%), pelvis (43%), femur (35%), and tibia (3%). In the head and neck, the clavaria, maxilla, and mandible are most commonly affected.[295] In 80% of patients, the degree of skeletal involvement is limited and found fortuitously on radiographic studies or at autopsy. The facial bones are rarely involved; however, whenever the maxilla and mandible are affected, the calvarium is invariably also involved.[295] Advanced calvarial involvement may lead to a characteristically enlarged head, and the reduced size of the cranial cavity secondary to calvarial and skull base bony ingrowth can lead to altered mental status, dementia, and other neurologic abnormalities. Platybasia is associated with cranial nerve deficits. Encroachment into the orbits, neurovascular canals, and sinonasal cavities has led to proptosis, visual loss, neurologic deficits, facial deformity, and nasal congestion. Despite the thickness of the bone, it is extremely vascular and fragile and may be prone to fracture.

The initial radiographic and CT appearance of Paget's disease of the calvarium often reveals a lytic phase that produces osteoporosis circumscripta, usually involving the frontal region to the greatest degree. A ''mixed'' phase may follow. This phase shows foci of sclerotic, woven bone

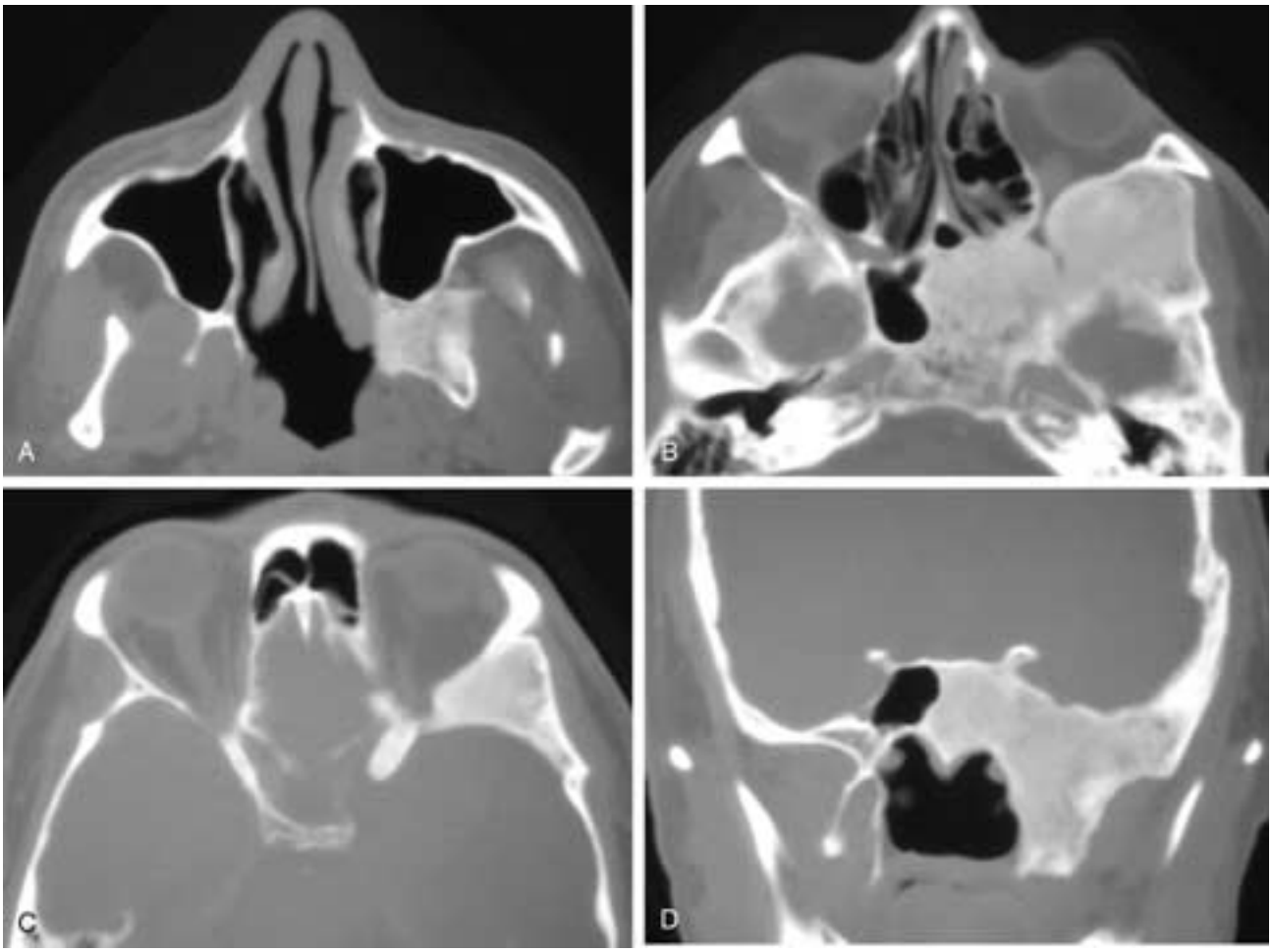

FIGURE 6-152 Serial axial CT scans (**A** through **C**) and coronal CT scans (**D**) show a ''ground glass'' expanded left sphenoid bone. The left sphenoid sinus is obliterated, and all portions of the bone are affected.

VIEW IMAGE

Copyright © 2003, Mosby, Inc. All rights reserved.

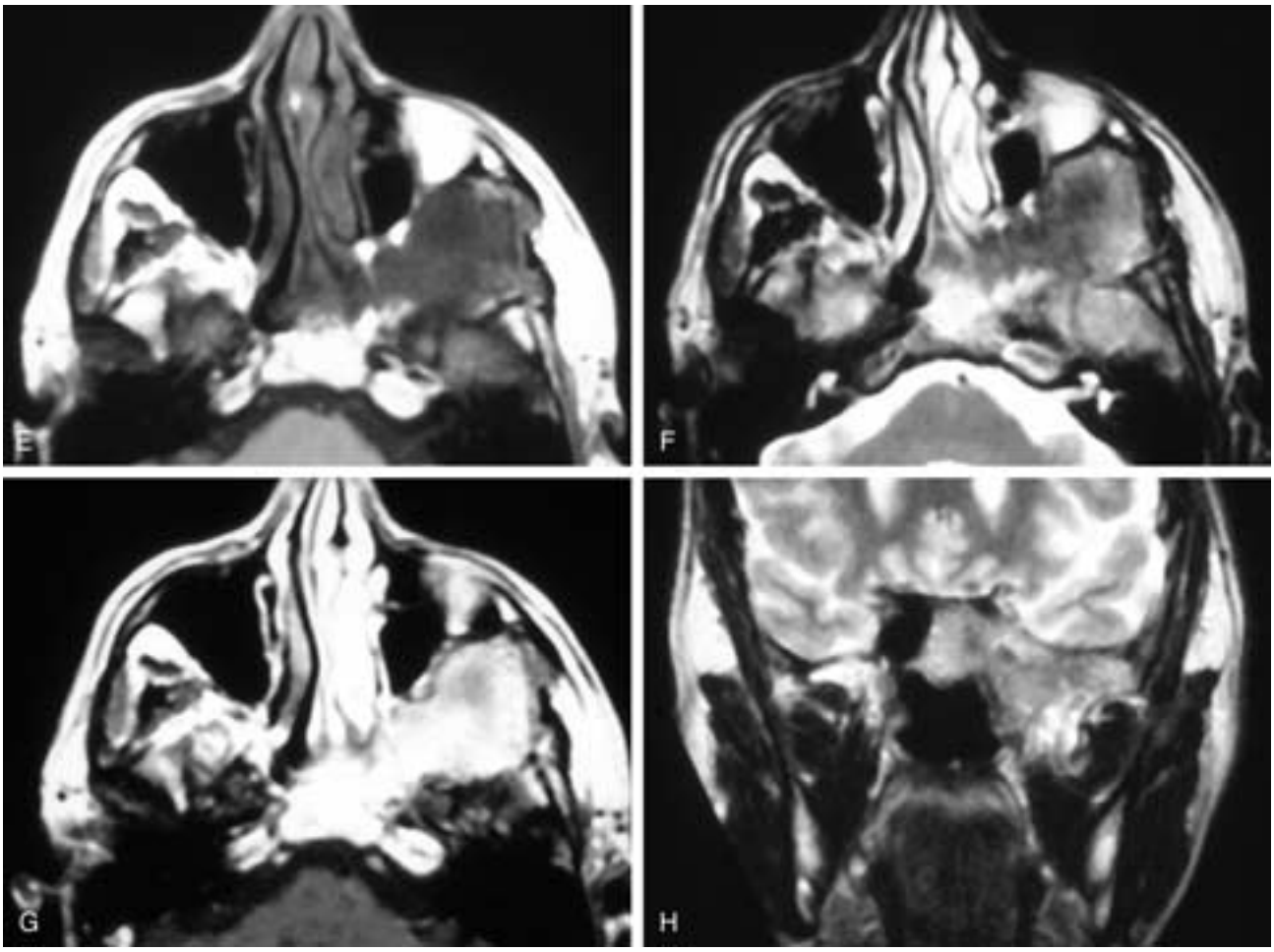

VIEW IMAGE

FIGURE 6-152 *Continued.* Axial T1-weighted (**E**), T2-weighted (**F**), and T1-weighted, contrast-enhanced (**G**) MR images and a coronal T2-weighted (**H**) MR image show the low to intermediate T1-weighted and T2-weighted signal intensity and the marked enhancement of the process. This patient had fibrous dysplasia.

within areas of lower density, which represent sites of fibrous myeloid production. The remaining bone often gives a moderately diffuse radiopacity producing a ''cotton wool'' appearance. Eventually, there can be a sclerotic phase, with poor corticomedullary differentiation. The calvarium itself is thickened; usually the greatest degree of thickening is anterior, and one side of the skull tends to be more affected than the other. Inner table irregularity is usually greater than that of the outer surface. It is the sclerotic form of Paget's disease that usually affects the facial bones. This results in a thickened, dense bone with slightly irregular cortical surfaces and poor corticomedullary differentiation (Figs. 6-160 to 6-163).[295]

On MR imaging, the dense foci of bone give rounded foci of signal void on all imaging sequences. The marrow tissues give high T1-weighted and fairly high T2-weighted signal intensities, reflecting the fat and blood protein in these regions. The background matrix gives an intermediate signal intensity on all imaging sequences. The facial area demonstrates a mixed, low to intermediate signal intensity on all imaging sequences. The lesion usually enhances nonhomogeneously.[295]

Histologically, pagetoid bone reflects an erratic resorption pattern and new production of bone that fails to mature normally. This is seen as predominantly woven mosaic bone, with increased osteoclastic and osteoblastic activity.

Sarcomas may develop in 5% to 10% of patients with multifocal Paget's disease and in less than 2% of patients with limited bone involvement. The prognosis of Paget's sarcoma is grave; most patients die within 2 years. The development of multiple tumors is frequent; autopsy studies suggest a multicentric rather than a metastatic origin for these tumors. Most Paget's sarcomas are osteogenic sarcomas (50% to 60%) or fibrosarcomas (20% to 25%).[296] In the facial area, benign GCTs can also occur. On plain films and CT, GCTs usually appear as sharply localized, nonosseous masses. Because the bone seen in Paget's disease, as well as in the sarcomas, tends to give an intermediate signal intensity on all MR imaging sequences, it is often more difficult to diagnose and map these malignancies or tumors on MR imaging than on CT (Fig. 6-163).[295]

Sarcomas

Osteogenic Sarcoma and Chondrosarcoma

Primary bone sarcomas occur over a wide age range; osteogenic sarcoma (OS) occurs most commonly after the

Copyright © 2003, Mosby, Inc. All rights reserved.

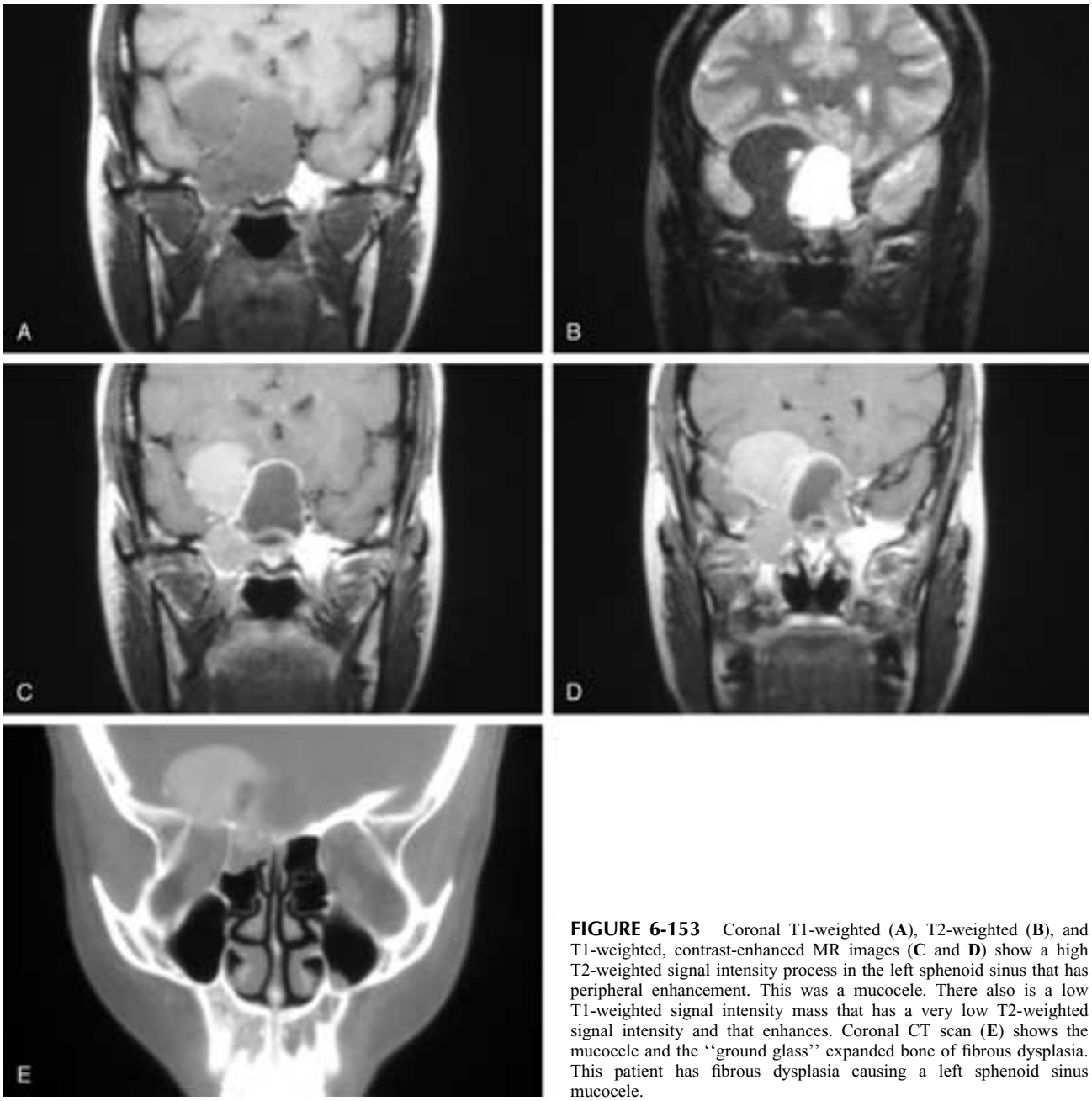

FIGURE 6-153 Coronal T1-weighted (**A**), T2-weighted (**B**), and T1-weighted, contrast-enhanced MR images (**C** and **D**) show a high T2-weighted signal intensity process in the left sphenoid sinus that has peripheral enhancement. This was a mucocele. There also is a low T1-weighted signal intensity mass that has a very low T2-weighted signal intensity and that enhances. Coronal CT scan (**E**) shows the mucocele and the ''ground glass'' expanded bone of fibrous dysplasia. This patient has fibrous dysplasia causing a left sphenoid sinus mucocele.

VIEW IMAGE

first decade of life, whereas chondrosarcoma (CS) occurs most commonly after the fourth decade. Primary OS, that is, OS in the absence of previous irradiation or Paget's disease, most commonly occurs prior to closure of the growth plates within the distal femur. Huvos reported on over 1000 cases of OS from Memorial Sloan-Kettering Cancer Center and found that half of them occurred around the knee, and that the femur was the most common bone affected.[297] Only 7% of these OSs occurred in the head and neck, usually in the jaws (55 of 77 cases in the head and neck, followed by craniofacial bones and calvaria).

Primary CSs occur most commonly in the pelvic region and femur.[298]

In a series of almost 500 CSs from Memorial Sloan-Kettering Cancer Center, only 5% (25 cases) occurred in the head and neck. Secondary CS of the head and neck can be seen after radiation therapy or in the setting of Maffucci syndrome or Ollier disease.[299] In a review of 56 craniofacial CSs, 25 (44.6%) involved the alveolar maxilla and maxillary sinus; 23 (41.1%) involved the nasal septum, ethmoid, and sphenoid; 6 (10.7%) involved the mandible; and 2 (3.6%) involved the nasal tip.[300–302]

Histologic diversity characterizes OS. OS, by definition, is a tumor in which the malignant cells produce an osteoid matrix. Histologic subtypes of OS include (1) osteoblastic OS, which produces abundant osteoid matrix; (2) chondroblastic OS, which produces abundant chondroid matrix, yet the osteoid present merits the classification of OS rather than CS; (3) telangiectatic OS, a highly vascular sarcoma with a lytic radiographic appearance; (4) fibroblastic (fibrosarco-

Copyright © 2003, Mosby, Inc. All rights reserved.

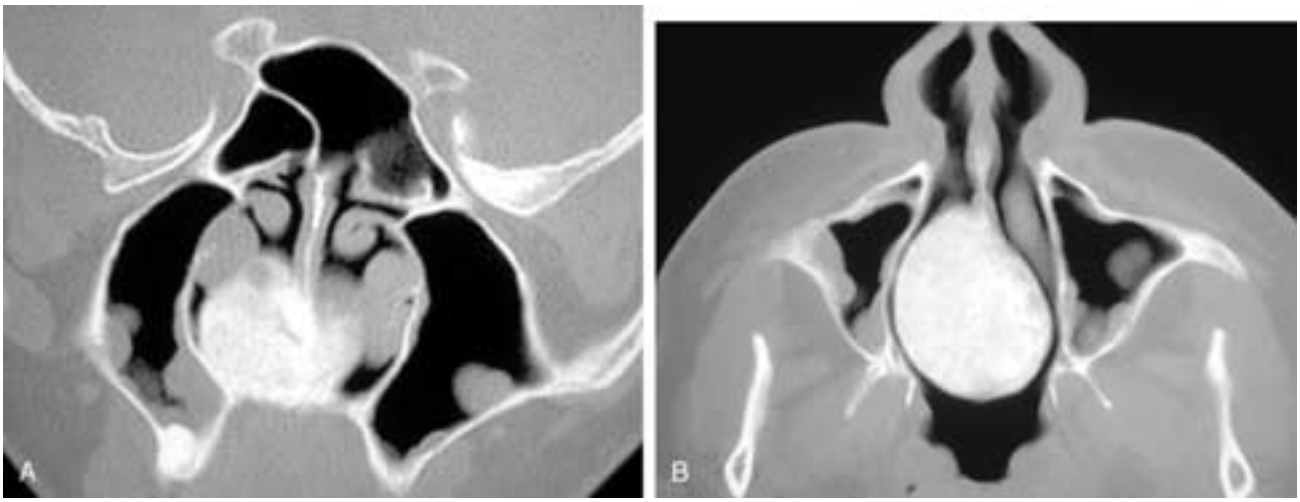

VIEW IMAGE

FIGURE 6-154 Coronal (**A**) and axial (**B**) CT scans show a densely ossified mass in the nasal septum. Two months earlier, this was a nonossified mass. This patient had a healed brown tumor from hyperparathyroidism.

matous) OS, composed predominantly of malignant fibroblast-like cells with some osteoid production; (5) fibrohistiocytic (malignant fibrous histiocytoma [MFH]) OS, which contains malignant multinuclear tumor giant cells in addition to the fibrosarcomatous component; and (6) round cell OS, composed predominantly of small round malignant cells with occasional osteoid production (Fig. 6-164). Many OSs display multiple histologic patterns, thereby precluding neat categorization. Despite the wealth of clinicopathologic data, there is little to indicate that histologic subclassification for OS has prognostic significance over classic tumor staging and grading (Broder's grading) schemata.

CS is generally more histologically uniform than OS. Abundant chondroid matrix is the rule. CS is graded (I, II, III) according to tumor cellularity and cytologic atypia.

VIEW IMAGE

FIGURE 6-155 Coronal multidirectional tomogram shows an expansile lesion in the maxillary alveolus and hard palate (*arrows*). This patient had a central-type giant cell granuloma.

FIGURE 6-156 Lateral view shows an expansile, loculated, and destructive lesion of the maxilla. This patient had an aneurysmal bone cyst.

VIEW IMAGE

Copyright © 2003, Mosby, Inc. All rights reserved.

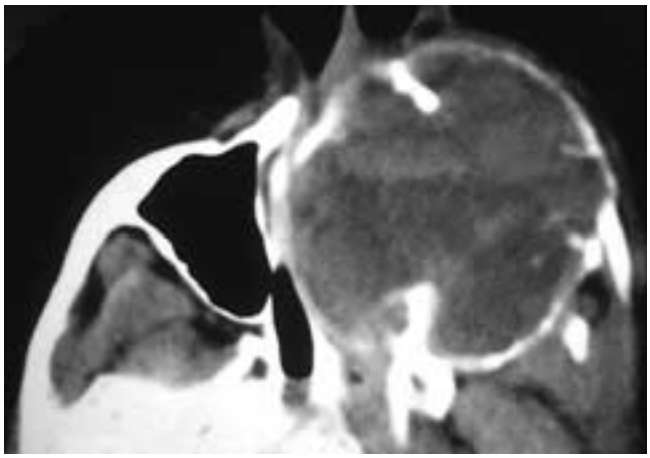

VIEW IMAGE

FIGURE 6-157 Axial CT scan shows an expansile mass in the left maxillary sinus. The surrounding bone is remodeled and not eroded. This patient had an aneurysmal bone cyst. (Courtesy of Dr. Revel and Dr. Vanel.)

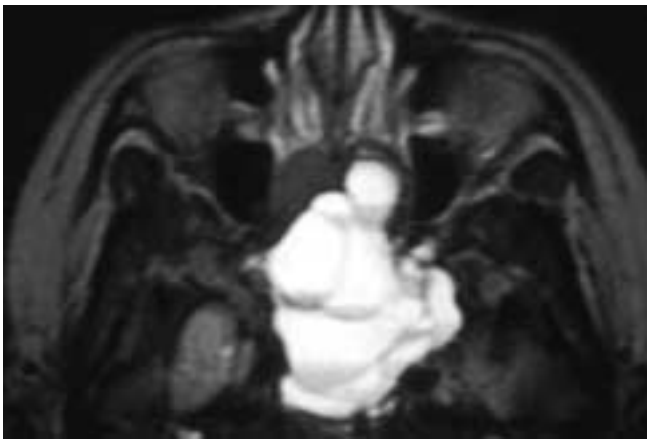

VIEW IMAGE

FIGURE 6-159 Axial T2-weighted MR image shows a mass in the sphenoid bone and sphenoid sinus. This lesion is composed of multiple cystic areas, each with a fluid-fluid level. This patient had an aneurysmal bone cyst.

Grade I CS is composed of invasive lobulated tumor producing abundant matrix, with binucleate chondrocytes (Fig. 6-165). Distinguishing it from a benign chondroma may not be possible with limited material and requires radiographic correlation to establish an aggressive, invasive growth pattern. Grade II CS has greater cellularity and pleomorphism than a grade I tumor and is easily identified as both malignant and chondroid in nature. A grade III neoplasm is very cellular and pleomorphic. The chondroid matrix may be limited. Spindle cell CS (so-called dedifferentiated CS) is an unusual variant in which a high-grade undifferentiated sarcoma ''springs forth'' from a lower-grade CS.

Surgery and adjuvant chemotherapy is indicated for OS. Establishing a preoperative diagnosis of OS allows for neoadjuvant chemotherapy. The chemotherapeutic effect can then be histologically assessed based on postoperative (postchemotherapy) tumor viability, and thus the postoperative completion of chemotherapy can be tailored based on the observed response. Complete surgical resection is indicated for CS; adjuvant chemotherapy and radiotherapy have not been shown to improve survival. Proton beam therapy may be considered as primary therapy for unresectable cases. Survival of patients with head and neck OS and CS is dependent upon tumor stage, grade, and site. Jaw OS has a 5-year disease-free survival rate of between 30% and 50%. The prognosis for OS in Paget's disease, as mentioned, is known to be particularly poor. The 5-year disease-free survival rate for craniofacial CS is around 40%.[303] Fu and Perzin emphasize that sinonasal CS is less amenable to resection than CS at other sites.[209] For both OS and CS, the metastatic rate (predominantly to the lungs, liver, brain, bones, and lymph nodes) directly correlates with the tumor grade. Overall, only 7% of sinonasal CSs develop metastases. Patients with mesenchymal CS in general have a 5-year survival rate ranging from 42% to 54.6% and a 10-year survival rate of 28%. Mesenchymal CS of the jaw bones (5- and 10-year survival rates of 82% and 56%, respectively) appears to have a more indolent course than axial skeletal or soft tissue mesenchymal CS.[304, 305]

On imaging, CS tends to occur at the cartilaginous junctions of the facial bones or in the cartilaginous nasal septum. Marginal bone erosion is typically present, and calcifications within the mass may or may not be seen. These tumors have fairly low T1-weighted and high T2-weighted signal intensities, and they enhance after contrast administration, either uniformly or nonuniformly. Without the presence of gross tumoral calcifications, the imaging appearance is not characteristic enough to establish a definitive diagnosis (Figs. 6-166 to 6-172). Rarely, a large, aggressive pituitary adenoma that extends into the nasal fossa may have similar imaging findings (Fig. 6-173).

With OS, there typically is a ''sunburst'' periosteal reaction, although this need not be present. Focal destruction is usually seen; however, dense sclerotic bone may be present, especially in the maxillary alveolus. Depending on the bone content of the tumor, the signal intensities can vary, usually being primarily a low T1-weighted and an intermediate T2-weighted signal intensity. Enhancement after contrast administration is present, although not usually to the degree seen in CS (Figs. 6-174 to 6-180).

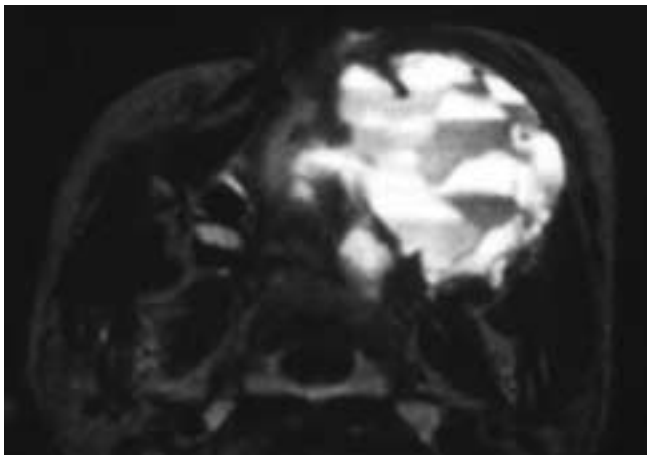

VIEW IMAGE

FIGURE 6-158 Axial T2-weighted MR image shows multiple cystic components with fluid-fluid levels within a left maxillary sinus mass. This patient had an aneurysmal bone cyst. (Courtesy of Dr. Revel and Dr. Vanel.)

Copyright © 2003, Mosby, Inc. All rights reserved.

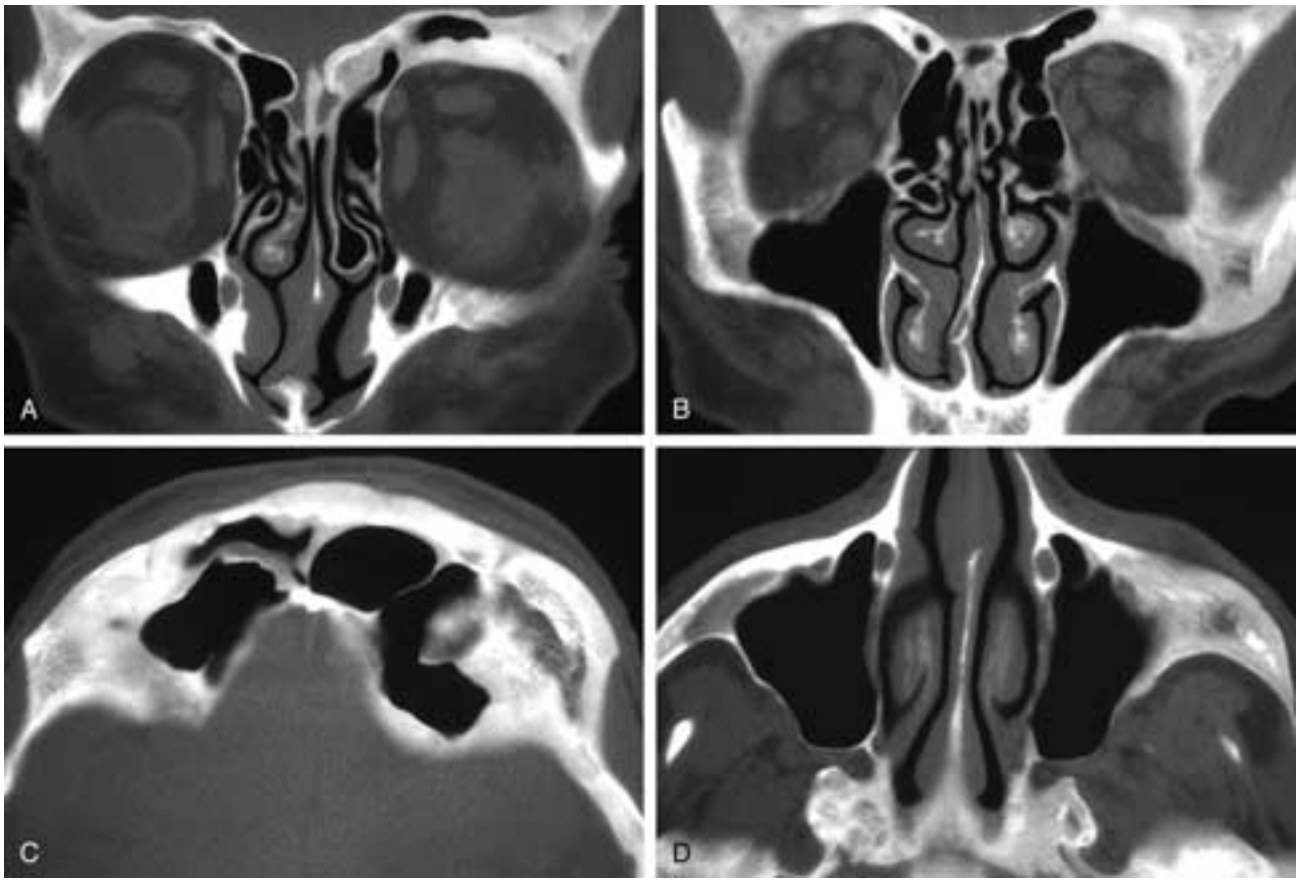

VIEW IMAGE

FIGURE 6-160 Coronal (**A** and **B**) and axial (**C** and **D**) CT scans show the facial bones to be thickened, denser than normal, and with poorly defined trabeculae. Similar changes were present in the calvarium. This patient had Paget's disease.

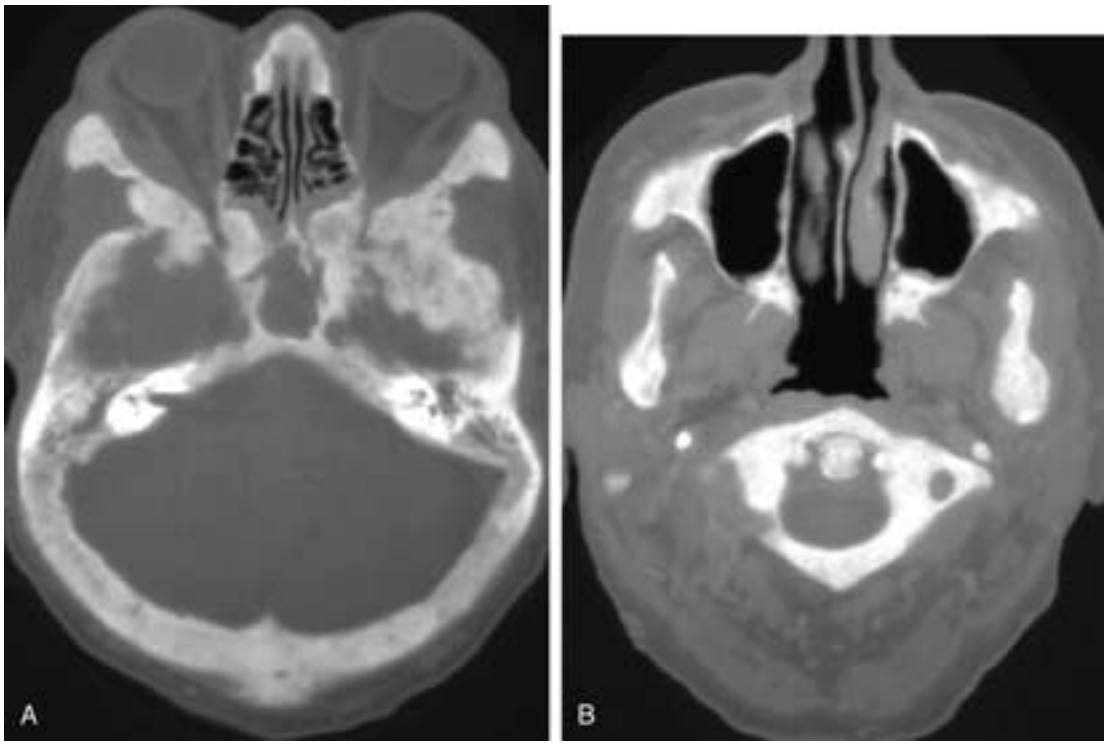

VIEW IMAGE

FIGURE 6-161 Axial CT scans through the orbits (**A**) and the maxillary sinuses (**B**) show that the bones of the skull base, upper cervical vertebra, and face are thicker and denser than normal. The bones have a slightly irregular contour, and there is poor detail of the trabeculae. This patient had Paget's disease.

Copyright © 2003, Mosby, Inc. All rights reserved.

VIEW IMAGE

FIGURE 6-162 Sagittal (**A**) and coronal (**B**) T1-weighted MR images show diffusely thickened bone in the facial region and the calvaria. The areas of high signal intensity in the calvaria correspond to regions of marrow, while the areas of low signal intensity correspond to regions of dense woven bone formation. The thickened calvaria has reduced the size of the intracranial compartment. The majority of the abnormal bone has a nonhomogeneous low to intermediate signal intensity. This patient had Paget's disease.

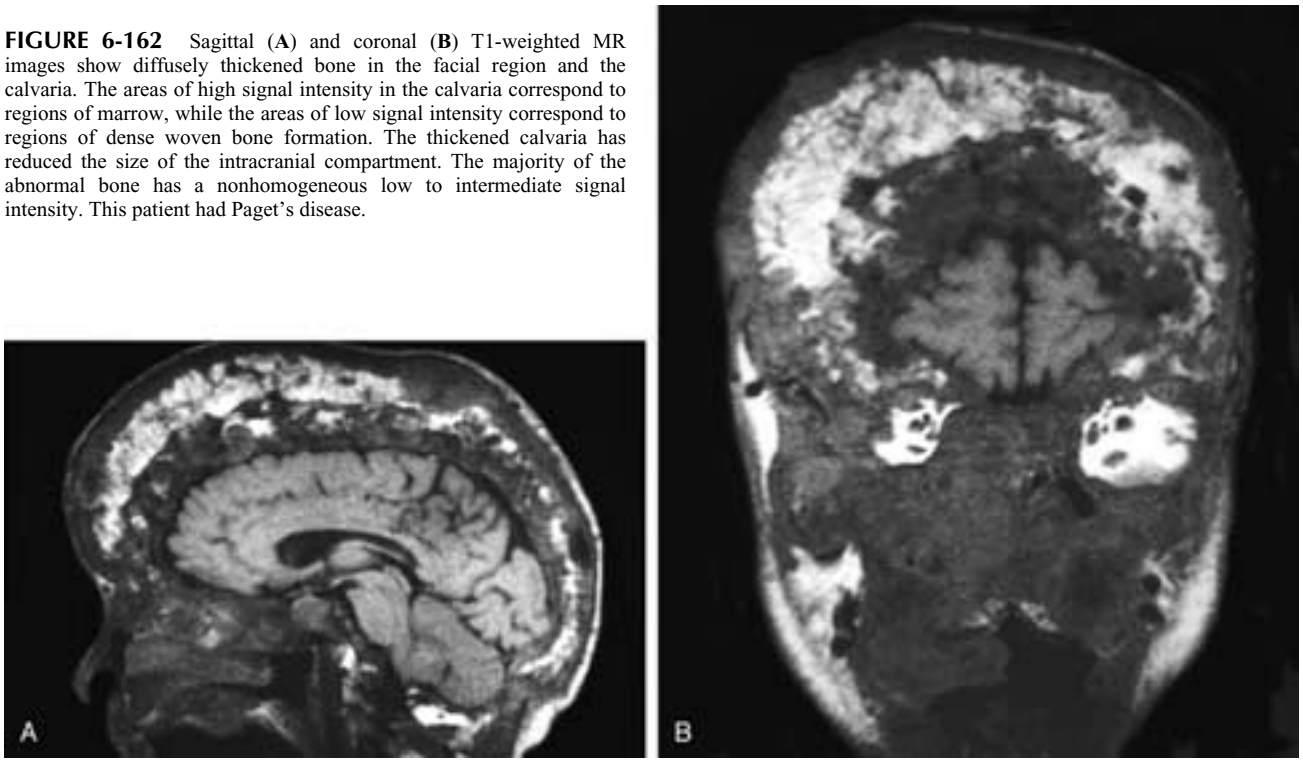

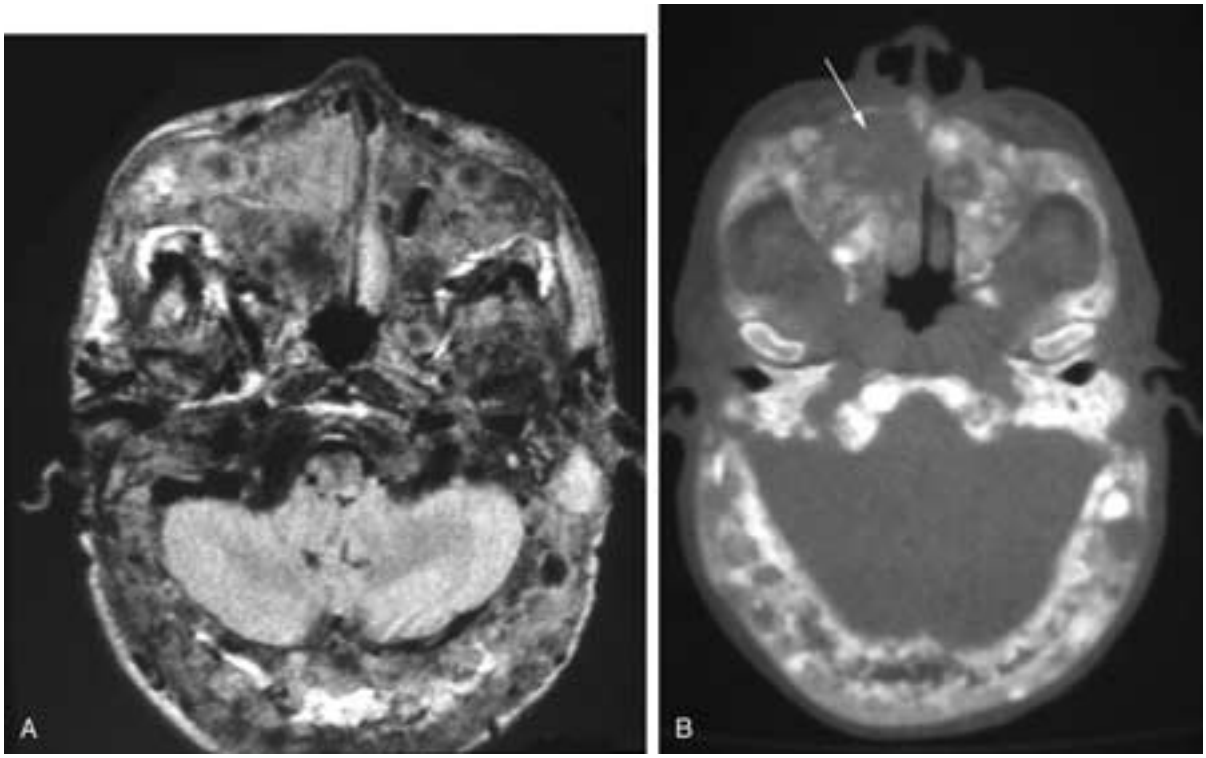

VIEW IMAGE

FIGURE 6-163 Axial proton density MR image (**A**) and a corresponding axial CT scan (**B**) show marked thickening of the calvaria, with localized areas of dense woven bone. The expanded bone has virtually obliterated the maxillary sinuses. In **B** there is an area in the anterior medial right maxilla that is almost devoid of bone (*arrow*). This region, in retrospect, can be identified in **A**, but it is not as clearly evident. This patient had Paget's disease, and this localized area was an osteosarcoma.

Copyright © 2003, Mosby, Inc. All rights reserved.

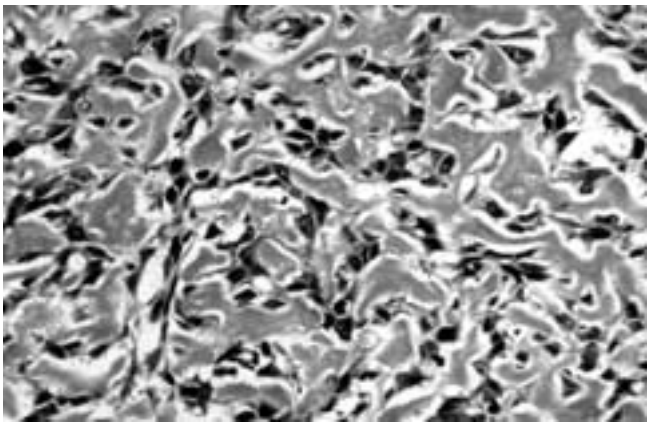

VIEW IMAGE

FIGURE 6-164 Osteogenic sarcoma: The malignant cells of this poorly differentiated OS are producing a lacelike osteoid stroma.

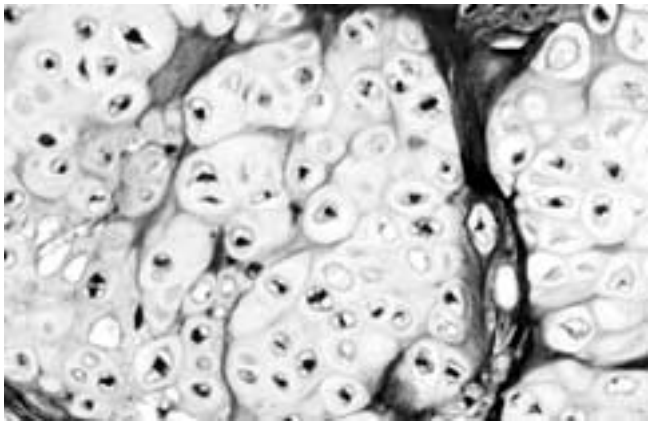

VIEW IMAGE

FIGURE 6-165 Chondrosarcoma grows in a lobulated fashion. These chondrocytes are atypical and crowded.

VIEW IMAGE

FIGURE 6-166 Axial (**A**) and coronal (**B**) CT scans show a destructive mass in the left ethmoid sinuses. The tumor has broken into the left orbit and the anterior cranial fossa. Gross, discrete calcifications are present within the mass. This patient had a chondrosarcoma.

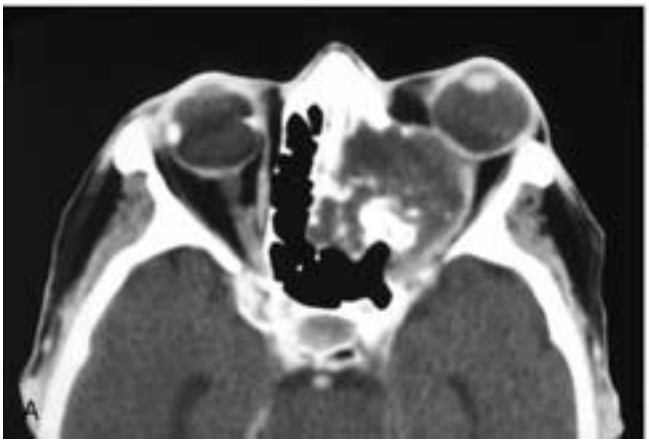

Mesenchymal Chondrosarcoma

Mesenchymal CS is a rare variant of CS, representing approximately 10% of all CSs.[306] It can occur as an osseous (60% to 70%) or soft tissue (30% to 40%) neoplasm. Among 35 patients with mesenchymal CS seen at the Memorial Sloan-Kettering Cancer Center, 14% occurred in the head and neck, most commonly in the maxilla.[306] The craniospinal meninges and orbital soft tissues are the most common extraskeletal sites. These tumors also have been reported in the ethmoid sinuses. The majority of affected patients are 40 years old or younger (average, 26 years old). Mesenchymal CS is a bimorphic tumor composed of islands of well-differentiated hyaline cartilage juxtaposed to a small cell undifferentiated malignancy.

ODONTOGENIC LESIONS AND TUMORS

Odontogenic and developmental cysts arise from the cystic expansion of epithelial remnants of various components of the dental apparatus or entrapped epithelium. They are generally uncommon entities and can be classified as either follicular cyst, periodontal cyst, odontogenic keratocyst, calcifying odontogenic cyst, nasopalatine cyst, median palatine cyst, and nasolabial cyst. The following discussion is limited to those jaw cysts that can present as maxillary or palatal lesions (also see Chapter 17).

Jaw Cysts

Follicular Cyst

Follicular cysts (also referred to as dentigerous cysts) represents up to 24% of all odontogenic cysts. There is a pronounced predisposition for males and for African Americans. Most affected patients are diagnosed between the second and fourth decades of life. These cysts develop as

Copyright © 2003, Mosby, Inc. All rights reserved.

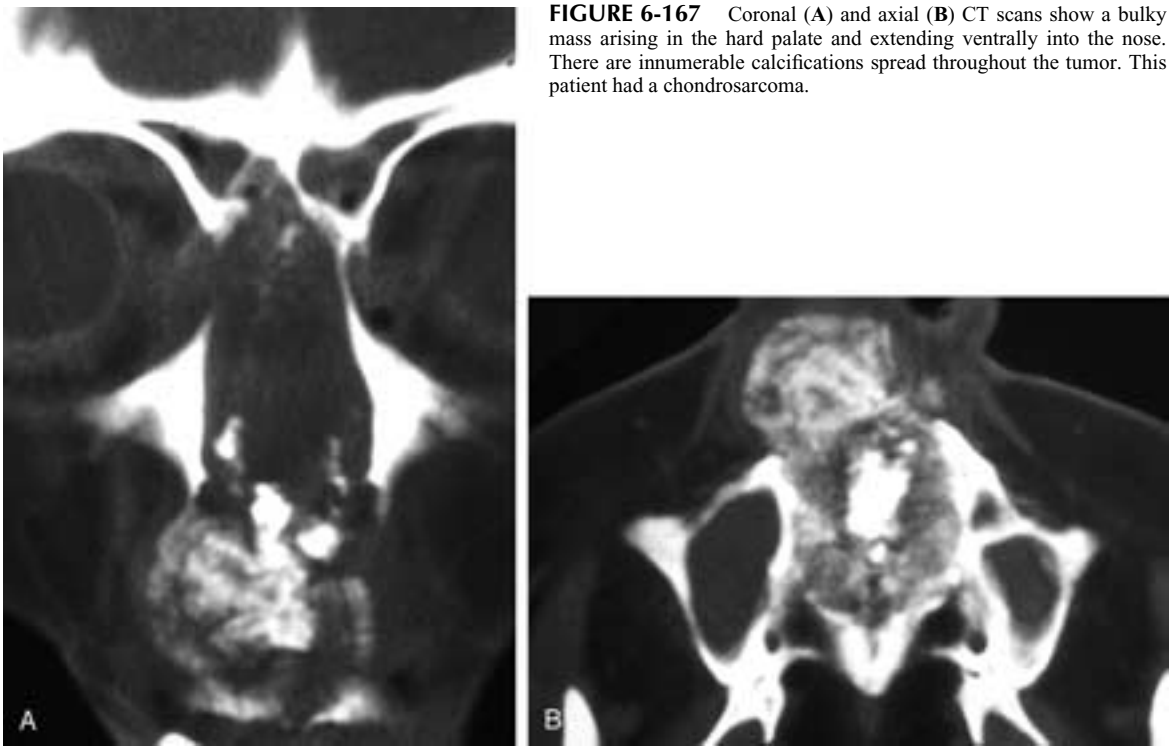

FIGURE 6-167 Coronal (**A**) and axial (**B**) CT scans show a bulky mass arising in the hard palate and extending ventrally into the nose. There are innumerable calcifications spread throughout the tumor. This patient had a chondrosarcoma.

VIEW IMAGE

a result of fluid accumulation either around the tooth crown or within the enamel organ. They are invariably associated with impacted or unerupted teeth. The most commonly affected teeth are the mandibular third molars, maxillary canines, and third molars. Follicular cysts may also be associated with supernumerary teeth.[307]

Radiographically, one sees a well-circumscribed cyst that contains the crown of the tooth. As the cyst grows, it pulls the unerupted tooth with it. Small dentigerous cysts are unilocular. Large cysts may be multilocular, and the confined tooth may be displaced from its normal location. Resorption of adjacent teeth roots can occur.[308]

The dentigerous cyst must be distinguished radiographically from a normal dental follicle. If a dental follicle measures 2 cm or more, it is highly likely that the unerupted tooth will develop a dentigerous cyst. Similarly, a pericoronal space of 2.5 mm or more heralds an 80% likelihood that the unerupted tooth will become a dentigerous cyst.[309]

If the cyst erodes into the maxillary sinus, it may grow rapidly, remodeling the antral walls. Often the inferior maxillary sinus cortex is elevated over portions of the cyst. In the axial view, this can be detected by noting what appear to be two bony walls in the posterior sinus. Here the most posterior bone represents the true sinus wall, while the anterior bone represents the elevated sinus floor. If multiple dentigerous cysts are present, the patient should be examined for the basal cell nevus syndrome (see below). On MR imaging, the cyst fluid has intermediate signal intensity

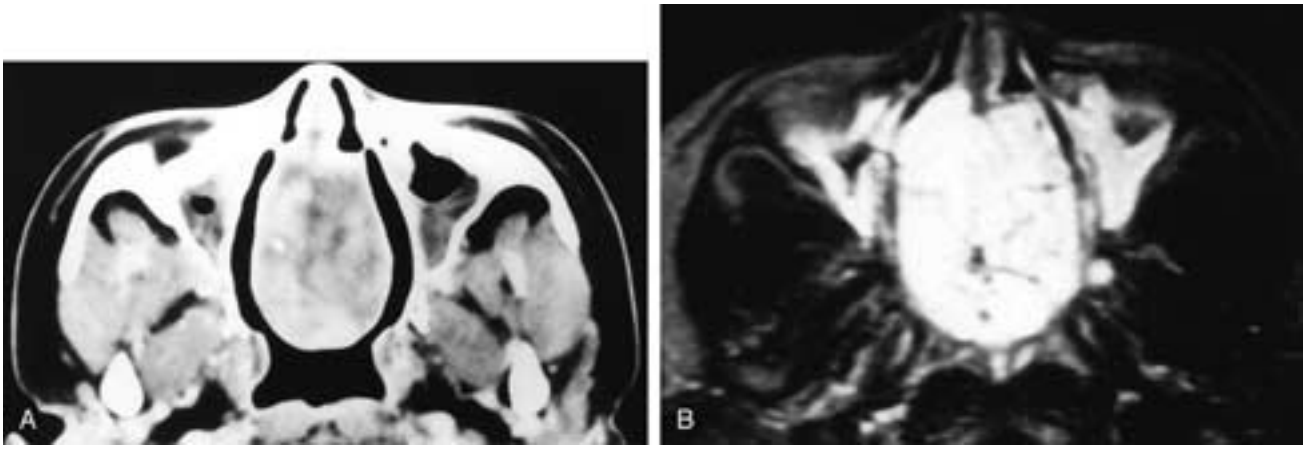

FIGURE 6-168 Axial CT scan (**A**) and axial T2-weighted MR image (**B**) show a bulky mass arising from the nasal septum. Scattered calcifications are present within the mass. The lesion had an intermediate T1-weighted signal intensity. Obstructive inflammatory changes are present in the maxillary sinuses. This patient had a chondrosarcoma.

VIEW IMAGE

Copyright © 2003, Mosby, Inc. All rights reserved.

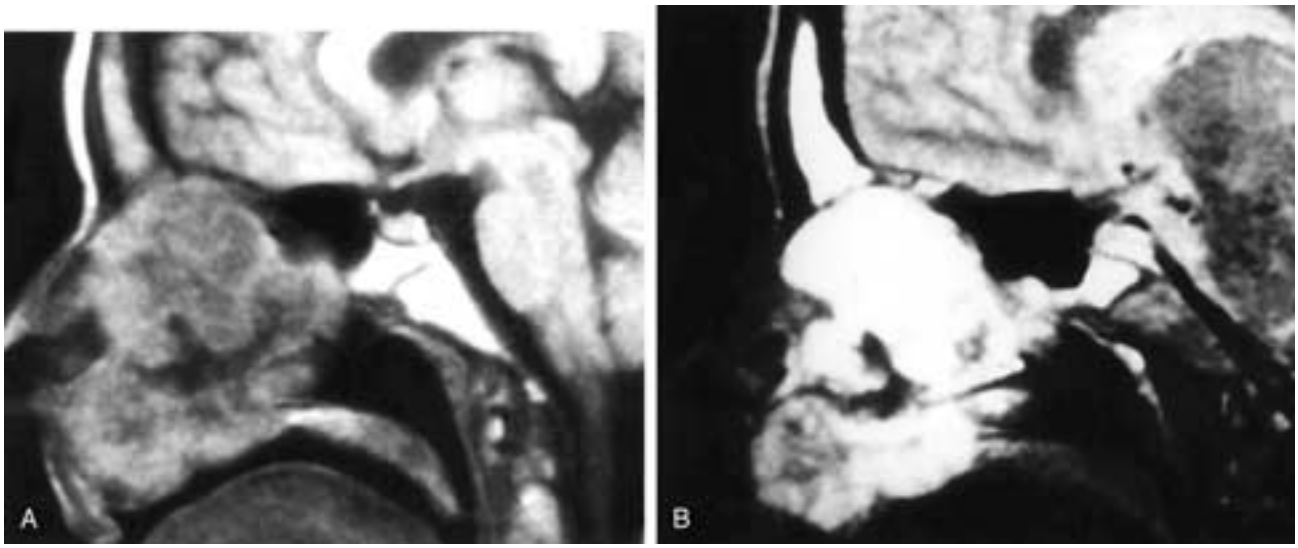

VIEW IMAGE

FIGURE 6-169 Sagittal T1-weighted (**A**) and T2-weighted (**B**) MR images show a slightly nonhomogeneous nasal septal mass that has a low to intermediate signal intensity in **A** and a high signal intensity in **B**. The frontal sinuses are obstructed by the tumor. This patient had a chondrosarcoma.

on T1-weighted images and high signal intensity on T2-weighted images; the displaced tooth gives a signal void on all imaging sequences. In this regard, the MR imaging appearance may be similar to that of an antral aspergilloma (Figs. 6-181 to 6-186).

Small dentigerous cysts are cured by curettage. Larger multiloculated cysts may require marsupialization. An ameloblastoma may arise within the wall of the dentigerous cyst. This mural or cystic ameloblastoma is often diagnosed only by the pathologist; the radiographic findings in such cases are those of a simple dentigerous cyst.[307, 309] There is a familial predisposition toward this transformation. The prognosis of a cystic ameloblastoma arising in a dentigerous cyst is excellent, as curettage is usually curative.

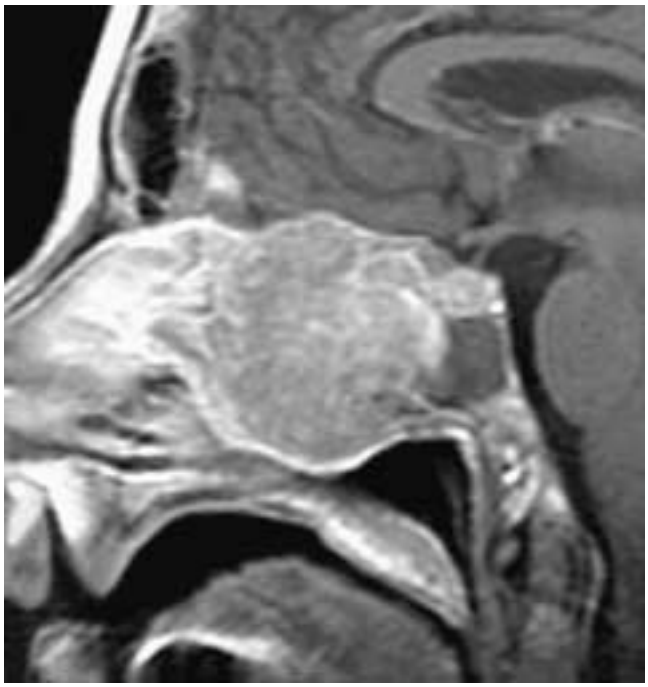

VIEW IMAGE

FIGURE 6-170 Sagittal T1-weighted, fat-suppressed, contrast-enhanced MR image shows an enhancing nasal septal mass that has extended into the sphenoid bone. A mucocele is present within the obstructed sphenoid sinus. This patient had a chondrosarcoma.

Periodontal Cyst

Periodontal cysts are also referred to as periapical, radicular, apical periodontal, or dental cysts. They represent the most common jaw cyst and arise in erupted, infected carious teeth as sequelae to periapical granulomas. Maxillary teeth are most commonly involved. Maxillary periodontal cysts can erode into the maxillary sinus, remodeling the antral walls and elevating the inferior sinus cortex (Figs. 6-187 to 6-189).[309, 310]

The term *residual periodontal cyst (residual cyst)* refers to a periapical cyst developing after tooth extraction. Treatment of these cysts consists of simple enucleation.[306]

The lateral periodontal cyst (also referred to as a paradental cyst) is a noninflammatory developmental cyst that arises lateral to the tooth root. This cyst probably arises from proliferation of rests within the dental lamina. This cyst occurs most often in adults in the premolar and cuspid areas. Radiographically, there is an incidental multiloculated cyst along the lateral tooth root.

Odontogenic Keratocyst

Odontogenic keratocysts (OKCs) can be subclassified as central (intraosseous), which are further subclassified as parakeratotic, orthokeratotic, or mixed, versus peripheral or mucosal. The central parakeratotic OKC (POKC) is most commonly encountered and is also referred to as a primordial cyst. POKC represents up to 16.5% of all jaw cysts and is most commonly seen in patients within the second and third decades of life. The mandible is affected two to four times more often than the maxilla, with a predilection for posterior jaws. Half of patients with POKC

Copyright © 2003, Mosby, Inc. All rights reserved.

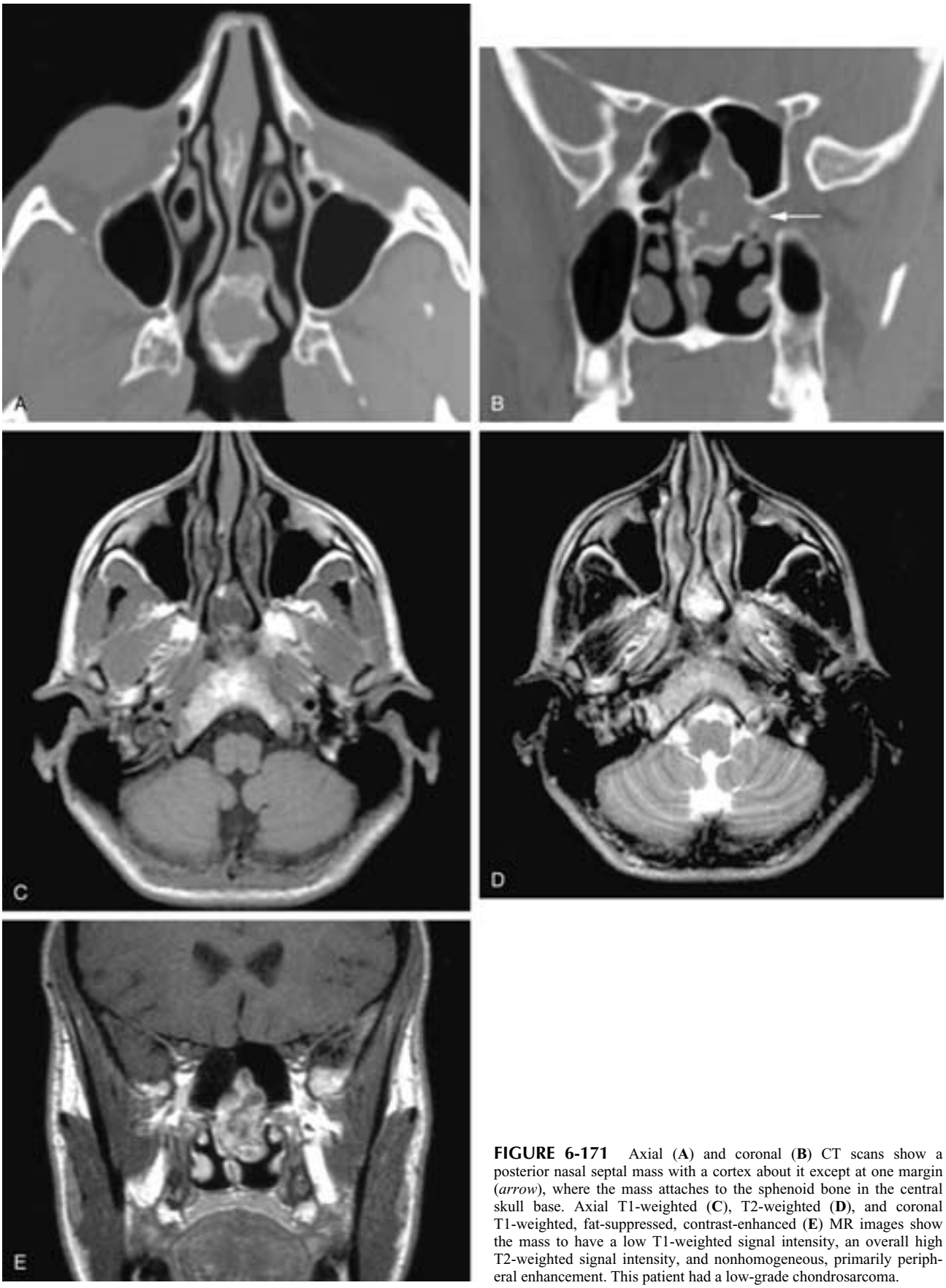

FIGURE 6-171 Axial (**A**) and coronal (**B**) CT scans show a posterior nasal septal mass with a cortex about it except at one margin (*arrow*), where the mass attaches to the sphenoid bone in the central skull base. Axial T1-weighted (**C**), T2-weighted (**D**), and coronal T1-weighted, fat-suppressed, contrast-enhanced (**E**) MR images show the mass to have a low T1-weighted signal intensity, an overall high T2-weighted signal intensity, and nonhomogeneous, primarily peripheral enhancement. This patient had a low-grade chondrosarcoma.

VIEW IMAGE

Copyright © 2003, Mosby, Inc. All rights reserved.

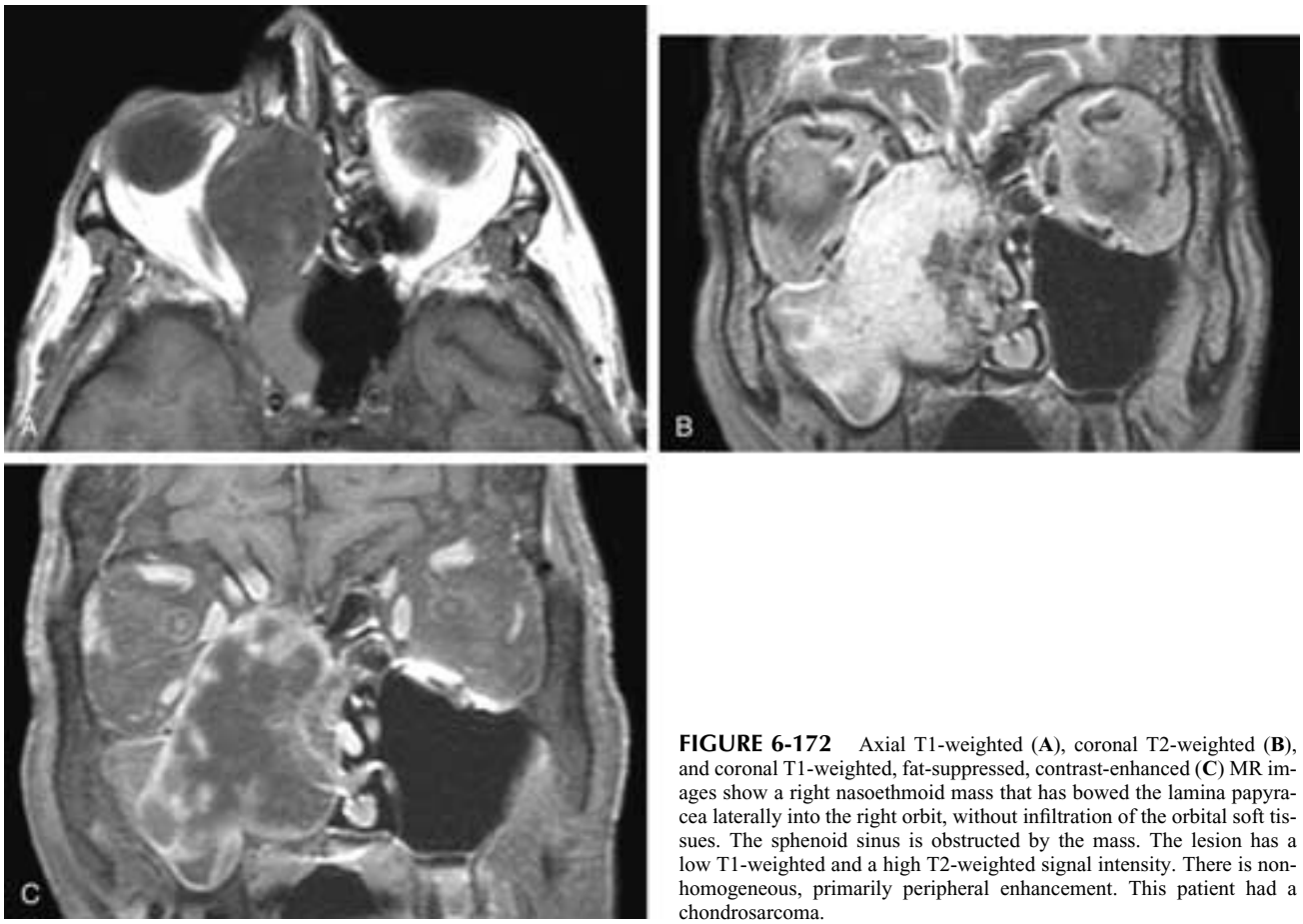

FIGURE 6-172 Axial T1-weighted (**A**), coronal T2-weighted (**B**), and coronal T1-weighted, fat-suppressed, contrast-enhanced (**C**) MR images show a right nasoethmoid mass that has bowed the lamina papyracea laterally into the right orbit, without infiltration of the orbital soft tissues. The sphenoid sinus is obstructed by the mass. The lesion has a low T1-weighted and a high T2-weighted signal intensity. There is nonhomogeneous, primarily peripheral enhancement. This patient had a chondrosarcoma.

VIEW IMAGE

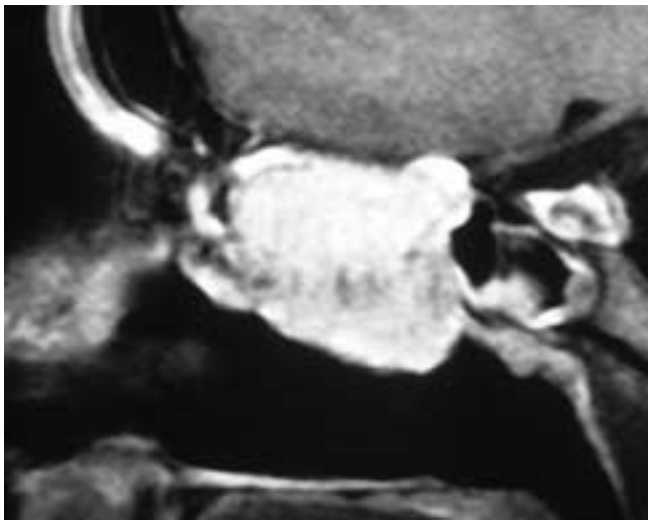

VIEW IMAGE

FIGURE 6-173 Sagittal T1-weighted, fat-suppressed, contrast-enhanced MR image shows an enhancing mass that fills the nasal fossae and sphenoid sinuses. The tumor extends caudally into the roof of the nasopharynx. A small nodule of tumor projects above the sella turcica. This patient had an aggressive pituitary adenoma.

FIGURE 6-174 Lateral view shows an aggressive tumor of the maxilla that has caused a ''sunburst'' periosteal reaction anteriorly. This patient had an osteogenic sarcoma.

VIEW IMAGE

Copyright © 2003, Mosby, Inc. All rights reserved.

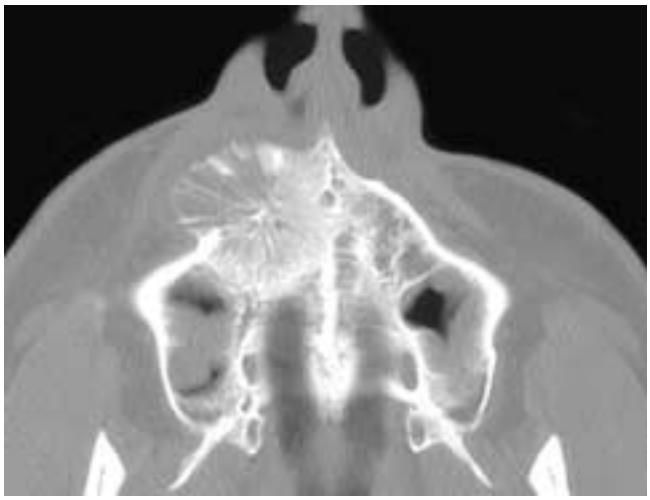

VIEW IMAGE

FIGURE 6-175 Axial CT scan shows a destructive mass in the right anterior maxilla with a typical ''sunburst''-type periosteal reaction. This patient had an osteogenic sarcoma.

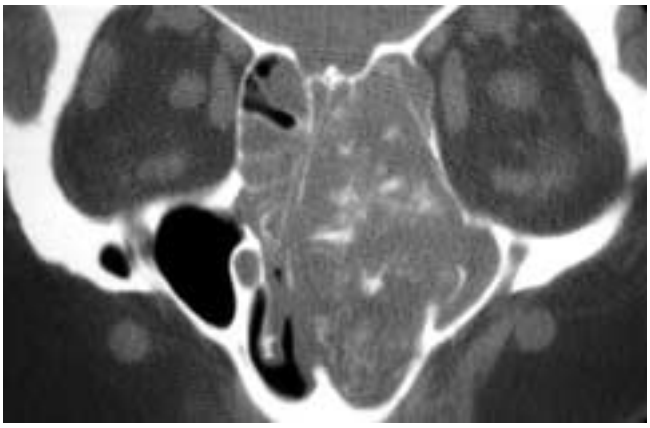

VIEW IMAGE

FIGURE 6-176 Coronal CT scan shows a destructive mass in the nasal cavity and ethmoid sinuses, sphenoid sinuses, and right maxillary sinus. The tumor erodes the central skull base and the floor of the anterior cranial fossa. Within the mass are irregular areas of calcification or ossification. This appearance is highly suggestive of a sarcoma rather than a carcinoma. This patient had an osteogenic sarcoma.

complain of pain. Maxillary POKC can extend into the antrum, causing nasal obstruction.[307]

Historically, the term *primordial cyst* reflects the idea that these cysts were derived from degenerated stellate reticulum of the enamel organ prior to mineralization. However, these cysts are now believed to originate from dental lamina or its remnants or from extensions of basal cells from the overlying epithelium. Most are believed to develop from supernumerary teeth. When a rare cyst develops in place of a tooth, it is considered a replacement type of keratocyst.[307]

Radiographically, POKCs appear as unilocular or multilocular radiolucencies that may have a thin, reactive, sclerotic bony rim and smooth or scalloped margins or appear destructive, invading adjacent bone. Pathologically, these cysts are lined by stratified squamous epithelium, producing corrugated parakeratosis. The term *parakeratosis* refers to retained nuclei within the compact hyperkeratosis. The basal reserve cells reveal reverse palisading, which refers to the fact that the nuclei are oriented away from the basement membrane.

Multiple odontogenic keratocysts are associated with the nevoid basal cell carcinoma syndrome (Gorlin's syndrome). This condition is transmitted in an autosomal dominant fashion as a result of loss of a tumor suppressor gene on chromosome 9q22. Nevoid basal cell carcinoma syndrome is associated with the early development of multiple basal cell carcinomas, which can occur within preexisting sebaceous nevi, palmar and plantar pitting, and skeletal developmental abnormalities, as well as within the above-mentioned POKC. POKCs have also been associated with Marfan's syndrome. They are known for their aggressive potential for invasion and recurrence; up to 62.5% may recur. Simple POKC may be treated by enucleation, keeping the cyst intact. Multilocular or more destructive POKCs are better treated by en bloc resection.

Orthokeratosis is defined as compact keratin without retained nuclei. An orthokeratotic-type keratocyst (OOKC) represents 13% of OKCs. There is a male predisposition and no increased predominance in African Americans. OOKCs have a predilection for the mandible, but unlike POKCs, OOKCs are more likely to affect the anterior jaws. OOKCs are noteworthy in that they are generally unilocular.[307]

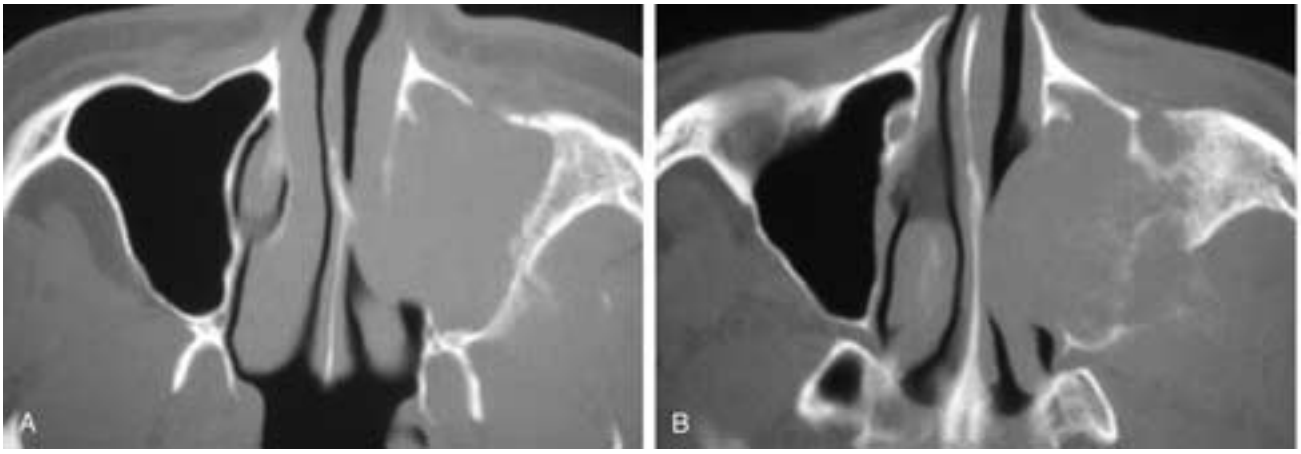

VIEW IMAGE

FIGURE 6-177 Axial CT scans (**A** and **B**) show a mass in the left maxillary sinus, with destruction of portions of the anterior, medial, and posterior sinus walls. In addition, there is an aggressive periosteal reaction in the posterior sinus wall.

Copyright © 2003, Mosby, Inc. All rights reserved.

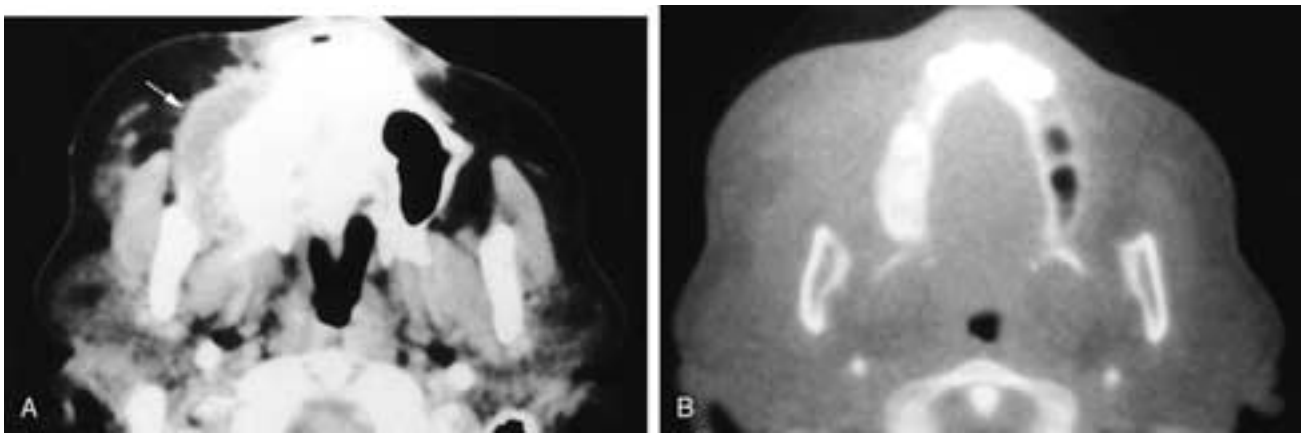

VIEW IMAGE

FIGURE 6-178 Axial CT scans viewed at ''soft-tissue'' (**A**) and ''bone'' (**B**) window settings show a nonossified mass along the outer margin of the right maxillary alveolus (*arrow*). The alveolus in this area is minimally enlarged and very dense. This patient had an osteogenic sarcoma.

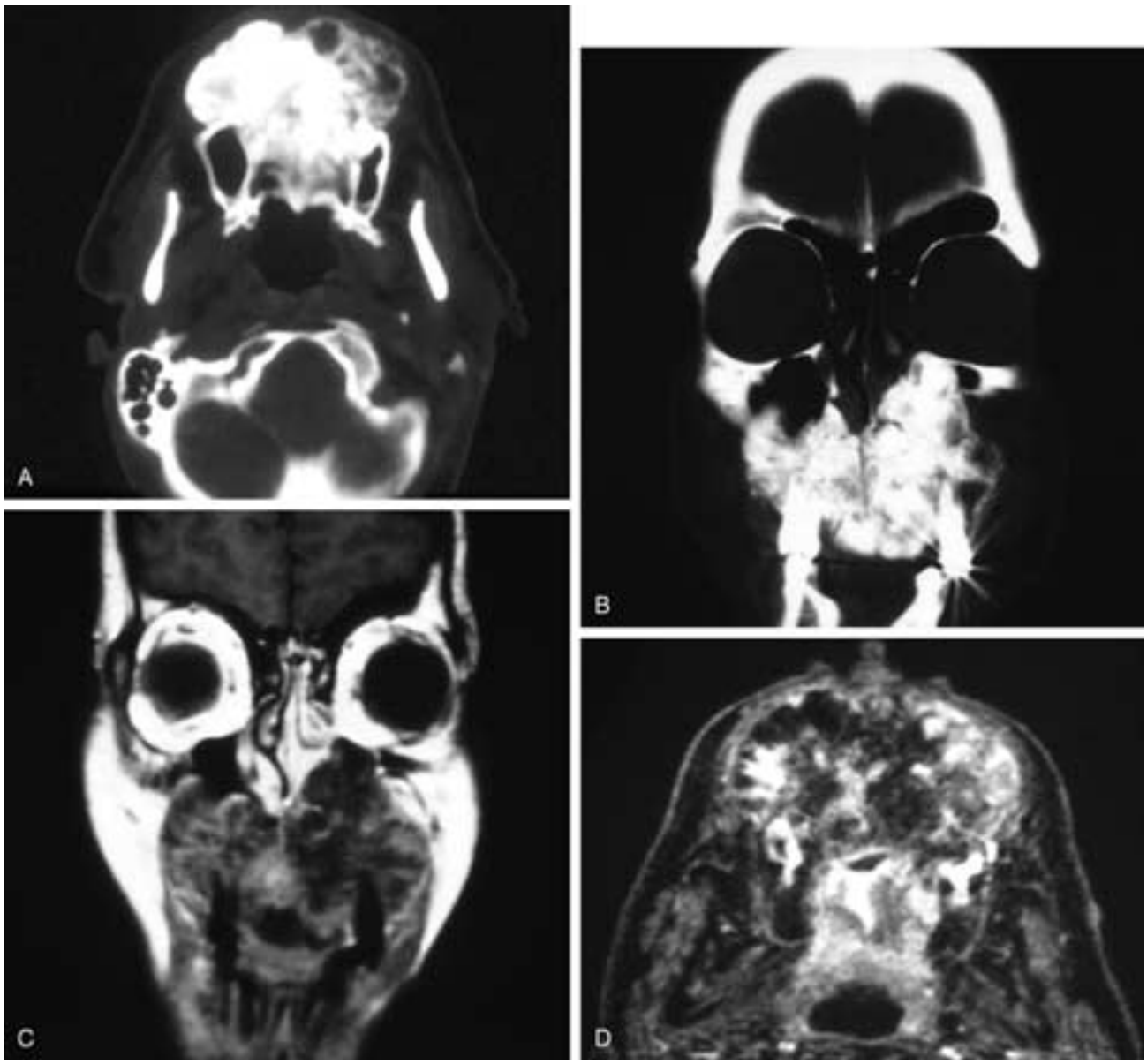

VIEW IMAGE

FIGURE 6-179 Axial (**A**) and coronal (**B**) CT scans show a dense area of bony production in the hard palate. No intact cortex is identified in the region of the mass. Coronal T1-weighted (**C**) and axial T2-weighted (**D**) MR images show that this mass is quite nonhomogeneous. The areas of dense bone seen on the CT scan are for the most part of low signal intensity, but the lesion is not as clearly separated from the adjacent uninvolved maxilla and maxillary sinuses as it is on the CT scan. This patient had an osteogenic sarcoma.

Copyright © 2003, Mosby, Inc. All rights reserved.

VIEW IMAGE

FIGURE 6-180 Coronal CT scan on a patient who previously had a craniofacial resection for an osteogenic sarcoma shows a recurrent bony mass with aggressive periosteal production. This patient had a recurrent osteogenic sarcoma.

FIGURE 6-182 Coronal CT scan shows an expansile mass in the left antrum. A molar tooth is present in the uppermost wall of the lesion. This patient had a dentigerous cyst.

VIEW IMAGE

Radiographically, one sees a unilocular radiolucent cyst. CT shows the bone morphology better than plain films; however, contrast-enhanced MR images provide the essential macroscopic detail, including focal wall enhancement and isointense intraluminal soft-tissue masses, which correlates with the histologic findings of focal inflammatory ulceration of the cyst lining, orthokeratosis, and cell debris. The cyst lining lacks the prominent corrugated proliferating basaloid reserve cells of POKC. Rather, these basal reserve cells are more flattened. The hyperkeratosis lacks retained nuclei, hence the classification ''orthokeratosis.'' Curettage is curative. OOKCs are less aggressive than POKCs and recur infrequently.

Calcifying Odontogenic Cyst

This cyst has a variety of names, including keratinizing ameloblastoma, keratinizing and calcifying ameloblastoma, melanotic ameloblastic odontoma calcifying cyst, cystic calcified odontogenic tumor, ghost cell tumor, and atypical adamantinoma.[307] The calcifying odontogenic cyst is an uncommon lesion, comprising only about 2% of all benign odontogenic lesions.[307] These cysts affect the maxilla and mandible equally. About 78% are intraosseous (central), and 22% are confined to the peripheral soft tissues. They are either unilocular or multilocular radiolucent cysts that frequently contain radiopaque material ranging from small flecks to large masses. The lesion can be well circumscribed or poorly demarcated. Radiographically, it resembles a calcifying epithelial odontogenic tumor, an odontoma, an ossifying fibroma, and fibrous dysplasia. The lining of a calcifying odontogenic cyst consists of ameloblastic epithelium and ''ghost cells,'' which undergo dystrophic calcification. Treatment can be by curettage, enucleation, or conservative surgical excision; unlike the keratocyst, recurrences are unlikely.[310]

Fissural Cyst

The term *fissural cyst* refers to a cystic expansion that had been attributed etiologically to entrapped epithelium within

VIEW IMAGE

FIGURE 6-181 Caldwell view shows an expansile process in the left maxillary sinus with a tooth in the medial antral wall (*arrows*). This patient had a dentigerous cyst.

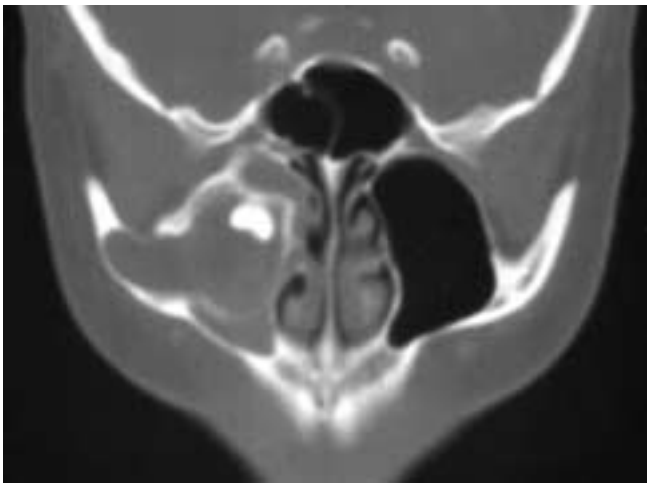

FIGURE 6-183 Coronal CT scan shows an expansile right maxillary sinus mass with a tooth within the antrum. This patient had a dentigerous cyst.

VIEW IMAGE

Copyright © 2003, Mosby, Inc. All rights reserved.

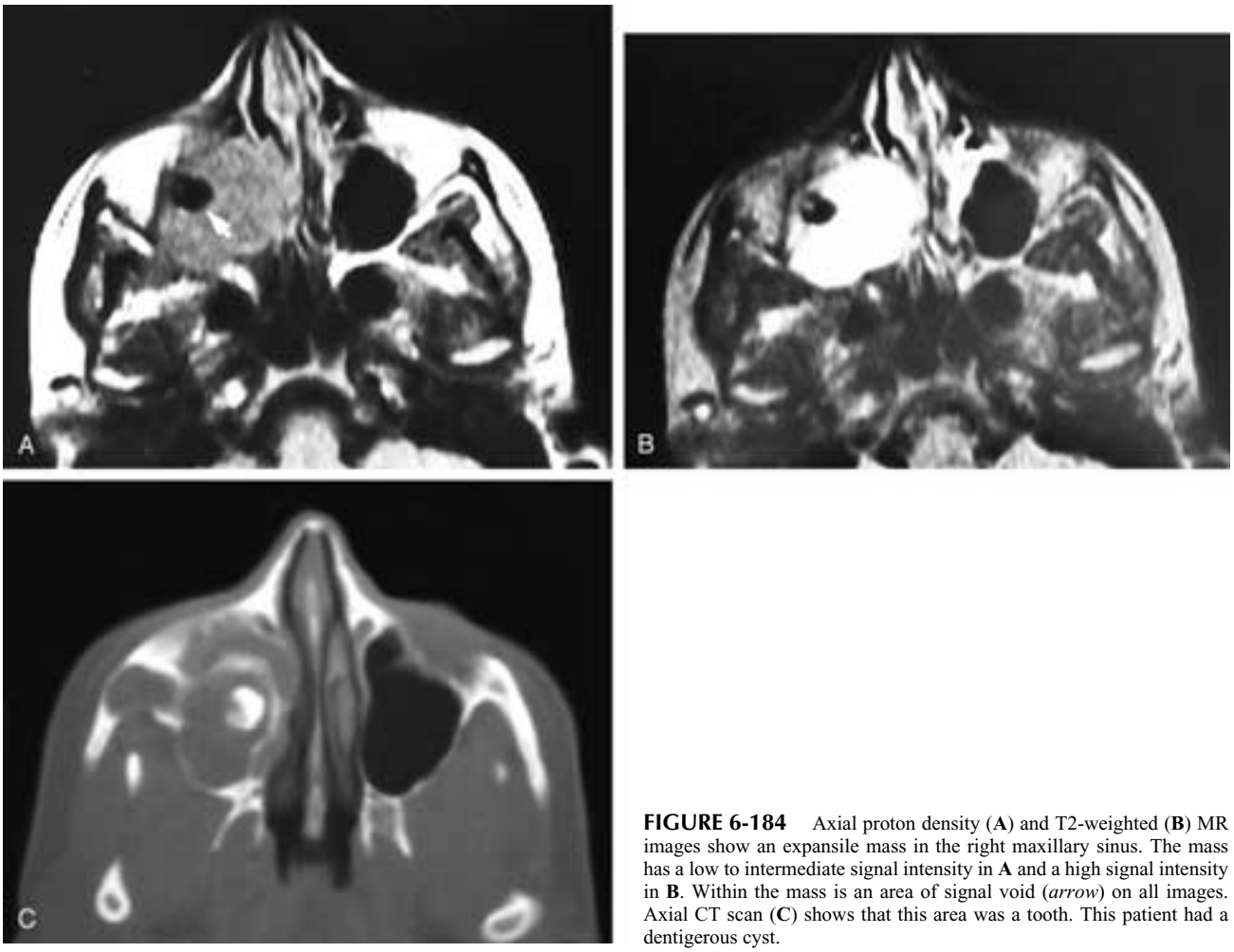

FIGURE 6-184 Axial proton density (**A**) and T2-weighted (**B**) MR images show an expansile mass in the right maxillary sinus. The mass has a low to intermediate signal intensity in **A** and a high signal intensity in **B**. Within the mass is an area of signal void (*arrow*) on all images. Axial CT scan (**C**) shows that this area was a tooth. This patient had a dentigerous cyst.

VIEW IMAGE

the fusion lines of the frontonasal and maxillary processes. However, it is apparent that these rare cysts may actually result from a variety of inflammatory as well as developmental etiologies. These cysts are classified as either globulomaxillary or median mandibular cysts.[307] Figure 6-190 is a diagrammatic overview of all of the cysts related to the maxillary alveolus and the palatal region.

The globulomaxillary cyst is found between the maxillary lateral incisor and canine teeth and represents less than 3% of all jaw cysts and 20% of maxillary cysts. Most occur in patients under 30 years of age. Radiographically, the globulomaxillary cyst appears as an inverted pear-shaped or ovoid cyst in the maxillary alveolus (Fig. 6-191). It often pushes apart the roots of the lateral incisor and canine teeth and can distort the lower anterior aspect of the maxillary sinus.[309]

Radiographically, the median mandibular cyst appears as a well-circumscribed radiolucency between the mandibular central incisors. The histologies of both cysts are nonspecific, and the diagnoses are confirmed radiographically.

Developmental Cyst

Developmental cysts are the most commonly encountered nonodontogenic jaw cysts, representing 73% of these cysts.[307] They develop from entrapped ductal epithelium and may be classified anatomically as either nasopalatine duct (also known as median anterior maxillary cysts), median palatal, or nasolabial cysts (Figs. 6-190, 6-192, and 6-193). Nasopalatine or median anterior maxillary cysts may be further subclassified as either incisive canal cyst (ICC) or palatine papilla cyst. The latter cyst is uncommon, derived from the incisor papilla soft tissue, and does not manifest itself radiographically. The ICC is thought to arise from remnants of the nasopalatine duct or as a result of degeneration of the contents of the incisive canal.[307] Patients with ICC present with a swelling of the anterior palate behind the central incisors.

Radiographically, ICC appears as a well-defined radiolucency above or between the root apices of the maxillary central incisors, exceeding 0.6 cm, that does not extend into the paranasal sinuses.[307] The cyst may be lined by either squamous or respiratory mucosa and may contain glandular or connective tissue remnants.

The median palatal cyst is an ICC that has extended posteriorly. Clinically, it appears as a midline palatine swelling that may also extend to the nasal floor. Radiographically, it appears as a midline palatal radiolucency. The histology is similar to that of ICC.

Lastly, the nasolabial (also referred to as nasoalveolar) cyst is thought to be derived from the nasolacrimal duct apparatus. Clinically, it appears as a small cystic mass in the upper lip, nasal vestibule, or nasal alae, obliterating the

Copyright © 2003, Mosby, Inc. All rights reserved.

nasolabial fold. Nasolabial cysts are primarily soft-tissue based and therefore are rarely seen on plain films. If large, they may scallop the adjacent bone.

Odontogenic Tumors

Odontogenic tumors arise from the dental apparatus, mimicking the various stages of odontogenesis; ameloblastoma, cementoma, odontoma, and fibromyxoma are the most common of these tumors, which can involve the paranasal sinuses (also see Chapter 17).

Ameloblastoma (Including Unicystic Ameloblastoma)

Ameloblastoma represents only 1% of all pathologic lesions of the jaw and 18% of all odontogenic tumors.[307] Characteristically, this is a slowly growing solid and cystic tumor. Most affected patients are in the third and fourth decades of life. The ratio of mandibular to maxillary tumors is approximately 4:1, and the posterior mandible is the most common site. The majority of maxillary tumors (90%) involve the premolar-molar area. Noncentral ameloblastomas (those arising from peripheral, soft-tissue, nonosseous, or noncentral sites) are not considered in this discussion. An ameloblastoma presents as an enlarging, painless swelling, and large maxillary tumors can cause nasal obstruction. Other signs and symptoms include pain, bleeding, unhealed extraction sites, trismus, and neural involvement.[311, 312]

Radiographically, the ameloblastoma appears as a multiloculated, honeycombed lytic lesion devoid of mineralization. If the tumor extends into the antrum, the sinus will be clouded and the walls remodeled or destroyed. On CT, ameloblastomas have a nonenhancing, nonhomogeneous appearance, and on MR imaging they have nonhomogeneous mixed signal intensities. On T1-weighted images these tumors demonstrate intermediate signal intensity,

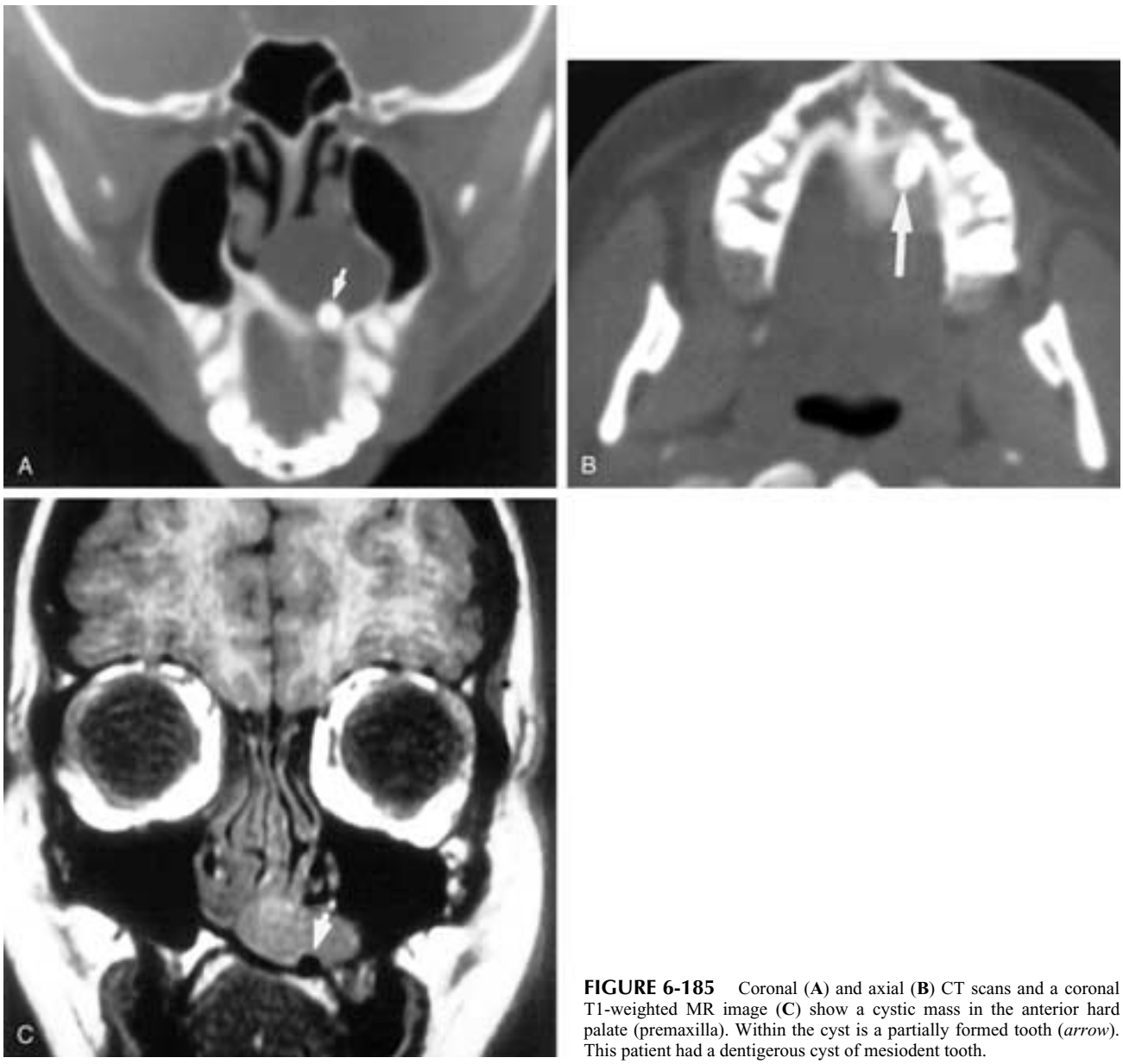

FIGURE 6-185 Coronal (**A**) and axial (**B**) CT scans and a coronal T1-weighted MR image (**C**) show a cystic mass in the anterior hard palate (premaxilla). Within the cyst is a partially formed tooth (*arrow*). This patient had a dentigerous cyst of mesiodent tooth.

VIEW IMAGE

Copyright © 2003, Mosby, Inc. All rights reserved.

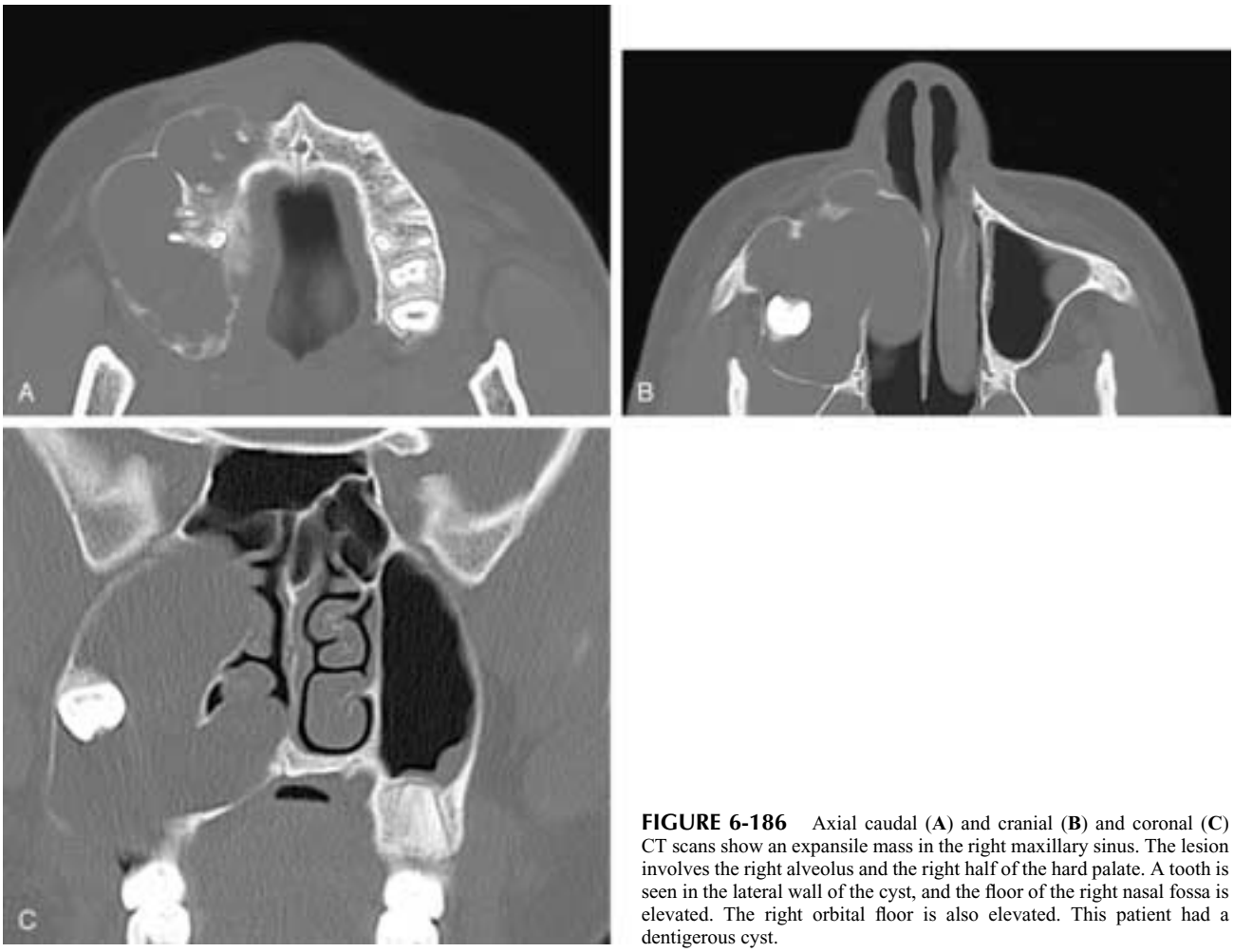

FIGURE 6-186 Axial caudal (**A**) and cranial (**B**) and coronal (**C**) CT scans show an expansile mass in the right maxillary sinus. The lesion involves the right alveolus and the right half of the hard palate. A tooth is seen in the lateral wall of the cyst, and the floor of the right nasal fossa is elevated. The right orbital floor is also elevated. This patient had a dentigerous cyst.

VIEW IMAGE

whereas on T2-weighted studies they have variable intermediate and high signal intensities (Figs. 6-194 and 6-195).

Histologically, the epithelial component is characterized by basaloid cells forming ribbons or lining the perimeter of nests and islands. These islands can contain spindled cells mimicking (and thus called) stellate reticulum. The epithelial component can also contain squamous cells or granular cells. The latter contain lysosomal granules and may represent a degenerative phenomenon.[307] The stromal component of ameloblastoma contains mature fibroblastic and myofibroblastic elements.

The clinical course of ameloblastomas is characterized by slow, destructive growth without metastatic capacity. The tendency toward recurrence is dependent upon tumor site, stage, and primary therapy. A low recurrence rate (15%) can be seen after complete resection with negative margins.[307] Conversely, curettage or enucleation can be associated with a much greater likelihood of local tumor recurrence. Maxillary ameloblastomas are more likely to present with cortical destruction and invasion of soft tissues than mandibular tumors, and hence are inherently more likely to recur after resection. Skull base invasion and intracerebral extension can thus lead to death. There are two rare malignant variants of ameloblastoma: malignant ameloblastoma and ameloblastoma carcinoma. Malignant ameloblas-

FIGURE 6-187 Waters view shows a mass in the lower right antrum that has elevated the inferior mucoperiosteal white line (*arrow*). This indicates that the mass arose in the alveolus below the sinus. This patient had a radicular cyst.

VIEW IMAGE

Copyright © 2003, Mosby, Inc. All rights reserved.

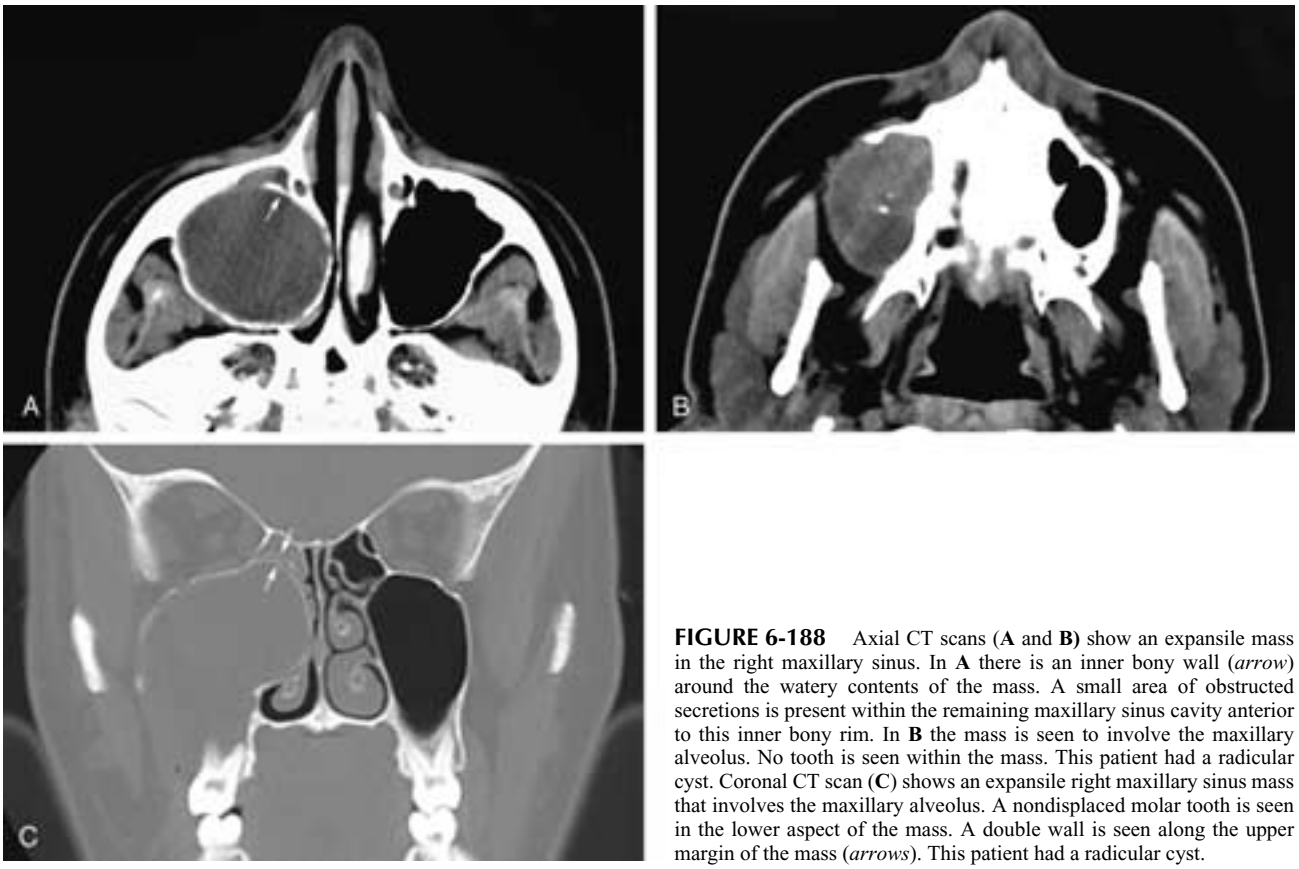

FIGURE 6-188 Axial CT scans (**A** and **B**) show an expansile mass in the right maxillary sinus. In **A** there is an inner bony wall (*arrow*) around the watery contents of the mass. A small area of obstructed secretions is present within the remaining maxillary sinus cavity anterior to this inner bony rim. In **B** the mass is seen to involve the maxillary alveolus. No tooth is seen within the mass. This patient had a radicular cyst. Coronal CT scan (**C**) shows an expansile right maxillary sinus mass that involves the maxillary alveolus. A nondisplaced molar tooth is seen in the lower aspect of the mass. A double wall is seen along the upper margin of the mass (*arrows*). This patient had a radicular cyst.

VIEW IMAGE

toma is histologically benign, yet it metastasizes. This usually occurs after a long history of multiple unsuccessful surgical procedures or after radiation therapy. Most metastases occur in the lungs, pleura, and regional lymph nodes.[312]

Ameloblastic carcinoma is histologically malignant, and the metastases are less differentiated than the primary tumor.

Complete surgical resection is the treatment of choice for all ameloblastomas. Chemotherapy appears to be relatively ineffective against both the primary lesion and the metastases, and most lesions are not radiosensitive.[312]

Unicystic ameloblastoma deserves special mention. It represents 5% to 15% of all intraosseous ameloblastomas and occurs almost exclusively in the mandible.[307] This lesion appears radiologically as a unilocular mandibular cyst.

Histologically, one sees a unilocular simple or plexiform cyst lined by ameloblastomatous tissue (as described above). Unicystic ameloblastomas may be treated more conservatively than typical ameloblastomas, by curettage or enucleation, with a low recurrence rate.

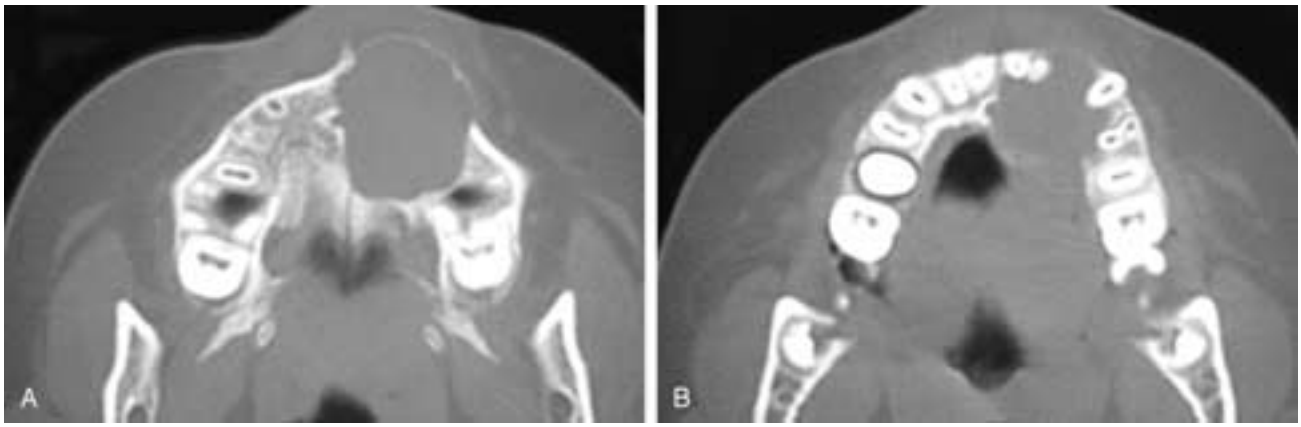

VIEW IMAGE

FIGURE 6-189 Axial CT scans (**A** and **B**) show an expansile cystic mass in the left alveolus and hard palate. The cyst wall is seen in relationship to the left lateral incisor tooth. This patient had a radicular cyst.

Copyright © 2003, Mosby, Inc. All rights reserved.

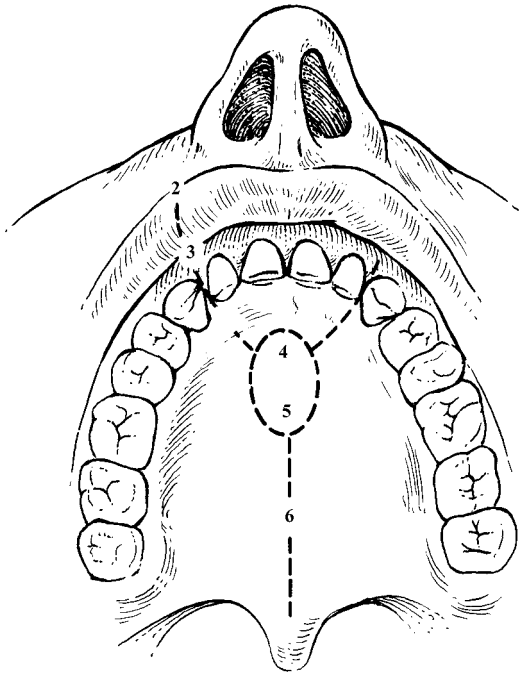

VIEW IMAGE

FIGURE 6-190 Diagram of distribution of fissural cyst. *1,* Nasolabial cyst; *2,* nasoalveolar cyst; *3,* globulomaxillary cyst; *4,* nasopalatine cyst; *5,* cyst of palatine papilla; and *6,* median palatal cyst.

Cementoblastoma

Cementum-producing tumors can be classified as either benign cementoblastoma, gigantiform cementoma, periapical cemental dysplasia (previously discussed), and cemento-ossifying fibroma (previously discussed with fibroosseous jaw lesions). Cementoblastoma (also referred to as cementoma) is an uncommon neoplasm arising from the mesodermal periodontal ligament, which surrounds the tooth roots and contains cells able to produce cementum, bone, and fibrous tissue. Most patients are in their fourth decade of life or younger and present with a mandibular mass in the premolar-molar region. Because cementomas are attached to the tooth roots, tooth innervation can be disrupted and affected teeth can appear nonresponsive to vitality tests.[312]

Radiographically, these lesions appear as single or multiple well-defined radiopaque masses in continuity with the root apices of affected teeth. A zone of lucency, or ''halo,'' surrounds each lesion (Figs. 6-196 to 6-198). The radiographic differential diagnosis is primarily hypercementosis, which refers to the excessive accumulation of cementum along the surface of the involved tooth root(s). Hypercementosis is associated with Paget's disease, periapical inflammation, and elongation of a tooth as a result of the loss of its antagonistic opposing tooth.[312]

Histologically, cementum appears as coalescing trabeculae of eosinophilic matrix with basophilic reversal lines. Numerous active cementoblasts can be seen in cementoblastomas. These tumors have limited growth potential and are usually cured by local excision.

The gigantiform cementoma (familial multiple cementoma, cemento-osseous dysplasia) is a rare lesion characterized by single or multiple nodular, irregular masses ranging from 1 to 10 cm in one or both jaws. Only the alveolar processes are affected, independent of the teeth. Radiographically, one sees expansion of the cortical plates with concomitant simple bone cysts. Serum alkaline phosphatase is not elevated, thus excluding Paget's disease.

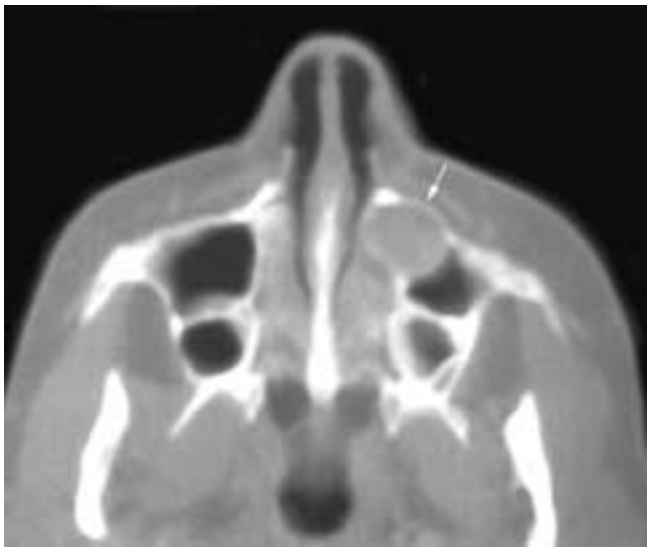

FIGURE 6-191 Axial CT scan shows an expansile soft-tissue mass (*arrow*) in the left anterior maxilla. The caudal aspect of the lesion extends down into the alveolus, separating the canine and lateral incisor teeth. This cyst has a thin rim of bone around its margin. This patient had a globulomaxillary cyst.

VIEW IMAGE

Histologically, one sees solid sheets of acellular cementum and some proliferative areas. Clinically, this is a self-limiting process, and treatment depends on the clinical course. Osteomyelitis is the most common complication.

FIGURE 6-192 Intraoral occlusal film shows a well-demarcated cyst of the palate. This patient had a fissural cyst.

VIEW IMAGE

Copyright © 2003, Mosby, Inc. All rights reserved.

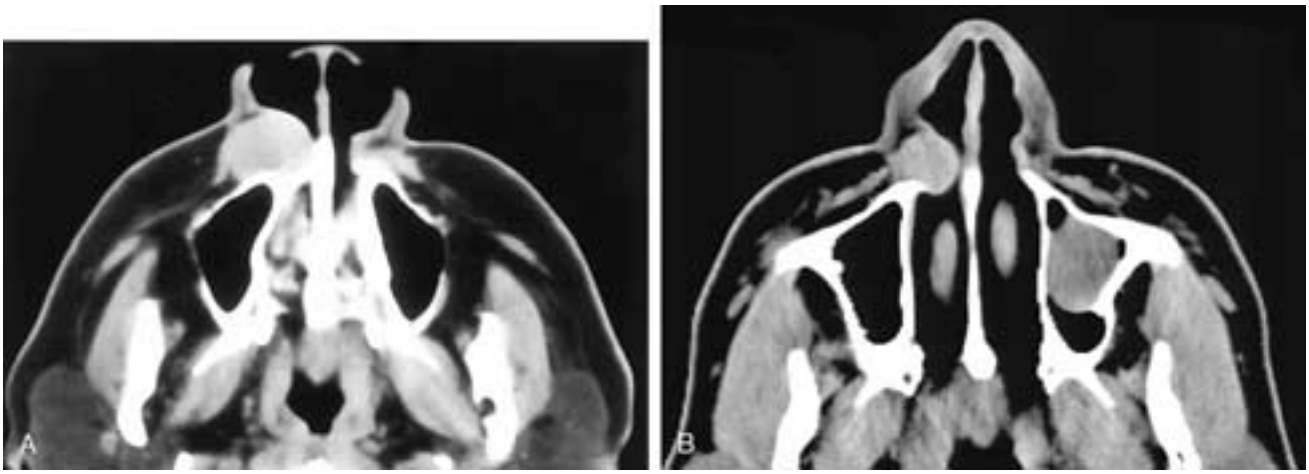

VIEW IMAGE

FIGURE 6-193 Axial CT scan (**A**) shows a soft-tissue density ovoid mass in the soft tissues of the right face deep to the lateral margin of the nose. The adjacent maxillary bone is uninvolved. In **B** a CT scan on another patient shows an ovoid mass in the lateral nostril region anterior to the medial maxilla. The bone is not involved. An incidental retention or polyp is present in the left antrum. Both of these patients had nasoalveolar cysts.

Odontoma

Odontomas are tumors that produce both the epithelial and mesenchymal components of the dental apparatus with complete, mature differentiation. Enamel, dentin, cementum, and pulp production can be seen within these tumors. These lesions usually occur within the second decade of life, affecting both genders equally; 59% occur in the maxilla.[307] Odontomas can be classified as either complex or compound; both occur with equal frequency. The complex odontoma has a haphazard arrangement of the elements. In compound odontomas the elements have a normal, more mature relationship to one another.[313]

Radiographically, the complex odontoma appears as an amorphous radiopacity. The compound odontoma has

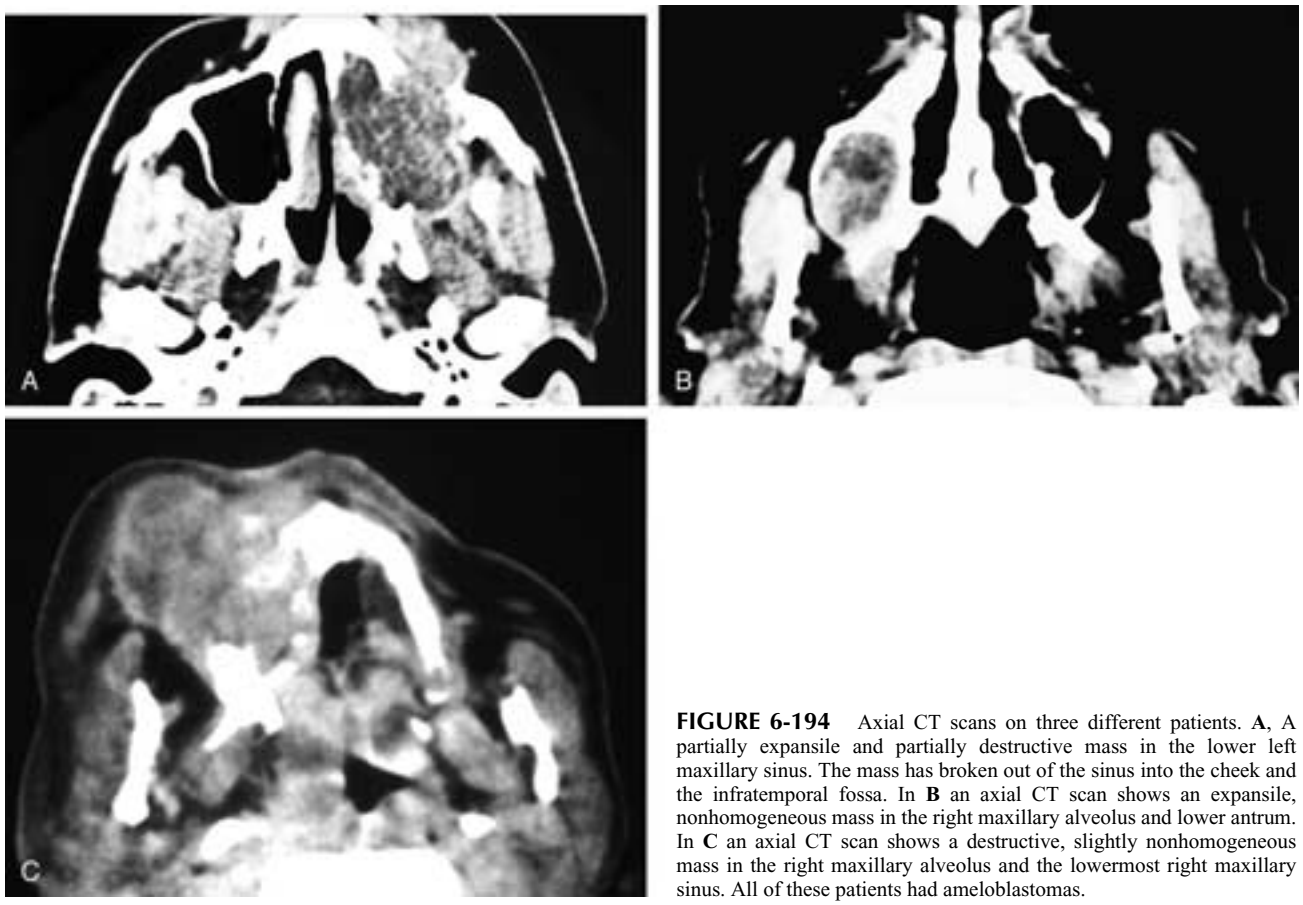

VIEW IMAGE

FIGURE 6-194 Axial CT scans on three different patients. **A**, A partially expansile and partially destructive mass in the lower left maxillary sinus. The mass has broken out of the sinus into the cheek and the infratemporal fossa. In **B** an axial CT scan shows an expansile, nonhomogeneous mass in the right maxillary alveolus and lower antrum. In **C** an axial CT scan shows a destructive, slightly nonhomogeneous mass in the right maxillary alveolus and the lowermost right maxillary sinus. All of these patients had ameloblastomas.

Copyright © 2003, Mosby, Inc. All rights reserved.

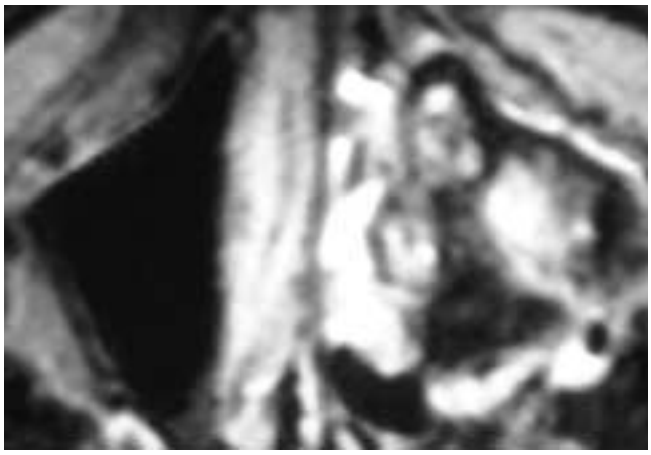

FIGURE 6-195 Axial T2-weighted MR image shows a nonhomogeneous mass in the left maxillary sinus. The lesion has extended into the nasal fossa and the infratemporal fossa. This patient had an ameloblastoma. The imaging appearance is similar to that of a minor salivary gland tumor in this sinus.

anywhere from 3 to 2000 miniature teeth (or denticles), with single roots or no roots (Figs. 6-199 through 6-201). All odontomas are surrounded by a thin, radiolucent halo that represents the fibrous capsule. Radiographically, the differential diagnosis includes prior bone grafting.

Bone grafting to the maxillary floor can be performed for patients who require dental implants but have insufficient native bone to support them (Fig. 6-202). This imaging appearance should not be confused with that of an odontogenic tumor.

FIGURE 6-196 Intraoral occlusal film shows a calcified palatal mass with a surrounding lucent zone (*arrows*). Note the small radiopaque densities surrounding the tooth roots (hypercementosis). This patient had a cementoma.

FIGURE 6-197 Lateral view shows a calcified mass with a surrounding lucent zone in the maxillary alveolus and in the mandible. This patient had two cementomas.

Histologically, complex odontomas contain a disorganized array of dentin, cementum, enamel, and tooth pulp. In compound odontomas, one sees actual attempts at tooth formation. Treatment involves complete surgical excision; recurrences are rare.

Calcifying Epithelial Odontogenic Tumor

The calcifying epithelial odontogenic tumor (Pindborg tumor) is a benign odontogenic neoplasm that constitutes

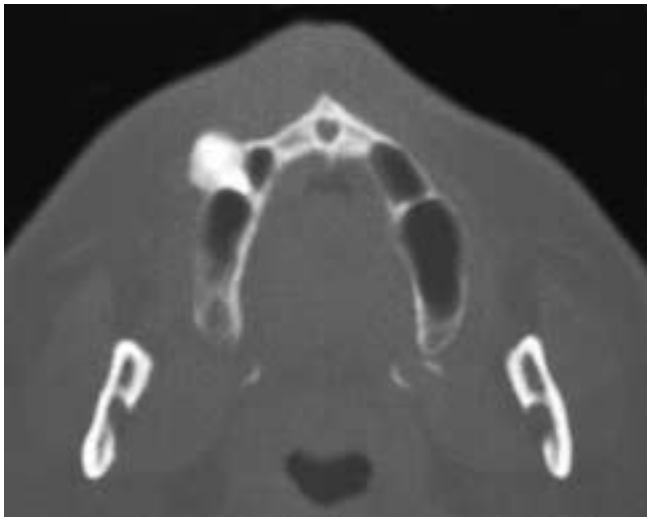

FIGURE 6-198 Axial CT scan shows a dense osseous mass arising in the right maxillary alveolus. The lesion is localized to one area, and the remaining alveolus is normal. This patient had a cementoma.

Copyright © 2003, Mosby, Inc. All rights reserved.

VIEW IMAGE

FIGURE 6-199 Lateral view shows a large, expansile mass in the left maxillary alveolus and antrum. There are innumerable discrete, toothlike densities (denticles). This patient had a compound odontoma.

1% of this class of tumors. It usually occurs in patients in the fourth and fifth decades of life, although it has been reported in patients with an age range of 2 to 82 years.[307] These tumors are equally divided between males and females and occur twice as often in the mandible as in the maxilla. Most often the premolar teeth are affected. Although most tumors are asymptomatic and are discovered incidentally on dental radiographs, they also may cause jaw expansion. Between 35% and 45% of cases are associated with an impacted tooth.[307]

Pathologically, there are sheets of polyhedral or spindle cells, with sharply defined borders and prominent nuclei. The ultrastructure of the spindle cells has characteristics of myoepithelial cells. A capsule is variably present. Calcospherites composed of apatite crystals form laminations (Liesegang's rings) throughout the tumor. A variation of the tumor is a clear cell type, whose cells contain glycogen.[307]

Radiographically, most of these tumors are initially radiolucent, multilocular lesions with indistinct margins. The calcifications generally appear later and may be extensive or may not be seen on plain films, being too small. On CT and MR imaging these tumors are usually partially expansile, bulky maxillary sinus lesions with areas of calcification (Fig. 6-203). The differential diagnosis includes ameloblastoma, odontogenic myxoma, central GCG, follicular cyst, and OKC.

Metastatic renal cell carcinoma may at first be included in the differential diagnosis when there is a prominent clear cell population, but the presence of sheets of epidermoid-appearing cells in the Pindborg tumor helps eliminate this possibility.[307] A malignant variant with the capacity for metastasis has been described. This tumor revealed marked nuclear and cellular hyperchromatism, giant cells, and abnormal mitoses.[307]

Treatment of the Pindborg tumor varies from curettage for small lesions to en bloc resection for larger lesions. If not completely removed, these tumors will recur.

HAMARTOMAS, TERATOMAS, AND TERATOCARCINOMAS

The term *hamartoma* refers to an abnormal, oncologically benign proliferation of indigenous tissues. The sinonasal tract is the most common site for head and neck hamartomas, usually in the area of the nasal septum. Histologically, one sees benign disorganized epithelium, salivary glands, muscle, and cartilaginous and vascular tissues.[314, 315]

An epithelial variant, respiratory epithelial adenomatoid hamartoma, has been reported. Clinically, these neoplasms appear similar to inflammatory polyps, but are more

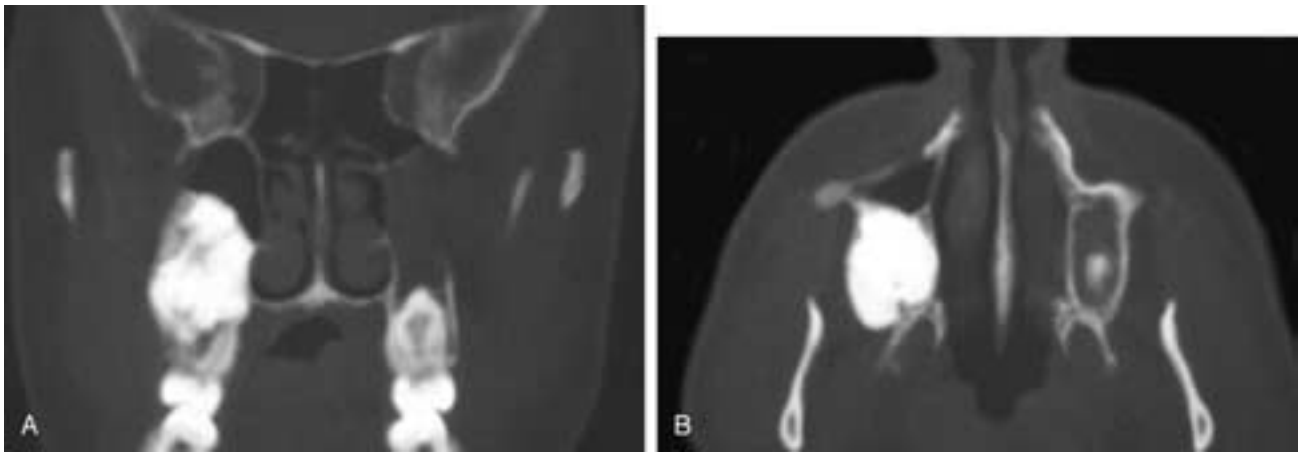

VIEW IMAGE

FIGURE 6-200 Coronal (**A**) and axial (**B**) CT scans show a very dense nodular mass arising from the right maxillary alveolus and extending into the right antrum. This patient had a complex odontoma.

Copyright © 2003, Mosby, Inc. All rights reserved.

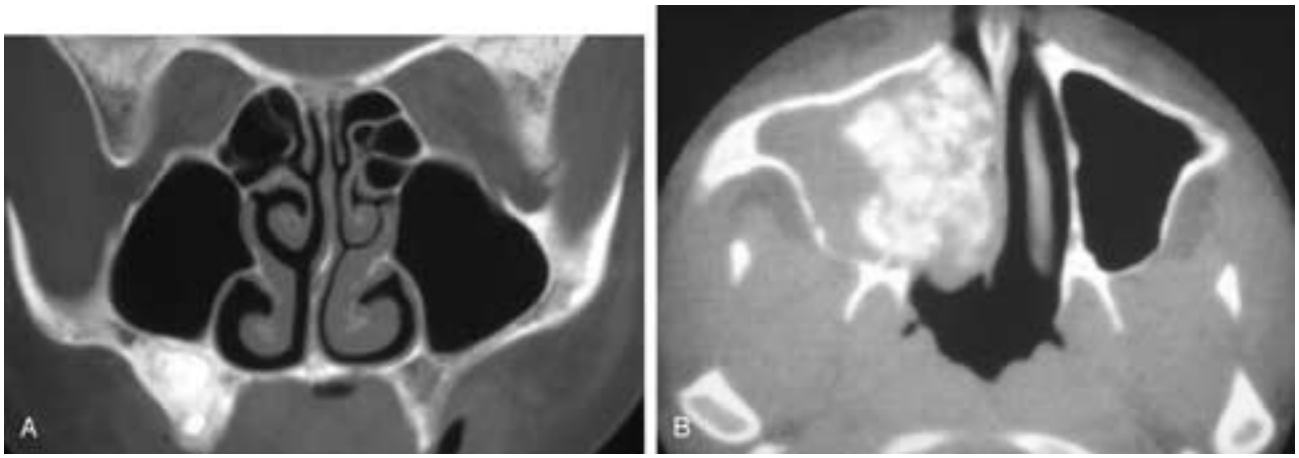

VIEW IMAGE

FIGURE 6-201 Coronal CT scan (**A**) shows a very dense nodular mass in the right maxillary alveolus. Axial CT scan (**B**) on another patient shows a mass in the right maxillary sinus with numerous discrete radiodensities. Obstructed secretions are present laterally in the sinus. Both of these patients had a complex odontoma.

indurated and occur at sites atypical for inflammatory polyps (posterior nasal septum). These differ from conventional sinonasal hamartomas in that there is a prominent glandular proliferation mimicking inverted Schneiderian papillomas or intestinal-type adenocarcinomas.

The term *teratoma* refers to a neoplasm-producing tissue that recapitulates all three germ layers (ectodermal, mesodermal, and endodermal). Teratomas may be histologically mature and oncologically benign, such as a dermoid cyst. A ''hairy polyp'' is essentially a polypoid, epithelium-lined dermoid of the nasopharynx that is seen in the pediatric population. It may be considered a benign teratoma; however, others believe it to be choristomatous since, unlike dermoids, it has limited growth potential.[316] Teratomas may also be histologically immature while being oncologically benign, or they may harbor malignant components and have aggressive biologic potential. As a general rule, pediatric head and neck teratomas tend to be oncologically benign, whereas adult teratomas tend to be histologically and thus oncologically malignant.[317] An epignathus, or ''fetus-in-fetus'' (unequal conjoined twins in which the smaller, incomplete one [the parasite] is attached to the larger twin [the autosite] at the jaw), is an extreme example of a neonatal teratoma originating from the jaw and presenting as a massive, protruding oral neoplasm. Other neonatal teratomas can originate from the soft tissues of the thyroid and cervical region. While these tumors are grotesquely manifest and can cause fatal upper airway obstruction, they are usually oncologically benign. Thus, prenatal surgical intervention can convert an otherwise moribund situation. Sinonasal teratomas (teratocarcinoma, malignant teratoma, teratocarcinosarcoma) have been reported predominantly in the adult population, with a male predominance.[314] The presenting symptoms are those associated with a sinonasal mass. Radiographically and grossly, these tumors are heterogeneous, with solid and cystic components. Histologically, one sees a mixture of immature, benign teratomatous tissue (e.g., epithelial, mesenchymal, differentiated cartilaginous) and a histologically malignant component that is usually carcinomatous but may be of any derivation. Sinonasal teratomas are associated with a high mortality rate, despite multimodality treatment.

METASTATIC DISEASE TO THE SINONASAL CAVITIES

Metastasis from primary tumors below the clavicles to the sinonasal cavities is infrequent. Only about 100 have been reported, the most common of which is metastatic renal cell carcinoma (RCC). Tumors found in the sinonasal cavities precede the diagnosis of the primary tumor in 8% of patients.[13] Next in frequency are tumors of the lung and breast; these are followed considerably less frequently by tumors of the testis, prostate, and gastrointestinal tract.[13, 318, 319] Soft-tissue sinonasal metastasis from esophageal carcinoma, initially mimicking acute sinusitis, has been rarely reported.[320]

The average age of patients with metastatic renal cell tumors to the sinonasal cavities is the sixth decade of life,

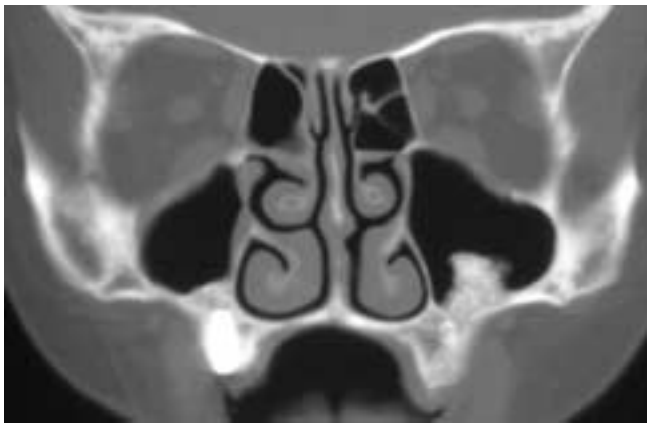

FIGURE 6-202 Coronal CT scan shows a dental implant in the right maxillary alveolus. In the floor of the left antrum, there is a bony prominence that represents transplanted bone placed to support a future left-sided dental implant.

VIEW IMAGE

Copyright © 2003, Mosby, Inc. All rights reserved.

similar to that of patients with breast carcinoma metastases. Bronchogenic and gastrointestinal tract metastases generally appear in the fifth decade of life.

Symptoms of metastases are nonspecific, except for the renal cell lesions, which commonly cause epistaxis.[321] Generally, metastatic neoplasia to the sinonasal tract is associated with a poor prognosis. However, isolated metastatic RCC to the sinonasal tract, in the absence of disease dissemination, may be associated with a good survival after resection.[322, 323]

We have recently seen a patient with histologically confirmed metastatic RCC to the sinonasal tract in the radiologic absence of a primary renal neoplasm. This metastasis presumably occurs with a regressed primary RCC, since spontaneous regression of primary or metastatic RCC can occur as a rare phenomenon (Fig. 6-204).[324, 325]

Squamous and basal cell carcinomas of facial and scalp skin may metastasize to the central skull base, usually along neurogenic pathways. These metastases can occur despite negative specimen margins of the resected primary skin tumor. In these cases, the most accurate prognostic finding is perineural tumor invasion in the primary lesion.[326–328] In rare instances, skin melanomas metastasize to the sinonasal cavities. Along with the metastases from RCCs, these lesions are the most vascular metastases and often manifest with epistaxis.

Thyroid carcinoma metastatic to the paranasal sinuses is rare.[329–334] The patient may have symptoms related to the distant metastasis rather than the primary tumor. Such metastases in differentiated thyroid carcinoma portend a poor prognosis.

A case of an endometrial carcinoma metastatic to the paranasal sinuses has also been reported, as has a rare case of metastatic choriocarcinoma to the nasal cavity from testicular teratoma in a patient who presented with intractable epistaxis.[335, 336]

On CT, metastases from lung, breast, distal genitourinary tract, and gastrointestinal tract tumors are aggressive, bone-destroying soft-tissue masses that enhance minimally, if at all. The metastases are usually indistinguishable from a primary sinonasal SCC. By comparison, metastases from primary RCCs and melanomas are enhancing masses that may remodel the sinonasal walls as well as destroy them. Prostate carcinoma is one of the few primary tumors that may give a purely blastic metastasis to the facial bones and skull. Although a

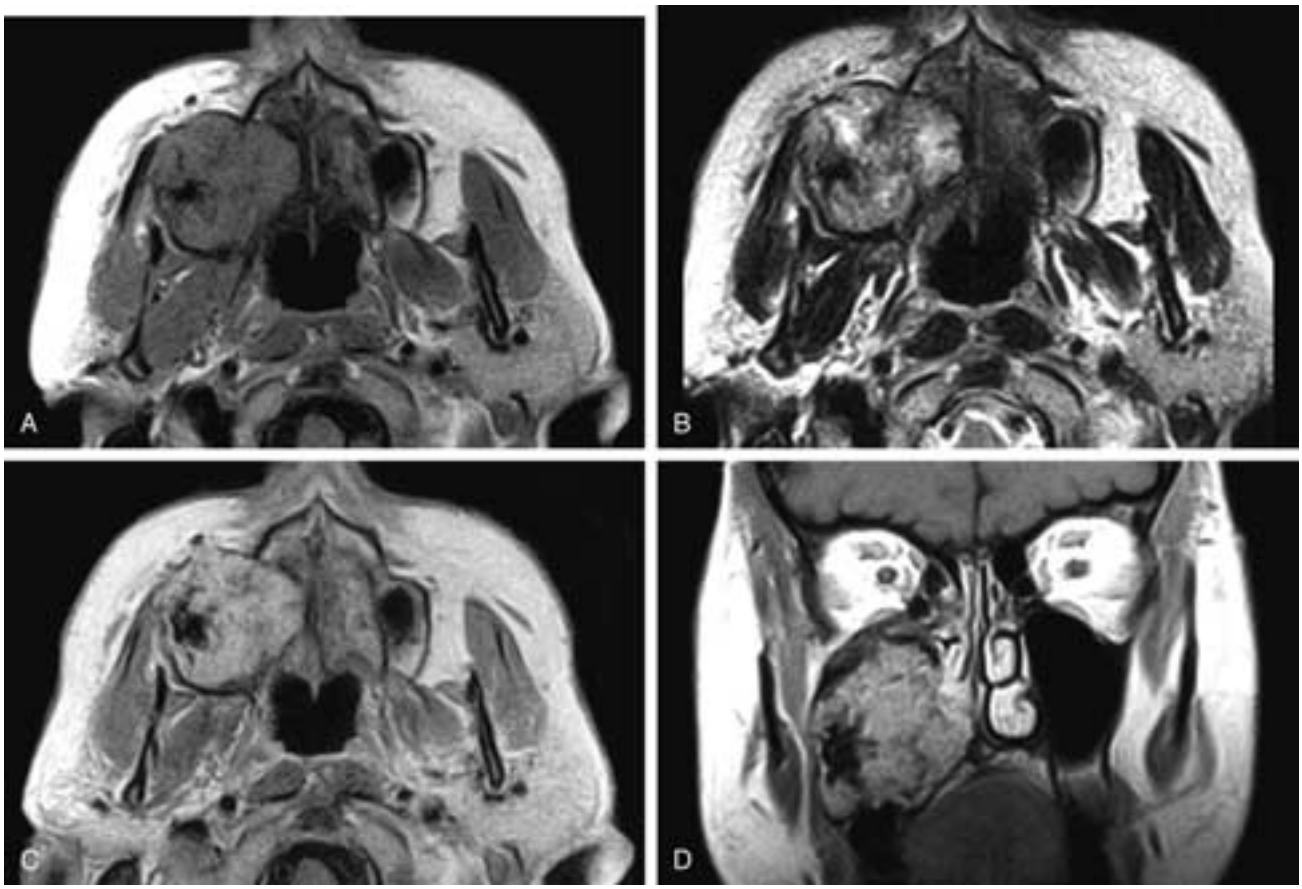

FIGURE 6-203 Axial T1-weighted (**A**), T2-weighted (**B**), and axial (**C**) and coronal (**D**) T1-weighted, contrast-enhanced MR images show a soft tissue mass in the right maxillary sinus with a low T1-weighted signal intensity and a nonhomogeneous T2-weighted signal intensity. The mass enhances slightly. There are areas of signal void within the lower lateral aspect of the mass on all sequences that were calcifications. This patient had a calcifying epithelial odontogenic tumor.

VIEW IMAGE

Copyright © 2003, Mosby, Inc. All rights reserved.

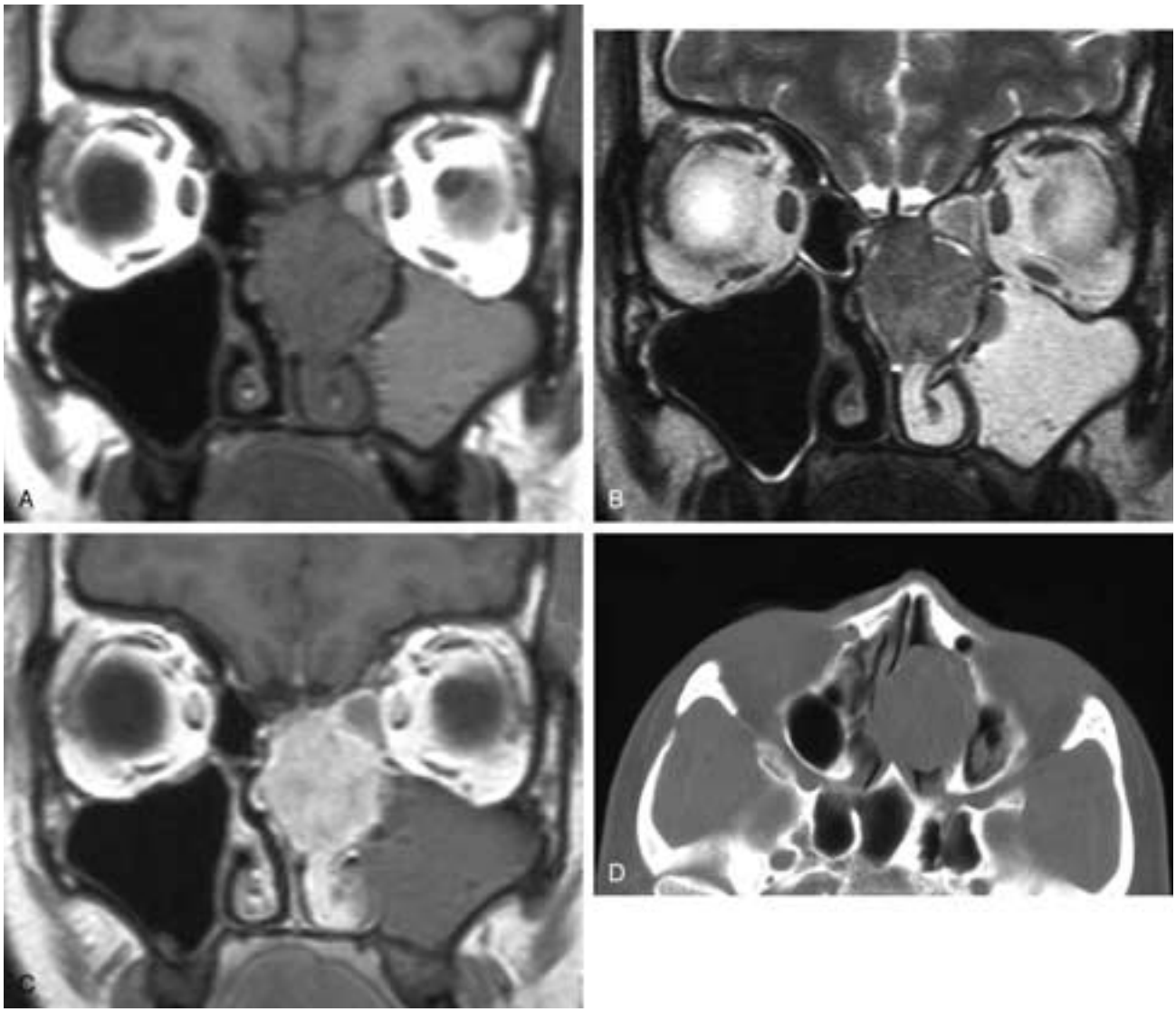

VIEW IMAGE

FIGURE 6-204 Coronal T1-weighted (**A**), T2-weighted (**B**), and T1-weighted, fat-suppressed, contrast-enhanced (**C**) MR images and an axial CT scan (**D**) show a spherical noninvasive mass in the upper left nasal fossa. The mass obstructs the remaining left ethmoid cells and the left maxillary sinus. The mass has a low T1- and T2-weighted signal intensity, and it enhances. The spherical shape suggests that this is either a minor salivary gland tumor or a lesion such as a schwannoma. This was a clear cell tumor metastatic from renal cell carcinoma.

Copyright © 2003, Mosby, Inc. All rights reserved.

FIGURE 6-205 Axial CT scan shows multiple discrete areas of lytic bone destruction (*arrows*). This patient had metastatic lung carcinoma.

VIEW IMAGE

soft-tissue mass may occur, often only a sclerotic, slightly thickened bone with an abnormal, irregular trabecular pattern is seen. On CT this pure bone disease can be overlooked unless wide windows are used to evaluate the bone.

The most important radiographic indication of metastasis is the presence of more than one lesion, particularly because sinonasal tumors usually do not erode multiple areas of bone. Rather, contiguous sites of bone erosion spread from an area of initial involvement. Thus, two areas of bone erosion with intervening normal bone suggest metastatic disease. However, a solitary destructive lesion may always represent a metastasis and the imaging appearance is nonspecific, often overlapping with that of other lesions that arise within the central skull base and sella (Figs. 6-205 to 6-214).

FIGURE 6-206 Axial contrast-enhanced CT scan shows an enhancing mass in the left ethmoid sinuses and nasal cavity and a second mass in the occipital horn. This patient had metastatic melanoma.

VIEW IMAGE

Copyright © 2003, Mosby, Inc. All rights reserved.

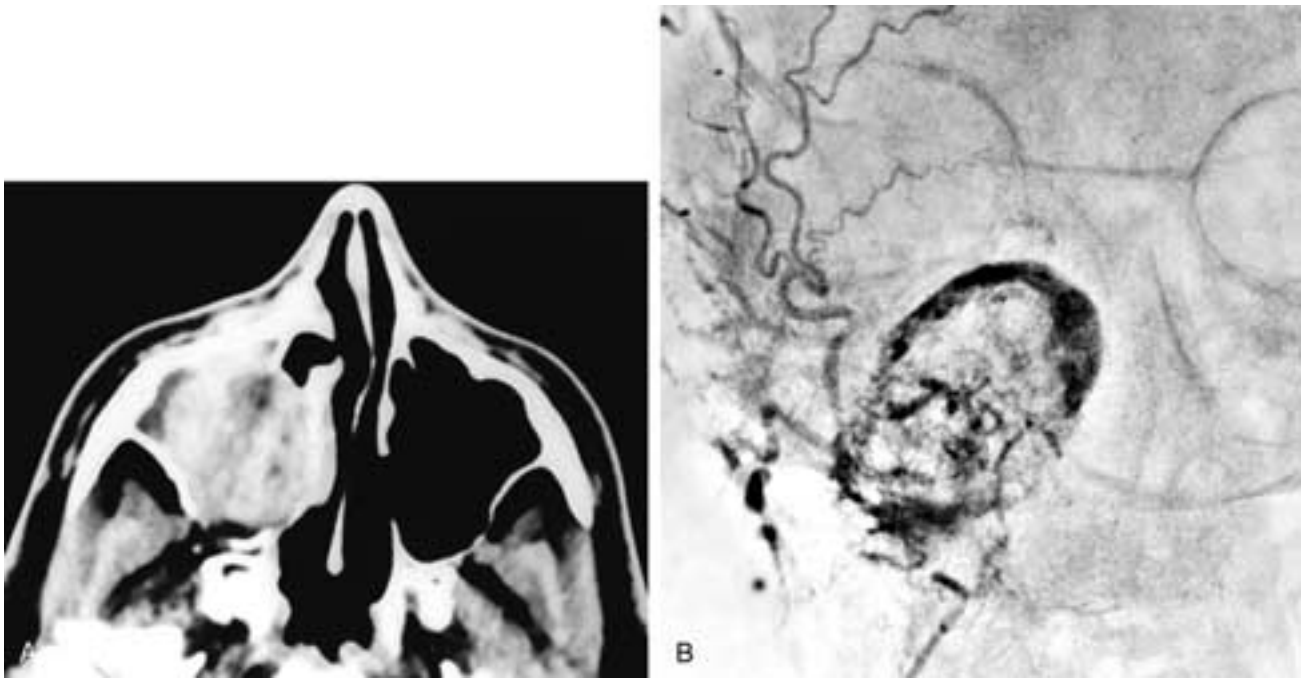

VIEW IMAGE

FIGURE 6-207 Axial contrast-enhanced CT scan (**A**) and coronal subtraction angiogram (**B**) show an expansile enhancing and vascular mass in the right maxillary sinus. This patient had metastatic hypernephroma.

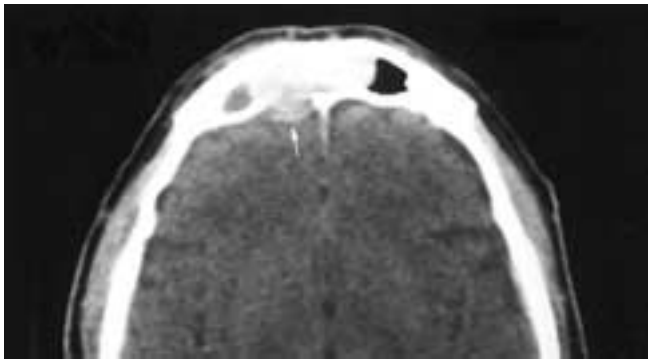

VIEW IMAGE

FIGURE 6-208 Axial contrast CT scan shows an enhancing frontal sinus mass that has eroded the posterior sinus table (*arrow*). This patient had metastatic hypernephroma.

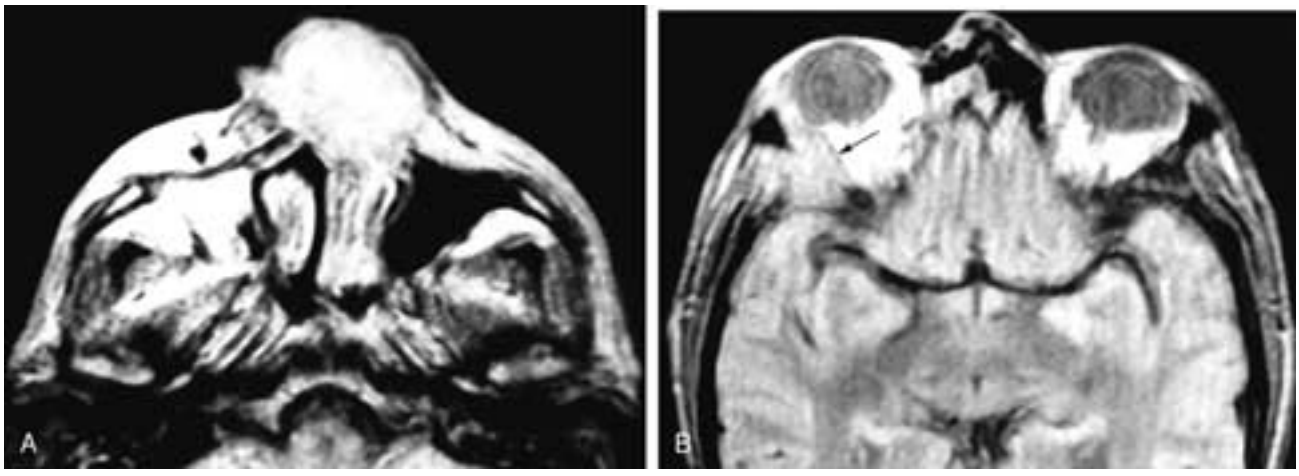

VIEW IMAGE

FIGURE 6-209 Axial proton density MR images through the level of the lower nasal fossa (**A**) and the orbits (**B**) show two distinct masses: one in the nose and one in the right lateral orbital wall (*arrow*). Both masses are homogeneous and of an intermediate to high signal intensity. This patient had metastatic lung carcinoma.

Copyright © 2003, Mosby, Inc. All rights reserved.

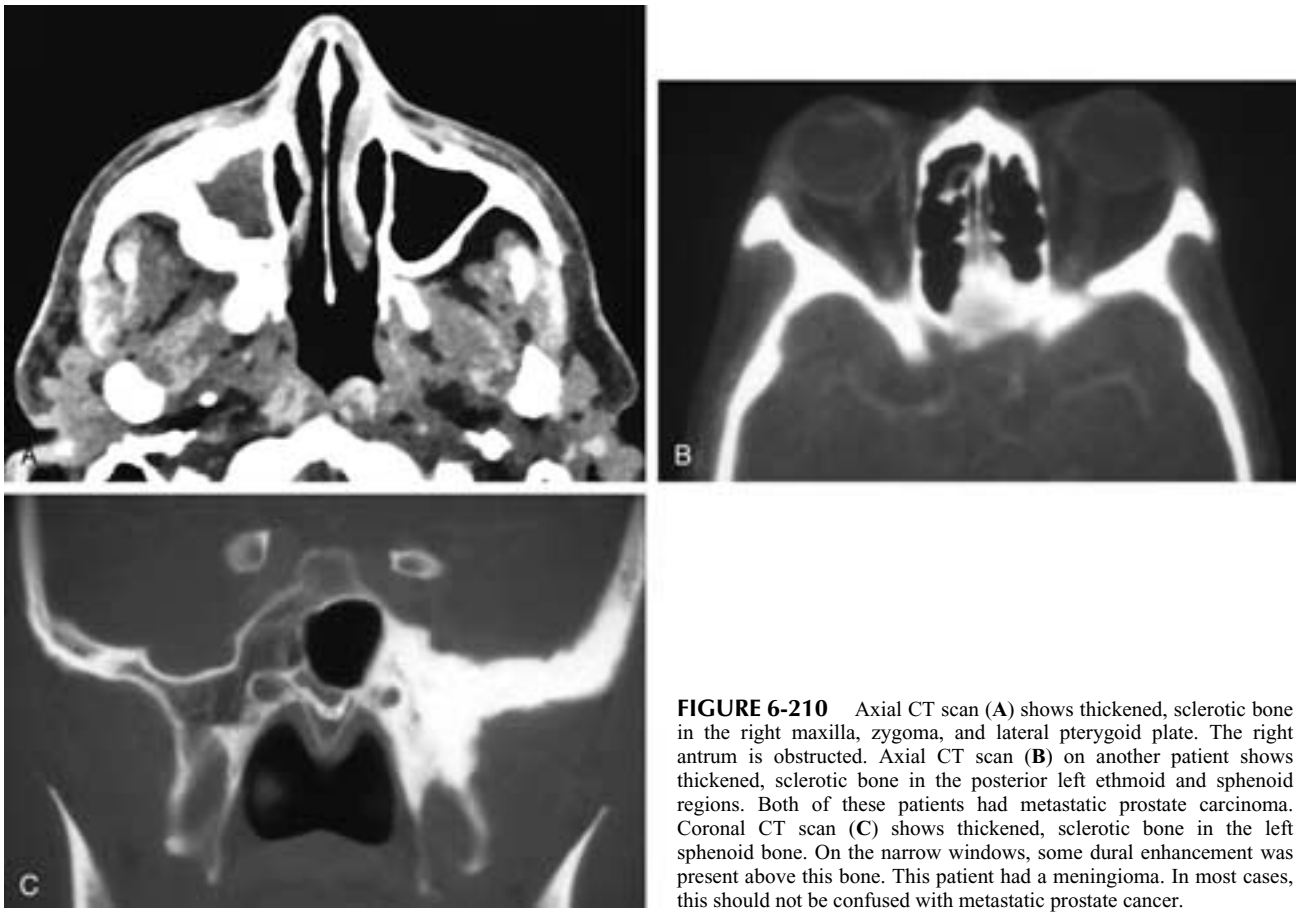

FIGURE 6-210 Axial CT scan (**A**) shows thickened, sclerotic bone in the right maxilla, zygoma, and lateral pterygoid plate. The right antrum is obstructed. Axial CT scan (**B**) on another patient shows thickened, sclerotic bone in the posterior left ethmoid and sphenoid regions. Both of these patients had metastatic prostate carcinoma. Coronal CT scan (**C**) shows thickened, sclerotic bone in the left sphenoid bone. On the narrow windows, some dural enhancement was present above this bone. This patient had a meningioma. In most cases, this should not be confused with metastatic prostate cancer.

VIEW IMAGE

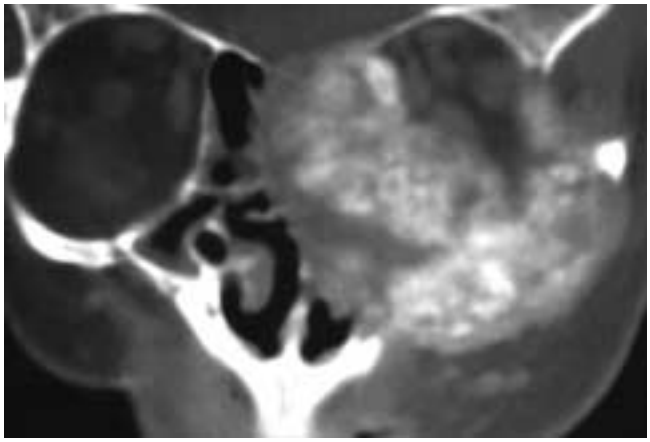

FIGURE 6-211 Coronal CT scan shows diffuse, irregular tumoral calcifications in the left face invading the ethmoid, anterior cranial fossa floor, nasal fossa, orbit, maxillary sinus, and cheek. This patient had metastatic sarcoma with calcium deposition.

VIEW IMAGE

Copyright © 2003, Mosby, Inc. All rights reserved.

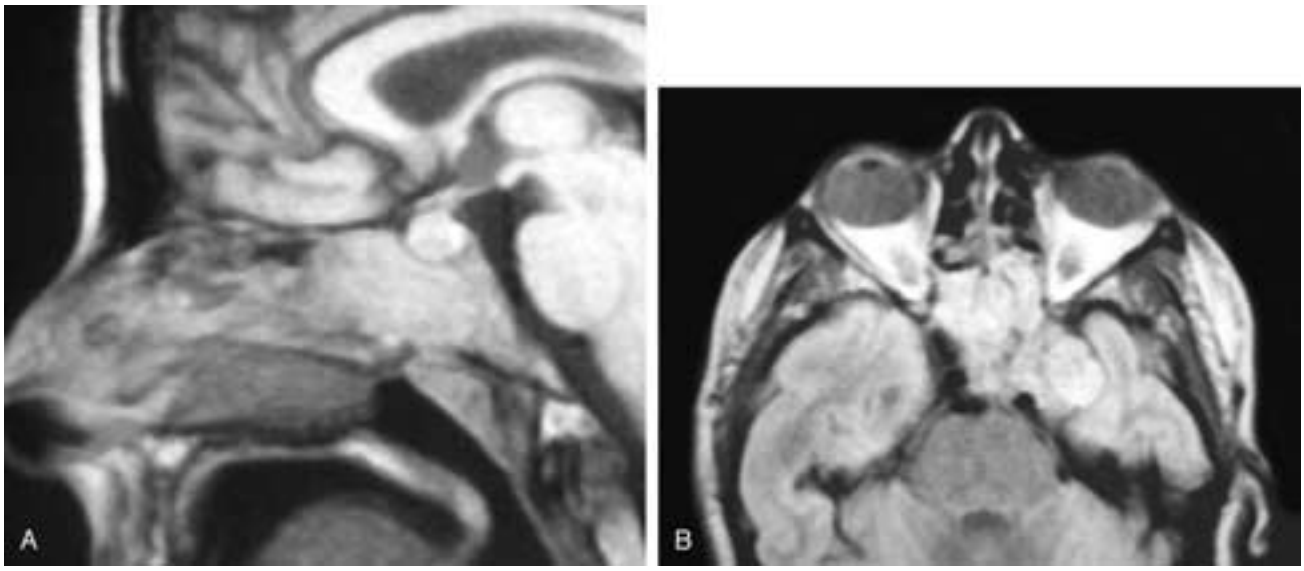

VIEW IMAGE

FIGURE 6-212 Sagittal (**A**) and axial (**B**) T1-weighted MR images show an intermediate signal intensity mass in the sphenoid sinus and clivus with invasion of the left temporal lobe. This patient had a rare metastatic pheochromocytoma.

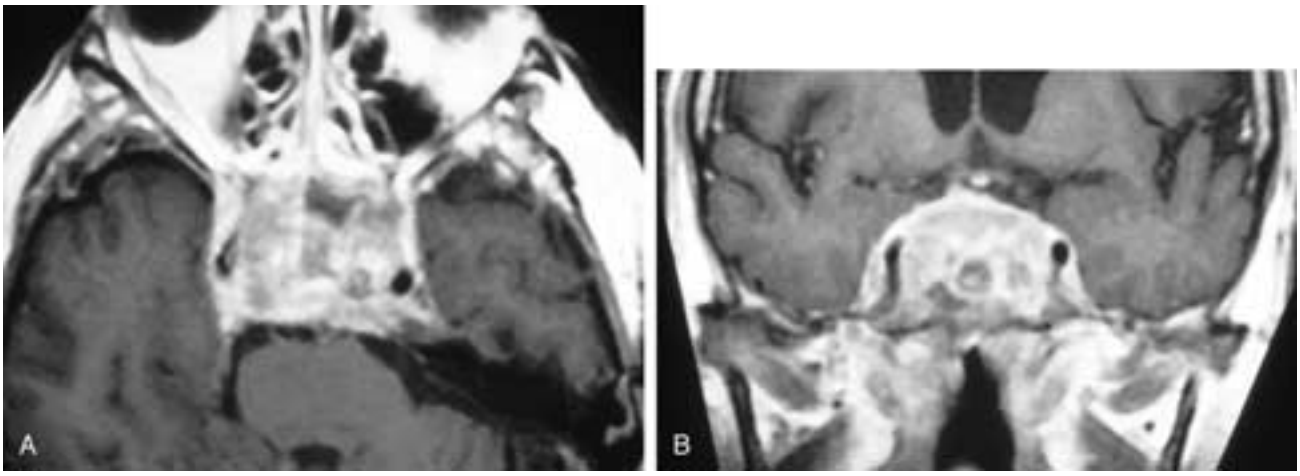

VIEW IMAGE

FIGURE 6-213 Axial (**A**) and coronal (**B**) T1-weighted, fat-suppressed, contrast-enhanced MR images show an enhancing mass in the sphenoid sinus, sella turcica, and both cavernous sinuses. This patient had metastatic prostate carcinoma.

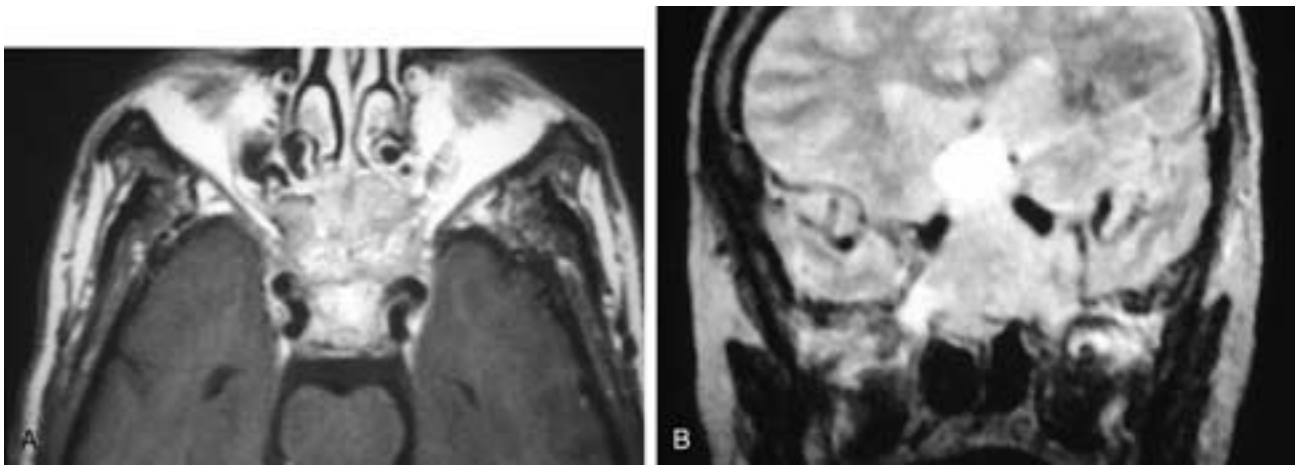

VIEW IMAGE

FIGURE 6-214 Axial (**A**) and coronal (**B**) T1-weighted, fat-suppressed, contrast-enhanced MR images show an enhancing mass in the sphenoid sinus extending into both cavernous sinuses and into the suprasellar region. This patient had an aggressive pituitary adenoma.

Copyright © 2003, Mosby, Inc. All rights reserved.

REFERENCES

1. Batsakis J, ed. Tumor of the Head and Neck: Clinical and Pathological Considerations. 2nd ed. Baltimore: Williams and Wilkins, 1979;177–187.
2. Muir C, Weland L. Upper aerodigestive tract cancers. Cancer (Suppl) 1995;75:147–153.
3. Harrison D. The management of malignant tumors of the nasal sinuses. Otolaryngol Clin North Am 1971;4:159–177.
4. Harrison D. Problems in surgical management of neoplasms arising in the paranasal sinuses. J Laryngol 1976;90:69–74.
5. Jeans W, Gilani S, Bullimore J. The effect of CT scanning on staging of tumours of the paranasal sinuses. Clin Radiol 1982;33:173–179.
6. Nishijima W, Takooda S, Tokita N, et al. Analysis of distant metastases in squamous cell carcinoma of the head and neck and lesions above the clavicles at autopsy. Arch Otolaryngol Head Neck Surg 1993;119:65–68.
7. Elkeslassy A, Meder JF, Lafitte F, Rezeai K, Fredy D. [Imaging of non-osseous malignant tumors of the anterior skull base. Preoperative evaluation]. Neurochirurgie 1997;43:68–75.
8. Lloyd G, Lund V, Phelps PD, et al. Magnetic resonance imaging in the evaluation of nose and paranasal sinus disease. Br J Radiol 1987;60:957–968.
9. Som P, Shapiro M, Biller H, Sasaki C, Lawson W. Sinonasal tumors and inflammatory tissues: differentiation with MR imaging. Radiology 1988;167:803–808.
10. Dubois P, Schultz J, Perrin R, Dastur K. Tomography in expansile lesions of the nasal and paranasal sinuses. Radiology 1977;125:149–158.
11. Som P, Shugar J. The significance of bone expansion associated with the diagnosis of malignant tumors of the paranasal sinuses. Radiology 1980;136:97–100.
12. Som P, Shugar J. When to question the diagnosis of anaplastic carcinoma. Mt Sinai J Med 1981;48:230–235.
13. Barnes L, Verbin R, Gnepp D. Diseases of the nose, paranasal sinuses and nasopharynx. In: Barnes L, ed. Surgical Pathology of the Head and Neck. Vol 1. New York: Marcel Dekker, 1985;403–451.
14. Hyams V. Papillomas of the nasal cavity and paranasal sinuses: a clinicopathologic study of 315 cases. Ann Otol Rhinol Laryngol 1971;80:192–206.
15. Lasser A, Rothfeld P, Shapiro R. Epithelial papilloma and squamous cell carcinoma of the nasal cavity and paranasal sinuses: a clinicopathologic study. Cancer 1976;38:2503–2510.
16. Vrabec D. The inverted schneiderian papilloma: a clinical and pathological study. Laryngoscope 1975;85:186–220.
17. Brandwein M, Steinberg B, Thung S. HPV 6/11 and 16/18 in Schneiderian inverted papillomas. Cancer 1989;63:1708–1713.
18. McLachlin C, Kandel R, Colgan T. Prevalence of HPV in sinonasal papillomas. A study using PCR and in-situ hybridization. Mod Pathol 1992;5:406–409.
19. Norris H. Papillary lesions of the nasal cavity and paranasal sinuses. I Exophytic (squamous) papillomas: a study of 28 cases. Laryngoscope 1962;72:1784–1797.
20. Shohet JA, Duncavage JA. Management of the frontal sinus with inverted papilloma. Otolaryngol Head Neck Surg 1996;114:649–652.
21. Lund V, LLoyd G. Radiological changes associated with inverted papillomas of the nose and paranasal sinuses. Br J Radiol 1984;57:455–461.
22. Sukenik M, Casiano R. Endoscopic medial maxillectomy for inverted papillomas of the paranasal sinuses: value of the intraoperative examination. Laryngoscope 2000;110:39–42.
23. Momose K, Weber A, Goodman M. Radiological aspects on inverted papilloma. Radiology 1980;134:73–79.
24. Yousem D, Fellows S, Kennedy D, et al. Inverted papilloma: evaluation with MR imaging. Radiology 1992;185:501–505.
25. Woodruff W, Vrabec D. Inverted papilloma of the nasal vault and paranasal sinuses: spectrum of CT findings. AJR 1994;162:419–423.
26. Som P, Lidov M. The significance of sinonasal radiodensities: ossification, calcification, or residual bone? AJNR 1994;15:917–922.
27. Dammann F, Pereira P, Laniado M, et al. Inverted papilloma of the nasal cavity and the paranasal sinuses: using CT for primary diagnosis and follow-up. AJR 1999;172:543–548.
28. Slootweg P, Richardson M. Squamous cell carcinoma of the upper aerodigestive system. In: Gnepp D, ed. Diagnostic Surgical Pathology of the Head and Neck. Philadelphia: WB Saunders, 2001;19–78.
29. Barton R. Nickel carcinogenesis of the respiratory tract. J Otolaryngol 1977;6:412–422.
30. Perzin K, Lefkowitch J, Hui R. Bilateral nasal squamous carcinoma arising in papillomatosis: report of a case developing after chemotherapy for leukemia. Cancer 1981;48:2375–2382.
31. Weimert T, Batsakis J, Rice D. Carcinoma of the nasal septum. J Laryngol Otol 1978;92:209–213.
32. Baredes S, Cho H, Som M. Total maxillectomy. In: Blitzer A, Lawson W, Friedman W, eds. Surgery of the Paranasal Sinuses. Philadelphia: WB Saunders, 1985;204–216.
33. Harrison D. Critical look at the classification of maxillary sinus carcinoma. Ann Otol 1978;87:3–9.
34. Fleming I, Cooper J, Henson D, et al. American Joint Committee on Cancer Staging Manual. 5th ed. Philadelphia: Lippincott Raven, 1997.
35. Chaudhry A, Gorlin R, Mosser D. Carcinoma of the antrum: a clinical and histopathologic study. Oral Surg Oral Med Oral Pathol 1960;13:269–281.
36. Larsson L, Martensson G. Maxillary antral cancers. JAMA 1972;219:342–345.
37. Som M. Surgical management of carcinomas of the maxilla. Arch Otolaryngol 1974;99:270–273.
38. St. Pierre S, Baker S. Squamous cell carcinoma of the maxillary sinus: analysis of 66 cases. Head Neck Surg 1983;5:508–513.
39. Chowdhury AD, Ijaz T, el-Sayed S. Frontal sinus carcinoma: a case report and review of the literature. Australas Radiol 1997;41:380–382.
40. Kocak A, Erten SF, Mizrak B, et al. Unusual presentation of a sinonasal carcinoma mimicking an aneurysm rupture. Childs Nerv Syst 1998;14:338–342.
41. Ogura J, Schenck N. Unusual nasal tumors: problems in diagnosis and treatment. Otolaryngol Clin North Am 1973;6:813–837.
42. Conley J, ed. Concepts in Head and Neck Surgery. Stuttgart: Georg Thieme Verlag, 1970.
43. Phillips CD, Futterer SF, Lipper MH, Levine PA. Sinonasal undifferentiated carcinoma: CT and MR imaging of an uncommon neoplasm of the nasal cavity. Radiology 1997;202:477–480.
44. Som PM, Silvers AR, Catalano PJ, et al. Adenosquamous carcinoma of the facial bones, skull base, and calvaria: CT and MR manifestations. AJNR 1997;18:173–175.
45. Acheson E, Gowdell R, Jolles B. Nasal cancer in the Northamptonshire boot and shoe industry. Br Med J 1970;1:385–393.
46. Hadfield E. A study of adenocarcinoma of the paranasal sinuses in woodworkers in the furniture industry. Ann R Coll Surg Engl 1970;46:301–319.
47. Franquemont D, Fechner R, Mills S. Histologic classification of sinonasal intestinal-type adenocarcinoma. Am J Surg Pathol 1991;15:368–375.
48. Barnes L. Intestinal-type adenocarcinoma of nasal cavity and paranasal sinuses. Am J Surg Pathol 1986;10:192–202.
49. Batsakis J, ed. Tumor of the Head and Neck: Clinical and Pathological Considerations. 2nd ed. Baltimore: Williams and Wilkins, 1979;76–99.
50. Klintenberg C, Olofsson J, Hellquist H, et al. Adenocarcinoma of the ethmoid sinuses: a review of 38 cases with special reference to wood dust exposure. Cancer 1984;31:482–488.
51. Spiro R, Koss L, Hajdu S, et al. Tumors of minor salivary origin: a clinicopathologic study of 492 cases. Cancer 1973;31:117–129.
52. Yamamoto Y, Saka T, Makimoto K, et al. Histological changes during progression of adenoid cystic carcinoma. J Laryngol Otol 1992;106:1016–1020.
53. Goepfert H, Luna MA, Lindberg RD, White AK. Malignant salivary gland tumors of the paranasal sinuses and nasal cavity. Arch Otolaryngol 1983;109:662–668.
54. Tran L, Sidrys J, Horton D, et al. Malignant salivary gland tumors of the paranasal sinuses and nasal cavity. The UCLA experience. Am J Clin Oncol 1989;12:387–392.
55. Conley J, Dingman D. Adenoid cystic carcinoma in the head and neck (cylindroma). Arch Otolaryngol 1974;100:81–90.
56. Compagno J, Wong R. Intranasal mixed tumors (pleomorphic adenomas): a clinicopathologic study of 40 cases. Am J Clin Pathol 1977;68:213–218.
57. Suzuki K, Moribe K, Baba S. A rare case of pleomorphic adenoma of nasal cavity in Japan. Nippon Jibiinkoka Gakkai Kaiho 1990;93:740–745.
58. Freeman S, Kennedy K, Parker G, et al. Metastasizing pleomorphic adenoma of the nasal septum. Arch Otolaryngol Head Neck Surg 1990;116:1331–1333.

Copyright © 2003, Mosby, Inc. All rights reserved.

59. Sigal R, Monnet O, de Baere T, et al. Adenoid cystic carcinoma of the head and neck: evaluation with MR imaging and clinical-pathologic correlation in 27 patients. Radiology 1992;184:95–101.
60. Jin XL, Ding CN, Chu Q. Epithelial-myoepithelial carcinoma arising in the nasal cavity: a case report and review of literature. Pathology 1999;31:148–151.
61. Alarcos A, Matesanz A, Alarcos E. A glomus tumor of the nasal fossa and ethmoid sinus. Acta Otorrinolaringol 1992;34:291–295.
62. Staehler H. Paraganglioma of the nasal cavity. Laryngol Rhinol Otol 1985;64:399–402.
63. Sharma HS, Madhavan M, Othman NH, et al. Malignant paraganglioma of frontoethmoidal region. Auris Nasus Larynx 1999;26:487–493.
64. Shimono T, Hayakawa K, Yamaoka T, et al. Case report: glomus tumour of the nasal cavity and paranasal sinuses. Neuroradiology 1998;40:527–529.
65. Barnes L, Verbin R, Gnepp D. Diseases of the nose, paranasal sinuses and nasopharynx. In: Barnes L, ed. Surgical Pathology of the Head and Neck. Vol 1. New York: Marcel Dekker, 1985;659–724.
66. Elkon D, Hightower S, Lim M, et al. Esthesioneuroblastoma. Cancer 1979;44:1087–1094.
67. Kadish S, Goodman M, Wine C. Olfactory neuroblastoma: a clinical analysis of 17 cases. Cancer 1976;37:1571–1576.
68. Miyamoto R, Gleich L, Biddinger P, Gluckman J. Esthesioneuroblastoma and sinonasal undifferentiated carcinoma: impact of histological grading and clinical staging on survival and prognosis. Laryngoscope 2000;110:1262–1265.
69. Som P, Lawson W, Biller H, et al. Ethmoid sinus disease: CT evaluation in 400 cases. Part III: Cranio-facial resection. Radiology 1986 Jun; 159(3):605–609.
70. Morita A, Ebersold M, Olsen K. Esthesioneuroblastoma: prognosis and management. Neurosurgery 1993;32:706–715.
71. Levine P, Gallagher R, Cantrell R. Esthesioneuroblastoma: reflections of a 21-year experience. Laryngoscope 1999;109:1539–1543.
72. Dulgurov P, Calcaterra T. Esthesioneuroblastoma: the UCLA experience 1970–1990. Laryngoscope 1992;102:843–849.
73. Mack E, Prados M, Wilson C. Late manifestations of esthesioneuroblastoma in the central nervous system: report of two cases. Neurosurgery 1992;30:93–97.
74. Regenbogen V, Zinreich S, Kim K. Hyperostotic esthesioneuroblastoma: CT and MR findings. JCAT 1988;12:52–56.
75. Derdeyn C, Moran C, Wippold FI. MRI of esthesioneuroblastoma. JCAT 1994;18:16–21.
76. Som P, Lidov M, Brandwein M, et al. Sinonasal esthesioneuroblastoma with intracranial extension: marginal tumor cysts as a diagnostic MR finding. AJNR 1994;15:1259–1262.
77. Silva E, Butler J, MacKay B, Goepfert H. Neuroblastomas and neuroendocrine carcinomas of the nasal cavity: a proposed new classification. Cancer 1982;50:2388–2405.
78. Frierson H, Mills S, Fechner R, et al. Sinonasal undifferentiated carcinoma: an aggressive neoplasm derived from Schneiderian epithelium and distinct from olfactory neuroblastoma. Am J Pathol 1986;10:771–779.
79. Gallo O, Graziana P, Fini-Storchi O. Undifferentiated carcinoma of the nose and paranasal sinuses: an immunohistochemical and clinical study. ENT J 1993;72:588–595.
80. Freedman H, DeSanto L, Devine K, et al. Malignant melanoma of the nasal cavity and paranasal sinuses. Arch Otolaryngol 1973;97:322–325.
81. Batskis J, Sciubba J. Pathology. In: Blitzer A, Lawson W, Friedman W, eds. Surgery of the Paranasal Sinuses. Philadelphia: WB Saunders, 1985;74–113.
82. Brandwein M, Rothstein A, Lawson W, et al. Sinonasal melanoma—a clinicopathologic study of 25 cases and literature meta-analysis. Arch Otolaryngol Head Neck Surg 1997;123:290–296.
83. Welkosky H, Sorger K, Knuth A, et al. Malignant melanoma of the mucus sinuses of the upper aerodigestive tract. Clinical, histological and immunohistological characteristics. Laryngorhinootologie 1991; 70:302–306.
84. Franquemont D, Mills S. Sinonasal malignant melanoma: a clinicopathologic and immunohistological study of 14 cases. Am J Clin Pathol 1991;96:689–697.
85. Jayaraj SM, Hern JD, Mochloulis G, Porter GC. Malignant melanoma arising in the frontal sinuses. J Laryngol Otol 1997;111:376–378.
86. Stowens D, Lin T. Melanotic progonoma of the brain. Hum Pathol 1974;5:105–113.
87. Kapadia S, Frisman D, Hitchcock C, et al. Melanotic neuroectodermal tumor of infancy. Clinicopathological, immunohistochemical, and flow cytometric study. Am J Surg Pathol 1993;17:566–573.
88. Huvos AG, ed. Bone Tumors: Diagnosis, Treatment, and Prognosis. 2nd ed. Philadelphia: WB Saunders, 1991;525.
89. Kapadia S. Tumor and tumor-like lesions of the soft tissue. In: Barnes L, ed. Surgical Pathology of the Head and Neck. Vol 2. 2nd ed. New York: Marcel Dekker, 2000;787–888.
90. Howard D, Daniels H. Ewing's sarcoma of the nose. Ear Nose Throat J 1993;72:277–279.
91. Lane S, Ironside J. Extra-skeletal Ewing's sarcoma of the nasal fossa. J Laryngol Otol 1990;104:570–573.
92. Klein E, Anzil A, Mezzacappa P, et al. Sinonasal primitive neuroectodermal tumor arising in a long-term survivor of heritable unilateral retinoblastoma. Cancer 1992;70:423–431.
93. Saw D, Chan J, Jagirdar J. Sinonasal small cell neoplasm developing after radiation therapy for retinoblastoma: an immunohistologic, ultrastructural and cytogenetic study. Hum Pathol 1992;23:896–899.
94. Klein E, Anzil A, Mezzacappa P. Sinonasal primitive neuroectodermal tumor arising in a long-term survivor of heritable unilateral retinoblastoma. Cancer 1992;70:423–431.
95. Chowdry K, Manoukian J, Rochon L. Extracranial primitive neuroectodermal tumor of the head and neck. Arch Otolaryngol Head Neck Surg 1990;116:475–478.
96. Schmidt D, Herrmann C, Jurgens H. Malignant peripheral neuroectodermal tumor and its necessary distinction from Ewing's sarcoma. A report from Kiel Pediatric Tumor Registry. Cancer 1991;68:2251–2259.
97. Hillstrom R, Zarbo R, Jacobs J. Nerve sheath tumors of the paranasal sinuses: electron microscopy and histopathologic diagnosis. Otolaryngol Head Neck Surg 1990;102:257–263.
98. Donnelly M, Saler M, Blayney A. Neurogenic sarcoma of the sinonasal tract. J Laryngol Otol 1992;105:186–190.
99. Som P, Biller H, Lawson W. An approach to parapharyngeal space masses: an updated protocol based upon 104 cases. Radiology 1984;153:149–156.
100. Sharma R, Tyagi I, Banerjee D, Pandey R. Nasoethmoid schwannoma with intracranial extension. Case report and review of literature. Neurosurg Rev 1998;21:58–61.
101. Fujiyoshi F, Kajiya Y, Nakajo M. CT and MR imaging of nasoethmoid schwannoma with intracranial extension [letter]. AJR 1997;169:1754–1755.
102. Hunt J, Pugh D. Skeletal lesions in neurofibromatosis. Radiology 1961;76:1–19.
103. Oberman H, Sullenger G. Neurogenous tumors of the head and neck. Cancer 1967;20:1992–2001.
104. D'Agostino A, Soule E, Miller R. Sarcomas of the peripheral nerves and somatic soft tissues associated with multiple neurofibromatosis (von Recklinghausen's disease). Cancer 1963;16:1015–1027.
105. Hellquist H, Lundgren J. Neurogenic sarcoma of the sinonasal tract. J Laryngol Otol 1991;105:186–190.
106. Guccion J, Enzinger F. Malignant schwannoma associated with von Recklinghausen's neurofibromatosis. Virchows Arch 1979;383:43–57.
107. Cadotte M. Malignant granular cell myoblastoma. Cancer 1974;33: 1417–1422.
108. Farr H, Gray GJ, Vrana M. Extracranial meningioma. J Surg Oncol 1973;5:411–420.
109. Lopez D, Silvers D, Helwig E. Cutaneous meningioma: a clinicopathologic study. Cancer 1974;34:728–744.
110. Taxy J. Meningioma of the paranasal sinuses: a report of two cases. Am J Surg Pathol 1990;14:82–86.
111. Brunori A, Scarano P, Colacecchi R, Chiappetta F. A case of primary meningioma of the frontal sinus. Neurochirurgie 1999;45: 307–311.
112. Bertrand B, Devars F, Aouadi A, et al. [Primitive extracranial meningioma: a case report of intratemporal and naso-sinusal localization]. J Otolaryngol 1996;25:182–187.
113. Som P, Sacher M, Strenger S, et al. ''Benign'' metastasizing meningioma. AJNR 1987;8:127–130.
114. Chakrabarty A, Mitchell P, Bridges LR. Craniopharyngioma invading the nasal and paranasal spaces, and presenting as nasal obstruction. Br J Neurosurg 1998;12:361–363.

Copyright © 2003, Mosby, Inc. All rights reserved.

115. Jiang RS, Wu CY, Jan YJ, Hsu CY. Primary ethmoid sinus craniopharyngioma: a case report. J Laryngol Otol 1998;112:403–405.
116. Barnes L, Verbin R, Gnepp D. Diseases of the nose, paranasal sinuses and nasopharynx. In: Barnes L, ed. Surgical Pathology of the Head and Neck. Vol 2. New York: Marcel Dekker, 1985;912–1044.
117. Shugar J, Som P, Krespi Y. Primary chordoma of the maxillary sinus. Laryngoscope 1980;90:1825–1830.
118. Miro JL, Videgain G, Petrenas E, et al. Chordoma of the ethmoidal sinus. A case report. Acta Otorrinolaringol Esp 1998;49:66–69.
119. Wright D. Nasopharyngeal and cervical chordoma: some aspects of their development and treatment. J Laryngol 1967;81:1337–1355.
120. De las Casas L, Singh H, Halliday B, et al. Myxoid chondrosarcoma of the sphenoid sinus and chondromyxoid fibroma of the iliac bone: cytomorphologic findings of two distinct and uncommon myxoid lesions. Diagn Cytopathol 2000;22:383–389.
121. Rosenberg A, Nielsen G, Keel S, et al. Chondrosarcoma of the base of skull: a clinicopathologic study of 200 cases with emphasis on its distinction from chordoma. Am J Surg Pathol 1999;23:1370–1378.
122. Zacay G, Eyal A, Shacked I, et al. Chordoma of the cervical spine. Ann Otol Rhinol Laryngol 2000;109:438–440.
123. Hug E, Loredo L, Slater J, et al. Proton radiation therapy for chordomas and chondrosarcomas of the skull base. J Neurosurg 1999;91:432–439.
124. Yuh W, Flickinger F, Barloon T. MR imaging of unusual chordomas. JCAT 1985;12:30–35.
125. Fischbein NJ, Kaplan MJ, Holliday RA, Dillon WP. Recurrence of clival chordoma along the surgical pathway. AJNR 2000;21:578–583.
126. Pe'er J, Ilsar M. Ectopic lacrimal gland under the nasal mucosa. Am J Ophthalmol 1982;94:418–419.
127. Furukawa M, Takeuchi S, Umeda R. Ectopic tonsillar tissue in the nasal septum. Auris Nasus Larynx 1983;10:37–41.
128. Downs B, Shores C, Drake A. Choristoma of the nasopharynx. Otolaryngol Head Neck Surg 2000;123:523.
129. Esteban F, Ruiz-Avila I, Vilchez R, et al. Ectopic pituitary adenoma in the sphenoid causing Nelson's syndrome. J Laryngol Otol 1997;111:565–567.
130. McGurk M, Goepel J, Hancock B. Extranodal lymphoma of head and neck: a review of 49 consecutive cases. Clin Radiol 1985;36:455–458.
131. Fellbaum C, Hansmann M, Lennert K. Malignant lymphomas of the nasal and paranasal sinuses. Virch Arch A Pathol Anat Histopathol 1989;414:399–405.
132. Cleary K, Batsakis J. Sinonasal lymphomas. Ann Otol Rhinol Laryngol 1994 Nov;103:911–914.
133. Quraishi M, Bessell E, Clark D, et al. Non-Hodgkin's lymphoma of the sinonasal tract. Laryngoscope 2000;110:1489–1492.
134. Rodriguez J, Romaguera J, Manning J, et al. Nasal-type T/NK lymphomas: a clinicopathologic study of 13 cases. Leuk Lymphoma 2000;39:139–144.
135. Cuadra-Garcia I, Proulx G, Wu C, et al. Sinonasal lymphoma: a clinicopathologic analysis of 58 cases from the Massachusetts General Hospital. Am J Surg Pathol 1999;23:1356–1369.
136. Vidal R, Devaney K, Ferlito A, et al. Sinonasal malignant lymphomas: a distinct clinicopathological category. Ann Otol Rhinol Laryngol 1999;108:411–419.
137. van de Rijn M, Bhargava V, Molina-Kirsch H, et al. Extranodal head and neck lymphomas in Guatemala: high frequency of Epstein-Barr virus–associated sinonasal lymphomas. Hum Pathol 1997;28:834–839.
138. Pomilla P, Morris A, Jaworek A. Sinonasal non-Hodgkin's lymphoma in patients infected with human immunodeficiency virus: report of three cases and review. Clin Infect Dis 1995;21:137–149.
139. Strickler J, Meneses M, Habermann T, et al. Polymorphic reticulosis: a reappraisal. Hum Pathol 1994;25:659–665.
140. Arber D, Weiss L, Albujar P. Nasal lymphoma in Peru: high incidence of T-cell immunophenotype and Epstein-Barr virus infection. Am J Surg Pathol 1993;17:392–399.
141. Weiss L, Gaffey M, Chen Y, Frierson HJ. Frequency of Epstein-Barr viral DNA in ''Western'' sinonasal and Waldeyer's ring non-Hodgkin's lymphomas. Pathol Annu 1992;16:156–162.
142. Han J, Seo E, Kwon H, et al. Nasal angiocentric lymphoma with hemophagocytic syndrome. Korean J Intern Med 1999;14:41–46.
143. King AD, Lei KI, Ahuja AT, et al. MR imaging of nasal T-cell/natural killer cell lymphoma. AJR 2000;174:209–211.
144. Ooi GC, Chim CS, Liang R, et al. Nasal T-cell/natural killer cell lymphoma: CT and MR imaging features of a new clinicopathologic entity. AJR 2000;174:1141–1145.
145. Harnsberger H, Bragg D, Osborn A. Non-Hodgkin's lymphoma of the head and neck: CT evaluation of nodal and extranodal sites. AJNR 1983;8:673–679.
146. Kondo M, Hashimoto T, Shiga H. Computed tomography of sinonasal non-Hodgkin's lymphoma. JCAT 1984;8:216–219.
147. Duncavage J, Campbell B, Hanson G. Diagnosis of malignant lymphomas of the nasal cavity, paranasal sinuses and nasopharynx. Laryngoscope 1983;93:1276–1280.
148. Marsot-Dupuch K, Raveau V, Aoun N. Lethal midline granuloma: impact of imaging studies on the investigation and management of destructive midfacial disease in 13 patients. Neuroradiology 1992;34:155–161.
149. Borges A, Fink J, Villablanca P, et al. Midline destructive lesions of the sinonasal tract: simplified terminology based on histopathologic criteria. AJNR 2000;21:331–336.
150. Barnes L, Verbin R, Gnepp D. Diseases of the nose, paranasal sinuses and nasopharynx. In: Barnes L, ed. Surgical Pathology of the Head and Neck. Vol 2. New York: Marcel Dekker, 1985;1045–1209.
151. Uyesugi W, Watabe J, Petermann G. Orbital and facial granulocytic sarcoma (chloroma): a case report. Pediatr Radiol 2000;30:276–278.
152. Bassichis B, McClay J, Wiatrak B. Chloroma of the masseteric muscle. Int J Pediatr 2000;9:57–61.
153. Pomeranz S, Hawkins H, Towbin R, et al. Granulocytic sarcoma (chloroma): CT manifestations. Radiology 1985;155:167–170.
154. Castro E, Lewis J, Strong E. Plasmacytoma of paranasal sinuses and nasal cavity. Arch Otolaryngol 1973;97:326–329.
155. Fu Y-S, Perzin K. Nonepithelial tumors of the nasal cavity, paranasal sinuses and nasopharynx: a clinicopathologic study—IX plasmacytomas. Cancer 1978;42:2399–2406.
156. Bachmeyer C, Levy V, Carteret M, et al. Sphenoid sinus localization of multiple myeloma revealing evolution from benign gammopathy. Head Neck 1997;4:347–350.
157. Kondo M, Hashimoto S, Inuyama Y. Extramedullary plasmacytoma of the sinonasal cavities: CT evaluation. JCAT 1986;10:841–844.
158. Soo G, Chan A, Lam D, et al. Extramedullary nasal plasmacytoma—an unusual clinical entity. Ear Nose Throat J 1996;75:171–173.
159. Willman C, Busque L, Griffith B, et al. Langerhan's-cell histiocytosis (histiocytosis X), a clonal proliferative disease. N Engl J Med 1994;331:154–160.
160. Devaney K, Putzi M, Ferlito A, Rinaldo A. Head and neck Langerhan's cell histiocytosis. Ann Otol Rhinol Laryngol 1997;106:526–532.
161. Lieberman P, Jones C, Steinman R. Langerhans cell (eosinophilic) granulomatosis. A clinicopathologic study encompassing 50 years. Am J Surg Pathol 1996;20:519–552.
162. Alessi DM, Maceri D. Histocytosis x in the head and neck in a pediatric population. Arch Otolaryngol Head Neck Surg. 1992;118:945–948.
163. Hussain SS, Simpson RD, McCormick D, Johnstone CI. Langerhan's cell histiocytosis in the sphenoid sinus: a case of diabetes insipidus. J Laryngol Otol 1989;103:877–879.
164. Stromberg JS, Wang AM, Huang TE, et al. Langerhan's cell histiocytosis involving the sphenoid sinus and superior orbital fissure. AJNR 1995;16:964–967.
165. Jaffe H, Lichtenstein L. Eosinophilic granuloma of bone; condition affecting one, several or many bones, but apparently limited to skeleton, and representing mildest clinical expression of peculiar inflammatory histiocytosis also underlying Siwe disease and Schuller-Christian disease. Arch Pathol 1944;37:99–118.
166. Ide F, Iwase T, Saito I. Immunohistochemical and ultrastructural analysis of the proliferating cells in histiocytosis X. Cancer 1984;53:917–921.
167. De Schepper A, Ramon F, Van Marck E. MR imaging of eosinophilic granuloma: report of 11 cases. Skeletal Radiol 1993;22:163–166.
168. Goodnight JW, Wang MB, Sercarz JA, et al. Extranodal Rosai-Dorfman disease of the head and neck. Laryngoscope 1996;106:253–256.
169. Gregor RT, Ninnin D. Rosai-Dorfman disease of the paranasal sinuses. J Laryngol Otol 1994;108:152–155.

Copyright © 2003, Mosby, Inc. All rights reserved.

170. Ku P, Tong M, Leung C, et al. Nasal manifestation of extranodal Rosai-Dorfman disease—diagnosis and management. J Laryngol Otol 1999;113:275–280.
171. Innocenzi D, Silipo V, Giombini S, et al. Sinus histiocytosis with massive lymphadenopathy (Rosai-Dorfman disease): case report with nodal and diffuse muco-cutaneous involvement. J Cutan Pathol 1998;25:563–567.
172. Smithson L, Lipper M, Hall JJ. Paranasal sinus involvement in thalassemia major: CT demonstration. AJNR 1987;8:564–565.
173. Olivieri N. The beta-thalassemias. N Engl J Med 1999;341: 99–109.
174. Tunaci M, Tunaci A, Engin G, et al. Imaging features of thalassemia. Eur Radiol 1999;9:1804–1809.
175. Apostol JV, Frazell E. Juvenile nasopharyngeal angiofibroma. Cancer 1965;18:869–878.
176. Som P, Cohen B, Sacher M. The angiomatous polyp and the angiofibroma: two different lesions. Radiology 1982;144:329–334.
177. Som P, Shugar J, Cohen B. The nonspecificity of the antral bowing sign in maxillary sinus pathology. JCAT 1981;5:350–352.
178. Bryan R, Sessions R, Horowitz B. Radiographic management of juvenile angiofibromas. AJNR 1981;2:157–166.
179. Som P, Lanzieri C, Sacher M. Extracranial tumor vascularity: determination by dynamic CT scanning. II The unit approach. Radiology 1985;154:407–412.
180. Herman P, Lot G, Chapot R, et al. Long-term follow-up of juvenile nasopharyngeal angiofibromas: analysis of recurrences. Laryngoscope 1999;109:140–147.
181. Lloyd G, Howard D, Phelps P, Cheesman A. Juvenile angiofibroma: the lessons of 20 years of modern imaging. J Laryngol Otol 1999;113:127–134.
182. Murray A, Falconer M, McGarry GW. Excision of nasopharyngeal angiofibroma facilitated by intra-operative 3D-image guidance. J Laryngol Otol 2000;114:311–313.
183. Fitzpatrick P, Briant D, Berman J. The nasopharyngeal angiofibroma. Arch Otolaryngol 1980;106:234–236.
184. Batsakis J, et al. Tumors of the Head and Neck: Clinical and Pathological Considerations. 2nd ed. Baltimore: Williams and Wilkins, 1979;139–143.
185. Barnes L, Verbin R, Gnepp D. Diseases of the nose, paranasal sinuses and nasopharynx. In: Barnes L, ed. Surgical Pathology of the Head and Neck. Vol 1. New York: Marcel Dekker, 1985;725–880.
186. Enziger F, Weiss S. Soft Tissue Tumors. 3rd ed. St Louis: CV Mosby, 1995.
187. Barnes L. Tumor and tumor-like lesions of the soft tissue. In: Barnes L, ed. Surgical Pathology of the Head and Neck. Vol 2. 2nd ed. New York: Marcel Dekker, 2000;991–993.
188. Kurien M, Nair S, Thomas S. Angiosarcoma of the nasal cavity and maxillary antrum. J Laryngol Otol 1989;103:874–876.
189. Solomons N, Stearns M. Haemangiosarcoma of the maxillary antrum. J Laryngol Otol 1990;104:831–834.
190. Kimura Y, Tanaka S, Furuka M. Angiosarcoma of the nasal cavity. J Laryngol Otol 1992;106:368–369.
191. Dorfman H, Steiner G, Jaffe H. Vascular tumors of bone. Hum Pathol 1971;2:349–375.
192. Joachims H, Cohen Y. Hemangioendothelioma of mastoid bone. Laryngoscope 1974;84:454–458.
193. Enzinger F, Smith B. Hemangiopericytoma: an analysis of 106 cases. Hum Pathol 1976;7:61–82.
194. El-Naggar A, Batsakis J, Garcia G, et al. Sinonasal hemangiopericytomas: clinicopathologic and DNA content study. Arch Otolaryngol Head Neck Surg 1992;118:134–137.
195. Hekkenberg RJ, Davidson J, Kapusta L, et al. Hemangiopericytoma of the sinonasal tract. J Otolaryngol 1997;26:277–280.
196. Catalano PJ, Brandwein M, Shah DK, et al. Sinonasal hemangiopericytomas: a clinicopathologic and immunohistochemical study of seven cases. Head Neck 1996;18:42–53.
197. Kauffaman S, Stout A. Hemangiopericytoma in children. Cancer 1960;13:695–710.
198. Herve S, Abd Alsamad I, Beautru R, et al. Management of sinonasal hemangiopericytomas. Rhinology 1999;37:153–158.
199. Gnepp D, Chandler W, Hyams V. Primary Kaposi's sarcoma of the head and neck. Ann Int Med 1984;100:107–114.
200. Lothe F, Murray J. Kaposi's sarcoma: autopsy findings in the African. Acta Unio Int Contra Cancrum 1962;18:429–452.
201. Greenberg J, Fischl M, Berger J. Upper airway obstruction secondary to AIDS-related Kaposi's sarcoma. Chest 1985;88:638–640.
202. Levy F, Tansek K. AIDS-associated Kaposi's sarcoma of the larynx. J Ear Nose Throat 1990;69:177–183.
203. Fliss D, Parikh J, Freeman J. AIDS-related Kaposi's sarcoma of the sphenoid sinus. J Otolaryngol 1992;21:235–237.
204. Barnes L, Verbin R, Gnepp D. Diseases of the nose, paranasal sinuses and nasopharynx. In: Barnes L, ed. Surgical Pathology of the Head and Neck. Vol 2. New York: Marcel Dekker, 1985;1834–1836.
205. Landis S, Murray T, Bolden S, Wingo P. Cancer statistics. CA Cancer J Clin 1999;49:8–31.
206. National Cancer Institute. (March 26, 2002). Surveillance, Epidemiology, and End Results [On-line]. Available: www-seer.ims.nci.nih.gov.
207. Lawrence WJ, Donegan W, Natarajan N, et al. Adult soft tissue sarcomas. A pattern of care survey of the American College of Surgeons. Ann Surg 1987;205:349–359.
208. Enziger F, Weiss S. Soft Tissue Tumors. 2nd ed. St Louis: CV Mosby, 1988.
209. Fu Y-S, Perzin K. Nonepithelial tumors of the nasal cavity, paranasal sinuses and nasopharynx: a clinicopathologic study. Cancer 1974;33: 1289–1305.
210. Ardekian L, Samet N, Talmi Y, et al. Vascular leiomyoma of the nasal septum. Otolaryngol Head Neck Surg 1996;114:798–800.
211. Nall A, Stringer S, Baughman R. Vascular leiomyoma of the superior turbinate: first reported case. Head Neck 1997;19:63–67.
212. Murono S, Ohmura T, Sugimori S, Furukawa M. Vascular leiomyoma with abundant adipose cells of the nasal cavity. Am J Otolaryngol 1998;19:50–53.
213. Huang C, Chien C, Su C, Chen W. Leiomyoma of the inferior turbinates. J Otolaryngol 2000;29:55–56.
214. Lippert B, Godbersen G, Luttges J, Werner J. Leiomyosarcoma of the nasal cavity. Case report and literature review. ORL 1996;58:115–120.
215. Strasser M, Gleich L, Hakim S, Biddinger P. Pathologic quiz case 2. Nasal leiomyosarcoma, low grade. Arch Otolaryngol Head Neck Surg 1998;124:715, 717.
216. Harcourt J, Gallimore A. Leiomyoma of the paranasal sinuses. J Laryngol Otol 1993;107:740–741.
217. Kuruvilla A, Wenig B, Humphrey D, et al. Leiomyosarcoma of the sinonasal tract: a clinicopathologic study of nine cases. Arch Otolaryngol Head Neck Surg 1990;116:1278–1286.
218. Dropkin L, Tang C, Williams J. Leiomyosarcoma of the nasal cavity and paranasal sinuses. Ann Otol Rhinol Laryngol 1976;85: 399–403.
219. Barnes L. Tumor and tumor-like lesions of the soft tissue. In: Barnes L, ed. Surgical Pathology of the Head and Neck. Vol 2. 2nd ed. New York: Marcel Dekker, 2001;889–1048.
220. Kapadia S, Meis J, Frisman D, et al. Fetal rhabdomyoma of the head and neck: a clinicopathologic and immunophenotypic study of 24 cases. Hum Pathol 1993;24:754–765.
221. Kapadia S, Meis J, Frisman D, et al. Adult rhabdomyoma of the head and neck: a clinicopathologic and immunophenotypic study. Hum Pathol 1993;24:608–617.
222. Young JJ, Miller R. Incidence of malignant tumors in U.S. children. J Pediatr 1975;86:254–258.
223. Sercarz J, Mark R, Tran L, et al. Sarcomas of the nasal cavity and paranasal sinuses. Ann Otol Rhinol Laryngol 1994;103:699–704.
224. Callender T, Weber R, Janjan N, et al. Rhabdomyosarcoma of the nose and paranasal sinuses in adults and children. Otolaryngol Head Neck Surg 1995;112:252–257.
225. Lee J, Lee M, Lee B, et al. Rhabdomyosarcoma of the head and neck in adults: MR and CT findings. AJNR 1996;17:1923–1928.
226. Licameli G, Tunkel D, Westra W. Pathologic quiz case 2. Rhabdomyosarcoma (RMS), alveolar type, of the paranasal sinus. Arch Otolaryngol Head Neck Surg 1997;123:881–883.
227. Daya H, Chan H, Sirkin W, Forte V. Pediatric rhabdomyosarcoma of the head and neck: is there a place for surgical management? Arch Otolaryngol Head Neck Surg 2000;126:468–472.
228. Golledge J, Fisher C, Rhys-Evans P. Head and neck liposarcoma. Cancer 1995;76:1051–1058.
229. Dooms G, Hricak H, Sollitto R, et al. Lipomatous tumors and tumors with fatty component: MR imaging potential and comparison of MR and CT results. Radiology 1985;157:479–483.

Copyright © 2003, Mosby, Inc. All rights reserved.

230. Gnepp D, Henley J, Weiss S, Heffner D. Desmoid fibromatosis of the sinonasal tract and nasopharynx: a clinicopathologic study of 25 cases. Cancer 1996;78:2572–2579.
231. Heffner D, Gnepp D. Sinonasal fibrosarcomas, malignant schwannomas, and ''Triton'' tumors: a clinicopathologic study of 67 cases. Cancer 1992;70:1089–1101.
232. Bortnick E. Neoplasms of the nasal cavity. Otolaryngol Clin North Am 1973;6:801–812.
233. Frankenthaler R, Ayala A, Hartwick R, Goepfert H. Fibrosarcoma of the head and neck. Laryngoscope 1990;100:799–802.
234. Barnes L, Kanbour A. Malignant fibrous histiocytoma of the head and neck. A report of 12 cases. Arch Otolaryngol Head Neck Surg 1988;114:1149–1156.
235. Brookes G, Rose P. Malignant fibrous histiocytoma of the ethmoid sinus. J Laryngol Otol 1983;97:279–289.
236. Nemes Z, Thomazy V, Adany R, Muszbek L. Identification of histiocytic reticulum cells by immunohistochemical demonstration of Factor XIII (F-XIIIa) in human lymph nodes. J Pathol 1986;149:121–132.
237. Nemes Z. Differentiation markers in hemangiopericytoma. Cancer 1992;69:133–140.
238. Merrick R, Rhone D, Chilis T. Malignant fibrous histiocytoma of the maxillary sinus. Arch Otolaryngol 1980;106:365–367.
239. Dai J, Shi M, Li G. [Computed tomographic features of malignant fibrous histiocytoma]. Chung Hua Chung Liu Tsa Chih 1996;18:140–142.
240. Basak S, Mutlu C, Erkus M, et al. Benign fibrous histiocytoma of the nasal septum. Rhinology 1998;36:133–135.
241. Som P, Brandwein M, Maldjiian C. Inflammatory pseudotumor of the maxillary sinus: CT and MR findings in six cases. Am J Roentgenol 1994;163:689–692.
242. Batsakis J, El-Naggar A, Luna M, Goepfert H. Pathology consultation—''inflammatory pseudotumor'': What is it? How does it behave? Laryngology 1995;104:329–331.
243. Takimoto T, Kathoh T, Ohmura TR. Inflammatory pseudotumor of the maxillary sinus mimicking malignancy. Rhinology 1990;28: 123–127.
244. Coffin C, Watterson J, Priest J, Dehner L. Extrapulmonary inflammatory myofibroblastic tumor (inflammatory pseudotumor). A clinicopathologic and immunohistochemical study of 84 cases. Am J Surg Pathol 1995;19:859–872.
245. Hytiroglu P, Brandwein M, Strauchen J. Inflammatory pseudotumor of the parapharyngeal space: case report and review of the literature. Head Neck 1992;14:230–234.
246. Chan Y, Ma L, Young C, Lam K. Parapharyngeal inflammatory pseudotumor presenting as a fever of unknown origin in a 3 year old girl. Pediatr Pathol 1988;8:195–203.
247. Keen M, Conley J, McBride T. Pseudotumor of the pterygomaxillary space presenting as anesthesia of the mandibular nerve. Laryngoscope 1986;96:560–563.
248. Drucker C, Brodin A, Wolff A. Pathological quiz. Arch Otolaryngol 1989;115:998–1000.
249. Zukerberg L, Rosenberg A, Randolph G, et al. Solitary fibrous tumor of the nasal cavity and paranasal sinuses. Am J Surg Pathol 1991;15:126–130.
250. Kohmura T, Nakashima T, Hasegawa Y, Matsuura H. Solitary fibrous tumor of the paranasal sinuses. Eur Arch Otorhinolaryngol 1999;256:233–236.
251. Kessler A, Lapinsky J, Berenholz L, et al. Solitary fibrous tumor of the nasal cavity. Otolaryngol Head Neck Surg 1999;121:826–828.
252. Barnes L. Tumor and tumor-like lesions of the soft tissue. In: Barnes L, ed. Surgical Pathology of the Head and Neck. Vol 2. 2nd ed. New York: Marcel Dekker, 2001;948.
253. Shugar J, Som P, Meyers R, et al. Intramuscular head and neck myxoma: report of a case and review of the literature. Laryngoscope 1987;97:105–107.
254. Barnes L, Verbin R, Appel B, Peel R. Diseases of bones and joints. In: Barnes L, ed. Surgical Pathology of the Head and Neck. Vol 2. 2nd ed. New York: Marcel Dekker, 2000;1049–1232.
255. Hurwitz JJ, Fine N, Howarth DJ, DeAngelis D. Lacrimal obstruction due to a nasal osteoma. Can J Ophthalmol 1999;34:296–298.
256. Osguthorpe J, Hungerford G. Benign osteoblastoma of the maxillary sinus. Head Neck Surg 1983;6:605–609.
257. Attane F, Tannier C, Vayr R. Pneumocephalus complicating osteoma of the frontal sinus. Rev Neurol (Paris) 1996;152:279–282.
258. Marras LC, Kalaparambath TP, Black SE, Rowed DW. Severe tension pneumocephalus complicating frontal sinus osteoma. Can J Neurol Sci 1998;25:79–81.
259. Koivunen P, Lopponen H, Fors AP, Jokinen K. The growth rate of osteomas of the paranasal sinuses. Clin Otolaryngol 1997;22:111–114.
260. Evans H, Ayala A, Romsdahl M. Prognostic factors in chondrosarcoma of bone: a clinicopathologic analysis with emphasis on histologic grading. Cancer 1977;40:818–831.
261. Chaudhry A, Robinovitch M, Mitchell D, et al. Chondrogenic tumors of the jaws. Am J Surg 1961;102:403–411.
262. McCoy J, McConnel F. Chondrosarcoma of the nasal septum. Arch Otolaryngol 1981;107:125–127.
263. Gay I, Elidan J, Kopolovic J. Chondrosarcoma of the skull base. Ann Otol Rhinol Laryngol 1981;90:53–55.
264. Huvos AG, ed. Bone Tumors: Diagnosis, Treatment, and Prognosis. 2nd ed. Philadelphia: WB Saunders, 1991;68.
265. Som P, Bellot O, Blitzer A. Osteoblastoma of the ethmoid sinus: the fourth reported case. Arch Otolaryngol 1979;105:623–625.
266. Coscina W, Lee B. Concurrent osteoblastoma and aneurysmal bone cyst of the ethmoid sinus: case report. CT J Comput Tomogr 1985;9:347–350.
267. Lucas D, Unni K, McLeod R, et al. Osteoblastoma: clinicopathologic study of 306 cases. Hum Pathol 1994;25:117–134.
268. Engelbrecht V, Preis S, Hassler W, Lenard HG. CT and MRI of congenital sinonasal ossifying fibroma. Neuroradiology 1999;41: 526–529.
269. Lawton MT, Heiserman JE, Coons SW, et al. Juvenile active ossifying fibroma. Report of four cases. J Neurosurg 1997;86:279–285.
270. Tobey JD, Loevner LA, Yousem DM, Lanza DC. Tension pneumocephalus: a complication of invasive ossifying fibroma of the paranasal sinuses. AJR 1996;166:711–713.
271. Barnes L, Verbin R, Appel B, Peel R. Tumor and tumor-like lesions of the soft tissue. In: Barnes L, ed. Surigcal Pathology of the Head and Neck. Vol 2. 2nd ed. New York: Marcel Dekker, 2000;1091–1095.
272. Dehner L. Fibro-osseous lesions of bone. In: Ackerman L, Spjut H, Abell M, eds. Bones and Joints. Vol Monograph No. 17. Baltimore: International Academy of Pathology, 1976;209–235.
273. Som P, Lidov M. The benign fibro-osseous lesion: its association with paranasal sinus mucoceles and its MR characteristics. JCAT 1992;16:871–876.
274. Sterling K, Stollman A, Sacher M. Ossifying fibroma of sphenoid bone with coexistent mucocele: CT and MRI. JCAT 1993;17:492–494.
275. Commins DJ, Tolley NS, Milford CA. Fibrous dysplasia and ossifying fibroma of the paranasal sinuses. J Laryngol Otol 1998;112:964–968.
276. Barnes L, Verbin R, Gnepp D. Diseases of the nose, paranasal sinuses and nasopharynx. In: Barnes L, ed. Surgical Pathology of the Head and Neck. Vol 1. New York: Mercel Dekker, 1985;883–1044.
277. Von Wowern N, Odont D. Cherubism: a 36-year long-term follow-up of 2 generations in different families and review of the literature. Oral Surg Oral Med Oral Pathol Oral Radiol Endod 2000;90:765–772.
278. Hitomi G, Nishide N, Mitsui K. Cherubism: diagnostic imaging and review of the literature in Japan. Oral Surg Oral Med Oral Pathol Oral Radiol Endod 1996;81:623–628.
279. Yamaguchi T, Dorfman H, Eisig S. Cherubism: clinicopathologic features. Skeletal Radiol 1999;28:350–353.
280. Huvos AG, ed. Bone Tumors: Diagnosis, Treatment, and Prognosis. 2nd ed. Philadelphia: WB Saunders, 1991;432–441.
281. Kujas M, Faillot T, Van Effenterre R, Poirier J. Bone giant cell tumour in neuropathological practice. A fifty year overview. Arch Anat Cytol Pathol 1999;47:7–12.
282. Auclair P, Cuenin P, Kratochvil F, et al. A clinical and histomorphologic comparison of the central giant cell granuloma and the giant cell tumor. Oral Surg Oral Med Oral Pathol 1988;66:197–208.
283. Stolovitzky J, Waldron C, McConnel F. Giant cell lesions of the maxilla and paranasal sinuses. Head Neck 1994;16:143–148.
284. Barnes L, Verbin R, Appel B, Verbin R. Tumor and tumor-like lesions of the soft tissue. In: Barnes L, ed. Surgical Pathology of the Head and Neck. Vol 2. 2nd ed. New York: Marcel Dekker, 2000;1156–1169.

Copyright © 2003, Mosby, Inc. All rights reserved.

285. Som P, Lawson W, Cohen B. Giant cell lesions of the facial bones. Radiology 1983;147:129–134.
286. Rhea J, Weber A. Giant cell granuloma of the sinuses. Radiology 1983;147:135–137.
287. Friedman W, Pervez N, Schwartz A. Brown tumor of the maxilla in secondary hyperparathyroidism. Arch Otolaryngol 1974;100:157–159.
288. Smith G, Ward P. Giant cell lesions of the facial skeleton. Arch Otolaryngol 1978;104:186–190.
289. Becelli R, Cerulli G, Gasparini G. Surgical and implantation reconstruction in a patient with giant-cell central reparative granuloma. J Craniofac Surg 1998;1:45–47.
290. Citardi MJ, Janjua T, Abrahams JJ, Sasaki CT. Orbitoethmoid aneurysmal bone cyst. Otolaryngol Head Neck Surg 1996;114:466–470.
291. Kaffe I, Naor H, Calderon S, Buchner A. Radiological and clinical features of aneurysmal bone cyst of the jaws. Dentomaxillofac Radiol 1999;28:167–172.
292. Som P, Schatz C, Flaum E, Lanman T. Aneurysmal bone cyst of the paranasal sinuses associated with fibrous dysplasia: CT and MR findings. JCAT 1991;15:513–515.
293. Baker H, Papsidero M, Batsakis J, Krause C. Aneurysmal bone cyst of the ethmoid. Head Neck Surg 1982;5:177–180.
294. Barnes L, Verbin R, Appel B, Peel R. Tumor and tumor-like lesions of the soft tissue. In: Barnes L, ed. Surgical Pathology of the Head and Neck. Vol 2. 2nd ed. New York: Marcel Dekker, 2001;1084.
295. Som P, Hermann G, Sacher M. Paget disease of the calvaria and facial bones with an osteosarcoma of the maxilla: CT and MR findings. JCAT 1987;11:887–890.
296. Epley KD, Lasky JB, Karesh JW. Osteosarcoma of the orbit associated with Paget disease. Ophthalmol Plast Reconstr Surg 1998;14:62–66.
297. Huvos AG, ed. Bone Tumors: Diagnosis, Treatment, and Prognosis. 2nd ed. Philadelphia: WB Saunders, 1991;87.
298. Huvos AG, ed. Bone Tumors: Diagnosis, Treatment, and Prognosis. 2nd ed. Philadelphia: WB Saunders, 1991;349.
299. Hyde G, Yarington CJ, Chu F. Head and neck manifestations of Maffucci's syndrome: chondrosarcoma of the nasal septum. Am J Otolaryngol 1995;16:272–275.
300. Saito K, Unni K, Wollan P, Lund BC. Chondrosarcoma of the jaw and facial bones. Cancer 1995;76:1550–1558.
301. Gadwal S, Fanburg-Smith J, Gannon F, Thompson L. Primary chondrosarcoma of the head and neck in pediatric patients: a clinicopathologic study of 14 cases with a review of the literature. Cancer 2000;88:2181–2188.
302. Rassekh C, Nuss D, Kapadia S, et al. Chondrosarcoma of the nasal septum: skull base imaging and clinicopathologic correlation. Otolaryngol Head Neck Surg 1996;115:29–37.
303. Huvos AG, ed. Bone Tumors: Diagnosis, Treatment, and Prognosis. 2nd ed. Philadelphia: WB Saunders, 1991;399.
304. Vencio E, Reeve C, Unni K, Nascimento A. Mesenchymal chondrosarcoma of the jaw bones: clinicopathologic study of 19 cases. Cancer 1998;82:2350–2355.
305. Lockhart R, Menard P, Martin J, et al. Mesenchymal chondrosarcoma of the jaws. Report of four cases. Int J Oral Maxillofac Surg 1998;27:358–362.
306. Huvos AG, ed. Bone Tumors: Diagnosis, Treatment, and Prognosis. 2nd ed. Philadelphia: WB Saunders, 1991;382.
307. Verbin R, Barnes L. Cysts and cyst-like lesions of the oral cavity, jaws, and neck. In: Barnes L, ed. Surgical Pathology of the Head and Neck. Vol. 3. 2nd ed. New York: Marcel Dekker, 2001;1437–1555.
308. Verbin R, Barnes L. Cysts and cyst-like lesions of the oral cavity, jaws and neck. In: Barnes L, ed. Surgical Pathology of the Head and Neck. Vol 2. New York: Marcel Dekker, 1985;1278–1281.
309. Stafne E, Gibilisco J. Oral Roentgenographic diagnosis. 4th ed. Philadelphia: WB Saunders, 1975;147–168.
310. Barnes L, Verbin R, Gnepp D. Diseases of the nose, paranasal sinuses and nasopharynx. In: Barnes L, ed. Surgical Pathology of the Head and Neck. Vol 2. New York: Marcel Dekker, 1985;1233–1329.
311. Batsakis J, ed. Tumor of the Head and Neck: Clinical and Pathological Considerations. 2nd ed. Baltimore: Williams and Wilkins, 1979;531–560.
312. Mehhlisch D, Dahlin D, Masson J. Ameloblastoma: a clinicopathologic report. J Oral Surg 1972;30:9–22.
313. Barnes L, Verbin R, Gnepp D. Diseases of the nose, paranasal sinuses and nasopharynx. In: Barnes L, ed. Surgical Pathology of the Head and Neck. Vol 2. New York: Marcel Dekker, 1985;1331–1409.
314. Ferlito A, Rinaldo A. Developmental lesions of the head and neck. In: Barnes L, ed. Surgical Pathology of the Head and Neck. Vol 3. 2nd ed. New York: Marcel Dekker, 2000;1649–1671.
315. Heffner D. Problems in pediatric otorhinolaryngic pathology, III. Teratoid and neural tumors of the nose, sinonasal tract, and nasopharynx. Int J Pediatr Otorhinolaryngol 1983;6:1–21.
316. Heffner DK, Thompson LD, Schall DG, Anderson V. Pharyngeal dermoids (''hairy polyps'') as accessory auricles. Ann Otol Rhinol Laryngol 1996;105:819–824.
317. Batsakis J, el-Naggar A, Luna M. Teratomas of the head and neck with emphasis on malignancy. Ann Otol Rhinol Laryngol 1995;104:496–500.
318. Som P, Norton K, Shugar J, et al. Metastatic hypernephroma to the head and neck. AJNR 1987;8:1103–1106.
319. Maschka DA, McCulloch TM, Nerad JA. Prostate cancer metastatic to the orbit [see comments]. Ann Otol Rhinol Laryngol 1996;105:70–71.
320. Aw CY, Hwang JS, Brett RH, Lu PK. Metastatic oesophageal carcinoma to the paranasal sinuses—a case report. Singapore Med J 1999;40:539–541.
321. Batsakis J, ed. Tumor of the Head and Neck: Clinical and Pathological Considerations. 2nd ed. Baltimore: Williams and Wilkins, 1979;240–250.
322. Bernstein J, Montgomery W, Balogh K. Metastatic tumors to the maxilla, nose and paranasal sinus. Laryngoscope 1966;76:621–650.
323. Gottlieb MD, Roland JT Jr. Paradoxical spread of renal cell carcinoma to the head and neck. Laryngoscope 1998;108:1301–1305.
324. Vogelzang N, Priest E, Borden L. Spontaneous regression of histologically proved pulmonary metastases from renal cell carcinoma: a case with 5-year follow up. J Urol 1992;148:1247–1248.
325. Kallmeyer J, Dittrich O. Spontaneous regression of metastases in a case of bilateral renal cell carcinoma. J Urol 1992;148:138–140.
326. Cottel WI. Perineural invasion by squamous-cell carcinoma. J Dermatol Surg Oncol 1982;8:589–600.
327. Goepfert H, Dichtel W, Medina J, et al. Perineural invasion in squamous cell skin carcinoma of the head and neck. Am J Surg 1984;148:542–547.
328. Hanke C, Wolf R, Hochman S, et al. Chemosurgical reports: perineural spread of basal cell carcinoma. J Dermatol Surg Oncol 1983;9:742–747.
329. Altman KW, Mirza N, Philippe L. Metastatic follicular thyroid carcinoma to the paranasal sinuses: a case report and review. J Laryngol Otol 1997;111:647–651.
330. Freeman JL, Gershon A, Liavaag PG, Walfish PG. Papillary thyroid carcinoma metastasizing to the sphenoid-ethmoid sinuses and skull base. Thyroid 1996;6:59–61.
331. Yamasoba T, Kikuchi S, Sugasawa M, et al. Occult follicular carcinoma metastasizing to the sinonasal tract. J Otorhinolaryngol Relat Spec 1994;56:239–243.
332. Mochimatsu I, Tsukuda M, Furukawa S, Sawaki S. Tumours metastasizing to the head and neck—a report of seven cases. J Laryngol Otol 1993;107:1171–1173.
333. Renner GJ, Davis WE, Templer JW. Metastasis of thyroid carcinoma to the paranasal sinuses. Otolaryngol Head Neck Surg 1984;92:233–237.
334. Cinberg JZ, Terrife D. Follicular adenocarcinoma of the thyroid in the maxillary sinus. Otolaryngol Head Neck Surg 1980;88:157–158.
335. Scott A, Raine M, Stansbie JM. Ethmoid metastasis of endometrial carcinoma causing mucocele of maxillary antrum. J Laryngol Otol 1998;112:283–285.
336. Tariq M, Gluckman P, Thebe P. Metastatic testicular teratoma of the nasal cavity: a rare cause of severe intractable epistaxis. J Laryngol Otol 1998;112:1078–1081.

Copyright © 2003, Mosby, Inc. All rights reserved.

7

Facial Fractures and Postoperative Findings

Peter M. Som and Margaret S. Brandwein

SECTION ONE: FACIAL FRACTURES
INTRODUCTION
FACIAL BUTTRESSES
CLINICAL DIAGNOSIS AND TREATMENT
IMAGING
NASAL FRACTURES
CENTRAL MIDFACIAL FRACTURES
- Nasoorbital Fractures
- Isolated Maxillary/Palatal Fractures
- Le Fort I Fractures
- Le Fort II Fractures
- Le Fort III Fractures

LATERAL MIDFACIAL FRACTURES
- Trimalar (Zygomatic) Fractures
- Zygomaticomaxillary Fractures
- Zygomaticomandibular Fractures
- Zygomatic Arch Fractures
- Blow-out and Blow-in Orbital Wall Fractures

FRONTAL SINUS FRACTURES
SPHENOID SINUS FRACTURES
PEDIATRIC FACIAL FRACTURES
SECTION TWO: POSTOPERATIVE SINONASAL CAVITIES
IMAGING EVALUATIONS
OPERATIVE PROCEDURES
NASAL SURGERY
FRONTAL SINUS SURGERY
- Trephination
- Lynch Procedure
- Killian Procedure
- Riedel Procedure
- Osteoplastic Flap Procedure

ETHMOID SINUS SURGERY
- External Ethmoidectomy
- Internal Ethmoidectomy
- Transantral Ethmoidectomy

MAXILLARY SINUS SURGERY
- Intranasal Antrostomy and the Caldwell-Luc Procedure

SPHENOID SINUS SURGERY
SURGERY FOR SINUS MALIGNANCY
- Medial Maxillectomy
- Total Maxillectomy

EXTENSIVE NASOETHMOID SURGERY
CRANIOFACIAL RESECTION

SECTION ONE

FACIAL FRACTURES

INTRODUCTION

The paranasal sinuses develop within and are protected by the facial bones. The facial bones also surround and protect the orbits, nasal fossae, and mouth, they support the maxillary dentition, and they serve as attachments for the facial muscles. The facial skeleton can be considered as a honeycombed structure of varying thickness and form that develops strength along stress zones by forming buttressed arches. In general, the most superficial portion of the facial skeleton is physically the strongest and serves the additional function of protecting the more delicate central part of the face. The honeycombed construction of the middle third of the facial skeleton evolved to resist the vertical masticatory forces, and in this regard it provides excellent stability. However, external impact forces directed toward the midface can disrupt this central structure, and the fracture of even one buttress can weaken the entire lattice, causing it to

Copyright © 2003, Mosby, Inc. All rights reserved.

collapse. Fortunately, such collapse is often prevented by the strength of these same facial buttresses and the additional support of the skull base.[1, 2]

FACIAL BUTTRESSES

The facial skeleton can be analyzed in terms of the supporting buttresses that comprise its structure. There are two main sagittal buttresses on either side of the face. There is a medial buttress that extends from the anterior maxillary alveolus up the lateral wall of the pyriform aperture, which is the opening in the facial skeleton that defines the margins of the nasal fossae, and into the medial orbital wall. This nasomaxillary buttress is thus formed by the lower maxilla, the frontal process of the maxilla, the lacrimal bone, and the nasal process of the frontal bone. There is also a lateral buttress, the zygomaticomaxillary buttress, which is formed on either side by the lateral wall of the maxilla, the body of the zygoma, and the orbital process of the frontal bone in the lateral orbital wall. A third buttress has been suggested, the pterygomaxillary buttress, which extends from the posterior maxillary alveolus (tuberosity) cranially along the pterygoid plates to the skull base.

These buttresses have evolved as mechanical adaptations of the skull to masticatory forces, and the greatest occlusal forces are absorbed by the zygomaticomaxillary buttress, as evidenced by the thick cortical bone present in the lateral maxillary-zygomatic region when compared with the more fragile medial maxillary wall. In addition to these sagittal buttresses, some authors believe that there is also a median buttress formed by the nasal septum. Overall these craniocaudal buttresses are curved, and analysis suggests that they need reinforcement by axial struts. Thus these sagittal buttresses are interconnected by three axial (horizontal) struts that are formed by the floor of the anterior cranial fossa, the orbital floor and zygomatic arches, and the maxillary alveolus and hard palate. In addition, the skull base, which is oriented at approximately a 45° angle to the occlusal plane of the maxilla, acts as an additional axial buttress. Together these buttresses or struts form an interconnecting facial support system.

The facial skeleton can also be conceptualized as being formed by two coronal buttresses: an anterior plane formed by the vertical portion of the frontal bone (glabellar region), the orbital rims, the anterior maxilla, and the alveolus; and a posterior plane formed by the posterior wall of the maxilla and the pterygoid processes.[1, 3, 4]

Such analyses, first studied experimentally by Le Fort, have led to an understanding of the major lines of weakness in the midfacial skeleton, and these, in turn, have helped explain why certain fractures follow an overall predictable course. The efforts of Le Fort are recognized today by the Le Fort types I, II, and III fractures. The forces he used experimentally are similar to the low-velocity impact forces that occur today in fist fights and sporting events. However, at present there are also high-velocity impact injuries such as those that occur in high-speed vehicular accidents and with violence involving blunt devices or gunshot wounds. Despite the much greater order of magnitude of these impact forces, the same fracture lines are still encountered, albeit in various combinations other than those originally observed by Le Fort.[1, 2]

In addition to causing complicated facial fractures, such high-impact trauma rarely may be associated with cervical spine injury. In one study of 582 consecutive patients with facial fractures, 1.04% (6) were found to have a cervical spine injury, all of which were the result of a car accident.[5] Thus, the proper workup of a patient with severe facial fractures should also include evaluation of the cervical spine. In addition, imaging of these patients should include the brain and the carotid arteries for associated trauma.

CLINICAL DIAGNOSIS AND TREATMENT

The diagnosis of facial fractures usually is accomplished by a combination of clinical and imaging examinations. The clinician is primarily concerned with the detection of malocclusion, abnormal mobility, and crepitation as signs of fracture. Often, deformity of the facial skeleton is initially concealed by overlying edema, hemorrhage, and soft-tissue injury. Any evidence of a palpable step-off at the orbital rim, diplopia, hypertelorism, midfacial elongation, cerebrospinal fluid (CSF) rhinorrhea, or flattening of the cheek further helps the clinician identify the type of fracture present. However, only after imaging studies can the fractures be completely identified and characterized. It is now recognized that the information gained from CT scans is of greater net value than that gained from a combination of routine radiographs and clinical examination. Thus imaging is essential for proper treatment planning in these cases.[1, 2, 6]

In many instances, clinicians wait several days after the trauma before reducing the fracture(s). This delay allows some of the soft-tissue injury to subside and may be necessary if the patient has other life-threatening injuries that require immediate attention (before the less critical facial fractures are addressed). However, if possible, a delay of more than 7 days is to be avoided, because after this time fibrous fixation of the fracture occurs and fracture reduction becomes more difficult, often requiring refracturing to attain normal positioning.

The basic principles of treating midfacial fractures are (1) reduction of the fractures and (2) fixation of the fractured bones to one another and to the skull. Absolute immobilization of the fractures is the main prerequisite for rapid and undisturbed healing because the main interferences with fracture healing are local mechanical factors. In the early phase of fracture healing, mobility can disturb the normal course of bone regeneration and lead to faulty differentiation of the callus.[1, 2, 7–9] Of primary clinical concern is the restoration of occlusion and facial form, because these provide a means of restoring the essential masticatory function. Midfacial restoration is accomplished by means of arch bars applied to the maxillary and mandibular teeth and then, after manipulation is held in good occlusion, by fixing the arch bars together with small rubber bands. Such fixation of the midface must be maintained until bony union and consolidation are achieved. If internal wire fixation is used, immobilization usually takes 6 to 8 weeks. Intermaxillary fixation alone requires 3 to 4 weeks to prevent further occlusal malalignment.[8, 9] However, today most internal fixation is accomplished by the use of microplates or

Copyright © 2003, Mosby, Inc. All rights reserved.

miniplates and screws (Fig. 7-1).[8–10] With this technique, intermaxillary fixation is accomplished without a waiting interval. In addition, the growing use of microplate fixation has almost made obsolete the complex internal fixation schemes accomplished with wire sutures and wire suspensions (Fig. 7-2). External fixation for facial fractures using a halo frame with fixation bars is also less common due to the utilization of microplates.

Infections of the fracture line are among the most serious complications of facial fractures. Any fracture must be considered potentially infected if it traverses the alveolus, the walls of the nasal skeleton, or the paranasal sinuses or communicates with a soft-tissue wound. Such fractures are called *compound fractures,* and appropriate antibiotic therapy reduces the chances of infection in these fractures.[1, 2, 8, 9] With good treatment the risk of infection of a maxillary or midfacial fracture is only about 2%, and the risk of osteomyelitis is 0.5%. However, a treatment delay of 2 to 3 weeks raises the incidence of osteomyelitis to 1.3%.[8, 9] Similarly, posttraumatic sinusitis occurs in 7.25% to 9% of all the patients with midfacial fractures, and proper maintenance of sinus drainage must be a therapeutic consideration.[7]

It is not uncommon to encounter multiple bone fragments during open reduction of facial bone fractures. When these fragments are few and their size is large, there is no problem. However, multiple small, thin bone fragments are difficult to handle, making accurate reduction with interfragmentary wires problematic. This is frequently encountered in fractures of the anterior maxillary wall, orbital floor, orbital roof, and frontal sinus. Therefore, many surgeons reconstruct the larger segments and discard the smaller segments. In one study, 10 patients who sustained facial fractures with multiple small, thin fragments were treated with tissue adhesive (*n*-butyl-2-cyanoacrylate). Postoperative three-dimensional (3D) CT scans demonstrated excellent reconstruction following this technique.[11]

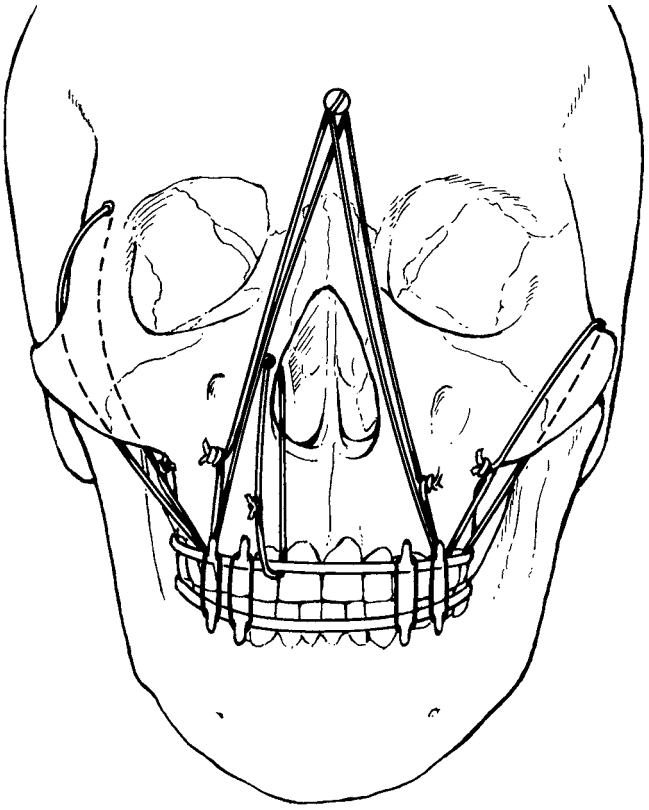

FIGURE 7-2 Frontal diagram of the different types of intraosseous wiring. The maxillary and mandibular teeth are fitted with arch bars, which are held together with rubber bands. With the patient in good occlusion, fixation can be achieved by frontomalar suspension, glabella (screw) suspension, pyriform aperture suspension, or circumzygomatic suspension.

VIEW IMAGE

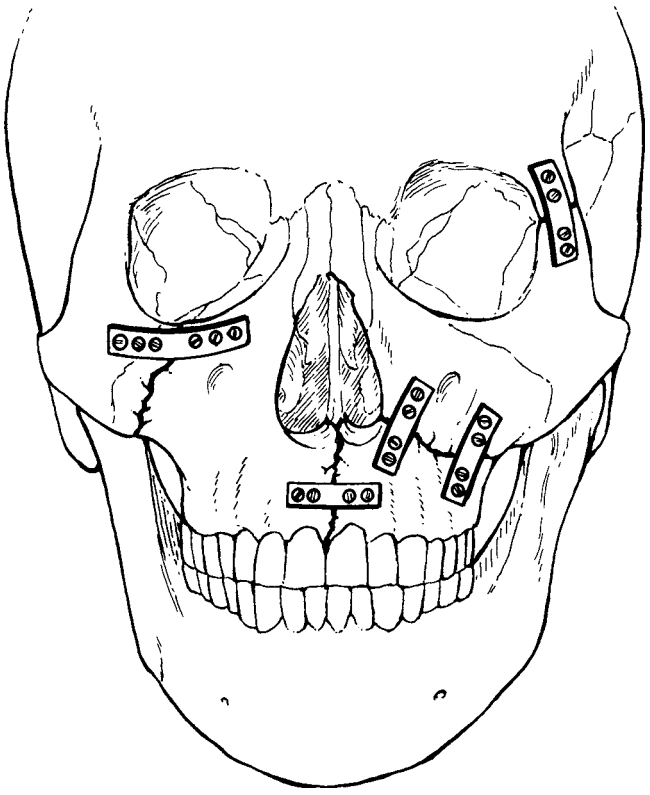

FIGURE 7-1 Frontal diagram of the use of microplates or miniplates in the fixation of midfacial fractures at typical fracture sites.

VIEW IMAGE

Thus, the concepts of treating craniomaxillofacial fractures have changed over the last 15 years, and modern imaging techniques play a central part in establishing a proper diagnosis. In addition, advanced life support and intensive care medicine now allow for early primary fracture treatment. The former principles of minimal exposure of bone fragments using small incisions have been replaced by principles from reconstructive craniofacial surgery comprising extensive subperiosteal dissection, exposure of all fracture lines, open reduction, and rigid internal fixation. Missing bony structures are replaced primarily by autogenous bone grafts or the use of exogenous materials. By using these concepts, most late esthetic and functional sequelae of facial fractures can be dramatically reduced.[12]

The final goal in reconstructing the facial skeleton of trauma patients is to obtain good cosmetic and functional outcomes. To accomplish those goals, many surgeons believe that the key to repairing midfacial fractures is the correct placement of the zygomatic arch in relation to the cranial base and the midface. In this way the transverse,

Copyright © 2003, Mosby, Inc. All rights reserved.

vertical, and sagittal diameters are regained in their correct spacial relationships.[13]

IMAGING

CT is the modality of choice for the most complete evaluation of the facial skeleton and facial soft tissues.[14] Although contrast-enhanced CT scans can assess the brain and dural spaces, which so often have associated damage in the severe accidents that cause facial trauma, these structures are better evaluated with MR imaging.[15] The most useful diagnostic information is gained by utilizing both axial and coronal CT scans.[16, 17] That is, a single-plane CT study does not provide as detailed information as an orthogonal two-plane examination. Specialized sagittal or oblique plane studies, although helpful in specific cases, are generally considered optional.[8] These specialized reconstructions usually appear degraded when compared to the original acquisition plane images; however, with the use of multidetector CT units, such deficiency may be a thing of the past.

Helical CT provides a means of obtaining better-quality two-dimensional (2D) reconstructions in any plane and provides excellent 3D reconstructions. Although some detail is lost as part of the smoothing algorithm, the 3D images serve as an excellent communication tool with the surgeons.[18, 19] These 3D images usually allow clinicians to visualize the fracture segments and their relationship to one another better than on a series of 2D scans in any one plane. Although these 3D images have been shown to be of little value in the temporal bone, they have considerable value in the skull base and the facial skeleton, especially if surfaces are involved or fragments are displaced.[20] With the newer 3D software, the fracture segments can be manipulated on screen so that the clinician can evaluate a particular treatment approach or the results of a treatment plan. In addition, 3D models can now be constructed from the CT data, allowing hands-on preoperative planning in complex cases.[18] It has been shown that measurement of the skull and facial bone landmarks by 3D reconstruction is quantitatively accurate for surgical planning and treatment evaluation of craniofacial fractures.[21]

Because MR imaging does not visualize the bone directly, small yet unstable nondisplaced facial fractures may not be seen. Although MR imaging can be helpful in differentiating blood from inflammatory reactions and edema fluid, such a distinction is rarely of clinical importance. By 48 hours after the trauma, intrasinus blood has a high methemoglobin content. If MR imaging is performed at this time, the blood has a high T1-weighted signal intensity, while edema and infection have intermediate to low T1-weighted signal intensities.[22]

In addition to evaluating the facial bones, the skull base also must be carefully examined, as fractures of the anterior cranial fossa are found in 7.1% of central midfacial fractures, 14.7% of centrolateral midfacial fractures, and 1.1% of lateral midfacial fractures.[7] The midfacial area is formed by the paired maxillae, palatal bones, inferior turbinates, lacrimal bones, nasal bones, zygomas, and solitary vomer and ethmoid bones. Central midfacial fractures include all forms of fractures that occur between the root of the nose and the alveolar processes of the maxillae, without involvement of the zygomas. These fractures include the alveolar process fracture of the maxilla, with detachment of teeth; the transverse fracture just above the floor of the nasal cavity, with separation of the palate and alveolus (Le Fort I, or Guérin's, fracture); the median or paramedian sagittal fracture of the hard palate; the pyramidal fracture, with separation of the midface either with the nasal bones (Le Fort II and Wassmund II) or without the nasal bones (Wassmund I); and fractures of the nasal bones and the nasoethmoidal region.[7]

Lastly, it must be remembered that with minor trauma, no fracture may be present and yet there are reportable findings. Thus, intrasinus hemorrhage, subcutaneous edema, subcutaneous hematomas, and foreign bodies may be present (Fig. 7-3). These findings must be noted, as they serve to explain

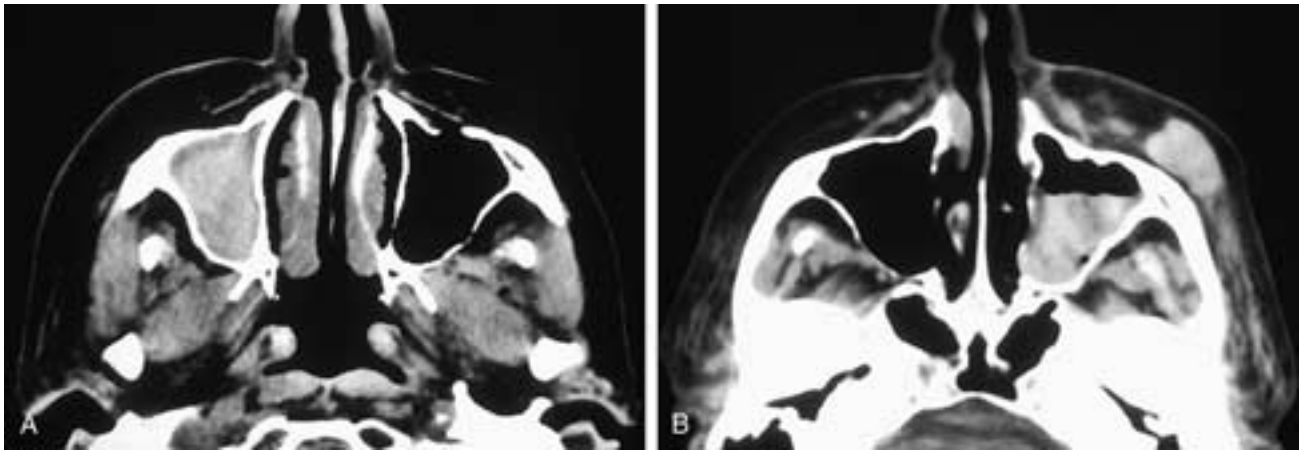

VIEW IMAGE

FIGURE 7-3 Axial CT scan (**A**) shows high-attenuation hemorrhage within the right maxillary sinus. There is slight fullness of the soft tissues in the right cheek area. This patient had received blunt trauma to the right face and presented with epistaxis. No fractures were present. Axial CT scan (**B**) on another patient shows high-attenuation fluid within the left maxillary sinus. There is also edema and a hematoma within the subcutaneous tissues of the left cheek. This patient was in the passenger seat during a low-velocity car accident and presented with a cheek deformity and epistaxis. No fractures were present.

Copyright © 2003, Mosby, Inc. All rights reserved.

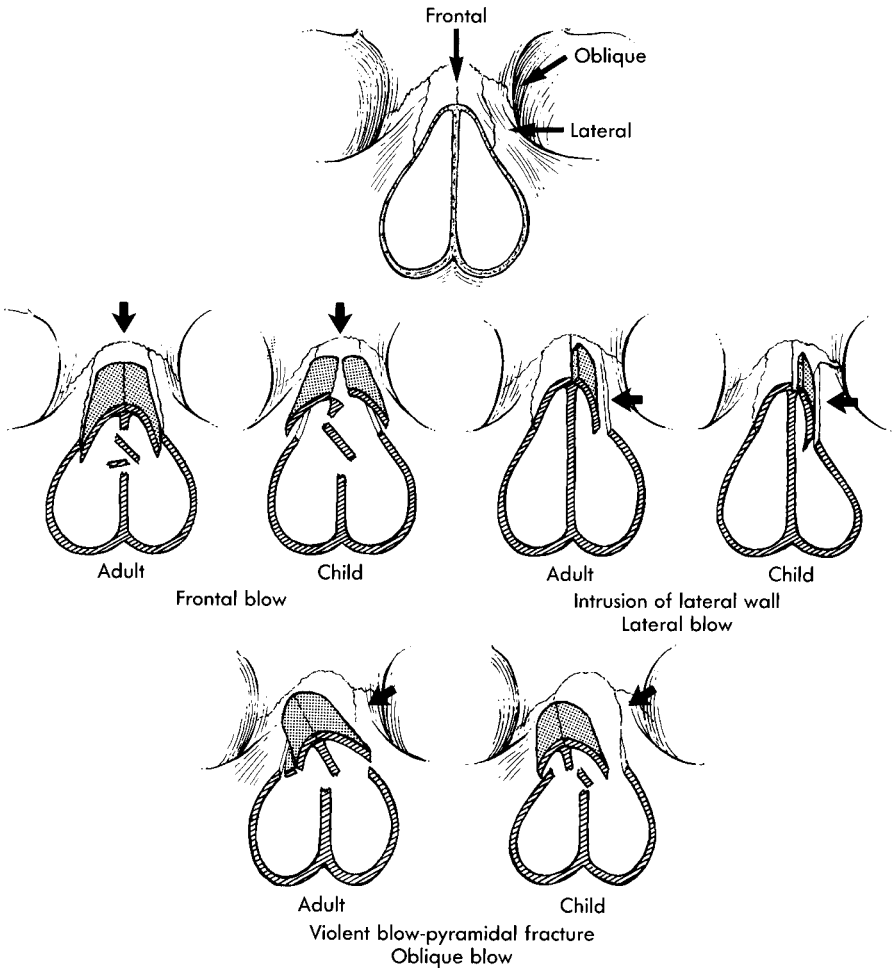

FIGURE 7-4 Frontal diagram showing different common types of nasal fractures in children and adults that result from frontal, lateral, and oblique blows.

VIEW IMAGE

facial deformity and epistaxis that may clinically suggest a fracture.

NASAL FRACTURES

Nasal injuries are the most common fractures of the facial skeleton; about 50% of facial fractures are isolated fractures of the nasal pyramid.[10, 14] That is, nasal fractures can occur either as isolated fractures or in association with other facial injuries. A distinction should be made between fractures of the cartilaginous nasal structures and those of the nasal bones because they represent different types of injuries.[1, 2]

The extent of disruption of the nasal structure relates to the direction and degree of the force causing the injury (Fig. 7-4). The lateral impact injury is more common than the frontal injury; 66% of nasal fractures result from a lateral force, but only 13% are the result of a frontal impact.[23] Although not universally used, one of the main classification systems for nasal bone fractures divides the frontal injuries into three types. In plane 1 injuries, the injury does not extend dorsal to a plane that extends from the caudal tip of the nasal bones to the anterior nasal spine. The majority of the impact is absorbed by the lower nasal cartilages and the nasal tip. Separation and avulsion of the upper lateral nasal cartilages occur, and occasionally there is posterior dislocation of the septal and alar cartilages. In plane 2 injuries, the external nose, the nasal septum, and the anterior nasal spine are all involved. There is splaying or flattening of the nasal bones; septal cartilage tears and overriding may occur. In plane 3 injuries, the orbital and possibly the intracranial structures are also involved. Typically there are comminuted nasal bone fractures, and fractures of the frontal processes of the maxillae, the lacrimal bones, and the ethmoid labyrinth. Severe nasal septal injuries can result in upward extension that may involve the cribriform plate and orbital roof.[23]

With weak lateral (oblique) impacts, plane 1 injuries result and involve only the ipsilateral nasal bone. Typically the lower nasal bone, the frontal process of the maxilla, and possibly the pyriform aperture margin are medially displaced. Lateral plane 2 injuries result from a greater force than plane 1 injuries. The fracture results in medial displacement of the ipsilateral nasal bone and lateral displacement of the contralateral nasal bone and nasal septum. Lateral plane 3 injuries are still more severe and result in nasal bone fractures with involvement of the nasal septum, the frontal process of the maxilla, and the lacrimal bone.[23]

In summary, the majority of nasal bone fractures involve the thinner, distal third of the nasal bones, and the nasoethmoid margin remains intact.[1, 2, 10] A lateral blow to

Copyright © 2003, Mosby, Inc. All rights reserved.

the nose usually causes a simple cartilage depression or fracture of only the ipsilateral nasal bone (Fig. 7-5). However, an anteriorly placed nasal blow usually fractures both nasal bones at their lower ends, and because the force is absorbed by the nasal septum, the septum is also displaced and fractured.

With a greater force, the entire nasal pyramid, including the frontal processes of the maxillae, may become detached (Fig. 7-6).[10] When the nasal bones and septum are displaced posteriorly, a saddle nose deformity and splaying of the nose result.[1, 2] In more severe fractures, traumatic hypertelorism and telecanthus may occur, and hemorrhage caused by rupture of the anterior or posterior ethmoidal arteries may be severe.

In adults, the internasal suture is solidly ossified so that the nasal bones function as a unit between the frontal processes of the maxilla. However, in children the internasal suture is not yet ossified, and the nasal bones are essentially hinged on each other while resting on the frontal processes of the maxillae. As a result, the frontal processes usually are

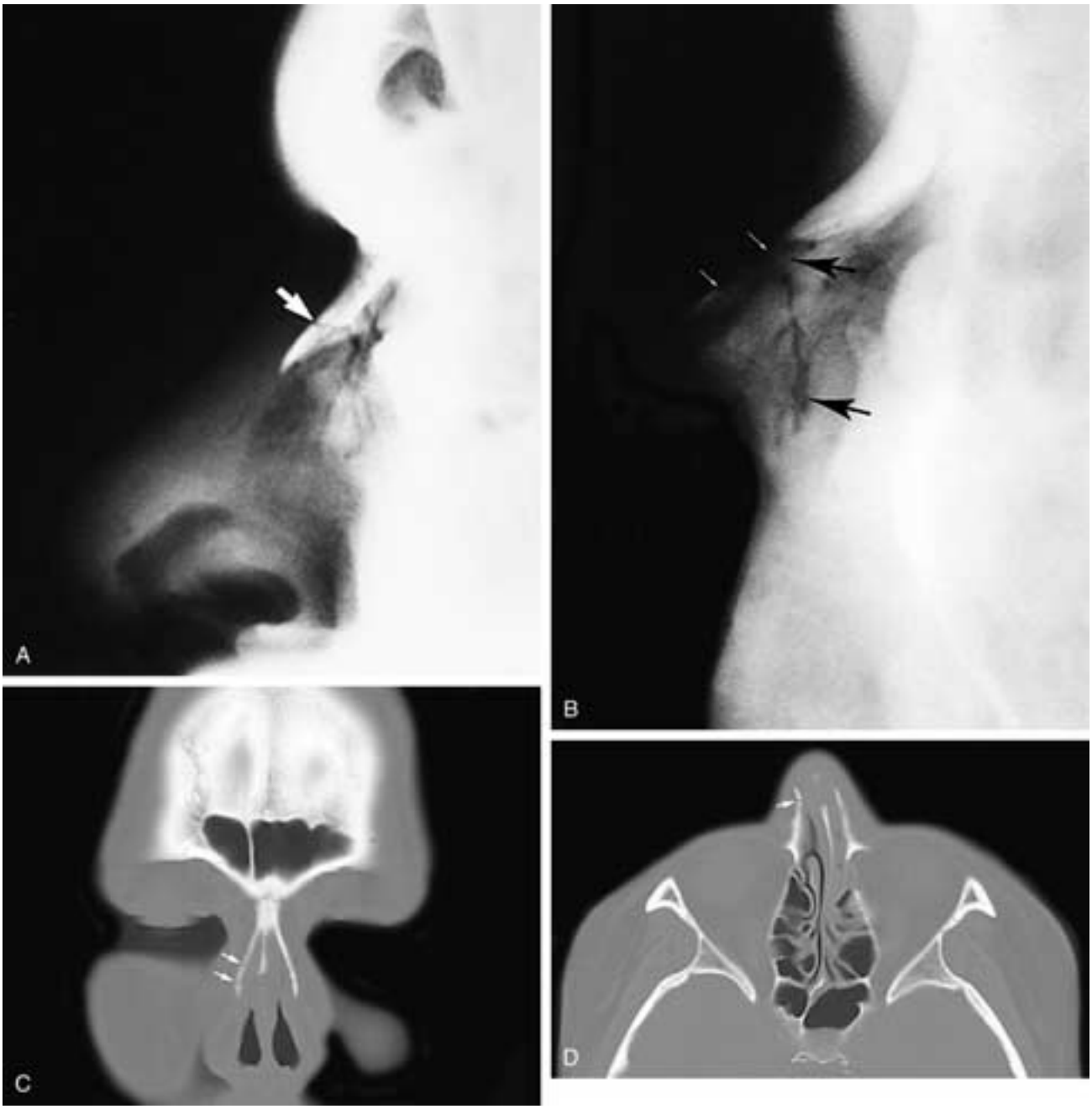

VIEW IMAGE

FIGURE 7-5 Lateral plain film (**A**) shows a nondisplaced fracture (*arrow*) extending from the midline nasal bones laterally. Lateral plain film (**B**) shows comminuted nasal bone fractures (*small arrows*) with extension into the frontal processes of the maxilla (*arrows*). Coronal (**C**) and axial (**D**) CT scans on another patient show minimally displaced right nasal fractures (*arrows*).

Illustration continued on following page

Copyright © 2003, Mosby, Inc. All rights reserved.

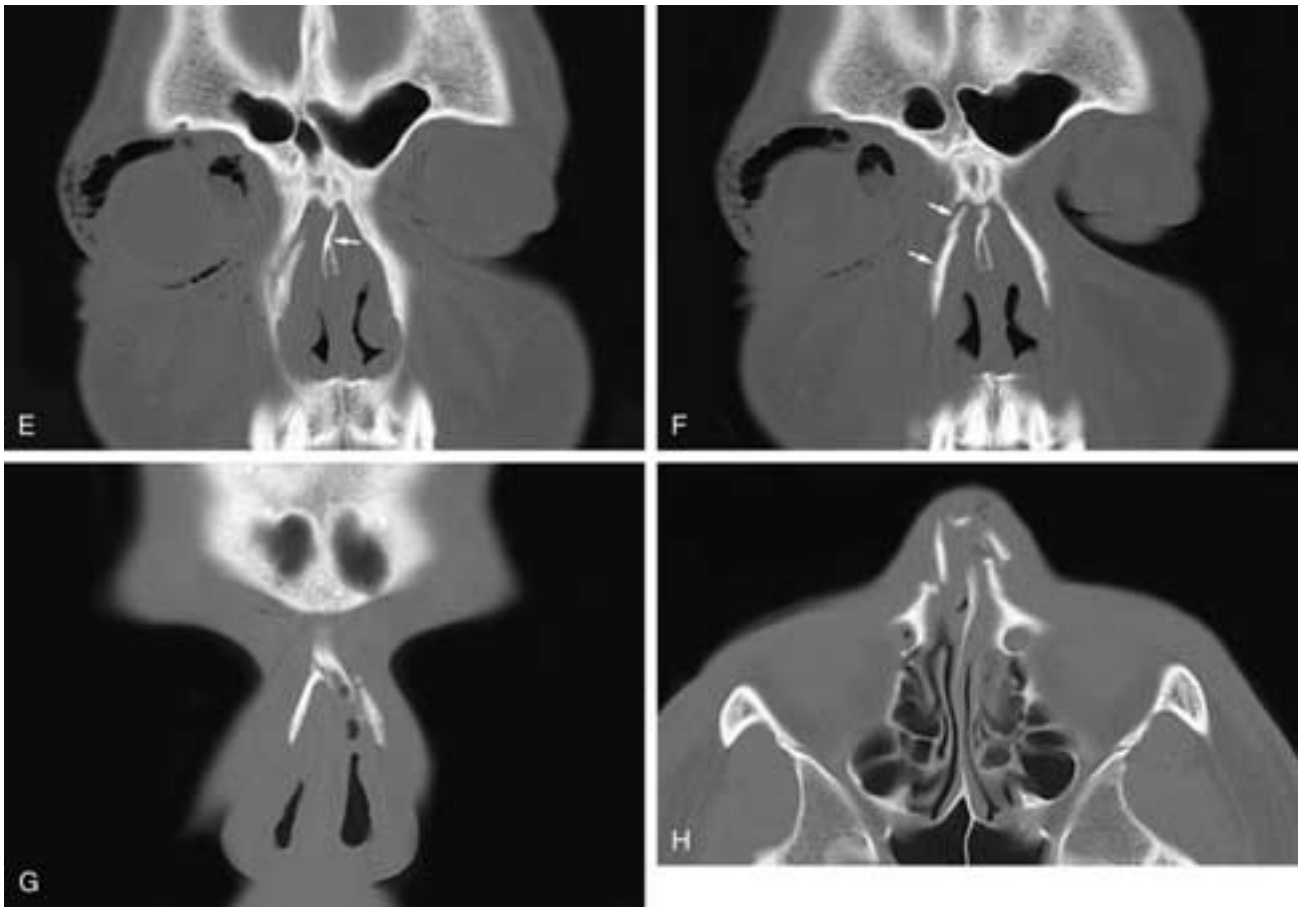

VIEW IMAGE

FIGURE 7-5 *Continued.* Coronal CT scans (**E, F**) on a different patient show medially displaced comminuted fractures of the right nasal bone (*arrow* in **E**) and a displaced fracture of the anterior bony nasal septum (*arrows* in **F**). There is also orbital emphysema on the right side from an ethmoid fracture. Coronal (**G**) and axial (**H**) CT scans on yet another patient show comminuted fractures of the nasal bones and the right frontal process of the maxilla.

not fractured in childhood nasal injuries.[1, 2] In fact, it has been noted that in children there is a less prominent nasal projection (the nasal bone length is almost equal to the width), and there is increased elasticity and stability of the midface due to the presence of developing bone, the relative lack of sinus pneumatization, and the state of mixed dentition. There is also increased shielding of the facial skeletal structure due to the disproportionate amount of soft tissue relative to bone, and the small weight and size of the child decrease inertial impact forces.[23]

If the nose is struck from the side and near its base, the lateral cartilaginous walls may be displaced, and this type of injury is not identified radiographically. Further, edema and hemorrhage usually fill in the resulting surface depression and obscure clinical detection of the deformity. If these injuries and simple nasal fractures initially go undetected, especially if they occur in conjunction with more serious injuries, the inadequately treated nasal trauma may result in cosmetic deformity and functional impairment.[1, 2]

If the nasal trauma results in buckling of the nasal septal cartilage, the fractured cartilage fragments may overlap one another, thereby separating the perichondrium from the cartilage. This event allows a hematoma to develop in the space between the perichondrium and the cartilage, and this hematoma interferes with the cartilage's overlying mucoperiosteal vascular supply. Eventual cartilage necrosis occurs. If such a septal hematoma is not initially identified and treated, it becomes an organized hematoma that causes a firm, unyielding thickening of the septum and impaired breathing.

If a septal hematoma becomes infected after mucosal injury, a septal abscess develops, with fever, pain, septal swelling, eventual cartilage necrosis and resulting loss of nasal support and the development of a saddle nose deformity, and possible intracranial spread of the infection.[1, 2] To avoid these complications, it is essential to have careful clinical examination of the nasal septum and early evacuation of a septal hematoma. If imaging studies of the nose and nasal fossae are also performed, the radiologist should always direct attention to the nasal septum to identify any localized septal swelling or traumatic deviation (septal bone fracture and/or cartilage dislocation).[1, 2]

One study demonstrated that, based on clinical examination, 25% of patients required surgical reduction of a nasal fracture or dislocation despite a negative plain film examination.[24] In addition, there is a poor correlation (6.6% to 10%) between the plain film demonstration of a fracture and the need for surgical reduction.[23] In more severe injuries, a higher detection rate and better clinical correlation are achieved with the use of CT. Actual fracture of

Copyright © 2003, Mosby, Inc. All rights reserved.

cartilage may not be imaged by any modality. However, in these cases, cartilage dislocation or a focal hematoma usually draws attention to the injury.

CENTRAL MIDFACIAL FRACTURES

Nasoorbital Fractures

The nasoorbital fracture most often results from a blow over the bridge of the nose. The force displaces the nasal pyramid posteriorly, fracturing the nasal bones, frontal processes of the maxillae, lacrimal bones, ethmoid sinuses, walls of the frontal sinuses, cribriform plate, and nasal septum. The ethmoid lamina usually fractures on itself in an accordion fashion, and this is best visualized on CT in the axial plane. Posttraumatic hypertelorism and telecanthus may result, as well as associated damage to the lacrimal apparatus and the medial canthal tendon (Fig. 7-7). Careful attention also should be given to any fractures involving the bones near the optic canal, as a surgical attempt to reduce the facial bone fractures may displace such an optic canal fracture and cause blindness.

In the floor of the anterior cranial fossa the dura is thin and firmly adherent to the bone. Thus the skull base and dura in the anterior cranial fossa function as a unit, and a fracture through this region invariably tears the dura. Dural tears provide a pathway for CSF rhinorrhea and the development of an intracranial pneumocele or infection (Fig. 7-8).[1, 2] In one series, motor vehicle accidents accounted for nearly 70% of these cases, and 63% of the patients had associated severe nonfacial injuries. In addition, 51% of the cases had central nervous system injury and 42% of the patients had CSF leakage. Telecanthus was present in 12% of the cases.[25, 26] Thus, if a fracture in the region of the nasion is identified on imaging, a careful search should always be made for any associated intracranial traumatic complications.

VIEW IMAGE

FIGURE 7-6 Lateral plain film shows a nasal fracture through the frontonasal suture (*arrow*) with posterior displacement of the nasal bones.

Isolated Maxillary/Palatal Fractures

Alveolar fractures are the most common isolated maxillary fractures. An upward blow to the mandible can thrust the mandible into the maxilla and push the maxillary teeth upward and outward. This movement, in turn, fractures the alveolus. Because of the strong soft-tissue support over the alveolus, these isolated fractures rarely are displaced. The involved teeth often are displaced or devitalized, and such alveolar fractures in children may damage the tooth germs.[7] Partial fractures of the maxilla can result from a blow delivered by a narrow object directly over the anterior maxillary wall. The fractures usually involve the anterior and lateral antral walls and extend toward the pyriform aperture and down into the maxillary alveolus (Figs. 7-9 to 7-12).

Sagittal fractures of the palate result from either an axial or an oblique blow to the chin or a direct blow to the upper jaw. The fracture passes through the weakest portion of the palatine process of the maxilla, which is in a sagittal plane just off of the midline. The midline itself is reinforced by the vomer, whereas the lateral hard palate is supported by the alveolus. In more violent trauma a sagittal midline fracture can occur, and comminuted palatal fractures are associated with other central or centrolateral facial fractures.[7]

Le Fort I Fractures

The Le Fort I (Guérin's) fracture results from a blow delivered over the upper lip region and is characterized by detachment, at a level just above the floor of the nasal cavity, of the upper jaw with the tooth-bearing segments from the caudal portions of the maxillary sinuses and the lower nasal septum. The fracture extends through the lower nasal septum, the lower walls of the maxillary sinuses, and the lower pterygoid plates. Thus the fracture segment includes the entire palate, maxillary alveolus and teeth, and portions of the pterygoid plates. This ''floating palate'' is displaced posteriorly, resulting in malocclusion and hemorrhaging into the antra (Figs. 7-13 and 7-14).[7]

The presence of upper arch dentures can modify the fracture patterns occurring in midfacial trauma. In a group of such patients with predominantly Le Fort I fractures, an atypical fracture path was noted, with a vertical fracture passing from the main Le Fort I fracture to the inferior orbital rim. Full upper arch dentures generally protected the upper alveolus from fracture but, where there was discontinuity of the prosthesis, alveolar fractures mirrored the edge of the denture as it crossed the alveolus. Thus the clinician should be alerted to the possibility of unusual maxillary fractures in denture wearers.[27]

Copyright © 2003, Mosby, Inc. All rights reserved.

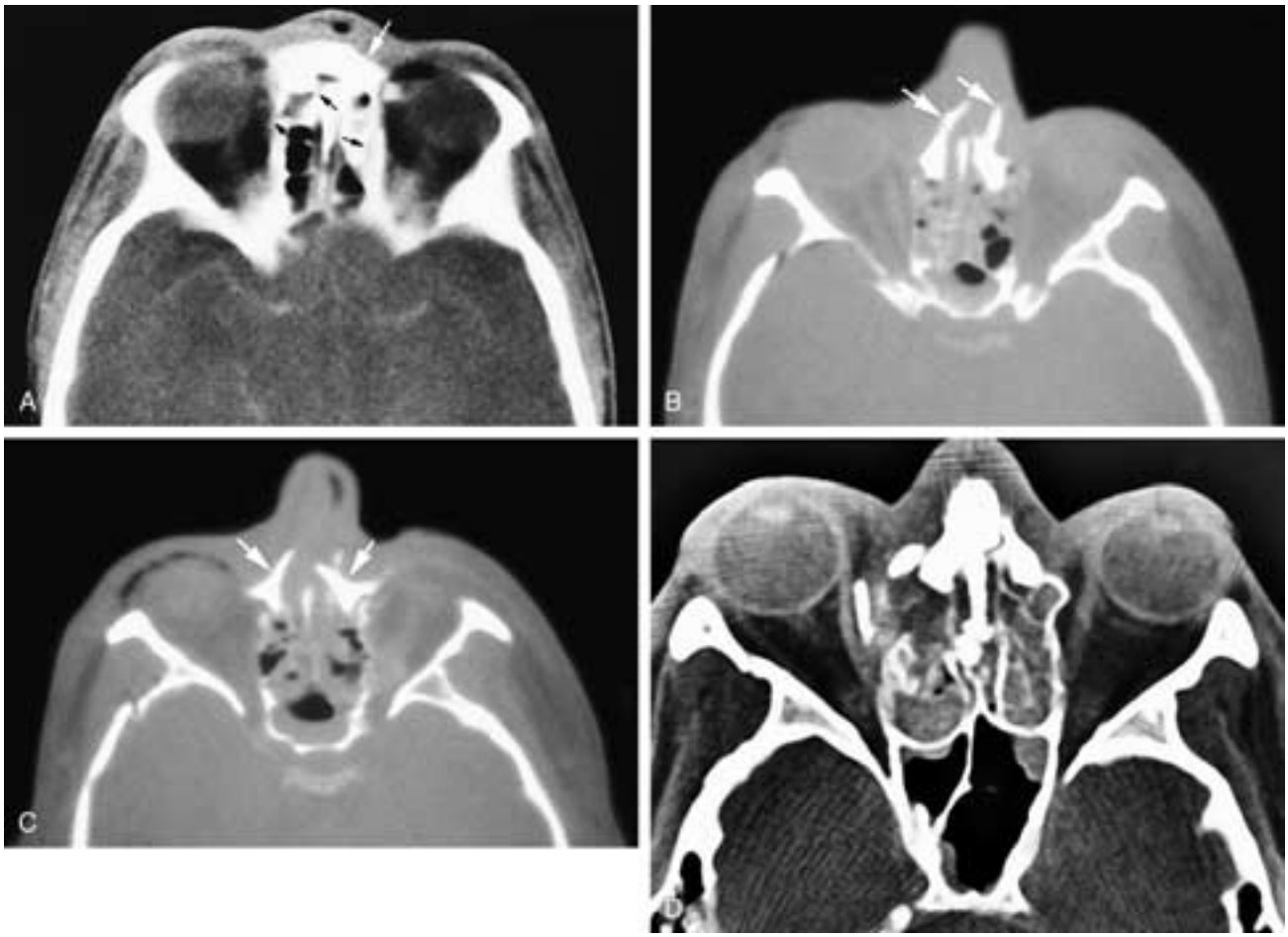

VIEW IMAGE

FIGURE 7-7 Axial CT scan (**A**) shows a nasoorbital fracture with posterior displacement of the region of the nasion (*white arrow*) and fractures through the fovea ethmoidalis (*small arrows*). Axial CT scan (**B**) shows a nasoorbital fracture with posterior displacement and rotation to the left side of both nasal bones and the frontal processes of each maxilla (*arrows*). There are also fractures of the ethmoids with some hypertelorism. Axial CT scan (**C**) shows a nasoorbital fracture with posterior and medial displacement of both nasal bones and each frontal process of the maxilla. There are also multiple fractures of the ethmoid complex and some hypertelorism. Axial CT scan (**D**) shows a nasoorbital fracture with posterior displacement of the nasal bones and fractures and hypertelorism of the ethmoid complex.

Le Fort II Fractures

A strong, broad blow over the central facial region causes a pyramidal fracture, one of the most severe midfacial fractures. The high, central midface fracture (Le Fort II) is characterized by a fracture line that extends through the root of the nose, then runs bilaterally to involve the lacrimal bones and medial orbital walls. On each side the fracture line then turns anteriorly along the floor of the orbit near the infraorbital canal and extends down the zygomaticomaxillary suture and the anterior wall of the maxilla; posteriorly the fracture goes down across the infratemporal surface of the maxilla and finally extends through the lower pterygoid plates. This creates a pyramid-shaped central facial fracture segment. The deep central midface (Wassmund I) fracture spares the nasal bones and extends from the lateral edges of the pyriform aperture back across to the lacrimal bones and into the medial orbital walls. From this point the fracture is the same as the Le Fort II (Figs. 7-15 and 7-16).[7] In the Le Fort II and Wassmund I fractures the zygomatic bones remain attached to the cranium. The pyramid-shaped fracture segment (the central midface) is posteriorly displaced, resulting in a ''dishface'' deformity, malocclusion, and hemorrhage. Anesthesia or paresthesia of one or both of the infraorbital nerves occurs in 78.9% of the cases.[10]

Le Fort III Fractures

Centrolateral midfacial fractures are characterized by separation of the entire facial skeleton from the skull base. Such a craniofacial dysjunction has a fracture line that extends through the root of the nose, then runs bilaterally across the lacrimal bones and medial orbital walls, to continue posterolaterally across the floor of each orbit to the inferior orbital fissure. At this point on each side, one portion of the fracture line extends laterally and upward across the lateral orbital wall to end near the zygomaticofrontal sutures. A second fracture line extends from the

Copyright © 2003, Mosby, Inc. All rights reserved.

VIEW IMAGE

FIGURE 7-8 The Caldwell view (**A**) shows massive intracranial air in a patient who had a nasoorbital fracture. Coronal CT scan (**B**) shows intracranial air in another patient with a nasoorbital fracture.

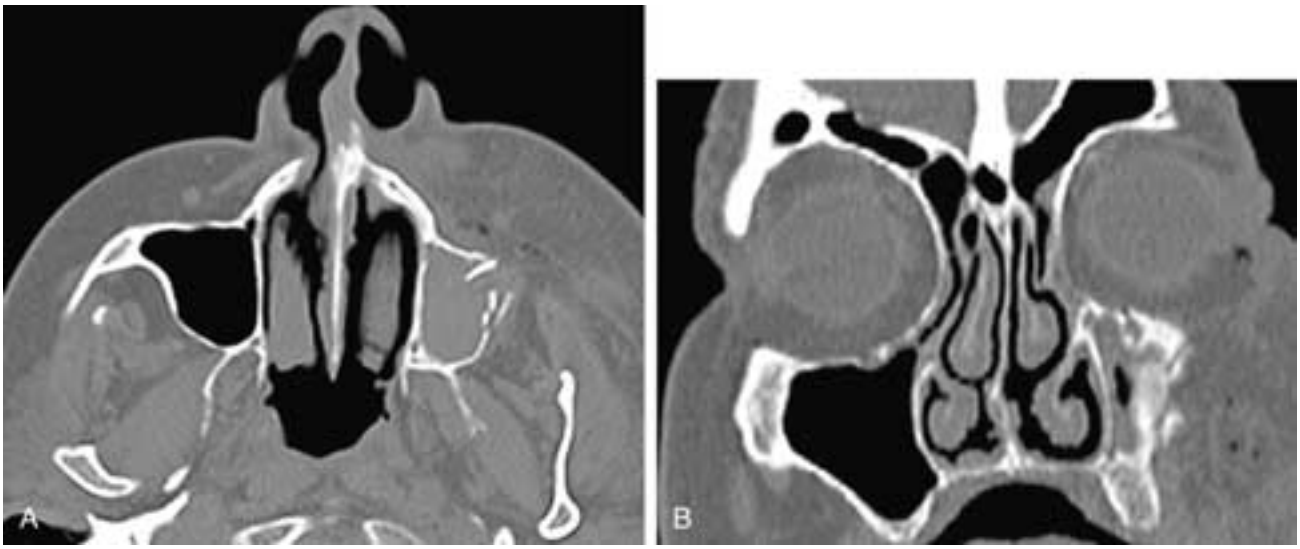

VIEW IMAGE

FIGURE 7-9 Axial (**A**) and Coronal (**B**) CT scans show a comminuted fracture of the anterolateral left antral wall. This type of fracture usually is the result of a blow from a narrow object.

Copyright © 2003, Mosby, Inc. All rights reserved.

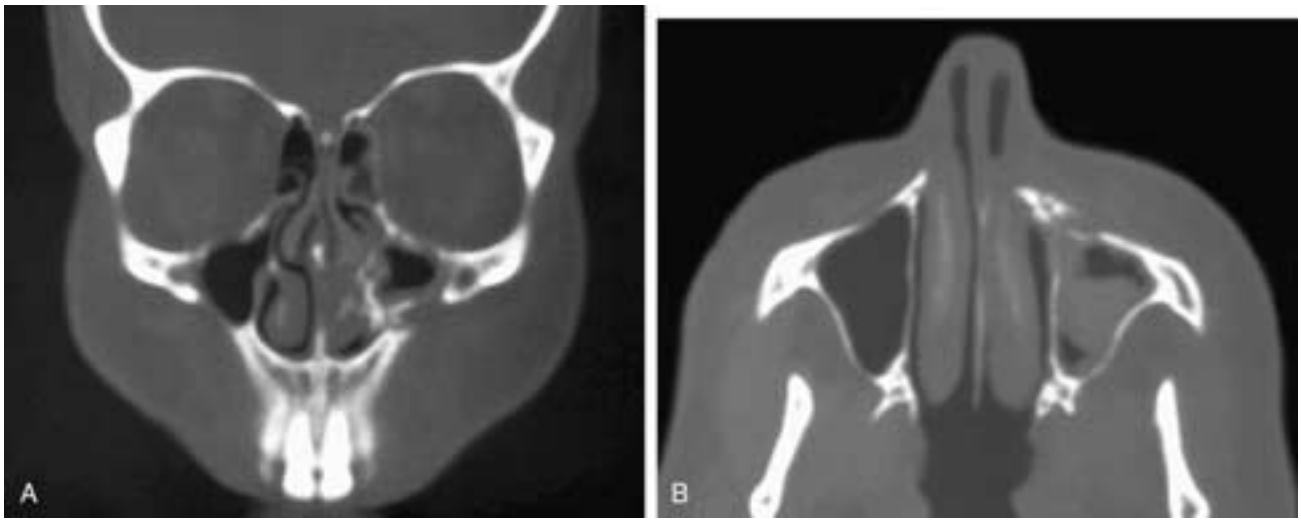

VIEW IMAGE

FIGURE 7-10 Coronal (**A**) and axial (**B**) CT scans show comminuted fractures involving the left anteromedial maxilla.

orbital floor down across the back of each maxilla to the lower portion of the pterygoid plates. The zygomatic arches also are fractured, thereby completing the separation of the facial skeleton from the skull base. Such a fracture is called a Le Fort III or Wassmund IV fracture (Figs. 7-17 to 7-19). The same fracture without inclusion of the nasal bones is called a Wassmund III fracture (Fig. 7-17B), and the fracture line extends from each side of the pyriform aperture up to the lacrimal bones. The fracture then continues as a Le Fort III fracture. The distinguishing feature between the Le Fort III fracture and the Le Fort II fracture is the inclusion in the Le Fort III fractured segment of the zygomas and lateral orbital walls. These patients have a dishface deformity, CSF rhinorrhea, hemorrhage, damage to the lacrimal apparatus, and malocclusion. The infraorbital nerves are involved in 69.3% of cases.[10]

FIGURE 7-11 Coronal CT scan (**A**) shows a maxillary fracture involving the anterior lower antral wall. The fracture segments are prolapsed into the antrum and nasal cavity. There is also orbital and subcutaneous emphysema. Axial (**B**) and coronal (**C**) CT scans on another patient show fractures limited to the lateral walls and roof of the right maxillary sinus with subcutaneous emphysema.

VIEW IMAGE

Copyright © 2003, Mosby, Inc. All rights reserved.

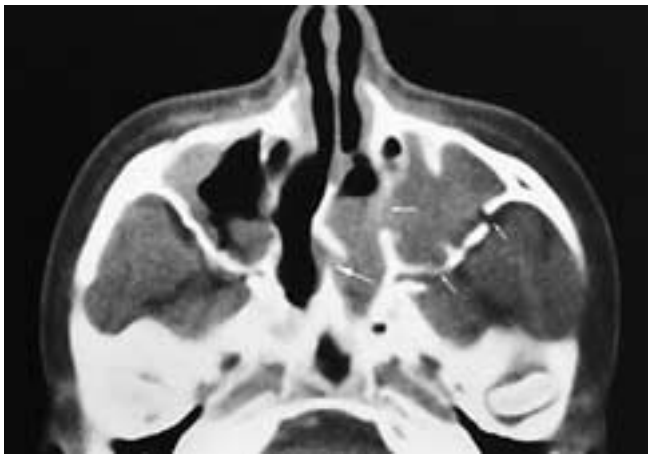

FIGURE 7-12 Axial CT scan shows fractures of the left maxillary sinus's posterolateral and medial walls (*small arrows*) and a fracture of the nasal septum (*large arrow*).

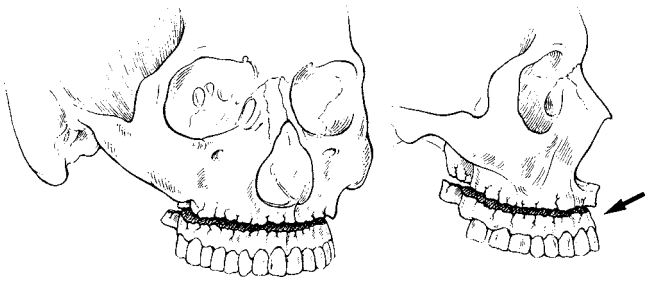

FIGURE 7-13 Diagram of a Le Fort I fracture, which results in a ''floating'' palate.

LATERAL MIDFACIAL FRACTURES

Lateral midfacial fractures include the zygomatic fractures (trimalar, or tripod), zygomatic arch fractures, zygomaticomaxillary fractures, zygomaticomandibular fractures, and fractures of the floor of the orbit (blow-out fractures).

Trimalar (Zygomatic) Fractures

Zygomatic fractures are the second most common facial fractures after nasal bone trauma. The fracture line in a zygomatic fracture extends from the lateral orbital wall (zygomaticofrontal suture and the zygomaticosphenoid suture) to the inferior orbital fissure, then across the orbital floor near the infraorbital canal, down the anterior maxilla near the zygomaticomaxillary suture, and up the posterior maxillary wall back to the inferior orbital fissure. There is also a fracture through the weakest part of the zygomatic arch, which is about 1.5 cm dorsal to the zygomaticotemporal suture. The infraorbital nerve is impaired in 94.2% of the cases.[10] These fractures are usually and traditionally referred to as trimalar or tripod fractures because these are fractures through the three bony connections of the zygoma. That is, there are fractures (1) through the lateral orbital wall, (2) separating the zygoma and maxilla, and (3) through the zygomatic arch. Rarely these fractures have been referred to as quadramalar fractures, because the fractures extend through four suture lines (zygomaticofrontal, zygomaticosphenoid, zygomaticotemporal, and zygomaticomaxillary). Nonetheless, the more common term is trimalar fracture, recognizing that there is one fracture line through the

FIGURE 7-14 Coronal (**A**) and lateral (**B**) multidirectional tomograms show a Le Fort I fracture (*curved arrows*) and its extension through the pterygoid plates (*arrows*).

Copyright © 2003, Mosby, Inc. All rights reserved.

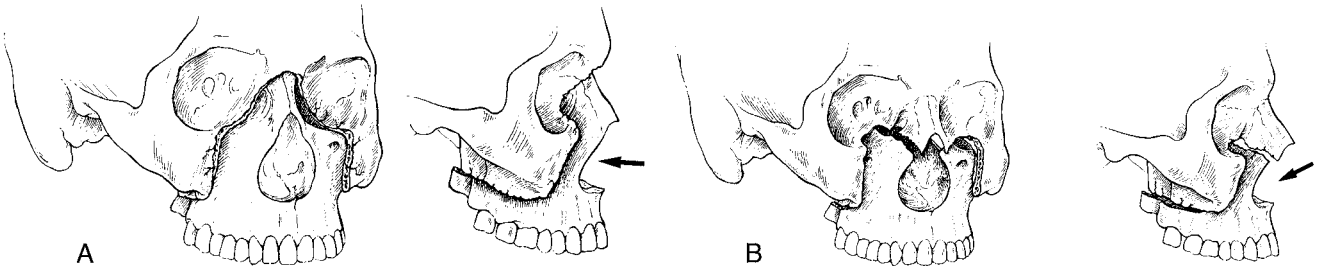

VIEW IMAGE

FIGURE 7-15 Diagram (**A**) of a Le Fort II fracture. The midfacial fracture segment is pyramidal in shape, and these fractures are often called *pyramidal fractures.* Diagram (**B**) of a Wassmund I fracture. This is the same type of fracture as Le Fort II, except that the nasal bones are spared.

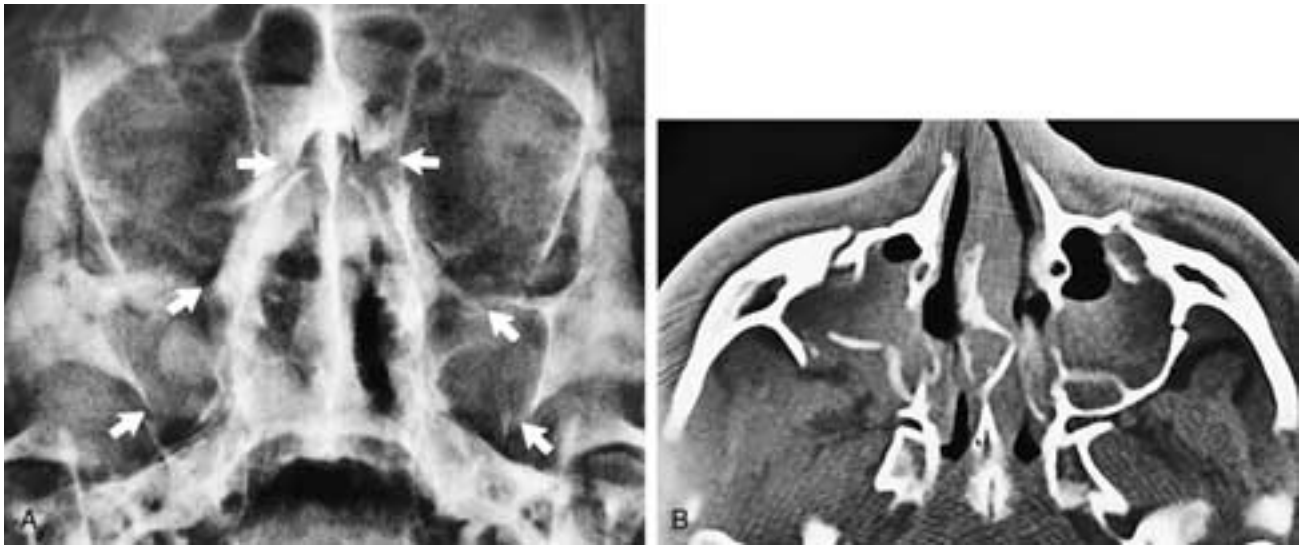

VIEW IMAGE

FIGURE 7-16 Waters view (**A**) shows a Le Fort II fracture (*arrows*) that creates a pyramid-shaped fracture segment. Axial CT scan (**B**) shows a Le Fort II fracture. The midface fracture segment is clearly seen, and the zygomas are uninvolved. On more caudal scans the pterygoid plates were fractured, and on more cranial scans the ethmoid sinuses and orbital floors were fractured.

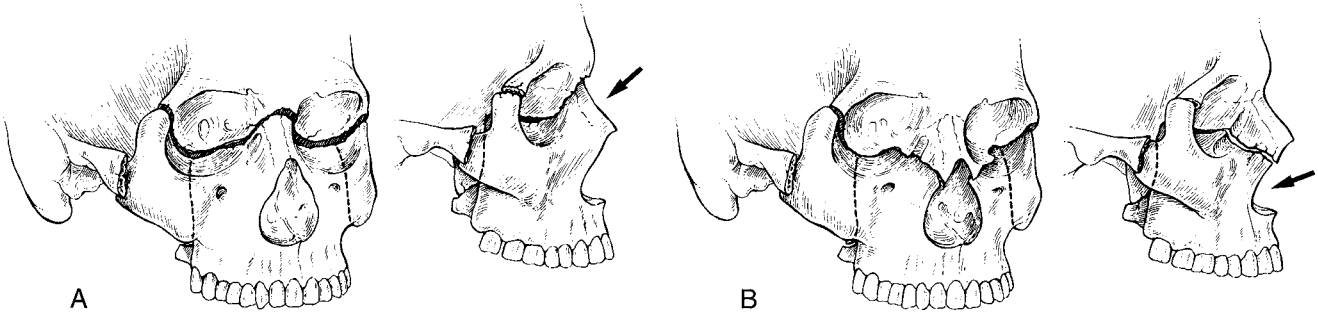

VIEW IMAGE

FIGURE 7-17 Diagram (**A**) of a Le Fort III fracture. There is separation of the viscerocranium and the facial bones. The dotted fracture lines extend down the posterior maxillary sinus walls. The fracture involves the lateral orbital walls and the zygomatic arches. Diagram (**B**) of a Wassmund III fracture. This fracture is similar to the Le Fort III fracture, except that the nasal bones are not involved. The dotted fracture lines extend down the posterior maxillary sinus walls.

Copyright © 2003, Mosby, Inc. All rights reserved.

VIEW IMAGE

FIGURE 7-18 Waters view shows a Le Fort III fracture (*arrows*). Hemorrhage is present in both antra.

lateral orbital wall that actually goes through two suture lines (zygomaticofrontal and zygomaticosphenoid).

In one study, as many as one-third of all patients who suffered comminuted malar fractures had an ocular disorder, but only 16.7% of patients with a blow-out fracture had ocular problems. Decreased visual acuity was the primary problem accompanying the majority of significant eye injuries.[28–30]

Several classifications of lateral midface fractures have been proposed.[31] Each considers the displacement of the zygoma as it relates to the clinical severity of the fracture and how the malar position may be used to plan treatment. Zygomatic fractures account for 49% to 53% of the midface fractures, and in one study 69% of midfacial fractures involved the zygomatic complex, either alone or in combination with other midface fractures.[7, 31] The reports vary considerably as to the frequency of the different malar fracture positions. One of the more complete classifications, including the fracture type, frequency, and postreduction stability, is shown in Table 7-1.

Table 7-1
TYPE, FREQUENCY, AND POSTREDUCTION STABILITY OF ZYGOMATIC FRACTURES

Fracture Type	Frequency	Postreduction Stability (%)
Nondisplaced	11	100
Isolated arch	16	93
Rotation around vertical axis	12	
Medial	3.5	57
Lateral	8.5	88
Rotation around horizontal axis	6	
Medial	10	
Lateral	5	50
Displacement without rotation	31	
Medial	11.5	39
Lateral	1	0
Posterior	12	92
Inferior	6.5	0
Isolated rim	9.5	47
Complex	14.5	0

Before the use of miniplates and microplates, this type of classification allowed the clinician to better predict the postoperative stability of the fracture and thus influence the degree of fixation needed (Figs. 7-20 to 7-25). When the malar eminence is rotated in more than one axis or displaced in more than one direction, the primary rotation and displacement are usually used to classify the fracture. However, these complex cases point out the limitation of any of these classification systems. In the present era, the use of miniplates and microplates is common, and there is little

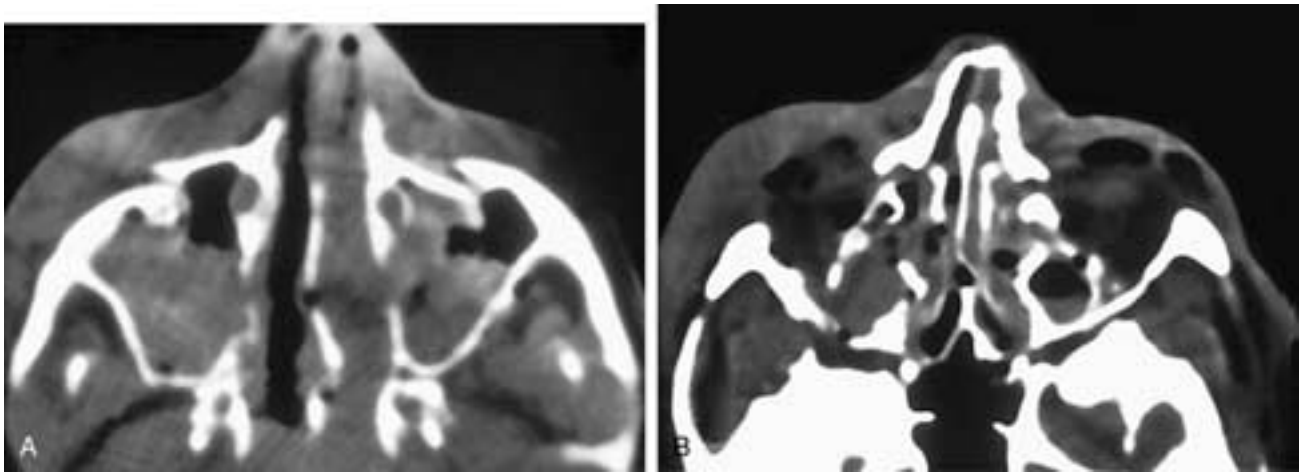

VIEW IMAGE

FIGURE 7-19 Axial CT scans show a Le Fort III fracture. The more caudal aspects of the fracture (**A**) are similar to those of a Le Fort II fracture. However, the more cranial fractures (**B**) separate the facial bones from the cranium.

Copyright © 2003, Mosby, Inc. All rights reserved.

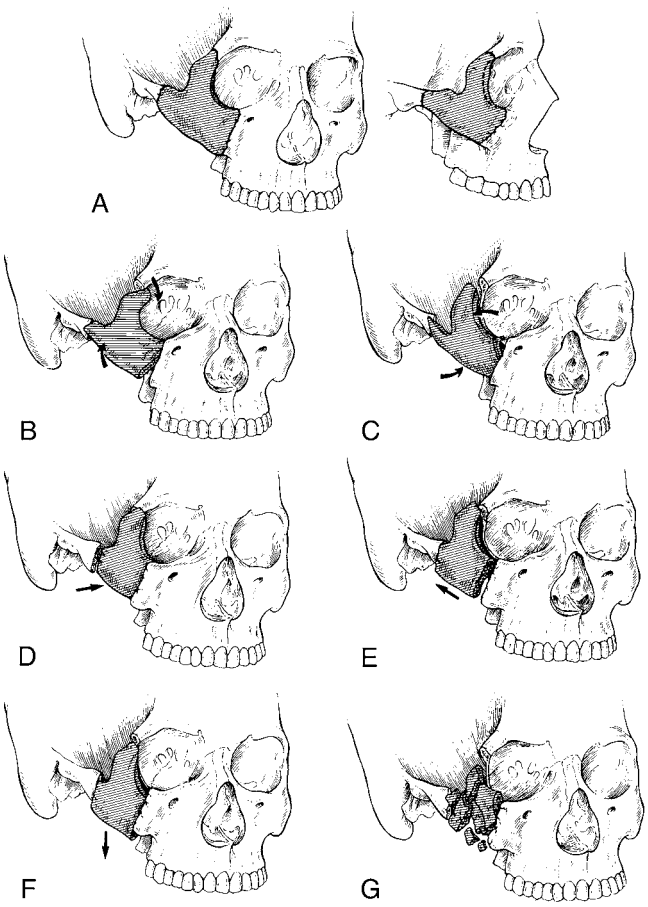

VIEW IMAGE

FIGURE 7-20 Diagram (**A**) of a nondisplaced trimalar zygomatic fracture. Diagram (**B**) of a zygomatic fracture with clockwise (medial) rotation around a horizontal axis (anterior to posterior) through the zygoma. Diagram (**C**) of a zygomatic fracture with counterclockwise (lateral) rotation around a horizontal axis (anterior to posterior) through the zygoma. Diagram (**D**) of a zygomatic fracture with pure medial displacement. Diagram (**E**) of a zygomatic fracture with pure posterior displacement. Diagram (**F**) of a zygomatic fracture with pure inferior displacement. Diagram (**G**) of a zygomatic comminuted (complex) fracture.

reliance on a classification system to determine the treatment type. It is used by the few surgeons who believe that not all zygomatic fractures need fixation after reduction. It is generally believed that the primary cause of movement of a reduced but nonfixed malar fracture is the masseter muscle's pulling force on the zygoma.[32]

Zygomaticomaxillary Fractures

Zygomaticomaxillary fractures differ from trimalar fractures in that the former fractures include a maxillary segment. Thus, a zygomaticomaxillary fracture involves the orbital floor, extends down the anterior maxilla (often more medially than in a typical trimalar fracture) near the infraorbital foramen, runs to the premolar region, and then extends across the palate to the maxillary tuberosity and lower pterygoid plates.

Zygomaticomandibular Fractures

Zygomaticomandibular fractures differ from zygomatic fractures only by the additional fracture of the mandibular condyle, coronoid process, or both.

Zygomatic Arch Fractures

When there are isolated fractures of the zygomatic arch, there usually are at least three discrete fracture lines, creating two fracture segments. These pieces are displaced medially and downward, reflecting the direction of the impact force. The fracture pieces may impinge on the temporalis muscle or coronoid process of the mandible and interfere with movement of the lower jaw (Figs. 7-26 and 7-27). Trismus is reported in 45% of zygomatic arch fractures and in about 33% of all zygomatic fractures.

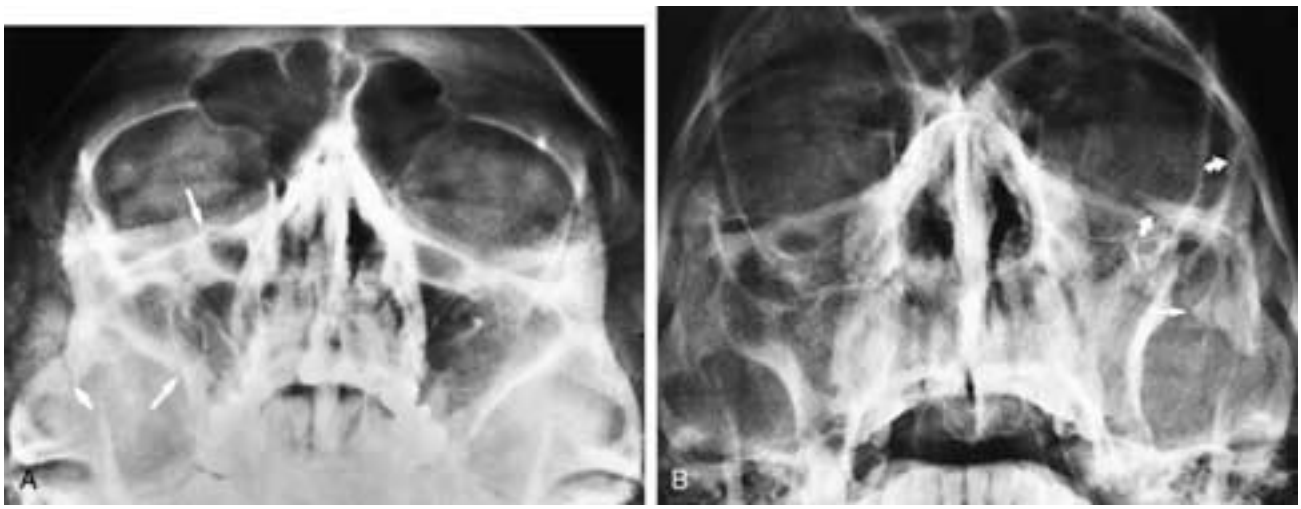

VIEW IMAGE

FIGURE 7-21 Waters view (**A**) shows a nondisplaced right zygomatic fracture. The fractures through the maxilla and the zygomatic arch are seen (*arrows*). However, the zygomaticofrontal fracture is not visualized because there was only a slight diastasis at this point. Waters view (**B**) shows a left zygomatic fracture that is laterally displaced (*arrow*) and slightly clockwise rotated (*curved arrows*).

Copyright © 2003, Mosby, Inc. All rights reserved.

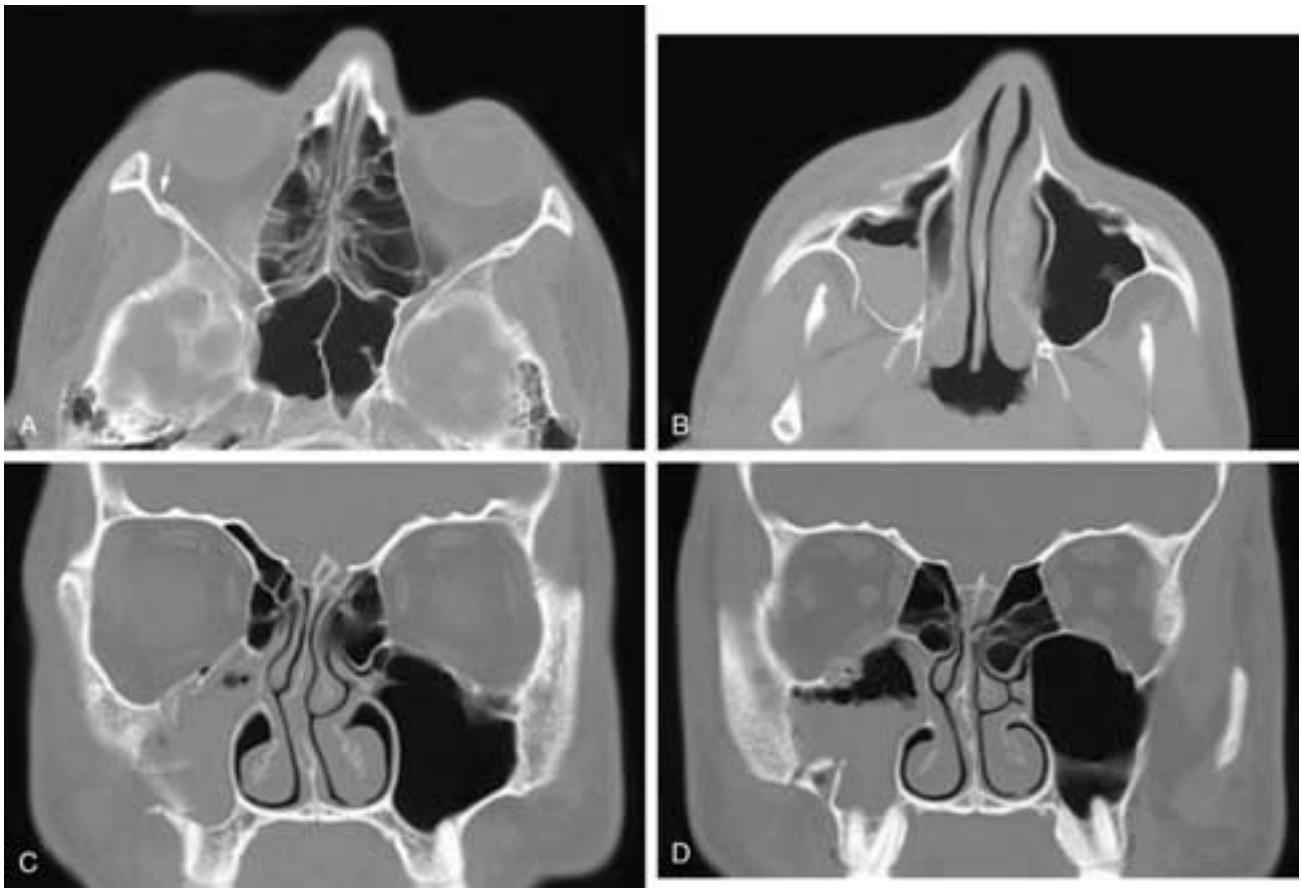

VIEW IMAGE

FIGURE 7-22 Axial images through the orbit (**A**) and the maxilla (**B**) and coronal images (**C**, **D**) show a right trimalar fracture. The right frontosphenoid fracture is minimally displaced (*arrow* in **A**), and the zygoma is inferiorly and posteriorly displaced. Hemorrhage is present in the right antrum, and a small amount of orbital emphysema is present.

Blow-out and Blow-in Orbital Wall Fractures

Fractures of the orbital floor may occur as either simple or comminuted fractures in conjunction with midfacial fractures, with atypical periorbital fractures (orbital roof), or as isolated blow-out fractures.

The term *orbital blow-out fracture* describes the injury that results from a blow to the orbit by an object that is too large to enter the orbit (fist, baseball, etc.). The force of the blow is absorbed by the orbital rim and is transmitted to the thinner orbital floor, which shatters, usually in the middle third near the infraorbital canal (presumably the floor is

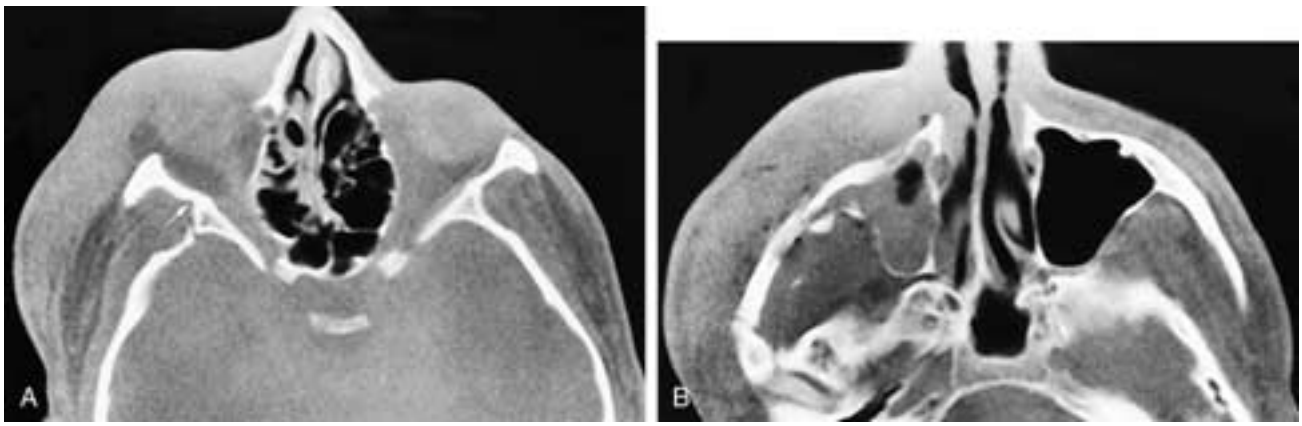

VIEW IMAGE

FIGURE 7-23 Axial CT scans through the orbit (**A**) and the zygomatic arch (**B**) show a right zygomatic fracture with posterior displacement and clockwise (medial) rotation of the zygoma. The site of the zygomatico-frontosphenoid fracture is also seen (*arrow* in **A**).

Copyright © 2003, Mosby, Inc. All rights reserved.

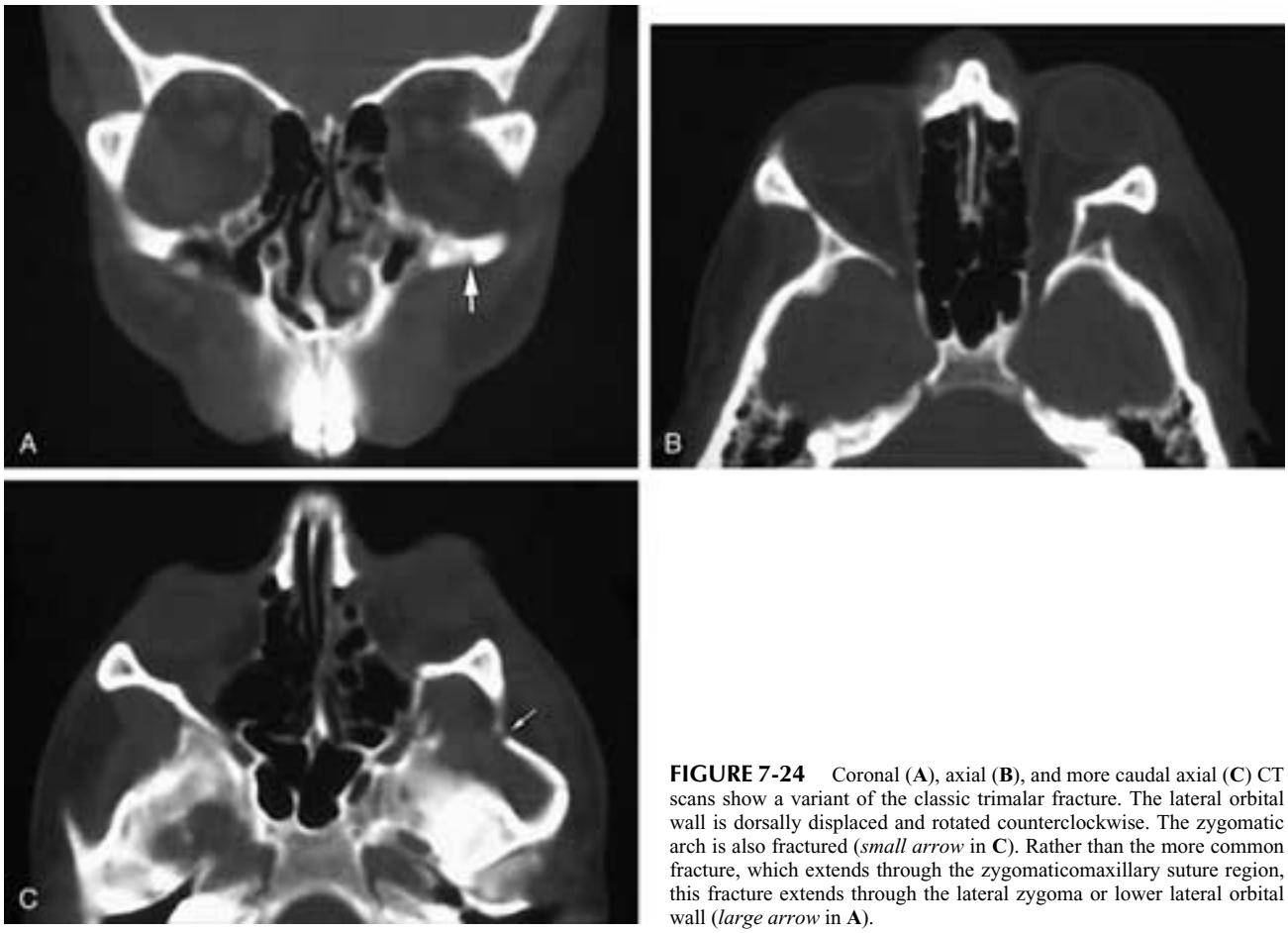

FIGURE 7-24 Coronal (**A**), axial (**B**), and more caudal axial (**C**) CT scans show a variant of the classic trimalar fracture. The lateral orbital wall is dorsally displaced and rotated counterclockwise. The zygomatic arch is also fractured (*small arrow* in **C**). Rather than the more common fracture, which extends through the zygomaticomaxillary suture region, this fracture extends through the lateral zygoma or lower lateral orbital wall (*large arrow* in **A**).

VIEW IMAGE

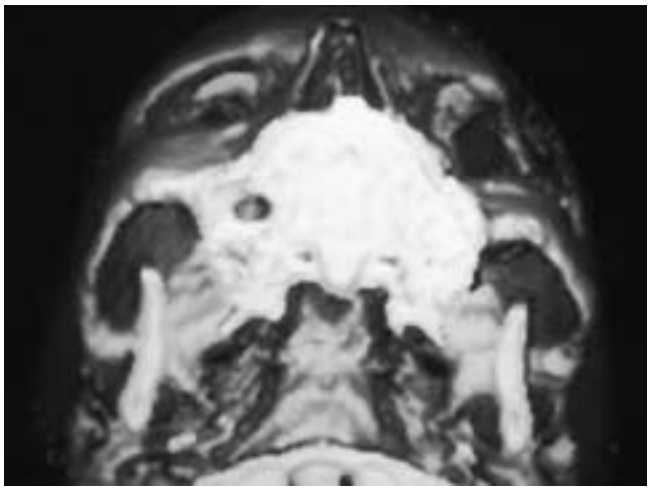

VIEW IMAGE

FIGURE 7-25 Three-dimensional reconstruction on a patient with a left trimalar fracture. The zygoma is posteriorly displaced compared with the normal right side. The white area in the center of the picture is the hard palate seen en face. Most of the mandible was removed from the computerized picture.

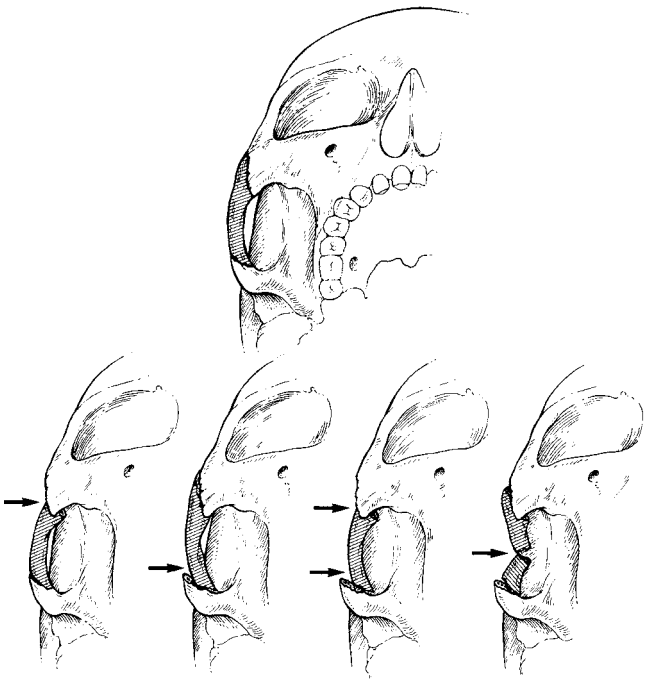

FIGURE 7-26 Diagram of different types of isolated zygomatic arch fractures. The last type may impinge medially on the coronoid process of the mandible.

VIEW IMAGE

Copyright © 2003, Mosby, Inc. All rights reserved.

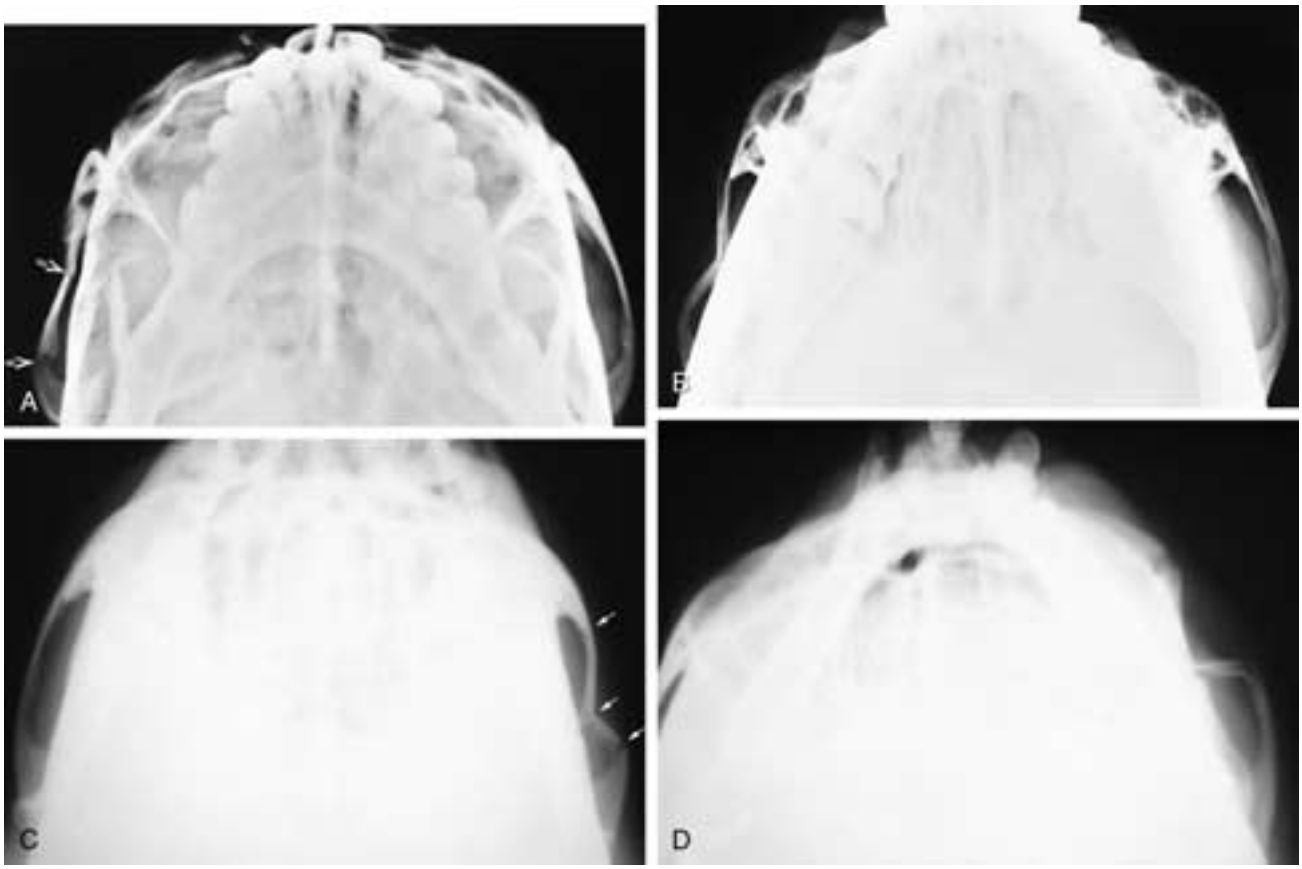

VIEW IMAGE

FIGURE 7-27 Underpenetrated base views on different patients. In (**A**) there are slightly depressed right zygomatic arch fractures (*arrows*). In (**B**) there is a solitary right depressed zygomatic arch segment. In order to create this type of depression, there must be at least three fractures. In (**C**) a left zygomatic arch depressed fracture similar to that seen in (**B**) is present, and the actual three fractures (*arrows*) are more clearly seen. In (**D**), there is a more severely depressed left zygomatic arch fracture that impinges on the coronoid process of the mandible and locked mandibular motion.

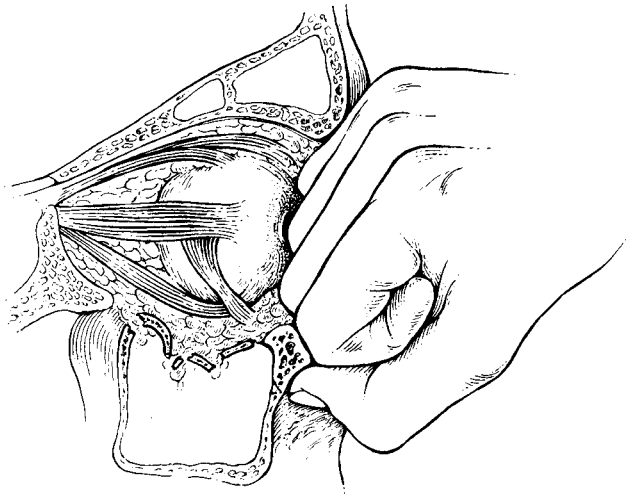

VIEW IMAGE

FIGURE 7-28 Diagram of blow-out fracture. The impacting object is larger than the orbital rim diameter. The blow fractures the orbital floor and pushes the eye back. The eye then displaces the fractured floor into the maxillary sinus.

weakened by the presence of the infraorbital canal, which is often also dehiscent). As the eye is pushed back into the conical orbital apex, it increases intraorbital pressure and this ''blows out'' the fractured floor into the maxillary sinus. Usually the orbital rim is not fractured (pure blow-out fracture) and the globe remains undamaged. Less commonly the inferior orbital rim also is fractured; this is referred to as an impure blow-out fracture. Blow-out fractures represent only 3% to 5% of all midface fractures (Figs. 7-28 to 7-34).[33]

Herniation of orbital fat, inferior rectus muscle, and inferior oblique muscle can occur with occasional muscle entrapment in the fracture line, resulting in diplopia on upward gaze. However, diplopia is the most frequent complaint in all patients with blow-out fractures and may occur solely because of periorbital edema and hemorrhage, which exert pressure on the globe. This type of diplopia resolves in several days, whereas entrapment diplopia remains. If the cause of diplopia is in doubt, a traction test can be performed on the inferior muscles. Rarely a depression fracture of the orbital roof or superior orbital rim can impinge on the upper globe, prohibiting upward gaze and clinically mimicking an inferior muscle entrapment (Fig. 7-35). Imaging studies clarify this situation. In these

Copyright © 2003, Mosby, Inc. All rights reserved.

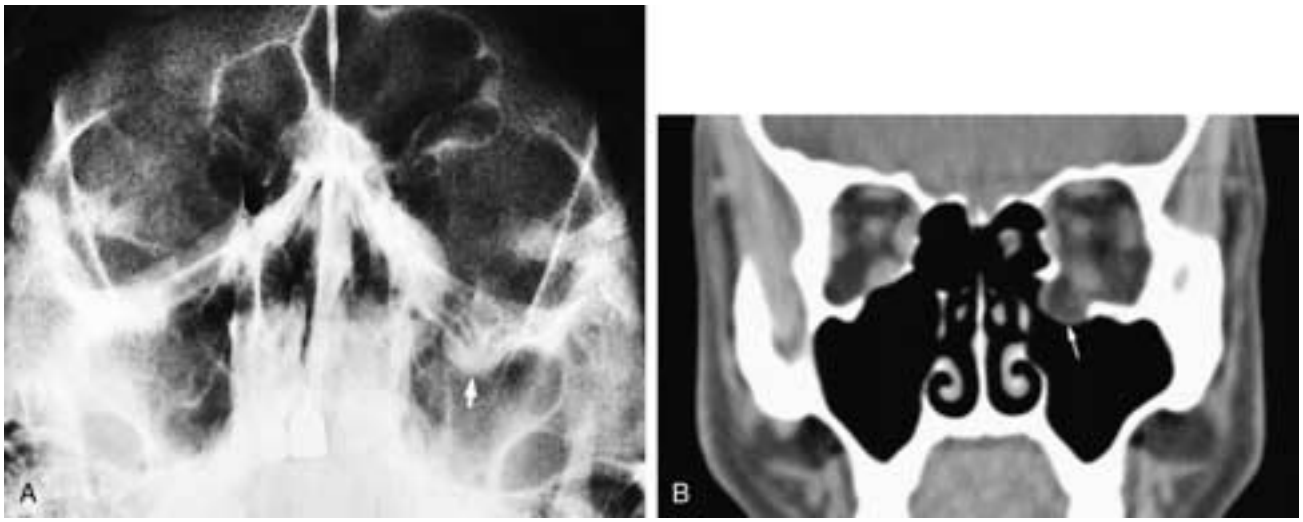

VIEW IMAGE

FIGURE 7-29 Waters view (**A**) shows polypoid soft-tissue mass in the roof of the left antrum (*arrow*). This was a blow-out fracture of the orbital floor. Coronal CT scan (**B**) shows a blow-out fracture of the left orbital floor. The herniated soft tissues (*arrow*) mimic an antral polyp on plain films.

latter cases, communication with the base of the anterior cranial fossa can lead to CSF leakage into the orbit or herniation of meninges or brain through the fracture line.

Rarely the orbital floor fracture segments can herniate upward into the orbit, impinging on the inferior orbital muscles or the globe. This unusual occurrence has been called a blow-in fracture, and on imaging it must be clearly identified so that the clinician can reposition this fractured bone. Laceration of the globe can rarely occur.[10, 34]

Despite the fact that many reports have indicated that the middle third of the orbital floor is the weakest portion of the orbit, the thin lamina papyracea of the medial wall should theoretically be the weakest area. In one study of clinically suspected orbital blow-out fractures evaluated with CT scans, the most common fracture was an isolated medial wall fracture (55%), followed by medial and inferior wall fractures (27%). The most common facial fracture associated with a medial wall fracture was a nasal fracture (51%), not an inferior wall fracture (33%). This suggests that the force causing a nasal fracture is an important causative factor in creating a pure medial wall fracture. Of patients with medial wall fractures, 25% had diplopia and 40% had enophthalmos.[35]

In another article analyzing 2741 patients with facial fractures, 273 patients (9.9%) were identified with 304 medial orbital wall fractures. The male-to-female ratio was 5:1, and most injuries involved the left orbit. Most fractures were caused by fist fights, but more complex injuries were noted secondary to car accidents and falls. The fractures were divided into types based on the location and severity of

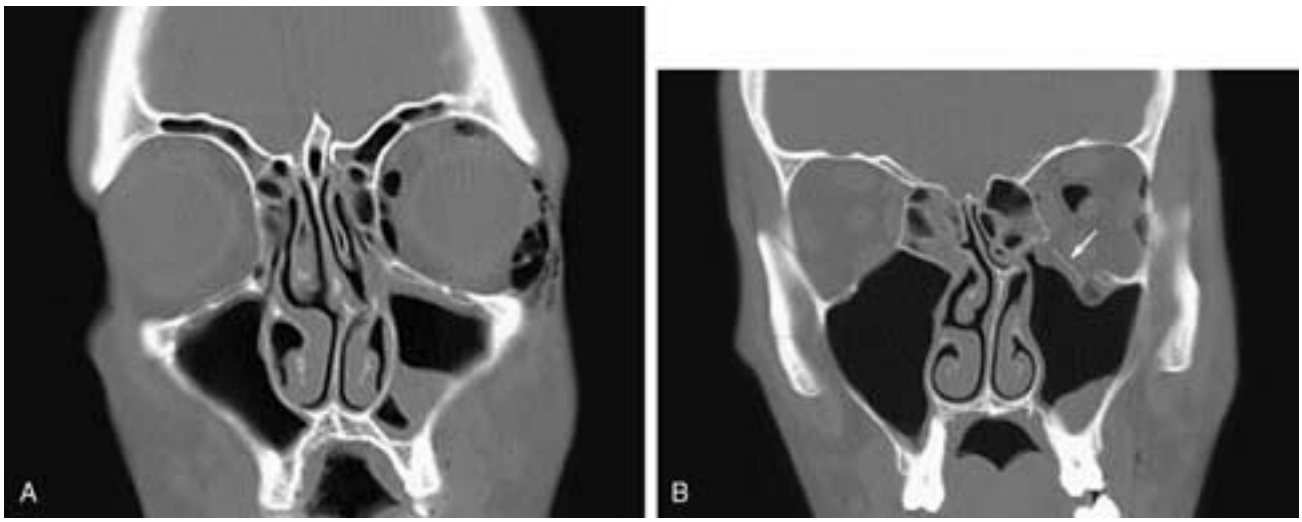

VIEW IMAGE

FIGURE 7-30 Coronal CT scans. In (**A**) there is an intact orbital rim anteriorly. In (**B**) there is an orbital floor fracture (*arrow*) in the midfloor just posterior to the orbital rim. This was a pure blow-out fracture. The fracture is just medial to the infraorbital canal, and this patient had hypesthesia in the cheek. Secretions are seen in both ethmoid sinuses, and hemorrhage occurred in the left antrum. There is also subcutaneous and orbital emphysema.

Copyright © 2003, Mosby, Inc. All rights reserved.

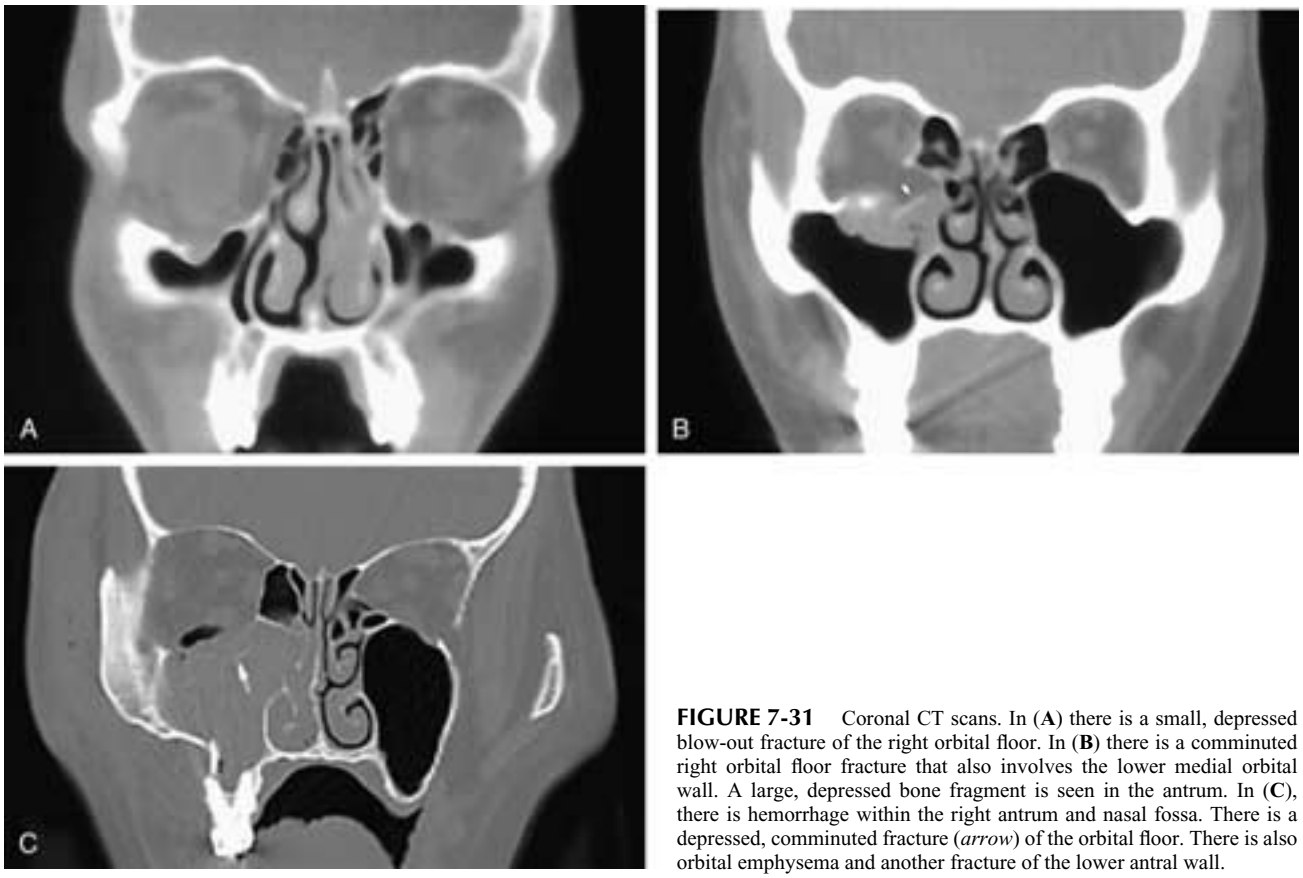

FIGURE 7-31 Coronal CT scans. In (**A**) there is a small, depressed blow-out fracture of the right orbital floor. In (**B**) there is a comminuted right orbital floor fracture that also involves the lower medial orbital wall. A large, depressed bone fragment is seen in the antrum. In (**C**), there is hemorrhage within the right antrum and nasal fossa. There is a depressed, comminuted fracture (*arrow*) of the orbital floor. There is also orbital emphysema and another fracture of the lower antral wall.

VIEW IMAGE

the injury. Type I fractures were confined to the medial orbital wall. Type II fractures involved the medial orbital wall and continuous orbital floor. Type III fractures involved the medial orbital wall and orbital floor and malar fractures. Type IV fractures involved the medial orbital wall and complex midfacial injuries. Although visual loss (2%), diplopia (41%), and enophthalmos (12%) were seen, diplopia and enophthalmos were commonly observed with type II injuries. Imaging studies showed that about 52% of the fractures were associated with prolapse of orbital fat, but only 43% could be diagnosed on plain films.[36]

Thus, fractures of the medial orbital wall can occur either as isolated fractures or in conjunction with orbital floor fractures or more complex fractures. Traditionally, such medial wall fractures were considered to accompany nearly 50% of orbital floor fractures, but as discussed, the incidence may be far greater. Often the ethmoid fracture is poorly visualized on plain films, with only some clouding of the

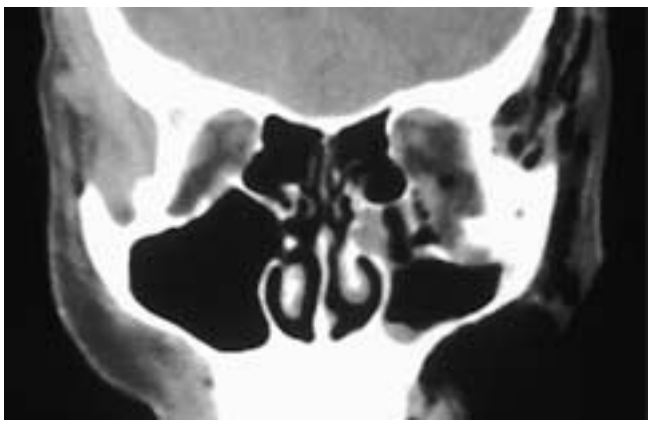

FIGURE 7-32 Coronal CT scan shows a moderately large blow-out fracture in the floor and medial wall of the left orbit. Orbital emphysema is also present.

VIEW IMAGE

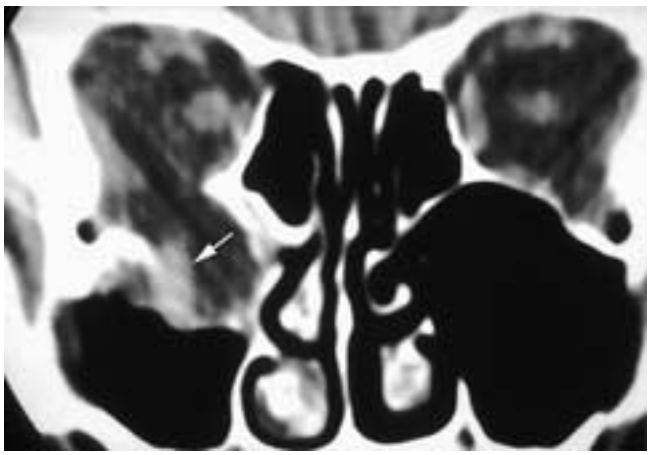

FIGURE 7-33 Coronal CT scan shows a large right orbital floor blow-out fracture. The inferior rectus muscle (*arrow*) is depressed into the fracture. This muscle was entrapped on the lateral fracture margin.

VIEW IMAGE

Copyright © 2003, Mosby, Inc. All rights reserved.

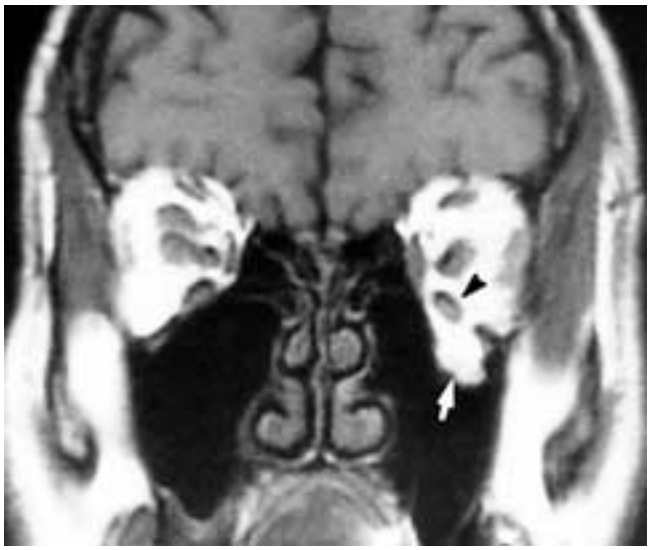

VIEW IMAGE

FIGURE 7-34 Coronal T1-weighted MR image shows a left blow-out fracture. Fat has herniated into the left antrum (*arrow*), and there is minimal depression of the inferior rectus muscle (*arrowhead*).

ethmoid cells being evident. Even on CT scans, if there is no bone displacement, the actual fractures may not be identified. However, on CT, fat that has herniated into the fractured ethmoid complex is well visualized (Figs. 7-36 to 7-41). Herniated fat can also be identified on MR imaging, although small fracture segments may not be identified. Muscle entrapment in these fractures is rare.[37] The only imaging differential diagnosis is a congenital dehiscence of the lamina papyracea (actually, a hypoplasia of the ethmoid complex). In congenital dehiscence, on CT and MR imaging, portions of the lamina papyracea are either not visualized or are medially bowed and orbital fat lies in the ethmoid complex. However, unlike in trauma cases, the margins of the defect are smooth and there is no history of trauma.

Medial wall fractures can also be inferred by the presence of orbital emphysema. Such orbital air most commonly comes from an ethmoid sinus fracture and rarely results from an isolated maxillary fracture. The infrequent occurrence of orbital emphysema with orbital floor blow-out fractures is attributed to the rapid sealing of the fracture by edema, hemorrhage, and periorbital herniation of orbital fat

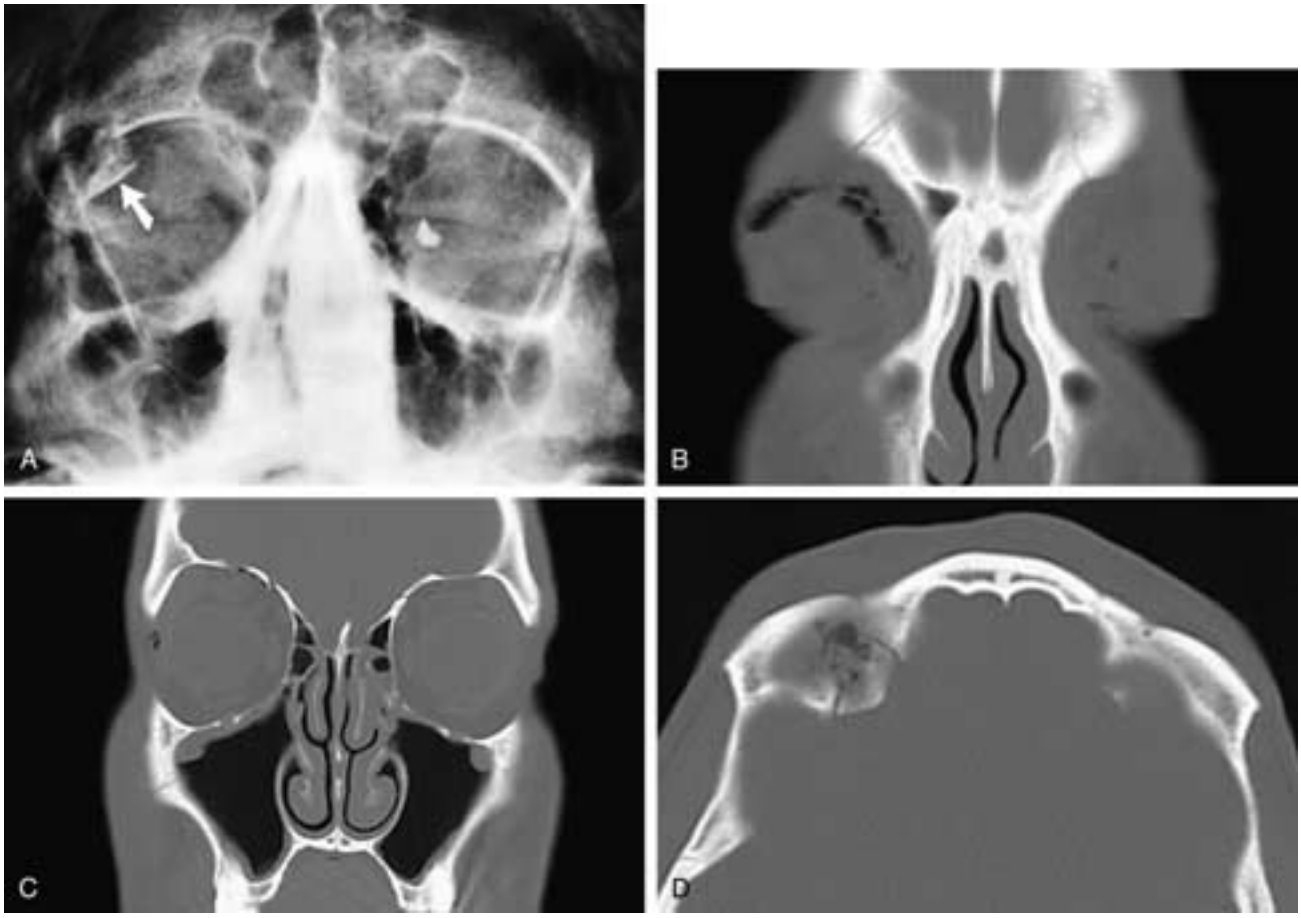

VIEW IMAGE

FIGURE 7-35 Waters view (**A**) shows a depressed orbital roof fracture (*arrow*) that impinged on the globe and clinically mimicked a blow-out fracture of the orbital floor with entrapment. A foreign body is also seen in the left eye. Coronal anterior (**B**) and posterior (**C**) and axial (**D**) CT scans on another patient with a fracture of the right frontal bone and orbital roof. There is minimal displacement of the right orbital roof fracture, as well as orbital emphysema and a small amount of extradural air. There is also a similar nondisplaced left frontal and orbital roof fracture.

Copyright © 2003, Mosby, Inc. All rights reserved.

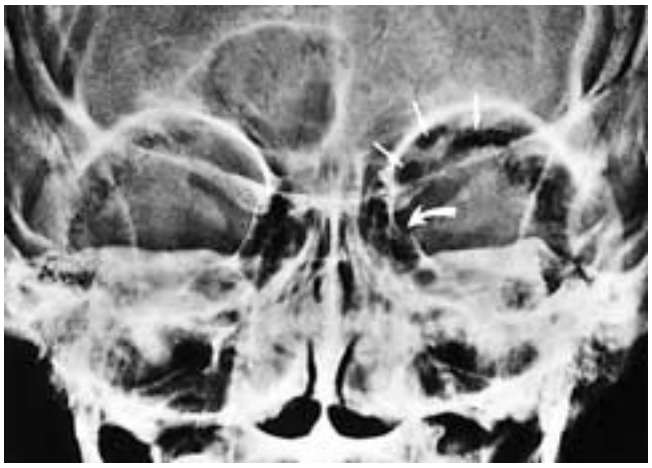

VIEW IMAGE

FIGURE 7-36 Caldwell view shows orbital emphysema (*three arrows*) and a defect in the left lamina papyracea (*curved arrow*). This was a medial wall blow-out fracture.

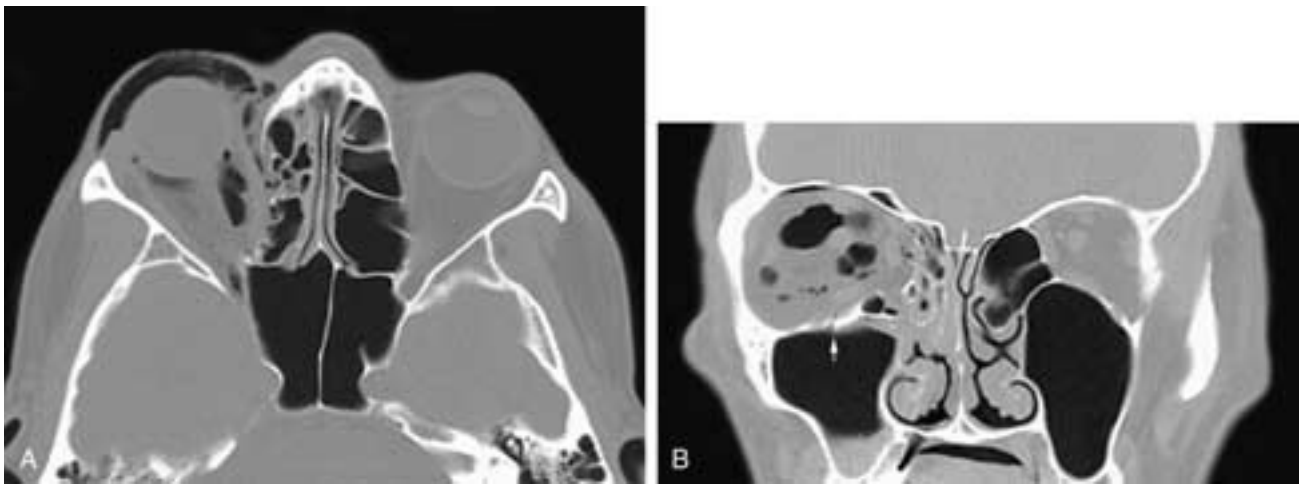

VIEW IMAGE

FIGURE 7-37 Axial (**A**) and coronal (**B**) CT scans show a comminuted right medial wall blow-out fracture with extensive orbital emphysema. There is also a right orbital floor fracture (*arrow* in **B**). Hemorrhage is present in the right ethmoid sinuses.

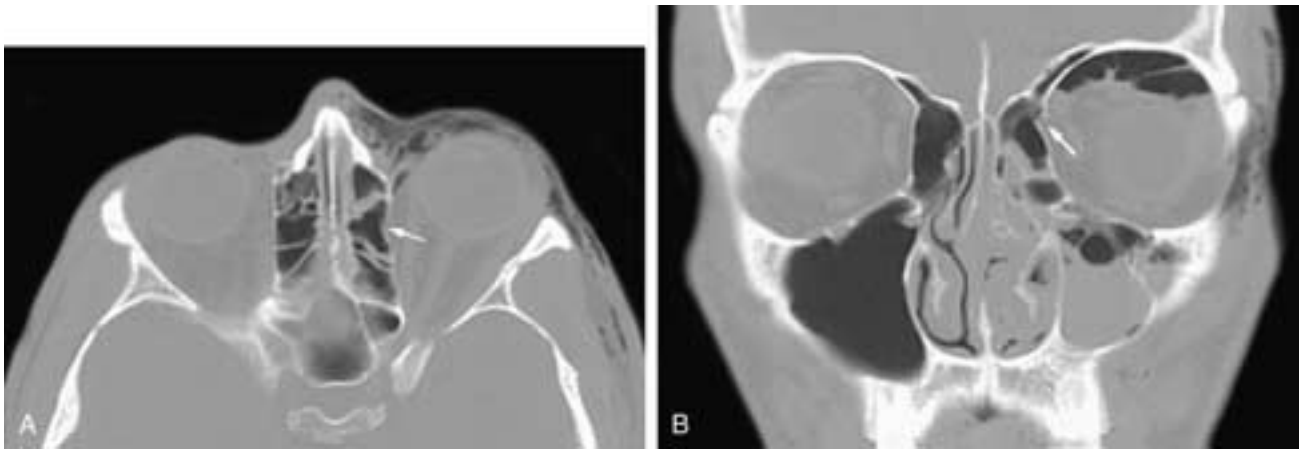

VIEW IMAGE

FIGURE 7-38 Axial (**A**) and coronal (**B**) CT scans show left orbital emphysema. In (**A**), the medial wall fracture is not as well seen (*arrow*) as it is in (**B**) (*arrow*). Minimal hemorrhage is present in the left ethmoid sinuses. Hemorrhage and secretions are present in the left maxillary sinus.

Copyright © 2003, Mosby, Inc. All rights reserved.

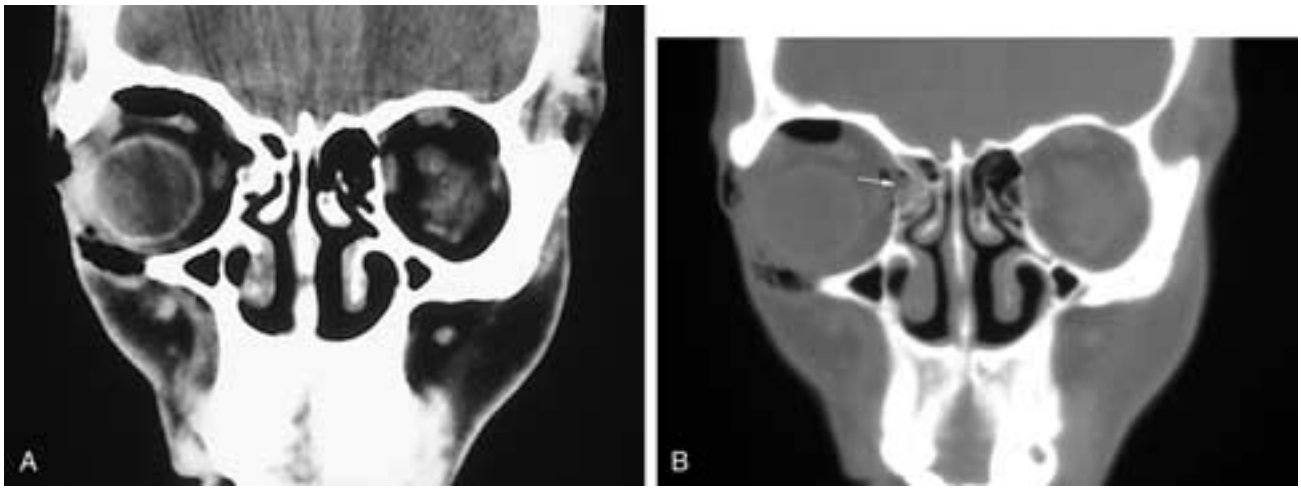

VIEW IMAGE

FIGURE 7-39 Coronal CT scans at soft-tissue (**A**) and bone (**B**) settings show a medial wall right blow-out fracture (*arrow* in **B**). There is also orbital emphysema. Note how much more difficult it is to detect the findings in (**A**).

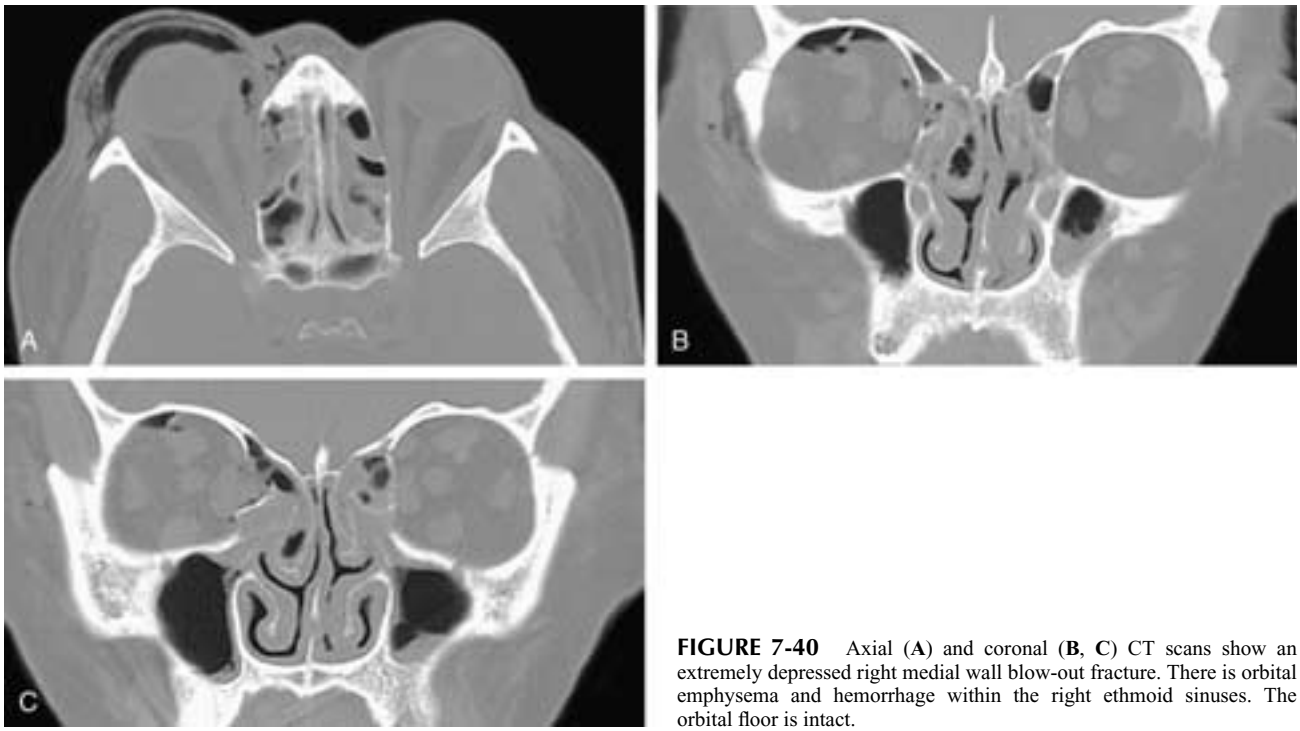

FIGURE 7-40 Axial (**A**) and coronal (**B**, **C**) CT scans show an extremely depressed right medial wall blow-out fracture. There is orbital emphysema and hemorrhage within the right ethmoid sinuses. The orbital floor is intact.

VIEW IMAGE

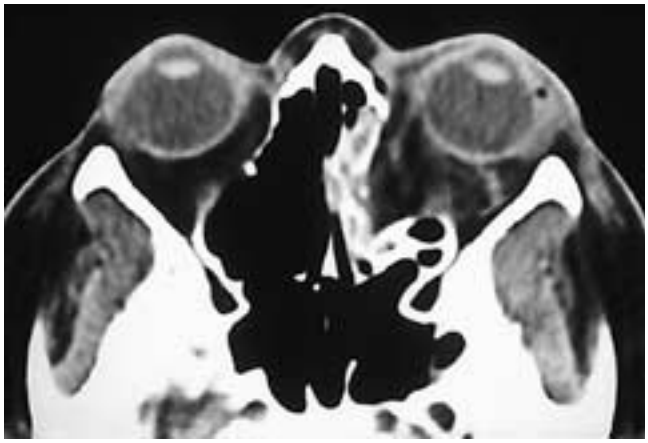

FIGURE 7-41 Axial CT scan shows a left medial wall blow-out fracture with a large herniation of orbital fat into the fracture site. This is the type of fracture that can result in chronic enophthalmos.

VIEW IMAGE

Copyright © 2003, Mosby, Inc. All rights reserved.

and muscle. Orbital emphysema develops after an ethmoid fracture when nose blowing by the patient increases intranasal pressure, which in turn raises the intrasinus pressure and forces air into the orbit. In most patients, refraining from nose blowing allows the fracture line to seal and the orbital air to resorb.[10]

Rarely, air can enter the orbit from a complex fracture involving the frontal or sphenoid sinuses. However, these cases are associated with severe facial trauma, and the source of the air becomes evident on imaging studies. Even more rarely, pneumomediastinum can occur following a blow-out fracture.[38]

The two clinical indications for immediate surgery on an orbital blow-out fracture are definite muscle entrapment and acute enophthalmos. In the most dramatic case, the globe is almost completely displaced into the maxillary sinus and there are reports of complete globe herniation into a fractured maxillary sinus.[39–41] However, milder and more common degrees of acute enophthalmos may take several days to confirm clinically because of the presence of periorbital edema and hemorrhage.

The development of chronic enophthalmos is also to be avoided, because it leads to cosmetic deformity and in some cases diplopia. Chronic enophthalmos develops when too much orbital fat has herniated from the orbit. Although initially the increased orbital volume clinically goes unnoticed because of compensatory intraorbital edema, the subsequent loss of edema, scarring, and lipogranulation of the herniated tissues eventually cause sufficient volume loss that the globe recedes. The patients who are at greatest risk are those who have sizable herniations of fat into one sinus (maxillary or ethmoid) or moderate herniations into both medial wall and orbital floor fractures. The imager must draw the clinician's attention to any such cases that may have the potential to develop chronic enophthalmos, even in the absence of acute enophthalmos or muscle entrapment.

Alloplasts are often used to reconstruct the orbital floor where they have been effective in the long-term reconstruction of this orbital margin. However, such products rarely work effectively in the long-term attempted repair of the medial orbital wall, as invariably there is movement of the alloplast. The products most often used include Teflon, Silastic, and Marlex mesh, all of which have the benefit of not being absorbed.[42] However, these alloplasts have the disadvantages of extrusion and infection. They can be identified on CT, which is a useful modality to detect early displacement of the graft.

On plain films, soft-tissue swelling over the inferior orbital rim, antral opacification with or without an air-fluid level, and subcutaneous emphysema in the cheek are often the only indirect signs of a blow-out fracture. An actual depressed or displaced orbital floor bone fragment may not be seen. Occasionally a soft-tissue polypoid density can be visualized in the antral roof. This may represent the site of the blow-out fracture filled with orbital contents and hemorrhage or it may represent an unrelated antral cyst or polyp. Only on coronal CT or MR imaging can the actual fracture and herniated tissue be clearly seen. A completely displaced piece of bone, a trapdoor fracture, or a hinged fracture can then be identified, as can the typical ''teardrop'' herniation of orbital contents. On CT the orbital fat may be of a higher attenuation than expected because of hemorrhage; in some cases an antral air-blood level may be present.[22] On MR imaging, the high T1-weighted signal intensity of the orbital fat and any hemorrhage can be well seen; however, a small bone fracture segment may not be identified.

Supraorbital roof fractures are uncommon, and the incidence has been reported to be between 1% and 5%. In one study of 621 patients with facial fractures, 9.3% had supraorbital roof fractures. The average age of these patients was 31 years, and the predominant mechanism of injury was from motor vehicle accidents. Sixty-nine percent of the patients had associated skull fractures and 54% had frontal sinus fractures. Dural tears were present in 14 patients, traumatic encephalocele in 3, proptosis in 6, pulsatile proptosis in 3, orbital apex syndrome in 1, persistent CSF leak in 3, and meningitis in 5. A majority of the patients had associated intracranial bleeds.[43]

FRONTAL SINUS FRACTURES

Frontal sinus fractures are the result of either direct trauma or an extension of a calvarial fracture into the sinus. Of all the fractures involving the frontal sinuses, 67% are limited to the anterior table, 28% involve both the anterior and posterior sinus walls, and only 5% are limited to the posterior sinus table.[44] Most commonly a linear fracture occurs in the anterior sinus wall. This fracture tears the mucosa and produces hemorrhage, edema, and sinus opacification. The fracture line may extend downward, often involving the superomedial orbital rim (Figs. 7-42 to 7-48).

FIGURE 7-42 Caldwell view shows a comminuted fracture of the frontal bone (*arrows*) that extends into the frontal sinus.

VIEW IMAGE

Copyright © 2003, Mosby, Inc. All rights reserved.

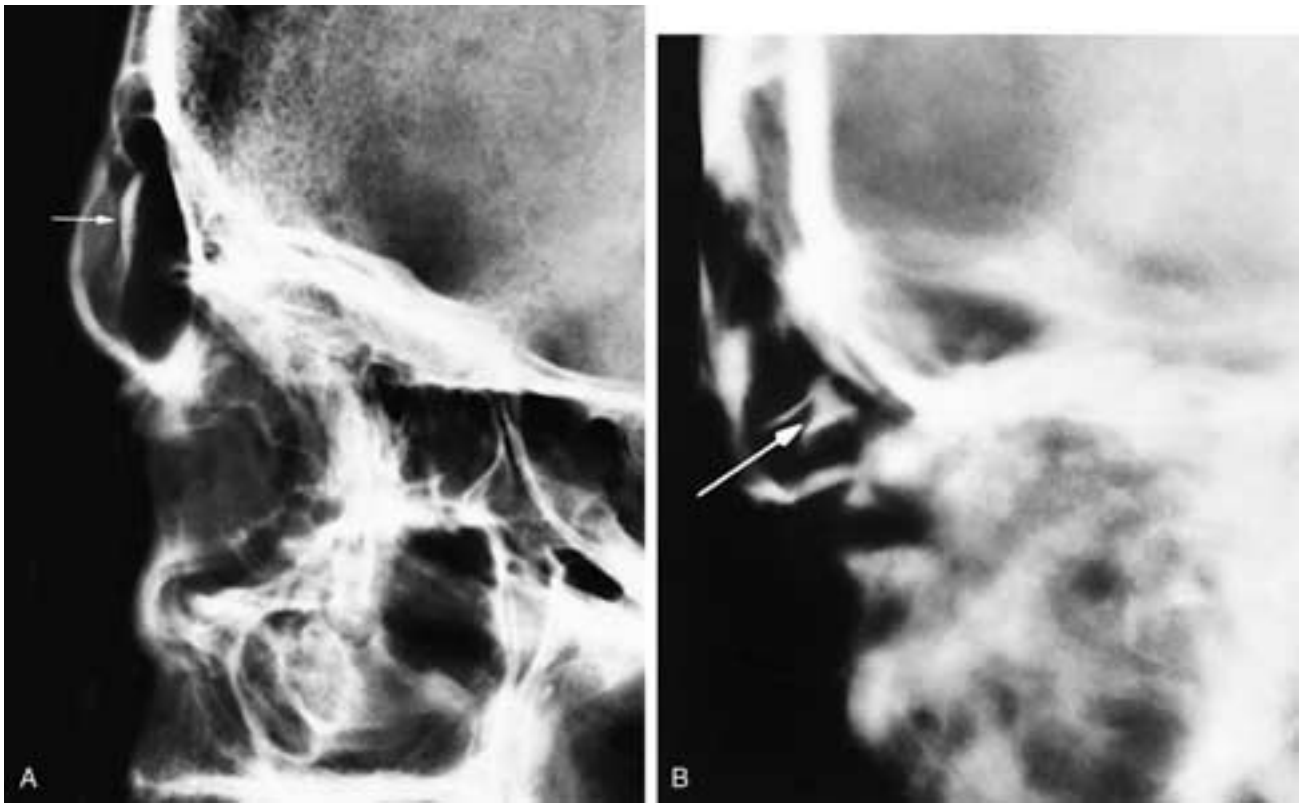

VIEW IMAGE

FIGURE 7-43 Lateral plain film (**A**) shows a depressed anterior frontal sinus wall fracture (*arrow*). Lateral tomogram film (**B**) shows a depressed fracture (*arrow*) of the anterior wall and floor of the frontal sinus.

Comminuted fractures of the anterior wall also occur and frequently reflect the size and shape of the object causing the fracture. On plain film Caldwell and Waters views, only a vague density may appear in the frontal sinus. However, on a lateral view, bone fragments may be identified within the sinus. Axial CT most clearly confirms the presence of such depressed fractures, which often are clinically unobserved because the forehead soft-tissue depression is filled by edema and hemorrhage.[45]

Complex fractures of both the anterior and posterior frontal sinus tables usually are associated with other midfacial fractures. Isolated fractures of the posterior sinus wall are rare. They occur either as an extension of a skull base fracture or as an extension of a calvarial fracture.[46–49] Any fracture involving the posterior frontal sinus wall opens communication with the dural spaces, and CSF leakage into the sinus and intracranial infection or a pneumocele can develop. Rarely, orbital emphysema or CSF leakage into the orbit can result from frontal sinus fractures. In one study of CT scans on patients with suspected intracranial posttrau-

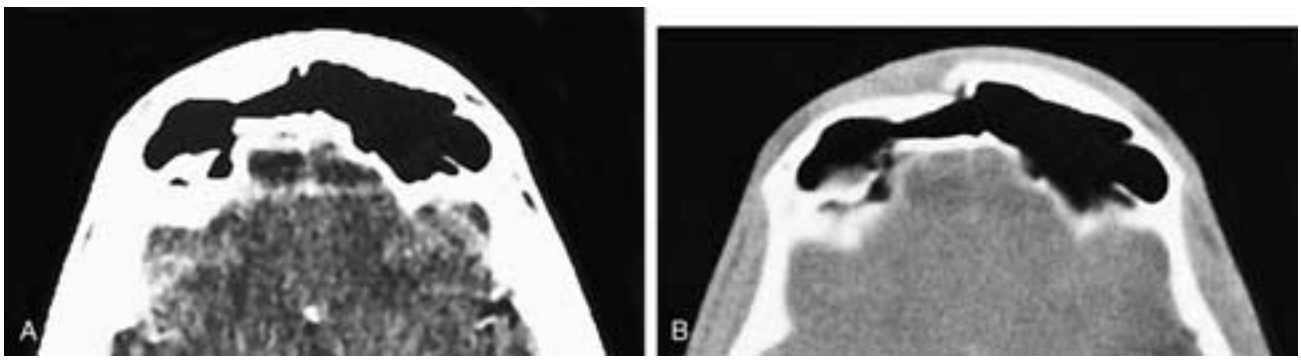

VIEW IMAGE

FIGURE 7-44 Axial CT scans seen at narrow window settings (**A**) and wide window settings (**B**). In (**A**) there is no obvious depression of the forehead, nor is there an obvious fracture of the right anterior frontal sinus table. In (**B**) the fracture is clearly seen. There was no soft-tissue depression in the forehead because the defect was filled with hemorrhage and edema fluid.

Copyright © 2003, Mosby, Inc. All rights reserved.

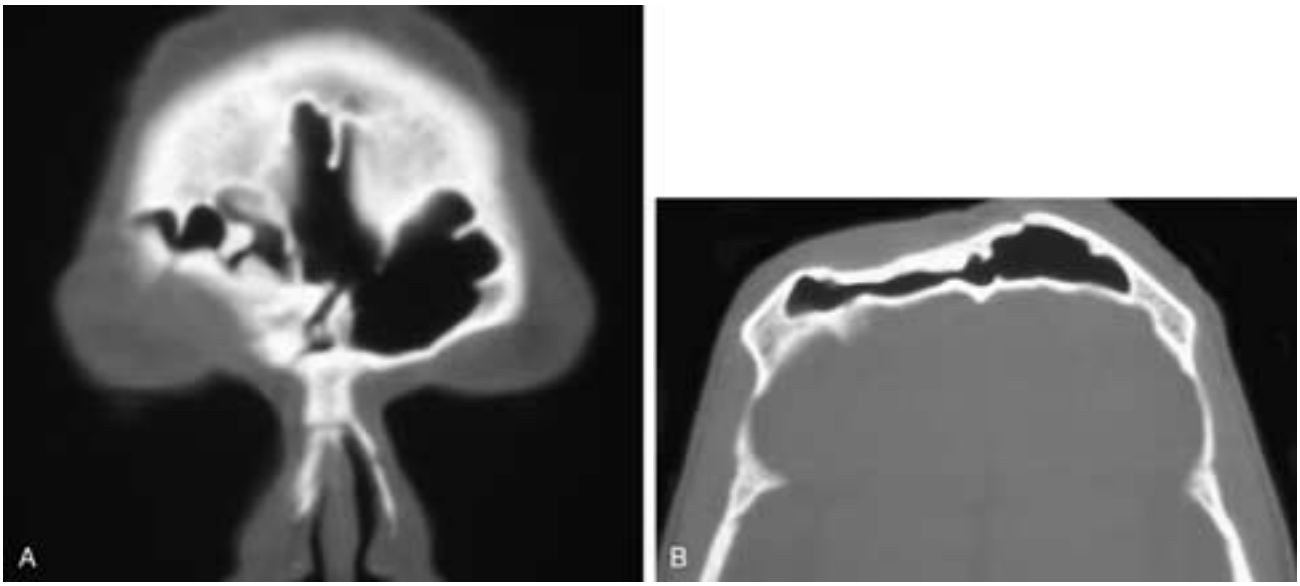

VIEW IMAGE

FIGURE 7-45 Coronal (**A**) and axial (**B**) CT scans show a depressed comminuted fracture of the right anterior frontal sinus table that also involves the right orbital roof.

matic injuries, 90% of the patients had a frontal sinus fracture identified on the initial CT scan. Complex fractures involving the anterior and posterior walls accounted for 65% of the cases, and isolated anterior wall (24%) or posterior wall (11%) fractures were less common.[45] This study reflects the severity of the trauma that led to both the fractures and the intracranial damage. In fact, it has been determined that it takes two to three times the force to fracture the frontal sinus than it does to fracture the zygoma, maxilla, or mandible.[50]

In general, nondisplaced frontal sinus fractures are treated conservatively. Uncomplicated anterior table fractures with cosmetic deformity are treated by fragment reduction and stabilization, usually with microplates or miniplates. Nasofrontal duct obstruction is usually managed by sinus obliteration. Finally, comminuted, displaced anterior and posterior table fractures, especially those associated with persistent CSF leakage, are often treated by frontal sinus cranialization.[47]

SPHENOID SINUS FRACTURES

Fractures of the sphenoid sinus seldom occur, but when they do, they are associated with severe cranial trauma and basilar skull fractures. Often, these patients are recumbent due to the associated intracranial injuries. In these cases, sphenoid opacification or a sphenoid sinus air-fluid level may indicate intrasinus hemorrhage, leakage of CSF directly into the sinus from a sphenoid sinus fracture, CSF drainage into the sinus via the nasopharynx from a temporal bone fracture in a patient with an intact tympanic membrane, poor sinus drainage due to supine position, and edema around indwelling nasogastric or orotracheal tubes. Rarely, milder trauma to the midfacial region may extend back into the sphenoid sinus. If the fracture injures the adjacent internal carotid arteries or cavernous sinuses, these events may be life-threatening.

PEDIATRIC FACIAL FRACTURES

When compared with the adult skeleton, the pediatric facial bones behave differently with regard to fracture patterns, healing, and treatment. The inherent elasticity of the facial bones in a young patient is advantageous in trauma because the bone yields more easily and does not fracture as readily as it does in an adult.[1] When a fracture does occur, the thick, elastic periosteum usually prevents bone displacement and a green-stick fracture results. In addition, fractures heal faster in children than in adults, so the period of immobilization is shorter. However, if treatment is delayed, the fragments may become fixed, making fracture reduction more difficult. Malocclusions in the primary dentition that are not completely corrected may be spontaneously compensated for by the secondary dentition or may be treated by orthodontic therapy.[1]

Although children have many advantages in terms of healing, they are at a disadvantage with regard to dentition. In 30% to 50% of pediatric facial fractures, the tooth germs lie in the fracture. These teeth fall out during healing or have delayed development and deformities that do not manifest clinically until the permanent teeth erupt. Facial fractures also can damage the bony growth centers and result in osseous hypoplasia, functional abnormalities, and cosmetic deformities. Some clinicians believe that the child's parents should be informed of these potential problems at the time of the initial injury.

Children generally have too few teeth for fixation splints,

Copyright © 2003, Mosby, Inc. All rights reserved.

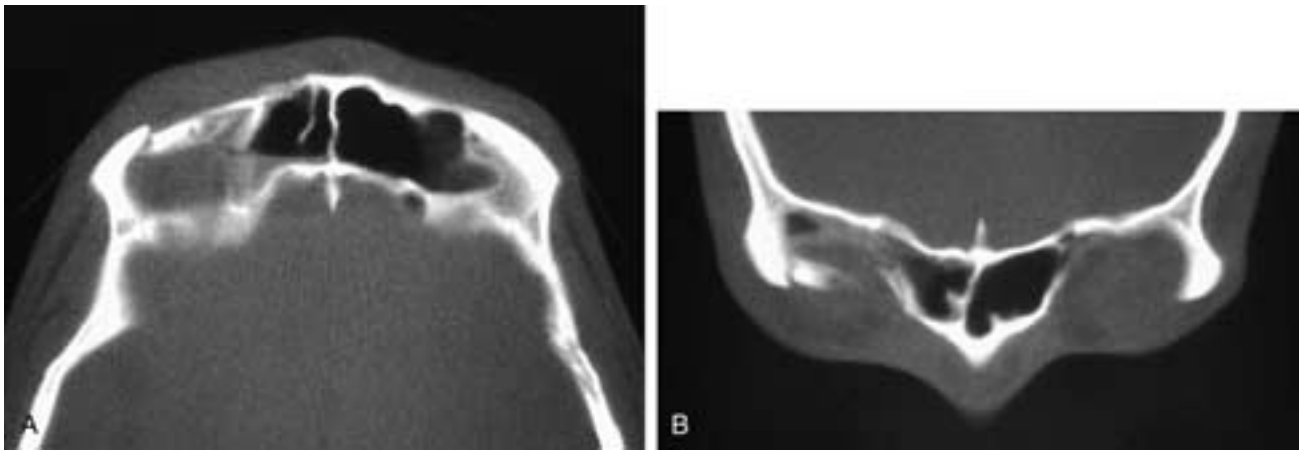

VIEW IMAGE

FIGURE 7-46 Axial (**A**) and coronal (**B**) CT scans show a fracture involving the right orbital roof and the lower anterior frontal sinus table.

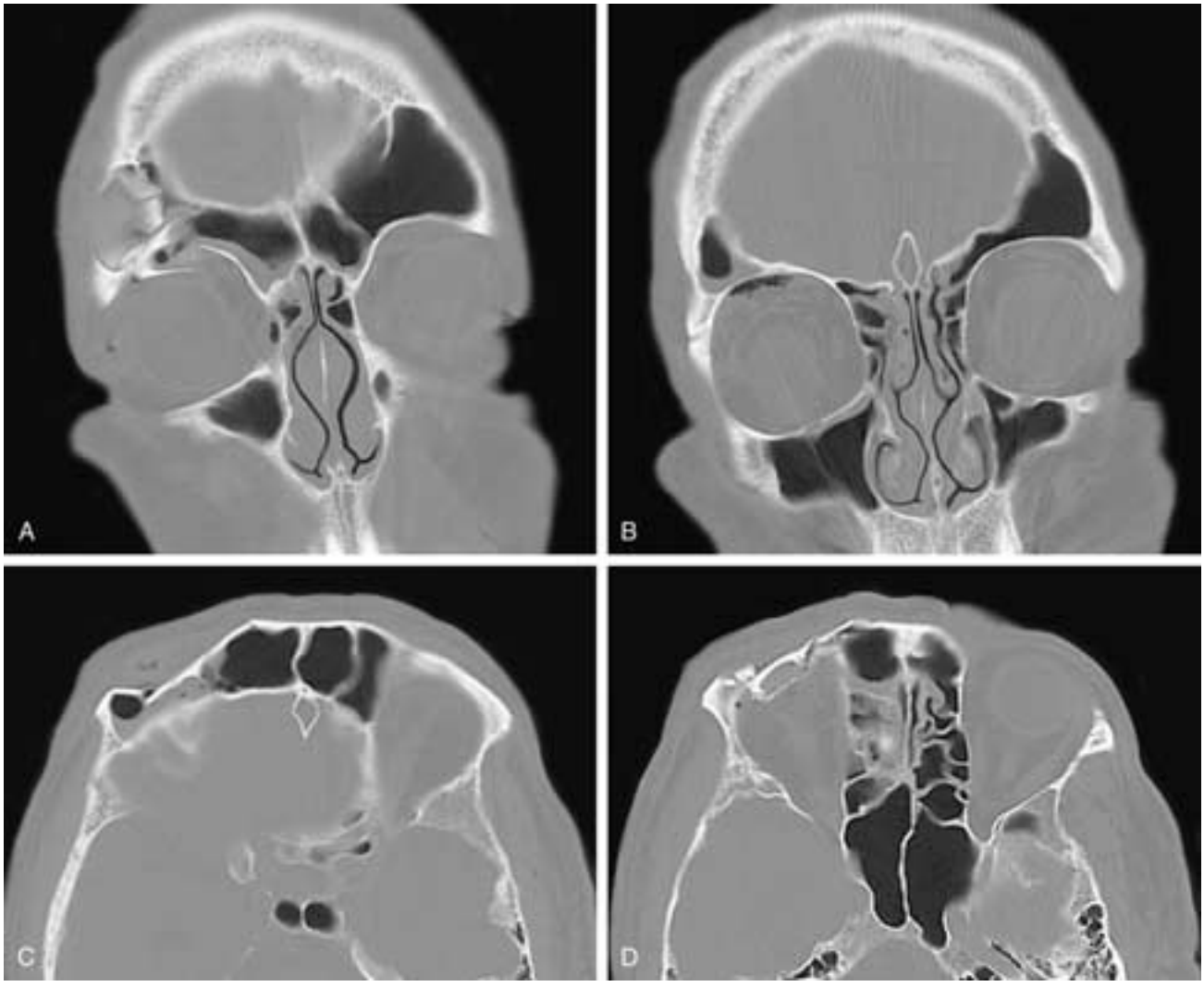

VIEW IMAGE

FIGURE 7-47 Coronal anterior (**A**) and posterior (**B**) CT scans and axial cranial (**C**) and caudal (**D**) CT scans show a comminuted right frontal sinus fracture that involves the anterior table and the roof of the orbit. A fracture segment impinges on the upper globe and prevents upward gaze. Orbital emphysema is also present.

Copyright © 2003, Mosby, Inc. All rights reserved.

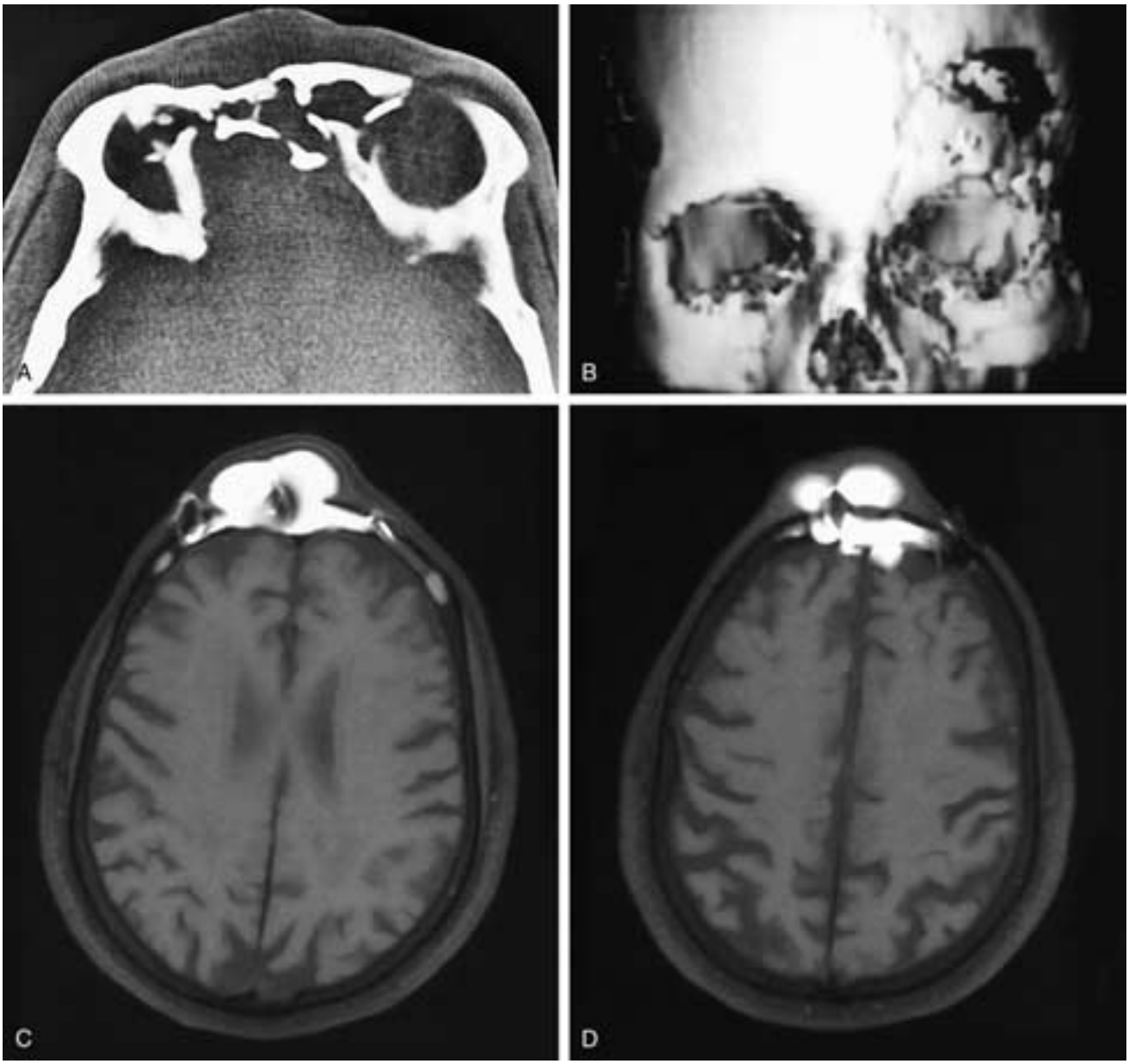

VIEW IMAGE

FIGURE 7-48 Axial CT scan (**A**) shows a comminuted midfacial fracture that involves the orbital roof bilaterally, as well as the anterior and posterior frontal sinus walls. Coronal 3D reconstructed image (**B**) on a different patient shows a markedly depressed left frontal bone fracture that involved the lateral margin of the left frontal sinus. As in Figure 7-42, frontal bone fractures often may involve the frontal sinuses. Axial T1-weighted, fat-suppressed MR images (**C, D**) on a patient who had prior frontal sinus trauma and an osteoplastic flap repair and then reinjured the frontal sinus. Hemorrhage has occurred within the flap fat, expanding it through the anterior and posterior fracture defects. *Illustration continued on following page*

and treatment plans must be modified from those used in adult patients. No wire ligatures can be placed in children under 2 years of age. After this age, it may be possible to fix interdental wires and arch bars if the primary teeth have not been damaged by caries and their crowns have an adequately retentive form. However, with the appearance of interdental spaces caused by eruption of the secondary teeth, the possibility of fixing dental splints becomes less likely. Similarly, erupted permanent teeth can accept such ligatures only after their greatest convexity has passed the gingival margin. This period lasts from about the fifth to the eighth years of life.[1]

Copyright © 2003, Mosby, Inc. All rights reserved.

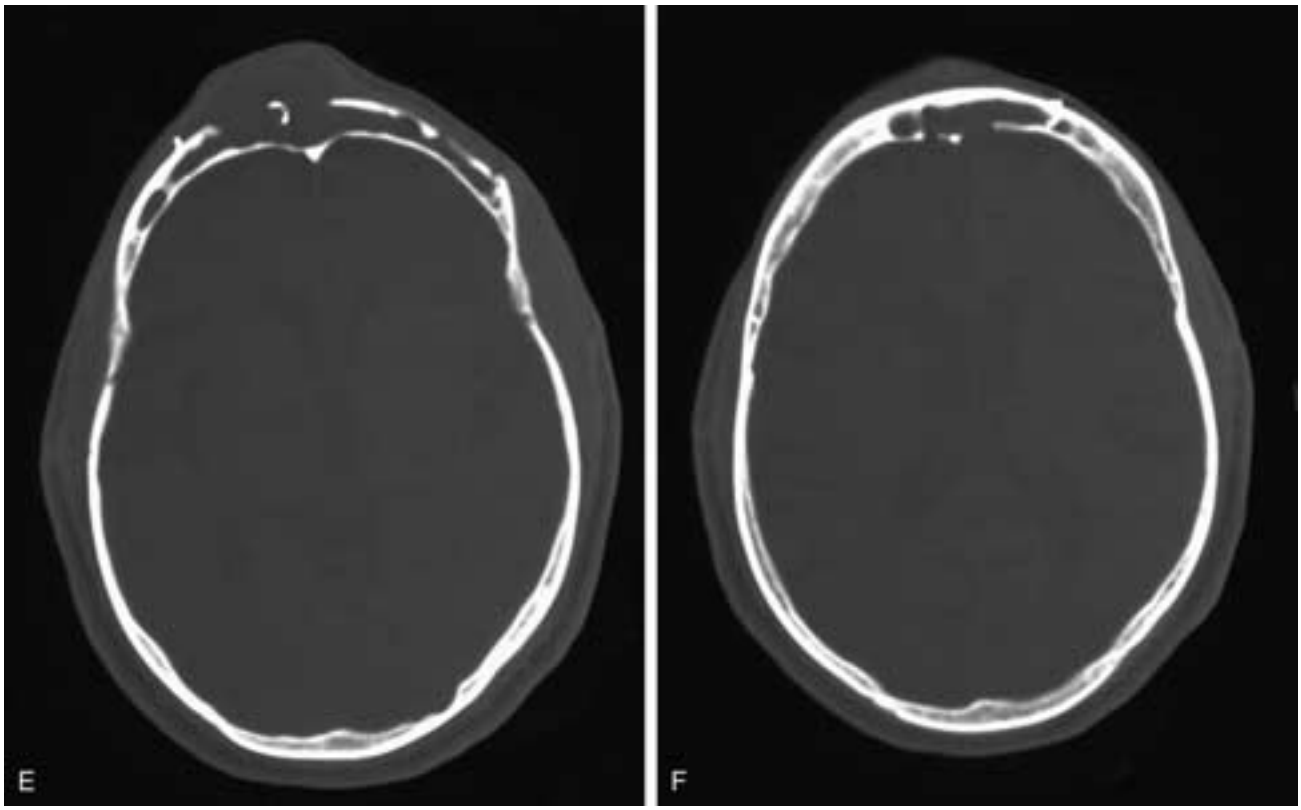

FIGURE 7-48 *Continued.* Corresponding axial CT scans (**E, F**) show the bone defects.

VIEW IMAGE

SECTION TWO

POSTOPERATIVE SINONASAL CAVITIES

IMAGING EVALUATIONS

The proper imaging evaluation of the postoperative patient requires the radiologist to be knowledgeable about a number of facts, some of which are often obscure at the time of performing and then interpreting the imaging examination. Ideally, the radiologist should know what operation was performed, when it was done, and what disease prompted it. Familiarity with the various surgical procedures enables the radiologist to determine which bone(s), if any, can be expected to be removed, what soft-tissue defects may be created, and what soft tissue or foreign material is usually placed to repair the surgical defect. This knowledge is essential for proper imaging interpretation and should help prevent the misdiagnosis of a surgical defect as a site of bone erosion or a muscle-fascia graft as a tumor recurrence.

The interval between the surgery and the time of imaging helps the radiologist determine the type of soft-tissue reaction to expect. For recent surgery, the primary healing reaction is active inflammation with edema and possible hemorrhage. However, if the surgery was performed months to years ago, the primary expected healing reaction is mature granulation tissue or vascularized scar with varying degrees of fibrosis. In some patients, a reactive bony sclerosis may occur after those procedures that denude mucosa. Such a reaction requires time to develop and produce sufficient bone thickening to possibly reduce the sinus cavity size. This is a reactive process to the surgery and, although it may appear the same on imaging as the sclerosis associated with chronic inflammation, there is no evidence of active disease or pain in the majority of these patients. However, in some patients, recurrent sinusitis can coexist with the reactive postoperative changes. In these cases, one cannot know whether the bone changes are attributable to the active inflammation, the postoperative reaction, or both.

Knowledge of the disease process that initially prompted the surgery allows the radiologist to anticipate the types of imaging changes to expect. Thus, if the initial disease was chronic infection, one may commonly expect recurrent sinus mucosal thickening, reactive bone sclerosis and thickening, and possible nasal polyposis. If the initial disease was a granulomatous process, one may expect sinus mucosal thickening, nasal mucosal changes, septal erosions, and bone erosions intermixed with areas of reactive bone. If the initial disease was a tumor, the concern will be to characterize any nodular or localized soft-tissue disease, differentiate recurrent tumor from infection, and observe the presence of progressive bone erosion or soft-tissue extension to areas not normally involved by the surgery.

The best and most efficacious way to interpret a

Copyright © 2003, Mosby, Inc. All rights reserved.

postoperative imaging study, especially on a patient with a malignancy, is to compare it with a prior examination. Initially, this is best accomplished by comparing a follow-up study to a baseline postoperative CT or MR examination. This baseline scan is important for the imaging monitoring of a patient after surgery because it provides an anatomic reference with which all future examinations can be compared. If this baseline study is obtained too close to the time of surgery, the imaging findings are dominated by changes of hemorrhage and edema and thus may give a false impression of what the eventual stable postoperative appearance will be. However, if one waits too long after surgery, recurrent disease may be present. The best compromise appears to be a postoperative waiting period of 6 to 8 weeks. This time allows most of the hemorrhage and edema to resolve, whereas few if any tumors (or chronic inflammatory diseases) will recur within this period.[51, 52]

Although the baseline study is less important in patients with inflammatory disease, it still provides a reference standard against which future imaging studies can be compared, and a few physicians routinely obtain such a study for future comparison.

On subsequent follow-up CT or MR examinations, any progressive soft-tissue resolution can be interpreted as a further reduction of any postoperative edema and inflammation. However, the appearance of any new soft-tissue changes, or sites of bone erosion, must be considered recurrent disease until proven otherwise. Patients who have been operated on for inflammatory disease usually do not need periodic follow-up scans and are only imaged if symptoms reappear. By comparison, those patients who have been operated on for tumors should have scheduled periodic follow-up scans if early tumor recurrences are to be diagnosed. The time interval between these examinations usually is 4 to 6 months for the first 2 or 3 postoperative years and then 6 to 12 months for the next 2 to 3 years.[51, 52]

Plain films do not allow detailed evaluation of the postoperative patient because of the overall survey nature of these studies and the unique anatomy of the paranasal sinuses, where focal soft-tissue disease is best assessed by its relationship to the adjacent bone (which may now be resected) and sinus cavity air (which may be obscured by fibrosis or disease). Thus CT and MR imaging are the examinations of choice in monitoring the course of postoperative patients. CT allows the detailed evaluation of bone and a fairly accurate assessment of the soft tissues, provided that both axial and coronal views are available. The use of contrast is desirable because it provides some distinction between inflammatory tissue, tumor, and scar.

MR imaging offers the possibility of further differentiating recurrent tumors from sites of active infection. However, even when contrast is used, the distinction between vascularized scar and tumor may be impossible and early bone erosions may go undetected.[53] Tumor invasion into marrow-containing bone is, however, usually detected earlier on MR imaging than on CT.

Ultimately the examination of choice depends on the surgical procedure and the disease. In general, recurrent inflammatory disease is best followed on CT. The appearance of mucosal thickening is easily identified, and interval changes can be assessed by comparison to a previous CT study.

The radiologist is presented with more serious diagnostic problems when following a patient with a tumor, as the distinction between inflammatory disease, scar, and tumor is of critical importance. On CT, inflammatory secretions and reactions tend to have lower attenuation than most sinonasal tumors. On contrast-enhanced CT, active inflammatory changes tend to enhance more than most tumors. However, variations in this pattern commonly exist, and in many cases vascularized scar tissue cannot be confidently differentiated from either inflammation or tumor.

On MR imaging, inflammatory tissues usually have a low to intermediate T1-weighted and a high T2-weighted signal intensity. As mentioned in Chapter 6, about 95% of sinonasal tumors have intermediate signal intensity on all imaging sequences. Thus, in most cases, a good distinction can be made between tumor and adjacent inflammation.[54] On contrast-enhanced MR imaging, inflammatory tissues enhance intensely, and they tend to follow the contour of the sinus cavity wall fairly smoothly. Tumors, on the other hand, usually enhance only moderately and have a distinctly nodular configuration. As mentioned, the vascularized scar tissue that often develops in the postoperative sinonasal cavities has the identical imaging characteristics as tumor on both CT and MR imaging. Ultimately the distinction between these tissues is made either by comparing the imaging findings on serial studies or by biopsy of any suspicious regions. In general, MR imaging is the preferred modality to follow patients with sinonasal tumors. Newer approaches to detect early tumor recurrence include the use of MR spectroscopy and PET scanning. These topics are discussed in Chapter 45.

OPERATIVE PROCEDURES

NASAL SURGERY

Although surgery on the nose is primarily cosmetic, posttraumatic airway reconstruction accounts for many procedures. Surgery confined to the nasal or septal cartilages rarely leaves an imaging identification. However, during a rhinoplasty, use of the saw, chisel, and file to remove bone leaves a slight irregularity along the midline contour of the nasal bones. This is best seen on lateral plain films of the nose (Fig. 7-49). The nasal bones are also purposely fractured in cases of nasal bone ''hump'' removal. Once this bony mound has been removed, the resulting broad nasal base is cosmetically too wide. Because of this, the lateral nasal walls are fractured and turned inward, re-creating a thin midline nasal contour. Such iatrogenic fractures may mimic a recent traumatic fracture, and only the patient's history may resolve any confusion. After 6 to 12 months, the sharp edges of all nasal fractures become smooth, and the fracture lines are less sharply identified. Old fractures also can prove confusing when evaluating recent nasal trauma.

In more severe nasal injuries in which the nasal bones have been crushed, cartilage or rib implants may be used to reconstruct a normal nasal contour. These implants give a unique radiographic appearance that, once identified, indicates to the imager that reconstructive surgery was performed (Figs. 7-50 to 7-52).

Copyright © 2003, Mosby, Inc. All rights reserved.

VIEW IMAGE

FIGURE 7-49 Lateral plain film shows a patient who has had a prior rhinoplasty. The irregularity of the nasal bone contour is postsurgical in etiology.

The topics of endoscopic sinonasal surgery and the postoperative complications associated with this surgery are covered in Chapters 3 and 4. The following discussion concerns those more classic, nonendoscopic operations.

FRONTAL SINUS SURGERY

Trephination

Statistically, most frontal sinus disease stems from infection and can be classified as acute or chronic. In acute infections, especially if an air-fluid level is found on plain films or imaging, factors such as the time to diagnosis and the patient's immediate response to treatment determine whether a trephination (essentially an incision and drainage) procedure should be performed. The operation consists of drilling a small hole 0.5 to 1 cm to the side of the midline, usually near the upper edge of the eyebrow. After the sinus is entered and drained (the sinus mucosa is not stripped), a drainage tube or cannula is placed in the sinus for 8 to 14 days, after which it is removed to prevent a foreign body reaction in the sinus mucosa.[55] Most often the surgeon determines, by means of a Caldwell view, the sinus size and the presence of any sinus loculations. Care must be taken so that the drill does not enter either the orbit below, the anterior cranial fossa through the posterior sinus wall, or, for a small sinus, the calvarium outside of the sinus margin. The surgical defect is poorly visualized on coronal and axial CT unless the scans happen to pass directly through the site (Fig. 7-53). If the scan is performed while the drain is in place, the drain can be followed to its exit point from the sinus.

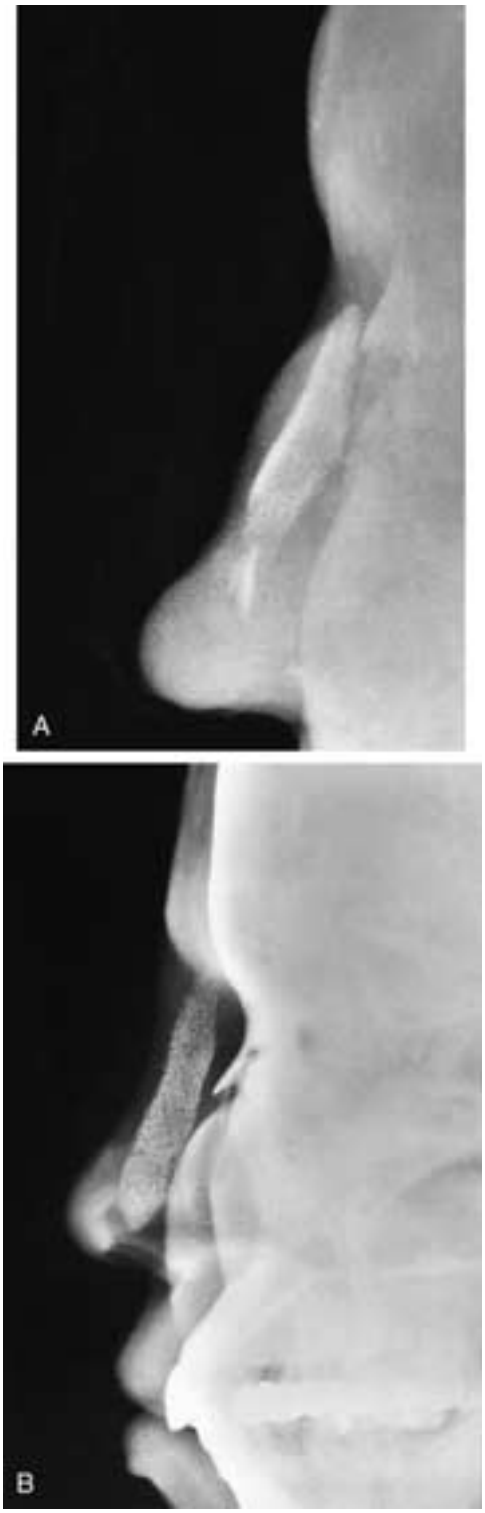

VIEW IMAGE

FIGURE 7-50 Lateral plain film (**A**) shows a patient with a rib nasal graft replacing badly fractured nasal bones. Lateral plain film (**B**) shows a patient with a partially calcified cartilage graft replacing crushed nasal bones.

In patients with chronic inflammatory disease, two types of procedures can be performed: those that do not obliterate the sinus cavity and the more commonly performed procedures that obliterate the sinus cavity. Although not commonly performed today, there are mainly three frontal sinus

Copyright © 2003, Mosby, Inc. All rights reserved.

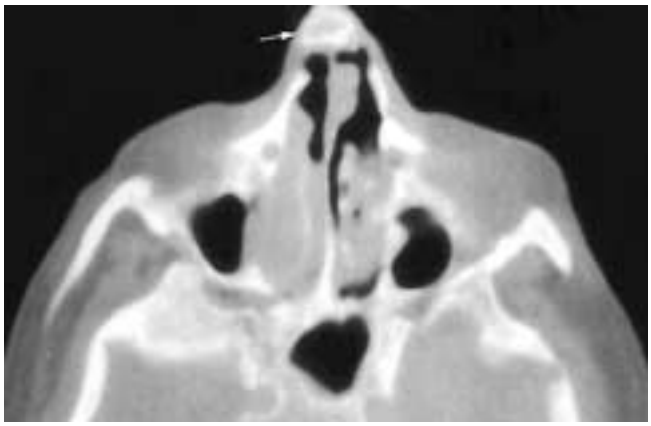

VIEW IMAGE

FIGURE 7-51 Axial CT scan shows a rib (*arrow*) used in a nasal reconstruction. There is unrelated inflammatory disease in the nasal cavities.

VIEW IMAGE

FIGURE 7-52 Axial (**A**) and coronal (**B**) CT scans show a free flap reconstruction of the lower nose after a rhinectomy. The bulk of the graft is fatty.

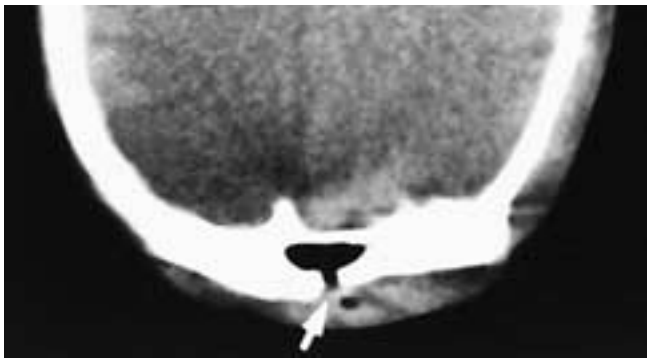

VIEW IMAGE

FIGURE 7-53 Coronal CT scan shows a frontal sinus that was trephined because of an acute unresponsive sinusitis. The site of the trephination is seen as a hole in the anterior sinus wall (*arrow*).

nonobliterative procedures: the Lynch, Killian, and Riedel procedures. For the most part, these operations have been replaced by endoscopic approaches or, for large sinuses, the obliterative osteoplastic flap procedure.

Lynch Procedure

The Lynch procedure is utilized primarily for disease in the ethmoid sinuses and supraorbital ethmoid cells. However, it also provides good entrance into a small to moderate-sized frontal sinus. The Lynch incision is buried in the creases and concavity of the lateral nose and the superomedial orbital margin. The frontal sinus is entered from below and behind the orbital rim, and the region of the nasofrontal duct is exposed by a lateral (external) ethmoidectomy. The diseased frontal sinus and ethmoid mucosa are removed, and a tube is placed in the nasofrontal duct to promote sinus drainage through a reconstructed duct. This tube remains in place for 6 to 8 weeks and then is removed intranasally (Figs. 7-54 to 7-56).

If the frontal sinus is too large for all of its diseased mucosa to be effectively removed by the standard Lynch procedure, an extended Lynch incision can be used, extending the incision more laterally over the orbit. Alternatively, in past years, a larger bony defect was made in the anterior frontal sinus wall, using either the Killian or Riedel procedure.

Killian Procedure

In a moderately large frontal sinus the Killian procedure can be used. Via two bony defects, this approach creates a larger entrance into the frontal sinus than can be obtained with an extended Lynch procedure. In the Killian approach the first bony defect is created above the orbital rim in the anterior frontal sinus wall, and the second defect is created below and behind the orbital rim in the frontal sinus floor (via a standard Lynch incision). The intact superior orbital rim partially prevents the overlying soft tissues of the forehead from collapsing into the sinus, and when compared with the Riedel procedure, the resulting cosmetic deformity is minimized (Fig. 7-57). However, the soft tissues of the forehead region do partially prolapse into the sinus cavity and create a noticeable cosmetic deformity, which is well

Copyright © 2003, Mosby, Inc. All rights reserved.

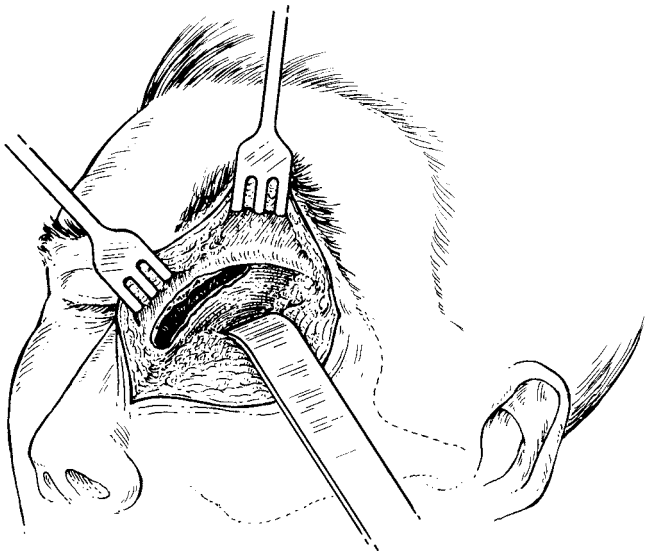

VIEW IMAGE

FIGURE 7-54 Diagram of a Lynch procedure. The ethmoid sinuses, supraorbital ethmoid cells, and small frontal sinuses can be approached by this procedure. The incision is buried in the creases of the lateral nose and the superomedial orbital rim.

seen on axial scans. As in the Lynch procedure, the nasofrontal duct is reconstructed through an external ethmoidectomy.

Riedel Procedure

For the reliable removal of diseased sinus mucosa in a large frontal sinus, the Riedel procedure can be used. In this approach the two surgical defects created in the Killian procedure are joined into one large defect, which includes the superior orbital rim (Fig. 7-58). At the completion of the procedure the soft tissues of the forehead are laid on the posterior frontal sinus wall, which has been denuded of its mucosa. This effectively obliterates the upper sinus cavity but creates a cosmetically undesirable soft-tissue defect in the forehead. The nasofrontal duct is reconstructed as in the Lynch procedure.[55, 56]

Because of the cosmetic deformities associated with these procedures, particularly the latter two techniques, and because the nasofrontal duct becomes obstructed postoperatively in about 50% of these patients, the cosmetically less deforming obliterative osteoplastic flap procedure has gained great popularity, especially in the moderate to large frontal sinuses in which mucosa cannot be removed by a Lynch approach.

Osteoplastic Flap Procedure

The osteoplastic flap incision is either a curved coronal scalp incision that is hidden in the scalp hair or a brow incision that extends between the eyebrows, crossing the intervening skin crease near the root of the nose or nasion. Once the periosteum over the frontal bone is exposed, a template made from a Caldwell view is used to trace the frontal sinus contour on the bone and periosteum. This template should come from a film taken on a dedicated head unit such as the Franklin head unit, which has a magnification factor of only 3.4% (compared with 10.3% on a standard 40-inch posteroanterior Caldwell film).[57] The template is made by cutting out on this film the sinus contour and the contour of the upper orbits. The resulting template is then gas sterilized. The orbital contours can be used to localize the template on the patient, and then the sinus outline is traced on the patient's exposed frontal bone with its intact periosteum.

The periosteum is incised on all except its inferior margin, and the frontal sinus contour is drilled into the anterior frontal sinus table. The drill line is beveled medially and downward into the sinus to help ensure that the frontal sinus and not the anterior cranial fossa is entered. The inferior margin of this anterior wall is not drilled but is fractured from side to side, elevated, and turned downward off of the sinus, with its overlying periosteum intact. This technique yields a viable bone flap. The sinus mucosa is then drilled out, and the sinus cavity is obliterated with fat or muscle, usually taken from the abdominal wall. The anterior sinus wall is then replaced, the periosteum sutured, and the skin closed, leaving literally no cosmetic deformity (Fig. 7-59).

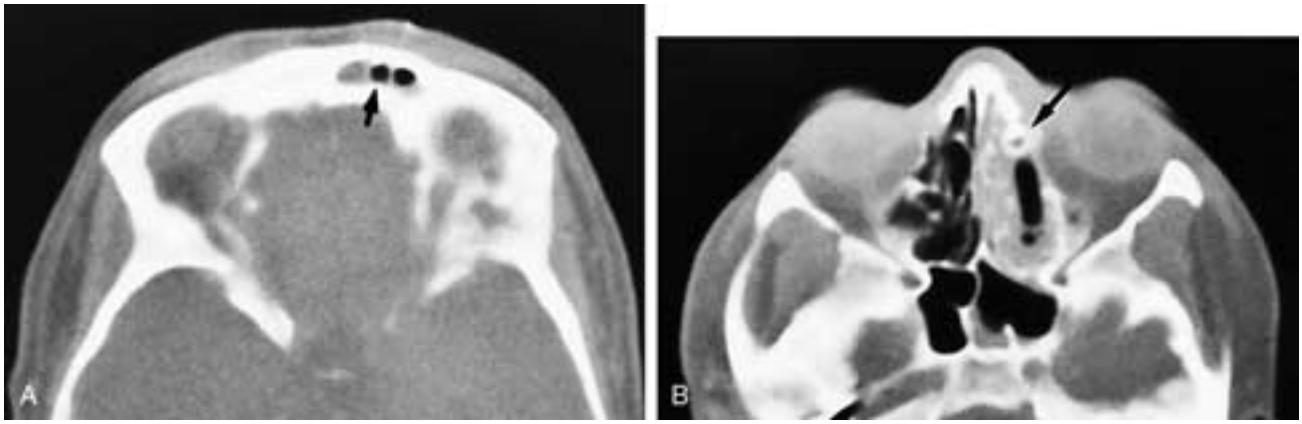

VIEW IMAGE

FIGURE 7-55 Axial CT scan (**A**) shows an air-filled tube (*arrow*) in the left frontal sinus. The sinus is partially filled with secretions. Axial CT scan (**B**) through the ethmoid sinuses shows the drainage tube (*arrow*) extending down into the nose. There has been an external ethmoidectomy, and the anterior lamina papyracea has been removed. The left ethmoid cavity and the left sphenoid sinus have inflammatory changes.

Copyright © 2003, Mosby, Inc. All rights reserved.

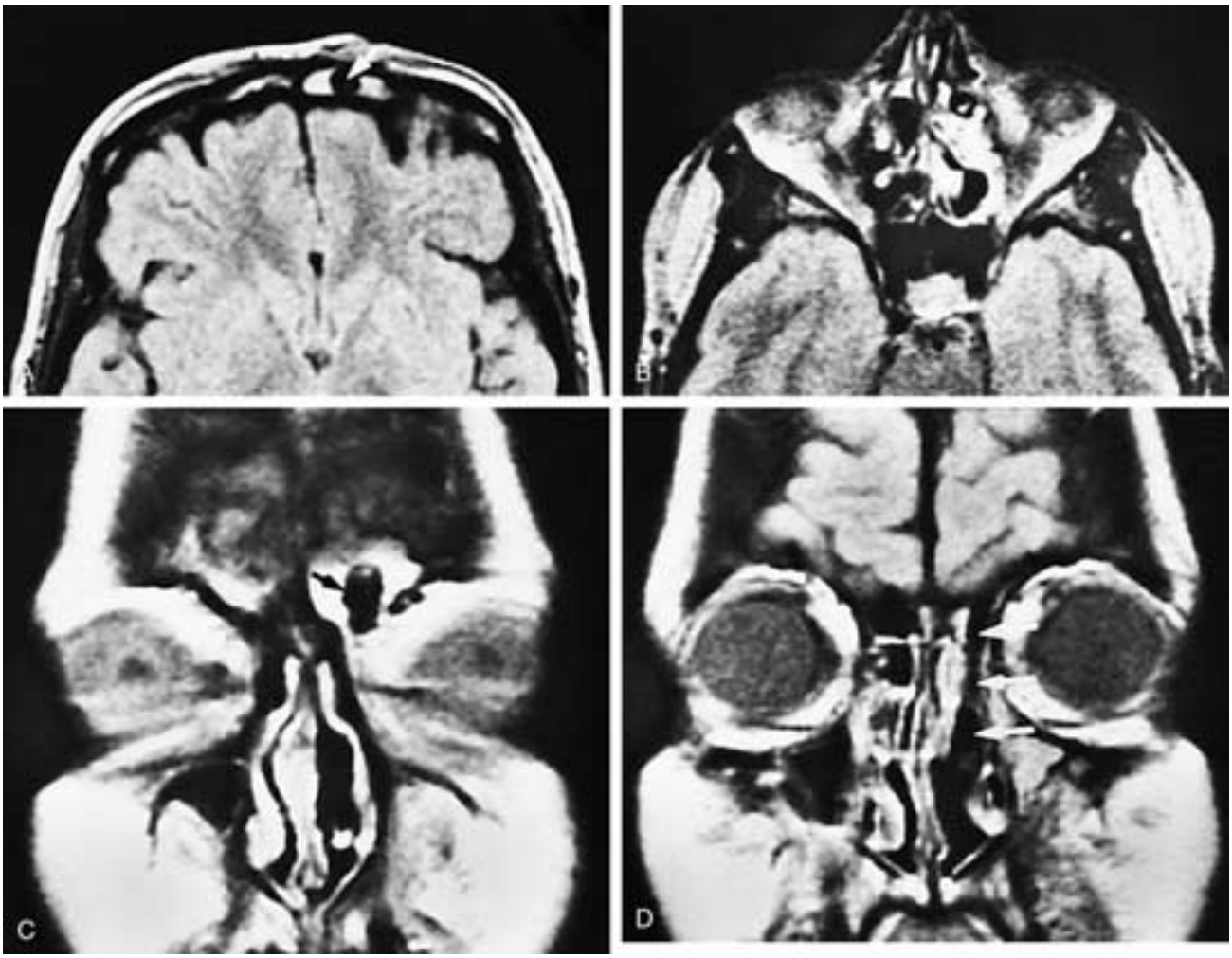

VIEW IMAGE

FIGURE 7-56 Axial proton density MR images (**A**, **B**) show a drainage tube in the left frontal sinus (**A**) (*arrow*) and sinus secretions. In (**B**), the drainage tube can barely be seen in the left ethmoid sinuses (*arrow*), and inflammatory changes are present as well. On the MR images, it is almost impossible to appreciate that an external ethmoidectomy has been performed. Coronal proton density MR images (**C**, **D**) show the tube in the left frontal sinus (*black arrow*) and the drainage tube extending through the ethmoid sinuses into the nasal fossa (*arrows*).

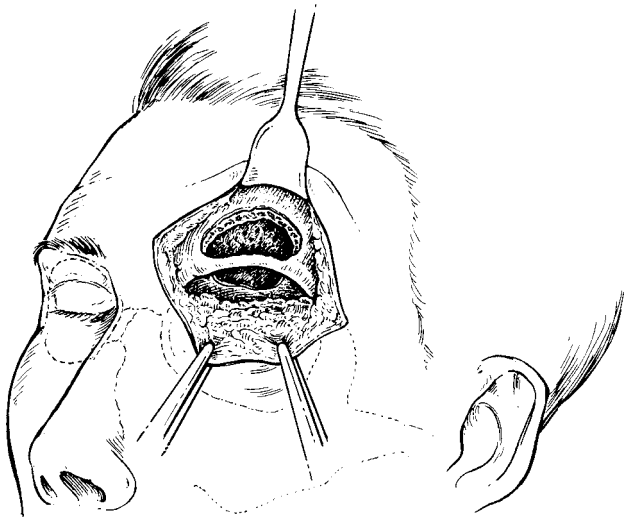

VIEW IMAGE

FIGURE 7-57 Diagram of a Killian procedure in which the superior orbital rim remains intact. Because of the forehead deformity, this procedure has for the most part been abandoned.

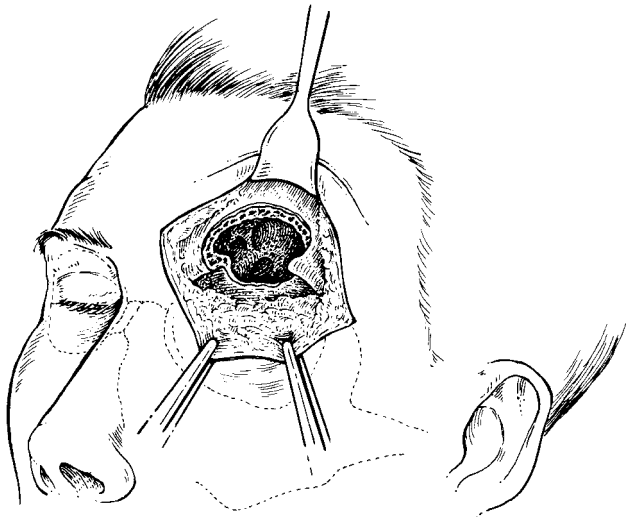

FIGURE 7-58 Diagram of a Riedel procedure in which the superior orbital rim has been removed. Because this operation causes a large deformity of the forehead, it has been almost entirely abandoned.

VIEW IMAGE

Copyright © 2003, Mosby, Inc. All rights reserved.

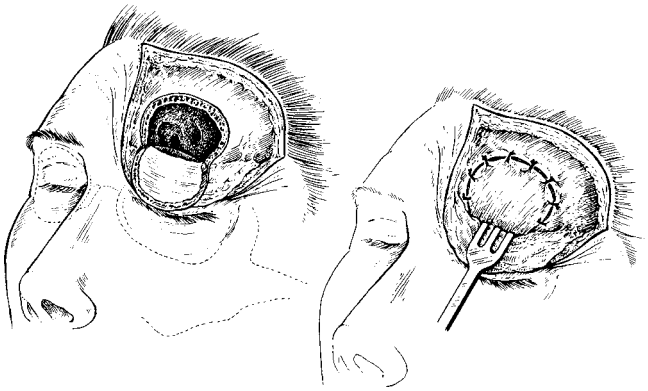

VIEW IMAGE

FIGURE 7-59 Diagram of an osteoplastic flap procedure. The anterior sinus wall is flipped down, with the inferior periosteum left intact. After the sinus mucosa and disease are removed, the sinus is obliterated with fat and then the flap is replaced. This procedure leaves almost no cosmetic deformity.

The fat progressively and gradually undergoes fibrosis, usually until the fibrosis represents one-third to one-half the volume of the obliterating material. More extensive fibrosis of the fat does not appear to occur normally. Throughout this fibrosing process, no volume loss occurs so that the sinus remains obliterated.

Infection of the bone flap or the operative margins, with or without associated osteomyelitis, and infection of the obliterating fat are the two most significant complications of the osteoplastic flap procedure. If the infection cannot be controlled with antibiotic treatment, reoperation is necessary. This often necessitates the removal of the anterior sinus wall bone flap, with some resulting inward prolapse of the forehead soft tissues. A plastic reconstruction can then be performed at a later date once the infection is cured.

If the osteoplastic flap procedure was performed to obliterate a mucocele that thinned or destroyed a portion of the posterior or anterior sinus tables, these defects will also be visualized on subsequent imaging studies. On plain films the osteoplastic bone flap is identified by a variably thin zone of lower density at its margins. This zone represents the bone that was drilled out of the frontal table during surgery (Figs. 7-60 and 7-61). In a few cases the flap fit may be so good as to make visualization of the surgical margin almost impossible on Caldwell or Waters views. However, a lateral view clearly shows the beveled surgical defect. In fact, if a history of prior surgery is not obtained, this defect may be misinterpreted as an anterior frontal table fracture (Fig. 7-62). If the sinus margin was altered before surgery, it will remain so after surgery. Thus the mucoperiosteal white line may be absent or replaced by a thick zone of sclerosis, and the sinus contour may be remodeled. Although this appearance can be confusing and suggests that whatever caused these changes is still present in the sinus, these sinus alterations merely reflect whatever process originally necessitated the surgery. The fat used to obliterate the sinus usually causes the sinus to have a hazy soft-tissue density on plain film, suggesting sinusitis. The surgical bony margins should be sharp and of a normal texture even though the bone flap does not fit precisely against the adjacent frontal bone. An air-fluid level indicates reinfection of the sinus, a serious complication.

On CT the bone flap may go unnoticed if only narrow window images are available. At wide window settings the bone flap should have a normal texture (Fig. 7-63). However, the edges of the flap and the adjacent frontal bone occasionally have a ragged, irregular appearance that reflects the beveling surgical procedure. Without any associated clinical or soft-tissue changes of infection, this irregular bone should not elicit a diagnosis of osteomyelitis. Frank osteomyelitis appears as areas of bone demineralization, erosion, or sequestration accompanied by swelling and cellulitis of the overlying forehead soft tissues. There usually is also evidence of infection in the underlying fat (Fig. 7-64).

FIGURE 7-60 Waters view shows a patient after bilateral osteoplastic flap surgery. The flap margins can barely be identified (*arrows*).

VIEW IMAGE

The bone flap should be in a normal alignment with the adjacent frontal bone contour, that is, the flap should not be either depressed into the sinus or elevated over the adjacent frontal bone. When the flap is elevated, infection of the underlying obliterating fat must be considered. The obliter-

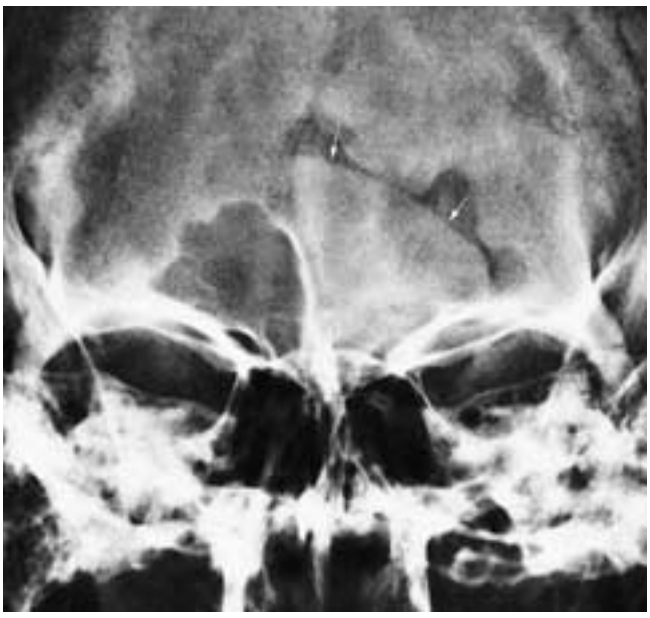

FIGURE 7-61 Caldwell view shows a patient after left osteoplastic flap surgery. The margins of the flap are well seen (*arrows*). The space between the flap and the calvarium is a normal postoperative finding resulting from the bone removal that occurs during surgery.

VIEW IMAGE

Copyright © 2003, Mosby, Inc. All rights reserved.

ated sinus is best examined at both narrow and wide windows. The entire sinus cavity should be airless and filled with fat that has randomly scattered strands of soft-tissue-dense fibrous tissue. Whenever a focal mass of soft-tissue density is seen within the fat or whenever more than half of the fat content is of fibrous density, the imager should raise the possibility of infection (Figs. 7-64, 7-66, and 7-68 to 7-70). This type of infection is usually associated with elevation of the flap secondary to swelling of the fibrous fatty material (Figs. 7-65, 7-69, and 7-70). In these cases the intracranial compartment should also be examined for evidence of spread of the infection.

Occasionally the osteoplastic bone flap fractures during surgery; however, as long as the overlying periosteum remains intact, the fracture pieces usually remain viable. The imager should verify that the bony pieces have a normal texture, that there are no sites of osteomyelitis, and that the bone fragments are not elevated. In rare instances after many years, some calcification can occur in the obliterating fat; this should be considered a normal postoperative variant.

On MR imaging the signal intensities in the normal postosteoplastic flap sinus reflect the obliterating fat. Thus there is a high T1-weighted and an intermediate T2-weighted signal intensity (Fig. 7-71). Although infection in the fat will produce a high T2-weighted signal intensity, occasionally areas of high T2-weighted signal intensity are seen in noninfected sinuses (Fig. 7-72). The precise cause of this is unclear. Thus, the mere presence of a high T2-weighted signal intensity within the obliterating fat should not warrant a diagnosis of postoperative infection. Infection should be considered if there is high T2-weighted signal intensity in the obliterating fat, elevation of the bony flap, and evidence of swelling and inflammation in the surrounding forehead soft tissues.

VIEW IMAGE

FIGURE 7-62 Lateral multidirectional tomogram shows a patient's status after an osteoplastic flap procedure. The surgical margin of the flap (*arrow*) is seen and may simulate a fracture.

ETHMOID SINUS SURGERY

Although today the ethmoid sinuses are most often approached endoscopically, traditionally the ethmoid complex can be partially resected via three major approaches: the external, the internal (intranasal), and the transmaxillary (transantral) (Fig. 7-73). These procedures are performed for inflammatory disease, and the aim is to progressively remove the disease from each cell until all of the pathologic material is extirpated. The primary areas of complication are entrance into the floor of the anterior cranial fossa and damage to the orbital contents.[51, 52, 57]

External Ethmoidectomy

The external approach provides the best overall access and visualization of the ethmoid cells. After a Lynch incision, the periorbita is elevated and the surface of the lamina papyracea is viewed to identify prior fractures and any areas of dehiscence or erosion. The anterior and posterior ethmoidal canals are exposed. A line connecting these canals lies just below the floor of the anterior cranial fossa, and if the surgeon stays caudal to this line, entrance into the anterior cranial fossa should not occur. The surgical field can be enlarged to the frontal sinus, supraorbital cells, orbit, anterior sphenoid sinus, or base of the skull; the nasofrontal duct is best opened with this approach. In an external ethmoidectomy, the anterior cells are first entered through the lamina papyracea, and then the posterior cells are progressively opened as needed. As a Lynch incision must be made, this external approach has a scar hidden in the crease of the medial orbital margin.

Internal Ethmoidectomy

The internal ethmoidectomy is an intranasal approach and usually includes resection of the middle turbinate to provide better access to the ethmoid and sphenoid cells. The ethmoid complex is usually entered via the bulla ethmoidalis; the anterior cells are resected and then the more posterior cells are opened. Although in experienced hands the lamina papyracea is not violated in this procedure, dehiscence of the lamina papyracea or a prior external ethmoidectomy is a contributing factor to inadvertant entrance into the orbit. The internal ethmoidectomy approach is used for isolated ethmoid sinus disease, for biopsies in patients who do not have coexistent antral disease, and in patients who do not wish to have an external incision.

Transantral Ethmoidectomy

The transantral approach is used when the antral cavity has coexistent sinusitis or when the intranasal approach is not possible for anatomic or technical reasons. The antrum is entered using a Caldwell-Luc approach,

Copyright © 2003, Mosby, Inc. All rights reserved.

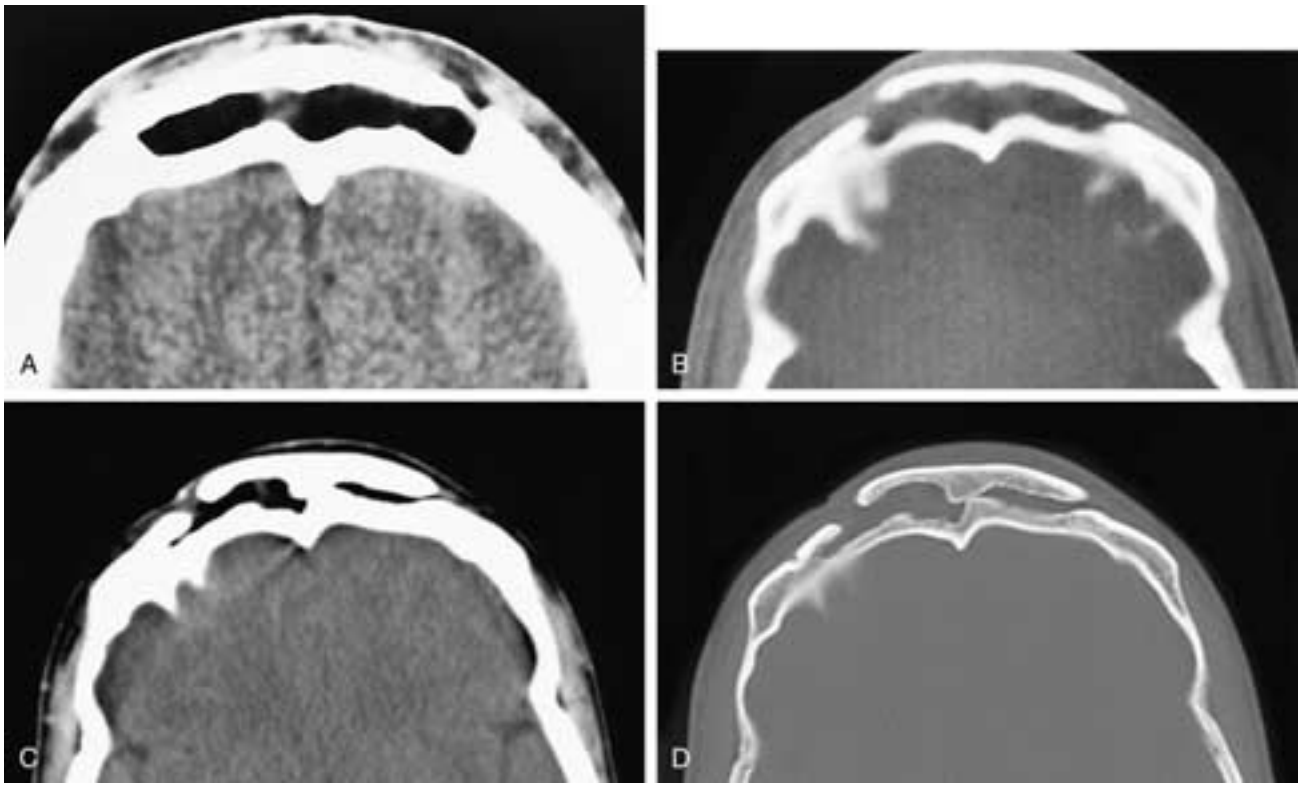

VIEW IMAGE

FIGURE 7-63 Axial CT scans at narrow (**A**) and wide (**B**) window settings. The patient has had an osteoplastic flap procedure. The sinus is filled with fat, and the flap is clearly seen in a good position. In (**A**), the presence of the flap can be easily overlooked. Axial CT scans at narrow (**C**) and wide (**D**) window settings on another patient who has also had an osteoplastic flap procedure. The sinus is filled with fat; however, the bone flap appears elevated. This is secondary to abutting of the residual sinus septum on the flap bone and the posterior sinus wall. This will be the new normal frontal sinus appearance for this patient and demonstrates why baseline postoperative scans should be obtained.

and the medial, upper maxillary sinus wall (ethmoidomaxillary plate) is taken down so that the ethmoid cells can be entered. The ethmoid cells are then progressively resected.

In all of these ethmoidectomy procedures, the surgeon is essentially blindly cutting through the most inaccessible ethmoid septa, those located at the cranial and posterior margins of the ethmoid complex. Even when the surgeon believes that the resection extended back into the sphenoid sinus, CT often shows that the most posterior ethmoid cells and the sphenoid sinus remain untouched. Because entrance into the anterior cranial fossa is to be avoided, most surgeons favor caution and many of the most cranial ethmoid cells also remain intact. These remaining cells point out the difficulty of intraoperatively estimating one's precise anatomic position. Because disease can recur in these remaining cells, postoperative scans should be obtained if the patient's symptoms persist or recur (Figs. 7-74 to 7-84).[51, 52]

Because of the relatively small, boxlike anatomy of the ethmoid complex, postoperative hemorrhage can fill some unresected cells, and on occasion, rather than resorb, the blood becomes fibrosed or even ossified. Such en bloc fibrosis does not often occur after surgery in the other paranasal sinuses, but it is fairly common in the ethmoid complex. The imaging differentiation of recurrent disease from fibrosis can be difficult, as the attenuation values frequently are not sufficiently different to establish a definitive diagnosis. In general on CT, recurrent inflammation enhances and the fibrosis does not.

Uncommonly, a dense fibrous scar develops within the postoperative ethmoid bed. This usually has low T1-weighted and T2-weighted signal intensity and thus can be distinguished from active infection on the T2-weighted

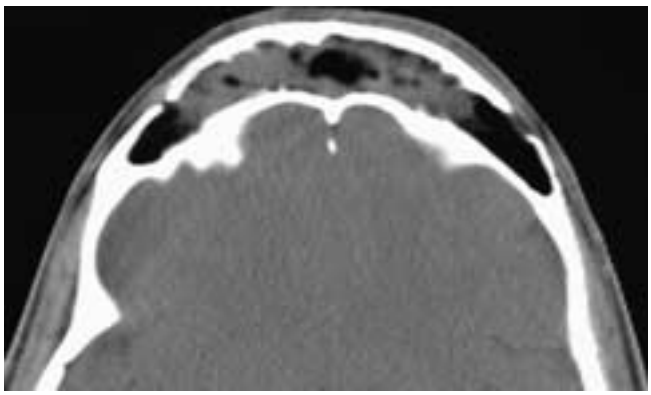

FIGURE 7-64 Axial CT scan shows an osteoplastic flap. Although over half of the fat has soft tissue rather than fat attenuation, the bone flap is in a good position and there are no inflammatory changes in the overlying soft tissues. This is a normal imaging variant of this procedure.

VIEW IMAGE

Copyright © 2003, Mosby, Inc. All rights reserved.

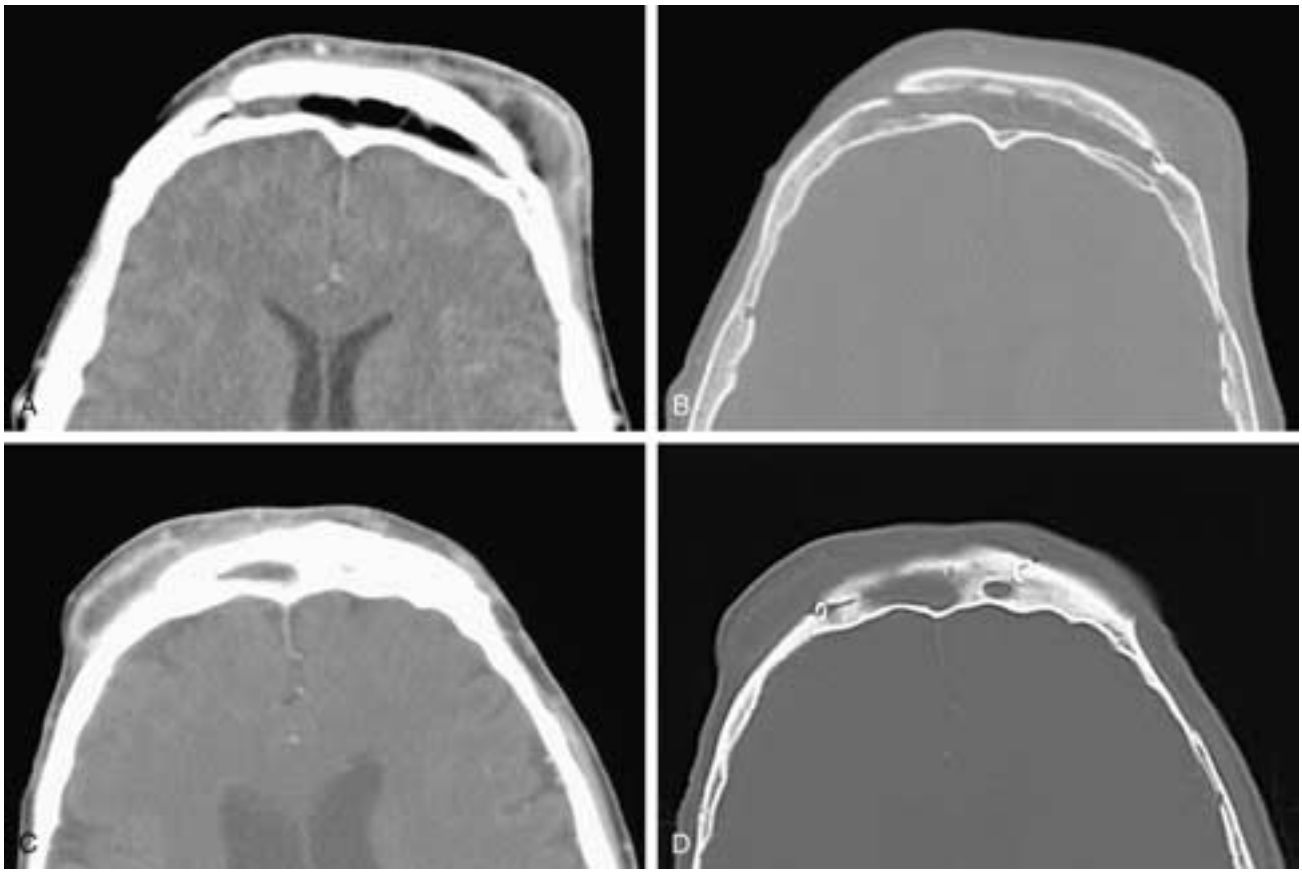

VIEW IMAGE

FIGURE 7-65 Axial CT scans at narrow (**A**) and wide (**B**) window settings. The patient has had an osteoplastic flap procedure. Despite the presence of primarily fat attenuation within the sinus, the right side of the bone flap is elevated, there is an abscess at the left margin of the flap, and there is swelling of the forehead soft tissues. This was an infected flap. Axial CT scans at narrow (**C**) and wide (**D**) window settings on another patient. In (**C**), an abscess is seen in the forehead soft tissues. Although it lies at the right margin of an osteoplastic flap, the bony flap cannot be seen clearly. In (**D**), the bony flap is clearly seen. This was an early abscess, developing after local head trauma to the region. The flap is otherwise normal on imaging.

scans. The denuded ethmoid bone may also develop a hyperostotic reaction that produces variable amounts of bone. In some cases, a localized osteoma-like bone develops; in other cases, the entire postoperative cavity may be obliterated by the bone that often mimics the appearance of fibrous dysplasia. This type of bone reaction also occurs in the maxillary sinus and to a lesser degree in the sphenoid sinus. It is rare that this reactive bone develops in the postoperative frontal sinus.

In addition to noting how extensive is the removal of the ethmoid septae, the imager should anticipate (1) an absent anterior third to half of the lamina papyracea from an

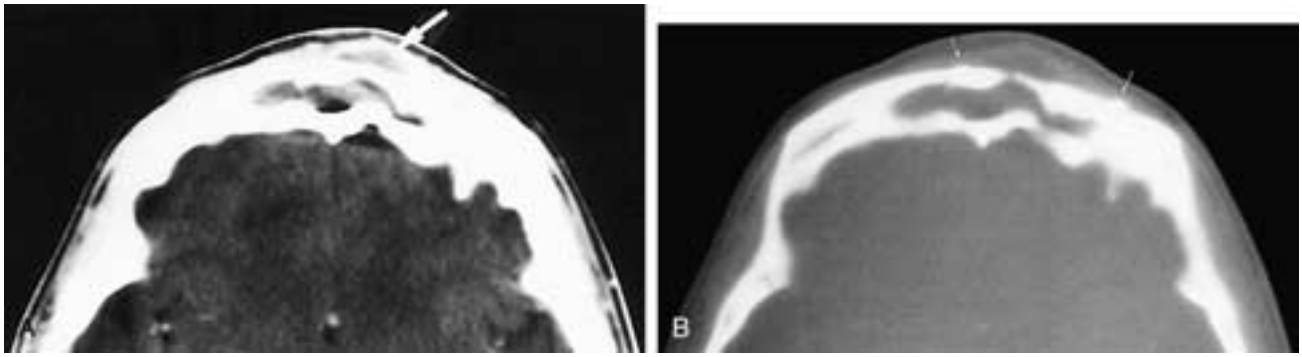

VIEW IMAGE

FIGURE 7-66 Axial CT scans at soft tissue (**A**) and bone (**B**) window settings show a patient who had a left osteoplastic flap. The small wire sutures stabilizing the flap can barely be seen in (**B**) (*small arrows*). There is erosion of the midanterior bone flap, and an abscess is present in the forehead (*arrow* in **A**). The fat used to obliterate the sinus is also dense, reflecting infection.

Copyright © 2003, Mosby, Inc. All rights reserved.

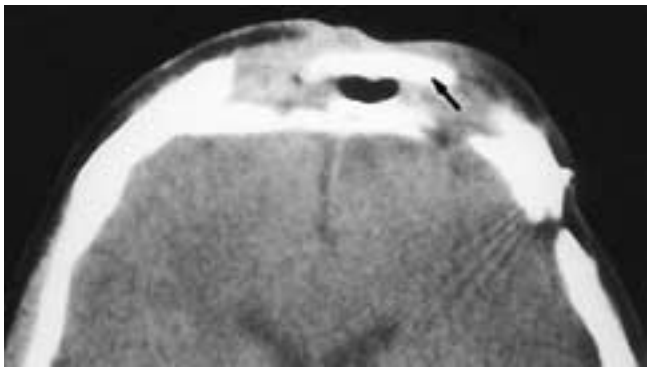

VIEW IMAGE

FIGURE 7-67 Axial CT scan shows an infected osteoplastic flap. There is swelling of the overlying forehead soft tissues, and the bone flap (*arrow*) has been partially eroded. In addition, just behind the flap there is air, which should not be present in an obliterated sinus. The defect in the left posterior sinus table was related to the surgery.

VIEW IMAGE

FIGURE 7-68 Axial contrast CT scan shows a patient's status after a right osteoplastic flap procedure. Although the obliterating fat is only slightly denser than expected, there is elevation and rotation of the bone flap (*arrow*) and swelling of the forehead soft tissues. This was an infected flap.

external approach, (2) an absent medial ethmoid wall and probably an absent middle turbinate from an internal approach, and (3) a Caldwell-Luc defect in the lower anterior antral wall, absent bone in the upper medial antral wall, and possibly an absent middle turbinate from a transantral approach. Any residual soft tissues in the remaining ethmoid cells should be clearly noted by the imager for future reference.

If a postethmoidectomy cavity becomes obstructed after mucosal reepithelialization, a postoperative mucocele may develop (Fig. 7-85). This mucocele usually does not grow like a typical ethmoid mucocele, which tends to expand laterally into the orbit. Rather, this postoperative mucocele takes the course of least resistance and expands within the enlarged postoperative ethmoid cavity. It is only after the entire ethmoid cavity is filled that the mucocele bulges into the orbit. On imaging, characteristically there is a collection of entrapped secretions within the postoperative ethmoid.[58]

MAXILLARY SINUS SURGERY

Today the most common diagnostic and therapeutic procedures performed on the antrum and the osteomeatal complex are endoscopic. However, intranasal antrostomy and the Caldwell-Luc operation are still performed. The endoscopic techniques and their postoperative appearances are discussed in Chapters 3 and 4.

Intranasal Antrostomy and the Caldwell-Luc Procedure

In an intranasal antrostomy the membranous and bony lateral nasal wall of the inferior meatus is partially resected in an attempt to create better gravity drainage for the sinus. In the Caldwell-Luc procedure, in addition to the intranasal antrostomy, the maxillary sinus is entered via the canine fossa region in the lower anterior antral wall. Because this entrance scar is intraoral, there is no facial scarring (Fig. 7-86). Once the sinus is entered, the diseased mucosa is removed. Initially the anterior wall bony defect is closed by a hematoma that eventually undergoes fibrosis (Figs. 7-87 to 7-90). However, this hematoma can uncommonly become infected, and in rare instances an oroantral fistula may be created. If this complication occurs, it is usually within the first or second postoperative week.

Via the Caldwell-Luc approach, the bone of the posterior sinus wall can also be removed to provide access for internal maxillary artery ligation or to expose the pterygopalatine fossa, vidian nerve, and pterygopalatine ganglion.[55] In such cases, a bony defect in the upper medial and posterior antral wall also can be seen on imaging.

In some patients, synechiae develop between the posterior maxillary sinus wall and the margins of the canine fossa/Caldwell-Luc defect in the anterior sinus wall. Such synechiae may form the basis for the development of a membrane that extends across the sinus between the anterior and posterior walls. Once formed, this membrane may obstruct the drainage of the lateral portion of the maxillary sinus and lead to the appearance of a postoperative antral

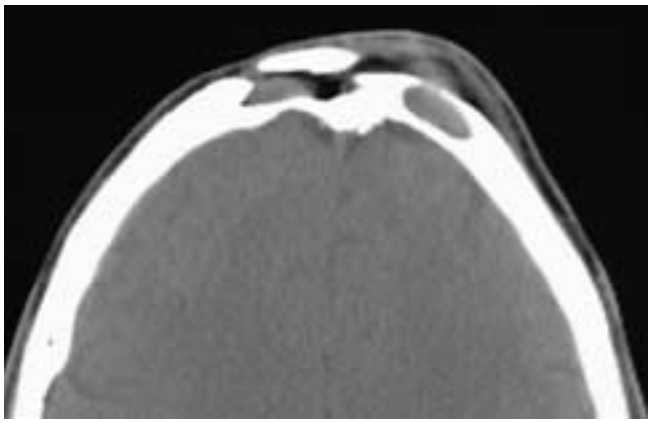

VIEW IMAGE

FIGURE 7-69 Axial CT scan of a patient who had a right osteoplastic flap procedure. There is an ovoid soft tissue density within the right sinus. The bone flap is elevated, and there is thickening of the forehead soft tissues. In addition, the left frontal sinus is opacified, and there is a soft tissue mass in the overlying forehead with thinning of the intervening anterior frontal sinus bone. This patient had a recurrent mucopyocele in the right frontal sinus. There was a mucocele in the nonoperated left frontal sinus.

Copyright © 2003, Mosby, Inc. All rights reserved.

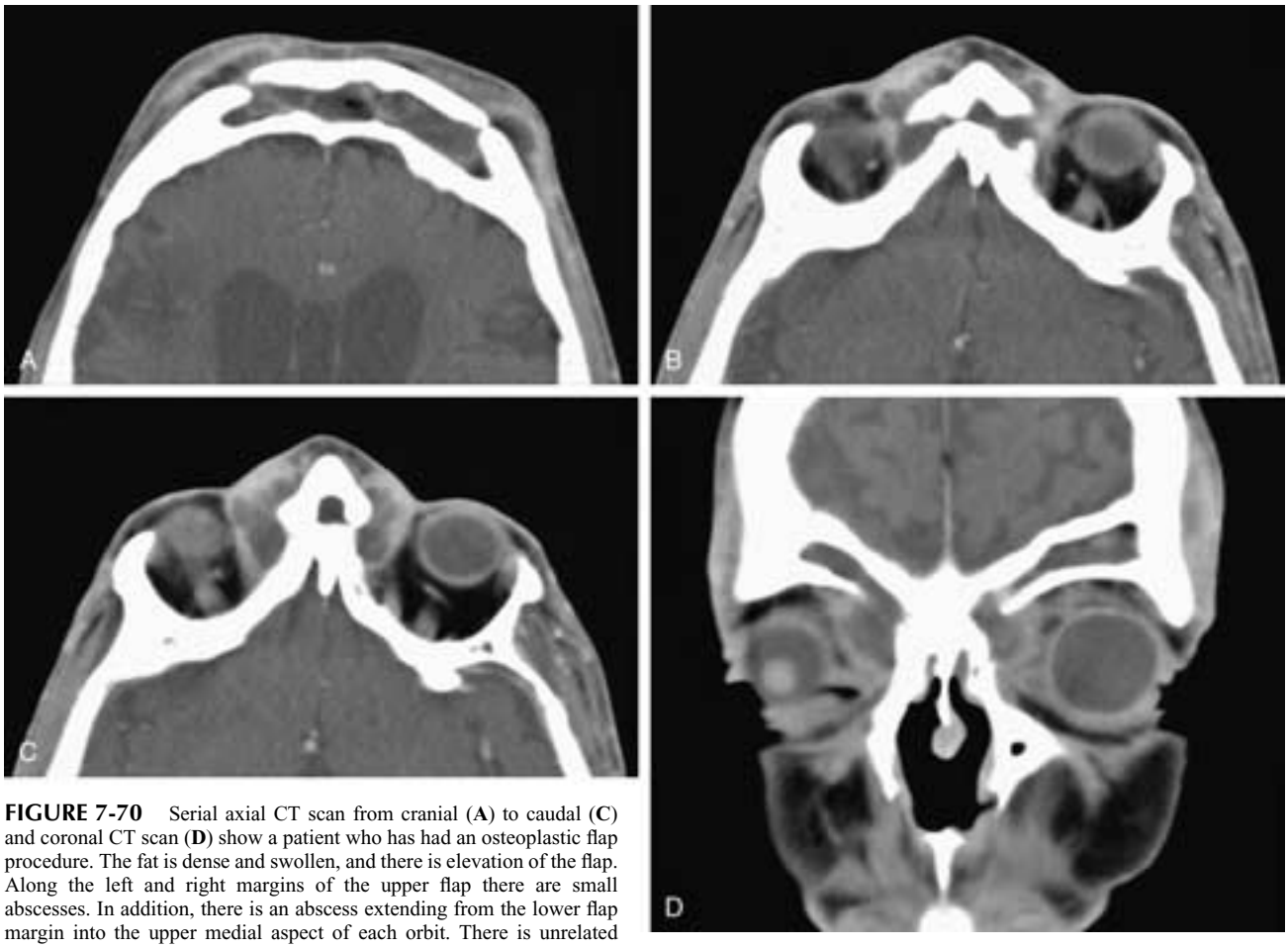

VIEW IMAGE

FIGURE 7-70 Serial axial CT scan from cranial (**A**) to caudal (**C**) and coronal CT scan (**D**) show a patient who has had an osteoplastic flap procedure. The fat is dense and swollen, and there is elevation of the flap. Along the left and right margins of the upper flap there are small abscesses. In addition, there is an abscess extending from the lower flap margin into the upper medial aspect of each orbit. There is unrelated ventricular dilatation.

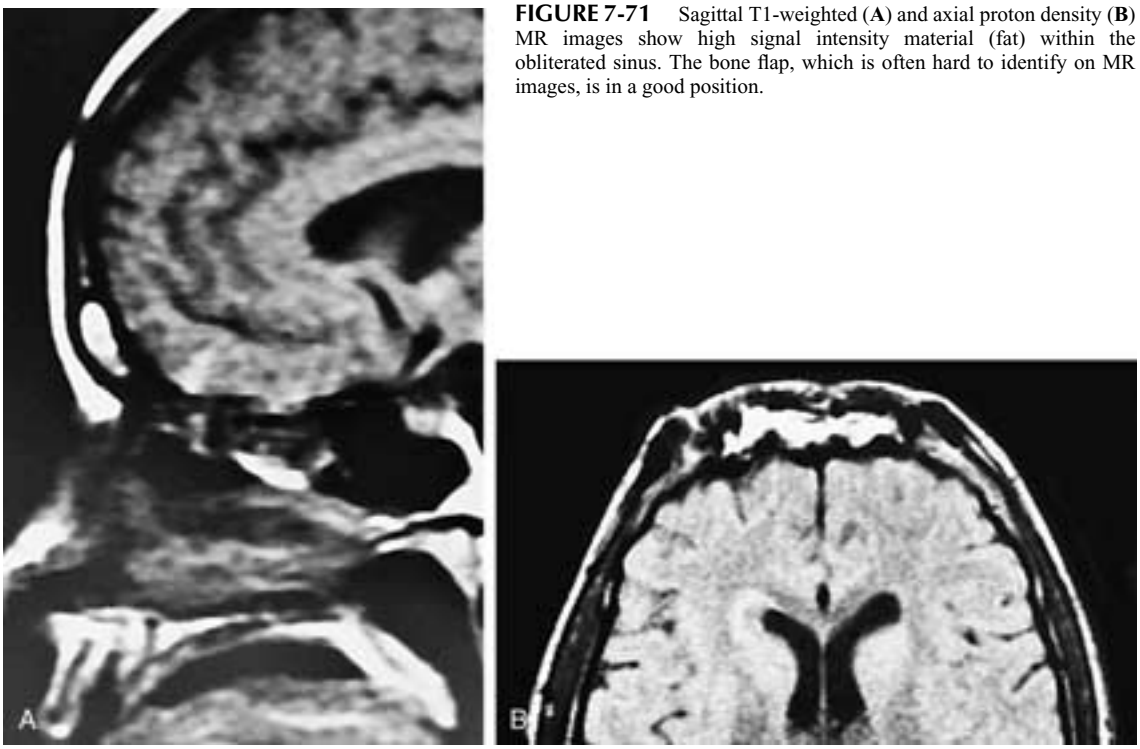

FIGURE 7-71 Sagittal T1-weighted (**A**) and axial proton density (**B**) MR images show high signal intensity material (fat) within the obliterated sinus. The bone flap, which is often hard to identify on MR images, is in a good position.

VIEW IMAGE

Copyright © 2003, Mosby, Inc. All rights reserved.

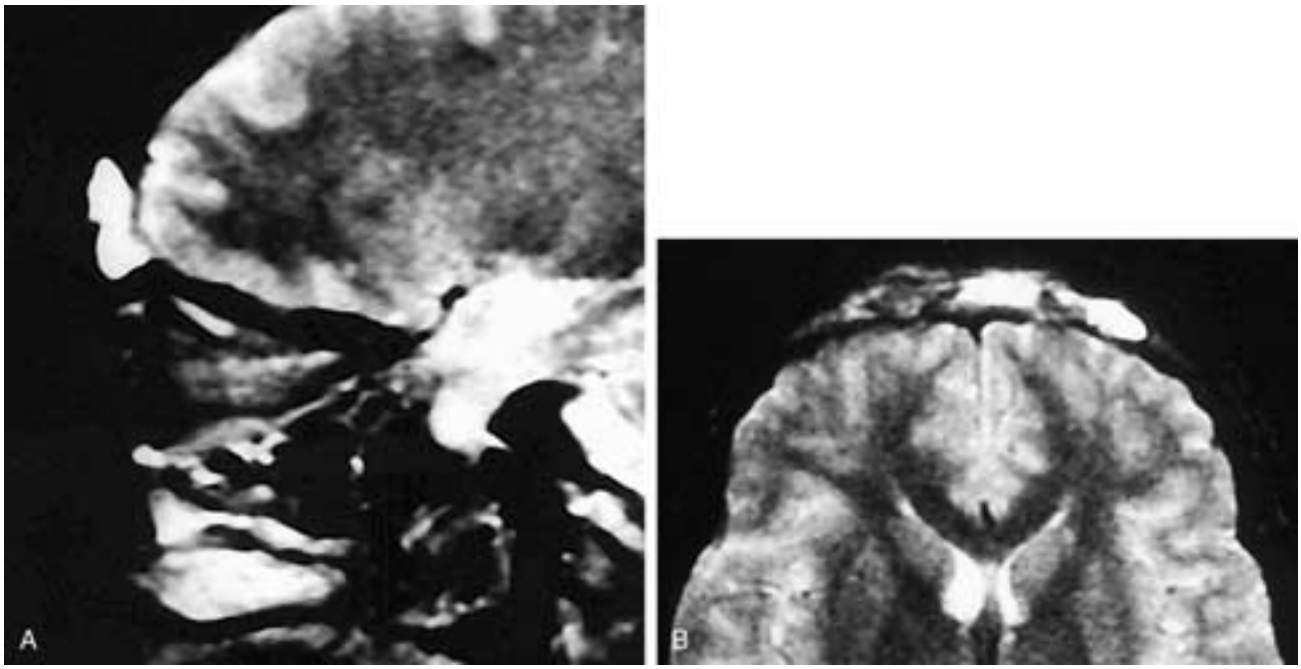

VIEW IMAGE

FIGURE 7-72 Sagittal (**A**) and axial (**B**) T2-weighted MR images on a patient who has had an osteoplastic flap procedure. The right side of the obliterated sinus has a normal fat signal intensity. However, the middle and left regions of the sinus have high signal intensity. This usually indicates the presence of infection, but this patient was asymptomatic. Such high T2-weighted signal intensity may be a normal postoperative MR finding. There is no elevation of the bone flap, and there are no inflammatory changes in the forehead soft tissues.

mucocele. In these cases, the medial postoperative sinus cavity remains aerated, while the lateral sinus cavity first becomes obstructed and then, as a mucocele develops, expanded. The imaging appearance of a laterally expanded mucoid mass in such a sinus signifies the presence of a postoperative mucocele (Figs. 7-91 and 7-92). Less often, postoperative antral mucoceles can occur in the maxillary recesses in the tuberosity and in the hard palate.

As previously mentioned, once the sinus mucosa has been stripped from the sinus wall, a bony reaction may be elicited that results in reactive bone formation, thickening of the sinus wall, and reduction or obliteration of the sinus cavity. Such a reaction is an expected consequence of the procedure and should not necessarily signify to the radiologist that active infection is present (Figs. 7-88 and 7-89).[59]

Optic nerve compression and decreased visual acuity in

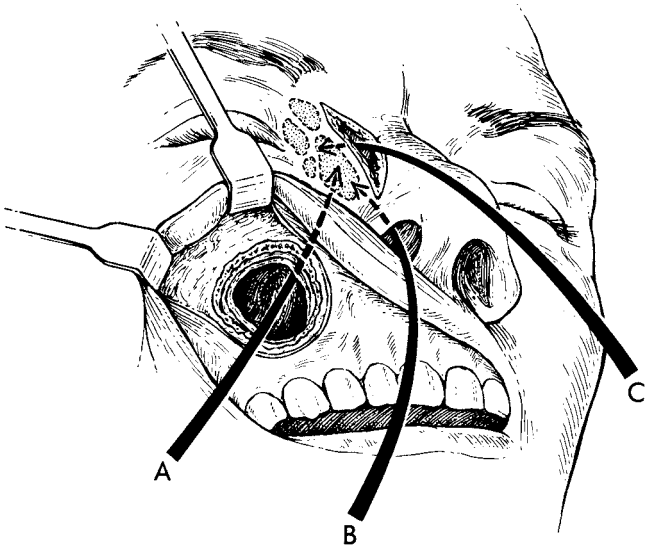

VIEW IMAGE

FIGURE 7-73 Diagram of the three major surgical approaches to the ethmoid sinuses. (**A**) Transmaxillary or transantral. (**B**) Internal or intranasal. (**C**) External (Lynch).

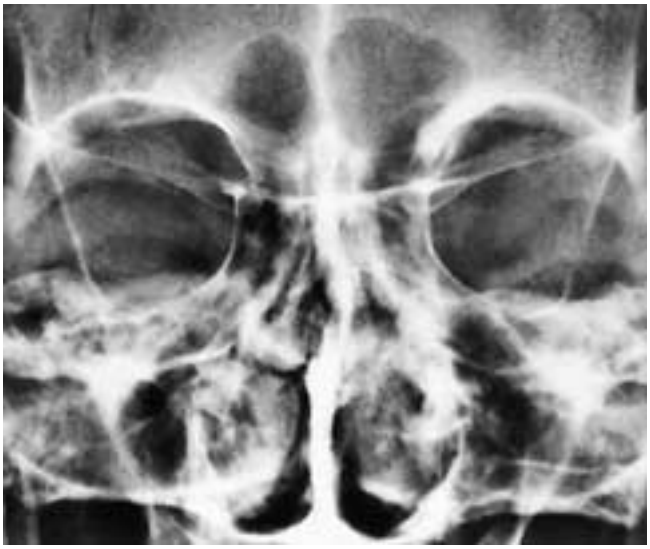

FIGURE 7-74 Caldwell view shows clouding of the left ethmoid sinuses. This appearance suggests infection. However, in this patient it was due to fibrosis after an ethmoidectomy.

VIEW IMAGE

Copyright © 2003, Mosby, Inc. All rights reserved.

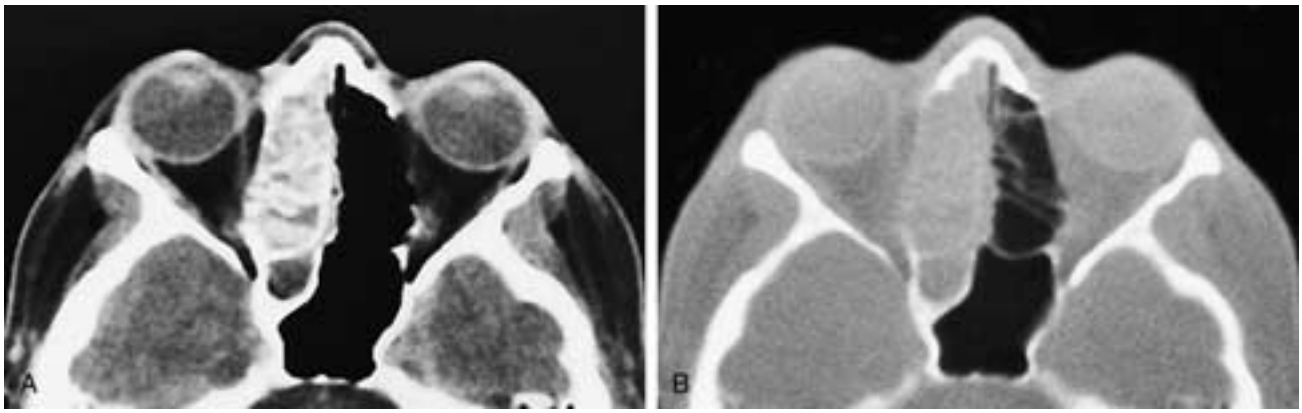

VIEW IMAGE

FIGURE 7-75 Axial CT scans at narrow (**A**) and wide (**B**) window settings show inflammatory disease in the right ethmoid and sphenoid sinuses. In (**A**), there appears to have been a left sphenoethmoidectomy, as the septations are not seen. However, in (**B**), the left ethmoid septa and the anterior sphenoid sinus wall are intact, indicating that no surgery was performed. In order to avoid such mistakes, these cases should always be viewed at wide window settings.

patients with thyroid ophthalmopathy may be treated by surgical decompression of the orbit. The procedures most commonly employed are a lateral orbitotomy (Krönlein's procedure); an antral (orbital floor) decompression using a Caldwell-Luc approach; an ethmoid decompression using an external ethmoidectomy approach; and an orbital roof decompression accomplished via a craniotomy. Of these operations, the greatest degree of decompression from a single procedure is obtained from the orbital floor approach. However, this procedure must be performed bilaterally so that the visual axes are not made asymmetric, resulting in diplopia and cosmetic deformity. The lateral and ethmoid decompressions can be combined with antral decompressions to achieve maximal relief of exophthalmos and a decrease in intraorbital pressure. The orbital roof approach provides relatively little decompression, and because it is a

Text continued on page 420

FIGURE 7-76 Axial CT scan (**A**) shows the postoperative appearance of a complete left internal ethmoidectomy. Axial (**B**) and coronal (**C**) CT scans show another patient who has had bilateral ethmoidectomies. On the left side, the lamina papyracea is intact and the operation was an internal ethmoidectomy. On the right side, the anterior lamina papyracea is not seen (*arrow* in **B**). This is a result of an external ethmoidectomy.

VIEW IMAGE

Copyright © 2003, Mosby, Inc. All rights reserved.

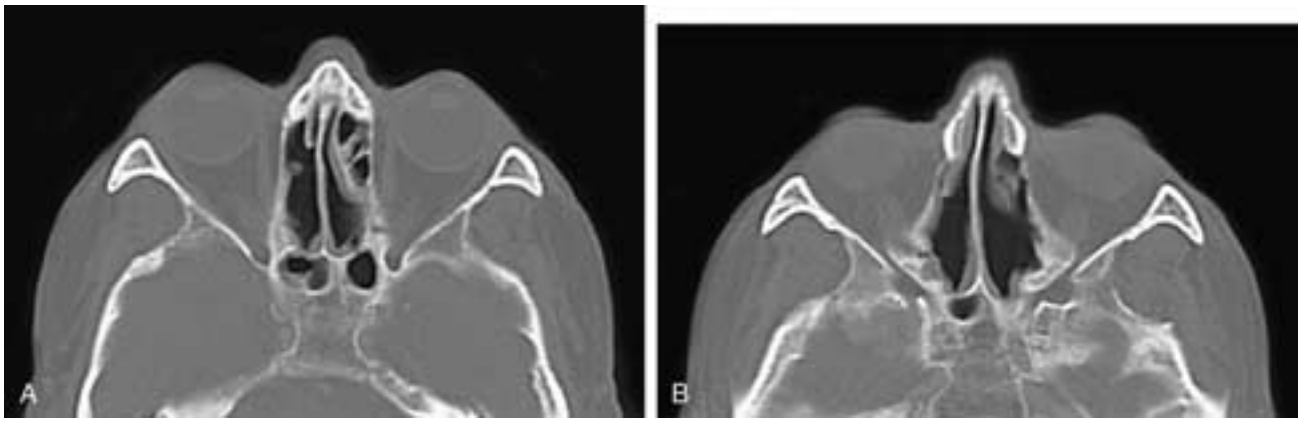

VIEW IMAGE

FIGURE 7-77 Axial CT scans at cranial (**A**) and caudal (**B**) levels of the ethmoid complex on a patient who has had bilateral internal ethmoidectomies. On the right side, almost all of the cells were removed. On the left side, the uppermost anterior cells remain. This appearance is typical of this operation, and the location of any remaining cells should be noted in the imaging reports of these cases.

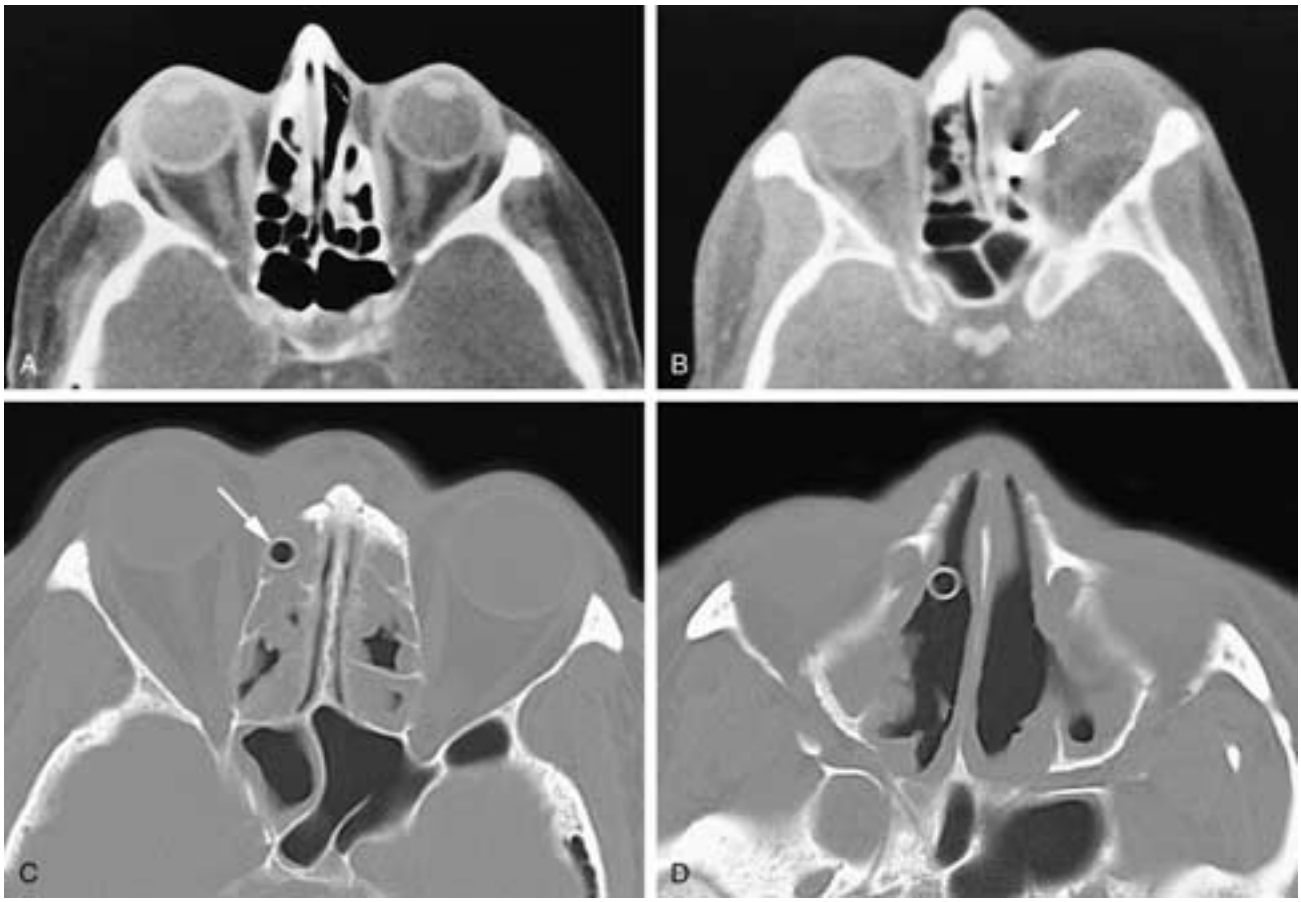

VIEW IMAGE

FIGURE 7-78 Axial CT scan (**A**) shows the postoperative appearance of a left external ethmoidectomy. The anterior lamina papyracea has been surgically removed and is replaced by fibrosis (*arrow*). Axial CT scan (**B**) shows a patient's status after a left external ethmoidectomy. The surgical clip (*arrow*) is used to control bleeding from the ethmoidal vessels. The soft tissue in the anterior ethmoid cavity was fibrosis and granulation tissue in this asymptomatic patient. Axial CT scans (**C, D**) on another patient show that a Lynch procedure was performed on the right side, and the drainage tube extends from the frontal sinus down through the ethmoid (*arrow* in **C**) sinus into the right nasal fossa (**D**).

Copyright © 2003, Mosby, Inc. All rights reserved.

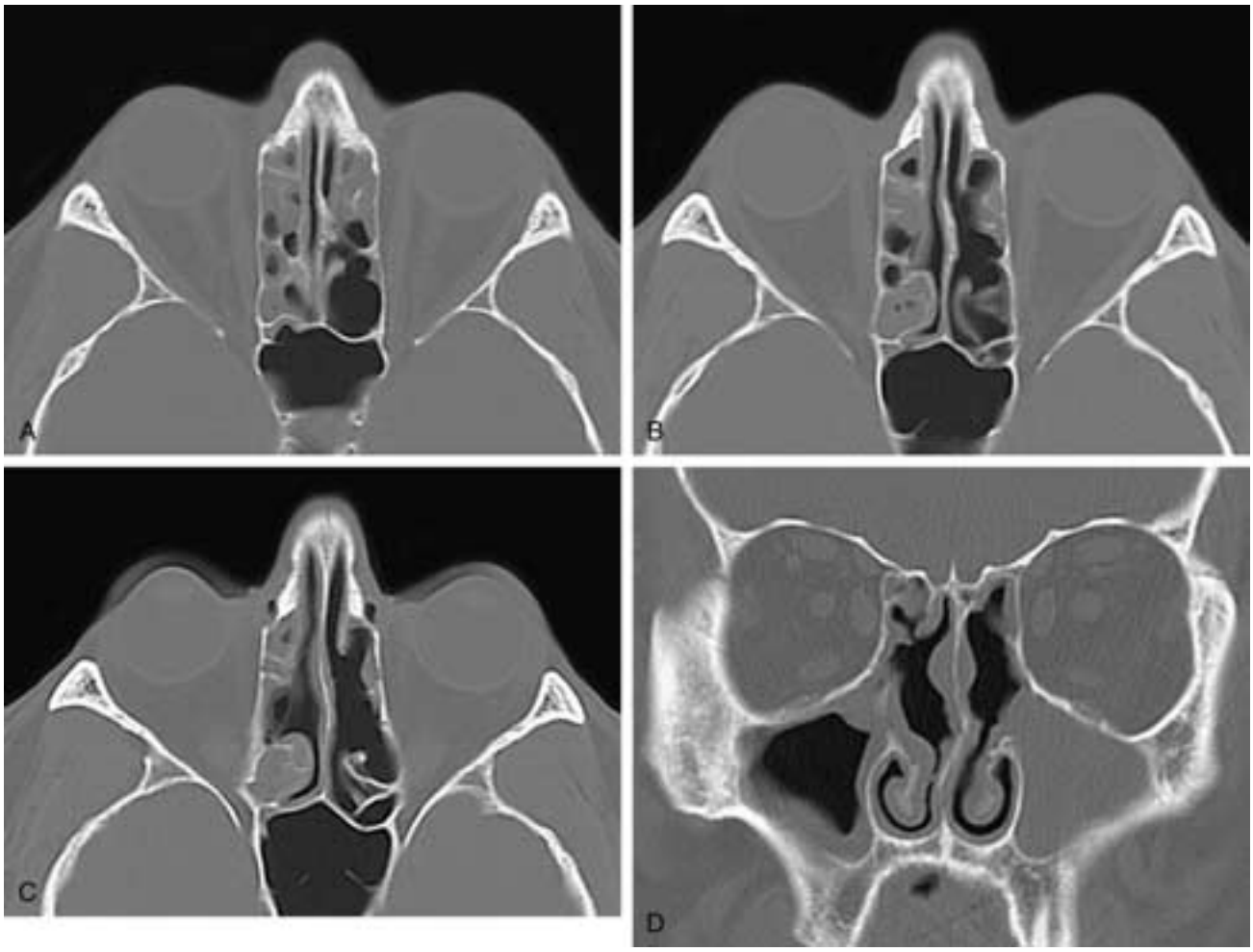

VIEW IMAGE

FIGURE 7-79 Serial axial CT scans from cranial (**A**) to caudal (**C**) and a coronal CT scan (**D**) on this patient who has had bilateral internal ethmoidectomies. The most superior cells remain anteriorly on both sides. The upper middle and posterior cells are also still present on the right side. Inflammatory disease is present in these remaining cells. Typically, the upper and posterior cells are not removed in internal ethmoidectomies because the surgeon does not want to enter the anterior cranial fossa inadvertently. The middle turbinates were removed at surgery, and inflammatory disease is present in both maxillary sinuses.

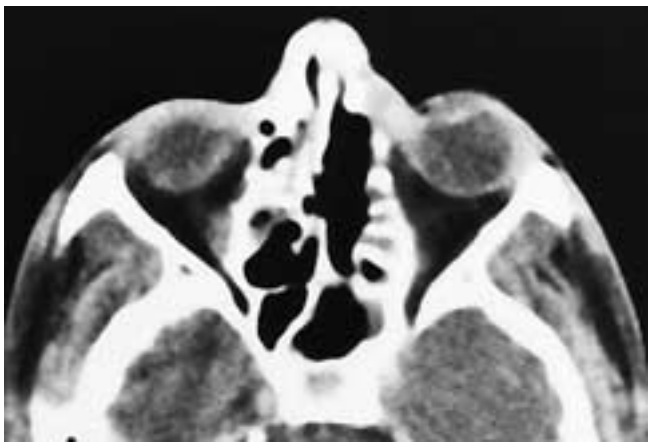

VIEW IMAGE

FIGURE 7-80 Axial CT scan shows the appearance of a left ethmoidectomy. Several of the posterior and more cranial ethmoid septa are still seen. This is a common finding, and these areas may be sites of residual disease.

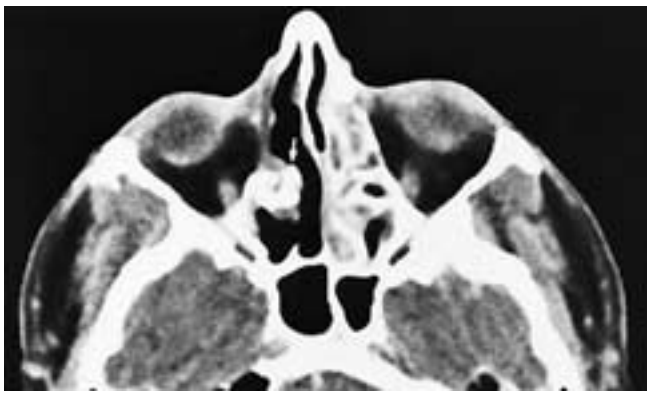

FIGURE 7-81 Axial CT scan shows a patient who has had a right ethmoidectomy. There is a focal area of bone production within the postoperative cavity (*arrow*). This represents reactive bone in response to surgery occurring in residual septae. It has no pathologic significance.

VIEW IMAGE

Copyright © 2003, Mosby, Inc. All rights reserved.

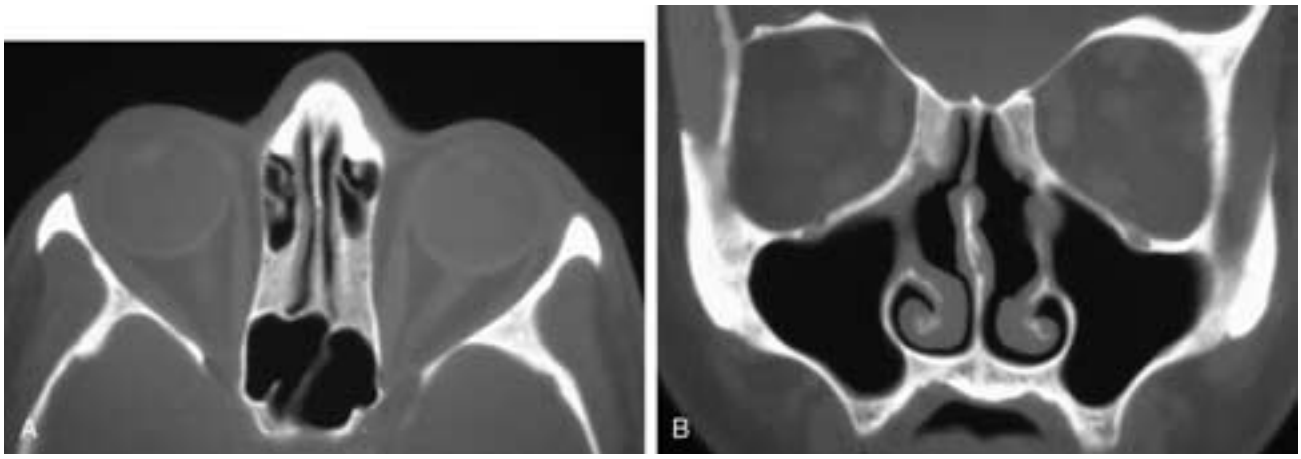

VIEW IMAGE

FIGURE 7-82 Axial (**A**) and coronal (**B**) CT scans on a patient who has had bilateral internal ethmoidectomies. ''Ground glass''–appearing bone is present in the upper posterior and middle postoperative cavities, partially obliterating the postoperative ethmoid cavities. This is a normal postoperative bony reactive change and should not be misinterpreted as an abnormality.

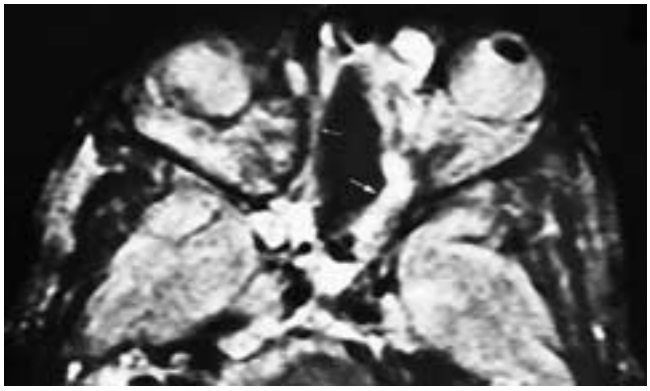

VIEW IMAGE

FIGURE 7-83 Axial T2-weighted MR image shows the appearance of prior complete bilateral internal ethmoidectomies. Part of the postoperative cavity is lined with fibrotic tissue (*small arrow*), and other areas have inflammatory tissue with a high T2-weighted signal intensity (*large arrow*).

VIEW IMAGE

FIGURE 7-84 Axial CT scan shows a destructive mass in the left posterior sphenoethmoid region (*arrow*). This patient had a limited left ethmoidectomy for suspected infectious disease. No preoperative scan was obtained. It was only when postoperative left eye signs developed that a scan was obtained. This patient had both infection and a squamous cell carcinoma.

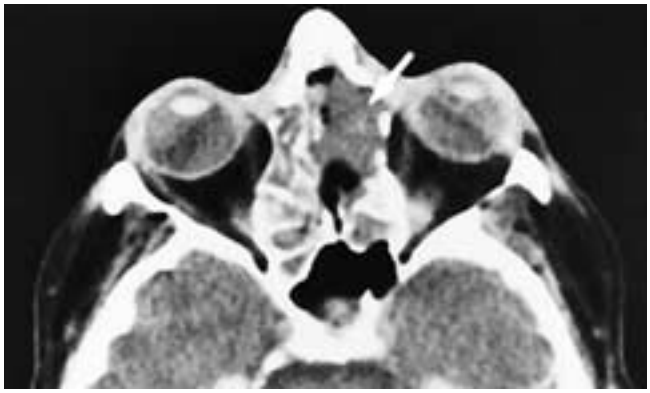

VIEW IMAGE

FIGURE 7-85 Axial CT scan shows the appearance of a left ethmoidectomy that has an accumulation of mucoid material within the postoperative cavity (*arrow*). Rather than extending into the left orbit as a typical ethmoid mucocele, the postoperative mucocele tends to fill the post-ethmoidectomy cavity first.

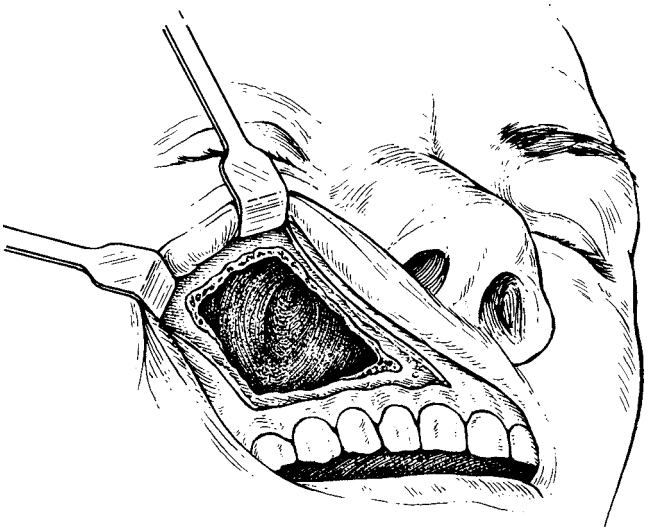

VIEW IMAGE

FIGURE 7-86 Diagram of the Caldwell-Luc approach. The maxillary sinus is entered anteriorly under the lip via the canine fossa. The hole in the sinus can be variable in size.

Copyright © 2003, Mosby, Inc. All rights reserved.

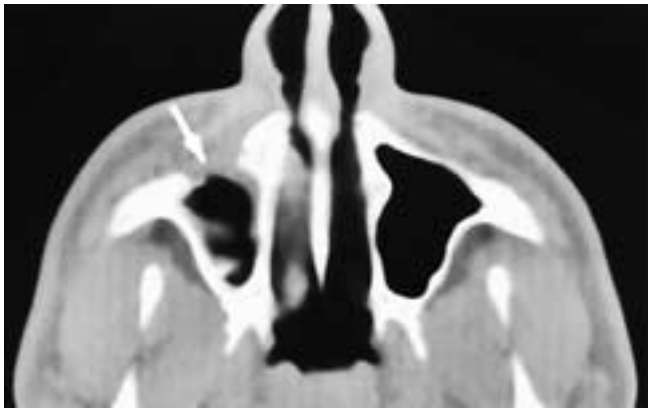

VIEW IMAGE

FIGURE 7-87 Axial CT scan shows the anterior sinus wall Caldwell-Luc defect (*arrow*). The soft tissues in the sinus were senechia.

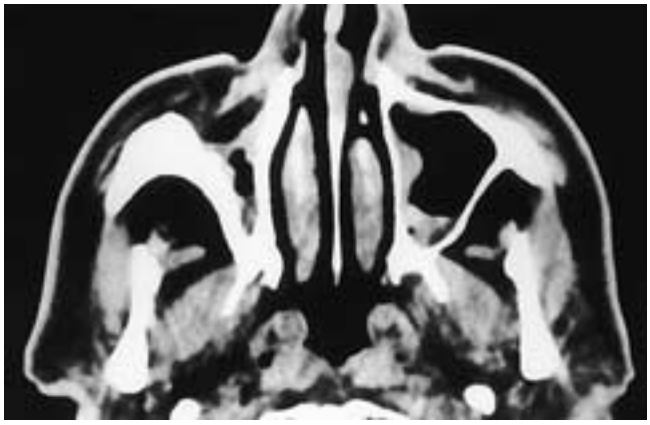

VIEW IMAGE

FIGURE 7-88 Axial CT scan shows a patient after a right Caldwell-Luc procedure. Fat from the cheek has partially prolapsed into the defect, and some inflammatory mucosal thickening is present bilaterally.

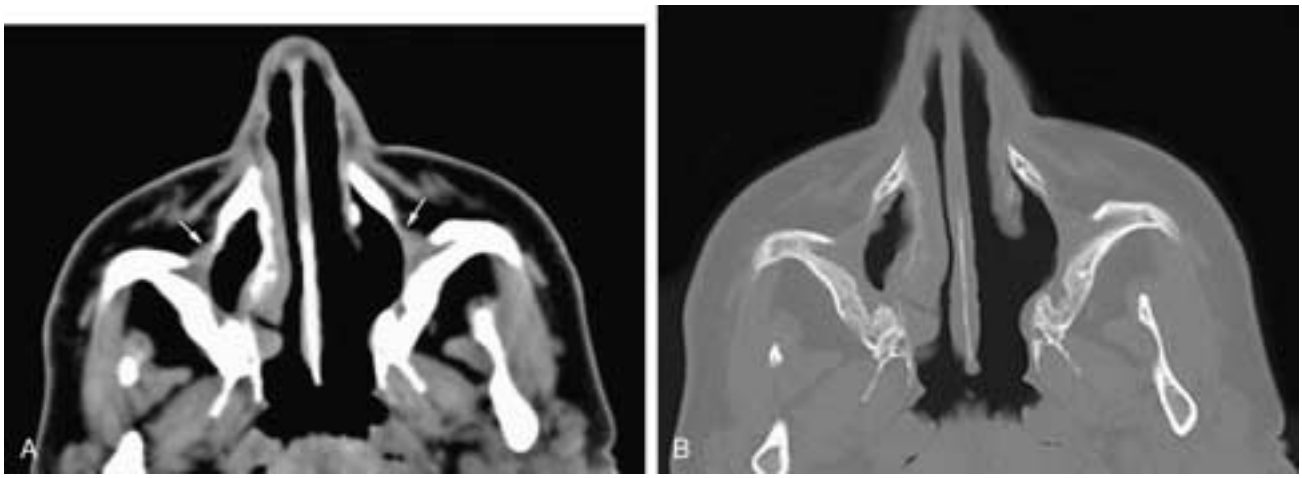

VIEW IMAGE

FIGURE 7-89 Axial CT scans seen at narrow (**A**) and wide (**B**) window settings on a patient after bilateral Caldwell-Luc procedures. The thickening of the posterolateral sinus bony walls is a reaction to the denuding of the sinus mucosa during the procedure and is an expected postoperative finding. Note the fibrous tissue that closes off the anterior sinus wall defect (*arrows* in **A**).

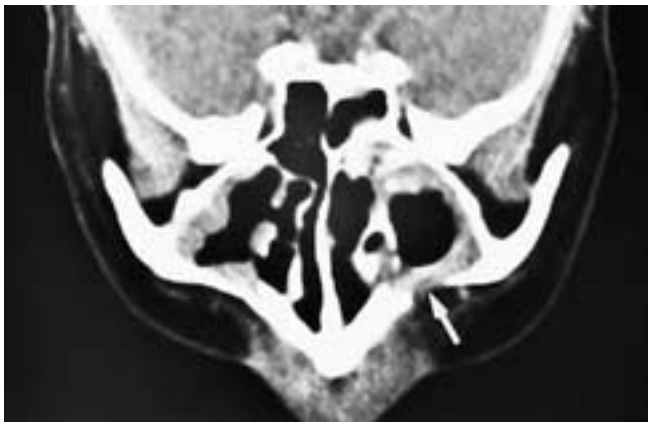

VIEW IMAGE

FIGURE 7-90 Coronal CT scan shows the Caldwell-Luc defect in the anterior left maxillary sinus wall (*arrow*) and inflammatory mucosal thickening in both antra.

Copyright © 2003, Mosby, Inc. All rights reserved.

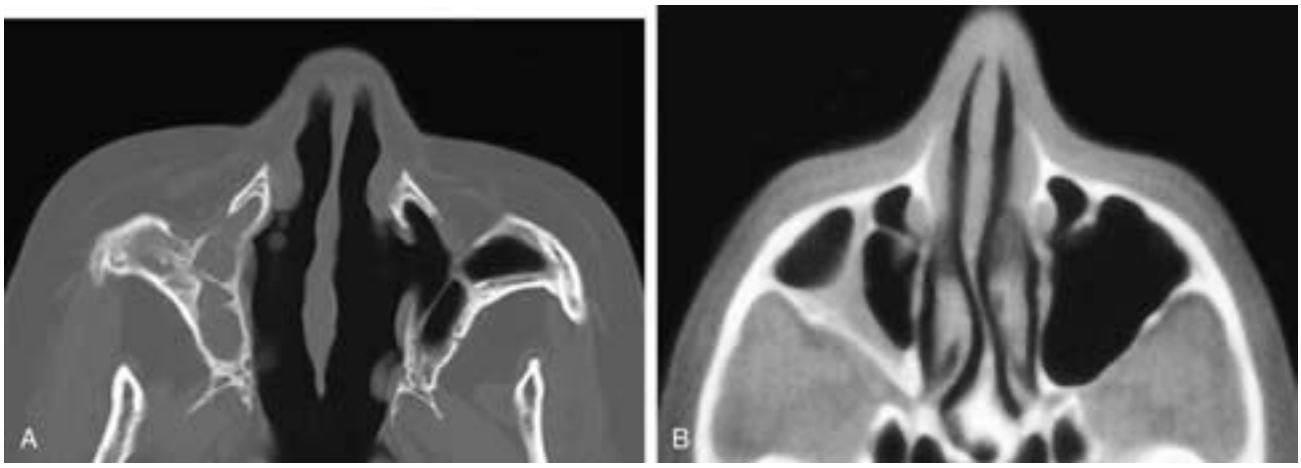

VIEW IMAGE

FIGURE 7-91 Axial CT scan (**A**) on a patient who has had bilateral Caldwell-Luc procedures. On the right side, the defect is fibrosed over and the sinus cavity is opacified. On the left side, fibrous strands extend from the surgical defect to the posterior sinus wall. Axial CT scan (**B**) on a patient after a right Caldwell-Luc procedure. On this more cranial scan through the antrum, a septum has formed between the anterior and posterior sinus walls. If this septum completely obstructs the lateral portion of the sinus, a postoperative mucocele will develop.

more extensive surgical approach, it is reserved for the most severe cases.

On sectional imaging, the absence of the lateral portion of the orbital wall may at first elude detection, the imager's attention being drawn by pronounced proptosis with muscle enlargement. However, careful evaluation of the bony orbital walls will show that a Krönlein procedure was performed (Figs. 7-93 and 7-94). The ethmoid decompression has the same appearance as an external ethmoidectomy, and it is the orbital muscle findings of thyroid ophthalmopathy that suggest the diagnosis (Figs. 7-93 to 7-95). The antral decompression reveals prolapse of the orbital fat and inferior muscles into the upper maxillary sinuses. Without a history, on axial scans this operation may present a confusing picture, often mimicking unusual antral disease. However, coronal scans reveal that most of the orbital floor bone is missing, a finding that differentiates this postoperative appearance from the rare event of bilateral orbital floor blow-out fractures, in which the displaced fracture's segments can be identified (Figs. 7-94 and 7-96).

SPHENOID SINUS SURGERY

The sphenoid sinuses can be approached through the anterior sinus wall for biopsy, to improve sinus drainage, or to remove inflammatory tissue. The sphenoid sinusotomy opens the anterior wall of the sinus and creates a wide-open cavity that leads into the nasopharynx (Fig. 7-97). The sinus can be reached by intranasal, transseptal, transmaxillary, or transethmoidal approaches.

In the transnasal approach, portions of the posterior middle turbinate, the superior turbinate, and some of the posterior ethmoid cells are removed to gain exposure. In the transseptal approach, portions of the cartilaginous and bony nasal septum (vomer) are removed. The transmaxillary

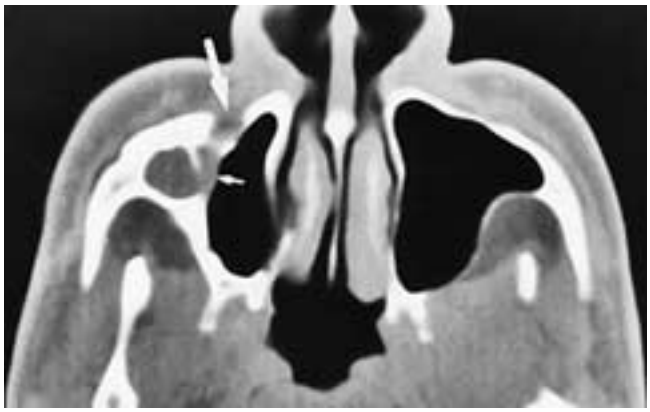

VIEW IMAGE

FIGURE 7-92 Axial CT scan shows an anterior Caldwell-Luc defect in the right maxillary sinus wall (*large arrow*). There is an expansile mass in the lateral portion of the right antrum (*small arrow*). This patient had a postoperative antral mucocele.

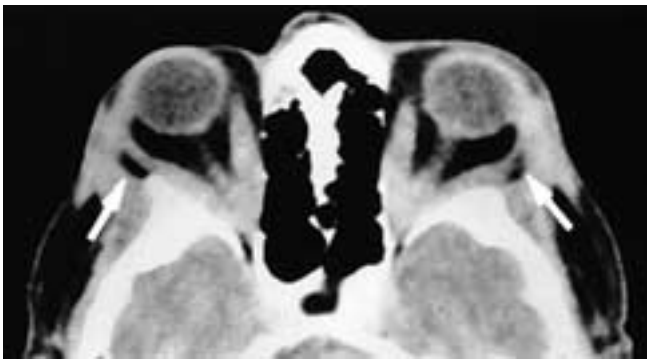

FIGURE 7-93 Axial CT scan shows a patient with the changes of thyroid ophthalmopathy. All of the extraocular muscle bellies are enlarged, and there is tapering at the tendon insertions. There is also bilateral proptosis. The lateral orbital walls (*arrows*) have been surgically removed, making the proptosis appear even greater than it is. This patient has had bilateral lateral orbitotomies (Krönlein's approaches).

VIEW IMAGE

Copyright © 2003, Mosby, Inc. All rights reserved.

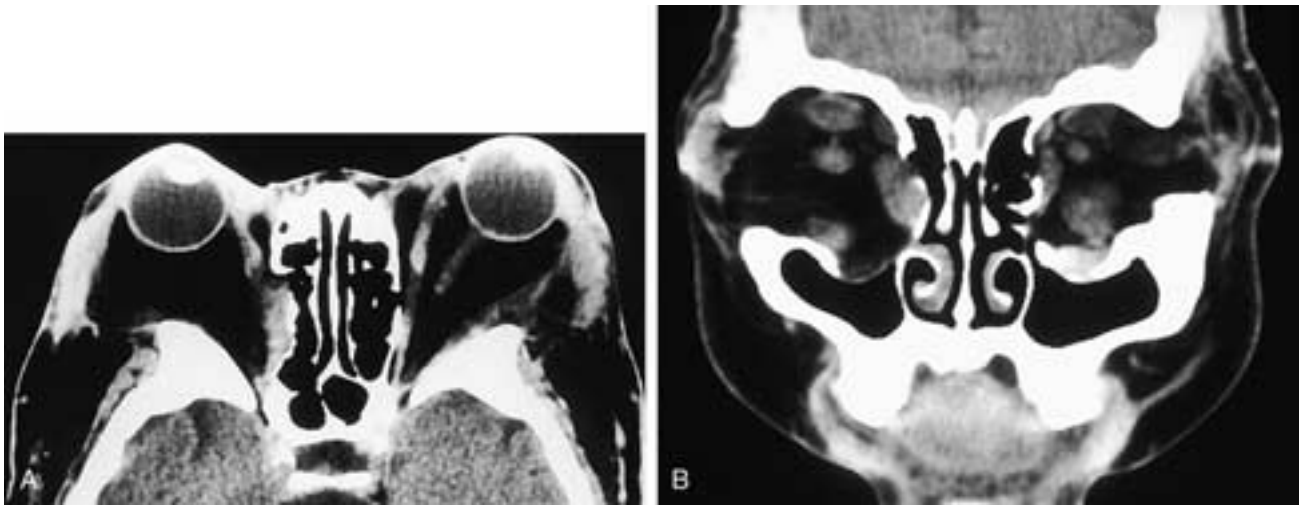

VIEW IMAGE

FIGURE 7-94 Axial (**A**) and coronal (**B**) CT scans show a patient with bilateral thyroid ophthalmopathy and bilateral Krönlein's and orbital floor decompression procedures. A medial right ethmoid decompression was also performed.

approach is an extension of a Caldwell-Luc procedure in which a transmaxillary ethmoidectomy is extended to include the anterior sphenoid sinus wall. The transethmoidal approach is simply a posterior extension of an external ethmoidectomy procedure. Thus, depending on the approach used, in addition to a widened ostium or an absence of one or both anterior sphenoid sinus walls, the respective surgical defects just described should be observed on images.[55, 56]

When a sphenoid sinusotomy is performed, care must be taken to avoid trauma to the carotid artery. In 17% of patients the bony wall separating the sinus and artery is so thin that it provides little if any protection from trauma, and carotid artery damage may lead to a posttraumatic aneurysm or a carotid-cavernous fistula.[60, 61] Similarly, damage can occur to the cavernous sinus and to the vidian, maxillary, and optic nerves in those patients who have these nerves running within the sinus (see Chapters 2 and 3).

A transsphenoidal hypophysectomy can be performed as an extension of a sphenoid sinusotomy. Once the sphenoid sinus cavity is surgically exposed, portions of the anterior wall and the floor of the sella turcica can be removed and the pituitary fossa entered from below. Muscle, fat, cartilage, or bone may be used to seal the surgical defect. On sectional imaging, in addition to the site of surgical bone removal, sclerotic thickening of the remaining portions of the anterior wall and the floor of the sella turcica may be observed. Some postoperative prolapse of sellar contents, including fat, into the sphenoid sinus can occur, and without benefit of the surgical history, the imaging picture can simulate that of a large pituitary tumor with extension into the sphenoid sinus.

In the preoperative evaluation of patients being considered for a transsphenoidal hypophysectomy, the imager must direct special attention to the thickness of the bone forming the anterior wall of the sella turcica. In nearly 99% of patients, the sphenoid sinus development extends back to within 1 mm of the anterior wall or under the sellar floor. However, in the 1% of patients in whom a thick margin of bone remains between the sinus and sella, the transsphenoi-

VIEW IMAGE

FIGURE 7-95 Axial CT scan shows large muscle bellies in the extraocular muscles with tapering at the anterior tendon insertions. The ethmoid complexes have been collapsed by a decompression. This patient had thyroid ophthalmopathy.

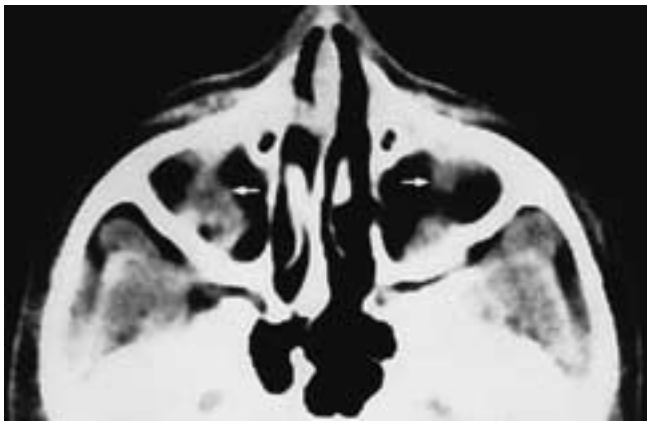

FIGURE 7-96 Axial CT scan through the upper maxillary sinuses shows the inferior rectus muscles (*arrows*) and orbital fat in the upper antra. The orbital floors have been surgically removed. This patient had thyroid ophthalmopathy and bilateral orbital floor decompressions.

VIEW IMAGE

Copyright © 2003, Mosby, Inc. All rights reserved.

FIGURE 7-97 Axial CT scan (**A**) shows a patient with bilateral ethmoidectomies and sphenoid sinusotomies. The anterior sphenoid sinus walls have been removed (*arrows*). Coronal CT scan (**B**) on another patient who has had bilateral sphenoid sinusotomies. Note that the lower anterior sinus walls (*arrows*) have been removed. An axial CT scan (**C**) on another patient shows that bilateral internal ethmoidectomies and a left sphenoid sinusotomy (*arrow*) have been performed.

VIEW IMAGE

dal approach is not desirable; instead, an intracranial approach is used often.[31]

SURGERY FOR SINUS MALIGNANCY

The type of tumor-curative operation performed on the maxillary sinus varies, depending upon the precise location of the primary neoplasm. Thus a tumor affecting the lower portion of the antrum may require an infrastructure-type partial maxillectomy, while a nasal tumor may require a medial maxillectomy. More extensive tumor necessitates a total maxillectomy with or without removal of the pterygoid plates and adjacent structures. A partial or total ethmoidectomy is often combined with a maxillectomy for complete tumor extirpation.

Medial Maxillectomy

For localized nasal tumors that only involve a portion of the medial antral wall, a partial or medial maxillectomy is performed, usually in association with a partial ethmoidectomy and a resection of the nasal tumor. If the lower antral wall is involved, portions of the adjacent hard palate and maxillary alveolus may also be included in the resection (Fig. 7-98). Thus, in a partial maxillectomy, the medial antral wall, the inferior turbinate, often the middle turbinate, the lower ethmoid cells, and, if appropriate, portions of the hard palate and alveolus are removed. The lateral portion of the antrum and its mucosa remain intact.

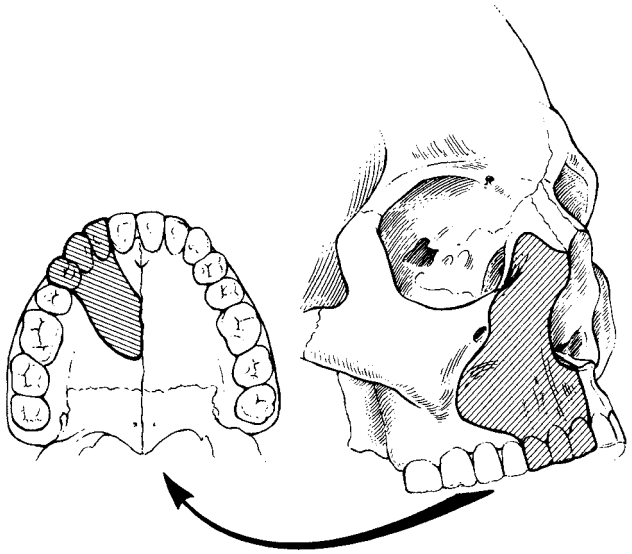

FIGURE 7-98 Diagram of a typical medial maxillectomy resection. A portion of the palate is removed if needed to obtain a tumor-free margin. The medial antral wall and inferior turbinate are also included in the resection.

VIEW IMAGE

Copyright © 2003, Mosby, Inc. All rights reserved.

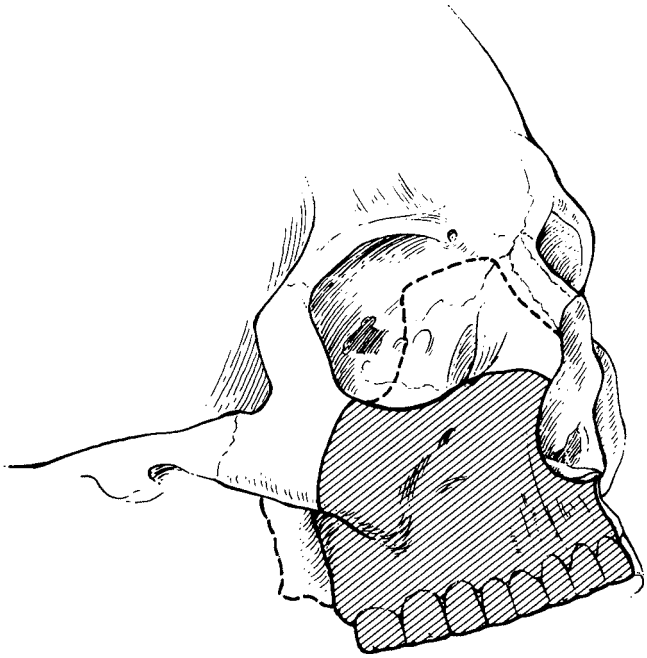

VIEW IMAGE

FIGURE 7-99 Diagram of a typical total maxillectomy resection. Variable portions of the zygoma and pterygoid plates may be included in the resection. Similarly, the orbital floor may be taken in its entirety, and an ethmoid resection (*dotted line*) may also be included to obtain a tumor-free margin.

Total Maxillectomy

For more extensive tumors, a total maxillectomy is performed (Fig. 7-99). In addition to resection of the maxilla, there is some variation as to what is included in the resection. Such surgery may include the body of the zygoma, the ipsilateral hard palate and alveolus, the inferior turbinate, and often the pterygoid plates and portions of the ethmoid sinuses.[62, 63] Modifications are made to fit the specific tumor location. Thus the orbital floor may be left in place or it may be included along with an orbital exenteration. The latter is performed when there is gross tumor extension into the orbit.

Erosion of the bones lining the orbit may necessitate an orbital exenteration, and the degree of orbital involvement must be noted by the imager in order to aid the clinician in planning surgery. Gross orbital invasion almost always requires an orbital exenteration. However, erosion of bone, without gross penetration of the periorbita, may or may not necessitate an orbital exenteration. To some degree, this depends on the particular philosophy of the clinician and the tumor histology.

Today, there is a tendency not to exenterate an orbit for minimal disease, especially if the periorbita remains intact. This is a less aggressive approach than that of several decades ago, when exenteration was almost always performed. This is due in part to better chemo/radiation treatments and in part to a change in philosophy based on statistics noting tumor recurrences.

For squamous cell carcinoma, the initial involvement of any orbital bone must be considered when surgery is performed, even if preoperative chemo/radiation has shrunk the tumor away from the orbit. Failure to do so usually results in an orbital margin recurrence. With other tumors such as olfactory neuroblastomas, initial involvement of the orbital wall need not result in an exenteration. If there is a good preoperative tumor response to chemo/radiation and the orbit becomes grossly free of tumor, in most cases tumor resection without an exenteration may be curative.

After the bone is resected, the postmaxillectomy cavity can be lined with a split-thickness skin graft to create an immediate epithelial surface, or a muscle graft can be placed to fill the cavity. If the orbital floor was removed, various synthetic grafts can be placed to help support the orbital contents. Similarly, bone and prosthetic material can be placed to support the anterior and lateral facial structure, and prostheses can be placed to fill the surgical defects created in the hard palate and alveolus. These foreign substances can cause imaging problems either because they may degrade the image quality or because, in the case of some plastics and musculofascial grafts, on MR imaging they may simulate normal bone and go undetected. Eye prostheses also may cause degradation artifacts on scans.

As mentioned, there is a tendency today to obliterate the postoperative maxillectomy cavity created, with or without an ethmoidectomy, by using a rotated myocutaneous graft. Such a graft brings muscle, fat, and soft tissues into an area in which they normally are not present, and recognition of such a graft will obviate difficulties in interpreting postoperative CT and MR images.

The sinus cavity in a partial maxillectomy patient is lined by normal mucosa. The defect after a total maxillectomy can be lined either by a split-thickness skin graft or a myocutaneous graft. In any case, after a 6- to 8-week postoperative interval, nearly all of the operative-related edema and hemorrhage will have subsided and a baseline scan should be performed. This scan maps the patient's new anatomy and establishes the contour and thickness of the postoperative mucosal surfaces. The normal postoperative mucosa is smooth and moderately thin. Any localized area of soft-tissue nodularity or mucosal-submucosal thickening must be suspected of representing recurrent tumor until proven otherwise. If such an area develops that was not noted on the baseline scan, the imager should direct the clinician specifically to this site for biopsy (Figs. 7-100 to 7-109). This approach has led to more positive biopsy specimens than are obtained from clinical assessment alone. The routine postoperative imaging follow-up of patients has also led to identification of small, early recurrences that were overlooked on routine clinical follow-up.[62]

EXTENSIVE NASOETHMOID SURGERY

The lateral rhinotomy provides access to the entire nasal cavity and the maxillary, ethmoid, and sphenoid sinuses. Modifications and extensions of this approach can be used to include access to the frontal sinuses. The typical incision extends from just below the medial end of one eyebrow, caudally between the nasal dorsum and medial canthus of the eye, down the nasofacial crease, and along the nasal alar rim. The incision is then extended down the upper lip if necessary. The nose is turned to the side, thereby exposing the pyriform aperture. This procedure gives access to the entire lateral nasal wall and nasal septum. Usually removed

Copyright © 2003, Mosby, Inc. All rights reserved.

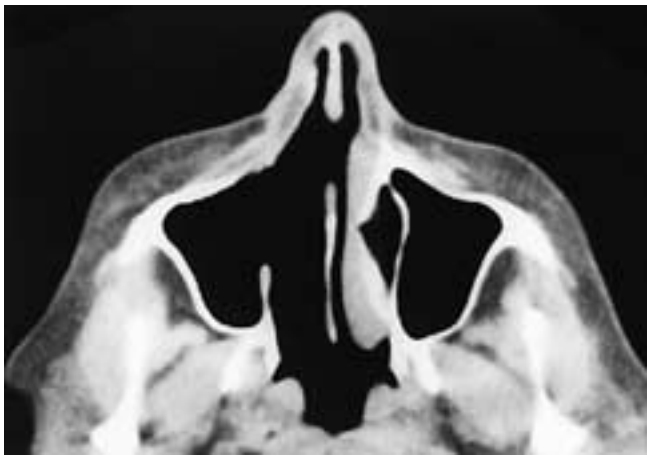

VIEW IMAGE

FIGURE 7-100 Axial CT scan shows the normal appearance after partial right maxillectomy. The medial antral wall has been removed, and the soft tissues in and around the antrum should be smooth.

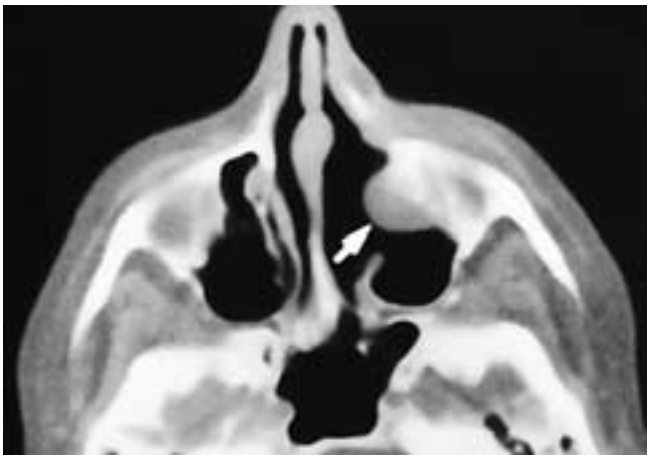

VIEW IMAGE

FIGURE 7-101 Axial CT scan on a patient after partial left maxillectomy with a smooth nodular mass (*arrow*) in the antrum. Although this could be an inflammatory mass, tumor should be suspected until proven otherwise. This patient had tumor recurrence.

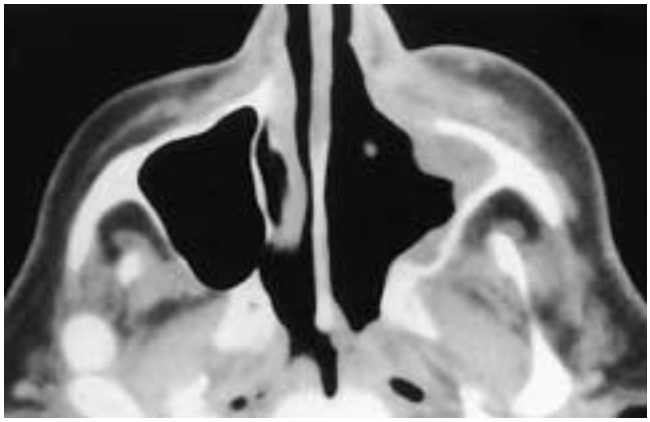

VIEW IMAGE

FIGURE 7-102 Axial CT scan on a patient after a left medial maxillectomy. There is a nodular fullness in the soft tissues filling the postoperative cavity. This smooth nodule was a retention cyst and not recurrent tumor.

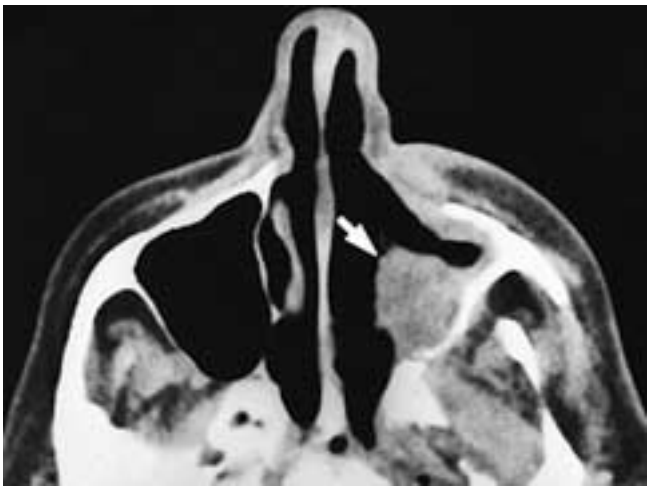

VIEW IMAGE

FIGURE 7-103 Axial CT scan on a patient after partial left maxillectomy with irregularly nodular tumor recurrence (*arrow*) in the antrum. The smooth soft tissues lining the anterior left antrum were scar tissue.

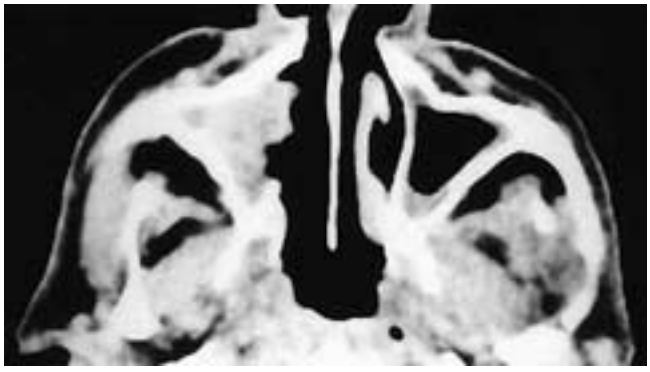

VIEW IMAGE

FIGURE 7-104 Axial CT scan on a patient after right medial maxillectomy. The soft tissues within the right sinus have a nodular contour and suggest recurrent tumor. Inflammatory disease is present in the left antrum. This patient had recurrent inverted papilloma.

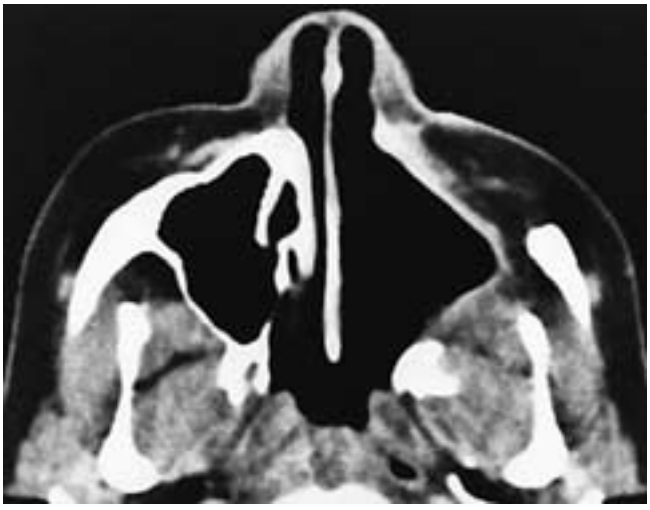

VIEW IMAGE

FIGURE 7-105 Axial CT scan on a patient who has had a total left maxillectomy. The postoperative cavity is smoothly lined with thin soft tissue from a split-thickness skin graft. This is the normal appearance of a total maxillectomy. The pterygoid plates were not resected in this patient.

Copyright © 2003, Mosby, Inc. All rights reserved.

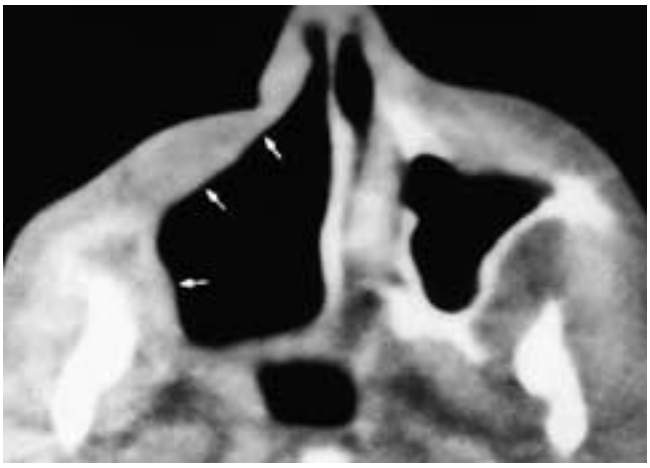

VIEW IMAGE

FIGURE 7-106 Axial CT scan shows the normal postoperative appearance of a right total maxillectomy. The postoperative cavity is smoothly lined (*arrows*). The pterygoid plates were resected in this patient.

at surgery are the medial antral wall, the ethmoid cells, and the inferior and middle turbinates. The anterior sphenoid wall can be resected via this procedure, and the operation can be extended to include the entire nasal septum and contralateral nasal cavity structures, resulting in a total rhinotomy. In general, the operation of choice for a unilateral nasal tumor is a medial maxillectomy with a lateral rhinotomy and ethmoidectomy. Despite the extent of the resection, the cosmetic and functional results are excellent. Regarding patient follow-up, as with the postmaxillectomy patient, the same general imaging rules apply, namely, one must suspect tumor at sites of soft-tissue nodularity and mucosal thickening (Figs. 7-110 to 7-113).

CRANIOFACIAL RESECTION

This large operation is reserved for patients with tumors of the superior nasal cavity, ethmoid sinuses, frontal sinuses, anterior sphenoid sinuses, and orbits. The operation essentially combines a frontal craniotomy with a resection of the

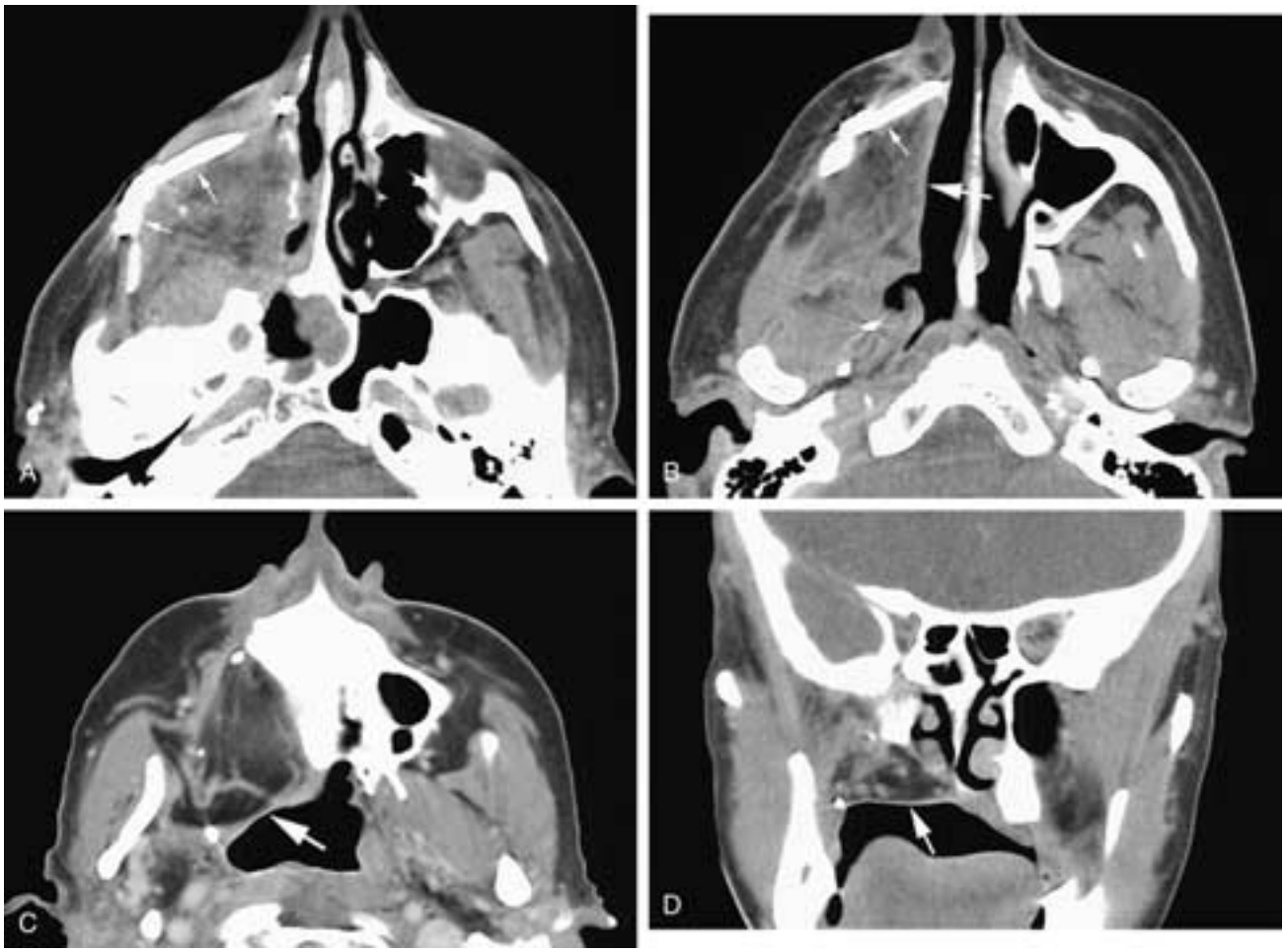

VIEW IMAGE

FIGURE 7-107 Serial axial CT scans from cranial (**A**) to caudal (**C**) and a coronal CT scan (**D**) on a patient who has had a right total maxillectomy with a graft reconstruction. Plated bone (*small arrows*) is present superficially to give a better contour to the cheek. The fat of the graft fills most of the postoperative cavity and forms the right side of the reconstructed palate. Notice that the free margins of the graft (*large arrows*) are smooth, with a thin mucosal lining. This is the expected normal postoperative appearance for such an operation.

Copyright © 2003, Mosby, Inc. All rights reserved.

FIGURE 7-108 Axial CT scans (**A**, **B**) at narrow window settings and axial (**C**, **D**) and coronal (**E**) CT scans at wide window settings on a patient who has had a right maxillectomy with an osteomyocutaneous flap reconstruction. Transplanted bone has been used to reconstruct the palate (*large arrow*) and the malar contour (*small arrows*). Tooth implants (*black arrows*) were then placed in the reconstructed palate/alveolar region.

VIEW IMAGE

Copyright © 2003, Mosby, Inc. All rights reserved.

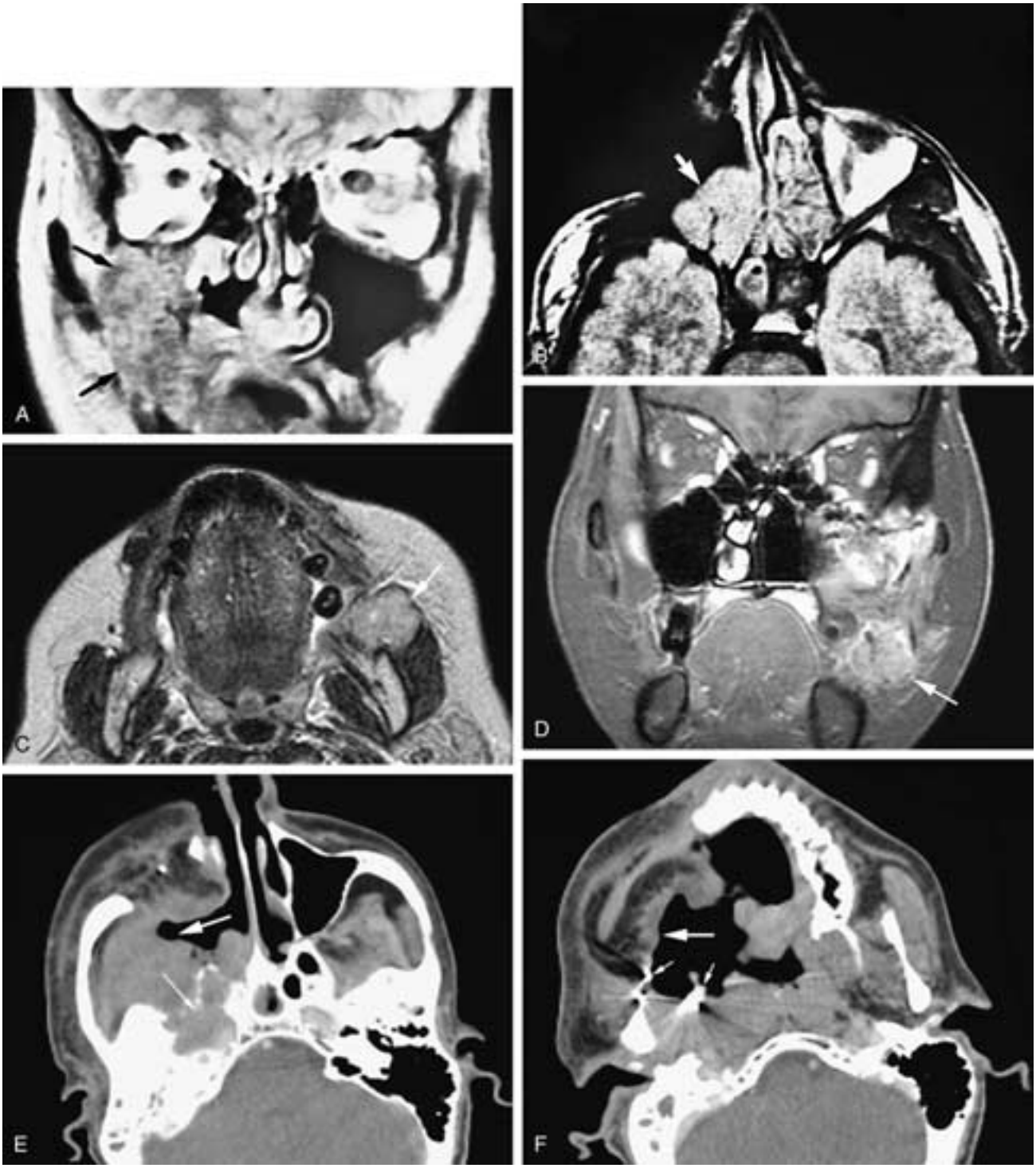

VIEW IMAGE

FIGURE 7-109 Coronal proton density MR image (**A**) shows a large right recurrent tumor with an intermediate signal intensity (*arrows*) in a patient who has had a total right maxillectomy. Axial proton density MR image (**B**) shows a patient who has had a total right orbital exenteration and a total maxillectomy. Tumor recurrence is seen in the right orbital apex (*arrow*). Axial FSE T2-weighted (**C**) and coronal T1-weighted, fat-suppressed, contrast-enhanced MR image (**D**) on a different patient who has had a left maxillectomy with a graft reconstruction. A tumor nodule is seen at the lower lateral margin of the graft (*arrows*). This was not clinically evident and points out the value of surveillance imaging. Axial CT scans (**E, F**) on another patient who has had a right total maxillectomy with a flap reconstruction. Tumor is present along the upper margin of the flap, eroding the skull base (*thin arrow*). Tumor fills the flap, and the medial side of the flap has become necrotic and ulcerated (*large arrow*). In (**F**), surgical clips that were within the flap are now exposed (*small arrows*) at the necrotic surface of the flap.

Copyright © 2003, Mosby, Inc. All rights reserved.

VIEW IMAGE

FIGURE 7-110 Coronal CT scan through the anterior antrum (**A**) and posterior antrum and sphenoid sinus (**B**) in a patient who has had a left lateral rhinotomy. There has been a left ethmoidectomy and a medial maxillectomy. The upper nasal septum has also been removed. This is the typical appearance of this operative procedure. Coronal (**C**) and axial (**D**) T1-weighted, fat-suppressed, contrast-enhanced MR images of another patient who has had a lateral rhinotomy including a right total maxillectomy and ethmoidectomy and a left medial antrostomy and a partial ethmoidectomy. Note the absence of any focal enhancing nodules.

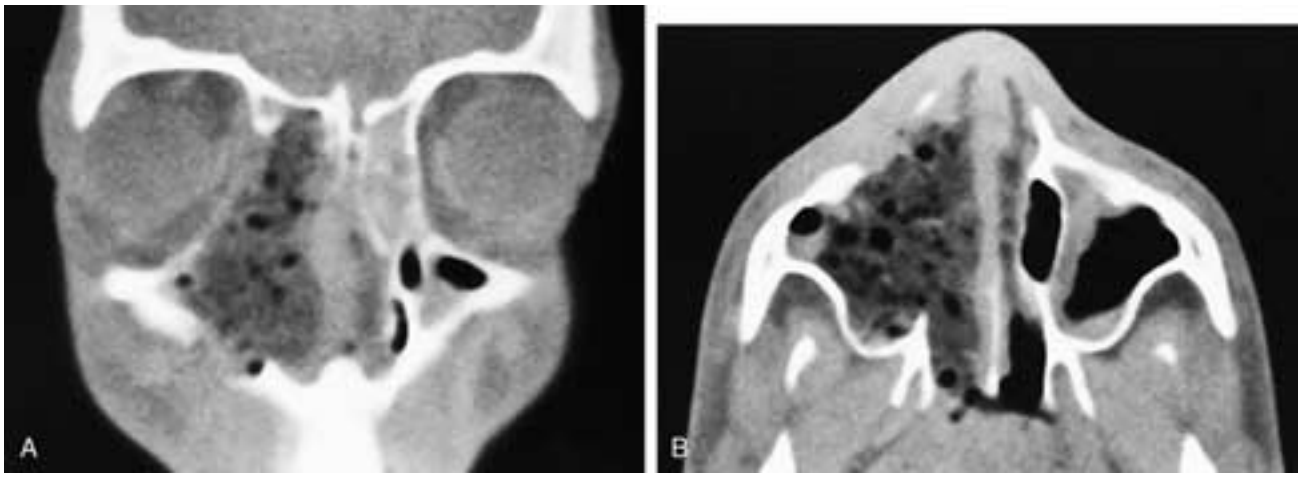

VIEW IMAGE

FIGURE 7-111 Coronal (**A**) and axial (**B**) CT scans show a patient who has had a right lateral rhinotomy. The postoperative cavity is filled with packing.

Copyright © 2003, Mosby, Inc. All rights reserved.

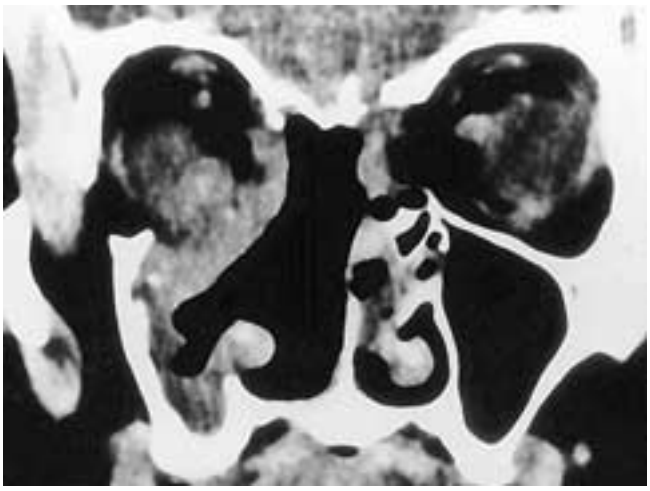

VIEW IMAGE

FIGURE 7-112 Coronal CT scan on a patient after an extended right lateral rhinotomy. The floor and medial wall of the right orbit have been removed. Although the thickened soft tissues along the orbital margin could be either scar or recurrent tumor, the smooth margin suggests that tumor is not present. The best way to evaluate this disease is to compare this scan with a previous study. Biopsy may be necessary. No tumor was present in this patient.

midportion of the floor of the anterior cranial fossa and an extended lateral rhinotomy. The surgery is often performed by a skull-base team comprised of a neurosurgeon and an otolaryngologist. Initially, one of several types of frontal or bifrontal craniotomies is performed, the frontal lobes are elevated, and any tumor extension into the brain is resected. The bone and dura in the floor of the anterior cranial fossa are then incised. The typical resection includes the posterior wall of the frontal sinuses, the cribriform plate, the fovea ethmoidalis on each side, and as much of the medial orbital roof as is necessary to obtain a margin around the tumor. The posterior incision runs along the posterior roof of the sphenoid sinus, and it can extend back to the tuberculum sella. An extended lateral rhinotomy is then performed, and the resection includes one or both ethmoid sinuses (including the corresponding medial orbital wall), the nasal septum, and if necessary a portion of the medial maxilla. Once the entire specimen is free, the surgeons proceed with an en bloc extirpation. An anterior dural flap and a temporalis free musculofascial graft are used to close and support the cranial floor defect, and the lateral rhinotomy is closed separately (Fig. 7-114).[51, 64, 65]

Postoperative CT scans contain several areas that may cause diagnostic difficulties. First, the anterior dura adjacent to the frontal osteotomy becomes thickened and enhances on contrast studies. This appearance may persist indefinitely and relates to a low-grade reactive process that obliterates the dural spaces (Fig. 7-115). Second, the musculofascial flap that supports the central region of the floor of the anterior cranial fossa can bulge slightly downward into the upper postoperative nasoethmoid cavity (Figs. 7-116 and 7-117). This can simulate a tumor mass on axial CT scans and MR images, but usually can be identified as representing the graft region on coronal studies. This is especially true during the period before the free flap becomes completely fibrosed, usually between 2 and 8 months after the surgery. Although the CT appearance is not effectively altered once the flap is completely fibrosed, the MR imaging findings are changed. The initial intermediate T1-weighted and high T2-weighted signal intensities are gradually replaced by low signal intensities or signal voids on all imaging sequences. This change corresponds to replacement of the graft by scar. The thickness of the fibrosed graft may occasionally be sufficiently similar to that of the remaining bony floor of the adjacent anterior cranial fossa that on coronal MR images the radiologist may not detect that bone has been removed (Fig. 7-118). Only the altered contour of the bony floor of the anterior cranial fossa (absent the crista galli and fovea ethmoidalis) may signify that the surgery included the bone in this region. Such bone defects are seen easily on coronal CT. There are slight variations in the imaging appearance of patients who have had craniofacial procedures, primarily reflecting variations in the surgical approach (Figs. 7-119 and 7-120).

Any nodularity along the cranial or nasal margin of the graft or postoperative sinonasal cavity must be suspected of

Text continued on page 435

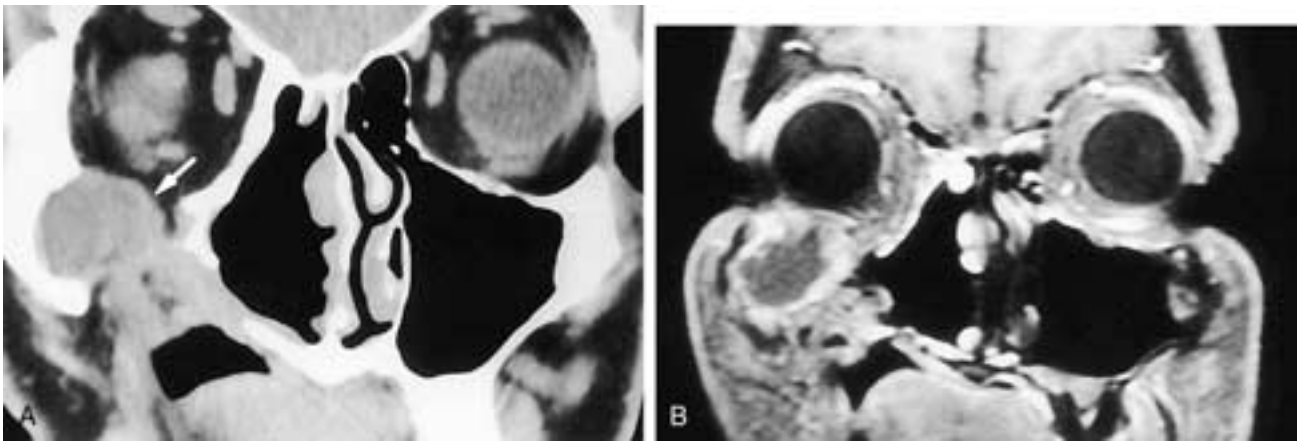

VIEW IMAGE

FIGURE 7-113 Coronal CT (**A**) and coronal T1-weighted, contrast-enhanced, fat-suppressed MR (**B**) image show a patient's status after an extended right lateral rhinotomy. No nodularity is present within the postoperative cavity. However, there is a mass (*arrow* in **A**) in the right zygomatic recess of the right antrum, which has broken into the floor of the right orbit. The lesion has surrounding mucosal enhancement, but the secretions within it do not enhance. This patient had a postoperative mucocele.

Copyright © 2003, Mosby, Inc. All rights reserved.

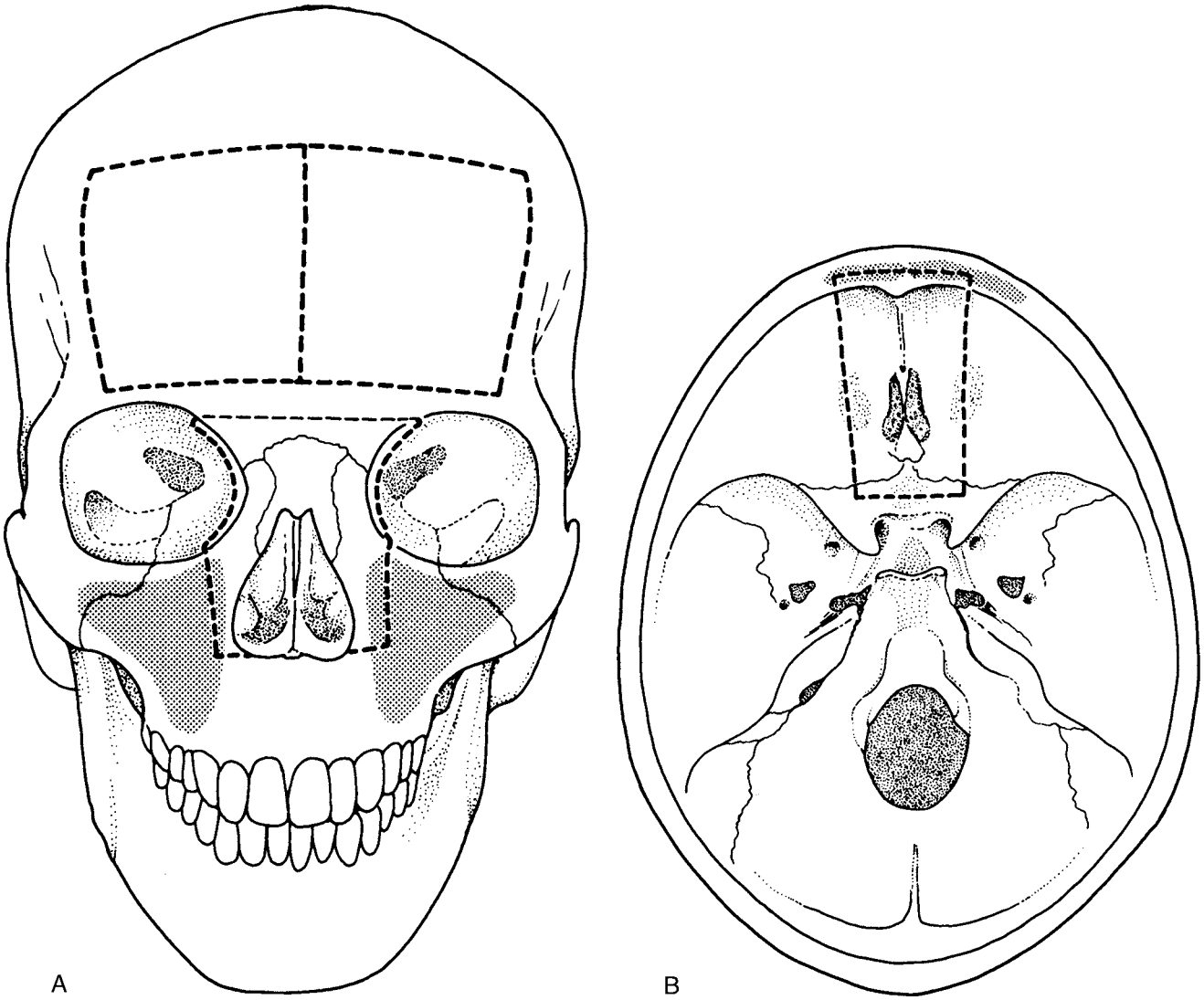

VIEW IMAGE

FIGURE 7-114 Diagrams of the skull in the frontal view (**A**) and the axial view (**B**) as seen from above with the calvarium removed. The osteotomies typically performed in the craniofacial procedure (*dashed lines*) are outlined.

Copyright © 2003, Mosby, Inc. All rights reserved.

VIEW IMAGE

FIGURE 7-115 Axial contrast-enhanced CT scan shows dural thickening and enhancement (*large arrow*) that normally is seen as a postoperative finding in a patient who has had a craniofacial resection. The osteotomy sites in the frontal bones (*small arrows*) are also seen.

VIEW IMAGE

FIGURE 7-116 Coronal CT scans through the anterior (**A**) and posterior (**B**) ethmoid sinus levels in a patient who has had a craniofacial procedure. The ethmoid bones including the medial wall of the left orbit, the medial wall of the left antrum, and most of the roof of the left orbit were removed. Note the smooth margins of the intracranial portion of the flap and the sinonasal and orbital margins. Any focal nodule or mass should raise suspicion of a tumor recurrence.

Copyright © 2003, Mosby, Inc. All rights reserved.

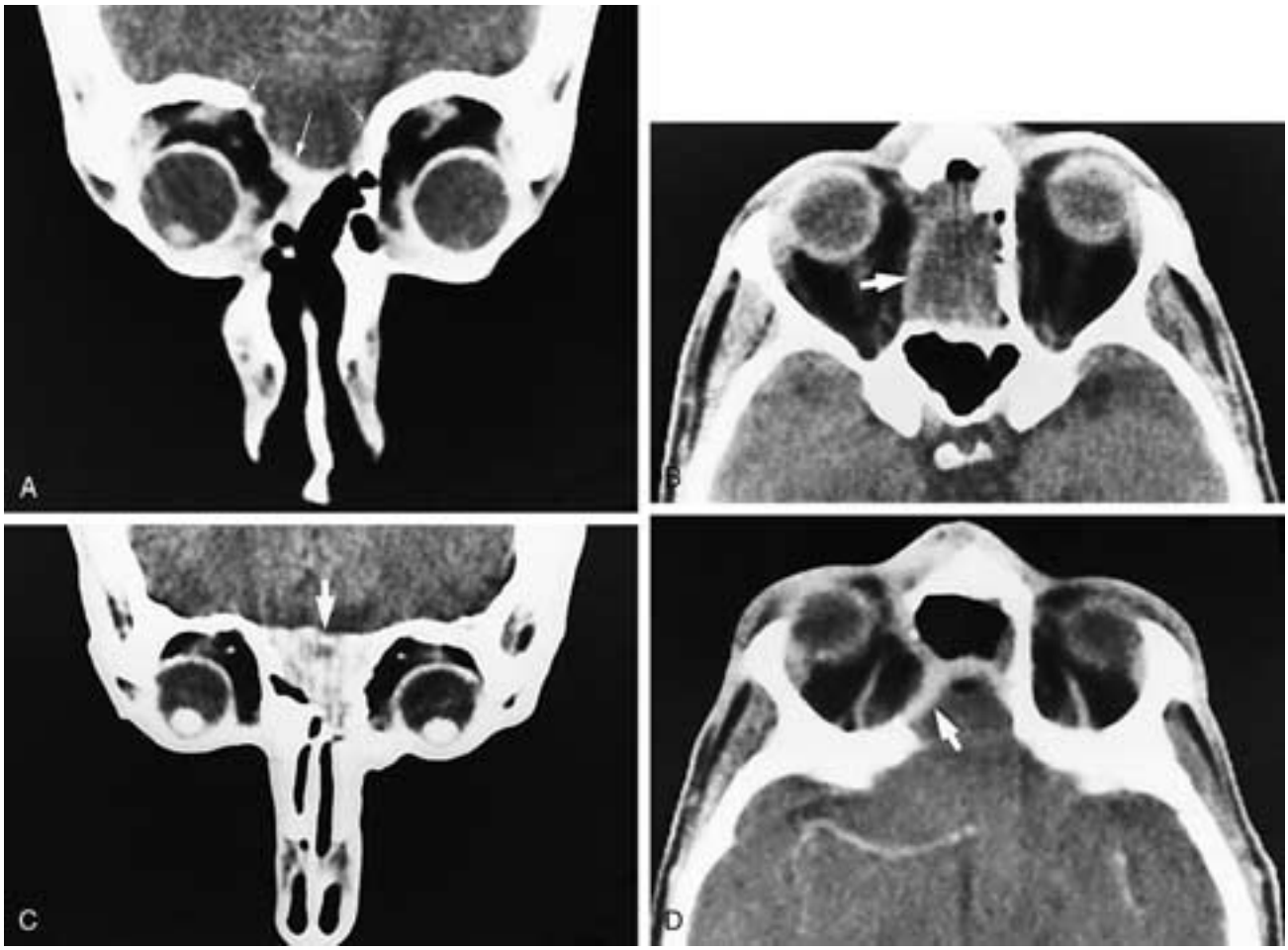

VIEW IMAGE

FIGURE 7-117 Coronal contrast-enhanced CT scan (**A**) on a patient who has had a craniofacial procedure. There is enhancement of the muscle fascial graft (*large arrow*) between the margins of the bony resection (*small arrows*). The intracranial and sinonasal contours of the graft are smooth. Axial CT scan (**B**) shows a soft-tissue mass (*arrow*) in the postoperative upper nasoethmoid cavity. This is the fascial-muscle graft of an osteoplastic flap as it prolapses slightly below the level of the anterior skull base. Any confusion regarding this ''pseudomass'' can be resolved with a coronal study. Coronal contrast-enhanced CT scan (**C**) on a patient who has had a craniofacial resection. The fascial-muscle graft and adjacent dura enhance (*arrow*), filling the surgical defect in the floor of the anterior cranial fossa. The graft hangs down into the postoperative nasoethmoid cavity. Axial contrast-enhanced CT scan (**D**) shows enhancement of dura and granulation tissue (*arrow*) partially below the level of the fascial-muscle graft in a patient who has had a craniofacial resection. The air anteriorly is actually in the upper postoperative nasoethmoid cavity.

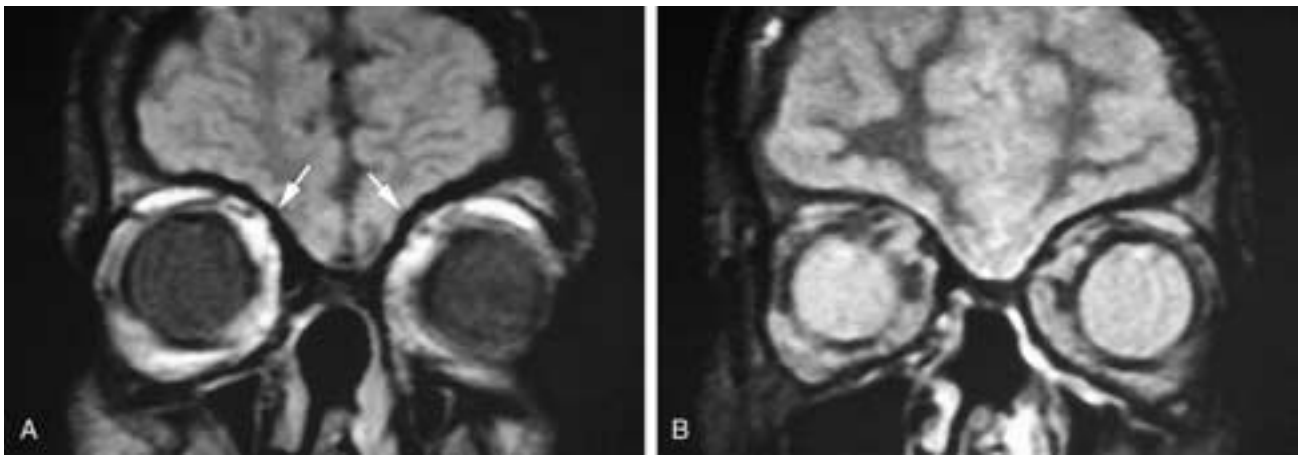

VIEW IMAGE

FIGURE 7-118 Coronal T1-weighted (**A**) and proton density (**B**) MR images on a patient who has had a craniofacial resection. The graft has fibrosed, giving it signal void on all sequences. Because the graft has about the same thickness as the adjacent bone (*arrows* in **A**) in the remaining floor of the anterior cranial fossa, no obvious defect is seen. The imaging key to identifying that this surgery was performed is the absent normal contour of the crista galli and fovea ethmoidalis. Note that the cranial and sinonasal margins of the graft site are smooth.

Copyright © 2003, Mosby, Inc. All rights reserved.

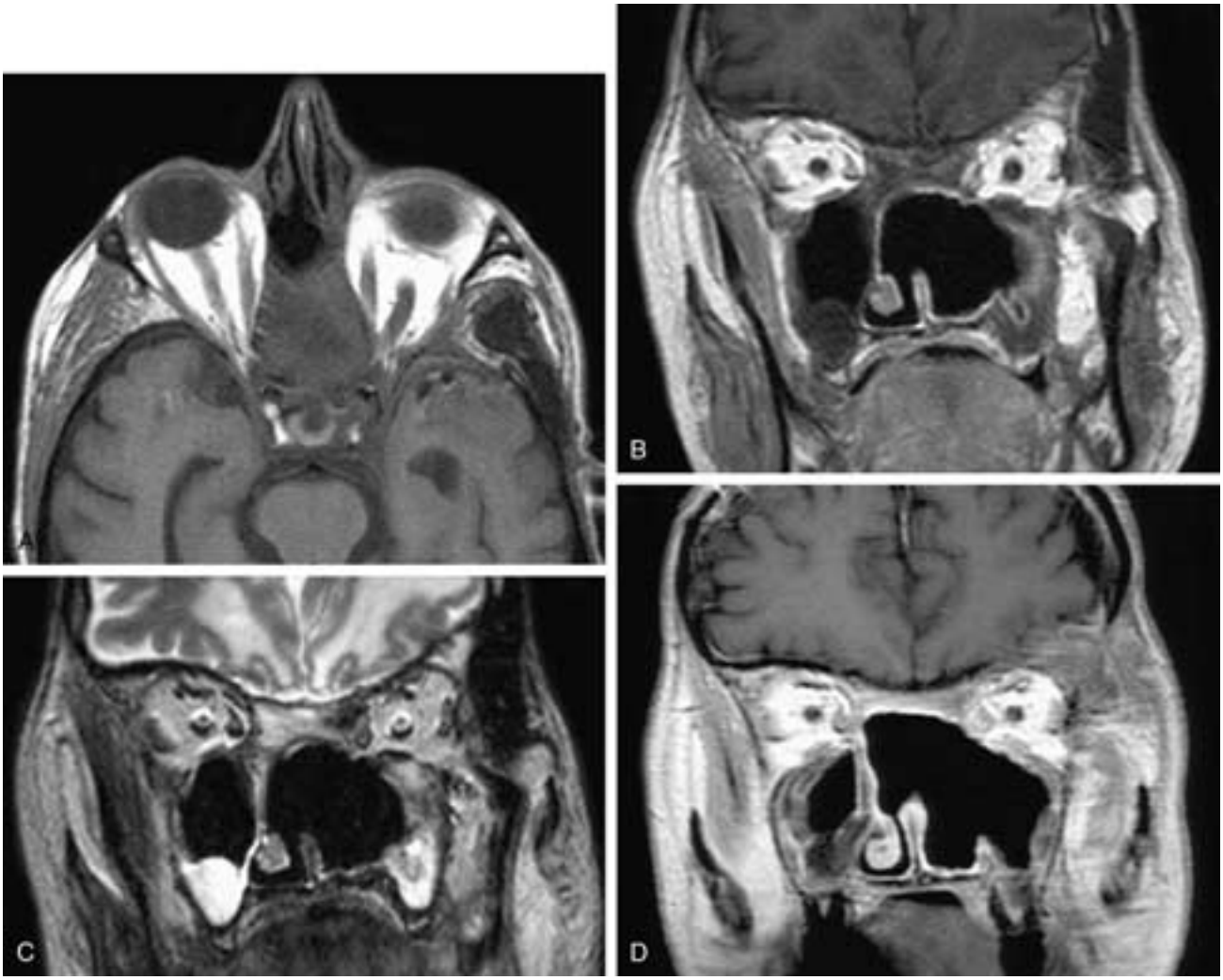

VIEW IMAGE

FIGURE 7-119 Axial T1-weighted (**A**) and coronal T1-weighted (**B**), T2-weighted (**C**), and T1-weighted, fat-suppressed, contrast-enhanced (**D**) MR images on a patient who has had a craniofacial procedure. In (**A**) a ''pseudomass'' is seen in the midline upper nasoethmoid region. This is the flap as it hangs down into the upper sinonasal cavity. This is confirmed on the coronal images, where smooth margins are seen along the intracranial, sinonasal, and orbital margins. Incidental inflammatory disease is present in the right maxillary sinus. This is the normal postoperative appearance of a patient who has had a craniofacial procedure.

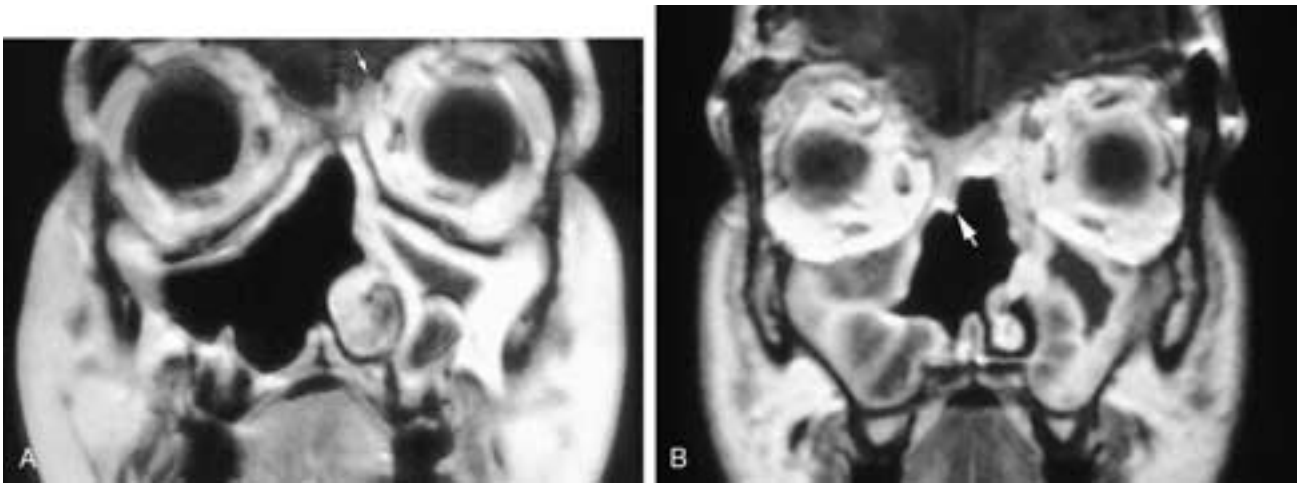

VIEW IMAGE

FIGURE 7-120 Coronal T1-weighted, contrast-enhanced MR images on two different patients who have had craniofacial procedures. In (**A**) the mucosa lining the postoperative nasal cavity and the right maxillectomy cavity is smooth and normal. There is a sinusitis with entrapped secretions in the left antrum. The graft in the floor of the anterior cranial fossa enhances minimally, and if one is not careful, one may overlook the extent of the removed bone, especially in the skull base. A focal area of nodularity is seen (*arrow*) along the intracranial margin near the left attachment of the graft to the bone. This remained stable in appearance over several postoperative years. In this patient, this was a postoperative variant, and it points out the value of obtaining baseline postoperative images. In (**B**) the intracranial margin is smooth, but there is a focal nodule along the right sinonasal margin (*arrow*). Although this area is easily accessible to clinical observation, it was also present on the baseline scan and remained unchanged. There is also bilateral antral inflammatory disease.

Copyright © 2003, Mosby, Inc. All rights reserved.

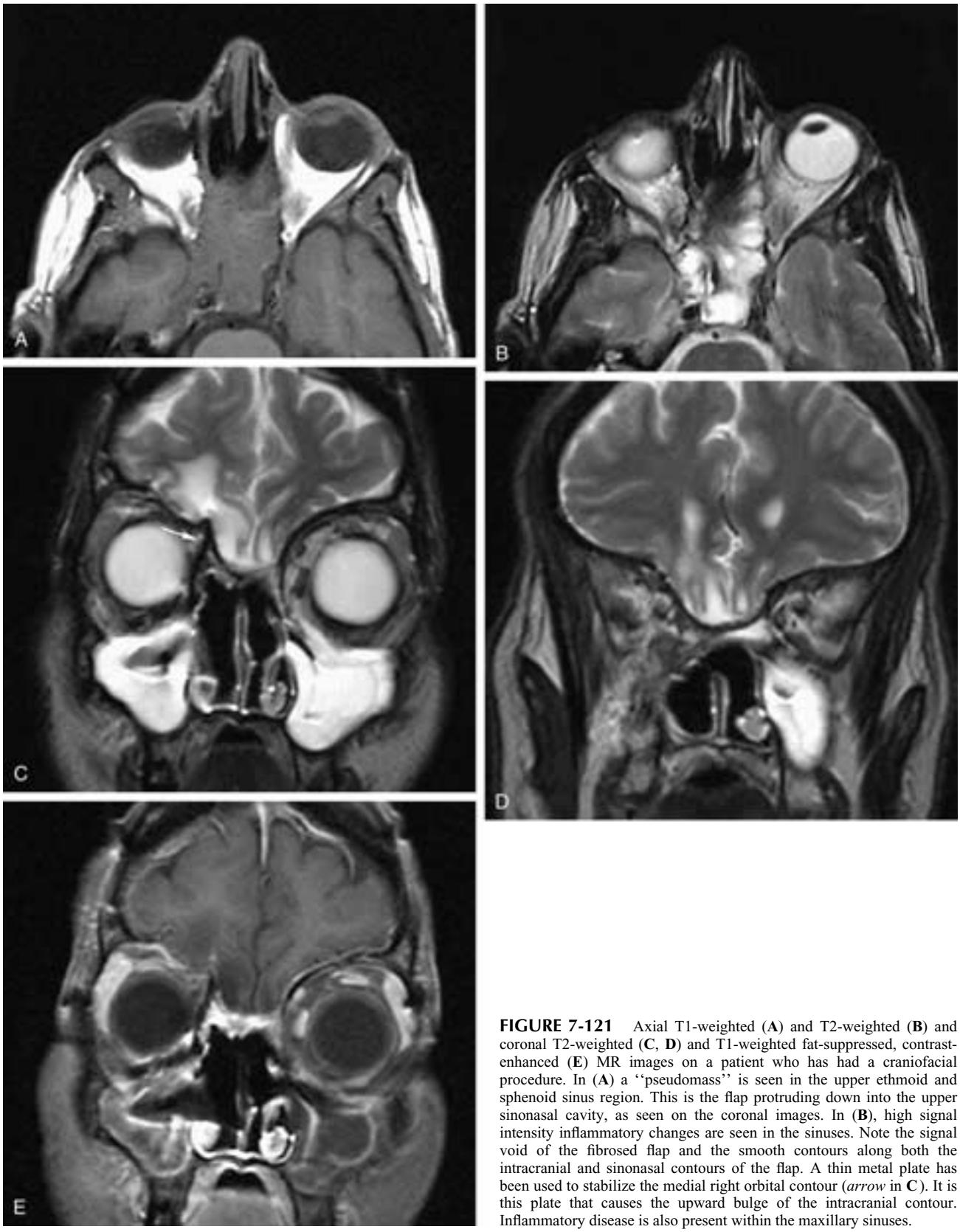

FIGURE 7-121 Axial T1-weighted (**A**) and T2-weighted (**B**) and coronal T2-weighted (**C**, **D**) and T1-weighted fat-suppressed, contrast-enhanced (**E**) MR images on a patient who has had a craniofacial procedure. In (**A**) a ''pseudomass'' is seen in the upper ethmoid and sphenoid sinus region. This is the flap protruding down into the upper sinonasal cavity, as seen on the coronal images. In (**B**), high signal intensity inflammatory changes are seen in the sinuses. Note the signal void of the fibrosed flap and the smooth contours along both the intracranial and sinonasal contours of the flap. A thin metal plate has been used to stabilize the medial right orbital contour (*arrow* in **C**). It is this plate that causes the upward bulge of the intracranial contour. Inflammatory disease is also present within the maxillary sinuses.

VIEW IMAGE

Copyright © 2003, Mosby, Inc. All rights reserved.

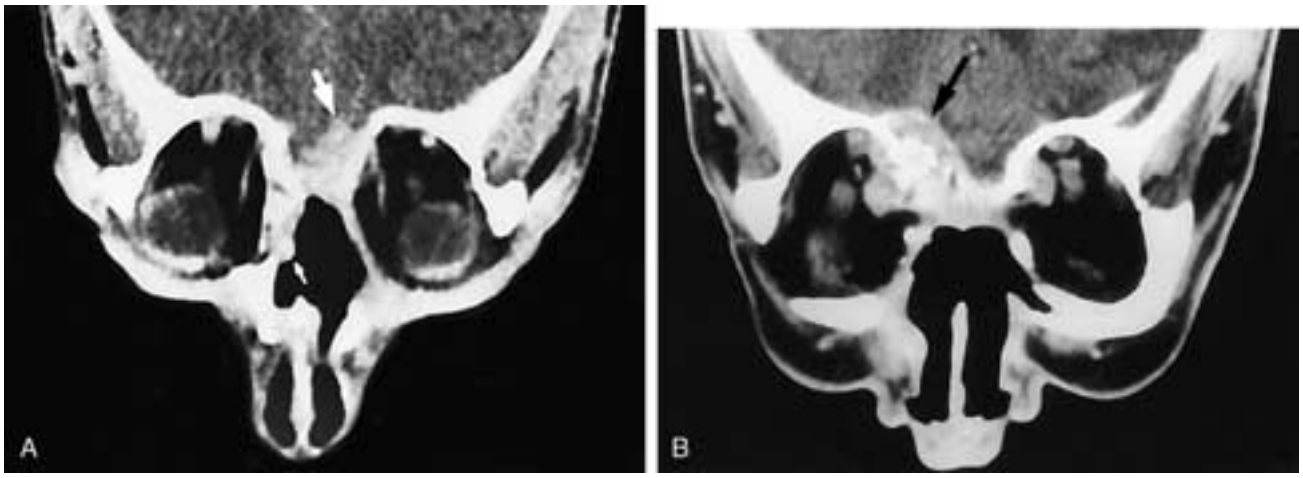

VIEW IMAGE

FIGURE 7-122 Coronal contrast-enhanced CT scan (**A**) on patient who has had a craniofacial resection. The upper fascial-muscle graft contour is nodular (*arrow*). This should raise the suspicion of early tumor recurrence. This patient had recurrent tumor. Coronal CT scan (**B**) on a patient who has had a craniofacial resection. There is a soft-tissue mass (*arrow*) along the graft margin in the floor of the anterior cranial fossa. The mass has also invaded the right orbit. This patient had recurrent adenocarcinoma.

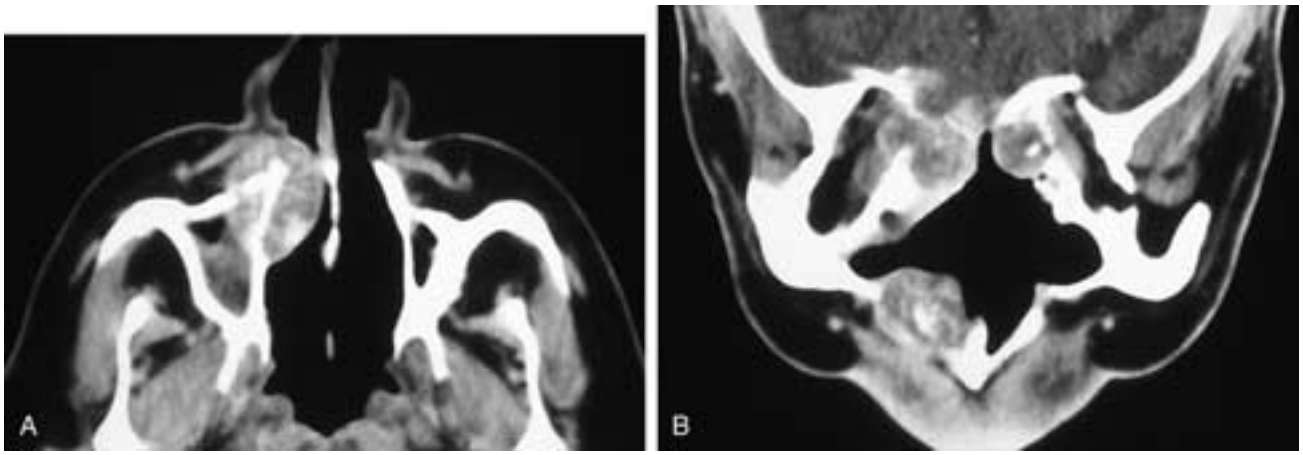

VIEW IMAGE

FIGURE 7-123 Axial (**A**) and coronal (**B**) CT scans on a patient who has had a craniofacial procedure. There are tumor nodules along the upper sinonasal cavity, in the right orbit, and along the right intracranial graft margin. There is also tumor in the right anterior maxilla. Speckled calcifications are seen within each tumor nodule. This patient had recurrent adenocarcinoma.

representing tumor. Progressive thickening of the graft or an upward convexity along the cranial margin of the graft are possible signs of tumor recurrence. Unfortunately, a vascularized scar tissue develops postoperatively that has imaging findings similar to those of recurrent tumor on both CT and MR imaging, with or without contrast. However, this tissue will not progressively grow on serial imaging studies. Thus, tumor recurrence in these patients is best detected by a change in the mucosal or graft surface contour or thickness.[51] Occasionally, inflammatory disease including abscess formation may be seen after surgery. However, in these cases, the clinical presentation usually suggests the diagnosis (Figs. 7-121 to 7-124).

Although technically large graft replacements of the facial area can be performed, the cure rate of such major surgery is often disappointing. Tumor recurrences can occur either deep within the graft or adjacent to the surgical bed (Figs. 7-125 and 7-126).

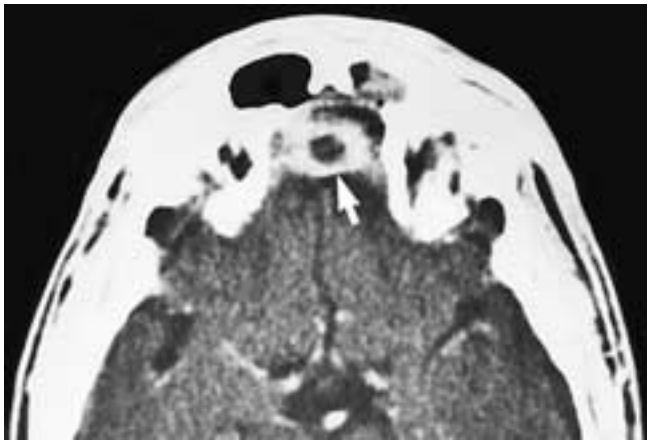

FIGURE 7-124 Axial contrast-enhanced CT scan shows a ring-enhancing mass (*arrow*) just cranial to the fascial-muscle graft in a patient who has had a craniofacial resection. This patient had a postoperative abscess.

VIEW IMAGE

Copyright © 2003, Mosby, Inc. All rights reserved.

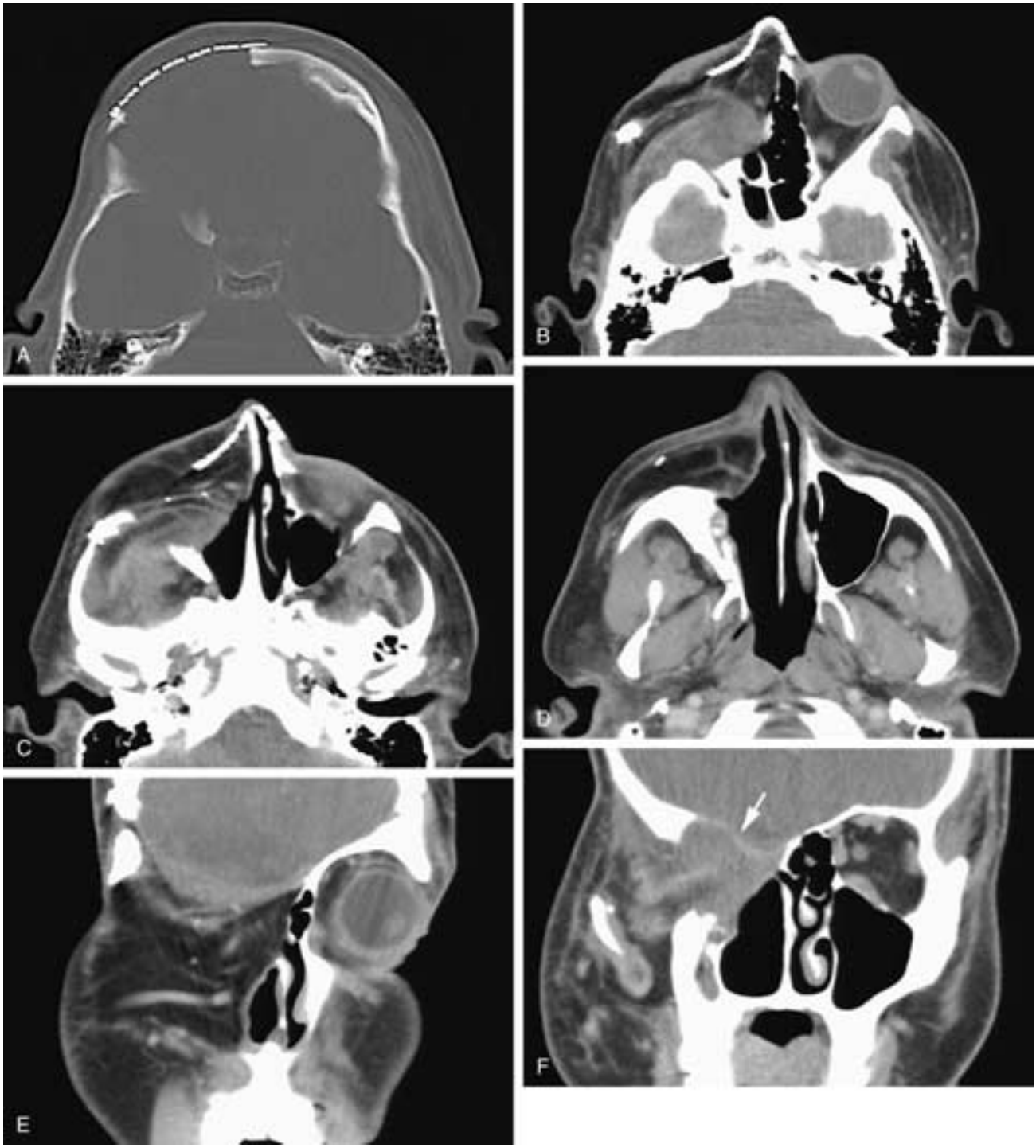

VIEW IMAGE

FIGURE 7-125 Serial axial CT scans from cranial (**A**) to caudal (**D**) and coronal CT scans from anterior (**E**) to posterior (**F**) on a patient who has had a craniofacial procedure, with a myocutaneous graft replacing the right orbit and face. Metal plates have been used to form a nasal contour. Although soft-tissue attenuation is seen near the cranial margin of the craniofacial graft, the intracranial margin (*arrow*) is smooth, as is the sinonasal margin. No recurrence is present.

Copyright © 2003, Mosby, Inc. All rights reserved.

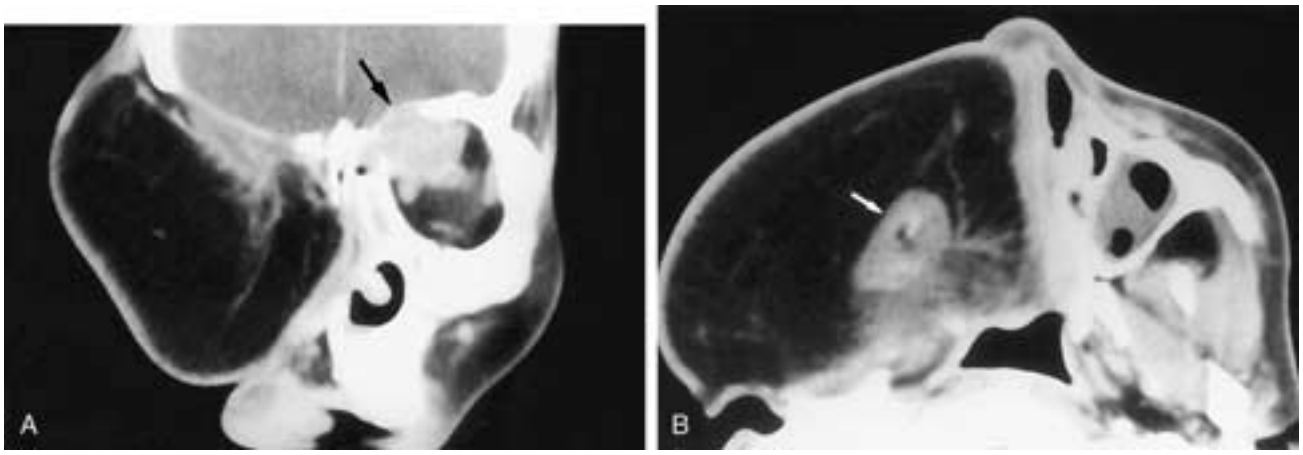

VIEW IMAGE

FIGURE 7-126 Coronal (**A**) and axial (**B**) CT scans on a patient who has had multiple recurrences of a rhabdomyosarcoma after chemotherapy, irradiation, and numerous operations. Finally, a large myocutaneous graft was used to replace her entire right facial region. The bulk of this graft makes clinical detection of a recurrence within it extremely difficult. Imaging shows the muscle (*arrow* in **B**) within the graft and no evidence of tumor recurrence. However, tumor has now recurred on the left side of the craniofacial graft and in the upper left orbit (*large arrow* in **A**).

REFERENCES

1. Stanley RB Jr, Nowak GM. Midfacial fractures: importance of angle of impact to horizontal craniofacial buttresses. Otolaryngol Head Neck Surg 1985;93:186–192.
2. Stanley RB Jr. Use of intraoperative computed tomography during repair of orbitozygomatic fractures. Arch Facial Plast Surg 1999;1: 19–24.
3. Gentry LR, Manor WF, Turski PA, Strother CM. High-resolution CT analysis of facial struts in trauma: 1. Normal anatomy. AJR 1983;140:523–532.
4. Gentry LR, Manor WF, Turski PA, Strother CM. High-resolution CT analysis of facial struts in trauma: 2. Osseous and soft-tissue complications. AJR 1983;140:533–541.
5. Beirne JC, Butler PE, Brady FA. Cervical spine injuries in patients with facial fractures: a 1-year prospective study. Int J Oral Maxillofac Surg 1995;24:26–29.
6. Manson PN, Iliff N. Management of blow-out fractures of the orbital floor. II. Early repair for selected injuries. Surv Ophthalmol 1991;35:280–292.
7. Schwenzer N. [Corrective operations following primary surgical management of facial cleft patients]. Fortschr Kieferorthop 1986;47:540–546.
8. Kreipke DL, Moss JJ, Franco JM, et al. Computed tomography and thin-section tomography in facial trauma. AJR 1984;142:1041–1045.
9. Kreipke DL, Lingeman RE. Cross-sectional imaging (CT, NMR) of branchial cysts: report of three cases. J Comput Assist Tomogr 1984;8:114–116.
10. Rowe NL. Maxillofacial injuries—current trends and techniques. Injury 1985;16:513–525.
11. Kim DB, Sacapano M, Hardesty RA. Facial fractures in children. West J Med 1997;167:100.
12. Schierle HP, Hausamen JE. [Modern principles in treatment of complex injuries of the facial bones]. Unfallchirurg 1997;100:330–337.
13. Becelli R, Renzi G, Frati R, Iannetti G. [Maxillofacial fractures in children]. Minerva Pediatr 1998;50:121–126.
14. Manson PN, Markowitz B, Mirvis S, et al. Toward CT-based facial fracture treatment. Plast Reconstr Surg 1990;85:202–212; discussion 213–214.
15. Brant-Zawadzki MN, Minagi H, Federle MP, Rowe LD. High resolution CT with image reformation in maxillofacial pathology. AJR 1982;138:477–483.
16. Zilkha A. Computed tomography in facial trauma. Radiology 1982;144:545–548.
17. Zilkha A. Multiplanar reconstruction in computed tomography of the orbit. Comput Radiol 1982;6:57–62.
18. Lill W, Solar P, Ulm C, et al. Reproducibility of three-dimensional CT-assisted model production in the maxillofacial area. Br J Oral Maxillofac Surg 1992;30:233–236.
19. Carls FR, Schuknecht B, Sailer HF. Value of three-dimensional computed tomography in craniomaxillofacial surgery. J Craniofac Surg 1994;5:282–288.
20. Bruning R, Quade R, Keppler V, Reiser M. [3-D CT reconstruction of fractures of the skull base and the facial skeleton]. Rofo Fortschr Geb Rontgenstr Neuen Bildgeb Verfahr 1994;160:113–117.
21. Cavalcanti MG, Haller JW, Vannier MW. Three-dimensional computed tomography landmark measurement in craniofacial surgical planning: experimental validation in vitro. J Oral Maxillofac Surg 1999;57:690–694.
22. Zimmerman R, Bilaniuk L, Hackney D, et al. Paranasal sinus hemorrhage: evaluation with MR imaging. Radiology 1987;162: 499–503.
23. Arden RL, Crumley RL. Cartilage grafts in open rhinoplasty. Facial Plast Surg 1993;9:285–294.
24. Clayton MI, Lesser TH. The role of radiography in the management of nasal fractures. J Laryngol Otol 1986;100:797–801.
25. Stranc MF. The pattern of lacrimal injuries in naso-ethmoid fractures. Br J Plast Surg 1970;23:339–346.
26. Stranc MF. Primary treatment of naso-ethmoid injuries with increased intercanthal distance. Br J Plast Surg 1970;23:8–25.
27. Cooter RD, Dunaway DJ, David DJ. The influence of maxillary dentures on mid-facial fracture patterns. Br J Plast Surg 1996;49: 379–382.
28. al-Qurainy IA, Titterington DM, Dutton GN, et al. Midfacial fractures and the eye: the development of a system for detecting patients at risk of eye injury. Br J Oral Maxillofac Surg 1991;29:363–367.
29. al-Qurainy IA, Stassen LF, Dutton GN, et al. Diplopia following midfacial fractures. Br J Oral Maxillofac Surg 1991;29:302–307.
30. al-Qurainy IA, Stassen LF, Dutton GN, et al. The characteristics of midfacial fractures and the association with ocular injury: a prospective study. Br J Oral Maxillofac Surg 1991;29:291–301.
31. Yanagisawa E, Smith H. Normal radiographic anatomy of the paranasal sinuses. Otolaryngol Clin North Am 1973;6:429–457.
32. Ellis E 3rd, Ghali GE. Lag screw fixation of mandibular angle fractures. J Oral Maxillofac Surg 1991;49:234–243.
33. Smith PH. Blow out fracture of the floor of the orbit. Aust NZ J Surg 1967;36:319–322.
34. Gruss JS, Hurwitz JJ. Isolated blow-in fracture of the lateral orbit causing globe rupture. Ophthalmol Plast Reconstr Surg 1990;6: 221–224.

Copyright © 2003, Mosby, Inc. All rights reserved.

35. Burm JS, Chung CH, Oh SJ. Pure orbital blowout fracture: new concepts and importance of medial orbital blowout fracture. Plast Reconstr Surg 1999;103:1839–1849.
36. Nolasco FP, Mathog RH. Medial orbital wall fractures: classification and clinical profile. Otolaryngol Head Neck Surg 1995;112:549–556.
37. Coker NJ, Brooks BS, El Gammal T. Computed tomography of orbital medial wall fractures. Head Neck Surg 1983;5:383–389.
38. Almog Y, Mayron Y, Weiss J, et al. Pneumomediastinum following blowout fracture of the medial orbital wall: a case report. Ophthalmol Plast Reconstr Surg 1993;9:289–291.
39. Berkowitz RA, Putterman AM, Patel DB. Prolapse of the globe into the maxillary sinus after orbital floor fracture. Am J Ophthalmol 1981;91:253–257.
40. Raghav B, Vashisht S, Keshav BR, Berry M. The missing eyeball—CT evaluation (a case report). Ind J Ophthalmol 1991;39: 188–189.
41. Pelton RW, Rainey AM, Lee AG. Traumatic subluxation of the globe into the maxillary sinus. AJNR 1998;19:1450–1451.
42. Lee FY, Hazan EJ, Gebhardt MC, Mankin HJ. Experimental model for allograft incorporation and allograft fracture repair. J Orthop Res 2000;18:303–306.
43. Martello JY, Vasconez HC. Supraorbital roof fractures: a formidable entity with which to contend. Ann Plast Surg 1997;38:223–227.
44. Shockley WW, Stucker FJ Jr, Gage-White L, Antony SO. Frontal sinus fractures: some problems and some solutions. Laryngoscope 1988;98:18–22.
45. Olson EM, Wright DL, Hoffman HT, et al. Frontal sinus fractures: evaluation of CT scans in 132 patients. AJNR 1992;13:897–902.
46. Whelan MA, Reede DL, Meisler W, Bergeron RT. CT of the base of the skull. Radiol Clin North Am 1984;22:177–217.
47. Rohrich RJ, Hollier LH. Management of frontal sinus fractures. Changing concepts. Clin Plast Surg 1992;19:219–232.
48. Rohrich RJ, Hollier LH, Watumull D. Optimizing the management of orbitozygomatic fractures. Clin Plast Surg 1992;19:149–165.
49. Rohrich RJ, Shewmake KB. Evolving concepts of craniomaxillofacial fracture management. Clin Plast Surg 1992;19:1–10.
50. Nahum AM. The biomechanics of facial bone fracture. Laryngoscope 1975;85:140–156.
51. Som PM, Lawson W, Biller HF, et al. Ethmoid sinus disease: CT evaluation in 400 cases. Part III. Craniofacial resection. Radiology 1986;159:605–609.
52. Som PM, Lawson W, Biller HF, Lanzieri CF. Ethmoid sinus disease: CT evaluation in 400 cases. Part II. Postoperative findings. Radiology 1986;159:599–604.
53. Som PM, Urken ML, Biller H, Lidov M. Imaging the postoperative neck. Radiology 1993;187:593–603.
54. Som P, Shapiro M, Biller H, et al. Sinonasal tumors and inflammatory tissues: differentiation with MR imaging. Radiology 1988;167: 803–808.
55. Naumann H, Buckingham R. Head and Neck Surgery: Indications, Techniques, Pitfalls. Vol. 1. Philadelphia: WB Saunders, 1980; 173–462.
56. Ballantyne J, Harrison D. Operative Surgery: Nose and Throat. London: Butterworth, 1986;1–177.
57. Urken M, Som P, Lawson W, et al. The abnormally large frontal sinus. Part I: a practical method for its determination based upon an analysis of 100 normal patients. Laryngoscope 1987;97:602–605.
58. Som P, Shugar J. The CT classification of ethmoid mucoceles. J Comput Assist Tomogr 1980;4:199–203.
59. Unger JM, Dennison BF, Duncavage JA, Toohill RJ. The radiological appearance of the post-Caldwell-Luc maxillary sinus. Clin Radiol 1986;37:77–81.
60. Johnson D, Hopkins R, Hanafee W. The unprotected parasphenoidal carotid artery studied by high resolution computed tomography. Radiology 1985;155:137–141.
61. Pedersen R, Troost B, Schramm V. Carotid-cavernous sinus fistula after external ethmoid-sphenoid surgery. Arch Otolaryngol 1981;107:307–309.
62. Som P, Shugar J, Biller H. The early detection of antral malignancy in the post maxillectomy patient. Radiology 1982;143: 509–512.
63. Baredes S, Cho H, Som M. Total maxillectomy. In: Blitzer A, Lawson W, Friedman W, eds. Surgery of the Paranasal Sinuses. Philadelphia: WB Saunders, 1985;204–216.
64. Lund V, Howard D, Lloyd G. CT evaluation of paranasal sinus tumors for craniofacial resection. Br J Radiol 1983;56:439–446.
65. Nuss D, Janecka I. Surgery of the anterior and middle cranial base. In: Cummings C, Fredrickson J, Harker L, et al, eds. Otolaryngology—Head and Neck Surgery. Vol 4. St. Louis: CV Mosby, 1993; 3300–3337.

Copyright © 2003, Mosby, Inc. All rights reserved.

Section II

Orbit and Visual Pathways

Copyright © 2003, Mosby, Inc. All rights reserved.

Copyright © 2003, Mosby, Inc. All rights reserved.

8

The Eye

Mahmood F. Mafee

EMBRYOLOGY OF THE EYE
- Optic Nerves, Macular Area, and Fovea Centralis
- Lens
- The Ciliary Body and Suspensory Ligaments of the Lens
- The Iris and the Aqueous Chamber
- The Vitreous
- The Choroid
- The Sclera
- The Cornea
- Vascular System

IMAGING TECHNIQUES
- MR Imaging
- CT Technique
- MR Imaging and Evaluation of Intraocular Foreign Bodies
- MR Imaging Artifacts

NORMAL OCULAR ANATOMY
- Ocular Structures
- Tenon's Capsule
- Sclera
  - Blood Supply and Nerve Supply of the Sclera
- Cornea
  - Blood Supply and Nerve Supply of the Cornea
- Uvea (Choroid, Ciliary Body, and Iris)
  - Bruch's Membrane
  - Choriocapillaris
  - Choroidal Stroma
  - Suprachoroidea
  - Blood Supply of the Choroid
  - Function
  - Nerve Supply of the Choroid
- Ciliary Body
- Iris
- Retina
  - Blood Supply of the Retina
- Vitreous

INTRAOCULAR POTENTIAL SPACES

NORMAL IMAGING OF OCULAR ANATOMY

LENS

OCULAR PATHOLOGY
- Congenital Anomalies
  - Anophthalmia
  - Microphthalmia
  - Macrophthalmia
    - *Buphthalmos and Megalophthalmos*
  - Staphyloma
  - Cryptophthalmos
  - Coloboma and Morning Glory Anomaly
    - *Diagnostic Imaging*

OCULAR DETACHMENTS
- Posterior Hyaloid Detachment
- Retinal Detachment
- Choroidal Detachment, Choroidal Effusion, and Ocular Hypotony
- Ocular Inflammatory Disorders
- Other Inflammatory Conditions
  - Lymphoid Hyperplasia
  - Papilledema
  - Episcleritis
  - Scleritis
  - Uveitis
  - Parasitic Infections
  - Intraocular Calcifications

LEUKOKORIA

RETINOBLASTOMA
- Trilateral Retinoblastoma
- Tetralateral Retinoblastoma
- Clinical Diagnosis
- Diagnostic Imaging
- MR Imaging
- Intraocular Mass and Mass-Like Lesions Simulating Retinoblastoma

PERSISTENT HYPERPLASTIC PRIMARY VITREOUS
- Clinical Diagnosis
- MR Imaging

Copyright © 2003, Mosby, Inc. All rights reserved.

RETINAL DYSPLASIA
- **Norrie's Disease**
  - **Diagnostic Imaging**
- **Warburg's Syndrome**
  - **Clinical Diagnosis**
  - **Diagnostic Imaging**
- **Retinopathy of Prematurity**
  - **Ophthalmoscopic Picture**
    - ***Regressive Phase***
    - ***Cicatricial Phase***
  - **Diagnostic Imaging**
- **Coats' Disease**
  - **Clinical Presentation and Diagnosis**
  - **Diagnostic Imaging**
- **Ocular Toxocariasis (Sclerosing Endophthalmitis)**
  - **Diagnostic Imaging**
- **Ocular Astrocytic Hamartoma (Retinal Astrocytoma)**
- **Combined Hamartoma of the Retinal Pigment Epithelium and Retina**
- **Incontinentia Pigmenti**
- **Juvenile Xanthogranuloma**
- **Glioneuroma**
- **Papillitis**
- **Optic Nerve Head Drusen**
- **Choroidal Osteoma**
  - **Clinical Diagnosis**
  - **Imaging Diagnosis**
  - **Differential Diagnosis**
- **Retina Gliosis**
- **Myelinated Nerve Fibers**
- **X-Linked Retinoschisis**
- **Retinal Detachment**
- **Subretinal Neovascular Membranes**
- **Vitreous Opacities**
- **Von Hippel-Lindau Retinal Angiomatosis**
- **Choroidal Hemangioma**
- **Malignant Uveal Melanoma**
  - **Clinical Diagnosis**
  - **Diagnostic Imaging**
  - **Differential Diagnosis**
- **Melanocytoma**
- **Uveal Metastasis**
- **Uveal Nevus**
  - **Diagnostic Imaging**
- **Choroidal and Retinal Hemangiomas**
  - **Clinical Features**
  - **Diagnostic Imaging**
- **Angiomatosis Retinae and Von Hippel-Lindau Disease**
- **Choroidal Hemorrhage and Choroidal Detachment**
- **Choroidal Cyst**
- **Other Tumors of the Uvea**
  - **Ocular Lymphoma**
  - **Ocular Leukemia**
  - **Primary Ocular Schwannoma (Neurilemoma)**
  - **Leiomyoma**
- **Ocular Adenoma and Adenocarcinoma**
- **Medulloepithelioma**
- **Retinal Detachment in the Differential Diagnosis of Uveal Melanoma**
- **Senile Macular Degeneration**
- **Ocular Trauma**
  - **Globe Injury**
  - **Postsurgical Changes**
  - **Anophthalmic Socket and Orbital Implant**

EMBRYOLOGY OF THE EYE

The globe is formed from the neuroectoderm of the forebrain, the surface ectoderm from the head, the mesoderm lying between these layers, and neural crest cells.[1] The neural tube ectoderm (neuroectoderm) gives rise to the retina, the fibers of the optic nerve, and the smooth muscles (the sphincter and dilator papillae) of the iris.[1] The surface ectoderm on the side of the head forms the corneal and conjunctival epithelium, the lens, and the lacrimal and tarsal glands.[1, 2] Although the mesenchymal cells are derived from mesenchyme, neural crest cells also migrate into this mesenchyme, and it is from this combined mesenchyme that the corneal stroma, the sclera, the choroid, the iris, the ciliary musculature, part of the vitreous body, and the cells lining the anterior chamber are formed.[2]

The rudimentary eyes appear as two neuroectodermally lined hollow diverticula (grooves) extending from the lateral aspects of the forebrain (diencephalon) (Fig. 8-1). It is in the third week of gestation (22 days) that these diverticulae appear, one on either side of the neural groove. These are the optic pits, and they deepen to form the optic vesicles, which can be identified in the 4 mm embryo (less than 4 weeks of gestation)[3] (Fig. 8-1). The diverticula grow out laterally, and their ends come into close apposition with the overlying surface ectoderm. The apposition of the outer wall of each optic vesicle to the overlying surface epithelium is essential for the transmission of inductive messages that stimulate the surface ectoderm to form a small area overlying the optic vesicle that thickens and forms the lens placode. As the process of lens induction proceeds, the outer surface of the optic vesicle flattens and then becomes concave toward

Copyright © 2003, Mosby, Inc. All rights reserved.

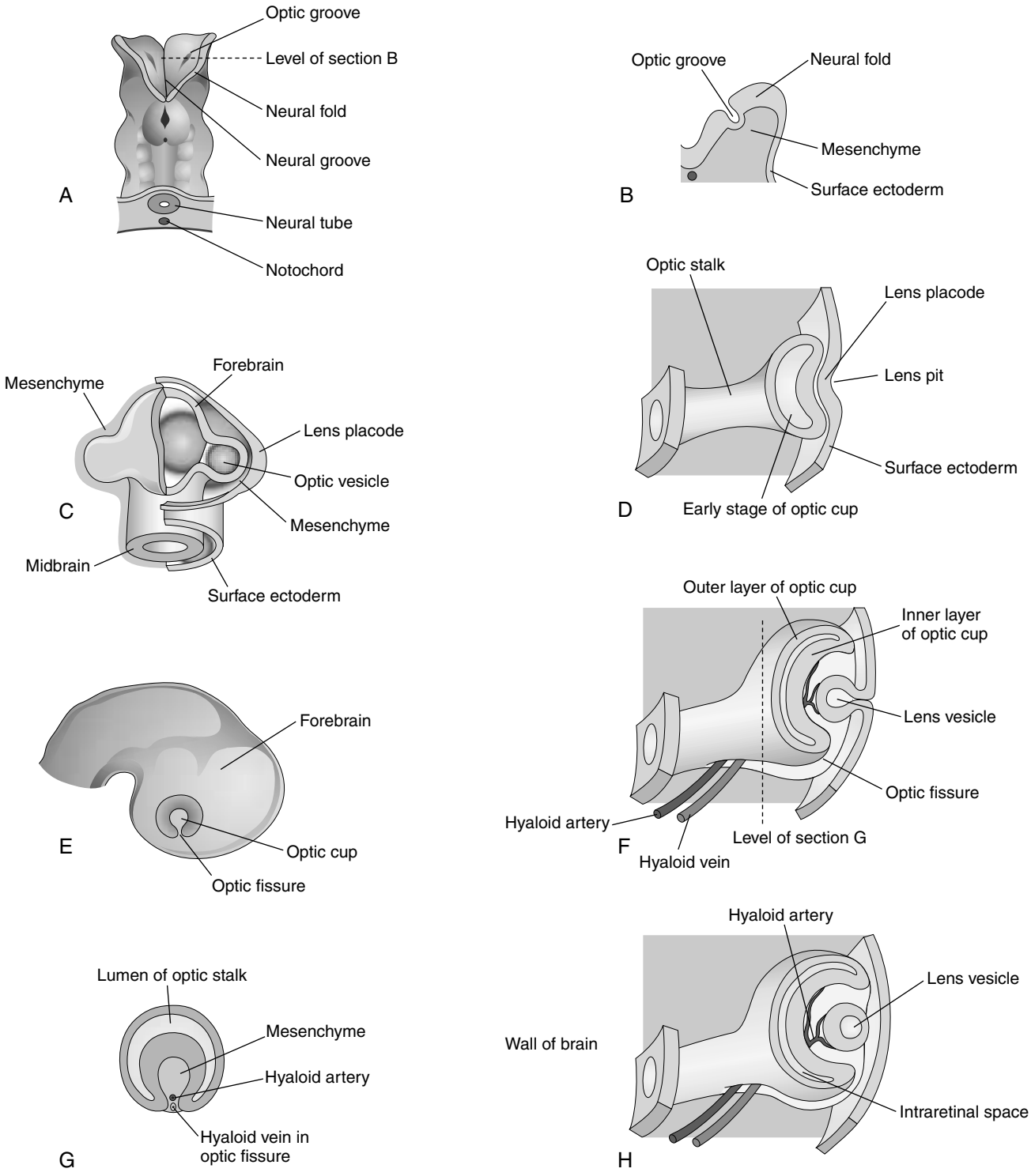

VIEW IMAGE

FIGURE 8-1 Drawings showing early eye development. **A**, Optic sulci or grooves are seen in the cranial end of an embryo at about 22 days of gestation. The neural folds have not yet fused to form the primary forebrain vesicles. **B**, Transverse section of a neural fold showing the optic sulcus. **C**, Schematic drawing of an embryo at about 28 days of gestation shows the covering layers of mesenchyme and surface ectoderm. **D**, **F**, and **H**, Schematic sections of the developing eye showing the successive stages in the development of the optic cup and lens vesicle. **E**, Lateral view of the brain of an embryo at about 32 days of gestation showing the external appearance of the optic cup. **G**, Transverse section of the optic stalk showing the optic fissure and its contents. Note that the edges of the fissure are growing together, thereby completing the optic cup and enclosing the central artery and vein of the retina in the optic stalk and cup. (From Moore KL, Persaud TVN. The Developing Human: Clinically Oriented Embryology 6th ed. Philadelphia, Pa: Saunders, 1998; 493.)

Copyright © 2003, Mosby, Inc. All rights reserved.

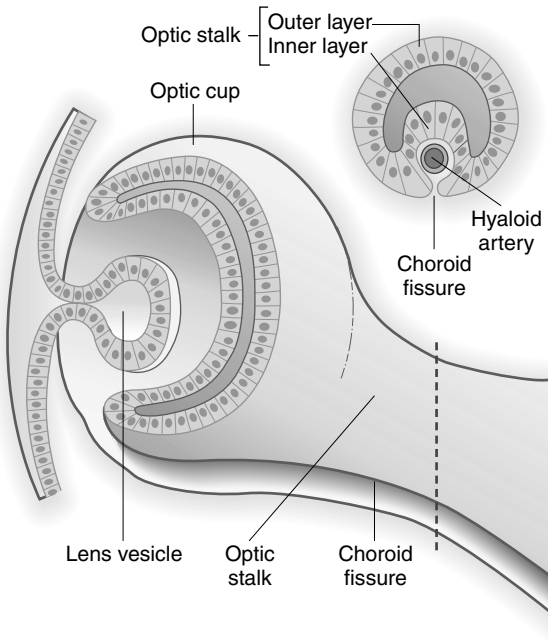

VIEW IMAGE

FIGURE 8-2 Drawing of the optic cup and stalk showing the choroid fissure containing the hyaloid artery. The cross section (top) is through the level of the dashed line. (From Carlson BM. Human Embryology and Developmental Biology, 2nd ed. St. Louis, Mo: Mosby, 1994; 265.)

the surface of the embryo. This results in the transformation of the distal end of the optic vesicle into the double-layered optic cup. The proximal portion of each optic vesicle becomes constricted to form the optic stalk[1–6] (Figs. 8-1 and 8-2). The lens placode invaginates and sinks below the surface ectoderm to become the lens pit, and its edges come together and fuse to enclose a hollow lens vesicle[1–6] (Figs. 8-2 and 8-3). By the fifth week, the lens vesicle loses contact with the surface ectoderm and lies within the mouth of the optic cup, the edges of which form the future pupil[1–7] (Figs. 8-1 and 8-3). The lens vesicle initiates a new series of inductive reactions by acting on the overlying surface ectoderm to begin development of the cornea.

In the 5 mm embryo, the invagination is not limited to the outer wall of the optic vesicle, but also involves its caudal surface and extends in the form of a groove for some distance along the optic stalk[2] (Figs. 8-1 and 8-2). Thus, for a time, a wide hiatus, the optic fissure or choroidal fissure (embryonic fissure), exists in the inferior edge of the optic cup.[1, 2] The embryonic fissure remains open for some distance along the optic stalk at the inferior and slightly nasal aspect of the optic cup (Figs. 8-1 and 8-2). Through the embryonic fissure, the mesenchyme extends into the optic stalk and cup, carrying the hyaloid artery with it to the posterior surface of the lens[1–3] (Fig. 8-3). The hyaloid artery, a branch of the ophthalmic artery, supplies the inner layer of the optic cup, the lens vesicle, and the mesenchyme in the optic cup (Figs. 8-4 and 8-5). The hyaloid vein drains blood from these structures. Later, as growth proceeds, the edges of this fissure become narrowed, and by the seventh week of embryonic development the fissure closes, forming a narrow tube, the optic canal, inside the optic stalks. Failure of the choroidal fissure to close completely results in a coloboma (a notched defect) formation, which may include the iris, ciliary body, choroid, retina, or optic nerve.

The retina develops from the optic cup (Figs. 8-2 and 8-3). For purposes of description, the retina may be divided into two developmental layers, the pigment layer and the neural layer. Its two layers are at first equipotential and mutually interchangeable. The pigment layer is formed from the outer thinner layer of the optic cup. It is a single layer of cells that becomes columnar in shape, and pigment granules develop within the cytoplasm of these cells. The neural layer is formed from the inner layer of the optic cup.[1–6] It is

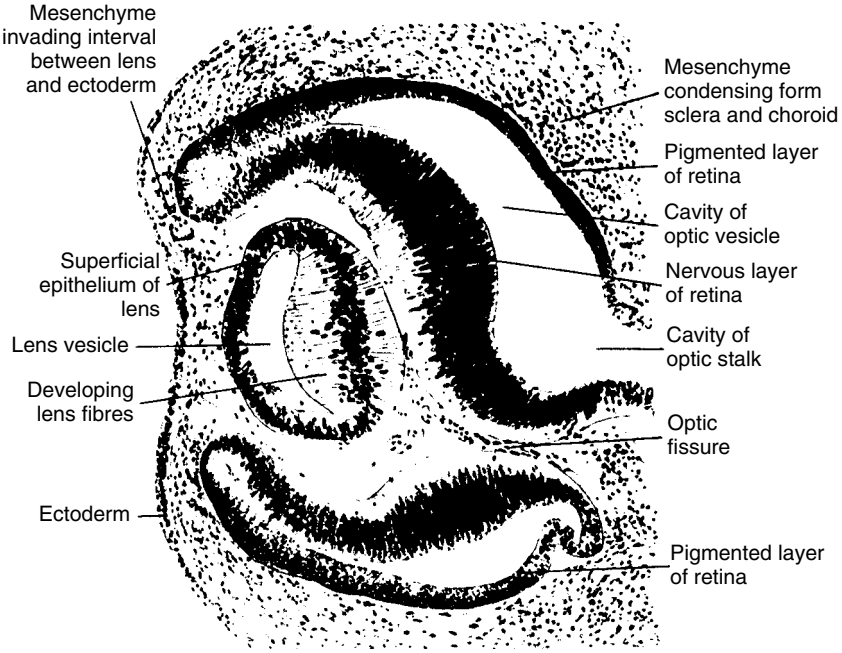

FIGURE 8-3 A lateral section through the developing eye of a human embryo 13.2 mm long. (From Bannister LH, Berry MM, Collins P, Dyson M, et al. (eds). Gray's Anatomy, 38th ed. Edinburgh: Churchill Livingstone, 1999; 259.)

VIEW IMAGE

Copyright © 2003, Mosby, Inc. All rights reserved.

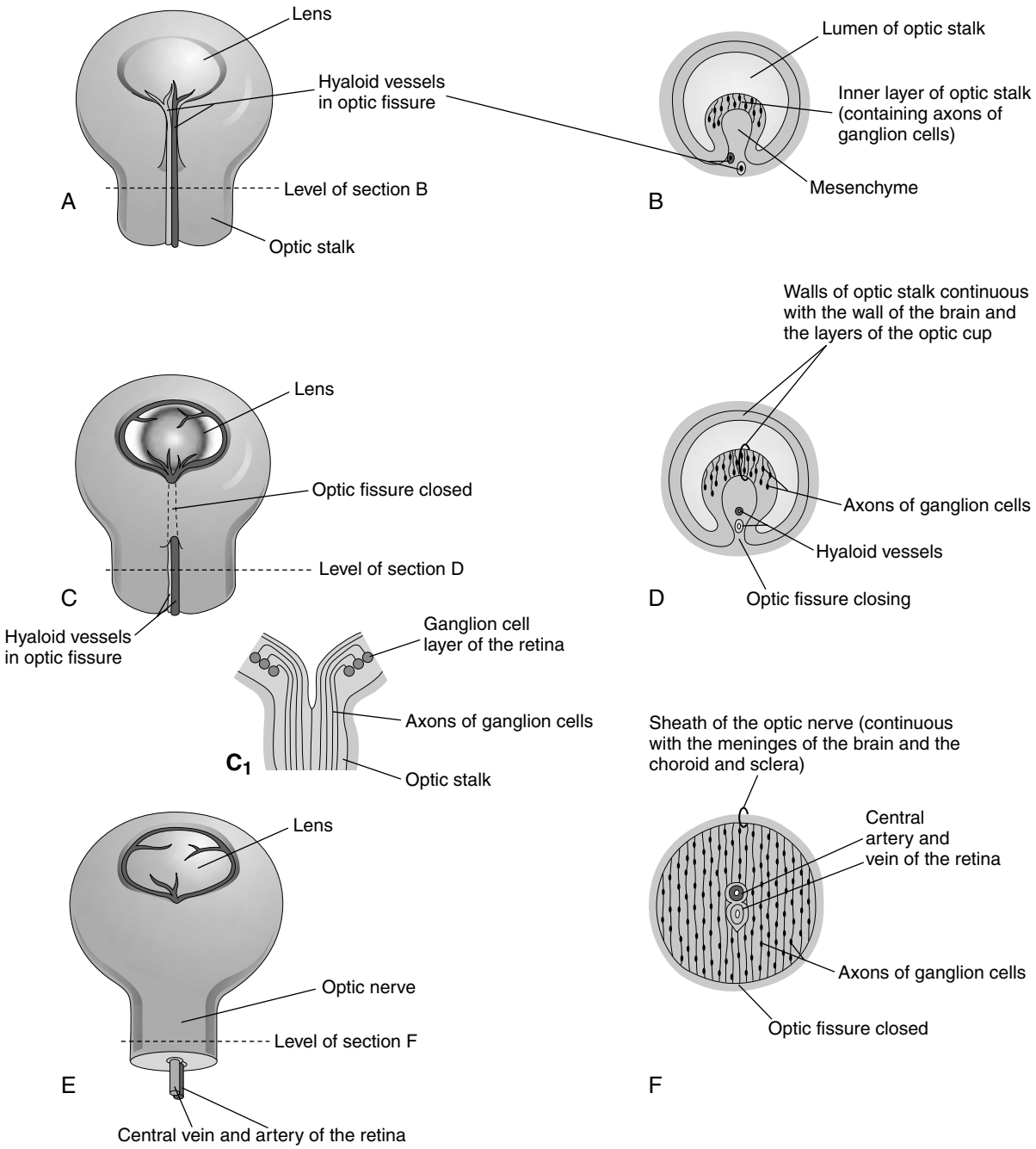

FIGURE 8-4 Diagrams showing the closure of the optic fissure and the formation of the optic nerve. **A**, **C**, and **E**, Views of the inferior surface of the optic cup and stalk showing progressive stages in the closure of the optic fissure. $\mathbf{C_1}$, Schematic drawing of a longitudinal section of a part of the optic cup and stalk showing axons and ganglion cells of the retina growing through the optic stalk to the brain. **B**, **D**, and **F**, Transverse sections of the optic stalk showing successive stages in the closure of the optic fissure and the formation of the optic nerve. (From Moore KL, Persaud TVN. The Developing Human: Clinically Oriented Embryology 6th ed. Philadelphia, Pa: Saunders, 1998; 495.)

important to realize that in the region of the cup that overlaps the lens, the inner layer is not differentiated into neural elements. This anterior one-fifth of the inner layer persists as a layer of columnar epithelium, which, together with the corresponding part of the pigmented epithelium of the outer layer, extend forward onto the posterior surface of the developing ciliary body and iris to form the double epithelium of the ciliary body and iris.[1, 2] The posterior four-fifths of the inner layer of the optic cup undergoes cellular proliferation, forming an outer nuclear zone and an inner marginal zone devoid of nuclei (Fig. 8-3). Later, at the 12 mm stage, the cells of the nuclear zone invade the marginal zone, so that at the 17 mm stage, the neural part of the retina consists of an inner and an outer neuroblastic

Copyright © 2003, Mosby, Inc. All rights reserved.

layer.[2] The inner neuroblastic layer of the retina forms the ganglion cells, the amacrine cells, and the somata of the sustentacular fibers of Müller.[1, 2, 8, 9] The outer neuroblastic layer of the retina gives rise to the horizontal cells, the nuclei of the bipolar rod and cone nerve cells, and probably the rod and cone cells as well (Fig. 8-6).[1, 2]

By the eighth month of fetal life, all the layers of the retina can be recognized[1, 2] (Fig. 8-7). Thus, the inner layer of the optic cup may be divided into a small nonneural portion near the edge of the cup and a large photosensitive portion, the two being separated by a wavy line, the ora serrata. It is interesting to remember that the cavity of the optic vesicle is continuous through the optic stalk (optic canal) with the cavity of the diencephalon (i.e., the part that forms the third ventricle) (Figs. 8-1 and 8-2). Early in development, the outermost layer of cells of the nuclear zone have cilia, which are continuous with the ciliated ependymal cells of the third ventricle.[2] Later, during the seventh week of development, the cilia of the cells of the nuclear zone disappear and are believed to be replaced by the outer segments of the rods and cones during the fourth month of gestation.[2]

Optic Nerves, Macular Area, and Fovea Centralis

The deepest part of the optic (embryonic) fissure is at the center of the floor of the optic cup[1] (Figs. 8-1 and 8-2). In this region, which later is the site of the optic disc, the inner (neural) cell layer of the cup is continuous with the corresponding invaginated cell layer of the optic stalk (Fig. 8-3). As a result, the developing nerve fibers of the ganglion cells can pass directly into the wall of the stalk to become the optic nerve.[1] At the 7.5 mm embryonic stage, the area in the optic cup where the optic nerve head will develop can be identified.[5] It is referred to as the primitive epithelial papilla and is located at the superior end of the embryonic fissure.[10] Once the axons pass through the primitive epithelial papilla, it is referred to as the optic nerve head.[5, 10, 11]

The macular area first develops as a localized increase of superimposed nuclei in the ganglion cell layer, lateral to the optic disc, just after midterm. During the seventh month there is a peripheral displacement of the ganglion cells, leaving a central shallow depression, the fovea centralis. The foveal cones decrease in width in their inner segments, but

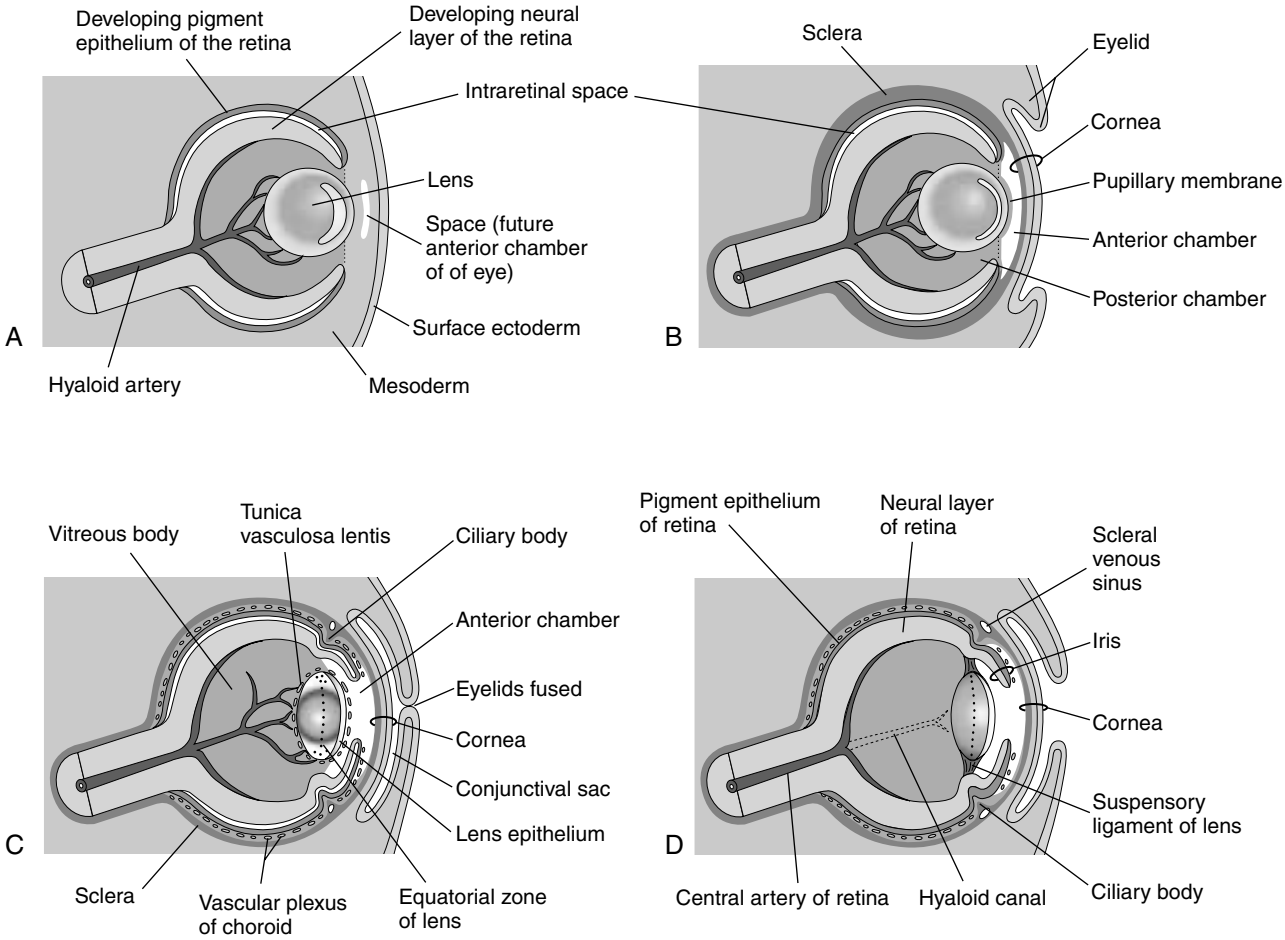

FIGURE 8-5 Drawings of sagittal sections of the eye showing successive developmental stages of the lens, retina, iris, and cornea. **A**, 5 weeks; **B**, 6 weeks; **C**, 20 weeks; **D**, newborn. Note that the layers of the optic cup fuse to form the retinal pigment epithelium and neural retina and extend anteriorly as the double epithelium of the ciliary body and its iris. The retina and optic nerve are formed from the optic cup and stalk (outgrowths of the brain). At birth the eye is about three quarters of its adult size. Most successive growth occurs during the first year of life. (From Moore KL, Persaud TVN. The Developing Human: Clinically Oriented Embryology 6th ed. Philadelphia, Pa: Saunders, 1998; 498.)

VIEW IMAGE

Copyright © 2003, Mosby, Inc. All rights reserved.

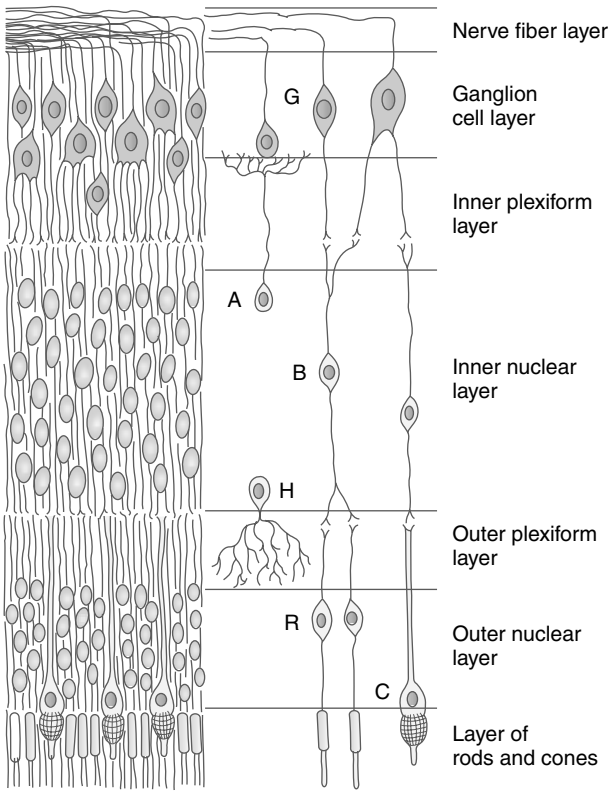

VIEW IMAGE

FIGURE 8-6 Drawing of the tissue and cellular organization of the neural retina of the human fetus. **A**, Amacrine cell; **B**, bipolar cell; **C**, cone, **G**, ganglion cell; **H**, horizontal cell. **R**, Rod. (From Carlson BM. Human Embryology and Developmental Biology, 2nd ed. St. Louis, Mo: Mosby, 1994; 271.)

their outer segments are elongated. This permits an increase in foveal cone density.[2] At birth, the ganglion cells have been reduced to a single layer in the fovea, and by 4 months of age, the cone nuclei in the center of the fovea have no ganglion cells covering them. The reason for the newborn's imperfect central fixation is that the cones do not fully develop until several months after birth.[2]

The ganglion cells of the retina develop axons that converge to a point where the optic stalk leaves the posterior surface of the optic cup (Fig. 8-3). This site will later become the optic disc.[1–3, 9] The axons now pass among the cells that form the inner layer of the stalk. Gradually, the inner layer encroaches on the cavity of the stalk until the inner and outer layers fuse. The cells of the optic stalk form neuroglia-supporting cells to the axons, and the cavity of the stalk disappears. The stalk, together with the optic axons, forms the optic nerve. The surrounding mesenchyme condenses and later differentiates into the meninges, which form a sheath for the optic nerve. The axons of the optic nerve begin to develop their myelin sheaths just before birth, but the process of myelination continues for some time after birth.[1–3] After the eyes have been exposed to light for about 10 weeks, myelination is complete. The hyaloid artery and vein become the central artery and vein of the retina, running for a distance within and along the optic nerve.[1, 2]

Lens

As described, the rudimentary lens is first seen as a thickening of the surface ectoderm, the lens placodes, at 22 days of gestation; it overlies the optic vesicle (Figs. 8-1 and 8-2). The lens placode invaginates and sinks below the surface ectoderm to form the lens vesicle, which is overlapped by the margin of the optic cup and becomes separated from the overlying ectoderm by mesenchyme.[1, 2] The cells forming the posterior wall of the lens vesicle rapidly elongate and form transparent lens fibers known as the primary lens fibers (Fig. 8-3). At the cellular level, the relatively unspecialized lens epithelial cells undergo a

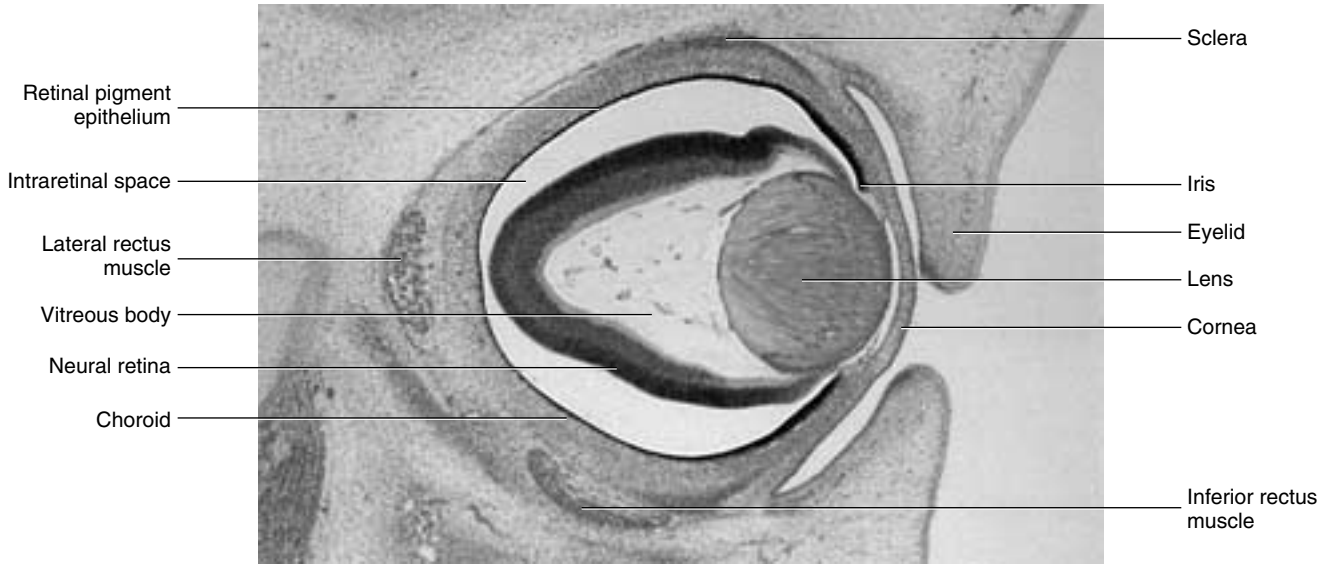

VIEW IMAGE

FIGURE 8-7 Sagittal section of the eye of an embryo at about 56 days of gestation. Note the developing neural retina and the retinal pigment epithelium. The intraretinal space normally disappears as these two layers of the retina fuse. (From Moore KL, Persaud TVN, Shiotak: Color Atlas of Clinical Embryology. Philadelphia, WB Saunders, 1994.)

Copyright © 2003, Mosby, Inc. All rights reserved.

profound transformation into transparent, elongated cells that contain large quantities of crystallin proteins, the primarily proteins being α, β, and γ.[12] With the increase in length of these cells, the cavity of the lens vesicle gradually becomes obliterated.[2] The primary lens fibers become attached to the apical surface of the anterior lens epithelium.[2] All additional lens fibers are formed by the division of the anterior epithelial cells at the equatorial zone or rim of the lens (Figs. 8-8 and 8-9). These are known as the secondary lens fibers, and new secondary lens fibers are formed throughout life.

By the second month of gestation, the lens is invested by a vascular mesenchymal condensation termed the *vascular capsule of the lens*, the ventral part of which, covering the lens, is named the pupillary membrane. The blood vessels supplying the dorsal part of this capsule are derived from the hyaloid artery, and those for the ventral part are derived from the anterior ciliary arteries.[1, 2] By the sixth month, all the vessels of the capsule are atrophied except the hyaloid artery, which becomes occluded during the eighth month of gestation.[1, 2] With the loss of its blood vessels the vascular capsule of the lens disappears (Fig. 8-4, 8-5), but sometimes the pupillary membrane persists at birth, giving rise to the condition termed *congenital atresia of the pupil*.[1, 2] In the fetus the lens grows rapidly because it is supplied by the hyaloid artery, which forms a plexus on the posterior surface of the lens capsule. By the time the infant is born, the anteroposterior diameter of the lens is nearly that of an adult. Its equatorial diameter is about two-thirds of that reached in the adult.[2]

The lens capsule is formed from the mesenchyme that surrounds the lens. As mentioned, in the earliest stages of development, it receives an abundant arterial supply from the hyaloid artery as the tunica vasculosa lentis. Later, this blood supply regresses, and it disappears before birth. In the 40 mm human embryo, the layers of the retina, developing lens, pupillary membrane, cornea, conjunctival sac, anterior and posterior aqueous chambers, the developing vitreous body, the condensing circumoptic mesenchyme, and the fused eyelids are recognized (Fig. 8-7).[1]

Throughout most of its life, the lens is under the influence of the retina. Thus, following induction of the lens, chemical secretions from the retina accumulate in the vitreous humor behind the lens and appear to stimulate the formation of lens fibers.[12]

The Ciliary Body and Suspensory Ligaments of the Lens

The mesenchyme, situated at the edge of the optic cup, differentiates into the connective tissue of the ciliary body,

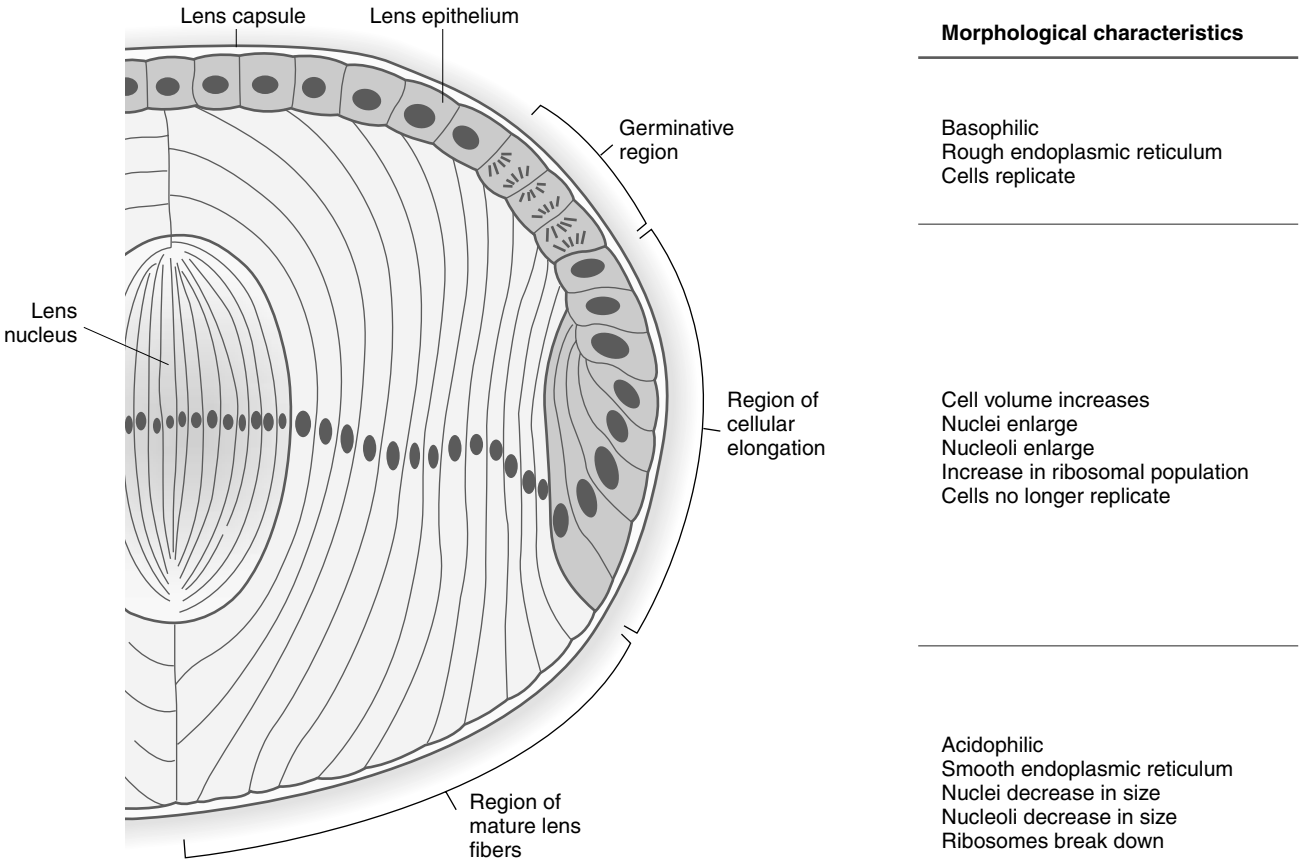

FIGURE 8-8 Drawing of the organization of the vertebrate lens. As the lens grows, epithelial cells from the germinative region stop dividing, elongate, and differentiate into lens cells that produce lens crystallin proteins. (Papaconstantinou J. Molecular aspects of lens cell differentiation. Science 156:338–346, 1967.)

VIEW IMAGE

Copyright © 2003, Mosby, Inc. All rights reserved.

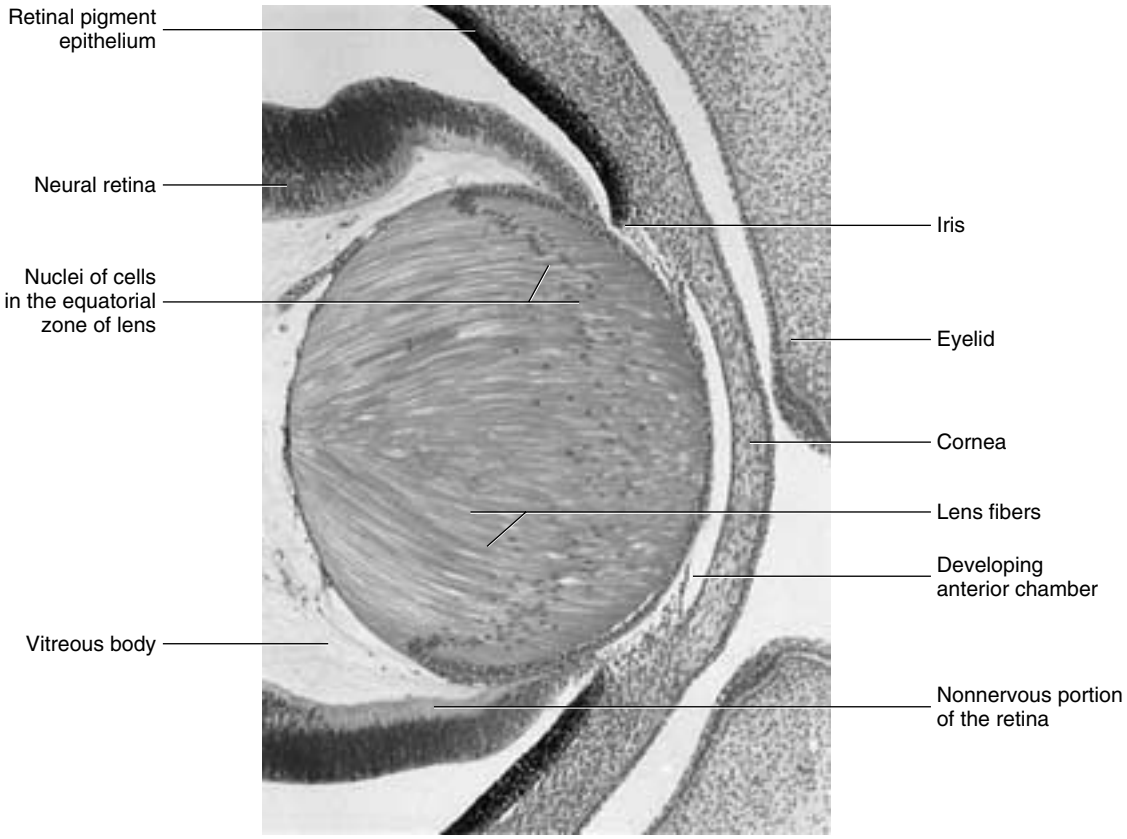

VIEW IMAGE

FIGURE 8-9 Higher magnification of a portion of the developing eye seen in Figure 8-7. Note that the lens fibers have elongated and obliterated the cavity of the lens vesicle. The inner layer of the optic cup has thickened to form the neural retina, and the outer layer is heavily pigmented (retinal pigment epithelium). (From Moore KL, Persaud TVN, Shiotak: Color Atlas of Clinical Embryology. Philadelphia, WB Saunders, 1994.)

the smooth muscle fibers of the ciliary muscle, and the suspensory ligaments of the lens. The two layers of neuroectoderm (the outer pigment layer and the anterior one-fifth of the inner layer) forming the edge of the optic cup grow onto the posterior surface of the ciliary muscle, forming the two epithelial layers covering the ciliary body.[2] The fibers of the ciliary muscles are derived from the mesoderm, but those of the sphincter and dilator pupillae are of ectodermal origin, being developed from the cells of the pupillary part of the optic cup (Fig. 8-10).[1, 2]

The Iris and the Aqueous Chamber

The mesenchyme, situated on the anterior surface of the lens, condenses to form the pupillary membrane. The two layers of neuroectoderm (the pigment layer of the retina and the neural layer of the retina) forming the growing edge of the optic cup, having covered the ciliary muscle, now extend onto the posterior surface of the pupillary membrane. These structures fuse to become the iris.[2] The sphincter and dilator muscles of the pupil are derived from the pigment cells of the neuroectoderm. The mesenchyme forms the connective tissue and blood vessels of the iris. Pigment cells derived from the neuroectoderm penetrate the sphincter muscle and enter the connective tissue. The opening in the central part of the iris becomes the pupil. The pupillary membrane begins to separate from the iris, and at about the eighth month of gestation, the pupillary membrane starts to degenerate and eventually disappears.[2]

The anterior (aqueous) chamber of the eye appears as a cleft in the mesenchyme between the surface ectoderm and the developing iris.[1, 2] The posterior chamber develops as a slit in the mesenchyme posterior to the developing iris and anterior to the developing lens (Fig. 8-5). The mesenchyme superficial to the cleft forms the substantia propria of the cornea. The mesenchyme deep to the cleft forms the mesenchymal stroma of the iris and the pupillary membrane (Fig. 8-10).[1] When the pupillary membrane disappears, the anterior and posterior chambers of the eye communicate with each other through a circumferential scleral venous sinus (sinus venosus sclerae, canal of Schlemm).[1] This sinus (canal) is the outflow site of aqueous humor from the anterior chamber of the eye to the venous system. Temporally, the anterior and posterior chambers communicate when the pupillary membrane disappears and the pupil is formed.[1]

The Vitreous

The vitreous body develops between the developing lens and the optic cup. The primitive or primary vitreous body consists of a network of delicate cytoplasmic processes that

Copyright © 2003, Mosby, Inc. All rights reserved.

are derived partly from the ectodermal cells of the developing lens and partly from the neuroectoderm of the retinal layer of the optic cup. The mesenchyme that enters the cup through the choroidal (embryonic or optic) fissure and around the equator of the lens becomes intimately united with this reticular tissue and also contributes to the formation of the vitreous body, which is therefore derived partly from the ectoderm and partly from the mesoderm.[1, 2] It contains many vascular elements, including the vasa hyaloidea propria, which join the primitive vitreous. At this stage, the primitive vitreous is supplied by the hyaloid artery and its branches. The definitive or secondary vitreous arises between the primitive vitreous and the retina. It is at first a homogeneous gel, which rapidly increases in volume and pushes the primitive vitreous anteriorly behind the iris. Hyalocytes, derived from the mesenchyme around the hyaloid vessels, now migrate into the secondary vitreous. Later the hyaloid vessels atrophy and disappear, leaving the acellular hyaloid canal.[2] The hyaloid artery becomes occluded during the eighth month of intrauterine life.[2] Prior to this, during the fourth month, the hyaloid artery gives off retinal branches, and its proximal part persists in the adult as the central artery of the retina.[2] The hyaloid canal, which carries the artery through the vitreous during development of the primitive (primary) vitreous, persists after the vessel has become occluded.[1, 13–15]

The Choroid

Outside the optic cup, there is a layer of mesenchymal cells that are primarily of neural crest origin. As a result of induction from the pigmented epithelium of the retina, these mesenchymal cells differentiate into structures that provide the vascular and mechanical support of the eye.[12] The innermost cells of this mesenchymal layer become the highly vascular choroid, and the anterior part of the choroid is eventually modified to form the ciliary body and ciliary processes.

The Sclera

The sclera is also derived from the mesenchyme surrounding the optic cup, outside the choroid. This mesenchyme forms a densely collagenous covering, the sclera, which is continuous with the cornea. It first forms near the future insertion of the rectus muscle.[1]

The Cornea

The formation of the cornea is the last in the series of inductive events in the formation of the eye. Corneal development is induced by the lens and the optic cup.[1] The corneal epithelium is formed from the surface ectoderm and the mesothelium of the anterior chamber from the mesenchyme[2] (Figs. 8-5, 8-9). The substantia propria and the endothelium covering the posterior surface of the cornea are formed from mesenchyme.[1] Bowman's membrane, which lies immediately beneath the basal lamina of the corneal epithelium, is formed from mesenchyme.[1] Descemet's membrane, which is the basement membrane of the endothelial cells, is synthesized by the endothelial cells

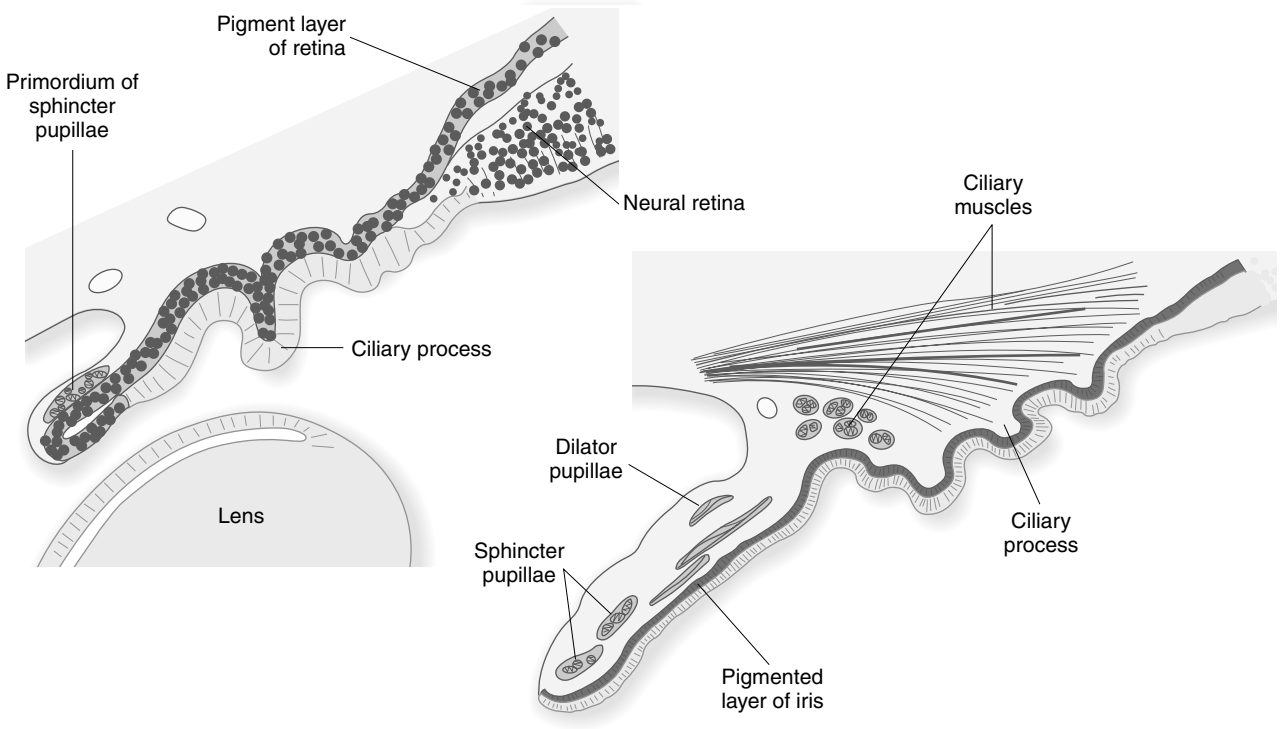

FIGURE 8-10 Drawing of two stages (earlier on the left) in the development of the iris and ciliary body, including the sphincter and dilator pupillae muscles. (From Carlson BM. Human Embryology and Developmental Biology, 2nd ed. St. Louis, Mo: Mosby, 1994; 274.)

VIEW IMAGE

Copyright © 2003, Mosby, Inc. All rights reserved.

formed from mesenchyme.[1] Listed from outside to inside, the layers that form the mature cornea are the outer epithelium, Bowman's membrane, the secondary stroma, Descemet's membrane, and the corneal endothelium.

Vascular System

The development of the vascular system of the eye is a complex process that involves the appearance of vessels to meet the nutritional needs of the developing eye and subsequent regression of those same vessels.[3] In the early embryo, the internal carotid artery supplies a fine capillary plexus to the dorsal aspect of the optic cup (dorsal ophthalmic artery). Soon afterward, a second branch of the internal carotid artery is given off to supply the medial aspect of the optic cup.[3] This branch is called the ventral ophthalmic artery and is anastomosed with the dorsal ophthalmic artery.[3] The hyaloid artery is a branch of the dorsal ophthalmic artery that passes through the embryonic fissure into the optic cup. Simultaneously, the orbital tissues are supplied by the stapedial artery, a branch of the internal carotid artery.[3] The hyaloid artery extends toward and around the lens vesicle and projects a vascular meshwork across the lens to form the tunica vasculosa lentis.[3] During the sixth week of gestation, the primitive dorsal ophthalmic artery is transformed into the definitive ophthalmic artery, and the ventral ophthalmic artery regresses and transforms into the posterior nasal ciliary artery.[3] The ophthalmic artery's branches become the central retinal artery, the temporal long posterior ciliary artery, and the short posterior ciliary artery.[3] In the third trimester, the hyaloid system begins to regress and the tunica vasculosa lentis becomes thin and atrophic, and eventually disappears.[3–5] Remnants of this system may sometimes be seen in the adult as a persistent pupillary membrane.[6] The hyaloid artery is no longer patent and loses its connection to the disc in the eighth month of intrauterine life (Figs. 8-4 and 8-5). Occasionally, a connective bud may remain attached to the disc as Bergmeister's papilla.[3]

IMAGING TECHNIQUES

Computed tomography (CT) provided a major imaging advance over conventional radiography and multidirectional tomography in examining the eye. However, the development of magnetic resonance (MR) imaging has proven to be an even greater breakthrough in diagnostic medical imaging and biomedical research.[16–20] This section discusses CT and MR imaging of the normal globe and the features of ocular pathology, with particular emphasis on the potential of MR imaging in the practice of ophthalmology.

MR Imaging

The success of MR imaging depends on the cooperation of the patient and, in the case of infants and children, appropriate sedation. The procedure should be carefully explained to the patient and the family or accompanying persons, especially to the person who will stay in the MR scanner room with the patient. For sedation, oral chloral hydrate (75 to 100 mg/kg body weight) usually affords satisfactory sedation in children up to 2 to 4 years of age. When this proves inadequate, intramuscular diphenhydramine (Benadryl, a one-time dose of 1 mg/kg) or midazolam (Versed, 0.05 to 0.08 mg/kg) for children 5 to 8 years of age can be added.[7] Other children may need intravenous medication or general anesthesia, and there may be variations among institutions regarding the doses and medications used. Because of the importance of monitoring sedated patients, sedation procedures should be performed by a trained, dedicated MR imaging nurse. The patient should be monitored during MR imaging using pulse oximetry, allowing evaluation of the arterial oxygen saturation. When general anesthesia is required, anesthesiologists use MR-compatible monitoring and ventilation equipment.

The majority of MR imaging studies described in this section were performed on a 1.5-T Signa unit (General Electric, Milwaukee) with 3 or 5 mm thick sections, with no gap or a 0, 0.6 to 1.5 mm interslice gap. A complete MR evaluation of the eye should consist of high-resolution axial, coronal, and sagittal images of the eye and surrounding structures. The globe can be successfully evaluated with the standard head coil. The field of view, however, should be maintained between 12 and 16 cm and in plane resolution of 256×192, 256×256, or 512×256. Orbital surface coils are used to improve the spatial resolution of MR images.[21] If they are available, they should be used primarily for lesions limited to the globe and for smaller lesions that may not be detected by a head coil. For intraocular lesions that have invaded the optic nerve and retrobulbar space, a head coil is preferred. The use of contrast-enhanced MR imaging of the orbit and brain, using a head coil, is recommended for the evaluation of children with suspected retinoblastoma and, in particular, for patients with possible subarachnoid seeding of retinoblastoma and those with bilateral disease. This technique allows early detection of optic nerve involvement, orbital spread, or asymptomatic pineoblastoma and suprasellar tumors.[21] Although the examination should always be tailored to the problems of the individual patient, in general for ocular lesions the routine MR imaging examination consists of both T1- and T2-weighted images and precontrast and postcontrast T1-weighted images with and without fat suppression. The suggested head coil or surface coil protocol for ocular MR imaging is as follows:

Axial View
- TR 2000–3000 ms, TE 30/80–120 ms
- 256×192, 3 mm slice thickness, 0.5 mm skip
- Field of view (FOV) 16×16 cm, 2 number of excitation (NEX), no phase wrap (NP)
- This may be replaced by a fast spin echo, single echo, T2-weighted, fat suppression acquisition technique

Precontrast Axial View
- TR 500 ms, TE 20 ms
- 256×192, 3 mm slice thickness, 0.5 mm skip
- FOV 14–16, 2 or 3 NEX, NP

Postcontrast Axial and Coronal Views
- TR 500 ms, TE 20 ms
- 256×192, 2 or 3 mm slice thickness, 0.5 mm skip
- FOV 14–16, 3 NEX, NP

Copyright © 2003, Mosby, Inc. All rights reserved.

Postcontrast Fat Suppression Axial View
TR 500 ms, TE 20 ms
256 × 192, 3 mm slice thickness, 0.5 mm skip
FOV 14–16, 3 NEX, NP

An additional postcontrast, fat suppression, T1-weighted sagittal view may be obtained according to the findings in the axial or coronal sections.

Postcontrast Axial View of the Orbit and Head Using a Head Coil
TR 500 ms, TE 20 ms
256 × 192, 5-mm slice thickness, 1.5-mm skip
FOV 22–24 cm, 1 NEX

Because motion artifact is more pronounced on images obtained with a surface coil due to the inherent sensitivity of the coil, a lesion is sometimes seen better on images obtained with a head coil.[21] With the surface coil, a 3 mm section thickness is used to reduce the problem of partial volume averaging. The thin section has the disadvantage of generating less signal (a small volume), and this may result in a decreased amount of T2-weighted information in later echoes, particularly in rapidly decaying T2-weighted signals. For these reasons, at times a uveal melanoma may be better seen on T2-weighted images obtained with a head coil rather than with a surface coil. This is extremely important because the hypointensity of melanotic tissues in T2-weighted images is an important diagnostic feature of these lesions.[19, 21] Despite the difficulties encountered with inhomogeneity in the face and orbit, fat suppression MR techniques are most often utilized. Fat suppression pulse sequences are important for the detection of intraocular (small) lesions and for the evaluation of extraocular extension of eye tumors and inflammation. Fat suppression is also useful in the T2-weighted acquisitions of the optic nerve and optic pathway.

CT Technique

The CT protocol for intraocular lesions includes 1.5 to 3 mm axial sections of the globe. For all foreign bodies and lesions at 6 o'clock and 12 o'clock, additional direct 3 to 5 mm coronal sections are obtained. Additional 1.5, 3, or 5 mm axial sections (depending on the size of the lesion) of the orbit are obtained following administration of iodinated contrast material (meglumine diatrizoate, 1 ml per pound of body weight). In cases of suspected retinoblastoma and uveal melanoma, additional 5 to 10 mm axial sections of the head are obtained to investigate the possibility of an intracranial abnormality. The major application of CT for ocular lesions is the detection of foreign bodies and intraocular calcification. For intraocular tumors and other intraocular pathology, MR imaging is the preferred initial study.

MR Imaging and Evaluation of Intraocular Foreign Bodies

Despite the many advantages of MR imaging, it may not be indicated as a primary modality in the evaluation of the traumatized eyes harboring a possible intraocular foreign body. This cautionary advice is based on the possibility of additional damage to the injured eye by ferromagnetic foreign bodies that are induced to move during the imaging process. A study conducted in vitro and in vivo (rabbit) experiments to examine the effects of MR imaging (1.5 Tesla Units) on intraocular foreign bodies showed that diamagnetic and paramagnetic foreign bodies were imaged without artifacts and without movement during the imaging process, and ferromagnetic foreign bodies produced large amounts of artifact that prevented meaningful images.[22] All ferromagnetic foreign bodies moved during in vitro imaging. During in vivo imaging, three of four ferromagnetic foreign bodies moved, producing substantial retinal injury. It was concluded that MR imaging is contraindicated in the patient with a traumatized eye and a suspected ferromagnetic foreign body. For those patients with a remote history of a traumatic foreign body, or in metal workers or other high-risk individuals, high-resolution 1.5 mm or thinner CT scans of the orbits and 5 to 10 mm thick CT scans of the head are recommended to rule out the possibility of foreign bodies. Patients with stapedectomy (metallic) or other metallic prostheses that have proved to be safe for 1.5T MR unit should be carefully screened for MR study using a 3T or higher field. Not enough data are available to demonstrate that these devices may not move at field strengths higher than 1.5T.

MR Imaging Artifacts

Motion artifacts may result in marked degradation of MR images. It is important to tell patients to close their eyes during the examination. Artifacts may occur as a result of tattooing of eyelids with iron oxide and even from the external application of eye cosmetics (Fig. 8-11). The artifacts arising from tattooing or related to eye cosmetics usually appear as distortion of the skin contours in the location of the iron oxide. There also may be distortion of the shape of the globe and multiple artifacts consisting of hyperintense areas around the contour of the eyelids.

NORMAL OCULAR ANATOMY

Ocular Structures

The eyeball (eye or globe) is made up of the segments of two spheres of different sizes placed one in front of the other. The anterior, smaller segment is transparent (cornea) and forms about one-sixth of the eyeball. The posterior, larger segment is opaque (sclera) and forms about five-sixths of the eyeball.[23] The anterior pole of the eyeball is the center of curvature of the transparent segment, or cornea. The posterior pole is the center of the posterior curvature of the eyeball, and it is located slightly temporal to the optic nerve. The geometric or optic axis is a line connecting the two poles. The equator lies midway between the two poles. Because the fovea centralis is temporal and slightly inferior to the posterior pole, the visual axis and the optic axis do not coincide.[24]

The eye consists of three primary layers (Fig. 8-11): (1) the sclera, or outer layer, which is composed primarily of

Copyright © 2003, Mosby, Inc. All rights reserved.

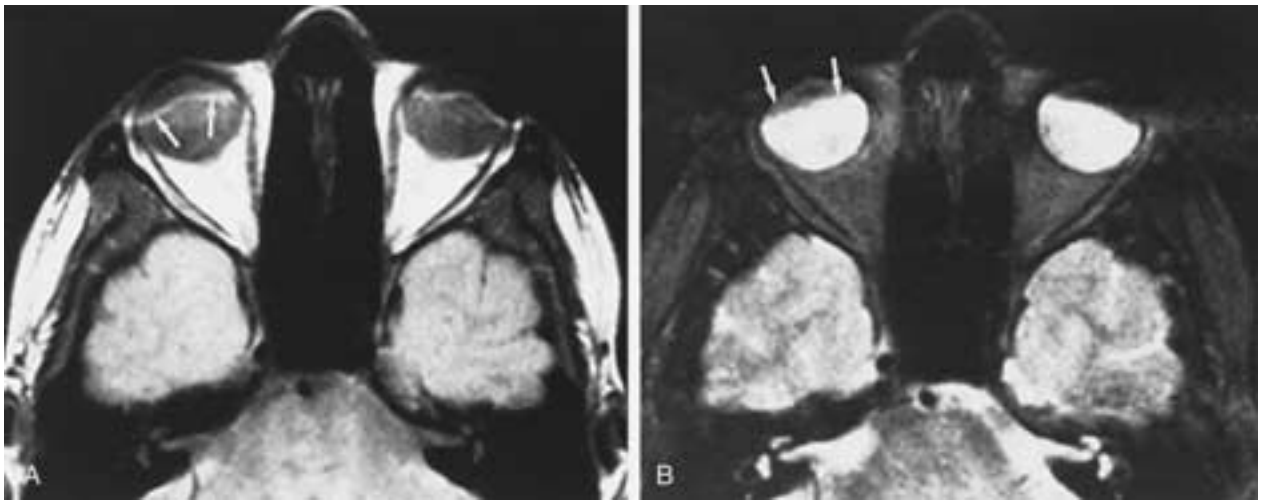

FIGURE 8-11 Axial PW (**A**) and T2-weighted (**B**) MR images show makeup artifacts (*arrows*).

VIEW IMAGE

collagen-elastic tissue; (2) the uvea, or middle layer, which is richly vascular and contains pigmented tissue consisting of three components: the choroid, ciliary body, and iris; and (3) the retina, or inner layer, which is the neural, sensory stratum of the eye.

Tenon's Capsule

The fascial sheath of the eyeball, also called the fascia bulbi or Tenon's capsule, is a thin membrane that envelops the eyeball and separates it from the central orbital fat. It thus forms a socket for the eyeball.[23] Tenon's capsule blends with the sclera just behind the corneoscleral junction and fuses with the bulbar conjunctiva. Tenon's capsule is perforated behind by the optic nerve and its sheath, the ciliary nerves and vessels. The capsule fuses with and extends to the sheath of the optic nerve and the sclera around the entrance of the optic nerve.[25] Septa of fibrous tissue are attached to the outer surface of Tenon's capsule, and near the equator it is perforated by the vortex (vorticose) veins (draining veins of the choroid and sclera).[25] The inner surface of Tenon's capsule is smooth and shiny and is separated from the outer surface of the sclera by the episcleral (Tenon's) space.[25] This is a potential space that is traversed by fibers of loose connective (areolar) tissue, which extend between the fascia and the sclera.[26] The episcleral space starts anteriorly, at the bulbar conjunctiva near the sclerocorneal junction, and extends to the optic nerve, where it firmly attaches to the nerve and then is continuous with the subdural and subarachnoid spaces about the nerve.[26] The tendons of all extrinsic ocular muscles pierce the capsule to reach the sclera. At the site of perforation, the fascial sheath is reflected back along the tendons of these muscles to form on each a tubular sleeve.[23] The connection between the muscle fibers and the sheath is especially strong at the point where the two fuse.[25, 26] For this reason, the muscles retain their attachment to the capsule and do not retract extensively after enucleation (tenotomy).[25, 26] The superior oblique muscle sleeve extends as far as the trochlea. The inferior oblique muscle sleeve extends to the origin of the muscle on the floor of the orbit.[23] The tubular sleeves for the four recti muscles have important expansions. Those for the medial and lateral recti are strong and are attached to the lacrimal and zygomatic bones. Because these expansions may limit the actions of these muscles on the eyeball, they are called medial and lateral check ligaments.[23] Thinner and less distinct expansions extend from the superior rectus tendon to that of the levator palpebrae superior, and from the inferior rectus to the inferior tarsal plate. The inferior part of the fascial sheath of the eyeball is thickened and is continuous medially and laterally with the medial and lateral check ligaments.[23] This hammock-like arrangement of the fascial sheath constitutes what is known as the suspensory ligament of Lockwood.[23] This thickened area receives contributions from the fascia of the inferior rectus and inferior oblique muscles as they cross each other below the eyeball. The close relationship between the suspensory ligament of Lockwood and the tendons of the inferior oblique and inferior rectus muscles makes operations on these muscles very difficult and the results unpredictable.[23] The suspensory ligament is strong enough to provide the eyeball with adequate support in case of maxillectomy. Inflammatory and intraocular neoplastic processes are the most common lesions to involve Tenon's space. In posterior scleritis, episcleritis, Tenon's fasciitis, and pseudotumor, an inflammatory effusion produces a characteristic circular or semicircular distention of Tenon's capsule (Fig. 8-12). Retinoblastomas (Fig. 8-13) and melanomas (Fig. 8-14) also may invade Tenon's space.[21]

Sclera

The sclera is the globe's outer white leathery coat. It extends from the limbus at the margin of the cornea to the optic nerve, where it becomes continuous with the dural sheath.[27] The external side of the sclera lies against Tenon's capsule. The internal surface of the sclera blends with the suprachoroidal tissues.[27] Posteriorly the sclera is perforated by the vortex veins, the long posterior ciliary arteries and nerves, and the short posterior ciliary arteries and nerves.

Copyright © 2003, Mosby, Inc. All rights reserved.

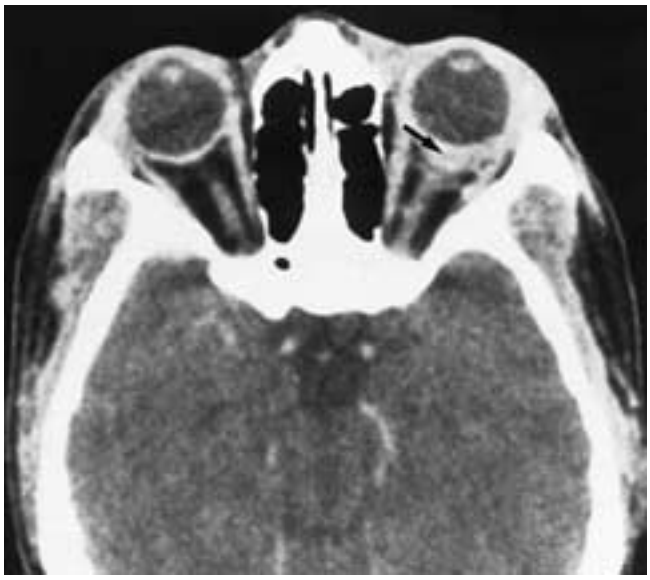

VIEW IMAGE

FIGURE 8-12 Pseudotumor. Axial CT scan shows fluid (*arrow*) and inflammatory infiltration in Tenon's space.

The sclera is composed predominantly of extracellular bundles of collagen. The sclera forms the posterior five-sixths of the eyeball and is opaque. In the adult the sclera is 1 mm thick posteriorly, thinning at the equator to 0.6 mm. It is thinnest, 0.3 mm, immediately posterior to the

VIEW IMAGE

FIGURE 8-13 Axial CT scan shows retinoblastoma with extension into Tenon's capsule. A mass with focal calcification (*arrows*) fills the entire left globe and extends into Tenon's space (*curved arrow*). (From Mafee MF et al. Malignant uveal melonoma and similar lesions studied by CT. Radiology 1985;156:403–408.)

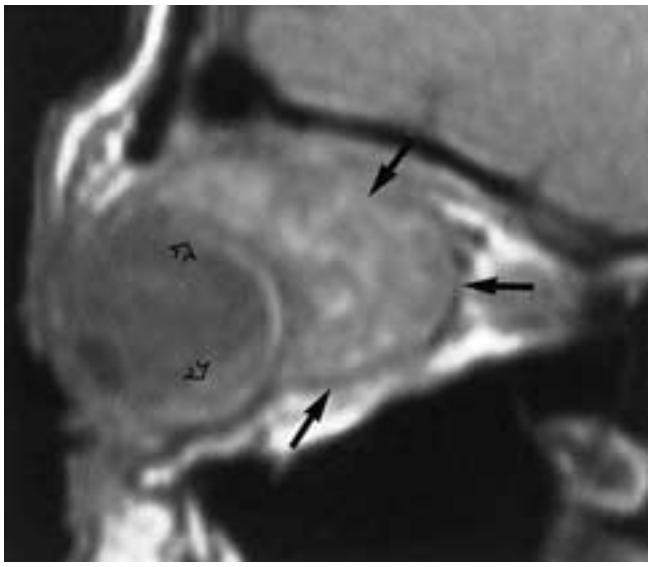

FIGURE 8-14 Uveal melanoma with extension into Tenon's capsule. Sagittal PW MR image shows a large, well-capsulated retrobulbar mass (*arrows*) in this patient with uveal melanoma (not seen in this section). Note the subretinal fluid (*open arrows*). Surgery confirmed the intraocular tumor and massive extension into Tenon's capsule.

VIEW IMAGE

tendinous insertions of the recti muscles.[23] At the corneoscleral junction the sclera is 0.8 mm thick. The medial rectus muscle inserts 5.5 mm posterior to the limbus; the inferior rectus 6.5 mm; the lateral rectus 6.9 mm; and the superior rectus 7.7 mm.[23] The insertions of the superior oblique and inferior oblique muscles are posterior to the scleral equator. The sclera is perforated posteriorly about 3 mm medial and 1 mm above the posterior pole by the optic nerve. The site of this perforation is referred to as the posterior scleral foramen.[23] Here the sclera is fused with the dural and arachnoid sheaths of the optic nerve. The lamina cribrosa is where the optic nerve fibers pierce the sclera. One of the openings in the lamina is larger than the rest and transmits the central retinal artery and vein. Since the lamina cribrosa is relatively a weak point, it can be made to bulge outward by a rise in intraocular pressure, producing a cupped disc. The sclera is pierced anteriorly at the insertion of the recti muscles by the branches of anterior ciliary arteries. Each rectus muscle has two anterior ciliary arteries, with the exception of the lateral rectus muscle, which only has one.[23]

The sclera is pierced about 4 mm posterior to the equator of the eye by the vortex veins (four or five). The posterior scleral apertures are numerous and are located around the optic nerve. They transmit the long and short ciliary nerves and vessels.[23] Anteriorly, the sclera is continuous with the cornea. Just posterior to the corneoscleral junction, and lying within the sclera, is a circularly running canal called the sinus venous sclerae or the canal of Schlemm. The sclera may be divided, for purpose of description, into three layers: (1) the episclera, (2) the scleral stroma, and (3) the lamina fusca.[23] The episclera is the outermost layer and consists of loose connective tissue. It is connected to Tenon's capsule by fine strands of tissue. Anteriorly, the episclera has a rich blood supply from the anterior ciliary arteries, which form a plexus that extends between the extrinsic muscle insertions and the corneoscleral junction. These vessels lie deep to the

Copyright © 2003, Mosby, Inc. All rights reserved.

conjunctiva and normally are nonconspicuous. However, in the presence of inflammatory disease they become very red and congested. The scleral stroma consists of dense fibrous tissue intermingled with fine elastic fibers. The lamina fusca is the innermost layer of the sclera. It is separated from the external surface of the choroid by a potential space, the suprachoroidal (perichoroidal) space. Connecting the lamina fusca with the choroid are fine collagen fibers that provide a weak attachment between the sclera and the choroid.[23]

Blood Supply and Nerve Supply of the Sclera

The sclera is a relatively avascular structure. However, anterior to the insertions of the recti muscles, the branches of the anterior ciliary arteries form a dense episcleral plexus. This plexus exists beneath the conjunctiva and is normally inconspicuous; however, in the presence of inflammation involving the cornea, iris, and ciliary body, marked vasodilatation may occur. This pronounced vasodilatation is known as a ciliary flush.[23] This rich blood supply to the anterior episclera results in rapid healing of surgical incisions.[23] The posterior sclera receives small branches from the long and short posterior ciliary arteries. The sclera is innervated by the ciliary nerves that arise from branches of the trigeminal nerve.

Cornea

Microscopically, the cornea consists of five layers. From front to back, they are (1) the corneal epithelium, (2) Bowman's layer (membrane), (3) the substantia propria, (4) Descemet's membrane, and (5) the corneal endothelium. Bowman's layer is acellular and consists of interwoven collagen fibers embedded in intercellular substances. It ends abruptly at the limbus. The substantia propria forms 90% of the corneal thickness. It is transparent and consists of many lamellae of collagen fibers that run parallel to the surface.[23] Descemet's membrane is the basement membrane of the endothelium. It is thicker than the endothelium. The corneal epithelium is stratified and consists of five layers of cells. The corneal endothelium consists of a single layer of flattened cells.[23]

Blood Supply and Nerve Supply of the Cornea

The cornea is avascular and devoid of lymphatic drainage. It is nourished by diffusion from the aqueous humor and from the capillaries of the sclera and conjunctiva that end at its edge. The cornea is innervated by the ophthalmic division of the trigeminal nerve, mainly through the long ciliary nerves.[23]

Uvea (Choroid, Ciliary Body, and Iris)

The uveal tract lies between the sclera and the retina (Fig. 8-15). The choroid is the section of the uveal tract that lies between the sclera and the retinal pigment epithelium, the outer layer of the retina (Fig. 8-15). It forms a membrane of predominantly vascular tissue extending from the optic nerve to the ora serrata (Fig. 8-15), beyond which it continues as the ciliary body.[23, 27] Its thickness varies from approximately 0.22 mm at the posterior pole to 0.10 mm near the ora, at the optic nerve, where it forms part of the optic nerve canal, and at the point of internal penetration of the vortex veins. Its inner surface is smooth and firmly attached to the retinal pigment epithelium; its outer surface is roughened. It is firmly attached to the sclera in the region of the optic nerve and where the posterior ciliary arteries and ciliary nerve enter the eye. It is also tethered to the sclera where the vortex veins leave the eyeball.[23] This accounts for the characteristic shape of choroidal detachment, which shows valleys at the site of the vortex veins.[28] The choroid can be divided into four layers, which are, extending from internally to externally, Bruch's membrane, the choriocapillaris, the stroma, and the suprachoroidea.[23, 28]

Bruch's Membrane

Bruch's membrane (2 to 4 μm thick) is a tough, acellular, amorphous, bilamellar structure situated between the retina and the rest of the choroid.[29] Microscopically, Bruch's membrane consists of five layers: the basement membrane of the retinal pigment epithelium, the inner collagenous zone, a meshwork of elastic fibers, the outer collagenous zone, and the basement membrane of the choroicapillaris.[23, 30] The function of Bruch's membrane is not exactly known, although it is believed to play a role in the passage of tissue fluid from the choriocapillaris to the retina.[23] When a choroidal tumor breaks through Bruch's membrane, it results in a characteristic mushroom-shaped growth configuration (Fig. 8-16).

Choriocapillaris

The choriocapillaris is the capillary layer of the choroid, lying immediately external to Bruch's membrane. The capillaries are drained by the vortex veins. The choriocapillaris is a visceral type of vasculature containing wide-bore

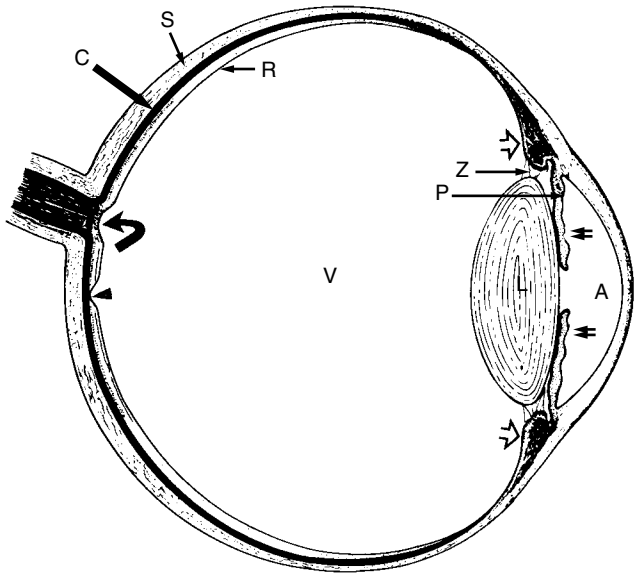

FIGURE 8-15 Ocular coats and chambers. The three ocular coats consist of the sclera (*S*), middle layer: uvea (*black layer*), consisting of choroid (*C*), ciliary body (*hollow arrows*), and iris (*double black arrows*); the inner layer: the retina (*R*). Note the optic nerve disc (*curved arrow*), fovea (*arrowhead*), vitreous chamber (*V*), lens (*L*), zonule fibers (*Z*), posterior chamber (*P*), and anterior chamber (*A*).

VIEW IMAGE

Copyright © 2003, Mosby, Inc. All rights reserved.

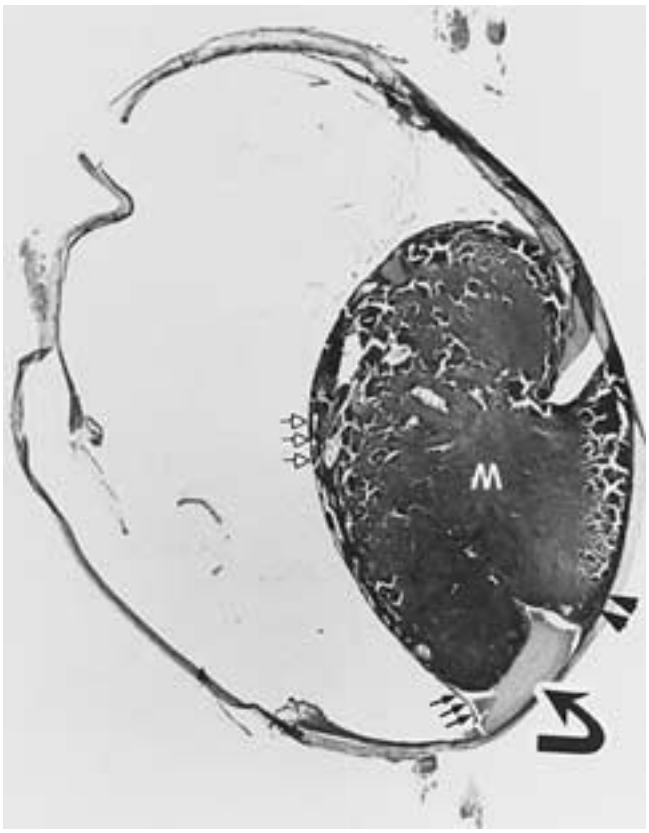

VIEW IMAGE

FIGURE 8-16 Uveal melanoma. Tissue section shows a mushroom-shaped uveal melanoma (*M*) arising from the choroid (*arrowheads*) and breaking through Bruch's membrane (*curved arrows*). The retina (*open arrows*) is elevated to the top of the tumor and is detached (*arrows*) at the slope of the tumor. (From Mafee MF et al. Malignant uveal melanoma and similar lesions studied by CT. Radiology 1985;156:403–408.)

capillaries with fenestrations in the vessels. These openings are covered by diaphragms, which permit the relatively free exchange of material between the choriocapillaris and the surrounding tissues.[31] By contrast, the retinal capillaries show no fenestrations and present a strong barrier to the interchange of material from capillary to retinal tissue.[27] It should be noted that the density of the capillaries is greatest and the bore is widest at the macula.

Choroidal Stroma

The choroidal stroma lies external to the choriocapillaris and consists of blood vessels, nerves, fibroblasts, a collection of immunologic cells, macrophages, lymphocytes, mast cells, plasma cells, and loose collagenous supporting tissue containing melanocytes. The blood vessels of the stroma are branches of the short posterior ciliary arteries and extend anteriorly. The veins are much larger and converge to join four or five vortex (vorticose) veins that drain into the ophthalmic veins.

Suprachoroidea

The suprachoroidea, also called the perichoroidal/suprachoroidal space, is a potential space, approximately 30 μm thick, that lies between the stroma and the sclera.[27] Running across this space are thin pigmented sheets of connective tissue called the suprachoroid lamina.[23] Running in the suprachoroidal space are the long and short posterior ciliary arteries and nerves. At the optic nerve the choroid becomes continuous with the pia and arachnoid.[23]

Blood Supply of the Choroid

The choroid receives its blood supply mainly from the posterior ciliary arteries. A number of recurrent branches arise from the anterior ciliary arteries. All of these arteries are branches of the ophthalmic artery. The four or five vortex (vorticose) veins drain the choroid into the ophthalmic veins.

Function

The most important functions of the uvea are to provide a vascular supply to the eye and to regulate the ocular temperature.[20] The choroid is also responsible for nourishing the pigment epithelium and the outer one-third of the retina.[27] The fenestrations in its capillaries permit proteins and other larger molecules to diffuse through Bruch's membrane, and the selectivity of passage of these materials anterior to Bruch's membrane depends on the retinal pigment epithelium.[27] It is also thought that changes in the blood flow in the choroidal blood vessels may produce heat exchange from the retina.[23] The pigment cells in the choroid absorb excess light, preventing reflection.[23]

Nerve Supply of the Choroid

The choroid is innervated by the long and short ciliary nerves. The long ciliary nerves are branches of the nasociliary nerve, a branch of the ophthalmic division of the trigeminal nerve. They carry sensory nerve and sympathetic fibers. The short ciliary nerves arise from the ciliary ganglion and carry sympathetic and parasympathetic fibers.[23]

Ciliary Body

The ciliary body is continuous posteriorly with the choroid and anteriorly with the peripheral margin of the iris (Fig. 8-15). Considered as a whole, the ciliary body is a complete ring that runs around the inside of the anterior sclera. It is about 6 mm wide and extends forward to the scleral spur (a projecting ridge of scleral tissue along the internal scleral sulcus) and backward to the ora serrata of the retina.[23] On cross section the ciliary body is triangular, with its small base facing the anterior chamber of the eye and its anterior outer angle facing the scleral spur. Its apex extends posteriorly and laterally to become continuous with the choroid.[23] The anterior surface or base is ridged or plicated and is called the pars plicata. The posterior surface is smooth and flat and is called the pars plana. It is the pars plicata that surrounds the periphery of the iris and gives rise to the ciliary processes. The fibers of the zonule of the lens attach to the surface of the pars plicata (Fig. 8-15). The posterior margin of the pars plana has a scalloped edge that fits into and corresponds with the tooth-like edge of the ora serrata. Surgically, the pars plana is an important anatomic structure. Because of its relative avascularity and its position anterior to the retina, incisions through the sclera and choroid into the vitreous should be made at this point to avoid hemorrhagic complications and retinal detachments.

Copyright © 2003, Mosby, Inc. All rights reserved.

The ciliary body is made up of (1) the ciliary epithelium, (2) the ciliary stroma, and (3) the ciliary muscle. The epithelium consists of two layers of cuboidal cells that cover the inner surface of the ciliary body.[23] Embryologically, they represent the two layers of the optic cup. The inner layer of cubical cuboidal cells is nonpigmented and constitutes the anterior continuation of the nervous layer of the retina. These cells also line the anterior chamber.[23] The deeper outer layer consists of cuboidal cells that are packed with melanin pigment and constitutes the anterior continuation of the pigmented layer of the retina.[23] These cells rest against the stroma of the ciliary body. The structures of the two layers of ciliary epithelium on electron microscopy appear to suggest that both layers are involved in producing aqueous humor.[23] The ciliary stroma consists of loose connective tissue, rich in blood vessels and melanocytes, containing the embedded ciliary muscle. The ciliary muscle consists of smooth muscle fibers. It is innervated by the postganglionic parasympathetic fibers derived from the oculomotor nerve. The nerve fibers reach the muscle via the short ciliary nerves.

Iris

The iris is a thin, contractile, pigmented diaphragm with a central aperture, the pupil (Fig. 8-15). It is suspended in the aqueous humor between the cornea and the lens. The periphery of the iris that is attached to the anterior surface of the ciliary body is called the ciliary margin or root of the iris.[23, 32] The iris divides the space between the lens and the cornea into an anterior and a posterior chamber. The aqueous humor, formed by the ciliary processes in the posterior chamber, circulates through the pupil into the anterior chamber and exits into the sinus venosus (canal of Schlemm) at the iridocorneal angle.[23, 32] The iris consists of a stroma and two epithelial layers located posteriorly and derived from the neural ectoderm. The stroma consists of highly vascular connective tissue containing melanocytes. The stroma also contains nerve fibers, the smooth muscle of the sphincter pupillae, and the myoepithelial cells of the dilator pupillae.[23] The nerve supply of the sphincter pupillae is from the parasympathetic postganglionic fibers in the short ciliary nerves. They are derived from the oculomotor nerve. The dilator pupillae muscle is a thin layer of myoepithelium.[23] The myoepithelial cells are derived from the anterior layer of the iris pigment epithelium that covers the posterior surface of the iris.[23] The arterial blood supply of the iris is from the major arterial circle located in the stroma of the ciliary body. The major arterial circle is formed from the two long posterior ciliary arteries and the seven anterior ciliary arteries.[23]

Retina

The retina is the internal layer of the eyeball. It is a thin, transparent membrane having a purplish-red color in living subjects. The external surface of the retina is in contact with the choroid and the internal surface with the vitreous body. Posteriorly the retina is continuous with the optic nerve. The optic nerve and the inner layer of the eye represent an anteriorly protruding portion of the brain. Grossly the retina has two layers: (1) the inner layer, which is the sensory retina, that is, photoreceptors, and the first- and second-order neurons (ganglion cells) and neuroglial elements of the retina (Müller's cells, or sustentacular gliocytes); and (2) the outer layer, which is the retinal pigment epithelium (RPE), consisting of a single lamina of cells whose nuclei are adjacent to the basal lamina (Bruch's membrane) of the choroid.[20, 32]

The retina is very thin, measuring 0.056 mm near the disc and 0.1 mm anteriorly at the ora serrata.[32, 33] It is much thinner at the optic disc and thinnest at the fovea of the macula. The retina consists of a single-layer outer RPE and an inner neurosensory layer, which are both derived from neuroectoderm. The sensory retina extends forward from the optic nerve to a point just posterior to the ciliary body. Here the nervous tissues of the retina end and its anterior edge forms a crenated wavy ring called the ora serrata (Fig. 8-15). The anterior, nonreceptive part of the retina at the ora serrata becomes continuous with the pigmented and nonpigmented columnar cell layers of the ciliary body and its processes. At the iris, both layers of cells continue on its posterior surface, and they both become pigmented. The macula, the center of the retina, lies 3.5 mm temporal to the margin of the optic nerve (Fig. 8-15). The retina is attached tightly at the margin of the optic disc and at its anterior termination at the ora serrata. It is also firmly attached to the vitreous but loosely to the RPE, and it is nourished by the choroid and the RPE.[27] The macula lutea is the retinal area for the most distinct vision.[23] The optic disc is pierced by the central retinal artery and vein. At the disc there is a complete absence of rods and cones. Thus, it is insensitive to light and is referred to as the blind spot. On ophthalmoscopic examination the optic disc is paler than the surrounding retina. The RPE cells contain numerous round or ovoid melanin granules. The cells have numerous functions, including the absorption of light, participation in the turnover of the outer segments of the photoreceptors, and the formation of rhodopsin and iodopsin by storing and releasing vitamin A, which is a precursor of the photosensitive pigment.[23, 33] The RPE cells are joined to each other by tight junctions. This arrangement forms a barrier (blood retinal barrier) that limits the flow of ions and prevents diffusion of large toxic molecules from the choroid capillaries to the photoreceptors of the retina. In oculocutaneous and ocular albinism, there is a lack of melanin pigment in the pigment cells of the retina and the uvea.[23, 33] The neural retina consists of three main groups of neurons: (1) the photoreceptors (cone and rod cells), (2) the bipolar cells, and (3) the ganglion cells. Its also possesses other important neurons, the horizontal cells and the amacrine cells, that modulate their activity.[23, 33] Supporting cells (Müller cells) are also present. The photoreceptors are similar to other sensory receptors elsewhere in the body. The bipolar cells are similar to the neurons in the posterior root ganglia and form the first-order neurons. The ganglion cells are similar to the relay neurons found in the spinal cord and brainstem and form the second-order neurons.[23] The axons of the ganglion cells form the optic nerve, and its fibers become myelinated after they have passed through the lamina cribrosa. The myelin sheaths of these axons are formed from oligodendrocytes rather than Schwann cells. The nerve cells of the lateral geniculate body form the

Copyright © 2003, Mosby, Inc. All rights reserved.

third-order neurons, and their axons terminate in the visual cortex. Thus, the number of neurons involved in conducting light impulses from the retina to the visual cortex is the same as that found in other sensory pathways.[23] Based on light microscopic findings, the retina is said to be composed of 10 layers. These are, from peripheral (farthest away from the center of the eye) to central, (1) the pigment epithelium, (2) the rods and cones, (3) the external limiting membrane, (4) the outer nuclear layer, (5) the outer plexiform layer, (6) the inner nuclear layer, (7) the inner plexiform layer, (8) the ganglion cells, (9) the nerve fiber layer, and (10) the internal limiting membrane. The outer nuclear layer consists of the nuclei of the rod and cone cells. The outer plexiform layer is made up of the synapses between the terminal processes of the rod and cone cells, the bipolar cells, and the horizontal cells. The inner nuclear layer consists of the nuclei of the bipolar cells, the horizontal cells, the amacrine cells, and the Müller cells. The inner plexiform layer is made up of synaptic connections between the bipolar, amacrine, and ganglion cells. The ganglion cell layer consists of the nuclei of the ganglion cells. The nerve fiber layer consists of the axons of the ganglion cells that are converging toward the optic disc. The external and internal limiting membranes are formed by the cell processes of the supporting Müller cells.[23, 33] There are two types of photoreceptors, the rods (110 to 125 million) and the cones (6.3 to 6.8 million).[23] The cones are responsible for vision in dim light. The rods are absent at the fovea. The cones, by contrast, are most dense at the fovea. There are approximately 1 million ganglion cells in each retina and about 100 photoreceptor cells per ganglion cell. The rod cells contain rhodopsin. The cone cells contain several photochemicals, similar in composition to rhodopsin, and are known as iodopsins.[23] The bipolar cells have a radial orientation. One or more dendrites of the bipolar cells pass outward to synapse with the photoreceptor cell terminals. The single axon is directed inward to synapse with ganglion and amacrine cells. The ganglion cells resemble cells found in nervous ganglia. They are situated in the inner part of the retina. The ganglion cells are the second type of neurons in the visual pathway. Most of them are small (midget ganglion cells), but a small number are large.[23] They are absent at the fovea. The ganglion cells are multipolar cells, and their dendrites synapse with the axons of bipolar and amacrine cells. The axons of ganglion cells converge at the exit of the optic nerve at the optic disc. After piercing the lamina, the nerve fibers become myelinated. In some individuals, the ganglion cell axons are partially myelinated; such areas are non-seeing and will produce a blind spot.[23] In addition to rod and cone cells, bipolar cells, and ganglion cells, there are two types of neurons in the retina called horizontal and amacrine cells. The horizontal cells are located close to the terminal expansion of the rods and cones. The horizontal cells respond to the neurotransmitter liberated by the rods and cones following excitation by light.[23] It is believed that the horizontal cells integrate visual stimuli. The amacrine cells are situated close to the ganglion cells. These cells are stimulated by the bipolar cells, which in turn excite the ganglion cells.[23]

The retinal supporting cells are similar to the neuroglial cells. One of them runs radially and is called the Müller cell. These cells fill in most of the space of the neural retina not occupied by the neurons. Other glial-like cells, called retinal astrocytes, perivascular glial cells, and microglial cells, have also been described.[23]

The macula lutea is an oval, yellowish area at the center of the posterior part of the retina. It measures about 4.5 mm in diameter and lies about 3 mm to the lateral side of the optic disc. Its yellow coloration is caused by a yellow carotenoid pigment, xanthophyll, which is present in the retina layers from the outer nuclear layer inward. The fovea centralis is a depression in the center of the macula lutea. It measures about 1.5 mm in diameter. The depression is made by the peripheral displacement of the nerve cells and fibers of the inner layers of the retina, leaving only the photoreceptors in the center. This greater light accessibility explains why this central depression has the most distinct vision. There are no blood vessels overlying the fovea and no rod cells in the floor of the fovea. It is here that the highest concentration of cones exists. The optic disc measures about 1.5 mm in diameter. A rise in CSF pressure causes the optic disc to bulge into the eyeball. It is believed that the pressure on the optic nerve impedes the axoplasmin flow of its fibers, and this causes the optic disc to swell.

Blood Supply of the Retina

The blood supply of the retina is from two sources. (1) The outer lamina, including the rods and cones and outer nuclear layer, is supplied by the choroidal capillaries; the vessels do not enter these laminae, but tissue fluid exudes between these cells. (2) The inner laminae are supplied by the central retinal artery. The retinal arteries are anastomotic end arteries, and there are no arteriovenous anastomoses. The retina depends on both of these circulations, neither of which alone is sufficient.[23] The central retinal artery is the first branch of the ophthalmic artery,[23, 33] measuring about 0.3 mm in diameter, and runs forward adherent to the dural sheath of the optic nerve. It enters the inferior and medial side of the optic nerve about 12 mm posterior to the eyeball. The artery is surrounded by a sympathetic plexus and accompanied by the central vein. It pierces the lamina cribrosa to enter the eyeball. At this location the posterior ciliary arteries form an anastomotic circle in the sclera around the optic nerve. Small branches from this circle penetrate the choroid to supply the optic disc and the adjacent retina. Small anastomoses occur between the branches of the posterior ciliary arteries and the central retinal artery (cilioretinal artery). The central vein of the retina leaves the eyeball through the lamina cribrosa. The vein crosses the subarachnoid space and drains directly into the cavernous sinus or the superior ophthalmic vein. The retina has no lymphatic vessels.

Vitreous

The vitreous body occupies the space between the lens and retina and represents about two thirds of the volume of the eye or approximately 4 ml.[34, 35] All but 1% to 2% of the vitreous is water, which is bound with a fibrillar collagen meshwork of soluble proteins, some salts, and hyaluronic acid.[20, 23, 34, 35] It possesses a network of fine collagen fibrils that form a scaffolding.[23] The vitreous is the largest and simplest connective tissue present as a single structure in the human body.[32] Any insult to the vitreous body may result in

Copyright © 2003, Mosby, Inc. All rights reserved.

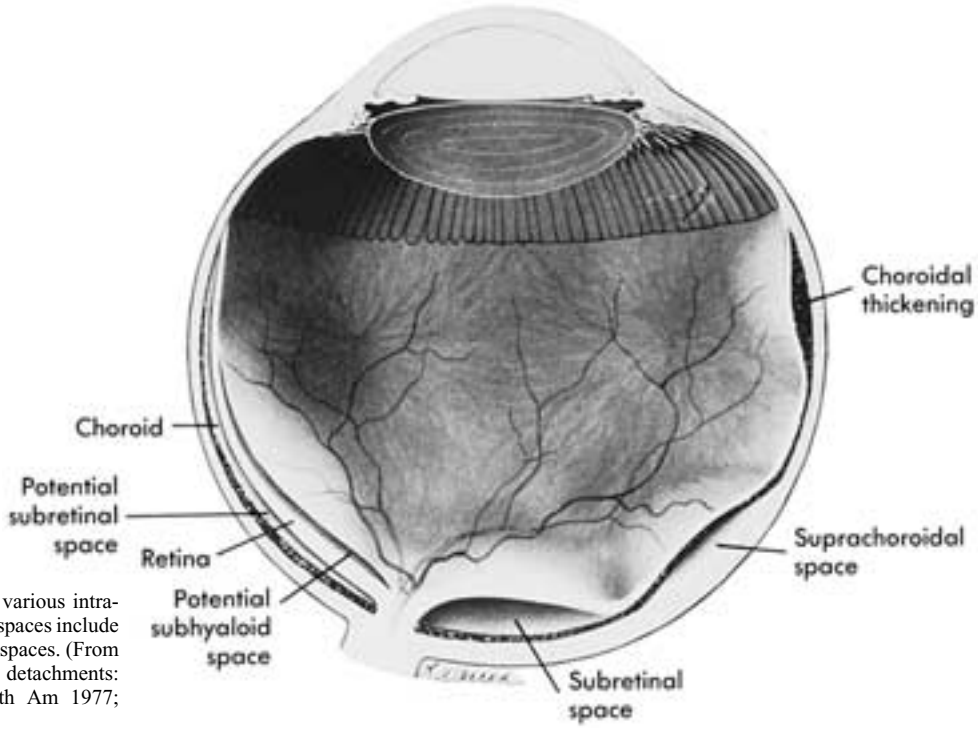

VIEW IMAGE

FIGURE 8-17 Diagram demonstrates various intraocular potential spaces. Principal potential spaces include subretinal, suprachoroidal, and subhyaloid spaces. (From Mafee MF et al. Retinal and choroidal detachments: role of MRI and CT. Radiol Clin North Am 1977; 25:487–507.)

a fibroproliferative reaction (such as proliferative vitreoretinopathy), which can subsequently result in a tractional retinal detachment.[20] The vitreous body has been said to be bounded by membranes, such as the anterior and posterior hyaloid membranes.[23] Anteriorly the vitreous body has a saucer-shaped depression for the lens called the hyaloid fossa.[23] The vitreous body is attached to the sensory retina, especially at the ora serrata and the margin of the optic disc.[23] It is also attached to the ciliary epithelium in the region of the pars plana.[23] The attachment of the vitreous to the lens along the periphery of the hyaloid fossa is firm in young people and weakens with age.

Within the vitreous, the hyaloid (Cloquet's) canal (channel) runs forward from the optic disc to the posterior pole of the lens. During fetal life this channel contains the hyaloid artery, a branch of the central artery of the retina. In developing eyes it nourishes the lens. The hyaloid artery disappears about 6 weeks before birth, and the canal becomes filled with liquid.[23] The vitreous body transmits light, supports the posterior surface of the lens, and assists in holding the sensory retina against the RPE.

INTRAOCULAR POTENTIAL SPACES

There are basically three potential spaces in the eye that can accumulate fluid, resulting in detachment of the various coats of the globe (Fig. 8-17)[20, 32, 36, 37]: (1) the posterior hyaloid space, the potential space between the base of the hyaloid (posterior hyaloid membrane) and the sensory retina (Fig. 8-17). Separation of the posterior hyaloid membrane from the sensory retina is referred to as posterior hyaloid detachment[35] (see Fig. 8-17); (2) the subretinal space, the potential space between the sensory retina and the RPE. Separation of the sensory retina from the retinal pigment epithelium is referred to as retinal detachment (Fig. 8-17); and (3) the suprachoroidal space, the potential space between choroid and the sclera. The RPE and Bruch's membrane are tightly adherent to the choroid and become separated only when both layers are torn. However, the choroid is loosely attached to the sclera and can be separated, resulting in choroidal detachment (Fig. 8-17). The hyaloid fossa (patellar fossa) on the anterior surface of the vitreous for the lens is also a potential space called the retrolenticular space. Exudates and hemorrhage can accumulate in this space in some pathologic conditions.[23] Another potential space is the episcleral or Tenon's space, which was described earlier.

NORMAL IMAGING OF OCULAR ANATOMY

Regarding the anatomy and pathology of the globe, MR imaging is a modality that provides both excellent contrast for ocular imaging and good sensitivity for detecting gross as well as incipient pathology.[20, 21, 23, 37, 38] The globe is unique in that it contains both the most (vitreous) and least (lens) water-laden soft tissues in the body.[37, 38] Since the MR appearance of the vitreous and lens is a function of the interaction between tissue protein and water and because of the wide variation in water content of the eye's various tissues, the eye is an ideal organ for an MR imaging study (Fig. 8-18). The vitreous water content is 98% to 99%, that of the cornea is 80%, and that of the lens is 65% to 69%; these differences produce different water proton relaxation times for each of these tissues.[19, 32, 38]

Copyright © 2003, Mosby, Inc. All rights reserved.

The vitreous represents about two thirds of the volume of the eye, or approximately 4 ml.[29] The vitreous humor is a gel-like transparent extracellular matrix composed of a meshwork of 0.2% collagen fibrils interspersed with 0.2% hyaluronic acid, polymers, water (98% to 99%), and a small amount of soluble proteins.[17, 32, 38] In a number of ocular disease states and as part of the aging process, the vitreous can degenerate to a liquid state devoid of collagen.[18, 32, 39] The vitreous is both viscous and gel-like, and has characteristics associated with both the hyaluronic acid and collagen components, respectively. In a manner similar to that of synovial fluid, the vitreous serves as somewhat of a biologic shock absorber.[39] Because the vitreous is a gel composed of long, fixed collagen fibrils bathed only with dilute dissolved proteins, just a fraction of its water content is in contact with macromolecules.[38] Consequently, the bulk of the water in the vitreous relaxes on MR imaging as pure water, with only a small protein–water interaction.[19, 38] Thus the vitreous has T1 and T2 relaxation times that are longer than those of most tissues but are shorter than those of water (Fig. 8-18).

LENS

The lens is made up of three parts: (1) an elastic capsule, (2) a lens epithelium, which is confined to the anterior surface of the lens, and (3) the lens fibers. The capsule envelops the entire lens. The lens epithelium is cuboidal and lies beneath the capsule. It is found only on the anterior surface of the lens. The lens fibers constitute the main mass of the lens. The fibers are formed by the multiplication and differentiation of the lens epithelial cells at the equator. The lens is held in position by a series of delicate fibers known as the suspensory ligament of the lens, or zonule. The zonule fibers arise from the epithelium of the ciliary process.

The lens is approximately 9 mm in diameter and 4 to 4.5 mm thick. Anterior to the lens are the iris and the aqueous humor; posteriorly, the lens is bordered by the vitreous humor (Fig. 8-15). The zonular fibers (zonules of Zinn) are inserted on the outermost surface of the equatorial lens capsule and extend to the ciliary body (Fig. 8-15). Chemically, the lens is 66% water, making the lens the least hydrated organ of the body.[23] The remainder of the lens is composed of protein forming a liquid crystal. On MR imaging the normal lens is characteristically darker than the surrounding fluid-laden tissue on T2-weighted pulse sequences, predominately because of the dominance of its ultrashort T2 relaxation time (Fig. 8-18).[38] The lens nucleus has both a lower water content and a shorter T2 relaxation time than the cortex.

MR imaging provides precise information regarding other ocular structures as well. The anterior chamber is crescent-shaped, is just anterior to the lens, and is almost isointense to the vitreous humor on both short and long TR images (Fig. 8-18A and 8-18B).[32, 38] The ciliary body may be seen on T2-weighted MR images as a hypointense area running from the edge of the lens to the wall of the globe (Fig. 8-19). Differentiation by MR imaging of individual layers of the sclera, choroid, and retina is impossible in the normal eye.[18, 19, 32]

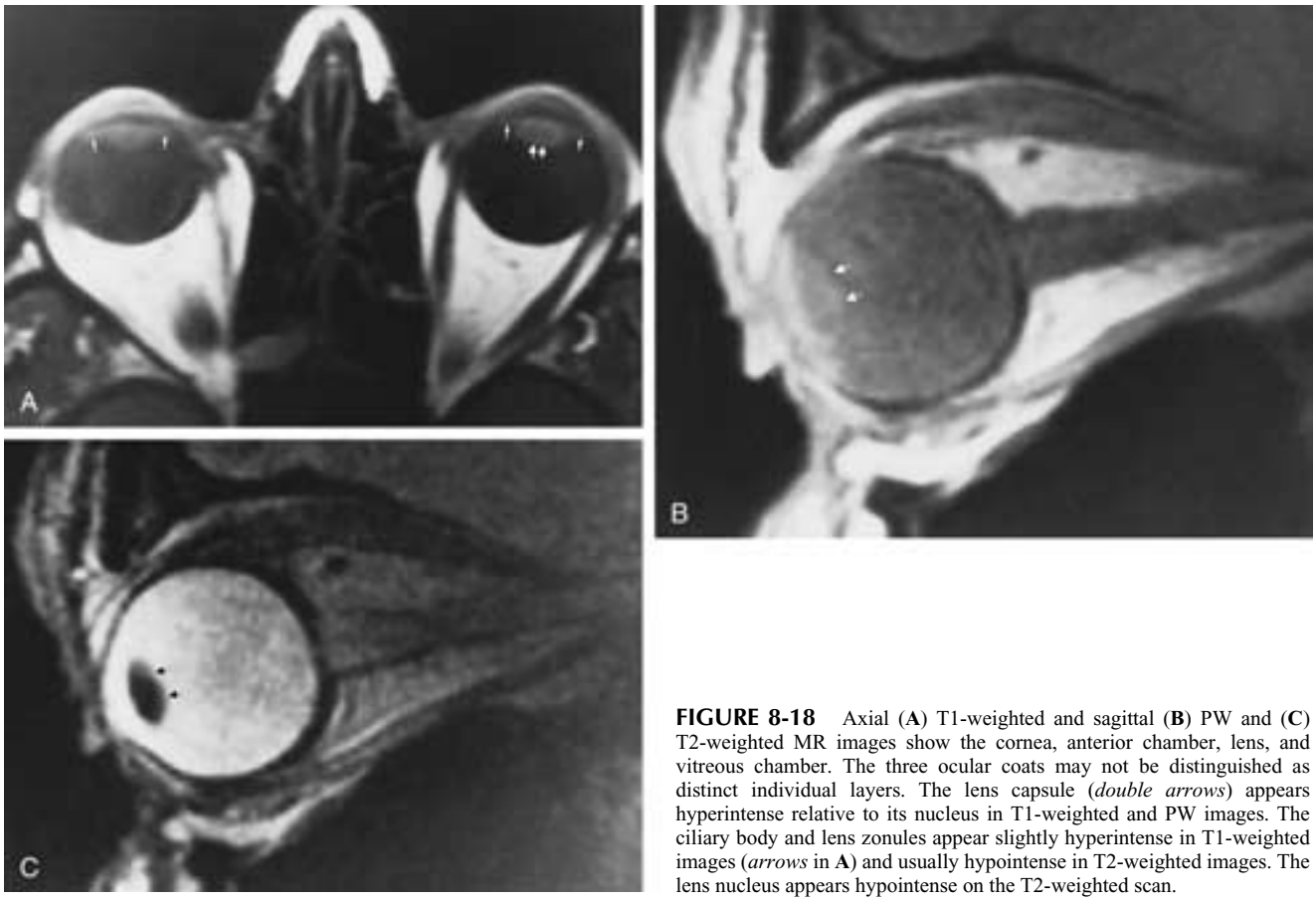

FIGURE 8-18 Axial (**A**) T1-weighted and sagittal (**B**) PW and (**C**) T2-weighted MR images show the cornea, anterior chamber, lens, and vitreous chamber. The three ocular coats may not be distinguished as distinct individual layers. The lens capsule (*double arrows*) appears hyperintense relative to its nucleus in T1-weighted and PW images. The ciliary body and lens zonules appear slightly hyperintense in T1-weighted images (*arrows* in **A**) and usually hypointense in T2-weighted images. The lens nucleus appears hypointense on the T2-weighted scan.

VIEW IMAGE

Copyright © 2003, Mosby, Inc. All rights reserved.

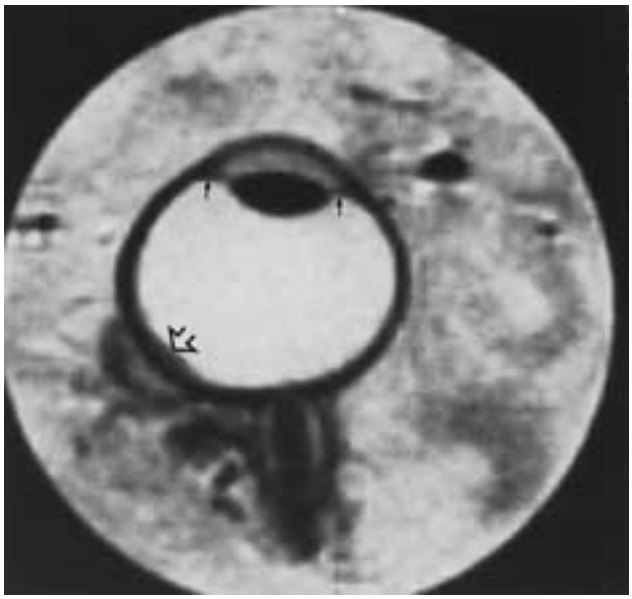

VIEW IMAGE

FIGURE 8-19 Uveal melanoma. T2-weighted MR image of an enucleated eye shows a hypointense posterior uveal melanoma (*hollow arrow*). Note the hypointensity of the lens and the hyperintensity of the vitreous humor. The ciliary body and lens zonules appear hypointense (*arrow*).

The anterior chamber is a small cavity (3 mm anteroposteriorly) lying behind the cornea and in front of the iris (Fig. 8-15). The chamber contains aqueous humor. Its volume is about 0.2 ml. The aqueous fluid nourishes the corneal epithelium and the lens.[27] The iris, which is the most anterior extension of the uveal tract, lies at the anterior surface of the lens (Fig. 8-15). The ciliary body, which is just posterior to the iris, is responsible for producing aqueous fluid, which drains from the eyeball through the trabecular meshwork at the angle formed by the joining of the root of the iris, the anterior margin of the ciliary body, and the corneoscleral junction.[27] The ciliary body divides the globe into two compartments (segments)—the anterior segment and the posterior segment. The anterior and posterior chambers belong to the anterior segment. The anterior chamber is anterior to the iris and posterior to the cornea (Fig. 8-15). It is filled with aqueous humor. Its volume is about 0.2 ml. It measures about 3 mm anteroposteriorly in its central portion.[23] The posterior chamber is a small stilt-like cavity posterior to the iris and anterior to the lens. Its volume is about 0.6 ml. It is filled with aqueous fluid and communicates with the anterior chamber through the pupil. The posterior chamber is bounded anteriorly by the iris, peripherally by the ciliary processes, and posteriorly by the lens and the zonule (Fig. 8-15).

OCULAR PATHOLOGY

Congenital Anomalies

Anophthalmia

Anophthalmia denotes the complete absence of an eye due to a developmental defect and is extremely rare.[40] More commonly, a small cystic remnant is seen and the term *clinical anophthalmia* is used. Bilateral cases suggest an early teratogenic event related to failure of the optic pit to develop.[40] In true anophthalmia, there is absence of neuroectodermal tissue within the orbit. Those structures not derived from neuroectoderm such as extraocular muscles, eyelids, conjunctiva, lacrimal apparatus, and bony orbit are present; however, the orbit is diminished in size, and orbital soft tissues including the optic nerve and extraocular muscles are rather hypoplastic. In true anophthalmia, in addition to absence of the globes, the optic nerves and the optic chiasm may be absent. The optic tracts may be rudimentary, and the lateral geniculate nuclei may be gliotic.[41] On CT and MR imaging there may be either rudimentary tissue or no globe present. At times, dystropic calcification may be present within the rudimentary tissue. The extraocular muscles, lacrimal glands, and eyelids are present.

Microphthalmia

Microphthalmia refers to a congenital underdevelopment of or acquired diminution in the size of the globe (Fig. 8-20). Congenital microphthalmia (microphthalmos) is a continuation of a spectrum that begins with anophthalmia. Microphthalmos is defined as an eye that has an axial length less than 21 mm in an adult or less than 19 mm in a 1-year-old child.[40] Microphthalmia can occur as an isolated disorder or may be associated with other ocular, craniofacial anomalies (Hallerman-Streiff syndrome) or systemic abnormalities such as MIDS (microphthalmos, dermal aplasia, and sclerocornea).[40] Other causes of microphthalmia include the congenital rubella syndrome, persistent hyperplastic primary vitreous (PHPV), and retinopathy of prematurity (ROP). Bilateral microphthalmia and cataract may be seen in Lowe's syndrome (oculocerebral renal disease).[41] Microphthalmia results from an insult to the embryo after the outgrowth of the optic vesicle. If the insult occurs before complete invagination of the optic vesicle, an orbital cyst may result. This condition is referred to as microphthalmos with *cyst*. It can present as a progressive swelling from birth. The cyst may course along the optic nerve, with free communication with the intraocular contents.

In some cases in which a baby is born with a unilateral small orbit and no visible eye, a small microphthalmic globe is present in the orbital soft tissues. All such children have hypoplastic orbits. CT and MR imaging in congenital microphthalmia demonstrate a small globe as well as a small, poorly developed orbit. In older patients microphthalmia may occur as the result of trauma, surgery, inflammation, radiation, or other processes, which result in disorganization of the eye (phthisis bulbi). In these patients, CT and MR imaging demonstrate a small, shrunken globe, often with extensive intraocular calcification or ossification (Fig. 8-21). The principal conditions with which microphthalmia may be associated are listed in Table 8-1.

Macrophthalmia

Buphthalmos and Megalophthalmos

Macrophthalmia, or enlargement of the globe, is seen in patients with axial myopia, congenital glaucoma (buphthalmos), Sturge-Weber syndrome, and neurofibromatosis. As many as 50% of patients with lid and facial involvement in neurofibromatosis exhibit glaucoma on the affected side. Up to 30% of patients with Sturge-Weber syndrome have glaucoma, and nearly two thirds of these patients develop

Copyright © 2003, Mosby, Inc. All rights reserved.

buphthalmos.[24] The hallmark of all forms of glaucoma in infants and young children is ocular enlargement (Fig. 8-22), which occurs because the immature and growing collagen that constitutes the cornea and sclera in the young eye still responds to increased intraocular pressure by stretching.[40] All parts of the globe may stretch in response to the elevated intraocular pressure until 3 to 4 years of age, and glaucoma-related axial myopia may be seen until the early teenage years.[40] Buphthalmos, the most extreme form of macrophthalmia, consists of elevated intraocular pressure and an enlarged globe, as well as an enlarged cornea. Megalocornea is characterized by bilateral anterior segment enlargement with a corneal horizontal diameter of more than 12 mm at birth and more than 13 mm after 2 years of age. Megalocornea may be present without other ocular abnormalities. Megalophthalmos is an enlarged cornea in an overall enlarged eye that does not have glaucoma. There is an increased ocular axial length, often more than 30 mm. The condition is most likely autosomal recessive, and its findings are similar to those of X-linked megalocornea.[40] The most common cause of macrophthalmia is axial elongation of the eye associated with high myopia.[41] The normal adult eye has an axial length of about 24 mm. Using CT data, the axial length and width of the globe have been

FIGURE 8-20 **A**, Axial CT scan shows a microphthalmic left eye associated with a small calcification. **B**, Axial CT scan in another patient shows bilateral microphthalmia with marked calcifications. **C**, Coronal CT scan of the same patient in **B** showing normal development of the extraocular muscle but hypoplastic optic nerves. **D**, Axial CT scan shows bilateral microphthalmia. There is an air pocket in the remnant of the right dysplastic globe. **E**, Axial PW (2000/30, TR/TE) image (same patient as in **D**), showing a dysplastic right eye and a microphthalmic left eye.

VIEW IMAGE

Copyright © 2003, Mosby, Inc. All rights reserved.

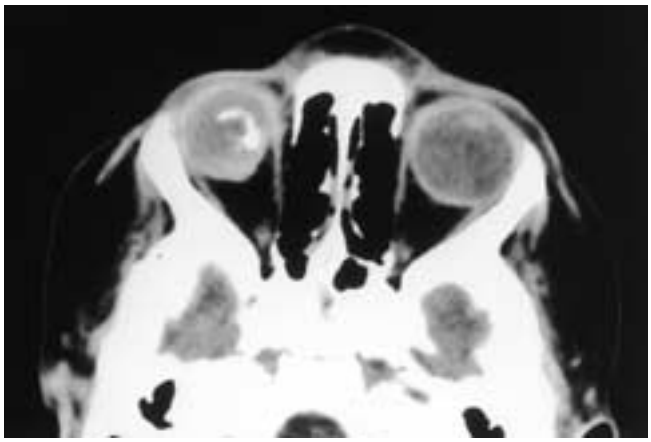

VIEW IMAGE

FIGURE 8-21 Phthisis bulbi: Axial CT scan shows a dense right eye with irregular calcification. This child with acquired immune deficiency syndrome developed cytomegalovirus chorioretinitis, resulting in a disorganized eye with associated dystrophic calcification.

published.[42] In addition to ocular elongation, CT and MR imaging may demonstrate thinning of the posterior scleral-uveal rim.

Staphyloma

Staphyloma refers to thinning and stretching (ectasia) of the scleral-uveal coats of the eyeball. Progressive myopia (megamyope) results in posterior staphyloma. The progressively myopic eye expands in all of its posterior dimensions, and the formation of an equatorial staphyloma with scleral dehiscences is not uncommon,[40] especially in the superotemporal quadrant. As the scleral shell expands, the retina and choroid stretch and thin to accommodate the area they cover. Staphyloma has also been reported in glaucoma, scleritis, necrotizing infection after surgery or radiation therapy, and with trauma. Anterior staphyloma also may occur as a result of inflammatory or infectious corneal thinning.[40]

Table 8-1
MICROPHTHALMIC EYE, ISOLATED AND ASSOCIATED WITH SOME SYNDROMES

Isolated microphthalmia
Microphthmos with orbital cyst
Persistent hyperplastic primary vitreous
Retinopathy of prematurity
Congenital rubella syndrome
Congenital toxoplasmosis
Congenital syphilis
Posttraumatic
Postinflammation (herpes, cytomegalovirus)
Postradiation therapy
Hallerman-Streipp syndrome
MIDS syndrome
Lowe's syndrome
Norrie's syndrome
Warburg's syndrome
Meckel's syndrome
Other craniofacial and systemic syndromes

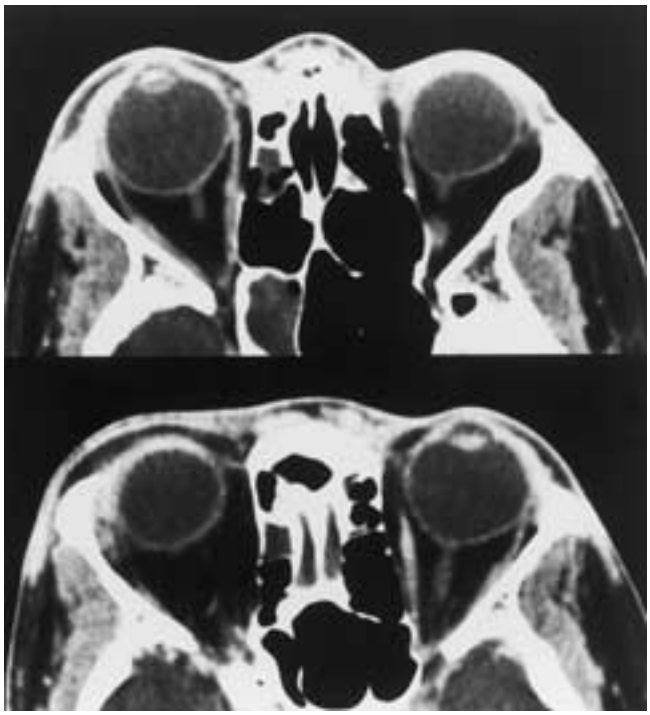

VIEW IMAGE

FIGURE 8-22 Glaucoma and enlarged eye. Axial CT scans shows moderate enlargement of the right globe (top). This child presented with eye pain and was found to have cataracts, anterior uveitis of unknown etiology, and glaucoma on the right side. Note the irregularity of the right lens as well as a shallow right anterior chamber (bottom).

Cryptophthalmos

Cryptophthalmos consists of partial or complete failure of development of the eyelids (eyebrow, palpebral fissure, eyelashes, and conjunctiva). It may be unilateral or bilateral. It may be associated with a skin-like cornea, an incompletely developed anterior segment, or a rudimentary cyst-like globe. Cryptophthalmos may be associated with systemic anomalies such as syndactyly and genitourinary anomalies.

Coloboma and Morning Glory Anomaly

A coloboma (Greek, a mutilation) is a notch, gap, hole, or fissure that is congenital or acquired and in which a tissue or portion of a tissue is lacking. Ocular coloboma may involve the iris, lens, ciliary body, retina, choroid, optic nerve, or sclera.[43] Three types of optic nerve colobomas occur: (1) isolated coloboma of the optic nerve, (2) retinochoroidal coloboma, and (3) Fuchs' coloboma.[44–46] In a typical coloboma, the cleft appears in the inferonasal quadrant of the globe and results from the failure of the embryonic fissure to close.[44–46] Fuchs' coloboma (tilted disc syndrome, nasal fundus ectasia syndrome) is a form of coloboma in which there is a congenital, inferiorly tilted optic disc in conjunction with an inferonasal crescent or conus along the border of the disc in the direction of the tilt.[45, 46] Myopia and astigmatism accompany these changes.[45, 46] Ophthalmoscopically, optic nerve coloboma characteristically shows enlargement of the papillary areas, with partial or total excavation of the disc (Fig. 8-23A). The embryonic derivation of the ocular structures was discussed previously in this chapter. A study of this embryology is important to understand the origin of optic nerve colobomas. Isolated

Copyright © 2003, Mosby, Inc. All rights reserved.

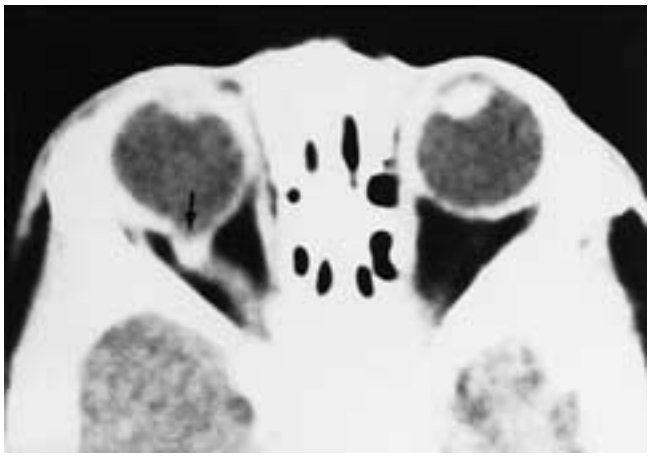

VIEW IMAGE

FIGURE 8-23 Typical coloboma of the optic disc. Axial CT scan shows a large posterior global defect (*arrow*) with optic disc excavation on the right side. The defect appears to be surrounded by an enhancing, deformed sclera and seems to have a direct connection with the vitreous body. (From Mafee MF et al. CT of optic nerve colobomas, morning glory anomaly, and colobomatous cyst. Radiol Clin North Am 1987; 25:693–699.)

optic nerve colobomas arise from failure of closure of only the most superior end of the embryonic fissure.[45–47] Failure of closure of other parts of the embryonic fissure causes iridic, lenticular, ciliary body, and retinochoroidal colobomas.[48] The visual acuity in eyes with optic nerve colobomas is variable and may range from normal to abnormal light perception. Both nonrhegmatogenous and rhegmatogenous (tear of the retina) retinal detachments have been well described in association with optic nerve coloboma.[45, 48] Optic nerve colobomas have been observed in association with ocular abnormalities, including congenital optic pit, cyst of the optic nerve sheath, posterior lenticonus, and remnant of the hyaloid artery.[45, 46] These colobomas also have been associated with nonocular abnormalities including cardiac defects, dysplastic ears, facial palsy, and transsphenoidal encephalocele.[49] A coloboma can form in normal-sized eyes as well as microphthalmic eyes. In a small percentage of microphthalmic eyes with coloboma, a defect in the sclera allows an extraocular herniation of the intraocular neural ectoderm to form an orbital cyst with a tunnel-like connection to the globe.[43] The relative sizes of the microphthalmic eye and colobomatous cyst, and the direction of cyst growth, are quite variable (Figs. 8-24 and 8-25). Colobomatous cysts have been associated with a number of systemic syndromes, chromosomal anomalies, and familial cases (Table 8-2).[43]

Morning glory disc is an anomaly that was first characterized by Kindler in 1970.[50] He described a unilateral congenital anomaly of the optic nerve head in 10 patients. Because of the similarity in appearance between the nerve head and a morning glory flower, he referred to the anomaly as the morning glory syndrome. Ophthalmoscopically, the disc is enlarged and excavated and has a central core of white tissue. The disc is surrounded by an elevated annulus of light and also by variable pigmented subretinal tissue.

Diagnostic Imaging

The CT and MR appearance of optic disc coloboma includes a posterior global defect with optic disc excavation (Fig. 8-23). The imaging appearance of the morning glory anomaly is characteristic and corresponds to its clinical appearance as a large funnel-shaped disc (Fig. 8-24). The colobomatous cyst associated with coloboma of the optic nerve head can be readily identified on CT and MR imaging (Figs. 8-25 and 8-26).

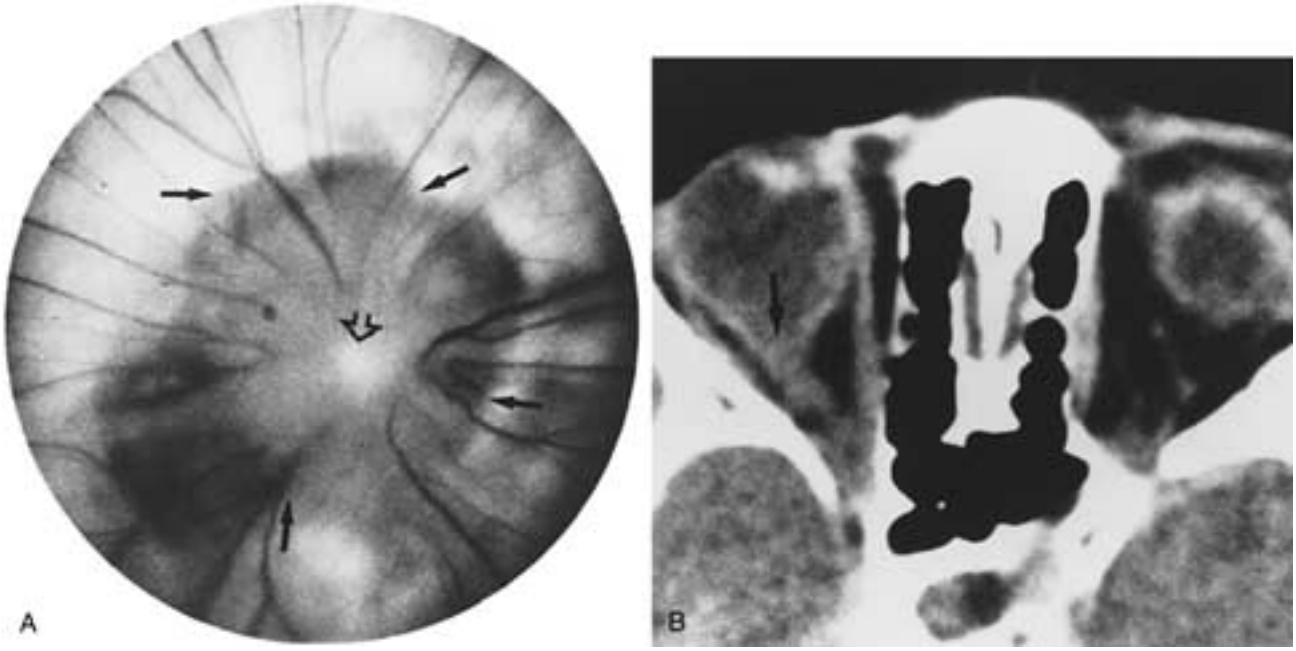

VIEW IMAGE

FIGURE 8-24 Morning glory anomaly. **A**, Disc is enlarged (*solid arrows*) and has a central core of white glial tissue (*open arrows*). **B**, Axial CT scan shows a funnel-shaped deformity of the posterior globe (*arrow*). (From Mafee MF et al. CT of optic nerve colobomas, morning glory anomaly, and colobomatous cyst. Radiol Clin North Am 1987;25:693–699.)

Copyright © 2003, Mosby, Inc. All rights reserved.

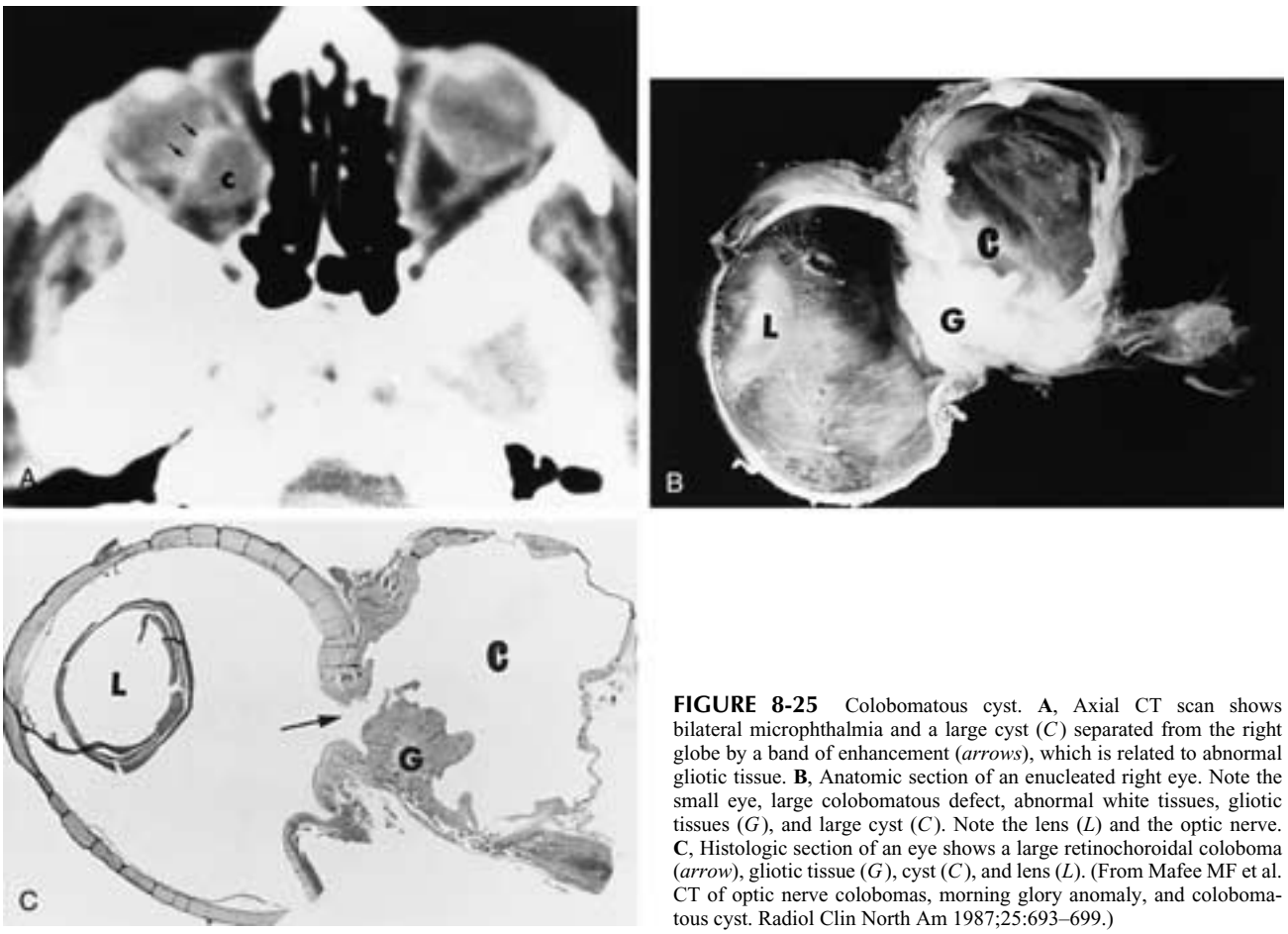

FIGURE 8-25 Colobomatous cyst. **A**, Axial CT scan shows bilateral microphthalmia and a large cyst (*C*) separated from the right globe by a band of enhancement (*arrows*), which is related to abnormal gliotic tissue. **B**, Anatomic section of an enucleated right eye. Note the small eye, large colobomatous defect, abnormal white tissues, gliotic tissues (*G*), and large cyst (*C*). Note the lens (*L*) and the optic nerve. **C**, Histologic section of an eye shows a large retinochoroidal coloboma (*arrow*), gliotic tissue (*G*), cyst (*C*), and lens (*L*). (From Mafee MF et al. CT of optic nerve colobomas, morning glory anomaly, and colobomatous cyst. Radiol Clin North Am 1987;25:693–699.)

VIEW IMAGE

Table 8-2
COLOBOMATOUS CYSTS ASSOCIATED WITH SYSTEMIC SYNDROMES

Oculocerebrocutaneous syndrome (Dellman's syndrome)
Focal dermal hypoplasia (Goltz's syndrome)
Brachio-oculofacial syndrome
CHARGE association
VATER association
Aicardi's syndrome
Proboscis lateralis
Lenz's syndrome
Meckle's syndrome
Warburg's syndrome
Triploidy
Trisomy 13
Trisomy 18
Cat-eye syndrome
4p depletion

Source: Adopted from Kaufman LM, Villablanca PJ, Mafee MF. Diagnostic imaging of cystic lesions in the child's orbit. Radiol Clin North Am 1998;36:1149–1163.

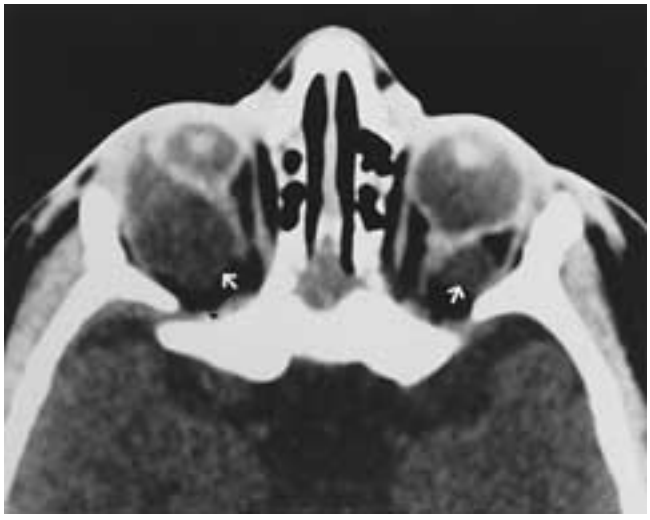

FIGURE 8-26 Colobomatous cyst. Axial CT scan shows microphthalmic eyes with large cysts (*arrows*).

VIEW IMAGE

Copyright © 2003, Mosby, Inc. All rights reserved.

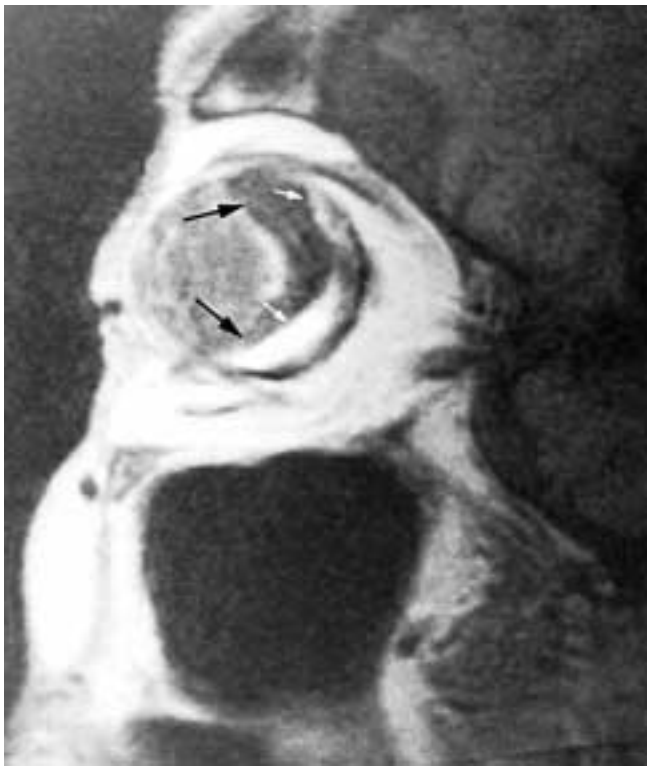

VIEW IMAGE

FIGURE 8-27 Posterior hyaloid detachment and retinal detachment in a patient with complicated macular degeneration. Sagittal T1-weighted MR image shows two semilunar regions; the posterior region (*white arrows*) is caused by chronic subretinal hemorrhage, and the anterior region (*black arrows*) is caused by posterior hyaloid detachment. Surgery confirmed these findings.

OCULAR DETACHMENTS

Posterior Hyaloid Detachment

Posterior hyaloid detachment usually occurs in adults over the age of 50 years but may occur in children with persistent hypertrophic primary vitreous (PHPV).[37, 39, 40] In the older population, the vitreous tends to undergo degeneration and liquefaction. This process may lead to posterior vitreous detachment and predispose to retinal detachment.[23] Posterior hyaloid detachment in adults may be associated with macular degeneration (Fig. 8-27).

The posterior hyaloid membrane is very thin and is invisible on MR imaging or CT, but it can be made visible when blood or other fluid fills the posterior hyaloid space, causing thickening of this membrane (Fig. 8-27). Fluid in the retrohyaloid space is seen on CT and MR imaging as a layered abnormality that shifts its location in the lateral decubitus position (Figs. 8-28 and 8-29). The retrohyaloid-layered fluid is shifted in the decubitus position because it is not within the substance of the vitreous (Fig. 8-28B). Hemorrhage within the vitreous mixes with the vitreous humor, which is a gel-like extracellular material and therefore does not show intragel layering. Fluid in the retrohyaloid space and the subretinal space may not be differentiated from each other on CT and MR imaging.[36]

Retinal Detachment

Retinal detachment occurs when the sensory retina is separated from the retinal pigment epithelium. The retinal pigment epithelium has a barrier function that, once damaged, allows fluid to leak into the potential subretinal space.[20, 36] Retinal detachment resulting from a hole (or tear) in the retina is referred to as rhegmatogenous retinal

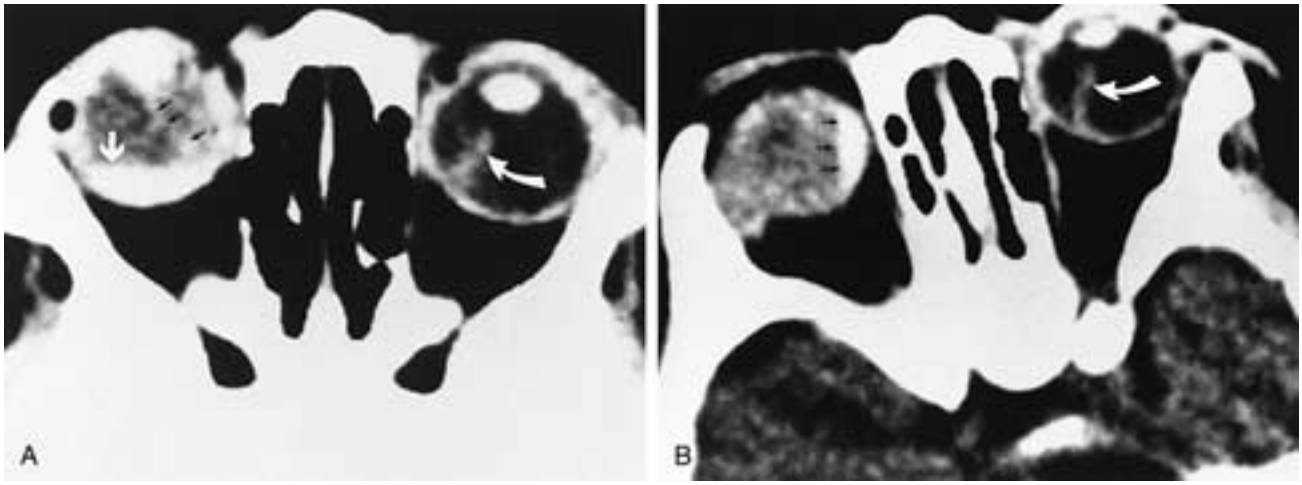

VIEW IMAGE

FIGURE 8-28 Posterior hyaloid detachment and congenital nonattached retina. Axial CT scans obtained without contrast in the supine position (**A**) and the decubitus position (**B**) show gravitational layering fluid (*white arrow* in **A**), which is related to hemorrhage in the subhyaloid space. Fluid shifts more freely in the subhyaloid space than in the subretinal space (*black arrows* in **B**). Note the congenitally nonattached retina of the left eye (*curved arrows*). Increased density, as well as retrolental soft tissue of the right eye (*black arrows* in **A**), are related to PHPV. (From Mafee MF et al. CT in the evaluation of patients with persistent hyperplastic primary vitreous [PHPV]. Radiology 1982;145:713–717.)

Copyright © 2003, Mosby, Inc. All rights reserved.

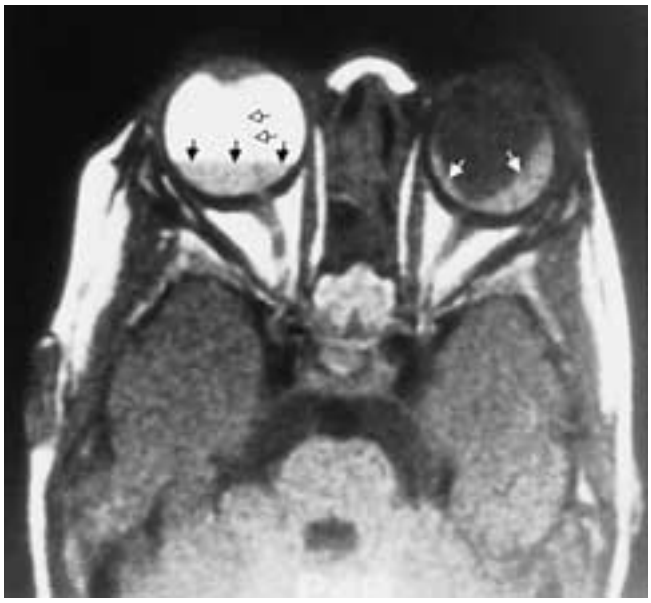

VIEW IMAGE

FIGURE 8-29 Posterior hyaloid and retinal detachment. Axial T1-weighted MR image shows the fluid-fluid level (*black arrows*) in the right vitreous chamber. This is thought to be caused by chronic (hyperintense) and acute (hypointense) hemorrhage in the subhyaloid or subretinal space. Note the detached leaves of the retina of the left eye (*white arrows*). The patient was diagnosed as having Warburg's syndrome. (From Mafee MF et al. Persistent hyperplastic primary vitreous [PHPV]: role of CT and MRI. Radiol Clin North Am 1987;25:683–692.)

detachment. The sensory retina is part of the central nervous system, so if there is a tear, the sensory retina cannot heal. By contrast, retinal pigment epithelium has healing potential. In laser treatment for retinal detachment, the energy of the laser beam is absorbed by RPE at the retinal detachment, and the resultant heat heals and closes the tear. Fluid in the subretinal space can be detected by CT and MR imaging (Fig. 8-30). Rhegmatogeneous retinal detachments are rare in the pediatric population. The majority of retinal detachments in children are nonrhegmatogenous and are secondary to other ocular diseases (Fig. 8-31). Retinal detachment usually is the result of retraction caused by a mass, a fibroproliferative disease in the vitreous such as vitreoretinopathy of prematurity or vitreoretinopathy of diabetes mellitus, or accompanying an inflammatory process such as the larval granuloma of toxocara endophthalmitis.[20, 36] Retinal detachment also may occur because of retinal vascular leakage, which is seen in patients with Coats' disease, a primary vascular anomaly of the retina characterized by telangiectasia. The telangiectatic vessels leak serum and lipid, resulting in accumulation of a lipoproteinaceous exudate in the subretinal space (Fig. 8-32). Retinal detachment is sometimes the result of subretinal hemorrhage and occurs following trauma, senile macular degeneration, or persistent hyperplastic primary vitreous. Any choroidal lesions can cause retinal detachment (Figs. 8-33 and 8-34). In an axial CT or MR imaging scan taken below or above the lens, the retinal detachment appears as a homogeneous increased density (Fig. 8-32A). Although the retina is very thin and is beyond the limits of resolution of CT and MR scanners, it may be shown when outlined by the significant contrast difference between the density or intensity of the subretinal effusion on one side and the vitreous cavity on the other side (Fig. 8-35). The appearance of the retinal detachment varies with the amount of exudation (Figs. 8-32 to 8-37) and organization of the subretinal materials. In a section taken at the level of the optic disc, retinal detachment is seen with a characteristic indentation at the optic disc (Figs. 8-36 and 8-37). When total retinal detachment is present and the entire vitreous cavity is ablated, the leaves of the detached retina may not be clearly detected (Fig. 8-38). Retinal detachment is seen on coronal MR imaging as a characteristic folding membrane (Fig. 8-39). The subretinal fluid of an exudative retinal detachment is rich in protein, giving higher CT numbers and stronger MR signal intensities (on T1-weighted MR images) than those seen in the subretinal fluid (transudate) of a rhegmatogenous detachment. A rhematogeneous retinal detachment is produced by a retinal tear and subsequent ingress of vitreous fluid into the subretinal space.[20, 36] In many cases of shallow retinal detachment, the

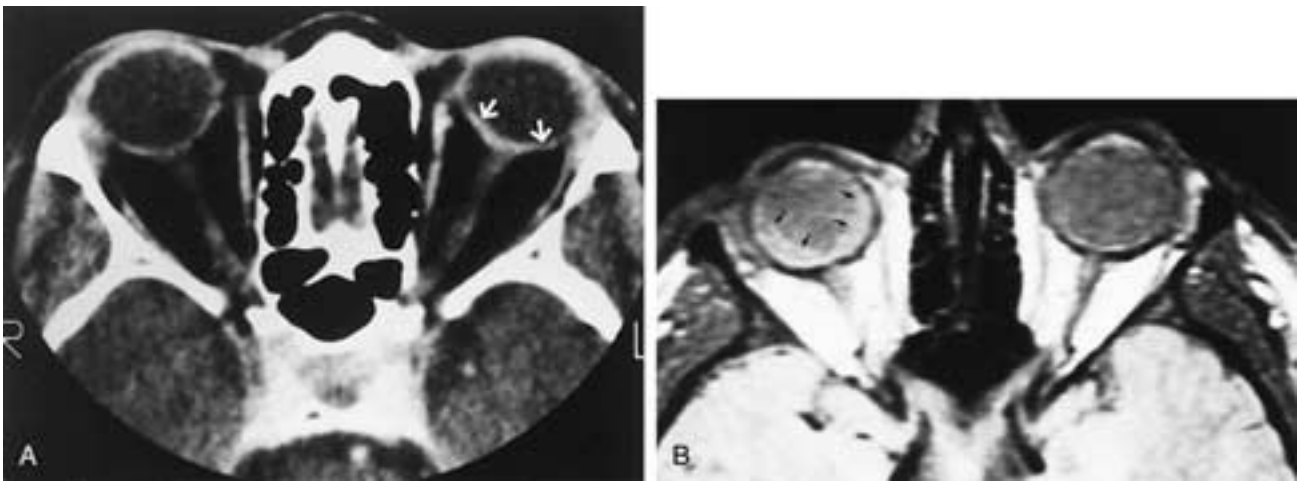

VIEW IMAGE

FIGURE 8-30 Retinal detachment. **A**, Axial CT scan shows a dependent image of increased density (*arrows*) of the left eye caused by retinal detachment. **B**, Axial PW MR image shows a dependent hyperintense image (*arrows*) of the right vitreous chamber caused by a subretinal exudate.

Copyright © 2003, Mosby, Inc. All rights reserved.

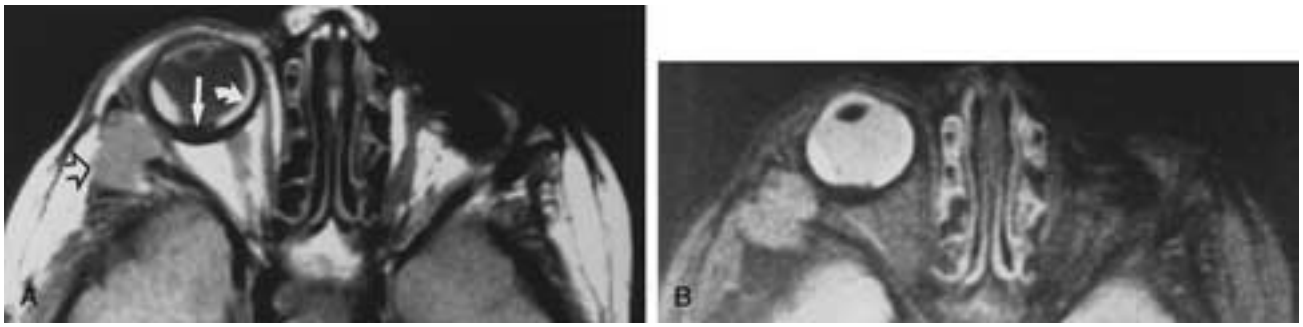

VIEW IMAGE

FIGURE 8-31 Exudative retinal detachment and regressed retinoblastoma after radiation therapy. **A**, Axial PW and **B**, T2-weighted MR images. **A** and **B** show a mass (*white arrow*) and a hyperintense subretinal exudate (*curved arrows*). The mass is hypointense in PW and T2-weighted MR images because of calcification. Note the destructive lesion (*open arrow*), presumably a sarcoma, that developed in the field of radiation therapy. The left eye has been enucleated in this patient, who had bilateral Rb.

MR image and in particular the CT scan may not show the detached retina. In these patients, ultrasonography is superior to MR imaging and CT. Retinal detachment is characteristically seen on CT or MR imaging as a V-shaped abnormality, with its apex at the optic disc and its extremities toward the ciliary body (Figs. 8-36 and 8-37). This appearance of retinal detachment may be confused with the appearance of choroidal detachment. However, choroidal detachment, in the region of the optic disc and macula, involves detachment of the choroid that is restricted by the anchoring effect of the vortex veins, short posterior ciliary arteries, and nerves. This restriction usually results in a characteristic appearance of the leaves of the detached choroid, which, unlike the detached

FIGURE 8-32 Retinal detachment caused by Coats' disease. **A**, Axial CT scan. **B**, Axial PW and **C**, Axial T2-weighted MR images. All images show total retinal detachment (*arrows*).

VIEW IMAGE

Copyright © 2003, Mosby, Inc. All rights reserved.

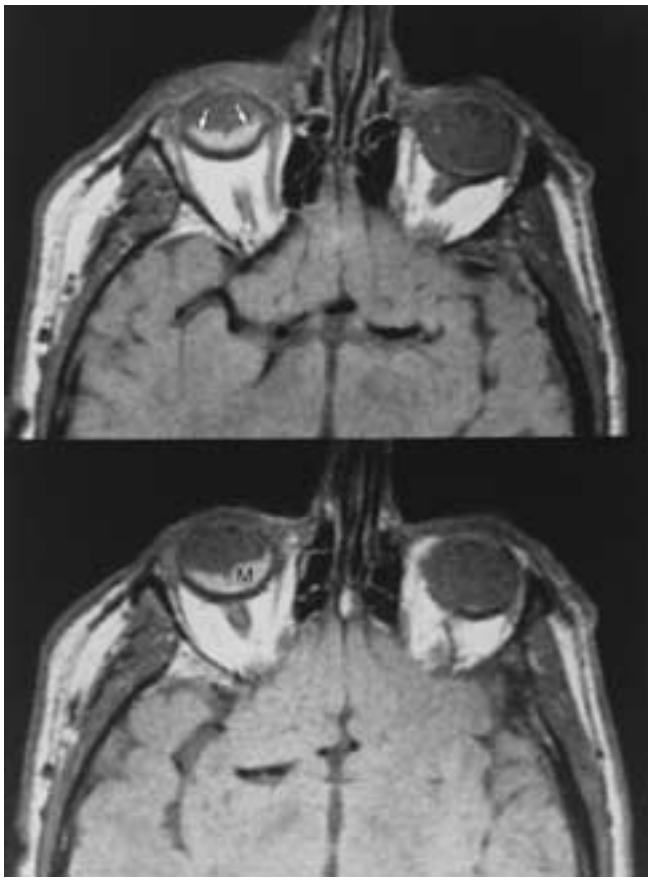

VIEW IMAGE

FIGURE 8-33 Retinal detachment caused by uveal melanoma. Axial PW MR images shows a mass (*M*) and exudative retinal detachment (*arrows*).

retinal leaves, do not extend to the region of the optic disc (Fig. 8-40).[20, 36]

Inflammatory diseases of the uvea are seldom limited to this vascularized layer of the eye. The sclera and retina are usually involved, producing scleritis or chorioretinitis, respectively. Inflammation of the choroid can damage the retinal pigment epithelial cells. Such damage causes breakdown of the ocular blood barrier, with subsequent outpouring of proteinaceous fluid (exudate) into the subretinal space, producing an exudative retinal detachment.[20] The sensory retina subsequently detaches. Interestingly, neoplastic diseases of the choroid may produce similar changes in the retinal pigment epithelium; however, these changes usually occur in a more advanced stage of the disease (Figs. 8-33 and 8-34).

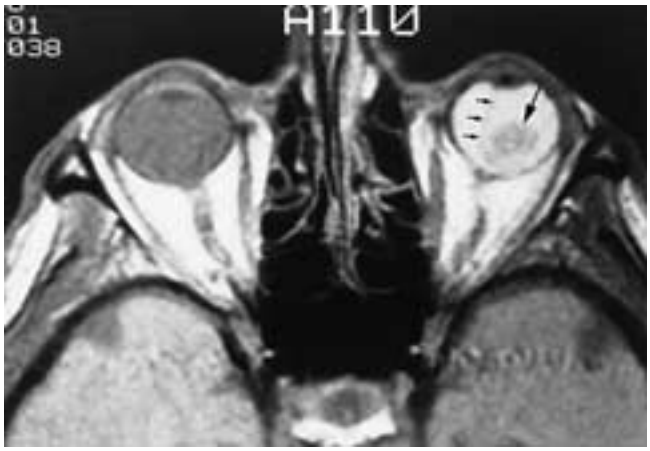

FIGURE 8-34 Total retinal detachment. Axial PW MR image shows a mass (*arrow*) with total retinal detachment (*arrows*). The subretinal exudate is hyperintense.

VIEW IMAGE

Malignant melanomas and choroidal hemangiomas are the most common choroidal neoplasms producing retinal detachment in adults (Figs. 8-33 and 8-34).[19, 36] These tumors produce various degrees of subretinal fluid accumulation, depending on the size and location of the tumor (Figs. 8-33 and 8-34). These tumors produce shifting fluid when the retinal detachment approaches at least one quarter of the circumference of the eye.[20] The subretinal exudate

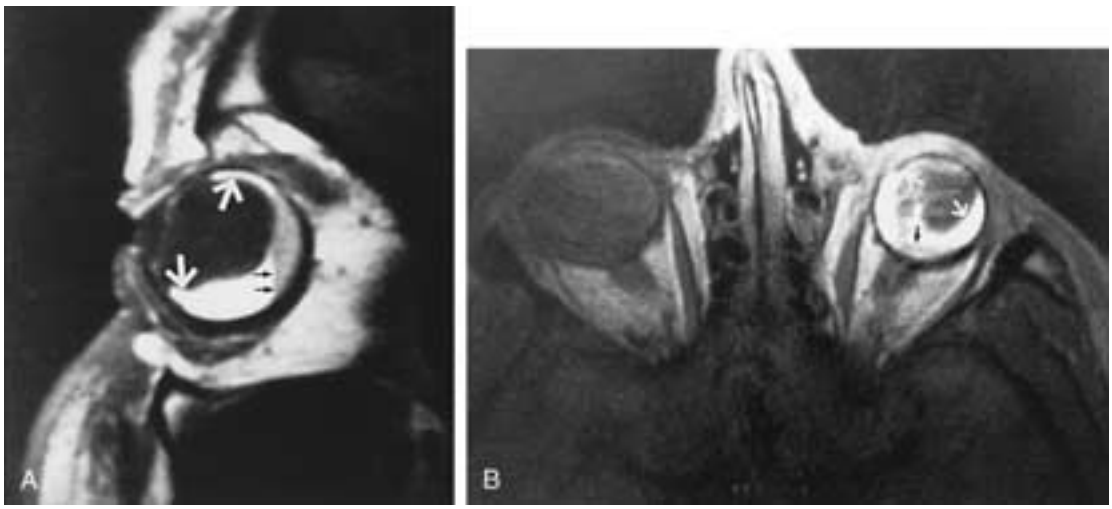

VIEW IMAGE

FIGURE 8-35 Retinal detachment. **A**, Sagittal T1-weighted sagittal MR image shows the leaves of a detached retina (*white arrows*). Subretinal fluid is hyperintense because of either exudate or chronic hemorrhage. Note the layered fluid (*black arrows*) caused by recent hemorrhage. **B**, Axial PW axial MR image shows leaves of a detached retina (*white arrows*) and layered recent hemorrhage (*black arrow*).

Copyright © 2003, Mosby, Inc. All rights reserved.

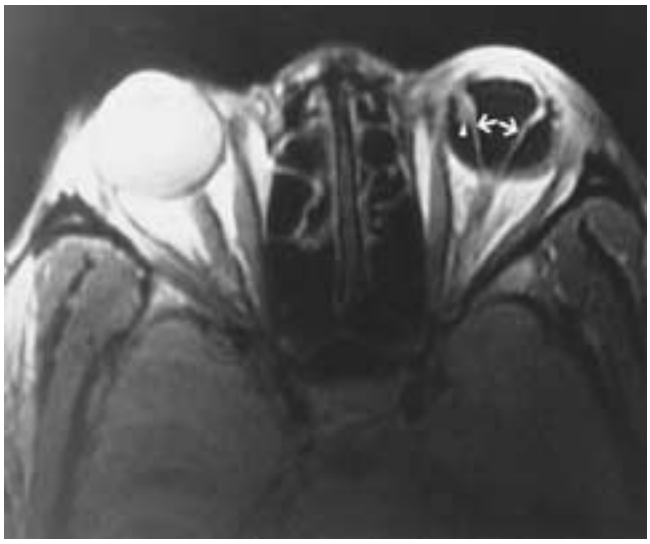

VIEW IMAGE

FIGURE 8-36 Total retinal detachment. Axial T2-weighted MR image shows a detached retina (*arrows*) with the characteristic V-shaped configuration with the apex at the optic disc. Hypointensity of the left globe is caused by injection of silicone oil into the vitreous, which also has escaped into the subretinal space. The arrowhead points to residual subretinal fluid not replaced by silicone oil. (From Mafee MF et al. Retinal and choroidal detachments: role of MRI and CT. Radiol Clin North Am 1977;25:487–507.)

often has a high density on CT and high signal intensity on MR imaging. MR imaging is superior to CT in differentiating choroidal lesions and suprachoroidal fluid from retinal lesions and subretinal fluid. Ultrasonography is superior to MR imaging and CT in the evaluation of retinal detachment.[20]

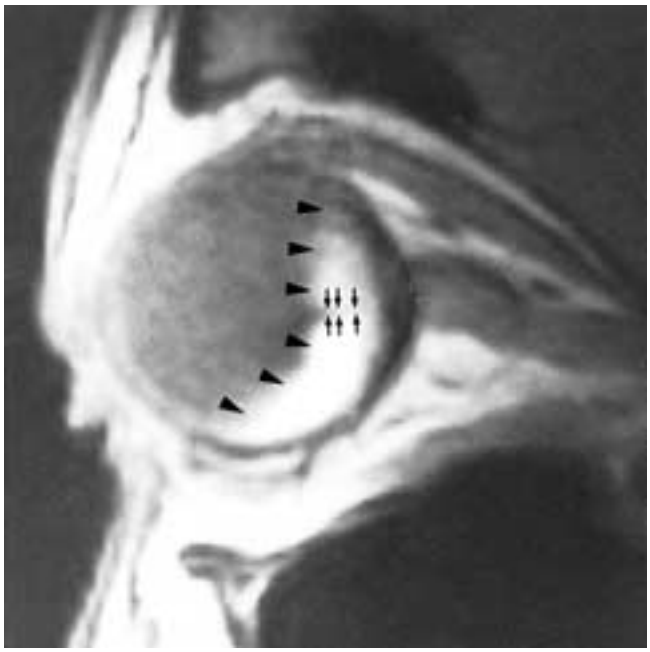

VIEW IMAGE

FIGURE 8-37 Retinal detachment. Sagittal PW MR image shows a detached retina (*arrowheads*) with characteristic folding of the retinal leaves (*arrows*) toward the optic disc.

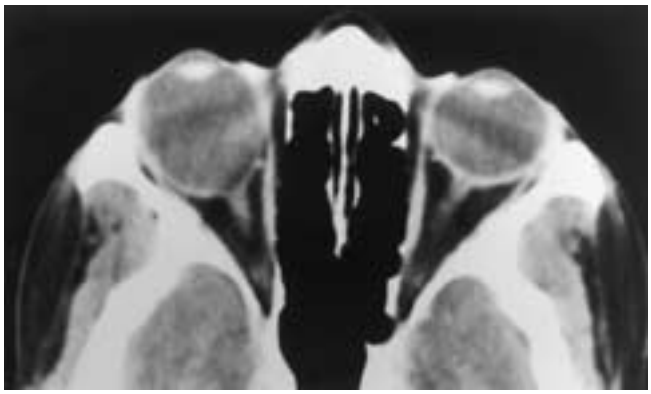

VIEW IMAGE

FIGURE 8-38 Axial myopia and staphyloma. Axial CT scan shows marked enlargement of the right globe associated with thinning of the sclera and bulging of the posterior globe including the peripapillary region.

Choroidal Detachment, Choroidal Effusion, and Ocular Hypotony

Choroidal detachment is caused by the accumulation of fluid (serous choroidal detachment) or blood (hemorrhagic choroidal detachment) in the potential suprachoroidal space.[20, 51–54] Serous choroidal detachment (Fig. 8-40) frequently occurs after intraocular surgery, penetrating ocular trauma, or inflammatory choroidal disorders.[52] Hemorrhagic choroidal detachment often occurs after a contusion, after a penetrating injury, or as a complication of intraocular surgery. Such detachment significantly influences the prognosis of the involved eye.[52] In these cases, ophthalmoscopic visualization of the fundus may be precluded by hyphema (blood in the anterior chamber) or vitreous hemorrhage. Ultrasound, although useful, has

VIEW IMAGE

FIGURE 8-39 Retinal detachment. T1-weighted coronal MR image shows the characteristic appearance of retinal folds (*arrows*) and a hyperintense subretinal exudate (*E*).

Copyright © 2003, Mosby, Inc. All rights reserved.

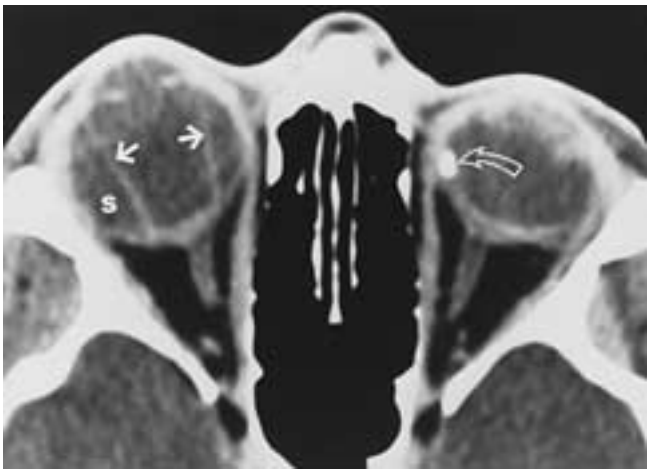

VIEW IMAGE

FIGURE 8-40 Serous choroidal detachment. Axial CT scan shows two prominent linear images (*solid arrows*) in the right eye. Because of the anchoring effect of posterior ciliary arteries and nerves, detached leaves of choroid usually do not appear to converge at the disc, unlike retinal leaves in retinal detachment. The suprachoroidal space (*S*) is isodense with vitreous, indicating serous choroidal detachment. The enlarged right globe results from known congenital glaucoma. Note the postsurgical changes in the left eye and the scleral-encircling silicone band (*curved arrow*). (From Mafee MF et al. Malignant uveal melanoma and simulating lesions: MRI evaluation. Radiology 1986;160:773–780.)

certain shortcomings in examining the traumatized eyes in the presence of an opaque medium. Contact B-scan ultrasound can expel the intraocular contents, is not tolerated by a patient with a painful eye, and increases the risk of inflammation.[54, 55] A-scan ultrasound, though less traumatic, is not often used because it is time-consuming and its interpretation requires experience. If air or gas is present in the vitreous cavity, the ultrasound postoperative evaluation of choroidal detachment is difficult. CT is best suited for the evaluation of a lacerated globe. If there is no suspicion of a ferromagnetic foreign body, MR imaging may be used.

Ocular hypotony is the essential underlying cause of serous choroidal detachment.[52] Ocular hypotony may be the result of inflammatory diseases (uveitis, scleritis), accidental perforation of the eyeball, ocular surgery, or intensive glaucoma therapy.[52–55] The pressure within the suprachoroidal space is determined by the intraocular pressure, the intracapillary blood pressure, and the oncotic pressure exerted by the plasma protein colloids.[51] The capillaries of the choriocapillaris differ from those of other capillary beds in the body because the choriocapillaris is a visceral type of vasculature with fenestrations in the vessels.[27, 31] These openings are covered by diaphragms, which permit the relatively free exchange of material between the choriocapillaris and the surrounding tissues.[27] Ocular hypotony causes increased permeability of the choroidal capillaries. This increased permeability leads to the transudation of fluid from the choroidal vasculature into the uveal tissue and causes diffuse swelling of the entire choroid (choroidal effusion). As the edema of the choroid increases, fluid accumulates in the potential suprachoroidal space, resulting in serous or exudative choroidal detachment.[51, 52, 54, 56] Choroidal effusion, like choroidal hematoma, may be preceded by surgery or other types of trauma to the eye.[57, 58] In fact, choroidal effusion may be a common, albeit transient, occurrence after intraocular surgery.[59] Other causes of choroidal effusion include inflammatory disorders of the eyeball, myxedema, photocoagulation, retinal cryopexy, Vogt-Koyanagi-Harada syndrome, and the uveal effusion syndrome.[59, 60] Clinically the choroidal detachment appears as a smooth gray-brown elevation of the choroid extending from the ciliary body to the posterior segment.[52, 54] Even when the ocular media are clear in pigmented eyes, it is difficult with ophthalmoscopy to differentiate between a serous and a hemorrhagic choroidal detachment.[52, 54] The appearance of serous choroidal detachment on CT has been described.[52] It appears as a semilunar or ring-shaped area of variable attenuation. The degree of attenuation depends on the cause but is generally greater with inflammatory disorders of the eyeball. Inflammatory diseases of the choroid (uveitis) seldom appear as a localized mounding of the choroid; however, they generally produce a diffuse thickening with no localized area of mounding unless there is a choroidal abscess.[20]

Hemorrhagic choroidal detachments appear as either a low or high mound-like area of high density on CT, which can be quite large and irregular (Fig. 8-41). In a fresh hemorrhagic choroidal detachment, the choroid and hemorrhage in the potential suprachoroidal space are isodense. However, in a patient with chronic choroidal hematoma or a serosanguineous choroidal detachment, it may be possible to separate choroid and suprachoroidal fluid accumulation (Fig. 8-42).[52]

MR imaging, with its direct multiplanar imaging ability, is an excellent method for evaluating the eye in patients with choroidal detachment, particularly if ultrasound or CT, in conjunction with the clinical examination, has not provided sufficient information. MR imaging shows a choroidal hematoma as a focal, well-demarcated, lenticular mass in the wall of the eyeball (Fig. 8-43). This characteristic configuration usually does not change as the hematoma ages.[53] However, a decrease in the size of the choroidal hematoma may be observed. Multiple lesions occasionally may be seen (Fig. 8-43). The signal intensity of the choroidal hematoma depends on its age. Within the first 48 hours or so, the hematoma is isointense to slightly hypointense relative to

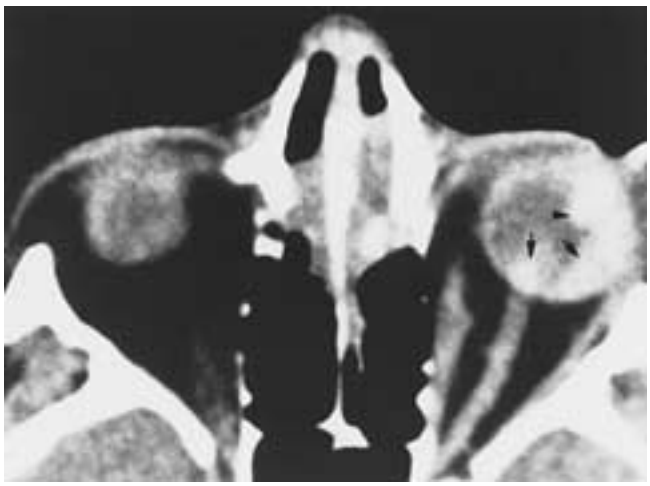

FIGURE 8-41 Acute choroidal hemorrhage (detachment). Axial CT scan shows choroidal hematomas (*arrows*).

VIEW IMAGE

Copyright © 2003, Mosby, Inc. All rights reserved.

VIEW IMAGE

FIGURE 8-42 Choroidal detachment. Axial CT scan shows detached choroid (*arrows*). Note the air in the right vitreous caused by air-fluid exchange from a detached choroid.

the normal vitreous body on T1-weighted and proton density MR images (Fig. 8-43A) but is markedly hypointense on T2-weighted images (Fig. 8-43B). After 5 days, its signal intensity characteristics are different, being relatively hyperintense on T1-weighted and proton density images (Fig. 8-44A) and only slightly hypointense on T2-weighted images (Fig. 8-44B).[20, 52, 53] At this stage, the choroidal hematoma may be confused with a choroidal melanoma.[53] The hematoma usually continues to increase in signal intensity on T1-weighted, proton density, and T2-weighted images (Fig. 8-44) and usually becomes markedly hyperintense by 2 weeks on all MR sequences (Figs. 8-44 and 8-45).[20, 52, 53]

Serous choroidal detachment (Figs. 8-46 and 8-47) and choroidal effusion (Figs. 8-48 and 8-49) have a different appearance on CT and MR imaging from choroidal hematoma (Figs. 8-41 and 8-43). Serous choroidal detachment is caused by a nonhemorrhagic accumulation of fluid in the suprachoroidal potential space. The choroidal detachment appears as a smooth elevation of the choroid (Figs. 8-46 and 8-47), the fluid in the suprachoroidal space is often hypodense on CT (Fig. 8-46), and its MR appearance is that of an exudate (Fig. 8-47). A choroidal effusion usually is seen as a crescentic or ring-shaped lesion on both CT and MR imaging (Figs. 8-48 and 8-49).[20, 52, 53] It does not resemble the lenticular appearance of a hematoma. Inflammatory choroidal effusions usually appear as increased signal intensity on all MR images (Figs. 8-48 and 8-49). This high signal intensity is thought to be due to the high protein content of the effusion fluid.[53] Posttraumatic effusions, although also demonstrating increased signal on T1-weighted and T2-weighted images, are not as hyperintense as the inflammatory effusions.[53] At times it may be difficult to differentiate retinal detachment and choroidal detachment, since the distinction of choroidal effusion from subretinal effusion is not always clear.[20, 53, 54] Shifting of subretinal fluid occurs rather rapidly, whereas shifting of suprachoroidal fluid occurs slowly.[20] Therefore, rapidly shifting fluid within the wall of the eye, demonstrated on CT or MR imaging, favors the diagnosis of retinal detachment.

Ocular Inflammatory Disorders

The eye may be affected by either known systemic or idiopathic ocular inflammatory processes. A host of infectious diseases may affect the glove. Viral diseases include herpes simplex, rubella, rubeola, mumps, variola, varicella, cytomegalovirus (Fig. 8-50), and infectious mononucleosis. Bacterial diseases include syphilis, brucellosis, tuberculosis, and leprosy. Fungal infections, particularly candidiasis, may also involve the globes in diabetic and immunocompromised patients.[41] Chronic inflammatory processes may cause calcification of the sclera, choroid and

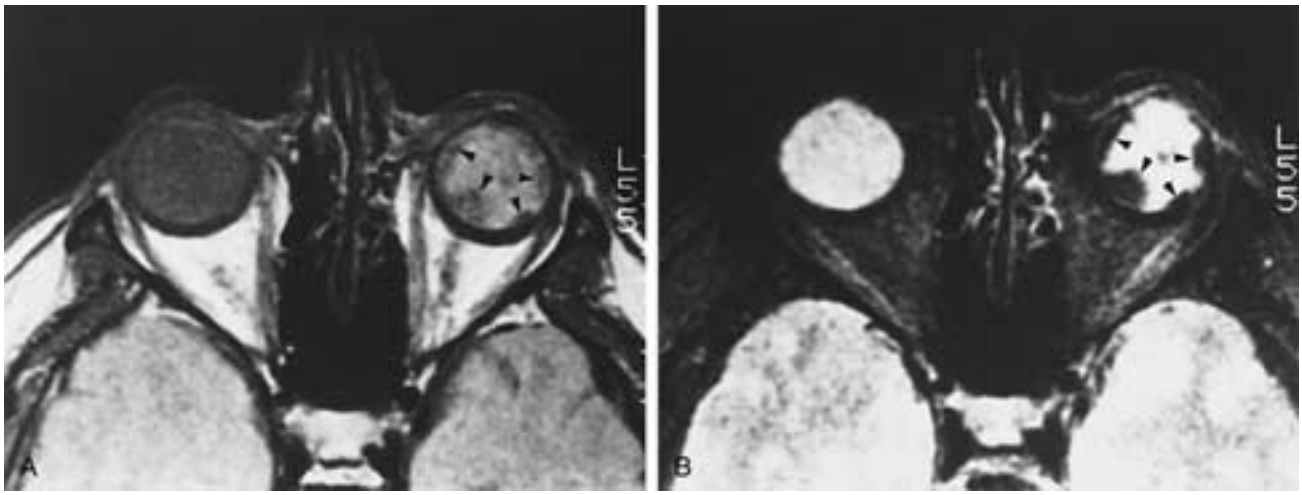

VIEW IMAGE

FIGURE 8-43 Acute choroidal hemorrhage (detachment). **A**, Axial PW and **B**, T2-weighted MR images. Scans show choroidal hematomas (*arrowheads*). The increased intensity of the left globe is probably caused by protein leaking into the vitreous as a result of an impaired retinal-blood barrier. (From Mafee MF et al. Retinal and choroidal detachments: role of MRI and CT. Radiol Clin North Am 1977;25:487–507.)

Copyright © 2003, Mosby, Inc. All rights reserved.

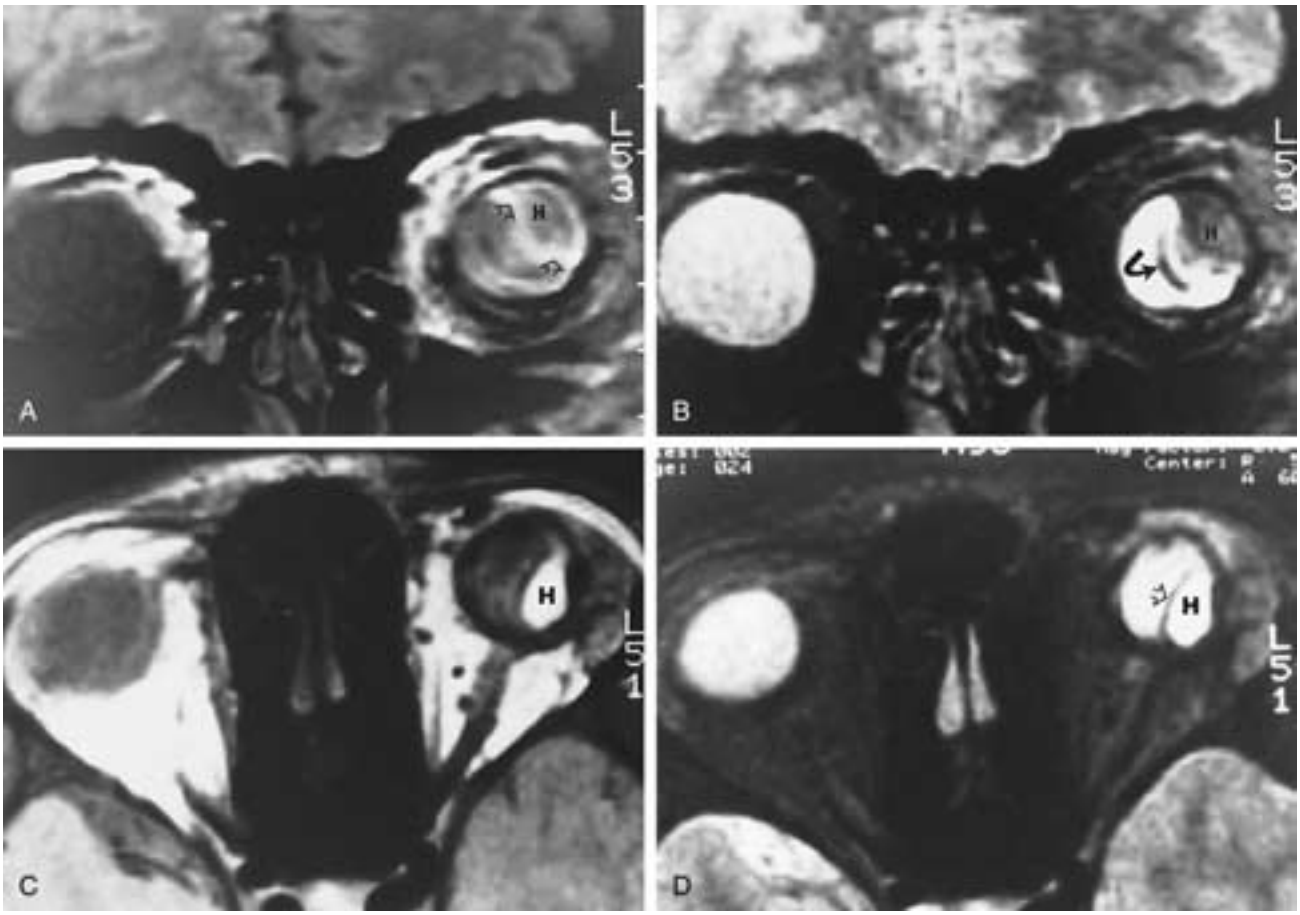

VIEW IMAGE

FIGURE 8-44 Subacute and chronic hemorrhagic choroidal detachment. **A**, Coronal PW MR image shows choroidal hematoma (*H*) as an area of mixed signal intensity. The peripheral part of the hematoma is hyperintense (*arrows*). **B**, Coronal T2-weighted MR image shows a choroidal hematoma (*H*) as a hypointense area. The curved image (*curved arrow*) is thought to be caused by residual intravitreal silicone oil. **C**, Axial PW and **D**, T2-weighted MR images. Scans obtained about 9 days after the scans in **A** and **B** show that the hematoma is markedly hyperintense.

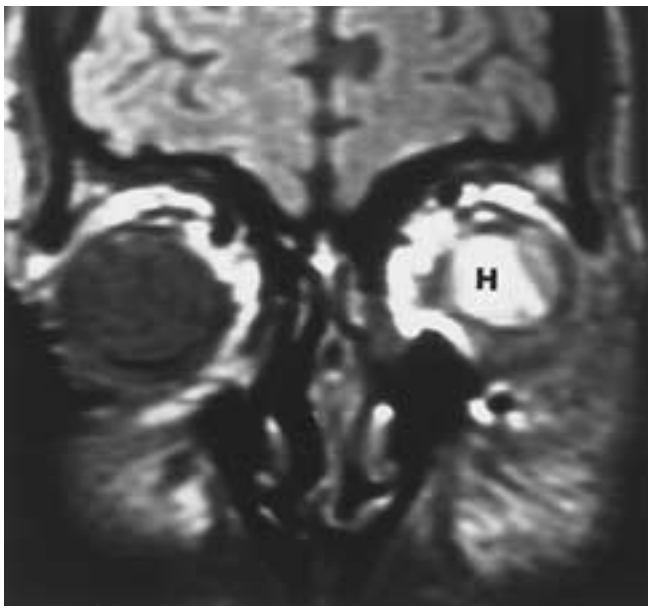

VIEW IMAGE

FIGURE 8-45 Chronic hemorrhagic choroidal detachment. Coronal PW MR image shows a hyperintense choroidal hematoma (*H*).

lens. Extensive disease may result in irregular calcific intraocular masses and a small, deformed globe (phthisis bulbi) (Fig. 8-21).

Other Inflammatory Conditions

Lymphoid Hyperplasia

Lymphoid hyperplasia of the uvea may cause thickening of the posterior wall of the globe, a finding that can simulate melanoma, uveitis, and posterior scleritis (see Fig. 8-12). Lymphoma and leukemic infiltration of the globe may also simulate uveitis.

Papilledema

Increased intracranial pressure may result in papilledema with elevation of the optic discs. On CT and MR scans, elevation and bulging of the optic disc into the posterior aspect of the globe is observed (Fig. 8-51). The diameter of the optic nerve sheath complex may be increased. On postcontrast T1-weighted MR imaging scans, there may be increased enhancement of the optic discs (Fig. 8-51).

Copyright © 2003, Mosby, Inc. All rights reserved.

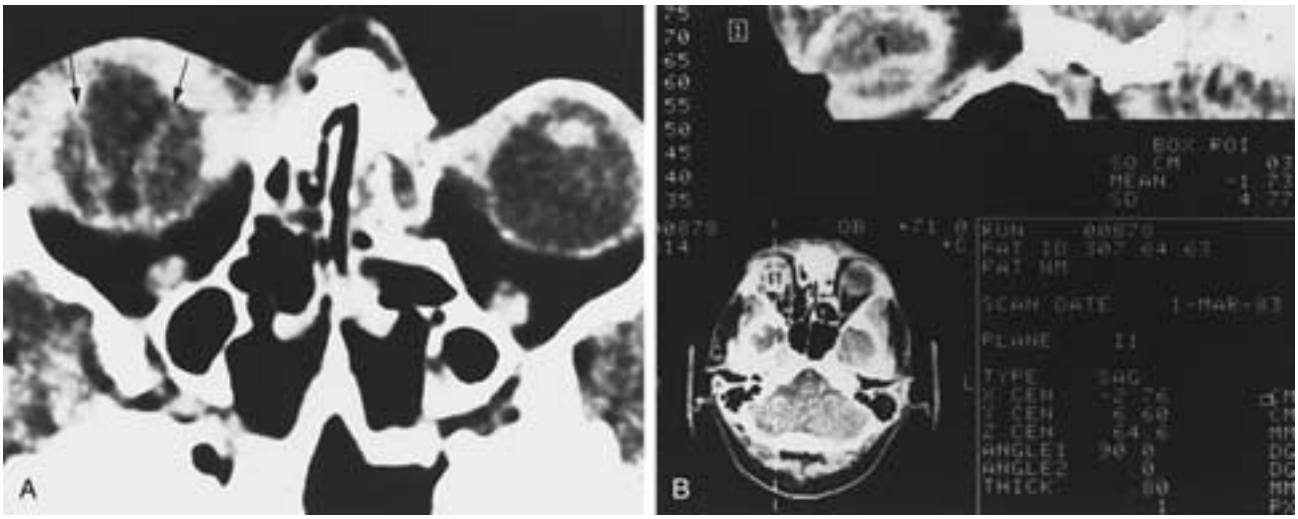

VIEW IMAGE

FIGURE 8-46 Serous choroidal detachment. **A**, Axial CT scan. **B**, Reformatted sagittal CT image. Scans show detached choroid (*arrows* and *arrowhead*). The suprachoroidal space is isodense to vitreous compatible with serous fluid.

Episcleritis

Episcleritis is a relatively common idiopathic inflammation of the thin layer of tissue lying between the conjunctiva and the sclera. It may be unilateral (66%) or bilateral. In some cases, episcleritis is associated with deeper inflammation (scleritis). Episcleritis is usually self-limited and resolves within 1 to 2 weeks. Imaging evaluation is not indicated in episcleritis.

Scleritis

Scleritis can occur either as an idiopathic condition or in association with systemic diseases.[41] The process may be unilateral or bilateral. Patients with anterior scleritis present with pain, erythema, photophobia, and tenderness.[41, 61] Scleritis may be caused by collagen-vascular disorders, granulomatous diseases, metabolic disorders, infections, and trauma. The sclera is basically an avascular structure deriving its blood supply from the choroidal episcleral plexus.[62] Scleritis may be bacterial, fungal, or viral in origin.[62] It may be caused by metabolic disease (gout) or by a group of autoimmune disorders, including rheumatoid arthritis, polyarthritis nodosa, lupus erythematosus, Wegener's granulomatosis, and relapsing polychondritis.[41, 61] Inflammatory bowel disease, especially Crohn's disease, can be associated with scleritis. Sarcoidosis and Cogan's syndrome also can be associated with scleritis. In most cases of posterior scleritis, however, no underlying cause is found.[61] Scleritis is classified as anterior or posterior scleritis. Scleritis may be acute or chronic. Posterior scleritis results in thickening of the sclera and choroid.[61, 62] There may be associated thickening of Tenon's capsule, as well as secondary serous or exudative retinal detachment (Fig. 8-52).[61, 62] Histopathologically, posterior scleritis is classified into two forms: (1) nodular and (2) diffuse. Nodular posterior scleritis is a focal or zonal necrotizing granulomatous inflammation surrounding a discrete sequestrum of scleral collagen.[61, 62] This type can mimic uveal melanoma (Fig. 8-53). Diffuse posterior scleritis appears as diffuse thickening of the uveoscleral coat, with some degree of contrast enhancement on both CT and MR scans.[61, 62] Fluid between the sclera and Tenon's capsule often causes choroidal detachment, which can be detected by CT and MR imaging or ultrasonography. Perforation of the sclera may be seen in necrotizing scleromalacia, a rare disease usually associated with severe rheumatoid arthritis.[41] At times, in addition to posterior scleritis, other features in support of a diagnosis of pseudotumor may be present on CT and MR scans. These findings suggest that several entities (posterior scleritis, scleritis, sclerotenonitis, periscleritis, and orbital pseudotumor) represent a continuum of the same disease.[62]

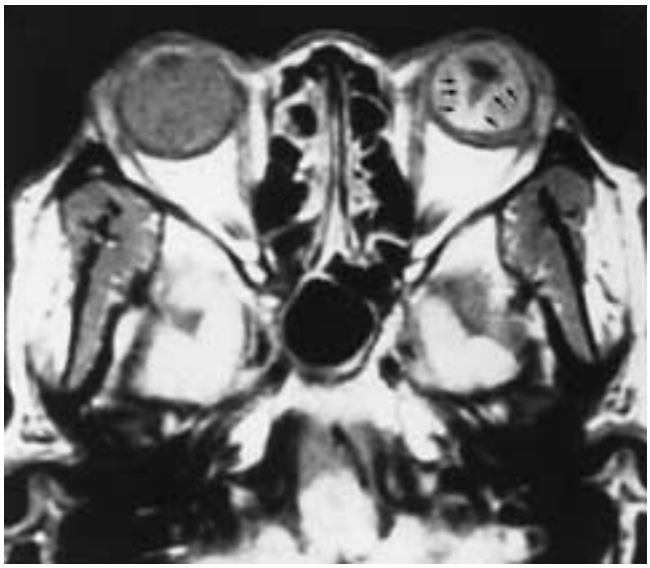

VIEW IMAGE

FIGURE 8-47 Serous choroidal detachment. Axial PW MR image shows a kissing choroidal detachment. Suprachoroidal fluid is slightly hyperintense compared with that of the normal right vitreous. The detached choroid (*arrows*) appears thick, and its hyperintensity is caused by accumulation of fluid in its interstitium.

Copyright © 2003, Mosby, Inc. All rights reserved.

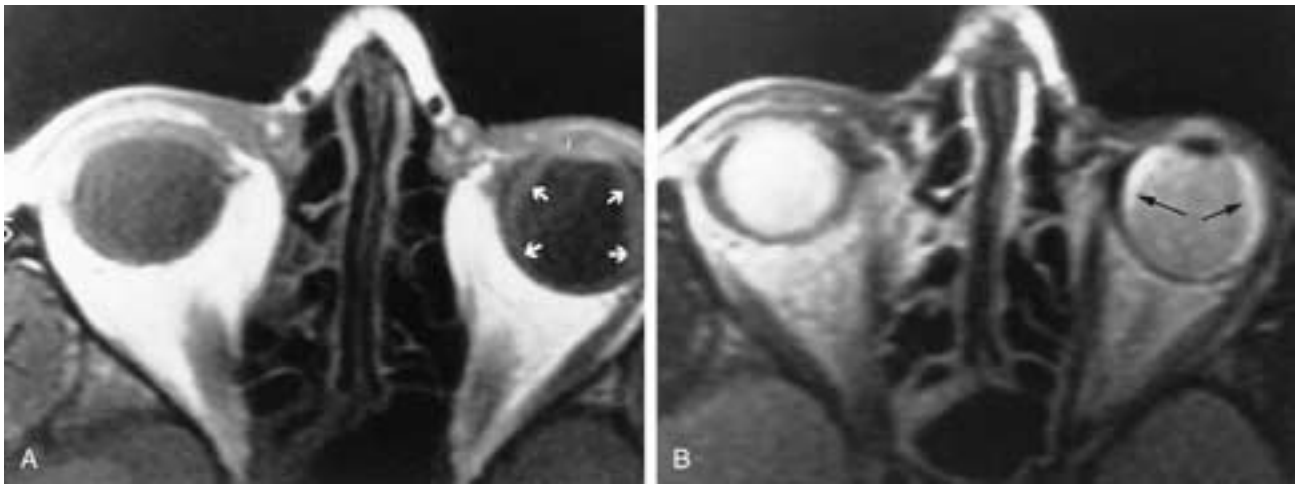

VIEW IMAGE

FIGURE 8-48 Choroidal detachment. **A**, Axial PW and **B**, T2-weighted MR images. Scans show the choroidal effusion of the left eye as a ring-shaped area of increased signal intensity (*arrows*).

Uveitis

Uveitis is an inflammatory process of the intraocular contents, often prominently involving the uveal tract.[41] The etiology of uveitis is often unknown. Many patients appear to have a perturbation of lymphocytic control mechanisms.[41] Intraocular lymphoma can mimic posterior uveitis, pars planitis, or pars plana endophthalmitis; the last condition is an idiopathic form of uveitis. Uveitis may be caused by a specific organism such as *Toxoplasma* or cytomegalovirus. Ocular tuberculosis results from endogenous spread of systemic disease (Fig. 8-54). Toxoplasmosis is a common cause of posterior chorioretinitis. In congenital toxoplasmosis, the fetus is infected in utero and the infection is arrested by the time of diagnosis. Many of these children have cerebral toxoplasmosis and the detection of CNS calcifications by CT helps to establish the etiology.[41] In the adult form of ocular toxoplasmosis, associated CNS involvement is much less common.

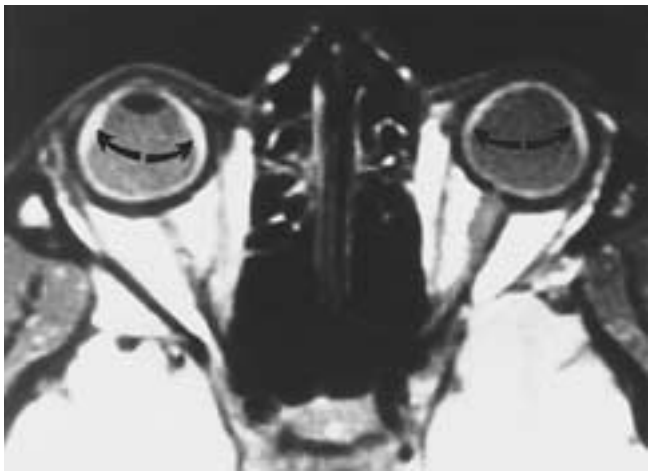

VIEW IMAGE

FIGURE 8-49 Bilateral choroidal effusion. Axial PW MR image shows bilateral ring-shaped areas of increased signal intensity (*arrows*). This MR appearance may be difficult to differentiate from that of retinal detachment. (From Mafee MF et al. Choroidal hematoma and effusion: evaluation with MRI. Radiology 1988;168:781–786.)

Parasitic Infections

Larval granulomatosis usually affects children between 2 and 8 years of age. The process causes uveitis resulting from ingestion of the eggs of the nematode *Toxocara canis* or *T. cati* (Fig. 8-55).[41] Three clinical patterns occur: (1) a unilateral localized granuloma that may mimic retinoblastoma, (2) endophthalmitis, and (3) pars plana disease.[41]

Intraocular Calcifications

Deposition of calcium in ocular tissues is a complex process, the pathophysiology of which depends on the specific site of calcification. Intraocular calcifications may be metastatic (hypercalcemic states) or dystrophic, and arise in association with diverse degenerative ocular conditions (neoplasia, inflammation, congenital dysplasias, and senescent or traumatic degeneration).[41, 63] Calcifications in neoplasms may be a result of tumor necrosis. Such neoplasms include retinoblastoma and astrocytic hamartomas seen in tuberous sclerosis or neurofibromatosis Type I. Fifty percent of patients with tuberous sclerosis may develop retinal hamartomas, which often calcify. Ocular calcification or ossification may also occur in congenital vascular lesions such as Sturge-Weber syndrome and Von Hippel-Lindau disease.[41] Scleral calcification has been reported in patients with linear sebaceous nevus syndrome.[41] The association of the nevus sebaceous syndrome of Jadassohn with seizures, mental deficiency, and ocular abnormalities has been reported.[41] The ocular anomalies may include coloboma of the iris and choroid, conjunctival lipodermoids, horizontal and rotational nystagmus, and vascularization of the cornea.[41] Chronic posttraumatic degeneration is probably the most common cause of dystrophic intraocular calcification. Choroidal osteoma, episcleral choristoma, and optic disc drusen are other causes of intraocular calcification.[41] Retinopathy of prematurity also may cause delayed unilateral or bilateral ocular calcification.[63] Scleral calcification may be seen in elderly people at or anterior to the sites of insertion of the horizontal extraocular muscles.[63] *Phthisis bulbi* refers to calcification or ossification within a shrunken or atrophic globe. It may be the result of any ocular insult with subsequent degeneration. It is most commonly a result

Copyright © 2003, Mosby, Inc. All rights reserved.

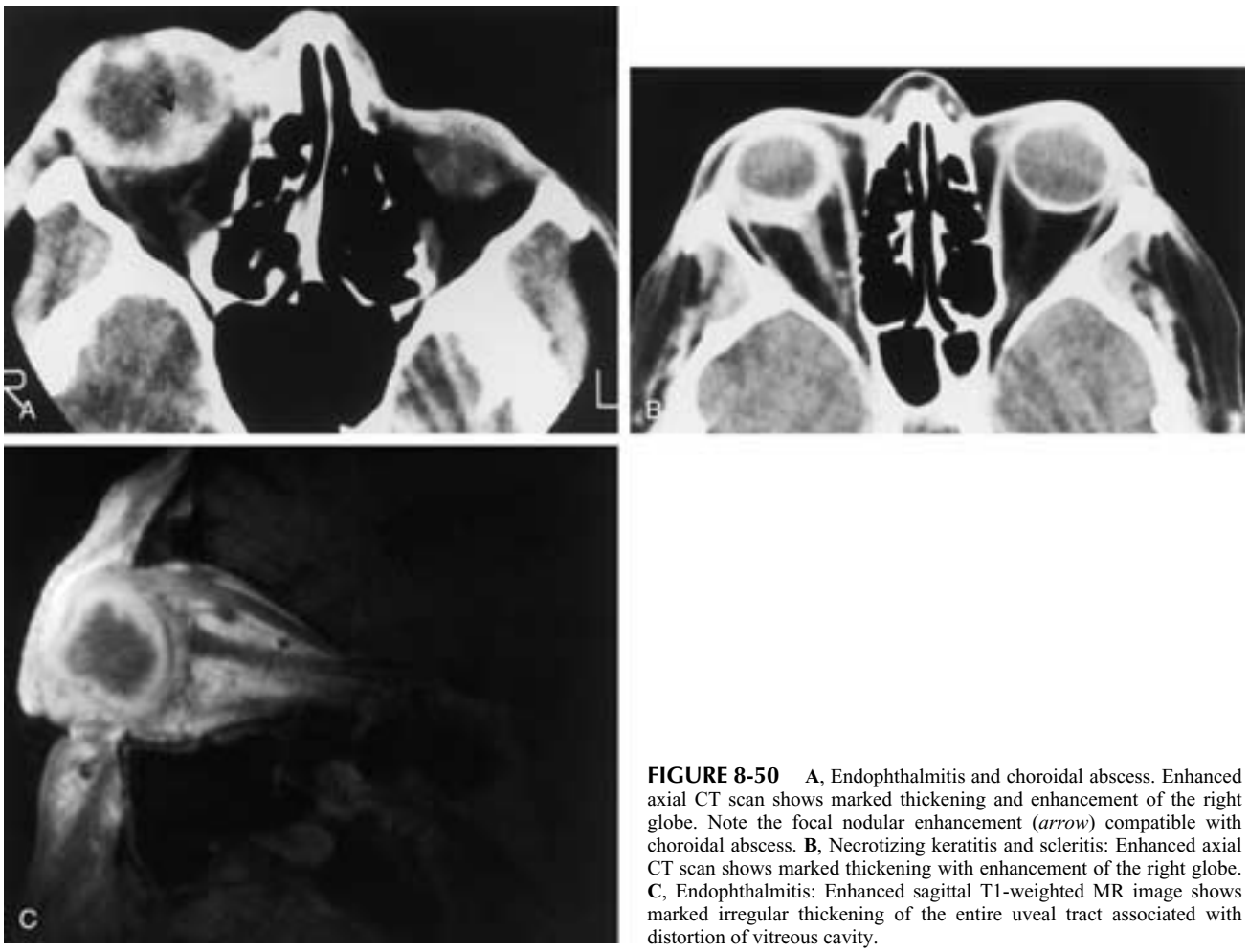

FIGURE 8-50 **A**, Endophthalmitis and choroidal abscess. Enhanced axial CT scan shows marked thickening and enhancement of the right globe. Note the focal nodular enhancement (*arrow*) compatible with choroidal abscess. **B**, Necrotizing keratitis and scleritis: Enhanced axial CT scan shows marked thickening with enhancement of the right globe. **C**, Endophthalmitis: Enhanced sagittal T1-weighted MR image shows marked irregular thickening of the entire uveal tract associated with distortion of vitreous cavity.

VIEW IMAGE

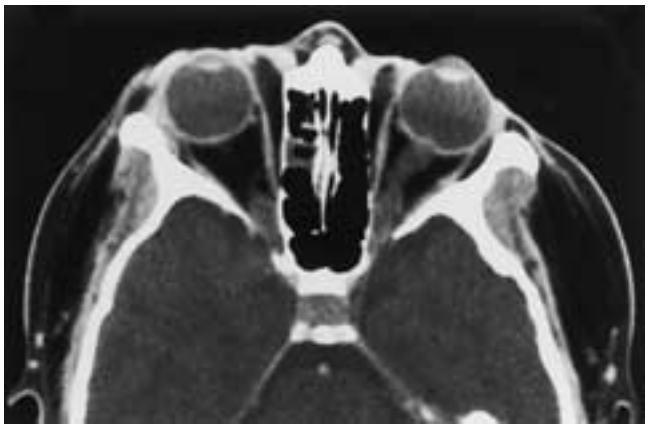

VIEW IMAGE

FIGURE 8-51 Optic papilledema. Axial CT scan shows bulging of the left optic disc in this patient with bilateral papilledema. There was bilateral optic disc enhancement on enhanced T1-weighted MR images.

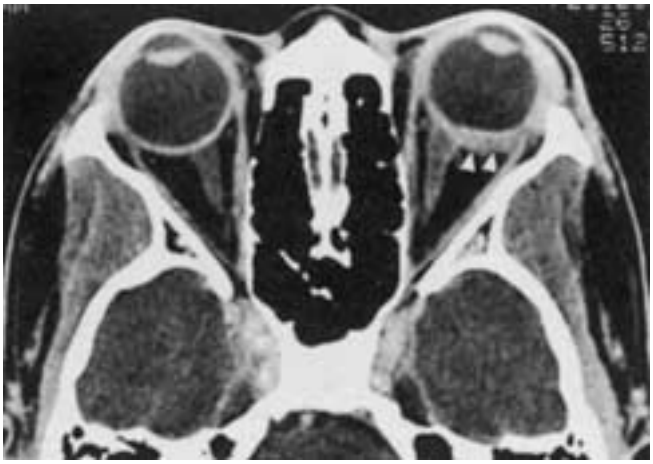

FIGURE 8-52 Posterior scleritis. Enhanced axial CT scan shows thickening with enhancement of the posterior scleral-uveal coat (*arrowheads*). (Courtesy of M.F. Mafee, MD, FACR, Chicago.)

VIEW IMAGE

Copyright © 2003, Mosby, Inc. All rights reserved.

of trauma or infection.[63] Table 8-3 lists the most frequent causes of intraocular calcifications.[63]

LEUKOKORIA

Leukokoria is a white, pink-white, or yellow-white pupillary reflex (cat's eye). It is a sign that results from any intraocular abnormality that reflects the incident light back through the pupil toward the observer. This reflection of light is the result of a white or light-colored intraocular mass, membrane, retinal detachment, or a retinal storage disease.[40, 64] Leukokoria is dependent on the size, location, and pigmentation of the intraocular pathology. When examining a child with leukokoria, the major diagnostic considerations are retinoblastoma, persistent hyperplastic primary vitreous (PHPV), retinopathy of prematurity (ROP), congenital cataract, Coats' disease, toxocariasis, total retinal detachment, and a variety of other nonspecific diseases.

Leukokoria is the most common presenting sign of retinoblastoma, the highly malignant primary retinal cancer. Howard and Ellsworth studied 500 consecutive patients in whom the diagnostic possibility of retinoblastoma was raised.[65] Of these 500 patients, diagnoses other than retinoblastoma were made in 265 cases (53%). Out of 27 different conditions, the most common was PHPV, followed by ROP, posterior cataract, coloboma of the choroid or optic disc, uveitis, and larval granulomatosis. Identification of the cause of the leukokoria is critical to ensure prompt recognition and appropriate treatment, and diagnostic accuracy is particularly important because retinoblastoma is one of the few human cancers for which definitive treatment is carried out without a confirmed histopathologic diagnosis.[21] Common ocular and orbital disorders in children are listed in Table 8-4.

RETINOBLASTOMA

Retinoblastoma (Rb) is the most common intraocular tumor of childhood. It is a highly malignant primary retinal tumor that arises from neuroectodermal cells (nuclear layer of the retina) that are destined to become retinal photoreceptors.[66, 67] The manner of intraocular and extraocular extension, patterns of metastasis and recurrence, ocular complications, and associated malignancies make the diagnosis of retinoblastoma one of the most challenging problems of pediatric ophthalmology and radiology. To ensure appropriate therapy, retinoblastoma must be differentiated from a host of benign lesions that stimulate it (Table 8-5). This diagnosis must be established rapidly to permit maximum ocular salvage and to minimize tumor-associated mortality.[64, 68] When the disease extends beyond the eye, mortality approaches 100%.[68] With earlier diagnosis, the 5-year survival rate with tumors limited to the globe is greater than 90%.[32, 69] The classification of retinoblastomas has been established in regard to expected results of therapy. Group I includes tumors with a very favorable prognosis. These are either solitary tumors or multiple tumors less than four disc diameters in size at or behind the equator. Useful vision in the treated eye is attained in 90% of these patients and overall in about 75% of eyes that are not enucleated.[69] In group II the prognosis is also favorable, including patients with one or several tumors measuring between 4 and 10 disc diameters. In group III the tumors are anterior to the equator or there is a solitary tumor larger than 10 disc diameters. In these cases the prognosis is guarded. Group IV includes tumors that are multiple and extend up to the ora serrata. Group V includes those tumors that involve half of the retina or tumors that also have vitreous seeds. Groups IV and V have unfavorable prognoses.[21, 32]

Virchow was the first to postulate that retinoblastoma is of glial origin. He used the term *glioma of the retina* to describe the tumor.[32] Bailey and Cushing divided Rb into two types: (1) medulloblastoma and (2) neuroepithelioma. It is now well known that retinoblastoma is derived from primitive embryonal retinal cells (either photoreceptor or neuronal retinal cells).[70] This tumor can be undifferentiated or well-differentiated and can display evidence of photoreceptor differentiation in the form of Flexner-Wintersteiner rosettes and fleurettes.[66, 67, 71, 72] The tumor is composed of small round or ovoid cells with scant cytoplasm and relatively large nuclei. There is marked variability in the histologic features of retinoblastoma. Some tumors display

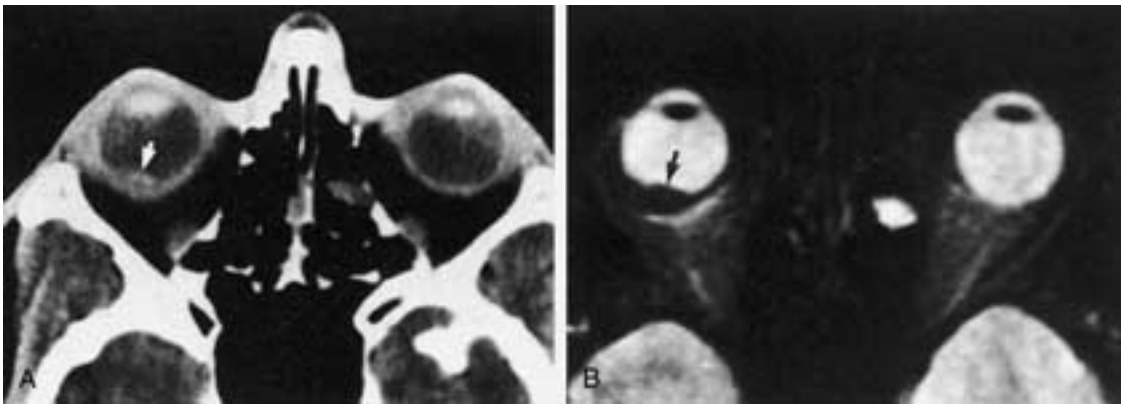

FIGURE 8-53 Posterior nodular scleritis. **A**, Axial CT scan shows a mass-like lesion (*arrow*). **B**, Axial T2-weighted MR image. The lesion (*arrow*) appears hypointense, simulating a choroidal melanoma. It was barely recognized on T1-weighted images (not shown). The patient improved and his symptoms resolved following a short course of steroid therapy. (Courtesy of M.F. Mafee, MD, FACR, Chicago.)

VIEW IMAGE

Copyright © 2003, Mosby, Inc. All rights reserved.

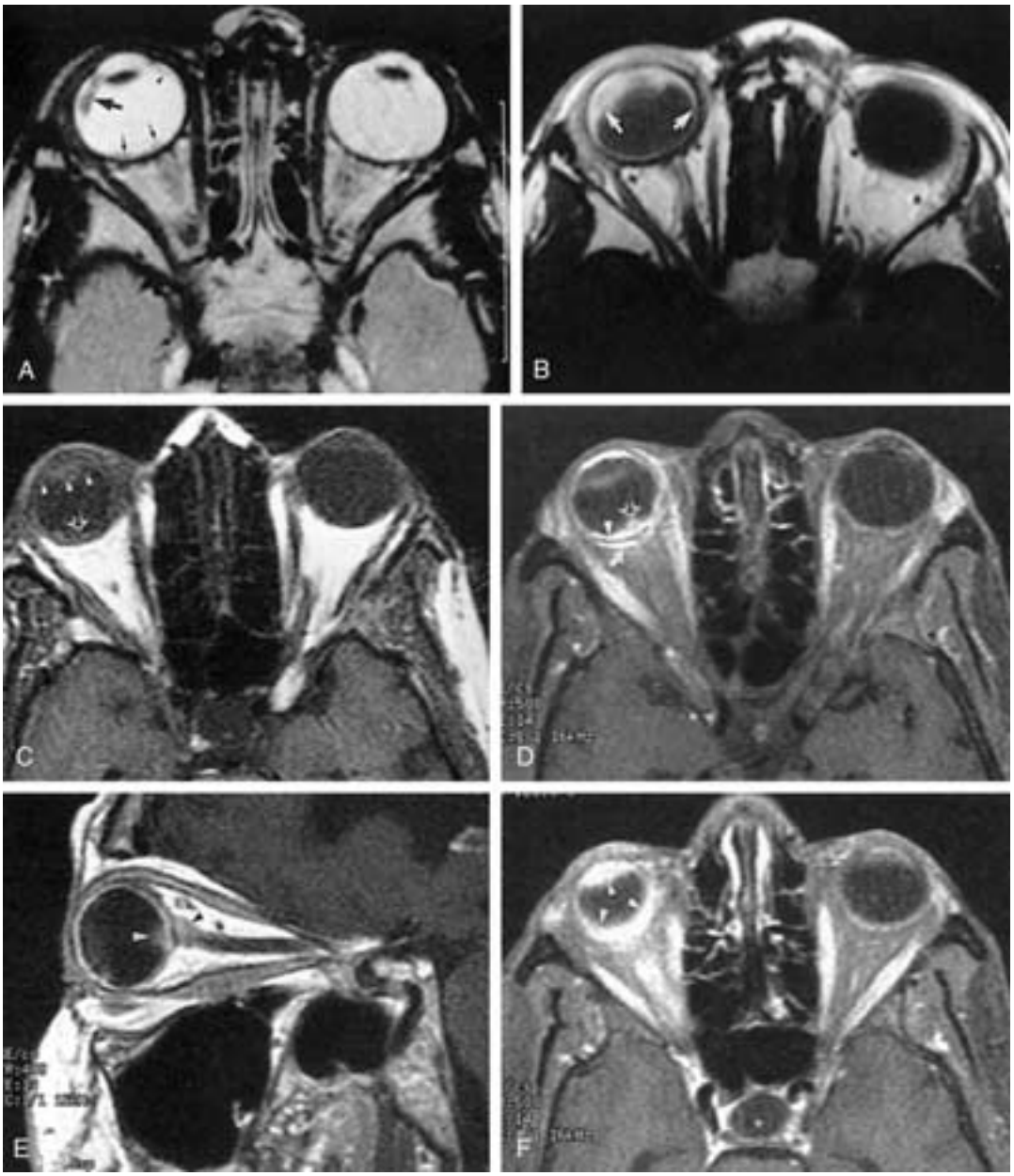

VIEW IMAGE

FIGURE 8-54 (1) Granulomatous uveitis. **A**, Axial T2-weighted (2800/95, TR/TE) MR image shows hypointense lesions (*arrows*). **B**, Axial enhanced, T1-weighted (400/15, TR/TE) MR image shows marked enhancement of the entire uveal tract (*arrow*). Rb is unlikely because the lesion appears to have arisen within the uvea rather than the retina. (2) Ocular sarcoidosis panuveitis. **C**, Unenhanced axial T2-weighted (500/13, TR/TE) MR image shows nodular thickening of the posterior aspect of the right globe (*arrow*) and thickening of the anterior segment (*arrowheads*) of the right globe. **D**, Enhanced axial fat-suppressed, T1-weighted (500/13, TR/TE) MR image shows nodular enhancement of the posterior aspect of the right globe (*arrowhead* and *open arrow*) related to granulomatous involvement of the choroids. Note the enhancement of the anterior segment of the right globe and the abnormal enhancement of Tenon's capsule (*curved arrow*). **E**, Enhanced sagittal T1-weighted (400/13, TR/TE) MR image shows granuloma at the optic disc (*white arrowhead*) as well as involvement of the optic nerve (*black arrowhead*). **F**, Enhanced axial fat-suppressed, T1-weighted (500/14, TR/TE) MR image shows enhancement of the markedly thickened uveal tract (*arrowheads*).

significant necrosis and prominent foci of calcification. A few tumors show areas of glial differentiation.[67, 71] The occurrence of a second cancer arising outside the treatment radiation field was pointed out by Jensen and Miller[73] and Abramson, Ellsworth, Kitchin, and Tung.[74] Abramson et al.[74] demonstrated that patients with heritable retinoblastoma are highly susceptible to the development of other nonocular cancers, usually osteogenic sarcomas, and other neoplasms at sites of irradiation. The worldwide incidence of retinoblastoma has been reported to be 1 in 18,000 to 30,000 live births.[75] Although the tumor is congenital in origin, it usually is not recognized at birth.[32] However,

Copyright © 2003, Mosby, Inc. All rights reserved.

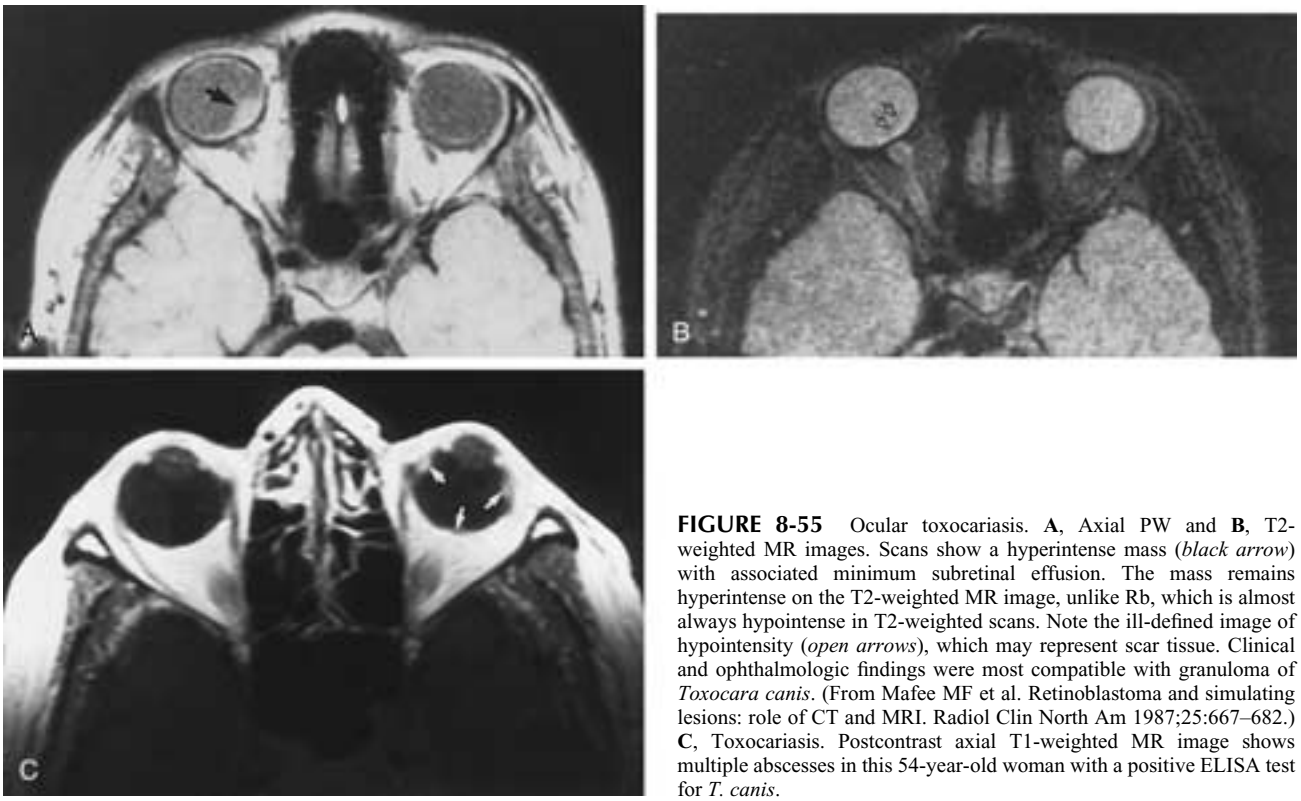

FIGURE 8-55 Ocular toxocariasis. **A**, Axial PW and **B**, T2-weighted MR images. Scans show a hyperintense mass (*black arrow*) with associated minimum subretinal effusion. The mass remains hyperintense on the T2-weighted MR image, unlike Rb, which is almost always hypointense in T2-weighted scans. Note the ill-defined image of hypointensity (*open arrows*), which may represent scar tissue. Clinical and ophthalmologic findings were most compatible with granuloma of *Toxocara canis*. (From Mafee MF et al. Retinoblastoma and simulating lesions: role of CT and MRI. Radiol Clin North Am 1987;25:667–682.) **C**, Toxocariasis. Postcontrast axial T1-weighted MR image shows multiple abscesses in this 54-year-old woman with a positive ELISA test for *T. canis*.

VIEW IMAGE

Table 8-3
CAUSES AND SITES OF CALCIUM DEPOSITION IN INTRAOCULAR TISSUE

Site of Calcification	Description	Causes
Cornea	Basement membrane of corneal epithelium, Bowman's membrane, anterior stromal lamellae	Chronic iridocyclitis
Sclera	Focal, near insertion of rectus muscles	Idiopathic sclerochoroidal calcification Hypercalcemia* Rheumatoid arthritis* Microphthalmic with cyst* Metastatic calcification* Linear sebaceous nevus syndrome
Lens	Focal or diffuse, in the subcapsular or equatorial region (especially in hypermature cataracts)	Any condition that causes hypermature cataract
Ciliary body	Focal	Trauma Medulloepithelioma (teratoid)* Myopia
Choroid/RPE	Focal or diffuse (from RPE metaplasia or choroid osteoma)	Trauma Uveitis, *Toxocara* granuloma* Sturge-Weber syndrome* Choroidal osteoma*
Retina	Focal, scattered or diffuse	Retinoblastoma Drusen Phthisis bulbi Subretinal membrane Periretinal membrane PHPV* ROP* Coats' disease* Astrocytoma* CMV retinitis* Tuberous sclerosis* Von Hippel-Lindau disease* Chronic organized retinal detachment Medulloepithelioma*
Optic nerve	Focal, near the surface of the optic nerve	Drusen Astrocytoma* Optic nerve sheath dural idiopathic calcification*

*Uncommon causes.
RPE, retinal pigment epithelium; *PHPV*, persistent hyperplastic primary vitreous; *ROP*, retinopathy of prematurity; *CMV*, cytomegalovirus.
Source: Yan X, Edward DP, Mafee MF. Ocular calcification: radiologic–pathologic correlation and literature review. Int J Neuroradiol 1998;4:81–96.

Copyright © 2003, Mosby, Inc. All rights reserved.

Table 8-4
COMMON OCULAR AND ORBITAL DISORDERS OF CHILDREN

Retinoblastoma—most common malignant ocular cancer in children
Persistent hyperplastic primary vitreous
Retinopathy of prematurity
Coats' disease
Microphthalmos with or without orbital cyst
Ocular trauma
Ocular inflammation, including granulomatous conditions
Toxocara larval granulomatosis
Orbital cellulitis—most common cause of proptosis in children
Dermoid and epidermoid cysts—most common orbital masses
Capillary hemangioma and lymphangioma—most common vascular masses
Optic nerve glioma—most common optic nerve tumor in children
Rhabdomyosarcoma—most common primary malignant orbital tumor in children
Leukemia
Pseudotumor
Neurofibroma
Metastatic neuroblastoma—most common metastatic cancer of the orbit in children
Subperiosteal hematoma

ocular involvement and metastasis may be present at birth.[62] In the United States, the average age of the child at diagnosis is 13 months.[76] In other countries, the disease is often not detected until the fourth year of life, when it is usually far advanced.[77] Over 90% of all diagnoses are made in children younger than 5 years of age. The sex distribution is equal, and there is no preference for either the right or the left eye.[78] Retinoblastoma results when an individual retinal cell has inactivation or loss of both alleles of the Rb1 gene on chromosome 13q14.[79–83] Transformation of the retinal cell occurs only if the genetic events occur during the age of vulnerability, usually when the patient is less than 3 years old. Retinoblastoma occurs in two distinct patterns: (1) a nonfamilial sporadic form and (2) a familial, hereditary form that appears at the clinical level to be autosomal dominant.[21] In both forms, the biology of the retinoblastoma tumor is identical. In nonfamilial retinoblastoma, an individual somatic retinal cell undergoes two sequential genetic events resulting in the loss or inactivation of both Rb1 alleles. All of the patients with nonfamilial retinoblastoma have unilateral solitary tumors. In the familial form, the patient's first loss or inactivation of an Rb1 allele occurs during gametogenesis at the germ cell level (either an inherited or a new mutation), so that every cell in the patient has only one working Rb1 allele. Retinoblastoma results if one of the patient's ''primed'' retinal cells has loss or inactivation of the second Rb1 allele (statistically, a 90% chance). With familial retinoblastoma, 85% of the cases are bilateral and 15% are unilateral.[21] Overall, approximately one third of the patients with retinoblastoma have bilateral disease.[19, 78, 84]

A parent with bilateral retinoblastoma has about a 50% chance of passing retinoblastoma on to one child.[78] Some affected children have been found to have an associated deletion of the long arm of chromosome 13 involving band 13q14.[81, 82] The association between retinoblastoma and deletion of the q14 band of chromosome 13j (13q14) has been convincingly documented.[81–83, 85] Esterase D, an electrophoretically polymorphic human enzyme, has also been mapped to chromosomal band 13q14.[86] In several families with hereditary retinoblastoma with no apparent chromosomal deletion, the gene for retinoblastoma has been shown to be closely linked to that for esterase D and assigned to chromosome band 13q14.[86, 87] Compilation of data from recent studies suggests an approximately 7% incidence of 13q chromosomal deletion in patients with retinoblastoma.[88, 89] Only a few of the patients with retinoblastoma have a sufficiently large chromosomal deletion to produce systemic dysmorphic features such as microcephaly, genital malformations, ear abnormalities, mental retardation, and toe and finger abnormalities.[89] Karyotype analysis of these children with congenital dysmorphic features may allow detection of chromosome 13 deletion involving band 13q14, prompting ophthalmic examination and therefore allowing early diagnosis of retinoblastoma.[89] Patients with familial Rb are highly susceptible to the development of other nonocular cancers, usually osteogenic sarcoma, as well as other neoplasms at the site of external beam irradiation (see Fig. 8-31).[32] A second neoplasm may also arise outside the field of radiation.[32] Of 688 patients who survived therapeutic external beam irradiation for retinoblastoma, 89 developed second tumors, 62 in the field of radiation and 27 outside of the field.[32, 74] Of 23 patients who received no radiation, five developed second tumors, either osteosarcoma or soft tissue

Table 8-5
INTRAOCULAR MASS AND MASS-LIKE LESIONS SIMULATING RETINOBLASTOMA

Coats' disease	Uveitis
Toxocariasis	Vitreous hemorrhage
Medulloepithelioma	Endophthalmitis
Retinal astrocytoma	Organized vitreous
Combined hamartoma of retinal pigment epithelium and retina	Retinal detachments
Choroidal osteoma	Persistent hyperplastic primary vitreous
Incontinetia pigmenti	Retinopathy of prematurity
Juvenile xanthogranuloma	X-linked retinoschisis
Mesoectodermal leiomyoma	Retinal dysplasia
Papillitis	Syndrome
Optic nerve head drusen	Norrie's disease
Retinal gliosis	Developmental retinal cyst
Myelinated nerve fibers	Falciform fold
Chorioretinal coloboma	Familial exudative vitreoretinopathy
Optic disc coloboma	Trauma
Walker-Warburg morning glory disc	Myopia
Von Hippel-Landau retinal angiomatosis	Stickler's syndrome
Choroidal hemangioma	Congenital cataract
Subretinal neovascular membrane	Congenital glaucoma
Vitreous opacities	Myiasis

Copyright © 2003, Mosby, Inc. All rights reserved.

sarcoma.[74] The incidence of second tumors is 20% 10 years after initial diagnosis, 50% at 20 years, and 90% at 30 years.[32, 65, 74]

Trilateral Retinoblastoma

The occurrence of ectopic retinoblastoma in the pineal body or in a parasellar region (*trilateral retinoblastoma*) has been reported by Jakobiec et al.[90] and Bader et al.[91, 92] The association of retinoblastoma with pinealoblastoma suggests that these tumors may be related.[93] In addition to having a common neuroectodermal origin, it is well known that in lower vertebrates the pineal gland has photoreceptor functions (similar to those seen in their retinas) and endocrine functions.[93] The development of an ectopic midline neuroblastic tumor in a patient with bilateral retinoblastoma probably represents an additional focus of a multicentric malignancy rather than a second primary tumor or metastatic disease.[91] It is also well known that the histologic appearance of retinoblastomas and pinealoblastomas may not be distinguished from each other.[90] It is postulated that, because of their similar origin, the same mutations may be cancerogenic for both retinoblasts and pinealoblasts. The failure of pineoblastomas to develop in all patients with heritable retinoblastoma may be due to a smaller cell population in the pineal gland or to other unrecognized factors.[94]

Tetralateral Retinoblastoma

Trilateral retinoblastoma is the syndrome of bilateral retinoblastoma with a solitary midline intracranial tumor in the pineal gland, suprasellar region, or parasellar region.[70] El-Nagger et al.[95] reported an 11-month-old infant with bilateral and two distinct partially calcified intracranial tumors: a large mass in the area of the pineal gland and a second tumor in the suprasellar region. On biopsy, the pineal mass was compatible with a neuroblastic tumor (pinealoblastoma). The authors coined the term *tetralateral retinoblastoma* for this case of two distinct midline intracranial neuroblastic tumors associated with bilateral Rb.

Clinical Diagnosis

Retinoblastoma accounts for about 1% of all deaths from childhood cancer in the United States.[96] The diagnosis of retinoblastoma usually can be made by an ophthalmoscopic examination. However, the detection and clinical differentiation of retinoblastoma from a host of benign simulating lesions may be difficult.[35, 82–99] The most common sign associated with retinoblastoma is leukokoria, which is present in 60% of patients (Fig. 8-56).[21, 32, 78] Strabismus (deviation of the eye) is the second most common sign. Pain caused by secondary glaucoma, often with heterochromia (different-colored irides), is the next most common symptom and sign, which leads to ophthalmologic evaluation. The ophthalmologic recognition of retinoblastoma is quite reliable. Small lesions are seen as gray-white intraretinal foci. Because of the difference in color from the surrounding retina and choroid, retinoblastomas can be seen when they are as small as 0.02 mm.[71] Other characteristic ophthalmoscopic findings include tumor calcification and vitreous seeding. As tumors grow in size, they often assume a convex configuration and produce three growth patterns: (1) In endophytic retinoblastoma, the tumor projects anteriorly, breaks through the internal limiting membrane of the retina, and grows into the vitreous. (2) In exophytic retinoblastoma, the tumor arises intraretinally and subsequently grows into the subretinal space, causing elevation of the retina.[64, 86] With continued tumor growth, there is an associated exudation and, rarely, a subretinal hemorrhage, which progressively cause retinal detachment; ophthalmoscopically, the exophytic tumors can simulate a traumatic retinal detachment. (3) In diffuse retinoblastoma, the tumor grows along the retina, appearing as a placoid mass. This diffuse form presents a perplexing diagnostic difficulty because of its atypical ophthalmoscopic feature (which simulates inflammatory or hemorrhagic conditions), its characteristic lack of calcification, and its occurrence usually outside of the typical age group.[64] All three growth forms, but especially the exophytic and diffuse infiltrating forms, may result in a tractional or exudative retinal detachment. Vitreous seeding of the tumor is more common in the endophytic and diffuse forms. Thus retinoblastoma may present as (1) a retinal or subretinal mass, with or without an associated retinal detachment or vitreous opacity; (2) a retinal detachment, with little indication of its etiology; (3) an opaque vitreous, with a limited view of the retinal structures and few clues to the etiology of the vitreous changes; or (4) some combination of the above forms.[64]

Diagnostic Imaging

Although ophthalmoscopic recognition of retinoblastoma is often reliable, imaging modalities should be used on all patients suspected of harboring a retinoblastoma to determine the presence of gross or subtle retrobulbar spread, intracranial metastasis, and the presence of a second tumor. In addition, imaging techniques may allow differentiation of retinoblastoma from lesions such as PHPV, Coats' disease, ROP, toxocariasis, retinal detachment, organized subretinal hemorrhage, organized vitreous, endophthalmitis, retinal dysplasia, retinal astrocytoma (hamartoma), retinal gliosis, myelinated nerve fibers, choroidal hemangioma, coloboma, morning glory anomaly, congenital cataract, choroidal osteoma, drusen of the optic nerve head, and other so-called pseudogliomas and leukokorias. These lesions may have a clinical appearance similar to that of retinoblastoma (Table 8-6). Ultrasonography, CT, and MR are the most useful imaging techniques in the evaluation of these lesions. The tumor and calcification can be diagnosed by ultrasonography; however, the accuracy of ultrasonography for this condition is only 80%.[88] Diagnosis of tumor extension to the medial and lateral aspects of the orbit and extraocular extension are particularly limited with ultrasound.

High-resolution, thin-section (1.5 mm) CT can detect tumor and calcification within it with a high degree of accuracy.[24, 32, 84, 100] More than 90% of retinoblastomas show evidence of calcification on CT.[100] Calcification may be small and single, large and single, multiple and punctate

Copyright © 2003, Mosby, Inc. All rights reserved.

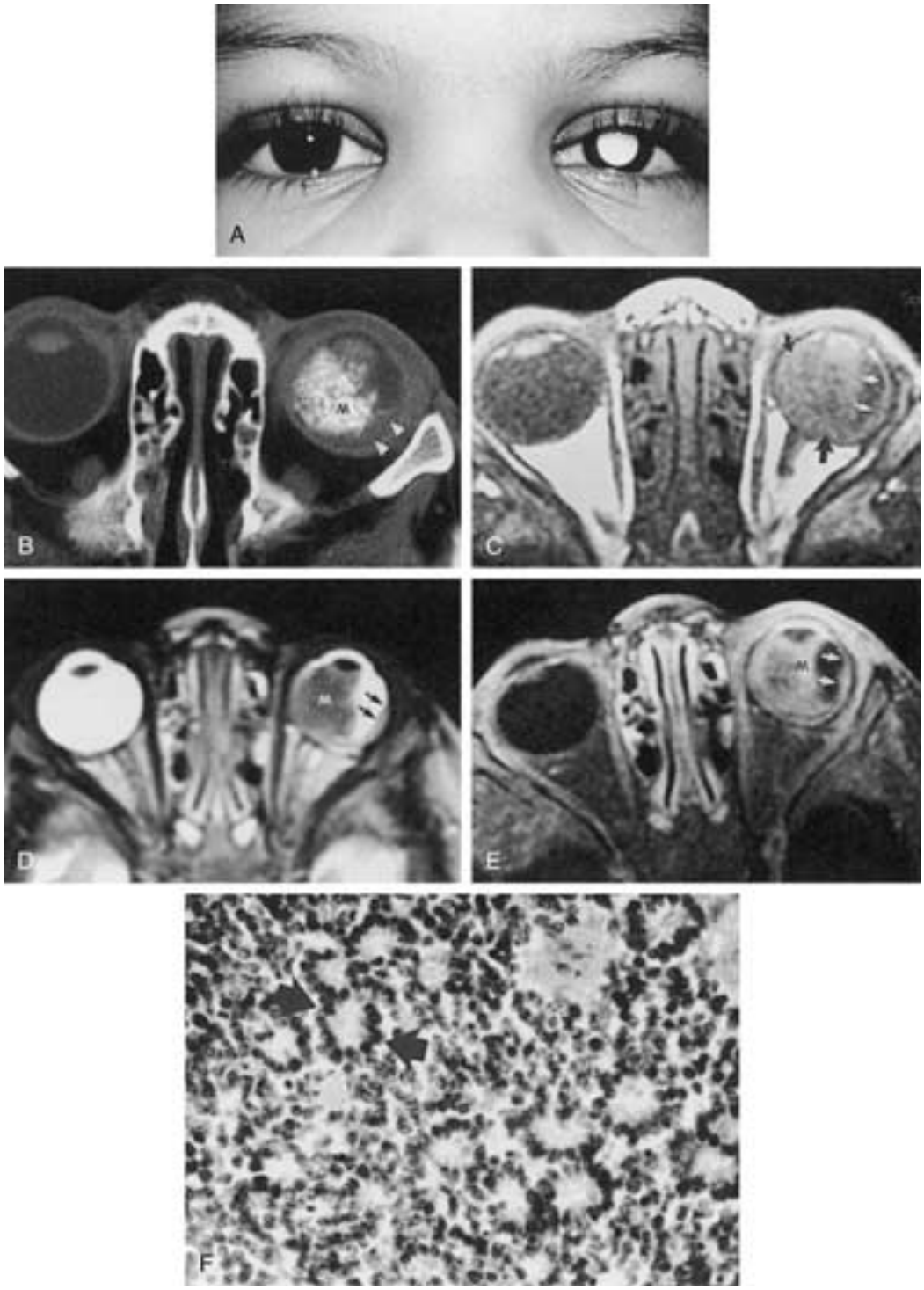

VIEW IMAGE

FIGURE 8-56 Retinoblastoma. **A**, Leukokoric left eye (whitish papillary reflex). **B**, Axial CT scan shows a large calcified intraocular mass (*M*). Note the noncalcified component (*arrowhead*). **C**, Axial T1-weighted (500/15, TR/TE) MR image shows a relatively hyperintense infiltrative mass (*arrows*). **D**, Axial T2-weighted (2000/102) MR image shows a hypointense infiltrative mass (*M*). Note the extension along the temporal aspect of the globe (*arrows*). **E**, Axial enhanced, fat-suppressed, T1-weighted (400/15, TR/TE) MR image shows moderate enhancement (*arrows*) of the mass (*M*). Note the enhancement along the temporal aspect of the globe (*arrows*). **F**, Histopathologic examination reveals well-differentiated retinoblastoma with numerous Flexner-Winterstein rosettes (*arrows*).

Copyright © 2003, Mosby, Inc. All rights reserved.

Table 8-6
CT AND MR IMAGING DIFFERENTIAL DIAGNOSIS OF CHOROIDAL OSTEOMA

Choroidal hemangioma
Amelanotic choroidal nevus or melanoma
Regressed retinoblastoma
Metastatic carcinoma to choroid (prostate)
Idiopathic or dystrophic sclerochoroidal calcification
Posttraumatic or postinflammatory ocular calcification
Bone formation in phthisical eyes
Neurilemoma or neurofibroma of choroid
Intraocular foreign body
Calcification related to macular degeneration
Peripapillary choroidal calcification in chronic retinal detachment

(Fig. 8-56), or a few fine-speckled foci.[84] The DNA released from necrotic cells in retinoblastoma has a propensity to form a DNA–calcium complex. It is the frequent presence of this calcified complex that allows the intraocular tumor to be identified by fundoscopic, ultrasonic, and CT imaging.[32, 84, 100–102] In the extraocular component of retinoblastoma, calcification is rarely present.[84] The presence of intraocular calcification in children under 3 years of age (98% of cases present prior to age 6 months) is highly suggestive of retinoblastoma because none of the simulating lesions, except microphthalmos and colobomatous cyst, contain calcification.[32, 84] Retinoblastoma in a microphthalmic eye is extremely rare. In children over 3 years of age, some of the simulating lesions, including retinal astrocytoma, ROP, toxocariasis, and optic nerve head drusen can produce calcification.[32, 84] The diffuse infiltrating form of retinoblastoma is rare and may have no calcification (Fig. 8-57).[40, 86]

A retinal astrocytoma (astrocytic hamartoma) may initially appear like a retinoblastoma,[32, 76, 84] and the retinal astrocytoma may be present before any of the neurologic or dermatologic manifestations of tuberous sclerosis appear.[84] The CT appearance of these myelinated nerve fibers may also be similar to that of retinoblastoma.[84]

MR Imaging

MR imaging has been used to evaluate retinoblastoma and other simulating lesions.[84, 96, 99, 103–105] In the diagnosis of retinoblastoma, MR imaging is not as specific as CT (Fig. 8-56) because of its lack of sensitivity in detecting calcification. However, the MR imaging appearance of retinoblastoma may be specific enough to differentiate retinoblastoma from simulating lesions (Fig. 8-57).[105] Retinoblastomas appear slightly or moderately hyperintense in relation to normal vitreous on T1-weighted (Fig. 8-56) and proton density images. On T2-weighted images, they appear as areas of markedly (Fig. 8-56) to moderately low signal intensity. Tumors elevated 3 to 4 mm in height may not be definitely identified on MR imaging,[84, 105] and lesions less than 2 to 3 mm in height are not confidently recognized by present MR imaging technology. Calcifications on MR imaging may be seen as varied degrees of hypointensity in all pulse sequences (Fig. 8-56). In contrast to CT scanning, which is highly specific for calcification, MR imaging may be nonspecific. In many cases a calcification may not be recognized on MR imaging (Fig. 8-58). Thus, in the diagnosis of retinoblastoma, CT is more specific because of its superior sensitivity for detecting calcifications. Calcifications as small as 2 mm can be reliably detected by CT.[105] MR imaging, however, has better contrast resolution than CT, and MR imaging provides more information for differentiation of leukokoric eyes.[21, 105] The use of paramagnetic gadolinium contrast material has improved the sensitivity of MR imaging. Retinoblastomas show moderate to marked enhancement on postcontrast MR images (Figs. 8-56 and 8-57).

In a study of 27 patients with leukokoria, MR in all retinoblastomas (17 cases) showed a mass.[105] These masses had relatively short T1 and short T2 relaxation times. All retinoblastomas were seen as mildly to moderately hyperintense lesions on T1-weighted and proton density MR imaging (Figs. 8-56 to 8-58), and this appearance was very similar to that of uveal melanoma. None of the patients with PHPV, ROP, Coats' disease, or toxocariasis demonstrated MR imaging characteristics similar to those of retinoblastomas.[105]

Of the various imaging modalities, MR imaging has become the most useful in evaluating the challenging retinoblastoma patient.[21, 32] Ultrasound is limited by the presence of complex intraocular interfaces when vitreous opacities, retinal masses, subretinal fluid, and retinal detachments are present. As stated, CT is valuable in demonstrating calcification, but both ultrasound and CT are of lesser value in showing local spread of retinoblastoma (Fig. 8-59) or in distinguishing retinoblastoma from stimulating lesions. In the study of eyes with suspected retinoblastoma, our protocol includes plain CT (1.5 to 3 mm thick sections) of the eyes and MR imaging of the eyes and brain, because optic nerve (Fig. 8-59), extracranial (Figs. 8-60 and 8-61) and intracranial involvement (Figs. 8-62 and 8-63) may be better evaluated by MR imaging than by CT scanning. Both techniques can detect the intra- and extraocular lesions; however, MR imaging provides more information about the differentiation of other pathologic intraocular conditions that cause leukokoria, as well as other lesions such as medulloepithelioma and mesoectodermal leiomyoma.[21, 32] Patients with familial retinoblastoma are highly susceptible to the development of other nonocular cancers, usually osteogenic sarcoma as well as other neoplasms at the site of external beam radiation (see Fig. 8-31). Second neoplasms may also arise outside the field of radiation.[21, 32]

Intraocular Mass and Mass-Like Lesions Simulating Retinoblastoma

There are other pediatric intraocular disorders that may clinically simulate retinoblastoma by presenting as a retinal or subretinal mass or mass-like lesion, retinal detachment, or a vitreous opacity.[21, 32] Further taxing the clinician's skills, (1) many of these other intraocular masses or mass-like lesions may secondarily result in retinal detachment or

Copyright © 2003, Mosby, Inc. All rights reserved.

vitreous opacity, (2) the vitreous opacity disorders may secondarily result in a retinal detachment, (3) retinal detachments may undergo organization and contracture so as to resemble an intraocular mass, and (4) secondary cataracts may prevent direct viewing of the primary intraocular condition.

In a study of 500 consecutive patients with leukokoria in whom the diagnostic possibility of retinoblastoma was raised, diagnoses other than retinoblastoma were made in 265 cases.[65] The most common causes of leukokoria include retinoblastoma, PHPV, ROP, Coats' disease, posterior cataract, coloboma of the choroid or optic disc, uveitis, larval granulomatosis, and a variety of other processes (see Table 8-5).[21]

PERSISTENT HYPERPLASTIC PRIMARY VITREOUS

PHPV is a condition that needs to be differentiated from retinoblastoma. Clinically, this condition is characterized by a unilateral leukokoria in a microphthalmic eye of a full-term baby. Rarely, PHPV may be bilateral. It is caused by the failure of the embryonic hyaloid vascular system to regress normally. The basic lesion is caused by a persistence of various portions of the primary vitreous and tunica vasculosa lentis, with hyperplasia and extensive proliferation of the associated embryonic connective tissue. In a study by Howard and Ellsworth,[65] of 500 children with leukokoria, PHPV accounted for 51 of the 265 non-Rb

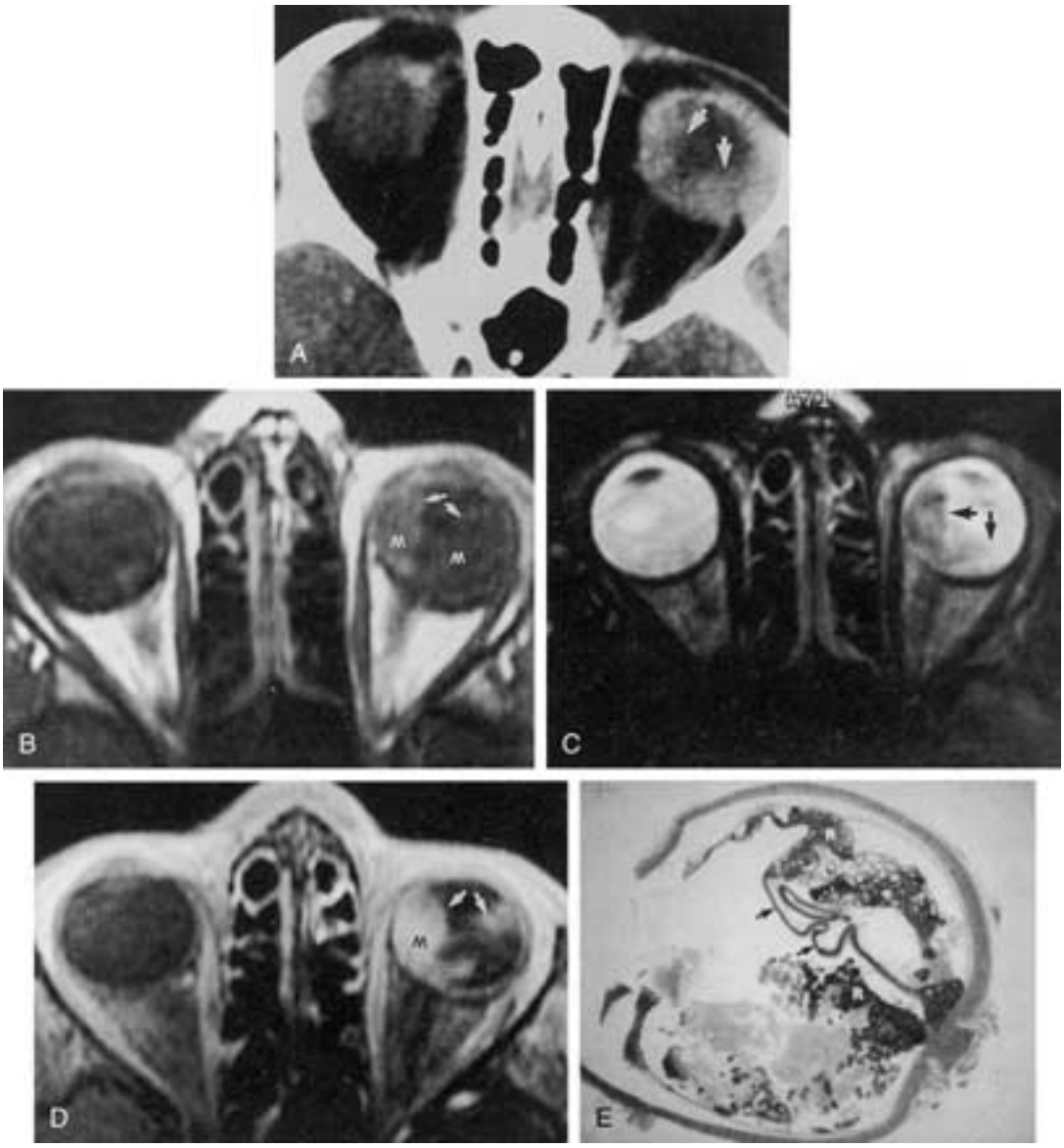

FIGURE 8-57 Diffuse infiltrating retinoblastoma. **A**, Axial CT scan shows an infiltrative noncalcified mass (*arrows*). **B**, Axial T1-weighted MR image shows a slightly hyperintense infiltrative exophytic mass (*MR*) under a detached retina (*arrows*). **C**, Axial T2-weighted MR image shows a hypointense infiltrative mass (*arrows*). **D**, Axial enhanced, fat-suppressed, T1-weighted MR image shows moderate enhancement of the tumor (*M*) under the associated retinal detachment (*arrows*). **E**, Photomicrograph of an enucleated eye showing diffuse retinoblastoma (*R*) with a detached retina (*arrows*) and no calcification.

VIEW IMAGE

Copyright © 2003, Mosby, Inc. All rights reserved.

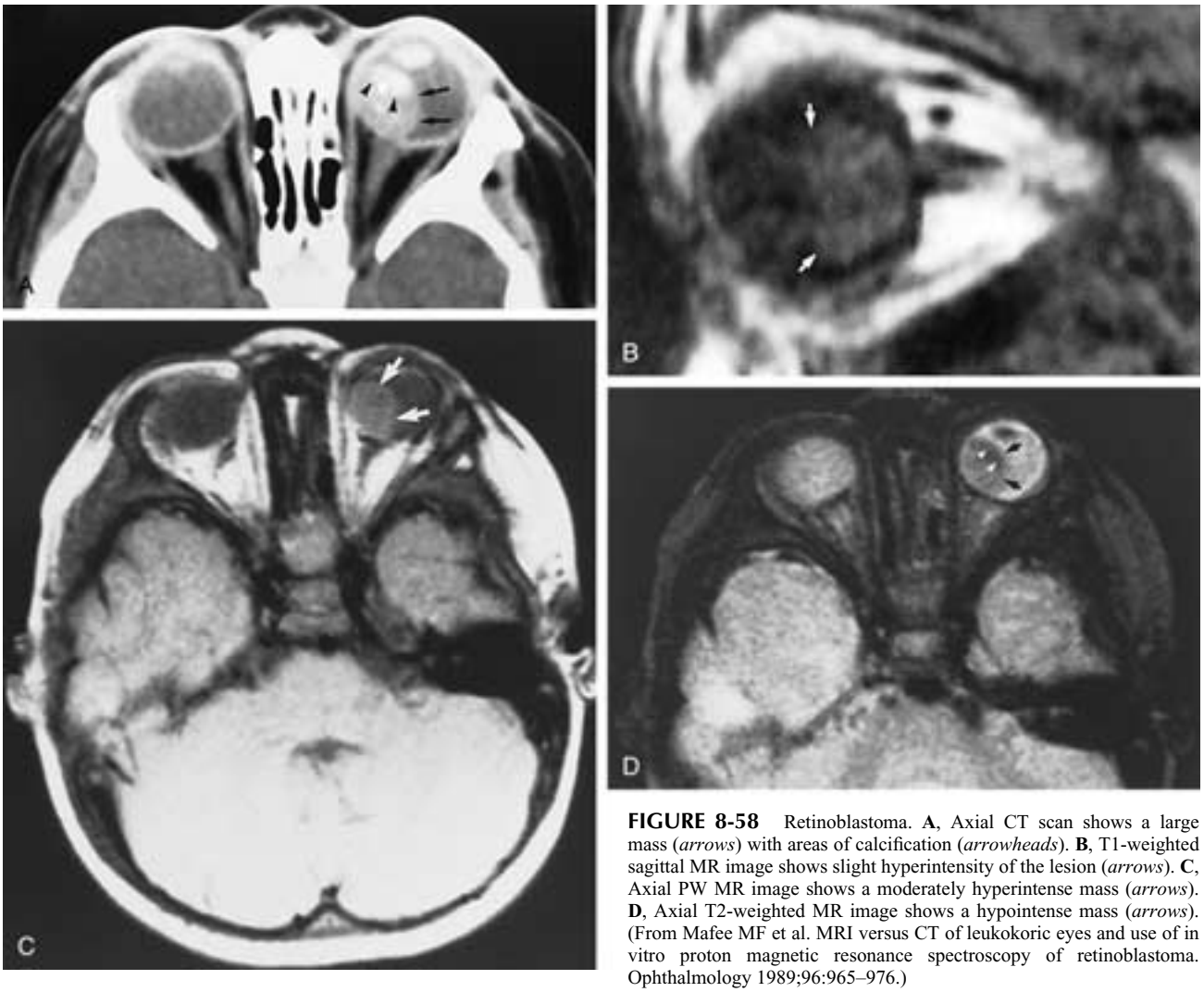

FIGURE 8-58 Retinoblastoma. **A**, Axial CT scan shows a large mass (*arrows*) with areas of calcification (*arrowheads*). **B**, T1-weighted sagittal MR image shows slight hyperintensity of the lesion (*arrows*). **C**, Axial PW MR image shows a moderately hyperintense mass (*arrows*). **D**, Axial T2-weighted MR image shows a hypointense mass (*arrows*). (From Mafee MF et al. MRI versus CT of leukokoric eyes and use of in vitro proton magnetic resonance spectroscopy of retinoblastoma. Ophthalmology 1989;96:965–976.)

VIEW IMAGE

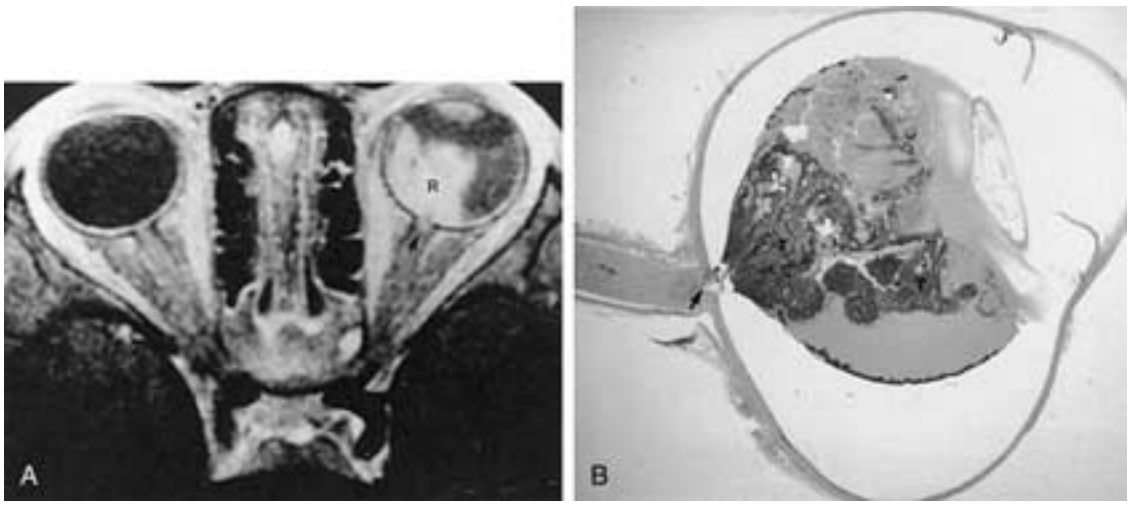

VIEW IMAGE

FIGURE 8-59 Retinoblastoma with optic nerve involvement. **A**, Enhanced, fat-suppressed, axial T1-weighted MR image shows marked enhancement of a retinoblastoma (*R*) with extension into the optic nerve (*arrow*). **B**, Photomicrograph of an enucleated eye showing the tumor (*T*) as well as extension into the optic nerve head (*arrow*). (Courtesy of D. Ainbinder, MD, Tacoma, WA.)

Copyright © 2003, Mosby, Inc. All rights reserved.

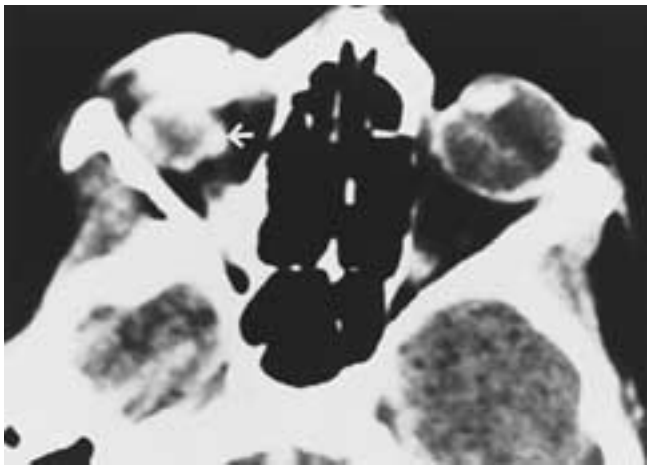

FIGURE 8-60 Recurrent retinoblastoma. Axial CT scan shows recurrent disease (*arrow*) after enucleation. Note the right false eye. (Courtesy of Dr. G. Schullman.)

VIEW IMAGE

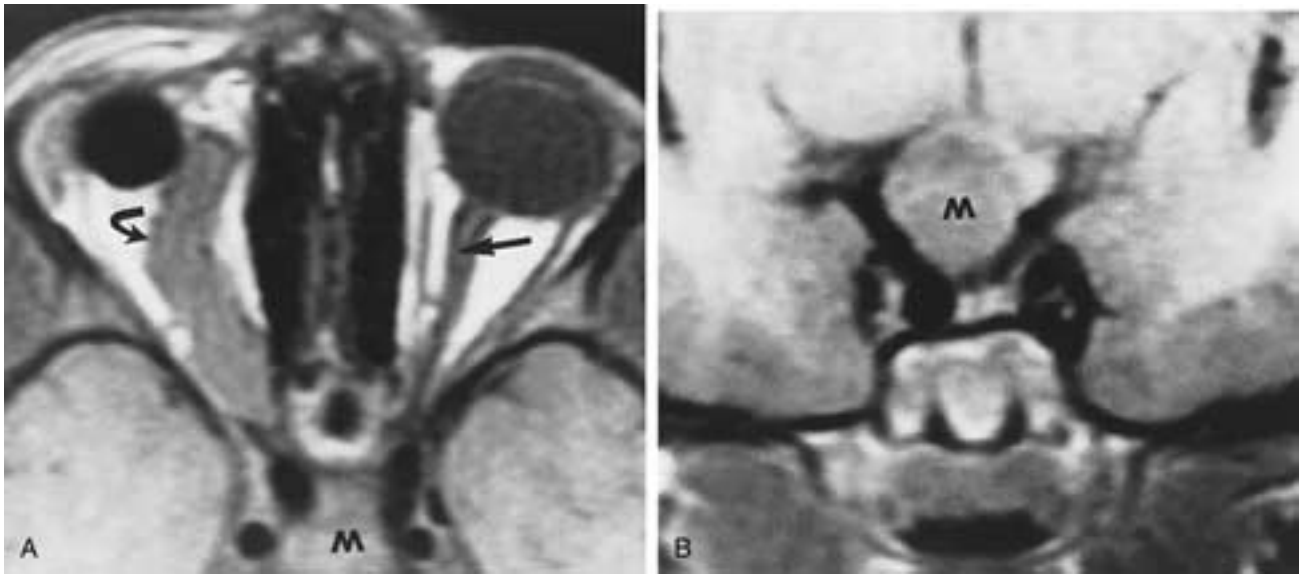

VIEW IMAGE

FIGURE 8-61 Recurrent retinoblastoma. **A**, Axial PW MR image shows a right false eye and marked tumor along the right optic nerve (*curved arrow*). Note the normal left optic nerve (*arrow*) and the tumor mass (*M*) in the sellar region. **B**, Coronal PW MR image shows a marked tumor mass (*M*) in the sellar and suprasellar region.

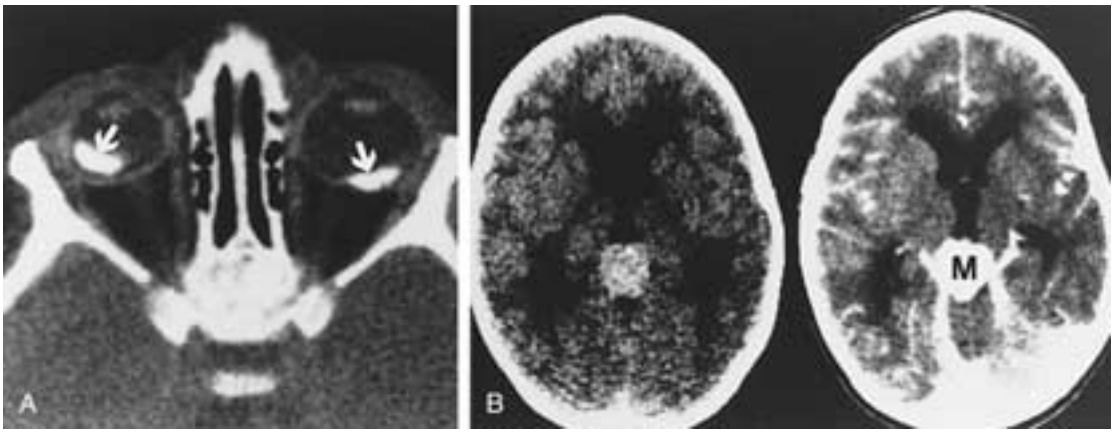

VIEW IMAGE

FIGURE 8-62 Presumed trilateral retinoblastoma. **A**, Axial CT scan shows bilateral calcified retinoblastomas (*arrows*). **B**, Axial CT scans with and without contrast enhancement show a large mass (*M*) in the region of the pineal gland with associated moderate hydrocephalus. This presumed pinealoma (retinoblastoma?) developed 2 years after external irradiation to both eyes through lateral ports. (From Mafee MF et al. Retinoblastoma and simulating lesions: role of CT and MRI. Radiol Clin North Am 1987;25:667–682.)

Copyright © 2003, Mosby, Inc. All rights reserved.

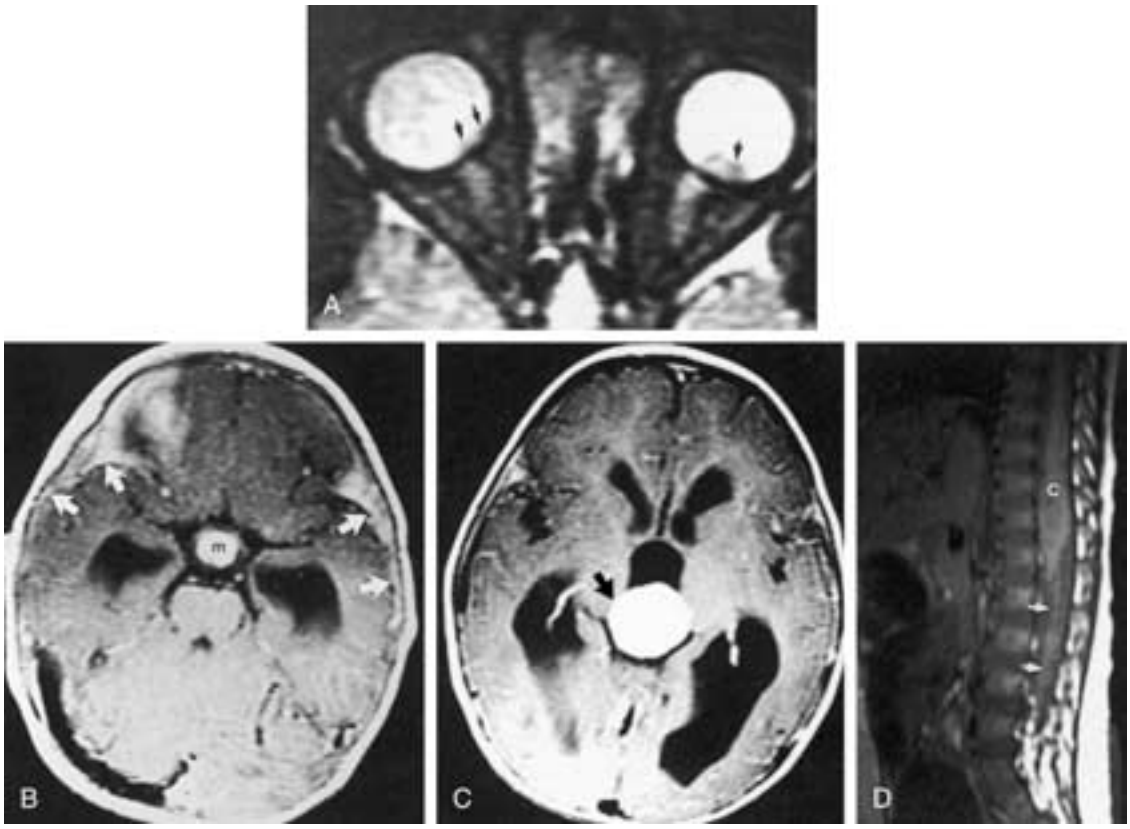

VIEW IMAGE

FIGURE 8-63 Tetralateral retinoblastoma. **A**, Axial T2-weighted MR image shows bilateral retinoblastoma (*arrows*). **B**, Enhanced axial T1-weighted MR image shows a markedly enhancing suprasellar mass (*m*). Note the subarachnoid spread of the tumor, seen as leptomeningeal enhancement along the sylvian fissures (*arrows*). **C**, Enhanced axial T1-weighted MR image shows marked enhancement of a pinealoblastoma (*arrow*). **D**, Enhanced sagittal T1-weighted MR image obtained a few months later shows diffuse distal spinal cord (*C*) and subarachnoid metastases (*arrows*).

cases. The authors concluded that except for retinoblastoma, PHPV is the most frequent cause of leukokoria in childhood. The nosology of PHPV is extremely complex.[105–107] The ocular malformation can reflect either an isolated congenital defect or a manifestation of more extensive ocular or systemic involvement. The term *persistent hyperplastic primary vitreous* therefore is a marked oversimplification that has no etiologic precision and only the grossest prognostic implications.[108] The embryonic intraocular vascular system may be divided into two components: an anterior system in the region of the iris and a posterior (retrolental) component within the vitreous. The anterior system is composed of the pupillary membrane, which is formed by small vascular buds that grow inwardly to vascularize the iris mesoderm anterior to the lens.[29] The posterior system includes the main hyaloid artery, vasa hyaloidea propria, and tunica vasculosa lentis.[29, 35] The first vessels to undergo regression are the vasa hyaloidea propria, followed by the tunica vasculosa lentis and eventually the main hyaloid artery.[29, 35, 108] During the first month of gestation, the space between the lens and the retina contains the primary vitreous. It consists of two parts: mesodermally derived tissue, including the hyaloid vessel and its branches, and a fibrillar meshwork that is of ectodermal origin.[109] In the second month of embryonic development, collagen fibers and a ground substance or gel component consisting of hyaluronic acid are produced. They form the secondary vitreous and begin to replace the vascular elements of the primary vitreous. By the fourteenth week, the secondary vitreous begins to fill the vitreous cavity.[109] By the fifth to sixth month of development, the cavity of the eye is filled primarily with the secondary vitreous that represents the adult vitreous. The primary vitreous is thus reduced to a small central space, Cloquet's canal, which runs in an S-shaped course between the optic nerve head and the posterior surface of the lens.[35, 36]

Clinical Diagnosis

Diagnosis of PHPV often is made difficult by its extremely broad array of clinical manifestations, etiologic heterogeneity, and frequently opaque ocular media.[106, 108, 110] Complete inspection of the interior of the eye may be precluded not only by cataract but also by vitreous hemorrhage or by opaque retrolental fibrovascular tissue. This condition usually manifests clinically as unilateral leukokoria in a microphthalmic eye. At birth the lens is clear, with a white to pinkish fibrovascular mass behind it; later, the lens usually becomes swollen and cataractous.[111] In the natural course of untreated PHPV, the eye often develops glaucoma and eventually buphthalmos or phthisis,

Copyright © 2003, Mosby, Inc. All rights reserved.

sometimes leading to loss of the globe.[111] The clinical presentation of PHPV is variable. Its main features include a unilateral (rarely bilateral) presentation, usually with leukokoria, microphthalmos, lens opacity, retinal detachment, and vitreous hemorrhage. In severe forms, elongated ciliary processes, elongated radial iris vessels, a shallow anterior chamber, and phthisis may occur. The diagnosis of the different types or causes of PHPV can sometimes be inferred from the family and birth histories, as well as from the details of the clinical examination.[108] Direct visualization of remnants of the fetal hyaloid vascular system offers the best evidence. However, direct visualization by ophthalmoscopy or microscopy is sometimes impossible because of the opaque media. In these circumstances, indirect visualization by CT and MR imaging can be diagnostically useful.[35, 108] The CT findings of PHPV were first reported by Mafee and Goldberg and their colleagues.[35, 108] Maximum information was derived from the use of CT following intravenous contrast administration and repeated scanning in the lateral decubitus position.[35] The CT findings include (1) microphthalmos, which is usually detectable, although it may be minimal or absent, and other deformities in the globe configuration, which may have been undetectable by physical examination or ultrasonography;[108] (2) calcification is absent within or around the globe; (3) generalized increased density of the entire vitreous chamber may be visible (Fig. 8-64), although minimally affected patients may show normal attenuation values in the vitreous chambers; (4) enhancement of abnormal intravitreal tissue may be seen after intravenous administration of a contrast medium; (5) tubular, cylindrical, triangular, or other discrete intravitreal densities suggest the persistence of fetal tissue in Cloquet's canal or congenital nonattachment of the retina (Fig. 8-65); (6) decubitus positioning may show a gravitational effect on a fluid level within the vitreous chamber (see Fig. 8-28), reflecting the presence of serosanguineous fluid in either the subhyaloid or subretinal space; and (7) the lens may be small and irregular, and the anterior chamber may be shallow.

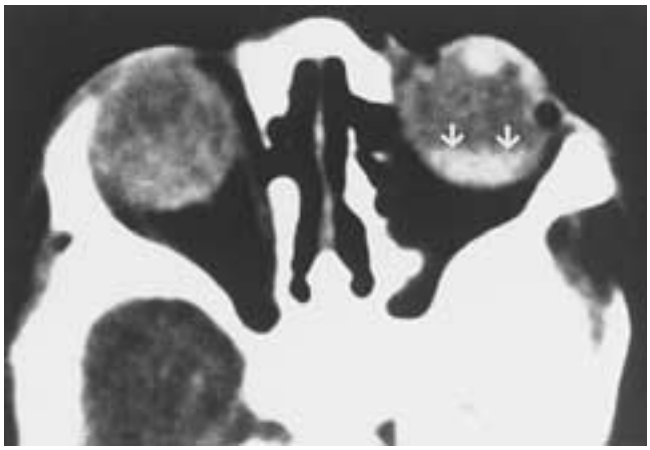

VIEW IMAGE

FIGURE 8-64 PHPV. Axial CT scan shows an increase in the density of both vitreous chambers, with gravitational layering of high-density fluid in the left eye (*arrows*). The high-density fluid is most likely caused by blood in the subhyaloid space.

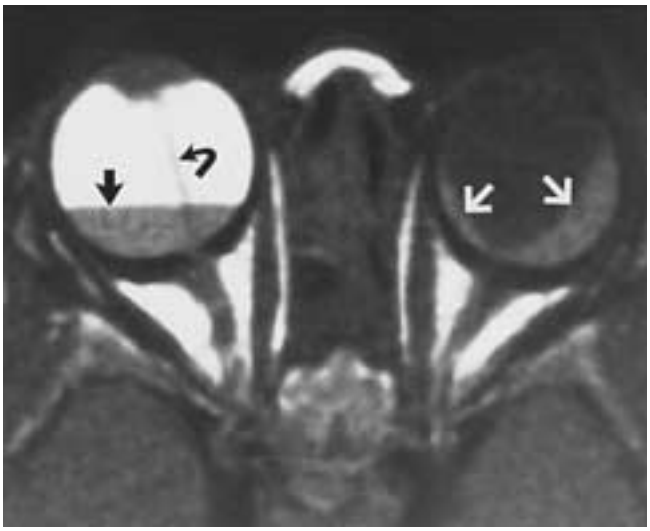

VIEW IMAGE

FIGURE 8-65 PHPV. This 5-month-old girl was diagnosed as having Warburg's syndrome (congenital oculocerebral disorder). Axial T1-weighted MR image shows hyperintense subretinal fluid in the left eye with a detached retina (*arrows*). Note the fluid-fluid level in the right vitreous (*solid arrow*). This is thought to be caused by chronic (hyperintense) and acute (hypointense) hemorrhage in the subhyaloid or subretinal space. Note the tubular image (*curved arrow*), which suggests a congenital nonattached retina or Cloquet's canal.

MR Imaging

The MR appearance of the different types of PHPV may be different. Early experience with MR imaging in patients with PHPV has revealed marked hyperintensity of the vitreous chamber on T1-weighted, proton density, and T2-weighted images.[36] The MR appearance of eyes with ROP may be identical to that of eyes with PHPV. The appearance of retinal detachment in PHPV has two forms: (1) retinal elevation into the vitreous from the optic nerve, resembling acquired forms of retinal detachment (Fig. 8-65), and (2) retinal elevation from a point in the wall of the eye that was eccentric to the optic nerve, suggesting a falciform fold or congenital nonattachment of the retina.[106, 108] Contrast-enhanced CT or MR imaging may demonstrate an enhanced retrolental mass (Fig. 8-66), and there may be increased enhancement in the anterior segment of the involved eye (Fig. 8-66). PHPV is often associated with severe malformations of the optic nerve and retina.[108] The ocular malformation usually reflects a manifestation of more extensive disease including Norrie's disease, Warburg's syndrome, primary vitreoretinal dysplasia, and other congenital defects. Nonetheless, the clinical or imaging detection of PHPV alerts the clinician to the appropriate diagnostic and prognostic possibilities. CT and MR imaging certainly are not indicated if the diagnosis and management of PHPV can be determined easily by conventional techniques. On the other hand, any procedure such as CT or MR imaging that aids the complex diagnostic and therapeutic decision-making that is often required for such affected children should be considered clinically useful and employed in these selected circumstances. In a CT study by Goldberg and Mafee[108] of eight children referred with several

Copyright © 2003, Mosby, Inc. All rights reserved.

diagnoses, including Rb, congenital cataract, and microphthalmos, after collation of data from clinical examinations under anesthesia and from CT scanning, although PHPV was not the initial diagnosis in any case, it proved to be the most acceptable diagnosis for all patients. MR imaging provides even more information in the diagnosis of PHPV because no patient with PHPV has the hypointensity of the vitreous chamber that is characteristic of retinoblastoma (Figs. 8-56 and 8-57). However, on CT, differentiation of a retinoblastoma from PHPV is not always easy.

RETINAL DYSPLASIA

Retinal dysplasia includes a group of disorders, such as Norrie's disease and Walker-Warburg's syndrome, in which abnormal proliferation and folding of the developing outer retina leads to congenital retinal detachment.[21] PHPV is manifested with more severe malformation in diseases such as Norrie's disease, Warburg's syndrome, and retinal dysplasia.

Norrie's Disease

Norrie's disease, or congenital progressive oculoacousticocerebral degeneration, is a rare X-linked recessive syndrome consisting of retinal malformation, deafness, and mental retardation or deterioration.[112] In 1927, Norrie described seven cases in two families with the same hereditary blindness.[113] In 1961, Warburg described the entity with other congenital eye diseases, coined the eponym *Norrie's disease*,[114] and later added the features of hearing loss and mental retardation. Warburg also described the disorder as *congenital progressive oculoacousticocerebral degeneration*.[115] Warburg established that Norrie's disease has an X-linked recessive pattern of inheritance, affects only males, and has ophthalmologically unaffected female carriers.[116] The affected males can exhibit ocular changes, including partial or complete retinal detachment; vitreoretinal hemorrhage, which can be present in the early neonatal period;[112] a retrolental mass; cataract; glaucoma; optic nerve atrophy; choroidal hypercellularity; and phthisis bulbi, which after varying periods of time lead to bilateral blindness.[112] Other findings include progressive high-tone sensorineural hearing loss,[116, 117] congenital nystagmus,[112] mild to severe mental retardation, and psychotic symptoms.[112, 116, 117]

The pathogenesis of Norrie's disease is unknown. Warburg[116] postulated that the basic lesion is a genetically determined biochemical defect that causes primary arrest in the development of the embryonic neuroectodermal structures of the retina, with consequent changes within the primary and secondary vitreous. Neuroectodermal changes also occur in the cerebral cortex.

Histopathologically, in the early stage the condition is characterized by absence of retinal ganglion cells and absence of normal nerve fiber layer structures in the retina.[118] In the more advanced stages of the disease, most authors have been impressed with the similarity between Norrie's disease and Coats' disease.[119] However, Apple, Fishman, and Goldberg[118] believed that in the earlier stages it is possible to differentiate Norrie's and Coats' diseases. Associated changes in Norrie's disease that may be present include optic nerve atrophy, atrophy of visual pathways, incomplete stratification of the brain cortex, and abnormalities of the brain.[115]

Diagnostic Imaging

The CT findings in Norrie's disease were first reported by Mafee and Goldberg.[35, 108] These included bilaterally dense vitreous chambers (Fig. 8-67A), a retrolental mass, retinal detachment, microphthalmia,[36] optic nerve atrophy, a shallow anterior chamber, and a small, highly dense lens.[36] There was no evidence of intraocular or extraocular calcification, nor was there any evidence of gravitational layering of intravitreal fluid. The MR imaging findings of Norrie's disease include bilateral hyperintense vitreous caused by chronic vitreous or subretinal hemorrhage (Fig. 8-67B,C); persistence of the primary vitreous may be present, the optic nerves may be hypoplastic, and there may be associated developmental anomalies of the brain (Fig. 8-67D).

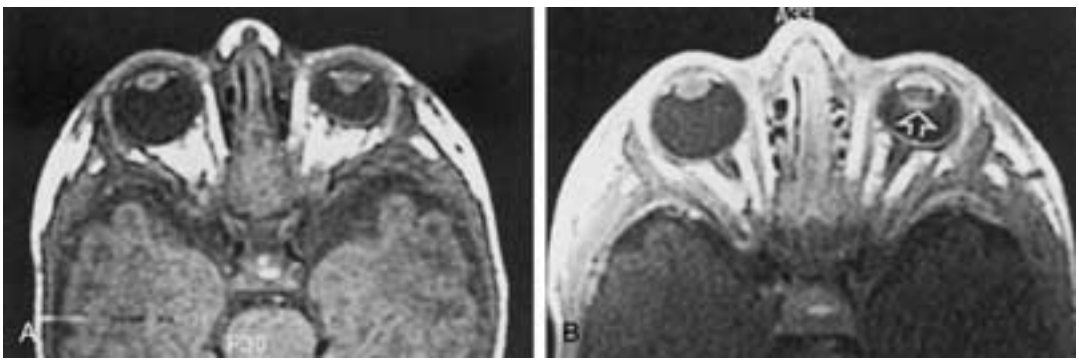

FIGURE 8-66 PHPV. Axial Precontrast (**A**) and postcontrast (**B**) T1-weighted (450/15, TR/TE) MR images show a microphthalmic left eye. Note the abnormal signal of the left lens, the retrolental enhancing mass (*arrow*), and the increased enhancement in the left anterior chamber related to elongated ciliary processes, possibly caused by leaking vessels.

VIEW IMAGE

Copyright © 2003, Mosby, Inc. All rights reserved.

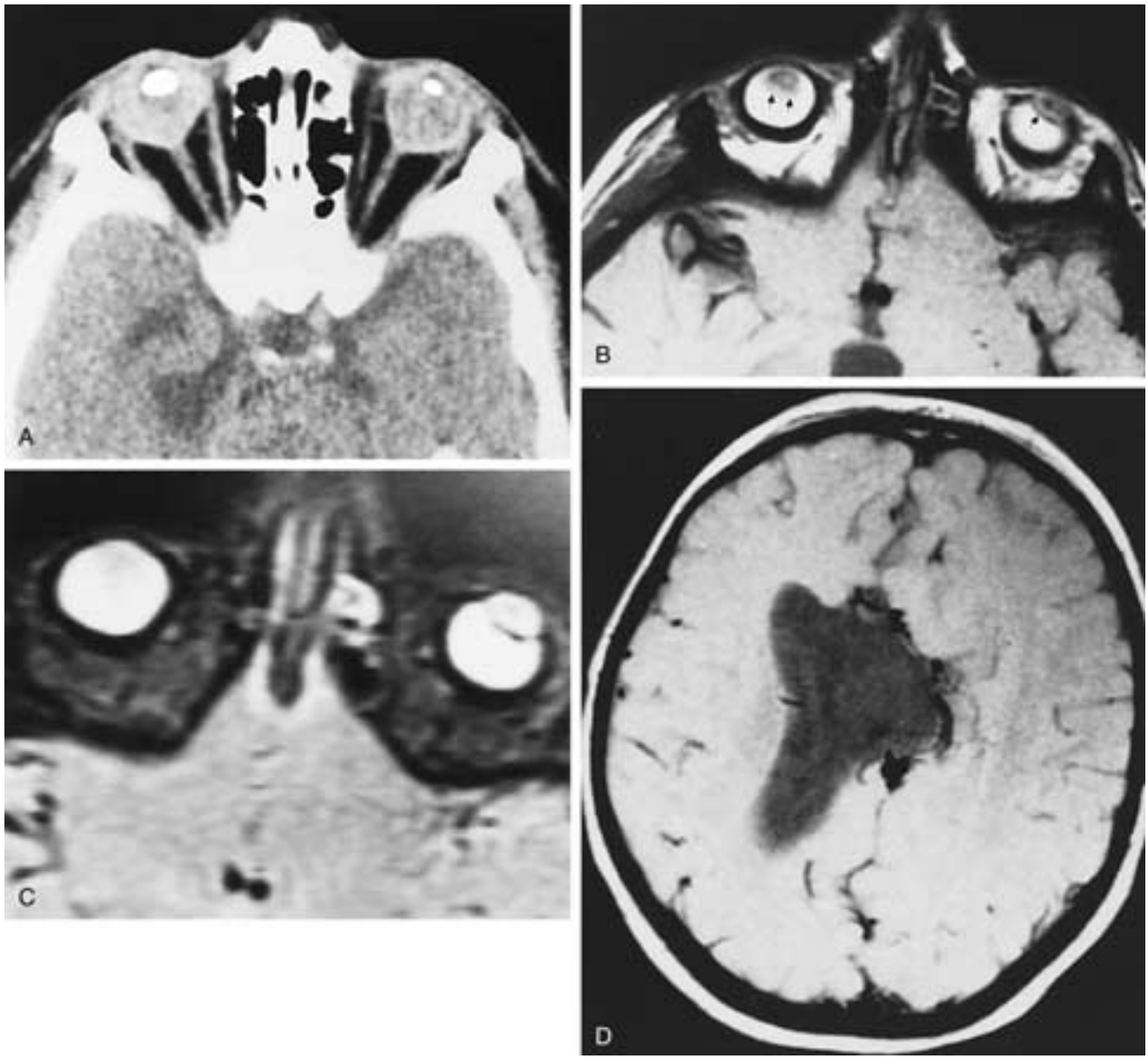

VIEW IMAGE

FIGURE 8-67 Norrie's disease with bilateral PHPV. **A**, Axial CT scan shows bilateral dense vitreous chambers and small eyes. The left lens is smaller than the right lens, and both are rather peculiar in shape. **B**, Axial PW MR image shows marked hyperintensity of both globes. **C**, Axial T2-weighted MR image shows hyperintensity of both globes. These changes are caused by proteinaceous fluid or chronic hemorrhage in the subhyaloid or subretinal space or within the vitreous chamber. Note the abnormal tissue in the retrolental regions (*arrows*), better seen in **B** than in **C**. These changes may be difficult to differentiate from ROP. **D**, Axial PW MR image shows a developmental anomaly of the lateral ventricles, a cavum septum pellucidum, and flattening of some of the cortical gyri (lissencephaly). (**A** to **C** from Mafee MF et al. Persistent hyperplastic primary vitreous (PHPV): role of CT and MRI. Radiol Clin North Am 1987;25:683–692.)

Warburg's Syndrome

Complex syndromes with congenital malformations of the central nervous system, microphthalmia, and congenital unilateral or bilateral retinal nonattachment have been described in a number of disorders such as Meckel's syndrome, a disorder with malformations of the central nervous system, including encephalocele, cleft palate, polydactyly, cysts of the liver and kidneys, genital malformations, and microphthalmia.[120]

In 1971, Warburg suggested that such patients might suffer from a nosologically distinct syndrome.[121] She described an autosomal recessive disorder consisting of profound mental retardation with death in infancy, hydrocephaly, microphthalmia, and congenital nonattachment of the retina.[121] Subsequent postmortem studies confirmed these clinical observations and noted the coexistence of lissencephaly in these patients.[122, 123]

In 1978 the syndrome was redescribed and the mnemonic HARDTE was coined to point out the following characteristic features: hydrocephaly, agyria, and retinal dysplasia (detachment), with or without encephalocele.[124] The

Copyright © 2003, Mosby, Inc. All rights reserved.

HARDTE, or Warburg's syndrome, is a congenital oculocerebral disorder caused by a genetic defect that simultaneously affects ocular and cerebral embryogenesis and specifically involves the retina and the brain.[125] The syndrome emphasizes the developmental and morphologic similarities between the cerebral cortex and the retina. The syndrome is characterized by congenital bilateral leukokoria.

The ophthalmic findings associated with this syndrome include microphthalmos and retinal dysplasia with congenital retinal nonattachment.[115, 126] Associated anomalies may include vitreous hemorrhage, a large intravitreal vessel, opaque retrolental tissue, persistent hyperplastic primary vitreous, and a hypoplastic optic disc.[125] The lens may have a pear-shaped configuration because of a posterior bulge (posterior lenticonus).[125] Postmortem studies of the brain attest to the poor growth of the cerebral hemisphere, with disorganization and dysgenesis of the cerebral and cerebellar gray and white matter.[122, 123, 125]

Clinical Diagnosis

Microphthalmia and hydrocephaly may be seen in children with congenital toxoplasmosis, rubella syndrome, congenital syphilis, and herpes and cytomegalovirus (CMV) infections. In toxoplasmosis, there may be characteristic chorioretinal scars and a positive serologic test. The presence of significant serum antibody titers against rubella, CMV, herpes virus, and syphilis should serve to distinguish Warburg's syndrome from these simulating disease entities.[32]

Diagnostic Imaging

The CT and MR imaging findings in the eyes of patients with Warburg's syndrome include bilateral retinal detachment (Fig. 8-68A), subretinal hemorrhage, vitreous hemorrhage, and gravitational intravitreal fluid (Fig. 8-68B). Persistence of the primary vitreous also may be present.[125] The congenital nonattached retina or the totally detached retina exhibits a characteristic narrow funnel shape or a triangular intravitreal mass adjacent to Cloquet's canal (see Figs. 8-28 and 8-65).

Retinopathy of Prematurity

In contrast to PHPV, ROP (retrolental fibroplasia, retinal fibroplasia) is seen in premature low-birth-weight infants. ROP is usually bilateral and fairly symmetric. The essential feature of ROP appears to be prematurity. The smaller the infant, the greater the risk of developing this disease. ROP usually develops as a response to prolonged exposure to supplemental oxygen therapy. It is possible that excessive oxygen plays only a participating role in the development of ROP. Eller et al.[127] noted that 14 patients had an associated persistent hyaloid vascular system. A massive persistent hyaloid vascular system was found in seven of their patients. The authors concluded that ROP may be related to a combination of developmental and environmental factors that prevent normal retinal vasculogenesis outside the womb.

Ophthalmoscopic Picture

In ROP, proliferation of abnormal peripheral retinal vessels occurs, with subsequent hemorrhage and cicatrization, which may organize and contract, leading to tractional retinal detachment in the advanced stages. The detachment may be partial or total, anterior or posterior, or in an open or closed funnel configuration. The ophthalmoscopic findings of ROP have been divided into active, regressive, and cicatricial phases. The initial active phase is characterized by arteriolar narrowing caused by a spastic response of the vessels to hyperoxia.[128] The vessels then start to dilate and become tortuous. A subsequent sign is the presence of fine, delicate neovascularization in the periphery, changes that are most marked in the temporal periphery because this is the region where the retinal vascularization develops last. Commonly, as long as premature infants are under oxygen therapy, there is no vascular dilatation or tortuosity, which

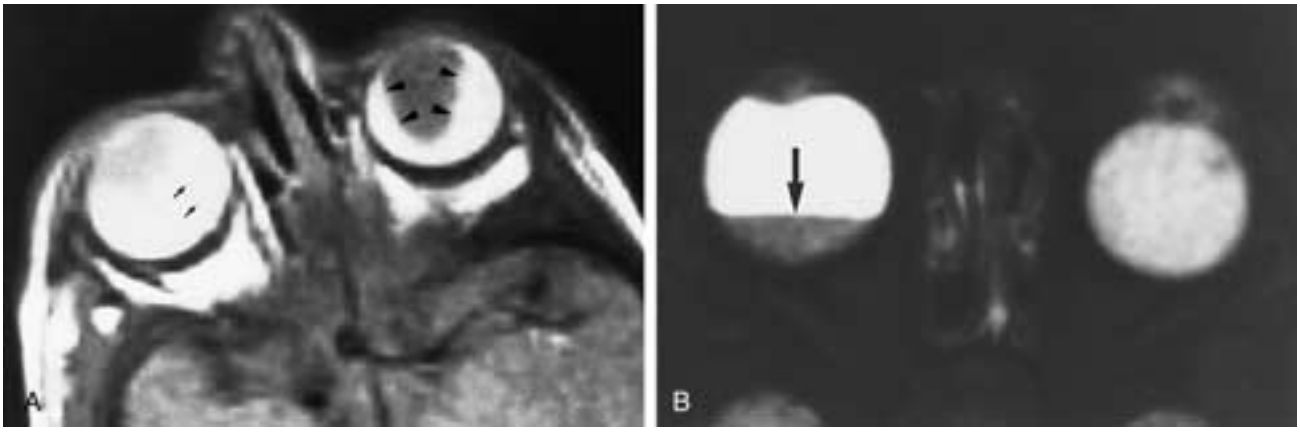

VIEW IMAGE

FIGURE 8-68 Warburg's syndrome. **A**, Axial T1-weighted MR image shows subretinal effusion with a detached retina (*arrows*) of the left eye. Hyperintensity of the right globe is caused by chronic hemorrhage in the subhyaloid or subretinal space. Note the congenitally nonattached retina or Cloquet's canal and the abnormal retrolental soft tissue. **B**, Axial T1-weighted MR image obtained 4 months later reveals progression of disease in both eyes with a fluid-fluid level (*arrow*) caused by chronic (hyperintense) and acute (hypointense) hemorrhage in the subhyaloid or subretinal space.

Copyright © 2003, Mosby, Inc. All rights reserved.

FIGURE 8-69 ROP. **A**, Axial CT scan shows increased density of the globes and left microphthalmos. **B**, Axial PW MR image shows hyperintensity of both globes, presumably caused by subretinal hemorrhage. Note the retrolental abnormal tissues (*arrows*) and detached retina (*curved arrow*). **C**, Axial T2-weighted MR image shows hyperintensity of the globes and abnormal retrolental soft tissues (*arrows*). Note the detached retina (*curved arrow*) and the layered acute hemorrhage in the right subretinal space (*arrowhead*).

VIEW IMAGE

occurs 24 to 48 hours after the infants are removed rapidly from the oxygen incubator.[129] Gradually, strands containing new vessels pass into the vitreous from the retina. There may be vitreous hemorrhage, which may be massive, and the retina may become partially or completely detached.[129]

Regressive Phase

A characteristic of the disease is that during the early stage, there is a tendency to regress spontaneously, with disappearance of the neovascularization and even of a general detachment of the retina.[129] The detached retina, however, may not always become reattached. About 85% to 90% of cases show spontaneous regression.[129]

Cicatricial Phase

Finally, a dense membrane or a gray-white vascularized mass will be left as permanent evidence of the active phase. The lens always remains clear. The retina is detached, with associated retinal scars. The growth of the eye is often inhibited, with microphthalmos as the final outcome.

Diagnostic Imaging

The early stage of ROP may have no specific CT and MR imaging findings except that the eyes may be microphthalmic. In more advanced cases, the CT and MR differential diagnosis between ROP (Fig. 8-69) and PHPV, retinoblastoma, endophthalitis, or a number of pathologic conditions wherein retinal detachment is a common feature may be difficult.[36, 84, 126, 129] The history of incubator treatment, birth weight, bilaterality, and the ophthalmoscopic, ultrasound, and CT findings are usually sufficient to establish the diagnosis. Calcification is rare in ROP. However, in the more advanced stage, calcification may be present. In the most advanced cases of ROP, both eyes are microphthalmic, with very shallow anterior chambers. Calcification in a microphthalmic eye is less indicative of retinoblastoma, although rarely retinoblastoma has been reported in microphthalmic eyes with or without ROP or PHPV. ROP may on occasion present as unilateral leukokoria. However, in the majority of cases, ROP presents as bilateral but often markedly asymmetric disease.[110] A persistent hyaloid vascular system may be an associated finding in patients with ROP, and the recognition of a massive persistent hyaloid vascular system on clinical examination, MR imaging, CT, or ultrasound is of prognostic importance.[127] In these cases, the surgical dissection of the retrolental membrane in the presence of a persistent hyaloid vascular system is more difficult because these vessels tend to bleed, and the retrolental membrane is tightly adherent to the detached retina.[127]

Coats' Disease

Coats' disease (primary retinal telangiectasis) is a primary vascular anomaly of the retina characterized by idiopathic retinal telangiectatic and aneurysmal retinal vessels, with progressive deposition of intraretinal and

Copyright © 2003, Mosby, Inc. All rights reserved.

subretinal exudates that leads to massive exudative retinal detachment (exudative retinopathy).[27, 130, 131] The condition occurs more frequently in juvenile males than in females. However, it is also seen in adults, in whom it is almost always unilateral.[27, 130, 132, 133] The formation of retinal telangiectasia, and the breakdown in the blood-retinal barrier with leakage of a lipoproteinaceous exudate at the telangiectasis, are the essential underlying causes of the pathologic changes that occur in Coats' disease.[27] The primary cause for the telangiectasis, and for the leakage of serum and lipid and eventual closure of the retinal vessels in the area of the telangiectasis, is unknown.[27] The degree of lipoproteinaceous subretinal exudation in Coats' disease appears to be proportional to the extent of the retinal telangiectasis.[134] The spectrum of pathologic changes in Coats' disease includes intraretinal or subretinal exudation, hemorrhages, lipid and fibrin deposition, phagocytic proliferation (ghost cells), and, ultimately, glial and fibrous tissue organization of the retina.[27] The vascular anomaly of Coats' disease, although present at birth, usually does not cause symptoms until the retina detaches and central vision is lost.[135]

Clinical Presentation and Diagnosis

Coats' disease usually occurs in young boys, with the onset of symptoms in most patients occurring before age 20. Although the incidence peaks between 6 and 8 years,[134] cases have been reported in patients ranging from 4 months old to the seventh decade.[134] The modes of presentation include leukokoria, strabismus, a failed school screening test, or painful glaucoma secondary to angle closure. Although the cause of Coats' disease remains unknown, there are isolated reports associating the disease with fasciocapsulohumeral muscular dystrophy, Turner's syndrome, Senior-Loken syndrome (familial renal-retinal dystrophy), the ichthyosis hystrix variant of epidermal nevus syndrome, inversion on chromosome 3, and a deletion of chromosome 13.[134] The ophthalmoscopic findings in Coats' disease vary with the stage of disease. In the early stages, the telangiectasis can be observed. In the later stages, when the retina is filled with and detached by a mass of cholesterol exudate (total bullous exudative retinal detachment), the telangiectasis can be seen only on fluorescein angiography.[27] In the early stage of the disease, while the retinal disease is not too extensive and the retinal detachment is shallow, photocoagulation, cryotherapy, or both usually obliterate the telangiectatic vessels and reduce or eliminate the exudative retinal detachment.[134] When there is extensive retinal telangiectasis and a total bullous exudative retinal detachment, cryotherapy and photocoagulation may not be sufficient to obliterate the leaking vessels. Such eyes commonly progress to secondary angle closure or iris neovascularization, becoming blind and painful as a result of acute congestive (neovascular) glaucoma.[134, 135]

Diagnostic Imaging

The ophthalmoscopic and biomicroscopic features of eyes with advanced Coats' disease may closely resemble findings in eyes with exophytic retinoblastoma and leukokoria.[136] It is important to distinguish retinoblastoma from Coats' disease. Many eyes with advanced Coats' disease are enucleated because retinoblastoma cannot be excluded.[135] In a study of 62 eyes satisfying the histologic diagnostic criteria of Coats' disease submitted to the Armed Forces Institute of Pathology, Chang, McLean, and Merritt[131] found that 52 (79%) were enucleated, with the diagnosis of retinoblastoma or to rule out retinoblastoma. Coats' disease is almost always unilateral, and it usually appears in boys slightly older (4 to 8 years) than those who have retinoblastoma.[21, 32] Many diagnostic techniques, including ultrasound, CT, and MR imaging, are available that help the ophthalmologist to diagnose clinical conditions, and CT and MR imaging have been shown to be extremely valuable in the diagnosis of Coats' disease.[84, 105, 134]

The CT and MR imaging findings in Coats' disease vary with the stage of the disease. In the early stages, both techniques may yield little information. In the later stages, retinal detachment accounts for all the pathologic findings in CT and MR imaging. Sherman, McLean, and Brallier[137] reported two children with Coats' disease. They concluded that CT could not differentiate between Coats' disease and unilateral noncalcifying retinoblastoma. Haik et al. reported the CT findings in 14 patients with Coats' disease; total retinal detachment (Fig. 8-70A) was routinely seen in advanced disease.[99] Calcification is not a feature of Coats' disease; however, in advanced Coats' disease, in up to one fifth of all cases, there is a fibrous submacular nodule that occasionally is calcified or ossified.[134] These nodules might represent exuberant proliferation and metaplasia of the retinal pigment epithelium (RPE).[134] MR imaging is superior to CT in differentiating Coats' disease from retinoblastomas and other leukokoric eyes.[105, 134] The subretinal exudation of Coats' disease is usually seen as hyperintense on T1-weighted, proton density, and T2-weighted MR images (Fig. 8-70B,C). In retinoblastomas, MR characteristically shows a mass that can be easily differentiated from an associated subretinal exudate. The retinoblastoma is relatively hyperintense on T1-weighted and proton density images (Figs. 8-56 and 8-57) and becomes hypointense on T2-weighted images (Figs. 8-56 and 8-57). The subretinal fluid of an associated retinal detachment is seen as various degrees of hyperintensity in all pulse sequences. Although Coats' disease can produce a subretinal mass resembling retinoblastoma, the mass in Coats' disease is caused by cholesterol, organized hemorrhage, and fibrosis, and therefore its signal is presumed to be inhomogeneous in character. The MR findings in patients with Coats' disease are compatible with retinal detachment without the presence of an intraocular mass (Fig. 8-71). In Coats' disease the detached retina may show enhancement following intravenous injection of Gd-DTPA contrast (Fig. 8-71D). The enhancement is due to idiopathic intraretinal telangiectasia and microaneurysms, the underlying pathology of Coats' disease. The MR findings in some of these patients in the early stages of the disease are normal.

In general, if an ophthalmologist suspects advanced Coats' disease but is uncertain about the correct clinical diagnosis and is unable to rule out retinoblastoma conclusively, a diagnostic imaging study should be requested.[135] When a patient presents with what appears to be a retinoblastoma with total retinal detachment, there are basically three diagnoses to consider: PHPV, Coats' disease, and ROP. In the appropriate clinical setting, the MR imaging and CT findings of Coats' disease should help establish a correct diagnosis.[21, 32, 134]

Copyright © 2003, Mosby, Inc. All rights reserved.

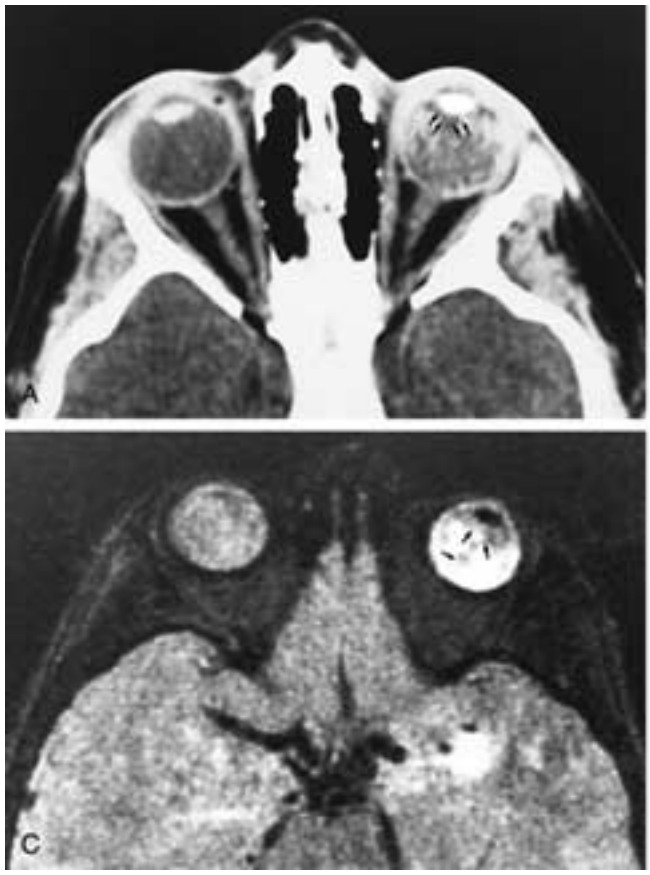

FIGURE 8-70 Coats' disease. **A**, Axial CT scan shows generalized increased density of the left globe caused by bullous retinal detachment. The leaves of the detached retina are faintly seen, as shown by the arrows. **B**, Axial PW MR image shows hyperintensity of the left globe caused by subretinal lipoproteinaceous effusion. Note the leaves of the detached retina (*arrows*). **C**, Axial T2-weighted MR image shows the detached retina (*arrows*).

VIEW IMAGE

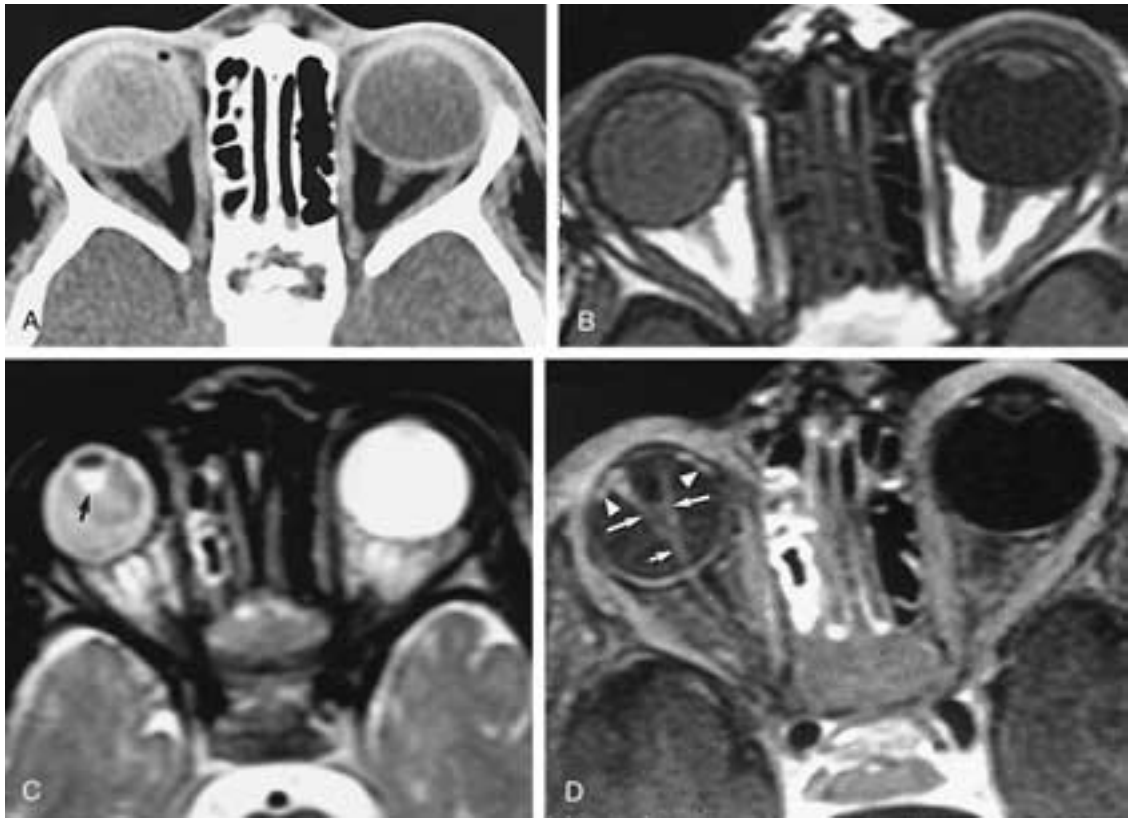

VIEW IMAGE

FIGURE 8-71 **A**, Axial CT scan shows the diffuse increased density of the right globe caused by total retinal detachment. A retinoblastoma cannot be excluded. **B**, Nonenhanced axial T1-weighted MR image shows slightly increased intensity of the right globe caused by total exudative retinal detachment. **C**, Axial T2-weighted MR image shows mixed signal intensities caused by a lipoproteinaceous exudate. The collapsed remaining part of the vitreous (*arrow*) appears hyperintense. **D**, Axial fat-suppressed, contrast-enhanced, T2-weighted MR image shows enhancement of the thickened, detached sensory retina (*arrows*). Note the enhancement of the peripheral retina (*arrowheads*) characteristically seen in Coats' disease, consistent with enhancement of telangiectatic vessels seen in **F** and **G**. A retinoblastoma can now be excluded.

Copyright © 2003, Mosby, Inc. All rights reserved.

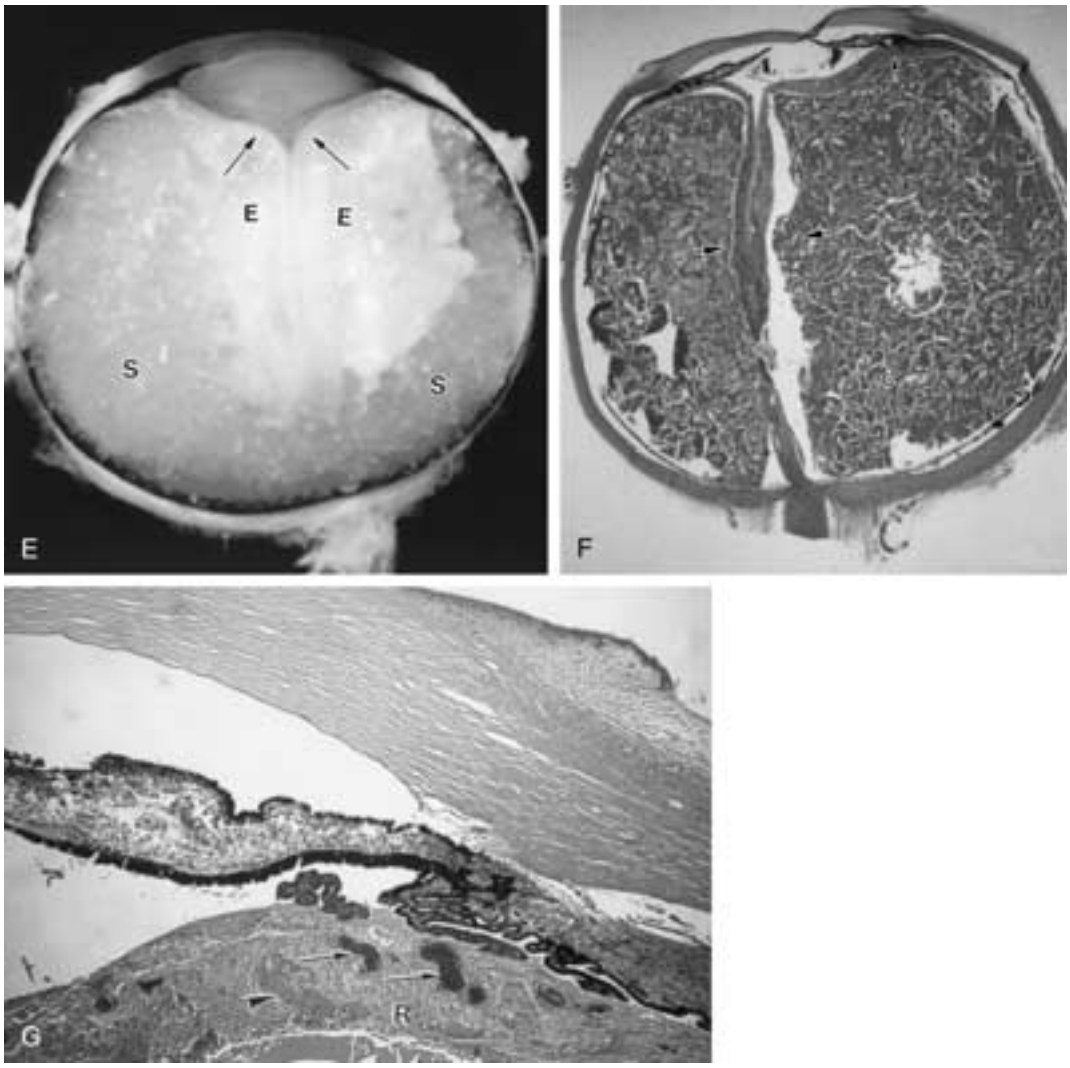

VIEW IMAGE

FIGURE 8-71 *Continued.* **E**, Gross photomicrograph of the eye. Note the large exudative detachment, with retinal elevation touching the posterior lens surface. The peripheral retina is markedly thickened (*arrows*). Areas of thick subretinal exudate (*E*) and cholesterol crystals are seen in the subretinal space (*S*). **F**, Photomicrograph of the eye. Note the bullous retinal detachment (*long arrows*) with peripheral telangiectatic vessels (*short arrow*). The subretinal space contains an eosinophilic exudate with cholesterol crystals (*C*). **G**, Peripheral detached retina (*R*) behind the iris showing telangiectatic blood vessels (*arrows*) and an intraretinal (*arrowhead*) and subretinal exudate. (Hematoxylin-eosin; original magnification × 10.)

Ocular Toxocariasis (Sclerosing Endophthalmitis)

Ocular toxocariasis is a chorioretinitis caused by an inflammatory response to the nematode *Toxocara canis*.[21] Infected puppies excrete worm ova that may survive in soil for years. The granuloma of *T. canis* is actually an eosinophilic abscess that contains the second-stage larva of *Toxocara* within it.[21] The infection results from ingestion of the ova (eggs) in contaminated soil. In these patients the death of the larva results in a wide spectrum of intraocular inflammatory reactions,[138–140] the more severe of which has the characteristic pathologic appearance of sclerosing endophthalmitis.[139, 140] Ocular toxocariasis is usually unilateral and is seen in older children. Clinically, it may present as endophthalmitis with vitreous haze from a profound inflammatory response or as posterior or peripheral retinal granuloma.[32] The granuloma appears a white, elevated lesion in the retina and may have associated adherent vitreous bands, vitreous traction, tractional retinal detachment, and dragging of the retina and optic disc.[32] In most but not all instances, the anterior segment is uninvolved, and a funnel-shaped retinal detachment is typically associated with an organized vitreous.[138] The histologic changes of the globe are characterized by an infiltration with lymphocytes, plasma cells, eosinophils, and giant cells. Retinal, subretinal, and vitreous hemorrhages may frequently occur. Remnants of the secondary larval stage of *T. canis* are often difficult to find. In 46 cases originally reported by Wilder,[139] larvae were present in 24. However, in the remaining 22 cases, larvae were not identified. In many cases, the diagnosis of ocular nematode infection is based presumptively on the characteristic histopathologic features of sclerosing endophthalmitis. A diagnostic enzyme-linked immunosorbent assay

Copyright © 2003, Mosby, Inc. All rights reserved.

(ELISA) for *Toxocara* is now available. In addition, analysis of vitreous fluid by ELISA testing reveals eosinophils. Eosinophilia may not be seen in peripheral blood.[64]

Diagnostic Imaging

Margo et al.[138] reported the CT findings in three cases of histopathologically proven sclerosing endophthalmitis. These findings consisted of a homogeneous intravitreal density that corresponded to a detached retina, an organized vitreous, and an inflammatory subretinal exudate. These investigators concluded that the findings are similar to those seen in Coats' disease and noncalcified retinoblastoma. Three cases of toxocariasis in young adults appeared on CT as a localized or diffuse ill-defined mass with no significant enhancement (Fig. 8-72). Clinical examination in these patients frequently shows vitreous, retinal, or choroidal signs of previous inflammation.[78] This inflammatory process (chronic abscess) is seen on CT as an irregularity of the uveoscleral coat with a diffuse or locally thickened, slightly enhanced uveoscleral coat (Fig. 8-72). This CT appearance usually favors a diagnosis of toxocariasis or another granulomatous disease of the globe and is due to diffuse inflammatory infiltration of the choroid and sclera (Fig. 8-72).[84]

In the appropriate clinical setting, the CT findings of the granuloma of *T. canis* should be relied on to establish a presumptive diagnosis.[84] MR imaging has been reported to have the ability to detect the site of the larval granuloma.[99] The MR images of a patient with a presumptive diagnosis of toxocariasis are shown in Figure 8-55A,B. In general, the proteinaceous subretinal exudate produced by the inflammatory response to the larval infiltration is seen as variably hyperintense on T1-weighted, proton density, and T2-weighted images. These MR imaging characteristics were found in two patients with suspected toxocariasis. Further studies are needed to establish the spectrum of MR imaging characteristics of this relatively uncommon ocular disease. The postcontrast MR imaging appearance of multiple *Toxocara* abscesses in a patient with a positive ELISA test is shown in Figure 8-55C. It should be noted that at times it may be very difficult to differentiate the MR imaging and CT appearances of chronic retinal detachment and organized vitreous from *Toxocara* granuloma, Coats' disease, and even ROP, PHPV, and noncalcified retinoblastoma.[84]

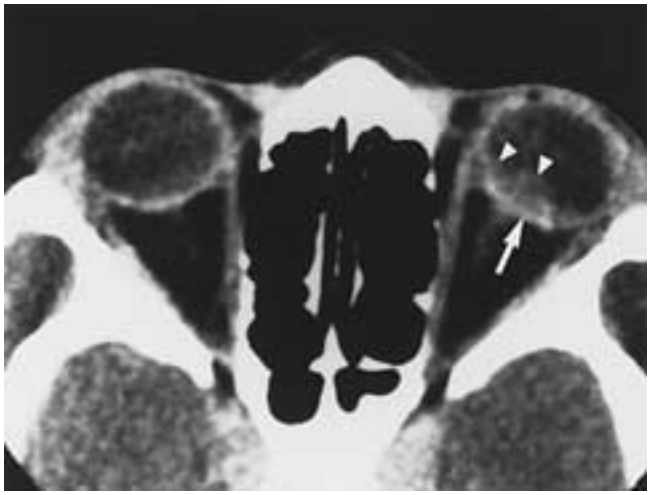

VIEW IMAGE

FIGURE 8-72 Ocular toxocariasis. Axial CT scan shows an irregular, moderately enhancing mass (*arrowheads*) with irregularity of the uveoscleral coat (*arrow*).

FIGURE 8-73 Astrocytic hamartoma. Axial CT scan shows a mass (*arrow*) in the posterior aspect of the right eye.

VIEW IMAGE

Ocular Astrocytic Hamartoma (Retinal Astrocytoma)

Although retinoblastoma is the major life-threatening cause of leukokoria in children, a host of other simulating conditions (pseudogliomas) can cause diagnostic confusion.[21, 32, 138] In some cases of leukokoria, it is exceedingly difficult to exclude the possibility of retinoblastoma without having to resort to enucleation.[138] Retinal astrocytoma is a benign yellow-white rare retinal tumor that occurs in association with tuberous sclerosis or neurofibromatosis or in isolation.[141] Early retinal astrocytoma (astrocytic hamartoma) may look exactly like early retinoblastoma and may be present before any neurologic or dermatologic manifestations of tuberous sclerosis appear.[32, 78] These tumors may appear in the retina or in the optic nerve. The usual appearance is that of a single nodule or multiple nodules elevated 1 or 2 mm above the surface of the retina. At this stage, CT and MR imaging cannot visualize the lesions. Tumors elevated more than 3 mm can be demonstrated on CT and MR imaging. The CT appearance of astrocytic hamartomas is similar to that of retinoblastoma (Fig. 8-73). If typical features of tuberous sclerosis are not present, the differentiation between astrocytic hamartomas and other ocular lesions may be very difficult. The CT appearance of myelinated nerve fibers in astrocytic hamartomas also may be similar to that of retinoblastoma (Fig. 8-74). In several patients with known tuberous sclerosis and clinical evidence of retinal nodules (dots), because of the small size of the lesions the ocular nodules were not seen on MR imaging.

Copyright © 2003, Mosby, Inc. All rights reserved.

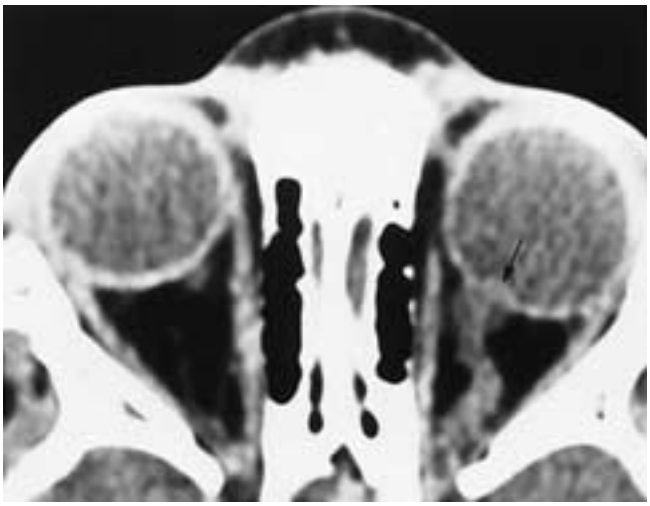

VIEW IMAGE

FIGURE 8-74 Myelinated nerve fiber (retinal gliosis). Axial CT scan shows a tortuous left optic nerve and soft tissue density at the optic disc (*arrow*). (From Mafee MF et al. Retinoblastoma and simulating lesions: role of CT and MRI. Radiol Clin North Am 1987;25:667–682.)

Combined Hamartoma of the Retinal Pigment Epithelium and Retina

Combined hamartoma of the retinal pigment epithelium and retina is a rare congenital ocular tumor, and patients present with painless loss of vision.[21] This benign proliferation of mature cells involving the retinal pigment epithelium, retina, and vitreous leads to an elevated lesion in the posterior pole or optic disc and occurs with varying pigmentation. The less pigmented lesions simulate retinoblastoma clinically.[21]

Incontinentia Pigmenti

Incontinentia pigmenti is a disorder associated with abnormalities of the skin, eye, and skeletal system.[21] The disease is inherited in an X-linked dominant pattern, although sporadic cases may occur. This condition is lethal in boys. Infants with this condition exhibit pigmentary skin abnormalities including erythematous skin with linear bullae at birth.[21] Ocular involvement is bilateral but often asymmetric. Retinal vascular abnormalities, pigmentary changes, and proliferation of retinal pigment epithelium lead to an intraocular nodular mass (pseudoglioma) that is usually seen in the first year of life. Peripheral fibrovascular proliferation may lead to tractional retinal detachment.[21]

Juvenile Xanthogranuloma

Juvenile xanthogranuloma (non-Langerhans' cell histiocytosis) is a benign cutaneous disorder affecting the skin and eye.[21] The cutaneous lesions are yellow-orange granulomatous nodules composed of histiocytes. This condition usually affects the iris and ciliary body,[142–144] but lesions in the choroid, retina, or optic nerve have also been reported.[143] Juvenile xanthogranuloma has also been noted to present as a solitary orbital granulomatous mass (Fig. 8-75). Infiltration of the iris can cause spontaneous hyphema, glaucoma, and uveitis.

Glioneuroma

Glioneuroma is an exceedingly rare neoplasm that arises from neuroepithelial cells that compromise the anterior margin of the embryonic optic cup.[145] The lesion usually appears at birth or in early childhood but is occasionally diagnosed in adulthood.[145] The tumor appears as a yellow or pink mass in the iris. Histopathologically, the ganglioneuroma is composed of an admixture of glial cells and neurons.[145]

Papillitis

Papillitis, inflammation of the optic nerve head, has multiple causes including ischemia, infections, and autoim-

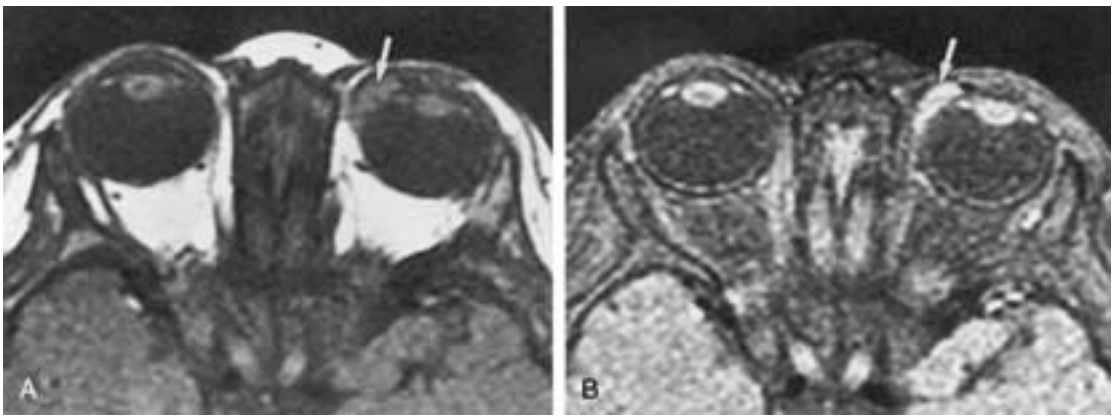

VIEW IMAGE

FIGURE 8-75 Juvenile xanthogranuloma. Precontrast axial T1-weighted (500/23, TR/TE) (**A**) and postcontrast T1-weighted (533/23, TR/TE) (**B**) MR images show an infiltrative enhancing mass involving the left eye (*arrow*). (Courtesy of A. Hidayat, MD, Washington, DC.)

Copyright © 2003, Mosby, Inc. All rights reserved.

mune diseases. If the inflammatory process is severe, the optic disc can be massively enlarged and hemorrhagic so as to resemble Rb.[21]

Optic Nerve Head Drusen

Optic nerve head drusen is a benign, usually bilateral cause of pseudopapilledema and is occasionally inherited as an autosomal dominant condition.[146, 147] Disc drusen or hyaline bodies are spherical, acellular, laminated concretions from an unknown source, often partially calcified and possibly related to accumulation of axoplasmic derivatives of degenerating retinal nerve fibers.[146, 147] Drusen are buried within the substance of the nerve head, usually anterior to the lamina cribrosa. They are covered by axonal and glial tissue, together with the vascular supply of the nerve head. Therefore, drusen of the optic nerve head are recognizable because of characteristic distortion in the shape of the nerve head. Drusen of the optic nerve head are usually bilateral. Clinically, the term *drusen* is more frequently applied to the very common multiple small, round, discrete punctate subretinal nodules (drusen of the pigmented retinal epithelium) at the posterior pole. From the standpoint of pathology, drusen of the optic disc should not be confused with drusen of the pigmented retinal epithelium, which are deposits of basement membrane material between the pigment epithelium of the retina and Bruch's membrane. Bruch's membrane is a tough, acellular, amorphous, bilamellar structure situated between the outer layer of the retina, that is, the RPE, and the choroid. Microscopically, Bruch's membrane consists of five layers: (1) basement membrane of the RPE, (2) inner collagenous zone, (3) elastic layer, (4) outer collagenous zone, and (5) basement membrane of the choriocapillaris. RPE drusen are extracellular deposits that lie between the basement membrane of the RPE and the inner collagenous zone of Bruch's membrane. It has been suggested that apoptosis, a process by which cells cast off part of their cytoplasm, may lead to formation of drusen.[63, 146, 147] The RPE drusen are believed to develop by the shedding of basal cytoplasm of RPE through its basement membrane. Over time, RPE and optic disc drusen change their size, shape, and consistency and may become calcified.[63, 146, 147] Drusen contain sialic acid, cerebrosides, calcium, carbohydrate, mucopolysaccharides, and iron. Optic disc drusen may vary in size (from 59 to 750 mm in diameter) and number; often, smaller drusen appear to coalesce to form larger aggregates. Once their calcified component is more than 1 to 1.5 mm, they should be recognized on thin-section (1 to 1.5 mm) CT scans.[146] RPE drusen are not large enough to be visible on CT scans.

Although optic disc drusen are rarely seen in early childhood, most drusen are believed to be present at birth.[146, 147] They become more apparent in later life as they enlarge and approach the disc surface, becoming ophthalmologically visible as hyaline or colloid bodies.[146] Drusen are rarely detected by CT scanning in early childhood. In order to suggest the diagnosis in early childhood, the CT scans should be carefully evaluated, as the optic disc drusen is not calcified enough at this age. Careful evaluation of the optic disc may reveal a small area that is slightly more dense than the rest of the disc. Some children and adults with drusen of the optic disc may undergo a number of diagnostic studies, including cranial CT and MR imaging, to exclude an intracranial process. Optic disc drusen have been reported in 20 to 24 per 1000 patients at autopsy and are bilateral in 73% of cases.[146, 147] When drusen are located well beneath the surface of the disc, they may blur the disc margin and may lead to misdiagnosis of papilledema. Clinically, drusen are usually asymptomatic, but arcuate field defects (arcuate scotomas) or peripheral field constrictions may be present. These field defects are usually not apparent until adulthood, which further emphasizes the slowly progressive nature of drusen. There also appears to be an association between drusen of the optic disc and retinal hemorrhages.[146] Clinical findings in optic disc drusen range from a small, subtle elevation of the disc to a large, globular yellow-white mass containing calcified concretions.[21] On CT drusen appear as discrete, rounded, high-density or calcified bodies that are confined to the optic disc surface and are found at any level within the prelaminar zone of the optic nerve (Fig. 8-76). Optic nerve drusen are difficult to visualize by MR imaging.

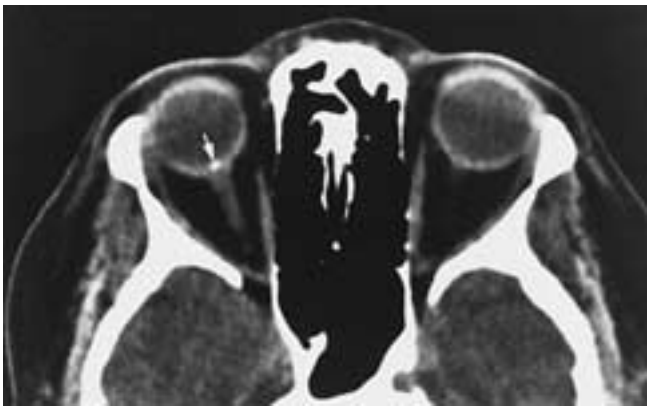

FIGURE 8-76 Optic nerve head drusen. Axial CT scan shows increased density at the optic disc (*arrow*).

VIEW IMAGE

Choroidal Osteoma

Choroidal osteoma is a benign tumor that is typically found unilaterally in young white girls.[21, 63] Histopathologic evaluation reveals mature bone with marrow spaces containing loose fibrovascular tissue.[63] Choroidal osteoma originally was classified as a choristoma (a benign congenital tumor composed of normal tissue elements that do not normally occur at that site), but currently it is regarded by some as an acquired benign choroidal neoplasm of unknown etiology.[145]

Clinical Diagnosis

Patients with choroidal osteoma present with painless progressive loss of vision over several months or years or abrupt recent blurring of central vision. Some lesions are detected initially on routine eye examination.[145] The tumor appears as a yellow-white or orange-red choroidal mass, depending on the amount of depigmentation or hyperplasia of the overlying retinal pigment epithelial layer. This calcified lesion is found in the macula or in the juxtapapil-

Copyright © 2003, Mosby, Inc. All rights reserved.

lary region extending toward the macula.[21] Small vessels can be seen on the surface of the osteoma. Choroidal osteoma involves one eye only in 70% to 80% of cases and both eyes in 20% to 30%.[145] If the lesion involves the macular choroid, visual acuity can be impaired because of degeneration of the overlying RPE and the neurosensory retina.[145] In other cases, a choroidal neovascular membrane arises from the inner surface of the lesion and produces a serous or serosanguineous macular retinal detachment that results in loss of vision.[145]

Imaging Diagnosis

Ultrasound and CT are useful in detecting choroidal osteoma. On a CT scan, choroidal osteomas appear as a plate-like calcified thickening of the posterior ocular wall, typically in the juxtapapillary region; unlike drusen, calcification typically does not involve the center of the optic disc (Fig. 8-77).

Differential Diagnosis

The most important lesions in the differential diagnosis of choroidal osteoma are listed in Table 8-6.

Retinal Gliosis

Retinal and optic nerve astrocytes are analogous to fibroblasts in the body.[21] *Retinal gliosis* refers to reactive proliferation and hypertrophy of astrocytes in the retina, especially occurring in response to injury. Gliotic tissue growth may appear mass-like or may cause tractional retinal detachment.

Myelinated Nerve Fibers

Oligodendrocytes and myelin are not usually present in the human retina.[21] Approximately 1% of eyes have myelinated nerve fibers within the retina, however, usually in a peripapillary distribution. This myelination results in a slightly elevated white retinal plaque and, if extensive, can produce leukokoria. The CT appearance of myelinated nerve fibers may be similar to that of noncalcified retinoblastoma (see Fig. 8-74).

VIEW IMAGE

FIGURE 8-77 Choroidal osteoma. Axial CT scan shows a peripapillary calcified mass (*arrows*) compatible with choroidal osteoma.

X-Linked Retinoschisis

X-linked retinoschisis is a congenital disorder in which there is splitting of the retina within the nerve fiber layer. This causes the inner layers of the retina to be elevated, or the schisis may result in retinal holes, eventually leading to a full-thickness retinal tear and detachment. The CT and MR imaging appearance of X-linked retinoschisis is nonspecific and compatible with retinal detachment.[21]

Retinal Detachment

Retinoblastoma may produce a retinal detachment, which in turn can obscure from view the underlying tumor. Therefore, a retinal detachment resulting from any other etiology can simulate Rb.[21, 32] Rhegmatogenous retinal detachments arise from full-thickness retinal breaks that occur secondarily from retinal atrophy, deterioration, trauma, or vitreous traction. The retinal break allows passage of liquified vitreous into the subretinal space,[21] subsequently causing retinal detachment. Predisposing conditions include trauma, high myopia, Stickler's syndrome, congenital cataract surgery, congenital glaucoma, and myiasis.[21] Nonrhegmatogenous retinal detachments result from traction on the surface of the retina or from exudation under or within the retina, as seen in conditions such as familial exudative vitreoretinopathy, falciform fold, or retinal cyst.[21]

Subretinal Neovascular Membranes

Subretinal neovascular membrane is an acquired abnormality in which growth of new blood vessels from the choriocapillaris occurs beneath the neurosensory retina, usually in response to some retinal injury. These new vessels may hemorrhage or leak, leading to serous retinal detachment. The lesion may organize, resulting in a gliotic, elevated retinal scar and retinal traction.[21]

Vitreous Opacities

Any disease, such as uveitis (see Fig. 8-38), vitreous hemorrhage, endophthalmitis, or organized vitreous, associated with cells in the vitreous can simulate retinoblastoma with vitreous seeding.[21, 32] These vitreous cells or opacities often obscure the view of the retina, causing more difficulty for the clinician in differentiating the etiology of the vitreous cells.

Von Hippel-Lindau Retinal Angiomatosis

Von Hippel-Lindau retinal angiomatosis is an autosomal dominant disorder characterized by retinal capillary heman-

Copyright © 2003, Mosby, Inc. All rights reserved.

giomas.[21] Ophthalmoscopic examination of the fundus reveals a red-orange mass lesion with tortuous feeder and draining vessels.[21] The lesion is usually located in the midperipheral retina and may be associated with exudates and retinal detachment. Aside from ocular conditions, these patients may develop cerebellar hemangioblastoma, optic nerve or optic chiasm hemangioblastoma, renal cell carcinoma, pheochromocytoma, cysts in the kidney or pancreas, and endolymphatic sac tumors.[21]

Choroidal Hemangioma

Choroidal hemangiomas are congenital vascular hamartomas of the choroid that are typically seen in middle-aged individuals. Normal retinal vessels overlie the mass. Choroidal hemangioma in children can simulate retinoblastoma.[21] The CT and MR imaging characteristics of choroidal hemangioma are described elsewhere in this chapter.

Malignant Uveal Melanoma

The uvea (choroid, ciliary body, and iris) is derived from both the mesoderm and the neuroectoderm and may harbor tumors from both of these origins. Because it is the most highly vascular portion of the eyeball, the uvea provides a suitable substrate for tumor cells. Most primary and metastatic ocular neoplasms involve the choroid, and the most common tumor is malignant melanoma.[148] Malignant melanomas of the uvea are unusual in blacks, with the white/black patient ratio being about 15:1.[149] Those melanomas involving the ciliary body and choroid are thought to originate from preexisting nevi.[148] The neoplasm has a capacity to metastasize hematogenously. Its favored metastatic site is the liver. The incidence of malignant melanoma of the choroid has been estimated to be 5.2 to 7.5 cases per million per year.[150] The incidence of uveal melanoma increases with age. Less than 2% of tumors are seen in patients below 20 years of age.[62] Congenital melanosis, ocular melanocytosis, oculodermal melanocytosis, and uveal nevi are predisposing lesions that precede the development of uveal melanoma.[62]

Callender's classification of melanotic lesions, which is based on cellular features, offers the best indication of the prognosis.[151, 152] The spindle-A tumors, which are composed of spindle cells with elongated nuclei, characteristically lacking nucleoli, have the best prognosis. The next best prognoses involve the spindle-B tumors, whose cells have the same shape as spindle-A lesions but are slightly larger and have a nucleus containing a prominent nucleolus. The next worst prognosis concerns the epithelioid-cell tumors, which are composed of larger, more pleomorphic cells than the spindle-cell tumors. Finally, there are mixed-cell tumors composed of both spindle and epithelioid cells.[148, 152] Some of the tumors may be amelanotic, especially the spindle-cell tumors.

Clinical Diagnosis

An iris melanoma is seen as a visible spot on the iris or as a discoloration of the iris in one eye. The typical ciliary body melanoma appears as a highly elevated, nodular, dark brown lesion in the peripheral fundus.[153] The typical choroidal melanoma appears as a dark brown solid tumor and has a biconvex, lenticular cross-sectional shape.[153] The tumor initially grows flat within the choroid, later elevates Bruch's membrane, and finally ruptures through it so that the melanoma assumes a characteristic mushroom shape, growing toward the vitreous cavity. The retina over the surface of the tumor becomes elevated and detached (solid retinal detachment). This detachment gradually extends as a serous detachment over the slopes of the tumor.

Ophthalmoscopically, the lesion is seen as a circumscribed mass of varied pigmentation along with a solid retinal detachment, and the retinal vessels over the surface of the mass are elevated. The retina usually is attached to the mass and does not float easily, as seen in rhegmatogenous retinal detachments. In some cases, the subretinal fluid extends only around the base of the lesion; in others, it accumulates to the extent that the retina is extensively or even totally detached.[153] In some cases, the subretinal fluid is bloody, almost exclusively in eyes that have tumor eruption through Bruch's membrane.[153]

If the tumor is not treated, it may cause secondary glaucoma and eventually break through the eye into the retrobulbar region. Metastases occur primarily to the liver. Management of clinically suspected choroidal melanomas has been the subject of some controversy in recent years. Enucleation has been a standard treatment for more than a century.[154] However, enucleation has not been proven to prevent metastasis. Furthermore, Zimmerman, McLean, and Foster have hypothesized a potentially harmful effect from intraoperative dissemination of tumor cells.[155] The controversy over the efficacy of enucleation remains unresolved.[156]

In general, relatively small choroidal melanomas measuring less than 10 mm in diameter and 3 mm in thickness have a relatively favorable prognosis, with a 10% to 15% incidence of death in 5 years.[157] Biologic aggressiveness has been judged by a clinically visible increase in the size of the tumor. Clinically stable choroidal melanomas are managed with longitudinal observations by clinical examination, echography, CT, and MR imaging, and no treatment. Nevertheless, visibly stationary melanomas have been capable of extensive extraocular extension and possibly even distant metastasis.[158, 159] Furthermore, it has been suggested that tumor cell dissemination may occur early in the course of the disease, with distant metastasis appearing many years later.[160] Thus the clinical management of even small and relatively stable choroidal melanomas warrants careful consideration and the use of all reasonable clinical aids.[156] If there is evidence of tumor growth, enucleation, or local excision, other modes of therapy such as photocoagulation and radiation therapy are indicated.[157, 161] Some advocate early enucleation of all melanomas to prevent metastasis.[160] Metastatic sites of primary uveal melanoma include liver, lung, bone, kidney, and brain in order of decreasing frequency, and a thorough search for metastasis is important to save the patient an unnecessary enucleation.[156]

Diagnostic Imaging

Although uveal melanomas can be accurately diagnosed by ophthalmoscopy, fluorescein angiography, or ultrasonog-

Copyright © 2003, Mosby, Inc. All rights reserved.

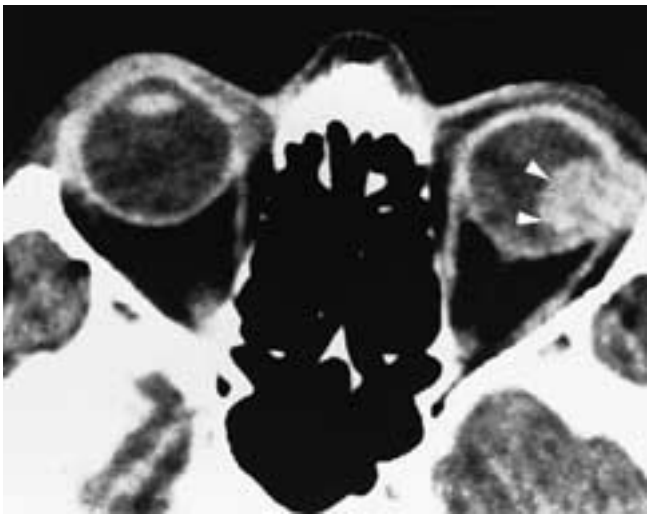

VIEW IMAGE

FIGURE 8-78 Malignant melanoma of the choroid. Axial CT scan shows a mushroom-shaped mass with increased density in the temporal quadrant of the left globe (*arrowheads*). (From Mafee MF et al. Malignant uveal melanoma and similar lesions studied by CT. Radiology 1985;156: 403–408.)

raphy, misdiagnosis continues to occur, particularly when opaque media preclude direct visualization.[137, 162–164] CT has proven to be a highly accurate method for demonstrating uveal melanoma, and dynamic CT can provide information about the vascularity and perfusion of intraocular lesions and can help distinguish uveal melanomas from other lesions such as choroidal hemangiomas. Most uveal melanomas are seen on CT as an elevated, hyperdense, sharply marginated lenticular or mushroom-shaped lesion (Figs. 8-78 and 8-79A).

MR imaging has been used to diagnose intraocular lesions.[21, 32, 165] On T1-weighted and proton density images, uveal melanomas are seen as areas of moderately high signal (greater signal intensity than in the vitreous) (Fig. 8-79B top). On T2-weighted images, melanomas are seen as areas of moderately low signal (lesser intensity than in the vitreous) (Fig. 8-79B bottom). These MR characteristics of uveal melanomas are very similar to those of retinoblastomas (Fig. 8-80). Associated retinal detachment is better visualized by MR imaging than by CT (Fig. 8-81). Exudative retinal detachment is usually depicted on MR imaging as a dependent area of moderate to very high signal intensity in T1-weighted, proton density, and T2-weighted images (Figs. 8-79 and 8-81), and total retinal detachment may be present. Chronic retinal detachment and hemorrhagic subretinal fluid have varied MR imaging appearances. Most uveal melanomas appear as a well-defined solid mass (Figs. 8-82 and 8-83). However, atypical features of ocular melanoma may be present. When necrotic or hemorrhagic foci are present within the uveal melanoma, the inhomogeneity present within the tumor can be problematic (Fig. 8-82). Some melanomas may be seen better on T1-weighted images (Fig. 8-82); discoid or ring melanomas may be difficult to detect if they are flat. Additionally, an organized subretinal exudate, with or without associated hemorrhage, may have MR characteristics similar to those of a uveal melanoma (Fig. 8-84). Tumor invasion of the sclera, optic disc, Tenon's capsule, and the extraocular orbit can be easily detected by MR imaging (Fig. 8-85). Paramagnetic contrast material is very useful in the diagnosis of uveal melanomas, in particular for evaluation of the optic nerve, as well as retrobulbar extension of ocular tumors (Fig. 8-86). Uveal melanomas demonstrate moderate enhancement on postgadolinium T1-weighted MR images. On fat suppression, the T1-weighted MR images demonstrate marked expansion of gray scale with apparently increased signal intensity of the extraocular muscles and lacrimal gland (Fig. 8-86C). Therefore, one should look carefully for extraocular tumor extension adjacent to the area of contact of extraocular muscles with the globe. Fat-suppressed T1-weighted MR images are prone to artifacts related

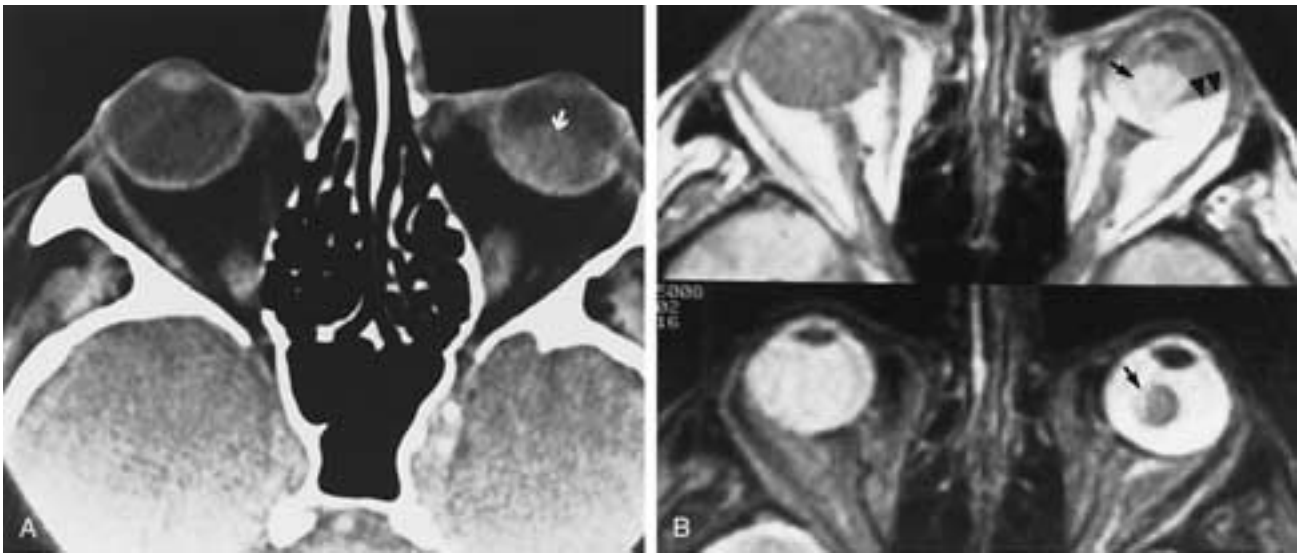

VIEW IMAGE

FIGURE 8-79 Malignant melanoma of the choroid. **A**, Axial CT scan shows a mass (*arrow*). **B**, Axial PW MR image (top) and T2-weighted MR image (bottom) show a mass (*arrow*) and exudative retinal detachment (*arrowheads*). Retinal detachment is distinguished better on MR imaging than on CT.

Copyright © 2003, Mosby, Inc. All rights reserved.

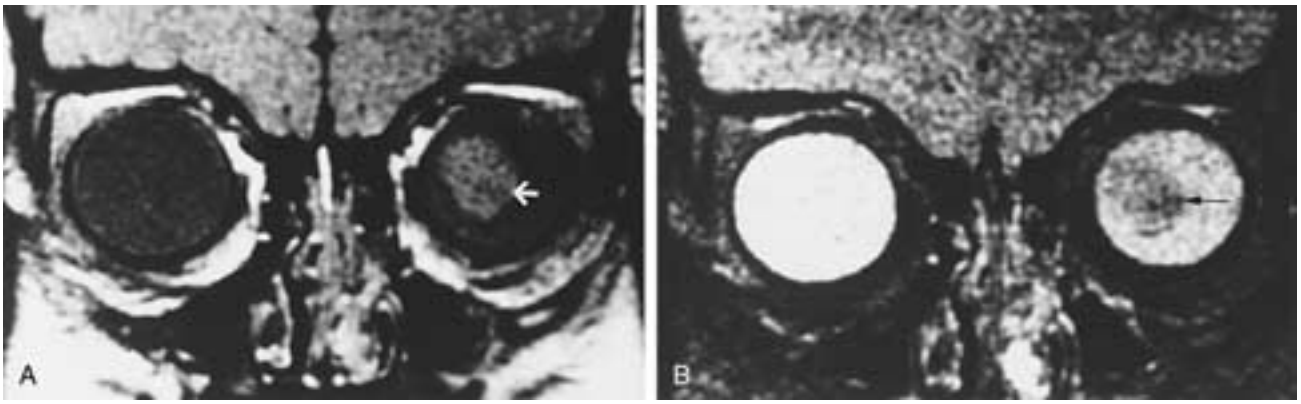

VIEW IMAGE

FIGURE 8-80 Retinoblastoma. **A**, Coronal PW and **B**, T2-weighted MR images. Scans show retinoblastoma (*arrows*). (From Mafee MF et al. Retinoblastoma and simulating lesions: role of CT and MRI. Radiol Clin North Am 1987;25:667–682.)

FIGURE 8-81 Malignant uveal melanoma. **A**, Macroscopic section showing a mushroom-shaped melanoma (*curved arrows*) and a detached retina (*open arrows*). **B**, Sagittal PW MR image of another patient shows a hyperintense mass (*arrows*) and retinal detachment (*arrowhead*). **C**, Sagittal T2-weighted MR image shows a mushroom-shaped hypointense melanoma (*arrows*). The subretinal effusion remains hyperintense.

VIEW IMAGE

Copyright © 2003, Mosby, Inc. All rights reserved.

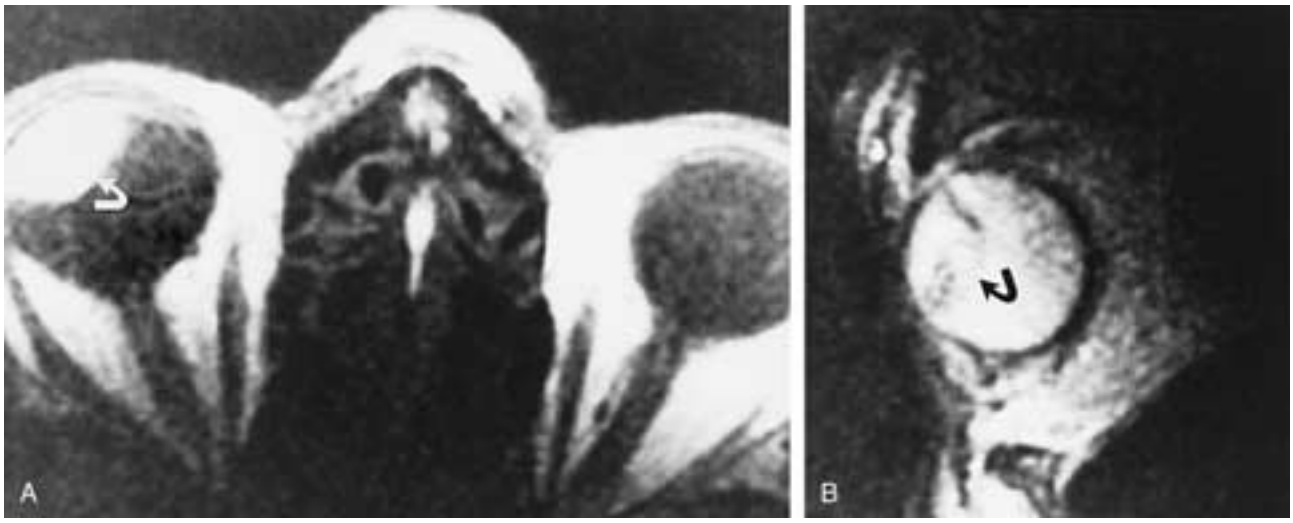

VIEW IMAGE

FIGURE 8-82 Malignant uveal melanoma. **A**, Axial T1-weighted MR image shows a hyperintense mass (*arrow*). **B**, Sagittal T2-weighted MR image shows the mixed signal appearance of the lesion (*arrow*). The anterior portion is hyperintense because of necrosis or hemorrhage.

to dental fillings or other foreign bodies around the orbit (Fig. 8-87).

Choroidal lesions elevated more than 3 mm are usually well visualized on MR imaging. Any lesion less than 3 mm is better studied with ultrasound.[21, 32] The MR imaging characteristics of melanotic lesions are believed to be related to the paramagnetic properties of melanin.[166–168] Damadian et al. reported that, unlike other tumors, melanomas have short T1 relaxation times, which the authors attributed to paramagnetic proton relaxation by stable radicals in melanin.[166] Electron spin-resonance studies have shown that melanin produces a stable free radical signal under all known conditions, and these stable radicals cause proton relaxation enhancement that shortens both T1 and T2 relaxation time values.[167] However, a recent study[169] has shown that with the use of synthetic models, the content of free radicals in melanin (10^{18} spins per gram or one free radical per 3000 subunits), at the average concentration of melanin estimated within melanoma tissue (15 mg/ml), is too low to affect substantially the tissue TI relaxation time.[169]

It has been shown that melanin has a high affinity and binding capacity for metal ions,[169] and natural melanin contains a wide variety of bound metals in vivo (iron,

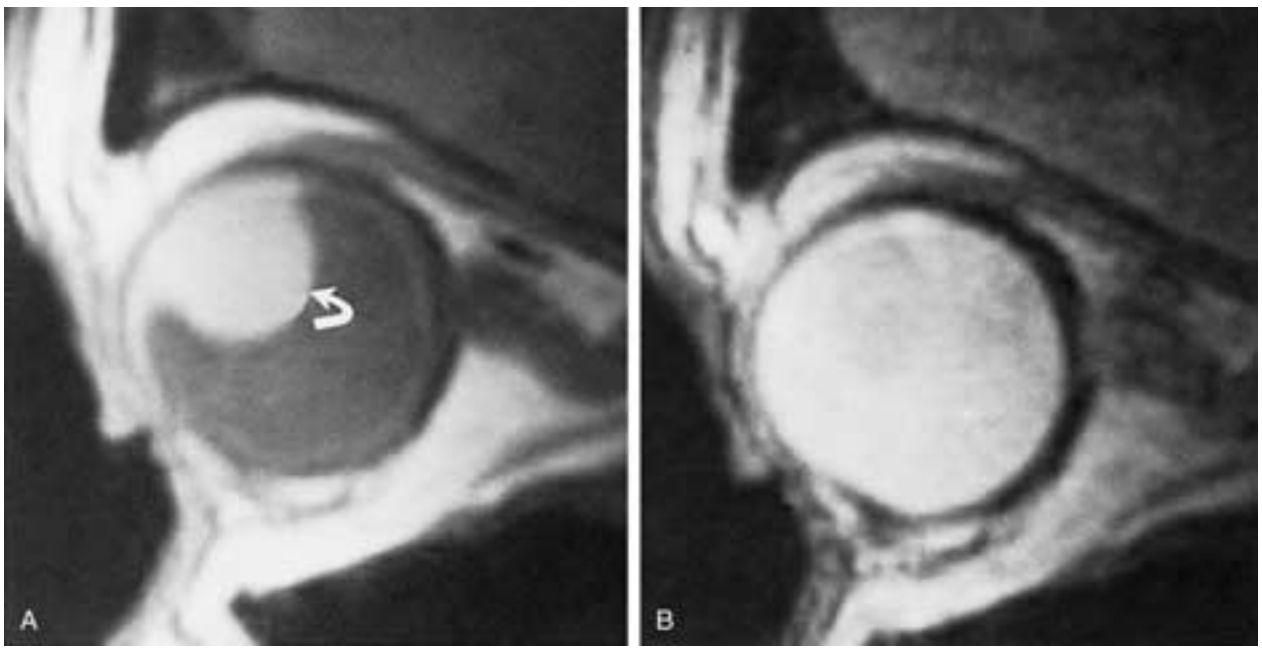

VIEW IMAGE

FIGURE 8-83 Malignant uveal melanoma. **A**, Sagittal PW and **B**, T2-weighted MR images. Scans show a mass (*arrow*), which is better seen in the PW MR image. The lesion remains slightly hypointense on the T2-weighted MR image.

Copyright © 2003, Mosby, Inc. All rights reserved.

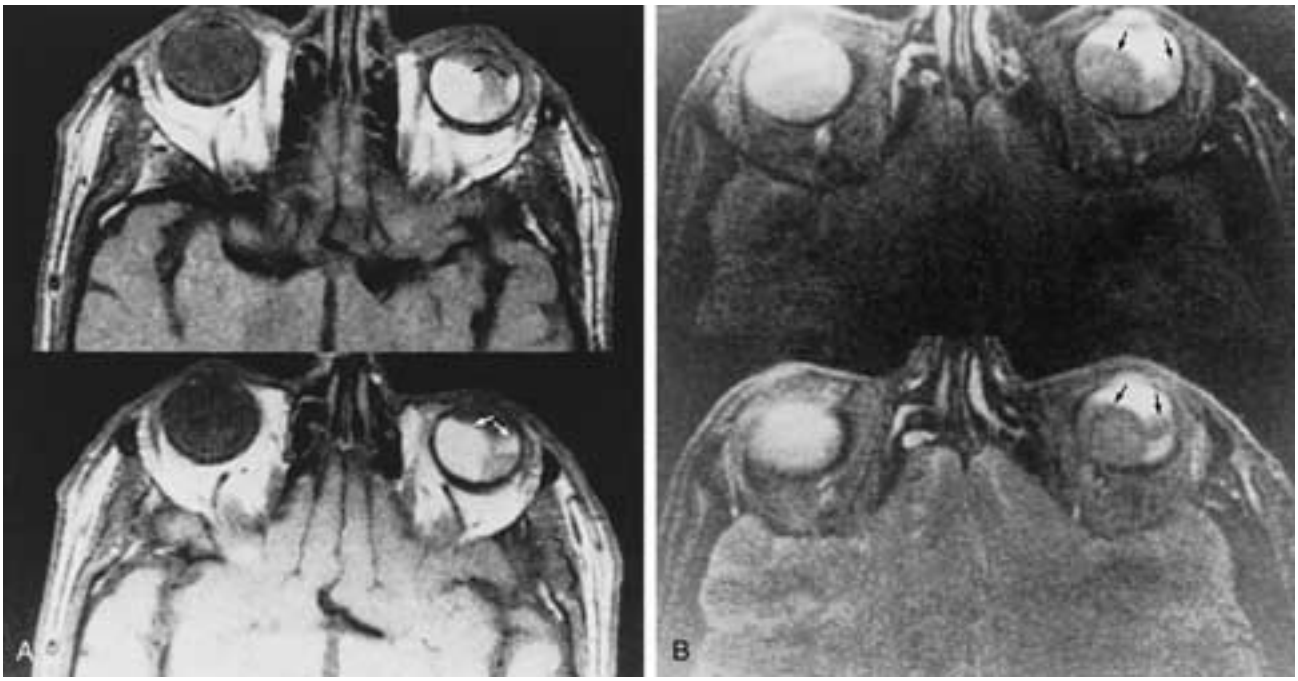

VIEW IMAGE

FIGURE 8-84 Malignant uveal melanoma and postradiation retinal detachment simulating recurrent tumor. **A**, Axial PW MR images show hyperintense masses (*arrows*). **B**, Axial T2-weighted MR images show hypointense masses. The eye was enucleated, and masses were found to be caused by highly proteinaceous, organized subretinal fluid with some degree of hemorrhage as well. The uveal melanoma was seen as a small, partially necrotic lesion. The MR imaging appearance of these subretinal changes is identical to the MR imaging characteristics of melanotic lesions. Therefore, caution must be exercised in MR imaging interpretation of intraocular lesions. When highly proteinaceous lesions are present, such as in this case or in the case of mucin-producing metastatic adenocarcinoma, MR imaging may not differentiate them from uveal melanomas.

copper, manganese, and zinc).[62] This indicates that melanin may have a cytoprotective function as an intracellular scavenger of free metals. The work of Enochs and associates[169] revealed that it is the binding of paramagnetic metals (paramagnetic metal scavenging) that is responsible for the high signal intensities of melanomas on T1-weighted MR images. Uveal melanomas therefore are unique in that both T1 and T2 relaxation values are relative shortened. Hence, on T1-weighted images, the lesion should be relatively hyperintense, the opposite of that predicted for T2-weighted images, and these signal intensities have been observed in the overwhelming majority of uveal melanomas. At times, uveal melanomas may have mixed or high signal intensity on T2-weighted scans (Fig. 8-83). The MR imaging diagnosis of uveal melanomas is greatly enhanced by the use of gadolinium contrast material. Uveal melano-

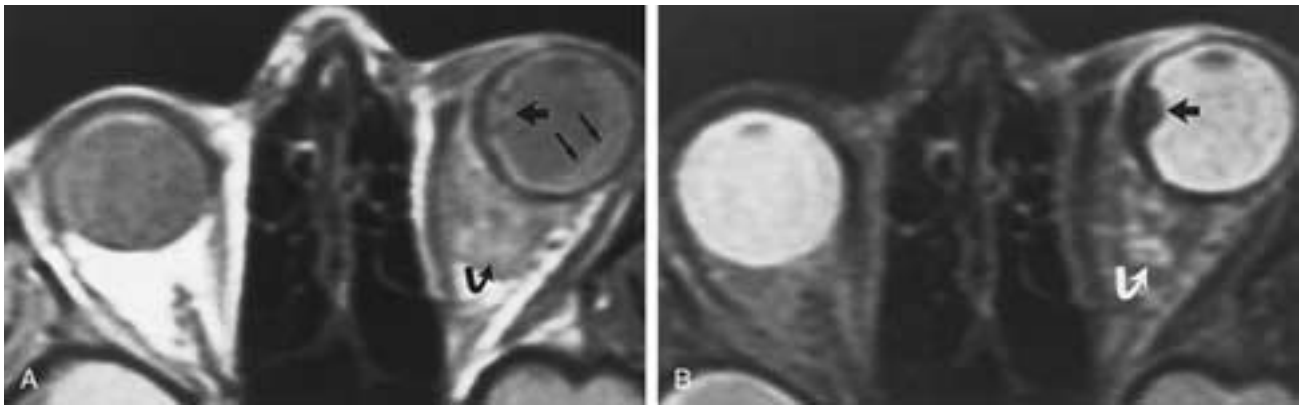

VIEW IMAGE

FIGURE 8-85 Uveal melanoma with massive retrobulbar extension. **A**, Axial PW and **B**, T2-weighted MR images. Scans show uveal melanoma (*large arrow*), subretinal fluid (*small arrows*), and massive extraocular tumor extension (*curved arrow*).

Copyright © 2003, Mosby, Inc. All rights reserved.

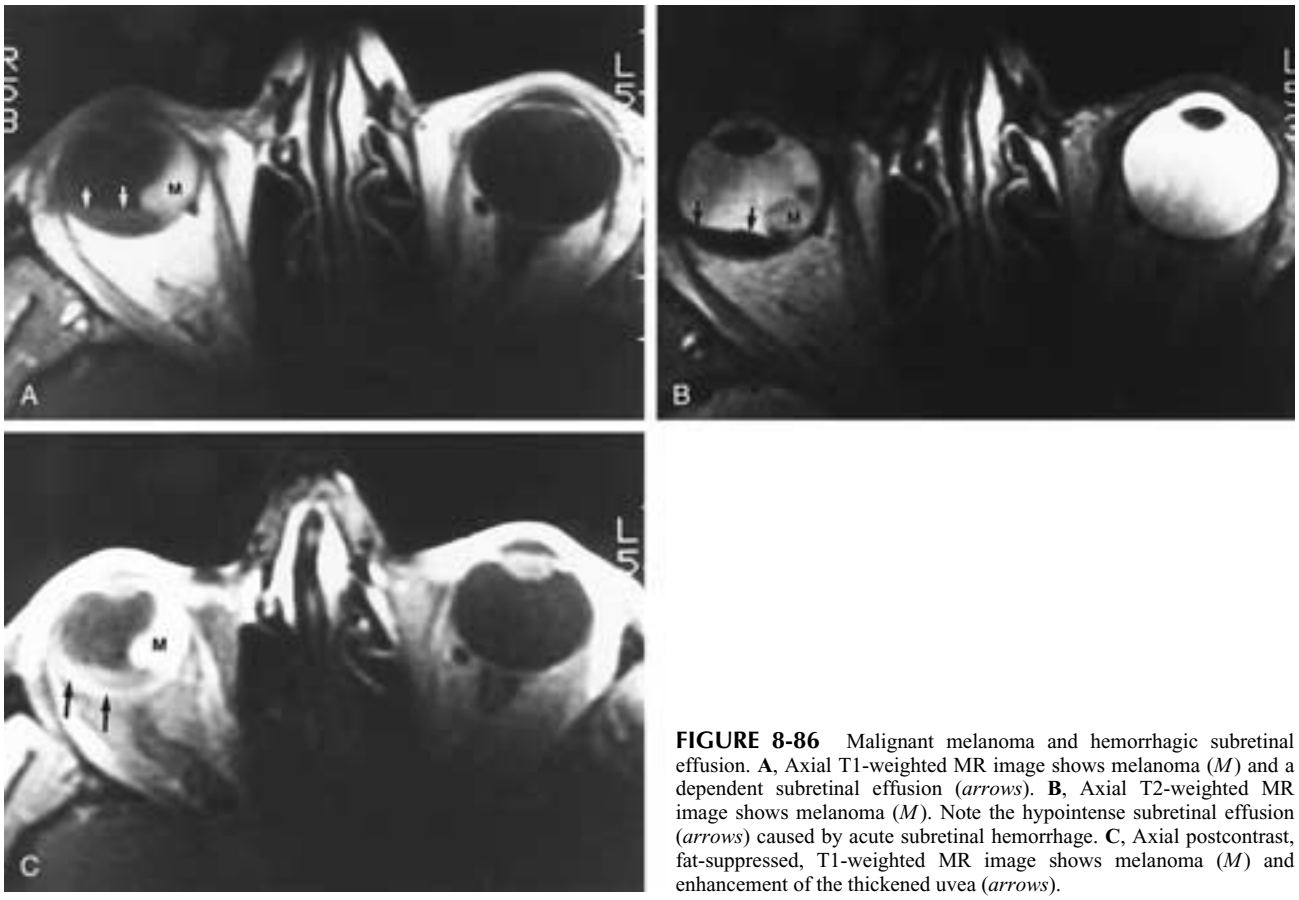

FIGURE 8-86 Malignant melanoma and hemorrhagic subretinal effusion. **A**, Axial T1-weighted MR image shows melanoma (*M*) and a dependent subretinal effusion (*arrows*). **B**, Axial T2-weighted MR image shows melanoma (*M*). Note the hypointense subretinal effusion (*arrows*) caused by acute subretinal hemorrhage. **C**, Axial postcontrast, fat-suppressed, T1-weighted MR image shows melanoma (*M*) and enhancement of the thickened uvea (*arrows*).

VIEW IMAGE

mas show moderate enhancement (Figs. 8-86 and 8-87), and ocular and extraocular invasion can be easily detected on postcontrast, fat-suppressed, T1-weighted scans. Extension into the orbit of a primary ocular melanoma is not common. The size of the extraocular extension is independent of the size of the ocular tumor (Fig. 8-85).

Differential Diagnosis

A number of benign and malignant lesions of the eye may be confused with malignant uveal melanomas. These conditions include metastatic tumors (Fig. 8-88), choroidal detachment, choroidal nevi, choroidal hemangioma, choroidal cyst, neurofibroma and schwannoma of the uvea,

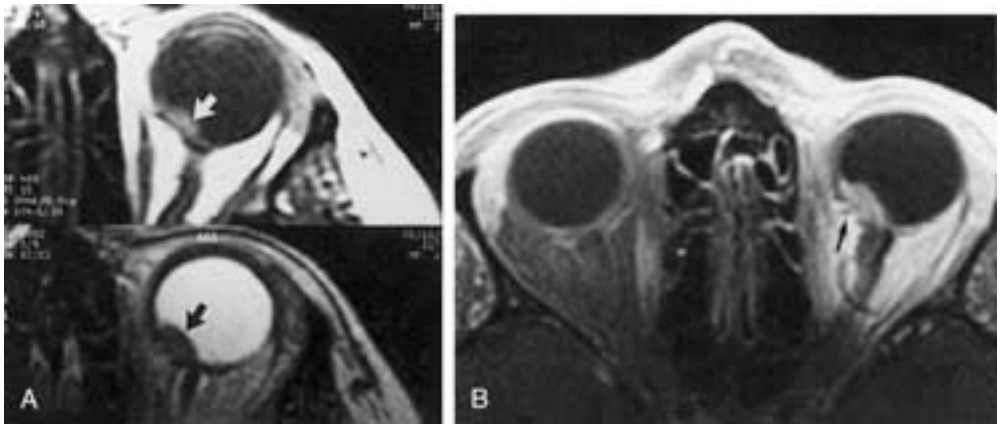

FIGURE 8-87 Malignant uveal melanoma. **A**, Axial T1-weighted (top) and T2-weighted (bottom) MR images showing a choroidal melanoma (*arrows*). **B**, Enhanced, fat-suppressed, T1-weighted MR image showing moderate tumor enhancement. Note the irregularity of the scleral and tumor nodule (*arrow*) caused by scleral invasion and retrobulbar extension, confirmed on histologic examination. The hyperintensity of the retrobulbar fat on the left in this image is due to dental metallic filling, causing a problem in suppressing the fat. (Courtesy of M.F. Mafee, MD, FACR, Chicago.)

VIEW IMAGE

Copyright © 2003, Mosby, Inc. All rights reserved.

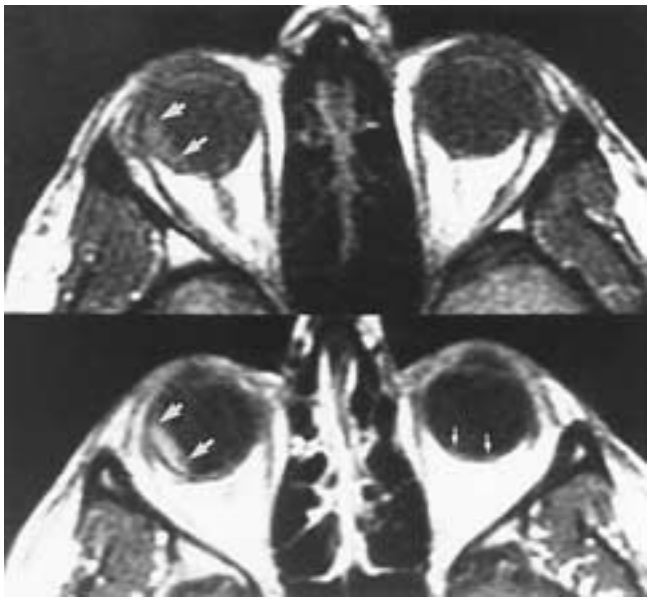

VIEW IMAGE

FIGURE 8-88 Uveal metastasis. Axial precontrast (top) and postcontrast (bottom) T1-weighted MR images show bilateral choroidal metastases (*arrows*).

leiomyoma, choroidal lymphoma (Fig. 8-89), adenoma of the ciliary body, medulloepithelioma, retinal detachment, and disciform degeneration of the macula.[19, 170, 171] The most important lesions in the differential diagnosis of iris melanomas and choroidal and ciliary body melanomas are listed in Tables 8-7 and 8-8.

Melanocytoma

Melanocytoma is a deeply pigmented benign tumor that usually occurs at the optic disc but may also arise anywhere in the uvea. Iris melanocytomas are rare and have a predisposition to release pigment into the anterior chambers, which causes a secondary open-angle glaucoma. Approximately 50% of melanocytomas develop in blacks, whereas the incidence of malignant uveal melanoma in blacks is less than 1%.[150] The MR imaging appearance of melanocytoma is similar to that of malignant uveal melanoma (Fig. 8-90). Melanocytomas are special types of uveal nevus. Melanocytoma of the optic disc usually is composed entirely of maximally pigmented, polyhedral nevus cells (magnocellular nevus cells).[40] Clinically, the lesion is a dark tumor that involves the substance of the optic disc. The melanocytomas appear homogeneously very hypointense on T2-weighted MR images (Fig. 8-90). Primary malignant melanoma of the optic nerve head is an exceedingly rare tumor.[172] Most melanomas of the optic nerve head are related to extension of a peripapillary choroidal melanoma.[173] The tumors are found to involve the choroid adjacent to the optic disc. Figure 8-91 shows a clinicopathologically proved primary malignant melanoma of the optic disc without choroidal involvement. The clinical appearance simulated that of a melanocytoma so precisely that the proper diagnosis was delayed. MR imaging demonstrated a discoid mass with

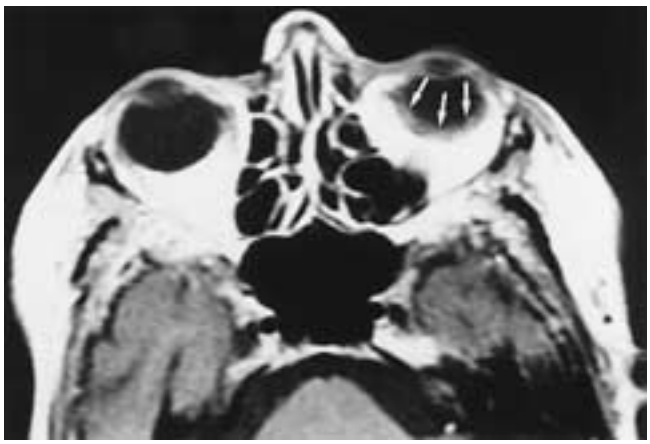

VIEW IMAGE

FIGURE 8-89 Choroidal lymphoma. Axial postcontrast T1-weighted MR image shows an irregular, infiltrative, moderately enhancing mass (*arrows*) involving the left globe. The appearance cannot be differentiated from that of uveal metastasis.

Table 8-7
DIFFERENTIAL DIAGNOSIS OF IRIS MELANOMAS

Nevus of the iris
Medulloepithelioma
Metastasis
Juvenile xanthogranuloma
Adenoma and adenocarcinoma of the ciliary epithelium
Cyst of the iris
Inflammatory granuloma
Leiomyoma of the iris and ciliary body
Choristoma, teratoma

Table 8-8
DIFFERENTIAL DIAGNOSIS OF CHOROIDAL AND CILIARY BODY MELANOMAS

Choroidal nevus including ocular melanocytosis
Melanocytoma of optic disc
Melanocytoma of choroid
Metastasis (often bilateral)
Choroidal hemangioma
Choroidal osteoma
Inflammatory granuloma of the uvea (tuberculosis, sarcoidosis)
Nodular posterior scleritis
Localized choroidal-suprachoroidal hematoma
Localized subretinal or subpigment epithelial hematoma (senile macular degeneration)
Medulloepithelioma
Choroidal lymphoma (almost always bilateral)
Primary ocular adenoma and adenocarcinoma
Hemangiopericytoma (ciliary body)
Leukemic infiltration of the uvea
Pseudotumor of the uvea
Massive gliosis of the retina
Astrocytoma of the retina
Uveal neurilemoma/neurofibroma

Copyright © 2003, Mosby, Inc. All rights reserved.

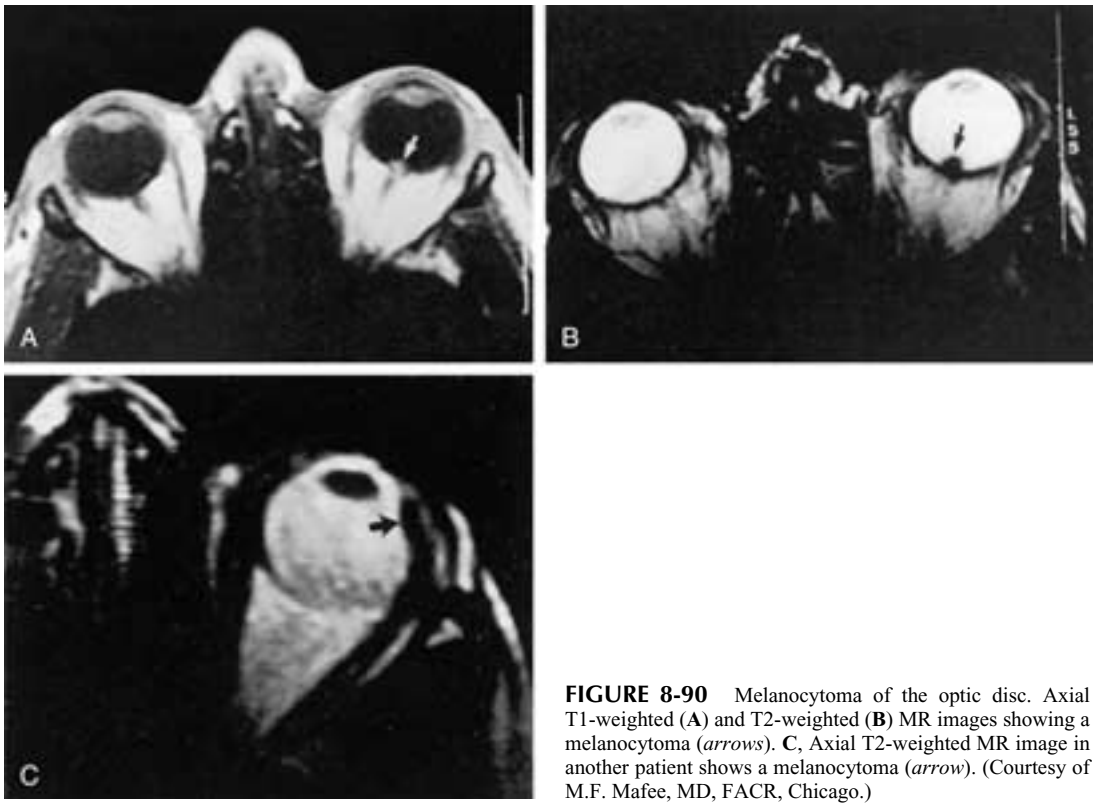

FIGURE 8-90 Melanocytoma of the optic disc. Axial T1-weighted (**A**) and T2-weighted (**B**) MR images showing a melanocytoma (*arrows*). **C**, Axial T2-weighted MR image in another patient shows a melanocytoma (*arrow*). (Courtesy of M.F. Mafee, MD, FACR, Chicago.)

VIEW IMAGE

involvement of the optic nerve (Fig. 8-91), and the patient underwent enucleation of the right eye. Even though 17 mm of nerve was obtained, tumor was present at the point of surgical resection. Later, the patient underwent right frontotemporal craniotomy to remove the remainder of the optic nerve to the chiasm.

Uveal Metastasis

Uveal metastasis can be confused with uveal melanoma both clinically and on imaging. Metastatic lesions of the uvea extend chiefly in the plane of the choroid, usually with relatively little increase in thickness. Unlike uveal melanomas, which tend to form a protuberant mass, metastatic lesions have a mottled appearance and a diffuse outline, causing relatively little increase in their thickness.[62] The malignant cells (emboli) obtain access to the eye via the bloodstream by means of the short posterior ciliary arteries, and this may be the reason that the majority of metastases occur in the posterior half of the eye. The most common source of secondary carcinoma within the eye is from the breast or lung. Tumor metastasis may occur in both the retina and the choroid, both eyes being affected in about one-third of the cases. Unlike uveal metastasis, bilateral uveal melanomas are rare. Metastatic carcinoma of the pancreas and stomach also have been reported in the retina.[62] On CT, uveal metastasis may be difficult to differentiate from uveal melanoma.[19, 62, 174] MR imaging has been shown to be superior to CT in differentiating uveal metastasis from uveal melanoma.[19] However, uveal metastases may have signal characteristics similar to those of uveal melanomas (Fig. 8-92). Metastatic lesions of the choroid may lead rapidly to prominent and widespread detachment of the retina. In these patients, the mottled appearance and diffuse outline of the lesion may be rather different from those of uveal melanoma. Gd-DTPA has increased the sensitivity of MR for detection of uveal metastasis (Fig. 8-89). A mucin-producing metastatic lesion (adenocarcinoma) may also simulate a uveal melanoma because the proteinaceous fluid tends to decrease the T1 and T2 relaxation times of the lesion. We have seen metastatic carcinoid as well as hypernephroma that were indistinguishable from other uveal metastasis on MR imaging.

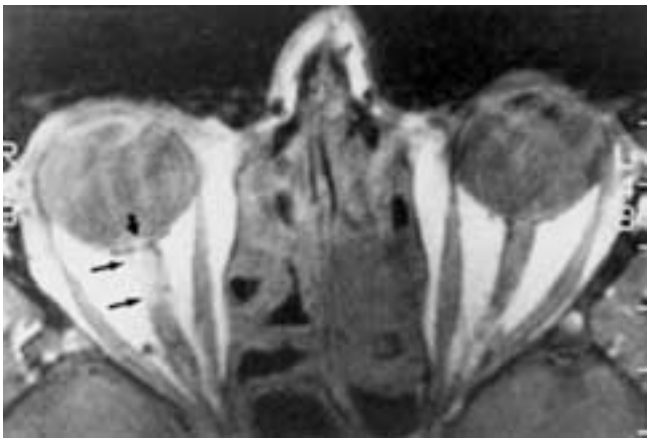

FIGURE 8-91 Melanoma of the optic nerve with optic nerve involvement. Enhanced, fat-suppressed, proton density MR image shows an optic nerve head lesion (*curved arrow*) with marked extension into the optic nerve (*arrows*). (Courtesy of M.F. Mafee, MD, FACR, Chicago.)

VIEW IMAGE

Copyright © 2003, Mosby, Inc. All rights reserved.

Uveal Nevus

Uveal nevi are congenital lesions, usually recognized late in the first decade of life and most frequently located in the posterior one third of the choroid.[40] Most choroidal nevi are less than 5 mm in basal diameter and less than 1 mm in thickness, but occasionally lesions of this type attain a basal diameter of 10 mm or more and a thickness of 3 mm or more.[40] They appear clinically as a flat or minimally elevated slate-gray choroidal mass with slightly indistinct margins. The color of these lesions depends largely on the composition of cell types within the nevus. Occasionally, choroidal nevi may be associated with shallow serous retinal detachment, with or without subretinal neovascularization.[168, 175, 176] If the macula becomes involved, this may cause visual field defects with decreased vision.[176] Under such circumstances, a choroidal nevus may simulate a choroidal melanoma both ophthalmoscopically and angiographically. The choroidal nevus is one of the most commonly misdiagnosed lesions to be enucleated under the misdiagnosis of malignant melanoma.[163, 164, 170] It is sometimes extremely difficult to differentiate these two lesions, with long-term follow-up being the only possible solution.[176] Most of the important lesions in the differential diagnosis of uveal nevi include melanoma of the iris, ciliary body, and choroid, metastatic carcinoma to the uvea, inflammatory granuloma, leiomyoma of the iris and ciliary body, juvenile xanthogranuloma of the iris and ciliary body, circumscribed choroidal hemangioma, choroidal osteoma, choroidal neurilemoma, subretinal or suprachoroidal hematoma, and foreign body in the iris.

Diagnostic Imaging

CT and MR imaging studies of several patients in whom uveal nevus was considered the likely ophthalmoscopic diagnosis showed that many lesions could not be visualized because of their small size, with most uveal nevi being less than 2 mm. In two uveal nevi seen on CT and MR imaging, the appearance was identical to that of uveal melanoma. Both of these patients underwent internal eye wall resection of the lesions, and a histopathologic study led to a diagnosis of choroidal nevus. It should be emphasized that CT and MR imaging are unable to differentiate uveal nevi from uveal melanomas. Internal eye wall resection may provide an alternative approach for suspicious lesions near the posterior pole, and this procedure has the advantage of preserving the globe.

Choroidal and Retinal Hemangiomas

Choroidal hemangiomas are seen usually in association with Sturge-Weber disease (encephalotrigeminal syndrome). Retinal angiomas (angiomatosis retinae), on the other hand, are seen in patients with von Hippel-Lindau disease. The diagnosis of choroidal hemangiomas on clinical grounds presents some difficulty. In the majority of cases, the lesion is discovered in the course of a pathologic examination, and in cases where an ophthalmoscopic examination had been performed, the tumor was concealed by the detachment of the retina.[177] The diagnosis of angiomatosis retinae of von Hippel-Lindau disease, by contrast, is chiefly dependent on the ophthalmoscopic appearance of the lesion. Sturge-Weber disease and von Hippel-Lindau disease belong to the general class of disorders referred to as phakomatoses. The major syndromes include neurofibromatosis, tuberous sclerosis (Bourneville's disease), encephalotrigeminal syndrome (Sturge-Weber disease), cerebelloretinal hemangioblastomatosis (von Hippel-Lindau disease), and ataxia-telangiectasia (Louis-Bar disease).

Sturge-Weber disease consists of capillary or cavernous hemangiomas that have a cutaneous distribution along the trigeminal nerve and of a predominantly venous hemangioma of the leptomeninges.[177, 178] The intracranial or cutaneous lesions may occur separately. The most familiar manifestation takes the form of the port-wine stain, or capillary nevus of the face, varying in its extent and sometimes being limited to the skin of the eyelids and conjunctiva. The eye changes are usually ipsilateral to the changes elsewhere, may be bilateral, and may be found without any surface angiomas. The ophthalmic changes consist of an angioma of the choroid, buphthalmos, or chronic glaucoma with atrophy and cupping of the optic nerve.[62, 177] The glaucoma may be explained by the angiomatous changes in the ciliary body or the angle of the anterior chamber.

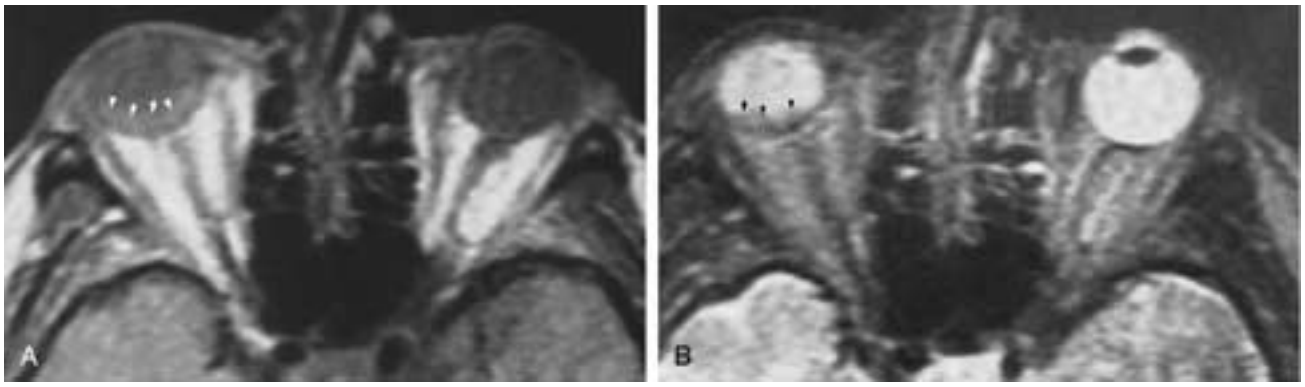

FIGURE 8-92 Choroidal metastasis. **A**, Axial PW MR image shows a hyperintense lesion (*arrows*) consistent with an ophthalmoscopic finding of choroidal metastasis. Note the irregularity of the lesion's surface. **B**, The lesion remained slightly hyperintense in this axial T2-weighted MR image.

VIEW IMAGE

Copyright © 2003, Mosby, Inc. All rights reserved.

Choroidal hemangiomas are congenital vascular hamartomas that are typically seen in middle-aged to elderly individuals, although they can be seen in children. Two different forms have been reported: (1) a circumscribed or solitary type not associated with other abnormalities and (2) a diffuse angiomatosis often associated with facial nevus flammeus or variations of Sturge-Weber syndrome.[62]

Clinical Features

Uveal hemangiomas are classified histologically into three descriptive categories: (1) cavernous, (2) capillary, and (3) mixed type. Regardless of their histologic classification, these lesions follow two major growth patterns: (1) the solitary circumscribed choroidal form and (2) the diffuse form associated with Sturge-Weber syndrome. Solitary choroidal hemangioma is confined to the choroid, shows distinct margins, and characteristically lies posterior to the equator of the globe.[62, 177] It is typically seen as a focal reddish orange choroidal tumor located in the juxtapapillary or macular regions of the fundus. In contrast, the hemangioma associated with Sturge-Weber syndrome is a diffuse process that may involve the choroid, ciliary body, iris, and occasionally other nonuveal tissues such as the episclera, conjunctiva, and limbus.

Diagnostic Imaging

Although uveal hemangiomas can be diagnosed by ophthalmoscopy, fluorescein angiography, or ultrasound, the clinical diagnosis may be difficult.[62, 177] In recent years, increased awareness of the various lesions of the uvea that may mimic melanoma (pseudomelanomas), combined with CT and MR imaging, has greatly decreased the frequency of erroneous diagnosis, so fewer eyes with choroidal hemangioma are enucleated.[62] A choroidal hemangioma is seen on plain CT as an ill-defined mass (Fig. 8-93A) that demonstrates marked enhancement with contrast infusion (Fig. 8-93B,C) and on dynamic CT (Fig. 8-93D). In some cases, the choroidal angioma may be concealed by the detachment of the retina (Fig. 8-93C). On MR imaging, a choroidal hemangioma may be seen as a hypointense area on T1-weighted (Fig. 8-93E) and T2-weighted images (Fig. 8-93F). Some choroidal hemangiomas are seen as a moderately intense area on T1-weighted, proton density, and T2-weighted images (Figs. 8-94 and 8-95). Whenever a choroidal hemangioma cannot be definitely differentiated from a uveal melanoma by MR imaging, contrast-enhanced CT is recommended using a combination of infusion-bolus (Fig. 8-93B) or dynamic CT techniques (Fig. 8-93D).[19, 36] Alternatively, gadolinium MR imaging may differentiate these entities (Fig. 8-95). The diagnosis of angiomatosis retinae of von Hippel-Lindau disease is chiefly dependent on the ophthalmoscopic appearance of the lesion. Because of the small size of the lesion (1.5 to 2 mm), retinal angiomas usually are not identified on MR imaging.

Angiomatosis Retinae and Von Hippel-Lindau Disease

Angiomatosis retinae and *von Hippel-Lindau disease* are interchangeable names for phakoma of the retinal angioma.[27] This syndrome consists of a vascular malformation of the retina and cerebellum. The retinal lesion usually has the characteristics of a malformation, and the cerebellar lesion consists of a slowly growing cystic hemangioblastoma(s). The cerebellar lesions may be multiple and associated with one or more spinal hemangioblastomas. Von Hippel described the ocular changes in 1895 and the clinical and pathologic changes in 1911. In 1926, Lindau described the frequent occurrence of von Hippel's ocular findings in patients with hemangioblastoma in the cerebellum, medulla, and spinal cord, with angiomas or cysts of the pancreas, liver, kidney, adrenals, epididymis, or ovaries.[27] This combination has been recognized as von Hippel-Lindau disease. Not all patients have a retinal lesion, the von Hippel part of the disease. Both eyes are affected in about 50% of cases, and 25% of the patients with retinal angioma manifest systemic involvement.[27, 40] Retinal angiomas are present at birth as hamartomatous collections of small nests of angioblastic and astroglial rest cells, but it is not until the second or third decade of life that an angioma grows sufficiently large to be clinically detected.[27] Among the conditions that must be considered in the differential diagnosis of angiomatosis retinae of von Hippel-Lindau disease are Eales' disease, Coats' disease, multiple retinal aneurysms (Leber's disease), and capillary angiectasis of the retina.[27, 40] Eales' disease, or retinal periphlebitis, occurs in young men (15 to 35 years old) and is characterized by vessel sheathing of the retina and vitreous hemorrhage. The retinal veins show sheathing with exudates, hemorrhage, and vasoproliferation.[40] There are also recurrent vitreous hemorrhages from affected veins.

Choroidal Hemorrhage and Choroidal Detachment

In discussing the differential diagnosis of uveal melanoma, choroidal hemorrhage and choroidal detachment must be considered because they may be easily mistaken for a choroidal tumor. A massive choroidal hemorrhage that has failed to rupture the lamina of Bruch may simulate the ophthalmoscopic, CT, and MR imaging appearance of a choroidal tumor because it forms a round, even globular, dark brown prominence that is opaque to transillumination (Figs. 8-96 and 8-97). The covering of the pigmented choroid, if the hemorrhage is in the suprachoroidal space, and of the retinal pigment layer may cause the hemorrhage's color to be even darker than that of the majority of melanomas. Such hemorrhage may become encapsulated and subsequently absorbed, leaving behind a more- or less-dense membrane. Choroidal effusion (uveal effusion) is another pathologic entity that can be confused with a ring melanoma.[53, 54] The CT and MR imaging appearances of choroidal hemorrhage (Figs. 8-41 and 8-97), choroidal detachment (Figs. 8-40, 8-46, and 8-47), uveal effusion (Fig. 8-48), were discussed earlier in this chapter.

Choroidal Cyst

Choroidal cysts are very rare. However, they can be mistaken for a choroidal tumor. They may be bilateral, and they may cause retinal detachment. The cyst may be successfully treated by the removal of its fluid content.

Copyright © 2003, Mosby, Inc. All rights reserved.

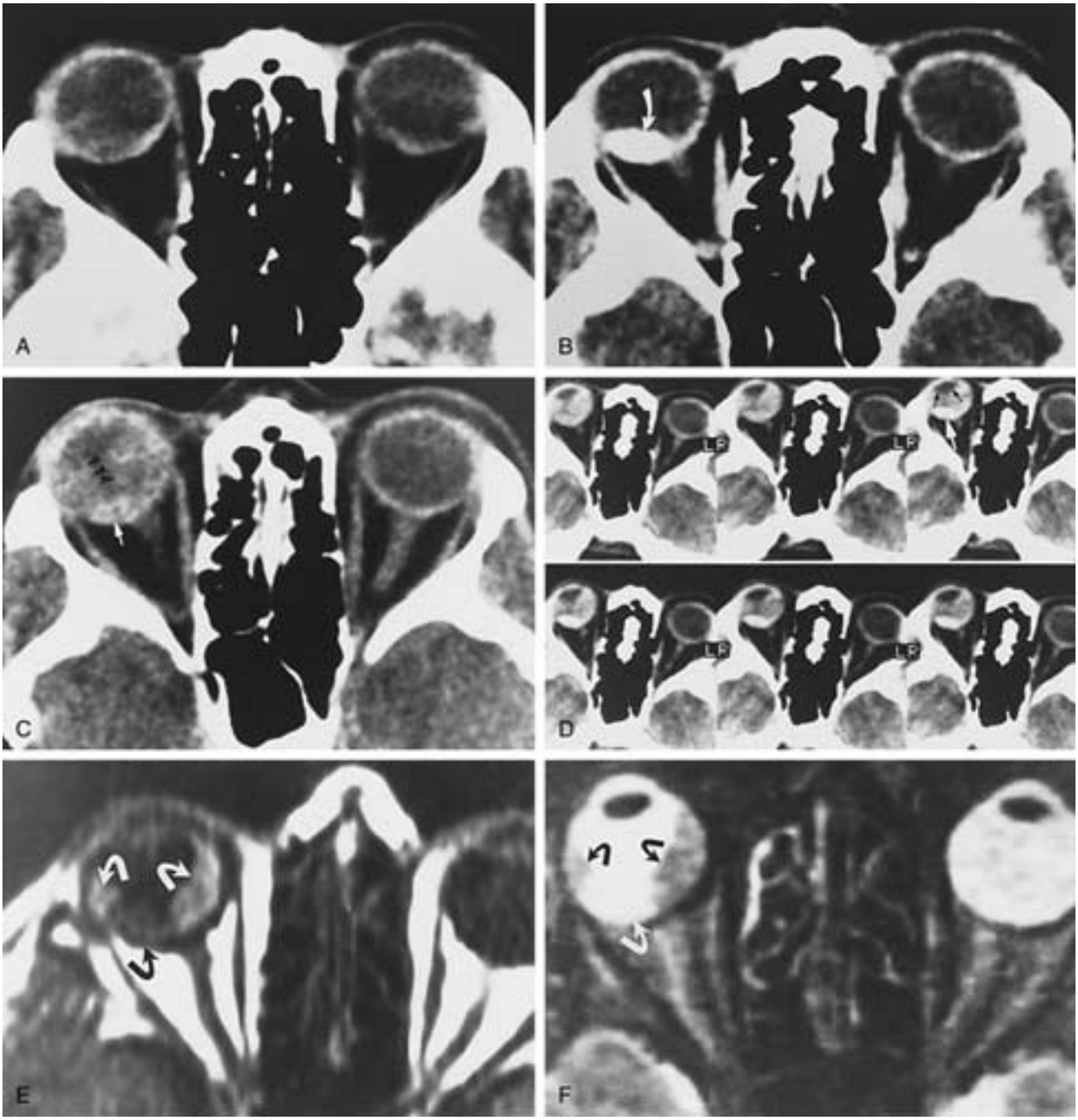

VIEW IMAGE

FIGURE 8-93 Choroidal hemangioma. **A**, Noncontrast axial CT scan shows a faint lesion of the right globe. **B**, Contrast axial CT scan obtained with rapid injection of contrast shows marked enhancement of a hemangioma (*arrow*). This patient later developed total retinal detachment. **C**, Routine axial contrast enhancement shows a mass (*arrow*) and retinal detachment (*arrowheads*). **D**, Dynamic CT scans show a hemangioma (*white arrow*), differentiating it from total retinal detachment (*black arrows*). **E**, Axial T1-weighted MR image shows hemangioma (*black arrow*) and chronic subretinal effusion (*white arrows*). **F**, Axial T2-weighted MR image shows the hemangioma as a hyperintense image (*white arrow*) and chronic subretinal effusion as a hypointense image (*black arrows*). The hypointensity of the subretinal effusion is thought to be caused by highly organized proteinaceous fluid. (From Mafee MF et al. Malignant uveal melanoma and simulating lesions: MRI evaluation. Radiology 1986;160:773–780.)

Copyright © 2003, Mosby, Inc. All rights reserved.

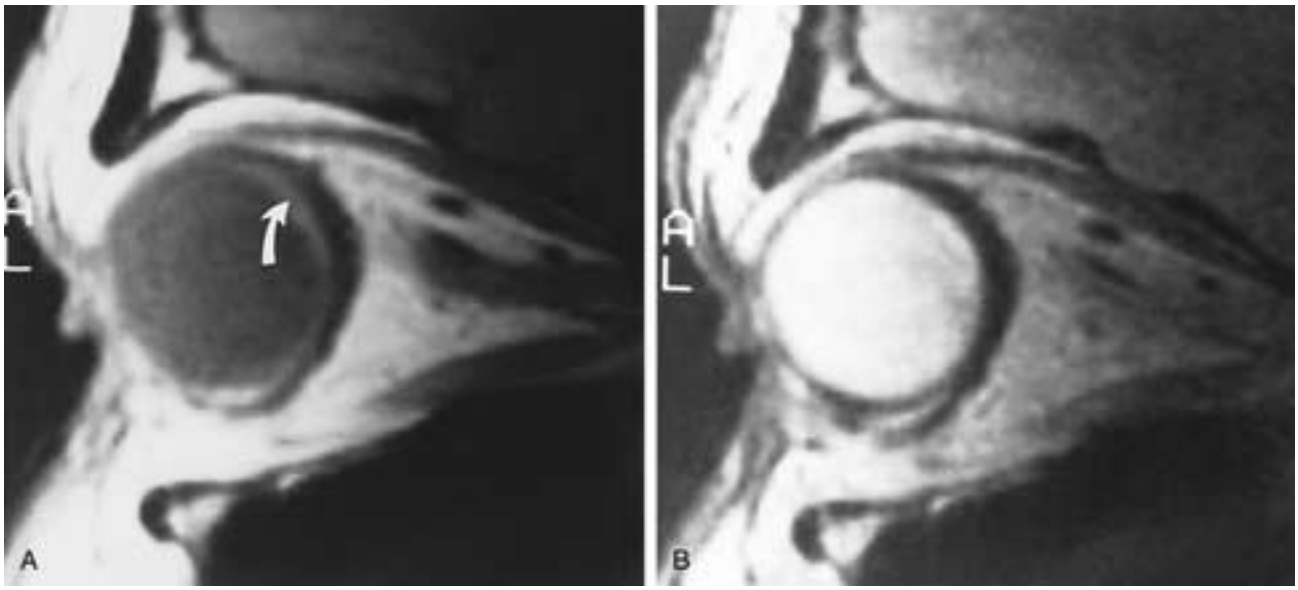

VIEW IMAGE

FIGURE 8-94 Choroidal hemangioma. **A**, Sagittal PW MR image shows a hyperintense mass (*arrow*). **B**, Sagittal T2-weighted MR image shows that the mass remains hyperintense. Ophthalmoscopic findings were most compatible with hemangioma. This MR imaging appearance may be difficult to differentiate from retinal detachment. Combined clinical and MR imaging findings should help the clinician make the right diagnosis.

Other Tumors of the Uvea

Ocular Lymphoma

Primary non-Hodgkin's lymphoma involving the eye is a rare condition. Modern immunohistochemical analysis shows that primary lymphomas of the retina and central nervous system (CNS) are usually large B-cell lymphomas.[40] The number of primary lymphomas of the retina and CNS has increased because of patients with acquired immune deficiency syndrome (AIDS) and other causes of immunodeficiency.[40] In contrast to primary ocular lymphoma, secondary ocular involvement by a systemic malignant lymphoma manifests itself mainly as a uveal tumor. Most often, the disease presents initially with signs of uveitis. Primary lymphoma of the eye is typically bilateral. Primary lymphoma of the retina can masquerade as a corticosteroid-resistant chronic uveitis.[40] Extensive infiltration of the retina and optic nerve head may lead to coagulative necrosis. Many atypical presentations of intraocular lymphoma have been reported, including a hemorrhagic retinal vasculitis that mimics a viral retinitis.[40] A secondary glaucoma may be present. The most important differential diagnosis includes the majority of cases of granulomatous uveitis, particularly ones that involve the retina, such as toxoplasmosis.[40] Ocular lymphoma can be mistaken for choroidal tumor.[62] On MR imaging, ocular

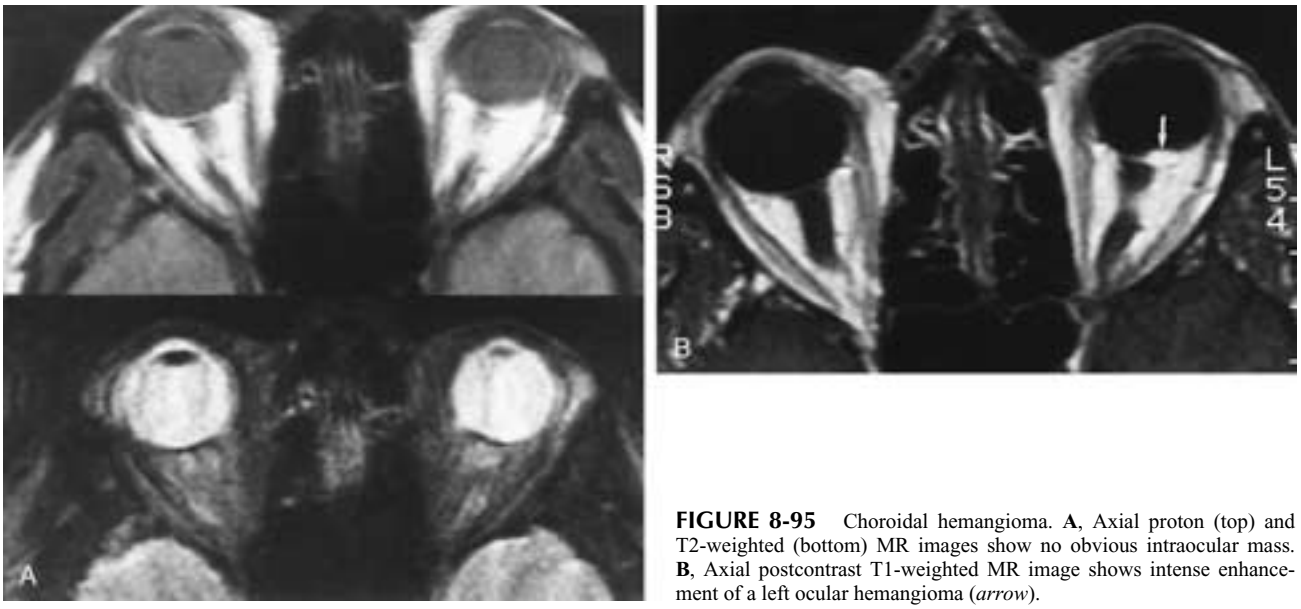

FIGURE 8-95 Choroidal hemangioma. **A**, Axial proton (top) and T2-weighted (bottom) MR images show no obvious intraocular mass. **B**, Axial postcontrast T1-weighted MR image shows intense enhancement of a left ocular hemangioma (*arrow*).

VIEW IMAGE

Copyright © 2003, Mosby, Inc. All rights reserved.

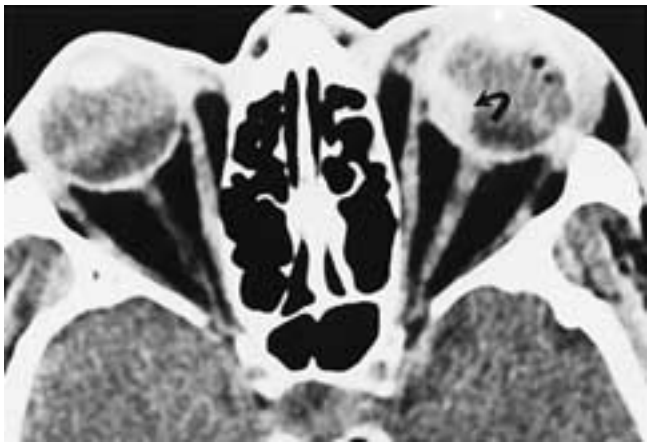

VIEW IMAGE

FIGURE 8-96 Acute choroidal hematoma. Axial CT scan shows a hyperdense mass (*arrow*) related to traumatic choroidal hematoma. Note the air bubbles in the left globe.

lymphoma may have signal characteristics similar to those of uveal melanomas (Fig. 8-98). They are often bilateral (Fig. 8-98). Bilateral melanomas are extremely rare.

Ocular Leukemia

Leukemic intraocular infiltration may involve the uvea, retina, optic disc, or vitreous. This is an uncommon ophthalmic disorder and unfortunately has a poor prognosis.[40] Leukemic intraocular infiltrates can present in one eye or both eyes. On MR imaging, leukemic infiltrates may have signal characteristics similar to those of uveal melanomas, metastasis, and intraocular inflammation (microbial and nonmicrobial).

Primary Ocular Schwannoma (Neurilemoma)

Primary ocular schwannoma is an extremely rare lesion that can cause diagnostic confusion with uveal melanoma. This benign neoplasm arises from the Schwann cells of the peripheral nerves in the uvea or sclera.[40] Primary ocular schwannoma occurs either in patients who have neurofibromatosis Type I or in patients who do not have this condition. It usually occurs as an amelanotic mass in the choroid or ciliary body that is indistinguishable clinically, by fluorescein angiography, and by ocular ultrasonography from a uveal melanoma.[40] The tumor consists of an encapsulated proliferation of amelanotic Schwann cells. Tumor cells exhibit positive immunoreactivity to S-100 protein but negative immunoreactivity to HMB-45 (melanoma-specific antigen) and muscle-specific markers (muscle-specific action).[40] The CT and MR imaging appearance of primary ocular schwannoma cannot be distinguished from that of uveal melanoma.[62] Primary intraocular neurofibroma is an extremely uncommon lesion that occurs in patients with neurofibromatosis Type I, although it has been reported in patients who have no manifestations of this syndrome.[40] The tumor is composed of an admixture of Schwann cells, fibroblasts, connective tissue, and neural axons and is usually nonencapsulated. The tumor typically arises in the choroid or ciliary body as an amelanotic mass that is indistinguishable from an amelanotic uveal melanoma by clinical examination and on imaging studies. At times in patients with neurofibromatosis Type I, the entire choroid may become thickened due to diffuse neurofibroma.

Leiomyoma

Smooth muscle tumors of the ciliary body are extremely rare and must be distinguished from other spindle-cell tumors, especially the more common amelanotic spindle-cell melanoma.[179, 180] Electron microscopic examination is necessary to prove the smooth muscle origin of these tumors.[179] Pathologically, leiomyoma consists of amelanotic spindle-shaped cells of benign appearance. Immunohistochemical staining shows positive immunoreactivity to muscle markers (muscle-specific action and smooth muscle action). Jakobiec et al.[180] reported two benign tumors of the ciliary body (one in a 37-year-old woman and another in a 20-year-old woman), which were diagnosed as neurogenic tumors by light microscopy but which on electron microscopic examination were found to be composed of smooth

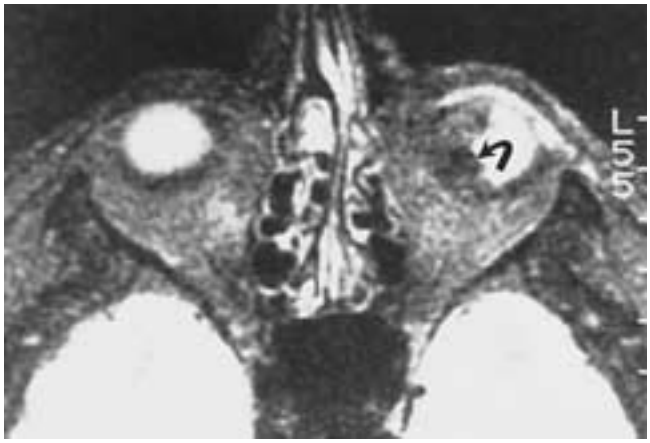

VIEW IMAGE

FIGURE 8-97 Acute choroidal hematoma. Axial T2-weighted MR image shows hypointense fresh choroidal hematoma (*arrow*).

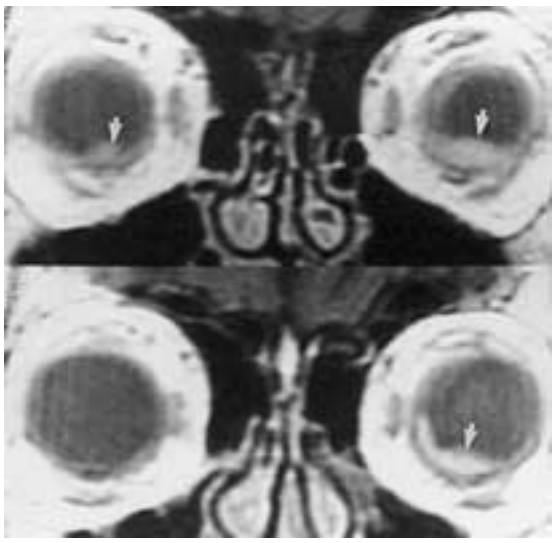

FIGURE 8-98 Uveal lymphoma. Enhanced T2-weighted MR images showing bilateral, intraocular, irregular enhanced masses (*arrows*). (Courtesy of M.F. Mafee, MD, FACR, Chicago.)

VIEW IMAGE

Copyright © 2003, Mosby, Inc. All rights reserved.

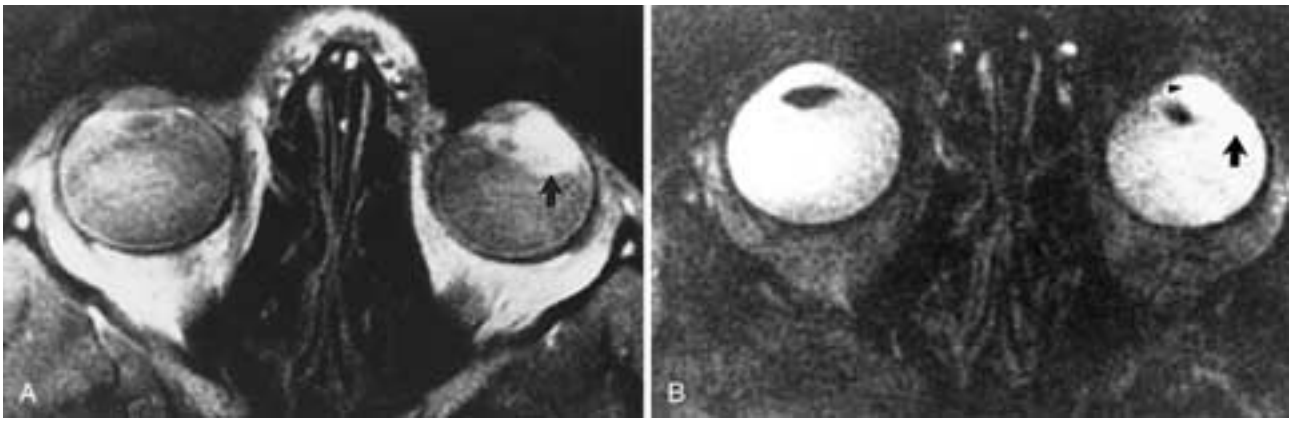

VIEW IMAGE

FIGURE 8-99 Leiomyoma of the ciliary body. **A**, Axial PW MR image shows a large, hyperintense mass (*arrow*). **B**, Axial T2-weighted MR image shows that the lesion remains hyperintense (*arrow*). Note the extension into the anterior chamber (*arrowhead*). (From Mafee MF et al. Retinoblastoma and simulating lesions: role of CT and MRI. Radiol Clin North Am 1987;25:667–682.)

muscle cells with unusual morphologic features. The authors concluded that myogenic and neurogenic characteristics reside in the neural crest origin smooth muscle of the ciliary body (mesectoderm) and that these tumors constitute a new nosologic entity of myogenic neoplasia. They coined the term *mesectodermal leiomyoma of the ciliary body* because the cells of the neural crest that contribute to the formation of bone, cartilage, connective tissue, and smooth muscle in the region of the head and neck have been called mesectoderm.[180] The MR appearance of a mesectodermal leiomyoma of the ciliary body has been reported.[84, 105] The lesion appeared as a well-defined noninfiltrative mass that demonstrated hyperintensity on T1-weighted, proton density, and T2-weighted images (Fig. 8-99). The CT and MR imaging appearance of ocular leiomyoma cannot be confidently distinguished from that of uveal melanoma and uveal neurogenic tumors.

Ocular Adenoma and Adenocarcinoma

Ocular adenoma and adenocarcinoma may arise from the pigment epithelium of the iris, ciliary body, or retina. Adenomas and adenocarcinomas of the ciliary epithelia appear as solid nodular lesions in the ciliary body region.[40] Those that arise from the pigmented ciliary epithelium are darkly melanotic, whereas those that arise from the nonpigmented ciliary epithelium are amelanotic. Ocular adenoma and primary adenocarcinoma are extremely rare tumors and may not be differentiated from ocular melanoma by CT and MR imaging.

Medulloepithelioma

Medulloepithelioma, or dictyoma, is a rare primary intraocular neoplasm derived from neuroectoderm, which characteristically arises from the primitive nonpigmented epithelium of the ciliary body.[40] Medulloepithelioma is usually seen in young children, although it can be seen in adults.[170, 181] Histologically, the tumor resembles embryonic retina and neural tissue.[181] This tumor has been divided into teratoid and nonteratoid types. The nonteratoid type (diktyoma) is a pure proliferation of cells of the medullary epithelium.[62] The teratoid type is distinguished by the additional presence of heteroplastic elements, particularly cartilage, skeletal muscle, and brain tissue.[62] Although most medulloepitheliomas are cytologically malignant, distant metastasis is uncommon.[62] From its point of origin on the ciliary body, the tumor may spread forward along the surface of the iris or backward along the surface of the retina.[62]

Medulloepithelioma generally occurs in the first decade of life as a nonpigmented ciliary body mass. In children, medulloepithelioma should be considered in the differential diagnosis of retinoblastoma, nematoid granuloma, and juvenile xanthogranuloma. In adults, this tumor may simulate amelanotic uveal melanoma and leiomyoma on ciliary body ophthalmoscopic evaluation, fluorescein angiography, ultrasonography, and CT (Fig. 8-100).[36] On MR imaging, medulloepithelioma appears similar to retinoblastoma and uveal melanoma.

FIGURE 8-100 Medulloepithelioma. Axial CT scan shows a hyperdense mass (*arrow*).

VIEW IMAGE

Copyright © 2003, Mosby, Inc. All rights reserved.

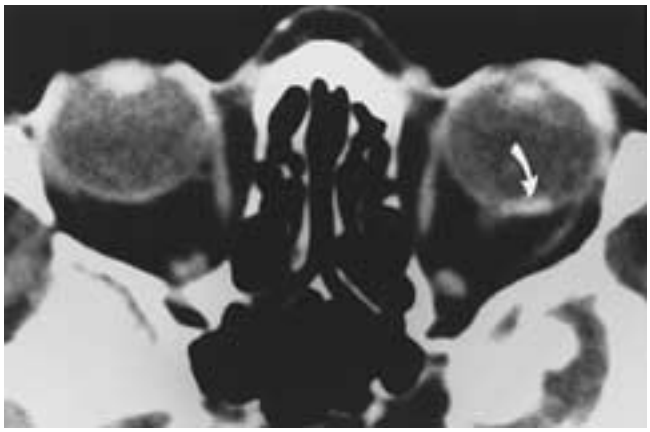

VIEW IMAGE

FIGURE 8-101 Senile macular degeneration. Axial PW MR image shows a hyperintense mass (*arrow*) compatible with discoid macular degeneration. The lesion remained mixed in signal intensity on a T2-weighted image with a small, ill-defined area that appeared hypointense.

Retinal Detachment in the Differential Diagnosis of Uveal Melanoma

The ophthalmoscopic appearance of a smooth globular outline of an elevated retina, characteristic of most cases of malignant uveal melanoma, on occasion may be caused by a simple retinal detachment. However, in practically all cases of simple retinal detachment, there is a retinal hole. On MR imaging, the appearance of a simple retinal detachment is characteristic, and provided that a mass is elevated more than 3 mm, the absence or presence of the mass can be readily assessed (Fig. 8-33). However, chronically organized or hemorrhagic subretinal fluid may have MR characteristics identical to those of uveal melanomas (Fig. 8-84).

Senile Macular Degeneration

Macular degeneration in the elderly is a leading cause of legal blindness. Arteriosclerosis of the choriocapillaries, dysfunction of the pigment epithelial cells, and loss of neuroepithelial cells are the fundamental causes of the macular degeneration syndrome in the elderly.[27] The earliest change at the macula is hyalinization and thickening of Bruch's membrane. Later, ingrowth of choroidal neovascularization into the subpigment epithelial space occurs, and eventually this results in detachment of the pigment epithelium. The serous fluid that accumulates in the subpigment space eventually finds its way into the subretinal space. One of the serious possible complications is hemorrhage, which is limited at first to the subpigment epithelial space but later extends into the subretinal space, eventually forming an organized fibrous scar, with consequent loss of almost all function of the involved macular.[27] The process of senile macular degeneration may be associated with liquefaction of the vitreous, which may cause posterior hyaloid detachment. The CT appearance of senile macular degeneration may be similar to that of uveal melanoma (Fig. 8-101). However, there may be more iodinated contrast enhancement in macular degeneration than in uveal melanomas. The MR imaging appearance of macular degeneration varies, depending on the stage of the disease. The lesion may show hyperintensity on all pulse sequences because of fluid in the subretinal space (Fig. 8-102), or there may be varied MR characteristics if there is associated hemorrhage and other complications (Fig. 8-102).

Ocular Trauma

Ocular trauma can be categorized as blunt or penetrating. Either mechanism can cause corneal tear, scleral rupture, lens dislocation, hemorrhage, retinal detachment, or choroidal detachment. Because of the pressure changes and radial distortions of the globe, blunt trauma may actually cause more damage to the eye than a small projectile passing through the globe.[182] There are imaging findings that may suggest many of the ocular injuries, but most are clinically obvious on clinical examination, and imaging is not usually ordered to assess these problems primarily. Ultrasound may

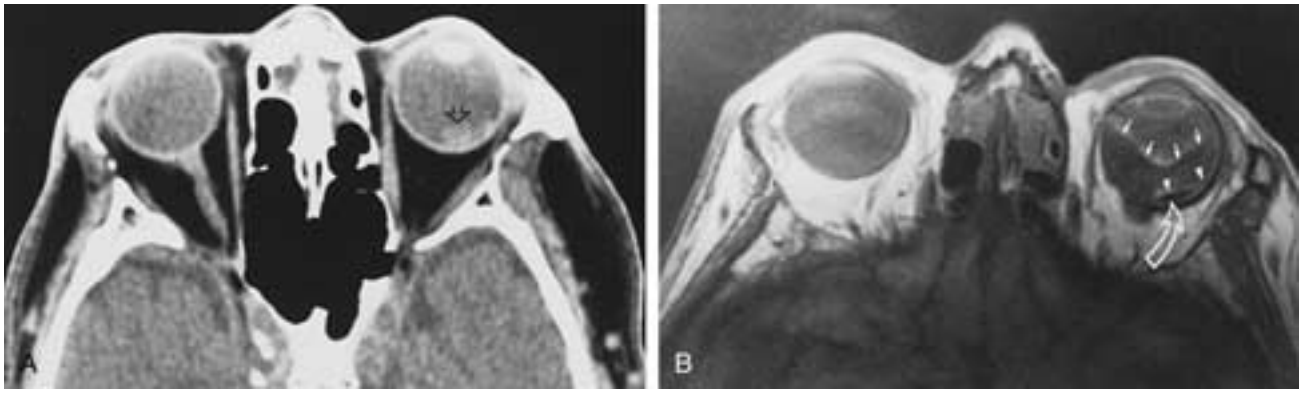

VIEW IMAGE

FIGURE 8-102 Senile macular degeneration associated with complications. **A**, Axial CT scan shows a mass (*arrow*) and a dependent image probably caused by effusion in the subretinal space. **B**, Axial T1-weighted MR image shows the characteristic posterior hyaloid detachment (*arrows*). Unlike retinal detachment, a detached posterior hyaloid membrane does not extend toward the optic disc. Note the detached retina (*arrowheads*) and the hypointense image (*curved arrow*) related to scar tissue in the subretinal and retinal regions. Surgery confirmed these findings. Notice that information obtained by MR imaging is far superior to that obtained by CT.

Copyright © 2003, Mosby, Inc. All rights reserved.

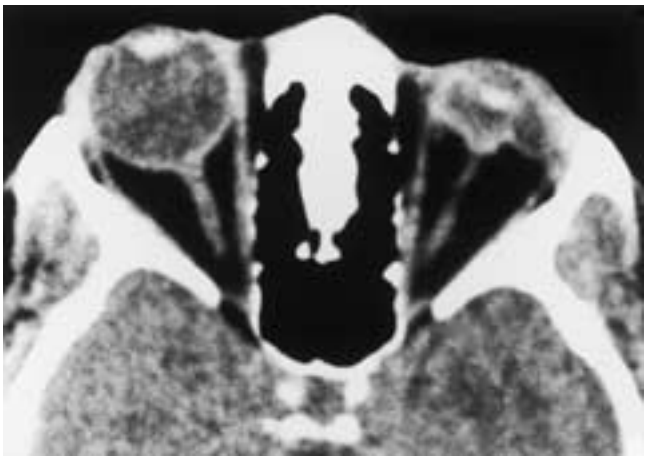

VIEW IMAGE

FIGURE 8-103 Ocular rupture. Axial CT scan shows deformity of the left eye with uveoscleral infolding due to ocular hypotony related to a rupture.

be used as part of an assessment, but the study is difficult to perform in the traumatized eye and is contraindicated in an open globe injury. Usually the most immediate concern for imaging is the possible presence of a foreign body, and the type of possible foreign body will determine the imaging modality used.

Intraocular foreign bodies (IOFBs) constitute a large percentage of ocular traumas, and advanced diagnostic and surgical techniques are required to manage them successfully.[183] Factors that influence the prognosis of IOFBs include the size, type of material, location, trajectory, reactivity, inflammatory response, degree and type of tissue damage, and length of time since the injury.

Patients presenting with ocular trauma are always examined for the presence of retained IOFBs. Indirect ophthalmoscopy, standard x-rays including the soft tissue (bone free) technique, CT, ultrasound, and, rarely, MR imaging are used to locate the foreign body. Localization of IOFBs is most often accomplished by CT, and this modality has proven valuable not only in detecting of IOFBs, but also in detecting ocular rupture (Fig. 8-103) and choroidal hematoma (Figs. 8-104 and 8-105).[52] Ultrasound is useful to examine the relationship of IOFBs to soft tissue pathology such as retinal detachment.[183]

The advent of endovitreal microsurgery has allowed a spectrum of treatment possibilities to be offered to the patient with a severely injured eye as well as for the removal of IOFBs. Therefore, a detailed diagnostic imaging study is vital to evaluate these patients properly. Of all ocular perforations, IOFBs occur in about 40%.[184] DeJuan et al.,[185] who reported a series of 453 cases seen at the Wilmer Eye Institute, found ocular perforations to be caused by projectiles (41%), lacerations (37%), and blunt trauma (22%). Of the 35 cases of IOFB studied by Coleman et al.,[183] 30 (86%) were due to metallic IOFBs; the remaining 5 (14%) consisted of three glass fragments and two concrete particles. Twenty-five of the metallic IOFBs proved to be magnetic. This means that magnetic IOFBs constitute 71% of all IOFBs and 83% of all metallic IOFBs. Three foreign bodies (8.5%) were due to BB guns. The high compressive and concussive forces seen in BB injuries are usually regarded as the reason for the poor prognosis.[183] The natural course of a retained IOFB varies widely. Small IOFBs may be completely resorbed,[186] and the IOFB may become encapsulated. Sederosis bulbi may develop in an eye with a retained iron-containing IOFB. The siderotic changes may stabilize or regress[187]; the foreign body may lose its magnetic properties or become radiolucent on x-ray.[187] Patients with a clinical diagnosis of siderosis bulbi may develop iris heterochromia, papillary mydriasis, cataract formation, retinal pigmentary degeneration, and occasionally optic disc hyperemia.[187] The diagnosis of IOFB is often made ophthalmoscopically or by slit-lamp examination. Gonioscopy will detect a foreign body in the anterior chamber angle. The removal of an IOFB should be strongly entertained in an eye with siderosis if a diminished electroretinographic response is noted or in an eye with a mobile foreign body in the vitreous or a nonencapsulated foreign body in the retina. Because up to 90% of IOFBs are magnetic,[183] the use of magnets has long been advocated for their removal. The magnets used in ophthalmic surgery

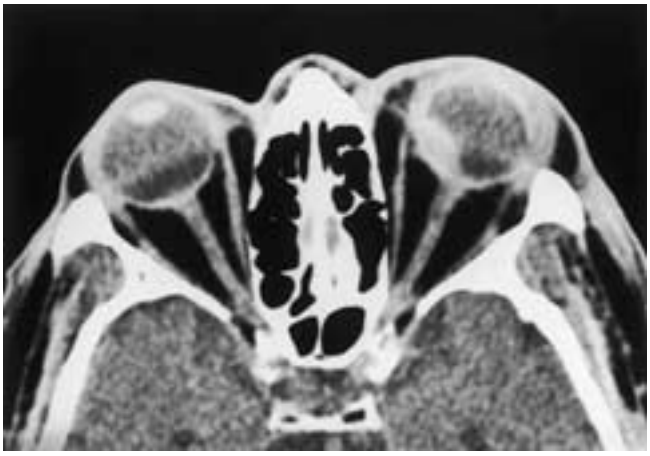

VIEW IMAGE

FIGURE 8-104 Ocular trauma and choroidal hematoma. Axial CT scan shows a hyperdense left choroidal hematoma. This can be confused with a choroidal melanoma.

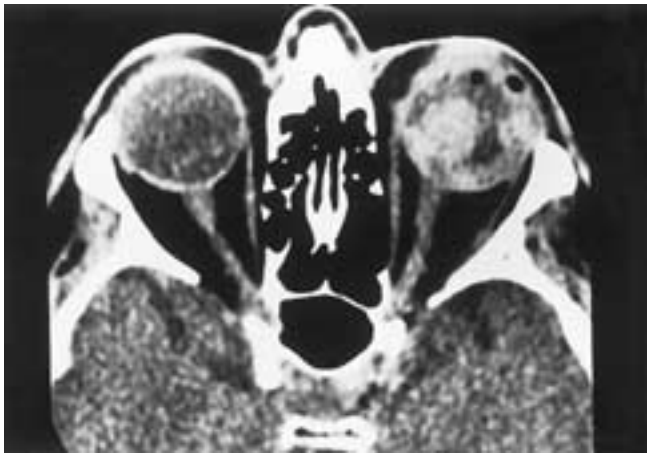

FIGURE 8-105 Choroidal hematoma following ocular surgery. Axial CT scan shows multiple choroidal hematomas of various sizes involving the left eye.

VIEW IMAGE

Copyright © 2003, Mosby, Inc. All rights reserved.

are of two general types: electromagnets and rare earth magnets.

Nonmagnetic IOFBs and even ferromagnetic foreign bodies are currently extracted in conjunction with posterior vitrectomy, endocoagulation, and removal of the foreign body by a forceps or other instrument. Retinal breaks may result from IOFBs. A retinal break encountered during vitrectomy generally is treated with retinopexy, often followed by fluid gas exchange and sometimes scleral buckling. Amber et al.[188] suggested that retinopexy may be avoided for retinochoroidal injury from a posteriorly situated metallic IOFB when there is no associated retinal detachment. The avoidance of retinopexy and fluid gas exchange may decrease the risk of retinal detachment and periretinal macular fibrosis.[188] Intraocular gas is known to cause breakdown of the blood-retina barrier, a situation that is significant in the stimulation of proliferative vitreoretinopathy.[188] Retained IOFBs are associated with endophthalmitis in approximately 7 to 13% of cases.[189] The use of intravitreal antibiotics in high-risk injuries and the possible use of vitrectomy surgery may reduce the incidence and severity of endophthalmitis.[189] Mieler et al.,[189] based on their experience, recommended prompt evaluation and surgical removal of acute retained IOFBs.

The optimal CT evaluation of intraocular pathology may consist of contiguous 1.5 mm axial sections parallel to the canthomeatal line. Thin sections are particularly valuable when evaluating small foreign bodies. Coronal and sagittal orbital reconstructions are helpful in confirming the intraocular location of a foreign body, especially when it is peripherally located. Direct coronal scanning is the best means of evaluating suspected foreign bodies at the 6 or 12 o'clock position in the globe. Plastic IOFBs are better demonstrated at a narrow window width, as described for intraorbital wood fragments.[190, 191] The plastics have a wide range of CT attenuation values (−125 to +364).[192] Most of the plastics are polyethylene, polystyrene, and polystyrene mixtures, which are inexpensive plastics often found in cheap disposable products such as fireworks.

CT scanning may fail to detect retained nonmetallic foreign bodies, especially when they are composed of organic material such as plastic[193, 194] or wood.[195] Ultrasound has the disadvantage of being technically difficult to perform; usually it is contraindicated in an open globe, and it does a poor job of identifying IOFBs when more than one is present.[193] MR imaging is contraindicated in the presence of a metallic foreign body.[193] Lobue et al.[193] performed CT and MR imaging on 10 enucleated eyes with wood, glass, and plastic foreign bodies. MR imaging detected all eight of the IOFBs compared to seven of eight found by CT. The authors noted that in three cases utilizing CT and involving wood or radiolucent plastic foreign bodies, confusion existed regarding whether a foreign body or merely an air bubble was detected. The authors stated that if a CT scan is normal and has ruled out a metallic IOFB, MR imaging may be useful in detecting and localizing a small nonmetallic foreign body. Williamson et al.[196] inserted a variety of magnetic and nonmagnetic IOFBs in 15 eyes. MR imaging (performed with a low-field MR unit) was accurate in locating 11 of the 15 foreign bodies that were nonmagnetic. The two foreign bodies not detected were located in the suprachoroidal space, suggesting that as with CT scanning, foreign bodies located near the sclera are hard to detect. Small steel foreign bodies produced artifact obscuring all intraocular details. Using a low-field MR unit caused no intraocular injuries and was considered safe by these authors. However, higher field strength MR imaging units have been demonstrated to apply torque to ferromagnetic foreign bodies, which are then capable in both animals[195] and humans[197] of causing intraocular damage. In general, MR imaging is contraindicated in traumatized eyes with suspected ferromagnetic foreign bodies. For those patients with a remote history of traumatic foreign body to the eye or in those people with jobs in a high risk field such as metal lathe work, a high-resolution 1.5 mm thick CT scan of the orbits and a 5 to 10 mm thick CT study of the head are recommended to rule out the possibility of foreign bodies.[198] An MR imaging study may be recommended after CT has ruled out the presence of a magnetic (metallic) foreign body.

Lagouros and associates[195] conducted in vitro and in vivo experiments to study MR imaging of IOFBs. Diamagnetic and paramagnetic foreign bodies were imaged without artifact and without movement during the imaging process, while ferromagnetic foreign bodies, as expected, produced large amounts of artifact that prevented meaningful imaging. All ferromagnetic foreign bodies moved during in vitro imaging. During in vivo imaging, three of four ferromagnetic foreign bodies moved, producing substantial retinal injury.

In general, all substances are influenced by a magnetic field, and their behavior in it is determined by their magnetic susceptibility according to the following equation:

$$X = \frac{\text{Intensity of Magnetization}}{\text{Magnetic Force}}$$ [199]

If X is negative, the substance is said to be diamagnetic; if X is positive, the substance is considered paramagnetic. In diamagnetic materials, the molecular currents (caused by electrons revolving in their orbit around their parent nuclei) in one direction are equal to those in the other direction. In the absence of an external field, the molecules of these substances have no net magnetic moment.[195] Paramagnetism occurs when the molecules of a substance have a permanent magnetic movement. A magnetic field acts on a molecule by aligning it with the external field and adding the molecular field to the external field. When an insulated wire is wound around a ring of any substance and an electrical current is passed through this system, a magnetic field is generated. With paramagnetic substances, this field is greater than that of the current in the winding alone. This field is 100 to 1000 times greater in a subclass of paramagnetic substances known as ferromagnetic substances. At room temperature, iron, nickel, cobalt, and gadolinium are the only ferromagnetic elements.[195] Alloys containing these elements also may be ferromagnetic.

The CT appearance of various plastics has been described by Henrikson and associates.[192] The authors concluded that plastics may not be readily apparent on a CT scan when they are small and in the negative CT number range (<−30 HU). Lagouros and associates[195] were able to image polystyrene with MR imaging, which had a CT density of −35 HU in the study by Henrikson et al.[192] It would seem that all plastics, being relatively hydrogen poor, have a signal void on MR

Copyright © 2003, Mosby, Inc. All rights reserved.

images, especially when they are in a relatively hydrogen-rich vitreous.[195]

The detection of an intraorbital wooden foreign body is difficult, particularly in cases of apparently minor trauma.[200–204] Orbital x-rays rarely detect wooden fragments.[203] CT has been shown to detect intraorbital wood associated with metallic paint[205] or a granuloma.[206] Wooden orbital foreign bodies are seen on CT scans as a site of low density; they often are mistaken for air or partial volume averaging of orbital fat. Both experimental[207] and clinical[208] studies have shown that CT has little value in detecting dry wood alone. Tate and Cupples[207] found that the high-resolution CT scanner could not detect small pieces of wood. Myllyla et al.[208] reported that CT scanning did not detect intraorbital wood in their two patients. They noted that the CT density of wood ranged from −618 to +23 HU. Orbital ultrasound also has some limitation in detecting intraorbital wood.[209] Intraorbital wooden foreign bodies are seen on MR imaging as an area of low signal intensity on T1-weighted, proton density, and T2-weighted images. They are particularly well delineated in T1-weighted MR images.[200] The usefulness of MR imaging in detecting orbital wooden foreign bodies was first reported by Green et al.[200] The authors recommended that MR imaging be done in all cases where orbital penetration by a wooden foreign body is suspected and the CT scan has not shown a foreign body. The possibility of an IOFB should be suspected in any patient sustaining minor lid trauma, especially when there is a history of injury caused by a pointed object. Second, if orbital fat is seen on direct physical examination, indicating violation of the orbital septum, an IOFB must be excluded. If standard x-rays and CT scans reveal a radiolucent focus anywhere within the orbit, particularly in a linear configuration, within the setting of orbital trauma, there should be a high index of suspicion for an organic foreign body.[210]

Globe Injury

The globe can be torn by penetrating injury or by blunt trauma. A projectile can perforate the globe or simple compression of the globe can cause tears in weak areas.[182] Pressure waves transmitted through the globe contribute to injury to the retina and choroid. In blunt trauma, the globe is usually compressed posteriorly, diminishing the anterior-to-posterior dimension. When this happens there is transient radial expansion at the equator followed by rebound in all directions.[182] This rapid variation in shape can tear the globe wall at various weak points. There can be vitreous extrusion and collapse of the globe. The sclera will fold inward, giving a wrinkled grape or ''crenated'' globe appearance (Figs. 8-106 to 8-108). More minor injuries can cause loss of pressure limited to the vitreous compartment or the aqueous chamber, and the aqueous chamber may appear less voluminous than normal (Fig. 8-109). There may slight distortion of the vitreous chamber. With slight loss of tone, the lens may appear to move slightly anteriorly or posteriorly, depending on the chamber involved.[211] In some cases, air is demonstrated in the globe and hemorrhage into the vitreous can be present. Of note, the globe may be normal in appearance; thus, imaging is not relied upon for exclusion of open globe injury or perforation of the globe.[212]

Hemorrhage into the eye is appreciated as increased density on CT. A hyphema, blood in the anterior chamber, may not be identifiable because the volume is small. Larger hemorrhages into the vitreous are more obvious. Hemorrhage may be seen as an isolated phenomenon or associated with wall rupture. Small foci of hemorrhage may mimic a foreign body. Retinal or choroidal detachments can be immediate or delayed. The retina can be torn by the acute injury, with hemorrhage pushing the retina away from the wall of the globe and into the vitreous compartment. Alternatively, injury to the vitreous can cause a fibrotic reaction, and subsequent retraction of scar can cause a delayed tractional detachment. Retinal and choroidal detachments were discussed earlier in this chapter.

The lens itself can be dislocated (Fig. 8-110; see also 8-106 and 8-107). With penetrating injury, the lens can be pushed directly into the vitreous cavity. In blunt trauma, the rapid changes in the shape of the globe can disrupt the zonule and suspensory fibers, destroying the supporting structure of the lens. In addition, the lens can be dislocated completely or can be dislocated along one margin if only a partial disruption occurs. The normal lens is a liquid crystal

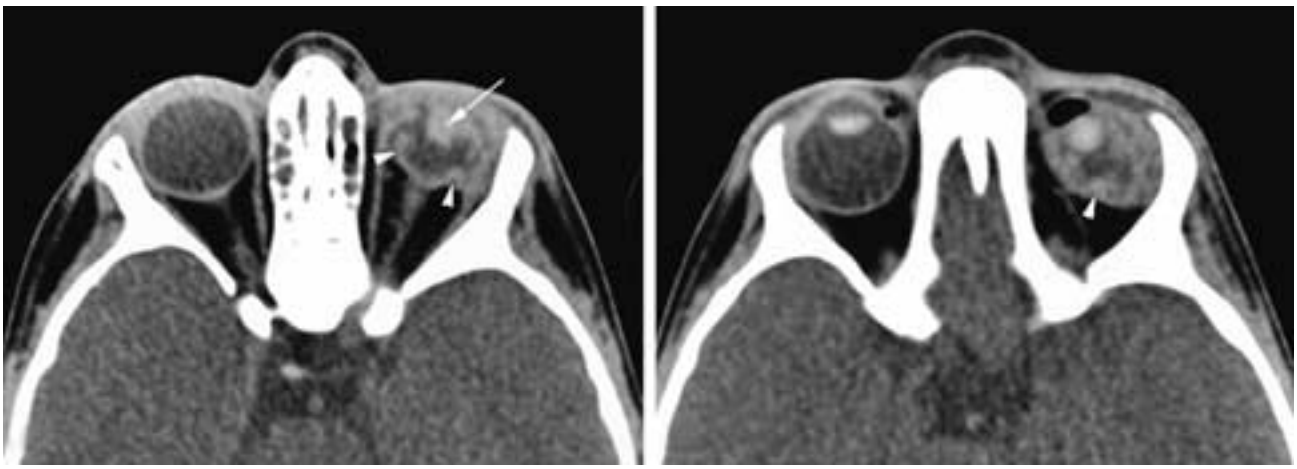

VIEW IMAGE

FIGURE 8-106 Perforation and collapse of the globe. Axial CT scans show infolding (*arrowheads*) of the posterior aspect of the globe, and the lens (*arrow*) is partially displaced.

Copyright © 2003, Mosby, Inc. All rights reserved.

VIEW IMAGE

FIGURE 8-107 Perforated globe with loss of tone and lens displacement on the left side. Intraocular lens implant, right side. **A**, Axial CT scan shows the intraocular lens (*arrow*) on the right side. Note that the left globe has lost tone and has partially collapsed, with infolding of the posterior sclera. **B**, Sagittal reconstruction shows the displacement of the lens (*arrowhead*) into the posterior aspect of the vitreous compartment.

structure with an extremely high protein content, and therefore is visible as a high density on CT contrasted against the vitreous. Any deviation from its normal position should suggest the possibility of zonular rupture with complete or partial dislocation. Patients with Marfan's syndrome are particularly prone to dislocations of the lens. Dislocations can be bilateral and can occur with minor trauma.

The lens capsule can be perforated. Fluid then moves into the lens, diluting the normally high protein (Fig. 8-111). On CT, the density decreases.[213–215] This decreased density represents early cataract formation. Later calcification can occur.

Avulsions of the extraocular muscles can give the appearance of a shorter, fatter muscle displaced or contracted posteriorly into the orbit. Because the sheath of the muscle may remain intact, a linear structure may remain, connecting the enlarged muscle belly to the globe. The optic nerve can also be torn or avulsed from the posterior globe.

Postsurgical Changes

Many surgical interventions result in a change in the appearance of the globe that is detectable on CT or MR imaging. Most of these findings relate to surgery for detached retina or cataracts.

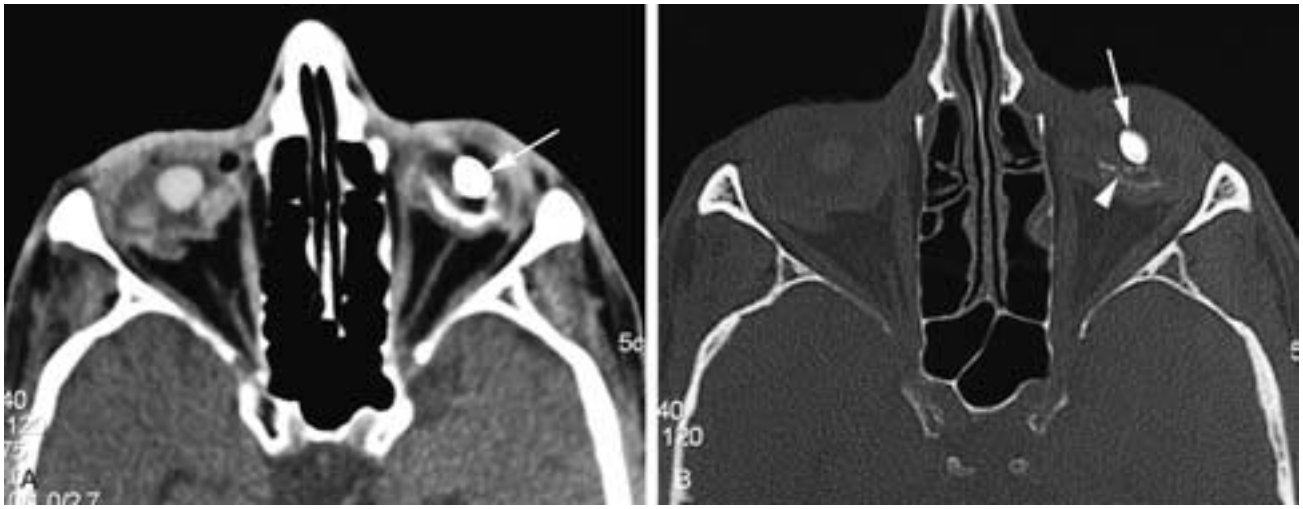

VIEW IMAGE

FIGURE 8-108 Acute perforation of the globe on the right side. Phthisis bulbi and calcified lens on the left side. Axial CT scans at narrow (**A**) and wide (**B**) window settings. There is inward buckling of the sclera of the right globe after acute trauma. There is calcification along the wall of the globe on the left, with a calcified lens (*arrow*) from a previous insult.

Copyright © 2003, Mosby, Inc. All rights reserved.

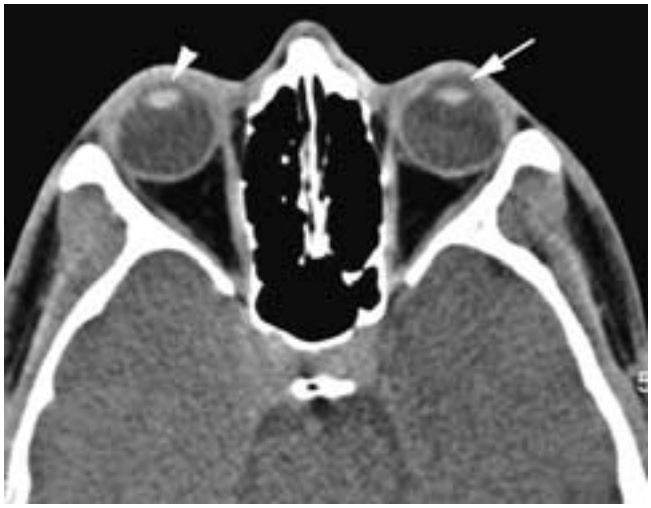

VIEW IMAGE

FIGURE 8-109 Perforation of the cornea. Axial CT scan shows perforation of the cornea with hypotony of the aqueous chamber. The fluid space between the cornea and the lens on the right side (*arrowhead*) is diminished compared to the left. A normal aqueous chamber is seen on the left side (*arrow*).

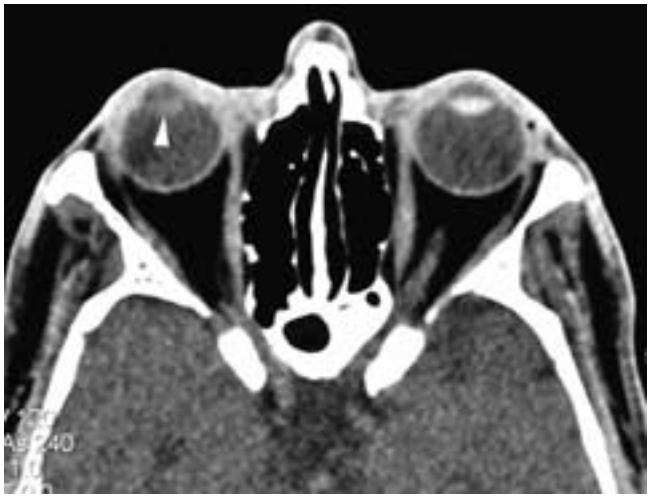

FIGURE 8-111 Axial CT. Acute perforation of the lens capsule. The abnormal lens (*arrowhead*) has low density due to the influx of fluid diluting the normally high protein of the lens. Compare with the opposite side.

VIEW IMAGE

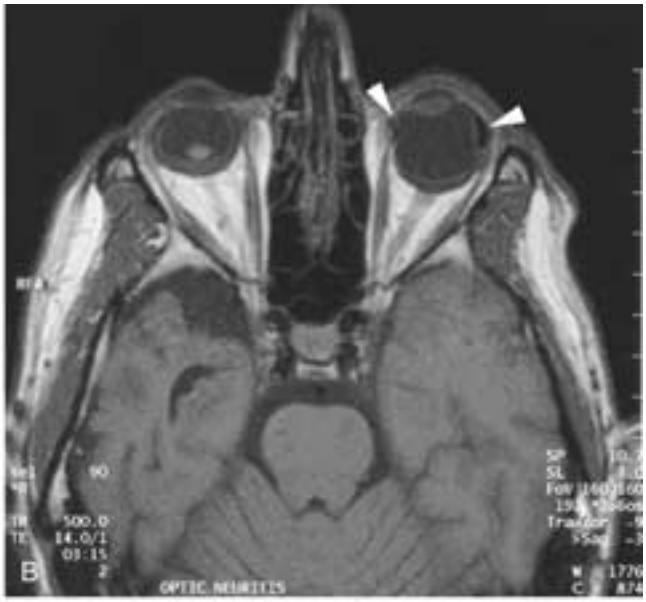

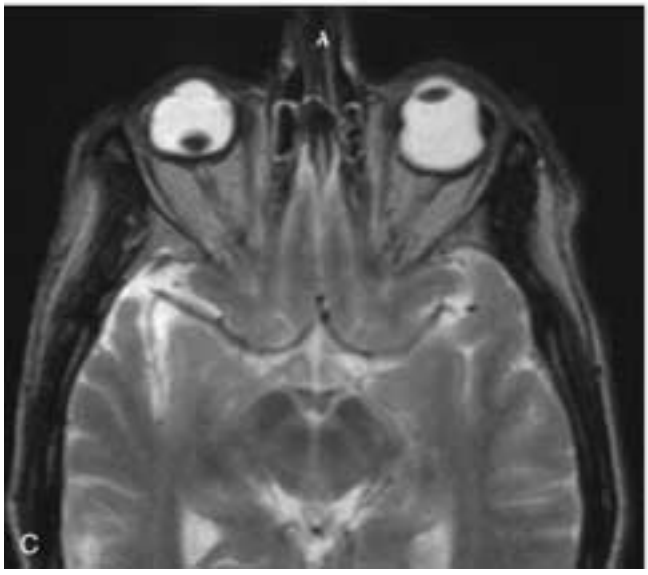

FIGURE 8-110 Dislocated lens, right eye; scleral buckle, left eye. MR imaging. **A**, Axial T1-weighted image shows the dislocated lens (*arrow*) posteriorly positioned in the right globe. **B**, Axial T1-weighted axial image. On the left side, the low-signal areas (*arrowheads*) on the medial and lateral aspect of the globe represent the scleral buckle. **C**, Axial T2-weighted image shows the dislocated lens on the right and the scleral buckle (low signal) on the left.

VIEW IMAGE

Copyright © 2003, Mosby, Inc. All rights reserved.

Scleral buckle or banding, a procedure done for a detached retina, produces a very typical appearance.[216, 217] A plastic or composite band is placed completely around the equator of the globe, passing close to the insertion points of the rectus muscles (Fig. 8-112; see also Fig. 8-110). The inward ''squeeze'' decreases the likelihood that the retina will pull away from the wall of the globe once the retina has been reattached or reapproximated to its normal position. Most scleral buckles are made of silicone or hydrogel, are dense on CT, and have low signal intensity on MR imaging.[217] A silicone sponge can give the appearance of air and thus can be of low density on CT. The appearance of some materials can be variable, particularly on MR imaging, but the characteristic position of the buckle circling the globe usually makes the banding obvious. The inward ''girdling'' or bowing of the wall of the globe is also usually appreciable on imaging.

After the detached retina is repositioned against the wall of the globe, a laser or cryoprobe is used to fuse the retina to the more peripheral layers. The ophthalmologist may place a gas or fluid into the vitreous chamber to push the retina outward and tamponade the retina against the wall of the globe. Silicone oil, fluorosilicone oil, perfluorocarbon liquid, saline, and various other substances including expanding gases have been used for such tamponade retinopexy procedures. The appearance varies with the materials used.[217–220] Many materials are dense on CT and variable on MR imaging (Fig. 8-113). Some materials can be confused with diffuse hemorrhage if the history of previous surgery is not given. Silicone, for example, is dense on CT and has high signal intensity on T1-weighted images and low signal intensity on T2-weighted images.[221]

Probably the most common postsurgical change seen at imaging is the artificial intraocular lens (IOL) placed after cataract extraction. The lens is surgically removed via an incision in the sclera or a phacoemulsification is performed. In phacoemulsification, an instrument or probe is inserted into the lens, and ultrasound is used to disrupt and liquify the inner structure of the lens

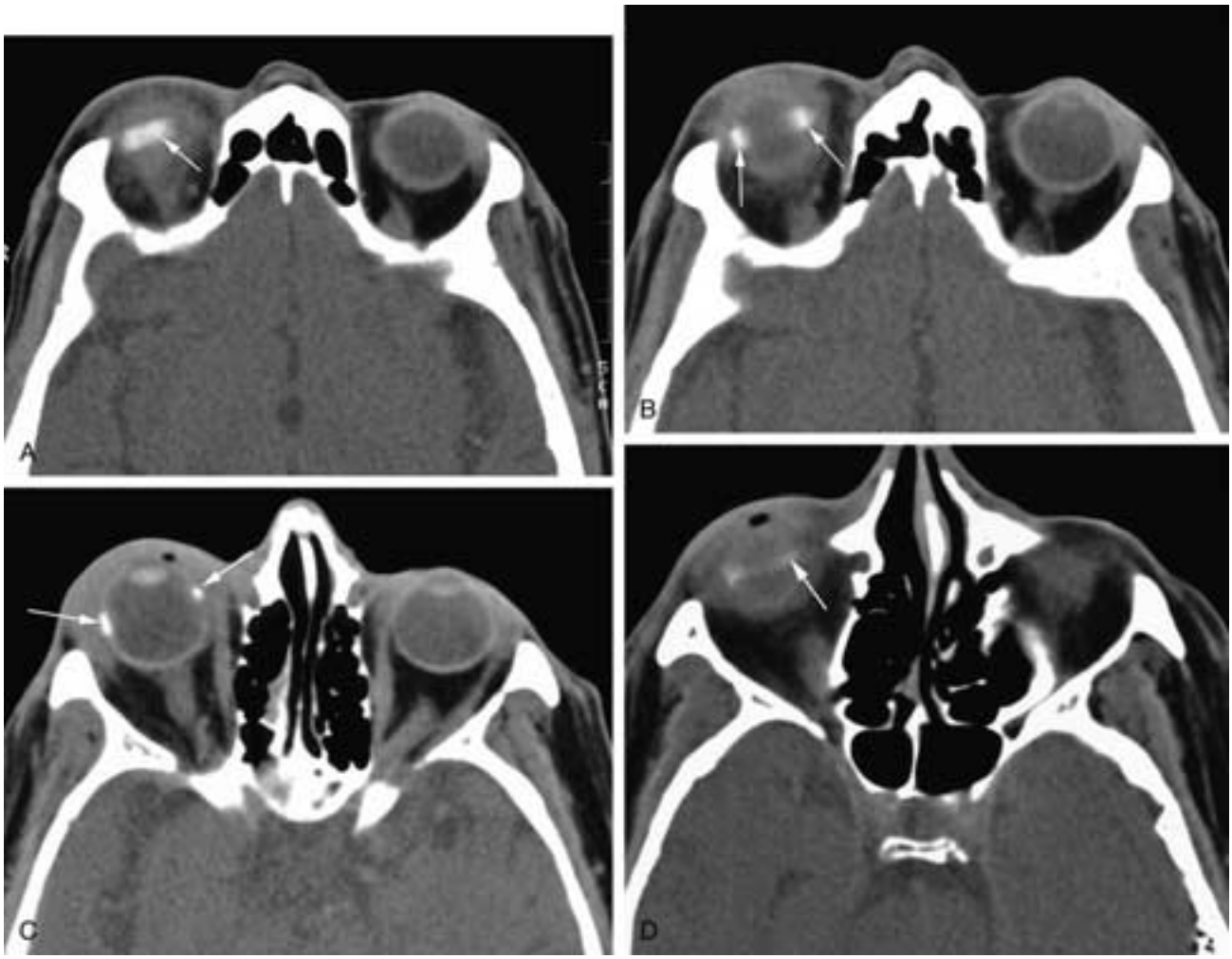

FIGURE 8-112 Scleral buckle in retinal detachment. **A** to **D**, Axial CT images showing the linear radial density encircling the globe (*arrows*). Note that if followed on all images, the radiodensity makes a complete ring around the globe.

VIEW IMAGE

Copyright © 2003, Mosby, Inc. All rights reserved.

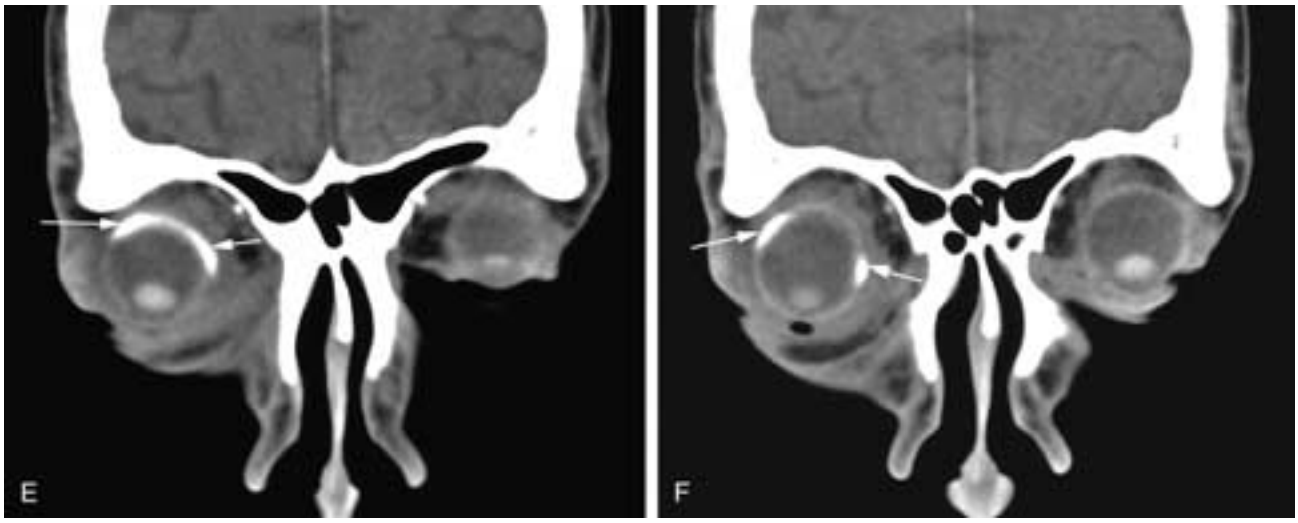

VIEW IMAGE

FIGURE 8-112 *Continued.* **E** and **F**, Coronal images show the encircling band (*arrowheads*).

including the cataract. The contents are then removed by suction. After either procedure, an IOL is then usually inserted.

With CT, rather than the biconvex structure characteristic of a normal lens, an IOL implant is typically seen as a thin, radiodense line (Fig. 8-107). A similar linear structure frequently can be appreciated on MR imaging. IOLs are commonly seen incidentally in patients undergoing imaging for nonorbital problems.

Finally, various drainage shunts and filters can be placed as decompression procedures in patients with glaucoma (Fig. 8-114), and the aqueous humor may collect in a reservoir-like ''bleb'' beneath the conjunctiva. Such a collection may be visible along the margin of the globe, usually close to the limbus.

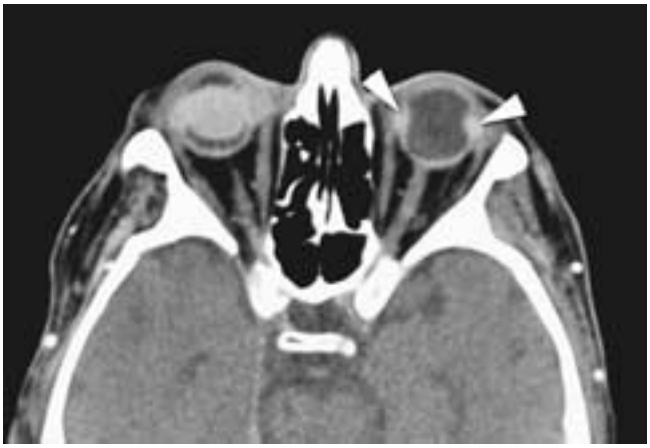

VIEW IMAGE

FIGURE 8-113 Silicone tamponade for retinal detachment of the right eye. Axial CT scan shows the radiodensity of the silicone in the globe. As with the normal lens, though radiodense on CT, the silicone is transparent to visible light. Note the scleral buckle (*arrowheads*) on the left side.

Anophthalmic Socket and Orbital Implant

CT and MR imaging play an important role in the examination of the anophthalmic socket and the orbital implant.[222] There are two types of orbital implants: (1) spherical orbital implants, used following enucleation, and (2) reconstructive orbital implants, including plates, sheets, and fixation screws, which are used to repair nonsurgical and surgical trauma.[222] The spherical orbital implant is sutured within the intraconal space (Fig. 8-115). The layered closure includes the rectus muscles, Tenon's capsule, and the conjunctiva. An external custom-fit ocular prosthesis is then worn on the ocular surface (Fig. 8-115). Spherical orbital implants can be made of nonporous materials, such as silicone and polymethylmethacrylate, or of porous materials, such as porous polyethylene or hydroxyapatite (Fig. 8-116). Postenucleation imaging requests frequently involve such concerns as porous spherical orbital implant vascularization (Fig. 8-117), migration, exposure, orbital tumor recurrence, and associated craniofacial abnormalities.[222] Gadolinium-enhanced MR imaging has proven to be very valuable in determining the vascularization of hydroxyapatite implants following enucleation (Fig. 8-117).[223, 224] Based upon the extent of relative MR imaging enhancement within the implant, surgeons determine the appropriate time to integrate the spherical orbital implant surgically with an overlying external ocular prosthesis.[222–224] Integration involves drilling a hole through the overlying soft tissues into the spherical orbital implant and placing an integrational peg.[222] The peg, which is positioned inside the conjunctiva-lined hole is coupled with the external ocular prosthesis to improve motility.[222] A sufficient blood supply to the orbital implant must be present to support a conjunctival lining of the drilled interface.[222] Motility coupling pegs for porous polyethylene orbital implants recently have been introduced, and surgeons may request an MR study prior to placement of a peg.[225] MR documentation of fibrovascular ingrowth has broad clinical importance, and the rate of fibrovascular ingrowth is both patient and surgical technique dependent.[222]

Copyright © 2003, Mosby, Inc. All rights reserved.

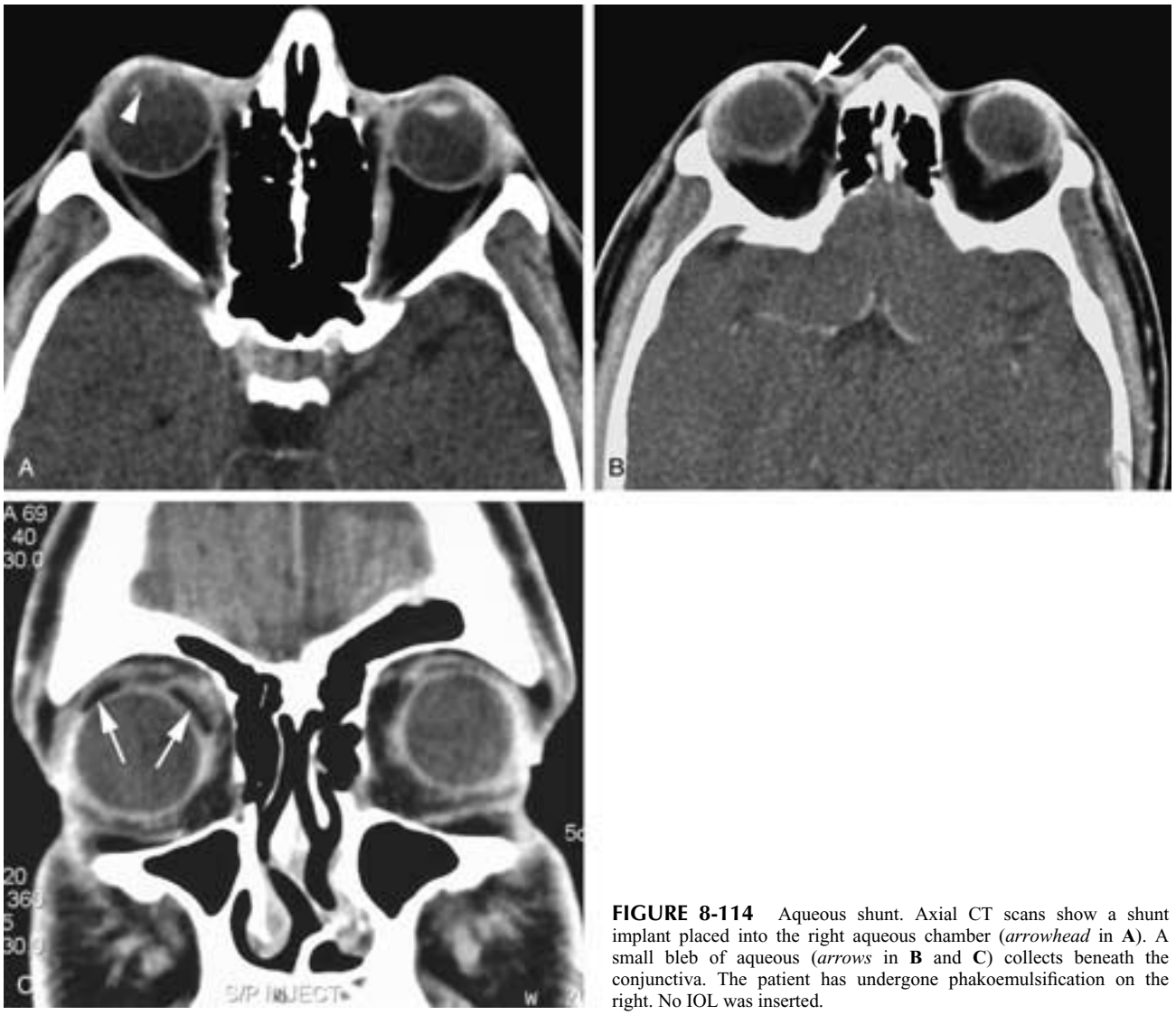

FIGURE 8-114 Aqueous shunt. Axial CT scans show a shunt implant placed into the right aqueous chamber (*arrowhead* in **A**). A small bleb of aqueous (*arrows* in **B** and **C**) collects beneath the conjunctiva. The patient has undergone phakoemulsification on the right. No IOL was inserted.

VIEW IMAGE

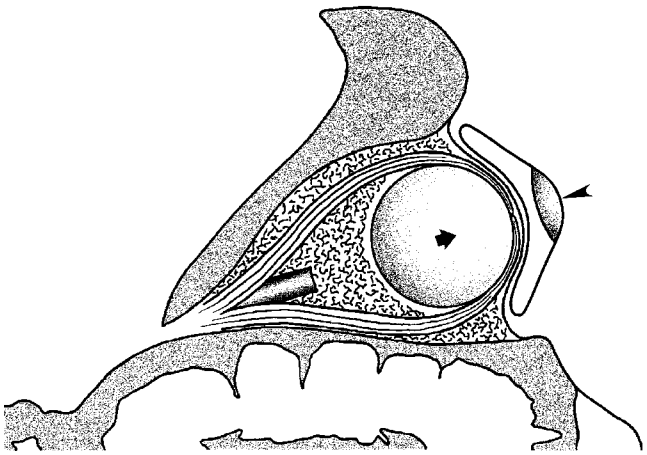

VIEW IMAGE

FIGURE 8-115 Enucleation with placement of an orbital implant. The orbital implant is sutured within the intraconal space (*arrow*). The layered closure includes the rectus muscles, Tenon's capsule, and the conjunctiva. A custom-fit ocular prosthesis is worn on the ocular surface (*arrowhead*).

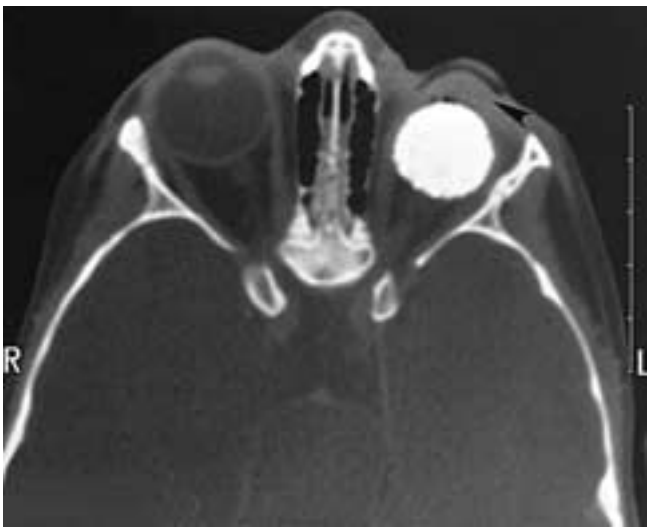

FIGURE 8-116 Enucleation with placement of an unwrapped hydroxyapatite orbital implant. Axial CT scan shows the coarse surface of the hydroxyapatite implant and the position of the overlying prosthesis (*arrowhead*).

VIEW IMAGE

Copyright © 2003, Mosby, Inc. All rights reserved.

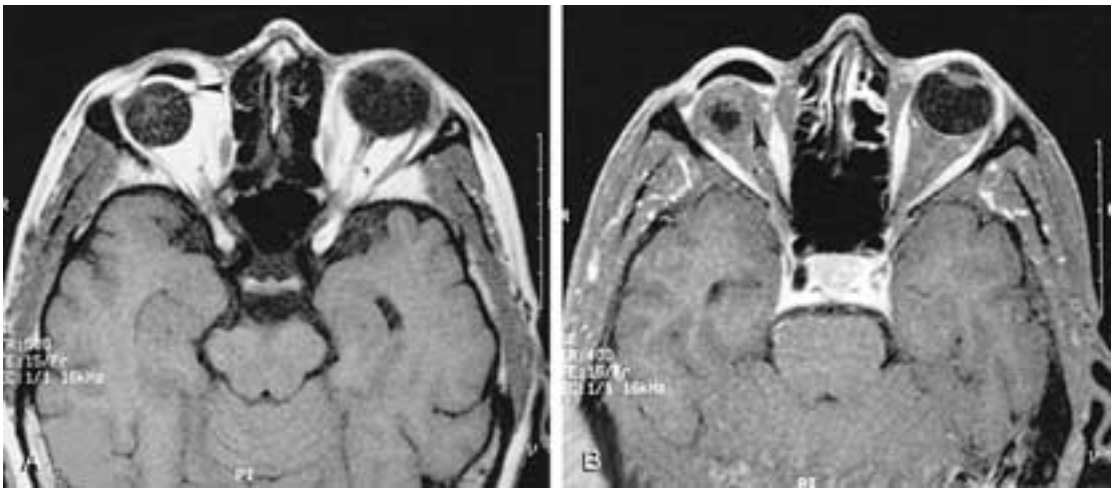

VIEW IMAGE

FIGURE 8-117 Enucleation with a porous polyethylene implant and an overlying dermis fat graft. **A**, Axial T1-weighted MR image shows the hyperintense signal of the dermis fat graft (*arrowhead*) anterior to the orbital implant and posterior to the ocular prosthesis. **B**, Axial T1-weighted, gadolinium-enhanced, fat-suppressed MR image shows the hyperintense signal of the rectus muscles consistent with a favorable blood supply. The hyperintense signal of the periphery of the orbital implant is consistent with early vascularization of the porous implant (*arrowhead*).

REFERENCES

1. Warwick R, Williams PL. Gray's Anatomy, 35th British ed. Philadelphia: WB Saunders, 1973;145–147.
2. Snell RS, Lemp MA (eds). Clinical Anatomy of the Eye. Boston: Blackwell Scientific, 1989;1–15.
3. Mann IC. Developmental Abnormalities of the Eye, 2nd ed. Philadelphia: JB Lippincott, 1957;74–78.
4. Mann IC. On the development of the fissure and associated regions in the eye of the chick and some observations of the mammal. J Anat 1921;55:113–118.
5. Mann IC. The Development of the Human Eye. New York: Grune & Stratton, 1969.
6. Yanoff M, Duke JS, eds. Ophthalmology. Philadelphia: CV Mosby, 1999;3.1–3.6.
7. Mafee MF, Jampol LM, Langer BC, Tso M. Computed tomography of optic nerve colobomas, morning glory anomaly, and colobomatous cyst. Radiol Clin North Am 1987;25:693–699.
8. Driell D, Provis JM, Billson FA. Early differentiation of ganglion, amacrine, bipolar and Müeller cells in the developing fovea of the human retina. J Comp Neurol 1990;291:203–219.
9. Hollenberg J, Spira AW. Human retinal development. Ultrastructure of the outer retina. Am J Anat 1973;137:357–386.
10. Mann IC. On the morphology of certain developmental structures associated with the upper end of the choroidal fissure. Br J Ophthalmal 1922;6:145–163.
11. Brown G, Tasman W (eds). Congenital Anomalies of the Optic Disc. New York: Grune & Stratton, 1983;97–191.
12. Carlson BM. Human Embryology and Developmental Biology. St. Louis: CV Mosby, 1994;252–268.
13. Jack RL. Regression of the hyaloid vascular system: an ultrastructural analysis. Am J Ophthalmal 1972;74:261–271.
14. Renz BE, Vygantas CM. Hyaloid vascular remnants in human neonates. Ann Ophthalmal 1977;9:179–184.
15. Mafee MF, Goldberg MF, Valvassori GE, et al. Computed tomography in the evaluation of patients with persistent hyperplastic primary vitreous (PHPV) Radiology 1982;145:713–717.
16. Aguayo JB, Glaser B, Mildvan A, et al. Study of vitrous liquifaction by NMR spectroscopy and imaging. Invest Ophthalmol Vis Sci 1985;26:692–697.
17. Wehrli FW, Shimakawa A, Gullberg GT, et al. Time of flight MR flow imaging. Selective saturation recovery with gradient refocusing. Radiology 1986;160:781–785.
18. Mafee MF, Peyman GA, Grisolano JE, et al. Malignant uveal melanoma and simulating lesions: MR imaging evaluation. Radiology 1986;160:773–780.
19. Mafee MF, Puklin J, Barany M, et al. MRI and in vivo proton spectroscopy of the lesions of the globe. Semin Ultrasound CT MR 1988;9:59–71.
20. Mafee MF, Peyman GA. Retinal and choroidal detachments: role of MRI and CT. Radiol Clin North Am 1987;25:487–507.
21. Kaufman LM, Mafee MF, Song CD. Retinoblastoma and simulating lesion: role of CT, MR imaging and use of GD-DTPA contrast enhancement. Radiol Clin North Am 1998;36:1101–1117.
22. Lagouros PA, Langer BG, Peyman GA, et al. Magnetic resonance imaging and intraocular foreign bodies. Arch Ophthalmol 1987;105: 551–553.
23. Snell RS, Lemp MA (eds). Clinical Anatomy of the Eye. Boston: Blackwell Scientific, 1989.
24. Zion VM. Phakomatoses. In: Tasman W, Jaeger EA, eds. Duane's Clinical Ophthalmology, Vol 5. Chapter 36:1–12.
25. Reeh MF, Wobij JL, Wirtschafter JD. Ophthalmic Anatomy: A Manual with Some Clinical Applications. San Francisco: American Academy of Ophthalmology, 1981;11–54.
26. Mafee MF, Putterman A, Valvassori GE, et al. Orbital space-occupying lesions: role of computed tomography and magnetic resonance imaging. An analysis of 145 cases. Radiol Clin North Am 1987;25:529–559.
27. Siegelman J, Jakobiec FA, Eisner G, eds. Retinal Diseases: Pathogenesis, Laser Therapy and Surgery. Boston: Little, Brown, 1984;1–66.
28. Rutmin U. Fundus appearance in normal eye. I. The choroid. Am J Ophthalmol 1967;64:821–857.
29. Anderson H, Apple D. Anatomy and embryology of the eye. In: Peyman GA, Sanders DR, Goldberg MF, eds. Principles and Practice of Ophthalmology, Vol 1. Philadelphia: WB Saunders, 1980;3–68.
30. Nakaizumi Y. The ultrastructure of Bruch's membrane. II. Eyes with a tapetum. Arch Ophthalmol 1964;72:388–394.
31. Wudka E, Leopold IM. Experimental studies of the choroidal blood vessels. Arch Ophthalmol 1956;55:857–885.
32. Mafee MF. Magnetic resonance imaging: Ocular anatomy and pathology. In: Newton TH, Bilanuik LT, eds. Modern Neuroradiology, Vol 4. Radiology of the Eye and Orbit. New York: Clavadel Press/Raven Press, 1990;2.1–3.45.
33. Warwick R, Williams PL, eds. Gray's Anatomy, 35th British ed. Philadelphia: WB Saunders, 1973.
34. Balaz EA. Physiology of the vitreous body. In: Schepens CL, ed. Importance of the Vitreous Body in Retinal Surgery with Special Emphasis on Reoperations. St. Louis: CV Mosby, 1960;29–48.
35. Mafee MF, Goldberg MF, Valvassori GE, et al. Computed tomography in the evaluation of patients with persistent hyperplastic primary vitreous (PHPV). Radiology 1982;145:713–714.

Copyright © 2003, Mosby, Inc. All rights reserved.

36. Mafee MF, Goldberg MF. CT and MR imaging for diagnosis of persistent hyperplastic primary vitreous (PHPV). Radiol Clin North Am 1987;25:683–692.
37. Aguayo JB, Blackband SJ, Schoeniger J, et al. Nuclear magnetic resonance imaging for a single cell. Nature 1986;322:190–191.
38. Penning DJ, et al. MRI imaging of enucleated human eye at 1.5 Tesla. J Comput Assist Tomogr 1986;10:55.
39. Balaz EA. The molecular biology of the vitreous. In: McPhearson A, ed. New and Controversial Aspects of Retinal Detachment. New York: Harper & Row, 1968;3–15.
40. Yanoff M, Duker JS. Ophthalmology. Philadelphia: CV Mosby, 1999.
41. Char DH, Unsold R. Computed tomography: ocular and orbital pathology. In: Newton TH, Bilanuik LT, eds. Modern Neuroradiology, Vol 4. Radiology of the Eye and Orbit. New York: Clavadel Press/Raven Press, 1990;9.1–9.64.
42. Mafee MF, Pruzansky S, Corrales MM, et al. CT in the evaluation of the orbit and the bony interorbital distance. AJNR 1986;7:265–269.
43. Kaufman LM, Villablanca PJ, Mafee MF. Diagnostic imaging of cystic lesions in the child's orbit. Radiol Clin North Am 1998;36:1149–1163.
44. Lyle DJ. Coloboma of the optic nerve. Am J Ophthalmol 1932;15:347–349.
45. Brown G, Tasman W, eds. Congenital Anomalies of the Optic Disc. New York: Grune & Stratton, 1983;97–191.
46. Mafee MF, Jampol LM, Langer BG, et al. Computed tomography of optic nerve colobomas, morning glory anomaly, and colobomatous cyst. Radiol Clin North Am 1987;25:693–699.
47. Mann I. Developmental Abnormalities of the Eye, 2nd ed. Philadelphia: JB Lippincott, 1957;74–78.
48. Savell J, Cook JR. Optic nerve colobomas of autosomal dominant heredity. Arch Ophthalmol 1976;94:395–400.
49. Pollock JA, Newton TH, Hoyt WF. Transsphenoidal and transethmoidal encephaloceles. Radiology 1968;90:442–453.
50. Kindler P. Morning glory syndrome: unusual congenital optic disc anomaly. Am J Ophthalmol 1970;69:376–384.
51. Capper SA, Leopold IH. Mechanism of serous choroidal detachment. Arch Ophthalmol 1956;55:101–113.
52. Mafee MF, Peyman GA. Choroidal detachment and ocular hypotony: CT evaluation. Radiology 1984;153:697–703.
53. Mafee MF, Linder B, Peyman GA, et al. Choroidal hematoma and effusion: evaluation with MR imaging. Radiology 1988;168: 781–786.
54. Peyman GA, Mafee MF, Schulman JA. Computed tomography in choroidal detachment. Ophthalmology 1984;91:156–162.
55. Iijima Y, Asanagi K. A new B-scan ultrasonographic technique for observing ciliary body detachment. Am J Ophthalmol 1983;95: 498–501.
56. Wing GL, Schepens CL, Trempe CL, et al. Serous choroidal detachment and the thickened choroid sign detected by ultrasonography. Am J Ophthalmol 1982;84:499–505.
57. Archer DB, Canavan YM. Contusional eye injuries: retinal and choroidal lesions. Aust J Ophthalmol 1983;11:251–264.
58. Gole GA. Massive choroidal hemorrhage as a complication of krypton red laser photocoagulation for disciform degeneration. Aust N Z J Ophthalmol 1985;13:37–38.
59. Maumenee AE, Schwartz MF. Acute intraoperative choroidal effusion. Am J Ophthalmol 1985;100:147–154.
60. Schepens CL, Brockhurst RJ. Uveal effusion. I. Clinical picture. Arch Ophthalmol 1963;70:189–201.
61. Chaques VJ, Lam S, Tessler HH, Mafee MF. Computed tomography and magnetic resonance imaging in the diagnosis of posterior scleritis. Ann Ophthalmol 1993;25:89–94.
62. Mafee MF. Uveal melanoma, choroidal hemangioma, and simulating lesions: role of MR imaging. Radiol Clin North Am 1998;36:1083–1099.
63. Yan X, Edward DP, Mafee MF. Ocular calcification radiologic–pathologic correlation and literature review. Int J Neuroradiol 1998;4:81–96.
64. Weiter JJ, Ernest JT. Anatomy of the choroidal vasculature. Am J Ophthalmol 1974;78:583–590.
65. Howard GM, Ellsworth RM. Differential diagnosis of retinoblastoma: a statistical survey of 500 children. I. Relative frequency of the lesions which stimulate retinoblastoma. Am J Ophthalmol 1965;60: 610–618.
66. Popoff NA, Ellsworth RM. The fine structure of retinoblastoma: in vivo and in vitro observations. Lab Invest 1971;25:389–402.
67. Tso MO. Clues to the cells of origin of retinoblastoma. Int Ophthalmol Clin 1980;20(2):191–210.
68. Kodilyne HC. Retinoblastoma in Nigeria: problems in treatment. Am J Ophthalmol 1967;63:467–481.
69. Abramson DH, Ellsworth RM, Tretter P, et al. Treatment of bilateral groups I through III retinoblastoma with bilateral radiation. Arch Ophthalmol 1981;99:1761–1762.
70. Kyritsis AP, Tsokos M, Triche TJ, et al. Retinoblastoma: origin from a primitive neuroectodermal cell? Nature 1984;307:471–473.
71. Tso MOM, Fine BS, Zimmerman LE. The nature of retinoblastoma. I. Photoreceptor differentiation: a clinical and histopathologic study. Am J Ophthalmol 1970;69:339–349.
72. Tso MOM, Zimmerman LE, Fine BS, et al. A cause of radioresistance in retinoblastoma: photoreceptor differentiation. Trans Am Acad Ophthalmol Otolaryngol 1970;74:959–969.
73. Jenson RD, Miller RW. Retinoblastoma: epidemiologic characteristics. N Engl J Med 1971;285:307–311.
74. Abramson DH, Ellsworth RM, Kitchin DF, Tung G. Second nonocular tumors in retinoblastoma survivors. Ophthalmology 1984;91:1351–1355.
75. Pendergrass TW, Davis S. Incidence of retinoblastoma in the United States. Arch Ophthalmol 1980;98:1204–1210.
76. Ellsworth RM. The management of retinoblastoma. Trans Am Ophthalmol Soc 1969;67:462–534.
77. Lennox EL, Draper GJ, Sanders BM. Retinoblastoma: a study of natural history and prognosis of 268 cases. Br Med J 1975;3: 731–734.
78. Abramson DH. Retinoblastoma: diagnosis and management. Cancer J Clin 1982;32:130–140.
79. Kundson AG. Retinoblastoma: a prototype heredity neoplasm. Semin Oncol 1978;5:57–60.
80. Kundson AG Jr. Mutation and cancer: a statistical study of retinoblastoma. Proc Natl Acad Sci USA 1971;68:820–823.
81. Lele KP, Penrose LS, Stallard HE. Chromosome deletion in a case of retinoblastoma. Ann Hum Genet 1963;27:171–174.
82. Kundson AG Jr, Meadows AT, Nichols WW, et al. Chromosomal deletion and retinoblastoma. N Engl J Med 1976;295:1120–1123.
83. Yunis JJ, Ramsey N. Retinoblastoma and subband deletion chromosome 13. Am J Dis Child 1978;132:161–163.
84. Mafee MF, Goldberg MF, Greenwald MJ, et al. Retinoblastoma and simulating lesions: role of CT and MR imaging. Radiol Clin North Am 1987;25:667–681.
85. Cavenee WX, Murphree AL, Shul MM, et al. Prediction of familial predisposition to retinoblastoma. N Engl J Med 1986;314:1201–1207.
86. Sparkes RS, Sparkes MC, Wilson MG, et al. Regional assignment of genes for human esterase D and retinoblastoma to chromosome band 13q14. Science 1980;208:1042–1044.
87. Sparkes RS, Murphree AL, Lingua RW, et al. Gene for hereditary retinoblastoma assigned to human chromosome 13 by linkage to esterase D. Science 1983;219:971–973.
88. Motegi T. High rate of detection of 13q-14 deletion mosaicism among retinoblastoma patients (using more extensive methods). Hum Genet 1982;61:95–97.
89. Seidman DJ, Shields JA, Augsburger JJ, et al. Early diagnosis of retinoblastoma based on dysmorphic features and karyotype analysis. Ophthalmology 1987;94:663–666.
90. Jakobiec FA, Tso MOM, Zimmerman LE, et al. Retinoblastoma and intracranial malignancies. Cancer 1977;39:2048–2058.
91. Bader JL, Miller RW, Meadows AT, et al. Trilateral retinoblastoma. Lancet 1980;2:582–583.
92. Bader JL, Meadows AT, Zimmerman LE, et al. Bilateral retinoblastoma with ectopic intracranial retinoblastoma: trilateral retinoblastoma. Cancer Genet Cytogenet 1982;5:203–213.
93. Judisch GF, Patil SR. Concurrent heritable retinoblastoma, pinealoma and trisomy X. Arch Ophthalmol 1981;99:1767–1769.
94. Stefanko SZ, Manschot WA. Pinealoblastoma with retinoblastomas differentiation. Brain 1979;102:321–332.
95. El-Naggar S, Kaufman LM, Chapman LI, Miller MT, Mafee MF. Tetralateral retinoblastoma. Ann Ophthalmol 1995;27(6):360–363.
96. Schulman JA, Peyman GA, Mafee MF, et al. The use of magnetic resonance imaging in the evaluation of retinoblastoma. J Pediatr Ophthalmol Strabismus 1986;23:144–147.

Copyright © 2003, Mosby, Inc. All rights reserved.

97. Robertson DM, Campbell RJ. Analysis of misdiagnosed retinoblastoma in a series of 726 enucleated eyes. Mod Probl Ophthalmol 1977;18:156–159.
98. Char DH. Current concepts in retinoblastoma. Ann Ophthalmol 1980;12:792–804.
99. Haik BG, Saint Louis L, Smith ME, et al. Magnetic resonance imaging in the evaluation of leukokoria. Ophthalmology 1985;92: 1143–1152.
100. Char DH, Hedges TR, Norman D. Retinoblastoma: CT diagnosis. Ophthalmology 1984;91:1347–1350.
101. Goldberg BB, Kotler MN, Ziskin MD. Diagnostic Uses of Ultrasound. New York: Grune & Stratton, 1975;100.
102. Danziger A, Price MI. CT findings in retinoblastoma. AJR 1979;133:695–702.
103. Daniel AF, Shurin SB, Bardenstein DS. Trilateral retinoblastoma: two variations. AJNR 1995;16:166–170.
104. Provenzale JM, Weber AL, Klintworth GK, et al. Radiologic–pathologic correlation. Bilateral retinoblastoma with coexistent pinealoblastoma (trilateral retinoblastoma). AJNR 1995;16:157–165.
105. Mafee MF, Goldberg MF, Cohen SB, et al. Magnetic resonance imaging versus computed tomography of leukokoric eyes and use of in vitro proton magnetic resonance spectroscopy of retinoblastoma. Ophthalmology 1989;96(7):965–976.
106. Warburg M. Retinal malformations: aetiological heterogeneity and morphological similarity in congenital retinal non-attachment and falsiform folds. Trans Ophthalmol Soc UK 1979;99:272–283.
107. Ohba N, Watanabe S, Fujita S. Primary vitreoretinal dysplasia transmitted as an autosomal recessive disorder. Br J Ophthalmol 1981;65:631–635.
108. Goldberg MF, Mafee MF. Computed tomography for diagnosis of persistent hyperplastic primary vitreous (PHPV). Ophthalmology 1983;90:442–451.
109. Peyman GA, Sanders DR. Vitreous and vitreous surgery. In: Peyman GA, Sanders DR, Goldberg MF, eds. Principles and Practice of Ophthalmology, Vol. 2. Philadelphia: WB Saunders, 1980;1327–1401.
110. Katz NNK, Margo CE, Dorwart RH. Computed tomography with histopathologic correlation in children with leucocoria. J Pediatr Ophthalmol Strabismus 1984;21:50–56.
111. Caudhill JW, Streeten BW, Tso MOM. Phacoanaphylactoid in persistent hyperplastic primary vitreous. Ophthalmology 1985;92: 1153–1158.
112. Liberfarb RM, Eavey RD, DeLong GR, et al. Norrie's disease: a study of two families. Ophthalmology 1985;92:1445–1451.
113. Norrie G. Causes of blindness in children: twenty-five years experience of Danish institutes for the blind. Acta Ophthalmol 1927;5:357–386.
114. Warburg M. Norrie's disease: a new hereditary bilateral pseudotumour of the retina. Acta Ophthalmol 1961;39:757–772.
115. Warburg M. Norrie's disease (atrofia bulborum hereditaria): a report of eleven cases of hereditary bilateral pseudotumour of the retina, complicated by deafness and mental deficiency. Acta Ophthalmol 1963;41:134–146.
116. Warburg M. Norrie's disease: a congenital progressive oculo-ocoustico cerebral degeneration. Acta Ophthalmol 1966(suppl 89);1–47.
117. Holmes LB. Norrie's disease: an X-linked syndrome of retinal malformation, mental retardation, and deafness. J Pediatr 1971;79:89–92.
118. Apple DJ, Fishman GA, Goldberg MF. Ocular histopathology of Norrie's disease. Am J Ophthalmol 1974;78:196–203.
119. Blodi FC, Hunter WS. Norrie's disease in North America. Doc Ophthalmol 1969;26:434–450.
120. Mecke S, Passarge E. Encephalocele, polycystic kidneys and polydactyly as an autosomal recessive trait simulating certain other disorders: the Meckel syndrome. Ann Genet 1971;14:97–103.
121. Warburg M. The heterogeneity of microphthalmia in the mentally retarded. Birth Defects 1971;7:136–154.
122. Chemke J, Czernobilsky B, Mundel G, et al. A familial syndrome of central nervous system and ocular malformation. Clin Genet 1975;7:1–7.
123. Chan CC, Egbert PR, Herrick MK, et al. Oculocerebral malformations: a reappraisal of Walker's ''lissencephaly.'' Arch Neurol 1980;37:104–108.
124. Pagon RA, Chandler JW, Collie MR, et al. Hydrocephalus, agyria, retinal dysplasia, encephalocele (HARDTE) syndrome: an autosomal recessive condition. Birth Defects 1978;14(6B):233–241.
125. Levine RA, Gray DL, Gould N, et al. Warburg syndrome. Ophthalmology 1983;90:1600–1603.
126. Warburg M. Hydrocephaly, congenital retinal nonattachment, and congenital falciform fold. Am J Ophthalmol 1978;85:88–94.
127. Eller AW, Jabbour NM, Hirose T, et al. Retinopathy of prematurity: the association of a persistent hyaloid artery. Ophthalmology 1987;94:444–448.
128. Ashton N, Ward B, Sperpell G. Role of oxygen in the genesis of retrolental fibroplasia: a preliminary report. Br J Ophthalmol 1953;37:513–520.
129. Michaelson IC. Retrolental fibroplasia. In: Michaelson IC, ed. Textbook of the Fundus of the Eye. Edinburgh: Churchill Livingstone, 1980;303–315.
130. Coats G. Forms of retinal disease with massive exudation. R Lond Ophthalmol Hosp Rep 1908;17:440–525.
131. Chang M, McLean IW, Merritt JC. Coats' disease: a study of 62 histologically confirmed cases. J Pediatr Ophthalmol Strabismus 1984;21:163–168.
132. Reese AB. Telangiectasis of the retina and Coats' disease. Am J Ophthalmol 1956;42:1–8.
133. Woods AC, Duke JR. Coats' disease. I. Review of the literature, diagnostic criteria, clinical findings, and plasma lipid studies. Br J Ophthalmol 1963;47:385–412.
134. Edward DP, Mafee MF, Valenzuela EG, Weiss RA. Coats' disease and persistent hyperplastic primary vitreous: Role of MRI and CT. Radiol Clin North Am 1988;36:1119–1131.
135. Silodor SW, Augsburger JJ, Shields JA, et al. Natural history and management of advanced Coats' disease. Ophthalmic Surg 1988;19: 89–93.
136. Shields JA. Diagnosis and Management of Intraocular Tumors. St. Louis: CV Mosby, 1983;497–533.
137. Sherman JL, McLean IW, Brallier DR. Coats' disease. CT pathologic correlation in two cases. Radiology 1983;146:77–78.
138. Margo CE, Katz NN, Wertz FD, et al. Sclerosing endophthalmitis in children: computed tomography with histopathologic correlation. Pediatr Ophthalmol Strabismus 1983;20:180–184.
139. Wilder HC. Nematode endophthalmitis. Trans Am Acad Ophthalmol Otolaryngol 1950;55:99–104.
140. Zinkham WM. Visceral larva migrans: a review and reassessment indicating two forms of clinical expression, visceral and ocular. Am J Dis Child 1978;132:627–633.
141. Reesner FH, Aaberg TM, VanHorn DL. Astrocytic hamartoma of the retina not associated with tuberous sclerosis. Am J Ophthalmol 1978;86:688–698.
142. Zimmerman LE. Ocular lesions of juvenile xanthogranuloma. Trans Am Acad Ophthalmol Otolaryngal 1965;69:412.
143. Wertz FD, Zimmerman LE, McKeown CA, et al. Juvenile xanthogranuloma of the optic nerve, disk, retina, choroid. Ophthalmology 1982;89:1331–1335.
144. Shields CL, Shields JA, Buchanon HW. Solitary orbital involvement in juvenile xanthogranuloma. Arch Ophthalmol 1990;108:1587.
145. Augsburger JJ, Guthoff R. Benign intraocular tumors. In: Yanoff M, Duker JS, eds. Ophthalmology. St. Louis: CV Mosby, 1999;9.9.1–9.14.2.
146. Mafee MF. Calcifications of the eye. Head and Neck Disorders (Fourth Series) test and syllabus. Reston, Va: American College of Radiology, 1992;70–116.
147. Friedman AM, Henkind P, Gartner S. Drusen of the optic disk: a histopathological study. Trans Ophthalmol Soc UK 1975;95:4–9.
148. McMahon RT. Anatomy, congenital anomalies, and tumors. In: Peyman CA, Sanders DR, Goldberg MF, eds. Principles and Practice of Ophthalmology. Philadelphia: WB Saunders, 1980;1491–1553.
149. Yanoff M, Fine BS. Ocular Pathology. A Text and Atlas. Hagerstown, Md: Harper & Row, 1975;831.
150. Depotter P, Shields JA, Shields CL, eds. MRI of the Eye and Orbit. Philadelphia: JB Lippincott, 1995;35–92.
151. Callender GR. Malignant melanotic tumors of the eye: a study of histologic types in III cases. Trans Am Acad Ophthalmol Otolaryngol 1931;36:131–142.
152. McLean JW, Foster WU, Zimmerman LE. Prognostic factors in small malignant melanomas of choroidal and ciliary body. Arch Ophthalmol 1977;95:148–158.
153. Augsburger JJ, Damato BE, Bornfeld N. Malignant intraocular tumors. In: Yanoff M, Duker JS, eds. Ophthalmology. St. Louis: CV Mosby, 1999;9.3.1–9.8.4.

Copyright © 2003, Mosby, Inc. All rights reserved.

154. Donders PC. Malignant melanoma of the choroid. Trans Ophthalmol Soc UK 1973;93:745–751.
155. Zimmerman LE, McLean IW, Foster WD. Does enucleation of the eye containing a malignant melanoma prevent or accelerate the dissemination of tumor cells? Br J Ophthalmol 1978;62: 420–425.
156. Duffin RM, Straatsma BR, Foos RY, et al. Small malignant melanoma of the choroid with extraocular extension. Arch Ophthalmol 1981;99:1827–1830.
157. Char DH. The management of small choroidal melanomas. Surv Ophthalmol 1978;22:377–387.
158. Canny CLB, Shields JA, Kay ML. Clinically stationary choroidal melanoma with extraocular extension. Arch Ophthalmol 1978;96: 436–439.
159. Ruiz RS. Early treatment in malignant melanomas of the choroid. In: Brockhurst RJ, Boruchoff SA, Hutchinson BR, et al, eds. Controversy in Ophthalmology. Philadelphia: WB Saunders, 1977; 604–610.
160. Manschot WA, VanPeperzeel HA. Choroidal melanoma: enucleation or observation? A new approach. Arch Ophthalmol 1980;98:71–77.
161. Peyman GA, Juarez CP, Diamond DG, et al. Ten years' experience with eye wall resection for uveal melanomas. Ophthalmology 1984;91:1720–1725.
162. Mauriello JA Jr, Zimmerman LE, Rothstein TB. Intrachoroidal hemorrhage mistaken for malignant melanoma. Ann Ophthalmol 1983;15:282–284.
163. Ferry AP. Lesions mistaken for malignant melanoma of the posterior uvea: a clinicopathologic analysis of 100 cases with ophthalmoscopically visible lesions. Arch Ophthalmol 1964;72S:463–469.
164. Shields JA, Zimmerman LE. Lesions simulating malignant melanoma of the posterior uvea. Arch Ophthalmol 1973;89:466–471.
165. Peyster RG, Augsburger JJ, Shields JA, et al. Intraocular tumors: evaluation with MR imaging. Radiology 1988;68:773–779.
166. Damadian R, Zaner K, Hor D, et al. Human tumors by NMR. Physiol Chem Phys 1973;5:381–402.
167. Gomori JM, Grossman RI, Shields JA, et al. Choroidal melanomas: correlation of NMR spectroscopy and MR imaging. Radiology 1986;158:443–445.
168. Mafee MF, Peyman GA, McKusick MA. Malignant uveal melanoma and similar lesions studied by computed tomography. Radiology 1985;156:403–408.
169. Enochs SW, Petherick P, Bogdanova A, et al: Paramagnetic metal scavenging by melanin: MR imaging. Radiology 1997;204:417–423.
170. Zimmerman LE. Problems in the diagnosis of malignant melanomas of the choroid and ciliary body. Am J Ophthalmol 1973;75:919–929.
171. Depotter P, Shields JA, Shields JA, Shields CL. Computed tomography and magnetic resonance imaging of intraocular lesions. Ophthalmol Clin North Am 1994;7:333–346.
172. Erzurum SA, Jampol LM, Territo C, O'Grady R. Primary malignant melanoma of the optic nerve simulating a melanocytoma. Arch Ophthalmol 1992;110:684–686.
173. Deveer JA. Juxtapapillary malignant melanoma of the choroid and so-called malignant melanoma of the optic disk. Arch Ophthalmol 1973;51;147–751.
174. Mafee MF, Peyman GA, Peace JH, et al. Magnetic resonance imaging in the evaluation and differentiation of uveal melanoma. Ophthalmology 1987;94:341–348.
175. Naumann G, Yanoff M, Zimmerman LE. Histogenesis of malignant melanomas of the uvea: histopathologic characteristics of nevi of the choroid and ciliary body. Arch Ophthalmol 1966;76:784–796.
176. Gonder JR, Augsburger JJ, McCarthy FF, et al. Visual loss associated with choroidal nevi. Ophthalmology 1982;89:961–965.
177. Mafee MF, Ainbinder DJ, Hidayat AA, Friedman S: MRI and CT in the evaluation of choroidal hemangioma. Int J Neuroradiol 1995;1:67–77.
178. Adams RD, DeLong GR. Developmental and other congenital abnormalities of the nervous system. In: Harrison TR. Harrison's Principles of Internal Medicine. New York: McGraw-Hill, 1974; 1849–1863.
179. Meyer SI, Fine BS, Font RI, et al. Leiomyoma of the ciliary body: electron microscopic verification. Am J Ophthalmol 1968;66:1061–1068.
180. Jakobiec FA, Font RL, Tso MOM, et al. Mesectodermal leiomyoma of the ciliary body: a tumor of presumed neural crest origin. Cancer 1977;2102–2113.
181. Apt L, Heller MD, Moskovitz M, et al. Dictyoma (embryonal medulloepithelioma): recent review and case report. J Pediatr Ophthalmol 1973;10:30–38.
182. Pieramici DJ, Parver LM: A mechanistic approach to ocular trauma. Ophthalmol Clin North Am 1995;8(4):569–587.
183. Coleman DF, Lucas BC, Rondeau MJ, et al. Management of intraocular foreign bodies. Ophthalmology 1987;94:1647–1653.
184. Benson WE, Machemer R. Severe perforating injuries treated with pars plana vitrectomy. Am J Ophthalmol 1976;81:728–732.
185. de Juan E Jr, Stemberg P Jr, Michels RG. Penetrating ocular injuries: types of injuries and visual results. Ophthalmology 1983;90:1318–1322.
186. Begle HL. Perforating injuries of the eye by small steel fragments. Am J Ophthalmol 1929;12:970–977.
187. Scott RS, Weigeist TA. Management of siderosis bulbi due to a retained iron containing intraocular foreign body. Ophthalmology 1990;97:375–379.
188. Ambler JS, Sanford F, Meyers M. Management of intraretinal metallic foreign bodies without retinopexy in the absence of retinal detachment. Ophthalmology 1991;39:391–394.
189. Mieler WF, Ellis MK, Williams DF, et al. Retained intraocular foreign bodies and endophthalmitis. Ophthalmology 1990;97:1532–1538.
190. Grove AS. Orbital trauma and computed tomography. Ophthalmology 1980;403–411.
191. Grove AS Jr. Orbital trauma evaluation by computed tomography. Comput Tomogr 1979;3:267–278.
192. Henrickson GC, Mafee MF, Flanders AE, Kriz RJ, Peyman GA, et al. CT evaluation of plastic intraocular foreign bodies. AJNR 1987;8: 378–379.
193. Lobue TD, Deutsch TA, Lobick J. et al. Detection and localization of nonmetallic intraocular foreign bodies by magnetic resonance imaging. Arch Ophthalmol 1988;106:260–261.
194. Duker JS, Fisher DH. Occult plastic intraocular foreign body. Ophthalmic Surg 1989;20:169–170.
195. Lagouras PA, Langer BG, Peyman GA, et al. Magnetic resonance imaging and intraocular foreign bodies. Arch Ophthalmol 1987;105: 551–553.
196. Williamson THE, Smith FW, Forrester JV. Magnetic resonance imaging of intraocular foreign bodies. Br J Ophthalmol 1989;73: 555–558.
197. Kelly WN, Paglen PG, Pearson JA, et al. Ferromagnetism of intraocular foreign body causes unilateral blindness after MR study. AJNR 1986;7:243–245.
198. Zheutlin JD, Thompson JT, Shofner RS. The safety of magnetic resonance imaging with intraorbital metallic objects after retinal reattachment or trauma (letter). Am J Ophthalmol 1987;103:831.
199. Sears FW, Zenansky MW (eds). University Physics, ed 4. Reading, MA: Addison-Wesley, 1970.
200. Green BF, Kraft SP, Carter KD, et al. Intraorbital wood: detection by magnetic resonance imaging. Ophthalmology 1990;97:608–611.
201. Ferguson EC III. Deep, wooden foreign bodies of the orbit: a report of two cases. Trans Am Acad Ophthalmol Otolaryngol 1970;74: 778–787.
202. Macrae JA. Diagnosis and management of a wooden orbital foreign body: case report. Br J Ophthalmol 1979;848–851.
203. Brock L, Tanenbaum HL. Retention of wooden foreign bodies in the orbit. Can J Ophthalmol 1980;15:70–72.
204. Reshef DS, Ossoinnig KC, Nerad JA. Diagnosis and intraoperative localization of a deep orbital organic foreign body. Orbit 1987;6:3–15.
205. Weisman RA, Savino PJ, Schut L, et al. Computed tomography in penetrating wounds of the orbit with retained bodies. Arch Otolaryngol 1983;109:265–268.
206. Grove AS Jr. Computed tomography in the management of orbital trauma. Ophthalmology 1982;89:433–440.
207. Tate E, Cupples H. Detection of orbital foreign bodies with computed tomography: current limits. AJR 1981;137:493–495.
208. Myllyla V, Pyhtinen J, Pajvansalo M, et al. CT detection and location of intraorbital foreign bodies: experiments with wood and glass. ROFO 1987;146:639–643.
209. Coleman DJ. Reliability of ocular and orbital diagnosis with B-scan ultrasound orbital diagnosis. Am J Ophthalmol 1972;74:704–718.
210. Macrae JA. Diagnosis and management of a wooden orbital foreign body: case report. Br J Ophthalmol 1979;63:848–851.

Copyright © 2003, Mosby, Inc. All rights reserved.

211. Weissman JL, Beatty R, Hirsch WL, Curtin HD. Enlarged anterior chamber: CT finding of a ruptured globe. AJNR 1995;16(4 Suppl):936–938.
212. Joseph DP, Pieramici DJ, Beauchamp NJ Jr. Computed tomography in the diagnosis and prognosis of open-globe injuries. Ophthalmology 2000;107(10):1899–1906.
213. Segev Y, Goldstein M, Lazar M, Reider-Groswasser I. CT appearance of a traumatic cataract. AJNR 1995;16(5):1174–1175.
214. Boorstein JM, Titelbaum DS, Patel Y, Wong KT, Grossman RI. CT diagnosis of unsuspected traumatic cataracts in patients with complicated eye injuries: significance of attenuation value of the lens. AJR 1995;164(1):181–184.
215. Almog Y, Reider-Groswasser I, Goldstein M, Lazar M, Segev Y, Geyer O. ''The disappearing lens'': failure of CT to image the lens in traumatic intumescent cataract. J Comput Assist Tomogr 1999;23(3): 354–356.
216. Bressler EL, Weinberg PE, Zaret CR. Silicone encircling bands for retinal detachment: CT appearance. J Comput Assist Tomogr 1984;8(5):960–962.
217. Girardot C, Hazebroucq VG, Fery-Lemonnier E, et al. MR imaging and CT of surgical materials currently used in ophthalmology: in vitro and in vivo studies. Radiology 1994;191(2):433–439.
218. Herrick RC, Hayman LA, Maturi RK, Diaz-Marchan PJ, Tang RA, Lambert HM. Optimal imaging protocol after intraocular silicone oil tamponade. AJNR 1998;19(1):101–108.
219. Manfre L, Fabbri G, Avitabile T, Biondi P, Reibaldi A, Pero G. MRI and intraocular tamponade media. Neuroradiology 1993;35(5): 359–361.
220. Yoshida A, Cheng HM, Kwong KK, Ogasawara H, Garrido L, McMeel JW. Magnetic resonance imaging of intraocular tamponades. Ophthalmic Surg 1991;22(5):287–291.
221. Mathews VP, Elster AD, Barker PB, Buff BL, Haller JA, Greven CM. Intraocular silicone oil: in vitro and in vivo MR and CT characteristics. AJNR 1994;15(2):343–347.
222. Ainbinder DJ, Haik BG, Mazzoli RA. Anophthalmic socket and orbital implants: role of CT and MR imaging. Radiol Clin North Am 1998;36:1133–1147.
223. DePotter P, Shields CL, Shields JA, et al. Role of magnetic resonance imaging in the evaluation of the hydroxyapatite orbital implant. Ophthalmology 1992;99:824.
224. Shields CL, Shields JA, DePotter P. Hydroxyapatite orbital implant after enucleation: experience with initial 100 consecutive cases. Arch Ophthalmol 1992;110:333.
225. Rubin PA, Green JP, Keur C, et al. Medpur motility coupling post: primary placement in humans. Am Soc Ophthal Plast Reconstr Surg 28th Annual Symposium, 1997.

Copyright © 2003, Mosby, Inc. All rights reserved.

9

Orbit: Embryology, Anatomy, and Pathology

Mahmood F. Mafee

EMBRYOLOGY OF THE ORBIT
- The Orbit
- Extraocular Muscles
- The Eyelids
- The Lacrimal Gland
- The Lacrimal Sac and Nasolacrimal Duct

INTRODUCTION TO THE ORBIT
BONY ORBIT
- Orbital Roof
- Medial Orbital Wall
- Orbital Floor
- Lateral Orbital Wall

ORBITAL APEX
- Superior Orbital Fissure
- Inferior Orbital Fissure
- Pterygopalatine Fossa

PERIORBITA
ORBITAL SEPTUM AND EYELIDS
ORBICULARIS OCULI
TENON'S CAPSULE (FASCIA BULBI) AND TENON'S SPACE
ORBITAL FATTY RETICULUM
EXTRAOCULAR MUSCLES
- Spiral of Tillaux
- Retractors
- Levator Muscle
- Lower Eyelid Retractors
- Movements of Eyelid and Eyeball
- Blood Supply to the Extraocular Muscles

OPTIC NERVE
- Meningeal Sheaths (Dura, Arachnoid, Pia)
- Blood Supply of the Optic Nerve

PERIPHERAL NERVES
SENSORY INNERVATION
MOTOR INNERVATION
- Oculomotor Nerve (III)
- Trochlear Nerve (IV)
- Abducens Nerve (VI)

OTHER NERVES
AUTONOMIC NERVES
VASCULAR ANATOMY
VENOUS DRAINAGE OF THE ORBIT AND EYEBALL
LACRIMAL APPARATUS
TECHNIQUE FOR ORBITAL CT AND MR IMAGING
- General Considerations
- Computed Tomography
- MR Imaging Techniques
  - Inversion Recovery and Application of Fat-Suppression Technique
  - T1-Weighted Fat-Suppression Technique
- Normal CT and MR Imaging Anatomy
  - Extraocular Muscles
  - Orbital Compartments
  - Lacrimal Gland
  - Vascular and Neural Structures
  - Optic Nerve
  - Globe

BONY INTERORBITAL DISTANCE
PATHOLOGY
- Hypertelorism, Hypotelorism, Exophthalmos, and Exorbitism
- Congenital and Developmental Abnormalities
- Anatomic and Developmental Considerations
- Bony Abnormalities
- Bony Orbit in Craniofacial Dysostosis
- Primary Congenital Isolated Craniosynostosis
- Orbit in Plagiocephaly
- Orbit in Crouzon's and Apert's Diseases
- Saethre-Chotzen Syndrome (Acrocephalosyndactyly Type II)
- Neurofibromatosis
- Orbital (Mesodermal) Defects
- Mandibulofacial Dysostosis

Copyright © 2003, Mosby, Inc. All rights reserved.

- Orbital Defects
- Bony Orbital Defects
- Bony Orbit in Craniofacial Microsomia
- Developmental Orbital Cysts
- Diagnostic Imaging
- Other Less Common Congenital Anomalies and Acquired Cysts of the Orbit and Optic System
- Congenital Cystic Eye
- Other Orbital Cysts
- Optic Nerve Sheath Meningocele
- Enterogenous Cysts
- Dentigerous Cysts
- Cystic Vascular Lesions: Lymphangioma, Varix, Chocolate Cyst
- Epithelial and Appendage Cysts
- Epithelial Implantation Cysts
- Lacrimal Gland Cysts
- Dacryoceles
- Hematic Cysts and Cholesterol Granuloma
- *Diagnostic Imaging*
- *MR Imaging Findings in Various Stages of Orbital Hematoma*
- *Orbital Cholesterol Granulomas*
- *Diagnostic Imaging*
- Aneurysmal Bone Cysts
- Cystic Myositis
- Orbital Abscesses (Inflammatory Orbital Cysts)
- Parasitic Cysts
- *Hydatid Cysts*
- *Cysticercosis*
- *Diagnostic Imaging*

INFLAMMATORY DISEASES

- Orbital Cellulitis and Sinusitis
- Bacterial Orbital Cellulitis Classification
- Bacterial Preseptal Cellulitis and Preseptal Edema
- Postseptal Orbital Cellulitis
- Subperiosteal Phlegmon and Abscess
- Cavernous Sinus Thrombosis
- Mycotic Infections
- Acute, Subacute, and Chronic Idiopathic Orbital Inflammatory Disorders (Pseudotumors)
- Histopathology
- Anterior Orbital Inflammation
- Diffuse Orbital Pseudotumor
- Orbital Myositis
- Perineuritis and Periscleritis
- Lacrimal Adenitis
- Apical Orbital Inflammation
- Painful External Ophthalmoplegia (Tolosa-Hunt Syndrome)
- Thyroid Orbitopathy (Graves' Dysthyroid Ophthalmopathy)
- Pathology
- *Immunopathology*
- *Histopathology*
- Diagnosis
- Diagnostic Imaging
- Sarcoidosis
- Pathologic and Immunologic Features
- Clinical Features
- Optic Nerve Sarcoidosis
- *Diagnostic Imaging in Optic Nerve Sarcoidosis*
- Sjogren's Syndrome
- Vasculitides (Angiitides)
- Wegener's Granulomatosis
- B-Cell and T-Cell Lymphoma
- Periarteritis Nodosa (Polyarteritis Nodosa)
- Hypersensitivity (Leukocytoclastic) Angiitis
- Lupus Erythematosus
- Amyloidosis

MISCELLANEOUS GRANULOMATOUS AND HISTIOCYTIC LESIONS

- Langerhans' Cell Histiocytosis
- Historical Background
- Clinical Features
- Ocular Manifestations
- Histopathologic Features
- Immunohistochemistry
- Diagnostic Imaging
- Juvenile Xanthogranuloma
- Clinical Features
- Histopathologic Features
- Diagnostic Imaging
- Erdheim-Chester Disease
- Pseudorheumatoid Nodules
- Necrobiotic Xanthogranuloma

TUMORS

- Orbital Lymphoma
- Diagnostic Imaging
- Lymphoplasmacytic Tumor (Plasma Cell Tumor)

ORBITAL LEUKEMIA

ORBITAL VASCULAR CONDITIONS

- Capillary Hemangioma (Benign Hemangioendothelioma)
- Cavernous Hemangioma
- Lymphangioma
- Orbital Varix
- Carotid Cavernous Fistulas and Arteriovenous Malformations
- Hemangiopericytoma

Copyright © 2003, Mosby, Inc. All rights reserved.

NEURAL LESIONS
Orbital Schwannoma
Neurofibroma
TUMORAL AND NONTUMORAL ENLARGEMENT OF THE OPTIC NERVE SHEATH
OPTIC NEURITIS
PNEUMOSINUS DILATANS
FIBROUS TISSUE TUMORS OF THE ORBIT
Fibrous Histiocytoma
Fibroma and Fibrosarcoma
Nodular Fasciitis
RHABDOMYOSARCOMA OF THE ORBIT
Diagnostic Imaging
MESENCHYMAL CHONDROSARCOMA OF THE ORBIT
LACRIMAL GLAND AND FOSSA LESIONS
Diagnostic Imaging
MISCELLANEOUS LACRIMAL GLAND LESIONS
Amyloid Tumor of the Lacrimal Gland
Kimura's Disease
SECONDARY ORBITAL TUMORS
ADDITIONAL PATHOLOGIES OF THE EXTRAOCULAR MUSCLES
Ocular Motility Disorders
Acquired Ocular Motility Disturbances Associated with Orbital Pathology
Brown's Superior Oblique Tendon Sheath Syndrome
Double Elevator Palsy
Other Causes
Traumatic Injury of the Ocular Muscles
Blowout Fracture
Congenital Anomalies of the Extraocular Muscle
Congenital Syndromes
Noncomitant Strabismus Without Associated Malformations

EMBRYOLOGY OF THE ORBIT

The Orbit

The orbital bones develop from the mesenchyme that encircles the optic vesicle (see also the discussion of embryology in Chapter 8).[1, 2] The medial wall forms from the lateral nasal process. The lateral wall and inferior wall develop from the maxillary process. The superior wall forms from the mesenchymal capsule of the forebrain. The posterior orbit is formed by the bones of the base of the skull.[2] The bones of the orbit form as membranous bone, except for the ethmoid, which is enchondral in origin.[1, 2] It is interesting to note that early in development, the eye develops at a faster rate than the orbit, so that in the sixth month of fetal life the anterior half of the eye projects beyond the orbital opening. The eye increases rapidly in size during the first years of life. The rate of growth then slows but increases again at puberty. The cornea, which is relatively large at birth, reaches adult size by the time the child is 2 years old.[2] Pigmentation of the iris stroma occurs during the first years after birth.[2] The lens grows rapidly after birth and continues to grow throughout life. At birth the eye is hypermetropic (hyperopic or farsighted). Later, as the anteroposterior axis of the eye increases in length, this condition is corrected. A further increase in the anteroposterior axis could cause myopia, but generally this is prevented by the simultaneous flattening of the lens as growth proceeds.[2]

Extraocular Muscles

The extraocular muscles of the eye are formed from the mesenchyme in the region of the developing eye (preotic myotomes).[1] Originally represented as a single mass of mesenchyme, they later separate into distinct muscles, first at their insertions and later still at their origins. The levator palpebrae superioris is formed last, splitting off from the mesenchyme that forms the superior rectus muscle. During their development, the extraocular muscles become associated with the third, fourth, and sixth cranial nerves.[1]

The Eyelids

The eyelids develop as folds of surface ectoderm above and below the developing cornea (Figs. 9-1 and 9-2). As they grow, they become united with each other at about the third month of gestation.[1] The lids remain fused until about the fifth month of gestation, when they start to separate. Separation of the eyelids is completed by the seventh month of intrauterine life.[1] While the lids are fused, a closed space, the conjunctival sac, exists in front of the cornea. The mesenchymal core of the lids forms the connective tissue and tarsal plates. The mesenchyme of the second pharyngeal arch invades the eyelids to form the orbicularis oculi muscle supplied by the seventh cranial nerve. The cilia develop as epithelial buds from the surface ectoderm. The ciliary glands of Moll and Zeis grow out from the ciliary follicles. The tarsal glands (meibomian glands) develop as columns of ectodermal cells from the lid margins.[1] The epithelium of the cornea and conjunctiva is of ectodermal origin, as are the eyelashes and the lining cells of the tarsal and other glands opening onto the margins of the eyelids.[2]

The Lacrimal Gland

The lacrimal gland forms as a series of ectodermal buds that grow superolaterally from the superior conjunctival

Copyright © 2003, Mosby, Inc. All rights reserved.

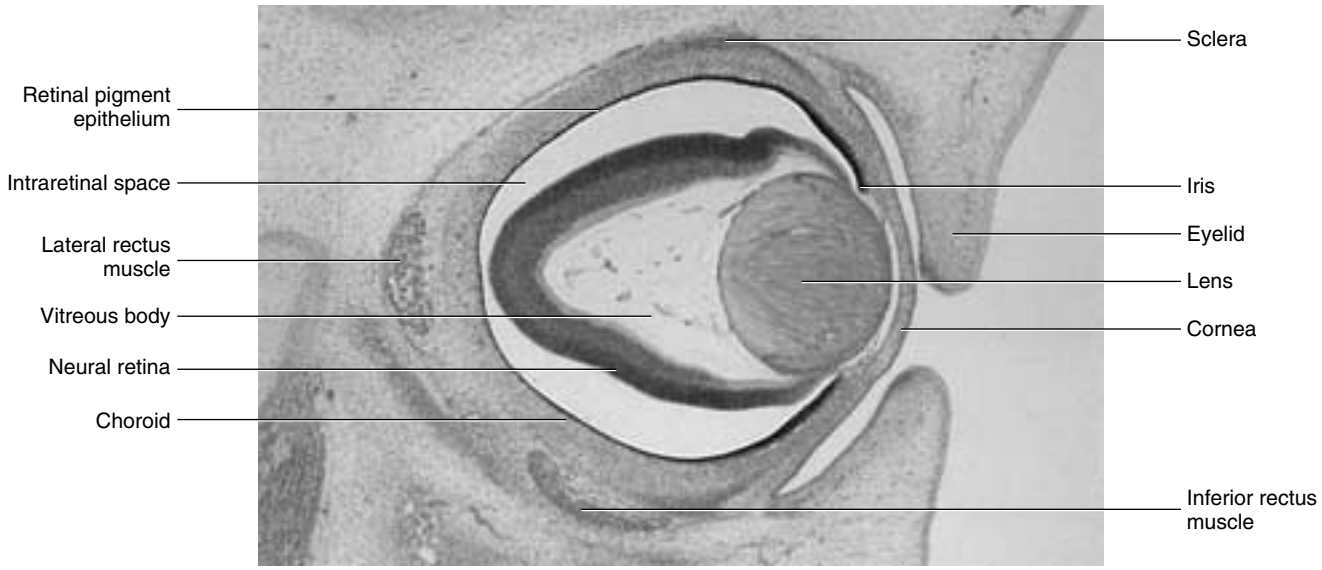

VIEW IMAGE

FIGURE 9-1 Photomicrograph of a sagittal section of the eye of an embryo (×50) at Carnegie stage 23, about 56 days. Observe the developing neural retina and the retinal pigment epithelium. The intraretinal space normally disappears as these two layers of the retina fuse. (From Moore KL, Persaud TVN, Shiota K: *Color Atlas of Clinical Embryology*. Philadelphia, WB Saunders, 1994.)

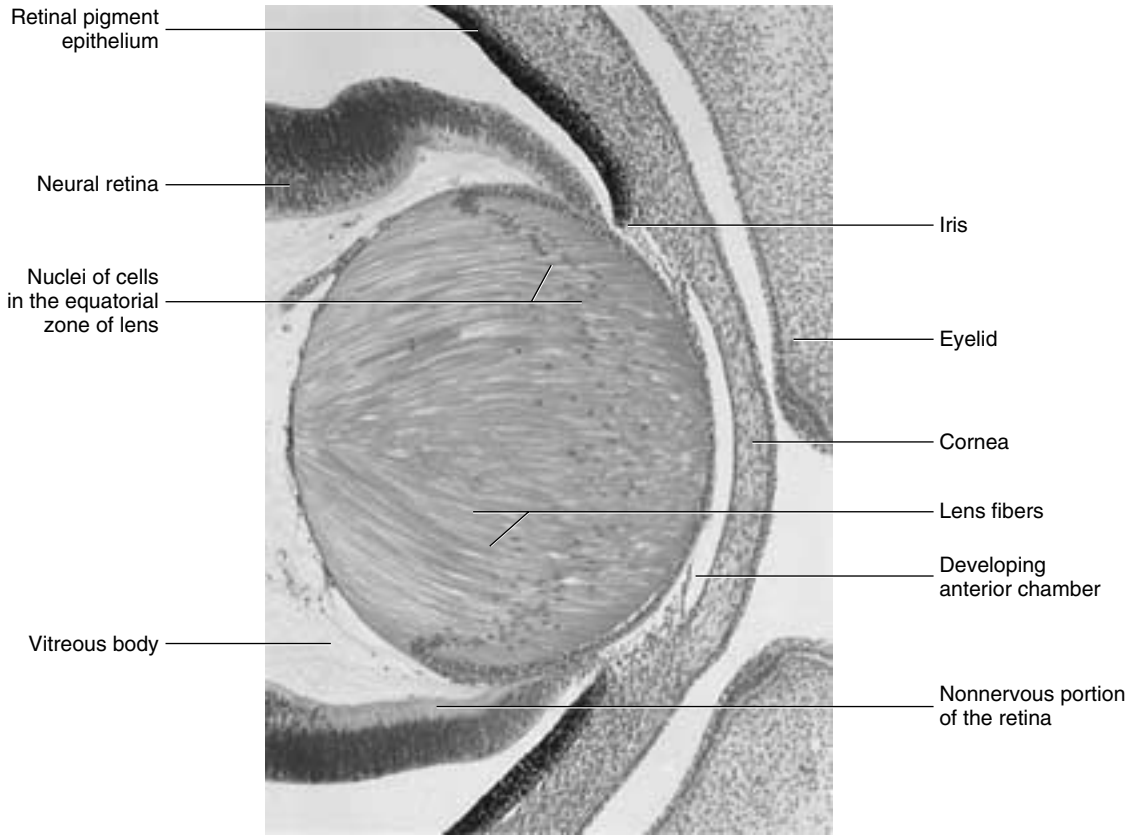

VIEW IMAGE

FIGURE 9-2 Higher magnification of a portion of the developing eye of the embryo shown in Figure 9-1. Observe that the lens fibers have elongated and obliterated the cavity of the lens vesicle. Note that the inner layer of the optic cup has thickened greatly to form the neural retina and that the outer layer is heavily pigmented (retinal pigment epithelium). (From Moore KL, Persaud TVN, Shiota K: *Color Atlas of Clinical Embryology*. Philadelphia, WB Saunders, 1994.)

Copyright © 2003, Mosby, Inc. All rights reserved.

fornix into the underlying mesenchyme.[1] These buds are arranged in two groups, one forming the gland proper and the other its palpebral process.[2] These buds later canalize, forming the secretory units and multiple ducts of the gland. The gland becomes divided into orbital and palpebral parts with the development of the levator palpebral superioris. Tears are usually not produced until 1 to 3 months after birth.

The Lacrimal Sac and Nasolacrimal Duct

The lacrimal sac and nasolacrimal duct initially develop as a solid cord of ectodermal cells in the nasomaxillary groove between the lateral nasal elevation and the maxillary process of the developing face.[1, 2] Later, this solid cord of cells sinks into the mesenchyme, and during the third month of embryonic life, the central cells of the cord break down and the cord becomes canalized to form the nasolacrimal duct. The superior end becomes dilated to form the lacrimal sac. Incomplete canalization, particularly in the lower end of the system, is common, even in full-term infants. Further cellular proliferation results in the formation of the inferior, superior, and common lacrimal ducts. The lacrimal canaliculi (superior and inferior) arise as buds from the upper part of the cord of cells and secondarily establish openings (puncta lacrimalia) on the margins of the lids.[2]

INTRODUCTION TO THE ORBIT

The orbits are two recesses that contain the globes, extraocular muscles, blood vessels, nerves (cranial nerves II, III, IV, V, VI and the sympathetic and parasympathetic nerves), adipose and connective tissues, and most of the lacrimal apparatus. The orbit is bordered by the periosteum of seven bones (frontal, sphenoid, ethmoid, lacrimal, maxilla, zygoma, and palatine), and it is separated from the globe by Tenon's capsule.[1, 3, 4] Anteriorly are the orbital septum and the lids. The orbital cavity is pyramidal in shape, with its apex directed posteromedially and its base, the orbital opening, directed anterolaterally. Its bony walls separate it from the anterior cranial fossa superiorly; the ethmoid air cells, sphenoid sinus, and nasal cavity medially; the maxillary sinus inferiorly; and the lateral face and temporal fossa laterally and posteriorly. The volume of the orbit in adult is about 30 cc. The orbital entrance averages about 35 mm in height and 45 mm in width, and the maximum width occurs about 1 cm behind the anterior orbital margin.[5, 6] In adults, the depth of the orbit varies from 40 to 45 mm from the orbital entrance to the orbital apex.

BONY ORBIT

Each orbit presents a roof, floor, medial wall, lateral wall, base (or orbital opening), and apex (Figs. 9-3 and 9-4). The orbital ventral margin or rim forms a quadrilateral spiral. The superior margin is formed by the frontal bone, which is interrupted medially by the supraorbital notch or foramen that transmits the supraorbital blood vessels and the supraorbital nerve, a branch of the ophthalmic division of the trigeminal nerve. The medial margin is formed by the frontal bone above and by the posterior lacrimal crest of the maxillary bone and the anterior lacrimal crest of the lacrimal bone below. The inferior margin is formed by the maxillary and zygomatic bones, while the lateral margin is formed by the zygomatic and frontal bones.

Orbital Roof

The orbital roof is formed from the orbital plate of the frontal bone and most of the lesser wing of the sphenoid bone (Fig. 9-3). Anteromedially is the floor of the frontal sinus, and anterolaterally is the lacrimal fossa, in which lies the orbital part of the lacrimal gland. Posteriorly, at the junction of the roof and the medial wall, are the optic canal and optic foramen (Fig. 9-4), which establish communication between the orbit and the suprasellar cistern and cavernous sinuses. The optic canal contains the optic nerve, ophthalmic artery, and sympathetic fibers. Medially and anteriorly is the fovea (fossa) trochlearis, which is located approximately 4 mm from the superior orbital margin. From it is formed the trochlea or pulley of the superior oblique muscle. The trochlea is a curved plate of hyaline cartilage attached to the trochlear fossa. Calcification of the trochlea is common.

Medial Orbital Wall

The medial wall is exceedingly thin, except at its most posterior part. This wall is formed by a small portion of the frontal process of the maxilla, the lacrimal bone, the ethmoid bone, and the body of the sphenoid (Figs. 9-3, 9-4). The medial wall slopes gently downward and laterally into the floor. Anteriorly is the lacrimal groove for the lacrimal sac. The groove communicates below with the nasal cavity through the nasolacrimal canal, which is about 1 cm long

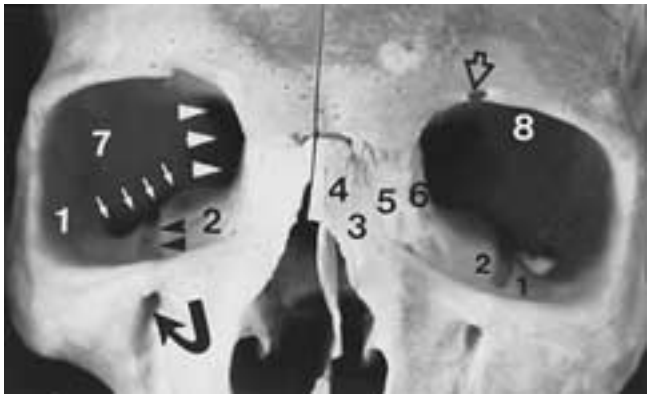

FIGURE 9-3 Frontal view of orbits. *1*, Orbital process of zygomatic bone; *2*, orbital process of maxilla; *3*, frontonasal process of maxilla; *4*, nasal bone; *5*, lacrimal bone; *6*, orbital plate of ethmoid bone (lamina papyracea); *7*, orbital surface of greater wing of sphenoid bone; *8*, orbital surface of frontal bone. Note supraorbital foramen (notch) (*hollow arrow*), superior orbital fissure (*white arrowheads*), inferior orbital fissure (*white arrows*), infraorbital groove (*black arrowheads*), and infraorbital foramen (*curved arrow*).

VIEW IMAGE

Copyright © 2003, Mosby, Inc. All rights reserved.

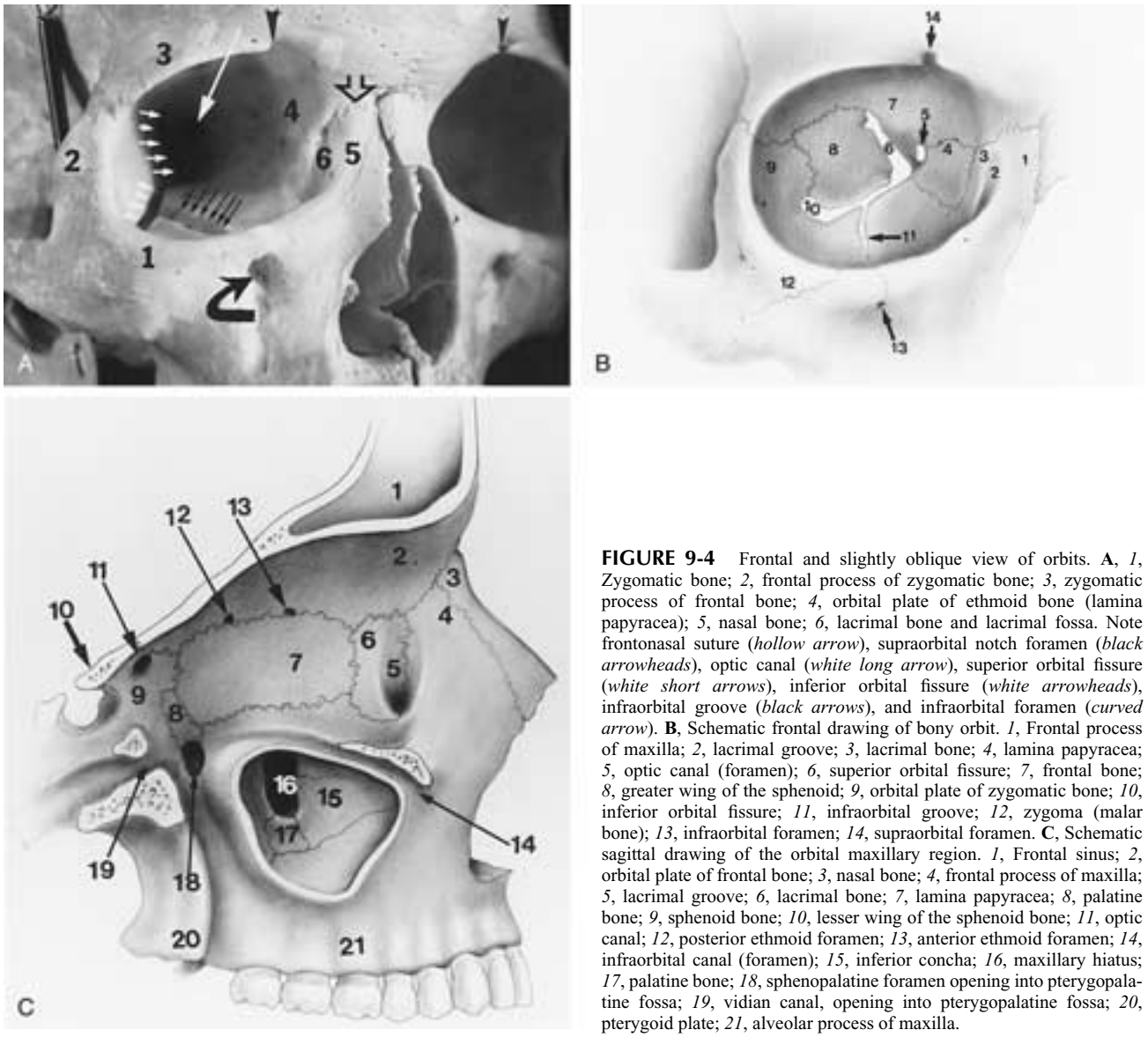

FIGURE 9-4 Frontal and slightly oblique view of orbits. **A**, *1*, Zygomatic bone; *2*, frontal process of zygomatic bone; *3*, zygomatic process of frontal bone; *4*, orbital plate of ethmoid bone (lamina papyracea); *5*, nasal bone; *6*, lacrimal bone and lacrimal fossa. Note frontonasal suture (*hollow arrow*), supraorbital notch foramen (*black arrowheads*), optic canal (*white long arrow*), superior orbital fissure (*white short arrows*), inferior orbital fissure (*white arrowheads*), infraorbital groove (*black arrows*), and infraorbital foramen (*curved arrow*). **B**, Schematic frontal drawing of bony orbit. *1*, Frontal process of maxilla; *2*, lacrimal groove; *3*, lacrimal bone; *4*, lamina papyracea; *5*, optic canal (foramen); *6*, superior orbital fissure; *7*, frontal bone; *8*, greater wing of the sphenoid; *9*, orbital plate of zygomatic bone; *10*, inferior orbital fissure; *11*, infraorbital groove; *12*, zygoma (malar bone); *13*, infraorbital foramen; *14*, supraorbital foramen. **C**, Schematic sagittal drawing of the orbital maxillary region. *1*, Frontal sinus; *2*, orbital plate of frontal bone; *3*, nasal bone; *4*, frontal process of maxilla; *5*, lacrimal groove; *6*, lacrimal bone; *7*, lamina papyracea; *8*, palatine bone; *9*, sphenoid bone; *10*, lesser wing of the sphenoid bone; *11*, optic canal; *12*, posterior ethmoid foramen; *13*, anterior ethmoid foramen; *14*, infraorbital canal (foramen); *15*, inferior concha; *16*, maxillary hiatus; *17*, palatine bone; *18*, sphenopalatine foramen opening into pterygopalatine fossa; *19*, vidian canal, opening into pterygopalatine fossa; *20*, pterygoid plate; *21*, alveolar process of maxilla.

VIEW IMAGE

and contains the nasolacrimal duct. The duct opens into the inferior meatus of the nasal cavity. Also in the medial wall are two canals for the anterior and posterior ethmoidal nerves and vessels. These canals are situated at the level of the floor of the anterior cranial fossa, as their lower margins are formed by the ethmoid bone and their upper margins are formed by the frontal bone. The anterior ethmoidal foramen is located at the frontal-ethmoidal suture and transmits the anterior ethmoidal vessels and nerve. The posterior ethmoidal foramen transmits the posterior ethmoidal vessels and nerve.[1, 3–6] If an external ethmoidectomy is performed and the surgeons keep their bone incision caudal to a line between these canals, the incision will be into the ethmoid complex and not into the anterior cranial fossa.

Orbital Floor

The inferior wall, or floor of the orbit, is relatively thin, and in most of its extent it is also the roof of the maxillary antrum or sinus (Figs. 9-3 and 9-4). The floor actually is made up of the orbital part of the maxilla, the orbital process of the zygomatic bone, and the orbital process of the palatine bone (Figs. 9-3 and 9-4). The orbital process of the palatine bone forms a small triangular area in the posteromedial corner of the orbital floor, where the floor meets the medial wall. The floor is not horizontal, but slants upward so that the posteromedial portion is higher than the flatter anterolateral portion.[1] Anteriorly, for about 1.0 to 1.5 cm, the floor is continuous with the lateral orbital wall. However, posterior to this area, the floor and lateral wall are separated by the inferior orbital fissure (Figs. 9-3 and 9-4). This fissure connects the orbit medially and posteriorly with the pterygopalatine fossa, and laterally and anteriorly with the retromaxillary and temporal fossae. The medial lip of the fissure is notched by the infraorbital groove, or fissure (Figs. 9-3 and 9-4), which passes forward in the orbital floor (usually in the middle third of the orbital floor), sinks into the orbital floor about 1 cm behind the orbital rim, and becomes the infraorbital canal that opens on

Copyright © 2003, Mosby, Inc. All rights reserved.

the anterior face of the maxilla as the infraorbital foramen, about 1 cm below the inferior orbital rim (Figs. 9-3 and 9-4).[1] The groove, canal, and foramen transmit the infraorbital nerve, the continuation of the maxillary nerve (V_2).[1, 3–6] The inferior oblique muscle arises from the floor of the orbit just lateral to the opening of the nasolacrimal canal.[5, 6] It is the only extraocular muscle that does not originate from the orbital apex.

Lateral Orbital Wall

The lateral wall of the orbit is the thickest wall, and it is formed by the orbital surface of the greater wing of the sphenoid bone behind and the orbital surface of the frontal process of the zygomatic bone in front (Figs. 9-3 and 9-4). The two bones meet at the sphenozygomatic suture. This aspect of the zygomatic bone presents the openings of two minute canals, one for the zygomaticofacial nerve and artery (near the junction of the floor and lateral walls) and the other for the zygomaticotemporal nerve and artery, which are slightly higher on this wall.[1, 5, 6] The lateral orbital tubercle, a small elevation of the orbital margin of the zygoma, lies approximately 11 mm below the frontal-zygomatic suture. This important landmark is the site of attachment for (1) the check ligament of the lateral rectus muscle, (2) the suspensory ligament of the eyeball, (3) the lateral palpebral ligament, and (4) the aponeurosis of the levator palpebrae muscle.[5, 6]

ORBITAL APEX

The apex of the orbit is basically formed by the optic canal and the superior orbital fissure.[1, 3] The optic canal and the superior and inferior orbital fissures allow various structures to enter and exit the orbit. The optic canal, having virtually no length at birth, becomes 4 mm long by 1 year of age and is up to 9 mm long in adults. The optic canal is directed forward, laterally (about 45° from the midsagittal plane), and somewhat downward (about 12° from the horizontal plane) and has orbital and intracranial openings (foramina). The configuration of the intracranial opening is oval, with its long axis in the horizontal plane. The configuration of the midportion of the optic canal is circular, and the configuration of the orbital opening is an oval with its long axis in the vertical plane. The optic canal is bounded medially by the body of the sphenoid bone (Figs. 9-5 and 9-6),

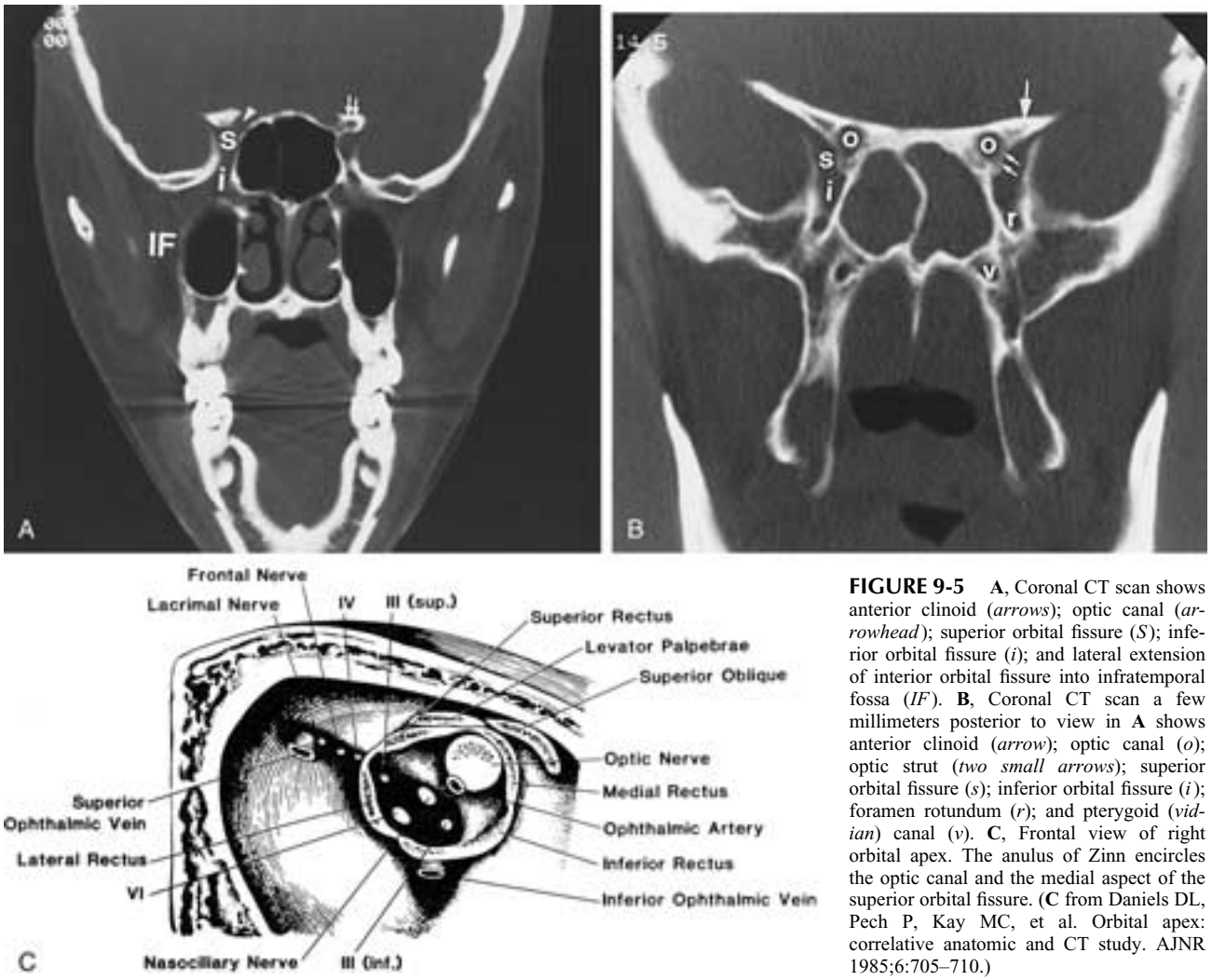

FIGURE 9-5 **A**, Coronal CT scan shows anterior clinoid (*arrows*); optic canal (*arrowhead*); superior orbital fissure (*S*); inferior orbital fissure (*i*); and lateral extension of interior orbital fissure into infratemporal fossa (*IF*). **B**, Coronal CT scan a few millimeters posterior to view in **A** shows anterior clinoid (*arrow*); optic canal (*o*); optic strut (*two small arrows*); superior orbital fissure (*s*); inferior orbital fissure (*i*); foramen rotundum (*r*); and pterygoid (*vidian*) canal (*v*). **C**, Frontal view of right orbital apex. The anulus of Zinn encircles the optic canal and the medial aspect of the superior orbital fissure. (**C** from Daniels DL, Pech P, Kay MC, et al. Orbital apex: correlative anatomic and CT study. AJNR 1985;6:705–710.)

VIEW IMAGE

Copyright © 2003, Mosby, Inc. All rights reserved.

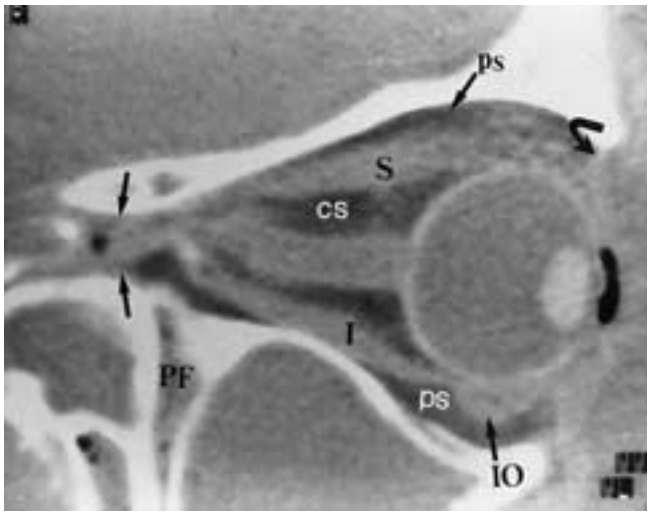

VIEW IMAGE

FIGURE 9-6 Orbital CT anatomy. Direct parasagittal CT scan of cadaver head shows peripheral orbital space (*ps*); central orbital (intraconal) space (*CS*); optic nerve; superior rectus muscle (*S*) and inferior rectus muscle (*I*); inferior oblique muscle (*IO*); orbital septum (*curved arrow*); and common tendon of Zinn (*arrows*). Periosteum (periorbita) lines bony orbit as orbital fascia and is loosely attached to bony orbit. Periosteum is united with dura mater and sheath of optic nerve at optic canal. Normally, periosteum cannot be differentiated from adjacent soft tissues. Periosteum is continuous with periosteum of the bones of the face and is also continuous with layer of dura at superior orbital fissure. Note continuity of periorbita with periosteum of pterygomaxillary fossa (*PF*). Infection or infiltrative process of pterygomaxillary fossa may invade orbital subperiosteal space (periorbita) or vice versa. (CT scan courtesy of FW Zonneveld.) (From Mafee MF et al. Orbital space-occupying lesions: role of CT and MRI: an analysis of 145 cases. Radiol Clin North Am 1987;25:529.)

superiorly by the superior root of the lesser wing of the sphenoid bone, and inferiorly and laterally by the inferior root (optic strut) of the lesser wing of the sphenoid bone.[4] Attached to the orbital wall surrounding the opening of the optic canal (and thus the optic nerve, ophthalmic artery, and sympathetic nerves) and extending around the lower aspect of the vertical portion of the superior orbital fissure (encircling cranial nerves III and VI) is the common tendinous ring (annulus) of Zinn, which gives origin to the inferior, medial, lateral, and superior rectus muscles (Fig. 9-6).[1] Usually the inferior ophthalmic vein is below the annulus of Zinn in the lower aspect of the superior orbital fissure. Above the annulus of Zinn and within the superior orbital fissure are the superior ophthalmic vein, the recurrent meningeal artery, the lacrimal nerve, the frontal nerve, and cranial nerve IV.

Superior Orbital Fissure

Just inferolateral to the optic canal and separated from it by the optic strut is the superior orbital fissure, located between the greater and lesser wings of the sphenoid bone (Fig. 9-5). This fissure is approximately 22 mm long and is somewhat comma-shaped, with the bulbous or wider portion inferomedially and the thin portion superolaterally. The inferior part of the superior orbital fissure is divided from the superior part by the origin of the lateral rectus muscle.[1, 6] Where the fissure begins to widen, its lower border is marked by a bony projection, often sharp in character, which gives attachment to the lateral part of the common tendinous ring of Zinn. The superior orbital fissure communicates with the middle cranial fossa and transmits the oculomotor, trochlear, and abducens nerves and the terminal branches of the ophthalmic nerve (V_1) and the ophthalmic veins. The lacrimal, frontal, and trochlear nerves traverse the narrow lateral part of the fissure, which also transmits the meningeal branch of the lacrimal artery and the occasional orbital branch of the middle meningeal artery. The trochlear nerve is situated more medially and lies just outside the common tendinous ring of Zinn.[1] The two divisions (superior and inferior) of the oculomotor nerve, the nasociliary nerve (a branch of the ophthalmic nerve), the abducens nerve, and the sympathetic plexus pass within the tendinous ring and therefore traverse the wider medial part of the fissure. They may be accompanied by the superior and inferior ophthalmic veins, but the superior ophthalmic vein may also accompany the trochlear nerve, and the inferior ophthalmic vein may pass through the medial end of the fissure below the ring.[1]

Inferior Orbital Fissure

At the posterior aspect of the orbit, the inferior and lateral walls of the orbit are separated by the inferior orbital fissure (Figs. 9-3 to 9-5). The fissure lies just below the superior orbital fissure and is bounded above by the greater wing of the sphenoid, below by the maxilla and the orbital process of the palatine bone, and laterally by the zygomatic bone (the zygomaticomaxillary suture). The inferior orbital fissure extends obliquely as a gently curving continuation of the more medial pterygopalatine fossa (Figs. 9-6 and 9-7). The maxillary nerve is the most important structure traversing the inferior orbital fissure. The inferior orbital fissure also transmits the infraorbital vessels, the zygomatic nerve, and a few minute twigs from the pterygopalatine ganglion. Through the anterior part of the inferior orbital fissure, a vein passes to connect the inferior ophthalmic vein with the pterygoid plexus in the infratemporal fossa.[1] The inferior ophthalmic vein passes through its lower portion before entering the cavernous sinus.[6]

Pterygopalatine Fossa

The pterygopalatine fossa is a small, narrow pyramidal space situated below the apex of the orbit and tapering inferiorly[7] (Fig. 9-6). It is bounded above by the body of the sphenoid, in front by the maxilla, behind by the pterygoid processes and the greater wing of the sphenoid, and medially by the palatine bone (Fig. 9-6). It communicates with the infratemporal fossa through the pterygomaxillary (retromaxillary) fissure. The five foramina that open into this fossa are (1) the foramen rotundum, (2) the pterygoid (vidian) canal, (3) the pharyngeal (palatovaginal) canal (Fig. 9-5B), (4) the sphenopalatine foramen, and (5) the pterygopalatine canal. The most important contents of the fossa are the maxillary nerve, the pterygopalatine (sphenopalatine) ganglion, and the terminal part of the maxillary artery. The maxillary nerve (V_2) runs from the inferior aspect of the cavernous sinus and

Copyright © 2003, Mosby, Inc. All rights reserved.

exits the skull base through the foramen rotundum. The nerve then runs through the upper part of the pterygopalatine fossa, just above the pterygopalatine ganglion, and enters the inferior orbital fissure, passing forward and laterally to reach the posterior end of the infraorbital groove in the floor of the orbit. The nerve finally exits to the face through the infraorbital foramen.

Below and medial to the foramen rotundum, the pterygoid (vidian) canal (Fig. 9-5B) transmits the vidian nerve and vidian artery. The vidian nerve is formed by the joining of the superficial petrosal nerve (from the geniculate ganglion of the facial nerve containing parasympathetic and motor fibers) and the deep petrosal nerve, a branch from the sympathetic plexus on the internal carotid artery. The pterygoid nerve ends in the pterygopalatine ganglion.

The pharyngeal (palatovaginal) canal transmits the pharyngeal branch of the maxillary artery and the pharyngeal nerve, a branch of the pterygopalatine ganglion, to the roof of the pharynx. This nerve is distributed to the mucous membrane of the nasal part of the pharynx, behind the auditory tube.[1] The sphenopalatine foramen is on the medial wall of the pterygopalatine fossa. It is bounded above by the body of the sphenoid, in front by the orbital process of the palatine bone, behind by the sphenoidal process, and below by the upper border of the perpendicular plate of the palatine bone. It transmits the nasopalatine nerve and accompanying vessels from the pterygopalatine fossa to the nasal cavity.

FIGURE 9-7 Direct parasagittal CT scan shows lateral extension of inferior orbital fissure (*curved arrow*) into infratemporal fossa (*IF*). Note inferior oblique muscle (*white arrow*) and superior rectus muscle (*black arrow*).

VIEW IMAGE

The pterygopalatine canal extends from the inferior margin of the pterygopalatine fossa, at the junction of the anterior and posterior walls, to the greater palatine canal opening in the palate. The greater palatine canal transmits the greater (anterior) and lesser (middle and posterior) palatine nerves and the palatine vessels. In general, the pterygopalatine ganglion supplies parasympathetic innervation to the pharynx, palate, nasal cavity, and lacrimal gland.[4] Thus, in summary, the pterygopalatine fossa communicates with five major anatomic regions: (1) the nasal cavity via the pterygopalatine (sphenopalatine) foramen, (2) the oral cavity via the pterygopalatine canals, (3) the infratemporal fossa via the pterygomaxillary (retromaxillary) fissure, (4) the orbit via the inferior orbital fissure, and (5) the middle cranial fossa via the foramen rotundum and the vidian canal.

PERIORBITA

The periosteum of the bony orbit is known as the *periorbita* or the *orbital fascia*.[8] The periosteum is a specialized connective tissue structure that covers the bones. It consists of two strata: a superficial fibrous mantle and an active inner layer known as the *cambium*.[9] Duhamel is credited with the first scientific investigation of the osteogenic properties of the periosteum.[10] The periorbita (orbital fascia) is generally loosely adherent to the surrounding bones except at the anterior orbital margin, trochlear fossa, lacrimal crests, and margins of the fissures and canals.[1, 3, 4, 8] Anteriorly, it is continuous with the periosteum of the orbital margins (Figs. 9-6 to 9-8). Posteriorly, it is continuous with the dura of the optic nerve and the dura surrounding the superior orbital fissure. Thus, posteriorly located surgery or trauma may result in cerebrospinal fluid (CSF) leaks.[3] The dura matter is composed of a meningeal layer and a periosteal layer. These two layers are so closely bound together that they can be separated only with difficulty.[4, 7] After these layers pass through the optic foramen, however, they become separated. The meningeal layer continues as the sheath of the optic nerve, and the periosteal layer lines the bony orbit as the orbital fascia or periorbita. Numerous septae and fascial bands from various structures in the orbit are attached to the inner surface of this periosteum.[4] In front, the periorbita is fused with the orbital septum along the margins of the base (anterior rims) of the orbit.[5] The orbital septum is the continuation of the periosteum.[4, 8]

ORBITAL SEPTUM AND EYELIDS

The orbital septum is a thin sheet of fibrous tissue that forms the fibrous layer of the eyelids and is attached to the margins of the bony orbit, where it is continuous with the periorbita. In the upper eyelid, it fuses with the levator aponeurosis. In the lower eyelid, the orbital septum fuses with the capsulopalpebral fascia (see below) approximately 3 to 5 mm below the inferior tarsal border. The fused capsulopalpebral fascia/orbital septum complex, along with a small contribution from the inferior tarsal smooth muscle, inserts on both the posterior and inferior tarsal surfaces, as well as on the tapered inferior border of the tarsus.[5] The

Copyright © 2003, Mosby, Inc. All rights reserved.

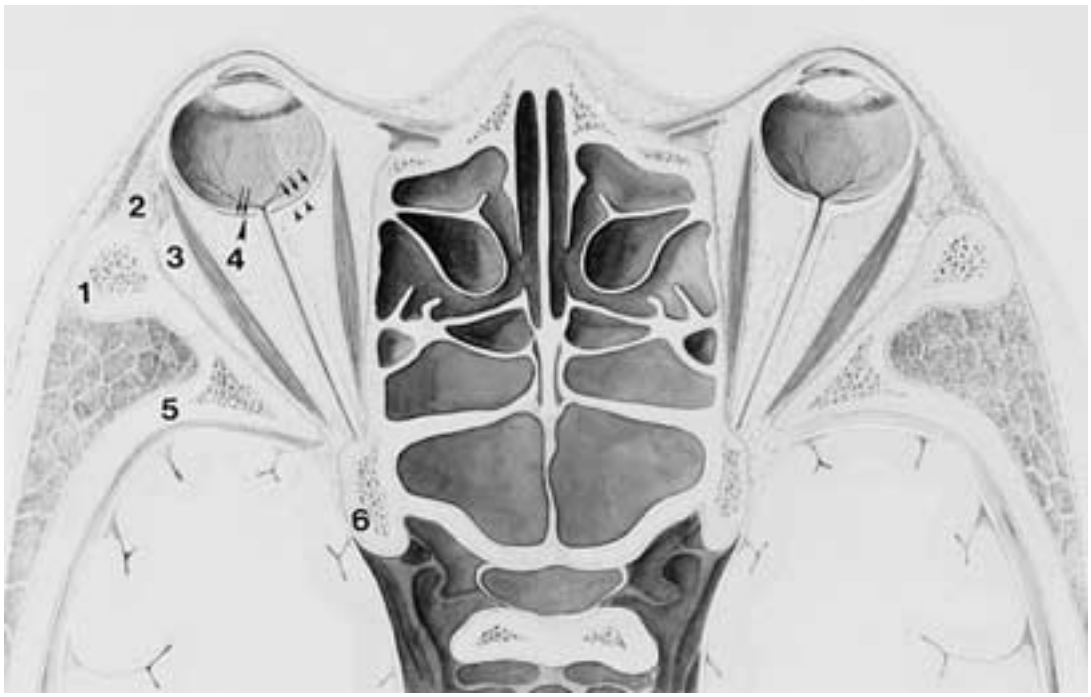

VIEW IMAGE

FIGURE 9-8 Diagram of the orbital-cranial region showing the zygomatic bone, (*1*); lacrimal gland, (*2*); peripheral orbital fatty reticulum, (*3*); central orbital fatty reticulum, (*4*); greater wing of the sphenoid, (*5*); lesser wing (anterior choroid) of the sphenoid, (*6*). Notice the retina (*three arrows*), choroid (*two arrows*), sclera (*arrowhead*), and Tenon capsule (*two arrowheads*).

palpebral portion of the orbicularis oculi muscle lies in front of the orbital septum (Fig. 9-8).[5] Moving from the skin inward toward the orbit, in general, each eyelid or palpebra consists of skin, subcutaneous areolar tissue, fibers of the orbicularis oculi, the tarsus and orbital septum, tarsal glands (meibomian), and conjunctiva. The conjunctiva is the transparent vascularized mucous membrane that covers the inner surfaces of the eyelids, and is reflected over the front part of the sclera and cornea.[1, 5] The line of reflection of the conjunctiva from the eyelids on the eyeball is called the *conjunctival fornix*. The palpebral conjunctiva is highly vascular, and its deeper part contains a considerable amount of lymphoid tissue, especially near the fornices. It is intimately adherent to the tarsi.[1] The ocular conjunctiva is loosely connected to the eyeball. On reaching the cornea, the ocular conjunctiva continues as the corneal epithelium.[1] The palpebral conjunctiva is covered by a nonkeratinized epithelium that contains the mucin-secreting goblet cells and the accessory lacrimal glands of Krause and Wolfring.[5] Secretions from these accessory glands form the major components of the lacrimal secretion, in contrast to the reflex tear secretion from the parasympathetically innervated main lacrimal gland.[5] Thus, anteriorly, the orbit can be considered as being closed by the orbital septum (Figs. 9-6, 9-8), which forms the fibrous layer of the eyelids. Within each eyelid, the orbital septum is thickened to form a tarsal plate. The levator palpebrae superioris has a broad anterior aponeurosis. Some of its fibers attach to the superior tarsal plate, while other terminal filaments interdigitate with the superior tarsal muscle (Müller's muscle), a smooth muscle that extends along the upper margin of the superior tarsal plate. As a result, some of the action of the levator palpebrae superioris must extend through Müller's muscle before it affects the superior tarsal plate. In Horner's syndrome, the ptosis associated with that syndrome occurs because Müller's muscle is paralyzed and the upper eyelid cannot be elevated until this muscle has been passively stretched out to its full length by the action of the levator palpebrae superioris. This results in end-stage ptosis and minimal lid elevation after the complete contraction of the levator palpebrae superioris. A few fibers of the inferior rectus muscle are attached to the lower edge of the inferior tarsal plate.[5, 6] Posteriorly, each plate is covered by conjunctiva and has meibomian glands (modified sebaceous glands) embedded in its deep surface.

The tarsal plates consist of dense connective tissue and serve as the skeleton of the eyelids. They are attached to the orbital margin by the lateral and medial palpebral ligaments. The length (22 mm) and thickness (1 mm) of the upper and lower tarsal plates are similar.[6] The upper tarsus is more than twice as wide (11 mm) as the lower tarsus.[6] The tarsal (meibomian) glands are modified sweat glands, and their oily secretion passes through small orifices into the tear film.

ORBICULARIS OCULI

The orbicularis oculi muscle is a flat, elliptical muscle that surrounds the orbital margin, extending onto the temporal region and cheek (orbital portion), onto the eyelids (palpebral portion), and behind the lacrimal sac (lacrimal portion) (Fig. 9-8). The palpebral portion of the orbicularis muscle consists of thin bundles of fibers that arise from the medial palpebral ligament (Fig. 9-8). The fibers sweep

Copyright © 2003, Mosby, Inc. All rights reserved.

laterally and concentrically across the eyelids and in front of the orbital septum. At the lateral angle of the eye, the fibers interlace at the lateral palpebral raphe.

TENON'S CAPSULE (FASCIA BULBI) AND TENON'S SPACE

Tenon's capsule is a fibroelastic membrane that envelops the eyeball from the optic nerve to the level of the ciliary muscle. Tenon's capsule is also called the *fascial sheath*, *fascia bulbi*, and *bulbar fascia* of the eyeball. This fibroelastic socket, which encloses the posterior four fifths of the eyeball, separates it from the central orbital fat (Figs. 9-6 and 9-8).[4, 8] Movement of the eyeball is facilitated by the fascia bulbi, which invests but does not adhere to the sclera. The bulbar fascia is discussed in Chapter 8.

ORBITAL FATTY RETICULUM

Within the orbit, all structures are embedded in a fatty reticulum. The fibroelastic tissue that makes up the reticulum divides the fat into lobes and lobules.[4–8] The fatty reticulum is divided into (1) peripheral orbital fat, which is outside the muscle cone and its intermuscular membranes (Figs. 9-4, 9-6, and 9-8), and (2) central orbital fat, which is within the muscle cone (Figs. 9-6 and 9-8).

EXTRAOCULAR MUSCLES

The six striated extraocular muscles, including the four recti and two oblique muscles, control eye movement (Figs. 9-6, 9-8). The rectus muscles arise from the annulus of Zinn, which is a funnel-shaped tendinous ring that encloses the optic foramen and the medial end of the superior orbital fissure, where it is continuous with the dural sheath of the optic nerve and periorbita.[3, 8–11] The annulus has an upper portion, called the *superior orbital tendon* or the *upper common tendon of Lockwood*, and a lower portion, called the *lower common tendon of Zinn*.[12] Because of this intimate relationship, apical disease frequently affects all of these structures simultaneously. In addition, surgical removal of optic nerve tumors must be done within the annulus, which is most safely entered superomedially after removing the orbital roof.[3] The inferior rectus muscle originates from the common tendon of Zinn below the optic foramen. It inserts into the inferior sclera 6.5 mm from the limbus. The superior rectus (the longest of the four recti) originates from the common tendon of Lockwood above the optic foramen and from the sheath of the optic nerve. It passes below the levator aponeurosis and inserts into the upper sclera 7.7 mm from the limbus. The medial rectus muscle (the thickest of the recti) arises from the upper tendon of Lockwood, the lower tendon of Zinn, and the sheath of the optic nerve and inserts 5.5 mm from the limbus.[11, 12] The lateral rectus originates from the lower common tendon of Zinn and the upper common tendon of Lockwood and inserts 6.9 mm from the limbus.[12] The superior oblique (longest and thinnest of the extraocular muscles) originates from the periosteum of the body of the sphenoid bone, above and medial to the annulus of Zinn and the origin of the medial rectus.[11, 12] It passes anteriorly along the upper part of the medial orbital wall as a slender tendon and enters the trochlea, a fibrocartilaginous ring lined with a synovial-type sheath.[13] The tendon slides through the trochlea and then turns sharply posterolaterally and downward beneath the superior rectus muscle to insert in the lateral sclera, behind the equator of the eye. The inferior oblique muscle is the only extrinsic eye muscle that originates not from the orbital apex but from a shallow depression in the orbital plate of the maxilla at the anteromedial corner of the orbital floor just posterolateral to the orifice of the nasolacrimal duct. It passes under the inferior rectus and runs posteriorly, laterally, and superiorly before inserting into the inferolateral aspect of the globe.[14] All extraocular muscles are about 40 mm in length except for the 37 mm inferior oblique.[15] One important difference among these muscles is the ratio of tendinous tissue to muscle fibers. The inferior oblique muscle contains essentially no tendon, and the superior oblique has 20 mm of tendon.[15]

Spiral of Tillaux

The four rectus muscles insert on the anterior portion of the globe in a configuration called the *spiral of Tillaux*.[6] The medial rectus muscle inserts closest to the limbus, and the superior rectus muscle inserts farthest from the limbus. The relationship between the muscle insertions and the ora serrata is clinically important, as a malpositioned bridle suture could pass through the insertion of the superior rectus muscle and perforate the retina.[6]

Retractors

The retractors of the upper eyelid are the levator muscle, the levator aponeurosis, and the sympathetically innervated superior tarsal muscle (Müller's muscle).[5] In the lower eyelid, the retractors are the capsulopalpebral fascia and the inferior tarsal muscle (Müller's muscle).[5]

Levator Muscle

The levator palpebrae superioris muscle originates in the apex of the orbit from the periorbita of the lesser wing of the sphenoid, just above the annulus of Zinn.[5] The body of the levator muscle overlies the superior rectus as it travels anteriorly toward the lid. The levator muscle and its tendon in adults is 50 to 60 mm long. The muscle portion, which is approximately 40 mm long, is innervated by the superior division of the oculomotor nerve and elevates the upper eyelid. The levator palpebra is often called the *seventh extraocular muscle*. The superior transverse ligament (Whitnall's ligament) is a condensation of the sheath of the levator muscle located in the approximate area of the transition from levator muscle to levator aponeurosis.[5] Whitnall's ligament functions primarily as a suspensory support for the upper eyelid and the superior orbital tissues.[5] Its analog in the lower eyelid is Lockwood's ligament.[5] As

Copyright © 2003, Mosby, Inc. All rights reserved.

the levator aponeurosis continues forward, it inserts into the anterior surface of the tarsus and by medial and lateral horns into the canthal tendons.[5, 6] The lateral horn of the levator aponeurosis is strong, and it divides the lacrimal gland into orbital and palpebral lobes, attaching firmly to the orbital tubercle.[5] As mentioned, the superior tarsal muscle (Müller's muscle) also inserts on the superior tarsal border, and this muscle provides approximately 2 mm of lift for the upper eyelid. If this muscle is paralyzed, as in Horner's syndrome, a mild proptosis will result.[5]

Lower Eyelid Retractors

The capsulopalpebral fascia is the lower eyelid analog to the levator palpebra muscle and aponeurosis.[5] It is a layer of dense connective tissue that originates at the capsulopalpebral head from the terminal muscle fibers and tendon of the inferior rectus muscle.[5] The capsulopalpebral head divides into two portions as it encircles and fuses with the sheath of the inferior oblique muscle. Anterior to the inferior oblique muscle, the two portions of the capsulopalpebral head join to form Lockwood's suspensory ligament, where it becomes known as the *capsulopalpebral fascia*.[5] The capsulopalpebral fascia fuses with the orbital septum. This fused fascial layer proceeds upward to insert on the inferior tarsus.[5]

Movements of Eyelid and Eyeball

The levator palpebra superioris is the main, striated voluntary muscle that elevates the upper eyelid. It is opposed by the orbicularis oculi.[1, 6] When the smaller inferior stratum of nonstriated Müller's muscle is denervated, it is responsible for the ptosis in Horner's syndrome. Blinking results in distribution of the lacrimal secretions. The height at which the upper lid is maintained is in part related to the brightness of the light entering the eye. In very bright conditions, the lid is lower, thereby limiting glare.

Within its fascial sheath, the eyeball is rotated by the extraocular muscles, which displace the gaze upward (elevation), downward (depression), medially (adduction), and laterally (abduction). Rotation about an anteroposterior axis (torsion) may also occur.[11, 12, 14, 15] The actions of the medial and lateral recti are adduction and abduction, respectively. They are antagonists, and by reciprocal adjustment of their lengths, the visual axis can be swept through a horizontal arc. The superior rectus muscle's primary action is elevation. This muscle also has a secondary, less powerful action of medial rotation (adduction).[1, 12] Its primary antagonist is the inferior rectus, which depresses and adducts the eyeball. The superior oblique muscle acts on the eyeball from the trochlea. Because the attachment of the inferior oblique is for practical purposes vertically inferior to this, both muscles approach the eyeball at the same angle, being attached in approximately similar positions in the superior and inferior posterolateral quadrants of the eyeball.[1] From these attachments, it is easy to understand that the inferior oblique elevates the gaze and the superior oblique depresses it. Both oblique muscles produce abduction.[1, 12] Like the superior and inferior recti, the two oblique muscles have opposed forces with respect to the other (antagonist). However, acting together, they can assist the lateral rectus in abduction of the visual axis.[1]

Blood Supply to the Extraocular Muscles

The blood supply for the extraocular muscles is derived from the inferior and superior muscular branches of the ophthalmic artery, the lacrimal artery, and the infraorbital artery. Except for the lateral rectus muscle, each rectus muscle receives two anterior ciliary arteries that communicate with the major arteriole circle of the ciliary body. The lateral rectus is supplied by a single vessel derived from the lacrimal artery.

OPTIC NERVE

The optic nerve is not a nerve but actually a nerve fiber tract of the central nervous system formed by over 1 million axons that originate in the ganglion cell layer of the retina.[6, 16] The nerve has an organization similar to that of the white matter of the brain. Its fibers are surrounded by glial rather than Schwann cell sheaths.[6, 16] The optic nerve (Fig. 9-6), along with the ophthalmic artery, traverses the optic canal and passes forward and laterally within the cone of rectus muscles to enter the eyeball just medial to its posterior pole. The optic nerve is about 3.5 to 5.5 cm long and about 3 to 4 mm in diameter.[3, 6] It is divided into four portions: intraocular (1 mm), intraorbital (3 cm), intracanalicular (5 to 6 mm), and intracranial (1 cm).[3] The intraocular portion can be divided into three parts: (1) prelaminar, (2) laminar, and (3) retrolaminar. The surface of the prelaminar portion is visible ophthalmoscopically. It is a 1.5×1.75 mm oval with a disc-shaped depression (the physiologic cup) located slightly temporal to its geometric center.[5, 6] The optic nerve head (optic disc) is composed of nonmyelinated axons from the retinal ganglion cells, blood vessels, and astrocytes that form a thin basal lamina on its inner surface. Myelinated nerve fibers in the retina result from oligodendrocytes that have migrated beyond the lamina cribrosa and have formed a lamellar envelope around ganglion cell axons.[5, 6] As ganglion cell axons enter the optic nerve head, they become segregated into bundles or fascicles by neuroglial cells. These astrocytes enclose groups of nerve fibers throughout the ocular and orbital portions of the optic nerve.[5] The bundles continue to be separated by connective tissue all the way to the chiasm. This connective tissue is derived from the pia mater and is known as the *septal tissue*.[5, 6] The retinal layers terminate as they approach the edge of the optic disc. The laminar portion of the optic disc is composed of astrocytes, elastic fibers, collagenous connective tissue from the scleral lamina, and small blood vessels. The lamina cribrosa functions as a scaffold for the optic nerve axons. The retrolaminar portion extends from the lamina cribrosa to the apex of the orbit. From the lamina cribrosa centrally, the retinal ganglion cells become myelinated as the cross-sectional diameter of the nerve increases to approximately 3 mm. After passing through the optic canal, the optic nerves lie above the ophthalmic arteries, and above and medial to the internal carotid artery. The anterior cerebral arteries cross over the optic nerves and are joined by

Copyright © 2003, Mosby, Inc. All rights reserved.

the anterior communicating artery. The optic nerves then pass posteriorly to join in the optic chiasm.

Meningeal Sheaths (Dura, Arachnoid, Pia)

The dura, the outer layer, is composed of collagenous connective tissue. The arachnoid is made up of fine collagenous fibers arranged in a loose meshwork lined by endothelial cells. The innermost layer, the pia, is made up of fine collagenous and elastic fibers and is highly vascularized. Elements from both the arachnoid and the pia are continuous with the optic nerve septa. The pial septa, which originate in the region of the posterior lamina cribrosa, enclose all neurofascicles. The septa continue throughout the orbital and intracanalicular portion of the nerve and end in the intracranial portion. They are composed of collagen, elastic tissue, fibroblasts, nerves, and small arterioles and venules. They provide mechanical support for the nerve bundles and nutrition to the axons and glial cells. Meningothelial cells cover the pia mater. The arachnoid mater is continuous with the subarachnoid space. It ends at the level of the lamina cribrosa. It is composed of collagenous tissue, small amounts of elastic tissue, and meningothelial cells. The dura mater encases the optic nerve and comprises the outer layer of the meningeal sheaths. It is 0.3 to 0.5 mm thick and consists of dense bundles of collagen and elastic tissue fused anteriorly with the outer layers of the sclera. The meninges of the optic nerve are supplied by sensory fibers, which accounts for the pain experienced by patients with inflammatory optic nerve diseases.

Blood Supply of the Optic Nerve

The prelaminar and lamina cribrosa regions are supplied by branches of the posterior ciliary arteries, while the surface of the optic disc is supplied by retinal arterioles that are branches of the central retinal artery or from branches of small cilioretinal arteries.[5, 6, 16] The intraorbital part of the optic nerve is supplied by intraneural branches of the central retinal artery and multiple recurrent pial branches arising from both the peripapillary choroid and the central retinal and ophthalmic arteries.[5] The intracanalicular portion of the optic nerve is supplied almost exclusively by the ophthalmic artery. The intracranial portion of the optic nerve is supplied primarily by branches of both the internal carotid artery and the ophthalmic artery. The actual distance from the back of the globe to the orbital apex is 20 mm. Thus, from the optic foramen, the optic nerve takes a tortuous, S-shaped course to the back of the globe. This longer length of the optic nerve allows movement of the eye without tension on the nerve. As mentioned, the intraorbital portion of the optic nerve increases to 3 mm in diameter due to myelination of the nerve fibers and surrounding meningeal sheaths. The orbital portion of the optic nerve lies within the muscle cone. Before passing into the optic canal, the nerve is surrounded by the annulus of Zinn, formed by the origins of the rectus muscles. The superior and medial rectus muscles partially originate from the sheath of the optic nerve. This may explain why patients with retrobulbar neuritis complain of pain when moving their eyes.[5] As previously mentioned, the optic nerve is covered by three layers: the pia mater, the arachnoid, and the dura, which sheathe the nerve and extend from the optic canal forward to the globe. The pia mater is highly vascular and is attached tightly to the optic nerve.[16, 17] The subarachnoid space is filled with CSF in continuity with the intracranial subarachnoid space. The subdural space surrounding the optic nerve, however, has no direct connection to the intracranial subdural space.[16, 17] The optic nerve is fixed to the apex of the orbit by fusion of the pia mater, the arachnoid membrane, and the dura mater to the periosteum at the optic canal.[17] At the optic canal, the dural sheath of the nerve fuses to the periosteum so that the nerve is completely immobilized.[5] The ophthalmic artery is encased by dura in the optic canal, where it lies inferolateral to the nerve. At the orbital end of the canal, it loses the dural coat and crosses medially in the intraconal space.[17]

PERIPHERAL NERVES

Several nerves reach the orbit from the middle cranial fossa and the pterygopalatine fossae. The optic nerve traverses the optic canal. Other nerves gain access to the orbit through the orbital fissures.

SENSORY INNERVATION

The major sensory innervation of the orbit is via the ophthalmic (V_1) and maxillary (V_2) divisions of the trigeminal nerve. The trigeminal nerve is the largest cranial nerve and possesses both sensory and motor divisions. The sensory portion (V_1 and V_2) subserves the greater part of the scalp, forehead, face, eyelids, eyes, lacrimal gland, extraocular muscles, ears, and dura. The motor portion innervates the muscles of mastication and the tensor tympani through the branches of the mandibular nerve. The trigeminal nuclear complex extends from the midbrain to the upper cervical segments, often as caudal as C_4.[5, 6] The cell bodies of the ophthalmic nerve are in the semilunar (Gasserian) ganglion. From the ganglion, the nerve courses along the lateral wall of the cavernous sinus, below the oculomotor and trochlear nerves, and enters the orbit through the superior orbital fissure. The ophthalmic nerve, before entering the orbit, divides into lacrimal, frontal, and nasociliary nerves, each of which enters the orbit through the superior orbital fissure.[3, 6] The frontal (largest branch) and lacrimal (smallest branch) branches of the ophthalmic nerve enter the orbit outside of the annulus of Zinn and run forward between the periorbita and the levator complex to supply the forehead and lacrimal gland. The nasociliary branch is intraconal, crosses medially over the optic nerve, continues forward along the medial wall of the orbit below the superior rectus and superior oblique muscles, and terminates as the ethmoidal (anterior and posterior) and infratrochlear nerves.[6] Its branches include one to the ciliary ganglion and two long ciliary nerves.[3, 6] The long ciliary nerves carry sympathetic vasoconstrictor fibers to supply vessels within the eyeball.[6]

Copyright © 2003, Mosby, Inc. All rights reserved.

MOTOR INNERVATION

Oculomotor Nerve (III)

The nucleus of the oculomotor nerve is in the midbrain tegmentum. The nerve appears in the interpeduncular fossa, courses above the other nerves in the most cephalic, lateral wall of the cavernous sinus, and enters the orbit through the superior orbital fissure. It has superior and inferior divisions, which are often formed before entering the orbit.[6] The nerve enters the muscle cone within the annulus of Zinn as a superior division (supplying the levator and superior rectus) and an inferior division (supplying the medial and inferior recti and the inferior oblique).

Trochlear Nerve (IV)

The nucleus of the trochlear nerve is in the midbrain tegmentum. Its fibers leave the central nervous system through the anterior medullary velum dorsally, cross to the opposite side, and pass rostrally and caudally to run in the lateral wall of the cavernous sinus between the oculomotor (III) and ophthalmic (V_1) nerves. The trochlear nerve then crosses the oculomotor nerve and passes through the superior orbital fissure above the other nerves to supply the superior oblique muscle.[5, 6]

Abducens Nerve (VI)

The nucleus of the abducens nerve is in the tegmentum of the pons. Its fibers leave the central nervous system in the ventral groove between the medulla and pons, and pass through the cavernous sinus between the internal carotid artery and the ophthalmic nerve (V_1). The abducens nerve then enters the orbit through the superior orbital fissure and passes forward on the inner surface of the lateral rectus, which it supplies.[5, 6]

OTHER NERVES

The seventh cranial nerve is the motor supply for the orbicularis oculi and its sensory division; the nervus intermedius gives the parasympathetic supply to the lacrimal gland. The facial nerve enters the parotid gland and then divides into upper temporal facial and lower cervical facial branches. It innervates the orbicularis via the upper division, which forms the temporofrontal and zygomatic branches.[3]

AUTONOMIC NERVES

The ciliary ganglion lies 1.5 to 2 cm behind the eyeball, lateral to the optic nerve and medial to the lateral rectus muscle. The ciliary ganglion measures about 1 to 2 mm in diameter. It receives sensory fibers from the nasociliary nerve, parasympathetic fibers from the oculomotor nerve, and sympathetic fibers from the internal carotid plexus in the cavernous sinus (via the superior orbital fissure).[3, 6] Only the parasympathetic fibers synapse in the ganglion. The sensory root subserves the cornea, iris, and ciliary body through short ciliary nerves that pass from the anterior part of the ciliary ganglion into the eyeball.[6] The parasympathetic fibers supply the ciliary muscle and iris sphincter (constricts pupil). The preganglionic fibers of the parasympathetics to the sphincter muscle arise in the Edinger-Westphal nucleus of the midbrain, travel with the oculomotor nerve, and run in its inferior division to end by synapsing in the ciliary ganglion. The postganglionic fibers arise from cells of the ciliary ganglion and leave the ganglion by short ciliary nerves that pierce the sclera and run to the iris. The sympathetic fibers supply ocular vessels, the iris dilator (by means of the ciliary nerves), the lacrimal gland, and the sympathetic muscles (Müller's muscles) of the upper and lower eyelids. The sympathetic fibers to the dilator pupillae muscle pass through the ciliary ganglion without synapse and run with the short ciliary nerves. The preganglionic fibers of the sympathetics to the dilator pupillae arise in the intermediolateral gray column of the upper thoracic cord, enter the sympathetic trunk, and ascend in the cervical sympathetic trunk to end by synapses in the superior cervical ganglion.[5] The postganglionic fibers arise in cells of the superior cervical ganglion and ascend through the carotid and cavernous nervous plexuses. Some fibers join the ophthalmic nerve to continue in its nasociliary branch and are carried to the eye with the long ciliary branches of this nerve. Other fibers from the cavernous plexus enter the sympathetic ''root'' of the ciliary ganglion, pass through this ganglion without synapse, and run with the short ciliary nerves.[5] Still other intraorbital sympathetic fibers travel with the oculomotor nerve to the smooth muscle component of the levator palpebrae superioris and inferior recti (Müller's muscles).[6]

The preganglionic parasympathetic fibers of the lacrimal gland arise from cells in the superior salivatory nucleus and run in the nervus intermedius with the facial nerve. They then leave the facial nerve, at the geniculate ganglion, as the greater superficial petrosal nerve, which becomes part of the nerve of the pterygoid (vidian) canal, to enter and synapse in the pterygopalatine ganglion. The postganglionic fibers arise from the cells of the pterygopalatine ganglion, pass through the pterygopalatine nerves to the maxillary nerve, and then pass through the zygomatic branch of this nerve.[5] These fibers then enter the zygomaticotemporal branch of the zygomatic nerve in the orbit and communicate with the lacrimal branch of the ophthalmic nerve to reach the lacrimal gland. The preganglionic sympathetic fibers of the lacrimal gland arise in the intermediolateral gray column of the upper thoracic cord, enter the sympathetic trunk, ascend in the cervical sympathetic trunk, and end by synapses in the superior cervical ganglion.[5] The postganglionic sympathetic fibers arise in cells of the superior cervical ganglion, pass through the carotid plexus, and continue rostrally in the deep petrosal nerve, to join the superficial greater petrosal nerve to become the pterygoid (vidian) nerve. Then the fibers pass through the pterygopalatine ganglion, without synapse, and are distributed in a manner similar to that of the postganglionic parasympathetic fibers to reach the lacrimal gland.[5]

Copyright © 2003, Mosby, Inc. All rights reserved.

VASCULAR ANATOMY

The major arterial supply to the orbit is from branches of the ophthalmic artery. This artery usually arises from the distal end of the cavernous sinus segment of the internal carotid artery. Rarely, it may arise from the middle meningeal artery and enter the orbit through the superior orbital fissure.[3] In the optic canal, it courses below and lateral to the optic nerve within the dural sheath, and at the orbital apex it penetrates laterally through the dura. In 82.6% of subjects it crosses to the medial orbit over the optic nerve, and in the remaining 17.4% of subjects the artery courses under the nerve.[3] The branches of the ophthalmic artery, with some variations in origin, are the lacrimal, supraorbital, anterior and posterior ethmoidal, nasofrontal, and dorsonasal arteries. The branches for the eyeball include the central artery of the retina and the ciliary arteries. The central artery of the retina is the first branch of the ophthalmic artery.[6] It crosses the optic nerve, pierces it, and runs in its center to spread over the retina.[5] The ciliary arteries are arranged in three groups: short posterior ciliary, long posterior ciliary, and anterior ciliary arteries.[5] The posterior ciliary arteries supply the globe via 15 to 20 short (to the choroid and ciliary processes and the optic nerve head) and 2 long (to the ciliary muscle, iris, and the anterior choroid) branches.[3] The long posterior ciliary arteries enter the sclera on either side of the optic nerve and run between the choroid and sclera to the ciliary body, where their branches form the anterior major arterial circle. The anterior ciliary arteries arise from the muscular branches that run with the tendons of the recti muscles and form the vascular zone under the conjunctiva. These arteries then pierce the sclera to join the major arterial circle.[5] The lacrimal artery branches into the recurrent meningeal, zygomatic, glandular, and lateral palpebral arteries (which form the arcades of the lid). The ophthalmic artery frequently has anastomotic branches to the external carotid system, by means of the middle meningeal and lacrimal arteries, which pass through the superior orbital fissure, and by means of the anterior deep temporal, superficial temporal, and lacrimal arteries.[3]

VENOUS DRAINAGE OF THE ORBIT AND EYEBALL

The venous blood from the eyeball and adjacent structures drains into the valveless inferior and superior ophthalmic veins. The superior ophthalmic vein drains into the cavernous sinus via the superior orbital fissure. The inferior ophthalmic vein passes through the inferior orbital fissure, anastomosing with the pterygoid venous plexus.[1, 3, 6] Both the superior and inferior ophthalmic veins communicate with the veins of the face.[1, 6] The superior ophthalmic vein is the larger of these two veins and arises behind the medial part of the upper eyelid by the union of a branch from the supraorbital vein and a branch from the facial vein (angular, supraorbital). The branch from the supraorbital vein enters the orbit through the supraorbital notch, while the branch from the facial vein pierces the orbital septum. The superior ophthalmic vein receives tributaries that correspond to most of the branches of the ophthalmic artery. It communicates with the central vein of the retina, and near the apex of the orbit it commonly receives the inferior ophthalmic vein. The superior ophthalmic vein also receives the two vorticose veins from the upper part of the eyeball (the vorticose veins correspond to the posterior ciliary veins). It has three sections, the first extending posterolaterally to the medial border of the superior rectus. The second section enters the muscle cone and passes superolaterally to the optic nerve and beneath the superior rectus muscle. The third section extends posteromedially along the lateral border of the superior rectus and extends to the superior orbital fissure.[3] The more variable inferior ophthalmic vein arises from a venous plexus on the anterior part of the floor of the orbital cavity. It communicates with the facial vein over the inferior orbital margin and with the pterygoid venous plexus through the inferior orbital fissure. It passes posteriorly in the orbital fat on the inferior rectus muscle and receives muscular branches and the two inferior vorticose veins from the lower part of the eyeball. The inferior ophthalmic vein often forms inferolaterally as a plexus and passes posteriorly adjacent to the inferior rectus muscle. It anastomoses with the superior ophthalmic vein and has a similar branch that connects with the pterygoid plexus through the inferior orbital fissure.[3] It may pass through the lower part of the superior orbital fissure and empty directly into the cavernous sinus.

LACRIMAL APPARATUS

The lacrimal gland lies in the superolateral angle of the orbit, in a shallow fossa (lacrimal fossa) behind the upper eyelid, and is deeply indented by the lateral border of the tendon of the levator palpebra superioris (Fig. 9-8).[1, 3, 17] The gland weighs 78 g and measures $20 \times 12 \times 5$ mm.[3] It is divided into palpebral and orbital (larger) lobes by the lateral border of the levator aponeurosis.[3] The orbital lobe is superior to the palpebral lobe. Small ducts (10 to 12) open from the deep surface of the gland into the conjunctival sac, and resection of the palpebral lobe functionally destroys the gland.[3] This is important to remember when attempting to biopsy the lacrimal gland. The borders of the gland are related anteriorly to the orbital septum, posteriorly to the periorbital fat, and medially to the superior rectus, globe, and lateral rectus (Fig. 9-8). The inferior surface rests on the lateral rectus.[3] The lacrimal gland is a serous gland. The gland has a nodular surface with a fine connective tissue pseudocapsule.[3] The gland is supported by Whitnall's ligament and by septal attachments to the superior periorbita. The lacrimal artery penetrates it posteriorly, and the vein from it drains into the superior ophthalmic vein. Its lymphatic drainage is by means of the lid and conjunctiva to the preauricular nodes.[3] The lacrimal nerve, and sometimes branches of the zygomatic nerve, carry the sensory afferents. The parasympathetic efferents are by the nervus intermedius, facial, greater superficial petrosal, vidian, sphenopalatine ganglion, infraorbital, and lacrimal nerves.[1, 3] The sympathetic efferents are from the internal carotid plexus through the sphenopalatine (pterygopalatine) ganglion. In addition to the main lacrimal gland, there are accessory glands (of Krause and Wolfring) in the lids and conjunctiva.

Copyright © 2003, Mosby, Inc. All rights reserved.

There are 20 to 40 glands of Krause in the upper fornix and 6 to 8 in the lower fornix. The glands of Wolfring are fewer, consisting of three at the upper border of the superior tarsus and one at the lower border of the inferior tarsus.[3] Tears produced by the gland pass medially toward the lacrimal puncta across the surface of the cornea, assisted by blinking of the eyelids. Evaporation of the fluid is retarded by the oily secretion of the tarsal glands. Tears are drained into the lacrimal sac through the lacrimal canaliculi of the upper and lower lids. The canaliculi originate at the puncta and have a 2 mm vertical portion and an 8 mm horizontal portion, which join into a common canaliculus. The superior canaliculus first is directed upward, then medially and downward. The inferior canaliculus first descends and then is directed medially. The common canaliculus enters the lateral wall of the lacrimal sac by means of the valve of Rösenmuller, which prevents reflux.[3] The lacrimal sac lies in the lacrimal groove, which is formed by the lacrimal bone and the frontal process of the maxillary bone.[1] The lacrimal canaliculi are lined by squamous epithelium, whereas the sac and nasolacrimal duct are lined by columnar epithelium, goblet cells, and ciliated cells. The lacrimal sac is 13 to 15 mm in vertical length. The tears drain through the nasolacrimal duct just beneath the inferior turbinate through a fold in the duct (called the *valve of Hasner*) in the lateral wall of the nasal cavity (also see Chapter 10).[3]

TECHNIQUE FOR ORBITAL CT AND MR IMAGING

General Considerations

CT and MR imaging are the two modalities commonly used for imaging the orbit. Each has advantages and disadvantages. In general, CT is the modality of choice for bony detail and for detecting calcifications and foreign bodies, but irradiation to the orbital structures is a disadvantage. The radiation dose to the lens, although less than that of a complex motion tomography orbital series, averages about 5 cGy per imaging plane. MR imaging, on the other hand, has no known biologic side effects and is superior to CT when evaluating soft-tissue detail in the globe. MR imaging is generally considered equivalent to or slightly better than CT when evaluating the orbital soft tissues. However, MR imaging should not be used for the evaluation of the orbit whenever a ferromagnetic foreign body is suspected to be present.

Computed Tomography

A routine CT examination of the orbits includes contiguous axial and coronal sectioning with a 3 mm slice thickness. When there is a suspicion of a smaller lesion, thinner sections (two 1 mm sections) should be obtained. Such thin sections are essential for optimal demonstration of the optic nerve's anatomy and pathology. Thin slices have the advantage of less volume averaging and thus provide finer spatial resolution. The radiologist should always tailor the examination according to the clinical information and the preliminary diagnosis. For foreign bodies, it is important to obtain 1.0 to 1.5 mm axial sections to increase the sensitivity for detection of smaller objects. Provided there is no patient motion, it is often unnecessary to obtain additional direct coronal sections for the localization of foreign bodies because the use of computer reformatting is helpful in producing images in other planes, especially if a multidetector scanner is utilized. For foreign bodies or lesions at the 6 or 12 o'clock position in a coronal view, it may be advisable to obtain direct coronal sections. However, the use of multidetector CT may obviate the need for such multiplanar acquisitions. For lesions of the globe, thin sectioning (1.0 to 1.5 mm) is exceedingly important, because one can easily miss an ocular lesion on routine 5 mm sections.[17] For bony lesions or orbital fractures, in addition to the routine study, retrospective high-resolution extended bone scale images should be obtained (4000 ms window width, 700 to 800 window level).[17]

For orbital CT scanning, the need for intravenous (IV) contrast medium administration should be determined by the clinical information and is best left to the discretion of the radiologist. Contrast material uniformly increases the density of most intraorbital soft-tissue structures.[18] Although it is not always easy to discriminate between orbital lesions based on their patterns of enhancement, contrast material is often necessary to evaluate their vascular characteristics and, more importantly, to evaluate any intracranial extension of an orbital lesion. Not uncommonly, an apical orbital mass may be an extension of an intracranial lesion such as a meningioma, which can be readily missed on a noncontrast CT study. In general, a contrast medium is not used when evaluating for foreign bodies, uncomplicated orbital fractures, uncomplicated thyroid ophthalmopathy, morphologic changes in or variations of the extraocular muscles, dermoid cysts (noninfected and unruptured), and bony lesions such as osteoma, osteoid osteoma, fibrous dysplasia, and Paget's disease. Contrast-enhanced CT is usually necessary in patients with osteogenic or chondrogenic sarcomas or metastatic bone disease.

The axial sections normally are obtained roughly parallel to the infraorbital-meatal line.[17, 18] This can be easily determined by obtaining a lateral digital scout view (scanogram). The inferior section should include the upper portion of the maxillary sinuses, and the upper section should include the sella and the entire frontal sinuses. For all orbital and ocular tumors, additional postcontrast 10 mm axial sections of the remainder of the head are usually obtained. Although brain metastasis from orbital and ocular tumors is uncommon, the additional sections may provide information about unsuspected lesions (meningioma, aneurysm, and arteriovenous malformation).[17] The coronal sections are obtained roughly perpendicular to the infraorbital-meatal line. However, in many instances, the angle of the coronal sections is made more oblique (semicoronal) when the patient has many dental fillings or other metallic prostheses. Patient positioning for imaging in the coronal plane can be in either the prone or supine position, and as for the axial sections, the coronal plane study can be determined easily by obtaining a lateral digital scout view of the orbit. The coronal examination of the orbits should be tailored according to the clinical information and the findings on the axial sections. In patients suffering from visual loss and when evaluating the

Copyright © 2003, Mosby, Inc. All rights reserved.

intracranial extension of an apical lesion, the coronal sections should be extended posteriorly to include the optic chiasm. For lesions involving the anterior ethmoid air cells and nasal cavity, and for lesions arising from the nasolacrimal sac and duct, coronal sections should be extended anteriorly to include the nasal bones.

Almost all CT scanners are capable of performing computer reformation of compiled data from axial sections into coronal, sagittal, or oblique planes. Although the quality of the images may be inferior to those obtained with direct scanning, in many instances additional information can be obtained, particularly if high-quality, thin (1.5 to 3 mm) direct axial or coronal sections are available. It should be noted, however, that the quality of such images on the newer multidetector CT scanners is excellent. If a multidetector scanner is not available, direct sagittal plane scans of the craniofacial structures can be achieved by laying the patient on a separate support and using a special head holder that is fitted to the standard tabletop.[19, 20]

MR Imaging Techniques

Almost all of the MR images presented in this section were obtained with a 1.5 Tesla Signa unit (General Electric, Milwaukee). Using a head coil, single echo spin-echo (SE) pulse sequences were obtained with a repetition time (TR) of 400 to 800 ms and an echo time (TE) of 20 to 25 ms (TR/TE, 400 to 800/20 to 25 ms). Multiecho SE pulse sequences were obtained with a TR of 1500 to 2800 ms and a TE of 20 to 100 ms. Although each examination should be specifically tailored to the patient's problem, the routine MR imaging examination of the orbit should include short TR, short TE sagittal images, 4 to 5 mm in thickness with 1 to 1.5 mm intersection spacing, using the routine head coil. These studies were most often performed with one excitation, a 256×192 or 256×256 matrix size, and a 20 to 24 cm field of view. Following the sagittal T1-weighted scans, an axial multiecho SE sequence (TR/TE 2000 to 2800/20, 80 ms) was obtained to include the entire orbital structures. For this multiecho SE pulse sequence, a section thickness of 4 to 5 mm with a 1.5 to 2.5 mm intersection gap was used, with a matrix size of 256×192 and a 20 cm field of view. An additional single echo or multiecho SE sequence in the coronal plane was obtained according to the findings on the sagittal and axial sections. Because T1-weighted images provide more spatial resolution than T2-weighted images, if more anatomic detail is essential, coronal T1-weighted images are preferred. On the other hand, T2-weighted images provide more contrast resolution than T1-weighted images, and if there is a need for more pathologic detail, coronal multiple SE pulse sequences are obtained (TR/TE, 2000/20, 80 ms). For optic nerve lesions, additional parasagittal images are obtained by using a head coil. For some of the orbital lesions, additional images were obtained using a surface coil. Images with a surface coil provide better spatial resolution than images obtained with a head coil. However, because of signal dropout, an apical lesion or intracranial extension of an orbital lesion cannot be fully evaluated. Paramagnetic contrast material, a gadolinium complex of diethylenetriamine pentaacetic acid (Gd-DTPA), should be used for suspected orbital abscesses, meningiomas, schwannomas, neurofibromas, hemangiopericytomas, fibrous histiocytomas, lacrimal gland tumors, metastases, lymphomas, pseudotumors, other specific or nonspecific orbital masses, and optic nerve lesions including optic neuritis. Contrast-enhanced, T1-weighted studies were obtained with an axial SE 600 to 800/20 (TR/TE) sequence with four excitations, a 16 to 20 cm field of view, and a 256×128 matrix size. Section thickness was 3 mm with a 0.5 mm intersection gap. A precontrast T1-weighted axial SE sequence was always obtained. This pulse sequence was identical to the postcontrast T1-weighted sequence, except that two rather than four excitations were used.

Inversion Recovery and Application of Fat-Suppression Technique

Short tau inversion recovery (STIR) images result in very high lesion conspicuity by suppressing the signal from fat and by adding T1-weighted and T2-weighted information together. Because most pathology has a long T1 and T2 relaxation time, pathology appears with a high signal intensity on STIR. Further, the lower fat signal intensity makes any pathology stand out. The optimal TI (time of inversion) for fat suppression may vary from one individual to another, depending on coil loading and fat composition. The optimal TI for fat suppression at 1.5 Tesla is in the 145 to 170 ms range. Usually the STIR image is obtained with a TR of 2000, a TI of 150 to 160, and a TE of 20 ms.

T1-Weighted Fat-Suppression Technique

Fat-suppressed T1-weighted images may be obtained using various techniques.[21, 22] In this chapter, fat-suppressed T1-weighted images were obtained using a presaturation technique. Before imaging, the spectral fat peak was determined in each patient. Subsequently, an RF pulse was applied, centered at the resonant frequency of fat. The RF pulse was followed by a spoil gradient. This fat-suppression technique (chemsat) is a standard feature on the Signa system and can be easily applied in the same time required for a standard T1-weighted sequence. After the postcontrast fat-suppressed images were obtained, a standard T1-weighted sequence in either the axial or coronal plane, with the same parameters used for the fat-suppressed T1-weighted images, was immediately obtained. This was done because the fat-suppression pulse sequences are more sensitive to magnetic susceptibility artifacts.[21–23] In addition, the enhancement of the extraocular muscles, and in particular the lacrimal glands, is exaggerated on the fat-suppressed images. There is thus the possibility of misinterpreting a lesion if it is adjacent to the lacrimal gland, the extraocular muscles, or the walls of the sinuses (air–bone–soft-tissue interface).[17]

Normal CT and MR Imaging Anatomy

The bony landmarks can be visualized best on CT with the aid of the bone extended scale and bone window technique (Fig. 9-9). The optic canal can be seen on both axial and coronal scans. The lateral and medial bony orbital margins, the superior and inferior orbital fissures, the lacrimal fossa, lacrimal sac, nasolacrimal canal, infraorbital canal, and paranasal sinuses are also equally well seen on

Copyright © 2003, Mosby, Inc. All rights reserved.

FIGURE 9-9 Nasolacrimal canals. Coronal CT scan shows nasolacrimal canals (*arrows*). Note the anterior ethmoid cells (*E*).

VIEW IMAGE

axial or coronal scans (Fig. 9-9). Coronal scans are best for assessing the floor and roof of the orbits. The lamina papyracea is a paper thin plate of bone that forms most of the medial orbital wall, separating it from the adjacent ethmoid air cells. This plate often appears to be dehiscent on CT, and therefore care should be taken not to make an erroneous diagnosis of bone destruction or fracture.

Extraocular Muscles

The extraocular muscles are well visualized on CT, and they are uniformly enhanced on postcontrast CT scans (Figs. 9-10 to 9-13). These muscles are also seen well on MR imaging (Figs. 9-14 to 9-26). The extraocular muscles generally have a course parallel to that of the adjacent orbital wall. Consequently, only the horizontal recti (lateral and medial) may be seen in their entirety in the axial plane (Figs. 9-12 and 9-16). Likewise, the vertical recti (inferior and superior) may be seen best in the parasagittal (oblique) plane (Figs. 9-6, 9-7, and 9-27). The tapering of these muscles in

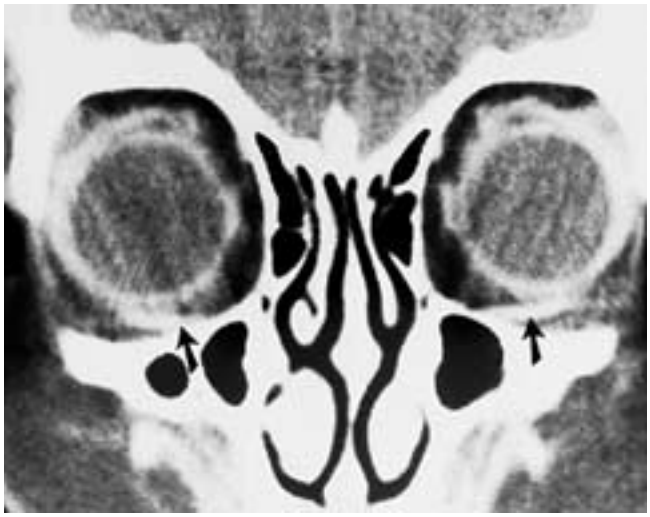

FIGURE 9-10 Inferior oblique muscles. Coronal CT scan shows inferior oblique muscles (*arrows*).

VIEW IMAGE

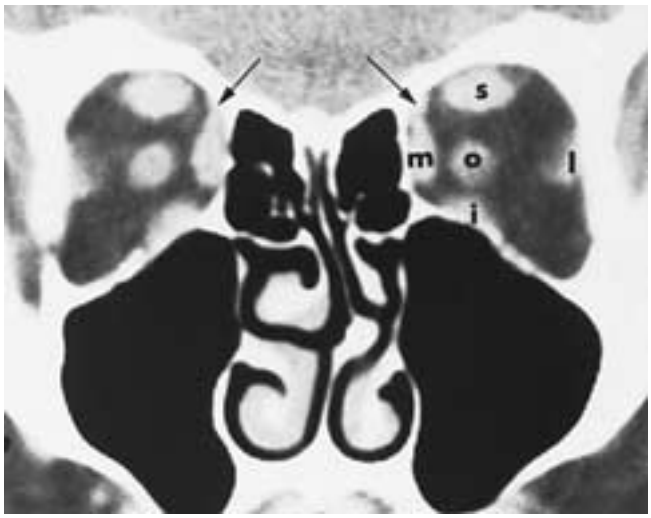

FIGURE 9-11 Extraocular muscles. Coronal CT scan shows inferior rectus muscle (*i*); lateral rectus muscle (*I*); medial rectus muscle (*m*); and superior rectus muscle (*s*). Note the superior oblique muscles (*arrows*) and optic nerve (*o*).

VIEW IMAGE

their tendinous portions and their origins at the annulus of Zinn are seen well in the parasagittal (vertical recti) and axial (horizontal recti) planes (Figs. 9-6 and 9-16). The superior and inferior recti are only partially visualized in any one axial plane (Figs. 9-14, 9-15, 9-20, and 9-21). On coronal scans, all of the recti muscles are seen in an oblique cross section (Figs. 9-22 and 9-24) related to their slanted orientation to the coronal plane as the walls of the orbit slant toward the orbital apex. For accurate determination of the cross-sectional size of these muscles, reformatted images or direct oblique MR imaging would have to be done separately for each muscle. This is obviously not practical, nor is it necessary unless there is a critical situation requiring the precise size of a particular muscle.[15] The levator palpebrae superioris is closely approximated to the superior rectus muscle, and it is identified as a separate muscle only on anterior coronal images (Fig. 9-22), where it diverges from the superior rectus. These two muscles can be visualized as separate muscles on sagittal and parasagittal (oblique) MR imaging (Fig. 9-27). The muscle portion of the superior oblique muscle can be visualized best on coronal scans, and its tendinous portion is seen best on axial scans (Figs. 9-11, 9-13, and 9-23). The reflected portion of the superior oblique muscle and its tendon are seen best on axial scans (Figs. 9-13 and 9-20). The trochlea is seen well on axial scans, and it is occasionally calcified. The inferior oblique muscle is seen best on coronal, sagittal, and parasagittal scans (Fig. 9-10). On axial scans the muscle belly is poorly seen, but its insertion is well visualized.

Orbital Compartments

In descriptive terms, the orbit has been divided into the extraperiosteal, subperiosteal, extraconal, conal, and intraconal spaces (Boxes 9-1 to 9-3). The intraconal space is separated from the other spaces by the rectus muscles and their intermuscular septa, which are denser in the anterior orbit and are seen best on coronal scans (Figs. 9-22 and 9-23). Because certain lesions have a predilection to present

Copyright © 2003, Mosby, Inc. All rights reserved.

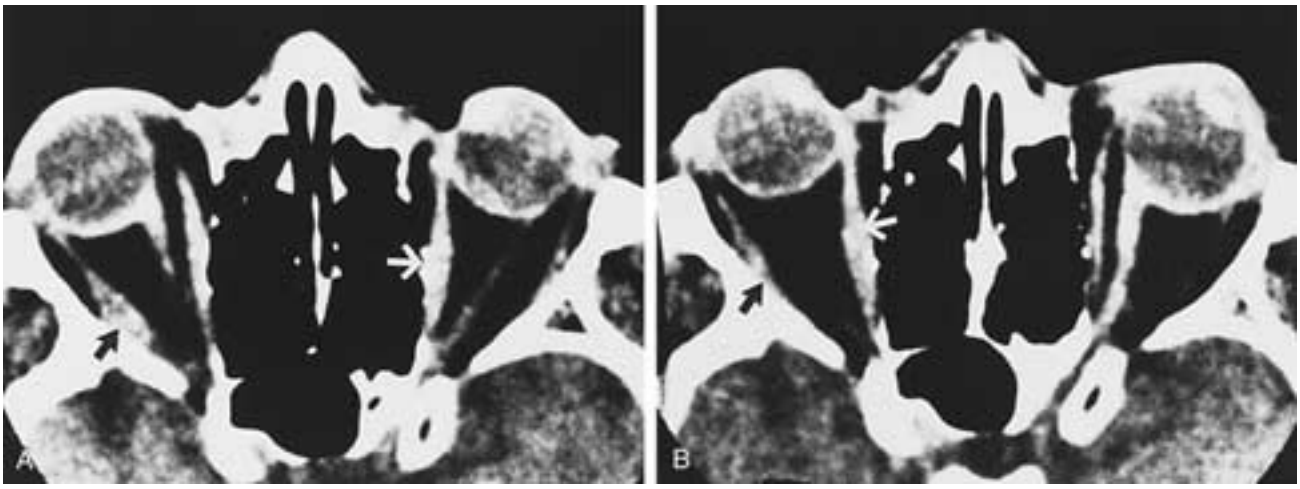

VIEW IMAGE

FIGURE 9-12 Demonstration of Sherrington's law of reciprocal innervation. **A**, Axial CT scan obtained during right lateral gaze. Note that the right lateral rectus muscle (*black arrow*) and the left medial rectus muscle (*white arrow*) contract, and the right medial and left lateral rectus muscles relax (lengthen). **B**, Axial CT scan obtained during left lateral gaze. Right medial rectus muscle (*white arrow*) and left lateral rectus muscle are contracted, and right lateral rectus muscle (*black arrow*) and left medial rectus muscle are relaxed (lengthened). (From Mafee MF et al. CT in the evaluation of Brown's superior oblique tendon sheath syndrome. Radiology 1985;154:691–695.)

in a specific orbital space, the concept of the orbital spaces has some practical value. It is useful for radiologic differential diagnosis and for surgical planning, and these lesions are discussed later in this chapter. The distinction of intraocular and extraocular locations within the orbit is also useful when evaluating metastatic and dystrophic orbital calcifications (Boxes 9-4 and 9-5).

Lacrimal Gland

With the exception of a portion of the superior ophthalmic vein, the lacrimal glands are the only prominent structures readily identified in the superolateral extraconal space.[18] Each lacrimal gland is about the size and shape of an almond. It is adjacent to the tendons of the superior and lateral rectus muscles and is separated from the globe by the lateral rectus muscle (Figs. 9-10, 9-13, and 9-19). The more anterior palpebral lobe is separated from the deeper orbital lobe by the lateral horn of the levator muscle aponeurosis.[24]

Vascular and Neural Structures

Although the vascular structures in the orbit frequently can be seen on noncontrast CT, they are highlighted with

VIEW IMAGE

FIGURE 9-13 Normal superior oblique muscles. Axial CT scan demonstrates the superior oblique tendon (*crossed arrows*); trochlea (*arrowhead*); reflected portion of the superior oblique muscle's tendon (*white arrows*); medial rectus (*hollow arrow*); and lacrimal glands (*curved arrow*). (From Mafee MF et al. CT in the evaluation of Brown's superior oblique tendon sheath syndrome. Radiology 1985;154:691–695.)

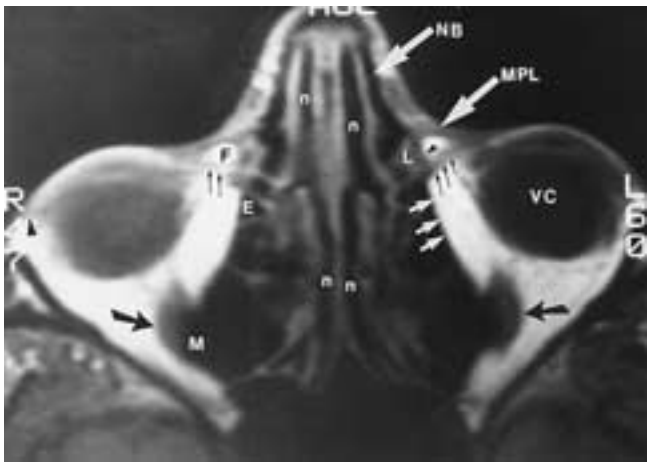

VIEW IMAGE

FIGURE 9-14 Normal MR imaging anatomy. T1-weighted MR image shows the nasal bone (*NB*); nasal cavities (*n*); medial palpebral ligament (*MPL*); lacrimal portion of the orbicularis oculi and orbital septum (*small black arrows*); lacrimal sac (*L*); lacrimal fascia (*small arrowhead*); periorbita (periosteum) (*three white arrows*); inferior rectus muscle (*large black arrows*); maxillary sinus (*M*); ethmoid air cells (*E*); nasal bone (*NB*); vitreous chamber of the eye (*VC*); fat pad (*F*) adjacent to the lacrimal sac; and the lateral palpebral ligament (*large black arrowhead*). The lacrimal sac is about 12 cm long, is situated in the lacrimal fossa, and is enclosed by the lacrimal fascia (*small black arrowhead*), which is attached behind to the posterior lacrimal crest of the lacrimal bone and in front to the anterior lacrimal crest of the maxilla. The fascia is formed from the periorbita (*three white arrows*).

Copyright © 2003, Mosby, Inc. All rights reserved.

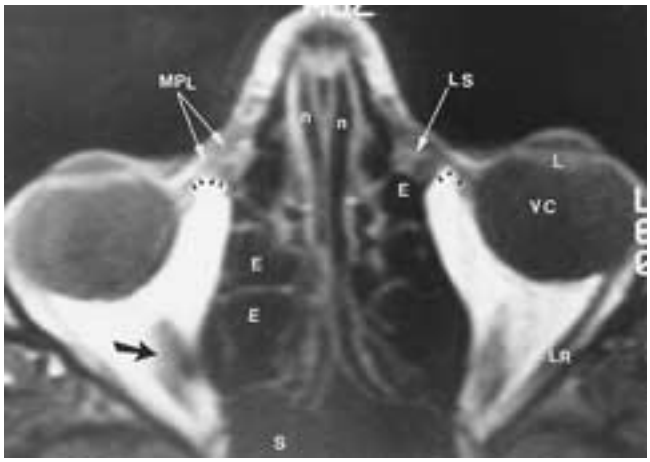

VIEW IMAGE

FIGURE 9-15 Normal MR imaging anatomy. T1-weighted MR image obtained 3 mm superior to the view in Figure 9-14 shows the medial palpebral ligament (*MPL*); lacrimal sac (*LS*); medial check ligament (*arrowheads*); nasal cavities (*n*); ethmoid air cells (*E*); sphenoid sinus (*S*); inferior rectus muscle (*black arrow*); and lateral rectus muscle (*LR*).

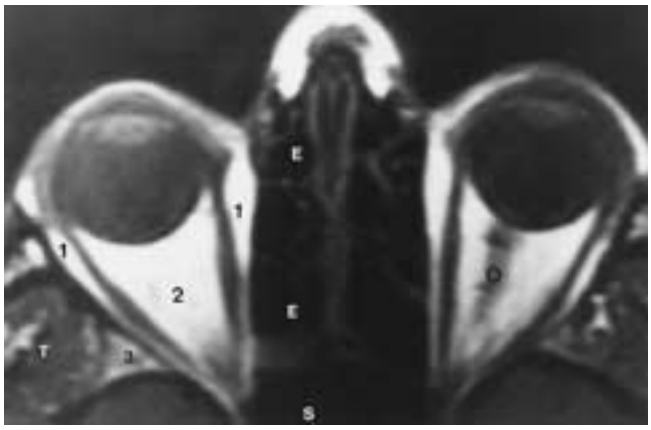

VIEW IMAGE

FIGURE 9-17 Normal MR imaging anatomy. T1-weighted MR image obtained 3 mm superior to the view in Figure 9-16 shows the optic nerve (*0*); extraconal fat (*1*); intraconal fat (*2*); bone marrow of the greater wing of the sphenoid (*3*); temporalis muscle (*T*); ethmoid (*E*); and sphenoid (*S*) sinuses.

contrast. On MR imaging the larger vessels usually have low signal intensity (signal void). The ophthalmic artery can be seen in the apex of the orbit on the inferior aspect of the optic nerve and then as it swings laterally before looping around and over the optic nerve to its superior medial aspect (Fig. 9-24). Several of its branches, including the anterior and posterior ethmoidal and posterior ciliary branches, usually can be identified.[3, 25, 26]

The superior ophthalmic vein originates in the extraconal space, in the anteromedial aspect of the orbit. It then courses near the trochlea to pass through the muscle cone beneath the superior rectus muscle and above the optic nerve. It then exits the intraconal space through the superior orbital fissure (Figs. 9-19 and 9-20). This vein is routinely identified in axial, coronal, sagittal, and parasagittal images. The inferior ophthalmic and connecting veins are seen inconsistently.[3] The intraconal and extraconal components of the small nerves of the orbit, particularly the frontal, supraorbital, and inferior divisions of the third nerve, as well as the infraorbital nerve, may be identified on CT. These nerves are identified better on MR imaging. The position of these nerves may be variable.[3] The frontal nerve can be seen between the levator palpebrae superioris muscle and the orbital roof (Figs. 9-22 and 9-23). Most of these small nerves can be seen on coronal scans of the orbital apex (Fig. 9-22).[26]

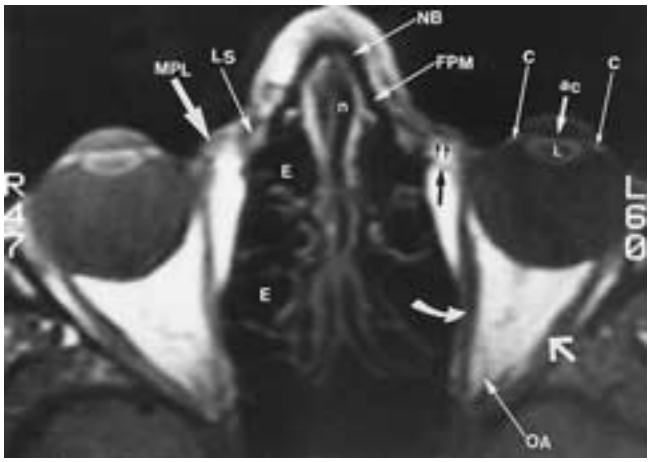

VIEW IMAGE

FIGURE 9-16 Normal MR imaging anatomy. T1-weighted MR image obtained 3 mm superior to view in the view in Figure 9-15 shows the nasal bone (*NB*); frontal process of the maxilla (*FPM*); ciliary body (*C*); anterior chamber (*ac*); lens (*L*); lacrimal sac (*LS*); medial palpebral ligament (*MPL*); ethmoid sinuses (*E*); medial rectus muscle (*curved arrow*); and lateral rectus muscle (*straight arrow*). Notice the expansion of the fascial sleeve of the medial rectus muscle as it forms the medial check ligament (*black arrow*). The medial check ligament is attached to the lacrimal bone. The orbital septum (*small black arrows*) is seen anterior to the medial check ligament.

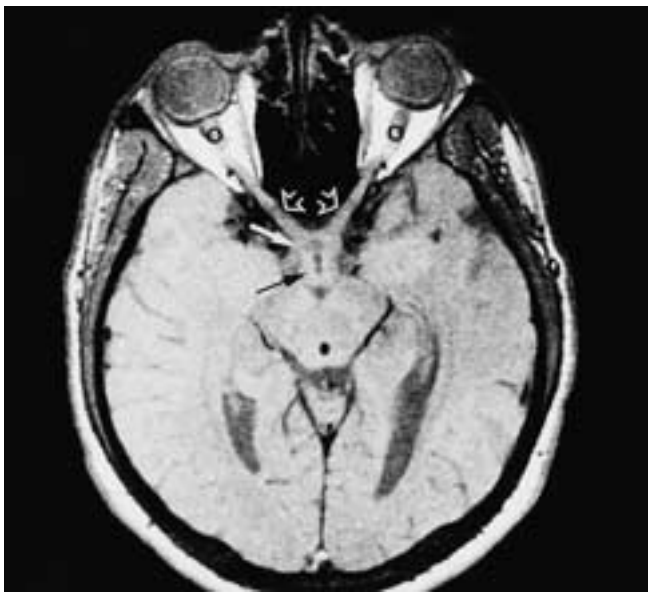

VIEW IMAGE

FIGURE 9-18 Normal MR imaging anatomy. PW MR image shows the intraorbital segment of the optic nerves (*o*); intracanalicular segment of the optic nerves (*hollow arrows*); chiasm (*white arrow*); and hypothalamus (*black arrow*).

Copyright © 2003, Mosby, Inc. All rights reserved.

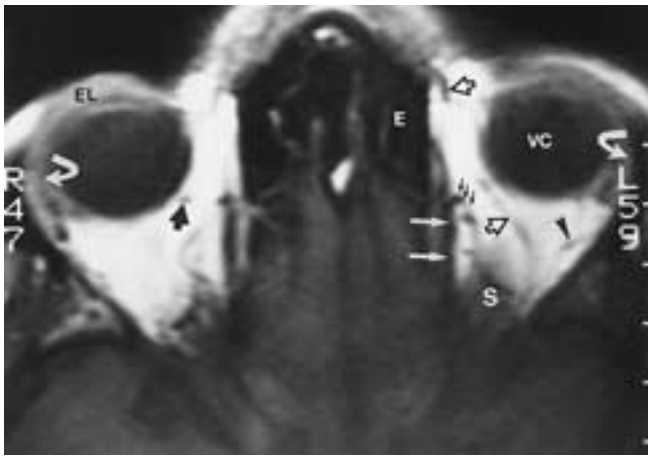

VIEW IMAGE

FIGURE 9-19 Normal MR imaging anatomy. T1-weighted MR image obtained 6 mm superior to the view in Figure 9-17 shows the superior rectus muscle (*S*); lacrimal vein (*arrowhead*); lacrimal glands (*curved arrows*); superior ophthalmic vein (*hollow arrows*); medial ophthalmic vein (*three small arrows*); superior oblique muscle (*white arrows*); presumed vorticose vein (*solid black arrow*); eyelid (*EL*); and vitreous chamber (*VC*).

Optic Nerve

The optic nerve arises from the ganglionic layer of the retina and consists of coarse myelinated fibers, like the white matter of the central nervous system.[1, 6, 16] The orbital segment of the optic nerve is 3 to 4 mm in diameter and 20 to 30 mm long (Fig. 9-18). It has a serpiginous course (with minimal inferior and lateral bowing in its midportion) in the orbit, which allows unrestricted movement of the globe. From its insertion on the posterior globe, it courses posteriorly, medially, and superiorly to exit the orbit at the optic canal. The optic nerve is covered by layers of pia, subarachnoid membrane, and dura mater. All these layers fuse as they approach the globe, becoming continuous with the sclera. The intracranial subarachnoid space extends around the optic nerve, ending at the sclera. The subdural space is a potential space and is not considered to be continuous with the intracranial subdural space. At the superior aspect of the intracanalicular portion of the optic nerve, the three layers of covering are fused to each other and to the optic nerve. The dural layer is fixed to the periosteum of the optic canal, protecting it from back-and-forth motion.[17] The intracranial segment of the optic nerve is located medially and then above the internal carotid artery in the suprasellar region (Fig. 9-18). The optic nerves join in the suprasellar cistern to form the optic chiasm (Fig. 9-18). The subarachnoid space around the optic nerve sheath has a low density on CT and can be imaged during the course of iodinated contrast cisternography. The meningeal layers of the optic nerve show enhancement on postcontrast CT. On coronal scans, immediately posterior to the globe, a small central density within the nerve represents the central retinal artery and vein.[3] The optic nerve and sheath measure 3 to 5 mm in the axial plane and 4 to 6 mm in the coronal plane.[17] The intracanalicular and prechiasmatic portions of the optic nerve are particularly well demonstrated by MR imaging (Fig. 9-18). Generally, on T1-weighted, proton density, and T2-weighted images, the optic nerve has signal intensities similar to those of normal white matter.[27] A ring of T1-weighted hypointensity and T2-weighted hyperintensity, representing CSF within the nerve sheath, is frequently seen on coronal sections. This should not be confused with well-defined areas of hypointensity bordering the nerve, which are caused by chemical shift artifact.

Globe

The three ocular coats (sclera, choroid, and retina) form a well-defined line on CT that enhances with IV contrast. The lens is normally hyperdense on CT, and the vitreous appears hypodense and shows no contrast enhancement. On MR imaging the ocular coats appear as a hypointense ring, and the vitreous has characteristics very similar to those of CSF. The lens is isointense to vitreous (low signal intensity) on T1-weighted images and has very low signal intensity on T2-weighted images. These signal intensities reflect the high

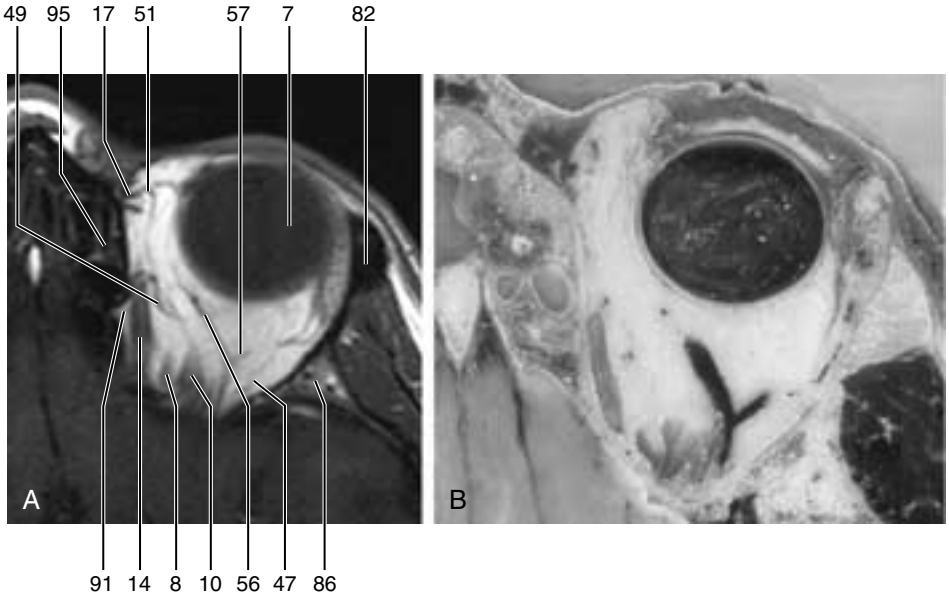

VIEW IMAGE

FIGURE 9-20 Normal MRI anatomy. T1-weighted MRI obtained 3 mm shows superior muscle complex (*S*); superior ophthalmic vein (*hollow arrows*); lacrimal artery (*LA*); lacrimal vein (*LV*); lacrimal gland (*curved arrow*); and reflected portion of superior oblique muscle tendon (*black arrows*).

Copyright © 2003, Mosby, Inc. All rights reserved.

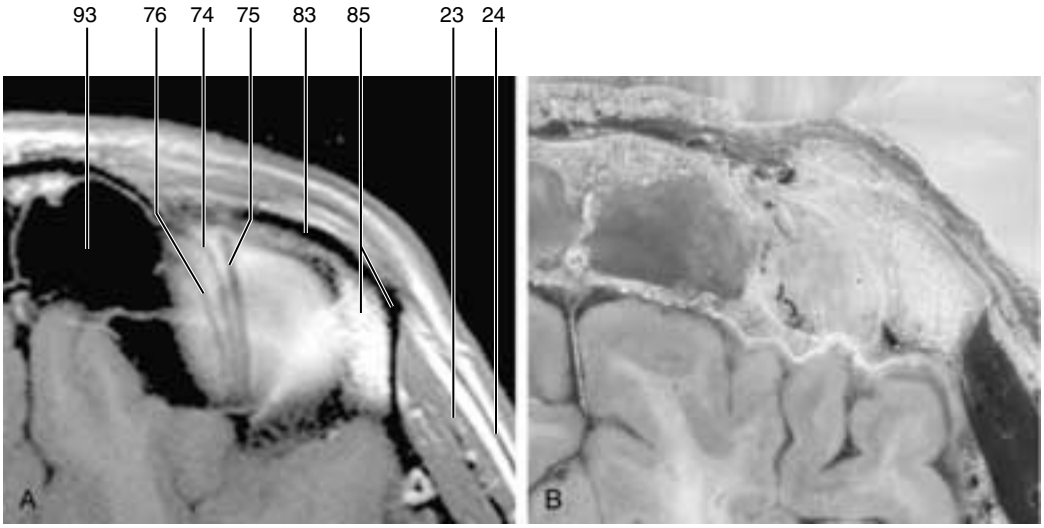

VIEW IMAGE

FIGURE 9-21 Normal MRI anatomy. T1-weighted MRI obtained 3 mm superior to view in Figure 9-20 shows superior rectus–levator palpebrae complex (*SMC*); superior ophthalmic vein (*SOV*); presumed frontal nerves (*hollow arrows*); presumed lacrimal nerve (*arrowheads*); lacrimal glands (*curved arrows*); sclera (*S*); trochlea (*white solid arrow*); presumed supratrochlear nerve (*two small black arrows*); frontal bone (*FB*); frontal sinus (*FS*); orbital septum (*curved black arrow*); and orbicularis oculi (*four black arrows*).

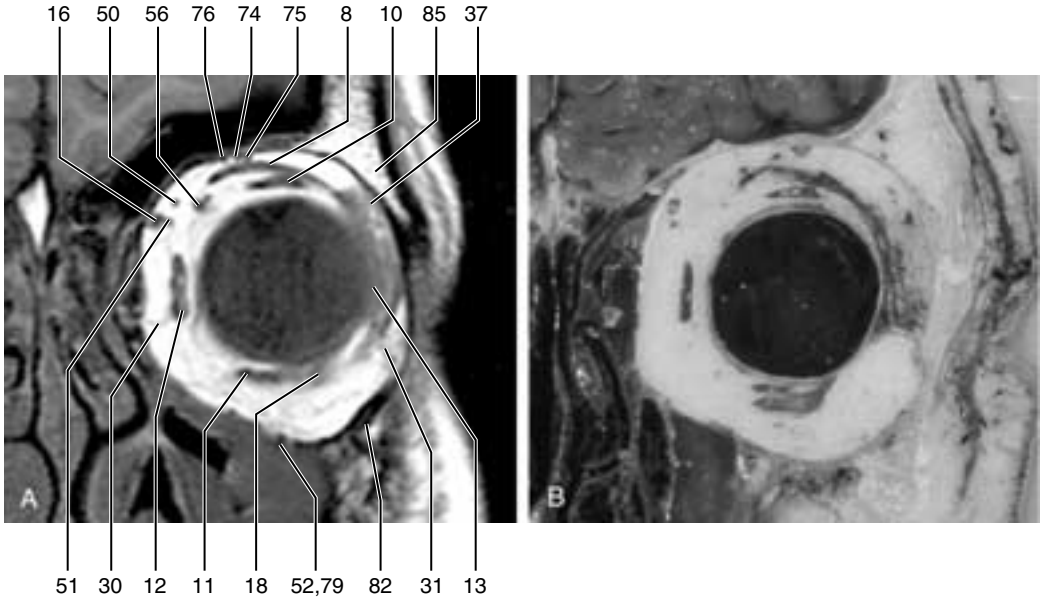

VIEW IMAGE

FIGURE 9-22 Normal MRI anatomy. Coronal T1-weighted MRI shows medial rectus muscle (*1*); superior oblique muscle tendon (*2*); superior ophthalmic/supratrochlear vein (*3*); levator palpebrae superioris (*4*); tendon of superior rectus (*single short arrow*); tendon of superior oblique muscle (*5*); inferior oblique muscle (*6*); tendon of inferior rectus muscle (*7*); tendon lateral rectus muscle (*8*); palpebral portion of lacrimal gland (*9*); supraorbital nerve (*white arrowhead*); and intermuscular septum (*black arrows*).

Copyright © 2003, Mosby, Inc. All rights reserved.

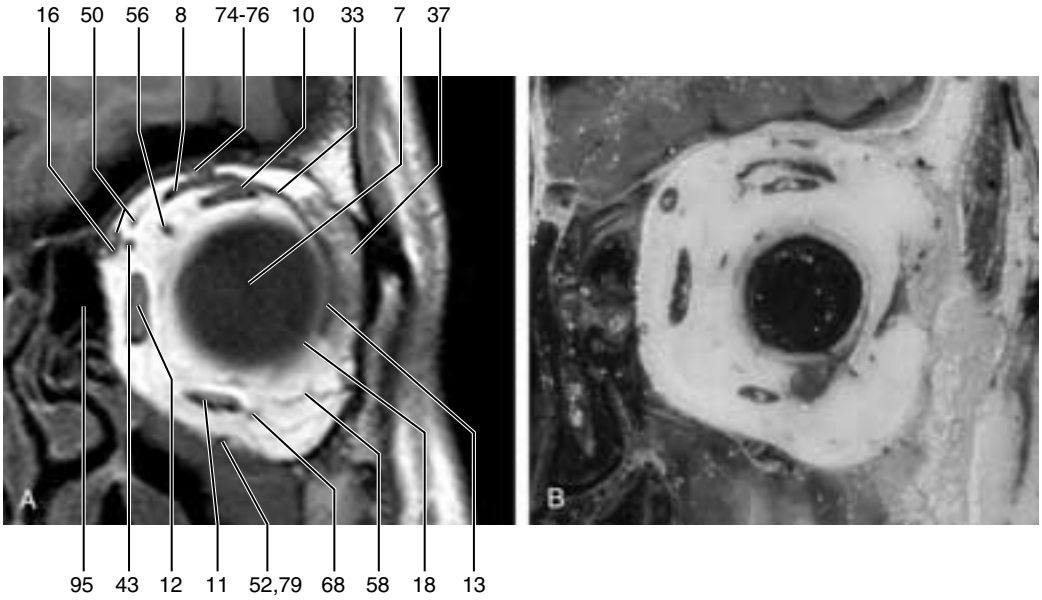

FIGURE 9-23 Normal MRI anatomy. Coronal T1-weighted MRI shows inferior rectus muscle (*1*); medial rectus muscle (*2*); superior oblique muscle (*3*); superior rectus muscle (*4*); levator palpebrae superioris (*5*); partially volumed lacrimal gland (*6*); lateral rectus (*7*); presumed branch of oculomotor nerve (*8*); collateral vein (*small arrowheads*); medial ophthalmic vein (*solid black arrow*); frontal nerve/supraorbital nerve (*hollow arrow*); supraorbital/ophthalmic artery (*single arrowhead*); vitreous (*V*); and maxillary antrum (*M*).

protein and liquid crystal composition of the lens. The imaging of the globe is discussed in detail in Chapter 8.

BONY INTERORBITAL DISTANCE

The distance between the orbits and their individual dimensions are important in the diagnosis of craniofacial anomalies. The orbits are often involved in craniofacial malformations, which include orbital clefts, orbital hypotelorism, and hypertelorism, and measurement of the bony interorbital distance (BID) is useful in establishing the severity of hypertelorism. This distance between orbits is commonly measured at the interdacryon level, the dacryon being the point of junction of the nasal bone, lacrimal bone, and maxilla.[19] Before CT, most observers relied on standard radiographs for measuring the BID, and normal values for adults and the younger age groups are available.[28-32] The BID was first defined by Cameron, in a small number of dried skulls, as the maximum distance between the medial

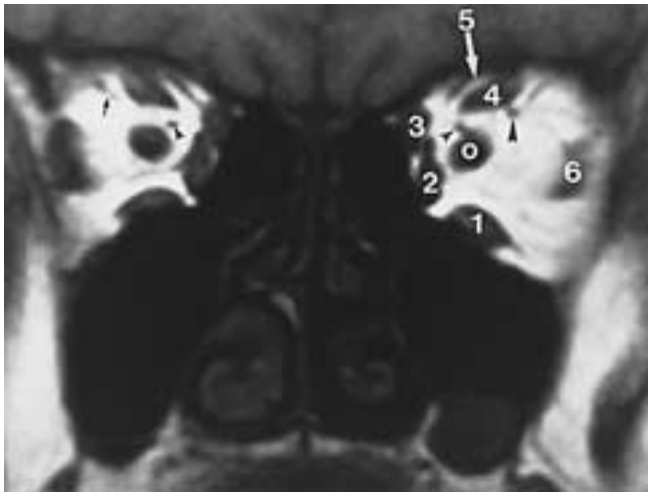

FIGURE 9-24 Normal MR imaging anatomy. T1-weighted MR coronal image shows the inferior rectus muscle (*1*); medial rectus muscle (*2*); superior oblique muscle (*3*); superior rectus muscle (*4*); levator palpebrae superioris (*5*); lateral rectus muscle (*6*); optic nerve (*o*); superior ophthalmic vein (*large arrowhead*); ophthalmic artery (*small arrowhead*); and lacrimal nerve (*black arrow*).

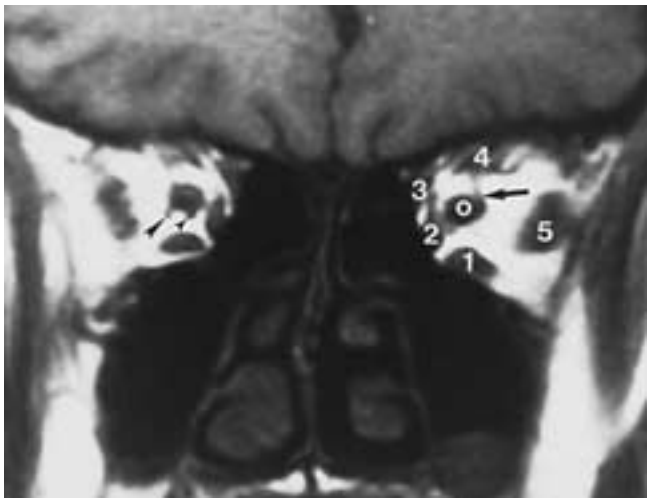

FIGURE 9-25 Normal MR imaging anatomy. T1-weighted MR coronal image shows the inferior rectus muscle (*1*); medial rectus muscle (*2*); superior oblique muscle (*3*); superior rectus muscle (*4*); lateral rectus muscle (*5*); optic nerve (*o*); long posterior ciliary arteries (*arrowheads*); and presumed ciliary ganglion (*arrow*).

Copyright © 2003, Mosby, Inc. All rights reserved.

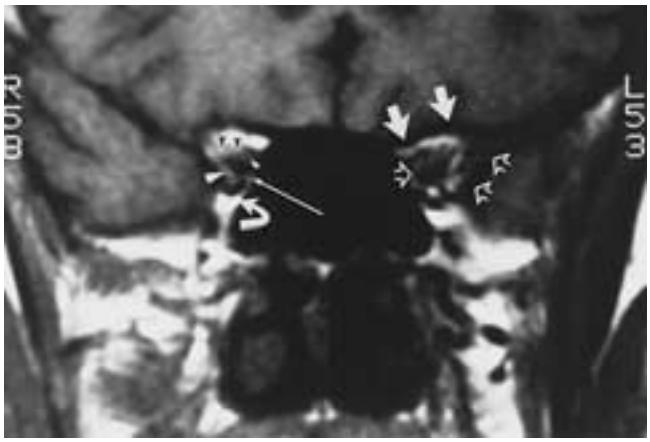

VIEW IMAGE

FIGURE 9-26 Normal MR imaging anatomy. T1-weighted MR coronal image shows the lesser (*double solid arrows*) and greater (*double hollow arrows*) wings of the sphenoid bone, medial rectus muscle (*single hollow arrow*); inferior rectus muscle (*long arrow*); lateral rectus muscle (*large white arrowhead*); superior muscle complex (*black arrowheads*); optic nerve (*short white arrowhead*); and fat in the apex of the orbit, along with the inferior orbital fissure (*curved arrow*). The common tendon of Zinn is seen as areas of hypointensity between the rectus muscles. The relative position of the nerves, veins, and ophthalmic artery entering orbital cavity through superior orbital fissure cannot be precisely resolved with current MR imaging technology.

BOX 9-1
INTRACONAL (CENTRAL ORBITAL) LESIONS

More Common

- Cavernous hemangioma
- Optic nerve meningioma
- Optic nerve glioma
- Optic nerve granulomatous disease (sarcoid)
- Optic neuritis (multiple sclerosis)
- Lymphoma
- Pseudotumor
- Lymphangioma
- Venous angioma
- Varix
- Arteriovenous malformation
- Carotid cavernous fistula
- Hemangiopericytoma
- Rhabdomyosarcoma
- Metastasis
- Orbital cellulitis and abscess

Less Common

- Capillary hemangioma
- Peripheral nerve tumors
  - Neurofibroma
  - Schwannoma
- Leukemia
- Hematocele
- Optic nerve sheath cyst
- Colobomatous cyst
- Hemangioblastoma (optic nerve)
- Chemodectoma (ciliary ganglion)
- Necrobiotic xanthogranuloma
- Lipoma
- Amyloidosis

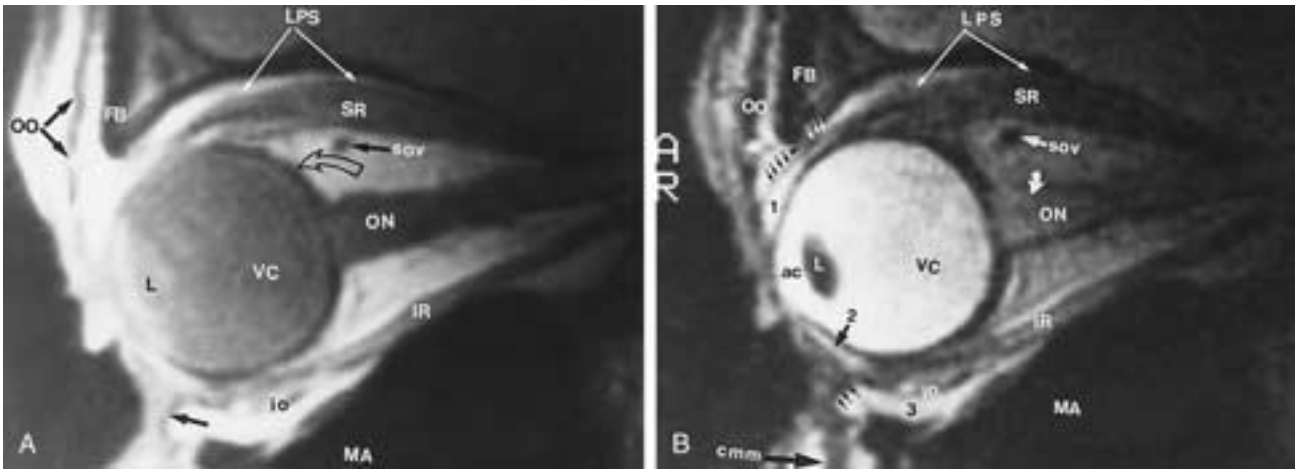

VIEW IMAGE

FIGURE 9-27 **A**, Normal MR imaging anatomy. Sagittal PW MR image shows fibers of the orbicularis oculi (*OO*); frontal bone (*FB*); levator palpebrae superioris (*LPS*); superior rectus muscle (*SR*); superior ophthalmic vein (*SOV*); sclera and Tenon capsule (*curved arrow*); optic nerve (*ON*); inferior rectus muscle (*IR*); maxillary antrum (*MA*); inferior oblique muscle (*io*); vitreous chamber (*VC*); lens (*L*); and orbital septum (*straight arrow*). **B**, Sagittal T2-weighted MR image shows fibers of the orbicularis oculi (*OO*); frontal bone (*FB*); levator palpebrae superioris (*LPS*); superior rectus muscle (*SR*); superior ophthalmic vein (*SOV*); optic nerve (*ON*); CSF along the optic nerve (*curved arrow*): inferior rectus muscle (*IR*); maxillary antrum (*MA*); inferior oblique muscle (*io*); extraconal fat (*3*); orbital septum (*three small arrows*); complex muscle of mouth (*cmm*); inferior (*2*) and superior (*1*) fornices; anterior chamber (*ac*); lens (*L*); and vitreous chamber (*VC*). Note the tendon of insertion of the levator palpebrae superioris (*small white arrows*). This tendon is an aponeurosis that descends posterior to the orbital septum. The orbital septum is depicted in this section as an ill-defined image (*arrowhead*). The tendinous fibers of the superior palpebrae muscle pierce the orbital septum and become attached to the anterior surface of the superior tarsal plate (*four black arrows*).

Copyright © 2003, Mosby, Inc. All rights reserved.

BOX 9-2
COMMON CAUSES OF ENLARGED EXTRAOCULAR MUSCLES AND SUBPERIOSTEAL LESIONS

Enlarged Extraocular Muscle

Graves' myositis
Inflammatory myositis, including cysticercosis
Granulomatous myositis (less common)—sarcoidosis
Pseudotumor (myositic type)
Lymphoma
Vascular lesions (hemangioma, arteriovenous malformation)
Aromegaly
Pseudorheumatoid nodule
Metastasis (breast, lung)

Orbital Subperiosteal Lesions

Subperiosteal cellulitis
Subperiosteal abscess
Infiltration of neoplastic lesions of paranasal sinuses
Infiltration of meningiomas (en plaque meningiomas)
Lymphomas
Leukemia
Plasmacytomas
Lacrimal gland tumors
Dermoid and epidermoid
Hematoma and hematic cyst
Cholesterol granuloma
Fibrous histiocytoma
Primary osseous or cartilaginous tumors
Metastasis (neuroblastoma)

BOX 9-3
EXTRACONAL PERIPHERAL ORBITAL LESIONS

More Common

Capillary hemangiomas
Cholesterol granulomas
Dermoids and epidermoids
Lacrimal gland lesions
- Inflammation
- Lymphoma
- Pseudotumor
- Sarcoidosis

Epithelial tumors
Lymphangiomas
Peripheral nerve tumors
Plasmacytomas
Rhabdomyosarcomas
Sarcoidosis

Less Common

Amyloidosis
Fibrous histiocytoma
Hemangiosarcoma
Hemangiopericytoma
Hematic cyst
Lipoma
Orbital encephalocele
Wegener's granulomatosis

BOX 9-4
DIFFERENTIAL DIAGNOSIS OF METASTATIC ORBITAL CALCIFICATION

Congenital
- Fanconi's syndrome (proximal renal tubular dysfunction)
- Milk-alkali syndrome
- Renal tubular acidosis

Endocrine
- Hyperparathyroidism, primary or secondary
- Hypoparathyroidism
- Pseudohypoparathyroidism

Idiopathic—sarcoidosis
Infectious
- Cytomegalovirus
- Leprosy
- Osteomyelitis
- Syphilis
- Toxoplasmosis
- Tuberculosis

Toxic
- Excessive ingestion of calcium phosphate or alkali
- Vitamin D intoxication

Traumatic—immobilization
Neoplastic
- Bronchogenic carcinoma
- Metastatic involvement of bone
- Multiple myeloma
- Parathyroid adenoma
- Parathyroid carcinoma

Modified from Froula PD et al. The differential diagnosis of orbital calcifications, as detected on computed tomographic scans. Mayo Clin Proc 1993;68:256-257.

walls of the bony orbits measured at the juncture of the crista lacrimalis posterior with the frontolacrimal suture.[31] Currarino and Silverman, in their studies of arhinencephaly and trigonocephaly, measured the BID between the medial walls at what was described to be the junction between each medial angular process of the frontal bone with the maxillary and lacrimal bones.[28]

To provide a statistically more reliable standard, Gerald and Silverman repeated the original work of Currarino and Silverman, using the same technical factors, and studied 100 patients at each year of age from birth to 12 years.[28, 29] Hansman, using radiographs of the skull and paranasal sinuses in a large group of healthy subjects, presented measurements of the BID and the thickness of the skull.[32] According to him, from infancy to adulthood, the BID for girls is consistently narrower than for boys. Starting at 1 year 6 months, there is a gradual increase in the size of the BID for both sexes. At about 13 years of age, girls' growth begins to level off. Since boys' growth continues to increase to the age of about 21 years, the measurements in girls fall more markedly below those of boys as growth is completed. The average adult measurement in women is 25 mm and in men is 28 mm.[32]

CT of the orbit provides, along with other information, an opportunity to evaluate the distance between the orbits and, if necessary, any other linear and angular measurements. On

Copyright © 2003, Mosby, Inc. All rights reserved.

BOX 9-5 DIFFERENTIAL DIAGNOSIS OF DYSTROPHIC ORBITAL CALCIFICATION

Intraocular
Cataract
Endophthalmitis
Granulomas (sarcoid, *Toxocara*)
Hyaline plaques
Idiopathic sclerochoroidal calcification
Optic nerve drusen
Phthisis bulbi
Retinal detachment
Retinal dysplasia
Retinoblastoma
Retinopathy of prematurity
Tuberous sclerosis
Von Hippel-Lindau disease

Extraocular
Within the Lacrimal Gland Fossa
Amyloid
Choristoma
Dermolipoma
Malignant and benign tumors of the lacrimal gland (more common in malignant tumor)
Plasmacytoma
Pleomorphic adenoma
Varix

Extrinsic to the Lacrimal Gland Fossa
Amyloid
Arteriovenous shunt or malformation
Calcified trochlea
Cartilaginous tumors
Cysticercosis (cestode or tapeworm; *Taenia solium*)
Glioma
Hemangioma
Hemangiopericytoma
Hemorrhage
Idiopathic inflammatory "pseudotumor"
Lymphangioma
Lymphoma
Melanoma
Meningioma
Metastatic colonic carcinoma
Mucocele
Neuroblastoma
Neurofibroma
Orbital bone fragment after trauma
Teratoma
Trichinosis (nematode, *Trichinella spiralis*)
Varix

From Froula PD et al. The differential diagnosis of orbital calcifications, as detected on computed tomographic scans. Mayo Clin Proc 1993;68:256-257.

CT, the lacrimal bones and orbital plates of the ethmoid (lamina papyracea) are seen as a thin line of bone, and the BID can be measured at any desired point.[19] From the CT studies of 400 adults (200 men aged 18 to 82, average age 52; 200 women aged 17 to 88, average age 54), the BID was measured between the medial walls of the orbits, along with certain other linear and angular measurements; these data are given in Table 9-1. These data were collected from patients with normal orbits who were studied because of a suspected diagnosis of brain infarction, hearing loss, or brain tumor. None of these patients had any underlying craniofacial anomaly or congenital malformation. The patients were Caucasian, except for a few who were Asian. In this study, data were collected only from nonrotated axial sections in the plane of the optic nerve (Fig. 9-28). On similar CT sections through the orbits, there are two configurations of the medial orbital walls. The first is a parallel separation of the medial orbital walls, and the second is a fusiform or lateral spread of the ethmoidal air cells, with the widest separation of the orbital walls occurring posterior to the posterior pole of the globe.[19] The distance between the medial walls of the bony orbits at various points, and other linear and angular measurements, are illustrated in Figure 9-28A,B. Several reference points have been used. The anterior pole (*A*) is applied to the central point of the anterior curvature of the eyeball, and the posterior pole (*P*) is the central point of its posterior curvature. A line joining the two poles forms the optic axis (*AP*), and the primary axes of the two globes are nearly parallel. The cranial opening of the optic canal is well demonstrated in Figure 9-28A. The optic canal lies between the root of the lesser sphenoid wing and the body of the sphenoid bone (Fig. 9-28A and 9-29). The anterior root is broad and flat and is continuous with the planum sphenoidale (Figs. 9-26 and 9-28A). The posterior root is shorter and thicker (optic strut), and is connected to the body of the sphenoid opposite the posterior border of the sulcus chiasmatis.[19]

As seen in Table 9-1, the normal BID, measured at the posterior border of the frontal processes of the maxilla on nonrotated CT scans in the plane of the optic nerve, ranges from 2.29 to 3.21 cm (average, 2.67 cm) in men and 2.29 to 3.20 cm (average, 2.56 cm) in women. The widest interorbital distance lies behind the posterior poles of the globes. This ranges from 3.16 to 4.10 cm (average, 3.37 cm) in men and 2.93 to 3.67 cm (average, 3.20 cm) in women. A line joining the lateral orbital margins in the axial plane (line DD in Table 9-1 (Figs. 9-26 and 9-28B) normally intersects the globe near its midportion, with at least one third of the globe posterior to this line.

PATHOLOGY

Hypertelorism, Hypotelorism, Exophthalmos, and Exorbitism

The terminology used to describe abnormalities of the orbit is complicated and may be confusing[33] to those unfamiliar with it. It will therefore be briefly reviewed. *Hypertelorism* is literally translated from Greek as ''increased distance'' (*hyper* meaning ''over'' and *tele* meaning

Copyright © 2003, Mosby, Inc. All rights reserved.

Table 9-1
CT ORBITAL MEASUREMENTS IN 400 ADULTS

	Measurement (cm)					
	Minimum		Maximum		Mean	
Line, Description	Male	Female	Male	Female	Male	Female
AA, Approximates interpupillary distance	6.26	6.21	7.51	7.50	6.78	6.63
BB, BID measured at posterior border of frontal processes of maxillae	2.29	2.29	3.21	3.20	2.67	2.56
CC, BID measured posteriorly or at level of orbital equator (useful orbits)	2.63	2.56	3.50	3.30	2.80	2.83
DD, Distance between anterior margin of frontal processes of zygomatic bones at level of plane of optic nerves	9.18	9.29	10.13	11.00	9.73	9.97
EE, Distance between optic nerves where they enter eyeballs	5.16	4.78	6.40	6.00	5.43	5.27
FF, BID measured at level of posterior poles of eyeballs	2.87	2.56	3.70	3.51	3.10	2.97
GG, BID measured at its widest part (usually posterior to FF line)	3.16	2.93	4.10	3.67	3.37	3.20
HH, BID measured at its most posterior part (apex of bony orbit)	2.16	2.43	3.37	3.23	2.73	2.80
II, Distance between superior orbital fissures at apex of bony orbit	2.90	2.70	3.83	3.63	3.10	3.00
JJ, Distance between central portion of cranial opening of optic canals	2.20	2.01	2.73	2.70	2.30	2.20
KK, Distance between tips of anterior clinoid processes	2.31	2.43	3.21	3.16	2.80	2.83
EI, Length of intraorbital part of optic nerve:						
Right	2.70	2.40	3.80	3.23	3.10	2.90
Left	2.60	2.40	3.80	3.21	3.20	2.80
AP, Anteroposterior diameter of eyeball:						
Right	2.50	2.39	2.90	2.70	2.80	2.50
Left	2.40	2.40	2.80	2.80	2.70	2.63
TT, Transverse diameter of eyeball:						
Right	2.50	2.40	2.80	2.90	2.70	2.71
Left	2.50	2.50	2.90	2.90	2.80	2.83
Angle between optic nerve axes (in degrees)	35°	36.5°	50°	51.5°	41°	42.3°

Note: *BID* = bony interorbital distance.

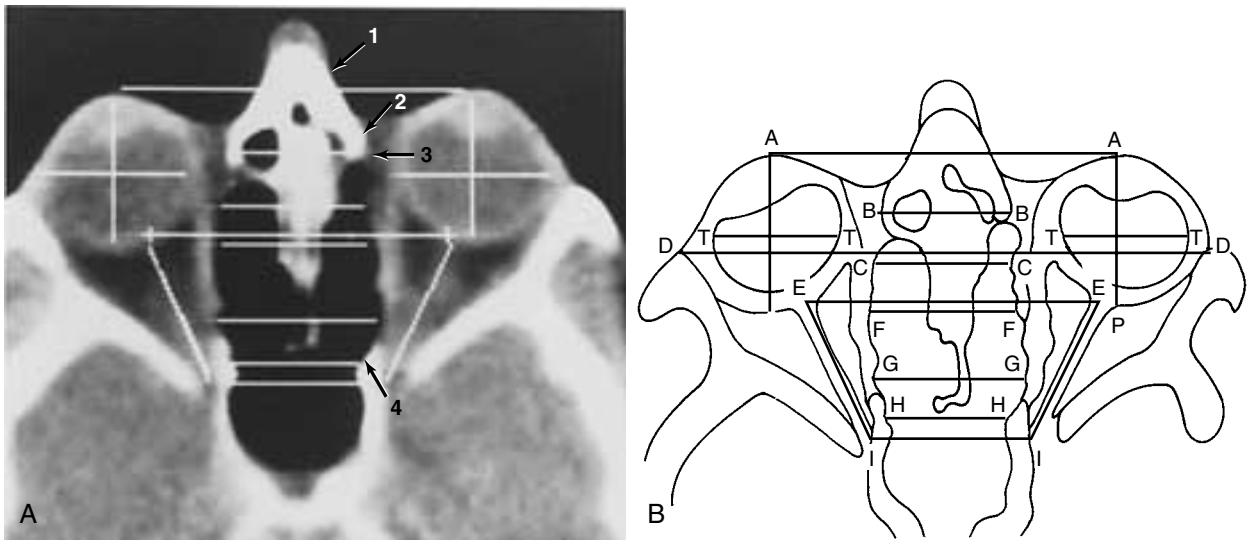

VIEW IMAGE

FIGURE 9-28 **A**, Axial CT scan of the orbits at the level of the plane of the optic nerves shows the outline of the globes, lenses, and vitreous bodies; level of the medial check ligament (*3*); medial and lateral rectus muscles; optic nerves; and retroorbital fat compartments. Note the nasal bone (*1*) and frontal process of the maxilla (*2*) on either side. The lamina papyracea is seen as a very thin density hardly distinguishable from the medial aspect of the medial rectus muscle. Posterior to that is the most posterior part of the medial wall of the bony orbit (*4*), which is related to the anterior part of the sphenoid sinus. **B**, Diagram shows different points selected for various measurements presented in Table 9-1. (From Mafee MF et al. CT in the evaluation of the orbit and the bony interorbital distance. AJNR 1986;7:265.)

Copyright © 2003, Mosby, Inc. All rights reserved.

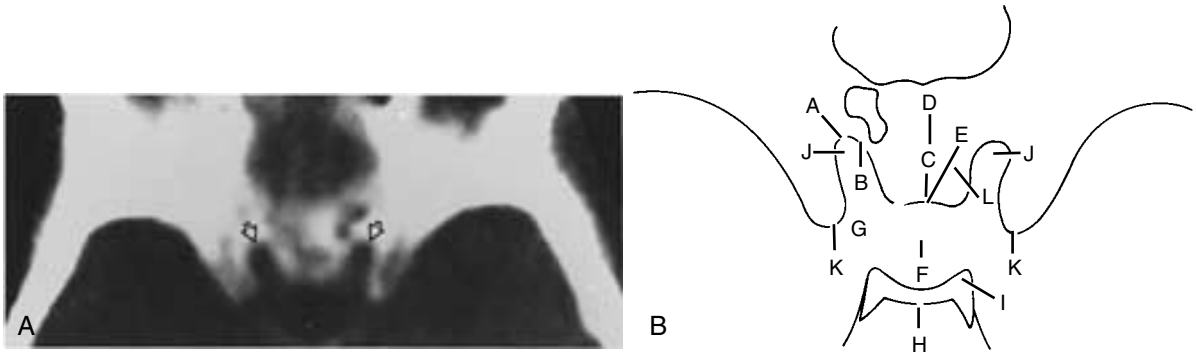

VIEW IMAGE

FIGURE 9-29 **A**, Axial CT scan of the head at the level of the planum sphenoidale and anterior roots of the lesser wings of the sphenoid bone shows the cranial openings (*arrows*) of the optic canals. **B**, Diagram shows structures in **A**. *A*, Cranial opening of the optic canal; *B*, anterior root of the lesser wing of the sphenoid; *C*, posterior border of the chiasmatic groove; *D*, planum sphenoidale; *E*, tuberculum sellae; *F*, pituitary fossa; *G*, middle clinoid; *H*, dorsum sellae; *I*, posterior clinoid; *J*, midportion of the cranial opening of the optic canal; *K*, anterior clinoid; *L*, anterior border of the chiasmatic groove. (From Mafee MF et al. CT in the evaluation of the orbit and the bony interorbital distance. AJNR 1986;7:265.)

''distant''). Orbital hypertelorism describes the anatomic situation in which the medial walls of the orbits are farther apart than normal.[33-35]

Patients with orbital hypertelorism almost always have eyes that are spaced more widely apart than normal. Telecanthus is a condition that may clinically mimic orbital hypertelorism. In telecanthus the distance between the apices of the medial canthal ligaments is increased, and the eyes are spaced more widely apart than normal. However, the BID is not increased; these patients do not have orbital hypertelorism. They do have medial canthal hypertelorism. Telecanthus may be congenital or acquired; when acquired, it is often a consequence of trauma.[33]

Orbital *hypotelorism* refers to a decrease in the BID. Patients with this condition may appear clinically to have either narrowly spaced or normally spaced eyes; surprisingly, they may even appear to have widely spaced eyes. For example, patients with Down's syndrome and trisomy 13 syndrome were classically described as having hypertelorism on the basis of clinical evaluation. However, in fact, these patients have orbital hypotelorism.[33, 35]

Exophthalmos describes abnormal prominence of the globe, and proptosis emphasizes abnormal protrusion of the globe. *Exophthalmos* and *proptosis*, however, commonly are used as synonyms. *Exorbitism*, on the other hand, refers to a decrease in the volume of the orbit. The orbital contents are greater in volume than the orbital capacity and generally protrude anteriorly (proptosis), causing the globe to be unusually prominent (exophthalmos).

Congenital and Developmental Abnormalities

There are many hereditary and sporadic abnormalities that involve the orbits, globe, adjacent orbital tissues, and other craniofacial and skeletal structures. The embryology of the eyes and orbits is presented in Chapter 8 and earlier in this chapter. The embryology of the midface is presented in Chapter 1. The study of these congenital and developmental conditions is complicated by the variety of names used for the same syndrome and by the overlapping criteria used to establish the diagnosis of a syndrome.[36] To list all of the congenital malformations or syndromes is beyond the scope of this chapter. Many excellent books have detailed descriptions of these disorders.[34-39] The eyes are often involved in craniofacial malformations, including orbital clefts and orbital hypotelorism and hypertelorism. CT and MR imaging have proven to be very useful in the preoperative evaluation of such patients, and imaging may show an encephalocele or a porencephalic cyst as an additional feature of the malformation.[19] The surgical treatment of hypertelorism involves translocation of the globes toward the midline by lateral wall osteotomy at a point posterior to the equator of the eye.[19]

Anatomic and Developmental Considerations

Congenital abnormalities of the orbit and eyes result from faulty development of the embryo and fetus, and the eighth week of gestation is the last week of true embryonic development.[36, 40-46] By the third week of gestation, the optic pits appear, one on either side of the forebrain. Disturbance of the prosencephalic organizing center (prechordal mesoblast) can cause cyclopia, synophthalmia, or arhinencephaly. Anophthalmia occurs as a result of failure of the neuroectoderm of the optic pit to develop from the anterior portion of the neural plate. A variety of ocular and systemic abnormalities may be seen with an optic nerve coloboma. These conditions have been described in Chapter 8. Craniosynostosis is due to abnormal development of the blastemic stage of the skull bone, including the basicranium. Mandibulofacial dysostosis and otocephaly probably are due to inhibition of mesodermal differentiation of the facial structures derived from the first branchial (visceral) arch. These conditions are discussed in Chapter 1.[36]

Under normal conditions, the eye directs orbital growth.

Copyright © 2003, Mosby, Inc. All rights reserved.

During the first year of life, the eye practically doubles in volume and attains more than 50% of its adult volume.[47] By the end of the third year, 75% of the adult volume is achieved (similar to neural growth).[47] The shape of the orbital cranial junction is also influenced by the development of the brain and skull.[47] When the brain is underdeveloped but the eye is normal, the orbital plate of the frontal bone is usually elevated into the anterior fossa of the skull.[19] In microcephaly the orbits are usually circular and the roofs are highly arched.[48] When the eye is underdeveloped but the brain is normal, the orbital plate of the frontal bone appears hypoplastic and the vertical or cranial part is usually normal (Fig. 9-30). Enucleation of the globe in infancy and early childhood, if untreated with a prosthesis, leads to arrested development of the orbit, resulting in a small orbit.[36]

In coronal suture synostosis, the orbit on the side of the fusion is elongated superiorly and laterally, imparting a harlequin appearance (Fig. 9-31). Correction of the cranial deformity can lead to spontaneous correction of the orbital deformity in some instances.[49, 50] In mandibulofacial dysostosis, the orbits may be defective inferolaterally because of malar bone hypoplasia. In cases of severe malar hypoplasia, the lateral wall of the orbit is formed by the greater wing of

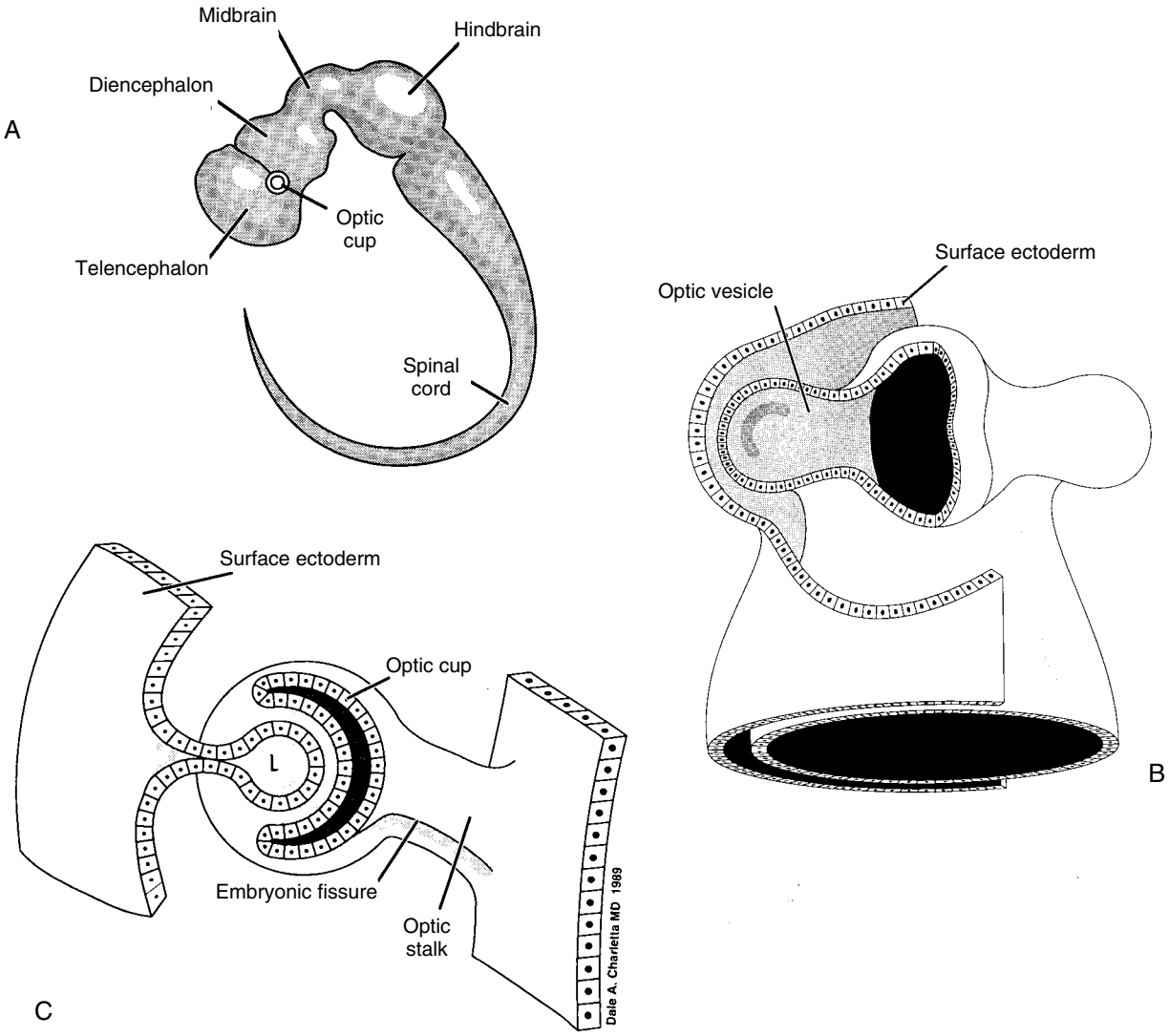

VIEW IMAGE

FIGURE 9-30 **A**, A 5-mm developing human embryo (4 weeks of gestation). By 3 weeks of gestation two indentations appear, one on either side of the neural groove. These are optic pits, which deepen to form the optic vesicles, one on either side of the forebrain. The optic vesicles give rise to an optic stalk and optic cup on either side. **B**, Development of the posterior ocular structures. In the 4 mm embryo, lateral diverticula on either side of the forebrain have given rise to two optic vesicles. The distal portions of the optic vesicles expand, and the proximal portions become the tubular optic stalks. **C**, At the 5 mm stage, the external surface of each optic vesicle invaginates to form the optic cup. The inner wall of the optic cup (formerly the outer wall of the optic vesicle) gives rise to the retina, and the outer wall of the cup becomes the retinal pigment epithelium. The optic vesicle is covered by a layer of surface ectoderm, which forms the lens (*L*). Note the embryonic fissure, through which mesenchyme extends into the optic stalk and cup. Failure of the embryonic fissure to close causes typical ocular colobomas. (From Mafee MF et al. CT of optic nerve colobomas, morning glory anomaly, and colobomatous cyst. Radiol Clin North Am 1987;25:693.)

Copyright © 2003, Mosby, Inc. All rights reserved.

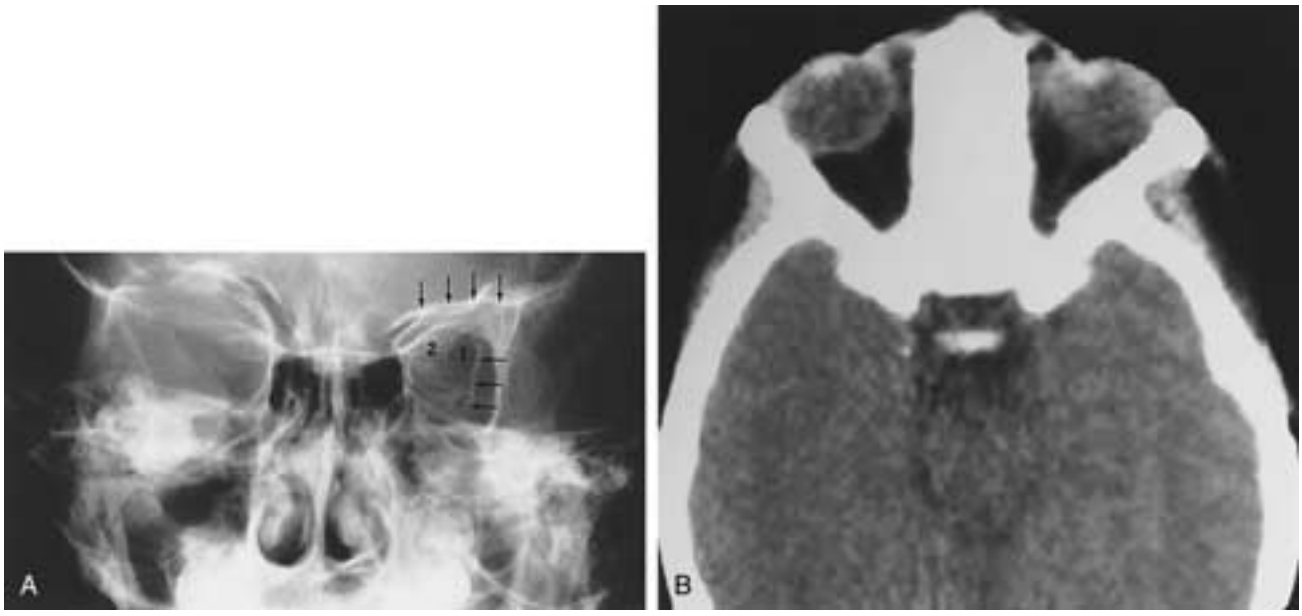

VIEW IMAGE

FIGURE 9-31 **A**, Microphthalmia. Posteroanterior view of the skull. The lesser wing of the sphenoid (*2*) and the left maxillary sinus are hypoplastic; superior orbital fissures are asymmetric (*1*). Note the difference between the oblique lines (*horizontal arrows*), which represent cortices of the temporal surface of the greater wings of the sphenoid bone. Notice the hypoplasia of the roof of the left orbit (*vertical arrows*). **B**, Microphthalmia. Four-year-old boy born without a nose and with left microphthalmos and apparent hypertelorism. The left globe is smaller than the right. Increased soft tissue between the medial wall or orbit and the globe anteriorly has the clinical appearance of hypertelorism. In fact, the interorbital bony distance is normal. (From Mafee MF et al. CT in the evaluation of the orbit and the bony interorbital distance. AJNR 1986;7:265.)

the sphenoid and the zygomatic process of the frontal bone (also see Chapter 1).

Bony Abnormalities

Minor degrees of facial and orbital asymmetry are the most common causes of pseudoproptosis.[4] For the most part, these patients have minor degrees of asymmetry involving all of the hemifacial structures.[3] However, in a few instances, the asymmetry may be related to maxillary hypoplasia resulting in a relatively retroplaced orbit on the affected side. In many cases, familial asymmetry may be evident when the siblings or parents are examined. These minor developmental abnormalities of the orbit are considered anatomic variations. Anomalies of ossification may result in accessory sutures and supernumerary ossicles in the orbital walls.[36] On rare occasions, congenital absence of bone in the frontal, maxillary, and orbital regions may result in deformity of the bony orbit. Asymmetric enlargement of one bony orbit may be due to eccentrically located lesions such as neurofibroma, hemangioma, lymphangioma, dermoid, and other slow-growing processes. A small orbit is seen in anophthalmia, microphthalmia, and postenucleation of the globe in infancy, if not followed by prompt prosthetic treatment.

Bony Orbit in Craniofacial Dysostosis

Craniofacial dysostosis and developmental anomalies may result in profound orbital abnormalities. Orbital malformations in craniofacial dysostosis result chiefly from coronal synostosis. Premature closure of one or more cranial sutures, termed *craniosynostosis* or *craniostenosis*, is the common denominator of many patients with craniofacial anomaly.[51–58]

Primary Congenital Isolated Craniosynostosis

Any cranial suture may undergo premature closure, but several patterns are recognizable more commonly than others.[50] The incidence of congenital suture synostosis reported by Harwood-Nash,[51] derived from a composite of his experience and from two large series reported by Anderson and Geiger[52] and Shillito and Matson,[53] is as follows: sagittal, 56%; single coronal, 11%; bilateral coronal, 11%; metopic suture, 7%; lambdoid, 1%; and three or more sutures, 14%. Depending on the suture that is prematurely closed, the skull and orbit, including the interorbital distance, have a characteristic shape. These can be grouped as follows: (1) metopic; trigonocephaly (triangular head); hypotelorism is a constant feature of the trigonocephaly;[48] (2) sagittal, scaphocephaly (dolichocephaly), in which the anteroposterior diameter of the bony orbit is usually increased and the vertical and transverse diameters of the bony orbit are usually decreased; (3) unilateral coronal or lambdoid; plagiocephaly; in this condition, if the coronal suture is involved, there is characteristic deformity of the bony orbit, which will be discussed later; (4) bilateral coronal or lambdoid, resulting in brachycephaly; (5) coronal and sagittal; oxycephaly or acrocephaly (turricephaly); and (6) coronal, lambdoid, and sagittal;

Copyright © 2003, Mosby, Inc. All rights reserved.

cloverleaf skull (kleeblattschädel). Primary craniosynostosis may be associated with congenital syndromes. These conditions include the following: Crouzon's disease (craniofacial dysostosis), Apert's disease (acrocephalosyndactyly, type I), Saethre-Chotzen syndrome (acrocephalosyndactyly, type II), Carpenter's syndrome (acrocephalopolysyndactyly), chondrodystrophia calcificans congenita (Conradi's syndrome, or punctate epiphyseal dysplasia), Brachmann-de Lange syndrome, Laurence-Moon-Biedl-Bardet syndrome, Treacher Collins syndrome (mandibulofacial dysostosis), and craniotelencephalic dysplasia.[39, 48, 50]

Orbit in Plagiocephaly

Plagiocephaly is due to unilateral closure of one of the paired sutures of the skull, frequently the coronal or lambdoid but rarely the temporosquamous sutures. Each produces a characteristic deformity of the skull. In practice, most of the time, plagiocephaly is seen in patients with hemicoronal premature synostosis, in which there is an ipsilateral elevation of the lesser wing of the sphenoid associated with upward extension of the superior lateral portion of the orbit, imparting a harlequin appearance to the orbit (Fig. 9-32A).[50] The flattening of the ipsilateral frontal bone is also characteristic of premature coronal synostosis (Fig. 9-32B). The volume of the anterior cranial fossa on the side of fusion is decreased. The greater wing of the sphenoid is expanded, displaced forward and downward, and forms a relatively large middle cranial fossa (Fig. 9-32B,C). This occurs in addition to upward elevation of the roof of the orbit, which produces a shallow orbit. The ethmoidal plate (roof of the ethmoidal sinus) also is elevated on the side of fusion (Fig. 9-32A). The nasal septum, crista galli, and ethmoidal complex are tilted to the side of fusion (Fig. 9-32A).

Premature fusion of both coronal sutures may occur with or without any other associated abnormality. This may result in marked shortening of the anterior cranial fossa and orbital depth, and the brain impressions become more prominent on the inner table of the frontal bone (Fig. 9-33). Both a harlequin appearance of the orbit and the bony changes of the unilateral coronal synostosis are duplicated in this bilateral form of premature fusion (Fig. 9-33). Lombardi noted a connection between sagittal or lambdoid synostosis, or both, in half of the reported cases of coronal suture synostosis.[55]

Orbit in Crouzon's and Apert's Diseases

Crouzon's disease, also known as *craniofacial dysostosis*, is an autosomal dominant disorder with considerable variability in expression.[50] Apert's disease, also known as *acrocephalosyndactyly type I*, is transmitted as an autosomal dominant disorder. The cranial and facial characteristics of Crouzon's disease are somewhat similar to those of Apert's syndrome, including brachycephaly, hypertelorism, bilateral exophthalmos, parrot-beaked nose, maxillary hypoplasia, relative prognathism, and a drooping lower lip that produces a half-open mouth. Bilateral exophthalmos is essentially a consequence of exorbitism, which in turn is a consequence of several factors that combine to produce a decrease in orbital volume. On the basis of the skull shape alone, Crouzon's and Apert's diseases cannot be distinguished.[50]

In any large series of patients with Crouzon's disease, there is no regular pattern of calvarial deformity. Oxycephaly, brachycephaly, scaphocephaly, and trigonocephaly may be present. In fact, there is too much heterogeneity to allow for a simplistic description. Generally, in Crouzon's disease, brachycephaly, or oxycephaly, is most often observed. Apert's disease is characterized by irregular craniostenosis with an acrobrachycephalic skull and syndactyly of the hands and feet. Associated skeletal abnormalities such as ankylosis of the elbow, hip, and shoulder, as well as malformations of the cardiovascular, gastrointestinal, and genitourinary systems, may be present.

The orbital malformation in Crouzon's and Apert's diseases is due mainly to premature coronal synostosis. A striking harlequin appearance of the orbits is seen that results from elevation of the roof and lateral walls of the orbits (Fig. 9-34). The supraorbital rim is recessed, and the infraorbital rim is hypoplastic. The orbital depth is markedly reduced as the result of verticalization of the roof (upward tilt of the lesser wing and orbital plate of the frontal bone). Displacement of the greater wing of the sphenoid into a more coronal orientation, which is referred to as *frontalization* of the greater wing of the sphenoid, and ballooning of the ethmoid are other factors contributing to exotropia. Hypoplasia of the maxilla and the intermaxillary component contributes in part to the exophthalmos and relative prognathism (Figs. 9-34 and 9-35). Hypoplasia of the maxilla causes recession of the infraorbital rim and foreshortening of the orbital floor.[50] The optic canal in Crouzon's and Apert's diseases is usually narrow. This may lead to optic atrophy.[3] The distance between the intracranial openings of the optic canals is usually normal, and this finding forms the basis for surgical procedures designed to correct orbital hypertelorism by moving the bony orbits closer together without damaging the optic or oculomotor nerves.[50] Of particular importance to the surgeon contemplating surgical correction of orbital hypertelorism are the orientation and degree of foreshortening of the lateral wall of the orbit. The type of lateral wall osteotomy performed (sagittal split or total mobilization) often depends on these anatomic factors.[33, 34] Patients with craniosynostosis syndromes may have marked extraocular muscle anomalies ranging from an apparent absence of ocular muscles to abnormally inserted muscles or very small extraocular muscles (Figs. 9-34 to 9-36).

Saethre-Chotzen Syndrome (Acrocephalosyndactyly Type II)

Saethre-Chotzen syndrome was described by Saethre in 1931 and in 1932 by Chotzen.[50, 55-57] The first family with this disease to be reported in the United States was described in 1970 by Bartsocas et al.[58] Saethre-Chotzen syndrome is characterized by synostotic malformation of multiple sutures, facial asymmetry, mild midface hypoplasia, ptosis of the eyelids, an antimongoloid slant of the palpebral fissures, a beaked nose, a low-set frontal hairline, variable brachycephaly, and variable cutaneous syndactyly, particularly of the second and third fingers. Other associated abnormalities

Copyright © 2003, Mosby, Inc. All rights reserved.

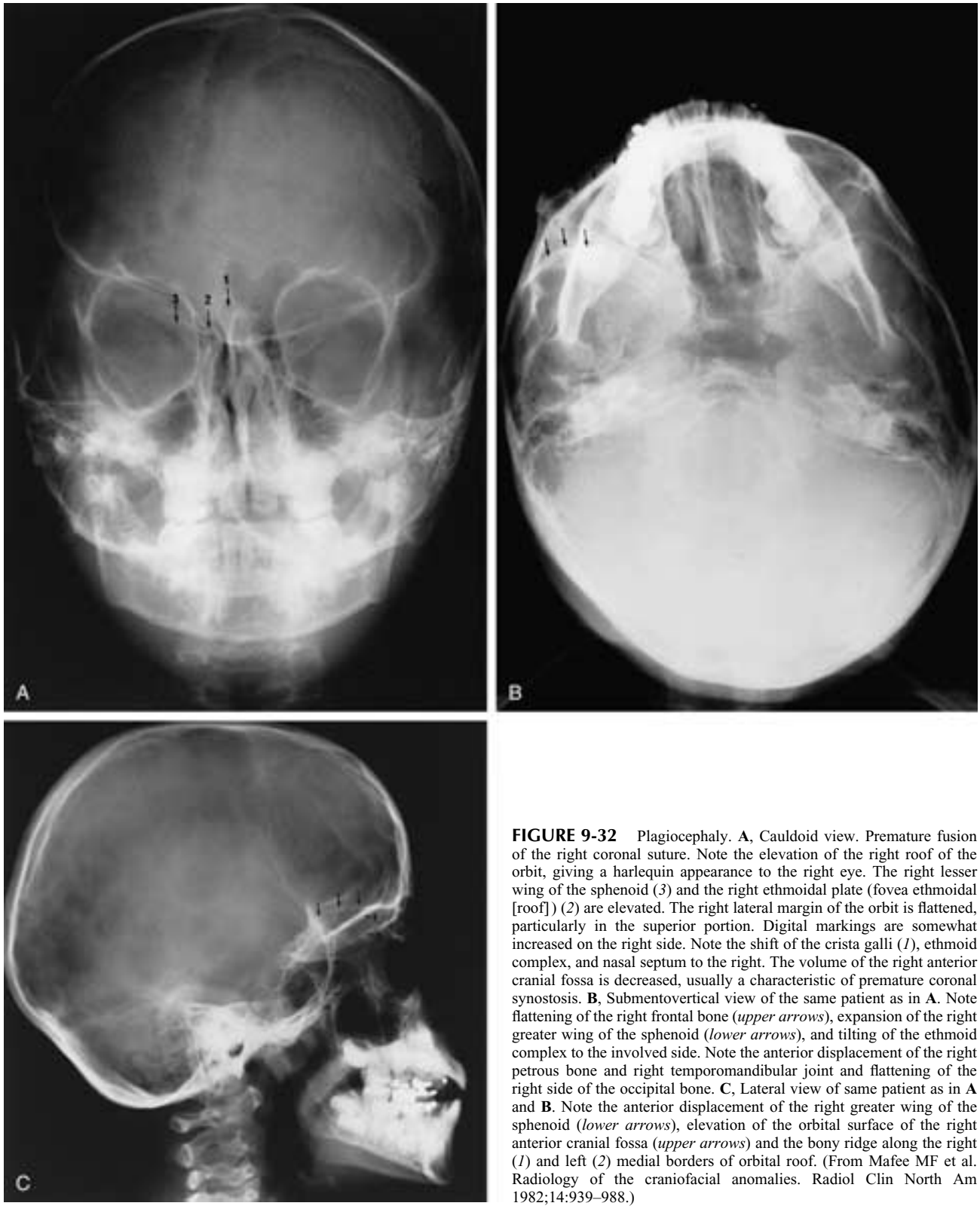

FIGURE 9-32 Plagiocephaly. **A**, Cauldoid view. Premature fusion of the right coronal suture. Note the elevation of the right roof of the orbit, giving a harlequin appearance to the right eye. The right lesser wing of the sphenoid (*3*) and the right ethmoidal plate (fovea ethmoidal [roof]) (*2*) are elevated. The right lateral margin of the orbit is flattened, particularly in the superior portion. Digital markings are somewhat increased on the right side. Note the shift of the crista galli (*1*), ethmoid complex, and nasal septum to the right. The volume of the right anterior cranial fossa is decreased, usually a characteristic of premature coronal synostosis. **B**, Submentovertical view of the same patient as in **A**. Note flattening of the right frontal bone (*upper arrows*), expansion of the right greater wing of the sphenoid (*lower arrows*), and tilting of the ethmoid complex to the involved side. Note the anterior displacement of the right petrous bone and right temporomandibular joint and flattening of the right side of the occipital bone. **C**, Lateral view of same patient as in **A** and **B**. Note the anterior displacement of the right greater wing of the sphenoid (*lower arrows*), elevation of the orbital surface of the right anterior cranial fossa (*upper arrows*) and the bony ridge along the right (*1*) and left (*2*) medial borders of orbital roof. (From Mafee MF et al. Radiology of the craniofacial anomalies. Radiol Clin North Am 1982;14:939–988.)

VIEW IMAGE

Copyright © 2003, Mosby, Inc. All rights reserved.

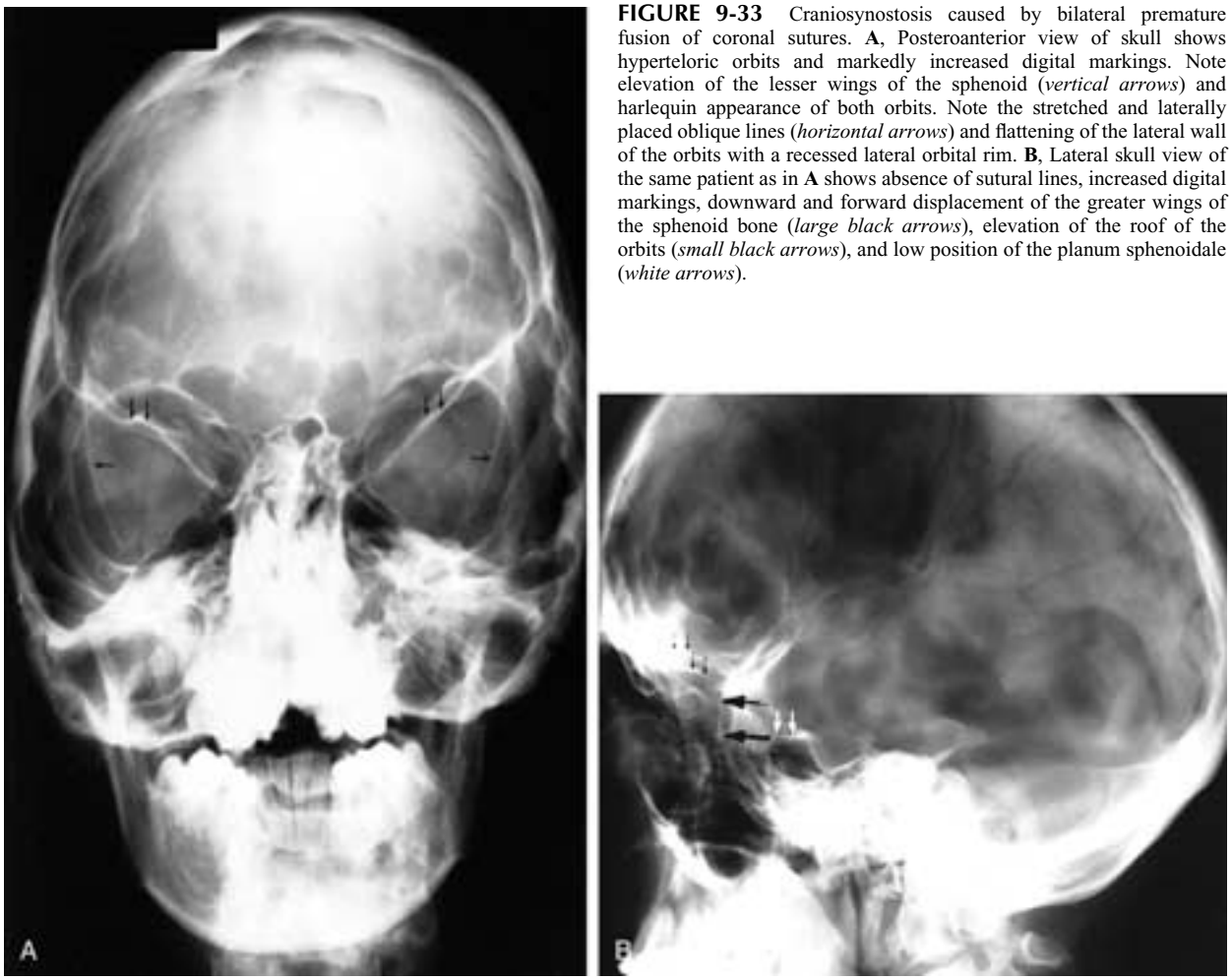

FIGURE 9-33 Craniosynostosis caused by bilateral premature fusion of coronal sutures. **A**, Posteroanterior view of skull shows hyperteloric orbits and markedly increased digital markings. Note elevation of the lesser wings of the sphenoid (*vertical arrows*) and harlequin appearance of both orbits. Note the stretched and laterally placed oblique lines (*horizontal arrows*) and flattening of the lateral wall of the orbits with a recessed lateral orbital rim. **B**, Lateral skull view of the same patient as in **A** shows absence of sutural lines, increased digital markings, downward and forward displacement of the greater wings of the sphenoid bone (*large black arrows*), elevation of the roof of the orbits (*small black arrows*), and low position of the planum sphenoidale (*white arrows*).

include a high-arched palate, cleft palate, and deformity of the external ear. The orbital abnormalities in these patients are similar to those in Crouzon's and Apert's diseases.

Neurofibromatosis

The classic description of neurofibromatosis was published by Friedrich Daniel von Recklinghausen in 1882. Clinical criteria for diagnosing neurofibromatosis include (1) six or more café-au-lait spots, each greater than 1.5 cm in diameter; (2) axillary or other intertriginous freckles; (3) cutaneous neurofibromas; and (4) one or more unequivocally affected parents or siblings.[59] The disease itself is characterized by abnormalities of both ectodermal and mesodermal origin. It is transmitted as an autosomal dominant disorder of variable penetrance.[33] The incidence of neurofibromatosis is approximately 1 in 3000 live births.[60] About 50% of these patients have a positive family history of the disease, and the other 50% are the result of a spontaneous mutation; the mutation rate is about 10:4.[61] The incidence of central nervous system tumors, including acoustic neuromas, gliomas, meningiomas, and ependymomas, is six times that of the general population.[62] Often multiple central nervous system tumors are present. Although 25% to 35% of neurofibromas occur in the head and neck region, orbital abnormalities are relatively uncommon.[60] Orbital abnormalities are often associated with exophthalmos, which may be pulsatile and generally can be classified into one of four categories: (1) orbital neoplasms; (2) plexiform neurofibromatosis; (3) orbital osseous dysplasia (Fig. 9-37); and (4) congenital glaucoma.[60] The most common orbital neoplasm seen in association with neurofibromatosis is optic glioma (Fig. 9-37A). Meningioma is not unusual. Both optic gliomas and meningiomas may occur bilaterally. Bilateral optic gliomas are almost pathognomonic of neurofibromatosis (Fig. 9-38), whereas bilateral meningiomas are only suggestive of neurofibromatosis. Orbital schwannoma, neurofibroma, and neurofibrosarcoma also can be seen in these patients.

Orbital (Mesodermal) Defects

Osseous dysplasia of the cranial bones, in particular the bony orbit, may be part of the abnormality associated with von Recklinghausen's disease. The orbital defect is a consequence of partial or complete absence of the greater or lesser wing of the sphenoid bone, or both. The body of the sphenoid bone may also be involved, producing

Copyright © 2003, Mosby, Inc. All rights reserved.

an abnormal and dysplastic sella turcica (Fig. 9-37).[33, 60] These osseous abnormalities allow the adjacent temporal lobe of the brain and its overlying, often thickened dural membrane to herniate anteriorly into the posterior aspect of the orbit, causing anterior displacement of the globe (Fig. 9-37). The normal CSF pulsations are transmitted to the globe, resulting in pulsatile exophthalmos. Associated findings include hypoplasia of the ipsilateral frontal and maxillary sinuses and hypoplasia of the adjacent ethmoid air cells.[33, 60]

Mandibulofacial Dysostosis

Orbital Defects

The malformation known as *mandibulofacial dysostosis* (MFD) was first reported in 1889 by an ophthalmologist, G.A. Berry.[63] Treacher Collins, whose name is attached to the disease of MFD, described the disease and noted the characteristic malar hypoplasia and the associated flattening of the cheeks.[64] In 1923, Pires de Lima and Monteior stated that MFD probably is due to a developmental defect affecting the branchial arches (the hallmark of MFD is its varied expressivity).[65] Franceschetti and Klein, who coined the name *mandibulofacial dysostosis*, classified the syndrome into five separate categories: complete, incomplete, abortive, unilateral, and atypical.[66] Gorlin et al. stated that there is no unilateral form of the syndrome and that such cases are better classified as hemifacial microsomia.[37] Poswillo, in his experimental study of a teratogenically induced phenocopy of MFD in an animal model, showed that the disorder results from disorganization of the preoptic neural crest at about the time of migration of cells to the first and second branchial arches.[67] There are now several recognized malformations in which abnormalities of the eye and associated abnormalities of structures derived from the first and second branchial arches are found.

VIEW IMAGE

FIGURE 9-34 Crouzon's disease. Coronal MR image shows the striking harlequin appearance of the orbits caused by elevation of the roofs and lateral walls or orbits. Note the deformity of the extraocular muscles and hypoplasia of the midface. One or more extraocular muscles may be absent in Crouzon's or Apert's disease.

Bony Orbital Defects

In MFD the maxilla and malar bones are usually poorly developed, with small antra and shallow or incomplete orbital floors (Fig. 9-39A).[50] The malar bones are hypoplastic, and the zygomatic arches are usually incomplete. The development of the zygomatic process of the maxilla varies among the cases described, and it may not be developed. The radiographic orbital characteristics of MFD are the downward-sloping floors of the orbits in line medially with a beak-like bony nasal contour. The lateral and lower rim of the orbit is often defective (Fig. 9-39A). CT shows the deficiency of the lateral orbital floor as an orbital cleft that varies considerably in degree. The greater wings of the sphenoid may be hypoplastic, and therefore the lateral orbital wall may be defective (Fig. 9-39A). Herring et al. reported a patient with MFD who had hypoplasia of the greater wing of the sphenoid and in whom the temporal squamous bone extended anteriorly, beyond its usual boundaries, to replace the very hypoplastic greater wing of the sphenoid.[68] The squamous bone articulated directly with the frontal bone, at the anterior end of the temporal fossa, and formed a section of the lateral orbital wall. In MFD the infraorbital foramen may be absent, the fossa of the lacrimal sac may be larger than normal, and the nasolacrimal canal is usually short.[68] The lacrimal bones are normal.

Bony Orbit in Craniofacial Microsomia

Craniofacial microsomia is known by many names, including *first and second branchial syndrome*, *otomandibular dysostosis*, and *oculoauriculovertebral dysplasia*.[37, 50, 69] In general, among the congenital oculoauriculocephalic syndromes, the term *first and second branchial arch syndrome* designates a characteristic congenital malformation that is usually unilateral but occasionally is bilateral. The term *hemifacial microsomia* was advocated by Gorlin et al. to refer to patients with unilateral microtia, microsomia, and failure of formation of the mandibular ramus and condyle.[37] Hemifacial microsomia includes as a variant of this complex such malformations as Goldenhar's syndrome and oculoauriculovertebral dysplasia, previously described as separate entities.[37] About 10% of the patients have bilateral involvement, but the disorder is nearly always more severe on one side.[37] The associated eye findings that are considered variable features of this syndrome include epibulbar dermoids or lipodermoids, microphthalmia, coloboma of the choroid and iris, and deformity of the bony orbit similar to MFD as a result of hypoplasia of the maxilla and malar bone.

Copyright © 2003, Mosby, Inc. All rights reserved.

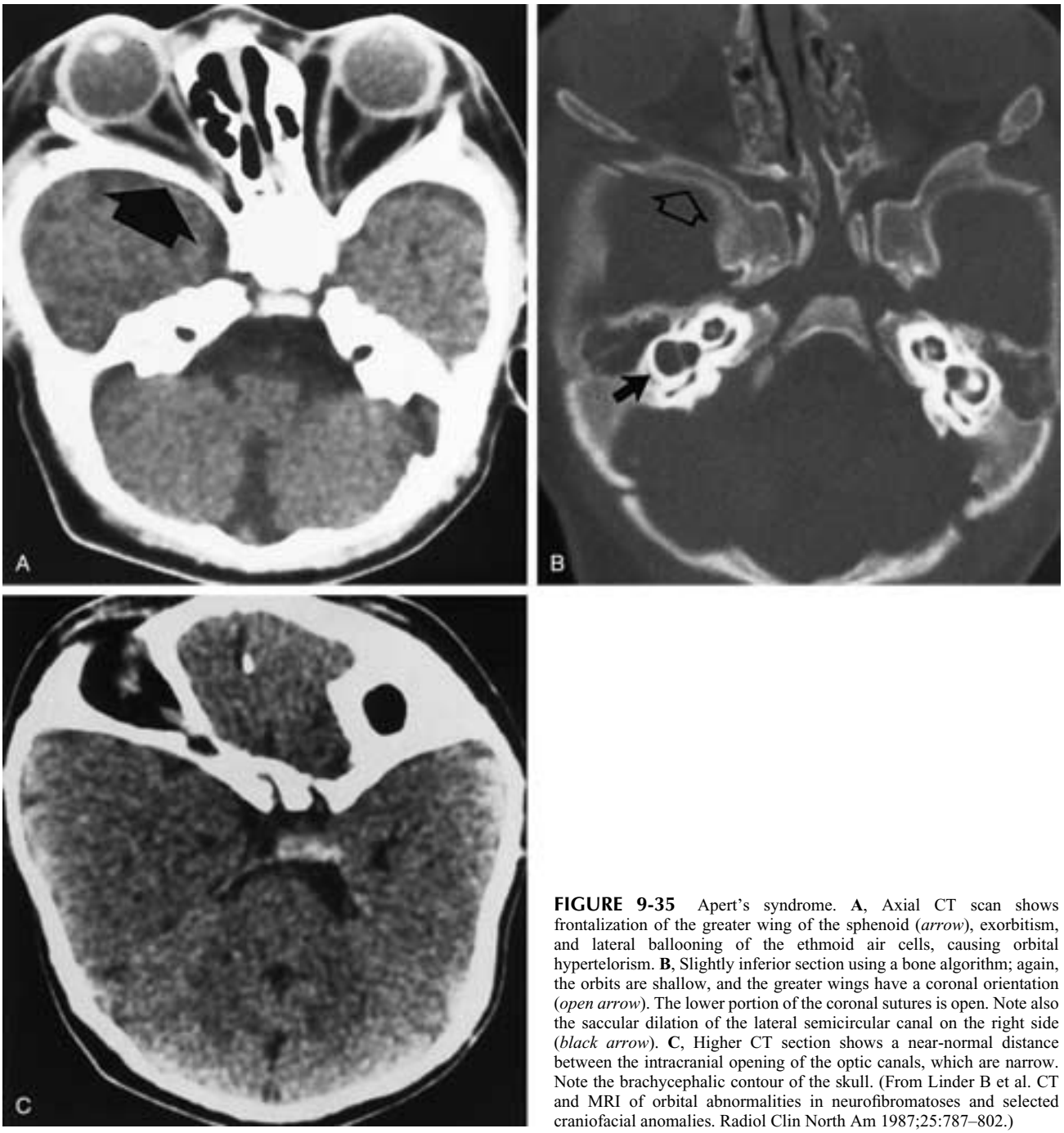

FIGURE 9-35 Apert's syndrome. **A**, Axial CT scan shows frontalization of the greater wing of the sphenoid (*arrow*), exorbitism, and lateral ballooning of the ethmoid air cells, causing orbital hypertelorism. **B**, Slightly inferior section using a bone algorithm; again, the orbits are shallow, and the greater wings have a coronal orientation (*open arrow*). The lower portion of the coronal sutures is open. Note also the saccular dilation of the lateral semicircular canal on the right side (*black arrow*). **C**, Higher CT section shows a near-normal distance between the intracranial opening of the optic canals, which are narrow. Note the brachycephalic contour of the skull. (From Linder B et al. CT and MRI of orbital abnormalities in neurofibromatoses and selected craniofacial anomalies. Radiol Clin North Am 1987;25:787–802.)

VIEW IMAGE

Developmental Orbital Cysts

The most frequent developmental cysts involving the orbit and periorbital structures are the dermoid and epidermoid cysts, choristomas, and teratomas.[3, 8, 17, 70–72] The relative frequency of these cysts compared to other orbital lesions is shown in Table 9-2. The age distribution of the common orbital diseases is shown in Table 9-3. Choristoma is a focus of tissue histologically normal for an organ or part of an organ at a site other than the site at which it is located.[5, 6, 73] A dermoid or epidermoid cyst is a choristoma that may be found in several locations in the orbit. Lipodermoids are solid tumors that are usually located beneath the conjunctiva over the lateral surface of the globe.[5, 6] A conjunctival lipodermoid is a true choristoma, since (adipose) fatty tissue usually is not found in this region. Conjunctival choristomas are relatively common congenital lesions that possess little growth potential. They contain both dermal and epidermal elements that are not normally found in the conjunctiva.[74] Three types of conjunctival choristomas are found—the solid limbal dermoid, the more diffuse dermolipoma, and the complex choristoma. Solid limbal dermoids typically occur unilaterally, at the inferotemporal limbus. Dermolipomas (lipoder-

Copyright © 2003, Mosby, Inc. All rights reserved.

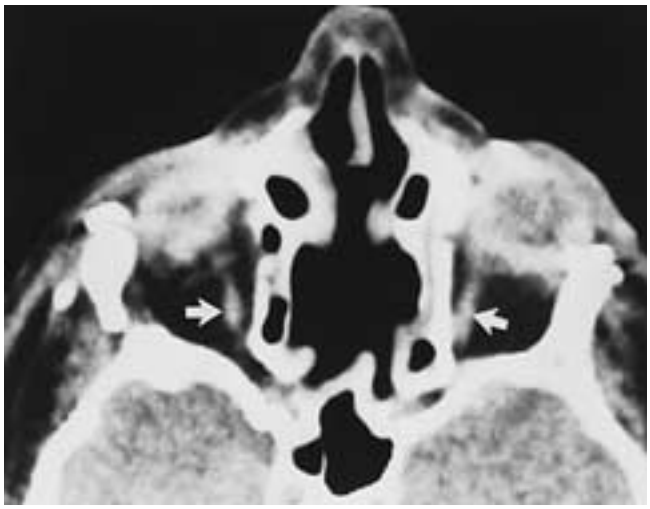

VIEW IMAGE

FIGURE 9-36 Crouzon's syndrome. CT scan shows the small inferior rectus muscles (*arrows*). Note the hypertelorism and postsurgical changes of the lateral orbital walls.

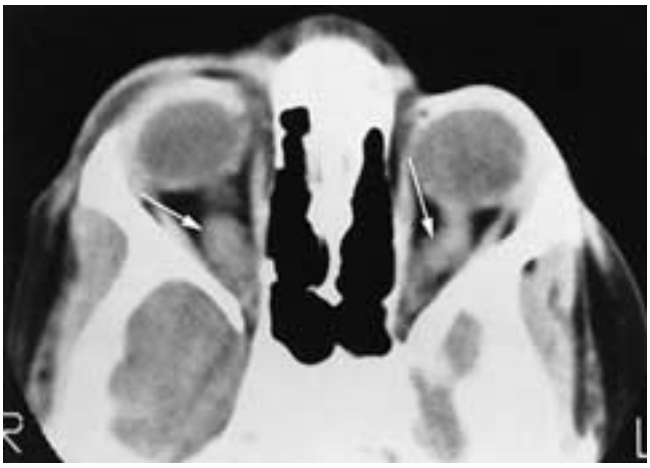

VIEW IMAGE

FIGURE 9-38 Axial CT scan. Neurofibromatosis with bilateral optic nerve gliomas (*arrows*).

moids) are less dense than solid dermoids and contain more adipose tissue. Typically they are found on the superior temporal bulbar conjunctiva near the levator and extraocular muscles[5, 6] (Fig. 9-40). These masses can extend from the limbus anteriorly to the posterior aspect of the globe and orbit between the superior and lateral rectus.[74] Care must be taken during surgical removal to avoid rupture of the cyst, with deposition of cells at the operative sites, and in particular not to damage the palpebral portion of the lacrimal gland, extraocular muscles, or levator palpebrae superioris.[73, 74] Bilateral limbal dermoids or dermolipomas are found in children who have Goldenhar's syndrome. Complex choristomas consist of variable combinations of ectopic tissues such as ectopic lacrimal gland, respiratory, eyelid gland, or brain tissues. Epibulbar osseous choristomas are solitary nodules that resemble dermoids. They are composed of mature, compact bone along with other typical choristomatous elements such as pilosebaceous units and hair follicles.[74] Dermoid and epidermoid cysts are choristomas that are among the most common orbital tumors of childhood. Both may be found in several locations in the orbit, most frequently superior and temporal. The tumor is congenital but may not be noted at birth. Many become evident only in the second and third decades.[6] Both result from the inclusion of ectodermal elements during closure of the neural tube. The dermal elements that are pinched off along the suture lines, diploe, or within the meninges or scalp in the course of embryonic development give rise to

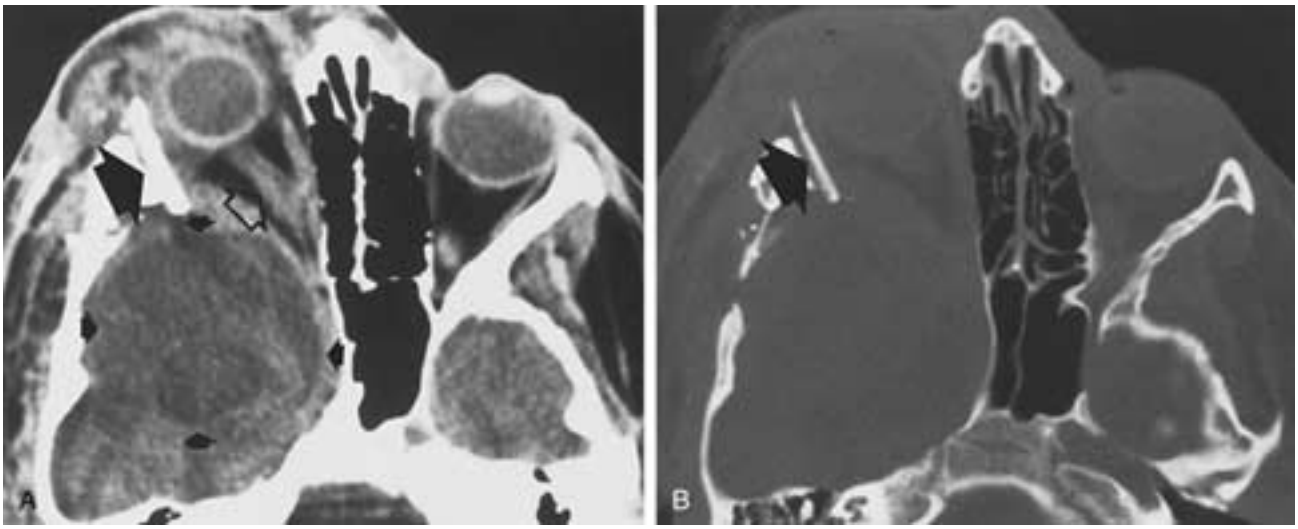

VIEW IMAGE

FIGURE 9-37 Neurofibromatosis. The patient had previous surgery for correction of an orbital deformity. **A**, Axial CT scan. Note the bone graft along the lateral margin of the right orbit (*large black arrow*). Note the normal left and dysplastic right greater wing of the sphenoid bone, with anterior herniation of the porencephalic cyst of the temporal lobe (*small arrows*) covered by dura. The right optic nerve is enlarged (*open arrow*), and the right globe is proptotic. Enlargement of the optic nerve is thought to be caused by optic nerve glioma. **B**, Osseous abnormalities are better seen on this bone detail image. (From Linder B et al. CT and MRI of orbital abnormalities in neurofibromatosis and selected craniofacial anomalies. Radiol Clin North Am 1987;25:787.)

Copyright © 2003, Mosby, Inc. All rights reserved.

VIEW IMAGE

FIGURE 9-39 **A**, Mandibulofacial dysostosis. Posteroanterior (PA) view of the skull shows a hypoplastic mandible, hypoplastic malar bones, hypoplastic maxillary antra, and hypoplastic lateral wall of the orbits (*arrow*). Oblique (innominate) lines are not visible because of hypoplasia of the greater wing of the sphenoid. **B**, Normal PA view of the skull for comparison.

these cysts.[6, 71] Both have a fibrous capsule with varying degrees of thickness. The epidermoid has a lining of keratinizing, stratified squamous epithelium. The dermoid contains one or more dermal adnexal structures such as sebaceous glands and hair follicles. Some dermoid cysts may also contain lobules of fat. These dermoid cysts should be considered well-differentiated teratomas, because they contain tissue derived from more than a single embryonic germ layer. Teratomas are choristomatous tumors that contain tissues representing two or more germ layers. Endodermal derivatives such as gut or respiratory epithelium, ectodermal tissues such as skin and its appendages, and neural and mesodermal tissues such as connective tissues, smooth muscles, cartilage, bone, and vessels may be present. These developmental cysts represent 24% of all orbital and lid masses, 6% to 8% of deep orbital masses, and 80% of cystic orbital lesions.[75] These cysts may contain fluid or solid components.[73, 76] Teratomas are evident at birth as grossly visible cystic orbital masses.[8, 71] Teratomas are tumors composed of cells originating from more than one embryonic germ layer and situated in a site that is not the normal location for the cells.[73] Orbital teratomas may arise from pluripotential stem cells delivered to the orbit hematogenously or from stem cells displaced during their migration.[73] The tumors can be both solid and cystic. However, they are usually cystic and can cause dramatic exophthalmos at birth. Although teratomas in other sites such as testes are commonly malignant, teratomas within the orbit are rarely malignant.[73] Orbital teratomas tend to affect girls, are unilateral, grow rapidly, and are not associated with other anomalies. Although exenteration is sometimes performed

Table 9-2
FREQUENCY OF ORBITAL LESIONS BY MAJOR DIAGNOSTIC GROUP

Diagnostic Group	Frequency (%)
Thyroid orbitopathy	47
Cystic lesions	8
Inflammatory lesions	8
Vascular lesions	5
Lacrimal gland lesions	4
Lymphoproliferative lesions	4
Secondary tumors	4
Myxomatous and adipose lesions	3
Mesenchymal lesions	2
Metastatic tumors	2
Optic nerve tumors	1
Fibrous and connective tissue lesions	1
Osseous and fibroosseous lesions	1
Histiocytic lesions	<1
Other and unclassified	17

From Dutton J. Orbital diseases. In: Yanoff M, Duker JS, eds. Ophthalmology. St. Louis: CV Mosby, 1999;14.1–14.7.

Copyright © 2003, Mosby, Inc. All rights reserved.

Table 9-3
AGE DISTRIBUTION OF COMMON ORBITAL DISEASES

Diagnostic Group	Frequency (%)		
	Childhood and Adolescence (0–20 Years)	Middle Age (21–60 Years)	Later Adult Life (61+ Years)
Thyroid orbitopathy	10	59	40
Infectious process	7	3	3
Inflammatory lesions	6	5	9
Cystic lesions	12	3	4
Vascular neoplastic lesions	15	2	1
Other vascular lesions	7	2	3
Trauma	7	4	2
Secondary orbital malignancies	1	2	9
Metastatic malignancies	1	1	8
Mesenchymal lesions	9	1	1
Lymphangiomas	6	1	0
Lymphoproliferative diseases	1	3	12
Optic nerve lesions	5	1	1
Other neurogenic lesions	5	3	2
Lacrimal gland fossa	1	1	1
Other	7	8	4

From Dutton J. Orbital diseases. In: Yanoff M, Duker JS, eds. Ophthalmology. St. Louis: CV Mosby, 1999;14.1–14.7.

because of the fear of malignancy, cystic teratomas can sometimes be removed with preservation of the eye.[6] Intraocular teratomas are distinctly rare and may appear similar to the teratoid medulloepithelioma, a usually benign tumor of the ciliary body and rarely of the optic disc and nerve, which is seen in young children. The dermoid and epidermoid cysts favor the upper portion of the orbit for their growth (Figs. 9-41 and 9-42). They grow slowly; however, at times these cysts can grow rapidly, particularly in adults.[72] They are most frequently located at the superior temporal quadrant of the orbit, where they are fixed to the periosteum near the frontozygomatic suture line (Figs. 9-41 and 9-42A,B).[70–72] Occasionally, they can be found at the frontoethmoidal or frontonasal sutures and can simulate an encephalocele (Fig. 9-42C).[6] These cysts may be entirely confined to the orbital adnexal tissues. Most of them appear clinically during childhood and present as subcutaneous nodules near the orbital rim. In adults the cysts most commonly arise behind the orbital rim, often near the lacrimal gland, and may be difficult to distinguish from lacrimal gland tumors.[71, 72] The cysts may contain cystic or solid components.

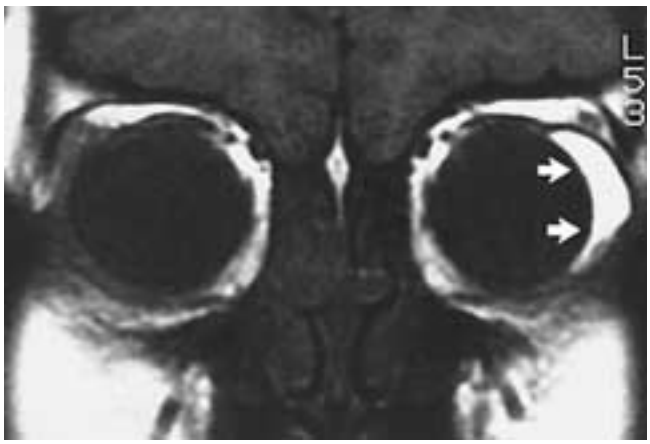

FIGURE 9-40 Coronal T1-weighted MR image shows a hyperintense mass (*arrows*) compatible with a dermolipoma. (From Kaufman LM et al. Diagnostic imaging of cystic lesions in the child's orbit. Radiol Clin North Am 1998;36:1149–1163.)

VIEW IMAGE

Diagnostic Imaging

The imaging modality of choice depends on the entity being considered. When a prominent feature of the suspected lesion is bone remodeling, bone destruction, bone or calcium deposition, or intralesional fat, CT scanning is indicated (Fig. 9-41). MR imaging may provide information about the characteristics of fluid and tissues within the cystic lesion. Both epidermoid and dermoid cysts appear on CT as unenhanced, well-circumscribed, smoothly marginated, low-density masses (Figs. 9-41, 9-42). If a dermoid cyst contains fatty tissues (well-differentiated teratomas), it has fat density on CT (Fig. 9-42A). Similarly, calcifications may be seen within these dermoid cysts. Calcification is not a feature of epidermoids. Although rare, we have seen calcification in intracranial epidermoid but not in orbital epidermoid cysts. Fat-fluid levels may be present in dermoid cysts. A ruptured dermoid/epidermoid cyst shows surrounding inflammatory changes. Some dermoid cysts may appear moderately to markedly hyperdense on CT scans. On MR imaging, dermoid and epidermoid cysts have low signal intensity on T1-weighted MR images and high signal intensity on T2-weighted, flair as well as diffusion-weighted MR images (Fig. 9-41B). A dermoid cyst that contains significant fatty tissue demonstrates the MR characteristics of fat (Fig. 9-42B). Both dermoid and epidermoid cysts may demonstrate marginal enhancement of their wall on postcontrast CT and MR images. The CT and MR imaging features of these lesions are shown in Table 9-4.

Copyright © 2003, Mosby, Inc. All rights reserved.

VIEW IMAGE

FIGURE 9-41 Epidermoid cyst. **A**, Postcontrast axial CT scan shows a nonenhanced low-density mass (*E*) compatible with an epidermoid cyst. Notice the scalloping of the lateral orbital wall (*arrows*). **B**, T2-weighted MR scan. The epidermoid cyst (*E*) appears as a homogeneous hyperintense mass.

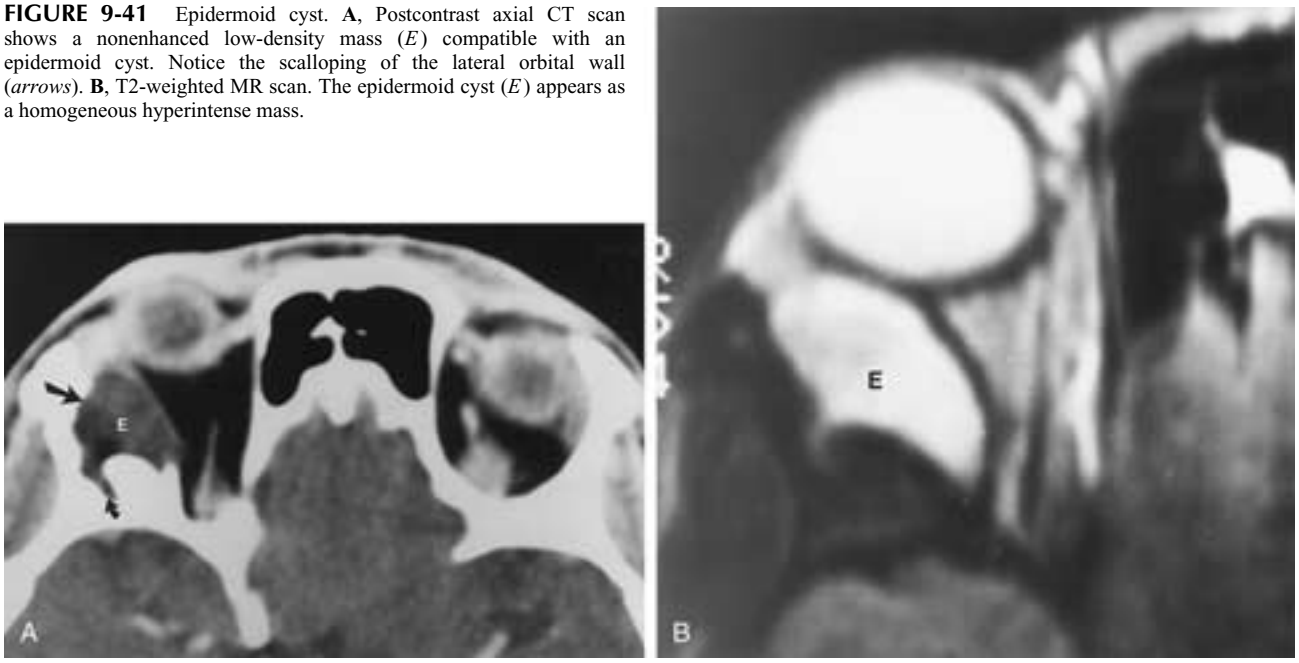

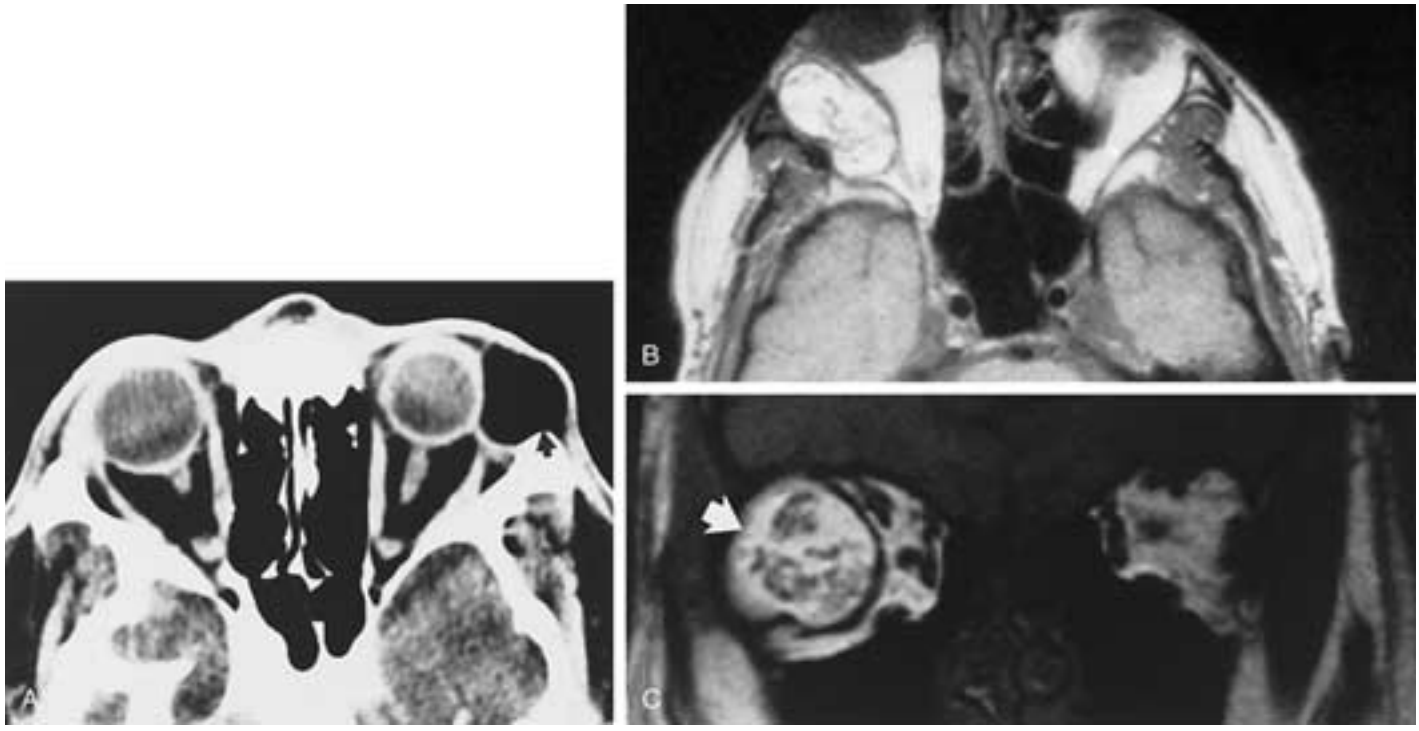

FIGURE 9-42 **A**, Dermoid. Axial CT scan shows a fat-containing lesion (*arrow*) compatible with an orbital dermoid. **B**, Another patient. Dermoid. PW axial MR image and T2-weighted coronal MR image (**C**) show a giant dermoid (*arrow*). The lesion is inhomogeneous and contains hyperintense areas caused by fat. The lesion is nearly isointense to fat on the T2-weighted MR image. **D**, Axial-enhanced CT scan shows a well-circumscribed, rounded, low-density dermoid cyst (*C*) in the nasal aspect of the anterior orbit. (From Kaufman LM et al. Diagnostic imaging of cystic lesions in the child's orbit. Radiol Clin North Am 1998;36:1149–1163.)

VIEW IMAGE

Copyright © 2003, Mosby, Inc. All rights reserved.

Table 9-4
CT AND MR IMAGING FEATURES OF ORBITAL CYSTS

Diagnostic Group	CT Characteristics	MR Imaging Characteristics
Epidermoid cyst	Nonenhancing mass with or without bone erosion Scalloping with sclerosis of the adjacent bone may be present No calcification Minimal enhancement of the capsule may be present	Hypointense on T1-weighted and hyperintense on T2-weighted images Minimal enhancement of capsule may be present Associated orbital inflammatory changes, when cyst is ruptured
Dermoid cyst	Nonenhancing mass with or without bone erosion Scalloping with sclerosis of the adjacent bone may be present Calcification, if present, is a characteristic feature Hypodensity (fat), if present, is characteristic (adipose tissue) Fat-fluid level may be present and is characteristic Minimal enhancement of the capsule may be present	Hypointense on T1-weighted and hyperintense on T2-weighted images Those containing fat demonstrate signal characteristics of fatty tissue Minimal enhancement of capsule may be present Associated orbital inflammatory changes, when cyst is ruptured
Conjunctival choristoma (dermolipoma)	Density of adipose tissue	Intensity of adipose tissue
Cholesterol granuloma (chronic hematic cyst)	Nonenhancing mass with or without bone erosion Lytic lesion with ragged bone destruction Often isodense to brain No sclerotic margin	High signal on T1-weighted and T2-weighted images Often homogeneous in signal characteristics Heterogeneous signal, particularly on T2-weighted images
Enterogenous cysts	Isodense or hyperdense, depending on the mucous content of the cyst	Hypointense or hyperintense on T1-weighted images, depending on the mucous content of the cyst, and hyperintense on T2-weighted images
Other orbital epithelial and appendage cysts, including implantation cysts	Nonenhancing low-density mass	Nonenhancing, hypointense on T1-weighted and hyperintense on T2-weighted images
Congenital cystic eye	Nonenhancing low-density mass	Hypointense on T1-weighted and hyperintense on T2-weighted images Nonenhancing mass
Dacryocele	Nonenhancing (unless infected) low-density mass	Hypointense on T1-weighted and hyperintense on T2-weighted images; nonenhancing mass, unless infected
Parasitic cysts (hydatid, cysticercosis)	Cystic lesions within or near an EOM Some degree of enhancement around the cyst wall Scolex can be identified Diffuse myositis may be present Cystic lesion within or near lacrimal gland or other part of the orbit	Cystic lesions within or near an EOM Hypointense on T1-weighted and hyperintense on T2-weighted images Some degree of enhancement around the cyst wall Scolex can be identified Diffuse myositis may be present

Other Less Common Congenital Anomalies and Acquired Cysts of the Orbit and Optic System

The orbit develops from mesodermal tissues, and the globe and optic pathway develop from ectodermal tissues. Developmental defects of the eyeball result in a small orbit. The majority of orbital changes are found in association with deformities of the skull (Fig. 9-30) and skeleton.[36] Cyclopia, synophthalmia, clinical anophthalmia, and microphthalmia (Figs. 9-30 and 9-31) are developmental anomalies of the globe that are seen in the fetal central system anomalies associated with problems in forebrain differentiation (holoprosencephaly). MR imaging is particularly noteworthy in the detection of these anomalies. In general, a variety of cysts and cyst-like lesions involve the orbit. The list includes developmental anomalies as well as acquired lesions arising in the orbit or in adjacent structures.[73] A *cyst* is defined as a closed sac with a membranous or cellular lining and a luminal space containing air, fluid, semifluid, or solid materials. Cysts typically result from developmental anomalies, obstruction of ducts, or parasitic infections or trauma, as listed in Table 9-5.

Congenital Cystic Eye

Congenital cystic eye is a rare congenital anomaly resulting from failure of the optic vesicle to invaginate during the fourth week of embryogenesis.[73] It presents at birth as a complex cyst occupying the orbit, without any vestige of a globe (Fig. 9-43). The cyst wall is lined by cells derived from undifferentiated retina and retinal pigment epithelium. Some remnant of an optic nerve–like structure and extraocular muscles may be present.[73] CT and MR imaging generally show an enlarged orbit containing a rounded or ovoid, septated cyst (Fig. 9-43). The superior orbital fissure may be enlarged (widened) ipsilaterally. On MR imaging, the signal intensity of the cyst may not be equal to that of the normal vitreous, because the cyst is generally filled with serum. A rudimentary connection to a thinned optic nerve may be seen. A nodular focus may be seen adjacent to the cyst wall, representing primitive ectopic lens tissue.[73] In the colobomatous orbital cyst, unlike the congenital cystic eye, the globe and optic nerve are seen on CT and MR imaging. The globe is, however, microphthalmic (Fig. 9-44). Orbital colobomatous cysts are described in Chapter 8.

Copyright © 2003, Mosby, Inc. All rights reserved.

Other Orbital Cysts

Optic Nerve Sheath Meningocele

Optic neural sheath meningocele (optic nerve sheath cyst, arachnoid cyst, perioptic hygroma, and dural ectasia, among others) is a saccular dilatation of the meninges surrounding the orbital portion of the optic nerve.[77] These meningoceles may occur primarily or secondarily in association with other orbital processes, such as meningioma, optic nerve pilocytic astrocytoma, and hemangioma. Clinically, these meningoceles may present with changes in visual acuity, visual field, and optic nerve appearance. The CT and MR imaging appearance of optic nerve meningocele or ectasia is that of a prominent focal or segmental enlargement of the dural arachnoid sheath around the optic nerve (Fig. 9-45). The optic nerve dural ectasia may be associated with an empty sella and enlarged subarachnoid cisterns, such as gasserian cisterns (Fig. 9-46).

Cephaloceles include meningocele, encephalocele, meningoencephalocele, and porencephalic cyst.[73] A cephalocele is a cyst-like herniation of brain or meningeal tissues into adjacent structures. The lesions are commonly congenital but can also be due to acquired defects in the bony orbit. The herniated tissue may be limited to meninges (meningocele); brain parenchyma (encephalocele); brain and meninges (meningoencephalocele); or expanding porencephalic cysts. Brain tissue may herniate into the orbit via natural orbital foramina, such as the superior orbital fissure; through dehiscences of the cranial sutures; or through bony orbital defects, such as those seen in patients with neurofibromatosis type 1. When a cleft associated with a midline craniofacial dysraphism affects the nose, there is an increased incidence of frontonasal and intraorbital encephaloceles, anophthalmos, or microphthalmos. Hypertelorism and a broad nasal root are also found in nearly all affected individuals.[73] MR imaging remains the study of choice to illustrate cephaloceles.

Table 9-5
ORBITAL CYST

I.	Developmental
	Choristoma (epidermal, dermoid, dermolipoma)
	Teratoma
	Colobomatous cyst
	Congenital cystic eye
	Optic nerve sheath meningocele
	Congenital dacryocele (mucocele)
II.	Cysts of Adjacent Structures
	Cephalocele (meningocele, encephalocele, meningoencephalocele, porencephalic cyst)
	Enterogenous cyst
	Dentigerous cyst
III.	Acquired Orbital Cyst
	Mucocele
	Mucopyocele
	Dacryocele
	Cystic vascular lesions (lymphangioma, orbital varix)
	Chocolate cyst (hemorrhagic cyst)
	Epithelial and appendage cysts
	Epithelial implantation cysts
	Lacrimal gland cyst
	Lacrimal sac cyst (dacryocele), mucocele
	Hematic cyst (subperiosteal)
	Cholesterol granulomatous cyst
	Aneurysmal bone cyst
	Cystic myositis
	Orbital abscess
	Parasitic cyst (hydatid cyst, cysticercoses)

Enterogenous Cysts

Enterogenous cysts are rare congenital choristomatous cysts of the central nervous system. They contain a single layer of mucin-secreting epithelial cells that resemble gastrointestinal epithelium. The lower cervical and cervicothoracic regions are the more common sites of the lesion. An orbital location is extremely rare.[78] Occasionally these cysts may be seen in the anterior cranial fossa and extending into the orbit. CT shows a well-circumscribed, homogeneous, rather hyperdense, lobular, nonenhancing mass. Extension through the superior orbital fissure may be present. Bony erosion due to compressive bone atrophy or bony remodeling including the greater wing of the sphenoid bone and ethmoid roof may be present. On MR imaging, the lesion usually appears hyperintense on T1-weighted images due to the mucous secretions elaborated by the epithelial lining cells. The T2-weighted MR images may show variable signal intensity, depending on the protein content of the fluid within the cyst. Enhancement of the mucosal rim may be seen on enhanced CT and MR images.[78]

Dentigerous Cysts

Dentigerous cysts, fluid-filled and lined by keratinizing (keratogenic cysts) or nonkeratinizing, stratified squamous epithelium, arise from the jaw. Infrequently, the cyst can enlarge into the maxillary sinus and erode into the orbit. These cysts appear as a nonenhancing low-density mass on CT scans. On MR imaging they appear with a low to intermediate signal on T1-weighted MR images and hyperintense on T2-weighted MR images. The signal characteristics on T1-weighted MR images depend on the cyst's protein content.

Cystic Vascular Lesions: Lymphangioma, Varix, Chocolate Cyst

Lymphangioma and varix will be described later in this chapter. Lymphangiomas contain numerous variably sized cystic spaces. Acute hemorrhage into these cystic spaces, whether spontaneous or after minor trauma, results in chocolate cysts. A varix is a venous anomaly and may include a single smooth-contoured, dilated vein. Intralesional hemorrhage in an orbital varix may result in the formation of a chocolate cyst.[73]

Epithelial and Appendage Cysts

Various acquired cysts involving the eyelids or superficial orbit may derive from the skin of the eyelids, the skin appendages (glands and cilia), or the conjunctiva.[73] Common in children is the chalazion, a cystic expansion at the meibomian sebaceous gland due to a blockage of its excretory duct. Other cysts include apocrine hidrocystoma (sudoriferous cyst), originating from a blocked excretory duct of Moll's apocrine sweat gland; eccrine hidrocystoma, derived from the lid eccrine sweat gland; sebaceous cyst (pilar cyst, retention cyst of the pilosebaceous structure); milia (cystic expansion of the pilosebaceous structure due to obstruction of the orifice); epidermal inclusion cyst (cutane-

Copyright © 2003, Mosby, Inc. All rights reserved.

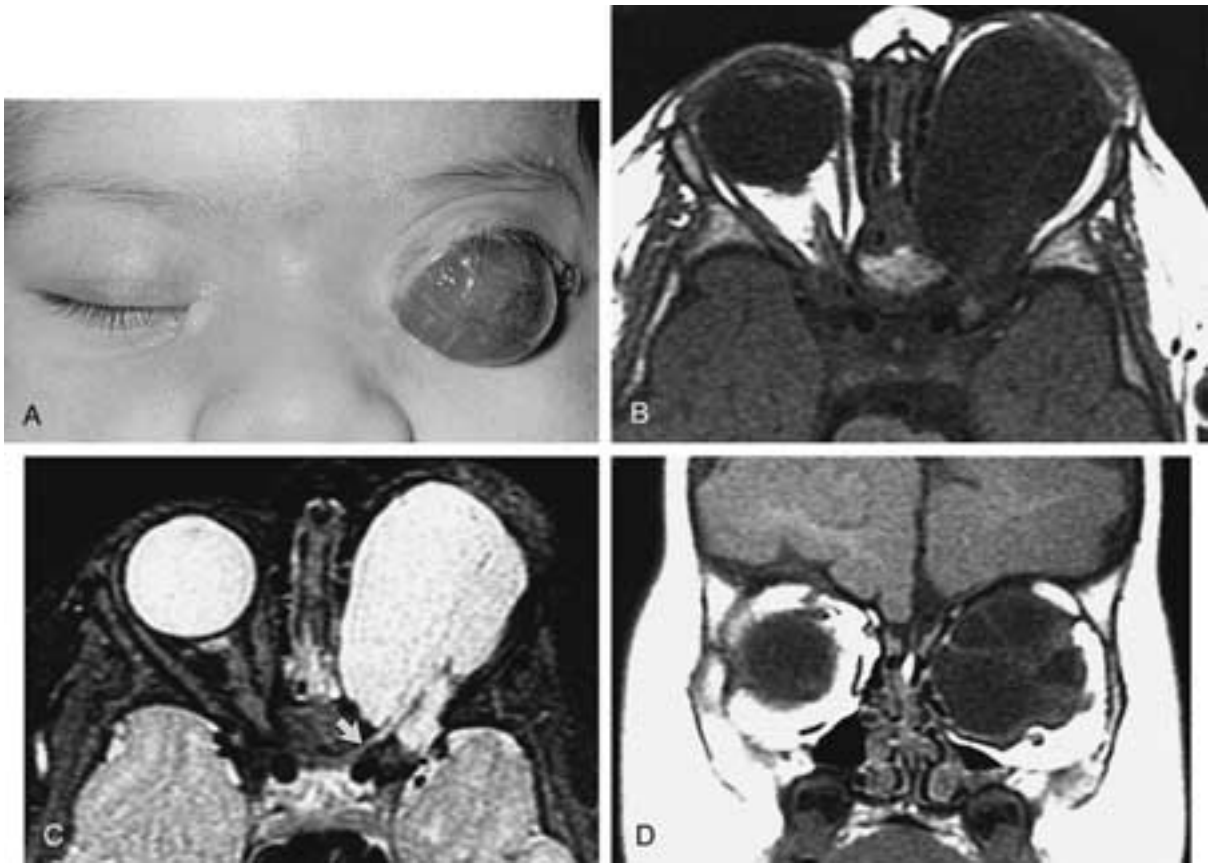

VIEW IMAGE

FIGURE 9-43 Congenital cystic eye. **A**, Four-month-old girl with a congenital cystic eye associated with Goltz's syndrome. **B**, Axial T1-weighted MR image through the orbit shows a large orbital cyst, an enlarged orbit, and no discernible normal bulbar structures on the left. **C**, Axial T2-weighted MR image shows a rudimentary optic nerve (*arrow*) leading into the lesion. Signal intensity is homogeneously high. **D**, Coronal contrast-enhanced, T1-weighted MR image shows thin, enhancing strands and a more focal amorphous tissue mass in the posterior aspect of the lesion (probably dysmorphic retinal tissue). (From Kaufman LM et al. Diagnostic imaging of cystic lesions in the child's orbit. Radiol Clin North Am 1998;36:1149–1163.)

ous or subcutaneous cyst lined by stratified squamous epithelium with a keratin-filled lumen); pilomatrixoma (calcifying epithelioma of Malherbe, a solid or cystic mass derived from hair matrix cells); and conjunctival inclusion cyst (a thin-walled, fluid-filled cyst lined by stratified, nonkeratinizing, cuboidal epithelium containing mucus-secreting goblet cells). Because most epithelial and appendage cysts remain small (less than 1 cm) and limited to the eyelid and the superficial orbit, medical imaging studies are rarely ordered by the ophthalmologist.

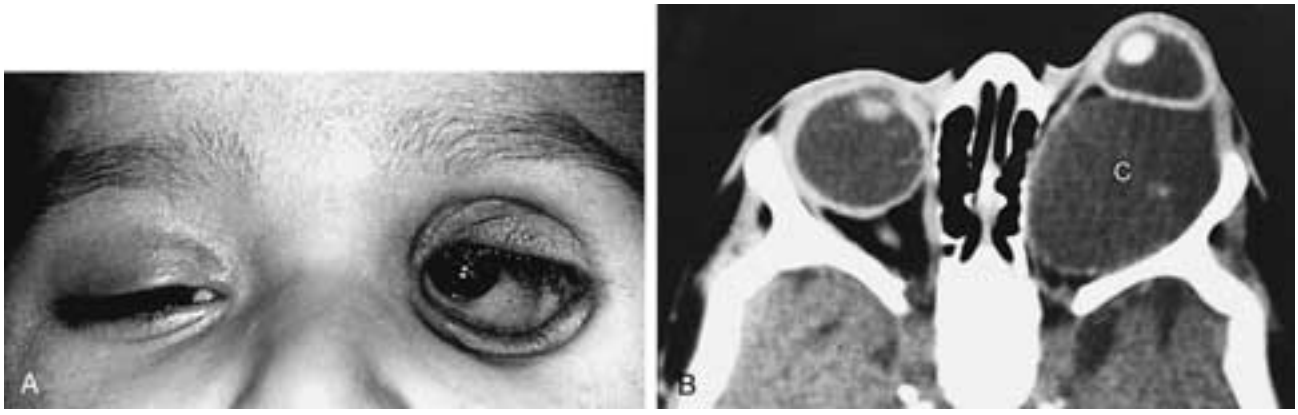

VIEW IMAGE

FIGURE 9-44 **A**, Six-month-old girl with proptosis of a microphthalmic eye with colobomatous cyst. **B**, CT image shows a large, low-density retrobulbar cyst (*C*) and a microphthalmic eye. The connection between the cyst and the globe is not evident in this image. (From Kaufman LM et al. Diagnostic imaging of cystic lesions in the child's orbit. Radiol Clin North Am 1998;36:1149–1163.)

Copyright © 2003, Mosby, Inc. All rights reserved.

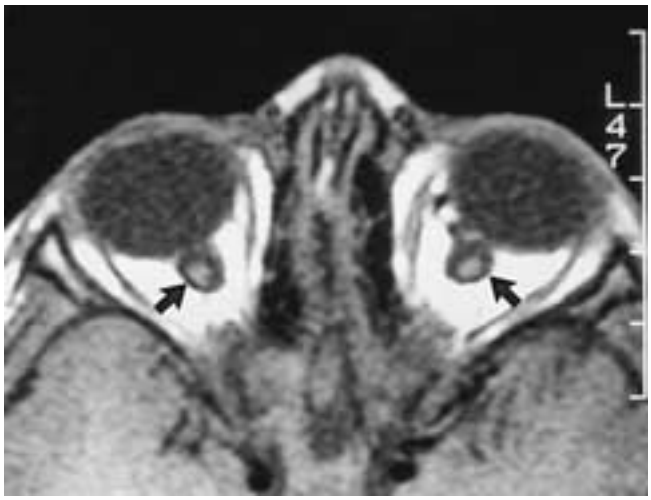

FIGURE 9-45 Ectasia of the optic nerve sheath (meningocele). Axial T1-weighted MR image shows the prominence of the subarachnoid space around the nerves (*arrows*). (From Kaufman LM et al. Diagnostic imaging of cystic lesions in the child's orbit. Radiol Clin North Am 1998;36:1149–1163.)

VIEW IMAGE

Epithelial Implantation Cysts

Epithelial implantation cysts are derived from cells of the cutaneous epithelium, conjunctival epithelium, or respiratory epithelium that are traumatically displaced under the skin of the eyelid or into the orbit. The CT and MR imaging appearance of these cysts is nonspecific and similar to that of any simple cyst (Fig. 9-47). A nonenhanced cystic orbital mass following orbital surgery or enucleation should raise the question of the presence of an epithelial implantation cyst.

FIGURE 9-46 Ectasia of the optic nerve sheath. T2-weighted MR image shows marked expansion of the subarachnoid space around the right optic nerve (*arrow*). Note the empty sella (*E*) and dilated Gasserian cisterns (*G*). (From Kaufman LM et al. Diagnostic imaging of cystic lesions in the child's orbit. Radiol Clin North Am 1998;36:1149–1163.)

VIEW IMAGE

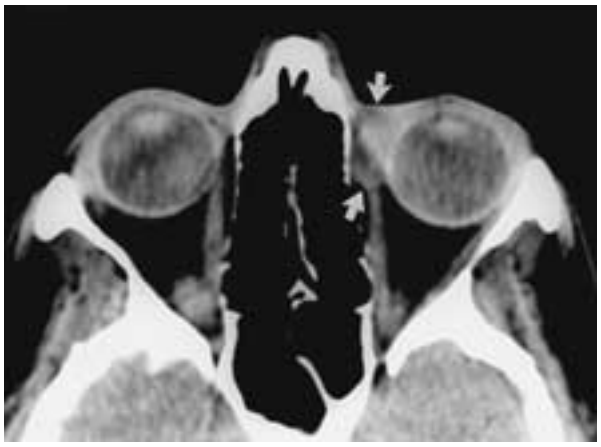

FIGURE 9-47 Axial CT scan shows a well-defined mass (*arrows*) compatible with an epithelial implantation cyst. (From Kaufman LM et al. Diagnostic imaging of cystic lesions in the child's orbit. Radiol Clin North Am 1998;36:1149–1163.)

VIEW IMAGE

Lacrimal Gland Cysts

Cysts of the lacrimal glands can be due to blockage of the gland's excretory ducts.[73] The cyst is then located in either the orbital or the palpebral lobe of the main lacrimal gland, or in the conjunctival fornices due to blockage of the accessory lacrimal glands of Krause and Wolfring.[73] The CT and MR imaging appearance of lacrimal gland cysts is similar to that of any simple cyst (Figs. 9-48 and 9-49).

Dacryoceles

A dacryocele (lacrimal sac mucocele) is a cystic expansion of the nasolacrimal sac or a diverticulum of the sac. The expansion is caused by a proximal or distal block of the nasolacrimal duct. Dacryoceles are considered a congenital anomaly of the lacrimal drainage system and are usually apparent in the first few days of life. On CT and MR imaging, dacryoceles appear as well-circumscribed, rounded lesions centered in the nasolacrimal sac region. On CT scans, the density of the lesion is homogeneous when noninfected. On MR imaging, a dacryocele appears hy-

FIGURE 9-48 CT scan shows a low-density image (*arrows*) compatible with a lacrimal gland cyst. (From Kaufman LM et al. Diagnostic imaging of cystic lesions in the child's orbit. Radiol Clin North Am 1998;36:1149–1163.)

VIEW IMAGE

Copyright © 2003, Mosby, Inc. All rights reserved.

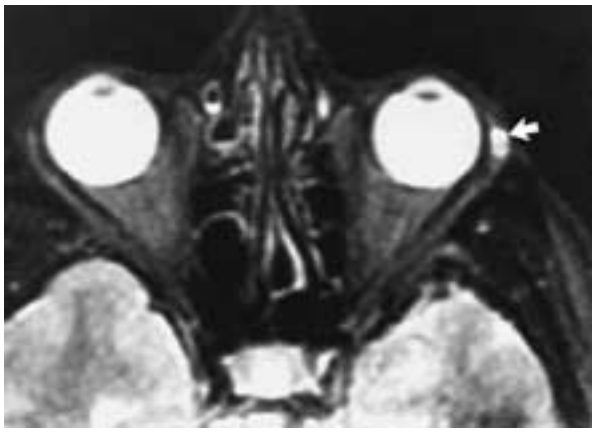

VIEW IMAGE

FIGURE 9-49 Axial T2-weighted MR image shows a lacrimal gland cyst (*arrow*). (From Kaufman LM et al. Diagnostic imaging of cystic lesions in the child's orbit. Radiol Clin North Am 1998;36:1149–1163.)

pointense on T1-weighted and hyperintense on T2-weighted images. If it is infected, there may be a rim of contrast enhancement (Fig. 9-50).

Hematic Cysts and Cholesterol Granuloma

Most orbital hematomas, like other localized collections of blood, resolve within days. The hematic cyst (organizing hematoma, hematocele), is a cyst-like mass that develops slowly as an acute orbital hemorrhage, is incompletely absorbed, and undergoes organization.[73] There may be a fibrous cyst wall with a lumen composed of degraded blood products, cholesterol, hemosiderin, hematoidin crystals, erythrocytes, histiocytes, giant cells, and granuloma tissue. The hematic cyst may occur anywhere in the orbit or in the orbital bones (cholesterol granuloma).[73, 79] The subperiosteal compartment of the orbit, a potential space, is an important entity due to its unique anatomy, location, and susceptibility to various pathologic processes, such as

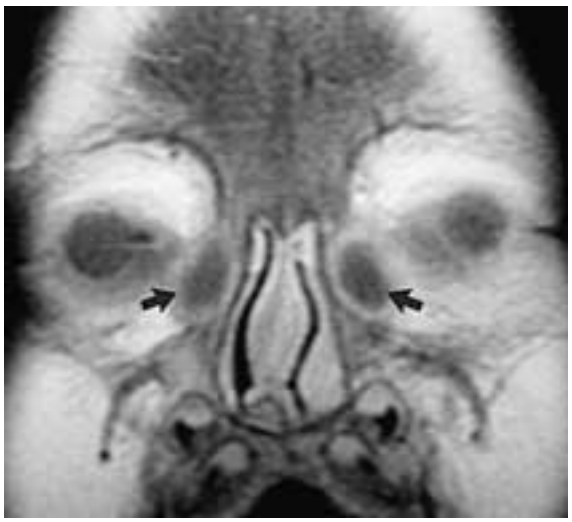

VIEW IMAGE

FIGURE 9-50 Enhanced coronal T1-weighted MR image shows bilateral dacryoceles (*arrows*). (From Kaufman LM et al. Diagnostic imaging of cystic lesions in the child's orbit. Radiol Clin North Am 1998;36:1149–1163.)

hemorrhage, infection, infiltration of lymphoproliferative disorders, infiltration of en plaque meningiomas, and metastasis.[17, 79] The etiology of subperiosteal hematomas is either traumatic or spontaneous. Traumatic hemorrhage is most common, but the time interval between the traumatic episode and the clinical manifestation may vary from immediate to months or years.[17, 79] Spontaneous hemorrhage can occur as a complication of leukemia, thrombocytopenia, blood dyscrasia, hemophilia, anticoagulant use, and other hemorrhagic systemic diseases, including sickle cell anemia.[79] Subperiosteal hematomas can be of several varieties. Acute subperiosteal hematoma is a rare complication of trauma, presenting as painful unilateral proptosis.[79] It may also develop so insidiously as to defy explanation, especially when there is no definite history of injury. Usually it is the result of bleeding from the subperiosteal blood vessels.[79] It may also develop as an extension of a subgaleal hematoma. At times it is continuous with an epidural hematoma after head trauma. In cases of trauma, blood tends to collect in the subperiosteal location superiorly, as the frontal bone is the largest continuous concave surface of the orbit and has a loose periosteal attachment.[79]

Diagnostic Imaging

CT is a very accurate diagnostic method to evaluate subperiosteal hematomas. Coronal sections, either direct or reformatted, are essential for accurate diagnoses. The CT appearance of acute and subacute subperiosteal hematomas is that of a sharply defined extraconal, homogeneous, high-density, nonenhancing mass with a broad base abutting the bone and displacing the peripheral orbital fat toward the center of the orbit (Figs. 9-51 to 9-53). The mass, like other subperiosteal lesions, is fusiform or biconvex, is confined by the sutures (frontozygomatic or frontoethmoidal), and is best seen in coronal or sagittal images. Prompt aspiration of the hematoma can lead to early decompression and prevent serious late sequelae. A chronic subperiosteal hematoma appears on CT as a heterogeneous, relatively hypodense, sharply defined extraconal mass with a broad base (Fig. 9-54). Long-standing chronic hematic cysts, the so-called cholesterol granulomas, appear as cystic lesions, associated with compression bone atrophy as well as expansion and erosions of adjacent bone (Fig. 9-55). On a CT scan, chronic hematic cysts may not be differentiated from epidermoid-dermoid cysts (Fig. 9-10). However, they can be easily differentiated by MR imaging (Fig. 9-56).

MR Imaging Findings in Various Stages of Orbital Hematoma

The diagnosis of hematoma is greatly aided by MR imaging, which can characterize all stages of blood degradation. The iron atoms of hemoglobin have a different magnetic effect, depending on the physical and oxidative state of the hemoglobin itself.[80] Fresh (hyperacute) oxygenated blood (hemorrhage no more than a few hours old) has approximately the same MR imaging characteristics as water, being hypointense on T1-weighted and hyperintense on T2-weighted images, using a high field (1.5 Tesla) MR unit. Acute hemorrhages (1 to 7 days old), because of the paramagnetic effect of deoxyhemoglobin, have a low signal on T1-weighted and in particular on T2-weighted images

Copyright © 2003, Mosby, Inc. All rights reserved.

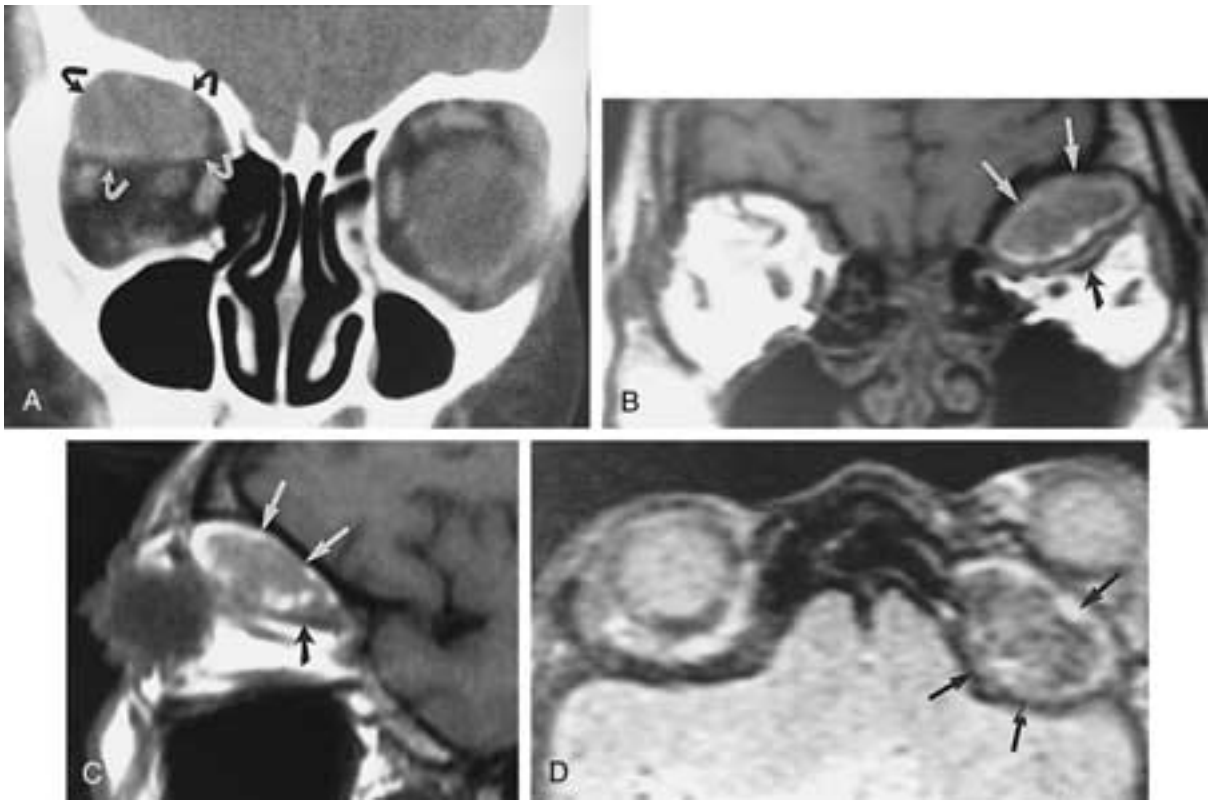

VIEW IMAGE

FIGURE 9-51 Acute subperiosteal hematoma. **A**, Coronal CT scan through the orbit showing a hyperdense acute subperiosteal hematoma (*arrows*) along the roof of the orbit and displacing the orbital contents inferiorly. **B**, Coronal T1-weighted (500/20, TR/TE) MR image in another patient showing the intermediate signal intensity of an acute subperiosteal hematoma (*white arrows*). Note the displaced periosteum (*black arrow*). **C**, Sagittal T1-weighted (600/20, TR/TE) MR image of the same patient in **B** showing the acute subperiosteal orbital hematoma (*white arrows*). Note the displaced periosteum (*black arrow*). **D**, Axial T2-weighted (200/80, TR/TE) MR image of the same patient in **B** through the orbit. Note the low signal intensity of the acute hematoma (*arrows*) on the T2-weighted image. (From Dobben GD et al. Orbital subperiosteal hematoma, cholesterol granuloma, and infection. Evaluation with MR imaging and CT. Radiol Clin North Am 1998;36:1185–1200.)

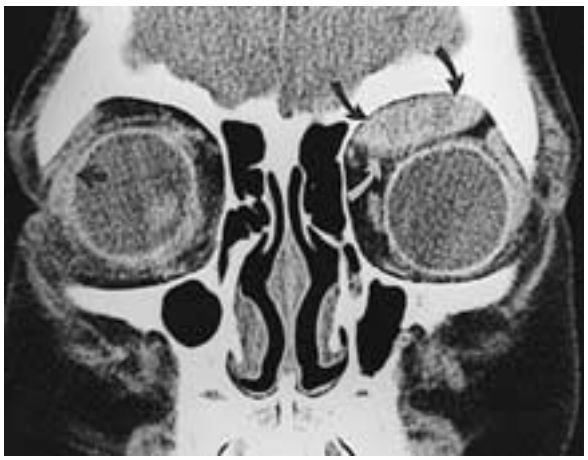

VIEW IMAGE

FIGURE 9-52 Acute subperiosteal hematoma. Coronal CT scan through the orbit of an 8-year-old boy showing an acute subperiosteal hematoma (*curved arrows*). Note its hyperdense nature and fusiform shape. Note the normal lacrimal gland (*arrow*) on the opposite side. (From Dobben GD et al. Orbital subperiosteal hematoma, cholesterol granuloma, and infection. Evaluation with MR imaging and CT. Radiol Clin North Am 1998;36:1185–1200.)

(Fig. 9-51). With progressive oxidation of deoxyhemoglobin to methemoglobin, hemorrhages older than 7 days become hyperintense on T1-weighted images (Fig. 9-56). The signal on T2-weighted MR images remains low if the methemoglobin is still intracellular (i.e., if oxidation occurred before erythrocyte lysis), therefore having limited motion. The signal is high if the methemoglobin has become extracellular (Fig. 9-56). Hemosiderin, which causes a low signal on both T1-weighted and T2-weighted sequences, is encountered in scars or organized hematoma.[80] The MR imaging of hematoma is presented in Table 9-6.

Orbital Cholesterol Granuloma

Cholesterol granulomas are bone-pushing and bone-destroying lesions characterized by granulomatous infiltration surrounding cholesterol crystals. The cholesterol granuloma may be etiologically related to the loss of aeration of normally pneumatized bone, such as the petromastoid bone. Negative pressure develops, leading to tissue edema and hemorrhage. Rupture of red blood cell membranes results in precipitation of cholesterol and membrane phospholipids. This crystallized cholesterol, in turn, acts as a foreign body and elicits a giant cell

Copyright © 2003, Mosby, Inc. All rights reserved.

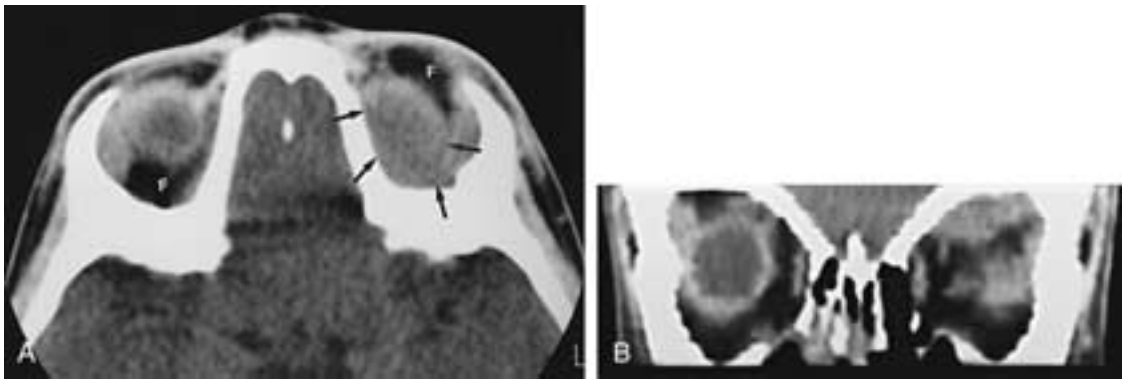

VIEW IMAGE

FIGURE 9-53 Subacute subperiosteal hematoma (less than 7 days). **A**, Axial CT scan of the orbit in a 2-year-old child. Note the subacute subperiosteal hematoma (*arrows*) and displacement of the peripheral orbital fat (F). **B**, Coronal reformatted images of the same patient showing the subacute hematoma. (From Dobben GD et al. Orbital subperiosteal hematoma, cholesterol granuloma, and infection. Evaluation with MR imaging and CT. Radiol Clin North Am 1998;36:1185–1200.)

granulomatous reaction. Histologically, there are no epithelial elements in the cholesterol granuloma. Histologically, the tissues consist of foci of reactive xanthogranulomatous infiltrates, cholesterol crystals, giant cells, and hemosiderin surrounded by a fibrous capsule (Fig. 9-55B). The initiating factors must be different in the lesions arising in nonpneumatized bone from those in the orbital region. In the orbit, cholesterol granulomas are secondary lesions that are formed due to a posttraumatic, postsurgical, or postinflammatory event. Various terms have been used to describe cholesterol granuloma including *lipid granuloma*, *cholesteatoma*, *xanthomatosis*, *histiocytic granuloma*, and *chronic hematic cyst*. Cholesteatomas are considered epidermoid cysts and should not be confused with cholesterol granulomas.

Diagnostic Imaging. On CT, cholesterol granulomas are seen as lytic lesions, usually with ragged bone destruction, that invariably extend extraperiosteally into the orbit, causing proptosis (Fig. 9-55A). Extension into the anterior and middle cranial fossae occurs less frequently.[79] On CT scans, the density of a cholesterol granuloma is approximately isodense with the brain, with the attenuation values ranging from 25 to 45 HU (mean, 34 HU). Unlike epidermoid cyst, no sclerotic margin is seen between the mass and normal diploic bone. The lesion demonstrates no enhancement on postcontrast CT scans. The differential diagnosis on the basis of CT scanning is limited to epidermoid and dermoid cysts or aneurysmal bone cyst. Aneurysmal bone cysts occur almost exclusively in children.[79] MR imaging can be of most value in the diagnosis of cholesterol granuloma. These lesions give rise to high signal on T1-weighted and T2-weighted sequences, characteristic of chronic hemorrhage (Fig. 9-57).[79]

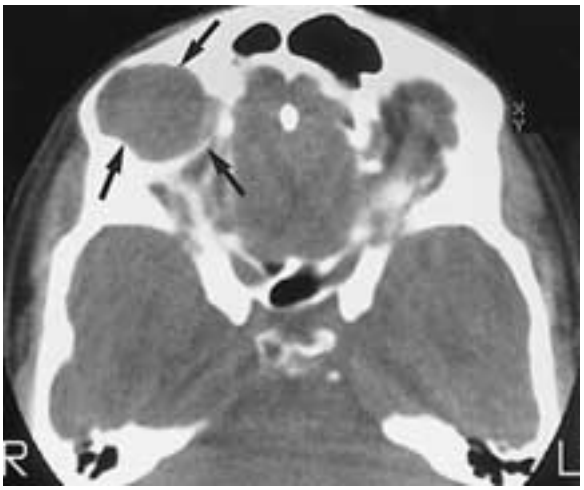

VIEW IMAGE

FIGURE 9-54 Chronic subperiosteal hematoma (cholesterol granuloma). Axial CT scan shows an expansile mass (*arrows*) compatible with a chronic hematic cyst. (From Dobben GD et al. Orbital subperiosteal hematoma, cholesterol granuloma, and infection. Evaluation with MR imaging and CT. Radiol Clin North Am 1998;36:1185–1200.)

Aneurysmal Bone Cysts

The term *aneurysmal bone cyst* (ABC) is a misnomer, because the lesion is histologically neither an aneurysm nor a cyst. Infrequently, ABC of the facial bones may involve the orbit in children.[73] ABC has been described as a benign lesion of bone characterized by a blood-filled cyst-like expansion within the bone. The expansion may be complex and multilobular, with septae of bony trabeculae, fibrous tissues, and stromal giant cells. The lesions remodel adjacent bone, but the surrounding periosteum remains intact. ABC is not an entity by itself but is always secondary to an underlying bony or fibroosseous condition, such as nonossifying fibroma, ossifying fibroma, fibrous dysplasia, juvenile pseudomonatous active (aggressive) ossifying fibroma (Fig. 9-58), chondroblastoma, chondromyxoid fibroma, osteoblastoma, giant cell tumor (osteoclastoma), fibrosarcoma, osteochondrosarcoma, hemangioendothelioma, or hemangioma.[73]

Cystic Myositis

Infrequently, nonspecific orbital myositis may result in cyst-like changes in an extraocular muscle.[73] These cysts may respond to treatment with oral corticosteroids, suggest-

Copyright © 2003, Mosby, Inc. All rights reserved.

ing that the cysts do not have a parasitic origin and probably represent edema in the muscles.[73]

Orbital Abscesses (Inflammatory Orbital Cysts)

Orbital abscesses are cyst-like pus pockets that develop subperiosteally, or in the orbit or lids, in association with orbital or preseptal cellulitis most often associated with sinonasal infections (Fig. 9-59). The CT and MR imaging of orbital abscesses will be described in a following section.

Parasitic Cysts

Hydatid Cysts

The occurrence of parasitic orbital cysts is limited to endemic regions with poor sanitation. The hydatid cyst is related to infection by the larval form of a parasitic tapeworm, *Echinococcus granulosus*. The adult worm lives in the intestines of carnivores (usually dogs but not humans). The infected carnivore passes the worm's ova in its feces. Grazing animals, acting as intermediate hosts, ingest the

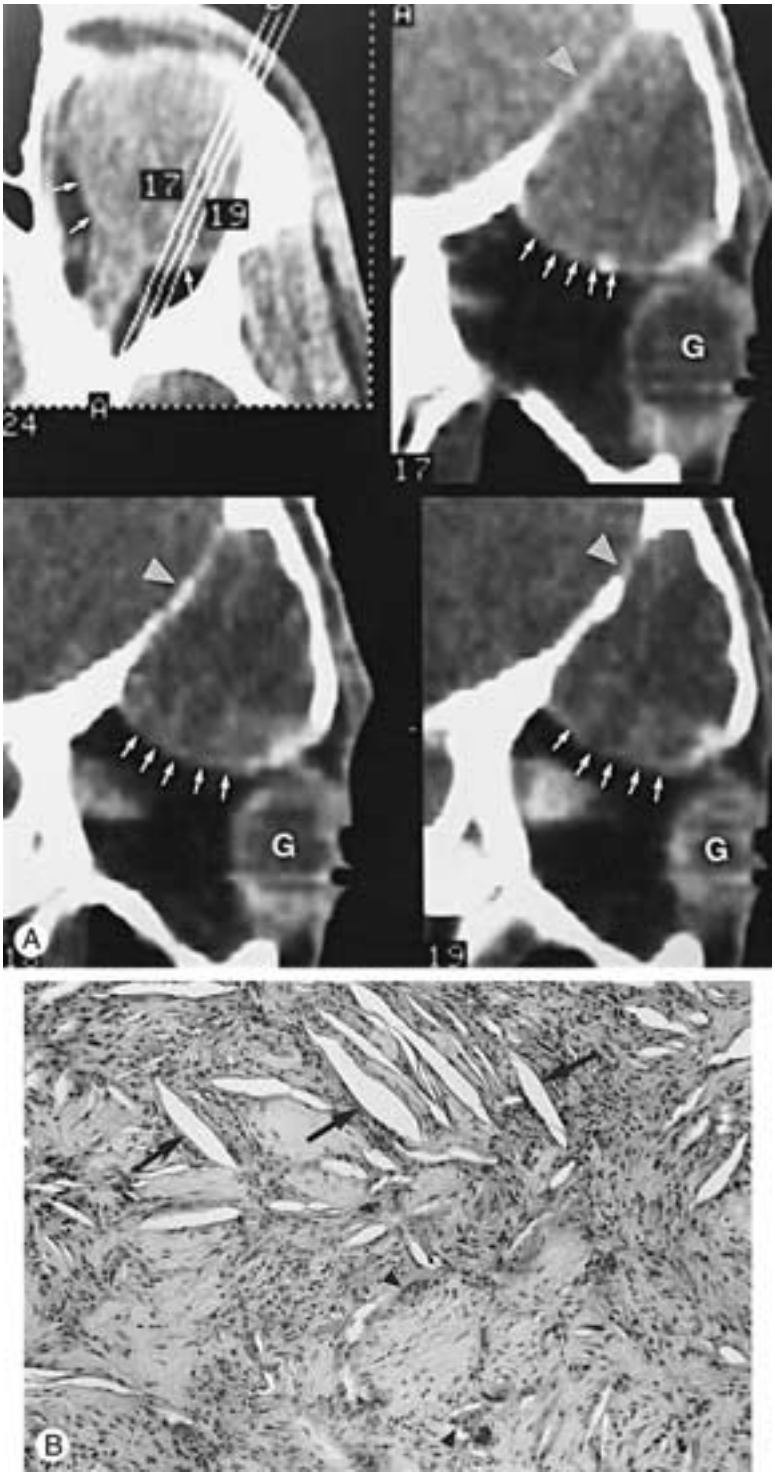

VIEW IMAGE

FIGURE 9-55 Chronic hematic cyst (cholesterol granuloma). **A**, Axial CT scan with oblique sagittal reformatting showing a cholesterol granuloma (*arrows*) of the left orbit. Note the displacement of the globe (*G*) inferiorly. The lesion, which is almost isodense with brain, has caused ragged bony destruction (*arrowheads*). On the axial image, the lesion may be mistaken for a lacrimal gland mass. **B**, Histopathologic examination of a cholesterol granuloma showing abundant cholesterol cells (*arrows*), foreign-body giant cells (*arrowheads*), and inflammatory cells (hematoxylin-eosin, original magnification ×40). (From Dobben GD et al. Orbital subperiosteal hematoma, cholesterol granuloma, and infection. Evaluation with MR imaging and CT. Radiol Clin North Am 1998;36:1185–1200.)

Copyright © 2003, Mosby, Inc. All rights reserved.

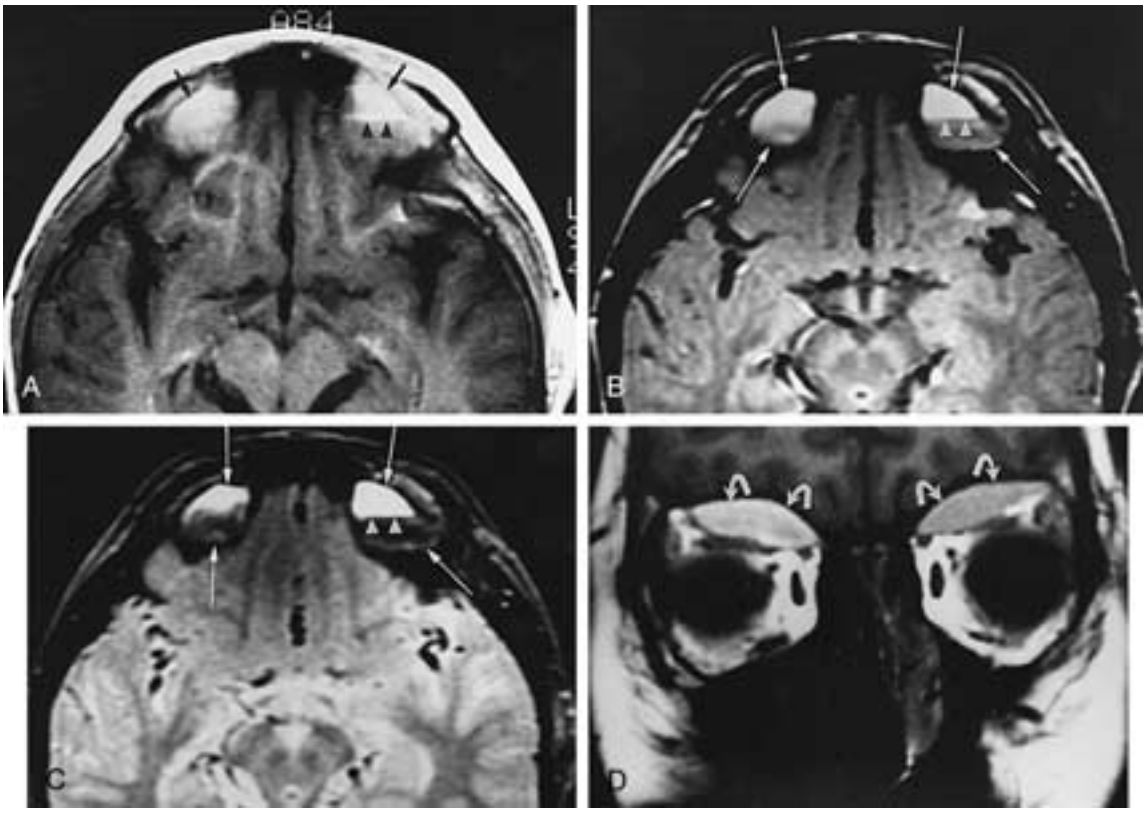

FIGURE 9-56 Subacute subperiosteal hematoma. **A**, Axial contrast-enhanced T1-weighted (350/16, TR/TE) MR image shows a subacute subperiosteal hematoma (*arrows*) in an 8-year-old child. Note the high to mixed signal intensity pattern on the T1-weighted sequence. Note the fluid-fluid level (*arrowheads*). **B**, Axial proton-density (2300/30, TR/TE) MR image of the same patient showing a fluid-fluid level (*arrowheads*) within the hematoma (*arrows*). **C**, Axial T2-weighted (2300/80, TR/TE) MR image showing a mixed signal intensity pattern with hypointensity images related to the intracellular methemoglobin portion of the subacute hematoma (*arrows*). Note the fluid-fluid level (*arrowheads*). **D**, Coronal T1-weighted (600/12, TR/TE) MR image reveals an excellent demonstration of the subacute subperiosteal hematoma (*arrows*). Note the high to intermediate signal intensity of the hematoma. (From Dobben GD et al. Orbital subperiosteal hematoma, cholesterol granuloma, and infection. Evaluation with MR imaging and CT. Radiol Clin North Am 1998;36:1185–1200.)

VIEW IMAGE

Table 9-6
MR IMAGING STAGING OF ORBITAL HEMATOMA

Stage	Hyperacute	Acute	Subacute	Subacute-Chronic	Chronic
Time	Few hours	1–3 days	3–7 days	7 days–weeks	Months–years
Type	Fresh blood	Early clot	Before cell lysis	After cell lysis	Organized/scars
Content	Oxyhemoglobin	Deoxyhemoglobin	Intracellular methemoglobin	Extracellular methemoglobin	Hemosiderin
T1-weighted MR image	Low-high	Low-iso	High	High	Low
T2-weighted MR image	High	Low	Low	High	Low

From Flanders AE, Espinosa GA, Markiewicz DA, et al. Orbital lymphoma. Radiol Clin North Am 1987;25:601-612.

Copyright © 2003, Mosby, Inc. All rights reserved.

ova, which develop into larval forms in the hosts' muscles. Humans are infected by eating the undercooked meat of an infected grazing animal. Traveling via the bloodstream, the hydatid can lodge in the orbit, resulting in a well-defined cystic mass with or without a fluid-fluid level containing the parasite. Clinically, patients present with slowly progressive, painless orbital signs.[73, 81]

Cysticercosis

Cysticercosis is a disease due to infestation by *Cysticercus cellulosae*, the larval form of the parasitic tapeworm *Taenia solium*. Clinically, patients present with either a visible subconjunctival cyst or orbital signs due to an extraocular muscle cyst that is unresponsive to treatment with oral corticosteroids.

Diagnostic Imaging

The CT and MR imaging characteristics of most parasitic cysts are nonspecific. There may be some degree of enhancement around the cyst wall.[73, 81] Nearly all patients with orbital cysticercosis examined by CT show a cystic lesion near or within an extraocular muscle. An intraocular mass or cyst may be present.[82] A scolex can be identified within the cystic lesions in nearly one half of patients by CT or MR imaging and is diagnostic (Fig. 9-60). CT or MR imaging evidence of a cystic lesion without a scolex or diffuse myositis in the presence of a positive enzyme-linked immunosorbent assay for anticysticercal antibodies is also diagnostic. Concurrent neurocysticercosis and orbital cysticercosis appear uncommonly (Fig. 9-60). Neurocysticercosis is generally associated with more morbidity than orbital cysticercosis.[73]

INFLAMMATORY DISEASES

Orbital infections account for about 60% of primary orbital disease processes.[3] The infection may be acute, subacute, or chronic. The majority of acute inflammatory disorders are of paranasal sinus origin. However, the

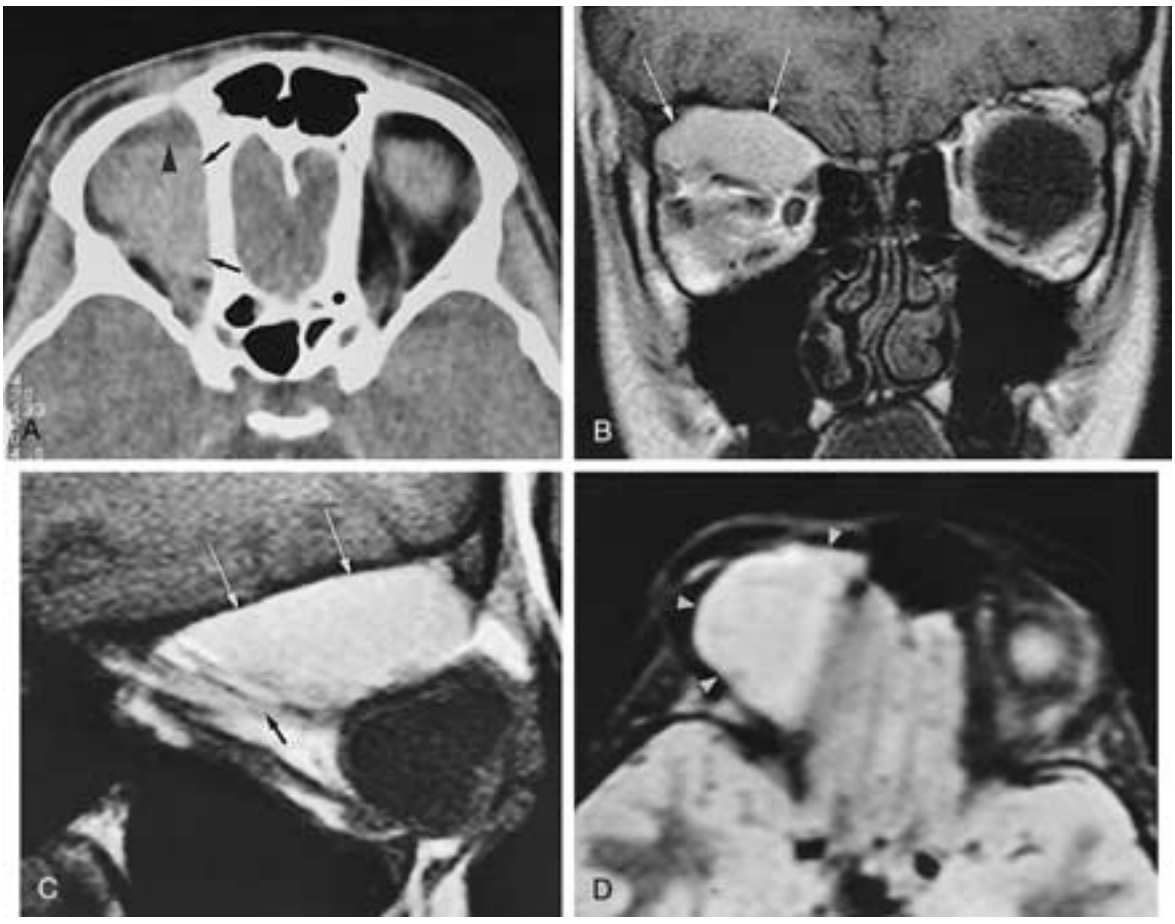

VIEW IMAGE

FIGURE 9-57 Chronic subperiosteal hematoma (about 12 days). **A**, Axial CT scan of the orbit showing a chronic subperiosteal hematoma (cholesterol granuloma) (*arrows*) seen as an isodense lesion with a fluid-fluid level (*arrowhead*). **B**, Coronal T1-weighted (500/20, TR/TE) MR image showing the cholesterol granuloma (*arrows*) in the same patient in **A** as a high-signal lesion, indicating its chronic nature. **C**, Sagittal T1-weighted (500/20, TR/TE) MR image illustrates the high signal pattern of the subperiosteal hematoma (*white arrows*), resulting in downward displacement of the optic nerve (*black arrow*). **D**, Axial proton density (2000/40, TR/TE) MR image shows this chronic hematoma (cholesterol granuloma) as a hyperintense lesion (*arrowheads*). (From Dobben GD et al. Orbital subperiosteal hematoma, cholesterol granuloma, and infection. Evaluation with MR imaging and CT. Radiol Clin North Am 1998;36:1185–1200.)

Copyright © 2003, Mosby, Inc. All rights reserved.

VIEW IMAGE

FIGURE 9-58 Aggressive psammomatoid ossifying fibroma. **A**, Coronal CT scan shows a large, expansile mass of mixed intensity. Note the psammomatoid bodies (*arrows*). **B**, Coronal CT scan in another patient shows an ossifying fibroma (*arrows*). The lesion is less aggressive than the lesion shown in **A**. Note the CT appearance of the psammomatoid bodies (*arrowheads*). **C**, Coronal CT scan in a 18-month-old child shows a soft-tissue mass, with involvement of the medial wall of the orbit as well as the roof of the ethmoid bone. Note the intralesional islands of calcification (*arrows*). Pathologic diagnosis was felt to be most consistent with an aggressive fibro-osseous lesion (fibrous dysplasia versus ossifying fibroma). (From Mafee MF et al. Fibro-osseous, osseous, and cartilaginous lesions of the orbit and paraorbital region. Radiol Clin North Am 1998;36:1241.)

infection may develop from infectious processes of the face or pharynx, trauma, or foreign bodies, or it may be secondary to septicemia. Nearly two thirds of orbital infections are estimated to occur secondary to sinusitis, and about one fourth of the infections are due to orbital foreign bodies. The bacteria most commonly involved are *Staphylococcus*, *Streptococcus*, *Pneumococcus*, *Pseudomonas*, Neisseriaceae, *Haemophilus*, and mycobacteria.[83, 84] Herpes simplex and herpes zoster are the major viral infections of the orbit. In immune-suppressed or immunocompromised patients and poorly controlled diabetic patients, opportunistic infections such as fungal and parasitic pathogens may be responsible for severe sinonasal-orbital infections. Acute inflammation is characterized by rapid onset associated with soft-tissue swelling and infiltration, loss of the normal soft tissue planes, local soft-tissue destruction, and abscess formation. The location of the process is clinically important because a preseptal infection (Fig. 9-61) rarely affects orbital functions. On the other hand, a retroseptal (postseptal) infection (Fig. 9-61) may have a profound and sudden

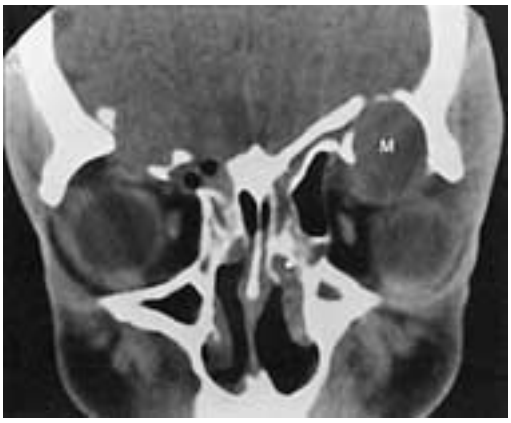

FIGURE 9-59 Extension of a supraorbital ethimoid mucocele into the orbit. Coronal CT scan shows an orbital cystic mass (*M*) related to extension of a mucocele. Note the postoperative changes of the contralateral orbital roof. (From Kaufman LM et al. Diagnostic imaging of cystic lesions in the child's orbit. Radiol Clin North Am 1998;36:1149–1163.)

VIEW IMAGE

Copyright © 2003, Mosby, Inc. All rights reserved.

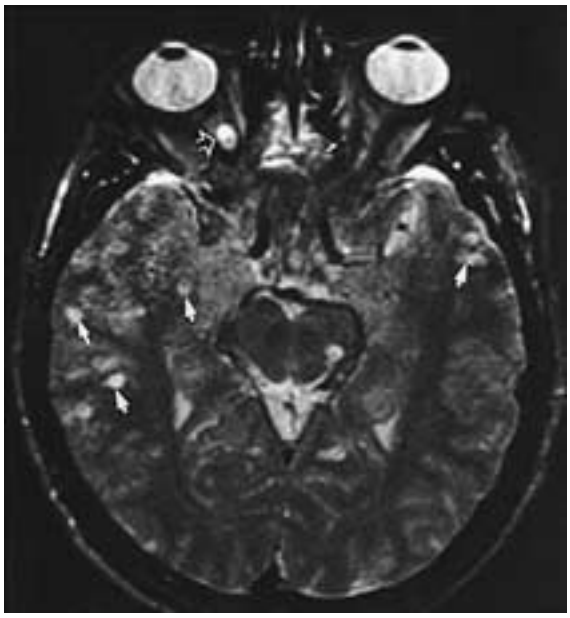

VIEW IMAGE

FIGURE 9-60 Cysticercosis. Axial T2-weighted MR image shows multiple intracranial abscesses (*arrows*) and an orbital abscess (*hollow arrow*). The orbital cyst shows a fluid-fluid level. Scolices are seen within the abscesses as tiny hypointense areas. (From Kaufman LM et al. Diagnostic imaging of cystic lesions in the child's orbit. Radiol Clin North Am 1998;36:1149–1163.)

effect on optic nerve and orbital motility function. Pathologically, in acute bacterial inflammation, polymorphonuclear leukocytes are usually the dominant cells, which, along with their pharmacologic intermediates, lead to necrosis and rapid involvement and destruction of tissue planes.

Orbital Cellulitis and Sinusitis

Sinusitis is the most common cause of orbital cellulitis. Even though antibiotics have reduced the incidence of complicated sinusitis with orbital involvement, it still occurs and may be the first sign of sinus infection in children.[71, 83, 84] In the preantibiotic era, morbidity and mortality from orbital cellulitis were significant, with 17% of cases resulting in death and 20% resulting in blindness. Orbital cellulitis is probably the most common cause of proptosis in children.[6] Pathophysiologically, infection originating within the sinuses can spread readily to the orbit via the thin and often dehiscent bony orbital walls and their many foramina or by means of the interconnecting valveless venous system of the face, sinuses, and orbit.[3] The classification of orbital cellulitis includes five categories or stages of orbital involvement: (1) inflammatory edema; (2) subperiosteal phlegmon and abscess; (3) orbital cellulitis; (4) orbital abscess; and (5) ophthalmic vein and cavernous sinus thrombosis.[3, 71, 84] Limiting a particular inflammatory lesion to one of these categories is often difficult because they tend to overlap.[71, 84]

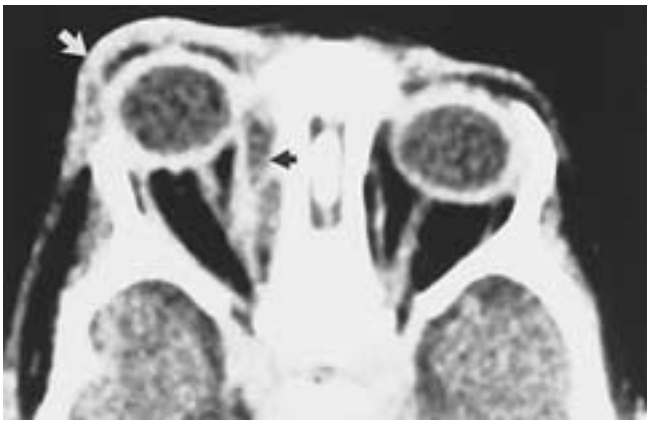

VIEW IMAGE

FIGURE 9-61 Preseptal and retroseptal orbital inflammation. Axial CT scan shows periorbital soft-tissue infiltration and edema (*white arrow*) and retroseptal subperiosteal inflammation and edema (*black arrow*).

Bacterial Orbital Cellulitis Classification

Based upon the anatomy and the presumed pathogenesis of orbital cellulitis of Chandler et al.,[85] classification of the orbital complications of sinus infections is recognized as most useful in clinical situations. The Chandler et al.[85] classification was devised prior to the advent of newer orbital imaging techniques, and modifications that make use of information obtained from these imaging techniques are indicated. We therefore recommend the classification scheme of periorbital infections,[86] outlined in Table 9-7.

Bacterial Preseptal Cellulitis and Preseptal Edema

Preseptal cellulitis defines infections limited to the skin and subcutaneous tissues of the eyelid anterior to the orbital septum.[86] Clinically, the patient has erythema and swelling

Table 9-7
STAGING OF ORBITAL CELLULITIS

State	Clinical Findings
Inflammatory edema	Eyelid swelling and erythema
Preseptal cellulitis	Eyelid swelling and erythema associated with inflammatory soft-tissue thickening of the orbit anterior to the orbital septum
	Chemosis may be present
Postseptal cellulitis	Edema of the orbital contents; proptosis, chemosis, and decreased extraocular movement
	Visual loss (unusual)
Subperiosteal abscess	A collection of inflammatory infiltrates and pus between the periorbita and involved sinuses
	Globe proptotic and displaced by abscess
	Visual loss with progression of the disease
Orbital abscess	Marked proptosis, ophthalmoplegia, and visual loss associated with abscess formation within the orbital fat or muscles
Cavernous sinus thrombosis	Proptosis and ophthalmoplegia with development of similar signs on the contralateral side associated with cranial nerve palsies (nerves III, IV, V, VI) and visual loss

Copyright © 2003, Mosby, Inc. All rights reserved.

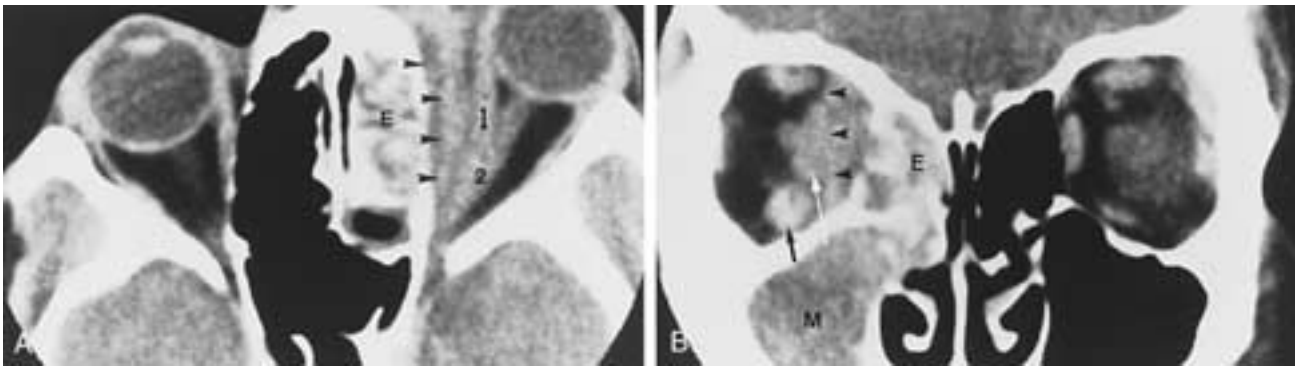

VIEW IMAGE

FIGURE 9-62 Orbital subperiosteal phlegmon. **A**, Axial CT scan shows proptosis of the left eye with mucoperiosteal thickening of the left ethmoid sinus (*E*), with soft-tissue induration in the medial subperiosteal space (*arrowheads*). Note the lateral displacement of the inflamed left medial rectus muscle (*1*). Optic nerve (*2*). **B**, Coronal CT scan, same patient as in **A**, shows clouding of the right ethmoid (*E*) and maxillary (*M*) sinuses, with subperiosteal soft-tissue induration (*arrowheads*) and swelling of the right medial rectus muscle (*white arrow*) and right inferior rectus muscle (*black arrow*). (From Mafee MF et al. CT assessment of periorbital pathology. In: Gozalez CA, Beeker MH, Flanagan JC, eds. Diagnostic Imaging in Ophthalmology. New York: Springer-Verlag, 1985;281–302.)

of the eyelids. There is no proptosis, chemosis, or limitation of ocular motility.[86] At a slightly more advanced stage, chemosis occurs. It is unusual for a preseptal infection to traverse the orbital septum and result in postseptal cellulitis.[86] Preseptal edema is the first stage of infection secondary to sinusitis. It is often clinically misdiagnosed as orbital or periorbital cellulitis. The infection in this early stage actually is still confined to the sinus; however, there is swelling of the eyelids with mild orbital edema reflecting congestion of the venous outflow of the eyelid. Usually the upper medial eyelid is affected, and if untreated, preseptal cellulitis will develop. CT or MR imaging demonstrates the eyelid edema and the inflammatory paranasal sinus disease.[8, 84]

Postseptal Orbital Cellulitis

Postseptal orbital cellulitis is an infectious process that occurs within the orbit proper, behind the orbital septum, and within the bony walls of the orbit.[86] Inflammatory edema characterizes the earliest stage of postseptal orbital infection. There is diffuse edema of the orbital contents with inflammatory cells and fluid, but no abscess formation.[86] The swelling of orbital tissues occurs when an increase in sinus venous pressure is transmitted to the orbital vasculature, resulting in transudation and leakage through the vessel walls.[86] Clinically, the patient has eyelid edema, mild proptosis, and chemosis. In severe cases, there may be generalized limitation of motility; however, visual acuity is not impaired.[86] Although contrast-enhanced diagnostic imaging of an isolated preseptal cellulitis usually is not clinically indicated, it can be useful in cases in which the clinical differentiation of preseptal and postseptal cellulitis is impossible or when the diagnosis is unclear.[86] It is important to recognize that based solely on CT and MR imaging, the differentiation between a cellulitis and allergic eyelid edema is impossible, particularly if the paranasal sinuses appear to be clear. The history is always essential in these cases. The CT and MR imaging findings include soft-tissue thickening of the eyelids. Usually the process is diffuse, and a localized eyelid abscess cavity is not seen. In postseptal orbital cellulitis, orbital imaging is indicated and a contrast-enhanced study is necessary to differentiate inflammatory edema, cellulitis, orbital phlegmon, and orbital abscess (Figs. 9-62 to 9-67).

Subperiosteal Phlegmon and Abscess

As the reaction of the orbital periosteum begins and gradually advances, the edema of the eyelids and conjunctivae becomes more generalized and the eye begins to protrude. Inflammatory tissue and edema collect beneath the periosteum to form a subperiosteal phlegmon (Fig. 9-62), which, subsequently, may develop into a subperiosteal abscess (Fig. 9-63). As the disease progresses, the inflammatory process infiltrates the periorbital and retroocular fat, giving rise to a true orbital cellulitis (Figs. 9-64, 9-66, and 9-67). The subperiosteal abscess and orbital cellulitis frequently coexist.[71, 84] At this stage, extraocular motility becomes progressively

FIGURE 9-63 Orbital subperiosteal abscess. CT scan shows proptosis of the left eye with mucosal thickening of the ethmoid air cells (*E*), with subperiosteal abscess (*hollow arrow*). Note the air bubble (*arrowhead*) within the abscess and the swollen left medial rectus muscle (*arrow*).

VIEW IMAGE

Copyright © 2003, Mosby, Inc. All rights reserved.

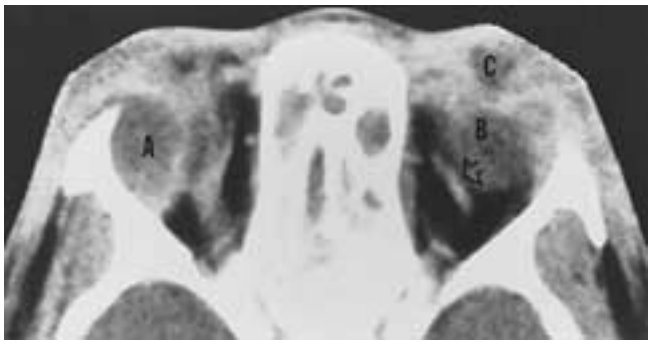

VIEW IMAGE

FIGURE 9-64 Orbital cellulitis and abscesses. CT scan shows right periorbital cellulitis and three abscesses. (*A*), Right retroseptal abscess. (*B*), Left retrobulbar abscess. (*C*), Left eyelid abscess. Note slightly engorged left superior ophthalmic vein (*hollow arrow*).

impaired. With severe involvement, visual disturbances can result from optic neuritis or ischemia (Fig. 9-62A). Progression of intraorbital cellulitis or spread from the subperiosteal space leads to intraconal or extraconal loculation and abscess formation (Fig. 9-64).[3, 71, 84] Progression of disease may lead to ophthalmic vein thrombosis (Fig. 9-68), cavernous sinus thrombosis, and associated mycotic aneurysm of the internal carotid artery (Fig. 9-69), all dire complications of orbital and sinonasal infections.

Cavernous Sinus Thrombosis

Cavernous sinus thrombosis (CST) arises from an infection in an area having venous drainage to the cavernous sinus.[83] Thus, the source infection is usually in the sinonasal cavities, in the orbits, and from infections involving the middle third of the face.[86] CST may develop from a septic thrombophlebitis arising in the ophthalmic vein (Fig. 9-68). Proptosis and ophthalmoplegia are common. Offending organisms may be aerobic or anaerobic, with *Staphylococcus aureus* and anaerobic streptococci being the most common organisms. Clinically, patients with CST are extremely ill, demonstrating signs of meningitis and multiple cranial nerve palsies bilaterally.[86] These patients usually have a headache, fever and chills, and an elevated white blood cell count with positive blood cultures.[83] The ophthalmologic findings include edema of the lids, exophthalmos, chemosis, paralysis of the eye muscles, engorgement of the retinal veins, and low-grade papilledema.[83] On contrast-enhanced CT scans, the normal cavernous sinus is seen as an enhancing parasellar structure with a sharply defined lateral border that is either straight or concave toward the adjacent middle cranial fossa. The internal carotid artery cannot normally be separated from the opacified venous sinuses within the cavernous sinus. When thrombosis is present, the cavernous sinus often has a low-attenuation, nonenhancing appearance. The lateral border may bow laterally toward the middle cranial fossa, and the contrast-enhanced internal carotid artery may be seen as a contrast-enhanced tubular structure within the cavernous sinus (Figs. 9-69B,C). Often the superior ophthalmic vein is markedly enlarged and possibly thrombosed. False-negative CT scans are common until late in the course of the disease.[86] Thrombosis of the superior ophthalmic vein (SOV) is seen on MR imaging as an enlarged vein that appears less hypointense than the vein on the normal opposite side. On T1-weighted and T2-weighted MR images, the thrombosed SOV may be seen as a hyperintense area within the lumen of the vein.[87–89] CST results in

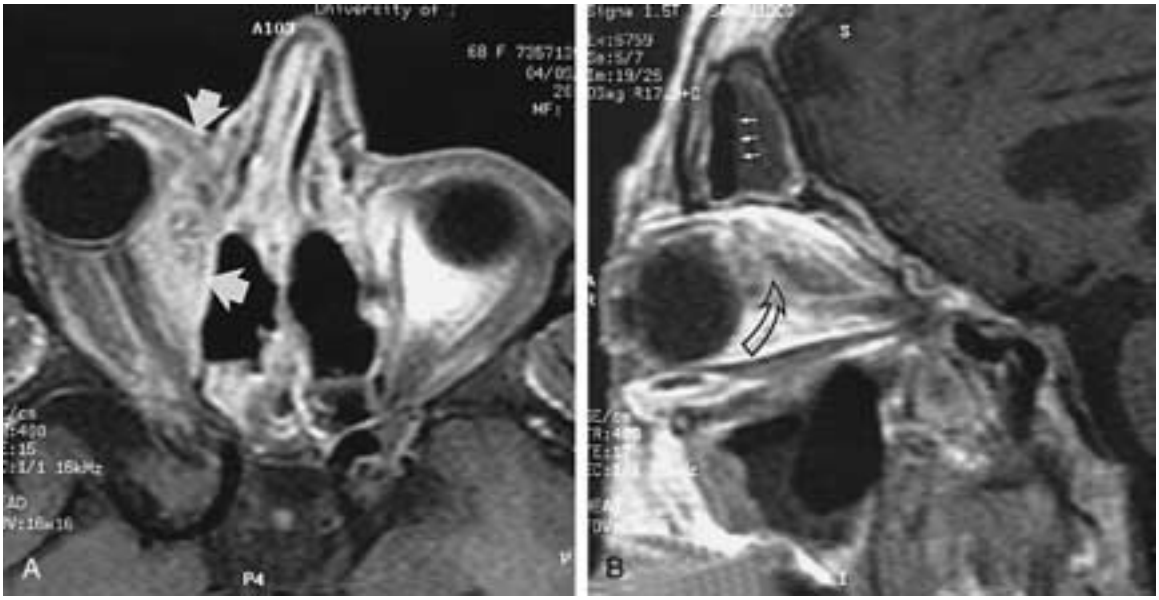

VIEW IMAGE

FIGURE 9-65 Orbital cellulitis. **A**, Enhanced, fat-suppressed, axial T1-weighted MR image showing diffuse enhancement of pre- and postseptal orbital tissue (*arrows*). **B**, Enhanced, fat-suppressed, sagittal T1-weighted MR image shows an air-fluid level in the frontal sinus (*arrows*) and diffuse orbital enhancement (*curved arrow*). There is no orbital abscess formation. (From Eustis HS et al. MR imaging and CT of orbital infections and complications in acute rhinosinusitis. Radiol Clin North Am 1998;36:1165–1183.)

Copyright © 2003, Mosby, Inc. All rights reserved.

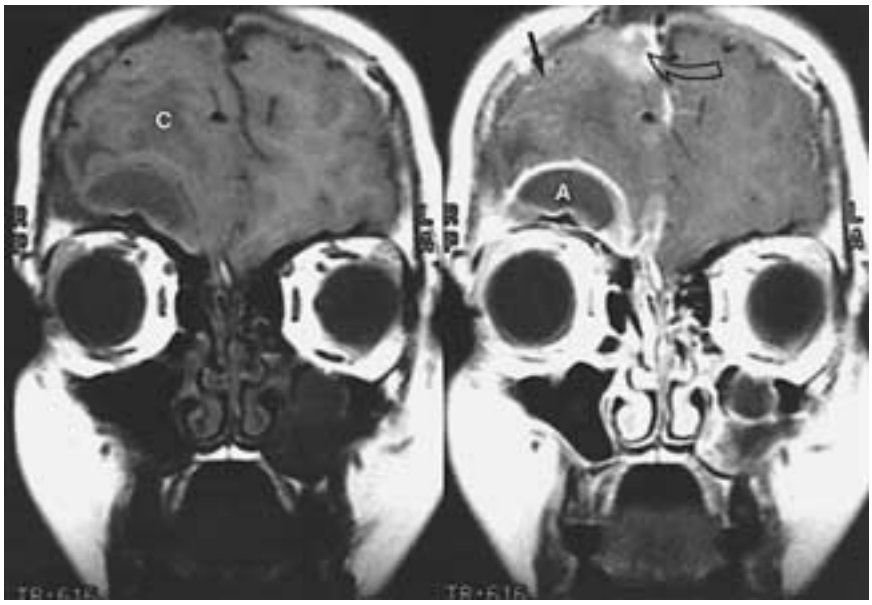

FIGURE 9-66 Epidural abscess, cerebritis, and meningitis in a child with acute sinusitis. Pre- and postcontrast-enhanced coronal MR image showing epidural abscess (*A*), edema adjacent to focal cerebritis (*C*), and leptomeningeal enhancement (*straight arrow*) related to meningitis. Note the enhancement of focal cerebritis (*curved arrow*). (From Eustis HS et al. MR imaging and CT of orbital infections and complications in acute rhinosinusitis. Radiol Clin North Am 1998;36: 1165–1183.)

VIEW IMAGE

engorgement of the cavernous sinus and ophthalmic veins and usually engorgement of the extraocular muscles.[86] MR imaging and MR venography are more sensitive than CT for revealing CST.[88] On MR imaging there is deformity of the cavernous portion of the internal carotid artery. The signal from the abnormal cavernous sinus is heterogeneous, and there is an obvious hyperintense signal intensity representing the thrombosed vascular sinus that often is seen on all pulse sequences. Mycotic (septic) aneurysm of the internal carotid artery is a serious complication of orbital infection. This can be suspected on CT or MR imaging and confirmed by MR angiography or standard angiography (Fig. 9-69).

Mycotic Infections

Orbital cellulitis secondary to infection with mycotic organisms occurs less frequently than bacterial infections, and usually these patients have a history of uncontrolled diabetes mellitus or are immunocompromised. Immunocompromised patients are particularly susceptible to infection by fungi such as *Candida* species, *Histoplasma capsulatum*, *Coccidioides immitis*, *Mucor*, and *Aspergillus* species.[86] *Mucor* and *Aspergillus* are by far the most

FIGURE 9-67 Sphenoid sinus abscess and subperiosteal abscess. Enhanced coronal T1-weighted MR image in a 12-year-old girl showing a sphenoid abscess (*A*) and a subperiosteal abscess (*arrows*). The patient lost her vision completely on the right. (From Eustis HS et al. MR imaging and CT of orbital infections and complications in acute rhinosinusitis. Radiol Clin North Am 1998;36:1165–1183.)

VIEW IMAGE

FIGURE 9-68 Thrombosis of the superior ophthalmic vein. Axial CT scan shows an engorged left superior ophthalmic vein with a filling defect (*arrow*), which was caused by a sphenoid sinus infection (moniliasis).

VIEW IMAGE

Copyright © 2003, Mosby, Inc. All rights reserved.

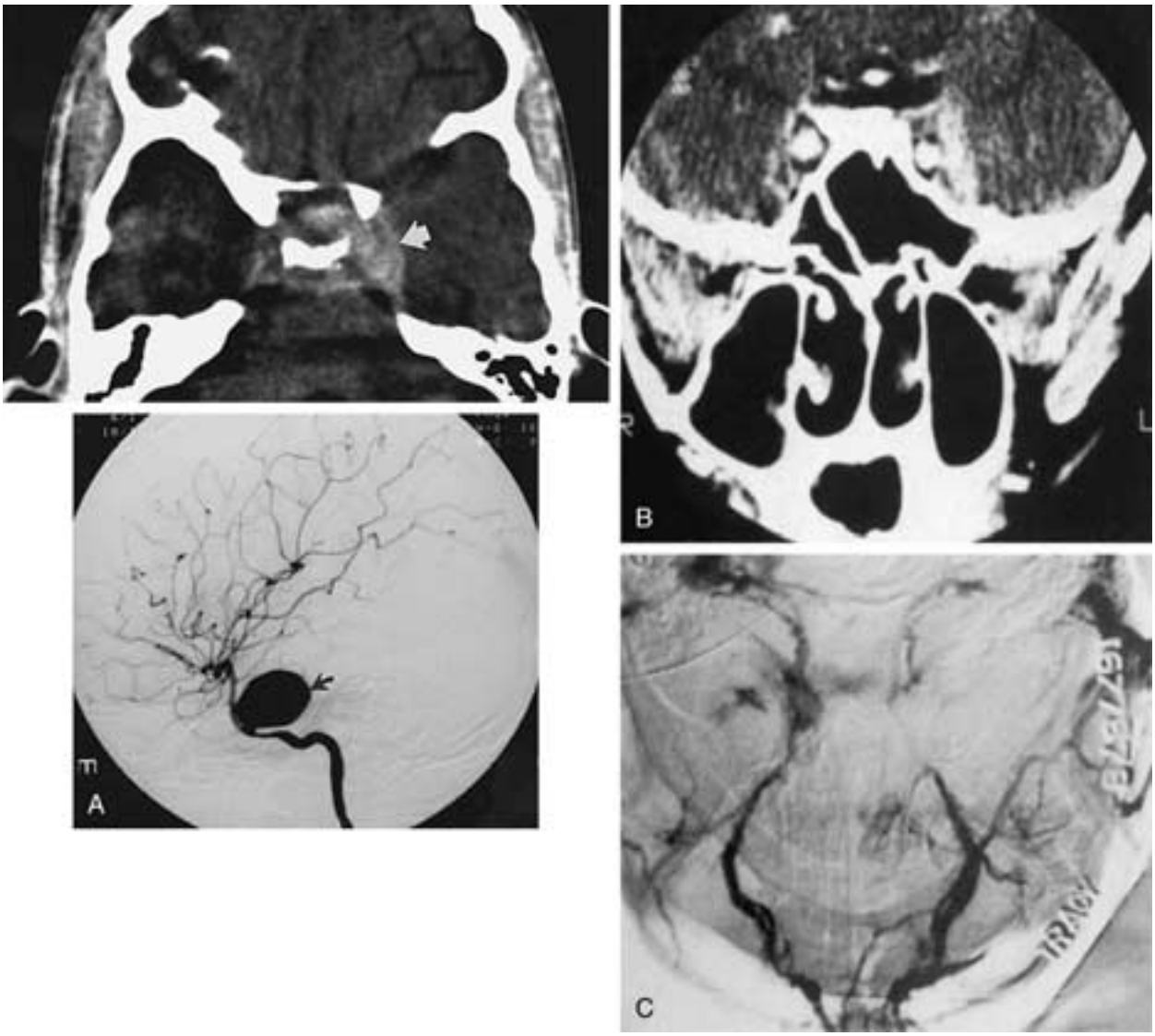

VIEW IMAGE

FIGURE 9-69 **A**, Mycotic (septic) aneurysm. **1**, Enhanced axial CT scan shows an enhancing mass (*arrow*) in the left cavernous sinus related to a mycotic artery. **2**, Lateral angiogram shows a large aneurysm (*arrow*) of the cavernous portion of the internal carotid artery. (From Eustis HS et al. MR imaging and CT of orbital infections and complications in acute rhinosinusitis. Radiol Clin North Am 1998;36:1165–1183.) **B**, Bilateral cavernous sinus thrombosis. Coronal CT section through the cavernous sinus following bolus injection reveals opacification of the internal carotid arteries bilaterally. The cavernous sinus reveals decreased attenuation in keeping with cavernous sinus thrombosis. Note enhancement of the dura bordering the left cavernous sinus. **C**, Right cavernous sinus thrombosis. Orbital venogram in the axial projection shows obstruction of the cavernous sinus on the right, secondary to thrombosis. Note the filling of the normal left cavernous sinus. (**B** and **C** from Weber AL, Mikulis DK. Inflammatory disorders of the paraorbital sinus and their complications. Radiol Clin North Am 1987;25:615–630.)

common fungal organisms incriminated. The fungi responsible for mucormycosis are ubiquitous and normally saprophytic in humans; they rarely produce severe disease, except in those with predisposing conditions.[71, 83, 90] There are four major types of mucormycosis: rhinocerebral, pulmonary, gastrointestinal, and disseminated, the most common of which is the rhinocerebral form.[90] The infection usually begins in the nose and spreads to the paranasal sinuses; then it extends into the orbit and cavernous sinuses.[71, 90] Orbital involvement results in orbital signs such as ophthalmoplegia, proptosis, ptosis, loss of vision, and orbital cellulitis.[71] The inflammatory process soon extends along the infraorbital fissure into the infratemporal fossa (Fig. 9-70) and may extend into the cavernous sinuses.

Black necrosis of a turbinate is a diagnostic clinical sign, but it may not be present until late in the course of the disease.[71, 90] The pathologic hallmark of mucormycosis is invasion of the walls of small vessels. For this reason, when the cavernous sinus is invaded, particularly in patients with mucormycosis and aspergillosis, rapid brain infarction may develop.[91]

Aspergillus is a ubiquitous fungus found primarily in agricultural dust. It may produce rhinocerebral disease and orbital involvement similar to that of mucormycosis,

Copyright © 2003, Mosby, Inc. All rights reserved.

although hematogenous spread from the lungs to the brain is more common.[90] This fungus also has a well-known propensity for invading blood vessels, including the internal carotid artery.[71] One important but not pathognomonic MR imaging finding of mycotic infections is the hypointensity of mycetoma on T2-weighted MR images (Fig. 9-71). This is thought to be due to paramagnetic materials produced by the fungi and the semisolid, cheesy nature of the mycetoma.

In general, and in the appropriate clinical setting, a multicentric or unicentric sinusitis with or without bone destruction, and orbital tissues with or without vascular thrombosis, should strongly raise the possibility of sino-orbital mycosis.[86] Although the combination of orbital and sinus involvement is not pathognomonic of rhinocerebral mucormycosis or aspergillosis, awareness of these diagnoses, particularly when any predisposing factors are present, helps establish an early diagnosis. Rapid diagnosis is important because early aggressive treatment is necessary to minimize morbidity and mortality from these usually fatal diseases. The main contribution of CT and MR imaging is their clear demonstration of the relationship between sinonasal, orbital, and intracranial disease (Fig. 9-71). One should realize that the CT and MR imaging findings of invasive aspergillosis are indistinguishable from those of mucormycosis and that advanced sino-orbital mucormyosis and invasive aspergillosis mimic aggressive tumors on CT and MR imaging.

Acute, Subacute, and Chronic Idiopathic Orbital Inflammatory Disorders (Pseudotumors)

Idiopathic inflammatory syndromes usually are referred to as *orbital pseudotumors*, a clinically and histologically confusing category of lesions.[3] In general, orbital pseudotumors represent a nongranulomatous inflammatory process in the orbit or eye with no known local or systemic causes.[92–94] This is a diagnosis of exclusion based on the history, the clinical course of the disease, the response to steroid therapy, laboratory tests, and biopsy in a limited number of cases.[92] There is a group of diverse disease entities that can mimic pseudotumors such as lymphoma, sarcoidosis, and other granulomatous diseases. By definition, the diagnosis excludes orbital inflammatory disease caused by entities such as Wegener's granulomatosis, retained foreign bodies, sclerosing hemangioma, trauma, and sinusitis. Among orbital disorders, after Graves' disease, pseudotumor is the next most common ophthalmologic disease. Pseudotumors account for 4.7% to 6.3% of orbital disorders, and the disease usually affects adults but may also affect children.[92] Pediatric orbital pseudotumor encompasses almost 6% to 16% of orbital pseudotumors. There is a higher incidence of bilateral orbital involvement, with approximately one third of the pseudotumors being bilateral.[92] Such pseudotumors are rarely associated with systemic disease. Children with orbital pseudotumor may also exhibit papillitis or iritis.[5, 6] Bilateral orbital pseudotumors in adults suggest the possibility of systemic vasculitis or a systemic lymphoproliferative disorder.[5, 6] Patients with pseudotumor typically present with the acute onset of orbital pain, restricted eye movement, diplopia, proptosis, and impaired vision from perioptic nerve involvement. Conjunctival vascular congestion and edema, as well as lid erythema and swelling, are common.[5, 6] Pseudotumors are often multicentric. In addition to the variety of classification systems and diagnostic criteria that have been offered over the years, the disease can include a wide range of clinical presentations and many of the symptoms are nonspecific. Pain is an important feature of pseudotumors; however, not all patients with pseudotumors present with pain.[5, 6] Some may have minimal proptosis or may even present with a totally scarred lesion (sclerosing pseudotumor) within a single muscle or in the retrobulbar fat pad.[5, 6]

Histopathology

The condition was first described in 1905 by Birch-Hirschfield[95] and has remained somewhat of an enigma in

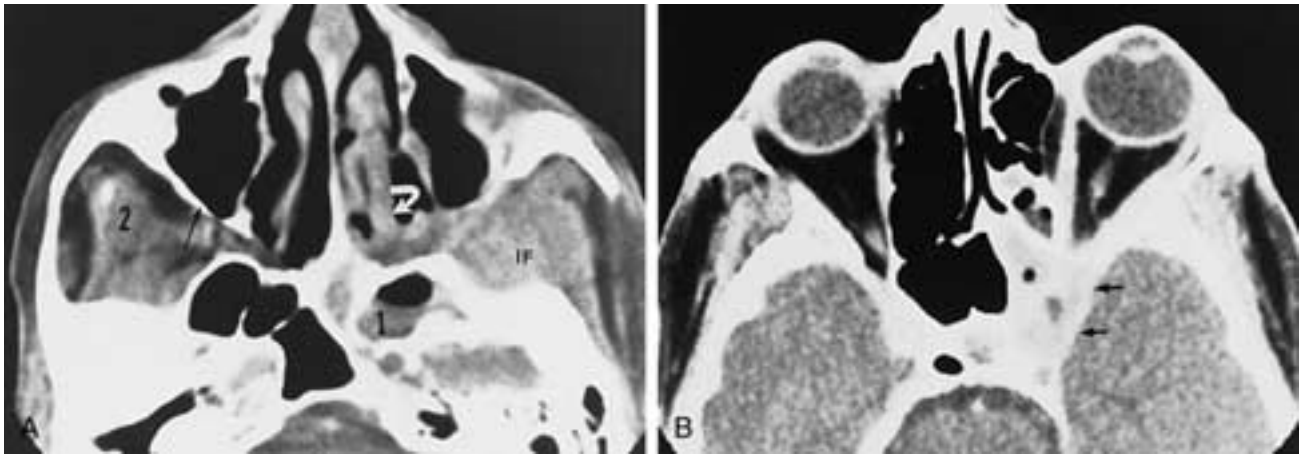

FIGURE 9-70 Mucormycosis. **A**, Axial CT scan shows soft-tissue induration in the left nasal cavity (*curved arrow*) and left infratemporal fossa (*IF*). Note the air-fluid level in the left sphenoid sinus (*1*). Fascial planes in the left infratemporal fossa (*IF*) region, compared with the right side (*2*), are obliterated. Note the rarefaction of the posterior wall of the left maxillary sinus compared with the normal right side (*black arrow*). **B**, Axial CT scan, same patient as in **A**, shows involvement of the left cavernous sinus (*arrows*) with enlargement (engorgement) of the left lateral and medial rectus muscles.

VIEW IMAGE

Copyright © 2003, Mosby, Inc. All rights reserved.

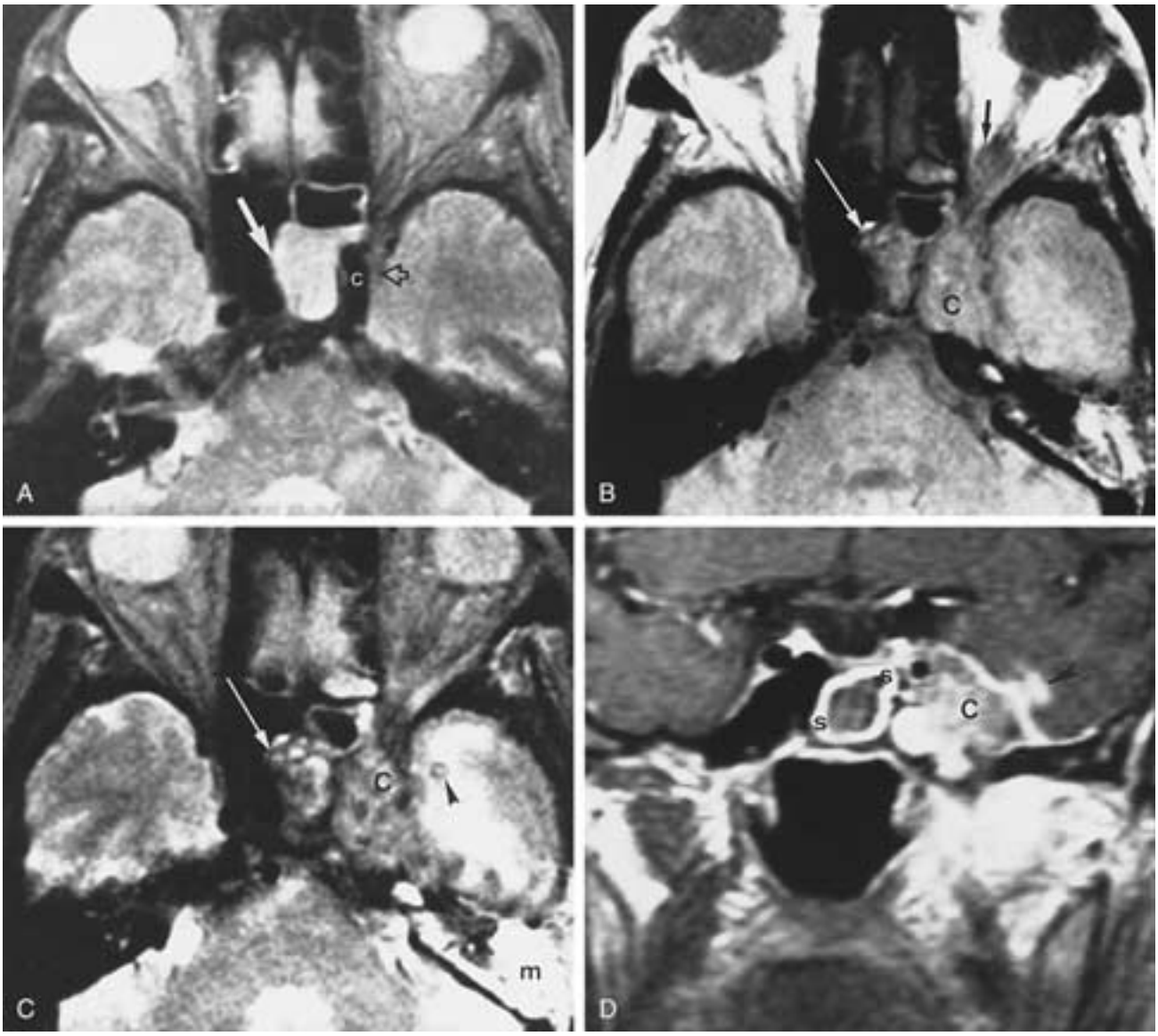

VIEW IMAGE

FIGURE 9-71 Aspergillosis. **A**, Axial T2-weighted MR image shows soft-tissue induration in the left sphenoid sinus (*white arrow*). Note the internal carotid (*C*) and early soft-tissue infiltration of the left cavernous sinus (*hollow arrow*). **B**, Axial PW MR image follow-up scan. **C**, Axial T2-weighted MR image follow-up scan. Scans show progression of the pathologic process, with marked infiltration of the left cavernous sinus (*C*) and formation of the left temporal lobe abscess (*arrowhead*) with marked peripheral edema. Note apical infiltration into the left orbit (*black arrow* in **B**) and inflammatory mycotic tissue in the left sphenoid sinus (*white arrow*). The mycotic process appears rather hypointense on the T2-weighted MR image, a not uncommon finding with fungal infections. Note the nonvisualization of the left internal carotid artery (compare with **A**); this results from invasion of the mycotic process, a finding confirmed by angiography and surgery. The mycotic process (*m*) has extended over the left petrous apex. **D**, Postcontrast (Gd-DTPA) coronal MR image shows enhancement of mucosal thickening of the left sphenoid sinus (*S*) and infiltrative process of the left cavernous sinus (*C*) and the temporal lobe abscess (*arrowhead*).

the ophthalmology, radiology, and pathology literatures.[94] The histopathology can vary from polymorphous inflammatory cells and fibrosis with a matrix of granulation tissue, eosinophils, plasma cells, histiocytes, lymphoid follicles with germinal centers and lymphocytes to a predominantly lymphocytic form (lymphoid hyperplasia) embedded in a loose fibrous stroma. It is the chronic lymphocytic variety that is related to lymphoma.[94] Many cases have been reported of lymphocytic pseudotumor that over a period of time are found to harbor a malignant lymphoma without any evidence of systemic lymphoma. The presence of germinal follicles and increased vascularity is indicative of a reactive lesion, often associated with a favorable prognosis and responsiveness to steroids. An association has been noted between diffusely distributed lymphoblasts, unresponsiveness to steroids, and a probable neoplastic lymphoid lesion.[94] However, not all steroid-resistant pseudotumors are destined to become lymphomatous. The peculiar behavior of pseudotumors has led some authors to speculate that some forms of pseudotumor are the result of an autoimmune

Copyright © 2003, Mosby, Inc. All rights reserved.

process.[94, 96] Pseudotumors are often multicentric, presenting with myositis, dacryoadenitis, sclerotenonitis (Tenon fasciitis), and inflammation of the dural sheath of the optic nerve and surrounding connective tissue.[5, 6] Pseudotumors may be classified as (1) acute and subacute idiopathic anterior orbital inflammation; (2) acute and subacute idiopathic diffuse orbital inflammation; (3) acute and subacute idiopathic myositic orbital inflammation; (4) acute and subacute idiopathic apical orbital inflammation; (5) idiopathic dacryoadenitis; and (6) perineuritis. Tolosa-Hunt syndrome (painful ophthalmoplegia) is a variant of pseudotumor in which the inflammatory process is restricted to the vicinity of the superior orbital fissure, the optic canal, or the cavernous sinus.[5, 6]

Anterior Orbital Inflammation

In the anterior orbital pseudotumor group, the main focus of inflammation involves the anterior orbit and adjacent globe.[3] The major features at presentation are pain, proptosis, lid swelling, and decreased vision. Other findings may be ocular and include uveitis, sclerotenonitis (Tenon's capsule), papillitis, and exudative retinal detachment. Extraocular muscle (EOM) motility is usually unaffected. CT and MR imaging show thickening of the uveal-scleral rim with obscuration of the optic nerve junction, which enhances with contrast infusion on CT (Fig. 9-72).[94] These findings are due to leakage of proteinaceous edema fluid into the interstitium of the uvea and Tenon's capsule secondary to the inflammatory reaction.[94] Fluid in Tenon's capsule has been well documented with ultrasound (the T sign). Patients with posterior scleritis can develop retinal detachment and fundal masses, which simulate intraocular tumors.[94] The differential clinical diagnosis of anterior orbital pseudotumor includes orbital cellulitis, ruptured dermoid cyst, or hemorrhage within a vascular lesion (hemangioma, lymphangioma), collagen vascular disease, rhabdomyosarcoma, and leukemic infiltration.

Diffuse Orbital Pseudotumor

Diffuse orbital pseudotumor is similar in many respects to acute and subacute anterior inflammation, with more severe signs and symptoms.[3] The diffuse, tumefactive, or infiltrative type of pseudotumor may fill the entire retrobulbar space and mold itself around the globe while respecting its natural shape. Even the largest mass usually does not invade or distort the shape of the globe or erode bone (Figs. 9-73 and 9-74). This type of disease can be very difficult to differentiate from lymphoma. These large, bulky masses can be intraconal, extraconal, or involve both spaces. This disease must be differentiated from true tumors of the orbit such as cavernous hemangioma, hemangiopericytoma, optic nerve sheath meningioma, optic nerve glioma, orbital schwannoma, and metastasis.[94] True tumors usually do not respect the boundaries of the globe, indenting or deforming its surface. Also, bone erosion and extraorbital extension are more typical of true tumors than of pseudotumors.

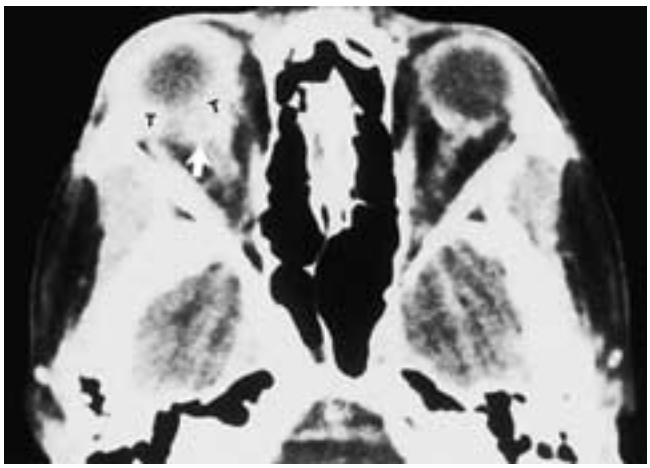

FIGURE 9-72 Pseudotumor: periscleritis/perineuritis. Postcontrast axial CT scan shows diffuse thickening of the scleral coat with inflammatory infiltration into Tenon's space (*T*) and perineuritis (*arrow*).

VIEW IMAGE

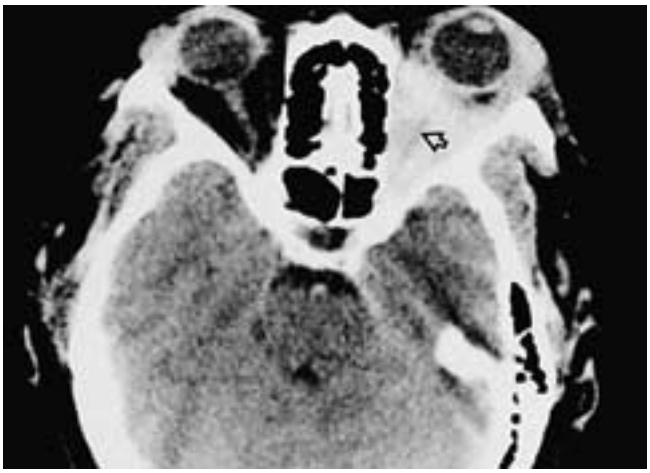

FIGURE 9-73 Pseudotumor. Axial CT scan shows diffuse infiltration of the entire retrobulbar space. The optic nerve appears as a lucent band (*arrow*) embedded within the lesion. (From Curtin HD. Pseudotumor. Radiol Clin North Am 1987;25:583.)

VIEW IMAGE

Orbital Myositis

Idiopathic orbital myositis is a condition in which one or more of the EOMs are primarily infiltrated by an inflammatory process (Figs. 9-75 to 9-79). The myositis can be acute, subacute, or recurrent, and the patient usually presents with painful extraocular movements, diplopia, proptosis, swelling of the lid, conjunctival chemosis, and inflammation over the involved EOM.[3, 94] This disorder may be bilateral. The most frequently affected muscles are the superior complex and the medial rectus (Fig. 9-75). The major differential diagnosis is Graves' disease. However, dysthyroid myopathy is usually painless in onset, asymmetric, slowly progressive, and associated with a systemic diathesis.[3] Trokel and Hilal state that the typical CT finding in orbital myositis is enlargement of the EOMs, which extends anteriorly to involve the tendon insertion (Figs. 9-75 and 9-76).[97] Other helpful indicators of inflammatory orbital myositis include a ragged, fluffy border of the involved muscle, with infiltration and obliteration of the fat in the peripheral surgical space between the periosteum of the orbital wall and the muscle cone. Also observed is an inward bowing of the medial contour of the muscle belly, forming a shoulder as it passes behind the globe (Fig. 9-75). All these findings can be attributed to local tendinitis, fasciitis, and

Copyright © 2003, Mosby, Inc. All rights reserved.

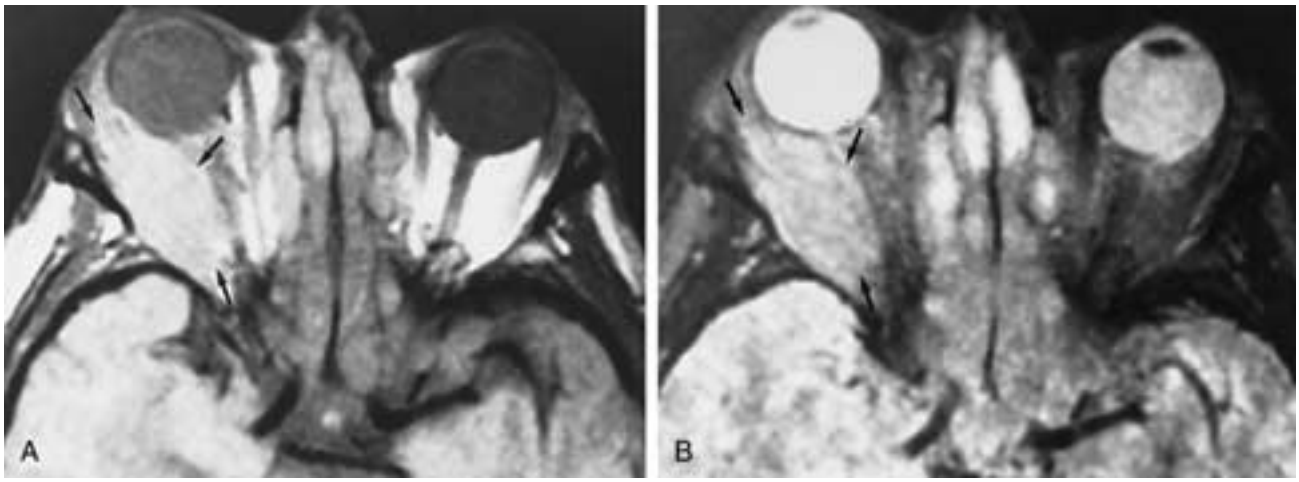

VIEW IMAGE

FIGURE 9-74 Pseudotumor. **A**, Axial PW MR image. **B**, Axial T2-weighted MR image. Scans show infiltrative process (*arrows*) compatible with pseudotumor. The lesion is isointense to brain on PW and T2-weighted MR scans. (From Curtin HD. Pseudotumor. Radiol Clin North Am 1987;25:583.)

myositis of the involved muscle. In contrast, the fusiform appearance of an enlarged muscle in thyroid myopathy is produced by a myositis without involvement of the muscle tendon insertion. The muscle borders are sharply defined, the fat in the peripheral surgical space is preserved, and there is no medial muscle bowing. Less common causes of EOM enlargement include arteriovenous fistula (e.g., carotid-cavernous fistula), granulomatous disease, and neoplasm (primary or metastatic).[94]

Perineuritis and Periscleritis

Idiopathic perineuritis (inflammation of the sheath of the optic nerve) can simulate optic neuritis by presenting with orbital pain, pain with extraocular motility, decreased visual acuity, and disc edema. In contrast to optic neuritis, pain is exacerbated with retrodisplacement of the globe, and there is mild proptosis.[94] CT and MR imaging show a ragged, edematous enlargement of the optic nerve sheath complex (Fig. 9-79A). If periscleritis is present, the inflammation involves the tissues immediately contiguous to the sclera (Fig. 9-79B).

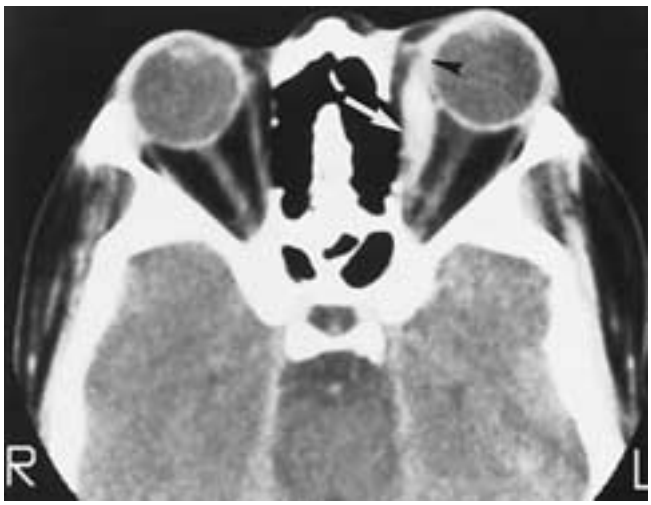

VIEW IMAGE

FIGURE 9-75 Myositic pseudotumor. Postcontrast Axial CT scan shows marked thickening and enhancement of the left medial rectus muscle (*arrow*). Note extension of the process into its tendinous insertion on the globe (*arrowhead*). (From Flanders AE et al. CT characteristics of orbital pseudotumor and other orbital inflammatory processes. J Comput Assist Tomogr 1989;13:40–47.)

Lacrimal Adenitis

Acute idiopathic lacrimal adenitis (pseudotumor) presents with tenderness in the upper outer quadrant of the orbit in the region of the lacrimal gland.[24, 94] Viral dacryoadenitis may present in a similar manner, although it is commonly associated with an etiology such as mumps, mononucleosis, or herpes zoster virus infection. Adenopathy and lymphocytosis can be present in these latter cases. The differential diagnosis of nonspecific lacrimal adenitis includes viral and bacterial dacryoadenitis, rupture of a dermoid cyst in the lacrimal gland region, specific lacrimal gland inflammations such as sarcoidosis and Sjogren's disease, lymphoproliferative disorders, cysts, and neoplasia in this region. Because of the wide variety and incidence of pathology that can involve the lacrimal gland, biopsy of this accessible site is necessary to obtain a definitive diagnosis (Fig. 9-80).[3]

Apical Orbital Inflammation

Pseudotumor may present with infiltration of the orbital apex, and these patients present with a typical orbital apex syndrome consisting of pain, minimal proptosis, and painful ophthalmoplegia. The CT and MR imaging findings include an irregular infiltrative process of the orbital apex with extension along the posterior portion of the EOMs or the optic nerve. Sarcoidosis (Fig. 9-81) and other granulomatous processes including Wegener's granulomatosis may be responsible for similar clinical and imaging presentations.

Painful External Ophthalmoplegia (Tolosa-Hunt Syndrome)

In 1954, Tolosa described a patient with unilateral recurrent painful ophthalmoplegia involving cranial nerves III, IV, VI, and V1.[98] Carotid arteriography in this case

Copyright © 2003, Mosby, Inc. All rights reserved.

showed segmental narrowing in the carotid siphon. The patient died after surgical exploration, and a postmortem study showed adventitial thickening in the cavernous carotid artery surrounded by a cuff of nonspecific granulation tissue that also involved the adjoining cranial nerve trunks. In 1961, Hunt et al. reported six patients, with similar clinical symptoms and signs.[99] After reviewing Tolosa's slides, these authors proposed a low-grade, nonspecific inflammation of the cavernous sinus and its walls as the cause of the syndrome. They also emphasized that angiography was essential to rule out an aneurysm or neoplasm.[99] In 1966, Smith and Taxdal applied the term *Tolosa-Hunt syndrome* to this entity.[100] They described five additional cases and stressed the diagnostic usefulness of the dramatically rapid therapeutic response to corticosteroids. In 1973, Sondheimer and Knapp reported three patients with Tolosa-Hunt syndrome on whom orbital venography was performed.[101] These investigators observed that the superior ophthalmic vein on the affected side was occluded in the posterior portion of the muscle cone in each case and that there was partial or complete obliteration of the ipsilateral cavernous sinus.

Painful external ophthalmoplegia, or Tolosa-Hunt syndrome, is now considered an idiopathic inflammatory process and a regional variant of idiopathic orbital pseudotumors that, because of its anatomic location (superior orbital fissure, cavernous sinus, or both), produces typical clinical manifestations.[98, 102] The disease manifests as recurrent attacks of a steady, dull, retroorbital pain, palsies of the third, fourth, or sixth cranial nerve and the first or second divisions or both of the trigeminal nerve, and venous engorgement. It is usually unilateral, but bilateral cases do

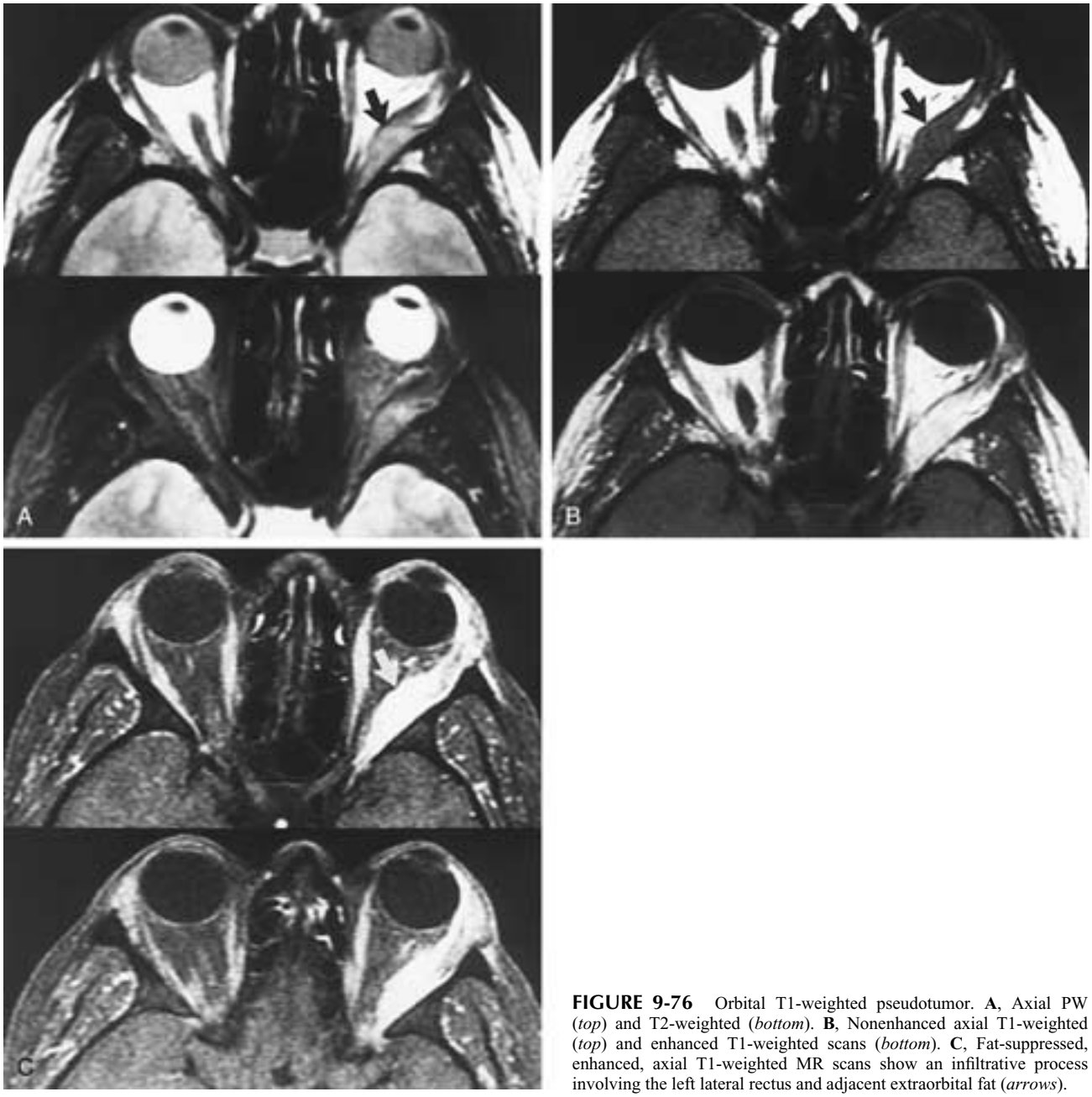

FIGURE 9-76 Orbital T1-weighted pseudotumor. **A**, Axial PW (*top*) and T2-weighted (*bottom*). **B**, Nonenhanced axial T1-weighted (*top*) and enhanced T1-weighted scans (*bottom*). **C**, Fat-suppressed, enhanced, axial T1-weighted MR scans show an infiltrative process involving the left lateral rectus and adjacent extraorbital fat (*arrows*).

VIEW IMAGE

Copyright © 2003, Mosby, Inc. All rights reserved.

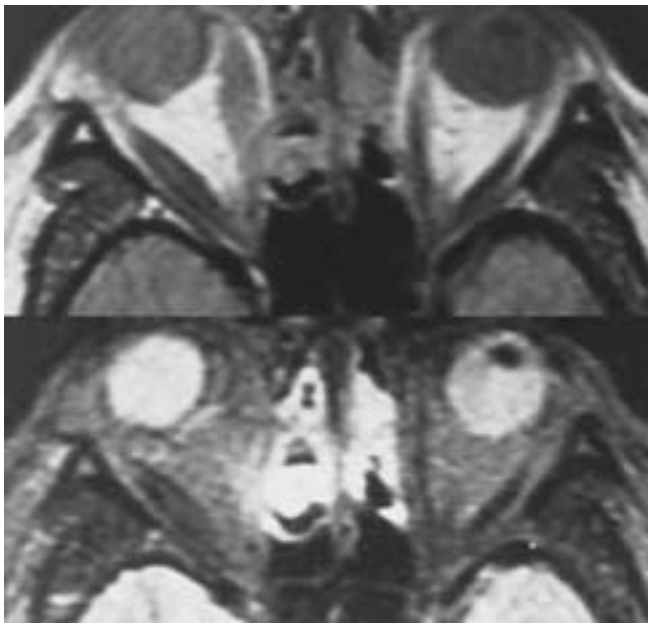

VIEW IMAGE

FIGURE 9-77 Pseudotumor (myositic type), axial PW (*top*) and T2-weighted (*bottom*) MR scans in another patient show enlargement of the right lateral and medial rectus muscles.

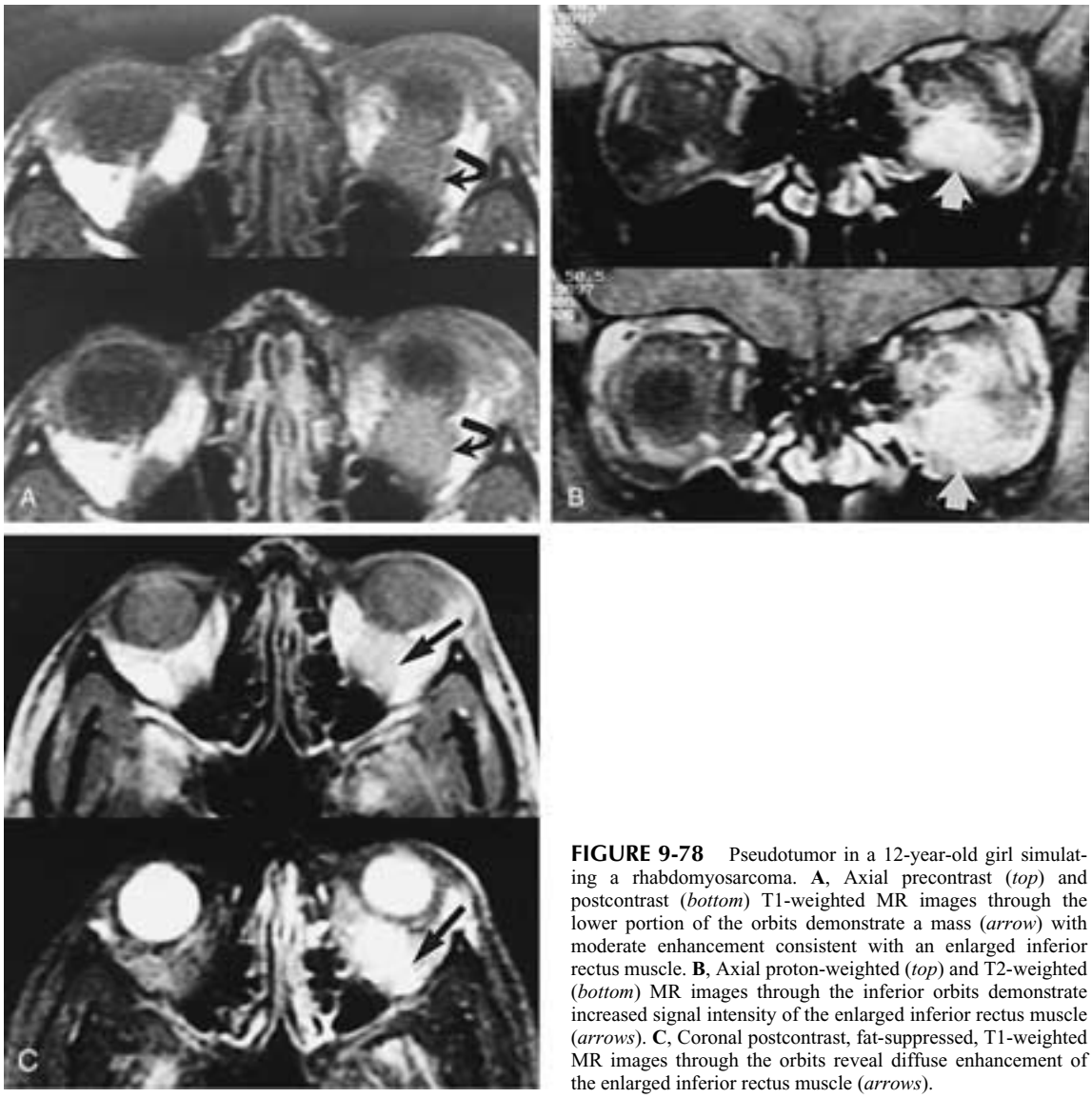

FIGURE 9-78 Pseudotumor in a 12-year-old girl simulating a rhabdomyosarcoma. **A**, Axial precontrast (*top*) and postcontrast (*bottom*) T1-weighted MR images through the lower portion of the orbits demonstrate a mass (*arrow*) with moderate enhancement consistent with an enlarged inferior rectus muscle. **B**, Axial proton-weighted (*top*) and T2-weighted (*bottom*) MR images through the inferior orbits demonstrate increased signal intensity of the enlarged inferior rectus muscle (*arrows*). **C**, Coronal postcontrast, fat-suppressed, T1-weighted MR images through the orbits reveal diffuse enhancement of the enlarged inferior rectus muscle (*arrows*).

VIEW IMAGE

Copyright © 2003, Mosby, Inc. All rights reserved.

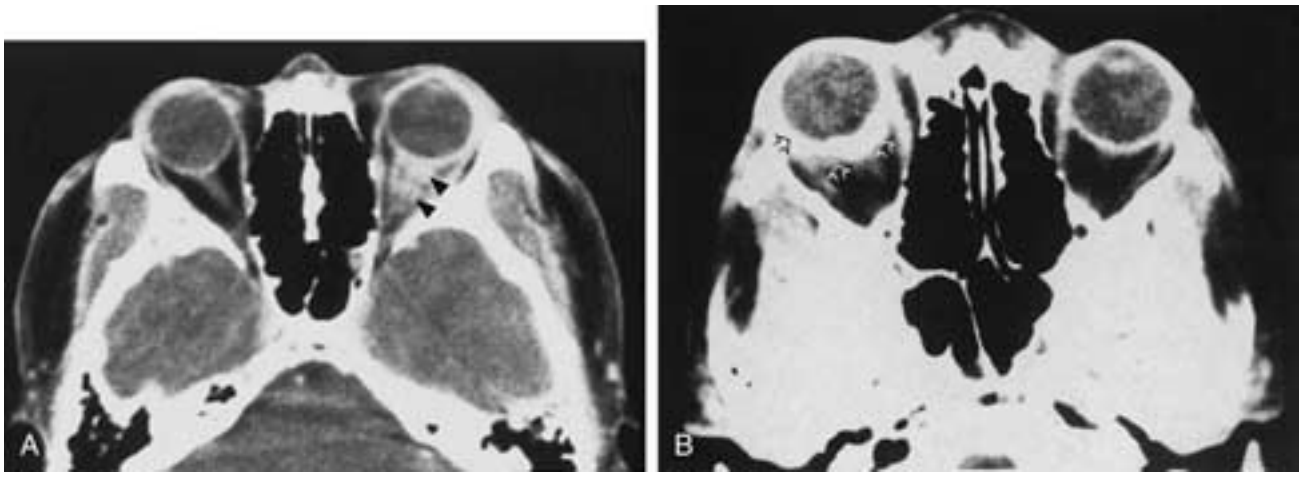

VIEW IMAGE

FIGURE 9-79 **A**, Pseudotumor (perineuritis type). Axial CT scan shows the intraconal region of infiltration (*arrowheads*) surrounding the left optic nerve. Slight thickening of the posterior sclera indicates posterior scleritis and fluid (exudate) in Tenon's space. **B**, Pseudotumor (scleritis and episcleritis type). Postcontrast axial CT scan shows a prominent ring of increased density and enhancement (*arrows*) due to reactive inflammatory effusion as well as infiltration in the potential Tenon's space (fasciitis). (**B** from Mafee MF et al. Lacrimal gland tumors and simulating lesions. Radiol Clin North Am 1999;37:219–239.)

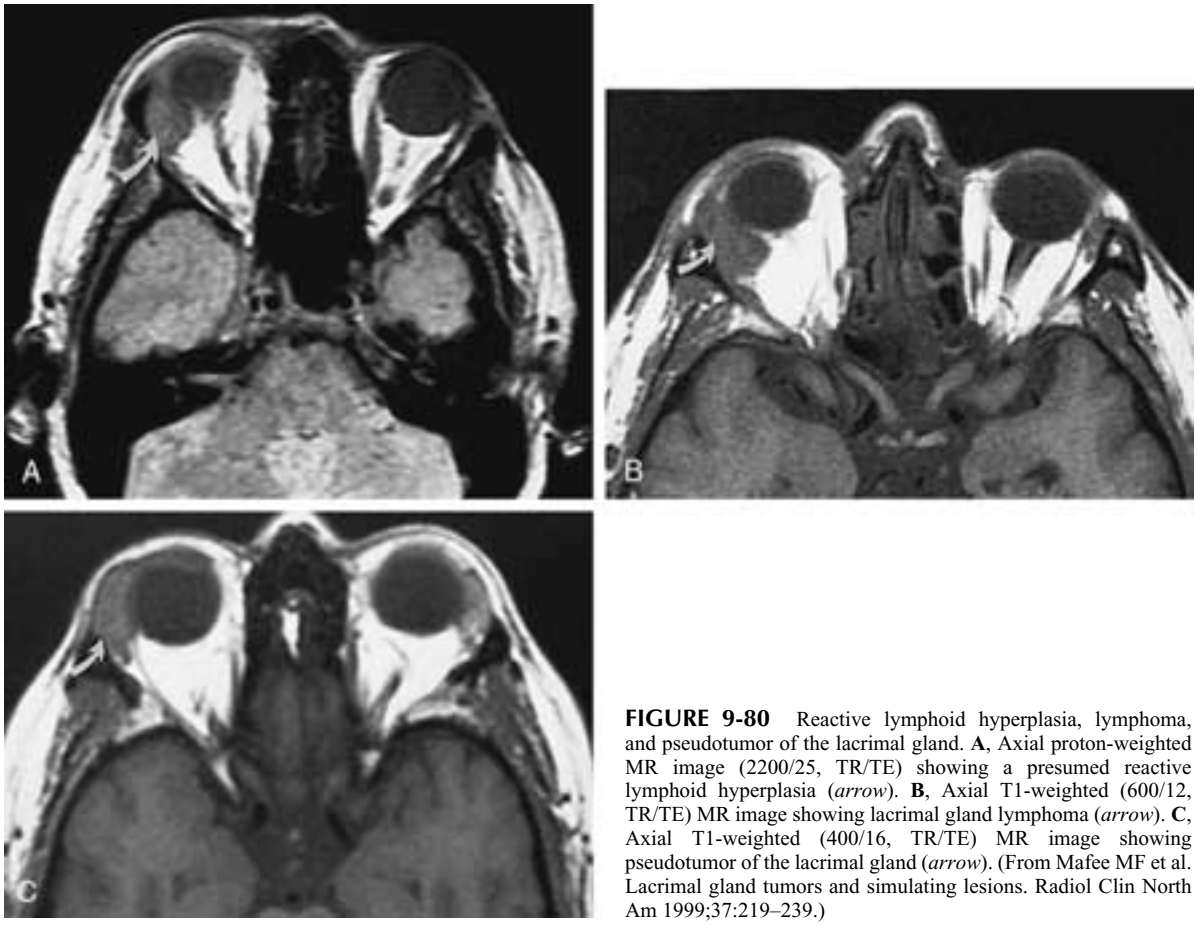

FIGURE 9-80 Reactive lymphoid hyperplasia, lymphoma, and pseudotumor of the lacrimal gland. **A**, Axial proton-weighted MR image (2200/25, TR/TE) showing a presumed reactive lymphoid hyperplasia (*arrow*). **B**, Axial T1-weighted (600/12, TR/TE) MR image showing lacrimal gland lymphoma (*arrow*). **C**, Axial T1-weighted (400/16, TR/TE) MR image showing pseudotumor of the lacrimal gland (*arrow*). (From Mafee MF et al. Lacrimal gland tumors and simulating lesions. Radiol Clin North Am 1999;37:219–239.)

VIEW IMAGE

Copyright © 2003, Mosby, Inc. All rights reserved.

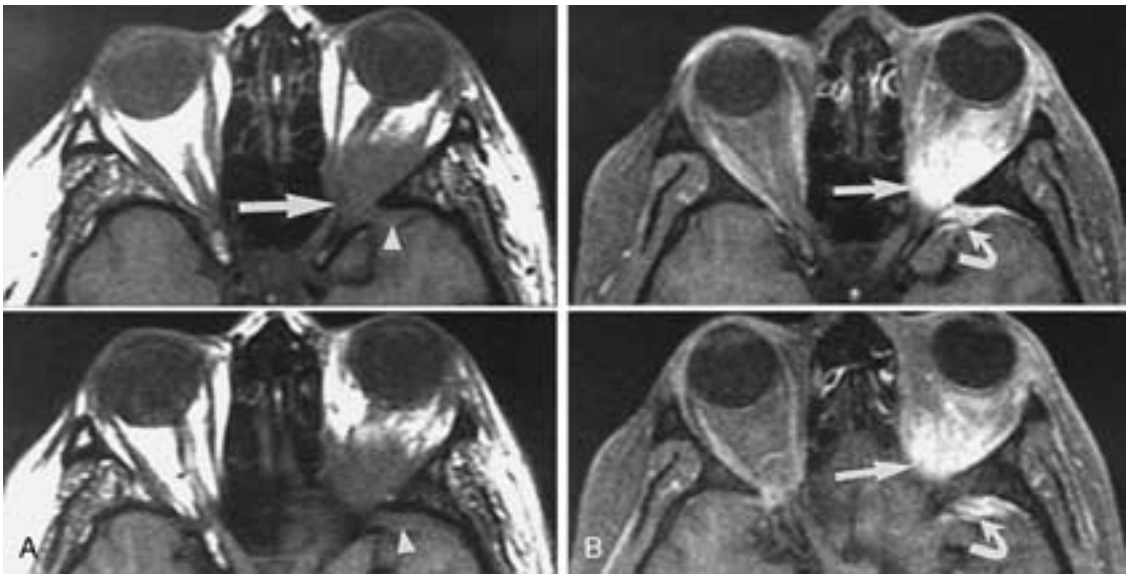

VIEW IMAGE

FIGURE 9-81 Orbital sarcoidosis presenting as superior orbital fissure syndrome. **A**, Unenhanced axial T1-weighted (400/25, TR/TE) MR images. Note the infiltrative process involving the orbital apex on the left side (*large arrow*). Note extension through the superior orbital fissure into the left temporal epidural space (*arrowheads*). **B**, Enhanced axial fat-suppressed, T1-weighted MR images show marked enhancement of this sarcoid granulomatous infiltration (*straight arrows*). Note the abnormal enhancement in the left temporal fossa (*curved arrows*). (From Mafee MF et al. Sarcoidosis of the eye, orbit, and central nervous system. Role of MRI. Radiol Clin North Am 1999;37:73–87.)

occur.[92] Immediate relief of symptoms following high doses of steroid therapy differentiate pseudotumor of the orbital apex and cavernous sinus from other lesions causing a superior orbital fissure syndrome.

Pathologically there is an infiltration of lymphocytes and plasma cells along with thickening of the dura matter, and it is important to exclude the possibility of a neoplastic (Fig. 9-82A), inflammatory (particularly mycotic) (Figs. 9-70 and 9-71), or vasogenic lesion. Carotid angiography and MR imaging are most useful in excluding an aneurysm as a cause of the clinical signs and symptoms.[103] Certain cavernous sinus, orbital apex, and parasellar lesions such as lymphoma, including Burkitt's lymphoma, leukemic infiltration, granulomatous diseases, pituitary adenomas, meningiomas, craniopharyngiomas, neurogenic tumors, dermoid cysts, orbital/sinonasal and nasopharyngeal carcinomas, invasive mycotic infections, aneurysm, and metastatic lesions (melanoma, lung, breast, kidney, thyroid, and prostate cancers) may produce similar symptoms.[103]

Thyroid Orbitopathy (Graves' Dysthyroid Ophthalmopathy)

Thyroid orbitopathy, or Graves' dysthyroid ophthalmopathy, is the most common cause of unilateral and bilateral exophthalmos in the adult population.[6, 103] The disease usually has its onset between the ages of 20 and 45 years.[6] The mean age of presentation for Graves' thyroid disease is 41 years, and the orbital disease occurs, on average, 2 to 5 years afterward.[104] Even though the disease is more common in women, its severity tends to be greater in men and in patients more than 50 years of age.[104] Graves' disease is a multisystem disease of unknown cause characterized by one or more of the three pathognomonic clinical entities: (1) hyperthyroidism associated with diffuse hyperplasia of the thyroid gland; (2) infiltrative ophthalmopathy; and (3) infiltrative dermopathy.[6] Thyroid orbitopathy (Graves' disease) includes any of the orbital and eyelid manifestations of this disorder. Among these clinical features are upper and lower eyelid retraction, exophthalmos, limitation of eye movements, eyelid edema, and epibulbar vascular congestion.[6] Although the majority of patients with thyroid orbitopathy have hyperthyroidism, the orbital manifestations of the disease may occur in individuals who are hypothyroid or euthyroid.[6] Occasionally, Graves' ophthalmopathy occurs in patients with Hashimoto's thyroiditis.[103]

Pathology

Immunopathology

Thyroid orbitopathy is presumed to be an autoimmune disease.[6, 103] It is postulated that the immune complexes (thyroglobulin and antithyroglobulin) reach the orbit via the superior cervical lymph channels that drain both the thyroid and the orbit.[6] These complexes bind to extraocular muscles and stimulate acute inflammation characterized by an influx of lymphocytes, plasma cells, mast cells, and fibroblast proliferation, glycosaminoglycan overproduction, and orbital congestions.[6, 103, 104] Circulating autoantibodies against a human eye muscle-soluble antigen have been detected in a significant percentage of patients with thyroid orbitopathy, and both humoral and cell-mediated immune mechanisms have been implicated.[6, 103] Immunohistochemical analysis and histologic findings have shown orbital infiltration with mononuclear cells sensitized to retro-orbital antigens.[103] Cytokines released by the infiltrating monocytes may stimulate immunomodulatory protein expression,

Copyright © 2003, Mosby, Inc. All rights reserved.

glycosaminoglycan production, and proliferative activity from orbital fibroblasts.

Histopathology

Generally, as in other forms of inflammatory myositis, the histopathology in Graves' ophthalmopathy consists early on of inflammatory cell infiltration, mucopolysaccharide deposition, and increased water content.[103] The EOMs are infiltrated by lymphocytes and contain an increased amount of hyaluronic acid, which binds to water and accounts for some of the orbital congestion.[6] In the chronic stage of the disease, the EOMs undergo degeneration of the muscle fibers and replacement fibrosis.[6, 103] Restrictive myopathy is caused by this fibrosis.

Diagnosis

The diagnosis of thyroid orbitopathy is based primarily on the patients' symptoms and clinical findings. Laboratory testing, including imaging studies, often is valuable in confirming the diagnosis.[6] The active phase of inflammation and progression tends to stabilize spontaneously 8 to 36 months after onset.[103] Exophthalmos, lid retraction, lid lag, prominence of the episcleral vessels, and lid edema are important clinical findings. In some patients, the disease is characterized by the gradual onset of primarily verical gaze diplopia.[11] In patients with Graves' ophthalmopathy, the forced duction test result is almost always abnormal, and limitation is the most common disturbance of ocular motility.[11, 14] The exophthalmos is the result of enlargement of the EOMs and/or increased orbital fat volume.[103] The exophthalmos is almost always bilateral and usually relatively symmetric, although occasionally it may be quite asymmetric.[103] The inferior rectus muscle is involved most commonly, followed by the medial rectus and the superior rectus.[103]

Diagnostic Imaging

CT and MR imaging in the acute congestive phase may show only markedly swollen retrobulbar orbital contents causing bilateral proptosis. The muscle bellies need not be

FIGURE 9-82 **A**, Wegener's granulomatosis in the sphenoid sinus with extension into the left orbit and optic canal. **A**, Axial CT section through the midorbits reveals a diffuse infiltrate in the region of the apex of the left orbit and optic canal. **B**, Axial CT section (bone window setting) through the optic canals reveals sclerosis in the region of the sphenoid sinus with irregularity and enlargement of the left optic canal. **C**, Coronal CT section through the sphenoid sinus reveals diffuse sclerosis in the outline of the sphenoid sinus along with soft-tissue thickening in the sphenoid sinus, especially on the left. Note destruction in the left lateral wall of the sphenoid sinus. (From Weber AL, Mikulis DK. Inflammatory disorders of the paraorbital sinus and their complications. Radiol Clin North Am 1987;25:615–630.) **B**, Neurosarcoidosis.

VIEW IMAGE

Copyright © 2003, Mosby, Inc. All rights reserved.

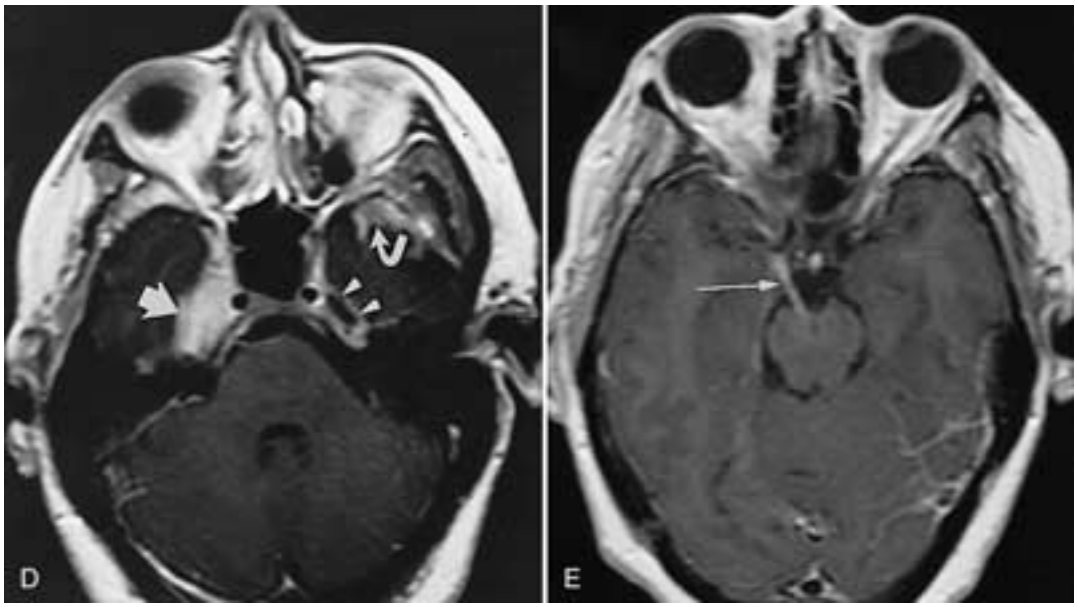

VIEW IMAGE

FIGURE 9-82 *Continued.* **D**, Enhanced axial T1-weighted (4501/11, TR/TE) MR image shows sarcoid granuloma involving the right Gasserian cistern (*large arrow*) and adjacent cavernous sinus, normal left Gasserian cistern (*arrowheads*), and abnormal enhancement in the left temporal fossa (*curved arrow*). **E**, Enhanced axial T1-weighted (450/11, TR/TE) MR image shows enhancement of the cisternal segment of the right third cranial nerve (*arrow*). The lateral gaze of the right eye is caused by the right oculomotor nerve palsy. (From Mafee MF et al. Sarcoidosis of the eye, orbit, and central nervous system. Role of MRI. Radiol Clin North Am 1999;37:73–87.)

enlarged. However, in this early stage of the disease, there also may be enlargement of the EOMs, and the coronal view is especially valuable in evaluating the degree of muscle enlargement and any optic nerve compression at the orbital apex. The increased orbital fatty reticulum results in anterior displacement of the orbital septum and at times prolapse of lacrimal glands. Strangulation of the optic nerve is seen best on axial CT scans.[3, 11]

About 90% of patients with thyroid orbitopathy have bilateral CT or MR imaging abnormalities (Figs. 9-83 and 9-84), even if the clinical involvement is unilateral.[3] Typically, enlargement involves the muscle belly, sparing the anterior tendinous insertion. However, there are rare patients who show thickening of the tendinous portion of the muscle.[3] Another helpful finding in thyroid myopathy is the presence of low-density areas within the muscle bellies. These are probably the result of focal accumulation of lymphocytes and mucopolysaccharide deposition.[3] Other CT and MR imaging findings in thyroid orbitopathy are increased orbital fat, enlargement (engorgement) of the lacrimal glands, edema (fullness) of the eyelids, proptosis, anterior displacement of the orbital septum, and stretching of the optic nerve with or without associated ''tenting'' of the posterior globe. On T2-weighted MR images, areas of high signal intensity may be present within the involved muscle. These areas presumably represent inflammation, and it is in these patients that a good clinical response to a trial of steroid therapy occurs. Later, a more chronic noncongestive phase follows, in which a restrictive type of limited eye movement often develops, secondary to fibrosis of the EOMs and to subsequent loss of elasticity.[11] At this stage, CT and MR imaging may show fatty replacement of the EOMs (Fig. 9-84B) or a string-like appearance of the EOMs (Fig. 9-84C). Although the muscles may be moderately to markedly attenuated, the orbital fatty reticulum volume remains increased, as may be evidenced by exophthalmos, anterior displacement of the orbital septum, and prolapse of the lacrimal glands. The differential diagnosis of Graves' dysthyroid orbitopathy on a clinical basis includes tumors that may be primary or metastatic, orbital inflammation including pseudotumor, and carotid cavernous or dural shunt fistulas. All of these conditions can usually be distinguished from Graves' orbitopathy on CT or MR images. However, at times, orbital myositis secondary to an inflammatory sinusitis, trichinosis, or a myositis due to

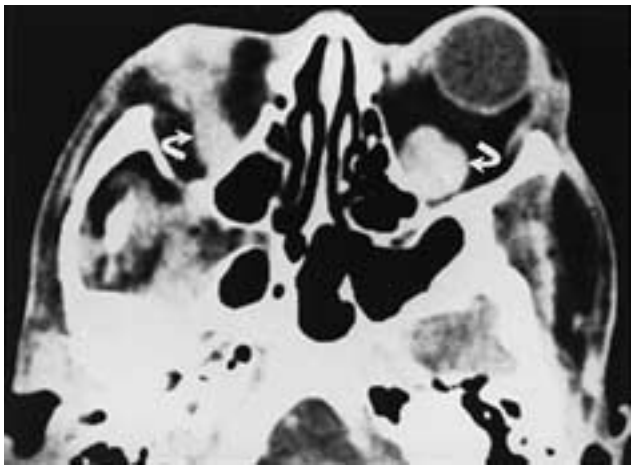

FIGURE 9-83 Thyroid myopathy. Axial CT scan shows enlargement of the inferior rectus muscles (*arrows*).

VIEW IMAGE

Copyright © 2003, Mosby, Inc. All rights reserved.

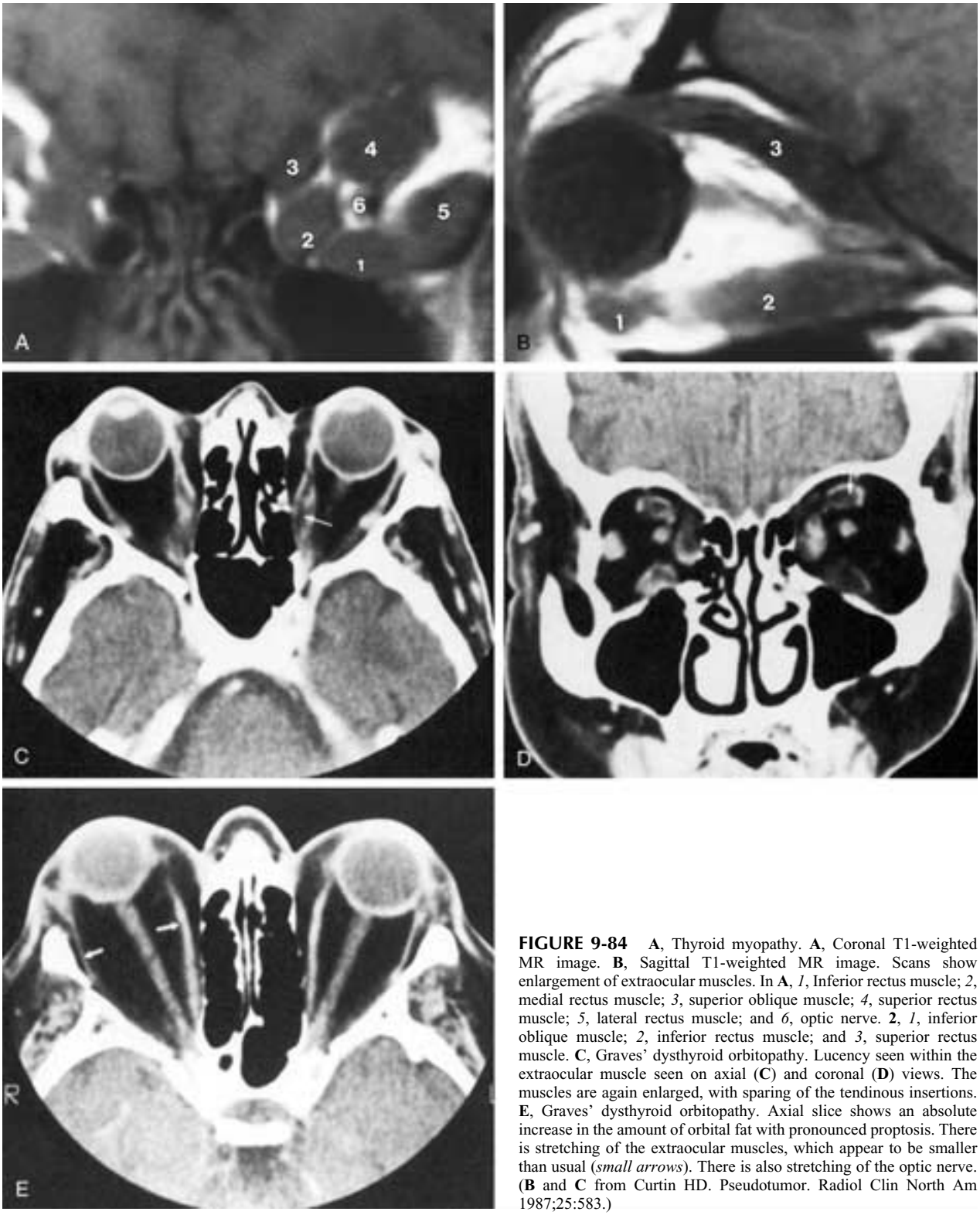

FIGURE 9-84 **A**, Thyroid myopathy. **A**, Coronal T1-weighted MR image. **B**, Sagittal T1-weighted MR image. Scans show enlargement of extraocular muscles. In **A**, *1*, Inferior rectus muscle; *2*, medial rectus muscle; *3*, superior oblique muscle; *4*, superior rectus muscle; *5*, lateral rectus muscle; and *6*, optic nerve. **2**, *1*, inferior oblique muscle; *2*, inferior rectus muscle; and *3*, superior rectus muscle. **C**, Graves' dysthyroid orbitopathy. Lucency seen within the extraocular muscle seen on axial (**C**) and coronal (**D**) views. The muscles are again enlarged, with sparing of the tendinous insertions. **E**, Graves' dysthyroid orbitopathy. Axial slice shows an absolute increase in the amount of orbital fat with pronounced proptosis. There is stretching of the extraocular muscles, which appear to be smaller than usual (*small arrows*). There is also stretching of the optic nerve. (**B** and **C** from Curtin HD. Pseudotumor. Radiol Clin North Am 1987;25:583.)

VIEW IMAGE

Copyright © 2003, Mosby, Inc. All rights reserved.

systemic diseases such as Crohn's disease or Wegener's granulomatosis, pseudotumor, lymphoma, and even metastases to extraocular muscles may be difficult to differentiate on imaging studies.

Sarcoidosis

Sarcoidosis is a granulomatous systemic disease that occurs worldwide, affecting persons of all races, both sexes, and all ages. It has a particular proclivity for adults under the age of 40 and for certain ethnic and racial groups. Estimates of the prevalence of sarcoidosis range from fewer than 1 to 40 cases per 100,000 population, with an age-adjusted annual incidence rate in the United States of 10.9 per 100,000 for whites and 35.5 per 100,000 for African Americans.[105] Higher annual incidence rates have been reported in other studies among African Americans, Irish, and Scandinavians. Sarcoidosis affects African Americans more acutely and more severely than it does people of other races. The cause of sarcoidosis remains obscure. The diagnosis of sarcoidosis is generally based on a biopsy finding of noncaseating granulomas with no other explanation.[3, 105]

The presenting features of sarcoidosis are protean, ranging from asymptomatic with abnormal findings on chest radiography in many patients to progressive multiorgan failure. Ophthalmic lesions develop in approximately 25% of patients, and virtually any part of the globe or orbit may be involved. There may be uveitis, chorioretinitis, and keratoconjunctivitis, and conjunctival inflammatory nodules may be seen.[3] The most common form of orbital involvement in sarcoidosis is chronic dacryoadenitis. This may be unilateral and may easily mimic a lacrimal gland tumor (Fig. 9-85A). Involvement of the lacrimal glands may also be very extensive (Fig. 9-85B), and when it occurs bilaterally in the lacrimal and salivary glands, it causes a Mikulicz-like syndrome of dry eyes and xerostomia.[17, 105] Sarcoid may also involve the optic nerve, and when this occurs, it may clinically resemble a primary neoplasm of the optic nerve (Fig. 9-86).[106, 107]

The classic symptoms of anterior uveitis have a rapid onset, with blurred vision, photophobia, and excessive lacrimation. These symptoms usually clear spontaneously within a year. Sarcoidosis may affect virtually any part of the nervous system. Among the 5% of patients so affected, involvement of the facial nerve is the most common and bilateral facial nerve palsy should be considered highly suspicious for sarcoidosis or Lyme disease. Any cranial nerve can be affected. The most common cranial nerves to be affected are the optic nerve, facial nerve, trigeminal nerve, acoustic nerve, oculomotor nerve, and abducens nerve in decreasing order of involvement. The illness can be self-limited or chronic, with episodic recrudescence and remissions.

It is not clear why some patients recover spontaneously, whereas others worsen. Visual system abnormalities are the most common extrathoracic manifestations of sarcoidosis. In addition to the globe, the conjunctiva, EOMs, retrobulbar space, lacrimal gland, optic nerve, chiasm, and optic radiations (meningovascular infiltration) may be affected.[105] These patients may present with confusing clinical and radiologic findings, especially if ophthalmic and neurologic involvement precedes systemic symptoms. Several investigators have characterized the MR imaging findings in neurosarcoidosis and in orbital and optic pathway sarcoidosis.

Pathologic and Immunologic Features

Sarcoidosis is a disorder mediated by excess helper T-lymphocyte activity at sites of disease activity. The noncaseating granulomas consist of mononuclear inflammatory cells, histiocytes, lymphocytes, plasma cells, and multinucleated giant cells.[105] Some of the granulomas may

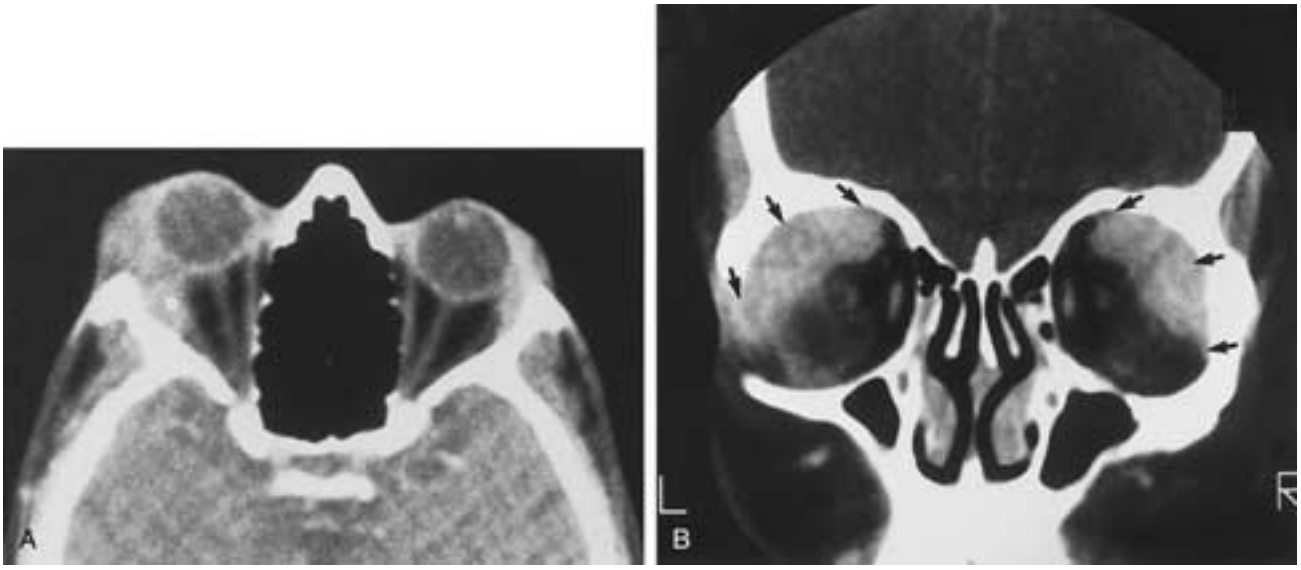

FIGURE 9-85 **A**, Sarcoidosis chronic dacryoadenitis. Axial CT scan shows enlargement of the right lacrimal gland. Note the mild enlargement of the left lacrimal gland. **B**, Sarcoidosis. Coronal-enhanced CT scan shows moderate enhancement of markedly enlarged lacrimal glands (*arrows*).

VIEW IMAGE

Copyright © 2003, Mosby, Inc. All rights reserved.

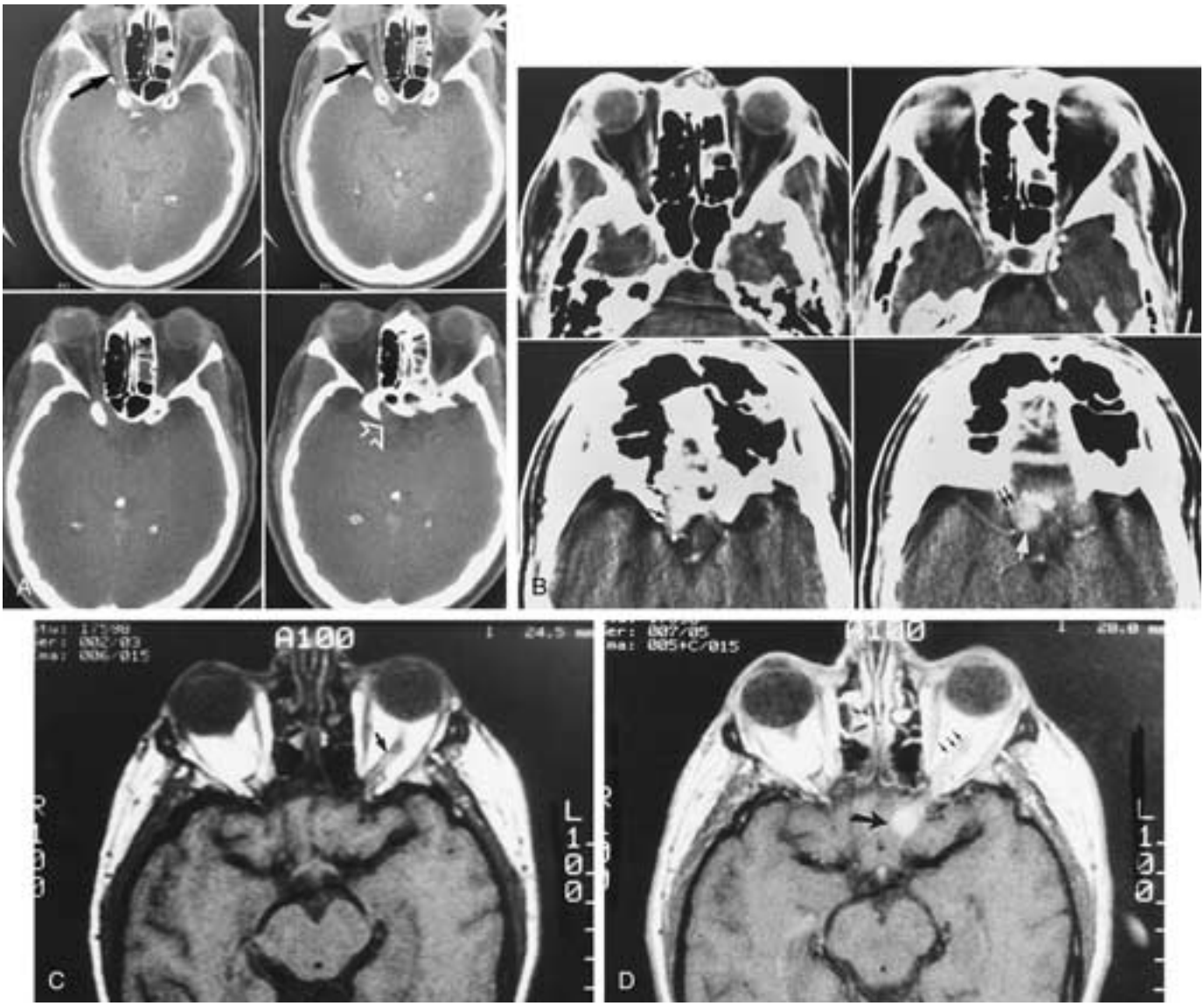

VIEW IMAGE

FIGURE 9-86 Sarcoidosis with optic nerve involvement. **A**, Serial axial CT scans show enlargement of the right optic nerve (*arrows*), including its intracranial segment. Note the soft-tissue mass in the right side of the chiasmatic cisterns (*hollow arrow*) and slight bilateral enlargement of the lacrimal glands (*curved arrows*). **B**, Serial axial CT scans obtained for soft-tissue detail, same patient as in **A**, show enhancing granulomas (*arrows*). **C**, Sarcoidosis-granuloma of the optic nerve. Axial T1-weighted MR scan shows no obvious lesion. There is a suggestion of slight thickening of the left optic nerve (*arrow*). **D**, Sarcoidosis-granuloma of the optic nerve. Enhanced axial T1-weighted MR scan shows increased enhancement of the left optic nerve (*arrows*) and a large granuloma involving the intracranial segment of the left optic nerve (*single arrow*).

have necrotic centers. Once mononuclear inflammatory cells accumulate in the target organ, macrophages aggregate and differentiate into epithelioid and multinucleated giant cells. Significant CD4 (helper-inducer) T cells are interspersed among these inflammatory cells. In time, CD4 and CD8 lymphocytes, and to a lesser extent B lymphocytes, form a rim around the granuloma. Except in the earliest stages of the granuloma, a dense band of fibroblasts, mast cells, collagen fibers, and proteoglycans begins to encase the cluster of cells in the granuloma. Fibrosis is an unfortunate outcome for many patients with sarcoidosis. Macrophages have a critical role in inducing fibroblasts to proliferate and to produce fibronectin and collagen in the lung. Most cells also contribute to the chronic fibrotic response in the granulomas.

Clinical Features

The clinical presentation of sarcoidosis may range from widespread disease to involvement of only one organ system at a time. Many asymptomatic cases are discovered during screening chest radiography, and these patients may or may not progress to clinically symptomatic disease. The majority of patients, however, present with systemic symptoms. In the United States, more than 50% of patients present with chronic respiratory symptoms and few constitutional symptoms. Lofgren's syndrome is referred to as the *constellation*

Copyright © 2003, Mosby, Inc. All rights reserved.

of erythema nodosum, bilateral hilar adenopathy, and *polyarthralgias*. Uveitis and parotiditis are referred to as *uveoparotid fever* or *Heerfordt's syndrome*. Lupus pernio is referred to as *nasal sarcoidosis*.[105]

There are no definitive diagnostic blood, skin, or radiologic imaging tests specific for the disorder. Although an elevated angiotensin converting enzyme (ACE) level helps to establish a diagnosis of sarcoidosis, measurement of serum ACE activity and gallium-67 scanning add little diagnostic value because of their lack of specificity.[105] Oksanen reviewed 50 cases of neurosarcoidosis and found that the ACE in the CSF was elevated in 18 of the 31 patients in whom it was measured.[105] The Kveim-Siltbach skin test is not widely available and is not approved for general use by the Food and Drug Administration. Respiratory tract involvement occurs at some time in the course of nearly all cases of sarcoidosis. Pulmonary involvement in sarcoidosis is typically bilateral, with four radiographic patterns: (1) bilateral lymphadenopathy without parenchymal abnormalities; (2) bilateral hilar lymphadenopathy with diffuse parenchymal changes; (3) diffuse parenchymal changes without hilar lymphadenopathy; and (4) diffuse parenchymal changes without hilar lymphadenopathy with upper lobe retraction. Hilar adenopathy is frequently accompanied by right paratracheal lymphadenopathy. Atypical radiographic presentations include unilateral lung or lobar infiltrates, unilateral lymphadenopathy, and predominant upper lobe involvement.[105]

Intrathoracic and peripheral lymphadenopathy are common, with radiographic evidence of hilar node enlargement in up to 90% of patients. Peripheral lymphadenopathies are typically nontender. Approximately 25% of patients have one or more skin manifestations. Dermatologists frequently detect sarcoidosis during a biopsy of atypical skin lesions. Lupus pernio produces indurated violaceous lesions principally on the cheeks, nose, lips, and ears.[105]

As mentioned, the ophthalmic lesions include uveitis (Fig. 9-87), infiltration of the lids, optic nerve (Fig. 9-88), orbit and EOMs (Fig. 9-81), granulomatous infiltration of lacrimal glands (Figs. 9-89 and 9-90), retinal vasculitis, uveitis, uveoretinitis, and vitritis. Dykhuizen and associates[108] reported a case of sarcoidosis that presented with recurrent headaches, transient right hemiparesis, and left-sided ophthalmoplegia. An excised left retrobulbar lesion demon-

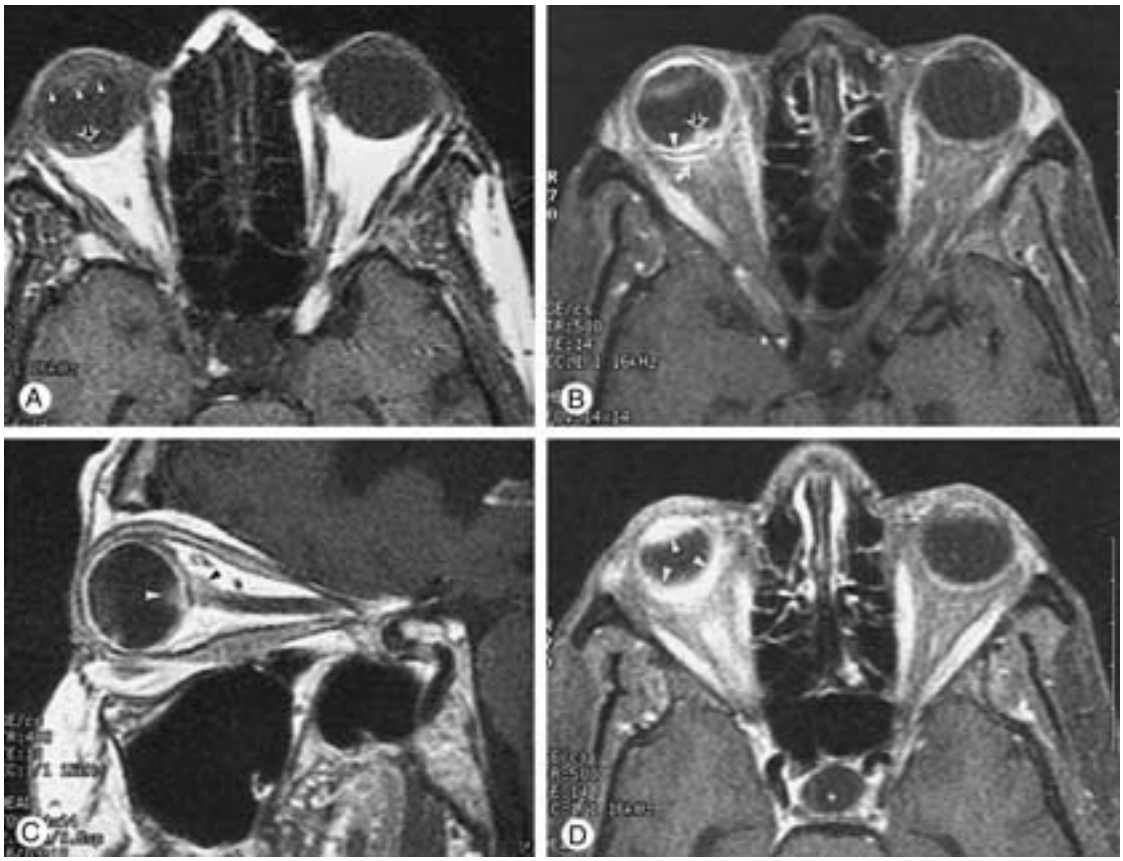

FIGURE 9-87 Ocular sarcoidosis panuveitis. **A**, Unenhanced, axial, T1-weighted (500/13, TR/TE) MR image shows nodular thickening of the posterior aspect of the right globe (*arrow*) and thickening of the anterior segment (*arrowheads*) of the right globe. **B**, Enhanced, axial, fat-suppressed T1-weighted (500/13, TR/TE) MR image shows nodular enhancement of the posterior aspect of the right globe (*arrowhead* and *open arrow*), related to granulomatous involvement of the choroid. Note enhancement of the anterior segment of the right globe. Notice abnormal enhancement of the Tenon's capsule (*curved arrow*). **C**, Enhanced, sagittal T1-weighted (400/13, TR/TE) MR image shows granuloma at the optic disc (*white arrowhead*) as well as involvement of the optic nerve (*black arrowhead*). **D**, Enhanced, axial, fat-suppressed T1-weighted (500/14, TR/TE) MR image shows enhancement of markedly thickened uveal tract (*arrowheads*). (From Mafee MF et al. Sarcoidosis of the eye, orbit, and central nervous system. Role of MRI. Radiol Clin North Am 1999;37:73–87.)

VIEW IMAGE

Copyright © 2003, Mosby, Inc. All rights reserved.

VIEW IMAGE

VIEW IMAGE

FIGURE 9-88 Optic nerve sarcoidosis. **A**, Enhanced, axial, T1-weighted (600/20, TR/TE) MR image shows increased enhancement of the right optic nerve (*arrow*). **B**, Enhanced, axial, T1-weighted (600/20, TR/TE) MR scan, taken 3 mm superior to **A**. Note nodular enhanced lesion (granuloma) involving right globe (*curved arrow*), enhancement of thickened intracranial segment of right optic nerve (*open arrow*), and abnormal enhancement along the anterior left sylvian fissure (*arrowheads*). **C**, Enhanced, coronal T1-weighted (650/20, TR/TE) MR image shows enlargement as well as marked enhancement of intracranial segment of the right optic nerve (*arrow*). **D**, Enhanced, axial, T1-weighted (600/20, TR/TE) MR image after corticosteroid treatment. Note absence of abnormal enhancement of the right globe as well as left anterior sylvian fissure (compare with **B**). **E**, Enhanced, axial, T1-weighted (612/25, TR/TE) MR image after corticosteriod treatment. Note decreased right optic nerve enhancement (*arrow*). **F**, Enhanced, coronal, T1-weighted (867/20, TR/TE) MR image. Note absence of enhancement of intracranial segment of right optic nerve, which was seen in **C**. (From Mafee MF et al. Sarcoidosis of the eye, orbit, and central nervous system. Role of MRI. Radiol Clin North Am 1999;37:73–87.)

Copyright © 2003, Mosby, Inc. All rights reserved.

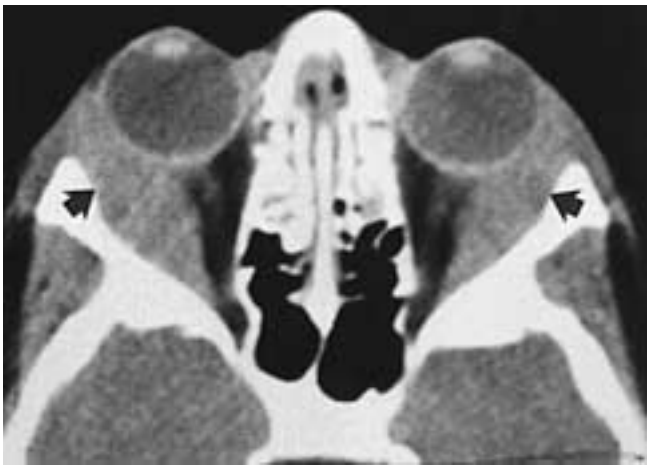

FIGURE 9-89 Presumed sarcoidosis of the lacrimal gland. Axial CT scan in this 7-year-old African American child shows marked enlargement of the lacrimal glands (*arrows*). (From Mafee MF et al. Sarcoidosis of the eye, orbit, and central nervous system. Role of MRI. Radiol Clin North Am 1999;37:73–87.)

strated sarcoid granulomatosis. Twelve years later, the patient developed a mass in the right lung. The excised lung mass was similar histologically to the previously removed left orbital mass. Idiopathic orbital inflammation displays a granulomatous inflammatory pattern that may mimic sarcoidosis. Raskin and associates[109] reported 12 patients with a diagnosis of sarcoidosis or another noninfectious granulomatous process involving the orbit. Five of these patients were diagnosed with sarcoidosis on histologic examination. In these patients, evaluation failed to reveal evidence of systemic involvement. The authors suggested that the clinicians should be aware of the existence of granulomatous idiopathic orbital inflammation not associated with systemic sarcoidosis as a distinct clinicopathologic entity. Monfort-Gouraud and associates[110] reported an inflammatory pseudotumor of the orbit and suspected sarcoidosis in a 13-year-old boy who had uveitis and symptoms of unilateral orbital inflammation. Mombaerts and associates[111] reported seven patients with unilateral idiopathic granulomatous orbital inflammation. Histopathologic analysis showed a spectrum of granulomatous inflammation admixed with nongranulomatous inflammation and fibrosis. They concluded that based on their study and review of the literature,

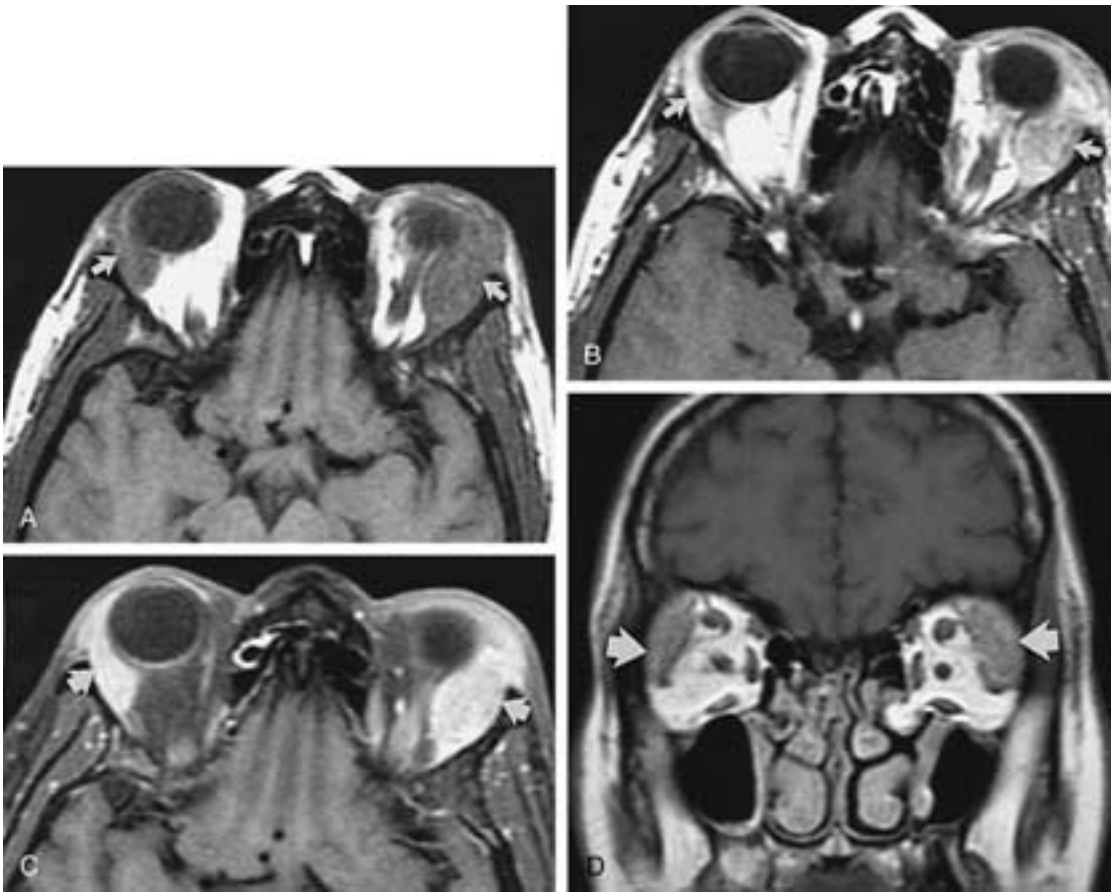

FIGURE 9-90 Sarcoidosis of lacrimal gland. Unenhanced, axial, T1-weighted (500/17, TR/TE) (**A**), enhanced, axial, T1-weighted (500/17, TR/TE) (**B**), enhanced, axial, fat-suppressed T1-weighted (500/17, TR/TE) (**C**), and enhanced, coronal, T1-weighted (600/18, TR/TE) (**D**) MR images show enlargement as well as increased enhancement of both lacrimal glands (*arrows*), more so on the left side. (From Mafee MF et al. Sarcoidosis of the eye, orbit, and central nervous system. Role of MRI. Radiol Clin North Am 1999;37:73–87.)

Copyright © 2003, Mosby, Inc. All rights reserved.

it appears that idiopathic granulomatous orbital inflammation is more closely related to orbital pseudotumor than to orbital sarcoidosis.

Carmody et al.[112] reported the MR imaging scans of 15 patients, 3 with presumed and 12 with proven orbital or optic pathway sarcoidosis. Eight patients had MR imaging evidence of optic nerve involvement by sarcoid granuloma. Perineural enhancement was seen in four cases and optic atrophy in one. Nine patients had optic chiasmal involvement. One patient had increased T2-weighted signal intensity in the optic radiations. Three patients had orbital masses that had MR imaging signal characteristics similar to those of idiopathic pseudotumor. Five patients had periventricular white matter abnormalities closely resembling multiple sclerosis.

Recently, Ing et al.[113] reported a 22-year-old white woman with optic nerve sarcoidosis without evidence of systemic or ocular disease. The authors found 17 cases similar to hers, with the diagnosis proved by optic nerve biopsy, reported in the English-language literature. In all of them, extensive prospective investigations revealed no systemic sarcoidosis. Most of these cases were initially mistaken for optic nerve sheath meningioma.

Neurosarcoidosis may produce anosmia and is frequently associated with ocular findings. In many cases of neurosarcoidosis, a diagnosis of meningioma is suspected preoperatively. Hypothalamic involvement in sarcoidosis is not uncommon and may mimic hypothalamic glioma. Lymphoma and Castleman's disease may involve the central nervous system including leptomeninges mimicking neurosarcoidosis and meningioma. Lymphoma may have primary intraorbital, intraocular, and intracranial involvement. Involvement of the optic nerve and other cranial nerves by angiocentric T-cell lymphoma, also known as *lymphomatoid granulomatosis*, has been reported.[105] Castleman's disease, a benign lymphoproliferative disorder related to lymphoma, is characterized by hyperplastic lymphoid follicles with capillary proliferation. This disorder was initially observed by Castleman in the mediastinum, but later reports described involvement elsewhere, including orbital and intracranial involvement.

Neurologic involvement with sarcoidosis takes two forms. In acute sarcoidosis, there tends to be involvement of a peripheral nerve, especially a cranial nerve and in particular the facial nerve. The optic nerve (which is not a peripheral nerve) is involved next most frequently. As mentioned, sarcoid uveitis in combination with a facial nerve palsy and fever is known as *Heerfordt's syndrome* or *uveoparotid fever*. The second form of nervous system sarcoidosis occurs in the chronic form of the disease with central nervous system involvement. Involvement of the optic nerve is more common in this form.[105] The involvement may be at the chiasm or in the intracanalicular or intraorbital segments of the optic nerve. Optic neuritis, granulomatous protrusions from the optic nerve head into the vitreous, and optic atrophy are manifestations of central nervous system and optic nerve sarcoid disease. Apart from the involvement of the lacrimal gland, involvement of the orbital tissues by true systemic sarcoidosis is rare.

Orbital pseudotumor may have a granulomatous pattern, which can easily be mistaken for sarcoidosis. Sarcoidosis-like lesions can be found in patients with syphilis, lymphogranuloma venereum, leprosy, tularemia, torulosis, histoplasmosis, blastomycosis, and coccidioidomycosis. The early lesions of sarcoidosis are much more likely to respond to corticosteroid therapy than are the late, fibrotic, hyalinized lesions. Lesions that demand systemic corticosteroid therapy are uveitis, optic neuritis, diffuse pulmonary and central nervous system lesions, persistent facial palsy, persistent hypercalcemia, and cutaneous lesions.

Optic Nerve Sarcoidosis

Certain inflammatory conditions, such as syphilis, tuberculosis, or sarcoidosis, may be responsible for a chronic and progressive loss of vision. Chronic optic neuropathy, however, is more frequently due to a compressive lesion, such as meningioma (intracanalicular, intraorbital, or tuberculum sellae), pituitary tumor, or paraclinoid aneurysm. Sarcoidosis frequently involves the nervous system and can present as an abrupt or chronic visual loss, with or without disc changes. In one series of 11 cases of sarcoidosis of the optic nerve in patients ranging in age from 16 to 48 years, only two patients were previously known to have the disorder.[114] Four patients showed disc granulomas, four had optic nerve granulomas, and five had posterior uveitis and retinitis. In this series, chest radiographs were characteristically abnormal in 8 of the 11 patients.[114] Only one third had elevated serum levels of ACE. CT scans in these 11 patients infrequently showed enlarged nerves or other findings. Although sarcoidosis is classically believed to commonly not involve the optic nerves, increasing numbers of cases of presumed optic nerve sarcoidosis have been seen on MR images and CT scans, some of them with histologic confirmation. Although neuroimaging does not distinguish optic nerve sheath meningioma from sarcoid of the optic nerve, in the absence of uveitis and systemic sarcoid disease certain imaging features should raise the possibility of optic nerve sarcoidosis, prompting a trial of corticosteroid therapy before proceeding to biopsy. Imaging features that may favor a diagnosis of sarcoidosis of the optic nerve include (1) enhancement of the optic nerve associated with prominent enlargement of the intracranial segment of this nerve; (2) enlargement of the intracranial segment of the optic nerve associated with contrast enhancement; and (3) abnormal enhancement of the optic nerve associated with abnormal dural and leptomeningeal enhancement. Bilateral optic nerve enlargement along with abnormal enhancement has not been seen. This finding should favor optic nerve sheath meningioma, demyelinating disease, optic glioma, lymphoma, leukemic infiltration, or pseudotumor. Optic nerve sarcoidosis in persons under age 16 years is extremely rare.[105] Enlargement and enhancement of the optic nerve in children is seen with optic nerve glioma, extension of retinoblastoma along the optic nerve, leukemic infiltration, and in very rare cases of optic nerve sheath meningioma and optic nerve medulloepithelioma.[105]

Diagnostic Imaging in Optic Nerve Sarcoidosis

When an ophthalmologist or neurologist suspects that an optic nerve is involved by sarcoidosis or that there is sarcoid of the central nervous system, a chest radiograph can be very useful. Active pulmonary sarcoidosis characteristically shows bilateral hilar adenopathy, with or without parenchymal disease. The nodes characteristically stand out from the

Copyright © 2003, Mosby, Inc. All rights reserved.

right heart border, and there is associated right paratracheal nodal involvement. Chest abnormalities are found in about 80% of patients with ocular sarcoidosis (uveitis). Gallium scintigraphy is more sensitive than chest radiography for showing pulmonary involvement in patients with sarcoidosis.[105] It lacks specificity, however, because other pulmonary diseases also show similar uptake. Lacrimal gland uptake of gallium-67 also occurs in more than 80% of patients with active sarcoidosis. This uptake is also nonspecific.[105]

In patients with ocular, orbital, and optic nerve sarcoidosis as well as neurosarcoidosis, MR imaging remains the imaging study of choice. Gadolinium-enhanced T1-weighted pulse sequences are the most informative part of the MR imaging study (Fig. 9-88), and enhanced fat-suppressed, T1-weighted MR images are essential for the diagnosis of optic nerve sarcoidosis or simulating lesions.[105]

Sjogren's Syndrome

Sjogren's syndrome is an autoimmune disorder characterized by keratoconjunctivitis sicca and xerostomia. Patients may have an associated autoimmune disease such as rheumatoid arthritis, systemic lupus erythematosus, polymyositis, scleroderma, or vasculitis. The lacrimal and salivary glands are initially infiltrated by periductal lymphocytes, and eventually atrophy of the acini with hyalinization and fibrosis occurs. The early disappearance of lysozymes from the tears in Sjogren's syndrome may help distinguish it from sarcoidosis, a disease in which the lysosomes in the tears are actually increased.

Vasculitides (Angiitides)

The vasculitides are an immunologically complex-mediated group of diseases that include a variety of inflammatory angiodestructive processes. Clinically, the vasculitides may show features of acute, subacute, and chronic inflammatory and vaso-obstructive signs and symptoms.[3] This group of diseases includes a wide variety of disorders that are usually classified on the basis of the symptoms they produce and the organs affected, as well as their histopathologic features.[3] The major ophthalmic or orbital diseases include polyarteritis nodosa, Wegener's granulomatosis, T-cell or B-cell lymphoma (previously called *idiopathic midline destructive disease*, *malignant midline reticulosis*, or *polymorphic reticulosis*), giant cell arteritis (temporal arteritis), hypersensitivity (leukocytoclastic) angiitis, and connective tissue disease, including systemic lupus erythematosus, rheumatoid arthritis, scleroderma, and polymyositis.

Wegener's Granulomatosis

Wegener's granulomatosis is a multisystem disease characterized by a triad of necrotizing granulomas in the upper and lower respiratory tracts, necrotizing vasculitis (focal necrotizing angiitis of small arteries and veins) of the lung, upper respiratory tract, and other sites, and glomerulonephritis.[3, 107] If left untreated, the disease is often fatal. The introduction of combined corticosteroid cyclophosphamide treatment has proven very successful.[3] The main chronic inflammatory or granulomatous processes that involve the sinus and the orbit include Wegener's granulomatosis and sarcoidosis.[102] Wegener's granulomatosis often mimics inflammatory, infectious, or malignant diseases and clinically involves the respiratory tract and kidneys.[102] However, ocular involvement is also common, occurring in 18% to 50% of the cases.[102] The disease may cause scleritis, episcleritis, uveitis, retinal vasculitis, and, rarely, conjunctival involvement. The condition is characterized by pain, proptosis, motility disturbance, chemosis, papilledema, and erythematous edema of the eyelids.[3, 107] Characteristically, ocular and orbital involvement is bilateral and either nonresponsive or transiently responsive to corticosteroids, often providing a clue to the diagnosis.[3] Involvement of the ocular adnexa includes lacrimal gland enlargement, nasolacrimal obstruction, and eyelid fistula formation.[3] The disease most commonly spreads from the paranasal sinuses to the orbit and produces pain, ophthalmoplegia, and loss of vision.[102] Although Wegener's granulomatosis characteristically occurs in the fifth decade of life, it has been documented in children.[102]

Orbital involvement with Wegener's granulomatosis should be differentiated from idiopathic pseudotumors, lymphoreticular proliferative disorders, and metastatic carcinoma.[107] The CT and MR imaging appearance of Wegener's granulomatosis is similar to that of pseudotumor and lymphoma (Figs. 9-91 and 9-92), and nasal and paranasal sinus involvement is present in the majority of cases (Fig. 9-82A). These diseases are definitively differentiated by biopsy, and a high titer of serum antineutrophil cytoplasmic antibodies is highly indicative of Wegener's granulomatosis. Treatment of the disease with glucocorticoids and cyclophosphamide results in complete remission in 75% of patients and partial remission in another 15%.[109]

B-Cell and T-Cell Lymphoma[109]

B-cell or T-cell lymphoma was formerly referred to as *idiopathic midline destructive disease*, *lethal midline granuloma*, *malignant midline reticulosis*, and *polymorphic reticulosis*. This disease is a clinical entity characterized by extensive destructive lesions of the nose, paranasal sinuses, and pharynx, often with associated involvement of the orbit and central facial bones. It has some similarity to Wegener's granulomatosis, but pulmonary disease is rare and renal involvement is absent.[107] This disease, which is not necessarily midline,[102, 115] is characterized by progressive unrelenting ulceration and necrosis, with destruction of the nasal septum. Most of these tumors are classified as T-cell lymphomas and are associated with Epstein-Barr virus infection.[102, 115] If the biopsy result indicates granulomatous vasculitis, the preferred treatment is cyclophosphamide and corticosteroids, as used for Wegener's granulomatosis. If the biopsy shows a lymphomatous process, radiotherapy is considered the treatment of choice.[107]

Periarteritis Nodosa (Polyarteritis Nodosa)

This condition is a vasculitis of the medium-sized and small arteries, adjacent veins, and occasionally arterioles and venules. The disease is segmental and leads to nodular aneurysms. The major ophthalmologic manifestations are retinal and choroidal infarcts that lead to exudative retinal

Copyright © 2003, Mosby, Inc. All rights reserved.

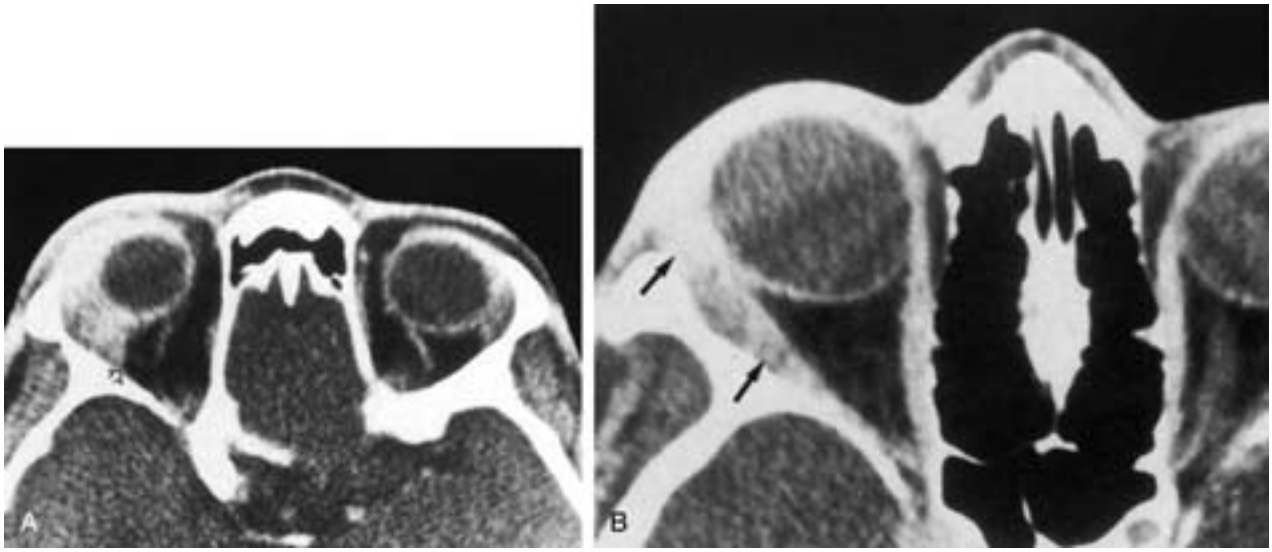

VIEW IMAGE

FIGURE 9-91 **A**, Wegener's granulomatosis with involvement of the lacrimal gland. Axial postcontrast CT scan shows diffuse enlargement of the right lacrimal gland. The lesion involves both palpebral and orbital lobes. Notice the rather straight configuration of the posterior aspect of the lesion (*hollow arrow*). In epithelial tumors of the lacrimal gland, the posterior border of the tumor has a rounded configuration. In Wegener's granulomatosis, enlargement of the lacrimal gland may be symmetric and extensive. Notice the slight enlargement of the involved left lacrimal gland in this patient. (From Mafee MF et al. Lacrimal gland and fossa lesions: role of computed tomography. Radiol Clin North Am 1987;25:767–779.) **B**, Wegener's granuloma. Axial CT scan showing an infiltrative process involving the right lacrimal gland and extending along the extraorbital space (*arrows*). (From Mafee MF et al. Orbital space-occupying lesions: role of CT and MRI: an analysis of 145 cases. Radiol Clin North Am 1987;25:529–559.)

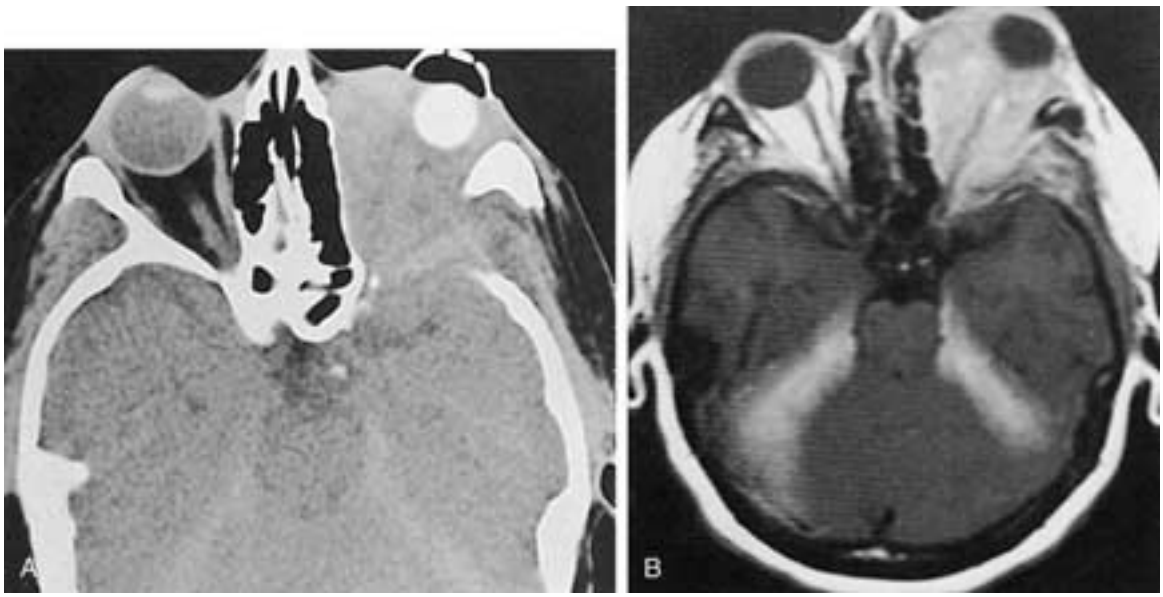

VIEW IMAGE

FIGURE 9-92 Progressive Wegener's granulomatosis of the left orbit. **A**, Axial CT scan demonstrates a diffuse homogeneous infiltrate obliterating the left orbit following exenteration of the left orbital contents. Note the anteriorly displaced prosthesis and a surgical defect in the lateral wall of the left orbit from previous surgery. **B**, Axial postcontrast T1-weighted MR image through the midorbits demonstrates marked enhancement of the inflammatory granulomatous process, which completely obliterates the left orbit, with stretching and anterior displacement of the globe. Note the diffuse enhancement of the tentorium cerebelli. (From Weber AL et al. Pseudotumor of the orbit: clinical, pathologic, and radiologic evaluation. Radiol Clin North Am 1999;37:151–168.)

Copyright © 2003, Mosby, Inc. All rights reserved.

detachment. Proptosis may occur secondary to severe inflammation of the orbital arteries, often leading to necrosis of the orbital connective tissues.[3, 107]

Hypersensitivity (Leukocytoclastic) Angiitis

This condition resembles periarteritis nodosa microscopically, but it affects smaller vessels. Pathologically, the arterioles, venules, and capillaries are usually but not necessarily necrotic, or they may simply have perivascular infiltration, with neutrophils undergoing karyolysis (leukocytoclasis). The spectrum of clinical disease varies from widespread multisystem involvement to primary dermatologic lesions.[3]

Lupus Erythematosus

Any of the connective tissue disorders may be associated with systemic vasculitis. The most common ones include systemic lupus erythematosus, rheumatoid arthritis, and dermatomyositis. Systemic lupus erythematosus is an autoimmune disease that affects many organs. It has a female/male ratio of 9:1 and occurs primarily in the second and third decades of life.[3] Histologically, the vasculitides in the connective tissue diseases resemble hypersensitivity angiitis.[3]

Evidence of antinuclear antibodies is universally present in this disorder. Of these patients, 20% have ocular involvement, primarily affecting the retinal vessels.[3] Orbital involvement is rare and is believed to be secondary to severe orbital vasculitis.[107] The CT and MR imaging appearance of orbital lupoid disease may resemble that of the pseudotumors and lymphoreticular proliferative disorders.

Amyloidosis

Amyloidosis is caused by deposition of an amorphous hyaline material (amyloid) in various tissues such as muscle, skin, nerve, submucosa, adrenal gland, and the orbit. Involvement of the orbit and ocular adnexa may occur as part of primary hereditary systemic amyloidosis, as part of secondary amyloidosis, or as a localized isolated process.[17, 83, 116] The clinical features of orbital and adnexal amyloidosis include blepharoptosis, caused by infiltration of the levator muscle of the upper eyelid, and oculomotor palsies resulting from involvement of multiple extraocular muscles. When the lacrimal gland is involved, the disease resembles a lacrimal gland tumor. On CT, amyloid deposits (homogeneous eosinophilic protein) simulate pseudotumors, vascular malformation, and other mass lesions, and the deposits can occasionally calcify (Figs. 9-93 and 9-94A).[83] On MR imaging, the amyloid deposits have signal intensities similar to those of skeletal muscle on all imaging sequences (Fig. 9-94B). Localized amyloid infiltrations may affect the paranasal sinuses, and bone destruction has been reported.[83]

MISCELLANEOUS GRANULOMATOUS AND HISTIOCYTIC LESIONS

A number of pathologic entities are recognized that, except for fibrous histiocytoma, rarely involve the orbit. These include histiocytosis X (Langerhans' histiocytosis), Erdheim-Chester disease, juvenile xanthogranuloma, pseudorheumatoid nodules, necrobiotic xanthogranuloma, and fibrous histiocytoma.[3] All of these lesions bear a common feature based on local or systemic infiltration by histiocytes.[3] Fibrous histiocytoma is the most common tumor in this category.[5]

Langerhans' Cell Histiocytosis

A granulomatous disease that occurs in children more often than sarcoidosis or Wegener's granulomatosis is Langerhans' cell histiocytosis; the disease has a predilection for children between 1 and 4 years of age.[102] The term *histiocytosis X* was coined to describe a group of histiocytic conditions, with the letter X indicating their unknown nature.[116] It is now known that these histiocytic conditions result from the proliferation and infiltration of abnormal histiocytes within various tissues. These cells are morphologically and immunologically similar to Langerhans' cells, leading to the name *Langerhans' cell histiocytosis* (*Hand-Schuller-Christian disease*, *Letterer-Siwe disease*, and *eosinophilic granuloma*).[117] Hand-Schuller-Christian disease typically involves the triad of diabetes insipidus, proptosis, and destructive bone lesions, often involving the sphenoid bone. Letterer-Siwe disease is seen in children under 2 years of age and is characterized by an acute disseminated form of Langerhans'cell histiocytosis associated with hepatosplenomegaly, adenopathy, fever, thrombocytopenia, anemia, and cutaneous lesions. The diagnostic feature is the presence of abnormal aggregates of Langerhans' cells. These cells, unlike other histiocytes, are characterized by immunochemical positivity for S-100 protein and CD1a and by the ultrastructural presence of membranous cytoplasmic structures, 200 to 400 mm in width and shaped like tennis rackets, that are known as *Birbeck granules*.[102]

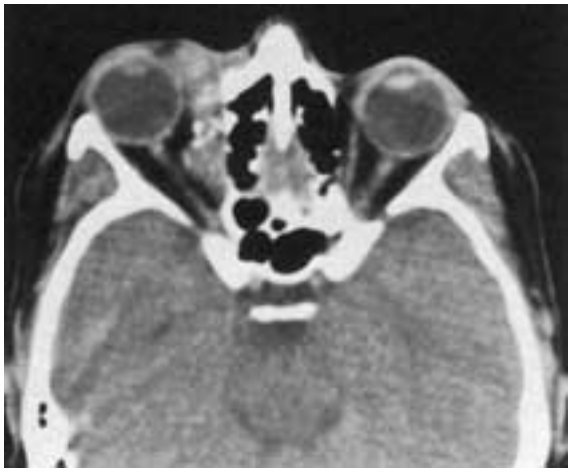

FIGURE 9-93 Amyloidosis of the right orbit with calcification. Axial CT section without infusion of contrast material reveals a mass in the extraconal space of the right orbit with a slight bulge into the intraconal space. Note the speckled calcifications within the amyloid deposit. The adjacent ethmoid sinus is normal. (From Weber AL, Mikulis DK. Inflammatory disorders of the paraorbital sinus and their complications. Radiol Clin North Am 1987;25:615–630.)

VIEW IMAGE

Copyright © 2003, Mosby, Inc. All rights reserved.

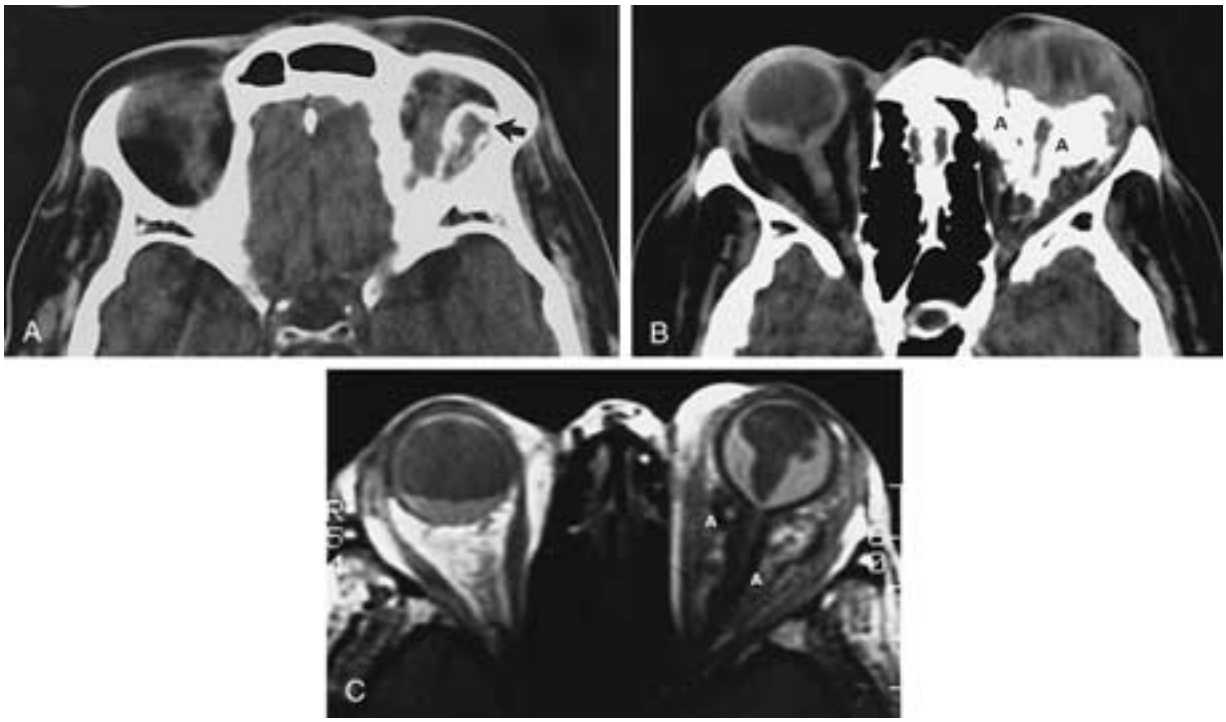

VIEW IMAGE

FIGURE 9-94 Amyloidosis of the lacrimal gland and orbit. **A**, Axial CT scan shows marked calcification of the left lacrimal gland (*arrow*). **B**, Axial CT scan shows a prominent cast-like calcification in the retrobulbar space caused by amyloidosis (*A*). Note the retinal detachment of the right eye. **C**, Axial T1-weighted (600/25, TR/TE) MR image shows hypointensity of the amyloid deposit (**A**). Note the bilateral exudative retinal detachment. The amyloid deposit appeared markedly hypointense on T2-weighted MR images (not shown). (From Mafee MF et al. Lacrimal gland tumors and simulating lesions. Radiol Clin North Am 1999;37:219–239.)

It is generally agreed that histiocytic disorders can be divided into two general categories: (1) X histiocytic (Langerhans' cell), Langerhans' cell histiocytosis (LCH), and (2) non–X histiocytic (monocyte-macrophage type) proliferation, including juvenile xanthogranuloma (JXG).[118] All of these disorders are characterized by a localized proliferation of histiocytes, but they differ in their morphology, histochemical and immunohistochemical staining patterns, and electron microscopic features.[119] Furthermore, they differ in their clinical presentation and radiologic appearance. Recently, the Histiocyte Society has redefined the classification of the histiocytoses of childhood. Class I includes LCH; class II includes all the histiocytoses of the mononuclear phagocytes other than Langerhans' cells, such as juvenile JXG; and class III includes the malignant histiocytic disorders. Orbital histiocytic disorders are classified as LCH (histiocytosis X); sinus histiocytosis with massive lymphadenopathy (Rosai-Dorfman syndrome); JXG; Erdheim-Chester disease; necrobiotic xanthogranuloma (NXG); pseudorheumatoid nodule; and sarcoidosis.[118]

Historical Background

In 1953, Lichtenstein[116] introduced the term *histiocytosis X* for a group of diseases that include eosinophilic granuloma, Hand-Schuller-Christian disease, and Letterer-Siwe disease. He believed that the pathologic common denominator of all three conditions was a distinctive and specific inflammatory histiocytosis. The letter X was used to underscore the unknown nature of the disease. Using the Birbeck granule as a marker, Nezelof and Barbey[117] in 1985 reported that the lesions of histiocytosis X were the result of inappropriate proliferation and infiltration of various tissues with abnormal histiocytic cells that are morphologically and immunologically similar to Langerhans' cells of the Langerhans' cell system. Consequently, the name of the disease was changed to *Langerhans' cell histiocytosis*.[118–120] This is a disease of unknown etiology. Some investigators suggested that LCH may be a disorder of immune regulation; however, recently, some investigators have provided strong evidence that all forms of LCH are a clonal proliferative disease.[119, 121]

Clinical Features

The disease has a predilection for children 1 to 4 years old.[102, 119] Lesions in children are most commonly located in bone or bone marrow. Although LCH is a rare disease, in patients with the disease orbital involvement is not uncommon, and with few exceptions it is usually seen in the chronic form of the disease, especially eosinophilic granuloma. The overall incidence of orbital involvement in a series of 76 children with LCH was 23%.[118] The most common signs and symptoms of orbital LCH were unilateral or bilateral proptosis, edema, erythema of the eyelid, and periorbital pain. Other signs and symptoms were ptosis, optic nerve atrophy, and papilledema. The frontal bone was most commonly involved by LCH, and the lesions were usually seen in the superior or superolateral wall of the orbit

Copyright © 2003, Mosby, Inc. All rights reserved.

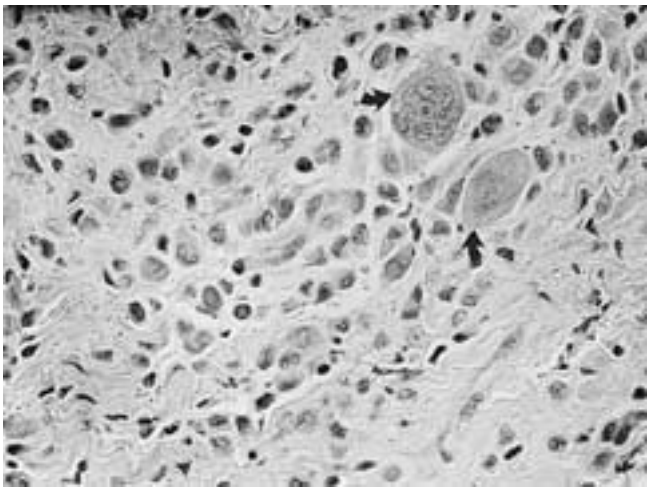

VIEW IMAGE

FIGURE 9-95 Langerhans' cell histiocytosis of the orbit. In addition to the mononuclear histiocytes, there are two multinucleated giant cells at the upper-right corner (*arrows*). ''Coffee bean'' nuclei are seen within the giant cells (hematoxylin-eosin, original magnification ×390). (From Hidayat AA et al. Langerhans' cell histiocytosis and juvenile granuloma of the orbit. Radiol Clin North Am 1998;36:1229–1240.)

in a rather anterior location. On rare occasions, the tumor may be noted in the orbital apex and superior orbital fissure without bone involvement. Classic cases of Hand-Schuller-Christian disease (the chronic disseminated form of LCH) with bilateral proptosis, diabetes insipidus, and bony defects of the skull are very rare.[118]

Ocular Manifestations

Intraocular involvement by LCH is rare and usually occurs as part of an acute disseminated form of the disease (i.e., Letterer-Siwe disease). In these cases, the uveal tract, particularly the choroid, is affected.[118]

Histopathologic Features

Grossly, the lesions are usually described as consisting of soft, friable, hemorrhagic, tan-yellow tissue. Histologically, the tumors are composed of sheets of large histiocytes with interspersed eosinophils, lymphocytes, and a few multinucleated giant cells (Fig. 9-95).

Immunohistochemistry

LCH cells are usually positive for the following immunologic markers: S-100 protein, peanut lectin, and CD1a (OKT-6).

Diagnostic Imaging

CT and MR imaging provide the most diagnostic assistance. Most lytic bony defects seen on standard plain films have been described as being irregular, serrated, and beveled, with or without a narrow zone of sclerosis. Orbital involvement may vary, but the most common orbital manifestation is a solitary lesion. In the typical case of orbital involvement, CT and MR imaging show an osteolytic lesion, commonly in the superior or superotemporal orbital region (Figs. 9-96 and 9-97). There is a fairly well-defined or diffuse soft-tissue mass encroaching on the lacrimal gland, the lateral rectus, or even the

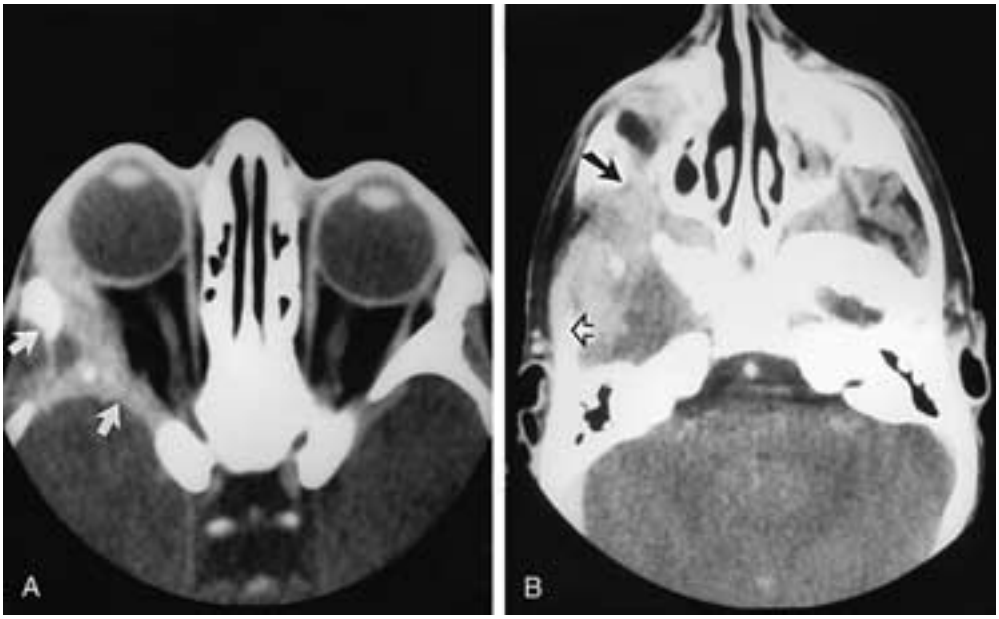

VIEW IMAGE

FIGURE 9-96 **A**, Langerhans' cell histiocytosis. Four-year-old boy with a history of gradual proptosis, diabetes insipidus, and skin lesions consistent with Hand-Schüller-Christian disease. Postcontrast axial CT scan shows replacement of the greater wing of the sphenoid bone (*arrows*) by soft tissue, which demonstrates marked enhancement. **B**, Langerhans' cell histiocytosis. Postcontrast axial CT scan in the same patient as in **A** showing a destructive lesion involving the squama of the right temporal bone (*hollow arrow*) as well as the posterior wall of the right maxillary sinus (*solid arrow*). Notice the marked soft-tissue infiltration into the right temporal fossa (*hollow arrow*). (From Hidayat AA et al. Langerhans' cell histiocytosis and juvenile granuloma of the orbit. Radiol Clin North Am 1998;36:1229–1240.)

Copyright © 2003, Mosby, Inc. All rights reserved.

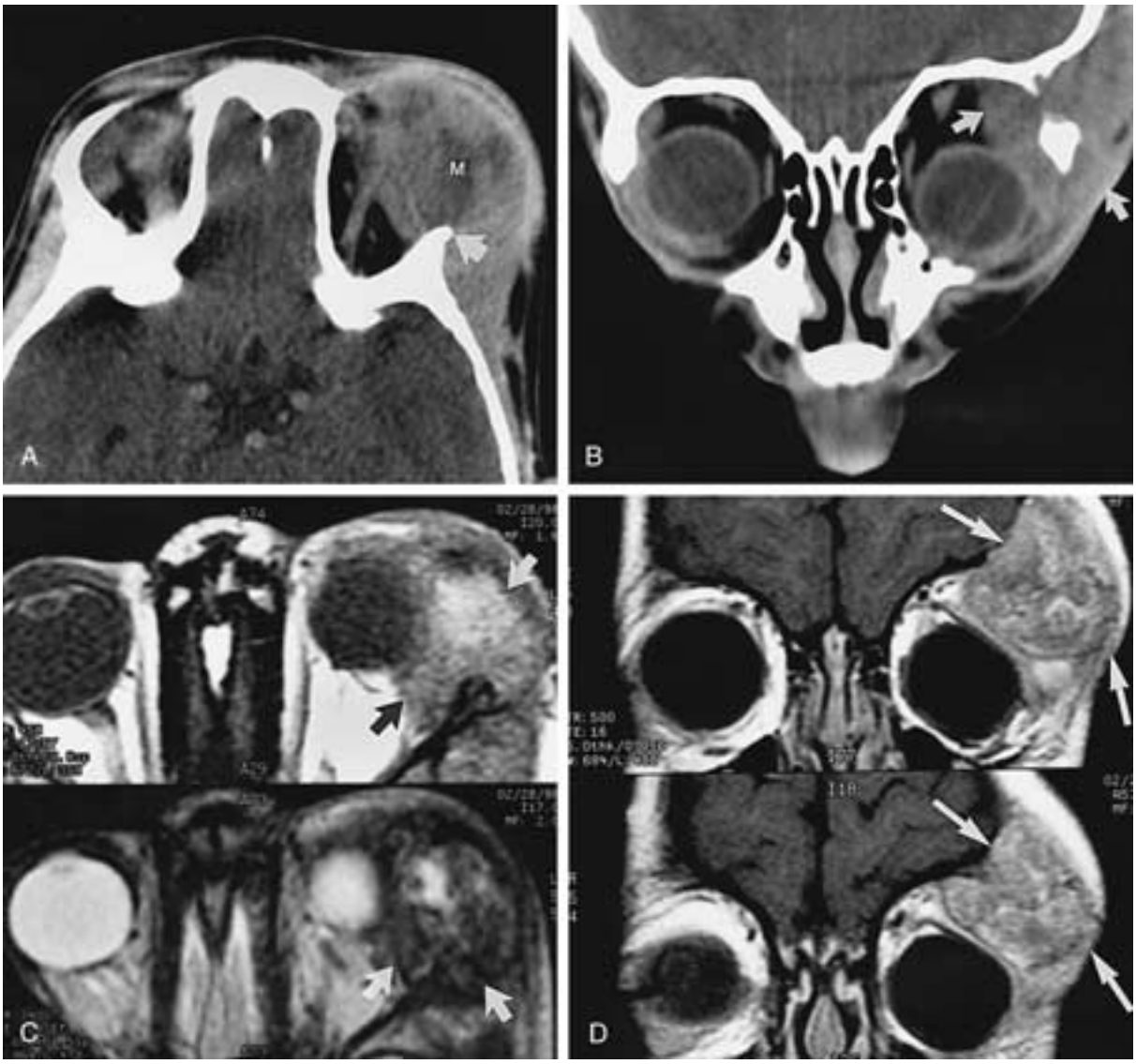

VIEW IMAGE

FIGURE 9-97 Langerhans' cell histiocytosis. **A**, Enhanced axial CT scan shows a prominent soft-tissue mass (*M*) with destruction of the orbital wall (*arrow*). **B**, Enhanced coronal CT scan shows a destructive mass involving the superolateral orbit (*arrows*). **C**, Axial proton-weighted (*top*) and T2-weighted (*bottom*) MR images show the mass (*arrows*). The mass appears hypointense on T2-weighted MR images caused by recent traumatic hemorrhage confirmed at surgery. **D**, Gadolinium contrast-enhanced, coronal T1-weighted MR images show marked enhancement of the lesion (*arrows*). (From Hidayat AA et al. Langerhans' cell histiocytosis and juvenile granuloma of the orbit. Radiol Clin North Am 1998;36:1229–1240.)

globe. There may be extension of the soft tissue into the epidural space, as well as into the temporal fossa. There may be marked infiltration of temporalis muscles (Fig. 9-96). At times, multiple lesions may be present, resulting in multiple bony defects, particularly in the superolateral orbital roof region. Similar osseous lesions may be seen in the sphenoid, ethmoid, temporal, occipital, and parietal bones, as well as in the facial bones. Rarely, the lesion may be totally extraosseous. On postcontrast CT and MR imaging, lesions demonstrate moderate to marked enhancement (Fig. 9-97). The differential diagnosis of LCH from an imaging viewpoint includes rhabdomyosarcoma, juvenile fibrosarcoma, aggressive fibromatosis, lacrimal gland tumors, lymphoma, pseudotumor, leukemic infiltration, granulocytic sarcoma or chloroma, sinus histiocytosis, metastatic neuroblastoma, metastatic Wilms' tumor, and metastatic Ewing's sarcoma.

Juvenile Xanthogranuloma

Juvenile xanthogranuloma (JXG) (nevoxanthoendothelioma)[121] is a benign, usually self-healing disorder of infants, children, and occasionally adults. The disease is of unknown etiology and pathogenesis and represents a proliferation of non-Langerhans' (monocyte-macrophage) types of cells. The term *juvenile xanthogranuloma* was first introduced in 1936, but recognition of the entity did not occur until 1954.[118] Recently, the Histiocyte Society has redefined the classification of the histiocytoses of childhood and included JXG in class II.[118]

Copyright © 2003, Mosby, Inc. All rights reserved.

Clinical Features

Characteristically, the disease affects children, particularly infants, and is sometimes noted at birth. Adults are affected less frequently. The most common site is the skin, where spontaneous resolution is frequent.

Orbital involvement with JXG is rare, with only 15 patients having been described in the English literature, mostly as case reports, except for the series of 5 infantile cases in Zimmermans's[121] report and 5 adult cases reported by Jakobiec and coworkers.[122] Eight of these patients were infants, mostly less than 9 months old. In four of these infants, the orbital lesion was present since birth. In 7 of the 15 orbital cases, the patients were adults ranging from 22 to 60 years of age (average, 45 years).

Inside the eye, the most common sites of involvement are the iris and the ciliary body.[118] The retina, choroid, and optic nerve are rarely involved. In the eye, the presenting clinical signs, as described by Zimmerman,[121] are (1) asymptomatic localized or diffuse tumor of the iris; (2) congenital or acquired heterochromia of the iris; (3) unilateral glaucoma; (4) spontaneous hyphema; and (5) a red eye with signs of uveitis.[118, 121]

Central nervous system involvement by JXG has been reported with associated seizures, ataxia, subdural effusions, increased intracranial pressure, developmental delay, diabetes insipidus, and other neurologic deficits.[118] T1-weighted MR imaging of the brain showed solid, gadolinium-enhancing masses without evidence of cerebral edema or displacement.

Histopathologic Features

Histologically, the lesions are composed of foamy histiocytes, epithelioid monocytes, lymphocytes, plasma cells, eosinophils, Touton giant cells, and spindle cells (Fig. 9-98).[118] Touton giant cells are multinucleated cells with the nuclei grouped in a wreath-like arrangement around a small central island of nonfoamy cytoplasm (Fig. 9-98). In contrast, the peripheral cytoplasm is foamy. The numbers of the different histiocytic cells are variable and form four distinctive patterns with varying degrees of overlap: (1) xanthomatous, (2) xanthogranulomatous, (3) fibrohistiocytic, and (4) combined patterns. It should be noted that the number of foamy or lipidized cells can be few, and Touton giant cells can be rare or absent in some cases, thus making the histologic diagnosis extremely difficult, as noted in one of the reported cases of orbital JXG.[121] In that case, there were many eosinophils and the lesion closely resembled those of LCH. Histologically, the differential diagnosis of orbital JXG includes Erdheim-Chester disease, particularly in adult patients. In both conditions there are Touton giant cells and foamy histiocytes. The only subtle difference between these disorders is the increased amount of fibrosis with collagenization and cholesterol clefts in Erdheim-Chester disease. In such cases, the clinical and paraclinical data, such as metaphyseal radiopacities, pulmonary infiltration and fibrosis, cardiac decompensation, chronic lipogranulomatous pyelonephritis, retroperitoneal xanthogranuloma, and hyperlipidemia in Erdheim-Chester disease, are extremely important for establishing the correct diagnosis.[123, 124] Inflammatory pseudotumor does not show xanthoma or Touton giant cells histologically. The differential diagnosis also includes LCH. In both lesions eosinophils are present, but the histiocytes are different morphologically and immunohistochemically. Touton giant cells are present only in JXG. The foamy histiocytes and Touton giant cells are negative for S-100 protein; however, a few S-100-positive dendritic cells were reported in the peripheral areas of JXG lesions.

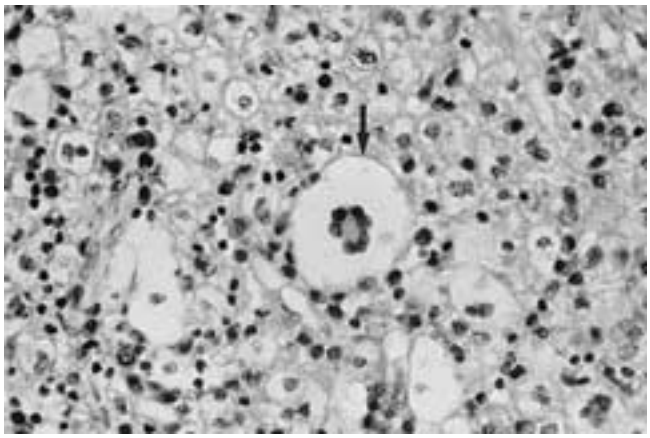

FIGURE 9-98 JXG of the orbit. Centrally, there is a characteristic multinucleated Touton giant cell (*arrow*), with the nuclei grouped in a wreath-like arrangement around a central small island of nonfoamy cytoplasm. The peripheral cytoplasm of the giant cell is pale and foamy. Other cells include xanthoma cells (lipidized histiocytes), with pale, foamy cytoplasm. A few lymphocytes are also present (hematoxylin-eosin, original magnification ×390). (From Hidayat AA et al. Langerhans' cell histiocytosis and juvenile granuloma of the orbit. Radiol Clin North Am 1998;36:1229–1240.)

VIEW IMAGE

Diagnostic Imaging

Radiologically, the most common ocular finding is involvement of the anterior portion of the eye (Fig. 9-99). It is important to know that the bony wall of the orbit may be involved.[119] These changes included simple erosions of the superior orbital rim in one patient, radiolucency in the malar eminence in another patient, and marked destruction of the roof and lateral wall of the orbit and of the greater wing of the sphenoid in a third patient.[119] Those cases with bone involvement may not be distinguished from LCH radiologically. There has also been a case in which the clinical and radiologic findings were typical of LCH (Hand-Schuller-Christian disease) in a 3-year-old girl who had bilateral proptosis and diabetes insipidus. However, the histopathology was more consistent with JXG (Fig. 9-100). Furthermore, the histiocytes were negative for the immunologic marker S-100 protein, and no Birbeck granules were found when electron microscopy was performed. The CT characteristics of orbital involvement of JXG in an adult are shown in Figure 9-101. It is important to realize that the inflammatory process, including the granulomatous disease involving the orbit, may simulate LCH. A case of orbital involvement by tuberculosis simulating LCH or JXG is shown in Figure 9-102.

Erdheim-Chester Disease

Erdheim-Chester disease is a peculiar form of systemic xanthogranulomatosis that occurs in adults.[123, 124] Most patients do not have orbital involvement. The first two cases

Copyright © 2003, Mosby, Inc. All rights reserved.

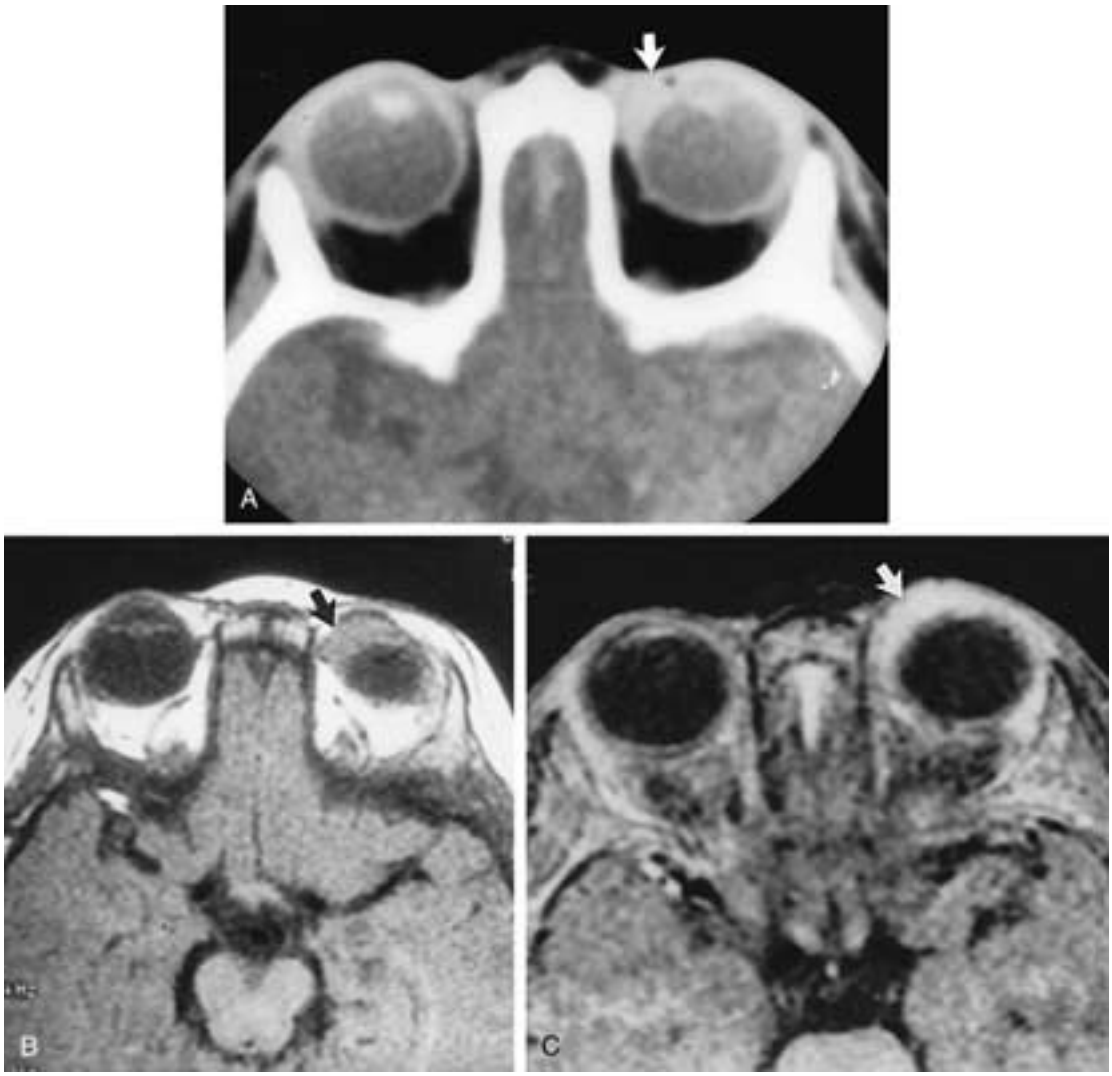

VIEW IMAGE

FIGURE 9-99 JXG of the orbit. **A**, Enhanced axial CT scan shows an enhancing infiltrative process involving the medial orbital region (*arrow*). **B**, Axial T1-weighted MR image shows the lesion (*arrow*) to be isointense to brain. **C**, Gadolinium-enhanced, fat-suppressed axial MR image shows marked enhancement of the orbital lesion (*arrows*). The lesion was adherent to the sclera. (From Hidayat AA et al. Langerhans' cell histiocytosis and juvenile granuloma of the orbit. Radiol Clin North Am 1998;36:1229–1240.)

VIEW IMAGE

FIGURE 9-100 JXG. **A**, Enhanced axial T1-weighted MR image shows an enhanced soft-tissue infiltrative process involving the lateral orbital walls (*open arrows*), epidural space (*white arrows*), and temporal fossa (*t*). **B**, Enhanced coronal T1-weighted MR image shows marked soft-tissue infiltration of both orbits (*arrows*), as well as involvement of the frontal bone on both sides. (From Hidayat AA et al. Langerhans' cell histiocytosis and juvenile granuloma of the orbit. Radiol Clin North Am 1998;36:1229–1240.)

Copyright © 2003, Mosby, Inc. All rights reserved.

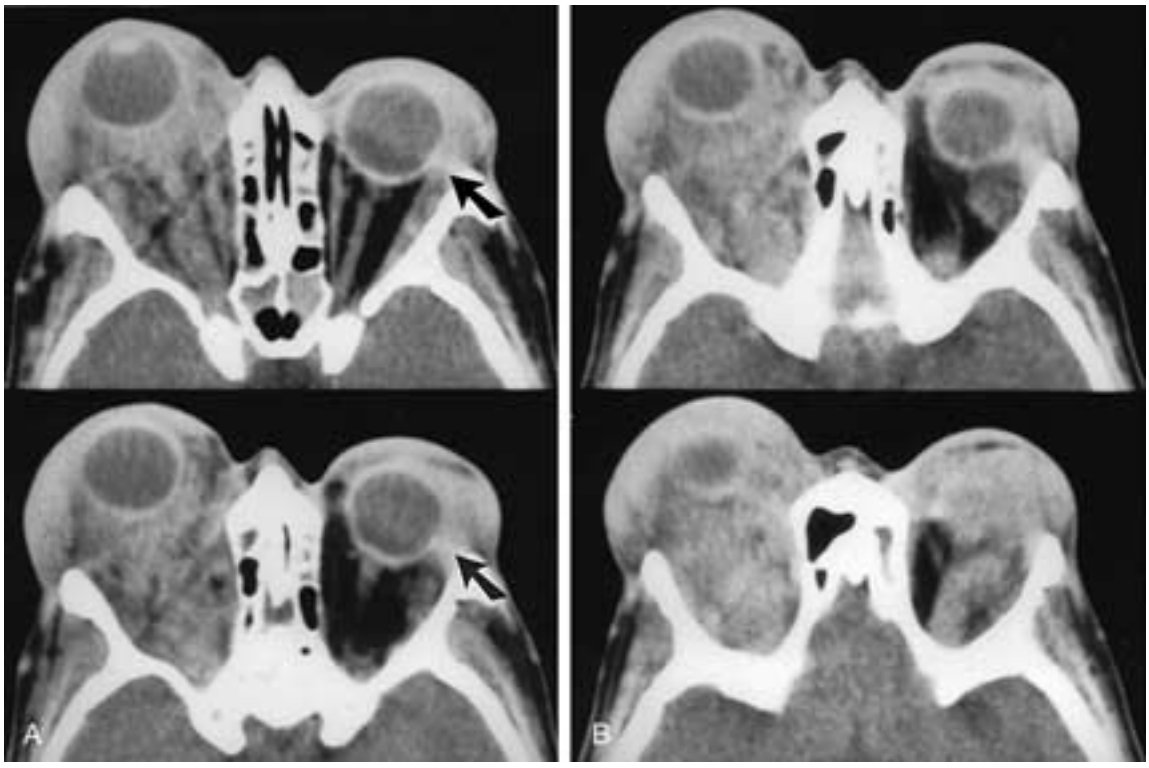

VIEW IMAGE

FIGURE 9-101 JXG of the orbit in an adult. **A**, Axial enhanced CT scans show proptosis and a diffuse infiltrative process involving the right orbit. There is abnormal soft-tissue thickening (*arrows*) of the left orbit as well. **B**, Enhanced axial CT scans show a marked infiltrative process involving the right orbit and, to a lesser extent, the left orbit. The differential CT diagnosis is bilateral pseudotumor, lymphoma, Wegener's granulomatosis, and necrobiotic xanthogranuloma. (From Hidayat AA et al. Langerhans' cell histiocytosis and juvenile granuloma of the orbit. Radiol Clin North Am 1998;36:1229–1240.)

were reported by Shields et al.[124] This disease is characterized by the infiltration of many organs including the lung, kidney, heart, bones, orbit, and retroperitoneal tissues. Orbital involvement tends to be bilateral. These patients present with progressive bilateral exophthalmos, which may lead to ophthalmoplegia, and visual loss secondary to compressive optic neuropathy.[92] CT and MR imaging may show extensive soft-tissue infiltration of the orbital fatty reticulum (Fig. 9-103).[107, 125] There may be no enhancement following the administration of Gd-DTPA contrast material.

Pseudorheumatoid Nodules

Pseudorheumatoid nodules usually occur as focal masses in the dermis of children. This disease may involve the

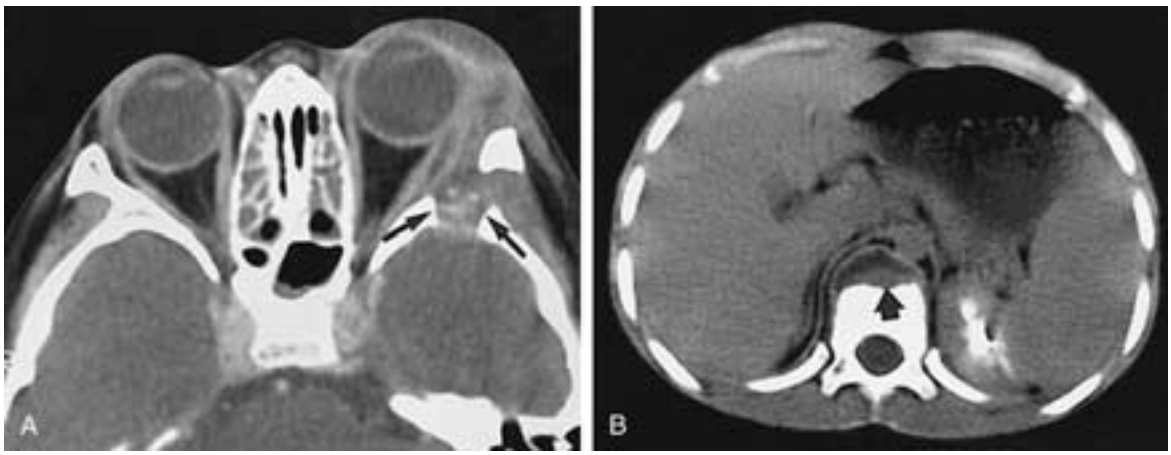

VIEW IMAGE

FIGURE 9-102 Tuberculosis. **A**, Enhanced axial CT scan shows a destructive lesion involving the left orbit (*arrows*). **B**, Axial CT scan through the abdomen shows a prevertebral tuberculous abscess (*arrows*). (From Hidayat AA et al. Langerhans' cell histiocytosis and juvenile granuloma of the orbit. Radiol Clin North Am 1998;36:1229–1240.)

Copyright © 2003, Mosby, Inc. All rights reserved.

VIEW IMAGE

FIGURE 9-103 Erdheim-Chester disease of both orbits. Axial CT scan through the midorbits reveals a diffuse infiltrate around the right globe laterally with extension into the lateral rectus muscles. A similar infiltrate is noted along the lateral part of the left globe and adjacent rectus muscle. (From Weber AL et al. Pseudotumor of the orbit: clinical, pathologic, and radiologic evaluation. Radiol Clin North Am 1999;37:151–168.)

anterior orbit and periorbital region. The subcutaneous nodules consist of zonular granulomas surrounding necrobiotic collagen. These are thought to be more common in sites of previous trauma and are easily managed by simple excision[3] (Fig. 9-104).

Necrobiotic Xanthogranuloma

Necrobiotic xanthogranuloma is a histocytic disease characterized by multiple indurated xanthomatous subcutaneous nodules in patients with paraproteinemia and proliferative disorders such as multiple myeloma and leukemia.[3, 107, 126] Pathologically, a zonular granulomatous inflammatory infiltrate, with Touton giant cells and xanthoma cells, surrounds an area of necrobiosis. Ophthalmic manifestations are common and include xanthogranulomas involving the eyelid, orbit, conjunctiva, and orbital fatty reticulum.

TUMORS

Orbital Lymphoma

Orbital lymphomas are solid tumors of the immune system composed primarily of (monoclonal) B cells. The extranodal presentation of non-Hodgkin's lymphoma is common, with an incidence ranging from 21% to 64%. Roughly 10% of the cases of non-Hodgkin's lymphoma present in the head and neck region, and lymphoid tumors account for 10% to 15% of orbital masses.[89]

Lymphoid neoplasms of the orbit span a large continuum of various classifications ranging from the malignant lymphomas, to the benign pseudolymphomas or pseudotumors, to the reactive and atypical lymphoid hyperplasias.[91] There are no absolute imaging, clinical, or even laboratory tests that distinguish all types of benign orbital lymphoid lesions from orbital lymphomas or lesions that can simulate them.[91-93] A pleomorphic cellular infiltrate is correlated with more benign biologic activity, and the more uniform the cellular appearance, the greater the likelihood that a malignancy is present.[91] Of all patients with orbital lymphoma, 75% have or will have systemic lymphoma.[91] There is extensive overlap histologically from one type to another, and some forms of the benign process can transform over time into a more aggressive variety of lymphoma. True lymphoid tissue in the orbit is found in the subconjunctival and lacrimal glands, and these two areas account for most of the lymphoreticuloses developing in the orbit.[91, 94] The most common cytologic forms of malignant lymphoma involving the orbit are histiocytic and lymphocytic, with various degrees of differentiation. Both benign and malignant lymphoid tumors of the orbit occur predominantly in adults and are extremely rare in children.[6] The two main types of lymphoid tumor that ophthalmologists deal with are reactive lymphoid hyperplasia, a localized benign disease of unknown cause, and malignant lymphoma, which may either arise in and be limited to the orbit, may arise in the sinonasal cavities and extend into the orbit, or may be one focus of a systemic lymphoma.[6] Clinically, both malignant lymphoma and reactive lymphoid hyperplasia can produce a painless progressive proptosis accompanied by extraocular motility disturbance, visual disturbance, and lacrimal gland enlargement.[6] Any orbital tissue or combination of tissues may be involved in either disease process.[6] All patients with benign and malignant lymphoid lesions of the orbit should be subjected to systemic evaluation to rule out a systemic lymphoproliferative disorder. Intracranial involvement is extremely uncommon in patients with lymphoma at the time of presentation, but such involvement occasionally occurs in some patients with persistent disease.[102] A few patients with Hodgkin's disease, Burkitt's lymphoma, and other non-Hodgkin's lymphomas have presented with the Tolosa-Hunt syndrome.[102] Outside the original lymphoid tissue of Waldeyer's ring, there is a mixed population of lymphocytes

FIGURE 9-104 Pseudotumor. Axial CT scan showing an extraconal infiltrative lesion (*arrow*) displacing the lateral rectus muscle medially. Histologic study showed a pseudorheumatoid nodule. (From Mafee MF et al. Orbital space-occupying lesions: role of CT and MRI: an analysis of 145 cases. Radiol Clin North Am 1987;25:529–559.)

VIEW IMAGE

Copyright © 2003, Mosby, Inc. All rights reserved.

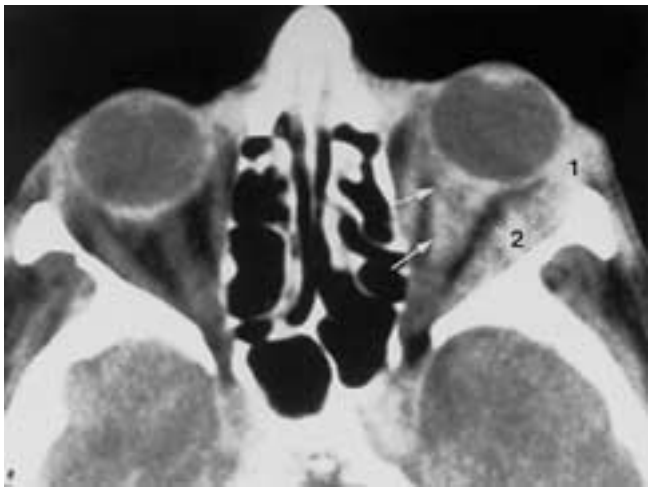

FIGURE 9-105 Lymphoma. Postcontrast axial CT scan shows an infiltrative process involving the left lacrimal gland (*1*), lateral orbital compartment (*2*), and perioptic nerve region (*arrows*).

FIGURE 9-106 Lymphomatoid granulomatosis. Contrast-enhanced axial CT scan shows diffuse infiltration of the intraconal space of the right orbit (*arrows*) with putty-like molding of the process around the posterior globe. CT features of this T-cell lymphoma precursor are virtually identical to those of true lymphoma, pseudotumor, lupoid infiltration, and metastatic carcinoma associated with marked proliferation of dense connective tissue surrounding malignant cells, such as in scirrhous carcinoma (breast, stomach).

that reside in the subepithelial area of the nasal cavity. A smaller population of lymphocytes is scattered among the submucosal glands and within the deep vascular stroma; extranodal B-cell non-Hodgkin's lymphoma derives from these cells.[115] In most cases, multiple sinuses are affected. Involvement of one or more paranasal sinuses is more typical of B-cell lymphoma, whereas involvement of the nasal cavity is more typical of T-cell lymphoma.[102] Less commonly, the lymphomas (generally those of a T-cell phenotype) invade adjacent sites such as the orbit, and patients present with diplopia, blurred vision, and paralysis of the cranial nerves.[102]

Diagnostic Imaging

Ultrasound, CT, and MR imaging can be used to evaluate orbital lymphomas. CT and MR imaging have made it possible to make a strong presumptive diagnosis of orbital lymphoma, especially when the CT and MR imaging features are examined in conjunction with the clinical signs and symptoms.[131] The CT and MR imaging findings are usually nonspecific, and based solely on imaging, it may be impossible to differentiate the lymphomas from orbital pseudotumors (Figs. 9-105 to 9-107), lacrimal gland tumors (Fig. 9-107), optic nerve tumors, Graves' orbitopathy, primary orbital tumors, or orbital cellulitis.[127–131] Orbital lymphomas are homogeneous masses of relatively high density and sharp margins, which are more often seen in the anterior portion of the orbit, the retrobulbar area (Fig. 9-108), or in the superior orbital compartment. CT and MR

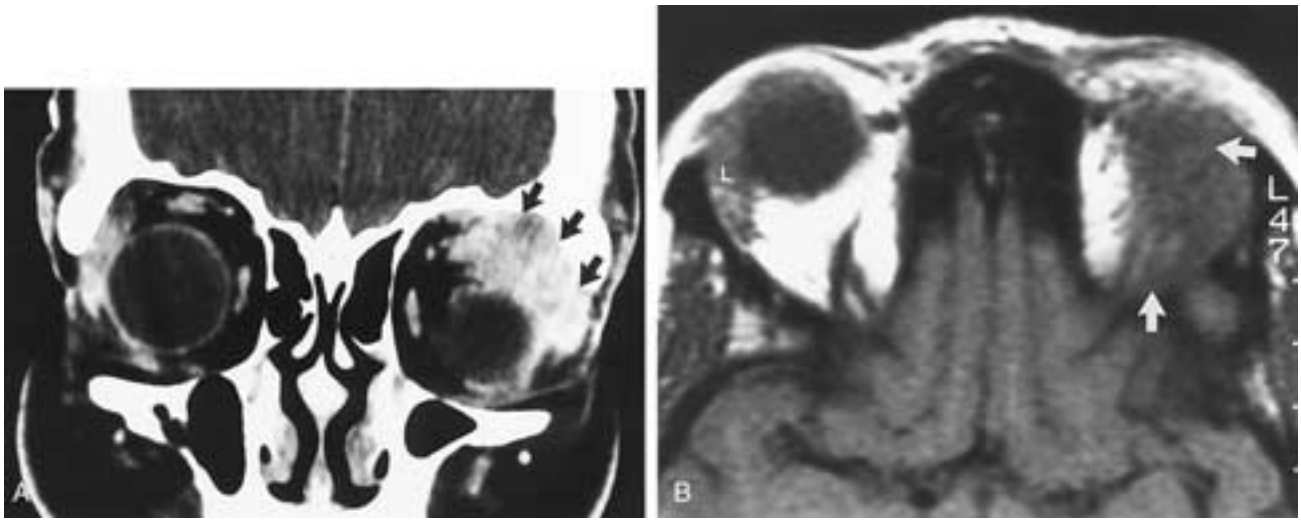

FIGURE 9-107 Orbital pseudotumor. **A**, Enhanced coronal CT scan. **B**, Axial T1-weighted axial MR scan showing an irregular mass involving the left lacrimal gland and adjacent orbital tissues (*arrows*).

Copyright © 2003, Mosby, Inc. All rights reserved.

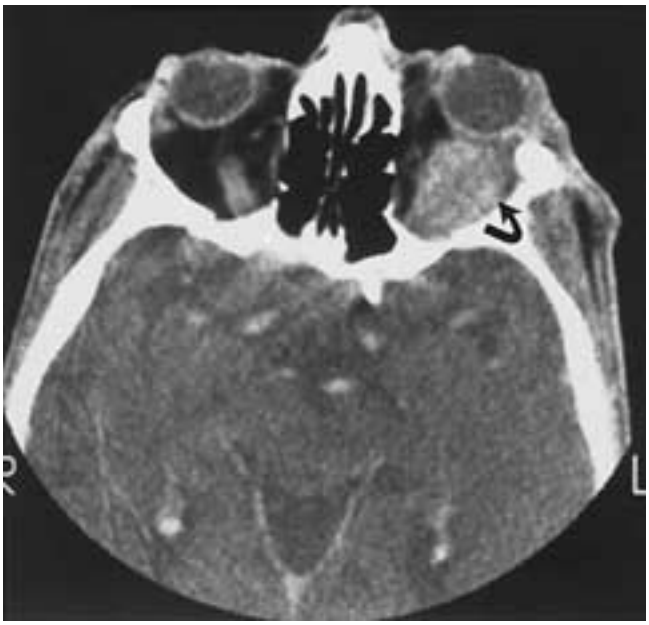

VIEW IMAGE

FIGURE 9-108 Lymphoma. Postcontrast axial CT scan shows a soft-tissue mass (*arrow*) in the left retrobulbar region.

imaging may reveal a putty-like molding of the tumor to preexisting structures without eroding the bone or enlarging the orbit.[127, 128] Mild to moderate enhancement is usually present (Figs. 9-106 to 9-108).[127, 131]

All orbital lymphoid tumors tend to mold themselves around the orbital structures without producing bony erosion (Figs. 9-108 and 9-109). Specifically, a bulky lesion in the region of the lacrimal fossa that does not produce bony erosion is most likely to be either inflammatory or lymphoid in character (Figs. 9-109 and 9-110).[17, 131] However, the aggressive malignant lymphomas can produce frank destruction of bone.[131] Lacrimal gland lymphoma displaces the globe medially and forward and appears as a moderately enhancing mass that diffusely involves the gland (Figs. 9-110 and 9-111).[127] Deformity of the globe's shape is rare.

MR imaging has proven to be as sensitive as CT for the diagnosis of orbital lymphoma and pseudotumors. Both pseudotumors and lymphoma may have intermediate or low signal intensity on T1-weighted and proton density images and appear isointense to fat on T2-weighted images (Figs. 9-111 and 9-112).[127]

Lymphoplasmacytic Tumor (Plasma Cell Tumor)

Tumors composed purely of plasma cells (plasmacytomas) and those composed of B lymphocytes and plasma cells (lymphoplasmacytoid tumors) are closely related to the various lymphomas.[3, 107] The plasma cell is actually a B lymphocyte that has become modified to produce large quantities of immunoglobulin.[107] These so-called plasmacytoid lymphomas may secrete IgM paraprotein in sufficient quantities to cause a monoclonal peak in the serum; this is classically seen in Waldenstrom's macroglobulinemia.[3] One of the important tumors composed of plasma cells is multiple myeloma (Fig. 9-113). There are also solitary forms of extramedullary plasmacytomas, which are not associated with systemic multiple myeloma.[107] These plasma cell tumors, particularly as they affect the orbit and ocular structures, display the same spectrum of clinical involvement seen in the lymphoproliferative disorders (Fig. 9-113).[3] Both isolated plasmacytoma and Waldenstrom's macroglobulinemia can produce a mass that can be visualized by both CT and MR imaging. The mass may be lobulated, densely enhancing, and well defined, and can be present with or without bone erosion (Fig. 9-114).[3] In systemic myelomatosis, a permeative or moth-eaten pattern of bone destruction or gross destruction may be present.[71]

ORBITAL LEUKEMIA

Leukemia is one of the most common childhood cancers. It is estimated that of the approximately 7100 cases of childhood cancer in the United States each year, 35% are leukemia.[107, 126] Leukemic disorders in children fall mainly into the lymphoid and myeloid groups. About 75% of the cases are acute lymphoblastic leukemia, 20% are acute myelogenous leukemia (AML), and 5% are chronic myelogenous leukemia.[107] Chronic lymphocytic leukemia is a disease of adulthood and almost never affects children.[107] The eye and adnexa are not infrequently involved (Fig. 9-115). Orbital involvement with leukemia is the result of direct infiltration of the orbital bone or soft tissue by leukemic cells (Fig. 9-116). In patients with AML, such infiltration most often occurs in the form of a granulocytic sarcoma (Fig. 9-117). A granulocytic sarcoma is commonly called a *chloroma* because the myeloperoxidase within the tumor imparts a green hue to it, as seen on gross examination.[107] This may be the first manifestation of AML in many patients. The lesion typically involves the orbital subperiosteal space, usually affecting the lateral wall of the orbit, with extensions to the temporal fossa. Medial orbital wall disease also occurs with involvement of ethmoid air cells, the cribriform plate, and the anterior cranial fossa. There may be dural or leptomeningeal infiltration, demonstrating enhancement on enhanced CT and MR imaging. The imaging differential diagnosis includes rhabdomyosarcoma, LCH, subperiosteal abscess, subperiosteal hematoma, lymphoma, pseudotumor, and metastasis (neuroblastoma, Ewing's sarcoma, and Wilms' tumor).

ORBITAL VASCULAR CONDITIONS

Vascular lesions of the orbit represent an important group of orbital pathologies, particularly in infants and children. They also are the most controversial group of lesions because of confusion regarding their nature, and a debate continues as to the classification of the various vascular malformations that may involve the orbit.[132] In general, orbital vascular lesions include capillary hemangioma, cavernous hemangioma (cavernoma, a venous malformation), varices (venous malformation), lymphangioma, lymph-

Copyright © 2003, Mosby, Inc. All rights reserved.

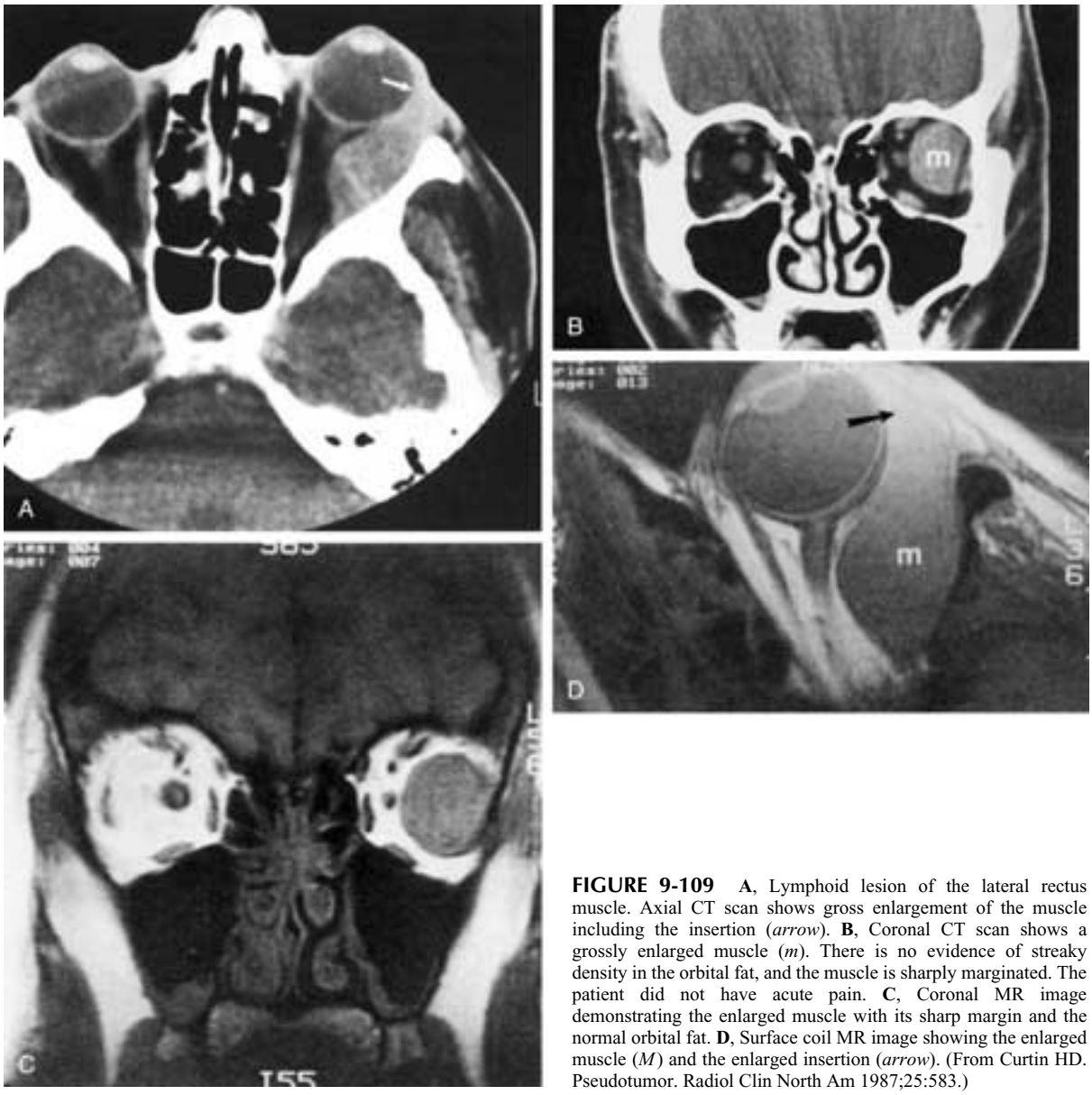

FIGURE 9-109 **A**, Lymphoid lesion of the lateral rectus muscle. Axial CT scan shows gross enlargement of the muscle including the insertion (*arrow*). **B**, Coronal CT scan shows a grossly enlarged muscle (*m*). There is no evidence of streaky density in the orbital fat, and the muscle is sharply marginated. The patient did not have acute pain. **C**, Coronal MR image demonstrating the enlarged muscle with its sharp margin and the normal orbital fat. **D**, Surface coil MR image showing the enlarged muscle (*M*) and the enlarged insertion (*arrow*). (From Curtin HD. Pseudotumor. Radiol Clin North Am 1987;25:583.)

VIEW IMAGE

angiovenous (venolymphatic) malformation, arteriovenous malformation, ''sclerosing hemangioma,'' hemangiopericytoma, and hemangioendotheliomas (angiosarcomas).

Capillary Hemangioma (Benign Hemangioendothelioma)

Capillary hemangiomas are tumors that occur primarily in infants during the first year of life. The tumor often increases in size for 6 to 10 months and then gradually involutes.[8, 17, 132, 133] It occurs most commonly in the superior nasal quadrant. Microscopically, the tumor is composed of endothelial and capillary vessel proliferations with benign endothelial cells surrounding small, capillary-sized vascular spaces.[8, 17, 132] Capillary hemangiomas in and

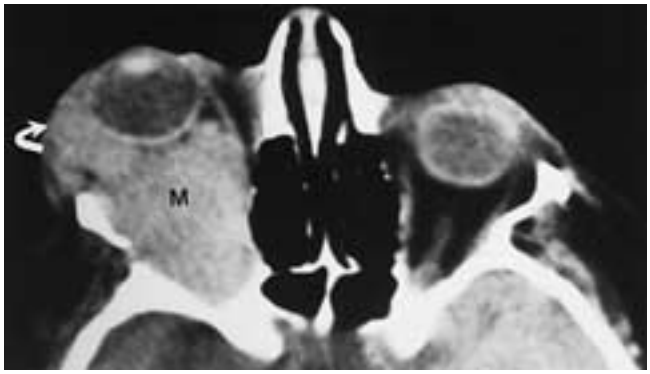

FIGURE 9-110 Lymphoma. Postcontrast axial CT scan shows a large mass (*M*) involving the right lacrimal gland (*arrow*) and retrobulbar region.

VIEW IMAGE

Copyright © 2003, Mosby, Inc. All rights reserved.

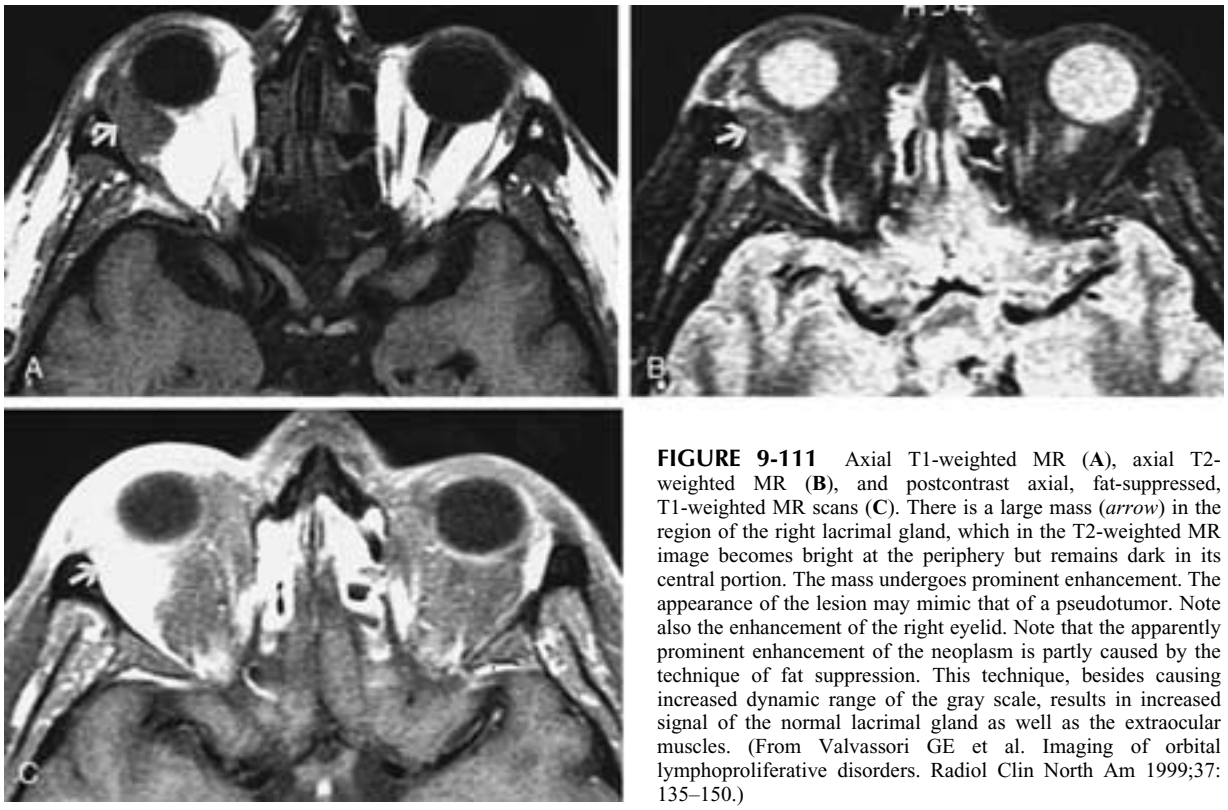

FIGURE 9-111 Axial T1-weighted MR (**A**), axial T2-weighted MR (**B**), and postcontrast axial, fat-suppressed, T1-weighted MR scans (**C**). There is a large mass (*arrow*) in the region of the right lacrimal gland, which in the T2-weighted MR image becomes bright at the periphery but remains dark in its central portion. The mass undergoes prominent enhancement. The appearance of the lesion may mimic that of a pseudotumor. Note also the enhancement of the right eyelid. Note that the apparently prominent enhancement of the neoplasm is partly caused by the technique of fat suppression. This technique, besides causing increased dynamic range of the gray scale, results in increased signal of the normal lacrimal gland as well as the extraocular muscles. (From Valvassori GE et al. Imaging of orbital lymphoproliferative disorders. Radiol Clin North Am 1999;37: 135–150.)

VIEW IMAGE

around the orbit may have an arterial supply from either the external carotid or internal carotid arteries, and these tumors are capable of bleeding profusely.[8, 132, 133] These hemangiomas may extend intracranially through the superior orbital fissure (Fig. 9-118), optic canal, and orbital roof. On CT these lesions are seen as fairly well-marginated (Fig. 9-118) to poorly marginated, irregular, enhancing lesions. Most are extraconal, although some of them may be seen in the intraconal space (Fig. 9-119). On dynamic CT, capillary hemangiomas characteristically show intense homogeneous enhancement (Fig. 9-120). On MR imaging, capillary hemangiomas appear as hypointense or slightly hyperintense to brain on T1-weighted images and hyperintense to brain on proton density and T2-weighted images. They show intense enhancement following the intravenous injection of Gd-DTPA contrast material. On MR angiography (MRA) the vascularity of these lesions may not be appreciated. Therefore, at present, one should not rely only on MRA for the diagnosis of these capillary hemangiomas.

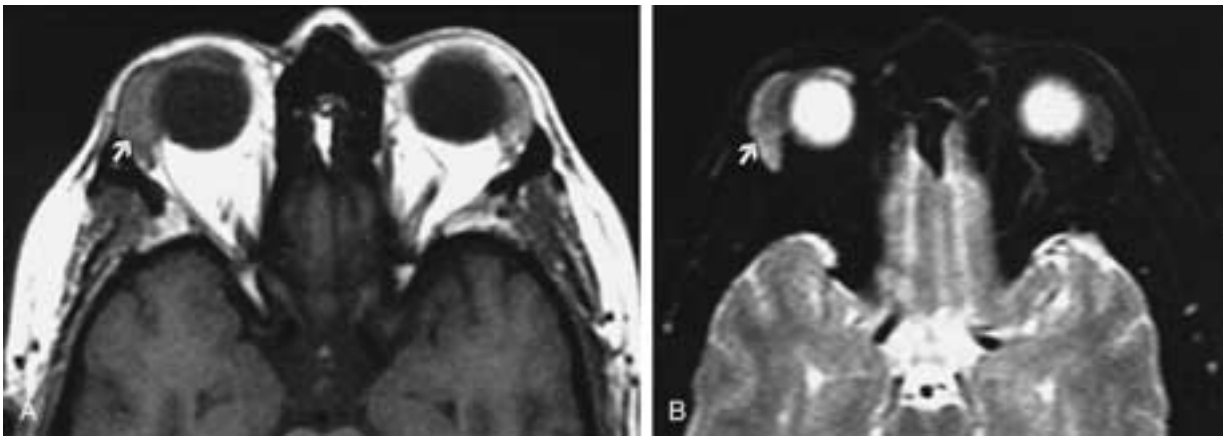

FIGURE 9-112 Pseudotumor. Axial T1-weighted MR (**A**) and axial T2-weighted MR (**B**) images. The right lacrimal gland is enlarged (*arrows*). The peripheral portion of the gland becomes brighter in the T2-weighted MR images, mimicking a lymphoma. (From Valvassori GE et al. Imaging of orbital lymphoproliferative disorders. Radiol Clin North Am 1999;37:135–150.)

VIEW IMAGE

Copyright © 2003, Mosby, Inc. All rights reserved.

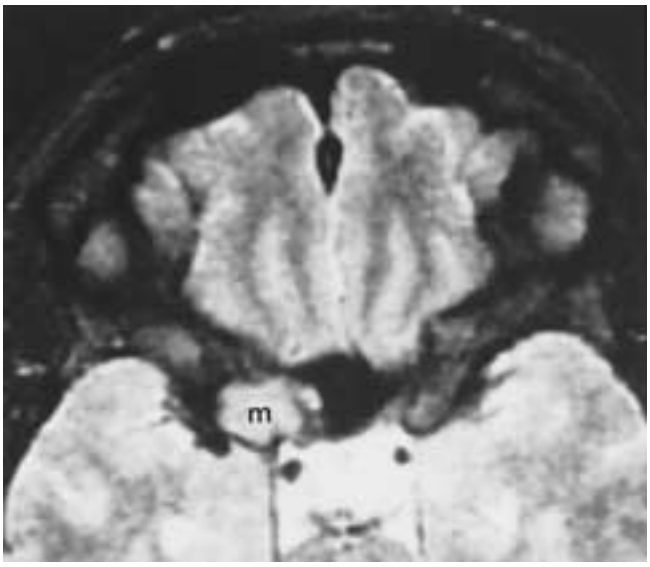

VIEW IMAGE

FIGURE 9-113 Multiple myeloma. Axial T2-weighted MR scan shows a mass (*m*) involving the right lesser wing and optic canal.

FIGURE 9-114 Orbital myeloma. Postcontrast coronal CT scan shows bone destruction of the superolateral aspect of the right orbit (*arrows*), with a large orbital mass (*M*). This patient initially showed symptoms of proptosis. Biopsy of this mass revealed features compatible with lymphoplasmacytic tumor.

VIEW IMAGE

Cavernous Hemangioma

Cavernous hemangioma of the orbit, the most common orbital vascular tumor in adults, has distinctive clinical and histopathologic features.[7, 17, 132] It tends to occur in the second to fourth decades of life. These tumors show a slowly progressive enlargement distinct from that of capillary hemangiomas, which gradually diminish in size. In contrast to capillary hemangiomas, a prominent arterial supply is usually absent.[8] Cavernous hemangiomas possess a distinct fibrous pseudocapsule and therefore, on CT and MR imaging, appear as well-defined masses (Figs. 9-121 and 9-122). This observation, in addition to the fact that they are usually independent of the general circulation, enables excision of the entire lesion without fragmentation.[8] These hemangiomas may be located anywhere in the orbit but frequently (83%) occur within the retrobulbar muscle cone (Figs. 9-121 to 9-123). On CT, cavernous hemangiomas appear as well-defined, smoothly marginated, homogeneous, rounded, ovoid, or lobulated soft-tissue masses of increased density and variable contrast enhancement (Fig. 9-121). Unless they are ruptured or surgically violated, cavernous hemangiomas always respect the contour of the globe (Fig. 9-124). The MR imaging characteristics of hemangiomas are shown in Figure 9-122. Histologically, cavernous hemangiomas are composed of large, dilated vascular channels (sinusoid-like spaces) lined by thin, attenuated endothelial cells.[8, 17, 132] At times, intraconal cavernous hemangiomas may be difficult to differentiate

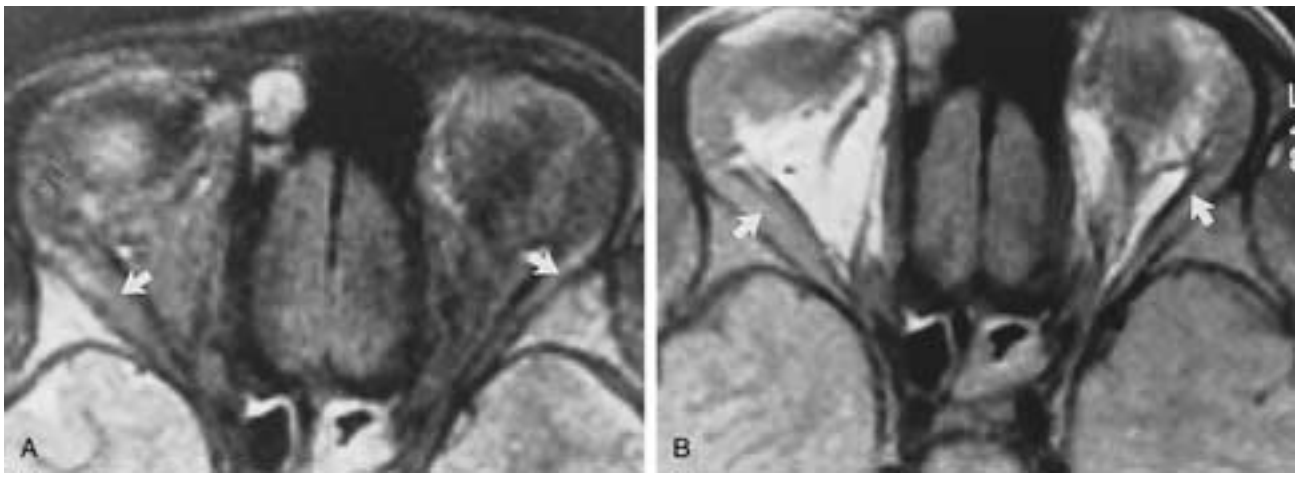

VIEW IMAGE

FIGURE 9-115 **A**, Axial PW scan. **B**, Axial T2-weighted MR imaging scan. Leukemic infiltration. Scans show bilateral subperiosteal leukemic infiltration (*arrows*).

Copyright © 2003, Mosby, Inc. All rights reserved.

from other intraconal lesions such as meningiomas, hemangiopericytomas, and schwannomas.[8, 17, 132] Uncommonly, an intramuscular hemangioma may occur (Fig. 9-125). Orbital bone modeling is not uncommon in cavernous hemangiomas, and at times, calcification may be seen in these lesions. *Sclerosing hemangioma* is another less well defined term used to describe hemangiomas that show prominent sclerosis. These lesions often show foci of calcification (Fig. 9-126).

Lymphangioma

Although the origin of lymphangioma may remain controversial, the lesion is an unencapsulated mass consisting mostly of bloodless vascular and lymph channels.[73] Connective tissue between the channels may contain foci of lymphoid cells that proliferate in viral infections, resulting in the clinical finding of worsening proptosis when the child has an upper respiratory tract infection.[73] Orbital lymphangiomas occur in children and young adults. In contrast to the rapid, self-limited growth of infantile capillary hemangiomas, lymphangiomas gradually and progressively enlarge during the first two decades of life.[8, 132] Cavernous lymphangiomas are composed of delicate endothelium-lined, lymph-filled sinuses (filled with clear fluid or chocolate-colored, unclotted fluid) that invade the surrounding connective tissue stroma.[8, 73, 132] The interstitial tissue often shows lymphoid follicles and lymphocytic infiltration.[8] Spontaneous (or after minor trauma) hemorrhage within the lesion is common, resulting in a chocolate cyst.[8, 17] Lymphangiomas may have distinct borders but are typically diffuse and not well encapsulated (Figs. 9-127 and 9-128), with portions of the lesion infiltrating normal tissues of the lid and orbit.[8, 17] They are usually multilobular (Fig. 9-128), and because complete surgical excision is seldom

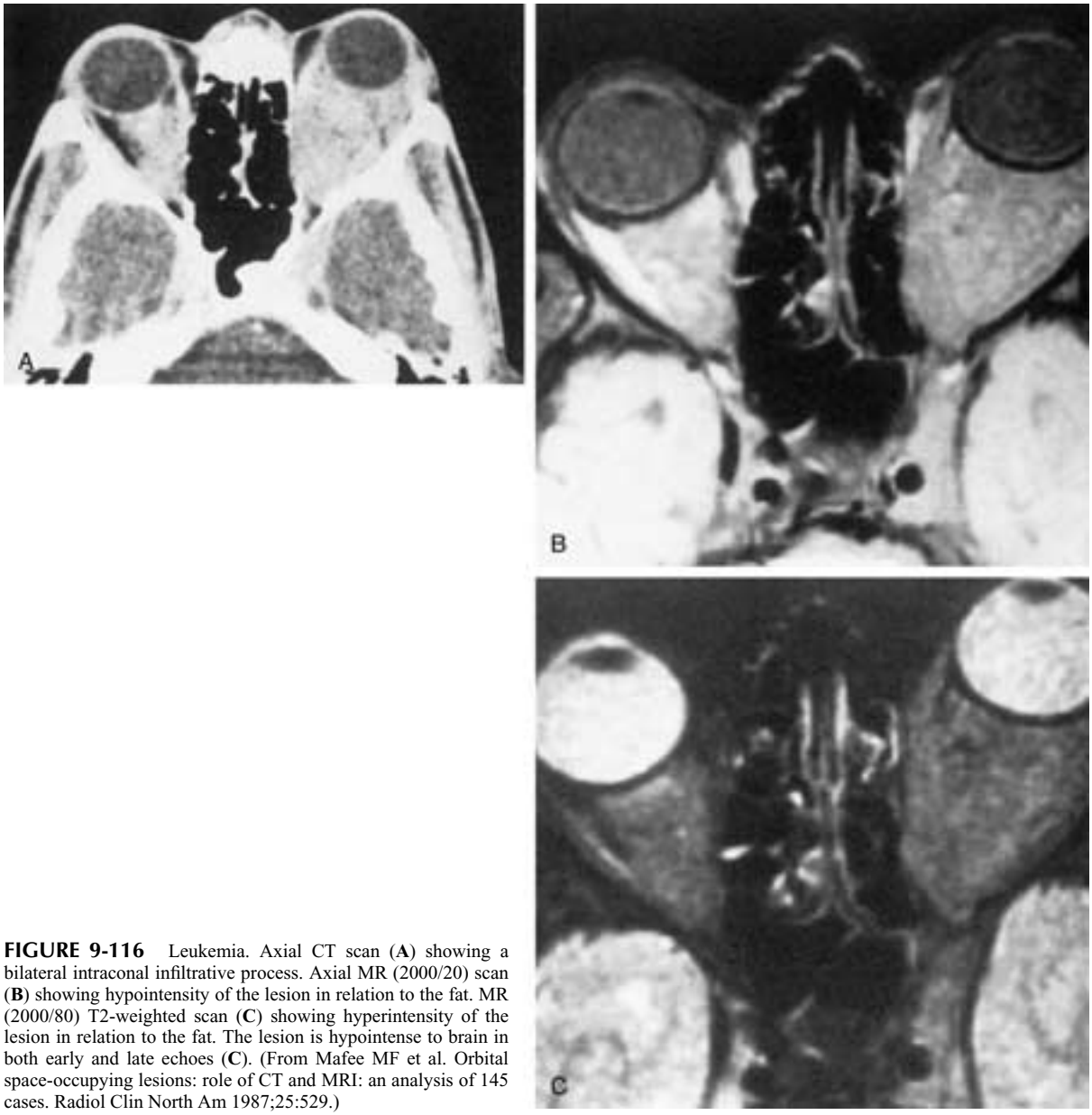

VIEW IMAGE

FIGURE 9-116 Leukemia. Axial CT scan (**A**) showing a bilateral intraconal infiltrative process. Axial MR (2000/20) scan (**B**) showing hypointensity of the lesion in relation to the fat. MR (2000/80) T2-weighted scan (**C**) showing hyperintensity of the lesion in relation to the fat. The lesion is hypointense to brain in both early and late echoes (**C**). (From Mafee MF et al. Orbital space-occupying lesions: role of CT and MRI: an analysis of 145 cases. Radiol Clin North Am 1987;25:529.)

Copyright © 2003, Mosby, Inc. All rights reserved.

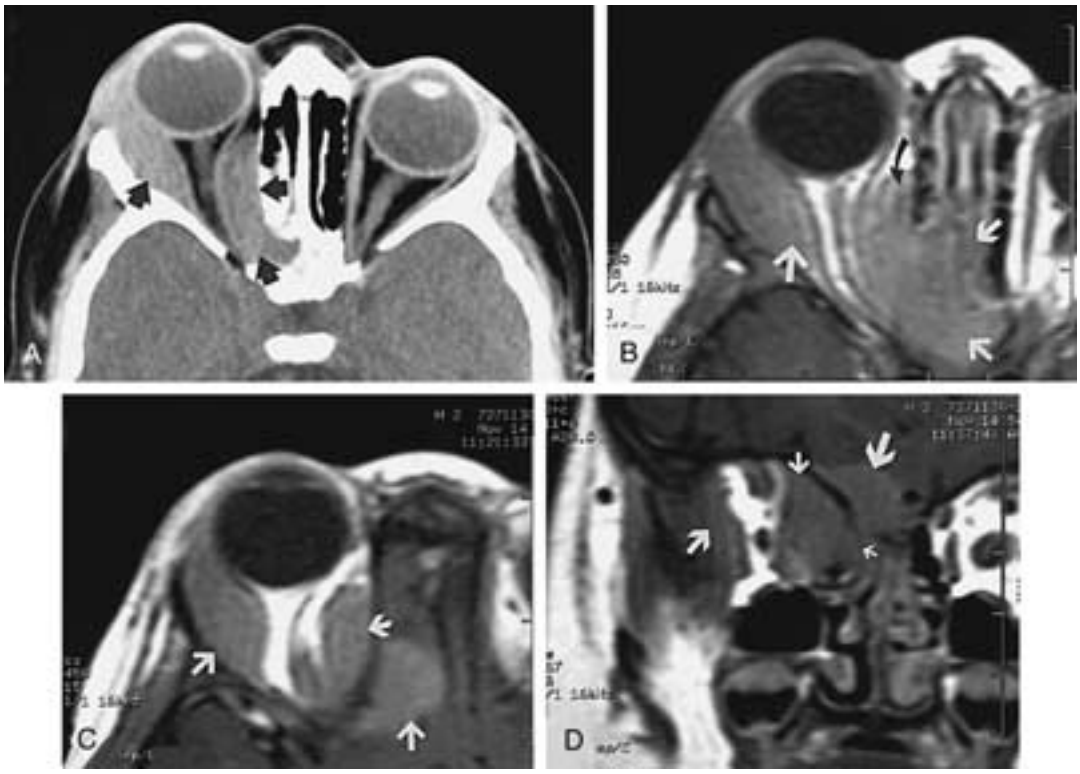

VIEW IMAGE

FIGURE 9-117 Granulocytic sarcoma (leukemia). Axial CT (**A**), postcontrast axial T1-weighted (**B** and **C**), and postcontrast coronal T1-weighted (**D**) MR scans demonstrate an extraconal infiltration involving both the medial and lateral aspects of the orbit (*arrows*). The lesion erodes into the ethmoid air cells and erodes the cribriform plate, with extension into the anterior cranial fossa. (From Valvassori GE et al. Imaging of orbital lymphoproliferative disorders. Radiol Clin North Am 1999;37:135–150.)

accomplished, recurrence is common.[8, 132] They are more common in the extraconal space.[8]

On CT these lymphangiomas appear as poorly circumscribed, often heterogeneous masses of increased density in the extraconal or intraconal space (Fig. 9-127). Bony remodeling may be present, calcification is rare, and minimal to marked contrast enhancement may be present (Fig. 9-127). On MR imaging, lymphangiomas are relatively hypointense or hyperintense to brain on T1-weighted images and usually very hyperintense on T2-weighted images (Figs. 9-128 and 9-129). Fluid-fluid levels related to hemorrhages of various ages are characteristic of lymphangioma. Their MR imaging characteristics should help differentiate them from pseudotumors and hemangiomas (Fig. 9-129).[8]

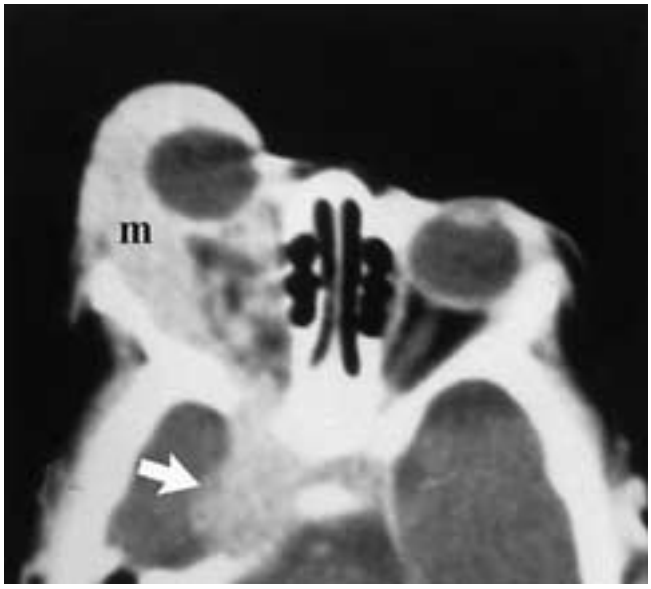

VIEW IMAGE

FIGURE 9-118 Capillary hemangioma. Postcontrast axial CT scan shows an enhancing mass (*m*) with involvement of the eyelid and extension into the right cavernous sinus (*arrow*).

Orbital Varix

Primary orbital varices are congenital venous malformations characterized by proliferation of venous elements and massive dilation of one or more orbital veins, presumably associated with congenital weakness in the venous wall.[8, 17, 73, 134] A varix may include a single smooth-contoured, dilated vein, a single vessel with segmental dilatation, or a tangled mass of venous channels.[73] Varices within the orbit may appear to have both cystic (chocolate) and solid components.[73] Orbital varices are the most common cause of spontaneous orbital hemorrhage.[135] Clinically, proptosis or globe displacement increases during a Valsalva maneuver, reflecting the varix's connection to the venous system.[73] The CT appearance of orbital varix may be normal in axial sections (Fig. 9-130A), but because of increased venous pressure, it is quite abnormal in coronal

Copyright © 2003, Mosby, Inc. All rights reserved.

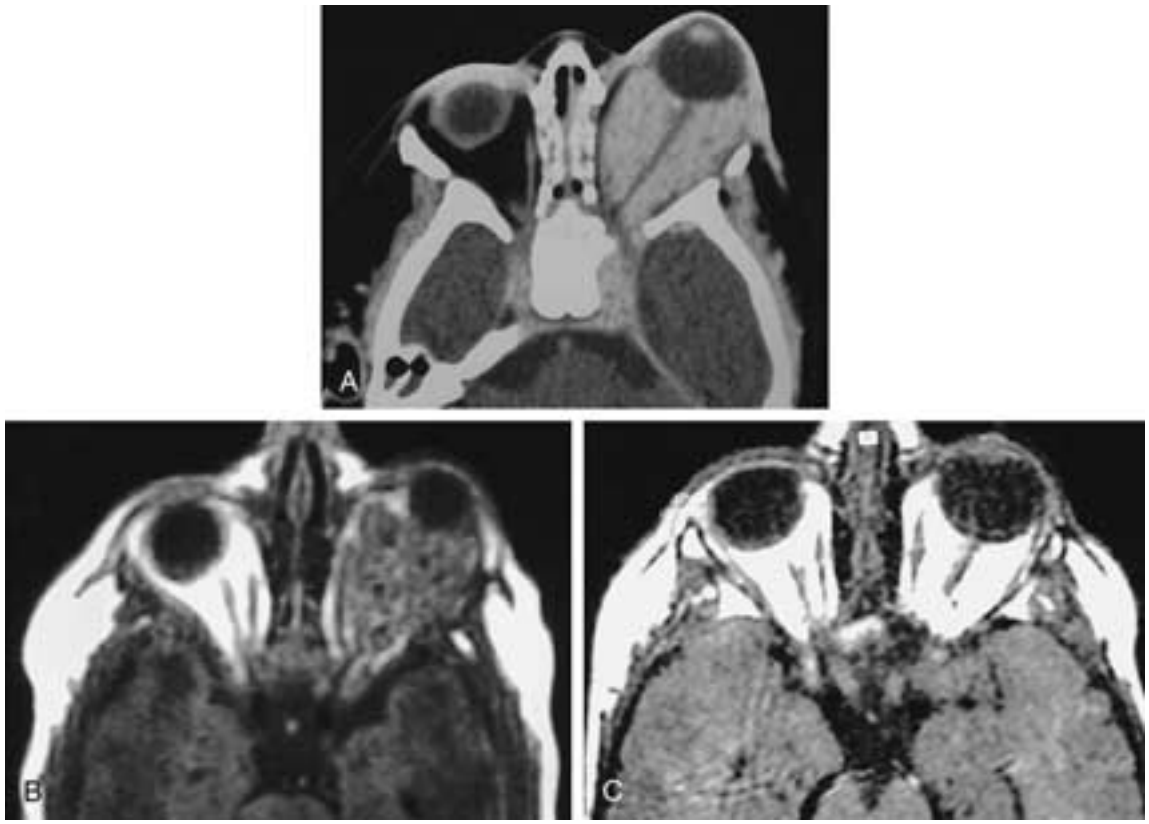

VIEW IMAGE

FIGURE 9-119 A baby boy with a left orbital capillary hemangioma that presented shortly after birth. **A**, Axial contrast-enhanced CT scan shows a mass filling and expanding the left orbit. The hemangioma appears to extend through the superior orbital fissure into the left cavernous sinus. The mass encircles and stretches the optic nerve sheath complex. Biopsy was performed but was inconclusive, and there was some discussion about further surgery. MR findings convinced the clinicians that this was a capillary hemangioma and the patient was treated with steroids instead. **B**, Axial T1-weighted MR image reveals a large, heterogeneous, finely lobulated mass expanding the left bony orbit. The focal regions of hypointensity are consistent with flow voids attributable to vessels. **C**, Axial T1-weighted MR scan shows that the capillary hemangioma involuted completely 2 years after the initial presentation. (From Bilanuik LT. Orbital vascular lesions: role of imaging. Radiol Clin North Am 1999;37:169–183.)

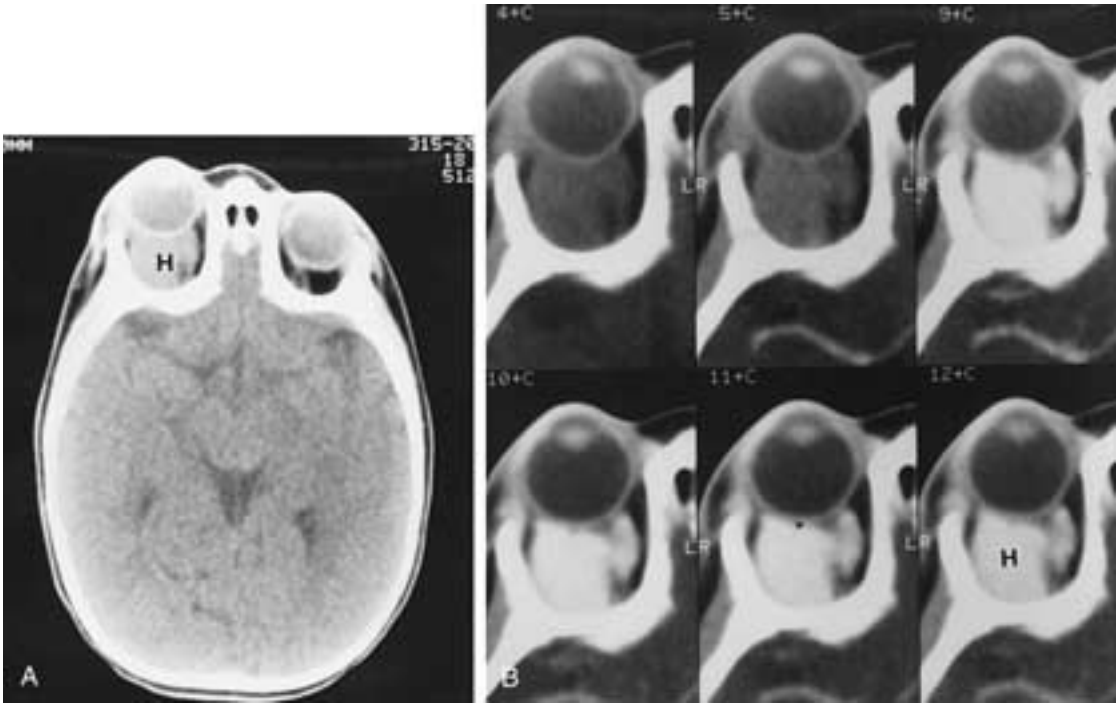

VIEW IMAGE

FIGURE 9-120 Capillary hemangioma. **A**, Enhanced axial CT scan showing a large retrobulbar mass compatible with a capillary hemangioma (*H*). **B**, Dynamic axial CT scanning reveals rapid wash-in of contrast in hemangioma (*H*). (From Mafee MF et al. Rhabdomyosarcoma of the orbit: evaluation with MR imaging and CT. Radiol Clin North Am 1998;36:1215–1227.)

Copyright © 2003, Mosby, Inc. All rights reserved.

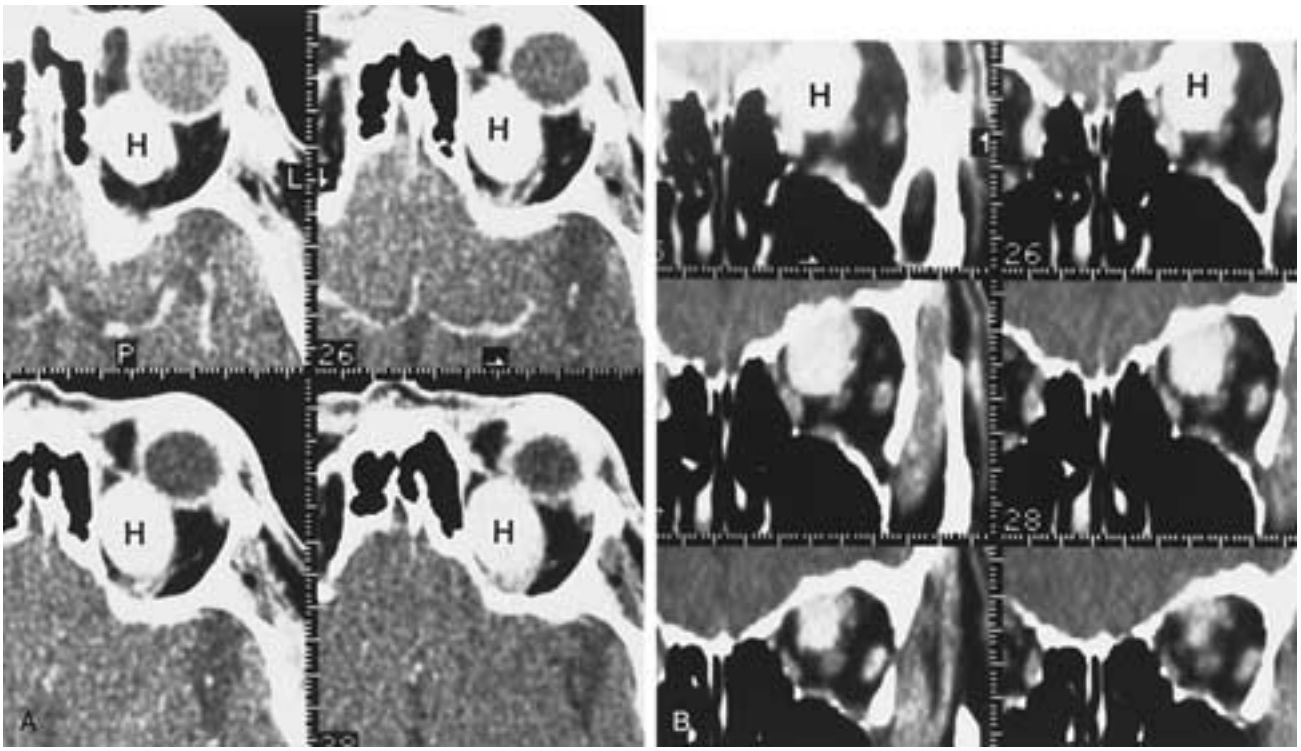

VIEW IMAGE

FIGURE 9-121 Cavernous hemangioma. **A**, Serial axial CT scan. **B**, Reformatted coronal CT scans. **A** and **B** show a well-defined intraconal markedly enhancing hemangioma (*H*).

sections, particularly those obtained in the prone position (Figs. 9-130B and 9-131). Because the varix may be completely collapsed or barely visible when the patient is lying quietly supine, any time an orbital varix is suspected, it is recommended that additional CT sections be obtained during a Valsalva maneuver. In a patient suspected of having an orbital varix, MR imaging also should be performed with the patient in the prone position. Some varices may have such a small communication with the systemic venous system that they are undistensible. Because they have stagnant blood flow, they manifest themselves by thrombosis and hemorrhage.[132] Venous anomalies of the orbit including varices may be associated with contiguous or noncontiguous intracranial venous anomalies.[132] Orbital varices may also be secondary to intracranial vascular malformations, particularly arteriovenous shunts.[172] MR imaging of orbital varices usually shows a varix to be hyperintense on T1-weighted, proton density, and T2-weighted images (Fig. 9-132). At times, an orbital varix may have the same MR imaging characteristics as a cavernous

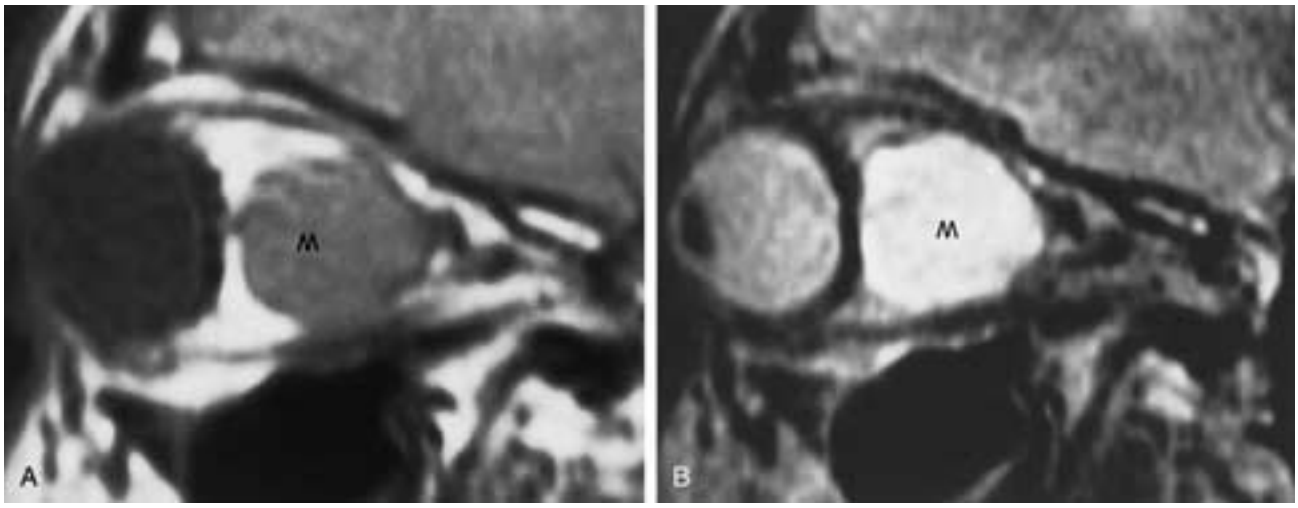

VIEW IMAGE

FIGURE 9-122 Cavernous hemangioma. **A**, Satittal PW MR scan. **B**, Sagittal T2-weighted MR scan. Scans show an intraconal mass (*M*), which was presumed to be a cavernous hemangioma.

Copyright © 2003, Mosby, Inc. All rights reserved.

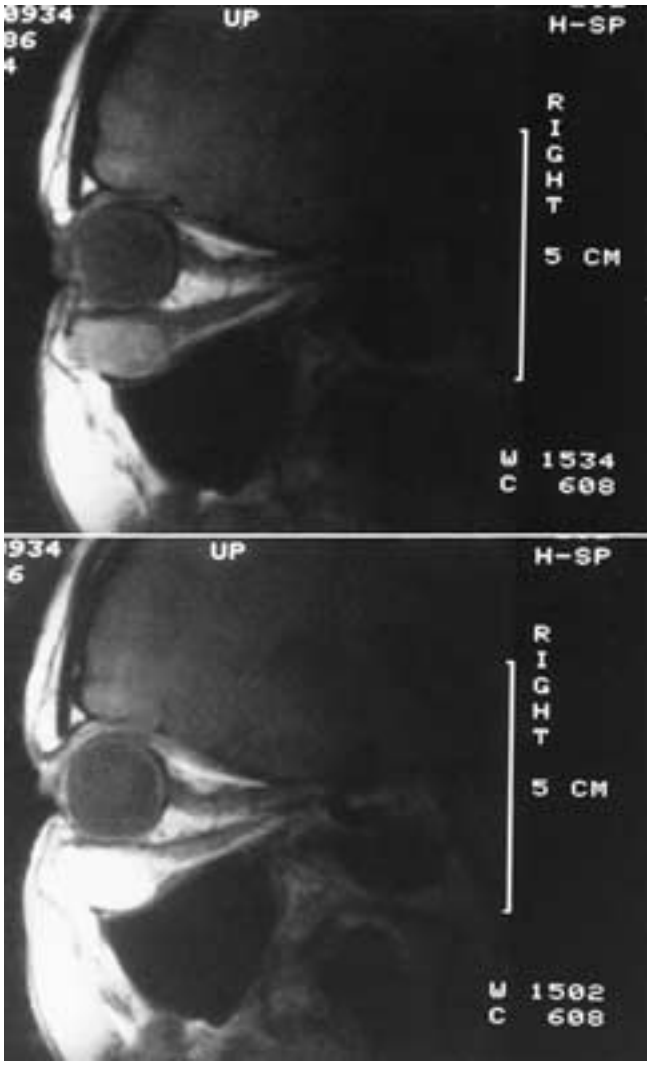

FIGURE 9-123 Orbital hemangioma. Sagittal MR images obtained without (*top*) and with (*bottom*) intravenous Gd-DTPA show a hemangioma in the anterior floor of the orbit. (Courtesy of Dr. August F. Markl.)

VIEW IMAGE

hemangioma or other orbital masses, being hypointense on T1-weighted, hyperintense on T2-weighted, and enhanced on postcontrast T1-weighted MR images. An orbital varix may also be seen as several round or tubular structures with associated calcifications (phleboliths) (Fig. 9-133).[8]

Carotid Cavernous Fistulas and Arteriovenous Malformations

Carotid cavernous fistulas produce proptosis, chemosis, venous engorgement, pulsating exophthalmos, and an auscultable bruit. Ischemic ocular necrosis resulting from a carotid-cavernous fistula has also been reported.[17, 136] A carotid cavernous fistula may result from trauma or surgery, or it may occur spontaneously. Spontaneous carotid-cavernous fistulas have been reported in patients with osteogenesis imperfecta, Ehlers-Danlos syndrome, and pseudoxanthoma elasticum. In these cases, the fistula probably

FIGURE 9-124 Cavernous hemangioma. Postcontrast axial CT scan shows an inhomogeneous enhancing mass (*M*) indenting the nasal aspect of the right globe. Note surgical defect (*arrow*).

VIEW IMAGE

resulted from weakness of the vessel walls related to the connective tissue disease.[136] CT and MR imaging demonstrate proptosis, with engorgement of the superior ophthalmic vein and frequent enlargement of the ipsilateral extraocular muscles (Fig. 9-134). There may be CT or MR imaging evidence of venous thrombosis in the lumen of the superior ophthalmic vein or cavernous sinus. Arteriovenous shunts within the orbit itself are rare.[132] At times, anomalous intracranial venous malformations, as well as dural vascular malformations and fistulas, may mimic the imaging appearance of carotid cavernous fistulas (Fig. 9-135).[136] Angiographic demonstration of the exact location of the carotid-cavernous fistula is essential to plan definitive therapy.

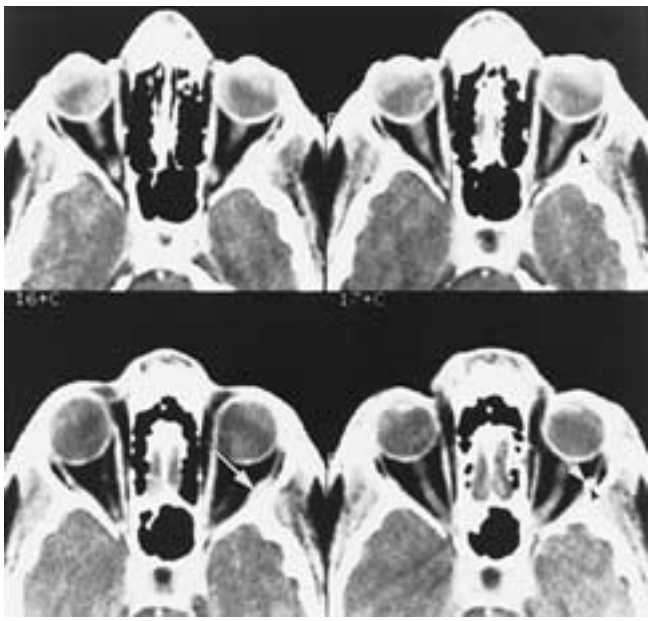

FIGURE 9-125 Hemangioma. Serial axial contrast-enhanced CT scans show an intramuscular hemangioma (*arrows*).

VIEW IMAGE

Copyright © 2003, Mosby, Inc. All rights reserved.

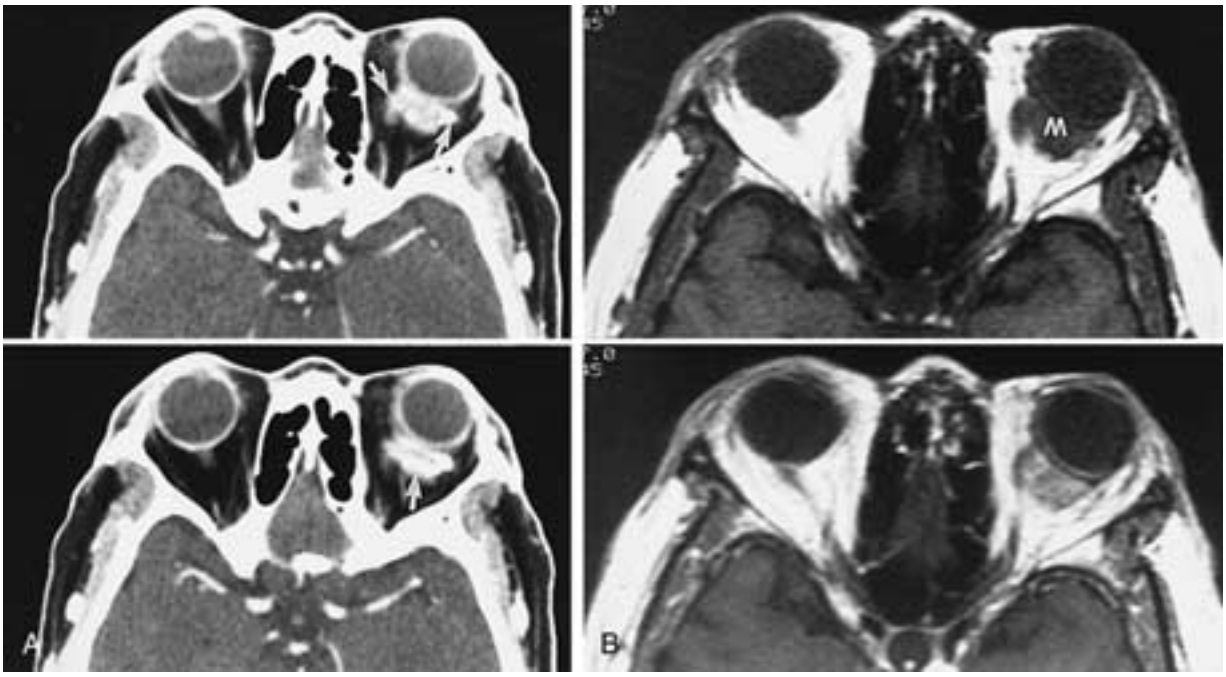

VIEW IMAGE

FIGURE 9-126 Sclerosing hemangioma. **A**, Axial-enhanced CT scans show an enhancing intraconal mass. Note several areas of calcifications. At histologic examination, there were foci of amyloidosis present in addition to calcifications. **B**, Axial T1-weighted (*top*) and enhanced T1-weighted (*bottom*) MR images show an intraconal mass (*M*) with moderate enhancement. (From Valvassori GE et al. Imaging of orbital lymphoproliferative disorders. Radiol Clin North Am 1999;37:135–150.)

Hemangiopericytoma

Hemangiopericytomas are rare, slow-growing vascular neoplasms that arise from unique cells called *pericytes of Zimmermann*, which normally envelop capillaries and postcapillary venules of practically all types of tissues.[8, 137–139] Histologically, these tumors are composed of scattered, capillary-like spaces surrounded by proliferating pericytes.[8] Hemangiopericytomas may be divided into lobules by fibrovascular septa.[8, 137] About 50% of the cases are malignant, and distant metastases, although uncommon, occur via the vascular and lymphatic routes.[8, 140] Most such metastases go to the lungs.[8, 137, 139] If not excised completely, these lesions tend to recur, and wide surgical excision is the treatment of choice.

On CT, the margins of an orbital hemangiopericytoma, in contrast to those of a cavernous hemangioma, may be slightly less distinct owing to its tendency to invade the adjacent tissues (Fig. 9-136).[8, 17] Erosion of the underlying bone may be present (Fig. 9-137), and marked contrast enhancement favors a diagnosis of hemangiopericytoma. MR imaging may not differentiate these tumors from cavernous hemangiomas, neurogenic tumors, meningiomas, and other lesions (Fig. 9-138), but angiography may

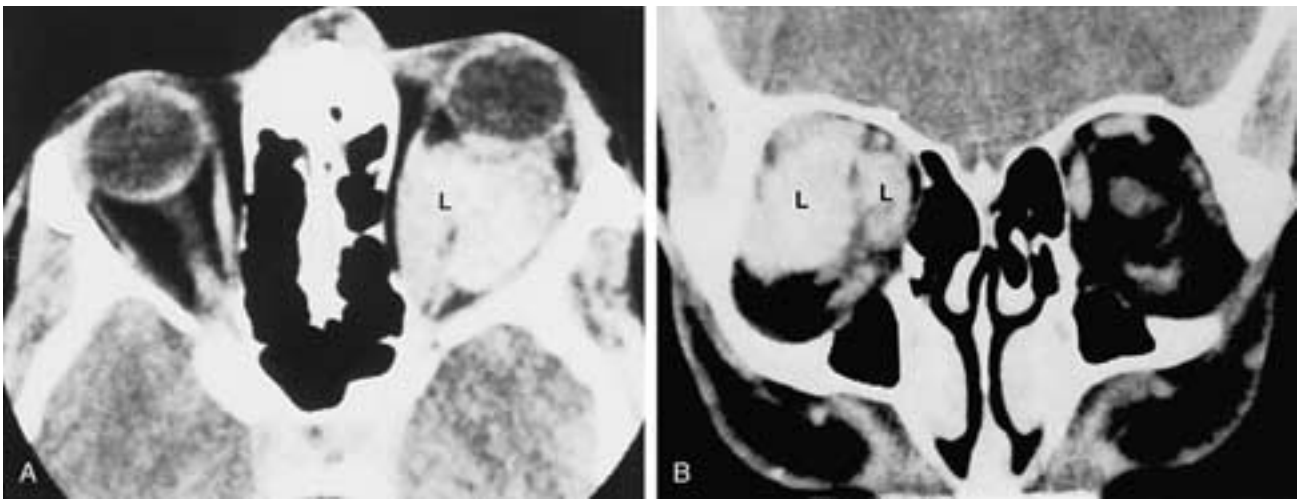

VIEW IMAGE

FIGURE 9-127 Lymphangioma. **A**, Contrast-enhanced axial CT scan. **B**, Coronal CT scan. **A** and **B** show a large lobulated lymphangioma (*L*).

Copyright © 2003, Mosby, Inc. All rights reserved.

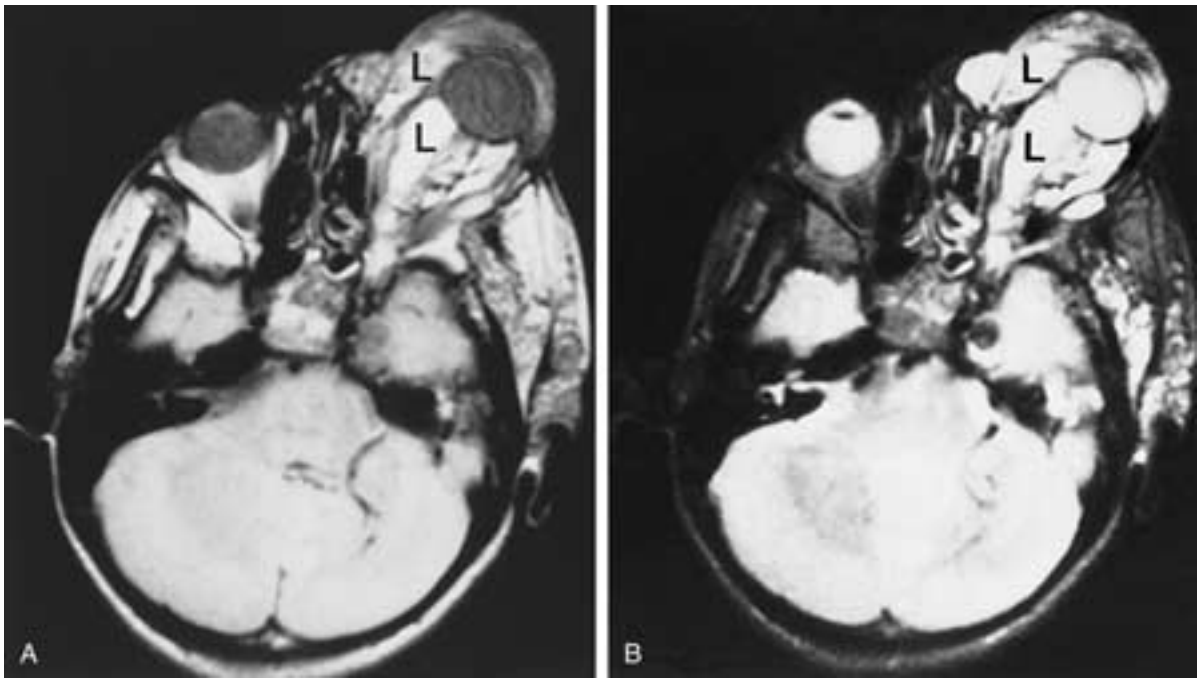

FIGURE 9-128 Lymphangioma. **A**, Axial PW MR scan. **B**, Axial T2-weighted MR scan. **A** and **B** show a large lymphangioma (*L*).

VIEW IMAGE

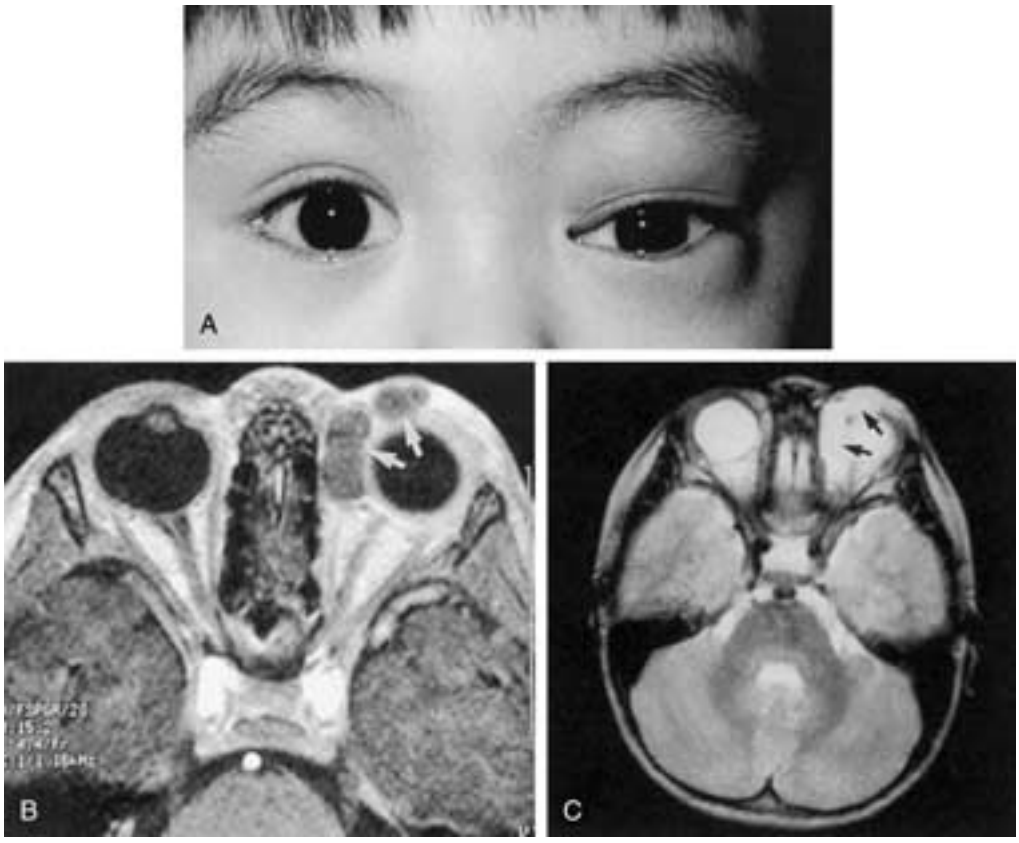

FIGURE 9-129 **A**, Clinical photograph of an 8-year-old boy who presented with acute upper-lid fullness on the left and inferior displacement of the globe caused by hemorrhage within a lymphangioma. **B**, Axial-enhanced T1-weighted MR image shows a lobular mass (*arrows*) in the anteromedial left orbit. The signal intensity of the lesion is hyperintense to vitreous and isointense to brain. There is no contrast enhancement. **C**, Axial T2-weighted MR image shows that the lesion (*arrows*) is homogeneously hyperintense to brain and isointense to vitreous. (From Kaufman LM et al. Diagnostic imaging of cystic lesions in the child's orbit. Radiol Clin North Am 1998;36:1149–1163.)

VIEW IMAGE

Copyright © 2003, Mosby, Inc. All rights reserved.

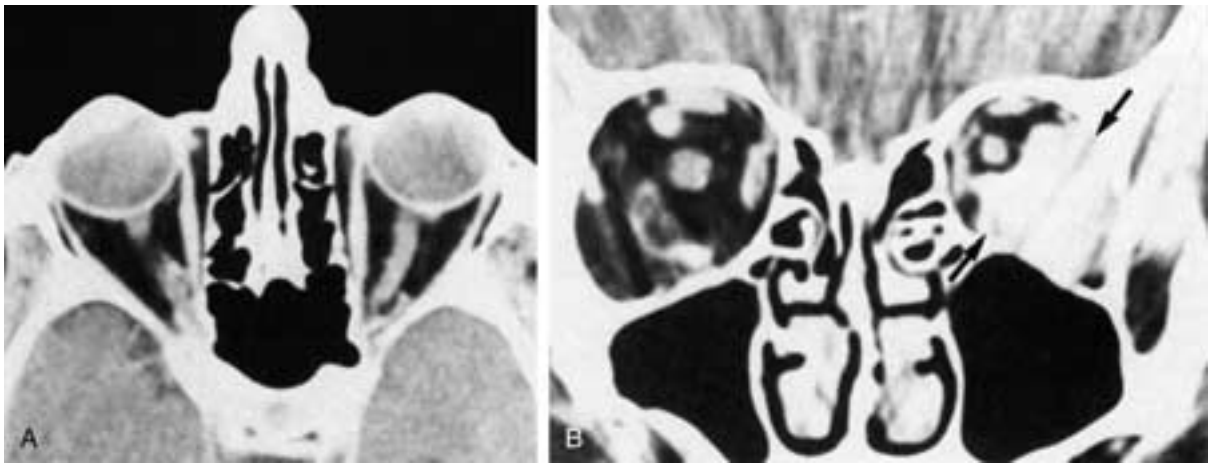

VIEW IMAGE

FIGURE 9-130 **A**, Orbital varix. Axial CT scan shows no obvious lesion. **B**, Coronal CT scan shows a large mass (*arrows*). (From Mafee MF et al. Orbital space-occupying lesions: role of CT and MRI: an analysis of 145 cases. Radiol Clin North Am 1987;25:529.)

differentiate the tumors from cavernous hemangiomas, meningiomas, and schwannomas.[8] Hemangiopericytomas usually have an early florid blush (Fig. 9-136C), and cavernous hemangiomas show a late minor pooling of contrast or often appear as avascular masses.[8, 134, 141] Meningiomas may show multiple tumor vessels and a late blush, and schwannomas may show no tumor blush.[8, 17, 140, 141] Hemangiopericytomas may be difficult to differentiate from other rare vasculogenic tumors such as angioleiomyomas, malignant hemangioendotheliomas (angiosarcomas), and fibrous histiocytomas.[8] Follow-up CT or MR imaging is extremely important to diagnose tumor recurrences (Fig. 9-137B).

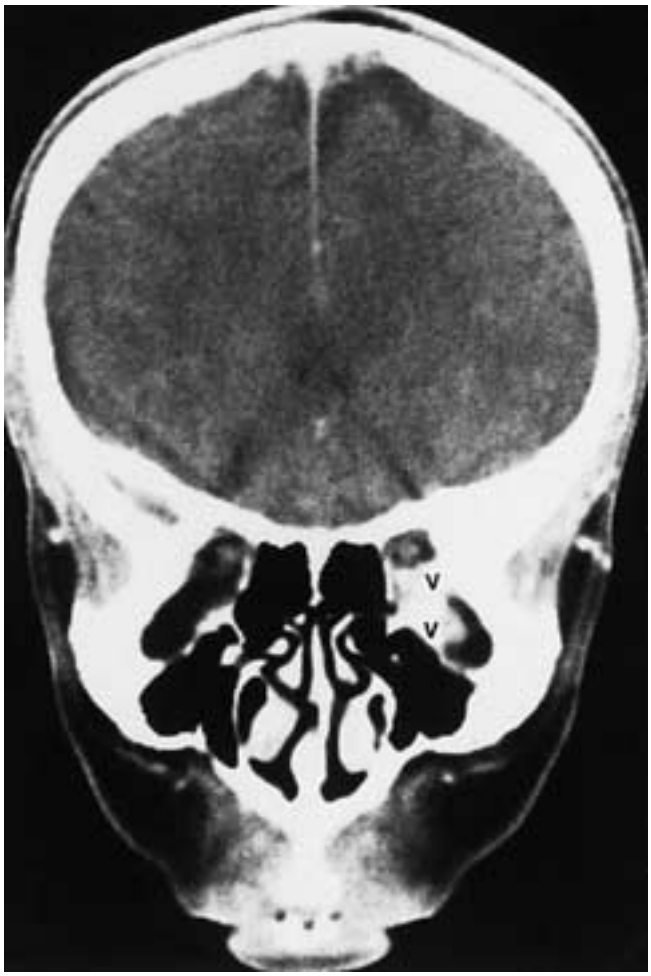

VIEW IMAGE

FIGURE 9-131 Orbital varix. Coronal contrast-enhanced CT scan shows several round, enhancing masses compatible with orbital varix (*V*).

NEURAL LESIONS

Orbital Schwannoma

The orbit is host to many peripheral nerves. Approximately 4% of all orbital neoplasms are peripheral nerve tumors and consist primarily of neurofibromas and neu-

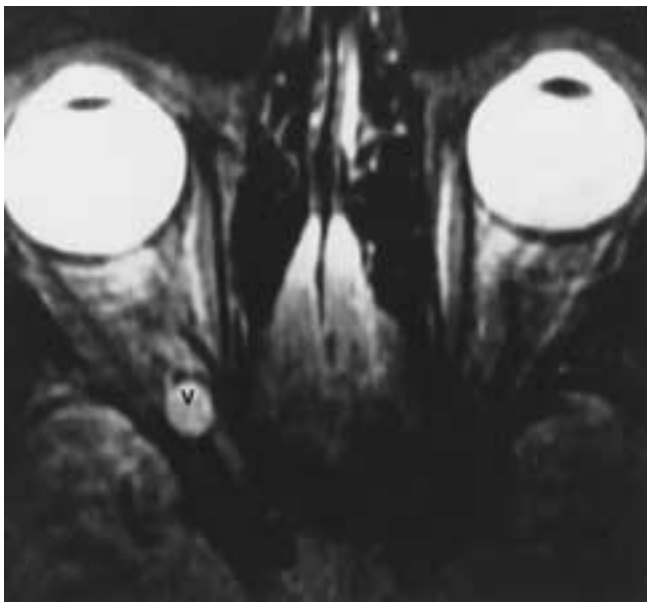

FIGURE 9-132 Orbital varix. Axial T2-weighted MR scan shows a round, hyperintense mass compatible with surgically proved orbital varix (*V*).

VIEW IMAGE

Copyright © 2003, Mosby, Inc. All rights reserved.

FIGURE 9-133 Orbital varix. Serial reformatted coronal sections showing multiple dilated veins in both eyes (*arrows*). Notice the calcifications (*arrowheads*). (From Mafee MF et al. Orbital space-occupying lesions: role of CT and MRI: an analysis of 145 cases. Radiol Clin North Am 1987;25:529.)

VIEW IMAGE

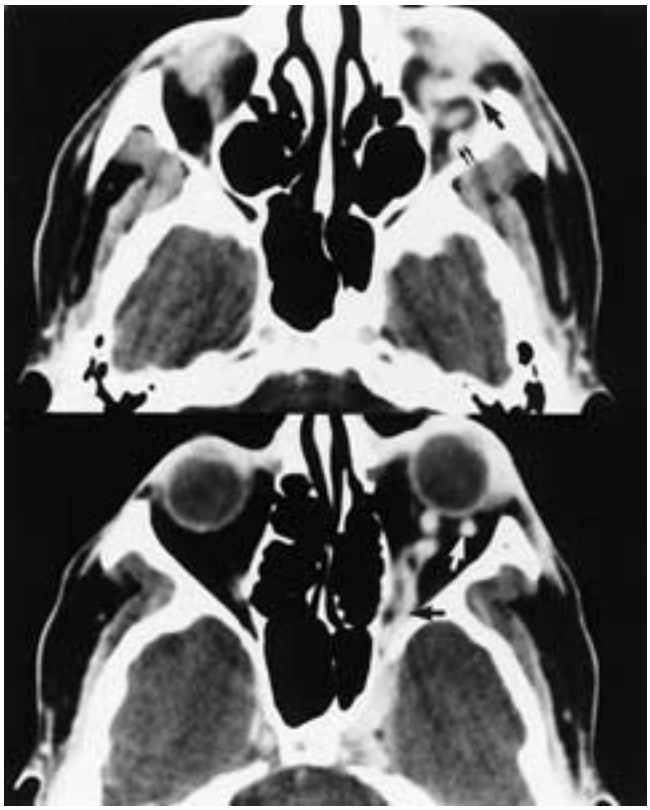

FIGURE 9-134 Carotid cavernous fistula. Enhanced axial CT scan shows enlarged intraorbital veins (*arrows*) and an enlarged left cavernous sinus.

VIEW IMAGE

rilemmomas or schwannomas.[142] Of these, 2% of the lesions are plexiform neurofibromatosis, 1% are isolated neurofibromas, and 1% are schwannomas.[142] Malignant peripheral nerve tumors (malignant schwannoma, neurofibrosarcoma) are extremely rare in the orbit.[142]

Neurofibroma

Neurofibromas may occur in one of four patterns: (1) plexiform, (2) diffuse, (3) localized or circumscribed, and (4) postamputation neuromas.[142] When most of the fascicles in a segment of peripheral nerve are involved, cylindrical enlargement of the entire nerve segment is observed. This clinical and gross pathologic configuration is referred to as *plexiform neurofibroma*.[7, 17, 142] Plexiform neurofibromas present in infancy or childhood and most commonly involve the eyelids. The tumor consists of cords and nodules giving rise to a ''bag of worms'' on palpation, and a plexiform neurofibroma involving the eyelid is considered to be virtually pathognomonic for neurofibromatosis (Von Recklinghausen's disease).[142] Diffuse neurofibromas have an appearance similar to that of plexiform neurofibromatosis, with infiltration of the orbital fat and EOMs, but these lesions are less likely to be associated with Von Recklinghausen's disease.[142] Circumscribed or localized neurofibromas often present as slow-growing tumors that exert a mass effect, with displacement of the globe. The tumor may occur along any sensory nerve but is more common in the superior quadrants. When arising from the lacrimal nerve, it may have the clinical appearance of a lacrimal gland tumor.

Copyright © 2003, Mosby, Inc. All rights reserved.

Histologically, plexiform neurofibromas are unencapsulated and have an organoid appearance, with proliferating units surrounded by perineurium enclosing axons, Schwann cells, and endoneurial fibroblasts. There is a marked increase in vascularity, which leads to profuse bleeding at the time of surgery.

This increased vascularity is responsible for marked contrast enhancement on CT and MR imaging. The CT and MR imaging appearance of plexiform neurofibromatosis in infants and children may be identical to that of a capillary hemangioma. Solitary neurofibromas often demonstrate a pseudocapsule, but a true perineurium is not seen. They are composed of wavy bundles of peripheral nerve sheath cells with comma-shaped nuclei and hyaluronic acid and collagen in the stroma.[142] The CT and MR imaging characteristics of neurofibroma are shown in Figures 9-138 to 9-140.

Schwannomas are benign, slow-growing nerve sheath tumors that account for 1% of all orbital tumors.[7,106, 107, 142] They may arise anywhere within the orbit, although they are most common in the intraconal space.[7] Their malignant counterpart, the malignant schwannoma (malignant neurolemma, neurogenic sarcoma, and fibrosarcoma of the nerve sheath), is exceedingly rare in the orbit.[7, 142] In general, neurofibromas and schwannomas are two benign tumors originating from Schwann cells that occur in the orbit as isolated lesions or in association with neurofibromatosis. The optic nerve has no Schwann cells; therefore, orbital schwannomas must arise from peripheral nerve fibers of

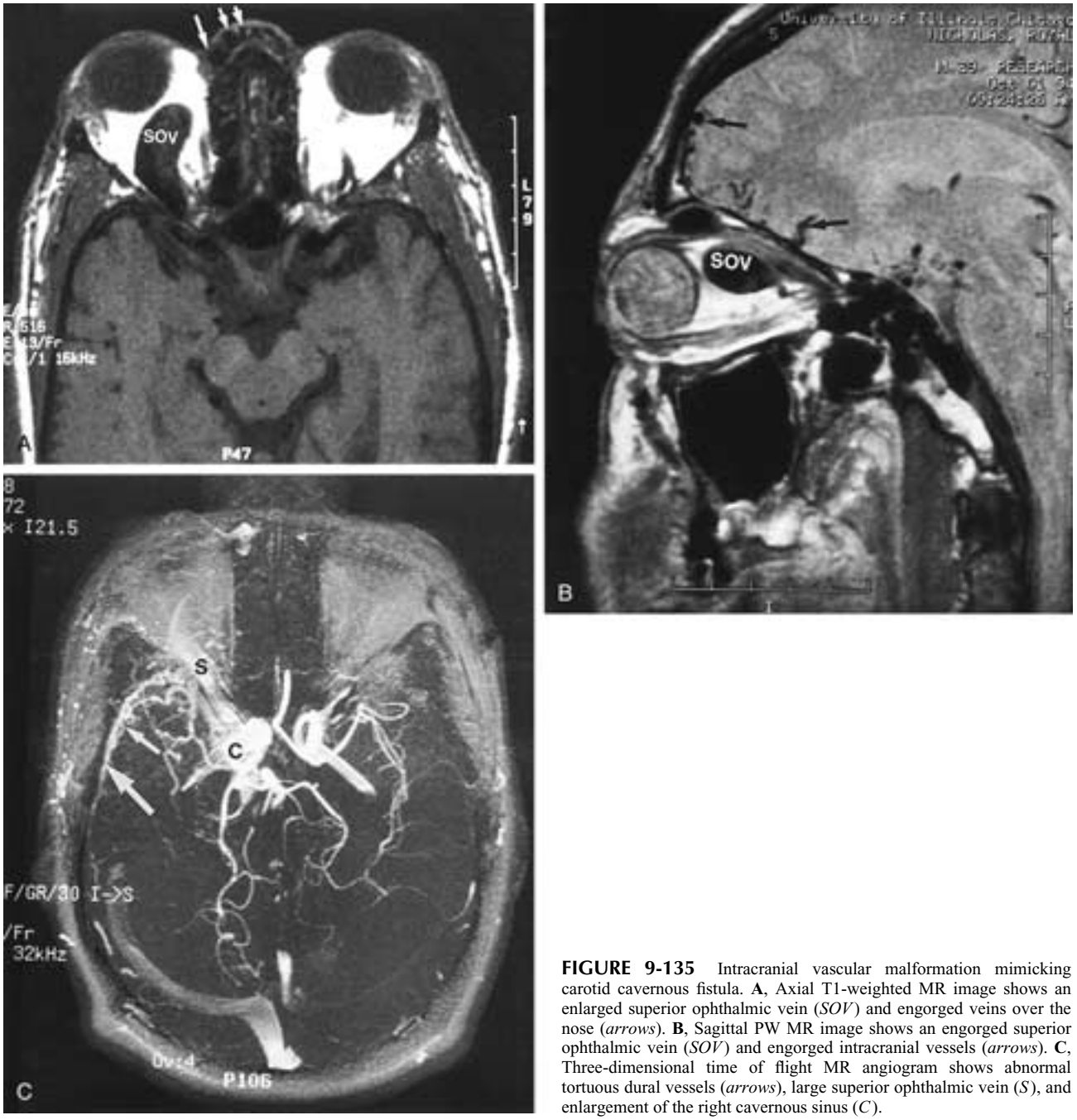

FIGURE 9-135 Intracranial vascular malformation mimicking carotid cavernous fistula. **A**, Axial T1-weighted MR image shows an enlarged superior ophthalmic vein (*SOV*) and engorged veins over the nose (*arrows*). **B**, Sagittal PW MR image shows an engorged superior ophthalmic vein (*SOV*) and engorged intracranial vessels (*arrows*). **C**, Three-dimensional time of flight MR angiogram shows abnormal tortuous dural vessels (*arrows*), large superior ophthalmic vein (*S*), and enlargement of the right cavernous sinus (*C*).

VIEW IMAGE

Copyright © 2003, Mosby, Inc. All rights reserved.

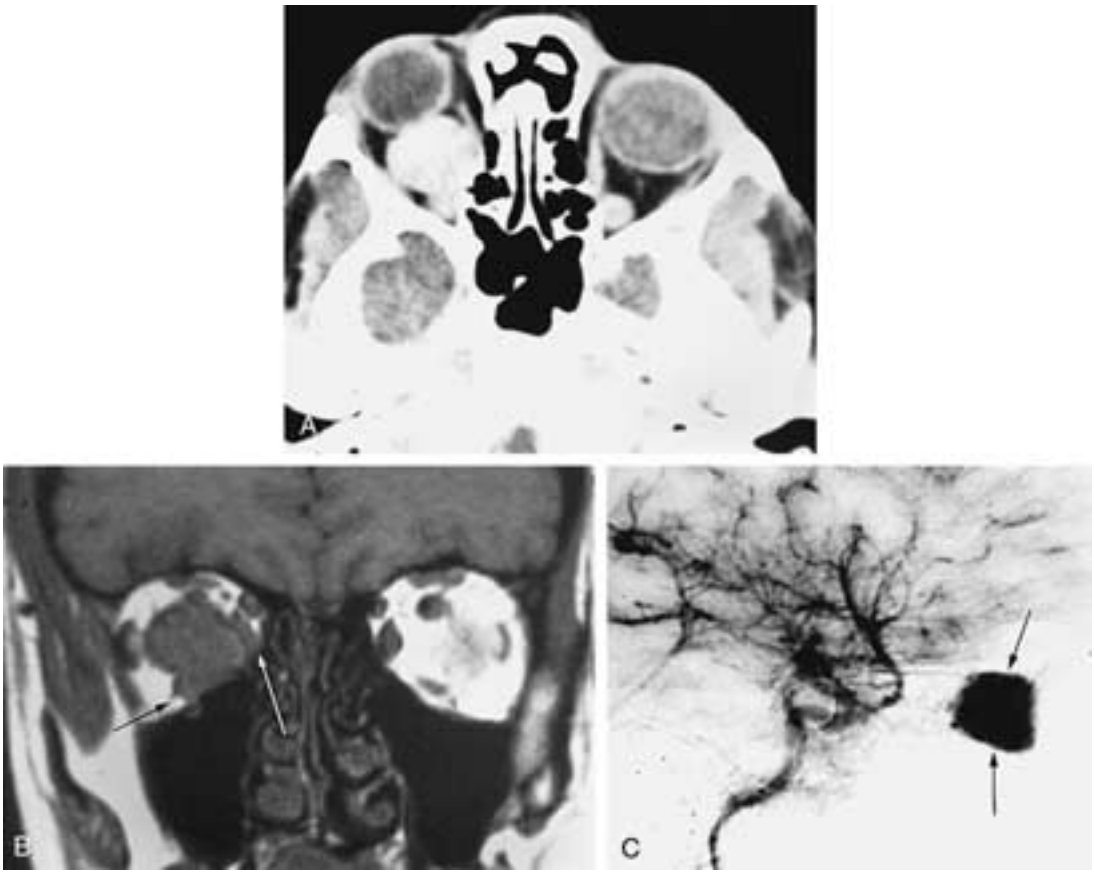

VIEW IMAGE

FIGURE 9-136 Hemangiopericytoma in a woman. **A**, Axial contrast-enhanced CT scan shows a large, enhancing mass in the right orbit that scallops the medial wall of the orbit and appears to have an irregular interface with the posterior right globe. **B**, Coronal T1-weighted MR image shows that the mass is irregular in outline, invades the inferior rectus muscle (*black arrow*), and extends around the left medial rectus muscle to infiltrate the extraconic fat (*white arrow*). **C**, Sagittal subtraction image of a conventional angiogram reveals marked enhancement of the hemangiopericytoma (*arrows*). This is an important differentiating point from a cavernous hemangioma, which usually shows no contrast pickup or a minimal amount in the venous phase. (Courtesy of Mahmood Mafee, MD, University of Illinois at Chicago, Chicago, Illinois. From Bilaniuk LT. Orbital Vascular Lesions: Role of Imaging. Radiol Clin North Am 1999 Jan;37(1):181.)

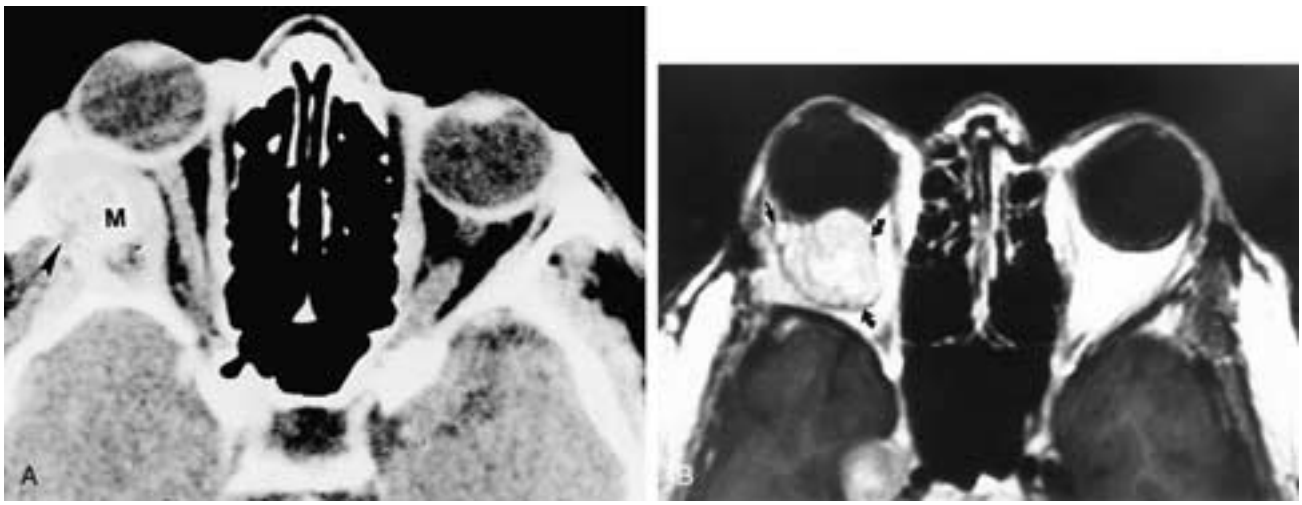

VIEW IMAGE

FIGURE 9-137 **A**, Hemangiopericytoma. Contrast-enhanced axial CT scan shows an enhancing mass (*M*) compatible with hemangiopericytoma. Note the erosion of the lateral orbital wall (*arrowhead*). **B**, Recurrent hemangiopericytoma. Enhanced axial T1-weighted MR scan shows a heterogeneously enhancing mass (*arrows*) compatible with recurrent hemangiopericytoma. (Courtesy of Dr. Michael Rothman.)

Copyright © 2003, Mosby, Inc. All rights reserved.

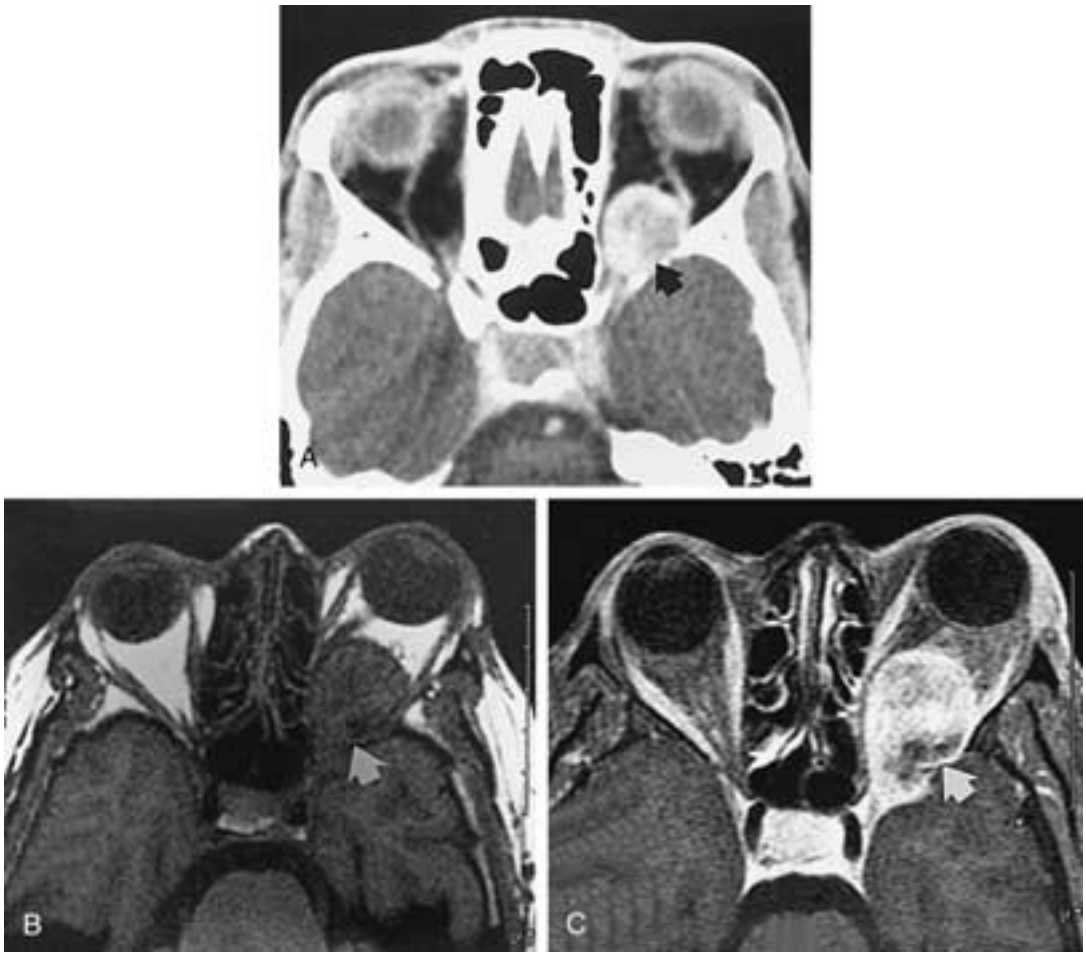

VIEW IMAGE

FIGURE 9-138 **A**, Postcontrast axial CT scan demonstrating a well-enhanced intraconal neurofibroma (*arrow*) of the posterior orbit. **B**, Axial T1-weighted MR scan of a posterior neurofibroma (*arrow*) as in **A**. Tumor is isointense to brain and hypointense to orbital fat. **C**, Axial fat-suppressed T1-weighted MR image of the tumor seen in **A** and **B** demonstrating the marked contrast enhancement of a posterior neurofibroma (*arrow*). (Courtesy of Mahmood Mafee, MD, University of Illinois at Chicago, Chicago, Illinois. From Carroll GS, Barrett GH, Fleming JC, et al. Peripheral Nerve Tumors of the Orbit. Radiol Clin North Am 1999 Jan;37(1):200.)

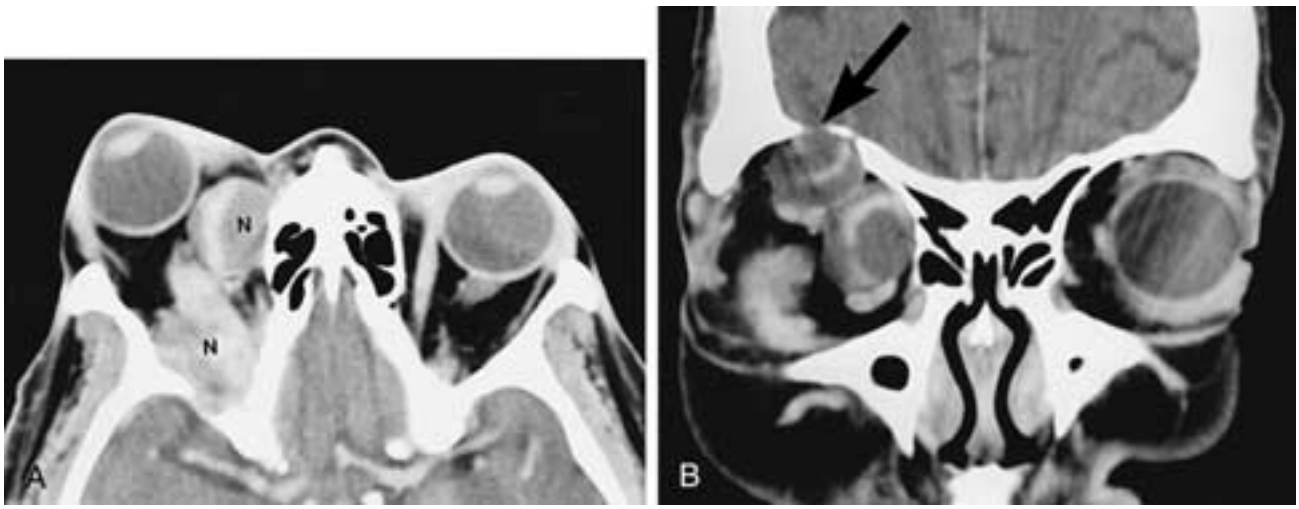

VIEW IMAGE

FIGURE 9-139 **A**, Axial postcontrast CT scan demonstrating an anterior medial orbital neurofibroma (*N*). **B**, Coronal CT scan of the tumor in **A** showing its multinodular configuration not readily seen in a single axial view. Note the compression atrophy of the orbital roof (*arrow*). (From Carroll GS, Barrett GH, Fleming JC, et al. Peripheral Nerve Tumors of the Orbit. Radiol Clin North Am 1999 Jan;37(1):198.)

Copyright © 2003, Mosby, Inc. All rights reserved.

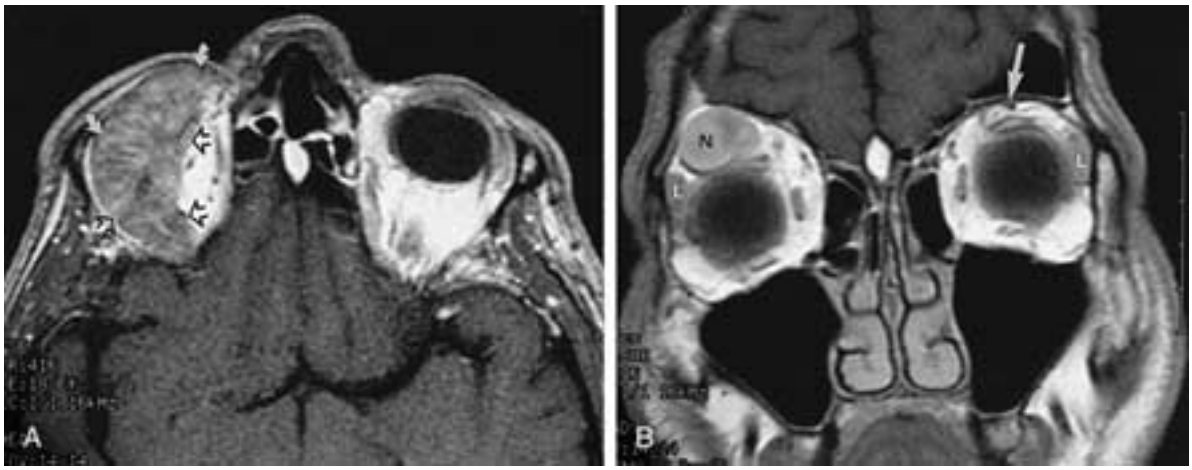

VIEW IMAGE

FIGURE 9-140 Neurofibroma of the frontal nerve. **A**, Axial-enhanced T1-weighted (416/18, TR/TE) MR image shows a large orbital mass (*arrows*), which shows moderate enhancement. **B**, Coronal-enhanced T1-weighted (500/16, TR/TE) MR image shows moderate enhancement of a neurofibroma (*N*). Note the normal lacrimal glands (*L*) and normal left frontal nerve (*arrow*). (From Mafee MF et al. Lacrimal gland tumors and simulating lesions. Radiol Clin North Am 1999;37:219–239.)

nerves III, IV, V, VI, VII, and the autonomic nerves. Schwannomas and neurofibromas are differentiated primarily on the basis of histopathology. Schwannomas are well encapsulated by the perineurium of the nerve of origin and, in contrast to neurofibromas, display clear evidence of Schwann cell origin.[142] Histologically, they are surrounded by a thin fibrous capsule that is formed by compression of perineural tissue. The tumor is composed of compactly arranged spindle-shaped cells that interlace in cords and whorls frequently oriented with their long axis parallel to one another. This cellular pattern is referred to as *Antoni type A*.[7, 107, 142] Commonly, the Antoni type B part of the tumor has a less cellular pattern characterized by haphazardly distributed cells in a collagenous matrix.[7, 17, 107, 142] On CT and MR imaging, orbital schwannomas appear as sharply marginated, oval or fusiform, intraconal or extraconal masses that demonstrate moderate to marked enhancement (Figs. 9-141 and 9-142). The optic nerve is always displaced and may be engulfed by the tumor (Fig. 9-141). The differential diagnosis includes cavernous hemangioma, meningioma, fibrous histiocytoma, neurofibroma, fibrocystoma, hemangiopericytoma, and metastasis.

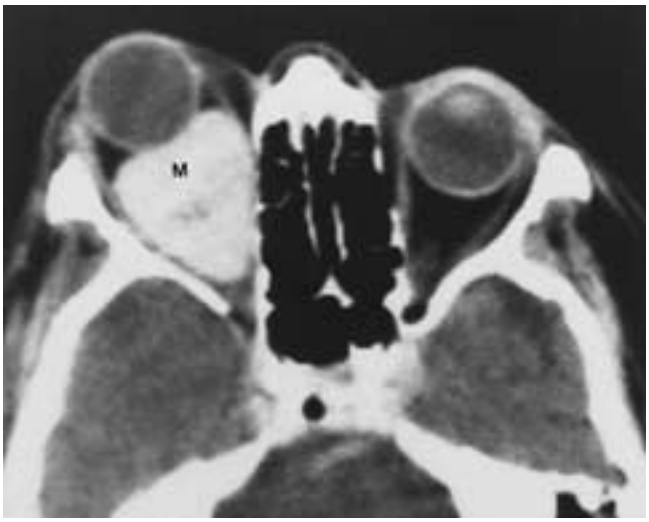

VIEW IMAGE

FIGURE 9-141 Orbital schwannoma. Contrast-enhanced axial CT scan shows a large enhancing mass (*M*).

TUMORAL AND NONTUMORAL ENLARGEMENT OF THE OPTIC NERVE SHEATH

Optic nerve sheath meningiomas and gliomas are the most common tumors involving the optic nerves, resulting in localized or diffuse enlargement of the optic nerve sheath complex (see Chapter 11). Primary or secondary involvement of the optic nerve in cases of lymphoma (Fig. 9-85), sarcoid (Fig. 9-86), leukemia, tuberculosis, toxoplasmosis, and syphilis has been reported.[16, 17, 27, 83] Optic nerve sarcoid manifesting as an enhanced tumor on CT and MR imaging scans can be easily mistaken for optic nerve sheath meningioma (Figs. 9-86, 9-88). Other rare causes of enlargement of the optic nerve include intradural cavernoma of the optic nerve and hemangioblastoma of the optic nerve, characteristically seen in patients with von Hippel-Lindau disease (Fig. 9-143).

OPTIC NEURITIS

This condition is an acute inflammatory process involving the optic nerve that may present as optic nerve enlargement.[16] Multiple sclerosis is the most common cause of optic neuritis and visual loss is typically unilateral, although it may be bilateral.[143] Optic neuropathies following chicken pox, rubella, rubeola, mumps, herpes zoster, mononucleosis, and viral encephalitis are referred to as *parainfections*, as opposed to those caused by direct tissue infiltration by microorganisms.[143] Visual loss is typically bilateral, occurring 10 to 14 days after the primary illness.

Copyright © 2003, Mosby, Inc. All rights reserved.

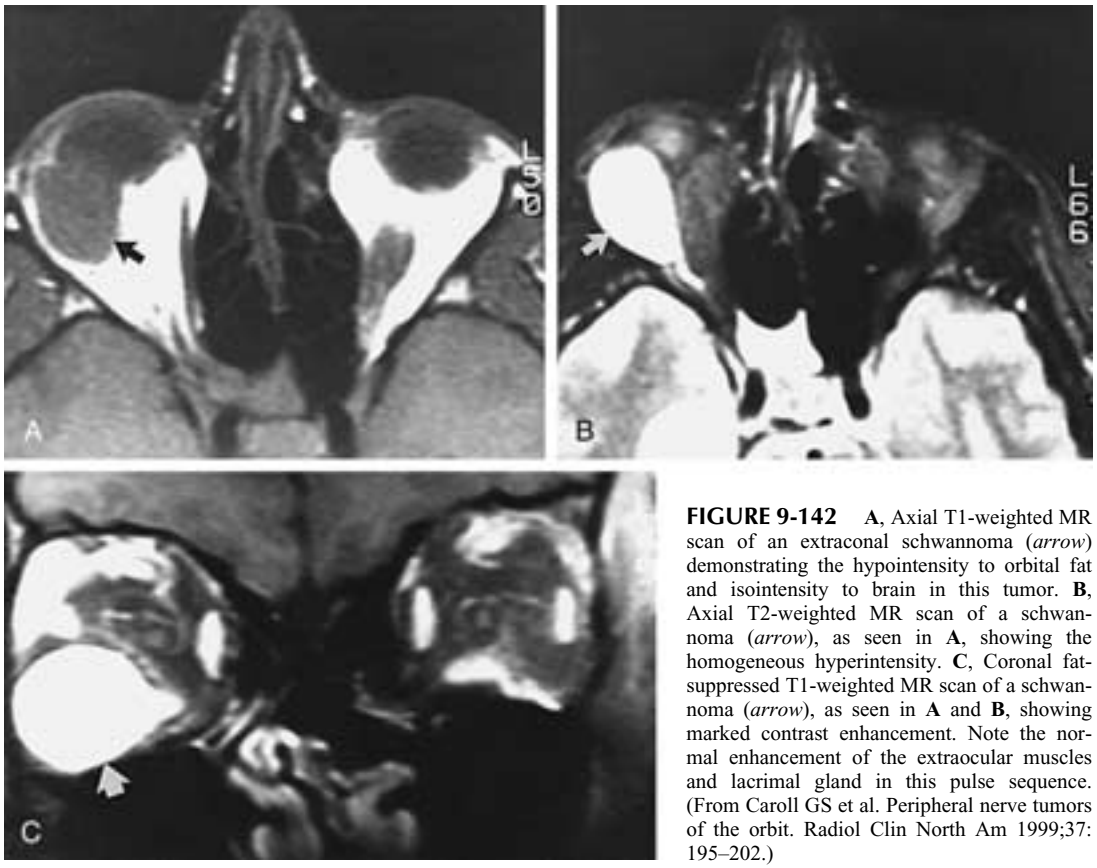

FIGURE 9-142 **A**, Axial T1-weighted MR scan of an extraconal schwannoma (*arrow*) demonstrating the hypointensity to orbital fat and isointensity to brain in this tumor. **B**, Axial T2-weighted MR scan of a schwannoma (*arrow*), as seen in **A**, showing the homogeneous hyperintensity. **C**, Coronal fat-suppressed T1-weighted MR scan of a schwannoma (*arrow*), as seen in **A** and **B**, showing marked contrast enhancement. Note the normal enhancement of the extraocular muscles and lacrimal gland in this pulse sequence. (From Caroll GS et al. Peripheral nerve tumors of the orbit. Radiol Clin North Am 1999;37: 195–202.)

VIEW IMAGE

This delay suggests a cascade of autoimmune mechanisms. Optic neuritis in patients with systemic lupus erythematosus or other autoimmune states is referred to as *autoimmune optic neuritis*.[143] Infective causes of optic neuritis include syphilis (neuroretinitis, papillitis, and perineuritis); toxoplasmosis; toxocariasis (papillitis); and, uncommonly, borreliosis (Lyme disease) and other granulomatous diseases.[143] Radiation optic neuropathy is another cause of optic neuritis. Optic neuritis in children differs from that in adults, including a greater incidence of disc swelling and a tendency toward bilateral simultaneous involvement.[143] Optic neuritis is often an early manifestation of multiple

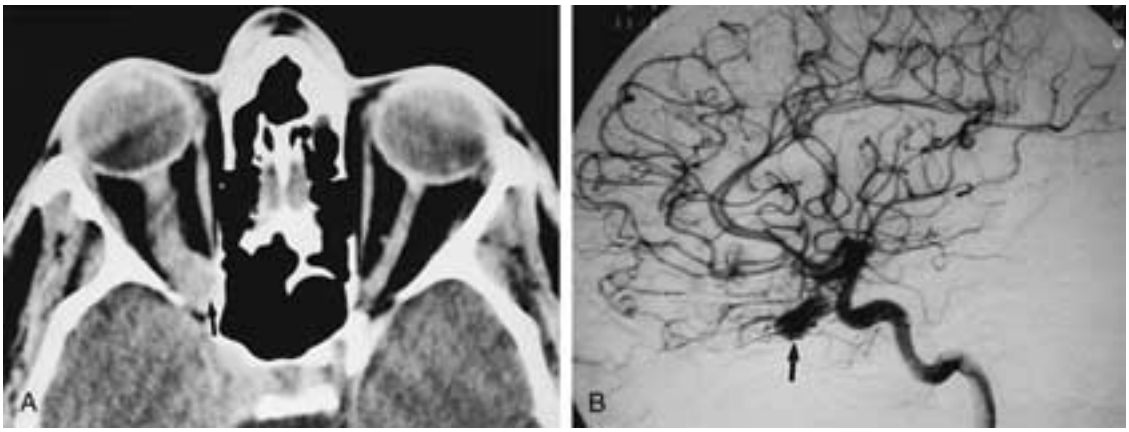

FIGURE 9-143 Optic nerve hemangioblastoma. Enhanced axial CT scan (**A**) and lateral angiogram (**B**) showing an optic nerve hemangioblastoma (*arrows*). (From Mafee MF et al. Optic nerve sheath meningiomas: role of MR imaging. Radiol Clin North Am 1999;37:37–58.)

VIEW IMAGE

Copyright © 2003, Mosby, Inc. All rights reserved.

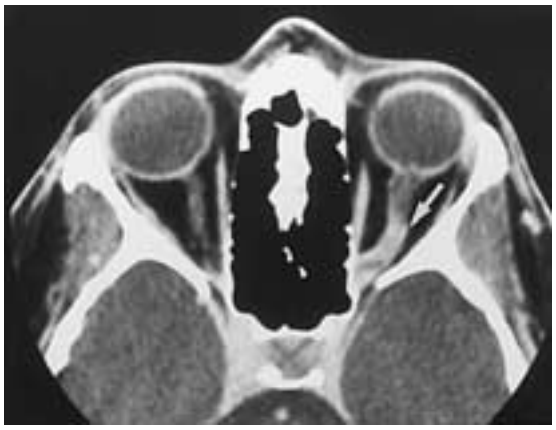

VIEW IMAGE

FIGURE 9-144 Optic neuritis. Enhanced axial CT scan shows enhancement of the left optic nerve (*arrow*). This may not be differentiated from sarcoidosis or meningioma.

sclerosis, and on CT there may be some enlargement of the optic nerve, usually with some degree of contrast enhancement (Fig. 9-144). On MR imaging the optic nerve may appear thickened and hyperintense on T2-weighted images (Fig. 9-145), and the MR visualization of multiple sclerosis plaques may be accentuated by inversion recovery (STIR) technique.[16, 83] Postcontrast fat-suppressed, T1-weighted MR images may be the best technique to demonstrate optic neuritis, and localized or diffuse areas of enhancement are typically seen within the nerve (Figs. 9-146 and 9-147). In general in patients with optic neuritis, contrast enhancement on CT and MR imaging is often subtle or present in a short segment of the optic nerve, particularly in the intracanalicular portion of the nerve (Fig. 9-146).

FIGURE 9-146 Postradiation optic neuritis. Enhanced, fat-suppressed, axial T1-weighted MR image shows enhancement of the intracanalicular segment of right optic nerve (*arrow*). Notice the postorbital exenteration on the left side.

VIEW IMAGE

PNEUMOSINUS DILATANS

Pneumosinus dilatans is a rare condition in which dilated paranasal sinuses lined by normal mucosa are present. In these hyperpneumatized paranasal sinuses, excessive pneumatization can lead to thinning and gross dehiscence of the bony wall. When there is actual bone dehiscence, the lesion is usually referred to as a *pneumocele* (see Chapter 5). The frontal sinus is most commonly affected, but the sphenoid sinus is the most important for visual loss because of its intimate relation with the optic canal.[144] Sphenoidal or sphenoethmoidal pneumosinus dilatans may be associated with visual symptoms.[144] Pneumosinus dilatans has been associated with meningioma and fibroosseous lesions, and pneumosinus dilatans without an associate pathologic process rarely causes visual loss (Fig. 9-148). The mechanism leading to optic neuropathy is uncertain, although with

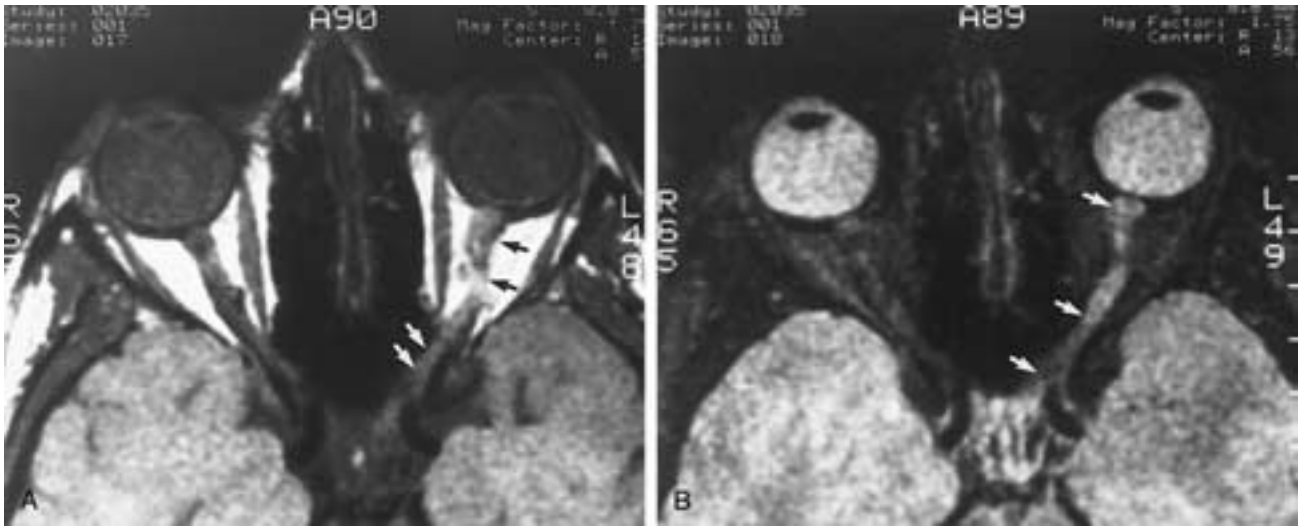

VIEW IMAGE

FIGURE 9-145 Optic neuritis. Axial PW (**A**) and T2-weighted (**B**) MR images show enlargement of the left entire optic nerve (*arrows*) in this 14-year-old girl with left optic neuritis.

Copyright © 2003, Mosby, Inc. All rights reserved.

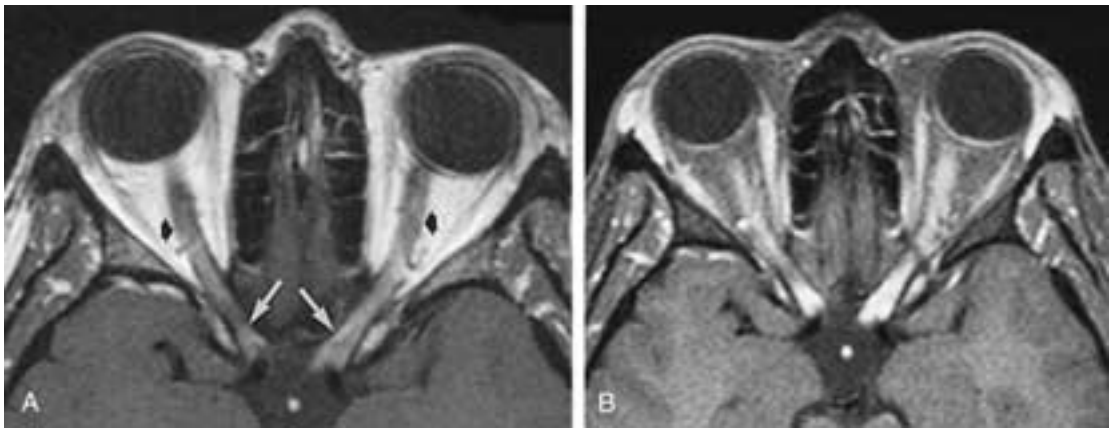

VIEW IMAGE

FIGURE 9-147 Optic neuritis. (**A**) Enhanced axial T1-weighted (600/18, TR/TE) and (**B**) enhanced axial fat-suppression T1-weighted (500/15, TR/TE) MR scans showing marked enhancement of intraorbital (*black arrows*) and intracanalicular segments (*white arrows*) of optic nerves. Biopsy revealed a demyelinating process. (From Mafee MF et al. Optic nerve sheath meningiomas: role of MR imaging. Radiol Clin North Am 1999;37:37–58.)

direct communication between the sinus and the optic canal present, one could postulate a direct compressive effect by mucosa or air leading to ischemic nerve damage.[144] It has been suggested that sudden elevation of the intrasinus pressure, as with sneezing or with altitude change (in airplanes), may cause direct damage to an exposed optic nerve.[144]

FIBROUS TISSUE TUMORS OF THE ORBIT

Fibrous tumors of the orbit are a group of lesions that present a confusing clinical, histologic, and imaging spectrum of disease. These include fibroma, fibrous histiocytoma, fibrocystoma, aggressive fibromatosis, nodular fasciitis, and fibrosarcoma. Fibrohistiocytic tumors are more common than fibroblastic (fibroma, fibromatosis) tumors.[145]

Fibrous Histiocytoma

Fibrous histiocytoma is a mesenchymal tumor that involves the fascia, muscle, and soft tissues of the body.[3, 145–148] It is considered by some authors to be the most common mesenchymal tumor of the orbit.[146] The neoplasm is made up of fibroblasts, myofibroblasts, undifferentiated mesenchymal cells, and fibrous-appearing histiocytic cells that tend to form a characteristic cartwheel or storiform pattern.[3, 145–148] Fibrous histiocytoma probably arises from a fibroblast precursor, and it bears no relationship to the systemic reticuloendothelioses or malignant histiocytoses. The tumor may be either benign or malignant.[146, 147] Malignant fibrous histiocytomas produce bone erosion. Benign lesions cause a mass effect with compressive bone atrophy (remodeling).[7] Fibrous histiocytomas are seen on CT and MR imaging as well-circumscribed masses that may be intraconal or extraconal and demonstrate

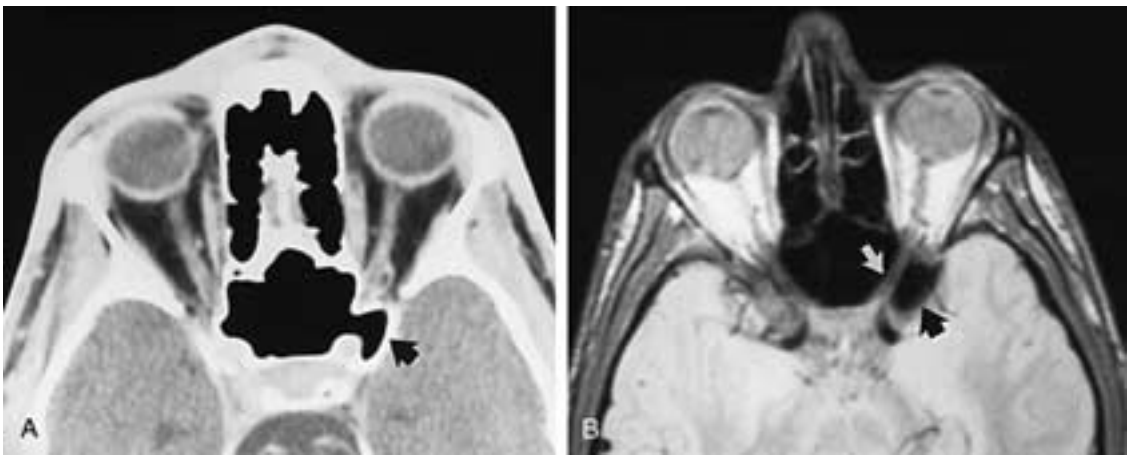

VIEW IMAGE

FIGURE 9-148 **A**, Sphenoid pneumosinus dilatans. Axial CT scan shows extension of sphenoid sinus pneumatization into the left lesser wing of sphenoid (*arrow*). **B**, Proton-weighted (2400/20, TR/TE) axial MR scan shows normal optic nerve (*white arrow*) and pneumatized lesser wing of sphenoid (*black arrow*). (From Mafee MF et al. Optic nerve sheath meningiomas: role of MR imaging. Radiol Clin North Am 1999;37:37–58.)

Copyright © 2003, Mosby, Inc. All rights reserved.

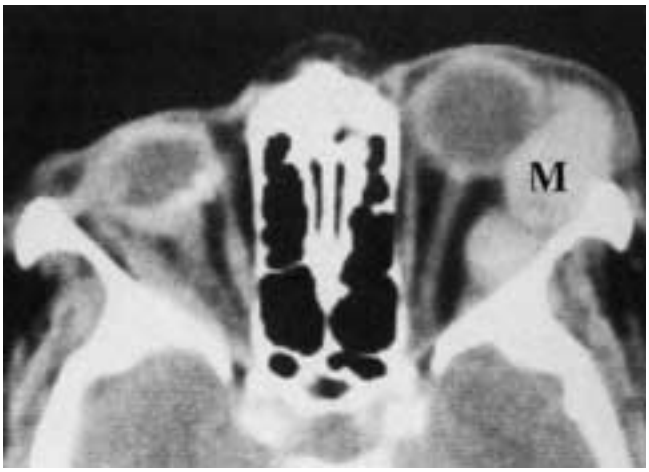

VIEW IMAGE

FIGURE 9-149 Fibrous histiocytoma. Axial postcontrast CT scan showing a bilobed enhancing mass (*M*) involving the peripheral orbital space. Notice the deformity of the right globe with calcifications representing pthisis bulbi. (From Mafee MF et al. Orbital space-occupying lesions: role of CT and MRI: an analysis of 145 cases. Radiol Clin North Am 1987;25:529–559.)

moderate to marked contrast enhancement (Figs. 9-149 and 9-150).[145] Some of the tumors may be bilobed. Some of the densely cellular fibrous histiocytomas may appear moderately to markedly hypointense on T2-weighted images, and these lesions may not be differentiated on imaging from some of the neurofibromas and other fibrous lesions (Fig. 9-151). The differential diagnosis should include cavernous hemangioma, hemangiopericytoma, schwannoma, meningioma, neurofibroma, fibrocystoma, vasculogenic leiomyoma, lymphoma, and metastasis. Malignant fibrous histiocytomas may be seen following irradiation of the orbit for retinoblastoma.[17]

Fibroma and Fibrosarcoma

Fibroma is the least common fibrous tumor of the orbit and is found mostly in young adults.[145] It is usually encapsulated and grows slowly over several years. It arises from the fascia of the EOMs or Tenon's capsule in the orbit. Fibrosarcoma is also rare in the orbit. Congenital, infantile, juvenile, and adult forms of fibrosarcoma are recognized.[145] Aggressive fibromatosis is a benign but locally invasive fibroblastic lesion lying clinically and pathologically in the spectrum between fibrosis and low-grade fibrosarcoma. Infantile deep (desmoid type), infantile myofibromatosis (congenital generalized fibromatosis), and adult (deep or musculoaponeurotic) forms are recognized (Fig. 9-152).

The lesion may be (1) solitary in about 73%; (2) multicentric, involving subcutaneous tissues, skeletal muscle, and the ends of long bones; or (3) generalized, with cutaneous, musculoskeletal, and visceral involvement.[145] Orbital involvement may rarely be bilateral.[145] Fibromatosis tends to be locally infiltrative and grows rapidly, which may cause it to be considered as a low-grade fibrosarcoma. Histologically, it is composed of well-differentiated, uniform fibroblasts, appearing similar to smooth muscle, but electron microscopy reveals that the lesion contains fibroblasts and myofibroblasts. Treatment is wide surgical excision. Fibromatosis recurs locally in 25% to 65% of cases and can be fatal. CT and MR imaging may show a lesion with either benign-appearing or invasive characteristics (Fig. 9-152).

Nodular Fasciitis

Nodular fasciitis is a common fibrous tumor found elsewhere in the limbs and trunk of adults, but head and neck involvement is seen more commonly in infants and children.[145] Orbital involvement may develop in the lid, conjunctiva, Tenon's capsule, or the deep orbit.[145] Microscopically, plump fibroblasts have a stellate appearance. Normal mitosis is present. The pathologic differential diagnosis should include fibromatosis, fibrosarcoma, leiomyoma, neurofibroma, schwannoma, myxofibrosarcoma, and myxoid liposarcoma.[145] Nodular fasciitis is best treated with complete excision and has a recurrence rate of 1% to 2%.[145] CT and MR imaging findings are nonspecific and similar to those of aggressive fibromatosis (Fig. 9-153).

RHABDOMYOSARCOMA OF THE ORBIT

Although rhabdomyosarcoma (RMS) is a rare tumor, it is still the most common primary orbital malignancy in children and the most common soft-tissue malignancy of childhood. Soft-tissue sarcomas account for 6% of all childhood cancers, and RMS accounts for approximately 50% of all pediatric soft-tissue sarcomas and 15% of all pediatric solid tumors.[149–153] Approximately 250 new pediatric patients are diagnosed with RMS each year in the United States. The head and neck area accounts for 35% of all RMS, the genitourinary system for 23%, and the extremities for 17%. The remainder are found in the trunk, retroperitoneum, chest, perineum, and gastrointestinal tract.[149–153] RMS occurs primarily in patients from ages 2 to 5; however, the tumor may occur at any age from birth to adulthood. In most cases, the average age at diagnosis is 7 to 8 years. RMS can be further divided into bimodal age peaks, depending on the histology. The embryonal and alveolar subtypes present in children, and the pleomorphic type presents more commonly in adults. The tumor may even be present at birth.[149] Orbital RMS is invariably unilateral, and although the tumor may involve any part of the orbit and adnexa, it tends to involve the superior portion of the orbit. The most characteristic presenting features of orbital RMS are a fairly rapid onset and progression, with proptosis and displacement of the globe.

RMS originates from embryonic tissue, either from immature prospective muscle fibers or pluripotential embryonic mesenchymal tissue, with a potential for aberrant differentiation into muscle fibers. Cytogenic analysis has found that many of these patients have a translocation between chromosomes 2 and 13 and abnormalities of chromosome 11.[149–153] This tumor does not originate from preformed extraocular striated muscles. The differential diagnosis also includes leukemic and metastatic deposits (neuroblastoma), lymphoma, LCH, aggressive fibromatosis, plexiform neurofibromatosis, ruptured dermoid cyst, sub-

Copyright © 2003, Mosby, Inc. All rights reserved.

periosteal hematoma after trauma, and a chocolate cyst related to hemorrhage in a lymphangioma. RMSs are pleomorphic tumors, and the cells may be anaplastic. On the basis of their histopathologic characteristics, RMSs are classified into one of three histologic types: (1) embryonal, (2) differentiated, and (3) alveolar. Differentiated RMS is the least frequent type and is rarely misdiagnosed because cells with eosinophilic cytoplasmic fibrils that are usually cross-striated are used to identify the tumor. Embryonal RMS, the most common histologic subtype, is believed to arise from the primitive muscle cell, because it is found in 7- to 10-week-old fetuses. The histologic differentiation between embryonal and alveolar RMS may be difficult. It has been estimated that up to 50% of proved cases of RMS are misdiagnosed on initial biopsy.[149]

RMS of the sinonasal tract and orbit often presents as a

FIGURE 9-150 Malignant fibrous histiocytoma. Axial (**A**) and coronal (**B**) contrast-enhanced CT. The contrast-enhanced CT studies on this 58-year-old man demonstrate a well-defined, moderately enhancing mass at the left lateral globe margin, which indents the globe without visibly invading the dense sclera. A small amount of gas is present in the mass after needle biopsy. **C**, Coronal T1-weighted image (TR/TE = 600/12) reveals that the mass is intermediate in signal intensity. **D**, Axial, fat-saturation, T1-weighted image (600/12) shows moderate gadolinium enhancement. **E**, Axial, conventional, STIR (TR/TE/T1 = 2000/43/170) image shows that the mass is hyperintense to temporalis muscle, slightly hypointense to the vitreous, and separated from the globe contents by the hypointense band of sclera. At surgery, it arose from the ciliary body near the tendinous insertion of the lateral rectus muscle. (From Dalley RW. Fibrous histocytoma and fibrous tissue tumors of the orbit. Radiol Clin North Am 1999;37:185–194.)

VIEW IMAGE

Copyright © 2003, Mosby, Inc. All rights reserved.

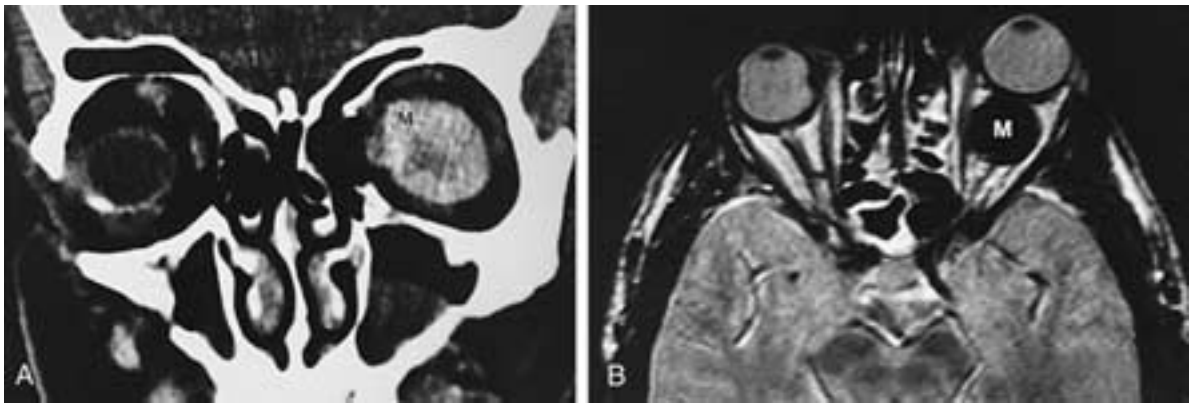

VIEW IMAGE

FIGURE 9-151 Fibrocytoma. **A**, Coronal contrast-enhanced CT scan shows moderately enhancing intraconal mass (*M*). **B**, Axial T2-weighted MR image shows markedly hypointense mass (*M*). This is related to marked dense collagen content. (From Dalley RW. Fibrous histocytoma and fibrous tissue tumors of the orbit. Radiol Clin North Am 1999;37:185–194.)

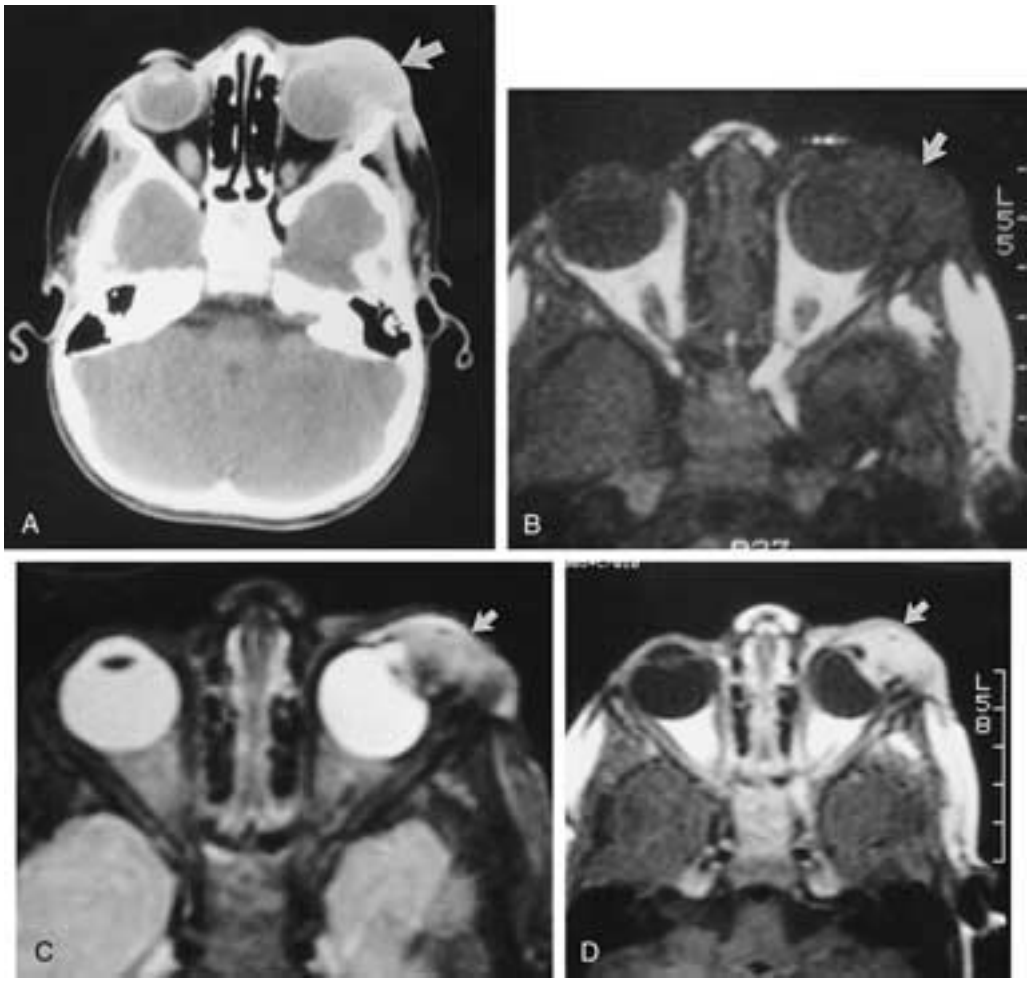

VIEW IMAGE

FIGURE 9-152 Aggressive fibromatosis. **A**, Enhanced axial CT scan shows a mass (*arrow*) with moderate enhancement. **B**, Axial T1-weighted MR image. The mass (*arrow*) is isointense to brain tissue. **C**, Axial T2-weighted MR image. The mass (*arrow*) appears hyperintense to muscles. **D**, Enhanced fat-suppression axial T1-weighted MR image. The mass (*arrow*) shows marked enhancement. Note invasion of the globe. (From Mafee MF et al. Rhabdomyosarcoma of the orbit: evaluation with MR imaging and CT. Radiol Clin North Am 1998;36:1215–1227.)

Copyright © 2003, Mosby, Inc. All rights reserved.

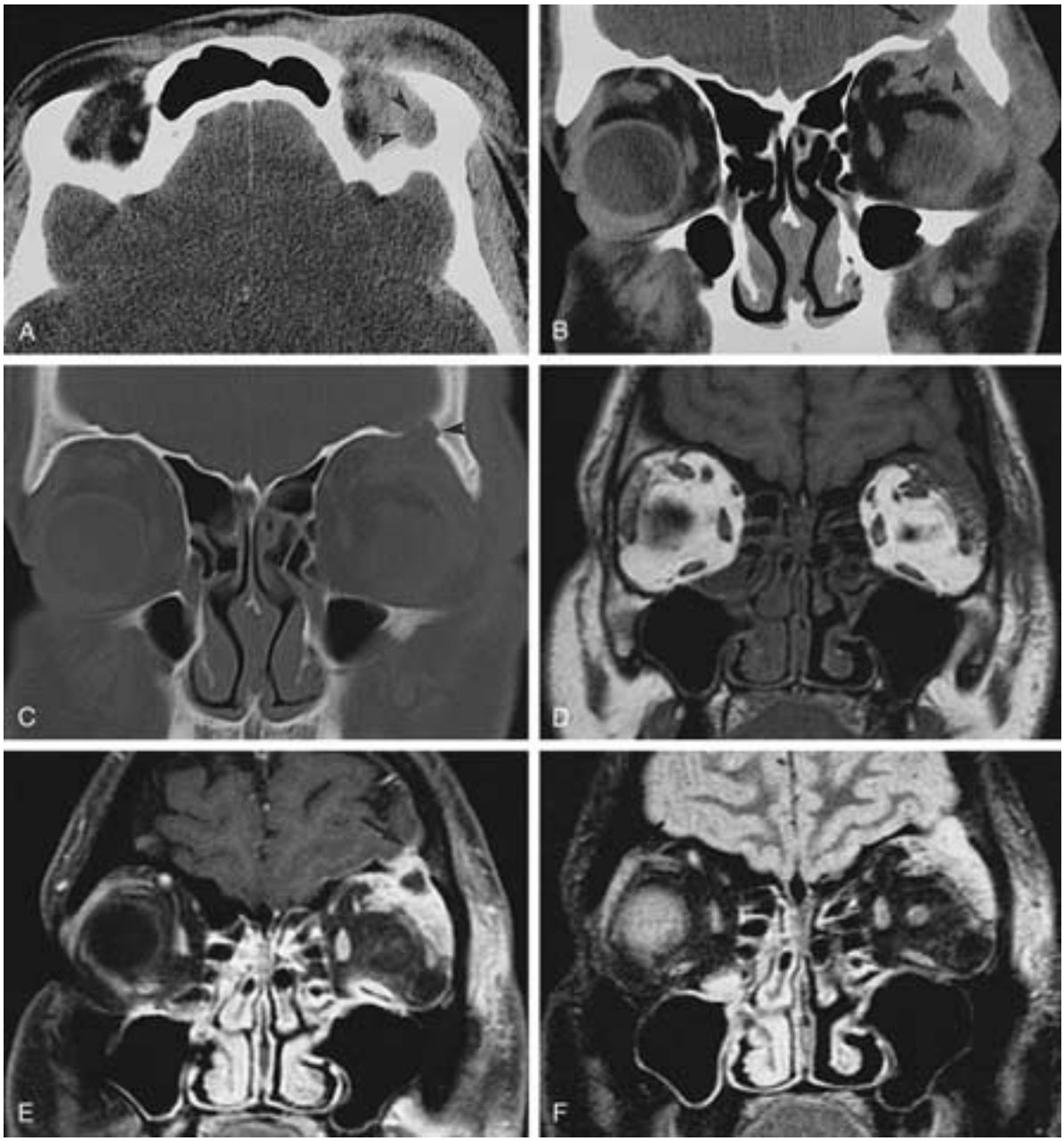

VIEW IMAGE

FIGURE 9-153 Nodular fasciitis. A 36-year-old man presented with an apparent inflammatory left orbital mass, which was unresponsive to 3 weeks of antibiotics. Axial (**A**) and coronal (**B**) contrast-enhanced CT. Soft-tissue windows show an ill-defined, enhancing, extraconal or subperiosteal soft-tissue mass in the left superior-lateral orbit, with a low-attenuation central area (*arrowheads*). Note the subtle enhancement along the anterior cranial fossa (*arrow*). **C**, Coronal CT bone windows demonstrate focal erosion in the frontal bone adjacent to this low-attenuation region (*arrowhead*). **D**, Coronal T1-weighted image (600/15) reveals an intermediate intensity extending lateral to the orbital rim in addition to eroding the frontal bone. **E**, Coronal, fat-saturation, postgadolinium, T1-weighted image (650/15). After gadolinium, most of the mass enhances, with a central, nonenhancing focus adjacent to the bone erosion. Note the intracranial dural reaction (*arrow*). **F**, Coronal, fast-STIR (2000/12/160) image. The mass is isointense to gray matter, with a focal area of hyperintensity corresponding to the cystic-appearing region on the postgadolinium image. The preoperative diagnosis was ruptured dermoid cyst or an aggressive lacrimal region abscess with osteomyelitis. (From Dalley RW. Fibrous histocytoma and fibrous tissue tumors of the orbit. Radiol Clin North Am 1999;37:185–194.)

relatively innocuous problem (e.g., recurrent sinusitis, proptosis, or a small nasoorbital mass). Secondary sinonasal tumors may arise from adjacent orbital spread of orbital or pharyngeal RMS. RMSs are aggressive bone-destroying and bone-pushing lesions. Although RMS of the orbit is most often seen in children and in adults under 20 years of age, at times it affects older patients.

RMS, nonrhabdomyosarcomatous soft-tissue sarcoma, and Ewing's sarcoma occur frequently in the head and neck of children. The nonrhabdomyosarcomatous sarcomas in-

Copyright © 2003, Mosby, Inc. All rights reserved.

clude fibrosarcoma, angiosarcoma, malignant fibrous histiocytoma, malignant schwannoma and neurofibroma, leiomyosarcoma, hemangiopericytoma, synovial sarcoma, and other less common sarcomas. Rao et al.[154] reported 110 cases of nonrhabdomyosarcomatous soft-tissue sarcomas. Head and neck sites accounted for only 15% of these tumors. The head and neck sites can be divided into three broad groups: (1) cranial parameningeal, (2) orbital, and (3) nonorbital-nonparameningeal.[149] Parameningeal RMS refers to those tumors arising in the nasopharynx, paranasal sinuses, nose, middle ear, temporal fossa, and pterygopalatine fossa. Nonorbital-nonparameningeal head lesions include superficial and deeply placed tumors, including tumors of the scalp and face, as well as deep tumors arising in the buccal mucosa, parapharyngeal space, larynx, salivary gland, and neck.[149]

Proptosis is an uncommon finding in children, but the vast majority of space-occupying lesions in the orbit causing proptosis in children are benign. These include inflammatory lesions (infection, abscess, and idiopathic orbital inflammation); developmental cysts (teratoma, dermoid, epidermoid); subperiosteal hematoma; benign and malignant mesenchymal tumors (osteogenic, chondrogenic, histiocytomatous, fibromatous [aggressive fibromatosis], lipomatous, myxomatous, rhabdomyomatous); tumors of vascular origin (hemangioma and lymphangioma); metastases; and neurogenic tumors (neurofibroma, plexiform neurofibromatosis, optic nerve glioma). Although malignant lesions are rare, clinically they can mimic more common benign processes, creating difficulty in diagnosis. Other orbital malignancies include lymphoma (including Burkitt's lymphoma), leukemia, extension of retinoblastoma, metastatic neuroblastoma, and secondary involvement by Ewing's sarcoma. Radiologic imaging is an essential aid to the clinician in differentiating the diagnostic possibilities.

Orbital RMS generally presents painlessly with rapidly progressive unilateral exophthalmos or, less commonly, as a superficial swelling with a palpable mass and proptosis. Patients may even present with a confusing or misleading history, such as recent trauma. Orbital RMS usually affects young children or adolescents up to age 16 years, with an average age of 7 years, but has been reported in older children and adults. Most tumors are retrobulbar, resulting in proptosis, but they can arise extraconally, especially superiorly or supranasally. They have also been reported to arise intraocularly from the ciliary body.[149] Tumors arising in the paranasal sinuses, nasal cavity, pterygopalatine fossa, nasopharynx, and parapharyngeal space may secondarily invade the orbit, and RMS arising elsewhere can metastasize to the orbit.[149]

Of the head and neck sites, orbital RMS has a better outlook, presumably because of the paucity of lymphatics and tumor confinement by the bony orbit. Parameningeal involvement is associated with the poorest outcome, presumably because of abundant lymphatics and the lack of confinement to prevent extension into the surrounding tissues.

Diagnostic Imaging

CT and MR imaging play an important role in the preoperative evaluation and staging of these tumors. Imaging should include CT and MR imaging of the primary and metastatic sites (i.e., lung, liver, brain, and so forth). CT and MR imaging are also important in evaluating recurrent and residual disease, and a baseline CT or MR imaging study is essential following completion of treatment. Without a baseline CT or MR scan, the follow-up studies may not be specific for tumor recurrence. Because of the dramatic improvement in survival of patients treated promptly with appropriate chemotherapy and radiation therapy, these tumors must be diagnosed as soon as possible.

On CT images, the RMSs are isodense in relation to normal muscles and appear as homogeneous, well-defined soft-tissue masses without bone destruction (Fig. 9-154). Larger tumors appear as less well defined soft-tissue masses with bone destruction or invasion of surrounding structures (Fig. 9-155). Tumors that have focal hemorrhage appear heterogeneous on CT scans. All tumors demonstrate moderate to marked contrast enhancement.[149]

On T1-weighted MR images, the RMSs are isointense or slightly hypointense compared with brain. On T2-weighted MR images, they appear to have increased signal intensity compared with brain (Fig. 9-156). Tumors that have chronic or subacute areas of hemorrhage demonstrate focal areas of increased signal on T1-weighted and T2-weighted images.[152] RMS demonstrates enhancement on contrast-enhanced CT and MR images (Fig. 9-157).[149] With the fat-suppression technique, T1-weighted images demonstrate marked expansion of the gray scale, with apparently increased signal intensity of the normal EOMs and lacrimal glands. Therefore, these normal structures should not be mistaken for tumor. The tumors appear more hyperintense on postcontrast fat-suppressed, T1-weighted images than on postcontrast non-fat-suppressed T1-weighted images.

When the diagnosis is suspected, cross-sectional imaging primarily with CT or MR imaging is performed to confirm the presence of an infiltrative mass and evaluate the extent of involvement of adjacent structures, including the brain. Although both may be equivalent in detecting an abnormal mass and determining its origin, MR imaging better delineates the full extent of involvement due to its superior soft-tissue contrast (Fig. 9-158).

Concomitant reactive sinus disease can be differentiated on MR imaging by differences in signal intensity on SE and postcontrast images. Superimposed fungal infection, during or following radiation therapy and chemotherapy, may pose

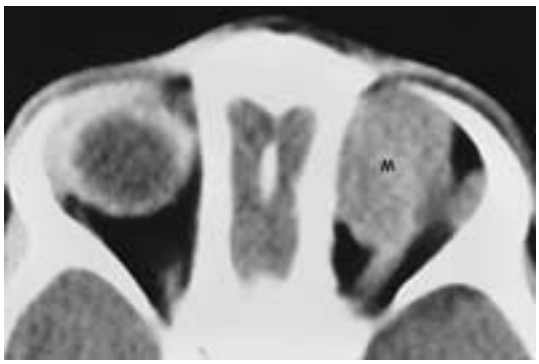

FIGURE 9-154 Rhabdomyosarcoma (5-year-old boy). Enhanced axial CT scan shows an orbital mass (*M*) with moderate contrast enhancement. (From Mafee MF et al. Rhabdomyosarcoma of the orbit: evaluation with MR imaging and CT. Radiol Clin North Am 1998;36:1215–1227.)

VIEW IMAGE

Copyright © 2003, Mosby, Inc. All rights reserved.

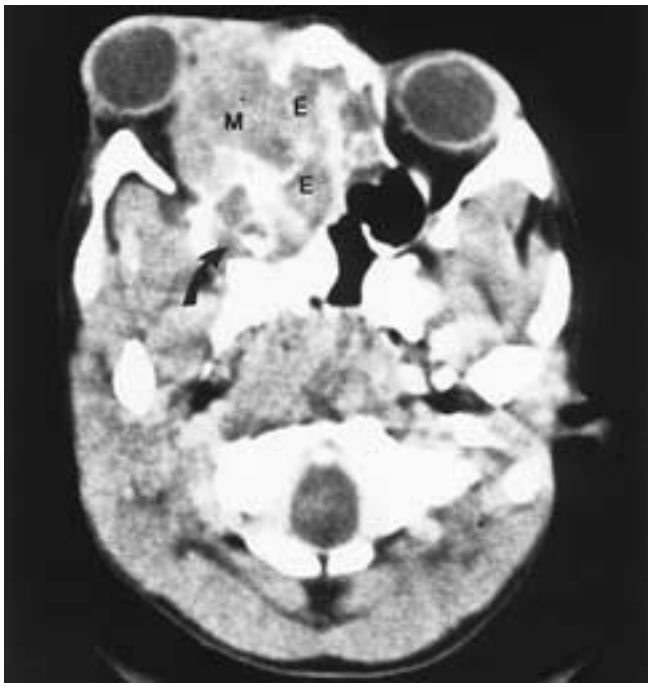

VIEW IMAGE

FIGURE 9-155 Rhabdomyosarcoma. Axial enhanced CT scan shows a large mass (*M*) in the right orbit extending into the right ethmoid air cells (*E*) and right infratemporal fossa (*arrow*).

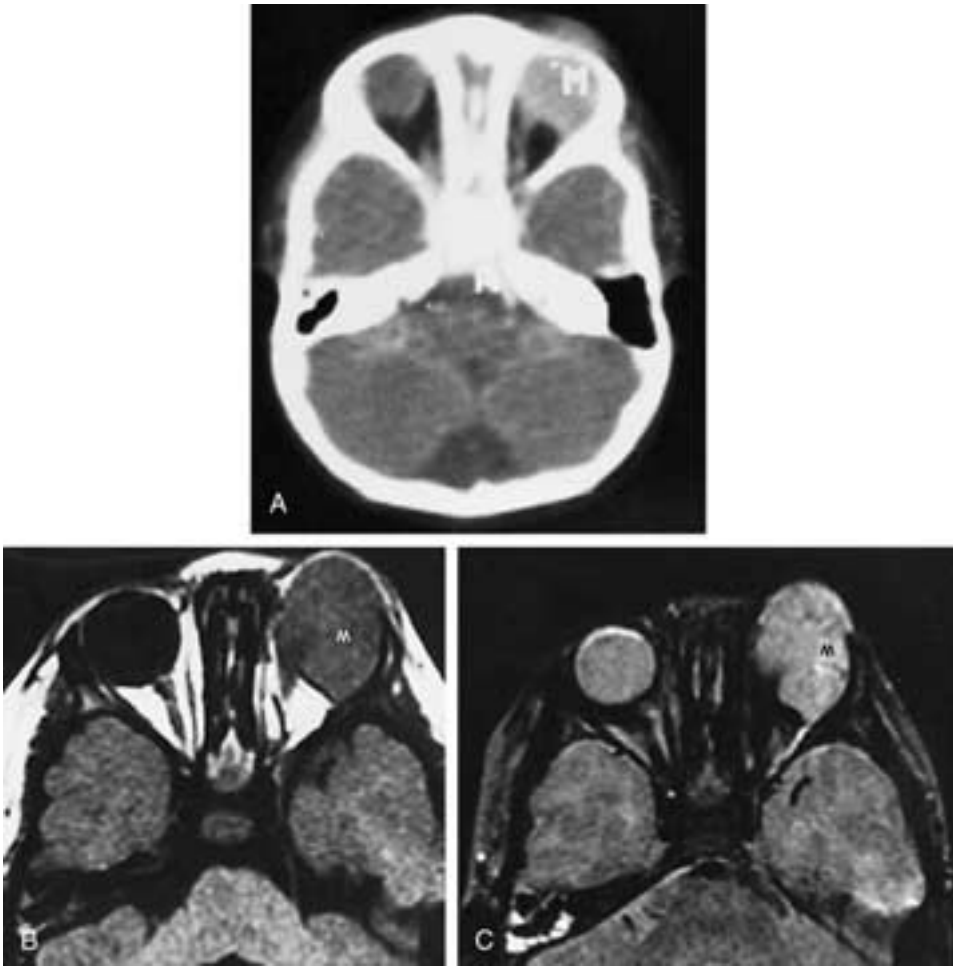

VIEW IMAGE

FIGURE 9-156 Rhabdomyosarcoma (2-year-old boy). **A**, Enhanced axial CT scan shows an orbital mass (*M*) that demonstrates moderate contrast enhancement. **B**, Axial T1-weighted MR image shows the mass (*M*), which is slightly hypointense to the brain. **C**, Axial T2-weighted MR image. The mass (*M*) appears hyperintense relative to the brain. (From Mafee MF et al. Rhabdomyosarcoma of the orbit: evaluation with MR imaging and CT. Radiol Clin North Am 1998;36:1215–1227.)

Copyright © 2003, Mosby, Inc. All rights reserved.

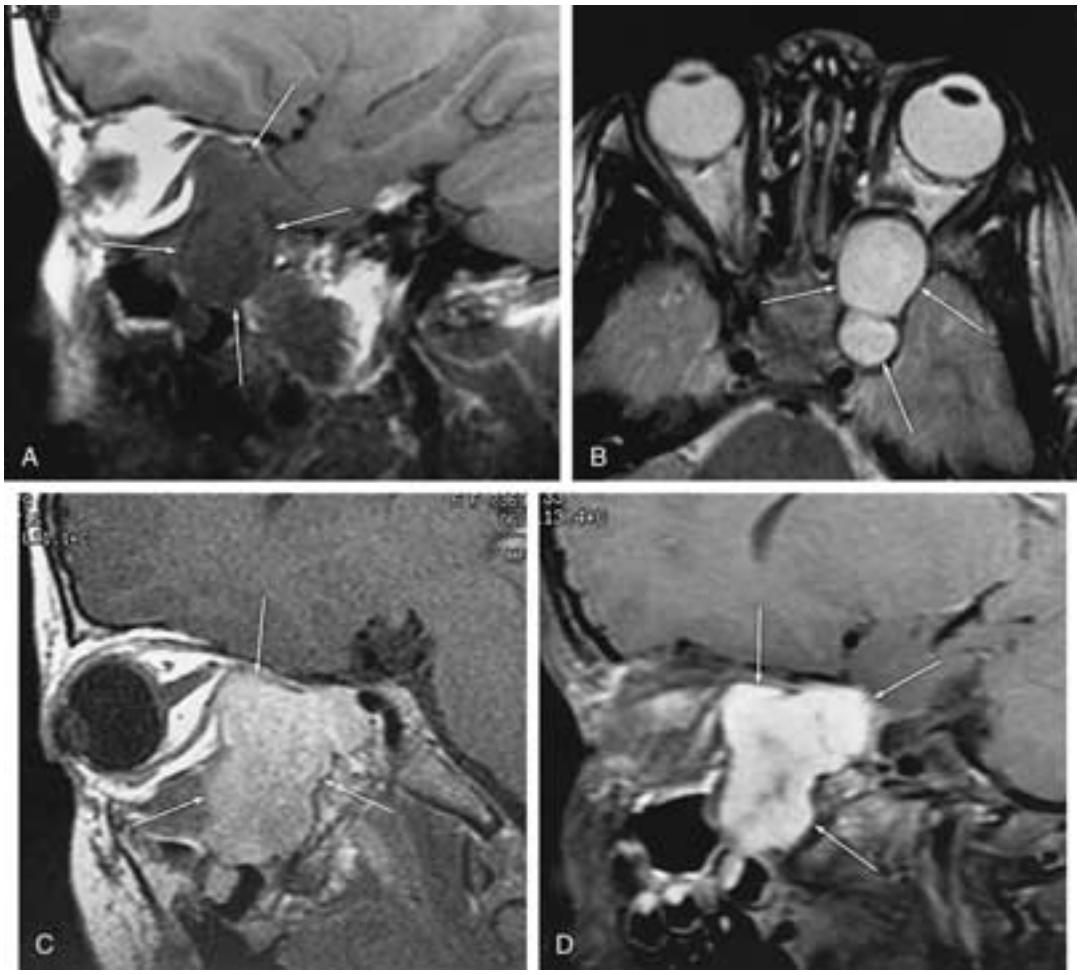

VIEW IMAGE

FIGURE 9-157 Rhabdomyosarcoma (6-year-old girl). **A**, Sagittal T1-weighted MR image shows a large mass (*arrows*) in the pterygopalatine fossa and infratemporal fossa. **B**, Axial T2-weighted MR image shows extension of tumor into the left orbital apex. Lesion appears hyperintense to brain. **C**, Enhanced sagittal T1-weighted MR image shows marked enhancement of tumor (*arrows*). Note extension into the orbital apex with elevation of the inferior rectus. Note also extension into the anterior aspect of the cavernous sinus. **D**, Enhanced fat-suppression sagittal T1-weighted MR image. Note apparent marked enhancement of tumor (*arrows*). (From Mafee MF et al. Rhabdomyosarcoma of the orbit: evaluation with MR imaging and CT. Radiol Clin North Am 1998;36:1215–1227.)

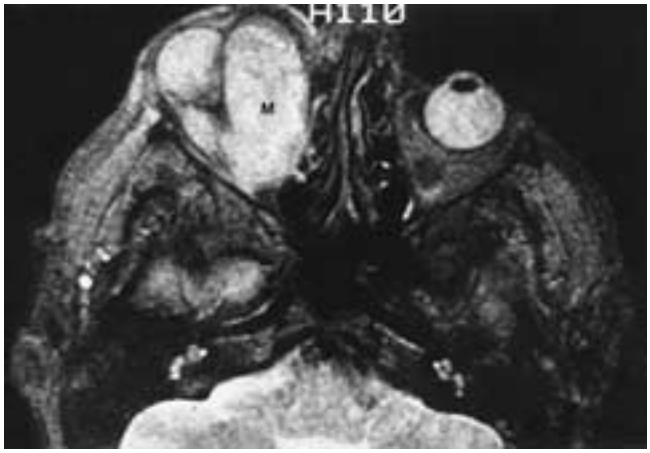

VIEW IMAGE

FIGURE 9-158 Rhabdomyosarcoma. Axial T2-weighted MR image shows a large orbital mass (*M*) in this 60-year-old man compatible with rhabdomyosarcoma.

a problem for the radiologist in distinguishing residual tumor from invasive fungal infection. The resultant bone destruction or remodeling about the orbit and cranium is common with advanced disease and is best evaluated with CT. It is still possible, however, to detect bony invasion by the distortion of the bone marrow signal on MR imaging, especially after the administration of contrast.

Many common and less common orbital and head and neck neoplasms, however, such as hemangiomas, lymphangiomas, lymphoma, leukemic infiltration, plexiform neurofibromatosis, aggressive fibromatosis, pseudorheumatoid nodule, and pseudotumor, can appear similar to RMS, with similar CT and MR imaging characteristics. Thus, the findings are nonspecific in many cases, necessitating a tissue diagnosis. Subperiosteal hematoma in children may simulate RMS. MR imaging in these cases may be extremely valuable to make the correct diagnosis. Orbital pseudotumors in children can simulate orbital RMS (Fig. 9-159), as can aggressive fibromatosis RMS (Fig. 9-152). Capillary hem-

Copyright © 2003, Mosby, Inc. All rights reserved.

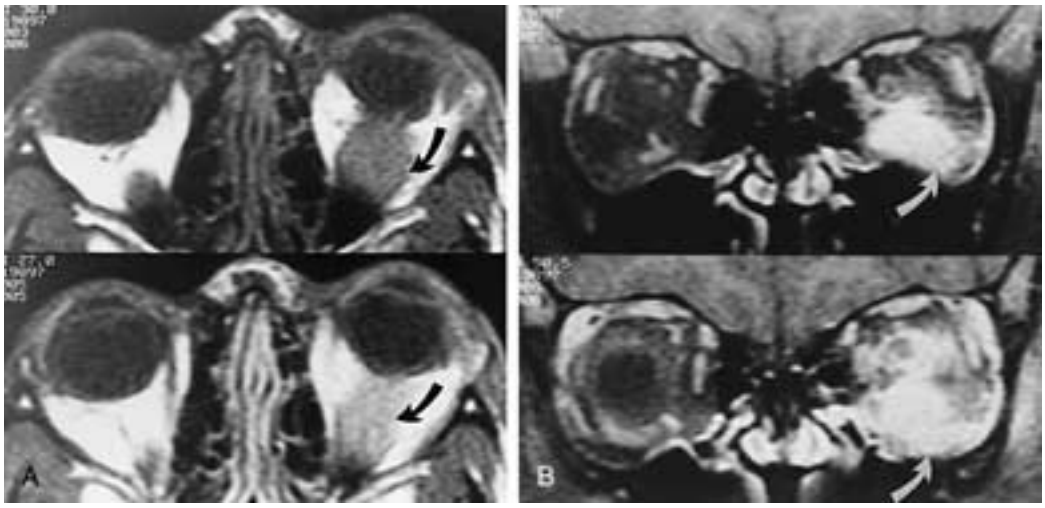

VIEW IMAGE

FIGURE 9-159 Pseudotumor. **A**, Nonenhanced (*top*) and enhanced (*bottom*) axial T1-weighted MR images showing thickening and enhancement of the left inferior rectus (*arrows*). **B**, Enhanced fat-suppression coronal T1-weighted MR images showing marked enhancement of this pseudotumor (*arrows*). This MR appearance can easily simulate rhabdomyosarcoma. (From Mafee MF et al. Rhabdomyosarcoma of the orbit: evaluation with MR imaging and CT. Radiol Clin North Am 1998;36:1215–1227.)

angiomas and other vasculogenic lesions (Fig. 9-160), including vascular malformations, may also simulate RMS, and dynamic CT may be very helpful in the diagnosis of capillary hemangiomas. At times, RMS may present with a clinical picture and imaging features of an orbital subperiosteal abscess.[155] In adults, lymphoma and primary and secondary orbital tumors should be included in the differential diagnosis (Fig. 9-161).

Imaging also allows planning of biopsy and surgery. Although superficial disease is easily accessible to the clinician, deeply seated masses present technical difficulties. Radiologic guidance (i.e., CT) may be used to direct aspiration biopsy safely, with minimal risk and morbidity. Further workup for staging should be performed including chest radiographs, a blood count, liver function tests, skeletal survey, bone marrow biopsy, etc. Surgery is performed to remove the maximum amount of tumor tissue that is safely feasible while minimizing the resulting deformity. Thus, staging depends on resection of the primary mass, the amount of residual tumor, and the presence of distant metastases, which usually involve the lung, bone marrow, lymph nodes, and brain. Due to the absence of lymphatics about the orbit, regional lymph nodes tend not to be involved, at least until advanced spread has occurred.

Once the diagnosis is confirmed by pathologic analysis, prompt treatment is initiated to maximize the patient's chances of survival. Currently, treatment includes biopsy or excision and radiation therapy with adjuvant chemotherapy. Smaller focal lesions may be entirely removed safely, whereas larger masses or metastatic lesions usually have

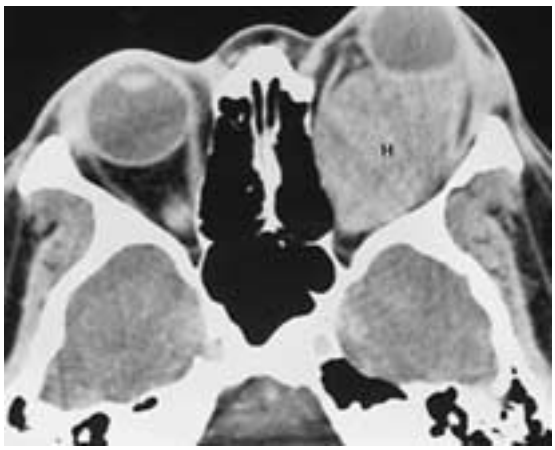

VIEW IMAGE

FIGURE 9-160 Sclerosing hemangioma (16-year-old girl). Enhanced axial CT scan shows a large, moderately enhancing intraconal mass compatible with hemangioma (*H*). (From Mafee MF et al. Rhabdomyosarcoma of the orbit: evaluation with MR imaging and CT. Radiol Clin North Am 1998;36:1215–1227.)

FIGURE 9-161 Malignant melanoma. Enhanced axial CT scan shows a large mass (*M*). This was diagnosed as primary orbital malignant melanoma, because no other primary could be identified. (From Mafee MF et al. Rhabdomyosarcoma of the orbit: evaluation with MR imaging and CT. Radiol Clin North Am 1998;36:1215–1227.)

VIEW IMAGE

Copyright © 2003, Mosby, Inc. All rights reserved.

VIEW IMAGE

FIGURE 9-162 Axial CT scans with coronal reconstruction show recurrence of rhabdomyosarcoma in a 5-year-old girl. (From Mafee MF et al. Rhabdomyosarcoma of the orbit: evaluation with MR imaging and CT. Radiol Clin North Am 1998;36:1215–1227.)

residual disease after extirpation. Regardless, radiation therapy helps control the local residual tumor, which may be microscopic and/or due to incomplete excision. The addition of combination chemotherapy has been shown to improve survival. Complete resection of a local tumor or minimal residual tumor after removal of regional disease allows 90% or greater survival after 5 years. With significant residual tumor, the prognosis drops to 35%. The major side effects of therapy are vision problems due to cataracts, retinopathy, and corneal scarring from keratoconjunctivitis. Other late side effects include bony orbital deformity and enophthalmos, secondary malignancy (leukemia), and leukoencephalopathy. Improvements in treatment regimens and decreases in radiation doses have decreased secondary complications.

After treatment is instituted, cross-sectional imaging can be used to objectively monitor tumor regression or residual and recurrent disease (Figs. 9-162 and 9-163). In fact, an increased risk of relapse is associated with posttreatment residual tissue, and residual tissue can be shown with CT or MR imaging prior to any clinical relapse. A relapse, in turn, denotes a poor prognosis; thus, early detection is essential. Clinical abnormalities and symptoms usually occur with recurrence, initiating further imaging to confirm the suspicion. Recurrent disease usually occurs locally in the surgical bed or regionally in the adjacent central nervous system. It is difficult to differentiate fibrosis and scarring from active tumor with CT and MR imaging, particularly if no baseline study is available. On the other hand, healing of bone destruction may signify a response to therapy and can be easily evaluated by CT. Furthermore, MR imaging of the brain may be helpful to monitor for, or follow up on, associated parenchymal leukoencephalopathic changes resulting from chemotherapy and radiation therapy, which may be subtle in the early stages. CT is less sensitive in this latter situation.

MESENCHYMAL CHONDROSARCOMA OF THE ORBIT

Extraskeletal malignant cartilaginous tumors are subdivided into two major categories: mesenchymal and myxoid chondrosarcoma. Mesenchymal chondrosarcomas commonly occur within the bones. Extraskeletal locations include the head and neck, the cranial and spinal dura mater, and, less frequently, the leg, especially the thigh.[156] Orbital mesenchymal chondrosarcoma (OMC) remains an extremely rare entity occurring more frequently in young women.[156–159] The most common presenting symptom of OMC is proptosis, with orbital pain, diplopia, and headache. Histologically, OMC is relatively distinct, containing islands of chondroid tissue. The cartilaginous areas have the appearance of mature cartilage. Most of them contain amorphic calcification and foci of ossification of the cartilaginous matrix.[156, 158] Other areas of undifferentiated mesenchymal tissue are seen, with a predominance of spindle-shaped cells. Mitoses are not frequent. In addition, areas of dilated vascular channels in the stroma can be seen that histologically resemble hemangiopericytoma.[156–159]

CT imaging characteristics include a relatively well-defined soft-tissue mass with areas of mottled, coarse calcification (Fig. 9-164A), and moderate, delayed contrast enhancement is noted. MR imaging characteristics include a signal intensity lower than or equal to that of brain on T1-weighted images and isointense to brain on T2-weighted images, with moderate enhancement after gadolinium contrast administration (Fig. 9-164B-F). The calcified component of the tumor shows low signal on both T1-weighted and T2-weighted MR images (Fig. 9-164B,F). On enhanced T1-weighted MR images, however, mild enhancement is seen even within the calcified components (Fig. 9-164D,E).[156]

The differential diagnosis for an intraorbital calcified mass includes meningioma, sclerosing hemangioma, hemangiopericytoma, vascular malformation, varix, and orbital amyloidosis.[8, 156] Calcification in cavernous hemangioma, fibrous histiocytoma, fibrocystoma, schwannoma, neurofibroma, and optic glioma is extremely rare. Hemangiopericytomas may occasionally demonstrate dystrophic calcification, which is usually seen after recurrence of the lesion.[156] Fibrous histiocytomas are the most common adult mesenchymal tumors of the orbit, presenting as well-circumscribed intraconal or extraconal masses with moderate to marked enhancement. The more cellular fibrous histiocytomas may have moderately or markedly low signal intensity on T2-weighted MR images.[156] This MR appearance may mimic that of OMC; however, unlike OMC, fibrous histiocytomas do not show calcification on CT scans. Orbital amyloidosis demonstrates a soft-tissue mass with coarse, streaky, amorphous calcification diffusely scattered throughout the lesion (Figs. 9-93 and 9-94). In addition, certain areas that appear to be calcific density actually represent amyloid (Figs. 9-93 and 9-94).[156]

Copyright © 2003, Mosby, Inc. All rights reserved.

LACRIMAL GLAND AND FOSSA LESIONS

The lacrimal gland is about the size and shape of an almond and is located in the superolateral extraconal orbital fat in the lacrimal fossa, adjacent to the tendons of the superior and lateral rectus muscles. The more anterior palpebral lobe is separated from the deeper orbital lobe by the lateral horn of the levator muscle aponeurosis.[24, 120] The lacrimal gland is a modified salivary gland, and it can be involved by a wide spectrum of orbital pathology. Meticulous clinical and preoperative imaging of these patients is imperative so that an inappropriate incisional biopsy is avoided. This situation is especially true when a benign mixed tumor of the lacrimal gland is suspected. This tumor requires en bloc excision through a lateral orbitotomy to ensure complete extirpation and prevent late recurrences.[24] If an incisional biopsy of a benign mixed tumor is performed, there is an increased likelihood of operative tumor spillage and thus late recurrences.[24, 160, 161] The excellent prognosis of benign mixed tumor, provided that it is completely removed at the first surgery, is now widely accepted.

Lesions of the lacrimal gland and fossa present special problems in diagnosis and management. Because of the importance of preoperative diagnosis, all clinical ancillary findings should be integrated into the assessment of individual cases. In general, epithelial tumors represent about 50% of the masses involving the lacrimal gland. The remaining 50% of lacrimal gland masses are either lymphoid or inflammatory in nature.[24, 160] Metastasis to the parenchyma of the lacrimal gland is rare.[24] Dermoid cysts are not true lacrimal gland tumors; rather, they arise from epithelial rests located in the orbit, particularly in the superolateral quadrant. Epithelial cysts, on the other hand, are intrinsic lesions that result from dilation of the lacrimal ducts.[24, 160]

Inflammatory diseases of the lacrimal gland can be divided into two categories, acute and chronic.[24] Acute dacryoadenitis (bacterial or viral) is more commonly seen in children and in younger people.[24, 156, 162, 163] It may be related to trauma and clinically is associated with local

VIEW IMAGE

FIGURE 9-163 Rhabdomyosarcoma (4-year-old boy). **A**, Axial T2-weighted MR image shows a predominantly hyperintense mass (*arrows*). **B**, Enhanced axial T1-weighted MR image. Note enhancement of tumor (*arrows*). Enhanced, fat-suppressed T1-weighted image. Note enhancement of tumor (*arrows*). Enhanced fat-suppression axial T1-weighted MR images (**C** and **D**), taken 6 months after completion of chemotherapy and radiation therapy. Note decreased size of mass (*arrows*). (From Mafee MF et al. Rhabdomyosarcoma of the orbit: evaluation with MR imaging and CT. Radiol Clin North Am 1998;36:1215–1227.)

Copyright © 2003, Mosby, Inc. All rights reserved.

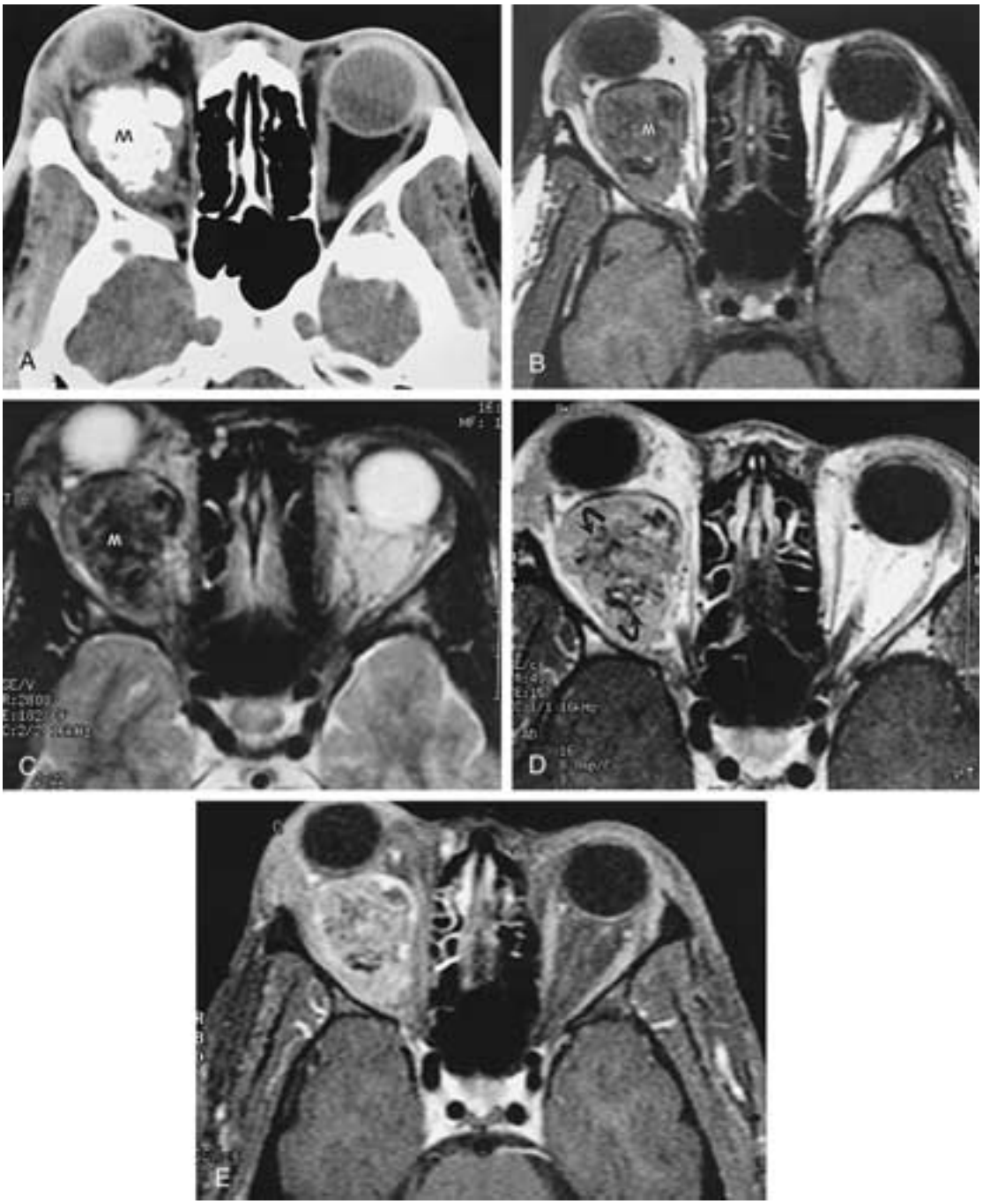

VIEW IMAGE

FIGURE 9-164 Mesenchymal chondrosarcoma. **A**, Enhanced axial CT scan shows a heavily calcified mass (*M*) in the right retrobulbar space. **B**, Axial nonenhanced T1-weighted MR image shows that the mass (*M*) is isointense to brain. Note areas of hypointensity related to more dense calcification. **C**, Axial, fast spin-echo, T2-weighted MR image shows that the mass (*M*) is heterogeneous but markedly hypointense, related to intratumoral foci of calcifications. **D**, Axial-enhanced T1-weighted MR image shows that the mass is rather hypervascular, as evidenced by marked contrast enhancement. The calcified component of the mass shows less enhancement (*arrows*). **E**, Axial fat-suppressed, enhanced T1-weighted MR image shows marked tumor enhancement. (From Koeller KK. Mesenchymal chondrosarcoma and simulating lesions of the orbit. Radiol Clin North Am 1999;37:203–217.)

tenderness, erythema, lid swelling, conjunctival chemosis, discharge or suppuration, enlarged preauricular and cervical nodes, and systemic findings.[24, 156] Acute dacryoadenitis is usually unilateral and tends to respond very rapidly to therapy.[24, 156] It may be part of the spectrum of idiopathic inflammatory orbital pseudotumor, and this diagnosis is made often on the basis of the clinical presentation, CT findings, and the prompt and favorable response to the administration of systemic corticosteroids.[24, 156, 163, 164]

Chronic dacryoadenitis may follow acute infection or may be caused by sarcoidosis (Fig. 9-165), thyroid ophthalmopathy, Mikulicz's syndrome, Sjogren's syn-

Copyright © 2003, Mosby, Inc. All rights reserved.

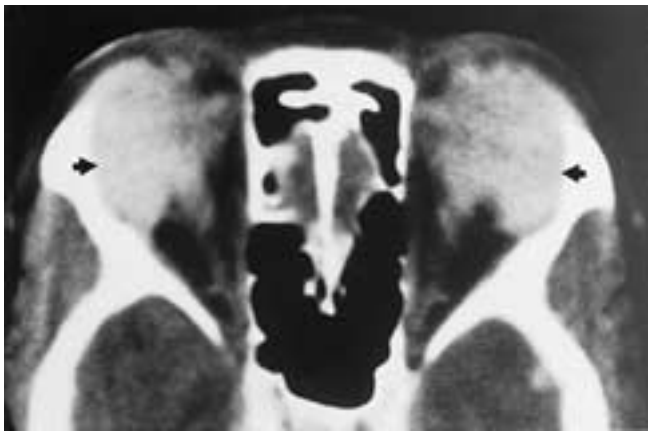

FIGURE 9-165 Sarcoidosis. Axial CT scan shows bilateral diffuse enlargement of entire lacrimal glands (*arrows*).

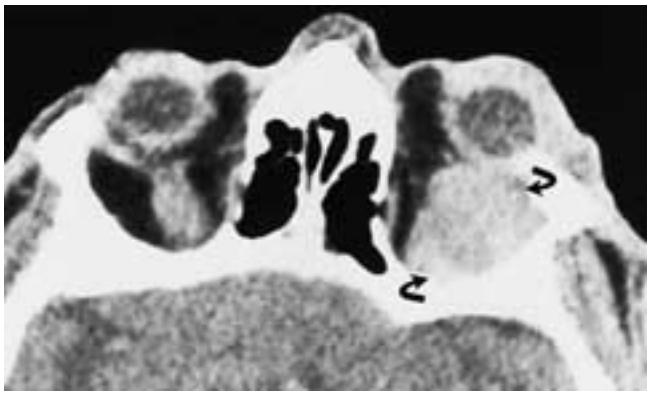

FIGURE 9-167 Lymphoma. Axial postcontrast CT scan shows a large mass in the superior temporal quadrant extending posteriorly to the orbital apex (*arrows*); the lacrimal gland is totally involved. Note the postsurgical changes in the lateral wall of the left orbit.

drome, ''sclerosing pseudotumors'' (Fig. 9-166), and Wegener's granulomatosis. In sarcoid there is usually bilateral disease, with either symmetric or asymmetric lacrimal gland enlargement (Fig. 9-165). Mikulicz's syndrome is a nonspecific swelling of the lacrimal gland and salivary glands associated with conditions such as leukemia, lymphoma, pseudotumor, tuberculosis, syphilis, and sarcoidosis. In Sjogren's syndrome, there is enlargement of and lymphocytic infiltration of the lacrimal glands. Half of these patients have a connective tissue disease such as rheumatoid arthritis, systemic lupus erythematosus, scleroderma, or polymyositis. Inflammatory pseudotumor in the region of the lacrimal gland accounts for about 15% of all orbital pseudotumors (Fig. 9-107).[156, 164] Although this disease is rare in the very young, the age variation is quite wide. The most common symptoms include proptosis, swollen lids, pain, and diplopia, and in the majority of patients the duration of symptoms is less than 6 months. Wegener's granulomatosis is characterized by necrotizing granulomas of the respiratory tract, renal failure, and a disseminated focal necrotizing angiitis of small arteries and veins.[24, 82, 165] Ocular involvement in Wegener's granulomatosis is common, affecting 40% of patients with generalized disease.[24, 82] Involvement of the lacrimal gland is not uncommon (Fig. 9-91). Histologic examination of involved lacrimal glands shows infiltration with histiocytes, plasma cells, lymphocytes, polymorphs, and eosinophils, with giant cell formation.[24, 164] Massive enlargement of lacrimal glands may be present and has been demonstrated on CT.[24, 164] Lymphomatous lesions of the lacrimal gland include a broad spectrum ranging from reactive lymphoid hyperplasia to malignant lymphomas of various types (Fig. 9-167). It can be very difficult to differentiate pathologically between benign lymphocytic infiltration and lymphoma other than to note in a general way that lymphomas tend to occur in older patients. Shield et al., in a review of 645 space-occupying orbital lesions that underwent biopsy, found 71 cases of lymphocytic and plasmacytic lesions.[165, 166] Of these, 12 were located in the lacrimal gland.

Benign mixed lacrimal gland tumors tend to occur in patients in the third to sixth decades of life. The tumors present with slowly progressive, painless upper lid swelling, proptosis, or both, without inflammatory symptoms or signs (Fig. 9-168). Malignant tumors also occur but may not be diagnosed as such on imaging unless there is adjacent bone destruction.

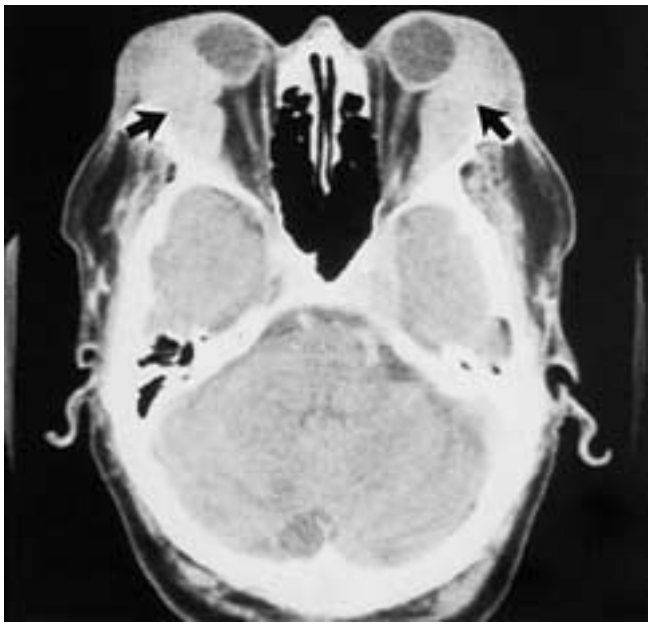

FIGURE 9-166 Lacrimal gland pseudotumor. An 80-year-old patient with swelling of both eyes. Axial postcontrast CT scan shows bilateral lobular enlargement of the lacrimal glands (*arrows*).

Diagnostic Imaging

Inflammatory lesions of the lacrimal gland cause diffuse enlargement of the gland. Contrast enhancement may be marked, and there may be associated acute lateral rectus muscle myositis. There may be associated scleritis with fluid in Tenon's space and a ring of uveoscleral enhancement. In chronic dacryoadenitis, the gland also shows diffuse oblong enlargement (Figs. 9-165 and 9-166). The glands may be massively enlarged in cases of sarcoidosis (Figs. 9-165), or in other conditions such as Mikulicz's syndrome, pseudotu-

Copyright © 2003, Mosby, Inc. All rights reserved.

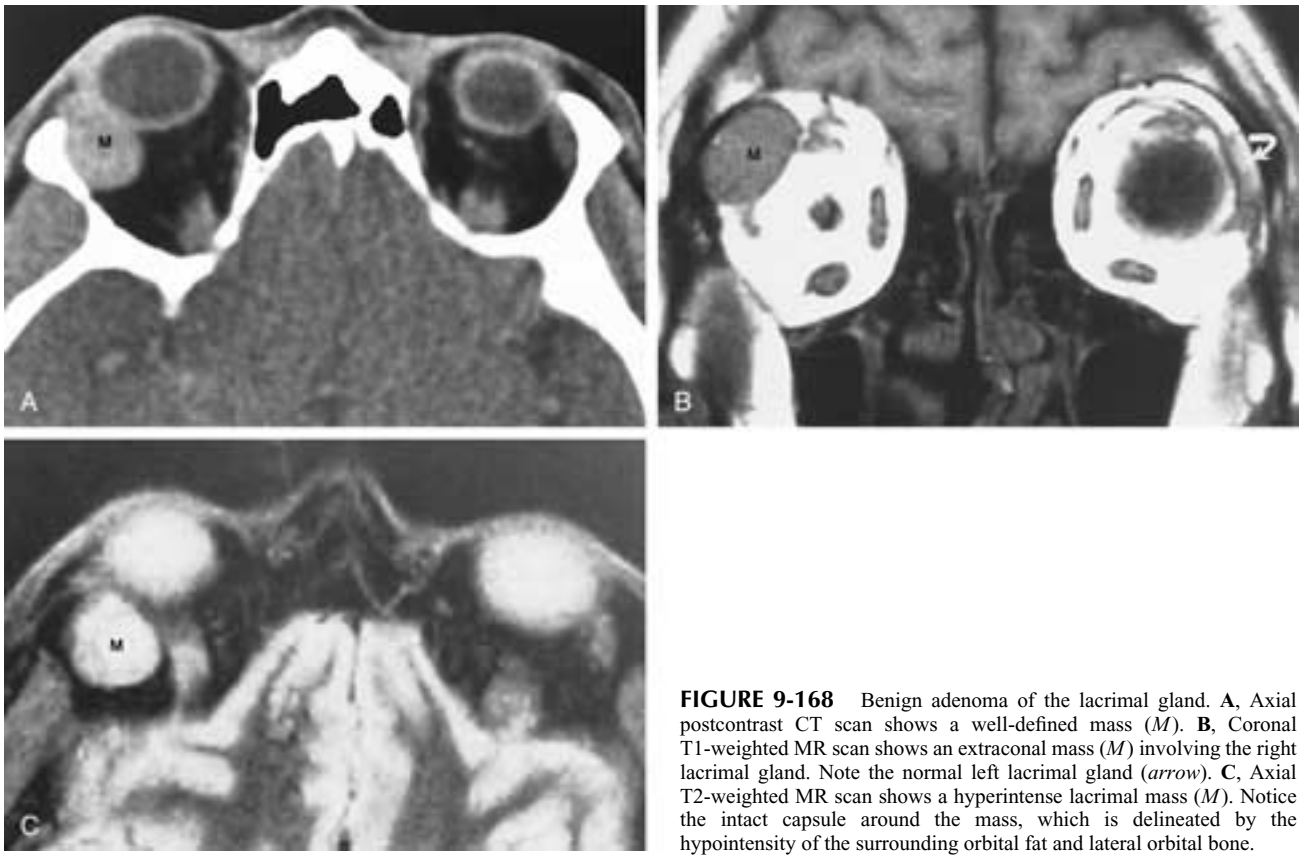

FIGURE 9-168 Benign adenoma of the lacrimal gland. **A**, Axial postcontrast CT scan shows a well-defined mass (*M*). **B**, Coronal T1-weighted MR scan shows an extraconal mass (*M*) involving the right lacrimal gland. Note the normal left lacrimal gland (*arrow*). **C**, Axial T2-weighted MR scan shows a hyperintense lacrimal mass (*M*). Notice the intact capsule around the mass, which is delineated by the hypointensity of the surrounding orbital fat and lateral orbital bone.

VIEW IMAGE

mor (Fig. 9-166), and Wegener's granulomatosis.[24, 82, 164] However, in these patients, scleral enhancement is not an associated feature, as it is in patients with acute inflammation.

Benign and malignant lymphoid tumors situated in the lacrimal gland also display diffuse enlargement with oblong contouring of the gland (Fig. 9-107).[24, 164] However, these lesions are usually bulky (Fig. 9-110), frequently have anterior and posterior extension, and mold and drape themselves on the globe. In general, inflammatory processes and lymphomas tend to involve all aspects of the lacrimal gland, often including its palpebral lobe (Figs. 9-107 and 9-110). By comparison, neoplastic lesions rarely originate in the palpebral lobe of the gland, and therefore there is often only posterior extension of the mass rather than anterior growth beyond the orbital rim (Figs. 9-168 to 9-170).

Because the lacrimal gland is histologically similar to a salivary gland, the diseases that affect these glands are similar and epithelial tumors represent 50% of the masses involving the lacrimal gland.[24, 160, 164] Half of these tumors are pleomorphic (benign mixed) adenomas, and the other half are malignant lesions. Of the malignant tumors,

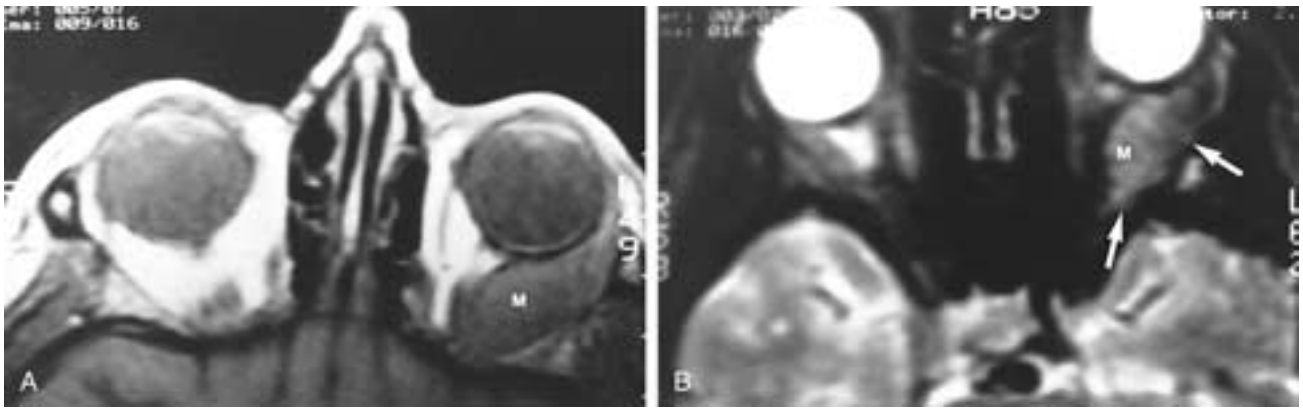

FIGURE 9-169 Adenocarcinoma of the lacrimal gland. (**A**) Axial T1-weighted MR scan and (**B**) Axial T2-weighted MR scan show a large mass (*M*). The lateral orbital wall is irregular (*arrows*). CT scans showed erosion of bone.

VIEW IMAGE

Copyright © 2003, Mosby, Inc. All rights reserved.

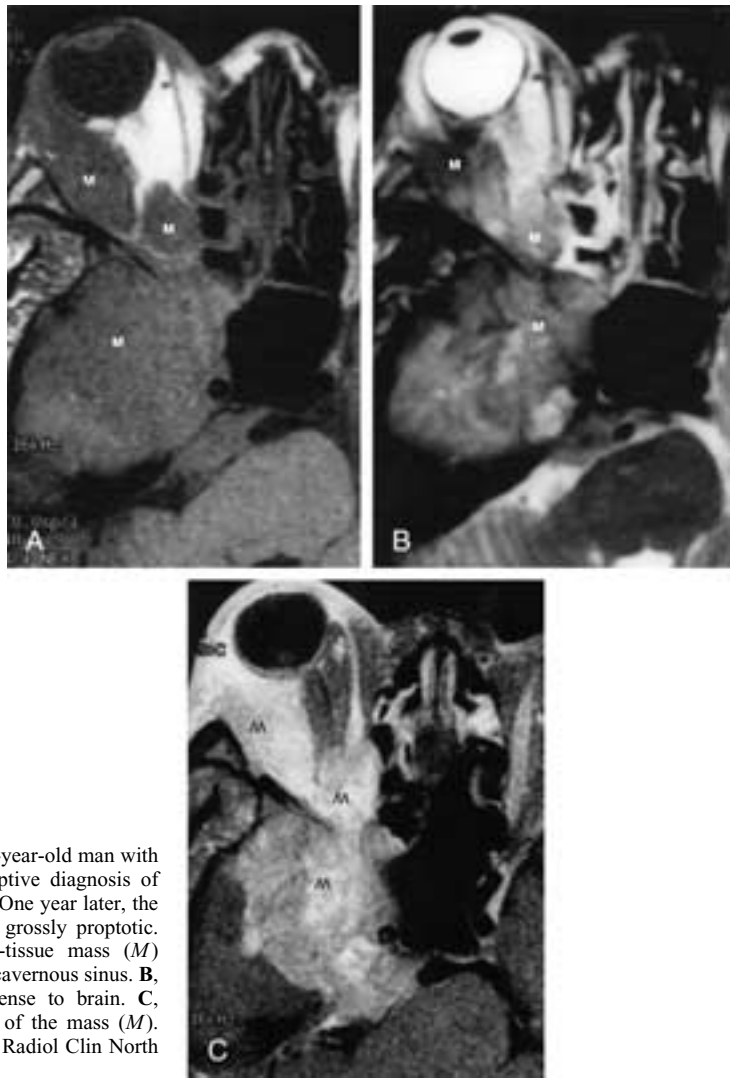

VIEW IMAGE

FIGURE 9-170 Adenoid cystic carcinoma of lacrimal gland. A 42-year-old man with decreased vision and painless proptosis of the right eye. A presumptive diagnosis of cavernous meningioma was made based on MR study (not shown). **A**, One year later, the patient returned for a follow-up study. Clinically, the right eye was grossly proptotic. Unenhanced axial T1-weighted MR image shows infiltrating soft-tissue mass (*M*) extending into right middle cranial fossa with involvement of adjacent cavernous sinus. **B**, Axial T2-weighted MR image shows that the mass (*M*) is isointense to brain. **C**, Axial-enhanced T1-weighted MR image shows diffuse enhancement of the mass (*M*). (From Mafee MF et al. Lacrimal gland tumors and simulating lesions. Radiol Clin North Am 1999;37:219–239.)

adenocystic carcinoma is the most common, followed by pleomorphic (malignant mixed tumor, carcinoma ex-pleomorphic adenoma), mucoepidermoid carcinoma, adenocarcinoma (Fig. 9-167), squamous cell carcinoma, and undifferentiated (anaplastic) carcinoma. A significant number of these tumors arise within pleomorphic adenomas as carcinoma ex-pleomorphic adenomas.[24, 158] Benign mixed tumors may undergo spontaneous malignant degeneration and are increasingly likely to undergo such malignant degeneration the longer they exist.[158, 161, 165] In such a malignant mixed tumor, the malignant cell clone develops from the preexisting benign mixed tumor, and the malignancy is often a poorly differentiated adenocarcinoma or an adenoid cystic carcinoma.[24, 164] In general, patients with these carcinomas have a poor prognosis.[24, 157]

In 1979 Stewart et al. described a scheme for the clinical diagnosis and management of lacrimal fossa pathology that classified these lesions using distinguishing clinical features and plain film radiographs.[157] Jakobiec et al.[161] performed a study evaluating the clinical and CT findings in 39 patients with four different kinds of lacrimal gland swelling. Sixteen of these patients had a parenchymal benign or malignant tumor. This study added a new diagnostic criterion, the ''contour analysis'' of the shape of the mass, as a factor to be combined with the clinical history. Stewart et al. reviewed 31 cases of benign and malignant lacrimal gland masses.[157] Fourteen patients had benign mixed lacrimal gland tumors, and 13 had pressure changes characterized by enlargement of the lacrimal fossa without destruction of bone. Sclerosis of bone was present in one patient. Malignant neoplasms accounted for 17 of the 31 tumors. Twelve patients had pressure changes, two had no bone changes, and three showed destructive changes. Three patients with pressure changes and malignant tumors had calcification in the lacrimal gland fossa. Two patients had sclerosis of bone adjacent to the lacrimal fossa.

In the series of Jakobiec et al.,[161] benign tumors had smooth, encapsulated outlines, whereas the malignant tumors displayed microserrations indicative of infiltration. In their series, inflammatory conditions demonstrated diffuse, compressed, and molded enlargement of the lacrimal gland in an oblong fashion, and there were no associated bone defects. This study concluded that well-encapsulated, rounded masses of long duration were likely to be benign mixed tumors. The epithelial neoplasms probably began unicentrally within the lacrimal gland and

Copyright © 2003, Mosby, Inc. All rights reserved.

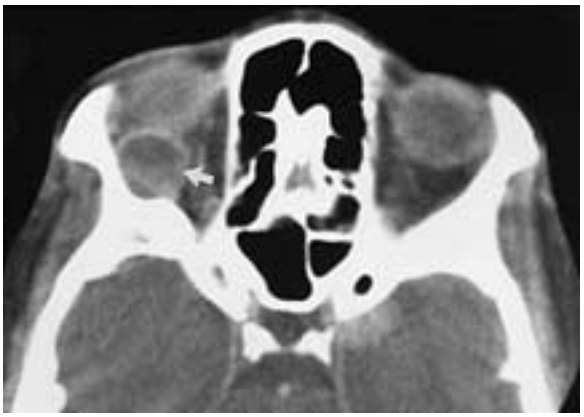

VIEW IMAGE

FIGURE 9-171 Lacrimal gland cyst. Axial CT scan shows a lacrimal gland cyst (*arrow*). This epithelial cyst developed in the orbital component of the lacrimal gland. (From Mafee MF et al. Lacrimal gland tumors and simulating lesions. Radiol Clin North Am 1999;37:219–239.)

grew in a centrifugal fashion in all directions, sometimes indenting the globe, distorting its muscle cone, and creating fossa or bone destruction in the orbital walls.[161] By contrast, inflammatory and lymphoid lesions of the lacrimal gland were seen as diffuse expansions of the lacrimal gland, and the lesions molded themselves to preexisting orbital structures without eroding bone or enlarging the orbit.[161, 164] The study found that the stroma of the epithelial tumors was often hyalinized or even cartilaginous and that this tissue was less likely than inflammatory or lymphoid tissue to mold, in a putty-like fashion, to the isthmus between the globe and the orbital bone.[161, 164]

Bony changes in the lacrimal gland fossa may be produced by either benign or malignant epithelial tumors.[24] However, bone changes also can be produced by a lacrimal gland cyst (Fig. 9-171) and by other orbital lesions such as schwannoma, neurofibroma, fibrous histiocytoma, and lesions originating within the subperiosteal space or bone such as a benign orbital cyst, hematic cyst (Fig. 9-172), cholesterol granuloma, LCH (in particular eosinophilic granuloma), dermoid cyst, epidermoid cyst, or metastatic carcinoma.[161] Lymphoid and inflammatory processes rarely produce bone changes.[24]

MISCELLANEOUS LACRIMAL GLAND LESIONS

Amyloid Tumor of the Lacrimal Gland

Infiltration of the lacrimal gland with amyloid is a very uncommon disorder.[164] Amyloidosis of the lacrimal gland and orbit usually is associated with the primary localized variant of the disorder, although it can be seen as a secondary form of the disease due to degeneration and amyloid depositions.[164] Isolated lacrimal gland involvement is rare and may mimic inflammatory, infiltrative, and even neoplastic diseases of the lacrimal gland. The CT and MR imaging findings of lacrimal gland amyloidosis consist of an enlarged lacrimal gland with or without calcification. Amorphous calcification of the lacrimal gland should raise the possibility of lacrimal amyloidosis (Fig. 9-94A), and calcifications may also be multiple, resembling phleboliths.[164]

Kimura's Disease

Kimura's disease is a chronic self-limited inflammatory condition of unknown etiology and a rare cause of a tumor-like mass in the head and neck.[164] Kimura et al.[167] reported this entity in 1948. Kimura's disease was long regarded as synonymous with angiolymphoid hyperplasia with eosinophilia; however, it is now clear that they are separate entities despite having some similar histologic features (also see Chapter 36).[164] Patients typically present with painless tumor-like nodules in the head and neck region, often associated with regional lymphadenopathy. Peripheral blood eosinophilia and an elevated serum level of IgE are almost always present.[164] Histologically, Kimura's disease is characterized by a mixed lymphoeosinophilic infiltration, reactive lymphoid follicles, ill-defined fibrosis, and capillary proliferation. Major salivary glands as well as the lacrimal gland may be involved in Kimura's disease.[164] The CT appearance of Kimura's disease is shown in Figure 9-173. The differential diagnosis of Kimura's disease of the lacrimal gland includes dacryoadenitis, sarcoidosis, pseudotumor, lymphoma, and lacrimal gland and fossa tumors.[164]

SECONDARY ORBITAL TUMORS

Malignant tumors of the sinonasal cavities may invade the orbit directly. Tumors of the skin of the face, such as basal cell and squamous cell carcinomas and malignant melanoma, can invade the orbit. The inferior orbital fissure is a pathway for tumors arising from or extending into the pterygopalatine or infratemporal fossae. Adenoid cystic tumors of the oral cavity and sinonasal cavities, as well as squamous cell carcinoma and lymphoma of the sinonasal-oral cavities, can extend along the perineural-perivascular pathways into the pterygopalatine fossa and then into the

VIEW IMAGE

FIGURE 9-172 Bilateral orbital metastases from a carcinoma of the breast. Axial postcontrast CT scan through the midorbits demonstrates a homogeneous mass in the retrobulbar space of the left orbit with no bony involvement. Note partial obliteration of the extraocular muscles and the optic nerve. There is asymmetric enlargement of the mid- to posterior portion of the right lateral rectus muscle. (Courtesy of Mahmood Mafee, MD, University of Illinois at Chicago, Chicago, Illinois. From Carroll GS, Barrett GH, Fleming JC, et al. Peripheral Nerve Tumors of the Orbit. Radiol Clin North Am 1999 Jan;37(1):166.)

Copyright © 2003, Mosby, Inc. All rights reserved.

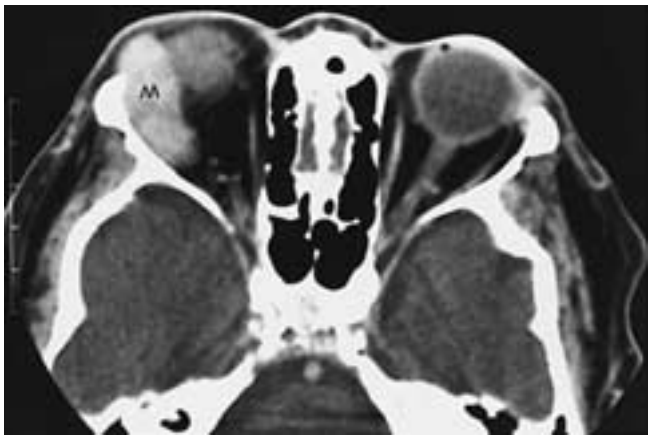

FIGURE 9-173 Kimura disease. Axial-enhanced CT scan shows moderate enhancement of a right lacrimal gland mass (*M*). This may not be differentiated from lymphoma, pseudotumor, sarcoid, Wegener's granuloma and even epithelial tumor of lacrimal gland. (From Mafee MF et al. Lacrimal gland tumors and simulating lesions. Radiol Clin North Am 1999;37:219–239.)

VIEW IMAGE

orbit. Intracranial lesions such as meningioma may extend through the posterolateral wall of the orbit, the optic canal, the sphenoid fissures, the ethmoidal foramina, or less resistant bony walls such as the lamina papyracea and orbital roof. Metastases to the orbit are most commonly the result of breast carcinoma in women (Fig. 9-172) and carcinoma of the lung, kidney, or prostate in men (Fig. 9-174). In children, metastases are from primary neuroblastoma, Ewing's sarcoma, and Wilms' tumor. Metastases can simulate primary tumors, myositis, or diffuse orbital pseudotumor (notably breast carcinoma), and a multiplicity of lesions can be helpful in suggesting the diagnosis of metastatic disease. Metastatic lesions may occur in any of the orbital compartments.[168] At times, a metastatic deposit may be single and well defined, simulating benign orbital tumors. This appearance has been seen in patients with known or unknown primary malignant melanoma and carcinoid tumor. In patients who have undergone enucleation for malignant uveal melanoma, retinoblastoma, and ocular medulloepithelioma, any tumor mass within the surgical bed should be considered a metastatic recurrence.

ADDITIONAL PATHOLOGIES OF THE EXTRAOCULAR MUSCLES

Ocular Motility Disorders

Ocular muscle disturbances (strabismus) are relatively common, occurring at a rate of approximately 2% to 4%.[15] While the onset is usually in infancy or early childhood, acquired forms may occur at any age. If the object being viewed does not fall on the macula of both eyes, strabismus exists and the position of the nonaligned eye determines the description of the type of deviation (esotropia = inward deviation, exotropia = outward deviation; vertical imbalance described as hyper- or hypotropia).[15]

Strabismus is frequently divided into two types based on the diagnostic and therapeutic implications. In comitant types of strabismus, movement is not limited in any field of gaze, nor is there evidence of a paretic muscle. The etiology is thought to be abnormalities in higher brain centers. By contrast, noncomitant strabismus is characterized by limited ocular movement due to lesions involving the brainstem, cerebral centers, or cranial nerves; to muscle damage; or to any process causing restricted movement of the EOMs and resulting in asymmetric movements. These two possible etiologies of noncomitant strabismus, neurologic and restrictive, can often be distinguished by a forced duction test that shows no impediment to passive movement of the eye with forceps when there is neurologic damage compared to limitation on attempted movement of the globe in restrictive disease of the EOM. For example, in a diabetic lateral rectus palsy, the eye may be passively moved freely, whereas in thyroid myopathy, when an attempt is made to rotate the eye with a forceps, the examiner experiences restriction to movement in one or more fields of gaze.[15]

The use of CT and MR imaging has improved our understanding of many congenital and acquired conditions causing strabismus. This results in more appropriate therapeutic intervention and gives insight into the pathophysiology of these conditions.[15]

When evaluating the relative size of EOMs, particularly the horizontal muscles (the medial rectus and lateral rectus), it is important to know where the patient is fixing his or her gaze at the time of scanning. The Sherrington law of reciprocal innervation states that when the agonist muscle contracts, an inhibitory impulse is sent to the antagonist muscle, which then relaxes and lengthens. These actions are essential for normal full range of ocular movement. Therefore, when the patient is looking at the right field of gaze, there is an increase in the size of the contracting right lateral and left medial rectus muscles and a decrease in the relaxed left lateral and right medial rectus muscles. If this is not appreciated when analyzing the CT scan, an inappropriate diagnosis of an enlarged muscle can be made (Fig. 9-12). In most clinical situations, it is preferable to have the patient fix his or her gaze in the straight-ahead position, and it is

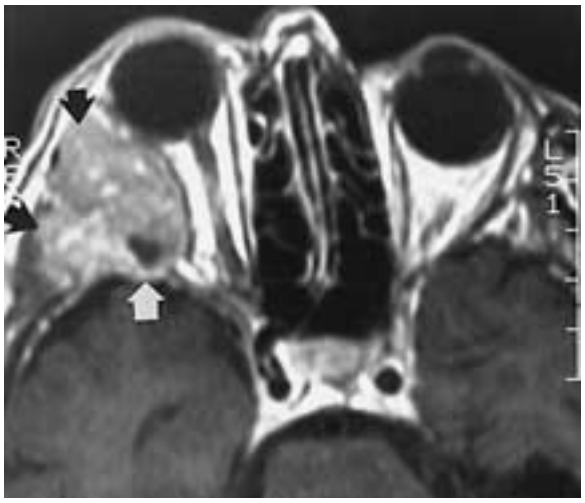

FIGURE 9-174 Orbital metastasis from a malignant histiocytoma. Axial-enhanced T1-weighted MR image shows a metastatic deposit involving the lateral wall of the right orbit (*arrows*).

VIEW IMAGE

Copyright © 2003, Mosby, Inc. All rights reserved.

useful to place some fixation target at a center point in the scanner unit.

Acquired Ocular Motility Disturbances Associated with Orbital Pathology

Many patients with classic hyperthyroidism show no ocular muscle involvement; conversely, patients manifesting severe eye muscle restriction often have normal thyroid function but are considered to have a form of euthyroid myopathy. Progressive limitation of movement may occur many years after active thyroid disease, or it may be the presenting symptom of thyroid dysfunction. Orbital myositis is a nonspecific orbital inflammation involving one or more EOMs, with characteristic clinical and CT findings, and it is often very responsive to systemic corticosteroids. Patients with orbital myositis or other conditions may present with an onset of limitation of ductions (monocular movement in test fields of gaze) in one or both eyes, with variable signs of inflammation and proptosis.[15] These conditions include carotid-cavernous fistula, infectious cellulitis, lymphomas, retrobulbar masses such as cavernous hemangioma, and occasional metastatic disease. In patients with carotid-cavernous sinus fistula resulting from an abnormal communication between the carotid arterial system and the cavernous sinus, orbital venous congestion occurs, with subsequent swelling of the EOMs and mechanical interference with movement. There may also be an associated neurologic palsy, especially of the sixth cranial nerve. CT and MR imaging may demonstrate enlarged EOMs in these patients with generalized ophthalmopathy that will revert to normal after closure of the fistula. Other lesions of the cavernous sinus such as aneurysm may also be responsible for limitation of ductions.[15]

Brown's Superior Oblique Tendon Sheath Syndrome

In 1973, Brown described a clinical syndrome (superior oblique tendon sheath or Brown's syndrome) characterized by an impaired ability to raise the eye in adduction. Typically, the patient may have straight eyes or a hypotropia (one eye lower in the primary position). Brown further classified this condition into true and simulated syndromes.[169] True (congenital) Brown's syndrome includes only those patients with a congenitally short or taut superior oblique tendon sheath complex. Patients with simulated (acquired) Brown's syndrome acquire the clinical features of the syndrome secondary to a variety of etiologies. Most authors, including Brown, have postulated that acquired Brown's syndrome is primarily a disease of the tendon sheath–trochlear complex of the superior oblique muscle secondary to an inflammatory process of the adjacent tissues.

Normal ocular movement of the superior oblique muscle requires a loose sheath and free movement of the tendon in the sheath. When the eye is adducted, the primary action of the inferior oblique muscle is elevation. When the eye is elevated in the adducted position, the superior oblique muscle normally relaxes, causing its tendon to lengthen and slide freely through the trochlea. If the superior oblique muscle cannot relax or its tendon cannot lengthen, the eye cannot be elevated while adducted. This limitation of elevation in adduction simulates an inferior oblique palsy, although the pathologic process is postulated to be located primarily in the superior oblique complex. This restriction in the physiologic passage of the tendon through the trochlea may be permanent or occur on an intermittent basis in the acquired form.

In acquired Brown's syndrome, the symptoms and findings often are intermittent. Affected patients usually complain of intermittent double vision (diplopia) on upward gaze and sometimes a ''clicking'' sensation in the area of the trochlea when attempting to look up (Fig. 9-175).

The CT appearance may show abnormalities in the area of the trochlea in acquired Brown's syndrome (Figs. 9-175 and 9-176). One patient who had a history of head trauma showed significant thickening of the reflected portion of the superior oblique tendon in the involved eye (Fig. 9-175), which was confirmed at the time of surgery.[169] The association of acquired Brown's syndrome and rheumatoid arthritis has been well documented in the literature and may spontaneously disappear (Fig. 9-177).

The CT scan enables an evaluation of three features of the superior oblique muscle: (1) the angle that the reflected tendon makes with the medial wall of the orbit; (2) the thickness of the tendon; and (3) the density of the tendon compared with that of surrounding tissues.[170] Under normal circumstances, these characteristics are nearly equal in both eyes. The CT scan makes this comparison of both eyes possible in a manner that no other procedure allows. The angle of the reflected tendon may be altered by surgery. CT scanning may also be used to compare the angle of the reflected tendon with the clinical function of the superior oblique muscles and to determine damage to the trochlear region. However, in congenital Brown's syndrome, relatively little abnormality of the superior oblique tendon has thus far been demonstrated by CT scan.

Double Elevator Palsy

Double elevator palsy is a weakness of both elevators of the same eye (weakness of superior rectus and inferior oblique muscles is almost always congenital and is characterized by limited elevation through the entire upper field). There have been very few descriptions of CT findings in these patients, but two interesting cases showed a small superior rectus muscle, although the inferior oblique muscle could not be definitely identified (Fig. 9-178). Interestingly, one patient also had a large inferior rectus muscle. It is not known whether the size change is primary or secondary in nature. Congenital double elevator palsy must be differentiated from acquired conditions that cause a restriction in upward gaze, such as a blowout fracture of the orbital floor, a downwardly displaced superior orbital wall fracture with impingement on the globe, atypical Brown's syndrome, or endocrine myopathy with involvement of the interior rectus. This differentiation can be aided by forced duction testing and the radiographic findings. Patients with symptomatic double elevator palsy may require muscle-transposing surgery in the affected eye.

Other Causes

Myositis of the EOMs with proptosis and signs of orbital inflammation have also been reported with systemic lupus erythematosus; proptosis has been noted with dermatomyo-

Copyright © 2003, Mosby, Inc. All rights reserved.

VIEW IMAGE

FIGURE 9-175 **A**, Acquired Brown syndrome showing the eyes in various gazing positions. The eyes are normal in the primary (phoria) (*E*), right lateral (*B*), left lateral (*H*), down and right (*C*), downward midline (*F*), and down and left positions (*I*). However, in the upward midline (*D*) and up and left positions (adduction of right eye) (*G*), elevation of the right eye is lacking. As the eye is abducted, the level of elevation remains the same until the midline is reached (*D*, *G*), at which point full elevation is usually possible (*A*). When the eye is adducted nasally (*G*) from the primary position (*E*), the primary action of the inferior oblique muscle is elevation; thus, lack of elevation of the right eye during adduction (*G*), as in this patient, simulates paralysis of the right inferior oblique tendon, which is the hallmark of Brown syndrome. This actually represents ''pseudoparalysis'' because the cause is not dysfunction of the right inferior oblique muscle but rather inadequate relaxation of its antagonist, the right superior oblique muscle. **B**, Axial CT scan demonstrates thickening of the reflected portion of the right superior oblique tendon (*arrowhead*). The belly of the superior oblique muscle can be seen on each side (*hollow arrow*). **C**, Scan taken 1.5 mm higher demonstrates marked thickening of the reflected tendon (*arrow*). (From Mafee MF, Folk ER, Langer BG, et al.: Computed tomography in the evaluation of Brown syndrome of the superior oblique tendon sheath. Radiology 1985;154:691–695.)

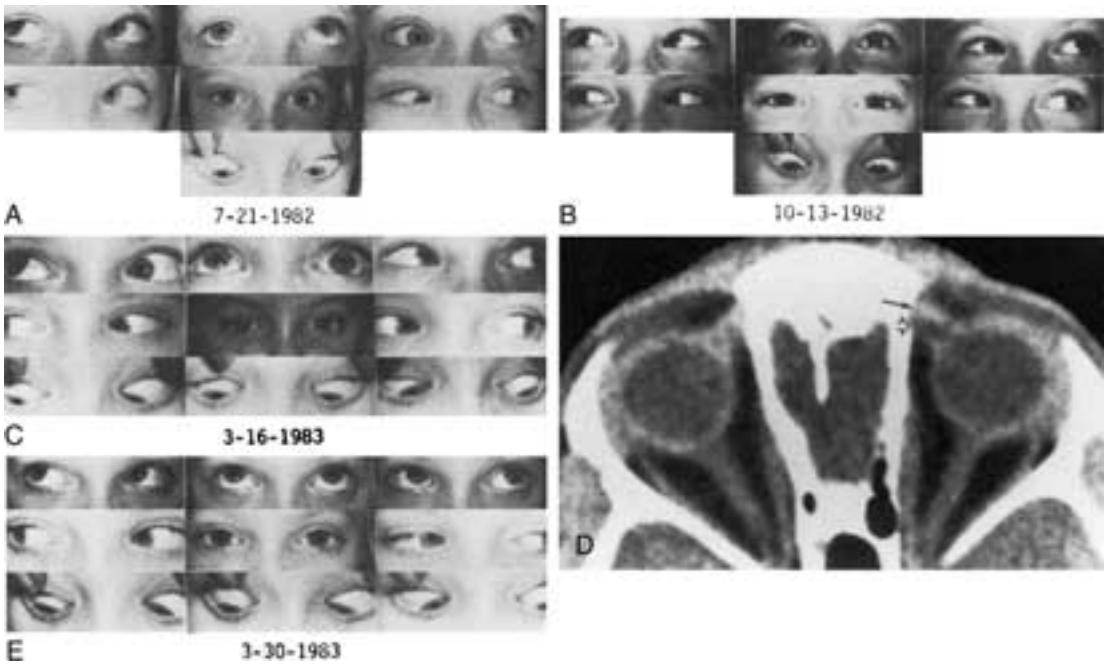

VIEW IMAGE

FIGURE 9-176 **A**, Congenital Brown syndrome showing the eyes in various gazing positions. Note the markedly limited elevation of the right eye in the upward midline position (*top middle*), which is even more pronounced on adduction of the right eye (*top right*). **B**, Eleven months after tenotomy of the right superior oblique muscle, elevation is markedly improved on both adduction and abduction. **C**, Acquired Brown syndrome developed on the opposite side following trauma. Note the limited elevation of the left eye in the straight-up position (*top middle*) and during adduction (*top right*). **D**, Axial CT scan demonstrates slight thickening of the reflected portion of the left superior oblique tendon (*arrow*). The open arrow points to area of edema. **E**, After 2 weeks of steroid therapy, elevation is markedly improved on both adduction and abduction. (From Mafee MF, Folk ER, Langer BG, et al.: Computed tomography in the evaluation of Brown syndrome of the superior oblique tendon sheath. Radiology 1985;154:691–695.)

Copyright © 2003, Mosby, Inc. All rights reserved.

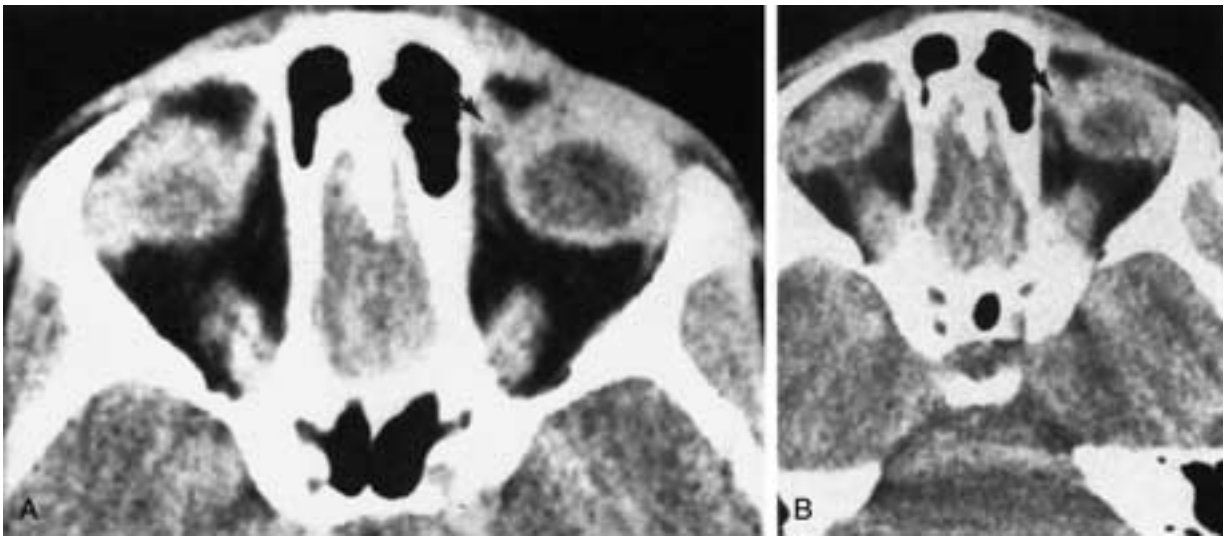

VIEW IMAGE

FIGURE 9-177 **A**, Axial CT scan demonstrates thickening of the reflected portion of the left superior oblique tendon (*arrow*). **B**, Scan taken 1.5 mm higher confirms the marked tendon thickening (*arrow*). (From Mafee MF, Folk ER, Langer BG, et al.: Computed tomography in the evaluation of Brown syndrome of the superior oblique tendon sheath. Radiology 1985;154:691–695.)

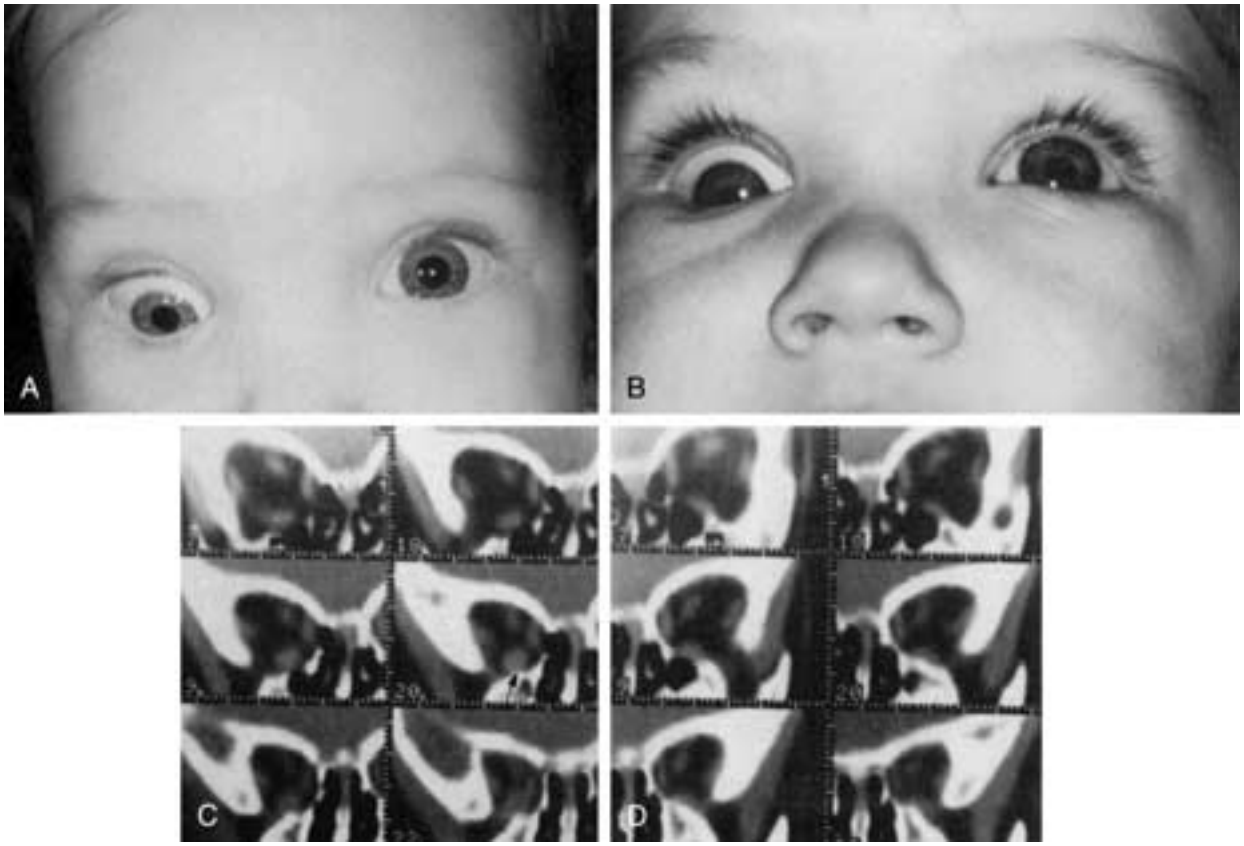

VIEW IMAGE

FIGURE 9-178 **A**, Double elevator palsy. Right hypotropia in the primary position in a patient with congenital double elevator palsy of the right eye. (Courtesy of D. Mittelman, MD.) **B**, Note limitation of elevation of the right eye. (Courtesy of D. Mittelman, MD.) **C**, Double elevator palsy. Serial reformatted coronal images showing enlarged right inferior rectus muscle. The superior rectus muscle is quite thin and hardly recognized as a distinct image. **D**, Serial reformatted coronal images of the normal left eye of the same patient in **C** for comparison.

Copyright © 2003, Mosby, Inc. All rights reserved.

sitis. Other rare causes of EOM enlargement include Crohn's colitis, sarcoidosis, cysticercosis, and carcinoma metastatic to an ocular muscle. CT studies have shown large EOMs in many cases of acromegaly. The increased size appeared to be related to the disease duration but not to growth hormone levels. These muscle findings have been observed even in treated cases.

Tychsen and coworkers described a group of patients with tenderness over the trochlea and discomfort on movement of the eye. CT scans demonstrated a soft-tissue density in the area of the trochlea that was believed to represent a localized subtype of idiopathic orbital inflammation.[171]

Traumatic Injury of Ocular Muscles

Blowout Fracture

The classic blowout fracture involves the floor of the orbit, usually sparing the orbital rim (see Chapter 7). Frequently, orbital tissues are trapped in the fracture site and ocular motility disturbances have been ascribed to entrapment of one or both inferior EOMs, but clinical and surgical experience has not supported the entrapment etiology of restricted ocular movement in many cases. Early positive forced duction tests do not necessarily prove entrapment, and these disturbances may be the result of hematoma or inflammation. Soft-tissue damage may play a significant role in causing the typical findings of a blowout fracture.

Congenital Anomalies of the Extraocular Muscles

Congenital Syndromes

Ocular motility disturbances frequently occur in craniosynostosis syndromes, and the observed patterns of abnormal movement are characteristically predictable. This is particularly true for the craniosynostosis syndromes of Apert and Crouzon. The type of abnormal movement noted in these two groups may be affected by mechanical factors induced by abnormal anatomy but also may show abnormalities in the size of muscles and the location of insertion.

Apert's and Crouzon's syndromes usually show strabismus in the primary position in addition to the presence of a V pattern, with an exotropia in the up position and straight eyes or esotropia in the down position, thus producing a V configuration. Most patients also have an associated overaction of the inferior oblique muscles and show limitation of movement in the field of action of the superior rectus and superior oblique muscles. This pattern (V) of ocular muscle imbalance is not unique to patients with certain craniofacial anomalies; it is present in many patients without bony abnormalities. What is unparalleled is the frequency of craniosynostosis patients who manifest this abnormality.

Another somewhat unexpected and well-documented finding in vertical ocular muscle imbalance in craniosynostosis patients is abnormal insertion or structure of the muscle. A number of case reports have noted the apparent absence of vertically acting muscles at the time of surgery. Diamond and coworkers reported EOM anomalies (primarily of the inferior and superior rectus muscles) in 42% of their patients with craniofacial dysostosis. Orbital high-resolution CT scanning with thin cuts (1 to 1.5 mm) demonstrates changes in the location and/or the size of EOMs. Axial, coronal, and sagittal projections are useful in obtaining an accurate estimate of the degree of abnormality. Patients with gross limitation of movement are most likely to demonstrate CT scan abnormalities. This type of evaluation is indicated to plan appropriate surgical procedures if ocular motility surgery is contemplated or to plan alternatives if the ocular muscles cannot be located.

Noncomitant Strabismus Without Associated Malformations

A few studies have utilized CT analysis of the EOMs in normal subjects, with attention to variation in size and location. This method of analysis has also been used to evaluate the position or slippage of the muscles as the eyes move to different gaze positions.

In some types of routine comitant strabismus, the degree of horizontal deviation is noted to change when the patient looks up and down. If there is a significant difference in the amount of esotropia (or exotropia) in upgaze and downgaze, the patient is described as having an A or V syndrome. Since a V pattern has been observed in most patients with craniosynostosis deviation, it has been postulated that this may be caused or enhanced by an abnormal vertical insertion of the horizontal recti. Following this reasoning, some strabismus patients who manifested a V or A pattern of horizontal strabismus, but did not have any evidence of craniofacial anomalies, were evaluated by CT. One group of investigators noted some change in the position of the horizontal recti in these patients. Further data are necessary to understand these relationships.

Diagnostic imaging studies such as CT and MR imaging are invaluable tools to demonstrate orbital and EOM anatomy in cases of strabismus following trauma or surgery, or loss of rectus muscle function following strabismus surgery, retinal detachment surgery, or ocular trauma. Traumatic disruption of the orbital tissues can simulate a lost muscle by many different mechanisms: severed nerves, neuropraxia, muscle crush, muscle entrapment in an orbital wall fracture, muscle slippage, muscle fibrosis and contracture, edema, hemorrhage, and adhesions. When an EOM is surrounded by tissue edema, hemorrhage, granulation tissue, or scar tissue, there may not be sufficient contrast to differentiate muscle from adjacent tissue by CT and MR imaging. When diagnostic imaging fails to reveal the muscle in question, however, exploratory surgery should still be considered before the diagnosis of lost muscle is accepted.

REFERENCES

1. Warwick R, Williams PL. Gray's Anatomy, 35th British ed. Philadelphia: WB Saunders, 1973;145–147.
2. Snell RS, Lemp MA (eds). Clinical Anatomy of the Eye. Boston: Blackwell Scientific, 1989;1–15.
3. Rootman J, ed. Diseases of the Orbit. Philadelphia: JB Lippincott, 1988.

Copyright © 2003, Mosby, Inc. All rights reserved.

4. Reeh MJ, Wobij JL, Wirtschafter JD. Ophthalmic Anatomy: A Manual with Some Clinical Applications. San Francisco: American Academy of Ophthalmology, 1981;11–54.
5. Smith MF. Orbit, eyelids, and lacrimal system. Basic and Clinical Science Course. San Francisco: American Academy of Ophthalmology, 1987–1988.
6. Wilson FM. Fundamentals and principles of ophthalmology. Basic and Clinical Science Course. San Francisco: American Academy of Ophthalmology, 1991–1992.
7. Daniels DL, Yu S, Pech P, et al. Computed tomography and magnetic resonance imaging of the orbital apex. Radiol Clin North Am 1987;25:803–817.
8. Mafee MF, Putterman A, Valvassori GE, et al. Orbital space-occupying lesions: role of CT and MRI, an analysis of 145 cases. Radiol Clin North Am 1987;25:529–559.
9. Canalis RF, Burstein FD. Osteogenesis in vascularized periosteum. Arch Otolaryngol 1985;3:511–518.
10. Duhamel HL. Sur le development et la crue des os des animax. Mem Acad R Sci 1742;55:354–370.
11. Mafee MF, Miller MT. Computed tomography scanning in the evaluation of ocular motility disorders. In: Gonzalez CF, Becker MH, Flanagan JC, eds. Diagnostic Imaging in Ophthalmology. New York: Springer-Verlag, 1985;39–54.
12. Dale RT, ed. Fundamentals of Ocular Motility and Strabismus. New York: Grune & Stratton, 1982.
13. Helveston EM, Merriam WW, Ellis FD, et al. The trochlea: a study of the anatomy and pathology. Ophthalmology 1982;89:124–133.
14. Fink WH. The anatomy of the extrinsic muscles of the eye. In: Allen JH, ed. Strabismus Ophthalmic Symposium. St. Louis: CV Mosby, 1950;17–62.
15. Miller TM, Mafee MF. Computed tomography scanning in the evaluation of ocular motility disorders. Radiol Clin North Am 1987;25:733–752.
16. Snell RS, Lemp MA, eds. Clinical Anatomy of the Eye. Boston: Blackwell Scientific, 1989.
17. Mafee MF. Imaging of the orbit. In: Valvassori GE, Mafee MF, Carter B, eds. Imaging of the Head and Neck. Stuttgart: Georg Thieme, 1995;248–327.
18. Zonneveld FW, Koorneef L, Hillen B, et al. Direct Multiplanar, High Resolution, Thin-Section CT of the Orbit. Eindhoven: Philips Medical Systems, 1986.
19. Mafee MF, Pruzansky S, Corrales MM, et al. CT in the evaluation of the orbit and the bony interorbital distance. AJNR 1986;7:265–269.
20. Mafee MF, Kumar A, Tahmoressi CN, et al. Direct sagittal CT in the evaluation of temporal bone disease. AJNR 1988;9:371–378.
21. Barakow JA, Dillon WP, Chew WM. Orbit, skull base and pharynx: contrast-enhanced fat suppression MR imaging. Radiology 1991;179: 191–198.
22. Tien RD, Hesselink JR, Szumowski J. MR fat suppression combined with Gd-DTPA enhancement in optic neuritis and perineuritis. J Comput Assist Tomogr 1991;15:223–227.
23. Tien RD, Chu PK, Hesselink JR, et al. Intra- and paraorbital lesions: value of fat-suppression MR imaging with paramagnetic contrast enhancement. AJNR 1992;12:245–253.
24. Mafee MF, Haik BG. Lacrimal gland and fossa lesions: role of computed tomography. Radiol Clin North Am 1987;25:767–779.
25. Langer BG, Mafee MF, Pollack S, et al. MRI of the normal orbit and optic pathway. Radiol Clin North Am 1987;25:429–446.
26. Zonneveld FW, Koornneef L, Hiller B, et al. Normal direct multiplanar CT anatomy of the orbit with correlative anatomic cryosections. Radiol Clin North Am 1987;25:381–407.
27. Ettl A, Salomonowitz E, Koornneef L, Zonneveld FW. High resolution MR imaging anatomy of the orbit. Correlation with comparative cryosectional anatomy. Radiol Clin North Am 1998;36: 1021–1045.
28. Currario G, Silverman FN. Orbital hypotelorism, arhinencephaly, and trigoncephaly. Radiology 1960;74:206–216.
29. Gerald BE, Silverman FN. Normal and abnormal interorbital distances with special reference to mongolism. AJR 1956;95: 154–161.
30. Morin J, Hiu J, Anderson J, et al. A study of growth in the interorbital region. Am J Ophthalmol 1936;56:895–901.
31. Cameron J. Interorbital width: new cranial dimension, its significance in modern and fossil man and in lower mammals. Am J Phys Anthropol 1931;15:509–515.
32. Hansman CF. Growth of interorbital distance and skull thickness as observed in roentgenographic measurements. Radiology 1966;86: 87–96.
33. Linder B, Campos M, Schafer M. CT and MRI of orbital abnormalities in neurofibromatosis and selected craniofacial anomalies. Radiol Clin North Am 1987;25:787–802.
34. Converse JM, McCarthy JG. Orbital hypertelorism. Scand J Plast Reconstr Surg 1985;15:265–276.
35. DeMyer WM. Neurologic evaluation associated forebrain maldevelopment and orbital hypotelorism. In: Symposium on Diagnosis and Treatment of Craniofacial Anomalies, Vol. 20. St. Louis: CV Mosby, 1979;153–163.
36. Becker MH, McCarthy JG. Congenital abnormalities. In: Gonzalez CF, Becker MH, Flanagan JC, eds. Diagnostic Imaging in Ophthalmology. New York: Springer-Verlag, 1985;115–187.
37. Gorlin RJ, Pindberg JJ, Cohen MM Jr. Syndromes of the Head and Neck, 2nd ed. New York: McGraw-Hill, 1976.
38. Smith DW. Recognizable Patterns of Human Malformation. Philadelphia: WB Saunders, 1970.
39. Taybi H. Radiology of Syndromes and Metabolic Disorders, 2nd ed. St. Louis: CV Mosby, 1983.
40. Mafee MF, Jampol LM, Langer BG, et al. Computed tomography of optic nerve colobomas: morning glory anomaly, and colobomatous cyst. Radiol Clin North Am 1987;25:693–699.
41. Mann I. Developmental Abnormalities of the Eye, 2nd ed. Philadelphia: JB Lippincott, 1957;74–78.
42. Mann I. The Development of the Human Eye. New York: Grune & Stratton, 1969.
43. Brown G, Tasman W, eds. Congenital Anomalies of the Optic Disc. New York: Grune & Stratton, 1983;97–191.
44. Arey LB. Developmental Anatomy, 6th ed. Philadelphia: WB Saunders, 1970.
45. Duke-Elder S, Wybar KC. System of Ophthalmology: The Anatomy of the Visual System, Vol. 2. St. Louis: CV Mosby, 1961.
46. Hamilton WJ, Boyd JD, Mossman HW, eds. Human Embryology: Development of Form and Function, 3rd ed. Baltimore: Williams & Wilkins, 1962.
47. Tessier P. The definitive plastic surgical treatment of the severe facial deformities of craniofacial dysostosis: Crouzon's and Apert's diseases. Plast Reconstr Surg 1971;48:419–442.
48. Campbell JA. Craniofacial anomalies. In: Newton TH, Potts DG, eds. Radiology of the Skull and Brain, Vol. 1, Book 2. St. Louis: CV Mosby, 1971;571–633.
49. Pruzansky S. Time: the fourth dimension in syndrome analysis applied to craniofacial malformations. Birth Defects 1977; 13:3–28.
50. Mafee MF, Valvassori GE. Radiology of the craniofacial anomalies. Otolaryngol Clin North Am 1981;14:939–988.
51. Harwood-Nash DC. Coronal sysostosis. In: Rogers LF, ed. Disorders of the Head and Neck Syllabus. Second Series. Chicago: American College of Radiology. 1977.
52. Anderson FM, Geiger L. Craniosynostosis: a survey of 204 cases. J Neurosurg 1965;22:229–240.
53. Shillito J Jr, Matson DD. Craniosynostosis: a review of 519 surgical patients. Pediatrics 1968;41:829–853.
54. Crouzon O. Dysostose cranio-faciale hereditaire. Bull Mem Soc Med Hop (Paris) 1912;33:545–555.
55. Lombardi G. Radiology in Neuro-Ophthalmology. Baltimore: Williams & Wilkins, 1967.
56. Saethre H. Ein beitrag zum turnschadel problem (pathogenese, erblickeit und symptomatologie). Deutsch Z Nervenh 1931;119: 533–555.
57. Chotzen F. Eine eigenartige familiare entwicklungsstorung (akrocephalo-syndaktylie), dysostosis craniofacialis and hypertelorisms). Mschr Kinder 1932;55:97–122.
58. Bartsocas CS, Weber AL, Crawford JD. Acrocephalosyndactyly type 3: Chotzen's syndrome. J Pediatr 1970;77:267–272.
59. Lewis A, Gerson P, Axelson K, et al. Von Recklinghausen neurofibromatosis II. Incidence of optic glioma. Ophthalmology 1984;91:929– 935.
60. Zimmerman RA, Bilaniuk LT, Mezger RA, et al. Computed tomography of orbitofacial neurofibromatosis. Radiology 1983;146: 113–116.
61. Kobrin JL, Block FC, Wiengiest TA. Ocular and orbital manifestations of neurofibromatosis. Surv Ophthalmol 1979;24:45–51.

Copyright © 2003, Mosby, Inc. All rights reserved.

62. Jacoby CG, Go RT, Beren RA. Cranial CT of neurofibromatosis. AJR 1980;135:553–557.
63. Berry GA. Note on a congenital defect (? coloboma) of the lower lid. R Lond Ophthalmol Hosp Rep 1889;12:225.
64. Treacher Collins E. Case with symmetrical congenital notches in the outer part of each lower lid and defective development of the malar bones. Trans Ophthalmol Soc 1900;20:190–191.
65. Pires de Lima JA, Monteior HB. Aparello branquiale suas pertur-bacoes evolutivas. Arch Anat Anthrop (Lisboa) 1923;8:185.
66. Francheschetti A, Klein D. The mandibulo-facial dysostosis, a new hereditary syndrome. Acta Ophthalmol 1949;27:141–224.
67. Poswillo D. The pathogenesis of the Treacher-Collins syndrome (mandibulofacial dysostosis). Br J Oral Surg 1975;13:1–26.
68. Herring SW, Rowlatt UF, Pruzansky S. Anatomical abnormalities in mandibulofacial dysostosis. Am J Med Genet 1979;3:225–259.
69. Pruzansky S, Miller M, Krammer JF. Ocular defects in craniofacial syndromes. In: Goldberg MF, ed. Genetic and Metabolic Eye Disease. Boston: Little, Brown, 1974;487, 498.
70. Henderson JW. Orbital Tumors. Philadelphia: WB Saunders, 1973;116–123.
71. Mafee MF, Dobben GD, Valvassori GE. Computed tomography assessment of paraorbital pathology. In: Gonzalez CA, Becker MH, Flanagan JC, eds. Diagnostic Imaging in Ophthalmology. New York: Springer-Verlag, 1985;281–302.
72. Grove AS. Giant dermoid cysts of the orbit. Ophthalmology 1979;86:1513–1520.
73. Kaufman LM, Villablanca JP, Mafee MR. Diagnostic imaging of cystic lesions in the child's orbit. Radiol Clin North Am 1998;36:1149–1163.
74. Rubenstein J. Disorders of the conjunctiva and limbus. In: Yanoff M, Duker JS, eds. Ophthalmology. St. Louis: CV Mosby, 1999;1.1–1.21.
75. Dutton J. Orbital diseases. In: Yanoff M, Duker JS, eds. Ophthalmology. St. Louis: CV Mosby, 1999;14.1–14.7.
76. Chang DF, Dallow RL, Walton DS. Congenital orbital teratoma: report of a case with visual preservation. J Pediatr Ophthalmol Strabismus 1980;17:88.
77. Garrity JA, Trautmann JC, Bartley GB, et al. Optic nerve sheath meningoceles: clinical and radiographic features in 13 cases with a review of the literature. Ophthalmology 1990;97:1519.
78. Laventer DB, Merriman JC, Defendini R, et al. Enterogenous cysts of the orbital apex and superior orbital fissure. Ophthalmology 1994;101:1614.
79. Dobben GD, Philip B, Mafee MF, et al. Orbital subperiosteal hematoma, cholesterol granuloma, and infection. Evaluation with MR imaging and CT. Radiol Clin North Am 1998;36:1185–1200.
80. Polito E, Leccisotti A. Diagnosis and treatment of orbital hemorrhagic lesions. Ann Ophthalmol 1994;26:85–93.
81. Gomez-Morales A, Croxatto JO, Croxatto L, et al. Hydatid cysts of the orbit: a review of 35 cases. Ophthalmology 1988;95:1027.
82. Mafee MF, Atlas SW, Galetta SL. In: Atlas SW, ed. Magnetic Resonance Imaging of the Brain and Spine, 3rd ed. Philadelphia: Lippincott Williams & Wilkins, 2002;1433–1524.
83. Weber AL, Mikulis DK. Inflammatory disorders of the paraorbital sinuses and their complications. Radiol Clin North Am 1987;25: 615–630.
84. Hawkins DD, Clark RW. Orbital involvement in acute sinusitis. Clin Pediatr 1977;16(5):464–471.
85. Chandler JR, Langenbrunner DJ, Stevens ER. The pathogenesis of orbital complications in acute sinusitis. Laryngoscope 1970;80: 1414.
86. Eustis HS, Mafee MF, Walton C, Mondonca J. MR imaging and CT of orbital infections and complication in acute rhinosinusitis. Radiol Clin North Am 1998;36:1165–1183.
87. Dolan RW, Choudhury K. Diagnosis and treatment of intracranial complications of paranasal sinus infection. J Oral Maxillofac Surg 1995;53:1080.
88. Igarishi H, Igarishi S, Fujio N, et al. Magnetic resonance imaging in the early diagnosis of cavernous sinus thrombosis. Ophthalmologica 1995;209:292.
89. Saah D, Schwartz A. Diagnosis of cavernous sinus thrombosis by magnetic resonance imaging using flow parameters. Ann Otol Rhinol Laryngol 1994;103:487.
90. Centeno RS, Bentson RJ, Mancuso AA. CT scanning in rhinocerebral mucormycosis and aspergillosis. Radiology 1981;140:383–389.
91. Courey WR, New PFJ, Price DL. Angiographic manifestations of craniofacial phycomycosis: report of three cases. Radiology 1972;103:329–334.
92. Weber AL, Vitale Romo L, Sabates NR. Pseudotumor of the orbit. Clinical, pathologic, and radiologic evaluation. Radiol Clin North Am 1999;37:151–168.
93. Blodi FC, Gass JDM. Inflammatory pseudotumor of the orbit. Br J Ophthalmol 1968;52:79–93.
94. Flanders AE, Mafee MF, Rao VM, et al. CT characteristics of orbital pseudotumors and other orbital inflammatory processes. J Comput Assist Tomogr 1989;13(1):40–47.
95. Birch-Hirschfield A. Zur diagnostik and pathologie der orbital-tumoren. Deutsche Ophth Ges 1905;32:127–135.
96. Motto-Lippa L, Jakobiec FA, Smith M. Idiopathic inflammatory orbital pseudotumor in childhood. II. Results of diagnostic tests and biopsies. Ophthalmology 1981;88:565–574.
97. Trokel SL, Hilal SK. Recognition and differential diagnosis of enlarged extraocular muscles in computed tomography. Am J Ophthalmol 1979;87:503–512.
98. Tolosa E. Periarthritic lesions of the carotid siphon with the clinical features of a carotid infraclinoid aneurysm. J Neurol Neurosurg Psychiatry 1954;17:300–302.
99. Hunt WE, Meagher JN, LeFever HE, et al. Painful ophthalmoplegia. Neurology 1961;11(Suppl):56–62.
100. Smith JL, Taxdal DSR. Painful ophthalmoplegia: the Tolosa-Hunt syndrome. Am J Ophthalmol 1966;61:1466–1472.
101. Sondheimer FK, Knapp J. Angiographic findings in the Tolosa-Hunt syndrome: painful ophthalmoplegia. Radiology 1973;106: 105–112.
102. Hurwitz CA, Faquin WC. Case record 5-2002. N Engl J Med 2002;346(7):513–520.
103. Rubin RM, Sadun AA. Ocular myopathies. In Yanoff M, Duker JS, eds. Ophthalmology. St. Louis: CV Mosby, 1999;11.18.1–11.18.8.
104. Kendler DL, Lippa J, Rootman J. The initial clinical characteristics of Graves' orbitopathy vary with age and sex. Arch Ophthalmol 1993;111:197–201.
105. Mafee MF, Dorodi S, Pai E. Sarcoidosis of the eye, orbit, and central nervous system: role of MR imaging. Radiol Clin North Am 1999;37:73–87.
106. Mafee MF. Case 25: optic nerve sheath meningioma. In: Head and Neck Disorders (fourth series) test and syllabus. Reston, VA: American College of Radiology, 1992;552–595.
107. Shields JA, ed. Diagnosis and Management of Orbital Tumors. Philadelphia: WB Saunders, 1989.
108. Dykhuizen RS, Smith C, Kennedy MM, et al. Necrotizing sarcoid granulomatosis with extrapulmonary involvement. Eur Respir J 1997;10:245–247.
109. Raskin EM, McCormick SA, Maher EA, et al. Granulomatous idiopathic orbital inflammation. Ophthalmol Plast Reconstr Surg 1995;11:131–135.
110. Monfort-Gouraud M, Chokre R, Dubiez M, et al. Inflammatory pseudotumor of the orbit and suspected sarcoidosis. Arch Pediatr 1996;3:697–700.
111. Mombaerts I, Schlingemann RO, Goldschmeding R, Koornep L. Idiopathic granulomatous orbital inflammation. Ophthalmology 1996;103:2135–2141.
112. Carmody RF, Mafee MF, Goodwin JA, et al. Orbital and optic pathway sarcoidosis: MR findings. AJNR 1994;15:775–783.
113. Ing EB, Garrity JA, Gross SA, Ebersold MJ. Sarcoid masquerading as optic nerve sheath meningioma. Mayo Clinic Proc 1997;72:38–43.
114. Beardsley TL, Brown SV, Sydner CF, et al. Eleven cases of sarcoidosis of the optic nerve. Am J Ophthalmol 1984;97:67–77.
115. Vidal RW, Devaney K, Ferlito A, et al. Sinonasal malignant lymphomas: a distinct clinicopathological category. Ann Otol Rhinol Laryngol 1999, 108:411–419.
116. Lichtenstein L. Histiocytosis X: integration of eosinophilic granuloma of bone, ''Letterer-Siwe disease'' and ''Hand Schuller-Christian disease'' as related manifestations of a single nosologic entity. Arch Pathol 1953;56:84–102.
117. Nezelof C, Barbey S. Histiocytosis: nosology and pathobiology. Pediatr Pathol 1985;3:1–41.
118. Hidayat AA, Mafee MF, Laver NV, Noujaim S. Langerhans' cell histiocytosis and juvenile xanthogranuloma of the orbit. Clinicopathologic, CT, and MR imaging features. Radiol Clin North Am 1998;36:1229–1240.

Copyright © 2003, Mosby, Inc. All rights reserved.

119. Stanley SS. Taking the X out of histiocytosis X. Radiology 1997;204: 322–324.
120. Nezelof C, Basset F. Langerhans' cell histiocytosis research: past, present, and future. Hematol Oncol Clin North Am 1998;12: 385–406.
121. Zimmerman LE. Ocular lesions of juvenile xanthogranuloma. Neoxanthoendothelioma. Trans Am Acad Ophthalmol Otolaryngol 1965;69:412–442.
122. Jakobiac FA, Mills MD, Hidayat AA, et al. Periocular xanthogranulomas associated with severe adult-onset asthma. Trans Am Opthalmol Soc 1993;91:99–129.
123. Alper MG, Zimmerman LE, LaPiana FG. Orbital manifestations of Erdheim-Chester disease. Trans Am Ophthalmol Soc 1983;8:64–68.
124. Shields AK, Karcioglu ZA, Shields C, et al. Orbital and eyelid involvement with Erdheim-Chester disease: a report of two cases. Arch Ophthalmol 1991;109:850–854.
125. Tien RD, Brasch RC, Jackson DE, et al. Cerebral Erdheim-Chester disease: persistent enhancement with Gd-DTPA on MR images. Radiology 1989;172:791–792.
126. Mafee MF. Eye and orbit. In: Som PM, Curtin HD, eds. Head and Neck Imaging. St. Louis: Mosby-Yearbook, 1996;1009–1128.
127. Flanders AE, Espinosa GA, Markiewicz DA, et al. Orbital lymphoma. Radiol Clin North Am 1987;25:601–612.
128. Peyster RG, Hoover ED. Computerized Tomography in Orbital Disease and Neuro-Ophthalmology. Chicago: CV Mosby, 1984;21–56.
129. Fitzpatrick PJ, Macko S. Lymphoreticular tumors of the orbit. Int J Radiat Oncol Biol Phys 1984;10:333–340.
130. Yeo JH, Jakobiec FA, Abbott GF, et al. Combined clinical and computed tomographic diagnosis of orbital lymphoid tumors. Am J Ophthalmol 1982;94:235–245.
131. Valvassori GE, Sabnis SS, Mafee RF, et al. Imaging of orbital lymphoproliferative disorders. Radiol Clin North Am 1999;37:135–150.
132. Bilaniuk LT. Orbital vascular lesions: role of imaging. Radiol Clin North Am 1999;37:169–183.
133. Mafee MF, Miller MT, Tan WS, et al. Dynamic computed tomography and its application to ophthalmology. Radiol Clin North Am 1987;25:715–731.
134. Ruchman MC, Stefanyszn MA, Flanagan JC, et al. Orbital tumors. In: Gonzalez CA, Becjer MH, Flanagan JC, eds. Diagnostic Imaging in Ophthalmology. New York: Springer-Verlag, 1985;201–238.
135. Krohel GB, Wright JE. Orbital hemorrhage. Am J Ophthalmol 1979;88:254–258.
136. Tan WS, Wilbur AC, Mafee MF. The role of the neuroradiologist in vascular disorders involving the orbit. Radiol Clin North Am 1987;25:849–861.
137. Panda A, Dayal Y, Singhal V, et al. Hemangiopericytoma. Br J Ophthalmol 1984;68:124–127.
138. Stout AP. Tumors featuring pericytes, glomus tumor and hemangiopericytoma. Lab Invest 1956;5:217–223.
139. Stout AP, Murray MR. Hemangiopericytoma. Ann Surg 1972;116: 26–32.
140. Bockwinkel KD, Diddams JA. Hemangiopericytoma: report of care and comprehensive review of literature. Cancer 1970;25:896–901.
141. Rootman J, Goldberg C, Robertson W. Primary orbital schwannomas. Br J Ophthalmol 1982;66:194–204.
142. Carroll GS, Haik BG, Fleming JC, et al. Peripheral nerve tumors of the orbit. Radiol Clin North Am 1999;37:195–202.
143. Mafee MF, Goodwin J, Dorodi S. Optic nerve sheath meningiomas: role of MR imaging. Radiol Clin North Am 1999;37:37–58.
144. Skolnick CA, Mafee MF, Goodwin JA. Pneumosinus dilatans of the sphenoid sinus presenting with visual loss. J Neuro-Ophthalmol 2000;20(4):259–263.
145. Dalley R. Fibrous histiocytoma and fibrous tissue tumors of the orbit. Radiol Clin North Am 1999;37:185–194.
146. Font RL, Hidayat AA. Fibrous histiocytoma of the orbit: a clinicopathologic study of 150 cases. Hum Pathol 1982;13:199.
147. Ros PR, Kursunoglu S, Batle JF, et al. Malignant fibrous histiocytoma of the orbit. J Clin Neuroophthalmol 1985;5:116.
148. Jacomb-Hood J, Moseley IF. Orbital fibrous histiocytoma: computed tomography in 10 cases and a review of radiological findings. Clin Radiol 1991;43:117–120.
149. Mafee MF, Pai E, Philip B. Rhabdomyosarcoma of the orbit. Evaluation with MR imaging and CT. Radiol Clin North Am 1998;36:1215–1227.
150. Vade A, Armstrong D. Orbital rhabdomyosarcoma in childhood. Radiol Clin North Am 1987;25:701–714.
151. Mafee MF. Case 10: myositic orbital pseudotumor. In: Head and Neck Disorders (fourth series) tested syllabus. Reston, VA: American College of Radiology, 1992;213–259.
152. Mafee MF. The orbit proper. In: Som PM, Bergeron RT, eds. Head and Neck Imaging. St. Louis: Mosby-Yearbook, 1991;747–813.
153. Mafee MF. Orbital and intraocular lesions. In: Edelman RR, Hesselink JR, Zlatkin MC, eds. Clinical Magnetic Resonance Imaging. Philadelphia: WB Saunders, 1995;985–1020.
154. Rao BN, Santana VM, Fleming ID, et al. Management and prognosis of head and neck sarcomas. Am J Surg 1989;158:373–377.
155. Seedat RY, Hamilton PD, deJager LP, et al. Orbital rhabdomyosarcoma presenting as an apparent orbital subperiosteal abscess. Int J Pediatr Otorhinolaryngol 2000;52:177–181.
156. Shinaver CN, Mafee MF, Choi KH. MRI of mesenchymal chondrosarcoma of the orbit: case report and review of the literature. Neuroradiology 1997;39:296–301.
157. Stewart WB, Krohel GB, Wright JE. Lacrimal gland and fossa lesions: an approach to diagnosis and management. Ophthalmology 1979;86:886–895.
158. Wright JE. Factors affecting the survival of patients with lacrimal gland tumors. Can J Ophthalmol 1982;17:3–9.
159. Koeller KK. Mesenchymal chondrosarcoma and simulating lesions of the orbit. Radiol Clin North Am 1999;37:203–217.
160. Zimmerman LE, Sanders LE, Ackerman IV. Epithelial tumors of the lacrimal gland: prognostic and therapeutic significance of histologic types. Int Ophthalmol Clin 1962;2:337–367.
161. Jakobiec FA, Yeo JH, Trokel SL, et al. Combined clinical and computed tomographic diagnosis for primary lacrimal fossa lesions. Am J Ophthalmol 1982;94:785–807.
162. Hesselink J, Davis K, Dallow R, et al. Computed tomography of masses in the lacrimal gland region. Radiology 1979;131:143–147.
163. Jones BR. Clinical features and etiology of dacryoadenitis. Trans Ophthalmol Soc UK 1955;75:435–452.
164. Mafee MF, Edward DP, Koeller KK, Dorodi S. Lacrimal gland tumors and simulating lesions. Clinicopathologic and MR imaging features. Radiol Clin North Am 1999;37:219–239.
165. Hoffman GS, Kerr GS, Leavitt RY, et al. Wegener granulomatosis: an analysis of 158 patients. Ann Intern Med 1992;116:488–498.
166. Shield SJA, Bakewell B, Augsburger JJ, et al. Classification and incidence of space-occupying lesions of the orbit: a survey of 645 biopsies. Arch Ophthalmol 1984;102:1606–1611.
167. Kimura T, Yoshimura S, Ishikawa E. Eosinophilic granuloma with proliferation of lymphoid tissue. Trans Soc Pathol Jpn 1948;37:179.
168. Char DH, Unsöld R. Computed tomography: ocular and orbital pathology. In: Newton TH, Bilaniuk LT, eds. Radiology of the Eye and Orbit. New York: Raven Press, 1990;9.1–9.64.
169. Brown HW. True and simulated superior oblique tendon sheath syndromes. Doc Ophthalmol 1973;34:123, 134.
170. Mafee MF, Folk ER, Langer BG, et al. CT in the evaluation of Brown syndrome of the superior oblique tendon sheath. Radiology 1985;154:691–695.
171. Tychsen L, Tse DT, Ossoining K, Anderson RL. Trochleitis with superior oblique myositics. Ophthalmology 1984;91:1075–1079.

Copyright © 2003, Mosby, Inc. All rights reserved.

10 Lacrimal Apparatus

Edward E. Kassel and Charles J. Schatz

INTRODUCTION
CONTRAST DACRYOCYSTOGRAPHY
- Equipment
- Contrast Materials
- Radiographic Techniques
- Injection Techniques

DIGITAL SUBTRACTION (MACRO) DACRYOCYSTOGRAPHY
CLINICAL TESTS
- Probing
- Irrigation
- Dye Tests
  - Jones 1 Test
  - Jones 2 Test
- Schirmer's Test
- Valsalva DCR Bubble Test

INDICATIONS FOR DACRYOCYSTOGRAPHY
SURGICAL PROCEDURES FOR EPIPHORA
THE NORMAL DACRYOCYSTOGRAM
- Anatomy

PATHOLOGY OF THE NASOLACRIMAL DRAINAGE SYSTEM
- Obstruction
- Fistulae
- Diverticula
- Lacrimal Sac Cysts
- Lacrimal Calculi
- Chronic Canaliculitis
- Posttreatment Considerations
  - Postsurgical Considerations
  - Postirradiation Considerations
  - Postchemotherapy Considerations

DACRYOSCINTIGRAPHY
- Technique
- Normal Examination
- Complete Obstruction
- Incomplete Obstruction: Functional Nasolacrimal Duct Obstruction
- Sensitivity of Dacryoscintigraphy

COMPUTED TOMOGRAPHY
- Radiographic Anatomy
- CT Pathology
  - Lacrimal Sac Tumors
  - Facial Trauma

COMBINED CT-DACRYOCYSTOGRAPHY
- Pediatrics
  - Congenital Atresia
  - Duplication

MAGNETIC RESONANCE DACRYOCYSTOGRAPHY
DACRYOCYSTOPLASTY AND STENT PLACEMENT
- Balloon Dacryocystoplasty
- Stents

ENDOSCOPY OF THE LACRIMAL DRAINAGE SYSTEM
SUMMARY

INTRODUCTION

Abnormalities of the nasolacrimal drainage system (NLDS) bring many patients to the eye clinic. The majority of these patients present with epiphora (tearing), with a smaller number presenting with swelling, discomfort, or a mass in the inferomedial orbit, the area of the lacrimal sac. Multiple diverse etiologies, intrinsic or extrinsic to the NLDS, may be responsible. To assess for causative factors, the clinician augments the clinical examination with specific clinical tests and/or an imaging referral to document the anatomy and functional capabilities, degrees and levels of patency of the NLDS itself, or to visualize the tissues extrinsic and adjacent to the NLDS.

This chapter will outline the various imaging tests available for such patients. Discussions of dacryocystogra-

Copyright © 2003, Mosby, Inc. All rights reserved.

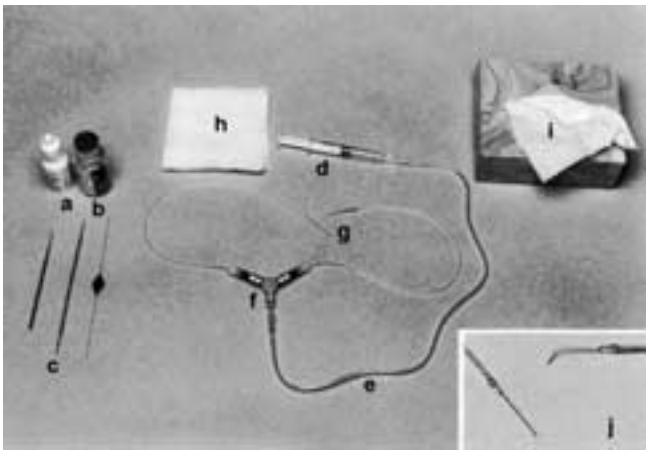

VIEW IMAGE

FIGURE 10-1 Equipment used in DCG: *a*, topical ophthalmic anaesthetic; *b*, low-osmolar, water-soluble contrast material; *c*, lacrimal dilators; *d*, 3 to 5 ml syringe; *e*, low-pressure tubing; *f*, Y-connector; *g*, lacrimal cannula; *h*, gauze pad; *i*, paper tissues; *j* (*inset*), magnified view of a commercially available lacrimal cannula. The cannula tip may be bent if clinically desired.

phy, dacryoscintigraphy, computed tomography, magnetic resonance imaging, and CT and MR imaging with topically or cannula introduced contrast media or solutions will outline the indications for and relative benefits of these various tests in specific patient populations. Radiographic anatomy, the more common pathologic processes, and their correlative imaging will be discussed in reference to the patient presenting with epiphora or a mass lesion of the inferomedial orbit. Applicable surgical procedures and the more recent experience with alternative dacryocystoplasty or stenting procedures provide a perspective on the current treatment options available to the patient.

CONTRAST DACRYOCYSTOGRAPHY

The radiographic evaluation of the NLDS by contrast dacryocystography (DCG) was first described by Ewing, and remains the definitive and usually the primary study in the evaluation of patients with tearing (epiphora) (Figs. 10-1[4] to 10-10).[1] Epiphora is a common cause of referral to the general ophthalmologist, and the treatment often requires surgery. DCG is capable of determining the patency of the canaliculi, lacrimal sac, and nasolacrimal duct. When disease is present, the site and degree of obstruction or stenosis or the presence of fistulae, diverticula, and concretions are well evaluated by DCG (Fig. 10-10).

Equipment

The equipment commonly used is illustrated in Figure 10-1. A dacryocystogram needle can be made by grinding off the sharp point of a 27-gauge lymphangiogram needle; the tip should be rounded and polished so that no metallic burrs remain. An alternative to this needle is a tapered catheter, as described by Iba and Hanafee,[2] made from no. 18 Teflon tubing, or commercially available Rabinov sialography catheters with a fine metallic cannula of 0.016 inch (27 gauge) diameter (Cook, Inc, Bloomington, Indiana). A punctal or lacrimal dilator (sharp or blunt Nettleship dilator) is also utilized, and for simultaneous injection and visualization of bilateral studies, a Y-connector may be helpful.

Contrast Materials

A variety of opaque contrast media have been used. Ewing used bismuth subnitrate in liquid petrolatum. Since then, ethiodized oil (ethiodol), iodized oil (lipiodol), and iophendylate (Pantopaque) have also been used.[1, 3–5] Such oil-based contrast media, (e.g., ultrafluid lipiodol) were felt to better fill the NLDS than water-soluble agents, were less irritating, and were undiluted by tears, offering better opacification. Such contrast entered the NLDS at negligible pressure, minimizing the chances of extravasation. However, oil-based agents have disadvantages in the NLDS. First, if extravasated, oily contrast can remain in the soft tissues for many years, inciting a granulomatous inflammatory response.[6] Second, oily opaque material is not completely miscible with tears and can fail to fill or coat the entire NLDS, limiting diagnostic capabilities. Third, oily

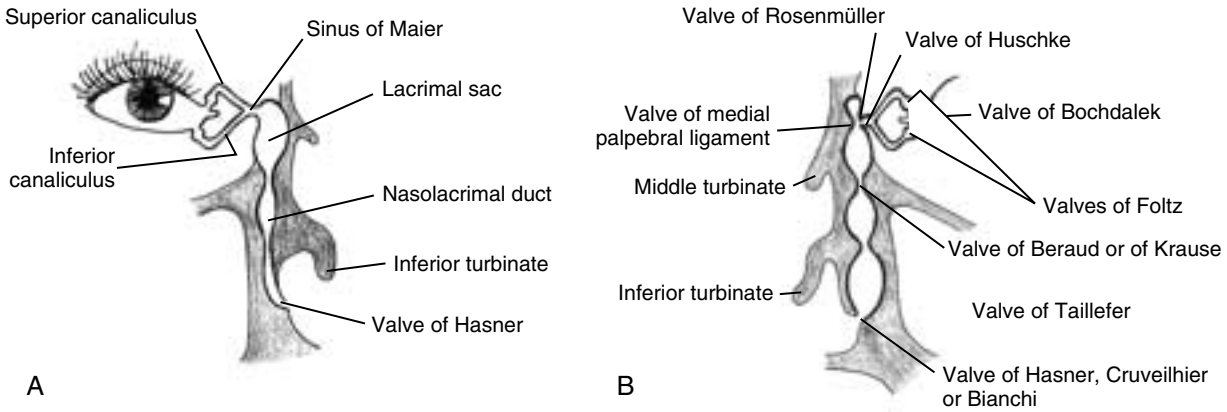

VIEW IMAGE

FIGURE 10-2 **A**, Anatomy of the NLDS. Right eye, frontal view. **B**, Drawing of the valves of the NLDS. Left eye, frontal view. (Modified from Warwick R. Eugene Woolf's Anatomy of the Eye and Orbit, 7th ed. Philadelphia: WB Saunders, 1976;232.)

Copyright © 2003, Mosby, Inc. All rights reserved.

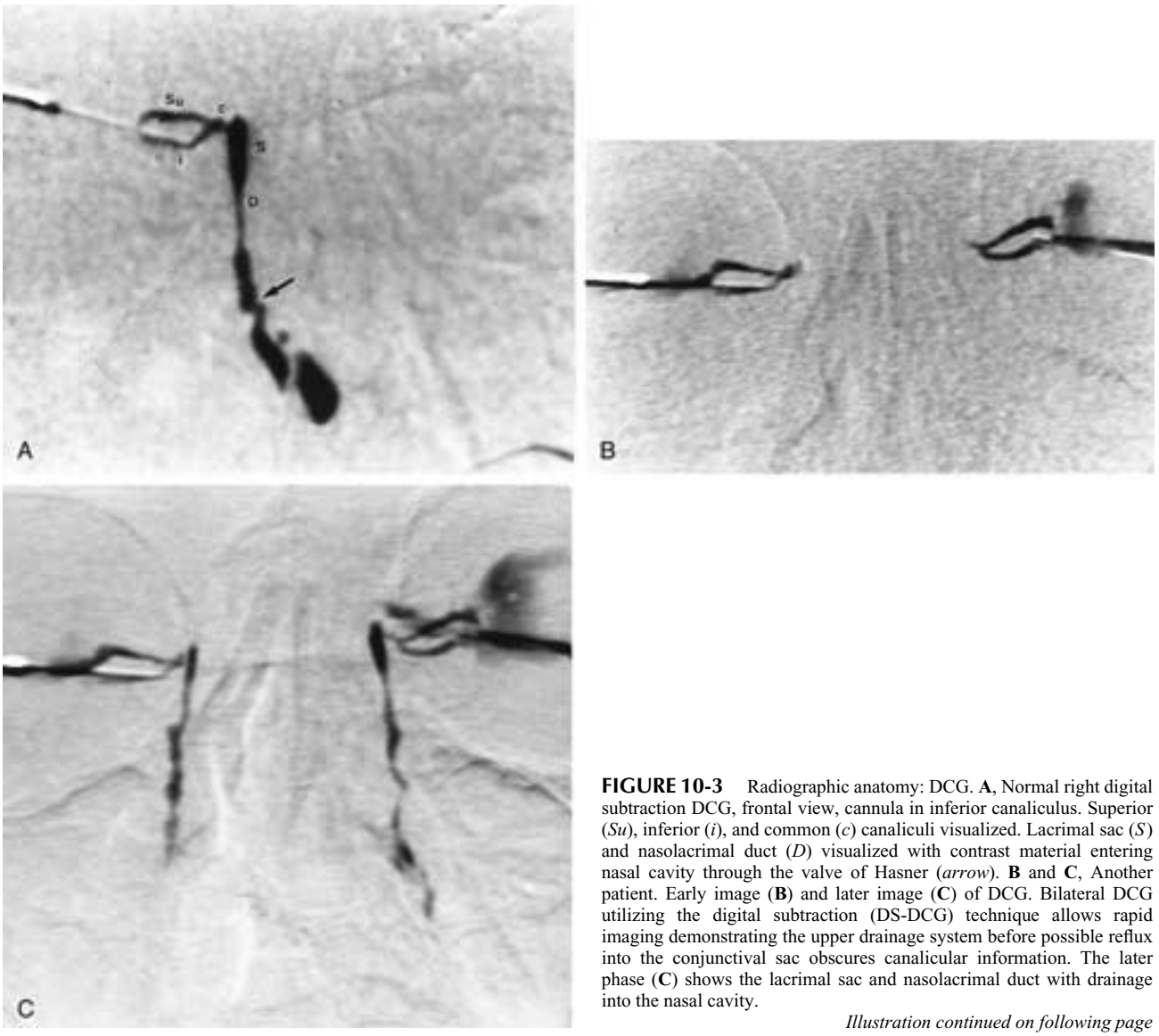

FIGURE 10-3 Radiographic anatomy: DCG. **A**, Normal right digital subtraction DCG, frontal view, cannula in inferior canaliculus. Superior (*Su*), inferior (*i*), and common (*c*) canaliculi visualized. Lacrimal sac (*S*) and nasolacrimal duct (*D*) visualized with contrast material entering nasal cavity through the valve of Hasner (*arrow*). **B** and **C**, Another patient. Early image (**B**) and later image (**C**) of DCG. Bilateral DCG utilizing the digital subtraction (DS-DCG) technique allows rapid imaging demonstrating the upper drainage system before possible reflux into the conjunctival sac obscures canalicular information. The later phase (**C**) shows the lacrimal sac and nasolacrimal duct with drainage into the nasal cavity.

Illustration continued on following page

VIEW IMAGE

contrast is more viscous than tears and often requires heating (especially with iodized oil) to reduce its viscosity before being injected.[7] If not heated, oily material requires a greater injection pressure than aqueous contrast material. Physiologic aqueous solution in the form of methylglucamine diatrizoate 40% (methylglucamine iodipamide 20%, Sinografin) was proposed by Sargent and Ebersole[6] as an excellent dacryocystographic contrast agent that was nonirritating, water soluble, miscible with tears, and similar in viscocity and pH to tears. Nonionic or lower osmolar aqueous solutions provide variable levels of iodine concentration and decreased viscosity, and are preferred for use when combining dacryocystography with digital subtraction techniques (see the section on Digital Subtraction (Macro) Dacryocystography). Munk et al.[8] noted some patient discomfort (a burning sensation) with sinografin and the nonionic solutions of 300 mg iodine per milliliter. Lipiodol offered the highest level of comfort and was the only ''tasteless'' solution. All the aqueous solutions have a disagreeable or mildly unpleasant taste but are safe to swallow.

Radiographic Techniques

Since the original description of Ewing,[1] many radiographic techniques for DCG have been described. The following are the more commonly used techniques:

- Macrodacryocystography, which uses a magnification (two and a half diameters optimum) technique after van der Plaat's description of radiographic magnification procedures.[9, 10]
- Kinetic DCG, which uses a cinematography format for evaluating the anatomy and function of the nasolacrimal apparatus.[11, 12]

Copyright © 2003, Mosby, Inc. All rights reserved.

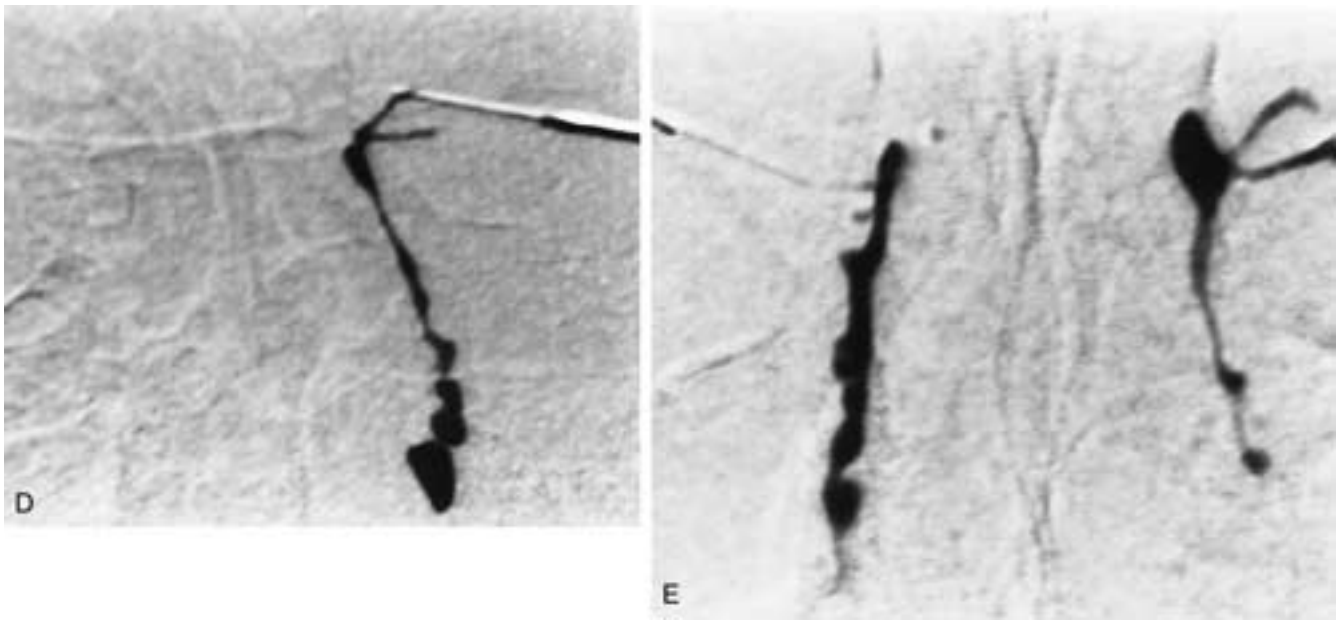

VIEW IMAGE

FIGURE 10-3 *Continued.* **D**, Anatomic variant with the left common canaliculus draining into the fundus of the lacrimal sac. **E**, Left common canaliculus empties into the lacrimal sac more inferiorly than usual. The left lacrimal sac is mildly dilated, with slight delay of drainage into the nasolacrimal duct.

- Distention DCG, which involves plain radiographs that are obtained during injection of the contrast material to better fill (distend) the NLDS.[2]
- Intubation macrodacryocystography, which combines distention DCG and macrodacryocystography.[13]
- Subtraction DCG, which combines intubation macrodacryocystography with a standard photographic subtraction technique.[14, 15]
- Tomographic DCG, which uses complex motion tomography to offer finer detail of the nasolacrimal apparatus. Thin-section images can be obtained in the frontal and lateral planes with improved detail compared to the above techniques[16] (Figs. 10-4 to 10-6).
- Digital subtraction DCG, which combines the techniques of dacryocystography with digital subtraction fluoroscopic capabilities.[17, 18] With the availability of higher-resolution digital capabilities, this technique has become the routine dacryocystographic study and is described separately in this chapter.

Injection Techniques

The study is performed with the patient supine on the examination table, and initial preliminary films are obtained to ensure patient positioning and image quality. The procedure is not uncomfortable, and in many patients no topical anesthetic is necessary. However, to make the patient more relaxed and to decrease blinking and lacrimation, one may instill into the conjunctival sac a very short-acting topical ophthalmic anesthetic (e.g., 0.5% proparacaine [Ophthaine]). Oxybuprocaine 0.4% is a very short-acting topical anesthetic that does not require shielding of the eye following the procedure, thus making it especially advantageous for bilateral studies. Approximately 2 ml of the radiopaque contrast material is drawn into a small syringe, which is then connected to the lacrimal cannula and tubing, and the system is cleared of any air bubbles. The inferior punctum is then dilated with a lacrimal dilator, with the lower lid slightly everted and with minimal lateral traction to help stabilize the punctum. To avoid damage (false passage) to the canaliculus, the dilator, and subsequently the cannula, are positioned initially perpendicular to the lid margin and then rotated 90° horizontally to be directed medially along the horizontal component of the canaliculus (with the lower lid stretched laterally). The lacrimal sac and medial canthus are then palpated to detect any mass lesion, fullness, or tenderness and to express any fluid present in the sac through the punctum or into the nose. Ideal procedure includes pre-DCG irrigation and careful expression of the lacrimal sac to flush out accumulation of thickened mucus within the duct system. Failure to irrigate the nasolacrimal duct system (NLDS) or express the lacrimal sac contents may lead to interpretive difficulties, including improper estimation of the size of the lacrimal sac or misdiagnosis of obstructions proximal to a stenosing lesion due to the retained secretions.[19] Residual fluid in the sac causes oil-based contrast media to form globules, giving a false impression of a polycystic sac or diverticula.[9] The lacrimal cannula is then

Copyright © 2003, Mosby, Inc. All rights reserved.

placed into the inferior punctum just far enough to remain stable during the study, and the tubing is taped to the patient's face. Care should be taken to avoid a common error, which is placement of the cannula too far into the inferior canaliculus. Frontal projection images approximating the Water's projection (40° occipitomental projection) are used to bring the nasolacrimal duct parallel to the imaging plane in an attempt to eliminate any distortion of the nasolacrimal duct. In this projection, the inferior orbital rim is approximately at the level of the junction of the middle and upper third of the nasolacrimal duct.[9] A coned occipitomental view is also obtained, centered midline at the inferior orbital margin. The injection is then made, and films are immediately obtained. If distention DCG, intubation DCG, or digital subtraction DCG is used, the films are obtained during the injection. Initial or subsequent cannulation of the superior punctum may be appropriate when there is difficulty with cannulation of the inferior punctum or when further assessment is required following the initial injection of the inferior punctum. A delayed upright film should be taken, especially if obstruction is suspected, to assess possible delayed drainage into or through the inferior drainage system.

The decision to perform specific unilateral or routine bilateral DCG varies with the individual or institutional philosophy. Routine bilateral DCG may be justified by the

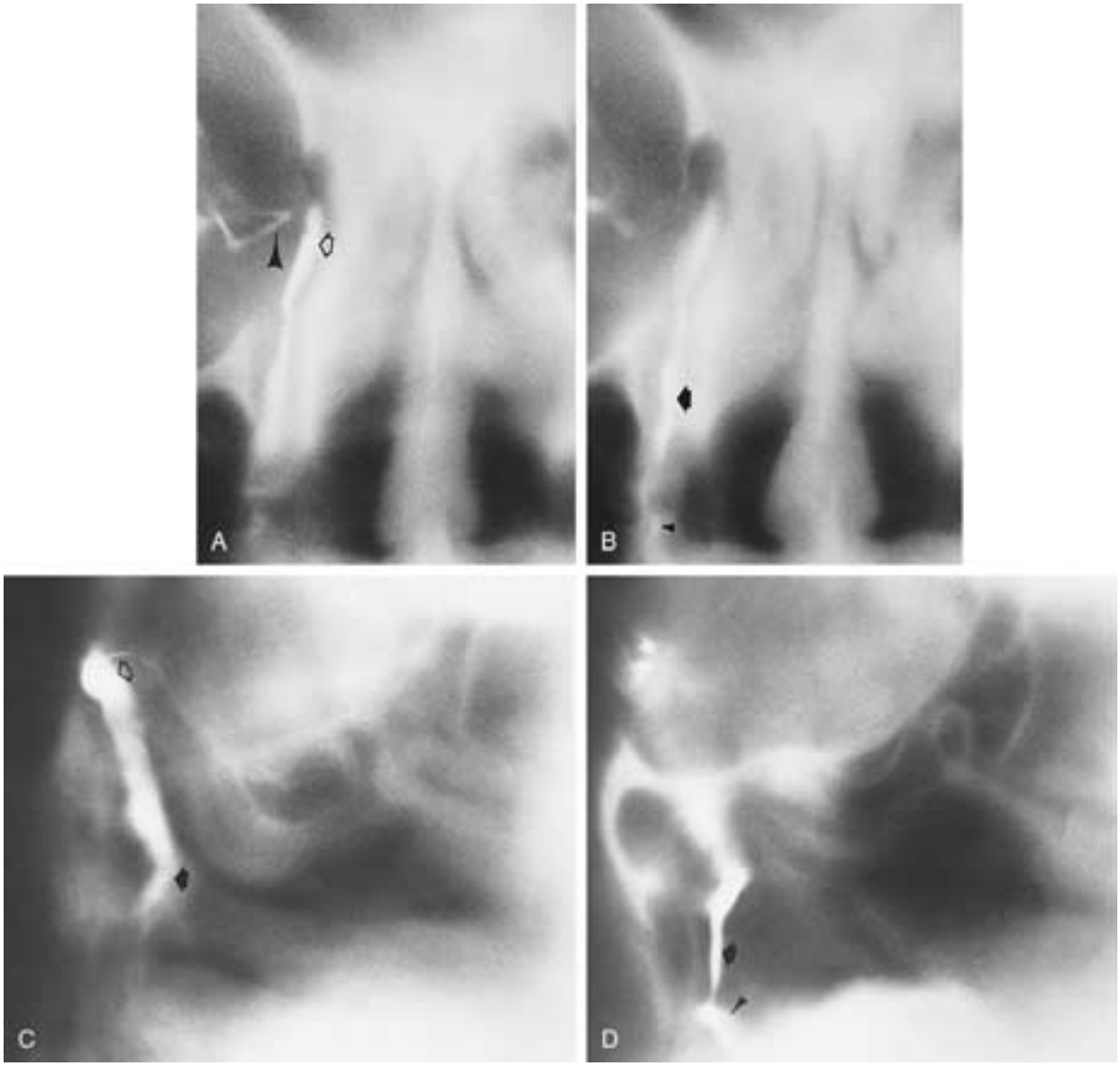

VIEW IMAGE

FIGURE 10-4 Tomographic DCG, which provides superb anatomic detail. **A**, Frontal plane tomography. Anterior section shows the canaliculi (*arrowhead*) and lacrimal sac (*open arrow*). **B**, More posterior tomographic section shows the nasolacrimal duct (*arrow*) and contrast material in the nasal cavity (*arrowhead*). **C** and **D**, Lateral tomograms show the lacrimal sac (*open arrow*), nasolacrimal duct (*closed arrow*), and contrast material in the nose (*arrowhead*). (See also Fig. 10-6.)

Copyright © 2003, Mosby, Inc. All rights reserved.

relative ease of the procedure; the lack of additional radiation, since the contralateral orbit is frequently included in the field of study; and the frequent finding of abnormalities in the clinically ''asymptomatic'' side.[20] Bilateral simultaneous injection, using a Y-connector, allows comparative flow characteristics through the NLDS. Other centers restrict the cannulation and visualization to those NLDSs that are symptomatic, eliminating any potential for iatrogenic insult to the noninvolved tear duct system.

DIGITAL SUBTRACTION (MACRO) DACRYOCYSTOGRAPHY

In contrast to intubation macrodacryocystography using a serial film changer, digital subtraction dacryocystography (DS-DCG) allows, under fluoroscopic control, proper positioning and subsequent real-time imaging during the introduction of contrast medium. Images are usually taken every 1 to 2 seconds and can be terminated as soon as

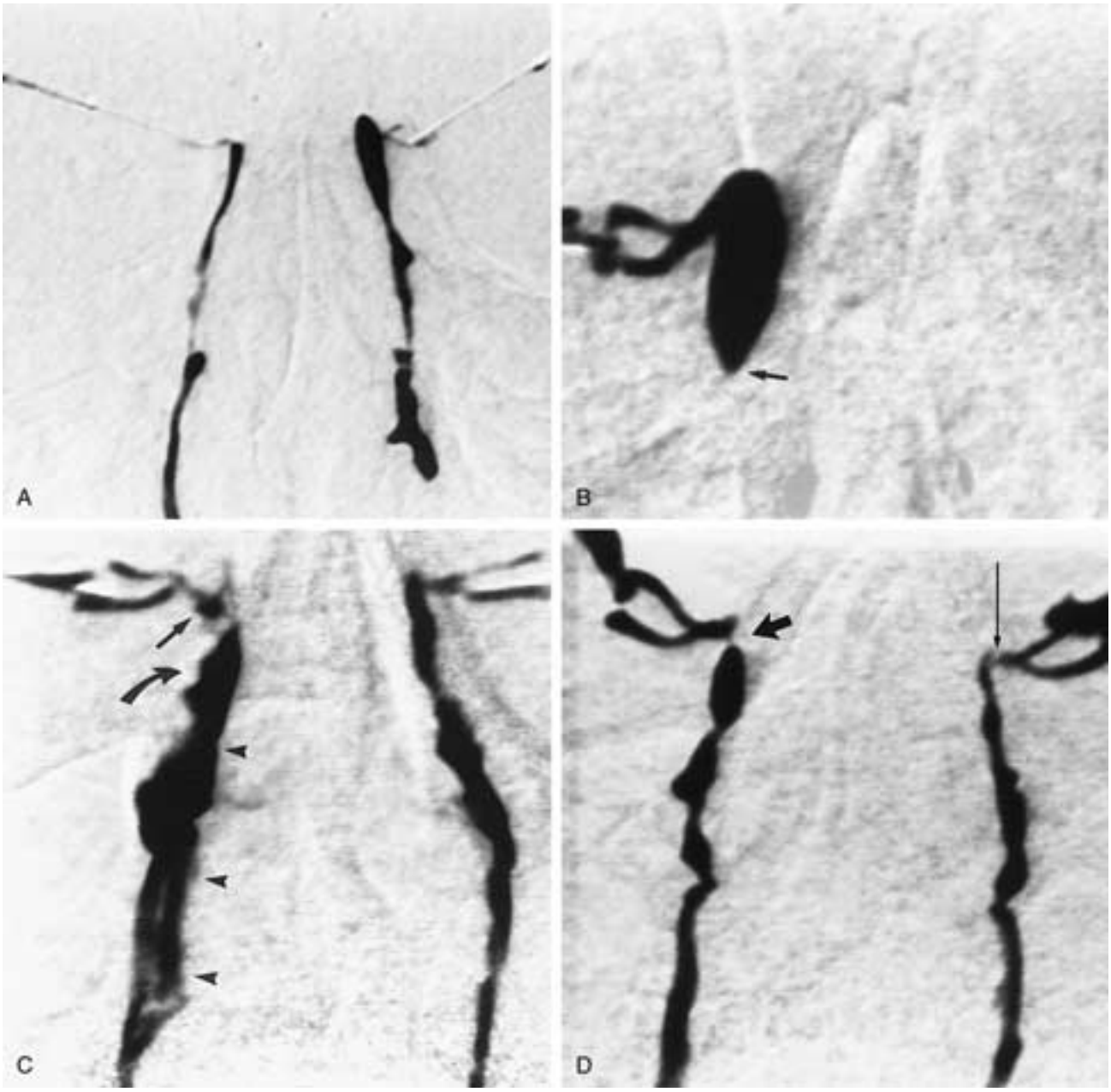

VIEW IMAGE

FIGURE 10-5 Stenosis-obstruction: DCG of the NLDS. Multiple patients. **A**, DCG with normal drainage bilaterally. Early distention of the left lacrimal sac compared with the more tubular configuration of the right lacrimal sac. Lack of reflux of contrast material into the right superior canaliculus. **B**, Complete obstruction of the distal lacrimal sac (*arrow*) at the junction with the nasolacrimal duct (*NLD*). Dilation (mucocele) of the lacrimal sac is present. **C**, Markedly irregular right lacrimal sac, contracted superiorly (*straight arrow*) and dilated inferiorly (*curved arrow*). The right NLD is also irregular and dilated (*arrowheads*). The left side is normal. Right chronic dacryocystitis is present. **D**, Stenosis at the junction of the right common canaliculus and lacrimal sac with contracture (*short arrow*) of the superior aspect of the lacrimal sac. Focal stenosis (*thin arrow*) is seen in the medial aspect of the left common canaliculus.

Copyright © 2003, Mosby, Inc. All rights reserved.

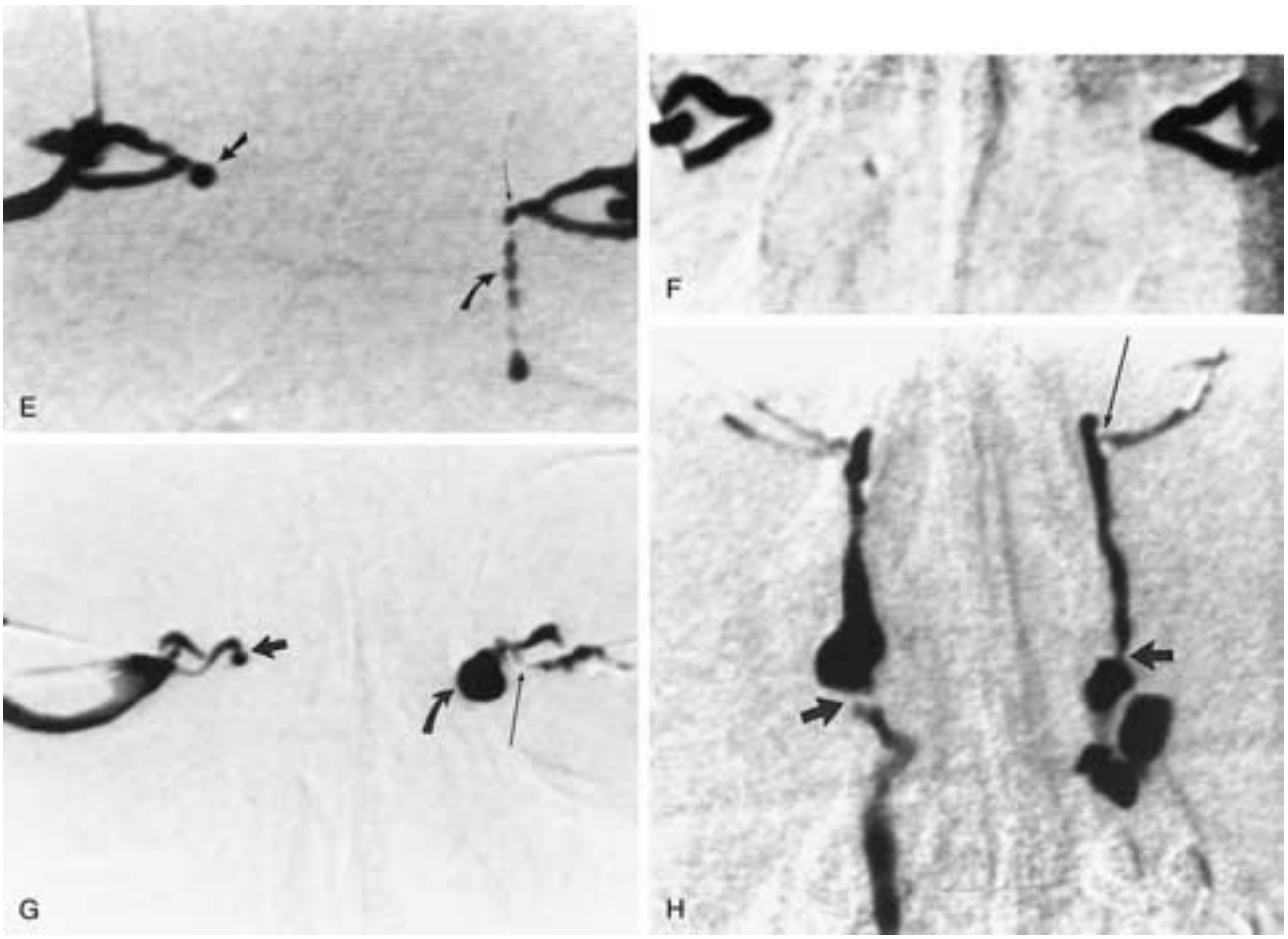

VIEW IMAGE

FIGURE 10-5 *Continued.* **E**, Bilateral DCG with an obstructed, cicatrized right lacrimal sac (*oblique arrow*). The left lacrimal sac is also scarred down (*thin arrow*), with irregularity and focal stenoses of the nasolacrimal duct (*curved arrow*). **F**, Bilateral obstruction of the lateral aspect of the common canaliculus with dilatation of the superior and inferior canaliculi bilaterally. **G**, Bilateral obstruction on DCG. Right cicatrized lacrimal sac (*straight arrow*). Left lacrimal sac mucocele (*curved arrow*). Stenosis also is present in the left inferior canaliculus (*thin arrow*). **H**, Stenosis at the valve of Hasner (*short arrows*), with distention of the distal right nasolacrimal duct. Mild stenosis in the left common canaliculus (*thin arrow*) with no reflux to the superior canaliculus.

Illustration continued on following page

patency or obstruction is defined. Fewer images (4 to 6) are usually acquired than for conventional DCG (6 to 10 images).[17] Digital adjustment of the data provides the most desired image quality on the ''hard copy'' film. The subtraction image is also digital, avoiding the time-consuming process of conventional photographic subtraction. The radiation dose to the lens is less in DS-DCG than in conventional DCG. Lead eye protection can reduce lens dosage, with further reduction achieved by noting early ductal patency using the real-time imaging capability of DS-DCG.[18, 21] The use of a carefully collimated high-kilovoltage primary beam; lead eye shields, which do not compromise the diagnostic quality of the study (placed lateral and anterior to the NLDS); and 30° oblique lateral projections for simultaneous bilateral DCG are simple measures that decrease by 97% the lens dosage required with conventional techniques. With these techniques, the radiation dosage for bilateral DCG can be limited to less than 1 mGy (1 mGy = 100 mrad) to the lens.[21] For conventional DCG, the patient lies supine, and the x-ray source is anterior to the patient. With DS-DCG the patient is also supine. However, the x-ray source is posterior to the patient, so that the cranium acts as a ''radiation shield'' to the lens. Galloway et al.[17] found the actual lens radiation dose/exposure to be 13 times greater for conventional DCG than for DS-DCG (270 vs. 20 mrad), with the total lens radiation dose per study (six exposures each) being 1644 versus 126 mrad. King and Haigh's[18] study had a mean radiation dose/DS-DCG run of 0.68 mSv compared with 1.53 mSv (l mSv = 100 mrem) for conventional two-film DCG, with the latter patients studied in the uncommon occipitomental position, and therefore having a lower reading than for the mentooccipital position usual for conventional DCG. Repeat studies needed as a result of suboptimal radiographic exposure factors were also obviated. Similarly, the ability to visualize the early flow of contrast medium through the canaliculi and upper drainage system obviates the need to repeat studies in which reflux into the conjunctival sac obscures information of canalicular patency.

In the early phase of injection, reflux can be minimized by an initial slow injection rate. Subsequently, the rate can be

Copyright © 2003, Mosby, Inc. All rights reserved.

increased to achieve greater sac distention or to overcome resistance caused by partial obstruction.[17] The ability of DS-DCG to clearly demonstrate the upper drainage system, especially the common canaliculus, further reduces the relative radiation exposure of conventional DCG by obviating the need for tomographic DCG. DS-DCG has also dramatically decreased the need for lateral radiographic images. In the majority of studies, a single dynamic injection is required. In those departments where lacrimal imaging is infrequently performed, the advantages of DS-DCG become more apparent in both radiation reduction and study quality.[18]

With the newer digital units, spatial resolution is superb, approaching that of conventional radiography, while the contrast resolution of digital imaging is markedly superior to that of conventional imaging. The immediate viewing (or reviewing) of DS-DCG images significantly reduces the proportionate length of the study, allowing more efficient use of time for the radiologist and the patient. The increased contrast sensitivity of digital imaging allows for greater flexibility of choice of contrast agents, with water-soluble agents being preferred because of their lower viscosity, greater miscibility with tears, and easier flow through the NLDS. These agents usually require smaller volumes and have lower iodine content than the agents used for conventional DCG. For appropriate DS-DCG images, the patient must be fully cooperative, and be able to lie still and follow instructions, although manipulation of the computed data can offset minor degrees of movement. The use of topical anesthetic and the choice of catheters and their placement within the canaliculus are similar to those of conventional DCG.

Inclusion of a late (delayed) image, after the patient has been in the upright position for 5 minutes, increases the sensitivity of DCG or DS-DCG, with the specific intention to assess for failure of gravitational drainage of contrast medium from the nasolacrimal duct system (NLDS). This delay also allows DCG and DS-DCG, more anatomically orientated imaging procedures, to offer a physiologic component to the procedure, augmenting the value of DCG and DS-DCG in the evaluation of patients with functional nasolacrimal duct obstruction (FNLDO).[22] (In the section on Dacryoscintography, see also Incomplete Obstruction and Functional Nasolacrimal Duct Obstruction.) FNLDO is diagnosed if there is poor emptying, with residual contrast material present in the lacrimal sac or nasolacrimal duct on the delayed image. In the normal patient, contrast medium almost immediately disappears from the NLDS with the patient placed in the upright position. Issues with viscosity and surface tension may affect contrast drainage. Oil-based contrast may be more easily detected as small droplets within the duct system.[22] Water-soluble contrast, although safer, may be partially absorbed by the epithelium of the NLDS during the delayed period. Although Zinreich et al.[23] have attempted contrast DCG by simply placing the radiographic contrast agent into the conjunctival sac, the display of anatomic structures is less detailed than with DCG using cannulation despite the sensitivity of digital subtraction imaging. The hope that such a topically applied contrast

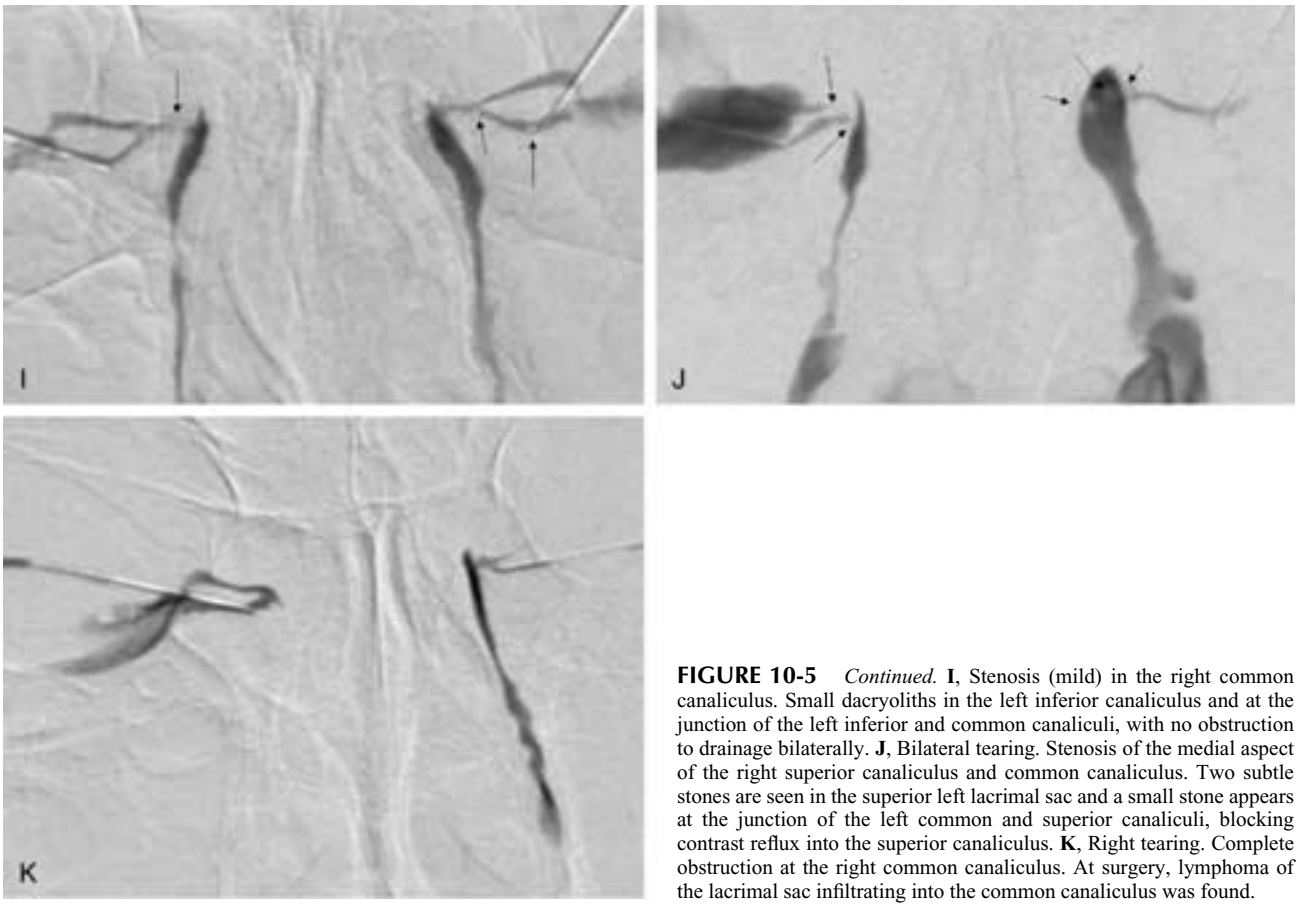

FIGURE 10-5 *Continued.* **I**, Stenosis (mild) in the right common canaliculus. Small dacryoliths in the left inferior canaliculus and at the junction of the left inferior and common canaliculi, with no obstruction to drainage bilaterally. **J**, Bilateral tearing. Stenosis of the medial aspect of the right superior canaliculus and common canaliculus. Two subtle stones are seen in the superior left lacrimal sac and a small stone appears at the junction of the left common and superior canaliculi, blocking contrast reflux into the superior canaliculus. **K**, Right tearing. Complete obstruction at the right common canaliculus. At surgery, lymphoma of the lacrimal sac infiltrating into the common canaliculus was found.

VIEW IMAGE

Copyright © 2003, Mosby, Inc. All rights reserved.

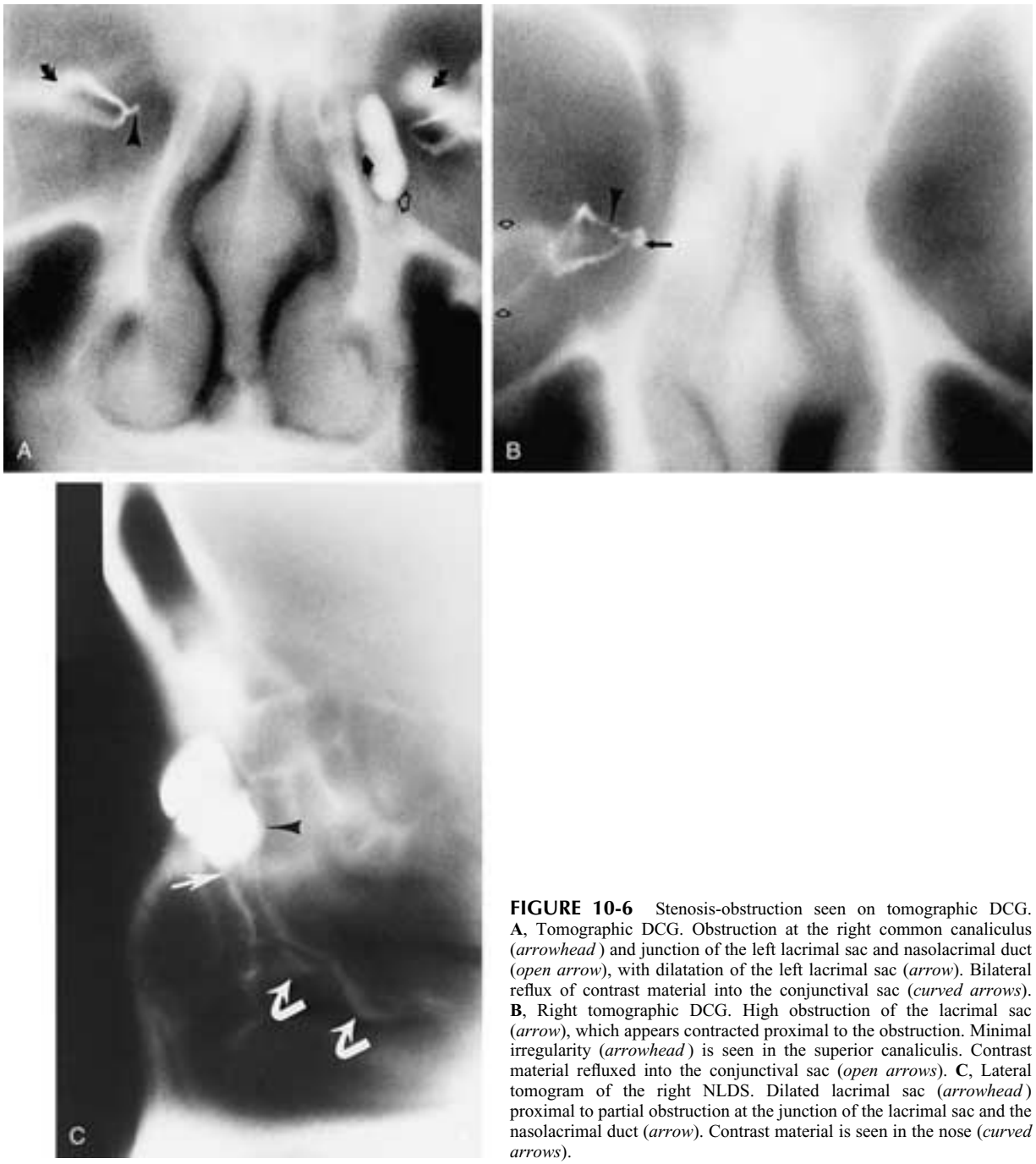

FIGURE 10-6 Stenosis-obstruction seen on tomographic DCG. **A**, Tomographic DCG. Obstruction at the right common canaliculus (*arrowhead*) and junction of the left lacrimal sac and nasolacrimal duct (*open arrow*), with dilatation of the left lacrimal sac (*arrow*). Bilateral reflux of contrast material into the conjunctival sac (*curved arrows*). **B**, Right tomographic DCG. High obstruction of the lacrimal sac (*arrow*), which appears contracted proximal to the obstruction. Minimal irregularity (*arrowhead*) is seen in the superior canaliculis. Contrast material refluxed into the conjunctival sac (*open arrows*). **C**, Lateral tomogram of the right NLDS. Dilated lacrimal sac (*arrowhead*) proximal to partial obstruction at the junction of the lacrimal sac and the nasolacrimal duct (*arrow*). Contrast material is seen in the nose (*curved arrows*).

VIEW IMAGE

DCG may allow the physiologic advantage of dacryoscintigraphy to be combined with the anatomic detail of cannulated DCG has yet to be fulfilled. The main acceptance of this technique is in its application to CT-dacryocystography or MR-dacryocystography techniques.

CLINICAL TESTS

Before referral for DCG, most patients are seen by an ophthalmologist, who performs a number of tests to assess epiphora.

Probing

Multiple calibers of fine flexible probes (Bowman probes 0000 to 0) may be used to ''palpate'' the nasolacrimal drainage lumen. Such probes can be passed to a ''hard stop'' representing the medial wall of the lacrimal sac. Slight withdrawal and downward angulation of the probe may allow entry into the nasolacrimal duct. A feeling of ''give'' or loss of resistance may be felt as the probe passes through the valve of Hasner. The upper drainage system is considered patent if a No. 0 probe passes through to the medial wall of the lacrimal sac.[24]

Text continued on page 669

Copyright © 2003, Mosby, Inc. All rights reserved.

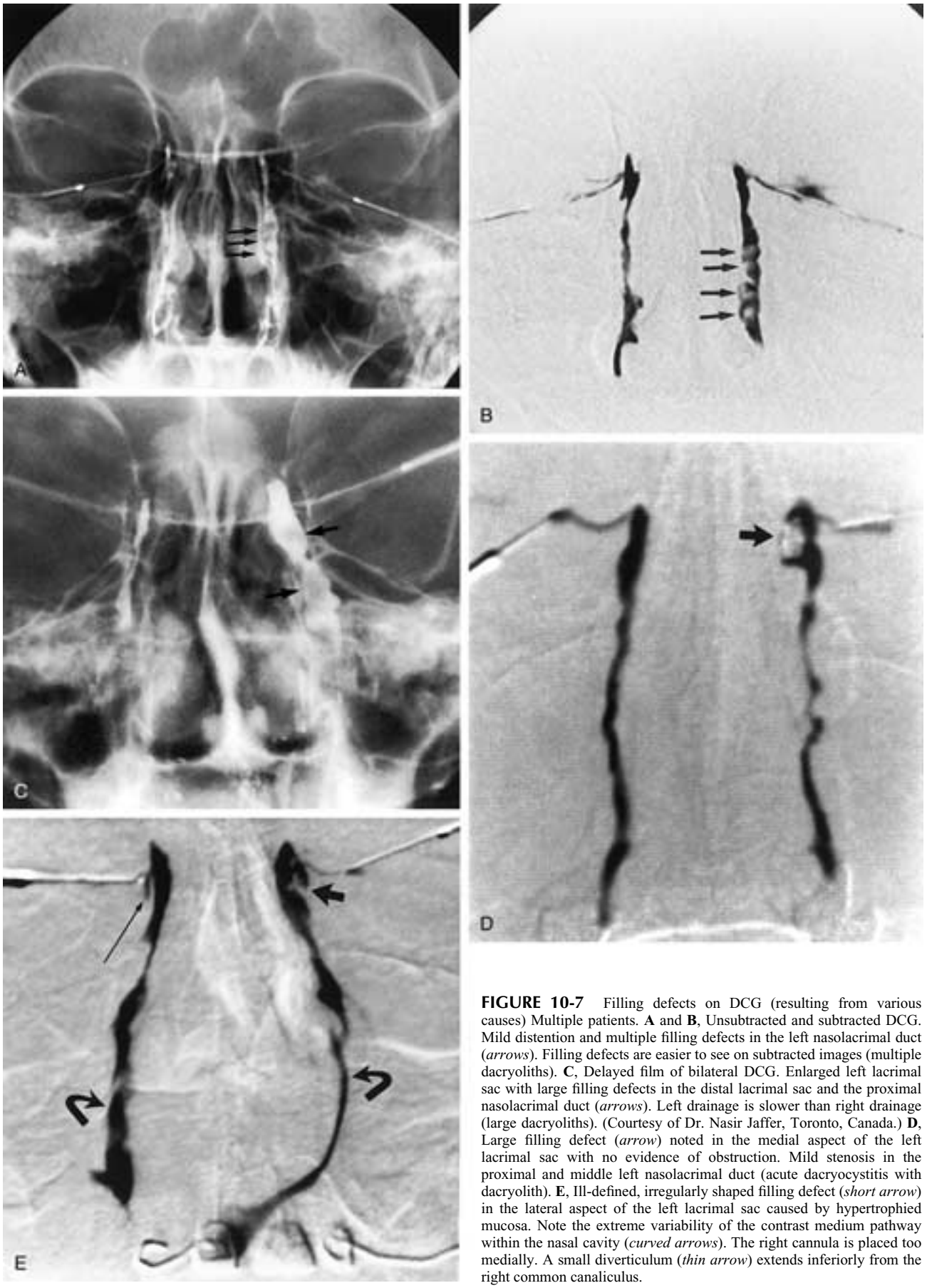

FIGURE 10-7 Filling defects on DCG (resulting from various causes) Multiple patients. **A** and **B**, Unsubtracted and subtracted DCG. Mild distention and multiple filling defects in the left nasolacrimal duct (*arrows*). Filling defects are easier to see on subtracted images (multiple dacryoliths). **C**, Delayed film of bilateral DCG. Enlarged left lacrimal sac with large filling defects in the distal lacrimal sac and the proximal nasolacrimal duct (*arrows*). Left drainage is slower than right drainage (large dacryoliths). (Courtesy of Dr. Nasir Jaffer, Toronto, Canada.) **D**, Large filling defect (*arrow*) noted in the medial aspect of the left lacrimal sac with no evidence of obstruction. Mild stenosis in the proximal and middle left nasolacrimal duct (acute dacryocystitis with dacryolith). **E**, Ill-defined, irregularly shaped filling defect (*short arrow*) in the lateral aspect of the left lacrimal sac caused by hypertrophied mucosa. Note the extreme variability of the contrast medium pathway within the nasal cavity (*curved arrows*). The right cannula is placed too medially. A small diverticulum (*thin arrow*) extends inferiorly from the right common canaliculus.

VIEW IMAGE

Copyright © 2003, Mosby, Inc. All rights reserved.

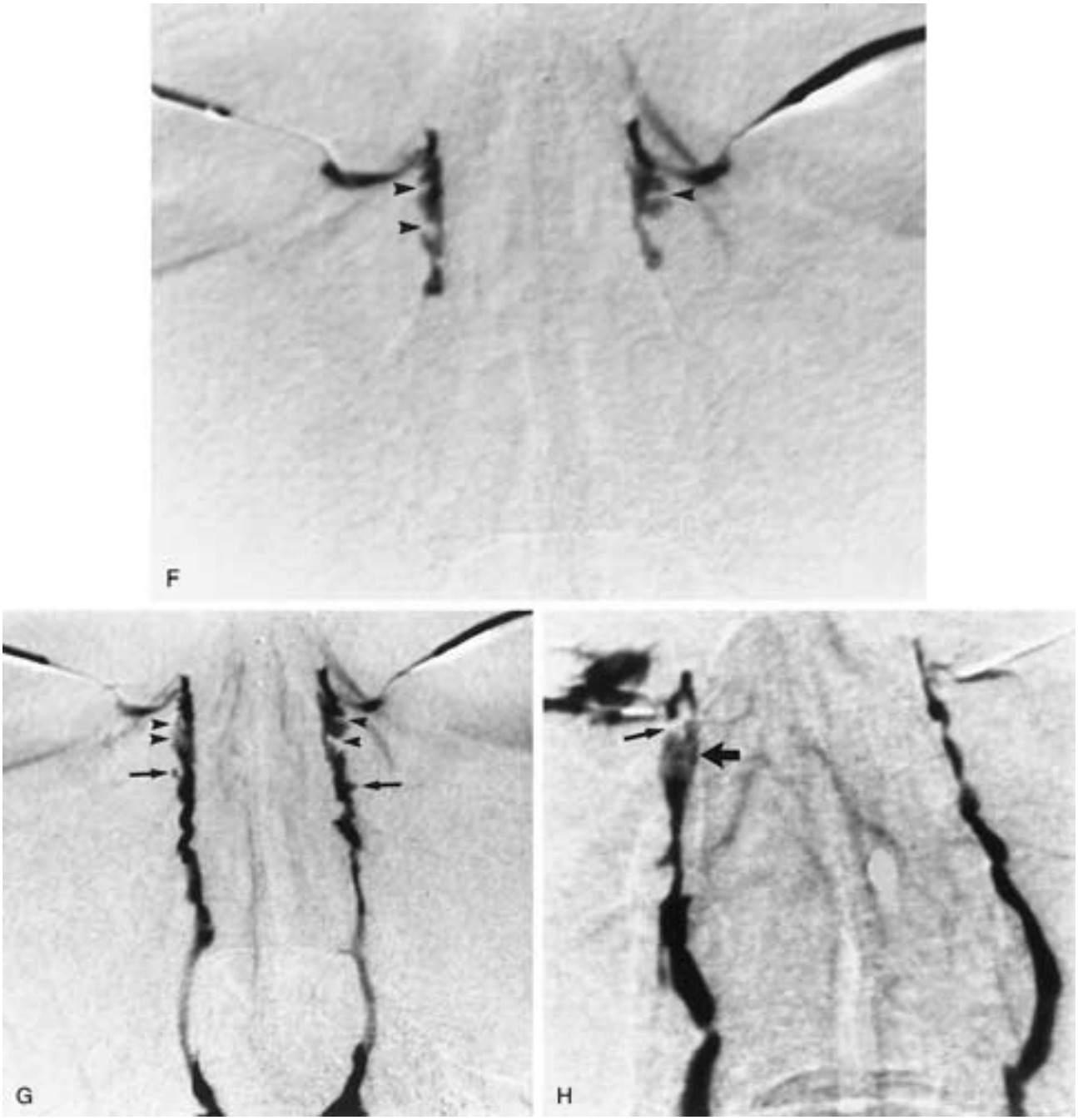

VIEW IMAGE

FIGURE 10-7 *Continued.* **F** and **G**, Early and late films of bilateral DCG. Lateral filling defects (*arrowheads*) and small diverticuli (*arrows*) are noted in the lacrimal sac and nasolacrimal duct bilaterally. Hypertrophic mucosal changes. **H**, Immediate drainage of the nasolacrimal system bilaterally. Filling defect in the right lacrimal sac (*thin arrow*) and decreased density in the inferior aspect of the right lacrimal sac (*short arrow*) caused by hematoma in the right lacrimal sac wall (pedestrian struck by a car).

Illustration continued on following page

Copyright © 2003, Mosby, Inc. All rights reserved.

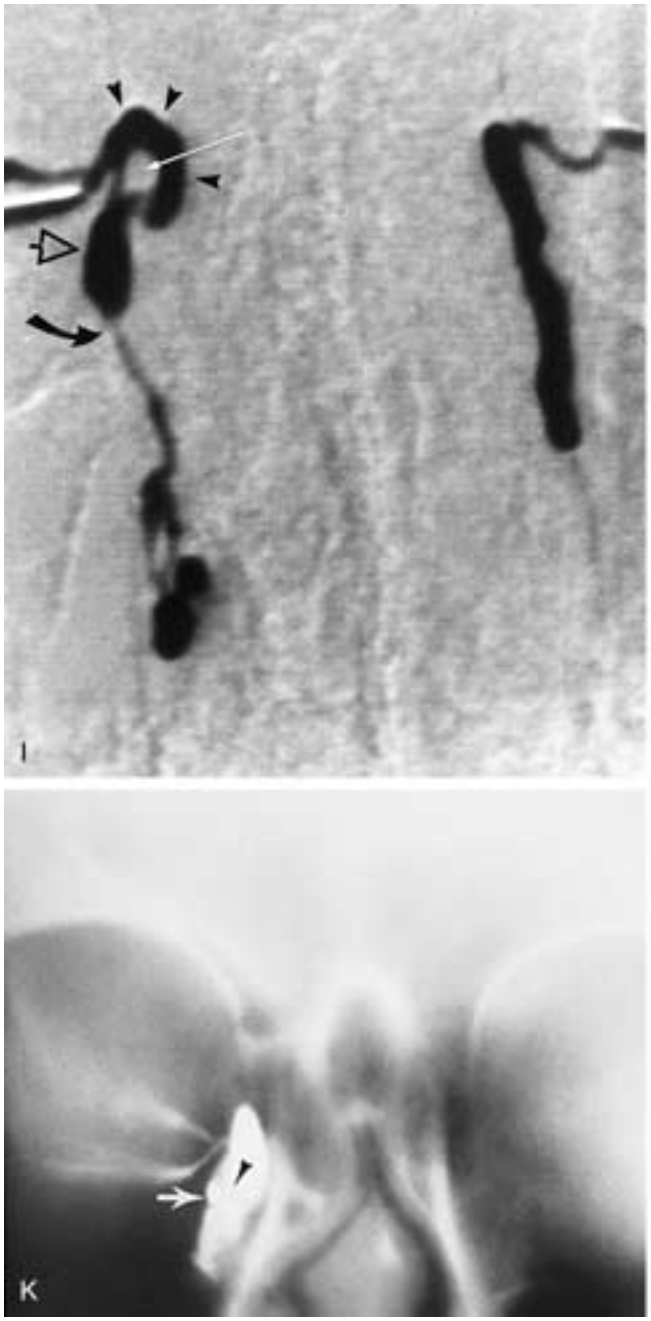

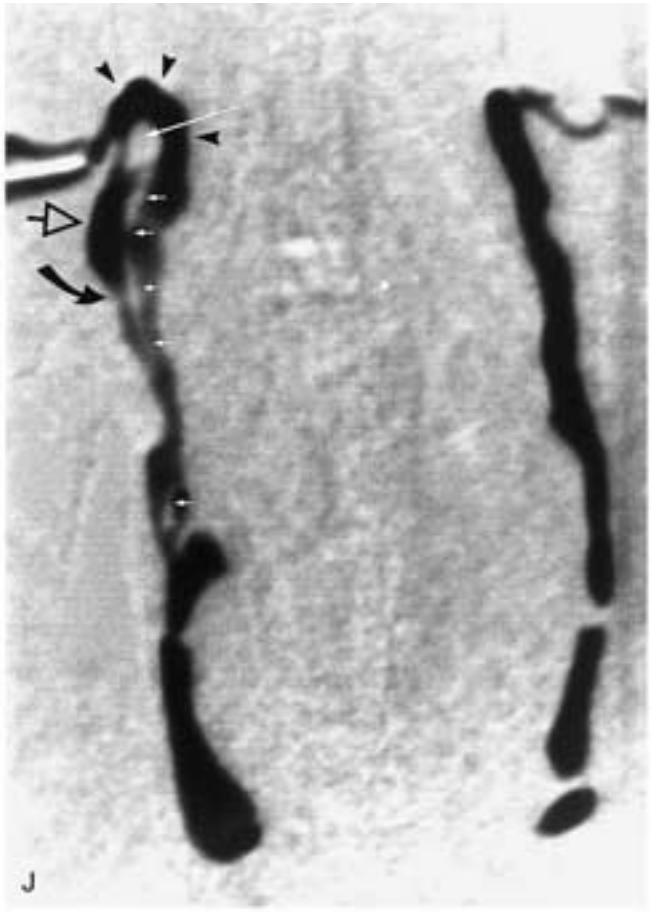

FIGURE 10-7 *Continued.* **I** and **J**, Early and late DCG images in a patient with previous DCR. The large filling defect in the abnormal right lacrimal sac represents prominent granulation tissue (*long white arrow*). Contrast superomedial to the filling defect represents the DCR pathway (*arrowheads*). The lacrimal sac is stenosed lateral to granulation tissue and then becomes dilated (*open arrow*) above the stenosis of the nasolacrimal duct (*curved arrow*). The elongated filling defect (*tiny white arrows*) represents the lateral wall of the nasal cavity separating the two channels of drainage (DCR to the nasal cavity and lacrimal sac to the nasolacrimal duct to the nasal cavity). **K** and **L**, AP and lateral tomographic DCG in a patient with a 10-year history of epiphora. Filling defect (*arrowhead*) in the dilated lacrimal sac (*arrow*) represents concretion of *Actinomyces israelii* (found at surgery). Lateral view shows contrast material in the inferior meatus (*open arrow*).

VIEW IMAGE

Copyright © 2003, Mosby, Inc. All rights reserved.

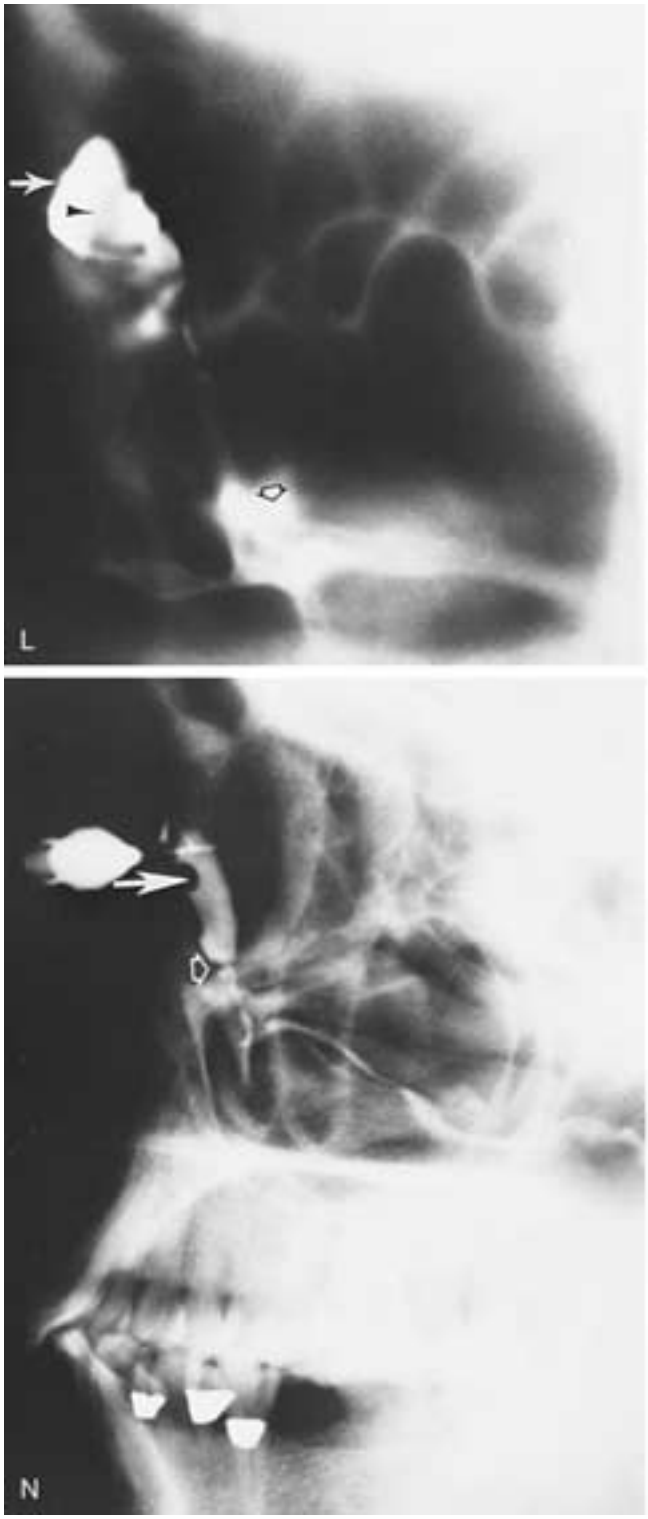

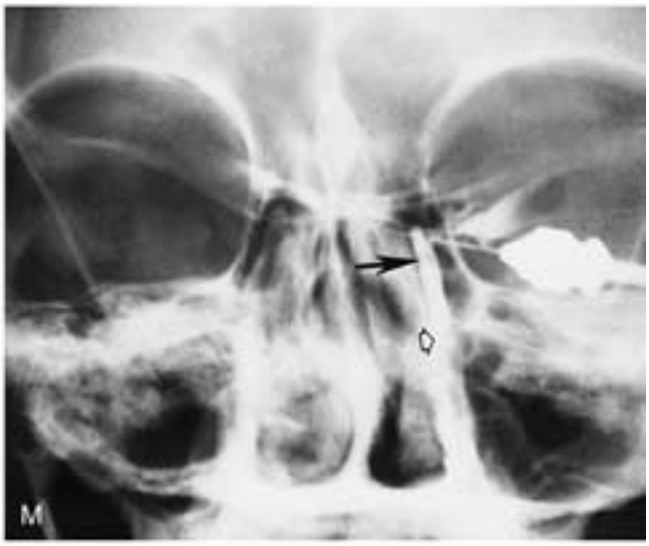

FIGURE 10-7 *Continued.* **M** and **N**, Left DCG, frontal view, and cross-table lateral projection. Air bubbles are present as a filling defect in the dilated lacrimal sac (*arrow*). On the cross-table lateral film, air bubbles rise in the lacrimal sac to differentiate it from concretions. Partial obstruction at the junction of the lacrimal sac and nasolacrimal duct (*open arrow*). (See also Figs. 10-17 to 10-19).

Illustration continued on following page

VIEW IMAGE

Copyright © 2003, Mosby, Inc. All rights reserved.

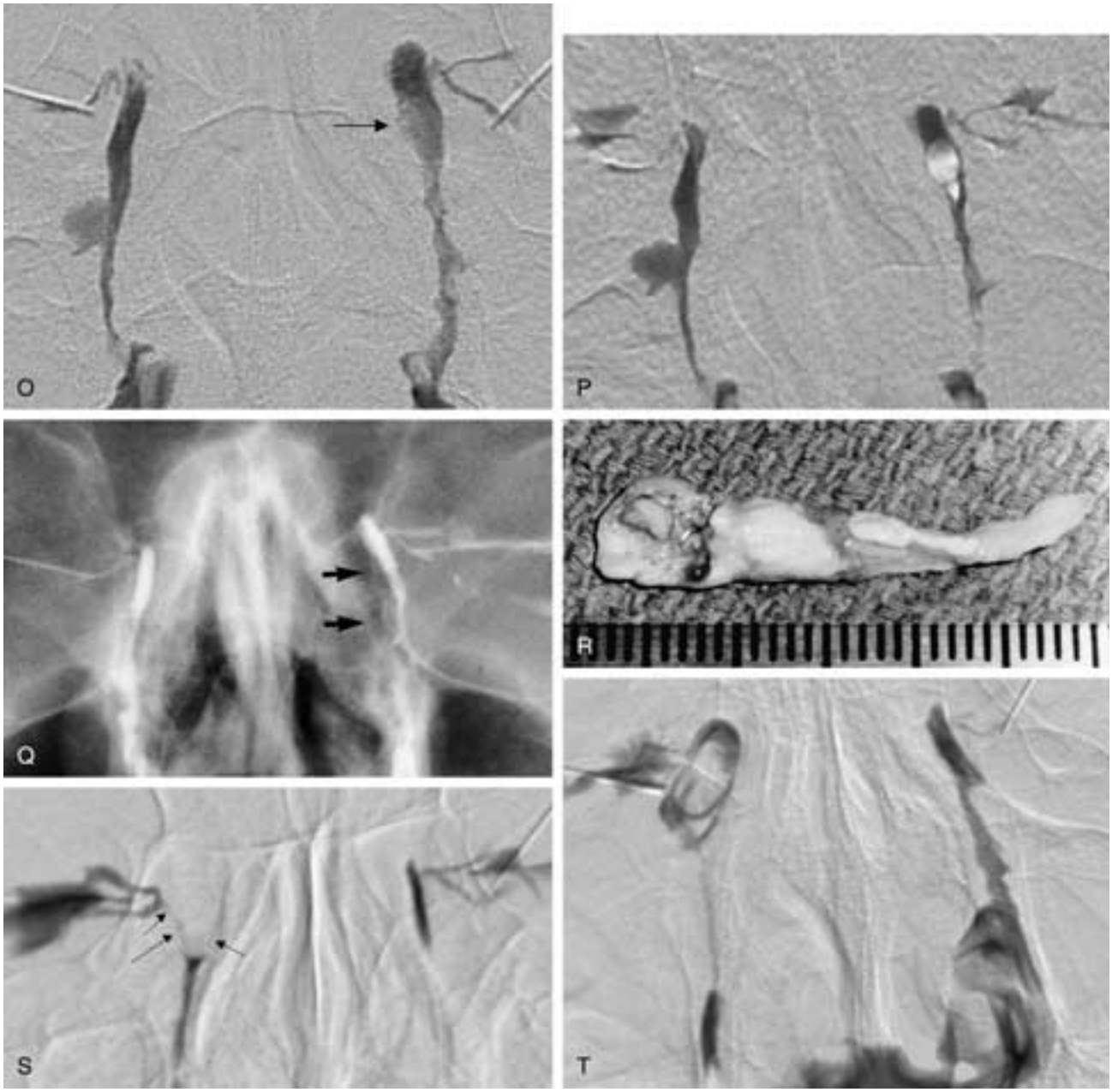

VIEW IMAGE

FIGURE 10-7 *Continued.* **O** and **P**, Tearing. Previous patency on irrigation. Recent intermittent patency. **O**, Subtle filling defect (*arrow*) is seen in the distended left lacrimal sac. **P**, Fourteen months later, a large dacryolith was more easily seen in the lacrimal sac. Incidental diverticulum at the junction of the right lacrimal sac and nasolacrimal duct. **Q** and **R**, Calculus in the left NLDS. The patient presented with tearing and patency on syringing. **Q**, DCG shows no evidence of obstruction. Contrast medium column is deflected laterally (*arrows*) from the expected position of the lacrimal sac. **R**, At surgery (DCR), a large stone was seen filling the entire sac and superior aspect of the nasolacrimal duct. **S**, Right tearing. Large filling defect distending the right lacrimal sac (*arrows*), with minimal contrast seen only peripherally. Common canaliculus not identified. Pathology: lymphoma lacrimal sac. (See also Fig. 10-5K). **T**, Large filling defect (dacryolith) in the right lacrimal sac, with limited contrast into the nasolacrimal duct. (**Q** and **R** From Hurwitz JJ, Kassel EE. Dacryocystography. In: Hurwitz JJ, ed. The Lacrimal System. Philadelphia: Lippincott-Raven, 1996;71.)

Copyright © 2003, Mosby, Inc. All rights reserved.

Irrigation

Standard lacrimal cannulation and irrigation are performed using saline solution. The patient is usually inclined forward, in a sitting position, to allow the irrigating solution to be readily assessed exiting from the nostrils. False-negative or false-positive tests may partly result from the variable ability (subjective) of the patient to detect the presence of saline entering the nasopharynx. A small amount of fluoroscein may be added to the saline to assist in the detection of patency of the drainage system. Syringing of the lacrimal system correlates poorly with DCG[25] and shows an 18% discordance with dacryoscintigraphy (DSG)[26] in detecting obstruction.

Dye Tests

Jones 1 Test

The fluoroscein 2% dye test (the primary dye test) detects functional obstruction, that is, defines the inability of the drainage apparatus to pump tears from the eye to the nose.[27] Two drops of dye placed into the conjunctival cul de sac should reach the nasal cavity within 1 to 3 minutes (positive test). It should be noted that in the Jones tests, a normal result is referred to as a positive test, unlike in most imaging examinations. The dye may be retrieved on a nasal applicator or confirmed by nose blowing or by nasal irrigation with saline.

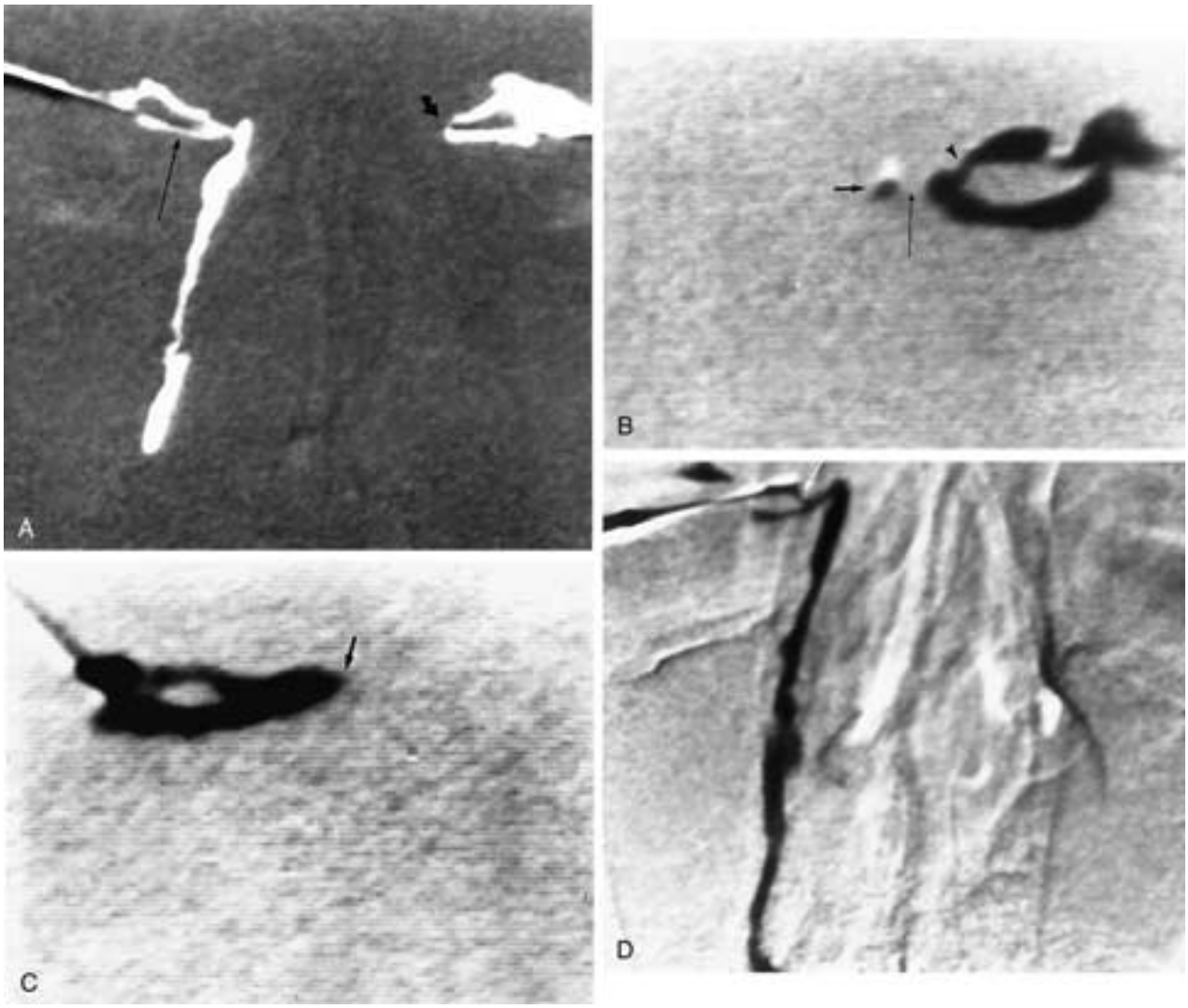

VIEW IMAGE

FIGURE 10-8 Canalicular obstruction. **A**, Bilateral DCG with complete obstruction of the lateral (proximal) left common canaliculus (*short arrow*). Mild stenosis of the distal right inferior canaliculus (*thin arrow*). **B**, Left superior canalicular injection shows severe stenosis of the medial left common canaliculus (*thin arrow*) with minimal contrast reaching the lacrimal sac (*short arrow*), which may be fibrosed. Mild stenosis of the medial aspect of the left superior canaliculus (*arrowhead*). **C**, Right DCG shows complete obstruction at the medial (distal) aspect of the common canaliculus (*arrow*). **D**, Superior canalicular injection. Focal tight stenosis (*arrow*) of the medial aspect of the superior canaliculus. No reflux into superior canaliculus had been seen from an inferior canalicular injection.

Illustration continued on following page

Copyright © 2003, Mosby, Inc. All rights reserved.

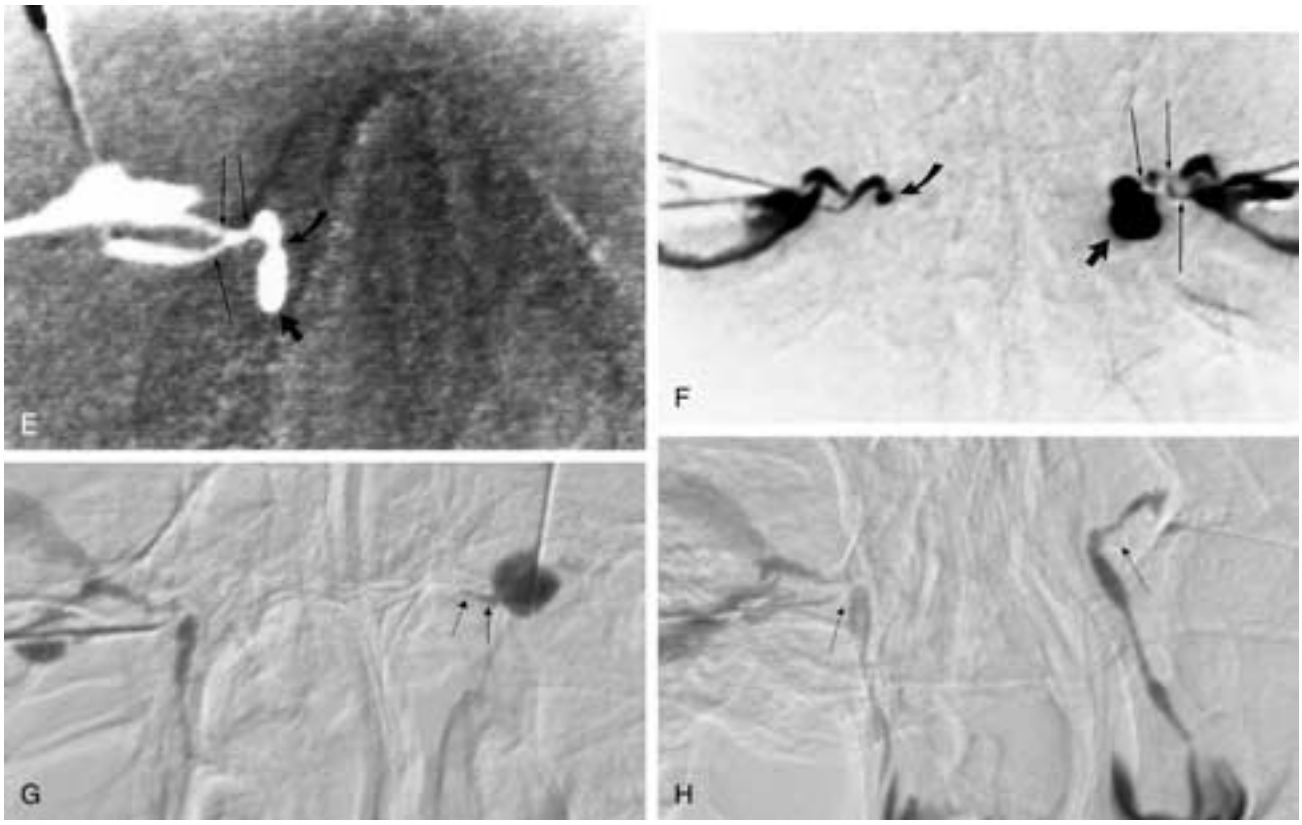

VIEW IMAGE

FIGURE 10-8 *Continued.* **E**, Superior canalicular injection. Mild stenosis (*thin arrows*) of the medial common canaliculus and the medial aspect of the right superior and inferior canaliculi. Obstruction of the distal right lacrimal sac (*short arrow*). Narrowed segment (*curved arrow*) of the lacrimal sac is due to fibrosis. **F**, Distended lobulated left lacrimal sac (mucocele) with outlet obstruction (*short arrow*). Severe stenosis (*thin arrows*) of the left common canaliculus (with focal dilatation) and inferior and superior canaliculi medially. Cicatrized right lacrimal sac (*curved arrow*). **G** and **H**, Bilateral tearing. **G**, Irregular dilated right superior canaliculus and stenosis at the junction of the common canaliculus and lacrimal sac, with contrast refluxing into the conjunctival sac. Obstruction at the medial aspect of the left inferior canaliculus (*arrows*), with contrast refluxing into the conjunctival sac. **H**, Repeat injection. The right cannula was moved closer to the punctum to better visualize the stenosis in the medial aspect of the right inferior canaliculus (*arrow*). Left injection through the superior punctum shows no obstruction to drainage. No reflux into the obstructed inferior canaliculus (*arrow*).

Jones 2 Test

If the Jones 1 test is negative (no dye reaches the nasal cavity), the Jones 2 test is performed by irrigating the NLDS with a saline solution (1 ml) after the conjunctival application of fluoroscein dye has been irrigated out of the conjunctival sac.[27]

1. Lack of fluid entering the nose is evidence of complete obstruction in the drainage system (negative test).
2. The presence of clear saline in the nasal cavity implies that the fluoroscein did not reach the lacrimal sac. The test is negative (abnormal). The canaliculi may be open, but they are not functioning, and the abnormality is localized to the upper NLDS.
3. Deeply stained fluid entering the nasal cavity implies that the fluoroscein reached the lacrimal sac physiologically but did not drain any further. The test is positive (the lacrimal pump and canaliculi are functioning, so that the lacrimal sac fills). There is incomplete obstruction of the nasolacrimal duct.

If both the Jones 1 and 2 tests fail to detect fluoroscein in the nasal cavity (negative tests), the lacrimal system is irrigated with fluoroscein to confirm total obstruction.[28]

Schirmer's Test

Schirmer's test is a measure of the eye's ability to produce tears in response to an external stimulus and can be estimated by the amount, in millimeters, of filter paper wetting by lacrimal fluid in 5 minutes. A dry eye may intermittently produce a large amount of tears, simulating epiphora. The test can differentiate hyposecretion and pseudoepiphora from normal secretions.[27]

Valsalva DCR Bubble Test

The Valsalva DCR bubble test offers confirmation of patency of a dacryocystorhinostomy site. A drop of saline is placed at the inner canthus, and the patient is asked to perform the Valsalva maneuver. The formation of a bubble

Copyright © 2003, Mosby, Inc. All rights reserved.

in the region of the punctum indicates a positive test.[29] Again as in the Jones test, the normal test is referred to as positive.

INDICATIONS FOR DACRYOCYSTOGRAPHY

DCG is indicated to investigate patients with epiphora after the clinical examination suggests a mechanical obstruction. Campbell[9] outlined the three fundamental principles in interpretation of DCG: (1) to describe the level of the obstruction, (2) to state whether the obstruction is complete or incomplete, and (3) to determine the cause of the obstruction. The suspected obstruction may be associated with various clinical conditions, including congenital obstructions, supernumerary canaliculi, lacrimal fistula or diverticula, concretions (dacryoliths), neoplastic or inflammatory processes, or posttreatment changes. When there is clinically assessed chronic obstruction, surgical or interventional treatment is indicated and DCG should offer maximum information to allow the appropriate procedure.

SURGICAL PROCEDURES FOR EPIPHORA

The most common surgical procedure for epiphora is a dacryocystorhinostomy (DCR), in which the medial wall of the lacrimal sac is opened into the nasal cavity, with specific attention being devoted to appropriate removal of adjacent bone (osteotomy) and suturing of the lacrimal sac and nasal mucosal flaps.[30] DCR is the procedure of choice to treat epiphora secondary to obstruction or severe stenosis of the distal lacrimal sac and the nasolacrimal duct. Stenoses or occlusion within the upper drainage system, proximal to the lacrimal sac, may require placement of fine stents (silastic or rubber) within the canaliculi to complement the DCR. Alternatively canaliculo-DCR may be performed, with resection of a canalicular stenotic segment and anastomosis to the lacrimal sac and incorporation into the DCR.[31] These stents are placed on a temporary basis. Construction of a conjunctival tract with insertion of permanent glass tubes (Pyrex) to bypass an occluded canaliculus (conjunctival DCR) has long-term implications for care and maintainance.[32] A limited canthocystostomy (lacrimal sac opened into the conjunctival fornix) procedure may be performed when the lacrimal sac and lower NLDS are intact and

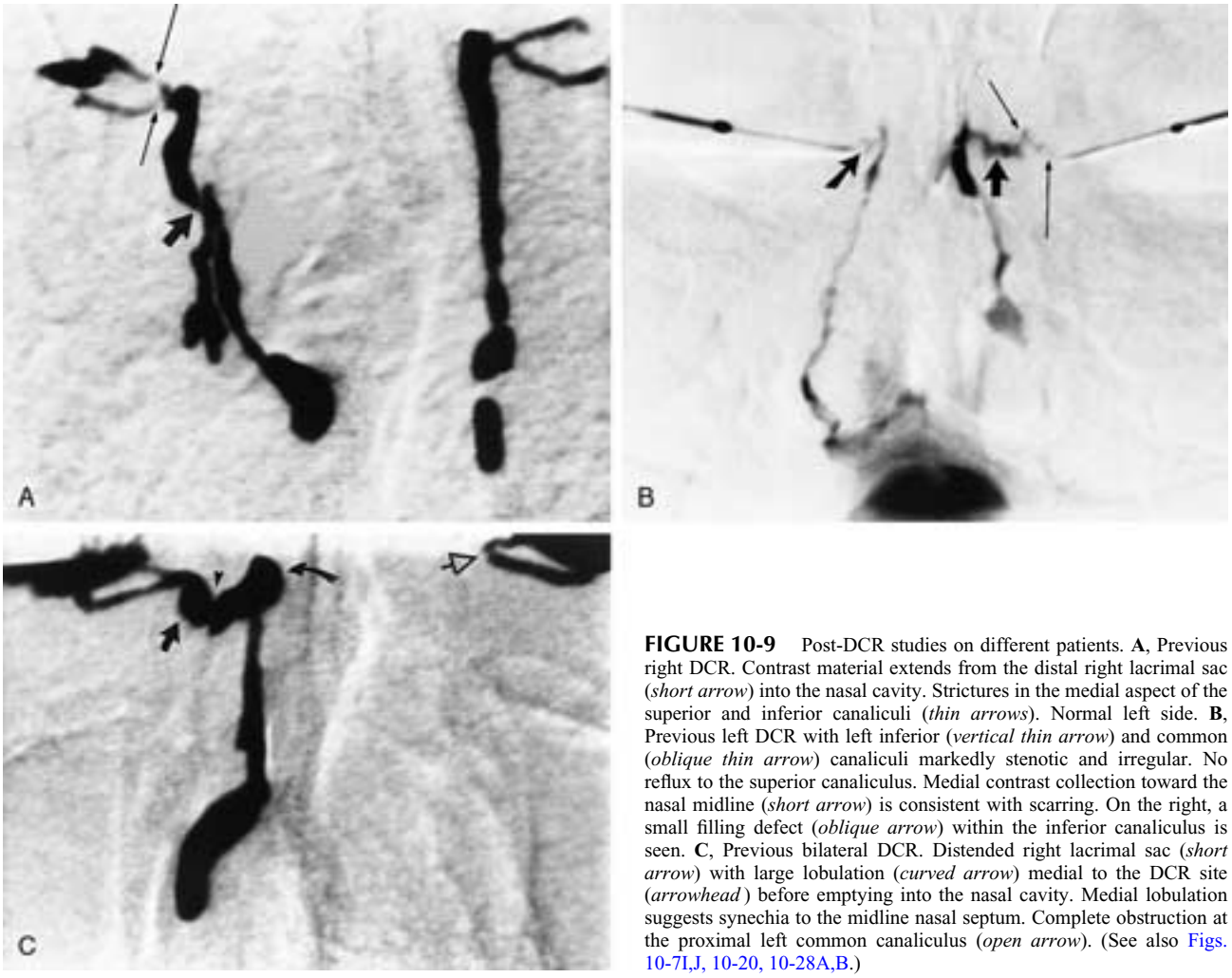

FIGURE 10-9 Post-DCR studies on different patients. **A**, Previous right DCR. Contrast material extends from the distal right lacrimal sac (*short arrow*) into the nasal cavity. Strictures in the medial aspect of the superior and inferior canaliculi (*thin arrows*). Normal left side. **B**, Previous left DCR with left inferior (*vertical thin arrow*) and common (*oblique thin arrow*) canaliculi markedly stenotic and irregular. No reflux to the superior canaliculus. Medial contrast collection toward the nasal midline (*short arrow*) is consistent with scarring. On the right, a small filling defect (*oblique arrow*) within the inferior canaliculus is seen. **C**, Previous bilateral DCR. Distended right lacrimal sac (*short arrow*) with large lobulation (*curved arrow*) medial to the DCR site (*arrowhead*) before emptying into the nasal cavity. Medial lobulation suggests synechia to the midline nasal septum. Complete obstruction at the proximal left common canaliculus (*open arrow*). (See also Figs. 10-7I,J, 10-20, 10-28A,B.)

VIEW IMAGE

Copyright © 2003, Mosby, Inc. All rights reserved.

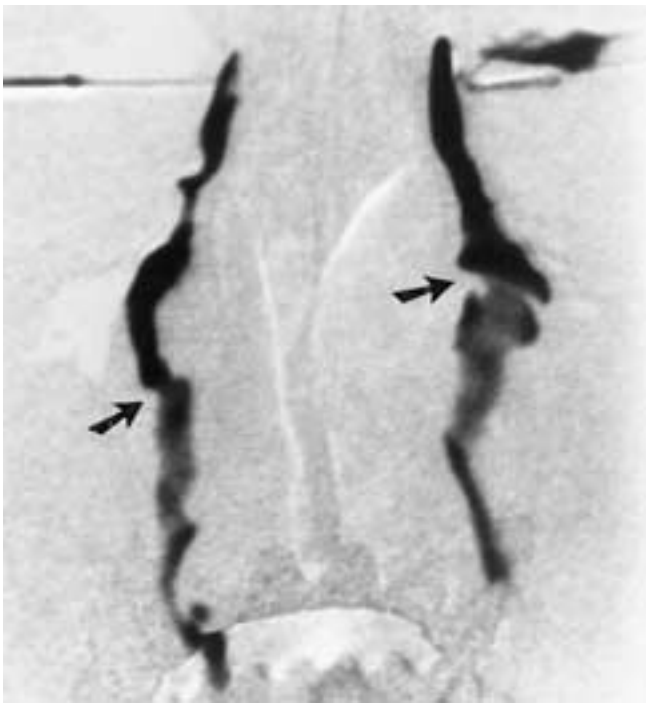

VIEW IMAGE

FIGURE 10-10 Shortened left nasolacrimal duct. Contrast material enters the left nasal cavity (*arrow*) more superiorly than usual (compare with the right side). There was previous resection of a left maxillary sinus neoplasm.

patent.[9] A canthoplasty (lateral) with resection and tightening of the preseptal and pretarsal orbicularis muscle may correct abnormal positions of the lid and allow tears to enter the punctum.

The increasing trend of minimally invasive surgical techniques, combined with the advancing technology of endoscopic visualization, has also been applied to the lacrimal patient. Endoscopic dacryocystoplasty (endonasal DCR), utilizing an endonasal endoscope to make an anastomosis (using traditional bone-removing instruments or a laser) between the lacrimal sac and the nasal cavity, circumvents the external approach (Toti's operation). With no external scar, the endoscopic approach offers better cosmesis. There is preservation of lacrimal pump function of the orbicularis oculi muscle, the presaccal fibers, the medial canthal tendon and their osseous supporting structures by approaching the lacrimal sac from the nasal cavity.[33–35] Compared to external DCR, endonasal DCR is less traumatic and offers minimal morbidity, less intraoperative bleeding, a shorter operative time, and a low complication rate.[36] Endoscopic DCR is a more difficult procedure to learn, is more technically challenging, and has the disadvantage of a smaller anastomotic opening and a higher recurrence rate of epiphora. Bone removal by drilling or by laser may cause overheating and increase the risk of postoperative fibrosis and closure of the lacrimal window.[35] As for external DCR, scarring of the ostium and errors in ostium location are the major reasons for surgical failure.[37] Epithelial anastomosis and continuous fluid flow are necessary for maintaining a patent surgical rhinostoma. For this purpose, a silicone stent is placed and is usually kept in place for at least 2 months.[36] Conversely, Kong et al.[38] suggest removal of the silicone tubes before 8 weeks to prevent granuloma formation and closure of the osteotomy site. Premature tube dislodgement may be associated with surgical failure.

Microendoscopy of the NLDS, endocanalicular and translacrimal DCR,[39] and fiberoptic laser probing are less frequently used surgical procedures for the treatment of lacrimal sac and nasolacrimal duct obstruction. Translacrimal and endocanalicular laser DCR techniques offer the advantage of less surgical dissection. The laser energy is directed away from the eye, avoiding the risks of laser injury to the globe that may occur with laser-assisted endonasal DCR.[39, 40] Thermal injury of the lacrimal sac may increase postoperative scarring and reduce patency.[41] (See also the section on Endoscopy of the Lacrimal Drainage System later in this chapter.)

THE NORMAL DACRYOCYSTOGRAM

Anatomy

The lacrimal system consists of the inferior canaliculus, superior canaliculus, common canaliculus, lacrimal sac, and nasolacrimal duct (Figs. 10-2 to 10-4). Tears from the conjunctival sac enter the punctum of both the inferior and superior canaliculi approximately 6 mm lateral to the medial canthus, briefly travel through a 2 mm vertical segment, and then turn abruptly medially to continue in the longer (7 to 10 mm) horizontal canalicular segment. There is a slight dilation, the ampulla, at the junction of the vertical and horizontal components of each canaliculus.[42] The superior and inferior canaliculi merge to form the common canaliculus (common ampulla) and enter a small diverticulum of the lateral wall of the lacrimal sac, the sinus of Maier. Occasionally the canaliculi enter the sinus of Maier separately. The upper canaliculus is slightly shorter and straighter than the lower, and the canalicular diameter is 0.5 mm, with a punctal diameter of 0.3 mm. The thin, elastic walls of the canaliculi allow the canaliculi to be dilated three times their normal diameter or to be straightened by lateral tension on the eyelid, an anatomic feature of significance for probing or instrumentation.[42] The punctal region is relatively avascular and therefore paler than adjacent tissues. This contrast is accentuated by lateral tension on the lid margin, helping to locate a stenosed punctum. The normal close contact between the puncta and the conjunctival tear fluid is essential (and should be noted for normal function) since the canaliculi fill by capillary extraction.

The common canaliculus is 1 to 5 mm in length and terminates medially through flaps of mucosa created by the acute angle with which the sinus of Maier enters the lacrimal sac. The superior flap is called the valve of Rosenmüller, and the inferior flap is called the valve of Huschke. The canaliculus enters the lateral aspect of the nasolacrimal sac just above the junction of its upper and middle thirds (i.e., 3 mm from the dome of the sac).[27]

In 1911, Schaeffer[43] described three different ways in which the canaliculi communicate with the lacrimal sac: (1) they can drain through a common canaliculus; (2) they can empty separately into a diverticulum of the lacrimal sac (sinus of Maier); or (3) in rare cases, they can empty separately into the lacrimal sac, with no common canaliculus or diverticulum present. Variations in the configuration

Copyright © 2003, Mosby, Inc. All rights reserved.

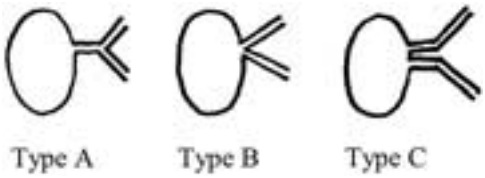

VIEW IMAGE

FIGURE 10-11 Forms of canalicular connection to the lacrimal sac. **Type A**: Upper and lower canaliculi join the common canaliculus. **Type B**: Upper and lower canaliculi join at the lacrimal sac wall to form a common opening. **Type C**: Upper and lower canaliculi enter the lacrimal sac separately. (Adapted from Yazici B, Yacizi Z. Frequency of the common canaliculus. A radiological study. Arch Ophthalmol 2000;118:1381–1385.)

of the common canaliculus have been noted. Approximately 90% of individuals have the typical configuration, that is, a common canaliculus clearly defined between the merged inferior and superior canaliculi laterally and the entry point into the lateral wall of the lacrimal sac medially.

For the 10% of the population for whom a common canaliculus is not present, there has been no clear description of how the canaliculi terminate. Jones and Wobig[27] reported that in 10% of individuals, the canaliculi actually open separately into a ''sinus of Maier,'' which in turn opens into the tear sac, implying only one common internal opening, also celled the inner punctum, into the tear sac. The term *sinus of Maier* is somewhat confusing since it has been used to describe three different anatomic entities: (1) the common canaliculus itself; (2) the terminal dilation of a common canaliculus; and (3) the lacrimal sac diverticulum into which the canaliculi open separately.[27, 42, 44] Yacizi and Yacizi[44] propose a functional term, *common opening*, to describe the configuration in which the common canaliculus is absent and the canaliculi unite at the sac wall and drain by one ostium. In a smaller number of patients, the upper and lower canaliculi drain separately and distinctly into the lacrimal sac.

In a recent study of 341 digital subtraction macrodacryocystograms on patients with obstructive epiphora, Yacizi and Yacizi[44] noted that 94.1% had the typical common canaliculus configuration (type A). In this study, 3.8% had an absent common canaliculus, with the lower and upper canaliculi united at a common opening in the lacrimal sac wall and draining into the lacrimal sac through this opening (type B). In only 2% of the studies did the upper and lower canaliculi drain separately into the lacrimal sac (type C) (Fig. 10-11).

In type B, the upper and lower canaliculi joined at a narrow angle at the lacrimal sac wall for a common opening. This pattern was unlikely to be confused with type C since the type C canaliculi maintained nearly parallel courses as they approached and maintained separate openings into the lacrimal sac. The authors[44] emphasize analysis of the early images of canalicular filling before a distended lacrimal sac may obscure a short common canaliculus and resemble a type B or type C pattern. There is no evidence that the presence or type of canalicular drainage affects the clinical course of nasolacrimal duct obstruction. Nasolacrimal duct obstruction, with resultant lacrimal sac distention, causes kinking of the common canaliculus (and probably of the superior and inferior canaliculi in type B and C configurations) due to compression by the lacrimal sac and may better explain further sac enlargement. Anatomic configurations have surgical implications for planned probings or silicone intubations at the time of DCR or for repairs of traumatized (lacerated) canaliculi to prevent the creation of false canalicular passages.

Review of the functional anatomy of the lacrimal outflow system at the junction of the common canaliculus and lacrimal sac may also be warranted. Mucosal folds at the superior and inferior borders of the common canaliculus–lacrimal sac junction have been described and respectively named the valve of Rosenmüller and the valve of Huschke. These valves have been seen or described inconsistently and occasionally have been omitted in the literature. Only the Hasner valve at the distal nasolacrimal duct has been shown to be a functional barrier to retrograde flow or reflux of fluid. However, the belief that the Rosenmüller valve prevents tear reflux from the lacrimal sac to the common canaliculus has persisted as the only explanation for the lack of reflux of lacrimal sac contents. The theory holds that the valve may become tighter with edema, inflammation, and distortion related to dacryocystitis, explaining the difficulty of cannulating the lacrimal sac in cases of dacryocystitis, dacryocystocele, or acute dacryocystic retention.[45]

Tucker et al.[46] have hypothesized that the Rosenmüller valve alone may be insufficient to explain the functional valve mechanism and offer an alternative finding and theory from their study of casts of lacrimal outflow systems. A consistent canaliculi configuration of an initial posterior vector at the level of the eyelids, followed by an anterior vector after passing posterior to the medial canthal tendon, with continuation in this anterior direction to enter the lacrimal sac at an acute angle suggests functional significance. The authors have postulated that the angle of entry of the common canaliculus into the lacrimal sac may explain the lack of reflux in pathologic conditions associated with an enlarged sac. As the lacrimal sac increases in size, its expansion is limited medially and posteriorly by the bony lacrimal sac fossa. Thus there is more expansion laterally and anteriorly. The lateral expansion may cause kinking of the canaliculus, which functionally blocks the canaliculus–sac junction (Fig. 10-12). External pressure applied to the sac may accentuate the functional valve. In patients with

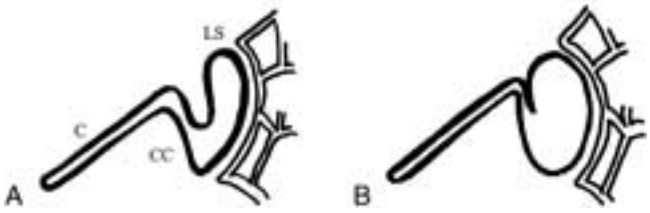

VIEW IMAGE

FIGURE 10-12 Pattern of angulation within the canalicular system at the canaliculus–lacrimal sac junction: hypothesis for one-way valve phenomenon. **A** and **B**, Looking at the right eye from above (i.e., anterior aspect is at the bottom of the image); the medial aspect (ethmoid sinuses) is at the right side of the image. **A**, Normal lacrimal anatomy. Canaliculi (*c*) bend posteriorly to pass behind the medial canthal tendon, and the common canaliculus (*cc*) bends anteriorly directly behind the medial canthal tendon to enter the lacrimal sac (mean angle of 58° to the lateral wall of the sac). **B**, Kinking and collapse of the common canaliculus at its junction with the lacrimal sac may occur with sac enlargement, leading to a one-way valve effect, preventing reflux of sac contents in certain cases of dacryocystitis, lacrimal sac mucoceles, and acute dacryocystic retention. (Adapted from Tucker NA, Tucker SM, Linberg JV. The anatomy of the common canaliculus. Arch Ophthalmol 1996;114:1231–1234.)

Copyright © 2003, Mosby, Inc. All rights reserved.

dilated lacrimal sacs not exhibiting a functional valve, the angulation of the common canaliculus, as it enters the sac, may not be acute enough to have a valve effect.[46]

Malik et al.[47] reported radiographic measurements of the lacrimal sac and nasolacrimal duct (Table 10-1). Any distention of the sac greater than 4 mm on the frontal radiograph is considered pathologic. The lacrimal sac ends in a slight taper inferiorly caused by a mucosal fold, the valve of Krause, just above the inferior rim of the orbit. The nasolacrimal duct, which extends 15 to 20 mm in length, begins at this level and may have a small portion of its course within the orbit before entering the bony canal (intraosseous component). This intraorbital segment is approximately 1 cm in length. Within the nasolacrimal duct there is a midsection mucosal constriction, the valve of Taillefer, just superior to the inferior turbinate bone, and a distal constriction, the valve of Hasner. The duct empties through the valve of Hasner into the inferior meatus of the nose, beneath the inferior turbinate. This inferior, or meatal, component usually opens into the nasal cavity 5 mm below the vault of the inferior meatus (anterior aspect) but may extend more inferiorly down the lateral wall of the inferior meatus before entering the nasal cavity. Such inferiorly located valves tend to have a more slit-like opening rather than the fold of mucosa forming Hasner's valve seen in the more superiorly located valves.

In the normal DCG, the canaliculi, lacrimal sac, and nasolacrimal duct are not dilated. On the frontal images, the lacrimal sac and nasolacrimal duct have a linear configuration. The fascia of the orbicularis oculi, which splits to enclose the lacrimal duct and sac, is thick and taut and indents the lumen at the junction of the lacrimal sac and nasolacrimal duct 0.7 cm above the bony canal opening.[9] On the lateral film, the nasolacrimal duct is seen to change direction slightly, inclining posteriorly. This marks the site of the valve of Krause. This combination of indentation and mild kinking caused by the change in nasolacrimal duct system (NLDS) direction may explain why the junction of the lacrimal sac and duct is the most frequent site of obstruction. A second change in direction, more acute, and also posteriorly inclined, is noted at the valve of Taillefer. On a lateral film, the course of the lacrimal sac and nasolacrimal duct should extend along a line from the medial canthus to the first maxillary molar.[42] The lacrimal sac may normally be three times as wide on the lateral image as on the frontal image.[9] Contrast material is identified entering the nasal cavity. In a patent system, the contrast medium will immediately drain from the nose into the pharynx and onto the base of the tongue, with the patient tasting the solution within a few moments. Normally 0.5 to 1.0 ml of contrast medium is injected per side. There should be free flow of contrast through the NLDS into the nasal cavity (inferior meatus). A mild increase in injection pressure may overcome an area of ''relative'' obstruction that may represent secretions or a partial stenosis, which would otherwise have been incorrectly interpreted as obstruction, with implications for treatment decisions. Three anatomic narrowings normally occur and may be noted: at the junction of the common canaliculus and lacrimal sac (valve of Rosenmüller or ''inner punctum''; at the junction of the distal lacrimal sac and nasolacrimal duct (valve of Krause); and at the distal valve of Hasner. These physiologic narrowings must not be mistaken for strictures or obstructions that are also more commonly located at these same sites.

Various mechanisms have been proposed to explain the drainage of tears. These anatomic and physiologic mechanisms, or their dysfunction, are poorly assessed by imaging modalities. Recent interest in the specialized vascular plexus, including cavernous tissue, which closely surrounds the lacrimal sac and nasolacrimal duct and connects caudally with the cavernous body of the nasal inferior turbinate, offers a further theory of tear outflow.[48, 49] Congestion within the vascular plexus affects the tear outflow system, allowing either obstruction or rapid transit of tear fluid. Paulsen et al.[50] propose that the previously described NLDS valves (Rosenmüller, Aubaret, Beraud, Krause, and Taillefer) may be based on different states of swelling of the cavernous body network and should be considered speculative (which may partly explain their inconsistent descriptions in the literature). (In the section Dacryoscintigraphy, see Normal Examination for further discussion of tear outflow.)

Table 10-1
NORMAL LACRIMAL DIMENSIONS

Area	Dimension (mm)	Mean (mm)	Range (mm)
Lacrimal sac	Vertical diameter	11.10	6–14
	Lateral diameter	2.43	1–4
	Anteroposterior diameter	4.00	1–6
Nasolacrimal duct	Vertical diameter	20.97	13–26
	Lateral diameter	2.30	1–4
	Anteroposterior diameter	2.84	1–4

From Malik SRK, Gupta AK, Chaterjee S, et al. Dacryocystography of normal and pathological lacrimal passages. Br J Ophthalmol 1969;53:174–179.

PATHOLOGY OF THE NASOLACRIMAL DRAINAGE SYSTEM

The lacrimal gland situated laterally and superiorly to the globe secretes tears. Under normal circumstances, the tears either evaporate from the surface of the globe or drain into the nasolacrimal passages and pass into the inferior meatus of the nose. Tearing may have several causes.[9] Excessive lacrimation may result in inadequate evaporation or drainage caused by a greater than normal volume of tears. In this situation, the DCG will appear normal. Much more commonly, excessive tearing represents obstructive epiphora, which results from complete or incomplete obstruction or from a functionally inefficient lacrimal system that cannot adequately handle the normal flow of tears. When there is an obstruction or stenosis, the DCG is abnormal. In a symptomatic patient, if contrast medium does not reflux into the superior canaliculus of an otherwise normal NLDS, a repeat study with cannulation of the superior canaliculus should be performed (Fig. 10-8D). There may be an inadequate or altered relationship of the puncta to the ocular surface or an abnormally small punctum inhibiting the transmission of tears into the lacrimal drainage system. In

Copyright © 2003, Mosby, Inc. All rights reserved.

such circumstances, the DCG will be normal. It must be emphasized that the introduction of a cannula into the puncta does not allow radiographic or physiologic assessment of the puncta. Observations regarding laxity of the lower lid, scarring or stenosis of the puncta, or other abnormalities of the lid may be better assessed clinically and should be commented on during the performance of the DCG. Such relationships may require functional assessment, such as with DSG. Permeable (patent) passageways, normal on DCG, may be functionally inefficient and better assessed with DSG. Finally, nasal obstruction may cause epiphora, occluding the valve of Hasner or the adjacent nasolacrimal canal. The venous plexus surrounding the NLDS is in direct communication with the venous plexus of the nasal mucosa. Edema within the nasal mucosa leads to venous plexus engorgement and secondary compression of the nasolacrimal duct.

Obstruction of the nasolacrimal duct system (NLDS) in the great majority of patients is due to idiopathic inflammation and scarring, which causes a spectrum of clinical symptoms ranging from partial occlusion to total obstruction.[51] Clear epiphora, secondary to nasolacrimal duct obstruction, represents a milder presentation. Mucoid epiphora results if bacterial overgrowth occurs in the stagnant fluid of the lacrimal sac. Clinical deterioration will include further signs of dacryocystitis (inflammation of the lacrimal sac) such as a medial canthal mass with increasing tenderness, mucopurulent discharge, secondary conjunctivitis, periorbital cellulitis, and a walled-off abscess in the lacrimal sac. The radiologist investigating the NLDS should be aware of this clinical spectrum and should understand that subtle cases of dacryocystitis require careful physical examination, including lacrimal irrigation.[51]

Dacryocystitis occurs because of obstruction of the flow of tears from the lacrimal sac. The obstructive etiology may be congenital or acquired, including inflammatory, infectious, infiltrative, traumatic, or neoplastic causes. All such processes must be considered as possible underlying factors in the presentation of dacryocystitis. In patients with nasolacrimal duct obstruction, the inflammation and fibrosis may be secondary to coexisting infectious colonization within the lumen of the lacrimal sac. Culture results of conjunctival and nasal specimens have not been predictive of lacrimal sac flora.[52] Assessment of the bacterial flora at the inferior lacrimal sac–nasolacrimal junction, using direct biopsy methods during 132 DCR procedures, to explore the possibility of primary bacteriologic etiology of the inflammatory response, gave positive culture results in 41.7% of the obstructed nasolacrimal duct systems undergoing DCR.[53] Of the isolates cultured, 78.5% were gram-positive bacteria (of this group 76.5% were *Staphylococcus* sp.) and 21.5% were gram-negative bacteria. Nine specimens yielded more than one organism. These organisms were found in patients with and without a history of infection, dacrycystitis, or the presence of a mucocele. Of the isolates, 69.2% were from patients with no history of dacryocystitis or mucocele, suggesting that the infection may have been the primary cause of the nasolacrimal duct obstruction. Conversely, the lack of positive cultures in a significant proportion of the above patients suggests etiologies other than bacterial invasion as the primary cause of obstruction, and organisms isolated may represent resident flora and not be causative.[54] DeAngelis et al.[53] have noted a greatly diminished prevalence of *Streptococcus pneumoniae* over the past 10 years. Others have noted a higher proportion of gram-negative bacteria associated with chronic dacryocystitis.[55]

One should try to distinguish between acute and chronic bacterial dacryocystitis. Acute dacryocystitis manifests as a painful swelling of the lacrimal sac, with surrounding erythema and edema. Pus may be expressible by pressure over a tender lacrimal sac. The bacteria reside in the wall of the sac, and treatment should be via the systemic route.[56] Complications include orbital cellulitis (usually limited to preseptal tissues), corneal involvement, lacrimal sac mucocele, and, rarely, orbital abscesses. The most common organisms implicated are *Staphylococcus aureus* in acquired cases and *S. pneumoniae* in congenital cases, although, due to the large number of potential causative organisms (gram positive or gram negative, aerobic or anaerobic), cultures and smears of expressed punctal secretions are desirable.

Chronic dacryocystitis is characterized by swelling of the lacrimal sac, which may or may not be painful, and with minimal if any surrounding inflammation. The bacteria reside in the lumen of the sac, necessitating treatment by local irrigation as well as by the systemic route.[56] A history of previous attacks of acute dacryocystitis may be present. Patients with chronic dacryocystitis and incomplete obstruction of the nasolacrimal duct may have superimposed bouts of acute dacryocystitis if duct patency is altered by swelling or debris in the duct system. For proper eradication of infection and resolution of dacryocystitis, the lacrimal obstruction must be eliminated to ensure adequate drainage of the nasolacrimal system. Chronic or recurrent dacryocystitis may require DCR. An obstructed lacrimal sac or lacrimal sac distention alone must be differentiated from dacryocystitis and its associated inflammatory changes.

Acute dacryocystitis is commonly associated with preseptal cellulitis. Infection of the lacrimal sac will preferentially localize in the preseptal space since the orbital septum inserts at the posterior lacrimal crest and acts as a significant anatomic barrier to prevent infections extending from the lacrimal sac posteriorly into the orbit. Orbital cellulitis rarely and orbital abscess very rarely result from acute dacryocystitis.[57, 58] The onset of a lacrimal sac abscess must be treated aggressively to prevent possible extension to adjacent tissues as an extraconal or intraconal orbital abscess.[57–60]

In a review of 148 patients with orbital abscesses, acute dacryocystitis was not the source of infection for a single patient.[61] Acute drainage of a lacrimal sac abscess is indicated, especially if it may be the source of orbital infection. In hyperacute dacryocystitis, treatment, although controversial, favors external drainage rather than intranasal (DCR) drainage. A DCR performed following resolution of the acute inflammation reduces the otherwise high risk of late failure due to extensive scarring.[58]

An intraconal abscess in a 1-month-old infant with congenital nasolacrimal duct obstruction (congenital dacryocystitis) suggests that anatomic barriers to infection may be less well defined in neonates than in adults.[62]

Subacute to chronic dacryocystitis may represent later stages of acute dacryocystitis that do not respond sufficiently to antibiotics or that may develop owing to persistent obstruction of the lacrimal system distal to the lacrimal sac.

Copyright © 2003, Mosby, Inc. All rights reserved.

A chronic lacrimal sac abscess (with the lacrimal sac swollen and filled with pus) or low-grade chronic dacryocystitis with intermittent exacerbations may result. Failure of antibiotic treatment of a lacrimal abscess due to chronic or subacute dacryocystitis is associated with obstruction of the lacrimal drainage system distal to the lacrimal sac, preventing drainage of pus from the lacrimal sac. Janssen et al.[60] have presented a subgroup of such patients who may be offered an alternative to DCR such as temporary stent placement within the nasolacrimal duct, along with systemic and topical broad-spectrum antibiotic coverage. This allows drainage of pus from the sac and relief of the infection, with no incidence of exacerbations or extension of the active inflammatory process. Long-term patency of the lacrimal duct system was not ensured by dacryocystoplasty. Surgical DCR was considered if reobstruction of the lacrimal duct system occurred.

Swelling (with or without fluctuance), erythema, and tenderness in the medial canthal area, extending inferior to the medial canthal tendon, simulating acute dacryocystitis or itis.[63, 64] Such cases of pseudodacryocystitis may be distinguished by the lack of a purulent discharge in the tear reflux, lack of a previous history of epiphora, or failure to note tearing between episodes of inflammation. Probing, irrigation, or DCG will confirm patent lacrimal systems. Inflammatory disease within the anterior ethmoid air cells may be noted on CT or MR imaging, with bone dehiscence of the lacrimal sac fossa better identified on CT. Such inner canthal fistulae associated with ethmoiditis are rare and tend to develop above the level of the medial palpebral ligament,[65] in contrast to acute dacryocystitis or lacrimal sac abscess, which extend inferior to the medial canthal tendon. An ethmoidectomy procedure rather than DCR is the treatment of choice for patients with primary sinonasal disease.

Obstruction

Obstruction may be due to various causes, including congenital stenosis, inflammatory diseases, calculi, trauma including foreign bodies, and tumors. Filling defects may be associated with an inflammatory process (see the section on Chronic Canaliculitis). DCG can assess both complete and incomplete obstructions (Figs. 10-5 to 10-8). The most common site of obstruction is the neck of the lacrimal sac, at its junction with the nasolacrimal duct, and it is usually due to inflammation (chronic dacryocystitis) and scarring of the nasolacrimal duct. Marked dilatation of the sac is usually clinically noted inferior to the level of the medial canthal tendon. Dilatation of the canaliculi is often associated with a dilated sac. Obstructions of the sac may be associated with a membrane at the medial end of the common canaliculus. Such a membrane must be identified and removed for a dacryocystorhinostomy (DCR) to be successful.[66] With pure sac obstructions, DCR should be successful in 100% of the cases, without the need for temporary intubation. Of the failed DCRs, 12% to 40% were due to common canaliculus problems.[66, 67] Thus high-quality images, especially of the canaliculi, are necessary to predict which patients will do poorly with simple DCR. The size of the lacrimal sac mucosal flap needed for the DCR may also be predicted from the DCG.

DCG may also define a cicatrized lacrimal sac, seen in chronic dacryocystitis. A cicatrized sac is more difficult to operate on, and is associated with poorer results than normal or enlarged lacrimal sacs when treated by endoscopic intranasal DCR in either primary treatment or revision patient populations. In these patients, the DCG can suggest that an external DCR should be the treatment procedure of choice.[37]

The next most frequent site of obstruction is the common canaliculus.[9, 16, 47] Common canalicular obstructions are most frequently related to chronic dacryocystitis or a ball valve effect of dacryoliths.[68] Accurate localization of canalicular obstruction has treatment implications (Fig. 10-8). Two thirds of common canalicular obstructions occur at the medial end, at the junction with the lacrimal sac, where a thin membrane, as a complication of inflammation within the sac, is present.[69] The common canaliculus appears as a well-defined structure on DCG. Treatment includes excision of the membrane and a DCR with temporary intubation (3 months) of the canaliculus. One third of common canalicular obstructions occur at its lateral end, as a result of mucosal obstruction where the superior and inferior canaliculi join. The entire common canaliculus is dissected out before mobilizing the lacrimal sac or periosteum. The scarred (stenosed) segment of canaliculus is excised, and the canaliculi are reanastomosed into the lateral wall of the lacrimal sac as a canaliculo-DCR. Occlusions or stenosis of the inferior or superior canaliculus may be due to traumatic laceration, canaliculitis, canalicular papillomas, and chronic pilocarpine or phospholine iodide use, and can be treated with DCR and temporary or permanent canalicular tubes or canaliculo-DCR reconstructive surgery.[68] Preoperative DCG diagnosis, with the exact location and length of occlusions/stenoses, therefore aids surgical planning and treatment decisions.

Less frequently, obstructions occur within the superior aspect of the lacrimal sac. Noncongenital obstructions of the distal nasolacrimal duct tend to be incomplete and are more frequently associated with adjacent sinus disease, inflammatory or neoplastic, than with intrinsic pathology of the nasolacrimal duct.[9] Neoplasms of the nasolacrimal duct (or sac) are rare, usually arise from pseudostratified columnar epithelium, and cause duct obstruction (Fig. 10-13A-C). On DCG, irregular duct obstruction, although nonspecific, should suggest or include this diagnostic possibility.[70]

Radiographically, the lacrimal sac above the obstruction will usually be dilated and have an ovoid or rounded configuration rather than a normal linear shape. The dilated sac or ‘‘mucocele of the lacrimal sac’’ is palpable below the medial canthus.[9] Occasionally the lacrimal sac will be constricted above the obstruction because of a cicatricial inflammatory response or fibrosis.[71]

Reflux of contrast medium into the conjunctival sac through the uncannulated punctum will occur when obstruction is present. This occurs early during the injection of a small volume of contrast medium. When the obstruction is incomplete, the DCG usually demonstrates dilation of the lacrimal sac above the incomplete obstruction. Contrast material must be visualized entering the nasal cavity to confirm the incomplete nature of the obstruction. Dilated

Copyright © 2003, Mosby, Inc. All rights reserved.

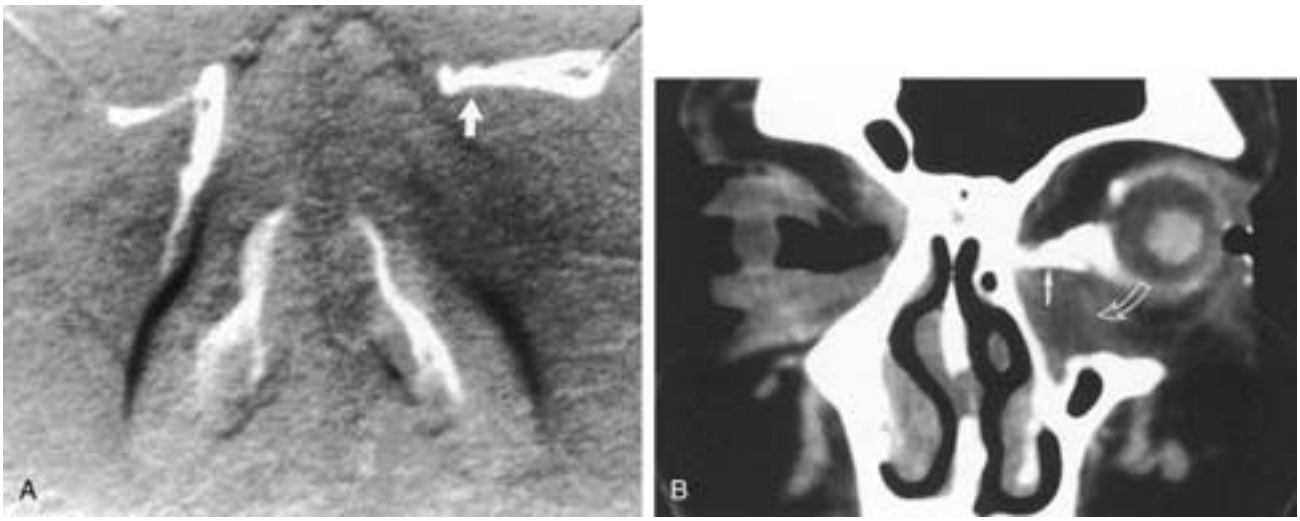

VIEW IMAGE

FIGURE 10-13 CT-DCG of mass lesions: inner canthus. CT-DCG allows better assessment of the extent of adjacent tissue involvement than DCG alone and better assessment of NLDS involvement than CT alone. **A** to **C**, Patient presents with left inner canthus prominence and epiphora. **A**, DCG shows superior displacement of the left canaliculi (*arrow*) with no visualization of the left lacrimal sac or nasolacrimal duct. **B**, Coronal CT-DCG shows displacement of the proximal NLDS (*solid arrow*) by a soft-tissue mass in the inner canthus (*open arrow*).

Illustration continued on following page

lacrimal sacs, distorted by fibrosis, must be differentiated from distended cystic diverticula or true cysts of the lacrimal sac (Fig. 10-14). Traumatic dislocation of the lacrimal sac must also be considered.

Obstructions in the lower part of the nasolacrimal duct occur less frequently. The diameter of the bony canal is one of the contributing factors for occurrence of strictures at this site. Women are affected much more frequently than men (up to 80%), probably related to their narrower bony canal.

Fistulae

Congenital lacrimal sac fistulae are relatively uncommon, estimated to occur in 1 per 2000 births.[72] Fistulae may also be postinflammatory (chronic dacryocystitis), posttraumatic, or postsurgical.[42, 72, 73] The fistula most commonly originates from the lacrimal sac (lacrimal sac-cutaneous fistula) but may arise from the canaliculi or nasolacrimal duct. Most of the fistulae are unilateral and located inferonasal to the medial canthus. Patients may be asymptomatic and overlooked for some time after birth or may demonstrate tearing from the fistula. the eye, or both.[74] Fistulae are usually associated with long-standing obstruction of the nasolacrimal drainage system (Fig. 10-15). A previous DCR may have been performed without recognition of the fistula's presence. The majority of patients present with epiphora, which may be delayed in onset; occasionally an inflammatory lesion of the lower lid may be the presenting sign.

Congenital lacrimal fistulae probably result from failure of involution of the lacrimal anlage, the thickened surface ectoderm of the nasooptic fissure, which becomes buried in the mesenchyme between the nasal and maxillary processes to form the nasolacrimal drainage system. Instead, this anlage proliferates, canalizes, and forms a fistula, whose cutaneous opening is just medial and inferior to the medial canthus.[27] The fistulous tract may also be incomplete and end blindly in the subcutaneous tissues near the lacrimal sac.[75] Welham and Bergin[76] have proposed that a congenital fistula may be caused by aberrant budding of the canaliculi, with the fistula representing a supernumerary or aberrant canaliculus. Absence of a superior or inferior canaliculus or absence of a punctum has been noted to be associated with lacrimal fistulae.[76, 77] The epithelial lining of the fistula is identical to that of a normal canaliculi.[75] A hereditary or familial pattern of presentation of lacrimal fistulae has also been noted.[27]

If the fistula is not clearly demonstrated by the DCG, placement of a lacrimal probe into the external opening, in conjunction with the DCG, may help show its origin from the nasolacrimal drainage system. Recommended treatment includes DCR, common canalicular dissection, fistula excision, and temporary canalicular intubation to bypass the distal obstruction and prevent common canalicular obstruction and recurrence of the fistula.[76] Others recommend excision alone or with nasolacrimal intubation, without DCR if there is no evidence of nasolacrimal obstruction.[74] Patients with very minor or no symptoms may simply be kept under observation.

Diverticula

Diverticula represent outpouchings of a lacrimal drainage pathway and are usually the result of a long-standing obstruction (Fig. 10-7F,G). They are most commonly asymptomatic, small, and clinically undetected. Occasionally they may be associated with episodic or permanent symptoms of nasolacrimal duct obstruction (chronic tearing discharge) and may present as a mass lesion without associated nasolacrimal duct obstruction.[78] Less often, they may present as an acute infection, either diverticulitis or

Copyright © 2003, Mosby, Inc. All rights reserved.

dacryocystitis secondary to duct obstruction. Congenital lacrimal sac diverticula most frequently result from the spontaneous rupture (outpouching) of the lacrimal sac wall in acute dacryocystitis associated with congenital nasolacrimal duct obstruction.[79]

Acquired lacrimal sac diverticula most commonly result from a weakening of the lacrimal sac wall after inflammation or trauma, including probing or irrigation, or after incision and drainage procedures for dacryocystitis.[78]

Diverticula of the lacrimal sac may be associated with dacryoliths, which may intermittently obstruct the opening of the lacrimal sac and increase the pressure of fluid within the sac, with resultant weakening of the lacrimal sac wall and diverticular formation in an asymptomatic patient.

Epiphora, associated with these diverticula, may result from mechanical pressure on the lacrimal drainage system rather than a primary intraluminal blockage of a duct or sac. Slow evolution of a lacrimal sac diverticulum is typical.[80] The most common location is at the junction between the lacrimal sac and the nasolacrimal duct. The communication between the diverticulum and the lacrimal sac may be clearly open or may be valvular and limited, limiting diverticular drainage. The relative rarity of reports of lacrimal diverticula in the literature more likely reflects their

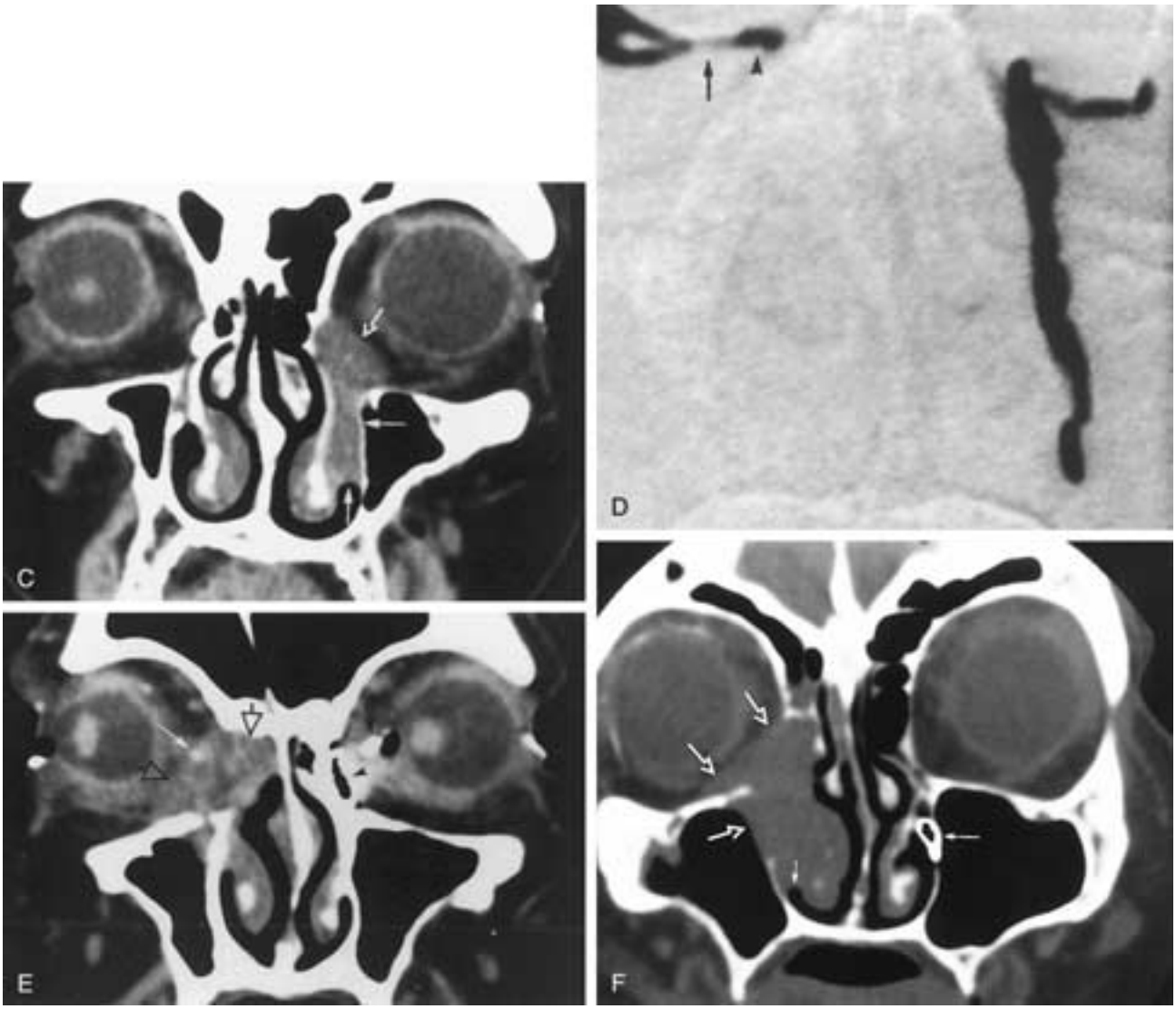

VIEW IMAGE

FIGURE 10-13 *Continued.* **C**, More posterior coronal image shows the soft-tissue mass (*open arrow*) extending into and widening the left nasolacrimal canal (*horizontal arrow*), reaching the inferior meatus (*vertical arrow*). CT-DCG offered significant information beyond that available by DCG alone. Pathology: transitional cell carcinoma in the left lacrimal sac. **D** to **F**, Right inner canthus mass with epiphora. **D**, DCG. Superior displacement of the right proximal NLDS (*arrow*). Only the most superior aspect of the lacrimal sac is visualized (*arrowhead*). **E**, Coronal CT-DCG. Large soft-tissue mass (*open arrows*) in the right medial canthus and adjacent ethmoid sinus, with destruction of the medial orbit wall. The lacrimal sac containing contrast medium is displaced laterally and superiorly (*thin arrow*). Normal left NLDS (*arrowheads*). **F**, Bone windows of a slightly more posterior coronal CT scan shows extension of the mass (*open arrows*) along the path of the nasolacrimal canal to the inferior meatus (*vertical arrow*) with adjacent bone destruction. Contrast material in the left inferior meatus (*horizontal arrow*). Pathology: squamous cell carcinoma.

Copyright © 2003, Mosby, Inc. All rights reserved.

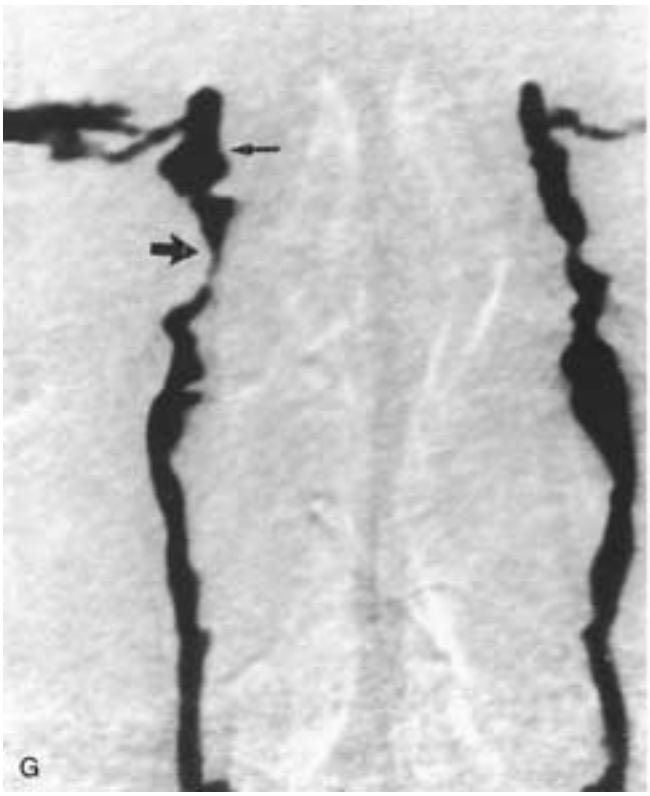

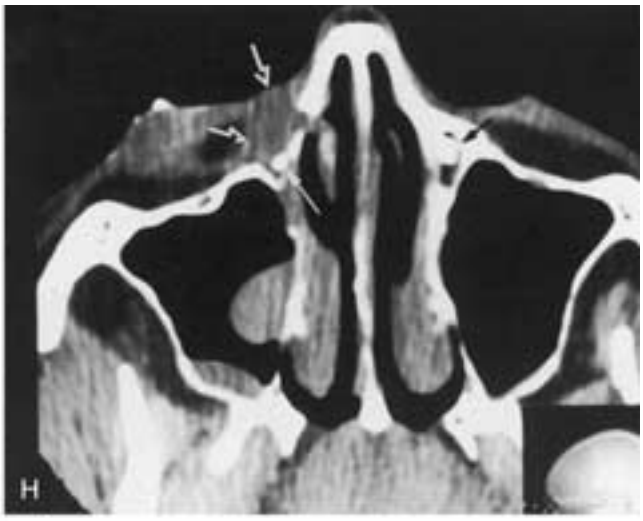

VIEW IMAGE

FIGURE 10-13 *Continued.* **G** and **H**, Mild prominence of the right inner canthus. **G**, DCG. Mass indenting the proximal right nasolacrimal duct (*larger arrow*) from the lateral aspect with mild distention of the lacrimal sac (*thin arrow*). **H**, Axial CT-DCG shows a soft-tissue mass in the right inner canthus (*open arrows*) displacing the lacrimal sac (*thin arrow*) posteromedially within the nasolacrimal fossa. Normal left NLDS (*black arrow*). Pathology: lymphocytic lymphoma in the wall of the lacrimal sac and duct. (Note also the nasopharyngeal lymphomatous mass.) (Courtesy of Dr. Nasir Jaffer, Toronto, Canada.)

frequently asymptomatic nature and difficulty in demonstrating them routinely by DCG. In many cases, only the obstruction or impression on the lacrimal sac due to the mechanical pressure of the diverticulum is noted. Only DCG or ultrasonography may reveal the narrow communication, while CT/MR imaging may better display the size, extent, and cyst-like characteristics of the diverticula, and their relationship to the nasolacrimal drainage system, for those lesions unable to be directly visualized by DCG.[78, 80]

Diverticula of the canaliculi, lacrimal sac, or nasolacrimal duct are usually the result of a long-standing obstruction (Fig. 10-7F,G), and the diverticula will remain until adequate drainage of the obstructed or partially obstructed nasolacrimal system is restored. It is not possible to diagnose diverticula preoperatively without a DCG. Clinically, distended cystic diverticula may resemble a dilated lacrimal sac or a true cyst of the lacrimal sac, which does not communicate with the NLDS.

Lacrimal Sac Cysts

Cysts arising from the lacrimal sac epithelium are rare. Although these cysts may be congenital, inflammatory, or traumatic in origin, most think they arise from diverticula of the lacrimal sac, with the cyst forming when the communication to the lacrimal sac closes off.[81] The cyst may communicate directly with the sac or may be anatomically separate. Lacrimal sac cysts usually present as a nonreducible, well-defined, slow-growing, painless mass in the inner canthus, below the level the medial canthal tendon.[82] Epiphora, which may be secondary to pressure on the sac, is a common symptom, and/or the cyst may be associated with a patent nasolacrimal drainage system.[81] Pressure over the mass will not alter the size of a lacrimal sac cyst but may reduce the size of a diverticulum. The pathologic description of a cystic cavity lined by columnar to cuboidal epithelium may not help differentiate a lacrimal sac cyst from a diverticulum or mucocele of lacrimal sac etiology. Treatment consists of total excision of the cyst. If there is any communication with the lacrimal sac, lacrimal sac wall repair and simultaneous DCR is indicated.

Lacrimal Calculi

Lacrimal sac dacryoliths may be present in 10% to 30% of patients presenting with chronic dacryocystitis.[83–85] In addition to tearing, patients with lacrimal sac calculi may present with a history of mucopurulent discharge, lacrimal sac distention, tenderness in the medial canthal region, and recurrent dacryocystitis. The frequency of partial nasolacrimal duct obstruction with dacryocystitis has been reported in as many as 65% to 70% of patients.[83, 84, 86, 87] Primary and

Copyright © 2003, Mosby, Inc. All rights reserved.

secondary dye tests indicate partial obstruction of the nasolacrimal duct (Figs. 10-7, 10-16C,D, 10-17D,E, and 10-18A-C).[85]

Wilkins and Pressly[86] stressed the intermittent but chronic nature of tearing unresponsive to treatment in patients with lacrimal calculi. There may be a history of repeated, painful lacrimal probings, occasionally with transient relief caused by either repositioning or fragmentation of the stone. The extreme inconsistency of nasolacrimal irrigation in patients with lacrimal calculi is most impressive, and by itself may suggest the diagnosis. Such variability of results may occur within a short period (minutes), with one irrigation showing reflux and suggesting obstruction and a second irrigation showing normal flow into the nasal cavity. Friable or fragmented calculi within the sac are subject to the currents produced by an irrigation, and cranial movement of the calculus will allow free flow, while caudal movement of the lacrimal sac calculus creates a ball-valve effect and complete nasolacrimal occlusion.[86] Weber et al.[88] have noted that dacryoliths do not change in size or shape, representing permanent filling defects in the DCG. Dacryoliths should be differentiated from retained thick secretions or air bubbles. Air bubbles injected into the nasolacrimal system represent an artifact that can simulate a concretion, although bubbles tend to be rounder and more sharply defined. A cross-table lateral view will demonstrate the air bubble floating in the lacrimal sac, while concretions tend to settle in the more dependent inferior posterior aspect of the sac and do not change location with altered positions of the head as quickly as air bubbles (Figs. 10-7M,N and

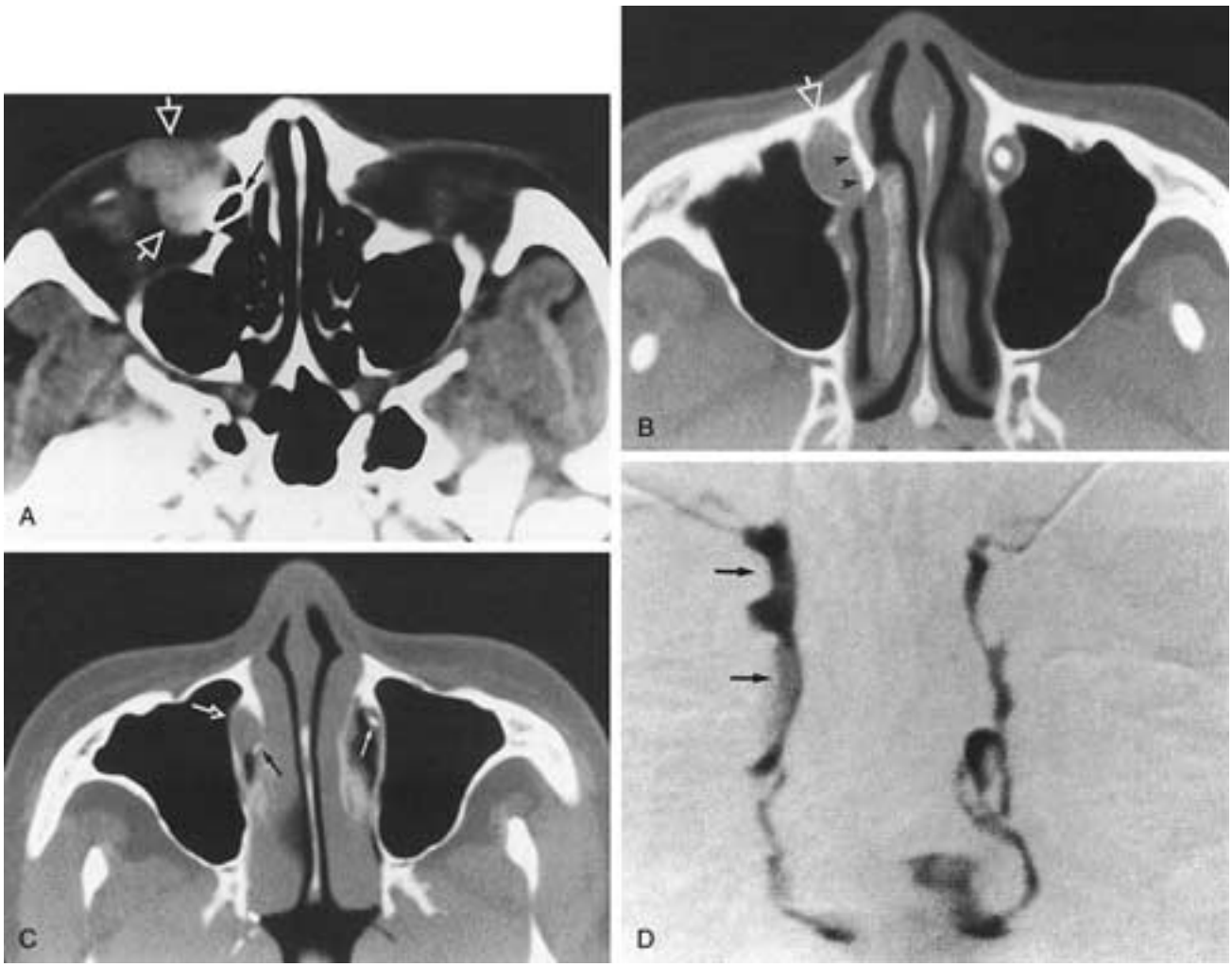

VIEW IMAGE

FIGURE 10-14 CT-DCG to identify the relationship between an inner canthus mass and the NLDS. **A** to **D**, Patient with a 2-year history of swelling of the right inner canthus. No epiphora. **A** to **C**, Axial CT-DCG scan from the superior to the inferior location. **A**, Large lobulated mass seen in the right inner canthus (*open arrow*) displacing the lacrimal sac (filled with contrast and seen as black because of density misregistration) (*solid arrow*) posteriorly within the nasolacrimal fossa. **B**, Enlarged right nasolacrimal canal (*open arrow*) with a contrast-filled nasolacrimal duct is compressed medially (*arrowheads*), resembling the bony wall of the canal. Normal left NLDS. **C**, At the level of the inferior meatus, normal termination of the left NLDS (*thin arrow*). Soft tissue on the right (*arrow*) displaces the contrast-filled nasolacrimal duct (*black arrow*) posteromedially. **D**, DCG. Prior to CT, only lateral indentation (*upper arrow*) of the dilated lacrimal sac was discussed, with less attention to the medial displacement of the nasolacrimal duct (*lower arrow*). Pathology: benign lacrimal sac cyst (from the wall of the lacrimal sac).

Copyright © 2003, Mosby, Inc. All rights reserved.

FIGURE 10-14 *Continued.* **E** to **L**, Second patient: right inner canthus swelling for 2 years. **E**, to **G**, Axial enhanced images, plus topical contrast, show a large, solid, well-defined mass in the right inner canthus displacing the globe laterally and extending into the nasolacrimal canal.

VIEW IMAGE

Illustration continued on following page

10-19A). Lacrimal sac calculi are often unsuspected at the time of surgery even though they are a common cause of epiphora. Preoperatively, such a diagnosis should be more strongly suspected in the younger patient (under age 50 years) with no obvious cause of epiphora.[86] In Jones'[84] and Wilkins and Pressly's series,[86] 65% and 53% of patients, respectively, under age 50 with epiphora of unknown etiology had calculi detected during DCR. Several reports have noted dacryoliths to be more common in younger and female patients. Reports indicate that 58% to 80% of patients with dacryoliths are under 50 years of age.[83, 84, 86, 87] Between 68% and 95% of patients with dacryoliths are female.[83, 84, 86, 87]

Most reports indicate that the frequency of lacrimal sac stones between 6% and 18% in patients undergoing dacryocystorhinostomy (DCR) for nasolacrimal duct obstruction. Yazici et al.'s[89] of 163 DCR cases noted a difference in the frequency of lacrimal sac dacryoliths in patients subcategorized as to etiology of obstruction. They report that 9.2% of the cases with primary acquired (idiopathic) nasolacrimal duct obstruction (PANDO) had dacryoliths. However, no dacryoliths were noted in a smaller group (38 cases) with a known cause of obstruction (congenital, traumatic, sinonasal surgery), a finding also noted in other series.[83, 84, 86] In analyzing the symptoms of patients with PANDO and dacryoliths compared to those without dacryoliths, Yazici et al.[89] noted the increased likelihood of acute medial canthal swelling (lacrimal sac distention or acute dacryocystic retention) without infection in patients with dacryoliths. They emphasized the distinction between lacrimal sac distention (no erythema or extreme tenderness, with a mucoid but not a purulent discharge) and dacryocystitis. Forty-two percent of the 12 patients with dacryoliths had simple acute lacrimal sac distention versus 5% of the 103 patients without dacryoliths. The previously reported greater frequency of acute dacryocystitis with dacryoliths may not have considered the distinction between lacrimal sac distention (retention) and acute dacryocystitis.

In these patients[89] with PANDO requiring DCR, the presence of lacrimal sac distention and male gender were more frequently associated with dacryoliths. There was no statistical significance related to age. Partial nasolacrimal duct obstruction and a history of cigarette smoking were relative risk factors for stone formation. Other studies[83, 84, 86] have noted a higher incidence of calculi in younger patients (under age 50) and in females.

The calculi may be fragmented, especially if the lacrimal drainage system has been probed. At surgery (DCR) the lacrimal sac must be carefully assessed and the puncta irrigated to ensure that all fragments are removed. Although the etiology of lacrimal calculi is obscure, predisposing factors such as stasis and infection are frequently associated

Copyright © 2003, Mosby, Inc. All rights reserved.

with calculus formation. An obstruction allowing partial drainage may facilitate the accumulation of debris. The etiology of dacryoliths, however, is more complex, with dacryolith formation noted in patients with no narrowing or compromise of the drainage system. The dacryolith is typically friable, often molding itself to the sac and duct. This friability helps explain the spontaneous passage of large dacryoliths through obstructed or anatomically narrowed ducts.[90, 91] The calculus consists of lamellae of cellular breakdown products and mucoproteins with or without calcium or ammonium salts.[89] Eyelashes, and occasionally particles of makeup, may be found in dacryoliths and may have acted as a nidus for dacryolith formation.[92–94] Herzig and Hurwitz,[95] in a series of 246

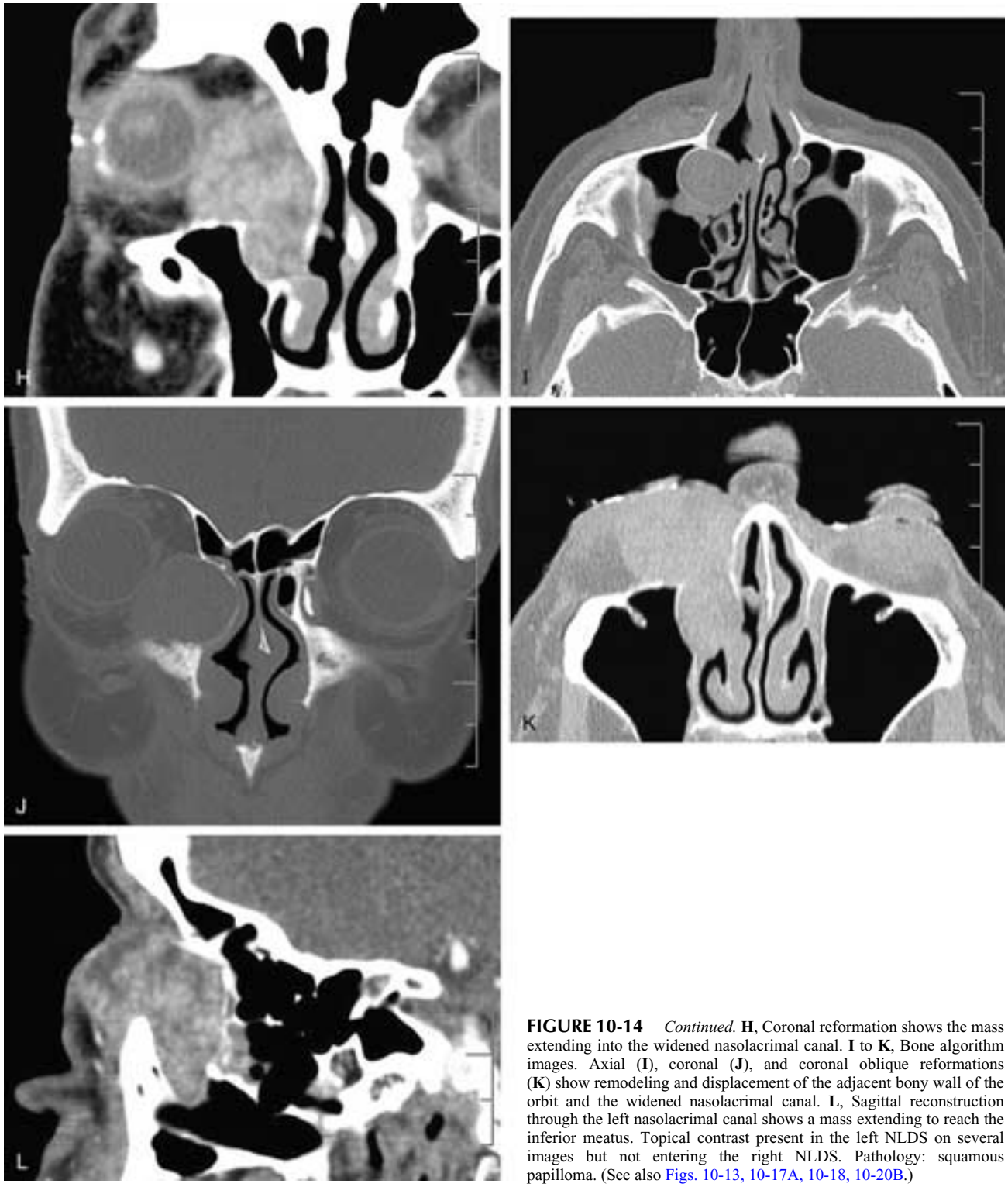

FIGURE 10-14 *Continued.* **H**, Coronal reformation shows the mass extending into the widened nasolacrimal canal. **I** to **K**, Bone algorithm images. Axial (**I**), coronal (**J**), and coronal oblique reformations (**K**) show remodeling and displacement of the adjacent bony wall of the orbit and the widened nasolacrimal canal. **L**, Sagittal reconstruction through the left nasolacrimal canal shows a mass extending to reach the inferior meatus. Topical contrast present in the left NLDS on several images but not entering the right NLDS. Pathology: squamous papilloma. (See also Figs. 10-13, 10-17A, 10-18, 10-20B.)

VIEW IMAGE

Copyright © 2003, Mosby, Inc. All rights reserved.

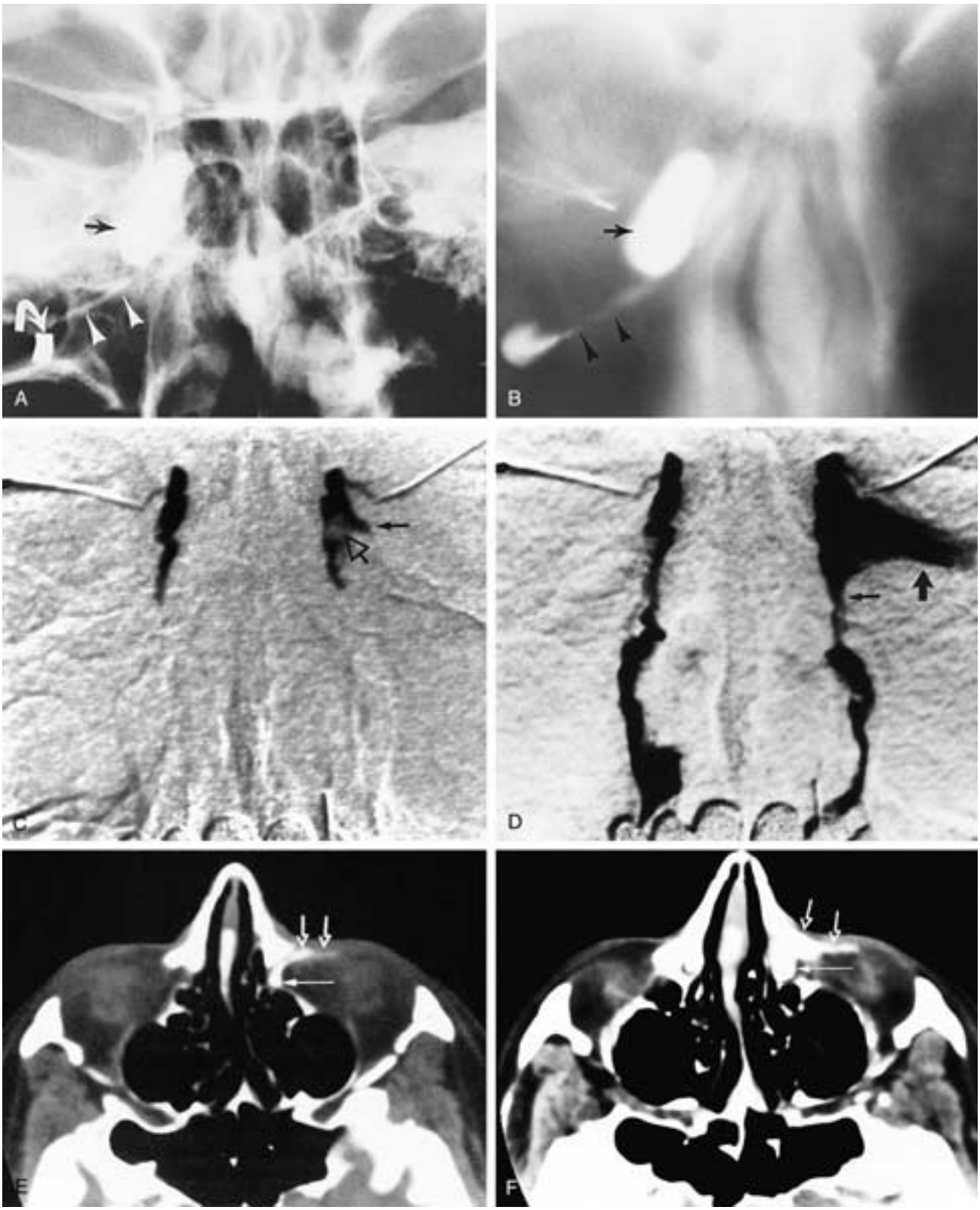

VIEW IMAGE

FIGURE 10-15 Fistulas and sinus tracts in preseptal tissues. **A** and **B**, Patient with epiphora and dacryocutaneous fistula draining below the inferior orbital rim. **A**, DCG, frontal view. **B**, Tomographic image. Dilated lacrimal sac (*arrow*). Fistula (*arrowheads*) seen extending from the distal lacrimal sac to the metallic marker on the skin surface at the cutaneous end of the fistula (*curved arrow*). **C** to **F**, Patient with a 2-year history of intermittent swelling of the left inferior eyelid causing closure of the eye and epiphora. Sinus tract into the lower lid in a patient with Crohn's disease. **C**, Early DCG image shows a suspicious ill-defined filling defect (*open arrow*) of the inferior left lacrimal sac, just above the origin of the nasolacrimal duct. Abnormal projection of contrast material in the lateral wall of the left lacrimal sac (*thin arrow*). **D**, Later DCG image. A large amount of contrast material extends inferolaterally toward the lower lid (*vertical arrow*). Contrast also enters the nasolacrimal duct (*horizontal arrow*) to empty into the nasal cavity. **E**, Axial CT-DCG shows contrast material extending from the lacrimal sac (*thin arrow*) to enter the soft tissues of the lower lid (*open arrow*). **F**, More inferior axial image shows the abnormal location of contrast material in the left inner canthus and lower lid (*open arrows*) and an enlarged collection of contrast material in or surrounding the left lacrimal sac (*thin arrow*).

Copyright © 2003, Mosby, Inc. All rights reserved.

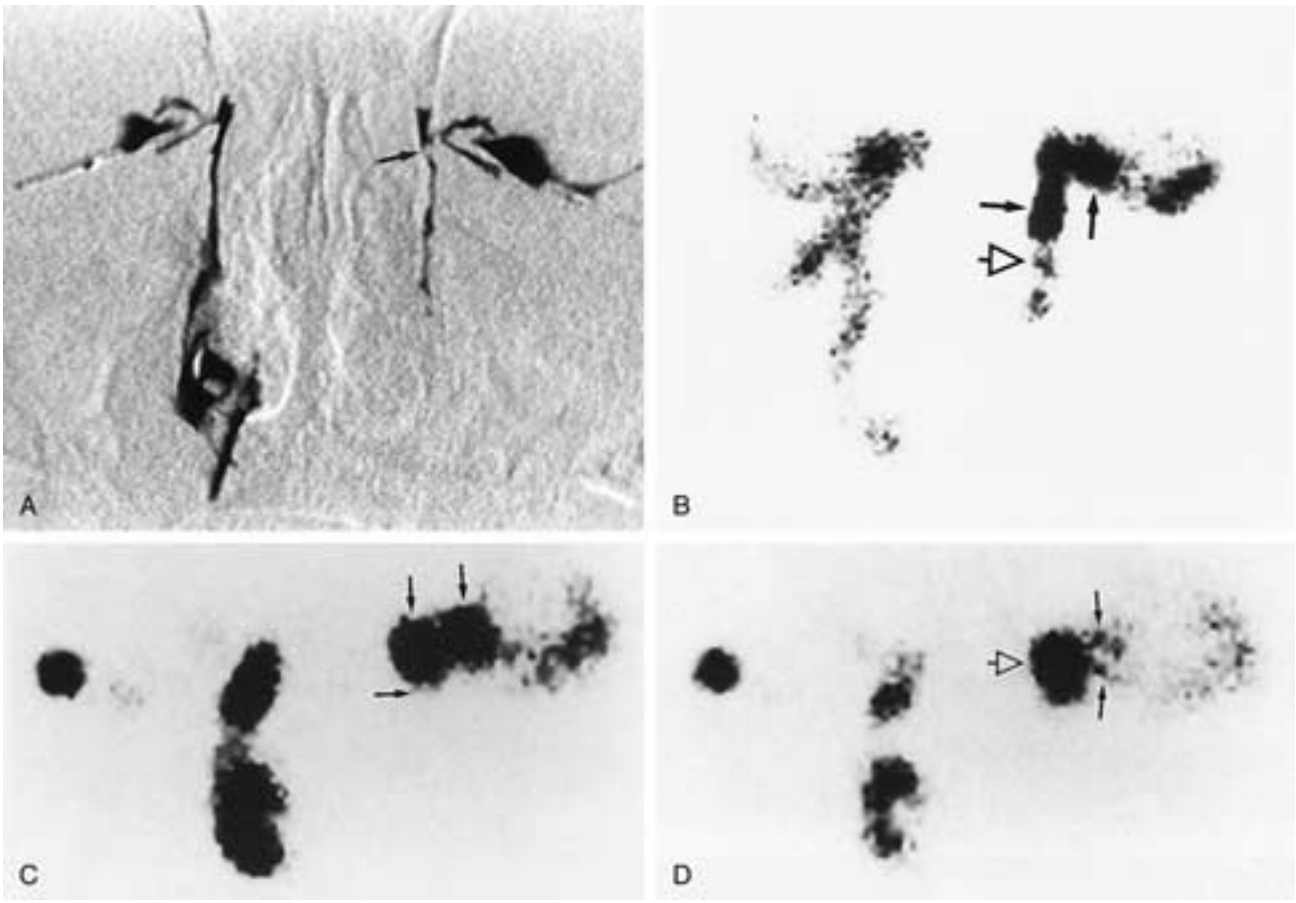

VIEW IMAGE

FIGURE 10-16 Comparison of DCG and DSG. **A** and **B**, Patient with left epiphora. **A**, DCG of the normal right side. Small filling defect of the distal left lacrimal sac (*arrow*) with delayed drainage into the nasolacrimal duct. **B**, DSG at 20 minutes. Normal drainage on the right side with decreased isotope activity within the NLDS. Persistent increased activity within the left lacrimal sac and canaliculi (*solid arrows*) with minimal activity entering the nasolacrimal duct (*open arrow*). **C** and **D**, Patient with left epiphora and a bloody discharge from the left tear duct. **C**, DSG at 15 minutes. Inferior portion of the left lacrimal sac is not seen (*horizontal arrow*). Increased activity in the proximal lacrimal sac and canaliculi (*vertical arrows*). Normal right drainage. **D**, Postrub DSG. Decreased activity in the right NLDS. Persistent increased activity in the left lacrimal sac (*open arrow*), superior canaliculus, and inferior canaliculus (*solid arrows*) caused by obstruction to outflow in the left lacrimal sac. Dacryolith in the left lacrimal sac. (See Fig. 10-18A-C for DCG and CT of the same patient.)

patients treated surgically, of whom 14 had calculi, were unable to demonstrate any systemic electrolyte abnormality predisposing to stone formation. They noted no abnormality of tear or serum calcium, phosphorus and uric acid concentrations, tear to serum calcium ratios or calcium-phosphate products. Accumulation (supersaturation) of electrolytes in an obstructed tear sac eventually leads to precipitation of a stone. Such precipitation can occur when obstruction is sudden (as in trauma or nasal surgery) or when obstruction is long-standing and associated with infection. The great majority of stones consist of calcium phosphate.[95]

The presence of a dacryolith, with persistent clinical features not responding to conservative treatment and requiring a DCR, may make endoscopic DCR more difficult or necessitate a larger opening for lacrimal sac exploration. An external approach may be necessary.[96]

Fungi have been noted in canalicular concretions but less frequently in lacrimal sac concretions. Anaerobic infection (*Actinomyces israelii*) is more common in canalicular stones (Fig. 10-7K,L), whereas *Candida*, an aerobic fungus, has been noted in lacrimal sac concretions.[97, 98] The relatively large size of fungi probably acts as the nidus, which, in a setting of chronic stasis, promotes or initiates calculus formation. The stasis, in a significant number of patients, is midlevel in the sac and probably results from the nature of the split fascia of the orbicularis muscle at this level, causing chronic dacryocystitis. The occurrence of lacrimal calculi is generally more frequent in female patients, but in at least one series male predominance was noted.[89] There have been variable results in identifying bacteria or fungi in association with lacrimal sac calculi. Jones[84] did not find any infectious agents in his results, while Berlin et al.[83] found bacteria or fungi rather commonly in lacrimal sac stones. They used routine hematoxylin-eosin stains as well as special fungal stains and recommended cultures for aerobes, anaerobes, and fungi. They noted DCG filling defects within the lacrimal sac in 4 of 11 patients found to have dacryoliths of the lacrimal sac at DCR.

Cast-like fungus obstruction of the nasolacrimal duct is uncommon.[98] When fungi occlude the lacrimal drainage

Copyright © 2003, Mosby, Inc. All rights reserved.

VIEW IMAGE

FIGURE 10-17 Cystic lesions of the inner canthus, CT-DCG. **A**, Mass in the left inner canthus (*open arrow*) is well defined and lies anterior to the left inferior canaliculus, which is filled with contrast medium (*closed arrow*). **B**, Well-defined right inner canthus mass (*arrow*) overlying the nasal bones. Tissue characteristics (-100 HU). Dermoid tumor. **C**, Neonate with a prominent left inner canthus. Hypodense mass (*open arrow*) contiguous with the nasolacrimal fossa (*solid arrow*). Dacryocystocele. **D** and **E**, DCG and enhanced axial CT in a patient with right epiphora and a questioned inner canthus mass. **D**, Mass indenting the medial aspect of the lacrimal sac inferiorly (*arrow*) with resultant dilation of the right lacrimal sac and a slight delay in drainage. **E**, Hypodense mass with a well-defined capsule (*open arrow*) extends into the nasolacrimal fossa (*arrowhead*) and represents a dilated lacrimal sac. Hyperdensity (*thin black arrow*) represents dacryolith in the medial wall of the sac, explaining the filling defect on DCG. Normal left lacrimal sac (*white thin arrow*). Pathology: chronic dacryocystitis with dacryolith. (See also Fig. 10-33, dacryocystocele.)

Copyright © 2003, Mosby, Inc. All rights reserved.

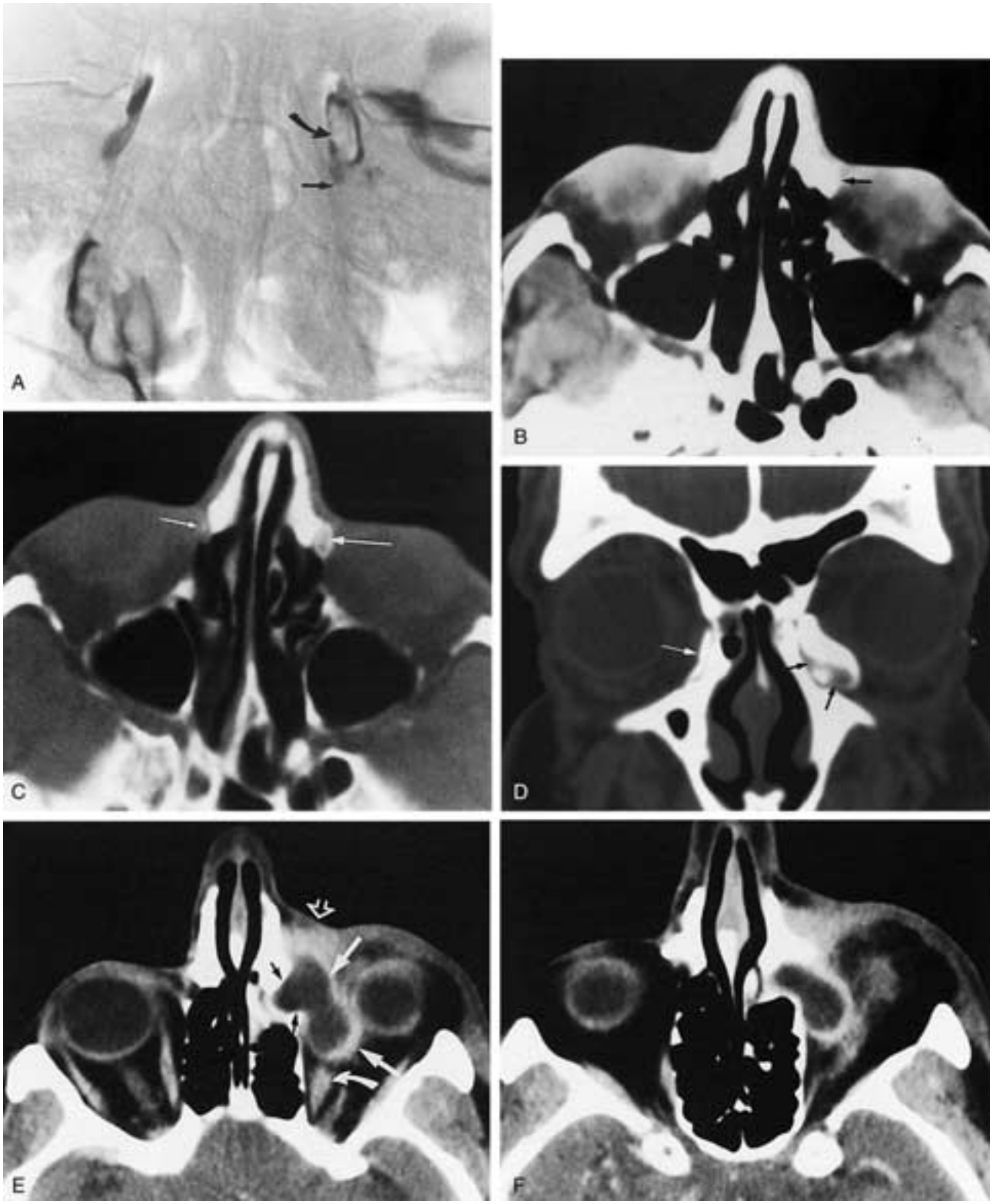

VIEW IMAGE

FIGURE 10-18 CT-DCG of intraluminal lesions. Multiple patients. **A**, Patient with a bloody discharge from the left tear duct. DCG shows a large filling defect (*curved arrow*) of the left lacrimal sac with a thin rim of contrast material peripherally. The nasolacrimal duct does not fill (*straight arrow*). **B**, CT-DCG. Soft-tissue window. See the prominent hyperdensity in the region of the left nasolacrimal fossa (*arrow*) compared with the right. **C**, Wider window of **B** shows a filling defect (*long arrow*) centrally in the enlarged left lacrimal sac within the nasolacrimal fossa. Contrast is faintly seen in the right lacrimal sac (*short arrow*). Pathology: dacryolith associated with gram-positive cocci. See Figure 10-16C,D for DSG on the same patient. **D**, Different patient with left inner canthus swelling. Coronal image shows a filling defect (*black arrows*) in the inferomedial aspect of the dilated left lacrimal sac. Normal right lacrimal sac (*white arrow*). Pathology: acute and chronic dacryocystitis with marked mucoid and cellular debris in a very distended lacrimal sac. **E** and **F**, Different patient. Cellulitis and chronic dacryocystitis with a lacrimal sac mucocele. **E**, Well-defined lobulated hypodensity of a lacrimal sac mucocele (*long arrows*) intimately associated with and enlarging the left nasolacrimal fossa (*short arrows*). The left globe is displaced laterally by the mass, which also abuts the optic nerve (not shown on this image). Preseptal soft-tissue swelling is present (*open arrow*). The medial rectus muscle is enlarged (*curved arrow*), representing a component of postseptal inflammatory involvement. **F**, More inferiorly located axial image emphasizes the relationship of the mucocele with the enlarged nasolacrimal fossa. Mucocele should not be mistaken for abscess cavity.

Copyright © 2003, Mosby, Inc. All rights reserved.

system, it is usually by formation of a stone or cast. *Aspergillus fumigatus* is an extremely rare cause of canalicular or lacrimal sac obstruction. *Aspergillus* produces hyphae, forming a ball or plug that obstructs the lacrimal system by mechanical obstruction without invading the surrounding tissues. Many cases have concomitant keratoconjunctivitis.[99] A lacrimal sac *Aspergillus* plug, presenting with initial intermittent obstruction and progressing to total obstruction, with discharge from the lacrimal punctum and extreme discomfort, may show no involvement of adjacent tissues (CT, operative and pathologic assessment), with CT only displaying an enlarged lacrimal sac. The discomfort is presumed to be caused by the stretched lacrimal sac capsule.[99] In patients with mechanical obstruction (i.e., plug) as an etiologic consideration, the planned DCR may be initiated with lacrimal sac exploration prior to osteotomy of the lacrimal fossa. The DCR may be abandonned if unnecessary.[99]

Calculi related to the canaliculi are discussed in the next section.

Since stasis secondary to an anatomic obstruction is likely to be the precipitating factor,[95] massaging, probing, or irrigation techniques to flush out the dacryoliths are restricted to incomplete obstructions and are limited in success due to the persistent stenosis of the nasolacrimal duct system (NLDS) or the increased size of the prestenotic dacryolith. Surgical removal of the dacryolith, in conjunction with an external DCR, is the standard treatment. The presence of calculi in the NLDS represents a limitation for endonasal DCR treatment. There have been attempts at nonsurgical management of dacryolithiasis using stent placement to correct an obstruction at the lacrimal sac–nasolacrimal junction. After fragmentation of the stones during stent implantation, the fragments passed through the stent with saline irrigation.[100]

In cases of dacryolithiasis associated with incomplete

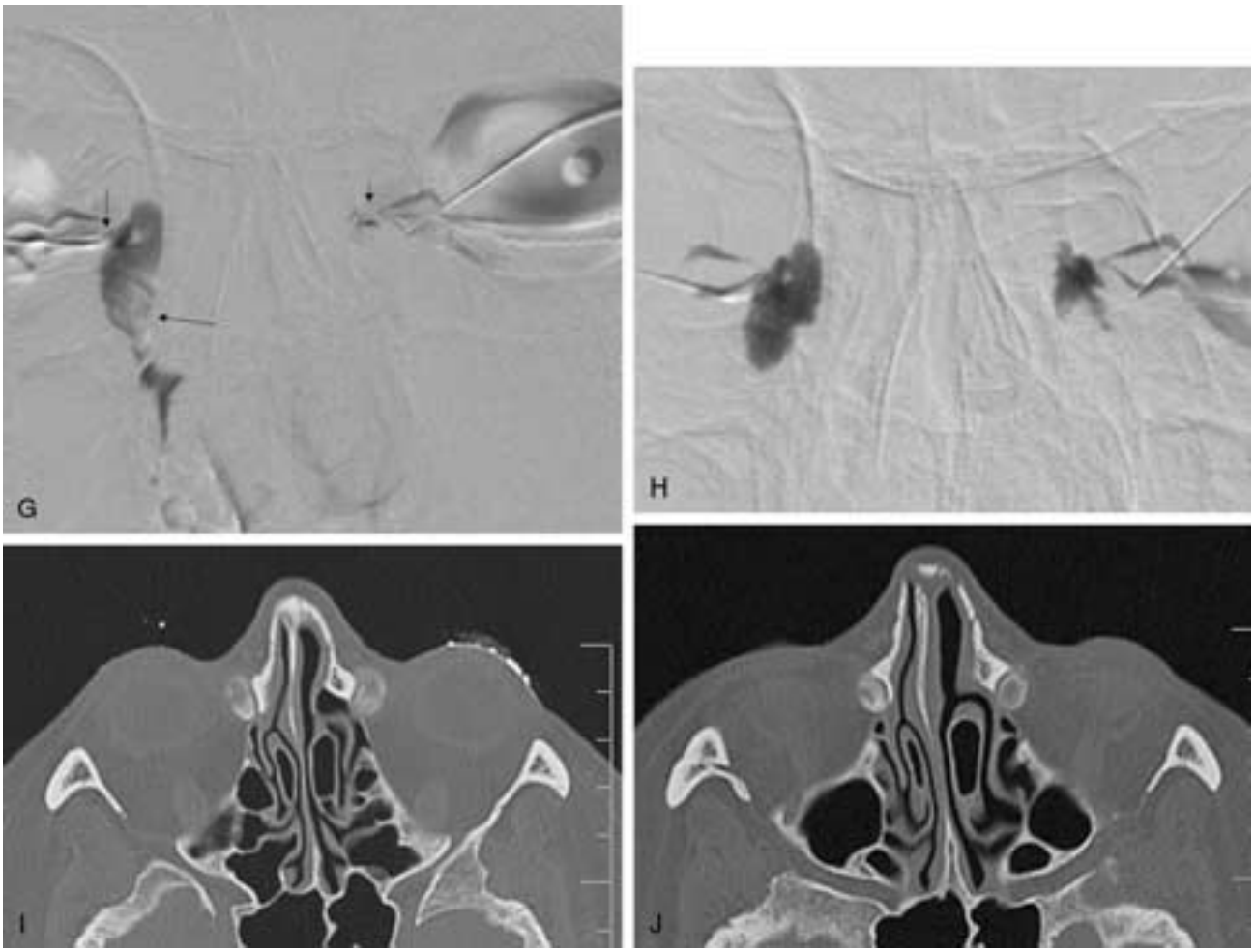

VIEW IMAGE

FIGURE 10-18 *Continued.* **G** to **N**, Lupus patient with bilateral tearing and intermittent facial swelling. **G**, DCG shows minimal filling of a stenosed left common canaliculus (*short arrow*). Contrast refluxes into the conjunctival sac. The right lacrimal sac is distended with secretions and debris (*horizontal arrow*) in the inferior medial aspect of the sac. Stenosis of the right superior canaliculus (*vertical arrow*). **H**, Repeat DCG study. Left lacrimal sac was distended and irregular, with a filling defect in the inferior aspect. Distended irregular right lacrimal sac. Contrast was not entering the nasolacrimal duct bilaterally. **I** and **J**, CT-DCG. Axial images show filling defects within the right and left lacrimal sacs.

Illustration continued on following page

Copyright © 2003, Mosby, Inc. All rights reserved.

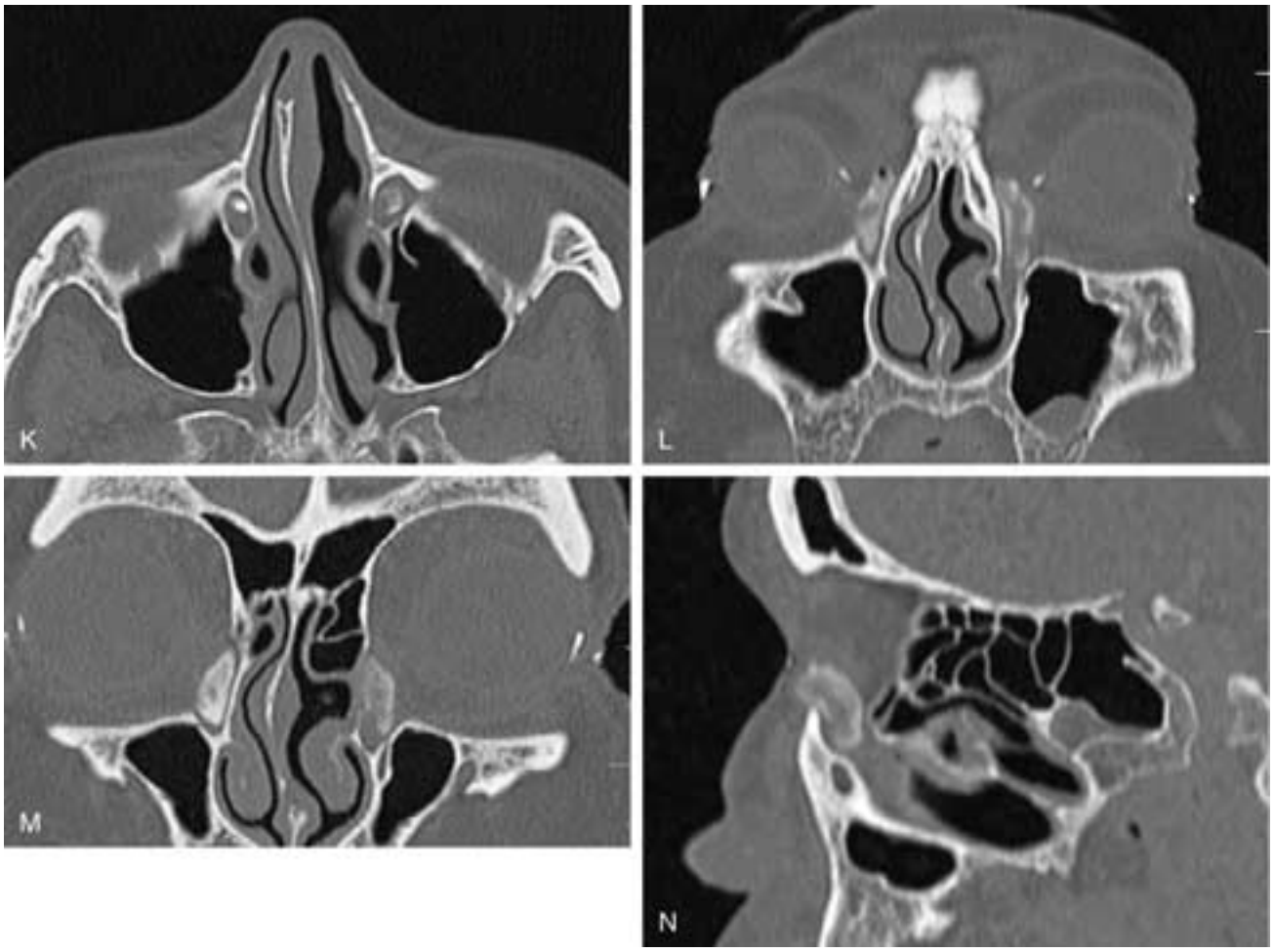

VIEW IMAGE

FIGURE 10-18 *Continued.* **K**, More inferior axial image shows a filling defect in the distended left nasolacrimal duct. **L** to **N**, Coronal (**L** and **M**) and left sagittal (**N**) reformations show intraluminal filling defects that lack sharp margins or definition. Pathology: chronic dacryocystitis with extensive mucoid and cellular debris.

(eight patients) or complete (two patients) obstructions, Wilhelm et al.[101] have performed balloon dilatation of the NLDS, principally to widen the stenosed obstructing segment, so that the dacryoliths may pass more easily into the nasal cavity during forced irrigation with saline. If stone passage was not achieved because of persistent stenosis or large dacryolith size, further balloon dilatation (eight patients) was used to crush the calculi. Incomplete washout of calculi by forced irrigation was supplemented by retrograde passage of a 6.3F sheath across the stenosis. With the tip inferior to the dacryolith, repeat forced irrigation is performed, with active aspiration of the fragments through the sheath. In two patients, additional fragmentation of the dacryolith with a gooseneck Amplatz snare, passed retrograde through the sheath, was followed by successful irrigation combined with aspiration. Attempts at stone removal may be unsuccessful when bending of the sheath occurs or if fragments are too large to pass through the sheath.[101] For those patients with preintervention complete obstruction, stent implantation was initially necessary to restore drainage function. Stone removal itself, by such nonsurgical techniques, should not be considered without concomitant treatment of the stenosis or obstruction.[100, 101] (See the section on Dacryocystoplasty and Stent Placement for a more detailed procedural discussion.)

Chronic Canaliculitis

Chronic infective canaliculitis, although relatively uncommon, is significant because of its specific radiologic and clinical features (Fig. 10-8). In 1854, von Graefe[102] was the first to attribute this condition to an infectious source. Although chronic canaliculitis was called *streptothrix*, since the anaerobic bacterium *A. israelii* was the most frequent causative agent. Numerous other anaerobic agents have been identified, including *Nocardia* and *Fusobacterium* species, *Arachnia propionica*, and *Bacteroides*, as well as aerobic fungi, including *Candida*, *Aspergillus*, and *Blastomyces*,[83, 103] emphasizing the need for both anaerobic and aerobic cultures. Secondary bacterial infections should be treated independently.

Chronic canaliculitis, as with most lacrimal drainage afflictions, affects women more often than men and the lower canaliculus more than the upper.[103] Involvement of more than one canaliculus rarely occurs,[104] and the disease

Copyright © 2003, Mosby, Inc. All rights reserved.

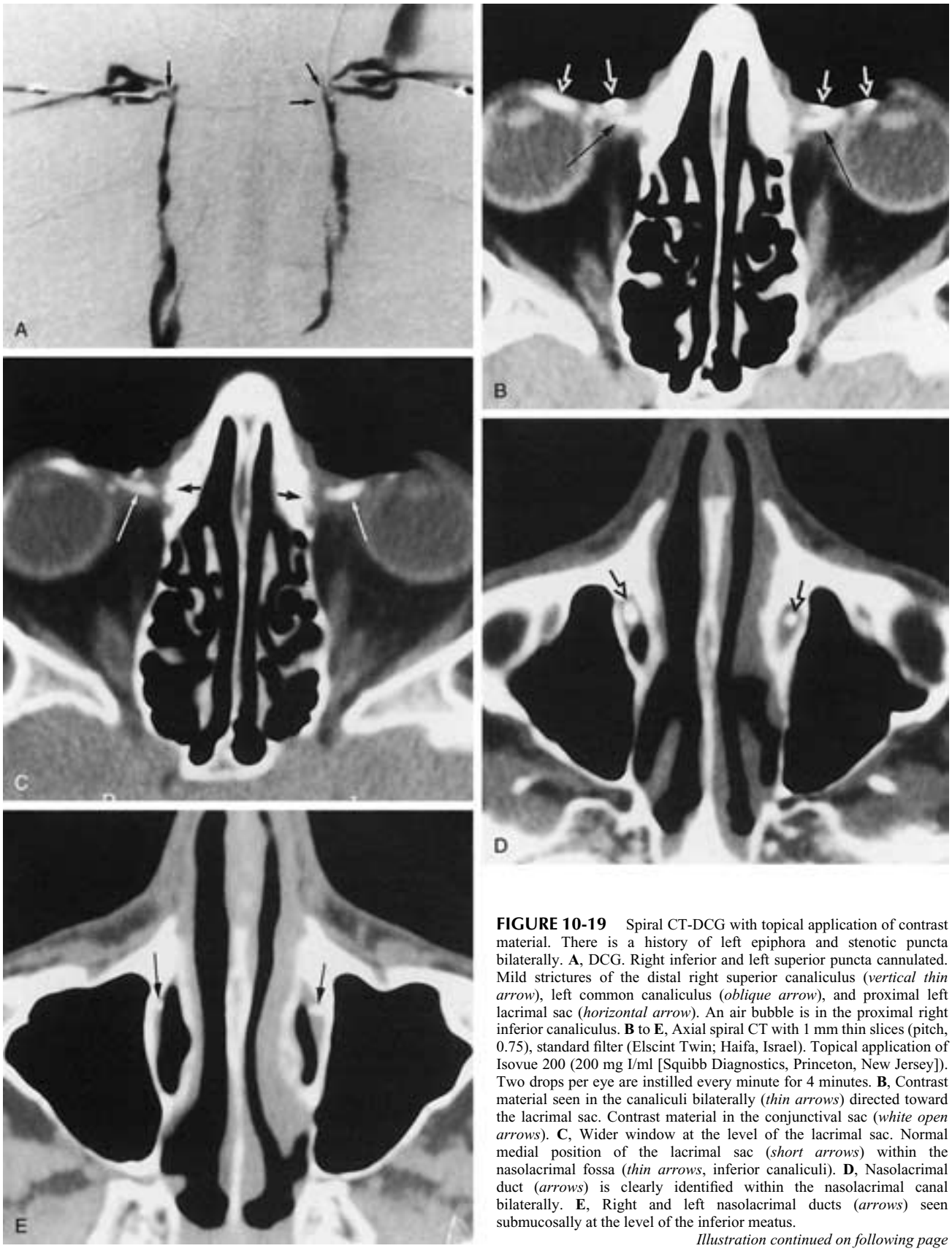

FIGURE 10-19 Spiral CT-DCG with topical application of contrast material. There is a history of left epiphora and stenotic puncta bilaterally. **A**, DCG. Right inferior and left superior puncta cannulated. Mild strictures of the distal right superior canaliculus (*vertical thin arrow*), left common canaliculus (*oblique arrow*), and proximal left lacrimal sac (*horizontal arrow*). An air bubble is in the proximal right inferior canaliculus. **B** to **E**, Axial spiral CT with 1 mm thin slices (pitch, 0.75), standard filter (Elscint Twin; Haifa, Israel). Topical application of Isovue 200 (200 mg I/ml [Squibb Diagnostics, Princeton, New Jersey]). Two drops per eye are instilled every minute for 4 minutes. **B**, Contrast material seen in the canaliculi bilaterally (*thin arrows*) directed toward the lacrimal sac. Contrast material in the conjunctival sac (*white open arrows*). **C**, Wider window at the level of the lacrimal sac. Normal medial position of the lacrimal sac (*short arrows*) within the nasolacrimal fossa (*thin arrows*, inferior canaliculi). **D**, Nasolacrimal duct (*arrows*) is clearly identified within the nasolacrimal canal bilaterally. **E**, Right and left nasolacrimal ducts (*arrows*) seen submucosally at the level of the inferior meatus.

Illustration continued on following page

VIEW IMAGE

Copyright © 2003, Mosby, Inc. All rights reserved.

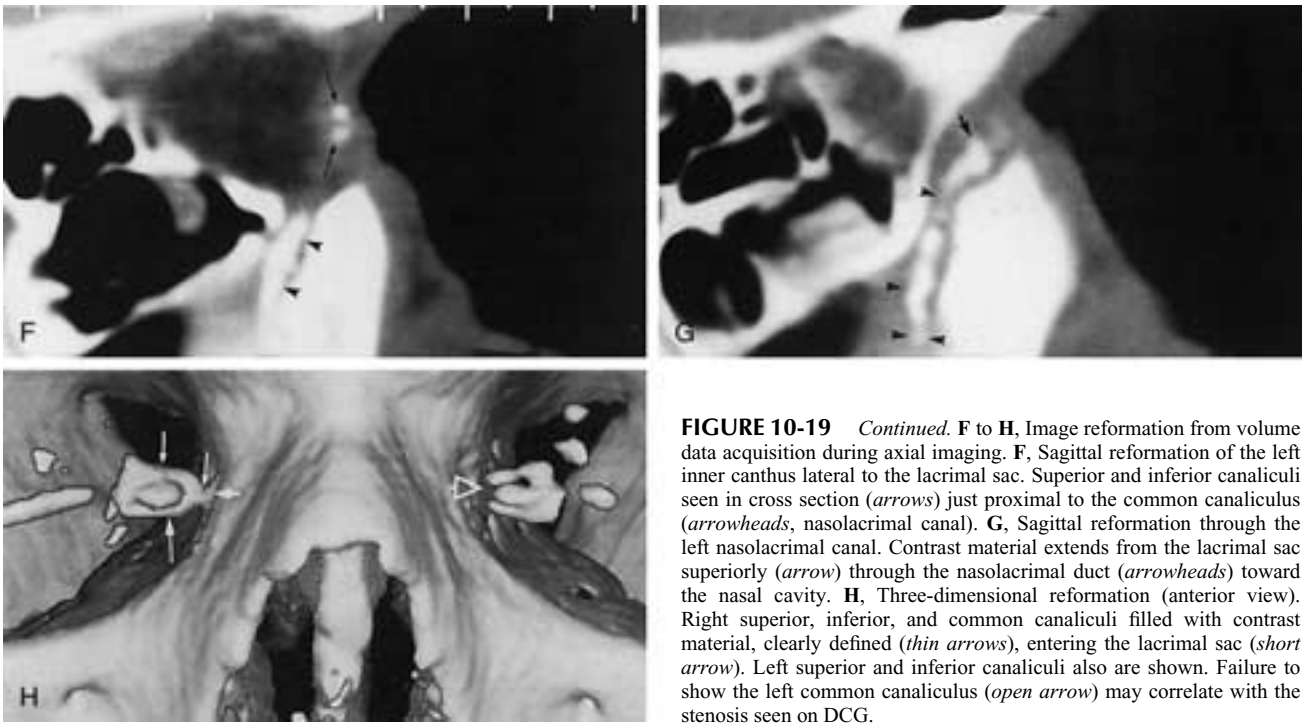

FIGURE 10-19 *Continued.* **F** to **H**, Image reformation from volume data acquisition during axial imaging. **F**, Sagittal reformation of the left inner canthus lateral to the lacrimal sac. Superior and inferior canaliculi seen in cross section (*arrows*) just proximal to the common canaliculus (*arrowheads*, nasolacrimal canal). **G**, Sagittal reformation through the left nasolacrimal canal. Contrast material extends from the lacrimal sac superiorly (*arrow*) through the nasolacrimal duct (*arrowheads*) toward the nasal cavity. **H**, Three-dimensional reformation (anterior view). Right superior, inferior, and common canaliculi filled with contrast material, clearly defined (*thin arrows*), entering the lacrimal sac (*short arrow*). Left superior and inferior canaliculi also are shown. Failure to show the left common canaliculus (*open arrow*) may correlate with the stenosis seen on DCG.

VIEW IMAGE

is almost always unilateral.[83, 103] Clinically, the affected lid is swollen from the lacrimal punctum to the medial canthus, with a chronic mucopurulent discharge or particulate matter expressed (with difficulty) from a pointing dilated punctum. Erythema and induration over the canaliculus may be noted. Demonstration of concretions within the canaliculus virtually establishes the diagnosis, although concretions can also form around small foreign bodies or hair (eyelash) in the canaliculi.[94, 103] Organisms such as *Actinomyces* or, less frequency, *S. aureus*, form filamentous aggregates (sulfur granules), which distend the canaliculus and impede the drainage of tears. However, the canaliculus is often patent to syringing, obscuring the correct diagnosis.[85] Adequate treatment requires complete removal of concretions, material that has accumulated within the canaliculus. Expression and curettage may be adequate, but often incision and debridement of the affected canaliculus is necessary. Antibiotics used without surgical correction are unsuccessful. Such patients therefore usually present with an extensive list of previously prescribed medications. Chronic unilateral conjunctivitis should always suggest the possibility of canaliculitis.

DCG shows dilation and irregularity of the affected canaliculi, with an appearance of sacculation, beading, or diverticula. Such dilation is nonspecific and may be noted proximal to any obstructive or stenosing lesion. Dilation without stenosis or the presence of irregular filling defects (due to concretions) within the canaliculi is more specific for a chronic infectious etiology such as actinomycosis. Filling defects in the absence of concretions or sulfur granules may represent actinomycotic filaments. The degree of dilation is related to the presence of filling defects and is unrelated to the infective organism.[103] Classically, the distal nasolacrimal system fills and is normal, with no evidence of inflammatory change despite the severity of the proximal canalicular duct involvement. The extent of involvement is characteristically limited to the proximal canaliculi such that the common canaliculus and lacrimal sac are usually normal (e.g., the common canaliculus was normal in 15 of 18 patients in one series).[103]

Concretions (dacryoliths) are more frequent in the lacrimal sac. Such concretions are less consistently associated with chronic infection than are concretions in the canaliculi.[83, 86] Chronic viral canaliculitis (e.g., ocular vaccinia, herpes zoster, or simplex ophthalmicus, viral conjunctivitis) tends to cause scarring, with stenosis or occlusion of the puncta and/or canaliculi, and therefore differs from the classic description of chronic infective canaliculitis.[105] Obstruction of the medial half of both canaliculi is often herpetic or trachomatous in origin.[106] In contrast to conjunctival infections caused by microbes, certain viral infections extend deeper into the stratified squamous epithelium of the canaliculi to involve the elastic layer, with resultant scarring and stenosis.[105]

Posttreatment Considerations

Postsurgical Considerations

Radiopaque tubes between the nasal cavity and medial canthus may be used in conjunction with DCR (canaliculo-DCR) to maintain patency within the canaliculi (Figs. 10-7I-J, 10-9, 10-20). Surgical clips may occasionally be present in the region of the medial canthus, and their relationship to the nasolacrimal drainage system may be important in cases of postsurgical obstruction. The relationship of the nasolacrimal sac to the DCR osteotomy site is assessed by CT. DCR is a relatively successful surgical procedure in 85% to 90% of cases, with an average failure rate of approximately 10%.[30, 107–110] DCR failure may be

Copyright © 2003, Mosby, Inc. All rights reserved.

due to delayed obstruction at the surgical anastomosis by granulation tissue, fibrosis, or osteogenic activity or by secondary stenosis of the canaliculi. The failed DCR patient will have recurrence of epiphora and frequently recurrent dacryocystitis. DCG shows DCR failure to be related to problems distal to the common canaliculus in 60% of cases.[66] A residual inferior portion of the sac, with its bony covering (incomplete osteotomy), may produce inadequate drainage requiring a direct surgical approach on the anastomosis. This is in contrast to a canaliculo-DCR, which is required in 12% to 40% of failed DCRs where the obstruction is in the common canaliculus.[66, 67] It may not be possible on DCG to differentiate an obstruction of the common canaliculus from a closed osteotomy site in patients with a previous DCR.[107] Scarring of the ostium (rhinostomy site) and errors in ostium location are the major causes of surgical failure.[111, 112] Adhesions to the nasal septum (synechia) from the rhinotomy site may case obstruction and DCR failure. These adhesions are detectable on CT.[111] On DCG, lacrimal sac diverticula, directed medially toward the midline, may suggest adhesions between the ostium and the nasal septum.[111]

The relatively increasing percentage of patients with postsurgical canalicular problems may reflect increasing attention to the lacrimal flap/osteotomy site and/or reflect the iatrogenic effects of dilations and probings of the canaliculi preoperatively or during surgery.

Hurwitz et al.[113] studied the effects of surgery and/or radiation treatment for paranasal sinus tumors on the NLDS of 19 patients. Of those patients treated surgically, the majority (75%) did not develop obstruction even though the NLDS was anatomically altered, with the nasolacrimal duct frequently being shortened and the lacrimal sac displaced (Fig. 10-10). During maxillary sinus surgery, the lacrimal bone and nasolacrimal canal are frequently removed, and these patients tended to have obstruction in the lower part of the NLDS and were amenable to treatment by DCR. Stenosis or irregularity of the lacrimal sac or one of the canaliculi may develop secondary to scar tissue formation but does not tend to cause obstruction.

Postirradiation Considerations

Patients treated with postoperative radiotherapy tended to have more profound abnormalities of the lacrimal system than those treated by surgery alone, with the delicate structure of the canaliculi most susceptible to irradiation injury and subsequent obstruction.[105, 106, 113] Such patients may need to be treated by prolonged intubation of the canaliculi (silicone tubing) or (canaliculodacryocystorhinostomy), with a success rate of only 60% to 70% versus 80% to 95% for uncomplicated lower NLDS obstruction.[114] Doucet and Hurwitz[114] postulated whether or not prophylactic placement of intubation tubes (silicone or glass stents) at the time of surgery would be beneficial for patients undergoing postoperative radiation therapy to prevent the canalicular stenosis or obstruction.

Postchemotherapy Considerations

The onset of epiphora, due to the development of punctal and canalicular fibrosis, soon after the weekly administration of docetaxel, an effective first- or second-line antineoplastic agent for the treatment of breast or prostate cancer,

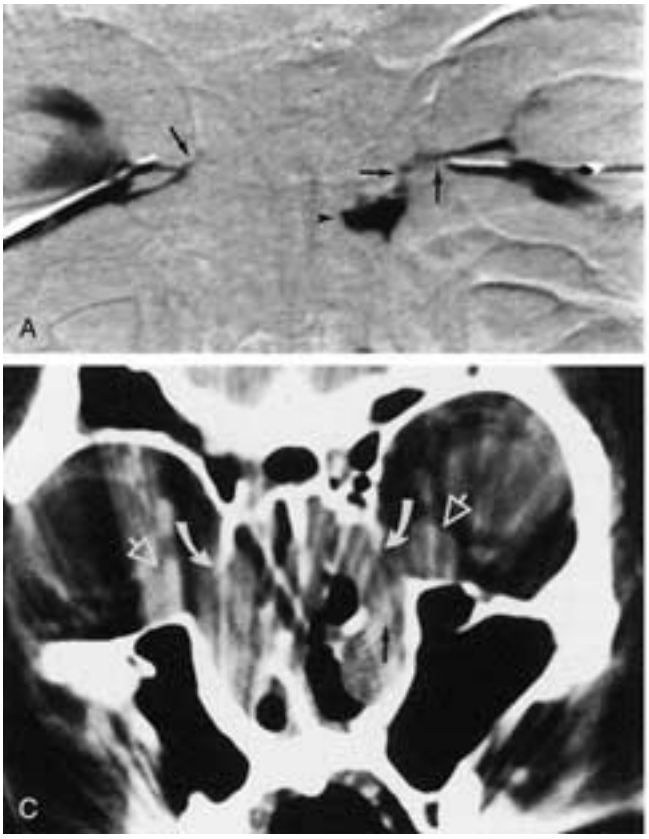

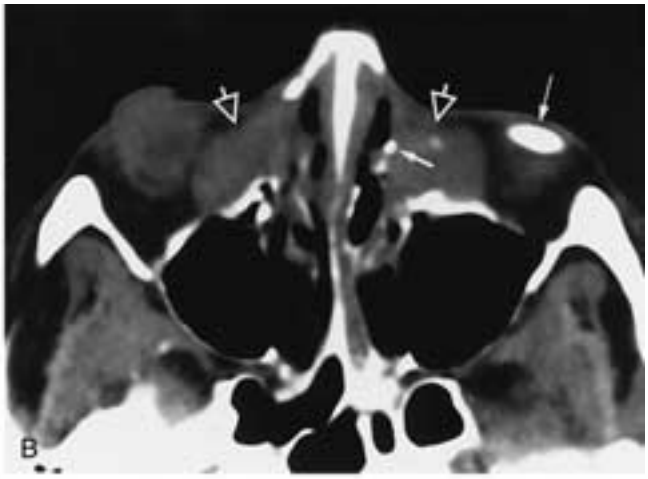

FIGURE 10-20 Bilateral inner canthal masses: previous bilateral DCG recurrent right epiphora. **A**, DCG. Right superior canalicular injection shows severe stenosis of the common canaliculus (*oblique arrow*), reflux into the inferior canaliculus, and no filling of the lacrimal sac. Left inferior canaliculus shows stenosis medially (*vertical arrow*) and a fibrosed lacrimal sac (*horizontal arrow*), with contrast entering the nasal cavity through the previous DCR (*arrowhead*) at the inferior aspect of the lacrimal sac. **B**, Axial CT-DCG shows bilateral inner canthus soft-tissue masses (*open arrow*). Contrast material is seen in the left NLDS (*solid arrow*) and conjunctival sac (*thin arrow*). **C**, Coronal CT-DCG (artifact from dental restorations). Inner canthus masses (*open arrows*) appear to be contiguous with soft-tissue densities of the nasal cavity through previous DCR osteotomy sites (*curved arrows*) and the left nasolacrimal canal (*black arrow*).

Illustration continued on following page

VIEW IMAGE

Copyright © 2003, Mosby, Inc. All rights reserved.

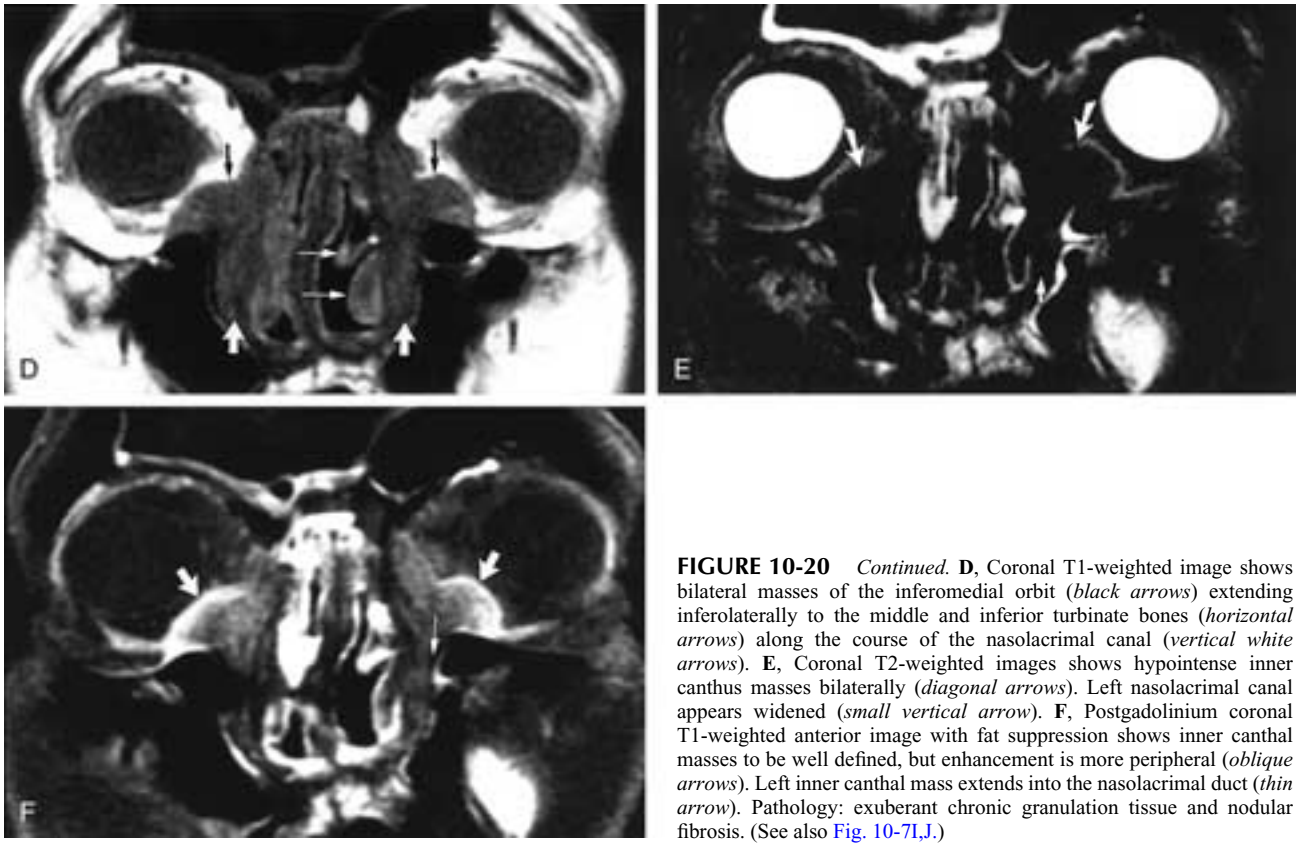

FIGURE 10-20 *Continued.* **D**, Coronal T1-weighted image shows bilateral masses of the inferomedial orbit (*black arrows*) extending inferolaterally to the middle and inferior turbinate bones (*horizontal arrows*) along the course of the nasolacrimal canal (*vertical white arrows*). **E**, Coronal T2-weighted images shows hypointense inner canthus masses bilaterally (*diagonal arrows*). Left nasolacrimal canal appears widened (*small vertical arrow*). **F**, Postgadolinium coronal T1-weighted anterior image with fat suppression shows inner canthal masses to be well defined, but enhancement is more peripheral (*oblique arrows*). Left inner canthal mass extends into the nasolacrimal duct (*thin arrow*). Pathology: exuberant chronic granulation tissue and nodular fibrosis. (See also Fig. 10-7I,J.)

VIEW IMAGE

has recently been described in three patients.[115] The pattern of fibrosis involved all four puncta and canaliculi. Discontinuation of the agent led to resolution of symptoms in only one of the three patients (who may have had less advanced fibrosis). The mechanism of canalicular stenosis may be secondary to secretion of the chemotherapeutic agent in the tear film, with fibrosis resulting from the direct contact (local) of the agent in the canaliculi. Alternatively, the mucous membrane lining the puncta and canaliculi may undergo fibrosis secondary to systemic effects of the drug, similar to the widespread edema and fibrosis noted elsewhere within the body.

Canalicular stenosis had previously been described in association with other chemotherapeutic agents, such as 5-fluorouracil.[116, 117] Screening for epiphora and canalicular stenosis has been advocated for this patient population, with early treatment consideration of silicone intubation or punctoplasty, while the patient is receiving the chemotherapeutic agent, to prevent complete closure of the canaliculi and the need for conjunctivo-DCR and Jones tube placement.

DACRYOSCINTIGRAPHY

In 1972, Rossomondo et al.[118] introduced a radionuclide technique to assess the lacrimal passages (Figs. 10-16, 10-21, and 10-22). This technique offers a more physiologic, less expensive, more sensitive, and more comfortable modality for assessing epiphora.[119–122] The ease of performance and the noninvasive nature of the procedure tend to encourage routine bilateral studies. DSG can also provide a quantitative dynamic analysis of tear drainage physiology. DCG, although the most commonly used imaging technique for evaluating the anatomy and pathology of the lacrimal drainage system, does not provide physiologic information.[113, 123] Because the pressure required to inject the DCG contrast material overcomes any functional occlusion of the NLDS, a normal DCG in a patient with epiphora offers no information related to functional stenosis or obstruction.

Technique

The patient is placed in a modified sitting position so that the head rests on a modified slit-lamp support that includes a chin rest, forehead support, and straps to immobilize the head for the study. Just before the instillation of radionuclide, manual pressure over the inner canthus empties the lacrimal sacs. With the head tilted back, a drop (approximately a 10 µl aliquot) of the solution technetium 99m pertechnetate or 99m-Tc-sulfur colloid is placed in the lateral conjunctival sac using an automatic micropipette. Instillation of larger volumes will simply overfill the conjunctival sac, resulting in spillage onto the face.[124] The patient's head is then placed within the supporting frame, and a micropinhole (1 mm) collimator is placed just anterior (e.g., 8 to 9 cm) to the nasion and between the two orbits in the upper central field of the gamma camera. Dynamic acquisition of scintigraphic images starts immediately after instillation of the radiopharmaceutical. Patients are instructed to blink every 5 seconds during data

Copyright © 2003, Mosby, Inc. All rights reserved.

acquisition. A computer is set up for a two-phase dynamic acquisition with the following protocol: phase 1 (stimulated phase, 0 to 2 minutes), 5 second scans for 24 frames; phase 2 (initial drainage phase, 2 to 12 minutes), 10 to 15 second scans for 40 frames. A variation of this technique has the patient remain still but blink normally, with the dynamic acquisition of tracer distribution imaged every 10 seconds for the first 160 seconds.[22] Static views are then taken routinely at 5, 10, 15, and 20 minutes.

An alternative technique includes an 8 µl drop of 99m-technetium-tin colloid, containing no more than 4 MBq and capturing 48 consecutive 15 second images, using a 2 mm pinhole collimator placed 2 cm from the eye, centered on the medial canthus.[26] Using this technique, each eye is imaged separately. The 2 mm aperture offers a preferred balance between resolution and increased sensitivity (sampling of radiation emitted). Other authors favor a 3 mm aperture or vary the distances (e.g., 1 cm subject to collimator, 5 cm nasion to collimator, or 8 cm subject distance).[125–127]

The passage of radioactivity is followed on a video display unit. An area of interest (e.g., interpalpebral fissure and canaliculi) can be outlined on a rapid-sequence video display terminal and quantitative data analysis achieved by the computer interfaced to the gamma camera (Fig. 10-22).

Radiopharmaceutical activity enters the canaliculi rapidly and then progresses along the NLDS, with activity increasing in the lacrimal sac and decreasing in the canaliculi. Data analysis and time activity curves for the radiopharmaceutical to leave an area of interest (various constructed points along the NLDS) can be obtained. The $T_{1/2}$ (the time required for one half of the radioactive dose to disappear) for a specific site can be estimated by finding the slope of the curve plotting the natural logarithm of counts per second from the region of interest against time.[128] The examination is terminated when the radiopharmaceutical reaches the nasal cavity. Residual radioactivity is flushed out by a saline eye bath at the end of the study (Fig. 10-16D). The radiation dose to the lens (4 to 21 mrad) is minimal, 1% of that from a DCG[129] or less than 2% of the radiation from an anterioposterior skull film (i.e., 4 vs. 200 to 370 mrad).[118, 130] The usual aliquot administered contains between 50 and 100 µCi of 99m-Tc.[118] The radiation dose will be increased if the lacrimal drainage system is blocked. If lacrimal fluid turnover is minimal and disappearance occurs only by physical decay, the maximum absorbed dose to the nearpoint of the lens will be 400 mrad.[129]

Normal Examination

Both lid margins are visualized, and the canaliculi are seen after approximately 10 seconds. The radiopharmaceu-

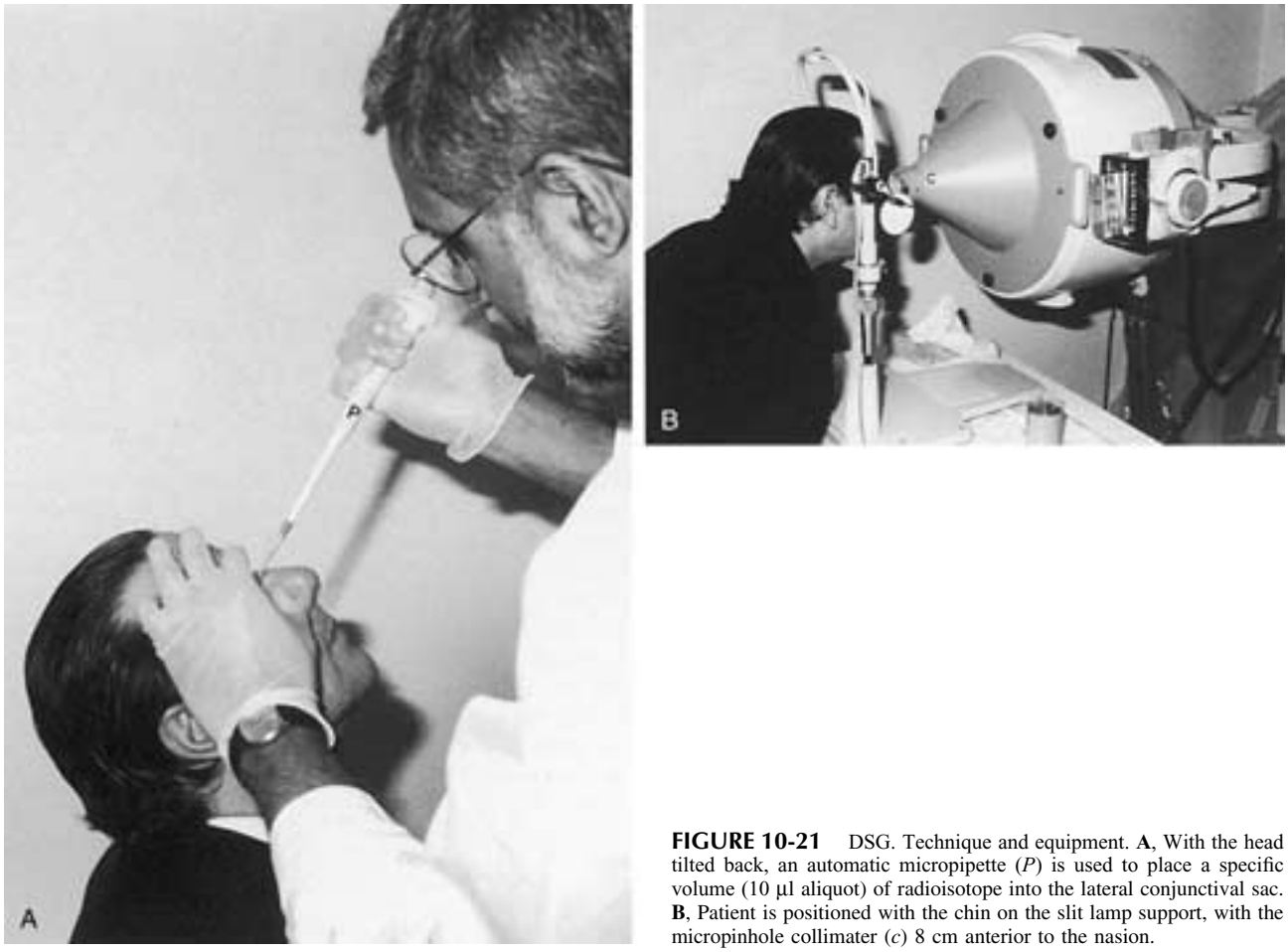

FIGURE 10-21 DSG. Technique and equipment. **A**, With the head tilted back, an automatic micropipette (*P*) is used to place a specific volume (10 µl aliquot) of radioisotope into the lateral conjunctival sac. **B**, Patient is positioned with the chin on the slit lamp support, with the micropinhole collimater (*c*) 8 cm anterior to the nasion.

VIEW IMAGE

Copyright © 2003, Mosby, Inc. All rights reserved.

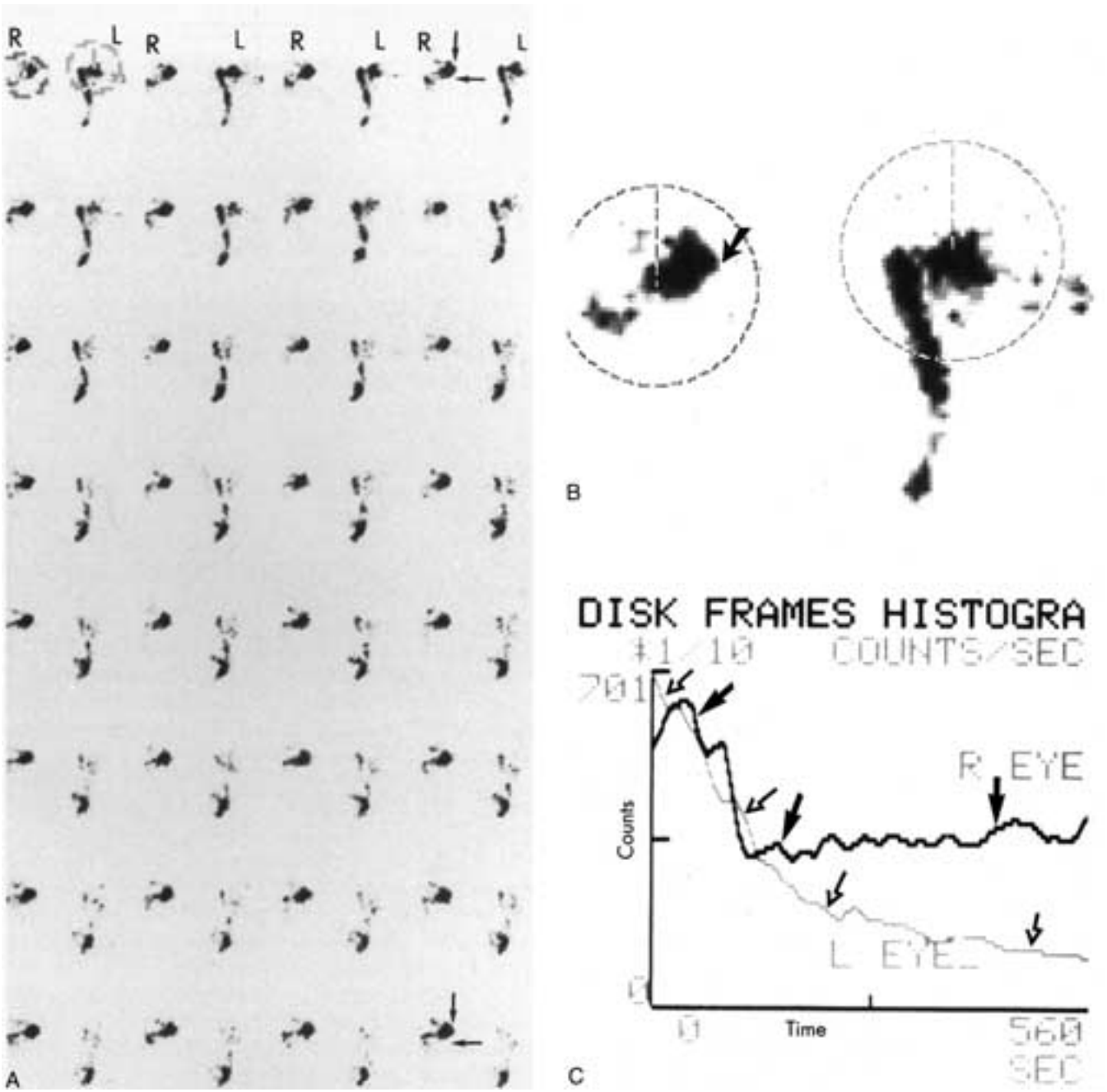

VIEW IMAGE

FIGURE 10-22 Bilateral DSG demonstrating isotope time activity patterns (normal and abnormal). **A**, Representative collection of images (each gathered at 10 second intervals) shows progression of activity (from superior to inferior) on the left (normal drainage). Obstruction at the right lacrimal sac (*vertical arrow*) with persistent proximal activity and no distal activity (*horizontal arrow*). **B**, Magnified image. The area of interest is outlined (*circles*) for the time–activity curve. Obstruction of the right lacrimal sac (*arrow*). **C**, Histogram of counts (activity) versus time. Normal slope indicates proper drainage from the left eye (*open arrows*). Right eye time–activity curve (*solid arrows*) shows failure of the normal slope, indicating a lack of drainage. ($T_{1/2}$ is beyond the limits of the scan time.)

tical can be seen progressively in the lacrimal sac and nasolacrimal duct, terminating in the nasal cavity. The valve of Hasner is usually seen as a reduction of scintillations at the lower end of the tracer column. A significant proportion of normal volunteers showed delayed passage of the radiopharmaceutical between the lacrimal sac and the nasal cavity, such that dacryoscintigraphy (DSG) is deemed unreliable for assessing the nasolacrimal duct, that is, the drainage system inferior to the lacrimal sac.[20, 125, 127] The flow of tears (radiopharmaceutical) from the conjunctival cul-de-sac to the lacrimal sac occurs in approximately 12 seconds, yet the radiopharmaceutical may not reach the nasal cavity for 10 to 20 minutes.[125] The elimination of tears is affected by the blink-driven ''lacrimal pump,''

Copyright © 2003, Mosby, Inc. All rights reserved.

which depends on the muscular blinking action of the eyelids, that is, the superficial and deep insertions of the preseptal and pretarsal orbicularis oculi of the lower and upper eyelids.[131] This component of the orbicularis envelops the lacrimal system, thus transmitting pressure through the tear outflow tract. With the eyelids closed, the ampulla and canaliculi are shifted medially, shortened, and compressed, and the tear fluid is driven into the lacrimal sac, which has a negative pressure. When the eyelids are open, pressure in the ampulla decreases and the pressure in the lacrimal sac increases, expelling fluid out through the nasolacrimal duct.[132]

The lacrimal pump can exert a suction effect at the punctum on the lacrimal secretions during blinking (Fig. 10-23)[124, 133, 134] Transit times of radioisotope to the lacrimal sac may be greatly prolonged in patients who do not blink but rather keep their eyelids closed. Occasional exceptions occur in patients with orbicularis contractions during lid closure. The elderly, with open lacrimal passages but inefficient tear fluid transportation, may also show delayed transit.[135] The greatest decay of tracer from the conjunctival sac occurs within the first few blinks.[136, 137] The relative drainage to the inferior and superior canaliculi remains controversial. Several studies concluded that activity was greater in the inferior than the superior canaliculus.[26, 128, 138] White et al.[126] showed that the superior and inferior canaliculi are of equal importance in lacrimal drainage and that no statistical difference exists between the amounts of tears that drain into either canaliculus. Similarly, Daubert et al.[139] showed no significant difference in tear flow between the upper and lower canaliculi in normal, patent, asymptomatic systems. If one canaliculus was blocked in an anatomically healthy NLDS, a compensatory increase in tear flow might occur in the other canaliculus such that no significant difference (statistical analysis $p < 0.05$) in time activity would be noted for $T_{1/2}$ of the interpalpebral fissure radioactivity (overall tear flow).[139] A single (upper or lower) canaliculus is sufficient for basal tear drainage but will not be sufficient to drain reflex tear secretion in 50% of cases.[140] The lacrimal drainage system is a closed system with a negative pressure, and occlusion of one canaliculus increases the suction effect and the subsequent increased tear flow through the patent canaliculus.[139]

The drainage of tears involves a number of different mechanisms including capillary action,[131, 133, 134] aided by contraction of the lacrimal part of the orbicularis oculi with blinking,[131, 141, 142] and craniocaudad distention of the sac with passive wringing of the sac because of its medial attachment and helically arranged fibrillar structure.[49] A vascular plexus, comparable to a cavernous body and embedded in the wall of the lacrimal sac and nasolacrimal duct, contains specialized blood vessels including regulatory arteries, a dense network of capillaries, capacitance veins, and cushion veins, which can reduce or interrupt venous blood outflow to allow large amounts of blood to accumulate inside the capacitance veins.[50] This cavernous body, which connects to that of the inferior turbinate of the nasal cavity, may facilitate closure and opening of the lumen of the nasolacrimal duct system (NLDS) by swelling and shrinkage of the cavernous body, with consecutive regulation of the tear outflow. When the net outflow of blood from the cavernous body is less than its inflow, there is mucosal expansion, functionally decreasing tear outflow. This represents a protective mechanism against foreign bodies or toxic stimuli that enter the conjunctival sac. In addition to increased lacrimal gland tear production, the decreased tear outflow, by the cavernous body response allows the increased tear pool to flush out the conjunctival sac while protecting the NLDS. The pathophysiology of functional lacrimal drainage insufficiency (epiphora despite a patent

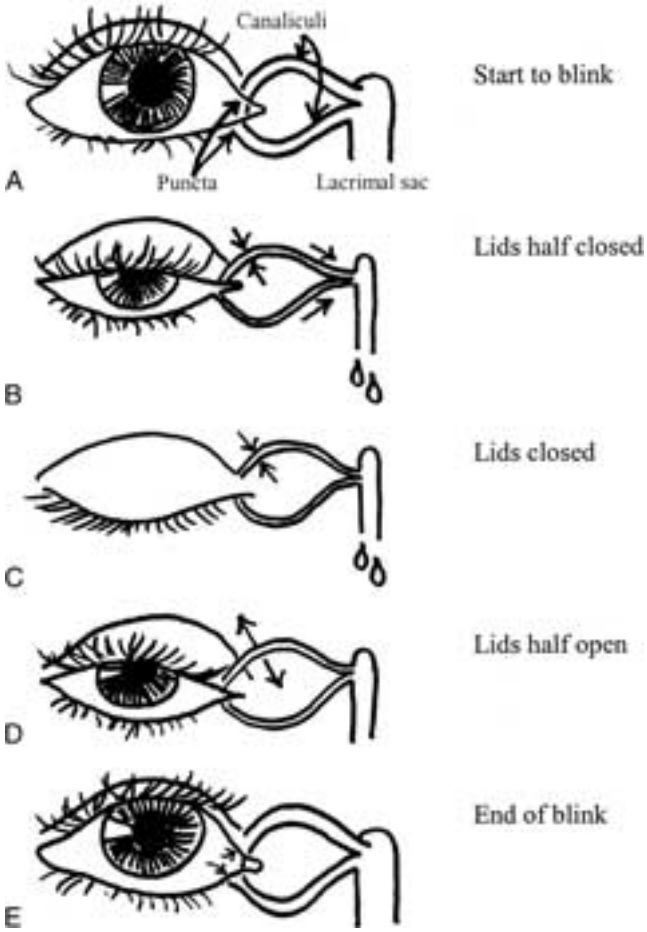

FIGURE 10-23 Lacrimal pump theory of Doane. **A**, Start of blink. The canaliculi and sac contain tear fluid from the previous blink. **B**, Lids half closed. As the upper lid descends, papillae containing punctal openings elevate from the medial lid margin, forcefully meeting the opposing lid margin, occluding the puncta, and preventing fluid regurgitation. Further lid closure squeezes the canaliculi and sac (through the action of the orbicularis oculi), forcing the contained tear fluid into the nasolacrimal duct. **C**, Lids closed. Maximum compression of the canaliculi and sac, with all fluid expressed into the nasal cavity. **D**, Lids half open. Puncta still occluded by opposing medial lid margins. Release of pressure by the orbicularis oculi with cessation of compression action. Elastic walls of the passages try to expand to their normal shape, with a resultant partial vacuum and negative pressure and with a suction effect forming within the canaliculi and sac. **E**, End of blink. As lid separation progresses, suction force holding the punctal region together is released and the punctal papillae ''pop'' apart, with negative intraluminal pressure drawing tear lake fluid into the canaliculi and sac. (Redrawn adaptation from Doane MG. Blinking and the mechanics of the lacrimal drainage system. Ophthalmology 1981;88:844–851 and adaptation of the above by Dale DL. Embryology, anatomy, and physiology of the lacrimal drainage system. In: Stephensen CM, ed. Ophthalmic, Plastic, Reconstructive, and Orbital Surgery. Boston: Butterworth-Heineman, 1997;19–30.)

VIEW IMAGE

Copyright © 2003, Mosby, Inc. All rights reserved.

NLDS during syringing) may be explained by the presence of the cavernous body.[50] Malfunctions within the vascular bed may lead to disturbances in the tear outflow cycle, ocular congestion, or total occlusion of the NLDS and may be caused more acutely by allergic conjunctivitis, rhinitis, or hay fever, or more chronically, as with stenoses after dacryocystitis or dacryolithiasis.[50] Persistent epiphora after dacryocystorhinostomy (DCR) may be due to destruction of the surrounding cavernous body. The cavernous body may also play a role in the absorption of tear fluid by the NLDS epithelial lining mucosa and alternative draining by the surrounding venous plexus before reaching the nasal cavity.[48]

Complete Obstruction

Total obstruction, if present, is identified on DSG (Fig. 10-16). Even though the lacrimal sac may be filled with lacrimal secretions, debris, or even concretions, there is physiologic reflux of the secretions into the conjunctival sac.[143, 144] Therefore, fresh secretions or radiopharmaceutical from the DSG will enter the lacrimal sac. The study is sensitive to the site of obstruction so that the appropriateness of surgery, such as DCR, or placement of drainage tubes can be determined. The smaller pinhole aperture helps improve resolution that may still be suboptimal in differentiating canalicular from proximal lacrimal sac pathology. However, DCG will provide anatomic information to complement DSG when necessary. If a DSG shows obstruction proximal to the lacrimal sac, the common canaliculus or the inferior and superior canaliculi or puncta may be obstructed.

Incomplete Obstruction: Functional Nasolacrimal Duct Obstruction

Patients with epiphora who have a normal DCG or a normal clinical lacrimal irrigation test usually have physiologic obstruction to the drainage of tears. FNDLO has been interpreted to mean symptomatic epiphora, with a lacrimal system patent to syringing and no detectable cause of epiphora external to the lacrimal drainage system (no cause for increased lacrimation and no lid abnormality present).[22] The main level of functional blockage (lacrimal drainage delay) in the lacrimal system was easier to detect objectively with DSG than with DCG. When discrepancies in the identified level of functional block occurred (41% of combined DSG-DCG studies of FNLDO patients), Wearne et al.[22] noted that the DSG detected an obstruction at a more proximal level in 16 of 20 patients. DSG/DCG discrepancies were most likely due to the pressure injection of DCG contrast dilating lesser degrees of more proximal stenosis. Positive scintigrams were subdivided into those demonstrating prelacrimal sac delay (13%), delay at the lacrimal sac–nasolacrimal duct junction (35%), or delay within the nasolacrimal duct (42%). Prelacrimal sac delay was defined as holdup at the inner canthus or failure of the tracer to reach the lacrimal sac by the end of the dynamic phase (160 seconds). Delay at the lacrimal sac–nasolacrimal duct junction (35%) was defined as preductal delay with early filling of the lacrimal sac but no sign of sac emptying on the static image at 5 minutes. Delay within the nasolacrimal duct (42%) was defined as intraductal delay with tracer noted in the upper part of the nasolacrimal duct at 5 minutes but no further drainage over the next 15 minutes. Of note, 72% of patients in the above series had clinically bilateral FNLDO.[22] The transit time through the distal part of the nasolacrimal duct and into the nasal cavity, known to show marked variability in normal individuals, was not calculated in their study. It is interesting to speculate whether the marked variability in transit time of normal individuals and patients with FNLDO may be related to functionality of the surrounding vascular plexus (cavernous body) or to variability of resorption of the tear fluid by the NLDS mucosa, as outlined by Paulsen et al.[50] (In the section Dacryoscintigraphy, see Normal Examination for further discussion.) Simultaneous bilateral DSG studies can compare and evaluate the delay in transit of the radiopharmaceutical on the involved side. Frequently, however, the clinically normal side will also reveal abnormal flow. Amanat et al.[20] noted in their patients with a clinically unilateral abnormality that 42% had an abnormal flow pattern by DSG on the contralateral side. Thus the contralateral side was clinically silent relative to the increased symptoms on the primary symptomatic side.

Sensitivity of Dacryoscintigraphy

DSG is more sensitive for detecting obstruction than macro-DCG.[127] Normal DSG was always associated with duct patency on DCG, allowing a protocol specifying that DSG should be the first investigation; if it is normal, DCG is unnecessary. In Rose and Clayton's series,[127] 26% of the NLDS showing obstruction on DSG had a normal DCG. In a series[22] limited to patients with a clinical diagnosis of FNLDO, both DSG and DCG were very sensitive in detecting abnormalities (95% and 93%, respectively), with DCG including the performance of a delayed upright 5 minute film and DSG results including quantitative analysis.[121] Hanna et al.,[26] in comparing syringing to DSG in patients with epiphora, found that 65% of apparently patent systems on syringing demonstrated abnormalities on DSG. Abnormalities included 40% with decreased entry into the NLDS or canalicular obstruction on DSG. In those patients with abnormal syringing, the most common site of obstruction on DSG was at the lacrimal sac outflow. In these patients, canalicular obstruction was seen with almost the same frequency as in those with patent syringing (35% vs. 33%).[26] Both DCG and syringing require cannulation. Either lid puncta and proximal canalicular functional or anatomic abnormalities may be missed on the basis of the cannulation or the pressure of the injection or irrigation.

In syringing, false negatives or false positives may result partly from the subjective nature of the patient's ability to interpret or be aware of saline entering the nasopharynx. In the Hanna et al. series, 18% of those who had a positive syringing test had a negative DSG.[26]

Weber et al.[88] found the greatest application for DSG to include children; puncta unable to be cannulated after surgery; posttrauma; and functional obstructions, especially if the DCG was normal.

Copyright © 2003, Mosby, Inc. All rights reserved.

COMPUTED TOMOGRAPHY

DCG cannot display information beyond that of the drainage lumen proper. Although displacement of the NLDS may be shown by DCG, the peripheral extent of mucosal or periductal disease cannot be defined. In these cases, CT may be indicated either initially or as a complementary study. The understanding that epiphora (or dacryostenosis) results from a multitude of etiologies should suggest a more selective imaging approach for each patient. When appropriate imaging studies are performed, diagnostic accuracy in dacryostenosis may be significantly improved, ensuring that diagnosis is not delayed and that the appropriate operation is done or that surgery can be avoided if contraindicated.[63, 145] Classifications of acquired lacrimal drainage obstruction further emphasize the need to understand the etiology of dacryostenosis.[145–148] Appropriate decisions are based on whether or not signs or symptoms result from processes arising outside the NLDS or whether abnormalities outside the NLDS are present that could adversely affect the outcome of the proposed lacrimal surgery. If such factors cannot be determined through clinical means, imaging tests should be performed that will limit surprises at the time of surgery.[149] Specific patients with epiphora and all patients presenting with an inferomedial orbital mass lesion are candidates for CT. The broader base of anatomic and pathophysiologic relationships to adjacent tissues offered by CT becomes helpful in making treatment decisions. As noted by others,[145, 150] dacryostenosis may be much more closely related to local nasal or sinus problems than has been previously emphasized. Similarly, the etiology of FNDLO and its relation to sinonasal disease has been largely unappreciated. High-resolution, thin-section CT imaging (1.0 to 2.5 mm slice thickness) may be an appropriate and useful modality for assessing the NLDS, its immediate bony confines, the lacrimal fossa, the adjacent orbit, the facial skeleton, paranasal sinuses (especially the agger nasi and ethmoid bulla air cells), and the nasal cavity. The increasing capabilities of volume acquisition thin-slice CT, with multiplanar and 3D reconstruction availability and shorter time acquisition, offer excellent imaging resolution and patient compliance. Anatomic depiction of the nasolacrimal sac and duct is well seen in the axial plane. Coronal assessment may be helpful, especially to display the junction of the lacrimal sac and duct and the relationship of the medial orbital floor or nasal cavity structures to the NLDS. Intravenous enhancement is routinely used (except in the trauma patient), since one is frequently assessing the possibility or the extent of an inflammatory or neoplastic lesion. The radiation dose absorbed by the lens during spiral CT for assessment of the NLDS has been measured at 1.8 to 2.6 mSv[151] compared to 0.68 mSv for DS-DCG.[18]

Radiographic Anatomy

Plain or intravenous enhanced CT (Fig. 10-24) does not identify the superior and inferior canaliculi or the common canaliculus. The canaliculi may be visualized by placement of topical contrast medium into the conjunctival sac (see the section on Combined CT-Dacryocystography).

The normal lacrimal sac and duct may be either tear-filled (soft-tissue density) or air-filled (Fig. 10-25). The lacrimal sac will normally not exceed a 2 mm diameter unless distended with air.[152] The sac itself is a membranous structure, noted within the bony lacrimal fossa.

The frontal process of the maxillary bone and the lacrimal bone form the lacrimal sac fossa. The fossa is a clearly demarcated depression bound anteriorly by the anterior lacrimal crest, contiguous with the inferior orbital rim, and posteriorly by the posterior lacrimal crest, a linear elevation along the anterior aspect of the lacrimal bone. The frontal process of the maxillary bone and the lacrimal bone contribute varying proportions to the formation of the lacrimal sac fossa. The anteroposterior position of the vertical suture between these components is variable. The lacrimal bone separates the upper half of the lacrimal fossa from anterior ethmoid air cells and the inferior part from the middle meatus of the nasal cavity. Closely surrounding the lacrimal sac is a rich venous plexus separating the sac from the adjacent lacrimal fascia, an anterior extension of the orbital periosteum, which splits at the posterior lacrimal crest to invest the lacrimal sac.

Enhancement of the venous plexus or the closely associated superficial and deep heads of the orbicularis oculi may help identify the lacrimal sac within the soft-tissue density of the medial canthal structures if the lacrimal sac is not air-filled. Horner's muscle represents the lacrimal component of the superficial and deep heads of the orbicularis oculi muscle attaching to the anterior and posterior lacrimal crests, respectively. These fibers act as a muscle envelope, surrounding the lacrimal fascia and sac. They are not distinguishable on CT from the anteriorly placed medial palpebral ligament, the subjacent lacrimal fascia, or the posteriorly positioned orbital septum.[42, 153]

The medial canthal ligament attaches to the anterior lacrimal crest and forms an anterior margin to the lacrimal sac. The medial orbital septum attaches just posterior to the posterior lacrimal crest. The lacrimal fossa and sac are therefore preseptal structures. Below the level of the medial palpebral ligament, the lacrimal sac is not enveloped by the orbicularis oculi muscle and therefore is potentially weaker at this site, offering less resistance to intraorbital spread of infection[153] or possibly to perforation by antegrade manipulation of instruments within the nasolacrimal drainage.[154]

In DCR, the opening in the bony wall between the lacrimal sac and the nasal cavity is initiated with perforation of the thin lacrimal bone at the inferior portion of the lacrimal sac fossa. In external DCR, a large bony opening measuring 1.5 cm is produced through the nasal wall of the lacrimal fossa, including the anterior lacrimal crest (thicker frontal process of the maxillary bone).[30] In endonasal DCR, the bony opening, at the same site, tends to be smaller and does not include the anterior lacrimal crest.[33] Because of the increasing popularity and frequency of use of endonasal DCR, using various laser and endoscopic techniques (and to a lesser extent endocanalicular laser DCR techniques), attention to the anatomic structures that need to be penetrated by the procedures has grown. Lacrimal bone thickness and variations in sinonasal configuration that may limit access or the feasibility of specific surgical approaches (endonasal or endocanalicular) have clinical treatment implications.[155, 156] The ability of various lasers to penetrate

Copyright © 2003, Mosby, Inc. All rights reserved.

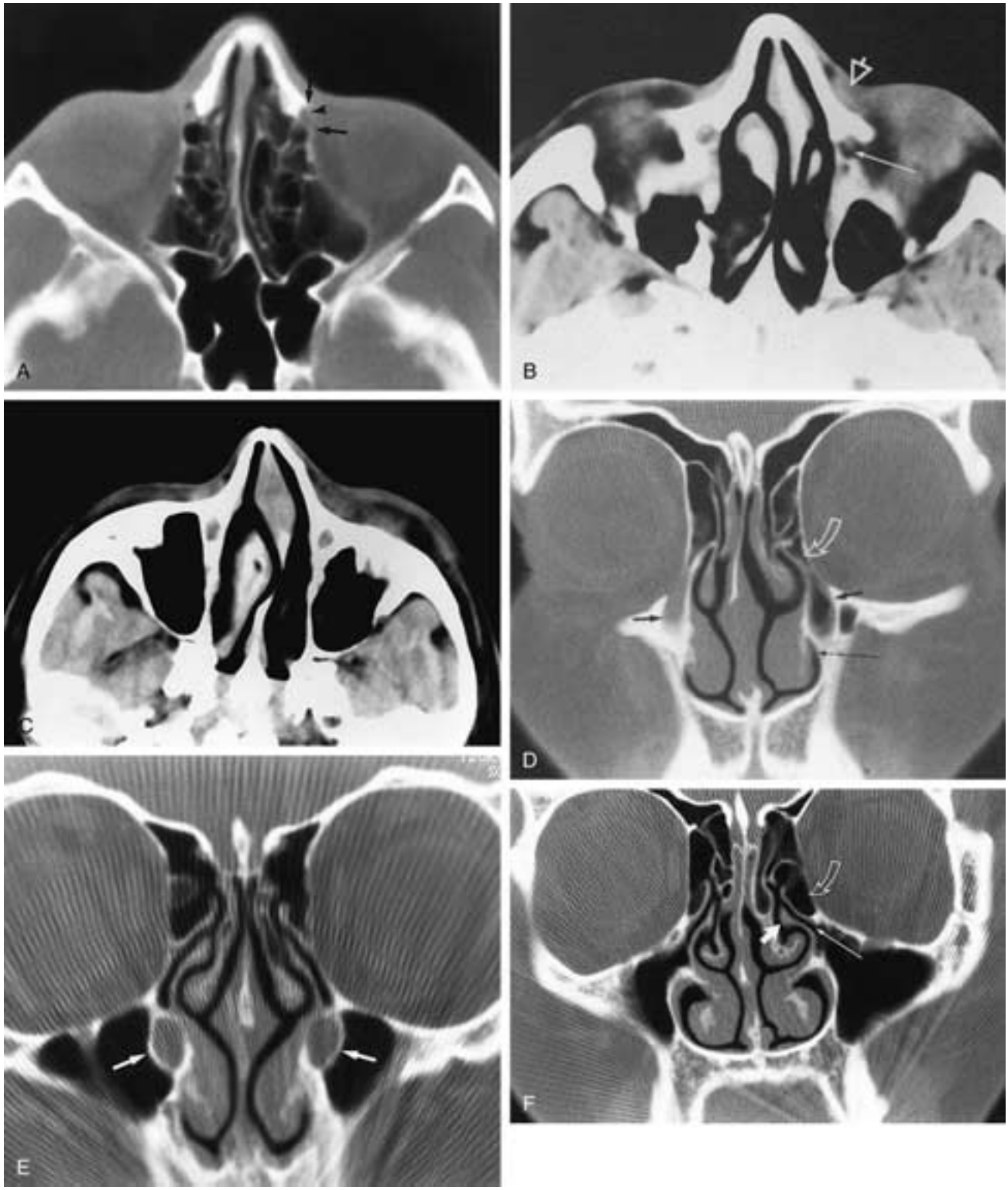

VIEW IMAGE

FIGURE 10-24 Normal CT anatomy. **A** to **C**, Axial. **A**, High-resolution axial CT scan shows the nasolacrimal fossa (*arrowhead*) and anterior and posterior lacrimal crests (*arrows*). **B** and **C**, Study done to assess preseptal lymphoma of the left orbit, noted as a soft-tissue density (*open arrow* in **B**) on both images. **B**, Fat-density tissue plane surrounding the lacrimal sac and proximal nasolacrimal duct (*thin arrow on the left*), which frequently is not identified (as in the nasolacrimal canal on the right) because of surrounding venous plexus, decreased fat content within the confined space, and artifact from adjacent bone. **C**, One slice, more inferiorly, is unable to define the nasolacrimal duct within the nasolacrimal canal. Compare this with the MR image of the nasolacrimal duct (Fig. 10-26). **D** to **F**, Coronal. **D**, Nasolacrimal canal (*short arrows*) is seen bilaterally lateral to the middle meatus and is directed inferiorly toward the inferior meatus (*thin arrow*). Note the normal cortical margin to the canal. Ethmoid bullae (*open arrow*) lie just medial to the superior aspect of the nasolacrimal canal. **E**, Nasolacrimal canals are oriented postinferiorly from superior to inferior. Depending on the angulation of coronal imaging, the canal may be obliquely transected (*arrows*). **F**, Just posterior to the nasolacrimal canal, a coronal image shows the osteomeatal unit. Ethmoid bulla (*open arrow*), infundibulum (*thin arrow*), and uncinate process (*short arrow*) are seen.

Copyright © 2003, Mosby, Inc. All rights reserved.

bone is less than that of the traditional mechanical instruments, especially when the fiberoptic laser is used through the endocanalicular route.[155]

Hartikainen et al.[155] noted the mean thickness of the lacrimal bone at the lacrimal fossa to be 106 µm, with 67% of patients having a mean thickness of less than 100 µm. Only 4% of patients had a mean thickness greater than 300 µm. A slightly decreased thickness of bone with increasing age was not significant. The lacrimal bone, although variable, tends to be thin, about 0.1 mm on average, and so can be easily penetrated with most surgical instruments. The osteotomy is then enlarged to include the thicker bone (frontal process of the maxilla) to the appropriate size required by the DCR technique.[155] Of 48 lacrimal patients with fossa dissections, only 1 displayed a significant anatomic variant, with no real lacrimal fossa bilaterally. The lacrimal sac was bounded, nasally and inferiorly, entirely by the frontal process of the maxillary bone, and the vertical suture was situated temporal to the tiny posterior lacrimal crest. Such a variation makes endoscopic or endocanalicular DCR techniques difficult or impossible.[155]

Yung and Logan,[156] in a smaller cadaveric series, reported an average thickness of 57 µm in nine dissections, excluding one abnormally thick lacrimal bone (296 µm). In all cases, the part of the lacrimal passage covered by the thin lacrimal bone corresponded to the upper part of the nasolacrimal duct and the lower part of the lacrimal sac. The thin lacrimal bone covered the posteromedial part of the upper nasolacrimal duct, with the thicker frontal process of the maxilla still covering the main part of the nasolacrimal duct. The authors note that the lacrimal bone is always situated immediately anterior to the mid-third of the uncinate process, an anatomic landmark in endonasal DCR procedures. An extremely large anterior ethmoidal air cell, the agar nasi, can be juxtaposed completely between the nasal cavity and the entire lacrimal fossa, leading to considerable confusion during DCR.[157]

A light source positioned within the lacrimal sac will transmit through the tiny lacrimal bone but not the thicker maxillary bone. Such transillumination can assist placement of the DCR osteotomy during endonasal DCR. Therefore, any surgical process (e.g., laser beam) directed at the area of maximum illumination (from the light source) tends to only remove the bone at the posteromedial portion of the inferior lacrimal sac–superior nasolacrimal duct rather than its entire width, with a resultant small lacrimal window.[156]

The lacrimal sac tapers inferiorly and is continuous with the nasolacrimal duct. The fascia investing the lacrimal sac also continues inferiorly to invest the nasolacrimal duct and become continuous with the periosteum surrounding the inferior meatus. The entire lacrimal drainage system remains continuous with the preseptal space even though the nasolacrimal duct is directed posteriorly and inferiorly.

The valve-like folds of mucosa (valves of Krause) separating the lacrimal sac from the nasolacrimal duct are not recognized on CT. An encircling bony canal along the medial aspect of the maxilla identifies the intraosseous component of the duct. The duct itself is usually collapsed and occupies only a small portion of the cross-sectional diameter of the bony canal. The most inferior portion of the nasolacrimal duct, approximately 5 mm in length, represents the membranous (or meatal) portion of the canal, passing beneath the nasal mucosa before emptying into the inferior meatus through a slit-like or funnel-shaped opening, the valve of Hasner.

The nasolacrimal canal represents the bony canal, which encloses and protects the nasolacrimal duct, connecting the inferior aspect of the lacrimal sac fossa to the inferior meatus of the nose. The maxilla contributes the greatest component, with the formation of a longitudinal groove, the lacrimal sulcus. The gap between the lips of this groove is completed by the articulation of two other component bones, the descending process of the lacrimal bone from above and the lacrimal process of the inferior nasal concha from below.[158] The form, dimension, and direction of the bony lacrimal

VIEW IMAGE

FIGURE 10-25 Air within the NLDS as a normal variant. **A**, Distended left nasolacrimal duct (*oblique arrow*) with air extending to the valve of Hasner (*vertical arrow*). Air also in the right lacrimal sac (*horizontal arrow*). Ethmoid agger nasi (*e*) immediately medial to the superior aspect of the lacrimal sac. **B**, Bilateral air-filled lacrimal sacs (*arrows*). Note the intimate relationship of the anterior ethmoid air cells (agger nasi) (*e*) and its importance in DCR planning. (See also Fig. 10-30C,D.)

Copyright © 2003, Mosby, Inc. All rights reserved.

Table 10-2
CAUSES OF SECONDARY ACQUIRED NASOLACRIMAL DUCT OBSTRUCTION

Primary Neoplasms	**Inflammation**
Papilloma	Granulomatous pseudotumor
Squamous cell carcinoma	Sarcoidosis
Hemangiopericytoma	Wegener's granulomatosis
Fibrous histiocytoma	
Oncocytic adenocarcinoma	
Melanoma	
Fibroma	
Secondary Involvement by Neoplasm	**Infections**
Lymphoma	Trachoma
Leukemia	Leprosy
Lethal midline lymphoma	Tuberculosis
Basal cell carcinoma	Rhinosporidiosis
Neurofibroma	
Maxillary sinus tumors	

From Linberg JV, McCormick SA. Primary acquired nasolacrimal duct obstruction: a clinicopathologic report and biopsy technique. Ophthalmology 1986;93:1055–1063.

passages show considerable variation, mainly due to the extent to which the individual bones participate in their formation, with the lacrimal bone being the most variable.[158]

The bony nasolacrimal canal has been reported to be a structure highly variable in size, with differences associated with age, sex, and race. There has been recent interest in CT imaging of the bony nasolacrimal canal to assess normal CT values and to establish values that may be causative or a component of factors leading to nasolacrimal duct obstruction. Assessment of an epiphora patient population with PANDO may indicate minimal bone canal diameter acceptable for balloon dacryocystoplasty (DCP) versus DCR.[159–161] PANDO is an idiopathic process, whereas secondary obstructions are attributed to a recognized causative factor.[146, 161] See Table 10-2. The prevalence of PANDO in women has generated interest in possible etiologies. Proposed mechanisms include heightened levels of inflammation in women, leading to tissue swelling and obstruction; hormonal imbalances causing transient changes in the mucous membranes; and anatomic differences between men and women.[146, 150, 161] A narrower bone environment, combined with inflamed mucosal tissues, would place the raw mucosal surfaces in close proximity, enhancing the chance that the mucosal walls will stick together, forming an obstruction secondary to scar tissue.[160] Generalized deepithelialization of mucous membranes occurs during the menstrual cycle, with smaller nasolacrimal passages being more easily obstructed with epithelial debris. Osteoporotic changes may also be a factor in the female predilection for PANDO. Chronic allergy or maxillary sinusitis may percolate through the porotic bony wall of the sinus and nasolacrimal duct, causing inflammatory changes in the canal and duct, leading to blockage.[162]

Groessl et al.[160] noted that women have significantly smaller anteroposterior dimensions in the inferior nasolacrimal fossa and the midnasolacrimal canal. Janssen et al.,[159] using 2 mm axial CT images photographed on bone windows to measure the minimal transverse diameter of the bony nasolacrimal canal, studied a control group of 50 men and 50 women, as well as a patient group with epiphora and PANDO treated by balloon DCP. The longer anteroposterior diameter of the canal (ranging in size from an average normal of 2.84 mm[47] to an upper limit of 8 mm[158]) was felt to be less useful due to the oblique posteroinferior orientation (15° to 25°) of the nasolacrimal canal relative to the axial image.[159] The smallest diameter of the bony canal appears to be the most relevant measure for ascertaining the origin of an obstruction of the lacrimal drainage system.[159] This smallest diameter is generally found midway along the canal.[160] The mean minimum transverse diameters of the bony canal in the control groups were 3.7 mm and 3.35 mm for men and women, respectively.[159] These measurements are considerably smaller than previously measured transverse diameters of 4 to 6 mm[158, 163] but correlate with the 3 mm diameter[157] or 2.3 mm[47] measurements of other studies, with variations reflecting the different measuring techniques or modalities used. The mean minimal diameter in the epiphora patient group was 3.0 mm, considerably smaller than that of the control groups, suggesting a relationship between a narrower bony canal and obstruction of the NLDS. The broad range of diameters found in the control group (1.5 to 6.3 mm) showed complete overlap with the range found in the symptomatic group (2.0 to 4.2 mm), suggesting that a relatively small minimal diameter of the bony canal is not the sole etiologic factor in PANDO.[159] Further research is needed to ascertain whether a minimum threshold value of the diameter of the bony canal can be determined, below which balloon DCP as a treatment for lacrimal obstruction is contraindicated, making surgical DCR the preferred treatment.[159]

While the majority of patients with clinically suspected PANDO will have histopathologic findings of inflammation and fibrosis, there is a low incidence of significant other pathology of the lacrimal sac, such as neoplasm. These cases can only be identified by biopsy of the lacrimal sac during DCR.[150, 161, 164] Malignant tumors, especially epitheliomas and lymphomas, may first appear as simple dacryocystitis for prolonged periods.[165] Defining the true incidence of unsuspected lacrimal sac neoplasms presenting clinically as PANDO has specific implications in determining whether routine biopsy during DCR is warranted. This would also determine if there is a significant risk of missing an underlying lacrimal sac tumor in patients not undergoing surgical intervention but having procedures such as DCP, or in those undergoing laser DCR, where direct visualization and biopsy of the lacrimal sac are not possible.[164]

When an asymptomatic, exceptionally enlarged nasolacrimal canal is observed, concern for the presence of a relatively uncommon lacrimal sac tumor is raised, since these tumors may grow down into and expand the nasolacrimal canal. Associated CT signs of lacrimal sac tumors should be sought, including a soft-tissue mass of the lacrimal sac, bone erosion, and extension of the mass into adjacent tissues.

There may be variable amounts of air or soft tissue within the confines of the nasolacrimal canal, with air occasionally extending from the inferior meatus to the lacrimal sac. In a large population of patients scanned for other reasons, soft-tissue opacification restricted to the nasolacrimal canal is routinely noted and is considered a normal variant. In 200 nasolacrimal ducts studied by coronal CT, 72% were opaque.[166] Of those ducts associated with normal paranasal

Copyright © 2003, Mosby, Inc. All rights reserved.

sinuses, 79% had an opacified nasolacrimal duct. However, in the lacrimal patient, soft-tissue opacity of the nasolacrimal duct may have more significance and reflect pathologic characteristics of the nasolacrimal duct itself, such as PANDO, or adjacent inflammatory or neoplastic processes extending to the nasolacrimal canal from the lacrimal sac, orbital origins, or sinonasal origins.[145] One should assess the tissues adjacent to the nasolacrimal canal and examine for prominence or abnormal thickness of the lacrimal sac wall. While the lacrimal patient may display soft-tissue opacification of the nasolacrimal canal more frequently on the side of epiphora,[145] the exact significance if this finding is unclear. With such opacification as the only CT finding, the need for further imaging investigations, such as DCG or CT-DCG, must be based on clinical correlation. Obstruction of the nasolacrimal duct with dilatation of the lacrimal sac (lacrimal sac mucocele, dacryocele, dacryocystocele) may cause pressure erosion and enlargement of the nasolacrimal canal, depending on the degree of lacrimal sac enlargement and the level of distal obstruction within the canal. The pressure within the obstructed NLDS results from obstruction at both the proximal and distal aspects and tends to be most profound in congenital dacryocystocele (nasolacrimal mucocele). In congenital dacryocystocele the distal obstruction tends to be at the valve of Hasner, with the classic triad of cystic dilatation of the lacrimal sac, a dilated nasolacrimal duct/canal, and an intranasal cystic mass from the inferior imperforate membrane ballooning into the nasal cavity. In two patients presenting with an intermittent obstruction, Rheeman and Meyer[167] hypothesized that the intraluminal pressure, great enough to cause pressure erosion and dilation of the bone canal, may also reach a level high enough to overcome the obstruction intermittently. Significant nasolacrimal canal enlargement may occur as an incidental normal variant, without evidence of erosion, displacement, or mass lesions. Such findings in asymptomatic patients usually warrant no further investigation. A DCR may help exclude any small neoplastic lesion of the lacrimal sac and nasolacrimal duct. A follow-up CT scan to show lack of change may be justified. Biopsy of the lacrimal sac or duct is not warranted in the absence of any clinical or radiologic evidence of tumor.[167]

Coronal CT (direct or reformatted) may better display the longitudinal course of the nasolacrimal canal but will not directly assess the membranous nasolacrimal duct (compare this to MR imaging of the nasolacrimal canal [Fig. 10-26] or CT-DCG [Figs. 10-19 to 10-27]).

CT Pathology

Dacryocystitis (inflammation and dilation of the lacrimal sac) is usually diagnosable clinically unless associated preseptal or periorbital cellulitis limits an adequate clinical assessment. Enhanced imaging studies are most useful and help differentiate preseptal inflammatory lesions from more specific acute and/or chronic dacryocystitis. CT demonstrates an enlarged lacrimal sac centered around the lacrimal fossa (Figs. 10-17 and 10-28 to 10-30). Axial CT (and/or MR imaging) also distinguishes the postseptal inflammatory lesions (periorbital or orbital abscess), which require urgent surgical intervention, from acute dacryocystitis, a preseptal inflammatory process that is treated nonsurgically (Fig. 10-29). Extrinsic compression or infiltration by an adjacent inflammatory, neoplastic, or traumatic process of the nasolacrimal duct or sac may result in obstruction, enlargement, or dilation of the lacrimal sac and must be considered in the differential diagnosis of medial canthal mass lesions. Mass lesions in the region of the medial canthus and lacrimal sac may represent lacrimal sac diverticula. While these lesions are most commonly small and asymptomatic, they may present as cystic mass lesions, with or without mechanical obstruction of the NLDS. DCG or ultrasound infrequently demonstrates the communication between the lacrimal sac lumen and the diverticulum, such that only indirect signs of compression, displacement, or obstruction are visualized on the DCG. The most common location of these diverticula is at the junction of the lacrimal sac and the nasolacrimal duct. Those larger clinically apparent cystic diverticula tend to appear tense and fluctuant, affixed to the deep tissues but not to the skin.[78] They are almost always located lateral to the lacrimal sac, frequently coursing along the inferior orbital rim deep to the medial aspect of the lower eyelid.[78] With gentle pressure, some may be decompressed through the punctum or into the nose if the communication between the diverticulum and the lacrimal system is patent. Air may be trapped in a diverticulum, enabling a pneumatocele to develop.

Pneumatocele should always be considered in this location, especially with a well-circumscribed roundish or cystic-appearing mass that may contain air or have an air-fluid level. There are usually no associated inflammatory changes and no evidence of lacrimal drainage system obstruction. In contrast to chronic dacryocystitis, which demonstrates a thick-walled lacrimal sac, diverticula tend to be surrounded by an extremely thin fibrous or epithelial/fibrous layer that may not be apparent on CT.[80] These masses do not enhance and suggest a cystic lesion rather than a neoplastic process. Lacrimal sac mucoceles and true lacrimal sac cysts may be difficult to differentiate by imaging. The tendency of lacrimal sac diverticula to extend more laterally at the inferior sac–duct junction, with thinner capsule, may help differentiate these lesions from the lacrimal sac mucocele that tends to expand more superiorly and to have a thicker, enhancing wall and an obstructed nasolacrimal system clinically. Topical administration of contrast medium (DCG-CT) may help define the lacrimal system's patency, as well as the possibility of contrast extending into the diverticulum. However, the communication between the lacrimal system and the diverticulum may be progressively sealed by chronic inflammation, forming an independent cyst (lined by lacrimal epithelium) containing increased caseous or proteinaceous content, and with inflammatory changes thickening its capsule, obscuring its more cystic nature and resembling a more solid mass. MR imaging may better demonstrate the cystic nature of the lesion in such a circumstance.

Lacrimal sac diverticula may be treated by ligation and excision. Those lesions (congenital or postinflammatory) located at the inferior lacrimal sac or nasolacrimal duct and causing obstruction are better treated by DCR.

Lesions arising within the orbit, paranasal sinuses, or nasal cavity may mimic lesions of the nasolacrimal drainage apparatus and present clinically with the same symptomatol-

Copyright © 2003, Mosby, Inc. All rights reserved.

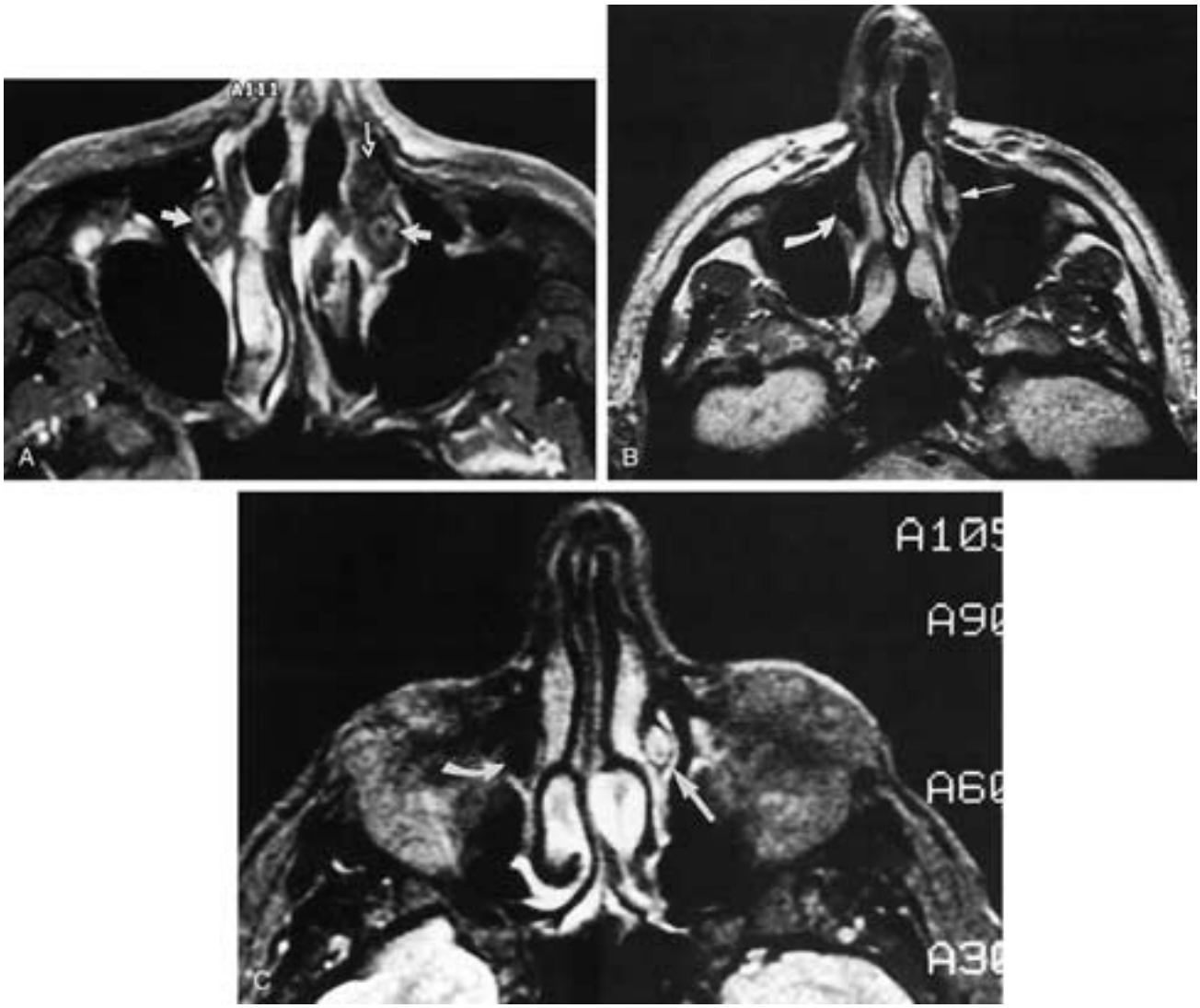

VIEW IMAGE

FIGURE 10-26 Nasolacrimal canal assessed by MR imaging. **A**, Patient with chronic inflammatory disease of the NLDS. Axial T1-weighted postgadolinium image shows mucosal enhancement of the nasolacrimal duct epithelium (*white arrows*). Nasal polypoid tissue is anterior to the nasolacrimal duct (*open arrow*). **B** and **C**, Another patient. **B**, Axial proton density image at the level of the inferior meatus shows the left nasolacrimal duct (*thin arrow*) just proximal to the valve of Hasner. Air in the right nasolacrimal canal is seen as signal void (*curved arrow*). **C**, Axial T2-weighted image scan shows the left nasolacrimal duct (*straight arrow*) within the canal. Air in the right nasolacrimal canal is seen as signal void (*curved arrow*). (See also Fig. 10-25.)

ogy as mass lesions of the inner canthus or inferomedial orbit (Fig. 10-30).[145, 152, 153]

A wide variety of neoplasms (benign and malignant) of the adjacent nasal cavity, maxillary, ethmoid, or even frontal sinuses may manifest as medial canthal masses. (See Table 10-3.) Squamous cell carcinoma and, less commonly, adenocarcinoma represent a majority of the malignant lesions. Inverted papilloma may arise within the lacrimal sac, although more commonly such tumors arise within the adjacent nasal cavity and paranasal sinuses and directly invade the lacrimal sac or spread from the nasal cavity up the nasolacrimal duct to reach the lacrimal sac and inner canthus.

Mucoceles arising in the anterior ethmoid air cells have an intimate relationship with the lacrimal fossa. CT may show opacified expanded anterior ethmoid air cells with thinning and remodeling of bone. Any bone destruction caused by pressure erosion, if present, will be more extensive than that seen with lacrimal sac dilations and will be eccentric relative to the nasolacrimal fossa. In these cases, the lamina papyracea bows toward the orbit.

Dermoids are well-defined lesions of the orbit that result from sequestration of ectodermal elements trapped along lines of embryonic fusion. Such masses tend to localize adjacent to suture lines. Although they are located most frequently adjacent to the frontozygomatic suture, a medial (nasal) extraconal location is also common. The presence of fat density, a fat-fluid level, or rim calcification may help suggest this diagnosis and differentiate a dermoid from a dilated lacrimal sac. Medial orbital or nasal dermoids also tend to be more superomedial. Unlike dacryocystitis or mucoceles of the nasolacrimal sac, such lesions do not

Copyright © 2003, Mosby, Inc. All rights reserved.

VIEW IMAGE

FIGURE 10-27 CT-DCG of normal anatomy. **A** to **D**, Coronal images of different patients. **E** and **F**, Axial images of the same patient. **A**, Coronal CT shows contrast in the left superior (*s*) and inferior (*i*) canaliculi, sinus of Maier (common canaliculus) (*c*), and lacrimal sac (*L*). **B**, Contrast material is seen in the proximal left nasolacrimal canal, left inferior meatus, and right distal nasolacrimal canal (*arrows*). Density artifact misregistration causes contrast material to appear black. The upper drainage system is not labeled. **C**, Coronal slice through the nasolacrimal canals bilaterally (*vertical arrows*) shows a small amount of contrast in the distal right nasolacrimal canal (*horizontal arrow*). *i*, Inferior meatus. **D**, Dilatation of the right lacrimal sac (*vertical arrow*) compared with the normal left sac (*horizontal arrow*). **E**, Left common canaliculus (*vertical arrow*) filled with contrast material. Slight prominence of the left lacrimal sac compared with the right (*black arrows*). *Open arrow*, Conjunctival sac. **F**, More inferior slice through the nasolacrimal canal shows contrast material within the nasolacrimal duct bilaterally (*arrows*). Normal variation with asymmetry in the diameter of the ducts. (See also Fig. 10-19.)

Copyright © 2003, Mosby, Inc. All rights reserved.

extend into the nasolacrimal duct. Coronal CT may be diagnostic by displaying continuity between the lacrimal sac and the nasolacrimal duct. Encephaloceles or meningoceles may present in the inner canthus as well-defined masses. Their extension superiorly within the nasoorbital tissues should suggest this diagnosis, and a defect in the skull base should be carefully sought. Hemangioma, lymphangioma, and neurofibroma are frequent benign tumors of the orbit. They may be associated with a mass effect and pressure erosion, but they do not cause bone invasion. Occasionally, an isolated varix of the angular vein may manifest as a medial canthal mass or may simulate a lacrimal sac mass. The patient usually presents with intermittent swelling. Tearing may be present if there is compression of the lacrimal drainage system. Regression of the mass with gentle pressure, or an alteration in the size of the mass with Valsalva maneuvers, or with alteration in head position, should suggest this diagnosis.[168, 169]

Malignant lesions arising within the orbit that may present as inner canthal masses include lymphoma, rhabdomyosarcoma, and metastases. Preseptal malignancies, including basal cell and squamous cell carcinomas of the skin and non-Hodgkin's lymphoma, commonly invade the medial canthal tissues. Rarely, plasmacytomas

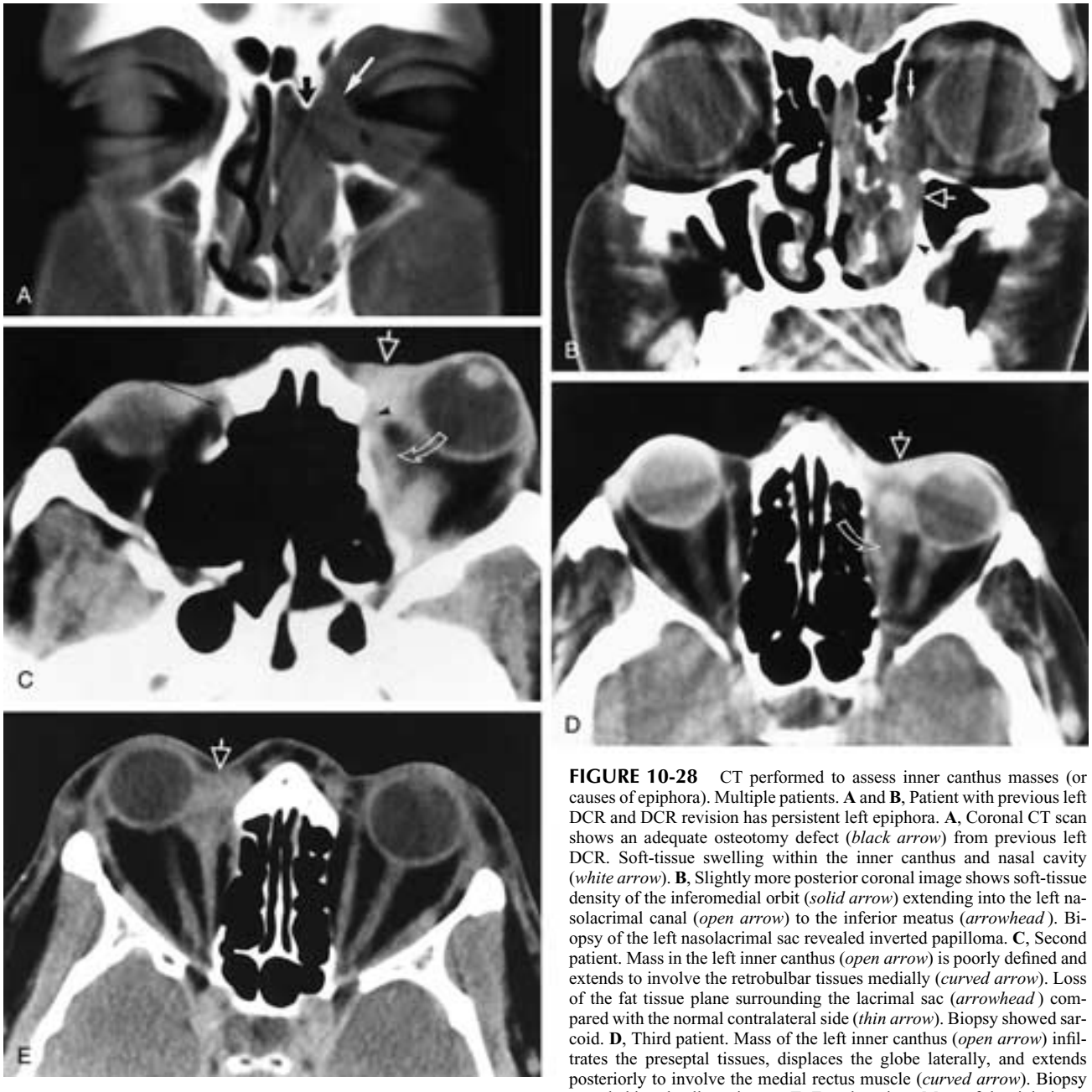

FIGURE 10-28 CT performed to assess inner canthus masses (or causes of epiphora). Multiple patients. **A** and **B**, Patient with previous left DCR and DCR revision has persistent left epiphora. **A**, Coronal CT scan shows an adequate osteotomy defect (*black arrow*) from previous left DCR. Soft-tissue swelling within the inner canthus and nasal cavity (*white arrow*). **B**, Slightly more posterior coronal image shows soft-tissue density of the inferomedial orbit (*solid arrow*) extending into the left nasolacrimal canal (*open arrow*) to the inferior meatus (*arrowhead*). Biopsy of the left nasolacrimal sac revealed inverted papilloma. **C**, Second patient. Mass in the left inner canthus (*open arrow*) is poorly defined and extends to involve the retrobulbar tissues medially (*curved arrow*). Loss of the fat tissue plane surrounding the lacrimal sac (*arrowhead*) compared with the normal contralateral side (*thin arrow*). Biopsy showed sarcoid. **D**, Third patient. Mass of the left inner canthus (*open arrow*) infiltrates the preseptal tissues, displaces the globe laterally, and extends posteriorly to involve the medial rectus muscle (*curved arrow*). Biopsy revealed basal cell carcinoma. **E**, Fourth patient. Mass of the right inner canthus (*arrow*) obscures insertion of the medial rectus into the globe. Biopsy found orbital pseudotumor. (See also Fig. 10-20.)

VIEW IMAGE

Copyright © 2003, Mosby, Inc. All rights reserved.

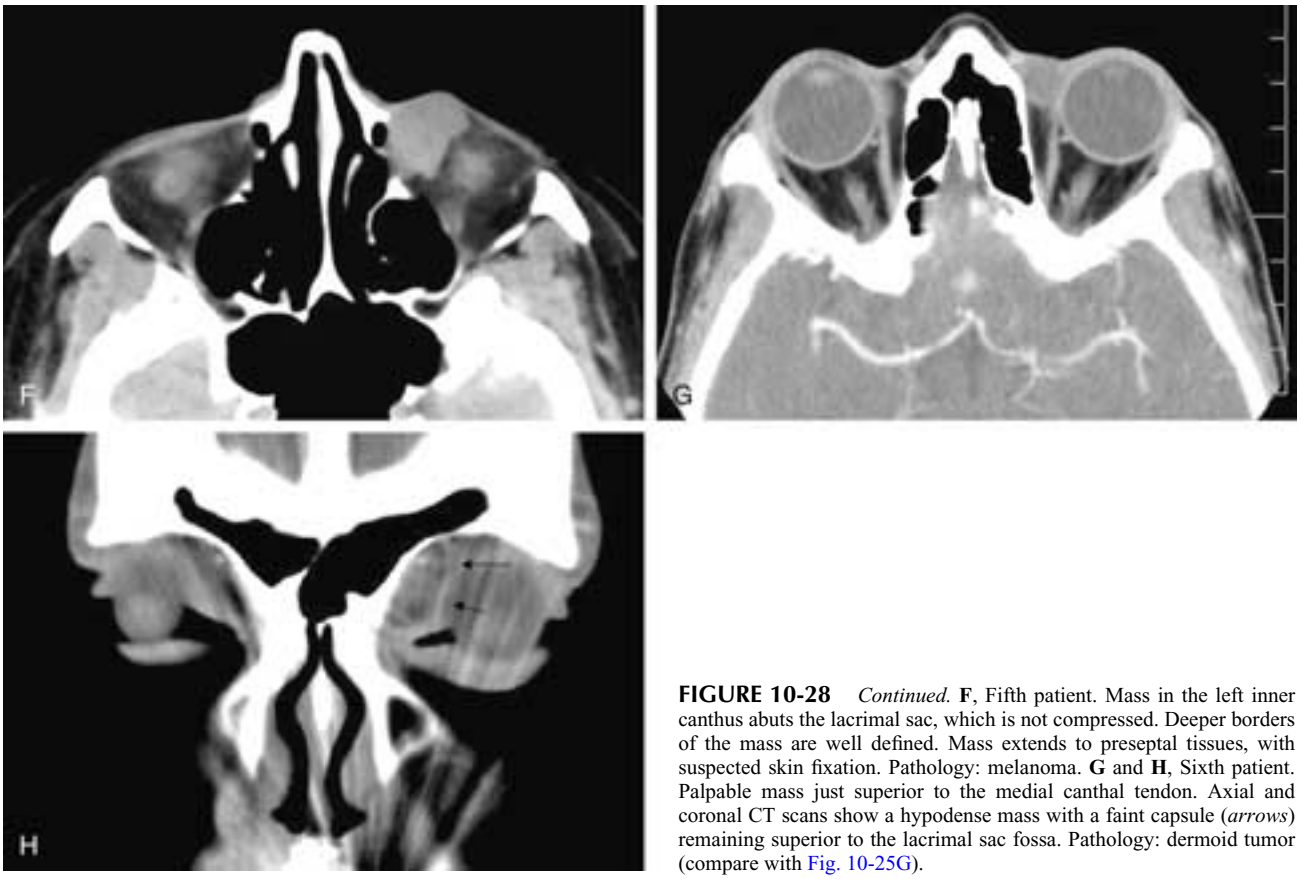

FIGURE 10-28 *Continued.* **F**, Fifth patient. Mass in the left inner canthus abuts the lacrimal sac, which is not compressed. Deeper borders of the mass are well defined. Mass extends to preseptal tissues, with suspected skin fixation. Pathology: melanoma. **G** and **H**, Sixth patient. Palpable mass just superior to the medial canthal tendon. Axial and coronal CT scans show a hypodense mass with a faint capsule (*arrows*) remaining superior to the lacrimal sac fossa. Pathology: dermoid tumor (compare with Fig. 10-25G).

VIEW IMAGE

and malignant fibrous histiocytomas may present at this location.

Orbital pseudotumor, especially if the medial rectus is primarily involved, can extend from the tendinous insertion to the adjacent lacrimal fossa. Radiographically, pseudotumor may be difficult to differentiate from malignant involvement, especially lymphoma. Sarcoidosis and other granulomatous inflammatory processes occasionally will be localized in the inferomedial orbit or within the nasolacrimal drainage apparatus (Fig. 10-20).

Lacrimal Sac Tumors

Tumors of the lacrimal sac are rare.[165, 170] These include a wide variety of epithelial and nonepithelial tumors (see Table 10-4). Epithelial neoplasms are subdivided histopathologically according to the Ryan and Font classification.[171] Benign epithelial tumors include papillomas (squamous, transitional, mixed) and are subdivided into exophytic or inverted growth patterns: oncocytomas, and benign mixed tumors. Malignant epithelial tumors (carcinomas) include squamous and transitional carcinomas, adenocarcinoma, oncocytic adenocarcinoma, and mucoepidermoid and adenoid cystic carcinomas, as well as poorly differentiated carcinoma and papilloma with carcinoma. Malignancies have been subdivided into those arising de novo or arising within or from a benign papilloma[170] (Fig. 10-13A-C).

There is a 55% malignancy rate for all tumors arising within the lacrimal sac.[170] Most tumors arise from the pseudostratified columnar epithelial lining of the sac. Epithelial tumors therefore predominate, representing 75% of all reported cases, with nonepithelial tumors accounting for the remaining 25%.[172] Poorly differentiated squamous cell (epidermoid) carcinomas, followed by transitional cell and mucoepidermoid carcinomas, are the most common malignancies. Benign epithelial masses, mainly papillomas, occur less than one third as frequently as the malignant epithelial tumors.

Nonepithelial tumors include those of mesenchymal origin (fibrous histiocytoma, hemangiopericytoma, lipoma); lymphoid lesions; reactive hyperplasia or malignant melanoma; granulocytic sarcoma (prior to peripheral blood or bone marrow involvement); and neural tumor. Fibrous histiocytoma and lymphoma are the most common nonepithelial tumors of the lacrimal sac. Fibrous histiocytoma displays varying patterns, fibroblastic to histiocytic predominance, and varying degrees of aggressiveness.

Lacrimal sac tumors present insidiously, with nonspecific symptoms of dacryostenosis or dacryocystitis. The tumors may be undiagnosed for months or years.[173] Treatment for a presumed infection may transiently improve swelling of the lacrimal sac and give a false impression of a clinical response, obscuring the underlying neoplastic disease.

The most common presenting signs and symptoms associated with lacrimal sac neoplasms include epiphora (53% of patients) with a mean duration of 3 years; dacryocystitis (38%, often chronic and irrigates freely); a mass or mucocele of the lacrimal sac (36%)[170]; and extension above the medial canthal tendon.[164] In 43% of patients in the Stefanyszyn et al. series,[170] the tumor was inadvertently found at the time of DCR for presumed

Copyright © 2003, Mosby, Inc. All rights reserved.

dacryostenosis. Bleeding from the puncta, either spontaneously or on applied pressure to the lacrimal sac, or bleeding from the nose was noted in 8% of patients, as an early sign in one patient with melanoma and as a late sign in all other neoplasms. The average duration of symptoms in this series preoperatively was 3 years. In a small percentage of cases, metastatic lymph nodes may be the initial manifestation of a malignant lacrimal sac tumor.[174]

The usual sequence of events with a lacrimal sac tumor begins with epiphora, followed by recurrent bouts of dacryocystitis, development of a nonreducible mass in the area of the lacrimal sac, with eventual extension outside the sac, and, later, in certain cases, epistasis, ulceration over the sac, regional nodal involvement (preauricular, submandibular, cervical) in approximately 28% and metastases.[170, 174, 175] Eyelid and orbital extension, with proptosis and decreased ocular motility, may then be noted in a high percentage of patients with malignant epithelial neoplasm.[174, 175] Signs to complement a high index of suspicion, necessary for an early diagnosis, include a painless, nonreducible, firm mass in the lacrimal sac region, especially if the mass extends superior to the medial canthal tendon,[164, 176] compared to the slightly lower position of the lacrimal sac mucocele associated with chronic dacryocystitis. There is a tendency for melanoma of the lacrimal sac to bleed (punctal or epistaxis) and disperse pigment.[176]

DCG tends to display findings earlier with a distended lacrimal sac and a filling defect, as well as mottled density (intraluminal growth), in conjunction with delayed drainage of the contrast material, when CT may still be negative. In early stages of tumor growth, the lacrimal drainage system will be patent.[176] DCG may be a more effective study for differentiating dacryocystitis from neoplasia and differentiating extrinsic from intrinsic lacrimal sac pathologic processes. CT better displays the extraluminal component of the soft-tissue lacrimal sac mass and its extension into

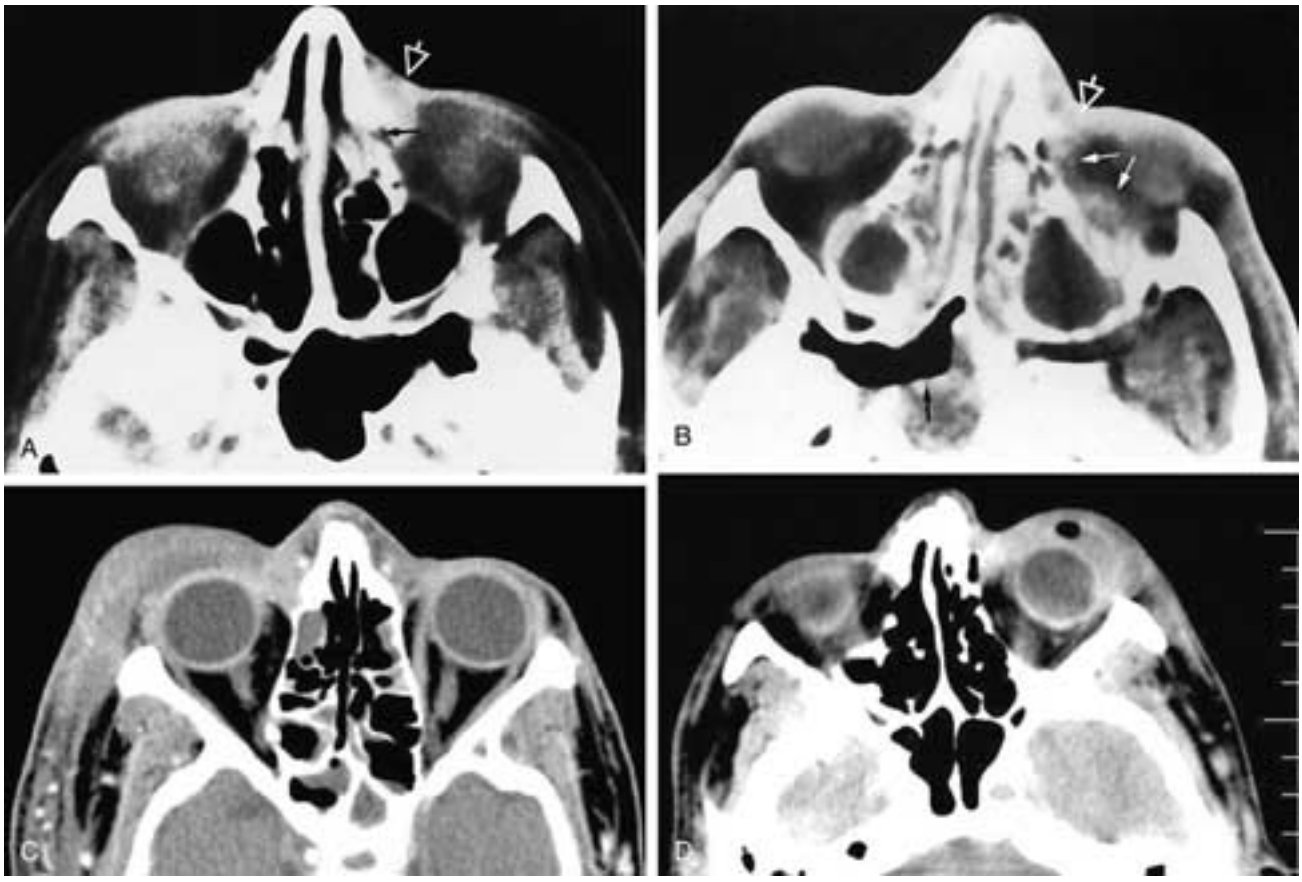

VIEW IMAGE

FIGURE 10-29 CT differentiating preseptal from orbital inflammatory lesions (which may be difficult on clinical examination). Multiple patients. **A**, Soft-tissue mass in the left inner canthus (*open arrow*) with faint peripheral enhancement contiguous with the left nasolacrimal fossa (partially obscured by beam-hardening artifact) (*thin arrow*). Mass is localized to the preseptal tissues. Pathology: chronic dacryocystitis with mucocele formation. **B**, Soft-tissue prominence (*open arrow*) of the left inner canthus, clinically noted on axial CT to involve the medial orbital soft tissues and inferior rectus muscle (*thin white arrows*). Pansinus opacification with fluid level in the right sphenoid sinus (*black arrow*). Sinusitis with left orbital cellulitis. **C**, Second patient. Preseptal orbital cellulitis secondary to dacryocystitis. Note the sharp posterior border of the inflammatory process due to orbital septum attachment to the posterior lacrimal crest. **D** and **E**, Third patient. Axial (**D**) and coronal (**E**) CT scans show a preseptal left orbital abscess containing air and pus. Soft-tissue edema extends medially to abut the normal air-containing lacrimal sac.

Copyright © 2003, Mosby, Inc. All rights reserved.

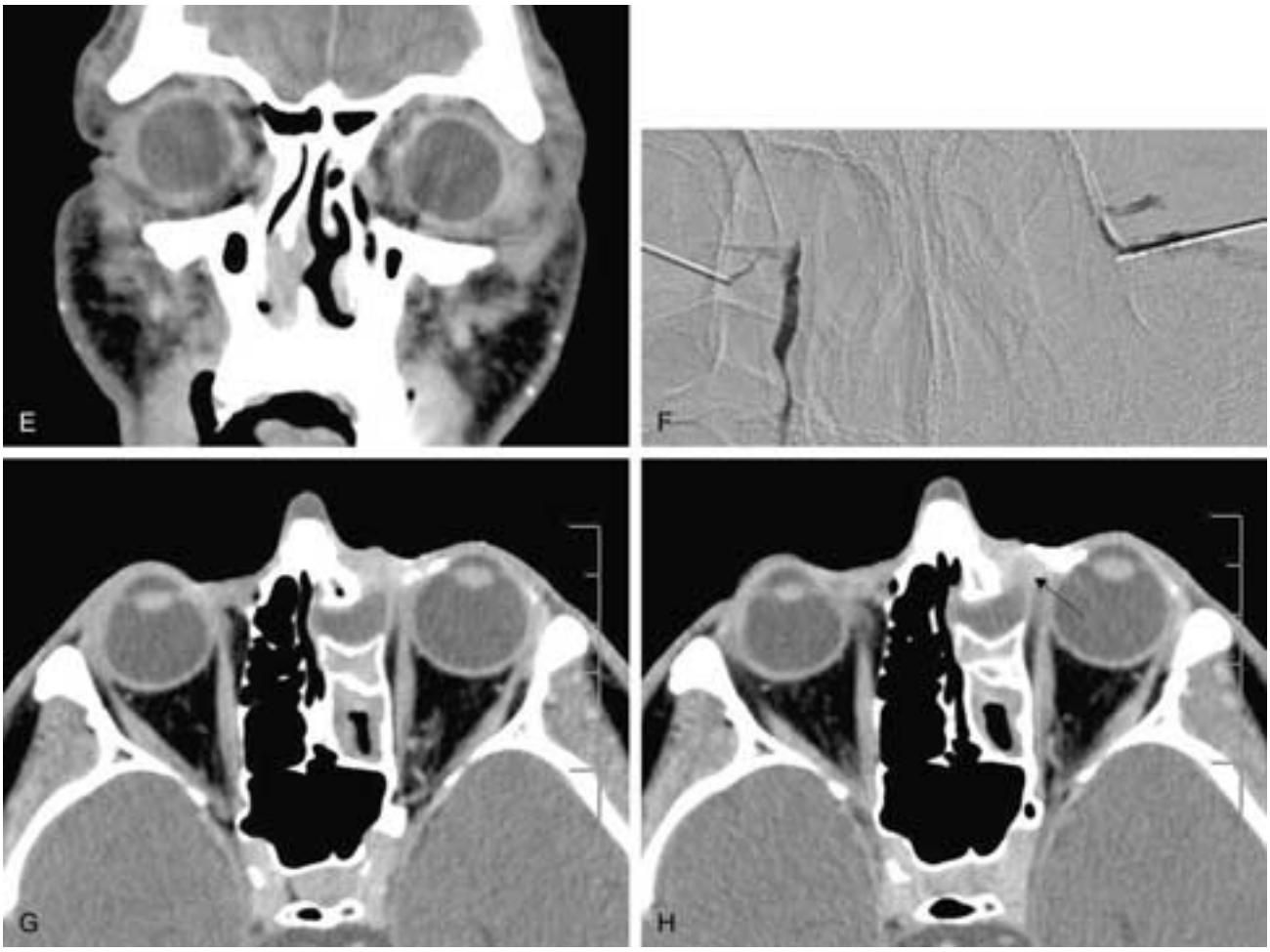

VIEW IMAGE

FIGURE 10-29 *Continued.* **F** to **J**, Fourth patient. Anterior ethmoid mucocele. **F**, DCG shows blocks at the common canaliculus, with dilatation of the superior and inferior canaliculi suggesting chronic canalicular inflammatory changes. **G** and **H**, Axial-enhanced CT scan shows a cystic mass centered within the anterior ethmoid air cell and projecting into the lacrimal sac fossa. Soft-tissue swelling of the left inner canthus and enlarged lacrimal sac (*arrow*).

Illustration continued on following page

surrounding tissues, bone erosion, or infiltration of the lacrimal sac fossa, nasolacrimal canal, or adjacent orbit and paranasal sinuses. CT-DCG will offer further information about the lacrimal sac lumen, allowing better assessment of the thickness or irregularity of the lacrimal sac wall (intramural growth) and the nasolacrimal duct than CT alone. MR imaging, with its superior soft-tissue resolution, may better display neoplastic extension of the lacrimal sac tumor into the nasolacrimal canal or into the adjacent soft tissues of the orbit.[177] Because of the desire for both bone and soft-tissue detail, CT usually is the primary modality for assessment, with MR imaging playing an adjunctive role in selective cases.

While benign lesions may allow a local resection, epithelial malignancies tend to grow along the epithelium of the lacrimal drainage system. Cure, therefore is dependent on a wide surgical excision of the lacrimal sac mass and the entire lacrimal drainage system (canaliculi, sac, and nasolacrimal duct), combined with a lateral rhinostomy and radiation therapy. CT remains the preferred posttreatment modality for follow-up of these patients. Persistent epiphora is frequently seen in the postradiation nonsurgical patient (e.g., with lymphoma). Postirradiation nasolacrimal duct stenosis is a frequent complication[178] that may be prevented by the insertion of nasolacrimal stents.[177] Epithelial carcinomas of the lacrimal sac have a recurrence rate of 50%.[171] The overall mortality of those treated with a combination of wide surgical excision and radiation is 37.5%.[174, 179]

CT findings of sac enlargement (dacryocystitis as a complication) should be distinguishable from the findings of solid tumor. Intraductal tumor and its relationship to the nasolacrimal bony canal or nasolacrimal fossa is best seen on CT, which also allows extracanalicular tumor spread to be assessed.[70] Bone destruction of the lacrimal fossa is common with intraductal malignant neoplasms.[152] DCG alone or in combination with CT may help better define small tumors arising from the lacrimal sac fundus or show the lumen irregularity caused by the tumor.[180]

Copyright © 2003, Mosby, Inc. All rights reserved.

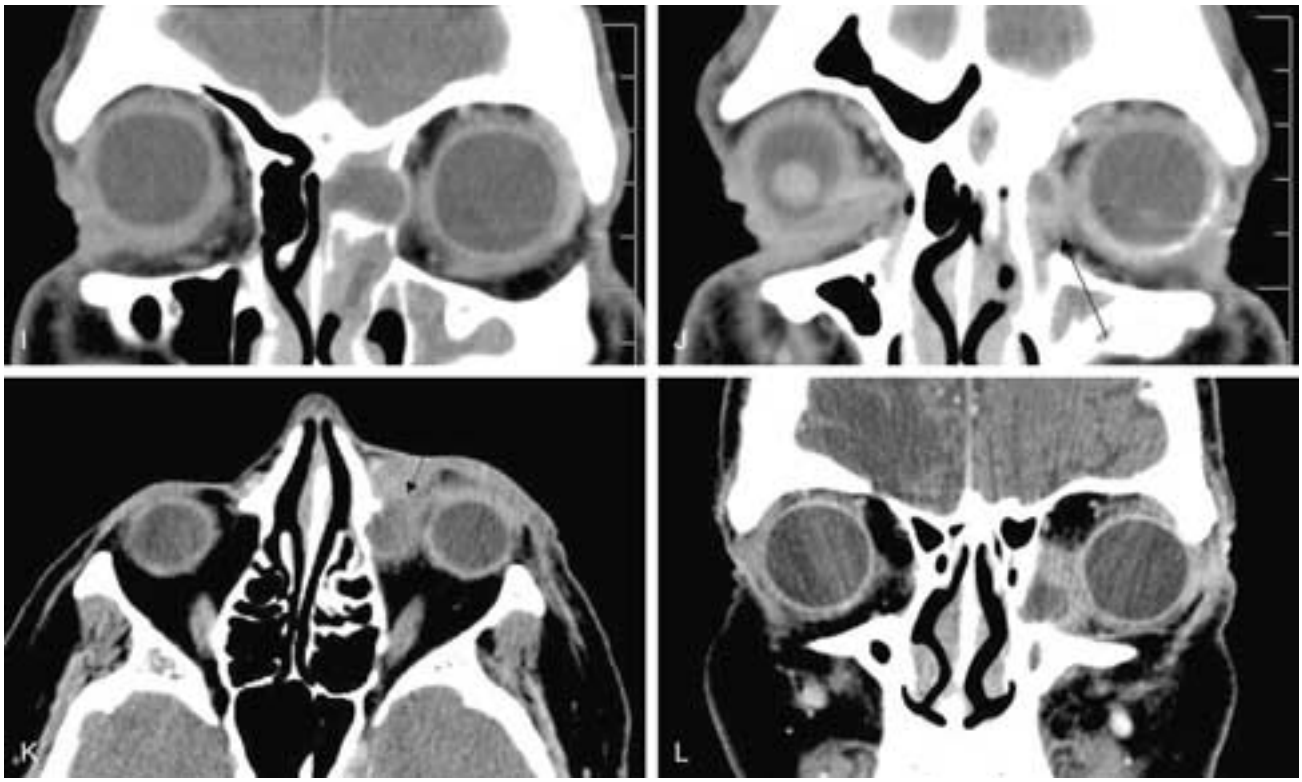

VIEW IMAGE

FIGURE 10-29 *Continued.* **I** and **J**, Coronal CT scans shows lateral displacement of the lamina papyracea and lacrimal fossa bed, as well as inflammatory changes of the lacrimal sac and surrounding tissues (*arrow*), with loss of normal tissue planes. Pathology: dacryocystitis secondary to anterior ethmoid inflammatory disease—mucocele. **K** and **L**, Fifth patient. Axial and coronal CT scans show a distended lacrimal sac with thickened walls, extensive preseptal swelling, and loss of adjacent tissue planes (*arrow*). Incidental right frontal lobe encephalomalacia. Pathology: lacrimal sac abscess.

Granulomatous pseudotumors, sarcoidosis, or other less common inflammatory or infiltrative diseases may involve the lacrimal sac and should be considered in the differential diagnosis.[181]

Facial Trauma

Traumatic lacerations of the canaliculi are poorly visualized by CT, and if clinical assessment is indefinite, DCG is the definitive study (Fig. 10-31). Similarly, CT may be insufficient to differentiate NLDS obstruction caused by acute edema or ecchymosis of adjacent tissues.[173] Persistent tearing (after subsidence of soft-tissue swelling) or recurrent dacryocystitis suggests a probable obstruction of the nasolacrimal duct system (NLDS) and the need for further assessment.

Fractures of the lacrimal fossa and nasolacrimal canal may lead to an acute and/or delayed obstruction of the nasolacrimal system. Such fractures or bone displacements are best assessed by CT, which may also help prevent a closed manipulation of a sharp, displaced fracture fragment that could further harm the lacrimal sac or duct. Demonstration of such bone fragments suggests that exploration and open reduction is a more prudent treatment.

Approximately 85% of obstructions associated with trauma occurred at the junction of the lacrimal sac and nasolacrimal duct. CT may suggest the level of obstruction by noting the location of fracture fragments. However, DCG remains a more exact and definitive method for locating the point of obstruction.

There is a relative infrequency of epiphora associated with severe facial trauma.[182] Campbell[9] noted only a 12% incidence in 100 cases of central midfacial fractures and postulated several reasons. In both the cranofacial (LeFort III)- and pyramidal (LeFort II)-type fractures, the lacrimal fossa and nasolacrimal canal tend to escape the fracture lines centered more superiorly at the nasofrontal suture and extending lateral to the nasolacrimal fossa and canal. The anterior and posterior lacrimal crests deflect the pyramidal fractures superior and then posterior to the lacrimal fossa into the orbital plate of the ethmoid. The transverse (LeFort I)-type fracture usually involves the lateral wall of the nasal cavity immediately above the floor of the nasal fossa, thereby sparing the nasolacrimal canal. Fistulae of the nasolacrimal duct into the maxillary antra may result from LeFort I type fractures.

Several series documenting orbital findings relative to facial fractures have noted symptomatic lacrimal obstruction in 0.2% of nasal fractures, 3.4% of LeFort II or III fractures, and 17% to 21% of nasoorbital-ethmoidal fractures.[182–187] Unger[188] noted that fractures involving the bony nasolacrimal fossa and canal were associated with simple unilateral facial fractures as well as the more complex midface fractures. Three patterns of fractures were noted: avulsion of the lacrimal sac fossa, comminuted fractures of the lacrimal

Copyright © 2003, Mosby, Inc. All rights reserved.

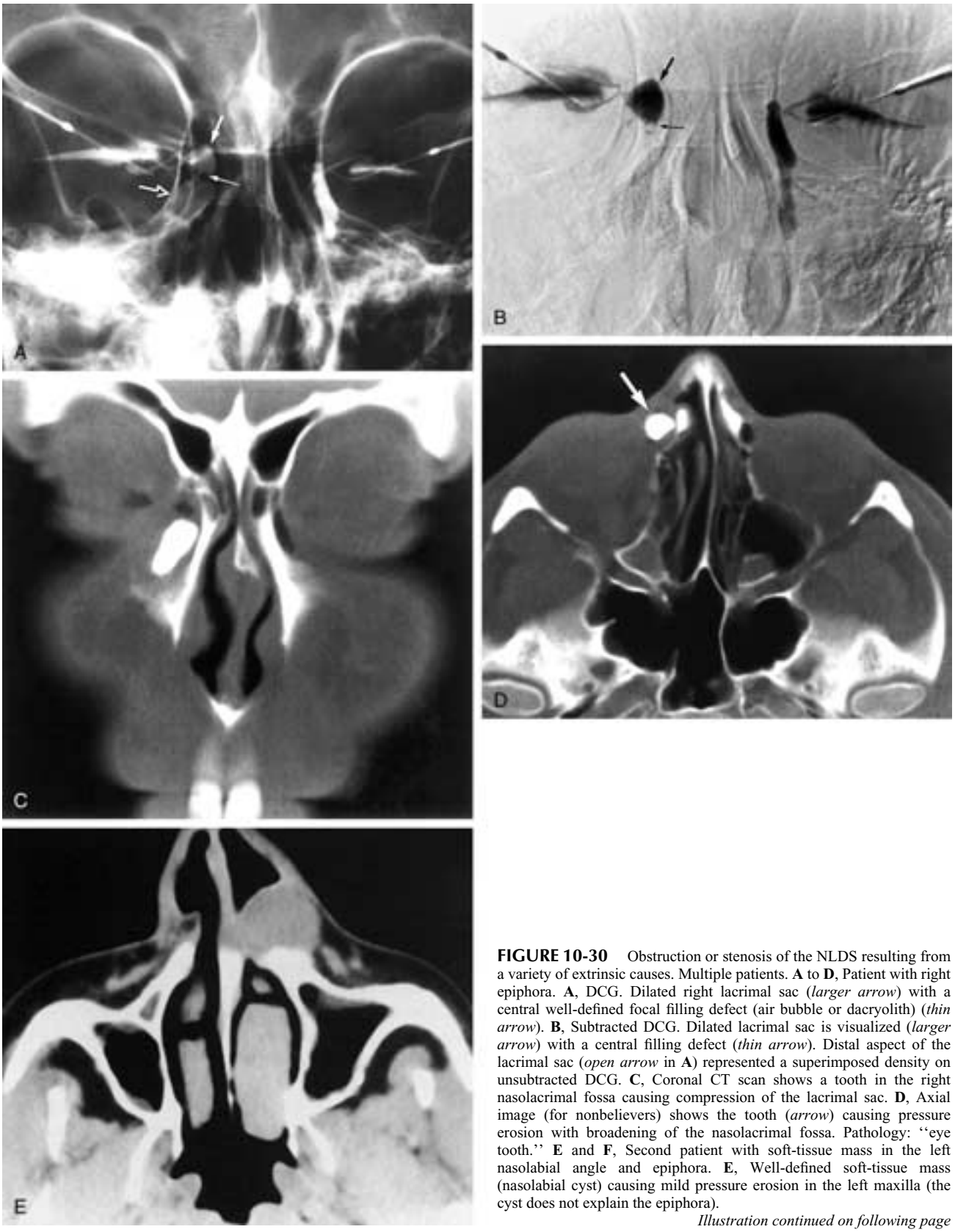

FIGURE 10-30 Obstruction or stenosis of the NLDS resulting from a variety of extrinsic causes. Multiple patients. **A** to **D**, Patient with right epiphora. **A**, DCG. Dilated right lacrimal sac (*larger arrow*) with a central well-defined focal filling defect (air bubble or dacryolith) (*thin arrow*). **B**, Subtracted DCG. Dilated lacrimal sac is visualized (*larger arrow*) with a central filling defect (*thin arrow*). Distal aspect of the lacrimal sac (*open arrow* in **A**) represented a superimposed density on unsubtracted DCG. **C**, Coronal CT scan shows a tooth in the right nasolacrimal fossa causing compression of the lacrimal sac. **D**, Axial image (for nonbelievers) shows the tooth (*arrow*) causing pressure erosion with broadening of the nasolacrimal fossa. Pathology: ''eye tooth.'' **E** and **F**, Second patient with soft-tissue mass in the left nasolabial angle and epiphora. **E**, Well-defined soft-tissue mass (nasolabial cyst) causing mild pressure erosion in the left maxilla (the cyst does not explain the epiphora).

Illustration continued on following page

VIEW IMAGE

Copyright © 2003, Mosby, Inc. All rights reserved.

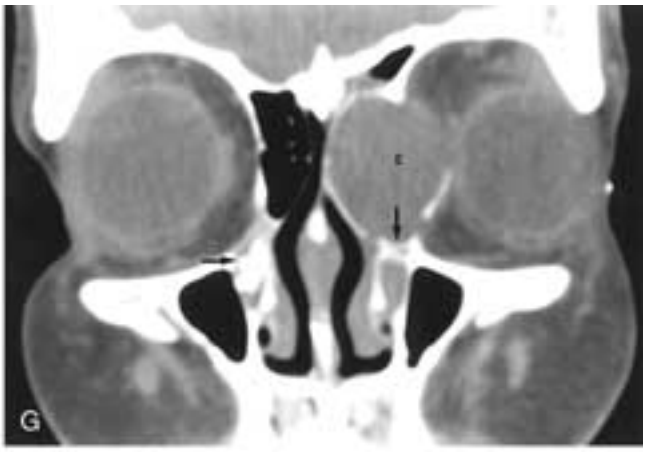

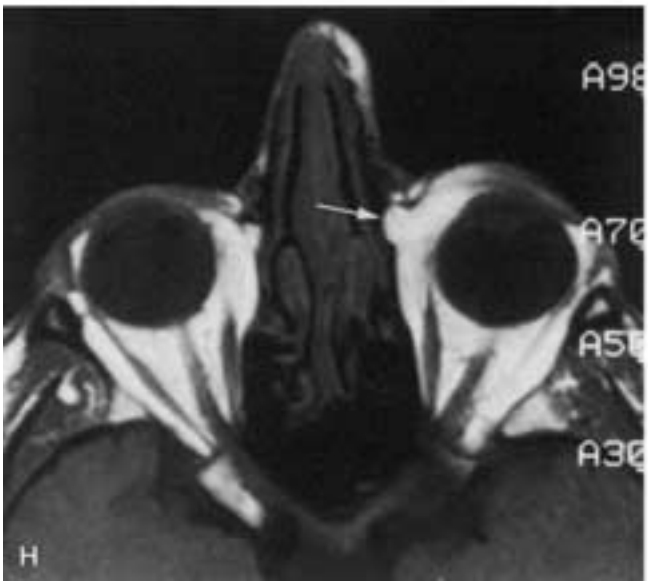

FIGURE 10-30 *Continued.* **F**, Coronal CT scan shows demineralization with loss of cortical bone of the left nasolacrimal canal (*open arrow*) compared with the normal right side (*solid arrow*). Pathology: posttraumatic inclusion cyst and suspected osteitis in the anterior maxilla. **G**, Soft-tissue mass centered about and expanding the left side of the ethmoid sinus (*E*). Medial wall of the orbit is displaced laterally, in contrast to a mass arising within the orbit. Bony partition (*vertical arrow*) is present between the mass and the nasolacrimal canal, in contrast to the mass arising in the nasolacrimal fossa. Contrast medium in the right nasolacrimal canal (*horizontal arrow*). Pathology: ethmoid mucocele. **H**, Intermittent left epiphora. Axial T1-weighted image shows increased fat content in the left inner canthus (compared with the right), with fat tissue herniating into and filling the left nasolacrimal fossa (*arrow*). (Courtesy of Dr. George Wortzman, Toronto, Canada.)

VIEW IMAGE

sac fossa or nasolacrimal canal, and linear fractures of the nasolacrimal canal. Fractures involving the nasolacrimal fossa most commonly were avulsions of an intact nasolacrimal fossa, with comminution of the nasolacrimal fossa being less frequent. Linear fractures of the fossa are rare. The anterior (frontal process of the maxilla) and posterior (lacrimal bone) lacrimal crests fortify the nasolacrimal fossa such that it maintains its integrity when displaced from the more fragile components of the adjacent orbital and nasal structures.[188] This CT finding correlates with the clinical observations that direct lacerations of the lacrimal sac are rare and that obstruction at the junction of the lacrimal sac and nasolacrimal duct is common.[189]

Although the superior aspect of the nasolacrimal canal is also formed by the lacrimal bone and maxilla, most of the canal continues within the medial (nasal) wall of the maxilla, which progressively thins toward the nasolacrimal canal opening just inferior to the inferior turbinate. The majority of fractures involving the nasolacrimal canal are comminuted, with the comminution being more common and more extensive where the bone is thinner at the more inferior aspect of the canal. Linear fractures of the nasolacrimal canal are relatively uncommon. Complication of drainage (epiphora) was seen in only 5 of 25 patients.[188]

Previous facial fracture repairs may add complexities to the performance of lacrimal surgery.[189] Bone grafts used in reconstruction may alter anatomic landmarks.[183, 190] Metallic plates, wires, and silastic or mesh sheets used for fracture repair may impede the lacrimal surgery or be causative factors in the lacrimal drainage symptoms and may require removal during the surgical repair or DCG.[183, 190] CT remains the primary modality of investigation for assessing facial fractures, malalignments, residual deformities, previous instrumentation, and their relationship to the NLDS. CT can also be used to show the bony anatomy in patients after surgery such as DCR (Fig. 10-32).

COMBINED CT-DACRYOCYSTOGRAPHY

DCG is the best modality to demonstrate obstruction of the NLDS itself, and CT is valuable in imaging the surrounding bone and soft-tissue structures of the face, sinuses, and orbit. Conventional CT alone cannot provide

Copyright © 2003, Mosby, Inc. All rights reserved.

Table 10-3
MASS LESIONS OF THE INNER CANTHUS

I. Nasolacrimal Drainage System
- A. Inflammatory/obstructive:
  1. lacrimal sac mucocele
  2. dacryocystitis
  3. lacrimal sac abscess
  4. cyst of the lacrimal sac
  5. granulomatous pseudotumor including sarcoid/Wegener's
- B. Benign tumors*
  1. Epithelial: inverting papilloma, benign mixed tumor
  2. Mesenchymal: fibroma, histiocytoma, hemangioma, neurogenic
- C. Malignant tumors*
  1. epithelial carcinomas
  2. lymphoma
  3. melanoma
  4. hemangiopericytoma
  5. granulocytic sarcoma

II. Orbit
- A. Preseptal
  1. Inflammatory: cellulitis, abscess
  2. Benign tumor: inclusion cysts, sebaceous cysts, dermoid
  3. Malignant skin or eyelid neoplasms: basal cell carcinoma, squamous cell carcinoma, meibomian gland carcinoma, sebaceous cell carcinoma, lymphoma, schwannoma
- B. Postseptal
  1. Inflammatory, including lymphatic: cellulitis, abscess, medial periorbital abscess, nasolabial pseudotumor, myositis
  2. Benign: dermoid, hemangioma
  3. Malignant: lymphoma, rhabdomyosarcoma, extramedullary plasmacytoma

III. Sinonasal
- A. Inflammatory: sinusitis, orbital cellulitis, periorbital abscess, orbital abscess, mucocele, ethmoid, frontal chronic granulation tissue
- B. Benign: polyposis, papilloma, oncocytoma
- C. Malignant: carcinoma (squamous cell, adenoca, minor salivary gland, etc.), lymphoma, melanoma, esthesioneuroblastoma

IV. Local—From Above (Skull Base, Dura, Brain)
- A. Meningioma
- B. Meningocele
- C. Encephalocele

V. Local Bone—Cartilage
- A. Fibro-osseous osteoma
- B. Osteosarcoma
- C. Chondrosarcoma
- D. Myeloma/plasmacytoma

VI. Geographic—Local Soft Tissues
- A. Neurogenic: neurofibroma
- B. Vascular: varix malformations, hemangioma, developmental or fissural cysts

VII. Trauma
- A. Hematoma: edema
- B. Displaced bone fragments
- C. Instrumentation of implants

VIII. Systemic
- A. Metastases
- B. Lymphoma, myeloma
- C. Histiocytosis

*See Table 10-4 for tumors of the lacrimal sac.

adequate information to suggest a focus of obstruction in the epiphora patient. Combining these two modalities shows the relationship between the NLDS and the surrounding soft tissue or bony structures to better advantage. This combined study (CT-DCG) is indicated in the assessment of more complex lacrimal problems such as medial canthal tumors, midface trauma, or previous lacrimal or adjacent sinonasal surgery (Figs. 10-13 to 10-15, 10-18, 10-19, and 10-27). The combined study can more confidently show masses to be intrinsic (e.g., dacryolith) or extrinsic to the duct system, and the full extent of an extrinsic mass can be more properly defined during CT-DCG. Either axial or coronal imaging may be preferred. Frequently these views are complementary. The continuing advances of spiral (volumetric) imaging with thinner overlapping slices allow improved image data accumulation in the axial plane. Reconstruction capabilities allow selective sagittal or coronal oblique images exactly along the axis of the NLDS. Reformatted studies reduce the total radiation exposure for such studies compared to direct imaging in multiple planes.

CT-DCG may better demonstrate the exact relationship of the lacrimal sac to the paranasal sinuses and advise the

Table 10-4
TUMORS OF THE LACRIMAL SAC (HISTOPATHOLOGIC CLASSIFICATION)

I. Epithelial Tumors
- A. Benign
  1. Papilloma: squamous, transitional
  2. Oncocytoma
  3. Benign mixed tumors
- B. Malignant epithelial tumors
  1. Papilloma with carcinoma
  2. Carcinoma: squamous, transitional adenocarcinoma, oncocytic adenocarcinoma, mucoepidermoid, poorly differentiated, adenoid cystic

II. Nonepithelial Tumors
- A. Mesenchymal
  1. Fibrous histiocytoma
  2. Hemangiopericytoma
  3. Hemangioma
  4. Lipoma
- B. Lymphoma
  1. Reactive
  2. Malignant
- C. Melanoma
- D. Granulocytic sarcoma
- E. Neurogenic
  1. Neurofibroma
  2. Neurilemmoma

Adapted from Stefanyszym MA, Hidayat AA, Pe'er JJ, Flanagan JC. Lacrimal sac tumors. Ophthal Plast Reconstr Surg 1994;10:169–184.

Copyright © 2003, Mosby, Inc. All rights reserved.

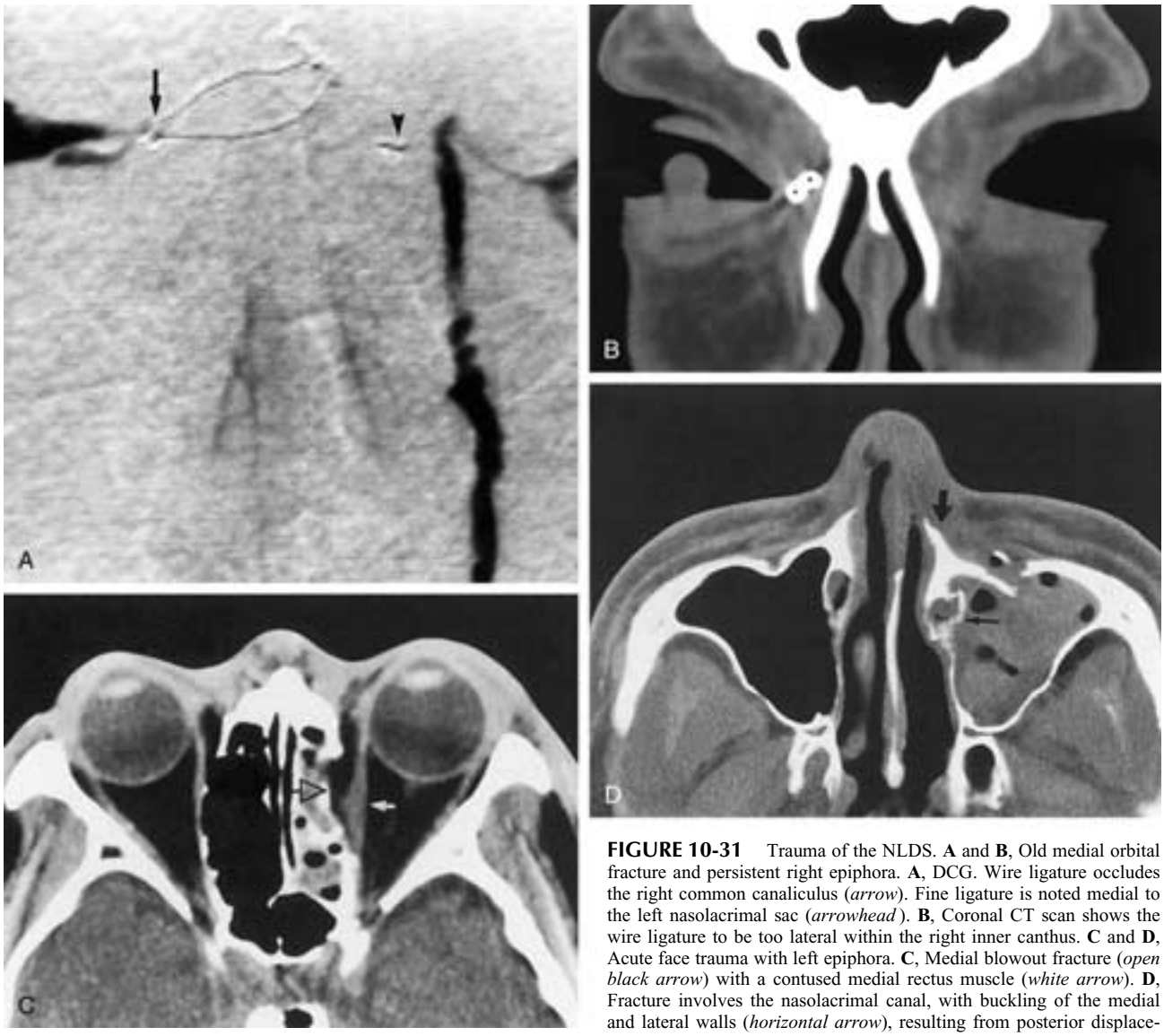

FIGURE 10-31 Trauma of the NLDS. **A** and **B**, Old medial orbital fracture and persistent right epiphora. **A**, DCG. Wire ligature occludes the right common canaliculus (*arrow*). Fine ligature is noted medial to the left nasolacrimal sac (*arrowhead*). **B**, Coronal CT scan shows the wire ligature to be too lateral within the right inner canthus. **C** and **D**, Acute face trauma with left epiphora. **C**, Medial blowout fracture (*open black arrow*) with a contused medial rectus muscle (*white arrow*). **D**, Fracture involves the nasolacrimal canal, with buckling of the medial and lateral walls (*horizontal arrow*), resulting from posterior displacement of an anteromedial maxillary fragment (*vertical arrow*). (**C** and **D** Courtesy of Dr. Lyne Noël de Tilly, Toronto, Canada.)

VIEW IMAGE

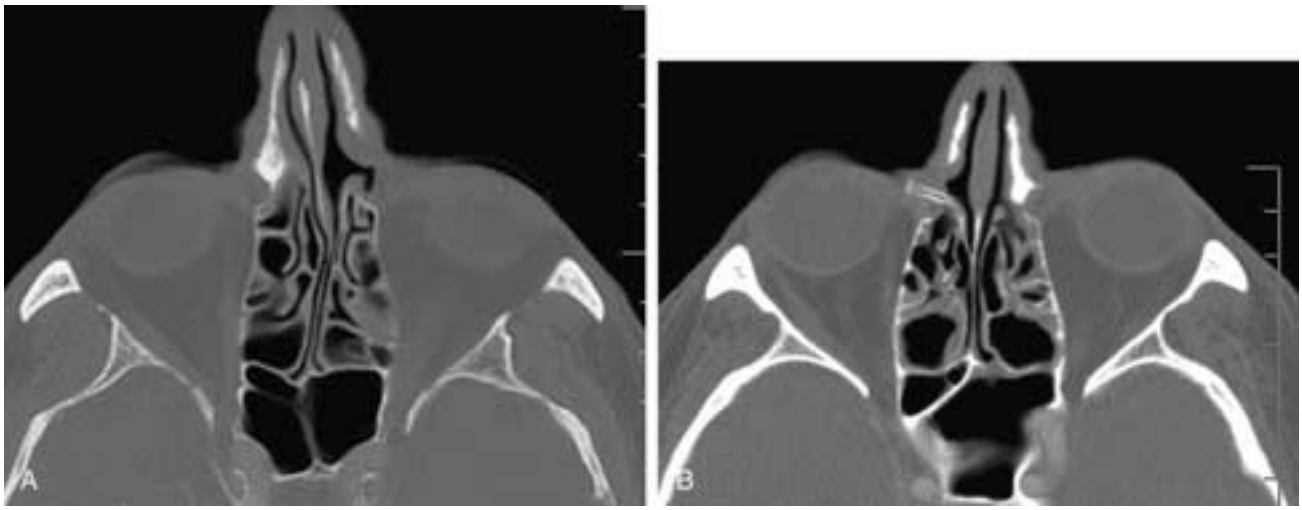

FIGURE 10-32 **A**, Typical bone defect from previous left external DCR. Open communication between the nasal cavity and lacrimal sac outlined by the presence of air. **B**, Canaliculo-DCR for reconstruction of the canaliculi, with postsurgery bone changes and the presence of a Jones tube (see ''Surgical Procedures for Epiphora'' in text).

VIEW IMAGE

Copyright © 2003, Mosby, Inc. All rights reserved.

surgeon whether the ethmoid sinus will be encountered in the course of the dacryocystorhinostomy (DCR). The most anterior ethmoid cells, the agger nasi cells, extend into bone adjacent to the lacrimal sac in 94% to 98.5% of patients, overlying the superior half of the lacrimal sac fossa.[191] Inappropriate osteotomy placement or inadvertent anastomosis of the lacrimal sac to an ethmoid air cell, rather than to the nasal mucosa, can lead to DCR failure.[191–193]

The location of the bony opening in patients who have undergone previous unsuccessful DCR is frequently invisible on DCG, but this surgically important information may be attained by CT-DCG.[194] Welham and Wulc's study[112] of 208 DCR failures, problems with the bony ostium were present in over half of the cases and represented the most common cause of DCR failure. Glatt et al.[194] emphasized the use of CT-DCG to show the relationship between the bony ostium of the failed DCR and the lacrimal sac, filled with radiographic contrast medium. Improper placement of the ostium, including too anterior, too inferior, or too small (improper size), was noted in their study. A proper osteotomy for external DCR should be relatively large, measuring at least 15 mm in diameter, all bone between the lacrimal sac and nasal mucosa should be removed, and no bone should be left within 5 mm of the common canaliculus.[24, 107, 112] A smaller bony ostium (5 to 7 mm in diameter) may be successful and appropriate for a transnasal laser DCR.[195] Bone regrowth at the osteotomy site after DCR is unusual, but may occur in children and can be a cause of DCR failure at the osteotomy site.[112] CT-DCG may show bone regrowth between the lacrimal sac and nasal cavity. Linberg et al.[196] showed that the average diameter of the intranasal ostium postoperatively shrinks to 2% of the original operative diameter, mainly because of soft-tissue scarring. CT or CT-DCG with proper use of bone and soft-tissue windows facilitates reoperation after DCR failure by determining what modifications are required in the bony ostium.[194] Such studies can also show whether anterior ethmoid air cell resection is required to allow proper mobilization of lacrimal and nasal mucosal flaps and appropriate internal anastomosis and drainage into the nasal cavity. Similarly, anatomic variants of the nasal cavity, anterior middle turbinate, inferior turbinate, or nasal septum may be noted. CT-DCG best shows the relationship of surgical clips, sutures, and fixation plates to the nasolacrimal sac or the osteotomy site. On routine intravenous enhanced CT or during surgery, it may be very difficult to identify the lacrimal sac on DCR failure patients because of exuberant granulation tissue or scarring and attenuation of anatomic landmarks. Such soft-tissue proliferation at the internal anastomosis may represent inadequate mucosal end-to-end suturing between the lacrimal sac and the nasal cavity.[112] CT-DCG facilitates the treatment of these more difficult patients by identifying the lacrimal sac's shape, location, and relationship to surrounding structures, especially the ostium and/or surgical clips. The more recent transnasal endoscopic approach to DCR failures requires knowledge that the bony ostium is of adequate size and location before considering this approach.

CT-DCG was more sensitive than MR-DCG in differentiating high-grade stenosis from total obstruction of the NLDS.[151] In the presence of postoperative scarring, MR-DCG was less helpful in assessing the site and size of a bone defect after rhinostomy. CT-DCG is preferred for such patients, better differentiating soft tissue from bone obstructions. Epiphora is a common complication following medial maxillectomy for lateral nasal wall neoplasms. Outlining the NLDS with contrast, in conjunction with CT, may better assess patients with poor lacrimal drainage and may differentiate possible causes including residual tumor, inflammatory changes, fibrosis, and postsurgical or postradiation effects on the sinus, the nasal cavity, or the NLDS itself.

In patient with a lacrimal outflow symptoms after trauma, CT-DCR offers all the advantages of routine CT with the additional benefits of more exact localization of the lacrimal drainage system. CT-DCR can assess the possible complexities of the lacrimal surgery (usually DCR) resulting from distorted anatomy secondary to trauma or previous reconstructions including grafting. Adjacent anatomic variations (anterior ethmoid air cells, proximity of the anterior middle turbinate process, or deviated nasal septum) are visualized, as are the locations of previous placed miniplates, wire, or silastic sheets that may need to be removed because of interference with lacrimal flow.[51]

Ashenhurst et al.[197] performed CT-DCG immediately following standard intubation macro-DCG. They left the DCG lacrimal cannula in place, with contrast medium reinjected just before CT scanning (Fig. 10-27). Images were obtained in the coronal and/or axial plane, depending on clinical and DCG information. Glatt et al.[194] similarly used an oil-based radiopaque contrast medium injected via an inferior canalicular catheter insertion and recommended CT-DCG immediately following the injection of contrast. In the assessment of failed DCRs, they found coronal images to be more helpful. Imaging should be obtained in both bone and soft-tissue modes for proper assessment of the soft tissues and adjacent bony landmarks. CT-DCG can be performed using water-soluble contrast medium eye drops placed into the conjunctival cul-de-sac.[23, 197–200] Although such topical application of contrast material may be less predictable in demonstrating the NLDS than cannulation CT-DCG, several advantages may be realized. Topical CT-DCG allows a more physiologic evaluation of the NLDS and increases patient comfort, tolerance, and acceptance of the study. The ease of the procedure obviates the need for skilled personnel to perform the lacrimal cannulation and eliminates any risk of procedural iatrogenic injury from the cannulation or injection of contrast medium. The increased sensitivity of CT for detection of subtle attenuation changes of contrast medium within the NLDS has allowed the option of decreased volumes and concentrations of such agents. The topically applied contrast used is low-osmolar, nonionic, and water soluble, with a concentration of 200 mg I/ml. One to two drops per minute, per eye, is given for 2 to 3 minutes before actual scanning starts. The patient is kept in a supine position for axial imaging or turned prone just before direct coronal imaging.

In a study[199] comparing instillation of topically applied contrast agents into the tear lake, iopamidol (Isovue 200; Squibb Diagnostics, Princeton, New Jersey) for CT and normal saline for MR-DCG, in healthy normal volunteers, CT-DCG consistently better displayed the smaller components of the NLDS (e.g., the superior, inferior, and common canulicula) than MR-DCG. These structures were seen

Copyright © 2003, Mosby, Inc. All rights reserved.

routinely on CT-DCG, while MR-DCG displayed the superior and inferior canulicular structures in approximately 50% and the common canaliculus in less than 20%.

While a variety of CT-DCG techniques allows personal preference and comfort, certain circumstances require techniques that are more specific. Routine placement of drops of contrast medium into the conjunctival cul-de-sac (tear lake) may offer inadequate visualization of the NLDS in those patients with known punctal or canalicular stenosis, other higher-grade stenoses, or conditions not favoring the flow of such contrast into or through the NLDS. For these patients, a less physiologic and more anatomic placement of contrast through cannulation is required. While some individuals may prefer the more pronounced attenuation of lipid-based contrast agents (e.g., Lipiodol ultrafluide; Guerbet, Villepinte, France), caution with the use of such agents is imperative. Their increased viscosity makes placement into the conjunctival sac impractical. Lipid-based contrast medium introduced through cannulation is more at risk for extravasation and related long-standing complications,[201] especially in the posttraumatic study or in assessing the patient with chronic inflammatory tissues of the NLDS. We routinely use water-soluble, low-osmolar contrast, with excellent results and increased safety. This approach provides excellent images. This CT-DCG technique better demonstrates the canaliculi of the upper drainage system (Fig. 10-19) than cannulation CT-DCG and offers further advantage when used with spiral (helical) CT and its volume data acquisition,[198–200] offering coronal and sagittal oblique reformations of superior quality along the axis of the NLDS. The extremely fast total data acquisition times (less than 20 to 30 seconds) ensures patient cooperation and almost no risk of movement, despite the acquisition of very thin (1 mm or less) overlapping axial scans through the area of interest. The high-quality reformations obviate the need for direct coronal imaging. Three-dimensional images of the NLDS can be reconstructed using a connectivity algorithm and viewed in relationship to adjacent orbital or facial skeletal structures. Patients may complain of slight dryness, burning, or irritation of the eye from the topical administration of water-soluble contrast material.[23, 199]

Pediatrics

Congenital Atresia

The nasolacrimal apparatus develops from a core of surface epithelium, the nasooptic fissure, trapped between the maxillary and frontonasal processes. Although canalization occurs uniformly throughout the length of the nasolacrimal drainage system, failure in this process is most common at the distal nasolacrimal canal. There is lack of perforation of the nasolacrimal canal at the inferior meatus (valve of Hasner), with a persistent layer of lacrimal and nasal epithelial cells, related to adhesions between the nasal mucosa and the nasolacrimal epithelium.[202] In some patients, a plug of epithelial cell debris causes obstruction.[203] Such distal obstruction may result in epiphora and mucoid discharge.[204]

Simple inspection allows diagnosis of congenital atresia of the lacrimal puncta. If only one punctum is involved, DCG should be performed through the opposite punctum to visualize the canaliculi. Retrograde filling of the canaliculus without reflux through the punctum indicates focal occlusion. If the canaliculus fails to visualize, there is atresia of the entire canaliculus.[88]

Congenital obstruction of the NLDS occurs commonly, but significant symptoms are relatively rare. Sevel[202] noted an incidence of NLDS obstruction in 30% of term fetuses and MacEwan and Young[205] noted such obstruction to be a common clinical problem, affecting as many as 20% of all infants, while Levy[206] noted epiphora occurring in only 6% of infants. Increased intraluminal pressure in the duct during initial respiratory efforts or crying at birth may rupture the distal membrane, forming the one-way valve of Hasner.[207, 208] These findings may partially explain the high proportion (85%) of spontaneous resolution of NLDS obstructions before the child reaches age 9 months.[209] The low rate of tear production during early infancy is also a factor in the low incidence of epiphora.

Rarely, concomitant obstruction is also present more proximally in the NLDS, creating a closed space that allows accumulation of fluid, causing a cystic swelling of the NLDS (Fig. 10-33). Such proximal obstruction occurs as the result of a valve-like unidirectional obstruction at the junction of the lacrimal canaliculi and sac (valve of Rosenmüller).[27] Cystic swelling may also result from some component of active intraluminal secretions. Berkowitz et al.[204] prefer the term *congenital nasolacrimal drainage system cyst* for this cyst, seen as a bluish mass below the medial canthal angle. The terms *mucocele*, *dacryocystocele*, and *amniotocele* are also applied to this entity. If a distended lacrimal sac is present at birth, without associated inflammatory changes, the cystic swelling is referred to as an *amniotocele containing sterile amniotic fluid*.[27] If the cyst is filled with epithelial debris and mucus generated by the NLDS, the term *mucocele* may be used.[208] Compression of the distended lacrimal sac does not tend to cause regurgitation through the puncta.[210] Conservative management is generally preferred. Probing may prevent dacryocystitis or pressure on the globes. Surgical intervention (usually probing only) is generally not recommended unless complications develop or obstruction persists after age 6 to 9 months. Complications of a congenital nasolacrimal cyst include epiphora, dacryocystitis, cellulitis, sepsis, and respiratory distress.

Cystic distention of the lacrimal sac expands the nasolacrimal fossa by pressure erosion, accentuating the posterior lacrimal crest. Nasal extension may cause respiratory distress. Probing of the nasolacrimal duct system, with relief of proximal and distal obstructions as initial treatment, may relieve respiratory distress.[211] However, intranasal marsupialization of the cyst is usually recommended if there is nasal airway compromise. Berkowitz et al.[204] suggest that NLDS cysts may be more common than was previously thought and that any neonate showing signs of NLDS obstruction should have a careful nasal examination to rule out an associated nasal mass. Obstruction to the NLDS may be an unrecognized cause of transient nasal mucosal congestion in the newborn.[204]

CT may help show the classic triad of a cystic medial canthal mass, dilation of the nasolacrimal duct, and a contiguous submucosal nasal cavity mass in the inferior meatus.[212, 213] Endoscopy may show this submucosal

Copyright © 2003, Mosby, Inc. All rights reserved.

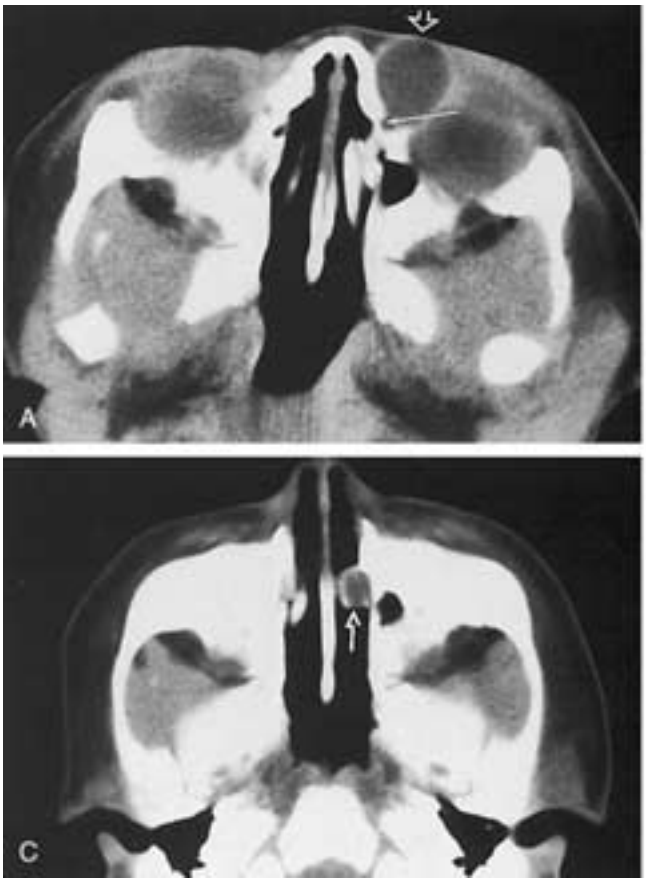

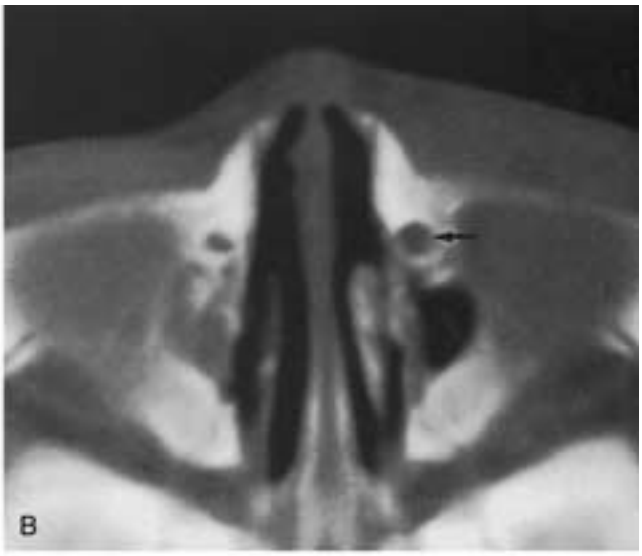

FIGURE 10-33 Congenital NLDS cyst (dacryocystocele) in a 10-day-old infant. **A**, Axial CT scan at the level of the inner canthus shows a low-density well-defined cystic mass (enlarged lacrimal sac) (*open arrow*) intimately associated with the left nasolacrimal fossa (*thin arrow*). **B**, Bone windows image at a level just inferior to the orbit floor shows a dilated left nasolacrimal canal (*arrow*). **C**, Soft-tissue axial image more inferiorly shows a well-defined soft-tissue mass (*arrow*) in the left nasal cavity. Classic triad of a cystic medial canthal mass, dilatation of the nasolacrimal duct, and contiguous submucosal nasal cavity mass in the inferior meatus. (Courtesy of Dr. Susan Blaser, Toronto, Canada.)

VIEW IMAGE

soft-tissue mass in the inferior meatus. Multiplanar MR imaging may better show the skull base and is useful in detecting findings that suggest other causes of medial nasoorbital mass lesions such as meningoceles, encephaloceles, and nasal gliomas. The presence of the classic triad suggests a congenital cyst or mucocele of the nasolacrimal duct, that is, a more distal duct obstruction. Obstructions that are more proximal tend to produce a lacrimal sac mucocele. However, mucoceles of the nasolacrimal duct system may extend either cranially or caudally; that is, mucoceles of the lacrimal sac may protrude downward into the nasolacrimal duct while mucoceles arising in the duct may extend upward to involve the lacrimal sac.[212] Mucoceles involving the lacrimal sac will have, as a clinical component, a mass in the medial canthus. Mucoceles of the distal nasolacrimal duct may present with cyst-like masses at the anteroinferior nasal cavity with a normal lacrimal sac and a superior nasolacrimal duct, because kinking of the thickened, inflamed mucosa in the upper portion of the mucocele prevents extension of secretions (or the mucocele) into the more proximal lacrimal apparatus.[212] The absence of a medial canthal mass therefore does not rule out obstruction of the NLDS or the diagnosis of a congenital NLDS cyst.

A variety of treatments have been described for congenital lacrimal system obstructions including massage (local), probing, irrigation, silicone intubation, and DCR. Although there is no consensus about the timing of or requirement for nasolacrimal probing, such probing is generally successful for treatment of nasolacrimal duct obstruction.[202, 214] However, the rate of failure of probing increases after the patient reaches 12 months of age. After 24 months of age, probing may fail in 67% of patients, and procedure-related complications increase significantly.[214, 215] Silicone intubation may be effective in those children in whom probing has failed; however, this technique also has associated complications such as laceration and erosion of the canaliculi, granuloma formation, corneal erosion, punctal injury, or premature intubation removal.[216] Formerly, DCR became the necessary procedure if silicone intubation failed. More recently, balloon dilation of the nasolacrimal system has been offered as a safe, effective alternative treatment for congenital nasolacrimal drainage obstruction, either as a primary procedure or after failure of probing or silicone intubation.[217, 218] Becker et al.[217] noted an overall postdilation patency rate of 95%, but the study had a limited follow-up period of 4 to 10 months.

Cho et al.[218] recently reported their hospital's treatment of 36 pediatric patients, older than 12 months of age, with congenital lacrimal system obstruction, 16 of whom had fluoroscopically guided balloon dilation (mean age, 33 months). Obstruction was most frequent at the valve of Hasner (15 eyes), with obstruction at the nasolacrimal duct in 2 eyes and at Krause's valve (junction of the lacrimal sac and duct) in 3 eyes; all but 2 eyes had complete obstruction. Seventy percent had had previous treatment with probing, irrigation, or silicone intubation (mean age, 34 months). The authors had a technical success rate (defined as free passage of contrast medium through the entire nasolacrimal system to the nasal cavity) in 95%, with clinical success (resolution of epiphora) in all patients in whom technical success was

Copyright © 2003, Mosby, Inc. All rights reserved.

achieved (mean follow-up of 16 months). Becker et al. performed balloon dilation through the superior canaliculus in an antegrade method after puncturing the obstruction with a probe, while Cho et al. used a retrograde approach, to better avoid canalicular damage, after puncturing the obstruction with a relatively stiff ball-tip guidewire. For both groups of authors, the results of balloon dilation in congenital nasolacrimal system obstruction were far more successful than dilation in adult nasolacrimal obstruction.[219–221] This is probably explained by the differences in pathogenesis. The majority of congenital obstructions are related to developmental anomalies such as a thin, persistent layer of nasolacrimal and nasal epithelial cells at the valve of Hasner.[106, 202, 203, 218] Such anomalies respond well to balloon dilation, with a low incidence of reobstruction secondary to adhesions and fibrosis, in contrast to the epiphora in adults caused by acquired etiologies such as chronic infection and/or inflammation, chronic fibrosis, involutional stenosis, or constriction secondary to the aging process. The one technical failure in Cho et al.'s series was in a patient with obstruction proximal to the valve of Hasner and may have represented a more diffuse nasolacrimal duct stenosis. (See also the section on Dacryocystoplasty and Stent Placement.)

Duplication

Canalicular duplication is usually asymptomatic. DCG will show the supernumerary duct as an opacified streak close to the superior or inferior canaliculus.[88]

MAGNETIC RESONANCE DACRYOCYSTOGRAPHY

Routine MR imaging, with or without intravenous gadolinium, may show disease processes, whether inflammatory or neoplastic, invading the region of the nasolacrimal duct system (NLDS) and the medial canthus. MR imaging was not utilized to assess intrinsic abnormalities of the NLDS proper (canaliculi, lacrimal sac, or nasolacrimal duct), although it could detect significant dilatation of the lacrimal sac or nasolacrimal duct (Figs. 10-20, 10-26, and 10-30). Conventional NLDS contrast media for DCG, whether oil based or water soluble, tended to be viscous and were routinely introduced by cannulation. Although oil based contrast can be identified within the NLDS by its specific fat intensity signal on MR imaging, the inconvenience of cannulation, the increased viscosity and poor miscibility of such contrast agents with tear fluid, and the risks of granuloma formation if extravasation occurs limit the use of MR imaging for assessment of intrinsic nasolacrimal drainage pathology. MR imaging has maintained a complementary role to Digital Subtraction DCG (DS-DCG), with DS-DCG assessing the NLDS and MR/CT assessing the adjacent extraluminal soft tissues. The increased soft-tissue resolution of MR imaging and the anterior location of the NLDS allowing surface coil imaging favor the strengths of MR imaging. In 1993, Goldberg et al.[222] utilized gadolinium (gadopentetate dimeglumine [Magnevist]; Berlex Laboratories, Wayne, New Jersey) in a diluted state, either topically or by cannulation, to visualize directly the canaliculi, lacrimal sac, and nasolacrimal duct. The gadolinium solution, initially diluted 10:1 in sterile saline, was further diluted 10:1 in a commercial liquid tear preparation such as methylcellulose. The prepared 1:100 solution represented a 0.5% concentration or 300 mOsm/L of gadolinium (from the initially commercial available 48.0% concentration). Used topically, the solution was introduced as an eyedrop into the conjunctival cul-de-sac, one drop per minute for 5 minutes immediately prior to scanning, with the patient in a supine position (Fig. 10-34). The authors recommended obtaining imaging within 5 to 10 minutes of introduction of the gadolinium solution. The contrast agent remains within the drainage system for approximately 20 minutes.

More recent studies[223] also suggest an interval of approximately 5 minutes between the final instillation of topical contrast into the conjunctival cul-de-sac and initial imaging to allow adequate passage of contrast through the NLDS (the time interval can be used for coil positioning, system tuning, localizer measurements, etc.). Blinking was encouraged between sequences since eyelid movements affect the lacrimal pump and tear transport.[141, 224] The required data acquisition of various sequences, including pre- and postintravenous contrast sequences, allows approximately 15 to 20 minutes for contrast medium distribution and visualization.

Rubin et al.[225] diluted gadolinium with sterile water to a 300 mOsm/L concentration for direct lacrimal sac infusion. Kirchhof et al.,[19] in an attempt to keep the viscosity of the eyedrops low, used saline instead of methylcellulose in the diluted gadolinium solution. They noted an accelerated passage of the eyedrops through the drainage system, making it difficult to trace the contrast agent in a patent nasolacrimal duct system.

Although topically applied gadolinium can assess functional outflow, canalicular injection of 1 ml of 0.5% gadolinium, using a lacrimal cannula, may be indicated in specific patients. The gadolinium solution in a 0.5% concentration is nonirritating to the ocular surface. MR-DCG has the potential to present information about the NLDS and the adjacent soft tissues, with superb soft-tissue resolution. DS-DCG, however, remains the gold standard for assessing the lacrimal drainage system. MR-DCG may be considered in patients with medial canthal masses or more complex tearing disorders, including congenital, postsurgical, or posttraumatic nasolacrimal obstruction or in those cases where a neoplastic process is suspected, either originating in the NLDS (lacrimal sac), adjacent paranasal sinuses, or orbit.[200, 222, 225] However, some suggest a role for MR-DCG in the assessment of the NLDS because DS-DCG fails to delineate the surrounding soft tissues and MR-DCG has increased sensitivity for detection of contrast more distally within the drainage system. MR-DCG does give detailed functional and morphologic information on the NLDS in a simple, noninvasive manner that does not use ionizing radiation. Newer MR-DCG techniques may be useful for depicting nasolacrimal obstruction, utilizing saline or water, without the use of chemical contrast media.[19, 199, 223, 226, 227]

In a study comparing DS-DCG and topical gadolinium-enhanced MR-DCG, Kirchhof et al.[19] found 100% sensitivity for demonstration of obstruction of the NLDS with either modality. The location of the obstruction was more precisely

Copyright © 2003, Mosby, Inc. All rights reserved.

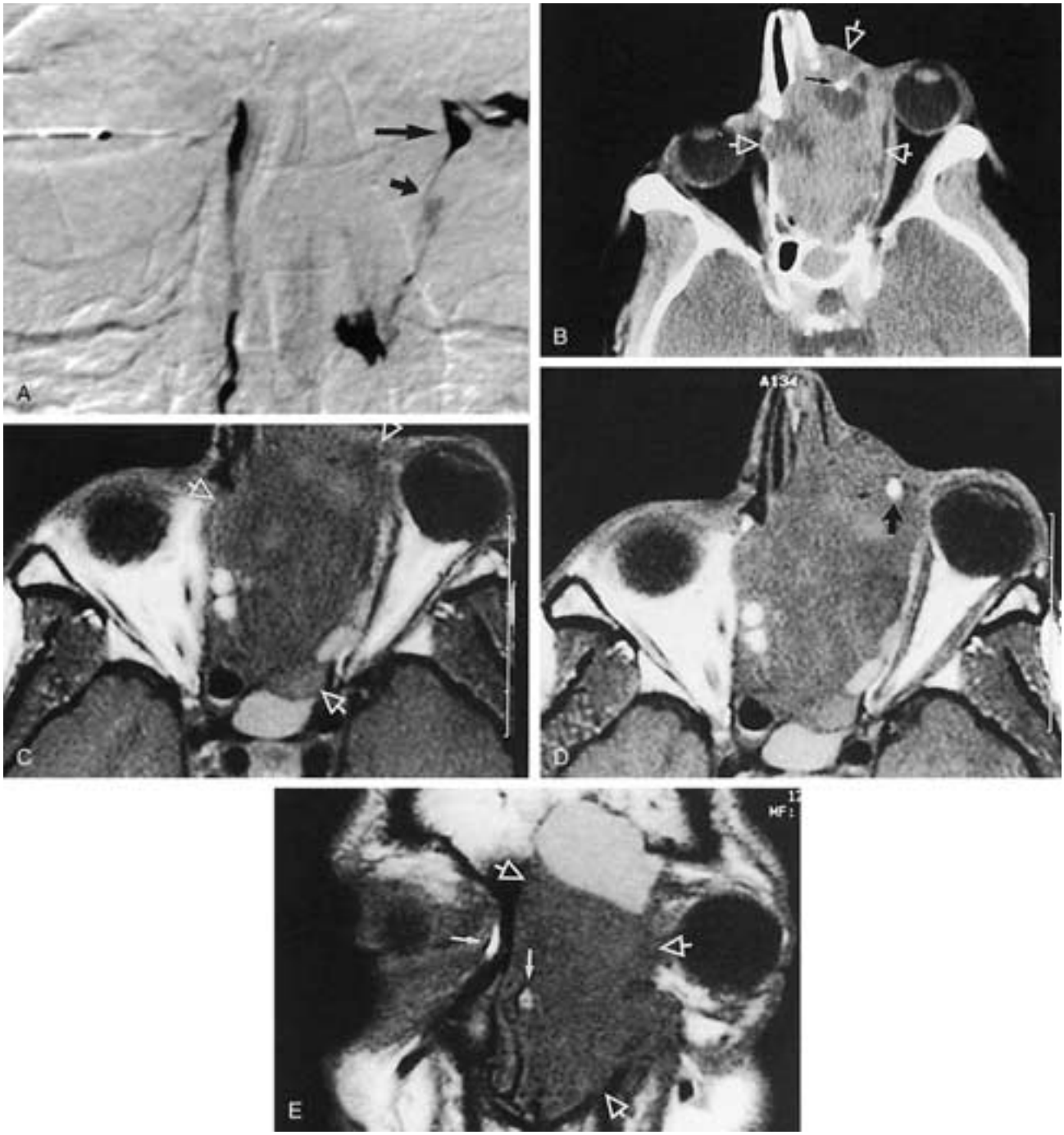

VIEW IMAGE

FIGURE 10-34 MR-DCG. Patient presented with a left inner canthus mass. There was no epiphora. **A**, DCG. Left lacrimal sac and canaliculi are displaced laterally (*large arrow*). Nasolacrimal duct courses inferomedially (*short arrow*) to drain into the nasal cavity. **B** to **E**, CT-DCG and MR-DCG performed to better show the relationship of the mass to the NLDS. **B**, Axial image of CT-DCG shows a large nasoethmoid mass (*open arrows*) invading the medial left orbit and inner canthus. NLDS with contrast medium (*thin arrow*) is seen coursing through the mass just anterior to the necrotic component of the mass. **C**, Axial T1-weighted pregadolinium image displays a large mass (*arrows*) within the nasal cavity and ethmoid sinuses, extending to the left inner canthus and displacing the left orbit contents laterally. **D**, Axial T1-weighted image with topical gadolinium (0.5% concentration) at the same level as **C** easily displays the left NLDS (*arrow*) surrounded by a mass. **E**, Coronal T1-weighted image shows a large left nasoethmoid mass (*open arrows*). Topical gadolinium is seen within the normal right lacrimal sac (*horizontal arrow*) and left nasal cavity (*vertical arrow*). Pathology: nasoethmoid squamous cell carcinoma.

Illustration continued on following page

Copyright © 2003, Mosby, Inc. All rights reserved.

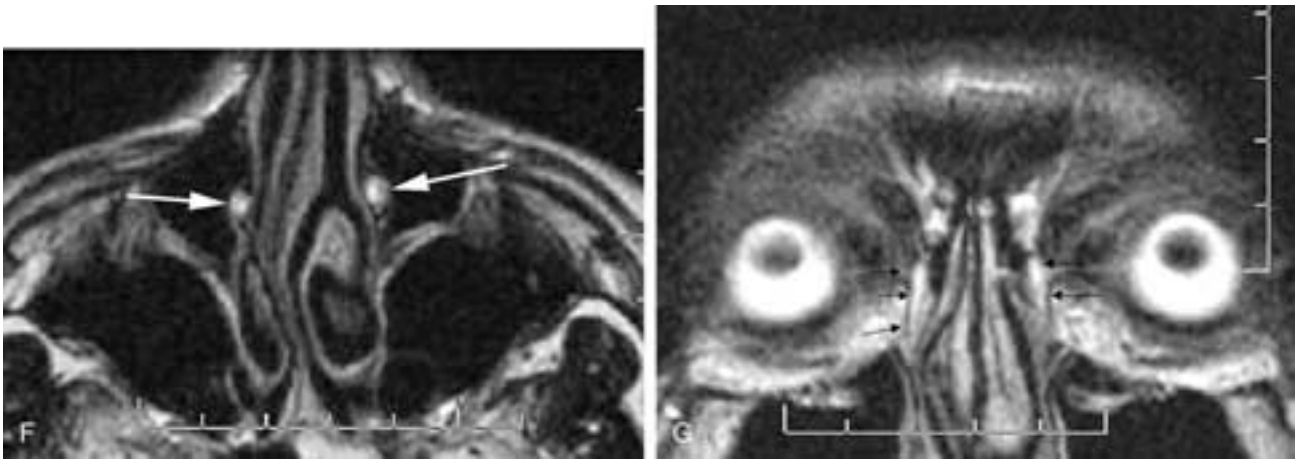

VIEW IMAGE

FIGURE 10-34 *Continued.* **F** and **G**, Second patient. Topical saline used as contrast medium. One or 2 drops per minute instilled into the conjunctival sac for 4 to 5 minutes prior to scanning may better demonstrate the lumen of the NLDS (*arrows*) on axial (**F**) and coronal (**G**) T2-weighted sequences. The saline flows more quickly through the drainage system than topical gadolinium, especially if the gadolinium is partially diluted with artificial tear drops.

detected on MR-DCG, with the contrast material traced further distally with MR-DCG than with DS-DCG in 3 of the 11 patients. MR-DCG, however, like other imaging modalities, may also diagnose NLDS obstruction too proximal due to accumulation of thickened mucus within the duct system. This problem may be avoided by performing irrigation and careful expression of the lacrimal sac prior to any DCG-type, contrast-enhanced NLDS imaging study. In contrast to the increased signal of contrast medium, mucus was isointense with mucosa on T1-weighted images and slightly hypointense on T2-weighted images. A fluid-fluid level may be seen between the contrast agent and mucus on coronal T1-weighted images.[19] MR-DCG may better distinguish soft-tissue obstruction from bone obstruction, a factor in deciding whether dilatation of a stenosis (dacrycystoplasty) is feasible or whether a surgical procedure (DCR) will be needed.

MR-DCG may better assess the amount of lacrimal sac mucosa present and available for mucosal flap manipulation (lacrimal sac to nasal mucosa anastomoses needed for external DCR surgery), with normal sac mucosa well delineated on T2-weighted, fat-saturated sequences. Although both DS-DCG and MR-DCG displayed the obstruction of the lacrimal sac 1 year after DCR in one patient, only MR-DCG directly displayed the postoperative cicatricial scarring.[19] DS-DCG and MR-DCG were equivalent in assessing size and filling defects within the lacrimal sac, a factor of importance for endoscopic intranasal DCR considerations, since scarring and dacryolithiasis are significant prognostic factors and potential contraindications. DS-DCG was superior in only one patient in whom MR-DCG failed to delineate fistulas distal to the nasolacrimal sac.[19]

Fat-saturated MR imaging sequences were preferred, with T2-weighted images considered superior to T1-weighted and with the fat-saturated sequences allowing better visualization of the contrast agent. Coronal slices (obtained at 70° to the hard palate to be parallel to the course of the lacrimal sac–nasolacrimal duct) were considered more helpful. Axial images were complementary and were preferred for measurement of the lumen of the lacrimal sac or nasolacrimal duct.[19] Acknowledging the additional information about the surrounding soft tissues, Kirchof et al.[19] noted that both MR-DCG and DS-DCG reliably depicted obstructions of the NLDS, but because of the increased expense of MR-DCG and the limited experience in differentiating between obstruction and stenosis of the NLDS, DS-DCG should be the first imaging study. MR-DCG should function as a complementary study except in the pediatric age group. In epiphora patients under age 6, MR-DCG, noninvasive and free of radiation, can be performed with sedation only (in contrast to DS-DCG, which is performed under general anaesthesia) and should be the primary imaging modality for assessment.

In Caldemeyer et al.'s[199] study of CT-DCG and MR-DCG utilizing topical contrast material, CT-DCG, with iopamidol (Isovue 200; Squibb Diagnostics, Princeton, New Jersey) and MR-DCG with normal saline, respectively, placed into the conjunctival cul-de-sac of healthy normal volunteers, CT better displayed the finer drainage system components better than MR-DCG. CT also displayed the adjacent bone anatomy.

In a study comparing DS-DCG and MR-DCG, Yoshikawa et al.[226] concluded that topical contrast-enhanced MR-DCG by itself may not be sufficient when precise information, including the length of the stenosis and the degree of narrowing is necessary to plan for DCG or nasolacrimal stenting. MR-DCG findings were not compatible with DCG findings in half of the 14 patients. On initial phantom studies, all sequences could visualize ducts equal to or smaller than 0.7 mm in diameter filled with contrast material. The lower spatial resolution of MR-DCG (11 cm rounded receiving surface coil, body coil for transmission) compared to DS-DCG and the absence of pressure (topical application) may result in an overexpression of stenosis or in interpreting stenosis as an obstructive lesion.[226] Cannulation MR-DCG may help eliminate these limitations.

Copyright © 2003, Mosby, Inc. All rights reserved.

Hoffman et al.[223] noted difficulties in detecting contrast medium (diluted gadolinium topically placed) in the most distal part of the NLD in some patients with mild epiphora, yet there was filling of the lacrimal sac and proximal duct. They postulate a physiologic obstruction at the distal end of the nasolacrimal due to resistance of the valve of Hasner. Similar findings have been previously noted in DSG,[144] with long transport delays (30 minutes or longer) even in asymptomatic eyes. Circumstances causing increased production of tears or minimal narrowing of the nasolacrimal duct may contribute to epiphora. The marked variation in tear transport times limits the assessment of the functional MR-DCG exam and must be interpreted with clinical and other imaging findings. For these reasons, DCG remains the standard exam for assessing obstructions of the NLDS.[223]

Recent MR-DCG studies have assessed other solutions (with associated MR technique alterations) to augment or possibly replace gadolinium as a contrast agent.[199, 226, 227] Yoshikawa et al.[226] combined T1-weighted (transverse thin slice) spin-echo and 3D-T1 fast field echo (FFE) sequences utilizing a topical diluted gadolinium solution, (with reconstructed Maximum Intensity Projection (MIP) images projected in the anteroposterior direction for the 3D-FFE sequence) as well as two T2-weighted sequences. The T2-weighted sequences included a transverse thin-slice fast spin echo (FSE) sequence and a coronal thick-slice section T2-weighted projected image, with the coronal sequences utilizing a topical saline solution rather than the diluted gadolinium solution. MR-DCG diagnoses were made by combining the findings on the saline-enhanced T2-weighted and gadolinium solution-enhanced T1-weighted images. The transverse images confirmed the diagnosis from the projected images. If discrepancies were noted between the T2-weighted projected images on the FFE-MIP images, the narrowed site was determined by the gadolinium-enhanced FFE-MIP images. In a preliminary study of 10 normal volunteers, the lacrimal sacs and proximal portion of the nasolacrimal ducts were seen in all patients; however, the caudal aspects of the nasolacrimal ducts and the canaliculi were not visualized on most sequences in approximately half of the cases. The inability to visualize the caudal portions of nasolacrimal ducts in normal volunteers may be due to the relatively fast flow in the narrowing lumen of the caudal duct or to an increase in the viscosity of the intraluminal fluid. The long echo time of the T2-weighted projected images may need to be adjusted to each patient's circumstance and may limit the discrepancies seen between the T2-weighted projected images and the FFE-MIP images. In the clinical study, inconsistent findings were also noted between the T2-weighted projected images and the FFE-MIP images or with the DS-DCG findings.[226]

The lacrimal sac residual lumen volume and the condition of the mucosa were better seen on the T2-weighted sequences. Mucosal thickening, including low signal intensity mucosal fibrous thickening, was noted on T2-weighted sequences, with intravenous gadolinium-enhanced images offering further information if required. The T2-weighted sequences also displayed the residual caudal lumen of an obstructed or narrowed site, which may help predict the effectiveness of conservative treatments (e.g., irrigation therapy). Despite limitations, combined complementary T1- and T2-weighted sequences, with respective diluted gadolinium or normal saline solutions as a less invasive study, may offer enough morphologic and functional information in the NLDS to have a screening role or potential to be the imaging examination of first choice for patients with lacrimal outflow disorders.[226]

Takehara et al.[227] have implemented MR-DCG techniques utilizing a less viscous combined normal saline–lidocaine hydrochloride solution as a contrast medium to emphasize the dynamic behavior of the fluid within the lacrimal pathway. The authors performed all studies via thin plastic lacrimal cannulas placed into the inferior lacrimal canaliculi bilaterally, with a Y-connector allowing bilateral simultaneous injection. Axial and coronal T2-weighted images were obtained using FSE or half Fourier single-shot FSE sequences without fat saturation. With the patient already in place within the gantry, the dynamic MR-DCG was performed while the patient injected the previously prepared combined saline-lidocaine solution by manual compression of the barrel of a single syringe. Thick-slice (20 to 30 mm), heavily T2-weighted images were repeatedly obtained during the injection. The section of study included the canaliculi, lacrimal sac, and nasolacrimal duct. Acquisition time for each image was less than 2 seconds. During the injection, imaging was repeated for 3 minutes with intervals of 4 to 5 seconds. Overall MR imaging time, including that for preliminary conventional T1- and T2-weighted sequences, was less than 20 minutes.

The solution's lower viscosity better filled the narrowed lumen of the NLDS. MR-DCG can be monitored and viewed during the course of the injection, so the patient can be directed to increase the injection rate if filling is incomplete or delayed. MR-DCG offers high temporal resolution, allows dynamic evaluation of fluid flow in the NLDS, and will not potentially miss the image that best demonstrates the obstructive segment. This concept parallels the advantages of DS-DCG compared to radiographic distention DCG and offers a dynamic capability superior to that of CT, without the radiation exposure. Such dynamic assessment, however, requires the facilitating solution to be introduced through lacrimal cannulas. Because of the decreased viscosity of the solution utilized, such cannulas, however, may be thinner and softer, allowing more comfortable, safer cannulation of the canaliculi.

In contrast to other MR-DCG techniques that are stationary or slow-flowing, this MR-DCG uses water injected into the lacrimal draining system as a substitute for other contrast media. The imaging strategy involves the acquisition of a series of heavily T2-weighted images since fluid-filled nasolacrimal ducts have long longitudinal and transverse relaxation times and will display high signal intensity on T2-weighted images. However, on these hydrographic images, everything looks black or white. The nasolacrimal abnormalities are evaluated indirectly using ''all-or-nothing'' images. The FSE sequence used was relatively immune to local magnetic field inhomogeneity (air in the maxillary sinus, dental prosthesis).[227] Dynamic MR-DCG, as a form of hydrographic imaging, does not reflect any soft-tissue contrast. Additional T1- and T2-weighted sequences are required for delineation of soft tissue (e.g., the presence of mucosal thickening or neoplasm). Half Fourier SS-FSE or FSE imaging using multiple thin slices provides static but detailed information. As also

Copyright © 2003, Mosby, Inc. All rights reserved.

noted in more static MR-DCG studies with saline placed topically into the conjunctival cul-de-sac and imaged with heavily T2-weighted sequences, mucosal disease of the NLDS or adjacent paranasal sinuses can make visualization of the NLDS more difficult.[199] Comparison of images before and after contrast administration is important to distinguish mucosal thickening from normal flow of saline. Image subtraction may be feasible. This technique is probably limited in detecting dacryolithiasis. Further investigations are necessary to assess the true potential and capabilities of dynamic MR-DCG.

DACRYOCYSTOPLASTY AND STENT PLACEMENT

Balloon Dacryocystoplasty

See the previous section on Congenital Atresia for further comments on dacryocystoplasty and stents. A small-bore soft[228] or ball-tip[229] guidewire (0.018 inch diameter) is introduced into the superior punctum and guided under fluoroscopic control through the NLDS into the inferior meatus. With nasal endoscopic assistance or lacrimal instruments and lateral fluoroscopy, the guidewire, which prefers to pass toward the nasopharynx, is directed through the nares. A hook was devised to grasp the guidewire under fluoroscopic control, shortening the procedure time and eliminating the need for nasal endoscopy.[230] A deflated angioplasty balloon catheter is introduced in a retrograde direction over the guidewire (in contrast to Becker and Berry's[231] initial report of antegrade balloon dilation of the nasolacrimal duct's nasal ostium). Proper positioning and dilation are controlled by fluoroscopic guidance, with injection of radiographic contrast media to inflate the balloon catheter (Figs. 10-35 and 10-36). The tibial arterial balloon angioplasty catheter (Cook Inc., Bloomington, Indiana), which dilates to 3 to 4 mm in diameter, is useful for Dacryocytoplasty (DCP). Different methods of dilation have been described, with Munk et al.[228] and Janssen et al.[219] recommending two or three dilations of 20 to 30 seconds each, while Song et al.[220] recommended that each dilation last for 5 minutes. Lee et al.[229] found that the soft tip and lack of tapering of the Balt balloon (Montmorency, France) made it preferable for dilations. After the final dilation, the balloon is withdrawn inferiorly and the guidewire superiorly (to avoid having the stiff segment of the guidewire pass through the area of recent dilation). Song et al.[220] leave the guidewire in place and perform DCG via the inferior punctum to verify passage of contrast medium. Balloon catheters with gradually increasing calibers ranging from 3 to 5 mm may be used. An irrigation of the NLDS with sterile saline, with or without dexamethasone, through the dilation catheter and/or flushing through the superior canaliculus is performed at the end of the procedure. Dexamethasone and antibiotic (gentamycin) eyedrops may be prescribed for 1 week postdilation, as well as acetylcysteine eyedrops if abundant mucus was present in the NLDS.[219] Blood clot formation in the NLDS, especially the dilated lacrimal sac, during or after balloon dilation may be a cause of treatment failure. Song et al.[220] noted such filling defects in 3 of 36 eyes in which DCG was performed immediately following dacryocystoplasty (DCP).

Janssen et al.[219] modified the Munk et al.[228] technique. In cases of complete obstruction in which reflux of contrast medium occurred through the opposite canaliculus, they recommend that DCG be repeated after occluding the noncannulated canaliculus by wedging within it a nonconducting lacrimal catheter. This may allow a small amount of contrast medium to outline an area of stenosis. For the DCP procedures, they favor a nontraumatizing 0.025 inch guidewire with a flexible curved tip (Terumo; Tokyo, Japan) to more easily negotiate the sharp curve between the common canaliculus and the lacrimal sac. Balloon catheter placement is restricted to the lacrimal sac or more caudally to prevent damage to the canaliculi. A balloon catheter with the balloon placed at the catheter tip allows dilation of stenoses high in the lacrimal sac and does not require the catheter tip to be passed into the common canaliculus.[221]

The study is performed under local anesthesia. Patients may experience some mild discomfort in the region of the medial canthus for 1 to 2 days after the procedure and a slightly blood-stained nasal discharge for 1 to 3 days. Evaluation of epiphora may be graded according to a subjective scale, as suggested by Munk et al.[228] This scale has proven useful in allowing comparisons in the epiphora patient population over time, as well as in comparing various patient groups and assessing degrees of success or benefits of treatment. In the system, Grade 0 is no epiphora; Grade 1 is occasional epiphora that requires drying or dabbing less than twice a day; Grade 2 is epiphora that requires drying 2 to 4 times a day; Grade 3 is epiphora that requires drying 5 to 10 times a day; Grade 4 is epiphora that requires drying more than 10 times a day; and Grade 5 is constant tear overflow. There is no standardized definition of success, with some results referring to Grade 0 or Grade 1 as a successful outcome posttreatment, while others may define an improvement of two or more grades as success. Still others may define Grade 2 to Grade 5 as poor outcomes despite improvement in the pretreatment status.

DCP may have a role in a defined patient population. Probing alone is frequently unsuccessful and has a greater risk of creating a false passage. In contrast to dilating probes, the use of balloon dilation offers radially directed dilating forces that are less likely to create severe tears. Fine guidewires of approximately one half the caliber of probes, with soft tips, especially when placed into a strictured or occluded NLDS, offer less risk of complication. Longitudinal shear forces by the larger catheters are reduced by the presence of a guidewire.

DCP is easily performed as an outpatient procedure, obviating the need for general anesthetic or controlled hypotension (used to control hemorrhage) and the relative invasiveness of DCR. More recent performance of DCR surgeries with local assisted anaesthesia and monitored sedation has improved operative field visibility and minimized blood loss while avoiding the hazards of general anaesthesia.[232] Still, the advantages of DCP, with diminished morbidity, cost, and operating room time, are obvious. No facial scarring or disfigurement occurs with DCP, and the procedure, if unsuccessful, does not preclude future DCR.

Copyright © 2003, Mosby, Inc. All rights reserved.

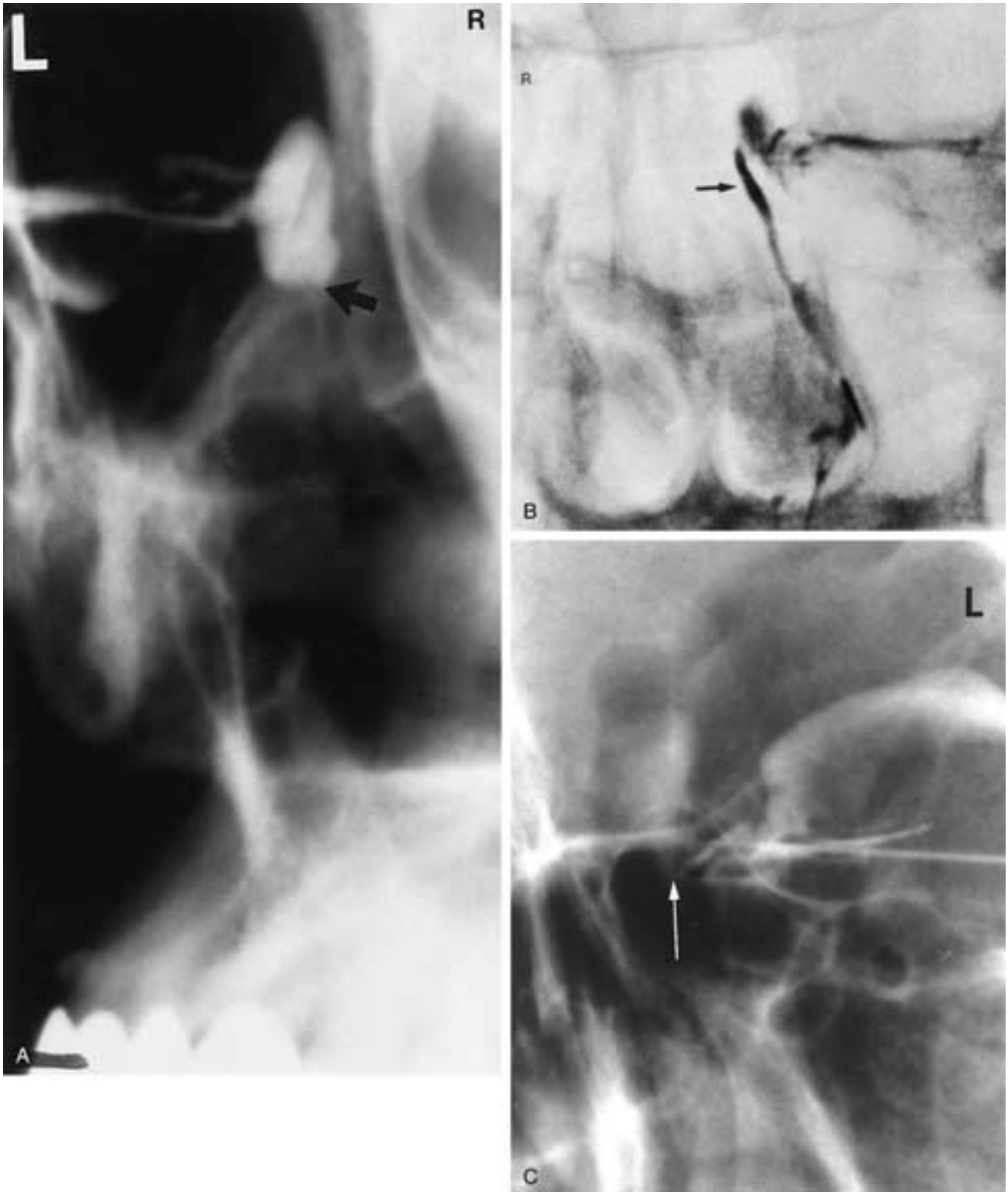

VIEW IMAGE

FIGURE 10-35 Balloon DCP. **A** and **B**, Case one. **A**, Predilatation DCG, viewing the left NLDS from a lateral oblique projection, shows a dilated lacrimal sac with complete obstruction (*arrow*) at the junction with nasolacrimal duct. **B**, Postdilatation DCG viewed anteriorly shows a normal-sized lacrimal sac (*arrow*) with spontaneous drainage through the nasolacrimal duct into the nasal cavity. **C** and **D**, Case two. **C**, Predilatation DCG (superior canaliculus injection) shows complete obstruction of the common canaliculus (*arrow*) with reflux into the inferior canaliculus and conjunctival sac.

Illustration continued on following page

Copyright © 2003, Mosby, Inc. All rights reserved.

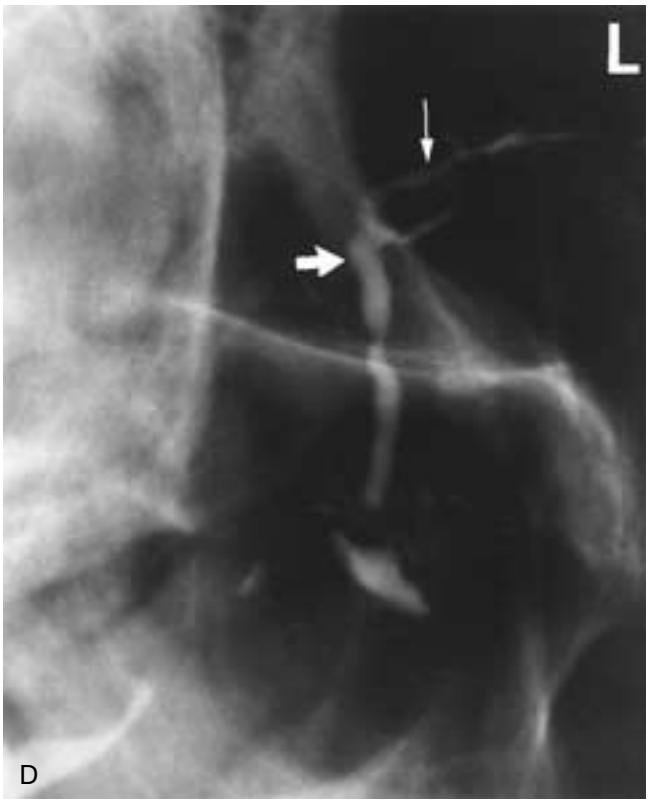

VIEW IMAGE

FIGURE 10-35 *Continued.* **D**, Postdilatation film (superior canalicular injection) (*vertical arrow*) shows contrast material draining through the lacrimal sac (*horizontal arrow*) and nasolacrimal duct into the nasal cavity. (Courtesy of Dr. Peter Munk, Vancouver, Canada.)

The use of ionizing radiation for balloon DCP (versus surgical treatment of epiphora) is a disadvantage to be addressed and controlled, to offer minimal radiation exposure since the eye, including the radiosensitive lens, remains in the field of the primary x-ray beam. Mean radiation doses to the lens of the treated eye varied from 1.37 mGy[233, 234] to 4.6 mGy[235, 236] and from 5.43 mGy[233, 234] to 38.5 mGy[235, 236] for the contralateral eye. In both series, the treated eye was always closer to the image intensifier, with the higher mean radiation dose values to the contralateral lens, closer to the x-ray tube. The measured dose to the treated eye may be reduced by limiting the number of digital images obtained. The dose to both eyes, especially to the untreated eye, can be limited by tight collimation, restricted to the treated eye, especially in the posteroanterior images. Phantom studies measured the dose to the untreated lens as only 25% of that to the treated eye (lens) on such collimated posteroanterior images.[233, 234] Much of the DCP procedure is performed using lateral fluoroscopy and digital image acquisition, such that radiation to the contralateral lens cannot be avoided. Approximately 90% of the overall radiation dose to the lens of the untreated eye, closer to the x-ray tube, results from lateral projection versus 65% for the lens of the treated eye.[236] Restricting lateral imaging to fluoroscopy and abandoning such digital image acquisition, the major source of the higher lens dose, will further reduce the lens dose.[236] DCG performed before and after DCP, with the exception of complex cases, should similarly be restricted to posteroanterior projection images.

Although preliminary, Munk et al.[228] experienced very favorable DCP results, with DCPs being technically successful in 16 of 18 cases, with improved epiphora in 13 (complete resolution in 11) patients and no change in 3 patients. Follow-up, however, was limited to 6 months maximum post-DCP, and only four patients had follow-up DCG, all within 3 weeks of the initial procedure. No correlation between degree of epiphora and severity of stenosis on the preprocedure DCG was noted. In the cases of partial stenosis, no change was noted in the appearance of the postdilation DCG, and Munk et al. anticipated that reproducibility of the DCG would be difficult since the nasolacrimal duct, when patent, is an open system, decompressed from below. Munk et al. did not have trouble passing the guidewire in the two cases of complete obstruction. They felt, however, that tight stenosis of the common canaliculus may represent an absolute or relative contraindication to DCP.

Song et al.[220] also noted difficulty defining success (or failure) in interpreting the results. Full dilation of obstructed areas may be noted technically, with the epiphora not resolving. They postulate that placement of stents may be useful in such patients. Song et al.[220, 237, 238] and Lee et al.[229] have followed patients for a more extended period. In further follow-up of those initial successes (in 56% of dilations) assessed at 7 days, 45% showed recurrence of symptoms at 2 months.[220] Although Lee et al. achieved 71% and 51% initial technical and clinical success rates for partial and complete obstruction, respectively, the 2-year clinical patency rates fell to 20% and 25%, respectively. The grade of stenosis did not influence the duration of patency. In assessing their initial results, technical success but clinical failure was noted in 29% and 44% of patients with partial and complete obstruction, respectively, for a 40% overall clinical failure. These patients tended to have clinical improvement of epiphora for 2 to 3 days only. No technical failures were noted in the partial occlusion subgroup, while 5% of those with complete obstruction were technical failures. Dilations of common canaliculus obstructions were more technically difficult. The authors avoided dilation of the superior and inferior canaliculi lateral to the common canaliculus to avoid damage to the canaliculi. Patency rates for complete obstructions remained the same from 6 months to 2 years post-DCP follow-up, while those for partial occlusion decreased such that there was no significant difference between the long-term patency rates of occlusions and stenosis.[229]

Janssen et al.[219] reported 90% substantial success in DCP treatment of 21 nasolacrimal duct system (NLDS) with severe epiphora followed for 14 to 70 weeks. These authors speculate that the finer atraumatic, nonmetallic guidewire (Terumo) and a dilated balloon diameter not exceeding 3 mm (vs. 3 to 4 mm for Munk et al.[228]) and 4 to 5 mm for Song et al.[220] may explain the difference in results. In normal adults, the diameter of the membranous nasolacrimal duct is 4 to 6 mm. Therefore, a larger catheter whose caliber is greater than 3 mm may traumatize the nasolacrimal duct or the rich venous plexus between the membranous portion of the duct and the bony canal.[219]

Continued follow-up of fluoroscopically guided balloon

Copyright © 2003, Mosby, Inc. All rights reserved.

DCP for recanalization of obstructed NLDS, as a viable alternative to operative treatments, has led to further scrutiny of such procedures due to some disappointing longer-term results, despite its initial technical successes.[219, 220, 228, 229, 239–241]

Various hypotheses have been put forward to improve results. Primary placement of stents, initially in conjunction with balloon DCP[237, 238, 242] and subsequently obviating balloon DCP,[230] were suggested. Others have suggested technique alterations to navigate the difficulties presented by canalicular or upper lacrimal sac strictures. Suggestions have been made to address the challenges of recanalizing the

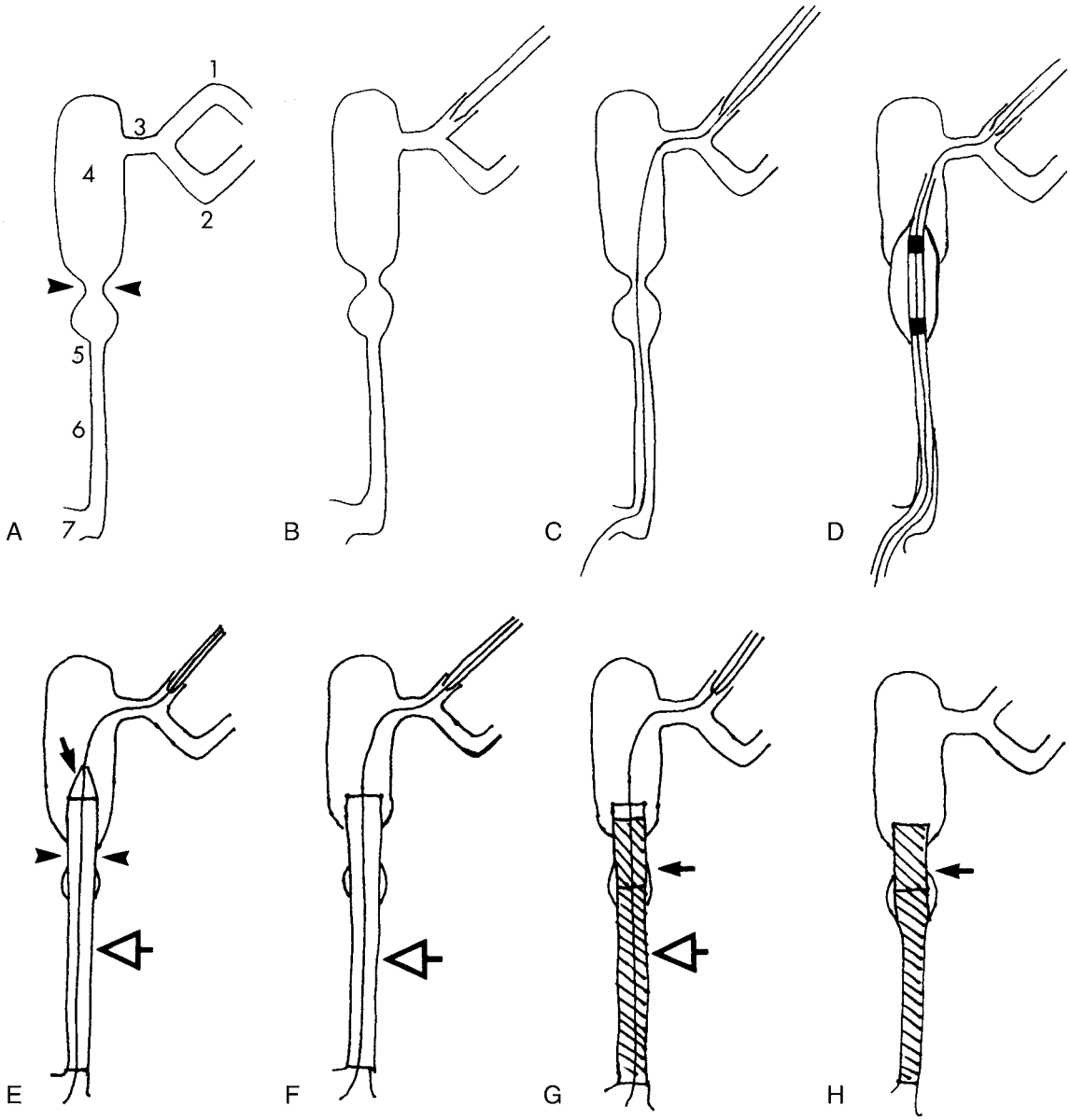

VIEW IMAGE

FIGURE 10-36 DCP technique. **A**, Normal NLDS. *1*, Superior canaliculus; *2*, inferior canaliculus; *3*, common canaliculus; *4*, lacrimal sac; *5*, junction of the lacrimal sac and nasolacrimal duct; *6*, nasolacrimal duct; *7*, valve of Hasner; *arrowheads*, stenosis in the lacrimal sac. **B** to **D**, Balloon DCP technique. **B**, Lacrimal catheter inserted into the superior canaliculus. **C**, Guidewire inserted through a lacrimal catheter in an antegrade manner and seen exiting through the valve of Hasner and manipulated through the nares. **D**, Balloon catheter inserted in a retrograde manner over a guidewire to an appropriate point to dilate the stenosis. (Modified from Janssen AG et al. Dacryocystoplasty: treatment of epiphora by means of balloon dilation of the obstructed nasolacrimal duct system. Radiology 1994;193:453–456.) **E** to **H**, Polyurethane stent technique. **E**, Steps **B** and **C** as above. No. 6 French sheath (*open arrow*) with dilator (*oblique arrow*) is passed retrograde over a guidewire through the lacrimal sac stenosis (*arrowheads*). **F**, Dilator removed from the sheath, which remains in place. **G**, Stent (*diagonal lines and horizontal arrow*) introduced retrograde over the guidewire into the sheath beyond the stenosis using a stent loader and pusher catheter (not shown). **H**, Sheath withdrawn while the stent is held in place by the pusher catheter. Once the stent is freed from the sheath, the pusher catheter is also withdrawn through the inferior nares, and the guidewire is withdrawn through the superior canaliculus. Stent extends inferiorly into the inferior meatus to ease retrieval if desired. (Modified from Song HY et al. Nonsurgical placement of a nasolacrimal polyurethane stent. Radiology 1995;194:233–237.)

Copyright © 2003, Mosby, Inc. All rights reserved.

more resistant occlusions extending the length of nasolacrimal duct. Such technical factors include flexible, steerable guidewires,[219, 221, 240, 243] hydrophilic-coated wires,[219, 221] nonmetal guidewires,[221] small-caliber catheters 2 to 3 mm in diameter,[221, 243] versus 3 to 4 mm catheters[228] or 4 to 5 mm catheters,[229, 240] decrease or absence of a catheter tip beyond the balloon,[221] shorter inflation period of 20 to 30 seconds,[228] 30 seconds,[221] 1 to 2 minutes,[243] versus 5 minutes,[229, 240] guiding cannulas,[221, 243] a Ritleng probe (through which guidewires may be passed),[224] and canalicular irrigation for flushing out or dislodging possible clots.[220, 221, 240, 245] The reason for consideration of the above factors is the desire to minimize ductal trauma as a factor in recurrence of epiphora, stenosis, or obstruction. Selection of the balloon catheter diameter and timing of inflation should be enough to tear the fibrotic component of the obstruction or stenosis, yet the catheter should be small enough in caliber or the duration of inflation should be short enough to prevent damage to the NLDS. The variety of options suggests that there is no universal solution. Personal preferences and individual choices are noted in the literature.

Strictures of the canaliculi and upper lacrimal sac can restrict the passage of steerable guidewires.[243] The floppy tip of the wire (of flexible systems) may become stuck or may coil in the small lumen of the lacrimal sac and not advance into the nasolacrimal duct. The relatively stiff ball-tip wire,[220] by elevating its handle superiorly, allows ease of manipulation of its tip into the lacrimal sac and the junction with the nasolacrimal duct but is more difficult to pass through stenotic lesions, increasing the risk of ductal wall damage or false passages.[243] Yet such stiff wires may be necessary to advance through the rigidity of complete obstructions of the nasolacrimal duct, where forceful advancement may be required.

Berkefeld et al.,[243] exploring beyond the technical issues in assessing their results in 85 patients treated with balloon DCP, looked at associated clinical factors that may predict reobstruction. They found recurrent episodes of active dacryocystitis; dacryolithiasis filling defects on initial DCG; posttraumatic strictures with bone canal narrowing; or long-segment rigid occlusions of the nasolacrimal duct, all factors in reobstruction, with 89% and 94% 12-month patency rates for focal stenoses or occlusions, respectively, if the above factors were not present. Otherwise, the reobstruction rate was 46% in patients with one of the above factors present.

In patients with active inflammatory changes, the potential benefit from removal of tight stenoses is limited to the short term, with active dacryocystitis involved with restenosis. Similarly, dacryolithiasis was seen to be a common cause of reobstruction after DCP, with filling defects seen on the preliminary DCG felt to be a contraindication to DCP. Posttraumatic stenoses frequently have bony narrowings that are too rigid for balloon dilation, with poor long-term outcomes and secondary inflammatory changes. Patients with multiple or diffuse stenoses or chronic (rigid) occlusions of the entire length of the nasolacrimal duct tend to have early reobstruction, probably secondary to the unavoidable trauma to the ductal wall and reactive mucosal overgrowth.[243] The high recurrence rates, between 45% and 80% in various series,[220, 229, 243] suggest a limited value for balloon DCP. While stent placement may improve technical success rates and midterm patency rates, the long-term implantation of such stents has been associated with recurrence rates as high as 64%, depending on the location of the obstruction.[246] The operative treatment of postsaccal stenosis has consistently shown long-term success rates of 85% to 90%[30, 107–110] for external DCR and at least 75% for endonasal endoscopic DCR.[109] Results are independent of the cause or length of the stenotic lesion, suggesting that DCR, either external or endoscopic in approach, is the preferred approach to these patients with factors suggesting a high rate of reobstruction. For those patients with focal partial obstructions, either junctional (lacrimal sac–nasolacrimal duct) or within the nasolacrimal duct, or with short-distance occlusions of the distal nasolacrimal duct, clinical long-term success with balloon DCP may be realized (80% or more) as a treatment preferable to surgery or stent placement.[243]

Janssen et al.,[221] in noting the varying results of DCP obtained by different authors, felt that the differences may be due to different DCP techniques, as well as patient selection.[239] Lee et al.'s[229] results may have been negatively affected by the inclusion of posttrauma obstruction and possible deformations of the bony lacrimal canal, as well as the inclusion of patients with stenosis of the common canaliculus. Similarly, Ilgit et al.[240] included stenotic common canaliculi in their series. Janssen et al.[221] excluded patients with canalicular stenoses from their series and included patients with posttraumatic obstruction, but only after CT was utilized to evaluate the bony lacrimal canal. Other exclusion criteria included acute dacryocystitis, tumors, sarcoidosis, and Wegener's granulomatosis. No relationship was noted between the duration of epiphora (more or less than 1 year) and initial or long-term success.[221] More interestingly, and in contrast to the findings by Berkefeld et al.,[243] the length of obstruction (short obstruction limited to one level versus obstructions extending to two, three, or four levels) also showed no relationship to initial or long-term success.[221] However, patients with partial obstruction had greater initial and long-term success than patients with complete obstruction.[221] Others also noted these findings.[229, 240, 245]

The mechanism of DCP in the treatment of epiphora due to lacrimal obstruction is relatively unknown. The majority of treated patients have PANDO. As outlined by Linberg and McCormick,[161] the membranous nasolacrimal duct has a loose structure of connective tissue around the stratified columnar epithelium of the lacrimal duct. Within this loose tissue, a venous plexus, lymphocytes, and some fibrous tissue were found. In patients with acquired obstruction, they noted vascular congestion, lymphocytic infiltration, and edema causing compression of the duct, in its earlier phase by active chronic inflammation along the entire length of the narrowed nasolacrimal duct. Such stenosis leads to pooling of tears and infection, which, in turn, increases inflammatory edema and eventually gives rise to fibrosis. At the same time, infection may cause reflex hypersecretion of tears. Janssen et al.[221] postulate that the success of DCP (or DCR) does not necessarily mean long-term patency of the nasolacrimal duct, but rather the breaking of this cycle of obstruction and infection. Balloon dilation may resolve the obstruction but does not remedy the primary inflammatory

Copyright © 2003, Mosby, Inc. All rights reserved.

process, which is likely to affect the recurrence of obstruction, with the dilatation crushing the mucosa of the duct at its stenotic segment, causing the development of a further inflammatory reaction and hemorrhage. Use of topical or systemic anti-inflammatory agents to reduce the early inflammatory reaction, flushing saline with or without antibiotics to dislodge clots, and intubation (or stents) to limit fibrosis and ensure patency have been attempted.

More recently, Kuchar and Steinkogler[247] have performed antegrade dilation of complete postsaccal stenosis patients, assessed by canalicular irrigation and transcanalicular endoscopy, using a Lacricath balloon catheter. Immediate postdilatation irrigation and endoscopy provided evidence of the reopened passage. Silicone intubation, for splinting the reopened stenoses, felt to be important for permanent patency during the initial scarring process, was performed immediately after the dilatation, with the tubes kept in place for 3 to 6 months. Such complementary postdilation silicone intubation, if consistently able to improve long-term patency rates, may offer an alternative to patients currently undergoing stenting. A 1 year patency rate of 73.3% was observed. Antegrade balloon dilatation, in conjunction with transcanalicular endoscopy, was felt to be easy and less expensive, without the need for more expensive imaging equipment the risks of radiation exposure.

The common canaliculus is second only to the lacrimal sac–nasolacrimal junction as the most common site for lacrimal drainage system obstruction.[47] In some patients, for canaliculodacryocystorhinostomy (with partial resection of the canalicular segment), silastic or rubber tubes are surgically placed for several months.[31] The standard surgical treatment of epiphora due to canalicular obstruction is conjunctival DCR, with a permanent bypass tube.[32, 248] Conjunctival DCR, indicated for obstructions at the canalicular level, forms a surgical tract between the conjunctiva and the internal anastomosis of the DCR. Glass (Pyrex) tubes are placed into the conjunctival tract as a permanent prosthesis, bypassing the canalicular obstruction. They require frequent, careful maintenance; may become dislodged or cause mild facial disfigurement; and require frequent cleaning and considerable patient commitment. Recurrent dacryocystitis, granuloma formation, eroded canaliculi, or, rarely, corneal irritation may result from the prolonged placement of such tubes. This surgery, in contrast to the standard DCR involving lacrimal sac or more distal obstructions, is more invasive and leads to a higher rate of recurrence at long-term follow-up. While these oculoplastic procedures have some patient compliance problems, which may suggest DCP as an alternative treatment, experience with DCP[220, 221, 228] suggests that such dilations of the NLDS should be limited to stenosis/obstructions of the distal lacrimal sac and nasolacrimal duct (i.e., the same patients for whom routine DCR is indicated).

Balloon catheter dilation of the canaliculi has been discouraged or considered contraindicated because of possible damage to the canaliculus or punctum.[51, 219, 221, 243] Recurrence rates of up to 60% to 70% were noted.[249] Stenosis in the canaliculi was not considered suitable for balloon dilation, and such dilation was limited to the diameter of the guidewire or lacrimal catheter. The risks of canalicular occlusion caused by laceration or recurrent stenosis seemed high, and operative reconstruction may be difficult in such cases. Those performing DCP must avoid damaging the canaliculi, thereby creating the need for conjunctival DCR and a permanent glass prosthesis that otherwise may not have been necessary.[51]

Other investigators, in small series, reported balloon catheter dilation of the common canaliculus to be safe and effective.[220, 229, 240, 250] These initial series, as well as the surgical limitations of canalicular DCR, have encouraged Ko et al.[251] to develop further their techniques for evaluation of the safety and long-term effectiveness of balloon DCP in the treatment of common canalicular obstruction. In a study of 195 eyes with common canalicular obstruction (84 complete and 111 partial), the authors achieved initial technical success in 90% and 94%, respectively, of these patients. Patency rates were 51% at 6 months, 43% at 1 year, and 40% at 2 years, sparing this group of patients from an operative procedure. Their improved results may be related to the use of a slightly larger 3 mm balloon and better stabilization of the balloon catheter during inflation by passing it further retrograde along the guidewire such that the distal radiopaque marker, instead of the catheter tip, is advanced beyond the punctum, for a more efficient ballooning effect. Technical failures included seven patients with false passages and four patients in whom the obstructed canaliculus could not be negotiated with a guidewire. The recurrence of obstruction seemed related to ductal wall damage from guidewire or balloon catheter manipulation and resultant mucosal overgrowth, fibrosis, and recurrent episodes of active dacryocystitis.[243]

A previously designed polyurethane stent and a technique for lacrimal canalicular obstruction have had only limited experience.[252] The flexibility of the stent led to difficulty in advancing the tapered portion of the stent retrograde through the obstruction from the lacrimal sac. A high rate of stent occlusion occurred secondary to granulation tissue growth into the ballooned-out portion.[252] A more suitable introducer system, as well as a stent with no interstices at the ballooned-out portion, may offer greater success in the nonsurgical treatment of canalicular obstruction.[252]

Stents

The tendency for obstructions to recur after dacryocystoplasty (DCP) may be due to the fibrotic nature of the stenosis/occlusion. Song et al.[238] addressed this problem in patients with obstruction of the nasolacrimal sac or duct with the placement of plastic stents immediately following balloon dilation. The plastic stent, with its distal tip left slightly protruding into the inferior meatus, may be easy to remove. This technique will not interfere with subsequent DCR. The firmness of these stents, however, led to patient discomfort and the need for a softer stent. Metallic stents, initially proposed for the creation of a larger, stable lumen, if blocked after placement, can only be removed surgically and may compromise subsequent DCR.[237, 238] Such metallic stents are also limited by a lack of longitudinal flexibility. Medium-type Palmaz balloon-expandable metallic stents offer greater longitudinal flexibility, with an articulated design for longer stenotic/occluded segments as well as a nonarticulated stent for more focal lesions. Although the

Copyright © 2003, Mosby, Inc. All rights reserved.

balloon and stent could be dilated to 4 mm, stenosis of the stented lumen was noted on follow-up studies.[242] Mucosal-lined tracts do not tolerate metal well.[253, 254] Mucosal hyperplasia and a local inflammatory foreign tissue reaction to the metallic stent by the ductal wall, with tissue ingrowth through the metallic struts, are probable causes of stent stenosis and obstruction. Although tissue ingrowth may stabilize with time, the limited caliber of the NLDS lacks any reserve capacity to tolerate this initial tissue response. Metallic stents in the NLDS have been replaced by softer nonmetallic stents and are no longer used.

Song et al.[230] introduced a soft polyurethane stent that could be positioned with an introducer set (a stent loader, a No. 6 French sheath, a dilator, and a pusher catheter), obviating the need for balloon dilation of a stenotic or occluding segment. This method of DCP has the guidewire placed in an antegrade manner, with the dilator, sheath, and stent positioned in a retrograde fashion (Fig. 10-36,E-H). Fluoroscopic placement of the stent was technically successful in 50 of 51 attempts. Complete resolution of severe epiphora was noted in 47 and partial resolution in 3 of the 50 nasolacrimal systems treated. Treated stenoses were limited to the lacrimal sac, junction, and nasolacrimal duct. During limited follow-up of these patients, no stents migrated. Obstruction of one stent (probably caused by a blood clot) required lacrimal irrigation. It was hoped that this technique, as well as reducing costs, shortening procedure time, and improving patient tolerance, might offer better long-term results.

Song et al.[246] reviewed their long-term patency rate of polyurethane stent placement for the treatment of epiphora in 236 patients (283 obstructed lacrimal systems) with a follow-up period greater than 1 year. Stent placement was technically successful in 270 systems (95%). Assessment of these 270 systems 7 days after stent placement showed 87% with complete resolution of epiphora, 10% with partial resolution, and 3% with no resolution. In 77 patients (29.5%) with initial improvement, recurrence of epiphora occurred at a mean duration of 16 weeks poststenting due to obstruction of the stent. Recurrence rates of stent obstruction were correlated with levels of initial obstruction, with the highest recurrence rates (64%) for obstruction of the lacrimal sac, compared to only 26% for obstruction at the junction of the lacrimal sac–nasolacrimal duct and 15% at the nasolacrimal duct.

The causes of partial resolution of epiphora at 7 days were inadequate placement of the stent or partial obstruction of the stent by blood clot (excluding those patients who also had coexistent common canalicular obstruction). Stent placement was deemed inadequate when its mushroom tip was not placed in the dilated area. In the 3% of patients with no resolution, DCG at 7 days showed patency, and the cause of lack of improvement was not identified. Stent migration was noted in two patients in whom markedly dilated lacrimal systems were noted proximal to the obstruction. The stents were replaced with second stents with wider muchroom tips. Approximately one third of the obstructed stents were able to be recanalized by forceful irrigation with saline through the superior punctum, suggesting that the stents may have been impacted by mucus. Of the 56 obstructed stents removed, mucoid material was found in 26 and granulation tissue in 30. The incidence of mucus plugging within the stent may be managed with acetylcysteine eyedrops[219] or by reinterventions to maintain patency.[246] The growth of granulation tissue into the stents may represent a foreign body reaction[255] and may be overcome by the use of stents without interstices in the ballooned-out portion or a coated drug-releasing stent.[246] Overgrowth of the proximal end of the stent by granulation tissue is a more serious complication.[246] Primary and secondary patency rates after DCP (with balloon dilatation) without stent placement have been higher than those for primary stent placement. In addition to obstruction of the stent, subclinical chronic infection from bacterial overgrowth contributing to a cycle of infection, mucosal swelling, increased obstruction and stasis may result. Rapid restenosis frequently results despite removal of a dysfunctional stent.[239] Total obstruction of the lacrimal sac or common canaliculus may occur, with resultant impossibility of the classic operative DCR. Balloon dilation DCP by itself will not preclude future DCR.

Those patients with epiphora of traumatic etiology had a technical failure rate of 29% (in 34 systems) compared to a 1% technical failure in the larger group of patients with idiopathic epiphora (249 systems) of nontraumatic etiology.[246] Malalignment of the fractured bone is a relative contraindication to nonsurgical placement of a lacrimal stent. The overall patency rates 1 year poststenting of 85% and 74% for stenting of obstructive lesions at the nasolacrimal duct or at the junction between the lacrimal sec and nasolacrimal duct, respectively, are only slightly lower than the patency rates (87%) for DCR.[30, 107–110] Patency rates for stenting obstructive lesions at the contracted lacrimal sac (46%) were considerably lower than those obtained with DCR. Stent placement in the obstructed lacrimal system is most valuable as initial therapy for obstructions below the junction between the lacrimal sac and the nasolacrimal duct.

Berkefeld et al.[243] have expressed reservations about implantation of plastic prostheses (stents) for predominantly benign stenoses of a small-caliber, slow-flow ductal system. Complications may render operative reconstruction difficult. The authors suggest operative treatment for those patients not suitable for balloon DCP. Although placement of stents in the NLDS offers interesting possibilities for duct patency, chronic infection and fibrotic reactions may occur in the end, suggesting that the number of patients who receive a stent as initial treatment of lacrimal system obstruction and the indications for stent placement should be reconsidered.[221]

Assessment of the NLDS prior to placement of a stent may help prevent stent failure. A small, fibrotic lacrimal sac that does not have the capacity to receive the expanded mushroom tip will allow the stent to migrate and occlude. The size of the sac should allow proper placement of the stent below the internal punctum (sinus of Maier) with complete expansion of the mushroom tip. If the head of the stent is placed high in the sac, the stent may contact and block the internal punctum, blocking tear drainage and causing common canaliculus obstruction.[238] Accumulation of tears under the head of the stent may predispose the lacrimal sac to infection.[244] An incorrect length of the stent, with the distal tip contacting the nasal floor, may also lead to poor drainage. False passages are occasionally created, usually with the stent noted to be too medial in position,

Copyright © 2003, Mosby, Inc. All rights reserved.

passing through the very thin bone of the medial wall of the inferior lacrimal sac fossa, during attempts to probe or pass the guidewire or stent through very tight obstructions. More recently, increased reporting of false passages during stent placement, either by the guidewire or by the stent, has been noted.[154, 156, 244] A site of relative weakness at the inferior medial aspect of the lacrimal sac, where Horner's muscle is incomplete or deficient, compared to the muscular envelope noted surrounding the remainder of the sac, was inferred to be a common site in four of five perforations.[154] The assistance of CT imaging, either routinely or if there is any concern about positioning of a guidewire or stent, during or after the procedure, may help identify malpositioned components.[154, 256]

Pabón et al.[256] noted that placement of the stent, confirmed in the proper anatomic tract, was a critical factor affecting long-term patency, with 73% of 61 such stents patent at 1 year compared to none of the 7 improperly positioned stents. Early stent blockage and the need for periodic irrigation may be indicative of malpositioning of the stent.

The presence of epiphora reflects abnormal drainage. The increased number of treatment options (probing, irrigation, intubation, external dacryocystorhinostomy (DCR), endocanalicular DCR, endoscopic DCR, dacryocystoplasty, stent placement) for the epiphora patient have led to a desire for increased functional and anatomic data from various imaging modalities to assist treatment decisions based on the site and nature of the obstruction or stenosis. For nasolacrimal duct obstruction, it is important to differentiate functional (incomplete or partial) from mechanical (complete) obstruction. If the stenosis is mild or incomplete and obstruction can be overcome during a pressure injection, then DCP or stent placement may be considered instead of DCR.[227] More static images, such as those obtained with CT-DCG or MR-DCG (especially if teardrop placement of contrast is used) or radiographic distention-DCG may not offer the required functional information.[227]

The role of CT-DCG immediately following DCG (with residual contrast in place) may assist patient selection for DCP for patients with posttraumatic obstruction,[189] patients with previous DCR failure,[194] or those in whom the guidewire cannot be passed with ease during DCP.[221] At the time of DCG, if imaging findings were suggestive of dacryocystitis, posttraumatic obstruction of the bony canal, tumors, sarcoidosis or Wegener's granulomatosis, these patients received CT for further assessment and possible exclusion from DCP consideration.[221] CT assessment of the nasolacrimal bony canal may reveal minimal diameters ranging from 2.5 to 4.0 mm,[221] in contrast to the assumed canal dimensions of 4 to 6 mm previously described.[158, 163]

Hurwitz[30] has outlined indications for DCR, including epiphora due to acquired obstruction within the nasolacrimal sac and duct; mucocele of the lacrimal sac; chronic dacryocystitis or conjunctivitis due to lacrimal sac obstruction; lacrimal sac infection that must be relieved before intraocular surgery; and congenital nasolacrimal duct obstruction that cannot be cured by probing. As noted by the recent number of articles on DCP or stenting,[246, 218, 221, 240] these are the same indications considered appropriate for DCP or stenting. Attempts to refine DCP techniques and patient selection criteria, as well as controlled studies, may better define which procedure is best suited for specific patients. More stringent definitions of success, including minimum 2 year follow-up, resolution of the patient's presenting complaint, and 100% patency on syringing tests, would allow more appropriate evaluation of comparative treatments (J.J. Hurwitz, personal communication). DCR remains the treatment of choice for patients with posttraumatic or congenital obstruction of the bony nasolacrimal canal or obstruction of the nasolacrimal canal due to polyps or granuloma. Contraindications to DCR—acute dacryocystitis and tumors of the lacrimal sac,[30]—are also contraindications for dacryocystoplasty.[221]

ENDOSCOPY OF THE LACRIMAL DRAINAGE SYSTEM

A prototype of a lacrimal canaliculoscope, develops in 1990, passed nicely into the canalicular system, was rigid, was less than 1 mm in external diameter—equivalent to a No. 0 lacrimal probe—and allowed direct visualization of the punctum and canaliculus.[257, 258] Newer-generation flexible endoscopes measure 0.3 to 0.5 mm in diameter and have good axial illumination and a 70° field of view, allowing direct visualization and excellent images of the canaliculi, lacrimal sac, nasolacrimal duct, and their mucous membranes[259] (Fig. 10-37). The endoscopic unit includes a Xenon light source, a video camera with an ocular attachment and a miniature camera system with a monitor and video camera. The above system can be combined with modified Jünemann probes, which have attachments for endoscopy and irrigation. Some probe models have a third attachment to couple a laser fiber.

Such procedures are performed in an outpatient setting with topical anaesthesia and a pericanalicular and perisaccal local anaesthetic. The punctum is dilated, and the endoscope is inserted and advanced during steady, gentle irrigation, which is necessary for good visibility. Patients experience discomfort similar to that of standard probing and irrigation.[259] Normal distention of the lacrimal system is seen as widening of the lumen and easy passage of the endoscope. Stenoses cannot be widened during irrigation and the endoscope meets with a degree of resistance, as in conventional probing. Mucosal characteristics can be identified and correlated with the type of obstruction. Normal lacrimal mucosa is smooth and pink; postinflammatory conditions show thickened reddish-gray mucosa with large papillae; stenosis (fibrotic plaque) presents as whitish-gray inelastic membranes; and submucosal folds are seen as thick gray strictures.[259] Heavy debris and secretions may be differentiated from complete stenosis by their clearance with irrigation. Partial obstruction may be visualized as a narrowed lumen, which widens during irrigation. Difficulties have been noted initially in the handling of the instruments, evaluation of the mucous membranes, or diagnosis of pathologic changes. There is improvement with experience and recognition of landmarks.[259] Endoscopy is currently utilized to visualize directly and localize more precisely obstructing lesions of the NLDS. Endoscopic examinations, combined with various types of lasers, may be utilized for treatment (endocanalicular laser-assisted DCR).

Copyright © 2003, Mosby, Inc. All rights reserved.

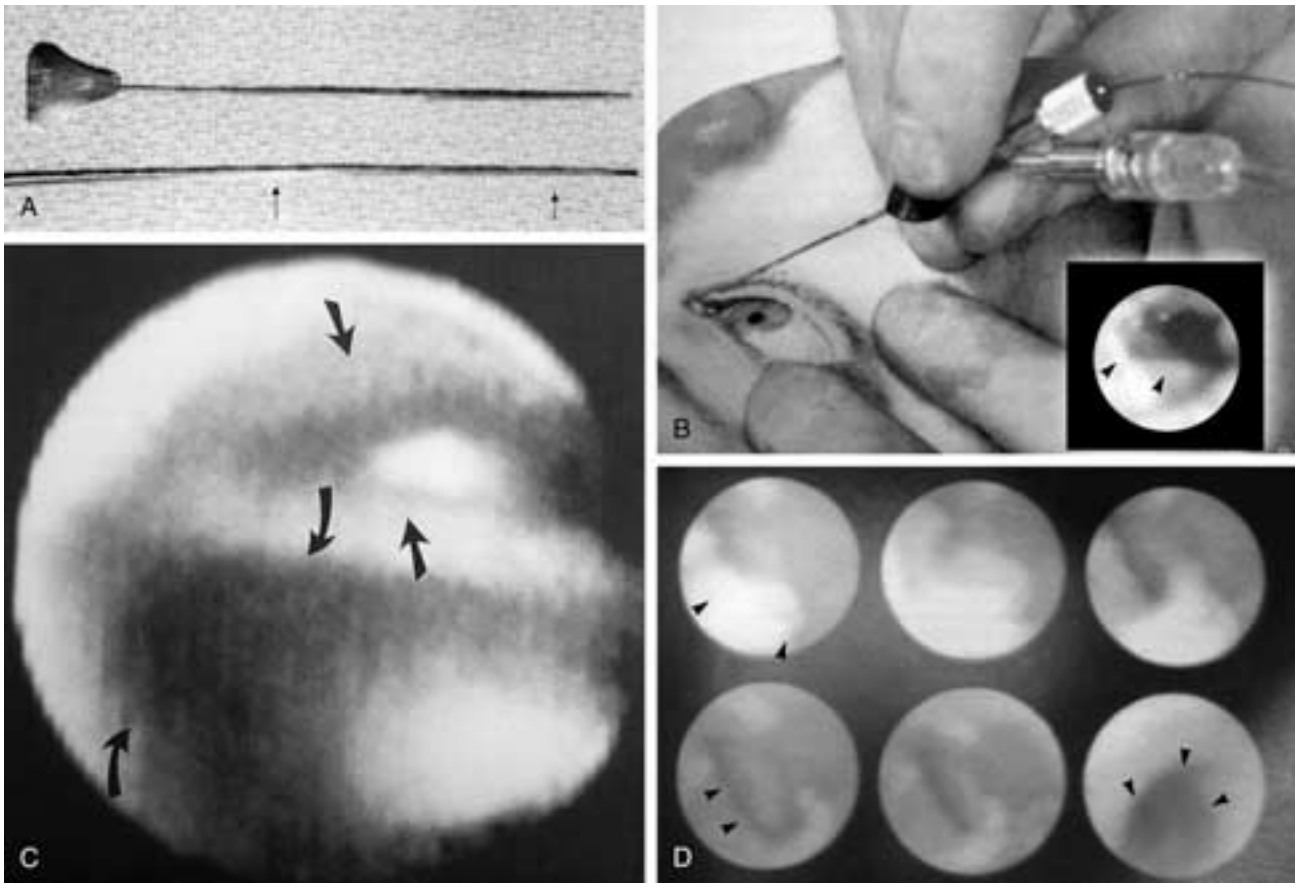

VIEW IMAGE

FIGURE 10-37 Lacrimal endoscopy. **A**, Canaliculoscope (*arrows*), less than 1 mm in external diameter, is equivalent in external diameter to No. 0 lacrimal probe. Newer canaliculoscopes now measure 0.5 mm in diameter. **B**, Endoscope (with attachment for irrigation) positioned in the inferior canaliculus. Inset shows debris and submucosal folds (*arrowheads*). **C**, Canaliculoscope image shows the junction of the superior and inferior canaliculi (darker areas outlined by *arrows*) approaching the common canaliculus. **D**, Lower canaliculus. Top three pictures show mucus and debris (*arrowheads*) occluding the canaliculus. Bottom left and middle pictures show a very narrow lumen (*arrowheads*) after cleansing of the canaliculus. Bottom right picture shows widening of the lumen under pressure irrigation (*arrowheads*). (**A** and **C** Courtesy of Dr. Jeffrey J. Hurwitz, Toronto, Canada, from Ashenhurst ME, Hurwitz JJ. Lacrimal canaliculoscopy. Development of the instrument. Can J Ophthalmol 1991;26:306. **B** and **D** Courtesy of Dr. Klaus Müllner, Graz, Austria, with permission from Müllner K, Bodner E, Mannor G. Endoscopy of the lacrimal system. Br J Ophthalmol 1999;83:949–952.)

However, to date, bone penetration and osteotomy formation have been less successful than for external DCR.[39]

SUMMARY

Epiphora is a common ophthalmologic complaint for which a number of imaging modalities are available. In our hands, intrinsic etiologies, based within or limited to the luminal component of the NLDS, remain routinely best assessed by digital subtraction (DS-DCG), with real-time images detailing the fine anatomic structures of the NLDS, including stenoses, obstructions (partial or complete), calculi, or morphologic abnormalities such as diverticulae or fistulae. CT and MR imaging display extrinsic lesions affecting the NLDS or mass lesions of the medial canthal and sinonasal-orbital regions. Without a proper index of suspicion, the lack of specificity of clinical signs in the epiphora patient may mask the opportunity to assess causal conditions arising within the wall, extramurally, extraorbitally, within the adjacent paranasal sinuses or nasal cavity. CT offers the advantage of better overall assessment of both bone and soft-tissue detail and tends to be used more frequently, when craniofacial information is desired, as in face trauma or involvement by tumor of the adjacent bone structures. MR imaging offers excellent soft-tissue resolution, especially with orbital surface coils. To better visualize the NLDS on CT or MR imaging, these studies may be complemented by cannulation, with administration of DCG contrast medium, or contrast may be placed topically into the conjunctival cul-de-sac, as a less invasive test that may offer limited functional information. Specific MR-DCG techniques, to highlight fluids (e.g., water, saline) introduced within the NLDS, as a noncontrast medium-detectable substance, show promise but currently do not offer the anatomic detail seen with DS-DCG or the functional analysis seen with DSG. DSG remains an excellent modality for assessing the dynamics of the NLDS, including canalicular dynamics and the lacrimal pump, functional obstruction, and delays in transit. Data analysis and

Copyright © 2003, Mosby, Inc. All rights reserved.

time-activity curves remain an important component of the study offering a quantitative picture of lacrimal drainage, and are especially useful in assessing those epiphora patients with no abnormality seen on DCG.

DCR remains the most consistent surgical treatment for epiphora secondary to an obstruction of the NLDS, with success rates approaching 90%. An alternative treatment, balloon DCP, is a less invasive, simple procedure performed under local anaesthetic on an outpatient basis. With careful patient selection, the most experienced clinicians have achieved encouraging results, approaching those for DCR. Stent placement may yet have a role, but it is no longer suggested as a primary alternative treatment. Knowledge of the criteria for patient selection for surgical procedures (external versus endoscopic DCR) or the alternative treatment, DCP, has led to greater awareness of NLDS factors and a more detailed analysis of lacrimal drainage imaging studies. Lacrimal endoscopy offers direct visualization of the NLDS membranes and precise localization of obstructing lesions. There is a learning curve. The exact role of lacrimal endoscopy, either as a diagnostic tool or in conjunction with surgical approaches such as laser DCR, has yet to be defined.

Acknowledgments

The authors wish to express their appreciation to Chris Bobkowski and Salvatore Ceniti for their assistance in the preparation of this manuscript and to Jeff Hurwitz, MD. The authors acknowledge the close working relationship between the Departments of Ophthalmology and Medical Imaging and the stimulation of the radiologists' interest in the pathology of the NLDS by their clinical colleagues.

REFERENCES

1. Ewing AE. Roentgen ray demonstration of the lacrimal abscess cavity. Am J Ophthalmol 1989;26:1–4.
2. Iba GB, Hanafee WN. Distension dacryocystography. Radiology 1968;90:1020–1022.
3. Campbell DM, Carter JM, Doub HP. Roentgen ray studies of the nasolacrimal passageways. Arch Ophthalmol 1922;51:462–470.
4. Hourn GE. X-ray visualization of the nasolacrimal duct. Ann Otol Rhinol Laryngol 1937;46:962–975.
5. Milder B, Demorest BH. Dacryocystography. I. The normal lacrimal apparatus. Arch Ophthalmol 1954;51:180–195.
6. Sargent EN, Ebersole C. Dacryocystography: the use of Sinografin for visualization of the nasolacrimal passages. AJR 1968;102: 831–839.
7. Law FW. Dacryocystography. Trans Ophthalmol Soc UK 1967;87: 395–407.
8. Munk FL, Burhenne LW, Buffam FV, et al. Dacryocystography: comparison of water-soluble and oil-based contrast agents. Radiology 1989;173:827–830.
9. Campbell W. The radiology of the lacrimal system. Br J Radiol 1964;37:1–26.
10. van der Plaat GF. X-ray enlargement technique. J Belg Radiol 1950;33:89.
11. Epstein E. Cine dacryocystography. Trans Ophthalmol Soc UK 1961;81:284–287.
12. Trokel SL, Potter GD. Kinetic dacryocystography. Am J Ophthalmol 1970;70:1010–1011.
13. Lloyd GAS, Jones BR, Welham RAN. Intubation macrodacryocystography. Br J Ophthalmol 1972;56:600–603.
14. Lloyd GAS, Welham RAN. Subtraction macrodacryocystography. Br J Radiol 1974;47:379–382.
15. El Gammal T, Brooks BS. Amipaque dacryocystography: biplane magnification and subtraction technique Radiology 1981;141: 541–542.
16. Schatz CJ. Tear duct system. In: Som PM, Bergeron RT, eds. Head and Neck Imaging, 2nd ed. St. Louis: CV Mosby, 1991;813–827.
17. Galloway JE, Kavic TA, Raflo GT. Digital subtraction dacryocystography: a new method of lacrimal system imaging. Ophthalmology 1984;91:956–962.
18. King SJ, Haigh SF. Technical report: digital subtraction dacryocystography. Clin Radiol 1990;42:351–353.
19. Kirchhof K, Hähnel S, Jansen O, Zake S, Sartor K. Gadolinium-enhanced magnetic resonance dacryocystography in patients with epiphora. J Comput Assist Tomogr 2000;24:327–331.
20. Amanat LA, Hilditch TE, Kwok CS. Lacrimal scintigraphy. II. Its role in the diagnosis of epiphora. Br J Ophthalmol 1983;67:720–728.
21. Jackson A, Hardcastle MP, Shaw A, Gibbon WW. Reduction of ocular lens dosage in dacryocystography. Clin Radiol 1989;40: 615–618.
22. Wearne MJ, Pitts J, Frank J, Rose GE. Comparison of dacryocystography and lacrimal scintigraphy in the diagnosis of functional nasolacrimal duct obstruction. Br J Ophthalmol 1999;83:1032–1035.
23. Zinreich SJ, Miller NR, Freeman LN, Glorioso LW, Rosenbaum AE. Computed tomographic dacryocystography using topical contrast media for lacrimal system visualization. Orbit 1990;9:79–87.
24. Hecht SD. Dacyocystorhinostomy. In: Hornblass A, Hanig CJ, eds. Oculoplastic, Orbital, and Reconstructive Surgery. Baltimore: Williams & Wilkins, 1990;1433–1440.
25. Nixon J. Birchall IWJ, Virjee J. The role of dacryocystography in the management of patients with epiphora. Br J Radiol 1990;63:337–339.
26. Hanna IT, MacEwan CJ, Kennedy N. Lacrimal scintigraphy in the diagnosis of epiphora. Nucl Med Commun 1992;13:416–420.
27. Jones LT, Wobig JL. Surgery of the Eyelids and Lacrimal System. Birmingham, Ala: Aesculapius, 1976;67, 141–151, 157–173.
28. Becker MH. The lacrimal drainage system. In: Gonzalez CF, Becker MH, Flanagan JC, eds. Diagnostic Imaging in Ophthalmology. New York: Springer-Verlag, 1986;88–91.
29. Mulligan NB, Ross CA, Francis IC, Moshegov CN. The valsalva DCR bubble test: a new method of assessing lacrimal patency after DCR surgery. Ophthal Plast Reconstr Surg 1994;10:121–123.
30. Hurwitz JJ. Dacryocystorhinostomy. In: Hurwitz JJ, ed. The Lacrimal System. Philadelphia: Lippincott-Raven, 1996;261–296.
31. Hurwitz JJ. Canaliculodacryocystorhinostomy. In: Hurwitz JJ, ed. The Lacrimal System. Philadelphia: Lippincott-Raven, 1996; 267–302.
32. Hurwitz JJ. Lacrimal bypass surgery. In: Hurwitz JJ, ed. The Lacrimal System. Philadelphia: Lippincott-Raven, 1996;303–316.
33. Hurwitz JJ. Endonasal dacryocystorhinostomy. In: Hurwitz JJ, ed. The Lacrimal System. Philadelphia: Lippincott-Raven, 1996; 317–321.
34. Whittet HB, Shun-Shin GA, Awdry P. Functional endoscopic transnasal dacryocystorhinostomy. Eye 1993;7:545–549.
35. Yung MW, Hardman-Lea S. Endoscopic inferior dacryocystorhinostomy. Clin Otolaryngol 1998;23:152–157.
36. Cokkeser Y, Evereklioglu C, Er H. Comparative external versus endoscopic dacryocystorhinostomy: results in 115 patients. Otolaryngol Head Neck Surg 2000;123:488–491.
37. Mannor GE, Millman AL. The prognostic value of preoperative dacryocystography in endoscopic intranasal dacryocystorhinostomy. Am J Opthalmol 1992;113:134–137.
38. Kong YT, Kim TI, Kong BW. A report of 131 cases of endoscopic laser lacrimal surgery. Ophthalmology 1994;101:1793–1800.
39. Levin PS, Stermogipson J. Endocanalicular laser assisted dacryocystorhinostomy. An anatomic study. Arch Ophthalmol 1992;110:1488–1490.
40. Pearlman SJ, Michalos P, Leib ML, Moazed KT. Translacrimal transnasal laser-assisted dacrycystorhinostomy. Laryngoscope 1997; 107:1362–1365.
41. Woog JG, Metson R, Puliafito CA. Holmium:YAG endonasal laser dacryocystorhinostomy. Am J Ophthalmol 1993;116:1–10.
42. Wolff E. Anatomy of the Eye and Orbit, 7th ed., revised by R. Warwick. Philadelphia: WB Saunders, 1976;226–237.
43. Schaeffer JP. Variations in the anatomy of the nasolacrimal passages. Am Surg 1911;54:148–152.

Copyright © 2003, Mosby, Inc. All rights reserved.

44. Yazici B, Yazici Z. Frequency of the common canaliculus: a radiological study. Arch Ophthalmol 2000;118(10):1381–1385.
45. Gonnering RS, Bosniak SL. Recognition and management of acute non-infectious dacryocystic retention. Ophthal Plast Reconstr Surg 1989;5(1):27–33.
46. Tucker NA, Tucker SM, Linberg JV. The anatomy of the common canaliculus. Arch Ophthalmol 1996;114:1231–1234.
47. Malik SRK, Gupta AK, Chaterjee S, ct al. Dacryocystography of normal and pathological lacrimal passages. Br J Ophthalmol 1969;53:174–179.
48. Paulsen F, Thale A, Kohla G, Schauer R, Rochels R, Parwaresch R, Tillman B. Functional anatomy of human lacrimal duct epithelium. Anat Embryol 1998;198:1–12.
49. Thale A, Paulsen F, Rochels R, Tillmann B. Functional anatomy of the human efferent tear ducts: a new theory of tear outflow mechanism. Graefes Arch Clin Exp Ophthalmol 1998;236:674–678.
50. Paulsen FP, Thale AB, Hallmann UJ, Schaudig U, Tillmann BN. The cavernous body of the human efferent tear ducts: function in tear outflow mechanism. Invest Ophthalmol Vis Sci 2000;41:965–970.
51. Glatt HJ. Dacryocystoplasty: an oculoplastic surgeon's perspective (letter). Radiology 1991;180:289–290.
52. Blicker JA, Buffam FV. Lacrimal sac, conjunctival, and nasal culture results in dacryocystorhinostomy patients. Ophthal Plast Reconstr Surg 1993;9:43–46.
53. DeAngelis D, Hurwitz J, Mazzulli T. The role of bacteriologic infection in the etiology of nasolacrimal duct obstruction. Can J Ophthalmol 2001;36:134–139.
54. Buffam FV. Discussion in DeAngelis D, Hurwitz J, Mazzulli T. The role of bacteriologic infection in the etiology of nasolacrimal duct obstruction. Can J Ophthalmol 2001;36:139.
55. Hartikainen J, Lehtonen OF, Saari KM. Bacteriology of lacrimal duct obstruction in adults. Br J Ophthalmol 1997;81:37–40.
56. Boruchoff SA, Boruchoff SE. Infections of the lacrimal system. Infect Dis Clin North Am 1992;6:925–932.
57. Mauriello JA Jr, Wasserman BA. Acute dacryocystitis: an unusual cause of life-threatening orbital intraconal abscess with frozen globe. Ophthal Plast Reconstr Surg 1996;12:294–295.
58. Ntountas I, Morschbacher R, Pratt D, Patel BC, Anderson RL, McCann JD. An orbital abscess secondary to acute dacryocystitis. Ophthalmic Surg Lasers 1997;28:758–761.
59. Molgat YM, Hurwitz JJ. Orbital abscess due to acute dacryocystitis. Can J Ophthalmol 1993;28:181–182.
60. Janssen AG, Mansour K, Bos JJ, Manoliu RA, Castelijns JA. Abscess of the lacrimal sac due to chronic or subacute dacryocystitis: treatment with temporary stent placement in the nasolacrimal duct. Radiology 2000;215:300–304.
61. Hornblass A, Herschorn BJ, Stern K, Grimes C. Orbital abscess. Surv Ophthalmol 1984;29:169–178.
62. Weiss GH, Leib LM. Congenital dacryocystitis and retrobulbar abscess. J Pediatr Ophthalmol Strabismus 1993;30:271–272.
63. Remulla HD, Rubin PAD, Shore JW, Cunningham MJ. Pseudodacryocystitis arising from anterior ethmoiditis. Ophthal Plast Reconstr Surg 1995;11:165–168.
64. Duvoisin B, Schnyder P, Agrifoglio A. CT diagnosis of occult anterior ethmoid sinusitis in a case of lacrimal sac abscess. AJR 1988;151:837–838.
65. Stivero J, Hadar T, Feinmesser R. Fistulae in the inner canthus associated with ethmoiditis. J Laryngol Otol 1992;106:1076–1078.
66. Keast-Butler J, Lloyd GAS, Welham RAN. Analysis of intubation macrodacryocystography with surgical correlations. Trans Ophthalmol Soc UK 1973;93:593–596.
67. Welham RAN, Henderson PM. Results of dacryocystorhinostomy: analysis of cause of failure. Trans Ophthalmol Soc UK 1973;93:601–609.
68. Millman AL, Liebskind A, Putterman AM. Dacryocystography: the technique and its role in the practice of ophthalmology. Radiol Clin North Am 1987;25:781–786.
69. Welham RAN. Canalicular obstructions and the Lester Jones tubes. Trans Ophthalmol Soc UK 1973;93:623–632.
70. Spira R, Mondshine R. Demonstration of nasolacrimal duct carcinoma by computed tomography. Ophthal Plast Reconstr Surg 1986;2:159–161.
71. Agarwal ML. Dacryocystography in chronic dacryocystitis. Am J Ophthalmol l961;52:245–251.
72. Francois J, Bacskulin J. External congenital fistulae of the lacrimal sac. Ophthalmologica 1969;159:249–261.
73. Masi AV. Congenital fistula of the lacrimal sac. Arch Ophthalmol 1983;81:701–704.
74. Toda C, Imai K, Tsujiguchi K, Komune H, Enoki E, Nomachi T. Three different types of congenital lacrimal sac fistulas. Am Plast Surg 2000;45:651–653.
75. Howard R, Caldwell J. Congenital fistula of the lacrimal sac. Am J Ophthalmol 1969;67:931–934.
76. Welham RAN, Bergin DJ. Congenital lacrimal fistulas. Arch Ophthalmol 1985;103:545–548.
77. Tsibidas P, Roussos J. Supernumerary lacrimal canaliculi. Ann Ophthalmol 1979;11:265–267.
78. Epley KD, Karesh JW. Lacrimal sac diverticula associated with a patent lacrimal system. Ophthal Plast Reconstr Surg 1999;15:111–115.
79. Bullock JD, Goldberg SH. Lacrimal sac diverticula. Arch Ophthalmol 1989;107:756.
80. Polito E, Leccisotti A, Menicacci F, Motolese E, Addabbo G, Paterra N. Imaging techniques in the diagnosis of lacrimal sac diverticulum. Ophthalmologica 1995;209:228–232.
81. Hosal BM, Hurwitz JJ, Howarth DI. Orbital cyst of lacrimal sac derivation. Eur J Ophthalmol 1996;6:279–283.
82. Hornblass A, Gross ND. Lacrimal sac cyst. Ophthalmology 1987;94:706–708.
83. Berlin AJ, Rath R, Rich L. Lacrimal system dacryoliths. Ophthalmic Surg 1980;11:435–436.
84. Jones LT. Tear-sac foreign bodies. Am J Ophthalmol 1965;60:111–113.
85. Viers ER: Lacrimal Disorders in Diagnosis and Treatment. St. Louis: CV Mosby, 1976;54–59.
86. Wilkins RB, Pressly JP. Diagnosis and incidence of lacrimal calculi. Ophthalmic Surg 1980;11:787–789.
87. Hawes MJ. The dacryolithiasis syndrome. Ophthal Plast Reconstr Surg 1988;4:87–90.
88. Weber AL, Rodriguez-DeVelasquez A, Lucarelli MJ, Cheng HM. Normal anatomy and lesions of the lacrimal sac and duct: evaluated by dacryocystography, computed tomography, and MR imaging. Neuroimaging Clin North Am 1996;6:199–217.
89. Yazici B, Hammad AM, Meyer DR. Lacrimal sac dacryoliths: predictive factors and clinical characteristics. Ophthalmology 2001;108:1308–1312.
90. Maltzman BA, Favetta JR. Dacryolithiasis. Am Ophthalmol 1979;11:473–475.
91. Kaye-Wilson LG. Spontaneous passage of a dacryolith. Br J Ophthalmol 1991;75:564.
92. McCormick SA, Linberg JV. Pathology of nasolacrimal duct obstruction. Clinicopathologic correlates of lacrimal excretory system disease. Contemp Issue Ophthalmol 1988;5:169–202.
93. Jay JL, Lee WR. Dacryolith formation around an eyelash retained in the lacrimal sac. Br Ophthalmol 1976;60:722–725.
94. Baratz KH, Bartley GB, Campbell W, Garrity JA. An eyelash nidus for dacryoliths of the lacrimal excretory and secretory systems. Am J Ophthalmol 1991;111:624–627.
95. Herzig S, Hurwitz JJ. Lacrimal sac calculi. Can J Ophthalmol 1979;14(1):17–20.
96. Berlin AJ. Success rate of endoscopic laser-assisted dacryocystorhinostomy (letter). Ophthalmology 2000;107:4–5.
97. Richards W. Actinomycotic lacrimal canaliculitis. Am J Ophthalmol 1973;75:155–157.
98. Wolter J, Stratford T, Harrell E. Cast-like fungus obstruction of the nasolacrimal duct. Arch Ophthalmol 1956;55:320–322.
99. Kristinsson JK, Sigurdsson H. Lacrimal sac plugging caused by *Aspergillus fumigatus*. Acta Ophthalmol Scand 1998;76:241–242.
100. Song HY, Jin YH, Lee HK, Sung KB. Non-operative management of dacryolithiasis. JVIR 1995;6:647–650.
101. Wilhelm KE, Hofer U, Textor HJ, Böker TH, Strunk HH. Dacryoliths; nonsurgical fluoroscopically-guided treatment during dacryocystoplasty. Radiology 1999;212:365–370.
102. von Graefe A. Koncretionen in unteren thraenenroerchen durch Pilzbildrung. Arch Ophthalmol 1854;1:284–288.
103. Sathananthan N, Sullivan TJ, Rose GE, Moseley IF. Intubation dacryocystography in patients with a clinical diagnosis of chronic canaliculitis (''streptothrix''). Br J Radiol 1993;66:389–393.

Copyright © 2003, Mosby, Inc. All rights reserved.

104. Francois J, Elewault-Ryssellaere M, De Vos E. Mycose et pseudo-mycoses des voies lacrymales. Ann Ocul 1966;199:1129–1142.
105. Bouzas AG. Virus aetiology of certain cases of lacrimal obstruction. Br J Ophthalmol 1973;57:849–851.
106. Hurwitz JJ, Welham RAN, Lloyd GAS. The role of intubation macrodacryocystography in management of problems of the lacrimal system. Can J Ophthalmol 1975;10:361–366.
107. McLachlan DL, Shannon GM, Flanagan JC. Results of dacryocystorhinostomy: analysis of the reoperations. Ophthalmic Surg 1980;11:427–430.
108. Tarbet KJ, Custer PL. External dacryocystorhinostomy. Surgical success, patient satisfaction, and economic cost. Ophthalmology 1995;102:1065–1070.
109. Hartikainen J, Antila J, Varpula M, Puukka P, Seppä H, Grénman R. Prospective randomized comparison of endonasal endoscopic dacryocystorhinostomy and external dacryocystorhinostomy. Laryngoscope 1998;108:1861–1866.
110. Allen K, Berlin AJ. Dacryocystorhinostomy failure: association with nasolacrimal silicone intubation. Ophthalmic Surg 1989;20:486–489.
111. Orcutt JC, Hillel A, Weymuller EA. Endoscopic repair of failed dacryocystorhinostomy. Ophthalmic Plast Reconst Surg 1990;6:197–202.
112. Welham RAN, Wulc AE. Management of unsuccessful lacrimal surgery. Br J Ophthalmol 1987;71:152–157.
113. Hurwitz JJ, Welham RAN, Maisey MN. Radiography in functional lacrimal testing. Br J Ophthalmol 1975;59:323–331.
114. Doucet TW, Hurwitz JJ. Canaliculodacryocystorhinostomy in the management of unsuccessful lacrimal surgery. Arch Ophthalmol 1982;100:619–621.
115. Esmaeli B, Valero V, Ahmadi MA, Booser D. Canalicular stenosis secondary to docetaxel (taxotere): a newly recognized side effect. Ophthalmology 2001;108:994–995.
116. Fezza JP, Wesley RE, Klippenstein KA. The treatment of punctual and canalicular stenosis in patients on systemic 5-FU. Ophthalmic Surg Lasers 1999;30:105–108.
117. Haidak DJ, Hurwitz BS, Yeung KY. Tear duct fibrosis (dacryostenosis) due to 5-fluorouracil. Ann Intern Med 1978;88:657.
118. Rossomondo RM, Carlton WH, Trueblood JH, Thomas RP. A new method of evaluating lacrimal drainage. Arch Ophthalmol 1972;88:523–525.
119. Brown M, El Gammal TA, Luxenberg MN, Eubig C. The value, limitations and applications of nuclear dacryocystography. Semin Nucl Med 1981;11:250–257.
120. Hilditch TE, Kwok CS, Amanat LA. Lacrimal scintigraphy. I. Compartmental analysis of data. Br J Ophthalmol 1983;67:713–719.
121. Hurwitz JJ, Maisey MN, Welham RAN. Quantitative lacrimal scintillography. I. Method and physiological application. Br J Ophthalmol 1975;59:308–312.
122. Hurwitz JJ, Maisey MN, Welham RAN. Quantitative lacrimal scintillography. II. Method and physiological application. Br J Ophthalmol 1975;59:313–322.
123. Hurwitz JJ, Welham RAN, Maisey MN. Intubation macrodacryocystography and quantitative scintillography: the ''complete'' lacrimal assessment. Trans Am Acad Ophthalmol Otolaryngol 1976;81:575–582.
124. Fraunfelder FT. Extraocular fluid dynamics: how best to apply topical ocular medication. Tr Am Ophthalmol Soc 1976;74:457–487.
125. Chavis RM, Welham RAN, Maisey MN. Quantitative lacrimal scintillography. Arch Ophthalmol 1978;96:2066–2068.
126. White WL, Glover AT, Buckner AB, Hartshorne MF. Relative canalicular tear flow as assessed by dacryoscintography. Ophthalmology 1989;96(2):167–169.
127. Rose JDG, Clayton CB. Scintigraphy and contrast radiography for epiphora. Br J Radiol 1985;58:1183–1186.
128. Rabinovitch J, Hurwitz JJ, Chin-Sang M. Quantitative evaluation of canalicular flow using lacrimal scintillography. Orbit 1984;3:263–266.
129. Robertson JS, Brown ML, Colvard DM. Radiation absorbed dose to the lens in dacryoscintigraphy with technetium 99m. Radiology 1979;133:747–750.
130. Rogers RT. Radiation dose to the skin in diagnostic radiology. Br J Radiol 1969;42:511–518.
131. Jones LT. An anatomical approach to problems of the eyelids and lacrimal apparatus. Arch Ophthalmol 1961;66:111–124.
132. Hill JC, Bethel W, Smirmaul HJ. Lacrimal drainage: a dynamic evaluation. Part I. Mechanics of tear transport. Can J Ophthalmol 1974;9:411–416.
133. Doane MG. Blinking and the mechanics of the lacrimal drainage system. Ophthalmology 1981;88:844–851.
134. Doane MG. Blinking and tear drainage. Adv Ophthalmic Plast Reconstr Surg 1984;3:39–52.
135. Hill JC, Bethel W, Smirmaul HJ. Lacrimal drainage: a dynamic evaluation. Part II. Clinical aspects. Can J Ophthalmol 1974;9:417–424.
136. Sorensen TB. Studies on tear physiology, pathophysiology and contact lenses by means of dynamic gamma camera and technetium. Acta Ophthalmol Suppl 1984;167:1–54.
137. White WL, Glover AT, Buckner AB. Effect of blinking on tear elimination as evaluated by dacryoscintigraphy. Ophthalmology 1991;98:367–369.
138. von Denffler HW, Dressler J, Pabst HW. Lacrimal dacryoscintigraphy. Semin Nucl Med 1984;14:8–15.
139. Daubert J, Nik N, Chandeyssoun PA, el-Choufi L. Tear flow analysis through the upper and lower systems. Ophthal Plast Reconstr Surg 1990;6:193–196.
140. Linberg JV, Moore CA. Symptoms of canalicular obstruction. Ophthalmology 1988;95(8):1077–1079.
141. Becker BB. Tricompartment model of the lacrimal pump mechanism. Ophthalmology 1992;99:1139–1145.
142. Rosengren B. On lacrimal drainage. Ophthalmologica 1972;164:409–421.
143. Amanat LA, Hilditch TE, Kwok CS. Lacrimal scintigraphy. I. Compartmental analysis of data. Br J Ophthalmol 1983;67:713–719.
144. Amanat LA, Hilditch TE, Kwok CS. Lacrimal scintigraphy. III. Physiological aspects of lacrimal drainage. Br J Ophthalmol 1983;67:729–732.
145. Francis IC, Kappagoda MB, Cole IE, Bank L, Dunn GD. Computed tomography of the lacrimal drainage system: retrospective study of 107 cases of dacryostenosis. Ophthal Plast Reconstr Surg 1999;15:217–226.
146. Bartley GB. Acquired lacrimal drainage obstruction: an etiologic classification system, case reports and a review of the literature. Part 1. Ophthal Plast Reconstr Surg 1992;8:237–242.
147. Bartley GB. Acquired lacrimal drainage obstruction: an etiologic classification system, case reports and a review of the literature. Part 2. Ophthal Plast Reconstr Surg 1992;8:243–249.
148. Bartley GB. Acquired lacrimal drainage obstruction: an etiologic classification system, case reports and a review of the literature. Part 3. Ophthal Plast Reconstr Surg 1992;9:11–26.
149. Zehavi C, Zadok J, Sacks D. The pitfalls of dacryostenosis. Ophthal Surg 1992;23:297–298.
150. Mauriello JA, Palydowycz S, DeLuca J. Clinicopathologic study of lacrimal sac and nasal mucosa in 44 patients with complete acquired nasolacrimal duct obstruction. Ophthal Plast Reconstr Surg 1992;8:13–21.
151. Hähnel S, Jansen O, Zake S, Sartor K. Ser wert der spiral-CT zur diagnose von stenosen der ableitenden Tranenwege. Röfo Fortschr Geb Röntgenstr Neuen Bildgeb Uerfahr 1995;163:210–214.
152. Friedman DP, Rao VM, Flanders AE. Lesions causing a mass in the medial canthus of the orbit: CT and MR features. AJR 1993;160:1095–1099.
153. Russell EJ, Czervionke L, Huckman M, Daniels D, McLachlan D. CT of the inferomedial orbit and lacrimal drainage apparatus: normal and pathologic anatomy. AJR 1985;145:1147–1154.
154. Pinto IT, Paul L, Grande C. Nasolacrimal polyurethane stent: complications with CT correlation. Cardiovasc Intervent Radiol 1998;21:450–453.
155. Hartikainen J, Aho HJ, Seppa H, Grenman R. Lacrimal bone thickness at the lacrimal sac fossa. Ophthalmic Surg Lasers 1996;27:679–684.
156. Yung MW, Logan BM. The anatomy of the lacrimal bone at the lateral wall of the nose: its significance to the lacrimal surgeon. Clin Otolaryngol 1999;24:262–265.
157. Dale DL. Embryology, anatomy, and physiology of the lacrimal drainage system. In: Stephensen CM, ed. Ophthalmic, Plastic, Reconstructive, and Orbital Surgery. Boston: Butterworth-Heinemann, 1997;19–30.

Copyright © 2003, Mosby, Inc. All rights reserved.

158. Whitnall SE. The Anatomy of the Human Orbit and Accessory Organ of Vision. H. Frowde, Hodder, Stoughton. Part 1. London: Oxford Medical Publication, 1921; chap. 5.
159. Janssen AG, Mansour K, Bos JJ, Castelijns JA. Diameter of the bony lacrimal canal: normal values and values bilateral to nasolacrimal duct obstruction. Assessment with CT. Am J Neuroradiol 2001;22: 845–850.
160. Groessl SA, Sires BS, Lemke BN. An anatomic basis for primary acquired nasolacrimal duct obstruction. Arch Ophthalmol 1997;115: 71–74.
161. Linberg JV, McCormick SA. Primary acquired nasolacrimal duct obstruction: a clinicopathologic report and biopsy technique. Ophthalmology 1986;93:1055–1063.
162. Well BA. Dacryocystitis. In: Viers ER, ed. The Lacrimal System. St. Louis; CV Mosby, 1971;118–119.
163. Duke-Elder S. Textbook of Ophthalmology. Vol. 1. The Development, Form, and Function of the Visual Apparatus. London: Kimpton, 1946;235.
164. Tucker N, Chow D, Stockl F, Codere F, Burnier M. Clinically suspected primary acquired nasolacrimal duct obstruction. Ophthalmology 1997;104:1882–1886.
165. Flanagan JC, Stokes DP. Lacrimal sac tumors. Ophthalmology 1978;85:1282–1287.
166. Loftus WK, Kew J, Metrewelic C. Nasolacrimal duct opacity on CT. Br J Radiol 1996;69:630–631.
167. Rheeman CH, Meyer DR. Enlargement of the nasolacrimal canal in the absence of neoplasia. Ophthalmology 1998;105:1498–1503.
168. Nasr AM, Huaman AM. Anterior orbital varix presenting as a lacrimal sac mucocele. Ophthal Plast Reconstr Surg 1998;14: 193–197.
169. Mudgil AV, Meyer DR, Dipillo MA. Varix of the angular vein manifesting as a Medial canthal mass. Am J Ophthalmol 1993;116: 245–246.
170. Stefanyszyn MA, Hidayat AA, Pe'er JJ, Flanagan JC. Lacrimal sac tumors. Ophthal Plast Reconstr Surg 1994;10:169–184.
171. Ryan SJ, Font RL. Primary epithelial neoplasms of the lacrimal sac. Am J Ophthalmol 1973;76:73–88.
172. Pe'er J, Hidayat AA, Ilsar M, Landau L, Stefanyszyn MA. Glandular tumors of the lacrimal sac. Their histopathologic patterns and possible origins. Ophthalmology 1996;103:1601–1605.
173. Powell JB. Nasolacrimal dysfunction. Laryngoscope 1983;93: 498–515.
174. Ni C, D'Amico DJ, Fan CQ, Kuo PK. Tumors of the lacrimal sac: a clinicopathological analysis of 82 cases. Int Ophthalmol Clin 1982;22(1):121–140.
175. Jones IS. Tumors of the lacrimal sac. Am J Ophthalmol 1956;42:561–566.
176. Hornblass A, Jakobiec FA, Bosniak S, Flanagan JC. The diagnosis and management of epithelial tumors of the lacrimal sac. Ophthalmol 1980;87:476–490.
177. Erickson BA, Massaro BM, Mark LP, Harris GJ. Lacrimal collecting system lymphomas: integration of magnetic resonance imaging and therapeutic irradiation. Int J Radiat Oncol Biol Phys 1994;29:1095–1103.
178. Nakamura Y, Mashima Y, Kameyama K, Mukai M, Oguchi Y. Detection of human papillomavirus infection in squamous tumours of the conjunctiva and lacrimal sac by immunohistochemistry, in situ hybridisation, and polymerase chain reaction. Br J Ophthalmol 1997;81:308–313.
179. Pe'er JJ, Stefanyszyn M, Hidayat AA. Non-epithelial tumors of the lacrimal sac. Am J Ophthalmol 1994;118:650–658.
180. Milder B, Smith ME. Tumors of the lacrimal excretory system. In: Milder B, Weils BA, eds. The Lacrimal System. Norwalk, Conn: Appleton-Century-Crofts, 1983;145–152.
181. Mruthyunjaya P, Meyer DR. Juvenile xanthogranuloma of the lacrimal sac fossa. Am J Ophthalmol 1997;123:400–402.
182. Gruss JS, Hurwitz JJ, Nik NA, Kassel EE. The pattern and incidence of nasolacrimal injury in naso-orbital-ethmoid fractures: the role of delayed assessment and dacryocystorhinostomy. Br J Plast Surg 1985;38:116–121.
183. Gruss JS. Naso-ethmoid-orbital fractures: classification and role of primary bone grafting. Plast Reconstr Surg 1985;75:303–315.
184. Stranc MF. The pattern of lacrimal injuries in naso-ethmoid fractures. Br J Plast Surg 1971;24:339–346.
185. Nik NA, Hurwitz JJ, Gruss JS. Management of lacrimal injury after naso-orbito-ethmoid fractures. Adv Ophthalmic Plast Reconstr Surg 1984;3:307–317.
186. Balle VH, Andersen R, Slim C. Incidence of lacrimal obstruction following trauma to the facial skeleton. Ear, Nose, Throat J 1988;67:66–70.
187. Osguthorpe JD, Hoang G. Nasolacrimal injuries: evaluation and management. Otolaryngol Clin North Am 1991;24:59–78.
188. Unger JM. Fractures of the nasolacrimal fossa and canal: a CT study of appearance, associated injuries, and significance in 25 patients. AJR 1992;158:1321–1324.
189. Glatt HJ. Evaluation of lacrimal obstruction secondary to facial fractures using computed tomography or computed tomographic dacryocystography. Ophthal Plast Reconstr Surg 1996;12:284–293.
190. Hurwitz JJ, Archer KF, Gruss JS. Double stent intubation in difficult post-traumatic dacryocystorhinostomy. Ophthalmic Surg 1988;19: 33–36.
191. Bolger WE, Bitzin CA, Parsons DS. Paranasal sinus bony anatomic variations and mucosal abnormalities: CT analysis for endoscopic sinus surgery. Laryngoscope 1991;101:56–64.
192. Blaylock WK, Moore CA, Linberg JV. Anterior ethmoid anatomy facilitates dacryocystorhinostomy. Arch Ophthalmol 1990;108:1774–1777.
193. Earwaker J. Anatomic variants in sinonasal CT. Radiographics 1993;13:381–415.
194. Glatt HJ, Chan AC, Barrett L. Evaluation of dacryocystorhinostomy failure with computed tomography and computed tomographic dacryocystography. Am J Ophthalmol 1991;112:431–436.
195. Gonnering RS, Lyon DB, Fisher JC. Endoscopic laser-assisted lacrimal surgery. Am J Ophthalmol 1991;111:152–157.
196. Linberg JV, Anderson RL, Bumsted RM, et al. Study of intranasal ostium external dacryocystorhinostomy. Arch Ophthalmol 1982;100: 1758–1762.
197. Ashenhurst M, Jaffer N, Hurwitz JJ, Corrin SM. Combined computed tomography and dacryocystography for complex lacrimal problems. Can J Ophthalmol 1991;26(1):27–31.
198. Moran CC, Buckwalter K, Caldemeyer KS, Smith RR. Helical CT with topical water-soluble contrast media for imaging of the lacrimal drainage apparatus, AJR 1995;164:995–996.
199. Caldemeyer KS, Stockberger SM, Broderick LS. Topical contrast-enhanced CT and MR dacryocystography: imaging the lacrimal drainage apparatus of healthy volunteers. AJR 1998;171:1501–1504.
200. Kassel EE, Schatz CJ. Lacrimal apparatus. In: Som PM, Curtin HD, eds. Head and Neck Imaging, 3rd ed. St Louis: CV Mosby, 1996;1129–1183.
201. Mansfield DC, Zeki SM, MacKenzie JR. Case report: extravasation of lipiodol—a complication of dacryocystography. Clin Radiol 1994;49:217–218.
202. Sevel D. Development and congenital abnormalities of the nasolacrimal apparatus. J Pediatr Ophthalmol Strabismus 1981;18: 13–19.
203. Busse HM, Müler KM, Kroll P. Radiological and histological findings of the lacrimal passages of newborns. Arch Ophthalmol 1980;98:528–532.
204. Berkowitz RG, Grundfast KM, Fitz C. Nasal obstruction of the newborn revisited: clinical and subclinical manifestations of congenital nasolacrimal duct obstruction presenting as a nasal mass. Otolaryngol Head Neck Surg 1990;103:468–471.
205. MacEwen CJ, Young JDH. Epiphora during the first year of life. Eye 1991;5:596–600.
206. Levy NS. Conservative management of congenital amnionotocele of the nasolacrimal duct. J Pediatr Ophthalmol Strabismus 1979;16: 254–256.
207. Guerry D III, Kendig EJ Jr. Congenital impatency of the nasolacrimal duct. Arch Ophthalmol 1948;39:193–202.
208. Meyer JR, Quint DJ, Holmes JM, et al. Infected congenital mucocele of the nasolacrimal duct. AJNR 1993;14:1008–1010.
209. Petersen RA, Robb RM. The natural course of congenital obstruction of the nasolacrimal duct. J Pediatr Ophthalmol Strabismus 1978;15:246–250.
210. Harris GJ, DiClementi D. Congenital dacryocystocele. Arch Ophthalmol 1982;100:1763–1765.
211. Edmond JC, Keech RV. Congenital nasolacrimal mucocele associated with respiratory distress. J Pediatr Ophthalmol Strabismus 1991;28:287–289.

Copyright © 2003, Mosby, Inc. All rights reserved.

212. Castillo M, Merten DF, Weissler MC. Bilateral nasolacrimal duct mucocele, a rare cause of respiratory distress: CT findings in two newborns. AJNR 1993;14:1011–1013.
213. Rand PK, Ball WS, Kulwin DR. Congenital nasolacrimal mucoceles: CT evaluation. Radiology 1989;173:691–694.
214. Katowitz JR, Welsh MG. Timing of initial probing and irrigation in congenital nasolacrimal duct obstruction. Ophthalmology 1987;94: 698–709.
215. Young JDH, MacEwen CJ, Ogston SA. Congenital nasolacrimal duct obstruction in the second year of life: A multicenter trial of management. Eye 1996;10:485–491.
216. Migliori ME. Endoscopic evaluation and management of the lacrimal sump syndrome. Ophthal Plast Reconstr Surg 1997;13:281–284.
217. Becker BB, Berry FD, Koller H. Balloon catheter dilatation for treatment of congenital nasolacrimal duct obstruction. Am J Ophthalmol 1996;121:304–309.
218. Cho YS, Song HY, Ko GY, Yoon CH, Ahn HS, Yoon HK, Sung KB. Congenital lacrimal system obstruction: treatment with balloon dilation. JVIR 2000;11:1319–1324.
219. Janssen AG, Mansour K, Krabbe GJ, van der Veen S, Helder AH. Dacryocystoplasty: treatment of epiphora by means of balloon dilation of the obstructed nasolacrimal duct system. Radiology 1994;193:453–456.
220. Song HY, Ahn HS, Park CK, Kwon SH, Kim CS, Choi KC. Complete obstruction of the nasolacrimal system. I. Treatment with balloon dilatation. Radiology 1993;186:367–371.
221. Janssen AG, Mansour K, Bos JJ. Obstructed nasolacrimal duct system in epiphora: long-term results of dacryocystoplasty by means of balloon dilation. Radiology 1997;205(3):791–796.
222. Goldberg RA, Heinz GW, Chiu L. Gadolinium magnetic resonance imaging dacryocystography. Am J Ophthalmol 1993;115:738–741.
223. Hoffman KT, Hosten N, Anders N. High resolution conjunctival contrast enhanced MRI dacryocystography. Neuroradiology 1999;41: 208–213.
224. Reifler DM. Early descriptions of Horner's muscle and the lacrimal pump. Surv Ophthalmol 1996;41:127–134.
225. Rubin PAD, Bilyk JR, Shore JW, Sutula FC, Cheng HM. Magnetic resonance imaging of the lacrimal drainage system. Ophthalmology 1994;101:235–243.
226. Yoshikawa T, Hirota S, Sugimura K. Topical contrast-enhanced magnetic resonance dacryocystography. Radiat Med 2000;18(6): 355–362.
227. Takehara Y, Isoda H, Kurihashi K, Isogai S, Kodaira N, Masunaga H, Sugiyama M, Ozawa F, Takeda H, Nozaki A, Sakahara H. Dynamic MR dacryocystography: a new method for evaluating nasolacrimal duct obstructions. AJR 2000;175:469–473.
228. Munk PL, Lin DTC, Morris DC. Epiphora: treatment by means of dacryocystoplasty with balloon dilation of the nasolacrimal drainage apparatus. Radiology 1990;177:687–690.
229. Lee JM, Song HY, Han YM, Chung GH, Sohn MH, Kim CS, Choi KC. Balloon dacryocystoplasty: results in the treatment of complete and partial obstructions of the nasolacrimal system. Radiology 1994;192:503–508.
230. Song HY, Jin YH, Rim JH, Huh SJ, Kim YH, Kim TH, Sung KB. Non-surgical placement of a nasolacrimal polyurethane stent. Radiology 1995;194:233–237.
231. Becker BB, Berry FD. Balloon catheter dilatation in lacrimal surgery. Ophthalmic Surg 1989;20:193–198.
232. Kratky V, Hurwitz JJ, Ananthanarayan C, Avram DR. Dacryocystorhinostomy in elderly patients: regional anaesthesia without cocaine. Can J Ophthalmol 1994;29:13–16.
233. Wilhelm K, Kramer S, Ewen E, Schuller H, Schild H. Radiation dose to the ocular lens, parotid and thyroid glands in dacryocystography and fluoroscopically-guided dacryocystoplasty. ROFO Fortschr Geb Rontgenstr Neuen Bildgab Verfahr 1998;168:270–274 (German).
234. Wilhelm KE. Radiation dose in fluoroscopically-guided dacryocystoplasty (letter). Radiology 2001;219:577.
235. Ilgit ET, Meric N, Bor D, Öznur I, Konus Ö, Isik S. Lens of the eye: radiation dose in balloon dacryocystoplasty. Radiology 2000; 217:54–57.
236. Ilgit ET, Bor D, Meric N. (Reply). Radiation dose in fluoroscopically-guided dacryocystoplasty. Radiology 2001;219: 577–578.
237. Song HY, Ahn HS, Park CK, Kwon SH, Rim CS, Choi KC. Complete obstruction of the nasolacrimal system. II. Treatment with expandable metallic stents. Radiology 1993;186:372–376.
238. Song HY, Jin YH, Kim JH, Sung KB, Han YM, Cho NC. Nasolacrimal duct obstruction treated non-surgically with use of plastic stents. Radiology 1994;190:535–539.
239. Janssen AG. Imaging and interventional procedures for the lacrimal duct system. In: Mukherji SK, Castelijns JA, eds. Medical Radiology: Modern Head and Neck Imaging. Berlin: Springer, 2000;211–235.
240. Ilgit ET, Yüksel D, Ünal M, Akpek S, Isik S, Hsanreisoglu B. Transluminal balloon dilation of the lacrimal draining system for the treatment of epiphora. AJR 1995;165:1517–1524.
241. Kumar EN. Technical note: non-surgical treatment of epiphora by balloon dacryoplasty—the technique. Br J Radiol 1995;68:1116–1118.
242. Ilgit ET, Yüksel D, Ünal M, Akpek S, Isik S. Treatment of recurrent nasolacrimal duct obstructions with balloon-expandable metallic stents: results of early experience. AJNR 1996;17:657–663.
243. Berkefeld J, Kirchner J, Müller HM, Fries U, Kollath J. Balloon dacryocystoplasty: indications and contraindications. Radiology 1997;205:785–790.
244. Yazici B, Yazici Z, Parlak M. Treatment of nasolacrimal duct obstruction in adults with polyurethane stent. Am J Ophthalmol 2001;131:37–43.
245. Yazici Z, Yazici B, Parlak M, Erturk H, Savci G. Treatment of obstructive epiphora in adults by balloon dacryocystoplasty. Br J Ophthalmol 1999;83:692–696.
246. Song HY, Jin YH, Kim JH, Suh SW, Yoon HK, Kang SG, Sung KB. Nonsurgical placement of a nasolacrimal polyurethane stent: long-term effectiveness. Radiology 1996;200:759–763.
247. Kuchar A, Steinkogler FJ. Antegrade balloon dilatation of nasolacrimal duct obstruction in adults. Br J Ophthalmol 2001;85:200–204.
248. Steinsapin KD, Glatt HJ, Putterman AM. A 16-year study of conjunctival dacryocystorhinostomy. Am J Ophthalmol 1990;109: 387–393.
249. Goo DF, Song HY, Yoon H, Sung K. Lacrimal canalicular strictures: safety and effectiveness of balloon dilatation (abstract). Radiology 1996;201(P):411.
250. Song HY, Lee CO, Park S, Suh SW, Yoon HK, Kang SG, Sung KB. Lacrimal canalicular obstruction: safety and effectiveness of balloon dilation. JVIR 1996;7:929–934.
251. Ko YK, Lee DH, Ahn HS, Yoon HK, Sung KB, Song HY. Balloon catheter dilation in common canalicular obstruction of the lacrimal system: safety and long-term effectiveness. Radiology 2000;214: 781–786.
252. Song HY, Lee CO, Park S, Suh SW, Yoon HK, Kang SG, Sung KB. Lacrimal canaliculus obstruction: non-surgical treatment with a newly designed polyurethane stent. Radiology 1996;199:280–282.
253. Palmaz JC. Balloon-expandable intravascular stent. Am J Roentgenol 1988;150:1263–1269.
254. Palmaz JC. Intravascular stents: tissue–stent interaction and design considerations. Am J Roentgenol 1993;160:613–618.
255. Howes EL, Rao NA. Basic mechanisms in pathology. In: Spencer WH, ed. Ophthalmic Pathology. An Atlas and Textbook, 4th ed. Philadelphia: WB Saunders, 1996;2973.
256. Pabón IP, Díaz LP, Grande C, de la Cal López MA. Nasolacrimal polyurethane stent placement for epiphora: technical long-term results. JVIR 2001;12(1):67–71.
257. Hurwitz JJ. Endoscopy canaliculus. In Hurwitz JJ, ed. The Lacrimal System. Philadelphia: Lippincott-Raven, 1996;103–104.
258. Ashenhurst ME, Hurwitz JJ. Lacrimal canaliculoscopy: development of the instrument. Can J Ophthalmol 1991;26:306–308.
259. Müllner K, Bodner E, Mannor GE. Endoscopy of the lacrimal system. Br J Ophthalmol 1999;83:949–952.

Copyright © 2003, Mosby, Inc. All rights reserved.

Copyright © 2003, Mosby, Inc. All rights reserved.

11

Visual Pathways

Robert A. Zimmerman, Larissa T. Bilaniuk, and Peter J. Savino

EMBRYOLOGY OF THE RETROCHIASMATIC VISUAL PATHWAY
ANATOMY OF THE VISUAL PATHWAYS
IMAGING TECHNIQUES
NORMAL CT AND MR IMAGING ANATOMY
PATHOLOGIC CONDITIONS
- Optic Nerve Visual Pathway Glioma
  - Clinical Findings
  - Pathologic Findings
  - CT Appearance
  - MR Imaging Appearance
- Perioptic Meningioma
  - Clinical Findings
  - Pathologic Findings
  - CT Appearance
  - MR Imaging Appearance
- Sarcoidosis
  - Clinical Findings
  - Pathologic Findings
  - CT Appearance
  - MR Imaging Appearance
- Lyme Disease
  - Clinical Findings
  - Pathologic Findings
  - CT Appearance
  - MR Imaging Appearance
- Craniopharyngioma
  - Clinical Findings
  - Pathologic Findings
  - CT Appearance
  - MR Imaging Appearance
- Rathke's Cleft Cyst
  - Clinical Findings
  - Pathologic Findings
  - CT Appearance
  - MR Imaging Appearance
- Pituitary Adenoma
  - Clinical Findings
  - Pathologic Findings
  - CT Appearance
  - MR Imaging Appearance
- Aneurysms
  - Clinical Findings
  - Pathologic Findings
  - CT Appearance
  - MR Imaging Appearance
- Infarction
  - Clinical Findings
  - Pathologic Findings
  - CT Appearance
  - MR Imaging Appearance
- Demyelinating Disease
  - Clinical Findings
  - Pathologic Findings
  - CT Appearance
  - MR Imaging Appearance
- Cerebral Neoplastic Disease
  - Clinical Findings
  - Pathologic Findings
  - CT Appearance
  - MR Imaging Appearance

The retrobulbar visual pathway (Fig. 11-1) includes all neural pathways involved in visual function from the point where the optic nerve originates in the posterior globe to the primary visual cortex lying within the medial aspects of the occipital lobes. The elements of the pathway can be affected by a variety of pathologic conditions, which, depending on their location, give rise to characteristic clusters of clinical symptomatology. The apparent symptoms therefore enable

Copyright © 2003, Mosby, Inc. All rights reserved.

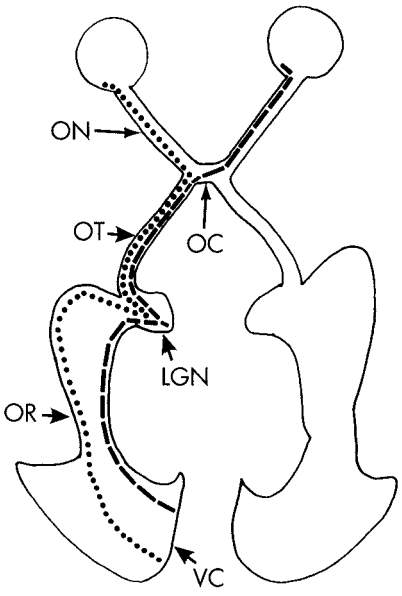

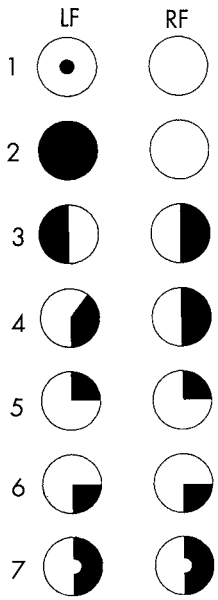

FIGURE 11-1 **A**, Diagram of left visual pathway. *Dots*, The pathway that starts in the temporal portion of the retinas of the left eye and ends in the left occipital cortex; *dashes*, pathway from the nasal portion of the retinas of the right eye that crosses to the left in the optic chiasm and ends in the left occipital cortex; *ON*, optic nerve; *OC*, optic chiasm; *OT*, optic tract; *LGN*, lateral geniculate nucleus; *OR*, optic radiations; *VC*, visual cortex. **B**, Visual field defects that can occur with abnormalities involving the left visual pathway. Each visual field is represented separately; the figure on the left represents the patient's left visual field. *LF*, left field; *RF*, right field. Site of lesion: *ON—1*. Left central scotoma: *ON—2*. Complete blindness left visual field. *ON—3*. Bitemporal hemianopia. *OT*, *LGN—4*. Right incongruous homonymous hemianopia. *OR—5*. Right congruous upper quadrantic hemianopia. *OR—6*. Right congruous inferior quadrantic hemianopia. *VC—7*. Right congruous homonymous hemianopia with macular sparing.

VIEW IMAGE

the pathologic condition to be localized along the visual pathway with a high degree of certainty. For this reason, imaging techniques may be tailored to display the expected condition optimally. In the past, these imaging techniques included plain radiographs, orbital venography, pneumoencephalography, and complex motion tomography. However, during the past two decades, computed tomography (CT) and magnetic resonance (MR) imaging have become the mainstays of visual pathway imaging because they allow direct visualization of the elements of the pathway and the pathologic processes contained therein. Today, MR imaging is the procedure of choice.

This chapter defines the anatomy of the visual pathway, discusses the relevant embryology, delineates the role of CT and MR imaging, discusses the various pathologic entities that can affect the visual pathway and their clinical symptomatology, and illustrates the appearance of these pathologic conditions.

EMBRYOLOGY OF THE RETROCHIASMATIC VISUAL PATHWAY

Embryologic development of the retrochiasmatic visual pathway is a complex process that occurs in a sequential, stepwise fashion. It involves the growth and development of both neural and vascular structures and is also affected by influences stemming from developing osseous structures.[1, 2] The embryology of the globe (discussed in Chapter 8) and optic nerve is described in general terms to place the development of the retrochiasmatic structures in perspective.

During the embryonic period of fetal life, specifically at 4 weeks of gestation, early vesicularization of the developing brain occurs.[1, 2] The optic pits appear on the surface of the rostral end of the developing embryo, and shortly thereafter, the optic vesicles evaginate from the prosencephalon, and the lens placode begins developing within the optic vesicle. By the end of 5 weeks of gestation, the optic vesicle has invaginated, forming the optic cup and the fetal fissure, a crease in the surface of the optic cup and stalk in which the hyaloid artery travels to vascularize the lens of the vesicle. Subsequently, early development of the various layers of the retina occurs. Within the developing retina, the axons of the ganglion cells begin to project into the optic stalk, giving rise to the first discernible structure of the optic nerve. By the end of 6 weeks of gestation, the lens capsule has formed around the lens vesicle, and progressive closure of the fetal fissure has begun.

The anlagen of the extraocular muscles begin to develop, arising from mesodermal tissues of the orbit, and by the end of 7 weeks of gestation, the fetal fissure has completely closed. At this time, the axons of the ganglion cells forming the optic nerve fibers reach the most proximal end of the optic stalk, with some crossing to form the chiasm. The lateral geniculate bodies begin to appear. The meningeal sheath surrounding the optic nerve forms and is contiguous with the dura covering the brain, as well as with the sclera enclosing the globe. Rods and cones begin to develop as a result of further retinal differentiation, and by the end of 8 weeks of gestation, retinal differentiation has progressed rapidly and the bony orbit has begun to develop. The optic stalk is entirely filled with nerve fibers, and as a result, the cavity of the optic vesicle no longer communicates with that of the forebrain. The optic chiasm is fully formed and separated from the floor of the third ventricle, with only the optic recess remaining as a remnant of the optic vesicle.

In the fetal period of intrauterine development, the optic pathway develops further, especially within the more central portions.[1, 2] By the end of 9 weeks of gestation, early differentiation of the occipital cortex is noted. At this point, the retina demonstrates a more mature, layered appearance, and by the end of 10 weeks of gestation, the optic tract has fully formed. The axons forming the optic nerve and tract reach the lateral geniculate bodies in the dorsolateral part of the mantle layer of the thalamus, and differentiation of the occipital cortex into marginal and mantle layers is completed by the end of 11 weeks of gestation, with full

Copyright © 2003, Mosby, Inc. All rights reserved.

elaboration of the peripheral cortical layer. By the end of 16 weeks of gestation, the adult form of retinal vascularization is seen with entry of the central retinal artery via the optic nerve head, resulting from progressive atrophy of the hyaloid system.

Myelination of the optic tracts begins at the lateral geniculate nuclei at 20 weeks of gestation and proceeds peripherally in a direction opposite to that of axonal growth. The choroid now demonstrates three distinct layers. Myelination of the optic tract and chiasm continues from 24 to 28 weeks of gestation, and progressive enfolding of the calcarine cortex forming the calcarine fissure is noted. By the end of 32 weeks of gestation, all layers of the retina have been entirely formed, and the eyelids, which previously were fused, are now unfused. By the end of 36 weeks of gestation, the optic nerve has completed its myelination to the lamina cribrosa. Myelination of the optic radiations does not begin until approximately the time of birth. It then proceeds centrifugally over a 4-month period, beginning from the calcarine cortex toward the lateral geniculate bodies.

ANATOMY OF THE VISUAL PATHWAYS

Light enters the globe via the cornea, passes through the aqueous humor, lens, and vitreous humor, and then strikes the retina, impinging on photoreceptor cells in the most posterior layer of its laminated structure. Depolarizations occur within the rods and cones, which transmit impulses to the bipolar cells in the intermediate layer of the retina. These bipolar cells are the primary afferent neurons of the visual system. Impulses are then transmitted to the ganglion cells, which lie in the more superficial anterior layer of the retina. The axons of the ganglion cells course upon the most anterior surface of the retina, converging on the posterior pole of the eye, where they initiate a 90° turn and pierce the sclera at the lamina cribrosa, coalescing to form the optic nerve. Myelination of the axons of the optic nerve occurs only within those axons that are outside the globe.[1] The axons anterior to the lamina cribrosa are not myelinated.

The optic nerves pass dorsomedially to the orbital apex, entering the skull via the optic canals.[3] They then combine at the optic chiasm, which is superior to the sella turcica in the suprasellar cistern at the base of the brain. Axons from the nasal half of the retina decussate to contribute to the contralateral optic tract, whereas axons from the temporal half of the retina remain uncrossed.

Each visual field projects on parts of both retinas, with the right visual field projected on the nasal half of the right retina and the temporal half of the left retina. A monocular crescent of the most peripheral area of the right visual field is projected only onto the nasal half of the right retina because of anatomic asymmetry, with the nasal retina being longer than the temporal retina. Fibers from both retinas, which carry information about the right visual field, combine at the optic chiasm, forming the left optic tract. Therefore the whole right visual field projects to the left hemisphere.[1]

The optic tract courses dorsolaterally around the hypothalamus and the rostral part of the cerebral peduncle within the perimesencephalic cistern, synapsing with cells of the lateral geniculate bodies (Fig. 11-1). A small number of fibers, the pupillary motor fibers, project in a medial caudal direction, forming the brachium of the superior colliculus, a projection to the superior colliculus and pretectal areas. The lateral geniculate nucleus lies in the dorsolateral aspect of the thalamus, ventral to the pulvinar and lateral to the medial geniculate body and cerebral peduncle. It is a precisely ordered six-layered structure. The contralateral half of the binocular visual field is represented in all layers of the lateral geniculate body. However, crossed and uncrossed fibers end in different layers. Crossed fibers project to layers 1, 4, and 6, whereas uncrossed fibers project to layers 2, 3, and 5.

Cell bodies of the lateral geniculate nucleus give rise to the optic radiations (geniculocalcarian tracts), which pass to the ipsilateral primary visual cortex lying on the medial aspect of the occipital lobes surrounding the calcarian sulcus (Fig. 11-1). Fibers of the optic radiations first pass through the retrolenticular part of the internal capsule (the most posterior part of the posterior limb of the internal capsule). They then arch laterally around the lateral ventricles and sweep posteromedially to synapse with cell bodies in the calcarine cortex. Fibers from the ventrolateral aspect of the lateral geniculate nucleus, carrying information from the inferior quadrant of the retina (superior visual field), sweep ventrally into the temporal lobe, pass laterally over the inferior horn of the lateral ventricle forming the so-called Myer's loop, and turn posteriorly to proceed to the calcarine cortex, inferior to the calcarine sulcus. Fibers from the dorsomedial aspect of the lateral geniculate nucleus, carrying information from the superior quadrant of the retina (inferior visual field), follow a more direct posterior course to the calcarine cortex, superior to the calcarine sulcus.

The calcarine cortex is topographically ordered in an anterior to posterior direction, as well as in a superior to inferior one.[1] The most posterior area receives information from the central (macular) visual field, the middle third receives binocular information from the contralateral visual field, and the most anterior third receives monocular information from the contralateral visual field. From the cell bodies lying within the calcarine cortex, axons project to the visual association cortex in surrounding areas.

As a result of precise topographic localization of the visual fields at each part of the visual pathway, discrete lesions can be localized clinically with a high degree of accuracy. Lesions causing interruption of the optic nerve result in monocular blindness (Fig. 11-2). Lesions interrupting the decussating fibers at the optic chiasm cause bitemporal hemianopsia (Fig. 11-3). Partial interruption of the retrochiasmal portion of the visual pathway results in incomplete hemianopsias that are localizing. With complete interruption and total homonymous hemianopsia, there is no localizing information. Interruption of the pathway at the optic tract causes contralateral homonymous hemianopsia. If the optic radiations are interrupted within the temporal lobe, a contralateral superior quadrantanopsia results (Fig. 11-4). Cortical lesions (Fig. 11-5) superior to the calcarine sulcus result in an inferior quadrantanopsia, whereas lesions inferior to the calcarine sulcus (Fig. 11-6) cause a superior quadrantanopsia. Lesions of the occipital pole result in central macular hemianopic deficits.

Copyright © 2003, Mosby, Inc. All rights reserved.

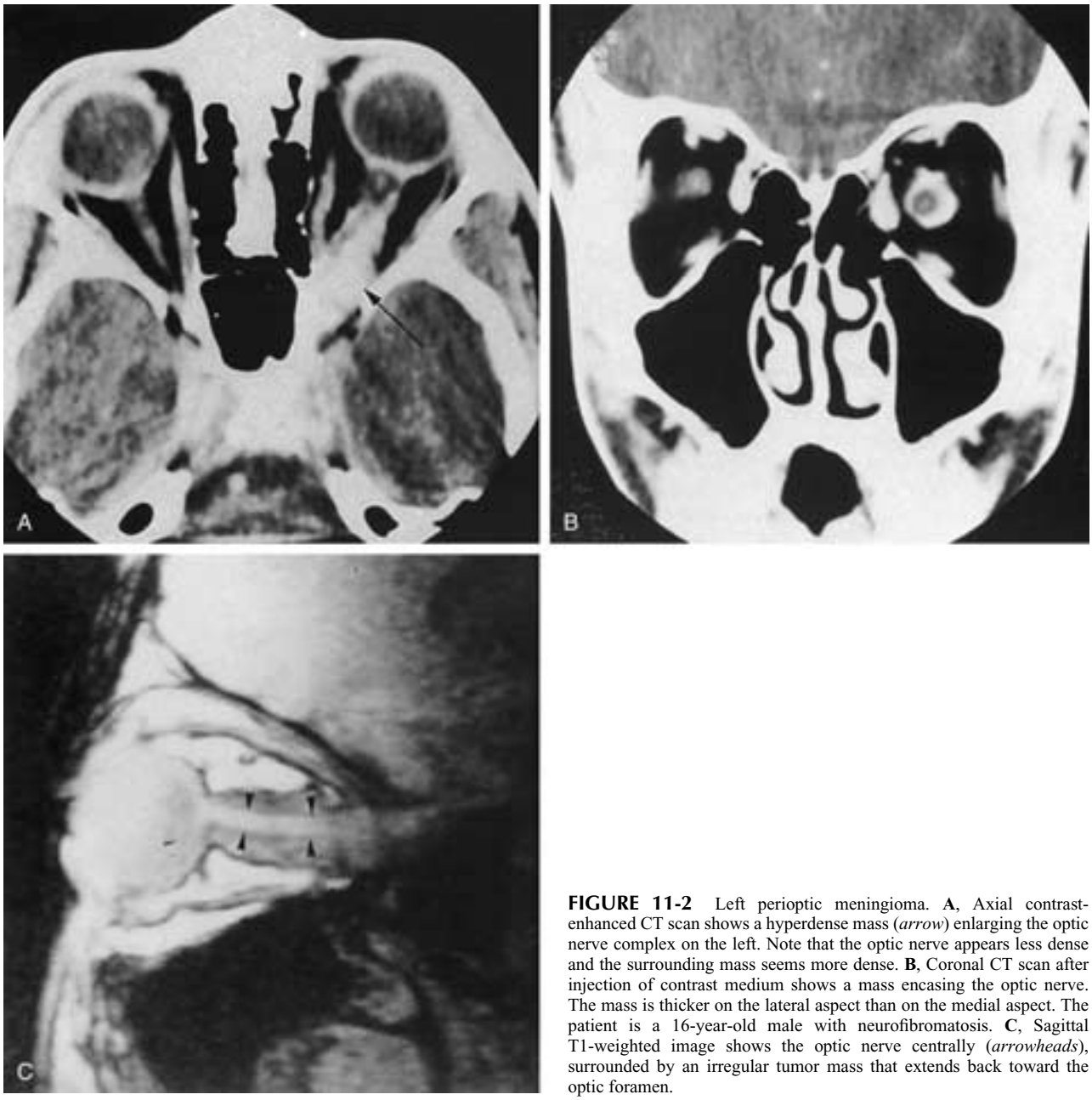

FIGURE 11-2 Left perioptic meningioma. **A**, Axial contrast-enhanced CT scan shows a hyperdense mass (*arrow*) enlarging the optic nerve complex on the left. Note that the optic nerve appears less dense and the surrounding mass seems more dense. **B**, Coronal CT scan after injection of contrast medium shows a mass encasing the optic nerve. The mass is thicker on the lateral aspect than on the medial aspect. The patient is a 16-year-old male with neurofibromatosis. **C**, Sagittal T1-weighted image shows the optic nerve centrally (*arrowheads*), surrounded by an irregular tumor mass that extends back toward the optic foramen.

VIEW IMAGE

IMAGING TECHNIQUES

The indications for imaging of the optic pathways are based on clinical findings and symptomatology, which include some form of visual loss. The rapidity of onset of visual loss suggests the type of pathologic condition responsible, whereas the specific visual field deficit suggests the location of the pathologic process within the visual pathway. In a patient under 45 years of age, sudden onset of monocular blindness, when associated with pain, suggests an optic nerve neuritis. Gradually progressive monocular blindness, especially if associated with proptosis, suggests a mass lesion such as perioptic meningioma involving the optic nerve sheath (Fig. 11-2) as one of the likely causes. The ophthalmoscopic findings of disk edema or optic atrophy are frequently associated with neoplasia and mass effect or an inflammatory process. If the finding is unilateral, the optic nerve is the likely site of involvement. However, if bilateral disk edema or optic atrophy is present, an intracranial cause is more likely. For example, papilledema is bilateral disk swelling due to increased intracranial pressure. Bitemporal hemianopsia is most commonly caused by a disease involving the optic chiasm; the most common disease is a pituitary adenoma (Fig. 11-3) that causes compression of the decussating fibers of the optic pathway. Other conditions with similar clinical findings include lesions that cause extrinsic compression of the chiasm (e.g., craniopharyngioma, meningioma, or carotid artery aneurysm) or intrinsic lesions of the chiasm, such as a chiasmatic glioma. Inflammatory conditions such as sarcoidosis, Langerhans' histiocytosis X, or tuberculosis may also involve the optic chiasm. Homonymous hemianopsia suggests a disease

Copyright © 2003, Mosby, Inc. All rights reserved.

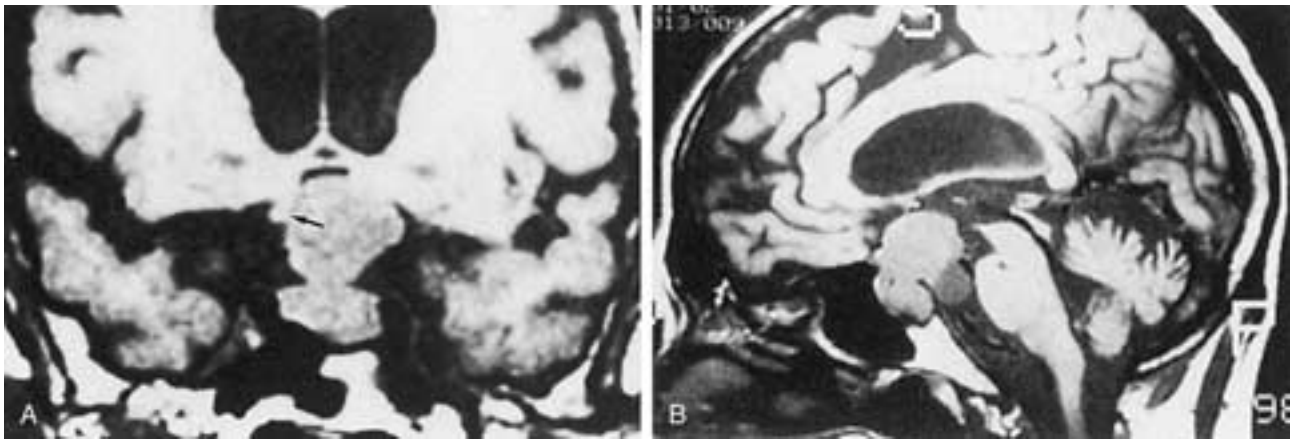

VIEW IMAGE

FIGURE 11-3 Pituitary adenoma with chiasmal compression in a 70-year-old male with bitemporal hemianopsia. **A**, Coronal T1-weighted image shows an isointense mass within the sella, expanding it to the left and extending through the diaphragma sella (site of the waist) into the suprasellar cistern. Note the compression of the right optic nerve (*arrow*). **B**, Sagittal T1-weighted image shows an intrasellar tumor mass. The optic chiasm is not distinguishable in this view.

process involving the retrochiasmatic portion of the visual pathway. Sudden onset of this visual field deficit suggests a vascular cause, whereas more gradual development suggests a mass lesion as the cause. If the deficit is incomplete and congruent (equally involving the superior and inferior quadrants of the contralateral visual field), the lesion is likely to lie within the calcarine cortex of the occipital lobe (Fig. 11-5). If the deficit is incomplete and incongruous, the lesion is likely to involve optic tracts, or it may lie either in the temporal lobe involving Meyer's loop (superior quadrantinopsia) (Fig. 11-4) or in the parietal lobe (inferior quadrantinopsia) (Fig. 11-7).

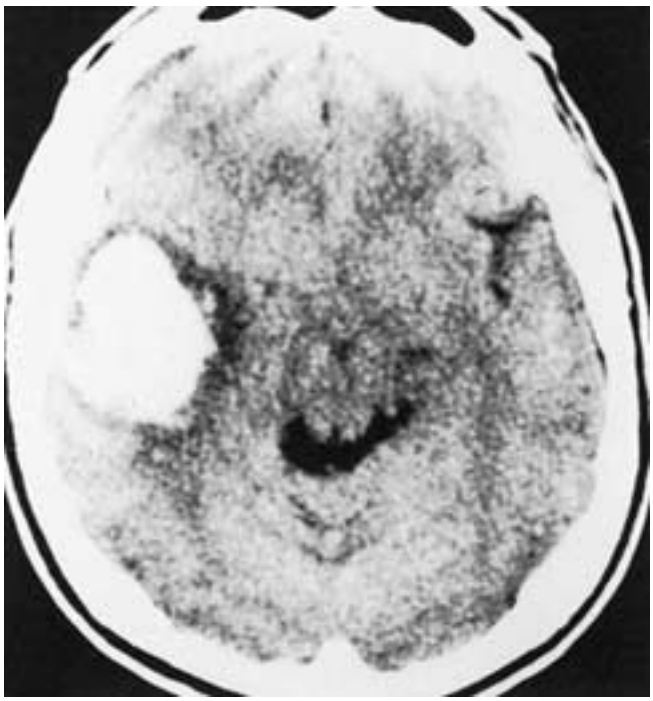

VIEW IMAGE

FIGURE 11-4 Temporal lobe hematoma. Axial CT image shows a hyperdense mass in the anterior aspect of the right temporal lobe.

CT evaluation of the visual pathway should be obtained with intravenous contrast enhancement unless the patient has experienced recent trauma or has a history of severe contrast reaction, or unless a foreign body, hemorrhage, or infarction along the course of the visual pathway is suspected. Axially oriented 5-mm-thick, contiguous CT sections should be obtained from the foramen magnum to the orbital floor; then 2-mm-thick sections should be obtained from the orbital floor to the orbital roof.[4] The remainder of the head can be imaged with contiguous 5-mm-thick scans. Coronal contiguous images 2 mm thick should be obtained with the patient's neck in maximally tolerated extension. The anatomic region included should extend from the dorsum of the sella to the anterior aspect of the globe and should include the sella turcica and the orbit.[5] A 20-cm field of view should be used for the axial images, with subsequent magnification of the orbital region to maximally display any pathology in the area. The coronal images should be obtained with a 12- to 15-cm field of view.

In general, MR imaging is the modality of choice for visualization of the elements of the visual pathway, except in patients with a history of trauma or when a fracture or foreign body with unknown ferromagnetic properties is suspected.[6–9] Once a modality for imaging has been chosen, the imaging protocol may be specifically altered to visualize optimally the region of the optic pathway most likely to contain the pathologic condition.

MR imaging of the elements of the optic pathway involves the use of a head coil. A dedicated orbit surface coil can be utilized to evaluate intraorbital lesions. Using the head coil, axial and coronal images with a TR of 500 to 800 msec and a TE of 20 msec should be obtained. Scans 3 mm thick, with no interscan space, one excitation, a 256 × 256 matrix, and a 14-cm field of view optimally display the structures of the orbit.[6, 10] The remainder of the intracranial optic pathway may be imaged using a sagittal TR 600, TE 20 spin-echo sequence with 5-mm-thick images, a 22-cm field of view, two excitations, and a 256 × 256 matrix. This should be followed by an axial study using a TR of 6000 and a TE of 100 msec, 5-mm-thick slices, one or two excitations,

Copyright © 2003, Mosby, Inc. All rights reserved.

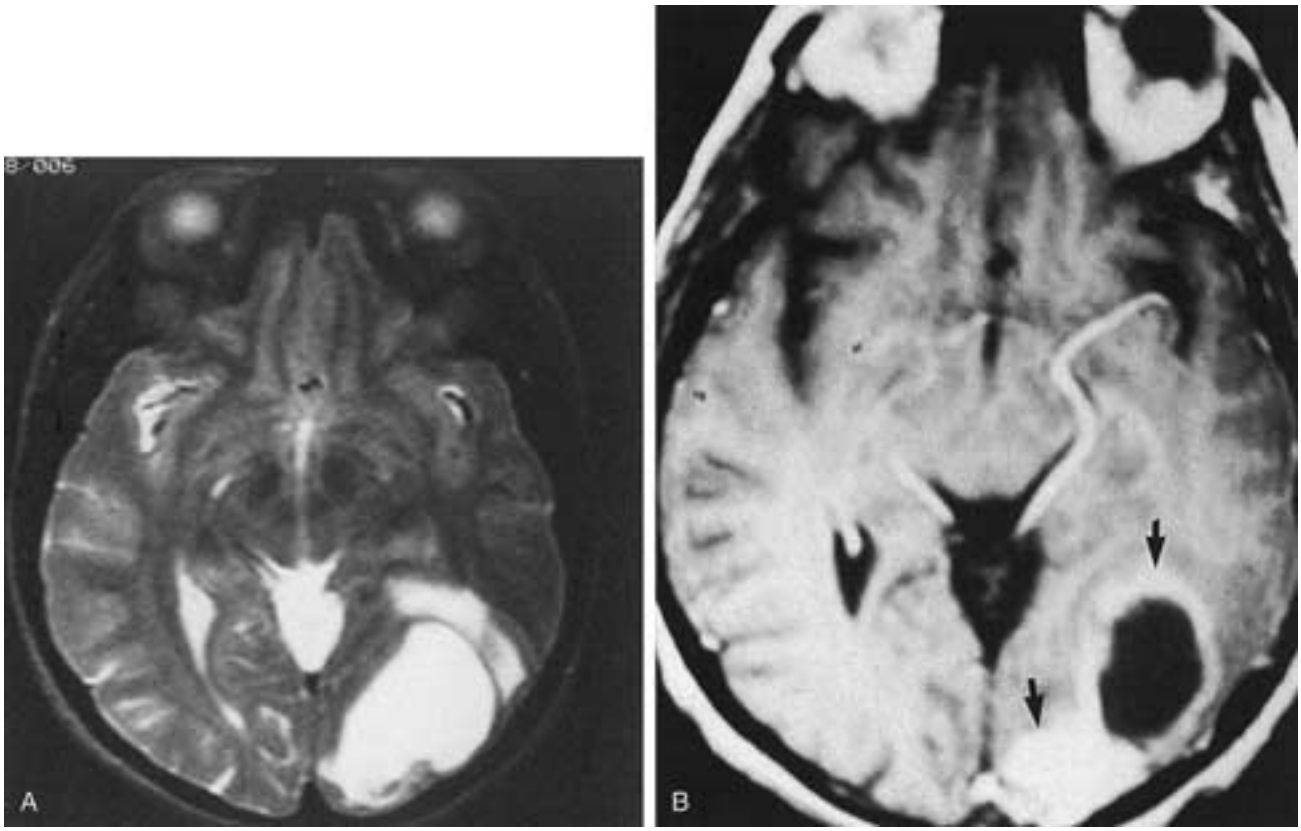

VIEW IMAGE

FIGURE 11-5 Occipital lobe metastasis from carcinoma of the lung. **A**, Axial T2-weighted image shows hyperintense mass in the left temporal occipital region; a point of separation exists between the most posterior portion of the mass and the anterior segment of high signal intensity edema in adjacent white matter. **B**, Axial T1-weighted image after injection of contrast medium shows tumor enhancement (*arrows*).

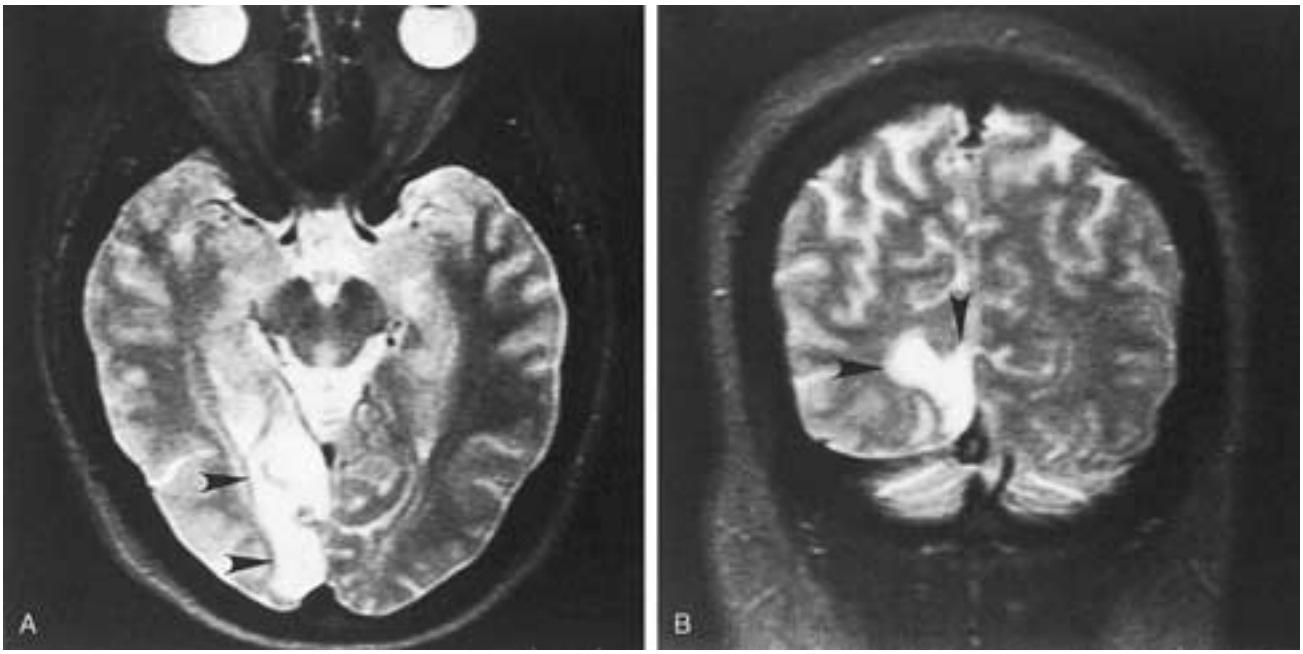

VIEW IMAGE

FIGURE 11-6 **A**, Axial T2-weighted image shows a high signal intensity occipital infarct (*arrowheads*). **B**, Coronal T2-weighted image. The infarct (*arrowheads*) lies below the calcarine fissure.

Copyright © 2003, Mosby, Inc. All rights reserved.

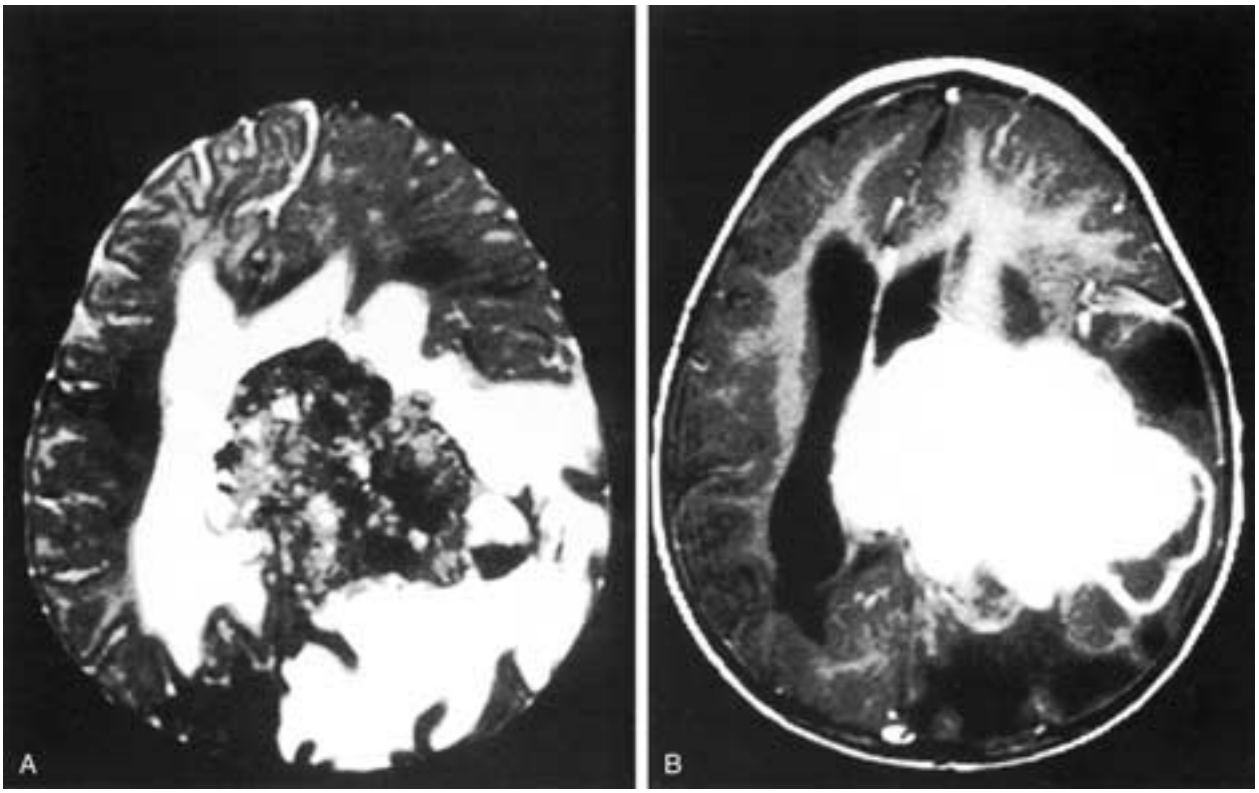

VIEW IMAGE

FIGURE 11-7 Choroid plexus carcinoma. Lateral ventricle, left side, invading the brain and producing right inferior quadrantic hemianopsia. **A**, Axial T2-weighted image shows a mass that is predominantly low in signal intensity, on its lateral margin is surrounded by vasogenic edema within the left cerebral hemisphere, and on its medial margin is within the displaced body of the left lateral ventricle. **B**, Axial T1-weighted image after gadolinium injection shows marked enhancement of the tumor mass.

a 512 × 512 matrix, and a 20-cm field of view.[8, 11] Techniques designed to suppress the signal from the orbital fat make pathologic conditions involving the optic nerve more visible and may be useful when subtle lesions are suspected.[12, 13] One such sequence involves the use of inversion recovery imaging (STIR).[14] Such a technique uses a TR of 2500, a TE of between 30 and 60, a TI of 150, two excitations, a 256 × 256 matrix, 3-mm-thick images, and a 1-mm interscan space. Fat suppressed, T2-weighted spin-echo images with a 256 × 256 matrix and a 2-mm slice thickness in the axial and coronal planes are also useful. In fluid attenuated inversion recovery imaging (FLAIR) the high signal of cerebrospinal fluid (CSF) is suppressed, while showing the abnormal high signal of increased water in pathologic tissue such as plaques of multiple sclerosis or areas of acute infarction.[15] FLAIR imaging can be obtained with turbo sequences in 3 minutes with a 256 × 256 matrix, one acquisition, and a 5-mm slice thickness. A typical pulse sequence uses a TR of 9000 msec, a TE of 120 msec, and a TI of 2200 msec. Contrast enhancement achieved with intravenous administration of gadolinium diethylenetriaminepentaacetic acid (DTPA) in a dose of 1 mmol/kg has demonstrated clinical utility in diagnosing both intraorbital and intracranial pathologic conditions, including neoplasms and inflammatory or infectious conditions. The use of fat-saturated, T1-weighted images with gadolinium enhancement in the axial (Fig. 11-8) and coronal (Fig. 11-9) planes is currently the procedure of choice for detecting abnormal enhancement of the optic nerve or surrounding tissues.

NORMAL CT AND MR IMAGING ANATOMY

The normal intraorbital optic nerve/sheath complex is well visualized on axial and coronal CT because of the natural contrast between it and the surrounding retrobulbar adipose tissue.[14] The normal optic nerves appear symmetric and homogeneous. The normal diameter of the nerve is 3 to 5 mm (average, 4.5 mm) on axial scans and 4 to 6 mm (average, 5 mm) on coronal scans.[4, 16] The intracanalicular portion of the optic nerve is poorly visualized with CT because of beam-hardening artifact from the surrounding bony canal. Unless intrathecal contrast material is used,[5, 17] the intracranial portion of the nerve, as well as the optic chiasm and optic tract, are poorly visualized on CT because of inadequate contrast between the CSF and the neural tissues.[5] Without contrast material in the CSF, the location of the intracranial portion of the nerve, the optic chiasm, and the optic tract is inferred on the basis of knowledge of their anatomic location relative to adjacent structures such as the suprasellar cistern, hypothalamus, medial aspect of the temporal lobes, and lateral aspect of the midbrain. The position of the lateral geniculate nucleus (LGN) is inferred by localizing the pulvinar of the thalamus, since the LGN is

Copyright © 2003, Mosby, Inc. All rights reserved.

not directly visualized on CT. The optic radiations also are not directly seen, but their expected location may be inferred by observing the appropriate area of the temporal lobe adjacent to the temporal horn of the lateral ventricle and the parietal lobe adjacent to the atrium of the lateral ventricle. The most distal portion of the optic radiation can also be inferred by its position relative to the occipital horns of the lateral ventricles. The calcarine cortex is directly visualized along the medial aspect of the occipital lobes.

On MR imaging, using spin-echo short TR/TE (600/20) and long TR/short TE (3000/30) sequences, the intraorbital optic nerve demonstrates signal intensity similar to that of cerebral white matter.[5] It is of low signal intensity relative to the high signal intensity of the retrobulbar adipose tissue. On spin-echo long TR/long TE (3000/90) images, the optic nerve has a signal intensity similar to that of orbital fat; however, often a small amount of high signal intensity CSF can be visualized in the subarachnoid space between the nerve sheath and the optic nerve. On turbo spin-echo long TR/long TE (6000/1000) images, the high signal intensity CSF outlines the optic nerve. The intracanalicular portion of the optic nerve is well visualized on MR imaging because of the absence of signal from the cortical bone forming the optic canal.[6] Short TR/short TE imaging sequences, particularly in the coronal projection, display the intracranial portion of the optic nerve as a relatively higher signal intensity structure within the lower signal intensity CSF of the suprasellar cistern.[18] The optic chiasm and optic tracts demonstrate similar characteristics and are best visualized in either the coronal or sagittal plane.[19] The LGN occasionally may be seen on long TR/long TE images as a high signal intensity nuclear aggregation. More commonly, the LGN is seen as a contour arising from the diencephalon and protruding into the ambiens cistern adjacent to the thalamus. The optic radiation may be seen as cerebral white matter intensity structures within the temporoparietal and occipital lobes; their course is inferred by knowledge of the anatomic location of this portion of the optic pathway. The calcarine cortex may be directly observed on either coronal, axial, or sagittal short or long TR images. The two gyri making up the primary visual cortex may be positively identified, since they are easily seen flanking the calcarine sulcus.

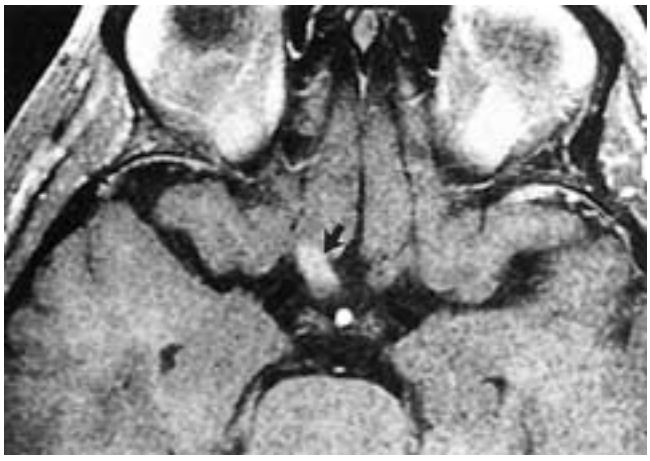

VIEW IMAGE

FIGURE 11-8 Multiple sclerosis in a 34-year-old woman with monocular visual loss of the right eye of recent origin. Axial fat-suppressed, gadolinium-enhanced, T1-weighted image shows enhancement of the enlarged right intracranial optic nerve (*arrow*).

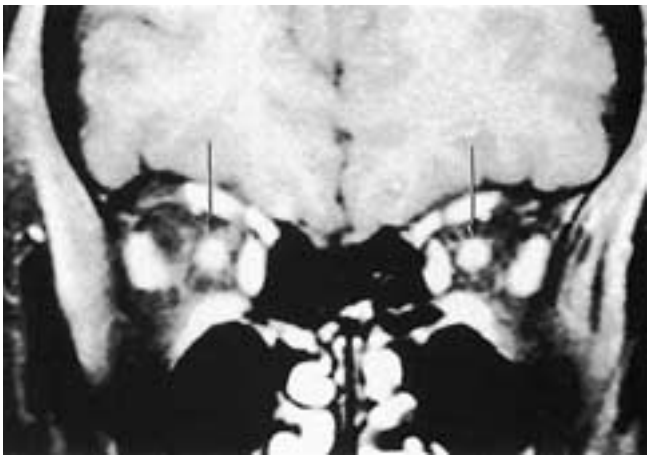

FIGURE 11-9 Multiple sclerosis in a 16-year-old female with bilateral scotomata and evidence of acute optic neuritis on fundoscopic examination. Coronal fat-suppressed, gadolinium-enhanced, T1-weighted MR image shows bilateral enlargement and enhancement of the intraorbital optic nerves (*arrows*).

VIEW IMAGE

PATHOLOGIC CONDITIONS

Optic Nerve Visual Pathway Glioma

Gliomas of the optic nerve or visual pathway are relatively uncommon low-grade neoplasms that can involve various portions of the retrobulbar visual pathway, including the optic nerve, chiasm, optic tracts, and radiations. These tumors appear most frequently during the first decade of life, and there is a slight female preponderance. There is also an association between optic nerve gliomas and intracranial visual pathway gliomas and neurofibromatosis type 1.

Clinical Findings

Optic nerve gliomas constitute approximately 3% of all orbital tumors; they outnumber perioptic meningiomas by approximately 4 to 1.[10] Optic nerve gliomas occur most frequently in the first decade of life (median age, 5 years); however, they may be present at birth and have been reported in patients as old as 60 years of age.[20, 21] They may occur at any point in the retrobulbar visual pathway, including the optic nerve, chiasm, or optic tract, lateral geniculate bodies, and optic radiations.[20–22] Involvement of the optic chiasm coexistent with gliomas of both optic nerves is more common than involvement of a single optic nerve.[20] Bilateral optic nerve gliomas imply neurofibromatosis type 1. Invasion of the globe by the tumor, although extremely rare, has been observed.[21]

Approximately 15% or more of patients with optic nerve gliomas demonstrate the findings of neurofibromatosis at the time of diagnosis (range, 12% to 38%).[20, 21] Visual pathway gliomas appear early in life, often before the clinical stigmata of neurofibromatosis become evident.

The clinical picture of patients with optic nerve gliomas depends on whether the primary involvement is orbital or intracranial. Intraorbital gliomas usually appear early, with

Copyright © 2003, Mosby, Inc. All rights reserved.

painless proptosis. Globe motility usually is not restricted. Optic atrophy is the most frequent ophthalmoscopic finding, with occasional disc edema.[20] Loss of or decreased vision occurs and may progress to total loss of vision. Occasionally, peripheral visual constriction may be observed. Clinically, intraobital optic nerve glioma and meningioma are difficult to differentiate.[21]

Intracranial visual pathway gliomas generally appear with symptoms related to the portion of the brain that is involved. These symptoms include seizures, nystagmus, hydrocephalus, and changes in mental status. Loss of vision is the most common initial symptom.[20] The presence of nystagmus is highly suspicious for chiasmal involvement.

Pathologic Findings

The cell of origin for optic nerve gliomas has not been definitively elucidated; thus, these neoplasms are included in the general classification as gliomas. Specifically, they are usually classified as grade I astrocytomas (juvenile pilocytic astrocytomas).[20, 22] The tumors are slow-growing, with no tendency to metastasize. Malignant transformation does not occur in childhood gliomas. Development of optic nerve gliomas is observed to occur in stages, from generalized hyperplasia of the glial cells within the nerve to complete disorganization with loss of landmarks within the nerve and the nerve sheath. The tumor usually causes smooth fusiform enlargement of the optic nerve (Fig. 11-10), although it may be somewhat asymmetric with respect to the nerve. A reactive meningeal hyperplasia may be incited, which extends beyond the position of the tumor itself, making it difficult to differentiate it from a perioptic meningioma.[22] Microscopically, the tumor is composed of round, spindle-shaped cells similar in appearance to those of the normal optic nerve. Because no mitoses are present, the tumors do not enlarge by cell division, but rather by hyperplasia of adjacent glial connective tissue and meninges, with

FIGURE 11-10 Neurofibromatosis type 1. Newly diagnosed optic nerve gliomas at age 15 months. The patient had recent onset of proptosis on the right. **A**, Axial T2-weighted image (TR 6000/TE 99) shows proptosis and expansion of the right optic nerve and flattening of the optic nerve head. **B**, Axial T1-weighted image with fat saturation (TR 650/TE 12/3 mm) shows diffuse enhancement of the right optic nerve glioma from the intracranial through the intracanicular to the intraorbital portion. There is faint enhancement of the intracranial portion of the left optic nerve. **C**, Postenhancement sagittal T1-weighted image with fat saturation image (TR 779/TE 12; 3-mm section) shows expansion and enhancement of the intracranial optic nerve just proximal to the optic canal. The chiasm is uninvolved.

VIEW IMAGE

Copyright © 2003, Mosby, Inc. All rights reserved.

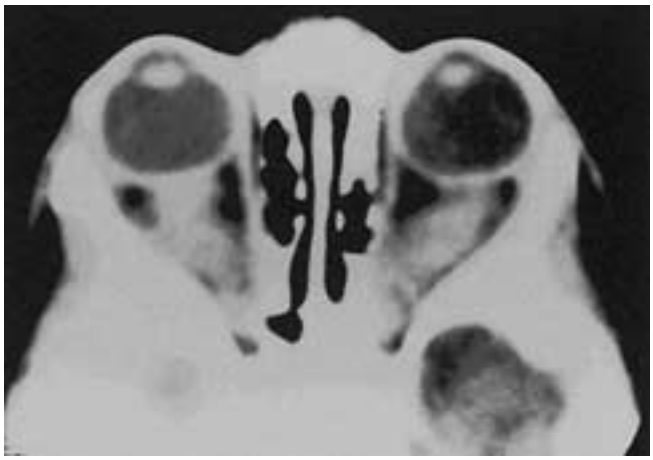

VIEW IMAGE

FIGURE 11-11 Bilateral optic gliomas with neurofibromatosis. Axial contrast CT scan shows bilateral enlargement and enhancement of optic nerve gliomas.

production of intracellular and extracellular mucopolysaccharides.

CT Appearance

Optic nerve gliomas may be unilateral or bilateral.[23] Unenhanced CT of these tumors typically demonstrates a marked diffuse, often fusiform, enlargement of an optic nerve, often with a characteristic kinking or buckling.[21, 24] Within the tumor, areas of lucency caused by mucinous or cystic changes may be observed, but calcification is not found in unirradiated optic nerve gliomas. Following administration of a contrast medium, a moderate to intense enhancement of the tumor is often observed, frequently containing irregular parenchymal lucencies.[21, 24] Bilateral optic nerve gliomas are thought to be characteristic of neurofibromatosis type 1 (Figs. 11-10 and 11-11).[24] Extension of the tumor through the optic foramen commonly results in enlargement of the optic canal. When the epicenter of the tumor involves the optic chiasm, both anterior and posterior components of the glioma may be seen. Such involvement is helpful in differentiating among lesions of the chiasm. Whatever imaging study is done, it must adequately evaluate the entire visual pathway, because frequently not only the optic nerve and chiasm but also the retrochiasmatic visual pathways are involved.[6]

MR Imaging Appearance

When evaluating the visual pathways (specifically the optic nerves) for optic nerve glioma, thin sections (3 mm or less) should be obtained, because excessive slice thickness may make lesions inapparent as a result of volume averaging.[23, 25] Precise anatomic definition of optic nerve gliomas is generally superior on MR imaging compared with CT, especially where the lesion passes through the optic canal (Figs. 11-10 and 11-12).[22] Sagittal MR imaging may give information not available with standard axial or coronal CT scanning techniques. In addition, the sensitivity of MR imaging to extensive visual pathway gliomas with involvement of the chiasm, optic tracts, lateral geniculate bodies, and optic radiations is much greater than that of CT (Fig. 11-12).[26] On MR imaging, a lesion involving the optic nerve is generally well defined, showing enlargement of the nerve (Fig. 11-10). On short TR/TE images, optic nerve gliomas are usually isointense to cortex and hypointense to white matter. Invariably they are hypointense to orbital fat. On long TR/TE images, the lesions demonstrate a mixed to homogeneous appearance that is hyperintense to white matter, cortex, and orbital fat.[27] Following administration of gadolinium contrast material, increased signal intensity on short TR/TE images is often seen (Figs. 11-10 and 11-12). The MR appearance of optic glioma is somewhat variable, depending on whether the tumor grows within the optic nerve (Fig. 11-12) or grows around the optic nerve into the perineural space. In the latter case, when the perineural portion enhances, it may mimic the perioptic meningioma and may be misdiagnosed, especially in the adolescent or adult patient. Intrinsic masses within the optic nerve, such as occult vascular malformations (Fig. 11-13), can be differentiated from intrinsic optic glioma by the presence of blood products on long TR images.

Perioptic Meningioma

Perioptic meningiomas are benign tumors arising from the meningoendothelial cells of the arachnoid. The rests from which these cells arise occur in a variety of locations within both the orbit and the cranial vault. Intraorbital meningiomas occur at the orbital apex, along the course of the optic nerve sheath, or unrelated to the optic nerve, usually in the extraconal space from the periosteum of the orbital wall.[21] Meningiomas make up approximately 5% to 7% of all primary orbital tumors, are more common in females than in males (4 to 1), and appear most frequently in the fourth and fifth decades of life (median age, 38 years).[28] They may occur in children (25% in the first decade), and they are much more frequent in patients with neurofibromatosis type 2 than in the general population.

Clinical Findings

The symptoms the patient displays depend on the size of the tumor and its location within the orbit. Small intracanalicular perioptic meningiomas may be difficult to detect and yet may cause significant visual symptomatology. Proptosis and visual loss are the usual symptoms in patients with perioptic meningiomas.[29] Disk elevation, optic atrophy with central or peripheral scotomata, or both are commonly seen because of the tumor's proximity to the optic nerve. Tumors that occur within the optic canal frequently appear with central scotomata, often without other symptoms.[29]

Pathologic Findings

Of the various histologic types of meningioma, the meningothelial variety is the most common within the orbit. Microscopically, the tumor consists of solid sheets of distinctively central vacuolated cells, with rare mitoses. Within the orbit, other histologic types of meningioma such as fibroblastic, transitional, syncytial, psammomatous, and angioblastic varieties are much less common. The rare orbital angioblastic meningioma is difficult to differentiate from hemangioblastoma and hemangiopericytoma.[24] Regardless of the histology, perioptic meningiomas in children tend to be more aggressive than those in adults. These

Copyright © 2003, Mosby, Inc. All rights reserved.

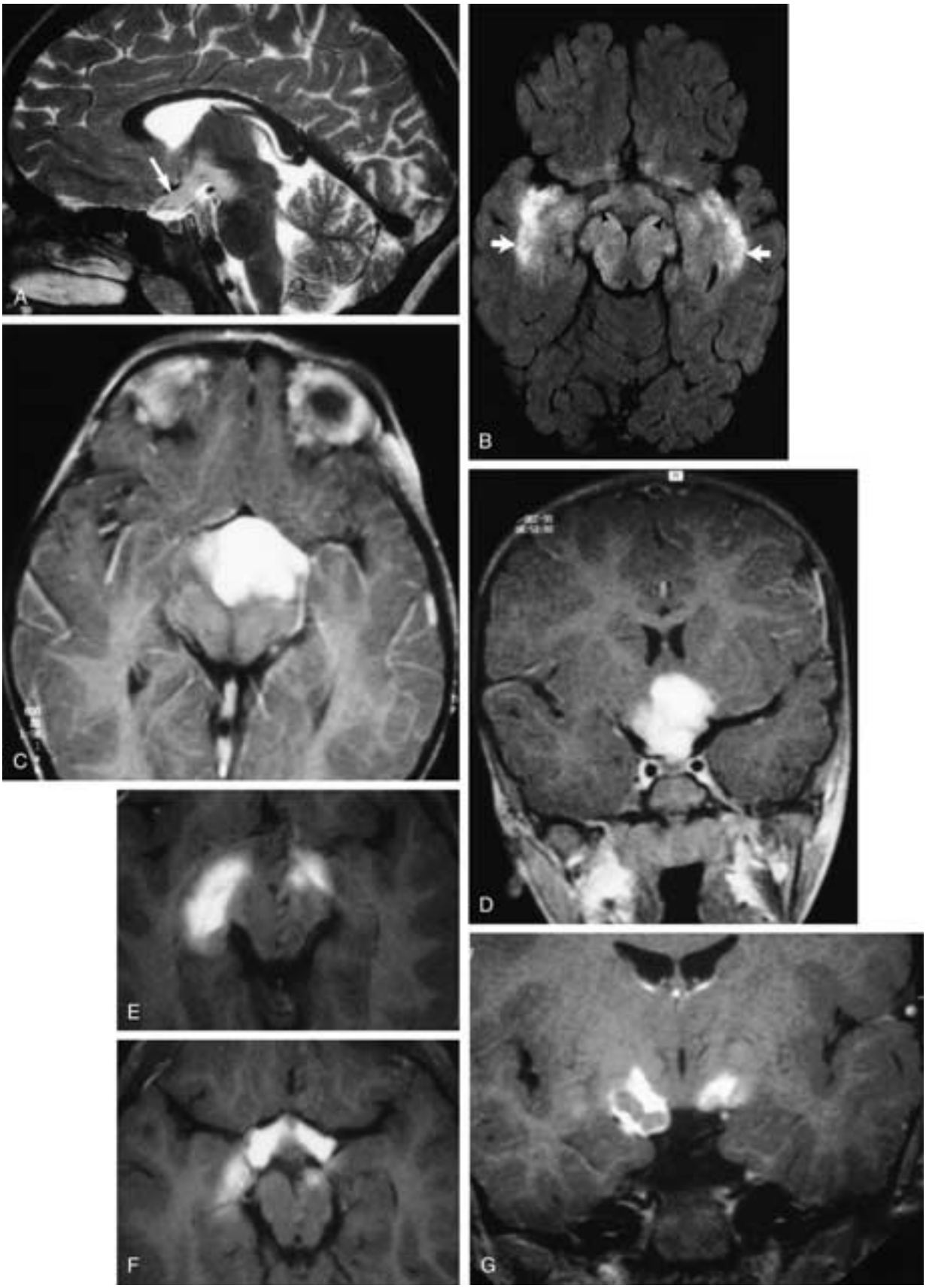

FIGURE 11-12 Visual pathway gliomas. **A**, Sagittal T2-weighted image in a 6-year-old male shows high signal intensity of an enlarged optic chiasm (*arrow*). Tumor extends posteriorly up against the brainstem and superiorly into the hypothalamus. **B**, FLAIR image in a 3-year-old female with neurofibromatosis type 1, shows involvement of the optic chiasm and optic tracts (*arrowheads*), as well as the brainstem and both medial temporal lobes (Meyer's loops) (*arrows*). **C** and **D**, Chiasmatic hypothalamic astrocytoma; **C**, T1-weighted axial image after contrast injection shows diffuse enhancement of the mass, as does the coronal image in **D**. **E** to **G**, Optic tract extension of chiasmatic glioma in a 6-year-old male with neurofibromatosis type 1. **E** and **F**, Axial T1-weighted, fat-suppressed images show contrast-enhanced tumor extending posteriorly from the chiasm into both optic tracts. Coronal T1-weighted, fat-suppressed image shows the right optic tract to be more involved than the left.

VIEW IMAGE

Copyright © 2003, Mosby, Inc. All rights reserved.

childhood tumors are often only partially encapsulated and have a propensity to grow by infiltration, breaking through the dura and involving other orbital structures. Orbital meningiomas, when adjacent to the bony wall, may induce a reactive hyperostosis, whereas those at or near the orbital apex may cause demineralization with enlargement of the optic canal.[28] Optic atrophy with a decrease in the number of axons within the nerve results from compression of the nerve by the tumor. The tumor grows either as an eccentric mass along one side of the optic nerve or as a circumferential lesion. Intratumoral psammomatous calcifications may be present, particularly within highly cellular areas of the tumor.

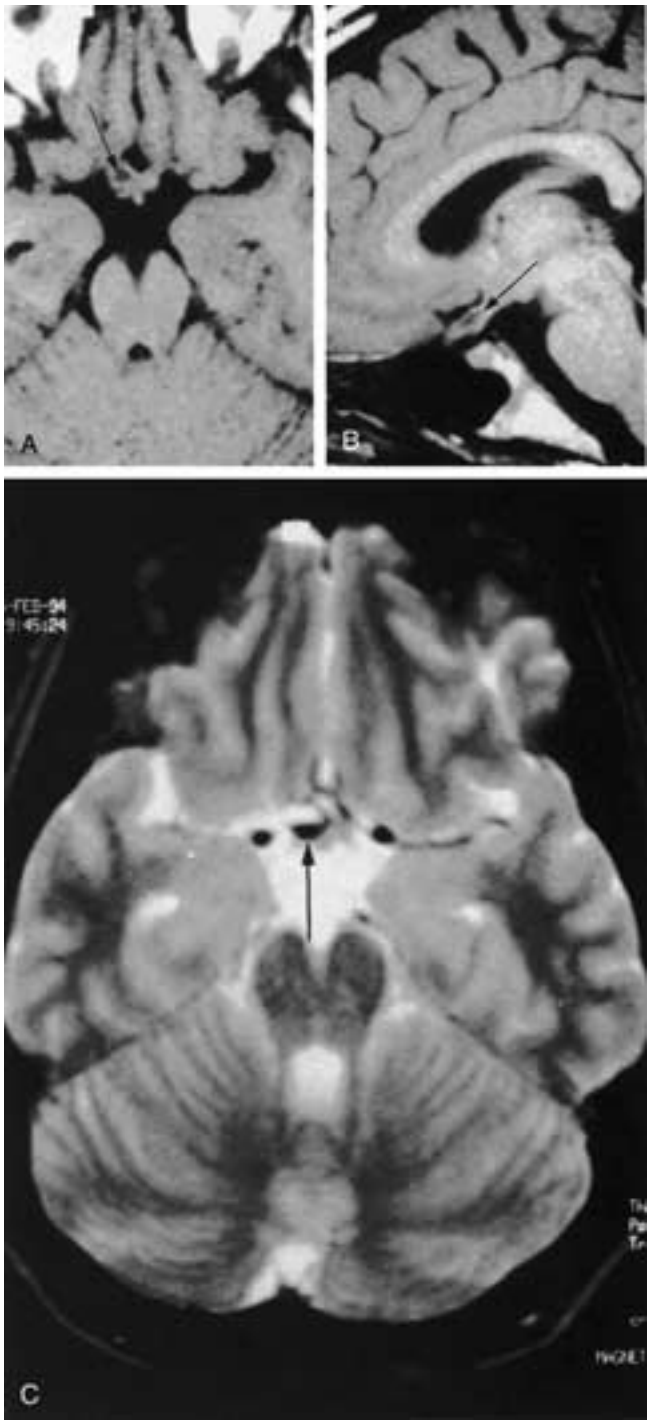

FIGURE 11-13 Occult vascular malformation of the right optic nerve in an 18-year-old female with monocular visual loss in the right eye for more than 1 year. The patient was referred with the diagnosis of right optic glioma. **A** and **B**, Axial and sagittal T1-weighted images without gadolinium enhancement show a hypointense, cystic expansion (*arrow*) of the intracranial portion of the optic nerve. **C**, Axial T2-weighted image shows hypointense blood (*arrow*), dependent within the cyst, the supernatant within the cyst being hyperintense. The findings are consistent with an occult vascular malformation. The same findings were present 1 year before this examination.

VIEW IMAGE

CT Appearance

On CT, perioptic meningiomas (Fig. 11-2) appear either as a localized eccentric mass at the orbital apex[14] or as a well-defined tubular thickening (64%) or fusiform enlargement (23%) of the optic nerve sheath complex.[21, 30–32] Stippled calcification within the tumor is common (Fig. 11-2), helping to differentiate it from the optic nerve glioma. Secondary enlargement of the optic canal, with bony hyperostosis, may be seen if the tumor is located in the appropriate position.[21, 24] Because the detection of calcification and bony change is helpful in making the diagnosis of perioptic meningioma, a noncontrast-enhanced CT scan with very thin sections (1 mm) may be considered superior to nonenhanced MR imaging in evaluating small perioptic lesions.[26] After administration of a contrast medium with CT, moderate to marked enhancement of the tumor is seen. The so-called tram-track sign of perioptic meningioma is caused by uniform enhancement of a circumferential meningioma (Fig. 11-3). This may simulate dural inflammation, a finding that may be present in cases of optic neuritis and idiopathic inflammatory pseudotumor.

MR Imaging Appearance

MR imaging displays the tumor as an abnormally enlarged optic nerve silhouette. Signal characteristics depend on the pulse sequence. On short as well as long TR/TE scans, perioptic meningiomas show diminished signal intensity relative to normal brain tissue.[21] Relative to orbital fat, on short TR/TE images the lesions are hypointense, whereas on long TR/TE images they are isointense. The calcifications within the tumor may be visualized as regions of signal void on MR imaging; however, most frequently intratumoral calcification is not seen. MR imaging may show meningiomatous bone involvement as a region of absence of the expected signal void within an area of cortical bone.[33] Chemical shift artifact, resulting in a dark line on one side of the optic nerve, may mimic calcification. Similarly, the subarachnoid space within the optic nerve sheath may appear dark on appropriate pulse sequences, mimicking circumferential calcification. This may be ruled out by using an appropriate pulse sequence designed to increase the signal intensity of CSF.[6] Gadolinium has become critical (Fig. 11-14B)[33] in the diagnosis of small perioptic tumors. Fat suppression is necessary with thin (2- to 3-mm) T1-weighted images in order to separate the enhancing tumor from the intraconal fat (Fig. 11-15).

Sarcoidosis

Sarcoidosis is a granulomatous disease of unknown cause that involves several organ systems, most commonly

Copyright © 2003, Mosby, Inc. All rights reserved.

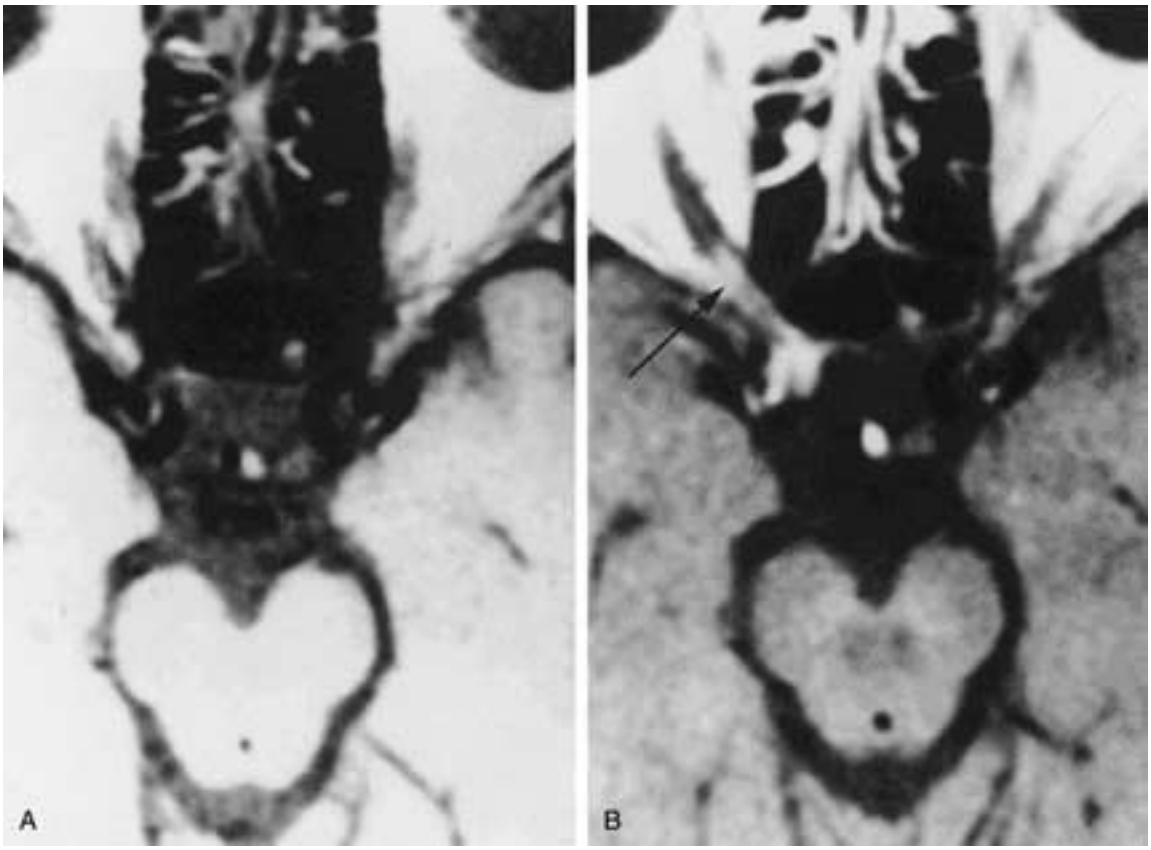

VIEW IMAGE

FIGURE 11-14 Perioptic meningioma. **A**, Axial T1-weighted image before administration of gadolinium shows no specific abnormality. **B**, Axial T1-weighted image after intravenous administration of gadolinium shows enhancement of tumor (*arrow*) that extends from the region of the anterior clinoid process on the right, through the optic canal, and along the optic nerve. Surgery revealed a perioptic meningioma.

mediastinal and peripheral lymph nodes, lungs, liver, spleen, skin, eyes, and lacrimal glands.[28, 34, 35] Pathologically, it is characterized by noncaseating granulomas, which may occur in any tissue or organ of the body. Ophthalmic changes caused by sarcoidosis occur in up to 60% of cases.[34] The most frequently involved area within the orbit is the lacrimal gland; however, infiltration may be seen in any orbital structure.[33, 36]

Clinical Findings

Two clinical presentations of sarcoidosis are noted. The subacute form generally occurs in patients under 30 years of age, particularly in women of Swedish, Puerto Rican, and Irish descent, and is characterized by rapid appearance of erythema nodosum, possibly with accompanying polyarthritis in association with bilateral hilar adenopathy. The second form is a chronic disease that affects patients over 30 years of age; the pulmonary parenchyma is involved, and the disease spreads beyond the thorax.[28] In general, the disease is seen predominantly in African Americans 20 to 40 years of age.[34] Patients with subacute sarcoidosis tend to exhibit peripheral and cranial nerve involvement, with the seventh cranial nerve most commonly involved and the optic nerve next most commonly affected. Involvement of the third, fourth, or sixth cranial nerves may produce extraocular muscle palsies. In the chronic form of sarcoidosis, CNS involvement is more common than peripheral nerve involvement, and the optic nerve is much more frequently affected than in the subacute form (recall that the optic nerve is an extension of a central brain tract and not a peripheral nerve). Optic nerve sarcoidosis may occur intracranially, with chiasmal involvement, or in the intracanalicular or intraorbital portions, and optic nerve involvement in this form of the disease may lead to optic atrophy.

Anterior uveitis, the most frequent sign of sarcoidosis, is characteristic of the subacute form of sarcoidosis, whereas a nonspecific granulomatous uveitis occasionally accompanied by cataract or secondary glaucoma is more indicative of the chronic form. Intracranial sarcoidosis is clinically evident in 5% of the cases, whereas 15% of autopsy cases demonstrate CNS involvement.[2] These patients may exhibit papilledema, disk edema secondary to increased intracranial pressure. Optic atrophy may be present as a result of inflammation of the optic nerve, compression by sarcoid granuloma, infarction due to sarcoid vasculitis, or glaucoma caused by intraocular inflammation.

Pathologic Findings

The basic lesion of sarcoidosis is a noncaseating epithelioid cell tubercle. Langerhans' giant cells are seen interspersed within the epithelioid cells centrally, and a thin rim of lymphocytes rings the individual tubercles. Inclusion bodies are characteristically seen within the giant cells in the tubercle. Although, as part of their natural course, the sarcoid granulomas may disappear without any evidence of scarring, they usually heal with sclerosis at the margins of

Copyright © 2003, Mosby, Inc. All rights reserved.

the tubercles, and calcification does not occur during the healing process.[28]

Intracranial involvement by sarcoidosis generally occurs in one of two patterns. The most common one is granulomatous leptomeningitis with involvement of the leptomeninges, including those investing the optic nerves. The second pattern is that of coalescence of sarcoid nodules into distinct parenchymal brain masses.[37] In the leptomeninges, the cranial nerves, pituitary gland, third ventricle, hypothalamus, and (in rare cases) pineal gland are involved.[33, 38] Hydrocephalus may result from sarcoid lesions of the aqueduct, fourth ventricular outlet foramina, or basal meninges, occasionally resulting in vessel obstruction with subsequent infarction.[39]

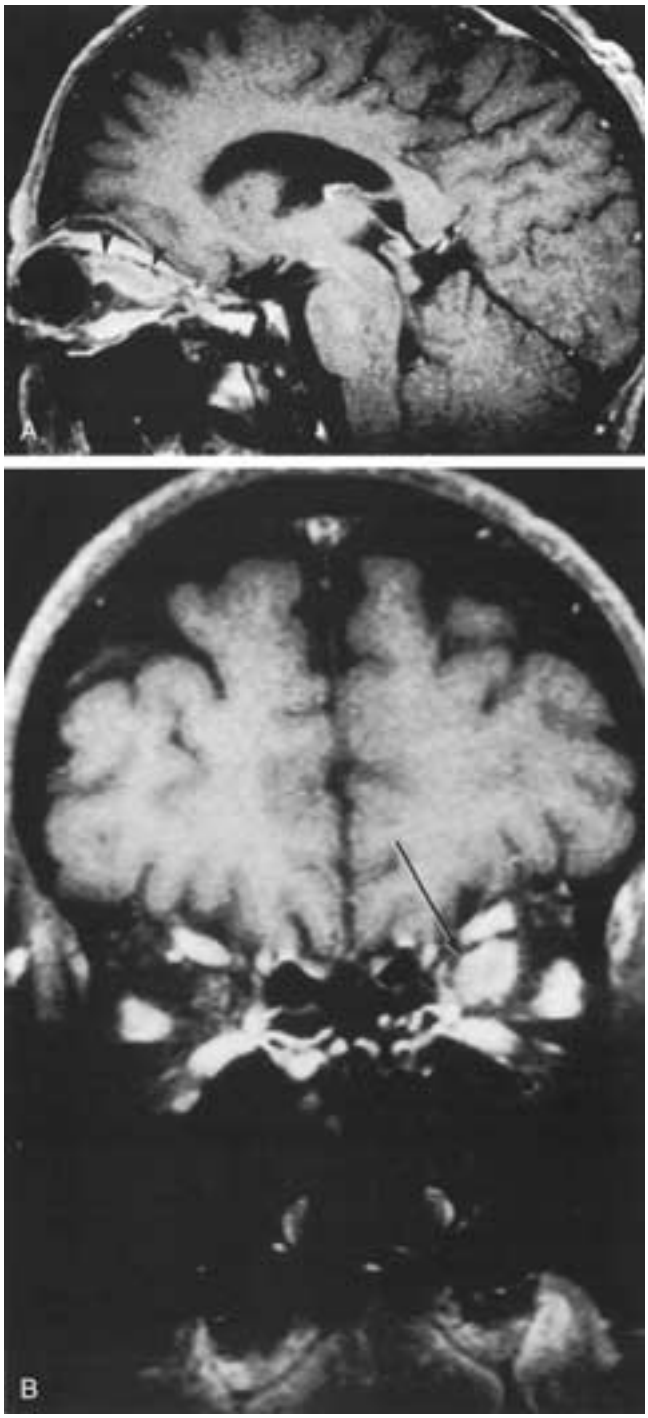

VIEW IMAGE

FIGURE 11-15 Perioptic meningioma in a 53-year-old male with left monocular visual loss and evidence of optic atrophy on fundoscopic examination. Symptoms had been progressive over a number of years. **A**, Oblique sagittal, fat-suppressed, gadolinium-enhanced T1-weighted MR image shows a mass (*arrowheads*) surrounding the optic nerve, extending from the globe back to the optic canal. **B**, Coronal fat-suppressed, T1-weighted, gadolinium-enhanced MR image shows that the left optic nerve (complex) is enlarged and enhancing (*arrow*).

CT Appearance

Diffuse infiltration of the leptomeninges is the most common CT finding. On the unenhanced study, areas of diffuse, irregularly increased attenuation along the leptomeninges may be seen. However, a normal study is the most frequent finding.[34, 40, 41] With orbital involvement the lacrimal gland may be enlarged, and irregular thickening of the meninges of the optic nerve may be present. Brain parenchymal involvement produces discrete nodules that, on an unenhanced CT scan, may be isodense or slightly hyperdense to the surrounding normal parenchyma. The nodules may be multiple or singular or may even form large, discrete masses upon coalescence. Surrounding edema is usually not present. Following administration of a contrast medium, diffuse, irregular enhancement along the basal cisterns can be seen. The borders of the cortical sulci may enhance similarly as a result of leptomeningeal spread within the perivascular spaces of Virchow-Robin.[34] Homogeneous enhancement of parenchymal nodules also occurs after administration of the contrast medium.[34, 39, 42] Obstructive hydrocephalus may be seen when structures adjacent to the third ventricle or the aqueduct or the outlet foramina of the fourth ventricle are involved. Cranial nerve involvement generally produces fusiform or irregular enlargement of the nerve with homogeneous enhancement after administration of contrast medium.[34] Compression or direct invasion of the cranial nerves may occur as a consequence of infiltration of the basal meninges. Calcification is not a feature of sarcoidosis.[38]

MR Imaging Appearance

Orbital sarcoidosis is evaluated well with MR imaging, which demonstrates a high degree of anatomic detail not seen with CT, particularly in areas where image degradation occurs on CT caused by beam-hardening artifact (i.e., in the intracanalicular and intracranial portions of the optic nerve).[43–47] MR imaging demonstrates sarcoid involvement of the optic nerve as diffuse enlargement of the optic nerve sheath complex of a variable signal intensity that is usually isointense to extraocular muscle on short TR/TE images and minimally hyperintense to orbital fat on long TR/TE images (Fig. 11-16).[33, 36, 48] Lacrimal gland involvement by sarcoid is generally seen as diffuse enlargement of the gland with a signal intensity pattern that may be either low or high on long TR/TE images.[33, 36] The two major pathologic changes of intracranial sarcoid are well demonstrated by MR imaging. They consist of abnormal tissue involving the meninges (Figs. 11-17 and 11-18) and the brain parenchyma (Fig. 11-16) in addition to

Copyright © 2003, Mosby, Inc. All rights reserved.

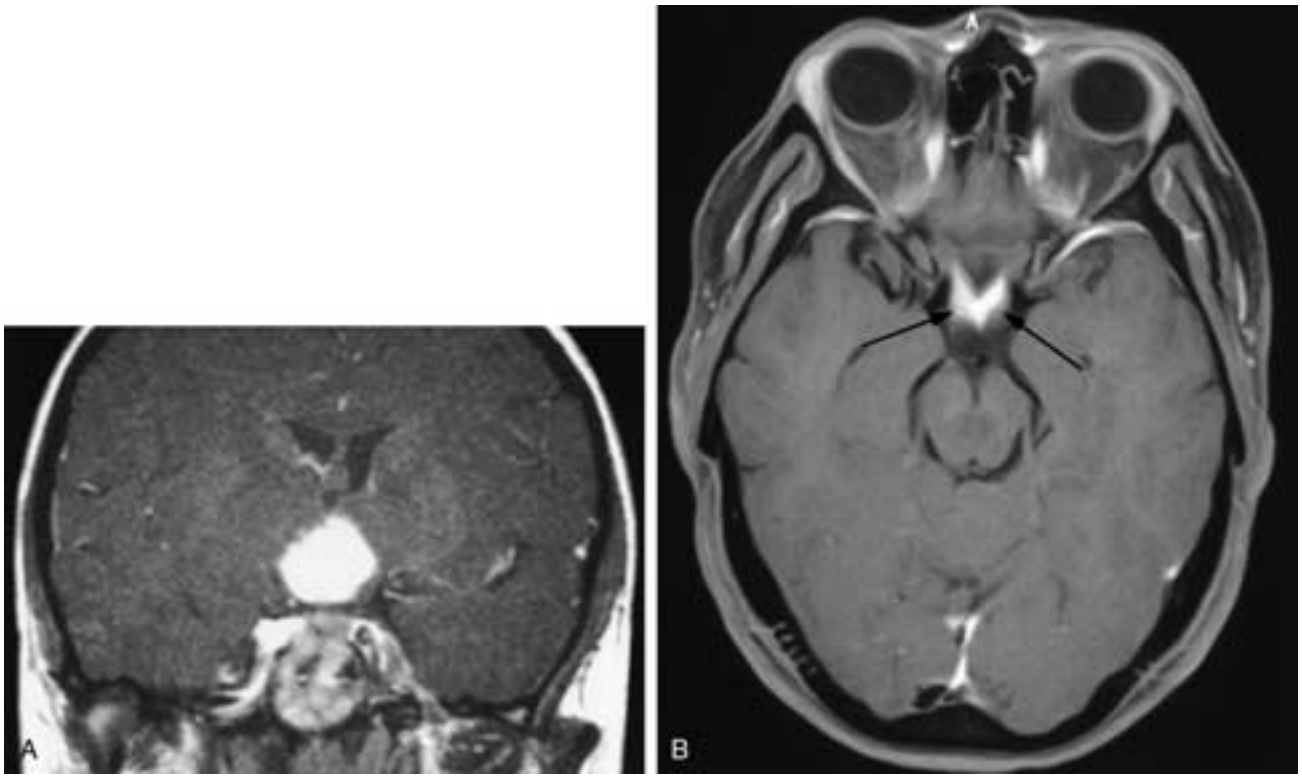

VIEW IMAGE

FIGURE 11-16 Sarcoidosis involving the hypothalamus and/or the optic chiasm. **A**, A 16-year-old female with hypothalamic dysfunction and visual impairment. Contrast-enhanced, T1-weighted coronal image shows a large enhancing mass. **B**, A 26-year-old female with chiasmatic and bilateral intracranial optic nerve involvement by sarcoid. Fat-suppressed, axial T1-weighted image after contrast injection shows enhancement of the areas of involvement (*arrows*).

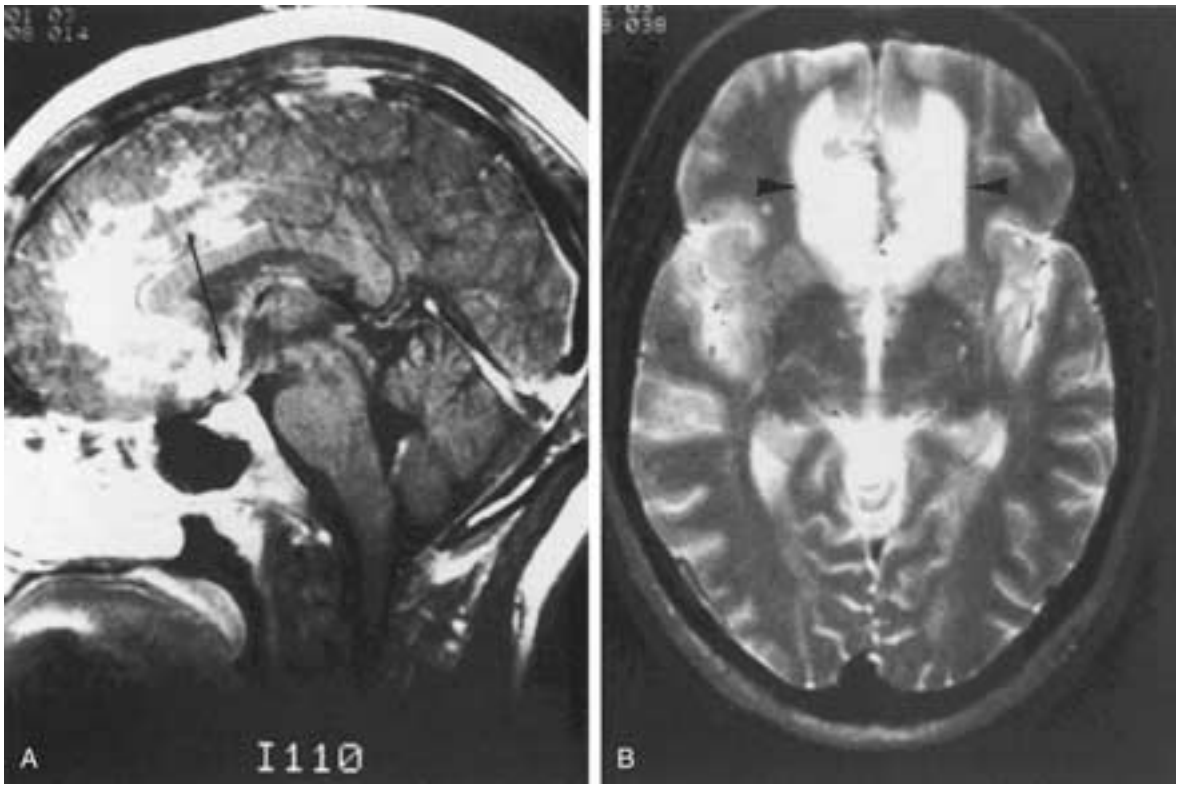

VIEW IMAGE

FIGURE 11-17 Leptomeningeal sarcoidosis. **A**, Sagittal T1-weighted image after injection of contrast material shows marked enhancement of leptomeninges between the frontal lobes, extending along the corpus callosum, and down onto the surface of the optic chiasm (*arrow*). **B**, Axial T2-weighted image shows bifrontal edema (*arrowheads*) within the cortex and white matter of the frontal lobes at the site of leptomeningeal involvement by sarcoid.

Copyright © 2003, Mosby, Inc. All rights reserved.

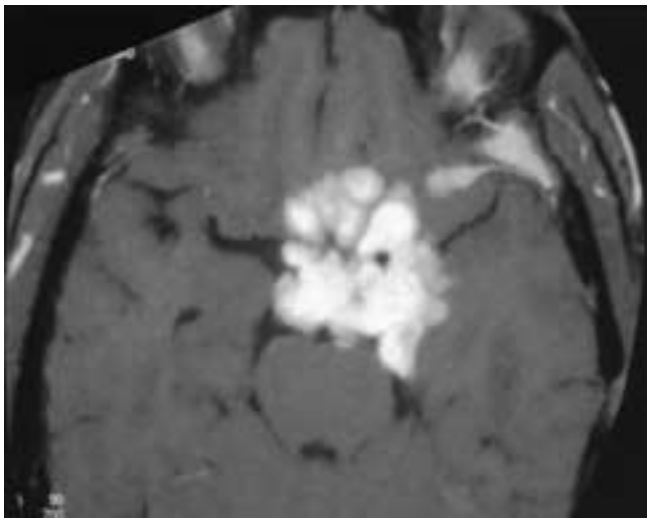

FIGURE 11-18 Leptomeningeal sarcoidosis presenting as a mass in a 45-year-old female with encasement of the chiasm and optic nerves. T1-weighted axial, fat-suppressed image after gadolinium injection. Except for the nodularity of the mass, its appearance mimicked a meningioma of the lesser wing of the sphenoid.

hydrocephalus and small areas of infarction.[49] Meningeal involvement by sarcoid tissue is most commonly seen in the region of the basal cisterns as focal areas of high signal intensity tissue on long TR/TE images (Fig. 11-17B). However, the signal intensity characteristics may vary, and the tissue occasionally may be hypointense to normal brain parenchyma on long TR/TE images. Periventricular involvement demonstrates similar signal intensity and is also a common location for visualization of abnormal sarcoid tissue. The parenchymal regions of sarcoidosis also have similar signal characteristics. MR imaging has greater sensitivity than CT for detecting regions of sarcoidosis, [45, 50] and the hydrocephalus associated with sarcoid involvement of the CSF pathway is clearly identified with MR imaging. The site of obstruction responsible for the hydrocephalus may also be determined with MR imaging techniques. Specifically, the absence of a flow void sign within the aqueduct or within the foramina of Magendie or Luschka may indicate these to be the primary sites of obstruction.[51] The use of gadolinium in evaluating sarcoid has proven helpful in demonstrating the extent of meningeal involvement (Figs. 11-17 and 11-18). However, the MR appearance of leptomeningeal sarcoid is not specific; a similar picture may be seen with tuberculosis and other bacterial meningitides such as pneumococcal meningitis (Figs. 11-19 and 11-20). In these circumstances, the clinical picture as well as CSF laboratory studies are important in the differential diagnosis.

Lyme Disease

Lyme disease is a worldwide tick-transmitted spirochetosis with endemic foci in North America and Europe. The spirochete is *Borrelia burgdorferi*, and the ticks that transmit the disease infect both deer and white-footed mice.

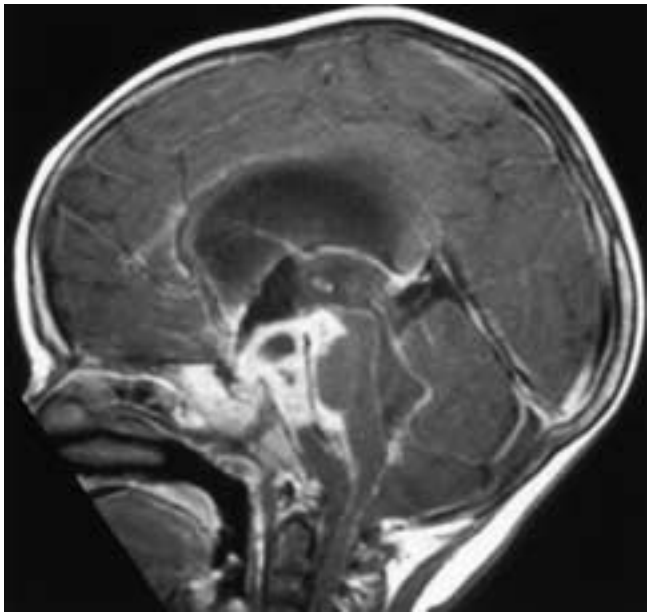

FIGURE 11-19 Tuberculous meningitis. Infant with hydrocephalus and cranial nerve palsies. Sagittal T1-weighted image after gadolinium injection shows a contrast-enhancing suprasellar subarachnoid collection encasing the chiasm and anterior brainstem. Findings are consistent with granulomatous meningitis at the base of the brain.

FIGURE 11-20 Pneumococcal meningitis in a comatose 1-year-old infant with hydrocephalus. Axial thin-section, postgadolinium injection, T1-weighted scan shows that the optic chiasm (*arrow*) is coated by a contrast-enhancing subarachnoid infiltrate. Note that the temporal horns are markedly dilated secondary to hydrocephalus.

Copyright © 2003, Mosby, Inc. All rights reserved.

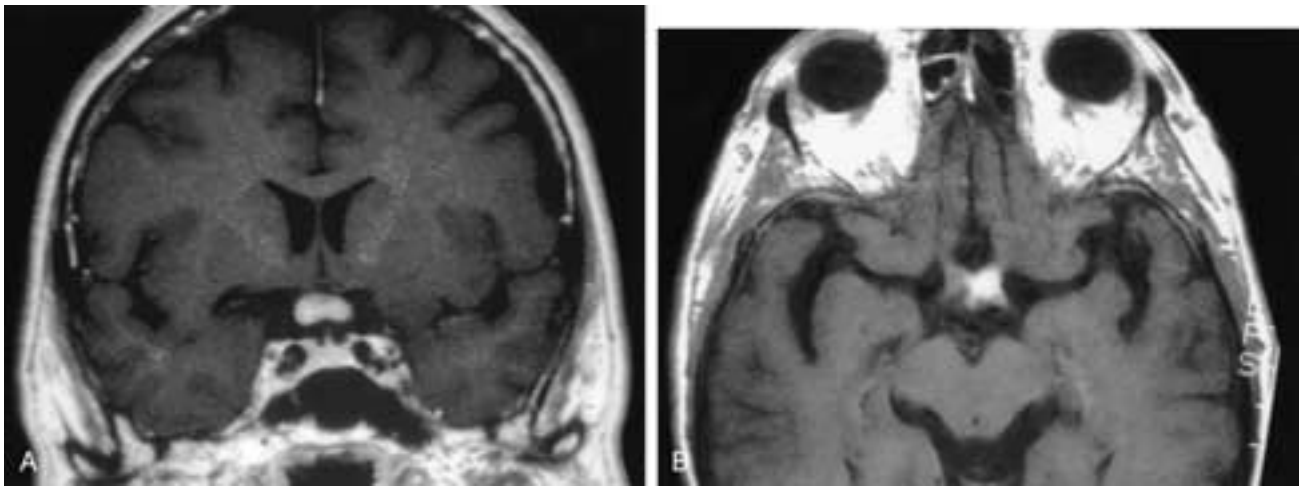

VIEW IMAGE

FIGURE 11-21 Lyme disease involving the optic chiasm in a 66-year-old female. Coronal (**A**) and axial (**B**) T1-weighted images after contrast injection show enhancement and enlargement of the optic chiasm. **A** is before treatment and **B** is 1 week after the beginning of treatment, showing some response to antibiotic therapy.

Clinical Findings

A bite by an infected tick can result in Lyme disease, causing a variety of manifestations, including arthritis, rash, cardiac manifestations and CNS involvement in 15% to 20% of cases.[52] In the CNS, cranial neuropathies (facial palsy, 80%), meningitis, headache, and cerebral parenchymal involvement resulting in mental changes can occur. [52]

Pathologic Findings

Lymphoplasmacytic perivascular and meningitic infiltration has been recognized in association with a CSF lymphomonocytic pleocytosis. Beyond these manifestations the CNS findings have not been well described pathologically.

CT Appearance

The CT findings that have been recognized are those occurring in the white matter as areas of hypodensity mimicking the lesions of multiple sclerosis. CT is not reliable in recognizing the cranial nerve findings seen on MR imaging as focal enlargement and contrast enhancement.

MR Imaging Appearance

The MR imaging findings most often consist of cranial nerve enhancement after gadolinium injection, with the seventh cranial nerve(s) most frequently involved.[53] However, high signal intensity lesions in the white matter can occur that mimic the lesions of multiple sclerosis.[54] Involvement of the optic nerves and/or chiasm (Fig. 11-21) is seen as swelling with high signal on T2-weighted scans and FLAIR and as contrast enhancement after gadolinium injection.[54] A positive serologic test should be followed by a full course of antibiotics. MR imaging can be used to follow the response to treatment.

Craniopharyngioma

Craniopharyngioma is a benign tumor that arises from remnants of Rathke's pouch. These tumors occur most commonly in a suprasellar location, as well as within the sella turcica. They represent 1% to 3% of intracranial tumors and are found most frequently in children. However, they have two other age peaks, one in young adulthood and one in the fifth decade.[55]

Clinical Findings

Patients with craniopharyngioma most frequently complain of a headache and visual disturbances occur commonly, related to impingement of the tumor on the optic pathway at the level of the chiasm or optic tracts.[56] Hypothalamic and pituitary dysfunction may be seen, and when the tumor occurs in a child, growth failure may result.[57]

Pathologic Findings

Craniopharyngiomas originate from squamous cell epithelial rests arising from Rathke's pouch. They are benign, slow-growing tumors. Grossly, the tumor is well encapsulated and adherent to (and possibly superficially invasive into) the surrounding tissues. As the tumor enlarges, the adjacent structures are compressed, including the optic chiasm anteriorly, the pituitary gland inferiorly, the hypothalamus superiorly, and the elements of the circle of Willis peripherally.[55] The tumor is usually cystic, with interspersed solid areas. The cystic region contains either a liquid or semisolid dark brown, greasy material composed of cholesterol crystals, keratin, and calcified debris. Microscopically, the solid portions of the tumor consist of nests of stratified squamous or columnar epithelium within a fibrous stroma similar to that of the enamel organ of the tooth. For this reason, these tumors are considered to have an adamantinomatous histologic pattern.[57] Approximately 75% of craniopharyngiomas contain significant amounts of calcium.

CT Appearance

On CT, craniopharyngiomas usually appear as rounded, lobulated, or irregularly marginated masses occupying the suprasellar cistern (85% of the time) and occasionally involving the sella turcica (20% of the time).[58] Cystic

Copyright © 2003, Mosby, Inc. All rights reserved.

components are noted in 85% of the lesions. These cystic regions demonstrate a variable attenuation ranging from markedly hypodense to isodense relative to CSF (Fig. 11-22). The attenuation probably depends on the cholesterol content. Calcification is present in approximately 75% of the cases, varying from 70% to 90% in craniopharyngiomas occurring in children to 35% to 50% in those occurring in adults. The character of the calcification is generally conglomerate, although rim-like calcifications may occur about the cystic portions of the lesion (Fig. 11-22). After administration of a contrast medium, the solid portions of the tumor usually enhance markedly.

MR Imaging Appearance

Because of its multiplanar imaging capabilities, MR imaging displays very well the anatomic configuration of the lesion relative to adjacent brain structures.[57] On short TR/TE images, the tumor generally has increased to intermediate signal intensity as a result of T1 shortening (Fig. 11-23A). This is most likely the result of increased protein concentration (greater than 9000 mg/100 ml), the presence of free methemoglobin, or both.[59] In rare cases the signal intensity is diminished, particularly if the lesion is predominantly cystic (Fig. 11-23C), with a low protein concentration within the cyst fluid. Focal areas of diminished signal intensity on short TR/TE and long TR/TE images may be secondary either to elevated keratin content within the cystic portions of the tumor or to calcification within the solid portions. As a rule, hyperintense signal is seen on long TR/TE images as a result of T2 prolongation.[57, 60] Comparison of CT and MR imaging shows CT's greater sensitivity in displaying calcification; this makes it a more specific radiologic procedure for craniopharyngioma identification, particularly when used in conjunction with the clinical history. MR imaging, on the other hand, is more sensitive to the presence of a tumor and gives a more accurate preoperative demonstration of the extent and location of the tumor, which is important in planning the surgical approach.[57, 60, 61] It has been shown that the craniopharyngioma's wall and solid portions enhance after administration of gadolinium (Fig. 11-24B). Thus, gadolinium increases the sensitivity of MR imaging in the evaluation of craniopharyngiomas, particularly in regard to tumor residual and recurrence after surgical excision.

MR proton spectroscopy has proven useful in differentiating craniopharyngiomas from hypothalamic astrocytomas and pituitary adenomas in children and adolescents.[62] Craniopharyngiomas show a peak in the lipid, lactate part of the scale (1 to 2 ppm), while hypothalamic astrocytomas show elevated choline to Naa ratios (e.g., 2.6 vs. a normal ratio of 0.75) and pituitary adenomas show no metabolites.[62]

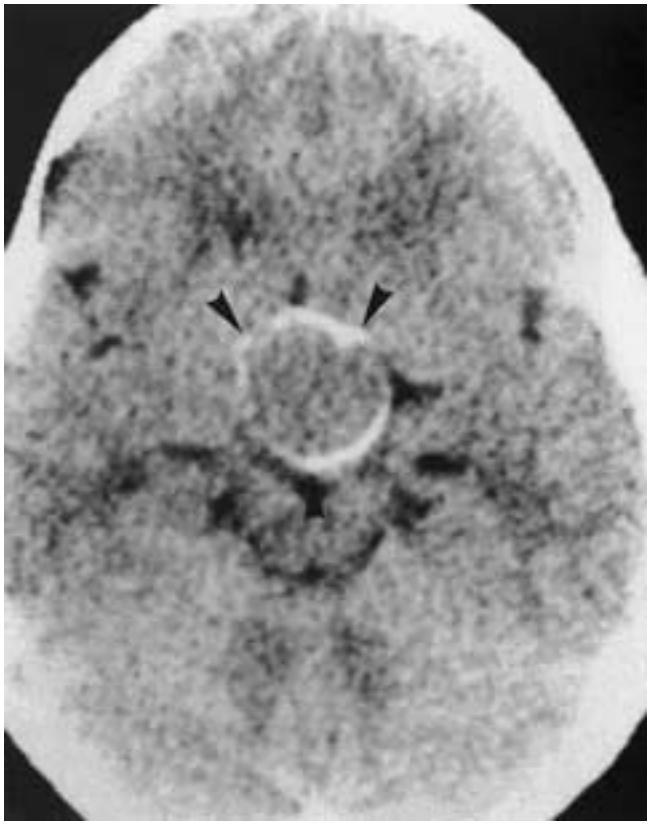

VIEW IMAGE

FIGURE 11-22 Craniopharyngioma. Axial nonenhanced CT image shows a suprasellar tumor with a peripheral rim of calcification (*arrowheads*) and a central region that is isodense to brain.

Rathke's Cleft Cyst

Rathke's cleft cyst is a benign lesion consisting of a cystic remnant of Rathke's pouch that occurs within the anterior portion of the sella turcica or the anterior aspect of the suprasellar cistern.

Clinical Findings

Rathke's cleft cysts usually are small and without discernible clinical symptoms. If they are symptomatic, patients may have hypopituitarism, diabetes insipidus, headache, or visual disturbances related to impingement on the visual pathway at the level of the optic chiasm or the optic tracts; however, only 60 symptomatic cases have been reported in the world literature.[63]

Pathologic Findings

The anterior lobe of the pituitary, the pars tuberalis and the pars intermedia, are derived from Rathke's pouch, which is also the origin of the Rathke's cleft cyst. The cyst is generally a simple structure lying primarily within the anterior portion of the sella turcica, occasionally with protrusions into the suprasellar cistern region, forming a dumbbell-shaped lesion. Microscopically, the wall of the cyst in the intrasellar portion is lined by a simple cuboidal epithelium, which may be ciliated, whereas the suprasellar portion may be lined by stratified squamous epithelium.[55] The single-cell layer forming the wall of the cyst often contains goblet cells, and the cystic contents usually have a serous or mucoid consistency, with varying amounts of cellular debris. This variable protein content probably accounts for the variable appearance of the cystic portion of the lesion on CT and MR imaging.

CT Appearance

Rathke's cleft cyst usually appears as a well-circumscribed cystic structure that has a mass effect, lies

Copyright © 2003, Mosby, Inc. All rights reserved.

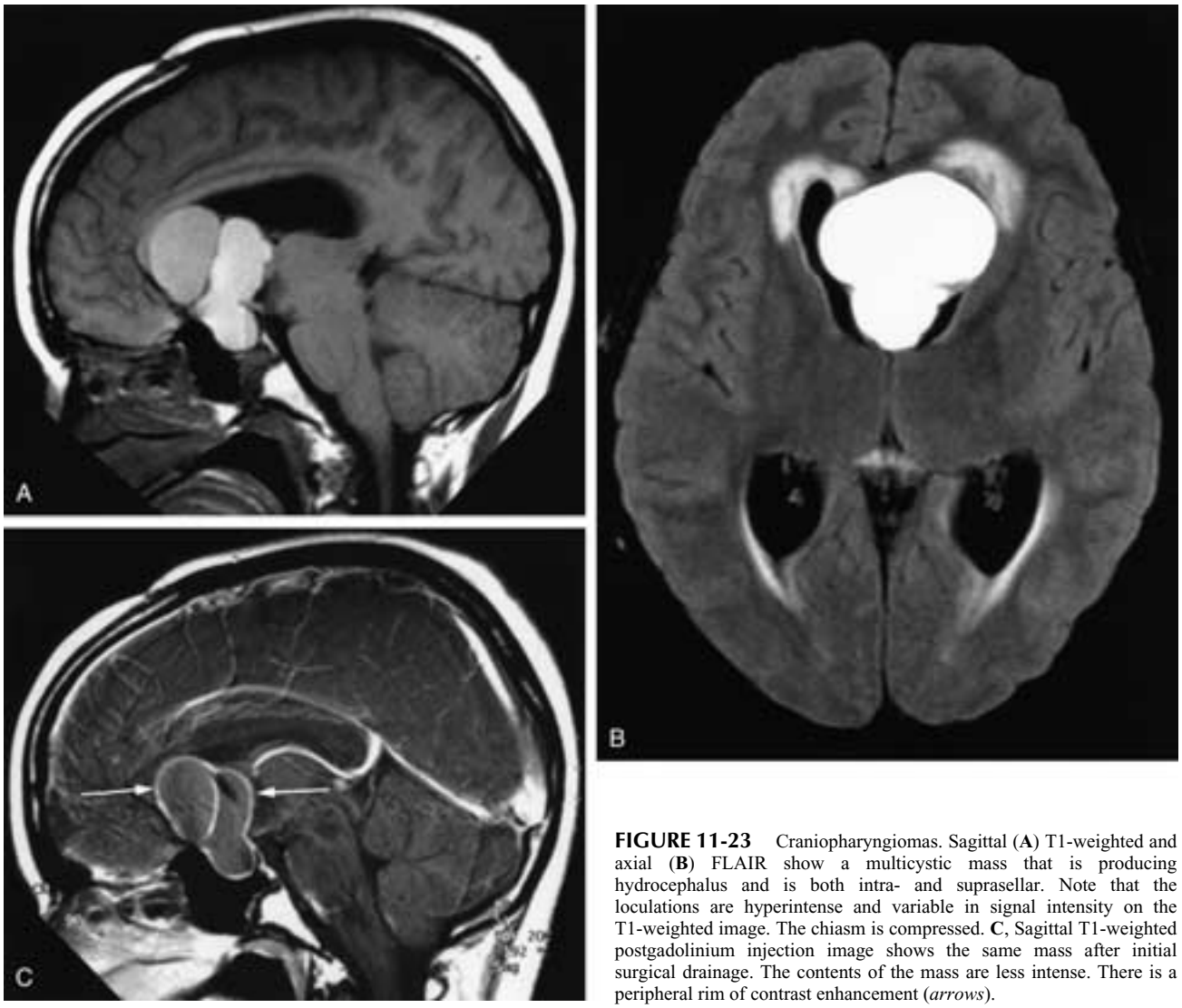

FIGURE 11-23 Craniopharyngiomas. Sagittal (**A**) T1-weighted and axial (**B**) FLAIR show a multicystic mass that is producing hydrocephalus and is both intra- and suprasellar. Note that the loculations are hyperintense and variable in signal intensity on the T1-weighted image. The chiasm is compressed. **C**, Sagittal T1-weighted postgadolinium injection image shows the same mass after initial surgical drainage. The contents of the mass are less intense. There is a peripheral rim of contrast enhancement (*arrows*).

VIEW IMAGE

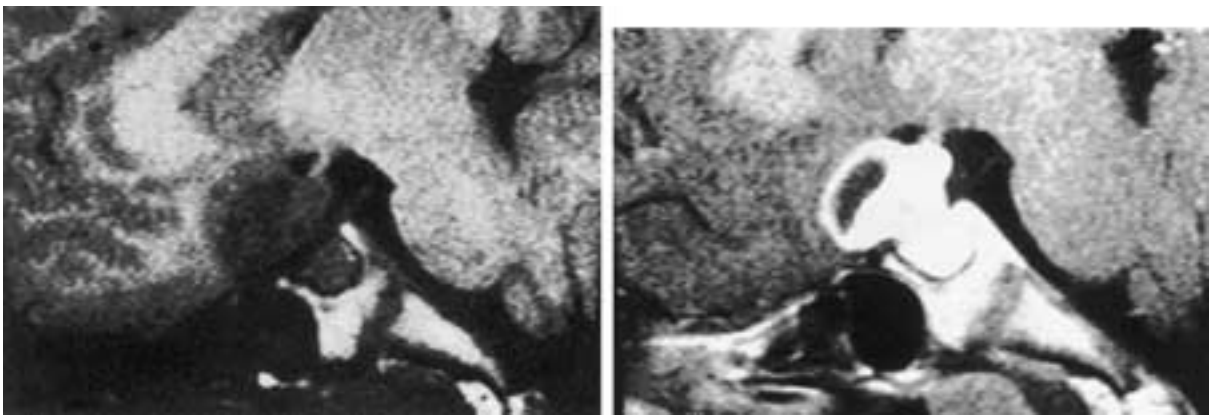

FIGURE 11-24 Craniopharyngioma in a 10-year-old male with evidence of clinical involvement of the left optic tract in the form of an incongruous homonymous hemianopsia. **A**, Sagittal T1-weighted MR image before gadolinium enhancement shows a soft-tissue mass both within and above the sella turcica; the mass abuts on the optic tract. **B**, T1-weighted MR image following gadolinium injection shows enhancement of the partially cystic mass.

VIEW IMAGE

Copyright © 2003, Mosby, Inc. All rights reserved.

within the sella turcica, and occasionally has suprasellar extension.[64] The wall of the cyst is generally thin, and the cyst contents usually are similar to CSF, although they may appear hypodense. The rim of tissue may enhance after administration of a contrast medium, and it occasionally contains small amounts of calcium. More complex cysts display a slightly increased density, with septa partitioning the cystic portion.[63] Differential considerations for the simple form of Rathke's cleft cyst include arachnoid cyst and cystic pituitary adenoma, whereas the more complex cysts may be impossible to differentiate from craniopharyngioma.

MR Imaging Appearance

Simple cysts generally have signal intensity characteristics similar to those of CSF; that is, they usually appear hypointense to brain parenchyma on short TR/TE images and hyperintense to brain parenchyma on long TR/TE pulsing sequences. If the cyst fluid contains significant amounts of cholesterol, increased signal intensity is noted on short TR/TE images, with diminishing intensity on progressively longer TR/TE images. Complex cysts, which represent a transitional form between a simple Rathke's cleft cyst and a craniopharyngioma, demonstrate signal heterogeneity on long TR/TE images, with an isointense to hyperintense signal on short TR/TE images (Fig. 11-25). MR imaging better displays the relationship of the Rathke's cleft cyst to adjacent structures, particularly the optic chiasm and hypothalamus (Fig. 11-26).

Pituitary Adenoma

Pituitary adenomas are benign neoplasms arising within the substance of the pituitary gland. They occur with equivalent frequency in males and females between 20 and 50 years of age. MR imaging has become the procedure of choice for evaluating tumors of the pituitary gland.

Clinical Findings

Adenomas of the pituitary gland can be separated into microadenomas (less than 1 cm in diameter) and macroadenomas (greater than 1 cm in diameter). The microadenomas typically appear with endocrine abnormalities, the specific findings depending on which hormone is being elaborated by the adenoma. Macroadenomas, on the other hand, appear more often with symptoms caused by mass effect, such as those resulting from chiasmatic compression or pituitary insufficiency.

Lateral extension of the pituitary adenoma into the cavernous sinus can involve cranial nerves III, IV, and VI. This can produce motility disturbances on the basis of isolated or combined cranial neuropathies. If there is an acute increase in the size of the adenoma, such as can occur with pituitary apoplexy, there can be rapid lateral expansion and the patient can suffer rapid onset of an ocular motility disturbance, with or without a sudden decrease in vision.

Pathologic Findings

Pituitary adenomas are usually unencapsulated solid tumors that may penetrate adjacent structures.[65] The tumors

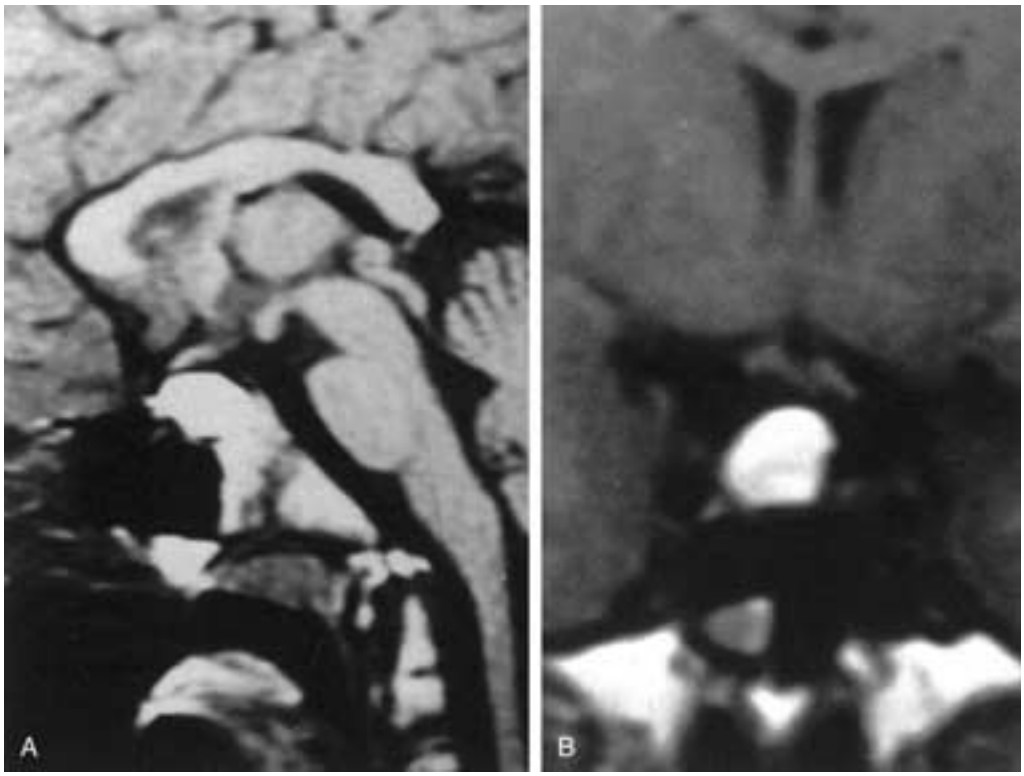

FIGURE 11-25 Cyst of Rathke's pouch. **A**, Sagittal T1-weighted image shows a hyperintense intrasellar mass bowing upward into the chiasmatic cistern just below the optic chiasm. **B**, Coronal T1-weighted image shows an intrasellar mass with suprasellar extension; note that chiasm is not compressed.

VIEW IMAGE

Copyright © 2003, Mosby, Inc. All rights reserved.

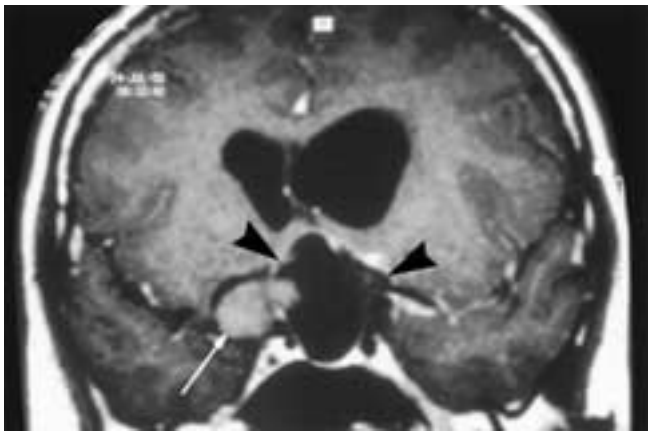

VIEW IMAGE

FIGURE 11-26 Cyst of Rathke's pouch. Contrast-enhanced coronal T1-weighted image shows a multilobulated intra- and suprasellar cystic mass (*arrowheads*) with one component (*arrow*) isointense to brain. There is no enhancement of the mass. The chiasm was compressed. Hydrocephalus is present.

can contain necrotic, cystic, or hemorrhagic regions and rarely contain calcification.[66] Of these adenomas, 25% to 30% are nonfunctional, 25% are prolactin-secreting tumors, 20% elaborate growth hormone, and 10% secrete adrenocorticotropic hormone (ACTH).[66] Microscopically, the adenomas are composed of sheets and cords of cells with a delicate stroma, and the functional adenomas usually contain highly granulated cells indicative of their cytochemical activity. Ischemia with consequent necrosis and hemorrhage may occur secondary to compromise of the blood supply, which results from compression at the diaphragma sellae. This eventually may cause a rapidly expanding sellar mass, with consequent optic nerve compression, headache, and occasional meningeal irritation. The incidence of malignant degeneration among pituitary adenomas is exceedingly small.

CT Appearance

The specific findings associated with pituitary adenoma vary, depending on the size of the lesion.[67, 68, 69] Microadenomas typically are seen as focal hypodense areas within the surrounding pituitary gland, causing convexity of the upper surface of the gland and an increase in the height of the gland greater than 9 mm. Associated displacement of the infundibulum away from the side of the lesion may be seen, and thinning of the ipsilateral sellar floor may be present. These findings are more often found in lesions elaborating prolactin. Lesions elaborating growth hormone or ACTH may be more difficult to visualize because they tend to be less well defined. Also, the ACTH-producing adenomas may be very small. After administration of a contrast medium, microadenomas tend to be hypodense relative to the surrounding normally enhancing pituitary gland.

Macroadenomas display findings that depend on the size of the lesion (Fig. 11-27). They tend to enlarge the sella, causing sloping of the sellar floor, with possible extension into the sphenoid sinus. Depending on the degree of suprasellar extension, macroadenomas may displace the chiasm, the temporal lobes, and even the third ventricle.[68] After administration of a contrast medium, the macroadenomas generally appear isodense to slightly hypodense compared with the cavernous sinuses. If the lesion is solid, homogeneous enhancement occurs (Fig. 11-28A), whereas cystic or necrotic areas within a lesion tend to remain less dense relative to the remainder of the lesion. Macroadenomas may contain calcification, either homogeneously distributed throughout the tumor or deposited in a rim. If infarction of the tumor occurs, a hypodense area secondary to edema may be seen; alternatively, a hyperdense area secondary to hemorrhage may be seen (Fig. 11-29A). However, these findings are often difficult to delineate on CT.[62]

MR Imaging Appearance

MR imaging usually allows accurate delineation of pituitary adenomas greater than 3 mm.[63] Smaller adenomas may also be diagnosed, but with less reliability.[70] A more specific diagnosis of a sellar mass may be achieved with MR imaging than with CT, and MR imaging is clearly better able to characterize subacute hemorrhage within the tumor.[61, 63, 71] Overall anatomic definition is more accurate with MR imaging than with CT (Figs. 11-29B, 11-30 and 11-31). Equivalent demonstration of sellar or dorsum sellae erosion is noted with the two imaging modalities,[72] but CT is better able than MR imaging to demonstrate intratumoral calcification.

Findings of a pituitary adenoma on MR imaging are similar to those noted on CT. Specifically, the primary findings are an upward bulge on the superior surface of the pituitary gland, with contralateral deviation of the infundibulum and sloping of the ipsilateral sellar floor (Fig. 11-31).[63] On short TR/TE images the adenomas tend to be slightly hypointense to the surrounding normal pituitary gland and may or may not be associated with a mass effect.[63] Occasionally pituitary adenomas may be isointense to the

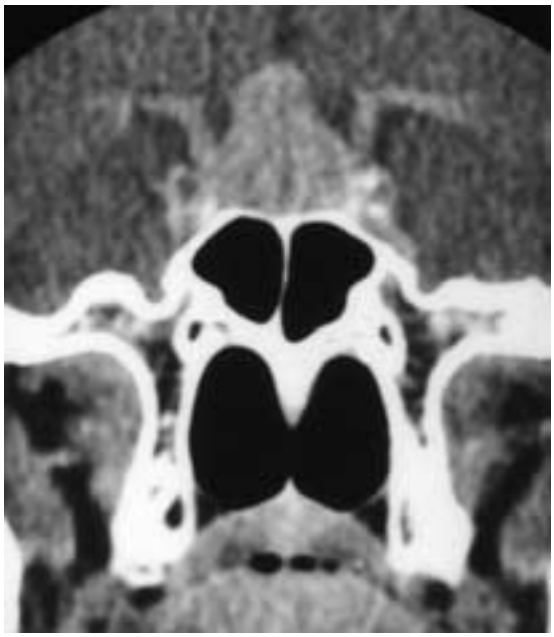

FIGURE 11-27 Pituitary adenoma; coronal contrast-enhanced CT image shows upward enlargement of the pituitary gland. The optic chiasm is affected.

VIEW IMAGE

Copyright © 2003, Mosby, Inc. All rights reserved.

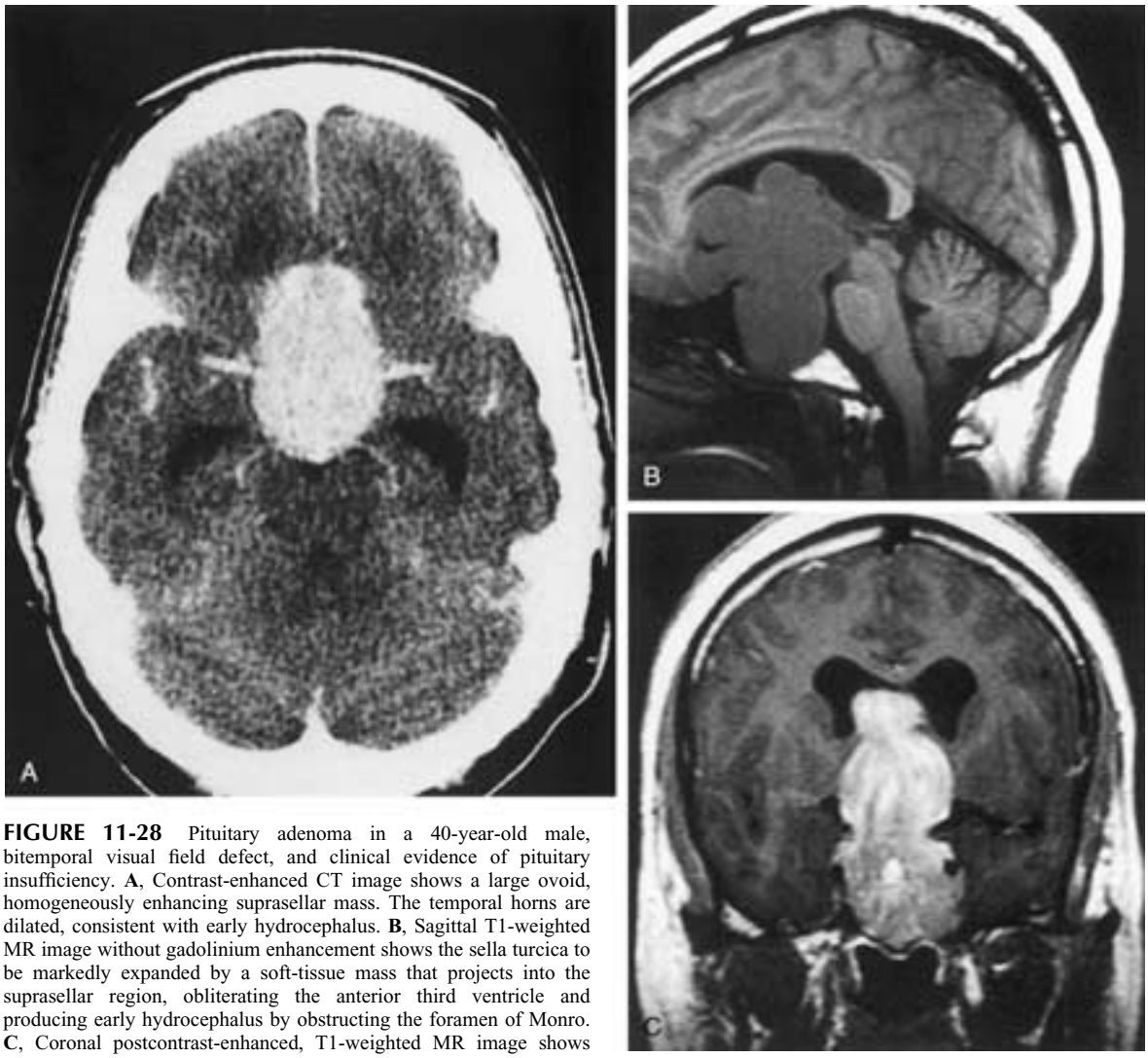

VIEW IMAGE

FIGURE 11-28 Pituitary adenoma in a 40-year-old male, bitemporal visual field defect, and clinical evidence of pituitary insufficiency. **A**, Contrast-enhanced CT image shows a large ovoid, homogeneously enhancing suprasellar mass. The temporal horns are dilated, consistent with early hydrocephalus. **B**, Sagittal T1-weighted MR image without gadolinium enhancement shows the sella turcica to be markedly expanded by a soft-tissue mass that projects into the suprasellar region, obliterating the anterior third ventricle and producing early hydrocephalus by obstructing the foramen of Monro. **C**, Coronal postcontrast-enhanced, T1-weighted MR image shows enhancement throughout the solid tumor.

surrounding normal pituitary tissue.[72] On long TR/TE images the appearance of the adenomas varies,[63] but they may be moderately hyperintense relative to surrounding pituitary tissue.[72] Pituitary adenomas usually demonstrate homogeneous signal intensity; however, occasionally they are of mixed intensity due to necrosis, hemorrhage, or cyst formations.[72]

Suprasellar extension with impingement on and displacement of the optic chiasm is best demonstrated on coronal and sagittal sections (Fig. 11-30).[61, 68] Coronal sections are also better for demonstrating tumor extension into the cavernous sinuses (Fig. 11-32).[73] Demonstration of extension into the cavernous sinuses is often difficult with MR imaging because the medial wall of the cavernous sinus is very thin, and violation of this tissue plane may be difficult to see. However, when the tumor extends around the intracavernous carotid artery, displacing it medially, or is found above it, displacing it downward, invasion of the cavernous sinus can be diagnosed.

There is no evidence of a difference in signal intensity between secretory and nonsecretory pituitary adenomas.[63] Cystic pituitary adenomas characteristically display high signal intensity on long TR/TE images and low signal intensity on short TR/TE images at the site of the cyst (Fig. 11-31). Subacutely hemorrhagic pituitary adenomas display high signal intensity on short TR/TE images because of the paramagnetic effect of methemoglobin (Fig. 11-33).[74] On short TR/TE images, after administration of a paramagnetic contrast agent such as gadolinium, a pituitary microadenoma is shown as a focal area of hypointensity relative to the surrounding enhancing normal pituitary tissue.[75, 76] This is true only if the images are acquired very early after administration of the contrast medium.[53] Dynamic scanning during contrast injection in the coronal plane through one thin section aids in diagnosis. On images obtained late after administration of the contrast medium, the microadenoma enhances and may not be distinguished from the normal pituitary gland. Macroadenomas show contrast enhancement.

Following performance of a transsphenoidal hypophysectomy, one possible complication is herniation of the optic chiasm, of the intracranial portion of the optic nerve, and/or

Copyright © 2003, Mosby, Inc. All rights reserved.

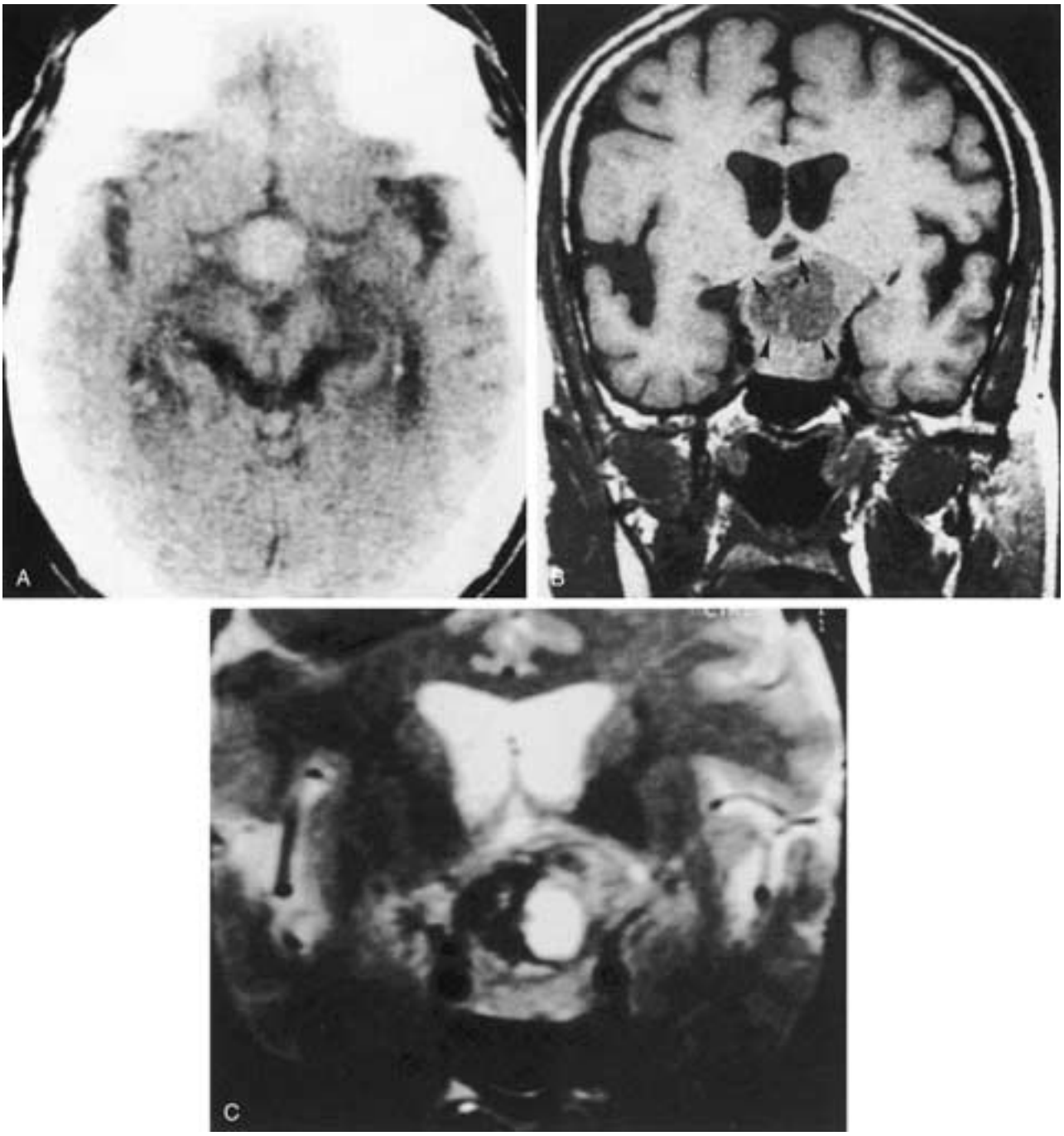

VIEW IMAGE

FIGURE 11-29 Pituitary apoplexy. **A**, Axial CT image without contrast medium shows a hyperdense suprasellar mass consistent with either bleeding or calcification. **B**, Coronal T1-weighted image shows an intrasellar and suprasellar mass extending slightly more to the left. The chiasm is displaced and compressed from below (*arrows*). The mass contains a slightly less intense zone (*arrowheads*) consistent with deoxyhemoglobin. **C**, Coronal T2-weighted image shows that the same area of hypointensity within the pituitary adenoma seen in **B** is of both high and low signal intensity. High signal intensity more to the left of the midline represents an area of cystic necrosis, whereas low signal intensity represents deoxyhemoglobin.

of the proximal aspect of the optic tracts into the surgically created empty sella. The herniation of the suprasellar visual system is well delineated with MR imaging. A visual deficit may or may not be present. The degree of deficit bears no relationship to the severity of herniation as seen on MR imaging.[77]

Aneurysms

Aneurysms may be responsible for visual symptoms if they impinge directly on the visual pathway.[78, 79] The most common aneurysms to do this arise from the internal carotid artery at the origin of the ophthalmic artery. Aneurysms

Copyright © 2003, Mosby, Inc. All rights reserved.

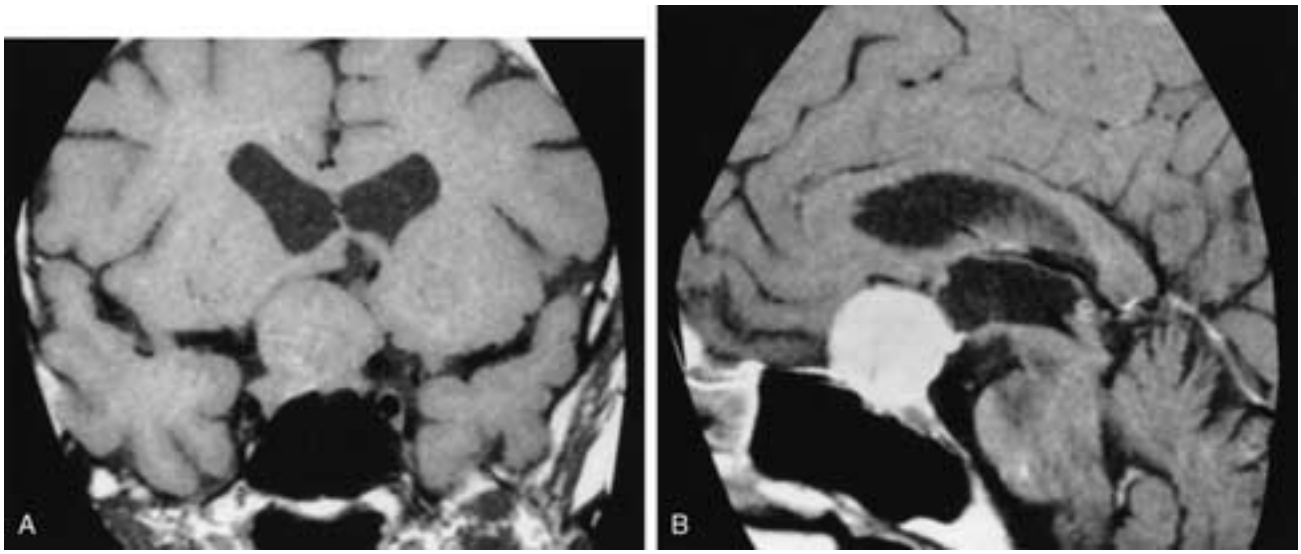

FIGURE 11-30 Pituitary adenoma in a 40-year-old male with bitemporal hemianopsia. **A**, Coronal T1-weighted image shows a large intra- and suprasellar mass stretching the chiasm from below. **B**, Sagittal T1-weighted image shows the adenoma enhancing. Note that the tumor did not expand into the aerated sphenoid sinus but upward, indicating an open diaphragma sellae.

VIEW IMAGE

occurring in this location compress either the optic chiasm, the intracranial portion of the optic nerve, or the proximal portion of the optic tract.

Clinical Findings

Aneurysms arising from the internal carotid artery at the origin of the ophthalmic artery most often appear in patients between 50 and 70 years of age, and most patients are female. Of the aneurysms in this location, 75% are discovered at the time of angiographic evaluation for subarachnoid hemorrhage that has originated from another

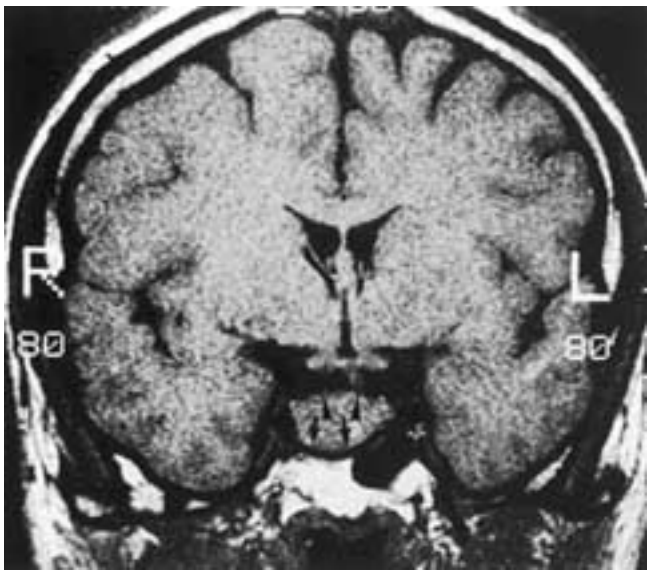

FIGURE 11-31 Pituitary adenoma. Coronal T1-weighted image shows downward bowing of an enlarged sella (*arrows*), upward convexity of the gland (*arrowheads*), and displacement of the infundibular stalk to the left.

VIEW IMAGE

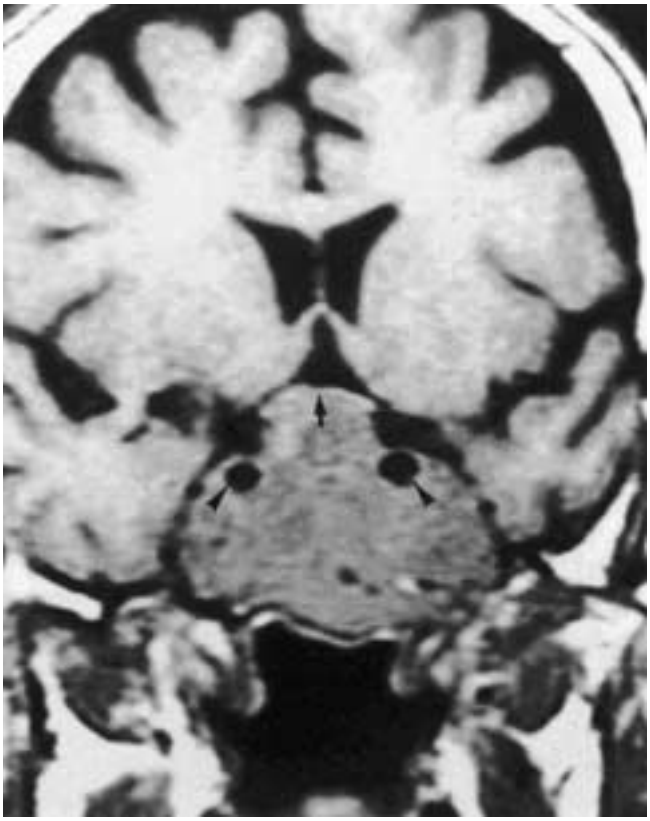

FIGURE 11-32 Pituitary adenoma. Coronal T1-weighted image shows a large pituitary adenoma elevating and compressing the optic chiasm (*arrow*). Both cavernous sinuses are invaded, and the tumor has extended lateral to the flow void of intracavernous internal carotid arteries (*arrowheads*). Note the outward convexity of the lateral margin of the cavernous sinuses.

VIEW IMAGE

Copyright © 2003, Mosby, Inc. All rights reserved.

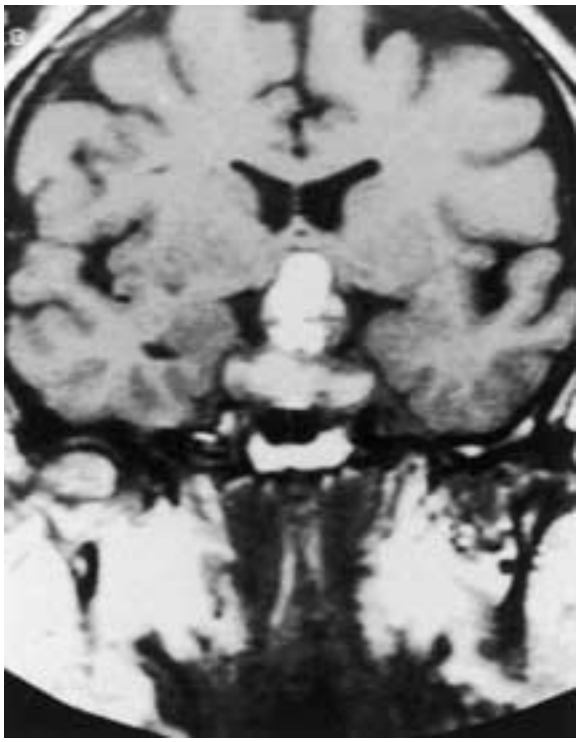

VIEW IMAGE

FIGURE 11-33 Pituitary adenoma with intratumoral hemorrhage. Coronal T1-weighted image shows an intrasellar and suprasellar mass of mixed signal intensity, which is caused by the presence of methemoglobin. Note that the mass extends laterally and compresses both cavernous sinus regions.

aneurysm. However, in approximately 25% of patients with these aneurysms, the presentation is solely because of visual symptoms. The aneurysms associated with visual symptoms are often found to be large (greater than 2.5 cm in diameter).[80, 81] Also, more than half of the patients with these aneurysms have at least one other intracranial aneurysm, and the most common site of the additional aneurysm is the same site on the contralateral side.[82]

A diverse range of visual abnormalities is encountered, but visual acuity is nearly always impaired. This usually begins on the side of the aneurysm and may progress over months or years, leading eventually to blindness. Visual field abnormalities are also diverse because of the variety of ways in which the optic nerves and chiasm can be displaced by the aneurysm. Most commonly, unilateral or bilateral temporal field defects are seen, and the clinical presentation of aneurysms in this location can mimic that of pituitary tumors.

Pathologic Findings

Grossly, these aneurysms tend to be saccular ones arising from the upper surface of the internal carotid artery at the origin of the ophthalmic artery.[83] Microscopically, within the aneurysm dome, there is fragmentation of the interna of the vessel with degeneration of the smooth muscle wall. Frequently the dome of the aneurysm contains layers of adherent thrombus of varying ages.

CT Appearance

Although aneurysms at the internal carotid-ophthalmic artery junction that cause visual pathway symptoms are usually intact, they are most frequently discovered when the patient seeks help for symptoms of a subarachnoid hemorrhage. Therefore, the CT findings of an aneurysm in this location often coincide with the findings of subarachnoid hemorrhage, which most commonly consist of high-density material lying within the sulci and cisternal spaces. Depending on the location of the ruptured aneurysm, high-density material reflecting hemorrhage may be seen within the ventricular system or within the brain parenchyma itself.

The appearance of the aneurysm causing visual pathway symptoms depends on whether there is partial thrombosis within the aneurysmal dome. If no thrombus is present, the aneurysm usually appears as a rounded area of slightly increased density lying cephalad to the cavernous sinus adjacent to the optic chiasm. The structures in the region may be displaced. After injection of a contrast medium, there is homogeneous enhancement of the aneurysm (Fig. 11-34), and rim calcification may or may not be present (Fig. 11-35). A partially thrombosed aneurysm appears on an unenhanced CT scan as a well-circumscribed mass with an isodense periphery and central hyperdensity. The hyperdense central patent lumen enhances upon administration of contrast medium, and a peripheral rim of enhancement may occur because of increased vascularity within the aneurysm wall. If the aneurysm is completely thrombosed, only isodense thrombotic material may be seen within its central portion.[84] Three-dimensional (3D) CT angiography is emerging as a useful technique for evaluation of intracranial aneurysms. Utilizing a continuous peripheral intravenous infusion of contrast material (1 ml/sec for a total dose of 2 ml/kg), rapid dynamic thin-section CT images are obtained through the circle of Willis. Surface-rendering 3D reconstruction algorithm software is then used to produce images of the circle of Willis, the cavernous and supraclinoid internal carotid arteries, and any associated aneurysms. Rotational evaluation of the produced images is then performed. This technique provides additional information regarding the position of an aneurysm relative to adjacent vascular and bony structures and, by inference, to adjacent neural structures, without the use of more contrast or imaging time than is required for a routine contrast-enhanced head CT scan.[85]

MR Imaging Appearance

Compared with CT, MR imaging more precisely characterizes giant aneurysms and defines their location relative to that of adjacent anatomic structures. However, MR imaging is much less sensitive than CT for detecting acute subarachnoid hemorrhage. Fluid-attenuated inversion recovery imaging is useful in showing subarachnoid hemorrhage on MR imaging as high signal intensity within cisterns and sulci between 3 to 45 days after the bleed.[86] Therefore, in the setting of symptoms suggesting acute subarachnoid hemorrhage, CT is the imaging modality of choice. However, MR angiography (MRA) is being used as a screening technique for detection and delineation of intracranial aneurysms in asymptomatic high-risk patient groups, and aneurysms as

Copyright © 2003, Mosby, Inc. All rights reserved.

small as 3 to 4 mm in diameter can be visualized. The sensitivity of MRA for detection of intracranial aneurysms varies between 70% and 95% (Fig. 11-36). Conventional contrast angiography remains the most sensitive modality for detecting intracranial aneurysms.[87, 88, 89] Nevertheless, this modality is limited by its ability to demonstrate only the patent portions of the lumen of the aneurysm, and because many aneurysms contain thrombus, which partially or completely obliterates the lumen, the full extent of the lesion often cannot be defined by conventional angiography.

The characteristic appearance of a partially thrombosed aneurysm on MR imaging has been well described.[84, 88, 90, 91] On spin-echo imaging, partially thrombosed aneurysms demonstrate a flow phenomenon, usually a flow void, within the patent portion of the lumen. The laminated thrombus along the margins of the aneurysm dome exhibits mixed signal intensities, reflecting the various stages of clot formation. A periluminal rim of hyperintensity is usually seen, reflecting methemoglobin surrounding the patent portion of the lumen (Fig. 11-34B). The parent vessel (i.e., the internal carotid artery) shows a signal void because of high-velocity flow. Gradient echo acquisition images, which display high-velocity flow as regions of high signal intensity, demonstrate blood flow within the lumen of the parent vessel and within the patent portion of the lumen of the aneurysm. On spin-echo images, aneurysms with no thrombus formation appear as areas of signal void (Figs. 11-37 and 11-38) and on gradient echo acquisition images as areas of high signal intensity. If the aneurysm is completely thrombosed, mixed signal intensity caused by various stages of clot formation is seen within the aneurysmal mass on spin-echo images (Fig. 11-38).

The relationship of the aneurysm to the elements of the visual pathway is delineated with MR imaging. The coronal plane is helpful in showing the relationship of the aneurysm to the optic chiasm, nerve, and tract, as well as the aneurysm's relationship to the structures of the sella turcica and the cavernous sinus. Additionally, mass lesions (other than aneurysms) impinging on the optic chiasm are well delineated with coronal MR imaging.[92, 93]

Infarction

Cerebral infarction, a localized area of tissue necrosis produced by circulatory insufficiency, is the most common

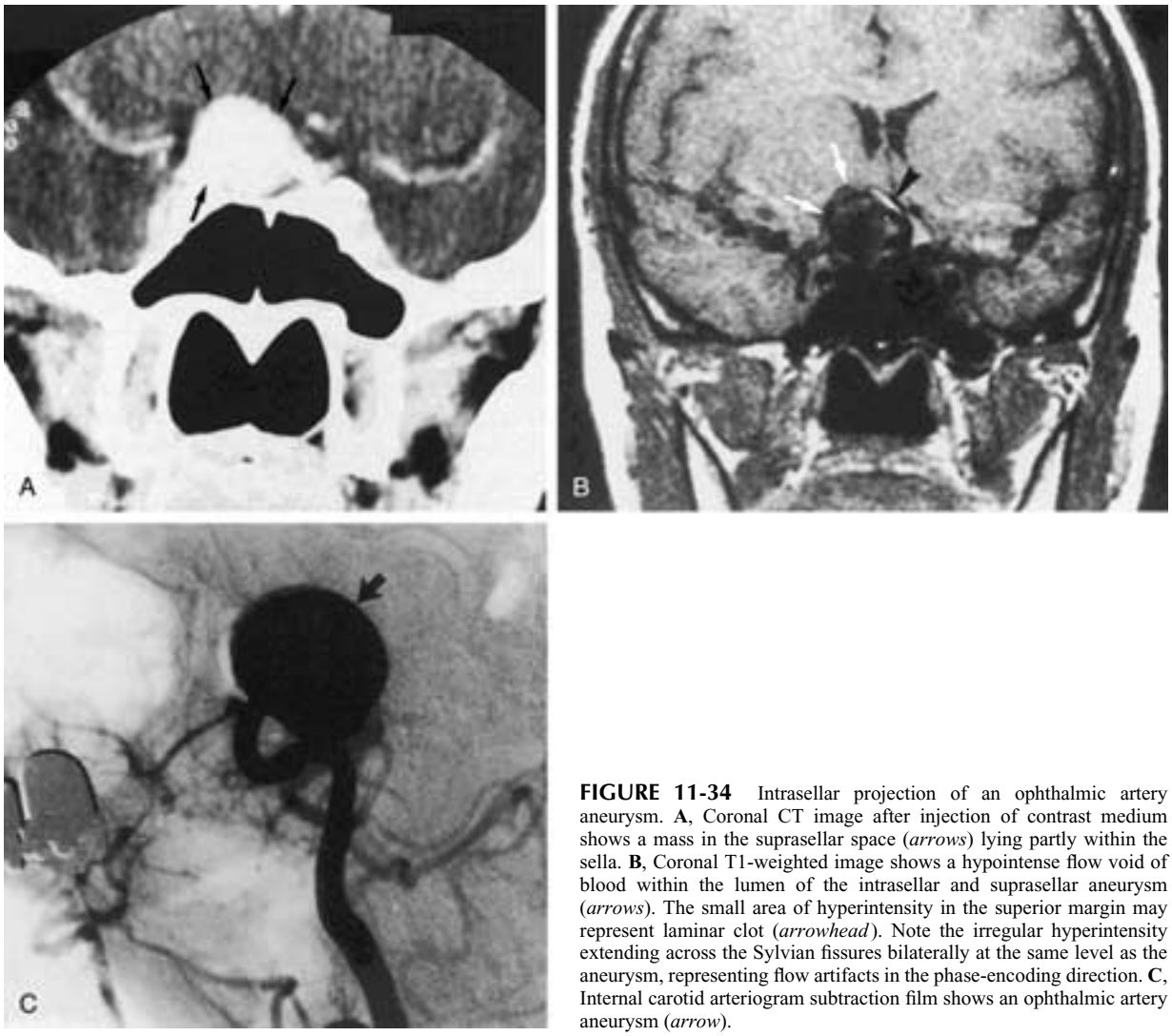

FIGURE 11-34 Intrasellar projection of an ophthalmic artery aneurysm. **A**, Coronal CT image after injection of contrast medium shows a mass in the suprasellar space (*arrows*) lying partly within the sella. **B**, Coronal T1-weighted image shows a hypointense flow void of blood within the lumen of the intrasellar and suprasellar aneurysm (*arrows*). The small area of hyperintensity in the superior margin may represent laminar clot (*arrowhead*). Note the irregular hyperintensity extending across the Sylvian fissures bilaterally at the same level as the aneurysm, representing flow artifacts in the phase-encoding direction. **C**, Internal carotid arteriogram subtraction film shows an ophthalmic artery aneurysm (*arrow*).

VIEW IMAGE

Copyright © 2003, Mosby, Inc. All rights reserved.

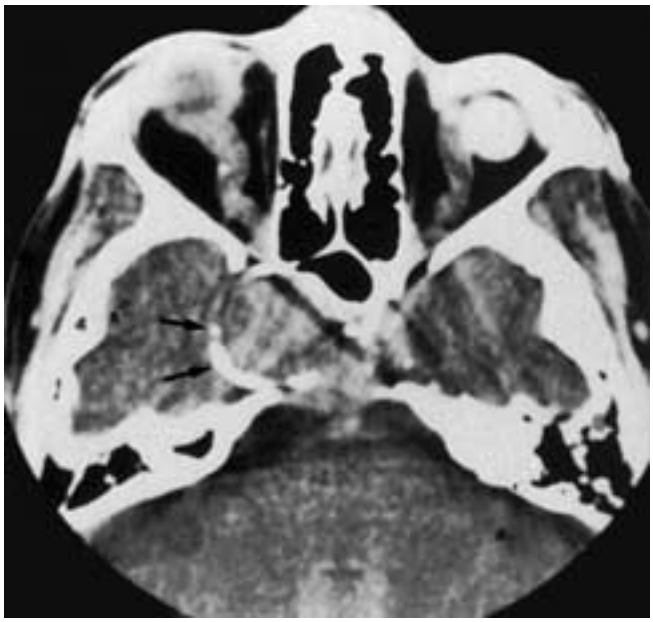

VIEW IMAGE

FIGURE 11-35 Intracavernous aneurysm. Plain axial CT image shows a mass with peripheral calcification (*arrows*) that is eroding the sphenoid bone and sella turcica.

pathologic disorder affecting the CNS. Cerebral infarctions may be further subdivided into ischemic and hemorrhagic forms. They may be due to arteriosclerosis, which may or may not be associated with thrombosis, emboli, or venoocclusive disease.

Clinical Findings

Circulatory insufficiency may be caused by involvement of the anterior cerebral circulation (internal carotid arteries and their branches) or the posterior cerebral circulation (the vertebral basilar system). Amaurosis fugax, or transient loss of vision in one eye, is the most common ocular symptom of internal carotid artery ischemia. Specific findings vary from altitudinal or arcuate visual field defects to complete loss of light perception in the affected eye. Vision may return after a few minutes, but permanent visual loss because of central retinal artery occlusion can and often does occur. Cholesterol emboli may be found in association with amaurosis fugax, and ophthalmoscopic evaluation reveals these emboli within the retinal arterioles as characteristic bright yellowish-orange plaques. Because the internal carotid artery and its branches supply the frontal lobes, parietal lobes, portions of the temporal lobes, the corpus striatum, and the internal capsule, an occlusion may produce a variety of contralateral motor and sensory dysfunctions in addition to the visual findings.

Insufficiency of the circulation of the vertebral basilar system causes transient ischemic attack or infarction with complex and diverse neurologic symptoms. In addition to ocular symptoms, vertigo and nausea may be present if the cochlear vestibular system is involved. Involvement of the auditory system may produce tinnitus or partial deafness. Headache, dysphagia, dysarthria, and hiccuping may also occur. The ocular symptoms include transient or permanent homonymous hemianopsia and possibly blurred vision with diplopia. The homonymous hemianopsia arises as a result of infarction of the occipital lobe's visual cortex, which is fed by branches of the posterior cerebral artery. Diplopia occurs because vascular insufficiency produces infarction in the fasciculi connecting the brainstem nuclei or in the brainstem nuclei of the third, fourth, and sixth cranial nerves. Internuclear ophthalmoplegia may occur as a result of interruption of the vascular supply to the medial longitudinal fasciculus (Figs. 11-39 and 11-40), but this does not usually manifest as diplopia.

Pathologic Findings

Infarcts may be divided into two basic categories, depending on the amount of hemorrhage that occurs in the involved tissue. Infarction caused by thrombotic events generally produces an anemic or nonhemorrhagic infarction, whereas infarctions of embolic cause often are associated with a variable degree of hemorrhage into the interstitial space.[47, 56] Infarctions affecting the elements of the visual pathway are not dissimilar to infarctions in other regions of the brain, showing no discernible histologic differences. Their distinguishing factor is their position relative to the various portions of the visual pathway. The mechanism of infarction, whether hemorrhagic or anemic, is the same: deprivation of blood supply to a given area. In hemorrhagic infarctions, transitory occlusion of a vessel results in ischemic change of the brain tissue and the involved blood vessel's walls. When the blood supply is reestablished, blood elements penetrate the damaged vascular wall into the interstitial space, creating parenchymal hemorrhage.

The earliest grossly visible change in the evolution of an ischemic infarction is a slight discoloration and softening of the affected tissue, which occurs approximately 6 to 8 hours after occlusion of the vessel. Histologically, at this point there is diffuse swelling of the neurons, with resultant

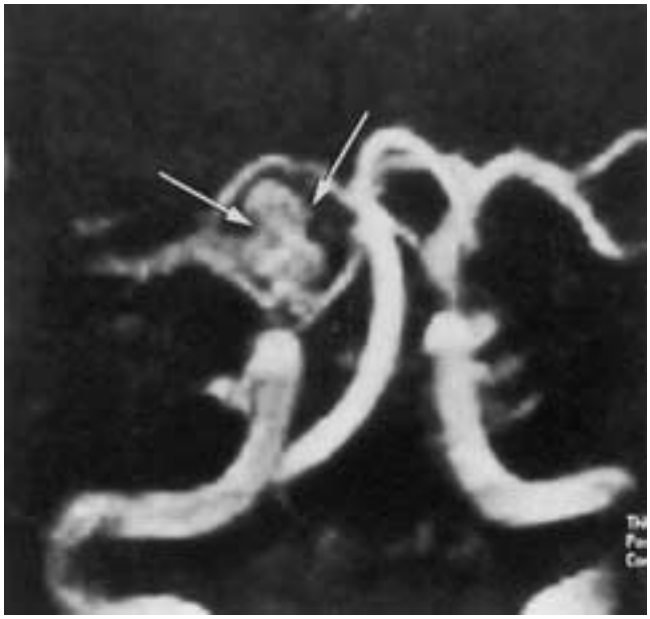

FIGURE 11-36 Aneurysm of the ophthalmic artery in a 53-year-old woman with right monocular visual loss; 3D time-of-flight MR angiography shows an aneurysm (*arrows*) arising from the internal carotid artery at the site of origin of the ophthalmic artery.

VIEW IMAGE

Copyright © 2003, Mosby, Inc. All rights reserved.

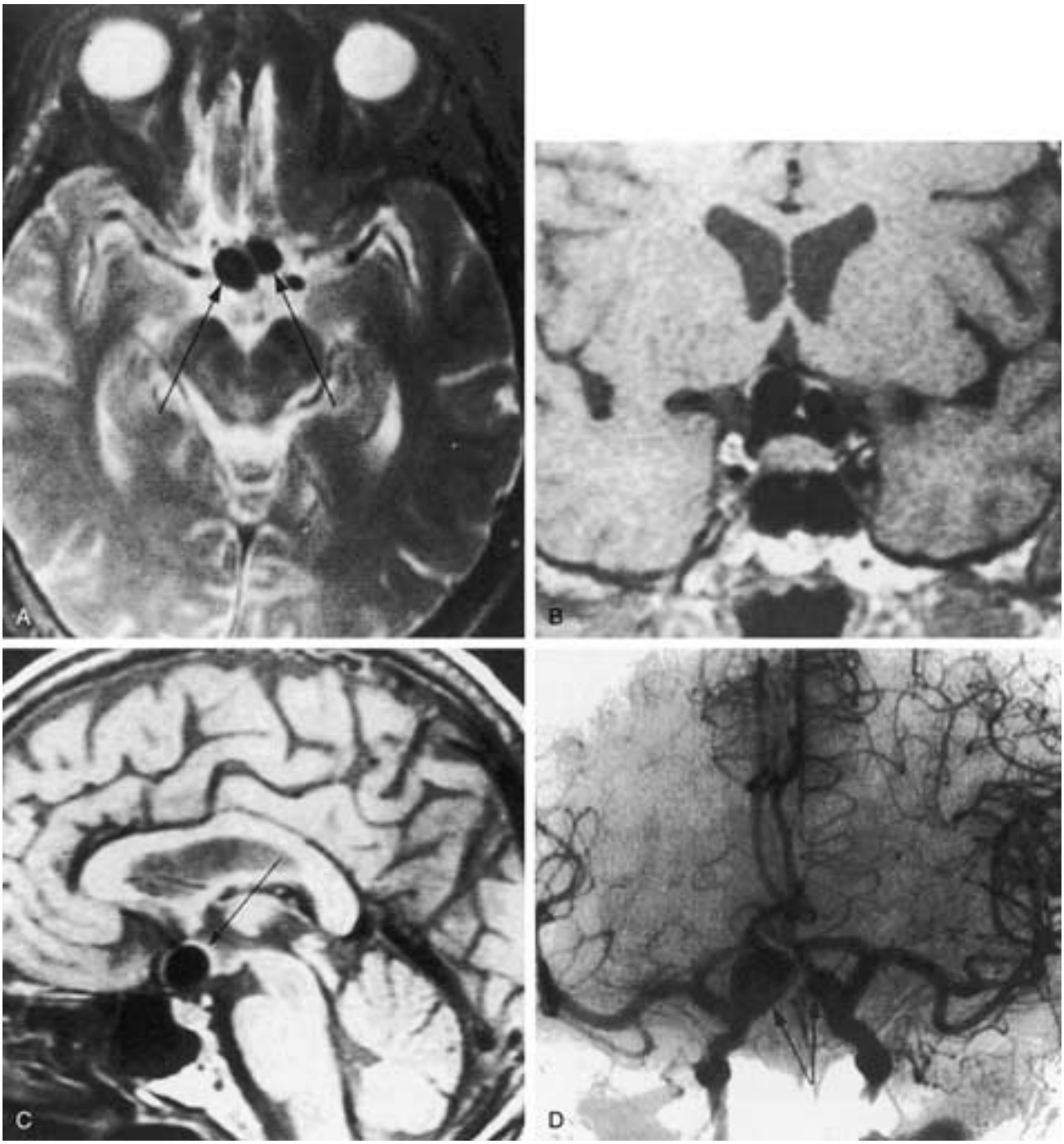

VIEW IMAGE

FIGURE 11-37 Bilateral ophthalmic artery aneurysms presenting with bitemporal hemianopsia. **A**, Axial T2-weighted image shows two areas of hypointensity (*arrows*) in the suprasellar cistern consistent with aneurysms. **B**, Coronal T1-weighted image shows two hypointense lumens of aneurysms projecting medially from the region of the internal carotid arteries and compressing the optic chiasm bilaterally. **C**, Sagittal T1-weighted image shows a larger aneurysm as a hypointense flow void and depicts the aneurysm's relationship to the chiasm (*arrow*), which is compressed from below. **D**, AP right and left carotid arteriogram subtraction films superimposed to show the relationships of both ophthalmic artery aneurysms, which project medially (*arrows*).

cytotoxic edema.[94] At 48 to 72 hours after occlusion of the vessel, tissue integrity is lost in the affected region and the surrounding tissue displays diffuse vasogenic edema. The combination of cytotoxic and vasogenic edema, with the resultant mass effect, may produce cerebral herniations that, depending on their site of occurrence, may damage neural transmission along the visual pathway (e.g., optic tract with temporal lobe herniation). Eventually, if the area of infarction is large enough, there is liquefaction and cyst formation surrounded by firm glial tissue. Histologically, in the final stages of evolution of an anemic infarction, gliosis both replaces and surrounds the necrotic region. Infarct evolution may take weeks to many months.[56] In addition to being associated with emboli, hemorrhagic

Copyright © 2003, Mosby, Inc. All rights reserved.

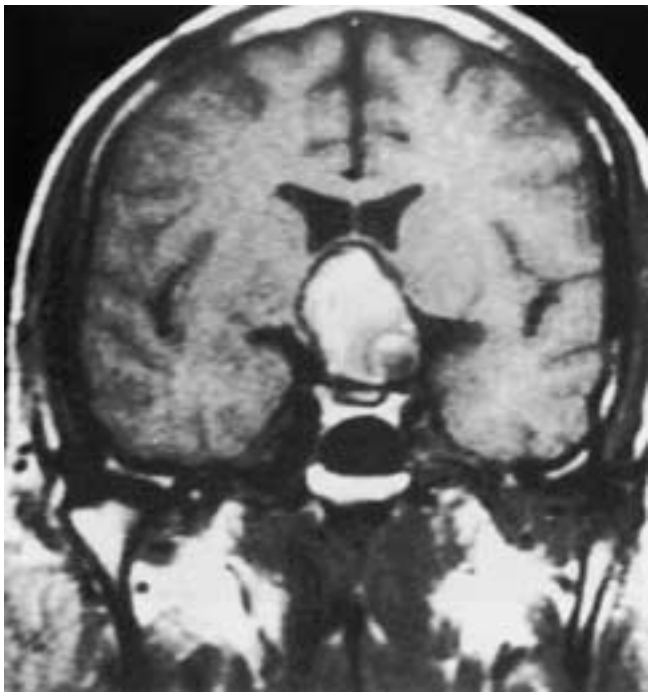

VIEW IMAGE

FIGURE 11-38 Thrombosed aneurysm. Coronal T1-weighted image shows a suprasellar mass composed of high signal intensity methemoglobin.

infarction may be seen in association with hypertension and venous occlusion (Fig. 11-40), bleeding dyscrasias, or anticoagulant administration.[95] After extravasation of blood into the interstitial tissue, significant mass effect may occur, resulting in herniation. In fact, hemorrhagic infarction may result from a herniation that caused temporary compression of a trapped blood vessel. With reperfusion of the vessel on reduction of the herniation, blood suffuses through the damaged vascular wall into the infarcted brain.

CT Appearance

The effects of an ischemic infarction may be visible as early as 3 to 6 hours after the ictus (Fig. 11-41A).[96] Occasionally, a thromboembolism within the vessel serving the area of infarction may be visualized on a CT scan as a region of hyperdensity in the vessel lumen before development of subsequent parenchymal changes (Fig. 11-42A).[97, 98] This finding is not, however, a reliable indicator of vessel occlusion or subsequent infarction, as it may be due to increased hematocrit or calcification within the vessel walls, as can occur with diabetes or hypertension.[99] However, changes may be seen more reliably between 8 and 24 hours after the onset of ischemia. These changes are regions of hypodensity in the involved vascular distribution, including both white and gray matter (Fig. 11-40A). The region of hypodensity, which represents intracellular (cytotoxic) edema, becomes more sharply defined over the next several days. Cytotoxic edema and tissue necrosis reach their maximum between the third and fifth days after the ictus, producing variable amounts of mass effect. In occipital lobe infarctions or infarctions involving the optic radiations, this may be perceived as effacement of the adjacent sulci and/or atrium and occipital horn of the lateral ventricle. Larger infarctions may cause marked mass effect and result in descending transtentorial herniation with occlusion of the posterior cerebral artery when it is trapped on the tentorial edge. Occlusion of the posterior cerebral artery results in infarction of the posterior temporal and occipital lobes.

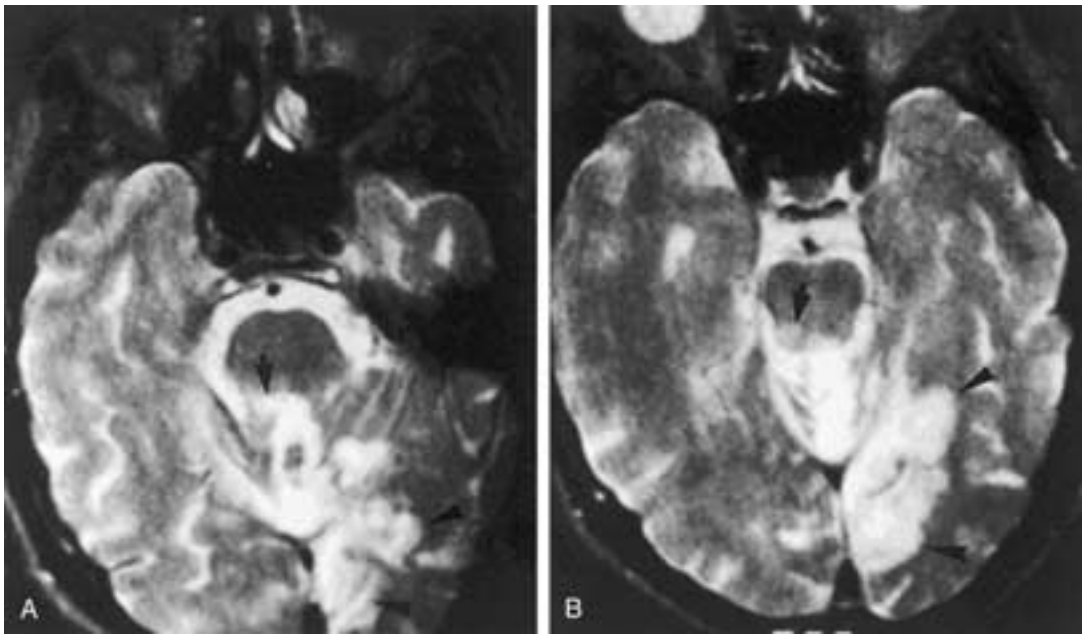

VIEW IMAGE

FIGURE 11-39 Left occipital lobe, midbrain, and upper brainstem infarction. **A**, Axial T2-weighted image shows hyperintense signal intensity at the site of the left occipital lobe infarct (*arrowheads*). Note the hyperintense focus of infarction in the periaqueductal region of the upper pons (*arrow*). **B**, Slightly higher axial T2-weighted image shows the further superior extent of a hyperintense infarct involving the left occipital and medial temporal lobes (*arrowheads*). A high signal intensity focus is present in the dorsal aspect of the right midbrain (*arrow*).

Copyright © 2003, Mosby, Inc. All rights reserved.

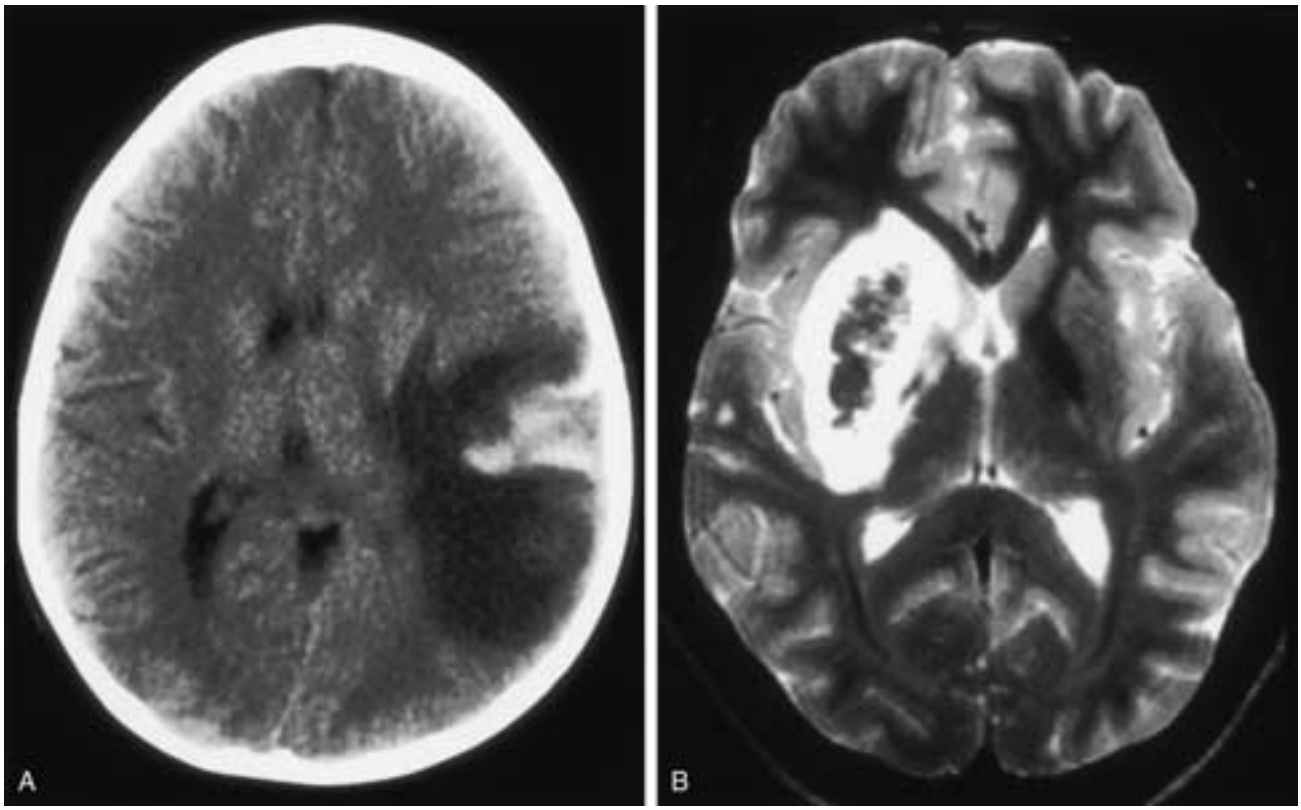

VIEW IMAGE

FIGURE 11-40 Hemorrhagic infarction. **A**, A 7-year-old female with cortical vein and transverse sinus thrombosis. Axial plain CT image shows a hypodense region in the left hemisphere with a central hyperdense hemorrhagic component. This hemorrhagic infarct causes a mass effect and a shift of midline structures to the right. **B**, A 15-year-old female with an embolic event. Axial T2-weighted MR image shows a right basal ganglionic region of both low (hemorrhage) and high (edema) signal intensity with mass effect.

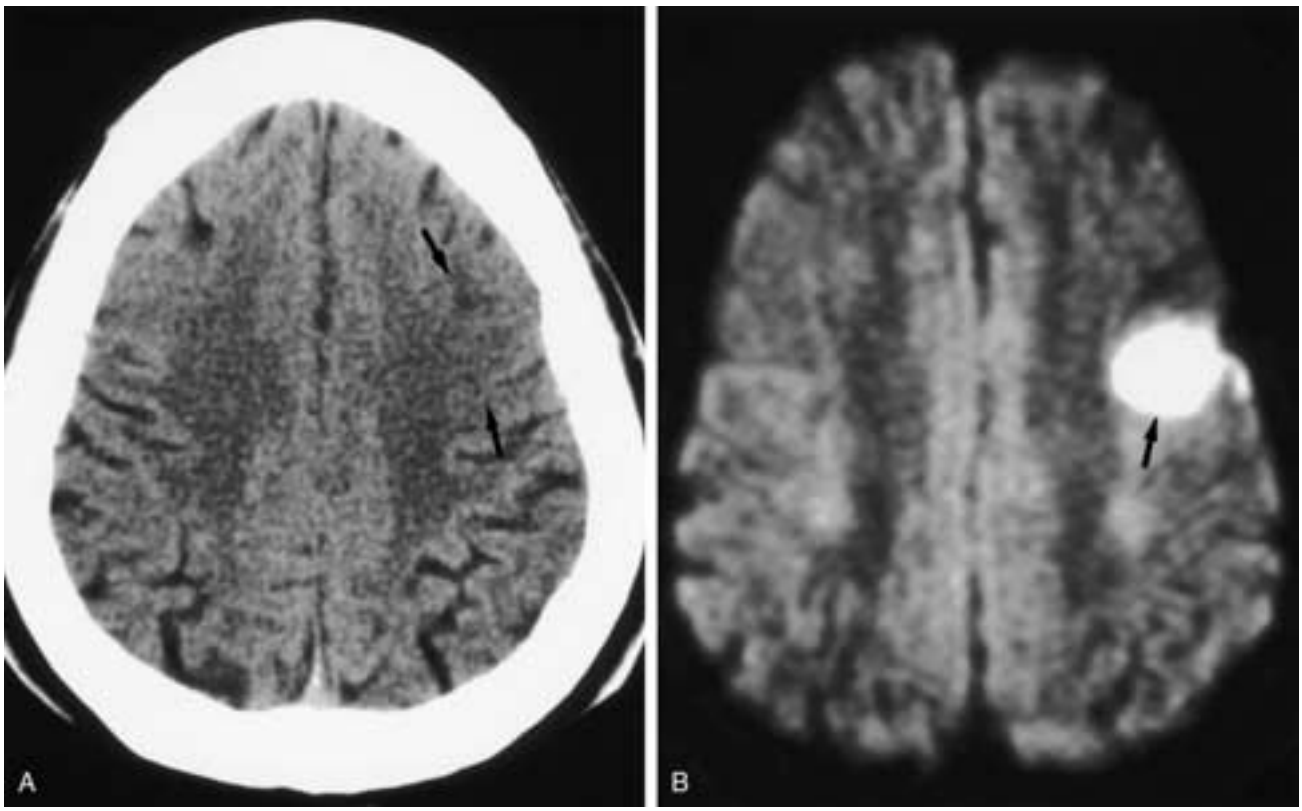

VIEW IMAGE

FIGURE 11-41 Acute embolic ischemic infarction in a 17-year-old female. **A**, CT image without contrast shows subtle posterior frontal cortical and subcortical hypodensity (*arrows*). **B**, Diffusion-weighted image shows acute infarction as high signal intensity (*arrow*).

Copyright © 2003, Mosby, Inc. All rights reserved.

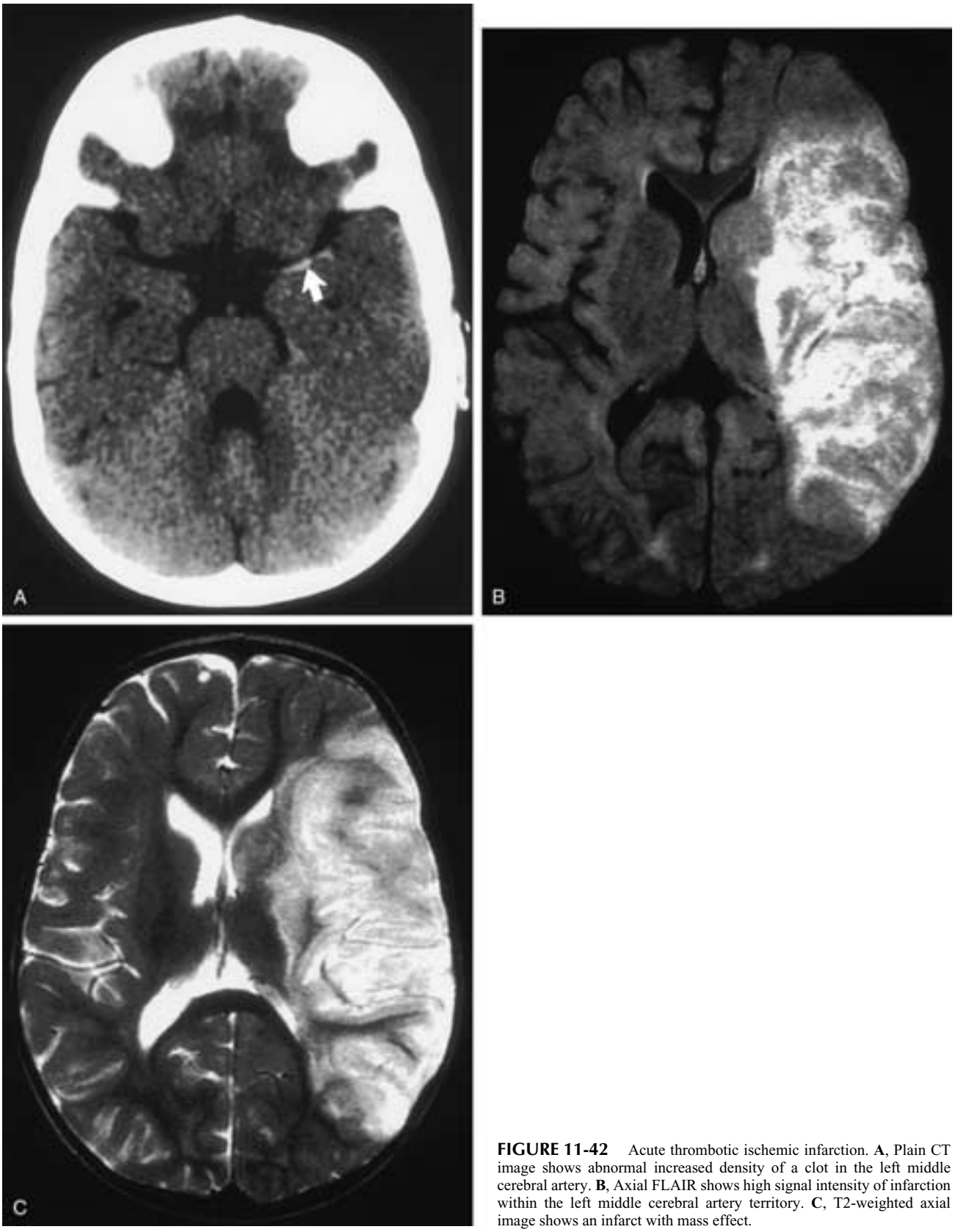

FIGURE 11-42 Acute thrombotic ischemic infarction. **A**, Plain CT image shows abnormal increased density of a clot in the left middle cerebral artery. **B**, Axial FLAIR shows high signal intensity of infarction within the left middle cerebral artery territory. **C**, T2-weighted axial image shows an infarct with mass effect.

VIEW IMAGE

Copyright © 2003, Mosby, Inc. All rights reserved.

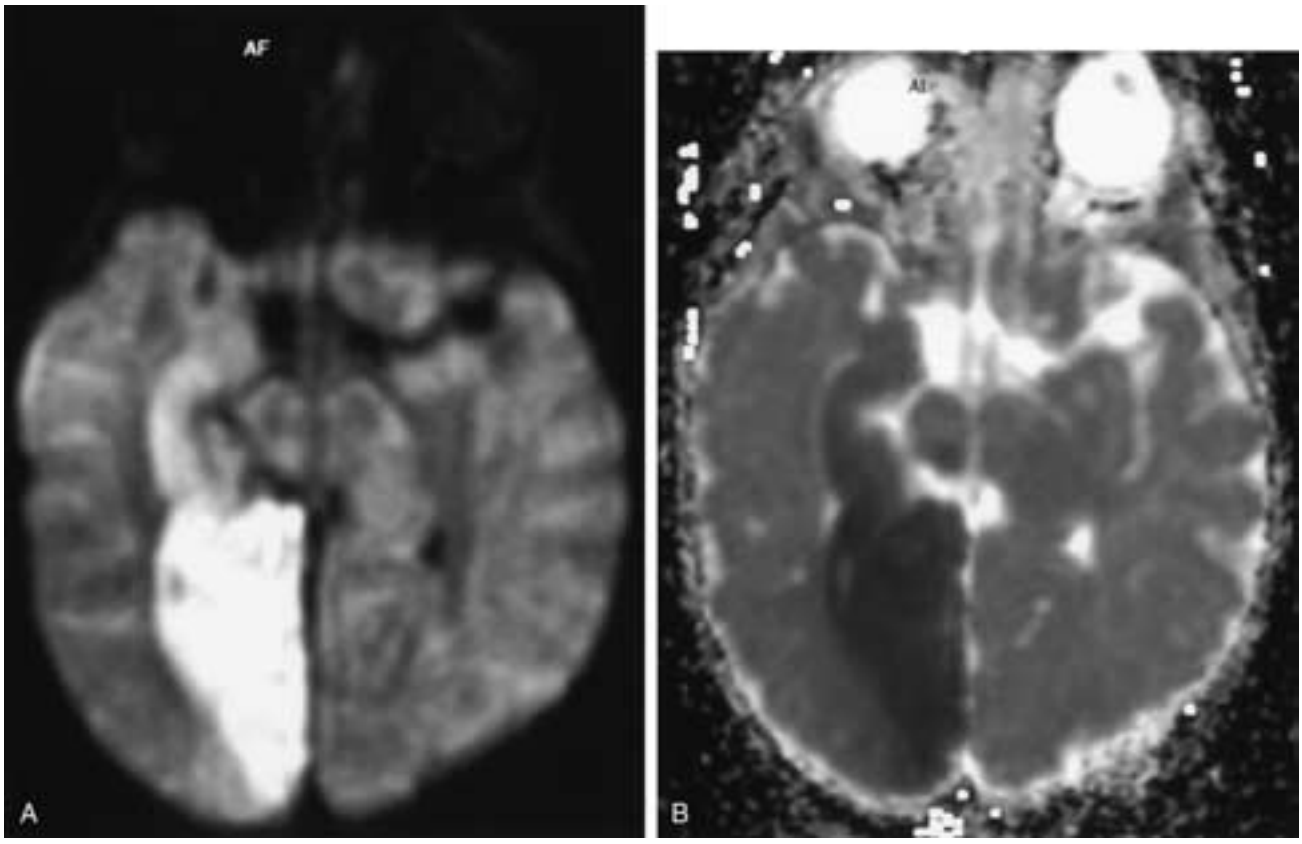

VIEW IMAGE

FIGURE 11-43 Acute embolic occlusion of the right posterior cerebral artery with ischemic infarction. **A**, Axial diffusion-weighted image shows high signal intensity indicating cytotoxic edema at the site of infarction. **B**, Axial ADC map shows low signal. Calculations of ADC measurements showed one-half normal values consistent with infarction.

Vasogenic (interstitial) edema is seen more often with embolic infarction. This follows reperfusion of the affected area, usually occurs 2 to 14 days after the acute event, and is responsible for a significant degree of mass effect. Approximately 1 month after the ictus, cystic cavitation in the infarcted region occurs pathologically and is responsible for increasingly sharp definition of the region of the infarct. The infarcted region also becomes smaller because of progression of gliosis, and there is resultant increase in the depth of the adjacent sulci and enlargement of the adjacent ventricle. Hemorrhagic infarctions, which result from embolic phenomena, overall are less frequent, representing only 20% of cases. The hemorrhage, when visible, is seen on an unenhanced CT scan as a region of high density involving the cortex or the deep white matter.

MR Imaging Appearance

MR imaging is the most valuable imaging tool in the evaluation of cerebral infarction because of its high sensitivity to increased tissue water content. The sensitivity of MR imaging in the early detection of infarction is much higher than that of CT.[100–103] Experimentally, infarctions may be detected with MR imaging 1 to 2 hours after the onset of ischemia.[104, 105] The earliest detectable changes are vascular flow-related abnormalities including absence of the flow void normally seen within the cerebral vessels. Also, on administration of gadolinium DTPA, enhancement of the arterial wall may occur, and these findings may be seen within minutes of onset. Early brain swelling can be detected on short TR/short TE images without associated parenchymal signal intensity changes on T2-weighted images.[105, 106] Diffusion weighted MR imaging, which evaluates local water mobility in vivo, can detect alterations in the involved brain parenchyma before the appearance of signal intensity changes on conventional T1-weighted and T2-weighted spin-echo images (Figs. 11-41A and 11-43).[94, 101, 102, 107, 108] The earliest parenchymal signal changes visible are caused by a prolongation of both T1 and T2 relaxation times, with resultant high signal intensity in the region of infarction on long TR/long TE images (Figs. 11-42C and 11-44A) and low signal intensity in the same region on short TR/short TE sequences (Fig. 11-45B).[109] This is frequently visible 6 to 12 hours after the onset of symptoms and is attributable to the development of cytotoxic edema. With further evolution of the infarction, absolute T1 and T2 prolongation becomes somewhat diminished, and only a slight alteration of signal intensity results in the affected area.[110] The mass effect produced by the region of infarction is clearly identified with MR imaging, with greater anatomic delineation of affected structures than is seen on CT. Contrast enhancement of the region may be demonstrated as early as 16 to 18 hours after the ictus and may be exaggerated in character.[105, 106, 111] Again, the region of enhancement correlates with areas of breakdown in the blood-brain barrier.[111, 112] Interestingly, as

Copyright © 2003, Mosby, Inc. All rights reserved.

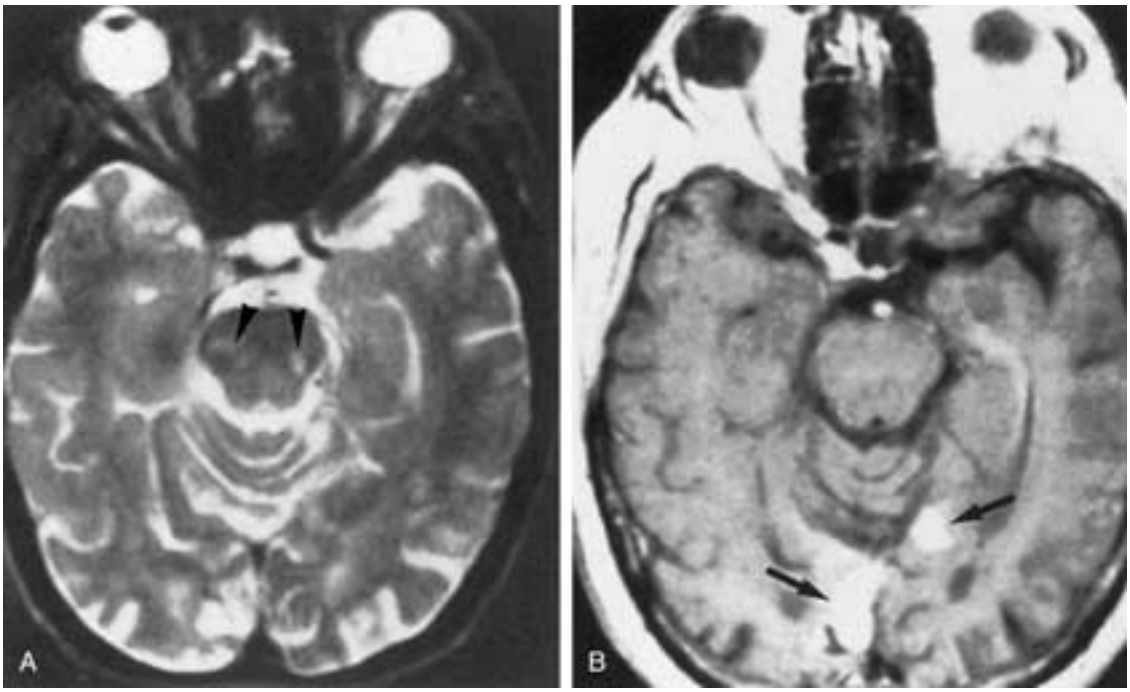

VIEW IMAGE

FIGURE 11-44 Multiple infarcts. **A**, Axial T2-weighted image shows several high-intensity foci in the upper pons (*arrowheads*) that are consistent with small infarcts. **B**, Axial T1-weighted image after injection of contrast medium shows enhancement of the right occipital lobe and left medial temporal lobe infarcts (*arrows*) not seen on the T2-weighted image.

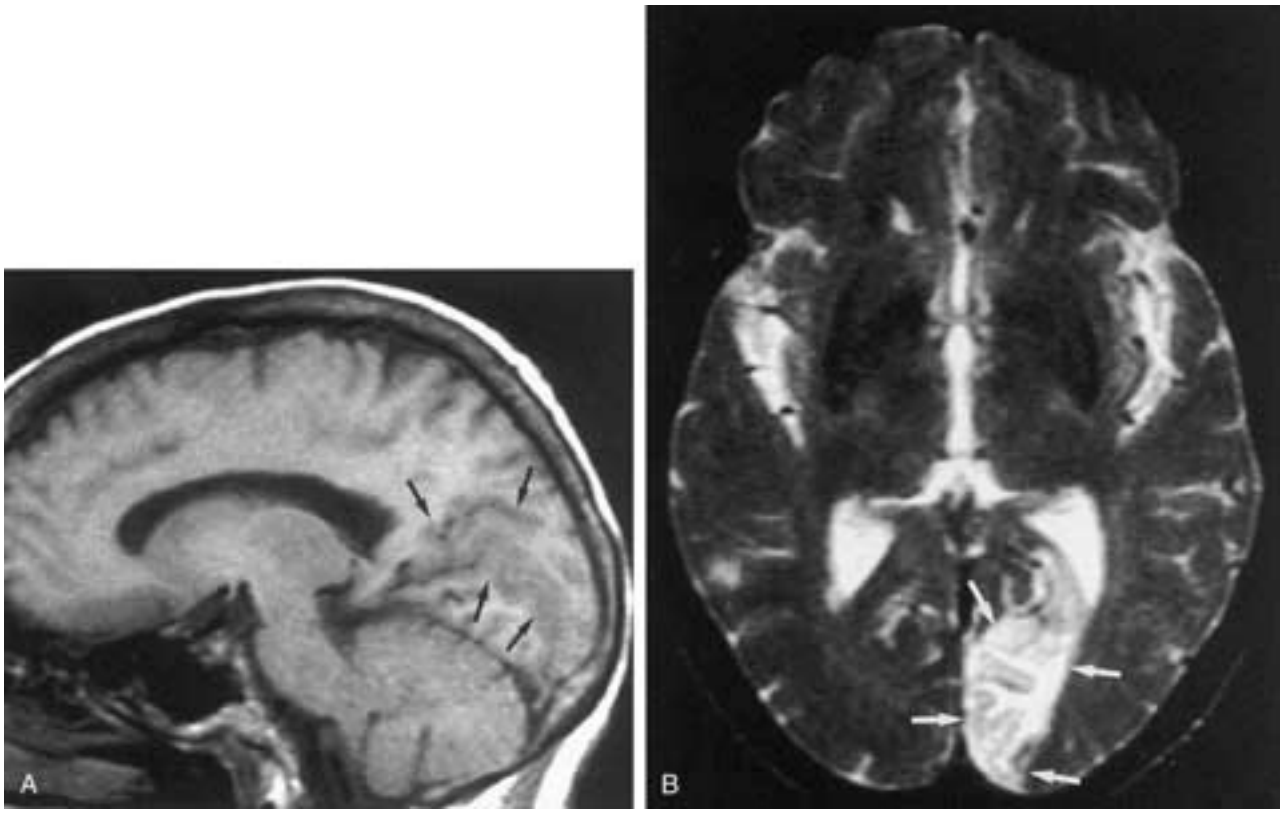

VIEW IMAGE

FIGURE 11-45 Left occipital infarct in a 50-year-old male with abrupt onset of right homonymous hemianopsia. **A**, Sagittal T1-weighted MR image without contrast injection shows decreased signal intensity involving the cortex (*arrows*) above and below the calcarine fissure. **B**, Axial T2-weighted MR image shows high signal intensity involving the cortex and subjacent white matter (*arrows*) in the left temporooccipital region including the calcarine cortex.

Copyright © 2003, Mosby, Inc. All rights reserved.

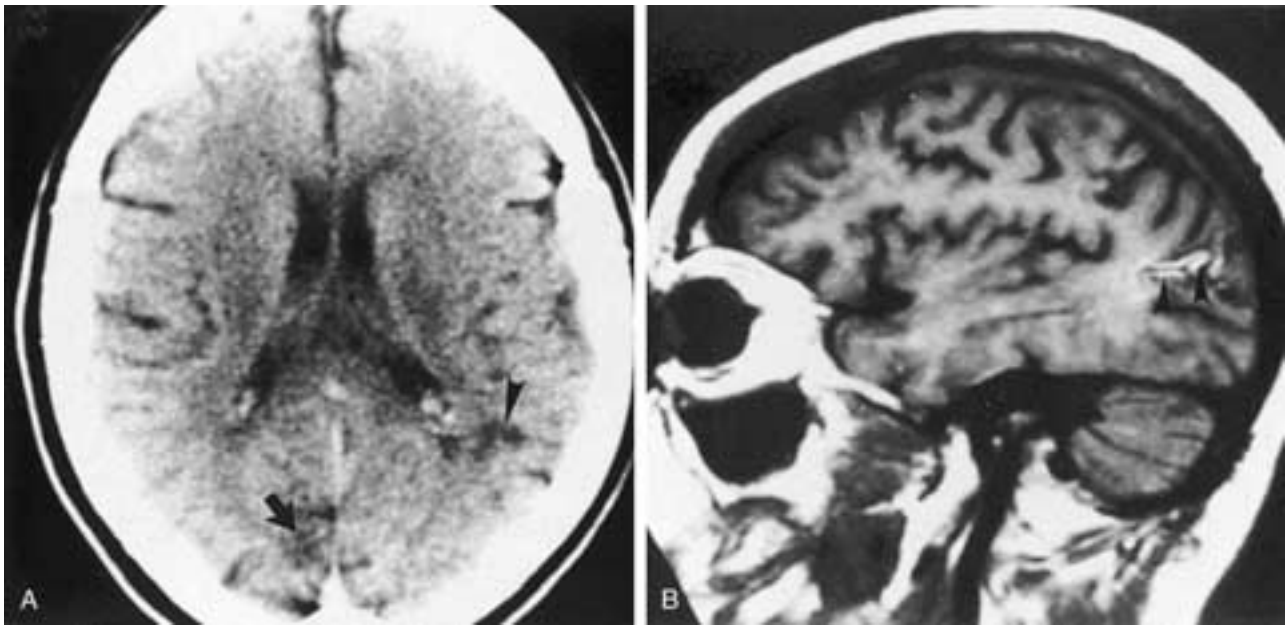

VIEW IMAGE

FIGURE 11-46 Hemorrhagic infarcts of the parietal and occipital lobes. **A**, Axial CT image without contrast shows a vague hypodensity in the right occipital lobe (*arrow*) and another vague hypodensity (*arrowhead*) in the left parietal lobe. **B**, Sagittal T1-weighted image shows hyperintense methemoglobin (*arrowheads*) in the cortex.

edema and mass effect develop, the rapidity with which enhancement occurs declines, presumably as a result of compression of the microvasculature. The regions of enhancement following administration of gadolinium are seen as areas of increased signal intensity on short TR/TE images (Fig. 11-44B). Brain parenchymal change secondary to ischemia caused by vasculitis shows the same basic characteristics with regard to signal intensity as ischemia from either embolic or thrombotic phenomena. However, there is a difference in distribution in that the regions of ischemia are more diffuse throughout the brain, tending to occur in the regions of gray and white matter interface.

Hemorrhagic infarction may be demonstrated as areas of high signal intensity on short TR/TE images (Fig. 11-46B) within the cortex or deep gray matter structures once deoxyhemoglobin within the extravasated blood has been oxidized to methemoglobin.[9] As evolution of the infarction proceeds and cystic encephalomalacia develops, the associated parenchymal volume loss is clearly delineated with MR imaging. Gliosis and demyelination within white matter tracts result in T2 prolongation and, consequently, high signal intensity in the affected areas on long TR/long TE images. Both deoxyhemoglobin and intracellular methemoglobin, as well as hemosiderin, produce loss of signal on T2-weighted images (Figs. 11-40B and 11-47).

Demyelinating Disease

The most common form of demyelinating disease to affect the optic pathway is multiple sclerosis. The characteristic changes seen in demyelination are caused by both plaque formation and gliosis, with resultant alteration in the appearance of the involved parenchyma. The neurophysiologic consequences of the loss of myelin are based on impaired transmission of neural impulses passing through the affected area.

Clinical Findings

Multiple sclerosis has a wide variety of signs and symptoms, which characteristically localize to at least two different anatomic areas within the CNS and occur with a series of relapses and remissions, separated by at least 1

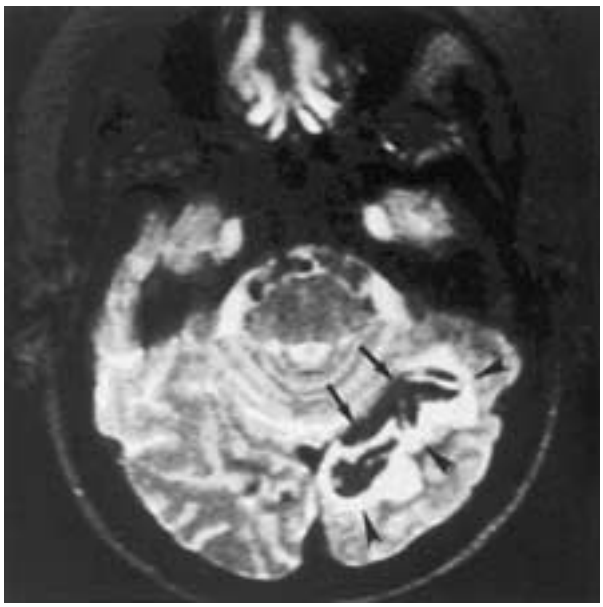

FIGURE 11-47 Hemorrhagic infarct. Axial T2-weighted image shows marked hypointensity of deoxyhemoglobin (*arrows*) in the cortex of portions of a hemorrhagic infarction. Surrounding hyperintensity is present (*arrowheads*).

VIEW IMAGE

Copyright © 2003, Mosby, Inc. All rights reserved.

month.[113] Initially the diagnosis may be difficult to confirm, since the presentation may be caused by a single lesion, or the course may be slowly progressive and not intermittent. Multiple sclerosis most characteristically affects patients between 10 and 50 years of age who reside in northern Europe or the northern United States, and females are affected more frequently than males in a ratio of 1.4 to 1.[114]

Approximately half of patients with multiple sclerosis show clinical signs of optic nerve involvement. Visual evoked responses and electrophysiologic tests of optic nerve and pathway function are positive in approximately 90% of patients with multiple sclerosis. However, only 20% of patients show isolated optic neuritis as their initial clinical symptom.[19] Visual involvement, when present, is typically unilateral, with dense regions of visual loss within the visual fields. Impaired color perception, ocular muscle palsies, and nystagmus are common, and internuclear ophthalmoplegia occasionally is present. Adrenal leukodystrophy (ADL) and Krabbe's disease are examples of dysmyelinating diseases that may cause visual symptoms and involve the visual pathway. ADL usually appears during childhood, with progressive ataxia and loss of hearing and sight. Patients with Krabbe's disease may show symptoms of developmental delay, irritability, and spasticity, often beginning at 3 to 6 months of age.

Pathologic Findings

In multiple sclerosis, the areas of demyelination are seen as focal lesions with well-circumscribed margins. Successive histologic changes occur, consisting of demyelination, a microglial reaction, and then astrocytic proliferation.[22] In the initial stages, oligodendrocytes and the myelin sheaths degenerate, without change in the axon. At this time, an associated vascular congestion with perivascular lymphocytic and plasma cell infiltrates is present. As a result, swelling is present in the acute stage of the inflammation. Later, microglia phagocytize the myelin debris, and this debris stimulates an intense gliosis that forms a firm glial scar in the late stage. Schilder's disease is characterized by large, symmetric zones of demyelination, with degeneration of neural fibers and gliosis. These zones occur throughout the CNS, including the optic nerve and optic radiation.[22] Histopathologically, the lesions are identical to those seen in multiple sclerosis.[115] Krabbe's disease, or globoid cell leukodystrophy, is caused by a deficiency of galactocerebroside beta-galactosidase, which leads to abnormal accumulation of galactoside and its derivative psychosine, which is toxic to oligodendroglial cells. As a consequence, multinucleated globoid cells (macrophages) accumulate in the white matter and are associated with extensive demyelination and astrogliosis.[116]

CT Appearance

The plaques of multiple sclerosis are sometimes detectable by nonenhanced CT as hypodense lesions within the periventricular white matter (Fig. 11-48). Occasionally, the plaques are large and demonstrate mass effect. However, they usually are less than 1.5 cm in greatest dimension. In approximately 5% of cases, multiple sclerosis plaques may be seen within the cortical gray matter or deep gray matter of the cerebral hemispheres.[117] After administration of a contrast medium, plaques in the acute phase may demonstrate enhancement. However, enhancement patterns vary, with none being characteristic of multiple sclerosis. High doses of contrast media have been used to increase the sensitivity of CT in the detection of multiple sclerosis plaques.[118] Steroid administration, however, suppresses the enhancement of acute multiple sclerosis plaques because of stabilization of the blood-brain barrier. With chronic multiple sclerosis, generalized cerebral atrophy may be seen as a result of extensive gliosis.

In adolescents with MS, the lesions observed tend to be more numerous and often confluent with a greater likelihood of infratentorial involvement and a decreased incidence of cortical atrophy.[119] The appearance of Schilder's disease on CT has been described as large, confluent areas of hypodensity within the deep cerebral hemispheric white matter, particularly the centrum semiovale. These areas may show peripheral contrast enhancement. CT scans of patients with Krabbe's disease typically demonstrate areas of low density in the cerebellum deep white matter, medial and lateral to the dentate nuclei. Interestingly, areas of increased density are noted symmetrically involving the thalami and subthalami, with extension to the corona radiata.[116, 120]

MR Imaging Appearance

Because MR imaging is the most sensitive method of evaluation for patients with multiple sclerosis, it has replaced CT in the diagnosis and follow-up of patients with this disease.[113, 114, 121–126]

Multiple sclerosis lesions characteristically demonstrate T2 prolongation, with consequent high signal intensity of the affected areas on long TR/TE scanning sequences (Fig. 11-48).[127] The plaques usually are located within the periventricular white matter (Fig. 11-49). The finger-like extensions radiating away from the lateral angle of the lateral ventricle have been labeled *Dawson's fingers*.[125] These are well seen on FLAIR images.[125] However, because of the sensitivity of MR imaging, increasingly, more plaques have been detected within the white matter of the cerebellum, brainstem, and spinal cord.[128–130] The activity of the plaques is difficult to ascertain. With intravenous administration of gadolinium, enhancement may be seen at the site of acute demyelination, with breakdown of the blood-brain barrier.[131–133] Additionally, enhancement of the leptomeninges may be seen as an inconstant occurrence. The cause and significance of plaque enhancement are in dispute; consequently, they cannot be taken as unequivocal supportive evidence of the presence or absence of MS or as an indicator of the activity of the disease process.[133–135] MR proton spectroscopy is able to differentiate areas of demyelination from regions of disrupted blood-brain barrier and consequent edema, both of which may exhibit enhancement following gadolinium DTPA administration. Proton spectroscopy (MRS) appears to be a more sensitive indicator of the true time course of demyelination in MS.[131] Short inversion time (inversion recovery sequences [STIR]), as well as other fat-suppressed MR techniques, are useful for evaluating the optic nerve in patients with clinically diagnosed optic neuritis[136] by demonstrating the plaque responsible for the observed clinical findings (Fig. 11-50B).[137, 138] However, visual potentials remain more sensitive than MR imaging for detection of optic nerve lesions. The MR imaging findings in Krabbe's disease appear to be

Copyright © 2003, Mosby, Inc. All rights reserved.

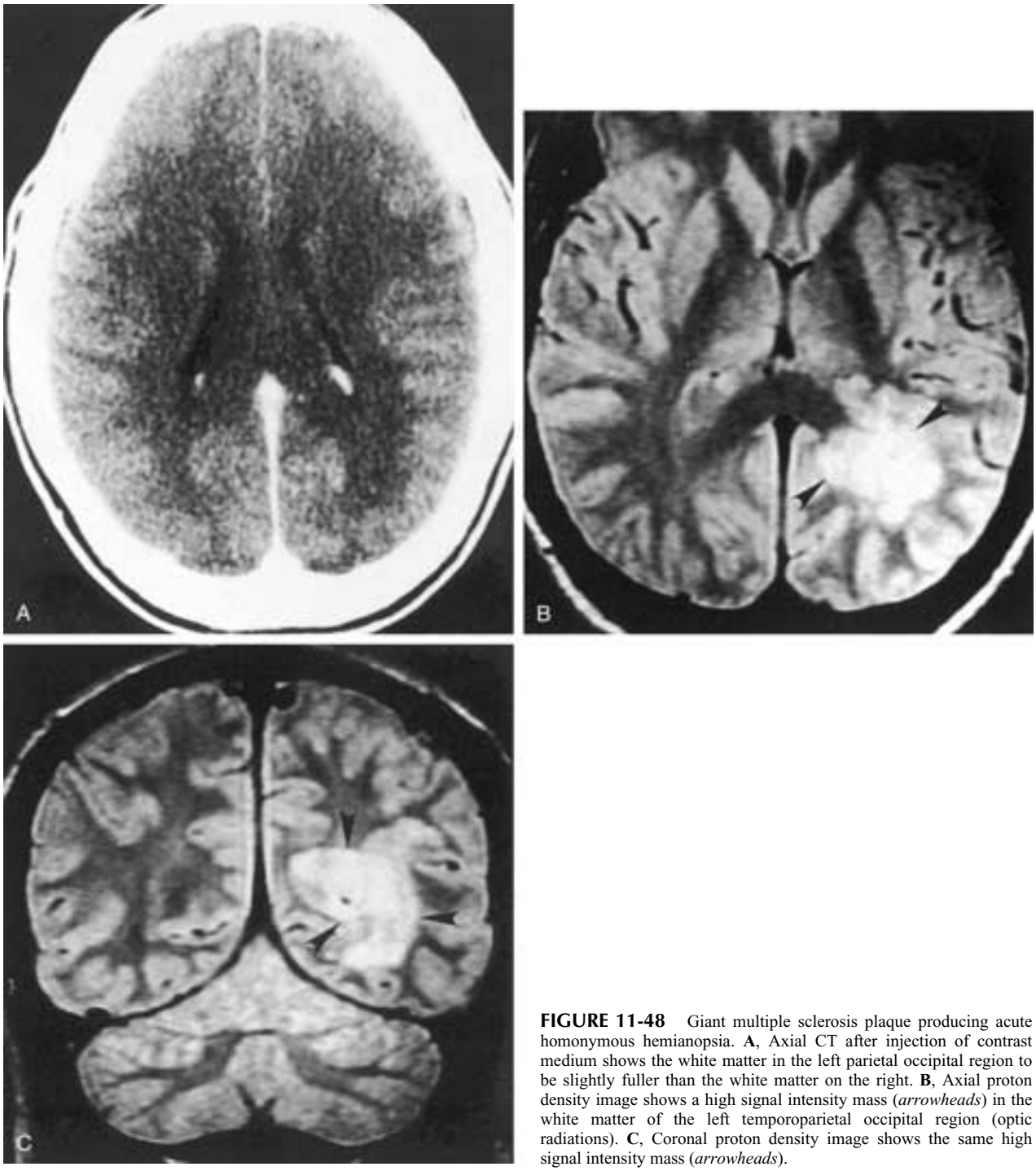

FIGURE 11-48 Giant multiple sclerosis plaque producing acute homonymous hemianopsia. **A**, Axial CT after injection of contrast medium shows the white matter in the left parietal occipital region to be slightly fuller than the white matter on the right. **B**, Axial proton density image shows a high signal intensity mass (*arrowheads*) in the white matter of the left temporoparietal occipital region (optic radiations). **C**, Coronal proton density image shows the same high signal intensity mass (*arrowheads*).

VIEW IMAGE

variable but usually consist of high signal intensity within the cerebral deep white matter on long TR/TE images. There does not appear to be a reproducible correlation between the areas of high density in the deep gray matter and deep white matter in the supratentorial brain demonstrated on CT and the alterations in these areas on MRS. Consequently, CT is used to demonstrate the characteristic changes in this disease.[116]

Cerebral Neoplastic Disease

Intracranial tumors affect the visual pathway either by disruption of the neural connections or by exertion of a mass effect, which causes distortion and subsequently impairs the functioning of the visual pathway. An extensive variety of neoplasms may involve the supratentorial brain and consequently the visual pathway.

Copyright © 2003, Mosby, Inc. All rights reserved.

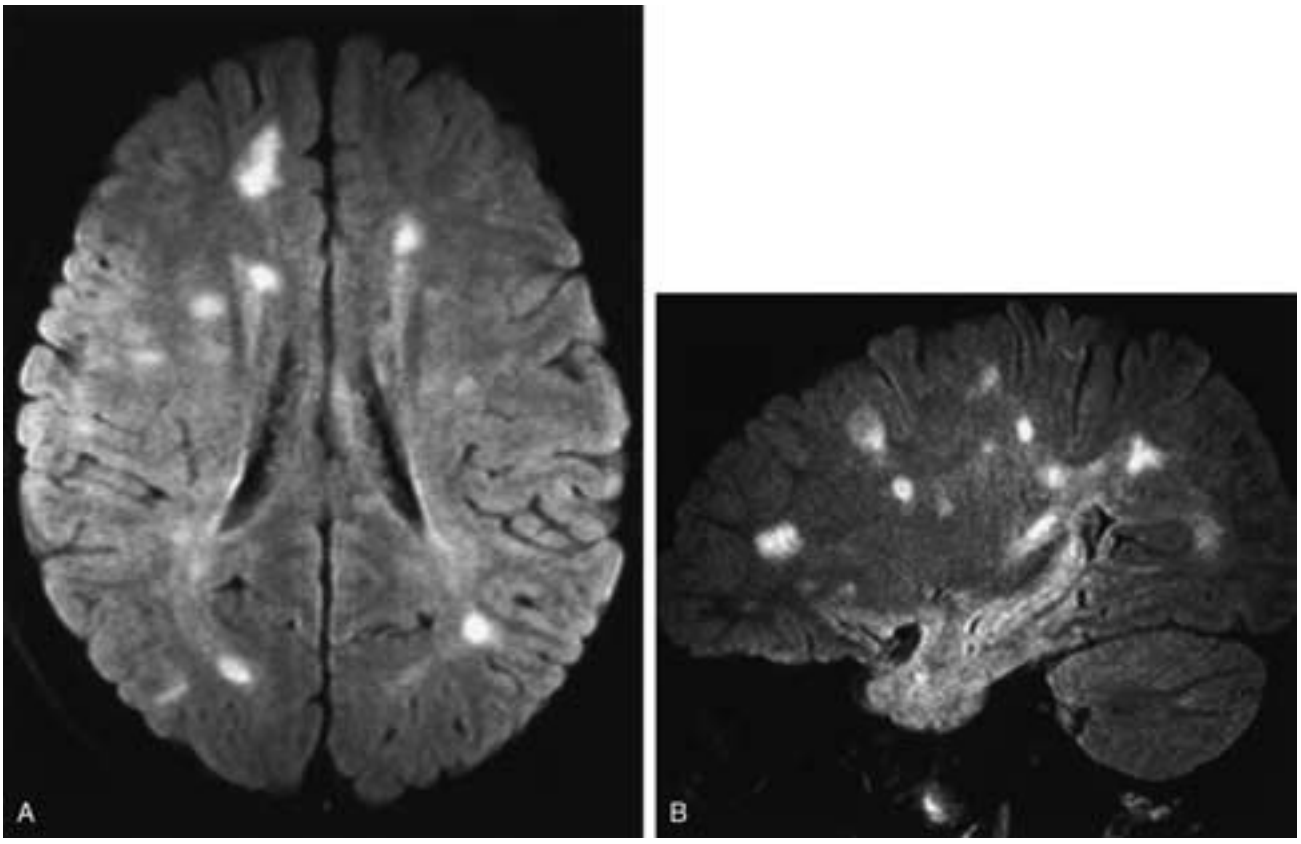

VIEW IMAGE

FIGURE 11-49 Multiple sclerosis. **A** and **B**, Axial and sagittal FLAIR images show multiple high-intensity multiple sclerosis plaques.

Clinical Findings

The location of a particular neoplasm within the brain often can be determined by clinical signs and symptoms. Large tumors that raise intracranial pressure result in papilledema. Hemiplegia is present if the tumor involves the primary motor cortex. Neoplasms within the parietal lobe often result in visual field defects, particularly those involving the superior parietal optic radiations and thus affecting the inferior quadrant of the contralateral visual field. If the neoplasm involves the angular gyrus of the dominant hemisphere, there may be an inability to recognize printed words (alexia) and an inability to write (agraphia).

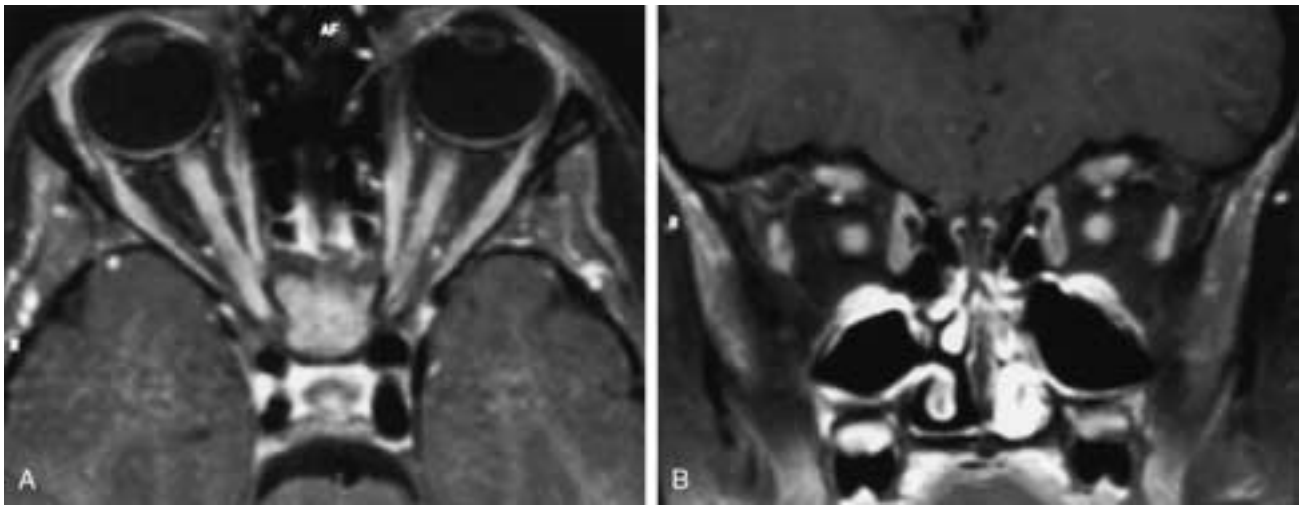

VIEW IMAGE

FIGURE 11-50 Multiple sclerosis. Bilateral optic neuritis. **A** and **B**, Axial and coronal T1-weighted images with fat suppression after gadolinium injection show symmetric enhancement of the intraorbital optic nerves.

Copyright © 2003, Mosby, Inc. All rights reserved.

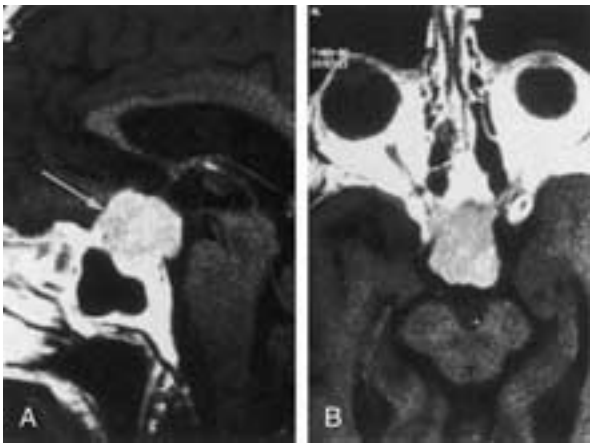

VIEW IMAGE

FIGURE 11-51 Suprasellar meningioma arising from the planum sphenoidale and diaphragma sellae in a 55-year-old female with bitemporal hemianopsia. **A**, Sagittal T1-weighted MR image following gadolinium injection shows enhancement of a suprasellar mass (*arrows*) that compresses the optic chiasm. **B**, Axial T1-weighted MR image after gadolinium injection shows the anterioposterior and lateral extent of the mass.

Within the temporal lobe, neoplasms can produce superior homonymous quadrantinopsia. If the tumor occurs at the confluence of the dominant frontal, temporal, and parietal lobes, an expressive aphasia frequently is present. Tumors occupying the occipital lobe often cause a congruous contralateral homonymous hemianopsia. If the tumor occupies the association areas of the occipital lobe, the patient may be unable to recognize familiar people (pragmatagnosia). Other clinical findings with intracranial neoplasm include morning headache, nausea, lethargy, and impaired consciousness, depending on the size and location of the tumor. Papilledema may be observed in patients with tumors anywhere in the supratentorial brain.

Pathologic Findings

A wide variety of different tumor types may involve the supratentorial brain and thus the visual pathway.[139] In general terms, the tissue types may be derived from the neural glia, which includes the astrocytes and oligodendrocytes, from the ependyma and its homologues, neurons, primitive undifferentiated cells, and meninges. The tumors may also be metastatic from other regions of the body. Tumors derived from astrocytes include astrocytomas, juvenile pilocytic astrocytomas, and oligodendrogliomas. Astrocytomas range from well-differentiated, histologically benign lesions to highly aggressive anaplastic forms such as glioblastoma multiforme. Intracranial meningiomas arise from the dura, impairing the visual pathway by exertion of a mass effect (Fig. 11-51). Epidermoid tumors arise from cell rests within the suprasellar cistern, enlarging to produce masses that can compress the optic chiasm (Fig. 11-52). FLAIR shows higher signal intensity in the epidermoid tumors than in arachnoid cysts, aiding in their diagnosis (Fig. 11-52).[140–142] Metastatic deposits to the brain from distant primary tumors are responsible for 20% to 25% of all intracranial tumors. The most frequent cell types are bronchogenic and breast carcinomas (Fig. 11-53). Metastatic foci usually are multiple and are found most frequently at the junction of the gray and white matter. The brain tissue surrounding the metastatic focus may show a high degree of vasogenic edema. Microscopically, the metastatic foci are usually identical to the primary neoplasm.

CT Appearance

On CT, intracranial neoplasms are most often identified as mass lesions with or without contrast enhancement and with or without varying degrees of peritumoral edema. Depending on the tumor's location, there may be associated hydrocephalus or other physical distortion of the neuraxis. Astrocytomas are usually isodense to hypodense to normal brain parenchyma on an unenhanced CT scan. The amount of peritumoral edema frequently reflects the grade of the tumor, as does the degree of enhancement after administration of a contrast medium. More aggressive tumor types, in general, demonstrate a greater degree of enhancement and more peritumoral vasogenic edema. Glioblastoma multiforme often demonstrates intense enhancement in a mixed or ring enhancing pattern and may have a markedly irregular margin (Fig. 11-54). Oligodendrogliomas tend to be of high density before administration of a contrast medium and to contain calcification in more than 90% of cases except in the pediatric population, in which calcification is seen in approximately 40% of cases (Fig. 11-55).[143, 144] On plain CT, meningiomas are usually hyperdense relative to normal brain parenchyma. Calcification is found in approximately 20% of cases. Peritumoral edema may be present, and enhancement is usually homogeneous and intense. Metastatic lesions may be either single or multiple and vary in size.[145] From 3% to 14% of metastatic deposits contain intratumoral hemorrhage.[146] The metastatic lesions on an unenhanced scan are hypodense to surrounding brain unless they contain intratumoral hemorrhage, and edema is almost always present to some degree. Enhancement characteristics vary, but enhancement is almost always present (97%).[145]

MR Imaging Appearance

In general, MR imaging demonstrates greater sensitivity in tumor detection than does CT.[147] With the exception of the demonstration of calcification and bone abnormalities associated with intracranial tumors, MR better characterizes a tumor once it is detected. With its lack of beam-hardening artifacts, direct multiplanar imaging, and greater contrast sensitivity, MR imaging better depicts the anatomic extent of a tumor than does CT. Acquisition of gadolinium-DTPA–enhanced images of brain neoplasms helps to define the integrity of the blood-brain barrier within the lesion and thus helps to characterize the tumor more completely and limit the differential diagnosis.[148, 149] The appearance of the various tumor types on MR imaging is a function of many factors, including variations in water content; the presence or absence of hemorrhage, fat, calcification, or paramagnetic material such as melanin; and the degree of vascularity of the tumor.[150]

Astrocytomas appear as mass lesions of high signal intensity on long TR/TE images (Fig. 11-56). Peritumoral edema may be seen on long TR/TE images as an area of high signal intensity spreading through the adjacent white matter. It is difficult to differentiate edema from tumor extension solely on the basis of spin-echo images (Figs. 11-56 and 11-57).[60] With increasing grade of the tumor, the tumor

Copyright © 2003, Mosby, Inc. All rights reserved.

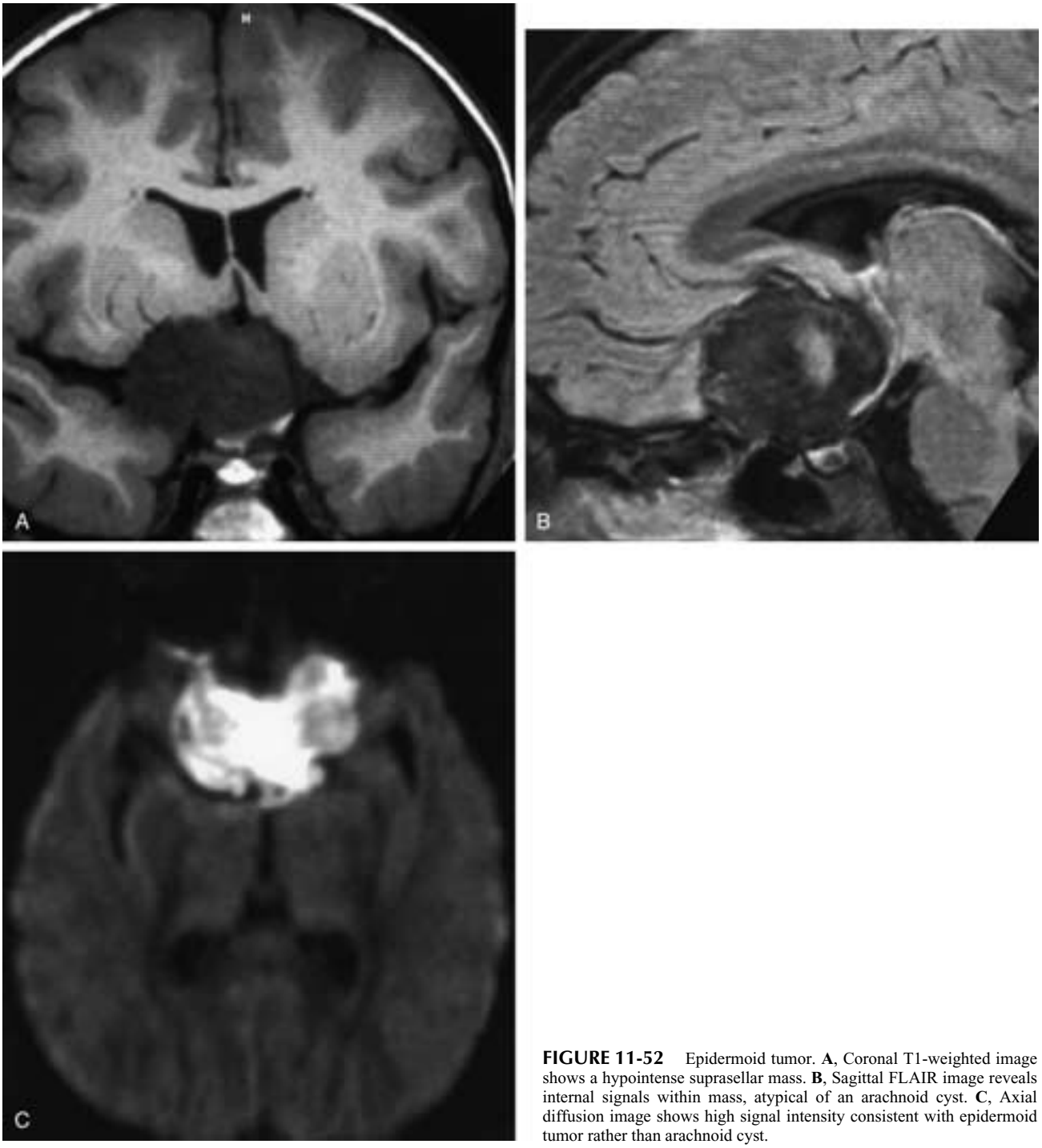

FIGURE 11-52 Epidermoid tumor. **A**, Coronal T1-weighted image shows a hypointense suprasellar mass. **B**, Sagittal FLAIR image reveals internal signals within mass, atypical of an arachnoid cyst. **C**, Axial diffusion image shows high signal intensity consistent with epidermoid tumor rather than arachnoid cyst.

VIEW IMAGE

Copyright © 2003, Mosby, Inc. All rights reserved.

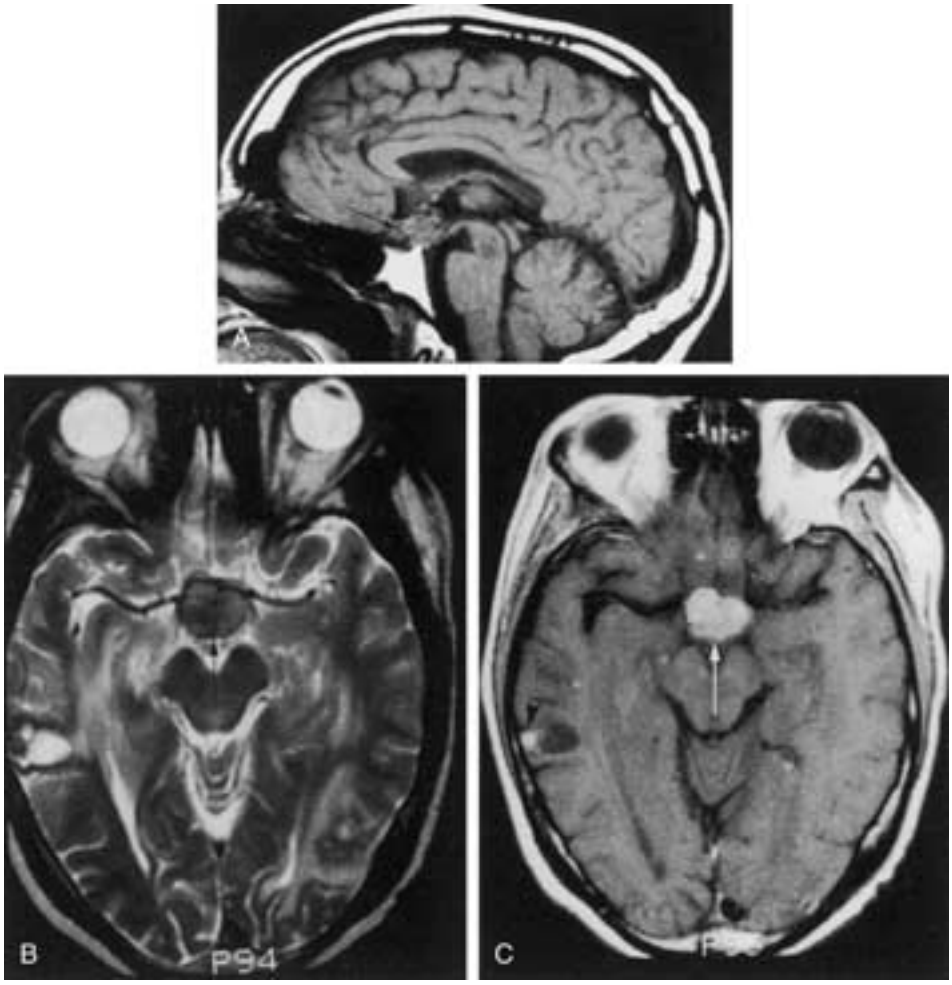

FIGURE 11-53 Metastatic carcinoma of the breast in a 60-year-old female with known carcinoma of the breast presenting with visual loss. **A**, Sagittal T1-weighted MR image shows an irregular mass (*arrow*) involving the optic chiasm. **B**, Axial T2-weighted image shows metastasis (*arrow*) to the optic chiasm to be hypointense, with a hypointense metastasis in the right temporal lobe surrounded by hyperintense vasogenic edema. There is a diffuse increase in signal intensity throughout the white matter secondary to prior radiation therapy. **C**, Axial T1-weighted MR image after gadolinium injection shows enhancement of both the chiasmatic mass (*arrow*) and the right temporal tumor (*arrowhead*).

VIEW IMAGE

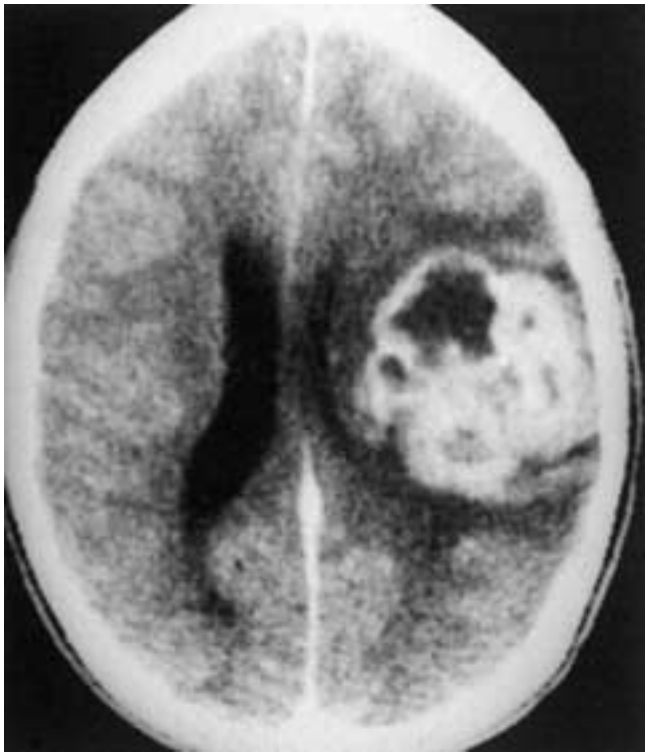

FIGURE 11-54 Glioblastoma multiforme. Axial CT image after injection of contrast medium shows marked enhancement of an irregular mass in the left frontal parietal region. The body of the left lateral ventricle is compressed.

VIEW IMAGE

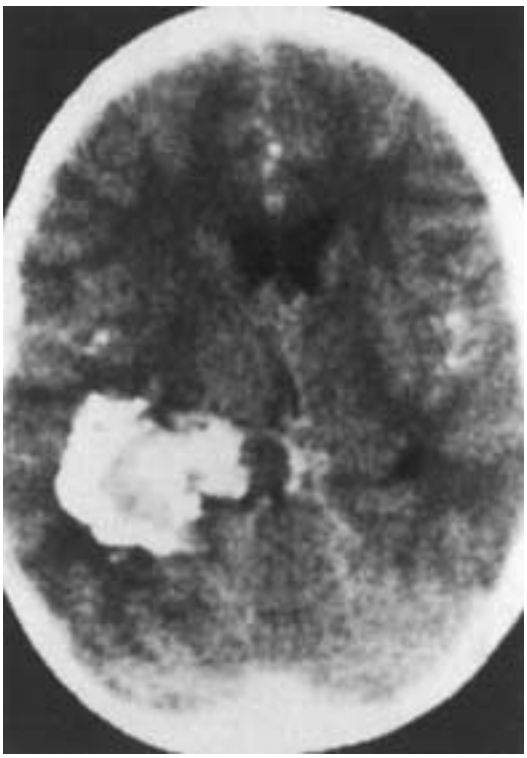

FIGURE 11-55 Oligodendroglioma. Axial CT image after enhancement shows a dense (calcified) right temporal lobe-thalamic mass.

VIEW IMAGE

Copyright © 2003, Mosby, Inc. All rights reserved.

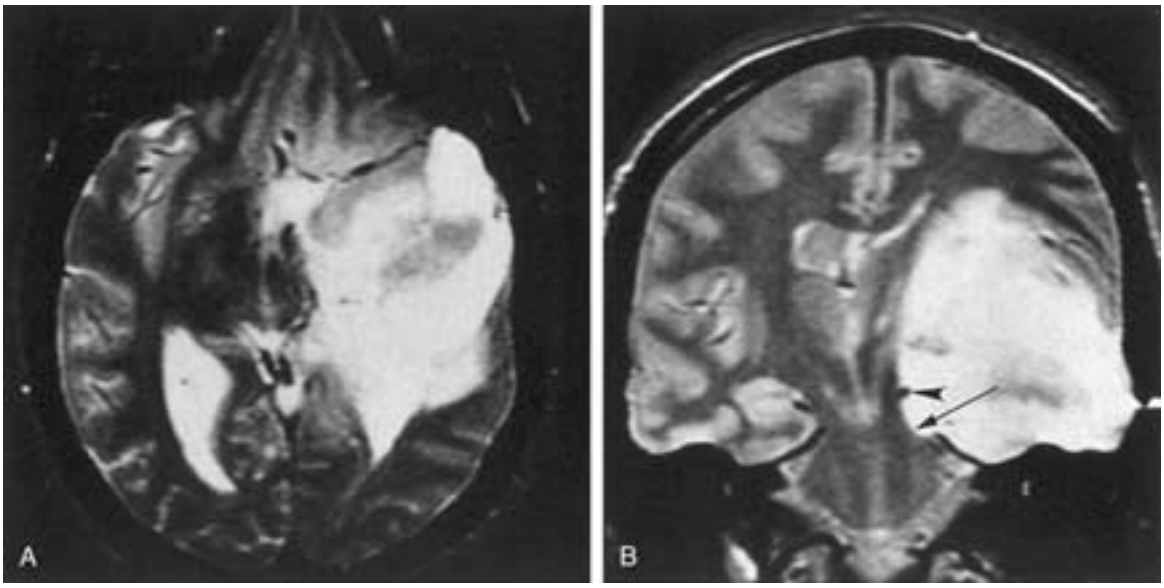

VIEW IMAGE

FIGURE 11-56 A 43-year-old-male with malignant degeneration of a low-grade astrocytoma of the temporal lobe. **A**, Axial T2-weighted image shows a hyperintense mass involving the left temporal lobe. Edema and tumor are not separable. **B**, Coronal proton density image shows the mass involving the temporal lobe on the left to have high signal intensity. The mass extends superiorly and medially. The tumor mass herniates (*arrow*) over the free edge of the tentorium and displaces medially the basilar vein of Rosenthal (*arrowhead*) against the mesencephalon. The optic tract is compressed.

margins tend to be more irregular. Glioblastoma multiforme, which is the most anaplastic form of astrocytoma, appears on long TR/TE images as a markedly hyperintense, irregularly bordered mass lesion. Also, with increasing tumor grade, there is progressive disruption of the blood-brain barrier, which, after intravenous administration of gadolinium, results in a progressively intense T1 shortening that is seen as increased signal intensity on short TR/TE images (Fig. 11-58). In pediatric patients, contrast enhancement can be seen in low-grade astrocytomas as well (Fig. 11-58). Oligodendrogliomas typically show hypointensity on short TR/TE images, with increased signal intensity on long TR/TE scans with signal void in areas of intratumoral calcification. Vasogenic peritumoral edema is infrequently seen, and enhancement following gadolinium-DTPA administration occurs in less than half of the cases.[143, 144]

VIEW IMAGE

FIGURE 11-57 Anaplastic astrocytoma of optic radiations. Axial T1-weighted image after administration of gadolinium shows an enhancing tumor mass involving the left optic radiations.

Meningiomas demonstrate signal characteristics that reflect the amount of calcification, vascularity, and interstitial fluid present within the mass.[151] In general, on short and long TR/TE images, meningiomas are isointense to hypointense to surrounding normal brain parenchyma (Fig. 11-59). As a result of the decreased conspicuity of meningiomas on MR imaging, detection is based on the displacement of normal structures of the neuraxis, including the white matter and vascular structures. On long TR/long TE images, surrounding edema, if present, helps to demarcate isointense meningiomas (Fig. 11-60). Intravenous administration of gadolinium delineates meningiomas much more clearly, because there is usually moderate to marked homogeneous enhancement.

Intracranial metastases display a variety of appearances on MR imaging. Characteristically, they appear on long TR/TE images as foci of increased signal intensity at the gray matter–white matter interface. Peritumoral edema is often present and may be difficult to distinguish from the tumor itself. Subtle differences in T1 and T2 relaxation time between the edema and the tumors may help in the differentiation. However, intravenous administration of gadolinium produces a clearer delineation (Fig. 11-61). The sensitivity for detection of single or multiple metastatic foci is increased with the use of gadolinium, thereby increasing

Copyright © 2003, Mosby, Inc. All rights reserved.

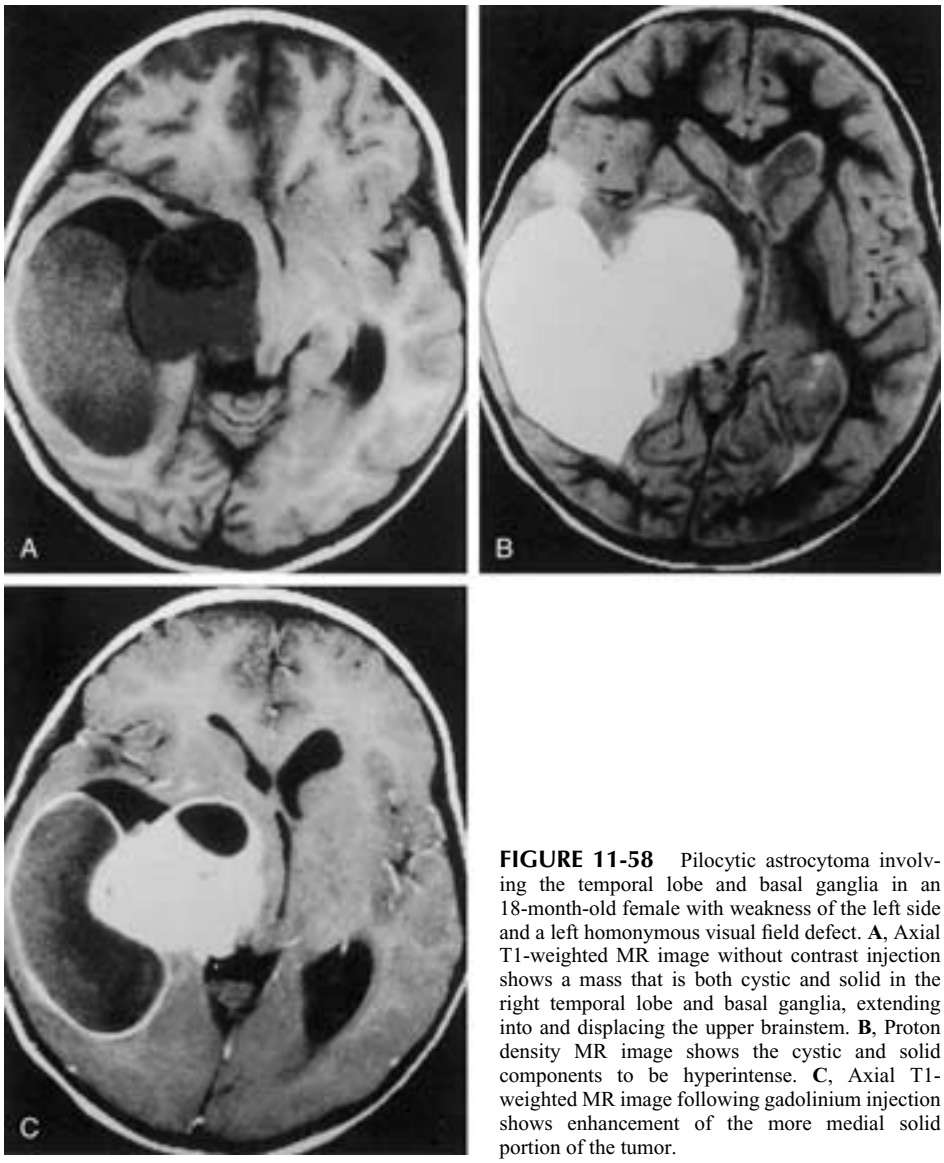

FIGURE 11-58 Pilocytic astrocytoma involving the temporal lobe and basal ganglia in an 18-month-old female with weakness of the left side and a left homonymous visual field defect. **A**, Axial T1-weighted MR image without contrast injection shows a mass that is both cystic and solid in the right temporal lobe and basal ganglia, extending into and displacing the upper brainstem. **B**, Proton density MR image shows the cystic and solid components to be hyperintense. **C**, Axial T1-weighted MR image following gadolinium injection shows enhancement of the more medial solid portion of the tumor.

VIEW IMAGE

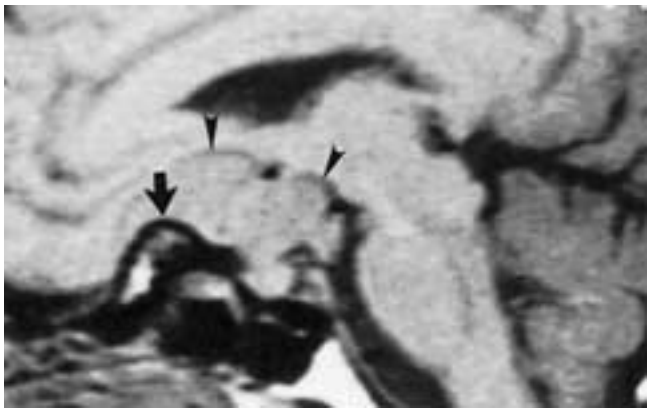

FIGURE 11-59 Suprasellar planum sphenoidal meningioma. Sagittal T1-weighted image shows a slightly hypointense suprasellar mass (*arrowheads*). Hyperostosis of the planum is present (*arrow*).

VIEW IMAGE

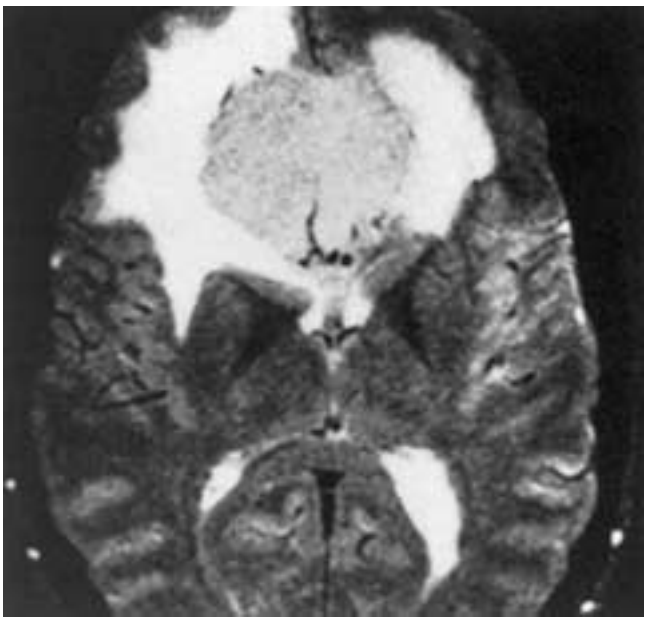

FIGURE 11-60 Olfactory groove meningioma. Axial T2-weighted image shows an isointense mass between the frontal lobes surrounded by high signal intensity edema.

VIEW IMAGE

Copyright © 2003, Mosby, Inc. All rights reserved.

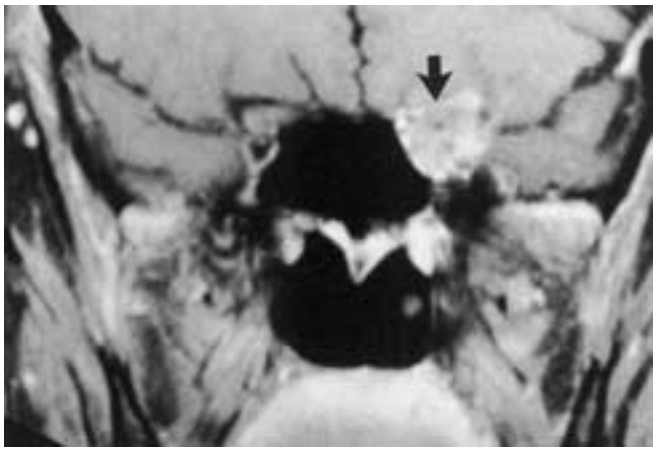

VIEW IMAGE

FIGURE 11-61 Metastatic breast carcinoma to the anterior clinoid process and optic canal in a 67-year-old female with a history of breast carcinoma presenting with visual loss in the left eye. Coronal T1-weighted, fat-suppressed, gadolinium-enhanced MR image shows a contrast-enhancing mass (*arrow*) involving the region of the left optic canal and anterior clinoid process.

the certainty of the diagnosis of a metastatic cause (Fig. 11-50).[152] In metastatic lesions to the wall of the orbit, fat-suppressed, gadolinium-enhanced images are important in demonstrating the disease (Fig. 11-58). In fact, in cases in which multiplicity of lesions is uncertain with the standard dose of 1.0 mmole/kg gadolinium-DTPA, doubling or tripling the dose has been shown to increase the likelihood that additional lesions will be detected.[153–155]

Aggressive infectious disease processes affecting immunocompromised patients, such as those with HIV, may mimic the appearance of metastatic lesions (Figs. 11-62 and 11-63).

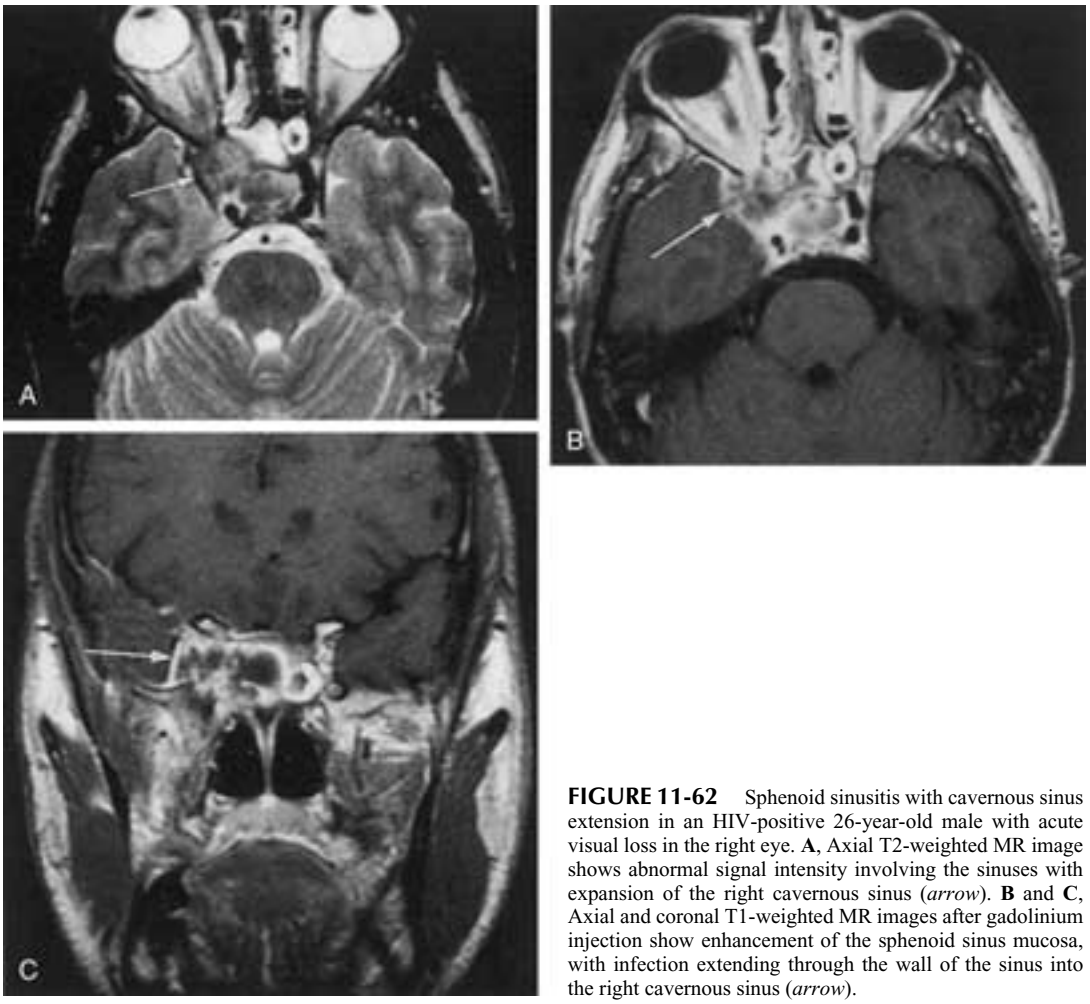

FIGURE 11-62 Sphenoid sinusitis with cavernous sinus extension in an HIV-positive 26-year-old male with acute visual loss in the right eye. **A**, Axial T2-weighted MR image shows abnormal signal intensity involving the sinuses with expansion of the right cavernous sinus (*arrow*). **B** and **C**, Axial and coronal T1-weighted MR images after gadolinium injection show enhancement of the sphenoid sinus mucosa, with infection extending through the wall of the sinus into the right cavernous sinus (*arrow*).

VIEW IMAGE

Copyright © 2003, Mosby, Inc. All rights reserved.

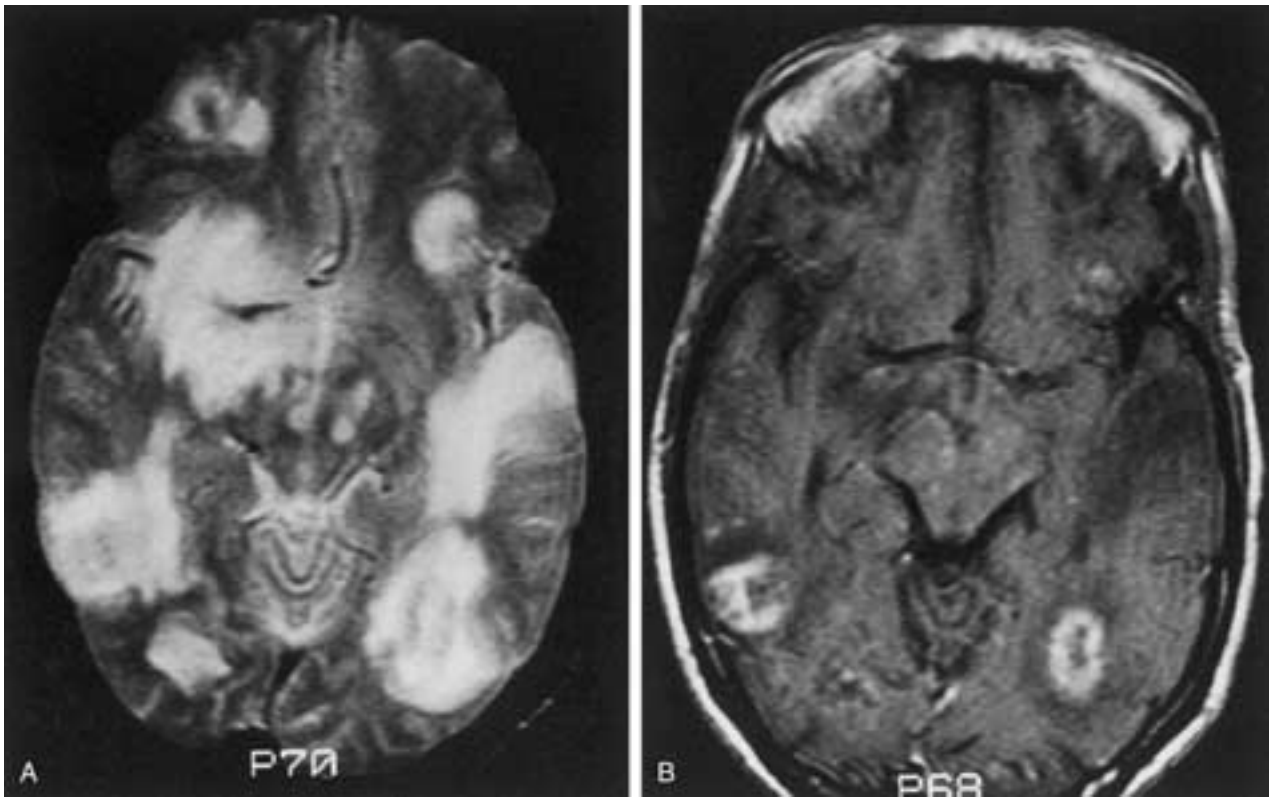

VIEW IMAGE

FIGURE 11-63 Toxoplasmosis abscesses in an HIV-positive 30-year-old male. **A**, Axial T2-weighted MR image shows multiple high signal intensity masses at the gray matter–white matter junctions and within the brainstem. **B**, Axial T1-weighted MR image after gadolinium injection shows enhancing masses with central necrosis.

REFERENCES

1. Duke-Elder, ed. System of Ophthalmology. London: Henry Kimpton, 1963.
2. Newell F, ed. Ophthalmology: Principles and Concepts. St. Louis: C.V. Mosby.
3. Gray H, ed. Anatomy of the Human Body. 29th ed. Philadelphia: Lea & Febiger, 1985.
4. Unsold R, DeGroot J, Newton TH. Images of the optic nerve: anatomic CT correlation. AJR 1980;135:767–773.
5. Daniels DL, Haughton VM, Williams AL, Gager WE. Computed tomography of the optic chiasm. Radiology 1980;137:123–127.
6. Bilaniuk LT, Atlas SW, Zimmerman RA. Magnetic resonance imaging of the orbit. Radiol Clin North Am 1987;25:509–528.
7. Azar-Kia B, et al. MR imaging evaluation of optic nerve (abstract). AJNR 1987;8:967.
8. Albert A, Lee BC, Saint-Louis L, et al. MRI of optic chiasm and optic pathways. AJNR 1986;7:255–258.
9. Hendrix LE, Kneeland JB, Haughton VM, et al. MR imaging of optic nerve lesions: value of gadopentetate dimeglumine and fat suppression technique. AJNR 1990;849–854.
10. Hershey BL, Peyster RG. Imaging of cranial nerve. II. Semin Ultrasound CT MR 1987;8(3):164.
11. Daniels DL, Herfkins R, Gager WE, et al. Magnetic resonance imaging of the optic nerves and chiasm. Radiology 1984;152:79–83.
12. Simon J, Szumowski J, Totterman S, et al. Fat suppression MR imaging of the orbit. AJNR 1988;9:961–968.
13. Jackson A, Sheppard S, Johnson AC. Combined fat and water suppressed MRI imaging of orbital tumors. AJNR 1999;20:1963.
14. Atlas SW, Grossman RI, Hackney DB, et al. STIR MR imaging of the orbit. AJR 1988;51:1025–1030.
15. Bastianello S, Bozzao A, Paolillo A, et al. Fast spin-echo and fast fluid-attenuated inversion-recovery versus conventional spin-echo sequences for MR quantification of multiple sclerosis lesions. AJNR 1997;18:699.
16. Ozgen A, Aydingoz U. Normative measurements of orbital structures using MRI. J Comput Assist Tomogr 2000;24:493.
17. Daniels DL, Pech P, Kay MC, et al. Orbital apex: correlative anatomic and CT study. AJR 1985;145:1141–1146.
18. Doyle AJ. Optic chiasm position on MR images. AJNR 1990;11: 553–555.
19. el Gammal TE. MR of normal optic chiasm. AJNR 1991;12:584.
20. Eggers H, Jakobiec FA, Jones IS. Optic nerve gliomas. In: Jones IS, Jakobiec FA, eds. Diseases of the Orbit. New York: Harper & Row, 1979;417–433.
21. Azar-Kia B, Naheedy MH, Elias DA, et al. Optic nerve tumors: role of magnetic resonance imaging and computed tomography. Radiol Clin North Am 1987;25:561–581.
22. Naumann GOH, Atle DJ. Optic nerve. In: Naumann GOH, Atle DJ, eds. Pathology of the Eye. New York: Springer-Verlag, 1987;723–770.
23. Davis PC, Hopkins KL. Imaging of pediatric orbit and visual pathways: computed tomography and magnetic resonance imaging. Neuroimaging Clin North Am 1999;9:93.
24. Mafee MF, Putterman A, Valvassori GE, et al. Orbital space occupying lesion: role of computed tomography and magnetic resonance imaging. Radiol Clin North Am 1987;25:529–559.
25. Sobel DF, Kelly W, Kjos BO, et al. MR imaging of orbital and ocular disease. AJNR 1985;6:259–264.
26. Atlas SW, Bilaniuk LT, Zimmerman RA, et al. Orbit: initial experience with surface coil spin-echo MR imaging at 1.5T. Radiology 1987;164:501–509.
27. Haik BG, Saint-Louis L, Bierly J, et al. Magnetic resonance imaging in the evaluation of optic nerve gliomas. Ophthalmology 1987;94: 709–717.
28. Jones IS, Jacobiec FA, eds. Diseases of the Orbit. New York: Harper & Row, 1979.

Copyright © 2003, Mosby, Inc. All rights reserved.

29. Sibony PA, Krauss HR, Kennerdell JS, et al. Optic nerve sheath meningiomas: clinical manifestations. Ophthalmology 1984;11: 1313–1326.
30. Hart WM, et al. Bilateral optic nerve meningiomas. AJNR 1980;1:375.
31. Daniels DL, Williams AL, Syvertsen A, et al. CT recognition of optic nerve sheath meningioma: abnormal sheath visualization. AJNR 1982;3:181–183.
32. Samples JR, Robertson DM, Taylor JZ, et al. Optic nerve meningioma. Ophthalmology 1983;90:1591–1594.
33. Atlas SW. Magnetic resonance imaging of the orbit: current status. Magn Resn Q 1989;5:39–96.
34. Hovda E, Wall M, Numaguchi Y, et al. Neurosarcoidosis involving optic nerves and leptomeninges: computed tomography findings. J Comput Assist Tomogr 1986;10:129–133.
35. Beardsley TL, et al. Eleven cases of sarcoidosis of the optic nerve (abstract). AJNR 1985;6:133.
36. Atlas SW, Grossman RI, Savino PJ, et al. Surface coil MR of orbital pseudotumor. AJR 148:803–808.
37. Urbach H, Kristof R, Zentner J, et al. Sarcoidosis presenting as an intra- or extra-axial cranial mass: report of two cases. Neuroradiology 1997;39:516.
38. Wall MJ, Peyster RG, Finkelstein SD, et al. A unique case of neural sarcoidosis with pineal and suprasellar involvement: CT and pathological demonstration. J Comput Assist Tomogr 1985;9: 381–383.
39. Mirfakhraee M, Crofford MJ, Guinto FC Jr, et al. Virchow-Robin space: a path of spread in neurosarcoidosis. Radiology 1986;158: 715–720.
40. Post MJD, Quencer RM, Tabei SZ, et al. CT demonstration of sarcoidosis of the optic nerve, frontal lobes and falx cerebri: a case report and literature review. AJNR 1982;3:523–526.
41. Hayes WS, Sherman JL, Stern BJ, et al. MR and CT evaluation of intracranial sarcoidosis. AJR 1987;149:1043–1049.
42. Clark WC, Acker JD, Dohan FC, et al. Presentation of central nervous system sarcoidosis as intracranial tumors. J Neurosurg 1985;63:851–856.
43. Walker FO, McLean WT Jr, Elster A, et al. Chiasmal sarcoidosis. AJNR 1990;11:1205–1207.
44. Engleken JD, Yuh WT, Carter KD, et al. Optic nerve sarcoidosis: MR findings. AJNR 1992;12:228–230.
45. Sherman JL, et al. MR evaluation of intracranial sarcoidosis: comparison with CT. AJNR 1987;8:940.
46. Sherman JL, Stern BJ, Sarcoidosis of the CNS: comparison of unenhanced and enhanced MR images. AJNR 1990;11:915–923.
47. Seltzer S, Mark AS, Atlas SW. CNS sarcoidosis: evaluation with contrast enhanced MR imaging. AJNR 1991;12:1227–1233.
48. Cooper SD, Brady MB, Williams JP, et al. Neurosarcoidosis: evaluation using computed tomography and magnetic resonance imaging. J Comput Assist Tomogr 1988;12:96–99.
49. Miller DH, Kendall BE, Barter S, et al. Magnetic resonance imaging in central nervous system sarcoidosis. Neurology 1988;38:378–383.
50. Ketonen L, Oksanen V, Kuuliaha I. Preliminary experience of magnetic resonance imaging in neurosarcoidosis. Neuroradiology 1987;29:127–129.
51. Hayes WS, Sherman JL, Stern BJ, et al. MR and CT evaluation of intracranial sarcoidosis. AJR 1987;49:1043–1049.
52. Packner AR, Duray P, Steere AC. Central nervous system manifestations of Lyme disease. Arch Neurol 1989;46:790–795.
53. Vanzieleghem B, Lemmerling M, Carton D. Lyme disease presenting with bilateral facial nerve palsy: MRI findings and review of the literature. Neuroradiology 1998;40:739.
54. Fernandez RE, Rothberg Ferencz G, Wujack D. Lyme disease of the CNS; MR imaging findings in 14 cases. AJNR 1990;11;479–481.
55. Kissane JM, Anderson WAD, eds. Anderson's Pathology. 9th ed. St. Louis: C.V. Mosby, 1989.
56. Crane TB, Yee RD, Hepler RS, et al. Clinical manifestations and radiologic findings in craniopharyngiomas in adults. Am J Ophthalamol 1982;94:220–228.
57. Pusey E, Kortman KE, Flannigan BD, et al. MR of craniopharyngiomas: tumor delineation and characterization. AJR 1987;149:383–388.
58. Price AC, et al. Craniopharyngioma: correlation of high resolution CT and MRI (abstract). AJNR 1985;6:465.
59. Ahmadi J, Destian S, Apuzzo ML, et al. Cystic fluid in craniopharyngiomas: MR imaging and quantitative analysis. Radiology 1992;182:783–785.
60. Lee BCP, Deck MF. Sellar and juxtasellar lesion: detection with MR. Radiology 1985;157:143–147.
61. Donovan JL, Nesbit GM. Distinction of masses involving the sella and suprasellar space: specificity of imaging features. AJR 1996;167:597.
62. Sutton LN, Wang ZJ, Wehrli SL, et al. Proton spectroscopy of suprasellar tumors in pediatric patients. Neurosurgery 1997;41: 388–394.
63. Kucharczyk W, Peck WW, Kelly WM, et al. Rathke cleft cysts: CT, MR imaging and pathologic features. Radiology 1987;165: 491–495.
64. Nagasaka S, et al. Rathke's cleft cyst (abstract). AJNR 1982;3:360.
65. Johnson CE, et al. Correlation of MR signal intensity, surgical findings and pathologic features of large pituitary adenomas: differentiation of soft cellular and firm fibrotic tumors (abstract). AJNR 1988;9:1013.
66. Robbins SL, Cotran RS, Kumar L, eds. Pathologic Basis of Disease. 3rd ed. Philadelphia: W.B. Saunders, 1984.
67. Taylor S. High resolution direct coronal CT of the sella and parasellar region (abstract). AJNR 1980;1:364.
68. Majos C, Coll S, Aguilera C. Imaging of giant pituitary adenomas. Neuroradiology 1998;40:651.
69. Davis PC, Hoffman JC Jr, Tindall GT, et al. CT surgical correlation in pituitary adenomas: evaluation of ••• in 113 patients. AJNR 1985;6:711–716.
70. Davis PC, Hoffman JC Jr, Spencer T, et al. MR imaging of pituitary adenoma: CT, clinical, and surgical correlation. AJR 1987;1797–1802.
71. Kunhara N, Takashi S, Hugano S. Hemorrhage in pituitary adenoma: correlation of MR imaging with operative findings. Eur Radiol 1998;8:971.
72. Karnaze MG, Sartor K, Winthrop JD, et al. Suprasellar lesions: evaluation with MR imaging. Radiology 1986;161:77–82.
73. Cottier J-P, Destrieux C, Brunereau L, et al. Cavernous sinus invasion by pituitary adenoma: MR imaging. Radiology 2000;215: 463–469.
74. Ostrov SG, Quencer RM, Hoffman JC, et al. Hemorrhage within pituitary adenomas: how often associated with pituitary apoplexy syndrome? AJR 1989;153:153–160.
75. Davis PC, et al. DTPA and MR imaging of the pituitary gland: preliminary report. AJNR 1987;8:817.
76. Newton DR, Dillon WP, Normal D, et al. Gadolinium DTPA enhanced MR imaging of pituitary adenomas. AJNR 1989;10: 949–954.
77. Kaufman B, et al. Herniation of the suprasellar visual system and third ventricle into empty sellae: morphologic and clinical considerations. AJNR 1989;10:65.
78. Bull J. Massive aneurysms at the base of the brain. Brain 1969;92:535–570.
79. Vinuela F, Fox A, Chang JK, et al. Clinico-radiological spectrum of giant super elinoid internal carotid artery aneurysms. Neuroradiology 1984;26:93–99.
80. Ferguson GG. Carotid ophthalmic artery aneurysms. In: Wilkins RH, Regarchary SS, eds. Neurosurgery. New York: McGraw-Hill, 1986;•••.
81. Banna M, Lasjaunias P. Intracavernous carotid aneurysm associated with proptosis in a 13 month old girl. AJNR 1991;12:969–970.
82. Deeb ZL, Schimel S, Rothfus WE, et al. Diagnosis of bilateral intracavernous carotid artery aneurysms by computed tomography. J Comput Assist Tomogr 1986;10:121–127.
83. Rhoton AL. Microsurgical anatomy of saccular aneurysms. In: Wilkins R, Rengarchary S, eds. Neurosurgery. New York: McGraw-Hill, 1986;•••.
84. Atlas SW, Grossman RI, Goldberg HI, et al. Partially thrombosed giant intracranial aneurysms: correlation of MR and pathologic findings. Radiology 1987;162:111–114.
85. Aoki S, Sasaki Y, Machida T, et al. Cerebral aneurysms: detection and delineation using 3D CT angiography. AJNR 1992;13:1115–1120.
86. Noguchi K, Ogawa T, Seto H, et al. Subacute and chronic subarachoid hemorrhage: diagnosis with fluid-attenuated inversion-recovery imaging. Radiology 1997;203:257–262.
87. Ross JS, Masaryk TJ, Modic MT, et al. Intracranial aneurysms: evaluation by MR angiography. AJNR 1990;11:449–455.
88. Hirsch W, et al. MRI in evaluation of parasellar aneurysms (abstract). AJNR 1987;8:957.

Copyright © 2003, Mosby, Inc. All rights reserved.

89. Pinto RS, Kricheff II, Butler AR. Correlation of computed tomographic, angiographic and neuropathological changes in giant cerebral aneurysms. Radiology 1979;132:85–92.
90. Olsen WL, Brant-Zawadzki M, Hodes J, et al. Giant intracranial aneurysms: MR imaging. Radiology 1987;163:431–435.
91. Becker RD, et al. MR appearance of intracranial aneurysms (abstract). AJNR 1987;8:964.
92. Slavin ML, Lam BL, Decker RE, et al. Chiasmal compression from fat packing after transsphenoidal resection of intrasellar tumor in two patients. Am J Ophthalmol 1993;115:368–371.
93. Cohen MM, Lessell S. Chiasm as syndrome due to metastasis. Arch Neurol 1979;36:565–567.
94. Beauchamp NJ Jr, Ulug AM, Passe TJ, van Zijl PCM. MR diffusion imaging in stroke: review and controversies. RadioGraphics 1998;18:1269.
95. Drake ME, et al. Conversion of ischemic to hemorrhagic infarction by anticoagulant administration: report of 2 cases with evidence from serial CT brain scans (abstract). Arch Neurol 1983;40:44–46.
96. Von Kummer R, Allen KL, Holle R, et al. Acute stroke: usefulness of early CT findings before thrombolytic therapy. Radiology 1997;205:327.
97. Tomsick TA, Brott TG, Chambers AA, et al. Hyperdense middle cerebral artery sign on CT: efficacy in detecting middle cerebral artery thrombosis. AJNR 1990;11:473–477.
98. Tomsick TA, Brott T, Barsan W, et al. Prognostic value of the hyperdense middle cerebral artery sign and stroke scale score before ultraearly thrombolytic therapy. AJNR 1996;17:79.
99. Rauch RA, Bazan C III, Larsson EM. Hyperdense middle cerebral arteries identified on CT as a false sign of vascular occlusion. AJNR 1993;14:669–673.
100. Drayer B. Imaging of cerebral infarction and intracerebral hematoma using MR, CT and SPECT (abstract). AJNR 1985;6:464.
101. Moseley ME, Kucharczyk J, Mintorovitch J, et al. Diffusion weighted MR imaging of acute stroke: correlation with T2 weighted and magnetic susceptibility-enhanced MR imaging in cats. AJNR 1990;11:423–429.
102. Fisher M, et al. Diffusion weighted MR imaging and ischemic stroke. AJNR 1992;13:1103.
103. Bryan RN, Levy LM, Whitlow WD, et al. Diagnosis of acute cerebral infarction: comparison of CT and MR imaging. AJNR 1991;12: 611–620.
104. Unger EC, Gado MH, Fulling KF, et al. Acute cerebral infarction in monkeys: an experimental study using MR imaging. Radiology 1987;162:789–795.
105. Yuh WTC, Crane MR, Loes DJ, et al. MR imaging of cerebral ischemia: findings in the first 24 hours. AJNR 1991;12:621–629.
106. Mueller DP, Yuh WT, Fisher DJ. Arterial enhancement in acute cerebral ischemia: clinical and angiographic correlation. AJNR 1993;14:661–668.
107. Chien D, Kwong KK, Gress DR, et al. MR diffusion imaging of cerebral infarction in humans. AJNR 1992;13:1097–1102.
108. Maier SE, Gudbjartsson H, Patz S, et al. Line scan diffusion imaging: characterization in healthy subjects and stroke patients. AJR 1998;171:85.
109. Marshal VG, Bradley WG Jr, Marshall CE, et al. Deep white matter infarction: correlation of MR imaging and histopathologic findings. Radiology 1988;167:517–522.
110. Brant-Zawadzki M, Pereira B, Weinstein P, et al. MRI of acute experimental ischemia in cats. Am J Neuroradiol 1985;7:7–11.
111. Elster AD. MR contrast enhancement in brainstem and deep cerebral infarction. AJNR 1991;12:1127–1132.
112. Virasponge C, Mancuso H, Quisling R. Human brain infarcts: Gd-DTPA–enhanced MR imaging. Radiology 1986;161:785–794.
113. Sheldon JJ, Siddharthan R, Tobias J, et al. MR imaging of multiple sclerosis: comparison with clinical and CT examinations in 74 patients. AJR 1985;145:957–964.
114. Uhlenbrock D, Seidel D, Gehlen W, et al. MR imaging in multiple sclerosis: comparison with clinical CSF and visually evoking potential findings. AJNR 1988;9:59–67.
115. Poser CM, Goutieres F, Carpentier MA, et al. Schilder's myelinoclastic diffuse sclerosis. Pediatrics 1986;77:107–112.
116. Choi S, Enzmann. Infantile Krabbe disease: complementary CT and MR findings. AJNR 1993;14:1164–1166.
117. Mikol F, et al. Computed tomography in multiple sclerosis. Rev Neurol 1980;136:481.
118. Spiegel SM, Vinuela F, Fox AJ, et al. CT of multiple sclerosis: reassessment of delayed scanning with high doses of contrast material. AJR 1985;145:497–500.
119. Osborn AG, Harnsberger HR, Smoker WR, et al. Multiple sclerosis in adolescents: CT and MR findings. AJR 1990;155:385–390.
120. Mehler MF, Rabinowich L. Inflammatory myelinoclastic diffuse sclerosis (Schilders disease): neuroradiologic findings. AJNR 1989; 10:176–180.
121. Paty DW, Oger JJ, Kastrukoff LF, et al. MRI in the diagnosis of MS: a prospective study with comparison of clinical evaluation, evoking potentials, oligoclonal banding and CT. Neurology 1988;38: 180–185.
122. Gebarski SS, Garbrielsen TO, Gilman S. The initial diagnosis of multiple sclerosis: clinical impact of magnetic resonance imaging. Ann Neurol 1985;17:469–474.
123. Johnson MA, Li DK, Bryant DJ, et al. Magnetic resonance imaging: serial observations in multiple sclerosis. AJNR 1984;5:495–499.
124. Ebner F, Millner MM, Justich E. Multiple sclerosis in children: value of serial MR studies to monitor patients. AJNR 1990;11:1023–1027.
125. Yhousry TA, Filippi M, Becker C, et al. Comparison of MR pulse sequences in the detection of multiple sclerosis lesions. AJNR 1997;18:959.
126. Kurihara N, Takahashi S, Furuta A, et al. MR imaging of multiple sclerosis simulating brain tumor. Clin Imag 1996;20:171.
127. Nowell MA, Grossman RI, Hackney DB, et al. MR imaging of white matter disease in children. AJR 1988;151:359–365.
128. De La Paz RL, et al. High field MR imaging of spinal cord multiple sclerosis (abstract). AJNR 1987;8:949.
129. Rosenblatt MA, Behrens MM, Zweifach PH, et al. Magnetic resonance imaging of optic tract involvement in multiple sclerosis. Am J Ophthalmol 1987;104:74–79.
130. Edwards MK, Farlow MR, Stevens JC. Cranial MR in spinal cord MS: diagnosing patients with isolated spinal cord symptoms. AJNR 1986;7:1003–1005.
131. Grossman RI, Lenkinski RE, Ramer KN, et al. MR proton spectroscopy in multiple sclerosis. AJNR 1992;13:1535–1543.
132. Larsson EM, Holtas S, Nilsson O. Gd DTPA enhanced MR of suspected spinal multiple sclerosis. AJNR 1989;10:1071–1076.
133. Simon JH. Contrast-enhanced MR imaging in the evaluation of treatment response and prediction of outcome in multiple sclerosis. J Magn Reson Imag 1997;7:29.
134. Grossman RI. Meningeal enhancement in multiple sclerosis: truth or coincidence. AJNR 1992;13:401–402.
135. Barkhoff F, Valk J, Hommes OR, et al. Meningeal Gd-DTPA enhancement in multiple sclerosis. AJNR 1992;13:397–400.
136. Merandi SF, Kudryk BT, Murtagh FR, et al. Contrast enhanced MR imaging of optic nerve lesions in patients with acute optic neuritis. AJNR 1991;12:923–926.
137. Jackson A, Sheppard S, Laitt RD, et al. Optic neuritis: MR imaging with combined fat- and water-suppression techniques. Radiology 1998;206:57.
138. Edwards MK, et al. Clinical utility of inversion recovery MR in the diagnosis of MS (abstract). AJNR 1989;10:898.
139. Hart MN, Earle KM. Primitive neuroectodermal tumors of the brain in children. Cancer 1973;32:890–897.
140. Ikushima I, Korogi Y, Hirai T, et al. MR of epidermoids with a variety of pulse sequences. AJNR 1997;18:1359–1363.
141. Lang ADP, Mitchell PJ, Wallace D. Diffusion weighted magnetic resonance imaging of intracranial epidermoid tumors. Australas Radiol 1999;43:16.
142. Kallmes DF, Provenzale JM, Cloft HJ, et al. Typical and atypical MR imaging features of intracranial epidermoid tumors. AJR 1997; 169:883.
143. Lee YY, Van Tassel P. Intracranial oligodendrogliomas: imaging findings in 35 untreated cases. AJR 1989;152:361–369.
144. Tice H, Barnes PD, Goumnerova L, et al. Pediatric and adolescent oligodendrogliomas. AJNR 1993;14:1293.
145. Pechova-Peterova V, Kalvach P. CT findings in cerebral metastases. Neuroradiology 1986;28:254–258.
146. Atlas SW, Grossman RI, Gomori JM, et al. Hemorrhagic intracranial malignant neoplasm: spin-echo MR imaging. Radiology 1987;164: 71–77.
147. Lee BCP, Kneeland JB, Cahill PT, et al. MR recognition of supratentorial tumors. AJNR 1985;6:871–878.

Copyright © 2003, Mosby, Inc. All rights reserved.

148. Haustein J, Landiado M, Niendorf HP, et al. Administration of gadopentitate dimeglumine in MR imaging of intracranial tumors: dosage and field strength. AJNR 1992;13:1199–1206.
149. Nägele T, Petersen D, Klose U, et al. Dynamic contrast enhancement of intracranial tumors with snapshot-FLASH imaging. AJNR 1993;14:89–98.
150. Spoto GP, Press GA, Hesselink JR, et al. Intracranial ependymoma and subependymoma: MR manifestations. AJNR 1990;11:83–91.
151. Sheporaitis LA, Osborn AG, Smirniotopoulos JG, et al. Intracranial meningioma. AJNR 1992;13:29–37.
152. Healy ME, Hesselink JR, Press GA, et al. Increased detection of intracranial metastases with intravenous Gd-DTPA. Radiology 1987;165:619–624.
153. Yuh WTC, Engelken JD, Muhonen MG, et al. Experience with high dose gadolinium MR imaging in the evaluation of brain metastasis. AJNR 1992;13:335–345.
154. Davis PC, Hudgins PA, Peterman SB, et al. Diagnosis of cerebral metastases: double dose delayed CT vs. contrast enhanced MR imaging. AJNR 1991;12:293–300.
155. Sze G, Milano E, Johnson C, et al. Detection of brain metastases: comparison of contrast enhanced MR with unenhanced MR and enhanced CT. AJNR 1990;11:785–791.

Copyright © 2003, Mosby, Inc. All rights reserved.

Copyright © 2003, Mosby, Inc. All rights reserved.

Section III

Central Skull Base

Copyright © 2003, Mosby, Inc. All rights reserved.

Copyright © 2003, Mosby, Inc. All rights reserved.

12

Central Skull Base: Embryology, Anatomy, and Pathology

Hugh D. Curtin, James D. Rabinov, and Peter M. Som

INTRODUCTION
EMBRYOLOGY
ANATOMY
- Bone
- Bordering Soft Tissues
  - Extracranial Soft Tissues
  - Intracranial Soft Tissues

IMAGING
NONNEOPLASTIC DISORDERS
- Congenital and Developmental Anomalies
- Cephaloceles
- Altered Ossification
- Vascular Variants
- Developmental Changes Caused by Extrinsic Factors
- Cartilage Dysplasias
- Inflammation and Obstruction

TUMORS AND TUMOR-LIKE CONDITIONS
- Chordomas
- Chondrosarcomas
- Chordoma Versus Chondrosarcoma
- Other Chondroid Tumors
- Meningiomas
- Craniopharyngiomas and Rathke's Pouch Cysts
- Juvenile Angiofibromas
- Pituitary Adenomas
- Neurogenic Tumors
- Giant Cell Lesions
- Aneurysmal Bone Cysts
- Langerhans Cell Histiocytosis
- Miscellaneous Tumors and Lesions of the Sphenoid Bone
- Mucoceles
- Aneurysms

SECONDARY TUMOR INVOLVEMENT OF THE SKULL BASE
- Direct Encroachment
- Perineural Spread
- Hematogenous Metastasis

TRAUMA
MISCELLANEOUS CONDITIONS
- Dysplasias
- Platybasia Versus Basilar Invagination
- Fibrous Dysplasia
- Paget's Disease
- Bone Dysplasias, Mucopolysaccharidosis, and Metabolic Diseases

CEREBROSPINAL FLUID LEAK
RHIZOTOMY INJECTIONS

INTRODUCTION

Advances in the techniques of skull base surgery could not have been realized without the developments made in modern imaging. The precise preoperative mapping of a lesion and the demonstration of its relationship to vital neural and vascular structures have allowed surgeons to plan an approach maximizing the chance for resection while minimizing morbidity. Before the CT and MR imaging era, the extent of a tumor was determined at the time of surgery, and the morbidity of the extensive approaches needed to stage a tumor was considered unwarranted in many cases. Today the surgeon can differentiate a tumor that has a possibility of complete resection from one where cure is unlikely and removal would cause unacceptably high morbidity.

Copyright © 2003, Mosby, Inc. All rights reserved.

The field of skull base surgery is still evolving, with many questions yet to be answered. Certainly there is controversy regarding what procedures are reasonable and appropriate. Thus, although technically a skull base lesion can be accurately mapped and surgically extirpated, it remains for further analysis to determine when a treatment represents a significant advantage to a patient.

Surgeons from several disciplines combine their skills to achieve approaches that, though extensive, are designed to keep manipulation of the crucial and fragile neurovascular structures to a minimum. The tenet of these procedures is to move bone, not brain.

Other therapeutic options such as proton and neutron beams, gamma knife radiosurgery, and various other focused beam radiotherapeutic technologies all require precise imaging definition of tumor boundaries if the lesion is to be treated and crucial radiosensitive structures spared.

The skull base can be divided into several regions—anterior, central, and posterior or posterolateral. The anterior skull base consists of the floor of the anterior cranial fossa and the frontal sinus, including the roof of the ethmoid sinuses, nasal cavity, and orbits. This topic is covered in Chapters 1 to 7. The posterolateral skull base is the temporal bone, and this topic is covered in Chapters 19 to 26. The present chapter covers the central skull base.

The primary component of the central basicranium is the sphenoid bone, with a smaller contribution from the basiocciput. In addition, the soft tissues immediately contiguous to these bony structures form an integral part of the central skull base, and such structures as the cavernous sinus, the pterygopalatine fossa, and the soft tissues adjacent to the foramen ovale and the superior orbital fissure are also discussed in this chapter.

EMBRYOLOGY

The basicranium develops primarily from cartilage precursors, with a small component from membranous bone. A review of certain details of basicranium development is important in understanding some of the normal and abnormal imaging findings.

The primordial embryonic germ disk is composed of the two primary germ layers, the epiblast and the hypoblast. The epiblast, which will evolve into the ectoderm, develops from the floor of the amniotic cavity, while the hypoblast develops from the roof of the yolk sac. At the fourteenth day of embryonic life, demarcation at the anterior pole of the embryonic disk occurs, and a thickening, the prechordal plate, arises in the future midcephalic region. This prechordal plate prefaces the development of the oropharyngeal region and eventually gives rise to the endodermal layer of the oropharyngeal membrane. In the third week of gestation, the mesoderm proliferates in all directions between the two primary layers of the embryo, adding thickness to the embryonic disk.[1] These mesodermal cells are derived from the primitive streak at the caudal end of the ectodermal side of the embryo. Within the mesoderm, as a result of proliferation and differentiation, a more condensed core of cells, the notochord, stretches from the cranial end of the primitive streak toward the cranial end of the embryo and the prechordal plate. The notochord acts as an axial skeleton for the embryo and has a profound effect on the later development of the spine and the skull base. The notochord induces the formation of the neural plate in the overlying ectoderm (neural ectoderm).

Embryonic differentiation continues, and the formation of the primitive brain and cranial nerves begins. Only after the positions of these neural primordia are established does the skull base itself begin to form. Condensations of the mesenchyme along the notochord (paraxial mesoderm) and contributions from the neural crest progress from the occipital level cranially. This process forms the basal condensation referred to as the *desmocranium*. This mesenchymal blastema extends beyond the level of the tip of the notochord into the prechordal area. It is within this desmocranium that chondrification eventually occurs.[2, 3]

The notochord is contained within the basal condensation of mesoderm and maintains a close relationship to the developing brain and primitive pharynx (Fig. 12-1). The terminus of the notochord is close to the oropharyngeal membrane, separating the ectoderm of the stomatodeum from the endoderm of the primitive pharynx. The formation of Rathke's (hypophyseal) pouch, from the mucosa of the stomatodeum (ectoderm), is thought to be influenced by the notochord. This pouch, which will generate the anterior pituitary gland, passes through the basal mesoderm just cephalad to the tip of the notochord on the way to meet the diverticulum of the diencephalon, which will pass downward, forming the posterior pituitary.[4] Rathke's pouch and tract pass through the mesoderm before chondrification occurs.

Before reaching the prechordal plate, the notochord comes into contact with the endoderm of the primitive pharynx, close to the position of Rathke's pouch, but on the endodermal side of the oropharyngeal membrane. It is at this level that a small outpouching from the pharyngeal mucosa develops, apparently drawn cranially by the notochord. This is the pouch of Luschka, and its position is identified by the pharyngeal bursa, a midline evagination from the nasopharyngeal wall.[1]

Chondrification centers appear within the basal mesodermal condensation. Those centers forming around the distal notochord are the parachordal cartilages. The cartilages from the occipital sclerotomes (from the four occipital somites) are incorporated into the basal cartilaginous plate. Together the parachordal- and sclerotome-derived cartilages are responsible for the formation of the basiocciput.[6]

At about the same time and slightly more cephalad, the prechordal cartilage centers are forming.[3, 6] The hypophyseal ossification centers form on either side of the hypophysis and fuse together (Fig. 12-2), completely obliterating the remnant of Rathke's duct.[3] The fused hypophyseal cartilages represent the precursors of the basisphenoid, forming most of the body of that bone. The paired presphenoid (or trabecular) cartilages fuse to become the precursor of the most anterior part of the sphenoid bone (anterior to the tuberculum sella) and give rise to the mesethmoid cartilage. The mesethmoid cartilage, in turn, develops into the perpendicular plate of the ethmoid and the crista galli.

The sphenoid bone is completed by a group of more laterally placed cartilages also developing from the basal mesoderm.[6] The orbitosphenoid cartilage forms the lesser wing of the sphenoid and contributes to the optic foramen, and the alisphenoid cartilage center produces the medial part

Copyright © 2003, Mosby, Inc. All rights reserved.

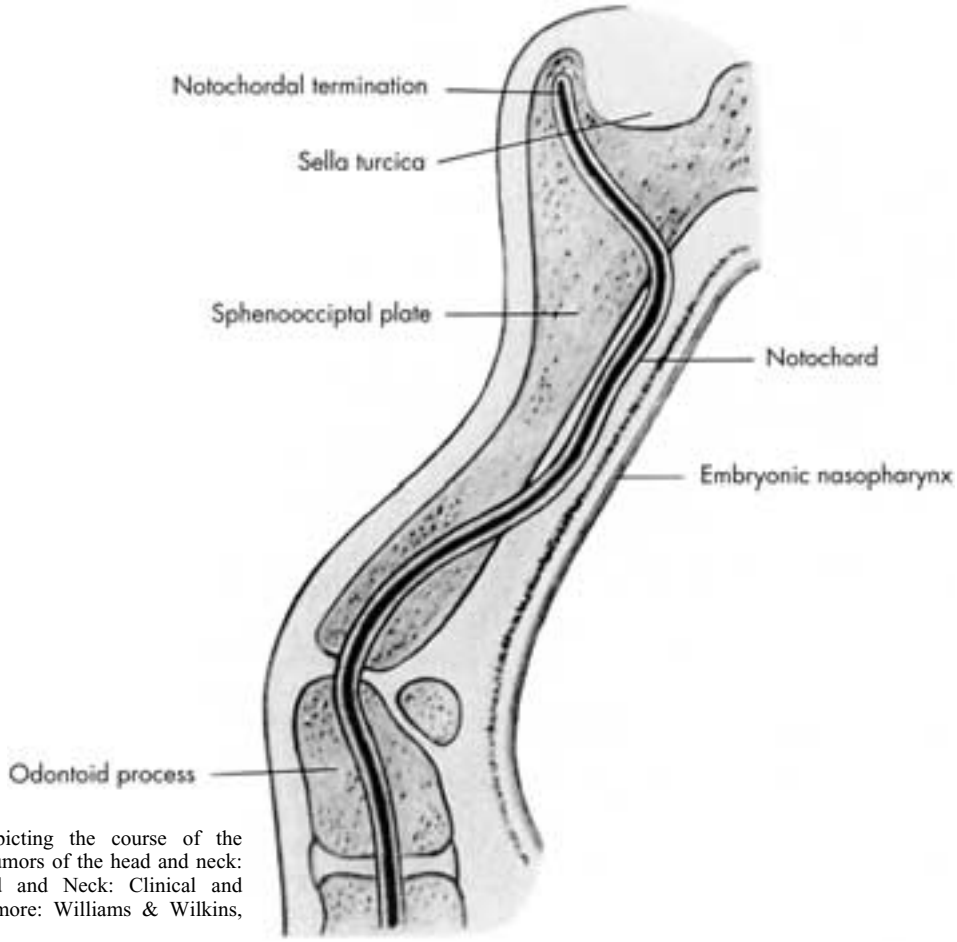

VIEW IMAGE

FIGURE 12-1 Midsagittal section depicting the course of the notochord. (From Batsakis JG. Soft tissue tumors of the head and neck: unusual forms. In: Tumors of the Head and Neck: Clinical and Pathological Considerations. 2nd ed. Baltimore: Williams & Wilkins, 1979; 353.)

of the greater sphenoid wing. The more lateral wing forms from condensed mesenchyme (intramembranous bone) rather than having a cartilaginous precursor.

The basiocciput and the various cartilage centers representing the sphenoid bone fuse into a cartilaginous continuum called the basal cartilaginous plate. The various foramina of the final basicranium are present within this primitive cartilaginous formation because the nerves and vessels have developed before chondrification begins and the cartilage is forced to develop around them. The bilateral otic capsule chondrifications also fuse to the parachordal cartilages and thus are joined with the basal plate.

Ossification centers now form within the cartilaginous precursor centers. This mechanism produces the presphenoid and postsphenoid as well as the lesser and greater wings. The pterygoid plates and portions of the greater wings form by intramembranous ossification. The small hamulus of the pterygoid develops endochondrally from a small chondroid center.

As ossification progresses, most of the cartilage between the centers is obliterated. Remaining cartilage can be found in various synchondroses, which persist into adult life. The most prominent ones are in the foramen lacerum and petroclival junction. The presphenoid and postsphenoid bones usually fuse by birth, but occasionally the separation persists in the newborn.[7] The bones of Bertin are two small, paired ossification centers that quickly fuse with the anterior sphenoid. It is here that pneumatization of the sphenoid bone begins. Thus, the initial air cells are formed in the

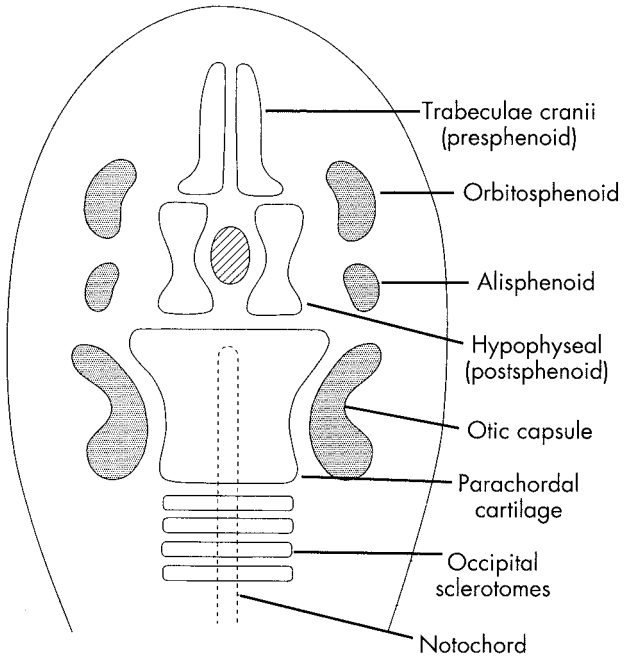

VIEW IMAGE

FIGURE 12-2 Diagram of the chondrification centers within the basal mesodermal condensation. The hypophyseal centers form on either side of the hypophysis and eventually fuse to form the sella and obliterate the pharyngohypophyseal canal. The postsphenoid is formed from these cartilage centers. The presphenoid forms more anteriorly. The orbitosphenoid and alisphenoid will contribute to the greater and lesser wings respectively.

Copyright © 2003, Mosby, Inc. All rights reserved.

presphenoid and progress into the more posterior and lateral ossification centers.

ANATOMY

The sphenoid bone is rightfully the focus of any discussion of the central skull base (Fig. 12-3).[8–11] The anterior basiocciput, articulating with the posterior inferior aspect of the sphenoid bone, also makes an important contribution to the central skull base. Equally crucial to imaging evaluation of the central skull base is an understanding of the contiguous soft tissues.

Bone

The sphenoid bone consists of a body, the greater and lesser wings, and the pterygoid processes (Fig. 12-4). The term *sphenoid* is derived from the Greek word for ''wedge,'' perhaps referring to its shape or its position between the basiocciput and the anterior skull base. The bone itself has been likened to the appearance of a diving horned owl when viewed from the anterior.

The central part of the sphenoid bone is a block-like structure variably hollowed out by the sphenoid sinus and bordered by many perforations, allowing passage of nerves and vessels. The great wings of the sphenoid sweep laterally, reaching and contributing to the lateral surface of the calvarium, just anterior to the squamous part of the temporal bone. Here the sphenoid bone articulates with the frontal bone, temporal bone, and parietal bone. The lesser wings are more medial in position and form the superior margin of the superior orbital fissure. The anterior clinoid is the posterior margin of the lesser wing. The pterygoid processes, with medial and lateral plates, drop inferiorly from the junction of the body and the greater wing.

Although much of the surface anatomy of the sphenoid bone, such as the sella turcica, the anterior and posterior clinoid processes, and the pterygoid plates, is familiar to the reader, other, slightly more obscure landmarks may be helpful in analyzing some of the imaging findings.

The superior surface of the sphenoid bone forms part of the floor of the anterior cranial fossa (Fig. 12-4B). Just posterior to the cribriform plate of the ethmoid bone, the ethmoid process of the sphenoid bone makes up the most anterior part of the planum sphenoidale. The planum is a flat region separating the cribriform area anteriorly from the chiasmatic sulcus, or groove, posteriorly. The planum is contiguous laterally with the flat superior surface of each lesser sphenoid wing.

The chiasmatic sulcus is a small, linear, transversely oriented depression just posterior to the planum (Fig. 12-4B-D). The anterior rim of the sulcus is referred to as the limbus and represents the most posterior ossification of the presphenoid ossification center. The posterior rim of the chiasmatic sulcus is the tuberculum, which represents the anterior ossification of the postsphenoid ossification center. The sulcus itself is thus the region that remains between these two ossification centers and is not the expected location of the optic chiasm, as its name implies. The turberculum separates the sulcus from the sella turcica. The optic canals enter the intracranial compartment at the level of the lateral margins of the chiasmatic sulcus.

The dorsum sella is a roughly rectangular plate of bone forming the posterior wall of the sella. The posterior surface of the dorsum is continuous with the posterior surface of the body of the sphenoid and basiocciput. This sloping surface is called the clivus.

On each side, the sphenoid bone is separated from the petrous apex of the temporal bone by the large foramen lacerum. The foramen lacerum is continuous with the smaller, more posterior petrooccipital fissure (petroclival synchondrosis). Both of these are filled with plates of cartilage.

The carotid artery exits the tip of the petrous apex and passes along the lateral aspect of the sphenoid body, causing a groove that reaches almost to the anterior clinoid process. This groove may cause an indentation on the lateral wall of the sphenoid sinus when viewed from within the sinus (Fig. 12-5).

The inferior surface of the sphenoid is very irregular, with many grooves and spurs (Fig. 12-4E,F). The pterygoid processes have already been mentioned. The free margin of the upper posterior edge of the medial pterygoid plate splits to form a shallow groove called the scaphoid fossa. The fossa extends posterolaterally toward the spine of the sphenoid. The tensor veli palatini muscle attaches to the scaphoid fossa and to the sphenoid spine. The sphenomandibular ligament also attaches to this spine.

More medially, the body of the sphenoid forms the roof of the nasopharynx. The rostrum of the sphenoid is in the midline and articulates with the vomer. More superiorly, on the anterior surface of the body, the midline ethmoid crest of the sphenoid articulates with the perpendicular plate of the ethmoid. The orifices to the sphenoid sinus are just lateral to this crest.

An understanding of the various perforations, foramina, and fissures of the sphenoid bone can be achieved best by studying cross-sectional images along with the pictures of specimens (Figs. 12-6 to 12-9).

In the axial plane (Fig. 12-7), the optic foramina (canals) converge toward the sella and optic chiasm and are almost perpendicular to one another. The cross-sectional shape of the optic canal changes from its intracranial to its extracranial margins. The intracranial margin of each optic canal has a slightly oval shape with the long axis horizontal. The midportion of the canal is circular and the intraorbital margin of the canal has an oval shape with the long axis vertical. The superior orbital fissure is a curving cleft when viewed from the front. When viewed in the axial plane, the fissure is directed toward the anterior cavernous sinus rather than toward the region of the sella. In the majority of cases a small amount of the orbital fat extends through the fissure to abut the cavernous sinus.

Just caudal to the superior orbital fissure, the foramen rotundum and the Vidian canal (pterygoid canal) pass from posterior to anterior through the skull base. The foramen rotundum is shorter, wider, and fairly straight, and it is found immediately inferior to the superior orbital fissure. In some individuals the foramen is extremely short, appearing only as a gap in the bone on axial images. The foramen rotundum passes from the cavernous sinus region to the pterygopal-

Copyright © 2003, Mosby, Inc. All rights reserved.

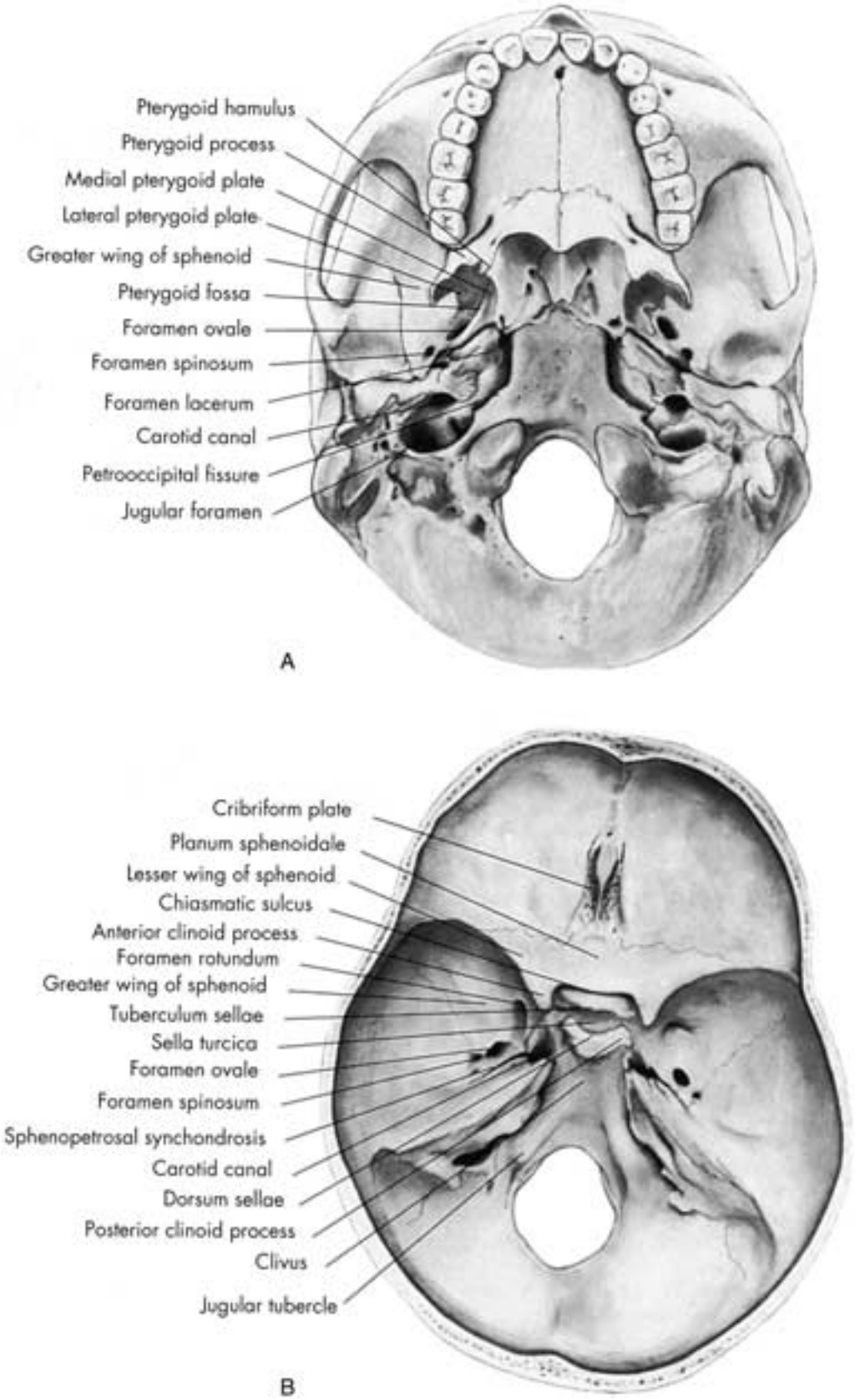

FIGURE 12-3 **A**, Exocranial view of the skull base. **B**, Endocranial view of the skull base.

VIEW IMAGE

Copyright © 2003, Mosby, Inc. All rights reserved.

atine fossa (Fig. 12-7D) and enters the fossa at the level of the inferior orbital fissure. The inferior orbital fissure separates the greater wing of the sphenoid from the more anteriorly located orbital floor.

The Vidian canal (pterygoid canal) (Fig. 12-7F) has its ventral margin more medial than its dorsal end, and its dorsal aspect points toward the carotid canal (petrous portion) rather than toward the cavernous sinus, as does the foramen rotundum. The Vidian canal is more inferior, slightly medial, longer, and narrower than the foramen rotundum. The anterior opening of the Vidian canal flairs (Vidian's trumpet) into the pterygopalatine fossa at the level of the sphenopalatine foramen. This foramen communicates between the pterygopalatine fossa and the posterior nasal cavity and nasopharynx.

The foramina ovale and spinosum (Fig. 12-7F) also extend through the sphenoid bone at the junction of the body and greater wing. They transmit the third division of the trigeminal nerve and the middle meningeal artery, respectively. The foramen ovale is anterior and medial to the foramen spinosum. The foramen ovale angles somewhat anteriorly and slightly laterally toward its extracranial opening. The foramen of Vesalius (emissary sphenoidal foramen) is an inconstant channel that passes anterior and slightly medial to the foramen ovale, carrying a small vein from the cavernous sinus. Other canals occasionally can be seen passing close to the foramen ovale through the medial greater wing of the sphenoid and root of the pterygoid. These are believed to carry venous connections from the cavernous sinus to the pterygoid plexus.[12]

The same anatomic landmarks also can be appreciated in the coronal plane (Figs. 12-8 and 12-9). Now the foramen

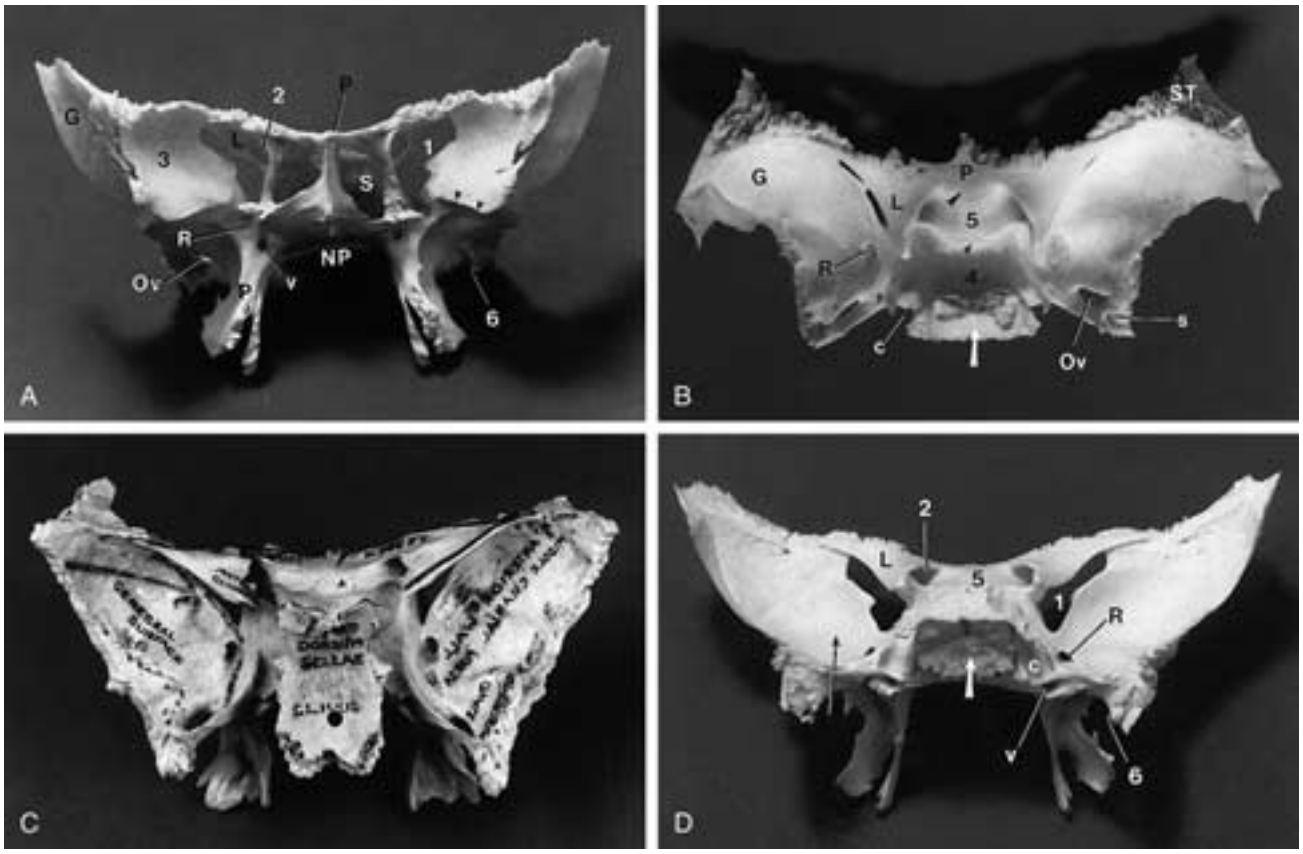

VIEW IMAGE

FIGURE 12-4 **A**, Anterior view of the sphenoid shows the superior orbital fissure (*1*), which can be followed down to the foramen rotundum (*R*). *G*, Greater wing; *L*, lesser wing of the sphenoid; *3*, orbital surface of the greater wing; *2*, optic canal; *V*, Vidian canal; *Ov*, foramen ovale; *6*, spine of the sphenoid; *NP*, nasopharyngeal area; *P*, planum sphenoidale; *S*, sphenoid sinus. The arrowheads are placed along the margin of the inferior orbital fissure. **B**, View from above. *G*, Greater wing; *L*, lesser wing of the sphenoid; *R*, foramen rotundum; *P*, planum sphenoidale; *Ov*, foramen ovale; *S*, foramen spinosum; *4*, sella turcica. The chiasmatic sulcus (*5*) can be followed out laterally to the intracranial end of the optic canal. *Large arrowhead*, limbus; *small arrowhead*, tuberculum sella; *large arrow*, sphenoid portion of the clivus; *C*, notch in the sphenoid bone through which passes the carotid artery. The dorsum sella has been broken off in this picture. **C**, View from posteriorly. (Courtesy Dr. Lewis E. Etter collection.) Posterior view of the clivus and dorsum sella with the clinoids intact. The relationship of the superior orbital fissure and foramen rotundum can be identified. The foramen ovale is seen further posteriorly. The tuberculum sella (*small arrowhead*) and the limbus (*larger arrowhead*) form the boundaries of the chiasmatic groove. **D**, View from posteriorly (the dorsum sella has been removed). The superior orbital fissure (*1*) can be followed toward the foramen rotundum (*R*). Optic canal intracranial opening (*2*) passing toward the chiasmatic sulcus (*5*). *L*, Lesser wing of the sphenoid; *C*, groove for the carotid artery; *v*, intracranial opening of the Vidian canal; *6*, spine of the sphenoid. The large white arrow shows the junctional surface of the basisphenoid at the sphenooccipital suture. The small black arrow passes through the foramen ovale.

Copyright © 2003, Mosby, Inc. All rights reserved.

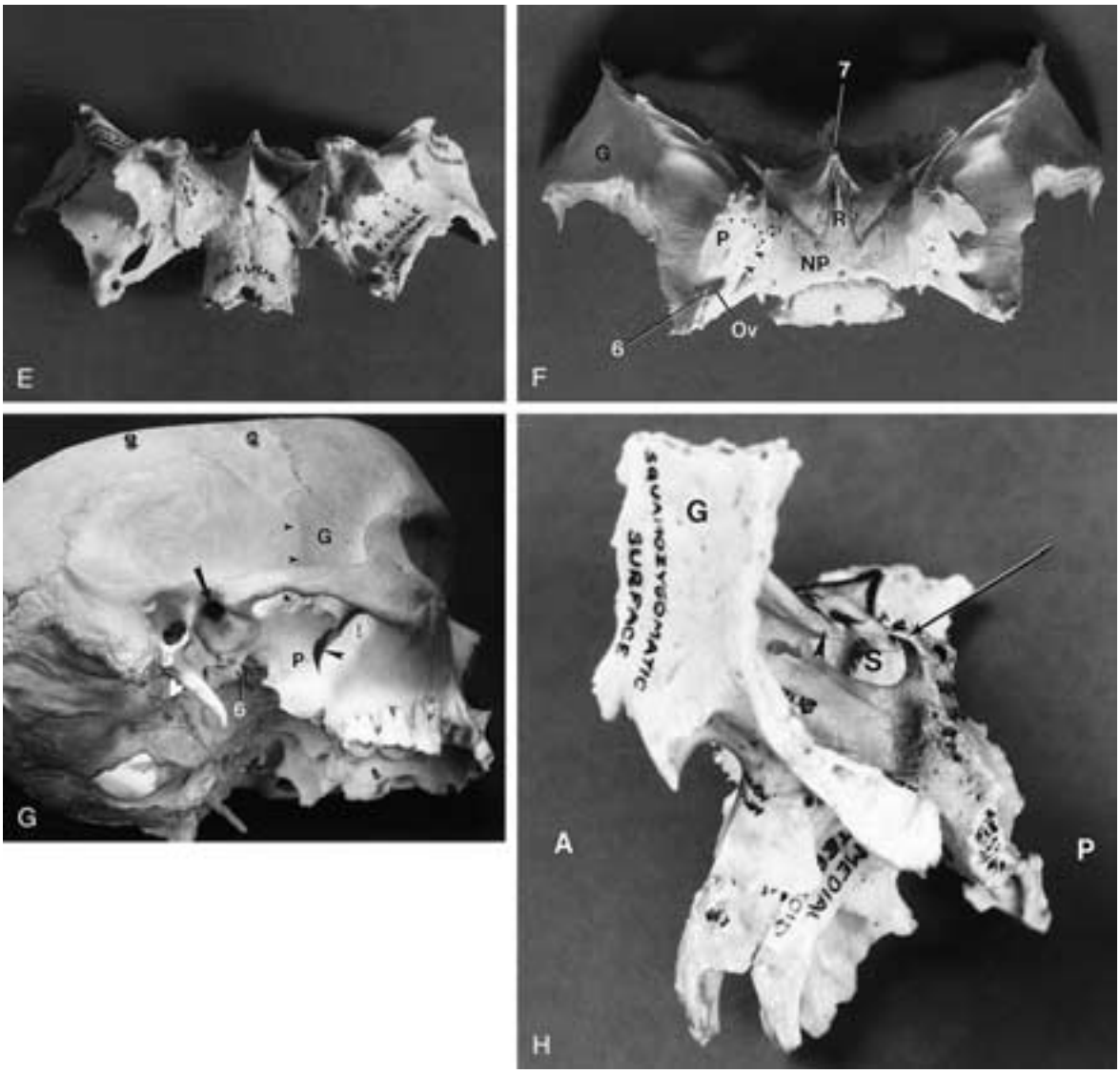

VIEW IMAGE

FIGURE 12-4 *Continued.* **E**, View from inferiorly showing the nasopharyngeal surface of the sphenoid bone. The pterygoid process (*P*) projects toward us. The scaphoid groove (*arrowheads*) is the attachment of the tensor veli palatini. The foramen ovale and foramen spinosum can be identified. **F**, View from inferiorly shows the rostrum (*R*) of the sphenoid, the sphenoid crest (*7*), the nasopharyngeal surface (*NP*), the greater wing of the sphenoid (*G*), and the pterygoid process (P). The letter P is on the lateral plate. The dotted line curves onto the medial plate indicated by the open arrow. The scaphoid fossa (*small arrowheads*) is the origin of the tensor veli palatini. The foramen ovale (*Ov*) and foramen spinosum (unlabeled) are partially obscured by the spine (*6*) of the sphenoid. **G**, Lateral view of the skull shows the pterygoid process (*P*) and the lateral surface of the greater wing (*G*) of the sphenoid. The large arrowhead indicates the pterygopalatine fossa. The small arrowheads are seen along the suture between the greater wing of the sphenoid and the squamosa of the temporal bone. The arrow indicates the glenoid fossa of the temporomandibular joint. *6*, Spine of the sphenoid. **H**, Lateral view of the sphenoid bone disarticulated. (Courtesy Dr. Lewis E. Etter collection.) Lateral view shows the greater wing of the sphenoid (*G*) and the pterygoid plates. More centrally, the posterior clinoid (*arrow*) is seen at the top of the dorsum sella. *Arrowhead*, Anterior clinoid; *S*, sella.

rotundum and the Vidian canal are seen in cross section, while the foramina ovale and spinosum are seen in longitudinal section. More posteriorly, Meckel's cave and the cavernous sinus structures are seen well in the coronal cross section.

At imaging, the normal appearance of the sphenoid bone depends on the degree of sinus development (Figs. 12-6 and 12-10) and the type of marrow present in the bone. The medullary space of the infant is predominantly red marrow. This is gradually replaced by fat of inactive yellow marrow.[13] This change begins in early childhood and progresses into adolescence. Usually by the late teens, the sphenoid medullary cavity is completely replaced by fat, giving a characteristic appearance at CT and MR imaging. For example, the medullary space of the basicranium in most infants less than 1 year of age has a uniformly low signal intensity on T1-weighted images. Areas of high signal intensity, representing fat, rapidly appear, and by the age of

Copyright © 2003, Mosby, Inc. All rights reserved.

7, some fatty marrow is present in virtually all people. Frequently, there are patches of both high and low signal intensity, giving an irregular MR pattern.[14, 15] By the age of 15, a uniformly fatty marrow with high signal intensity on T1-weighted images is present in most people, although some red marrow with lower T1-weighted signal intensity can persist into adulthood.

In the adult, fat is usually evenly distributed throughout the medullary space, interspersed around the remaining trabeculae. Some areas may be devoid of trabeculae, suggesting a cystic cavity such as a mucocele. However, the typical MR imaging signal intensities of fat or the typically low CT density allow the radiologist to make this differentiation (Figs. 12-11 and 12-12).

The sphenooccipital synchondrosis represents the junction of the occipital and sphenoid bones. This often can be seen on sagittal MR imaging or even on plain films in infants. It fuses in most children by the age of 8 years. The synchondrosis is a linear cleft that passes from the intracranial clivus to the pharyngeal surface of the basicranium. Sometimes the synchondrosis between the anterior and posterior ossification centers of the sphenoid can be seen in the infant (Fig. 12-13). This more ventral synchondrosis passes from the tuberculum or the anterior wall of the sella to the pharyngeal side of the sphenoid.[16, 17] This structure is anterior to the course of Rathke's pouch and tract and should not be confused with that embryonic structure.

Sphenoid sinus air cell development begins at birth. Initial air cell development is in the presphenoid region anteriorly, and further enlargement proceeds posteriorly to invade the basisphenoid.[18] Sinus development is slow for the first several years and then accelerates, so that by about the age of 7 or 8 years, the dorsal margin of the sinus has reached the anterior sella turcica.[13, 18] Expansion then continues in all directions, with sinus aeration frequently extending into the dorsum sella and anterior clinoids. Large sinuses can appear to extend down well into the basiocciput. Laterally, the air cells can extend between the foramen rotundum and the Vidian canal into the root of the pterygoid or even into the greater wing. If there is development of these lateral air cells, the space between the foramen rotundum and the Vidian canal is wider than if these air cells are not present. This increased separation should not be considered pathologic.[19]

The position of the septations within the sphenoid sinus varies considerably. Many of these septations pass from anterior to posterior. They can attach to the roof of the sphenoid (the floor of the sella). Some can curve laterally to attach to the bony wall separating the carotid artery from the sphenoid sinus. In this case, a fracture at the carotid groove is of concern if the septation is manipulated at surgery. The foramen rotundum may project into the lower lateral sinus wall, usually as a curved ridge. The Vidian canal may be in the sphenoid bone below the floor of the sphenoid sinus or it may be on a septum just above the sinus floor. A final normal variation of the architecture of the sphenoid bone is the formation of arachnoid granulations along the inner surface of the greater wing of the sphenoid, where the bone forms the anterior wall of the middle cranial fossa (Fig. 12-14). These ''pits'' can be visualized frequently on CT and should not be considered pathologic. In cases of nontraumatic CSF leaks these pits have been implicated as a causal factor. It has been suggested that the thin bone separating one of these pits from another may break, creating a communication with an air cell in the greater wing of the sphenoid.[20]

The occipital bone forms the margin of the foramen magnum and extends up to meet the basisphenoid at the sphenooccipital synchondrosis (Fig. 12-15). This synchondrosis is usually about one third up the length of the posterior surface of the clivus. It is the basilar part of the occipital bone that forms the region anterior to the foramen magnum. The lateral part of the occipital bone forms the lateral margin of the foramen magnum and includes the large occipital condyles, prominent landmarks on the caudal aspect of the skull. The jugular process of the occipital bone juts laterally and has a rounded prominence called the jugular tubercle along its superior margin. The hypoglossal canal passes just above the occipital condyle and just below the jugular tubercle. Posterior to the condyle is the condyloid canal, which enters this fossa carrying an emissary vein.[21, 22]

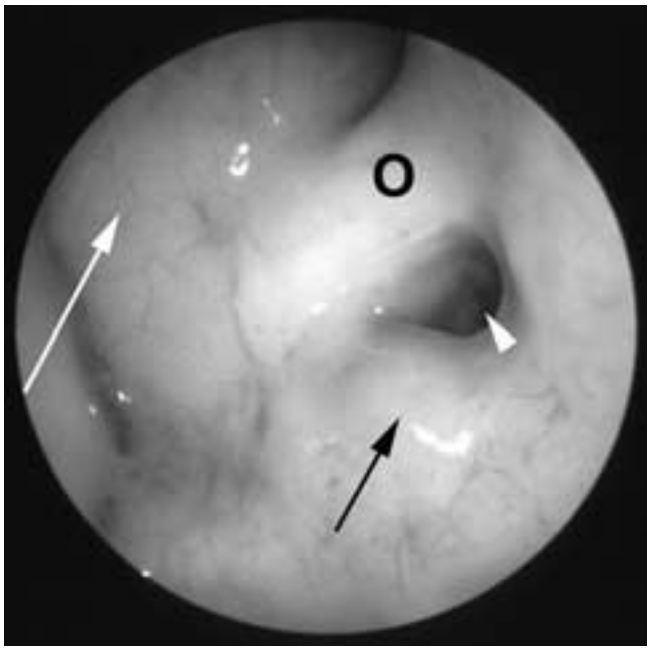

VIEW IMAGE

FIGURE 12-5 Endoscopic view of the sphenoid sinus. Note that the image is slightly rotated from the vertical plane due to the obliquity of the approach. Note the small recess (*arrowhead*) between the optic canal impression (*O*) and the bulge from the carotid artery (*black arrow*). The white arrow indicates the impression of the sella.

Bordering Soft Tissues

The evaluation of the soft tissues that border the skull base can be crucial in the analysis of disease. Just as lesions arising in the skull base itself can expand into these areas, lesions arising above or below the skull base can invade it. Importantly, the imaging demonstration of normal soft tissues between the skull base and a tumor is reassuring evidence that the skull base has not been invaded.

Extracranial Soft Tissues

The extracranial openings of the fissures and foramina of the skull base are bordered by soft tissues primarily

Copyright © 2003, Mosby, Inc. All rights reserved.

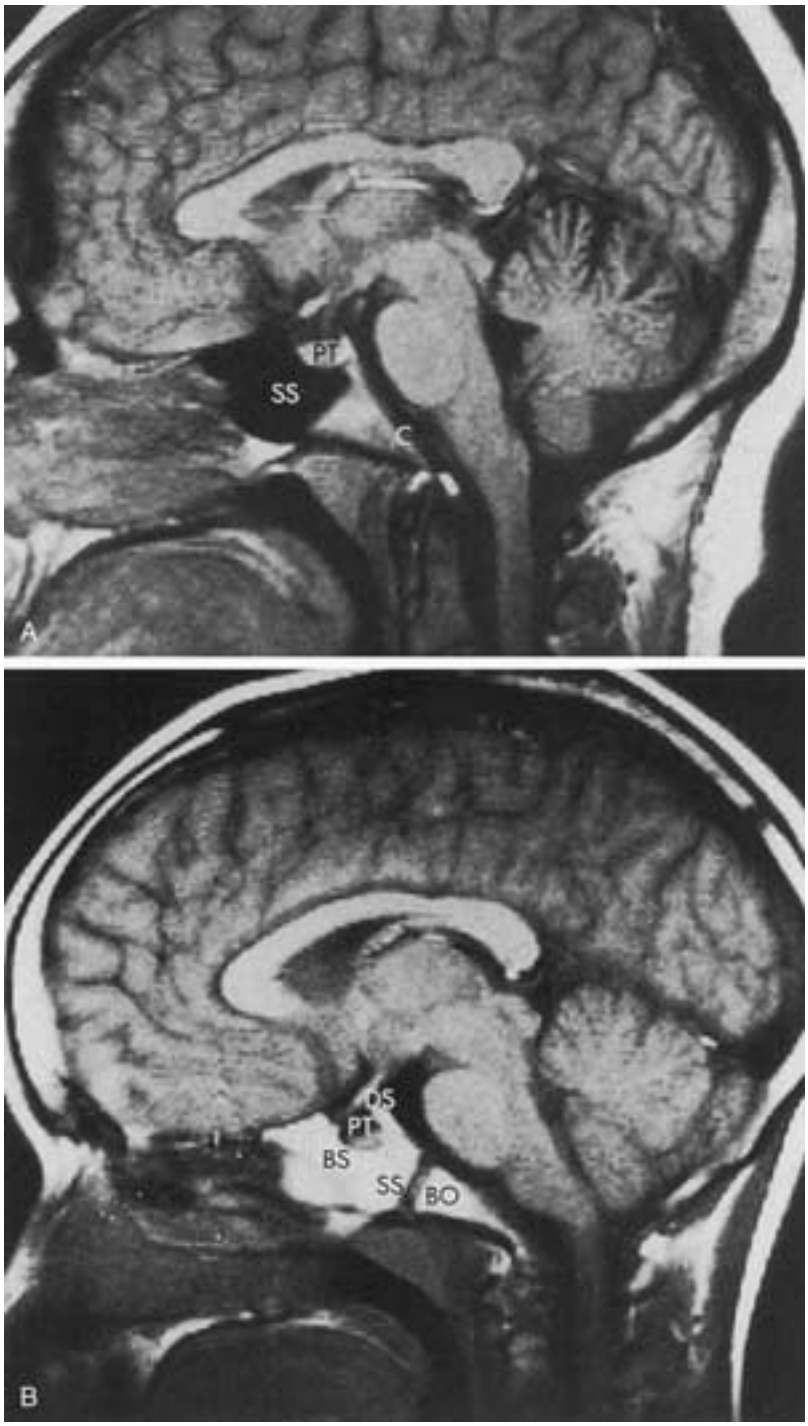

VIEW IMAGE

FIGURE 12-6 **A**, Midline sagittal T1-weighted MR image of the skull base in an adult. *PT*, Pituitary within the sella turcica; *SS*, sphenoid sinus; *C*, clivus. **B**, Midline sagittal T1-weighted MR image of the skull base in a child. *DS*, Dorsum sellae; *PT*, pituitary within the sella turcica; *BS*, basisphenoid; *SS*, sphenooccipital synchondrosis; *BO*, basiocciput.

containing fat, and just as in the remainder of the head and neck, this fat is important in the imaging analysis of the skull base. Because fat has a very characteristic appearance on CT and MR imaging, excellent contrast is afforded between normal tissue and most lesions, particularly cellular tumors. Thus, for instance, as a tumor approaches the base of the skull, the progressive obliteration of the fat planes allows detection of tumor infiltration.

The optic canal and the superior orbital fissure open into the orbit (Fig. 12-7), and although the optic nerve and the extraocular muscles occupy space in the orbital apex, there is still sufficient fat to allow detection of most lesions. Indeed, as mentioned, the orbital fat normally protrudes slightly through the superior orbital fissure into the region of the anterior cavernous sinus.

The foramen rotundum and the Vidian canal open into the pterygopalatine fossa. The fossa is filled almost entirely by fat (Figs. 12-7 and 12-8). This narrow cleft (Fig. 12-4G) behind the medial posterior wall of the maxillary sinus takes its name from the bones that make up the walls of this space. The pterygoid process of the sphenoid forms the posterior wall (Fig. 12-16), while the superiorly projecting orbital

Copyright © 2003, Mosby, Inc. All rights reserved.

process of the palatine bone makes up the anterior wall. The pterygopalatine fossa connects with five spaces: the central skull base and middle cranial fossa via the Vidian canal and the foramen rotundum, the orbit via the inferior orbital fissure, the infratemporal fossa via the retromaxillary or pterygomaxillary fissure, the nasal cavity via the sphenopalatine foramen, and the oral cavity via the pterygopalatine canals in which run the greater and lesser palatine nerves (Figs. 12-17 to 12-19). In addition, the second division of the trigeminal nerve branches in the pterygopalatine fossa before carrying sensory innervation to the face and to the mucosa of the palate (Fig. 12-17), and these nerves can be the pathway of tumor spread. Thus, the pterygopalatine fossa is an important landmark in staging of head and neck tumors.

Text continued on p. 797

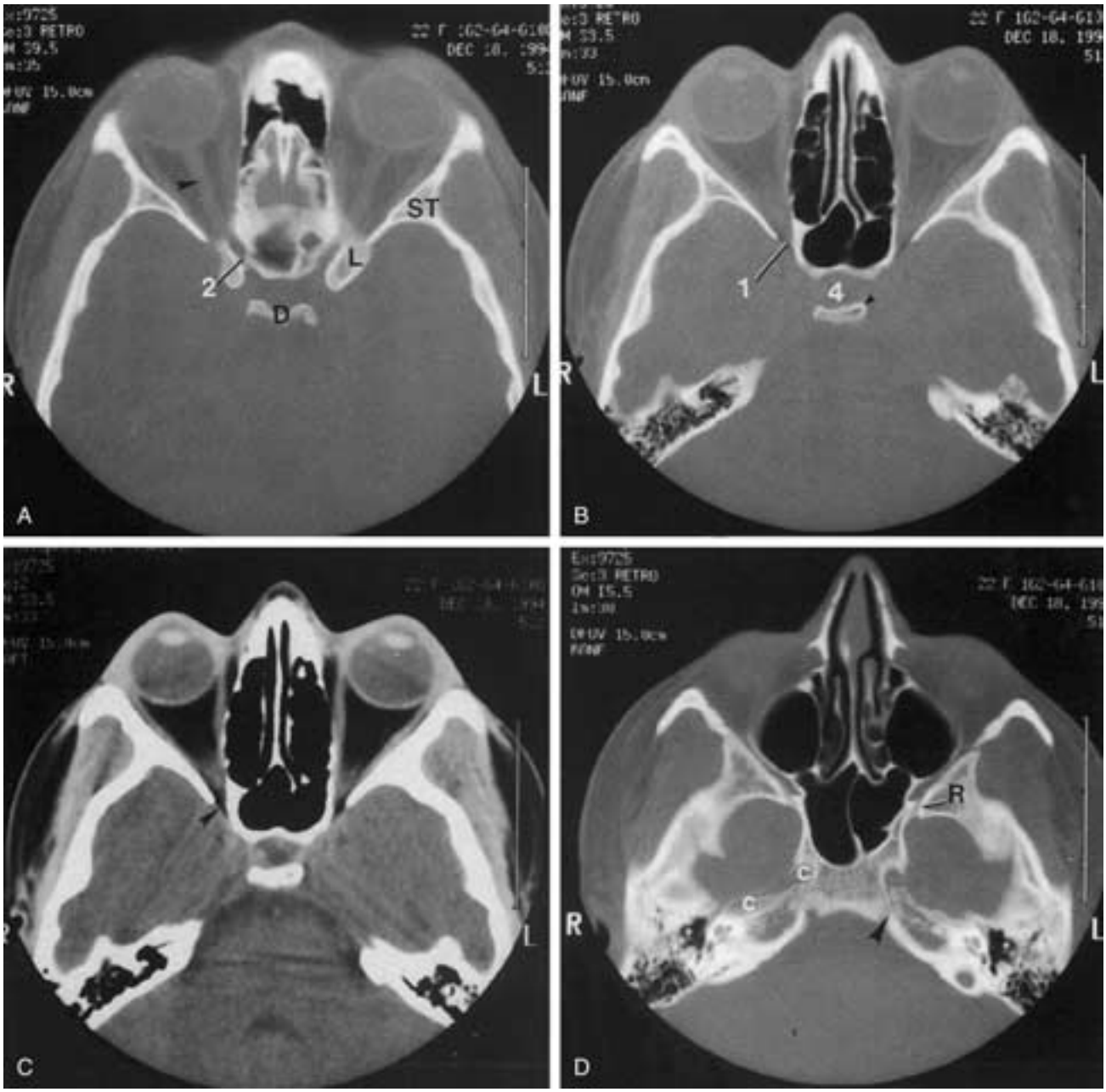

VIEW IMAGE

FIGURE 12-7 Axial CT scan of the skull base from superior to inferior. **A**, Level of the optic canal. *2*, Optic canal; *L*, lesser wing of the sphenoid; *D*, dorsum sella; *ST*, position of the ''sphenoid triangle.'' Note how the optic nerve (*arrowhead*) converges toward the optic canal. **B**, Level of the superior orbital fissure. *1*, Superior orbital fissure; *4*, sella turcica. The arrowhead indicates the posterior clinoid at the lateral aspect of the dorsum sella. Note how the superior orbital fissure is oriented anteriorly to posteriorly rather than converging toward the optic chiasm. **C**, Soft-tissue algorithm at the same level. Note how a small amount of fat (*arrowhead*) protrudes through the superior orbital fissure. **D**, Level of the foramen rotundum. The foramen rotundum (*R*) passes from the pterygopalatine fossa to the middle cranial fossa. *C*, Carotid canal. The medial *C* is immediately above the foramen lacerum. The medial *C* is in a small notch as the artery turns superiorly along the lateral aspect of the sphenoid bone. The petrooccipital (or petroclival) fissure is indicated by the arrowhead.

Copyright © 2003, Mosby, Inc. All rights reserved.

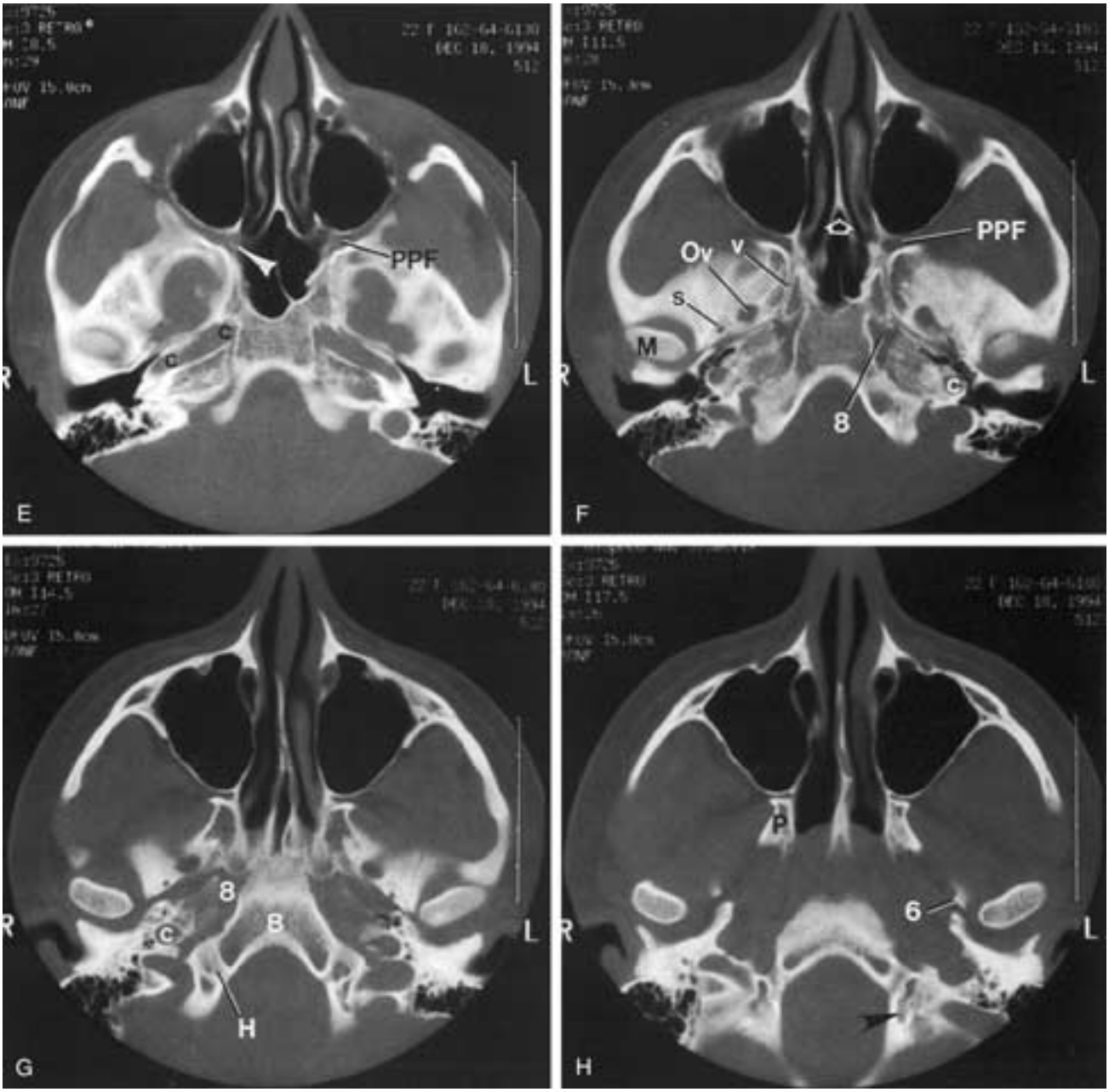

FIGURE 12-7 *Continued.* **E**, Level of the pterygopalatine fossa. The pterygopalatine fossa (*PPF*) is situated between the maxillary sinus anteriorly and the sphenoid bone posteriorly. The arrowhead indicates the sphenopalatine foramen, which connects the pterygopalatine fossa with the posterior nasal cavity and nasopharynx. *C*, Carotid canal. The more medial C is immediately above the foramen lacerum. **F**, Level of Vidian canal. *v*, Vidian canal; *Ov*, foramen ovale; *S*, foramen spinosum; *M*, mandible; *8*, foramen lacerum; *C*, inferior portion of the carotid canal; *PPF*, pterygopalatine fossa. The line indicating the PPF passes from the infratemporal fossa through the pterygomaxillary fissure into the pterygopalatine fossa. The open arrowhead indicates pneumatization extending into the rostrum of the sphenoid. Note how the Vidian canal passes from the pterygopalatine fossa posteriorly to the region close to the foramen lacerum rather than into the middle cranial fossa. **G**, Below the level of the Vidian canal. *B*, Basiocciput; *H*, hypoglossal canal; *8*, foramen lacerum; *C*, cross section of the lower vertical segment of the carotid canal. **H**, Through the level of the spine of the sphenoid. *6*, spine of the sphenoid. The small lucency just anterior to this point is the lower foramen spinosum. The arrowhead indicates the condyloid canal carrying an emissary vein. *P*, Pterygoid process.

Illustration continued on following page

VIEW IMAGE

Copyright © 2003, Mosby, Inc. All rights reserved.

FIGURE 12-7 *Continued.* **I**, Level of the occipital condyle. *9*, Occipital condyle; *large black arrowhead*, styloid process; *black arrow*, medial pterygoid plate; *open arrow*, lateral pterygoid plate; *small arrowhead*, pterygopalatine canal extending toward the palatine foramen; *NP*, nasopharynx.

VIEW IMAGE

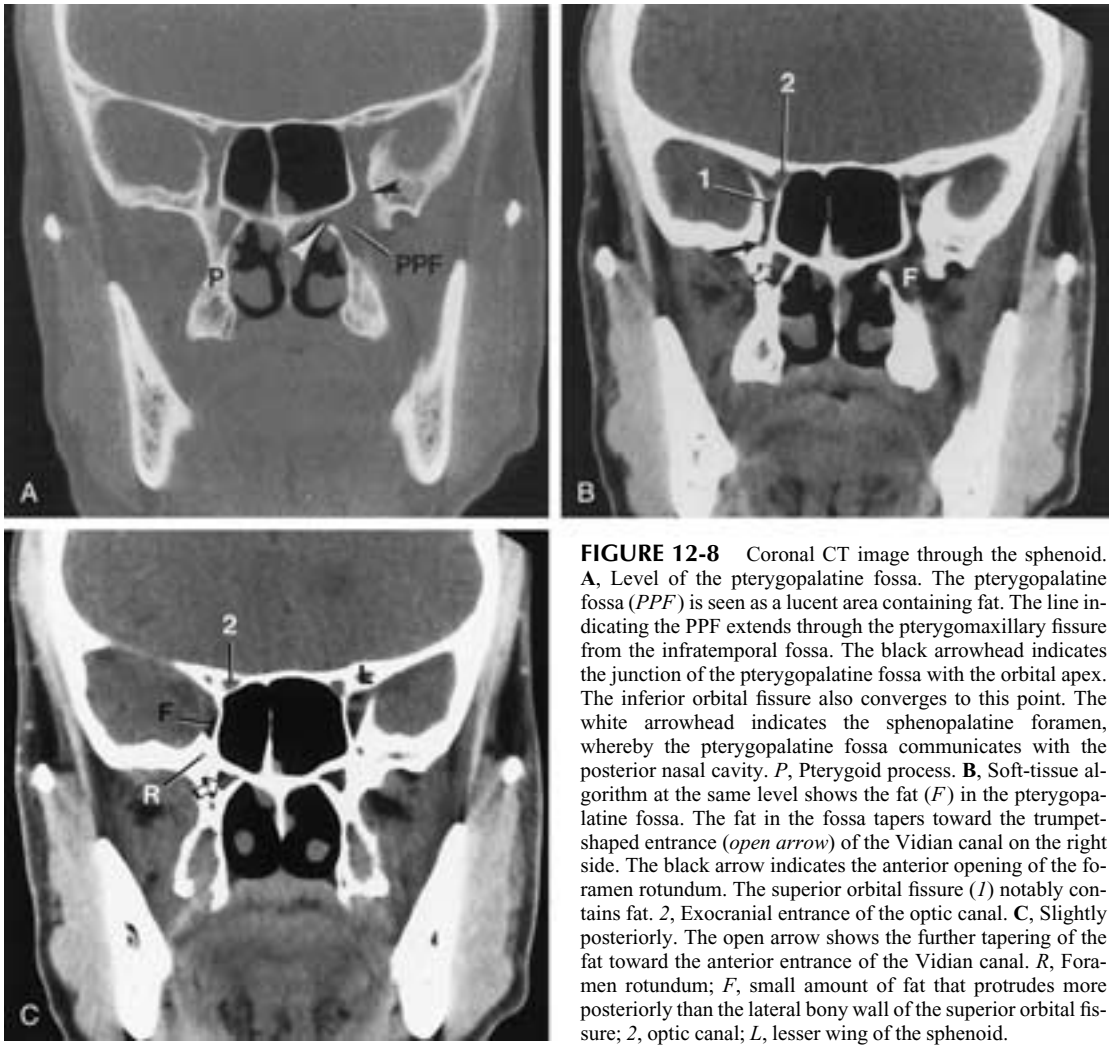

FIGURE 12-8 Coronal CT image through the sphenoid. **A**, Level of the pterygopalatine fossa. The pterygopalatine fossa (*PPF*) is seen as a lucent area containing fat. The line indicating the PPF extends through the pterygomaxillary fissure from the infratemporal fossa. The black arrowhead indicates the junction of the pterygopalatine fossa with the orbital apex. The inferior orbital fissure also converges to this point. The white arrowhead indicates the sphenopalatine foramen, whereby the pterygopalatine fossa communicates with the posterior nasal cavity. *P*, Pterygoid process. **B**, Soft-tissue algorithm at the same level shows the fat (*F*) in the pterygopalatine fossa. The fat in the fossa tapers toward the trumpet-shaped entrance (*open arrow*) of the Vidian canal on the right side. The black arrow indicates the anterior opening of the foramen rotundum. The superior orbital fissure (*1*) notably contains fat. *2*, Exocranial entrance of the optic canal. **C**, Slightly posteriorly. The open arrow shows the further tapering of the fat toward the anterior entrance of the Vidian canal. *R*, Foramen rotundum; *F*, small amount of fat that protrudes more posteriorly than the lateral bony wall of the superior orbital fissure; *2*, optic canal; *L*, lesser wing of the sphenoid.

VIEW IMAGE

Copyright © 2003, Mosby, Inc. All rights reserved.

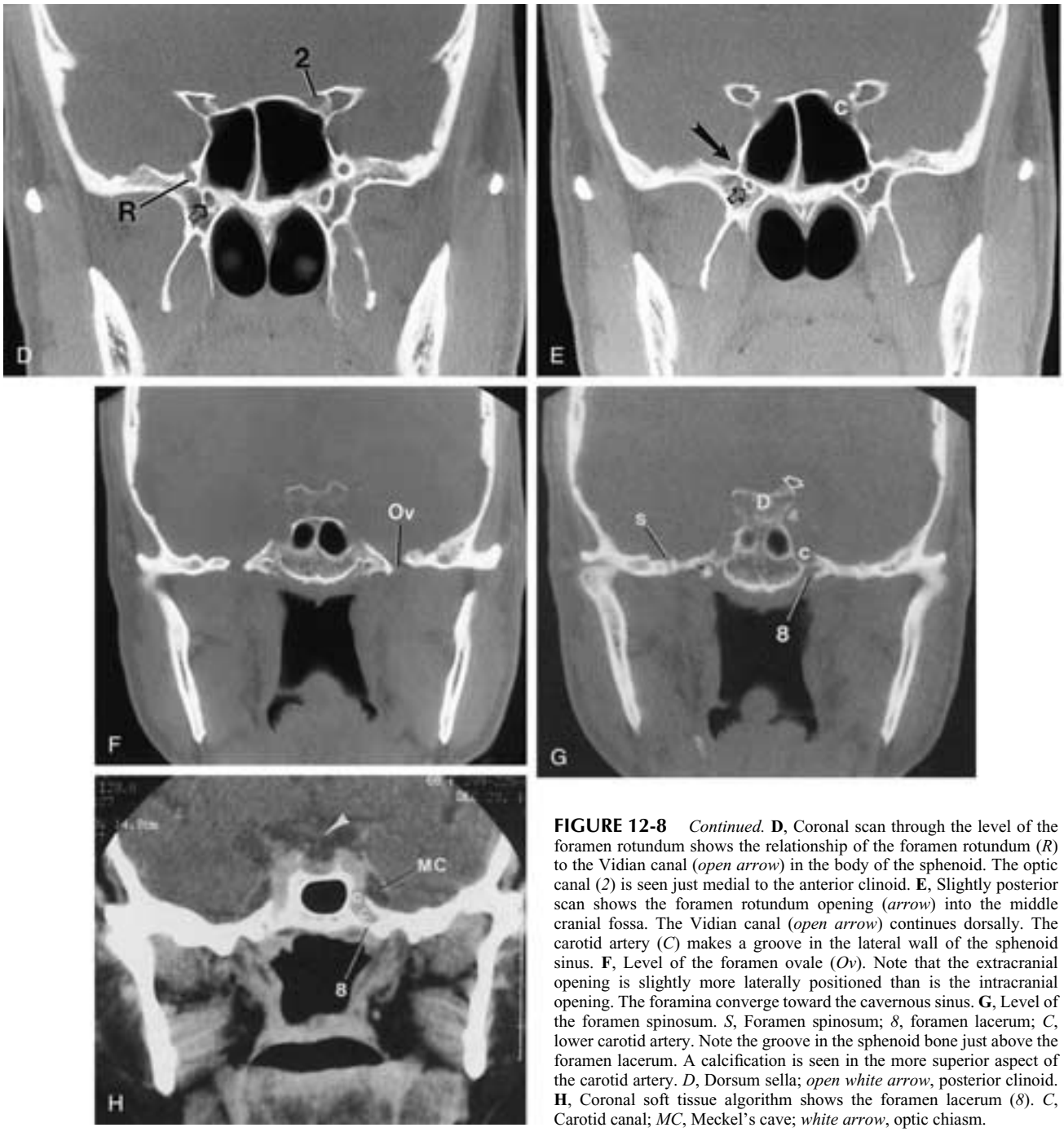

FIGURE 12-8 *Continued.* **D**, Coronal scan through the level of the foramen rotundum shows the relationship of the foramen rotundum (*R*) to the Vidian canal (*open arrow*) in the body of the sphenoid. The optic canal (*2*) is seen just medial to the anterior clinoid. **E**, Slightly posterior scan shows the foramen rotundum opening (*arrow*) into the middle cranial fossa. The Vidian canal (*open arrow*) continues dorsally. The carotid artery (*C*) makes a groove in the lateral wall of the sphenoid sinus. **F**, Level of the foramen ovale (*Ov*). Note that the extracranial opening is slightly more laterally positioned than is the intracranial opening. The foramina converge toward the cavernous sinus. **G**, Level of the foramen spinosum. *S*, Foramen spinosum; *8*, foramen lacerum; *C*, lower carotid artery. Note the groove in the sphenoid bone just above the foramen lacerum. A calcification is seen in the more superior aspect of the carotid artery. *D*, Dorsum sella; *open white arrow*, posterior clinoid. **H**, Coronal soft tissue algorithm shows the foramen lacerum (*8*). *C*, Carotid canal; *MC*, Meckel's cave; *white arrow*, optic chiasm.

VIEW IMAGE

Within the fat of the pterygopalatine fossa are the branches of the maxillary nerve, the pterygopalatine ganglion, and small vessels. Though a small amount of soft tissue can be identified in the fossa, the predominant imaging finding is fat, which serves as an important imaging landmark when evaluating potential tumor spread.

The foramen ovale opens into the masticator space below the skull base. As the third division of the trigeminal nerve exits the skull via this foramen, the nerve emerges into fat along the medial margin of the lateral pterygoid muscle.[23] The nerve passes just superficial (lateral) to the sphenomandibular ligament and the fusion of fascial layers that form the medial boundary of the masticator space. The tensor veli palatini muscle takes its origin along a line from the scaphoid fossa to the spine of the sphenoid bone. This small, thin muscle plays an important role in the fascial organization of the parapharyngeal spaces.

Intracranial Soft Tissues

Intracranially, most of the foramina converge to the region of the cavernous sinus and Meckel's cave (Figs. 12-7 and 12-8). The optic canals open into the suprasellar cistern. The cavernous sinus is a venous sinusoid structure situated between the layers of the dura, bordering the pituitary fossa

Copyright © 2003, Mosby, Inc. All rights reserved.

and the body of the sphenoid (Fig. 12-20). The cavernous sinus forms much of the medial wall of the middle cranial fossa.

The dural organization at Meckel's cave and the cavernous sinus is derived from the dural coverings of the contiguous inner surfaces of the skull. Two layers can be appreciated. The outer (peripheral) layer of the dura follows the bone of the skull base. The inner layer is reflected upward, forming the lateral wall of Meckel's cave and the cavernous sinus before attaching to the clinoids. This inner layer of dura has a secondary reflection that passes anteriorly from posteriorly, forming Meckel's cave. This cave can be thought of as a very loose root sleeve around the trigeminal nerve and ganglion.

The cavernous sinus is located at the superomedial aspect of Meckel's cave and extends anteriorly from that point. The cavernous sinus contains several nerves. The ophthalmic division of the trigeminal nerve passes into the cavernous sinus on the way to the superior orbital fissure. The maxillary division of the trigeminal nerve has a shorter course within the cavernous sinus before entering the foramen rotundum. The third division of the trigeminal nerve exits almost directly from Meckel's cave and does not truly enter the cavernous sinus. The semilunar or Gasserian ganglion, the convergence of the divisions of the nerve, lies along the lateral wall of Meckel's cave. The oculomotor, trochlear, and abducens nerves traverse the entire anteroposterior length of the cavernous sinus before exiting the skull at the superior orbital fissure.

The internal carotid artery also traverses the cavernous sinus. The artery curves superiorly immediately after exiting the petrous carotid canal. This brings the artery into the

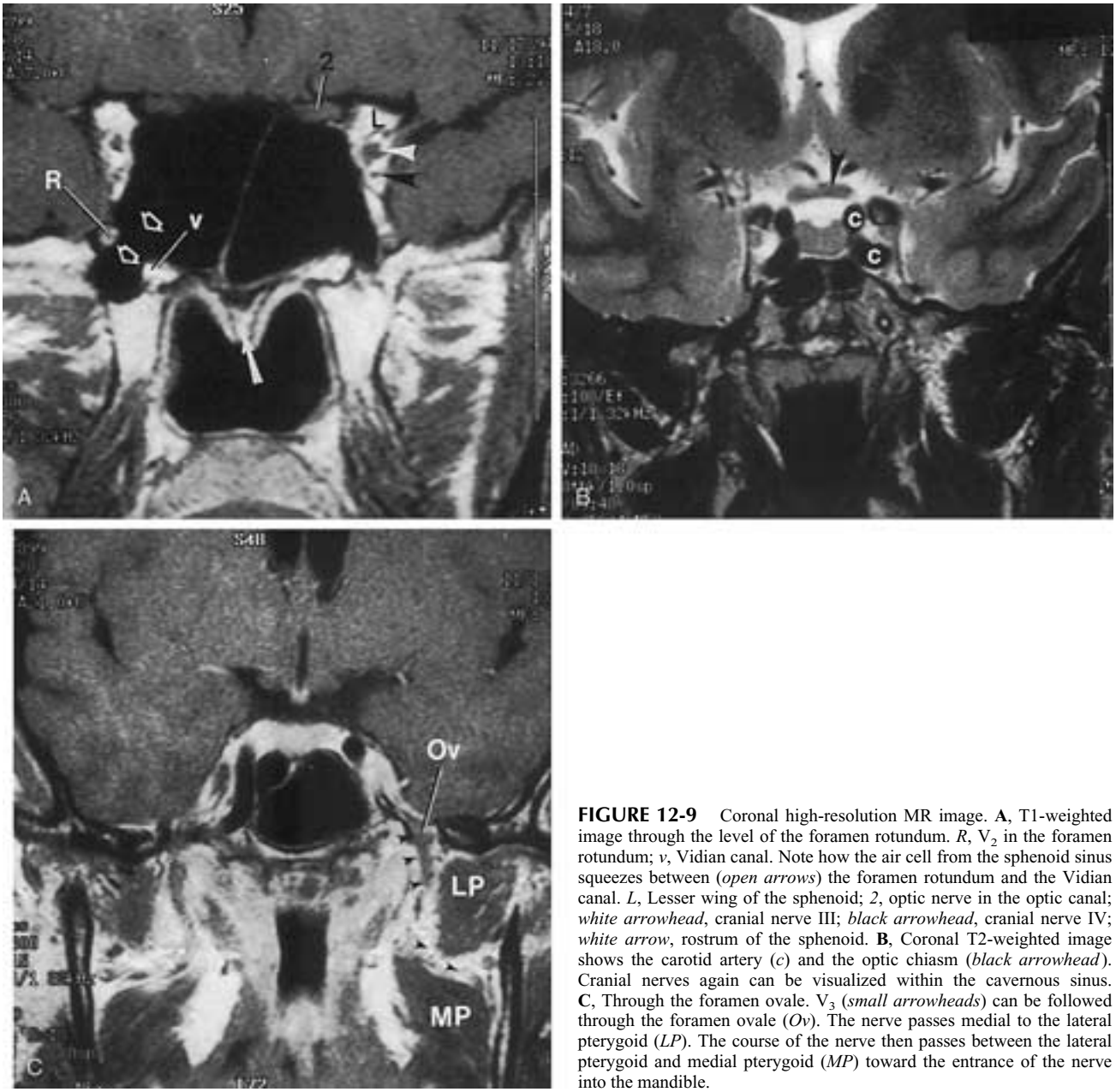

FIGURE 12-9 Coronal high-resolution MR image. **A**, T1-weighted image through the level of the foramen rotundum. *R*, V_2 in the foramen rotundum; *v*, Vidian canal. Note how the air cell from the sphenoid sinus squeezes between (*open arrows*) the foramen rotundum and the Vidian canal. *L*, Lesser wing of the sphenoid; *2*, optic nerve in the optic canal; *white arrowhead*, cranial nerve III; *black arrowhead*, cranial nerve IV; *white arrow*, rostrum of the sphenoid. **B**, Coronal T2-weighted image shows the carotid artery (*c*) and the optic chiasm (*black arrowhead*). Cranial nerves again can be visualized within the cavernous sinus. **C**, Through the foramen ovale. V_3 (*small arrowheads*) can be followed through the foramen ovale (*Ov*). The nerve passes medial to the lateral pterygoid (*LP*). The course of the nerve then passes between the lateral pterygoid and medial pterygoid (*MP*) toward the entrance of the nerve into the mandible.

VIEW IMAGE

Copyright © 2003, Mosby, Inc. All rights reserved.

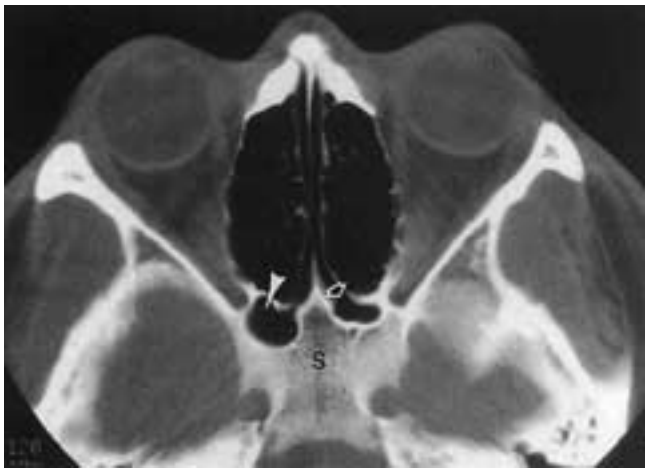

VIEW IMAGE

FIGURE 12-10 Normal but poorly pneumatized sphenoid. Small air cells (*arrowhead*) form in the anterior part of the sphenoid bone (*S*). The ostium (*open arrow*) can be followed into the sinus on the left side.

cavernous sinus between Meckel's cave and the lateral wall of the sphenoid sinus. The artery then curves anteriorly, making a short bend before passing through the dura just below the optic nerve.

IMAGING

Plain film investigation of the skull base has given way to CT and MR imaging. However, the skull base is ever present on any projectional image of the skull or of the sinuses. Indeed, a major factor in the development of the different views used in plain film radiography of the temporal bone and sinuses was an attempt to project the area of interest away from the confusing densities of the skull base. Although plain films are seldom used when skull base pathology is suspected, skull base problems can mimic various types of facial and sinus pathology. Thus, familiarity with the normal projectional anatomy is appropriate. This is discussed in Chapter 2.

CT can be performed in the axial and coronal planes. Other slice orientations and three-dimensional (3D) images can be reformatted. The advent of multidetector scanners with slice thicknesses approaching the dimensions of the pixel allows high-quality reformatting in any plane. This imaging advance is lessening, and in many cases eliminating, the need to perform direct coronal imaging. In turn, this eliminates the imaging-degrading beam-hardening artifacts from dental restorations so common on direct coronal CT. A slice thickness of no greater than 3 mm should be used, with thinner scans used to answer specific diagnostic questions regarding some of the smaller skull base foramina. The optimal slice thickness may change as more experience with the multidetector scanners is gathered.

Contrast is used whenever the cavernous sinus is examined or intracranial tumor is suspected. Bone algorithms are utilized to optimally visualize the thin cortices around the various foramina, and soft-tissue algorithms allow evaluation of the soft tissues adjacent to the skull base.

Although MR imaging can be performed in any plane, the routine examination should include the sagittal, axial, and coronal views, particularly in tumor cases. Gadolinium is used routinely to evaluate the cavernous sinus and potential intracranial tumor. Because some enhancing tumors can be as bright as fat, the interface between the lesion and the fat planes below the skull base can be lost unless either a precontrast sequence is obtained or fat suppression is used. One must be careful when fat suppression is employed, because the interface between the sphenoid sinus air and its wall often results in a significant susceptibility effect. This ''blooming'' can void the signal from important structures such as the cavernous sinus and the foramen rotundum (Fig. 12-21). The radiologist must be confident that the foramen

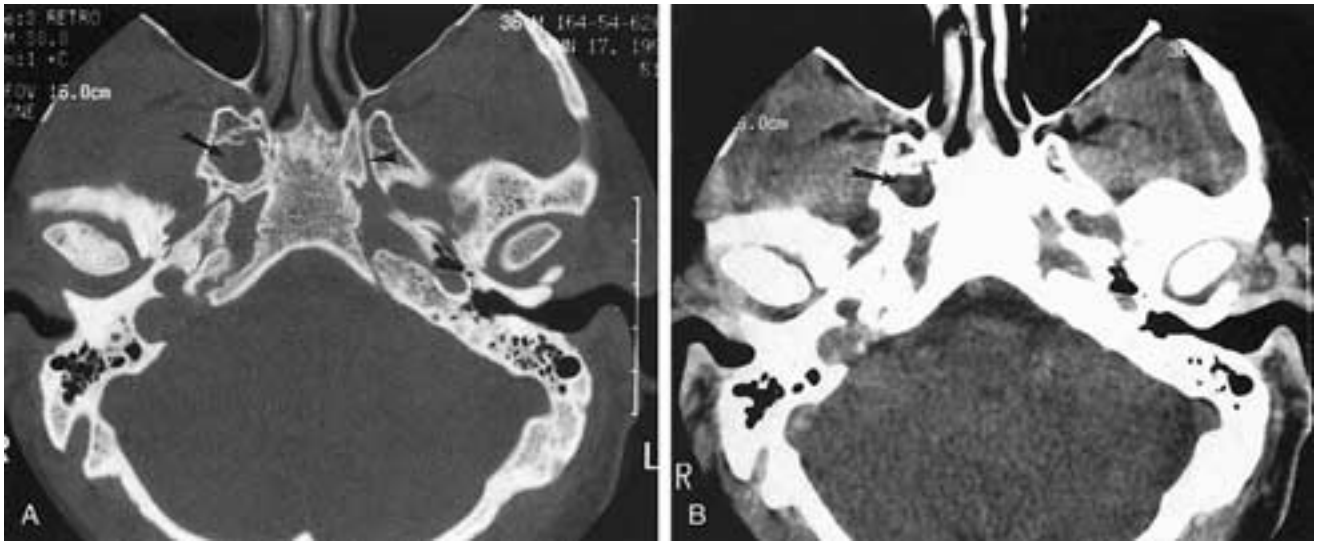

VIEW IMAGE

FIGURE 12-11 Normal variant in the sphenoid. **A**, Axial CT bone algorithm shows what appears to be a dilated cystic structure in the pterygoid process (*arrow*). The normal pterygoid (Vidian) canal is seen (*arrowhead*) on the opposite side. **B**, Soft-tissue algorithm shows that the area within this cystic structure contains fat, indicating that this represents a variation in ossification rather than obstructed secretions.

Copyright © 2003, Mosby, Inc. All rights reserved.

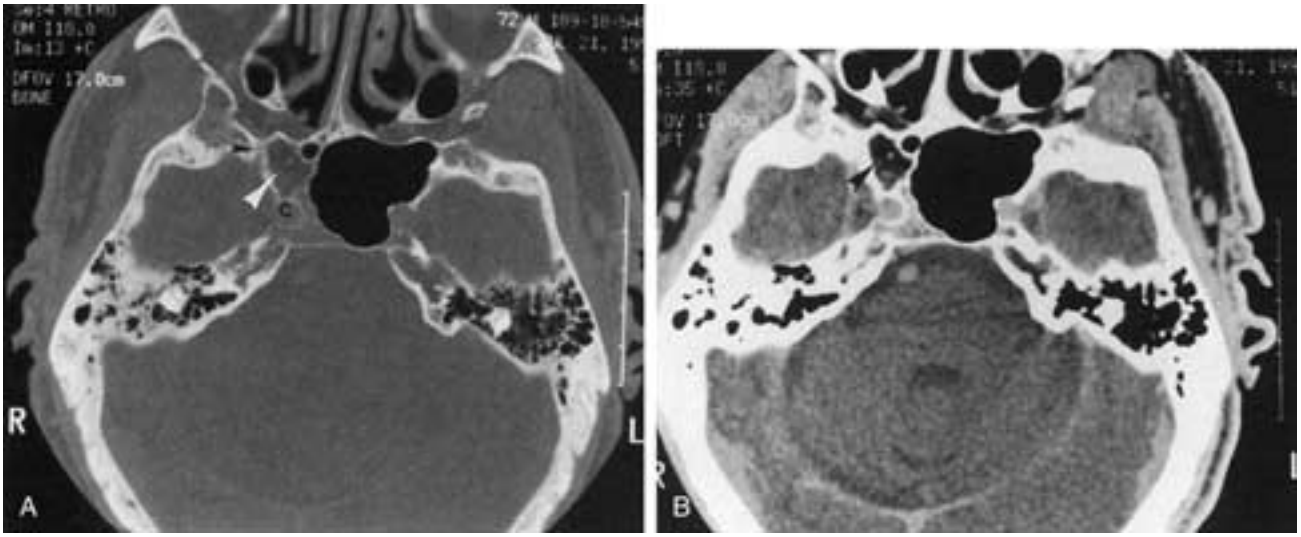

VIEW IMAGE

FIGURE 12-12 **A**, Normal nonpneumatized CT bone algorithm. An area (*white arrowhead*) in the right sphenoid initially can be confused with an obstructed sinus. However, on careful inspection, there appear to be trabeculae within the area. The foramen rotundum (*black arrowhead*) is seen just lateral to the area in question. **B**, On the soft-tissue algorithm at the same level, the area of concern shows a fatty density (*arrowhead*), indicating that this indeed represents normal fatty marrow.

VIEW IMAGE

FIGURE 12-13 Normal clivus in a child evaluated for thyroglossal duct remnant or cyst. T2-weighted image shows the thyroglossal abnormality in the tongue base (*white arrow*). The synchondrosis (*small white arrowhead*) between the pre- and postsphenoid ossification centers is easily identified, as is the synchondrosis between the sphenoid and occipital bones. *Large black arrowhead*, pituitary fossa; *small black arrowhead*, chiasmatic groove.

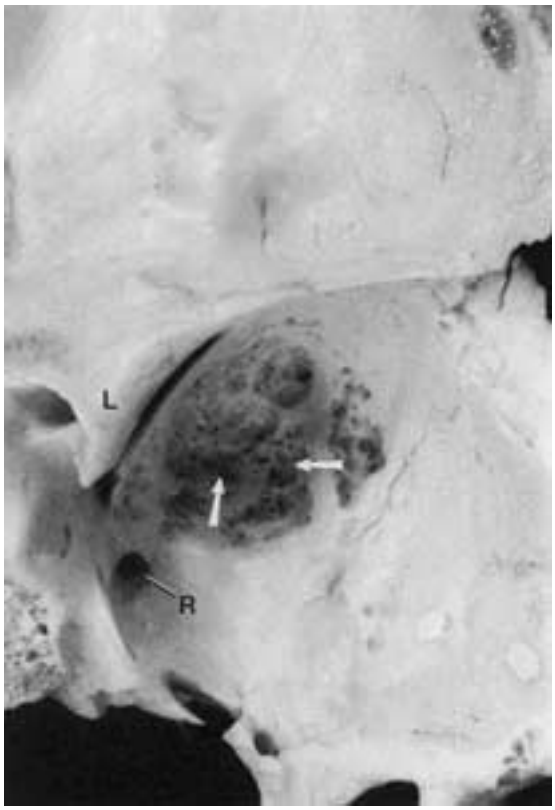

FIGURE 12-14 Arachnoid granulations extending into the sphenoid bone. Viewed from above, the arachnoid granulations extend through the intracranial cortex of the greater wing of the sphenoid, leaving rather extensive pitted perforations (*arrows*) of the cortex. The position of the small pits would put the granulations in close proximity to a laterally extending sphenoid air cell. *L*, Lesser wing of the sphenoid; *R*, foramen rotundum.

VIEW IMAGE

Copyright © 2003, Mosby, Inc. All rights reserved.

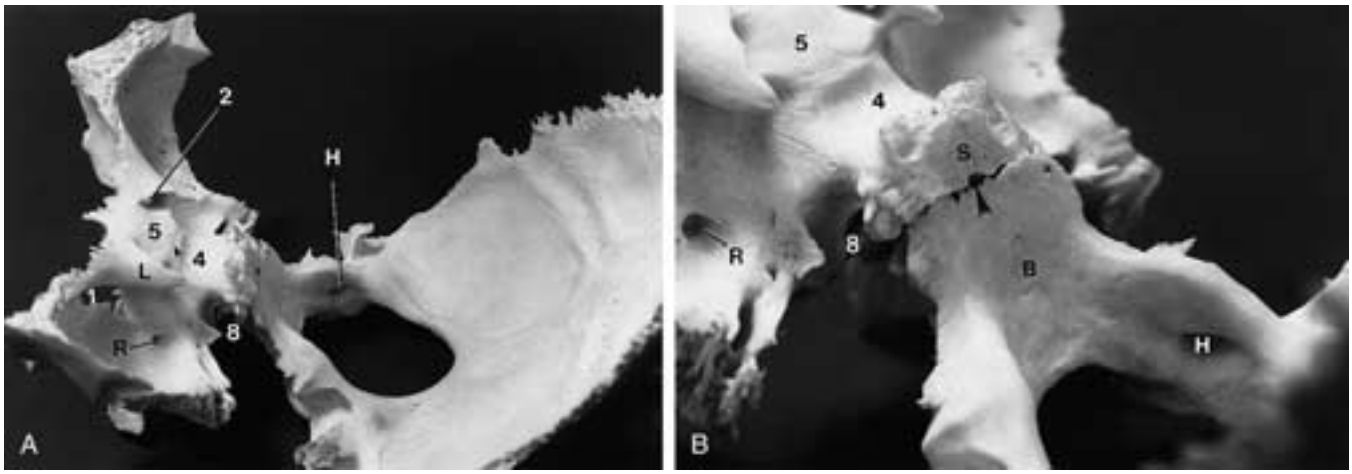

VIEW IMAGE

FIGURE 12-15 **A**, View from above and laterally of the sphenoid and occipital bones. *1*, Superior orbital fissure; *2*, optic canal; *4*, sella turcica; *5*, chiasmatic sulcus; *L*, lesser wing of the sphenoid; *R*, foramen rotundum; *H*, hypoglossal canal; *small arrowhead*, tuberculum sella; *8*, approximate position of the foramen lacerum at the tip of the temporal bone. **B**, Close-up of the sphenooccipital synchondrosis from above, laterally and slightly posteriorly. *8*, Approximate position of the foramen lacerum. The notch immediately above the 8 would hold the carotid artery. *R*, Foramen rotundum; *B*, basiocciput; *S*, posterior sphenoid; *4*, sella turcica; *5*, chiasmatic groove; *H*, hypoglossal canal; *arrowhead*, sphenooccipital structure.

has been adequately visualized either with or without fat suppression. Frequently, a subtle vascular plexus can be identified around the nerve within the foramen. Because of these plexes, symmetric slight enhancement of the cranial nerves as they exit the skull base may be seen routinely. It is only when there is asymmetric enhancement that pathology should be suspected. On the other hand, the Gasserian ganglion has sparse vascularity, and thus this ganglion should not enhance routinely on contrast MR sequences. If enhancement is seen within a Gasserian ganglion, it should be considered pathologic.

Fat suppression is often used with the newer fast spin-echo, T2-weighted sequences. On conventional spin-echo images, fat has a high T1-weighted and a low T2-weighted signal intensity. However, on fast spin-echo imaging, fat has a high signal intensity on both T1-weighted and T2-weighted images. Thus, on the T2-weighted fast spin-echo images, fat suppression can give an imaging appearance similar to that of the conventional spin-echo images. Again, the susceptibility effect of air and tissue can present imaging problems.

If the areas of the central skull base, cavernous sinuses, and sphenoid sinus are to be evaluated, a suggested protocol for the routine case includes T1-weighted sequences with and without gadolinium and T2-weighted scans; 3-mm-thick sections are used for the T1-weighted sequences, and 4- to 5-mm-thick sections are used for the T2-weighted scans.

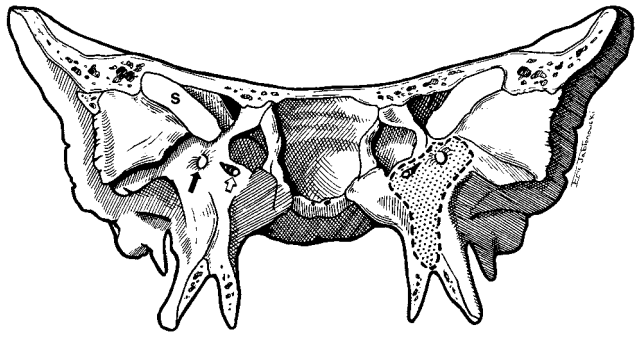

VIEW IMAGE

FIGURE 12-16 Anterior view of the sphenoid. The approximate projection of the pterygopalatine fossa is seen in the dotted outline. The foramen rotundum (*arrow*) and the Vidian canal (*open arrow*) enter the pterygopalatine fossa. *S*, Superior orbital fissure.

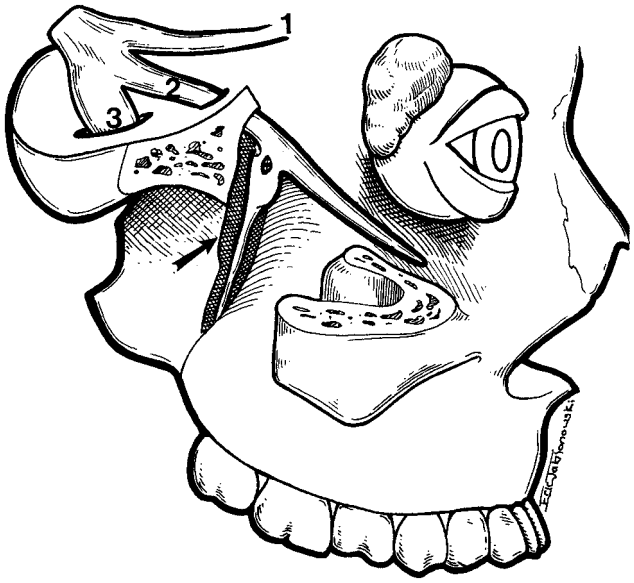

FIGURE 12-17 Branching of the trigeminal nerve. The trigeminal nerve forms three divisions in the region of Meckel's cave. The ophthalmic nerve (*1*) extends through the superior orbital fissure. The maxillary nerve (*2*) extends through the foramen rotundum into the pterygopalatine fossa (*arrow*). Here it branches into the infraorbital and palatine branches extending to the more superficial regions of the face and palate. The mandibular nerve (*3*) exits through the foramen ovale.

VIEW IMAGE

Copyright © 2003, Mosby, Inc. All rights reserved.

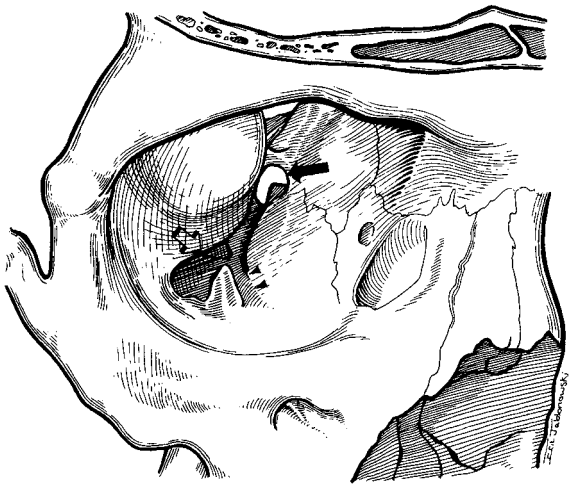

VIEW IMAGE

FIGURE 12-18 View of the foramen rotundum looking through the orbit. The foramen rotundum (*arrow*) barely can be seen poking up behind the inferior orbital fissure. The inferior orbital fissure (*open arrow*) extends between the orbital surface of the greater wing of the sphenoid and the orbit. The pterygopalatine fossa extends straight inferiorly from the point where the inferior orbital fissure appears to meet the foramen rotundum. The infraorbital canal (*arrowheads*) passes anteriorly from the inferior orbital fissure.

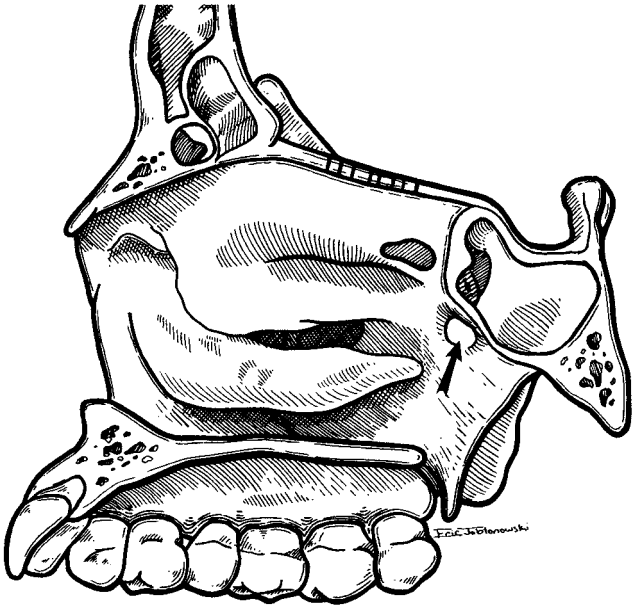

FIGURE 12-19 Medial view of the nasal cavity shows the position of the sphenopalatine foramen (*arrow*). Though covered by mucosa, this represents a passageway through the osseous structures between the posterior nasal cavity and the pterygopalatine fossa.

VIEW IMAGE

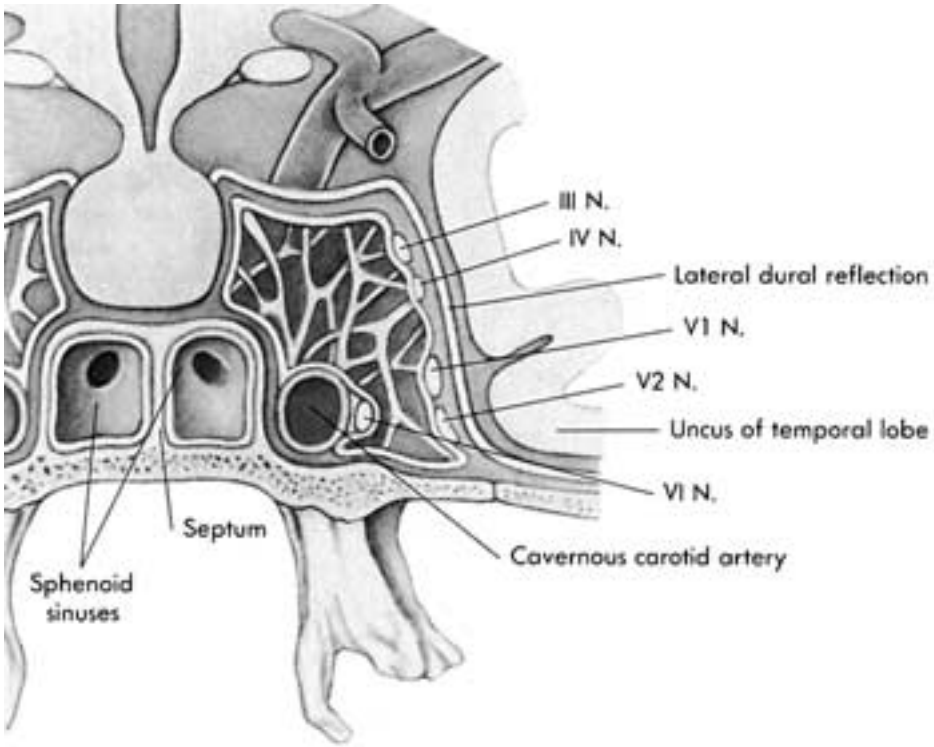

VIEW IMAGE

FIGURE 12-20 Coronal view of the cavernous sinus region.

Copyright © 2003, Mosby, Inc. All rights reserved.

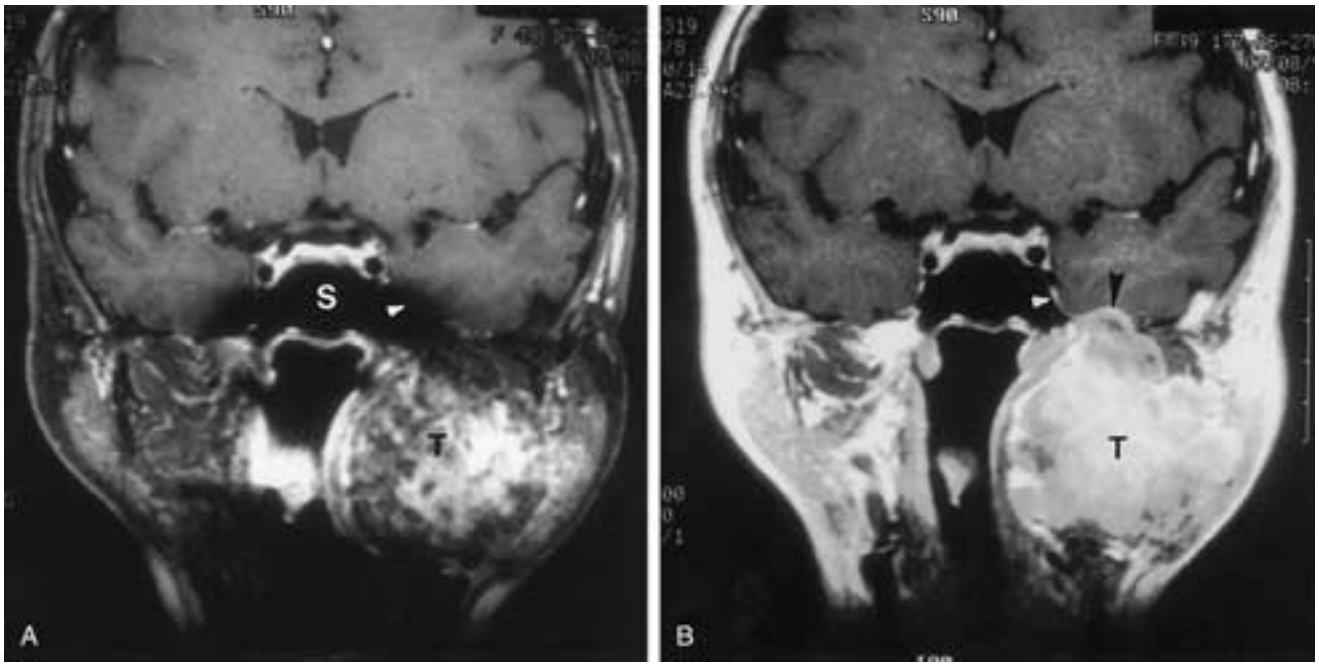

VIEW IMAGE

FIGURE 12-21 Very large benign tumor of the parotid gland extending through the floor of the middle cranial fossa. **A**, Coronal T1-weighted MR image with fat suppression after gadolinium administration. The tumor (*T*) can be readily visualized. The sphenoid sinus (*S*) is filled with air. The air causes ''blooming'' of the sinus laterally (*arrowhead*), obscuring the lower cavernous sinus in the region of the foramen ovale. This is due to the susceptibility effect. **B**, Without fat suppression, on a T1-weighted image after gadolinium administration, the lateral margin of the sphenoid sinus (*arrowhead*) is much better seen, as is the lower cavernous sinus. A small amount of tumor obscured with the previous image is well seen (*arrowhead*) protruding into the middle cranial fossa. *T*, Tumor.

Usually, high resolution (high matrix, low field of view) is included in the plane most likely to visualize a key structure.

In cases where a CSF leak is of concern or determination of the precise margin of the brain must be demonstrated relative to a defect in the skull base, either a high-resolution, T2-weighted sequence or a true inversion recovery sequence may be added.

NONNEOPLASTIC DISORDERS

Congenital and Developmental Anomalies

There are many normal variations in the sphenoid bone, most notably the degree of sinus pneumatization and the rate and final extent of replacement of red marrow by fatty yellow marrow. These variations were discussed previously under normal imaging appearance of the sphenoid bone.

Congenital or developmental abnormalities may represent either actual developmental problems of the sphenoid bone itself or reactions of the sphenoid bone to problems occurring elsewhere. For example, a cephalocele can occur through an actual deficiency in the sphenoid bone, whereas the distortion of the greater wing of the sphenoid that occurs in a patient with premature closure of the coronal suture represents an attempt of a normal sphenoid bone to compensate for an abnormality elsewhere. Although various dysplasias could be included in this section, they are discussed in this chapter and in Chapter 24.

Cephaloceles

A cephalocele is a protrusion of intracranial contents through a defect in the skull. The dura may be thinned or actually dehiscent. If the protrusion is composed of only the meninges and the subarachnoid space containing CSF, the term meningocele is used. If the sac also contains brain, the appropriate term is encephalocele. Though meningoceles can occur anywhere in the skull, most are found in the midline.

Cephaloceles occur sporadically, approximately once in 4000 births.[24] Most involve the cranial vault, with only about 20% of encephaloceles involving the anterior or central skull base. Of these, most are anterior in location (sincipital encephaloceles) and are considered to represent failures of neural tube fusion at the level of the anterior neuropore. A different mechanism must be postulated for those cephaloceles that pass through the region of the sphenoid.

Some authors have attributed the passage of encephaloceles through the sphenoid bone to persistence of the craniopharyngeal canal.[25] However, other authors question this concept, indicating that the adenohypophysis ascends too early, well before there is significant organization of the developing basicranium.[26] These authors have attributed the small canal occasionally identified traversing the sphenoid, between its pharyngeal surface and the pituitary fossa, to small blood vessels present in the embryo.

A second proposed theory is that these basal cephaloceles are herniations through defects related to problems with

Copyright © 2003, Mosby, Inc. All rights reserved.

fusion of the many ossification centers participating in formation of the skull base. These authors indicate that the route taken by most of these encephaloceles through the sphenoid bone conforms most closely to the synchondrosis between the presphenoid and postsphenoid ossification centers. This course passes from the region of either the tuberculum sella or the anterior wall of the sella, anteriorly and inferiorly toward the pharynx (Fig. 12-13). This theory also explains the occurrence of lateral basal encephaloceles that pass between the nonunited ossification centers of the postsphenoid and alisphenoid, precursors of the body and greater sphenoid wing, respectively.[27] Some encephaloceles appear to pass directly through the more lateral greater wing of the sphenoid.[28] This structure is formed by membranous bone, and perhaps in these cases a defect in formation of the bone itself can be implicated. This type of defect is seen in neurofibromatosis but can occur as an isolated abnormality as well.

The outer covering of the cephalocele is determined by the tissues found adjacent to the defect.[29] This may be a derivative of skin or mucous membrane, depending on the location. Most of the basal encephaloceles pass into the nose or nasopharynx and are covered by mucosa. By comparison, those cephaloceles that pass laterally into the infratemporal fossa have a fibrous wall derived from the dura and from the myofascial elements found in that location. Basal encephaloceles have been categorized depending on their point of passage through the skull base and on their final destination.[25, 28, 30] One system includes the following types: (1) transethmoidal, (2) sphenoethmoidal, (3) sphenorbital, (4) transsphenoidal, and (5) sphenomaxillary. Perhaps it is easiest to group the abnormalities into midline basal and lateral basal encephaloceles.

The transsphenoidal, sphenoethmoidal, and transethmoidal varieties occur in the midline (Figs. 12-22 and 12-23). The sphenoethmoidal passes through the sphenoethmoid area into the posterior nasal cavity or anterior nasopharynx. If the abnormality extends into the sphenoid sinus but does not perforate the floor to reach the nasopharynx, the term transsphenoidal is used. As the name suggests, transethmoidal encephaloceles are more anterior in location, passing through the anterior ethmoid and cribriform plate into the more anterior sinonasal system. Another term that may be encountered is sphenopharyngeal encephalocele. This type extends through the sphenoethmoid region into the nasopharynx and can be included in the sphenoethmoid group.

Lateral basal encephaloceles include the sphenorbital and sphenomaxillary types. The sphenorbital encephalocele passes through the region of the superior orbital fissure into the orbit, causing proptosis, often pulsatile proptosis. This type is commonly associated with neurofibromatosis and is considered to be an expression of the mesodermal component of this disease (Fig. 12-24) because the greater wing and often the lesser wing of the sphenoid do not develop normally and have defective ossification.[31] This gives the characteristic plain film appearance of a bare or empty orbit (Fig. 12-25).

The sphenomaxillary encephalocele is extremely rare, and few documented examples exist (Fig. 12-26).[27, 32–35] These lesions may squeeze into the pterygopalatine fossa and then pass laterally into the infratemporal fossa, presenting as a mass in the cheek. The more lateral transalar encephaloceles do not fit well into either the sphenomaxillary or sphenorbital groups, but they certainly could be included in the category of lateral basal encephalocele.

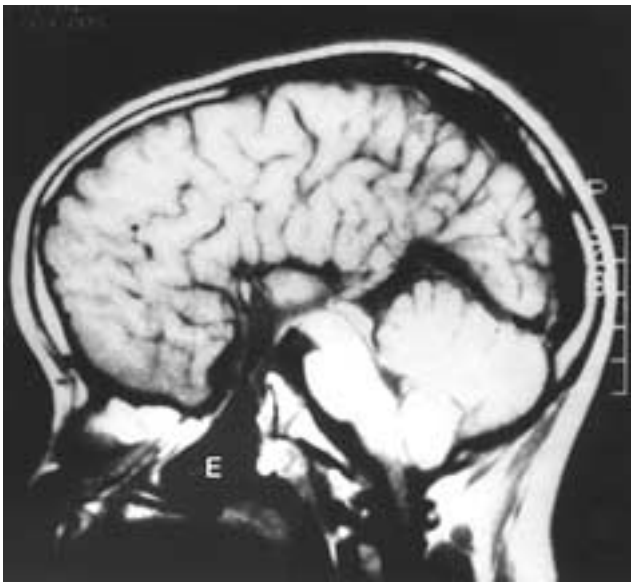

FIGURE 12-22 Sphenoethmoidal encephalocele. Sagittal T1-weighted MR image shows the encephalocele (*E*) extending into the nasal cavity, resting on the hard palate. The connection can be followed through the anterior sella and anterior sphenoid. This would be the approximate position of the fusion line of pre- and postsphenoids. The cystic abnormality did contain brain tissue along the wall and therefore qualifies as an encephalocele.

VIEW IMAGE

Patients with basal encephaloceles frequently have other anomalies. Most involve the midface. Hypertelorism is common, particularly with the more anterior varieties of encephaloceles. Cleft lip and cleft palate are also frequently associated findings, as is agenesis of the corpus callosum.[36]

The clinical presentation of cephaloceles varies; a submucosal mass in the nasal cavity or nasopharynx may present with airway obstruction, CSF leaks or recurrent meningitis may result from the weakened barrier between the sinonasal tract and the intracranial contents, and symptoms relating to involved central nervous system components can also be found. Herniations of the optic pathways, hypothalamus, or portions of the frontal lobes occur with midline defects. When the temporal lobe protrudes into the defect, the patient may present with seizures.

When imaging cephaloceles, the bony defect is better seen on CT than MR imaging. Usually there is a smooth cortical margin surrounding the tract, and the soft-tissue mass is identified passing into the extracranial region. Three-dimensional reformatted images can be used to show the relationship of the defect to the remaining basicranium.

Although MR imaging does not show the bony anatomy quite as well as CT, it better characterizes the contents of the herniated soft tissues and any related intracranial abnormalities.

Altered Ossification

If the presphenoid ossification extends further dorsally than normal, the postsphenoid ossification bone is corre-

Copyright © 2003, Mosby, Inc. All rights reserved.

spondingly shorter than normal. This results in the limbus, chiasmatic sulcus, and tuberculum being vertically oriented, elongating the anterior wall of the sella turcica. The resulting sella configuration is J-shaped, and this type of altered ossification occurs in such conditions as Turner's syndrome, achondroplasia, and the mucopolysaccharidoses. This represents a developmental J-shaped sella rather than one that occurs due to erosion of the dorsum sellae by a hypothalamic mass.

Vascular Variants

There are many minor variations of the arterial and venous vessels in and around the central skull base. Many represent normal variations of origin or course. The course of the carotid artery in the region of the cavernous sinus is quite constant; however, the artery can curve more medially than normal, pushing into the sphenoid sinus. The lateral sinus wall bone covering the medial aspect of the artery can be dehiscent, putting the vessel at risk during surgical procedures involving the sphenoid sinus (Fig. 12-27). Even when the artery is in a normal position, the bone separating the carotid artery from the sphenoid sinus may be quite thin. If a septation of the sphenoid sinus curves to attach to this thin bone, there is concern that manipulation of the septation may fracture the bony wall, injuring the vessel.

The persistent trigeminal artery is a large arterial variant that represents an abnormal persistent communication between the carotid artery and the basilar circulation (Figs. 12-28 and 12-29). This vessel is seen easily on arteriography and may be large enough to be visualized on CT or MR imaging. The vessel passes from the proximal cavernous carotid artery posteriorly to connect with the basilar artery.

The effect of the variations of venous passages through the skull base is thought to account for at least some of the

FIGURE 12-23 An 8-year-old child presenting with recurrent bouts of meningitis. Basal encephalocele (transsphenoid). Whether this passes through the synchondrosis or through a persistent cranial pharyngeal canal is controversial. **A**, Plain film of the skull, submental vertex view. A well-defined lucency surrounded by a thin rim of cortical bone is projected over the skull base (*arrows*). **B**, Coronal noncontrast CT scan through the central skull base shows the defect (*arrow*) in the sphenoid bone. **C**, Coronal T1-weighted image through the central skull base demonstrates herniation of the pituitary gland (*asterisk*) into the defect. Note the proximity of the pituitary gland to the roof of the nasopharynx. (Courtesy Dr. Das Narla.)

VIEW IMAGE

Copyright © 2003, Mosby, Inc. All rights reserved.

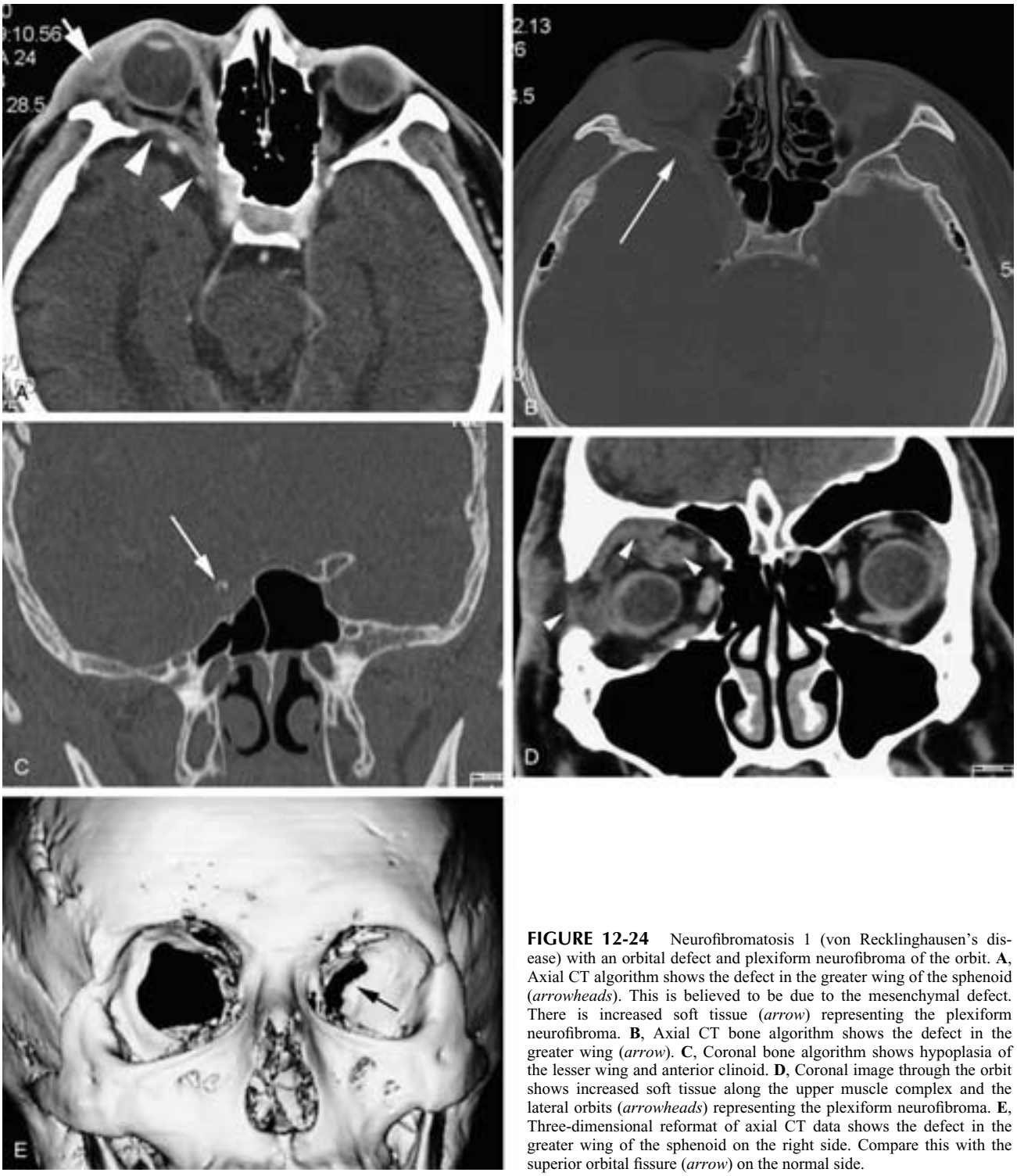

FIGURE 12-24 Neurofibromatosis 1 (von Recklinghausen's disease) with an orbital defect and plexiform neurofibroma of the orbit. **A**, Axial CT algorithm shows the defect in the greater wing of the sphenoid (*arrowheads*). This is believed to be due to the mesenchymal defect. There is increased soft tissue (*arrow*) representing the plexiform neurofibroma. **B**, Axial CT bone algorithm shows the defect in the greater wing (*arrow*). **C**, Coronal bone algorithm shows hypoplasia of the lesser wing and anterior clinoid. **D**, Coronal image through the orbit shows increased soft tissue along the upper muscle complex and the lateral orbits (*arrowheads*) representing the plexiform neurofibroma. **E**, Three-dimensional reformat of axial CT data shows the defect in the greater wing of the sphenoid on the right side. Compare this with the superior orbital fissure (*arrow*) on the normal side.

VIEW IMAGE

channels and foramina seen in the region of the foramen ovale. The best known of these variable channels is the foramen of Vesalius just anterior and medial to the foramen ovale. Ginsberg et al. used the term lateral rotundal canal to describe a channel passing vertically just lateral to the foramen rotundum.[12] They are thought to be channels connecting the cavernous sinus with the pterygoid plexus.

Developmental Changes Caused by Extrinsic Factors

The skull base develops in a complex environment, and the growth patterns of the sphenoid bone are modified by abnormalities occurring in the adjacent region. Craniosynostosis, or premature closure of a suture, prevents normal growth of a particular segment of the skull. The remaining

Copyright © 2003, Mosby, Inc. All rights reserved.

bones of the skull also become distorted as they attempt to make room for the growing brain (Fig. 12-30). The skull base has a limited ability to respond in these situations, but some characteristic changes are seen. Thus, coronal synostosis limits the ability of the calvarium to add to its length, yielding a brachiocephalic skull that is foreshortened from front to back and may be larger than normal in its vertical dimension. The greater wing of the sphenoid bone displaces anteriorly, as does the petrous bone, and the orbit is pushed forward and is somewhat shortened. These changes can occur on one or both sides, depending on the extent of sutural involvement.

Abnormalities in the contiguous soft tissues and CSF spaces also can have an effect on the shape, thickness, and position of the sphenoid bone. Primary or congenital arachnoid cysts are abnormal arachnoid or collagen-lined cavities that characteristically do not communicate with the ventricular system. They account for 1% of intracranial space-occupying lesions and usually appear in the first five decades of life.[37, 38] Men are more commonly affected than women. Although these abnormalities abut the skull base, they are developmental abnormalities of the subarachnoid space rather than of the skull base itself. In the early embryo there are no subarachnoid spaces around the brain. The forming brain is surrounded by loose mesenchyme, and all CSF is contained within the ventricles. It is hypothesized that as pulsations of the CSF force fluid into the subarachnoid space during normal development, some of the CSF becomes trapped between the developing pia and the arachnoid.[39] These cysts can occur in many locations; the middle cranial fossa is a frequent site. The cysts can expand progressively during antenatal development. The exact mechanism of this enlargement is unknown, although many theories have been proposed.[39] At imaging, the wings of the sphenoid can be remodeled. The greater wing is frequently thinned and pushed forward, and the lesser wing may be elevated. The cyst itself has a characteristic appearance on the imaging following the appearance of CSF on either CT or MR imaging. These cysts are dark (no restricted diffusion) on diffusion-weighted imaging, helping to differentiate them from an epidermoid in questionable cases.

Another congenital abnormality that has a secondary effect on the skull base is the Arnold-Chiari malformation. The inferiorly displaced brainstem can appear to cause a pressure effect on the clivus, giving it a scalloped, more vertical appearance. This is an incidental finding because the changes in the brain itself are far more obvious.

VIEW IMAGE

FIGURE 12-25 Neurofibromatosis with congenital defect of the sphenoid. The lesser wing of the sphenoid (*large black arrowhead*) and the superior orbital fissure (*small black arrowhead*) can be identified on the normal side. These two structures are not visualized on the abnormal side because of the maldevelopment of the lesser and greater wings of the sphenoid.

Cartilage Dysplasias

Because most of the sphenoid bone develops from cartilaginous precursors, various cartilage dysplasias will have an effect on the growth of the sphenoid bone. These are discussed later in this chapter.

Inflammation and Obstruction

A variety of inflammatory processes can involve the central skull base. Chief among them is sphenoid sinus infection. Infection can spread to the bone and to the cavernous sinus, causing cavernous sinus thrombosis.

Inflammatory changes in the sphenoid sinus have the same imaging appearance as sinusitis in other sinuses (Fig. 12-31) (see Chapter 5). Mucosal thickening and fluid can be identified, and chronic sinusitis can lead to sclerosis of the bony walls (Fig. 12-32). Fungal infections can invade the wall, reaching the cavernous sinus (Figs. 12-32 and 12-33), and thrombosis of the carotid artery and cavernous sinus can occur. Thrombosis can be identified on imaging as filling defects replacing the normal enhancement of the cavernous sinus (Fig. 12-34).[40] Venous channels leading to and from the cavernous sinus may be thrombosed. The inflammatory tissue does enhance and may blend with the enhancing sinus mucosa on CT. The cavernous sinus may bulge laterally, and the dura may enhance. Eventually, narrowing of the carotid artery can be seen within the sinus.

Necrotizing (malignant) otitis is an invasive pseudomonal infection that occurs almost exclusively in elderly diabetics and starts in the external auditory canal.[41–44] The infection can then spread across the soft tissues beneath the skull base and can even cross the midline. Invasion of the petroclival fissure or the central basicranium can occur in

Copyright © 2003, Mosby, Inc. All rights reserved.

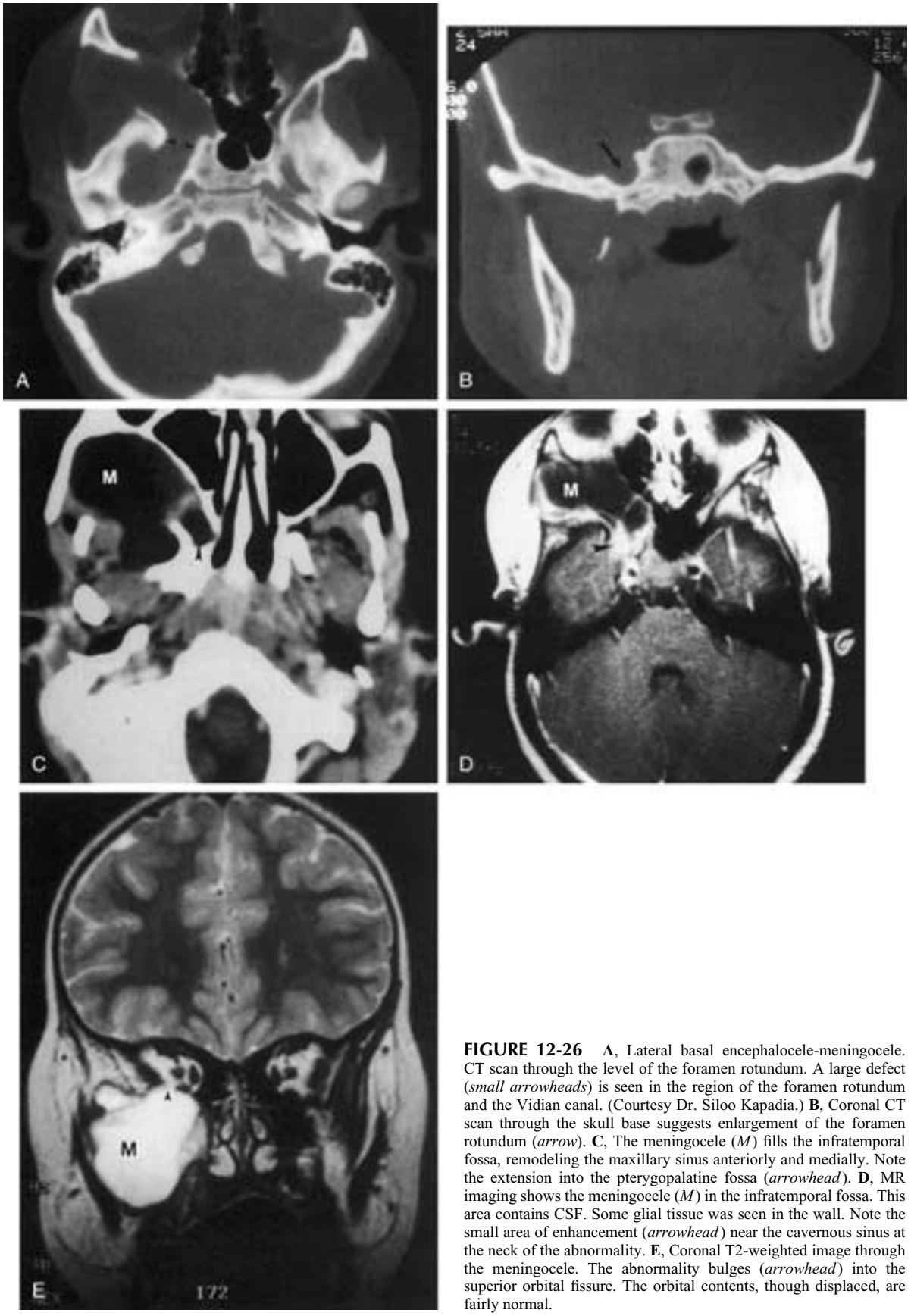

FIGURE 12-26 **A**, Lateral basal encephalocele-meningocele. CT scan through the level of the foramen rotundum. A large defect (*small arrowheads*) is seen in the region of the foramen rotundum and the Vidian canal. (Courtesy Dr. Siloo Kapadia.) **B**, Coronal CT scan through the skull base suggests enlargement of the foramen rotundum (*arrow*). **C**, The meningocele (*M*) fills the infratemporal fossa, remodeling the maxillary sinus anteriorly and medially. Note the extension into the pterygopalatine fossa (*arrowhead*). **D**, MR imaging shows the meningocele (*M*) in the infratemporal fossa. This area contains CSF. Some glial tissue was seen in the wall. Note the small area of enhancement (*arrowhead*) near the cavernous sinus at the neck of the abnormality. **E**, Coronal T2-weighted image through the meningocele. The abnormality bulges (*arrowhead*) into the superior orbital fissure. The orbital contents, though displaced, are fairly normal.

VIEW IMAGE

Copyright © 2003, Mosby, Inc. All rights reserved.

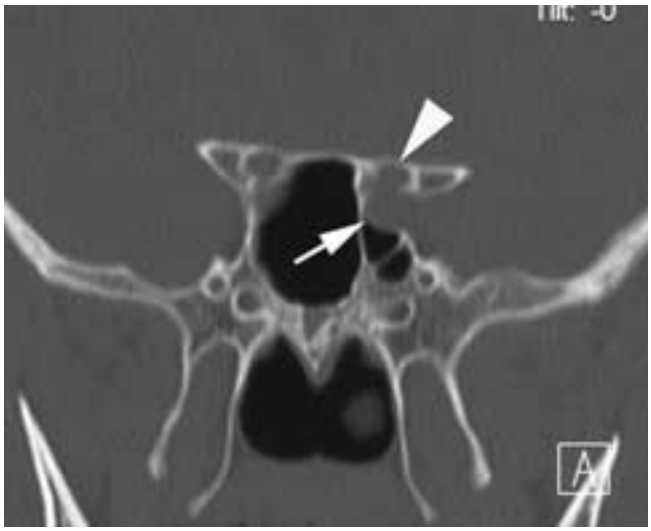

VIEW IMAGE

FIGURE 12-27 Medially positioned carotid artery impressing into the sphenoid sinus. The carotid artery (*arrow*) bulges into the sphenoid sinus. The bony plate separating the artery from the sinus may be thin or dehiscent. Optic canal (*arrowhead*).

later stages, and MR imaging can show obliteration of the clival fat.[45–47]

The Tolosa-Hunt syndrome is a presumed idiopathic inflammatory condition involving the orbital apex, superior orbital fissure, and cavernous sinus. This is discussed in Chapter 9.

Obstruction of the sphenoid sinus can result from the sequelae of inflammatory disease or rarely from tumor. Early in the process, the obstructed sinus secretions have a low (10 to 25 HU) CT attenuation. If the secretions become desiccated, their attenuation increases. *Aspergillus* colonization of the obstructed sinus cavity may add to the density as well. Eventually, the sinus may become very dense, mimicking the appearance of enhancement on nonenhanced scans. On MR imaging the signal intensities vary with the protein concentration of the obstructed secretions (Fig. 12-35).[48–50] With extreme desiccation, particularly when combined with *Aspergillus* colonization, the appearance may be ''black'' on all sequences. This topic is discussed in Chapter 5.

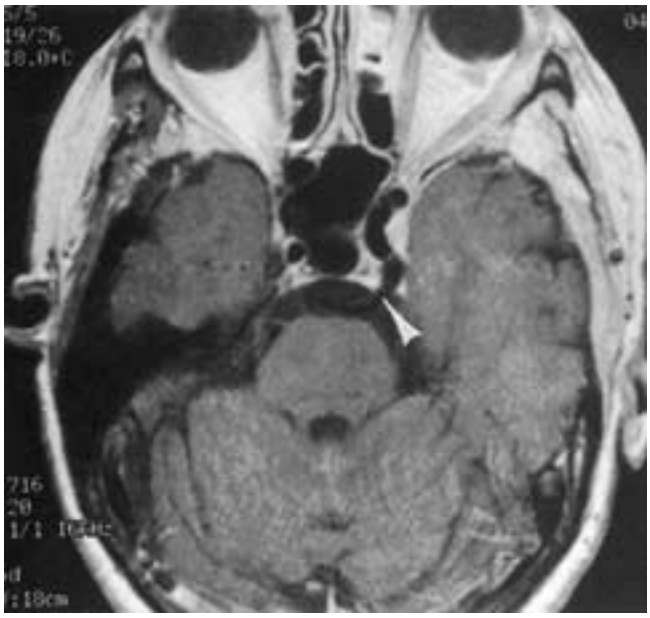

VIEW IMAGE

FIGURE 12-29 Persistent trigeminal artery. The postcontrast T1-weighted MR image shows the flow void connecting the intracavernous carotid artery with the basilar artery. *Arrowhead*, trigeminal artery.

A mucocele is the final result of sinus obstruction, with the pressures within the sinus eventually remodeling the bone outward. Sphenoid sinus mucoceles are discussed in the next section.

TUMORS AND TUMOR-LIKE CONDITIONS

Tumors can arise from the skull base itself or from any of the tissues adjacent to or passing through it.[51–54] The

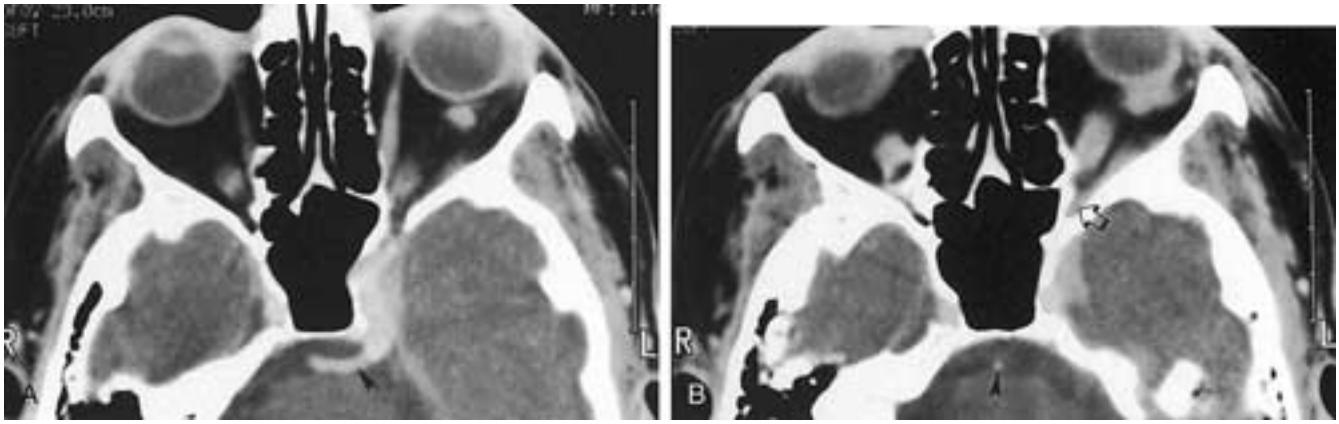

VIEW IMAGE

FIGURE 12-28 **A**, Persistent trigeminal artery shows the embryonic connection (*arrowhead*) between the carotid artery in the cavernous sinus and the basilar artery. **B**, Lower scan shows a very small basilar artery (*arrowhead*). Also note the obscuration of the fat at the junction of the upper pterygopalatine fossa and inferior orbital fissure (*open arrow*). This is a patient with perineural tumor extension along the branches of the trigeminal nerve. Adenoid cystic carcinoma.

Copyright © 2003, Mosby, Inc. All rights reserved.

VIEW IMAGE

FIGURE 12-30 Bilateral coronal synostosis. Axial CT scan through the skull base in a 2-year-old child shows the changes typical of coronal synostosis, including bilateral calvarial bulging of the region of the sphenozygomatic suture and fullness of both middle cranial fossae.

VIEW IMAGE

FIGURE 12-31 Sphenoid sinusitis and T1-weighted image after gadolinium administration. The patient has an air-fluid level in the sphenoid. *F*, Fluid; *open arrow*, enhancing mucosa.

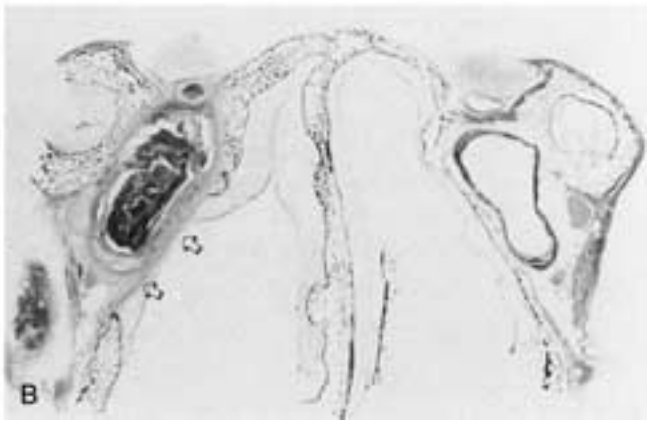

VIEW IMAGE

FIGURE 12-32 **A**, Chronic sphenoid sinusitis with fungus (*Aspergillus*) extending into the cavernous sinus. The sclerotic change (*black arrowheads*) along the margin of the sphenoid sinus indicates chronicity. Note the defect (*open arrow*) in the upper lateral cortex of the sphenoid sinus. The calcification just lateral to this point of erosion represents a calcification in the carotid artery. **B**, Autopsy section shows the bony defect (*open arrows*) between the cavernous sinus and the sphenoid sinus. Note the thrombosis in the carotid artery. (Courtesy of Dr. Berrylin J. Ferguson.)

Copyright © 2003, Mosby, Inc. All rights reserved.

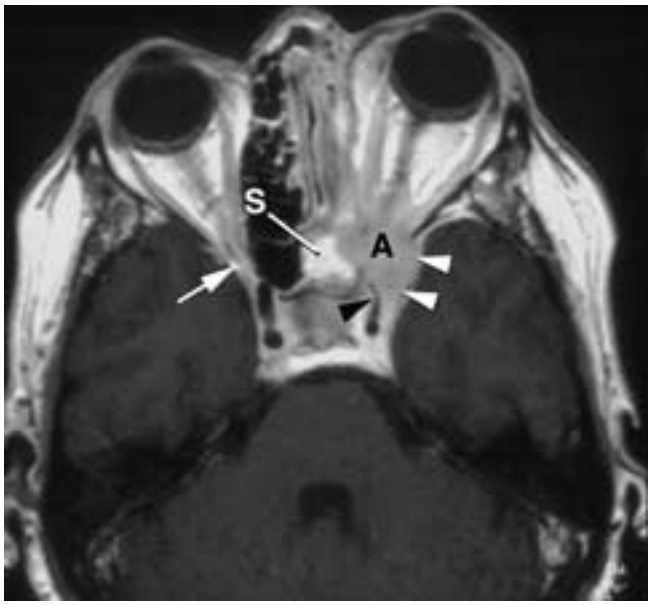

FIGURE 12-33 *Aspergillus* of the sphenoid sinus extending into the orbital apex and cavernous sinus. Axial postcontrast T1-weighted image shows the *Aspergillus* (*A*) with moderate enhancement. The lesion was intermediate to slightly dark on T2-weighted images. There is expansion of the anterior cavernous sinus (*white arrowheads*), with narrowing of the carotid artery (*black arrowhead*). There are retained secretions in the more medial sphenoid sinus (*S*). Note how the bright fat protruding through the superior orbital fissure is obliterated on the left side. Compare this to the normal fat on the right side (*white arrow*).

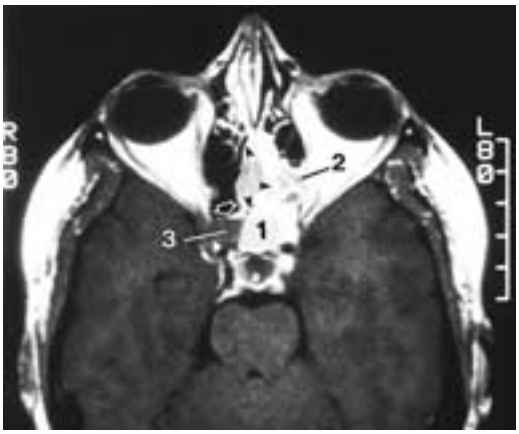

FIGURE 12-35 Esthesioneuroblastoma. The small tumor shows intermediate enhancement and causes the region of the nasal septum to bulge in all directions (*small black arrowheads*). The sinuses show various signal intensities reflecting various protein concentrations. The bright signal in the left sphenoid (*1*) could be due to a fairly high protein concentration or to hemorrhage. The intermediate signal intensity in the posterior left ethmoid (*2*) shows a lower protein concentration than in the left sphenoid. The low signal in the right sphenoid (*3*) is typical of relatively recent obstruction with high water and low protein concentrations. The enhancement of the mucosal margin (*open arrow*) also helps differentiate the obstructed sinus from the tumor.

apparent site of origin of a primary tumor is a helpful indicator of the lesion's histology, and subtle differences in location can cause the radiologist to favor one diagnosis over another.

Tumors develop according to the tissues present in a particular region. Hence, based on the anatomy, the skull base can be organized into three general regions (Fig. 12-36). In the midline, the sphenoid is a block of bone perforated by a sinus and covered by dura. Two important embryologic structures, the notochord and Rathke's pouch, pass through this part of the bone. Any of these tissues can contribute to pathology. Hence, in the midline, there can be chordomas (notochord), meningiomas, bone and sinus tumors, and rare lesions related to Rathke's pouch remnants.

Just off the midline in the sagittal plane of the fissures and formina, one still finds meningeal lesions. The lateral recess of the sphenoid sinus can extend into this area, so that pathology related to the sinus as well as rare bone lesions

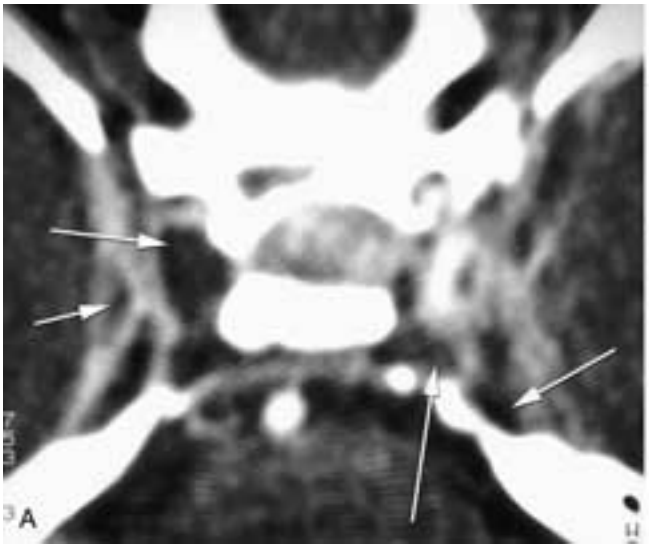

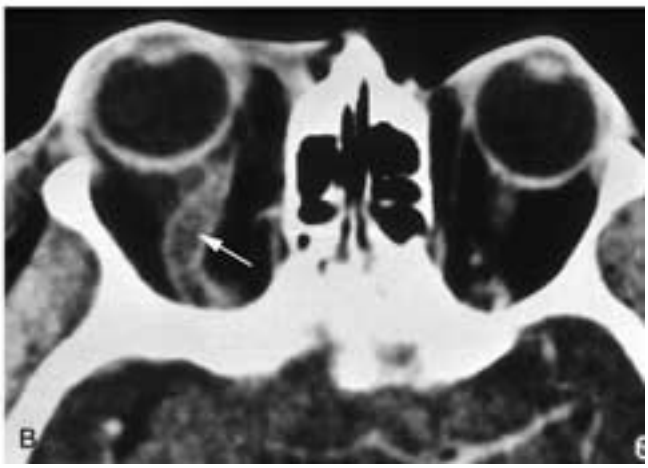

FIGURE 12-34 Thrombosis of the cavernous sinus. Postcontrast axial CT scan. **A**, There are filling defects (*arrows*) in places normally opacified in the cavernous sinus. **B**, There is a defect (*arrow*) filling the superior ophthalmic vein. (Courtesy of Bernard Schuknecht, Zurich.)

Copyright © 2003, Mosby, Inc. All rights reserved.

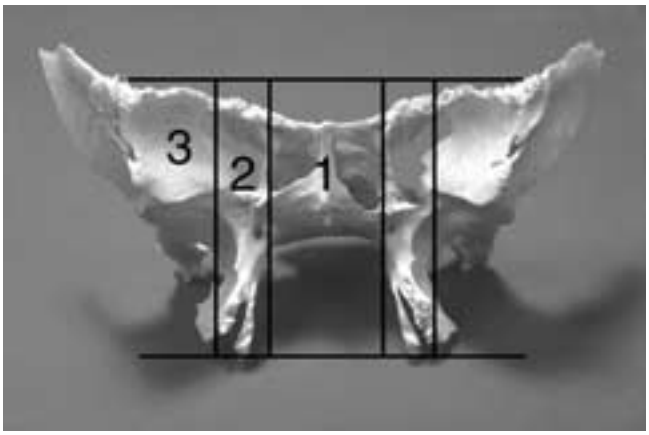

VIEW IMAGE

FIGURE 12-36 The sphenoid bone can be divided into three basic regions. In zone 1, the central sphenoid, lesions are predominantly related to bone, dura, sella, or the sphenoid sinus. Lesions arising in zone 2 may arise from dura but also arise from nerves and vessels. The lesions in zone 3 are usually related to the bone or dura. Metastases and meningiomas are common here.

can present here. Chondroid lesions are common here because the foramen lacerum and petrooccipital fissure contain cartilage. The various foramina carry nerves and vessels, so that nerve sheath tumors and aneurysms can arise here. Further laterally in the greater wing of the sphenoid, there are no fissures and foramina. This region is simply a bone covered by dura, and the lesions arising here reflect this simplicity. Most lesions are meningiomas or bone-related tumors. In this region, osseous metastases are also common. Certainly there is overlap in the anatomy and in the resultant pathology that occurs in these areas. However, analysis based on these general regions of the bone can be a helpful beginning to diagnosis.

Chordomas

Chordomas are malignant neoplasms arising from remnants of the embryonic notochord. More than one-third of these tumors arise in the skull base.[55–57] The terminus of the notochord is in the sphenoid bone just inferior to the sella turcica and the dorsum sella, and thus the skull base chordomas arise in the region of the clivus. Thirty-five percent of chordomas occur in the skull base compared with 50% in the sacrococcygeal region and 15% in the spine.[58]

Histologically, the lesion has a characteristic cell, the physaliphorous cell, with large vacuoles containing mucin and glycogen and with a ''bubbly'' appearance of the cytoplasm (Fig. 12-37).[58, 59] The cells tend to clump

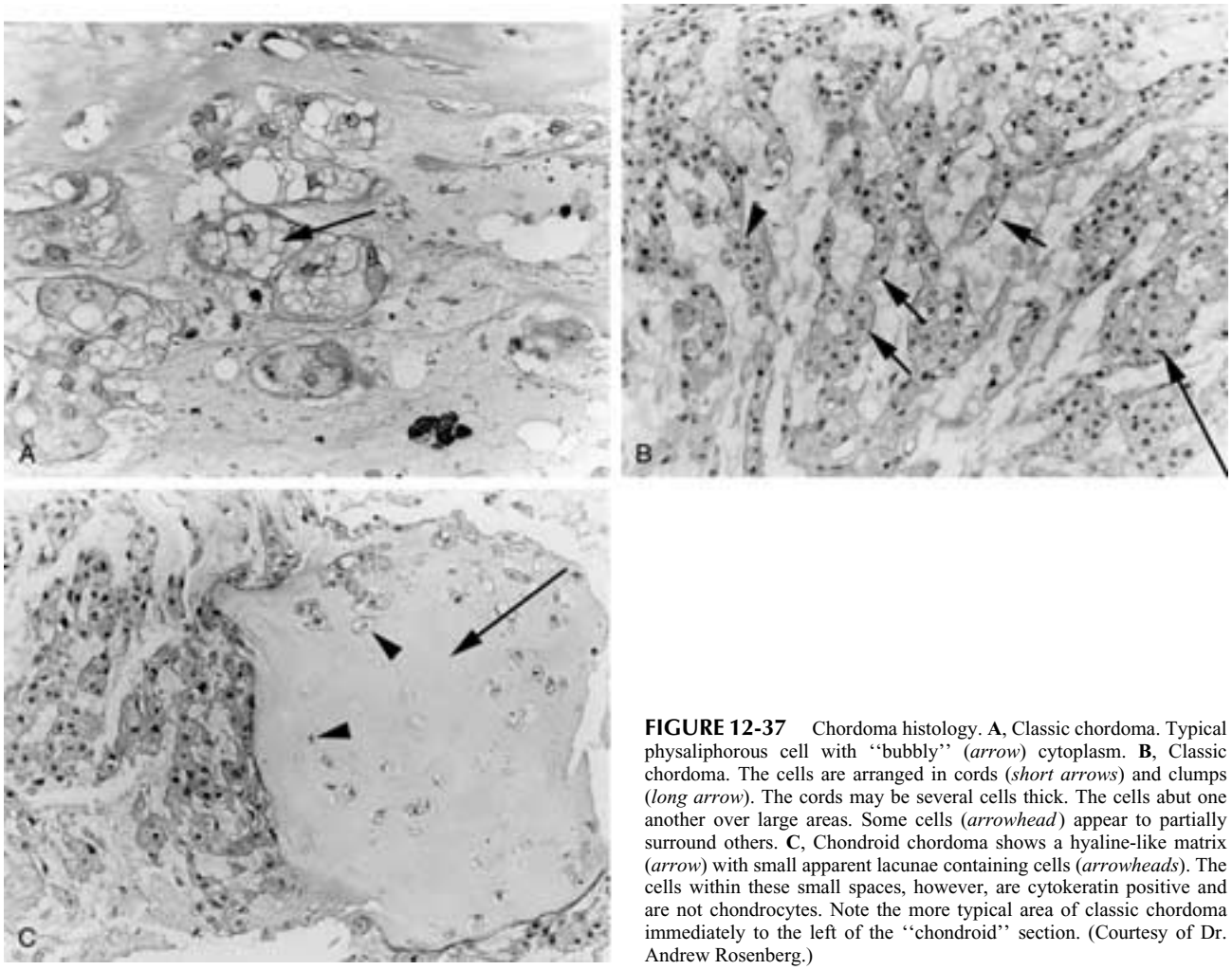

VIEW IMAGE

FIGURE 12-37 Chordoma histology. **A**, Classic chordoma. Typical physaliphorous cell with ''bubbly'' (*arrow*) cytoplasm. **B**, Classic chordoma. The cells are arranged in cords (*short arrows*) and clumps (*long arrow*). The cords may be several cells thick. The cells abut one another over large areas. Some cells (*arrowhead*) appear to partially surround others. **C**, Chondroid chordoma shows a hyaline-like matrix (*arrow*) with small apparent lacunae containing cells (*arrowheads*). The cells within these small spaces, however, are cytokeratin positive and are not chondrocytes. Note the more typical area of classic chordoma immediately to the left of the ''chondroid'' section. (Courtesy of Dr. Andrew Rosenberg.)

Copyright © 2003, Mosby, Inc. All rights reserved.

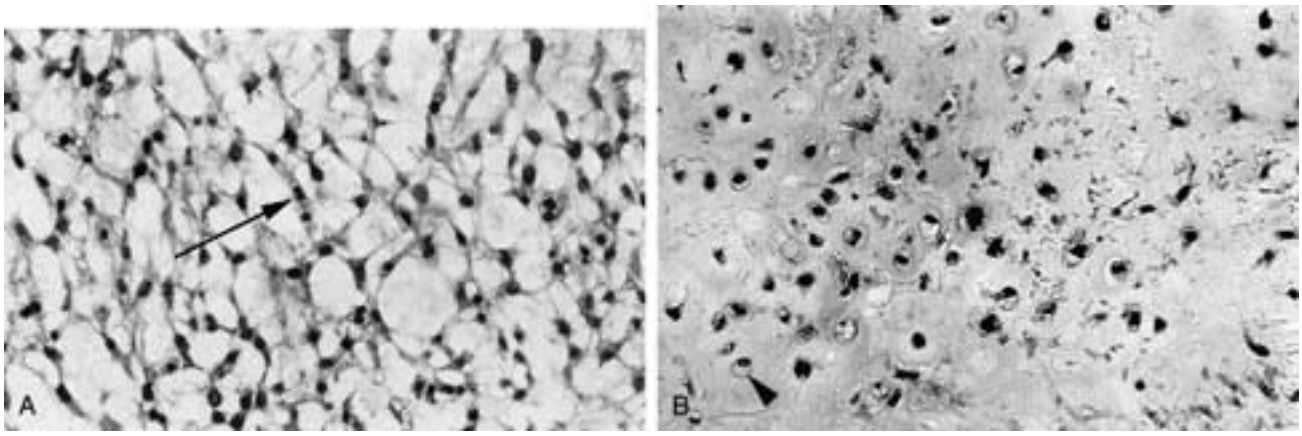

VIEW IMAGE

FIGURE 12-38 Chondrosarcoma histopathology. **A**, Myxoid chondrosarcoma. The cells (*arrow*) are true chondrocytes. They are negative for various epithelial markers including cytokeratin. Note how the cells abut one another end to end but do not form true cords. There are only small areas of contact between ends of cells. The cells are within a myxoid matrix. **B**, Hyaline-type chondrosarcoma. The cells are found within true hyalin matrix. The cells (*arrowheads*) are within small lacunae. These cells do not stain for various epithelial markers and are true chondrocytes. (Courtesy of Dr. Andrew Rosenberg.)

together into nests or chords (Fig. 12-37B), and adjacent cells have large segments of contact, at times partially wrapping around one another. The myxoid matrix surrounding the cells gives the tumor a gray, translucent appearance at gross examination. Small dystrophic calcifications and hemorrhages can also be seen.

A variant of chordoma has been described based on the histologic appearance (Fig. 12-37C), as regions within this variant resemble the hyaline type of chondrosarcoma (Fig. 12-38). This lesion was referred to as a ''chondroid chordoma'' by Heffelfinger et al. in 1973.[58] Small cells resembling chondrocytes are found in a matrix that resembles the hyaline matrix of the hyaline type of chondrosarcoma (see below). This tumor was thought to be a chordoma with cartilaginous differentiation. The variations in the designation received significant attention in the literature because of perceived differences in prognosis between classic chordoma and chondroid chordoma. However, immunohistochemical techniques have indicated that neither the cell nor the matrix of the ''chondroid'' portion of this variant is of true chondroid derivation. The cells in these regions stain positive for cytokeratin and for other epithelial markers such as epithelial membrane antigen and carcinoembryonic antigen. Such epithelial markers, particularly cytokeratin, are almost always negative in a true chondroid lesion but are positive in cells of classic chordoma and in notochordal tissue.[59] The term ''chondroid'' in chondroid chordoma, therefore, refers only to a histologic mimic. The lesion does not contain true cartilage or tissue of cartilage origin and thus is not a dimorphic tumor. Notably, both the original descriptions by Heffelfinger et al. and the cases labeled immunohistochemically as ''chondroid'' chordomas more recently by Rosenberg et al. contained not only regions of ''pseudocartilage,'' but also areas of the typical classic chordoma.[58, 59] The controversy regarding separation of chordoma and chondrosarcoma is further described later in this chapter under ''Chondrosarcoma.''

A final type of chordoma is the dedifferentiated chordoma. This type usually arises in the sacrococcygeal region rather than in the skull base. The dedifferentiated component is usually malignant fibrous histiocytoma or occasionally osteosarcoma. These tend to be very aggressive tumors with a poor prognosis.

Skull base chordomas arise within the basiocciput basisphenoid. Rarely, a chordoma can arise in the nasopharynx or can be completely intracranial in location. These locations are explained by the tortuous course of the notochord. Though most of the pathway of the notochord is within the osseous basicranium, short segments of the course transiently pass out of the bone into the soft tissue of the nasopharynx and into the posterior fossa. The passage of the notochord into the posterior fossa also explains a normal variant found in the dura or subarachnoid space of the midline posterior fossa at the level of the pons. A small amount of notochordal tissue occasionally can be present and is referred to as ecchordosis physaliphora. This tissue is also positive for cytokeratin and other epithelial immunohistochemical markers. Though usually small, this benign tissue occasionally can be fairly large. The descent of the notochord into the nasopharynx is believed to be related to the development of the pharyngeal bursa and therefore Thornwaldt's cyst. This is discussed in Chapter 28.

Chordomas can occur at any age, but in the craniovertebral area most cases are diagnosed between the ages of 30 and 50 years. This contrasts with the sacrococcygeal chordomas, which have a peak incidence in the 40- to 60-year age group. Men are more commonly affected than women. There have been cases reported of apparent familial lineage of chordoma.[60, 61] Cytogenetic analysis has been done in a few cases, with variable results.[60–62]

Common presenting symptoms of craniovertebral chordomas include orbitofrontal headaches and visual disturbances. The headache may result from involvement or stretching of the dura. Visual problems or ophthalmoplegia can result when the optic nerves and neural contents of the cavernous sinus are involved. Tumors can involve the trigeminal nerve and eventually can affect cranial nerves VII and VIII as the lesion approaches the internal auditory canal.

Copyright © 2003, Mosby, Inc. All rights reserved.

More inferiorly, cranial nerves IX through XII can be affected. Tumors can also cause symptoms by growing into the pituitary gland or by pushing the brainstem. Lesions extending into the nasopharynx can cause problems with breathing.

On CT, the chordoma is usually a midline clival lesion with both bone destruction and a soft-tissue mass. The margin between the tumor and normal bone is not sclerotic.[63] Radiodensities are frequently present and tend to be fairly large (Fig. 12-39). These densities are not calcifications and are thought to represent remaining fragments of the destroyed bone rather than new matrix formation.[64] Specifically, these tumors do not tend to show the small, calcified ringlets that may be present in chondrosarcomas. The expanding tumor may cross the petrooccipital fissure to reach the petrous bone or may extend intracranially, pushing the pons and brainstem posteriorly. Those rare tumors that occur outside of the bone, either intracranially or in the soft tissues of the nasopharynx, may or may not erode bone. At least part of the soft-tissue component of the tumor will enhance after intravenous contrast, but frequently there are regions that do not enhance and remain of relatively low density (Fig. 12-39). Cystic areas commonly are seen within the tumor.

The MR imaging appearance is quite variable. Usually there is a hypointense to isointense soft-tissue mass on

FIGURE 12-39 **A**, Chordoma. T1-weighted image without gadolinium administration. The tumor (*T*) is fairly homogeneous in the area of the lower basiocciput. The carotid (*arrowhead*) beneath the skull base is deviated laterally by the tumor. The nasopharynx, including the mucosa, is pushed forward. **B**, Axial T2-weighted image shows the high signal of the chordoma. **C**, CT scan done after intravenous contrast administration shows areas of low density (*arrow*) and fairly large ''calcifications'' representing residual bone from the destruction of the lower clivus.

VIEW IMAGE

Copyright © 2003, Mosby, Inc. All rights reserved.

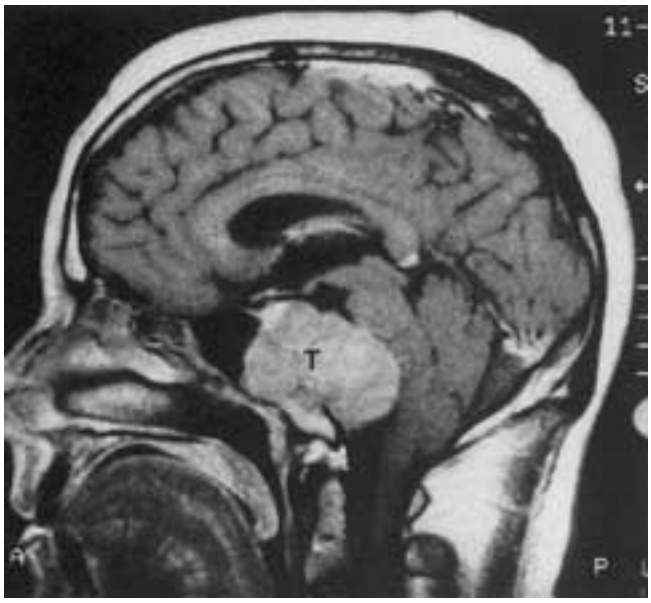

VIEW IMAGE

FIGURE 12-40 Chordoma. T1-weighted image after contrast administration shows the tumor (*T*), with fairly homogeneous intermediate enhancement without cystic areas.

T1-weighted images (Figs. 12-39 and 12-40).[65, 66] Cystic areas, large or small, containing hemorrhage or mucoid material, are frequently present and can be bright on T1-weighted images (Fig. 12-41). Occasionally, a remaining piece of bone is large enough to cause a signal void. On T2-weighted images, the tumors characteristically have a high signal intensity.[67] Old hemorrhage may be seen as dark areas on T2-weighted sequences (Fig. 12-42). MR imaging is excellent for detecting the margin of the lesion close to the cavernous sinus and for determining the relationship of the tumor to the brainstem.

Angiography shows a relatively avascular lesion without large intratumoral blood vessels. The normal vessels in and around the basicranium are frequently displaced by the tumor.

Chordomas grow slowly, and metastasis is quite rare. However, even after radical surgery, local recurrence is frequent.[68] Seeding along the surgical entrance pathway can also occur (Fig. 12-43).[69] ''Drop'' metastasis seeding the subarachnoid space of the spine has been reported but is uncommon.[70] The tumor's location within the clivus and its proximity to both carotid arteries and multiple cranial nerves make complete resection almost impossible in many cases. Treatment is frequently a combination of surgery and radiation therapy.[71] Chordomas are resistant to conventional radiotherapy, but success has been achieved with proton beam therapy, focused radiation therapy, and radiosurgery.[72–75] Often the tumor is partially resected to diminish the volume or to move the tumor away from critical structures prior to proton beam therapy.[76]

After radiation therapy, the lesion is not expected to disappear. Rather, control is considered if there is lack of growth and progression of symptoms. The indicated 5-year control rate after proton beam therapy has been 55% to 70%. A poorer prognosis has been described in women, in patients whose tumors show necrosis on imaging, and in patients who have tumors with measured volumes greater than 70 ml.[77, 78] Of note, a recent study indicated that chondroid chordoma (keratin positive) had the same prognosis as standard chordoma and did not share the better prognosis of

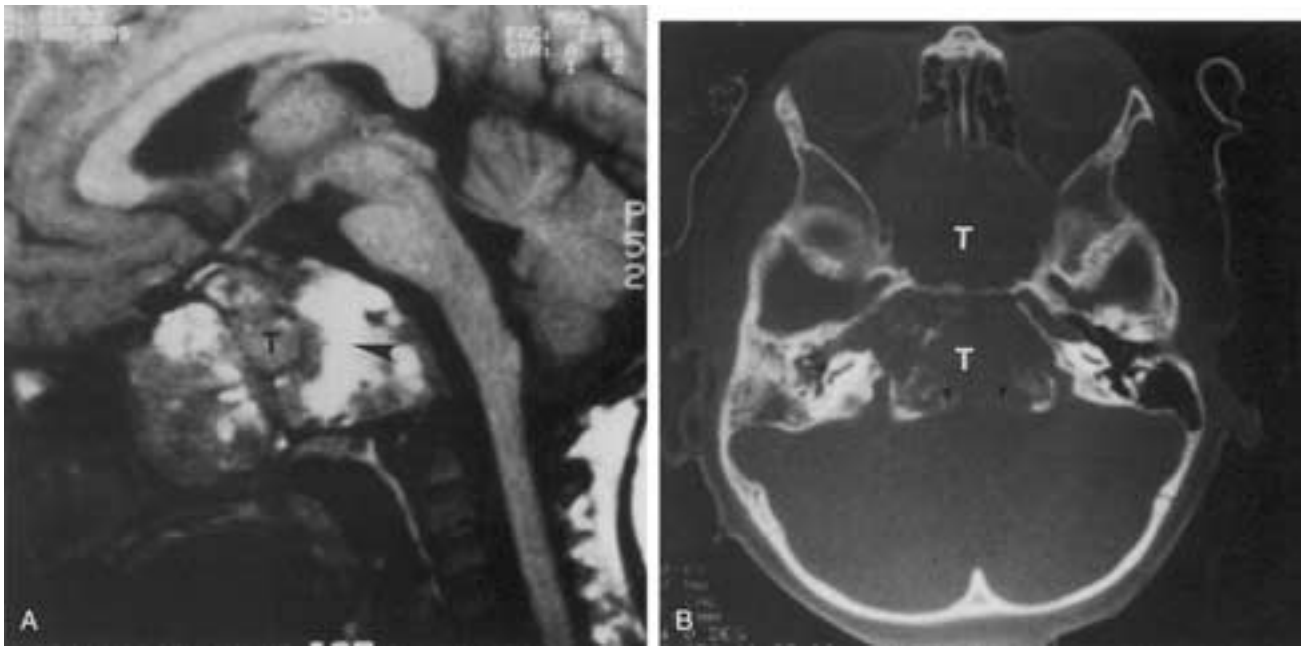

VIEW IMAGE

FIGURE 12-41 **A**, Chordoma of the skull base. Sagittal image shows the tumor replacing the sphenoid sinus. The tumor (*T*) has both intermediate and high (*large black arrowhead*) areas of signal intensity. Chordomas can have a variety of appearances, including areas of high signal representing either cystic areas or hemorrhage. **B**, Axial CT image shows the tumor with both anterior and posterior components (*T*). The expansion of the clival surface (*arrowheads*) is seen posteriorly.

Copyright © 2003, Mosby, Inc. All rights reserved.

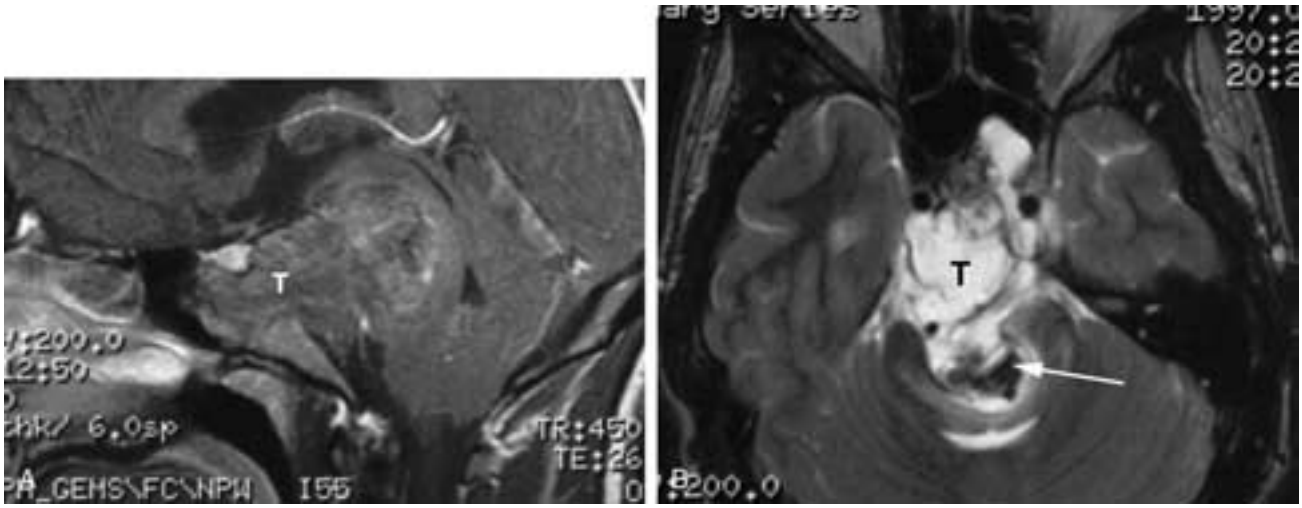

VIEW IMAGE

FIGURE 12-42 Chordoma of the basisphenoid. **A**, Postcontrast sagittal T1 image shows low enhancement of the tumor (*T*). Note how the lesion pushes posteriorly into the pons. **B**, Axial T2-weighted image shows the general high signal of the tumor (*T*), but there is an area of low signal representing hemosiderin from previous hemorrhage (*arrow*).

chondrosarcoma (see below).[79] Complications of radiation therapy, including proton beam therapy, include radiation optic neuritis and necrosis. Radiation change is frequently seen in the temporal lobes, where edema, gliosis, or even radiation necrosis can be present (Fig. 12-44).

Chondrosarcomas

Chondrosarcomas can arise from bone, cartilage, or even tissues without a cartilaginous component, and 6.5% of these tumors arise in the head and neck region.[80–82] In the skull base, chondrosarcomas are most commonly found in the region of the various synchondroses that remain after ossification replaces the embryonic chondroid basal plate. These tumors have a particular propensity for the petro-occipital (petroclival) synchondrosis or fissure (Figs. 12-45 to 12-47), and thus chondroid tumors in the deep skull base region tend to be off midline. The junction of the nasal septum and the rostrum of the sphenoid is another location where these tumors tend to arise (Fig. 12-48).[83] Chondrosarcoma can arise in the midline basisphenoid/basiocciput, presumably related to the sphenooccipital synchondrosis.

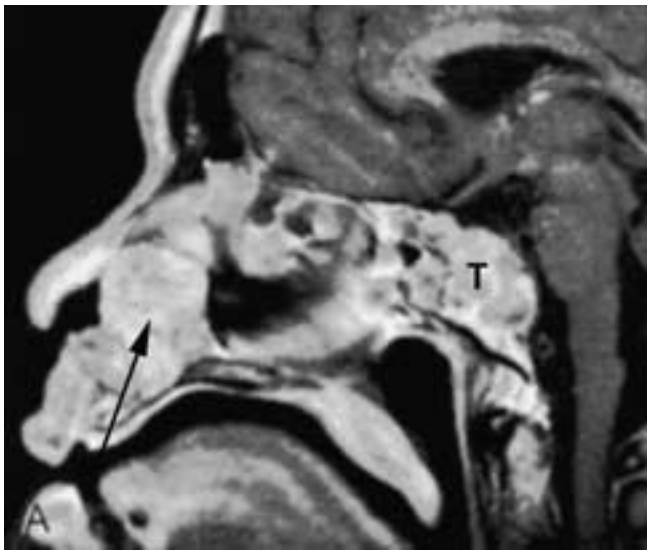

VIEW IMAGE

FIGURE 12-43 Recurrence of chordoma after the transsphenoidal approach to partial resection. Much of the tumor (*T*) remains in the upper basicranium. Note the recurrence (*arrow*) in the anterior part of the nasal septum.

Chondrosarcoma invades locally but seldom metastasizes.[84] Tumors spread away from the petrooccipital fissure, involve the clivus and petrous portion of the temporal bone, and bulge into the subarachnoid space cisterns or into the soft tissues beneath the skull base.

Chondrosarcomas vary in histologic type. Conventional chondrosarcoma includes the hyaline and myxoid types or a combination of the two (Fig. 12-38). Other types of chondrosarcoma include clear cell, dedifferentiated, and mesenchymal. Virtually all skull base chondrosarcomas are of the conventional type. A recent series of 200 cases showed the combination of hyaline and myxoid types to be most common, occurring in 63% of cases.[79] The relatively pure hyaline type accounted for 7.5% of cases, and the myxoid type accounted for 29.5% of cases. Both histologic patterns include true chondrocytes, but the surrounding matrix differs. The matrix in the hyaline type is more solid compared to the more mucinous or gelatinous matrix seen in the myxoid type. The hyaline matrix can mineralize, giving the characteristic ringlet calcification appearance on CT.

Conventional chondrosarcomas can be graded, reflecting degrees of differentiation. Almost all chondrosarcomas of the central skull base are well or moderately differentiated. Most are slow growing.

Chondrosarcomas can occur at almost any age, but most occur in middle age. The presentation depends on the location and local extension, and headaches or various cranial nerve palsies often cause the patient to seek medical attention.

Treatment may combine surgery with various types of

Copyright © 2003, Mosby, Inc. All rights reserved.

focused beam or particle radiation or may consist of radiation alone.[72, 85] Complete surgical removal is usually impossible due to the location of the lesion and its proximity to neural and vascular structures. These tumors grow slowly, and the prognosis is generally good.

On CT, chondrosarcomas have a varied appearance, depending on the amount of chondroid matrix present.[86] There is usually a significant soft-tissue component that has a dense appearance on noncontrast studies and enhances to some degree after contrast administration. Calcification of the tumor matrix is characteristic but is not always present. Thus, the degree of calcification is quite variable, with some chondrosarcomas having almost no calcification, while others, particularly the low-grade tumors, having extensive, even dense, calcification (Figs. 12-47 and 12-49). The calcifications tend to be small ringlets or incomplete rings, suggesting the cartilaginous nature of the matrix. Frequently, the margin between tumor and normal bone is fairly abrupt, and although this transition zone is fairly narrow, the tumor margin is not sclerotic.

On MR imaging, these tumors usually have an intermediate T1-weighted and a fairly high T2-weighted signal intensity. After gadolinium administration there is detectable enhancement, but the signal change is not profound (Fig. 12-50). Heavy calcifications may be detectable on MR imaging, but smaller ones cannot be seen. Indeed, even if there is fairly extensive calcification, this may not be evident on MR imaging. Therefore, there may be a significant difference between the amount of calcification seen on CT and the size of any MR signal voids that suggest the presence of calcifications.

Chondrosarcoma usually occurs as an isolated tumor, but it can occur as multiple tumors. Chondrosarcoma can occur in Ollier's disease (multiple enchondromatosis) and Maffucci syndrome (multiple enchondromas with associated cutaneous hemangiomas).[87, 88] Chondrosarcoma can also complicate Paget's disease.

Chordoma Versus Chondrosarcoma

Significant controversy surrounds the separation of some chordomas and chondrosarcomas of the central skull base. There is a significant overlap of the histologic patterns of these two tumors, potentially leading to ambiguity in diagnosis. This ambiguity can create problems in planning therapy and determining prognosis.

In the central skull base, there are two histologic types of chordoma and two histologic types of chondrosarcoma. Chordomas are either classic chordoma or chondroid chordoma (Fig. 12-37). Chondrosarcomas are either hyaline or myxoid (Fig. 12-38).[59, 79] The majority of chondrosarcomas are a mixture of myxoid and hyaline histologic types, and virtually all chondroid chordomas also contain regions of classic chordoma histology. There are histologic similarities between the ''chondroid'' part of the chondroid chordoma and hyaline chondrosarcoma and between the classic pattern of chordoma and the myxoid pattern of chondrosarcoma.

As mentioned previously, the term ''chondroid'' in chondroid chordoma refers to a histologic mimic rather than to true chondroid matrix. In the original descriptions of the chondroid chordoma, Heffelfinger et al. referred to a lesion that had areas of classic chordoma as well as regions that histologically resembled hyaline cartilage.[58] The lesion was thought to have cartilage differentiation within a chordoma. The so-called chondroid part of the chondroid chordoma resembles the hyaline-type chondrosarcoma, but the cells are actually typed immunohistochemically as epithelially derived cells rather than chondrocytes. Since the ''chondroid'' component of chordoma resembles hyaline-type chondrosarcoma, one would expect the controversy to be related to this overlapping appearance. However, most of the confusion has actually been between myxoid chondrosarcoma and classic chordoma.

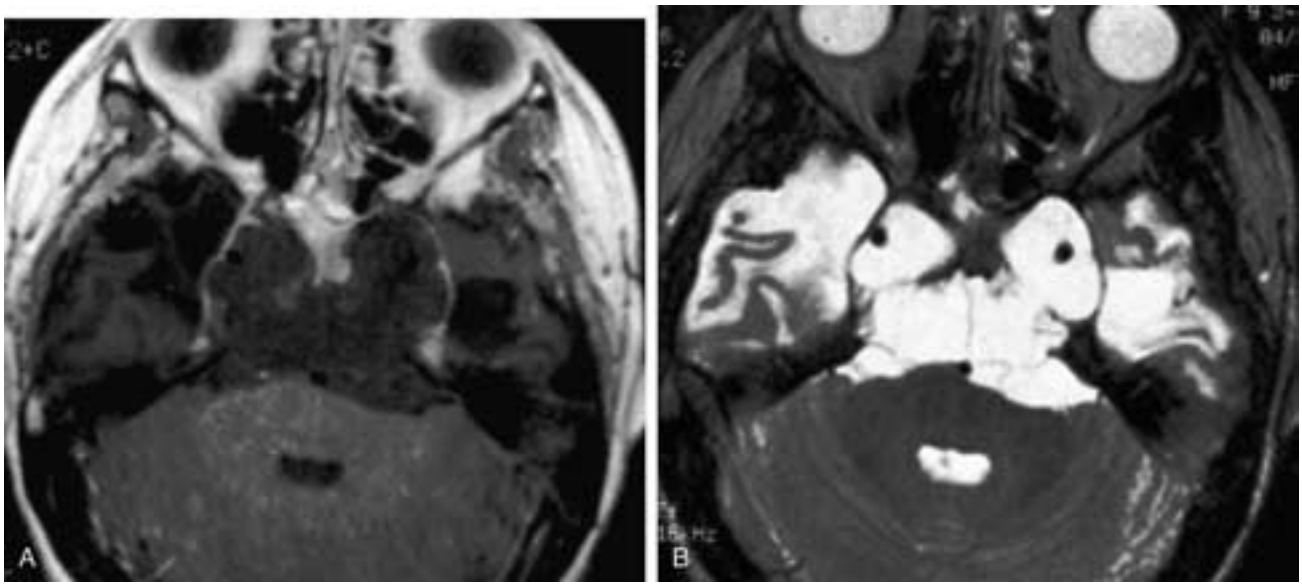

FIGURE 12-44 Chordoma after treatment. **A**, The expansile lesion of the basicranium shows very little enhancement. Note the changes in the contiguous temporal tips from radiation therapy. **B**, Axial T2-weighted image shows the typical high signal within the lesion and abnormal signal in the temporal lobes.

VIEW IMAGE

Copyright © 2003, Mosby, Inc. All rights reserved.

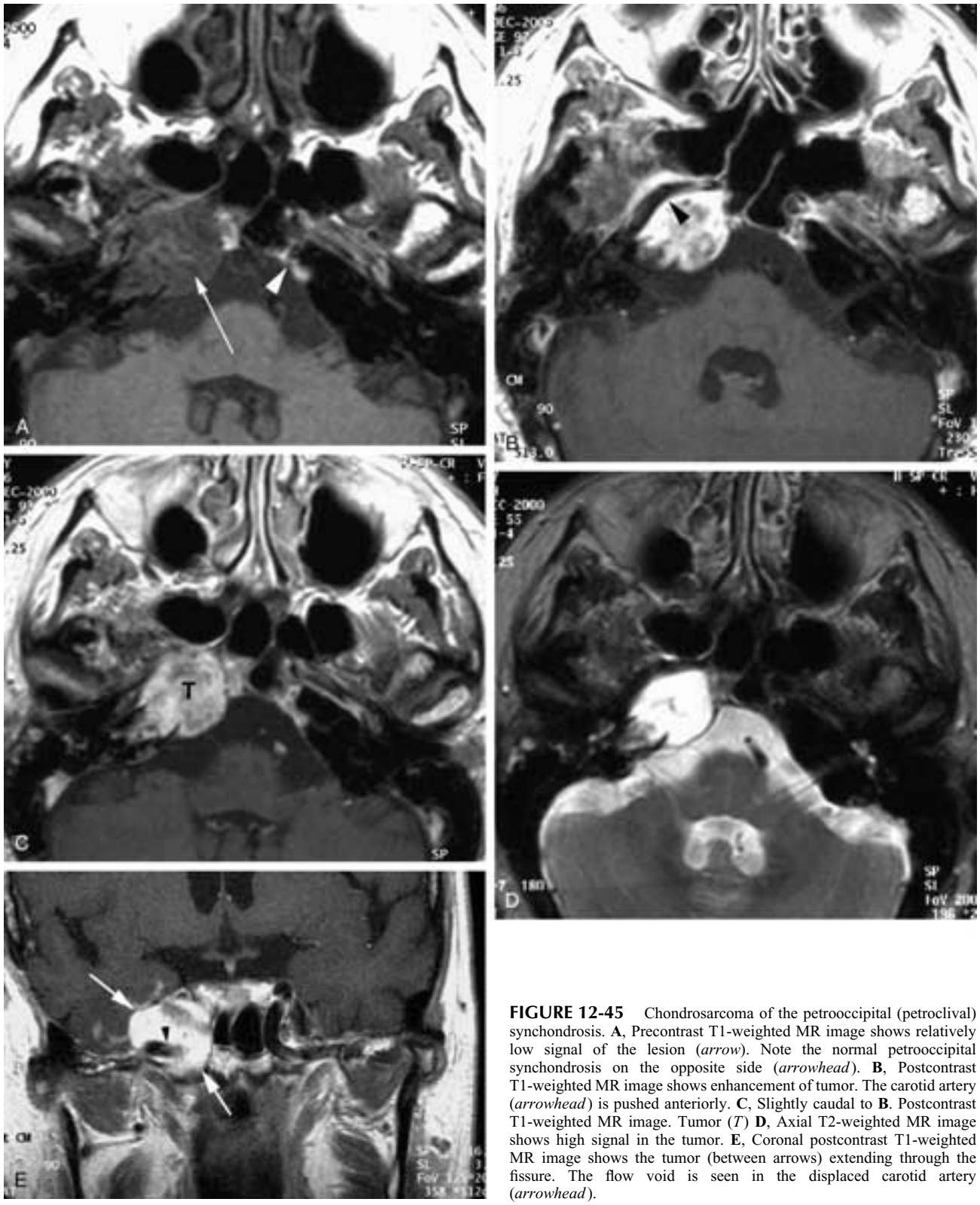

FIGURE 12-45 Chondrosarcoma of the petrooccipital (petroclival) synchondrosis. **A**, Precontrast T1-weighted MR image shows relatively low signal of the lesion (*arrow*). Note the normal petrooccipital synchondrosis on the opposite side (*arrowhead*). **B**, Postcontrast T1-weighted MR image shows enhancement of tumor. The carotid artery (*arrowhead*) is pushed anteriorly. **C**, Slightly caudal to **B**. Postcontrast T1-weighted MR image. Tumor (*T*) **D**, Axial T2-weighted MR image shows high signal in the tumor. **E**, Coronal postcontrast T1-weighted MR image shows the tumor (between arrows) extending through the fissure. The flow void is seen in the displaced carotid artery (*arrowhead*).

VIEW IMAGE

The myxoid type of chondrosarcoma also has some similarities to the chordoma. The myxoid matrix surrounding cells is similar to that seen in the classic pattern of chordoma. Cells can be found in strands resembling the chord pattern in chordoma. Vacuoles present in some chondrocytes give an appearance resembling the physaliphorous cell of the chordoma. These similarities lead to misdiagnosis of many myxoid chondrosarcomas as chordomas. However, differentiation can be made using the microscopic appearance and immunohistochemical staining.[79]

Copyright © 2003, Mosby, Inc. All rights reserved.

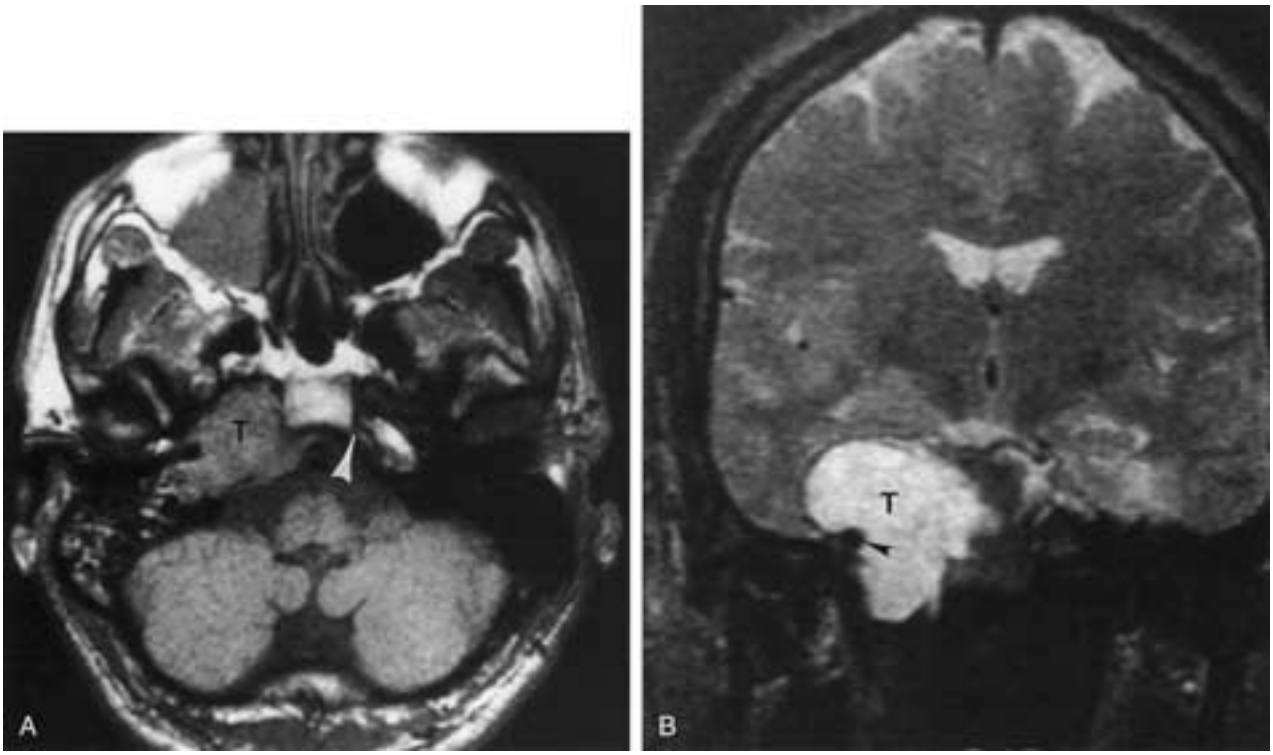

VIEW IMAGE

FIGURE 12-46 **A**, Chondrosarcoma of the petrooccipital synchondrosis. The tumor (*T*) shows an intermediate signal intensity on this T1-weighted image without contrast. Compare the position of this chondrosarcoma with the normal petrooccipital synchondrosis on the normal side (*arrowhead*). **B**, T2-weighted coronal image shows the tumor (*T*) extending inferiorly through the region of the petrooccipital synchondrosis and the foramen lacerum. The carotid artery (*arrowhead*) is pushed laterally.

In the myxoid chondrosarcoma, the cells tend to abut one another in only a small area at the end of each cell and thus they form chains or strands of cells. In the classic chordoma, cells abut along larger areas, forming larger groups of cells arranged into sheets, nests, and chords, a pattern not found in the chondrosarcoma. Cells may almost completely surround one another. In other words, the ''chord'' is differentiated from the strands found in the CSA by the greater length of cell contact. Chords tend to be more than one cell thick compared to the single-cell strands of cells in the CSA.

The most conclusive evidence, however, comes from immunohistochemical examination.[59, 79] The cells of chon-

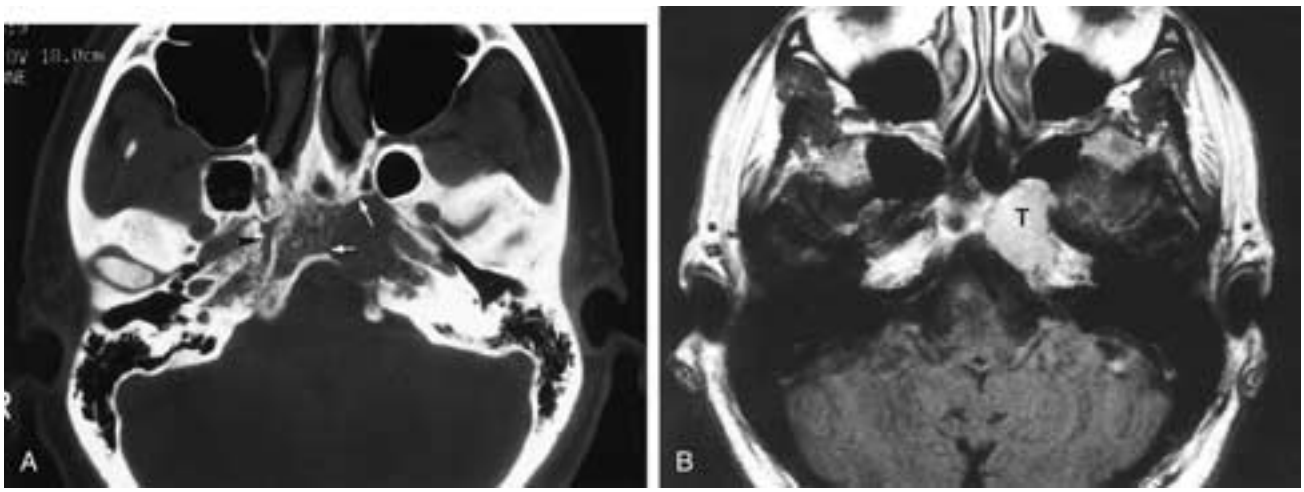

VIEW IMAGE

FIGURE 12-47 Chondrosarcoma arising in the foramen lacerum and petroclival fissure. **A**, CT bone scan algorithm shows a fairly smooth margin (*arrows*) of tumor arising in the region of the foramen lacerum. Note the normal foramen lacerum (*black arrowhead*) on the opposite side. **B**, T1-weighted postcontrast image. The tumor shows intermediate enhancement. The abnormality had a lower signal intensity on the T1-weighted precontrast image and relatively high signal intensity on the T2-weighted images (not shown).

Copyright © 2003, Mosby, Inc. All rights reserved.

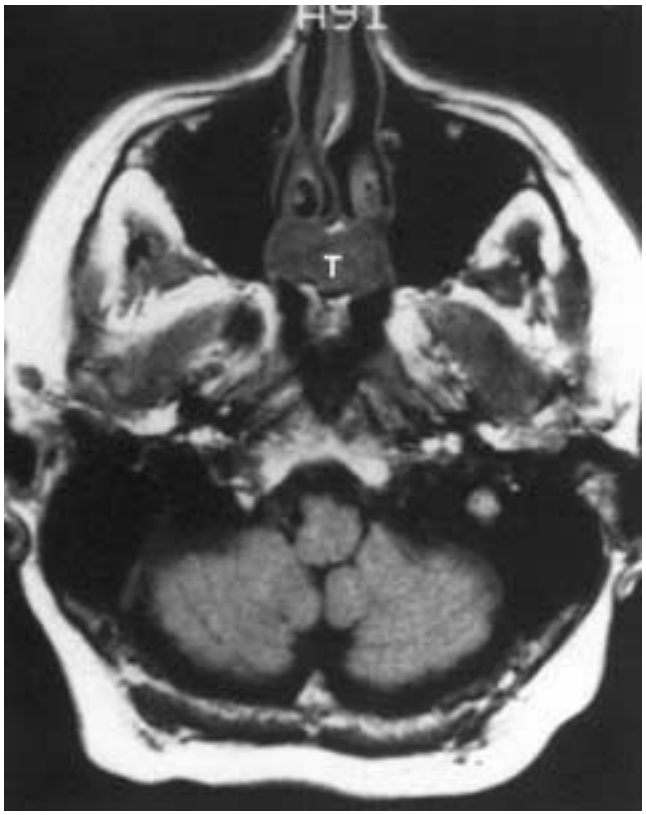

VIEW IMAGE

FIGURE 12-48 Chondrosarcoma of the nasal septum. The tumor (*T*) is seen in the posterior part of the nasal septum. Chondrosarcoma is a likely diagnosis for the rare tumor arising in this region.

drosarcoma (myxoid or hyaline) are true chondrocytes and do not stain for cytokeratin or other epithelial markers. This is true for chondroid lesions throughout the body. In the chordoma (classic and ''chondroid'') the cells do stain for these epithelial markers, reflecting their origin from the notochord. Notochordal tissue shows the same immunohistochemical profile as the chordoma.

Distinguishing the CSA from the chordoma is important, as the prognosis is quite different. In general, chordomas, including the ''chondroid'' variants, do more poorly than CSA. Although results vary, in a recent report of a large series of tumors treated with a combination of surgery and proton beam therapy, the 5-year control rate was about 51% for chordoma compared to over 90% for CSA.[79]

In the final analysis, one can say that chordoma virtually always arises in the midline and that a lesion arising in the region of the petroclival (petrooccipital) synchondrosis is very unlikely to be a chordoma, but rather is a chondrosarcoma. Chondrosarcomas, however, can arise in the midline related to either the sphenooccipital synchondrosis or the posterior nasal septum. Although the degree and appearance of calcification may give a clue to the identity of a lesion when the site of origin is ambiguous, the location of the tumor's origin is the dominant diagnostic indicator.

Other Chondroid Tumors

Other chondroid tumors of the skull base include chondromas, chondromyxoid fibroma, and, very rarely, chondroblastoma (Fig. 12-51). Truly benign chondromas are

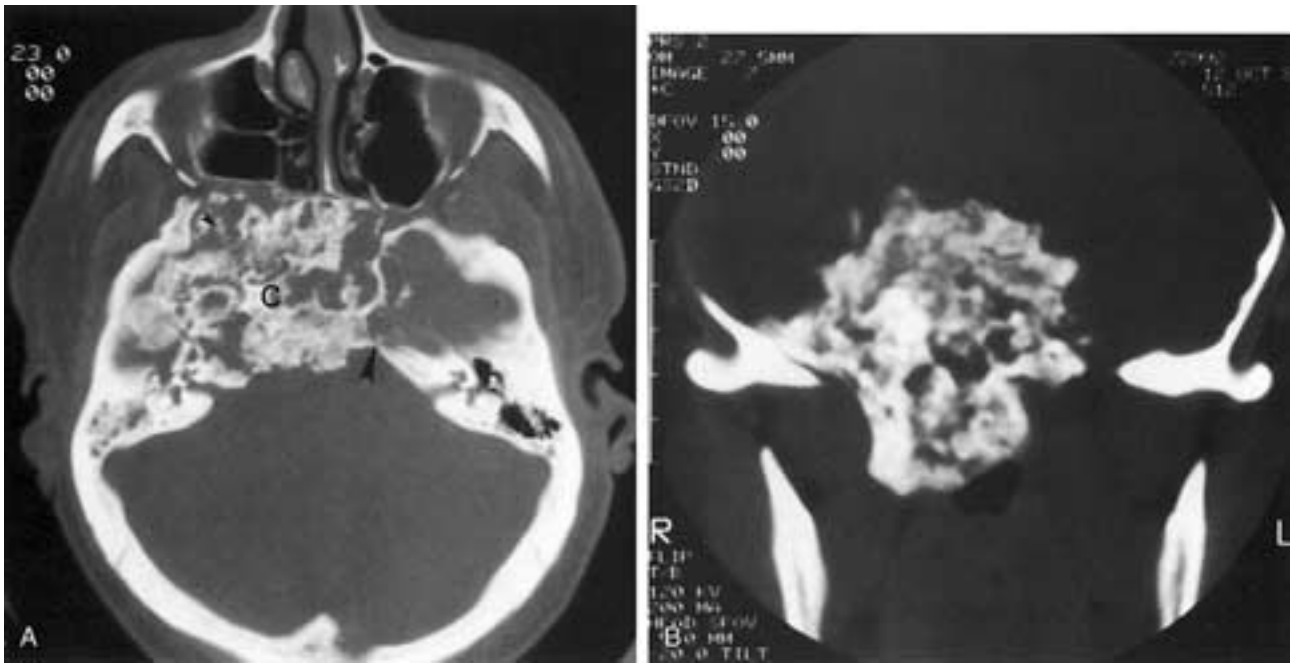

VIEW IMAGE

FIGURE 12-49 Chondrosarcoma of the skull base. **A**, The chondrosarcoma (*C*) replaces much of the body of the sphenoid and the right greater wing. Although the lesion definitely involves and extends across the midline, the center point of the tumor is close to the foramen lacerum. The petrooccipital fissure on the opposite side (*black arrowhead*) is normal. Small ringlets of calcification (*small black arrowhead*) are visualized within the tumor. **B**, Very heavy calcification is seen in this tumor.

Copyright © 2003, Mosby, Inc. All rights reserved.

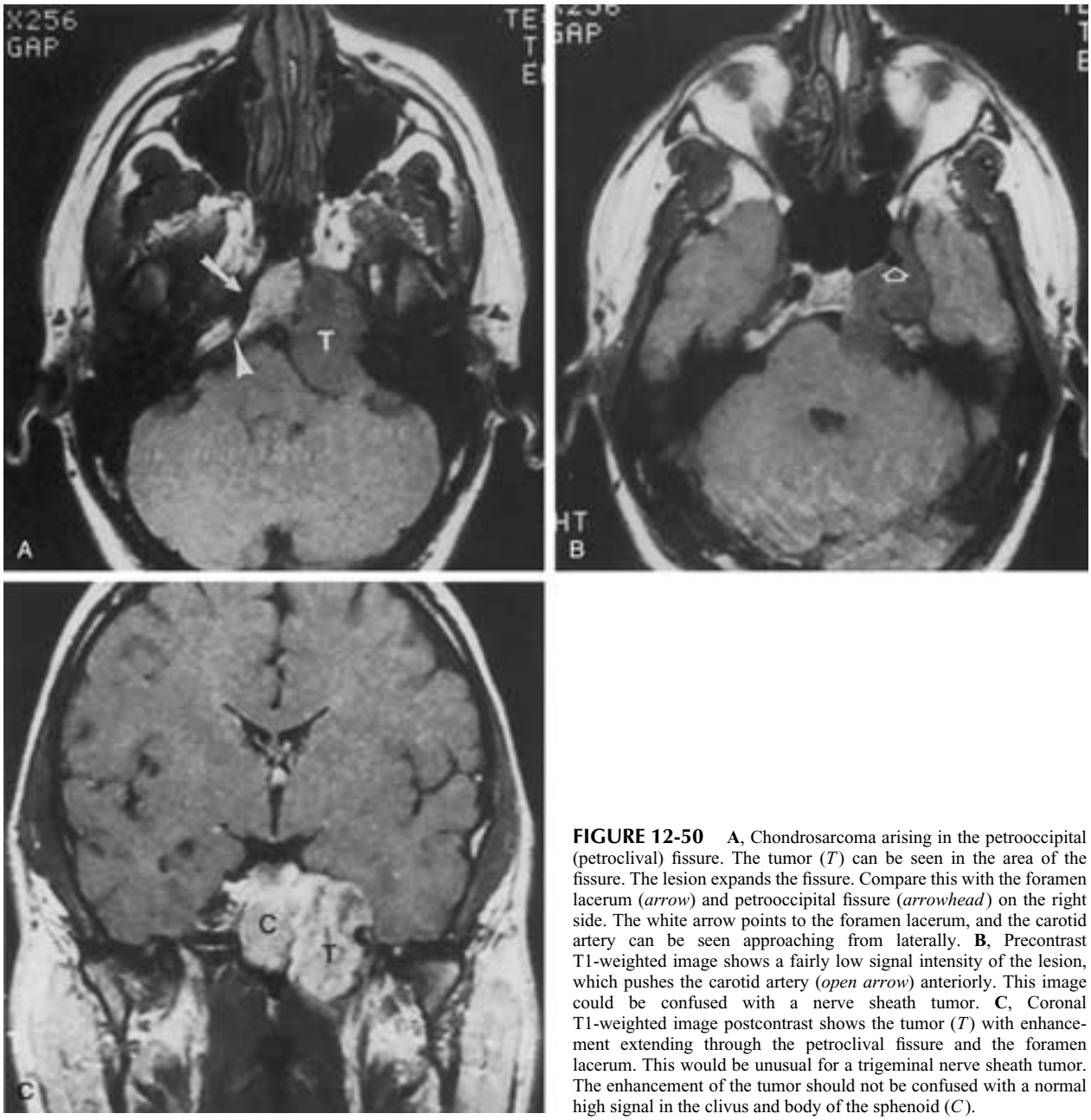

FIGURE 12-50 **A**, Chondrosarcoma arising in the petrooccipital (petroclival) fissure. The tumor (*T*) can be seen in the area of the fissure. The lesion expands the fissure. Compare this with the foramen lacerum (*arrow*) and petrooccipital fissure (*arrowhead*) on the right side. The white arrow points to the foramen lacerum, and the carotid artery can be seen approaching from laterally. **B**, Precontrast T1-weighted image shows a fairly low signal intensity of the lesion, which pushes the carotid artery (*open arrow*) anteriorly. This image could be confused with a nerve sheath tumor. **C**, Coronal T1-weighted image postcontrast shows the tumor (*T*) with enhancement extending through the petroclival fissure and the foramen lacerum. This would be unusual for a trigeminal nerve sheath tumor. The enhancement of the tumor should not be confused with a normal high signal in the clivus and body of the sphenoid (*C*).

VIEW IMAGE

sharply defined and may be calcified. Most are probably more appropriately considered low-grade chondrosarcomas. Rarely, chondromas of the skull base (in addition to the more common chondrosarcomas already mentioned) can be found in patients with Ollier's disease (multiple enchondromatosis) and the Maffucci syndrome (Fig. 12-52) (multiple enchondromas associated with subcutaneous hemangiomas).[87, 88] Several cases were reported in the region of the petrooccipital synchondroses, and astrocytomas can also occur in these conditions.

Chondromyxoid fibroma has been reported as an expansile mass in the skull base.[89, 90] The lesion is not infiltrating and is considered to be less destructive than chordoma, but it may overlap with chondrosarcoma in imaging appearance.

Meningiomas

Meningiomas are benign tumors that arise from the arachnoidal cells of the meninges.[91, 92] The peak incidence is between the ages of 20 and 60 years. Most meningiomas are found either along the convexities or parasagittally. A skull base origin is less common. Meningiomas can arise along almost any part of the sphenoid, including the greater wing, the planum sphenoidale, the tuberculum sella, and the wall of the cavernous sinus. From the initial site of origin, the tumor extends along the dural surfaces or intraosseously, and once it penetrates through the bone, a substantial extracranial mass can develop.

The clinical presentation depends on the site of origin, but headaches can be present with any of these tumors.

Copyright © 2003, Mosby, Inc. All rights reserved.

Meningioma of the planum sphenoidale may cause olfactory symptoms, and tumors closer to the chiasmatic sulcus can cause visual problems. Ophthalmoplegia can result as the nerves in the cavernous sinus are compromised.

The classification of meningiomas of the greater wing of the sphenoid is based on the location of the tumor. If the sphenoid wing is separated into thirds, both the degree of difficulty of resection and the likelihood of cranial neuropathy increase from laterally to medially. Tumors of the medial third, referred to as sphenocavernous meningiomas, are most likely to cause cranial neuropathies and represent the greatest surgical challenge. Recent surgical technical developments have improved surgical access to these difficult tumors, and if such surgery is planned, great precision in the imaging evaluation is required because of the close proximity of the lesion to critical neurovascular structures.

Meningiomas arising from the more lateral portion of the greater wing of the sphenoid may be fairly silent clinically because the cranial nerves are not directly involved. Although some of these meningiomas are globular in shape, many lesions in this location can be classified as hyperostosing en plaque meningiomas. Tumor growth can progress in any direction. As the tumor extends into the orbit, painless proptosis may occur. Inferior growth may cause a mass effect in the infratemporal fossa, presenting as a mass in the cheek or as problems with mastication. Lateral extension growth may displace the temporalis muscle. Medial growth can affect the trigeminal nerve, particularly the third division. Tumors from any location around the sphenoid bone can compress the brain, and seizures may be the presenting symptom.

Because arachnoid cells accompany the cranial nerves, it

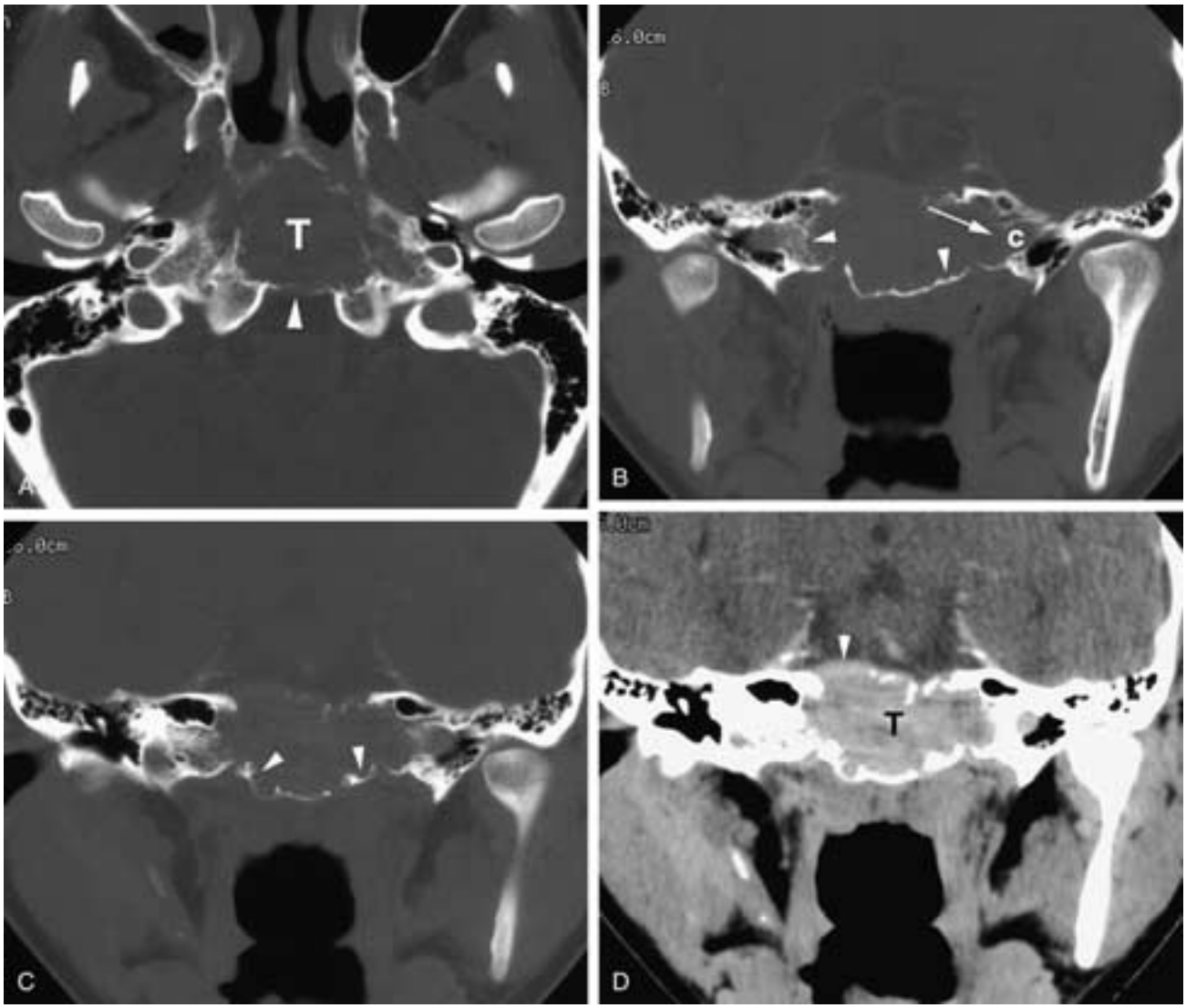

FIGURE 12-51 Chondromyxoid fibroma. **A**, Axial CT bone algorithm shows a tumor (*T*) bulging slightly through the posterior plate of the clivus (*arrowhead*). **B**, Coronal bone algorithm shows slight curvilinear scallops (*arrowheads*) along the margin. The bony wall (*arrow*) of the carotid canal (*C*) is eroded. **C**, Coronal bone algorithm shows slight scalloped areas (*arrowheads*). **D**, Coronal postcontrast soft-tissue window shows the tumor (*T*) bulging (*arrowhead*) into the posterior fossa.

VIEW IMAGE

Copyright © 2003, Mosby, Inc. All rights reserved.

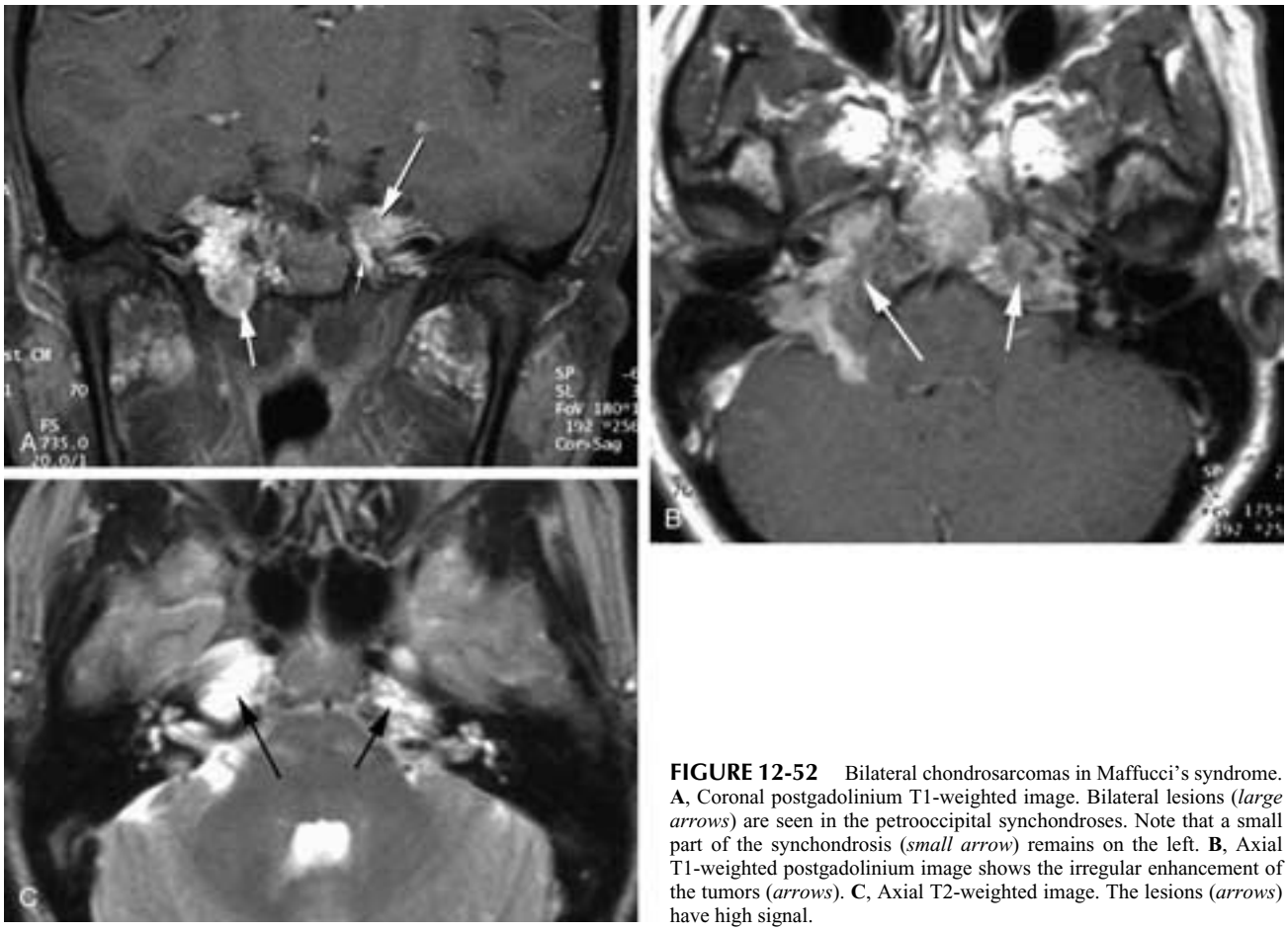

FIGURE 12-52 Bilateral chondrosarcomas in Maffucci's syndrome. **A**, Coronal postgadolinium T1-weighted image. Bilateral lesions (*large arrows*) are seen in the petrooccipital synchondroses. Note that a small part of the synchondrosis (*small arrow*) remains on the left. **B**, Axial T1-weighted postgadolinium image shows the irregular enhancement of the tumors (*arrows*). **C**, Axial T2-weighted image. The lesions (*arrows*) have high signal.

VIEW IMAGE

is not surprising that meningiomas can be found adjacent to and traversing various neural foramina.[93] These tumors can cause enlargement or erosion of these foramina, simulating a nerve sheath tumor. Gross destruction of the skull base can simulate malignancy.

On CT, there is enhancement of the soft-tissue component of the tumor. Calcifications may be detectable, and hyperostosis may be seen as thickening of the involved cortex or the trabeculae within the bone. Alternatively, as the meningioma extends through the skull base, a permeative bone pattern rather than a destructive or sclerotic pattern can be seen, often appearing on CT as a ''washed-out'' bone. Meningiomas arising from the planum sphenoidale may show characteristic sclerosis or upward ''blistering'' of the bone (Fig. 12-53). Both plain films and CT can demonstrate this finding.

Pneumosinus dilatans refers to enlargement of an air-filled sinus (Fig. 12-54). Pneumosinus dilatans of the sphenoid can occur either in isolation or in association with meningioma.[94–96] There is some controversy regarding terminology, as there are physicians who use the term ''pneumosinus dilatans'' only when referring to a dilated aerated sinus seen with adjacent tumor. Other people use the term to indicate any expanded air-filled sinus. When occurring with meningioma, the enlargement of the sinus may be focal or diffuse, depending on the position of the tumor, and focal hyperostosis may or may not be present. The enlarged sinus is not opacified unless there is additional inflammatory/obstructive pathology in the sinus itself. The cortex is usually intact, though a focal dehiscence may occur. Pneumosinus dilatans has been described with meningioma arising within the optic canal as well as on the intracranial surface of the sphenoid bone (Fig. 12-55).[97, 98] Apparent enlargement of the sinus can also occur in acromegaly, in fibrous dysplasia, and in Sturge-Weber and Klippel-Trenaunay-Weber syndromes.[99]

On MR imaging, meningiomas are usually isointense to brain parenchyma (Fig. 12-56). After the administration of gadolinium, these lesions enhance intensely (Fig. 12-57). A ''dural tail'' frequently can be seen extending along the dura at the margin of the tumor (Fig. 12-58). Hyperostosis is more difficult to visualize on MR imaging, but sometimes it can be appreciated as an enlargement of the signal void or as a low-signal area representing the cortical bone (Fig. 12-59).

Imaging is particularly important with those tumors in the sphenocavernous region, and the relationship of the tumor to the vital structures of the cavernous sinus is better defined on MR imaging than on CT.[100] Because the normal cavernous sinus often enhances slightly more intensely than the tumor, the interface between tumor and normal structures can be defined. The enlarging tumor often impinges on and may obliterate the CSF signal in Meckel's cave. Tumor also may extend through the bony medial wall of the cavernous sinus

Copyright © 2003, Mosby, Inc. All rights reserved.

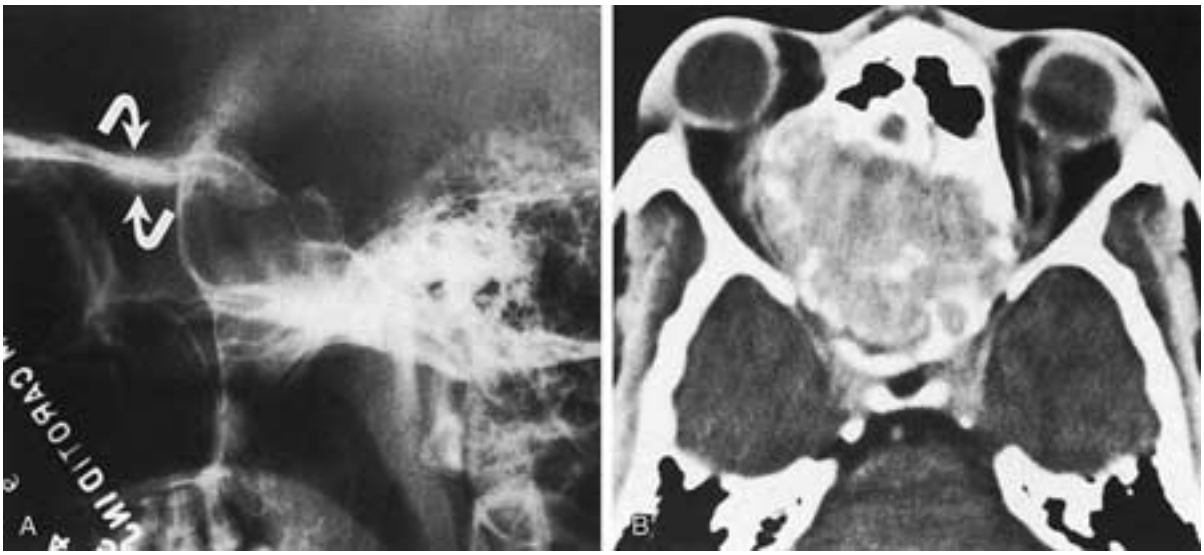

VIEW IMAGE

FIGURE 12-53 Meningioma in a 52-year-old female presenting with headache and altered mental status. **A**, Lateral plain film of the skull demonstrating hyperostosis in the region of the planum sphenoidale (*curved arrows*). **B**, Axial contrast-enhanced CT slice through the region of the planum demonstrating a large, expansile mass occupying the floor of the anterior cranial fossa emanating from the planum sphenoidale. Irregular enhancement and bony destruction are apparent.

to appear as an enhancing mass within the sphenoid sinus. Here there can be difficulty distinguishing the tumor from any inflammatory mucosal disease or primary malignancy within the sinus.

One of the most important relationships to note is the effect of the tumor on the internal carotid artery, as meningiomas can surround and frequently will narrow this vessel (Figs. 12-56 and 12-57).[101] A more superior tumor extent can involve the middle cerebral artery. Meningiomas also have been described following the carotid artery inferiorly into the petrous carotid canal.

Craniopharyngiomas and Rathke's Pouch Cysts

The craniopharyngioma arises from remnants of the pharyngohypophyseal (Rathke's) pouch, and most of these benign tumors are found in the sella or in the suprasellar cistern. Those lesions arising in the sellar or suprasellar region can grow into the sphenoid bone. Rarely, a craniopharyngioma occurs completely within the sphenoid bone, presumably developing from remnants of the pharyngohypophyseal duct trapped within the bone (Fig. 12-60).[102–104]

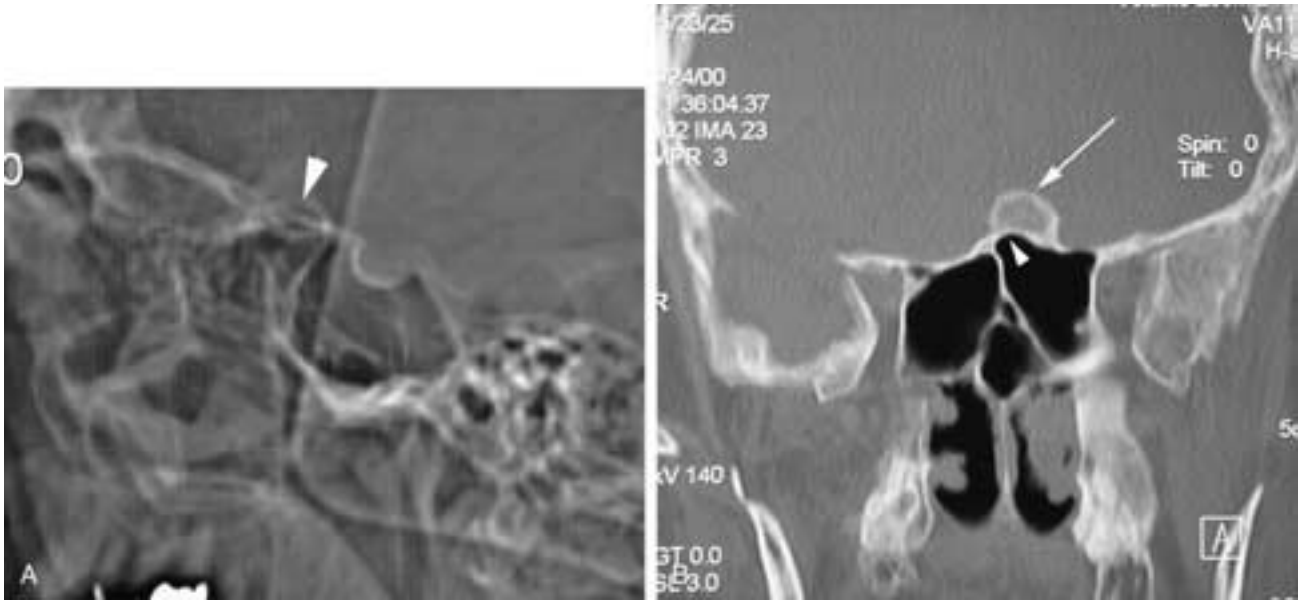

VIEW IMAGE

FIGURE 12-54 Pneumosinus dilatans adjacent to probable meningioma. **A**, Lateral skull view shows the expansion or ''blistering'' of the planum (*arrowhead*) just anterior to the limbus. **B**, A heavily calcified lesion (*arrow*) is seen adjacent to the upward expansion (*arrowhead*) of the sinus.

Copyright © 2003, Mosby, Inc. All rights reserved.

Although craniopharyngiomas are described in Chapter 11, they are included here because of the very rare intraosseous occurrence of the tumor. Though these lesions occur predominantly in the first two decades of life, they can occur at any age; indeed, several of those reported in sphenoid bone have occurred in older patients. Those that are predominantly in the sphenoid bone can extend upward into the pituitary fossa and result in decreased pituitary function. Optic nerve abnormalities are not common with these ''intraosseous'' tumors unless there is further extension into the suprasellar cistern or involvement of the optic canals.

The craniopharyngioma is very similar histologically to some odontogenic lesions, as the pharyngohypophyseal pouch is an ectodermal evagination from the embryonic oral cavity, anterior to the buccopharyngeal membrane, and may develop oral ectoderm-related histopathology.[105, 106] The similarity of the craniopharyngioma to the ameloblastoma has given rise to the term adamantinomatous craniopharyngioma. According to some authors, some of the histologic features of craniopharyngioma more closely approximate the keratinizing and calcifying odontogenic cysts than they do the ameloblastoma.[105]

Histologically, the adamantinomatous craniopharyngioma contains epithelial lobules with palisading nuclei along the periphery. Cystic spaces are filled with fluid or debris, and the so-called wet keratin is considered characteristic of this form of craniopharyngioma.[107] Wet keratin is a conglomeration of large, keratinized cells with ''ghost'' nuclei reflecting the necrobiotic nature of these cells. Calcifications are frequently seen within the lesion, and an inflammatory response along the periphery of the tumor can stimulate bone formation. This is the type of histology that accounts for the typical imaging appearance of the craniopharyngioma with cyst formation and calcification. Reports of infrasellar craniopharyngiomas are rare, but some of the findings that are characteristic of the suprasellar type are found in these infrasellar lesions. The tumor may have a

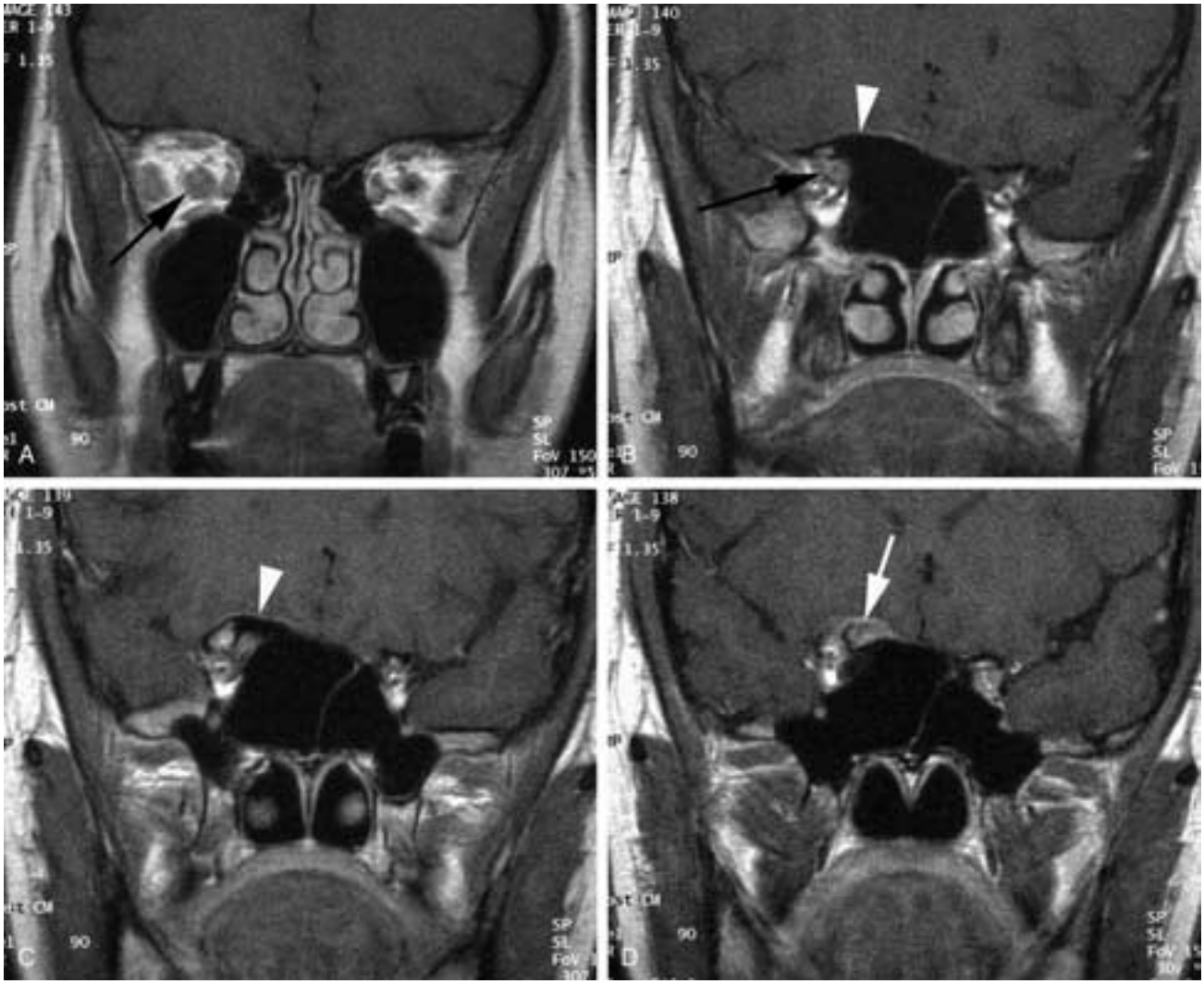

VIEW IMAGE

FIGURE 12-55 Pneumosinus dilatans of the sphenoid sinus with optic nerve meningioma. T1-weighted postgadolinium coronal images. **A**, Meningioma of the optic nerve sheath (*arrow*). **B**, Anterior to the optic foramen; enlargement of the nerve sheath (*black arrow*) and enlargement of the sphenoid sinus (*arrowhead*). **C**, Dilation of the air cell (*arrowhead*) extending into the anterior clinoid. **D**, The meningioma (*arrow*) extends intracranially at the opening of the optic canal.

Copyright © 2003, Mosby, Inc. All rights reserved.

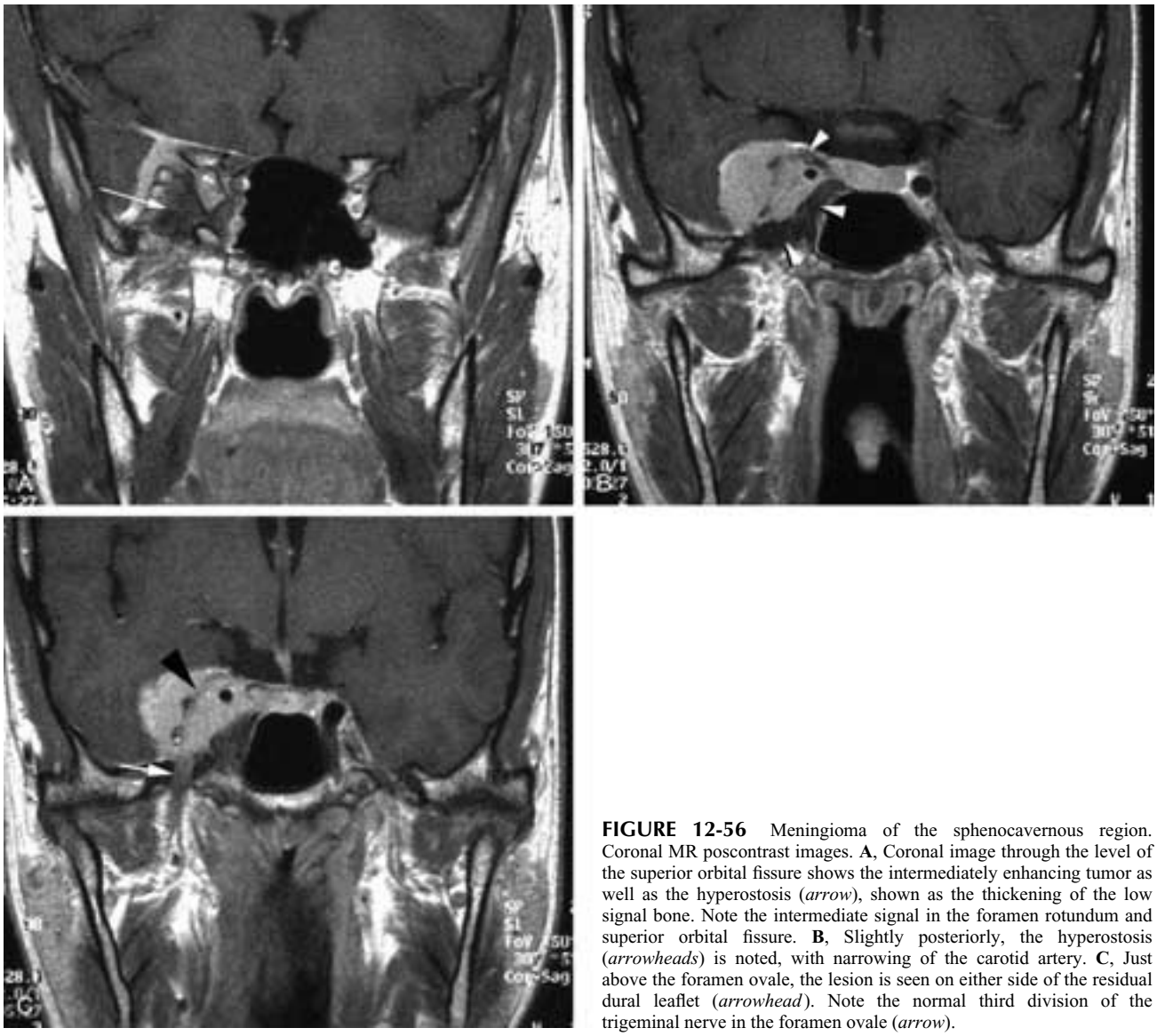

FIGURE 12-56 Meningioma of the sphenocavernous region. Coronal MR poscontrast images. **A**, Coronal image through the level of the superior orbital fissure shows the intermediately enhancing tumor as well as the hyperostosis (*arrow*), shown as the thickening of the low signal bone. Note the intermediate signal in the foramen rotundum and superior orbital fissure. **B**, Slightly posteriorly, the hyperostosis (*arrowheads*) is noted, with narrowing of the carotid artery. **C**, Just above the foramen ovale, the lesion is seen on either side of the residual dural leaflet (*arrowhead*). Note the normal third division of the trigeminal nerve in the foramen ovale (*arrow*).

VIEW IMAGE

soft-tissue component that can extend downward into the nasopharynx or anteriorly into the nasal cavity. Cyst formation and calcification can be found within the tumor or at its margin. Sclerotic changes within the sphenoid bone may reflect the inflammatory component of the lesion.[102]

A rare form of the tumor is the papillary or papillary-squamous craniopharyngioma, considered a distinct variant.[108–110] This tumor type is seen in adults and is frequently located in the region of the floor of the third ventricle. This entity is more cellular, typically lacks calcification, and appears to be more solid at imaging. Cystic components are less common than in the more common adamantinomatous type.

A second type of lesion related to the pharyngohypophyseal pouch is the Rathke's pouch or cleft cyst.[111] Unlike the craniopharyngioma, this cyst is lined by a single layer of epithelial cells, which may be cuboidal or columnar. Goblet cells also can be found frequently. Imaging shows a cystic mass, usually in the sella or suprasellar cistern, with no significant soft-tissue component and smooth, sharp margins. MR imaging can show a low or high T1-weighted signal intensity, depending on the protein content of the cyst fluid. T2-weighted images usually have high signal intensity.

Rathke's cleft cysts also can be found completely within the sphenoid bone (Fig. 12-61). In these cases, differentiation from a mucocele may be impossible. The MR imaging signal intensities are the same, and at biopsy the wall is very similar to that of a mucocele. The cyst contents may be helpful in this regard because the fluid of a Rathke's cleft cyst tends to be yellow and clear, with a low mucoid content.

Such a cyst within the sphenoid bone arises from the remnant of Rathke's pouch. Although the original location of this structure is within the body of the sphenoid, just below the floor of the sella, the variability of formation of the sphenoid sinus may ''push'' the cyst dorsally or superiorly, giving the cyst an eccentric location.

Copyright © 2003, Mosby, Inc. All rights reserved.

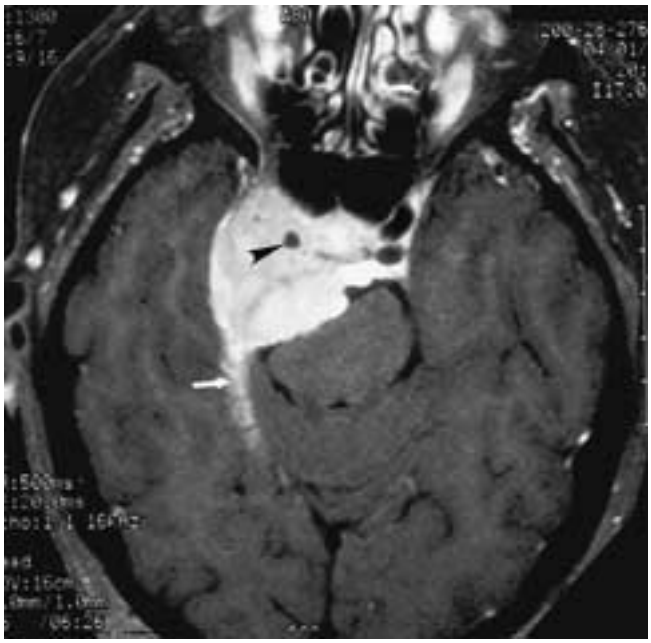

FIGURE 12-57 Meningioma. The tumor fills the region of the cavernous sinus. The carotid artery is narrowed (*black arrowhead*), and there is enhancement extending along the tentorium (*arrow*). Note that although the tumor enhances, one can still separate the margin of the lesion from the enhancement in the venous structures.

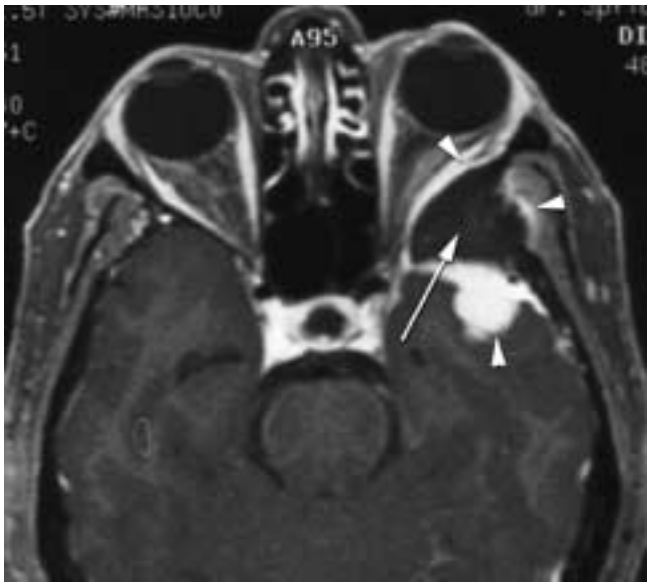

FIGURE 12-59 Meningioma of the sphenoid triangle (greater wing). There is hyperostosis, with an increase in the size of the bone of the sphenoid triangle (*arrow*). There is enhancement in the temporalis fossa, orbit, and middle cranial fossa (*arrowheads*). Note the globular appearance of the intracranial component.

Juvenile Angiofibromas

The juvenile angiofibroma is a benign tumor arising adjacent to the sphenopalatine foramen. Almost all of these tumors occur in adolescent males, and nasal obstruction and epistaxis are the most common presenting symptoms. The tumor is very vascular and thus has a characteristic appearance at imaging (Fig. 12-62). On CT and MR imaging the tumor enhances intensely, and on MR imaging there are flow voids representing the larger high-flow vessels. The location and routes of extension are characteristic and can be seen on either modality. On MR imaging, the tumor tends to have an intermediate signal intensity on T1-weighted

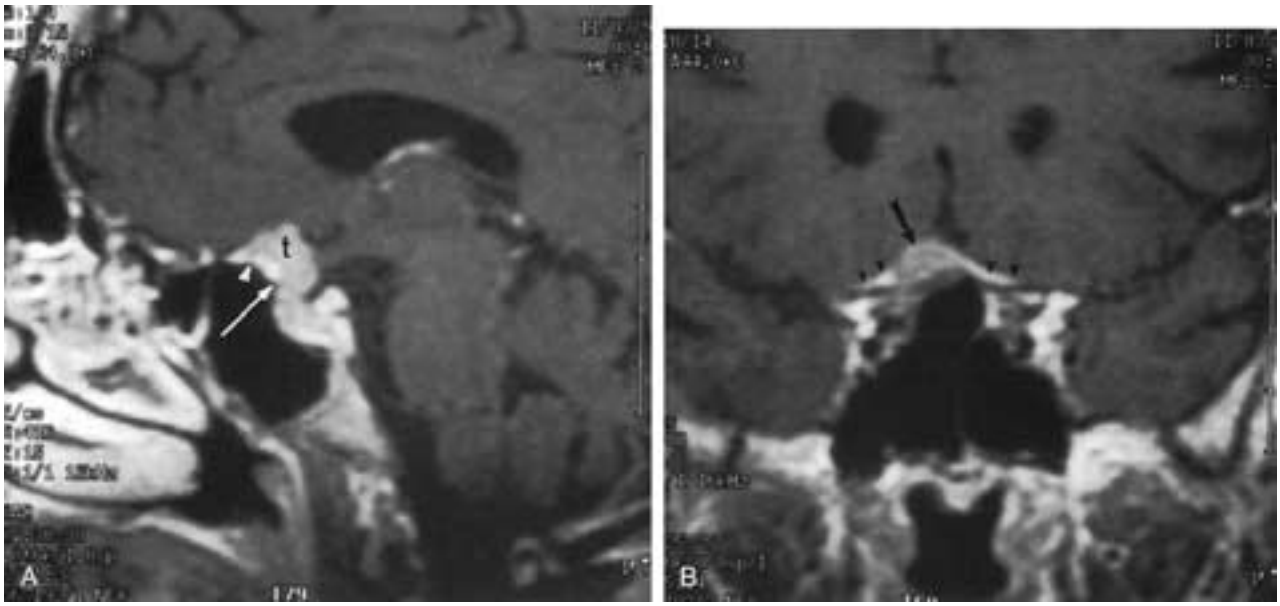

FIGURE 12-58 Meningioma of the chiasmatic groove and planium. **A**, Postgadolinium sagittal T1-weighted image shows the tumor (*t*) extending along the chiasmatic groove and onto the planium sphenoidale. The arrow indicates the position of the tuberculum sella, and the small white arrowhead indicates the limbus separating the chiasmatic groove from the planium. Note how the tumor spills over into the sella turcica. **B**, Coronal T1-weighted postcontrast image shows the tumor (*arrow*) with intermediate enhancement. Notice the enhancement of the dural tails (*small black arrowheads*) extending in either direction from the main tumor.

Copyright © 2003, Mosby, Inc. All rights reserved.

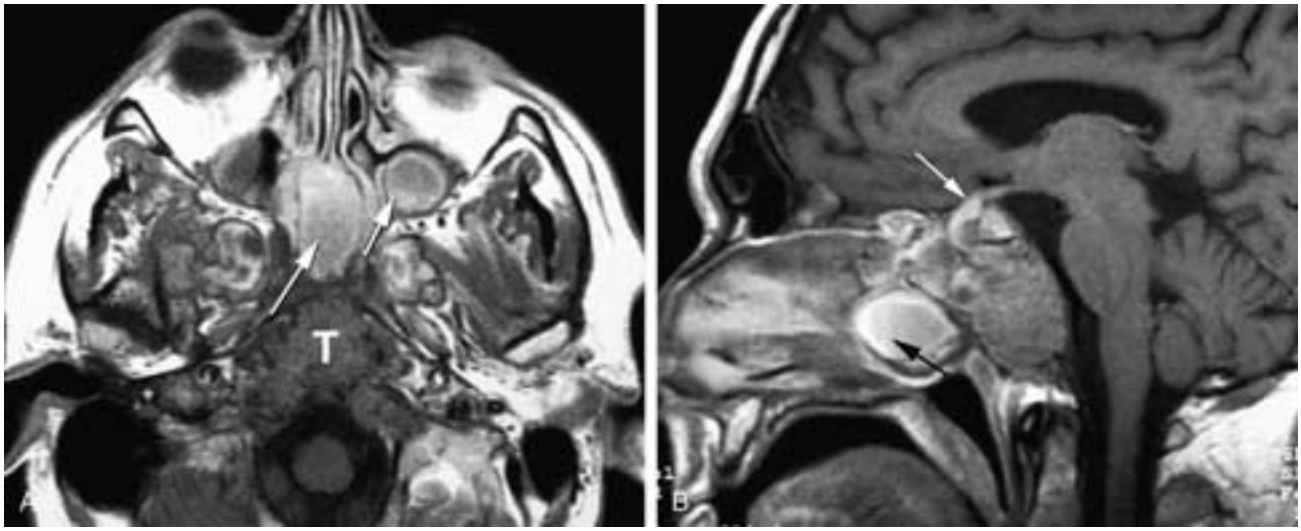

VIEW IMAGE

FIGURE 12-60 Craniopharyngioma. Predominantly infrasellar. **A**, Axial image shows the expansile lesion (*T*) extending into the nasal septum and the maxillary sinus (*arrows*). Note the small fluid levels of the cystic cavities within the anterior part of the tumor. **B**, Sagittal postcontrast image shows the lesion extending superiorly along the anterior pituitary stalk (*white arrow*). Fluid-fluid level (*black arrow*).

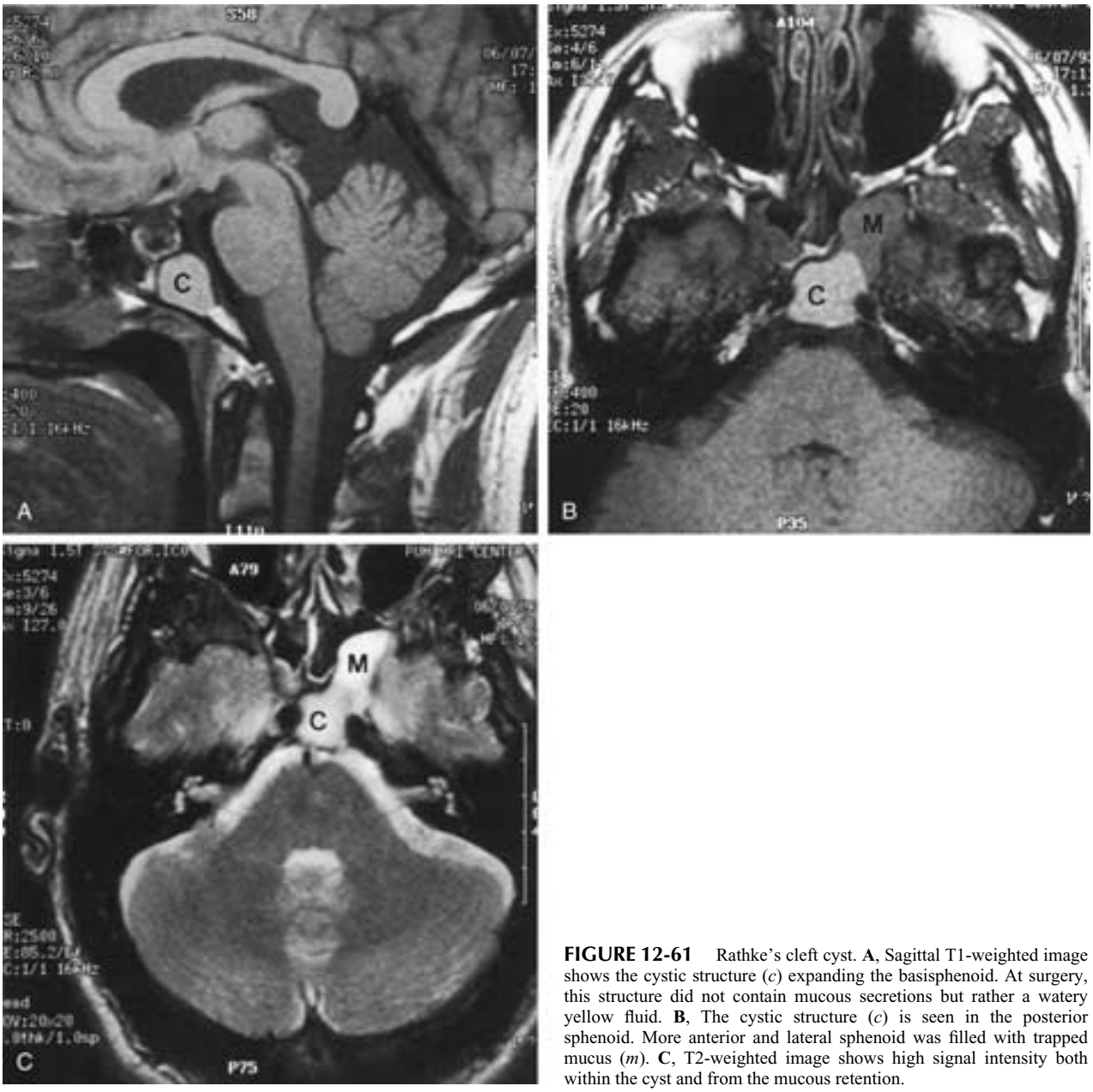

FIGURE 12-61 Rathke's cleft cyst. **A**, Sagittal T1-weighted image shows the cystic structure (*c*) expanding the basisphenoid. At surgery, this structure did not contain mucous secretions but rather a watery yellow fluid. **B**, The cystic structure (*c*) is seen in the posterior sphenoid. More anterior and lateral sphenoid was filled with trapped mucus (*m*). **C**, T2-weighted image shows high signal intensity both within the cyst and from the mucous retention.

VIEW IMAGE

Copyright © 2003, Mosby, Inc. All rights reserved.

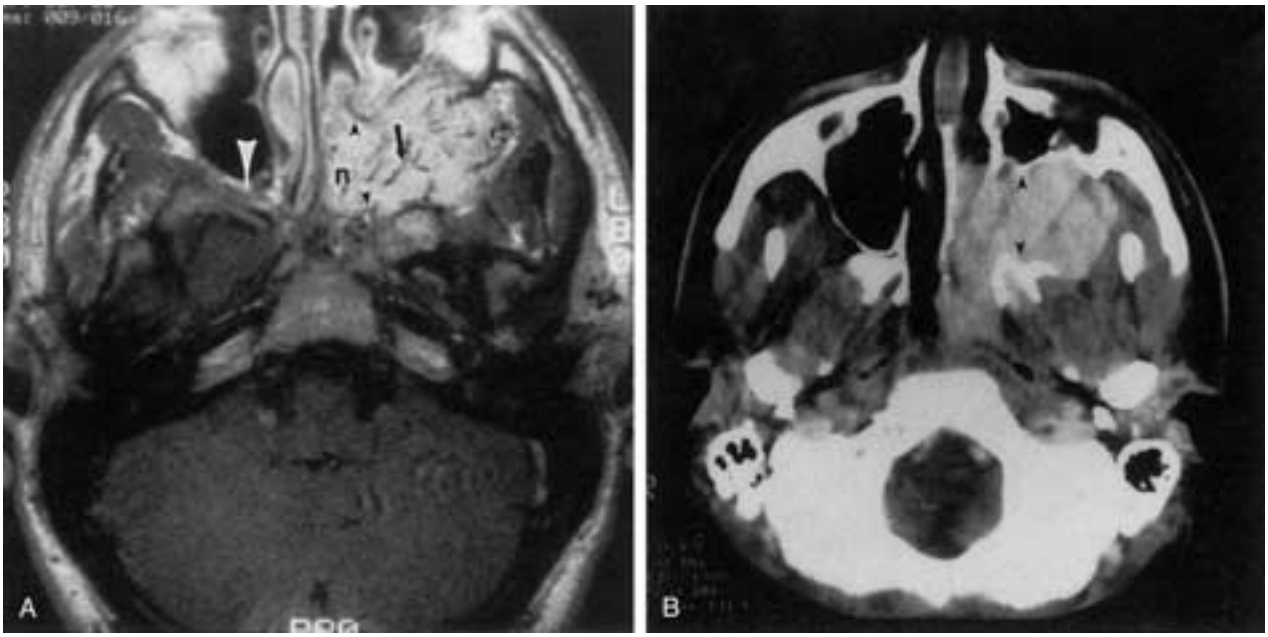

VIEW IMAGE

FIGURE 12-62 **A**, Juvenile angiofibroma expanding the pterygopalatine fossa. The T1-weighted postgadolinium MR image shows enhancing tumor in the region of the pterygopalatine fossa. It expands laterally (*open arrow*) into the infratemporal fossa, and medially the tumor passes through the region of the sphenopalatine foramen (*small black arrowheads*) into the posterior nasal cavity (*n*) and nasopharynx. Compare this with the normal pterygopalatine fossa (*white arrowhead*) on the opposite side. Flow voids representing large vessels (*black arrow*) can be seen within the tumor. **B**, CT scan shows the enlargement of the pterygopalatine fossa (*small black arrowheads*) by the enhancing mass. There is remodeling of the posterior wall of the maxillary sinus anteriorly. The pterygoid plates are pushed slightly posteriorly.

images and a relatively high signal intensity on T2-weighted sequences.

The tumor is locally invasive. In almost every case, tumor extends into the pterygopalatine fossa via the sphenopalatine foramen. The fossa is widened and its normal fat content obliterated. As the tumor grows, the posterior wall of the maxillary sinus is pushed anteriorly and the pterygoid plates are remodeled posteriorly. Actual bone erosion can occur at any margin but is frequently seen at the anterior surface of the upper pterygoid process. From this point the tumor can erode into the sphenoid sinus or posteriorly and superiorly through the more central skull base. As the tumor approaches the cavernous sinus and the middle cranial fossa, the dura remains intact initially. As the tumor continues to grow, the outer dural layer may be elevated so that, even if there is apparent tumor extension into the anterior cavernous sinus at imaging, the tumor still remains epidural in location at surgery. Once near the cavernous sinus, the tumor usually parasitizes intracranial vessels (Fig. 12-63). Eventually, though rare, larger tumors can break through the dural barrier and can even invade the brain.

The tumor can also grow laterally from the pterygopalatine fossa into the infratemporal fossa via the pterygomaxillary fissure. Anterior extension initially pushes the posterior antral wall anteriorly, but eventually the tumor can break through and expand into the sinus. Similarly, tumor in the pterygopalatine fossa can break through the pterygoid process or extend superiorly through the inferior orbital fissure into the orbit. Further extension through the superior orbital fissure is a common route of intracranial extension.

Although the tumor extent is mapped anatomically by CT and MR imaging, angiography is done to delineate the blood supply, often as a prelude to embolization. The primary blood supply is almost always from the terminal branches of the internal maxillary or the ascending pharyngeal arteries. Preoperative embolization effectively reduces intraoperative bleeding. Other arteries frequently may supply the tumor. Of particular concern are those coming from the internal carotid circulation. The arteries of the Vidian canal and the foramen rotundum usually fed from the termination of the sphenomaxillary artery can reverse the flow and carry the blood supply from the internal carotid artery to feed the tumor (Fig. 12-64). A blood supply from branches of the ophthalmic artery also has been demonstrated.

Pituitary Adenomas

Pituitary adenomas are discussed in Chapter 11. However, they are mentioned in this section because of their intimate relationship with the skull base. Two types are particularly pertinent to this discussion—the invasive pituitary adenoma and the infrasellar adenoma.

The invasive pituitary adenoma has its site of origin within the pituitary fossa.[112] As most pituitary adenomas enlarge, they extend superiorly through the diaphragm sella into the suprasellar cistern and toward the optic chiasm. Inferior enlargement displaces the sella floor downward. When a tumor actually breaks through the sella floor or grows laterally into the cavernous sinuses, it is considered an invasive pituitary adenoma (Fig. 12-65). The lesion can be

Copyright © 2003, Mosby, Inc. All rights reserved.

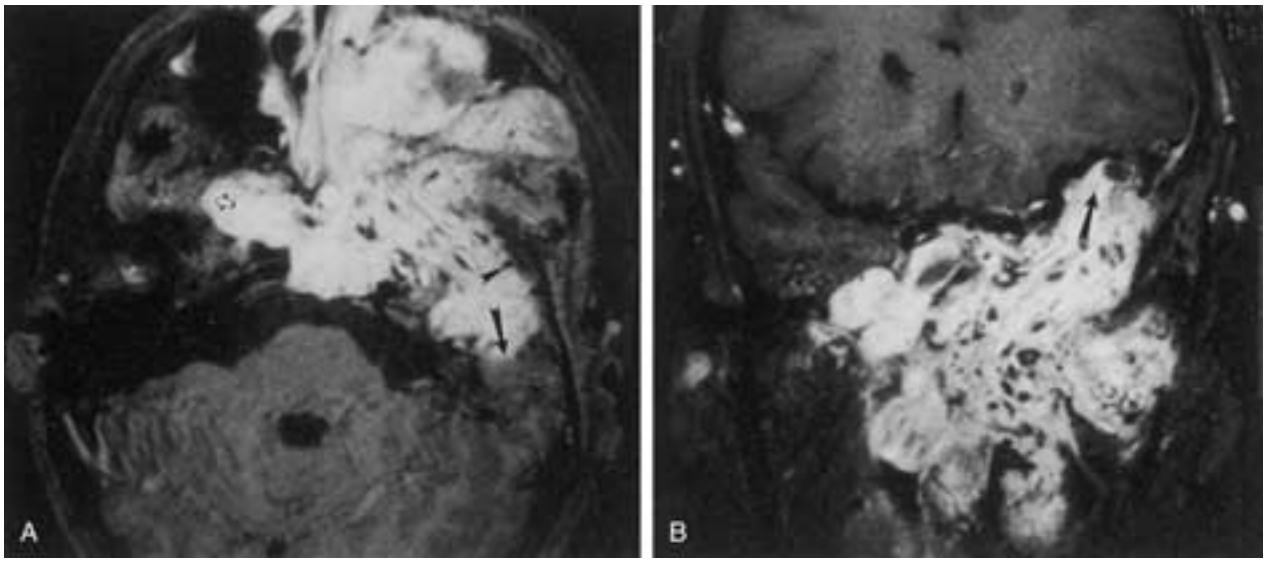

VIEW IMAGE

FIGURE 12-63 Juvenile angiofibroma. **A**, Axial postgadolinium T1-weighted image with fat suppression. This extensive tumor extends across the midline into the opposite infratemporal fossa (*open arrow*). There is extensive tumor (*black arrow*) extending intracranially. Flow voids (*arrowheads*) are seen within the tumor. **B**, Coronal postgadolinium T1-weighted image with fat suppression shows extensive intracranial tumor (*black arrow*) protruding superiorly. The lesion parasitized branches of the middle cerebral artery.

very large and destructive, at times reaching the nasopharynx or nasal cavity. In these cases, the imaging differentiation from a malignancy such as nasopharyngeal carcinoma can be quite difficult.[113] One differentiating point is that when a nasopharyngeal tumor invades the cavernous sinuses, it usually encases and narrows the carotid artery. However, when an invasive adenoma invades the cavernous sinuses, these arteries are surrounded but not narrowed. The lesion appears to squeeze around the vessel.

An extremely rare occurrence is a tumor of pituitary histology that is completely within the body of the sphenoid bone (Fig. 12-66).[114, 115] In these cases, the floor of the sella turcica has been reported to be intact. These extremely unusual tumors presumably arise from remnants of the

VIEW IMAGE

FIGURE 12-64 Lateral subtraction view of an internal carotid artery angiogram shows the presence of supply to this juvenile angiofibroma via dural branches of the cavernous carotid artery (*arrows*), consistent with tumor invasion of the cavernous sinus.

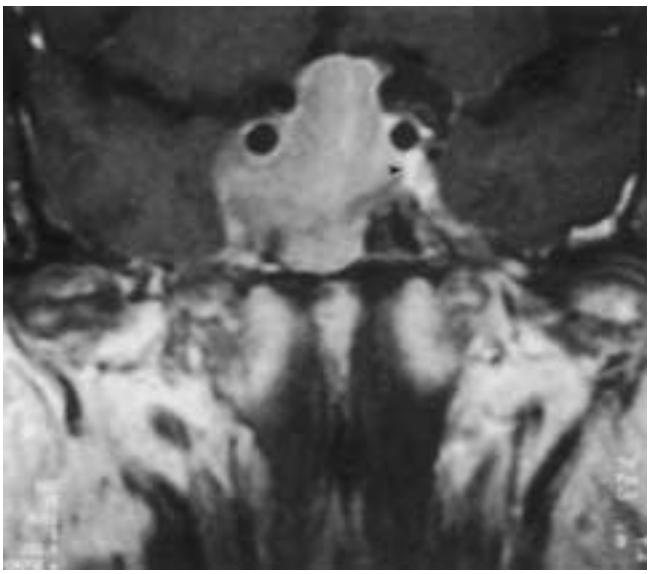

FIGURE 12-65 Invasive pituitary adenoma. Coronal postcontrast T1-weighted MR image. The adenoma shows intermediate enhancement, but the margin (*arrowhead*) between the adenoma and the normal cavernous sinus can be easily appreciated on the left-hand side. On the right side the adenoma extends further into the cavernous sinus, wrapping partially around the carotid artery. There is also inferior extension into the sphenoid body.

VIEW IMAGE

Copyright © 2003, Mosby, Inc. All rights reserved.

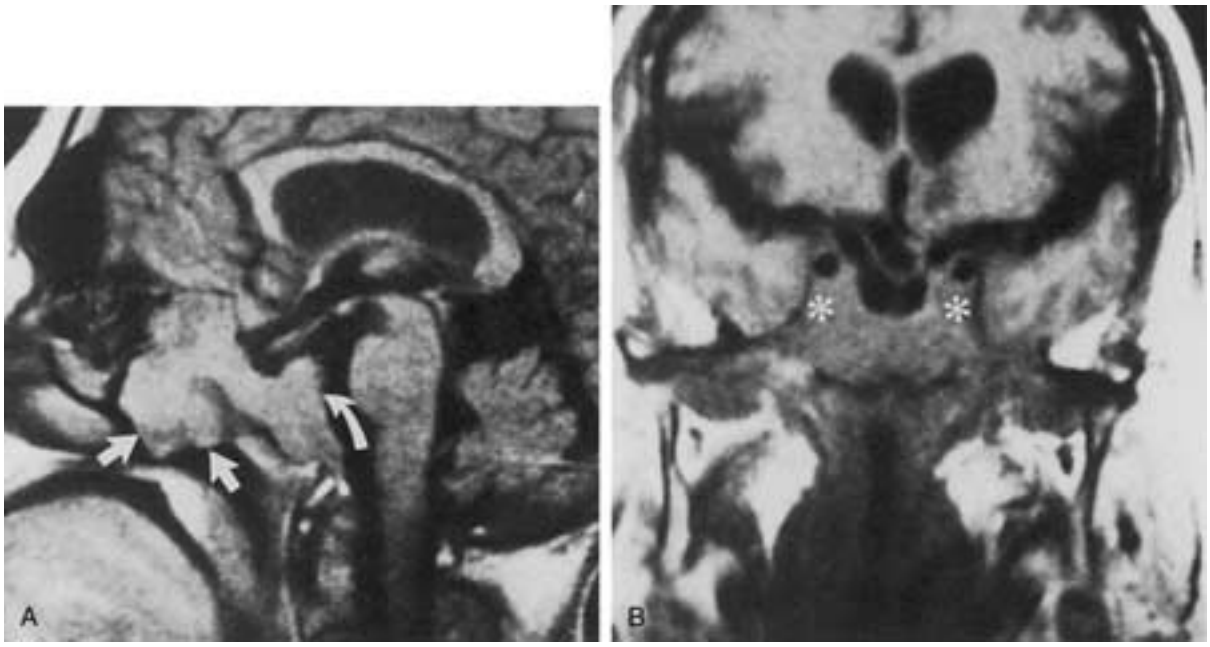

VIEW IMAGE

FIGURE 12-66 Intrasphenoid pituitary adenoma in a 38-year-old female presenting with amenorrhea, galactorrhea, and hyperprolactinemia. Midsagittal (**A**) and coronal (**B**) T1-weighted images show the presence of a mass involving the body of the sphenoid bone. The mass is relatively isointense to brain and extends inferiorly to the nasal fossa and nasopharynx (**A**, *straight arrows*), posteriorly to involve the clivus (**A**, *curved arrow*). It invades both cavernous sinuses (**B**, *asterisk*). A sphenoid sinus malignancy or chordoma also would be in the differential diagnosis.

pharyngohypophyseal pouch trapped by the closing ossification centers of the developing embryo. Another possibility is that the floor of the sella is not intact. In this case, the lesion invades the floor of the sella turcica and pushes or extrudes into the sphenoid sinus. The pulsation of the CSF transmitted through an incomplete diaphragm sella may help push the lesion down. As the lesion is pushed out of the sella, the appearance of an empty sella may be present.

Neurogenic Tumors

The numerous foramina of the sphenoid bone transmit several major cranial nerves and a variety of smaller nerves. Tumors can arise from these nerves.

Schwannomas (nerve sheath tumors) arise from the nerve sheath. Although the tumor can arise from virtually any nerve, the nerve most commonly affected in the central skull base is the trigeminal nerve. Hypoglossal nerve schwannomas are rare, as are lesions arising from cranial nerves III, IV, and VI in the region of the cavernous sinus. Schwannomas of cranial nerves IX, X, and XI arise at the margin of the basicranium in the medial jugular foramen.

The trigeminal schwannoma can arise in Meckel's cave or in the cistern along the course of the nerve (Fig. 12-67). Extension may occur through the foramen ovale, the foramen rotundum, or the superior orbital fissure (Figs. 12-68 and 12-69). When near the petrous apex, these schwannomas frequently have a dumbbell shape, with the anterior component enlarging the cavernous sinus and impinging on the middle cranial fossa, while the posterior component protrudes into the posterior fossa beneath the tentorium (Fig. 12-70). Other trigeminal schwannomas can remain isolated in either the posterior or the middle cranial fossae (Fig. 12-71). Rarely, a schwannoma can arise below the skull base in the masticator space or the pterygopalatine fossa. These tumors can protrude cranially, enlarging the foramen rotundum or the foramen ovale.

Like schwannomas elsewhere, trigeminal schwannomas can be solid or they can have a variable cystic component.

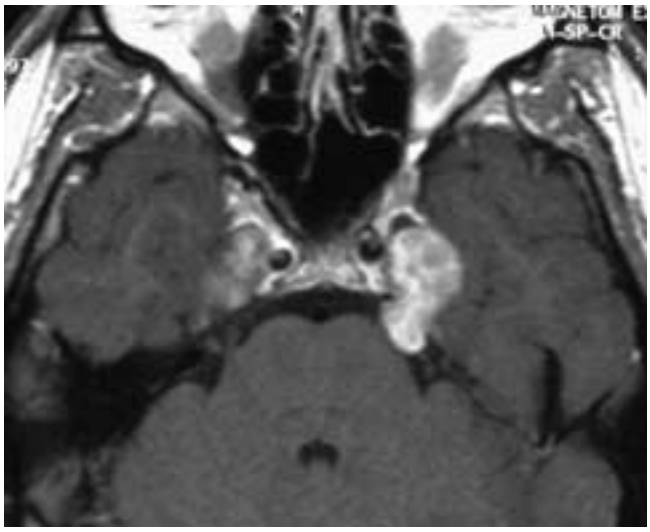

FIGURE 12-67 Schwannoma of Meckel's cave. The lesion on the left fills Meckel's cave and protrudes into the posterior fossa, giving it a dumbbell appearance.

VIEW IMAGE

Copyright © 2003, Mosby, Inc. All rights reserved.

VIEW IMAGE

FIGURE 12-68 Schwannoma extending through the superior orbital fissure. Note the lesion in the orbit (*black arrow*) extending through and obliterating the fat of the superior orbital fissure (*white arrowhead*) as the lesion extends into the anterior cavernous sinus (*black arrowhead*). Compare the obliteration of the fat on the left with the intact superior orbital fissure fat on the right (*white arrow*).

The smooth bony margin of an expanded foramen, if present, is best appreciated on CT. The cortex is usually maintained. These tumors enhance with contrast on either CT or MR imaging. On MR imaging, these tumors tend to have intermediate T1-weighted signal intensity. Cystic components can have low or high T1-weighted signal intensity. On T2-weighted images, these tumors have a fairly high signal intensity that is slightly higher than that of brain but is not as high as that of CSF.

Neurofibromas can affect the cranial nerves in neurofibromatosis type I (von Recklinghausen's disease). These lesions are made up of Schwann cells as well as perineural-like and fibroblastic cells.[116] Axons may be seen incorporated within the tumor. The nerve is enlarged and may follow through and expand the foramina (Figs. 12-72 and 12-73).

The plexiform neurofibroma is associated with neurofibromatosis type I. This abnormality is a more diffuse neurofibroma and is more infiltrative than either the localized neurofibroma or a classic schwannoma (Fig. 12-74). The tumor can follow and diffusely enlarge a branching nerve or plexus or can be a major component of a massive soft-tissue neurofibroma, a form of neurofibroma infiltrating diffusely through the soft tissues. Calcifications can sometimes be seen within these tumors on CT scans. The distribution of the trigeminal nerve can be affected, and when the tumor involves the orbit it often can be seen, with its irregular margins, extending into the orbital fat and around the orbital muscles. The plexiform neurofibroma may be associated with enlargement of the superior orbital fissure and with underdevelopment of the greater wing of the sphenoid, findings characteristic of neurofibromatosis I (Figs. 12-24 and 12-75). However, either the bony defect or the plexiform tumor can occur as an isolated lesion. Plexiform neurofibroma can also undergo malignant change. Primary malignant nerve sheath tumors are rare.

Giant Cell Lesions

Giant cell tumors (GCTs) are rare in the sphenoid bone. They have been reported in the body and in the greater sphenoid wing (Fig. 12-76). As in other areas of the body, the GCT of the sphenoid tends to occur in young adults. Most occur in the third or fourth decade of life but can occur at almost any age.[117, 118] A recent report described a series of pediatric patients with the lesion.[118] There is a slight female predominance.

The lesion expands the cortex of the bone but frequently leaves small gaps, producing an interrupted bony shell along the outer margin. There can be marginal sclerosis. With MR imaging, the lesion is described as having relatively low signal intensity on both T1-weighted and T2-weighted sequences. These lesions enhance moderately. Although cysts and fluid-fluid levels with areas of high signal intensity have been described, many GCTs are relatively homogeneous solid tumors.

The tumors may present with headache or cranial nerve palsies. Biopsy shows oval or plump spindle-shaped mononuclear cells and multinucleated giant cells evenly distributed throughout the lesion.[53] Each giant cell can have as many as 50 to 100 nuclei; most have 20 to 30. Reactive bone formation, hemorrhage, and cyst formation have also been described.

The GCT is one of the lesions considered to be a potential precursor of the aneurysmal bone cysts. Cysts can occur in part of the lesion or may replace the entire tumor. GCT can be primary or secondary. Secondary lesions can develop in pagetoid bone.

The giant cell granuloma (giant cell reparative granuloma, central giant cell granuloma) is most common in the mandible and maxilla but has been reported in the skull base, including the temporal bone and sphenoid.[119–123] The word ''central'' in the name central giant cell granuloma refers to a lesion whose origin is in bone rather than within the soft tissues of the oral cavity. Thus, a lesion arising in the gingiva is referred to as a peripheral giant cell granuloma. The giant cell granuloma is considered to be reactive rather than a true neoplasm. Trauma or hemorrhage have been suggested as inciting stimuli, but these are not definable in every case. There is a slight female predominance and the lesions occur at slightly younger ages than GCTs, typically between the ages of 10 and 25 years.[53]

The lesions are lytic and expansile and can have a sharp margin. The cortex is expanded, and the lesion is surrounded by a thin rim of bone. The cortex is frequently interrupted in some segments, and new bone formation has been reported.[123] On MR imaging, the giant cell granuloma tends to have low signal intensity on T1-weighted and T2-weighted sequences and the lesion enhances. There also can be significant hemorrhage into the lesion with cyst formation.

Histology shows giant cells, but they are not as evenly distributed throughout the lesion as in the GCT.[53] Each giant cell has fewer nuclei than the true GCT. In addition to the giant cells there are spindle-shaped fibroblasts, chronic inflammatory cells, and hemosiderin-laden macrophages, as well as collagen formation.

Brown tumors are indistinguishable histologically or radiologically from giant cell granuloma. They tend to occur later, in the fourth and fifth decades of life, and are seen in

Copyright © 2003, Mosby, Inc. All rights reserved.

patients with hyperparathyroidism.[120] They are more common in primary than secondary hyperparathyroidism, though they have been found in patients undergoing long-term dialysis. The serum calcium level is high, and the phosphorus level is low.

Aneurysmal Bone Cysts

Aneurysmal bone cysts (ABCs) occasionally are found in the sphenoid bone. On imaging, they appear as expansile masses with multiple cystic spaces. They have hemorrhage with large, blood-filled cavities, and fluid-fluid levels are characteristic. The patients are almost always less than 20 years old.

Several types of bone lesions have been considered to be precursors to ABCs. GCT, chondroblastoma, osteoblastoma, benign fibroosseous lesions, giant cell granuloma, chondromyxoid fibroma, bone cysts, eosinophilic granuloma, and hemangioma have all been mentioned.[53] Occasionally, an ABC can form within a malignancy. The ABC can have solid regions that mimic giant cell granuloma, with giant cells, fibroblasts, and hemorrhage.

Langerhans Cell Histiocytosis

Langerhans cell histiocytosis (LCH) is a proliferation of histiocytic and histiocytic like cells.[53] The typical histiocyte like cell is the Langerhans cell. The common histio-

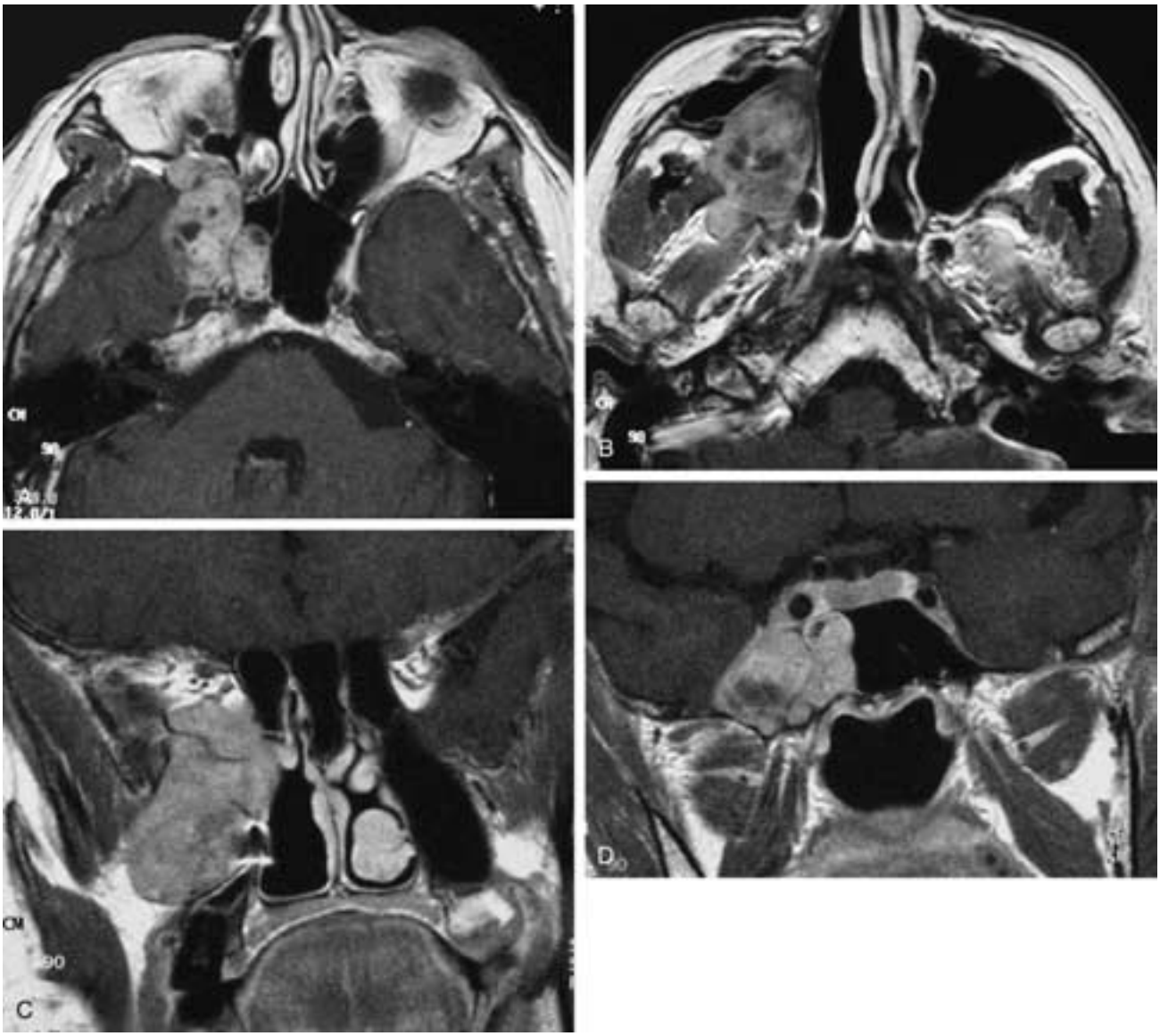

FIGURE 12-69 Schwannoma at V_2. **A**, Axial postcontrast image shows the tumor extending through the foramen rotundum into the upper pterygopalatine fossa. The lesion also extends into the sphenoid sinus. **B**, Image slightly caudal to **A** shows the tumor in the pterygopalatine fossa bowing the posterior wall of the maxillary sinus anteriorly. **C**, Coronal image shows the mass at the level of the pterygopalatine fossa extending up to the orbital fat. **D**, Coronal image at the level of the anterior cavernous sinus.

VIEW IMAGE

Copyright © 2003, Mosby, Inc. All rights reserved.

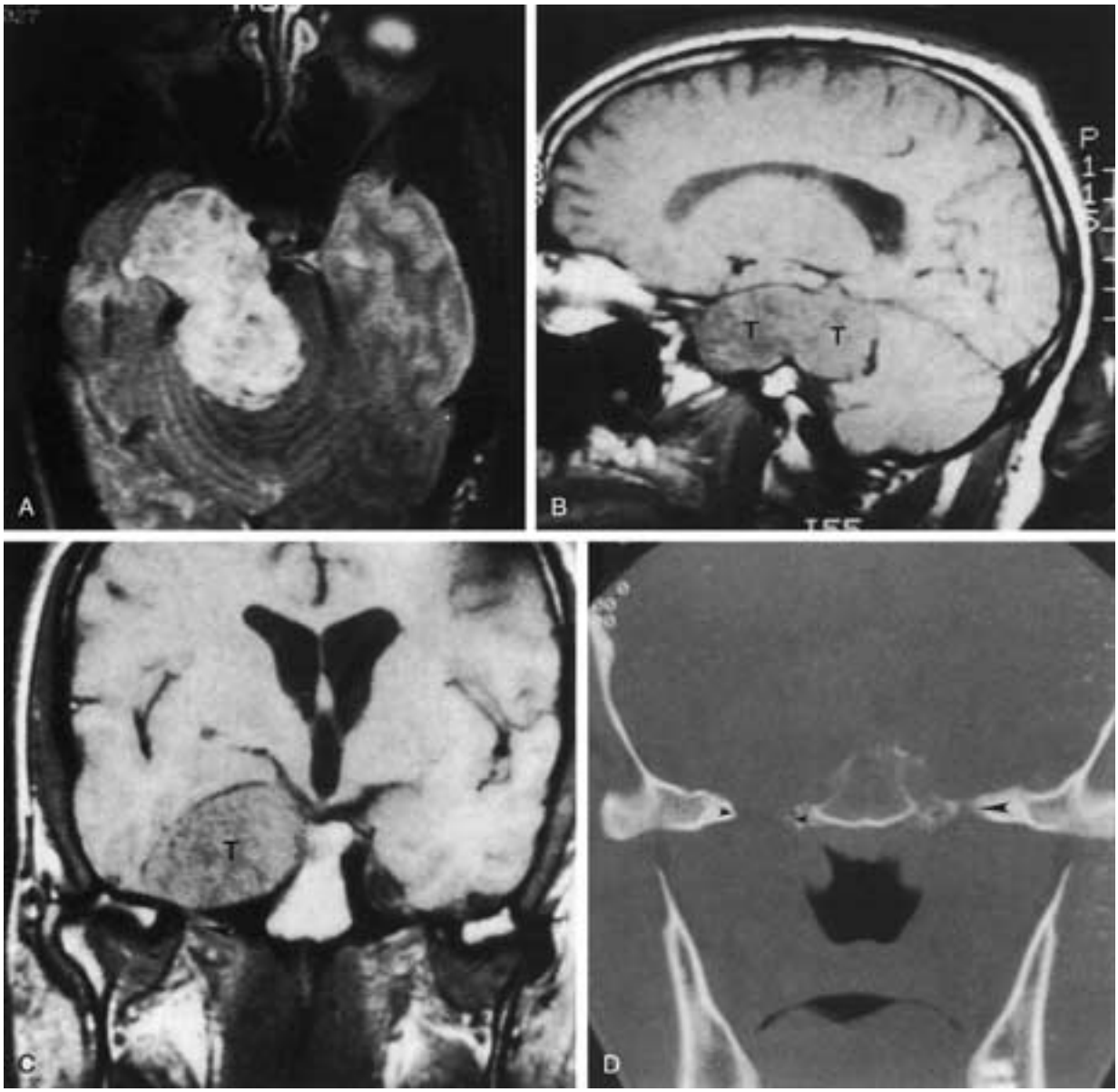

VIEW IMAGE

FIGURE 12-70 Nerve sheath tumor of the trigeminal nerve (schwannoma). The tumor (*T*) has both a middle cranial fossa and a posterior fossa component. Note that the carotid artery is pushed medially. **A**, The T2-weighted image shows relatively high signal but areas of intermediate signal as well. **B**, Sagittal image shows the dumbbell configuration of the tumor, with components both above and below the tentorium. The constriction is at the position of the tentorium. **C**, Coronal image shows the tumor expanding the region of the cavernous sinus and obscuring Meckel's cave. A small amount of fat (*arrowhead*) is seen just beneath the foramen ovale, indicating that the tumor did not spread by this route. **D**, Coronal bone algorithm. The foramen ovale between the small black arrowheads is enlarged even though the tumor did not extend through this foramen. Compare with the foramen ovale opposite (*large black arrowhead*).

cyte is a mononuclear cell with phagocytic ability, which contains many intracellular inclusions and lysosomes. The Langerhans cell has fewer lysosomes and less phagocytic ability than the usual histiocyte. The characteristic feature of the Langerhans cell is a folded large nucleus having a kidney or coffee bean shape. The lesion in LCH contains varying numbers of Langerhans cells mixed with eosinophils and more typical histiocytes.

The group of diseases included under the name Langerhans cell histiocytosis includes eosinophilic granuloma, Hand-Schuller-Christian (HSC), disease and Letterer-Siwe disease. These diseases, though related by histopathology, behave very differently. Eosinophilic granuloma (EG) usually has only one lesion at presentation and in such cases behaves clinically like a benign disease. If multiple lesions are present, a less benign course may be present. HSC disease is a chronic disease that is predominantly isolated to one organ complex such as the osseous system. It has a prognosis between those of EG and Letterer-Siwe disease. Letterer-Siwe disease is a multisystem, more acute disease that can be rapidly fatal. The classification is not exact, and there is often overlap. In general, the younger the patient, the

Copyright © 2003, Mosby, Inc. All rights reserved.

more severe the disease. Letterer-Siwe disease almost always presents in the first 3 years of life. HSC usually presents between 3 and 5 years of age and infrequently in slightly older persons. EG usually presents between the ages of 5 and 20 years.

The disease can involve almost any bone. LCH frequently involves the cranial vault and, less commonly, the skull base. The localized lesion of EG is the most likely variant to present as an isolated diagnostic problem in the skull base. Lesions can have a characteristic ''punched-out,'' sharply defined margin or can be more irregular, with a sclerotic margin. In the cranial vault, the lesion classically has a sharp margin with a beveled edge. A ''button sequestrum'' lesion is a lytic lesion in which residual bone remains. In the skull, most lesions are lytic, with or without sclerosis.

At radiography or CT scanning, the lesion may present as a ''punched-out'' abnormality, with a sharp margin and no sclerosis (Fig. 12-77). Alternatively, the lesion may have a more irregular sclerotic margin.[124, 125] On MR imaging, the lesion is seen as a solid mass, often obliterating the signal void of the cortex. The lesion usually has a high T2-weighted signal intensity but occasionally can have a fairly low signal intensity.[126] There is moderate enhancement. High signal intensity can be seen in contiguous soft tissues on T2-weighted images, reflecting the inflammatory nature of the lesion.[125]

Lesions involving the skull base can give cranial nerve palsies or present with pain and inflammatory symptoms. In the temporal bone, the lesion can mimic otitis media; however, there is no improvement on antibiotics. Systemic symptoms and peripheral eosinophilia are occasionally present. Lesions may be treated by curettage or by radiation therapy, depending on accessibility and proximity to crucial structures.

Miscellaneous Tumors and Lesions of the Sphenoid Bone

Though rare, osteosarcomas, Ewing's sarcoma, hemangiomas, and other miscellaneous tumors occasionally can be identified in the skull base. Similarly, lymphoma is uncommon, usually extending into the bone from contiguous soft-tissue disease. The rarity of these lesions precludes definitive statements about their imaging characteristics. However, anecdotal experience has shown that osteosarcoma can occur in the body or wing of the sphenoid.[127, 128] Imaging diagnosis relies on the identification of an osteoid matrix, seen best on CT. Lymphoma is very cellular and has a relatively low T2-weighted signal intensity. The primary mass is usually in the nasopharynx, but lymphoma can occasionally arise within the bone.

Plasmacytoma can affect the skull base and usually has a lytic, fairly homogeneous appearance on CT. On MR imaging, presumably because of cellularity, the tumor usually has an intermediate signal intensity on both T1-weighted and T2-weighted images. The lesion enhances

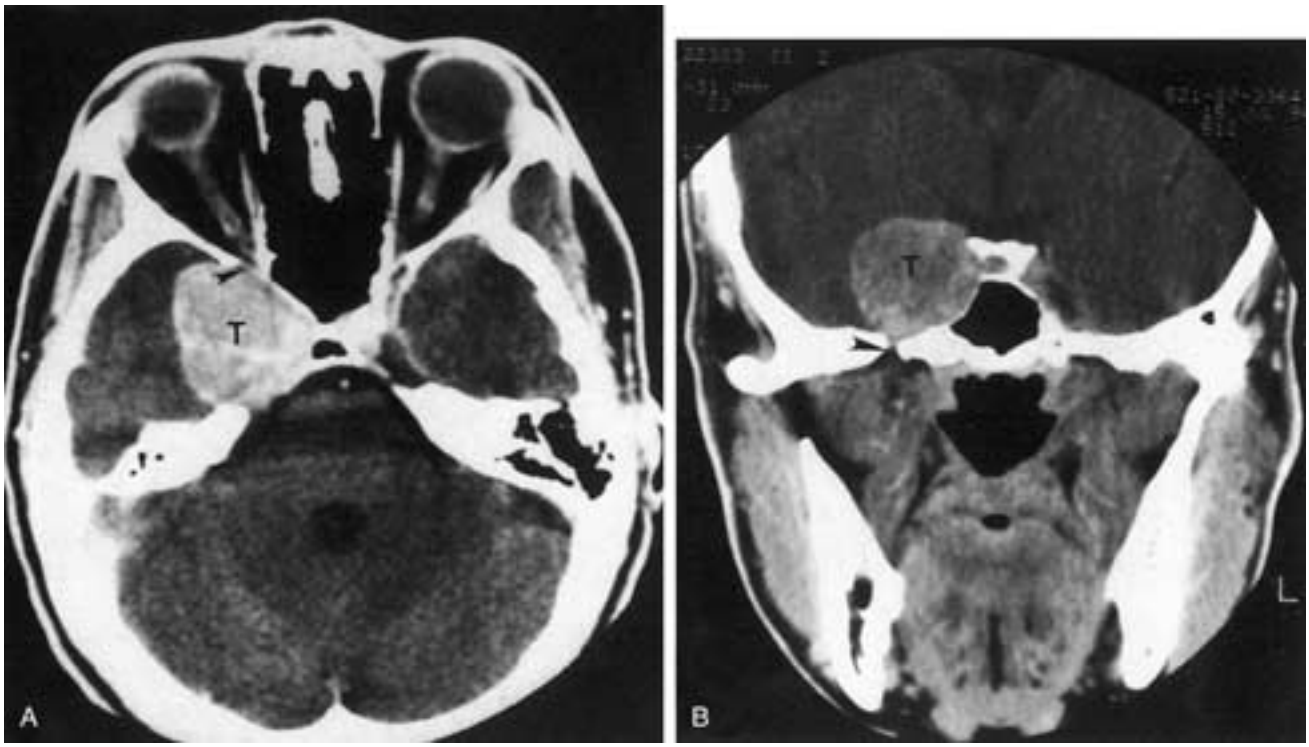

VIEW IMAGE

FIGURE 12-71 Neuroma of the cavernous sinus area. CT scan with contrast enhancement. **A**, Axial scan. The tumor (*T*) is seen at the level of the superior orbital fissure. The tumor bulges into and compresses the fat in the superior orbital fissure (*black arrowhead*) but does not protrude into the orbit. **B**, Coronal scan shows the tumor (*T*) scalloping and eroding the sphenoid sinus and dorsum sella. Again, it extends to but not through the foramen ovale. Note the maintenance of the normal fat (*black arrowhead*) just beneath foramen ovale.

Copyright © 2003, Mosby, Inc. All rights reserved.

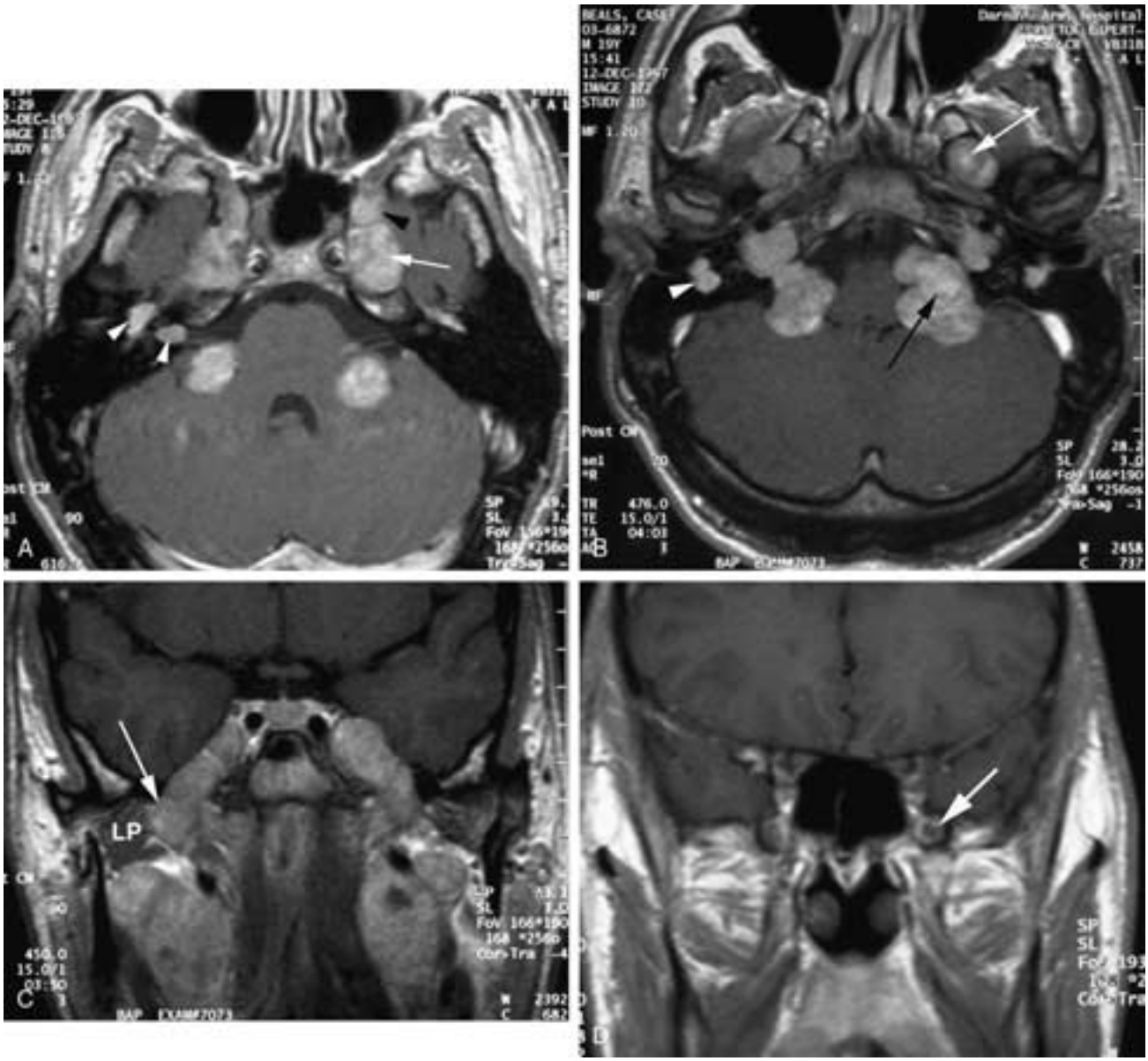

VIEW IMAGE

FIGURE 12-72 Neurofibromatosis 1 (von Recklinghausen's disease). Multiple neurofibromas involving multiple cranial nerves bilaterally. **A**, Axial postgadolinium image at the level of Meckel's cave shows bilateral lesions of the trigeminal nerve (*arrow*) as well as a lesion of the internal auditory canal following the facial nerve (*arrowheads*). The lesions of the trigeminal nerve follow the course of the foramen rotundum (*black arrowhead*). **B**, Axial postgadolinium scan slightly caudal to **A**. The neurofibroma extending through the foramen ovale is situated just medial to the lateral pterygoid muscle (*white arrow*). Lesion of the pars nervosa (*black arrow*) and lesion of the vertical facial nerve canal (*white arrowhead*). **C**, Coronal image shows the extension through the foramen ovale. Note how the lesion (*arrow*) just beneath the foramen ovale is situated just medial to the lateral pterygoid muscle (*LP*). Lesions are also seen lower in the neck. **D**, Coronal image through the region of the foramen rotundum shows the enlargement of the actual nerve (*arrow*) within the foramen surrounded by the small venous plexus.

on either CT or MR imaging. Although plasmacytoma can occur as an isolated lesion, many of these patients eventually develop multiple myeloma.

Carcinoma occasionally arises from the mucosal elements contained within the sphenoid sinus (Fig. 12-78). The tumor has an appearance similar to that of any invasive malignancy, and the diagnosis may be suggested by the relationship of the tumor to the sinus and surrounding structures.

Vascular lesions are rare in the skull base, and they may be benign or malignant.[129, 130] Benign lesions include hemangiomas or various vascular malformations. Hemangiomas have high T2-weighted signal intensity, may expand the bone, and enhance significantly. The bone may soften, and basilar invagination can result. Vascular malignancies potentially involving the skull base include angiosarcoma, hemangioendothelioma, hemangiopericytoma, and Kaposi's sarcoma.[53, 129]

Copyright © 2003, Mosby, Inc. All rights reserved.

Gorham's disease (massive osteolysis, disappearing bone disease, vanishing bone disease, phantom bone disease) is believed to develop from a vascular lesion.[4, 53, 131–137] Both hemangioma and lymphangioma have been mentioned as underlying lesions. This lesion at biopsy has a mixture of small-caliber blood vessels and fibrosis, with only a few osteoblasts. Both the skull and the skull base can be involved. At imaging, the bone is replaced by soft tissue, and there is a loss of bone volume (Fig. 12-79). The bone ''disappears'' or collapses. Malignancy, infection, and metabolic causes of bone loss must be excluded before the diagnosis is considered. The lesion may stop progressing spontaneously. Both surgery and radiotherapy have been attempted as curative therapies. The final diagnosis of many

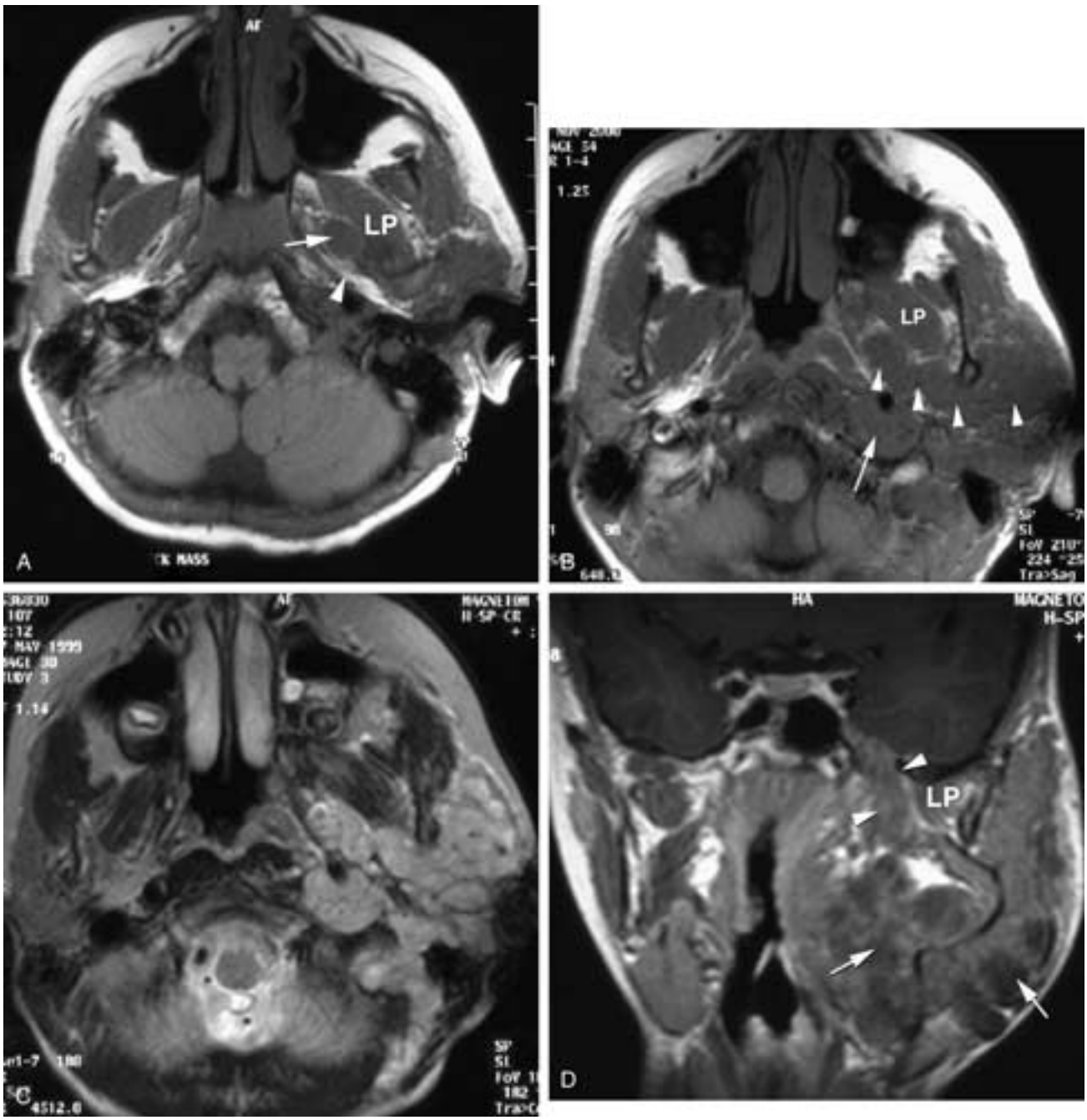

FIGURE 12-73 Neurofibromatosis 1 with neurofibroma extending along V_3 on the left side. Demonstration of the pathway of the auriculotemporal nerve. **A**, Axial T1-weighted precontrast image shows the tumor (*arrow*) just beneath foramen ovale along the medial margin of the lateral pterygoid muscle (*LP*). Note the fat (*arrowhead*) just beneath the skull base. **B**, The enlarged nerve can be followed along the course of the auriculotemporal nerve (*arrowheads*) extending posteriorly and laterally, just posterior to the upper mandible. *LP*, Lateral pterygoid muscle (*arrow*). A second lesion extends posterior to the carotid (*arrow*). **C**, T2-weighted image shows the relatively high signal of the lesions. **D**, Coronal T1-weighted postcontrast image shows the lesion extending up to and through the foramen ovale (*arrowheads*) just medial to the lateral pterygoid (*LP*). Lesions lower in the neck (*arrows*).

VIEW IMAGE

Copyright © 2003, Mosby, Inc. All rights reserved.

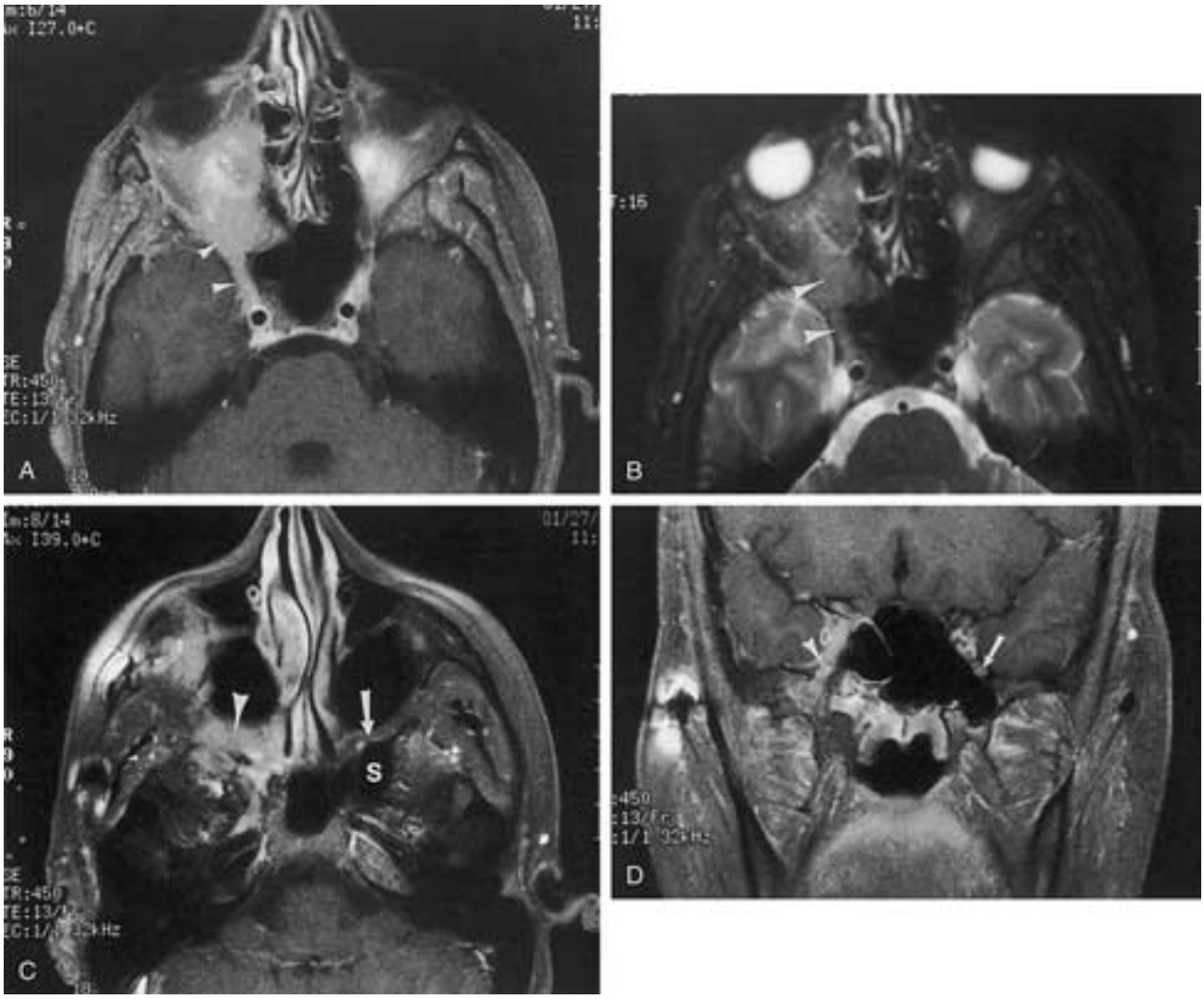

VIEW IMAGE

FIGURE 12-74 Diffuse neurofibroma extending along branches of the trigeminal nerve. **A**, Axial T1-weighted postcontrast image with fat suppression shows the tumor (*white arrowheads*) extending from the cavernous sinus anteriorly into the orbital apex and upper pterygopalatine fossa. **B**, T2-weighted image again shows the tumor (*arrowheads*), which has a fairly low signal intensity. **C**, Scan inferior to **A** shows the tumor (*white arrowhead*) filling and expanding the pterygopalatine fossa. Compare this with the normal pterygopalatine fossa (*arrow*) on the opposite side. In this fat-suppressed image, the signal within the normal pterygopalatine fossa is low. A laterally extending air cell from the sphenoid sinus (*S*) is seen extending into the attachment of the pterygoid plate. **D**, The tumor is seen in the anterior cavernous sinus and posterior superior orbital fissure (*open arrow*). The arrowhead indicates the approximate position of the foramen rotundum. The normal foramen rotundum on the opposite side (*arrow*) is identified. Again, note that the expanding sphenoid air cell on the normal side extends between the foramen rotundum and the Vidian canal. (Courtesy of Dr. Norman Leeds.)

of these rare tumors is made at biopsy, and usually the role of imaging is to accurately map the lesion.

Mucoceles

Obstruction of the sphenoid sinus ostium can result in a mucocele. The term mucocele is used by radiologists to indicate an airless, ‘‘mucus-filled’’ sinus, with an enlarged sinus cavity. Mucoceles can occur as isolated lesions or in association with polyps or other inflammatory disease. Any part of the sinus can be expanded. The anterior clinoid process is frequently pneumatized and thus can be enlarged by a mucocele (Fig. 12-80). If a mucocele forms near the root of the pterygoid process, where the air cells pass between the foramen rotundum and the Vidian canal, this bone can be enlarged. However, the separation of the Vidian and rotundum canals varies with the degree of air cell development and extension of air cells into the pterygoid process.[19] Thus, asymmetric separation of the foramina alone does not indicate mucocele. As the mucocele enlarges, it can erode or thin the bony cortex of the sphenoid sinus wall or the cortex of one of these foramina. When present, this erosion or scalloping is a reliable indicator of actual sinus expansion. As discussed in Chapter 5, the signal intensities on MR imaging can vary in relation to the protein

Copyright © 2003, Mosby, Inc. All rights reserved.

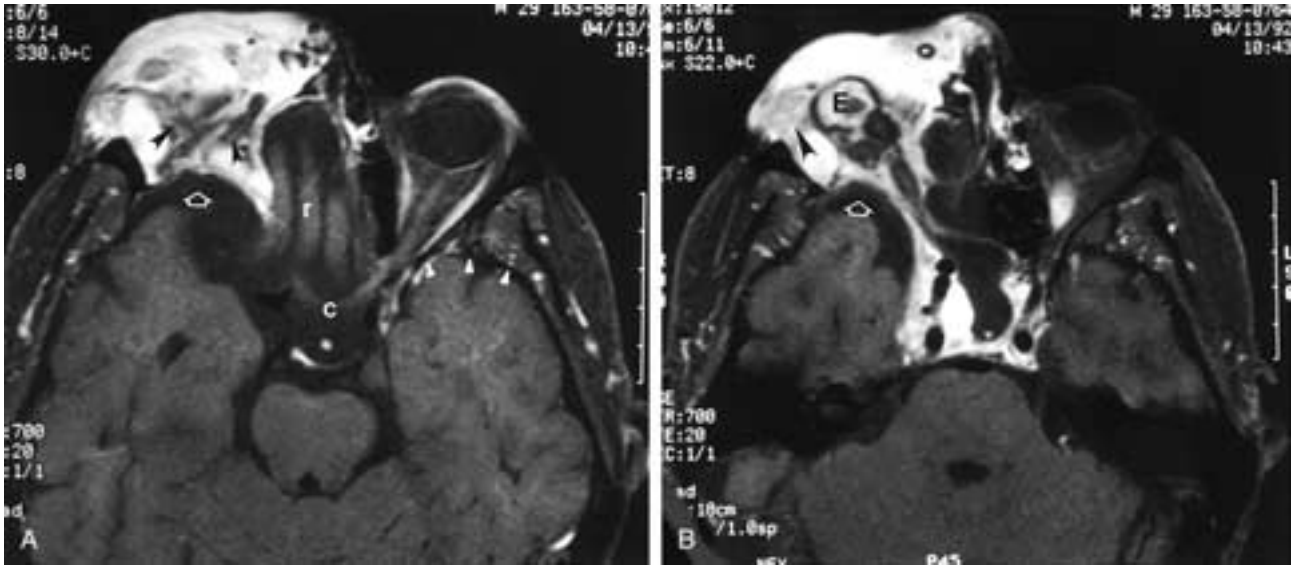

VIEW IMAGE

FIGURE 12-75 **A**, Neurofibromatosis with an orbital encephalocele and a plexiform neurofibroma. The abnormal neurofibroma (*arrowheads*) is seen within the malformed orbit. There is also a defect in the sphenoid bone, with herniation of the CSF space (*open arrow*) into the posterior orbit. *r*, Gyrus rectus; *c*, chiasm. Note the normal position of the anterior wall of the middle cranial fossa (*small white arrowheads*) on the opposite side. **B**, Axial postcontrast T1-weighted images after fat suppression. A plexiform neurofibroma (*arrowhead*) is seen within the malformed orbit. A small residual eye (*E*) can be identified. At this level, the temporal lobe can be seen following the CSF space (*open arrow*) into the posterior orbit.

FIGURE 12-76 GCT of the sphenoid. **A**, Sagittal T1-weighted image shows the tumor (*T*) in the skull base extending into and occluding the nasopharynx (*arrow*). **B**, Coronal postcontrast T1-weighted image shows moderate enhancement of the tumor (*T*). **C**, Axial T2-weighted image shows intermediate to low signal. **D**, Coronal CT image. The lesion extends to the cavernous sinuses on either side.

VIEW IMAGE

Copyright © 2003, Mosby, Inc. All rights reserved.

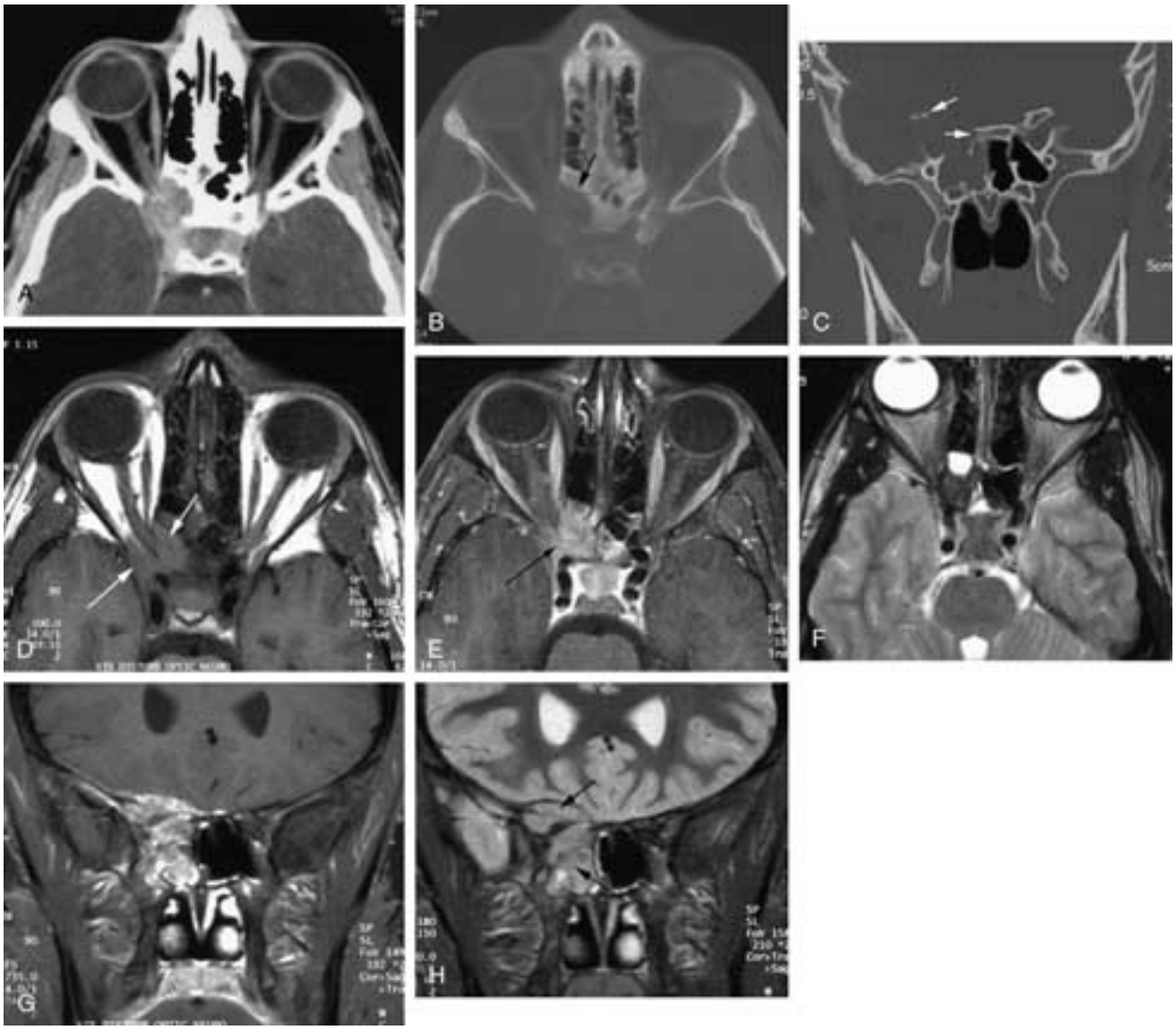

VIEW IMAGE

FIGURE 12-77 Langerhans histiocytosis (eosinophilic granuloma). **A**, Axial postcontrast CT algorithm shows a lesion in the orbital apex and lateral sphenoid with slight enhancement. **B**, Axial CT bone algorithm shows the lesion with a sharp margin (*arrow*). Note the demineralization around the optic nerve canal. **C**, Coronal bone algorithm shows a sharp nonsclerotic margin (*arrows*). **D**, T1-weighted MR image shows intermediate signal intensity of the lesion (*arrows*). **E**, Postgadolinium image shows moderate enhancement (*arrow*). **F**, Axial T2-weighted image shows the lesion to be relatively dark. **G**, Coronal postcontrast image shows the lesion bulging the dura superiorly and involving the apex as well as the lateral sphenoid. **H**, Coronal STIR (Short Tau Inversion Recovery) lesion (*arrows*).

concentration of the retained secretions (Fig. 12-81) and the presence of *Aspergillus* or other mycetomas. On contrast-enhanced MR images, a thin line of enhancing mucosa along the wall of the sinus identifies the obstructed nature of the sinus.[138]

Aneurysms

Aneurysms involving the central skull base can arise from the intracavernous portion of the carotid artery or extend from the petrous portion of the carotid, and though most aneurysms occur spontaneously, some occur after trauma (Figs. 12-82 to 12-86).[139] Despite the fact that transsphenoidal approaches to the pituitary gland, endoscopic explorations of the sphenoid, and various skull base approaches to the cavernous sinus put the artery at risk, postsurgical aneurysms (or pseudoaneurysms) are rare. Sphenoid sinus inflammatory disease, especially fungal disease, can extend into the cavernous sinus and cause an aneurysm.

Aneurysms can present with headache. Pressure on the nerves in the cavernous sinus can lead to ophthalmoplegia (with or without headache) or to facial pain. Hemorrhage is unusual. A small aneurysm confined to the cavernous sinus is unlikely to bleed, but larger ones occasionally can rupture.

Copyright © 2003, Mosby, Inc. All rights reserved.

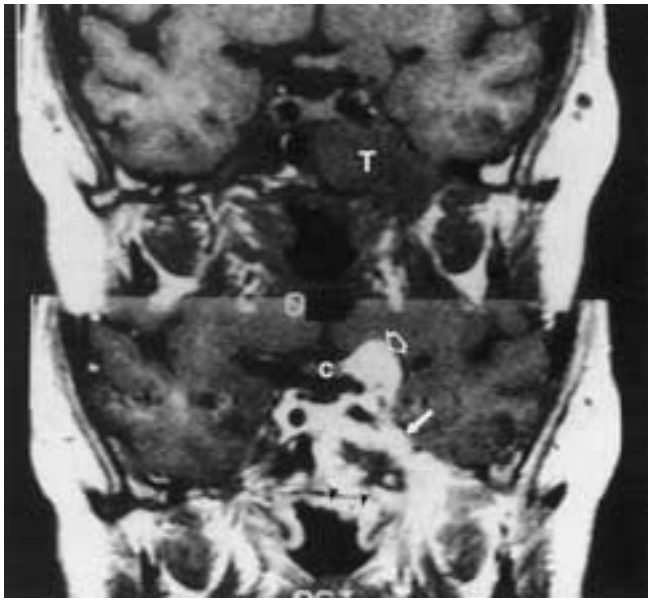

VIEW IMAGE

FIGURE 12-78 Carcinoma of the sphenoid sinus. Coronal T1-weighted MR images. The upper image shows the tumor (*T*) in the lateral sphenoid. The lower image (postcontrast) shows the enhancement (*white arrow*) extending into the cavernous sinus, with a fairly low signal in the central part of the tumor. A nodule of tumor (*open arrow*) is seen against the chiasm (*C*). The lower enhancement (*small black arrowheads*) represents the enhancing mucosa rather than the tumor itself. The mucosa is displaced slightly inferiorly by the tumor in the submucosal location.

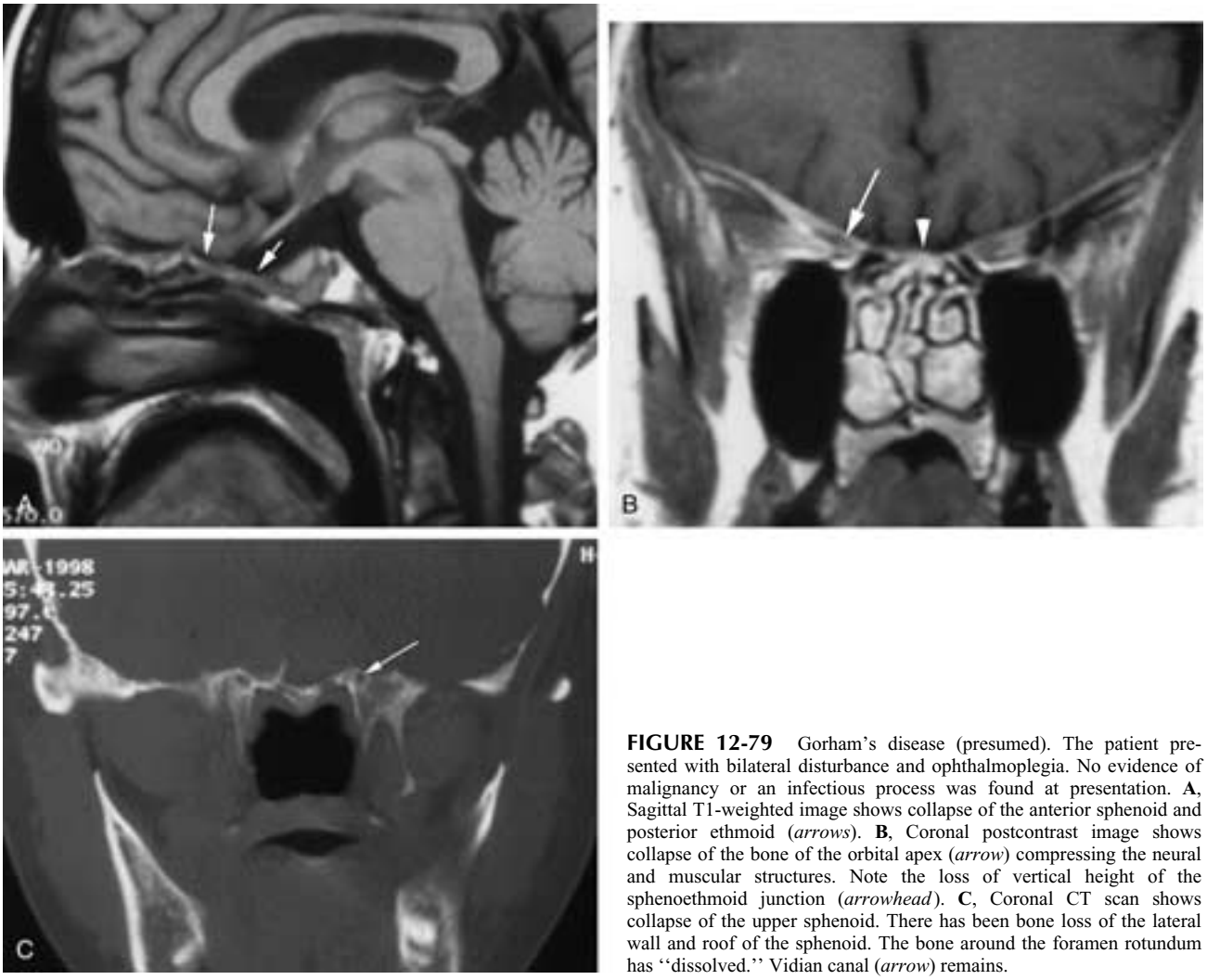

VIEW IMAGE

FIGURE 12-79 Gorham's disease (presumed). The patient presented with bilateral disturbance and ophthalmoplegia. No evidence of malignancy or an infectious process was found at presentation. **A**, Sagittal T1-weighted image shows collapse of the anterior sphenoid and posterior ethmoid (*arrows*). **B**, Coronal postcontrast image shows collapse of the bone of the orbital apex (*arrow*) compressing the neural and muscular structures. Note the loss of vertical height of the sphenoethmoid junction (*arrowhead*). **C**, Coronal CT scan shows collapse of the upper sphenoid. There has been bone loss of the lateral wall and roof of the sphenoid. The bone around the foramen rotundum has ''dissolved.'' Vidian canal (*arrow*) remains.

Copyright © 2003, Mosby, Inc. All rights reserved.

Depending on its direction of expansion, this type of aneurysm can rupture into the sphenoid sinus or into the subarachnoid space. The rupture can also be into the cavernous sinus, resulting in a carotid cavernous sinus fistula rather than a frank hemorrhage. If the aneurysm contains thrombosis, embolization to more distal arteries can lead to a central neurologic presentation.

An aneurysm of the cavernous portion of the internal carotid artery will enlarge the cavernous sinus; however, a small aneurysm may be undetectable. Usually, an aneurysm bows the lateral cavernous sinus wall laterally. The bony lateral sphenoid sinus wall may be bowed medially into the sinus. Small aneurysms are quite difficult to detect on planar imaging because of the normal tortuosity of the carotid artery. Careful examination of imaging done in multiple planes will lessen the likelihood of overlooking such an

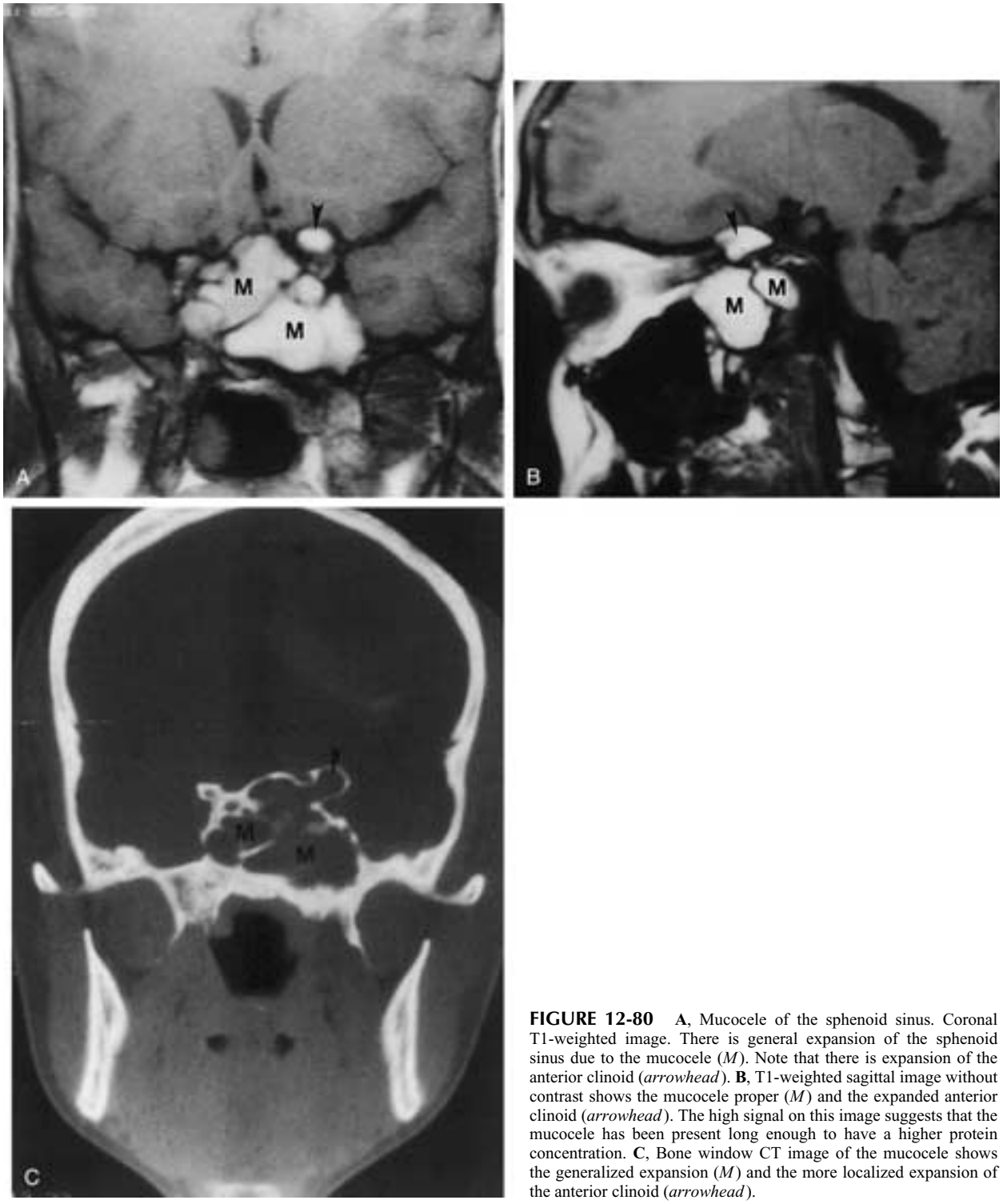

FIGURE 12-80 **A**, Mucocele of the sphenoid sinus. Coronal T1-weighted image. There is general expansion of the sphenoid sinus due to the mucocele (*M*). Note that there is expansion of the anterior clinoid (*arrowhead*). **B**, T1-weighted sagittal image without contrast shows the mucocele proper (*M*) and the expanded anterior clinoid (*arrowhead*). The high signal on this image suggests that the mucocele has been present long enough to have a higher protein concentration. **C**, Bone window CT image of the mucocele shows the generalized expansion (*M*) and the more localized expansion of the anterior clinoid (*arrowhead*).

VIEW IMAGE

Copyright © 2003, Mosby, Inc. All rights reserved.

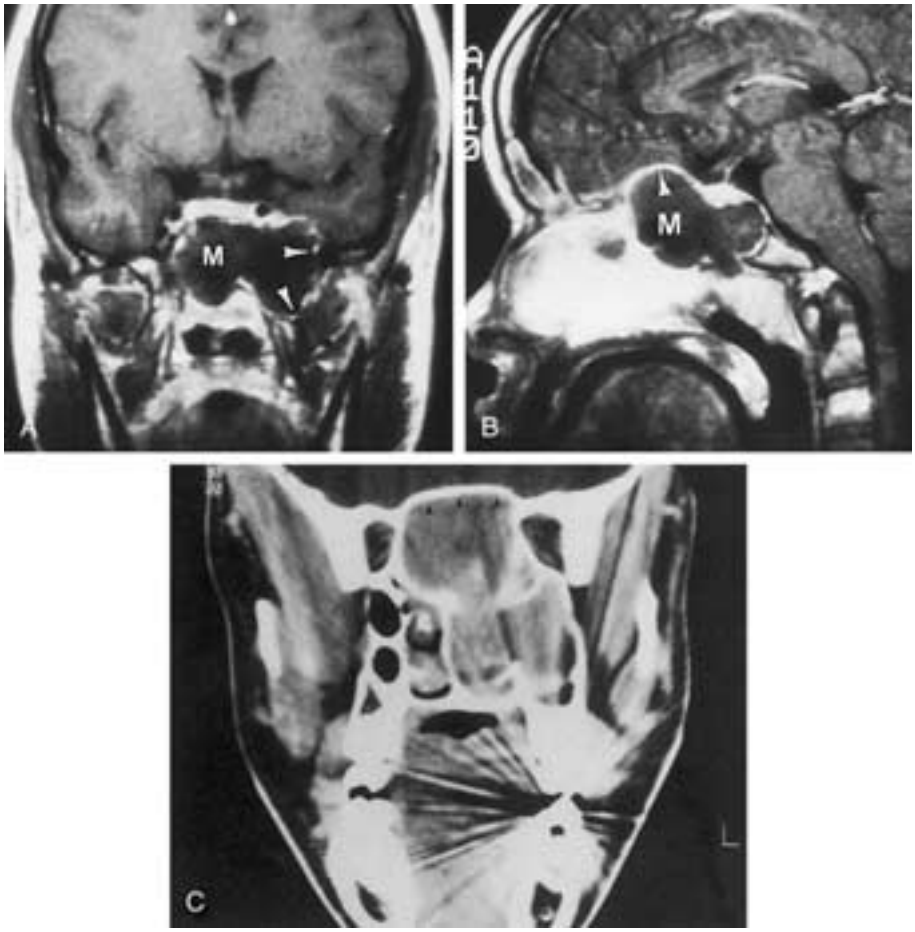

VIEW IMAGE

FIGURE 12-81 **A**, Mucocele of the sphenoid sinus. Coronal image shows the mucocele (*M*). There is expansion laterally (*white arrowheads*) in the position that would be typical of a lateral sphenoid air cell. The low signal on this postcontrast T1-weighted image is thought to be caused by very high protein content and desiccation. It might also be due to *Aspergillus*, which would give a very low signal. **B**, Postcontrast T1-weighted sagittal image shows the mucocele with upward expansion in the region of the planum (*white arrowhead*). Again, note the low signal and lack of enhancement in the mucocele cavity. **C**, Coronal CT image. The mucocele expands the planum and the cortex superiorly (*small arrowheads*).

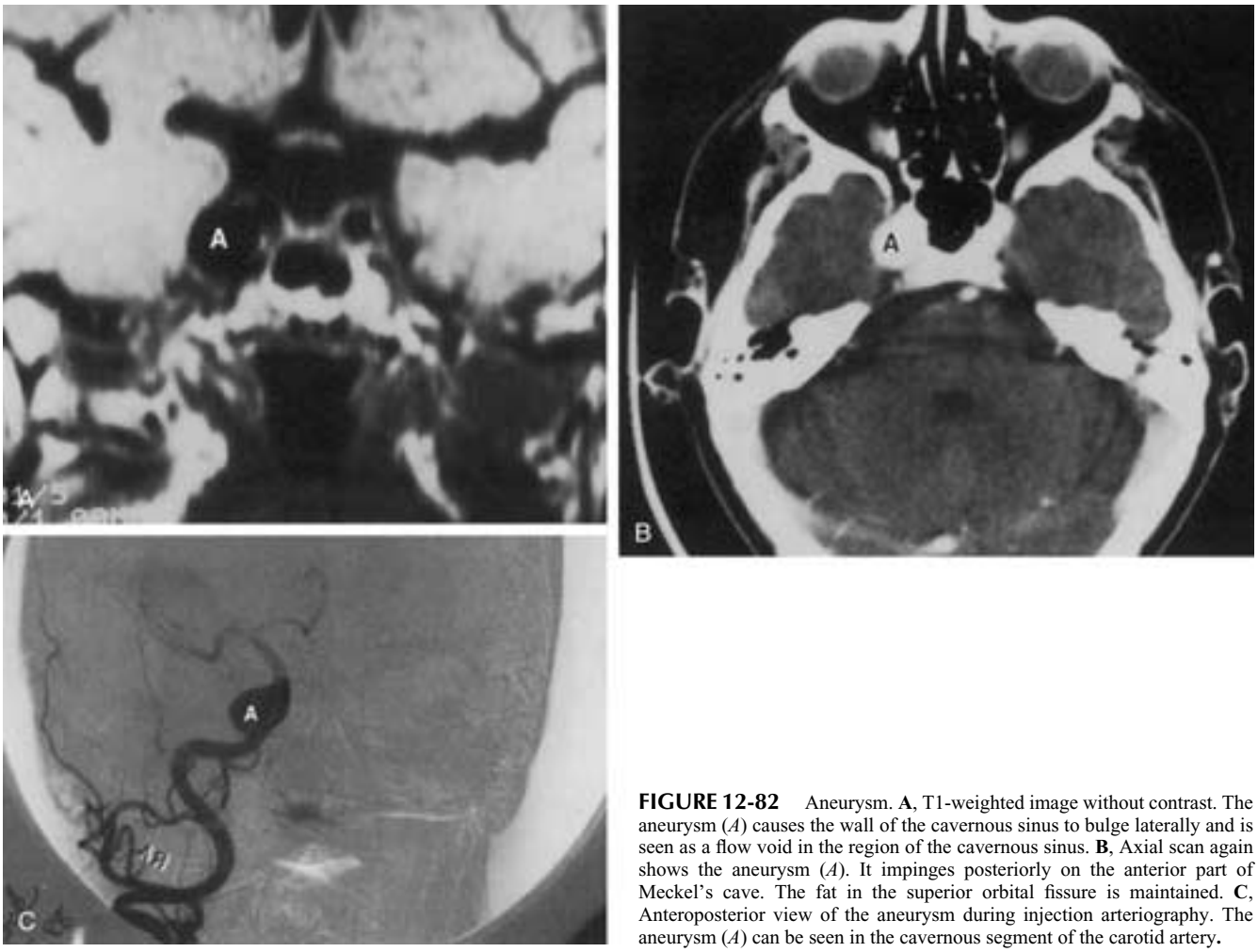

FIGURE 12-82 Aneurysm. **A**, T1-weighted image without contrast. The aneurysm (*A*) causes the wall of the cavernous sinus to bulge laterally and is seen as a flow void in the region of the cavernous sinus. **B**, Axial scan again shows the aneurysm (*A*). It impinges posteriorly on the anterior part of Meckel's cave. The fat in the superior orbital fissure is maintained. **C**, Anteroposterior view of the aneurysm during injection arteriography. The aneurysm (*A*) can be seen in the cavernous segment of the carotid artery.

VIEW IMAGE

Copyright © 2003, Mosby, Inc. All rights reserved.

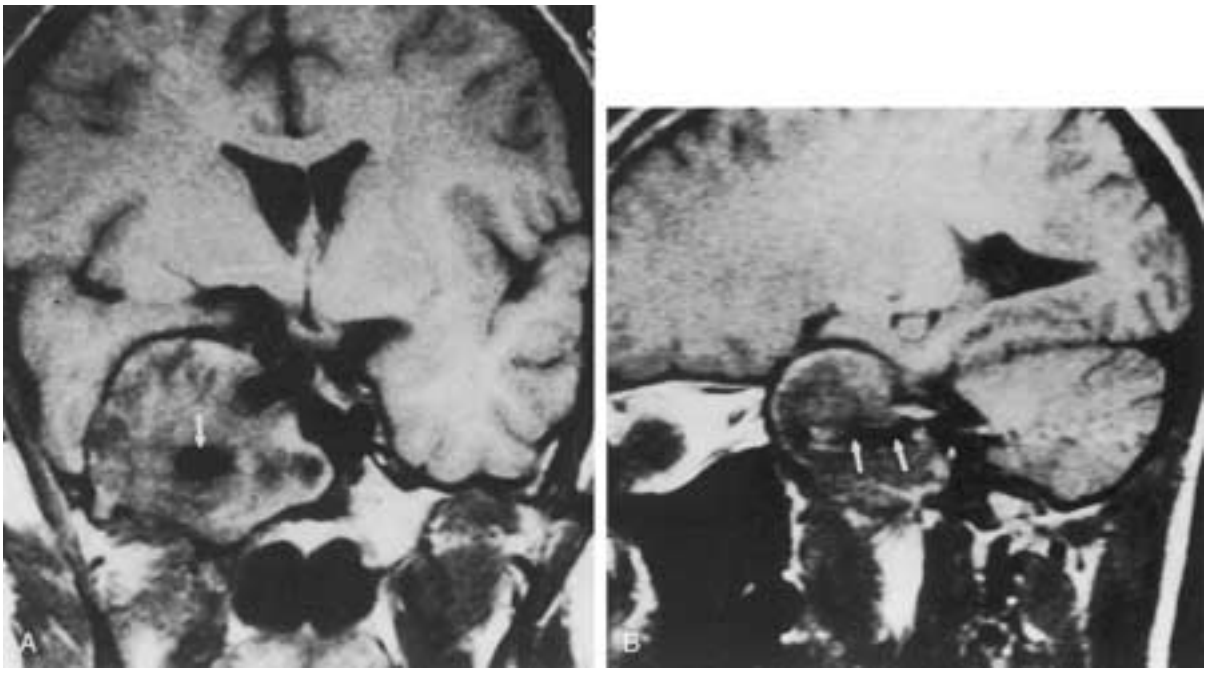

VIEW IMAGE

FIGURE 12-83 **A**, Coronal T1-weighted MR image. Partially thrombosed aneurysm of the petrous and cavernous carotid arteries. The flow void (*arrow*) is seen in the central part of the aneurysm. Most of the ''mass'' is filled with thrombus of varying signal intensities. **B**, Sagittal T1-weighted image without contrast again shows the flow void of the central lumen (*arrows*) within the larger mass, which is partially thrombosed.

aneurysm. If the lumen is patent, MRA or CT angiography may demonstrate the aneurysm. Catheter arteriography is not usually necessary for evaluation of a potential intracavernous aneurysm.

The imaging appearance of a large aneurysm is varied and depends on the patency of the lumen and the presence of partial thrombosis. If little thrombus is present, the lumen may completely opacify on enhanced CT, blending with and ''disappearing'' into the enhancing cavernous sinus. A dynamic CT scan's arterial phase may help separate the aneurysm from the normal cavernous sinus. If, on the other hand, thrombus fills part of the aneurysm, the lesion usually has a low density with an enhancing rim. A channel of opacification, representing residual lumen, occasionally can be seen. Calcification sometimes can be present in the aneurysm's wall.

On MR imaging, the appearance of an aneurysm also varies, depending on the presence or absence of partial thrombosis (Fig. 12-83). The lumen of a small aneurysm still may be detected if there is rapid blood flow causing a signal flow void. Larger aneurysms may be free of thrombus and appear as a large, rounded flow void. However, the flow in the aneurysm may be turbulent, giving a variety of signal intensities. The movement of the blood usually can be defined with various flow-sensitive sequences.

Thrombus, which partially or completely fills the lumen of an aneurysm, has a variable appearance on MR imaging. Layers of thrombus of varying age may be identified, and the appearance reflects the evolution of the blood products within the thrombus.[140] Thrombus of intermediate age is often bright on T1-weighted and T2-weighted images, reflecting concentrations of methemoglobin. This signal is seen most commonly bordering the residual lumen. Low signal areas, usually seen at the periphery of the aneurysm, reflect the presence of hemosiderin.

On rare occasions, these aneurysms, when large, can erode through the skull base, usually in the floor of the middle cranial fossa.[141]

Treatment of the aneurysm depends on its size, its location, and the presenting symptoms. Small aneurysms may be followed, but larger ones are usually treated. Alternatives to surgery include endovascular occlusion of the parent vessel or placement of balloons or coils within the aneurysm.

SECONDARY TUMOR INVOLVEMENT OF THE SKULL BASE

The skull base is frequently the site of tumor spread, involved most commonly by direct invasion from an adjacent primary neoplasm. Hematogenous metastasis from distant primary tumors also occurs. An important route of extension of primary head and neck tumors is perineural spread along the cranial nerves to and through the various skull base foramina.

Direct Encroachment

Tumors that arise close to the skull base frequently invade the bone because the fascial planes of the infratemporal fossa and nasopharynx preferentially direct the spread of neoplasm toward the skull base.[142] Nasopharyngeal cancer characteristically invades the midline skull base.[143] The strong pharyngobasilar fascia wrapping around the posterior

Copyright © 2003, Mosby, Inc. All rights reserved.

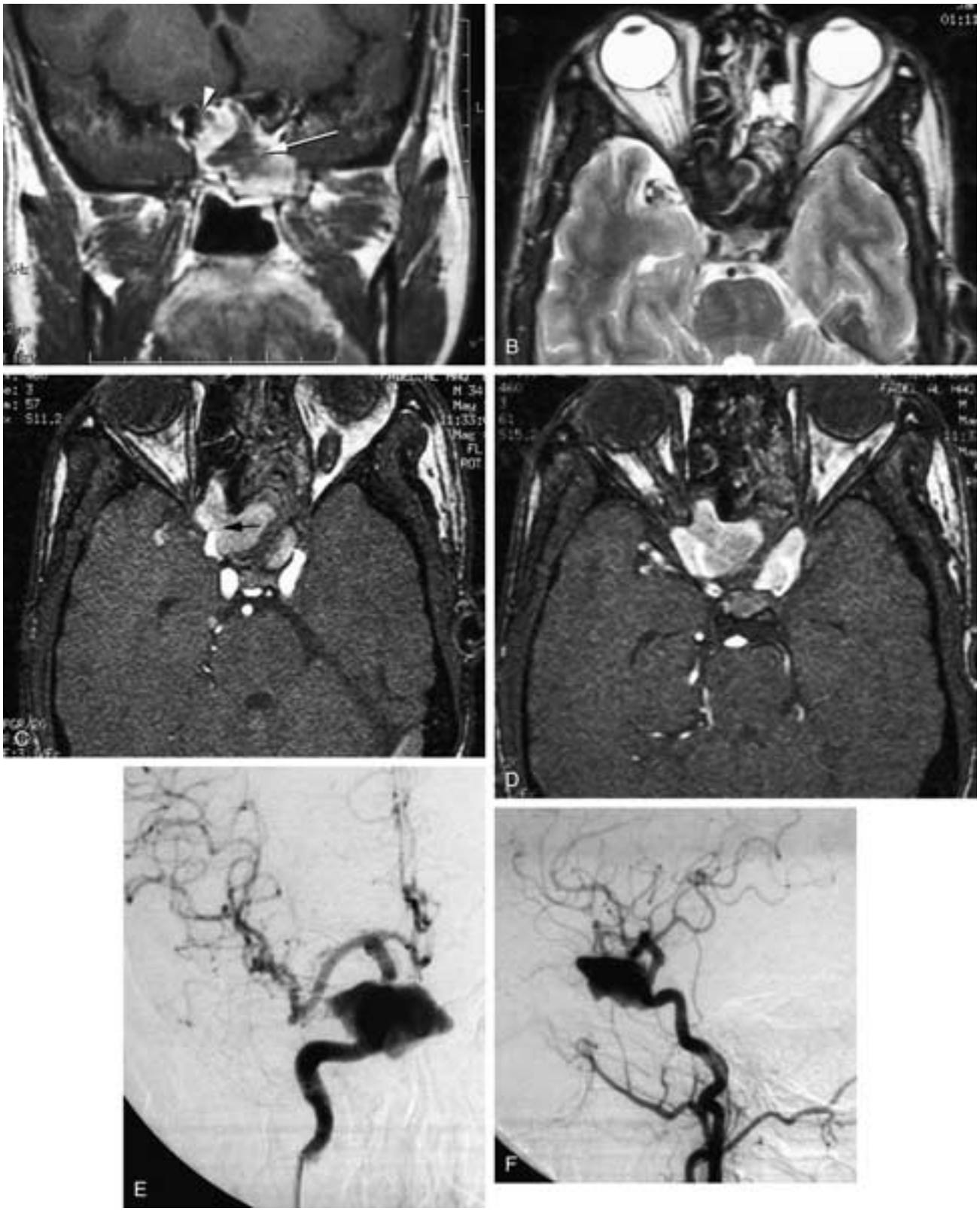

FIGURE 12-84 Carotid aneurysm (possible pseudoaneurysm) extending into the sphenoid sinus. **A**, Coronal T1-weighted image shows variable signal intensity (*arrow*) within an expanded sphenoid sinus. The enhancement along the margin might suggest mucocele. There is slight irregularity (*arrowhead*) adjacent to the right carotid artery. **B**, Axial T2-weighted image shows low signal within the sphenoid. **C**, SPGR image shows the proximity of the carotid artery (*arrow*) to the sphenoid sinus. **D**, Axial SPGR image slightly cephalad to **C** shows the expansion of the sinus. **E** and **F**, AP and lateral internal carotid injection and lateral common carotid injection shows the aneurysm filling the sphenoid sinus. (Courtesy of Dr. Mohammad Radwan, Ibn Sina Hospital, Kuwait.)

VIEW IMAGE

Copyright © 2003, Mosby, Inc. All rights reserved.

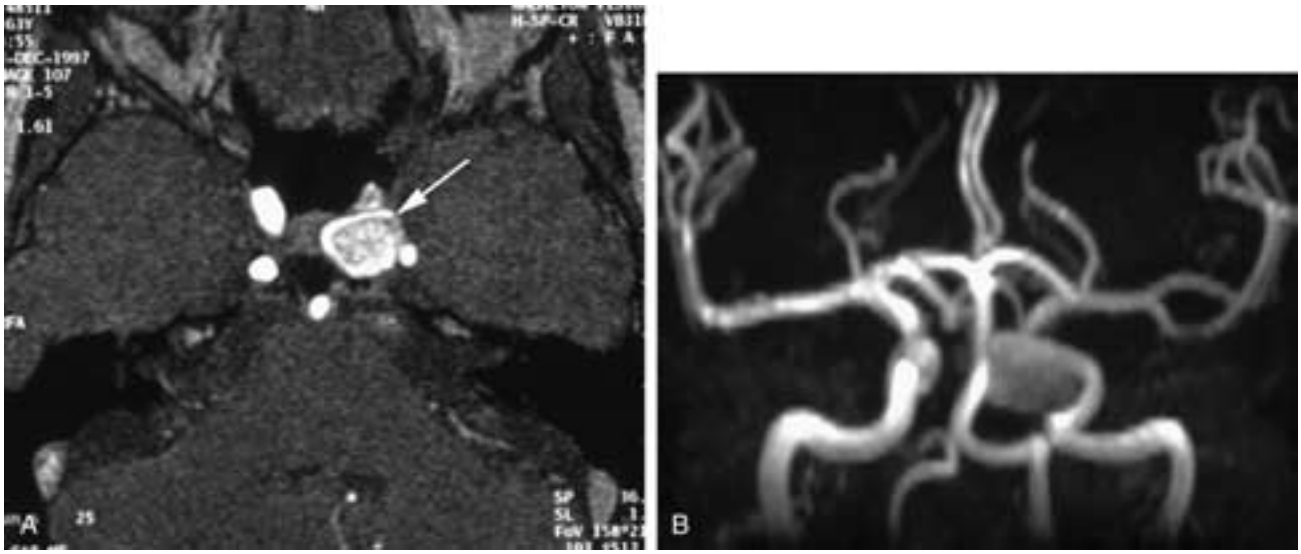

VIEW IMAGE

FIGURE 12-85 Aneurysm of the cavernous carotid extending into the sella. **A**, Axial gradient echo image shows high signal representing flow (*arrow*) within the aneurysm. **B**, MRA 3D time-of-flight shows the aneurysm extending medially from the cavernous carotid.

and lateral walls of the nasopharynx can limit lateral tumor growth, directing tumor growth superiorly toward the roof of the nasopharynx. Here the skull base, the undersurface of the sphenoid bone, is unprotected by any fascial layer, and thus the sphenoid bone is frequently eroded by nasopharyngeal carcinoma. Because many of these malignancies arise off midline in the region of the fossa of Rosenmuller, the foramen lacerum and the petrooccipital fissure immediately above this part of the nasopharynx are frequently invaded. Tumor spreading through this cleft, along the lateral aspect of the sphenoid body and basiocciput, can reach the cavernous sinus, middle cranial fossa, or posterior fossa. Such tumors encounter the carotid artery as soon as the foramen lacerum is breached. Erosion may extend through the cortex of the sphenoid bone proper to reach the clival marrow. Although erosion of the cortex is appreciated more easily on CT, high-resolution MR imaging better shows the presence and degree of marrow invasion (Fig. 12-87). Lateral tumor extension may pass over the pharyngobasilar fascia to reach the soft tissues in the upper masticator space, immediately below the foramen ovale. Tumor can then pass upward to reach the middle cranial fossa. Lateral extension also can occur along the eustachian tube toward the middle ear. Tumor can spread to the pterygoid process or through the sphenopalatine foramen into the pterygopalatine fossa. Here there is access to the Vidian canal and foramen rotundum. Usually the Vidian canal and the foramen rotundum are involved by direct tumor extension as tumor

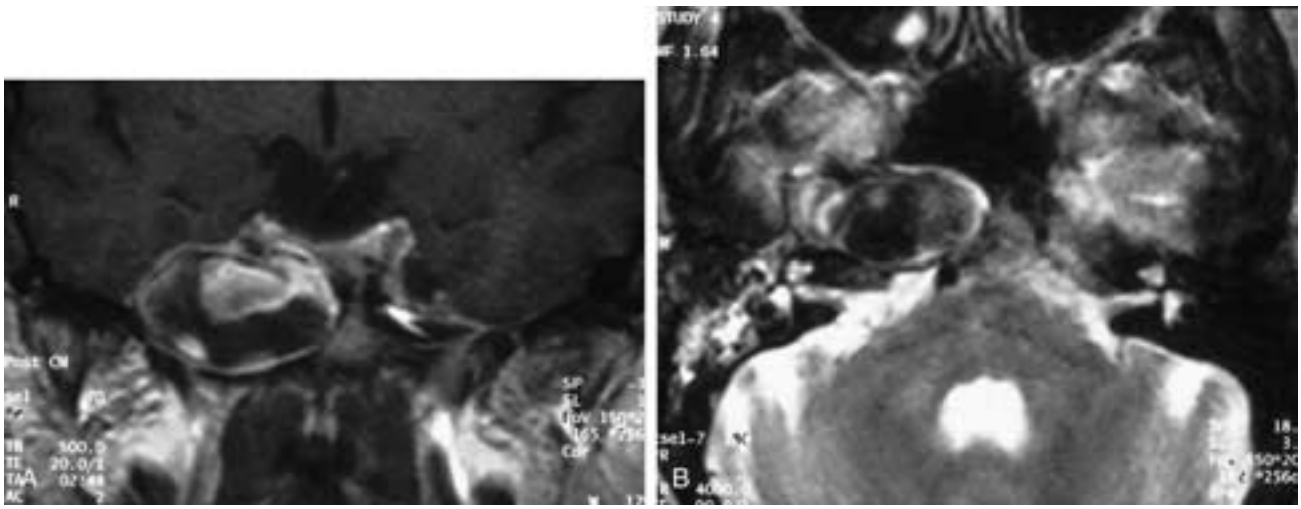

VIEW IMAGE

FIGURE 12-86 Petrous carotid aneurysm. **A**, Coronal T1-weighted postcontrast image shows partial thrombosis of the enlarged aneurysm of the petrous apex. Areas of bright signal represent enhancement indicating flow. **B**, Axial T2-weighted image shows the low signal of hemosiderin within portions of the aneurysm. Note the fluid in the middle ear and mastoid due to obstruction of the eustachian tube.

Copyright © 2003, Mosby, Inc. All rights reserved.

invades directly through the bone at the junction of the pterygoid process and body of sphenoid rather than by true perineural spread, where tumor follows the nerve selectively as a conduit.

Sarcomas, lymphomas, and other malignancies also invade directly into the skull base (Fig. 12-88).[144] Tumors can arise in the infratemporal fossa and erode into the greater wing of the sphenoid bone. The foramen ovale may represent the line of least resistance as a tumor expands within the masticator space.

Perineural Spread

Tumor can selectively follow a nerve or the sheath of a nerve to reach and ultimately pass through a foramen of the skull base.[145–148] Adenoid cystic carcinoma has a strong propensity for this type of spread. Other malignancies such as lymphoma, melanoma, and even squamous cell carcinoma have shown this type of tumor extension. The trigeminal nerve and its branches travel from the brainstem to many areas of the face, sinuses, and oral cavity, and this nerve is a primary route for perineural spread of tumors of the head and neck. The auriculotemporal nerve, a branch of the third division (V_3), can carry tumor from the parotid gland to the main trigeminal nerve and through the foramen ovale to reach the cavernous sinus.[149] Tumors from the palate, sinuses, and face can follow the second division (V_2) to the pterygopalatine fossa and then through the foramen rotundum.[150] Perineural spread along the first division (V_1) is less common, but occasionally a lacrimal gland or skin malignancy can extend along this nerve through the superior orbital fissure. As tumor follows the nerve, the nerve and foramen usually enlarge (Figs. 12-89 and 12-90). Less commonly, tumor may extend along a nerve without causing enlargement, and skip areas of tumor along the nerve can occur with adenoid cystic carcinoma.[1]

Enhancement of a normal-sized nerve on a gadolinium-enhanced MR image is considered suggestive of perineural tumor spread. However, neuritis or secondary edema also may cause nerve enhancement. Usually, once the tumor has passed intracranially through a neural foramen, the tumor enlarges, now free from the restriction of the canal.

A key concept in assessment of possible perineural extension relates to the presence of fat at the extracranial opening of the various neural foramina.[152] Each of the major neural trunks or branches that may serve as a pathway for perineural spread emerges from the skull base into a variable amount of fat, and effacement or obliteration of this fat suggests the presence of tumor. Conversely, if the fat at the appropriate location is normal, the presumption is that the tumor has not reached the skull base. This can be an important factor in planning potential surgery.

One of the most important perineural pathways to and through the central skull base is the second division of the trigeminal nerve (Fig. 12-17). The maxillary division of the trigeminal nerve passes through the foramen rotundum to reach the pterygopalatine fossa. Here the main trunk divides into the infraorbital, palatine, and superior alveolar branches, traveling to the anterior face, posterior hard palate, maxillary sinus, and maxillary teeth, respectively. The palatine nerves are particularly important because the mucosa covering the posterior hard palate contains a large concentration of minor salivary glands. Adenoid cystic carcinoma, with its propensity to spread along nerves, is a common occurrence in this location. If tumor follows the palatine nerves to the pterygopalatine fossa, the fat within the fossa is obliterated (Figs. 12-89, 12-91, and 12-92).

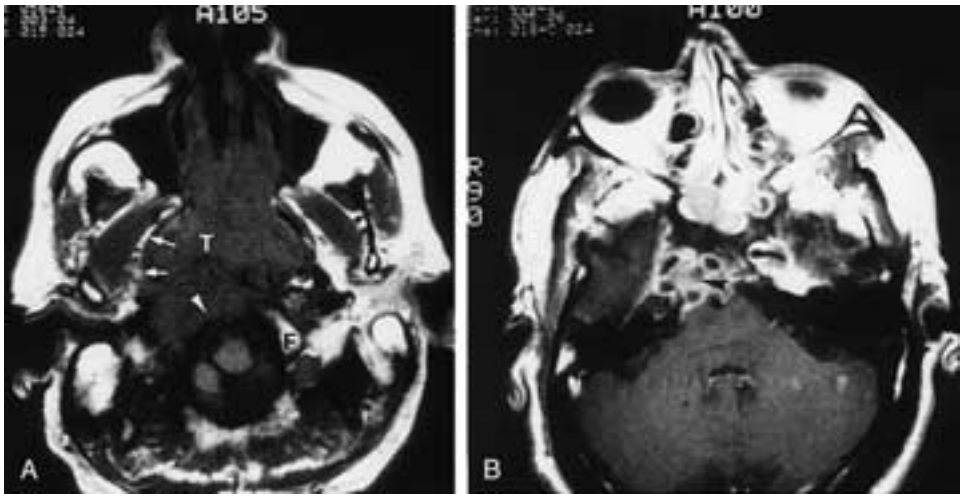

VIEW IMAGE

FIGURE 12-87 Nasopharyngeal carcinoma invading the basiocciput. **A**, The tumor (*T*) expands outward. There is a smooth expansion (*arrowheads*) of the wall of the nasopharynx without extension into the parapharyngeal fat. This demonstrates the strength of the fascial layers. Even though the tumor did not extend through the fascia, there is invasion of the bone (*arrowhead*), and there is obliteration of the fat within the medullary cavity and absence of the cortex. Compare this with the fat (*F*) in the occipital condyle on the normal side. MR imaging is very sensitive to tumor extension through the medullary fat. Small cortical erosions, however, can be missed. **B**, Postgadolinium image shows tumor extension (*arrowhead*) through the petrooccipital fissure at the lateral aspect of the sphenoid bone. Although enhancement can obscure the margins of the tumor below the skull base, it is helpful in demonstrating the tumor extent relative to the cavernous sinus and dural margin.

Copyright © 2003, Mosby, Inc. All rights reserved.

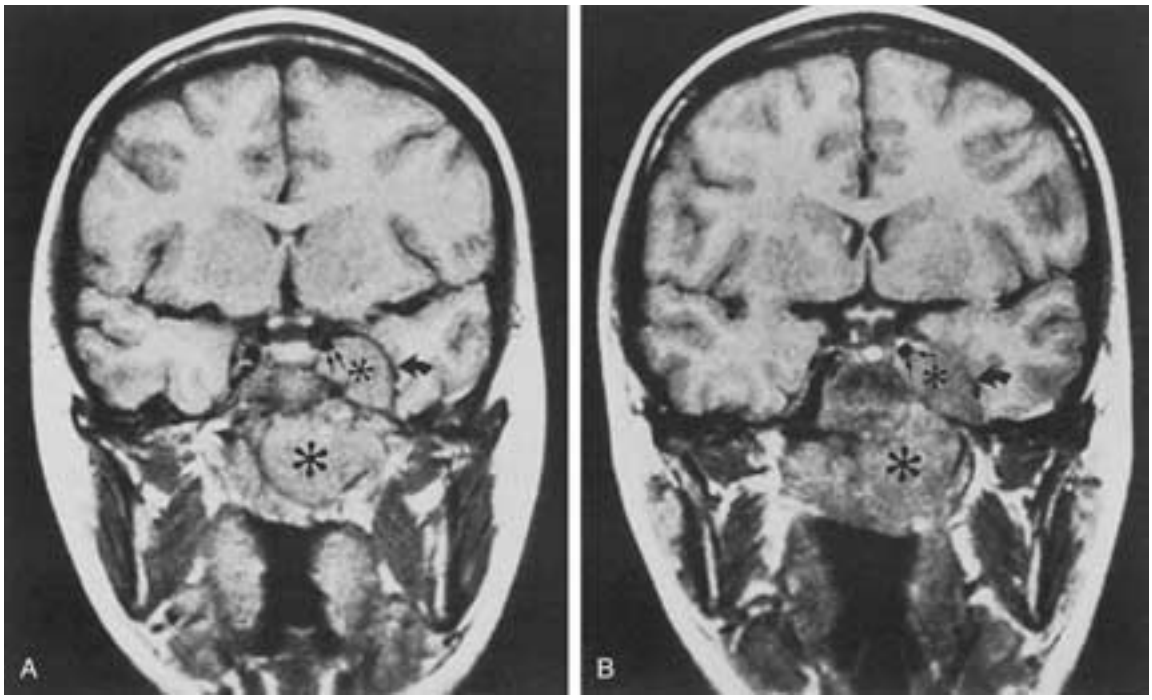

VIEW IMAGE

FIGURE 12-88 A 12-year-old male presents with restriction of ocular motion and nasal stuffiness. Rhabdomyosarcoma of the nasopharynx with extension through the skull base. Coronal T1-weighted image shows the presence of a mass within the nasopharynx (*large asterisk*), with skull base destruction and invasion of the left cavernous sinus (*small asterisk*). Note the lateral deviation of the lateral dural reflection of the cavernous sinus (*curved arrow*). The mass abuts the cavernous internal carotid artery (*small arrows*). (From Braun IF. MRI of the nasopharynx. Radiol Clin North Am 1989;27(2):315.)

From this fossa, tumor can follow nerves through the foramen rotundum and Vidian canal to the region of the cavernous sinus.

The trigeminal nerve exiting the foramen ovale passes into a small amount of fat in the upper masticator space just medial to the lateral pterygoid muscle (Fig. 12-73). If tumor follows the auriculotemporal nerve from the parotid gland to the foramen ovale, this fat is obliterated. This pathway is a significant problem, as the tumor may not yet be palpable and the finding can be quite subtle. The patient typically presents with facial pain, as the sensory branches of the trigeminal nerve are involved.

Tumor following branches of the trigeminal nerve may reach the lower lateral aspect of Meckel's cave in the region of the Gasserian ganglion. Normally, there is slight enhancement of the periganglionic venous plexus, giving the appearance of a thin V. The V appears to thicken as tumor enlarges (Fig. 12-89).[153] Finally, the tumor can grow posteriorly from the cavernous sinus, following the preganglionic fibers of the trigeminal nerve toward the brainstem.

Typically, perineural spread occurs in a retrograde manner, toward the brain. However, antegrade spread can occur from branch points. For example, a tumor of the hard palate with retrograde perineural extension can reach the pterygopalatine fossa. From there, the malignancy can spread in an antegrade manner along the infraorbital nerve and spread in a retrograde pathway through the foramen rotundum. Similarly, once tumor has reached Meckel's cave, it can pass back out of the skull in an antegrade fashion through the foramen ovale into the masticator space. The topic of perineural tumor spread is also covered in Chapter 13.

Hematogenous Metastasis

Hematogenous metastasis can reach the basicranium from primary tumors in the lung, kidney, breast, prostate, and a variety of other, more rare locations. The imaging findings are usually those of lytic destruction. Apparent bone expansion rarely can occur in tumors originating in the thyroid or the kidney. Sclerotic changes may be present in prostate metastasis and rarely with squamous cell carcinomas, giving an appearance much like that of a meningioma. Any part of the sphenoid bone may be involved. If the greater wing of the sphenoid is affected, the metastasis tends to grow outward in all directions. Thus, tumor is seen along the lateral wall of the orbit, along the dura of the middle cranial fossa, and elevating the temporalis muscle away from the destroyed calvarium (Fig. 12-93). A meningioma can give a similar appearance.

TRAUMA

Though the sphenoid and basiocciput are substantial bones, fractures are not uncommon.[154–157] Such fractures are almost always associated with other severe facial bone, cranial vault, and skull base fractures. Of the various

Copyright © 2003, Mosby, Inc. All rights reserved.

elements of the skull base, the orbital roofs, temporal bones, and posterior basiocciput are more likely to be fractured than the more central basicranium.[156] Any of these fractures should be carefully followed to determine if they extend into the more central skull base. Of particular concern are fractures of the temporal bone, as they frequently extend obliquely into the lateral wall of the cavernous sinus, where they can injure the carotid artery.

Fractures of the central basicranium can compromise the numerous neurovascular structures traversing the bone (Fig. 12-94). In addition, muscles of ocular motion, mastication, and eustachian tube function attach to the sphenoid bone,

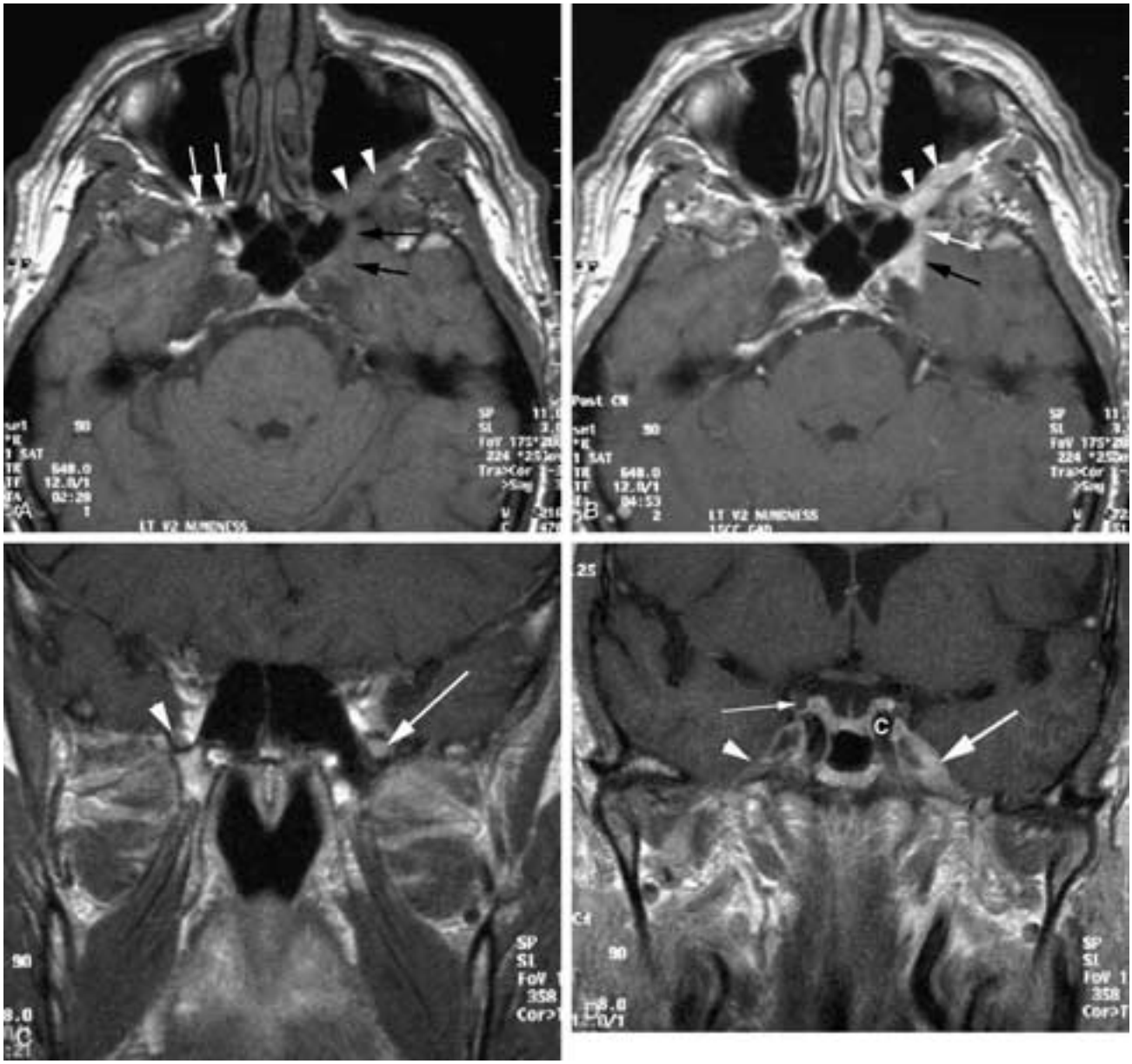

VIEW IMAGE

FIGURE 12-89 Perineural tumor from the hard palate extending through the pterygopalatine fossa and foramen rotundum into the region of the Gasserian ganglion. **A**, Axial precontrast T1-weighted image through the pterygopalatine fossa. There is obliteration of the fat as the tumor fills the pterygopalatine fossa (*arrowheads*). The lesion extends along the foramen rotundum into the anterior cavernous sinus (*black arrows*). Compare the appearance of the pterygopalatine fossa on the normal side (*white arrows*). **B**, Axial postcontrast image. There is enhancement of the tumor in the pterygopalatine fossa (*arrowheads*). It does not enhance to the signal intensity of fat. Again, the lesion is seen in the foramen rotundum (*white arrow*) and the anterior cavernous sinus (*black arrow*). **C**, Coronal postcontrast T1-weighted image. Note visualization of the actual enlargement of the nerve within the foramen rotundum (*arrow*). Compare this with the normal nerve on the opposite side (*arrowhead*) surrounded by a small, enhancing venous plexus. **D**, Coronal image through the involved region of the Gasserian ganglion. There is intermediate enhancement and thickening of the V (*arrow*) representing the region of the Gasserian ganglion. Note the normal venous plexus showing slight enhancement around the Gasserian ganglion (*arrowhead*) on the normal side. Third nerve (*small arrow*). *C*, carotid.

Copyright © 2003, Mosby, Inc. All rights reserved.

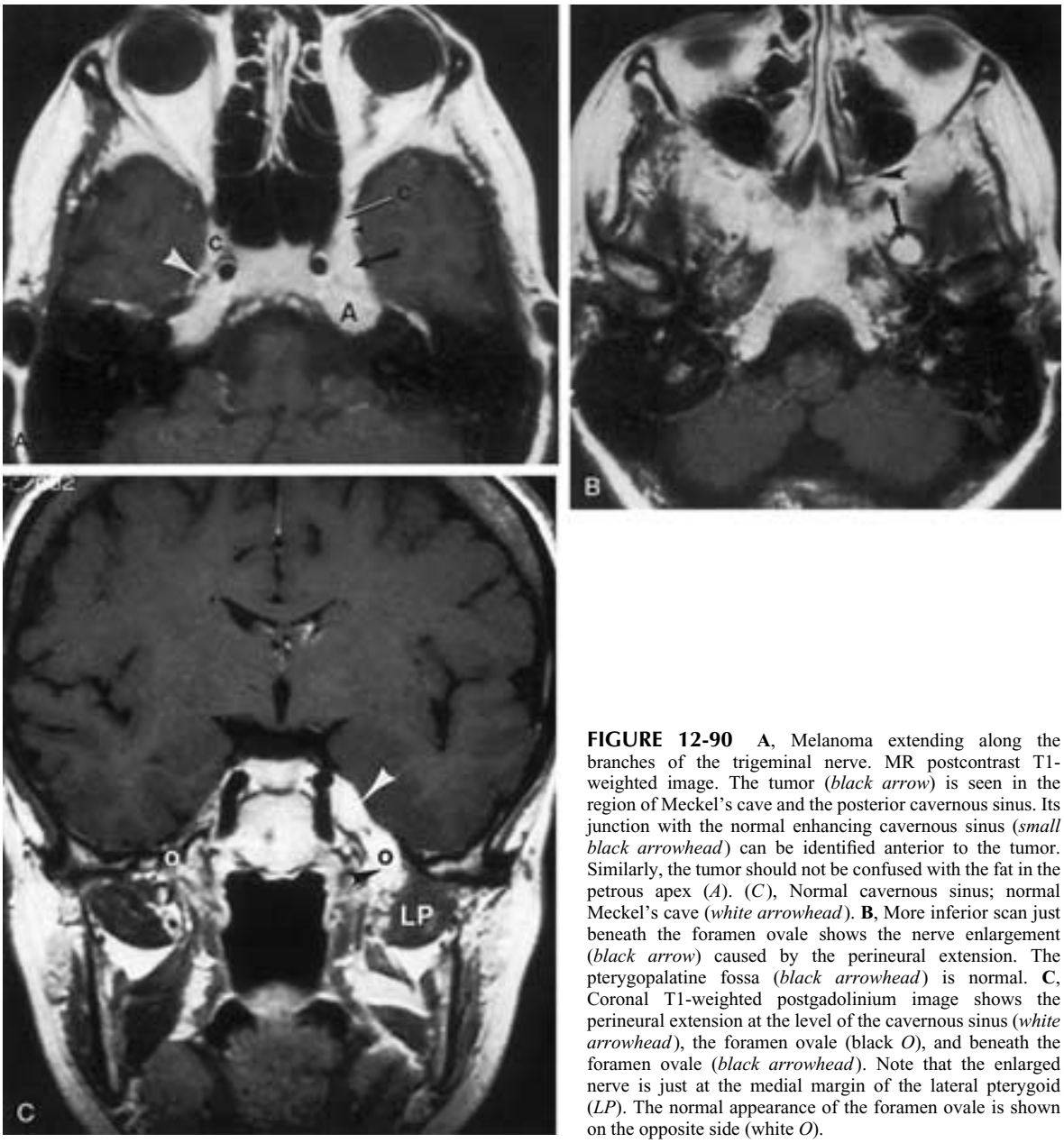

FIGURE 12-90 **A**, Melanoma extending along the branches of the trigeminal nerve. MR postcontrast T1-weighted image. The tumor (*black arrow*) is seen in the region of Meckel's cave and the posterior cavernous sinus. Its junction with the normal enhancing cavernous sinus (*small black arrowhead*) can be identified anterior to the tumor. Similarly, the tumor should not be confused with the fat in the petrous apex (*A*). (*C*), Normal cavernous sinus; normal Meckel's cave (*white arrowhead*). **B**, More inferior scan just beneath the foramen ovale shows the nerve enlargement (*black arrow*) caused by the perineural extension. The pterygopalatine fossa (*black arrowhead*) is normal. **C**, Coronal T1-weighted postgadolinium image shows the perineural extension at the level of the cavernous sinus (*white arrowhead*), the foramen ovale (black *O*), and beneath the foramen ovale (*black arrowhead*). Note that the enlarged nerve is just at the medial margin of the lateral pterygoid (*LP*). The normal appearance of the foramen ovale is shown on the opposite side (white *O*).

VIEW IMAGE

and separation of the attachments of these muscles can result in functional deficits. The thinner plates of bone such as the greater wing of the sphenoid and the pterygoid plates offer less resistance to fracture, and unless significantly displaced, these fractures can be inconsequential. Although dysfunction of the attached muscles can cause problems in mastication, frequently the patients are asymptomatic. Significant inward displacement of a fracture of the greater wing can tear the dura and traumatize the brain.

The pterygoid processes of the sphenoid bone represent the posterior supporting strut of the facial skeleton. As such, the pterygoid plates are involved in the Le Forte fractures, separating the facial bones from the skull base. These fractures are discussed in Chapter 7. Fractures that do involve the sphenoid body and basiocciput place the numerous traversing neurovascular structures at risk, because the various neural foramina represent weak points in the bone, and the nerve within may be crushed, contused, or lacerated. A displaced bone fragment may also impinge upon the nerve.

Any of the nerves can be involved, and ophthalmoplegia or paresthesias can be the sequelae. Severe trauma can result in the superior orbital fissure syndrome, including a dilated pupil, ptosis, and extraocular muscle dysfunction. The optic nerve is of particular concern, and in a patient with vision loss after trauma, the optic canal must be carefully examined (Fig. 12-95). Any fracture of the orbital roof or of the lamina papyracea should prompt careful analysis of the optic canal. A displaced fragment may put pressure on the nerve, and if it is not quickly corrected, permanent visual loss will result. Immediate loss of vision can represent either actual nerve injury or nerve compression.[158] On the other hand, a delayed

Copyright © 2003, Mosby, Inc. All rights reserved.

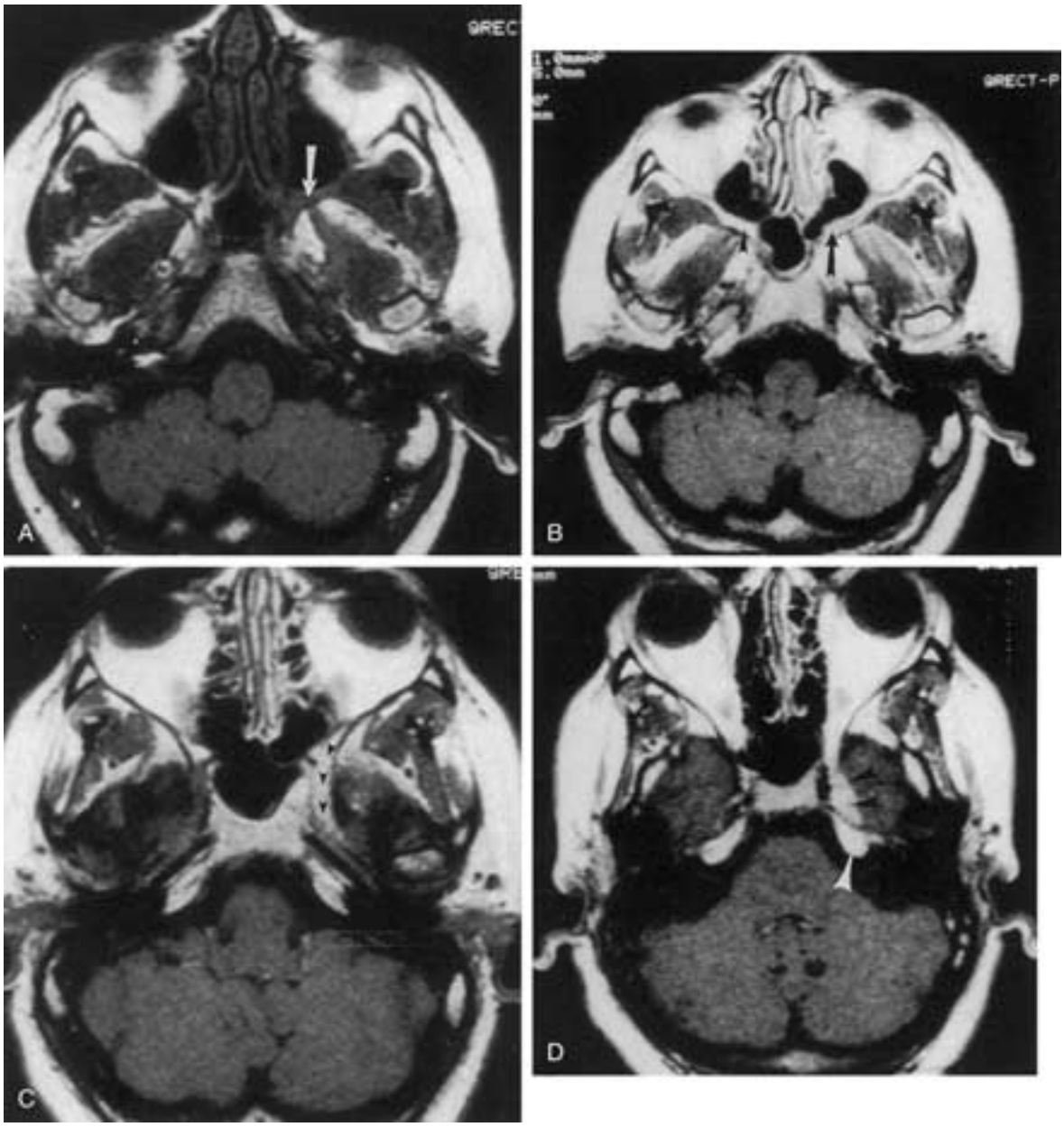

VIEW IMAGE

FIGURE 12-91 Adenoid cystic carcinoma of the palate extending along the branches of V_2. **A**, Axial T1-weighted image through the pterygopalatine fossa shows obliteration (*white arrow*) of the fat within the pterygopalatine fossa. Compare this with the normal fossa on the opposite side. Fat normally should be identified in this narrow structure. **B**, Postgadolinium T1-weighted image. Now the tumor enhances (*black arrow*). Without fat suppression (compare with the noncontrast study), this appearance might be considered normal. Compare it with the high signal of the fat in the normal pterygopalatine fossa on the opposite side. **C**, Postgadolinium T1-weighted image (slightly higher) shows enhancement of the tumor within the foramen rotundum (*black arrowheads*) leading toward Meckel's cave. **D**, Slightly higher postcontrast enhancement T1-weighted image shows the enhancement in the lower cavernous sinus (*black arrowheads*) obscuring Meckel's cave. The high signal of the fat in the petrous apex (*white arrowhead*) should not be confused with tumor.

Illustration continued on following page

Copyright © 2003, Mosby, Inc. All rights reserved.

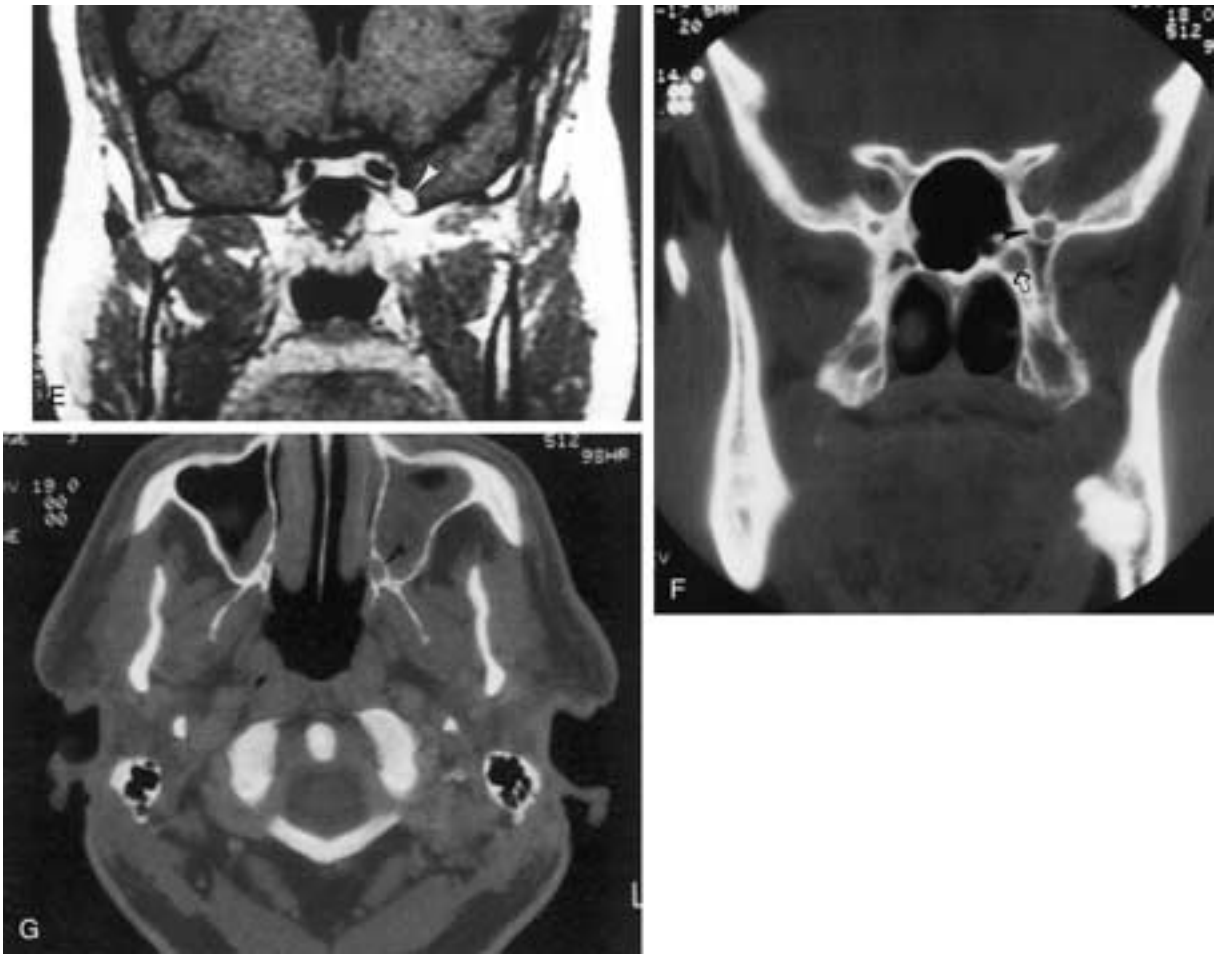

VIEW IMAGE

FIGURE 12-91 *Continued.* **E**, Coronal MR T1-weighted postgadolinium image shows the enlargement of the second division of the trigeminal nerve just posterior (*white arrowhead*) to the foramen rotundum. The nerve is enlarged and enhances, indicating tumor involvement. **F**, Coronal bone algorithm shows enlargement of the foramen rotundum (*black arrowhead*) and the Vidian canal (*open black arrow*). This indicates tumor extension along both nerves. **G**, Enlargement of the lower pterygopalatine canal (*black arrowhead*), which connects the pterygopalatine fossa with the hard palate.

onset or progressive loss of vision usually represents an accumulating hematoma or edema. The optic nerve and optic canal can be visualized by axial and coronal CT. Identification of small fracture lines requires high-resolution, thin slices using bone algorithms. Because an orbital hematoma also can affect the optic nerve, the soft tissues should be carefully examined.

Fractures crossing the course of the carotid artery and involving the bone contiguous to the artery may or may not injure the wall of this vessel. These fractures can affect the thin, bony wall of the lateral sphenoid sinus at the indentation caused by the segment of the artery entering the cavernous sinus or they can be associated with fractures of the area of the anterior clinoid. Significant tears can result in death or in a carotid cavernous (CC) fistula (Fig. 12-96). In CC fistula, CT and MR imaging may show enlargement of the venous structures extending away from the cavernous sinus. Streaky reticulation of the orbital fat due to edema is usually seen, as well as the enlargement of the venous structures.

A fracture of the sphenoid bone can create a connection between the CSF spaces and the sphenoid sinus, resulting in a CSF leak, demonstrable by cisternography (Fig. 12-97). Such a communication can lead to meningitis, which is often delayed in onset. As stated, fractures of the sphenoid are often associated with other fractures of the skull or the skull base. Anosmia, periorbital ecchymosis (''raccoon eyes''), hemotympanum, or mastoid region ecchymosis (Battle's sign) may be seen in conjunction with findings related to the central skull base.

MISCELLANEOUS CONDITIONS

Dysplasias

The basicranium develops primarily through enchondral bone formation. As such, the central skull base can be involved by any generalized disorder that affects cartilaginous bone formation. Many of the findings are incidental. However, bony enlargement, characteristic of some dysplasias, and bone softening, characteristic of others, can lead to

Copyright © 2003, Mosby, Inc. All rights reserved.

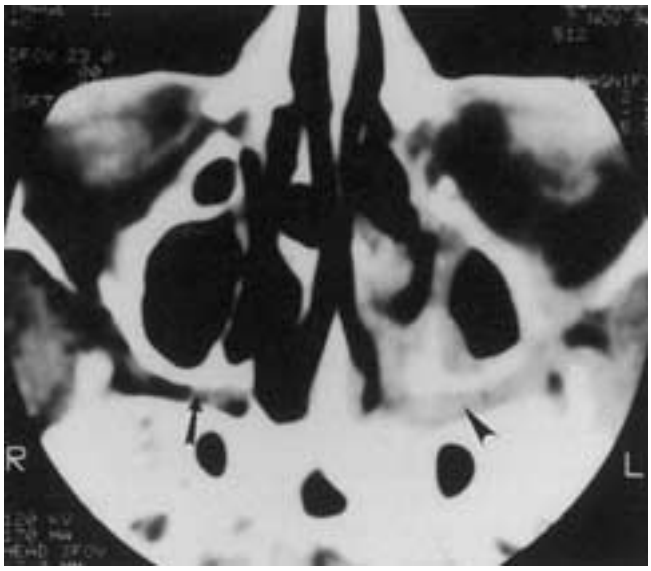

FIGURE 12-92 Axial CT image showing adenoid cystic carcinoma following the second division of the trigeminal nerve. The tumor (*black arrowhead*) obliterates the fat in the pterygopalatine fossa. Compare this with the fat (*arrow*) on the normal side.

VIEW IMAGE

significant problems resulting from compression of various cranial nerves or even of the brainstem and spinal cord. The base of the skull also is affected by generalized metabolic and hematologic diseases in which there are diffuse changes throughout the bony skeleton. Many of these entities cause softening of the bone, leading to a lack of support for the cranium. This can result in a protrusion of the upper spine into the foramen magnum or in a flattening of the skull base itself. These phenomena are referred to respectively as basilar invagination and platybasia.

Platybasia Versus Basilar Invagination

Platybasia and basilar invagination are terms used to characterize certain findings in patients with abnormal bony architecture of the basicranium. Although platybasia and basilar invagination may occur together, they represent different changes in the skull base. Platybasia is a flattening of the skull base. The basal angle of Weneke is the angle formed between a line drawn from the nasion to the center of the sella turcica and a line drawn from the center of the sella turcica down along the posterior aspect of the clivus. The normal adult basal angle is about 140°. If this angle is significantly increased, platybasia is present.

More frequently, the skull base softens and the upper cervical spine appears to push up into the base of the skull. Actually, the skull base is settling down around the focal pressure of the spine. This is true basilar invagination. There are several reference lines, developed to assess possible basilar invagination on plain films, that can be applied easily to midline sagittal MR imaging.

Chamberlain's line extends from the posterior margin of the hard palate to the posterior margin of the foramen magnum. If the tip of the odontoid is 5 mm or more above this line, basilar invagination is present. At times, the lip of the occipital bone, which makes up the posterior margin of the foramen magnum, is difficult to visualize on the lateral radiograph. To deal with this problem, McGregor's line was developed, extending from the posterior margin of the hard palate to the most inferior point on the cortex of the occipital bone posterior to the foramen magnum. This point is much easier to see on the lateral radiograph. Using this system, basilar invagination is considered to be present if the tip of the odontoid is 7 mm above the line or if more than one third of the height of the

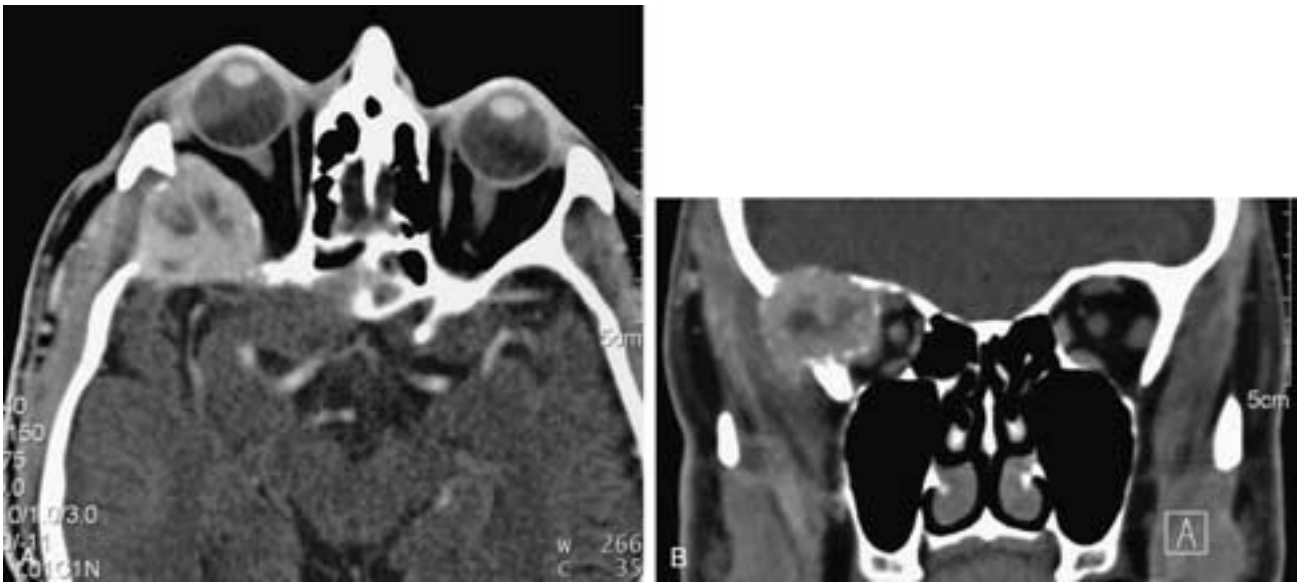

FIGURE 12-93 Metastatic renal carcinoma to the sphenoid triangle (greater wing of the sphenoid). **A**, The tumor is seen replacing the bone of the sphenoid triangle and extending into the orbit, temporalis fossa, and middle cranial fossa. **B**, Coronal CT postcontrast image.

VIEW IMAGE

Copyright © 2003, Mosby, Inc. All rights reserved.

VIEW IMAGE

FIGURE 12-94 A 23-year-old male following an automobile accident presents with superior orbital fissure syndrome and multiple cranial nerve deficits. Multiple skull base fractures. Axial CT scan through the skull base shows the presence of multiple fractures associated with fluid in the ethmoid and sphenoid sinuses. Multiple fractures causing narrowing of the orbital apex and inferior orbital fissure (*open arrow*) are appreciated, as well as a fracture involving the foramen ovale (*black arrow*).

odontoid process is above this line. Because on a sagittal MR image both the posterior lip of the foramen magnum and the lowest point on the occiput can be easily identified, either system can be used.

Although platybasia can occur in many situations, the findings are characteristic of abnormalities such as Paget's disease, osteogenesis imperfecta, and osteomalacia. These abnormalities are all associated with softened abnormal bone incapable of supporting the weight of the skull. On the other hand, basilar invagination has been reported in achondroplasia, ankylosing spondylitis, Arnold-Chiari malformation, atlantoaxial dislocation, cleidocranial dysplasia, congenital craniovertebral junction abnormalities, Crouzon's syndrome, Down's syndrome, familial primary basilar impression, fibrous dysplasia, Haju-Cherney syndrome, histiocytosis, chronic hydrocephalus, hyperparathyroidism, hypophosphatasia, Klippel-Feil syndrome, mucopolysaccharidosis, occipital craniotomy in a child, osteogenesis imperfecta, osteomalacia, osteomyelitis, osteopetrosis, osteoporosis, Paget's disease, pyknodysostosis, rheumatoid arthritis, rickets, and an unfused posterior arch of the atlas.[159]

Fibrous Dysplasia

Fibrous dysplasia is an abnormality of the bone with abnormal development of the fibroblasts and abnormal mineralization.[160–163] The bone is enlarged, and on CT, the cortex tends to be maintained and the enlarged medullary space can have a variety of appearances, depending on the amount of fibrous and osteoid matrix present. The appearance on CT varies from a fairly lucent medullary space to a densely calcified one. Some cases have a mixture of dense and sclerotic changes sometimes referred to as pagetoid. The

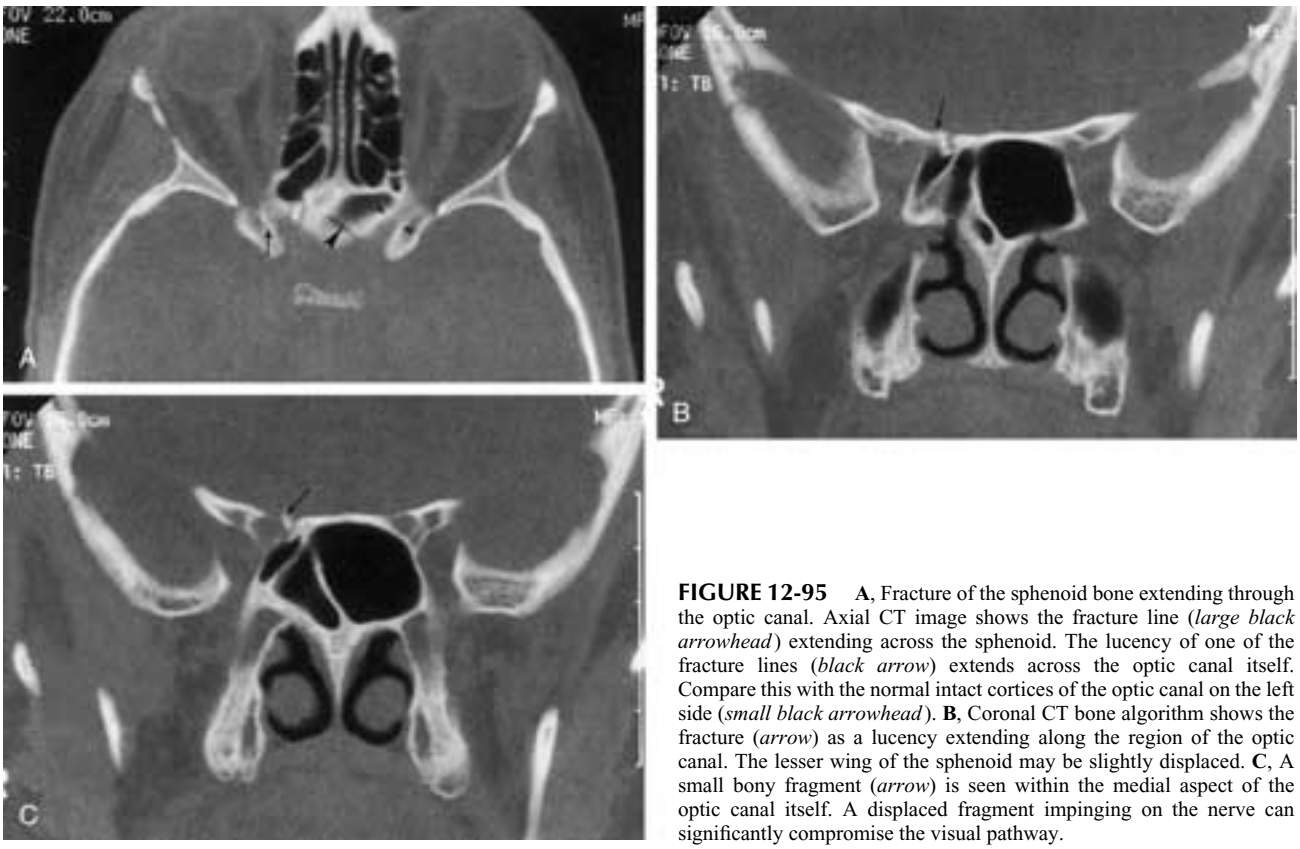

VIEW IMAGE

FIGURE 12-95 **A**, Fracture of the sphenoid bone extending through the optic canal. Axial CT image shows the fracture line (*large black arrowhead*) extending across the sphenoid. The lucency of one of the fracture lines (*black arrow*) extends across the optic canal itself. Compare this with the normal intact cortices of the optic canal on the left side (*small black arrowhead*). **B**, Coronal CT bone algorithm shows the fracture (*arrow*) as a lucency extending along the region of the optic canal. The lesser wing of the sphenoid may be slightly displaced. **C**, A small bony fragment (*arrow*) is seen within the medial aspect of the optic canal itself. A displaced fragment impinging on the nerve can significantly compromise the visual pathway.

Copyright © 2003, Mosby, Inc. All rights reserved.

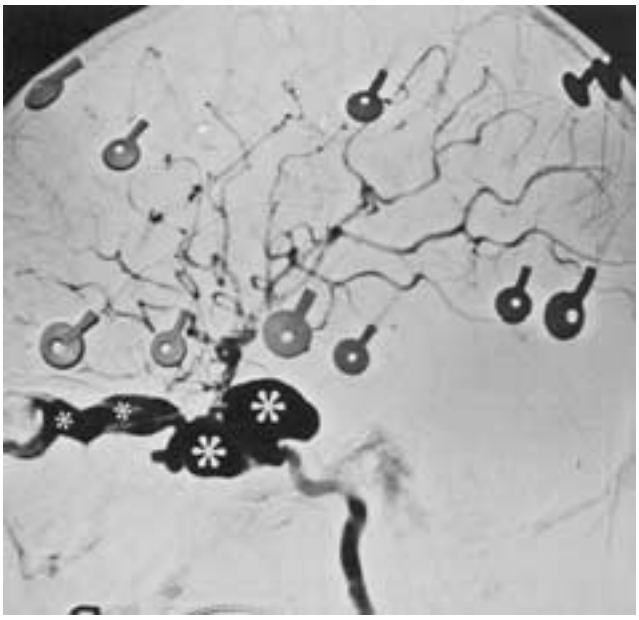

VIEW IMAGE

FIGURE 12-96 A 23-year-old male who presents with pulsatile exophthalmos and decreased visual acuity following a motorcycle accident. Skull base fracture with resultant cavernous carotid fistula. Lateral subtraction view of an internal carotid artery angiogram shows findings typical of a carotid cavernous fistula. Contrast from the arterial system has extravasated into the cavernous sinus (*large asterisks*) and subsequently into the superior ophthalmic vein (*small asterisks*). Arterial pressure transmitted to the venous system in the superior ophthalmic vein causes the pulsatile exophthalmos.

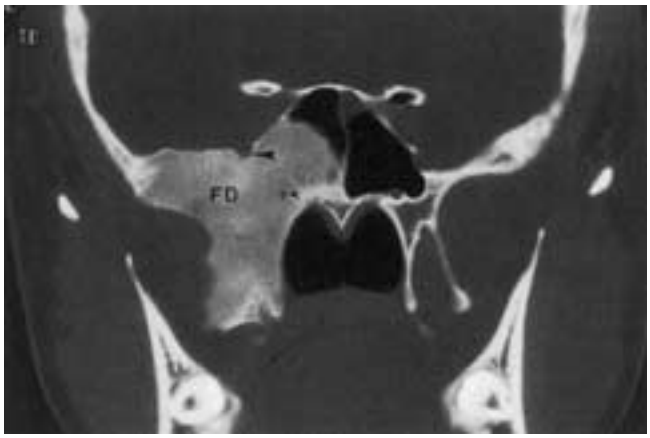

VIEW IMAGE

FIGURE 12-98 Fibrous dysplasia (*FD*) shows a typical ''ground glass'' appearance. The Vidian canal (*small black arrowhead*) and the groove for the second division of the trigeminal (*large black arrowhead*), just posterior to the foramen rotundum, have been incorporated or displaced by the expanding abnormality.

classic CT and plain film appearance is the ''ground glass'' medullary space surrounded by intact cortices (Fig. 12-98).

On MR imaging, the lesion has fairly low T1-weighted and T2-weighted signal intensity (Fig. 12-99). The internal matrix enhances with gadolinium, a phenomenon not as easily appreciated on CT. Although the classic appearance is one of a fairly homogeneous internal density on CT or signal intensity on MR imaging, inhomogeneous areas can be

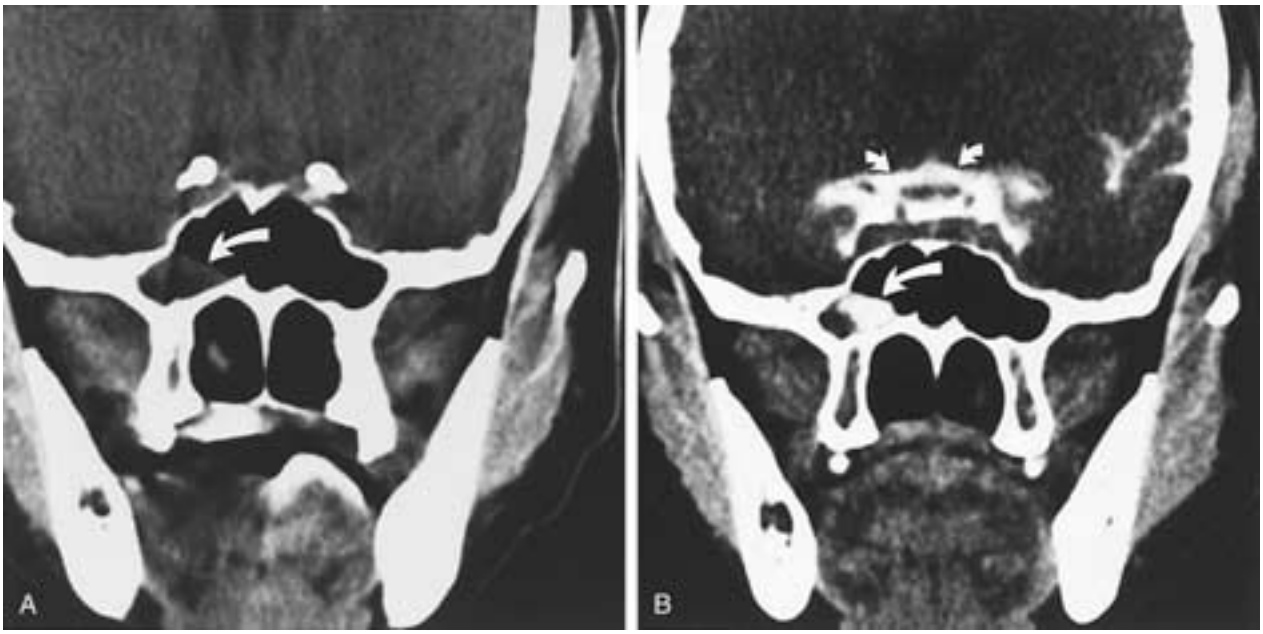

VIEW IMAGE

FIGURE 12-97 A 25-year-old male after head trauma with persistent CSF rhinorrhea and recurrent meningitis. Traumatic CSF fistula demonstrated by water-soluble contrast cisternography. Coronal CT scan through the sphenoid sinus obtained. Before **A** and following **B**, the intrathecal instillation of water-soluble contrast material. A soft-tissue density is appreciated involving the right lateral floor of the sphenoid sinus (*curved arrow*), as seen on the study before the instillation of contrast material. Following the instillation of contrast, increased density is appreciated in this region, consistent with the accumulation of contrast, documenting the presence of a CSF fistula. Also noted is the presence of contrast material within the suprasellar cistern (*small curved arrows*) outlining the chiasm and vascular structures. The fracture site was not identified.

Copyright © 2003, Mosby, Inc. All rights reserved.

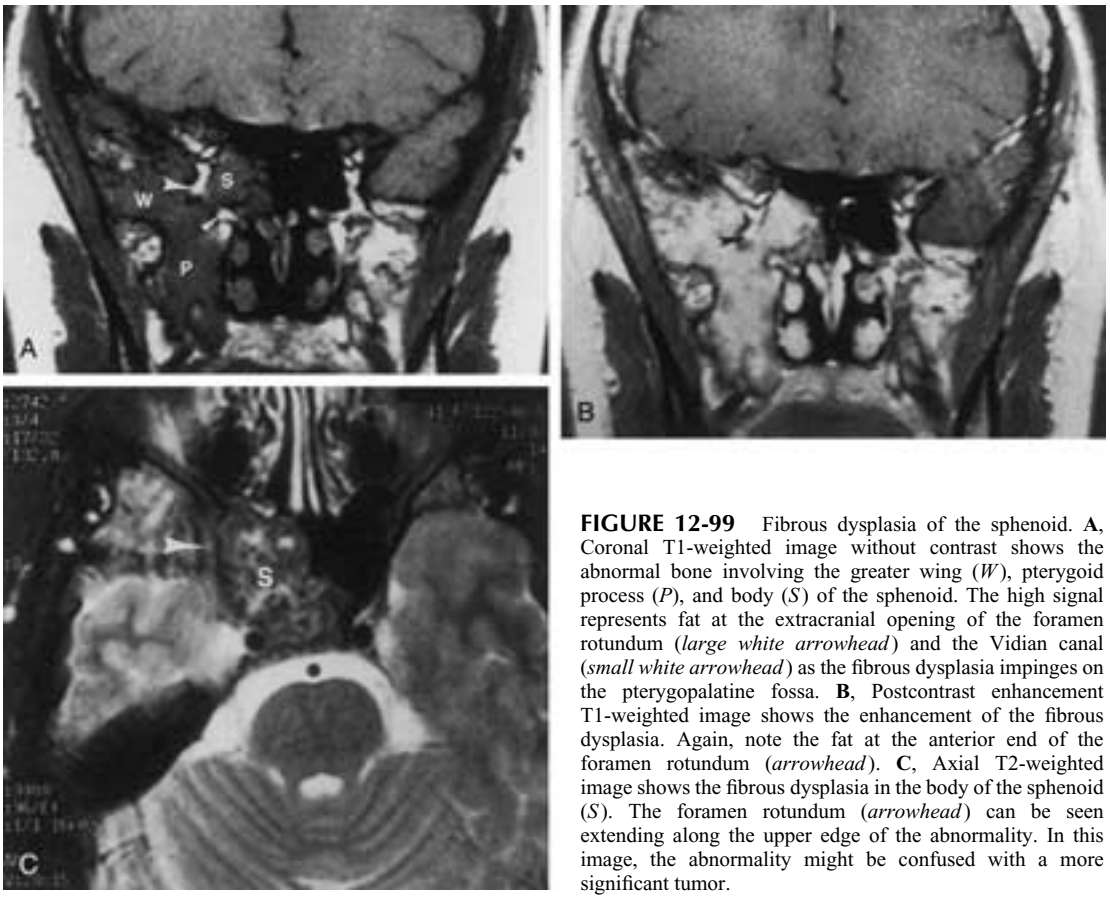

FIGURE 12-99 Fibrous dysplasia of the sphenoid. **A**, Coronal T1-weighted image without contrast shows the abnormal bone involving the greater wing (*W*), pterygoid process (*P*), and body (*S*) of the sphenoid. The high signal represents fat at the extracranial opening of the foramen rotundum (*large white arrowhead*) and the Vidian canal (*small white arrowhead*) as the fibrous dysplasia impinges on the pterygopalatine fossa. **B**, Postcontrast enhancement T1-weighted image shows the enhancement of the fibrous dysplasia. Again, note the fat at the anterior end of the foramen rotundum (*arrowhead*). **C**, Axial T2-weighted image shows the fibrous dysplasia in the body of the sphenoid (*S*). The foramen rotundum (*arrowhead*) can be seen extending along the upper edge of the abnormality. In this image, the abnormality might be confused with a more significant tumor.

VIEW IMAGE

present.[164] Some areas may be predominantly fibrous tissue with the appropriate CT and MR imaging findings. Some areas may represent hemorrhage and cyst formation. In the central skull base, parts of the sphenoid sinus may become isolated and obstructed. The trapped secretions can give signal intensities similar to those of the inhomogeneities of the fibrous dysplasia itself (Fig. 12-100). This can be of concern if the patient is evaluated for pain, as early mucocele formation cannot be differentiated from a static cystic region in fibrous dysplasia. Increasing size suggests mucocele formation. Most of the mineralized matrix is considered to be immature woven bone. Occasionally, small amounts of cartilage formation can occur, but this is unusual (Fig. 12-101).

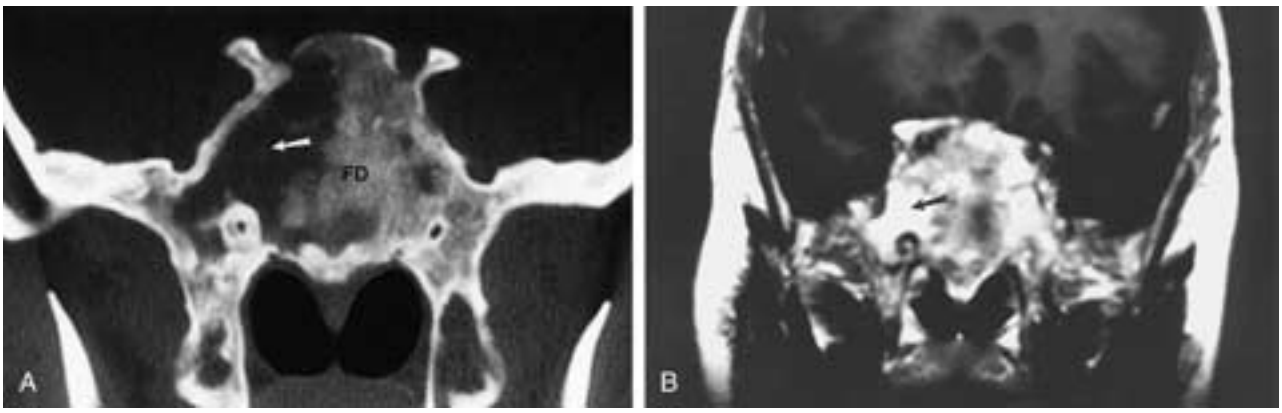

VIEW IMAGE

FIGURE 12-100 Fibrous dysplasia **A**, Fibrous dysplasia with low-density area on CT. The fibrous dysplasia (*FD*) fills and expands most of the body of the sphenoid. There are areas of low density (*arrow*), which could represent either cystic components of the fibrous dysplasia or areas of obstructed secretions because of the sinus mucosa. **B**, Coronal T1-weighted MR image shows high signal intensity consistent with the cystic portion of the fibrous dysplasia. However, note that this area extends between the Vidian canal and the foramen rotundum, which would be the usual position of a laterally extending air cell.

Copyright © 2003, Mosby, Inc. All rights reserved.

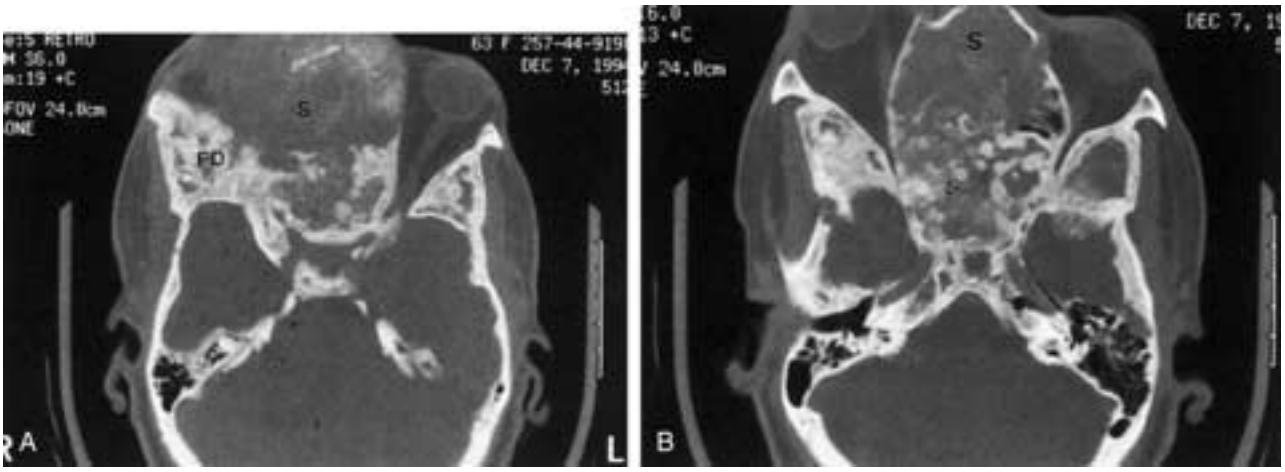

VIEW IMAGE

FIGURE 12-101 **A**, Fibrous dysplasia with secondary osteosarcoma. Fibrous dysplasia (*FD*) involves the greater wing of the sphenoid, extending into the sphenoid bone and including the lesser wing. It is bilateral. The sarcoma (*S*) is seen in the region of the nasal cavity extending into the orbit. **B**, More inferior scan shows the sarcoma (*S*) in the anterior nasal cavity. This fibrous dysplasia has small areas of cartilage formation histologically. This is shown as small rings of calcification (*open arrow*) on the CT scan.

Paget's Disease

Paget's disease is a process of unknown cause in which osteoclastic activity is abnormal.[165] The normal osseous structure is replaced by an abnormal matrix that is more vascular than normal. The osteoblasts continue to respond to this abnormal situation and lay down a thicker, more sclerotic, but softer bone. This bone involves the cortex and the trabeculae within the medullary cavity, and there is poor corticomedullary differentiation. There is more bone than usual, and the bone can be dense or lucent (Fig. 12-102). The findings in the temporal bone appear to be primarily lytic because they involve and demineralize the otic capsule. Again, because the bone is softer than normal, basilar invagination is frequently present. In this disease, the remodeling of the softened bone may be so extensive that there is true platybasia and basilar invagination. Secondary sarcoma canl occur.[166]

Bone Dysplasias, Mucopolysaccharidosis, and Metabolic Diseases

Many of the bone dysplasias cause abnormal density and shape of the skull base.[167, 168] Terminology varies, but this group of lesions includes the various osteochondrodysplasias, dysostoses, and osteopetroses.[160] Basilar invagination, though occurring occasionally, is not a typical finding in many of these bone disorders because the abnormal bone is not particularly soft. The distribution and appearance of the findings in the long bones and the craniofacial skeleton are used to establish the diagnosis. Thickening of the bone may take place at the expense of the neural foramina (Fig. 12-103), and cranial nerve palsies can result.[169, 170] Involvement of the sphenoid bone can lead to blindness or various ophthalmoplegias. Temporal bone involvement can lead to deafness and facial nerve paralysis.

Achondroplasia is an abnormality that affects the development of enchondral bone, and thus the skull base is predictably involved. The failure of growth at the sphenooccipital synchondrosis leads to a short clivus and a smaller sphenoid bone. The floor of the posterior fossa is higher and more horizontal than normal, with variable narrowing of the foramen magnum. If pronounced, this can lead to severe neurologic problems. A typical J-shaped sella is an incidental finding. Platybasia occurs because of maldevelopment of the occipital vertebral junction.

Osteogenesis imperfecta causes a deficient, weakened

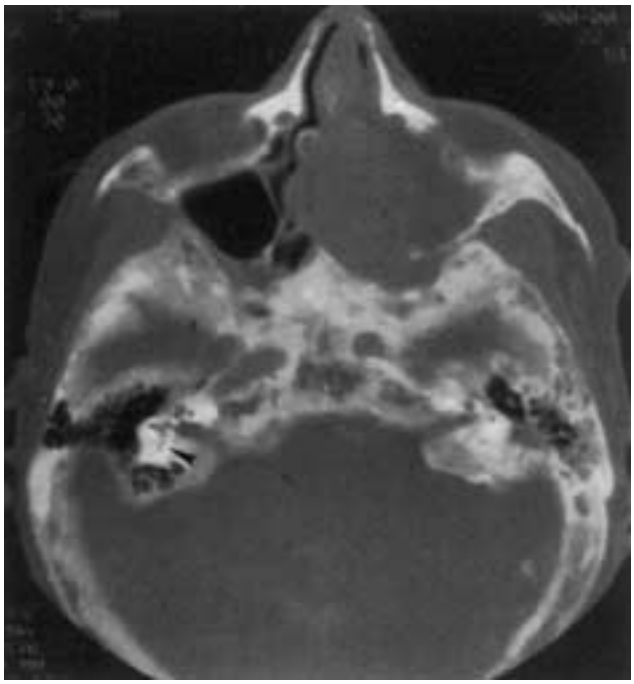

FIGURE 12-102 Paget's disease of the skull base. The diffuse, abnormally mineralized bone is seen in the temporal bone and sphenoid. There is relative sparing but some demineralization of the otic capsule (*arrowhead*). The patient had a sarcoma in the region of the maxillary sinus and nasal cavity.

VIEW IMAGE

Copyright © 2003, Mosby, Inc. All rights reserved.

bone structure, and basilar invagination occurs. The severity is quite variable in the tarda form. Wormian bones and narrowing of the foramen magnum also are present. The temporal bone can be involved with what appears to be extensive otosclerosis and production of undermineralized bone around the labyrinth.

The mucopolysaccharidoses (Morquio's, Hurler's, Hunter's, Maroteaux-Lamy, etc.) are lysosomal storage diseases. The skull base shows abnormal growth, and again, a J-shaped sella is present. The bone of the skull base may be thicker than usual, but because the bone is abnormal, basilar invagination can be present. Associated craniovertebral anomalies, with atlantoaxial instability, are considered more significant problems and can lead to severe neurologic deficits.

Hyperparathyroidism and other metabolic diseases also can result in an abnormal skull base with softening of the normal bone. However, the diagnosis usually is known or is made by evaluation of other parameters.

CEREBROSPINAL FLUID LEAK

A CSF leak may either be related to trauma, with a fracture creating the communication between the CSF space and the sinonasal cavities (Fig. 12-97), or may occur spontaneously.[171] The patient may present with clear rhinorrhea that is evident when the patient bends forward. Alternatively, the patient may swallow the CSF. Meningitis or intracranial abscesses may occur because the communication becomes an entrance pathway for microorganisms found in the sinonasal tract. The most common site of CSF

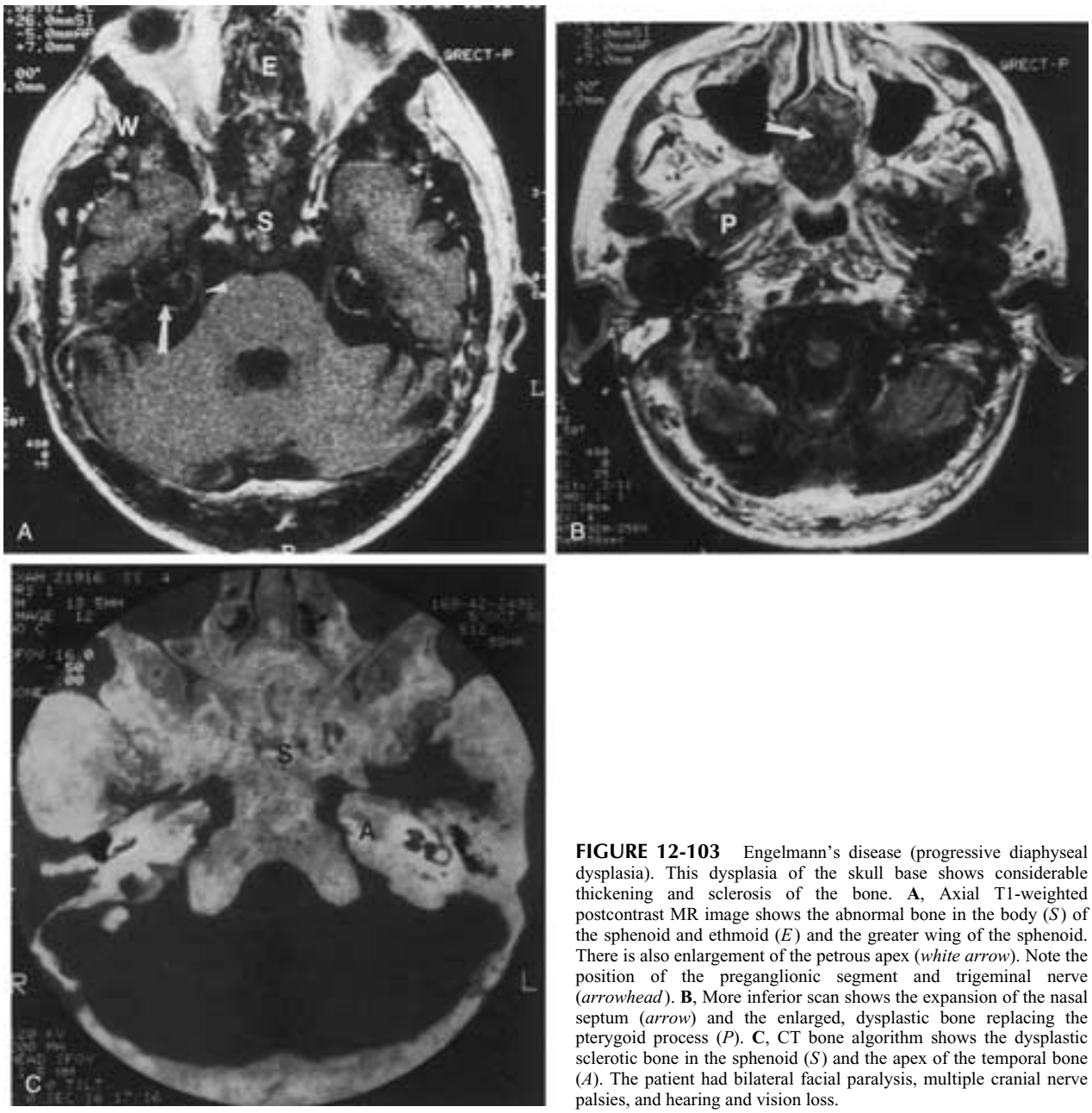

FIGURE 12-103 Engelmann's disease (progressive diaphyseal dysplasia). This dysplasia of the skull base shows considerable thickening and sclerosis of the bone. **A**, Axial T1-weighted postcontrast MR image shows the abnormal bone in the body (*S*) of the sphenoid and ethmoid (*E*) and the greater wing of the sphenoid. There is also enlargement of the petrous apex (*white arrow*). Note the position of the preganglionic segment and trigeminal nerve (*arrowhead*). **B**, More inferior scan shows the expansion of the nasal septum (*arrow*) and the enlarged, dysplastic bone replacing the pterygoid process (*P*). **C**, CT bone algorithm shows the dysplastic sclerotic bone in the sphenoid (*S*) and the apex of the temporal bone (*A*). The patient had bilateral facial paralysis, multiple cranial nerve palsies, and hearing and vision loss.

VIEW IMAGE

Copyright © 2003, Mosby, Inc. All rights reserved.

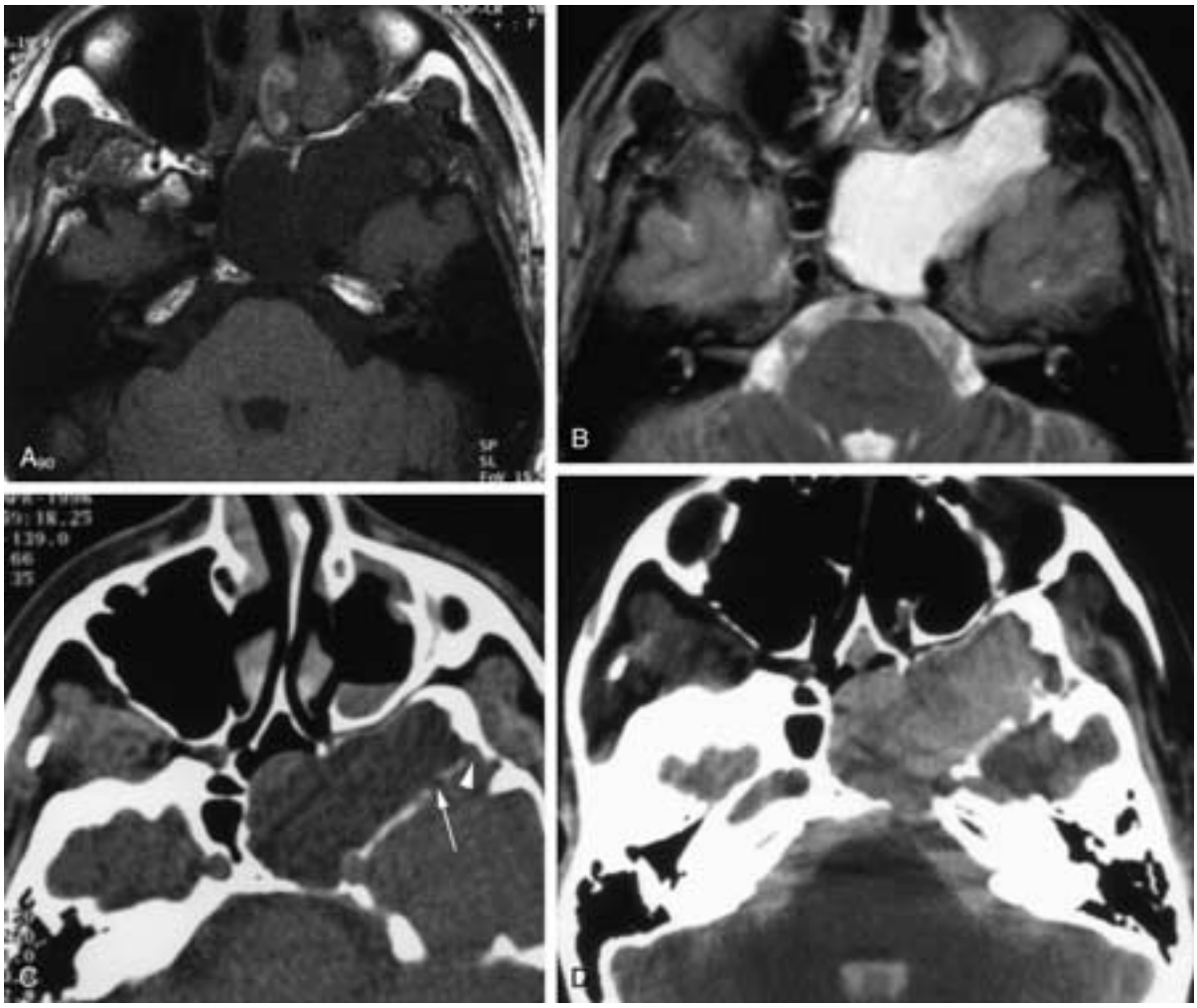

VIEW IMAGE

FIGURE 12-104 CSF leak into an enlarged sphenoid sinus. **A**, Axial T1-weighted image shows low signal equivalent to CSF in an expanded sphenoid sinus. The lateral extent of the sinus extends into the medial greater wing at the attachment of the pterygoid process. **B**, Axial T2-weighted image shows high signal compatible with CSF. **C**, Axial CT image prior to injection of intrathecal contrast shows a small pit (*arrow*) along the anterior wall of the middle cranial fossa. A small defect (*arrowhead*) appears to extend into the cystic cavity. This may represent extension of arachnoid granulations or a small fracture at that site. **D**, Postintrathecal contrast image shows filling of the cystic cavity as well as the prepontine cistern and fourth ventricle.

breech is anteriorly through the region of the cribriform plate or ethmoid roof. The second most common site is the temporal bone, where fractures may be associated with a CSF leak. If the tympanic membrane is ruptured, the fluid passes out into the external auditory canal as otorrhea. If the membrane is intact, the fluid passes through the eustachian tube into the nasopharynx and posterior nasal cavity. The patient can present with rhinorrhea, mimicking a fracture of the anterior skull base, and sphenoid sinus fluid levels, suggesting a fracture of the sphenoid sinus walls. CSF leaks through fractures of the sphenoid bone, communicating with the sphenoid sinus, are uncommon but do occur. The fracture must connect the sphenoid sinus and the CSF space, and so the location is usually over a lateral air cell at the root of the pterygoid process or in the floor of the middle cranial fossa. Here the cavernous sinus does not cover and ''protect'' the sinus. Of course, fractures through the sinus roof, especially if there is also an ''empty'' sella, can cause a CSF leak.

Tumors, especially those arising in the pituitary gland, can cause a nonsurgical CSF leak. Encephaloceles and congenital anomalies also rarely are responsible for CSF rhinorrhea. Spontaneous CSF rhinorrhea can pass along a communication through the anterior wall of the middle cranial fossa into a lateral air cell in the root of the pterygoid process or greater wing of the sphenoid.

Arachnoid granulations frequently are found in the anterior wall of the middle cranial fossa. A small defect in the dura can complete the communication through the thin bone. The communication is typically from the CSF space into the lateral or pterygoid air cell of the sphenoid sinus. This is the air cell protruding laterally between Vidian's canal and the foramen rotundum into the attachment of the pterygoid process. The CSF flows out through the sphenoid ostium into the posterior nasal cavity. Due to the pulsatile pressure of the CSF, an affected air cell may expand, mimicking a mucocele (Fig. 12-104).

CSF fistulas may be seen after skull base surgery.

Copyright © 2003, Mosby, Inc. All rights reserved.

Considerable effort is put into preventing this complication. One of the primary goals of reconstructive flap design is isolation of the CSF and the intracranial structures from the external world, particularly the sinonasal tract, with its plethora of potential pathogens. However, the pulsating pressure of the CSF works against the surgeon, and leaks occasionally occur. Because of the distorted postoperative anatomy, collections within the soft tissues or grafts may occur. These pseudomeningoceles may be clinically inconsequential if small, but they must be surgically corrected if large. The radiologic evaluation is done with CT or MR imaging. In the postoperative case, the area of primary concern is obvious, but the identification of the defect in the skull base often is not specifically useful because large defects are routine. Very useful is the identification of a fluid collection in the contiguous soft tissues or an intracranial air bubble near the site of the leak.

In the nonoperated patient, high-resolution CT is performed with a bone algorithm to look for a bony dehiscence.[172] Even if a defect is not seen, a collection of fluid within a sinus may suggest the location of the leak. Because the middle ear and mastoid are potential sites for the CSF leak, these areas must be carefully examined. In either the operated or the nonoperated patient, if the leak is not obvious, intrathecal contrast can be used. The patient is placed in the position that clinically is related to the CSF leak, and further CT imaging is done.[172, 173] Contrast cisternography is unlikely to be successful unless an active leak exists at the time of the study.

Radionuclide cisternography is considered to be more sensitive than these studies, but it does not accurately localize the leak site. The radionuclide is injected intrathecally, and pledgets are placed in the areas most likely to detect a leak (i.e., the pledgets may be placed high in the nasal cavity by the otolaryngologist). Later, the pledgets are retrieved and measured for radioactivity. Although this procedure can be done to confirm that a leak is present, it requires an active leaking at the time of the study. Recently, clinicians have been better able to verify that the rhinorrhea fluid is indeed CSF by testing the fluid for beta 2-transferrin, which is present in CSF but not in sinonasal secretions.

VIEW IMAGE

FIGURE 12-105 Radiopaque foreign body from glycerol rhizotomy. The radiopaque material (*large black arrowhead*) was added to the alcohol, which was injected into the area of Meckel's cave in the hope of relieving facial pain. The nerve (*small black arrowhead*) can be seen surrounded by this contrast.

RHIZOTOMY INJECTIONS

In order to control pain, alcohol may be injected into the Gasserian ganglion. Radiopaque material is often mixed with the injected alcohol. This appearance is characteristic and should not be confused with a calcified neoplasm (Fig. 12-105). The material is injected via the foramen ovale and can follow the nerve or can track along the dura.

REFERENCES

1. Sperber GH. Early embryonic development. In: Sperber GH ed. Craniofacial Embryology. 4th ed. London: Wright, 1989;7–30.
2. Burdi AR. Early development of the human basicranium: its morphogenic controls, growth patterns, and relations. In: Bosma JF ed. Symposium on Development of the Basicranium. DHEW Pub. No. (NIH) 76–989. Bethesda, Md: U.S. Dept. of Health, Education, and Welfare, Public Health Service National Institutes of Health, 1976;81–92.
3. Gasser RF. Early formation of the basicranium in man. In: Bosma JF ed. Symposium on Development of the Basicranium DHEW Pub. No. (NIH) 76–989. Bethesda, Md: U.S. Dept. of Health Education and Welfare Public Health Service National Institutes of Health, 1976; 29–43.
4. Romanoff AL. The Avian Embryo: Structural and Functional Development. New York: Macmillan, 1960.
5. Beltramello A, Puppini G, El-Dalati G, et al. Fossa navicularis magna. AJNR 1998;19(9):1796–1798.
6. Sperber GH. The cranial base. In: Sperber GH ed. Craniofacial Embryology. 4th ed. London: Wright, 1989;101–118.
7. Bosma JF. Introduction to the symposium on development of the basicranium. In: Bosma JF ed. Symposium on Development of the Basicranium. DHEW Pub. No. (NIH) 76–989. Bethesda, Md: U.S. Dept. of Health Education and Welfare Public Health Service National Institutes of Health, 1976;3–29.
8. Gray H, Williams PL, Bannister LH. Gray's Anatomy: The Anatomical Basis of Medicine and Surgery. 38th ed. New York: Churchill Livingstone, 1995.
9. McMinn RMH, Hutchings RT, Logan BM. Color Atlas of Head and Neck Anatomy. 2nd ed. London and Baltimore: Mosby-Wolfe, 1994.
10. Pernkopf E, Platzer W. Pernkopf Anatomy: Atlas of Topographic and Applied Human Anatomy. Vol. 1: Head and Neck. 3rd ed. Baltimore: Urban & Schwarzenberg, 1989.
11. Romrell LJ. Sectional Anatomy of the Head and Neck with Correlative Diagnostic Imaging. Philadelphia: Lea & Febiger, 1994.
12. Ginsberg LE, Pruett SW, Chen MY, Elster AD. Skull-base foramina of the middle cranial fossa: reassessment of normal variation with high-resolution CT. AJNR 1994;15(2):283–291.
13. Aoki S, Dillon WP, Barkovich AJ, Norman D. Marrow conversion before pneumatization of the sphenoid sinus: assessment with MR imaging. Radiology 1989;172(2):373–375.
14. Applegate GR, Hirsch WL, Applegate LJ, Curtin HD. Variability in the enhancement of the normal central skull base in children. Neuroradiology 1992;34(3):217–221.
15. Okada Y, Aoki S, Barkovich AJ, et al. Cranial bone marrow in children: assessment of normal development with MR imaging. Radiology 1989;171(1):161–164.

Copyright © 2003, Mosby, Inc. All rights reserved.

16. Shopfner CE, Wolfe TW, O'Kell RT. The intersphenoid synchondrosis. Am J Roentgenol Radium Ther Nucl Med 1968;104(1): 184–193.
17. Kier EL, Rothman SLG. Radiologically significant anatomic variations of the developing sphenoid in humans. In: Bosma JF ed. Symposium on Development of the Basicranium. DHEW Pub. No. (NIH) 76–989. Bethesda, Md: U.S. Dept. of Health Education and Welfare Public Health Service National Institutes of Health, 1976; 107–140.
18. Fujioka M, Young LW. The sphenoidal sinuses: radiographic patterns of normal development and abnormal findings in infants and children. Radiology 1978;129(1):133.
19. Lewin JS, Curtin HD, Eelkema E, Obuchowski N. Benign expansile lesions of the sphenoid sinus: differentiation from normal asymmetry of the lateral recesses. AJNR 1999;20(3):461–466.
20. Kaufman B, Yonas H, White RJ, Miller CF. Acquired middle cranial fossa fistulas: normal pressure and nontraumatic in origin. Neurosurgery 1979;5(4):466–472.
21. Ginsberg LE. The posterior condylar canal. AJNR 1994;15(5): 969–972.
22. Weissman JL. Condylar canal vein: unfamiliar normal structure as seen at CT and MR imaging. Radiology 1994;190(1):81–84.
23. Curtin HD. Separation of the masticator space from the parapharyngeal space. Radiology 1987;163(1):195–204.
24. James HE. Encephalocele, dermoid sinus, and arachnoid cyst. In: McLaurin RL ed. Pediatric Neurosurgery. 2nd ed. Philadelphia: WB Saunders, 1989;97–105.
25. Pollock JA, Newton TH, Hoyt WF. Transsphenoidal and transethmoidal encephaloceles. A review of clinical and roentgen features in 8 cases. Radiology 1968;90(3):442–453.
26. Silverman FN. Some features of developmental changes observed clinically in the sphenoid and basicranium. In: Bosma JF ed. Symposium on Development of the Basicranium. DHEW Pub. No. (NIH) 76–989. Bethesda, Md: U.S. Dept. of Health Education and Welfare Public Health Service National Institutes of Health, 1976; 319–345.
27. Kapadia SB, Janecka IP, Fernandes S, et al. Lateral basal encephalocele of the infratemporal fossa. Otolaryngol Head Neck Surg 1996;114(1):116–119.
28. Elster AD, Branch CL Jr. Transalar sphenoidal encephaloceles: clinical and radiologic findings. Radiology 1989;170(1 Pt 1): 245–247.
29. Nager GT. Cephaloceles. Laryngoscope 1987;97(1):77–84.
30. David DJ, Proudman TW. Cephaloceles: classification, pathology, and management. World J Surg 1989;13(4):349–357.
31. Kapadia SB, Janecka IP, Curtin HD, Johnson BL. Diffuse neurofibroma of the orbit associated with temporal meningocele and neurofibromatosis-1. Otolaryngol Head Neck Surg 1998;119(6): 652–655.
32. Leblanc R, Tampieri D, Robitaille Y, et al. Developmental anterobasal temporal encephalocele and temporal lobe epilepsy. J Neurosurg 1991;74(6):933–939.
33. Muller H, Slootweg PJ, Troost J. An encephalocele of the sphenomaxillary type. Case report. J Maxillofac Surg 1981;9(3):180–184.
34. Morris WM, Losken HW, le Roux PA. Spheno-maxillary meningoencephalocele. A case report. J Craniomaxillofac Surg 1989;17(8): 359–362.
35. Chapman PH, Curtin HD, Cunningham MJ. An unusual pterygopalatine meningocele associated with neurofibromatosis type 1. Case report. J Neurosurg 2000;93(3):480–483.
36. Sadeh M, Goldhammer Y, Shacked I, et al. Basal encephalocele associated with suprasellar epidermoid cyst. Arch Neurol 1982;39(4): 250–252.
37. Meche FGA, van der Braakman R. Arachnoid cysts in the middle cranial fossa: cause and treatment of progressive and nonprogressive symptoms. J Neurol Neurosurg Psychiatry 1983;46(12):1102–1107.
38. Sato K, Shimoji T, Yaguchi K, et al. Middle fossa arachnoid cyst: clinical, neuroradiological, and surgical features. Childs Brain 1983;10(5):301–316.
39. Naidich TP, McLone DG, Radkowski MA. Intracranial arachnoid cysts. Pediatr Neurosci 1985;12(2):112–122.
40. Schuknecht B, Simmen D, Yuksel C, Valavanis A: Tributary venosinus occlusion and septic cavernous sinus thrombosis: CT and MR findings. AJNR 1998;19(4):617–626.
41. Chandler JR. Malignant external otitis: further considerations. Ann Otol Rhinol Laryngol 1977;86(4 Pt 1):417–428.
42. Chandler JR. Malignant external otitis. Laryngoscope 1968;78(8): 1257–1294.
43. Nadol JB Jr. Histopathology of *Pseudomonas* osteomyelitis of the temporal bone starting as malignant external otitis. Am J Otolaryngol 1980;1(5):359–371.
44. Damiani J, Damiani K, SE K. Malignant external otitis with multiple cranial nerve involvement. Am J Otol 1979;1:115–120.
45. Curtin HD, Wolfe P, May M. Malignant external otitis: CT evaluation. Radiology 1982;145(2):383–388.
46. Grandis JR, Curtin HD, Yu VL. Necrotizing (malignant) external otitis: prospective comparison of CT and MR imaging in diagnosis and follow-up. Radiology 1995;196(2):499–504.
47. Rubin J, Curtin HD, Yu VL, Kamerer DB. Malignant external otitis: utility of CT in diagnosis and follow-up. Radiology 1990;174(2): 391–394.
48. Dillon WP, Som PM, Fullerton GD. Hypointense MR signal in chronically inspissated sinonasal secretions. Radiology 1990;174(1): 73–78.
49. Som PM, Dillon WP, Fullerton GD, et al. Chronically obstructed sinonasal secretions: observations on T1 and T2 shortening. Radiology 1989;172(2):515–520.
50. Zinreich SJ, Kennedy DW, Malat J, et al. Fungal sinusitis: diagnosis with CT and MR imaging. Radiology 1988;169(2):439–444.
51. Barnes L, Kapadia SB. The biology and pathology of selected skull base tumors. J Neurooncol 1994;20(3):213–240.
52. Batsakis JG. Vasoformative tumors. In: Batsakis JG ed. Tumors of the Head and Neck: Clinical and Pathological Considerations. 2nd ed. Baltimore: Williams & Wilkins, 1979;297–327.
53. Dorfman HD, Czerniak B. Bone Tumors. St. Louis: CV Mosby, 1998.
54. Campanacci M. Bone and Soft Tissue Tumors: Clinical Features, Imaging, Pathology, and Treatment. 2nd rev. ed. Padova, Vienna, New York: Piccin Nuova Libraria and Springer-Verlag, 1999.
55. Batsakis J, Kittleson A. Chordomas: otorhinolaryngologic presentation and diagnosis. Arch Otolaryngol 1963;78:168–172.
56. Burger PC, Scheithauer BW, Armed Forces Institute of Pathology (U.S.), Universities Associated for Research and Education in Pathology. Tumors of the Central Nervous System. Washington, DC: Armed Forces Institute of Pathology. 1994 Atlas of tumor pathology. Third series, fasc. 10.
57. Mabrey R. Chordoma: a study of 150 cases. Am J Cancer 1935;25:501–506.
58. Heffelfinger MJ, Dahlin DC, MacCarty CS, Beabout JW. Chordomas and cartilaginous tumors at the skull base. Cancer 1973;32(2): 410–420.
59. Rosenberg AE, Brown GA, Bhan AK, Lee JM. Chondroid chordoma—a variant of chordoma. A morphologic and immunohistochemical study. Am J Clin Pathol 1994;101(1):36–41.
60. Dalpra L, Malgara R, Miozzo M, et al. First cytogenetic study of a recurrent familial chordoma of the clivus. Int J Cancer 1999;81(1): 24–30.
61. Miozzo M, Dalpra L, Riva P, et al. A tumor suppressor locus in familial and sporadic chordoma maps to 1p36. Int J Cancer 2000;87(1):
68–72.
62. Buonamici L, Roncaroli F, Fioravanti A, et al. Cytogenetic investigation of chordomas of the skull. Cancer Genet Cytogenet 1999;112(1):49–52.
63. Weber A, Liebsch N, Sanchez R, et al. Chordomas of the skull base: radiological and clinical evaluation. Neuroimaging Clin North Am 1994;4(3):515–527.
64. Firooznia H, Pinto R, Lin J, et al. Chordoma: radiologic evaluation of 20 cases. AJR 1976;127:797–799.
65. Sze G, Uichanco LI, Brant-Zawadzki M, et al. Chordomas: MR imaging. Radiology 1988;166:187–191.
66. Meyers S, Hirsch WJ, Curtin H, et al. Chordomas of the skull base: MR features. AJNR 1992;13:1627–1636.
67. Oot R, Melville G, New P, et al. The role of MR and CT in evaluating clival chordomas and chondrosarcomas. AJNR 1988;9: 715–723.
68. Batsakis JG. Soft tissue tumors of the head and neck: unusual forms. In: Batsakis JG ed. Tumors of the Head and Neck: Clinical and Pathological Considerations. 2nd ed. Baltimore: Williams & Wilkins, 1979;353–385.

Copyright © 2003, Mosby, Inc. All rights reserved.

69. Fischbein NJ, Kaplan MJ, Holliday RA, Dillon WP. Recurrence of clival chordoma along the surgical pathway. AJNR 2000;21(3): 578–583.
70. Uggowitzer MM, Kugler C, Groell R, et al. Drop metastases in a patient with a chondroid chordoma of the clivus. Neuroradiology 1999;41(7):504–507.
71. al-Mefty O, Borba LA. Skull base chordomas: a management challenge. J Neurosurg 1997;86(2):182–189.
72. Debus J, Schulz-Ertner D, Schad L, et al. Stereotactic fractionated radiotherapy for chordomas and chondrosarcomas of the skull base. Int J Radiat Oncol Biol Phys 2000;47(3):591–596.
73. Hug EB, Loredo LN, Slater JD, et al. Proton radiation therapy for chordomas and chondrosarcomas of the skull base. J Neurosurg 1999;91(3):432–439.
74. Kondziolka D, Lunsford LD, Flickinger JC. The role of radiosurgery in the management of chordoma and chondrosarcoma of the cranial base. Neurosurgery 1991;29(1):38–45; discussion 45–46.
75. Sims E, Doughty D, Macaulay E, et al. Stereotactically delivered cranial radiation therapy: a ten-year experience of linac-based radiosurgery in the UK. Clin Oncol 1999;11(5):303–320.
76. Crockard A, Macaulay E, Plowman PN. Stereotactic radiosurgery. VI. Posterior displacement of the brainstem facilitates safer high dose radiosurgery for clival chordoma. Br J Neurosurg 1999;13(1):65–70.
77. O'Connell JX, Renard LG, Liebsch NJ, et al. Base of skull chordoma. A correlative study of histologic and clinical features of 62 cases. Cancer 1994;74(8):2261–2267.
78. Terahara A, Niemierko A, Goitein M, et al. Analysis of the relationship between tumor dose inhomogeneity and local control in patients with skull base chordoma. Int J Radiat Oncol Biol Phys 1999;45(2):351–358.
79. Rosenberg AE, Nielsen GP, Keel SB, et al. Chondrosarcoma of the base of the skull: a clinicopathologic study of 200 cases with emphasis on its distinction from chordoma. Am J Surg Pathol 1999;23(11):1370–1378.
80. Pritchard D, Lunke R, Taylor W, et al. Chondrosarcoma: a clinicopathologic and statistical analysis. Cancer 1980;45:149–152.
81. Jones H. Cartilaginous tumors of the head and neck. J Laryngol Otol 1973;87:135–138.
82. Lee Y, Van Tassel P. Craniofacial chondrosarcomas: imaging findings in 15 untreated cases. AJNR 1989;10:165–171.
83. Rassekh CH, Nuss DW, Kapadia SB, et al. Chondrosarcoma of the nasal septum: skull base imaging and clinicopathologic correlation. Otolaryngol Head Neck Surg 1996;115(1):29–37.
84. Guccion J, Font R, Enziger F, et al. Extraskeletal mesenchymal chondrosarcoma. Arch Pathol 1973;95:336–337.
85. Weber AL, Brown EW, Hug EB, Liebsch NJ. Cartilaginous tumors and chordomas of the cranial base. Otolaryngol Clin North Am 1995;28(3):453–471.
86. Brown E, Hug E, Weber A. Chondrosarcoma of the skull base. Neuroimaging Clin North Am 1994;4(3):529–541.
87. Ramina R, Coelho Neto M, Meneses MS, Pedrozo AA. Maffucci's syndrome associated with a cranial base chondrosarcoma: case report and literature review [see comments]. Neurosurgery 1997;41(1):269–272.
88. Balcer LJ, Galetta SL, Cornblath WT, Liu GT. Neuro-ophthalmologic manifestations of Maffucci's syndrome and Ollier's disease. J Neuroophthalmol 1999;19(1):62–66.
89. Keel SB, Bhan AK, Liebsch NJ, Rosenberg AE. Chondromyxoid fibroma of the skull base: a tumor which may be confused with chordoma and chondrosarcoma. A report of three cases and review of the literature. Am J Surg Pathol 1997;21(5):577–582.
90. Shek TW, Peh WC, Leung G. Chondromyxoid fibroma of skull base: a tumor prone to local recurrence. J Laryngol Otol 1999;113(4):380–385.
91. Ojemann R. Meningiomas: clinical features and surgical management. In: Wilkins R, Rengachary S, eds. Neurosurgery. New York: McGraw-Hill, 1985;635–654.
92. Cushing H. The meningiomas (dural endothelioma): their source and favoured seats of origin. Brain 1922;45:282–289.
93. Batsakis J. Other neuroectodermal tumors and related lesions of the head and neck. In: Batsakis J ed. Tumors of the Head and Neck: Clinical and Pathological Considerations. 2nd ed. Baltimore: Williams & Wilkins, 1979;348–352.
94. Miller NR, Golnik KC, Zeidman SM, North RB. Pneumosinus dilatans: a sign of intracranial meningioma. Surg Neurol 1996;46(5): 471–474.
95. Skolnick CA, Mafee MF, Goodwin JA. Pneumosinus dilatans of the sphenoid sinus presenting with visual loss. J Neuroophthalmol 2000;20(4):259–263.
96. Reicher MA, Bentson JR, Halbach VV, et al. Pneumosinus dilatans of the sphenoid sinus. AJNR 1986;7(5):865–868.
97. Hirst LW, Miller NR, Allen GS. Sphenoidal pneumosinus dilatans with bilateral optic nerve meningiomas. Case report. J Neurosurg 1979;51(3):402–407.
98. Hirst LW, Miller NR, Hodges FJ, et al. Sphenoid pneumosinus dilatans. A sign of meningioma originating in the optic canal. Neuroradiology 1982;22(4):207–210.
99. Spoor TC, Kennerdell JS, Maroon JC, et al. Pneumosinus dilatans, Klippel-Trenaunay-Weber syndrome, and progressive visual loss. Ann Ophthalmol 1981;13(1):105–108.
100. Hirsch WL Jr, Hryshko FG, Sekhar LN, et al. Comparison of MR imaging, CT, and angiography in the evaluation of the enlarged cavernous sinus. AJR 1988;151(5):1015–1023.
101. Young S, Grossman R, Goldberg H, et al. MR of vascular encasement in parasellar masses: comparison with angiography and CT. AJNR 1988;9(1):35–38.
102. Bret P, Beziat JL. [Sphenoido-nasopharyngeal craniopharyngioma. A case with radical excision by Le Fort I-type maxillotomy]. Neurochirurgie 1993;39(4):235–240.
103. Chakrabarty A, Mitchell P, Bridges LR. Craniopharyngioma invading the nasal and paranasal spaces, and presenting as nasal obstruction. Br J Neurosurg 1998;12(4):361–363.
104. Hillman TH, Peyster RG, Hoover ED, et al. Infrasellar craniopharyngioma: CT and MR studies. JCAT 1988;12(4):702–704.
105. Bernstein M, Buchino J. The histology similarity between craniopharyngioma and odontogenic lesions: a reappraisal. Oral Pathol 1983;56(5):502–511.
106. Alvarez-Garijo J, Froufe A, Taboada D, et al. Successful surgical treatment of an odontogenic ossified craniopharyngioma. J Neurosurg 1981;55:832–835.
107. Burger P, Scheihauer B. Craniopharyngiomas. In: Burger P, Scheihauer B, eds. Atlas of Tumor Pathology: Tumors of the Central Nervous System. Washington, DC: Armed Forces Institute of Pathology, 1994;349–354.
108. Lopez-Carreira M, Dominguez-Franjo P, Madero S, et al. Suprasellar papillary squamous craniopharyngioma. A case report. J Neurosurg Sci 1997;41(2):175–178.
109. Sartoretti-Schefer S, Wichmann W, Aguzzi A, Valavanis A. MR differentiation of adamantinous and squamous-papillary craniopharyngiomas. AJNR 1997;18(1):77–87.
110. Crotty TB, Scheithauer BW, Young WF Jr, et al. Papillary craniopharyngioma: a clinicopathological study of 48 cases. J Neurosurg 1995;83(2):206–214.
111. Hanna E, Weissman J, Janecka IP. Sphenoclival Rathke's cleft cysts: embryology, clinical appearance and management. Ear Nose Throat J 1998;77(5):396–399, 403.
112. Murphy F, Vesely D, Jordan R, et al. Giant invasive prolactinomas. Am J Med 1987;83(7):995–1002.
113. Hoffman JJ. Radiology of sellar and parasellar lesions. In: Wilkins R, Rengachary S, eds. Neurosurgery. New York: McGraw-Hill, 1985;822–834.
114. Slonin S, Haykal H, Cushing GW, et al. MRI appearance of an ectopic pituitary adenoma: a case report and review of the literature. Neuroradiology 1993;35:546–548.
115. Tovi F, Hirsch M, Sacks M, Leiberman A. Ectopic pituitary adenoma of the sphenoid sinus: report of a case and review of the literature. Head Neck 1990;12(3):264–268.
116. Scheithauer BW, Woodruff JM, Erlandson RA, Universities Associated for Research and Education in Pathology: Tumors of the peripheral nervous system. Washington, DC: Armed Forces Institute of Pathology, 1999. (Universities Associated for Research, Education in Pathology, eds. Atlas of tumor pathology. Third series; fasc. 24.)
117. Kioumehr F, Rooholamini SA, Yaghmai I, et al. Giant-cell tumor of the sphenoid bone: case report and review of the literature. Can Assoc Radiol J 1990;41(3):155–157.
118. Weber AL, Hug EB, Muenter MW, Curtin HD. Giant-cell tumors of the sphenoid bone in four children: radiological, clinical, and pathological findings. Skull Base Surg 1997;4:163–173.
119. Rhea JT, Weber AL. Giant-cell granuloma of the sinuses. Radiology 1983;147(1):135–137.
120. Som PM, Lawson W, Cohen BA. Giant-cell lesions of the facial bones. Radiology 1983;147(1):129–134.

Copyright © 2003, Mosby, Inc. All rights reserved.

121. Rogers LF, Mikhael M, Christ M, Wolff A. Case report 276. Giant cell (reparative) granuloma of the sphenoid bone. Skeletal Radiol 1984;12(1):48–53.
122. Lewis ML, Weber AL, McKenna MJ. Reparative cell granuloma of the temporal bone. Ann Otol Rhinol Laryngol 1994;103(10): 826–828.
123. Nemoto Y, Inoue Y, Tashiro T, et al. Central giant cell granuloma of the temporal bone. AJNR 1995;16(Suppl4):982–985.
124. Sampson JH, Rossitch E, Young JN, et al. Solitary eosinophilic granuloma. Neurosurgery 1992;31:755.
125. Hermans R, DeFoer B, Smet MH, et al. Eosinophilic granuloma of the head and neck. Pediatr Radiol 1994;24:33.
126. Brisman, Feldstein, Tarbell, et al. Eosinophilic granuloma of the clivus. Neurosurgery 1997;41:273–279.
127. Ashkan K, Pollock J, D'Arrigo C, Kitchen ND. Intracranial osteosarcomas: report of four cases and review of the literature [see comments]. J Neurooncol 1998;40(1):87–96.
128. Whitehead RE, Melhem ER, Kasznica J, Eustace S. Telangiectatic osteosarcoma of the skull base. AJNR 1998;19(4):754–757.
129. Rushing EJ, White JA, D'Alise MD, et al. Primary epithelioid hemangioendothelioma of the clivus. Clin Neuropathol 1998;17(2): 110–114.
130. Rajshekhar V, Chandy MJ. Haemangioma of the skull base producing basilar impression. Br J Neurosurg 1989;3(2):229–233.
131. Anavi Y, Sabes WR, Mintz S. Gorham's disease affecting the maxillofacial skeleton. Head Neck 1989;11(6):550–557.
132. Frankel DG, Lewin JS, Cohen B. Massive osteolysis of the skull base. Pediatr Radiol 1997;27(3):265–267.
133. Gorham LW, Wright AW, Schultz HH, Maxon FC. Disappearing bones: a rare form of massive osteolysis. Am J Med 1954;17(5):674–682.
134. Heffez L, Doku HC, Carter BL, Feeney JE. Perspectives on massive osteolysis. Report of a case and review of the literature. Oral Surg Oral Med Oral Pathol 1983;55(4):331–343.
135. Jackson JBS. A boneless arm. Boston Med Surg J 1838;10: 368–369.
136. Mawk JR, Obukhov SK, Nichols WD, et al. Successful conservative management of Gorham disease of the skull base and cervical spine. Childs Nerv Syst 1997;13(11–12):622–625.
137. Murphy JB, Doku HC, Carter BL. Massive osteolysis: phantom bone disease. J Oral Surg 1978;36(4):318–322.
138. Lanzieri CF, Shah M, Krauss D, Lavertu P. Use of gadolinium-enhanced MR imaging for differentiating mucoceles from neoplasms in the paranasal sinuses. Radiology 1991;178(2):425–428.
139. Chambers E, Rosenbaum A, Norman O, et al. Traumatic aneurysm of cavernous internal carotid artery, secondary epistaxis. AJNR 1981;2:405–409.
140. Atlas S, Grossman R, Goldberg H, et al. Partially thrombosed giant intracranial aneurysm: correlation of MR and pathologic findings. Radiology 1987;162:111–114.
141. Fisher A, Som P, Mosesson R, et al. Giant intracranial aneurysms with skull base erosion and extracranial masses: CT and MR findings. JCAT 1994;18:939–942.
142. Lederman M. Cancer of the Nasopharynx: Its Natural History and Treatment. Springfield, Ill: Charles C Thomas, 1961.
143. Chong VF, Mukherji SK, Ng SH, et al. Nasopharyngeal carcinoma: review of how imaging affects staging. JCAT 1999;23(6):984–993.
144. Malogolowkin M, Ortega J. Rhabdomyosarcoma of childhood. Pediatr Ann 1988;17(4):251–257.
145. Ballantyne A, McCarten A, Ibanez M. The extension of cancer of the head and neck through peripheral nerves. Am J Surg 1963;106:651–654.
146. Conley J, Dingman DL. Adenoid cystic carcinoma in the head and neck (cylindroma). Arch Otolaryngol 1974;100(2):81–90.
147. Dodd G, Dolan P, Ballantyne A, et al. The dissemination of tumors of the head and neck via the cranial nerves. Radiol Clin North Am 1970;8(3):445–453.
148. Spiro R, Huvos A, Strong E. Adenoid cystic carcinoma of salivary origin: a clinicopathologic study of 242 cases. Am J Surg 1974;128:512–520.
149. Laine F, Braun I, Jensen M, et al. Perineural tumor extension through the foramen ovale: evaluation with MR imaging. Radiology 1990;174:65–71.
150. Curtin H, Williams R, Johnson J. CT of perineural tumor extension: pterygopalatine fossa. AJNR 1984;5:731–737.
151. Nemzek WR, Hecht S, Gandour-Edwards R, et al. Perineural spread of head and neck tumors: how accurate is MR imaging? AJNR 1998;19(4):701–706.
152. Curtin HD. Detection of perineural spread: fat is a friend [editorial; comment]. AJNR 1998;19(8):1385–1386.
153. Williams LS. Advanced concepts in the imaging of perineural spread of tumor to the trigeminal nerve. Top Magn Reson Imaging 1999;10(6):376–383.
154. Ghobrial W, Amstutz S, Mathog R. Fractures of the sphenoid bone. Head Neck Surg 1986;8:447–451.
155. Gurdjian E, Webster J. Head Injuries: Mechanism, Diagnosis, and Management. Boston: Little, Brown, 1958.
156. McLaurin R, McLennan J. Diagnosis and treatment of head injury in children. In: Youmans J, ed. Neurological Surgery. 2nd ed. Philadelphia: WB Saunders, 1982;2084–2136.
157. Thomas L. Skull fractures. In: Wilkins R, Rengachary S, eds. Neurosurgery. New York: McGraw-Hill, 1985;1623–1626.
158. Manfredi S, Raji M, Sprinkle P, et al. Computerized tomographic scan findings in facial fractures associated with blindness. Plast Reconstr Surg 1981;68:479–482.
159. Taybi H, Lachman RS. Radiology of Syndromes, Metabolic Disorders, and Skeletal Dysplasias. 4th ed. St. Louis: CV Mosby, 1996.
160. Resnick D. Diagnosis of Bone and Joint Disorders. 3rd ed. Philadelphia: WB Saunders, 1995.
161. Daffner R, Kirks D, Gehweiler JJ, et al. Computed tomography of fibrous dysplasia. AJR 1982;139:943–946.
162. Fries J. The roentgen features of fibrous dysplasia of the skull and facial bones. AJR 1957;77:71–75.
163. Leeds N, Seaman W. Fibrous dysplasia of the skull and its differential diagnosis. Radiology 1962;78:570–578.
164. Casselman J, DeJonge I, Neyt L, et al. MRI in craniofacial fibrous dysplasia. Neuroradiology 1993;35:234–237.
165. Olmsted WW. Some skeletogenic lesions with common calvarial manifestations. Radiol Clin North Am 1981;19(4):703–713.
166. Smith J, Botet JF, Yeh SD. Bone sarcomas in Paget disease: a study of 85 patients. Radiology 1984;152(3):583–590.
167. Beighton P, Durr L, Hamersma H. Clinical features of sclerosteosis: a review of the manifestations in 25 affected individuals. Ann Intern Med 1976;84:393–397.
168. Beighton P, Hamersma H, Horan F. Craniometaphyseal dysplasia: variability of expression within a large family. Clin Genet 1979;15:252–258.
169. Hamersma H. Facial nerve paralysis in the osteopetroses. In: Fisch V, ed. Proceedings of the 3rd Symposium on Facial Nerve Surgery. Zurich: 1976;555–576.
170. Applegate L, Applegate G, Kemp S. MR of multiple cranial neuropathies in a patient with Camurati-Engelmann disease: case report. AJNR 1991;12:557–559.
171. Shetty PG, Shroff MM, Fatterpekar GM, et al. A retrospective analysis of spontaneous sphenoid sinus fistula: MR and CT findings. AJNR 2000;21(2):337–342.
172. Stone JA, Castillo M, Neelon B, Mukherji SK. Evaluation of CSF leaks: high-resolution CT compared with contrast-enhanced CT and radionuclide cisternography. AJNR 1999;20(4):706–712.
173. Drayer B, Wilkins R, Boehnke M, et al. Cerebrospinal fluid rhinorrhea demonstrated by metrizamide CT cisternography. AJR 1977;129:149–152.

Copyright © 2003, Mosby, Inc. All rights reserved.

Copyright © 2003, Mosby, Inc. All rights reserved.

13

Imaging of Perineural Tumor Spread in Head and Neck Cancer

Lawrence E. Ginsberg

INTRODUCTION
PERINEURAL INVASION VERSUS PERINEURAL SPREAD
THE MOST COMMON ANATOMIC LOCATIONS AND TUMOR HISTOLOGIES ASSOCIATED WITH PNS
SIGNS AND SYMPTOMS ASSOCIATED WITH PNS
COMMON CLINICAL SETTINGS ASSOCIATED WITH PNS
ANATOMIC NEUROLOGIC CONSIDERATIONS
- Ophthalmic Division of the Trigeminal Nerve (V_1)
- Maxillary Division of the Trigeminal Nerve (V_2)
- Mandibular Division of the Trigeminal Nerve (V_3)
- Facial Nerve
- Interconnections Between the Trigeminal and Other Cranial Nerves
- Spinal Nerves

IMAGING OF PERINEURAL TUMOR SPREAD
- Technical Considerations
- Imaging Diagnosis of PNS
- Secondary Imaging Findings

IMAGING PITFALLS
- Technique
- Questionable PNS
- Asymmetric Foraminal Enhancement

PERSISTENT POSTTREATMENT IMAGING ABNORMALITIES
MIMICS OF PNS
CONCLUSION

INTRODUCTION

In malignancies of the head and neck, tumor may spread along the neural sheath (via the endoneurium, perineurium, or perineural lymphatics) by a process known as perineural tumor spread (PNS). PNS most commonly occurs in a retrograde direction, toward the central nervous system, but also can occur in an antegrade manner. Early in the twentieth century there were scattered reports of this phenomenon.[1] The first comprehensive report on PNS was the frequently referenced work by A.J. Ballantyne et al., while in the imaging literature, the landmark article was by Dodd et al., who reported the plain film imaging findings in 40 patients.[2, 3] Despite the fact that PNS is well known, it remains a vexing clinical problem because it may be clinically silent and because it is often missed at imaging.

PERINEURAL INVASION VERSUS PERINEURAL SPREAD

It is important to distinguish between perineural invasion and perineural spread, as there is some confusion in the literature concerning the use of the term *perineural*. Perineural *invasion* is the microscopic finding of tumor cells surrounding very small nerve branches, and as such it cannot be seen on imaging.[4] It is an ominous prognostic sign associated with an increased local recurrence rate and decreased survival.[5, 6] This chapter is concerned with macroscopic or large nerve PNS, in which there is gross tumor spread, sometimes over a considerable length of the nerve.

Since PNS may be asymptomatic, it is critical that radiologists be vigilant in their efforts to detect it prior to the institution of therapy. The finding of PNS may convert a

Copyright © 2003, Mosby, Inc. All rights reserved.

lesion thought to be resectable into a nonresectable one. The presence of PNS may also mean that radiation fields need to be expanded to encompass the tumor spread. In the case of a parotid tumor, the finding of PNS may indicate that a temporal bone resection with a partial facial nerve resection may be needed to ensure a tumor-free margin along the facial nerve.

As mentioned, failure to diagnose PNS may have grave implications, particularly if the mode of therapy fails to address the disease extension along the nerve. Such failure virtually guarantees a tumor recurrence, which actually represents a progression of undetected residual disease. Furthermore, failure to recognize PNS on imaging studies is a not infrequent cause of legal action against radiologists. Reasons for failing to diagnose PNS include lack of familiarity with the types of cancers that commonly are associated with it, lack of familiarity with the common routes and imaging appearance of PNS, and inadequate imaging.

THE MOST COMMON ANATOMIC LOCATIONS AND TUMOR HISTOLOGIES ASSOCIATED WITH PNS

Though virtually any head and neck malignancy may be associated with PNS, certain primary sites and cancer types are clearly more likely to spread along the perineural route. Cutaneous malignancies, particularly squamous cell carcinomas and desmoplastic melanomas, tend to be associated with PNS, and such tumor spread is often associated with a recurrence of skin cancer.[6–10] Although these tumors may occur anywhere on the face, there is a predilection for the side of the nose and the lower lip, areas supplied by the maxillary division of the trigeminal nerve (V_2).[11, 12]

Mucosal primaries such as squamous cell carcinoma and especially minor salivary gland cancers such as adenoid cystic carcinoma are also associated with PNS.[13–16] In particular, primary tumors in the palate may gain direct access to the palatine nerves that innervate these mucosal surfaces, while nasopharyngeal tumors may spread to V_2 via extension into the pterygopalatine fossa (PPF) or to V_3 via extension into the masticator space.[13, 14, 17]

Virtually any salivary gland cancer, especially those arising in the parotid gland, may be associated with PNS. In such cases, although the facial nerve is at greatest risk for PNS, the auriculotemporal branch of the mandibular nerve may also provide a route for PNS.[13, 18] Another clinical setting involving the parotid gland that may result in PNS is either direct tumor extension or intraparotid metastases from an adjacent primary or recurrent skin cancer.[13, 19]

In addition to the cancers just mentioned, other malignancies, regardless of their histology or primary location, may also be associated with PNS if they involve anatomic sites such as the masticator space, PPF, or cavernous sinus/Meckel's cave.[13] For reasons that are unclear, cancers in certain locations do not often spread along perineural pathways. These sites include the submandibular gland, tongue, buccal mucosa, tonsil, larynx, pharynx, and floor of the mouth. Exceptions at these locations may occur, particularly if the tumor has extended to one of the areas mentioned that are associated with PNS.

SIGNS AND SYMPTOMS ASSOCIATED WITH PNS

The signs and symptoms most commonly associated with PNS include pain, paresthesias, numbness, formication (the sensation of ants and worms under the skin), and motor denervation weakness. The last is most often encountered as either facial paralysis or masticator muscle weakness when the facial nerve and V_3, respectively, are involved.[13, 19] Although microscopic perineural invasion may have similar symptoms, PNS should be considered when the neurologic symptoms suggest broader involvement than would be expected based on the location of the lesion (e.g., a small facial skin cancer with multiple divisions of the affected trigeminal nerve). Multiple cranial neuropathies are also an ominous finding, suggesting either PNS proximal to the cavernous sinus, tumor spread from one cranial nerve to another, or leptomeningeal disease.[7, 11] While the above-mentioned symptoms may suggest PNS, up to 40% of patients with PNS have either nonspecific symptoms or are asymptomatic.[7, 19, 20–22]

COMMON CLINICAL SETTINGS ASSOCIATED WITH PNS

In addition to the presence of a primary tumor in a high-risk location, there are postoperative clinical settings that are associated with PNS. These include the development of a cranial neuropathy in a patient who has had a previously resected tumor, with or without an obvious local recurrence.[7, 10, 11, 22] A typical history is that of a previous resection of a skin lesion thought either to be benign or malignant (often the specimen is no longer available for review, and occasionally the patient may not remember the surgery) associated with a new neurologic deficit along the corresponding branch of the trigeminal nerve or a more generalized trigeminal neuropathy.[10] Another common scenario is the development of a facial nerve paralysis in a patient who has had a prior resection of a parotid mass. Such histories should prompt a careful imaging search for PNS, and it is important that these patients not simply be diagnosed as having ''Bell's palsy'' or ''trigeminal neuralgia'' until more sinister causes are excluded.[10]

Unfortunately, the radiologist may not be aware that a lesion was previously resected, and the appropriate history must be specifically sought. On the other hand, if a neurologic deficit was caused by therapy or the initial presentation of the primary lesion, the patient may not report any new symptoms. Thus, if parotidectomy resulted in a facial nerve palsy, postoperative imaging may be the only way to establish the presence of PNS prior to the onset of additional cranial neuropathies.

Lastly, though rare, evidence of PNS may present clinically prior to detection of the associated primary cancer.[23] This might occur with an asymptomatic, submucosal, slow-growing tumor such as an adenoid cystic carcinoma. Several such tumors arising in the palate with PNS to the cavernous sinus have been reported.[23] Thus, an important corollary in the setting of no known primary tumor is that any patient who presents with a mass

Copyright © 2003, Mosby, Inc. All rights reserved.

in one of the common proximal locations associated with PNS (the PPF, Meckel's cave, or the cavernous sinus) should have a careful clinical and radiologic evaluation for a primary clinically silent head and neck malignancy.

ANATOMIC NEUROLOGIC CONSIDERATIONS

The cranial nerves most often involved in PNS from head and neck cancer are the trigeminal and facial nerves.[13, 15] Rarely, spinal nerve branches may be affected. In order to recognize PNS when it is visible on imaging studies, the radiologist must be familiar with the cranial nerve anatomy, including the branches that innervate a particular head and neck location and the proximal course of those nerves.

Ophthalmic Division of the Trigeminal Nerve (V_1)

The ophthalmic division of the trigeminal nerve (V_1) is uncommonly affected by PNS.[24–26] This nerve provides purely sensory innervation to the eye, lacrimal gland, conjunctiva, part of the nasal mucosa, and skin of the nose, eyelids, forehead, and scalp.[27] Figure 13-1 depicts the anatomy of the ophthalmic nerve. After emerging from the Gasserian ganglion in Meckel's cave, the ophthalmic nerve courses through the cavernous sinus, passes through the superior orbital fissure to enter the orbit, and then divides into the nasociliary, lacrimal, and frontal nerves (Fig. 13-1).

The frontal nerve is the largest branch; it divides into a smaller supratrochlear branch and a larger supraorbital branch (Fig. 13-1). The supratrochlear nerve runs anteromedially and exits the orbit to provide cutaneous innervation to the medial supraorbital region and the lower forehead near the midline. Cutaneous cancers in this region may have PNS along the supratrochlear nerve (Fig. 13-2). The supraorbital nerve courses anteriorly between the levator palpebrae and the orbital roof and then exits the orbit, where it divides into medial and lateral branches (Fig. 13-1). These branches provides sensory innervation to the scalp in the immediate supraorbital region and as far back as the lambdoidal suture.[27] Small branches also supply innervation to the frontal sinus mucosa and the pericranium. The supraorbital nerve is also at risk for PNS when a skin cancer arises in its region of innervation.

The lacrimal nerve provides innervation to the lacrimal gland, having first received a twig from the zygomaticotemporal nerve, which is a small branch of V_2 (containing postganglionic parasympathetic innervation from the pterygopalatine ganglion, originating in the greater superficial petrosal nerve, a branch of the facial nerve).[27] The nasociliary nerve provides small branches that innervate the frontal dura and the nasoethmoid mucosa. While it is theoretically possible that cancers along the distribution of these nerves (lacrimal gland, nasoethmoid, etc.) could be associated with retrograde PNS, such cases have not been reported.

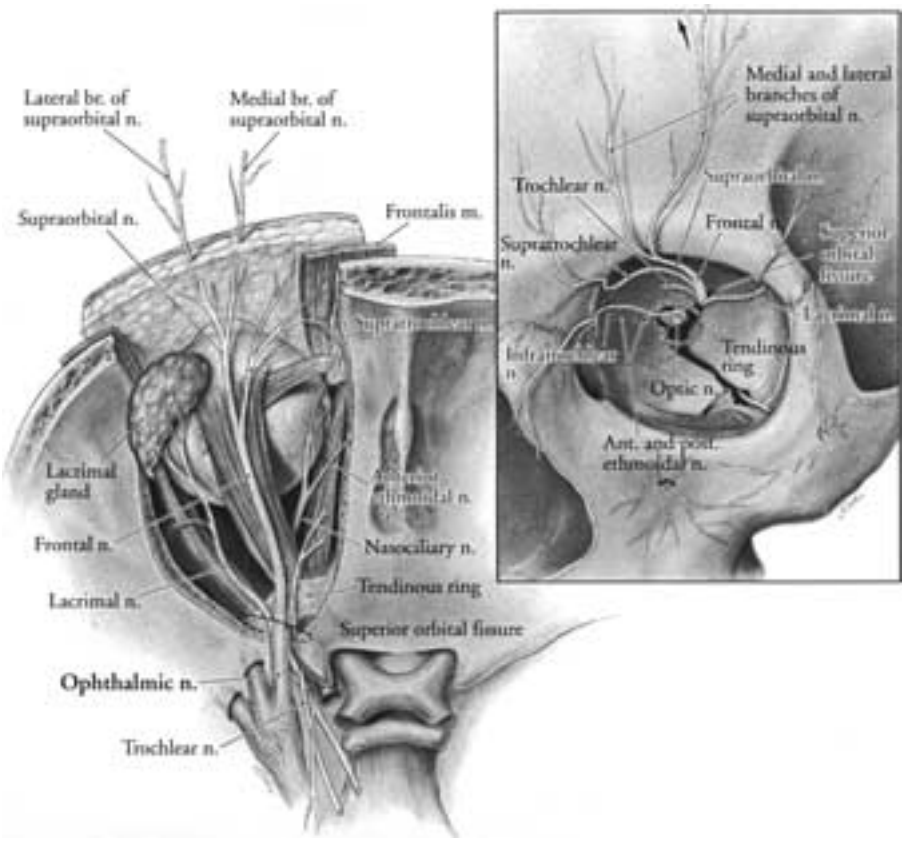

FIGURE 13-1 Diagrammatic representation of ophthalmic nerve (V_1) anatomy.

VIEW IMAGE

Copyright © 2003, Mosby, Inc. All rights reserved.

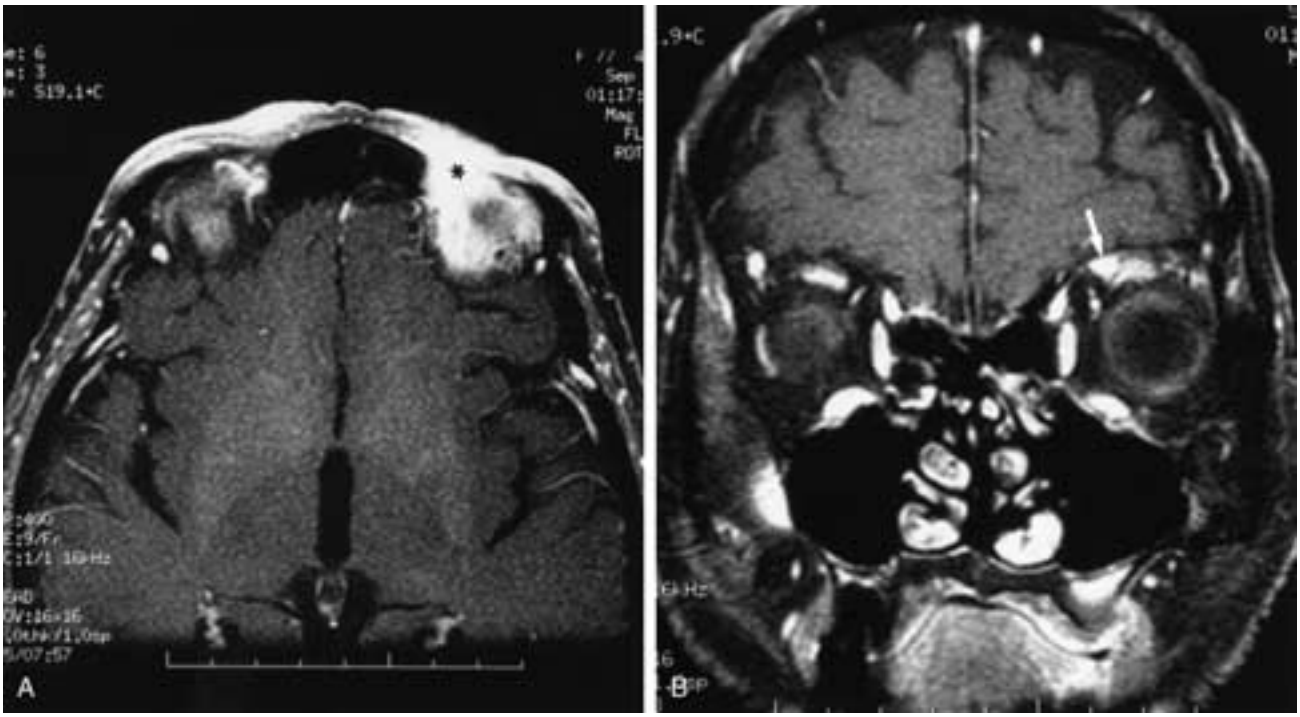

VIEW IMAGE

FIGURE 13-2 Squamous cell carcinoma in the left medial supraorbital region with PNS along the supratrochlear branch of the ophthalmic nerve. **A**, Contrast-enhanced axial T1-weighted MR image with fat suppression shows enhancing tumor in the left supraorbital region (*asterisk*). **B**, Contrast-enhanced coronal T1-weighted MR image with fat suppression shows thickening and abnormal enhancement of the supratrochlear branch of the ophthalmic nerve (*arrow*) just medial to the normally enhancing superior muscle complex.

Maxillary Division of the Trigeminal Nerve (V_2)

The maxillary division of the trigeminal nerve (V_2) provides sensory innervation to the skin of the midface, the mucosa of the palate, sinonasal region, and maxillary gingiva, and the maxillary teeth. Figure 13-3 depicts the anatomy of the maxillary nerve. The maxillary nerve courses through the cavernous sinus and then through the foramen rotundum to enter the PPF. Within the PPF, the maxillary nerve gives rise to several palatine branches as well as the zygomatic nerve. The palatine nerves course inferiorly through the greater and lesser palatine foramina to innervate the hard and soft palates, respectively.[14] The zygomatic nerve enters the orbit through the inferior orbital fissure, runs along the lateral orbital wall, and divides into the zygomaticofacial and zygomaticotemporal branches.[27] The zygomaticotemporal nerve sends a small twig to the lacrimal nerve, as mentioned earlier. Both the zygomaticotemporal and zygomaticofacial nerves exit the orbit through its lateral wall and supply innervation to the skin of the temporal region and lateral cheek (Fig. 13-3).[27] Also within the PPF, the maxillary nerve gives off the posterior superior alveolar nerve to the maxillary sinus.

More distally, the maxillary nerve enters the infraorbital canal as the infraorbital nerve and gives off the anterior and middle superior alveolar nerves to the maxillary teeth and gingiva. The infraorbital nerve then emerges from the infraorbital foramen and divides into its terminal branches, supplying the skin of the midfacial region and lateral nose (Fig. 13-3). Proximal or retrograde PNS from any of these innervated sites can occur along the respective distal branches of V_2, generally eventually involving the PPF.[28] Thus, tumors arising in the cheek are at particularly high risk of PNS along the infraorbital nerve, often with tumor in the PPF (Figs. 13-4, 13-5).[6, 8, 10, 13, 22, 28]

Skin cancers in the temporal region and upper lateral face may spread to the orbit via the zygomatic nerve (Fig. 13-5). A palate lesion can spread along the palatine nerves and then to the PPF (Figs. 13-6, 13-7).[14] Maxillary sinus tumors may have PNS along the superior alveolar nerves to enter the PPF.[28] If a nasopharyngeal carcinoma has extended into the nasal cavity, it may spread laterally through the sphenopalatine foramen to enter the PPF (Fig. 13-8).[13, 17] Once in the PPF, retrograde PNS can occur along the main trunk of V_2 through the foramen rotundum, with subsequent involvement of the cavernous sinus and Meckel's cave or even the more proximal main trigeminal nerve trunk (Figs. 13-7, 13-8).[13, 15, 28]

Once tumor is in the PPF, PNS may also occur along the vidian nerve (or nerve of the pterygoid canal) (Fig. 13-9).[13, 14, 29, 30] Antegrade PNS may occur once the PPF is involved. Commonly this occurs along branches of V_2, especially the infraorbital nerve (Fig. 13-7C).[3, 13, 15, 28] Once tumor has spread into Meckel's cave, antegrade PNS may also occur along V_3 (Fig. 13-7D).

Mandibular Division of the Trigeminal Nerve (V_3)

The mandibular division of the trigeminal nerve (V_3) provides sensory innervation to the skin of the lower face

Copyright © 2003, Mosby, Inc. All rights reserved.

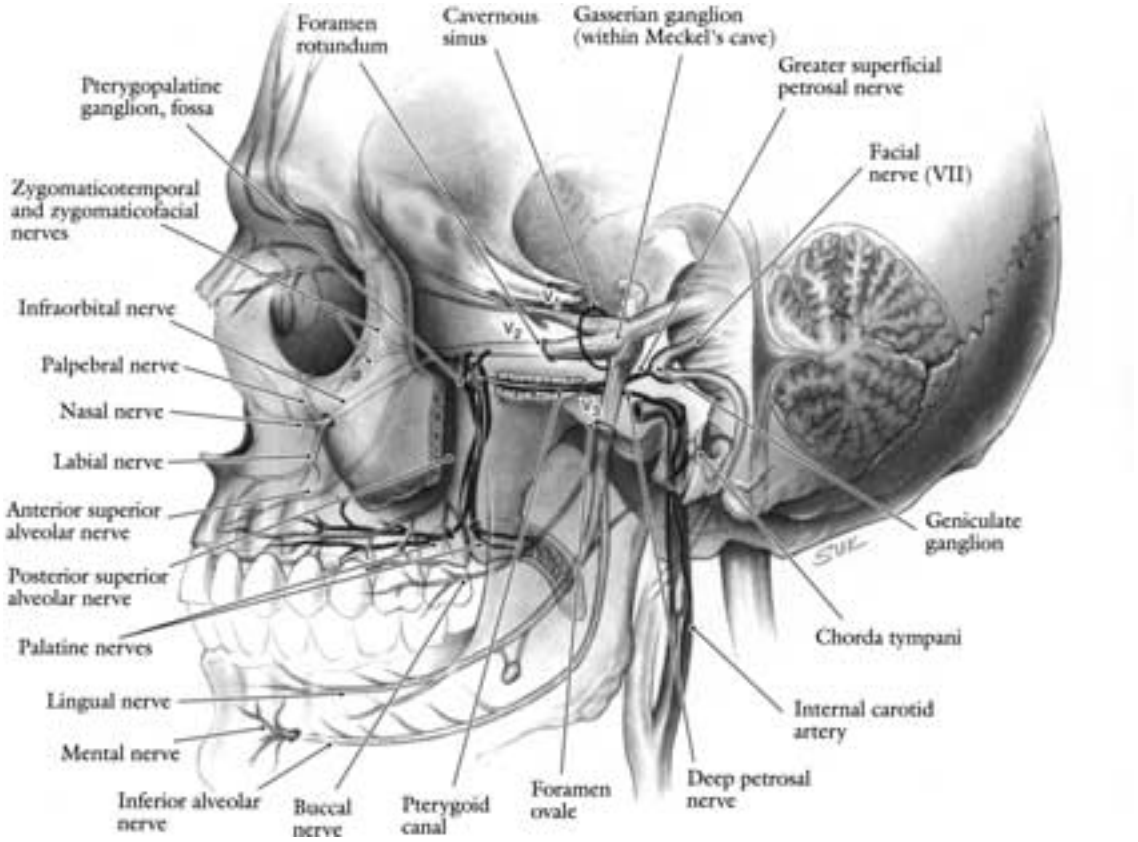

FIGURE 13-3 Diagrammatic representation of V_2 and V_3 anatomy. (From Ginsberg LE. Imaging of perineural tumor spread in head and neck cancer. Semin Ultrasound CT MR 1999;2:175–186.)

VIEW IMAGE

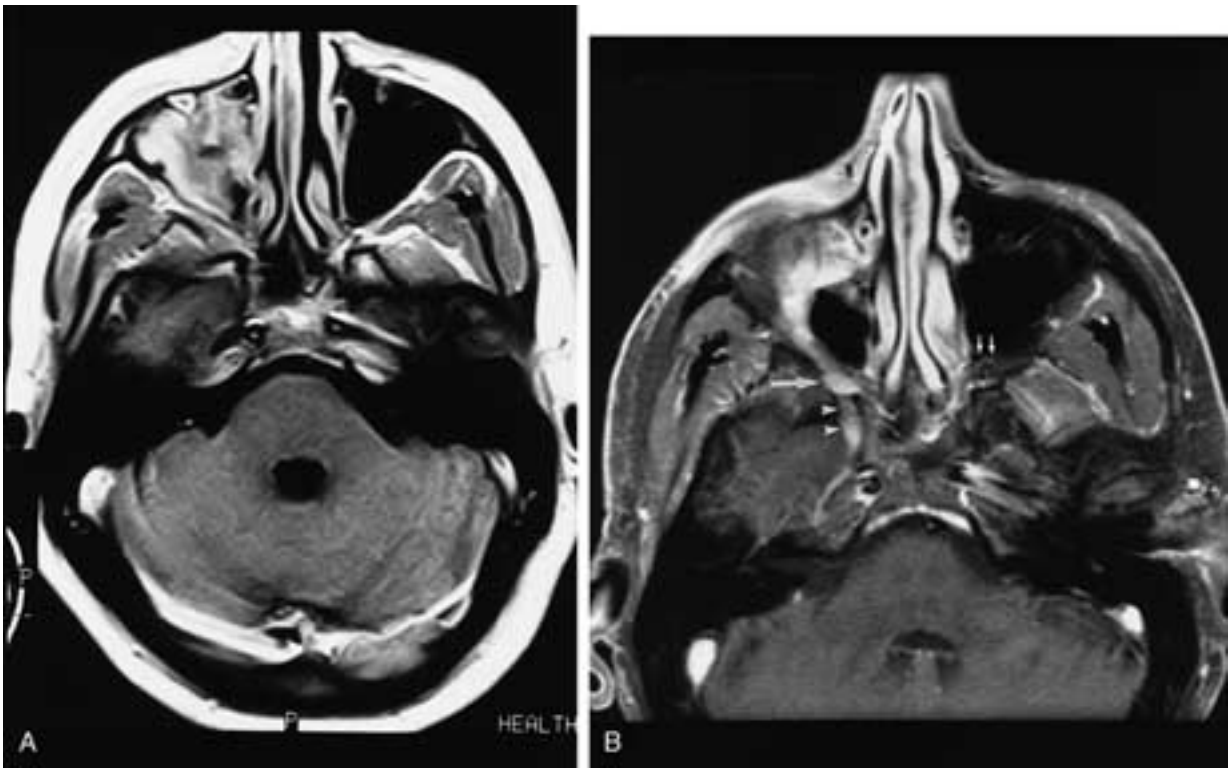

FIGURE 13-4 Squamous cell carcinoma in the right infraorbital region with PNS along the infraorbital branch of the maxillary nerve (V_2). **A**, Axial contrast-enhanced MR image without fat suppression. It is almost impossible to identify tumor within the right PPF. This scan was performed at an outside institution, and there was no precontrast T1-weighted imaging to help evaluate the PPF. **B**, Axial contrast-enhanced MR image with fat suppression allows visualization of excessive enhancement representing PNS in the right PPF (*long arrow*). Note the lack of significant enhancement in the normal left PPF (*short arrows*). On the right side, there is continued posterior or retrograde PNS within the foramen rotundum (*arrowheads*).

VIEW IMAGE

Copyright © 2003, Mosby, Inc. All rights reserved.

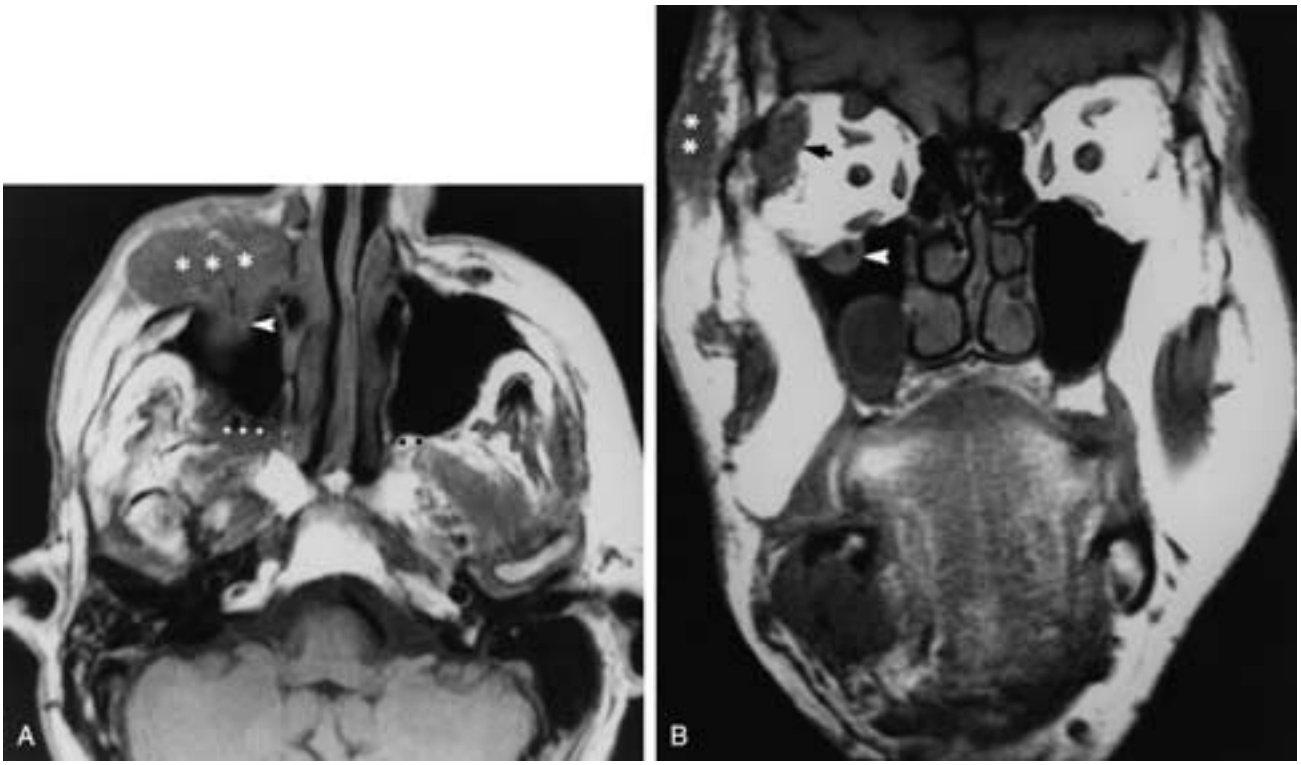

VIEW IMAGE

FIGURE 13-5 Recurrent desmoplastic melanoma in multiple facial locations with PNS along the zygomatic and infraorbital branches of the maxillary nerve (V_2). **A**, Axial T1-weighted MR image shows large right-sided cheek recurrence (*asterisks*) spreading posteriorly along the infraorbital nerve (*arrowhead*). Tumor can be seen widening and replacing the expected hyperintense fat within the right PPF (*white dots*). Note the normal hyperintense fat in the left PPF (*black dots*). **B**, Coronal T1-weighted MR image shows a grossly enlarged right infraorbital nerve representing perineural spread (*arrowhead*). Note the right-sided tumor recurrence in the temporal region (*asterisks*). The lateral intraorbital mass (*arrow*) likely represents PNS along the zygomaticotemporal/zygomaticofacial branches of V_2 (see Fig. 13-3). (From Ginsberg LE. Imaging of perineural tumor spread in head and neck cancer. Semin Ultrasound CT MR 1999;2:175–186.)

and the preauricular/temporal region, the mandibular teeth, and the mucosa of the mandibular gingiva, floor of the mouth, the tongue (anterior two thirds), and the buccal mucosa.[27] The mandibular nerve also provides motor innervation to the muscles of mastication and the mylohyoid and anterior belly of the digastric muscles. Figures 13-3 and 13-10 depict the anatomy of V_3. Exiting Meckel's cave, the mandibular nerve avoids the cavernous sinus and courses inferiorly through the foramen ovale to enter the masticator space, where it divides into anterior and posterior trunks. The anterior trunk primarily gives rise to motor branches (for the masseter, temporalis, and pterygoid muscles). The posterior trunk gives rise to the auriculotemporal and inferior alveolar nerves, branches commonly associated with PNS, and the lingual nerve, which is seldom associated with PNS.

The auriculotemporal nerve, depicted in Figure 13-10, arises just below the foramen ovale and provides cutaneous innervation to a broad area of the lateral and upper face. It also provides postganglionic parasympathetic innervation to the parotid gland though the fibers that originate in the facial and glossopharyngeal nerves as the lesser superficial petrosal nerve.[27, 31] The lesser superficial petrosal nerve has a very complicated course, but ultimately it synapses in the otic ganglion just beneath the foramen ovale and then uses the auriculotemporal nerve as a conduit to reach the parotid gland.[31]

The inferior alveolar nerve enters the mandible via the mandibular foramen on the medial surface of the mandibular ramus and provides sensory innervation to the mandibular teeth and gingiva. It terminates as the mental nerve, which exits the mental foramen in the anterior mandibular body and provides cutaneous innervation to the lower lip and chin.

Tumors in any anatomic location supplied by V_3 can have retrograde PNS, ultimately involving the main trunk of the mandibular nerve within the masticator space. Tumor may then spread upward through the foramen ovale to eventually affect Meckel's cave.[13, 15, 18, 20] Thus, a skin cancer of the lower lip or chin can spread along the mental nerve to involve the inferior alveolar branch of V_3 and the main trunk of V_3, and ultimately extend through the foramen ovale (Figs. 13-11, 13-12).[11, 13] Parotid or lateral facial tumors can spread along the auriculotemporal branch of V_3 and thus gain access to the main trunk of the mandibular nerve (Fig. 13-13).[13, 15, 18] Any tumor originating within or spreading to the masticator space may have PNS along the mandibular nerve and extend through the foramen ovale (Figs. 13-14, 13-15). As mentioned, once tumor affects Meckel's cave, it can spread posteriorly along the main trigeminal trunk (Figs.

Copyright © 2003, Mosby, Inc. All rights reserved.

13-12, 13-15). Antegrade PNS may also occur from Meckel's cave to involve the cavernous sinus and subsequently V_2 (Fig. 13-12) or V_3 (Fig. 13-7D).

Facial Nerve

The anatomy of the facial nerve is complicated and need not be covered here in its entirety (see Chapters 19, 20, and 21). Diagrammatic representations of the facial nerve can be found in Figures 13-3, 13-17, and 13-20. Almost always, PNS involving the facial nerve occurs with malignancies that arise in the parotid origin or with nearby skin cancers that secondarily invade or metastasize to the parotid gland. These lesions may have PNS along the distal facial nerve (Fig. 13-16).[3, 13, 15] Tumor may then spread along the facial nerve to involve the posterior genu, horizontal or tympanic segment, geniculate ganglion, labyrinthine segment, or ultimately the intracanalicular portion within the internal auditory canal (Fig. 13-16). Less commonly, PNS may

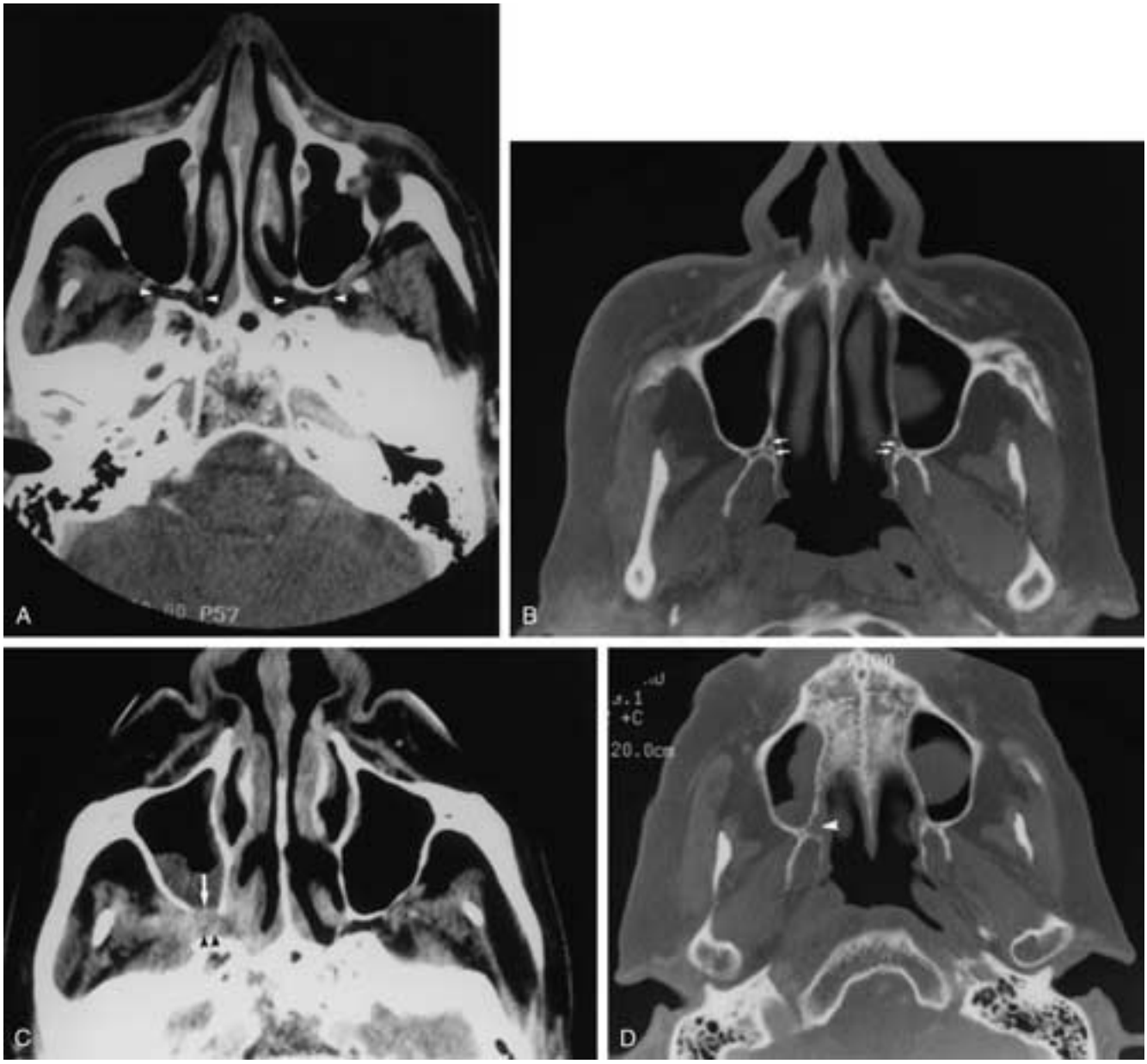

VIEW IMAGE

FIGURE 13-6 Squamous cell carcinoma of the right soft palate with development of perineural spread along the palatine nerves. Axial contrast-enhanced soft-tissue (**A**) and bone window (**B**) CT scans at the time of diagnosis of the palate lesion. The PPFs (*arrowheads*) are normal. On the bone window images through the pterygoid plates, the palatine foramen are normal (*arrows*). The palatine branches of V_2 traverse these foramina en route to/from the palate and PPF. Axial contrast-enhanced soft-tissue (**C**) and bone window (**D**) CT scans at levels similar to those of **A** and **B** obtained 3 months later. There is abnormal widening and enhancement representing PNS within the right PPF (*arrowheads*). The posterior wall of the right maxillary sinus is destroyed (*arrow*). On the bone windows, the right palatine foramina are now destroyed (*arrowhead*). Compare with **B**. (From Ginsberg LE, DeMonte F. Imaging of perineural tumor spread from palatal carcinoma. AJNR 1998;19: 1417–1422.)

Copyright © 2003, Mosby, Inc. All rights reserved.

VIEW IMAGE

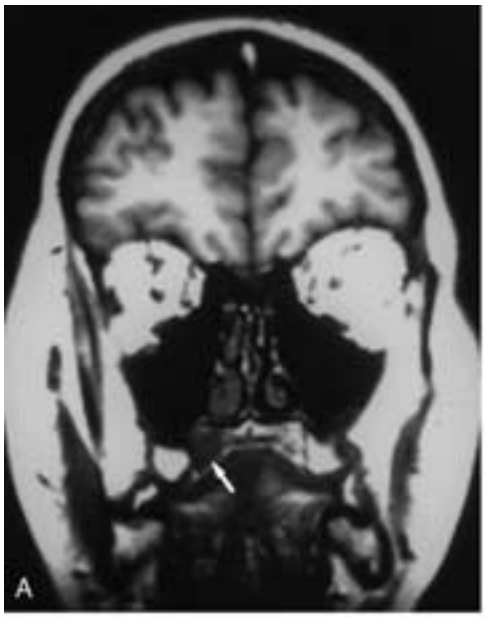

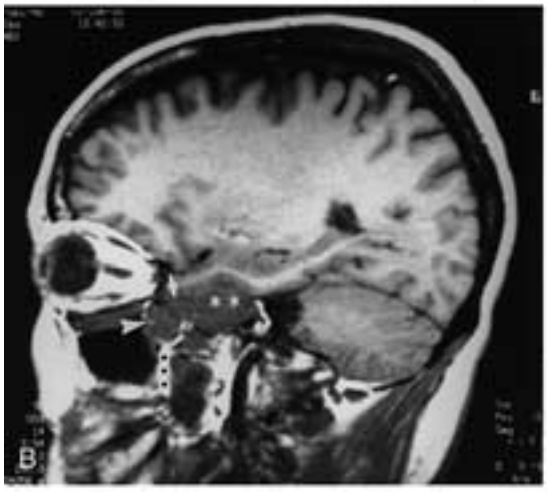

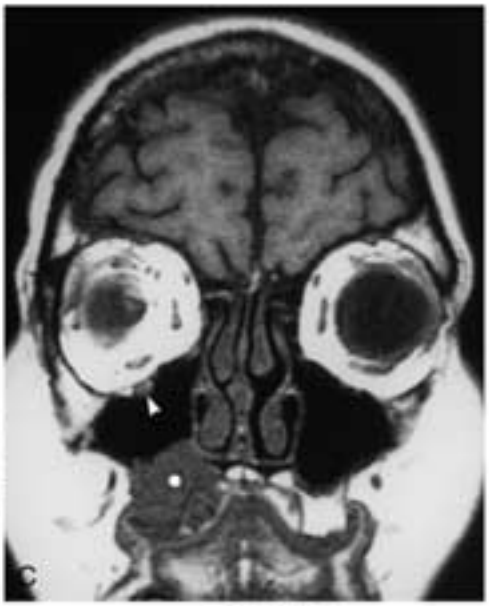

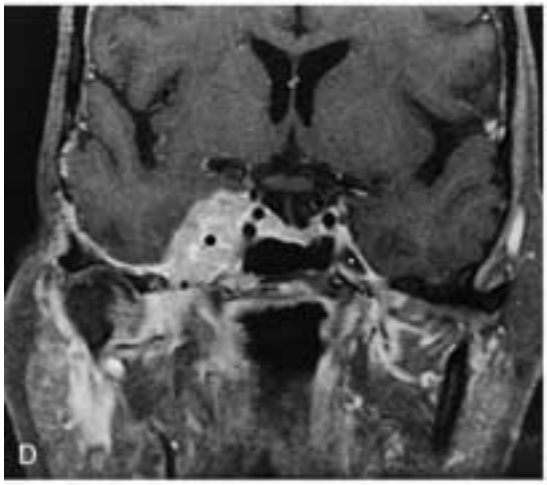

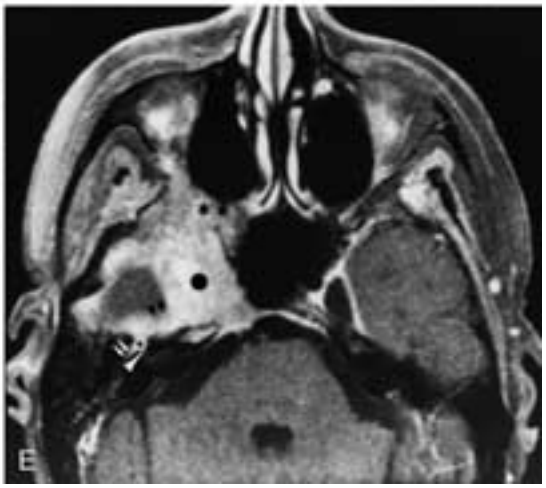

FIGURE 13-7 Adenoid cystic carcinoma of the right hard palate initially presenting with multiple cranial nerve palsies secondary to PNS to the cavernous sinus. **A**, Coronal T1-weighted MR image from brain MR imaging at the time of initial presentation shows a subtle submucosal mass in the right hard palate (*arrow*). This lesion was not appreciated clinically or radiographically. **B**, Sagittal T1-weighted MR image from the same study as **A** shows a large mass in the cavernous sinus (*asterisks*), in the foramen rotundum (*arrow*), and in the upper aspect of the PPF (*arrowhead*). Note that the fat in the lower PPF is normal (*black dots*), indicating a skip lesion from the palatal primary. Because the primary lesion went unnoticed, radiotherapy to the cavernous sinus was the sole therapy. **C** to **E**, MR images obtained 2 years after presentation. The patient now had recurrence of cranial neuropathies including a new right facial nerve paralysis. **C**, Coronal T1-weighted MR image shows that the right palatal primary lesion is much larger (*white dot*). Note the enlargement of the right infraorbital nerve, indicating antegrade perineural tumor spread. **D**, Coronal contrast-enhanced, fat-suppressed MR image shows massive tumor in Meckel's cave (*black dot*) with downward antegrade PNS through a widened foramen ovale (*asterisk*). Note the normal Meckel's cave on the left side (*white dot*) with peripheral but not central enhancement. **E**, Axial contrast-enhanced, fat-suppressed MR image shows massive tumor in the cavernous sinus and Meckel's cave (*large black dot*) and the PPF (*asterisks*). Tumor is also extending posterolaterally along the greater superficial petrosal nerve (*black arrowheads*), through the facial hiatus, and into the geniculate ganglion (*small black dot*). There is further tumor spread involving the labyrinthine (*white arrowhead*) and horizontal or tympanic segment (*white arrows*) of the right facial nerve. This latter finding accounts for the patient's facial nerve paralysis. (A, B, and D from Ginsberg LE, DeMonte F. Imaging of perineural tumor spread from palatal carcinoma. AJNR 1998;19:1417–1422. From Ginsberg LE, DeMonte F. Palatal adenoid cystic carcinoma presenting as perineural spread to the cavernous sinus. Skull Base Surg 1998;8(1):39–43.)

Copyright © 2003, Mosby, Inc. All rights reserved.

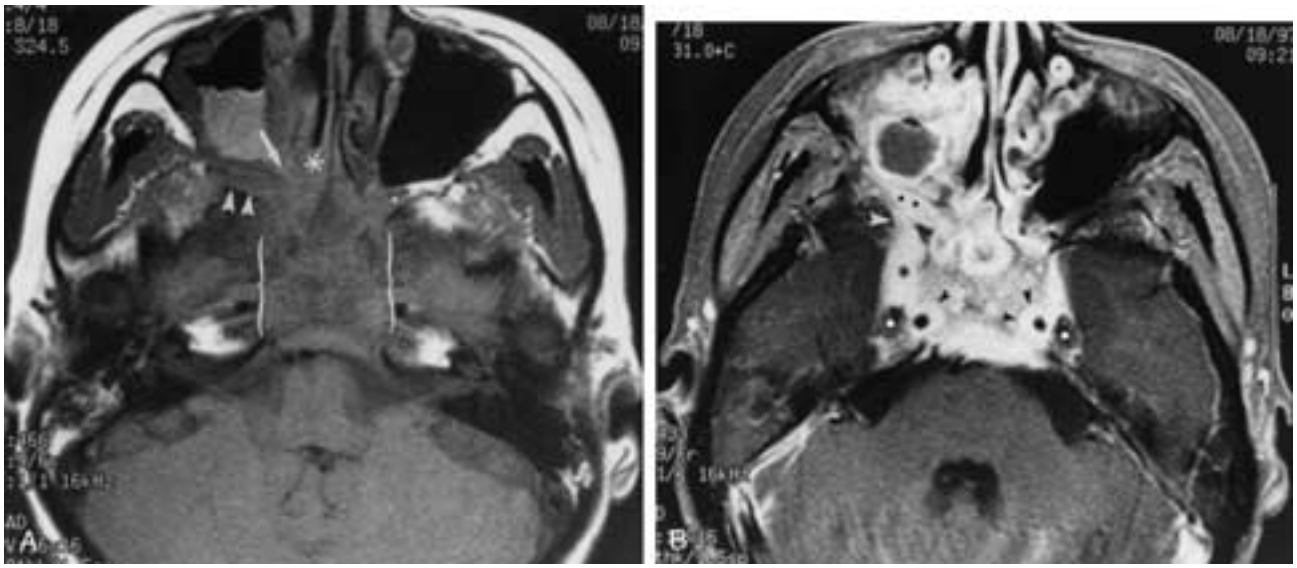

VIEW IMAGE

FIGURE 13-8 Nasopharyngeal carcinoma with V_2 perineural spread. **A**, Axial T1-weighted MR image shows tumor in the right nasal cavity (*asterisk*) with lateral extension through a widened sphenopalatine foramen (*arrow*) involving the right PPF (*arrowheads*). To a lesser extent, the left PPF is similarly affected (*white dot*). Note that the central skull base is diffusely infiltrated by tumor (*brackets*). **B**, Axial contrast-enhanced, fat-suppressed T1-weighted MR image shows enhancement of all tumor components including the right PPF (*black dots*). Tumor is extending posteriorly along the right maxillary nerve through the foramen rotundum (*white arrowhead*) to involve the cavernous sinus (*asterisk*). The left cavernous sinus is also infiltrated by tumor, which could have arrived there along the internal carotid artery, a common route of spread in nasopharyngeal cancer. Note the subtle abnormal enhancement surrounding the cavernous segment of both internal carotid arteries (*black arrowheads*). Bilaterally, Meckel's caves remain intact, with CSF signal intensity and no enhancement centrally (*white dots*). (From Ginsberg LE. Imaging of perineural tumor spread in head and neck cancer. Semin Ultrasound CT MR 1999;2:175–186.)

involve the facial nerve from a small facial nerve branch, the greater superficial petrosal nerve.

Interconnections Between the Trigeminal and Other Cranial Nerves

As alluded to earlier, small distal branches of the trigeminal nerve serve as terminal conduits for branches of other cranial nerves, primarily the facial nerve. This relationship has implications for PNS, and many of these interconnections are depicted in Figure 13-17. The most important of these connections involves the greater superficial petrosal nerve (GSPN). This nerve is a branch of the facial nerve that provides parasympathetic innervation to the lacrimal gland, palate, nasal cavity, and nasopharynx.[27, 30] The anatomy of the GSPN is depicted in Figures 13-3, 13-17, and 13-18. Facial nerve fibers, originating in the nervus intermedius, leave the geniculate ganglion as the GSPN. Exiting from the superior surface of the temporal bone through a small foramen known as the facial hiatus (Fig. 13-19), the intracranial segment of the GSPN courses medially and anteroinferiorly along the surface of the petrous bone to the foramen lacerum. There it joins the deep petrosal nerve of the sympathetic carotid plexus to enter the vidian or pterygoid canal as the vidian nerve or nerve of the pterygoid canal (Fig. 13-3).[30] Upon exiting the vidian canal, this nerve enters the PPF, where the preganglionic fibers synapse in the sphenopalatine (pterygopalatine) ganglion. In the PPF, some of the postganglionic fibers join the palatine nerves (branches of V_2) and course inferiorly to the hard and soft palates (Fig. 13-17).[14] Other postganglionic parasympathetic fibers from the sphenopalatine ganglion supply secretomotor and vasomotor innervation to the nasal cavity and lacrimal gland via other branches of V_2 (Fig. 13-17).[30]

While it is theoretically possible that a lacrimal malignancy could spread via the fibers that connect it to the GSPN, this has not been reported. In practical terms, PNS along the GSPN usually occurs after any tumor reaches the PPF. Via PNS, the tumor gains access to the vidian nerve, and then spreads in a retrograde manner along the GSPN and into the geniculate ganglion (Fig. 13-9).[30] Also, as can be seen from Figure 13-18, the GSPN lies immediately beneath Meckel's cave, and as a result of this anatomic relationship, tumor within Meckel's cave may spread to the GSPN and then continue in a retrograde manner (Figs. 13-7, 13-12).[13] In Figure 13-12, a squamous cell carcinoma of the lower lip first spread along the mental and inferior alveolar branches of V_3, up through the foramen ovale into Meckel's cave, and then ultimately into the temporal bone and geniculate ganglion via the GSPN (Fig. 13-12).

Spinal Nerves

In the head and neck, PNS generally involves branches of cranial nerves. However, cutaneous innervation to much of the neck, as well as parts of the face, is provided by branches of the superficial cervical plexus, derived from the ventral divisions of the first four cervical spinal nerves (Fig.

Copyright © 2003, Mosby, Inc. All rights reserved.

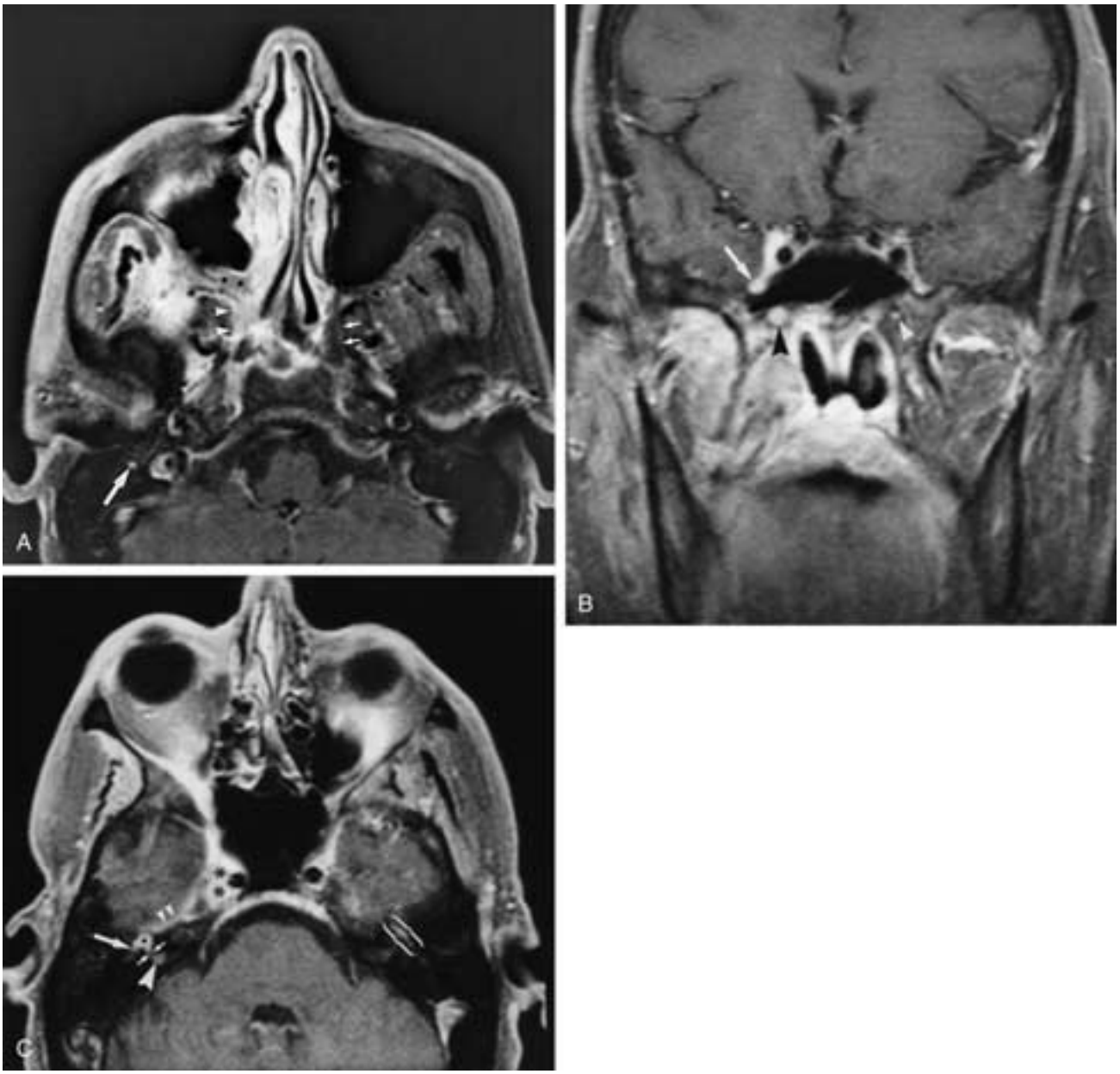

VIEW IMAGE

FIGURE 13-9 Palatal adenoid cystic carcinoma with extensive PNS. This patient was initially believed to have trigeminal neuralgia because of facial pain. A cavernous sinus/Meckel's cave mass was subsequently discovered on MR imaging. The palatal primary was not discovered until much later, and the patient ultimately developed a right-sided facial palsy. **A**, Axial contrast-enhanced, fat-suppressed T1-weighted MR image shows tumor enhancement in the right PPF (*black dots*). There is enlargement and excessive enhancement in the right vidian canal (*arrowheads*) indicating PNS along the vidian nerve. The normal left vidian canal is only faintly seen (*short arrows*). There is probably abnormal enhancement in the descending segment of the right facial nerve (*long arrow*). **B**, Coronal contrast-enhanced, fat-suppressed MR image shows enlargement and excessive enhancement representing PNS in both the right foramen rotundum (*arrow*) and the right vidian canal (*black arrowhead*). The cavernous sinus looks abnormal as well. The left vidian canal shows normal enhancement (*white arrowhead*). **C**, Axial contrast-enhanced, fat-suppressed MR image shows tumor involvement of the right cavernous sinus and the anterior aspect of Meckel's cave (*asterisks*). The greater superficial petrosal nerve courses directly beneath this area, as shown in Figure 13-18. There is abnormal enhancement indicating PNS along the greater superficial petrosal nerve (*small arrowheads*). The geniculate ganglion enhances brightly and is grossly enlarged (*black dot*). There is abnormal enhancement representing continued tumor spread to involve the labyrinthine (*small arrows*), intracanalicular (*large arrowhead*), and proximal tympanic (*large arrow*) segments of the right facial nerve. On the left side, the geniculate ganglion is of normal size (and enhances normally), and only the proximal GSPN and the proximal tympanic segment of the facial nerve enhance (*brackets*). (From Ginsberg LE, DeMonte F, Gillenwater AM. Greater superficial petrosal nerve: anatomy and MR findings in perineural tumor spread. AJNR 1996;17:389–393.)

Copyright © 2003, Mosby, Inc. All rights reserved.

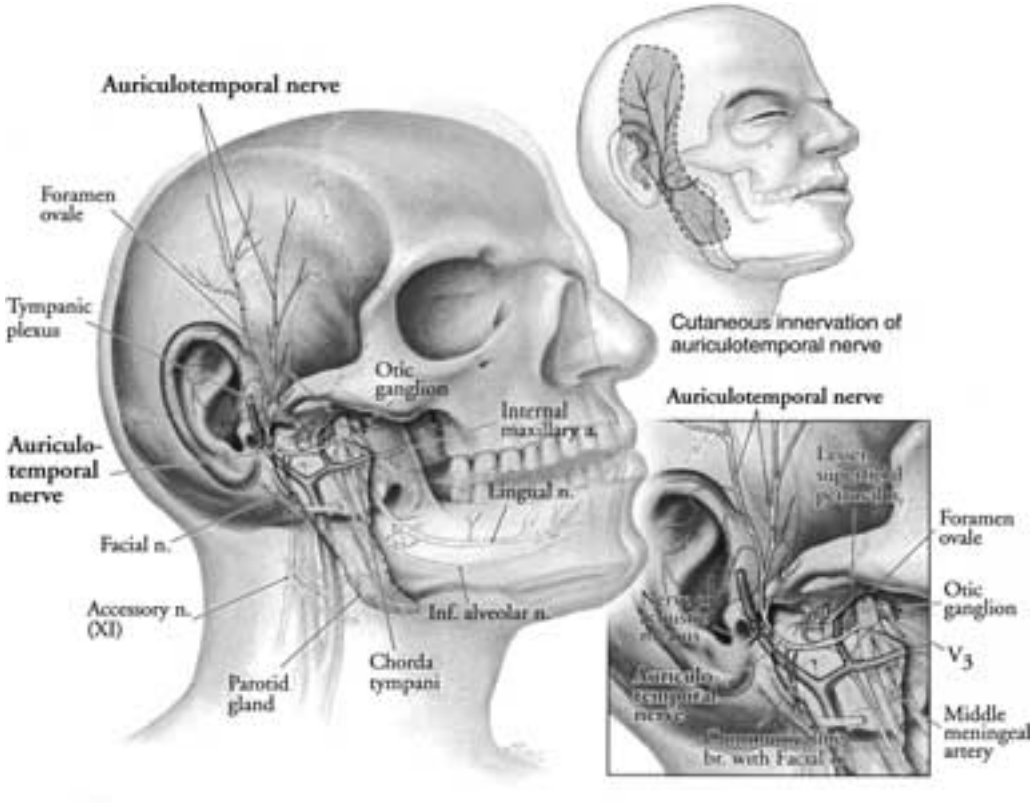

FIGURE 13-10 Diagrammatic representation of the auriculotemporal branch of V_3.

VIEW IMAGE

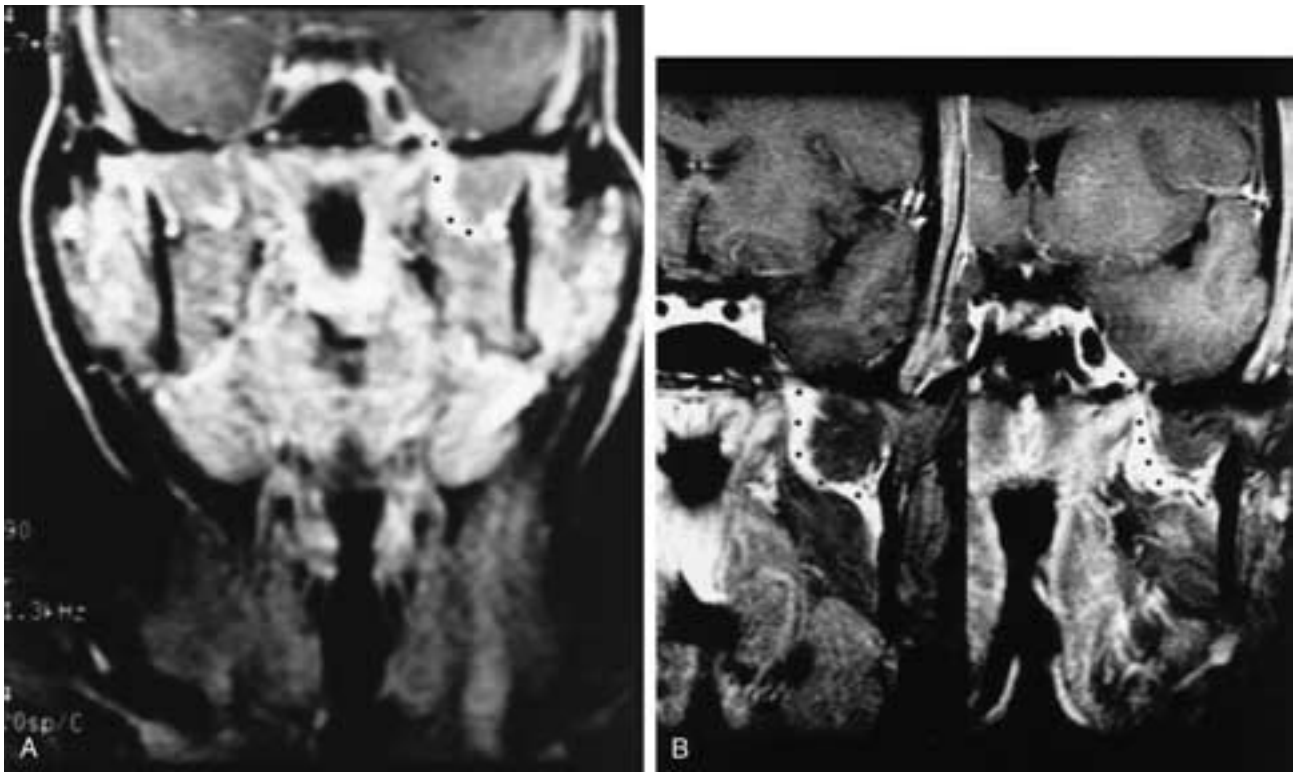

FIGURE 13-11 Squamous cell carcinoma of the left lower lip with PNS along the inferior alveolar branch of V_3. **A**, Coronal contrast-enhanced T1-weighted MR image without fat suppression obtained at an outside institution. Though visible, the perineural tumor along the proximal mandibular nerve and foramen ovale is hard to see (*black dots*). **B**, Repeat imaging with fat suppression; the tumor enhancement is far more conspicuous (*black dots*).

VIEW IMAGE

Copyright © 2003, Mosby, Inc. All rights reserved.

13-20).[27, 32] A case of PNS along the great auricular nerve, a branch of this plexus, secondary to a recurrent skin carcinoma in the lower parotid region has been reported (Fig. 13-21).[32] It is possible that cutaneous malignancies in other locations may spread along other branches of the superficial cervical plexus, such as the lesser occipital or transverse cutaneous nerves, and even spread intraspinally.

IMAGING OF PERINEURAL TUMOR SPREAD

Little is known about the sensitivity and specificity of imaging of PNS, as there are few studies that directly address this issue. Nemzek et al. reported a detection rate of 95% but found that the mapping of the entire extent of PNS

VIEW IMAGE

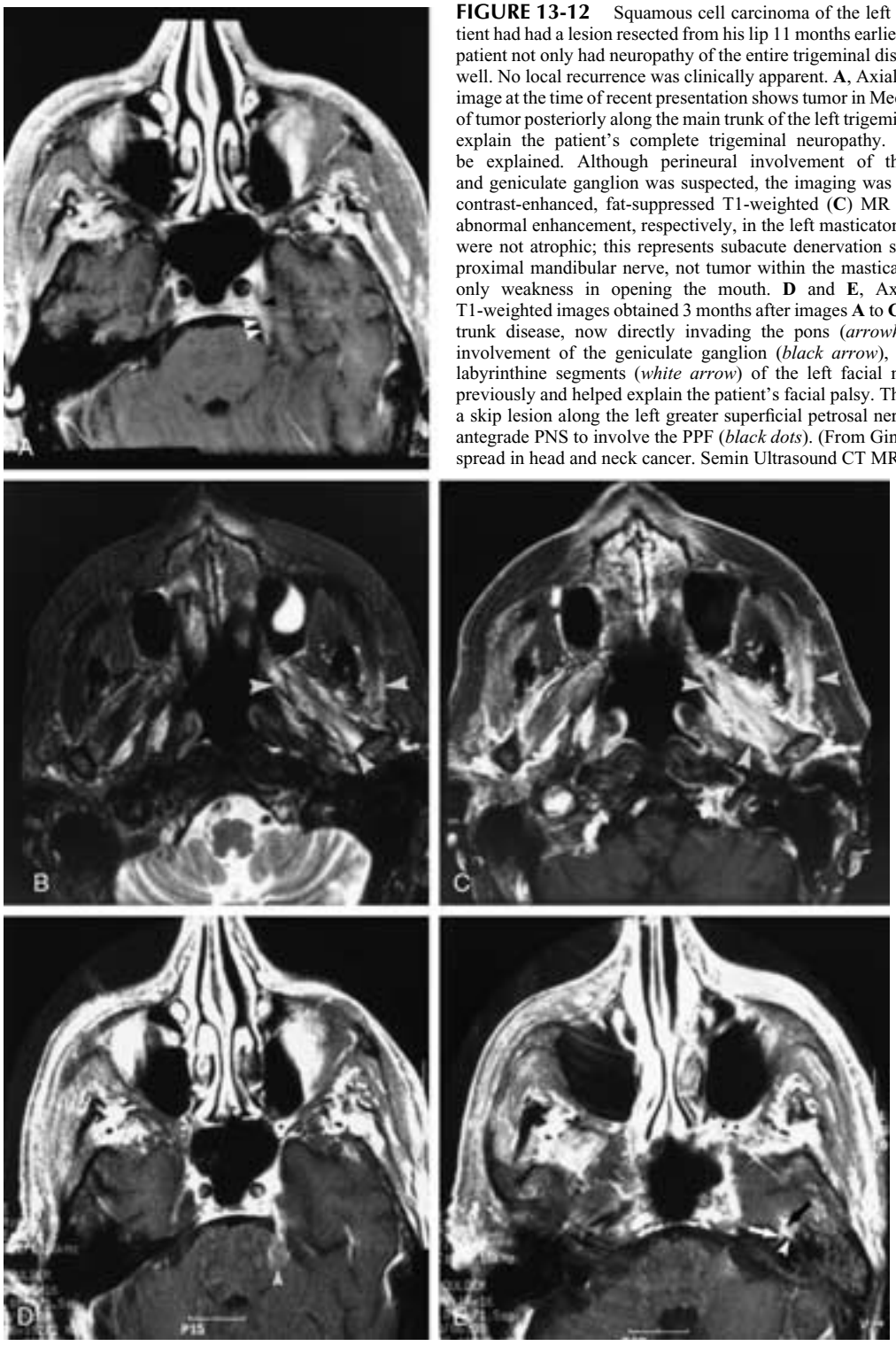

FIGURE 13-12 Squamous cell carcinoma of the left lower lip with extensive PNS. The patient had had a lesion resected from his lip 11 months earlier. At the time of recent presentation, the patient not only had neuropathy of the entire trigeminal distribution, but a facial nerve paralysis as well. No local recurrence was clinically apparent. **A**, Axial contrast-enhanced, fat-suppressed MR image at the time of recent presentation shows tumor in Meckel's cave (*black arrow*) and extension of tumor posteriorly along the main trunk of the left trigeminal nerve (*arrowheads*). These findings explain the patient's complete trigeminal neuropathy. However, the facial palsy could not be explained. Although perineural involvement of the greater superficial petrosal nerve and geniculate ganglion was suspected, the imaging was equivocal. Axial T2-weighted (**B**) and contrast-enhanced, fat-suppressed T1-weighted (**C**) MR images show hyperintense signal and abnormal enhancement, respectively, in the left masticator muscles (*arrowheads*). These muscles were not atrophic; this represents subacute denervation secondary to tumor involvement of the proximal mandibular nerve, not tumor within the masticator space. The patient had no trismus, only weakness in opening the mouth. **D** and **E**, Axial contrast-enhanced, fat-suppressed T1-weighted images obtained 3 months after images **A** to **C**. **D**, Progression of the main trigeminal trunk disease, now directly invading the pons (*arrowhead*), is seen. In **E**, there is tumor involvement of the geniculate ganglion (*black arrow*), proximal tympanic (*arrowhead*), and labyrinthine segments (*white arrow*) of the left facial nerve. This was not visible 3 months previously and helped explain the patient's facial palsy. This facial nerve disease was presumably a skip lesion along the left greater superficial petrosal nerve. In both **D** and **E**, there is probably antegrade PNS to involve the PPF (*black dots*). (From Ginsberg LE. Imaging of perineural tumor spread in head and neck cancer. Semin Ultrasound CT MR 1999;2:175–186.)

Copyright © 2003, Mosby, Inc. All rights reserved.

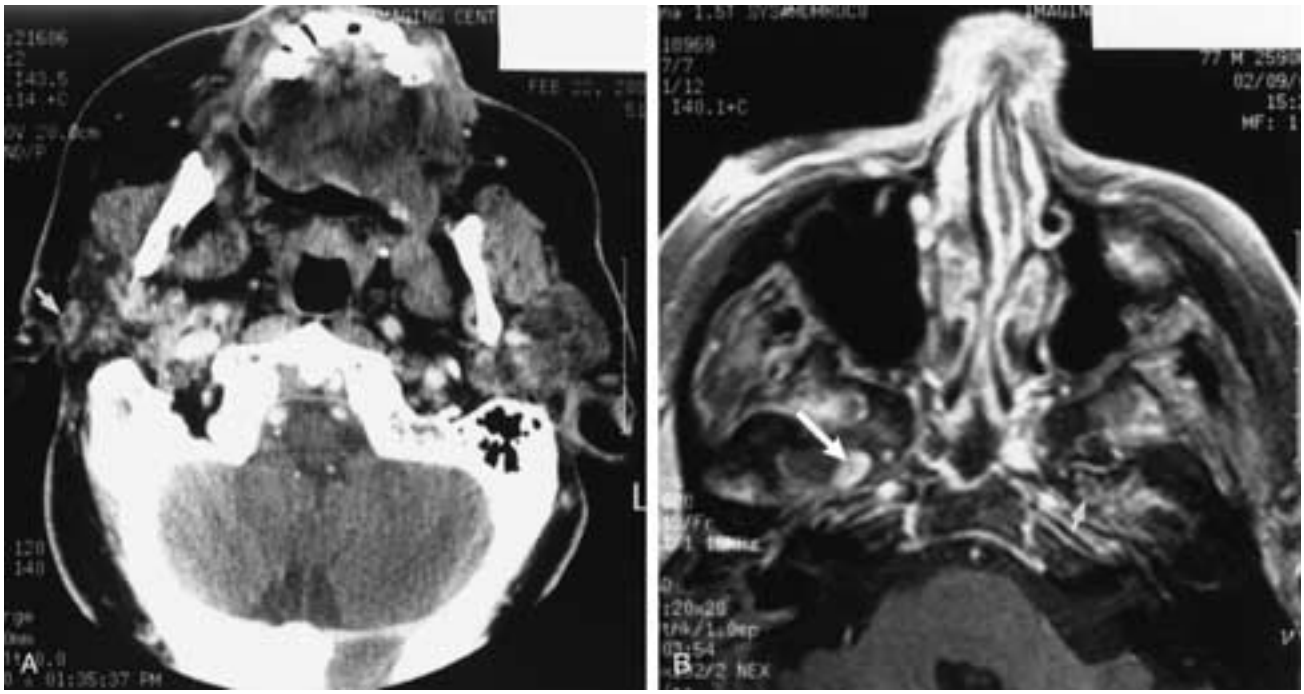

VIEW IMAGE

FIGURE 13-13 Recurrent preauricular cutaneous squamous cell carcinoma with parotid invasion and PNS along the auriculotemporal branch of V_3. **A**, Axial contrast-enhanced CT scan shows tumor in the superficial lobe of the right parotid gland (*arrow*). There was no bulky tumor extending into the masticator space. **B**, Axial contrast-enhanced, fat-suppressed T1-weighted image shows excessive enhancement representing tumor in the foramen ovale (*large arrow*). From the parotid gland, the only way tumor could spread to the foramen ovale is along the auriculotemporal nerve. Note that there is a small amount of normal enhancement in the normal left foramen ovale (*small arrow*).

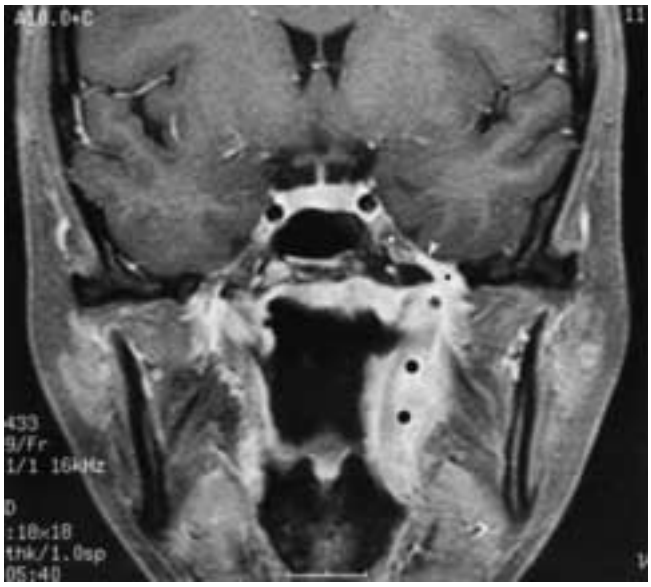

VIEW IMAGE

FIGURE 13-14 Nasopharyngeal carcinoma with lateral extension to the masticator space and mandibular nerve via PNS. Coronal contrast-enhanced, fat-suppressed T1-weighted image shows the left nasopharyngeal lesion (*large black dots*) with lateral extension to involve the upper masticator space (*asterisk*). Tumor is extending perineurally through the widened foramen ovale (*small black dot*). Although there is tumor in the most proximal aspect of the mandibular nerve (*arrowhead*), Meckel's cave (*white dot*) appears to be spared. (From Ginsberg LE. Imaging of perineural tumor spread in head and neck cancer. Semin Ultrasound CT MR 1999;2:175–186.)

was only 65% accurate.[21] The latter number might have been higher if fat suppression had been employed on the postcontrast sequences used in that study. For the imaging of PNS, sensitivity and specificity are difficult to measure with certainty because, in many cases, the imaging is so suggestive of PNS that biopsy is not performed.

Another factor limiting the imaging sensitivity and specificity for PNS is the imaging technique. Even in the presence of definite PNS, inadequate technique (or artifact, patient motion, etc.) can result in the disease being inconspicuous on the images and therefore not diagnosed. If proper imaging technique is adhered to, the overwhelming majority of PNS can be detected prior to initiating therapy.

Technical Considerations

One of the most important technical considerations is a knowledge of the indications for the imaging study prior to the examination. This allows the study to be tailored to the specific problem. Often, a CT or MR examination has been performed as a routine brain study with a 23 cm field of view (FOV). In this setting, detection of PNS is compromised, as the FOV is excessive and the images are too small to reveal fine neural structures. Whether the examination is a CT or an MR imaging study, the FOV should be no greater than 18 cm and preferably only 16 cm. Thin slices, 3 to 5 mm, should be obtained. For CT, high-resolution bone algorithm

Copyright © 2003, Mosby, Inc. All rights reserved.

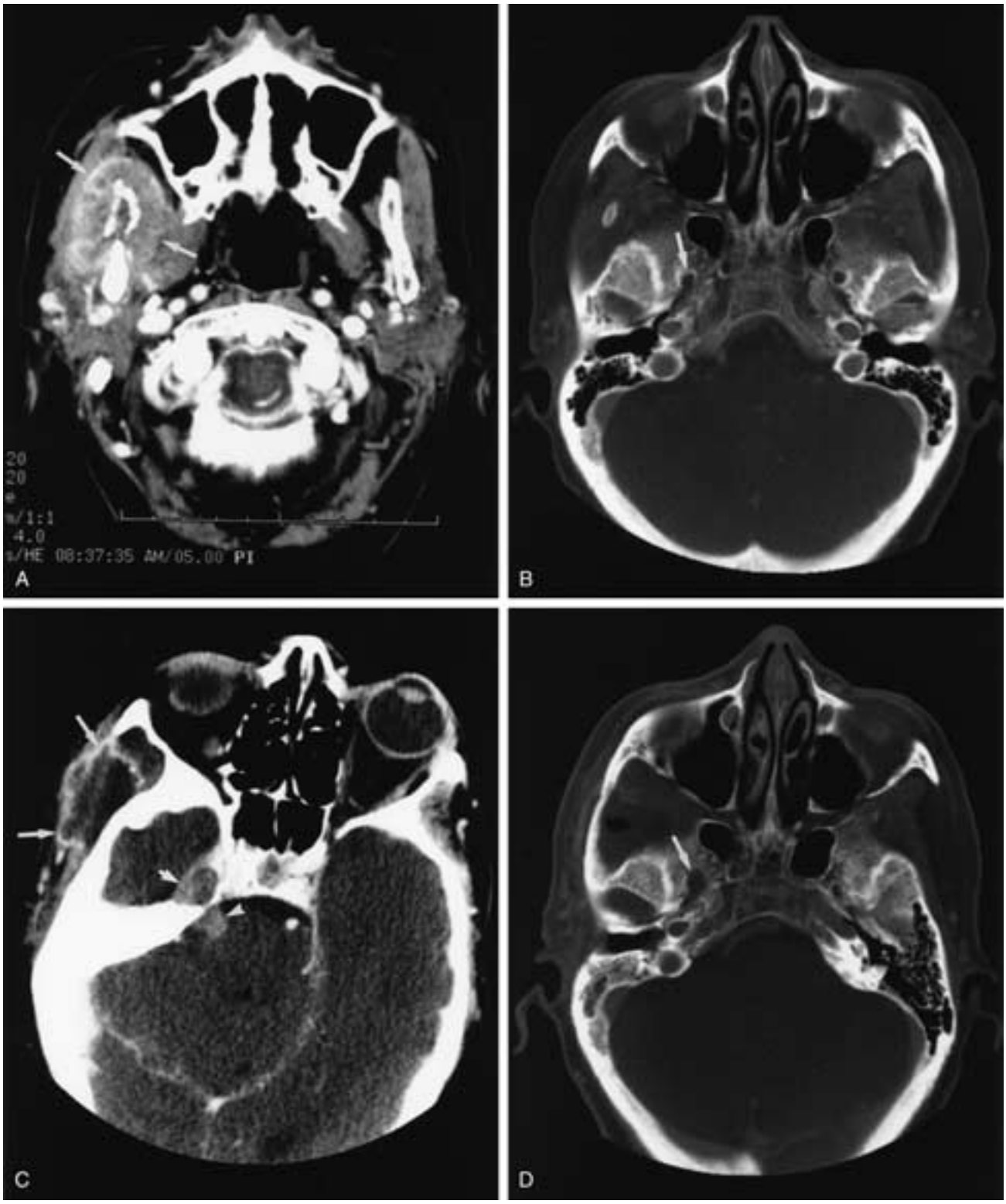

FIGURE 13-15 Squamous cell carcinoma of the right retromolar trigone with extension into the masticator space and subsequent PNS along V_3. Axial contrast-enhanced CT soft-tissue (**A**) and bone window (**B**) images at presentation show extensive tumor involvement of the right mandibular ramus and adjacent musculature (*arrows* in **A**). Note that the foramen ovale is normal, with intact cortical margins (*arrow* in **B**). No intracranial abnormality was visible on higher images at this time. Axial contrast-enhanced CT soft-tissue window (**C**) and bone window (**D**) images obtained 6 months after **A** and **B**. Despite surgery and radiotherapy, the patient had a large recurrence (*long arrows* in **C**). Note the enlargement and loss of the cortical margin in the right foramen ovale, suggesting PNS (*arrow* in **D**; compare this with the appearance of the foramen ovale in **B**). The soft-tissue window image shows enlargement and central enhancement indicating tumor in Meckel's cave (*short arrow* in **C**) with continued spread to involve the main right trigeminal trunk (*arrowhead*).

VIEW IMAGE

Copyright © 2003, Mosby, Inc. All rights reserved.

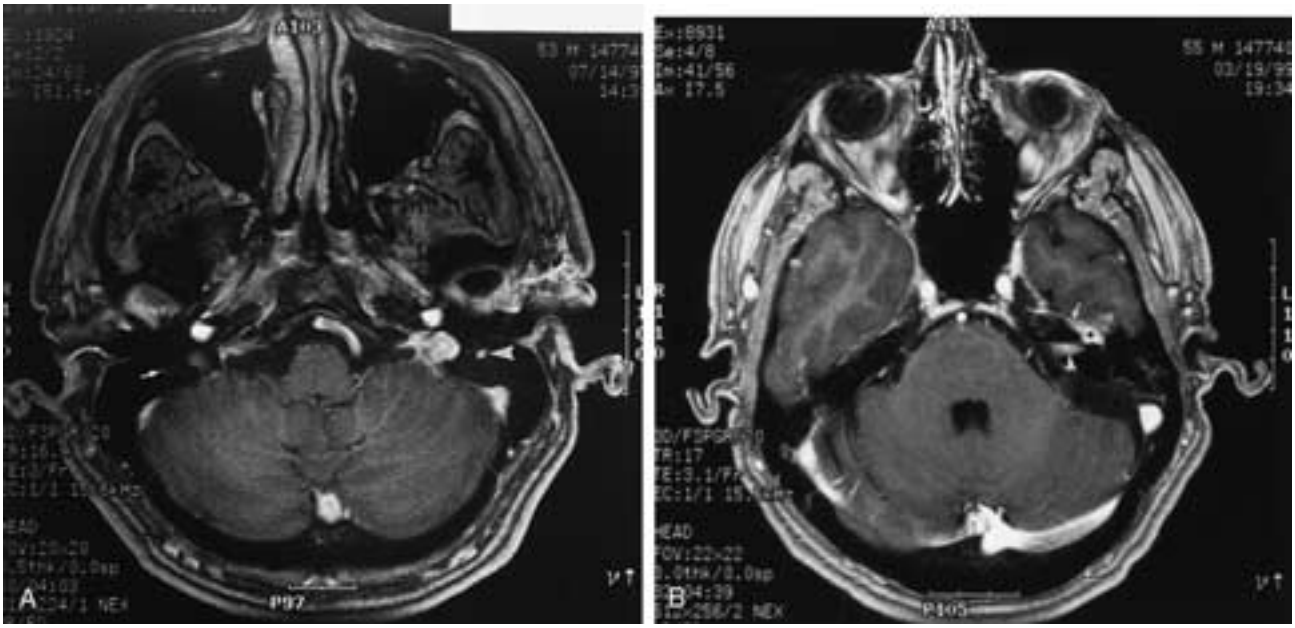

VIEW IMAGE

FIGURE 13-16 Adenocarcinoma of the left parotid gland with PNS along the facial nerve. **A**, Axial contrast-enhanced SPGR MR image obtained at an outside facility 1 month after left parotidectomy. The facial nerve was paralyzed postoperatively. This study was read as postoperative changes only; no mention was made of the abnormal enhancement and enlargement of the left descending facial nerve segment (*arrowhead*). The right descending facial nerve is normal (*arrow*). The tympanic and more anterior aspects of the left facial nerve are normal. Postoperatively, the patient had radiotherapy to the parotid region. **B**, Axial contrast-enhanced SPGR MR image obtained at an outside facility 20 months after **A**, by which time the patient had developed left-sided hearing loss. There is tumor in the geniculate ganglion (*black dot*), proximal greater superficial petrosal nerve (*arrow*), and internal auditory canal (*arrowhead*). This case demonstrates progression of PNS with initial failure to diagnose. The patient ultimately developed widespread leptomeningeal disease.

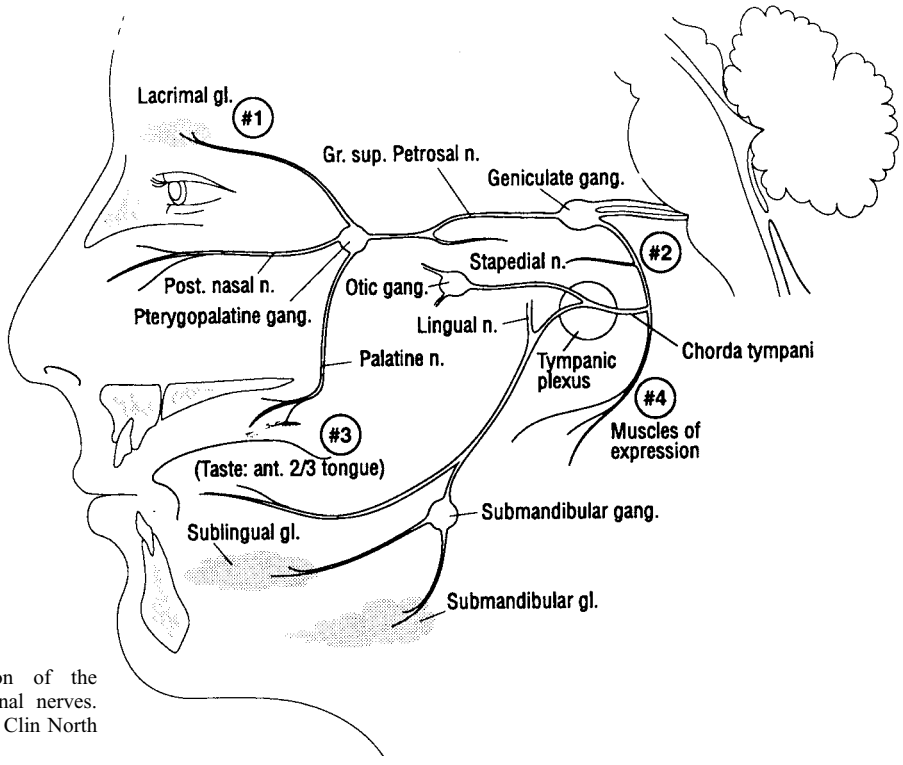

VIEW IMAGE

FIGURE 13-17 Diagrammatic representation of the interconnections between the facial and trigeminal nerves. (From Lane JI. Facial nerve disorders. Neuroimag Clin North Am 1993;3(1):129–151.)

Copyright © 2003, Mosby, Inc. All rights reserved.

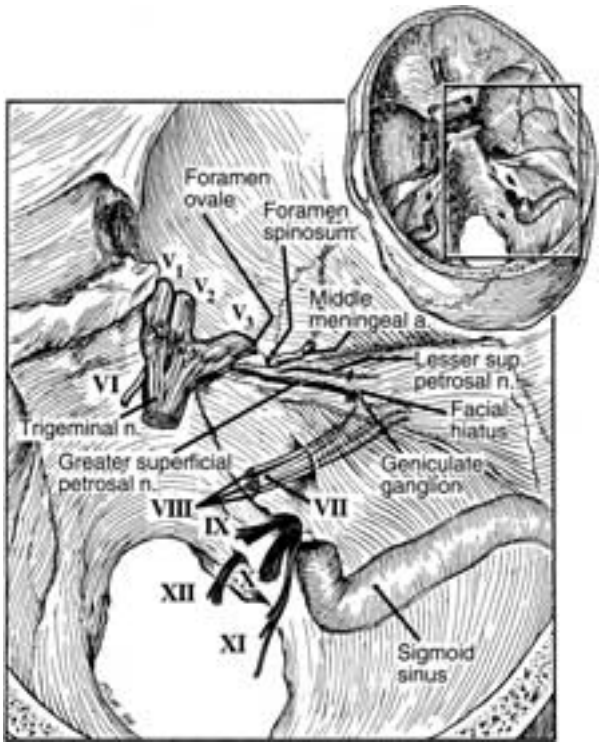

VIEW IMAGE

FIGURE 13-18 Diagrammatic representation of the greater superficial petrosal nerve. (From Ginsberg LE, DeMonte F, Gillenwater AM. Greater superficial petrosal nerve: anatomy and MR findings in perineural tumor spread. AJNR 1996;17:389–393.)

images should also be generated for evaluation of subtle bone erosion.

When MR imaging is performed, it is crucial to obtain axial T1-weighted images prior to the administration of contrast. This is necessary because the normal hyperintense signal intensity of fat in the PPF and foraminal areas is best assessed on this sequence. The presence of PNS has been overlooked, in part, because this sequence was omitted (Fig. 13-4). Although there is some controversy in the literature as to whether postcontrast MR imaging should be fat suppressed, it is generally agreed that in the evaluation of PNS, fat suppression should be used.[32] Though this technique is sometimes prone to artifact, there are numerous cases in which the lack of fat suppression has made PNS either difficult to see or completely inconspicuous (Figs. 13-4, 13-11). Postcontrast axial and coronal MR images should be obtained routinely.

Imaging Diagnosis of PNS

On CT, imaging findings suggestive of PNS include widening or destruction of neural foramina/canals, excessive enhancement within neural foramina/canals, or excessive enhancement or widening of the cavernous sinus, PPF, or Meckel's cave. In addition, the loss of fat planes immediately adjacent to neural foramina or within the PPF, even in the absence of abnormal enhancement, widening, or bone destruction, are highly suggestive findings of PNS (Figs. 13-6, 13-15).[13, 18, 28, 34–36] Caution should be used when interpreting bone destruction on CT, as it may simply be the direct effect of the tumor rather than PNS (Fig. 13-22).

VIEW IMAGE

On MR imaging, findings suggestive of PNS include any of the following: excessive enhancement of a cranial nerve branch (either within the cisternal portion or within a canal or foramen), loss of the normal fat pad adjacent to a foramen,[34, 35] or widening/excessive enhancement within the PPF, Meckel's cave, or the cavernous sinus (Figs. 13-2, 13-4, 13-5, 13-7 to 13-9, 13-11, 13-14, 13-16, 13-23). Again, loss of the normal T1-hyperintense fat in the PPF should be regarded as highly suspicious for PNS (Figs. 13-5, 13-8).

With regard to Meckel's cave, the site of the gasserian (trigeminal) ganglion, this space is filled primarily with CSF. As such, it should be of fluid density on CT and of fluid signal intensity on MR imaging. The ganglion has only some peripheral vascularity, and as such, there normally should be no central enhancement within Meckel's cave. Such enhancement is a strong indicator of the presence of disease (Figs. 13-7, 13-9, 13-12, 13-13, 13-15, 13-23).[13] In severe cases of PNS affecting the trigeminal nerve, it may be possible to observe thickening and abnormal enhancement of the main trigeminal trunk extending back from Meckel's cave toward the brainstem (Figs. 13-12, 13-13, 13-23). Although MR imaging is better at detecting PNS in the main trigeminal trunk, it can sometimes be seen with CT (Fig. 13-15).

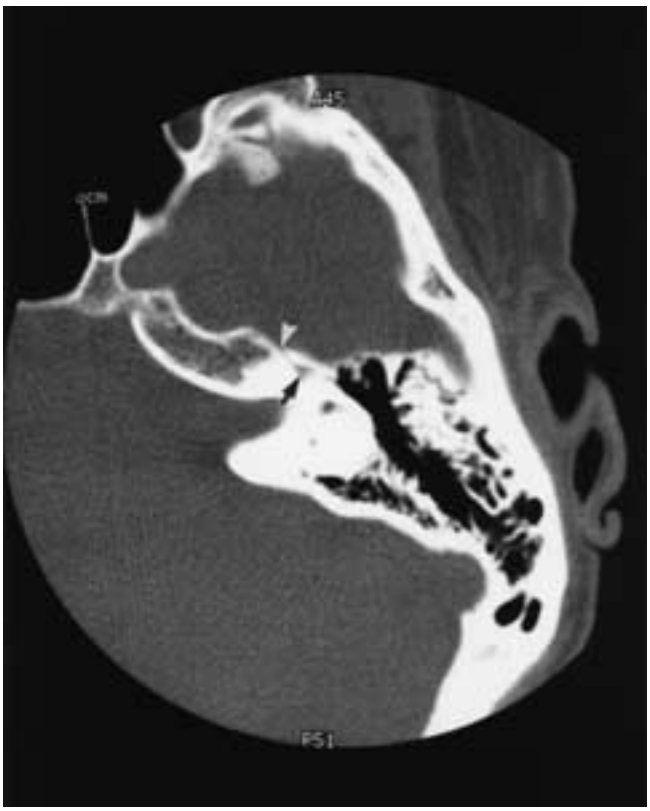

FIGURE 13-19 Axial CT bone window demonstrating the facial hiatus (*arrowhead*) for the greater superficial petrosal nerve, extending anteriorly from the geniculate ganglion (*arrow*). (From Ginsberg LE, DeMonte F, Gillenwater AM. Greater superficial petrosal nerve: anatomy and MR findings in perineural tumor spread. AJNR 1996;17:389–393.)

Copyright © 2003, Mosby, Inc. All rights reserved.

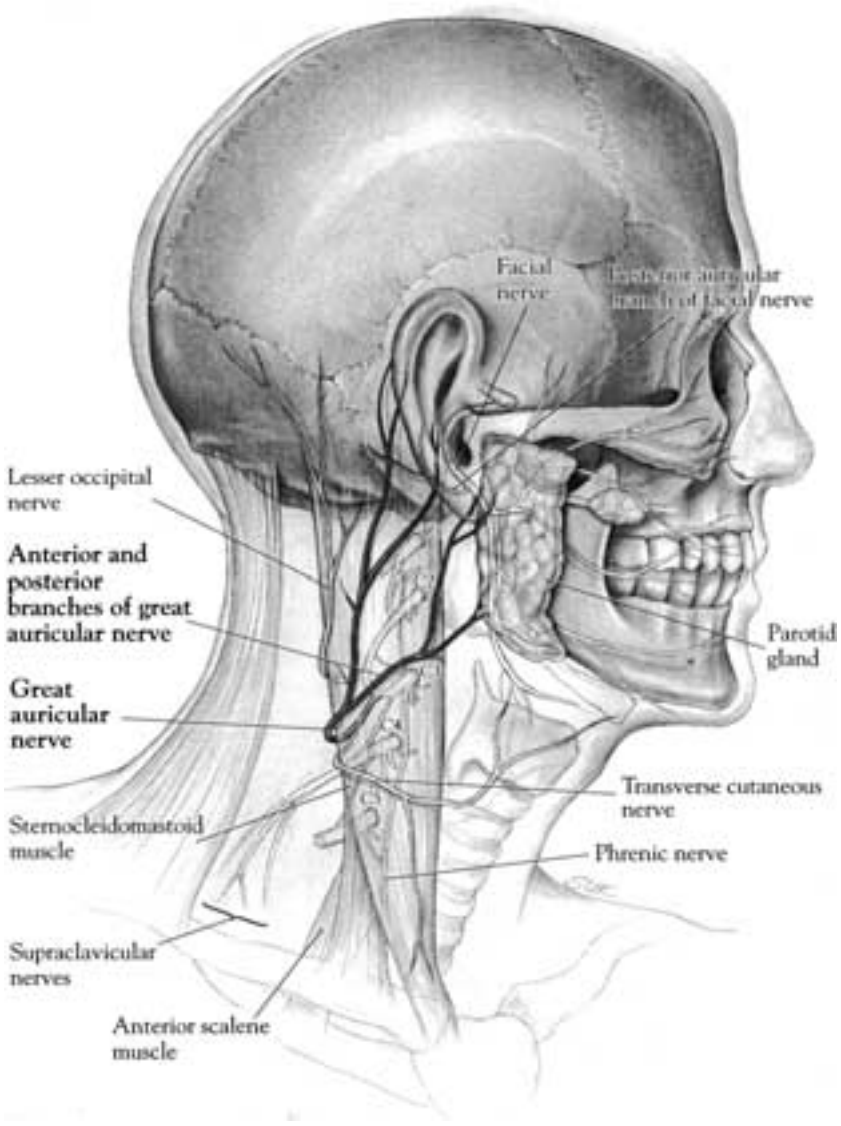

VIEW IMAGE

FIGURE 13-20 Diagrammatic representation of the cervical plexus and great auricular nerve. (From Ginsberg LE, Eicher SA. Great auricular nerve: anatomy and imaging of perineural tumor spread. AJNR 2000;21:568–571.)

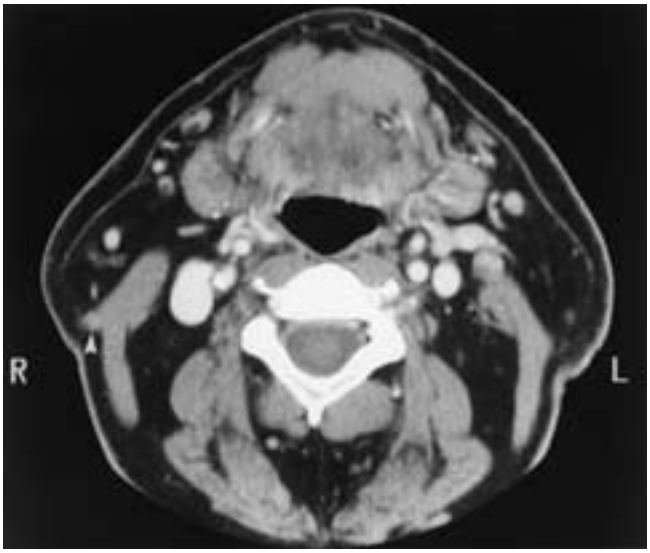

VIEW IMAGE

FIGURE 13-21 Recurrent cutaneous squamous cell carcinoma in the right lower parotid region with PNS along the great auricular nerve. Axial contrast-enhanced CT scan shows a subtly enhancing mass lateral to the right sternocleidomastoid muscle (*arrowhead*) representing PNS along the course of the great auricular nerve. (From Ginsberg LE, Eicher SA. Great auricular nerve: anatomy and imaging of perineural tumor spread. AJNR 2000;21:568–571.)

Copyright © 2003, Mosby, Inc. All rights reserved.

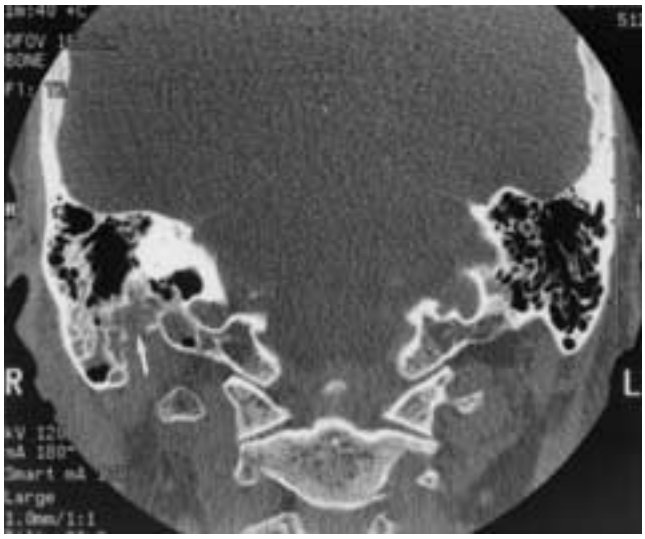

VIEW IMAGE

FIGURE 13-22 Squamous cell carcinoma of the right parotid gland with CT bone findings suggesting PNS along the descending facial nerve and stylomastoid foramen. The coronal CT bone window shows bone destruction at the stylomastoid foramen (*arrow*). The facial nerve canal was explored at surgery, and the nerve was found to be normal. These bone changes, though consistent with PNS, were secondary to the direct effects of the primary tumor.

VIEW IMAGE

FIGURE 13-23 Squamous cell carcinoma of the right forehead with very subtle PNS along the ophthalmic nerve (V_1). One year after excision of the primary skin cancer, the patient developed sensory neuropathy in the entire right trigeminal distribution. Axial (**A**) and coronal (**B**) contrast-enhanced, fat-suppressed T1-weighted MR images show very subtle abnormal enhancement within Meckel's cave on the right (*arrows* in **A** and **B**) and even subtler enhancement of the main trigeminal trunk (*arrowhead* in **A**). Biopsy of the right supraorbital region confirmed perineural infiltration of the supraorbital branch of V_1. The abnormal enhancement was presumed to represent a skip lesion originating on V_1, as there was no imaging evidence of tumor in the orbit, superior orbital fissure, or cavernous sinus. The patient received radiotherapy, as the disease was deemed inoperable. **C**, Axial contrast-enhanced, fat-suppressed T1-weighted MR image obtained 8 months after **A** and **B** shows massive disease recurrence/progression with bulky tumor in Meckel's cave (*asterisk*) and the pons (*black dot*).

Copyright © 2003, Mosby, Inc. All rights reserved.

The radiologist should also be alert to the potential for *skip lesions*, segments of normal intervening nerve between regions of PNS (Figs. 13-12, 13-23).[7, 10, 33, 37] In the literature, skip lesions have also been referred to as *resurfacing*. As previously mentioned, the radiologist should also be aware of the presence of antegrade PNS (Fig. 13-7).

Secondary Imaging Findings

The presence of secondary findings associated with PNS may either lend support to a case of suspected PNS or alert the radiologist to the presence of undiagnosed PNS. These findings chiefly are those of denervation of the mandibular division of the trigeminal nerve, whose branches innervate the muscles of mastication as well as the anterior belly of the digastric and mylohyoid muscles.[18, 38] In the chronic stages (more than 20 months following denervation), these muscles undergo fatty infiltration and/or atrophy, findings readily seen on CT or MR imaging (Fig. 13-24).[18, 38]

However, in the acute (less than 1 month) and subacute (1 to 20 months) stages of muscular denervation, there are findings that are seen only on MR imaging. These findings include increased T2-weighted signal intensity and abnormal enhancement within the affected muscles (Fig. 13-12).[38, 39] Although these imaging findings may suggest tumor involvement, particularly if the primary tumor is nearby, there are ways to differentiate tumor from denervation. On imaging, subacutely denervated muscle retains its internal striations, which are generally lost in the presence of tumor.[40] Clinically, a patient with tumor in the masticator muscles usually has trismus, whereas a patient with denervation has weakness of the masticator musculature.

VIEW IMAGE

FIGURE 13-24 Oral cavity squamous cell carcinoma with spread to the masticator space, V_3 PNS, and chronic denervation of the V_3-innervated musculature. Coronal contrast-enhanced CT scan shows tumor in the left pterygoid musculature (*large black dots*) and within the foramen ovale (*small black dot*). Note the atrophy of the mylohyoid (*arrowheads*), anterior belly of the digastric (*asterisk*), and masseter muscles (*arrows*) on the left side.

IMAGING PITFALLS

Various pitfalls exist in the imaging of PNS. Alone or in concert, they may result in PNS either not being diagnosed or being overdiagnosed.

Technique

As previously mentioned, if proper imaging technique is not employed, it is easy to overlook the diagnosis of PNS. The use of an excessively large FOV, the lack of a T1-weighted axial MR image to evaluate the PPF, and the lack of fat suppression on postcontrast MR imaging (Figs. 13-4, 13-11) are all problems that may contribute to the missed diagnosis of PNS.

Questionable PNS

In the early stages of PNS, the imaging findings can be extremely subtle. In some cases the findings are subtle but definite (Fig. 13-23), while in other cases the findings are so subtle as to be questionable. In the latter case, the radiologist must inform the surgeon of the possibility of PNS so that either a surgical exploration is performed to prove or disprove the presence of PNS or early follow-up imaging is obtained to evaluate the possible progression of PNS.

Asymmetric Foraminal Enhancement

All of the neural foramina and canals of the skull base normally contain emissary veins.[31] Slow-flowing blood within these veins usually results in some degree of enhancement after contrast administration, particularly on fat-suppressed MR images (Figs. 13-13B, 13-25).[41] Although most of the skull base foramina are quite symmetric, some normal asymmetry can occur.[31] If the patient is scanned with a slightly tilted or rotated scan angle, any asymmetry of these foramina should be viewed with caution prior to diagnosing an abnormality. That is, the radiologist should be certain that any asymmetry in the size of these foramina or in the degree of enhancement is truly caused by disease and not by asymmetric scanning of the patient.

PERSISTENT POSTTREATMENT IMAGING ABNORMALITIES

Following treatment for proven or strongly suspected PNS, the imaging findings may remain abnormal for an indefinite period of time. The imaging findings may rival the original appearance of PNS despite the lack of clinical evidence of persistent or progressive disease.[42] Obviously, on a given imaging study, it is impossible to exclude active

Copyright © 2003, Mosby, Inc. All rights reserved.

VIEW IMAGE

FIGURE 13-25 Normal foraminal enhancement on MR imaging. Axial contrast-enhanced, fat-suppressed T1-weighted MR image shows normal enhancement of both vidian canals (*small arrowheads*), both foramina ovale (*arrows*), and the left foramen spinosum (*large arrowhead*).

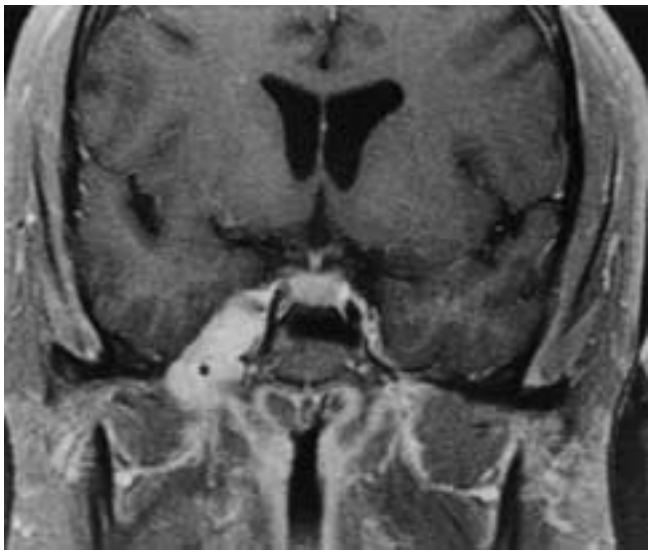

VIEW IMAGE

FIGURE 13-27 Right cavernous sinus/Meckel's cave schwannoma with extension through the foramen ovale. Coronal contrast-enhanced, fat-suppressed T1-weighted MR image shows an enhancing mass extending inferiorly through a grossly widened foramen ovale (*asterisk*). For Figures 13-26 and 13-27, prior to establishing the diagnosis, the possibility of PNS from a head and neck cancer should at least be considered and sought radiographically. (From Ginsberg LE. Imaging of perineural tumor spread in head and neck cancer. Semin Ultrasound CT MR 1999;2:175–186.)

disease in the face of findings that suggest PNS. However, one should be aware that imaging findings of PNS may not revert to normal even if the disease has been successfully treated.

It has been shown that once the PPF is violated surgically, images of this structure will appear abnormal indefinitely.[43] The persistent imaging findings consist of loss of the normal high T1-weighted fat signal intensity and the presence of excessive enhancement on contrast-enhanced images. Unfortunately, these findings are identical to those seen with PNS. Therefore, following surgery of the PPF, imaging studies should be interpreted with caution to avoid overdiagnosing PNS or local recurrence.[43] The best way to evaluate PPF is to compare serial follow-up imaging studies.

MIMICS OF PNS

The radiologist should be aware that there are other diseases that may have imaging and clinical findings identical to those of PNS. While there may be adjunctive clinical or radiologic signs that point to such a diagnosis, any given case may nonetheless present a diagnostic challenge. Thus, meningioma, occurring near a neural foramen, may extend through that foramen and mimic PNS (Fig. 13-26).[13]

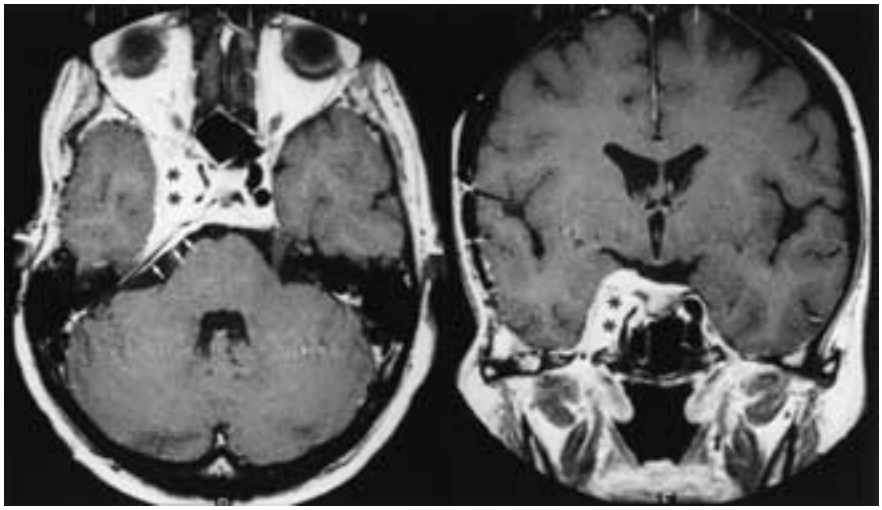

VIEW IMAGE

FIGURE 13-26 Cavernous sinus/Meckel's cave meningioma with extension through the foramen ovale. Left (axial) and right (coronal) contrast-enhanced T1-weighted MR images without fat suppression show a characteristic right cavernous sinus/Meckel's cave meningioma (*asterisks*). Note the dural tail extending posteriorly along the right petrous ridge (*arrows*). The lesion is seen on the coronal image to be extending inferiorly through a widened foramen ovale (*black dot*). (From Ginsberg LE. Imaging of perineural tumor spread in head and neck cancer. Semin Ultrasound CT MR 1999;2:175–186.)

Copyright © 2003, Mosby, Inc. All rights reserved.

Occasionally a schwannoma, particularly when it involves the trigeminal or facial nerves, may mimic PNS (Fig. 13-27). Finally, though uncommon and probably clinically obvious, advanced rhinocerebral mucormycosis may spread along cranial nerve branches and appear quite similar on imaging to PNS.[44]

CONCLUSION

It is clear that PNS is a serious complication and a major diagnostic challenge. Only by learning more about the relevant neuroanatomy and by obtaining a thorough clinical history of the head and neck cancer patient can the radiologist properly perform and interpret imaging studies so as to ensure that PNS is accurately diagnosed.

REFERENCES

1. Peet MM. Tumors of the gasserian ganglion. Surg Gynecol Obstet 1927;44:202–207.
2. Ballantyne AJ, McCarten AB, Ibanex ML. The extension of cancer of the head and neck through peripheral nerves. Am J Surg 1963;106: 651–667.
3. Dodd GD, Dolan PA, Ballantyne AJ, et al. The dissemination of tumors of the head and neck via the cranial nerves. Radiol Clin North Am 1970;8:445–461.
4. Batsakis JG. Pathology consultation: nerves and neurotropic carcinomas. Ann Otol Rhinol Laryngol 1985;94:426–427.
5. Soo KC, Carter RL, O'Brien CJ, et al. Prognostic implications of perineural spread of squamous carcinomas of the head and neck. Laryngoscope 1986;96:1145–1148.
6. Goepfert H, Dichtel WJ, Medina JE, et al. Perineural invasion in squamous cell skin carcinoma of the head and neck. Am J Surg 1984;148:542–547.
7. Woddruff WW, Yeates AE, McLendon RE. Perineural tumor extension to the cavernous sinus from superficial facial carcinoma: CT manifestations. Radiology 1986;161:395–399.
8. Majoie CB, Hullsmans FJH, Casteljins JA, et al. Perineural tumor extension of facial malignant melanoma: CT and MRI. J Comput Assist Tomogr 1993;17(6):973–975.
9. Batsakis JG, Raymond AK. Pathology consultation: desmoplastic melanoma. Ann Otol Rhinol Laryngol 1994;103:77–79.
10. Catalano PJ, Chandranath S, Biller HF. Cranial neuropathy secondary to perineural spread of cutaneous malignancy. Am J Otol 1995;16: 772–777.
11. Banerjee TK, Gottschalk PG. Unusual manifestations of multiple cranial nerve palsies and mandibular metastasis in a patient with squamous cell carcinoma of the lip. Cancer 1984;53:346–348.
12. Anderson CA, Krutchkoff D, Ludwig M. Carcinoma of the lower lip with perineural extension to the middle cranial fossa. Oral Surg Oral Med Oral Pathol 1990;69:614–618.
13. Ginsberg LE. Imaging of perineural tumor spread in head and neck cancer. Semin Ultrasound CT MR 1999;2:175–186.
14. Ginsberg LE, DeMonte F. Imaging of perineural tumor spread from palatal carcinoma. AJNR 1998;19:1417–1422.
15. Parker GD, Harnsberger HR. Clinical-radiologic issues in perineural tumor spread of malignant diseases of the extracranial head and neck. RadioGraphics 1991;11:383–399.
16. Dodd GD, Jing BS. Radiographic findings in adenoid cystic carcinoma of the head and neck. Ann Otol Rhinol Laryngol 1972;81:591–598.
17. Chong VFH, Fan YF, Khoo JBK. Nasopharyngeal carcinoma with intracranial spread: CT and MR characteristics. J Comput Assist Tomogr 1996;20(4):563–569.
18. Laine FJ, Braun IF, Jensen ME, et al. Perineural tumor extension through the foramen ovale: evaluation with MR imaging. Radiology 1990;174:65–71.
19. Mendenhall WM, Parsons JT, Mendenhall NP, et al. Carcinoma of the skin of the head and neck with perineural invasion. Head Neck 1989;11:301–308.
20. Caldemeyer KS, Mathews VP, Righi RR, et al. Imaging features and clinical significance of perineural spread or extension of head and neck tumors. RadioGraphics 1998;18:97–110.
21. Nemzek WR, Hecht S, Gandour-Edwards R, et al. Perineural spread of head and neck tumors: how accurate is MR imaging? AJNR 1998;19:701–706.
22. Arcas A, Bescos S, Raspall G, et al. Perineural spread of epidermoid carcinoma in the infraorbital nerve: case report. J Oral Maxillofac Surg 1996;54:520–522.
23. Ginsberg LE, DeMonte F. Palatal adenoid cystic carcinoma presenting as perineural spread to the cavernous sinus. Skull Base Surg 1998;8(1):39–43.
24. McNab AA, Francis AC, Benger R, et al. Perineural spread of cutaneous squamous cell carcinoma via the orbit. Ophthalmology 1997;104:1457–1462.
25. Alonso PE, Bescansa E, Salas J, et al. Perineural spread of cutaneous squamous cell carcinoma manifesting as ptosis and ophthalmoplegia (orbital apex syndrome). Br J Plast Surg 1995;48:564–568.
26. Esmaeli B, Ginsberg LE, Goepfert H, et al. Squamous cell carcinoma with perineural invasion presenting as a Tolosa-Hunt-like syndrome: a potential pitfall in diagnosis. Ophthal Plast Reconstr Surg 2000;16(6): 450–452.
27. Berry M, Bannister LH, Stranding SM. Nervous system. In: Bannister LH, Berry MM, Collins P, Dyson M, Dussek JE, Ferguson MWJ, eds. Gray's Anatomy, 38th ed. New York: Churchill Livingston, 1995;901–1937.
28. Curtin HD, Williams R, Johnson J. CT of perineural tumor extension: pterygopalatine fossa. AJNR 1984;5:731–737.
29. Pandolfo I, Gaeta M, Blandino A, et al. Case report: MR imaging of perineural metastasis along the vidian nerve. J Comput Assist Tomogr 1989;13:498–500.
30. Ginsberg LE, DeMonte F, Gillenwater AM. Greater superficial petrosal nerve: anatomy and MR findings in perineural tumor spread. AJNR 1996;17:389–393.
31. Ginsberg LE, Pruett SW, Chen MY, et al. Skull-base foramina of the middle cranial fossa: reassessment of normal variation with high-resolutioon CT. AJNR 1994;15:283–291.
32. Ginsberg LE, Eicher SA. Great auricular nerve: anatomy and imaging of perineural tumor spread. AJNR 2000;21:568–571.
33. Barakos JA, Dillon WP, Chew WM. Orbit, skull base, and pharynx: contrast-enhanced fat suppression MR imaging. Radiology 1991;179: 191–198.
34. Matzko J, Becker DG, Phillips CD. Obliteration of fat planes by perineural spread of squamous cell carcinoma along the inferior alveolar nerve. AJNR 1994;15:1843–1845.
35. Curtin HD. Detection of perineural spread: fat is a friend. Editorial. AJNR 1998;19(8):1385–1386.
36. Curtin HD, Williams R. Computed tomographic anatomy of the pterygopalatine fossa. RadioGraphics 1985;5(3):429–440.
37. Lee YY, Castillo M, Nauert C. Intracranial perineural metastasis of adenoid cystic carcinoma of head and neck. J Comput Assist Tomogr 1985;9:219–223.
38. Russo CP, Smoker WRK, Weissman JL. MR appearance of trigeminal and hypoglossal motor denervation. AJNR 1997;18:1375–1383.
39. Davis SB, Mathews VP, Williams DW. Masticator muscle enhancement in subacute denervation atrophy. AJNR 1995;16:1292–1294.
40. Chong J, Chan LL, Langstein HN, Ginsberg LE. MR imaging of the muscular component of myocutaneous flaps in the head and neck. AJNR 2001;22(1):170–174.
41. Ginsberg LE. The posterior condylar canal. AJNR 1994;15:969–972.
42. Sohn-Williams L, Mancuso AA, Menhenhall W. Perineural spread of skin carcinoma: clinical significance and natural history of the MR and CT findings following radiation therapy. Presented at the 84th annual meeting of the Radiological Society of North America, Chicago, December 1, 1998.
43. Chan LL, Chong J, Gillenwater AM, Ginsberg LE. The pterygopalatine fossa: postsurgical MR imaging appearance. AJNR 2000;21: 1315–1319.
44. McLean FM, Ginsberg LE, Stanton CA. Perineural spread of rhinocerebral mucormycosis. AJNR 1996;17:114–116.

Copyright © 2003, Mosby, Inc. All rights reserved.

Copyright © 2003, Mosby, Inc. All rights reserved.

Section IV

Jaws and Temporomandibular Joints

Copyright © 2003, Mosby, Inc. All rights reserved.

Copyright © 2003, Mosby, Inc. All rights reserved.

14

Embryology and Anatomy of the Jaw and Dentition

James J. Abrahams, Reuben Rock, and Michael W. Hayt

EMBRYOLOGY OF THE JAWS
EMBRYOLOGY OF THE DENTITION
ANATOMY
  Dentition and General Considerations
MANDIBLE
  Anatomic Specimen
    Lingual Surface
    Buccal Surface
  CT Images: Cross-Sectional View
    Lingual Surface
    Buccal Surface
    Internal Anatomy
      Axial View
      Panoramic View
MAXILLA
  Anatomic Specimen
  CT Images
    Axial View
    Panoramic View
    Cross-Sectional View

EMBRYOLOGY OF THE JAWS

Embryologically, the maxilla, mandible, and facial soft tissues arise from a number of structures early in the fourth week of development. These structures are the central unpaired frontonasal prominence, the paired nasomedial processes, and the paired maxillary and mandibular prominences. The last three of these arise from the first branchial arch. These all surround a ventral depression, the stomodeum, which will later become the mouth. These structures arise from neural crest tissues (Fig. 14-1) and are also described in detail in Chapter 1.[1–4]

As the embryo develops, the nasomedial and maxillary processes become more prominent and fuse to form the upper lip and upper jaw. The two nasomedial processes fuse to form the intermaxillary segment that is the precursor for the philtrum of the upper lip, the primary palate, and the premaxillary component of the upper jaw. These structures merge by intermingling of the underlying mesenchyme and disintegration of the overlying epithelia. The frontonasal prominence is displaced as the nasomedial processes merge, and it does not contribute significantly to the upper jaw.[1,4]

The mandible forms from the enlargement and fusion of the bilateral mandibular prominences. The mandibular skeleton develops from a cartilaginous derivative of the first branchial arch called *Meckel's cartilage.* When the maxillary and mandibular processes fuse laterally, they form the corners of the lips, or commissures.

As these facial structures are formed, mesenchymal cells of the first and second branchial arches invade them and form the muscles of mastication (first branchial arch, supplied by cranial nerve V, the trigeminal nerve) and the muscles of facial expression (second branchial arch, supplied by cranial nerve VII, the facial nerve).

Most of the differential jaw and facial growth occurs between 4 and 8 weeks, but changes occur in the different regions at different rates throughout fetal development and the early neonatal period. Relative to the adult, the neonatal face is small due to the fact that the jaws are still rudimentary at birth, the teeth undeveloped and unerupted, and the paranasal sinuses small.

As mentioned above, the various components forming the jaws fuse and mesenchymal merging occurs, leaving only the two nostrils and mouth as normal openings. If there is any interference with this process, a number of anomalies can occur, resulting in cleft lip, cleft chin, cleft anterior palate, and clefts at the corners of the mouth. If the

Copyright © 2003, Mosby, Inc. All rights reserved.

commissures do not form correctly, a large mouth or macrostomia can occur (also see Chapter 1).

EMBRYOLOGY OF THE DENTITION

The process by which the teeth form is called odontogenesis. Humans have two sets of teeth: the primary dentition (deciduous) and the secondary dentition (permanent). The presence of teeth in the maxilla and mandible contributes to the formation of the jaws and to the final shape of the face. There are 20 deciduous teeth and 32 permanent teeth.

Each tooth develops from ectoderm and ectomesenchyme (mesenchyme of the head). The enamel arises from the ectoderm, while the other tissues (dentin, cementum, periodontal ligament, and pulp contents) arise from the mesenchyme. The mesenchyme (ectomesenchyme) represents a migration of neural crest cells into the developing arches of the mandible and maxilla. Tooth development begins with the formation of the primary dental lamina invaginating into that mesenchyme. This dental lamina is a thickening of the oral epithelium overlying the jaws. These cells migrate into the primitive jaws in the sixth week of development. In 10 places in each of the mandibular and maxillary arches, cells of this dental lamina start to multiply faster than the surrounding cells and condense to form the tooth buds or tooth germs.[1–4]

Each tooth will develop and erupt at a specific time, but the overall pattern of odontogenesis is common to all teeth. The tooth germs of the permanent succedaneous teeth (the permanent teeth replacing deciduous teeth) arise from the secondary dental lamina and appear lingual to each deciduous tooth germ. These permanent succedaneous teeth are the permanent central and lateral incisors, canines, and first and second premolars. The premolars arise from the secondary lamina associated with deciduous (primary) molars and erupt into their corresponding positions. The permanent first, second, and third molars arise from the primary dental lamina posterior to the primary second molar. All the tooth buds except for the second and third permanent molars are present and start developing before birth.

As the tooth bud grows, it develops into a cap shape by invagination of mesenchyme (Fig. 14-2). The ectodermal component forms the enamel organ, which is composed of the outer enamel epithelium, the stellate reticulum, and the

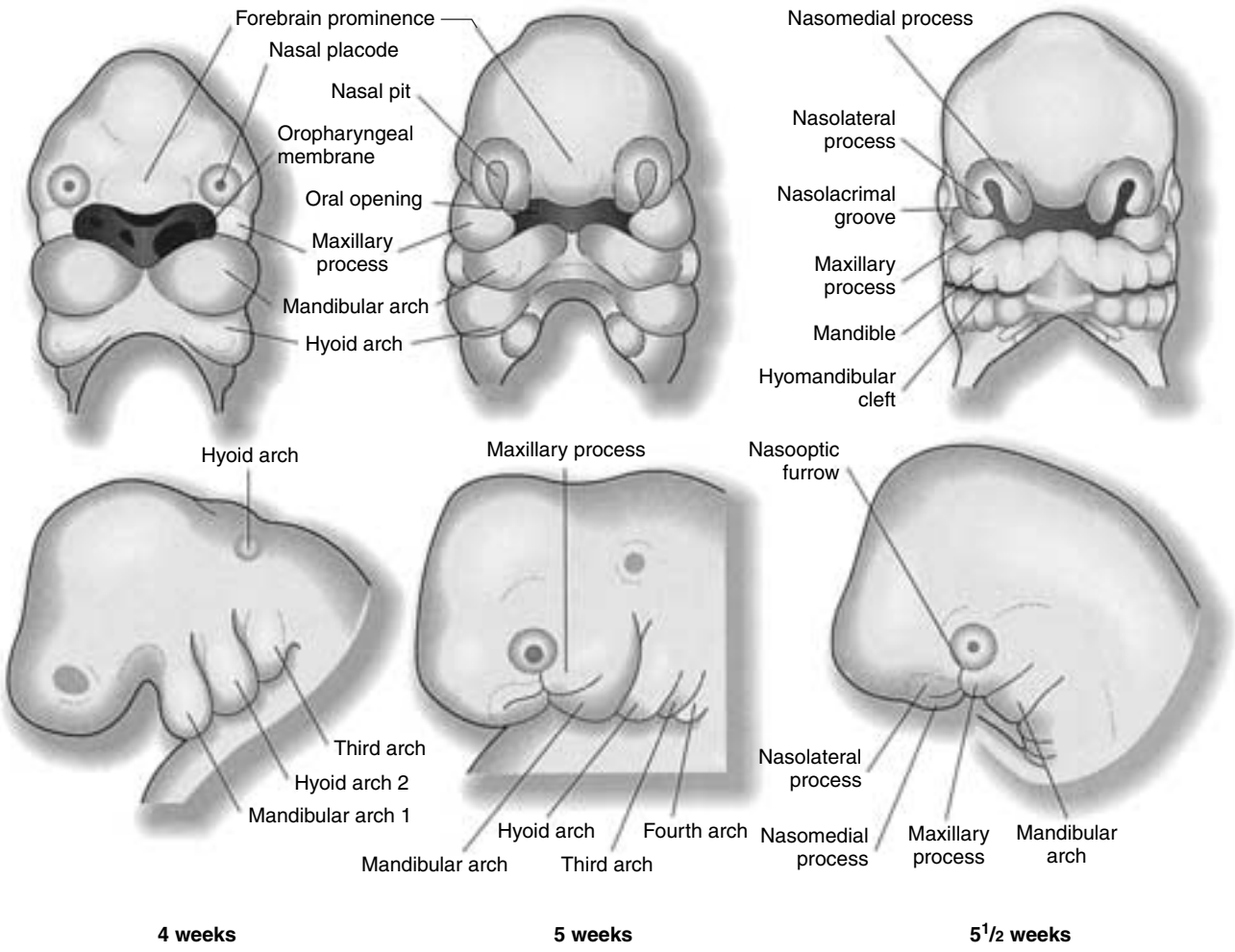

FIGURE 14-1 Frontal and lateral views of heads of human embryos from 4 to 8 weeks of age. (From Carlson BM. Human Embryology and Developmental Biology. St. Louis: CV Mosby, 1994.)

VIEW IMAGE

Copyright © 2003, Mosby, Inc. All rights reserved.

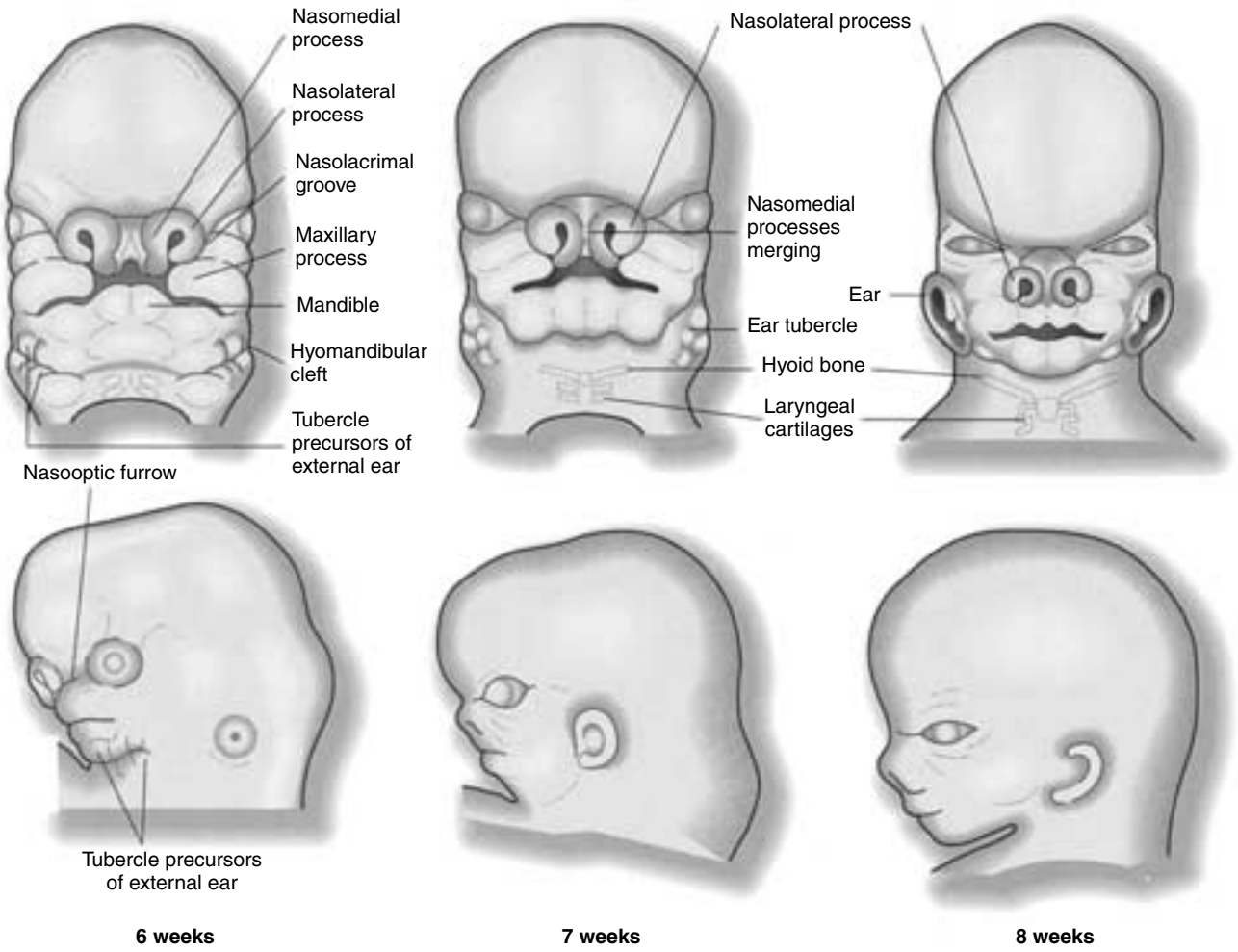

FIGURE 14-1 *Continued.* For legend see previous page.

VIEW IMAGE

inner enamel epithelium. A layer of more condensed cells develops from the stellate reticulum along the inner enamel epithelium, called the stratum intermedium. The enamel forms from the inner enamel epithelium, whose cells elongate into ameloblasts. Ameloblasts form the enamel of the tooth (Fig. 14-3).[2,3]

The invaginating mesenchyme forms the dental papilla. The peripheral cells of the dental papilla take on a columnar form and become known as *odontoblasts.* These cells will form the dentin of the tooth. The ameloblast and odontoblast layers are separated by a basement membrane. The future dentinoenamel junction is demarcated by the basement membrane. The dental papilla will later form the dental pulp, which is the soft tissue inside the root chamber of the tooth and contains nerves, vessels, and connective tissue.

At this stage, the tooth bud is starting to take on the shape of a bell and is called the *bell stage.* Later in the bell stage, the ameloblasts and odontoblasts start to produce the precursors of enamel and dentin. This starts to occur at about the fifth fetal month. The enamel is formed in a matrix in the shape of rods or a prism, but only after predentin is formed next to the inner enamel epithelium. In other words, enamel formation (amelogenesis) is induced by the production of dentin (dentinogenesis) (Fig. 14-4). Predentin later calcifies into dentin as the tooth develops. Both amelogenesis and dentinogenesis begin at the cusp or top of the tooth, and these processes continue toward the future apex or root. Enamel formation occurs only in the preeruptive tooth, while dentin deposition occurs throughout life. Enamel formation terminates with the development of an organic layer, the enamel cuticle. After this forms, the inner and outer enamel epithelia and the remains of the stratum intermedium form the reduced enamel epithelium, which fuses with the overlying oral epithelium to induce eruption of the teeth (movement of the tooth into the oral cavity).[2,3]

The dental laminae (primary and secondary) start to disintegrate at this stage. The cells of the dental lamina can disappear completely or can remain as groups of epithelial cells. These remnants may later give rise to lesions such as odontogenic (of tooth origin) cysts. As this occurs, further condensation of the mesenchyme around the tooth bud occurs, forming the dental sac. Also, the tooth buds become surrounded by islands of bone matrix that are developing in the jaws. Cells of the dental sac will produce other components of the teeth, such as cementum and the periodontal ligament. These will anchor the tooth in the bony socket (alveolus) of the jaws. As the teeth form, they start to migrate toward the surface of the jaws. Usually, no

Copyright © 2003, Mosby, Inc. All rights reserved.

teeth are seen in the mouth at birth, but natal teeth can occasionally be seen. Teeth erupt at different times during life in a fairly predictable pattern (Table 14-1).[3]

A number of anomalies of tooth development can occur.[5] These anomalies include too many teeth (supernumerary), too few teeth (hypodontia), the total lack of teeth (anodontia), or abnormal tooth shape and size, which may involve either the crown or the roots. Included are conditions such as fused teeth, enlarged teeth (macrodontia), or small teeth (microdontia); development of dentin and enamel can be faulty, resulting in conditions such as amelogenesis and dentinogenesis imperfecta. In these cases, the teeth are soft and prone to caries (dental decay), as well as to fracture from minor trauma, and anomalies of eruption, which include ectopia (tooth found in an abnormal position), impaction (impedance of eruption by bone or another tooth), ankylosis (the tooth is attached directly to bone, with no periodontal ligament), and delayed and premature eruption.

ANATOMY

Dentition and General Considerations

The teeth of the mandible and maxilla are each embedded in a horseshoe-shaped bony ridge called the alveolar process. Each process divides the oral cavity into two compartments: a more central one adjacent to the tongue called the oral cavity proper and a more peripheral one adjacent to the cheeks and lips called the oral vestibule. A horseshoe-shaped furrow formed where the mucous membrane of the lip and cheek reflect up onto the alveolar process is termed the fornix vestibuli. In the midline, vertically oriented folds of mucosa, the labial frenula, help connect the upper and lower lips to the alveolar process. The lingual frenum, or frenulum, is a similar structure in the midline on the undersurface of the tongue.

When fully dentured, the adult jaw contains 32 teeth—16

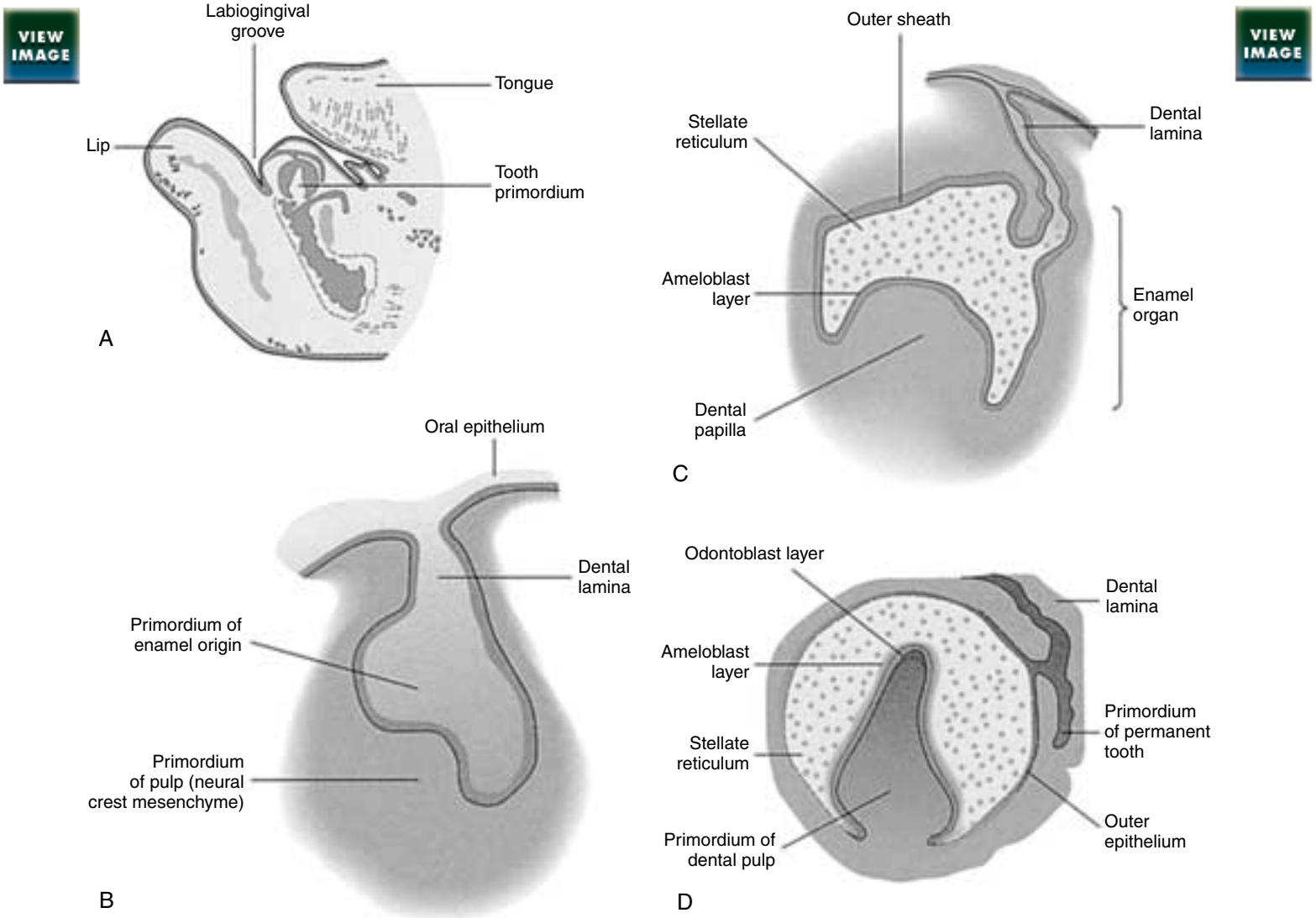

FIGURE 14-2 The development of a deciduous tooth. **A**, Parasagittal section through the lower jaw of a 14-week-old human embryo showing the relative location of the tooth primordium. **B**, Tooth primordium in a 9-week-old embryo. **C**, Tooth primordium at the cap stage in an 11-week-old embryo, showing the enamel organ. **D**, Central incisor primordium at the bell stage in a 14-week-old embryo before deposition of enamel or dentin.

Copyright © 2003, Mosby, Inc. All rights reserved.

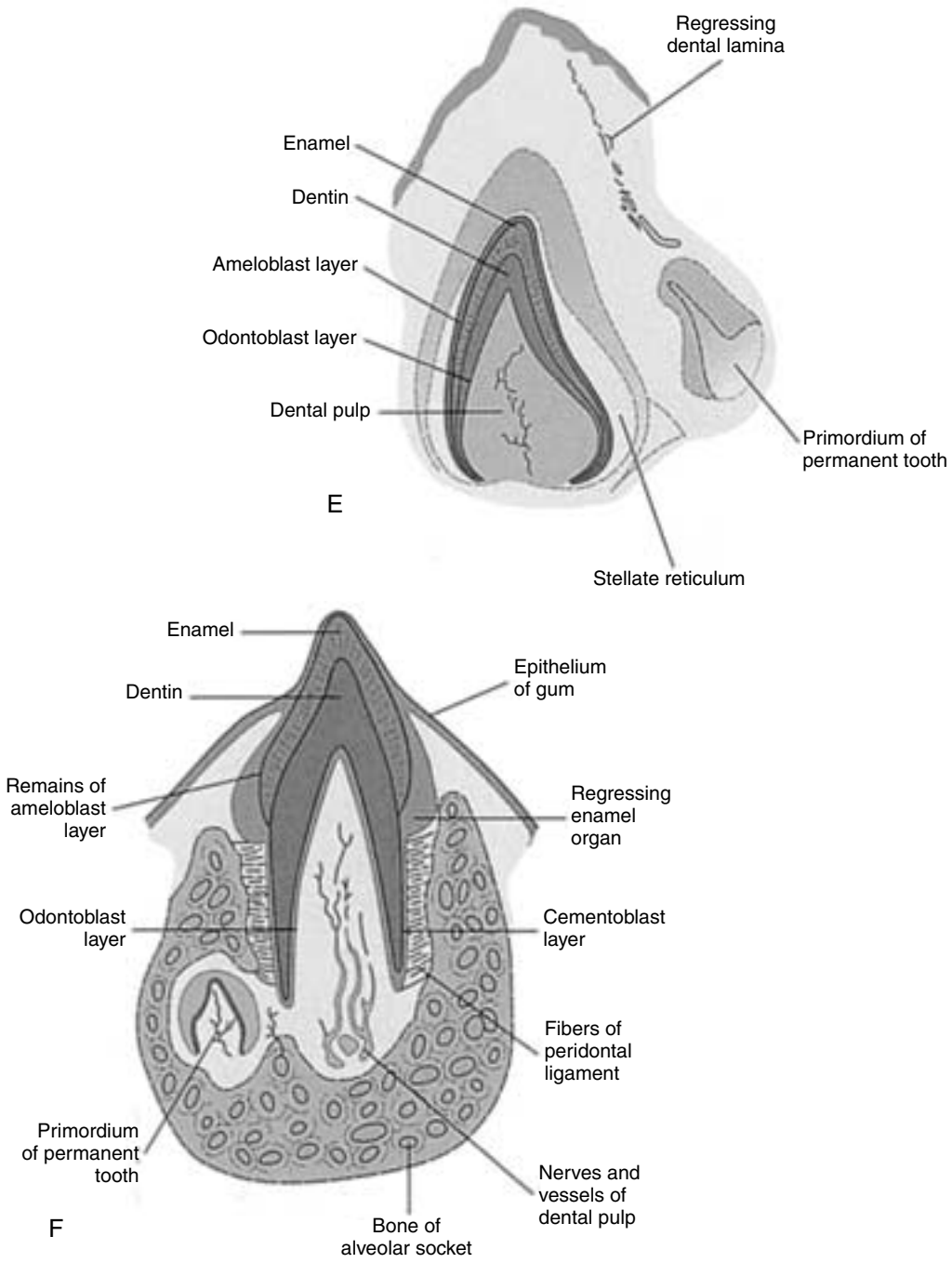

VIEW IMAGE

FIGURE 14-2 *Continued.* **E**, Unerupted incisor tooth in a term fetus. **F**, Partially erupted incisor tooth showing the primordium of a permanent tooth near one of its roots. (From Carlson BM. Human Embryology and Developmental Biology. St. Louis: CV Mosby, 1994.)

in the maxilla and 16 in the mandible. The teeth can be referred to by number or by name (Fig. 14-5). They are numbered sequentially, starting in the posterior right maxilla with tooth number 1 and continuing to number 16 in the posterior left maxilla. In the mandible they continue with tooth number 17 in the posterior left and end with tooth number 32 in the posterior right. The teeth are named beginning in the midline and moving distally on either side as follows: the central incisor, the lateral incisor, the canine, the first premolar, the second premolar, the first molar, the second molar, and the third molar.

The dentition of the pediatric jaw is different than that of the adult jaw. When fully dentured, it contains 20 teeth, 10 in the maxilla and 10 in the mandible, instead of the 32 teeth in the adult. Children lack the premolars and third molars. Instead of numbers, the teeth can be referred to by letter or by name (Fig. 14-5). They are lettered sequentially starting in the posterior right maxilla with tooth letter A (maxillary

Copyright © 2003, Mosby, Inc. All rights reserved.

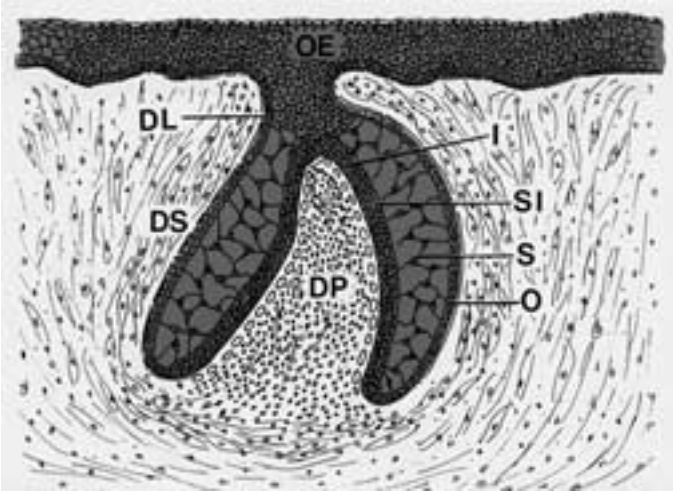

VIEW IMAGE

FIGURE 14-3 Illustration of a tooth germ. The four epithelial cell layers of the enamel organ (bell stage) are indicated as (*I*) inner, (*SI*) stratum intermedium, (*S*) stellate reticulum, and (*O*) outer. The dental papilla (*DP*) is enclosed within the four cell layers of the enamel organ and is continuous with the dental sac (*DS*), which surrounds the outer surface of the enamel organ. The dental lamina (*DL*) connects the enamel organ to the oral epithelium (*OE*). (From Melfi RC. Permar's Oral Embryology and Microscopic Anatomy. Philadelphia: Lea & Febiger, 1994.)

right second molar) and continuing to letter K (maxillary left second molar) in the posterior left maxilla. In the mandible, they continue with tooth letter L (mandibular left second molar) in the posterior left and end with letter U (mandibular right second molar) in the posterior right mandible. The teeth are named beginning in the midline and moving distally (posteriorly) on either side as follows: the central incisor, the lateral incisor, the canine, the first molar, and the second molar.

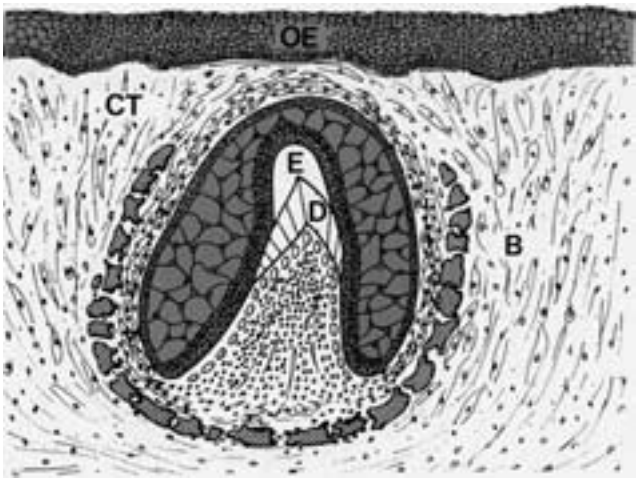

VIEW IMAGE

FIGURE 14-4 Illustration of an advanced tooth germ with enamel (*E*) and dentin (*D*) present in the coronalmost part. Ameloblasts are present around the enamel, whereas cervically the inner epithelial cells have not yet differentiated into ameloblasts. The dental sac surrounds the enamel organ and is continuous with the dental papilla. Developing bone (*B*) of the jaw is present, and the developing tooth is separated from the oral epithelium (*OE*) by connective tissue (*CT*). (From Melfi RC. Permar's Oral Embryology and Microscopic Anatomy. Philadelphia: Lea & Febiger, 1994.)

The portion of the tooth exposed in the oral cavity is called the anatomic crown (arrowheads in Fig. 14-6C), and the portion of the tooth embedded in the bony socket is referred to as the root (Fig. 14-7B). Most of the tooth is composed of dentine; however, the outer surface of the crown is covered by the smooth, dense enamel, and the outer surface of the root is covered by dense cementum, a tissue very similar to bone. A constriction where the crown and root meet is referred to as either the cervical constriction or the cementoenamel junction (Cc in Fig. 14-7B).

On CT, particularly in young people, the dense enamel appears separate from the dentine and looks like a dense band covering the crown of the tooth (E in Fig. 14-7B). With age, receding gingiva and bone cause portions of the root to be exposed in the oral cavity. The crown now differs from the original anatomic crown (that portion covered with enamel) and should be referred to as the functional crown. The arrows in Figure 14-6C point to the functional crown, and the arrowheads point to the anatomic crown.

The neurovascular bundle of the tooth enters the root apex via the apical foramen and travels through the root canal and into an expanded pulp chamber in the crown. The root canal and pulp chamber are seen on CT as a relatively radiolucent area in the center of the root and crown (Fig. 14-7B). Accessory apical foramina along the side of the root, rather than the apex of the root, may occasionally exist.

Each crown has five free surfaces.[6] The biting surface, or the surface where the upper and lower teeth oppose each other, is referred to as the occlusal surface (Figs. 14-6A and 14-7B). The surface facing toward the inside, or toward the oral cavity, is called the lingual surface in the mandible and the palatal surface in the maxilla (Fig. 14-6A). The outer surface of the tooth facing toward the lip and cheek is termed the labial surface for the incisors and canines and the buccal surface for the premolars and molars (Fig. 14-6C). This surface may more simply be referred to as the facial surface for all the teeth. The other tooth surfaces are the contact surfaces where one tooth contacts a neighboring tooth. Of

Table 14-1
THE USUAL TIMES OF ERUPTION AND SHEDDING OF DECIDUOUS AND PERMANENT TEETH

Teeth	Eruption	Shedding
Deciduous		
Central incisors	6–8 mo	6–7 yr
Lateral incisors	7–10 mo	7–8 yr
Canines	14–18 mo	10–12 yr
First molars	12–16 mo	9–11 yr
Second molars	20–24 mo	10–12 yr
Permanent		
Central incisors	7–8 yr	
Lateral incisors	8–9 yr	
Canines	12–13 yr	
First premolars	10–11 yr	
Second premolars	11–12 yr	
First molars	6–7 yr	
Second molars	12–13 yr	
Third molars	15–25 yr	

Source: Carlson BM. Human Embryology and Developmental Biology. St. Louis: CV Mosby, 1994;292.

Copyright © 2003, Mosby, Inc. All rights reserved.

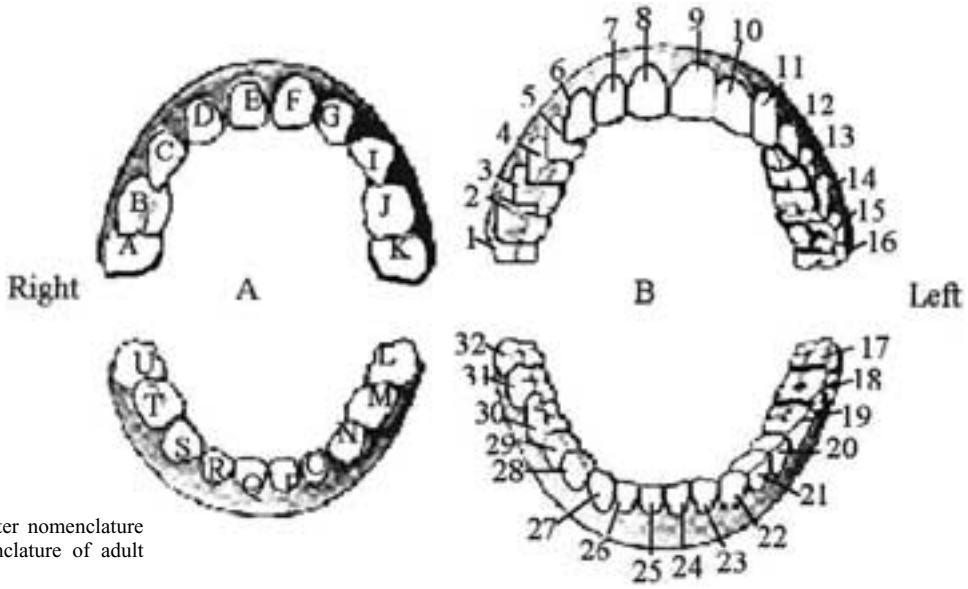

VIEW IMAGE

FIGURE 14-5 Illustration showing letter nomenclature of pediatric teeth (*A*) and number nomenclature of adult teeth (*B*).

these two surfaces, the one closest to the midline is referred to as the mesial surface, and the other is referred to as the distal surface (Figs. 14-6C and 14-7B). The mesial surface in the incisors and canines may also be called the medial surface, but in the premolars and molars it is termed the anterior surface. Likewise the distal surface in the incisors and canines may be called the lateral surface and in the premolars and molars the posterior surface.

Direction also can be described with this terminology. For example, toward the midline would be referred to as mesial, or anterior, and moving in the direction of the molars would be referred to as distal, or posterior. When referring to the crown of the tooth, one may move in the occlusal direction (toward the opposing tooth) or in the cervical direction (toward the cervical constriction), and when referring to the root, one may move in the cervical or apical direction. The use of this terminology is nicely exemplified by naming the roots of the teeth. For example, the first mandibular molar contains three roots, two buccal and one lingual. Of the two buccal roots, one is termed the mesiobuccal and the other is termed the distobuccal (Fig. 14-7B). The lingual one is simply called the lingual root.

The teeth are held in the bony socket by a highly specialized periodontal ligament that provides the teeth with small degrees of motion or ''give'' within the socket. On plain films, the ligament appears as a radiolucency between the cementum of the root and the lamina dura of the bony socket. The periodontal space normally measures between 0.1 and 0.2 mm and is therefore not typically identified on CT. Figure 14-7A, however, does show the lamina dura and to a lesser degree the periodontal space. A radiolucency seen on CT between the tooth root and the alveolar bone may represent a pathologic state such as periodontal disease, which is discussed later. In the cervical portion of the tooth, the fibers of the periodontal ligament radiate from the cementum of the root into the gingiva and serve to attach the gingiva to the tooth.

MANDIBLE

The anatomy of the mandible is described on the anatomic specimen in Figure 14-6 and on the illustrations of the neurovascular and muscular structures in Figures 14-8 and 14-9.[6–15] This anatomy is then labeled on the cross-sectional, axial, and panoramic CT images in Figure 14-10.[16]

Anatomic Specimen

Lingual Surface

The mandibular nerve, the third division of the trigeminal nerve, and the mandibular artery (Fig. 14-8A), enter the lingual surface of the mandible through the mandibular foramen (Mf in Fig. 14-6A). The foramen is situated in the center of the ramus, 1 to 2 cm posterior to the third molar at the craniocaudal level of the crowns of the teeth. The nerve and artery then travel anteriorly in the inferior alveolar canal (mandibular canal) (Fig. 14-8A). The canal typically hugs the lingual aspect of the mandible until it curves labially to exit the mandible at the mental foramen (M in Fig. 14-6C; Fig. 14-8A), which on the labial surface of the mandible is between the first and second premolars at the level of the roots. As the neurovascular bundle travels through the mandible, small nutrient canals extend coronally to supply the teeth (Fig. 14-8A, *arrow*). At the mental foramen the main trunk of the mandibular nerve exits as the mental nerve and supplies sensory fibers to the skin overlying the mandible and lower lip (Fig. 14-8A). A smaller branch, the incisive nerve, continues toward the midline within the mandible in the incisive canal (Fig. 14-11). It is accompanied by the incisive artery. This nerve innervates the canine and lateral incisor teeth, and the artery exits through the lingual foramen, which is located in the midline, inferiorly on the lingual aspect of the mandible (Lf in Figs. 14-6B and 14-11C). After exiting the mandible, this

Copyright © 2003, Mosby, Inc. All rights reserved.

artery anastomosis with the lingual artery of the tongue (Fig. 14-9A).

The mylohyoid nerve, a small branch of the mandibular nerve, rather than entering the mandibular foramen with the rest of the nerve, travels anteriorly in the mylohyoid groove on the lingual surface of the mandible (Mg in Fig. 14-6A). The mylohyoid nerve supplies the mylohyoid muscle (Fig. 14-9A,C,D), which fans out like a sling to form the functional floor of the oral cavity. This muscle inserts on the mandible along a bony ridge, the mylohyoid line (Ml in Fig. 14-6A). This line acts as a landmark, separating the oral cavity from the suprahyoid portion of the neck. Inferior to the mylohyoid muscle is the submandibular fossa (S in Fig. 14-6A), a slight concavity in the mandible for the submandibular gland. A small portion of the gland wraps around the posterior aspect of the mylohyoid muscle to enter the sublingual space (Fig. 14-9A). Superior to the mylohyoid line and muscle is the sublingual fossa (Sl in Fig. 14-6A), in which is situated the sublingual gland (Fig. 14-9A).

Also above the mylohyoid muscle are the geniohyoid and genioglossus muscles, which insert on a midline bony protuberance called the genial tubercle (Gt in Figs. 14-6B and 14-11C). It has four bony spines, two superior ones for the right and left genioglossus muscles and two inferior ones for the right and left geniohyoid muscles (Figs. 14-9C,D and

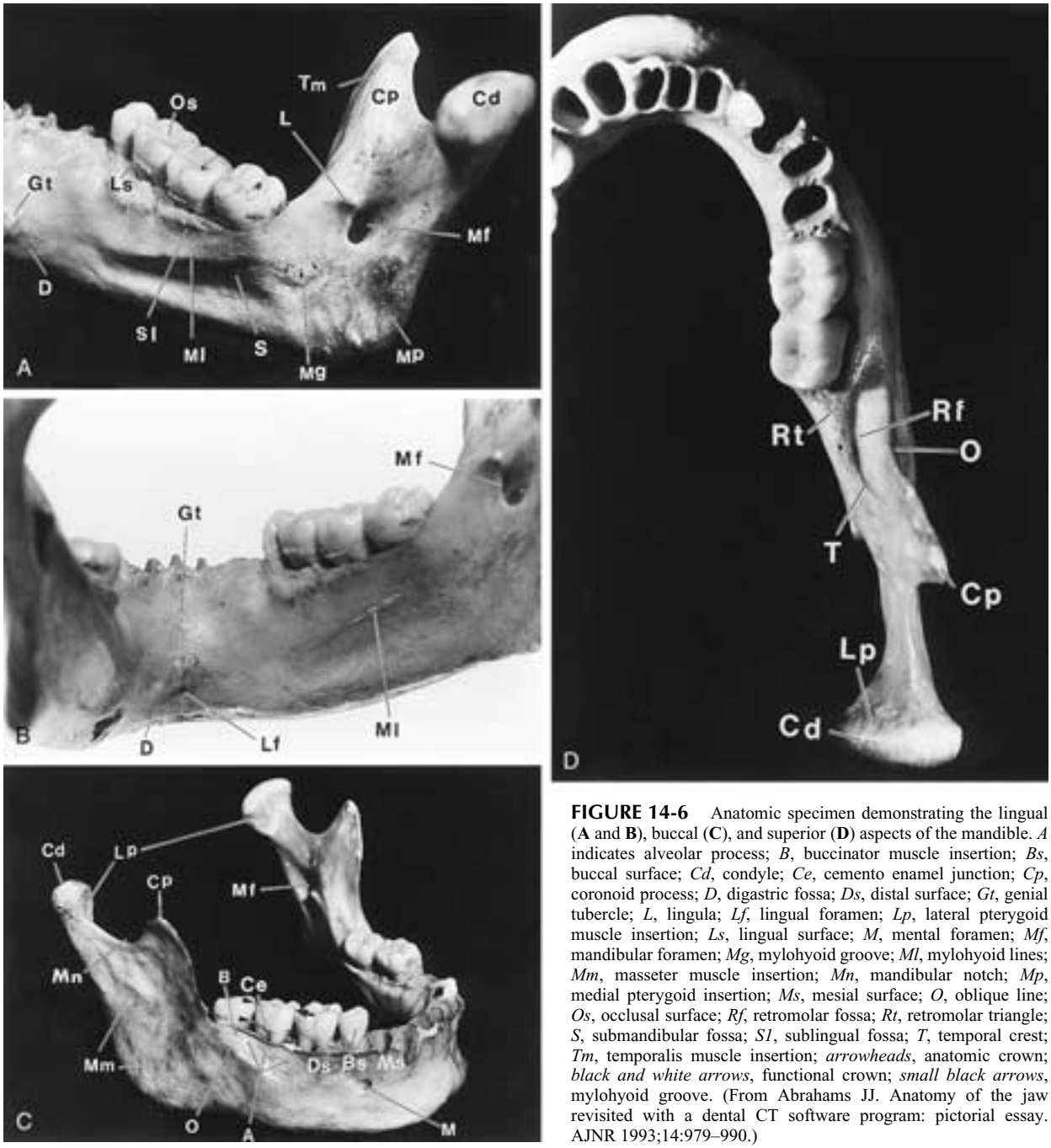

FIGURE 14-6 Anatomic specimen demonstrating the lingual (**A** and **B**), buccal (**C**), and superior (**D**) aspects of the mandible. *A* indicates alveolar process; *B*, buccinator muscle insertion; *Bs*, buccal surface; *Cd*, condyle; *Ce*, cemento enamel junction; *Cp*, coronoid process; *D*, digastric fossa; *Ds*, distal surface; *Gt*, genial tubercle; *L*, lingula; *Lf*, lingual foramen; *Lp*, lateral pterygoid muscle insertion; *Ls*, lingual surface; *M*, mental foramen; *Mf*, mandibular foramen; *Mg*, mylohyoid groove; *Ml*, mylohyoid lines; *Mm*, masseter muscle insertion; *Mn*, mandibular notch; *Mp*, medial pterygoid insertion; *Ms*, mesial surface; *O*, oblique line; *Os*, occlusal surface; *Rf*, retromolar fossa; *Rt*, retromolar triangle; *S*, submandibular fossa; *S1*, sublingual fossa; *T*, temporal crest; *Tm*, temporalis muscle insertion; *arrowheads*, anatomic crown; *black and white arrows*, functional crown; *small black arrows*, mylohyoid groove. (From Abrahams JJ. Anatomy of the jaw revisited with a dental CT software program: pictorial essay. AJNR 1993;14:979–990.)

VIEW IMAGE

Copyright © 2003, Mosby, Inc. All rights reserved.

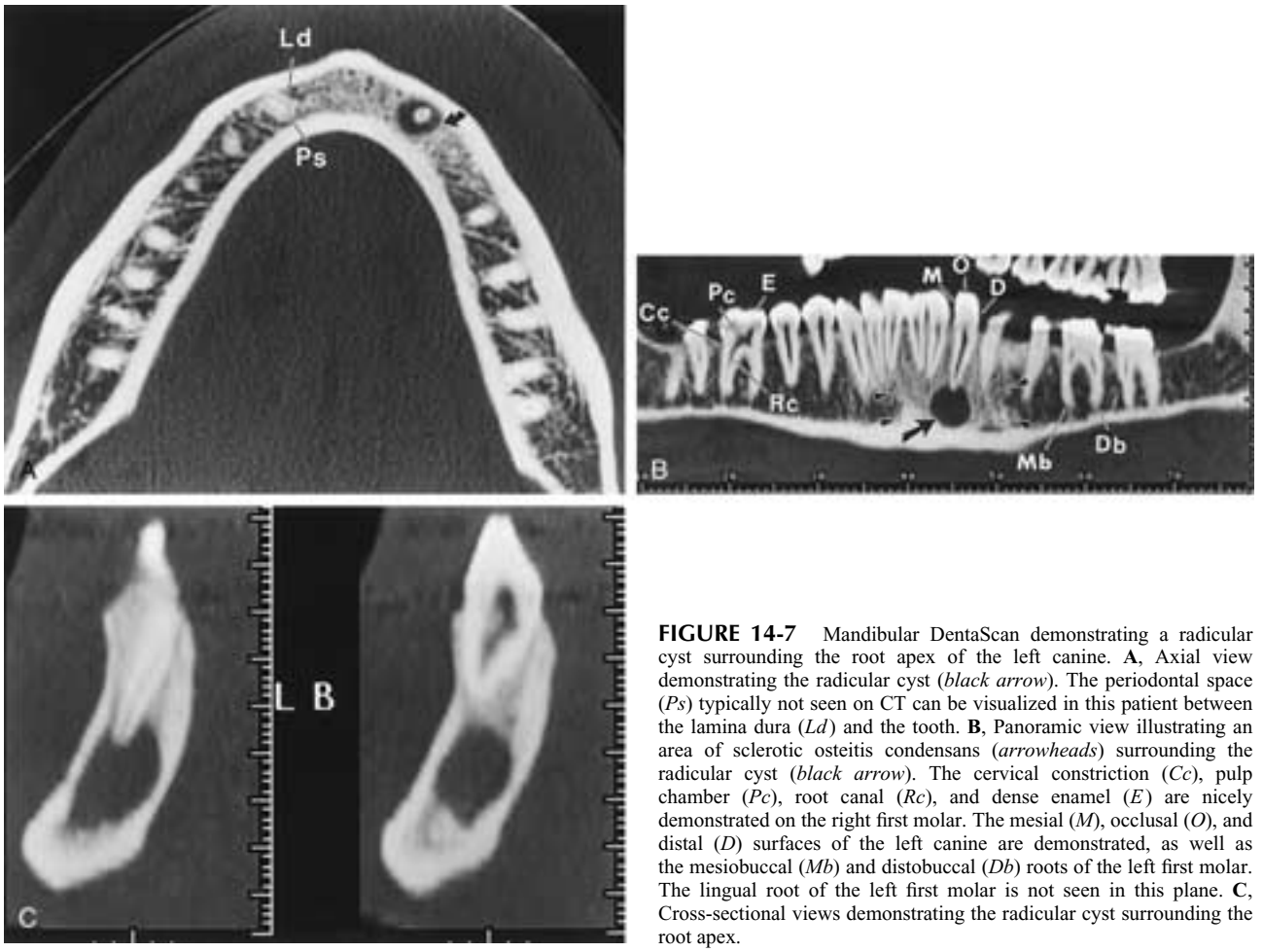

FIGURE 14-7 Mandibular DentaScan demonstrating a radicular cyst surrounding the root apex of the left canine. **A**, Axial view demonstrating the radicular cyst (*black arrow*). The periodontal space (*Ps*) typically not seen on CT can be visualized in this patient between the lamina dura (*Ld*) and the tooth. **B**, Panoramic view illustrating an area of sclerotic osteitis condensans (*arrowheads*) surrounding the radicular cyst (*black arrow*). The cervical constriction (*Cc*), pulp chamber (*Pc*), root canal (*Rc*), and dense enamel (*E*) are nicely demonstrated on the right first molar. The mesial (*M*), occlusal (*O*), and distal (*D*) surfaces of the left canine are demonstrated, as well as the mesiobuccal (*Mb*) and distobuccal (*Db*) roots of the left first molar. The lingual root of the left first molar is not seen in this plane. **C**, Cross-sectional views demonstrating the radicular cyst surrounding the root apex.

VIEW IMAGE

14-11C). Inferior to the mylohyoid muscle and to either side of the genial tubercle are the digastric fossae (D in Fig. 14-6A,B), each for the origin of the anterior belly of the digastric muscle (Fig. 14-9A).

The temporalis muscle (Fig. 14-9B) inserts on the coronoid process, the most superoanterior extension of the mandibular ramus (Cp in Fig. 14-6A,C). From here this muscle runs deep to the zygomatic arch to flare out over the lateral surface of the calvarium. Its function is to elevate the mandible, thus closing the jaw. Between the coronoid process and the more posterior articular condyle is the mandibular notch (Mn in Fig. 14-6C). The lateral pterygoid muscle (Fig. 14-9B) inserts on the anterior aspect of the condyle (Lp in Fig. 14-6C; Fig. 14-9D) and depresses, protrudes, and moves the jaw from side to side. The medial pterygoid (Fig. 14-9B) inserts more inferiorly on the angle of the mandible near the junction of the body and ramus (Mp in Fig. 14-6A; Fig. 14-9D) and serves to close the mandible along with the temporalis muscle.

Buccal Surface

On the buccal surface a bony ridge, the oblique line (O in Fig. 14-6C), is formed where the coronoid process (Cp in Fig. 14-6C) merges with the body of the mandible. The buccinator muscle (Fig. 14-9B), which compresses the cheeks to hold food between the teeth, inserts between the oblique line and the more medially (lingually) situated alveolar process (B in Fig. 14-6C; Fig. 14-9D). The deep and superficial portions of the masseter muscle (Fig. 14-9B,D) insert on the buccal surface of the ramus (Mm in Fig. 14-6C; Fig. 14-9D), having originated from the inferior and medial aspect of the zygomatic arch. This muscle acts to close the jaw along with the medial pterygoid and temporalis muscles. Portions of the platysma muscle also insert on the buccal aspect of the mandible along a line that runs inferiorly from the region of the molars to the mental protuberance (Fig. 14-9D). Anteriorly, between the first and second premolar teeth, the mental foramen is identified (M in Fig. 14-6C).

Superior Surface

The alveolar process, which houses the teeth, forms the most superior portion of the mandibular body. Its curved, or horseshoe, configuration is more acute than that of the body itself. This causes the alveolar process in its posterior (distal) aspect to be medially (lingually) positioned in relation to the mandibular body (Fig. 14-6D). The cross-sectional DentaScan images nicely illustrate how the alveolar process is situated on the lingual aspect of the mandible in image 10 (lower right) of Figure 14-10D.

Posterior to the teeth, the alveolar process tapers to form the retromolar triangle (Rt in Fig. 14-6D) that merges with

Copyright © 2003, Mosby, Inc. All rights reserved.

the lingual aspect of the ramus to form the temporal crest (T in Fig. 14-6D). Buccal to this, the anterior portion of the coronoid process (Cp in Fig. 14-6D) merges with the body of the mandible to form the oblique line (O in Fig. 14-6D). Between the oblique line and the temporal crest lies the retromolar fossa (Rf in Fig. 14-6D). The lateral pterygoid muscle inserts on the anterior lingual aspect of the condyle (Lp in Fig. 14-6D).

CT Images: Cross-Sectional View

Lingual Surface

Cross-sectional images 1 through 5 in Figure 14-10 are through the distal aspect of the right mandible, near the junction of the ramus and body. The mandibular foramen (Mf), the lingula (L), and the mylohyoid groove (Mg) are clearly seen on these images. More anteriorly (images 9

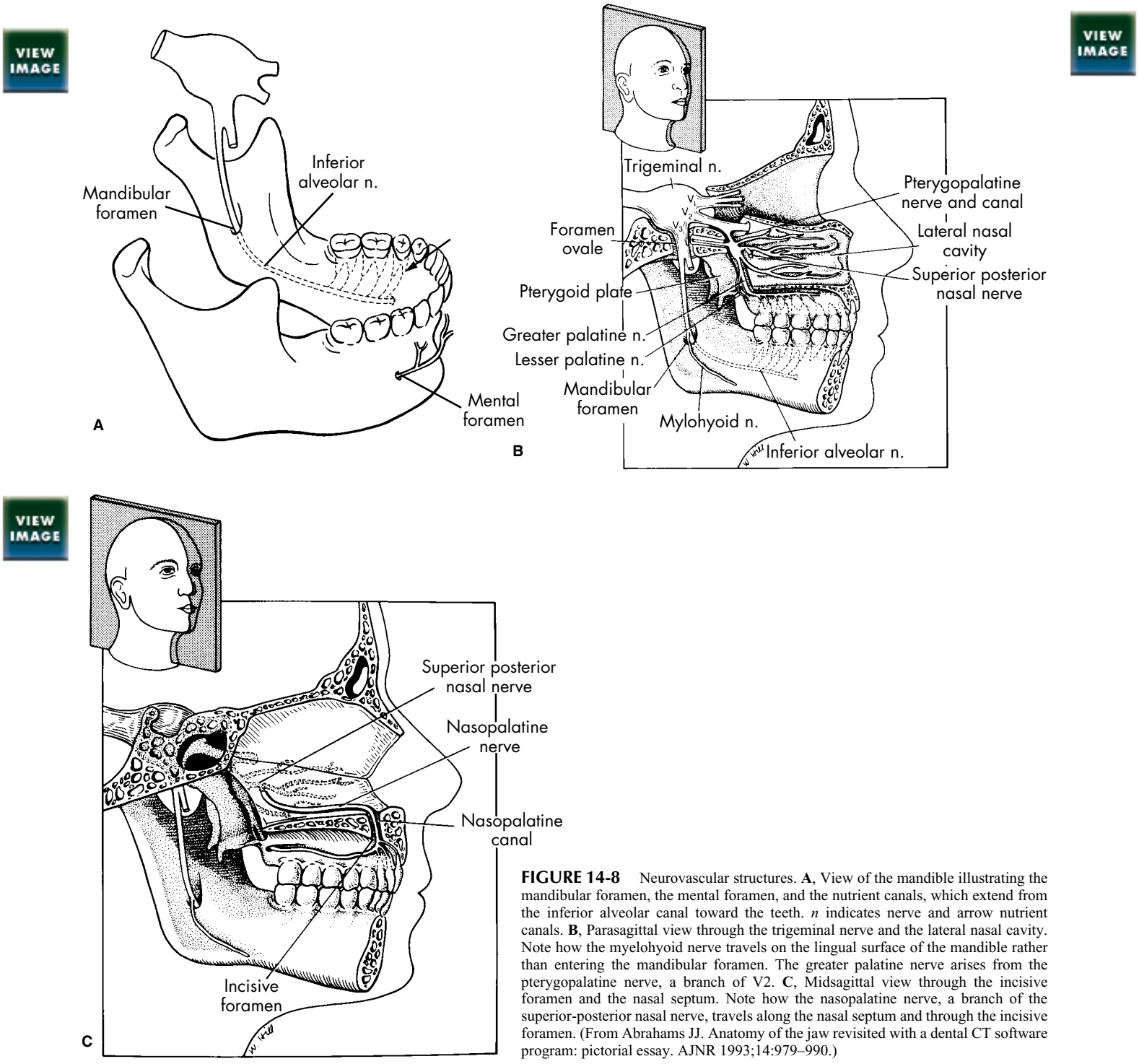

FIGURE 14-8 Neurovascular structures. **A**, View of the mandible illustrating the mandibular foramen, the mental foramen, and the nutrient canals, which extend from the inferior alveolar canal toward the teeth. *n* indicates nerve and arrow nutrient canals. **B**, Parasagittal view through the trigeminal nerve and the lateral nasal cavity. Note how the myelohyoid nerve travels on the lingual surface of the mandible rather than entering the mandibular foramen. The greater palatine nerve arises from the pterygopalatine nerve, a branch of V2. **C**, Midsagittal view through the incisive foramen and the nasal septum. Note how the nasopalatine nerve, a branch of the superior-posterior nasal nerve, travels along the nasal septum and through the incisive foramen. (From Abrahams JJ. Anatomy of the jaw revisited with a dental CT software program: pictorial essay. AJNR 1993;14:979–990.)

Copyright © 2003, Mosby, Inc. All rights reserved.

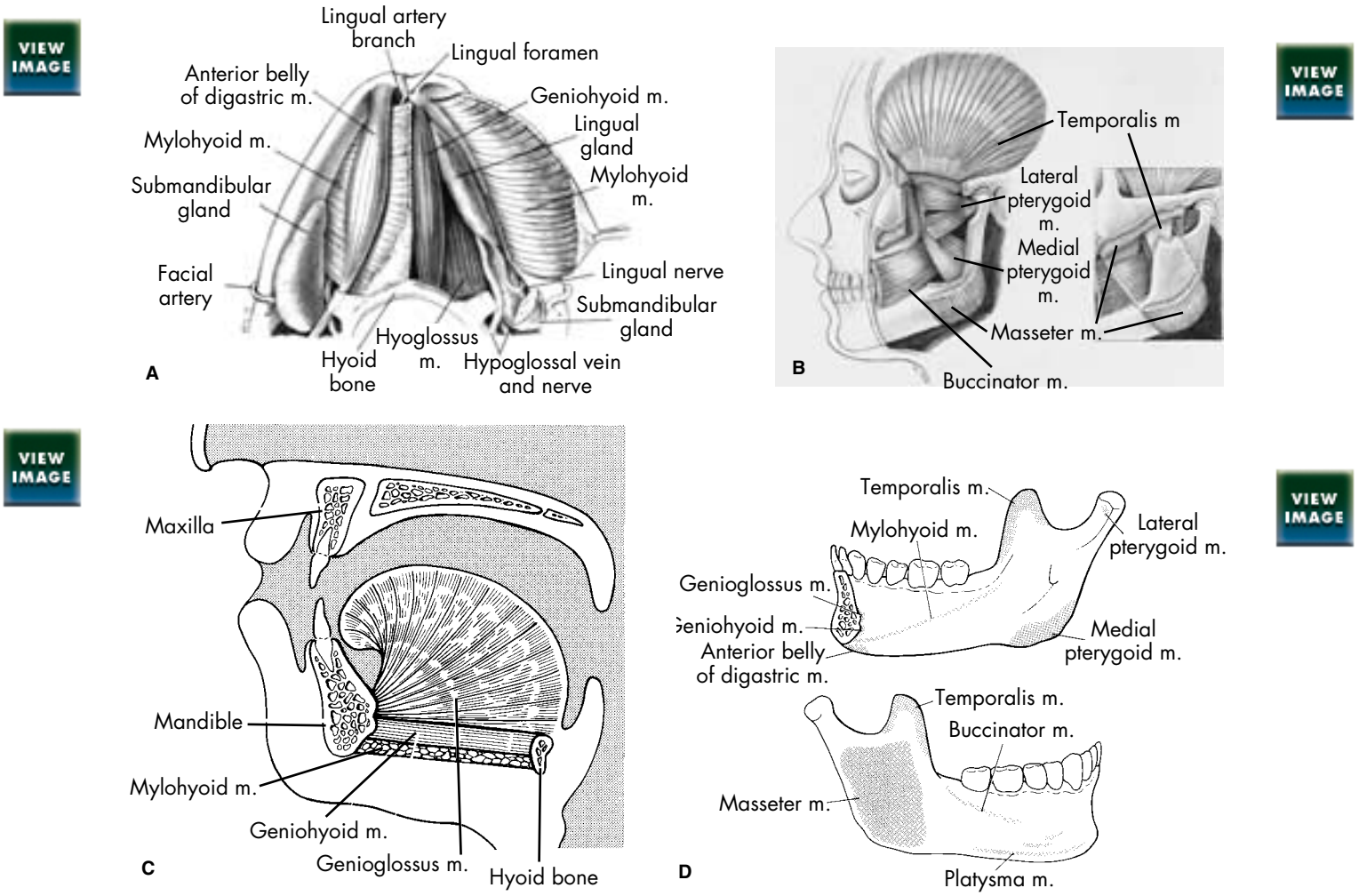

FIGURE 14-9 Muscles and insertions. **A**, Mandible viewed from below. *m* indicates muscle. **B**, Lateral view with zygomatic arch and coronoid process removed. **C**, Midline sagittal view through the genial tubercle. **D**, Muscle insertions. Lingual surface (*upper figure*). Buccal surface (*lower figure*). (From Abrahams JJ. Anatomy of the jaw revisited with a dental CT software program: pictorial essay. AJNR 1993;14:979–990.)

through 11 in Fig. 14-10D,E), the mylohyoid line (Ml), the submandibular fossa (S), and the sublingual fossa (Sl) are identified. In the region of the midline (images 27 and 28 in Fig. 14-10F), the genial tubercle (Gt) and the digastric fossa (D) can be seen. The superior (Gt-g) and inferior (Gt-h) processes of the genial tubercle, where the genioglossus and geniohyoid muscles insert, are better visualized in Figure 14-11C. This figure also demonstrates the lingual foramen (Lf) just below the genial tubercle.

Buccal Surface

The oblique line (O) that is formed where the coronoid process (Cp) merges with the body of the mandible is seen in the posterior images (images 4 through 7 in Fig. 14-10D). More anteriorly (image 20 in Fig. 14-10E), the mental foramen (M) can be seen in cross section. The course of the neurovascular bundle can be clearly traced on the cross-sectional images as it enters the mandibular foramen on the lingual surface, travels through the inferior alveolar canal (I), and finally exits the mental foramen on the buccal surface.

Superior Surface

On the buccal aspect of the superior surface, the coronoid process (Cp) is again visualized on the more distal images in Figure 14-10D. On more anterior images, the coronoid process merges with the mandible to form the oblique line (O) seen in image 7 of Figure 14-10D. On the lingual aspect of the superior surface, the temporal crest (T) is visualized on the more distal images (image 6 in Fig. 14-10D). More anteriorly the temporal crest becomes the retromolar triangle (Rt in image 8, Fig. 14-10D), and finally the alveolar process (A in image 10, Fig. 14-10D). The molars, which are normally seen in the alveolar process at this point, are absent in this edentulous patient. In the posterior mandible the alveolar process assumes a more lingual position in relation to the body of the mandible. This can be appreciated by comparing the position of the alveolar process to that of the mandible in image 10 (Fig. 14-10D) and image 17 (Fig. 14-10E). The retromolar fossa (Rf in Fig. 14-10D) is identified between the oblique line and the temporal crest.

Copyright © 2003, Mosby, Inc. All rights reserved.

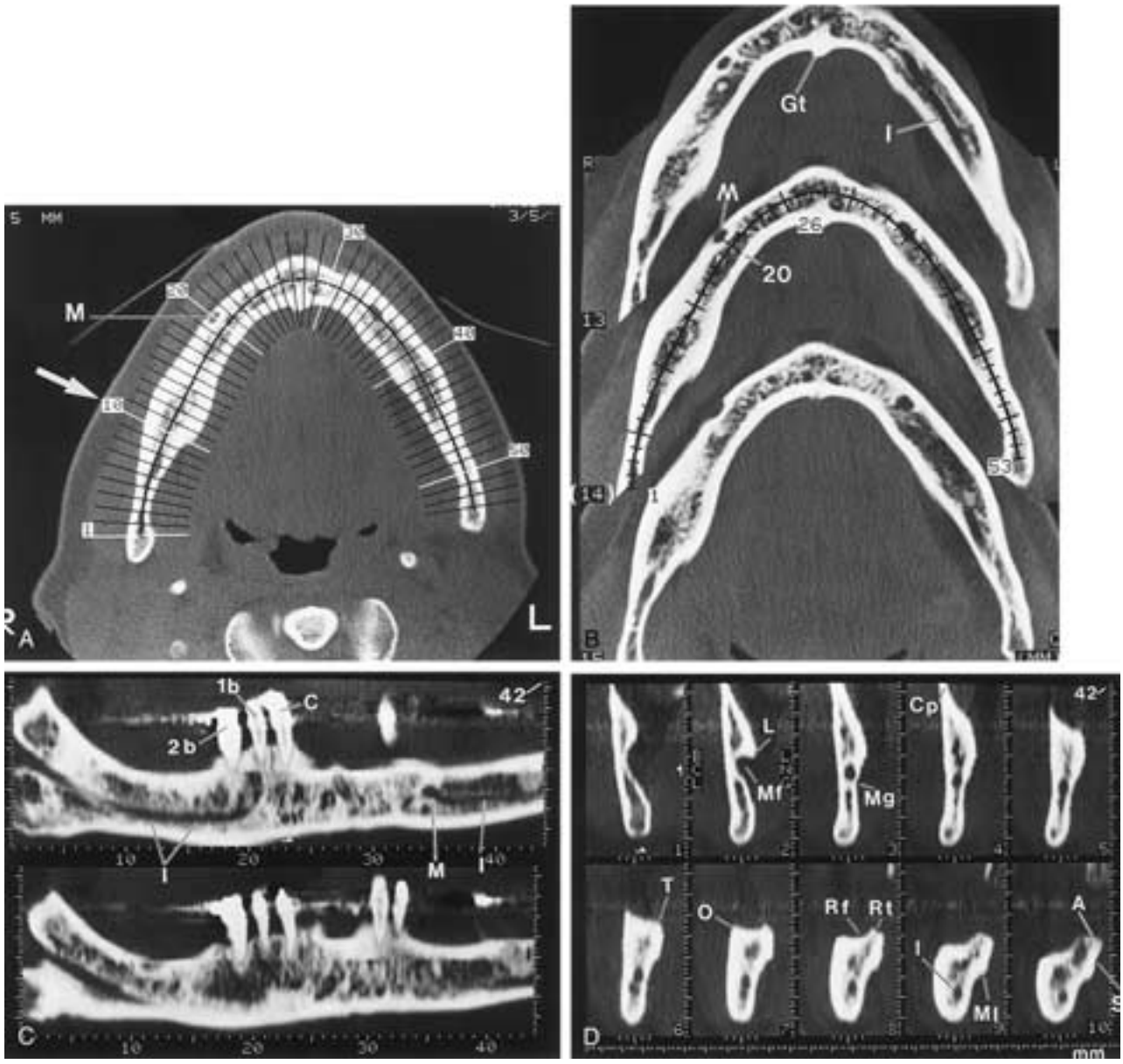

VIEW IMAGE

FIGURE 14-10 CT (DentaScan) image of mandible. The anatomy identified on the mandibular anatomic specimen in Figure 15-6 is now identified on these CT images. **A**, Axial image of mandible with superimposed curve. The curve defines the plane and location in which the panoramic images in **C** are reformatted. Numbered lines drawn perpendicular to this curve (*arrow*) define the plane and location in which the cross-sectional images viewed in **D** through **F** are reformatted. Mental foramen (*M*). **B**, Axial images illustrating the inferior alveolar canal (*I*), the mental foramen (*M*), and the genial tubercle (*Gt*). The numbers along the left side of the figure refer to the particular number of the axial image. Note that the mental foramen, which is seen on axial image number 14 at the twentieth perpendicular line, is also seen in **E** on cross-sectional image 20 (lower right) at the level of the fourteenth tick mark on the side of the image. The tick marks and numbers allow images to be correlated with one another. **C**, Panoramic views. The numbered tick marks along the bottom of the images correspond to the numbered perpendicular lines displayed on the axial image in **A**. The tick marks along the side of the image correspond to the axial images that were used to reformat these images. Note that there were 42 axial images acquired and thus 42 tick marks along the side of this image. Inferior alveolar canal (*I*), mental foramen (*M*), second bicuspid (*2b*), first bicuspid (*1b*), and cuspid (*C*). **D** through **F**, Cross-sectional views. Images 1 through 10 (**D**) are through the posterior right mandible (see perpendicular lines 1 through 10 in **A**).

Copyright © 2003, Mosby, Inc. All rights reserved.

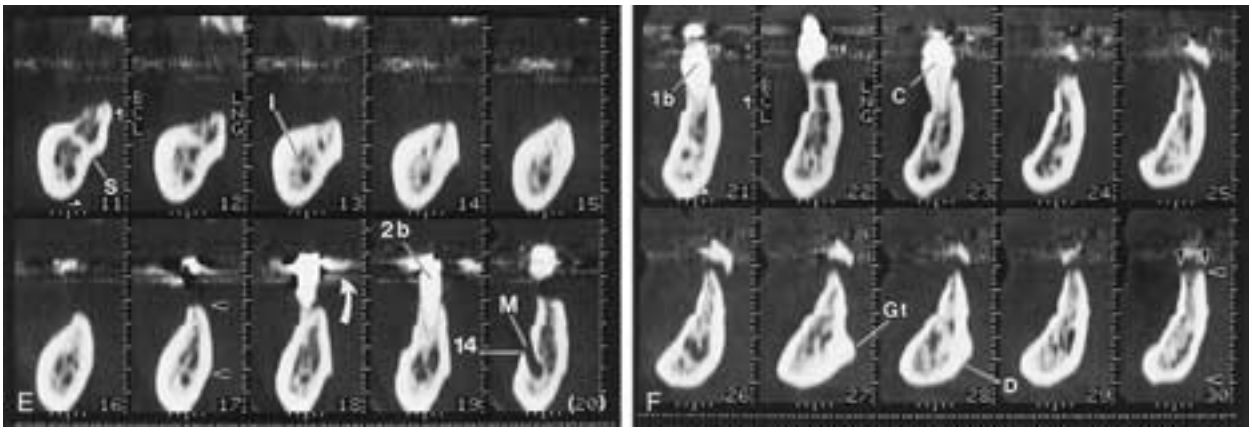

VIEW IMAGE

FIGURE 14-10 *Continued.* Images 11 through 20 (**E**) are more anterior. Images 21 through 30 (**F**) extend to the midline. The images of the left half of the mandible are not shown. Arrowheads in image 17 (**E**) indicate that the height of the mandible distal to the mental foramen is measured from the top of the alveolar process to the top of the mandibular canal, and mesial to the foramen it is measured from the top of the alveolar process to the bottom of the mandible (*arrowheads* in **F**, image 30). Measurement of the width is also demonstrated in image 30 (**F**). *mm* at the bottom of **D** indicates the millimeter scale. Note how streak artifact from dental restoration (*curved arrow* in **E**) does not degrade visualization of the bone. *A* indicates alveolar process; *C*, cuspid; *Cp*, coronoid process; *D*, digastric fossa; *Gt*, genial tubercle; *I*, inferior alveolar canal; *M*, mental foramen; *Mf* mandibular foramen; *Mg*, mylohyoid groove; *Ml* mylohyoid line; *O*, oblique line; *Rf*, retromolar fossa; *Rt*, retromolar triangle; *S*, submandibular fossa; *S1*, sublingual fossa; *T*, temporal crest; *1b*, first bicuspid; and *2b*, second bicuspid. (From Abrahams JJ. Anatomy of the jaw revisited with a dental CT software program: pictorial essay. AJNR 1993;14:979–990.)

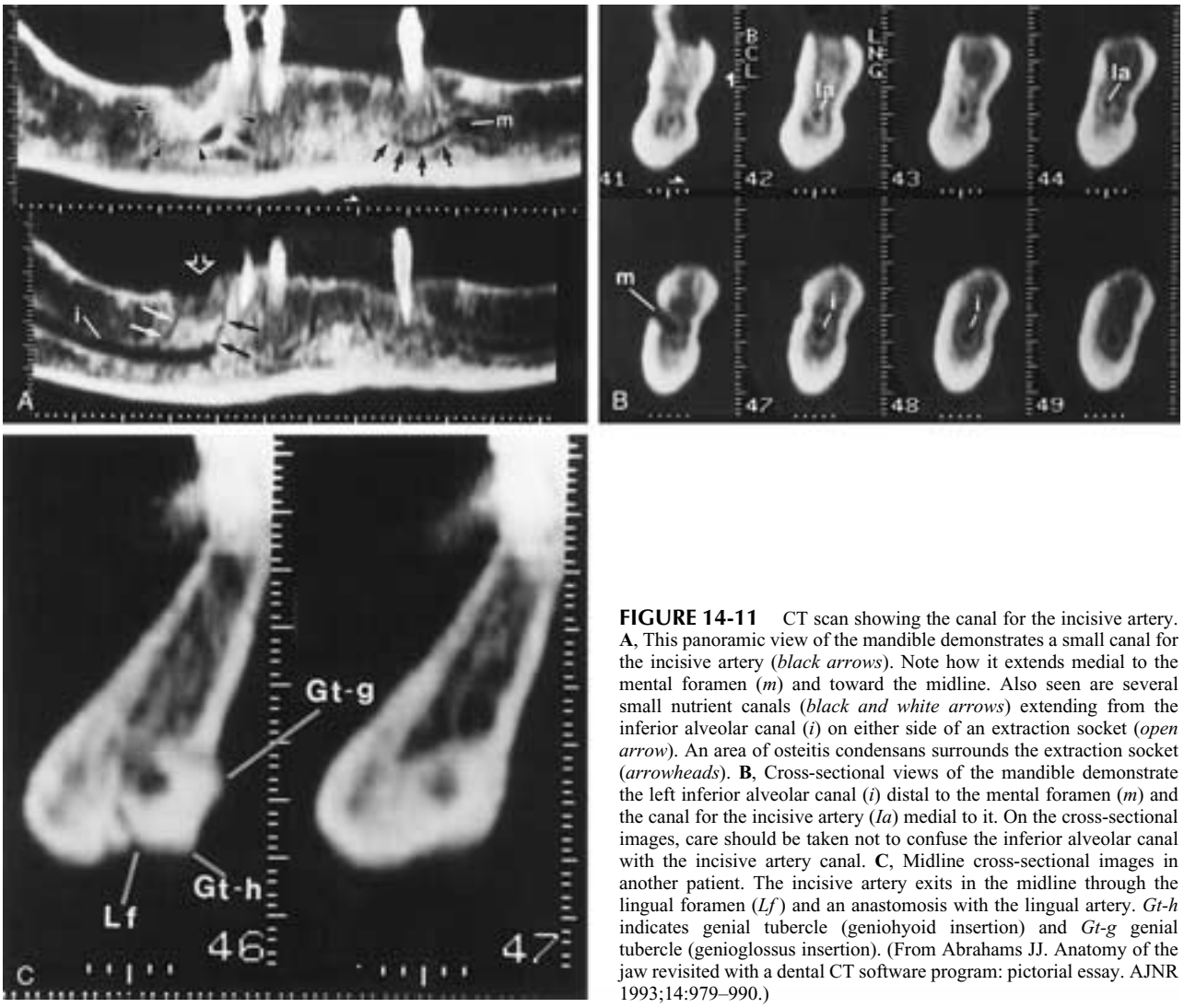

VIEW IMAGE

FIGURE 14-11 CT scan showing the canal for the incisive artery. **A**, This panoramic view of the mandible demonstrates a small canal for the incisive artery (*black arrows*). Note how it extends medial to the mental foramen (*m*) and toward the midline. Also seen are several small nutrient canals (*black and white arrows*) extending from the inferior alveolar canal (*i*) on either side of an extraction socket (*open arrow*). An area of osteitis condensans surrounds the extraction socket (*arrowheads*). **B**, Cross-sectional views of the mandible demonstrate the left inferior alveolar canal (*i*) distal to the mental foramen (*m*) and the canal for the incisive artery (*Ia*) medial to it. On the cross-sectional images, care should be taken not to confuse the inferior alveolar canal with the incisive artery canal. **C**, Midline cross-sectional images in another patient. The incisive artery exits in the midline through the lingual foramen (*Lf*) and an anastomosis with the lingual artery. *Gt-h* indicates genial tubercle (geniohyoid insertion) and *Gt-g* genial tubercle (genioglossus insertion). (From Abrahams JJ. Anatomy of the jaw revisited with a dental CT software program: pictorial essay. AJNR 1993;14:979–990.)

Copyright © 2003, Mosby, Inc. All rights reserved.

Internal Anatomy

Internally the inferior alveolar canal (I) is seen from its origin at the mandibular foramen to its termination at the mental foramen (M). From the region of the mental foramen, a smaller canal, the canal for the incisive artery (Ia), can be seen extending toward the midline (Fig. 14-11B). On the cross-sectional images, the canal distal to the mental foramen is the inferior alveolar canal and the canal mesial to the mental foramen is the canal for the incisive artery (Fig. 14-11A,B). In the midline, the canal for the incisive artery exits the lingual foramen (Lf in Fig. 14-11C) to anastomose with the lingual artery.

Axial View

On the axial view, the genial tubercle (Gt), mental foramen (M), and inferior alveolar canal (I) are identified in Figure 14-10A,B.

Panoramic View

On the panoramic view, the course of the inferior alveolar canal (I in Fig. 14-10C and i in Fig. 14-11A) can be traced to its exit point, the mental foramen (M). The canal for the incisive artery (Ia) is visualized extending from the mental foramen toward the midline in Figure 14-11A. Also in Figure 14-11A, nutrient canals (black and white arrows) can be seen extending cephalad from the inferior alveolar canal (i) toward the teeth.

MAXILLA

The anatomy of the maxilla is described first on the anatomic specimen in Figure 14-12 and then on the illustrations of the neurovascular structures in Figure 14-8.[7–15] This anatomy is then identified on the axial,

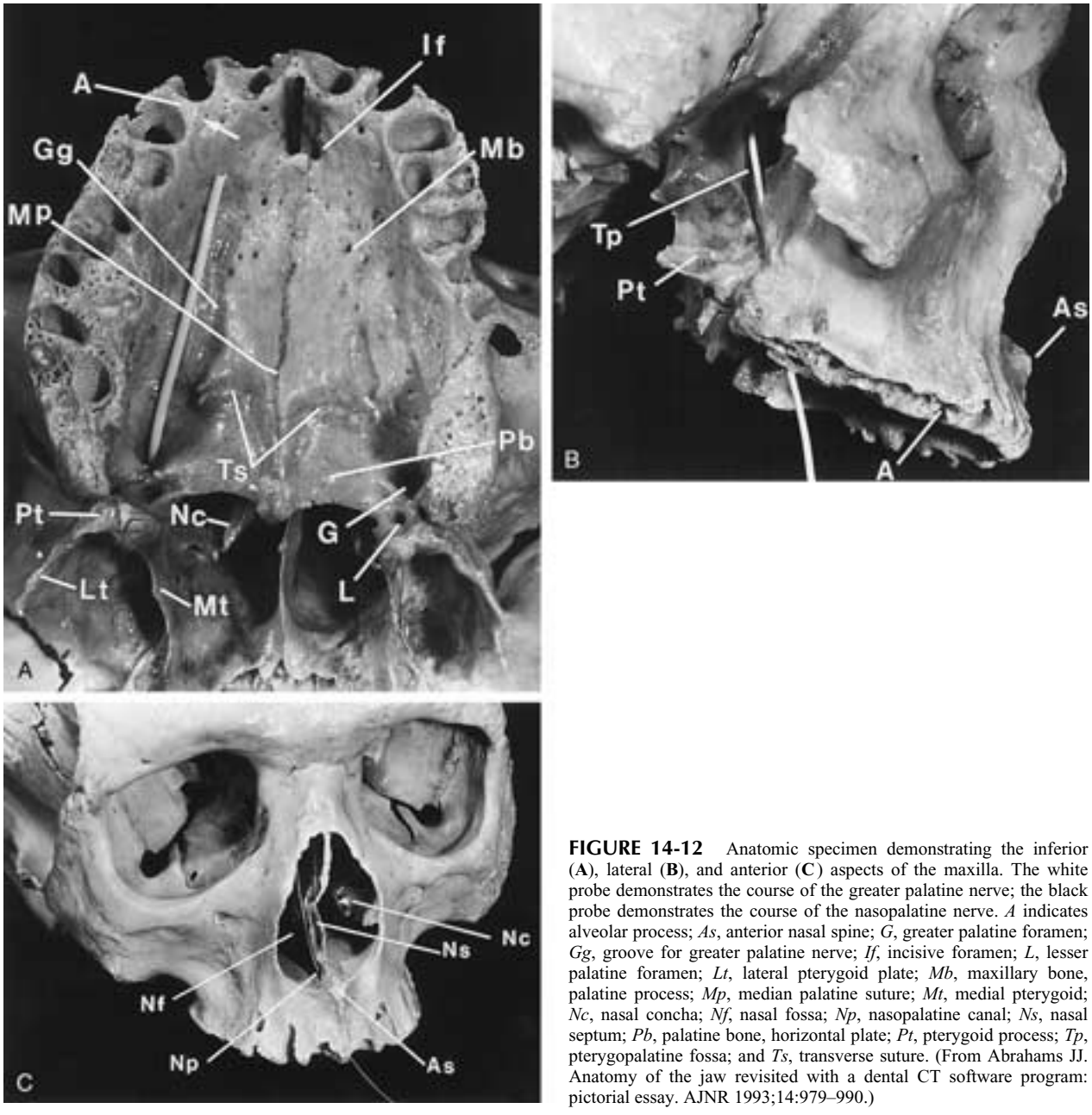

FIGURE 14-12 Anatomic specimen demonstrating the inferior (**A**), lateral (**B**), and anterior (**C**) aspects of the maxilla. The white probe demonstrates the course of the greater palatine nerve; the black probe demonstrates the course of the nasopalatine nerve. *A* indicates alveolar process; *As*, anterior nasal spine; *G*, greater palatine foramen; *Gg*, groove for greater palatine nerve; *If*, incisive foramen; *L*, lesser palatine foramen; *Lt*, lateral pterygoid plate; *Mb*, maxillary bone, palatine process; *Mp*, median palatine suture; *Mt*, medial pterygoid; *Nc*, nasal concha; *Nf*, nasal fossa; *Np*, nasopalatine canal; *Ns*, nasal septum; *Pb*, palatine bone, horizontal plate; *Pt*, pterygoid process; *Tp*, pterygopalatine fossa; and *Ts*, transverse suture. (From Abrahams JJ. Anatomy of the jaw revisited with a dental CT software program: pictorial essay. AJNR 1993;14:979–990.)

VIEW IMAGE

Copyright © 2003, Mosby, Inc. All rights reserved.

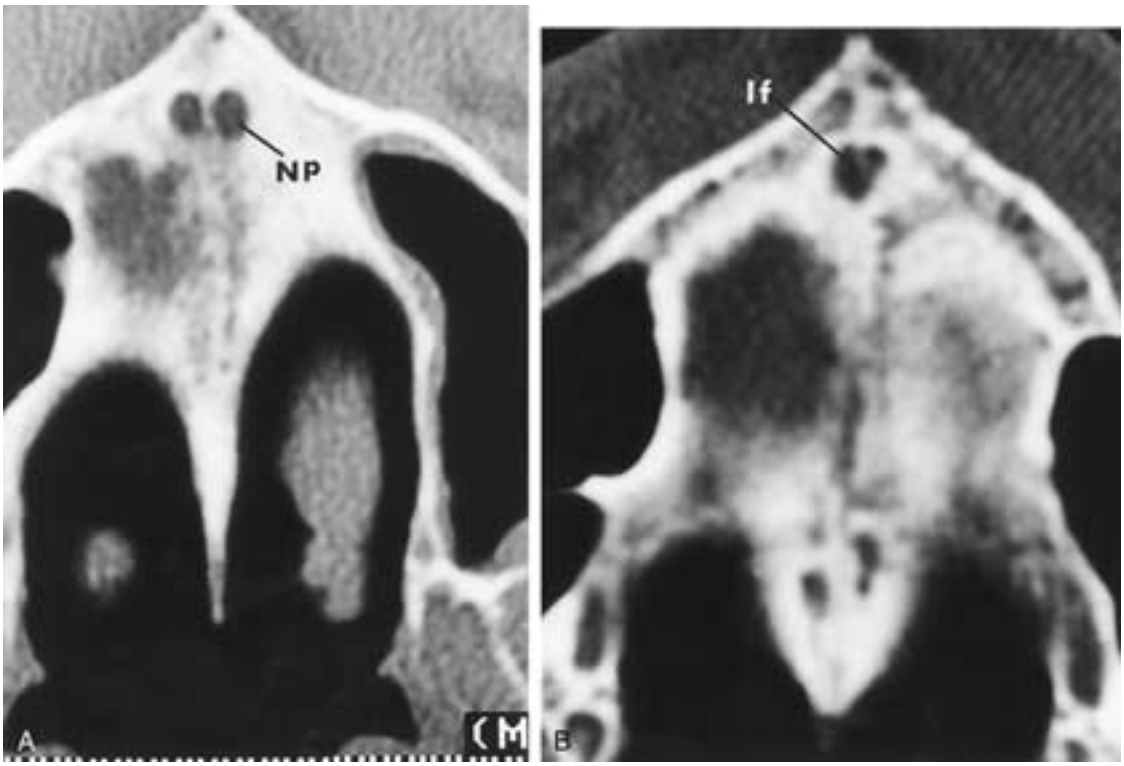

VIEW IMAGE

FIGURE 14-13 Axial views of the nasopalatine canal and the incisive foramen. **A**, The more superior axial image demonstrates the two nasopalatine canals (*Np*). **B**, The inferior slice demonstrates their common opening, the incisive foramen (*If*). (From Abrahams JJ. Anatomy of the jaw revisited with a dental CT software program: pictorial essay. AJNR 1993;14:979–990.)

panoramic, and cross-sectional CT images in Figures 14-13 and 14-14.[17]

Anatomic Specimen

The hard palate is composed of several bones delineated by sutures. The transverse suture (coronally oriented Ts in Fig. 14-12A) separates the horizontal plate of the palatine bone (Pb in Fig. 14-12A) from the palatine process of the maxillary bone (Mb in Fig. 14-12A). The median palatine suture (Mp in Fig. 14-12A), which runs in an anteroposterior (sagittal) direction, divides the palate into right and left halves. The pterygoid process of the sphenoid bone (Pt in Fig. 14-12A) is just posterior to the alveolar process. In younger patients, a coronally oriented suture also separates the premaxilla from the maxilla. This suture extends from the incisive foramen (If in Fig. 14-12A) to the lateral incisor-cuspid region (arrow in Fig. 14-12A).

As in the mandible, the teeth are housed in the alveolar process (A in Fig. 14-12A), a horseshoe-shaped bony process in the periphery of the anterior and lateral aspects of the hard palate. Cephalad to the alveolar process are the maxillary sinuses posteriorly and the nasal fossa anteriorly (Nf in Fig. 14-12C). Within the nasal fossa the nasal conchae (Nc in Fig. 14-12C) and nasal septum (Ns in Fig. 14-12C) are seen. A bony protuberance, the anterior maxillary spine (As in Fig. 14-12B,C), is situated just below the nasal fossae in the midline.

Posterior to the maxillary sinus and between it and the pterygoid process (Pt in Fig. 14-12A,B) lies the pterygopalatine fossa (Tp in Figs. 14-12B and 14-14C). The maxillary branch (V2) of the trigeminal nerve enters the pterygopalatine fossa after exiting the skull base through the foramen rotundum. From here a branch, the pterygopalatine nerve (Fig. 14-8B), travels inferiorly through the pterygopalatine canal to exit the greater (G in Fig. 14-12A) and lesser (L in Fig. 14-12B) palatine foramina as the greater and lesser palatine nerves. In Figure 14-12A, a white probe, representing the greater palatine nerve, is seen exiting the greater palatine foramen. After exiting, this nerve changes from a craniocaudal direction to run anteromedially (and horizontally) in a groove (Gg in Fig. 14-12A) in the hard palate. As it travels in the groove, sensory fibers are given off to supply the posterior two-thirds of the hard palate and teeth. The pterygopalatine nerve, represented by the other end of the white probe in Figure 14-12B, can be traced back into the pterygopalatine fossa (Tp in Fig. 14-12B).

Another branch of the pterygopalatine nerve, the superior posterior nasal nerve (Fig. 14-8B,C), enters the posterior nasal cavity through the sphenopalatine foramen. From here it gives off the nasopalatine nerve, a medial branch that runs anteroinferiorly along the nasal septum to enter the nasopalatine canal and incisive foramen (Figs. 14-8C and 14-12C). The incisive foramen is readily seen as a small, round opening in the hard palate just posterior to the central incisors (If in Fig. 14-12A). Sensory fibers supply the anterior hard palate and, along with the anterior superior alveolar nerve (a branch of the infraorbital nerve), supply the

Copyright © 2003, Mosby, Inc. All rights reserved.

central teeth. The terminal portions of the nasopalatine nerve anastomose with the terminal portion of the greater palatine nerve. In Fig. 14-12A,C, the black probe represents the course of the nasopalatine nerve. Note how the black probe enters the incisive foramen (If in Fig. 14-12A), travels through the nasopalatine canal (Np in Fig. 14-12C), and then along the nasal septum (Ns in Fig. 14-12C) to merge with the superior posterior nasal nerve (Fig. 14-8C). The right and left nasopalatine canals are situated in the anteroinferior nasal fossa on either side of the nasal septum.

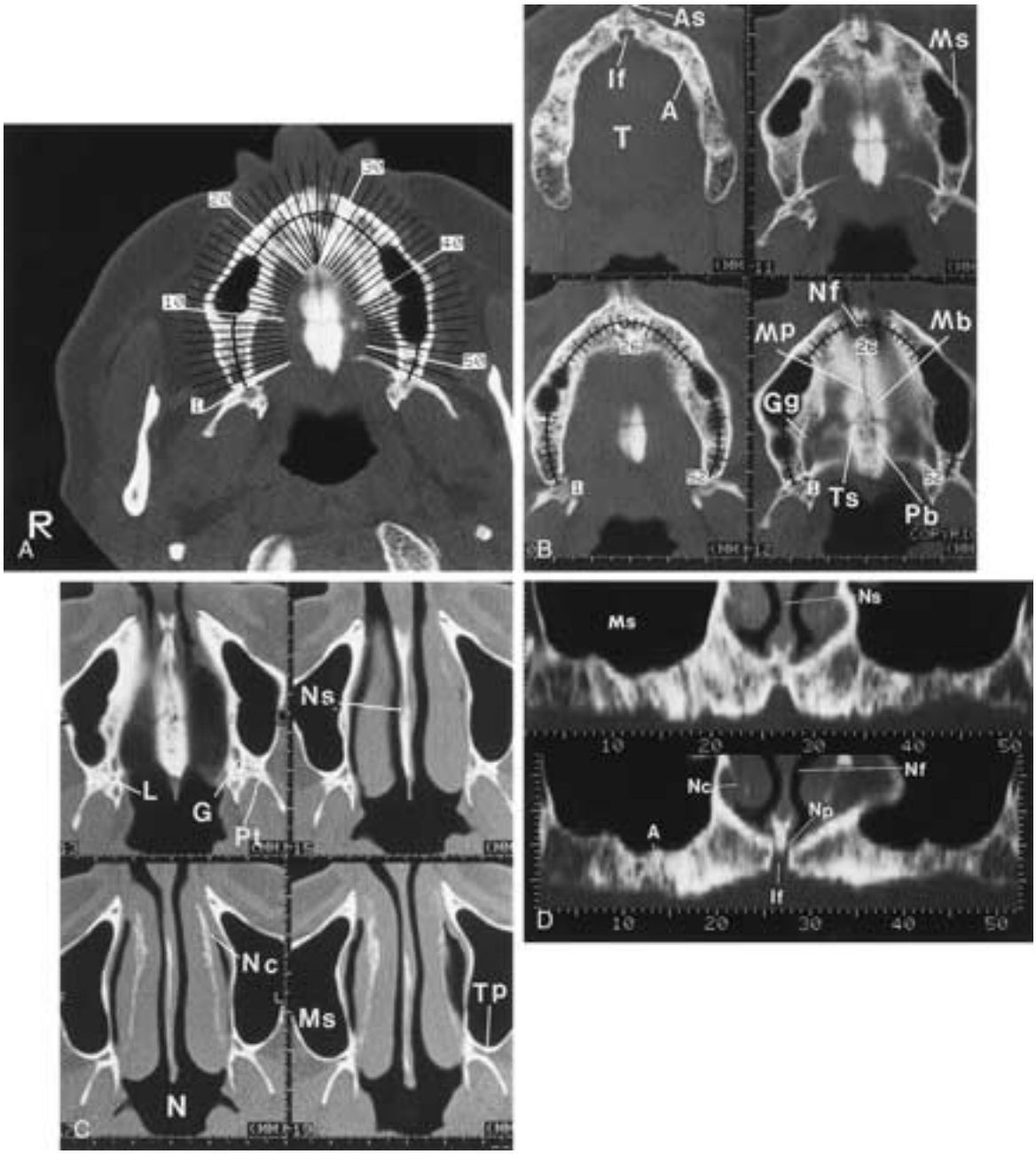

VIEW IMAGE

FIGURE 14-14 CT (DentaScan) image of maxilla. The anatomy identified on the maxillary anatomic specimen is now identified on these CT images. **A**, Axial image with superimposed curve. The curve defines the plane and location in which the panoramic images seen in **D** are reformatted. Numbered lines drawn perpendicular to this curve define the plane and location in which the cross-sectional images viewed in **E** and **F** are reformatted. **B,** Axial views through the alveolar ridge and hard palate. *A* indicates alveolar process; *As*, inferior nasal spine; *Gg*, groove for greater palatine nerve; *If*, incisive foramen; *Mb*, maxillary bone—palatine process; *Mp*, median palatine suture; *Ms*, maxillary sinus; *Nf*, nasal fossa; *Pb*, palatine bone—horizontal plate; *Ts*, transverse suture; and *T*, tongue. **C**, Axial views through the maxillary sinuses and the pterygopalatine fossa. *G* indicates greater palatine foramen; *L*, lesser palatine foramen; *Ms*, maxillary sinus; *Nc*, nasal concha; *Ns*, nasal septum; *Pt*, pterygoid process; and *Tp*, pterygopalatine fossa. **D**, Panoramic views. *A* indicates alveolar process; *If*, incisive foramen; *Ms*, maxillary sinus; *Nc*, nasal concha; *Nf*, nasal fossa; *Np*, nasopalatine canal; and *Ns*, nasal septum.

Copyright © 2003, Mosby, Inc. All rights reserved.

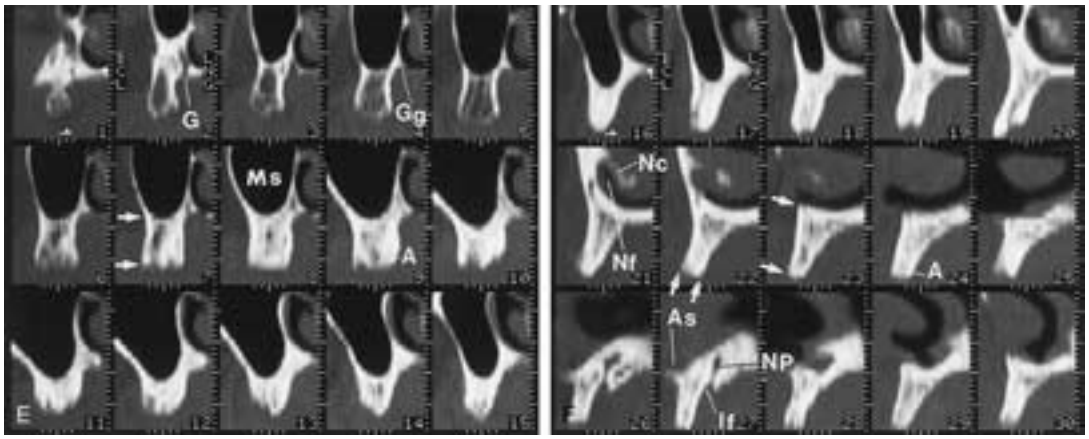

VIEW IMAGE

FIGURE 14-14 *Continued.* **E** and **F**, Cross-sectional views. Images 1 through 15 (**E**) are through the posterior right maxilla (see perpendicular lines 1 through 15 in **A**); images 16 through 30 (**F**) are more anterior on the right and extend to the midline (see perpendicular lines 16 through 30 in **A**). The arrows in image 7 (**E**) indicate how the height of the distal alveolar process is measured from the floor of the maxillary sinus to the top of the alveolar process and the mesial alveolar process (**F** in image 23) is measured from the floor of the nasal fossa to the top of the alveolar process (*arrows* in image 23). The arrows in image 22 (**F**) indicate how the width of the alveolar process is measured. *A* indicates alveolar process; *As*, anterior maxillary spine; *G*, greater palatine foramen; *Gg*, groove for greater palatine nerve; *If*, incisive foramen; *Ms*, maxillary sinus; *Nc*, nasal concha; *Nf*, nasal fossa; and *Np*, nasopalatine canal. (From Abrahams JJ. Anatomy of the jaw revisited with a dental CT software program: pictorial essay. AJNR 1993;14:979–990.)

CT Images

Axial View

The more caudal axial images in Figure 14-14B demonstrate the alveolar process (A), incisive foramen (If), and anterior maxillary spine (As). The teeth, which are normally visualized in the alveolar process at this level, are not seen in this edentulous patient. In the more cranial images the maxillary sinus (Ms) is visible cephalad to the posterior aspect of the alveolar ridge, and the nasal fossa (Nf) is seen cephalad to the anterior aspect of this ridge (Fig. 14-14B). The nasal septum (Ns), nasal concha (Nc), and nasopharynx (N) are visualized in Figure 14-14C. Figure 14-13 illustrates how the right and left nasopalatine canals appear as two separate openings on the more superior cuts but fuse to form a common opening, the incisive foramen, on the inferior images. This is also readily seen on the panoramic view (Fig. 14-14D).

The sutures are identified at the level of the hard palate (Fig. 14-14B). The maxillary bone (Mb) is separated from the palatine bone (Pb) by the transverse suture (Ts). The median palatine suture (MP) separates the right and left halves of the palatine bones. Also seen at the level of the hard palate is the groove for the greater palatine nerve (Gg). Just cephalad to the hard palate (Fig. 14-14C) the greater (G) and lesser (L) palatine foramina are seen.

If the greater palatine foramen is followed cephalad, it merges with the pterygopalatine fossa (Tp) (Fig. 14-14C), which is situated between the posterior wall of the maxillary sinus and the pterygoid process.

Panoramic View

The panoramic view in Figure 14-14D illustrates the position of the maxillary sinuses (Ms) and nasal fossae (Nf) just cephalad to the alveolar process (A). On either side of the nasal septum (Ns), the right and left nasal palatine canals (Np) are clearly visualized merging with the more inferior incisive foramen (If).

Cross-Sectional View

In Figure 14-14E,F, images 1 through 25 correspond to the right half of the maxilla, images 26 and 27 represent the midline with the incisive foramen, and images 28 through 30 represent the more medial aspect of the left maxilla. This may be more readily appreciated by looking at perpendicular lines 1 through 30, which are superimposed on the axial image in Fig. 14-14A. In the right posterior maxilla (Fig. 14-14E), the greater palatine foramen is visualized (G in image 2). As one moves toward the midline, the most proximal portion of the groove (Gg) for the greater palatine nerve can be seen in images 3 through 5. The maxillary sinuses (Ms) are visualized cephalad to the alveolar process on the more posterior images, and the nasal fossae (Nf) are visualized cephalad to the alveolar process on the more anterior images (21 to 23 in Fig. 14-14F). In the midline (images 26 and 27, Fig. 14-14F), the nasopalatine canal (Np), incisive foramen (If), and anterior maxillary spine (As) are seen.

REFERENCES

1. Sperber GH. Craniofacial Embryology 4th ed. London: Wright, 1989.
2. Melfi RC. Permar's Oral Embryology and Microscopic Anatomy: a textbook. Philadelphia: Lea & Febiger, 1994.
3. Carlson BM. Human Embryology and Developmental Biology. St. Louis: Mosby, 1994.
4. Moore KL, Persaud TVN. The Developing Human. Philadelphia: WB Saunders, 1988.
5. Farman AG, Nortjé CJ, Wood RE. Oral and Maxillofacial Diagnostic Imaging. St. Louis: CV Mosby, 1993.
6. Sicher H. The viscera of the head and neck. In: Sicher H. Oral Anatomy. 4th ed. St. Louis: CV Mosby, 1965;191–324.

Copyright © 2003, Mosby, Inc. All rights reserved.

7. Wishan M, Bahat O, Krane M. Computed tomography as an adjunct in dental implant surgery. Int J Periodont Restor Dentistry 1988; 8:30–47.
8. Ennis LM, Harrison MB Jr, Phillips JE. Normal anatomical landmarks of the teeth and jaws as seen in the roentgenogram. In: Ennis LM. Dental Roentgenology. 6th ed. Philadelphia: Lea & Febiger, 1967;334–407.
9. Gray H. Osteology. In: Gray H. Anatomy of the Human Body. 28th ed. Philadelphia: Lea & Febiger, 1969;107–293.
10. Gray H. The peripheral nervous system. In: Gray H. Anatomy of the Human Body. 28th ed. Philadelphia: Lea & Febiger, 1969;907–1042.
11. Gray H. The digestive system. In: Gray H. Anatomy of the Human Body. 28th ed. Philadelphia: Lea & Febiger, 1969;1161–1263.
12. Gray H. Arteries of the head and neck. In: Gray H. Anatomy of the Human Body. 28th ed. Philadelphia: Lea & Febiger, 1969;1161–1263.
13. Meschan I. The skull. In: Meschan I. An Atlas of Anatomy Basic to Radiology. Philadelphia: WB Saunders, 1975;209–287.
14. Sicher H. The skull. In: Sicher H. Oral Anatomy. 4th ed. St. Louis: CV Mosby, 1965;23–140.
15. Sicher H. The nerves of the head and neck. In: Sicher H. Oral Anatomy. 4th ed. St. Louis: CV Mosby, 1965;364–398.
16. Abrahams JJ. Anatomy of the jaw revisited with a dental CT software program: pictorial essay. AJNR 1993;14:979–990.
17. Abrahams JJ. The role of diagnostic imaging in dental implantology. Radiol Clin North Am 1993;31(1):163–180.

Copyright © 2003, Mosby, Inc. All rights reserved.

15

Dental CT Reformatting Programs and Dental Imaging

James J. Abrahams, Michael W. Hayt, and Reuben Rock

DENTAL CT PROGRAMS
- Scan Parameters
- Running the Dental Program
- Interpretation of Dental CT Program Images and Measurements
- Identifying the Mandibular Canal
- Dictated Report

ORTHOPANTOMOGRAPHIC (PANOREX) RADIOGRAPHY

INTRAORAL RADIOGRAPHY
- Periapical Radiographs
- Bitewing Radiographs
- Occlusal Radiographs

DENTAL PATHOLOGY SEEN ON RADIOGRAPHS
- Periodontal Disease
- Dental Caries

Edentulism is present in almost half of the population that is between 45 and 74 years of age.[1] Traditionally, edentulism has been treated with removable dentures; however, not all patients are candidates for dentures, and many have continued difficulty with speech, oral function, and reduced self-esteem. In response to these problems, dentists developed nonremovable bridges that are attached to oral implants, metal posts surgically embedded in the jaw (Fig. 15-1). During the past decade, it has been determined that CT, with a dental reformatting program, is the method of choice for the preoperative assessment of these patients, and as a result of this work, new dialogues and interactions have been created between the radiologist and the dentist and oral surgeon. This, in turn, has brought new territories and unfamiliar diseases to the radiologist's attention. Radiologists now evaluate the dental aspects of the oral cavity, including implants, periodontal disease, odontogenic tumors, and other lesions of the jaw.[2–8] The goal of this chapter is to present a comprehensive discussion of dental imaging, including dental CT reformatting programs, and orthopantomographic and intraoral films.

DENTAL CT PROGRAMS

Dental CT programs use thin, 1-mm axial CT images of the maxilla and mandible to reformat a series of multiple cross-sectional and panoramic images of the jaw. The orientation of the cross-sectional images, which can be confusing, is illustrated in Figure 15-2. The cross-sectional and panoramic images are illustrated in Figure 15-1. After the patient is scanned and the axial images have been acquired, the reformatting program is run to produce the panoramic and cross-sectional views described below.

Scan Parameters

The thin axial images are obtained in the following fashion. First, the patient is placed supine in the gantry, using a head holder, chin strap, and sponges on either side of the head to prevent motion. The patient is then instructed to remain motionless. A lateral digital scout view is first obtained to define the upper and lower limits of the study and to determine if the scan plane is parallel to the alveolar ridge. Because the DentaScan program does not permit angulation of the gantry, if the scan plane is not correctly positioned the patient should be repositioned and a repeat lateral digital scout scan performed. Once the scan plane is correct, 1-mm contiguous scans are obtained using a bone algorithm, dynamic mode, 15-cm field of view, 512 × 512 matrix, 140 kV and 70 mA. If both the mandible and maxilla are being studied, a separate run should be performed for

Copyright © 2003, Mosby, Inc. All rights reserved.

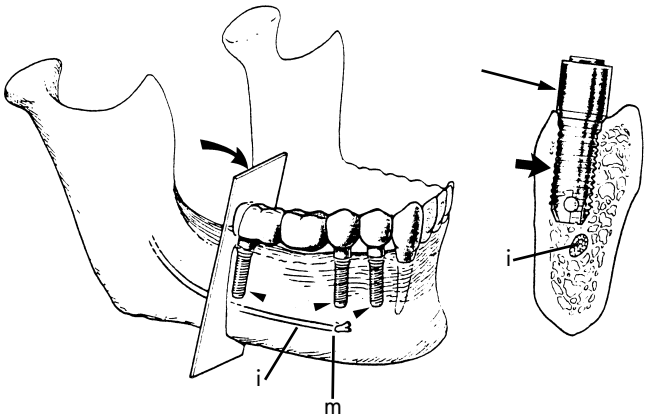

VIEW IMAGE

FIGURE 15-1 View of the mandible illustrating the plane of orientation of the cross-sectional DentaScan images. The top of the plane (*curved arrow*) corresponds to one of the numbered perpendicular lines on the axial image in Figure 15-2A. Note how the height and width of the alveolar process and the location of the mandibular canal can be readily determined on the cross-sectional image. Three root form implants are seen (*arrowheads*) supporting a four-tooth prosthesis. The abutment (*thin arrow*) attached to the fixture (*broad arrow*) raises it above the surface of the bone and gingiva and into the oral cavity. Inferior alveolar canal (*i*), mental foramen (*m*). (From Langer B, Sullivan D. Osseointegration: its impact on the relationship of periodontics and restorative dentistry. Part 1. Int J Periodont Res 1989;9:86.)

each because the scan angle of the mandible is slightly different than that of the maxilla.

Running the Dental Program

Once the axial images are acquired, they are processed with the dental CT reformatting program. Programs may vary slightly from manufacturer to manufacturer; however, the following guidelines generally apply. An axial image that nicely shows the curve of the mandible or maxilla at the level of the roots of the teeth is selected by the technologist and a curved line, along the midportion of the alveolus, is superimposed on the axial image (Figs. 15-2A and 15-3A) by depositing the cursor on approximately six different points along the curve of the jaw. The program then automatically connects these points to produce a smooth curve that will be superimposed on the jaw. This curved line defines the plane and location of the reformatted panoramic images (Figs. 15-2C and 15-3D). Several images are then reformatted both buccally and lingually to this curve.

The reformatted cross-sectional images (Figs. 15-2D–F and 15-3E,F) are defined by multiple numbered lines that the program automatically deposits perpendicular to the curved line (Figs. 15-2A and 15-3A). Figure 15-2A shows the plane and orientation of the cross-sectional images and the distance between the numbered perpendicular lines. The distance between the cross-sectional images can be varied. In general, a 2-mm spacing is used. If a stent with radiographic markers is utilized, 1-mm slices may be necessary to visualize the markers. The mandibular canal (neurovascular bundle) is easily visualized on the cross-sectional images, and the width and contour of the jaw can be readily assessed (Fig. 15-2D–F). Streak artifact, which degrades visualization of bone on direct coronal images, does not degrade the reformatted cross-sectional images because the artifact is projected at the level of the crowns of the teeth and not over the bony alveolus (curved arrow in Fig. 15-2E).

When the program is completed, three types of images are displayed: axial, cross-sectional, and panoramic. Typically there are approximately 30 to 50 axial images, 40 to 100 cross-sectional images, and 5 panoramic images. It is important to film these images in a consistent fashion to avoid confusing the referring dentist. Life-size (one to one magnification) cross-sectional and panoramic images are preferred. This can usually be accomplished with most programs by filming four images on a 14 × 17-inch x-ray film. If this cannot be accomplished, the manufacturer of the program should be consulted. A millimeter scale displayed on the films (mm at the bottom of Fig. 15-2D) is used to verify the degree of magnification and to obtain accurate measurements. One can place calipers on the bone image to be measured and transfer this caliper setting to the millimeter scale. Any minification or magnification of the images equally minifies or magnifies the scale and thus does not affect the measurements.

Optimally, filming is done on a laser printer. Most often the axial images are filmed with 12 images per film, while the cross-sectional and panoramic images are filmed with 4 images per film. Each cross-sectional and panoramic image actually contains multiple images (see Fig. 15-2). The images are typically photographed at a width (window) of 3000 to 4000 and a level (center) of 300 to 500 (Figs. 15-2 and 15-3).

Interpretation of Dental CT Program Images and Measurements

An understanding of the anatomy and pathology of the jaw is necessary to appropriately interpret the images displayed by the dental CT programs. It should first be noted that each CT view can be related to the others by a series of scale marks that appear on the films. The marks that run along the side of the cross-sectional and panoramic images (Fig. 15-2C,D) correspond to the direct axial slices that were used to reformat the images. For example, in Figure 15-2, 42 axial images were obtained to reformat the images; thus there are 42 scale marks along the side of the reformatted cross-sectional (Fig. 15-2D) and panoramic (Fig. 15-2C) images. The marks along the bottom of the panoramic images (Fig. 15-2C) correspond to the numbered cross-sectional images. The numbered scale lines correspond to the numbered lines drawn perpendicular to the curve superimposed on the axial image in Figure 15-2A. They therefore also correspond to the numbered cross-sectional images in Figure 15-2D–F. To illustrate how one view can be related to another, note how the right mental foramen (M) in Figure 15-2E, which is seen on cross-sectional image 20 (lower right) at the level of the fourteenth scale mark on the side of the image, is also seen in Figure 15-2B on axial image 14 at the twentieth perpendicular line. The same process can be applied to the panoramic view.

When the scan is performed as part of the preoperative workup of a dental implant patient, the status of the dentition and the proposed implant sites must be established. It should

Copyright © 2003, Mosby, Inc. All rights reserved.

be stated whether the patient is completely or partially edentulous and, if partially edentulous, where the teeth are absent. In the partially edentulous patient, it is presumed that the implants will be placed in the edentulous segments; thus measurements are obtained in these regions. The measurements are obtained from the cross-sectional images at about 10-mm intervals. If the cross-sectional images are 2 mm apart, then measurements are made on every fifth cross-sectional image. If the cross-sectional images are 1 mm apart, measurements are provided for every tenth image. The

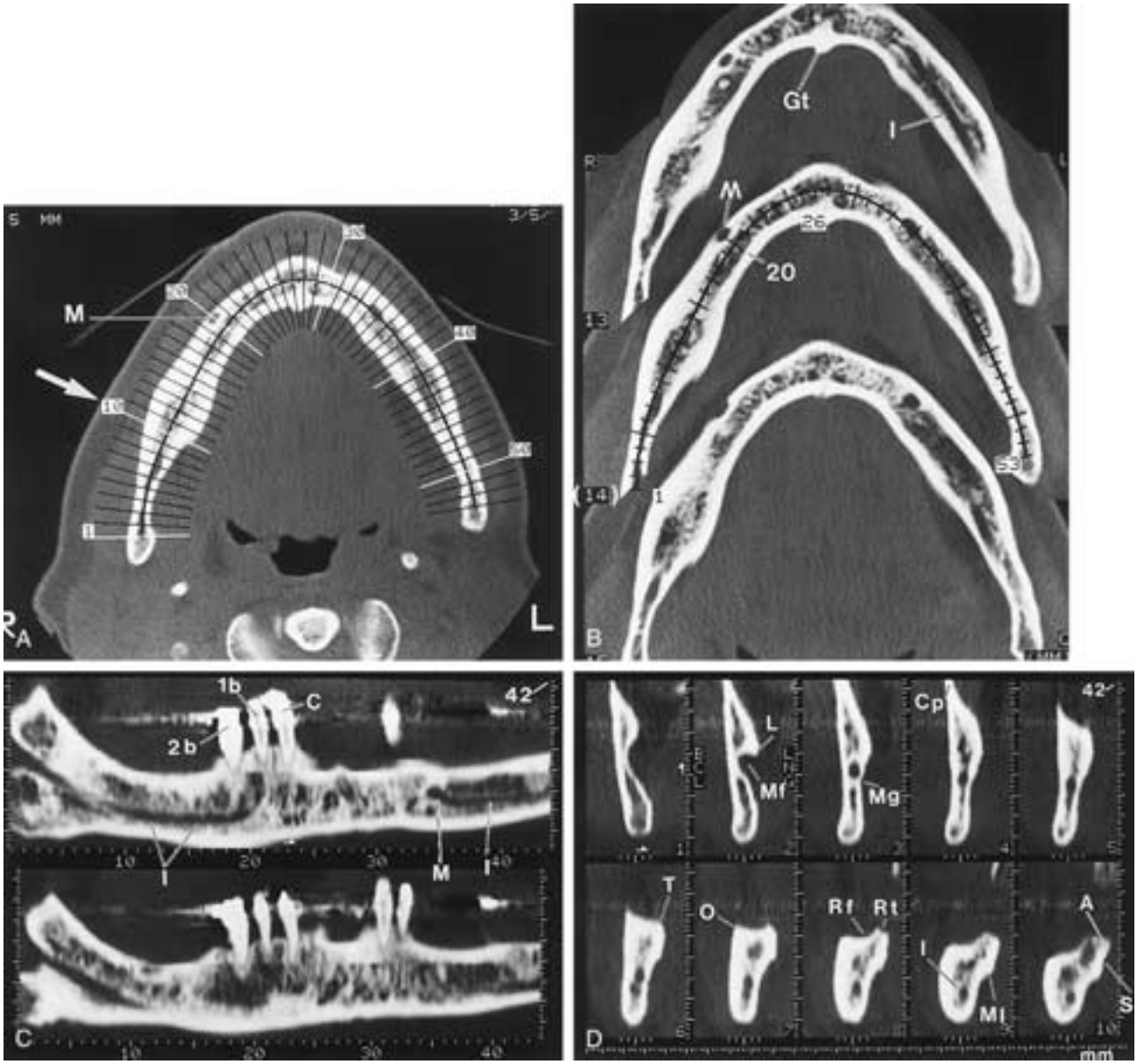

FIGURE 15-2 CT (DentaScan) scan of the mandible. The anatomy identified on the mandibular anatomic specimen in Figure 14-6 is now identified on these CT images. **A**, Axial image of mandible with a superimposed curve. The curve defines the plane and location in which the panoramic images in **C** are reformatted. Numbered lines drawn perpendicular to this curve (*arrow*) define the plane and location in which the cross-sectional images viewed in **D** through **F** are reformatted. Mental foramen (*M*). **B**, Axial images illustrating the inferior alveolar canal (*I*), the mental foramen (*M*), and the genial tubercle (*Gt*). The numbers along the left side of the figure refer to the particular number of the axial image. Note that the mental foramen, which is seen on axial image number 14 at the twentieth perpendicular line, is also seen in **E** on cross-sectional image 20 (lower right) at the level of the fourteenth tick mark on the side of the image. The tick marks and numbers allow images to be correlated with one another. **C**, Panoramic views. The numbered tick marks along the bottom of the images correspond to the numbered perpendicular lines displayed on the axial image in **A**. The tick marks along the side of the image correspond to the axial images that were used to reformat these images. Note that there were 42 axial images acquired and thus 42 tick marks along the side of this image. Inferior alveolar canal (*I*), mental foramen (*M*), second bicuspid (*2b*), first bicuspid (*1b*), and cuspid (*C*). **D** through **F**, Cross-sectional views. Images 1 through 10 (**D**) are through the posterior right mandible (see perpendicular lines 1 through 10 in **A**).

Illustration continued on following page

VIEW IMAGE

Copyright © 2003, Mosby, Inc. All rights reserved.

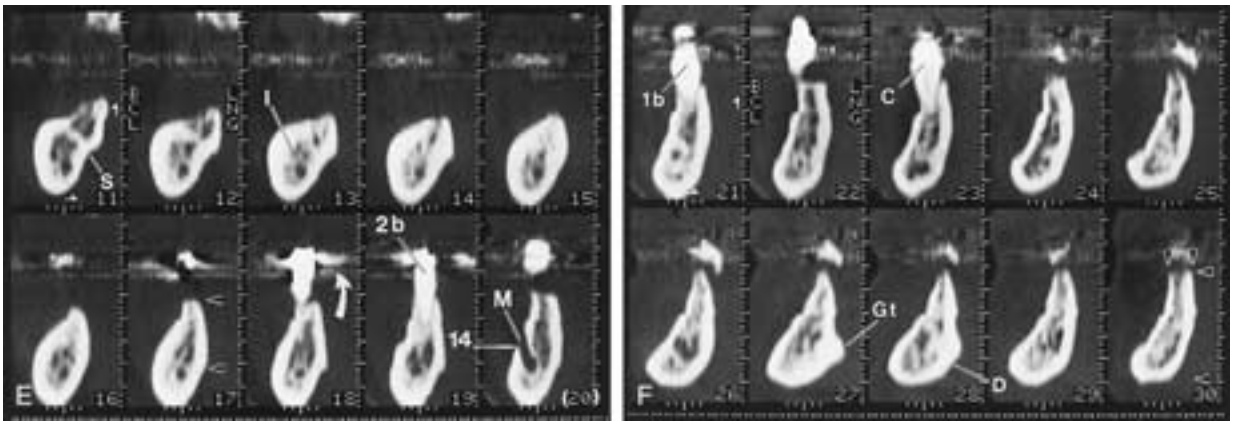

VIEW IMAGE

FIGURE 15-2 *Continued.* Images 11 through 20 (**E**) are more anterior. Images 21 through 30 (**F**) extend to the midline. The images of the left half of the mandible are not shown. Arrowheads in image 17 (**E**) indicate that the height of the mandible distal to the mental foramen is measured from the top of the alveolar process to the top of the mandibular canal, and mesial to the foramen it is measured from the top of the alveolar process to the bottom of the mandible (*arrowheads* in **F**, image 30). Measurement of the width is also demonstrated in image 30 (**F**). *mm* at the bottom of **D** indicates the millimeter scale. Note how streak artifact from the dental restoration (*curved arrow* in **E**) does not degrade visualization of the bone. *A* indicates alveolar process; *C,* cuspid; *Cp,* coronoid process; *D,* digastric fossa; *Gt,* genial tubercle; *I,* inferior alveolar canal; *M,* mental foramen; *Mf,* mandibular foramen; *Mg,* mylohyoid groove; *Ml,* mylohyoid line; *O,* oblique line; *Rf,* retromolar fossa; *Rt,* retromolar triangle; *S,* submandibular fossa; *S1,* sublingual fossa; *T,* temporal crest; *1b,* first bicuspid; and *2b,* second bicuspid. (From Abrahams JJ. Anatomy of the jaw revisited with a dental CT software program: pictorial essay. AJNR 1993;14:979–990.)

height and width of the alveolar process are measured as described in the following paragraph.

In the mandible, the height in the region distal (posterior) to the mental foramen is measured from the top of the alveolar process to the top to the mandibular canal (Fig. 15-2E, arrowheads in image 17). Methods of locating the mandibular canal, if it is not initially visualized on the cross-sectional images, are discussed later. In the region mesial (anterior) to the mental foramen, the full height of the mandible is obtained because the mandibular canal ends at the mental foramen and thus it is not present mesial to the foramen. Measurements in this area are provided from the top of the alveolar ridge to the bottom of the mandible (Fig. 15-2F, arrowheads in image 30). The width is measured near the top of the alveolar process (Fig. 15-2F, arrowheads in image 30). Occasionally, if the alveolar process comes to a point secondary to atrophy, it may be difficult to obtain a measurement. In this situation the surgeon may choose to remove the top pointed portion of the ridge (alveoloplasty), providing a broad base for an implant. This obviously affects the height of the alveolar ridge, and it is best to let the surgeon estimate how much of the ridge will be removed. Often under these circumstances, one simply states that the ridge is pointed, and a measurement for the width is not provided.

In the maxilla, the height in the distal (posterior) aspect is measured from the top (inferior surface) of the alveolar process to the floor of the maxillary sinus (Fig. 15-3E, arrows in image 7). More mesially (anteriorly), the height is usually not limited by the maxillary sinuses and is measured from the alveolar ridge to the nasal fossa floor (Fig. 15-3F, arrows in image 23). The width is measured in the same manner as that described for the mandible (Fig. 15-3F, arrows in image 22). In the completely edentulous patient, it is more desirable to place the implants centrally because the height of the alveolar process is not limited by the more distal mandibular canal or the maxillary sinuses.

Identifying the Mandibular Canal

It is extremely important to identify the mandibular canal on cross-sectional images and to provide the measurement from the top of the alveolar ridge to the top of this canal. If the canal is not properly identified, its injury during implant surgery can be quite debilitating for the patient, resulting in permanent paresthesia and hypesthesia of the face. Typically the canal is readily seen on cross-sectional images. However, there are times when portions of the canal or even the entire canal may be hard to visualize on the cross-sectional images. In this situation the following methods may be helpful in locating the canal.

The first method involves the cortical niche sign, which refers to an indentation along the inner or medullary margin on the lingual cortex of the mandible. This niche is created by the mandibular nerve as it traverses the mandible (Fig. 15-4). However, this niche can be quite subtle, unlike that shown in Figure 15-4, and it is not identified in all patients. When present, it is a good way to identify the canal. Care should be taken not to confuse other cortical irregularities with the cortical niche sign. The cortical niche is a continuous defect seen on multiple cross-sectional images. Other cortical irregularities are randomly situated and are not seen consecutively on multiple images. When the canal is identified with the cortical niche sign, its location should be confirmed with the other methods.

The next method, referred to as triangulation, utilizes the scale marks on the films to relate an anatomic structure well seen on one view to its location on another view. With this method, the panoramic and axial views can be

Copyright © 2003, Mosby, Inc. All rights reserved.

utilized to identify the canal on the cross-sectional views. For example, in Figure 15-5A, it is difficult to see the canal on the cross-sectional images, but the canal is readily seen in the panoramic view (Fig. 15-5B). The information from the panoramic view can be used to triangulate the location of the canal on the cross-sectional image, as shown in Figure 15-5.

To locate the canal on cross-sectional image 14 (Fig. 15-5A), first refer to the fourteenth scale mark along the bottom of the panoramic view (Fig. 15-5B). A vertical line from this point is then drawn up to the bottom of the canal and extended across in a perpendicular direction toward the scale marks on the left side of the panoramic image. Note

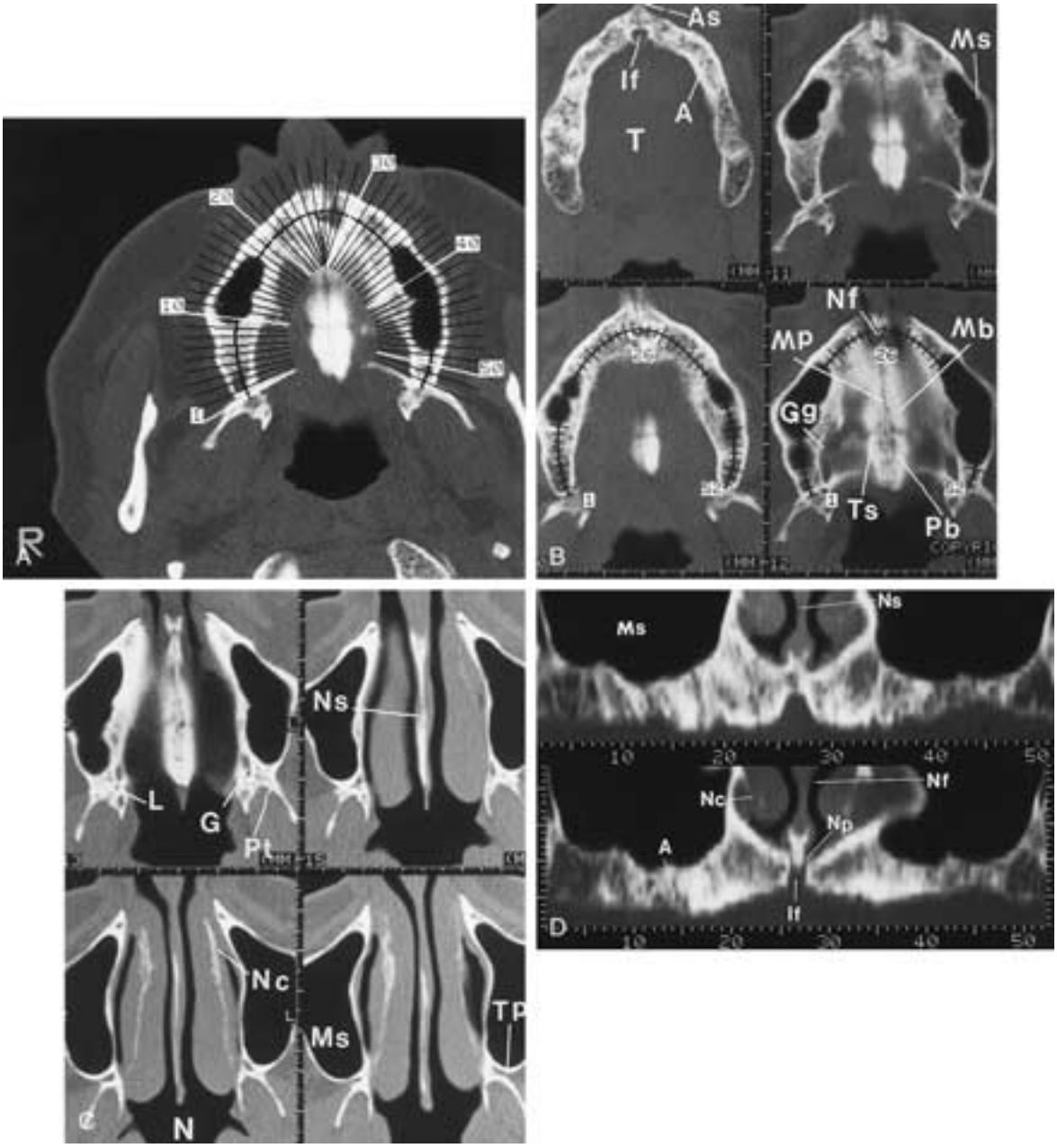

FIGURE 15-3 CT (DentaScan) scan of maxilla. The anatomy identified on the maxillary anatomic specimen in Figure 15-12 is now identified on these CT images. **A**, Axial image with superimposed curve. The curve defines the plane and location in which the panoramic images seen in **D** are reformatted. Numbered lines drawn perpendicular to this curve define the plane and location in which the cross-sectional images viewed in **E** and **F** are reformatted. **B**, Axial views through the alveolar ridge and hard palate. *A* indicates alveolar process; *As,* inferior nasal spine; *Gg,* groove for greater palatine nerve; *If,* incisive foramen; *Mb,* maxillary bone—palatine process; *Mp,* median palatine suture; *Ms,* maxillary sinus; *Nf,* nasal fossa; *Pb,* palatine bone—horizontal plate; *Ts,* transverse suture; and *T,* tongue. **C**, Axial views through the maxillary sinuses and the pterygopalatine fossa. *G* indicates greater palatine foramen; *L,* lesser palatine foramen; *Ms,* maxillary sinus; *Nc,* nasal concha; *Ns,* nasal septum; *Pt,* pterygoid process; and *Tp,* pterygopalatine fossa. **D**, Panoramic views. *A* indicates alveolar process; *If,* incisive foramen; *Ms,* maxillary sinus; *Nc,* nasal concha; *Nf,* nasal fossa; *Np,* nasopalatine canal; and *Ns,* nasal septum.

Illustration continued on following page

VIEW IMAGE

Copyright © 2003, Mosby, Inc. All rights reserved.

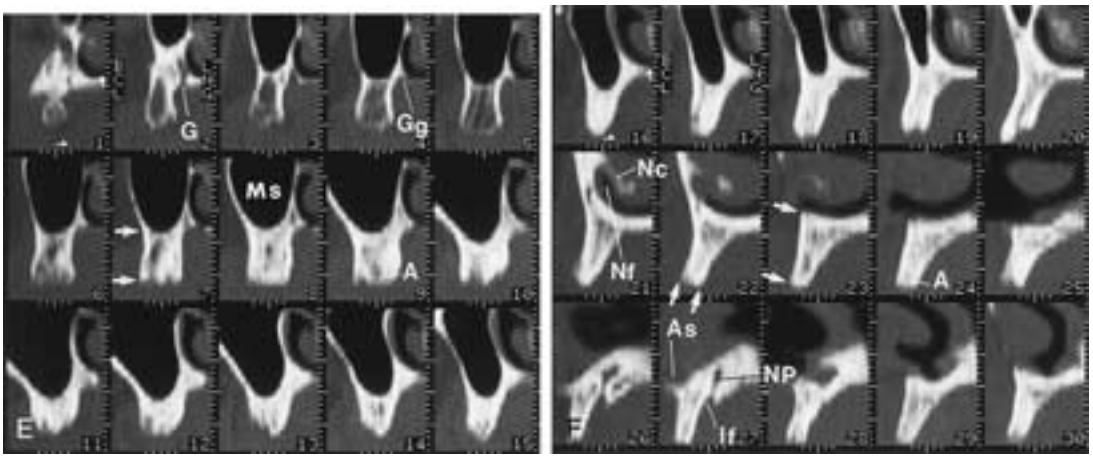

VIEW IMAGE

FIGURE 15-3 *Continued.* **E** and **F**, Cross-sectional views. Images 1 through 15 (**E**) are through the posterior right maxilla (see perpendicular lines 1 through 15 in **A**); images 16 through 30 (**F**) are more anterior on the right and extend to the midline (see perpendicular lines 16 through 30 in **A**). The arrows in image 7 (**E**) indicate how the height of the distal alveolar process is measured from the floor of the maxillary sinus to the top of the alveolar process and the mesial alveolar process (*F* in image 23) is measured from the floor of the nasal fossa to the top of the alveolar process (*arrows* in image 23). The arrows in image 22 (**F**) indicate how the width of the alveolar process is measured. *A* indicates alveolar process; *As,* anterior maxillary spine; *G,* greater palatine foramen; *Gg,* groove for greater palatine nerve; *If,* incisive foramen; *Ms,* maxilllary sinus; *Nc,* nasal concha; *Nf,* nasal fossa; and *Np,* nasopalatine canal. (From Abrahams JJ. Anatomy of the jaw revisited with a dental CT software program: pictorial essay. AJNR 1993;14:979–990.)

that this line intersects the twenty-first scale mark along the left side of the image. The level of the canal in cross-sectional image 14 can then be identified by counting up 21 scale marks along the side of the image (Fig. 15-5A). This same process can also be utilized with the axial images.

Finally, if a canal is identified on some cross-sectional images but not on others, the images on which it is identified can be utilized to estimate the position of the canal on the other images. This can be done because the distance from the bottom of the mandible to the bottom of the canal tends to be relatively constant. The only region where the distance is not constant is immediately adjacent to the mandibular foramen and the mental foramen. It is the distance from the top of the canal to the top of the alveolar process that varies secondary to atrophic changes. With this knowledge, one can extrapolate the location of the canal from the images in which it is visualized. For example, in Figure 15-2E, the distance from the bottom of the canal to the bottom of the mandible in image 11 is 5 mm, and in image 15 it is also 5 mm. Therefore, if the canal was not visualized in image 15, its location could be estimated by utilizing the position of the canal that was visible on image 11. Usually the right and left hemimandibles are symmetric, and the distance from the bottom of the mandible to the bottom of the canal on the right side at a particular point is approximately the same as the distance measured at that same point on the left. Thus, if the canal is identified on the cross-sectional images of the right half of the mandible, but not on the left side, this information can be used to estimate the position of the canal on the left side. It is recommended that one use several of these methods to confirm the location of the canal rather than relying on only one method.

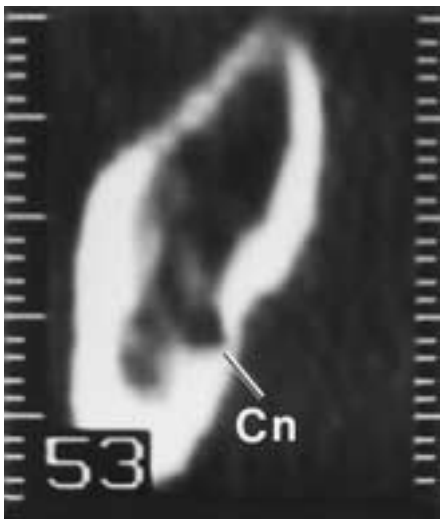

VIEW IMAGE

FIGURE 15-4 Cortical niche sign. This cross-sectional image of the mandible demonstrates an indentation on the lingual cortex of the mandible called the cortical niche sign (*Cn*), which is created by the mandibular nerve as it traverses the mandible. This sign, which is often more subtle than this, can be helpful in identifying the location of the mandibular canal. (From Abrahams JJ. CT assessment of dental implant planning. Oral Maxillofac Surg Clin North Am 1992;4:1–18.)

Dictated Report

A complete and comprehensive report should be provided for the referring dentist or oral surgeon. First, the report usually provides a discussion of the density and general health of the jaw. Also described are the presence of such conditions as maxillary sinus disease, periodontal disease, root canal procedures, extraction sockets, retained roots, atrophy, cysts, osteitis condensans, contour irregularities, surgical changes, and anomalies such as torus palatinus or mandibu-

Copyright © 2003, Mosby, Inc. All rights reserved.

larus. Next, the status of the dentition is discussed. State whether the patient is partially or completely edentulous. If the patient is partially edentulous, state whether the edentulous area is central or distally on the right or left.

If the scan is being performed for dental implants, then measurements of the alveolar ridge are provided of the edentulous regions where the implants are likely to be placed. The measurements are taken from the cross-sectional images at about 10-mm intervals, as described above, and reported in a tabular fashion. The location of the mental foramina and incisive foramen are identified as a reference point and for easier interpretation. For example, the following measurements were obtained from Figure 15-2E,F:

Image 17: Height 14 mm, width 4 mm
Image 20: Left mental foramen
Image 25: Height 26 mm, width 4 mm

If a stent with radiopaque markers is utilized, then the markers on the images are numbered with a wax pencil, measurements are obtained on the cross-sectional images where the markers appear, and the image number is provided in the report. In Figure 15-6, the measurements at the markers are as follows:

Marker 4 (Image 21): Height 13 mm, width 6 mm
Marker 5 (Image 27): Height 12 mm, width 5 mm

If the scan was performed to evaluate a lesion rather than implant placements, the alveolar measurements are not needed. Instead, a description of the lesion is provided. Is there expansion of the jaw or destruction of the cortex? Is the lesion lytic or opaque? Is it diffuse or focal? Are the roots of the teeth displaced or eroded?

Finally, the report should end with a brief impression, describing any pertinent pathology and the degree of atrophy of the alveolar process in the case of dental implants. One should also state that ''all measurements should be verified prior to surgery.'' This statement is included because the surgeon may choose to place the implant at a somewhat different angle than that measured by the radiologist and because, when the report is transcribed, it is possible for numbers to be typed incorrectly, and this may be difficult for the radiologist to notice.

ORTHOPANTOMOGRAPHIC (PANOREX) RADIOGRAPHY

Panoramic radiography is usually performed in a dentist's office. The typical use of this modality is to provide an overview for evaluating the jaws and dentition in a single radiograph (Fig. 15-7). This technique demonstrates the relationship of the teeth to the surrounding structures. It is extremely valuable before exodontia (removal of teeth) and for evaluating mandibular fractures. Since it shows the relationships of the teeth to the other teeth and surrounding structures, it is useful in orthodontic treatment planning and for demonstrating orthodontic movement of teeth. Other situations, such as abnormally erupted teeth, extractions, relationship of tumors to teeth, and so on, can also be assessed (Fig. 15-7).

Panoramic radiography of the jaws helps overcome limitations of conventional intraoral radiography. The radiation dose to the patient is 10 times less than that of the full-mouth intraoral radiography survey. Further, it allows overall coverage of the entire dental arches and associated structures on one radiograph. There can, however, be up to 25% distortion, and measurements may therefore be difficult. This is a relatively fast and painless procedure. It is also very useful when a patient cannot open the mouth due to trismus or trauma. The mandibular ramus, styloid process, temporo-

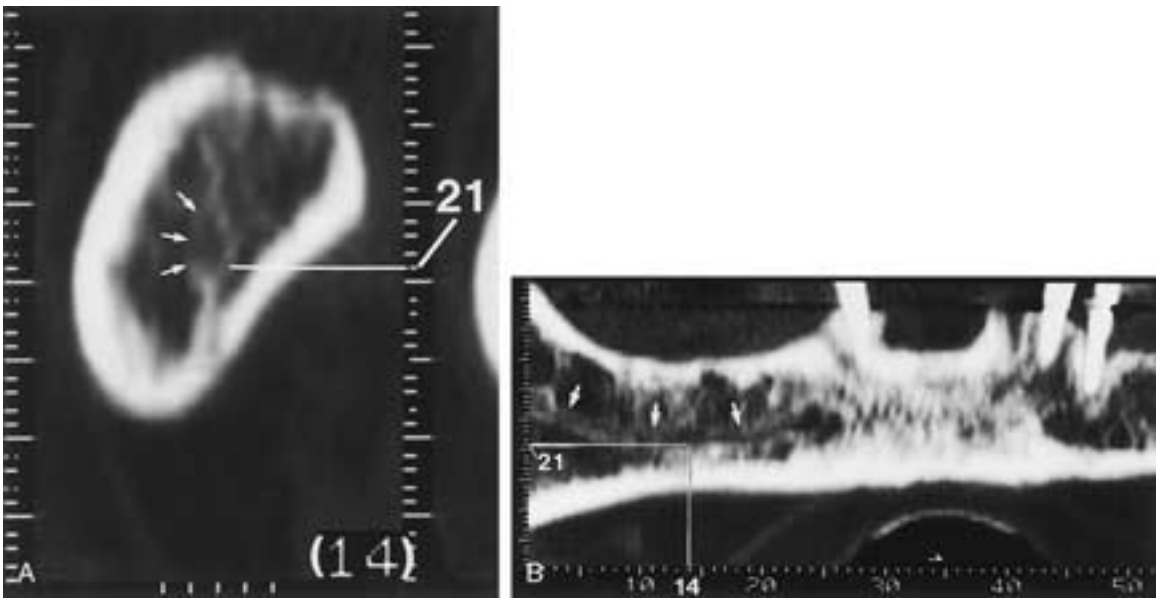

FIGURE 15-5 Triangulation. When the inferior alveolar canal is not initially seen on the cross-sectional images, as in this case (**A**), its location can be determined by triangulating from the panoramic (**B**) or axial image, as described in the section of text on ''Identifying the Mandibular Canal''. The inferior alveolar canal is indicated by arrows. (From Abrahams JJ. CT assessment of dental implant planning. Oral Maxillofac Surg Clin North Am 1992;4:1–18.)

VIEW IMAGE

Copyright © 2003, Mosby, Inc. All rights reserved.

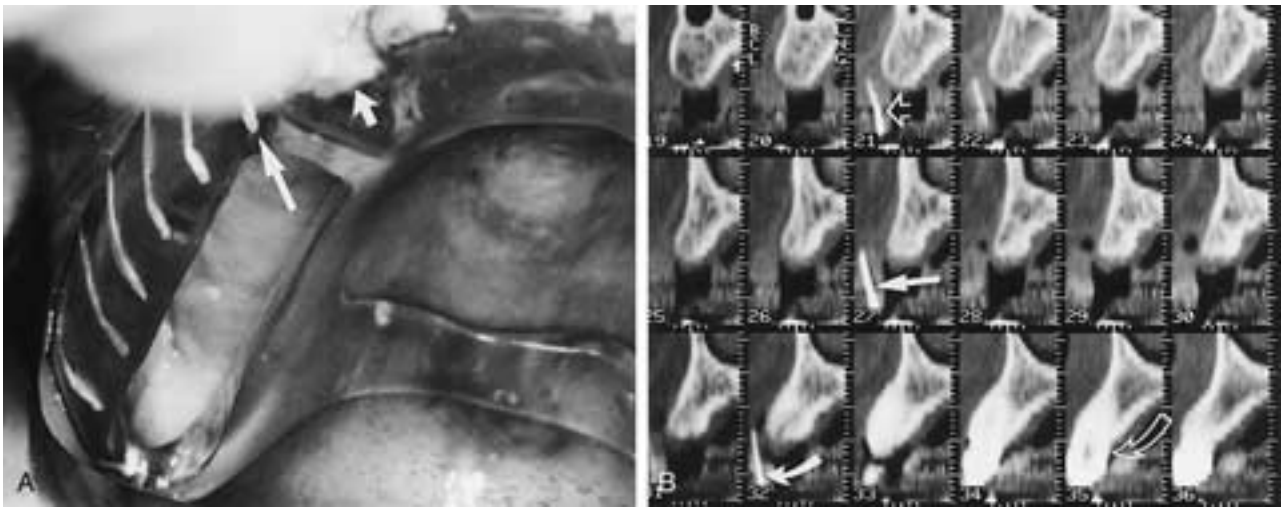

VIEW IMAGE

FIGURE 15-6 Surgical implant procedure. **A**, A stent with six vertical markers has been placed over the alveolar ridge and residual teeth. The sixth marker (*long arrow*) is adjacent to the right canine (*short arrow*) and will be demonstrated on the CT images. This marker appears as a dot on the axial image and as a line on the cross-sectional image. **B**, Cross-sectional views demonstrating markers 4 (*open arrow*), 5 (*straight arrow*), and 6 (*curved arrow*) of the stent. Note that marker number 6 is adjacent to the right canine (*open curved arrow*). By placing the stent on the patient during surgery, the surgeon knows that the bone under marker 6 is as depicted by cross-sectional image 32. (From Abrahams JJ. The role of diagnostic imaging in dental implantology. Radiol Clin North Am 1993;31(1):163–180.)

mandibular joint, superior maxillary sinus, and floor of the mouth structures are visualized. These structures cannot be seen with intraoral radiography. With this technique, some soft-tissue structures attenuate the x-ray beam enough to be visualized and cause artifacts. The panoramic radiograph is limited, when compared with conventional intraoral radiography, by the necessity for careful technique, sensitivity to patient motion, and relatively poor spatial resolution.

Rotational panoramic radiographs are obtained by rotating a slender x-ray beam in a horizontal axis that is positioned extraorally. The principle is very similar to that of conventional x-ray tomography. With this technique, the focal spot of the x-ray tube anode acts as the dimension of the projection. To eliminate scatter and artifact, the x-ray beam is angled beneath the occipital condyles of the skull approximately – 4° to –7°. The patient remains stationary as the x-ray tube and film cassette holder both rotate around the patient's face during the exposure. The film is exposed though a narrow opening in the cassette that is usually flexible. These films are very technique sensitive. If the patient is improperly positioned, certain structures will be out of the focal trough (blurred). Even in properly positioned patients, the midline structures may be flattened and spread out or may be projected as a double image.

The normal anatomic structure seen in panoramic radiography are listed below and shown in Figures 15-7 and 15-8.

1. Mandibular condyles
2. Ramus of the mandible
3. Cervical spine
4. Maxillary sinus
5. Inferior turbinate
6. Inferior alveolar canal
7. Mental foramen
8. Nasal fossae
9. Dentition
10. Sigmoid notch
11. Mandibular coronoid process
12. Developing tooth bud
13. Hyoid bone

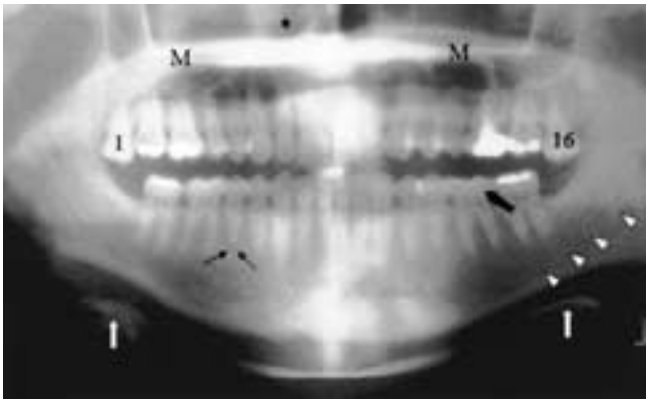

VIEW IMAGE

FIGURE 15-7 Panoramic radiograph of jaws in an adult with extractions of mandibular third molars. This has caused supereruption (occlusal migration due to lack of contact by the opposing tooth) of teeth numbers 1 and 16. Hyoid bone (*white arrow*). Inferior alveolar canal (*arrowheads*). Dentition (mandibular left second molar) (*bold black arrow*). Right mental foramen (*thin black arrow*). Inferior nasal turbinate (*). Maxillary sinus (*M*).

INTRAORAL RADIOGRAPHY

An intraoral radiograph is obtained by placing a film packet in the mouth and projecting the x-ray beam at different angles from a position outside of the mouth toward the teeth. There are three types of intraoral radiographs, which are described as periapical, bitewing, and occlusal.

Copyright © 2003, Mosby, Inc. All rights reserved.

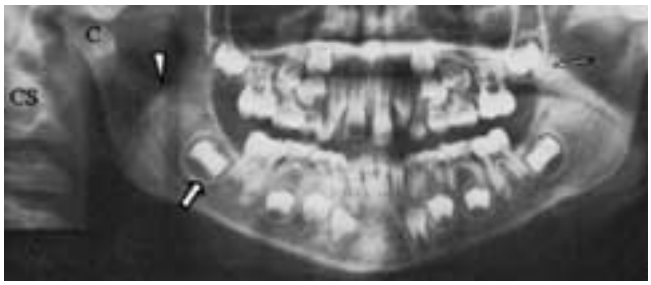

VIEW IMAGE

FIGURE 15-8 Panoramic radiograph of jaws in a child with mixed dentition (both primary and adult). Coronoid process (*thin white arrow*). Sigmoid notch of mandible (*arrowhead*). Mandibular condyle (*C*). Developing tooth bud of the permanent mandibular right first molar (*bold arrow*). Cervical spine (*CS*).

Periapical Radiographs

The word *periapical* comes from *peri,* meaning ''around,'' and *apical,* meaning ''at the apex or end of the tooth root'' (Fig. 15-9). This is the most common type of radiograph obtained in a dentist's office and has great spatial resolution, demonstrating exquisite detail compared with other techniques. Ideally, it is obtained by placing a film holder on the occlusal surface of the teeth and asking the patient to bite down to hold it in place. The film is attached to the end of the film holder within the patient's mouth on the lingual aspect, and an aiming guide is built into the other end of the film holder outside the patient's mouth. The aiming guide allows the dental x-ray tube to be aligned perpendicular to the film, thus preventing distortion. Periapical films allow the dentist to visualize the entire tooth, root, and surrounding structures, and to visualize the relationship of one tooth and its root to another. They allow the dentist to evaluate whether common entities such as caries and periodontal disease exist and, if so, their extent. This radiograph is also obtained during endodontal (root canal) procedures to measure tooth length and to determine whether the endodontal restoration (within the tooth root) is in the proper position. Periapical films have a vertical orientation, while the bitewing films have a horizontal orientation.

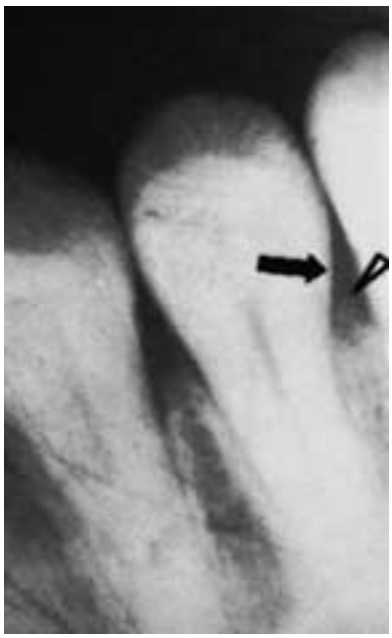

VIEW IMAGE

FIGURE 15-9 Periapical radiograph of mandibular first and second premolars. Cementoenamel junction (where enamel of tooth crown ends and cementum of root begins) (*black arrow*). The arrowhead points to the place where the alveolar crest of bone would normally be. Note that the bone is below this level secondary to loss from periodontal disease.

Bitewing Radiographs

Bitewing radiographs (Fig. 15-10) demonstrate on a single film the position and extent of the crowns and coronal one-third of the interalveolar bone and portion of the roots of the maxillary and mandibular teeth. These radiographs, too, have excellent spatial resolution. A special bitewing holding device is placed on the occlusal surface of the tooth and the patient gently bites down to hold it in place. As with the periapical radiograph, an aiming device is ideally used to maintain a perpendicular relationship between the film and the x-ray beam. These films are commonly obtained to detect interproximal caries (between teeth), iatrogenically malplaced dental restorations, periodontal disease, and calculus (tartar) deposits; to evaluate pulp chamber shape and size; and to evaluate the occlusal relationship of teeth. They are not usually helpful for visualization of the root apices or periapical lesions such as a cysts or abscesses.

Occlusal Radiographs

Occlusal radiographs are images of the incisal edges and occlusal surfaces of the teeth and a cross-section of the dental arches. The hard palate, upper lip, and base of the nose are seen in a maxillary occlusal radiograph. The mandibular occlusal radiograph records the floor of mouth, tongue, and lower lip. This type of radiograph is useful for determining the presence of foreign bodies, alveolar

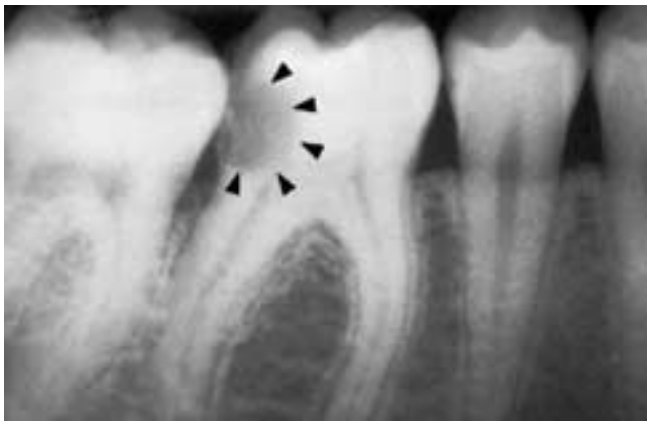

FIGURE 15-10 Bitewing radiograph of the mandibular second molar shows large interproximal carious lesion on the distal surface (*arrowheads*). Note that the root apices are not in the field of view on the bitewing radiograph.

VIEW IMAGE

Copyright © 2003, Mosby, Inc. All rights reserved.

fractures, and salivary duct calculi, as well as the position and relationship of impacted teeth.

DENTAL PATHOLOGY SEEN ON RADIOGRAPHS

Periodontal Disease

One of the most common abnormalities seen in dental radiographs is periodontal disease. This disease is a result of gingival inflammation (gingivitis), which leads to periodontitis (inflammation of the tooth socket) and then edentulism. Periodontal disease is very closely related to the patient's age and the amount of dental plaque accumulation. Accumulation of dental plaque at the free gingival margin causes the initial lesion of periodontal disease. Inflammatory exudates, gingival crevicular fluid, and leukocytes migrate into the gingival crevice. The collagen fibers within the gingiva near the free gingival margin become destroyed and replaced by inflammatory infiltrate and engorged vasculature. Subsequently, chemotactic substances from the maturing dental plaque cause a host response.

Initially, after about 4 days, early gingivitis develops, with associated swelling and erythema. Plaque then invades the periodontal ligament space, the gingival sulcus deepens through destruction of the junctional epithelium, and an inflammatory reaction against the plaque ensues at the free gingival margin. The periodontal membrane remains intact initially. After several weeks, inflammatory changes become more pronounced, and there is an increase in swelling and crevicular bleeding, with an associated increase in exudate. Predominantly plasma cells, along with T and B lymphocytes, are now found within the gingival sulcus. The lesion may exist for long periods, perhaps years, without progressing to the advanced lesion.[9]

As the lesion advances, plaque accumulates deep within the dental gingival junction, replacing the collagen fiber of the gingiva with inflamed connective tissue, ulceration of pocket epithelium, and increased crevicular fluid production. This results in destruction of the normal anatomy of the gingiva. Plaque and calculus then adhere to the root and tooth surface, attaching to irregularities in the cementum and absorbing bacterial endotoxin. Osteoclastic activity is then induced by factors from the dental plaque or inflammatory response. The supporting bone for the tooth is then lost.[10]

Some authors believe, however, that periodontal disease develops in response to infection by specific bacteria. Over 300 different microbial species have been identified that are associated with dental plaque and periodontal disease. Some, however, point to *Actinobacillus actinomycetemcomitans, Bacteroides indermedius,* and *Bacteroides gingivalis* as specific organisms that induce periodontal disease.

Most authors do agree that periodontal disease is a chronic disease that results in bone destruction (and supporting dental apparatus) at a rate of 0.2 mm per year. Some gingival plaque is thought of as inciting a host parasite response. This results in gingivitis followed by periodontal ligament attachment loss, increased gingival sulcus depth bone, and eventually tooth loss.

Normally, in the fully erupted dentition, the alveolar crest of bone is located adjacent to the cementoenamel junction of the tooth (where the enamel of the crown meets the cementum of the root). In Figure 15-9, one can see that early periodontal disease has caused the alveolar crest to be slightly below where it should be. As the disease progresses, there is more loss of bone and widening of the periodontal ligament space, which appears radiographically as a widening lucency between the bone and root (Fig. 15-11). Eventually more bone is lost, resulting in a moderate degree of disease (Fig. 15-12), and finally advanced bone loss ensues (Fig. 15-12). In addition to being focal, periodontal disease may be generalized to involve the entire maxilla or mandible.

FIGURE 15-11 Periapical radiograph of mandibular central incisors depicts mild loss of alveolar bone from periodontal disease. Alveolar crest (*arrowhead*) is eroded and is now located below the cementoenamel junction (*white arrow*). Concurrent minimal widening of the periodontal ligament space (*black arrows*) is noted.

VIEW IMAGE

Dental Caries

The next most common pathologic entity encountered on radiographs of the jaws is dental caries, an infectious disease associated with cavitation of the crown of an erupted tooth. Carious lesions are the result of mineral dissolution of the dental hard tissues by the acid metabolic products of carbohydrate fermenting bacteria. Since the enamel is composed primarily of inorganic salts, the process leads to formation of a cavity (carious lesion) due to demineralization from the altered pH. This is one of the most common diseases of humans and is more prevalent in societies that have a high percentage of processed, sugar-sweetened, sticky food. There is also a sex predilection, with a higher

Copyright © 2003, Mosby, Inc. All rights reserved.

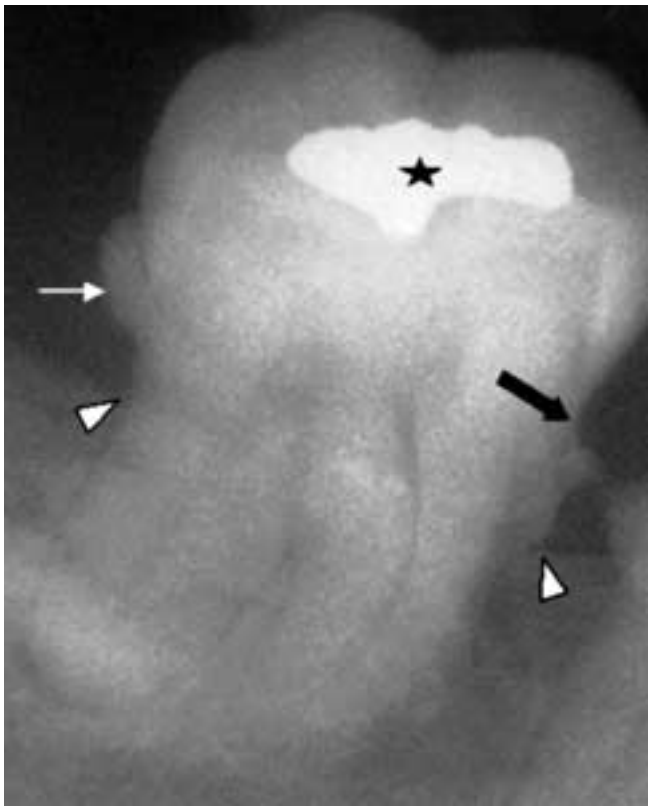

VIEW IMAGE

FIGURE 15-12 Periapical radiograph depicts moderate loss of alveolar bone (*arrowheads*). Cementoenamel junction (*black arrow*). The star denotes the occlusal amalgum dental restoration. Adherent calculus (tartar), which is frequently seen with periodontal disease, surrounds the clasp of the removed partial denture (*white arrow*).

frequency in women. Dental caries are the largest cause of tooth loss in people below the age of 35.

All dental caries start at the tooth surface and can be divided into the following types: pit and fissure, smooth surface, root (cemental), and recurrent types. They may also be either acute or chronic.

Pit and fissure caries are the most common type, often appearing at an early age. *Pits and fissures* refer to the normal anatomic irregularities predominantly seen along occlusal surfaces of the posterior teeth. Fissures are also present along the buccal and lingual surfaces of the molars and, to a lesser degree, along the lingual surfaces of the anterior teeth. Pit and fissure caries typically occur on the occlusal surfaces (surface facing an opposing tooth) (Fig. 15-14) and, less commonly, on the buccal surface (facing the cheek) of the primary and secondary posterior dentition. Occasionally, the lingual surface (surface facing the tongue) may be affected.

Smooth surface caries occur on those surfaces of the teeth that are smooth, without pits and fissures. The smooth surfaces are not involved in mastication. Smooth surface caries most commonly occur in interproximal regions where contiguous teeth abut. They most frequently occur at the mesial (anterior) (Fig. 15-15) and distal (posterior) (Fig. 15-10) surfaces at the contact point with the adjacent tooth, but may also occur in the cervical region buccally or lingually. Nursing bottle caries is a type of smooth surface caries caused by leaving the feeding bottle containing milk or juice in the infant's mouth when sleeping. This is commonly seen on the labial surface of the dentition. Additionally, in adults, smooth surface carious lesions are usually secondary to alteration in the quantity or quality of saliva produced. This may also be seen with dry mouth secondary to radiation therapy.

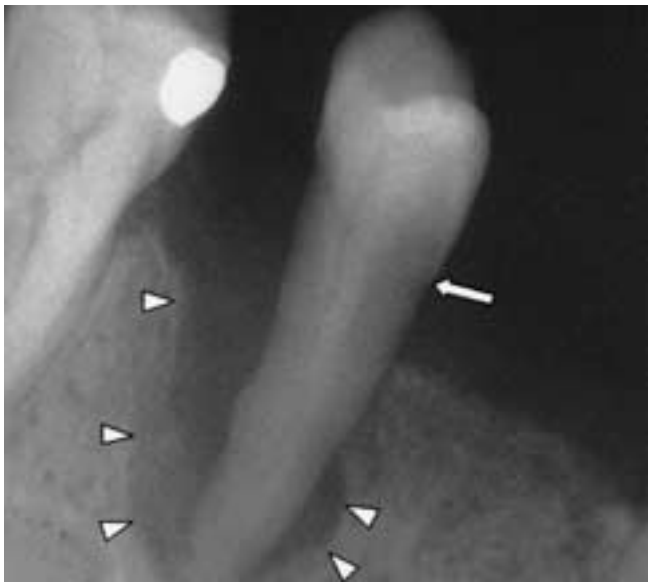

VIEW IMAGE

FIGURE 15-13 Periapical radiograph of the maxillary second premolar demonstrates severe loss of alveolar bone from advanced periodontal disease (*arrowheads*). Note the location relative to the cementoenamel junction (*white arrow*).

FIGURE 15-14 Periapical radiograph depicts a large pit and fissure carious lesion (*arrowheads*) of the occlusal surface. The lesion has invaded the pulp chamber of the tooth (*P*), as outlined by black arrows.

VIEW IMAGE

Copyright © 2003, Mosby, Inc. All rights reserved.

VIEW IMAGE

FIGURE 15-15 Periapical radiograph depicts a large interproximal carious lesion of the mesial surface (*arrowheads*). Concurrent moderate loss of alveolar bone is noted (*black arrow*).

Root (cemental) caries occurs in older adults secondary to gingival recession. The exposed root surface is thin and soft, making the root vulnerable to the abrasive action of tooth brushing. Chemical erosion from bacterial acid production may also affect the root surface, causing erosion of the thin dentin layer. This may quickly invade the pulp cavity, resulting in a nonvital tooth.

Recurrent caries is a term used for caries that have formed around a dental restoration. These lesions may be due to weakness in the integrity of a restoration that results in marginal leakage. This allows food and bacteria to insinuate between the restoration and the remaining tooth structure, outside of the area that is cleaned. These lesions progress at variable speed, depending on the patient's diet, oral hygiene habits, and the degree of sclerosis of adjacent dentin.[11]

Rampant caries are often found in young patients. They occur because young teeth have large pulp chambers with short and wide dentinal tubules containing little sclerosis. When this condition is combined with a diet high in refined carbohydrates and sugars and poor oral hygiene, rapid extensive caries may develop.[12]

REFERENCES

1. Laney WR, Tolman DE, Keller EE, et al. Dental implants: tissue-integrated prosthesis utilizing the osseointegrated concept. Mayo Clin Proc 1986;61:91–97.
2. Abrahams JJ. CT assessment of dental implant planning. Oral Maxillofac Surg Clin North Am 1992;4:1–18.
3. Abrahams JJ. The role of diagnostic imaging in dental implantology. Radiol Clin North Am 1993;31:(1):163–180.
4. Abrahams JJ, Levine B. Expanded applications of DentaScan: multiplanar CT of the mandible and maxilla. Int J Periodont Restor Dentistry 1990;10:464–467.
5. Abrahams JJ, Olivario P. Odontogenic cysts: improved imaging with a dental CT software program. AJNR 1993;14:367–374.
6. Delbalso AM, Greiner FG, Licata N. Role of diagnostic imaging in evaluation of the dental implant patient. Radiographics 1994;14: 699–719.
7. Fogelman D, Huang AB. Prospective evaluation of lesions of the mandible and maxilla: findings on multiplanar and three-dimentional CT. AJR 1994;163:693–698.
8. Yanagisawa K, Friedman C, Abrahams JJ. DentaScan imaging of the mandible and maxilla. Head Neck J 1993;15:1–7.
9. Ramfjord S, Ash M. Periodontology and Periodontics. Philadelphia: WB Saunders, 1979;Chaps 7, 10, 17, 23.
10. Regezi JA, Sciubba JJ. Oral Pathology. Philadelphia: WB Saunders, 1989;503–519.
11. Frank RM. Structural events in the caries process in enamel, cementum, and dentin. J Dent Res 1990;69:559–566.
12. Daculsi G, LeGeros RZ, Jean A, Kerebel B. Possible physico-chemical process in human dentin caries. J Dent Res 1987;66: 1356–1359.

Copyright © 2003, Mosby, Inc. All rights reserved.

16 Dental Implants and Related Pathology

James J. Abrahams

DENTAL IMPLANTS
IMPLANT SURGICAL PROCEDURE
- Fixture Placement
- Abutment Connection
- Prosthodontic Procedure

RADIOLOGY FOR ORAL IMPLANTS

RELATED PATHOLOGY
- Periodontal Disease
- Endodontal Disease
- Osteitis Condensans
- Maxillary Sinus Inflammation from Dental Disease
- Atrophy and Augmentation Procedures

DENTAL IMPLANTS

Dental implants are metal posts that are surgically implanted in the jaw to support a fixed dental prosthesis (Fig. 16-1). In the early development of implants, dentists attempted to imitate the natural anchorage system of the teeth, which are attached to the bony socket by the periodontal ligament. In addition to supporting the teeth, this ligament permits slight degrees of tooth motion within the socket. This ligament is visualized on plain radiographs as a thin radiolucent line situated between the lamina dura of the jaw and the tooth. The initial efforts to reproduce this ligament promoted growth of soft tissue between the oral implant and the bone.[1] These implants were often referred to as pseudoligaments or fibrous osseointegrated implants.[2, 3] However, the long-term results of these soft tissue–anchored implants were poor, and researchers redirected their efforts toward the possibility of anchoring the implants by direct contact with bone. Early long-term studies with these osseointegrated implants were optimistic, with success rates of 91% in the mandible and 81% in the maxilla.[4] Microscopic sections through bone-containing implants demonstrated the ability of osteoblasts to grow and integrate with the titanium posts, resulting in osseointegration.[5] The results of these early studies were corroborated by others, and this paved the road for the osseointegrated implants utilized today.[6]

There are three basic types of implants: root form (Fig. 16-1), blade (Fig. 16-2), and subperiosteal (Fig. 16-3). The osseointegrated, cylinder-shaped implants described previously are the root form because they simulate the shape of the root of a tooth. They are the ones most frequently used today and will be the type dealt with in this chapter. The blade implants are rectangular and are similar in shape to a razor blade. From the long side of the rectangle, one or more posts extend into the oral cavity to permit fixation of the prosthesis. The rectangular portion is implanted into the bone via a linear osteotomy, and the posts extend up above the gingiva. Lastly, the subperiosteal implants are metallic meshes that are custom built to fit over the alveolar process and under the periosteum. Several metallic posts extend from the mesh into the oral cavity (above the gingiva) to support the prosthesis. To customize these subperiosteal implants, the alveolar process must be surgically exposed so that a plaster impression can be obtained to manufacture the implant. After the implant is manufactured, the patient returns for a second surgical procedure that permits placement of the implant. The first surgical procedure can be eliminated if thin-slice axial CT is used to produce a 3D model of the jaw from which the prosthesis can be manufactured.

Osseointegrated root form implants are made up of several components (Fig. 16-4). The fixture is the portion of the implant that is surgically embedded in the osseous tissue of the jaw. It is made of titanium, a material that promotes osseointegration. The fixtures come in various sizes, typically ranging from 3.25 to 3.75 mm in diameter and 7 to 10 mm in length.[7] The size of the implant chosen is dependent upon the amount of available jaw bone. Dentists prefer the largest possible implant because it increases the surface area and thus provides stronger anchorage and more successful osseointegration. It is also preferable to have 1 to 1.5 mm of bone on either side of the implant and 1 to 2 mm of bone between the bottom of the implant and the adjacent structures (i.e., maxillary sinus, mandibular canal).[7] Fixtures can be threaded, unthreaded, or even coated with hydroxyapatite.[8]

The next component of the implant is the abutment (Figs. 16-1, 16-4), which is attached to the fixture to increase its

Copyright © 2003, Mosby, Inc. All rights reserved.

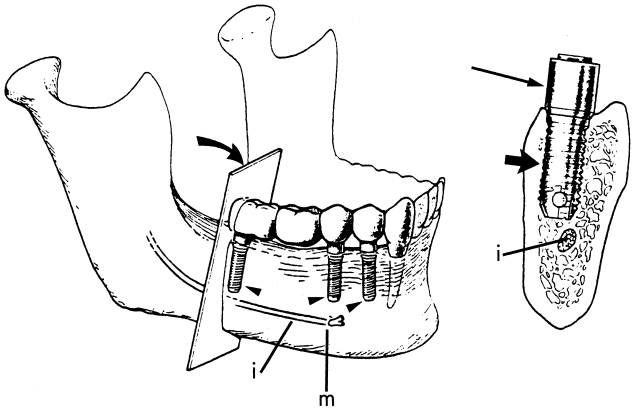

VIEW IMAGE

FIGURE 16-1 View of the mandible illustrating the plane of orientation of the cross-sectional DentaScan images. The top of the plane (*curved arrow*) would correspond to one of the numbered perpendicular lines on the axial image in Figure 16-2A. Note how the height and width of the alveolar process and the location of the mandibular canal can be readily determined on the cross-sectional image. Three root form implants are seen (*arrowheads*) supporting a four-tooth prosthesis. The abutment (*thin arrow*) that is attached to the fixture (*broad arrow*) raises it above the surface of the bone and gingiva and into the oral cavity. Inferior alveolar canal (*i*), mental foramen (*m*). (From Langer B, Sullivan D. Osseointegration: its impact on the relationship of periodontics and restorative dentistry. Part 1. Int J Periodont Res 1989;9:86.)

height to a level above the gingival surface. This occurs 3 to 6 months after the initial procedure, thus giving the fixture time to heal within the bone. The fixture is surgically exposed, and the abutment is attached with an abutment screw (Fig. 16-4). The top of the abutment screw itself has a small screw hole, which allows the dental prosthesis to be attached by a screw that runs through the prosthesis and into the abutment screw. This screw is designed to be the weakest portion of the implant so that in the event of unforeseen stress, it, rather than the fixture, will break. Angled abutments are also available to correct for implants that are inserted at an angle rather than parallel to the residual teeth.

The prosthesis is composed of a strong metal framework (Fig. 16-4) that supports the prosthetic teeth. Because the implants actually support this framework, patients can have a full 14-tooth dental prosthesis supported by only six implants or a 3-tooth prosthesis supported by two implants, as shown in Figure 16-4.

IMPLANT SURGICAL PROCEDURE

Dental implant surgery is a usually a two-stage procedure requiring a 4- to 6-month healing period between stages.[9] The healing period allows time for osseointegration to occur. In the first stage the fixture is installed; in the second stage the fixture is exposed, and the abutment is attached. The procedures are typically performed in the dentist's office, using local anesthetic.

Fixture Placement

The first stage of surgery, fixture installation, is more extensive than the second stage and usually takes about 2

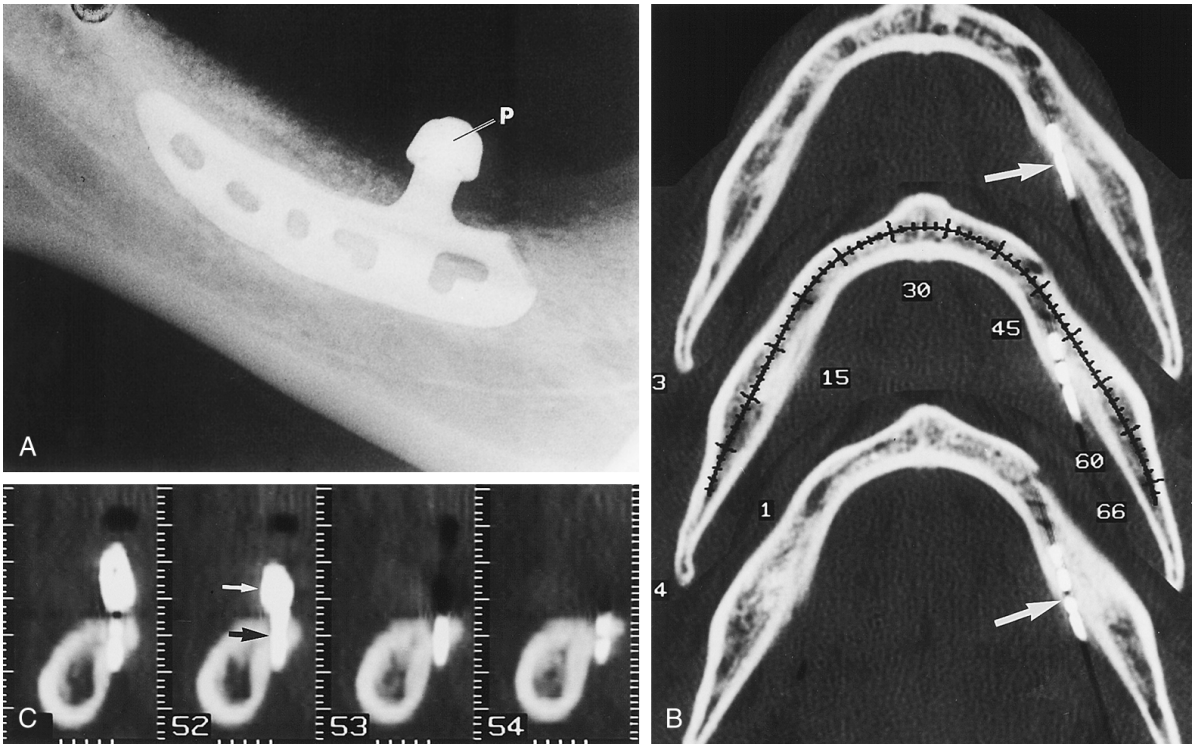

VIEW IMAGE

FIGURE 16-2 Blade implant in mandible. **A**, Plain film illustrating a single post-blade implant. Note how the blade is inserted in the mandible after a linear osteotomy, while the post (*P*) extends above the level of the bone and gingiva. **B**, Axial views demonstrating the blade implant in mandible (*arrow*). **C**, Cross-sectional views illustrating the blade within the mandible (*black arrow*) and the post (*white arrow*) extending into the oral cavity above the level of the bone and gingiva.

Copyright © 2003, Mosby, Inc. All rights reserved.

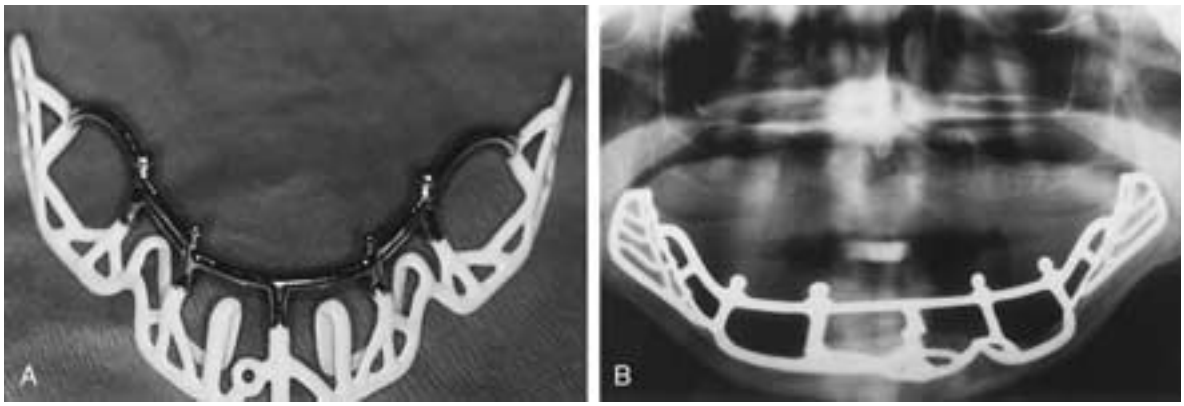

VIEW IMAGE

FIGURE 16-3 Subperiosteal implant. **A**, Photograph of a subperiosteal implant. The white portion fits under the periosteum and on top of the bone of the alveolar process, and the metallic-appearing portion extends above the gingiva to support the prosthesis. The subperiosteal portion (*white*) is often coated with hydroxyapatite to facilitate bone growth. **B**, Panoramic view demonstrating the subperiosteal implant on a severely atrophic mandible. The prosthesis has not been attached. (Courtesy of Dr. Wayne C. Jarvis, Williamsville, NY.)

hours, depending on the number of fixtures placed. Anesthesia is obtained by using local infiltration with lidocaine or a nerve block. A linear incision is then made along the buccal or lingual surface of the alveolar ridge, and a soft tissue flap, incorporating the periosteum, is reflected back (Fig. 16-5E). If the exposed bony ridge has a sharp or pointed surface secondary to buccolingual atrophy, an alveoloplasty may be performed to remove the sharp edge and provide a broad surface to install the fixtures. The anticipated implant site has been radiographically predetermined (Fig. 16-5A–D). Its position is then located on the patient either by measuring from an existing tooth or from another landmark that can be identified both on the films and on the patient or by using a stent with markers (Fig. 16-5B). Refer to the discussion of radiographic and surgical stents.

After the site has been identified on the patient, a series of graduated drill bits produce a hole in the bone. The hole is progressively widened to the appropriate size. A countersink widens the drill hole's entrance to accommodate the fixture head. The hole is then threaded with a titanium tap bur to accommodate the threaded fixture. Both drilling and threading are done at extremely low revolutions per minute (RPM), with copious irrigation to prevent heating and destruction of osteoblasts because osseointegration can only occur with viable cells. The top of the fixture has a threaded hole (Fig. 16-5G) to accommodate the abutment screw that is inserted during the second stage of the procedure. To prevent soft tissue and bone from growing into the hole while the patient is healing, a cover screw is used (Fig. 16-5E). The implant and cover screw are flush with the surface of the bone. To raise the height of the implant above the gingival surface, an abutment is later attached.

After the fixtures are placed, the tissue flap is sutured closed and the implants are allowed to heal for approximately 4 months in the mandible and 6 months in the maxilla (Fig. 16-5F). This promotes the process of osseointegration, thus forming a strong bond between the bone and the implant. Approximately 1 week after the initial surgery, the skin sutures are removed and the patient is fitted with an interim prosthesis, which typically is the one used before surgery. Because of the fixture, minor modifications of the old prosthesis may be necessary.

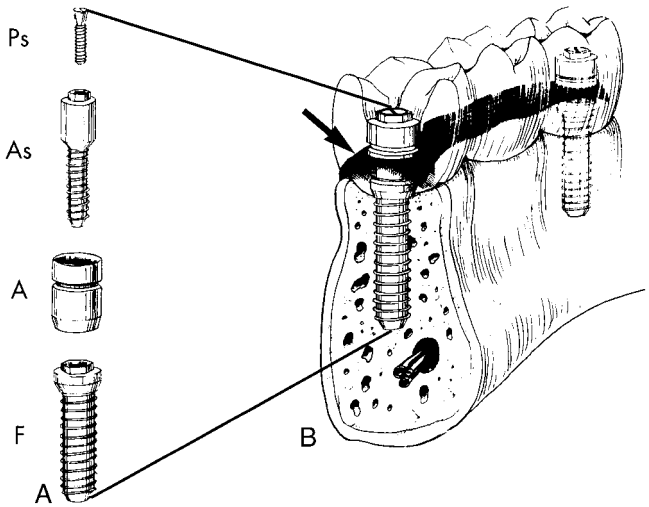

VIEW IMAGE

FIGURE 16-4 Illustration demonstrating the components of an implant (**A**) and two root form implants supporting a three-tooth prosthesis (**B**). For illustrative purposes, the black portion running through the prosthesis (*arrow*) represents the metal framework within the prosthesis. Prosthesis screw (*Ps*), abutment screw (*As*), abutment (*A*), and fixture (*F*).

Abutment Connection

The second stage of the procedure tends to be less traumatic for the patient and is typically carried out with only local infiltration of lidocaine. A pointed probe is used to locate the cover screws; after they are located, an incision is made to expose and remove them. Alternatively, a circular soft-tissue punch can be used to excise the tissue above the cover screw. The abutment is then attached to the fixture using the abutment screw. The top of the abutment screw has a screw hole that permits the prosthesis to be screwed into the fixture (Figs. 16-4 and 16-5H). Finally, a surgical pack is applied and retained for a short period by a healing cap.

Copyright © 2003, Mosby, Inc. All rights reserved.

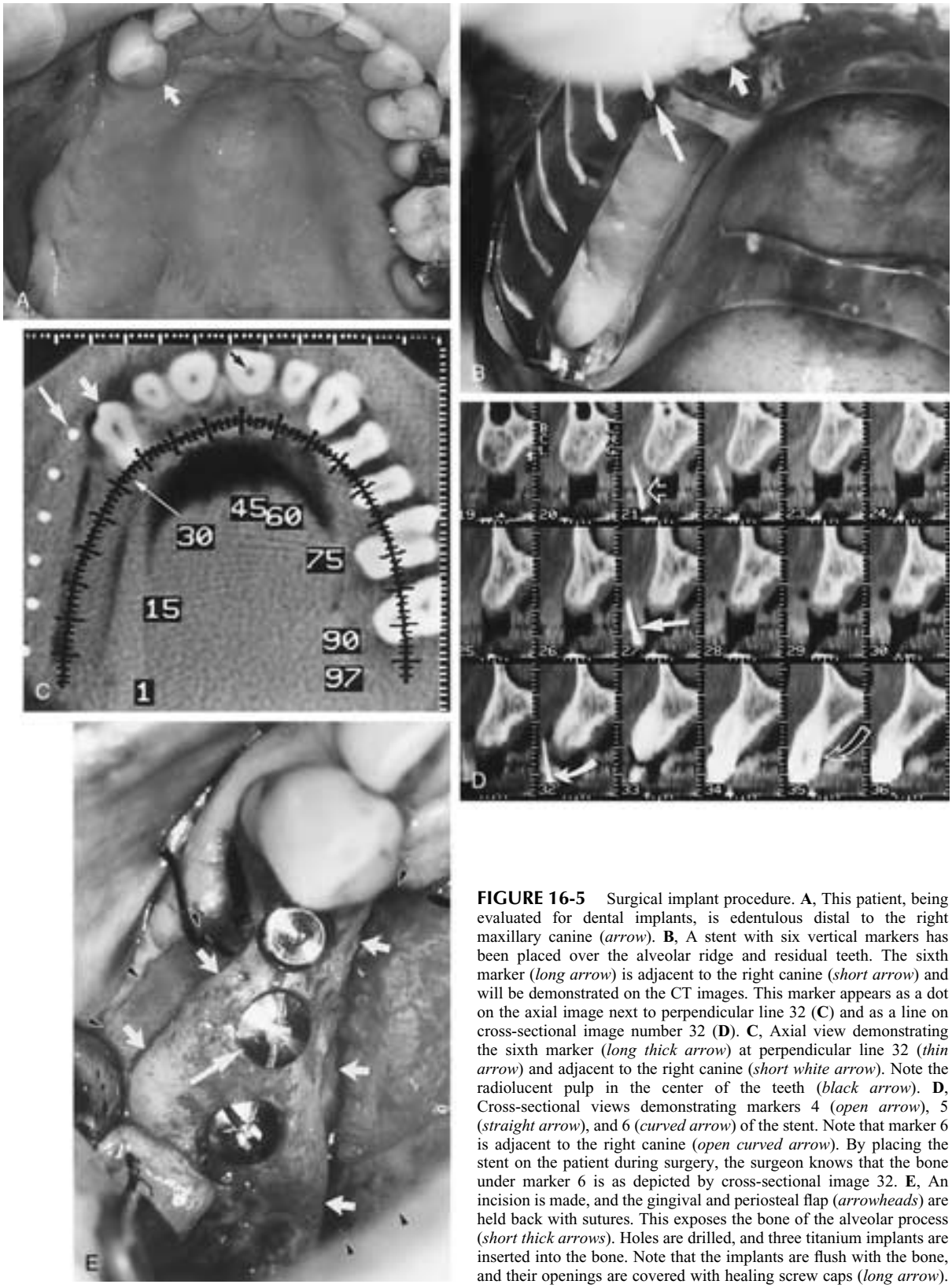

FIGURE 16-5 Surgical implant procedure. **A**, This patient, being evaluated for dental implants, is edentulous distal to the right maxillary canine (*arrow*). **B**, A stent with six vertical markers has been placed over the alveolar ridge and residual teeth. The sixth marker (*long arrow*) is adjacent to the right canine (*short arrow*) and will be demonstrated on the CT images. This marker appears as a dot on the axial image next to perpendicular line 32 (**C**) and as a line on cross-sectional image number 32 (**D**). **C**, Axial view demonstrating the sixth marker (*long thick arrow*) at perpendicular line 32 (*thin arrow*) and adjacent to the right canine (*short white arrow*). Note the radiolucent pulp in the center of the teeth (*black arrow*). **D**, Cross-sectional views demonstrating markers 4 (*open arrow*), 5 (*straight arrow*), and 6 (*curved arrow*) of the stent. Note that marker 6 is adjacent to the right canine (*open curved arrow*). By placing the stent on the patient during surgery, the surgeon knows that the bone under marker 6 is as depicted by cross-sectional image 32. **E**, An incision is made, and the gingival and periosteal flap (*arrowheads*) are held back with sutures. This exposes the bone of the alveolar process (*short thick arrows*). Holes are drilled, and three titanium implants are inserted into the bone. Note that the implants are flush with the bone, and their openings are covered with healing screw caps (*long arrow*).

VIEW IMAGE

Copyright © 2003, Mosby, Inc. All rights reserved.

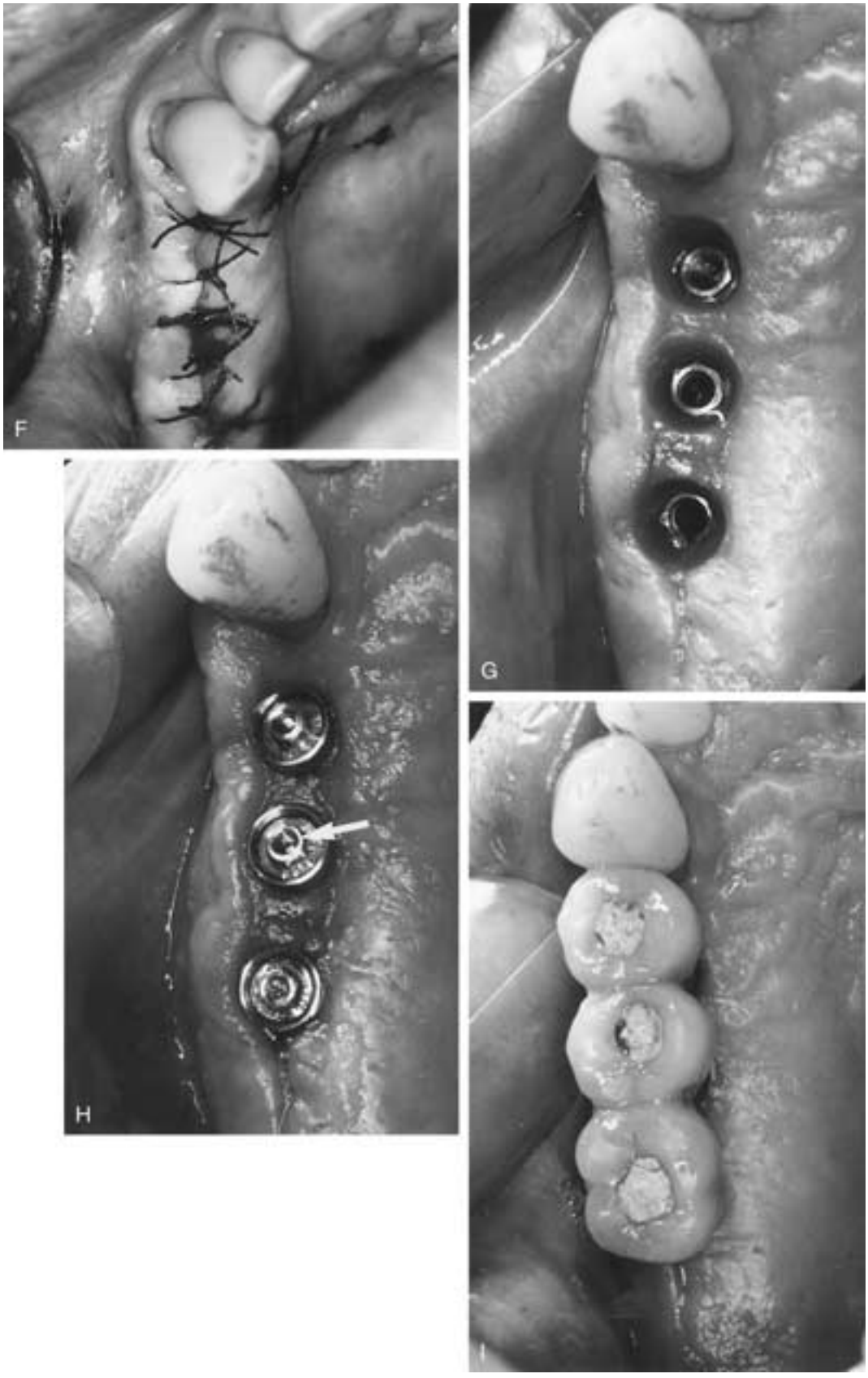

FIGURE 16-5 *Continued.* **F**, The incision is sutured closed and permitted to heal for 4 months in the mandible and 6 months in the maxilla. **G**, Before this photograph was taken, a small incision was made to remove the healing caps. Healing abutments, which were attached to the implants, have been removed. The threaded opening of the implant is visualized. **H**, The permanent abutments, which raise the fixture above the gingival surface, have now been attached. The screw hole (*arrow*) in the center of the abutment will accommodate the screw that fixes the prosthesis. **I**, The prosthesis is now attached to the three implants. The screw heads are covered with a white compound. (From Abrahams JJ. The role of diagnostic imaging in dental implantology. Radiol Clin North Am 1993;31(1):163–180.)

VIEW IMAGE

Copyright © 2003, Mosby, Inc. All rights reserved.

Prosthodontic Procedure

To make the prosthesis, an impression of the jaw with the abutments in place is made, using plaster or hydrocoloid. From this impression a cast of the mandible or maxilla is obtained. From this cast the prosthesis is made, aligning properly with the screw holes and properly aligning the prosthetic teeth with the occlusal plane. After the prosthesis is manufactured, it is fixed to the abutments with screws that typically come out the central fossa of the prosthetic teeth. A white compound is used to cover the screw holes (Fig. 16-5I).

RADIOLOGY FOR ORAL IMPLANTS

To perform the implant procedure, the oral surgeon and dentist need to know the precise height, width, and contour of the alveolar process, as well as its relationship to the maxillary sinus and mandibular canal. Injury to the neurovascular bundle within the mandibular canal results in paresthesia or hypesthesia of the face, whereas perforation into the maxillary sinus increases the likelihood of implant failure and creates the potential for an oroantral fistula and antral infection. The precise dimensions of the alveolar process are important to determine preoperatively because atrophy of the alveolar ridge, which occurs in edentulous patients, may preclude the use of implants.

Before the development of CT dental reformatting programs, attempts were made to obtain this information with panoramic, intraoral, and cephalometric films. However, the panoramic film produced up to 25% distortion, making accurate measurements almost impossible. In addition, the width (thickness) of the alveolar process could not be determined by any of these techniques. Therefore the surgeon had to rely primarily on clinical assessment to determine if the alveolar process was thick enough to accommodate an implant. Unfortunately, it was common to find during surgery that there was insufficient bone for the implants. As a result, radiologists and dentists began to evaluate the efficacy of using CT to assess these patients.[10, 11] Axial and coronal images were only marginally helpful because of the streak degradation artifacts created by any dental restorations. However, reformatted images using thin-slice axial CT were found to be extremely useful because the streak artifact could be avoided, the anatomy could be displayed in multiple planes, the width of the alveolar process could be accurately assessed, and accurate, reproducible millimeter measurements could be made.

Reformatting software programs, which display multiple panoramic and cross-sectional images, soon became available (Figs. 15-2 and 15-3; Chapter 15).[12–15] The particular program used in this chapter is DentaScan. Although these programs were initially developed to assess implant patients, they have also gained popularity for evaluating all lesions of the jaw (Fig. 16-6).[16–19]

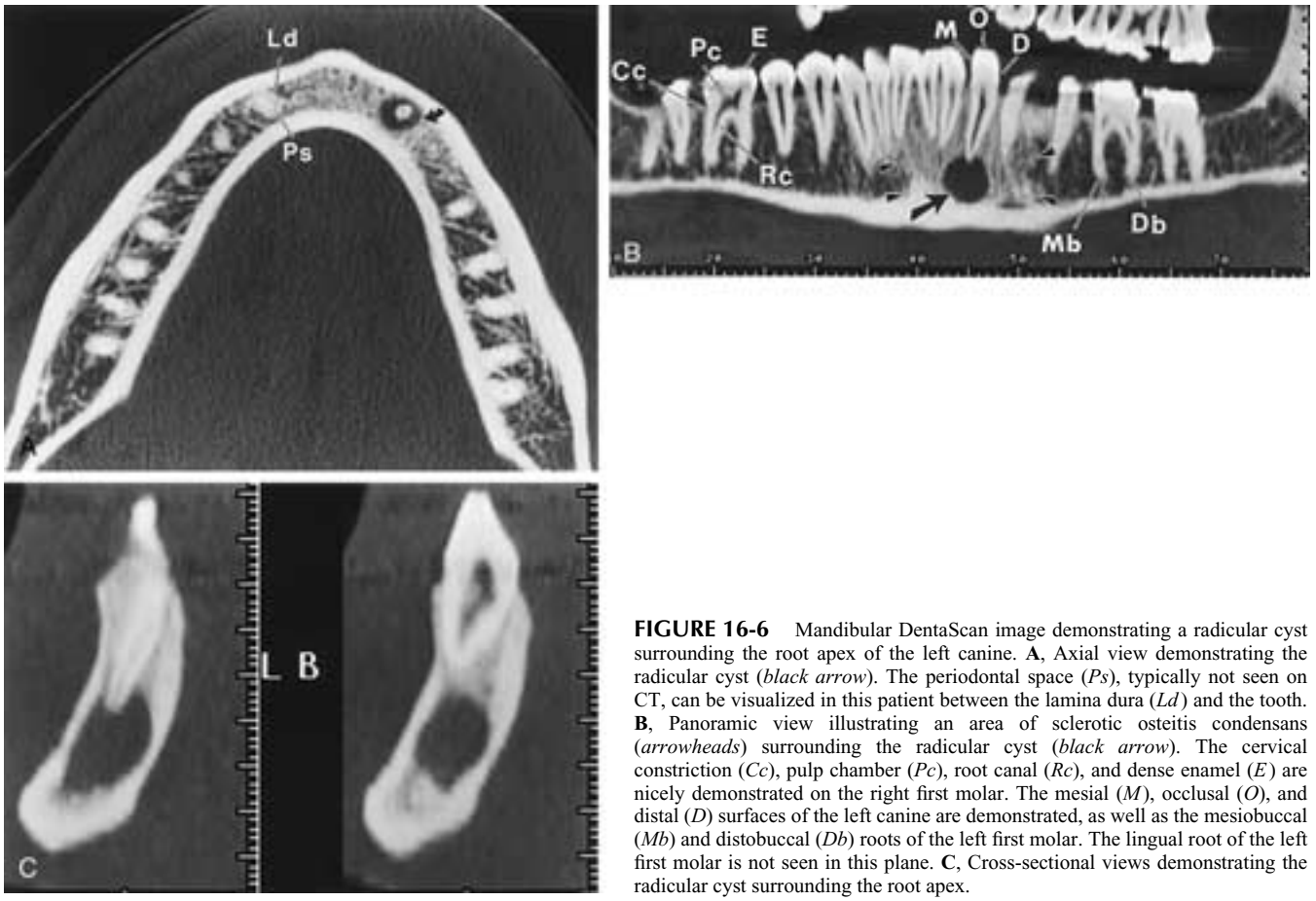

FIGURE 16-6 Mandibular DentaScan image demonstrating a radicular cyst surrounding the root apex of the left canine. **A**, Axial view demonstrating the radicular cyst (*black arrow*). The periodontal space (*Ps*), typically not seen on CT, can be visualized in this patient between the lamina dura (*Ld*) and the tooth. **B**, Panoramic view illustrating an area of sclerotic osteitis condensans (*arrowheads*) surrounding the radicular cyst (*black arrow*). The cervical constriction (*Cc*), pulp chamber (*Pc*), root canal (*Rc*), and dense enamel (*E*) are nicely demonstrated on the right first molar. The mesial (*M*), occlusal (*O*), and distal (*D*) surfaces of the left canine are demonstrated, as well as the mesiobuccal (*Mb*) and distobuccal (*Db*) roots of the left first molar. The lingual root of the left first molar is not seen in this plane. **C**, Cross-sectional views demonstrating the radicular cyst surrounding the root apex.

VIEW IMAGE

Copyright © 2003, Mosby, Inc. All rights reserved.

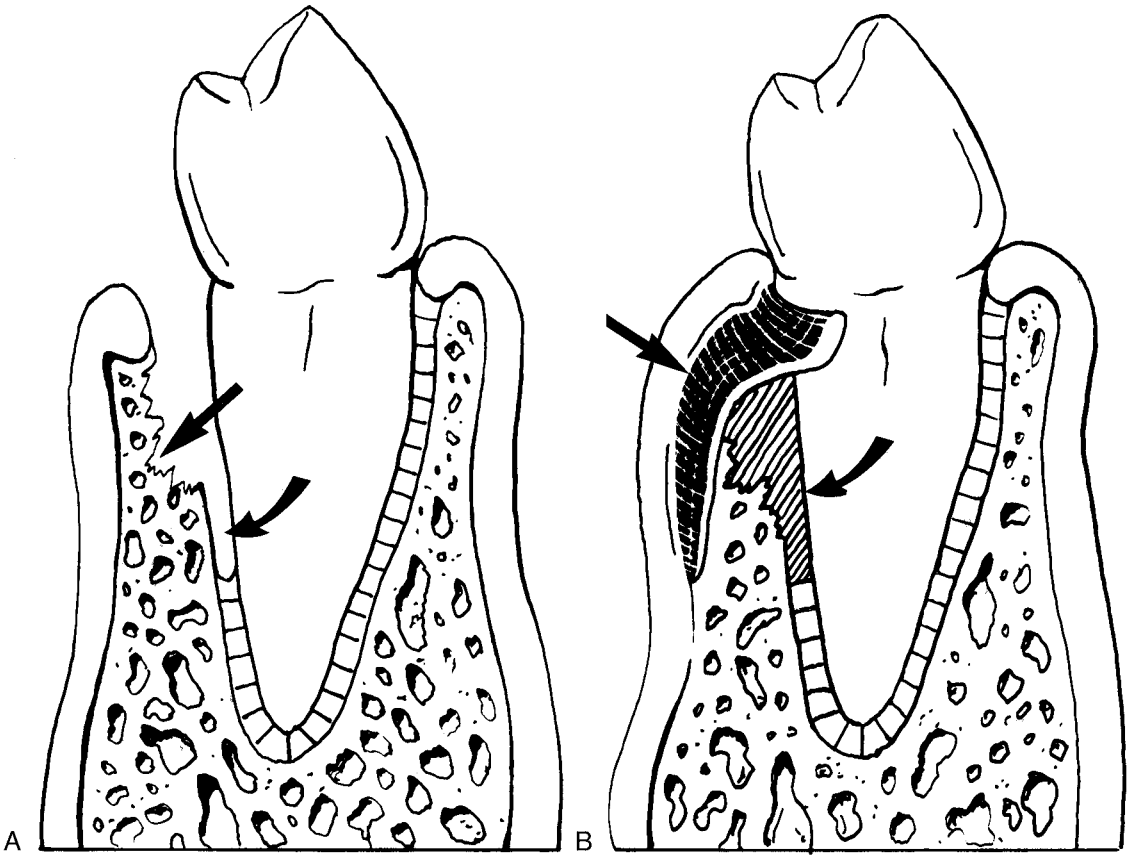

VIEW IMAGE

FIGURE 16-7 Illustration demonstrating a periodontal pocket and its repair. **A**, Bacterial overgrowth has attacked the periodontal ligament (*curved arrow*) and resorbed bone (*straight arrow*), creating this periodontal pocket. **B**, The periodontal pocket in **A** has now been packed with freeze-dried bone (*curved arrow*) and covered with a Gortex graft (*straight arrow*) to prevent ingrowth of soft tissue while the bone graft heals. The Gortex will be removed in approximately 6 weeks.

RELATED PATHOLOGY

Most patients being scanned for dental implants have considerable oral pathology, often related to the inflammatory process that likely caused their edentulism. The inflammatory disease, which often starts as gingivitis (inflammation of the gums), can be divided into periodontal and endodontal disease. Periodontal disease refers to infection of the periodontal ligament along the sides of the root and the adjacent surrounding bone. Endodontal disease refers to infection and resorption of bone at the root apex.

Periodontal Disease

Periodontal disease starts with gingivitis and the accumulation of bacteria-laden plaque around the teeth. This may harden into tartar or calculus, a tough, gritty material that is difficult to remove. The presence of this bacterial overgrowth produces inflammation of the gums, which presents clinically as swelling with frequent bleeding secondary to hyperemia from inflammation. If the infection is allowed to persist, the fibers that attach the gingiva to the tooth become involved, allowing bacteria to access the periodontal ligament (periodontitis). Once the periodontal ligament becomes involved, a periodontal pocket forms in which plaque accumulates adjacent to the root (Fig. 16-7A).

Routine dental hygiene at home does not adequately cleanse these infected regions, and the disease progresses. Eventually the periodontal ligament is destroyed, and the adjacent bone surrounding the root is resorbed.[20] Radiographically, periodontal disease is recognized by the associated bone loss that occurs. On CT, this bone loss appears as a radiolucency surrounding the root of the tooth (Fig. 16-8). The periodontal ligament, which appears as a radiolucency surrounding the root on radiographs (Fig. 16-9), is usually not resolved on CT because it is too thin. Therefore, radiolucency along the root of the tooth on CT usually implies periodontal disease. Because the resolution of radiographs exceeds that of CT, visualization of the periodontal ligament as a thin lucency between the root and lamina dura (surrounding cortical bone) (Fig. 16-9) is routinely seen. Widening of this periodontal space on radiographs implies periodontal disease (Fig. 15-10).

Endodontal Disease

Another frequently encountered condition in this patient population is an inflammatory cyst surrounding the root

Copyright © 2003, Mosby, Inc. All rights reserved.

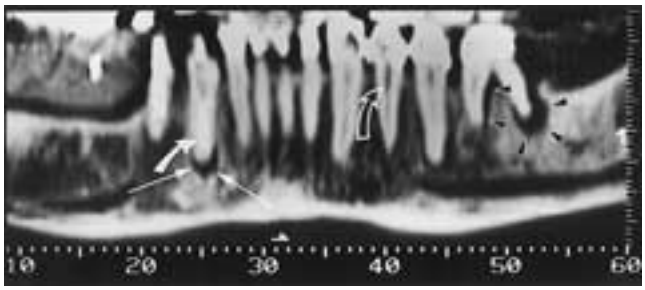

VIEW IMAGE

FIGURE 16-8 Panoramic CT scan of mandible demonstrating periodontal disease. The radiolucency surrounding the root of the left first molar (*arrowheads*) is due to bone resorption from periodontitis. The periapical lucency around the root apex of the right canine (*long arrows*) is a radicular cyst secondary to a periapical abscess. Note the metal post in the pulp chamber secondary to a prior root canal procedure (*solid curved arrow*), and compare this with the normal radiolucent pulp chamber of the left first premolar (*open curved arrow*). A zone of relatively dense sclerotic bone (osteitis condensans) is identified surrounding both areas of disease. (From Abrahams JJ. The role of diagnostic imaging in dental implantology. Radiol Clin North Am 1993;31(1):163–180.)

apex called a radicular cyst.[21] Bacteria gains access to the pulp chamber through dental caries and travels down the root canal to the root apex, where either an acute abscess or a more chronic granuloma forms. Bone loss develops around the root apex, and this appears as a periapical radiolucency on CT (Fig. 16-6). When bacteria enters the pulp chamber through dental caries, it causes pulpitis with inflammation and edema. Because the tooth cannot expand, pressure builds within the pulp chamber and the diminished blood flow causes the tooth to die. Radicular cysts are therefore associated with nonvital teeth. The treatment is to drill through the pulp chamber and drain the abscess (root canal procedure). After this drainage is accomplished, the root canal is filled with a radiopaque material that also plugs the apical foramen. This is readily seen on CT as a radiodensity, rather than a radiolucency, in the region of the pulp chamber and root canal (Fig. 16-8, *curved arrow*).

Osteitis Condensans

The chronic inflammatory changes of periodontal and endodontal disease can also cause reactive sclerosis in the adjacent bone, termed osteitis condensans. Radiographically, this appears as a relatively dense zone of bone surrounding an area of periodontal or endodontal disease (Fig. 16-8).[22] This condition is relatively benign, and treatment is directed at eradicating the underlying periodontal and endodontal disease.

Maxillary Sinus Inflammation from Dental Disease

The close proximity of the root apexes to the maxillary sinus makes periodontal and endodontal disease potential sources of infection to cause maxillary sinus disease. It is not uncommon to find mounds of inflammatory tissue within the sinus adjacent to the root apices of diseased teeth. These mounds frequently are misdiagnosed as mucous retention cysts or polyps on axial CT scans[23] (Fig. 16-10).

An oroantral fistula, which is an abnormal communication between the maxillary sinus and oral cavity, typically causes fluid and inflammatory changes in the maxillary sinus. These fistulas are often caused by tooth extractions but can also be caused by infection, trauma, tumors, etc.[24] Radiographically, the oroantral fistula presents as unilateral sinusitis with a bony defect in the floor of the maxillary sinus. This is best seen using dental CT reformatting programs (Fig. 16-11).

Atrophy and Augmentation Procedures

Periodontal and endodontal disease eventually lead to edentulism. The resorption of bone, however, continues even after the teeth are lost. This is because the normal vertical stress applied to the bone from the teeth is no longer present and disuse atrophy occurs. It is believed that the use of dental implants retards this atrophic process. The disuse atrophy affects both the height of the alveolar process (Fig. 16-12A) and the width (Fig. 16-12B). When it is severe, the mandibular canal, which is normally covered by a considerable amount of bone, may lie just under the gingival surface.

Several augmentation procedures are now available for patients who have severe atrophy and have insufficient bone for implants. In the sinus lift procedure, the surgeon elevates

FIGURE 16-9 Periapical radiograph of mandibular central incisors depicts mild loss of alveolar bone from periodontal disease. Alveolar crest (*arrowhead*) is eroded and is now located below the cemento-enamel junction (*white arrow*). Concurrent minimal widening of the periodontal ligament space (*black arrows*) is noted.

VIEW IMAGE

Copyright © 2003, Mosby, Inc. All rights reserved.

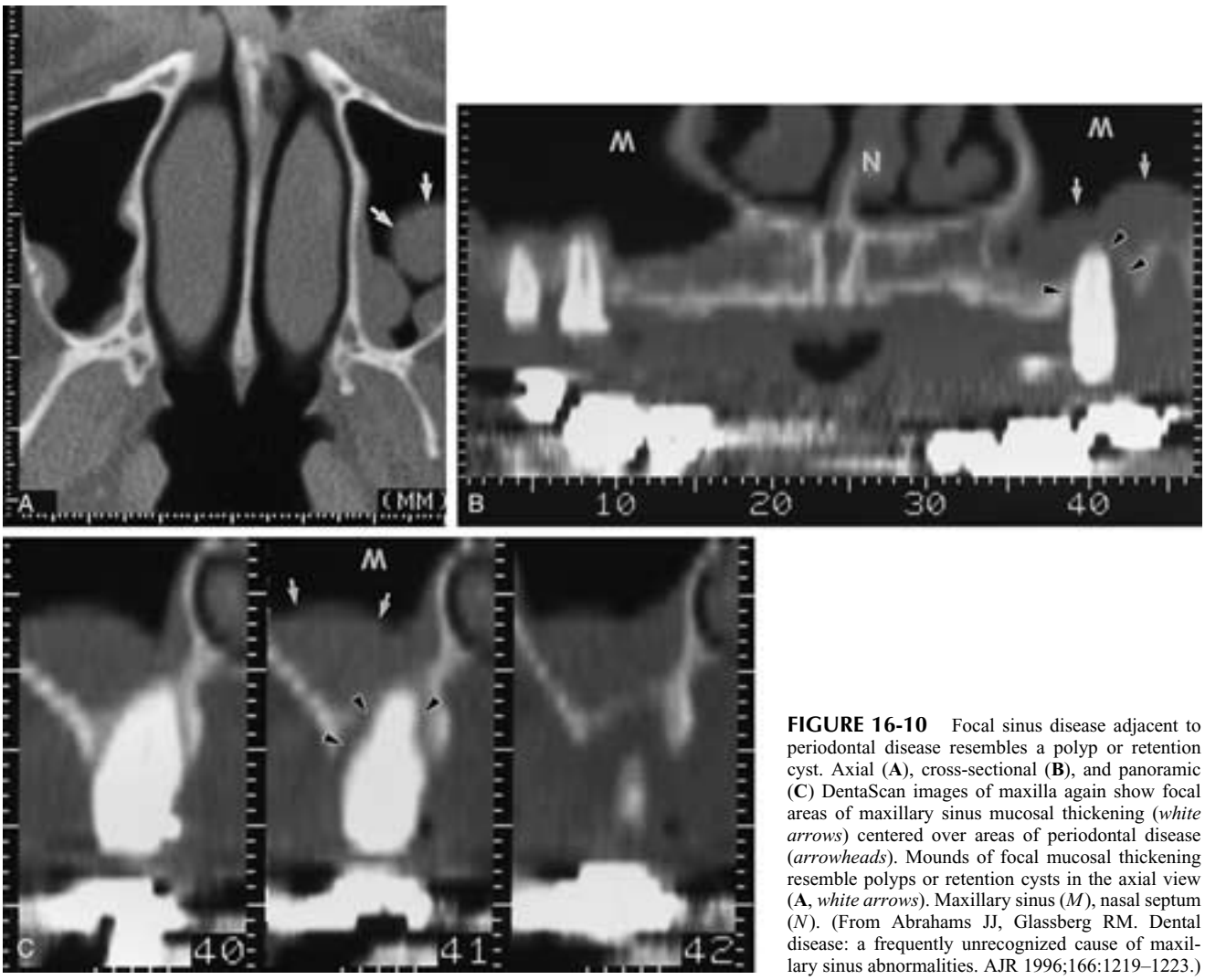

FIGURE 16-10 Focal sinus disease adjacent to periodontal disease resembles a polyp or retention cyst. Axial (**A**), cross-sectional (**B**), and panoramic (**C**) DentaScan images of maxilla again show focal areas of maxillary sinus mucosal thickening (*white arrows*) centered over areas of periodontal disease (*arrowheads*). Mounds of focal mucosal thickening resemble polyps or retention cysts in the axial view (**A**, *white arrows*). Maxillary sinus (*M*), nasal septum (*N*). (From Abrahams JJ, Glassberg RM. Dental disease: a frequently unrecognized cause of maxillary sinus abnormalities. AJR 1996;166:1219–1223.)

VIEW IMAGE

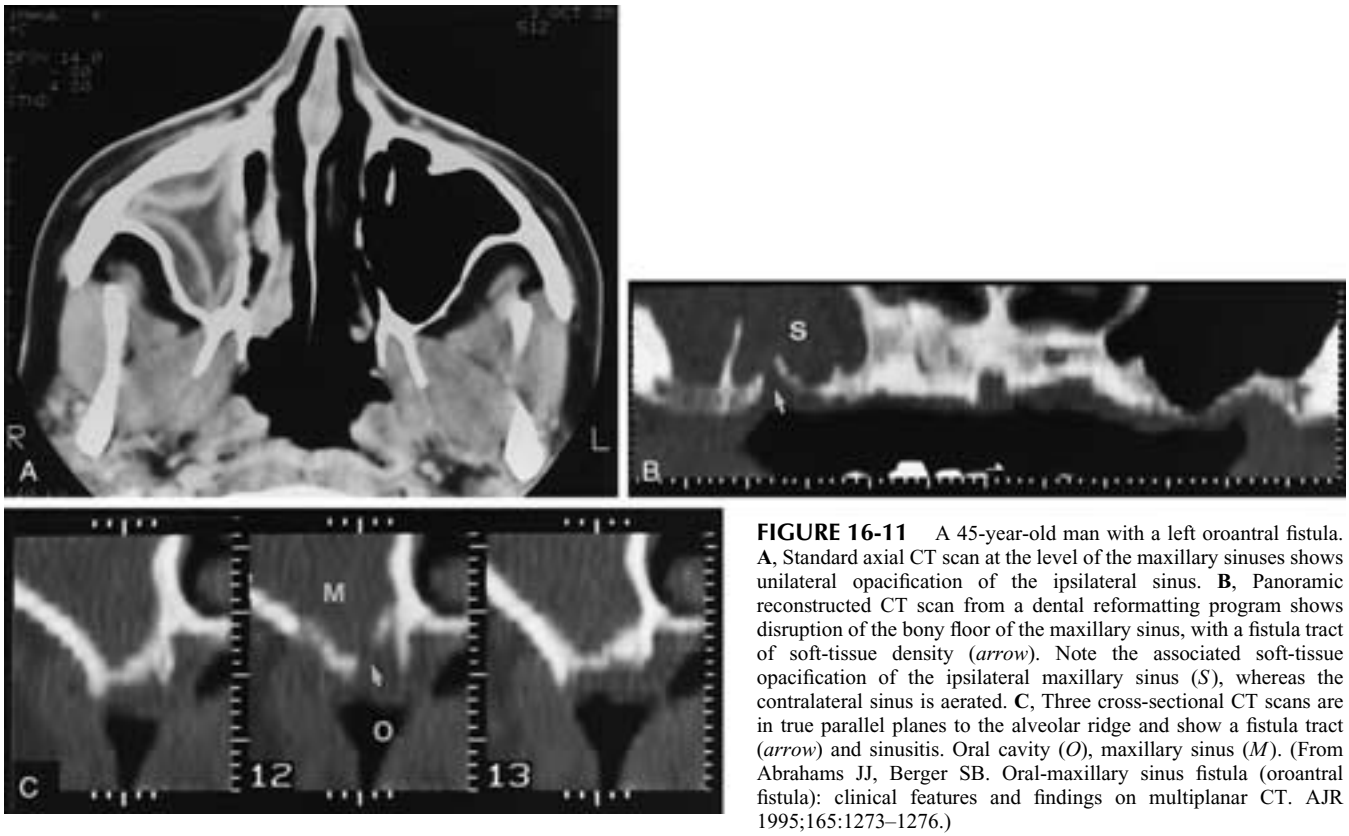

FIGURE 16-11 A 45-year-old man with a left oroantral fistula. **A**, Standard axial CT scan at the level of the maxillary sinuses shows unilateral opacification of the ipsilateral sinus. **B**, Panoramic reconstructed CT scan from a dental reformatting program shows disruption of the bony floor of the maxillary sinus, with a fistula tract of soft-tissue density (*arrow*). Note the associated soft-tissue opacification of the ipsilateral maxillary sinus (*S*), whereas the contralateral sinus is aerated. **C**, Three cross-sectional CT scans are in true parallel planes to the alveolar ridge and show a fistula tract (*arrow*) and sinusitis. Oral cavity (*O*), maxillary sinus (*M*). (From Abrahams JJ, Berger SB. Oral-maxillary sinus fistula (oroantral fistula): clinical features and findings on multiplanar CT. AJR 1995;165:1273–1276.)

VIEW IMAGE

Copyright © 2003, Mosby, Inc. All rights reserved.

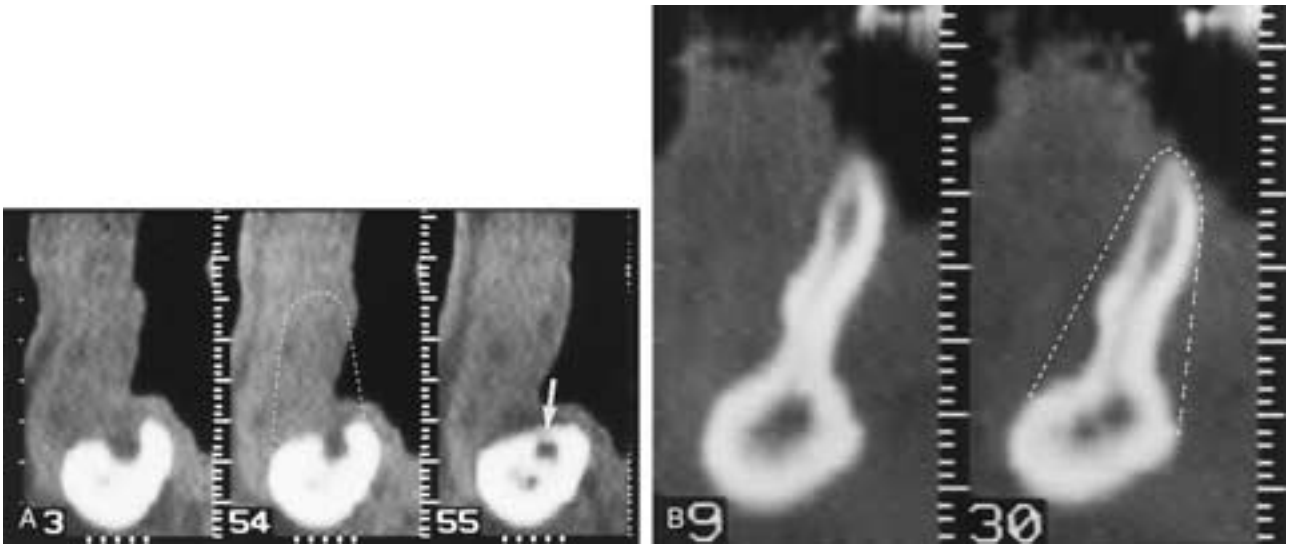

VIEW IMAGE

FIGURE 16-12 Cross-sectional views of the mandible in two different patients demonstrating bone resorption and atrophy. **A**, Bone loss and atrophy of the height of the mandible in this patient cause the mandibular canal (*arrow*) to sit immediately under the gingival surface. The dotted line demonstrates how the bone contour might have appeared before atrophy. The patient has insufficient bone for implants. (From Abrahams JJ. The role of diagnostic imaging in dental implantology. Radiol Clin North Am 1993;31(1):163–180.) **B**, The width of the mandible in this patient has been considerably diminished due to atrophy. The dotted line again demonstrates how the bone might have appeared before atrophy. (From Abrahams JJ. CT assessment of dental implant planning. Oral Maxillofac Surg Clin North Am 1992;4:1–18.)

the periosteum in the floor of the maxillary sinus and packs a freeze-dried bone graft between the elevated periosteum and the bony floor. After this heals, it will increase the height of the alveolar bone available in the maxilla. In both the mandible and maxilla, various bone grafts alone, often from iliac crest, have been used to increase the height and width of the alveolar process. These grafts may be supplemented with freeze-dried bone.

Finally, if the implant is placed and either the buccal or lingual surface is exposed and uncovered by bone, a procedure known as guided tissue regeneration, which utilizes Gortex as a physical barrier, can be performed to regenerate the bone adjacent to the implant in the following manner. Bone graft is first packed around the exposed surface of the implant, and then a piece of Gortex fabric is placed between the bone graft and soft tissues. The Gortex acts as a barrier, preventing the soft tissues from growing into the bone graft, thus allowing time for the graft to take. Typically the Gortex remains in place for about 6 weeks and is then removed. This procedure can also be used when placing an implant in a fresh extraction socket and for filling a periodontal pocket with bone graft, as illustrated in Figure 16-7B.

REFERENCES

1. Albrektsson T, Lekholm W. Osseo- integration: current state of the art. Dent Clin North Am 1989;33:537–544.
2. James R. The support system and perigingival defense mechanism of oral implants. J Oral Implant 1975;6:270–285.
3. Weiss C. Tissue integration of dental endosseous implants: description and comparative analysis of the fibro-osseous integration and osseous integration systems. J Oral Implant 1986;12:169–214.
4. Adell R, Lukholm U, Rockler B, et al. A 15-year study of osseointegrated implants in the treatment of the edentulous jaw. Int J Oral Maxillofac Surg 1981;10:387–416.
5. Branemark PI. Introduction to osseointegration. In: Branemark PI, Zarb G, Albrektsson T, eds. Tissue Integrated Protheses. Chicago and Berlin: Quintessence, 1985.
6. Albrektsson T. A multicenter report on osseointegrated oral implants. J Prosthet Dent 1988;60(1):75–84.
7. Delbalso AM, Greiner FG, Licata N. Role of diagnostic imaging in evaluation of the dental implant patient. Radiographics 1994;14: 699–719.
8. Krauser JT. Hydroxyapatite-coated dental implants. Dent Clin North Am 1989;33:879–903.
9. Moy PK, Weinlaender M, Kenney EB, et al. Soft tissue modifications of surgical techniques for placement and uncovering of osseointegrated implants. Dental Clin North Am 1989;4:665–699.
10. McGivney GP, Haughton V, Strandt JA, et al. A comparison of computed-assisted tomography and data-gathering modalities in prostodontics. Int J Oral Maxillofac Surg 1986;1:55–68.
11. Wishan M, Bahat O, Krane M. Computed tomography as an adjunct in dental implant surgery. Int J Periodont Restor Dentistry 1988; 8:31–47.
12. Rothman SLG, Chafetz N, Rhodes M, et al. CT in the pre-operative assessment of the mandible and maxilla for endosseous implant surgery. Radiology 1988;168:171–175.
13. Schwarz MS, Rothman SLGM, Chatetz N, et al. Computed tomography in dental implantation surgery. Dent Clin North Am 1989;33:555–597.
14. Schwarz MS, Rothman SLGM, Rhodes ML. Computed tomography. Part I. Pre-operative assessment of the mandible for endosseous implant surgery. Int J Oral Maxillofac Surg 1987;2:137–141.
15. Schwarz MS, Rothman SLGM, Rhodes ML, et al. Computed tomography. Part II. Pre-operative assessment of the mandible for endosseous implant surgery. Int J Oral Maxillofac Surg 1987;2:143–148.

Copyright © 2003, Mosby, Inc. All rights reserved.

16. Abrahams JJ. The role of diagnostic imaging in dental implantology. Radiol Clin North Am 1993;31(1):163–180.
17. Abrahams JJ, Olivario P. Odontogenic cysts: improved imaging with a dental CT software program. AJNR 1993;14:367–374.
18. Fogelman D, Huang AB. Prospective evaluation of lesions of the mandible and maxilla: findings on multiplanar and three-dimentional CT. AJR 1994;163:693–698.
19. Yanagisawa K, Friedman C, Abrahams JJ. DentaScan imaging of the mandible and maxilla. Head Neck J 1993;15:1–7.
20. Burgett F. Periodontal disease. In: Regezi JA, Sciubba JJ, eds. Oral Pathology: Clinical-Pathologic Correlations. Philadelphia: WB Saunders, 1989;503–519.
21. Regezi J, Sciubba J. Oral Pathology: Clinical-Pathological Correlation. Philadelphia: WB Saunders, 1989;301–336.
22. Regezi J, Sciubba J. Oral Pathology: Clinical-Pathological Correlation. Philadelphia: WB Saunders, 1989;390–404.
23. Abrahams JJ, Glassberg RM. Dental disease: a frequently unrecognized cause of maxillary sinus abnormalities? AJR 1995;166:1219–1223.
24. Abrahams JJ, Berger SB. Oral-maxillary sinus fistula (oro-antral fistula): clinical presentation and evaluation with multiplanar CT. AJR 1995;165:1273–1276.

Copyright © 2003, Mosby, Inc. All rights reserved.

17

Jaw: Cysts, Tumors, and Nontumorous Lesions

Alfred L. Weber, Takashi Kaneda, Steven J. Scrivani, and Shahid Aziz

SECTION ONE: PATHOLOGIC STATES
INTRODUCTION
CYSTS
- Definition and Classification
- Odontogenic Cysts
  - Periapical (Radicular) Cyst
  - Dentigerous (Follicular) Cyst
  - Odontogenic Keratocyst
    - *Basal Cell Nevus Syndrome (Gorlin's or Gorlin-Goltz Syndrome)*
  - Calcifying Odontogenic Cyst (Gorlin Cyst)
  - Other Odontogenic Cysts
- Nonodontogenic Cysts and Pseudocysts
  - Incisive Canal Cyst (Nasopalatine Duct Cyst)
  - Solitary, Simple, or Hemorrhagic Bone Cyst (Traumatic Bone Cyst)
  - Aneurysmal Bone Cyst
  - Static Bone Cavity (Stafne Cyst)
  - Medullary Pseudocyst

BENIGN ODONTOGENIC TUMORS AND RELATED TUMOR-LIKE CONDITIONS
- Ameloblastoma (Epithelial Origin)
- Calcifying Epithelial Odontogenic Tumor (Pindborg Tumor)
- Odontoma (Mixed Tumor)
  - Complex Odontoma
  - Compound Odontoma
  - Ameloblastic Fibroodontoma
  - Adenomatoid Odontogenic Tumor
  - Odontogenic Myxoma

CEMENTAL LESIONS
- Periapical Cemental Dysplasia and Florid Cemental Dysplasia (Florid Cementoosseous Dysplasia)
- Benign Cementoblastoma

BENIGN NONODONTOGENIC TUMORS
- Exostosis
- Osteoma
- Osteochondroma
- Chondroma
- Synovial Chondromatosis
- Giant Cell Lesions

LANGERHANS HISTIOCYTOSIS (HISTIOCYTOSIS X)
- Letterer-Siwe Disease
- Hand-Schuller-Christian Disease
- Eosinophilic Granuloma

FIBROOSSEOUS LESIONS
- Fibrous Dysplasia
- Ossifying Fibromas (Cemento-Ossifying Fibromas, Cementifying Fibromas)
- Paget's Disease (Osteitis Deformans)

VASCULAR LESIONS
- Hemangioma
- Vascular Malformation

NEUROGENIC TUMORS
MALIGNANT TUMORS
- Carcinoma
- Mucoepidermoid Carcinoma
- Metastatic Jaw Tumor
- Sarcoma
  - Osteogenic Sarcoma
  - Fibrosarcoma
  - Ewing's Sarcoma
- Malignant Lymphoma
- Multiple Myeloma
- Leukemia

INFLAMMATORY CONDITION OF THE MANDIBLE
- Osteomyelitis

Copyright © 2003, Mosby, Inc. All rights reserved.

Suppurative Osteomyelitis
Osteomyelitis with Periostitis
Tuberculous Osteomyelitis
Sclerosing Osteomyelitis
Osteoradionecrosis
SECTION TWO: SYSTEMATIC APPROACH TO IMAGING DIAGNOSIS OF JAW LESIONS
RADIOLUCENT LESIONS
Well-Defined Radiolucent Lesions
Ill-Defined Radiolucent Lesions
MIXED RADIOLUCENT-RADIOPAQUE LESIONS
RADIOPAQUE LESIONS
MR IMAGING
SECTION THREE: DENTAL ANOMALIES AND SYSTEMIC DISEASE
DENTAL ANOMALIES
Supernumerary Teeth
Hypodontia
Macrodontia and Microdontia
Dens in Dente (Dens Invaginatus)
Pulp Stones
Enamel Pearls
Amelogenesis Imperfecta
Dentinogenesis Imperfecta
Taurodontia
Dentin Dysplasias
DENTAL MANIFESTATION OF METABOLIC AND SYSTEMIC CONDITIONS

SECTION ONE

PATHOLOGIC STATES

INTRODUCTION

Lesions developing within the jaws can arise from the dental elements, bone, nerves, or blood vessels. Classifications of these jaw lesions have varied considerably, with no universally accepted terminology. Some of these classifications have emphasized the presumed cell of origin of various tumors, while the cysts have been classified as being either developmental or inflammatory in etiology. However, as the theories of derivation evolve, classifications change. The World Health Organization (WHO) classification published in 1992 is widely accepted (Table 17-1).[1] In this classification, the tumors are separated into benign and malignant types and further subdivided based on the odontogenic tissue types involved in the generation of the lesion. This section does not precisely follow the WHO classification, and not all of the rare tumors mentioned in it are included in this chapter. Several excellent and more complete reference works are cited in the References (also see Chapters 6, 15, and 27 for further discussions of these lesions).[2, 3]

It should be noted that the groupings in this section are not precise. For instance, the various cemental lesions are grouped together under benign odontogenic tumors and tumor-like conditions. Clearly, many of these lesions could have just as easily been included in the fibroosseous category. It is hoped that the organization of this chapter will be helpful to those who are less familiar with maxillofacial lesions and allow this complex topic to be more readily understood. The cystic lesions are discussed first, followed by true tumors and tumor-like conditions. Finally, infections of the jaw are discussed.

CYSTS

Definition and Classification

A cyst is characterized pathologically as an epithelium-lined cavity that contains fluid or semisolid material.[4] In most cases, microscopic examination of the lining tissue, as well as the clinical and radiographic findings, is necessary to achieve a diagnosis.

Cysts frequently occur in the jaw and appear radiographically as either unilocular or multilocular lucent areas of varying size and definition. Cysts of the mandible can come to clinical attention by remodeling bone and thus weakening the mandible, causing functional disturbances, or by the effects of secondary cyst infection. Delayed tooth eruption and displacement and resorption of tooth roots are often seen on imaging, and the cyst's relationship to a tooth is an important differential diagnostic feature. On the basis of the cell of origin, cysts have been subdivided into odontogenic and nonodontogenic types.

Odontogenic cysts arise from tooth derivatives.[5] Frequently, odontogenic cysts are divided into inflammatory and developmental types, with the developmental variety not being directly associated with inflammation. In some lesions the pathogenesis is unclear. Histologic analysis of the epithelial layers, the presence of cyst calcification, and the clinicial findings allow further subdivision of these cysts. The term *residual cyst* is frequently applied to any cyst (but specifically to a periodontal apical cyst) that remains or develops after surgical removal of a tooth.

Most odontogenic cysts are developmental in origin.[1] The fissural variety, as the name implies, arise along lines of fusion of the various bones and embryonic processes, and they are classified according to their anatomic location. Several cysts previously classified as fissural cysts have been moved into other categories, as their relationship to embryonic fusion or, alternatively, their worthiness of a separate category has been questioned. Developmental cysts

Copyright © 2003, Mosby, Inc. All rights reserved.

Table 17-1
WHO HISTOLOGIC CLASSIFICATION OF JAW TUMORS AND CYSTS
The classification is provided for completeness. Classifications of jaw lesions vary, and this chapter does not follow this classification exactly.

Histologic Classification of Odontogenic Tumors

Neoplasms and Other* Tumors Related to the Odontogenic Apparatus

Benign

*Odontogenic epithelium without odontogenic ectomesenchyme**
- Ameloblastoma
- Squamous odontogenic tumor
- Calcifying epithelial odontogenic tumor (Pindborg tumor)
- Clear cell odontogenic tumor

*Odontogenic epithelium with odontogenic ectomesenchyme, with or without dental hard-tissue formation**
- Ameloblastic fibroma
- Ameloblastic fibrodentinoma (dentinoma) and ameloblastic fibroodontoma
- Odontoameloblastoma
- Adenomatoid odontogenic tumor
- Calcifying odontogenic cyst
- Complex odontoma
- Compound odontoma

*Odontogenic ectomesenchyme with or without included odontogenic epithelium**
- Odontogenic fibroma
- Myxoma (odontogenic myxoma, myxofibroma)
- Benign cementoblastoma (cementoblastoma, true cementoma)

Malignant

Odontogenic carcinomas
- Malignant ameloblastoma
- Primary intraosseous carcinoma
- Malignant variants of other odontogenic epithelial tumors
- Malignant changes in odontogenic cysts

Odontogenic sarcomas
- Ameloblastic fibrosarcoma (ameloblastic sarcoma)
- Ameloblastic fibrodentinosarcoma and ameloblastic fibroodontosarcoma
- Odontogenic carcinosarcoma

Neoplasms and Other Lesions Related to Bone

Osteogenic neoplasms
- Cemento-ossifying fibroma (cementifying fibroma, ossifying fibroma)

Nonneoplastic bone lesions
- Fibrous dysplasia of the jaws

Cementoosseous dysplasias
- Periapical cemental dysplasia (periapical fibrous dysplasia)
- Florid cementoosseous dysplasia (gigantiform cementoma, familial multiple cementomas)
- Other cementoosseous dysplasias
- Cherubism (familial multiocular cystic disease of the jaws)
- Central giant cell granuloma
- Aneurysmal bone cyst
- Solitary bone cyst (traumatic, simple, haemorrhagic bone cyst)

Other Tumors
- Melanotic neuroectodermal tumor of infancy (melanotic progonoma)

Epithelial Cysts

Developmental

Odontogenic
- ''Gingival cysts'' of infants (Epstein pearls)
- Odontogenic keratocyst (primordial cyst)
- Dentigerous (follicular) cyst
- Eruption cyst
- Lateral periodontal cyst
- Gingival cyst of adults
- Glandular odontogenic cyst; sialoodontogenic cyst

Nonodontogenic
- Nasopalatine duct (incisive canal) cyst
- Nasolabial (nasoalveolar) cyst

Inflammatory
- Radicular cyst
- Apical and lateral
- Residual
- Paradental (inflammatory collateral, mandibular infected buccal) cyst

*The enamel organ derives from the odontogenic epithelium developing from the ectoderm of the oral cavity. The dental papilla and follicle are considered ectomesenchymal, derived partly from the neural crest. Lesions that contain odontogenic ectomesenchyme, as well as the odontogenic epithelium, have the capability of producing dentin and enamel. Those without ectomesenchyme cannot. Some lesions arise primarily from the mesenchyme and appear to incidentally include ''odontogenic epithelium,'' but the odontogenic epithelium does not play a key role in producing the lesion.

From Kramer IRH, Pindborg JJ, Shear M. Histological Typing of Odontogenic Tumours, 2nd ed. Berlin and New York: Springer-Verlag, 1992;7–9.

Copyright © 2003, Mosby, Inc. All rights reserved.

VIEW IMAGE

FIGURE 17-1 Radicular cyst of the left mandibular second molar tooth. Pantomogram of the mandible demonstrates a cystic, well-defined lesion around the apices of the lower left mandibular tooth. Note the sclerosis around the cyst and adjacent mandibular teeth, which is secondary to chronic osteitis.

include other cyst types derived from embryologic structures, such as dermoid cysts, and cysts arising from other causes, such as solitary bone cysts and aneurysmal bone cysts. Stafne's cyst is not a cyst at all but rather a variation in the development of the cortex of the bone.

Odontogenic Cysts

Periapical (Radicular) Cyst

Periapical (radicular) cyst is by far the most common odontogenic cyst.[1] It may form at any time during life, although the peak incidence is between 30 and 50 years of age. There is no sex predilection. This cyst is associated with carious teeth. Caries lead to infection of the pulp cavity and eventually pulp necrosis. Infection passes out of the apex of the root, resulting in apical periodontitis leading to an acute abscess or a more chronic granuloma. From these stages, the disease can quiesce and form the periapical (radicular) cyst. Most periapical cysts are discovered incidentally on radiography, but expansion of the cyst may cause a clinically noticeable displacement of teeth, and swelling and pain may occur when the cyst enlarges or becomes secondarily infected.

Radiographically, a radicular cyst is a well-circumscribed radiolucency arising from the apex of the tooth and bounded by a thin rim of cortical bone (Figs. 17-1 and 17-2). Large lesions may expand the cortical plates.[6] A radicular cyst can displace tooth structures and may cause slight root resorption. If the cyst occurs in the maxilla, extension into the maxillary sinus may be observed (Fig. 17-3). Radiographically, radicular cysts cannot be differentiated from periapical granulomas, which usually are less than 1.6 cm in diameter. On MR imaging, the lesions usually have high signal intensity on T2-weighted images and variable signal

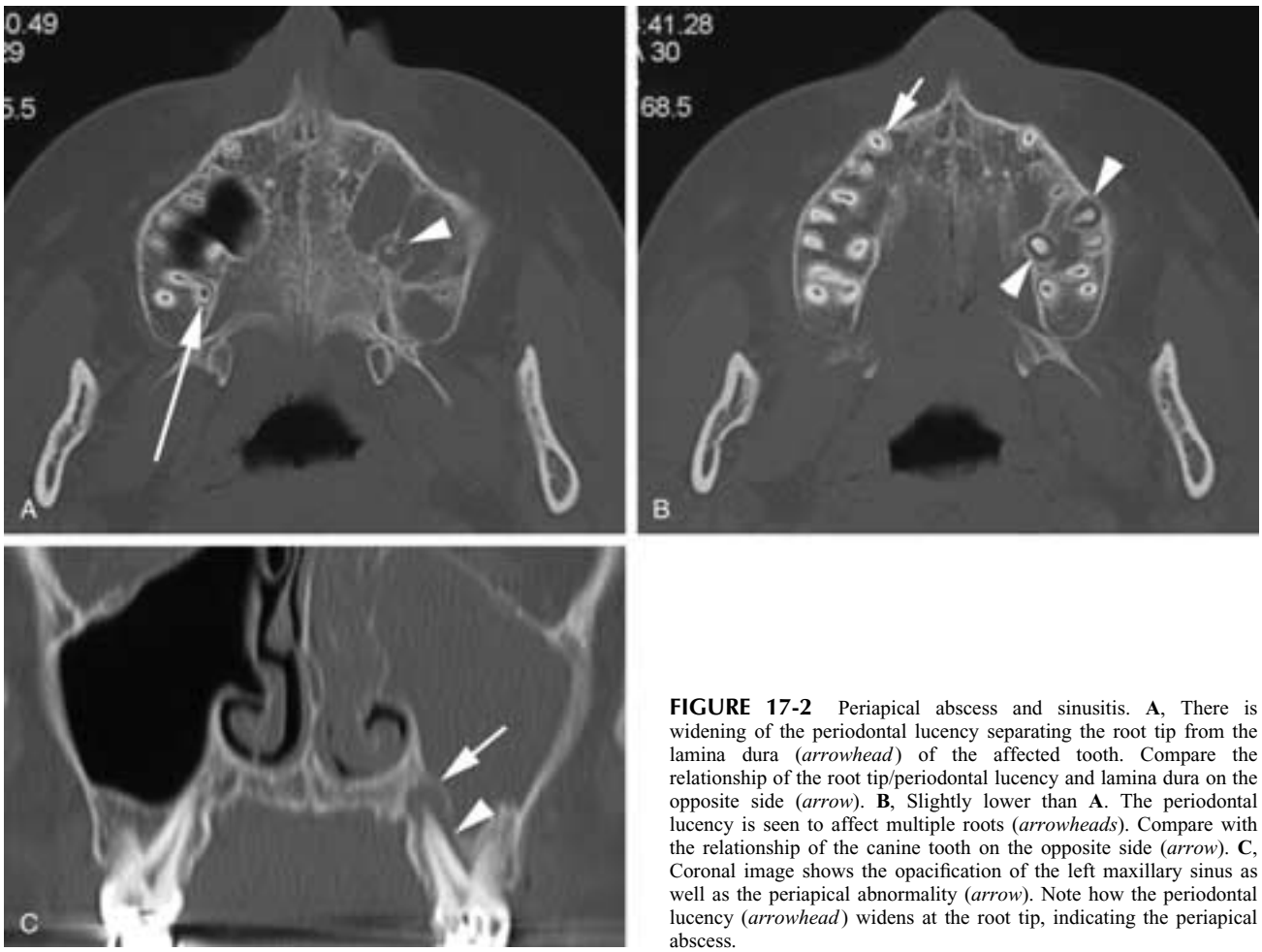

VIEW IMAGE

FIGURE 17-2 Periapical abscess and sinusitis. **A**, There is widening of the periodontal lucency separating the root tip from the lamina dura (*arrowhead*) of the affected tooth. Compare the relationship of the root tip/periodontal lucency and lamina dura on the opposite side (*arrow*). **B**, Slightly lower than **A**. The periodontal lucency is seen to affect multiple roots (*arrowheads*). Compare with the relationship of the canine tooth on the opposite side (*arrow*). **C**, Coronal image shows the opacification of the left maxillary sinus as well as the periapical abnormality (*arrow*). Note how the periodontal lucency (*arrowhead*) widens at the root tip, indicating the periapical abscess.

Copyright © 2003, Mosby, Inc. All rights reserved.

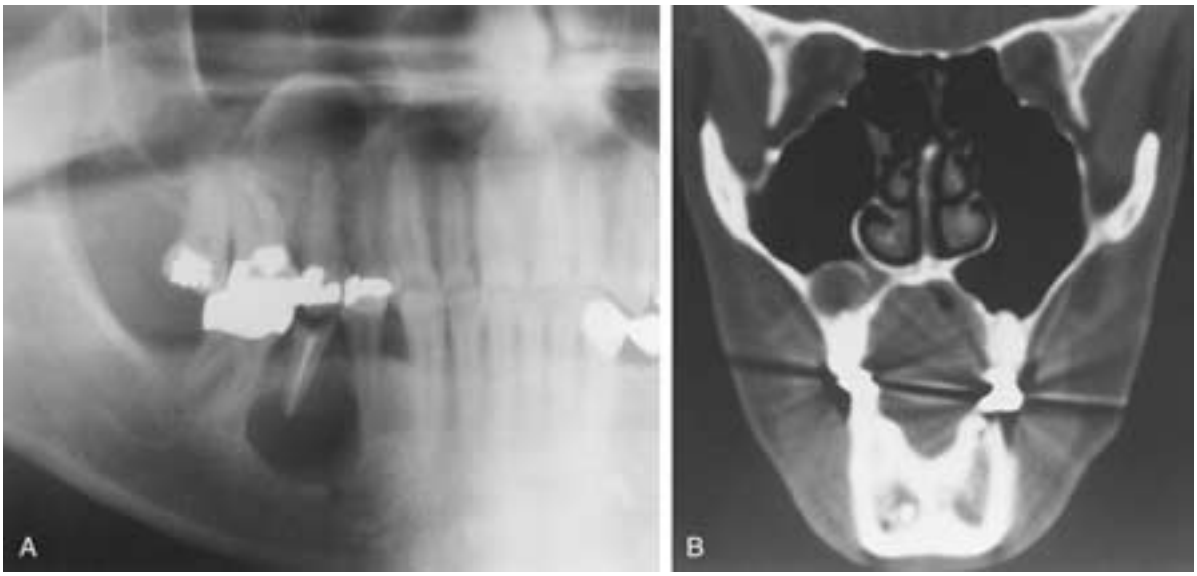

VIEW IMAGE

FIGURE 17-3 Radicular cyst. **A**, Pantomogram of the mandible and maxilla shows a radicular cyst around the apex of the right second premolar tooth within the mandible and around the apex of the upper right second premolar tooth. The upper radicular cyst bulges into the right antral cavity. **B**, Coronal CT of the paranasal sinuses shows the maxillary radicular cyst projecting into the floor of the right antrum.

intensity on T1-weighted images. On contrast-enhanced MR imaging, the cysts wall is usually thick and there is strong enhancement, probably representing inflammation.

Dentigerous (Follicular) Cyst

The dentigerous cyst is the second most common odontogenic cyst after the inflammatory periapical cyst . The dentigerous cyst forms around the crown of an unerupted tooth (Figs. 17-4 and 17-5). This tooth will never erupt. Fluid collects between layers of epithelium or between the epithelium and the enamel. Most dentigerous cysts become evident during the third and fourth decades of life, and most (75%) are located in the mandible. In the usual case, the tooth crown projects into the lumen of the cystic cavity. The wall of the cyst tends to converge to the cementoenamel junction. With continued cyst growth, only a limited portion of the tooth may be attached to the cyst lining.

Dentigerous cysts vary greatly in size, ranging from less than 2 cm in diameter to those that cause massive expansion of the jaw. They may cause displacement of teeth, but apical resorption of tooth structures is uncommon. Fractures and superimposed infection may develop in the cyst. Dentigerous cysts do not demonstrate an extracystic soft-tissue mass, as seen in ameloblastomas, but ameloblastomas, mucoepidermoid tumors, and carcinomas may develop in the wall of the cyst.

On imaging, a mandibular dentigerous cyst appears as a well-circumscribed unilocular area of osteolysis that incorporates the crown of a tooth. The adjacent teeth are displaced and may be partly eroded. Dentigerous cysts in the maxilla often extend into the antrum, displacing and remodeling the bony sinus wall (Fig. 17-6). Large cysts may project into the nasal cavity or infratemporal fossa and may elevate the floor of the orbit. In the mandible, buccal or lingual cortical expansion and thinning are noted. On MR imaging, the contents of the cyst show high signal intensity on T2-weighted images and low to intermediate signal intensity on T1-weighted images. The tooth itself is an area of signal void (Fig. 17-7). The lining of the cyst is thin and regular in thickness and may show slight enhancement after contrast injection.

FIGURE 17-4 Dentigerous cyst. Pantomogram of the mandible shows a sharply marginated, oval-shaped cyst in the body of the right mandible (*short arrow*). The crown (*long arrow*) of the impacted third molar tooth is incorporated into the posterior portion of the cyst.

VIEW IMAGE

Copyright © 2003, Mosby, Inc. All rights reserved.

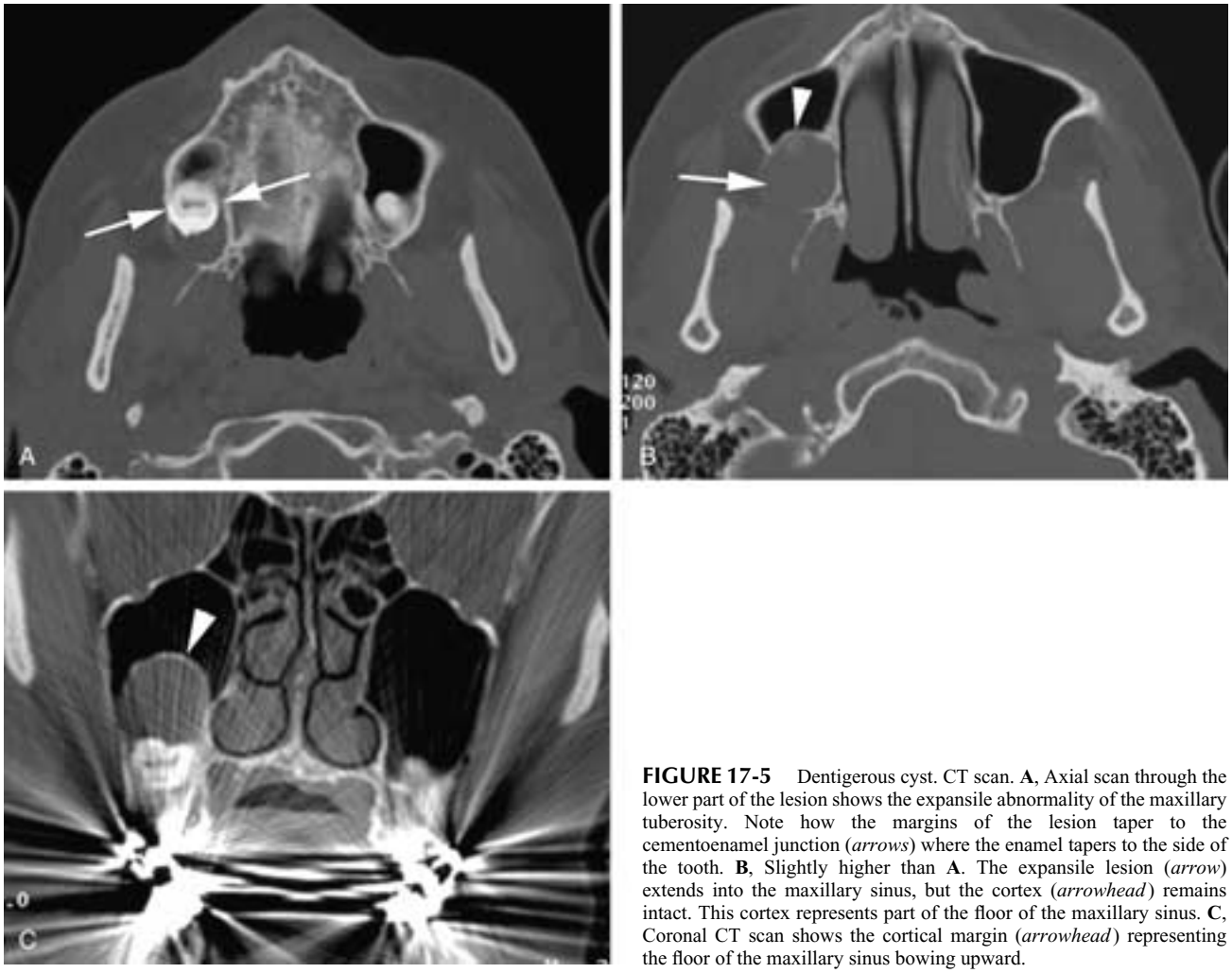

FIGURE 17-5 Dentigerous cyst. CT scan. **A**, Axial scan through the lower part of the lesion shows the expansile abnormality of the maxillary tuberosity. Note how the margins of the lesion taper to the cementoenamel junction (*arrows*) where the enamel tapers to the side of the tooth. **B**, Slightly higher than **A**. The expansile lesion (*arrow*) extends into the maxillary sinus, but the cortex (*arrowhead*) remains intact. This cortex represents part of the floor of the maxillary sinus. **C**, Coronal CT scan shows the cortical margin (*arrowhead*) representing the floor of the maxillary sinus bowing upward.

VIEW IMAGE

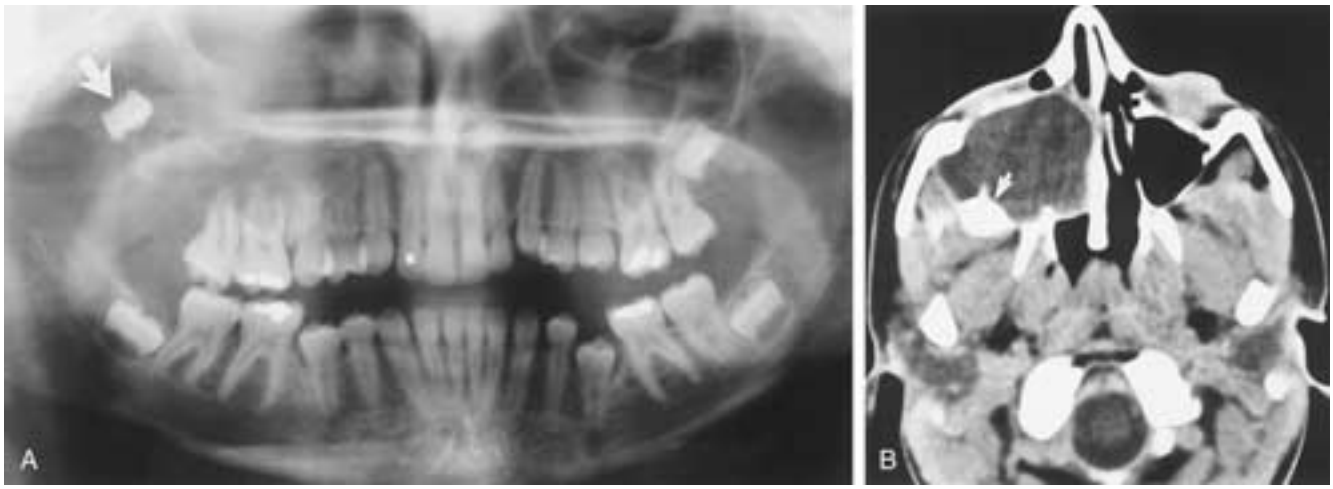

FIGURE 17-6 Dentigerous cyst. **A**, Pantomogram of the mandible and maxilla shows a displaced tooth in the upper lateral aspect of the right maxilla (*arrow*). There is a poorly defined expansile lesion in the same region. **B**, Axial CT demonstrates an expansile cystic lesion within the right antral cavity, with extension into the right nasal cavity and infratemporal fossa. Note the localized density at the posterior margin of this cyst representing a tooth that is incorporated into the cyst (*arrow*).

VIEW IMAGE

Copyright © 2003, Mosby, Inc. All rights reserved.

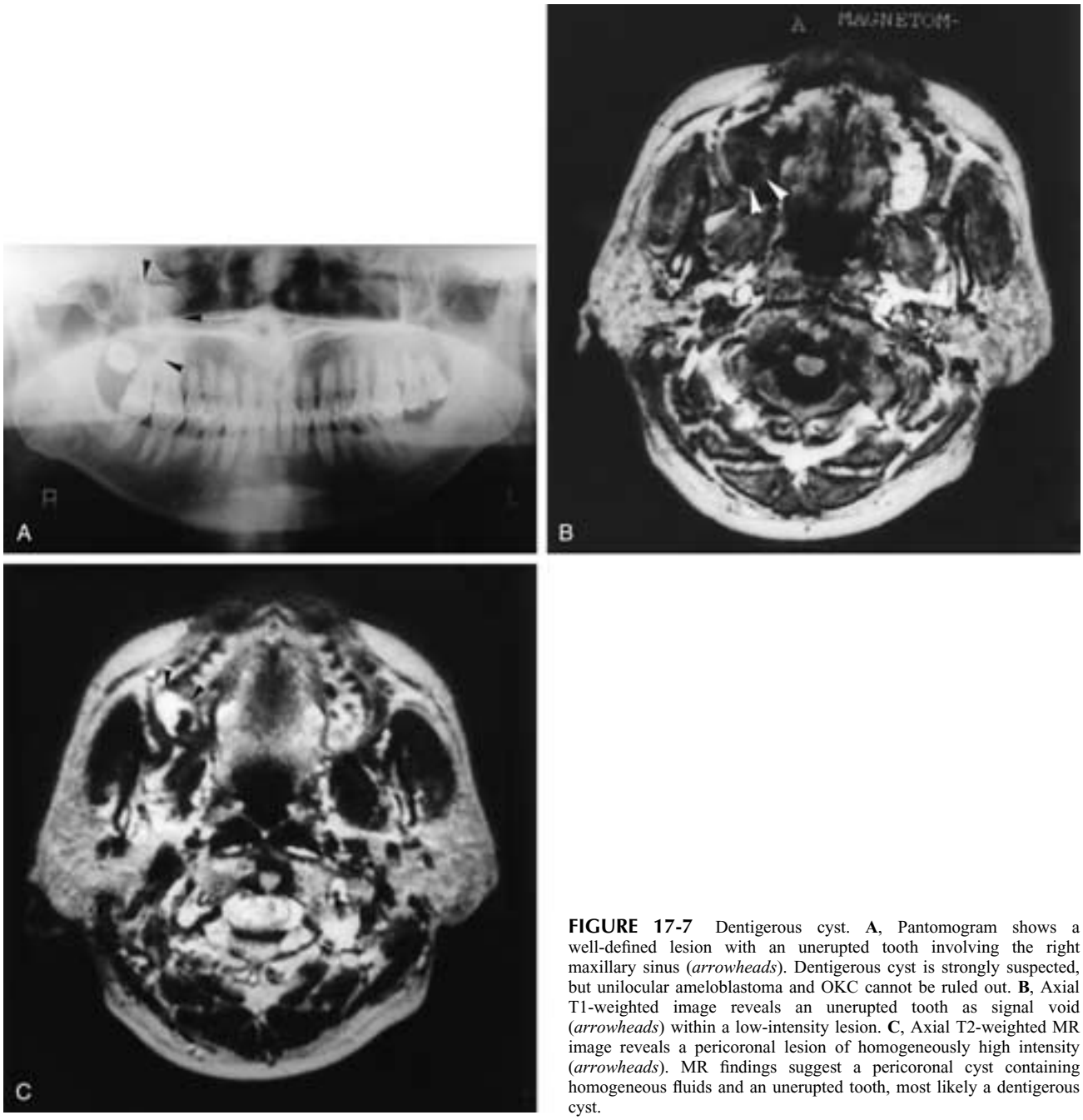

FIGURE 17-7 Dentigerous cyst. **A**, Pantomogram shows a well-defined lesion with an unerupted tooth involving the right maxillary sinus (*arrowheads*). Dentigerous cyst is strongly suspected, but unilocular ameloblastoma and OKC cannot be ruled out. **B**, Axial T1-weighted image reveals an unerupted tooth as signal void (*arrowheads*) within a low-intensity lesion. **C**, Axial T2-weighted MR image reveals a pericoronal lesion of homogeneously high intensity (*arrowheads*). MR findings suggest a pericoronal cyst containing homogeneous fluids and an unerupted tooth, most likely a dentigerous cyst.

VIEW IMAGE

Odontogenic Keratocyst

Odontogenic keratocysts (OKC) account for 3% to 11% of all jaw cysts and occur twice as often in the mandible as in the maxilla.[7–9] These cysts are found in patients of all ages, but the peak incidence is in the second and third decades of life. This cyst has been classified as a separate type of bone cyst because of its aggressive biologic behavior and histologic structure. Histologically, the cyst is lined by a stratified keratinizing squamous epithelium. The epithelium is characteristically thin, six to eight cell layers, and the keratinization is usually of the parakeratin type. Parakeratin has nuclei in the layer of keratin that borders the lining of the cyst. There is no keratogranular layer in the wall. Parakeratinization is a more disordered type of keratin formation than orthokeratinization. With the formation of orthokeratin, there is a granular layer and nuclei are not sloughed into the keratin. Orthokeratinizing epithelium is considered to reflect the normal keratinization process, as seen in the epithelial layer of the skin.

In the keratocyst, the interface between the epithelium and the connective tissue is flat, without rete ridge formation. The basal layer is prominent, with palisading cells containing darkly staining and enlarged nuclei. Daughter (satellite) cysts or microcysts may be observed microscopically. The recurrence rate has been variously reported as being between 20% and 60%. This high recurrence rate is thought to be the result of the specific abnormal biology of these cysts. Various hypotheses have

Copyright © 2003, Mosby, Inc. All rights reserved.

been proposed in an attempt to explain this rate and solve this problem.[10, 11]

The diagnosis depends on the cyst's microscopic features and is independent of its location and radiographic appearance. This cyst is a radiolucent lesion that may be multiloculated, with a smooth or scalloped border (Fig. 17-8). These cysts are characteristically located in the body and ramus of the mandible and may occur in conjunction with an impacted tooth (Figs. 17-9 and 17-10). The lesion usually grows along the length of the mandible and does not usually resorb teeth roots. CT shows a well-defined unilocular or multilocular cystic radiolucency with a bony sclerotic margin and bulging of the bony cortex (Fig. 17-11). Sometimes the content of the cyst shows higher density than water due to keratinized material.[12] The MR imaging appearance is variable but typically shows a cystic pattern with a regularly thin wall, heterogeneous intensity of fluid contents, and weak contrast enhancement of the cyst wall (Fig. 17-12).[13] The signal intensity on T2-weighted sequences is usually high but is variable, depending on the protein concentration of the contents.

One variant of the OKC has a true orthokeratinizing epithelial lining (see above). Although truly a keratocyst, the lesion exhibits significantly less aggressive behavior than the parakeratinizing variant. Some prefer to categorize these lesions separately as an orthokeratinizing keratocyst rather

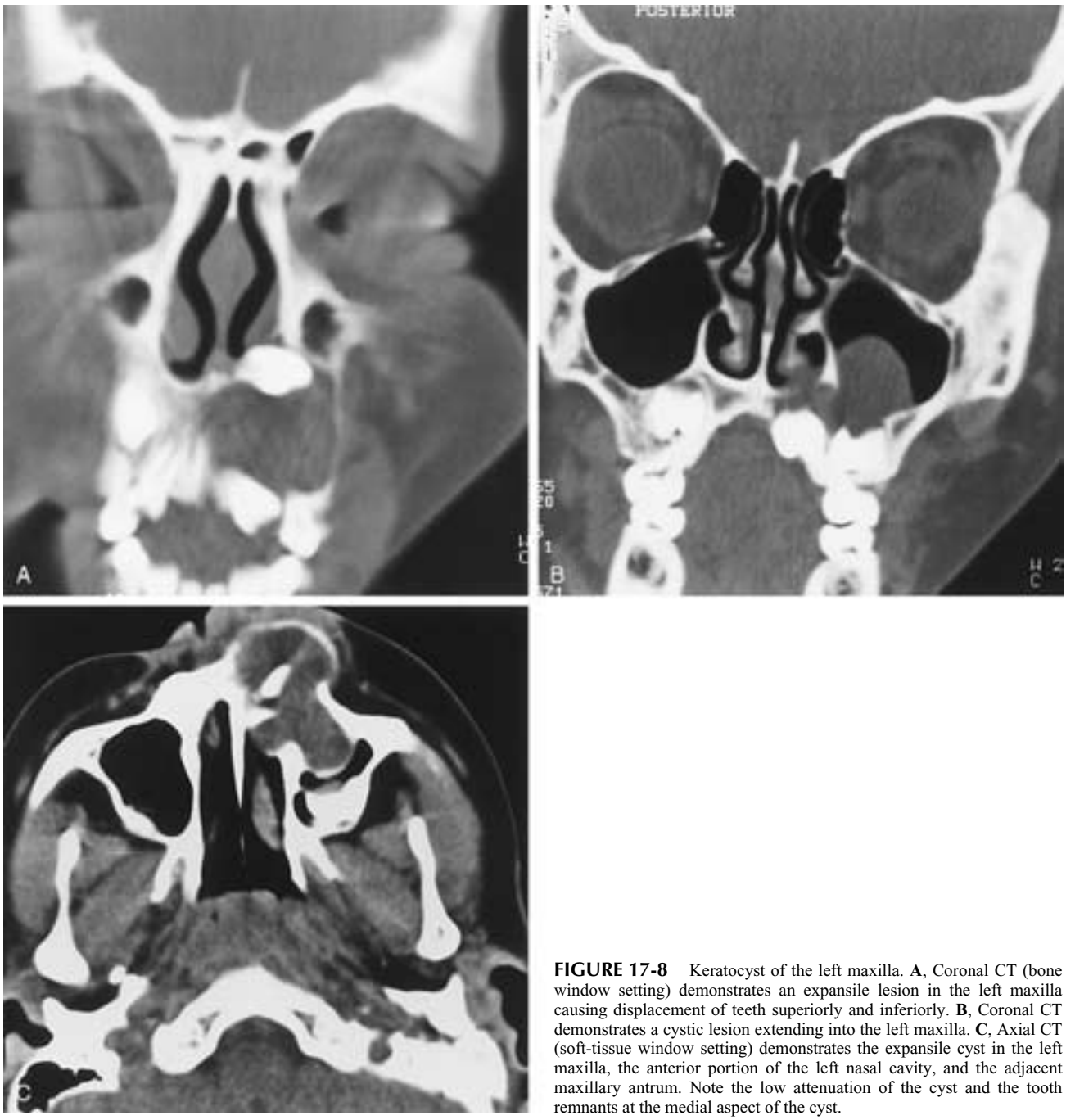

FIGURE 17-8 Keratocyst of the left maxilla. **A**, Coronal CT (bone window setting) demonstrates an expansile lesion in the left maxilla causing displacement of teeth superiorly and inferiorly. **B**, Coronal CT demonstrates a cystic lesion extending into the left maxilla. **C**, Axial CT (soft-tissue window setting) demonstrates the expansile cyst in the left maxilla, the anterior portion of the left nasal cavity, and the adjacent maxillary antrum. Note the low attenuation of the cyst and the tooth remnants at the medial aspect of the cyst.

VIEW IMAGE

Copyright © 2003, Mosby, Inc. All rights reserved.

VIEW IMAGE

FIGURE 17-9 Keratocyst. Oblique view of the mandible shows a multiloculated cyst in the posterior body of the mandible, angle of the mandible, and ramus. The third molar tooth is incorporated into the anterior part of the cyst. There is encroachment on the posterior aspect of the second molar tooth. Note that there is also expansion, with thinning of the anterior wall of the ascending ramus.

than a variant of the typical keratocyst. At imaging, the two lesions cannot be distinguished unless studies over time show the aggressive growth more typical of the parakeratinizing OKC.

The surgical management of OKC demands special attention because of the aggressive biologic behavior of these benign lesions.[14] Surgical treatment over the years has included decompression and marsupialization, enucleation and curettage, and local and en bloc resection and reconstruction. Various adjuvant methods of treatment have been used to decrease the potential for recurrence or to deal with a recurrence. These include extraction of teeth in continuity with the cyst, excision of overlying mucosa, and treatment of the surrounding bone with peripheral ostectomy, chemical cautery, or cryosurgery. Many of these lesions, especially recurrences, are treated with some combination of these surgical techniques. Regardless of the management strategy employed or the surgical outcome, these patients must be closely followed for many years.

The term *primordial cyst* is now usually considered to be synonymous with OKC. However, some consider the term to be more appropriately applied only to the rare cysts that contain nonkeratinized squamous epithelium rather than the typical keratinized lining typical of the keratocyst.[2] Primordial cysts are considered to arise from a degenerated enamel organ and are therefore found in place of a missing tooth (Fig. 17-13).

Basal Cell Nevus Syndrome (Gorlin's or Gorlin-Goltz Syndrome)

Basal cell nevus syndrome (nevoid basal cell carcinoma syndrome) is a genetic disorder inherited as an autosomal dominant trait with variable penetrance and expressivity.[15, 16] The syndrome becomes apparent between 5 and 10 years of age. There is no sex predilection, and many patients with this syndrome have slight mental retardation. The syndrome comprises a number of features that are classically grouped into five categories: cutaneous, skeletal, ophthalmologic, neurologic, and sexual. Among the most common features are multiple cysts of the jaw, multiple basal cell carcinomas, skeletal abnormalities, and ectopic calcifications. At least two of these findings must be present to establish a diagnosis.

The multiple jaw cysts develop early in childhood[17]; they may be either unilocular or multilocular and often prove to be keratocysts varying in size from 1 mm to several centimeters (Fig. 17-14). Many investigators have suggested that the OKCs in basal cell nevus syndrome are histologically and biologically different from the solitary OKCs not associated with this syndrome. Those associated with the syndome occur earlier and are more likely to recur after excision. However, this concept is not universally agreed upon. Some investigators believe that the cysts associated with this syndrome are just larger, multilocular, and tend to have more frequent satellite microcysts that may account for their clinical behavior. Nevoid basal cell carcinomas tend to appear later than cysts, usually before 30 years of age, and are found especially on the face, trunk, neck, and arms. The most common skeletal abnormalities are bifid ribs, synostosis of ribs, kyphoscoliosis, vertebral fusion, mild ocular hypertelorism, prognathism, polydactyly, and frontal and temporoparietal bossing. The ectopic calcifications occur most frequently in the falx cerebri and other areas of the dura.

Calcifying Odontogenic Cyst (Gorlin Cyst)

A calcifying odontogenic cyst is a rare developmental odontogenic lesion having features of both a cyst and a solid neoplasm. It was defined as a distinct entity by Gorlin et al. in 1962[18] and is listed by the WHO as an odontogenic epithelial cyst having odontogenic ectomesenchyme, with or without dental hard tissue formation. In the most recent WHO classification, the calcifying odontogenic cyst is also classified as a tumor.[1] The terms *calcifying odontogenic cyst* and *odontogenic ghost cell tumor* are used. The ghost cell tumor designation results from a characteristic cell found in the wall of the cyst. Ghost cells have eosinophilic cytoplasm and no nuclei. These cells can calcify.

The lesion occurs at many ages but is most commonly found in the second or third decade of life, with an almost equal sex distribution and a similar incidence in the mandible and the maxilla. Those in the maxilla are usually anterior. Radiographically, the cyst may present as a unilocular or multilocular radiolucency with discrete, well-defined margins containing scattered calcifications of irregular size (Figs. 17-15 and 17-16).[19–22] Such opacities may produce a ''salt-and-pepper-like'' appearance. Displacement of teeth or root resorption is occasionally seen. The lesion is sometimes associated with unerupted teeth. If it is seen along with a complex odontoma, those opaque components may be seen to merge (Fig. 17-15). The radiologic appearance may be similar to that of adenomatoid odontogenic tumor, ameloblastic fibro-odontoma, or calcifying epithelial odontogenic tumor (Pinborg).

Copyright © 2003, Mosby, Inc. All rights reserved.

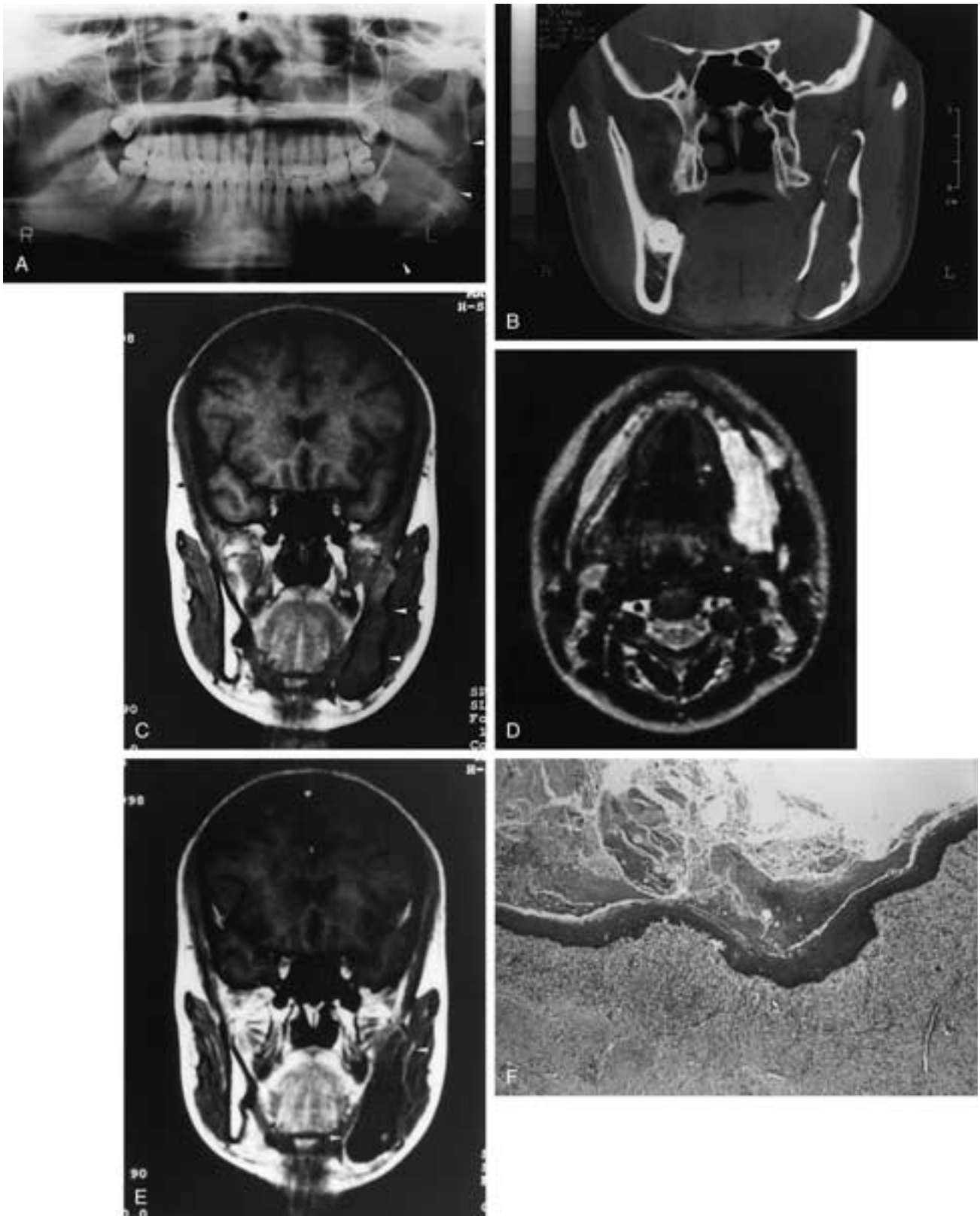

FIGURE 17-10 Unilocular odontogenic keratocyst in a 20-year-old woman. **A**, Panoramic radiograph shows a large, unilocular, expansile lesion (*arrowheads*) in the left side of the mandible. There is no root resorption of adjacent teeth. **B** Coronal CT shows an expansile unilocular lesion in the mandible. The bony sclerotic margin and bulging of the bony cortex can be seen. **C**, Axial T1-weighted MR image reveals a lesion of heterogeneously low to intermediate signal intensity in the mandible (*arrowheads*). **D**, On this axial T2-weighted MR image, the fluid contents of the cyst are heterogeneous in intensity. **E**, Gadolinium-enhanced MR image shows a thin cyst wall with weak enhancement. The cyst contents have heterogeneously low to intermediate signal intensity. The lack of solid tissue argues against the diagnosis of ameloblastoma, and OKC is suspected. **F**, Photomicrograph shows that the cyst has a uniformly thin wall with keratinization histopathologically (H & E. Original magnification ×100.)

VIEW IMAGE

Copyright © 2003, Mosby, Inc. All rights reserved.

Other Odontogenic Cysts

As stated, there is overlap in the descriptions of several entities. Several terms or named cysts deserve mention for completeness.[2, 3]

The lateral periodontal cyst is considered to be a developmental cyst arising from epithelial remnants in the periodontal ligament along the lateral aspect of the tooth root. It is not inflammatory and should be distinguished from the occasional occurrence of an inflammatory lateral radicular cyst that can occur here as well. The botryoid odontogenic cyst may simply be a multicystic variant of the lateral periodontal cyst.

Several cysts are thought by some to be most likely of an inflammatory origin, arising from epithelial rests in the periodontal space. The lateral radicular cyst has been mentioned as analogous to the periapical radicular cyst but occurring along the lateral aspect of the root. The term *paradental cyst* also describes an inflammatory cyst along the sides of the root. Originally described along the lateral aspect of the third molar, the term has been applied to other teeth as well.

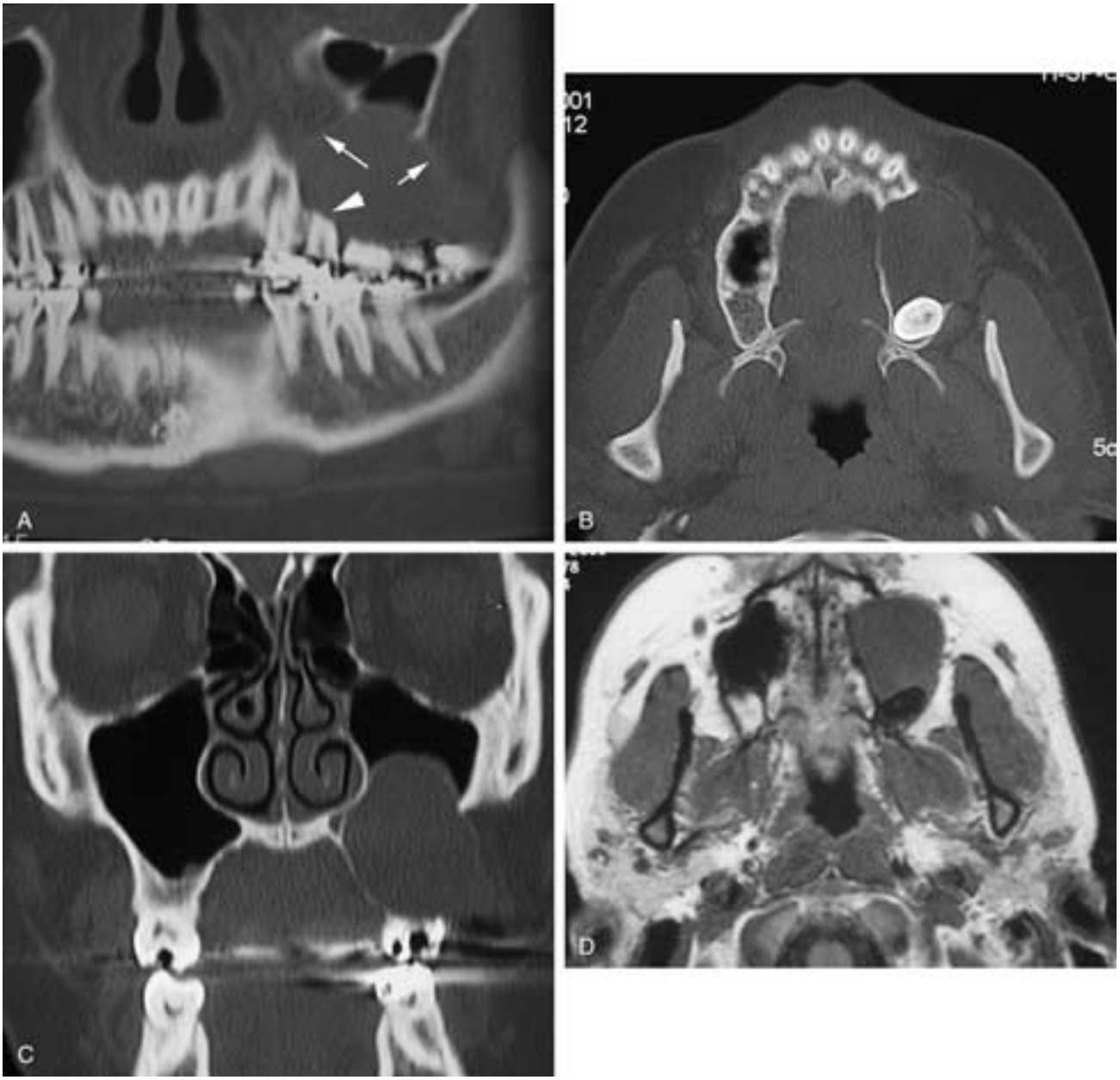

VIEW IMAGE

FIGURE 17-11 OKC. **A**, Panoramic reformat from multidetector spiral CT scan. The OKC is seen as an expansile abnormality in the left maxilla. Note the intact cortical line (*arrows*) as the lesion expands outward. Multiple root tips (*arrowhead*) are shortened and eroded. **B**, Axial bone algorithm CT shows the expansile abnormality in the lower maxilla. The lesion does have a relationship to the unerupted molar but does not show the typical configuration of a dentigerous cyst. **C**, Coronal CT shows the expanding abnormality enlarging the alveolar process and extending into the maxillary sinus. **D**, Axial T1-weighted MR image. The lesion shows low signal intensity.

Copyright © 2003, Mosby, Inc. All rights reserved.

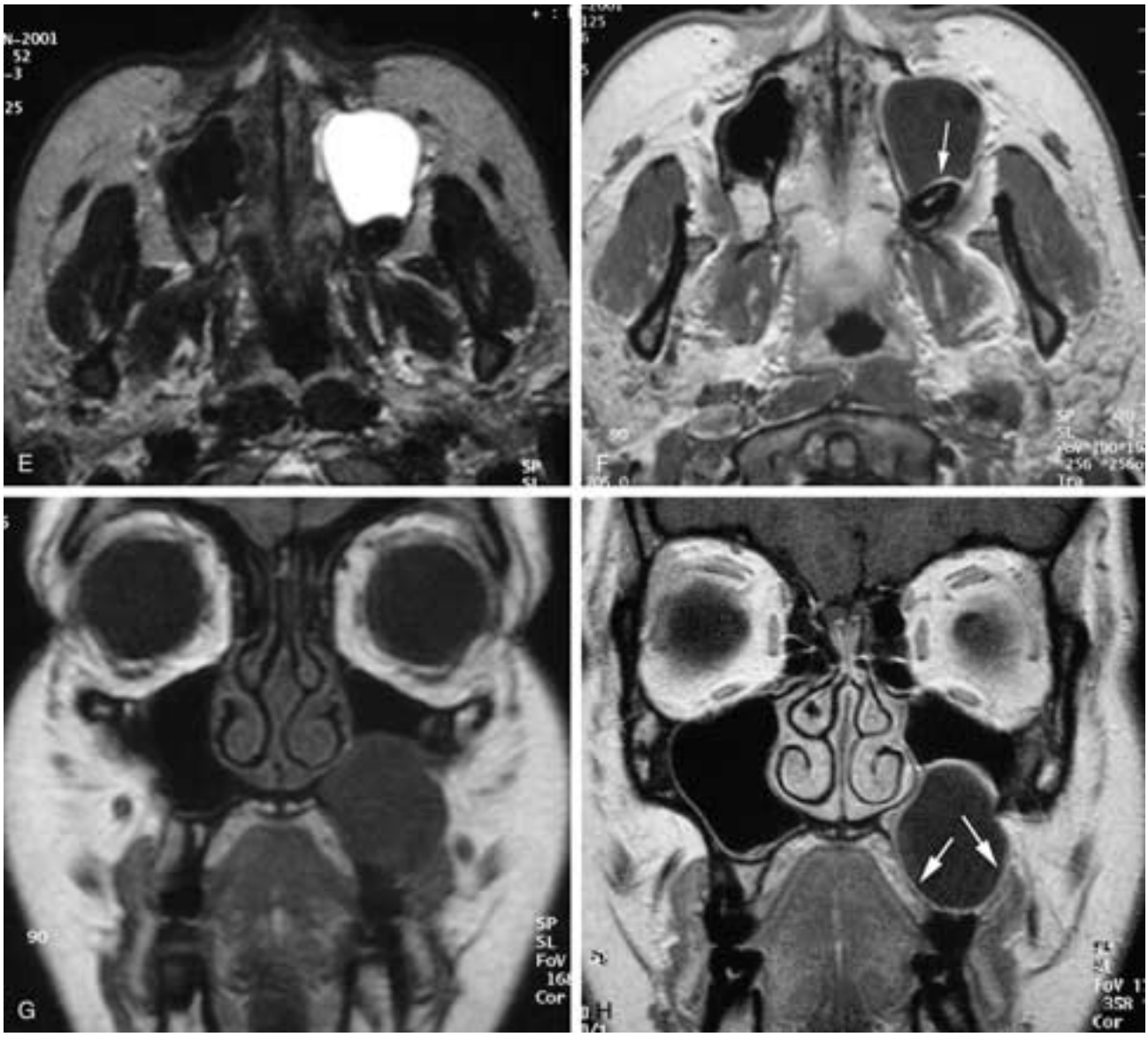

VIEW IMAGE

FIGURE 17-11 *Continued.* **E**, The lesion is homogeneously bright on this T2-weighted image. OKC can also be heterogeneous. **F**, Axial T1 postgadolinium image shows a thin, regular enhancing margin. Note that a thin soft-tissue enhancing margin (*arrow*) borders and ''covers'' the tooth. **G**, Coronal T1-weighted image. **H**, Coronal T1-weighted image after gadolinium enhancement shows the thin, regular enhancing wall (*arrows*) of the keratocyst.

The buccal bifurcation cyst arises from the periodontium at the bifurcation of the lateral (buccal) roots of the mandibular molars, usually the first. The roots tend to tip lingually. Although it is considered most likely related to inflammation, inflammation is not always present. The term *paradental cyst* (see above) has been applied to this lesion as well.[3]

Nonodontogenic Cysts and Pseudocysts

Incisive Canal Cyst (Nasopalatine Duct Cyst)

A nasopalatine duct cyst (incisive canal cyst) is a nonodontogenic developmental cyst or fissural cyst arising in the nasopalatine duct near the anterior palatine papilla.[23, 24] It is the most common nonodontogenic cyst. The cysts probably arise from epithelial remnants in the incisive canal. They can occur at any age but are most frequently found in the fourth and sixth decades of life, with no sex predilection. These cysts are usually asymptomatic, but some patients note swelling in the palate, especially when the cyst is primarily in the incisive papilla. Alternatively, the anterior maxilla can be remodeled forward, elevating the columella of the nose. Occasionally, patients notice a discharge of mucoid material and a salty taste through what are thought to be remnants of embryonic ductal structures on the palate.

Many of these cysts are small and are found on routine plain film radiographic surveys. It may be difficult on imaging to differentiate between an enlarged incisive fossa and an incisive canal cyst. The incisive canal cyst is always located at or close to the midline and usually is round or

Copyright © 2003, Mosby, Inc. All rights reserved.

ovoid, although it may be heart-shaped (Fig. 17-17). A condensed rim of cortical bone is often seen along the periphery, and the lesion may displace the roots of the central incisor teeth.

The nasolabial or nasoalveolar cyst is considered most likely a fissural cyst arising adjacent to bone at the root apex of the incisors just beneath the lip. It may scallop the bone along the anterior cortex of the maxilla. This lesion is also discussed in Chapter 6.

Several terms are no longer used. The term *globulomaxillary cyst* referred to a cyst located between the lateral incisor and the canine tooth, at the site thought to correspond to a developmental fusion line between the lateral nasal and maxillary processes.[25, 26] Today there is evidence that these cysts do not arise from ''trapped'' epithelium but are probably simply cysts of odontogenic origin (Fig. 17-18). A cyst in this location is now thought to be either a radicular cyst or perhaps a keratocyst.

The median palatal cyst is now frequently grouped with nasopalatine cysts rather than considered a separate entity.

Solitary, Simple, or Hemorrhagic Bone Cyst (Traumatic Bone Cyst)

Solitary, simple, or hemorrhagic bone cysts are seen more frequently in men than in women and are usually found in young people, with 70% occurring in the second decade of life.[27, 28] The etiologic factors are usually obscure. Yet, whether this cyst results from an injury not associated with a fracture that causes an intramedullary hematoma that disintegrates, producing the cyst within the bone, or is perhaps the result of aseptic necrosis or degeneration of an earlier benign tumor, the end result appears to be the same. A hemorrhagic bone cyst is a unilocular cavity that can be partly filled with a clear or sanguineous fluid. The cyst lining

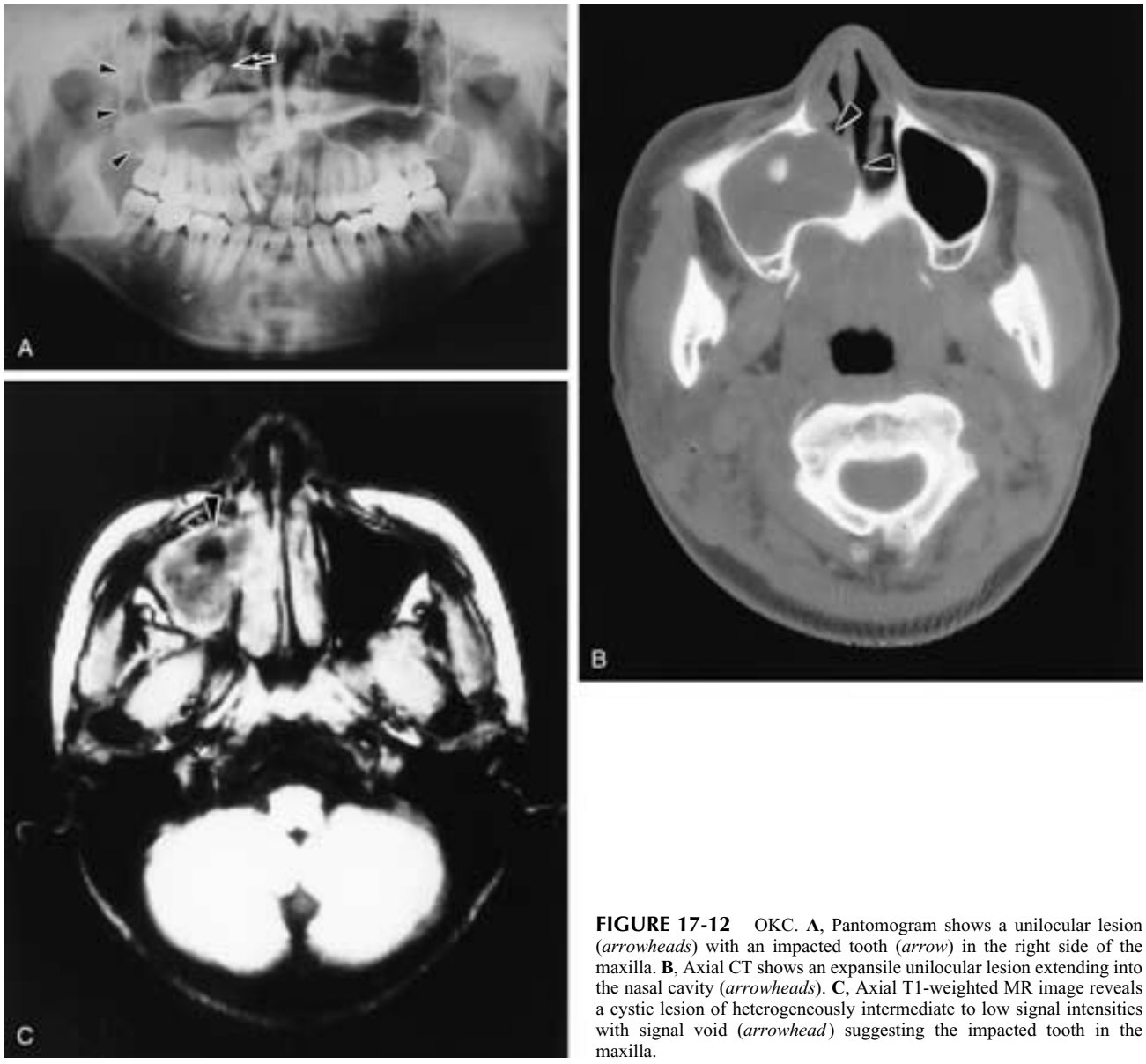

FIGURE 17-12 OKC. **A**, Pantomogram shows a unilocular lesion (*arrowheads*) with an impacted tooth (*arrow*) in the right side of the maxilla. **B**, Axial CT shows an expansile unilocular lesion extending into the nasal cavity (*arrowheads*). **C**, Axial T1-weighted MR image reveals a cystic lesion of heterogeneously intermediate to low signal intensities with signal void (*arrowhead*) suggesting the impacted tooth in the maxilla.

VIEW IMAGE

Copyright © 2003, Mosby, Inc. All rights reserved.

FIGURE 17-13 Primordial cyst in a 35-year-old man. **A**, Pantomogram shows a well-defined unilocular radiolucent lesion extending from the left upper premolar region into the left maxillary sinus (*arrowheads*). Differentiation between ameloblastoma, OKC, and primodial cyst is difficult. **B**, Axial T1-weighted MR image reveals an expansible low-intensity lesion in the left maxilla (*arrowheads*). **C**, Axial T2-weighted MR image shows the well-defined lesion of homogeneously high intensity. MR findings suggest a cyst other than OKC, but further differentiation is difficult.

VIEW IMAGE

consists of a loose vascular connective tissue that may have areas of recent or old hemorrhage.[29, 30]

Because these solitary bone cysts often are asymptomatic, most are discovered incidentally during examination of the teeth, and it is believed that some of them regress spontaneously. These lesions are most commonly located in the mandibular marrow space that extends posteriorly from the premolar region. Less often, they may occur in the incisor area of the mandible. Radiographically, these cysts are slightly irregular in shape and size and have poorly defined borders, and the outline of the cyst between the roots of the teeth has a scalloped appearance (Fig. 17-19). Larger cysts may extend into the interdental space. The ramus and body of the mandible may be slightly expanded (Fig. 17-20). The radiographic features are not sufficiently specific to be diagnostic. On MR T1-weighted images, the cyst may show variable signal intensities ranging from low to high according to the age of the hematoma. CT may be helpful to evaluate the contents of the cyst, as a relatively high density is consistent with blood products, but the density can be variable.

These lesions are usually investigated surgically with a single diagnostic and therapeutic procedure. Using a minimally invasive technique, the surgeon can evaluate the lesion and sample tissue. Healing usually takes place with reossification.

Aneurysmal Bone Cyst

These rare lesions are far more common in children than in adults, in females than in males, and in the mandible than in the maxilla or zygoma.[31–34] They usually present with a rapidly growing swelling that can be markedly disfiguring, and there is usually no pain or paresthesia. There can be spontaneous bleeding from around the teeth or from areas of mucosal trauma. Although there is often a history of prior trauma, these cysts can occur without this history, and they may be associated with a preexisting intraosseous pathologic process. Radiographically, these lesions are often multiloculated, with areas of bone destruction (Fig. 17-21). On CT or MR imaging, fluid-fluid levels may be present, a finding strongly suggestive of this entity. Histologically,

Copyright © 2003, Mosby, Inc. All rights reserved.

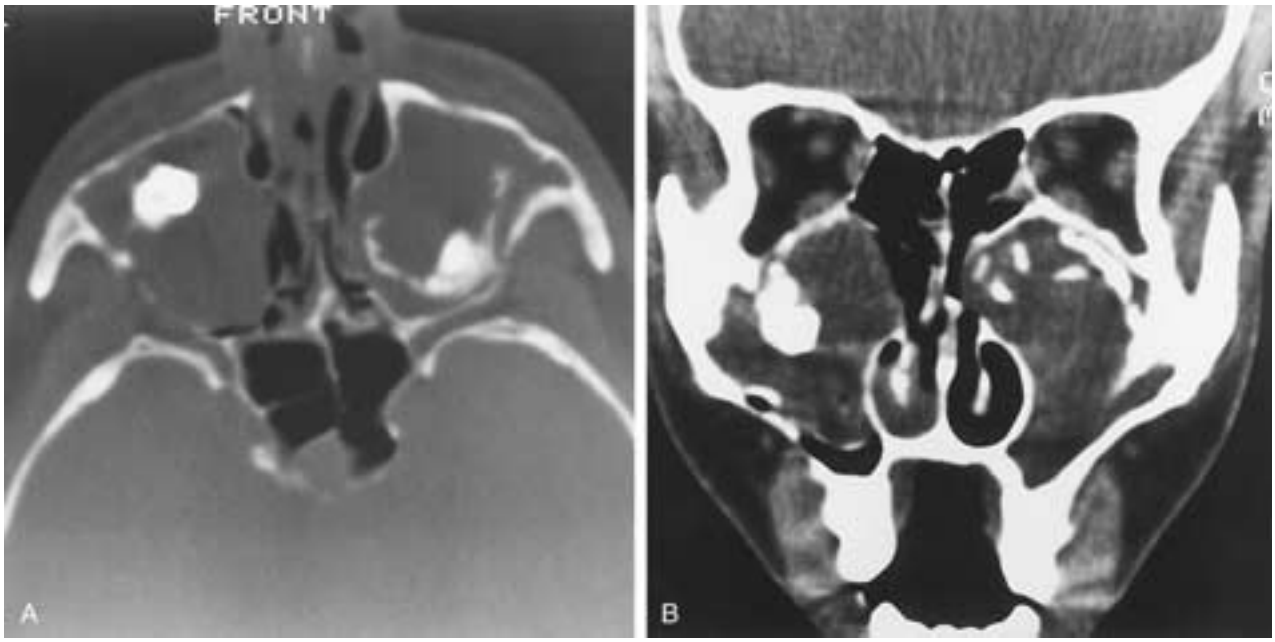

VIEW IMAGE

FIGURE 17-14 Bilateral maxillary keratocysts in a patient with the basal cell nevus syndrome. **A**, Axial CT (bone window setting) through the maxillary antra shows slightly expansile lesions in both antral cavities reflected by a cystic bony rim in the left antral cavity and some lateral expansion and thinning of the wall of the right antrum. Note the displaced teeth on the left and right within the cystic lesions. **B**, Coronal CT (soft-tissue window setting) demonstrates bilateral cystic lesions in the maxillary antra, with part of a thin rim of surrounding bone seen in the left antrum. Note the displaced tooth in the upper part of the right antral cavity and the low attenuation of the cyst contents.

they are epithelium-lined, blood-filled cavities with accumulations of immature connective tissue, multinucleated giant cells, osteoid, and inflammatory cells. Numerous approaches have been used to treat these lesions, including interventional radiologic procedures, low-dose radiation therapy, and multiple types of surgical enucleation and resection. More recently, these and other types of giant cell lesions have been treated with calcitonin, interferon, and direct intralesional steroid injections.[35, 36]

Static Bone Cavity (Stafne Cyst)

A Stafne cyst is a pseudocyst. The cortex of the mandible bows inward into the medullary space of the mandible. A

VIEW IMAGE

FIGURE 17-15 Calcifying odontogenic cyst. Occlusal radiograph shows a unilocular lesion (*arrowheads*) with odontoma (*arrow*) in the right side of the maxilla. Calcified tissue can be observed adjacent to the odontoma.

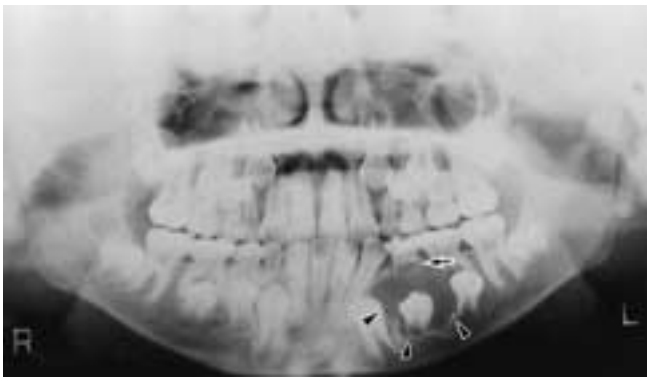

FIGURE 17-16 Calcifying odontogenic cyst. Pantomogram shows a pericoronal calcifying odontogenic cyst (*arrowheads*) with tiny calcifications. Root resorption can be observed at the left side of the milk tooth (*arrow*).

VIEW IMAGE

Copyright © 2003, Mosby, Inc. All rights reserved.

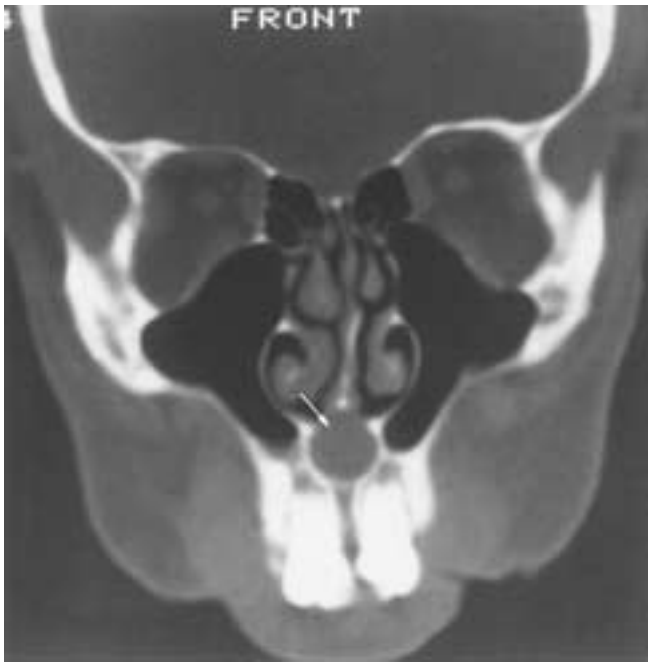

FIGURE 17-17 Nasopalatine cyst. Coronal CT (bone window setting) shows a cyst with bony expansion in the nasopalatine duct between the upper central incisor teeth (*arrow*). There is a slight bulge into the adjacent nasal cavity.

VIEW IMAGE

Stafne cyst appears as an elliptical ovoid or round radiolucency usually located on the medial surface of the posterior mandible, often near the angle of the mandible below the mandibular canal and the mylohyoid line of the mandible (Fig. 17-22). Stafne cysts occur more frequently in men than in women and have been reported in patients from 20 to 70 years of age. Most are discovered by 50 years of age. These asymptomatic lesions are usually detected incidentally on routine radiographs of the mandible. [37] The bone ''defect'' usually contains submandibular salivary gland tissue or fat.[38] The cortex is intact, separating the medullary space of the mandible from the soft tissues in the submandibular space along the medial aspect of the bone (Fig. 17-23). Bilateral lesions have been described.

FIGURE 17-18 ''Globulomaxillary cyst.'' Pantomogram shows a cystic structure (*arrow*) in the right maxilla causing divergence of the roots of the lateral incisor and canine tooth.

VIEW IMAGE

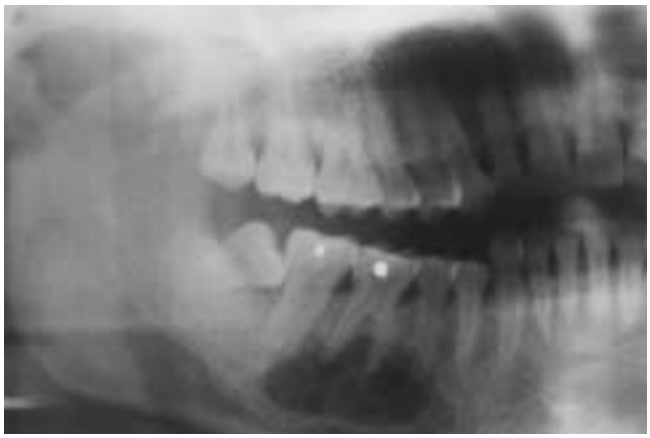

FIGURE 17-19 Hemorrhagic bone cyst in the body of the right mandible. Pantomogram of the mandible shows a sharply defined, oval-shaped cyst around the apices of the molar and premolar teeth of the right mandible.

VIEW IMAGE

Radiographically, the radiolucency has a well-defined border, often with a sclerotic margin, and varies in size from 1 to 2 cm (Figs. 17-22 and 17-23). The cortex follows along the lateral aspect of the abnormality, projecting into the bone. Diagnostic evaluation is usually needed to rule out lesions that are actually located within the bone.

Medullary Pseudocyst

The number of trabeculae crossing the medullary cavity of the mandible is variable. An area with relatively few trabeculae can give the appearance of a lucency mimicking a cyst on a plain film or parorex. Usually there is no sharp or sclerotic margin. In the adult, most of the medullary space is filled with fat, so the diagnosis of pseudocyst is readily made by the characteristic density on CT or signal intensity on MR imaging.

FIGURE 17-20 Traumatic simple (posttraumatic) bone cyst. The abnormality enlarges the body of the mandible, with some thinning of the bony wall (*arrow*).

VIEW IMAGE

Copyright © 2003, Mosby, Inc. All rights reserved.

VIEW IMAGE

FIGURE 17-21 Aneurysmal bone cyst of the left mandible. **A**, Coronal CT through the posterior portion of the mandible shows an expansile lesion in the left mandible. Note the thin, bony rim around the cyst and misplacement of teeth in the mandible at the lower aspect of the cyst. **B**, Axial CT through the ascending ramus of the mandible shows a cystic, expansile lesion with several fluid-fluid levels.

BENIGN ODONTOGENIC TUMORS AND RELATED TUMOR-LIKE CONDITIONS

Odontogenic tumors result from an abnormal proliferation of the cells and tissues involved in odontogenesis.[39, 40] They represent a diverse group of lesions that are classified according to the origin of the various layers of tooth development. Based on the histologic findings, these tumors have been divided into epithelial, mesodermal, and mixed tissue tumors of odontogenic origin.[3] The radiographic appearance of odontogenic tumors varies, and many of them cannot be differentiated from the cysts previously described.

Ameloblastoma (Epithelial Origin)

An ameloblastoma is a benign epithelial odontogenic tumor thought to arise from ameloblasts (enamel-forming cells).[41–43] It is found with about equal frequency in men and women and has a peak incidence in the third and fourth decades of life, with two thirds of cases occurring before 40 years of age. Ameloblastomas account for approximately 18% of odontogenic tumors; 81% are located in the mandible, and the remaining 19% are found in the maxilla. Half of the mandibular lesions are located in the molar regions. An ameloblastoma is a slow-growing, painless mass that may reach a considerable size; swelling is the most common presenting symptom. Ameloblastoma may mani-

FIGURE 17-22 Static bone cavity (Stafne cyst). Oblique view of the mandible shows an oval-shaped ''cavity'' in the angle of the mandible (*arrow*) below the mandibular canal. This lucency is simply a deformity of the medial cortex.

VIEW IMAGE

Copyright © 2003, Mosby, Inc. All rights reserved.

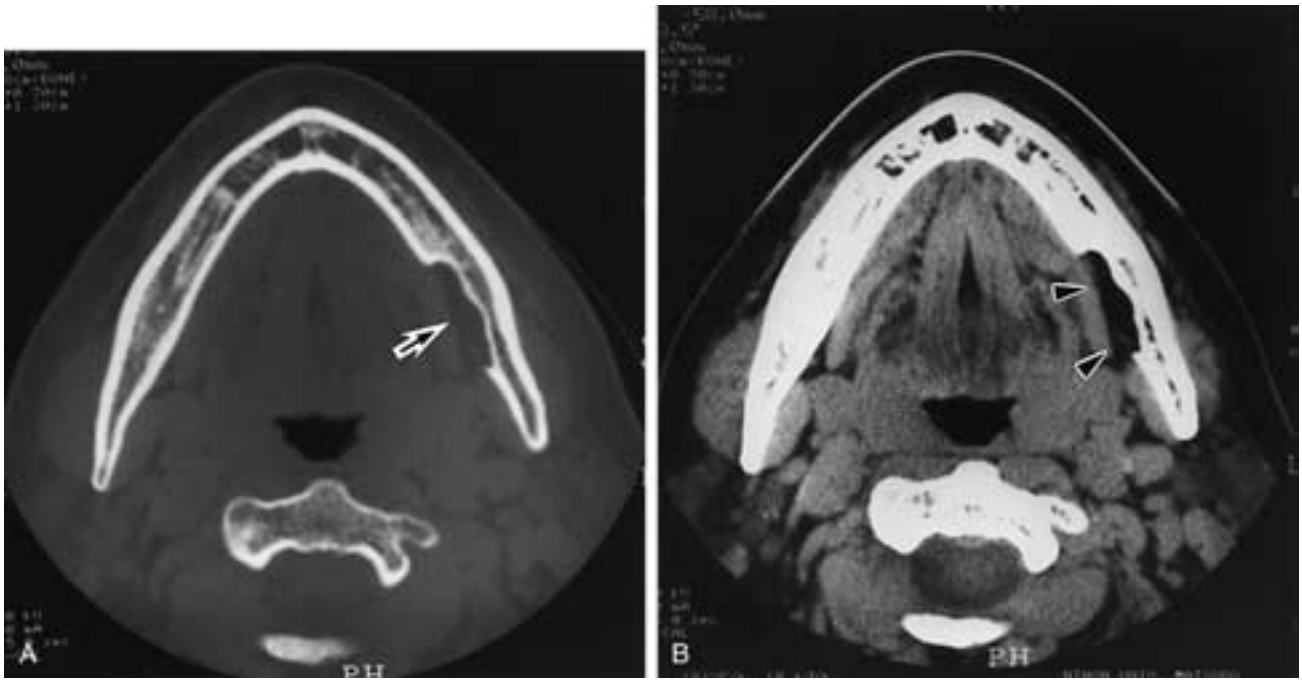

VIEW IMAGE

FIGURE 17-23 Static bone cavity (Stafne cyst). **A**, Axial CT (bone tissue window setting) shows a defect (*arrow*) with adjacent thinning of the lingual cortex. Note, however, that the cortex is complete along the lateral aspect of the abnormality. **B**, Axial CT (soft-tissue window setting) shows the static bone cavity containing adjacent fat (*arrowheads*).

fest in a number of histologic patterns, including the follicular, plexiform, acanthomatous, keratinizing, granular cell, basal cell, and clear cell types. In 1984 Eversole et al. described a desmoplastic variant of ameloblastoma.[44] This unusual variant was characterized histologically by an abundant densely collagenous stroma (desmoplasia) with small nests and strands of odontogenic epithelium.[3]

Radiographically, an ameloblastoma is radiolucent and either multilocular or unilocular (Figs. 17-24 and 17-25). The unilocular lesions occur most often in the maxilla (Fig. 17-26). The multilocular form often has been described as having a honeycombed or bubble-like appearance, and the loculi may be oval or spherical and vary in size. Ameloblastomas can vary in size from a small cyst confined to the alveolus to a large cyst that causes extensive destruction of the mandible or maxilla. The tumor has a tendency to break through the cortex of the bone, with subsequent tumor extension into the adjacent soft tissues (Figs. 17-27 and 17-28). There can be bony expansion of variable degree, sometimes with scalloped marginal sclerosis, and there is no periosteal new bone formation. Loss of the lamina dura, erosion of the tooth apex, and displacement of the teeth are also commonly seen. MR imaging findings in ameloblastomas include mixed patterns of solid and cystic components, irregularly thick walls, papillary projections, and marked enhancement of the walls and septa (Fig. 17-29). The demonstration of papillary projections and solid components on contrast-enhanced T1-weighted images is especially helpful in differentiating ameloblastomas from various other cysts (Fig. 17-30).[45] However, the desmoplastic variant of ameloblastoma shows unusual radiographic features such as a mixed radiolucent-radiopaque appearance with poorly defined borders. Because of its appearance, it can be mistakenly diagnosed as a fibroosseous lesion (Fig. 17-31).[46, 47]

The biologic behavior of these lesions has been of great interest and debate. Numerous clinical and histopathologic studies have evaluated the several varieties of ameloblas-

FIGURE 17-24 Ameloblastoma. Oblique view of the mandible shows a large cystic lesion in the body and ramus of the mandible, with attenuation and loss of bone superiorly. The lesion has broken through the upper part of the mandible.

VIEW IMAGE

Copyright © 2003, Mosby, Inc. All rights reserved.

toma in an attempt to relate the clinical picture, histologic pattern, and biologic behavior to provide more appropriate treatment. However, at this time, there does not seem to be any good correlation and the treatment strategies remain predominantly surgical. A variety of approaches have been advocated based on the individual patient. These include curettage and adjuvant treatment of the surrounding soft tissues, wide local excision, and large en bloc excisions with immediate or staged reconstruction. A malignant form of ameloblastoma accounts for 1% of the ameloblastomas. With recurrent tumors and delayed reconstructions, CT, MR imaging, and technetium bone scanning can be helpful in evaluating whether a soft-tissue mass is a recurrence or fibrous healing.

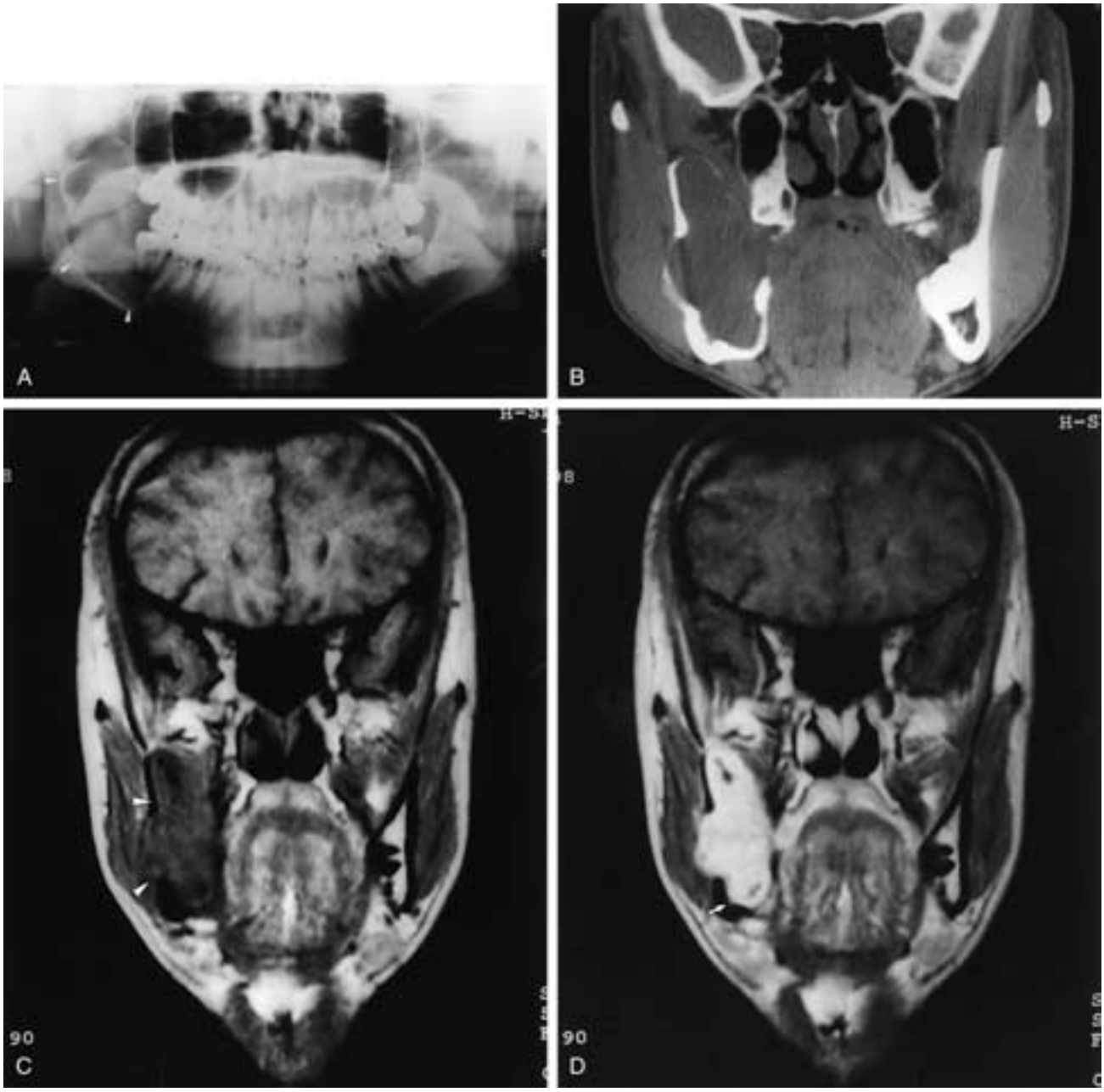

FIGURE 17-25 Multilocular ameloblastoma in a 25-year-old man. **A**, Pantomogram shows a large, multilocular, expansile lesion in the right side of the mandible (*arrowheads*). There is no root resorption of adjacent teeth. A cystic lesion is suspected. **B**, Coronal CT shows the expansile multilocular lesion, with bulging of the bony cortex without perforation. **C**, Coronal T1-weighted MR image reveals a lesion of homogeneously low signal intensity in the mandible (*arrowheads*). **D**, Enhanced coronal MR image shows the markedly enhanced solid lesion in the mandible. The mandibular canal can be seen under the solid mass (*arrow*).

VIEW IMAGE

Copyright © 2003, Mosby, Inc. All rights reserved.

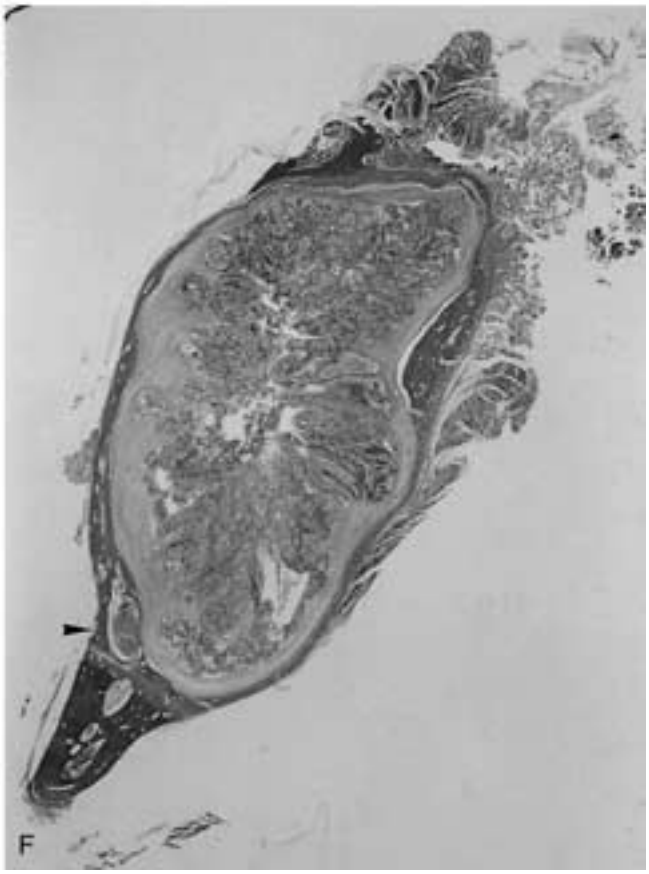

VIEW IMAGE

FIGURE 17-25 *Continued.* **E**, Coronal T2-weighted MR image reveals the tumor and fluid content to be of homogeneously high signal intensity. Solid ameloblastoma is suspected preoperatively, but other solid tumors cannot be ruled out. **F**, Photomicrograph shows complete solid tumor of ameloblastoma. (H&E. Original magnification ×100.) The mandibular canal is seen under the tumor (*arrowhead*).

Calcifying Epithelial Odontogenic Tumor (Pindborg Tumor)

A calcifying epithelial odontogenic tumor is composed of polyhedral epithelial cells in a fibrous stroma that contains acidophilic homogeneous structures that commonly calcify.[48–50] At first diagnosis the average age of the patient is about 40 years, with an age range of 12 to 78 years. There is no sex predilection. Many of these tumors are located in the premolar-molar area of the mandible, and in half of the cases they are associated with the crown of an impacted tooth.

Radiographically, the lesion usually is a mixed radiolucent and radiopaque mass that may be unilocular but more often is multilocular and honeycombed. It has poorly defined, irregular borders that reflect its aggressive behavior, which is similar to that of the ameloblastoma. Radiopaque densities of varying degree may be located close to the crown of an impacted tooth (Fig. 17-32). Curettage is the preferred treatment, but recurrence or extensive tumor involvement should be treated by resection.

Odontoma (Mixed Tumor)

An odontoma is a benign tumor made up of the various components of teeth (e.g., enamel, dentin, cementum, and pulp). It is also designated as a composite lesion because of the admixture of several types of tissue.[5, 51–54] During its maturation, an odontoma passes through the same stages as a developing tooth, but dentin and enamel are laid down in an abnormal pattern. In the initial stage of development, a radiolucent area develops because of bone resorption by the odontogenic tissues. In the intermediate and late stages, progressive calcification takes place, initially characterized by small, speckled calcific densities that eventually form radiopaque masses surrounded by a lucent ring. These tumors may be discovered in any location of the dental arches and are situated between the roots of teeth.

Both forms of odontoma (complex and compound) are frequently associated with unerupted teeth. It is noteworthy that compound odontomas occur most often in the anterior jaw, whereas complex odontomas tend to occur in the posterior jaw. A developing odontoma without calcification or with few calcifications is difficult to diagnose radiograph-

Copyright © 2003, Mosby, Inc. All rights reserved.

ically and usually cannot be differentiated from other similar-appearing lesions.

Complex Odontoma

Complex odontomas (complex composite odontomas) account for 24% of all odontomas.[52, 53] These lesions are composed of dental tissues arranged in a disorderly pattern and bearing no morphologic similarity to normal or rudimentary teeth (Figs. 17-33 and 17-34). Complex odontomas most commonly occur in patients aged 10 to 25 years, and males and females are affected equally. The lesion usually is asymptomatic and most frequently is located in the premolar and molar regions in the mandible, although it is sometimes found in the maxilla. Most lesions are small, measuring only a few millimeters, but some may reach a considerable size.

Radiographically, these lesions are well-demarcated radiopaque masses, often with radiating structures. Occasionally, the tumor is surrounded by a narrow radiolucent zone, and there usually is a nearby unerupted tooth. The preferred therapeutic treatment is enucleation. Cancellous bone grafting may be appropriate, depending on the size and location of the surgical defect.

Compound Odontoma

Compound odontoma (compound composite odontoma) consists of dental tissues that are similar to a normal tooth, having a more orderly pattern than that seen in complex odontoma.[54] The lesion is composed of many tooth-like structures, with enamel, dentin, cementum, and pulp arranged as in a normal tooth (Figs. 17-35 and 17-36). The

FIGURE 17-26 Ameloblastoma of the maxilla. **A**, Expansile abnormality with multiple loculations extends away from the alveolar process of the maxilla. Note the secondary cystic extension (*arrow*) to the midline. **B**, Soft-tissue algorithm (postcontrast) shows an enhancing septation (*arrowhead*) within the lesion. **C**, Coronal bone algorithm. The lesion elevates the floor of the nasal cavity. **D**, Coronal soft-tissue algorithm.

VIEW IMAGE

Copyright © 2003, Mosby, Inc. All rights reserved.

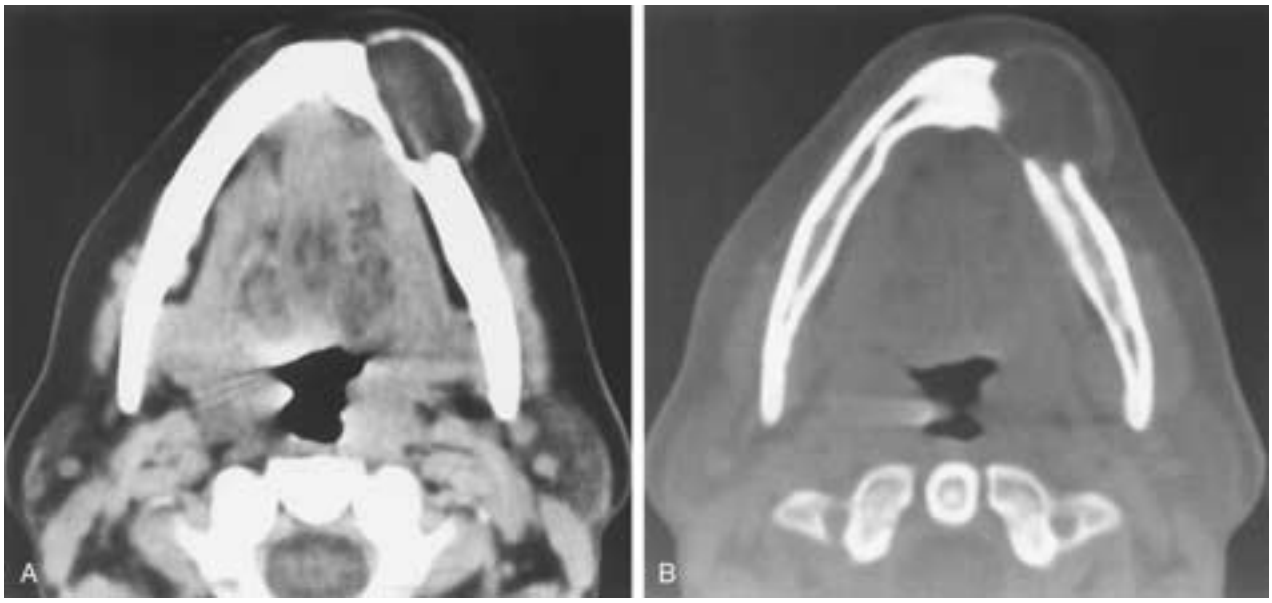

VIEW IMAGE

FIGURE 17-27 Ameloblastoma. **A**, Axial CT (soft-tissue window setting) shows an expansile lesion in the body of the left mandible and adjacent symphysis with marked lateral expansion. **B**, Axial CT (bone window setting) defines the boundary of this expansile lesion to better advantage. Also, note the erosion of the lingual surface of the mandible.

differentiation of teeth varies from case to case, and the number of teeth involved may be surprisingly high.

Most compound odontomas (60%) occur in the second and third decades of life, and there is no sex predilection. The tumor frequently is located in the incisor-canine region of the maxilla. It is usually small but may occasionally displace teeth or interfere with their eruption; the lesion is otherwise asymptomatic. Radiographically, several small, rather well-defined, malformed or rudimentary teeth are demonstrated, surrounded by a radiolucent zone that is caused by a fibrous capsule. The teeth contained in a compound odontoma are dwarfed and usually distorted, with simple roots (Fig. 17-37). Most of these lesions are well encapsulated and easily enucleated, and recurrences are not encountered after enucleation.

Ameloblastic Fibroodontoma

An ameloblastic fibroodontoma is a mixture of ameloblastic tissue and a composite odontoma. It is a rare lesion that can occur at any age but is more prevalent in children than in adults, being rare after the age of 13 years. This tumor is more common in the mandible (premolar-molar

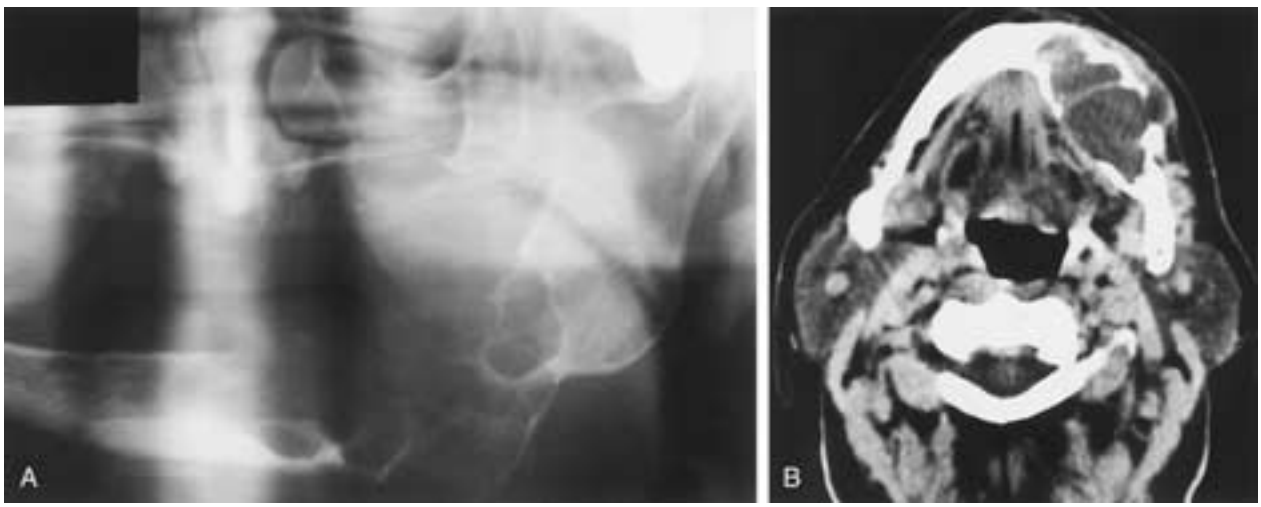

VIEW IMAGE

FIGURE 17-28 Ameloblastoma. **A**, Pantomogram of the mandible shows a multiloculated aggressive lesion in the body and ramus of the mandible with considerable loss of bone. **B**, Axial CT (soft-tissue window setting) shows the expansile lesion in the body and ramus. There is loss of bone medially and laterally. There is general low attenuation and slightly septated soft-tissue densities within the lesion. A small component of the tumor has penetrated through the lateral cortex into the adjacent soft tissues.

Copyright © 2003, Mosby, Inc. All rights reserved.

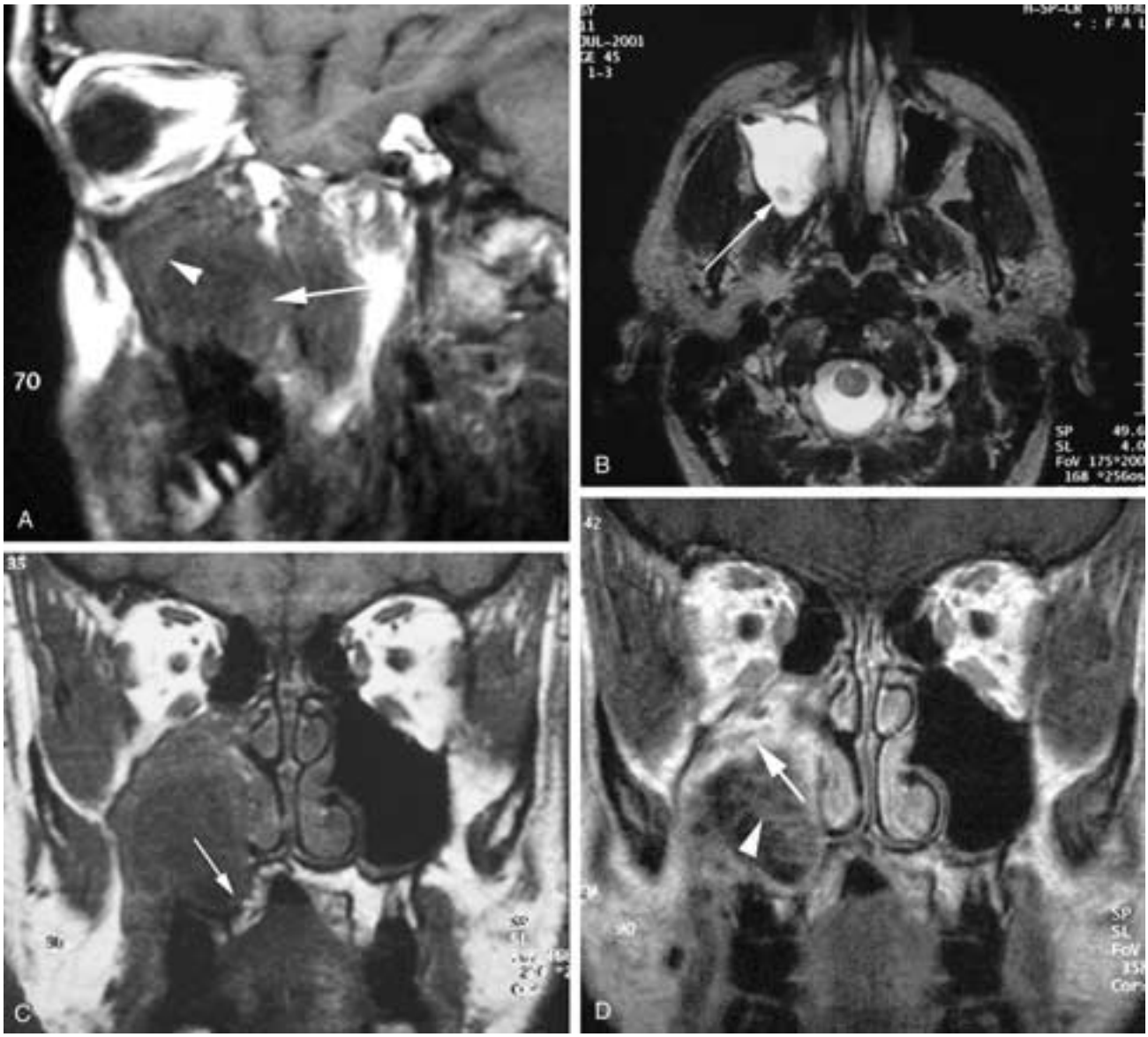

VIEW IMAGE

FIGURE 17-29 Ameloblastoma of the maxilla. **A**, Sagittal T1-weighted image shows an expansile lesion extending into the maxillary sinus. The superior margin of the lesion (*arrowhead*) extends into this sinus. An area of slightly higher signal (*arrow*) is a more nodular tissue extending into the primarily cystic abnormality. **B**, Axial T2-weighted image. The soft-tissue nodule (*arrow*) has lower signal than most of the cystic fluid. **C**, Coronal T1-weighted image. The lesion expands the palate and the alveolar process (*arrow*). **D**, Postcoronal T1-weighted image shows the nodular enhancement (*arrow*) along the margin. There is also an enhancing septation (*arrowhead*) within the lesion. Compare this to the pregadolinium image.

region) than in the maxilla, and it is always associated with developing teeth. Painless swelling or absence or displacement of teeth are the most common signs leading to its diagnosis.

Radiographically, the tumor has a lucent, well-defined margin with a solitary mass or several small radiopaque masses that may resemble miniature teeth (Fig. 17-38). Radiographic differentiation from other odontomas is not possible, and inadequate removal may be followed by a recurrence.

Adenomatoid Odontogenic Tumor

An adenomatoid odontogenic tumor, formerly known as adenoameloblastoma, is a tumor of odontogenic epithelium with duct-like structures and with varying degrees of inductive changes in the connective tissue.[3] It is relatively rare, accounting for approximately 3% of all odontogenic tumors.[55, 56] The tumor is seen more frequently in female patients. It usually occurs in the second decade of life and is present as a slow-growing, painless swelling. The maxilla is involved nearly twice as frequently as the mandible. Radiographically, the tumor is associated with the crown of an embedded tooth mimicking a dentigerous cyst. The radiolucency is well demarcated. Some tumors have a totally radiolucent center; others have punctate calcifications either sprinkled throughout (giving a cloud-like appearance) or in clusters (Fig. 17-39). The tumor can displace or prevent the

Copyright © 2003, Mosby, Inc. All rights reserved.

eruption of teeth, especially the canine. Root resorption is rarely encountered. The radiologic appearance may be similar to that of calcifying odontogenic cyst, ameloblastic fibroodontoma, and calcifying epithelial odontogenic tumor.[57]

Odontogenic Myxoma

An odontogenic myxoma appears to be a true odontogenic tumor, originating from the mesodermal portion of the odontogenic apparatus.[3] This tumor, which is not found in bones outside the jaw, accounts for about 3% to 6% of

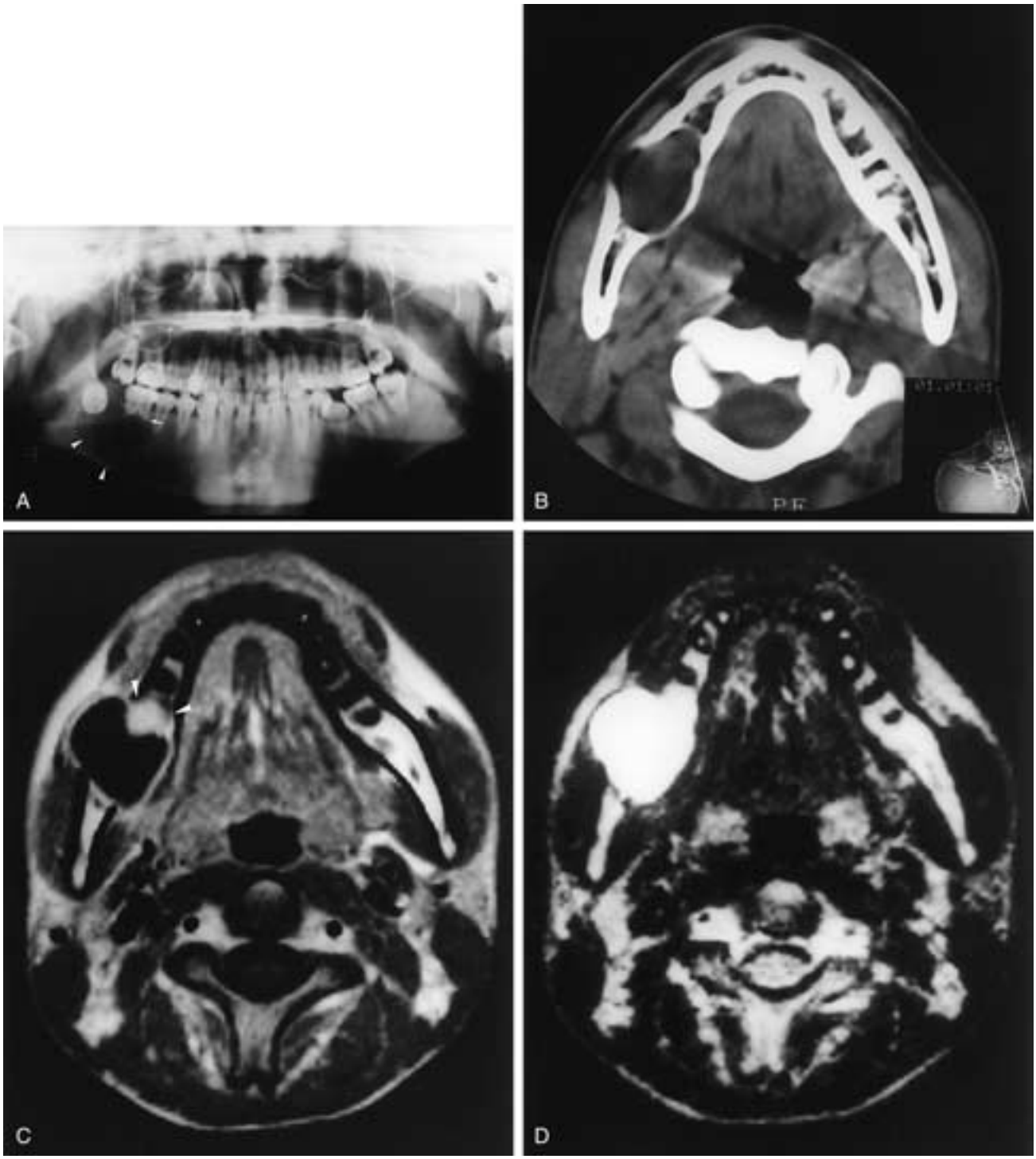

FIGURE 17-30 Unilocular ameloblastoma. **A**, Panoramic radiograph shows a large, unilocular, expansile lesion with an unerupted tooth in the right side of the mandible (*arrowheads*). There is root resorption of adjacent teeth (*arrow*). A cystic lesion is suspected. **B**, Axial CT shows an expansile unilocular lesion, with bulging of the bony cortex without perforation. **C**, Enhanced axial MR image shows a papillary projection (*arrowheads*) along the walls of the unilocular lesion. **D**, Axial T2-weighted MR image reveals the lesion to be of high signal intensity.

VIEW IMAGE

Copyright © 2003, Mosby, Inc. All rights reserved.

VIEW IMAGE

FIGURE 17-31 Desmoplastic variant of ameloblastoma in the mandible. **A**, Panoramic radiograph shows a diffuse, mixed radiolucent-radiopaque lesion in the mandible (*arrowheads*). **B**, Axial CT shows a definite buccal expansile radiolucent-radiopaque lesion (*arrowheads*). (Courtesy of Dr. T. Kurabayashi, Dept. of Dental Radiology, Tokyo Medical and Dental University, Tokyo.)

odontogenic tumors.[58, 59] It occurs most often in the second and third decades of life, with no sex predilection. The tumor consists of rounded and angular cells lying in an abundant mucoid stroma; the lesion is painless, locally invasive, and slow-growing. If untreated, odontogenic myxomas eventually may cause extensive destruction of bone with marked cortical expansion. The mandible and maxilla are involved with about equal frequency; however, in the mandible, the body and ramus are most commonly affected.

Radiographically, several radiolucent areas of varying size are present, septated by straight or curved bony trabeculae that form triangular, quadrangular, or square-shaped compartments (Figs. 17-40 and 17-41).[60, 61] Unilocular cysts have also been described. The radiographic margins of the tumor may be well or poorly defined, and the lesion may simulate ameloblastoma, central giant cell granuloma, or hemangioma. This tumor is benign but very aggressive and rapidly growing. It shows little encapsulation and often extends through bone, with a propensity to invade local soft tissues. It may appear to expand in thin layers into and through bone, as well as into the adjacent soft tissues.

Because of its histology and behavior, the treatment of choice has become wide en bloc resection rather than simple enucleation.[59] A tumor-free margin must be resected because of the tumor's local invasiveness and its tendency to recur. A recurrence rate of 25% after curettage has been reported.

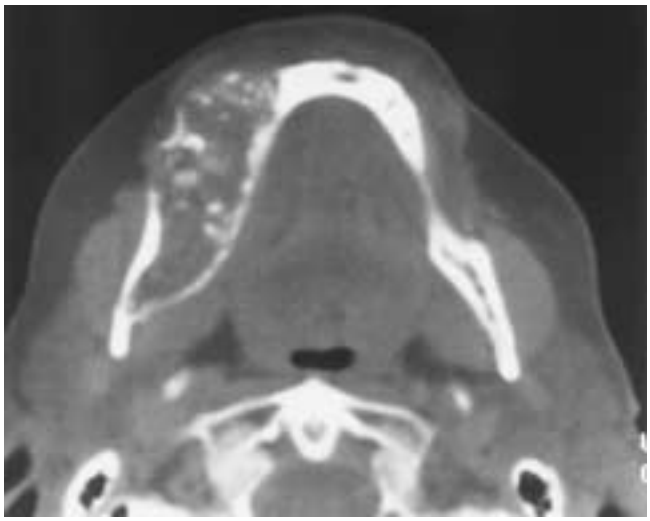

VIEW IMAGE

FIGURE 17-32 Pindborg tumor. Axial CT (bone window setting) shows marked expansion of the right mandible with loss of bone in the lateral cortex. Multiple calcific densities are noted within the lesion.

CEMENTAL LESIONS

Periapical Cemental Dysplasia and Florid Cemental Dysplasia (Florid Cementoosseous Dysplasia)

Periapical cemental dysplasia is a rare lesion that occurs most often in the mandibular region, although in rare cases the lesion may develop in the maxilla.[62–65] It always occurs at the roots of teeth. This lesion is more common in women (average age at diagnosis is 40 years) and among Africans/African Americans. In almost half of the patients, pain is the initial symptom; in other patients, a hard swelling may develop that may cause facial asymmetry.

The initial lesion, which is caused by a proliferation of connective tissue from the periodontal membrane, appears as a well-defined radiolucency.[63] However, it subsequently may be transformed into a radiopaque calcified mass. These lesions can be divided radiographically into three stages: (1) a rather well-defined radiolucency at the apex of a tooth (osteolytic or early stage); (2) a lesion that is partly radiolucent and partly radiopaque, with the dense tissue initially central in the lesion (cementoblastic or mixed stage); and (3) a lesion that is transformed into a mineralized radiopaque mass surrounded by a narrow radiolucent zone (mature stage) (Figs. 17-42 and 17-43). The in-

Copyright © 2003, Mosby, Inc. All rights reserved.

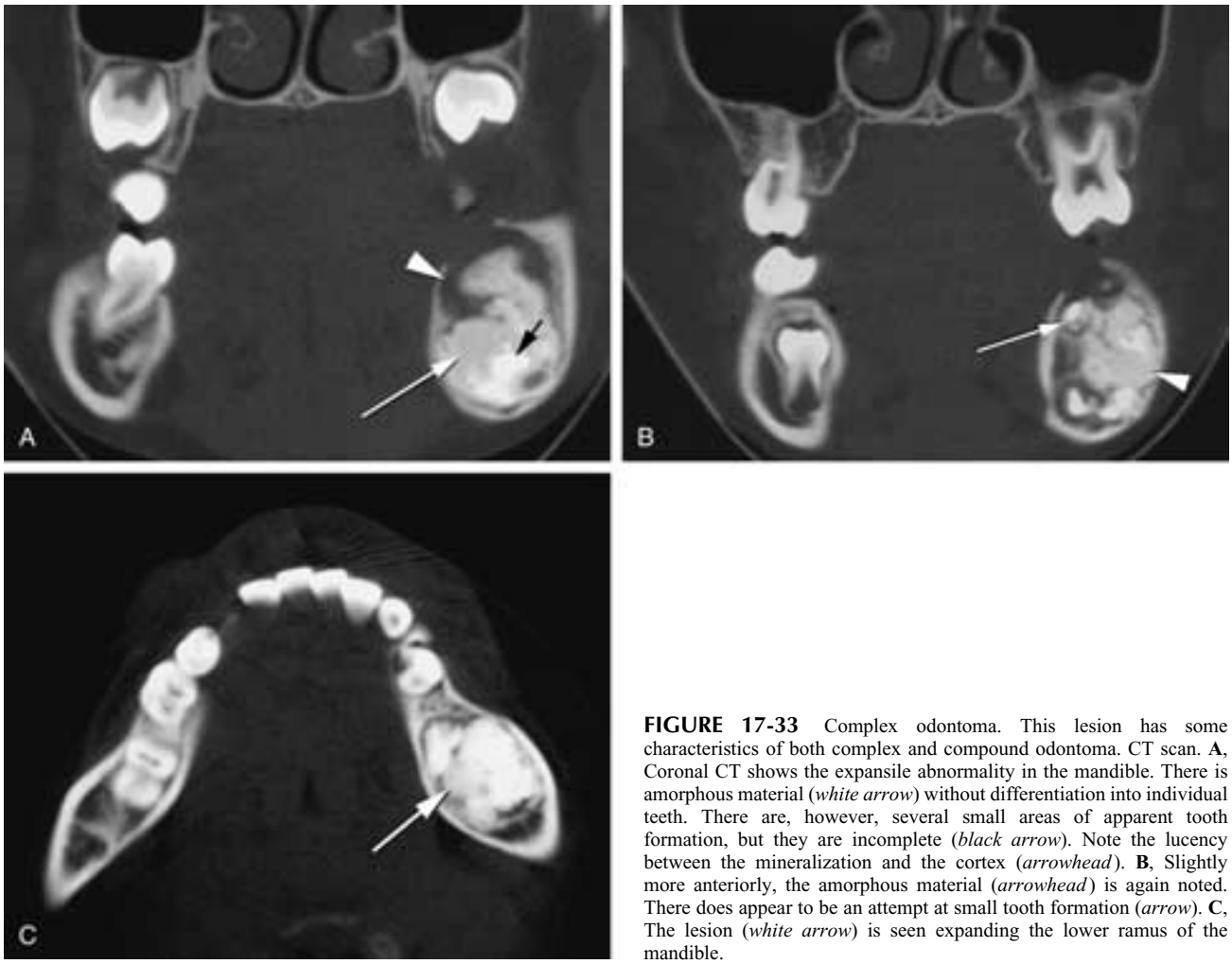

FIGURE 17-33 Complex odontoma. This lesion has some characteristics of both complex and compound odontoma. CT scan. **A**, Coronal CT shows the expansile abnormality in the mandible. There is amorphous material (*white arrow*) without differentiation into individual teeth. There are, however, several small areas of apparent tooth formation, but they are incomplete (*black arrow*). Note the lucency between the mineralization and the cortex (*arrowhead*). **B**, Slightly more anteriorly, the amorphous material (*arrowhead*) is again noted. There does appear to be an attempt at small tooth formation (*arrow*). **C**, The lesion (*white arrow*) is seen expanding the lower ramus of the mandible.

VIEW IMAGE

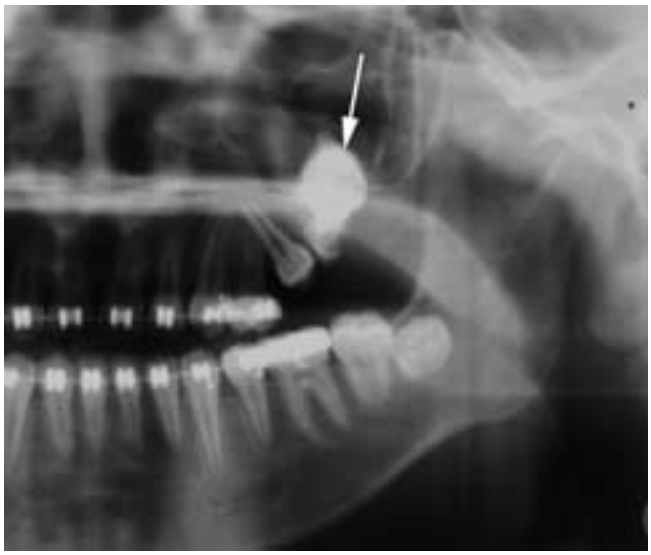

FIGURE 17-34 Complex odontoma, There is a focus of high density (*arrow*) in the region of the maxillary alveolus. There is disordered organization of dental tissue but no obvious true tooth element.

VIEW IMAGE

volved tooth is normal in color and responds normally to tests of vitality.

Periapical cemental dysplasia does not require treatment unless the lesion becomes infected or other disturbing symptoms occur. The treatment of choice is enucleation, with or without extraction of the involved tooth. No recurrences have been reported.

Florid cemental dysplasia (florid cementoosseous dysplasia) is a diffuse form of periapical cemental dysplasia (Fig. 17-44). Pain has been described, but many patients are asymptomatic. There is no clearly defined distinction between multiple periapical cemental dysplasia lesions and florid cemental dysplasia.

The diagnosis is made with plain films or occasionally with CT. MR imaging is not considered helpful (Fig. 17-45).

Benign Cementoblastoma

Also called a true cementoma, a benign cementoblastoma is a rare neoplasm of functional cementoblasts characterized by the formation of a cementum or cementum-like mass connected with a tooth root.[66, 67] The lesion occurs most

Copyright © 2003, Mosby, Inc. All rights reserved.

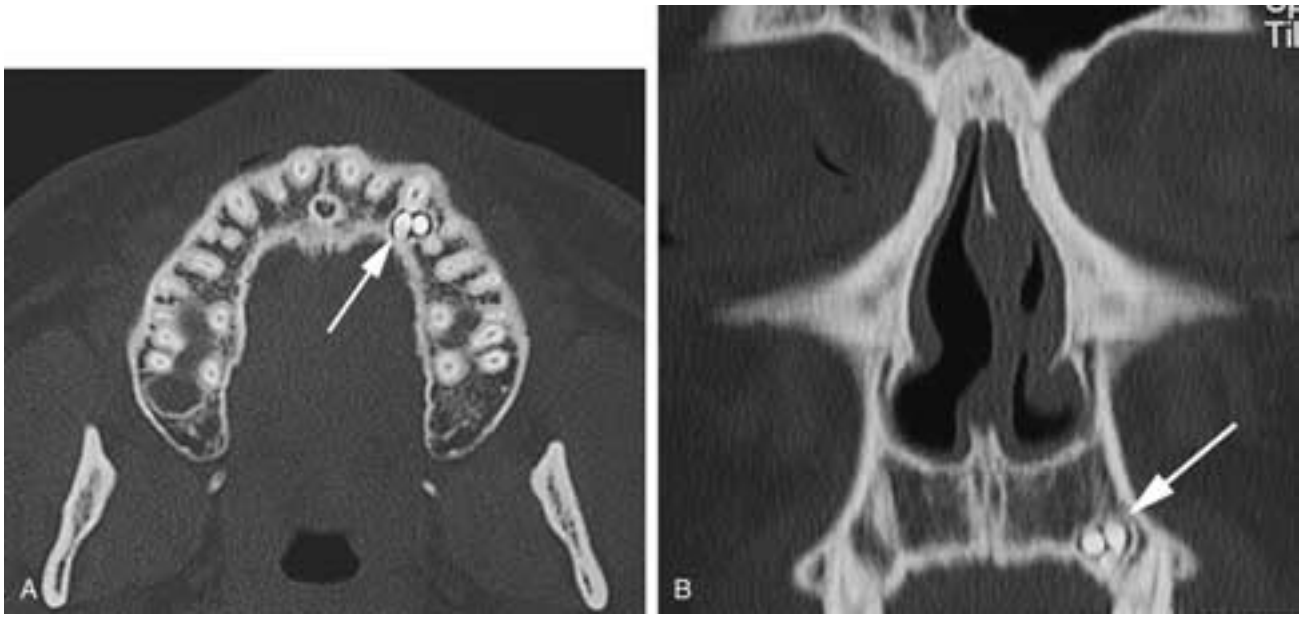

VIEW IMAGE

FIGURE 17-35 Compound odontoma. CT scan. **A**, Axial image shows small structures containing both enamel and dentine apparently forming small dental units (*arrow*). **B**, Coronal CT showing a small compound odontoma (*arrow*).

frequently in men under 25 years of age, is solitary, and usually is located in the molar or premolar region, with the mandibular first molar being most frequently involved. Benign cementoblastomas are most often associated with permanent teeth, but primary teeth may also be affected.

Radiographically, the tumor is well defined, with central dense radiopaque material being attached to the tooth root and a surrounding radiolucent zone of uniform width, which represents the peripheral nonmineralized tissues of the formative cellular layers.[68] These tumors have a tendency to expand the cortical bone of the jaws. The lesion is easily enucleated because it is benign and surrounded by a capsule.

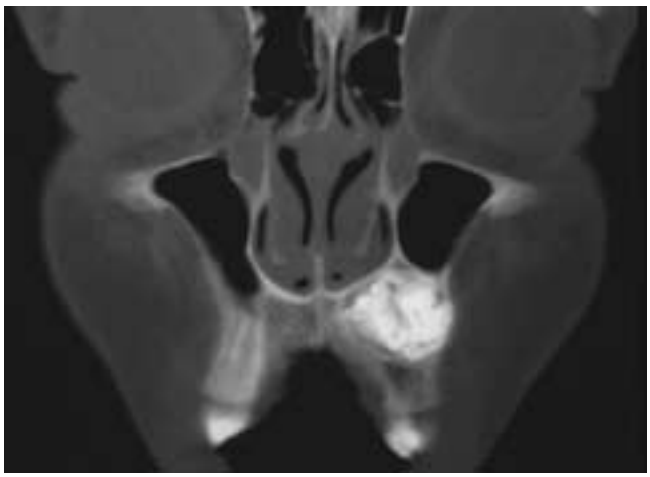

VIEW IMAGE

FIGURE 17-36 Compound odontoma. An expansile lesion with a well-defined cortical margin contains small, malformed dental structures similar to normal teeth.

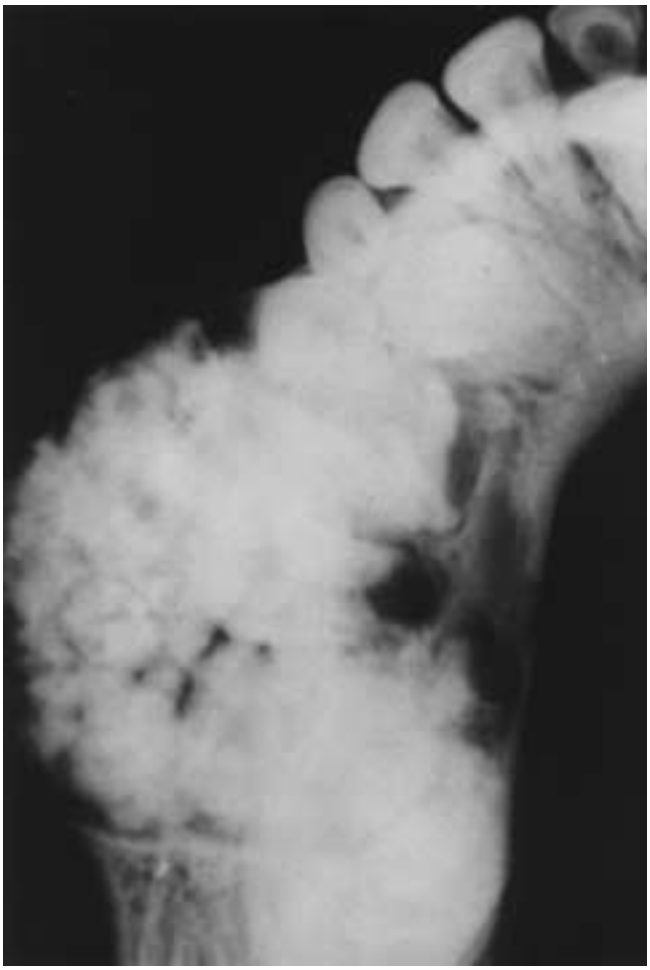

FIGURE 17-37 Compound odontoma. Semiaxial view of the mandible shows a calcified lesion expanding the outer cortex of the mandible. The lesion contains multiple malformed teeth. Note the surrounding lucent zone between the expanded cortex and the malformed teeth.

VIEW IMAGE

Copyright © 2003, Mosby, Inc. All rights reserved.

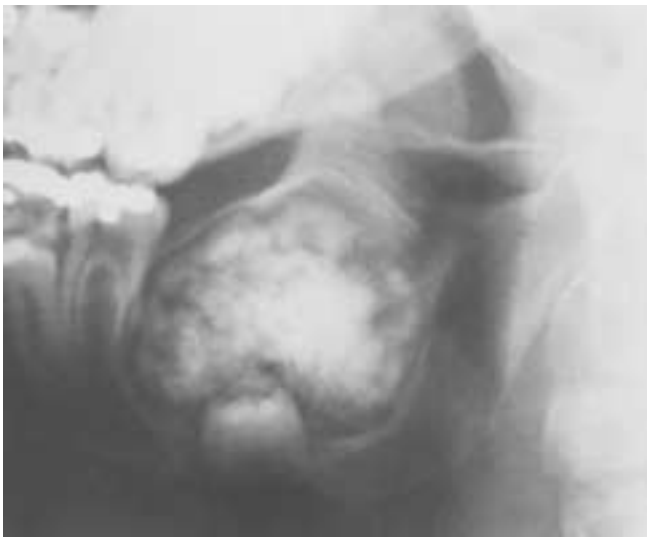

VIEW IMAGE

FIGURE 17-38 Ameloblastic fibroodontoma. Oblique view of the mandible shows an expansile lesion in the posterior body and ramus of the mandible. Amorphous calcific densities are noted within the lesion. There is a radiolucent zone between the calcified mass and the adjacent expanded cortex. Note the impacted third molar tooth, which is incorporated in the inferior part of the lesion.

VIEW IMAGE

FIGURE 17-40 Myxoma of the mandible. Pantomogram of the mandible shows multiple small, irregular lucent areas within the mandible bounded by thickened trabeculae. The lesion more anteriorly demonstrates an ill-defined lucent area beneath the molar teeth. There is extension of this myxoma through the cortex of the mandible, best illustrated inferiorly near the angle of the mandible.

BENIGN NONODONTOGENIC TUMORS

Benign nonodontogenic tumors are not unique to the jawbone, being found in other parts of the skeleton as well. Their radiographic appearance in the jaw does not differ significantly from their appearance in other bones if one takes into account any abnormalities the lesions may cause to adjacent tooth structures. The discussion of these lesions is based mainly on their tissue of origin.

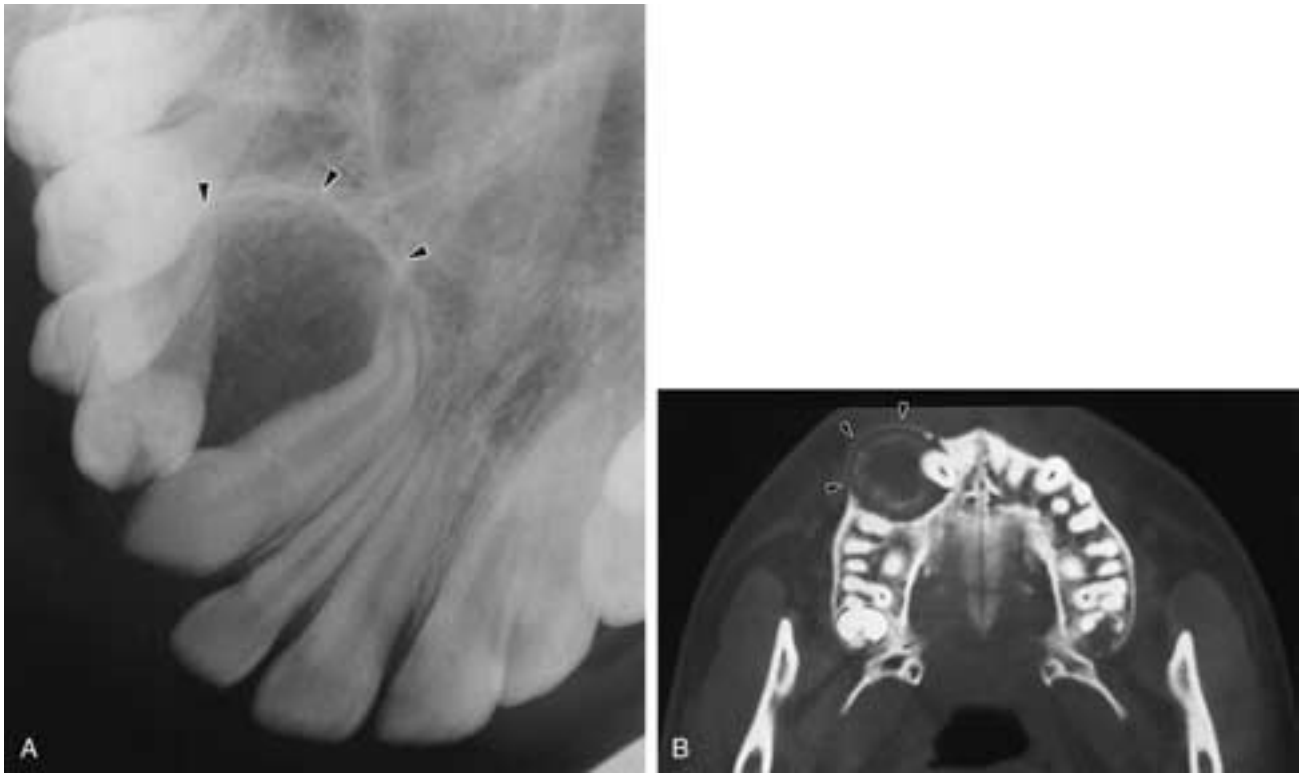

VIEW IMAGE

FIGURE 17-39 Adenomatoid odontogenic tumor. **A**, Occlusal view shows a well-defined radiolucent lesion with curved margins, tooth displacement, and small internal calcifications in the maxilla (*arrowheads*). **B**, Axial CT shows the well-defined rounded lesion with the incorporated canine and tiny calcifications (*arrowheads*).

Copyright © 2003, Mosby, Inc. All rights reserved.

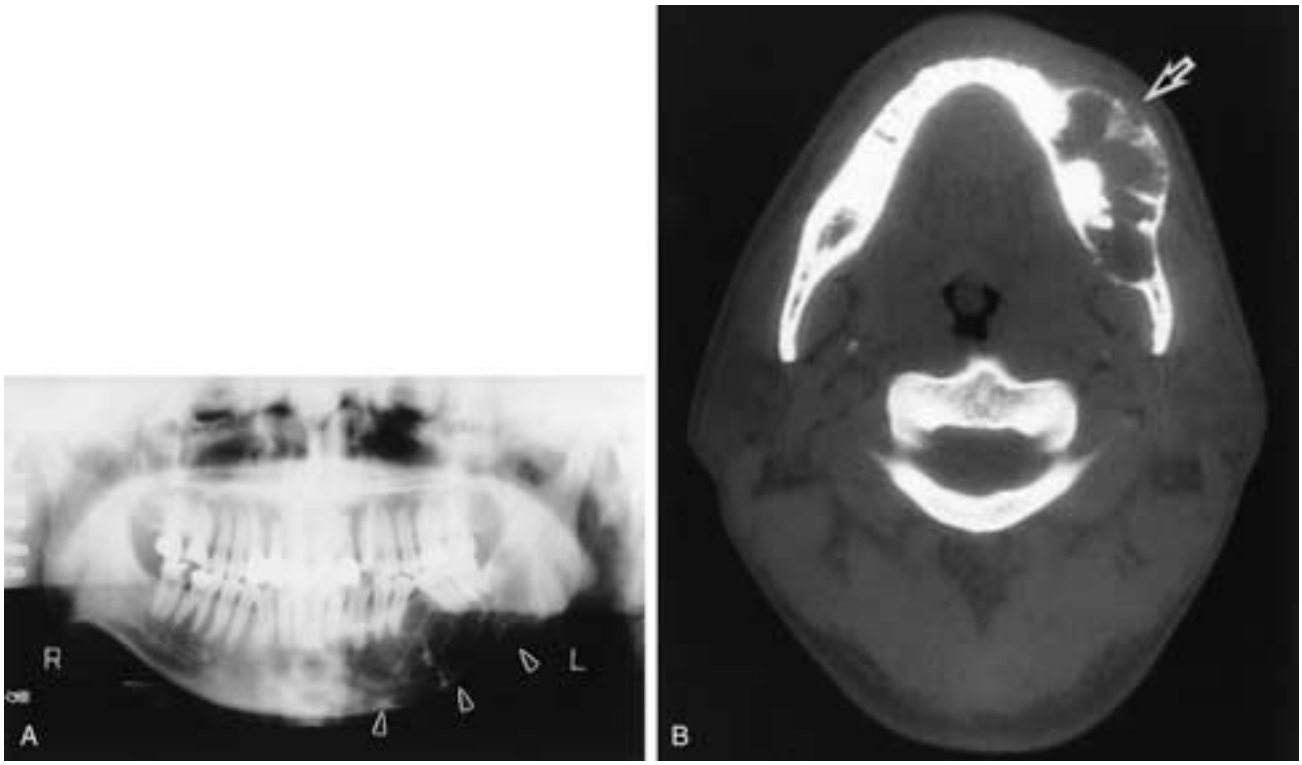

VIEW IMAGE

FIGURE 17-41 Myxoma of the mandible. **A**, Pantomogram shows an ill-defined lesion with straight septa and tooth displacement (*arrowheads*). **B**, Axial CT (bone window setting) shows buccal expansion of the lesion with straight septa (*arrow*).

Exostosis

Exostoses are localized outgrowths of bone that vary in size and can be either flat, nodular, or slightly pedunculated protuberances on the surface of the mandible or maxilla.[69–71] The cause of these exostoses of the jaw is unknown. Three types of exostosis are identified according to their location: the torus mandibularis, the torus palatinus, and multiple (maxillary) exostoses. They resemble the compact form of osteoma. The exostoses are differentiated primarily by their typical location.

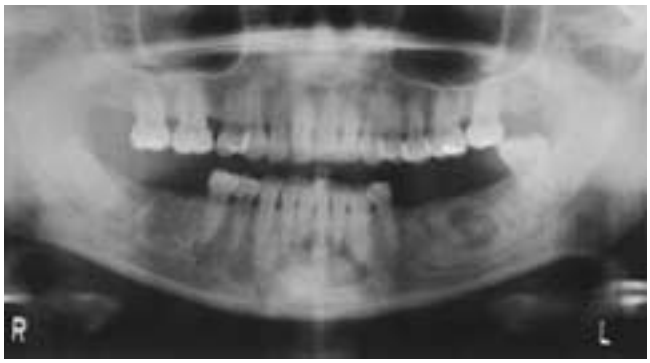

VIEW IMAGE

FIGURE 17-42 Periapical cemental dysplasia. Pantomogram of the mandible shows multiple sclerotic foci within the mandible, especially at the symphysis and body on the left. Some of these sclerotic areas merge imperceptibly with the mandible. Other densities are surrounded by a lucent ring. The radiographic appearance shows the evolution from lucent areas in the early stages, to mixed stages, and finally to the sclerotic stage.

Radiographically, exostoses are recognized as areas of increased bony density projecting from the mandible or maxilla. Exostoses composed of compact bone are of uniform radiopacity, whereas those that contain a marrow space have trabeculations. Some exostoses are difficult to demonstrate radiographically, particularly small ones and those that are superimposed on the teeth. An enostosis is a related lesion that originates from the inner cortex of the jaw as an area of osteosclerosis.

Torus mandibularis is an outgrowth of bone on the lingual surface of the mandible (Figs. 17-46 to 17-48). It usually is situated above the mylohyoid line, opposite the bicuspid teeth.[44] The size, shape, and number of exostoses vary. The mandibular tori are usually bilateral, but this condition has been found to be unilateral in 20% of cases. The reported incidence in the United States ranges between 6% and 8%, with no sex predilection.

Torus palatinus is a flat, spindle-shaped, nodular or lobular exostosis that arises in the middle of the hard palate (Figs. 17-49 and 17-50). The cause is unknown, but some theories suggest that it may be a hereditary condition.[63, 64] The incidence in the United States varies between 20% and 25%, with women being affected more often. Although torus palatinus may occur at any age, its peak incidence is before the age of 30 years. Radiographically, the torus palatinus is radiopaque, with distinct borders, and is composed of either dense compact bone or a shell of compact bone with a center of cancellous bone. Often a midline suture can be identified through the lesion. Surgical removal is indicated if the torus interferes with swallowing or if a denture must be constructed for prosthetic tooth replacement.

Copyright © 2003, Mosby, Inc. All rights reserved.

Multiple exostoses of the maxilla (Fig. 50) arise from the buccal or lingual surfaces of the maxilla, primarily in the molar region.[71] They appear as small, nodular, bony masses.

Osteoma

An osteoma is a benign neoplasm composed of compact or cancellous bone, usually in an endosteal or periosteal location.[72–74] These tumors vary greatly in size and, if large, can cause disfigurement. The average age at occurrence is 50 to 60 years, and twice as many women as men are affected. These lesions occur most often in the paranasal sinuses, especially in the frontal and ethmoid sinuses. The next most common site is the jaw, and the mandible is affected more often than the maxilla.

Osteomas have a characteristic radiographic appearance. They are well-circumscribed, sclerotic bony masses attached by a broad base or pedicle to the surface of the mandible. Root absorption may occur when the osteoma is located in the vicinity of a tooth. The need for surgical removal is determined clinically because osteomas have not been found to become malignant.

Gardner's syndrome, which is inherited as an autosomal dominant trait, consists of multiple osteomas, multiple colonic polyps, epidermoid and sebaceous cysts, desmoid tumors of the skin, and impacted supernumerary and permanent teeth (Fig. 17-51). The multiple osteomas often precede the onset of the colonic polyps, and these polyps almost always eventually become malignant.[75–78] Osteomas have a predilection for the frontal bone, maxilla, and mandible, although they may be observed in any of the bones of the cranium or facial skeleton. Osteomas of the jaw usually appear early in life, most often in the second decade.

Osteochondroma

An osteochondroma is a benign lesion thought to arise from overgrowth of cartilage at a growth site. These lesions have been reported most frequently in the coronoid and condylar processes.[79, 80] Radiographically, they usually appear as radiopaque extraosseous projections. Although it has been suggested that these tumors are very slow-growing and may have malignant potential, this is not universally agreed upon. Complete surgical removal is the treatment of choice, and recurrence is rare.

Chondroma

Chondromas are slow-growing lesions that presumably arise from cartilaginous remnants in bone.[81] They produce destruction of normal bone and appear as lytic lesions in the body of the mandible and occasionally in the condyle. Full delineation of condylar lesions often requires CT or MR imaging. Histologically, they are neoplasms of hyaline cartilage that are usually homogeneous in appearance. Therefore, these lesions have high signal intensities on T2-weighted MR images, while T1-weighted MR images often shows low signal intensities similar to those of water. It may be difficult to distinguish between benign and malignant lesions when unusual mitotic activity is identified. Surgical removal with wide margins is the preferred treatment.

Synovial Chondromatosis

Synovial chondromatosis is a proliferation of synovial tissues with the formation of cartilaginous particles in the

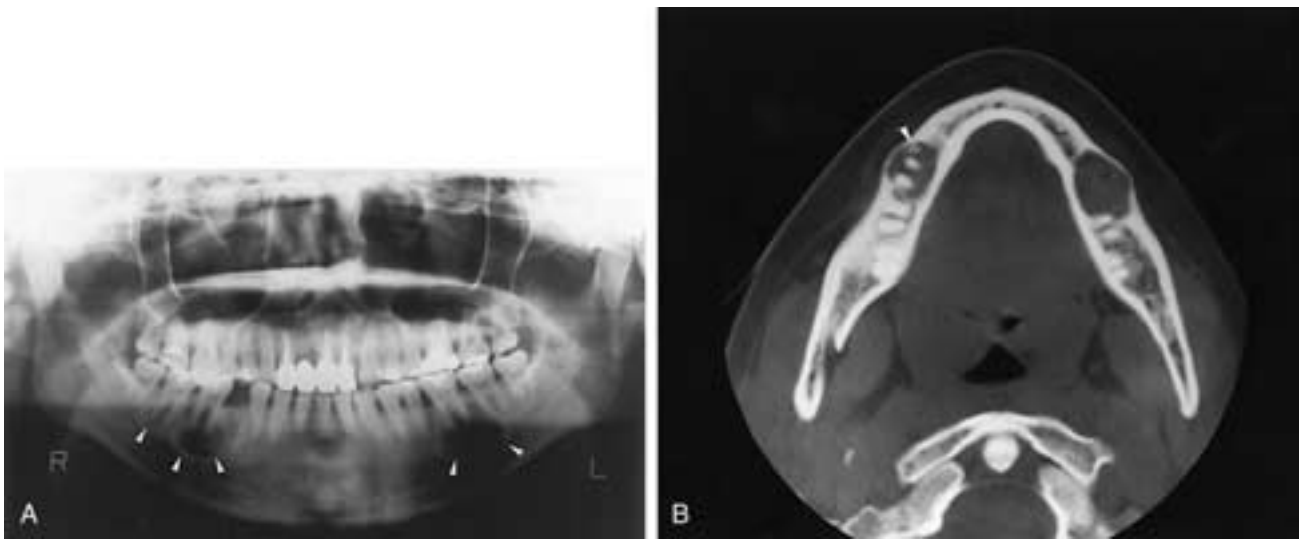

FIGURE 17-43 Cemental dysplasia in the mandible. **A**, Pantomogram shows multiple periapical radiolucent lesions with radiopaque areas in the mandible (*arrowheads*). This appearance may be indistinguishable from that of radicular cyst. **B**, Axial CT shows one expansile low-density lesion with tiny calcifications (*arrowhead*) and another expansile lesion without calcification. These are the early stages of cemental dysplasia.

VIEW IMAGE

Copyright © 2003, Mosby, Inc. All rights reserved.

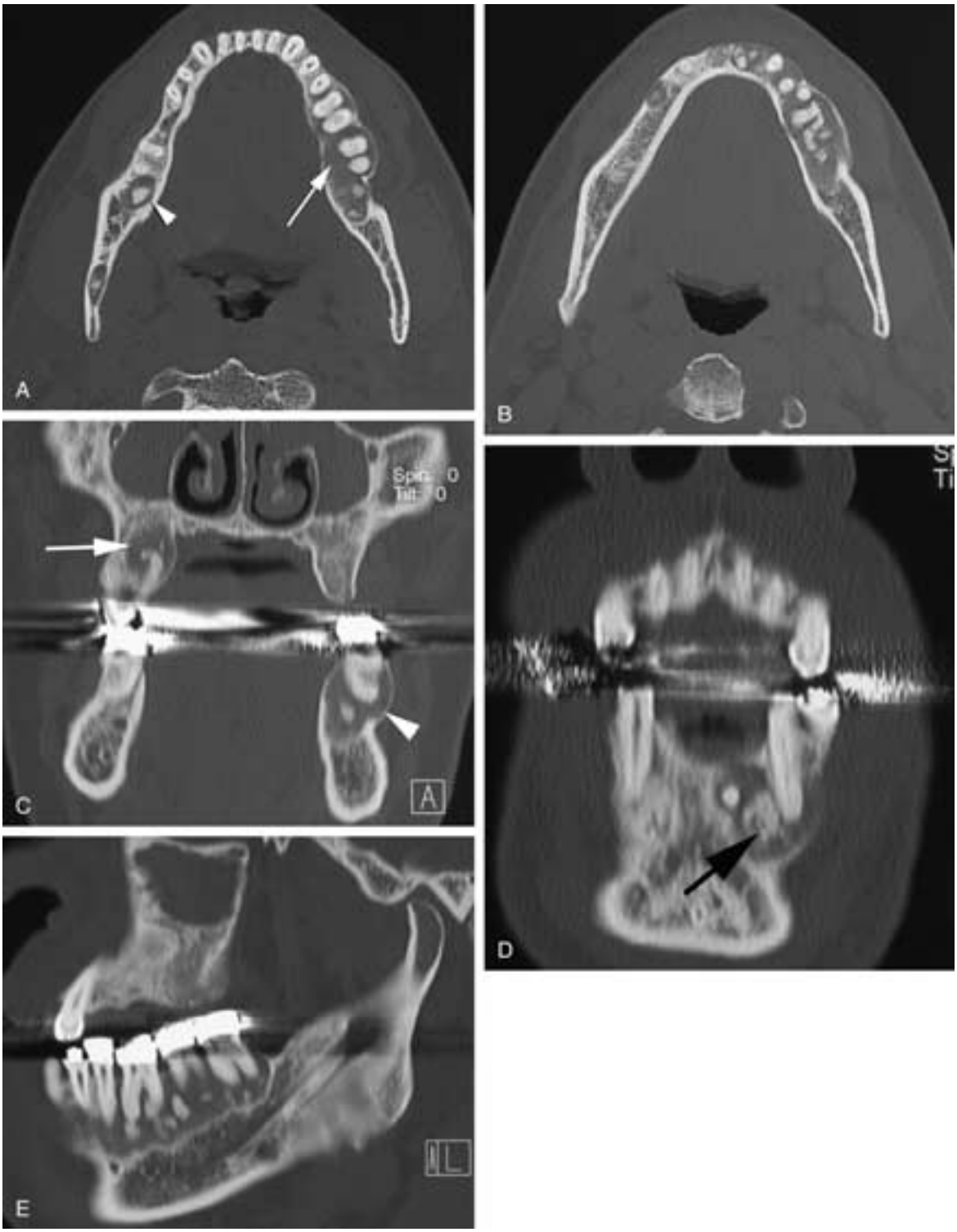

FIGURE 17-44 Florid cementoosseous dysplasia. **A**, Axial scan shows the expansile abnormality involving the mandible. The lesion is well corticated and has abnormal density (*arrow*) between the tooth roots and the margin of the lesion. An abnormality is also seen on the opposite side (*arrowhead*). **B**, Slightly caudad image shows that the lesion follows the mandible to the midline. Isolated root tips are involved on the opposite side. **C**, Coronal image shows the lesion in the mandible (*arrowhead*) as well as in the maxilla (*arrow*). There is expansion of bone. The abnormal bone is closely applied to the root tips. **D**, There is mineralization within the lesion (*black arrow*). This reflects the beginning of maturity of the lesion. **E**, Sagittal image shows the lesion involving multiple tooth roots. There are areas of mineralization within the lesion.

VIEW IMAGE

Copyright © 2003, Mosby, Inc. All rights reserved.

VIEW IMAGE

FIGURE 17-45 Cemental dysplasia of the mandible in a 38-year-old woman. Oblique sagittal T1-weighted MR image reveals multiple low signal intensities with tiny signal voids in the periapical region (*arrowheads*). Preoperative diagnosis of cemental dysplasia is made by radiography, and MR imaging is not useful for differentiation.

synovium that can ossify and migrate into the TMJ space. Symptoms vary widely, but patients often complain of intermittent periarticular swelling, pain, and limitation of motion. Radiographic findings depend on the extent of the proliferative process and include joint effusion, anatomic derangement of the normal joint structures with widening of the joint space, irregularity of the joint's articular surfaces, and evidence of calcified or ossified particles within the joint space. Surgical removal of the lesion and synovectomy is the usual treatment, and in most cases the articular disk does not need to be reconstructed. In cases where reconstruction is deemed necessary, the most common procedure is a vascularized, pedicled temporalis muscle flap interposed between the condyle and the articular fossa of the temporal bone (see Chapter 18).

Giant Cell Lesions

Giant cell lesions of the maxillofacial skeleton make up a continuum of clinically distinct yet histologically very similar pathologic conditions.[82–89] Giant cell granuloma, giant cell tumor, brown tumor of hyperparathyroidism, and cherubism are clinically separate entities that fall into this category. Whether or not the ''true'' giant cell tumor of long bones exists in the maxillofacial skeleton continues to be controversial. Most authors now believe that there is an analogy between the two lesions and that they may represent

FIGURE 17-46 Torus mandibularis. Dental view demonstrates bony exostoses along the lingual surface of the mandible bilaterally.

VIEW IMAGE

a spectrum of a similar pathologic process. Several groups have carried out histomorphometric studies to examine the biologic behavior of these lesions to classify them more correctly, with the aim of correlating histologic and clinical behavior. Based on the clinical, radiologic, and histologic findings, the designation of giant cell lesions of the jaws as either aggressive or nonaggressive may be of more help to the clinician than designation of all of these lesions as belonging to one group.

Giant cell granulomas occur most frequently in the second and third decades of life, and they occur twice as frequently in women as in men. Painless swelling is the most

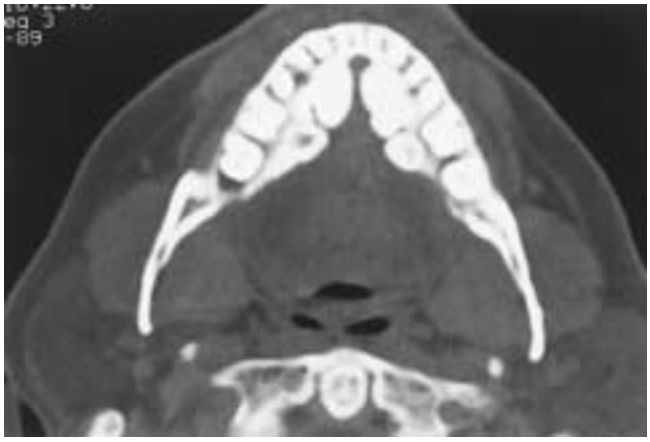

FIGURE 17-47 Torus mandibularis. Axial CT (bone window setting) through the mandible demonstrates bilateral bony exostosis of the lingual surface of the mandible.

VIEW IMAGE

Copyright © 2003, Mosby, Inc. All rights reserved.

VIEW IMAGE

FIGURE 17-48 Torus mandibularis. **A**, Axial image shows the thickening of the cortex (*arrow*) along the inner (lingual) margin of the mandible. **B**, Coronal image shows the torus (exostosis) in cross section (*arrows*).

common symptom, but some lesions may be noted as an incidental finding during routine radiographic screening. The mandible is affected in about two thirds of the reported cases, with most tumors being located in the anterior mandible between the second premolar and the second molar, often with extension across the midline. On occasion, these lesions may exhibit a more aggressive clinical and radiographic appearance.

Radiographically, the lesion most often has a radiolucent, multilocular, honeycombed appearance, with tiny bony septae traversing the involved area (Fig. 17-52). When present, the various loculi are irregular in shape and vary in size; however, unilocular tumors without trabeculation do occur.

VIEW IMAGE

FIGURE 17-49 A torus palatinus (*arrow*) extends from the midline of the palate.

Often there is rather marked expansion, with thinning of the cortical plates, and perforation may occur in large lesions. If the mass is adjacent to teeth, displacement and root resorption are seen. Lesions, especially those in the antral region, produce ''ground-glass'' radiopacities and occasional calcifications (Figs. 17-53 and 17-54). Treatment modalities include enucleation and curettage with local osteotomy, chemical cautery, electrocautery, cryotherapy, and en bloc resection.[82, 83] Calcitonin, interferon alpha, and intralesional steroids are newer modalities that have been somewhat successful in treating more aggressive and recurrent lesions.

LANGERHANS' HISTIOCYTOSIS (HISTIOCYTOSIS X)

Histiocytosis X is a spectrum of diseases with a proliferation of lipid-laden Langerhans' cells (histiocytes) accompanied by a significant inflammatory response.[90–99] This process can be focal or widely disseminated, acute or chronic, and benign or malignant. The cause of this disease remains unknown, although genetic factors, infectious agents, and immunologic abnormalities have been suggested. In 1987, the Writing Group of the Histiocyte Society proposed that the term *Langerhans' cell histiocytosis* replace *histiocytosis X* because Langerhans'-type histiocytes are a unique identifier for this disease.[98] Based on the clinical presentation, three variants have been described: Letterer-Siwe disease (disseminated acute histiocytosis), Hand-Schuller-Christian disease (disseminated chronic histiocytosis), and eosinophilic granuloma (localized histiocytosis).

Letterer-Siwe Disease

Letterer-Siwe disease is the acute, widely disseminated form of histiocytosis X.[95] It is generally fatal and usually

Copyright © 2003, Mosby, Inc. All rights reserved.

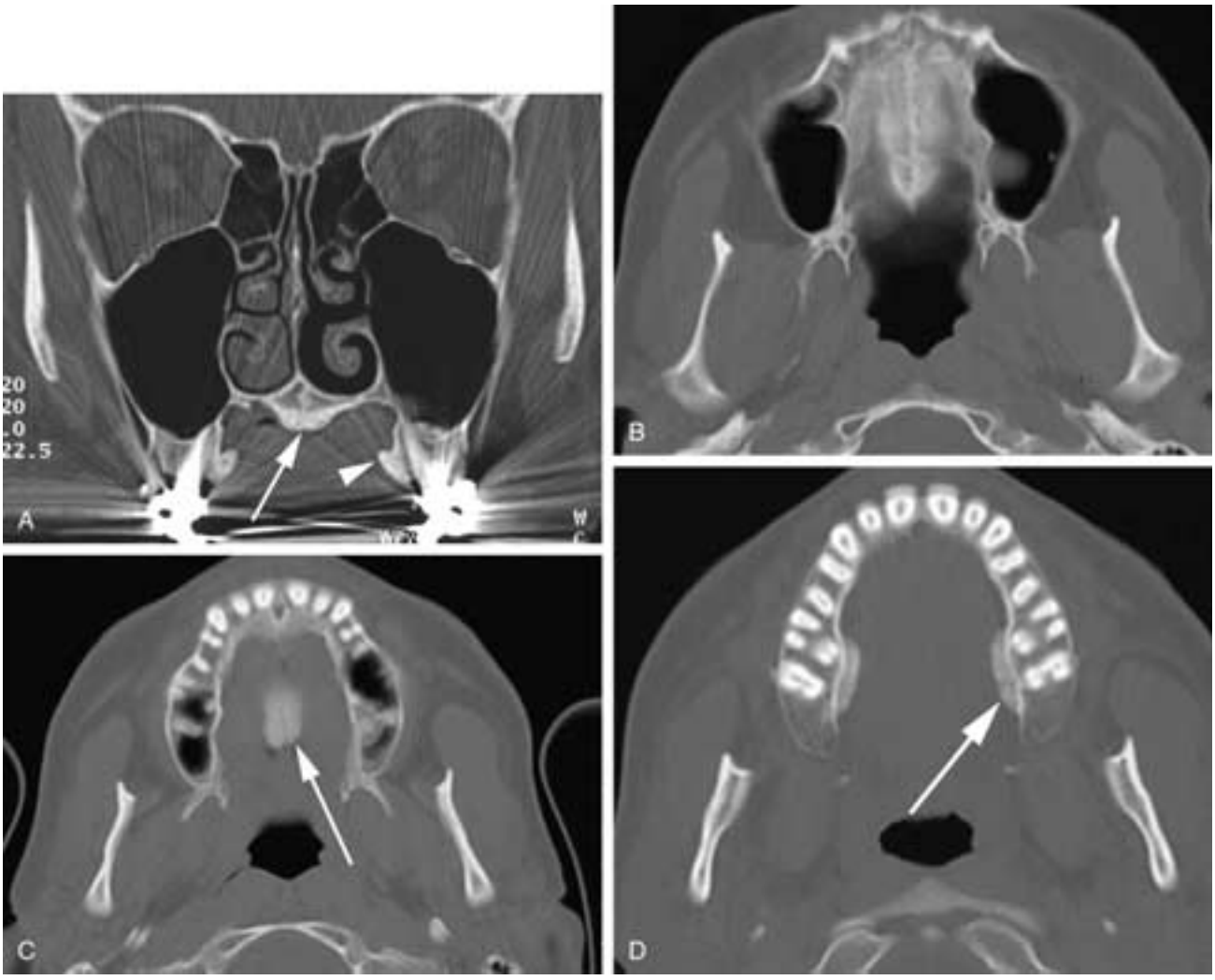

FIGURE 17-50 Torus palatinus and exostosis. CT scan. **A**, Coronal CT shows the torus palatinus (*arrow*) in the midline and the small bilateral maxillary exostosis (*arrowhead*) extending from the medial aspect of the alveolar process. **B**, Axial CT through the palate. **C**, Slightly inferiorly, the torus palatinus (*arrow*) is visualized. **D**, Slightly inferior to **C**. The maxillary exostosis (*arrow*) is identified. The lesion is bilateral.

VIEW IMAGE

occurs in infants under 1 year of age. Lesions are usually present in several bones and may appear as multiple small, rounded radiolucencies with well-defined borders. If teeth are present in the affected regions, they are frequently mobile, and there is associated gingival bleeding.

Hand-Schuller-Christian Disease

Hand-Schuller-Christian disease is the disseminated chronic skeletal and extraskeletal form of histiocytosis X.[96] It is the intermediate stage between eosinophilic granuloma and Letterer-Siwe disease. It occurs mostly in children (twice as often in boys as in girls) from the first to the tenth year of life. The three classic signs of the disease (single or multiple sharply defined calvarial defects, unilateral or bilateral exophthalmos, and diabetes insipidus) are noted in about 10% of patients. Other organs such as the lymph

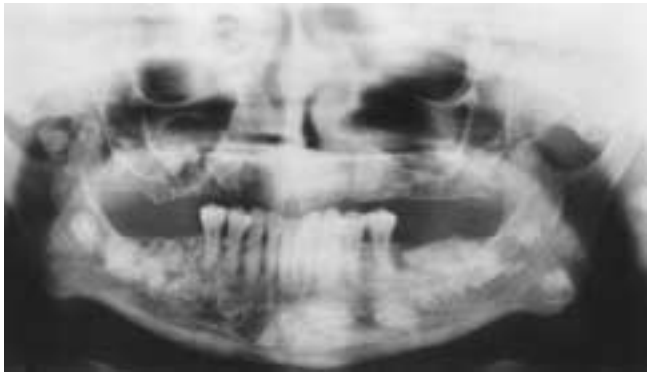

FIGURE 17-51 Gardner's syndrome. Pantomogram of the mandible and maxilla demonstrates multiple osteomas within the mandible and the alveolar portion of the maxilla. There is some conglomeration of the osteomas, especially in the body of the right mandible.

VIEW IMAGE

Copyright © 2003, Mosby, Inc. All rights reserved.

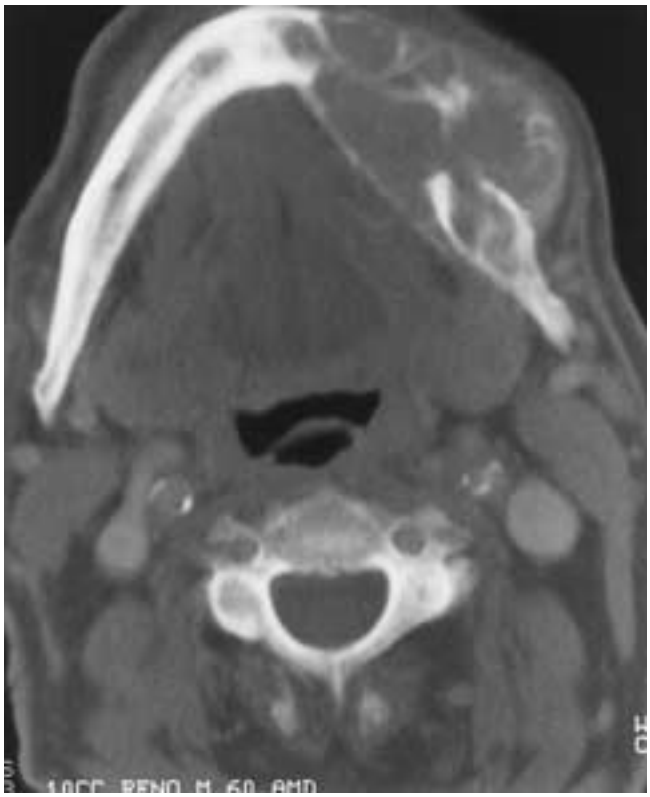

VIEW IMAGE

FIGURE 17-52 Giant cell granuloma of the left mandible. Axial CT (bone window setting) demonstrates a loculated, expansile lesion involving the ramus, body, and symphysis of the mandible.

nodes, liver, spleen, lungs, and skin may be involved. The first indication of the disease often appears in the oral structures, either in the form of red, spongy gingiva or premature loss of teeth. The typical radiographic appearance is one of irregular, lucent defects in the mandible and maxilla. The affected teeth appear to be ''floating in space'' as a result of marked destruction of the alveolar bone. The disease is slowly progressive, and the mortality rate may be as high as 60%.

Eosinophilic Granuloma

Eosinophilic granuloma is the mildest and most favorable form of histiocytosis X.[97] There is a male predilection, with a peak frequency in the third decade of life. The average age of patients with eosinophilic granuloma of the jaw is higher than that of patients with lesions in other parts of the body, and frequent sites are the skull and the tooth-bearing areas of the mandible. The lesion may be an incidental radiographic finding and may manifest as local pain, swelling, tenderness, or fever and general malaise. Eosinophilic granuloma of the mandible causes well-demarcated areas of osteolysis that may appear ''punched out.'' Maxillary lesions usually are not as well demarcated as those in the mandible.

The area of bone involvement is characterized by irregular lucent patches having no reactive sclerosis but often showing cortical destruction (Fig. 17-55). These patches may appear as single or multiple areas of rarefaction simulating jaw cysts, periapical granulomas, or periodontal disease (Fig. 17-56). Early radiographic findings include

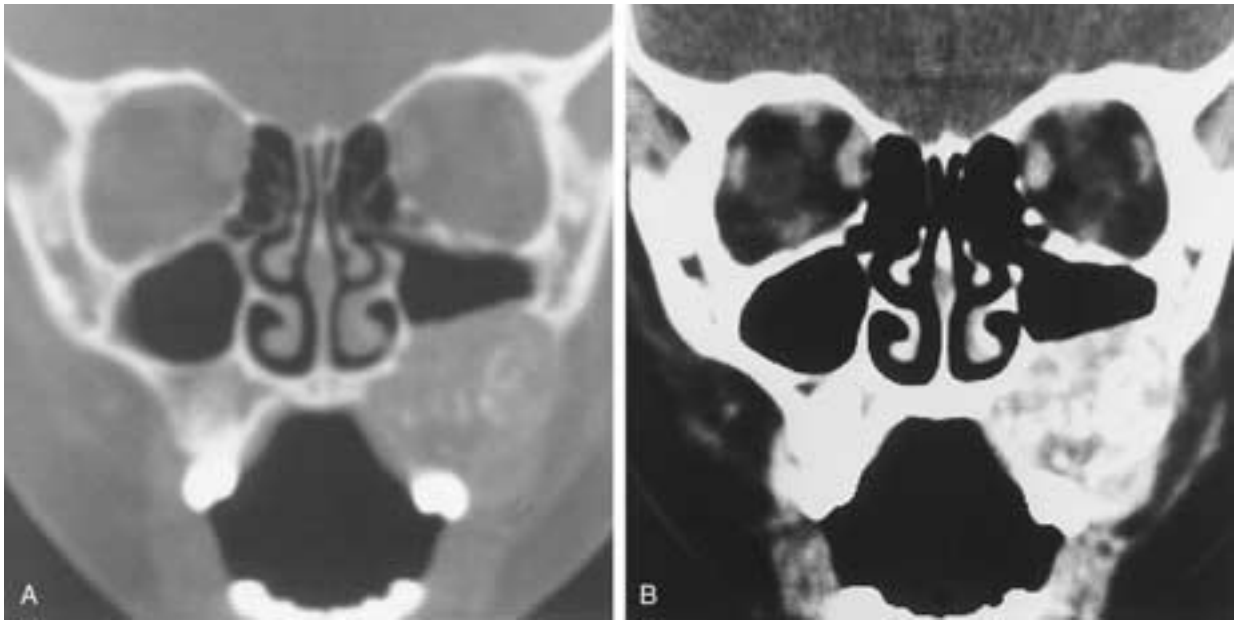

FIGURE 17-53 Giant cell granuloma of the left maxilla. **A**, Coronal CT (bone window setting) shows an expansile lesion in the left maxilla bulging into the left lower antrum and adjacent oral cavity. Note the calcific densities within the lesion. **B**, Coronal CT (soft-tissue window setting) demonstrates to better advantage the calcific and bony densities within the expansile lesion.

VIEW IMAGE

Copyright © 2003, Mosby, Inc. All rights reserved.

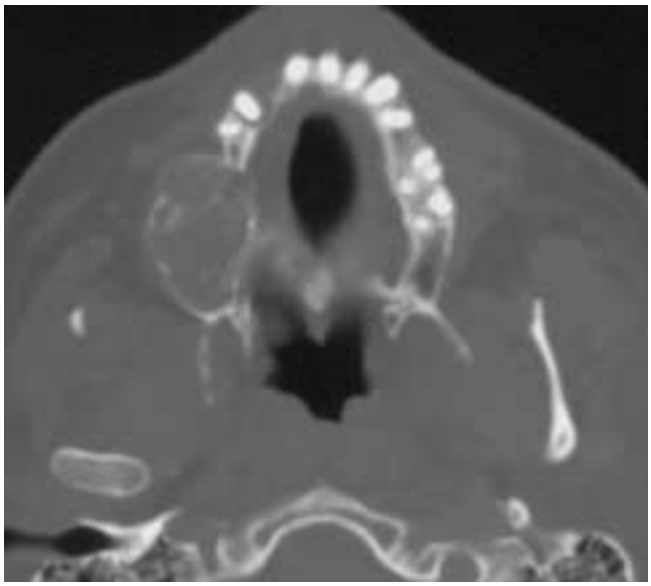

VIEW IMAGE

FIGURE 17-54 Giant cell lesion of the mandible. Axial CT scan. There is expansion of the alveolar process, and foci of mineralization are seen. The appearance of this lesion mimics that of fibrous dysplasia.

FIGURE 17-55 Eosinophilic granuloma in the right mandible. Pantomogram of the mandible shows a lucent, irregular, fairly well defined area in the body of the mandible between the second molar tooth and the first premolar tooth. There is some loss of the lamina dura of the lower second molar tooth.

VIEW IMAGE

destruction of the alveolar bone crest and interdental septum and loss of the cortical outline of a tooth follicle or the lamina dura. The teeth in the involved regions become loose, float in space, and are exfoliated.

Unifocal lesions may be curetted and packed with cancellous bone.[99] With several recurrences or persistent residual granulomas, low-dose irradiation and cortisone treatment may be beneficial. Cytostatic agents (vinblastine, cyclophosphamide, and etoposide) also have been used successfully. Other treatment modalities include immunotherapy (suppressin A, cyclosporin), hormonal therapy, intralesional steroids, and bone marrow transplantation.

FIBROOSSEOUS LESIONS

Fibrous Dysplasia

Fibrous dysplasia is a lesion of unknown cause, diverse histopathology, and uncertain pathogenesis that is most commonly seen in the first three decades of life.[100–106] It occurs more frequently in the maxilla than in the mandible, where it usually arises in the posterior regions of the bone. There are considerable microscopic variations in the different lesions, as evidenced by fibrous tissue alternating with trabeculae of coarse woven bone and less organized lamellar bone. The three forms of fibrous dysplasia are monostotic fibrous dysplasia, polyostotic fibrous dysplasia (in which multiple bony lesions, often unilateral, occur), and Albright's syndrome.

Monostotic fibrous dysplasia occurs equally often in males and females and is encountered frequently in children and young adults, with a mean age of 27 years.[102] The clinical symptom usually is painless swelling of the involved bone; however, neurovascular compromise may cause symptoms. Typically, there is involvement of the jaw, as noted by bulging of the labial or buccal plates, malalignment and displacement of teeth, protuberance of the maxilla, or enlargement of the maxilla or zygoma with proptosis. There also can be skull base disease.

Polyostotic fibrous dysplasia manifests early in life, often with an insidious onset. The disease is characterized by bone deformities, and in some cases there is associated bone pain. In this form of fibrous dysplasia, the skull and face are frequently involved, often with obvious asymmetry secondary to bone expansion. Jaw involvement develops slowly and usually presents with facial deformity, overgrowth of the alveolar bone, and displacement of teeth. There can be marked enlargement of the maxilla, with involvement of the maxillary sinuses, nasal cavities, orbit, and base of the skull. Craniofacial fibrous dysplasia is generally not a functionally devastating disease unless the lesion involves the orbit and skull base; when this happens, blindness, pituitary dysfunction, and vital neurovascular compromise may occur.

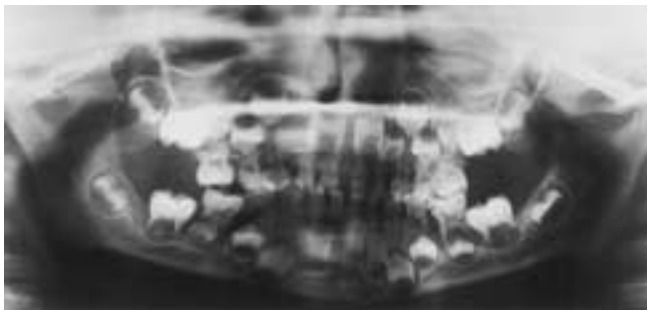

FIGURE 17-56 Diffuse eosinophilic granuloma in the mandible. Pantomogram of the mandible shows loss of the lamina dura of erupted and partially erupted tooth follicles. This is especially evident at the second lower right molar tooth.

VIEW IMAGE

Copyright © 2003, Mosby, Inc. All rights reserved.

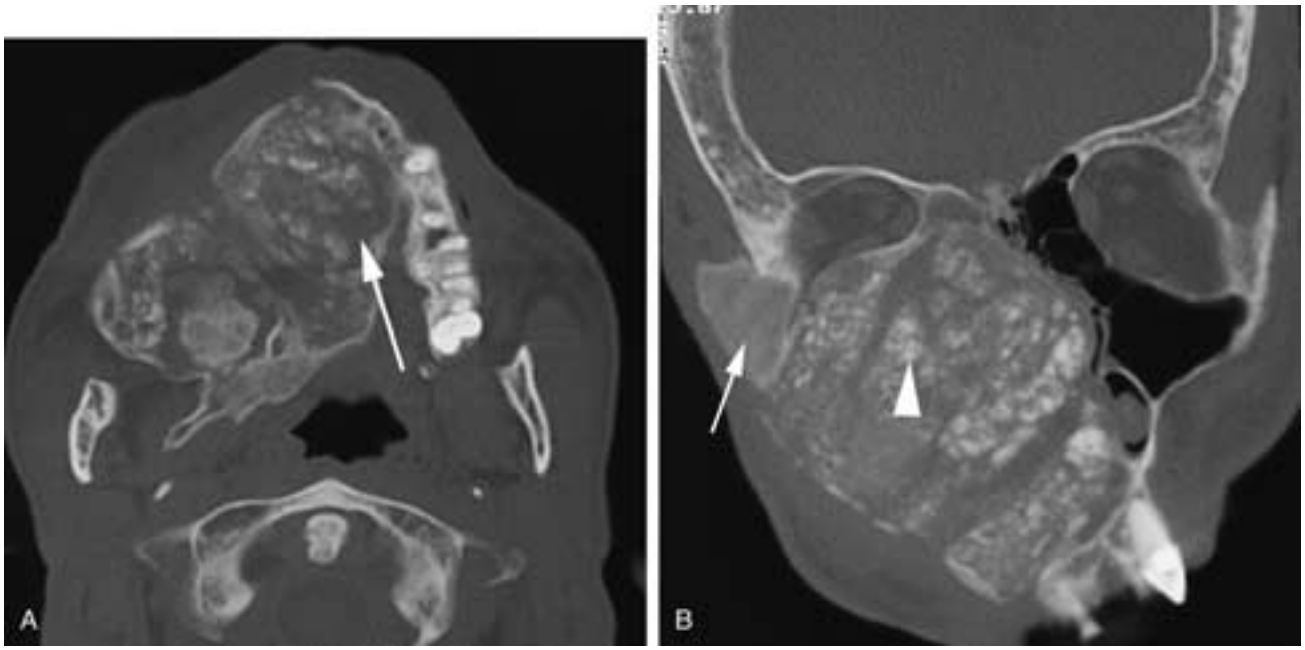

VIEW IMAGE

FIGURE 17-57 Fibrous dysplasia of the maxilla. There is gross expansion of the maxilla. The lesion contains multiple consistencies including soft tissue, bone, and perhaps cartilage. **A**, Axial image with multiple punctate areas of mineralization (*arrow*). The low density may represent fibrous tissue or a cystic component. **B**, Coronal image shows small foci of calcifications (*arrowhead*) that may represent chondroid matrix. This makes differentiation from chondrosarcoma difficult. The lateral part of the abnormality (*arrow*) has a typical ''ground glass'' appearance.

Albright's syndrome is a developmental defect of unknown cause. It consists of cutaneous pigmentation, precocious puberty, and multiple skeletal lesions. Young girls are affected most often.

The radiologic appearance of fibrous dysplasia can vary considerably, usually depending on the degree of bone present within the lesion (Figs. 17-57 to 17-60). One appearance is that of a unilocular or multilocular, primarily radiolucent lesion with a well-defined border. Interspersed bony trabeculae are often present within the lucent area, rendering the lesion partially radiopaque (Fig. 17-61). Another appearance is that of a marked homogeneous increase in bone density associated with bone expansion, which reflects the predominant histologic finding of bony

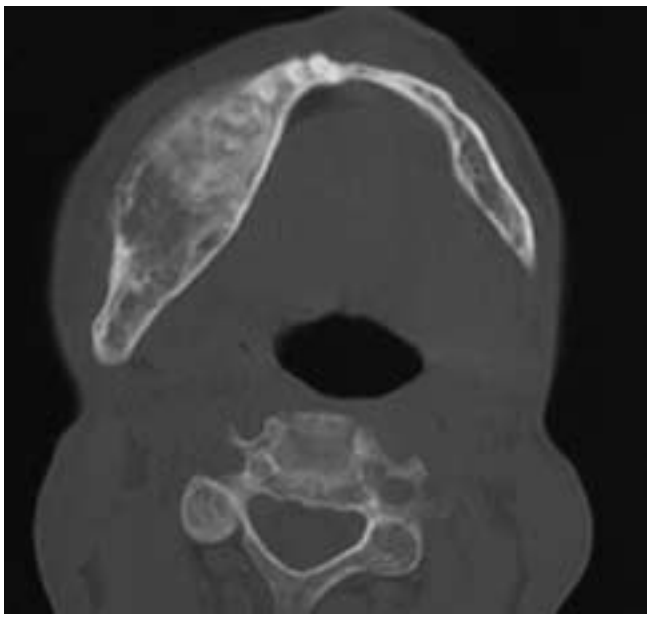

VIEW IMAGE

FIGURE 17-58 Fibrous dysplasia. There is an expansile abnormality of the mandible. The mineralization suggests osteoid as well as lucencies representing fibrous tissue.

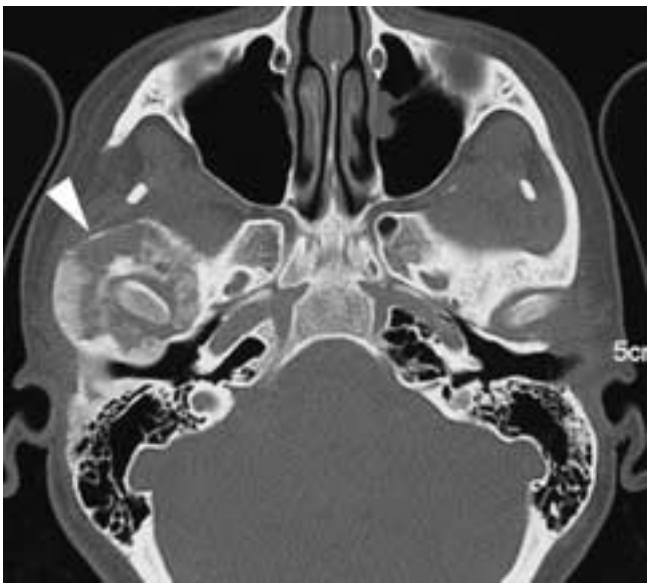

FIGURE 17-59 Fibrous dysplasia of the glenoid. There is expansion of the bone of the glenoid. This abnormality contains ''ground glass'' as well as soft-tissue density presumably representing fibrous tissue. Note that the cortex (*arrowhead*) is intact. The lesion does not involve the condylar head.

VIEW IMAGE

Copyright © 2003, Mosby, Inc. All rights reserved.

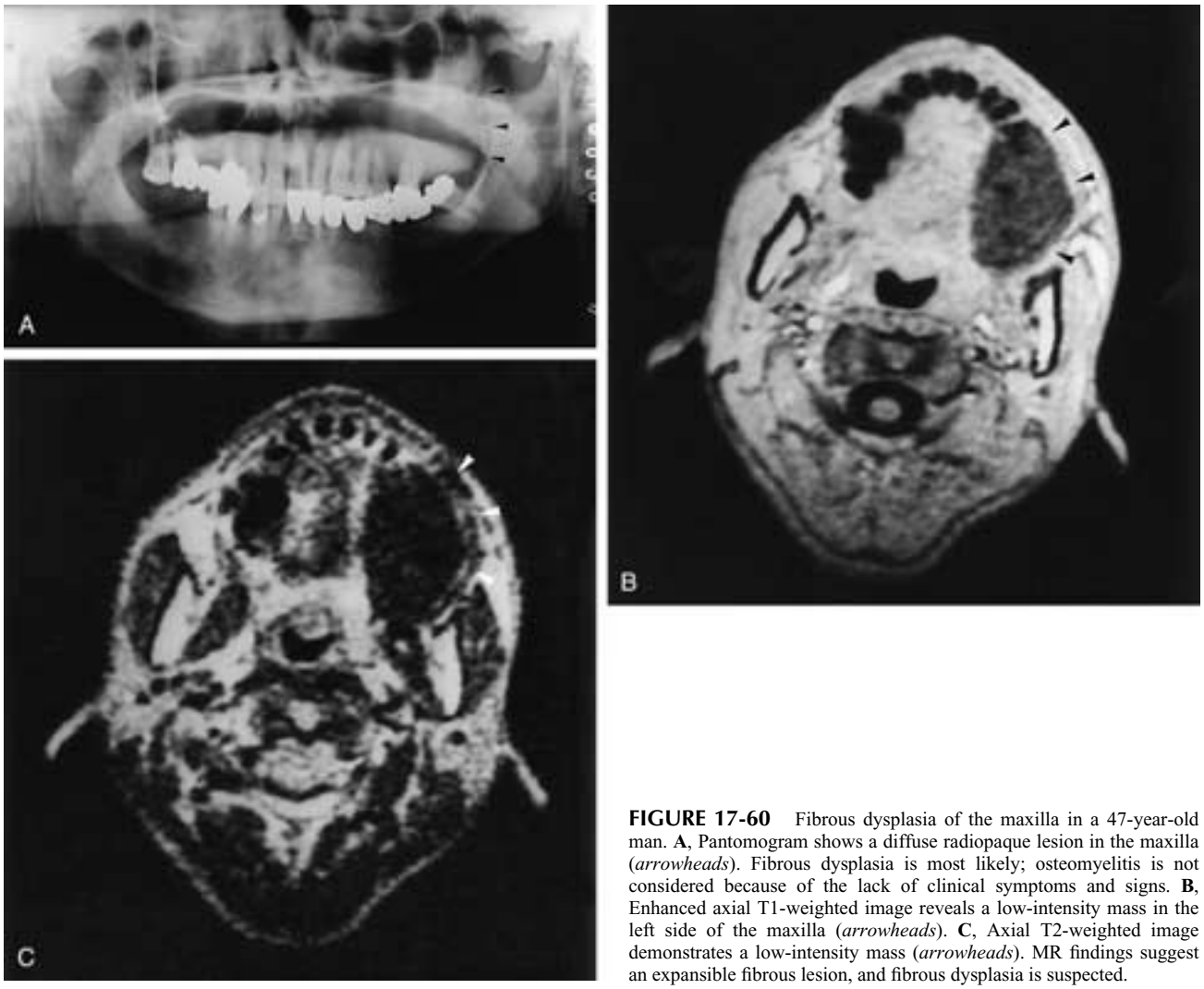

FIGURE 17-60 Fibrous dysplasia of the maxilla in a 47-year-old man. **A**, Pantomogram shows a diffuse radiopaque lesion in the maxilla (*arrowheads*). Fibrous dysplasia is most likely; osteomyelitis is not considered because of the lack of clinical symptoms and signs. **B**, Enhanced axial T1-weighted image reveals a low-intensity mass in the left side of the maxilla (*arrowheads*). **C**, Axial T2-weighted image demonstrates a low-intensity mass (*arrowheads*). MR findings suggest an expansible fibrous lesion, and fibrous dysplasia is suspected.

VIEW IMAGE

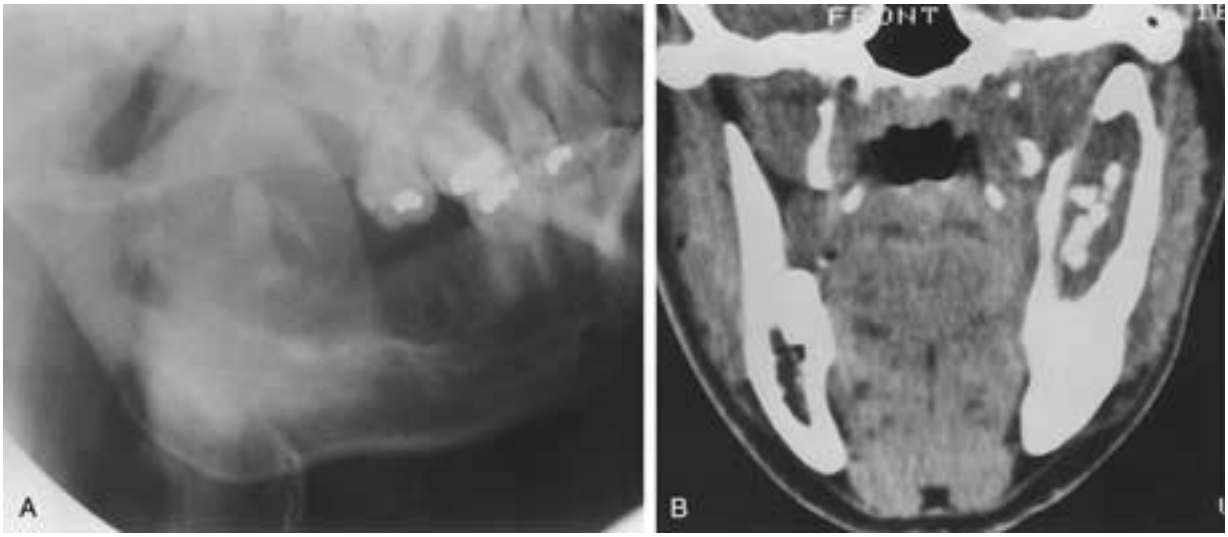

FIGURE 17-61 Monostotic fibrous dysplasia in the left mandible. **A**, Oblique view of the left mandible shows a sclerotic expansile lesion in the ramus of the mandible, with extension into the coronoid process. There are some calcific densities within the central anterior part of this lesion. **B**, Coronal CT (soft-tissue window setting) shows the expansile nature of the lesion in the ramus. Calcified densities are noted within the lesion.

VIEW IMAGE

Copyright © 2003, Mosby, Inc. All rights reserved.

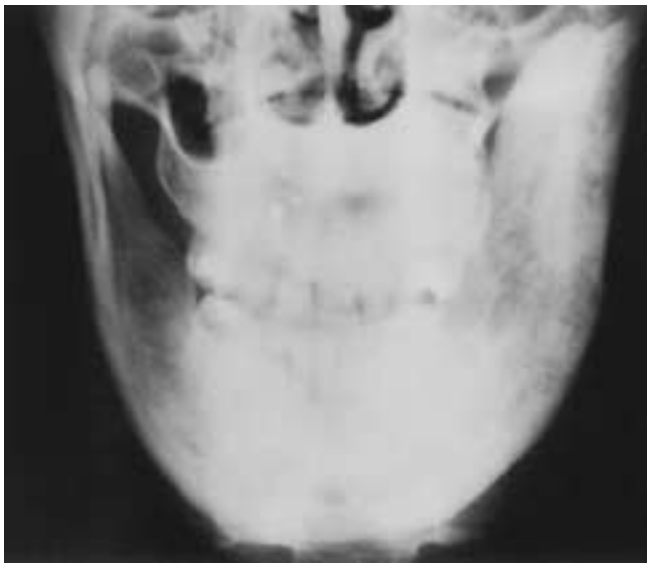

VIEW IMAGE

FIGURE 17-62 Monostotic fibrous dysplasia. Posteroanterior view of the mandible shows an expansile sclerotic lesion involving the left ramus of the mandible, with extension into the angle and body of the left mandible.

trabeculae with only a few scattered areas of fibrous tissue (Fig. 17-62). This is sometimes referred to as a ground-glass appearance, which is more evident on CT. Cystic lesions of appreciable size cause thinning and remodeling of the cortex, but they rarely perforate the cortex or produce new periosteal bone. Although the lesion may cause resorption of the roots of erupted teeth, this is rare. MR imaging findings also depend on the variety of components of the disease, especially on T2-weighted images. The fibrous components often shows enhancement after contrast administration. If the lesion has rich cartilaginous components or cystic changes, its signal intensities can be brighter: the former show gradual enhancement, while the latter show no enhancement.

The disease is usually self-limiting, often not progressing after the third decade of life. Surgical treatment usually is limited to a cosmetic debulking and recontouring of the bone. However, an accelerated progression of the disease has been noted with early and aggressive surgical manipulation, sometimes mandating additional surgery. Only small lesions can be removed by enucleation. Because there is a low incidence of malignant transformation of fibrous dysplasia, regular and careful follow-up should be maintained.

Ossifying Fibromas (Cemento-Ossifying Fibromas, Cementifying Fibromas)

The ossifying fibroma is an encapsulated, benign neoplasm consisting of fibrous tissue that contains various amounts of irregular bony trabeculae.[107, 108] As the lesion matures, the areas of ossification increase in number and coalesce, accounting for the lesion's progressively increasing radiodensity. These lesions may be difficult to distinguish from fibrous dysplasia histologically, but they are sharply demarcated and not uncommonly encapsulated masses that behave as benign neoplasms. In the recent WHO classification,[3] cemento-ossifying lesions (both neoplastic and dysplastic) are listed in the category of neoplasms and other lesions related to bone, although benign cementoblastoma, generally accepted as being essentially cementogenic, has been included in the neoplasms and other tumors related to the odontogenic apparatus category. Ossifying (cemento-ossifying) fibroma is found more often in females and may occur at any age, but it is most common in the third and fourth decades of life. The lesion develops predominantly in the mandible and is usually situated at the roots of the teeth or in the periapical region. It generally is asymptomatic, but a progressive increase in size may eventually cause swelling of the jaw.

Radiographically, the lesion usually has a distinct boundary, unlike fibrous dysplasia, and in the early stages it presents as a lucent area. As the lesion matures, bone densities appear, transforming the lesion into a radiopaque mass surrounded by a ''halo'' of less ossified tissue (Fig. 17-63). One aggressive variety of ossifying fibroma is referred to as juvenile ossifying fibroma. This term designates a very actively growing destructive lesion that is histologically identical to the routine ossifying fibroma. This lesion affects individuals younger than 15 years of age and occurs exclusively in the maxilla.

The treatment of ossifying fibroma is usually surgical enucleation. However, for some forms of this lesion, especially the juvenile form that is prone to recur, broader surgical resection should be considered.

Paget's Disease (Osteitis Deformans)

Paget's disease of bone is a chronic disease characterized by abnormal functioning of osteoblasts and osteoclasts resulting in poorly mineralized and deformed bones.[109, 110] There is a slightly higher male predominance, and the incidence increases with age. There are also reports of an occasional familial pattern. Although the exact cause remains unknown, numerous theories have been proposed regarding its development, including a slow viral infection, hormonal abnormalities, a vascular anomaly, an autoimmune-type connective tissue disorder, and a true neoplasia. Malignant transformation, although not a common occurrence, has been reported in the jaws and is a constant concern. This is of particular concern if the region has been previously irradiated.

In the craniofacial skeleton, involvement of the skull, maxilla, and mandible is common. Headache, dizziness, hearing loss, and other cranial nerve abnormalities may result from the skull base involvement. The maxilla is involved more commonly than the mandible. The jaw lesions cause bone enlargement, separation of teeth with generalized widening of the interdental spaces, ill-fitting dentures, and frequently neuralgia-type pain.

Radiographically, the jaw lesions have a variable appearance, depending on the stage of disease progression. There can be ''punched-out'' radiolucent areas, mixed areas giving a ''cotton wool-like'' appearance, and more densely sclerotic areas. The jaw lesions frequently show evidence of

Copyright © 2003, Mosby, Inc. All rights reserved.

rarefaction and sclerotic change in the alveolar bone, with loss of the lamina dura surrounding the teeth and hypercementosis of the roots of teeth. Radionuclide scanning can identify the presence of disease based on the presence of areas of biologic activity. Laboratory findings typically include elevations in serum alkaline phosphatase and urinary hydroxyproline. Serum calcium and phosphorus levels are usually normal.

Clinical management may consist of no more than closely following the patient. When more severe disease exists or when the bone lesions in the craniofacial skeleton cause symptoms, therapeutic intervention is usually indicated. Nonsurgical treatment can include steroids and the use of calcitonins and diphosphonates. Surgical procedures must be carried out with great care because the abnormal bone is often very vascular, and significant bleeding can occur.

VASCULAR LESIONS

Vascular lesions of the head and neck are a perplexing group of problems that have generated significant debate and confusion regarding terminology and classification.[111–117] Descriptive, anatomic-pathologic, and embryologic classification schemes have been devised and debated and generally have not offered clinicians significant treatment guidance. The classification developed by Mulliken and Glowacki in 1982 is based on the cellular kinetics of the anomalous vessels and provides a diagnostic and therapeutic approach based on the biologic behavior of the lesion.[114] In this classification, two entities exist: hemangiomas and vascular malformations.

Hemangioma

Hemangiomas are usually not identified at birth, but they appear soon thereafter. They are present in 12% of all children by 1 year of age. They go through a rapid proliferation phase during the first year of life followed by a much slower involution phase, which usually reaches partial or complete resolution by 5 to 7 years of age.

Hemangiomas are 2 to 2½ times more common in females than in males, and there is no racial predilection. Hemangiomas are found most often in the skull and vertebrae, and although common in the head and neck, they are rarely located in the jaw. They are benign tumors with vessels that have marked endothelial turnover, and there are increased numbers of mast cells that are thought to play a role in the pathophysiology of these lesions.

Although most hemangiomas can be diagnosed by the history and physical findings, some are difficult to fully evaluate clinically and warrant imaging studies. Radiographically, hemangiomas of the mandible appear as ill-defined radiolucent lesions usually involving the inferior alveolar canal (Fig. 17-64). Some lesions may have a cystic or occasionally a multilocular shape. CT and MR imaging are particularly helpful for deeper lesions and those thought to involve bone. Doppler ultrasound and angiography may also be employed. Angiography of hemangiomas shows a well-circumscribed mass, usually with prolonged parenchymal staining and tissue blush.

Treatment is based on correctly identifying the lesion and distinguishing it from a vascular malformation. Kaban and Mulliken pointed out, in their review of vascular anomalies of the maxillofacial region, that many reported hemangiomas were in fact vascular malformations.[113] Management of maxillofacial hemangiomas often consists of counseling and

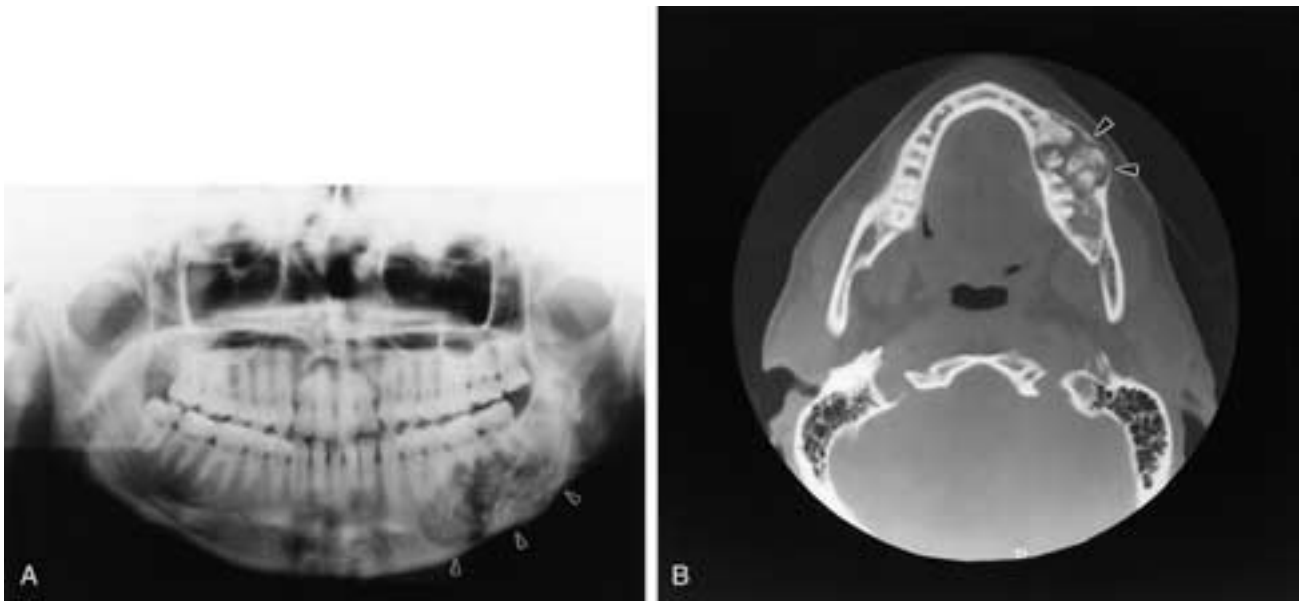

FIGURE 17-63 Cemento-ossifying fibroma in the mandible. **A**, Pantomogram shows a well-defined mixed radiolucent-radiopaque lesion (*arrowheads*). **B**, Axial CT (bone window setting) demonstrates a buccal expansile lesion with some calcifications in the mandible. The surrounding buccal bony cortex is barely preserved (*arrowheads*).

VIEW IMAGE

Copyright © 2003, Mosby, Inc. All rights reserved.

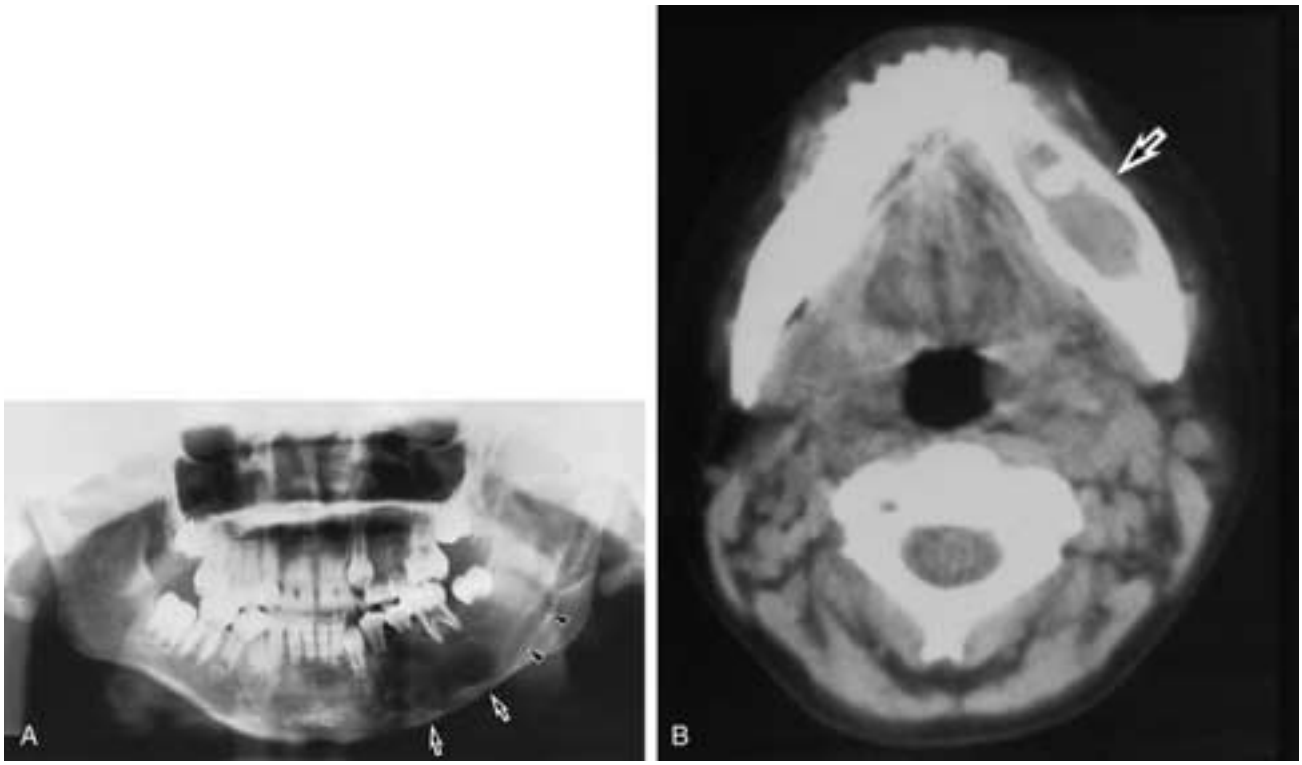

VIEW IMAGE

FIG. 17-64 Central hemangioma in the mandible. **A**, Pantomogram shows a large radiolucent lesion in the mandible (*arrows*). The inferior alveolar nerve canal has been widened, and its course has been altered (*arrowheads*). **B**, Axial CT (soft-tissue window setting) shows a well-defined, slightly expansile lesion (*arrow*). Note the increased density within the lesion suggesting blood rather than cystic fluid. (Courtesy of Dr. T. Kurabayashi, Dept. of Dental Radiology, Tokyo Medical and Dental University, Tokyo.)

parental support along with observation. If significant functional problems ensue, treatment consists of steroid therapy, compression therapy, radiotherapy, embolization, and treatment with interferon alpha.[116, 117] Surgery is reserved for small lesions and as a secondary procedure to correct cosmetic deformities.

Vascular Malformation

Vascular malformations are usually present at birth, but they may not be clinically evident until some inciting event occurs.[114] Their growth parallels normal body growth and is influenced by numerous additional factors. There is no sex predilection. Vascular malformations can be composed solely of capillary, venous, arterial, or lymphatic tissues or can be a combination of these tissues. They are subdivided into high-flow and low-flow lesions based on their clinical and angiographic patterns. In the maxillofacial region they frequently involve bone.

Radiographically, the lesion appears as a radiolucent area, often traversed by delicate bony trabeculae forming variously sized small cavities. In large vascular malformations the cortex may be thinned, remodeled, or eroded.[108] If the trabeculae are arranged in a radiating pattern, a sunburst or spoke wheel appearance results. In some cases, there may be a single radiolucent lesion with a sclerotic or ill-defined border that simulates a cyst. Root absorption, loss of the lamina dura, and exfoliation of teeth have also been reported, and a bruit may be heard or a thrill palpated over the lesion. Spontaneous bleeding around the involved teeth is a problem in the jaws.

Management of vascular malformations mandates a thorough knowledge of the pathologic process and the relevant anatomy. Small lesions may be treated with sclerosing agents, radiotherapy, cryotherapy, laser treatment, or conventional surgical techniques. Larger lesions, particularly high-flow and arteriovenous malformations, are best treated with embolization techniques, with or without surgical resection.

NEUROGENIC TUMORS

Benign neurogenic tumors, which include schwannomas (neurilemommas), neurofibromas, and traumatic neuromas, occasionally are found centrally within the jaw.[118–121] They may occur at any age, and there is little or no sex predilection. Most of these slow-growing lesions arise in the mandible and cause pain or paresthesia.

A schwannoma is usually encapsulated and composed of two distinct histologic components: Antoni type A tissue and Antoni type B tissue.[119] A neurofibroma arises from the connective tissue sheath of nerve fibers and has axons traversing the unencapsulated tumor.[118, 119] It may occur as a solitary lesion or as multiple lesions associated with neurofibromatosis. Solitary neurofibromas may originate in the oral mucosa or may occur within the jaws.

Copyright © 2003, Mosby, Inc. All rights reserved.

Radiographically, these lesions may present as solitary radiolucencies associated with the inferior alveolar canal or as multilocular radiolucencies that produce extensive bone damage, with cortical remodeling and even perforation. On occasion, the intraosseous tumor may perforate the cortex of the jaw and extend into the overlying soft tissues. A schwannoma, arising from the nerve within the inferior alveolar canal, may cause bulbous, elongated enlargement of the canal, and a neurofibroma adjacent to bone may produce a saucer-shaped erosive defect on the surface of the bone.

Treatment is surgical but depends on the size and location of the lesion. Smaller lesions can often be removed without significant damage to the nerve or surrounding tissues and without the need for major reconstructive surgery. Larger lesions, especially those with significant bone involvement, usually require larger surgical exposure with enucleation or en bloc surgical resection, often with additional treatment modalities such as cautery or cryotherapy of the bone. When these techniques are needed, surgical reconstruction is mandatory, often with a microsurgical nerve repair.

MALIGNANT TUMORS

Malignant tumors can be grouped into three categories: (1) lesions that invade the mandible and maxilla secondarily from adjacent soft-tissue structures of the oral cavity and sinuses, (2) tumors that arise primarily within the mandible and maxilla, and (3) metastatic tumors from distant sites. The radiographic appearance of malignant lesions often allows differentiation from benign tumors and cysts; however, a biopsy is necessary to establish the final diagnosis. For proper treatment planning, it is important to assess the extent of the malignant tumor radiographically before surgery or radiation therapy. CT and MR imaging have proven valuable in assessing the extent of tumors outside the mandible and maxilla, as well as in assessing disease extension within the bone or metastases to the neck.

Carcinoma

Most carcinomas encountered in the jaw originate in the oral cavity (lip, tongue, buccal mucosa, gingiva, floor of the mouth, and palate) and maxillary sinuses, and they secondarily invade the mandible and maxilla.[122–125]

Radiographically, the osseous involvement manifests early at the alveolar ridge with a saucer-shaped erosive defect. This defect may be shallow and well defined, but in time an irregular cavity can be formed. There is usually no evidence of bony sclerotic or periosteal reaction. Therefore, superficial erosion of the alveolar crest in the tooth-bearing regions may initially mimic periodontal disease. Radiographically, carcinoma usually appears as a radiolucency with irregular margins (Fig. 17-65). Permeative disease extension may create a ''moth-eaten'' appearance. The radiographic findings are nonspecific, and the tumor cannot be differentiated from other malignant lesions. Pathologic fractures are common complications in advanced cases.

Odontogenic carcinoma is a carcinoma arising within the bone without a lesion of the mucosa.[1] These rare malignancies arise from epithelial remnants left behind by the process of tooth formation, hence the use of the term *odontogenic*. Odontogenic carcinoma can be subcategorized according to its apparent origin. Malignant ameloblastoma represents transformation from a benign ameloblastoma. Primary intraosseous carcinoma arises without preexisting ameloblastoma. Some carcinomas may arise in preexisting odontogenic cysts.

Primary intraosseous carcinoma may develop from epithelial components that participate in the development of the teeth or from epithelial cells that become enclosed within the deeper structures of the jaw during embryonic development. About 90% of these lesions are found in the mandible; they occur more frequently in men than in women, and their peak incidence is in the sixth and seventh decades of life. Although uncommon, this lesion is now recognized as a distinct entity. The lesion typically has an irregular margin. No mucosal abnormality is seen.

Carcinomatous transformation of the epithelium in an odontogenic cyst is a rare event, although it has been reported in dentigerous cysts, radicular cysts, residual cysts, and keratocysts. None of the reported cases affected individuals over 40 years of age. Radiographically, the lesion resembles a cyst with a circumscribed margin. In the area of malignant degeneration the margin may become ill-defined, irregular, or moth-eaten.

Ameloblastoma is rarely malignant.[1–3] The WHO classification of 1992, however, does include malignant ameloblastoma[1] as a category. It defines malignant ameloblastoma as ''a neoplasm in which the pattern of an ameloblastoma and cytological features of malignancy are shown by the primary growth in the jaws and/or by any metastatic growth.'' There is controversy regarding exact terminology.[2, 126–128] Some advocate restriction of the term *malignant ameloblastoma* to an ameloblastoma that, although histologically benign, shows a malignant nature by metastasizing. The metastasis shows the histologic pattern of the original tumor, again without cytologic indicators of malignancy. There are tumors that do have typical cytologic findings of malignancy including increased and abnormal mitoses, nuclear pleomorphism, and so on. The term *ameloblastic carcinoma* has been advocated for these rare lesions. They may metastasize as well. Neither term should be applied to a histologically benign tumor that simply shows aggressive local extension even though involvement of key contiguous structures may be life-threatening. The radiologist should simply realize that the controversy related to terminology exists and that clarification of terms is appropriate in the individual case or in reports in the literature.

Malignant variants of ameloblastoma may arise de novo or in relation to a preexisting ameloblastoma. The lesions are most commonly found in the jaw. The imaging findings may be inseparable from those of benign ameloblastoma, but locally aggressive tumors can have a more irregular margin.

Other rare malignant epithelial lesions include clear cell odontogenic carcinoma and malignant odontogenic ghost cell tumor. The clear cell lesion must be distinguished from metastatic renal cell carcinoma. Immunohistochemical markers help make this differentiation. The term *malignant ghost cell tumor* (odontogenic ghost cell carcinoma) has

Copyright © 2003, Mosby, Inc. All rights reserved.

been applied to a histologically malignant solid tumor related to calcifying odontogenic cyst.

Mucoepidermoid Carcinoma

Mucoepidermoid carcinoma can also arise within the jaw.[129–132] Women are affected twice as often as men, and the average age at diagnosis is 46 years. The radiographic changes consist of ill-defined lytic or multilocular cystic areas that are often indistinguishable from squamous cell carcinoma (Fig. 17-66). CT and MR imaging are extremely helpful in delineating the extent of disease in the mandible and the surrounding soft tissues, as well as in identifying cervical lymph node involvement. An accurate tissue diagnosis is also mandatory to plan appropriate therapy, which usually consists of combined radiation therapy, chemotherapy, and surgery. A pretreatment oral examination and dental evaluation is necessary to diagnose any tooth and gum pathology that needs to be eliminated before initiating radiotherapy or chemotherapy. Also, when surgical resection is planned, appropriate prosthetic reconstruction strategies can be planned before surgery, allowing better functional results and greater patient satisfaction.

Metastatic Jaw Tumor

Metastatic tumors to the mandible or maxilla may be the first indication of an occult malignancy or the first evidence of dissemination of a known primary tumor. Patients with metastatic lesions may be asymptomatic or may complain of symptoms similar to those found with other primary malignant tumors. Metastases to the mandible are four times more frequent than those to the maxilla, and the most common primary tumors are in the breast, lung, kidney (hypernephroma), thyroid, prostate, and stomach.

FIGURE 17-65 Squamous cell carcinoma of the anterior mouth with secondary invasion of the mandible. **A**, Axial CT of the mandible (bone window setting) shows an erosion in the central and anterior parts of the mandibular symphysis. **B**, Axial CT (soft-tissue window setting) demonstrates a lesion in the anterior mouth, with extension into the mandible. Again, note the erosion in the anterior cortex and adjacent medullary portion of the mandible. **C**, Another patient. Axial T1-weighted MR image shows a large squamous cell carcinoma in the left cheek and retromolar trigone that has infiltrated the ramus of the mandible. The normal high signal intensity of marrow (*arrow*) is seen on the right side.

VIEW IMAGE

Copyright © 2003, Mosby, Inc. All rights reserved.

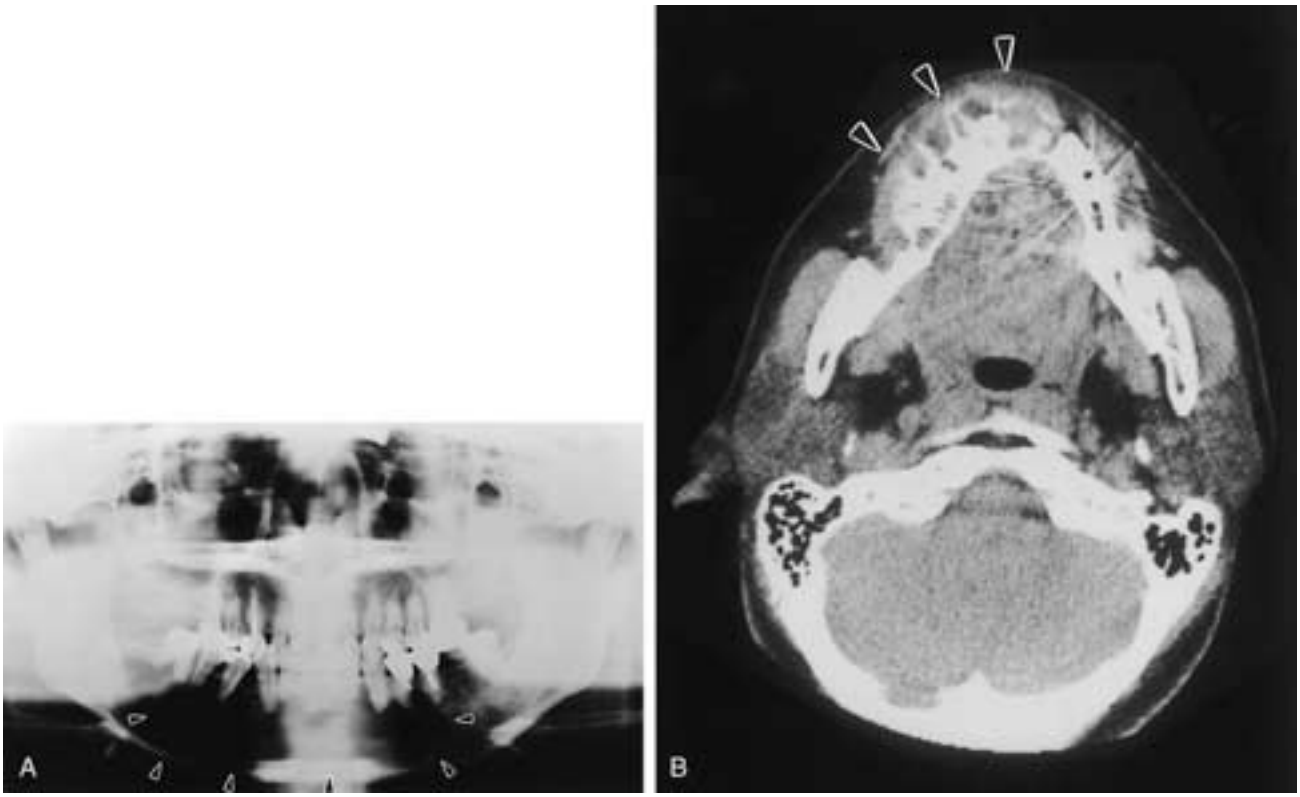

VIEW IMAGE

FIGURE 17-66 Mucoepidermoid tumor in the mandible. **A**, Pantomogram shows an ill-defined radiolucent lesion in the anterior part of the mandible (*arrowheads*). **B**, Axial CT of the mandible (soft-tissue window setting) demonstrates the ill-defined soft-tissue density lesion with multiple bony trabeculae. The surrounding buccal bony cortex is destroyed (*arrowheads*). (Courtesy of Dr. T. Kurabayashi, Dept. of Dental Radiology, Tokyo Medical and Dental University, Tokyo.)

In most instances, the bone destruction caused by a metastatic lesion is radiographically similar to that caused by a primary tumor, and the area of destruction within the mandible may be localized, bilateral, or diffuse (Fig. 17-67). On occasion a mixed lesion of lytic and blastic areas may be encountered, usually from a carcinoma of the breast. In rare cases, metastasis from a carcinoma of the prostate may cause diffuse osteoblastic change.

When metastatic disease is suspected, a thorough search for the primary site and other sites of metastatic involvement should be immediately initiated, and a biopsy for definitive tissue diagnosis should be performed. A team approach with coordination among the internist, radiologist, oncologist, surgeon, and other health care providers involved in the care of the cancer patient is the optimal approach to an often difficult problem.[133–140]

Sarcoma

Osteogenic Sarcoma

Osteogenic sarcoma is a malignant tumor of the bone in which neoplastic cells produce a variable amount of osteoid.[141–147] According to the predominant tissue observed microscopically, these lesions are classified as osteoblastic, chondroblastic, or fibroblastic. About 6.5% of osteogenic sarcomas arise in the jaw.

Primary osteogenic sarcoma usually affects children and young adults, with a peak incidence in the second decade of life. However, osteogenic sarcomas of the mandible and maxilla have their peak incidence a decade later. The mandible is affected more often than the maxilla, and there is no sex predominance. The main symptoms are swelling

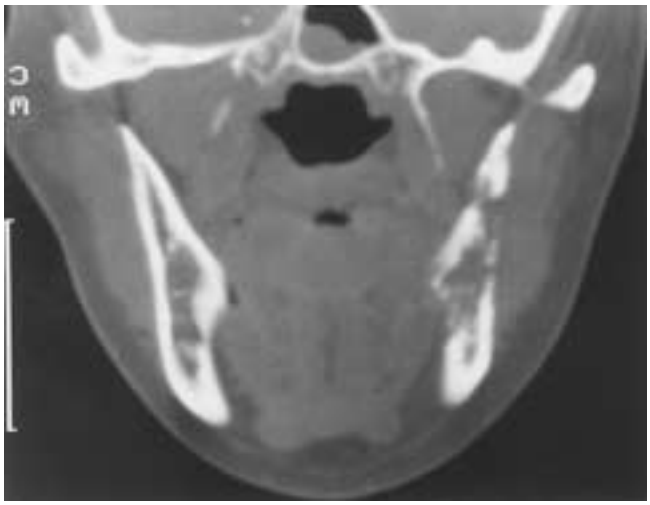

FIGURE 17-67 Carcinoma of the breast metastatic to the left mandible. Coronal CT through the mandible (bone window setting) shows a lytic destructive lesion in the ramus of the left mandible. There is no new bone formation.

VIEW IMAGE

Copyright © 2003, Mosby, Inc. All rights reserved.

VIEW IMAGE

FIGURE 17-68 Osteogenic sarcoma of the mandible. **A**, Oblique view of the mandible shows an ill-defined lucent area in the body of the right mandible. There is loss of the lamina dura of the remaining third molar tooth. There is also invasion of the mandibular canal. **B**, Axial CT (bone window setting) shows ill-defined destruction, with expansion of the body of the right mandible.

and pain, but paresthesias, loose teeth, and bleeding have been reported.

Radiographically, osteogenic sarcoma can cause lytic bone destruction with indefinite margins (osteolytic type) (Fig. 17-68), an area of sclerosis (osteoblastic type) (Figs. 17-69 and 17-70), or a mixed pattern. The osteoblastic type is the most common one in the jaw. Some osteosarcomas show a sunburst effect caused by radiating mineralized tumor spicules (Fig. 17-71). Cortical breakthrough, with tumor outside the jaw, is a common finding in advanced cases. Because a symmetrically widened periodontal membrane may be the earliest radiographic finding of osteogenic sarcoma of the jaw, this tumor must be differentiated from other diseases such as sclerodoma or acrosclerosis that also cause widening of the periodontal membrane.

Osteosarcomas can be easily assessed by CT because this modality identifies lesions that contain calcium, osteoid, or both. However, the extent of tumor spread within the marrow space or outside of the jaw may be seen better with MR imaging. Patients with mandibular osteosarcomas have a better prognosis than those with maxillary tumors; however, patients with mandibular or maxillary osteosarcomas are prone to develop either a recurrence or distant metastases, especially to the lungs. Treatment is surgical excision, usually followed by radiation therapy and possibly chemotherapy.

Fibrosarcoma

Fibrosarcoma of the jaw is a rare lesion that occurs predominantly in the mandible.[148, 149] Onset can occur at any age but is most common before the age of 50 years, with a peak incidence between 20 and 40 years of age. Among these tumors, peripheral and central fibrosarcomas have been differentiated. The rare central form most frequently develops in the mandibular canal and causes central bone

FIGURE 17-69 Osteogenic sarcoma of the left mandible. Pantomogram of the mandible shows a sclerotic lesion in the ascending ramus of the mandible and coronoid process. The boundaries of the mandible are poorly defined posteriorly. There is extension of this sclerotic tumor into the upper left mandibular canal.

VIEW IMAGE

Copyright © 2003, Mosby, Inc. All rights reserved.

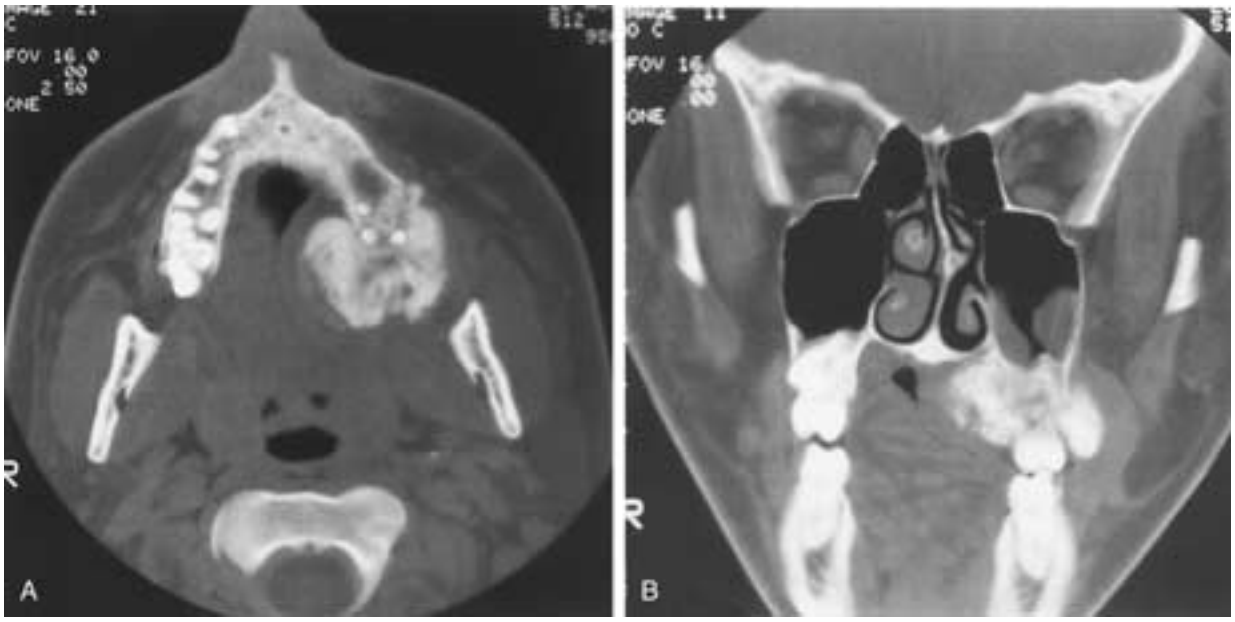

VIEW IMAGE

FIGURE 17-70 Chondroblastic osteosarcoma of the left maxilla. **A**, Axial CT through the maxilla demonstrates a sclerotic, destructive lesion in the left maxilla, with extension into the lower portion of the left antrum. **B**, Coronal CT demonstrates the sclerotic, destructive, expansile lesion in the left maxilla and in the lower left maxillary antrum.

destruction, with gradual expansion leading to cortical erosion in larger lesions. The more prevalent peripheral type originates from the periostium or the periodontal membrane, frequently in the body and angle of the mandible. Radiographically, erosive changes are encountered at the alveolar ridge or at the inferior border of the mandible; the depth of the defect varies, depending on the stage of tumor development. Usually an extramandibular soft-tissue mass of variable size is palpated.

An ameloblastic fibrosarcoma has been described as a mixed epithelial/mesenchymal lesion.[2] Only the mesenchymal component is malignant. The epithelial component most closely resembles an ameloblastic fibroma. This lesion is extremely rare. The terms *odontogenic sarcoma* and *ameloblastic fibro-odontosarcoma* have been used to refer to similar lesions.[150]

The term *carcinosarcoma* has been applied to a rare lesion in which both the epithelial and mesenchymal components are malignant.

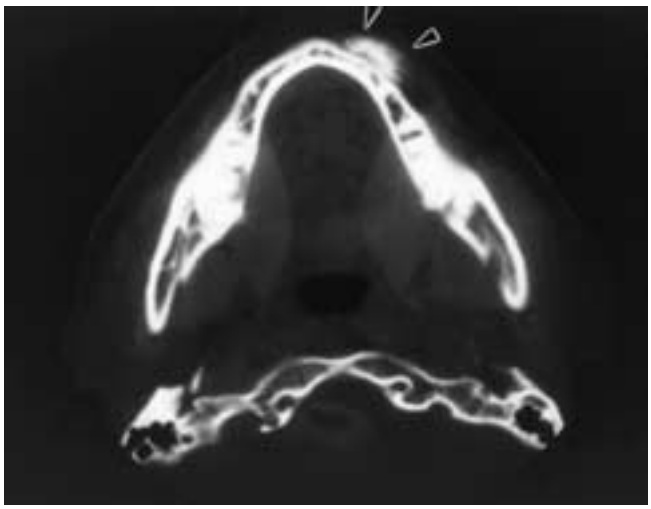

VIEW IMAGE

FIGURE 17-71 Osteogenic sarcoma in the anterior part of the mandible. Axial CT demonstrates a mass with periosteal reaction suggesting the typical ''sun-ray'' appearance in the mandible (*arrowheads*).

Ewing's Sarcoma

Ewing's sarcoma occurs predominantly in children and young adults between 5 and 25 years of age, and males are affected twice as frequently as females.[151–154] In one series of studies, jaw involvement occurred in 13% of cases, and this lesion occurs 10 times more frequently in the mandible than in the maxilla. Radiographically, the lesion has a mottled, irregular, lucent appearance, with sclerosis interspersed in a small percentage of tumors. Perpendicular bony spicules and extensive bone destruction may be found at the cortices. The characteristic onion-peel (onion skin) layering of new subperiosteal bone is often absent in the jaw. This tumor tends to metastasize early, often to multiple bony sites, making treatment difficult and the prognosis poor. Treatment usually involves a combination of radiotherapy and chemotherapy.

Malignant Lymphoma

Malignant lymphoma is derived from lymphocytes and reticulum (histiocytic) cells that are in different stages of development, and the disease can have either a regional or a systemic distribution.[155–157] Lymphomas in the head and neck occur predominantly in the neck nodes, oral cavity, nasopharynx, and occasionally in the sinuses. However, primary lymphoma of bone may occur in the mandible and

Copyright © 2003, Mosby, Inc. All rights reserved.

maxilla. Such bone lymphomas are predominantly histiocytic (large cell) lymphomas; they occur more frequently in the mandible than in the maxilla, and there is a male predominance. Radiographically, there are no pathognomonic findings. In the mandible, most often there are ill-defined lytic destructive areas of variable size (Fig. 17-72). Radiation therapy and chemotherapy are the primary treatment modalities.

Multiple Myeloma

Although single lesions may occasionally occur, multiple myeloma is characterized by multiple or diffuse bone involvement.[158–161] Myeloma occurs most frequently in patients 40 to 70 years of age, with males being affected twice as frequently as females. In patients with multiple myeloma of the jaw, mandibular lesions are far more common, and there is a predilection for the angle, ramus, and molar tooth regions. The typical radiographic appearance is that of ''punched-out,'' regular, circular, or ovoid radiolucencies with no circumferential bone reaction, especially when the skull is involved (Fig. 17-73). The cortex of the mandible may be perforated, but expansion of bone is not demonstrated. If the lesion is extensive, the entire bone may be destroyed, and bone destruction frequently is associated with hypercalcemia.

Treatment of multiple myeloma is primarily medical. Chemotherapy is the primary modality, often along with anabolic steroids, fluoride, calcium, and vitamin D. Solitary bone lesions most often are treated with radiation therapy. When surgery of jaw lesions is planned, consideration of the

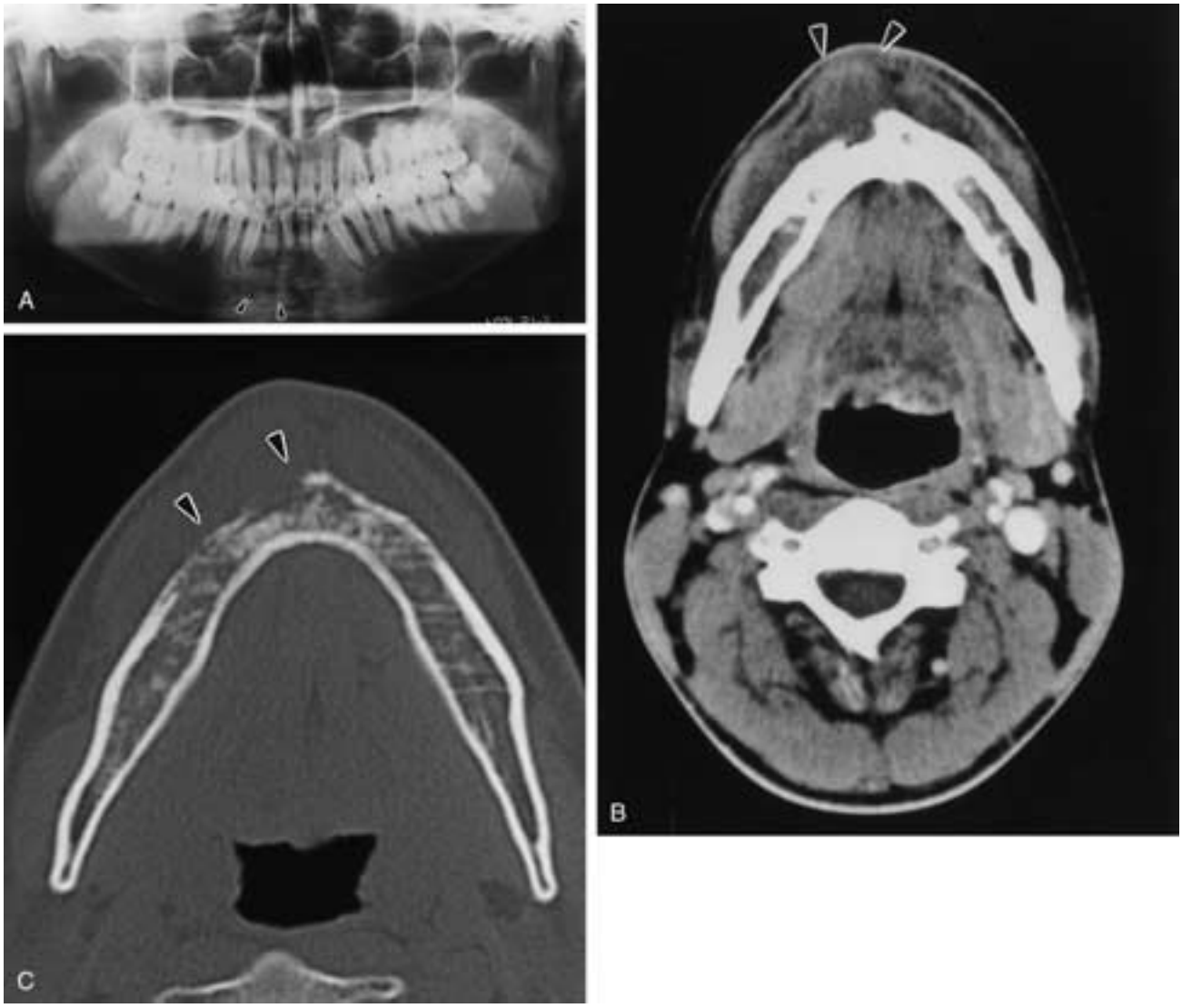

VIEW IMAGE

FIGURE 17-72 Lymphoma in the mandible. **A**, Pantomogram shows an ill-defined radiolucent lesion in the anterior part of the mandible (*arrowheads*). **B**, Axial CT of the mandible (soft-tissue window setting) demonstrates the soft-tissue density lesion in the anterior part of the mandible involving the surrounding soft tissue (*arrowheads*). **C**, Axial CT (bone window setting) demonstrates the ill-defined lesion (*arrowheads*), with permeative destruction of the buccal bony cortex (*arrowheads*). (Courtesy of Dr. T. Kurabayashi, Dept. of Dental Radiology, Tokyo Medical and Dental University, Tokyo.)

Copyright © 2003, Mosby, Inc. All rights reserved.

VIEW IMAGE

FIGURE 17-73 Multiple myeloma of the mandible. Pantomogram of the mandible shows a large, destructive lesion in the body and ramus of the left mandible, with extramandibular extension at the alveolus. There is the suggestion of a pathologic fracture at the anterior aspect of this lytic defect. Also, note the multiple ''punched-out'' lucent areas throughout the mandible, especially in the left ramus, consistent with foci of multiple myeloma.

patient's hematologic status is necessary to avoid untoward complications.

Leukemia

Leukemia may involve the jaw bones; in one series of patients with acute leukemia, 63% of cases had disease in the jaw.[162–164] An early radiographic finding is loss of the lamina dura with loosening of the teeth. This is often followed by varying degrees of lytic bone destruction (Fig. 17-74). Treatment is primarily medical management, and special attention should be paid to reducing the chance of oral infection and bleeding.

INFLAMMATORY CONDITION OF THE MANDIBLE

Osteomyelitis

Osteomyelitis, an inflammation of bone and bone marrow, may develop in the jaw as a result of odontogenic infection or the sequelae of various other conditions including underlying systemic diseases (immunocompromise) and focal injuries such as trauma, complicated fractures, and large doses of radiation therapy.[165–167] Development of osteomyelitis is rare in normal healthy people because of early administration of antibiotic therapy but can be associated with tuberculosis, diabetes, agranulocytosis, neutropenias, leukemia, uremia, sickle cell anemia, severe anemia, and febrile diseases such as typhoid.[165] The mandible is made up of a well-developed periosteum, a solid cortex, and a liberal spongiosa in the subapical region of the body of the mandible. The spongiosa also extends into the ascending ramus and the mental protuberance. The thick cortex is not easily penetrated by suppurative processes, and the infection can easily involve the whole mandible. Therefore, osteomyelitis of the mandible is more frequently and severely widespread than that of the maxilla.

Osteomyelitis may present radiographically as (1) suppurative osteomyelitis, (2) sclerosing osteomyelitis, (3) osteomyelitis with periositis, (4) tuberculous osteomyelitis, and (5) osteoradionecrosis.[160, 163] The disease may be either acute or chronic and may involve different clinical courses, depending on its nature.[166]

VIEW IMAGE

FIGURE 17-74 Leukemia of the mandible. **A**, Periapical film demonstrates general rarefaction and loss of the lamina dura (*arrowhead*). **B**, Axial T1-weighted MR image shows diffuse low signal intensity in the entire mandible (*arrowheads*). Normal fatty marrow has been completely replaced by leukemic infiltration.

Copyright © 2003, Mosby, Inc. All rights reserved.

Suppurative Osteomyelitis

Acute suppurative osteomyelitis is sudden in onset and runs a very acute course. Such cases are associated with a severe constitutional reaction: high fever, rapid pulse, vomiting, delirium, and prostration.[165] In some instances, the disease may run a chronic course with slow onset, slight fever, and moderate pain. Radiologic findings can differ, depending on the course of the disease. On conventional radiographs, the bone usually has a normal appearance in the early stage (the first 8 to 10 days) of the disease. Later radiographs can show single or multiple irregular radiolucencies with poorly defined margins.[167] Chronic osteomyelitis shows a variety of bone reactions including completely radiolucent areas, mixed radiolucent and radiopaque areas, and completely radiopaque areas.

Bone scintigraphy and MR imaging can detect the early stage of the diseases.[168–170] Bone scintigraphy is useful in examining patients with suspected osteomyelitis. Radionuclide studies may signify the possibility of early-stage osteomyelitis before osseous changes are apparent on plain radiographs. Technetium-99m methylene diphosphonate (^{99m}Tc-MDP) bone scans are sensitive indicators of altered osteoblastic activity, but local disturbances in vascular perfusion, clearance rate, permeability, and chemical binding also affect imaging.[168] On standard ^{99m}Tc-MDP bone scans, however, it is sometimes difficult to differentiate soft-tissue uptake from bone uptake in patients with known cellulitis and possible underlying osteomyelitis. MR imaging has been reported to be useful in the initial diagnosis of osteomyelitis. Its MR imaging appearance depends on a variety of factors, including the patient's age, the type and virulence of the offending organism, and the presence of an underlying medical conditions.[170] In a normal population of patients over 30 years old, the entire medulla of the mandible usually shows high signal intensities suggesting fatty marrow when spin echo images are used.[171] On MR imaging, bone marrow lesions of osteomyelitis show low signal intensity on T1-weighted images and high signal intensity on T2-weighted images. Sequestrum reveals low signal intensity on both T1- and T2-weighted images. Soft-tissue abnormalities are also evaluated on MR images, showing signal intensity patterns similar to those of marrow lesions, soft-tissue edema, blurring fat planes, and sometimes an abnormal fluid collection (Fig. 17-75).[169]

Contrast enhancement may improve the accuracy of the evaluation of osteomyelitis. Patients with active osteomyelitis show enhancement in medullary bony lesions. Infected areas are usually hypervascular, and the contrast moves into the extracellular fluid compartment because of altered vascular permeability.[172] This enhancement can be seen in soft-tissue components outside the infected areas of the mandible.

Osteomyelitis with Periostitis

Osteomyelitis with periostitis was erroneously described in the past as Garre osteomyelitis. It is simply a variant of osteomyelitis in which a periosteal reaction predominates, leading to subperiosteal deposition of new bone.[173, 174] This condition is characterized by the formation of new bone on the surface of the cortex over infected areas of spongiosa. The new bone formation is a response of the inner surface of the periosteum to stimulation by a low-grade infection that has spread through the bone and penetrated the cortex. The disease is seen almost exclusively in children and rarely occurs in persons over 30 years of age.[173] The mean age varies from 12 to 13.3 years, with a 1.4:1 male predominance. Patients have facial asymmetry resulting from a bony, hard swelling of the mandible.

Radiographs of this disease show laminar periosteal new bone (the so-called onion peel appearance), which is most evident on the inferior, buccal, or lingual aspect of the mandible (Fig. 17-76). In some cases, there may be accompanying radiolucent or osteosclerotic osteomyelitic changes, and small sequestra can often be seen. The differential diagnosis for a condition that resembles osteomyelitis with periositis includes Ewing's sarcoma, fibrous dysplasia, osteogenic sarcoma, infantile cortical hyperostosis, and peripheral osteomas.

Tuberculous Osteomyelitis

Tuberculous osteomyelitis is a specific infection caused by the acid-fast bacillus *Mycobacterium tuberculosis*. The oral tissue is involved by this organism via three routes: direct inoculation, extension from adjacent sites of infection, or hematogenous seeding.[175, 176] Radiographs of this disease show rarefaction with ill-defined borders and formation of sequestra, but sometimes there may be accompanying periosteal new bone formation (Fig. 17-77). The differential diagnosis includes nonspecific osteomyelitis, malignant tumors, and eosinophilic granuloma.

Sclerosing Osteomyelitis

Sclerosing osteomyelitis of the mandible is a predominantly proliferative reaction of bone representing resistance of the host to low-grade infection.[166] In patients with chronic sclerosing osteomyelitis, bone is deposited along the osseous cortex and existing trabeculae, resulting in thickening of the cortex and trabeculae and reduction or obliteration of the marrow spaces.[177]

Sclerosing osteomyelitis of the mandible has been divided into focal and diffuse types. The focal type, also known as periapical osteitis, is a common condition with a pathognomonic appearance. The radiographs show a well-circumscribed periapical radiopaque area of sclerotic bone (Fig. 17-78). The patient is easily cured by endodontic treatment or extraction of the affected tooth. The diffuse type is an uncommon disease that creates diagnostic and therapeutic problems.[177–179] Clinically, recurrent pain and swelling are typical symptoms. In the early stages of diffuse sclerosing osteomyelitis and in younger patients, the mandibular volume increases due to periosteal deposition of new bone. However, diffuse osteolytic changes are a more prominent feature than sclerosis. In the established chronic stages and in older patients with less prominent periosteal reactivity, the mandibular volume is reduced and sclerosis is more obvious, with smaller and fewer osteolytic zones. A distinctive radiographic and CT scan pattern is that of diffuse endosteal sclerosis with simultaneous involvement of the alveolar and basal bones and extension to the angle, ramus, or condyle, with indistinct borders. In the chronic stages, diffuse sclerosing osteomyelitis must be differentiated from other radiopaque lesions such as diffuse cemento-

Copyright © 2003, Mosby, Inc. All rights reserved.

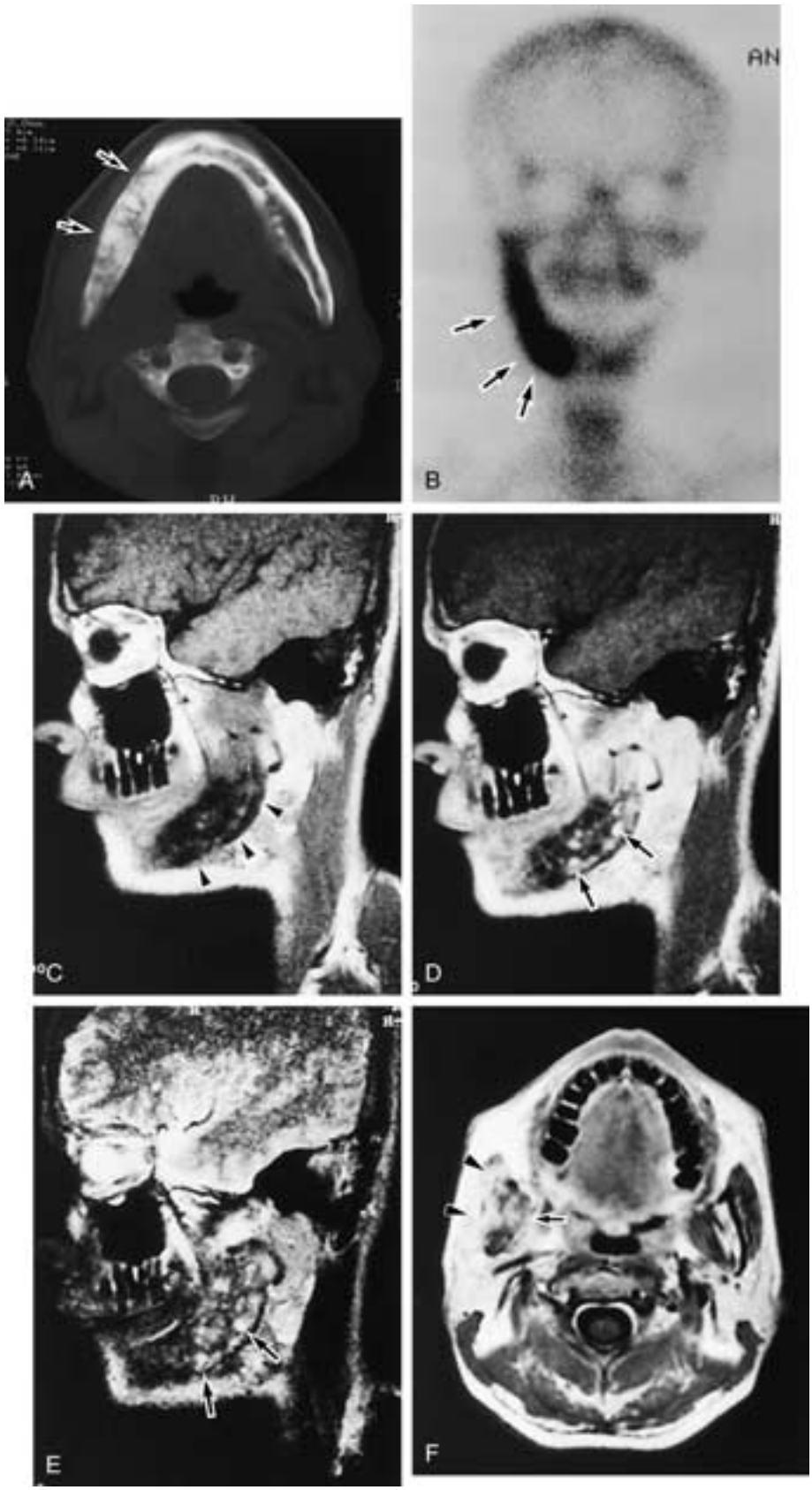

FIGURE 17-75 Chronic suppurative osteomyelitis. **A**, Axial CT shows osteolytic and sclerotic changes in the right side of the mandible. Cortex has been destroyed (*arrows*). **B**, Anterior view of bone scintigraphy shows increased activity in the right side of the mandible (*arrows*). **C**, Sagittal T1-weighted MR image shows low-intensity areas from the molar to the ramus region (*arrowheads*). **D**, Enhanced sagittal T1-weighted MR image demonstrates areas of patchy enhancement (*arrows*), which is consistent with residues of infected bone marrow. **E**, Sagittal T2-weighted MR image shows heterogeneous low to high signal intensities. Residues of inflammatory bone marrow show high-intensity foci (*arrows*). **F**, Enhanced axial T1-weighted MR image demonstrates enhancement in the ramus region (*arrow*). The right masseter muscle shows swelling and enhancement (*arrowheads*).

VIEW IMAGE

Copyright © 2003, Mosby, Inc. All rights reserved.

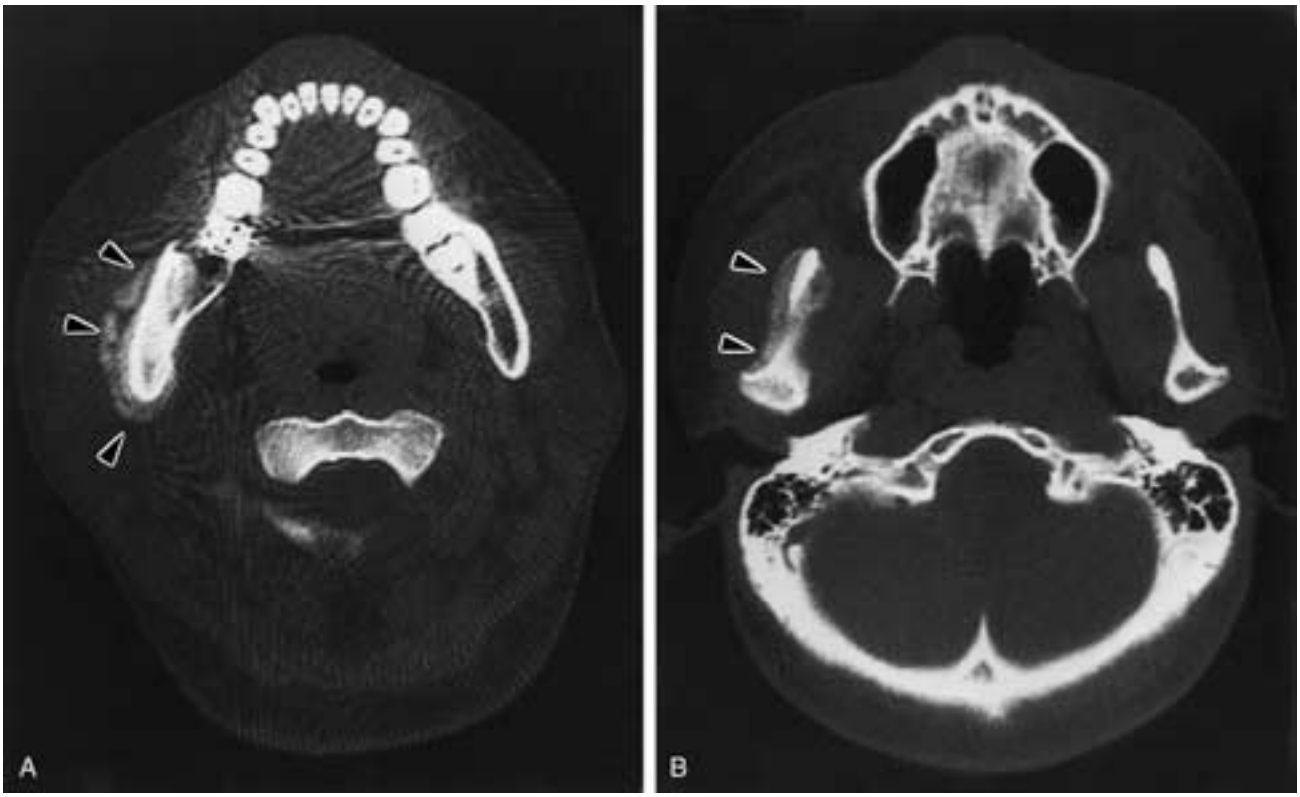

VIEW IMAGE

FIGURE 17-76 **A** and **B**, Osteomyelitis with periositis. Axial CT (bony window setting) shows multilayered periosteal reaction of irregular thickness in the right side of the mandible (*arrowheads*).

sis, sclerosing cemental masses of the jaw, and florid osseous dysplasia in radiographic examinations.[176]

MR imaging shows abnormally thickened cortex with a signal void. There may be defects in the cortex and decreased signal intensity of bone marrow on T1-weighted images. The medullary cavity has increased signal intensity on T2-weighted images. Diffuse enhancement with gadolinium can be seen outside of the mandible when soft tissue is involved. In management, some authors report that an early diagnosis is of the utmost importance, and the patient should be kept under observation for several years.[177–179] However, similarities to other radiopaque lesions such as diffuse cementosis, sclerosing cemental masses of the jaw, florid osseous dysplasia, Ewing's sarcoma, osteosarcoma, and metastasis, as well as the lack of pathognomonic features, signify that the diagnosis of this disease should be established by a combination of clinical, radiographic, and histologic findings.

VIEW IMAGE

FIGURE 17-77 Tuberculosis osteomyelitis. Pantomogram shows ill-defined borders and formation of sequestra (*arrowheads*).

Osteoradionecrosis

Osteoradionecrosis is a pathologic process that sometimes follows heavy irradiation of bone and is characterized by a chronic, painful necrosis accompanied by late sequestration and sometimes permanent deformity.[180, 181] The radiation effects are endothelial cell death, hyalinization resulting from amyloid degeneration, and thrombosis of vessels. The periosteum undergoes fibrosis, and bone osteocytes and osteoblasts become necrotic, with fibrosis of the marrow spaces. Bone trabeculae are reduced in width and number, so that there is an increase in the size of the marrow spaces, which contain necrotic debris. These changes are progressive and lead to necrosis of bone and sequestration, although there is no clear line of demarcation between vital and nonvital bones. Radiologically, the bone can be normal in the early stages. The progression of the bone change is slow and slight. In advanced cases, there are multiple radiolucent areas with poorly defined borders and enlarged, irregular trabecular spaces (with the typical moth-eaten appearance) containing areas of sequestra (Fig. 17-79).

Copyright © 2003, Mosby, Inc. All rights reserved.

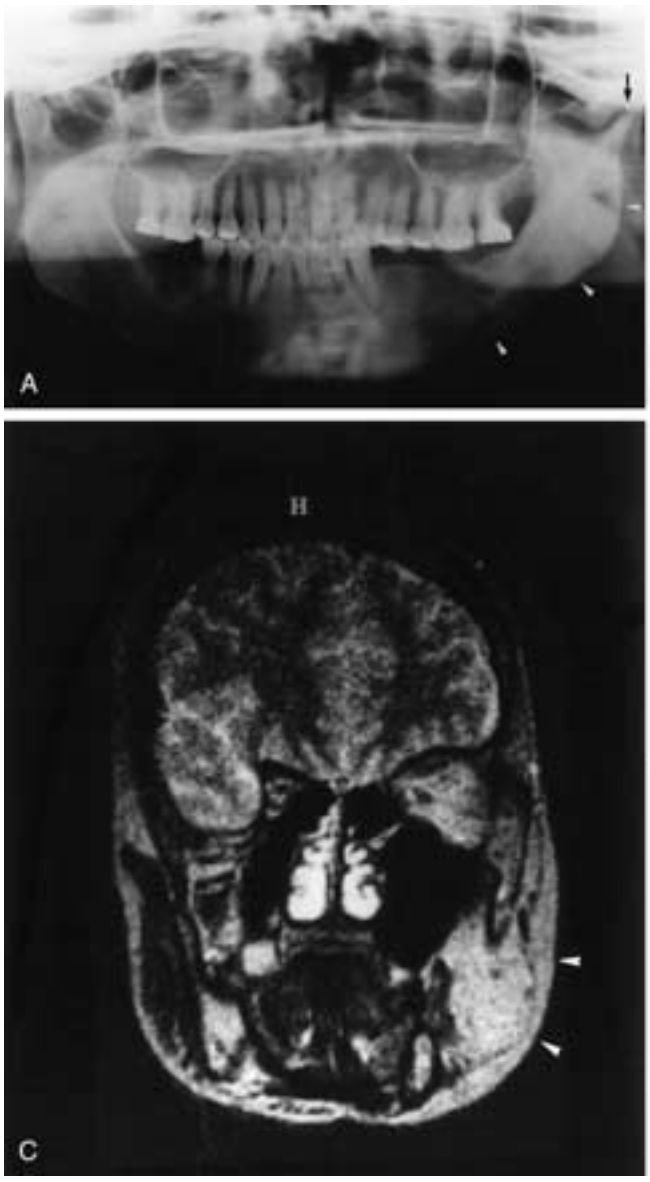

FIGURE 17-78 Sclerosing osteomyelitis. **A**, Pantomogram shows a radiopaque lesion in the left side of the mandible (*arrowheads*). The left head of the condyle is deformed (*arrow*). **B**, The entire mandible reveals low signal intensity in this axial T1-weighted MR image (*arrowheads*). Soft tissues around the left side of the mandible show high intensity and hemorrhage or fatty degeneration of the masseter muscle (*arrow*). **C**, Coronal T2-weighted MR image demonstrates expansile change of high intensity in the left side of the mandible (*arrowheads*). MR imaging reveals a larger extent of the lesion than does a pantomogram, and extensive inflammation was suspected.

VIEW IMAGE

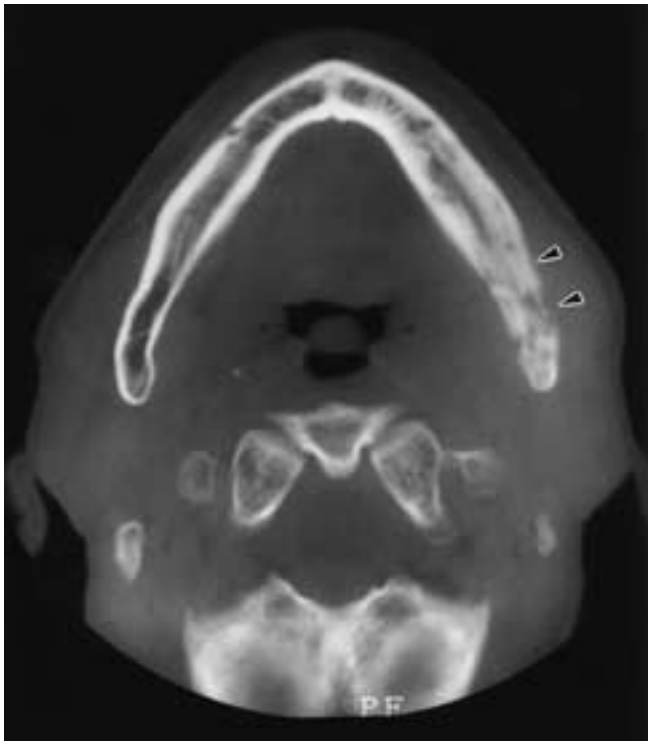

VIEW IMAGE

FIGURE 17-79 Osteoradionecrosis. Axial CT shows osteolytic and sclerotic changes in the left side of the mandible in a patient previously treated by radiation therapy. Destruction of the mandibular cortex can be seen (*arrowheads*).

Copyright © 2003, Mosby, Inc. All rights reserved.

SECTION TWO

SYSTEMATIC APPROACH TO IMAGING DIAGNOSIS OF JAW LESIONS

Takashi Kaneda, Manabu Minami, Hugh D. Curtin, Mitsuaki Yamashiro, Yoshiaki Akimoto, Kuni Ohtomo, Hiroyuki Okada, and Hirotsugu Yamamoto

The objective of this section is to present a systematic approach to the diagnosis of jaw lesions using various imaging findings.

Odontogenic tumors comprise about 10% of all tumors of the oral cavity and about 2.4% of all lesions biopsied by dentists in the United States.[3, 182] After clinical examination, the patient with a suspected jaw lesion is first referred for plain radiography, pantomogram, or sometimes CT. The radiologic examination is part of the overall diagnostic process. Oral surgeons need a differential diagnosis of the disease as well as an exact assessment of the topography and extent of the lesion. Infiltration into surrounding tissues must also be evaluated.

Radiologic diagnosis of jawbone lesions has used conventional radiography including dental and occlusal films, pantomography, conventional tomography, and CT.[183–185] More recently, MR imaging has allowed excellent soft-tissue differentiation, and its increasing application is beginning to have an impact on the diagnosis of dento-maxillofacial lesions.[186–190]

As discussed in the previous section, few radiographic or imaging appearances are pathognomonic for a specific lesion. Based on all imaging modalities, the disease pattern may indicate several different diseases of either odontogenic or nonodontogenic origin. The question is, ''How do we use the imaging modalities to differentiate these jawbone lesions?'' What is needed is an effective, systematic approach to solve this problem.

Conventional radiography and pantomography provide screening imaging in various pathologic conditions of the maxilla and mandible and may suggest the need for further radiologic examinations such as CT or MR imaging. Imaging in at least two planes is necessary to analyze the lesion and adjacent tissues properly. Currently, multidetector CT provides images in multiple planes from a single spiral scan acquisition. Dental reformatting software also provides cross-sectional as well as panoramic sectional imaging.

When a jaw lesion is first identified, inflammation related to a tooth is usually considered first because of the high incidence of caries and related periapical disease. Inflammation can progress and lead to several different pathologic

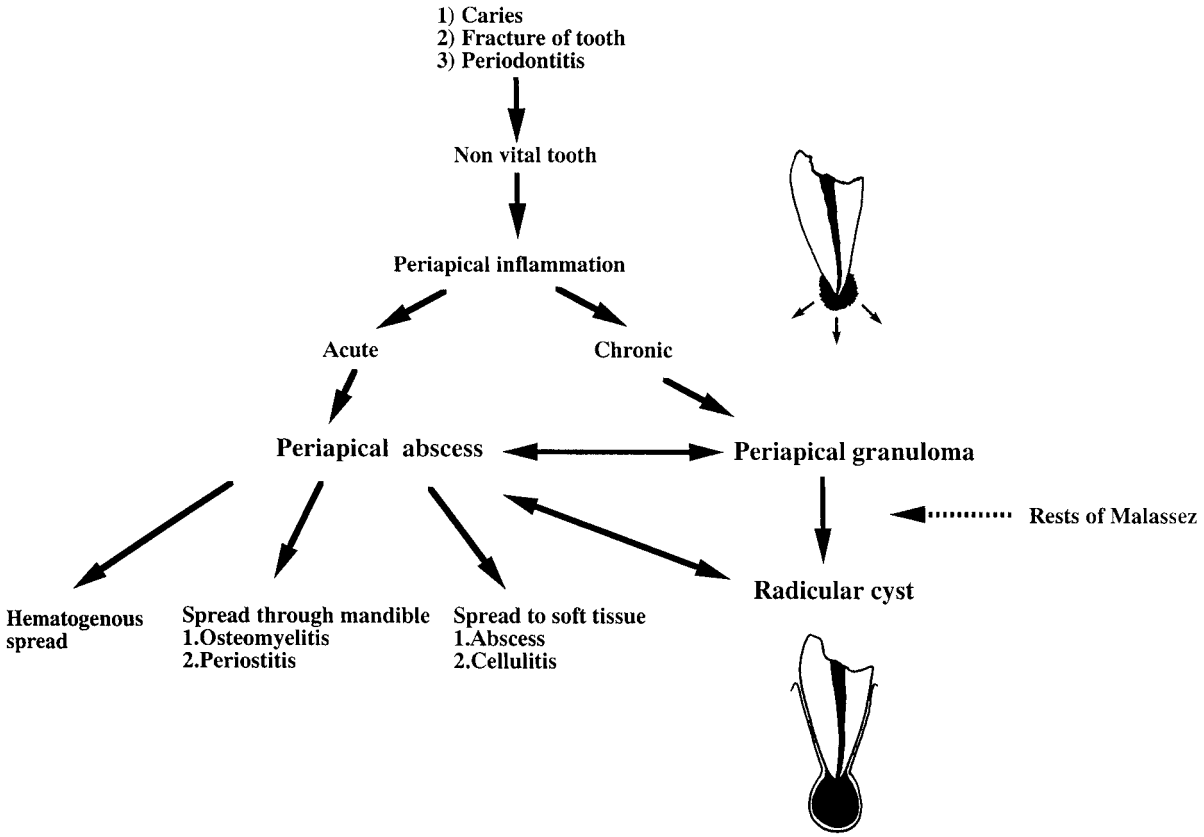

FIGURE 17-80 Sequelae of tooth infection.

VIEW IMAGE

Copyright © 2003, Mosby, Inc. All rights reserved.

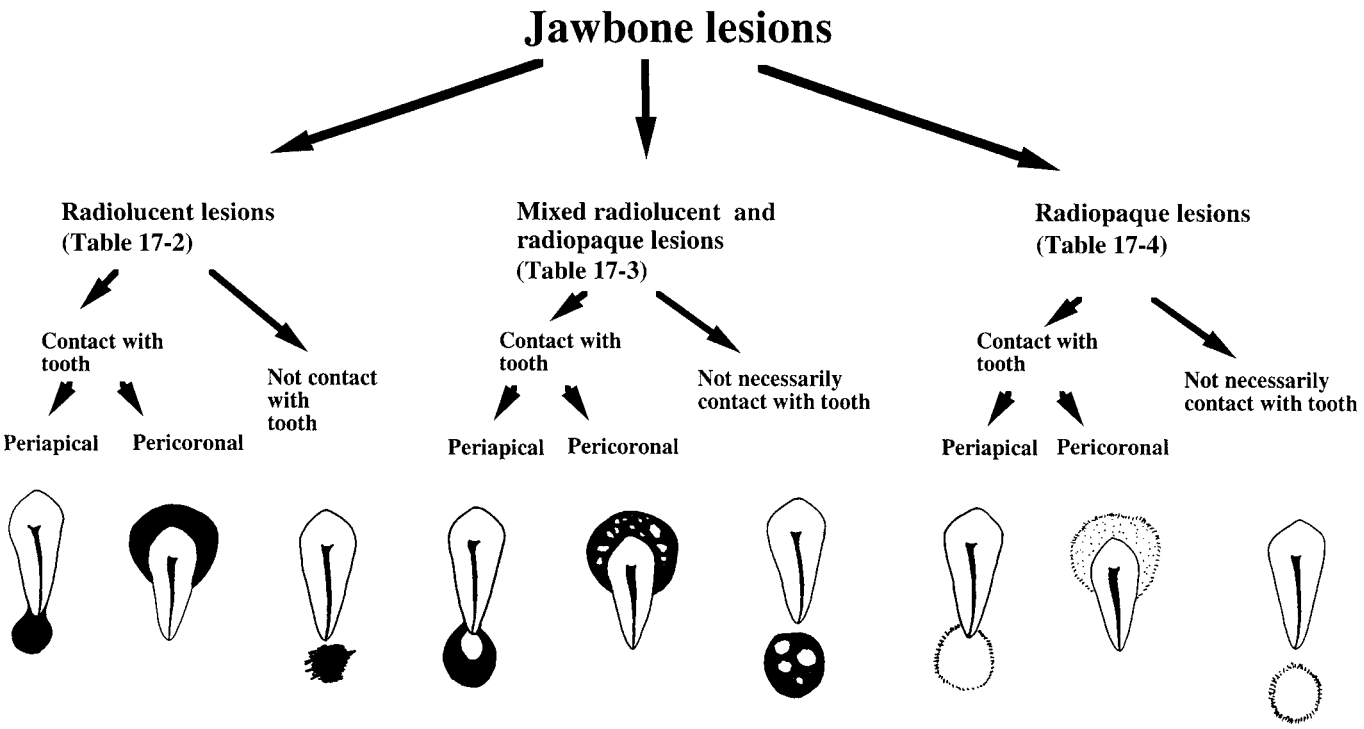

FIGURE 17-81 Systematic approach using radiologic examination of jawbone lesions.

VIEW IMAGE

conditions including periapical inflammation, periapical granuloma, periapical abscess, and radicular cyst (Fig. 17-80). Specifically, periapical inflammation or periapical granuloma is initiated and maintained by degeneration products of necrotic pulp tissue of a nonvital tooth. Stimulation of the resident epithelial rests of Malassez occurs in response to the products of inflammation. When the infection reaches the periapical tissue, many different tissue reactions may occur, depending on the nature of the infection and the resistance of the host.

If an inflammatory pathology can be excluded as a potential diagnosis, then the various tumors and cysts must be considered.

As previously discussed, the radiologic analysis for differential diagnosis primarily depends on changes in density, character of the margin, location, relationship to the teeth (including root resorption), and other radiologic findings (Fig. 17-81). The lesion may have a radiolucent, radiopaque, or mixed appearance. The margin may be sharp or indistinct, sclerotic or well corticated. Other useful radiologic findings are (1) the degree of extension, (2) the internal architecture of the lesion, (3) changes in the cortex of the mandible, and (4) periosteal reactions and soft-tissue changes. The relationship to a particular part of a tooth is extremely useful in the diagnosis of jaw lesions.[1, 191, 192]

RADIOLUCENT LESIONS

Well-Defined Radiolucent Lesions

Maxillomandibular lesions most frequently show a unilocular pattern or a multilocular pattern with internal septa.[1, 191, 192] A number of odontogenic and nonodontogenic lesions including periapical lesions, cyst of the globullomaxillary region, dentigerous cyst, primodial cyst, OKC, and ameloblastoma can present as well-defined radiolucent lesions (Table 17-2). When the lesion is equal or less than 2 cm in diameter, most of the lesions can be well evaluated by radiography alone. When radiolucent lesions are more than 2 cm in diameter, addition of MR imaging can be useful, especially for the evaluation of internal structures and the nature of the content, as stated below.[193]

Ill-Defined Radiolucent Lesions

Ill-defined radiolucent lesions are produced by inflammation and by malignancies of the jaw including carcinoma and osteosarcoma. Most carcinomas involving the jaws are invading from the lesions of the oral mucosa. Some may be metastatic deposits from primary tumors in distant sites.[185, 191, 192]

MIXED RADIOLUCENT-RADIOPAQUE LESIONS

A mixed radiolucent-radiopaque appearance (Table 17-3) can result from the presence of two or more tissues with different radiographic densities, varying degrees of maturation of the inflammatory soft tissue within the lesion, and localized resorption and apposition of new bone within or around the lesion. This appearance may indicate osteomyelitis, an immature fibroosseous lesion, or tumor.[185, 191, 192] The location of the lesion sometimes gives the clue for differentiation, but is not always a definite differential point.

Copyright © 2003, Mosby, Inc. All rights reserved.

Table 17-2
RADIOLUCENT LESIONS OF THE JAWS

	Periapical	Pericoronal	No Contact with Tooth
Cysts			
Common			
Radicular cyst (radicular granuloma)	○		
Residual cyst			○
Dentigerous cyst	△	○	
Primordial cyst			○
Odontogenic keratocyst		○	△
Globulomaxillary cyst			○
Nasopalatine duct cyst			○
Incisive canal cyst			○
Lateral periodontal cyst	○	△	
Static bone cavity			○
Uncommon			
Traumatic bone cyst			○
Aneurysmal bone cyst			○
Calcifying odontogenic cyst (early stage)		○	
Tumors			
Common			
Ameloblastoma (multilocular or unilocular)	△	○	○
Cemento-ossifying fibroma	○		△
Cementoblastoma (early stage)	○		
Periapical cemental dysplasia (early stage)	○		
Odontogenic fibloma		△	○
Giant cell granuloma	△	○	
Malignant neoplasm	△	△	○
Uncommon			
Ameloblastic fibroma and myxoma		○	
Calcifying epithelial odontogenic tumor (early stage)		○	
Odontogenic myxoma		△	○
Odontogenic fibloma		△	○
Odontoma (premineralized stage)			○
Cementifying and ossifying fibroma (early stage)	○		△
Histiocytosis X			○
Metastatic carcinoma			○
Others			
Osteomyelitis	○	○	△

○, Common; △, uncommon.

RADIOPAQUE LESIONS

Radiopacity in the jawbones is produced mainly by osteosclerosis, thickening of the cortex, cemental masses, or impacted teeth. Radiopaque lesions in the maxillomandibular region are usually fibroosseous lesions, inflammation, or tumors.[185, 191, 192] These lesions are considered to be best differentiated by a combination of plain radiography and high-resolution CT (Table 17-4).

MR IMAGING

MR imaging (Fig. 17-82) has an advantage over plain films and CT in that it directly visualizes bone marrow characteristics, is more sensitive to contrast enhancement, better evaluates soft-tissue involvement, and provides multiple planes of imaging without radiation. MR imaging is said to be less useful in examining cortical bone because of the lack of signal generated by compact bone. However, invading tumors involving the cortex can be identified, as the intermediate signal of the tumor replaces the signal void usually seen in the cortex. MR imaging is less frequently affected than CT by artifacts related to dental materials, but the images can be seriously distorted by dental materials with high ferrous content. Artifacts related to dental materials on MR imaging are mainly dependent on the strength of the magnetic field, the specific pulse sequence and scan direction, and the nature of the dental materials. In addition, some injury to the gingiva is unavoidable at dental treatment and subsequent implantation of dental bur

Copyright © 2003, Mosby, Inc. All rights reserved.

Table 17-3
MIXED RADIOLUCENT-RADIOPAQUE LESIONS OF THE JAWS

	Periapical	Pericoronal	Not Necessarily in Contact with Tooth
Common			
Cementoma (intermediate stage) (periapical cemental dysplasia)	○		
Calcifying odontogenic cyst	△	○	
Cemento-ossifying fibroma	○		△
Adenomatoid odontogenic tumor		○	
Calcifying epithelial odontogenic tumor		○	△
Odontoma (intermediate stage)	△	○	
Fibrous dysplasia, cherubism			○
Paget's disease			○
Osteitis	○	△	
Uncommon			
Cementoblastoma	○		
Ameloblastic fibroodonotoma		○	△
Odontogenic fibroma			○
Ameloblastic fibrodentinoma		○	△
Osteoblastoma			○
Hemangioma			○
Chondroma, chonodrosarcoma			○
Ewing's sarcoma			○
Lymphoma			○
Osteoblastic metastasis			○
Osteosarcoma			○
Histocytosis X			○
Osteomyelitis (chronic stage)			○
Osteoradionecrosis			○
Ossifying subperiosteal hematoma			○
Cemental mass	○		

○, Common; △, uncommon.

fragments into the gingiva may occur, resulting in local image distortion.[194]

MR imaging has been reported to be superior to CT in the evaluation of certain characteristics of apparently cystic lesions, giving better information about the inner consistency of the lesion with demonstration of cystic or solid components, thickness of cyst walls, and heterogeneity of fluid content. For example, an OKC frequently shows heterogeneous intensity of fluid contents on MR imaging, while other types of cysts usually show more homogeneous fluid intensity. Some cysts, especially inflammatory cysts, can be misdiagnosed as having a mixed or solid pattern on noncontrast studies and require contrast-enhanced examinations for accurate diagnosis.[190] These findings can be most easily evaluated in lesions larger than 2 cm in diameter.

MR imaging is also useful in differentiating ameloblastoma from larger cysts by demonstrating thick walls and papillary projections, especially on contrast examinations.[188] Other types of maxillomandibular benign tumors show well-defined solid components and some enhancement on contrast-enhanced T1-weighted images, but these findings are usually less helpful in separating various diagnoses. Maxillomandibular malignant tumors show ill-defined inhomogeneous enhancement on gadolinium-enhanced T1-weighted images. The findings are nonspecific but are useful in the evaluation of tumor extension for preoperative planning.

With osseous lesions in the maxillomandibular region, conventional tomography and CT are superior to MR imaging because of their better detection of calcification and cortical abnormality.

Acknowledgment

We thank Manabu Minami, M.D., Department of Radiology, the University of Tokyo, Japan, and Hugh D. Curtin, M.D., Department of Radiology, Massachusetts Eye and Ear Infirmary, and Harvard Medical School for their advice and editorial comments in helping us prepare this section.

Copyright © 2003, Mosby, Inc. All rights reserved.

Table 17-4
RADIOPAQUE LESIONS OF THE JAWS

	Periapical	Pericoronal	Not Necessarily in Contact with Tooth
Common			
Odontoma (complex, compound)		○	△
Cementoma (mature), periapical cemental dysplasia	○		
Fibrous dysplasia			○
Condensing osteitis, focal sclerosing osteitis	○	○	
Paget's disease			○
Sclerosing osteomyelitis	○		△
Unerupted or impacted tooth	○		△
Sclerotic cemental masses	○		
Unerupted or impacted tooth	○		△
Uncommon			
Cemento-ossifying fibroma	○		△
Chrondroma, chondrosarcoma			○
Exostosis, osteochondroma			○
Idiopathic osteosclerosis			○
Osteoblastoma, osteoid osteoma			○
Torus mandibularis or palatinus			○
Osteoblastic metastasis			○
Osteosarcoma			○

○, Common; △, uncommon.

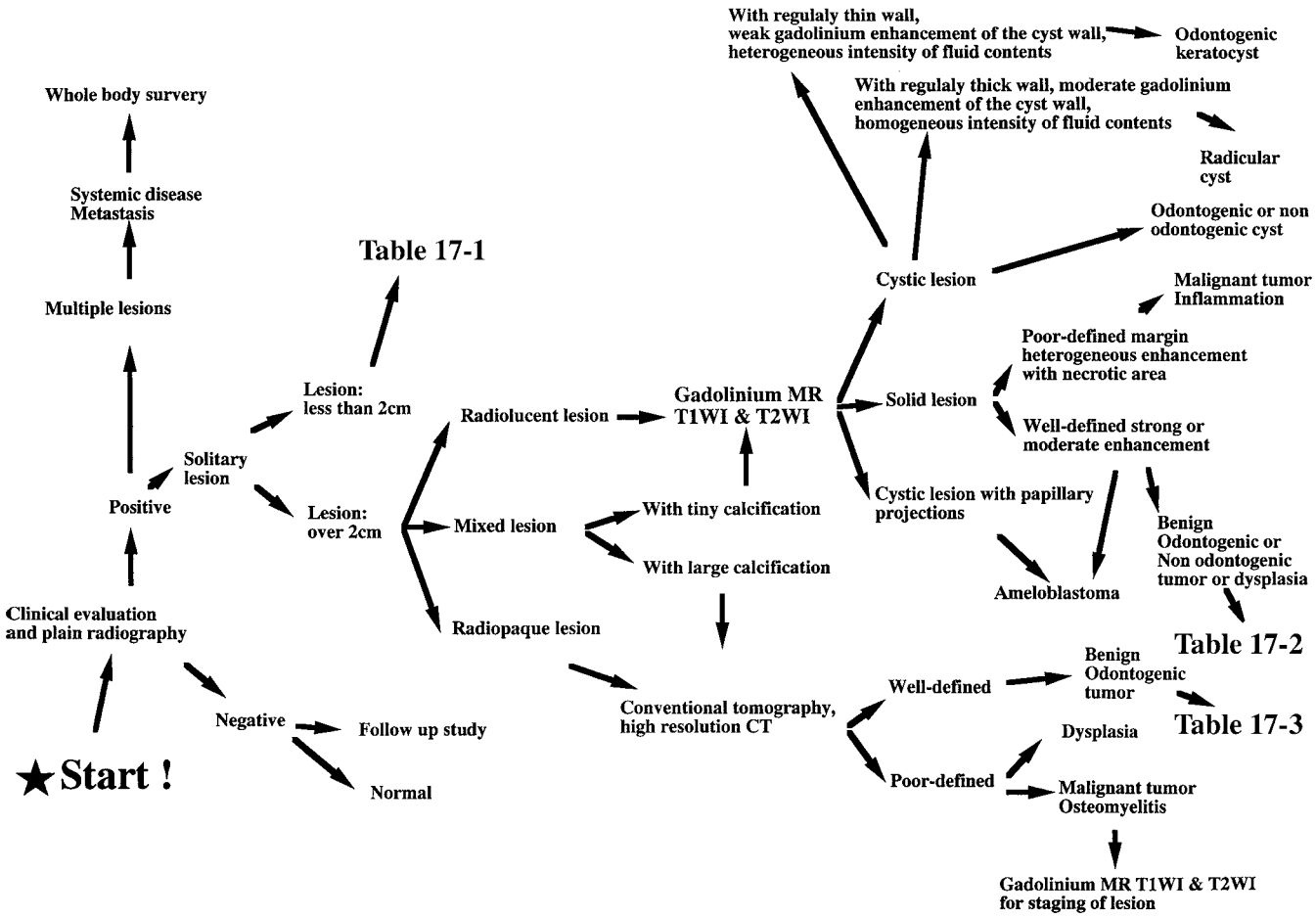

FIGURE 17-82 Systematic approach using radiologic examination and MR imaging of jawbone lesions.

VIEW IMAGE

Copyright © 2003, Mosby, Inc. All rights reserved.

SECTION THREE

DENTAL ANOMALIES AND SYSTEMIC DISEASE

Jorge Bianchi and Hugh D. Curtin

The purpose of this section is not to provide a complete description of every dental anomaly with a correlating imaging appearance or to discuss extensively the various manifestations of systemic disease. Rather, its purpose is to describe those conditions that may be seen incidentally during imaging of the head and neck and that may be questioned during interpretation of an examination done for an unrelated reason. It is hoped that some of the terminology will prove useful to the reader. A systemic disease will usually be obvious by the time the patient comes to imaging. Almost all of the dental anomalies described here are best shown by plain dental radiographs.

DENTAL ANOMALIES

Dental anomalies include variations in the shape, size, number, and morphology of the teeth. These types of abnormalities are relatively frequent and are usually diagnosed by the general dentist with plain radiographic films. Although most anomalies occur as isolated entities, some are associated with extraoral abnormalities. The various tooth structures (enamel, dentin, cementum, and periodontal ligament) have different embryologic origins, and abnormalities affecting a particular tooth structure may be associated with disorders of extradental tissues that have a similar embryologic origin.

Supernumerary Teeth

Supernumerary teeth are simply extra teeth (Fig. 17-83). They occur mainly in the anterior region of the maxilla. A supernumerary tooth in the anterior maxilla is called a mesiodens.[195] An extra tooth seen posterior to the molar area is called a distomolar or distodent. The term *paramolar* has been used to describe a supernumerary tooth in the region of the molars. It can be lingual (medial), buccal (lateral), or occur between the normal molars. The term has been used to describe a distomolar as well. Supernumerary teeth are usually smaller than normal teeth and are more common in the permanent dentition. They are present in 1% to 4% of the population.[196] Syndromes associated with supernumerary teeth include Gardner's syndrome and cleidocranial dysplasia, but a supernumerary tooth is most commonly seen as an isolated phenomenon.[197]

The presence of supernumerary teeth may affect the normal eruption of teeth and therefore future appropriate positioning of the teeth. Thus, the dentist may want to know the position and orientation of the mesiodens in the maxilla or jaw, as the position, orientation, and inclination of the mesiodens can be significant in potential treatment.

Palatal orientation refers to the position of the tooth facing the hard palate. Buccal orientation refers to the position of the tooth facing the cheek and the buccal mucosa of the alveolar process. The dentist can plan extractions or orthodontic treatment (teeth alignment) knowing the position and orientation of the mesiodens. Distomolars or paramolars may also have different inclinations and positions that can affect normal occlusion.

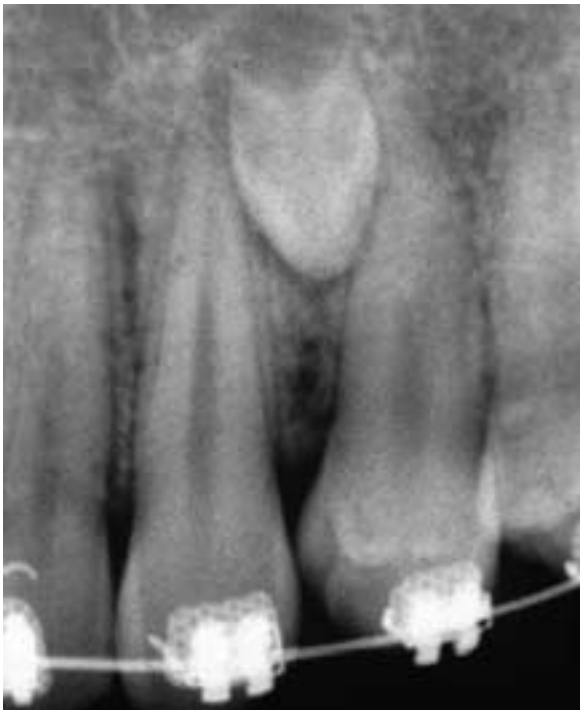

FIGURE 17-83 Supernumerary tooth. Periapical view of the anterior maxilla shows a supernumerary tooth between the left canine and first premolar.

VIEW IMAGE

Hypodontia

Hypodontia is the absence of one or more teeth.[198] This condition occurs in permanent dentition in 5% to 10% of the population. The most common missing teeth excluding the third molars are the mandibular second premolars and maxillary lateral incisors, respectively.[198, 199] Disorders associated with missing teeth include ectodermal dysplasia, epidermolysis bullosa, and a variety of other disorders.[200]

Ectodermal dysplasia is an X-linked recessive disorder characterized by the absence or deficient development of at least two derivatives of the ectoderm such as the teeth, hair, and nails (Fig. 17-84). Charles Darwin identified the first case in the 1860s.

Epidermolysis bullosa is a rare genetic disorder characterized by blister formation on the mucosa or skin that develops in response to minor trauma.

Radiation treatment can affect the normal development of the teeth, and missing teeth is a common consequence of radiation therapy in children.

Macrodontia and Microdontia

Macrodontia and microdontia refer to correlations between the size of a tooth and its correspondent on the opposite side of the arch.[199–201] Teeth may be bigger or smaller (Fig. 17-85) in a normal healthy individual. However, macrodontia and microdontia can affect the space available in the jaws for the teeth and therefore can affect normal occlusion. This may lead to misalignment of the teeth in the arch.

Copyright © 2003, Mosby, Inc. All rights reserved.

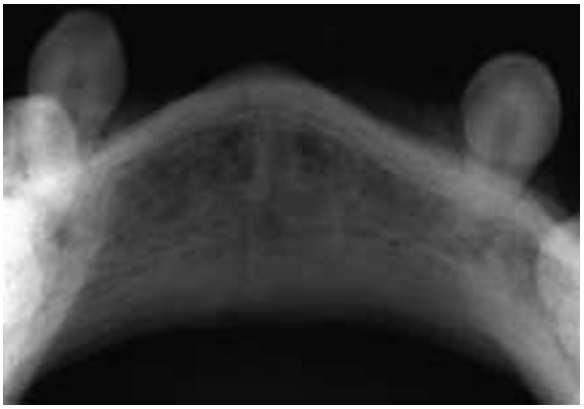

FIGURE 17-84 Ectodermal dysplasia. Occlusal view. Abnormal teeth with absence of central incisors.

Dens in Dente (Dens Invaginatus)

Dens in dente results from an invagination of the outer surface of the tooth into the inner part of the tooth (Figs. 17-86 and 17-87).[202, 203] It occurs most frequently in permanent upper lateral incisors. It can occur in any region of the tooth but usually affects the crown of the tooth, with the enamel folding inward. The vitality of the tooth may be compromised. When the abnormality involves the root of the tooth, the defect is lined by cementum.[202, 203]

Pulp Stones

Pulp stones are calcifications in the pulp chamber of the tooth (Figs. 17-88 and 17-89). The etiology is unclear, but there may be a direct relationship with increased age. The molar teeth are most commonly affected, but pulp stones can affect any tooth. At clinical inspection, a tooth with a pulp stone looks like any other tooth. A pulp stone may make root canal treatment difficult or impossible. Pulp calcifications have been found in association with tumoral calcinosis, dentin dysplasia, and Ehlers-Danlos syndrome.[204]

Enamel Pearls

Enamel pearls are small spherical enamel masses located at the root of the molars and are found in 2% of the population (Figs. 17-90 and 17-91).[205] There can be a small pulp chamber extending from the parent tooth. Enamel pearls can distort the periodontal space and may predispose the patient to periodontal disease, but usually they are not considered to have clinical significance. Occurring beneath the gingiva, they are not usually clinically obvious.

FIGURE 17-85 Microdontia. A periapical view of the right posterior maxilla shows a small second premolar (*arrow*).

FIGURE 17-86 Dens in dente. Periapical view shows an unerupted bicuspid with an invaginated cusp (*arrow*) consistent with dens in dente.

FIGURE 17-87 Dens in dente. Periapical view of the right maxilla shows a dens in dente in the lateral incisor. Invagination of the enamel (*arrow*) and pulp chamber is noted.

Copyright © 2003, Mosby, Inc. All rights reserved.

FIGURE 17-88 Periapical view of the right posterior maxilla. The first and second permanent molars show pulp stones in the pulp chamber (*arrow*).

Amelogenesis Imperfecta

Normal enamel is the densest material in the human body. Enamel covers the outer surface of the teeth and is almost 100% inorganic, composed mainly of hydroxyapatite crystals. Its attenuation value at CT is 3000 HU. Amelogenesis imperfecta is a developmental disorder that involves generalized abnormal enamel formation.[3] Strong autosomal and recessive X-linked associations have been documented.[206] The enamel is very thin (Fig. 17-92). The dentin can be seen through the enamel, giving the tooth a darker or, in some cases, a yellow-brown color. Frequently the enamel will fracture easily and the teeth wear down quickly. In some

FIGURE 17-89 Periapical view of the right posterior mandible. The right permanent canine and first bicuspid show pulp stones in the pulp chamber (*arrows*).

FIGURE 17-90 Enamel pearls. Periapical view of the right posterior maxilla. Enamel pearls are seen in the cervical portion of the first and second permanent molars (*arrows*).

variants the teeth readily absorb stains, adding a darkened component to the already abnormal appearance.[207]

The radiographic appearance varies with the subtype.[3, 207, 208] The enamel may be of normal density but very thin (hypoplastic form). The thickness initially may be relatively normal but the density is low, at times even lower than the radiographic appearance of dentin (hypomaturation or hypocalcified form). All forms erode or wear easily and the enamel may be worn down, giving a squared-off appearance to the crown.

Dentinogenesis Imperfecta

Dentinogenesis imperfecta (DI) is an autosomal dominant developmental disturbance of dentin formation.[209] Dentin is the inner layer of the tooth structure and has a more organic matrix than the enamel. DI can affect both primary

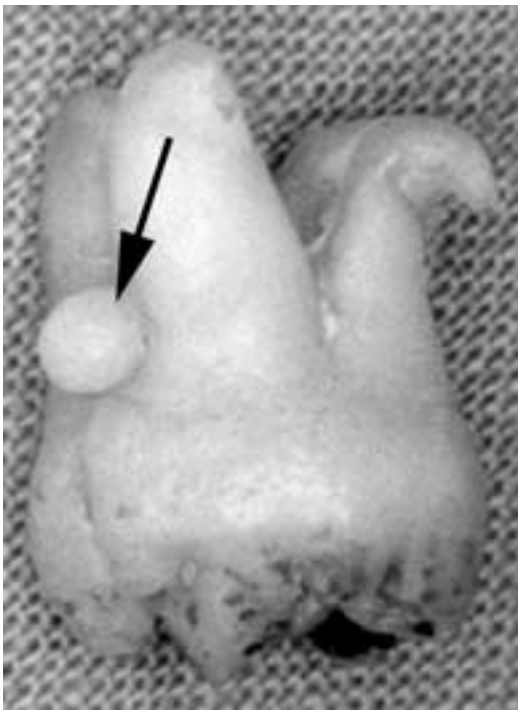

FIGURE 17-91 Enamel pearl. An enamel pearl (*arrow*) is seen on the cervical portion of the tooth.

Copyright © 2003, Mosby, Inc. All rights reserved.

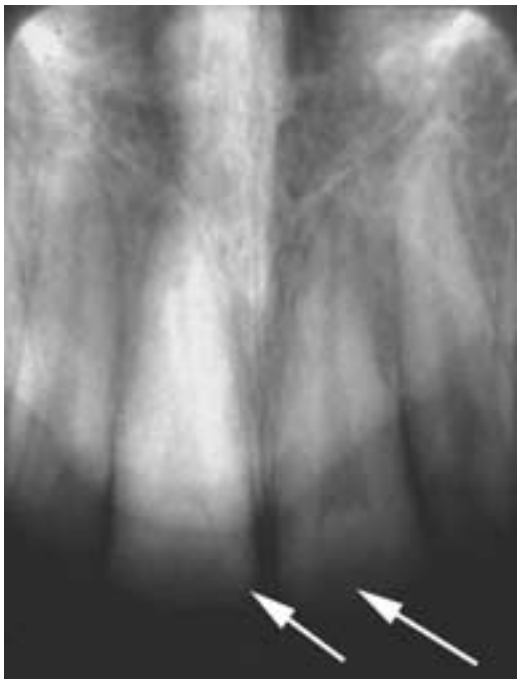

VIEW IMAGE

FIGURE 17-92 Amelogenesis imperfecta. Periapical view of the anterior maxilla. Dentin, pulp chamber, and cementum are present, but there is no or very thin enamel (*arrows*).

FIGURE 17-93 DI. Periapical view of the right maxilla shows pulp chamber obliteration and short teeth consistent with DI. An impacted canine is also seen.

VIEW IMAGE

and secondary dentitions and has no sex predilection. It may be associated with osteogenesis imperfecta but can occur in isolation, without associated skeletal abnormalities.[210] The term *hereditary opalescent dentin* has been applied to the isolated defect variant. The teeth may be translucent and vary in color from yellow to gray. The enamel fractures easily, and the teeth wear readily.[210]

Radiographic features of DI can include a variety of abnormalities. There can be a constriction of the cervical portion of the tooth (junction between enamel and cementum). The roots can be narrowed or short. There can be partial or complete obliteration of the pulp chamber (Fig. 17-93). The lucency is replaced by an opacity that is more characteristic of dentin.

Taurodontia

Taurodontia or taurodontism is an inherited anomaly characterized by enlarged pulp chambers of the teeth (Fig. 17-94). The pulp chamber's size is increased. Clinically, teeth with taurodontia appear no different than normal teeth. The radiographic identification of taurodonia is important because of the risk of exposing the pulp chamber during dental procedures.

Dentin Dysplasias

Dentin dysplasia is a rare dental anomaly. It is an autosomal dominant condition characterized by abnormal tooth and root formation.[211] Dentin dysplasias have two variants. Dentin dysplasia type 1 (radicular type) is characterized by poorly developed roots (chopped roots) and obliterated pulp chambers. The crown of the tooth may have normal color or may be slightly darker than normal. Radiologically, obliteration of the pulp cavity is present at birth. In dentin dysplasia type 2 (coronal type), the tooth has the same appearance as in DI. Clinically, the tooth is translucent. Radiography shows narrowing or obliteration of the pulp chamber occurs. Obliteration of the pulp chamber occurs later in dentin dysplasia than in DI. Dentin dysplasia is an uncommon condition.[211]

DENTAL MANIFESTATION OF METABOLIC AND SYSTEMIC CONDITIONS

A number of metabolic diseases that affect bone biology can also affect the teeth and surrounding structures including the bone, the lamina dura, and the periodontal ligament. Conditions such as hyperparathyroidism, osteoporosis, renal osteodystrophy, and rickets may lead to altered trabeculation of bone, loss or thinning of lamina dura, and a ''ground glass'' appearance of bone. The dentist may identify this radiographic sign during a regular plain film examination.

FIGURE 17-94 Taurodontia. Periapical views of the left and right posterior mandibles. Enlarged pulp chambers are noted.

VIEW IMAGE

Copyright © 2003, Mosby, Inc. All rights reserved.

Systemic conditions such as scleroderma (progressive systemic sclerosis) can present with generalized enlargement of the periodontal ligament (PDL) space.[212–214] The precise explanation of the finding is not known, but the abnormality has been attributed to an obliterative microvascuopathy and a thickened periodontal membrane.[212] The reduction in vascularity of the PDL space may predispose the patient to superimposed periodontal disease as well. This finding is not universal in patients with scleroderma. The differential diagnosis of enlarged PDL space includes occlusal trauma, orthodontic braces (alignment device), and malignancies. Orthodontic appliances pulling on the tooth will usually enlarge one aspect of the PDL space at the expense of the opposite side. The PDL space is narrowed on the side to which the tooth is being ''pulled.'' Malignancies in the jaws such as leukemia, lymphomas, sarcomas, primary lesions, or metastasis may present with teeth ''floating in space,'' localized alveolar bone destruction, and enlarged PDL spaces. ''Floating teeth'' are also seen in histiocytosis.

Patients with scleroderma can have bone changes as well, and there can be pronounced erosions at points of muscle attachment. Erosions or scalloping of the bone can be seen in the area of the angle of the mandible or more anteriorly where the anterior belly of the digastric attaches to the mandible. There can also be involvement of the coronoid process or condyle.

REFERENCES

1. Kramer IRH, Pindborg JJ, Shar M. Histological Typing of Odontogenic Tumours: World Health Organization: International Histological Classification of Tumours, 2nd ed. Berlin: Spring-Verlag;1992:1–42.
2. Sciubba JJ, Fantasia JE, Kahn LB. Tumors and cysts of the jaw. In: Rosai J, ed. Atlas of Tumor Pathology. Washington, DC: Armed Forces Institute of Pathology, 2001.
3. White SC, Pharoah MJ. Oral Radiology: Principles and Interpretation, 4th ed. St. Louis: CV Mosby, 2000.
4. Weber AL, Easter KM. Cysts and odontogenic tumors of the mandible and maxilla. I. Contemp Diagn Radiol 1982;5(25):1.
5. Borg G, Persson G, Thilander H. A study of odontogenic cysts with special reference to comparisons between keratinizing and non-keratinizing cysts. Swed Dent J 1974;67:311–325.
6. Shrout MK, Hall MJ, Hildebolt CE. Differentiation of periapical granulomas and radicular cysts by digital radiometric analysis. Oral Surg 1993;76:356–361.
7. Donoff RB, Guralnick WC, Clayman L. Keratocysts of the jaw. J Oral Surg 1972;30:800–884.
8. Brannon RB. The odontogenic keratocyst: a clinicopathologic study of 312 cases. I. Clinical features. Oral Surg 1962;42:54–72.
9. Brennon RB. The odontogenic keratocyst: a clinicopathologic study of 312 cases. II. Histologic features. Oral Surg 1977;43:233–255.
10. Shear M. Developmental odontogenic cysts: an update. J Oral Pathol Med 1994;23:1–11.
11. Forssell K, Forssell H, Kahnberg KE. Recurrences of keratocysts: a long-term follow up study. Int J Oral Maxillofac Surg 1988;17:25–28.
12. Yonetsu K, Bianchi JG, Troulis MJ, Curtin HD. Unusual CT appearance in an odontogenic keratocyst of the mandible: case report. AJNR 2001;22(10):1887–1889.
13. Minami M, Kaneda T, Ozawa K, et al. Cystic lesions of the maxillomandibular region: MR imaging distinction of odontogenic keratocysts and ameloblastomas from other cysts. AJR 1996;166: 943–949.
14. Williams TP, Connor FA. Surgical management of the odontogenic keratocyst: aggressive approach. J Oral Maxillofac Surg 1994;52: 964–966.
15. Koutnik AW, Kolodny SC, Hooker SP, et al. Multiple nevoid basal cell epithelioma, cysts, of the jaws, and bifid ribs syndrome: report of a case. J Oral Surg 1975;33:686–689.
16. Gorlin RJ, Goltz RW. Multiple nevoid basal cell epithelioma, jaw cysts, I and bifid ribs. N Engl J Med 1960;262:908–912.
17. Woolgar JA, Rippin JW, Browne RM. The odontogenic keratocyst and its occurrence in the nevoid basal cell carcinoma syndrome. Oral Surg Oral Med Oral Pathol 1987;64:727–730.
18. Gorlin RJ, Pindborg JJ, Clausen FP, Vickers RA. The calcifying odontogenic cyst: a possible analogue of the cutaneous calcifying epithelioma of Malherbe: an analysis of 15 cases. Oral Surg 1962;15:1235–1243.
19. Lello GE, Makek M. Calcifying odontogenic cyst. Int J Oral Maxillofac Surg 1986;15:637–644.
20. Tanimoto K, Tomita S, Aoyama M, et al. Radiographic characteristics of the calcifying odontogenic cyst. Int J Oral Maxillofac Surg 1988;17:29–32.
21. Buchner A. The central (intraosseous) calcifying odontogenic cyst: an analysis of 215 cases. J Oral Maxillofac Surg 1991;49: 330–339.
22. Devlin H, Horner K. The radiological features of calcifying odontogenic cyst. Br J Radiol 1993;66:403–407.
23. Abrams A, Howell FV, Bullock WK. Nasopalatine cysts. Oral Surg 1963;16:306–332.
24. Campbell JJ, Baden E, Williams AC. Nasopalatine cyst of unusual size: report of case. J Oral Surg 1973;31:776–779.
25. Christ TF. The globulomaxillary cyst: an embryologic misconception. Oral Surg 1970;30:515–526.
26. Little JW, Jakobsen J. Origin of the globulomaxillary cyst. J Oral Surg 1978;31:188.
27. Huebner GR, Turlington EG. So-called traumatic (hemorrhagic) bone cysts of the jaw. Oral Surg 1971;31:254–265.
28. Saito Y, Hoshina Y, Nagamine T. Simple bone cyst: a clinical and histopathological study of fifteen cases. Oral Surg Oral Med Oral Pathol 1992;74:487–491.
29. Suei Y, Tanimoto K, Wada T. Simple bone cyst: evaluation of contents with conventional radiography and computed tomography. Oral Surg Oral Med Oral Pathol 1994;77:296–301.
30. Biewald HF. A variation in the management of hemorrhagic, traumatic or simple bone cyst. J Oral Surg 1987;25:627.
31. Ellis DJ, Walters PJ. Aneurysmal bone cyst of the mandible. J Oral Surg 1972;34:26–32.
32. Gruskin SE, Dablin DC. Aneurysmal bone cyst of the mandible. J Oral Surg 1968;26:523–528.
33. Steidler NE, Cook RM, Reade PC. Aneurysmal bone cysts of the jaws: a case report and review of the literature. Br J Oral Surg 1970;16:254–261.
34. Reyneke JP. Aneurysmal bone cyst of the maxilla. Oral Surg 1978;45:441–447.
35. Karabouta I, Tsodoulos S, Trigonidis G. Extensive aneurysmal bone cyst of the mandible: surgical resection and immediate reconstruction. Oral Surg Oral Med Oral Pathol 1991;71:148–150.
36. Robinson PD. Aneurysmal bone cyst: a hybrid lesion? Br J Oral Maxillofac Surg 1985;23:220–226.
37. Stafne EC. Bone cavities situated near the angle of the jaw. J Am Dent Assoc 1942;29:19–69.
38. Buchner A, Carpenter WM, Merrell PW, Leider AS. Anterior lingual mandibular salivary gland defect. Oral Surg Oral Med Oral Pathol 1991;71:131–136.
39. Regezi JA, Kerr DA, Courtney RM. Odontogenic tumors: analysis of 706 cases. J Oral Surg 1978;36:771–778.
40. Weber AL, Easter KM. Cysts and odontogenic tumors of the mandible and maxilla. II. Contemp Diagn Radiol 1982; 5(36):1.
41. Small IA, Waldron CA. Ameloblastoma of the jaw. Oral Surg Oral Med Oral Pathol 1955;8(3):281–297.
42. Hylton RP, McKean TW, Albright JE. Simple ameloblastoma: report of case. J Oral Surg 1972;30:59.
43. Mehlish DR, Dahlin DC, Masson JK. Ameloblastoma: a clinicopathologic report. J Oral Surg 1972;30:9–22.
44. Eversole LR, Leider AS, Hansen LS. Ameloblastomas with pronounced desmoplasia. J Oral Maxillofac Surg 1984;42:735-740.
45. Minami M, Kaneda T, Yamamoto H, et al. Ameloblastoma in the maxillomandibular region: MR imaging. Radiology 1992;184: 389–393.

Copyright © 2003, Mosby, Inc. All rights reserved.

46. Kaffe I, Buchner A, Taicher S. Radiographic features of desmoplastic variant of ameloblastoma. Oral Surg 1993;76:525–529.
47. Ng KH, Siar CH. Desmoplastic variant of ameloblastomas in Malaysians. Br J Oral Maxillofac Surg 1993;31:299–303.
48. Franklin CD, Hindle MO. The calcifying epithelial odontogenic tumor: report of four cases, two with long-term follow-up. Br J Oral Surg 1976;13:230–238.
49. Franklin CD, Pindborg JJ. The calcifying epithelial odontogenic tumor. Oral Surg 1976;42:753–765.
50. Pindborg JJ. A calcifying epithelial odontogenic tumor. Cancer 1958;11:838–843.
51. Tratman EK. Classification of odontomes. Br Dent J 1951;91: 167–173.
52. Curreri RC, Masser JE, Abramson AL. Complex odontoma of the maxillary sinus: report of a case. J Oral Surg 1975;33:45–48.
53. Caton RB, Marble HB Jr, Topazian RG. Complex odontoma in the maxillary sinus. J Oral Surg 1973;36(5):658–662.
54. Thompson RD, Hale ML, McLeran JH. Multiple compound composite odontomas of maxilla and mandible: report of case. J Oral Surg 1968;26:478–480.
55. Regezi JA, Kerr DA, Courtney RM. Odontogenic tumors: analysis of 760 cases. J Oral Surg 1978;36:771–778.
56. Daley TD, Wysocki GP, Pringle GA. Relative incidence of odontogenic tumors and oral and jaw cysts in a Canadian population. Oral Surg 1994;77:276–280.
57. Philipsen HP, Reichart PA, Zhang KH, et al. Adenomatoid odontogenic tumor: biologic profile based on 499 cases. J Oral Pathol Med 1991;20:149–158.
58. Gundlach KK, Schulz A. Odontogenic myxoma: clinical concept and morphological studies. J Oral Pathol 1977;6(6):343–358.
59. Hendler BH, Abaza NA, Quinn P. Odontogenic myxoma, surgical management and an ultrastructural study. Oral Surg 1979;47: 203–217.
60. Davis RB, Baker RD, Alling CC. Odontogenic myxoma: clinical pathologic conference, case 24. J Oral Surg 1978;36:534–538.
61. Peltola J, Magnusson B, Happonen R-P, Borrman H. Odontogenic myxoma: a radiographic study of 21 tumours. Br J Oral Maxillofac Surg 1994;32:298–302.
62. Zegarelli EV, Kutscher AH, Napoli N, et al. The cementoma: a study of 235 patients with 435 cementomas. Oral Surg 1964;17:219–224.
63. Vegh T. Multiple cementomas (periapical cemental dysplasia). Oral Surg 1976;42:402–406.
64. Chaudhry AP, Spink JH, Gorlin RJ. Periapical fibrous dysplasia (cementoma). J Oral Surg 1958;16:483.
65. Waldron CA. Fibro-osseous lesions of the jaws. J Oral Maxillofac Surg 1993;51:828–835.
66. Hamner JE III, Scofield HH, Cornyn J. Benign fibro-osseous jaw lesions of periodontal membrane origin: analysis of 249 cases. Cancer 1968;22:861–878.
67. Cherrick HM, King OH Jr, Lucatorto FM, et al. Benign cementoblastoma: a clinicopathologic evaluation. Oral Surg 1974;37: 54–63.
68. Eversole LR, Sabes WR, Dauchess VG. Benign cementoblastoma. J Oral Surg 1973;36:824–830.
69. Suzuki M, Sakai T. A familial study of torus palatinus and torus mandibularis. Am J Phys Anthropol 1960;18:263.
70. King DR, Moore GE. An analysis of torus palatinus in a transatlantic study. J Oral Med 1976;31:44–46.
71. Bhaskar SN, Cutright DE. Multiple enostosis: report of cases. J Oral Surg 1968;26:321–326.
72. Weinberg S. Osteoma of the mandibular condyle: report of case. J Oral Surg 1977;35:929–932.
73. Noren GD, Roche WC. Huge osteoma of the mandible: report of a case. J Oral Surg 1978;36:375–379.
74. Alling CC, Martinez MG, Ballard JB, et al. Osteoma cutis: clinical pathologic conference, case 5 II. J Oral Surg 1974;32:195–197.
75. Halse A, Roed-Petersen B, Lund K. Gardner's syndrome. J Oral Surg 1975;33:673–675.
76. McFarland PH, Scheetz WL, Knisley RE. Gardner's syndrome: report of two families. J Oral Surg 1968;26:632–638.
77. Neal CG. Multiple osteomas of the mandible associated with polyposis of the colon (Gardner's syndrome). Oral Surg 1969;28: 628–631.
78. Witkop CJ. Gardner's syndrome and other osteognathodermal disorders with defects in parathyroid functions. J Oral Surg 1968;26:639–642.
79. Ramon Y, Horowitz I, Oberman M, et al. Osteochondroma of the coronoid process of the mandible. Oral Surg 1977;43:696–697.
80. Allan JH, Scott H. Osteochondroma of the mandible. Oral Surg 1974;37:556–565.
81. Chaudry AP, Robinovitch MR, Mitchell DF, et al. Chondrogenic tumors of the jaws. Am J Surg 1961;102:403–411.
82. Waldron CA, Shafer WG. Central giant cell reparative granuloma of the jaws. Am J Clin Pathol 1966;45:437–647.
83. Wesley RK, Horan M, Helfrick JF, et al. Central giant cell granuloma of the mandible: clinical pathologic conference, case 25 I. Oral Surg 1978;36:713.
84. Smith GA, Ward PH. Giant-cell lesions of the facial skeleton. Arch Otolaryngol 1978;104:186–190.
85. Curtis ML, Hatfield CG, Pierce JM. A destructive giant cell lesion of the mandible: report of a case. J Oral Surg 1979;37:432–436.
86. Chuong R, Kaban LB, Kozakewich H, et al. Central giant cell lesions of the jaws: a clinicopathologic study. J Oral Maxillofac Surg 1986;44:708–713.
87. Whitaker SB, Waldron CA. Central giant cell lesions of the jaws: a clinical, radiologic, and histopathologic study. Oral Surg Oral Med Oral Pathol 1993;75:199–208.
88. Pogrel MA. The use of liquid nitrogen cryotherapy in the management of locally aggressive bone lesions. J Oral Maxillofac Surg 1993;51:269–273.
89. MacIntosh RB. Surgical management of benign nonodontogenic lesions of the jaws. In: Peterson LJ et al, eds. Principles of Oral and Maxillo-Facial Surgery, Vol. 2. Philadelphia: Lippincott, 1992; 713–753.
90. Lichtenstein L. Histiocytosis X: integration of eosinophilic granuloma of bone: Letterer-Siwe disease and Schuler-Christian disease as related manifestation of a single nosologic entity. Arch Pathol 1953;56:84–102.
91. Rapidis AD, Langdon JD, Harvey PW, et al. Histiocytosis X. Int J Oral Surg 1978;7:76–84.
92. Scott J, Finch LD. Histiocytosis X with oral lesions: report of case. J Oral Surg 1972;30:748–753.
93. Soskolne WA, Lustmann J, Azaz B. Histiocytosis X: report of six cases initially in the jaws. J Oral Surg 1977;35:30–33.
94. Sigala JL, Silverman S Jr, Brody HA, et al. Dental involvement of histiocytosis. Oral Surg 1972;33:42–48.
95. Lieberman PH et al. A reappraisal of eosinophilic granuloma of bone, Hand-Schuller-Christian disease and Letterer-Siwe syndrome. Medicine 1969;48:375–400.
96. Maw RB, McKean TW. Hand-Schuller-Christian disease: report of case. J Am Dent Assoc 1972;85:1353–1357.
97. Ragab RR, Rake O. Eosinophilic granuloma with bilateral involvement of both jaws. Int J Oral Surg 1975;4:73–79.
98. Chu T, D'Angio GJD, Favara B. Histiocytosis syndromes in children. Lancet 1987;1:208–209.
99. David R, Oria RA, Kumar R, et al. Radiologic feature of eosinophilic granuloma of bone. AJR 1989;153:1021–1026.
100. Waldron CA, Giansanti JS. Benign fibro-osseous lesions of the jaws: a clinical-radiologic-histologic review of sixty-five cases. II. Benign fibro-osseous lesions of periodontal ligament origin. Oral Surg 1973;35:340–350.
101. Cangiano R, Stratigos GE, Williams FA. Clinical and radiographic manifestations of fibro-osseous lesions of the jaws: report of five cases. J Oral Surg 1971;29:872-881.
102. Hayward JR, Melarkey DW, Megquier J. Monostotic fibrous dysplasia of the maxilla: report of cases. J Oral Surg 1973;31:625–627.
103. Eversole LR, Sabes WR, Rovin S. Fibrous dysplasia: a nosologic problem in the diagnosis of fibro-osseous lesions of the jaws. J Oral Pathol 1972;1:189–220.
104. Waldron CA, Giansanti JS. Benign fibro-osseous lesions of the jaws: a clinical-radiologic-histologic review of sixty-five cases. I. Fibrous dysplasia of the jaws. Oral Surg 1973;35:190–201.
105. Waldron CA, Giansanti JS. Benign fibro-osseous lesions of the jaws: a clinical-radiologic-histologic review of sixty-five cases. II. Benign fibro-osseous lesions of periodontal ligament origin. Oral Surg Oral Med Oral Pathol 1973;35:340–350.
106. Schlumberger HG. Fibrous dysplasia (ossifying fibroma) of maxilla and mandible. Am J Orthod 1946;32:579–587.

Copyright © 2003, Mosby, Inc. All rights reserved.

107. Sherman RS, Sternbergh WCA. Roentgen appearance of ossifying fibroma of bone. Radiology 1948;50:595–609.
108. Waldron CA. Ossifying fibroma of mandible: report of 2 cases. Oral Surg Oral Med Oral Pathol 1953;6:467–473.
109. Anderson JT, Dehner LP. Osteolytic form of Paget's disease. J Bone Joint Surg (Am) 1976;58:994–1000.
110. Gee JK, Zambito RF, Argentieri GW, et al. Paget's disease (osteitis deformans) of the mandible. J Oral Surg 1972;30:223–227.
111. Lund BA. Hemangioma of the mandible and maxilla. J Oral Surg 1972;22:234.
112. Macansh JD, Owen MD. Central cavernous hemangioma of the mandible: report of two cases. J Oral Surg 1972;30:293–296.
113. Kaban LB, Mulliken JB. Vascular anomalies of the maxillofacial region. J Oral Maxillofac Surg 1986;44:203–213.
114. Mulliken JB, Glowacki J. Hemangiomas and vascular malformations in infants and children: a classification based on endothelial characteristics. Plast Reconstr Surg 1982;69:412–422.
115. Boyd JB, Mulliken JB, Kaban LB, et al. Skeletal changes associated with vascular malformations. Plast Reconstr Surg 1984;74:789–795.
116. Ezekowitz RAB, Mulliken JB, Folkman J. Interferon alpha-2a for life threatening hemangiomas of infancy. N Engl J Med 1992;326:1456–1463.
117. Ricketts RR, Hatly RM, Corden BJ, et al. Interferon alpha-2a for the treatment of complex hemangiomas of infancy and childhood. Ann Surg 1994;219:605–612.
118. Shklar G, Meyer I. Neurogenic tumors of the mouth and jaws. Oral Surg 1963;16:1075–1093.
119. Shimura K, Allen EL, Kinoshita Y, et al. Central neurilemmoma of the mandible: report of a case and review of the literature. J Oral Surg 1973;31:363–367.
120. Prescott GH, White RF. Solitary, central neurofibroma of the mandible: report of case and review of the literature. J Oral Surg 1978;28:305.
121. Singer CF, Gienger GL, Kulborn TL. Solitary intraosseous neurofibroma involving the mandibular canal: report of case. J Oral Surg 1973;31:127–129.
122. Nolan R, Wood NK. Central squamous cell carcinoma of the mandible: report of a case. J Oral Surg 1976;34:260–264.
123. Coonar HS. Primary intraosseous carcinoma of maxilla. Br Dent J 1979;147:47–48.
124. Lapin R, Garfinkel AW, Catania AF, et al. Squamous cell carcinoma arising in a dentigerous cyst. J Oral Surg 1973;31:354–358.
125. Sigal R, Zagdanski AM, Schwaab G, et al. CT and MR imaging of squamous cell carcinoma of the tongue and floor of the mouth. RadioGraphics 1996;16:787–810.
126. Eversole LR. Malignant epithelial odontogenic tumors. Semin Diagn Pathol 1999;16(4):317–324.
127. Slootweg PJ, Muller H. Malignant ameloblastoma or ameloblastic carcinoma. Oral Surg Oral Med Oral Pathol 1984;57(2):168–176.
128. Nagai N, Takeshita N, Nagatsuka H, et al. Ameloblastic carcinoma: case report and review. J Oral Pathol Med 1991;20(9):460–463.
129. Shear M. Primary intra-alveolar epidermoid carcinoma of the jaw. J Pathol 1969;97:645–651.
130. Sirsat MV, Sampat MB, Shrikhande SE. Primary intra-alveolar squamous cell carcinoma of the mandible. Oral Surg 1973;35:366–371.
131. Fredrickson C, Cherrick HM. Central mucoepidermoid carcinoma of the jaws. J Oral Med 1978;30:80–85.
132. Schultz W, Whitten JB. Mucoepidermoid carcinoma in the mandible: report of case. J Oral Surg 1969;27:337–340.
133. Adler CI, Sotereanos GC, Valdivieso JG. Metastatic bronchogenic carcinoma of the maxilla: report of case. J Oral Surg 1973;31:543–546.
134. Al-Ani S. Metastatic tumors to the mouth: report of two cases. J Oral Surg 1973;31:120–122.
135. Appenzeller J, Weitzner S, Long GW. Hepatocellular carcinoma metastatic to the mandible: report of case and review of literature. J Oral Surg 1971;29:668–671.
136. Carter DG, Anderson EE, Currie DP. Renal cell carcinoma metastatic to the mandible. J Oral Surg 1977;35:992–993.
137. Cherrick HM, Demkee D. Metastatic carcinoma of the jaws. J Am Dent Assoc 1973;87:180–181.
138. Moss M, Shapiro DN. Mandibular metastasis of breast cancer. J Am Dent Assoc 1969;78:756–757.
139. Aniceto GS, Penin AG, de la Mata Pages R, Moreno JJM. Tumors metastatic to the mandible: analysis of nine cases and review of the literature. J Oral Maxillofac Surg 1990;48:246–251.
140. Hishberg A, Leibovich P, Buchner A. Metastatic tumors to the jawbones: an analysis of 390 cases. J Oral Pathol Med 1994;23:337–341.
141. Garrington GE, Scofield HH, Cornyn J, et al. Osteosarcoma of the jaws: analysis of 56 cases. Cancer 1967;20:377–391.
142. Caron AS, Hajdu SI, Strong EW. Osteogenic sarcoma of the facial and cranial bones: review of 43 cases. Am J Surg 1971;122:719–725.
143. Wilcox JW, Dukart RC, Kolodny SC, et al. Osteogenic sarcoma of the mandible. Review of the literature and report of case. J Oral Surg 1973;31:49–52.
144. Clark JL, Unni KK, Dahlin DC, et al. Osteosarcoma of the jaw. Cancer 1983;51:2311–2316.
145. Wannfors K, Hammarstrom L. Periapical lesions of mandibular bone: difficulties in early diagnostics. Oral Surg 1990;70:483–489.
146. Lindquist C, Teppo L, Sane J, et al. Osteosarcoma of the mandible: analysis of nine cases. J Oral Maxillofac Surg 1986;44:759–764.
147. Yagan R, Radivoyevitch M, Beillon EM. Involvement of the mandibular canal: early sign of osteogenic sarcoma of the mandible. Oral Surg 1985;60:56–60.
148. Taconis WK, van Rijssel TG. Fibrosarcoma of the jaws. Skeletal Radiol 1986;15:10–13.
149. Wright JA, Kuehn PG. Fibrosarcoma of the mandible. Oral Surg 1973;36:16–20.
150. Slater LJ. Odontogenic sarcoma and carcinosarcoma. Seminars Diagn Pathol 1999;16:325–332.
151. Borhgelli RF, Barros RE, Zampieri J. Ewing sarcoma of the mandible: report of case. J Oral Surg 1978;36:473–475.
152. Carl W, Schaaf NG, Gaeta J, et al. Ewing's sarcoma. J Oral Surg 1971;31:472–478.
153. Wood RE, Nortje CJ, Hesseling P, Grotepas F. Ewing's tumor of the jaw. Oral Surg 1990;69:120–127.
154. Yalcin S, Turoglu HT, Ozdamar S, et al. Ewing's tumor of the mandible. Oral Surg 1993;76:362–367.
155. Steg RF, Dahlin DC, Gores RJ. Malignant lymphoma of the mandible and maxillary region. Oral Surg Oral Med Oral Pathol 1959;12:128.
156. Keyes GC, Balaban FS, Lattanzi DA. Periradicular lymphoma: differentiation from inflammation. Oral Surg 1988;66:230–235.
157. Cohen MA, Bender S, Struthers PJ. Hodgkin's disease of the jaws. Oral Surg Oral Med Oral Pathol 1984;57:413–417.
158. Miller CD, Goltry RR, Shenasky JH. Multiple myeloma involving the jaws and oral soft tissue. Oral Surg 1969;28:603–609.
159. Tabachnick TT, Levine B. Multiple myeloma involving the jaws and oral soft tissue. J Oral Surg 1976;34:931–933.
160. Tamir R, Pick AI, Calderon S. Plasmacytoma of the mandible: a primary presentation of multiple myeloma. J Oral Maxillofac Surg 1992;50:408–413.
161. Furutani M, Ohnishi M, Tanaka Y. Mandibular involvement in patients with multiple myeloma. J Oral Maxillofac Surg 1994;52:23–25.
162. Curtis AB. Childhood leukemias: osseous change in jaws on panoramic dental radiographs. J Am Dent Assoc 1971;88:844–847.
163. Michaud M, Baehner RL, Bixler D, et al. Oral manifestations of acute leukemia in children. J Am Dent Assoc 1977;95:1145–1150.
164. Sela MN, Pisanti S. Early diagnosis and treatment of patients with leukemia: a dental problem. J Oral Med 1977;32:46–50.
165. Shafer WG, Hine MK, Levy BM. A Textbook of Oral Pathology, 4th ed. Philadelphia: WB Saunders, 1983;479–510.
166. Parker ME. Infection of the teeth and jaws. In: Farman AG, Nortje CJ, Wood RE, eds. Oral and Maxillofacial Diagnostic Imaging. St. Louis: Mosby Year Book, 1993;181–209.
167. Hudson JW. Osteomyelitis of the jaws: a 50-year perspective. J Oral Maxillofac Surg 1993;51:1294–1301.
168. Rohlin M. Diagnostic value of bone scintigraphy in osteomyelitis of the mandible. Oral Surg Oral Med Oral Pathol 1993;75:650–657.
169. Kaneda T, Minami M, Ozawa K, et al. Magnetic resonance imaging of osteomyelitis in the mandible: comparative study with other radiological modalities. Oral Surg Oral Med Oral Pathol 1995;79:634–640.

Copyright © 2003, Mosby, Inc. All rights reserved.

170. Unger E, Moldofsky P, Gatenby R, Hartz W, Broder G. Diagnosis of osteomyelitis by MR imaging. AJR 1988;150:605–610.
171. Kaneda T, Minami M, Ozawa K, et al. Magnetic resonance appearance of bone marrow in the mandible at different ages. Oral Surg Oral Med Oral Pathol 1996;82:229–233.
172. Morrison WB, Schweitzer ME, Block GW, et al. Diagnosis of osteomyelitis: utility of fat-suppressed contrast-enhanced MR imaging. Radiology 1993;189:251–257.
173. Wood RE, Nortje CH, Grotepass F, et al. Periostitis ossificans versus Garre's osteomyelitis. 1. What did Garre's really say? Oral Surg 1988;65:773–777.
174. Nortje CH, Wood RE, Grotepass F, et al. Periostitis ossificans versus Garre's osteomyelitis. 2. Radiologic analysis of 93 cases in the jaws. Oral Surg 1988;66:249–260.
175. Sephariadou-Mavropoulo T, Yannoulopolous A. Tuberculosis of the jaws. Oral Maxillofac Surg 1986;44:158–162.
176. Wood RE, Housego T, Nortje CJ, Padayachee A. Tuberculous osteomyelitis in the mandible of a child. Pediatr Dent 1987;9: 317–320.
177. Van Merkesteyn JPR, Groot RH, Bras J, McCarrol RS, Bakker DJ. Diffuse sclerosing osteomyelitis of the mandible: a new concept of its etiology. Oral Surg Oral Med Oral Pathol 1990;70:414–419.
178. Jacobsson S. Diffuse sclerosing osteomyelitis of the mandible. Int J Oral Surg 1984;13:363–385.
179. Marx RE, Carlson ER, Smith BR, Toraya N. Isolation of *Actinomyces* species and *Eikenella corrodens* from patients with chronic diffuse sclerosing osteomyelitis. J Oral Maxillofac Surg 1994;52:26–33.
180. Marx RE. Osteoradionecrosis: a new concept in its pathology. J Oral Surg 1983;1:283–288.
181. Marx RE, Johson RD. Studies in the radiobiology of osteoradionecrosis and their clinical significance. Oral Surg Oral Med Oral Pathol 1987;64:379–390.
182. MacClatchey KD. Odontogenic lesions: tumors and cysts. In Batsakis JG, ed. Tumors of the Head and Neck: Clinical and Pathological Considerations, 2nd ed. Baltimore: Williams & Wilkins, 1979; 210–238.
183. Eversole LR, Rovin S. Differential radiographic diagnosis of lesions of the jaw bones. Radiology 1972;105:277–284.
184. Hertzanu Y, Mendelsohn DB, Cohn M. Computed tomography of mandibular ameloblastoma. J Comput Assist Tomogr 1984;8: 220–223.
185. Wood NK, Goaz PW. Differential Diagnosis of Oral and Maxillofacial Lesions, 5th ed. St. Louis: Mosby Year Book, 1997;238–518.
186. Belkin BA, Papageorage MB, Fakitsas J, Bankoff MS. A comparative study of magnetic resonance imaging versus computed tomography for the evaluation of maxillary and mandibular tumors. J Oral Maxillofac Surg 1988;46:1039–1047.
187. Cohn MA, Mendelsohn DB. CT and MR imaging of myxofibroma of the jaws. J Comput Assist Tomogr 1990;14:281–285.
188. Minami M, Kaneda T, Yamamoto H, et al. Ameloblastoma in the maxillomandibular region: MR imaging. Radiology 1992;184: 389–393.
189. Kaneda T, Minami M, Ozawa K, et al. Magnetic resonance imaging of osteomyelitis in the mandible: comparative study with other radiological modalities. Oral Surg Oral Med Oral Pathol 1995;79: 634–640.
190. Minami M, Kaneda T, Ozawa K, et al. Cystic lesions of the maxillomandibular region: MR imaging distinction of odontogenic keratocysts and ameloblastomas from other cysts. AJR 1996;166: 943–949.
191. Langlaris RP. Radiology of the jaws. In: Delbalso AM, ed. Maxillofacial Imaging. Philadelphia: WB Saunders, 1990;313–373.
192. Reeder MM, Bradley WG Jr. Gamuts in Radiology, 3rd ed. New York: Springer-Verlag, 1993;104–110.
193. Kaneda T, Minami M, Curtin HD, et al. Maxillomandibular lesions: assessment of gadolinium-enhanced MR images. Radiology 1998; 209(P):613–614.
194. Kaneda T, Minami M, Curtin HD, et al. Dental bur fragments causing metal artifacts on MR images. AJNR 1998;19:317–319.
195. Grahnen H, Lindahl B. Supernumerary teeth in the permanent dentition: a frequency study. Odont Rev 1961;12:290.
196. Grimanis GA, Kyriakides AT, Spyropoulos ND. A survey on supernumerary molars. Quintess Int 1991;22:989.
197. Yusolf WZ. Non-syndrome multiple supernumerary teeth: literature review. J Can Dent Assoc 1990;56:147.
198. Al Emran S. Prevalence of hypodontia and developmental malformation of permanent teeth in Saudi Arabian school children. Br J Orthod 1990;17:115.
199. Thorburn DN, Ferguson MM. Familial ogee roots, mobility, oligodontia and microdontia. Oral Surg Oral Med Oral Pathol 1992;74:576–581.
200. O'Dowling IB, McNamara TG. Congenital absence of permanent teeth among Irish school-children. J Ir Dent Assoc 1990;36: 136–138.
201. Garn SM, Lewis AB, Kerewsky BS. The magnitude and implications of the relationship between tooth size and body size. Arch Oral Biol 1968;13:129.
202. Soames JV, Kuyebi TA. A radicular dens invaginatus. Br Dent J 1982;152:308.
203. Yip WW. The prevalence of dens invaginatus. Oral Surg 1974;38:80.
204. Pope FM et al. Ehlers-Danlos syndrome type 1 with novel dental features. J Oral Pathol Med 1992;21:418–421.
205. Moskow BS, Canut PM. Studies on root enamel. II. Enamel pearls: a review of their morphology, localization, nomenclature, occurrence, classification. J Clin Periodontol 1990;17:275–281.
206. Witkop CJ Jr, Saulk JJ. Heritable defects of enamel. In: Stewart RE, Prescott GA, eds. Oral Facial Genetics. St. Louis: CV Mosby, 1976;151–226.
207. Crawford PJ, Aldred MJ. X-linked amelogenesis imperfecta: presentation of two kindreds and a review of the literature. Oral Surg 1992;73:449.
208. Via WF Jr. Enamel defects induced by trauma during tooth formation. Oral Surg 1968;25:49.
209. Witkop CJ Jr. Amelogenesis imperfecta, dentinogenesis imperfecta and dentin dysplasia revisited: problems in classification. J Oral Pathol 1988;17:547.
210. Schwartz S, Tsipouras P. Oral findings in osteogenesis imperfecta. Oral Surg 1984;57:161.
211. Ciola B, Bahn SL, Goviea GL. Radiographic manifestations of an unusual combination of type 1 and type 2 dentin dysplasia. Oral Surg Oral Med Oral Pathol 1978;45:317–322.
212. Wood RE, Lee P. Analysis of the oral manifestations of systemic sclerosis (scleroderma). Oral Surg Oral Med Oral Pathol 1988;65(2): 172–178.
213. White SC, Frey NW, Blaschke DD, et al. Oral radiographic changes in patients with progressive systemic sclerosis (scleroderma). J Am Dent Assoc 1977;94(6):1178–1182.
214. Alexandridis C, White SC. Periodontal ligament changes in patients with progressive systemic sclerosis. Oral Surg Oral Med Oral Pathol 1984;58(1):113–118.

Copyright © 2003, Mosby, Inc. All rights reserved.

18

Temporomandibular Joint

P.L. Westesson, Mika Yamamoto, Tsukasa Sano, and Tomohiro Okano

ANATOMY OF THE TMJ
FUNCTION OF THE TMJ
INTERNAL DERANGEMENT RELATED TO DISPLACEMENT OF THE DISK
- Disk Displacement with Reduction
- Disk Displacement without Reduction
- Disk Deformity
- Late-Stage Changes Following Disk Displacement
- Clinical Aspects of Internal Derangement

IMAGING
- Transcranial and Transmaxillary Projections
- Tomography
- Arthrography
  - Development of TMJ Arthrography
  - Single- and Double-Contrast Arthrography
  - Indications and Contraindications
  - Radiologic Equipment and Procedure
  - Technique for Single-Contrast Arthrography
  - Technique for Double-Contrast Arthrography
  - Arthrographic Findings of the Normal TMJ
  - Abnormal Findings
  - Complications Following Arthrography
- Computed Tomography
  - Technique for CT Scanning
  - CT Findings
- Magnetic Resonance Imaging
  - Magnetic Field Strength and Comparison with CT
  - Surface Coil and Scanning Technique
  - MR Imaging Findings of the Normal TMJ
  - Disk Displacement
  - Disk Deformity
- Other Findings and Conditions Related to Internal Derangement
  - Joint Effusion
  - Osteoarthritis
  - Marrow Abnormalities of the Mandibular Condyle
  - Osteochondritis Dissecans
  - Stuck Disk
  - Lock
- Accuracy of TMJ Imaging
- Imaging After Treatment
- Treatment Modalities for TMJ Internal Derangement
- Imaging Techniques after Surgical Treatment
- Alloplastic Implants
- Total Joint Replacement
- Costochondral Grafts
- Metallic Artifacts

MISCELLANEOUS CONDITIONS INVOLVING THE TMJ
- Tumors and Tumor-Like Conditions of the TMJ
  - Synovial Chondromatosis
  - Pigmented Villonodular Synovitis
  - Osteochondroma
  - Calcium Pyrophosphate Arthropathy (Pseudogout)
  - Synovial Cysts and Simple Bone Cysts
  - Rare Lesions and Tumors
  - Metastatic Disease in the TMJ Region
- Arthritides
- Acute Trauma
- Coronoid Hyperplasia
- Congenital Anomalies
  - Bifid Condyle
  - Hemifacial Microsomia
  - Asymmetry of the Mandible
- Atrophy of the Muscles of Mastication

MISCELLANEOUS IMAGING
- Radionuclide Imaging
- Thin-Section MR Imaging
- Dynamic MR Imaging
- MR Spectroscopy

Copyright © 2003, Mosby, Inc. All rights reserved.

The purpose of an imaging assessment of the temporomandibular joint (TMJ) is to graphically depict clinically suspected disorders of the joint. For many years, plain film radiography done mainly in a transcranial projection was the most commonly used method of making this assessment. This modality has major limitations because it is sensitive only to changes in the osseous components and depicts just the lateral aspect of the joint. With the evolution of newer imaging modalities such as arthrography, computed tomography (CT), and, most importantly, magnetic resonance (MR) imaging, the soft tissues of the joint could be appreciated. This allowed a better understanding of the anatomy and pathophysiology of internal derangements related to disk displacement.[1]

This chapter begins with descriptions of the anatomy and function of the TMJ and then provides an overview of the various imaging modalities available for evaluating the TMJ. Because most TMJ imaging is directed toward assessment of internal derangements or related degenerative joint changes, the sections addressing imaging methods emphasize the key findings in these important disorders. A variety of miscellaneous diseases that affect the TMJ are then covered, and an algorithm for imaging patients with TMJ problems is given.

ANATOMY OF THE TMJ

Interpreting TMJ imaging studies requires an understanding of the pathophysiology of the joint and a knowledge of both normal and pathologic anatomy of the joint and surrounding structures. Therefore, a description of joint anatomy, joint pathology, function, and dysfunction is presented in some detail.

The mandible and the temporal bone comprise the osseous components of the TMJ. The head of the mandibular condyle comprises the inferior component of the joint, and the temporal bone contributes the glenoid fossa and articular tubercle, forming the superior osseous (or skull base) part of the joint (Fig. 18-1). Unlike most other joints of the body, which have cartilaginous coverings, the articulating surfaces

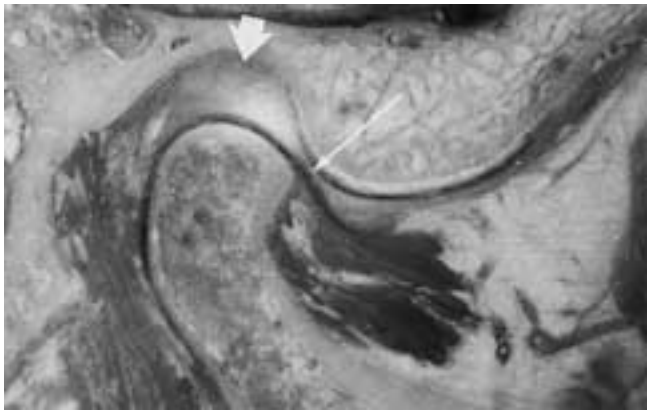

VIEW IMAGE

FIGURE 18-1 Normal TMJ in sagittal section. Biconcave disk in the normal superior position. The posterior band of the disk (*thick arrow*) is lying over the condyle. The central thin zone of the disk (*thin arrow*) is between the anterior prominence of the condyle and the articular eminence.

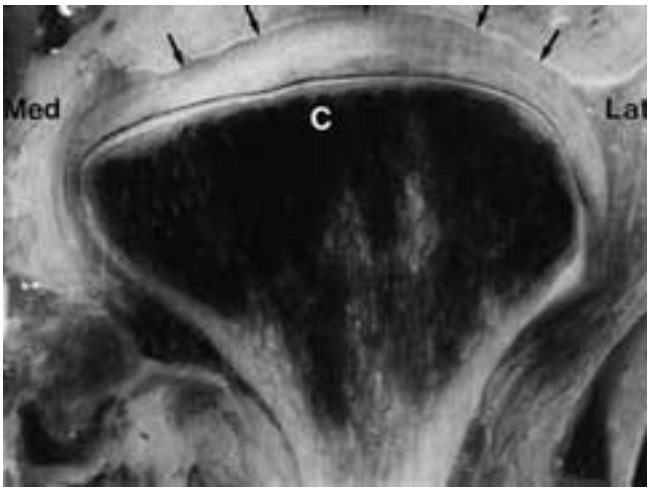

FIGURE 18-2 Normal TMJ in coronal section. The disk (*arrows*) is crescent-shaped and located over the condyle. Medially and laterally, the disk is attached to the condyle and capsule. The condyle (*C*) is indicated.

VIEW IMAGE

of the TMJ are covered by a thin layer of dense fibrous tissue.

The TMJ disk is a biconcave fibrous structure located between the mandibular condyle and the temporal component of the joint. The disk is round to oval, with a thick periphery and a thin central part. The mediolateral dimension of the disk is approximately 20 mm. In a sagittal section the normal disk appears biconcave, with the anterior and posterior thicker parts of the disk, respectively, referred to as the anterior and posterior bands.[2] In the normal joint the posterior band is located over the condyle, and the central thin zone is located between the condyle and the posterior part of the articular tubercle (Fig. 18-1). The anterior band is located under the articular tubercle. In the coronal plane, a section through the disk is crescent-shaped (Fig. 18-2). A joint capsule surrounds the joint, emerging from the temporal bone and extending like a funnel inferiorly to attach to the neck of the condyle. The medial and lateral edges of the disk attach to the capsule and then to the mandible at the inferior edge of the medial and lateral poles of the condyle (Fig. 18-2). Posteriorly, the disk is attached to the temporal bone and to the condyle by the posterior disk attachment. This attachment is extremely important in internal derangements of the TMJ. This region has also been referred to as the bilaminar zone or the retrodiskal tissue. The structure consists of loose fibrous connective and elastic tissue components. The posterior disk attachment has traditionally been called the bilaminar zone because initial histologic studies indicated that the upper part was elastic tissue and the lower part consisted of more connective tissue. However, more recent histologic studies have failed to confirm the bilaminar nature of the posterior disk attachment. Despite this, the term *bilaminar zone* continues to be used in both clinical and scientific work. The bilaminar zone also contains many small blood vessels. Anteriorly, the disk is attached to the joint capsule, and in the anteromedial portion of the joint the disk also merges with the upper head of the lateral pterygoid muscle.

There are two joint spaces, or compartments. The superior space separates the glenoid and articular eminence

Copyright © 2003, Mosby, Inc. All rights reserved.

of the temporal bone from the disk and its attachments. The inferior joint space separates the disk and its attachments from the condyle of the mandible. The anterior recess is a small space in the inferior joint compartment anterior to the condyle. The posterior recess is the part of the inferior joint space posterior to the condyle. The lower part of the bilaminar zone (posterior disk attachment) curves downward to attach to the condylar neck and thus forms the posterior boundary of the posterior recess of the inferior joint compartment.

FUNCTION OF THE TMJ

The function of the TMJ is complex because the upper and lower joint compartments principally act as two small joints within this same joint capsule. This allows for proportionally greater movement of the TMJ in relation to the actual size of the joint. The principal function of the disk is to permit relatively large movements within a small joint while maintaining stability. Rotation and translation occur in both the upper and lower joint spaces. However, translation occurs predominantly in the upper space, and rotation is more evident in the lower joint space. In the initial phase of jaw opening, the condyle rotates in the lower joint compartment. After this initial rotation, translation occurs in the upper and subsequently in the lower joint space. During translation, the condyle and the disk translate (slide) together under the articular tubercle. During all mandibular movements, the central thin part of the disk is located between the condyle and the articular tubercle. This suggests that the thick periphery of the disk and the thick posterior and anterior bands act as functional guides for the joint. This normal joint function can be identified in anatomic specimens of the TMJ (Fig. 18-3).

INTERNAL DERANGEMENT RELATED TO DISPLACEMENT OF THE DISK

Internal derangement is a general orthopedic term implying a mechanical fault that interferes with the smooth action of a joint.[3] Internal derangement is thus a functional diagnosis, and for the TMJ the most common internal derangement is displacement of the disk.[4–9] Most often the disk displaces in an anterior, anterolateral, or anteromedial direction. Thus the posterior band of the disk prolapses anteriorly, relative to the superior surface of the condyle (Figs. 18-4 and 18-5), instead of remaining in position between the condyle and glenoid fossa. As a consequence, the condyle is positioned under the posterior disk attachment rather than under the disk, and the condyle closes on the posterior attachment (bilaminar zone or retrodiskal tissues) rather than on the disk itself. The central thin part of the disk lies inferior to the articular tubercle.

Studies have shown that the disk frequently is also displaced in a medial (Fig. 18-6) or lateral direction.[10–13] Posterior disk displacement (Fig. 18-7) does occur, but it is rare. When present, it is frequently seen in combination with

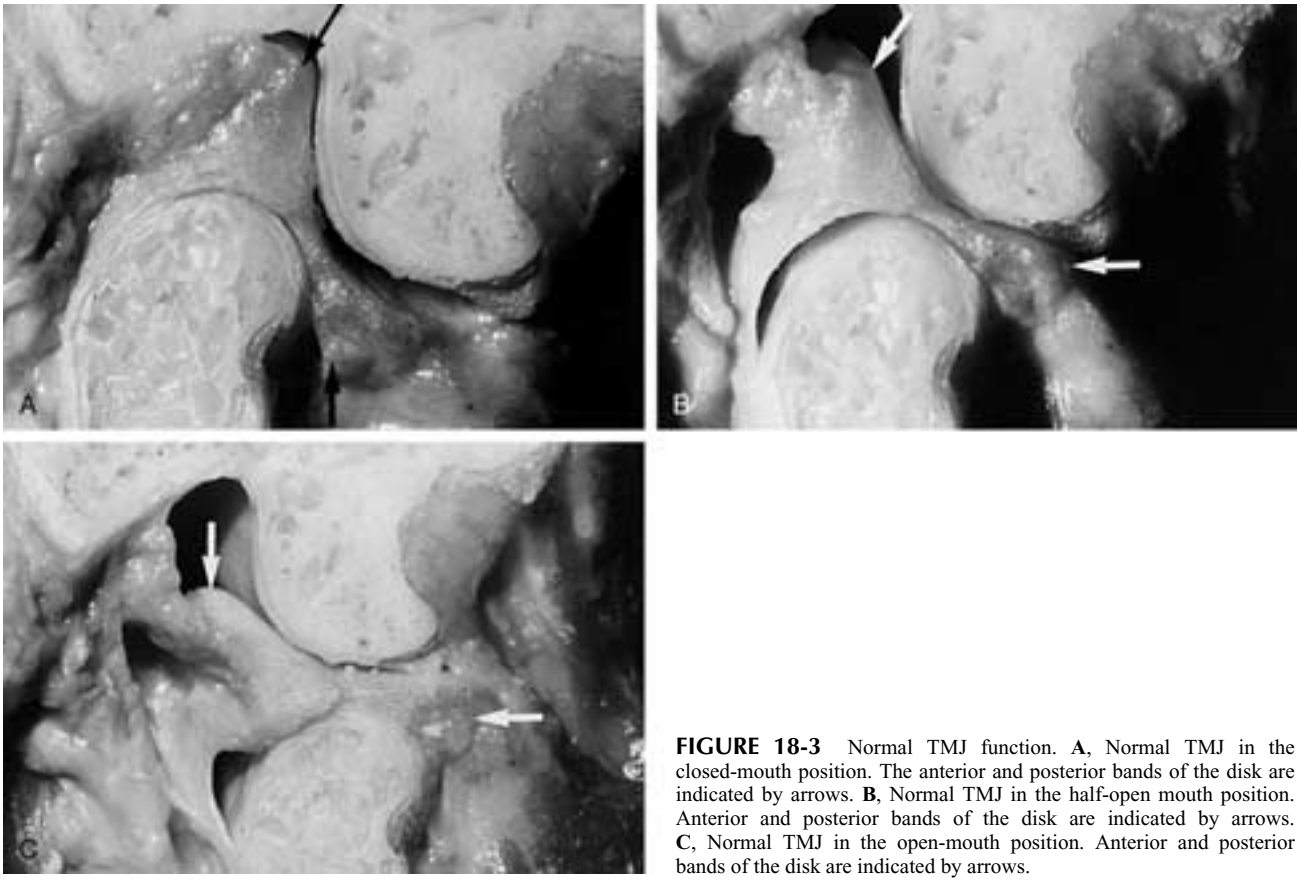

FIGURE 18-3 Normal TMJ function. **A**, Normal TMJ in the closed-mouth position. The anterior and posterior bands of the disk are indicated by arrows. **B**, Normal TMJ in the half-open mouth position. Anterior and posterior bands of the disk are indicated by arrows. **C**, Normal TMJ in the open-mouth position. Anterior and posterior bands of the disk are indicated by arrows.

VIEW IMAGE

Copyright © 2003, Mosby, Inc. All rights reserved.

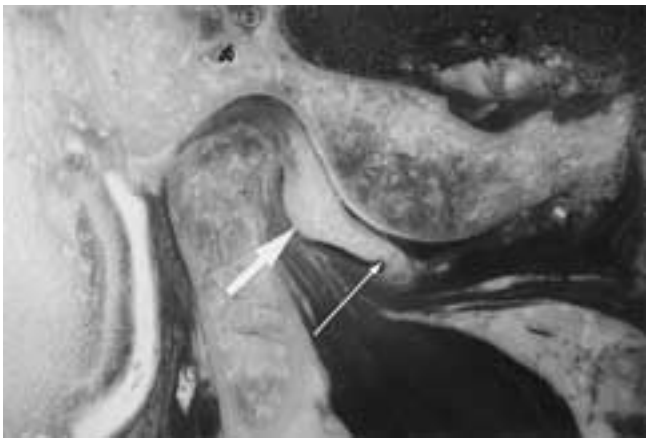

VIEW IMAGE

FIGURE 18-4 Anterior disk displacement. The disk is anteriorly displaced, with its posterior band (*thick arrow*) located forward of the condyle. Note that the central thin zone of the disk (*thin arrow*) is separated from the anterior prominence of the condyle.

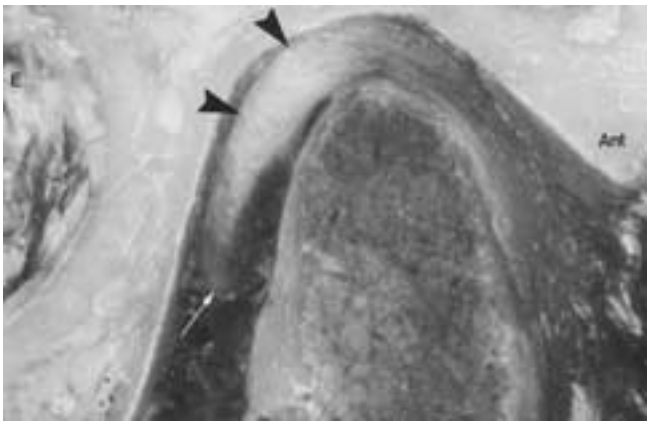

VIEW IMAGE

FIGURE 18-7 Posterior disk displacement. The disk (*arrowheads*) is posterior to the condyle. The external auditory canal (*E*) and anterior (*Ant*) are indicated for orientation. Inferiorly and posteriorly there is folding of the disk (*thin arrow*) similar to what is seen with anterior disk displacement.

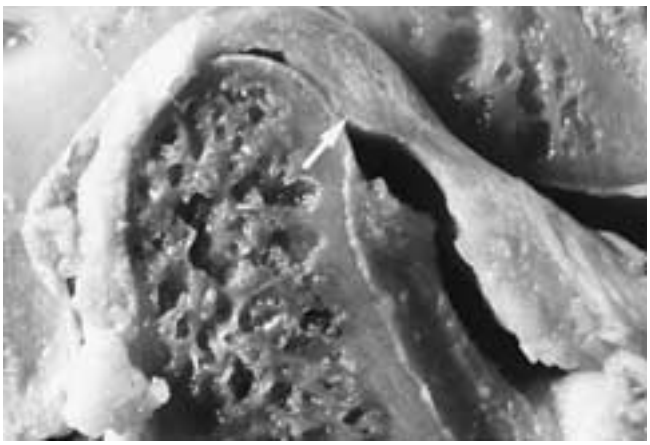

VIEW IMAGE

FIGURE 18-5 Anterior disk displacement. The disk is anteriorly displaced, with its posterior band (*arrow*) located slightly forward of the condyle.

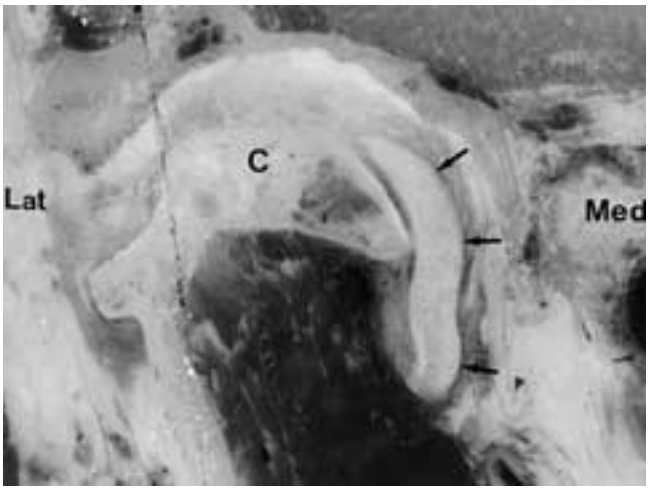

VIEW IMAGE

FIGURE 18-6 Coronal section of TMJ showing medial disk displacement. The disk is indicated by arrows. The condyle (*C*) is sclerotic.

medial disk displacement. A general classification of the different types of disk displacement of the TMJ is shown in Box 18-1. Pure lateral and pure medial sideways displacements of the disk also occur, but not as commonly as in combination with anterior displacement.[11–13] The combination of anterior and lateral or medial displacement is called rotational displacement, whereas pure lateral or pure medial displacement is called sideways displacement.[11]

The functional aspects of disk displacement include displacement with or without reduction. The functional categories of internal derangement are illustrated in Figure 18-8. In disk displacement with reduction (Fig. 18-8B) the disk is anteriorly displaced in the closed-mouth position but reverts to a normal superior position during opening. In disk displacement without reduction (Fig. 18-8C) the disk lies anterior to the condyle during all mandibular movements, and the normal condyle–disk relationship is not reestablished.

Disk Displacement with Reduction

When a displaced disk reduces to a normal position, a click is usually heard. When the jaw closes, the disk again

BOX 18-1

TERMINOLOGY FOR DESCRIBING THE POSTION OF THE DISK

Normal	Superior
Abnormal	Anterior, partial or complete
	Anteromedial rotation
	Anterolateral rotation
	Medial sideways
	Lateral sideways
	Posterior

Copyright © 2003, Mosby, Inc. All rights reserved.

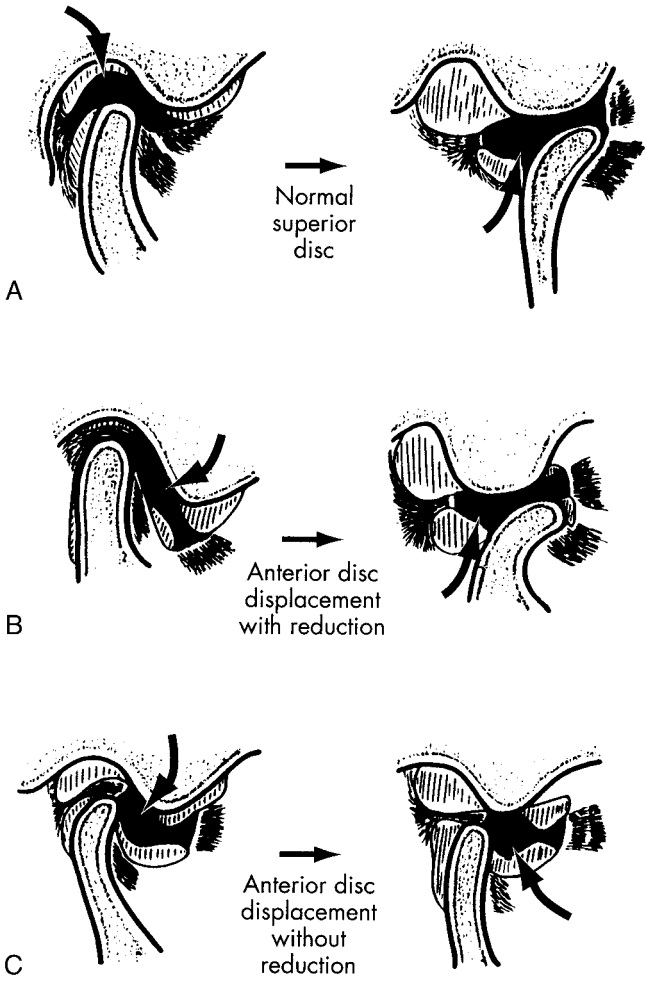

VIEW IMAGE

FIGURE 18-8 Schematic drawing of a normal TMJ and different categories of internal derangement. The disk is black and is indicated by the curved arrows. **A**, Normal. **B**, Anterior displacement with reduction. **C**, Anterior displacement without reduction.

displaces anteriorly, usually during the last phase of the closing movement of the jaw, and again a click is commonly heard. The closing click usually is less prominent than the opening click. The cyclic nature of disk displacement was described by Ireland in 1951.[14] The clicking sound has been shown to be caused by the impact of the condyle hitting the temporal bone component of the articulation after the condyle has passed under the posterior band of the disk.[15, 16]

Disk Displacement without Reduction

In disk displacement without reduction (Fig. 18-8C) the disk remains displaced relative to the condylar head, regardless of the jaw position. In the initial stages of this condition, jaw opening is typically limited and the jaw deviates to the side of the affected joint. However, this clinical characteristic is typical only during the initial (early) phase; with time, the opening capacity of the TMJ increases and the jaw no longer deviates to the affected side. This is the result of stretching or progressive elongation of the posterior disk attachment and, to a lesser extent, deformation of the disk itself. In the early stage, disk displacement without reduction is usually not associated with joint sounds.

Disk Deformity

The normal disk is biconcave when viewed in the sagittal plane (Fig. 18-3). In the early stages of internal derangement the disk remains normal in shape. However, the displaced disk begins to deform, as noted by thickening of the posterior band and shortening of the entire anteroposterior length of the disk (Fig. 18-9).[4, 9, 17–19] Additionally, both the central thin part and the anterior band decrease in size. The end result is a biconvex disk configuration and a stretched, elongated, and thinned posterior disk attachment. The gross changes of the disk are associated with histologic alterations within the disk that lead to metaplastic hyaline cartilage, hyalinization, and accumulation of foci of calcium deposits and abnormal collagen patterns.[20, 21] Changes also occur in the posterior disk attachment itself, leading to fibrosis and narrowing of vessels.[22, 23] Histologic studies of the posterior disk attachment in joints with disk displacement have shown narrowing of the arterial lumen, increased density of fibroblasts, and hyalinization of loose connective tissue.[24]

Late-Stage Changes Following Disk Displacement

In the late or chronic stages of disk displacement without reduction, the disk is deformed and has a stretched, torn, or detached posterior attachment; communications between the upper and lower joint spaces (perforation) are often seen.[8, 9, 19, 25] Most commonly the perforations are found in the posterior disk attachment, at its junction with the disk itself (Fig. 18-10). Infrequently, perforations are found in the disk per se.[19] Thus, although traditionally this condition has been designated *perforation of the disk*, this is not anatomically correct, as the perforations are usually found in the posterior disk attachment rather than in the disk proper.

Osseous changes involving the condyle and temporal

FIGURE 18-9 Anterior displacement and deformation of the disk. The disk (*arrow*) is biconvex. The condyle (*C*) articulates with the posterior disk attachment.

VIEW IMAGE

Copyright © 2003, Mosby, Inc. All rights reserved.

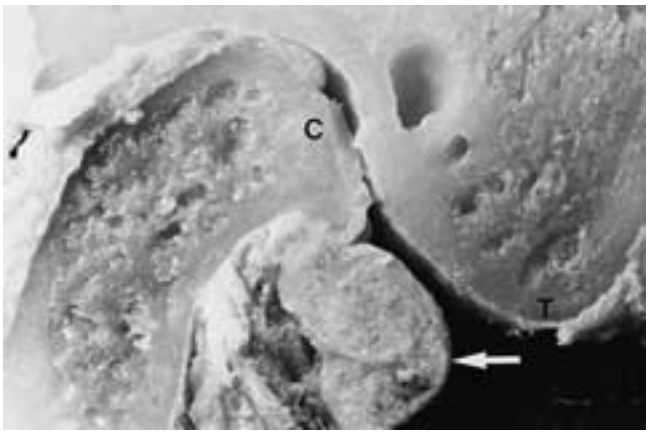

VIEW IMAGE

FIGURE 18-10 Anterior displacement and extensive deformation of the disk (*arrow*), with perforation of the posterior disk attachment. The condyle (*C*) is flattened, with an anterior osteophyte and surface irregularities.

bone often occur as sequelae of disk displacement.[7-9, 18, 26] Osseous changes consist of flattening and osteophytosis of the mandibular condyle and flattening of the temporal component of the articulation. These changes are more commonly observed in the lateral part of the joint and can be detected on plain film imaging. It should be noted that osseous changes are relatively late findings in the disease process, and it is often difficult to differentiate radiographically between advanced remodeling and degenerative joint disease.

Clinical Aspects of Internal Derangement

The preceding classification of disk position and function is based only on anatomic and functional aspects. In the clinical setting the patient's history, signs, and symptoms must be incorporated into the staging of the disease. Patients may complain of pain or of clicks when opening and closing the mouth. Physical examination may show tenderness on palpation of the joint or associated muscles. Palpable clicks or crepitus on movement of the jaw may be clinically evident, and abnormalities of occlusion or deviation of the jaw on opening may also suggest TMJ abnormality.

However, the clinical assessment of the TMJ has definite limitations. Multiple studies have shown that the accuracy of the physical examination in predicting the status of the joint is about 70%.[27–33] The intensity and location of pain in a study of more than 200 patients did not distinguish patients with internal derangement from those without internal derangement, and there was no consistent relationship between occlusion and the status of the joint. These studies indicate that physical examination alone is not reliable in determining the status of the joint.[28–34]

The situation is further complicated by the fact that clinical signs of TMJ internal derangement are relatively common in the general population. An epidemiologic study of more than 400 individuals ranging in age from 28 to 73 years showed clinical evidence of internal derangement in 39%. Most of these individuals had functional symptoms with clicking or limitation of opening, but the majority did not have any pain associated with the dysfunction. Studies of asymptomatic volunteers using both arthrography and MR imaging have shown disk displacement in approximately 20% to 25% of this population.[35–37] The finding of anatomic abnormalities in the joints of asymptomatic individuals is not unique to the TMJ. Similar observations have been shown in MR studies of the knee, cervical spine, and lumbar spine.[38–42]

The prevalence of disk displacement in symptomatic individuals is much higher than in a normal population.[43] In view of the high incidence of displacement in asymptomatic patients, the precise relationship of symptoms to the displacement is difficult to define. Disk displacement has been found in approximately 80% of patients with symptoms of TMD referred for MR imaging.[44] Several forms of disk displacement have been demonstrated in up to one third of asymptomatic volunteers.[44–46] One study analyzing the type of disk displacement in patients and asymptomatic volunteers showed that most of the volunteers have early stage disk displacement, and more severe displacements are seen in symptomatic patients.[47] However, complete disk dislocations are found incidentally in patients without complaints referable to the TMJ. Perhaps further investigation of these apparently asymptomatic patients could determine some degree of joint dysfunction, but clearly more work is necessary before the precise relationship between disk position and pain can be confidently defined.

Among patients presenting with TMJ symptoms, there is a significant prevalence of young females, and in the clinical population the female/male ratio has been between 5∶1 and 10∶1. The reason for the female dominance among TMJ patients is not fully understood. Cadaver studies have found that approximately 50% of elderly individuals have an internal derangement, with no significant difference between the sexes.[48]

Because of the difficulty in the clinical evaluation of a potential disk displacement, imaging must be done to define the anatomy of the joint and to determine the relationship of the disk to the condyle. The purpose of an imaging study is to identify and characterize the anatomy in a patient who presents with symptoms. Because of the overlap of morphologic abnormalities in symptomatic and asymptomatic individuals, imaging findings should always be interpreted in light of clinical findings. Similarly, the choice of imaging studies must depend on the clinical evaluation, and an algorithm for TMJ imaging can be made based upon prior clinical and imaging experience.

An appropriate patient evaluation integrates the imaging and clinical findings. A workable classification of TMJ disorders, related to internal derangement, is also necessary for communication among clinicians and radiologists. The classification developed by Wilkes[9] encompasses clinical, radiographic, and morphologic observations and categorizes internal derangement into early, intermediate, and late stages. This classification is presented in Box 18-2.

IMAGING

Transcranial and Transmaxillary Projections

The most common and most well-established plain film technique for examination of the TMJ is the transcranial

Copyright © 2003, Mosby, Inc. All rights reserved.

BOX 18-2

CLASSIFICATION OF INTERNAL DERANGEMENT

Early Stage	
Clinical	No significant mechanical symptoms other than reciprocal clicking (early in opening movement, late in closing movement, and soft in intensity); no pain or limitation in opening motion
Radiologic	Slight forward displacement; good anatomic contour of disk; normal tomograms
Surgical	Normal anatomic form; slight anterior displacement; passive incoordination (clicking) demonstrable
Early-Intermediate Stage	
Clinical	First few episodes of pain; occasional joint tenderness and related temporal headaches; beginning of major mechanical problems; increase in intensity of clicking sounds; joint sounds later in opening movement; and beginning transient subluxations or joint catching and locking
Radiologic	Slight forward displacement; slight thickening of posterior edge or beginning of anatomic deformity of disk; normal tomograms
Surgical	Anterior displacement; early anatomic deformity (slight to mild thickening of posterior edge); well-defined central articulating area
Intermediate Stage	
Clinical	Multiple episodes of pain, joint tenderness, temporal headaches, major mechanical symptoms: transient catching, locking, and sustained locking (closed locks); restriction of motion; difficulty (pain) with function
Radiologic	Anterior displacement with significant anatomic deformity or prolapse of disk (moderate to marked thickening of posterior edge); normal tomograms
Surgical	Marked anatomic deformity with displacement; variable adhesions (anterior, lateral, and posterior recesses); no hard-tissue changes
Intermediate-Late Stage	
Clinical	Characterized by chronicity with variable and episodic pain, headaches, variable restriction of motion; undulating course
Radiologic	Increase in severity over intermediate stage; abnormal tomograms; early to moderate degenerative remodeling; hard-tissue changes
Surgical	Increase in severity over intermediate stage; hard-tissue degenerative remodeling changes of both bearing surfaces; osteophytic projections; multiple adhesions (lateral, anterior, and posterior recesses); no perforation of disk or attachment
Late Stage	
Clinical	Characterized by crepitus on examination; scraping, grating, grinding; variable and episodic pain; chronic restriction of motion; and difficulty with function
Radiologic	Anterior displacement; perforation with simultaneous filling of upper and lower compartments; filling defects; gross anatomic deformity of disk and hard tissues; abnormal tomograms; essentially degenerative arthritic changes
Surgical	Gross degenerative changes of disk and hard tissues; perforation of posterior attachments; erosions of bearing surfaces; multiple adhesions equivalent to degenerative arthritis (sclerosis, flattening, and anvil-shaped condyle, osteophytic projections, and subcortical cystic formation).

From Wilkes CH. Internal derangement of the TMJ. Pathologic variations. Arch Otolaryngol Head Neck Surg 1989;115:469-477.

projection (Fig. 18-11). The lateral aspect of the joint is well visualized, but the central and medial parts of the joint are not clearly seen because the x-ray beam is not tangent to these articular surfaces. This disadvantage is partly compensated for by the fact that most of the early osseous changes occur laterally in the joint.[49]

It has been recommended that, in addition to the transcranial projection, an anteroposterior projection should be used to depict the central and medial parts of the condyle. A transmaxillary projection (Fig. 18-12) or a transorbital projection also is suggested.[50]

Tomography

Complex motion tomography has been recommended for detection of early osseous changes (Fig. 18-13). Studies have demonstrated that a clearer depiction of the osseous anatomy can be gained from tomography than can be gained from transcranial radiography.[51] Tomography may also be performed in the coronal plane, providing information about the medial and lateral poles of the condyle, which are usually not adequately depicted on the sagittal tomograms. The disadvantage of tomography is the rather large radiation

Copyright © 2003, Mosby, Inc. All rights reserved.

dose delivered to the lens of the eye. To a large extent, tomography has been replaced by CT, which probably represents the most effective modality for demonstrating osseous abnormalities.

Arthrography

Development of TMJ Arthrography

Early attempts at TMJ arthrography were undertaken by Nørgaard in the 1940s.[52, 53] However, this procedure was not adopted by many clinicians. It was considered technically difficult and painful for the patient, and the information gathered was not considered of great value for treatment planning and evaluation of prognosis. Only a few descriptions of TMJ arthrography appeared in the literature over the ensuing 25 years.

Toward the end of the 1970s several articles appeared, describing the clinical and arthrographic characteristics of internal derangement related to displacement of the disk.[7, 8, 54–56] These arthrographic studies were actually the first to depict displacement of the disk, a pathologic entity that had been suspected earlier.[14, 57-61] During the following years, considerable enthusiasm developed for TMJ arthrography, and a large number of publications describing the usefulness of the technique appeared. The changed attitude toward TMJ arthrography can be traced to the following factors: (1) use of an image intensifier to facilitate joint puncture and to study and document joint dynamics, (2) identification of disk displacement as a common cause of TMJ pain and dysfunction, and, probably most important, (3) introduction of new, conservative surgical methods for treating disk displacement.[7, 8, 54, 55, 62–66] These newer treatment methods required accurate information about the status and function of the joint. The use of a nonionic contrast medium, which made the examination less painful, and the combination of arthrography and tomography, also influenced the increased use of arthrography.[6, 25]

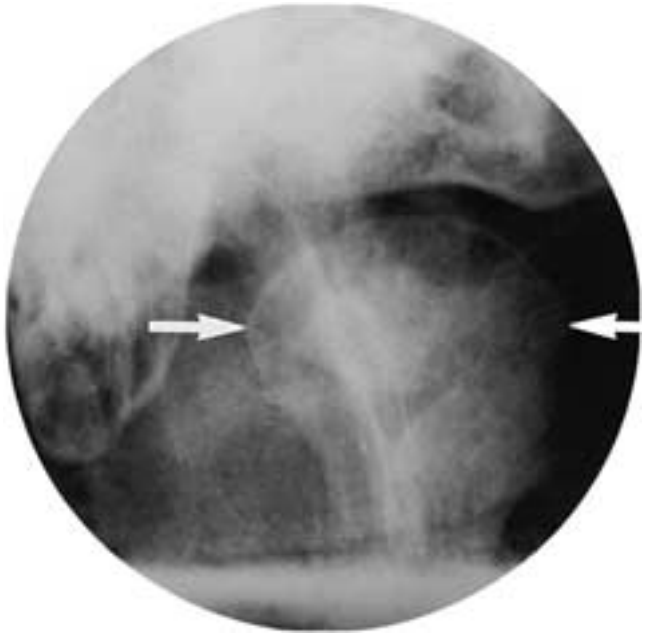

FIGURE 18-12 Transmaxillary radiograph of TMJ. The lateral and medial poles of the condyles are indicated by arrows.

VIEW IMAGE

Single- and Double-Contrast Arthrography

Injection of contrast medium into only the lower space (Fig. 18-14) is a simplification of the original arthrographic technique, in which contrast medium was injected into both upper and lower joint spaces.[5, 54, 55] This simplification

FIGURE 18-11 Transcranial radiograph of TMJ. The condyle (*C*), fossa (*F*), and tubercle (*T*) are indicated.

VIEW IMAGE

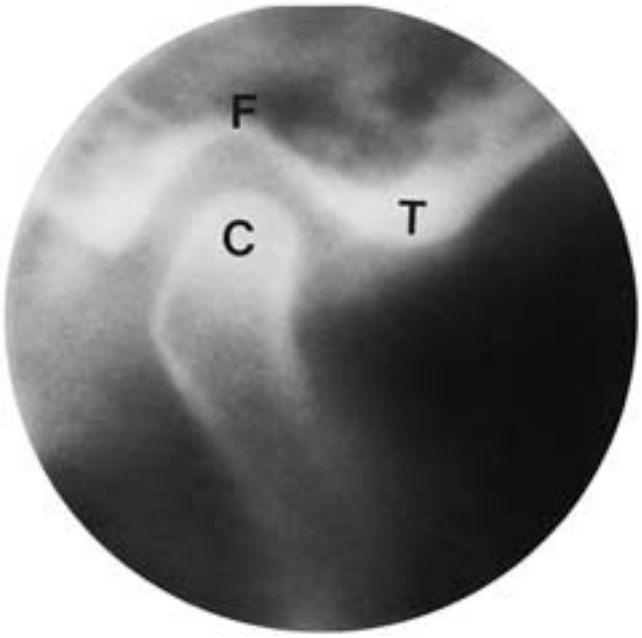

FIGURE 18-13 Sagittal tomogram of TMJ. The condyle (*C*), fossa (*F*), and tubercle (*T*) are indicated.

VIEW IMAGE

Copyright © 2003, Mosby, Inc. All rights reserved.

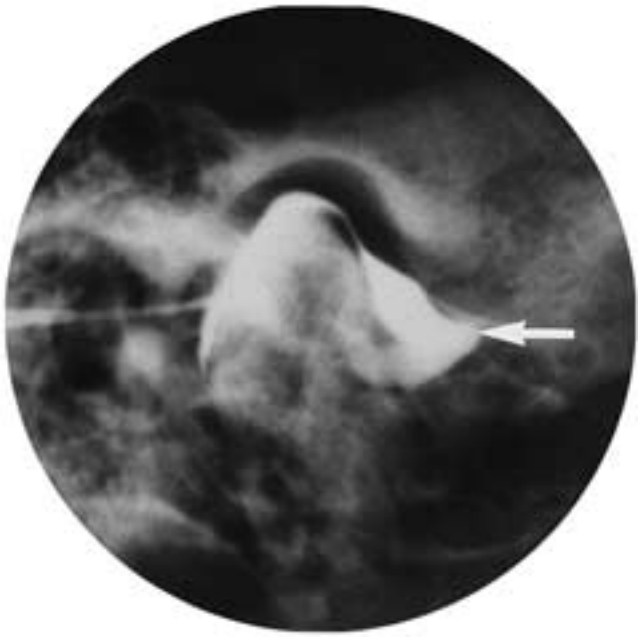

VIEW IMAGE

FIGURE 18-14 Lower compartment arthrogram of TMJ showing anterior disk displacement. The prominent anterior recess (*arrow*) of the lower joint space is a sign of disk displacement.

further popularized the use of arthrography; currently, single-contrast lower-compartment arthrography is the most commonly used arthrographic technique.[5, 54]

Double-contrast arthrography (Fig. 18-15) is a variant of arthrography in which injection of iodine contrast medium is combined with injection of air. [6, 17, 25, 56, 67, 68] The double-contrast study is superior to the single-contrast study in its demonstration of the configuration of the disk and the posterior disk attachment (Figs. 18-15 and 18-16). However, the double-contrast technique is technically more difficult to perform, because it requires cannulation of both the upper and lower joint spaces and the injection of both contrast medium and air.

Indications and Contraindications

MR imaging has almost completely replaced arthrography for establishing the position of the disk relative to the condyle, and many institutions have eliminated arthrography as a diagnostic procedure. Arthrography can still be done to assess the position and function of the disk in patients with pain and dysfunction suggesting internal derangement. Perforations of the disk or retrodiskal attachments can be identified as contrast injected into the inferior compartment passes freely into the superior compartment of the joint. Arthrography can be used in patients with TMJ disk displacement with reduction to determine the mandibular position that reestablishes a normal condyle–disk relationship.[54, 69] The purpose of this would be to establish the optimum position for initiating protrusive splint therapy (conservative therapy).[54, 69] Infrequently, arthrography is performed to delineate loose bodies within the joint spaces, for diagnostic aspiration of joint fluid, for intraarticular injection of cortisone, or for evaluation of the TMJ after trauma.

There are indications that arthrography occasionally relieves patients' symptoms.[70] Manipulation and lavage of the joint was shown to improve mobility and decrease pain in a small clinical study.[70] The mechanism is not fully understood, and the precise indications for therapeutic arthrography must await further studies.

An infrequent contraindication for TMJ arthrography is infection in the preauricular area, which could potentially result in contamination of the joint during the arthrographic procedure. In patients with previous reactions to contrast medium, other modalities such as MR imaging should be considered. However, arthrography has been performed on such patients without any premedication, and there was no untoward reaction. Bleeding disorders and anticoagulation medication also are relative contraindications to arthrography.

Radiologic Equipment and Procedure

A fluoroscopic table or a C-arm unit with an image intensifier is necessary equipment for this study. Because of the small size of the TMJ, it is also useful to be able to magnify the image to about three times its normal size. The capability for spot filming and videotape recording is valuable for documentation and the evaluation of joint dynamics. For double-contrast arthrography, tomography is also needed.

The examination is explained to the patient. The patient is placed on the tabletop in a laterally recumbent position, and the head is oriented so that the side to be injected faces up. The head is slightly tilted, and the transcranial projection is optimized with fluoroscopy. Opening and closing movements of the jaw, with attention to the condyle and fossa, are recorded on videotape before contrast medium is injected.

FIGURE 18-15 Dual space double-contrast arthrotomogram showing the disk (*arrow*) in a superior position. The mouth was half open, and the redundant posterior disk attachment (*arrowheads*) is seen between the disk and the posterior capsule. The upper and lower joint spaces are radiolucent due to the intraarticular injection of air.

VIEW IMAGE

Copyright © 2003, Mosby, Inc. All rights reserved.

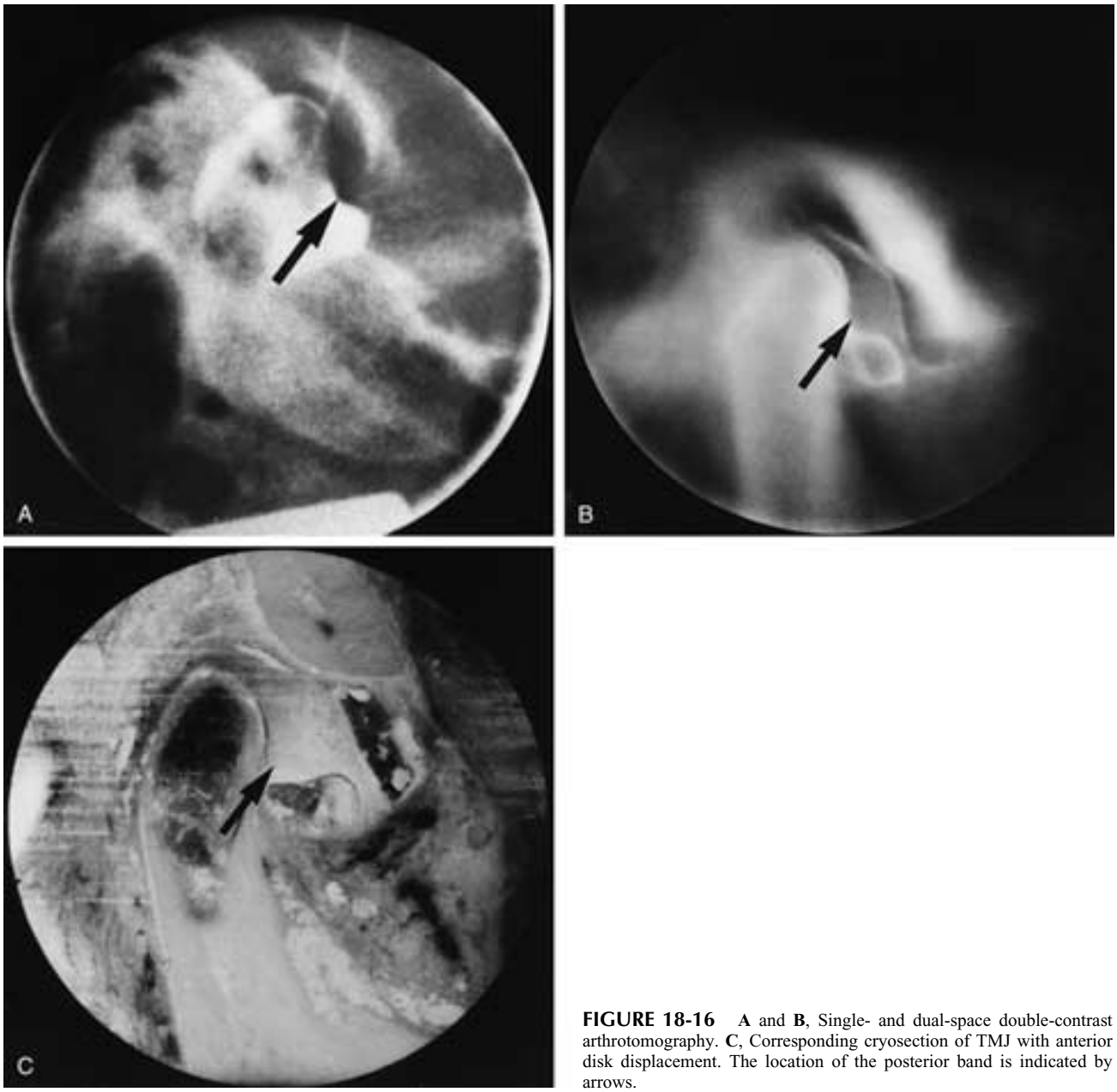

FIGURE 18-16 **A** and **B**, Single- and dual-space double-contrast arthrotomography. **C**, Corresponding cryosection of TMJ with anterior disk displacement. The location of the posterior band is indicated by arrows.

VIEW IMAGE

Technique for Single-Contrast Arthrography

The superoposterior aspect of the condyle is clinically and fluoroscopically identified and indicated on the skin by a metal marker.[71] The area is marked with a pen, and a local anesthetic (1% to 2% lidocaine) is injected. The joint is punctured with a 23-gauge, 3/4 to 1 inch scalp vein needle introduced perpendicular to the skin surface, and contrast medium (nonionic iodine, 300 mg/ml) is injected into the lower joint space (Fig. 18-17A). Contrast medium is injected until optimum visualization of the joint space has been achieved, as determined by fluoroscopic observation of the joint space. Usually between 0.2 and 0.4 ml of contrast medium is injected. The needle is then withdrawn from the joint space, but the tip of the needle is left in the soft tissue lateral to the joint. The patient is asked to open and close the mouth several times while the image is recorded on videotape. The free flow of contrast medium around the top of the condyle and into the anterior recess of the inferior space indicates a successful injection. Simultaneous filling of the upper joint space indicates a perforation of the disk or retrodiskal attachments. In joints with perforation, additional contrast medium usually needs to be injected for optimum image quality. Spot films are obtained in at least the closed- and open-mouth positions and at additional positions where abnormalities are clearly seen.

If the diagnosis is not clear from these images, it may be helpful to also inject contrast medium into the upper joint space (Fig. 18-17B). This can be done either by withdrawing the needle slightly and then directing it superiorly into the upper joint space (if the needle was left in place after the initial injection) or by reinserting it while the patient is holding the mouth half open. Injection of the upper joint

Copyright © 2003, Mosby, Inc. All rights reserved.

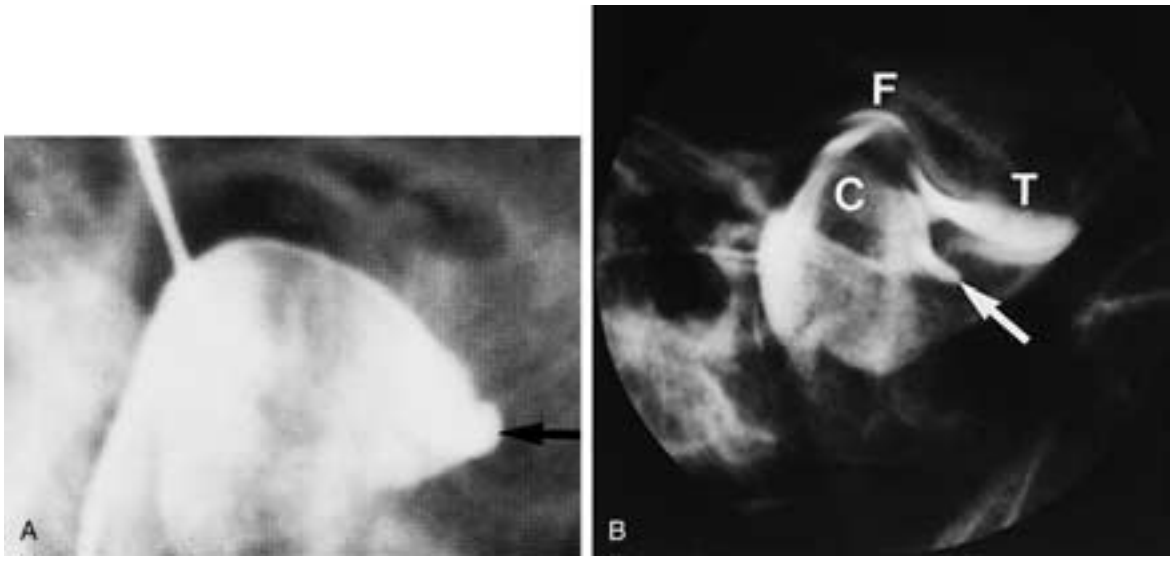

VIEW IMAGE

FIGURE 18-17 **A**, Single-contrast arthrogram of a normal TMJ with contrast injection into the lower joint compartment only. The small anterior recess of the lower joint compartment (*arrow*) suggests a normal superior disk position. **B**, Normal TMJ demonstrated by a single-contrast arthrogram with contrast injection into both the upper and lower joint spaces. The condyle (*C*), fossa (*F*), and tubercle (*T*) are indicated. The arrow indicates the anterior recess of the lower joint space.

space allows clearer delineation of the disk because both its inferior and superior surfaces are now coated by contrast medium.

Technique for Double-Contrast Arthrography

If double-contrast arthrography is to be performed, the joint spaces are punctured with catheters (Angiocath 0.8 mm in diameter and 25 mm in length) instead of needles.[17, 25] Contrast medium is injected via extension tubes and aspirated after the dynamic phase of the study. Room air is then injected via new extension tubes, and images are obtained on an upright tomographic unit such as the Phillips polytome. A complete description of the double-contrast technique is given elsewhere.[72]

Arthrographic Findings of the Normal TMJ

In a normal TMJ, the posterior band of the disk is located superior to the condyle in the so-called 12 o'clock position relative to the mandibular condyle (Fig. 18-18). The lower joint space has a relatively small anterior recess. However, studies of normal individuals without symptoms have shown great variation in the size of this recess despite the location of the disk in the superior position.[73] At maximum opening the disk is located inferior to the articular tubercle, and the

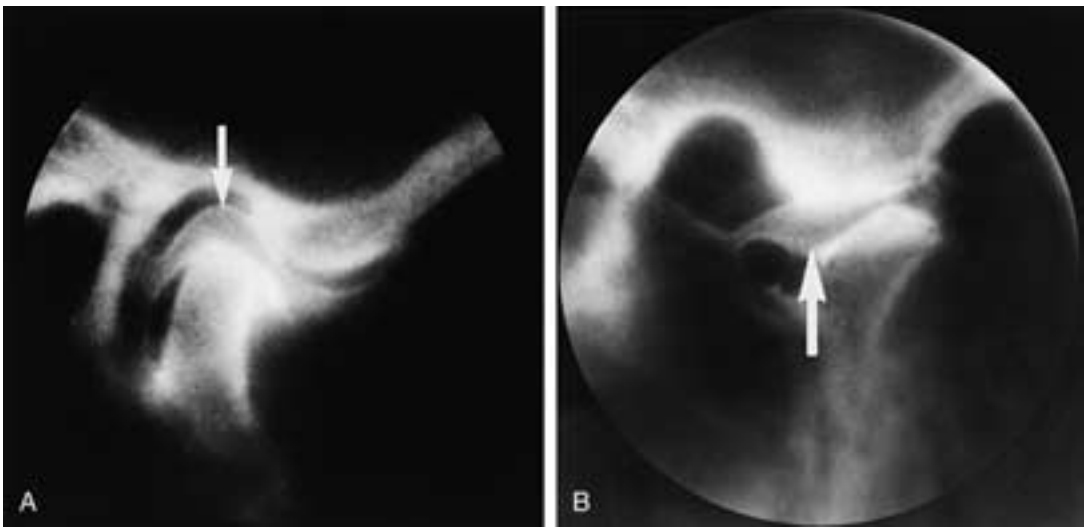

VIEW IMAGE

FIGURE 18-18 **A**, Normal TMJ with dual-space double-contrast arthrotomography in the closed-mouth position. The posterior band (*arrow*) of the disk is located over the condyle. **B**, Normal TMJ dual-space double-contrast arthrotomography in the open-mouth position. The posterior band (*arrow*) of the disk is located posterior to the condyle.

Copyright © 2003, Mosby, Inc. All rights reserved.

condyle articulates with the central thin zone and the posterior part of the disk (Fig. 18-18).

Abnormal Findings

Displacement of the disk with reduction (Fig. 18-19) and without reduction (Fig. 18-20) are the most frequent pathologic findings in TMJ arthrography. Principally this means that the posterior thick part (posterior band) of the disk is located anterior to the condyle in the closed-mouth position, and the condyle closes on the posterior disk attachment (bilaminar zone). An arthrographic sign of disk displacement in single-contrast lower compartment arthrography is enlargement of the anterior recess of the lower joint space (Fig. 18-19).

In disk displacement with reduction the disk is usually biconcave, although there may be some minor enlargement of the posterior band. This corresponds to the early-intermediate stage in the classification scheme described by Wilkes[9] (Box 18-2). In disk displacement without reduction a more extensive deformity of the disk is frequently encountered, and this corresponds to the late stage in the same classification scheme.[9] This is consistent with the deformities observed in pathologic specimens, which include thickening and shortening of the anteroposterior dimension of the disk. Perforation of the posterior disk attachment is another sign of late-stage internal derangement. Perforation is indicated by passage of contrast medium from the lower to the upper joint space (Fig. 18-21) when only the inferior space is injected.

Demonstration of pathology other than internal derangement is distinctly uncommon at TMJ arthrography. Patients with symptoms such as clicking and locking may occasionally have one or more loose bodies within the joint space.[74] Synovial chondromatosis, osteoarthrosis, or osteochondritis dissecans are the three principal causes of loose bodies in a joint.

Inflammatory joint disease such as rheumatoid arthritis is another pathologic entity that may affect the TMJ. However, this is usually diagnosed clinically, and patients with these diseases are rarely seen for TMJ arthrography. Osseous changes associated with rheumatoid arthritis can be clearly demonstrated with tomography or CT.

Complications Following Arthrography

Serious complications after arthrography are rare; no cases of infection following arthrography have been reported in the literature. Transient facial nerve palsy may result from extensive injection of a local anesthetic agent around the condyle and condylar neck, and the patient may have mild to moderate local discomfort for 1 to 2 days after the procedure. The use of nonionic or low-osmolality contrast media has been helpful in reducing the patient's discomfort.

Computed Tomography

CT scanning gives excellent definition of the bony contours of the mandibular head and the glenoid fossa. Axial imaging gives good definition of the head of the condyle, but sagittal and coronal planes are needed for evaluation of the actual joint surfaces. Though direct sagittal scanning of the TMJ (Figs. 18-22 and 18-23) has been done in the past, most institutions use axial scanning with sagittal reconstructions.[75–77] Both techniques have been reported to be successful in demonstrating internal derangement and

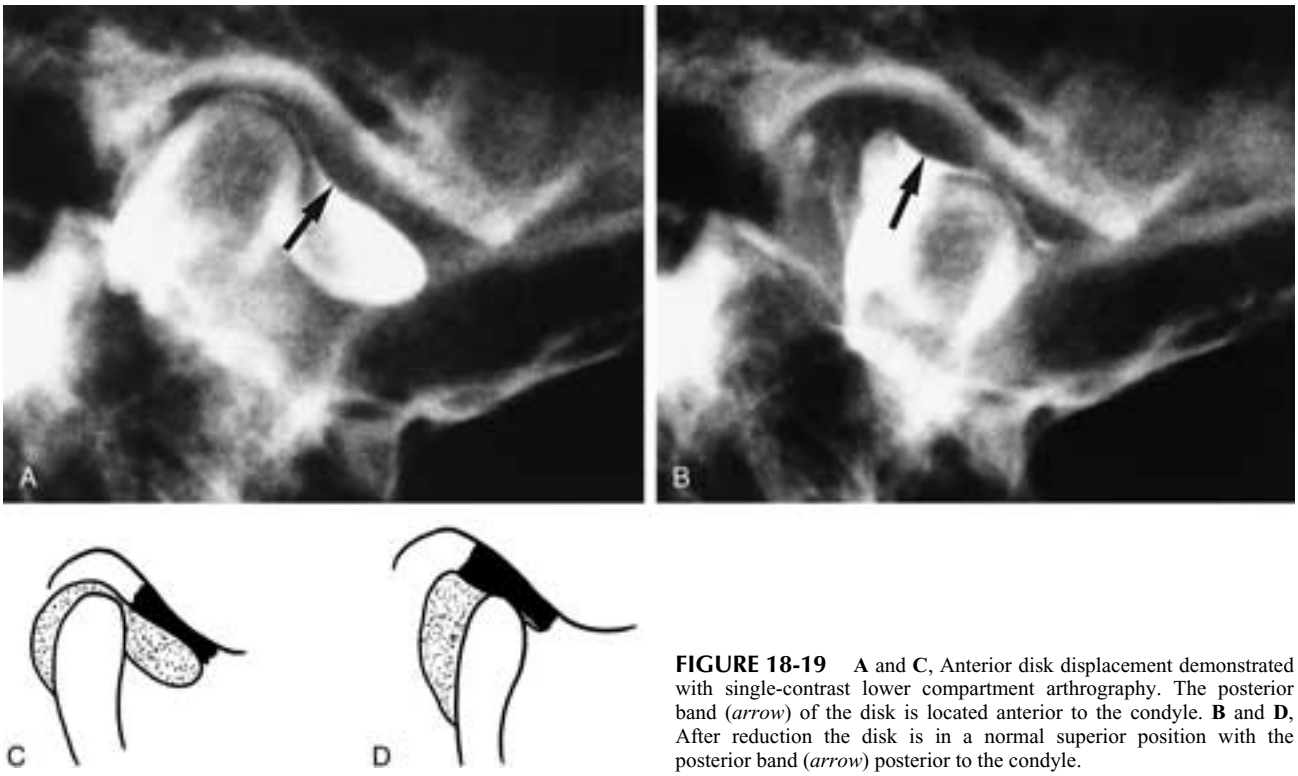

FIGURE 18-19 **A** and **C**, Anterior disk displacement demonstrated with single-contrast lower compartment arthrography. The posterior band (*arrow*) of the disk is located anterior to the condyle. **B** and **D**, After reduction the disk is in a normal superior position with the posterior band (*arrow*) posterior to the condyle.

VIEW IMAGE

Copyright © 2003, Mosby, Inc. All rights reserved.

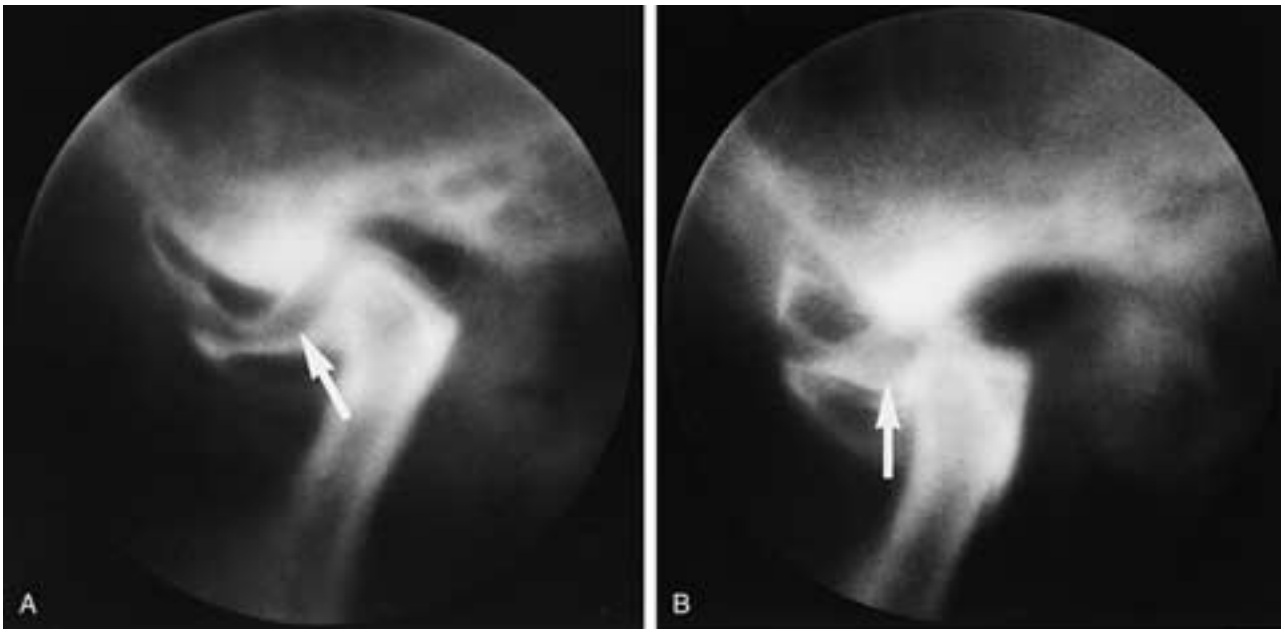

VIEW IMAGE

FIGURE 18-20 Anterior disk displacement without reduction, double-contrast arthrogram. **A** and **B**, With closed mouth and maximum mouth opening, the disk is located anterior to the condyle. The position of the posterior band is indicated by arrows.

osseous disease.[78–80] Currently, multidetector CT scan technology using very thin collimation allows coronal and sagittal reformatted images that rival direct scan images (Fig. 18-24). The use of CT for diagnosis of disk position has decreased rapidly during the past decade because of the superiority of MR imaging with surface coils (Fig. 18-25).[81] Although CT is not used for visualization of the disk, it is still the best means of examining the osseous structures of the joint.

The two main reasons to use CT in evaluation of the TMJ today are for evaluation of fractures and postsurgical changes involving the osseous components of the joint. Thus, CT can clearly demonstrate the integrity of the glenoid fossa and note the presence of extensive erosions. Perforation into the middle cranial fossa after alloplastic implants also is shown best on CT.

CT is also frequently used for evaluation of potential pathology in the contiguous tissues. Although MR imaging has certain advantages in evaluation of soft tissues, CT gives excellent information regarding the soft tissues and has the benefit of providing detailed images of the contiguous temporal bone and skull base. Calcifications are more easily appreciated on CT. This information can be gathered with the same single scan acquisition done to provide the images of osseous components of the joint.

Technique for CT Scanning

Sagittal images are preferable to axial or coronal images for disk visualization. Coronal and sagittal images are equally good when evaluating the integrity of the roof of the glenoid fossa, a common indication for CT in patients who have received alloplastic TMJ implants. Axial scanning is

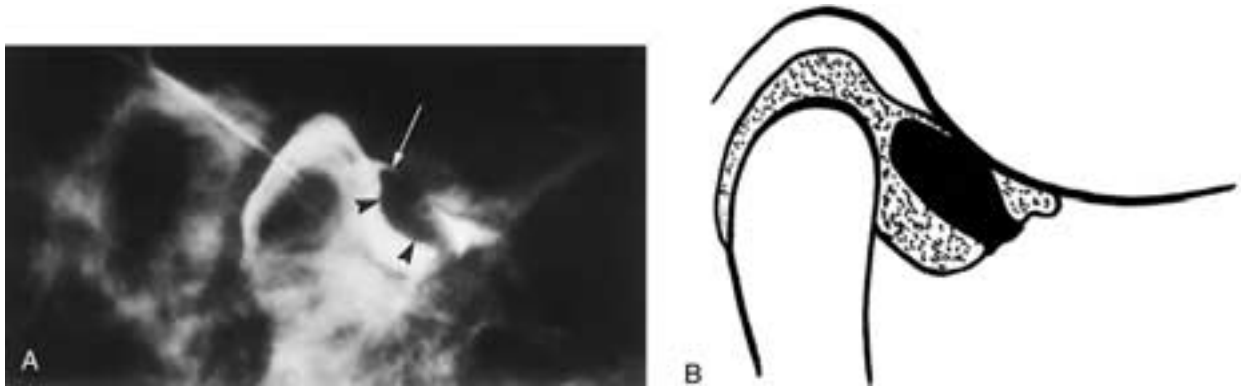

VIEW IMAGE

FIGURE 18-21 Perforation. **A**, Contrast material was injected into the lower joint space, and there is an overflow (*arrow*) to the upper joint space indicating perforation. The disk (*arrowheads*) is anteriorly displaced and deformed. **B**, Schematic drawing of **A**.

Copyright © 2003, Mosby, Inc. All rights reserved.

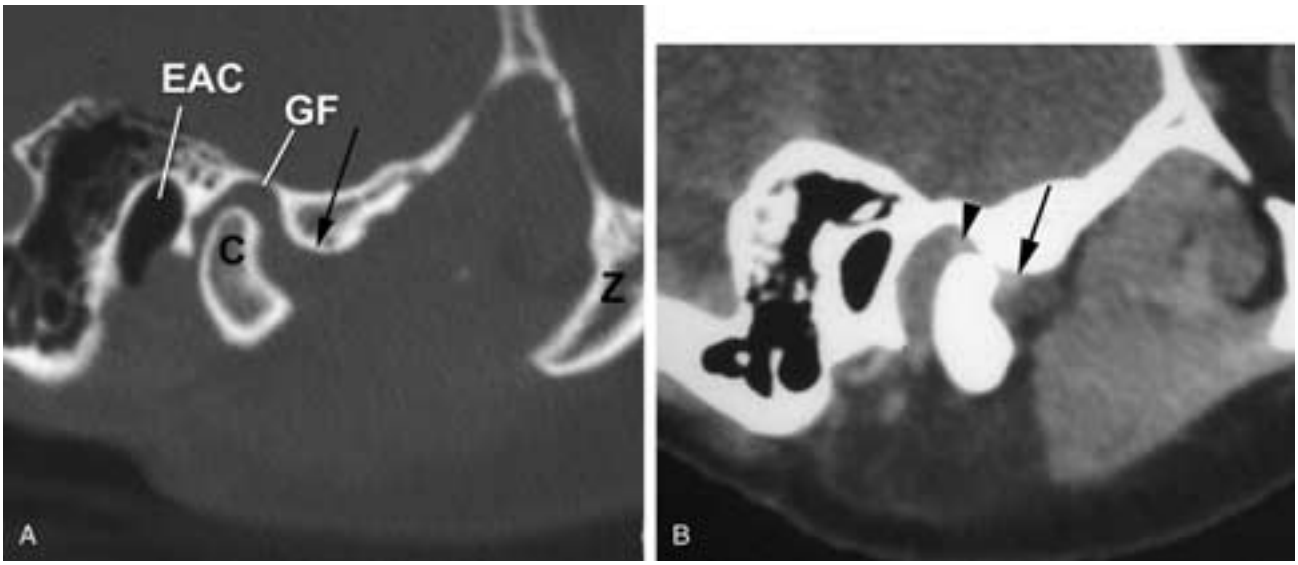

VIEW IMAGE

FIGURE 18-22 Direct sagittal CT of the TMJ. **A**, Bone algorithm shows the position of the condyle (*C*) in the glenoid fossa (*GF*) in the closed-mouth position. *EAC*, External auditory canal; *arrow*, articular eminence; *Z*, zygoma. **B**, Soft-tissue algorithm with the mouth slightly open. The condyle has moved slightly anteriorly and is not completely seated in the glenoid. There is good visualization of the disk. Anterior thick band (*arrow*), posterior thick band (*arrowhead*).

performed with 1 mm (or less) collimation, and sagittal and coronal images are reformatted from the original axial data. Three-dimensional reformatted images can be generated from the same data set (Fig. 18-26).

Before the advent of spiral CT machines, direct sagittal imaging required patients to be placed in uncomfortable positions, with the neck bent sharply to one side. In some cases, an additional stretcher was used to position the patient in the direct sagittal CT imaging plane.[75, 76] The stretcher was placed laterally at an angle with respect to the scanner table and the scanner gantry. Once the patient was in the correct position, scans were performed at 1 to 2 mm intervals from the medial to the lateral poles of the condyle. Additional images were obtained at maximum mouth opening. To minimize radiation, open-mouth images were taken in only a single plane through the center of the

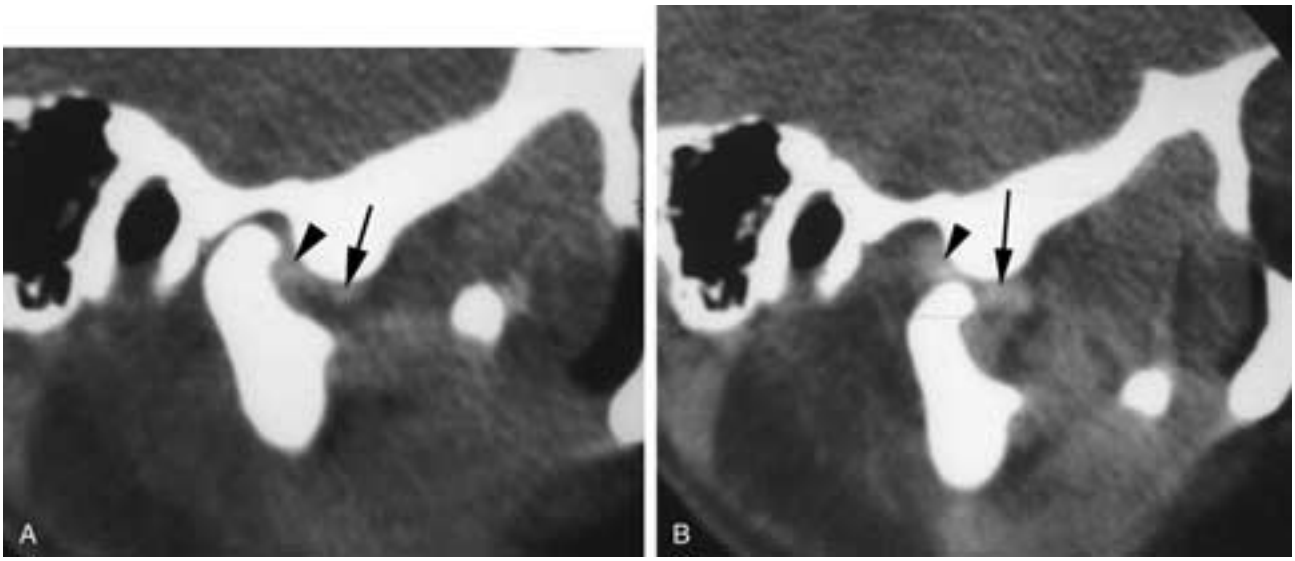

VIEW IMAGE

FIGURE 18-23 Direct sagittal CT. Anteriorly displaced disk with recapture (reciprocal click). **A**, Soft-tissue setting shows the condyle positioned posteriorly in the glenoid fossa. The posterior thick band (*arrowhead*) is demonstrated anterior to the condyle. The anterior thick band (*arrow*) is seen just inferior to the articular eminence. Normally, the condyle should articulate with the thin part of the disk visualized between the anterior and posterior thicker bands. **B**, Open-mouth position. The condyle now has a normal relationship to the disk articulating with the thin area between the posterior thick band (*arrowhead*) and the anterior thick band (*arrow*). The disk has been recaptured.

Copyright © 2003, Mosby, Inc. All rights reserved.

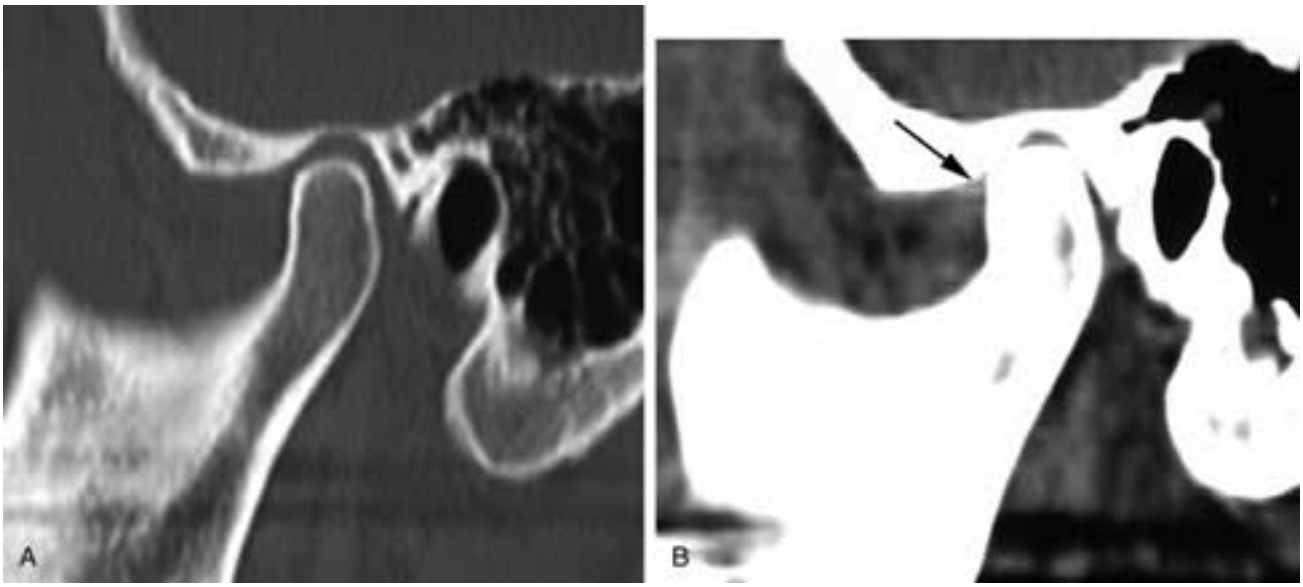

VIEW IMAGE

FIGURE 18-24 Multidetector CT with sagittal reformats. Normal TMJ. **A**, Sagittal reformatted image; the bone algorithm shows the normal relationship of the condyle to the glenoid and the articular eminence. **B**, Soft-tissue sagittal reformat shows a small focus of high density (*arrow*) just anterior to the condylar head. This represents the anterior thick band. This position is considered to be normal.

condyle. CT scans are reconstructed for both bone detail and soft-tissue detail, eliminating the need for conventional radiography or tomography.

CT Findings

When the disk is normal and thus positioned superior to the condyle, it is usually relatively difficult to visualize (Fig. 18-24). Indeed, the inability to see the disk anterior to the condyle and inferior to the tubercle has been interpreted as a diagnosis of normal disk position (Fig. 18-25). The lateral pterygoid fat pad is the fat around the lateral pterygoid muscle. Some fat is also seen between the two bellies of the lateral pterygoid muscle. If the disk is dislocated, it will distort this fat (Fig. 18-27). Scans with a wide mouth opening usually produce optimum images of the disk but are seldom performed, as MR imaging has become the preferred modality for identifying the disk and its position.

When the disk is anteriorly displaced, it appears as a high-attenuation small mass anterior to the condyle, inferior to the tubercle, and within the low-attenuation lateral pterygoid fat pad (Fig. 18-27). The configuration of the disk typically cannot be determined by CT because the soft-tissue separation is not sufficient for this purpose. The depiction of the disk on CT depends on the disk's density and size. Thus, if the disk is thin and small, it usually is not identified on CT, leading to a higher incidence of false-negative diagnoses. On the other hand, if the disk is large, it can be demonstrated by CT.

Magnetic Resonance Imaging

MR imaging has been used to image the TMJ since 1984, and imaging quality has continuously improved since that time.[1, 10, 82–89] A major advantage of MR imaging over all other radiographic imaging techniques is the absence of radiation to the patient. This is especially pertinent for TMJ imaging, because a significant number of the patients are young females.[64] The soft-tissue differentiation of MR imaging is also superior to that of all other imaging modalities that have been applied to this joint, and at this time MR imaging is the primary imaging technique for most clinical presentations.

The objective of MR imaging of the TMJ is to document soft- and hard-tissue abnormalities of the joint and its surrounding structures. The ability of MR imaging to visualize the soft-tissue structures around the joint is another advantage of this modality over arthrography, and a comparison of these two imaging modalities on the same joint shows this fact (Fig. 18-28).

Magnetic Field Strength and Comparison with CT

Scanners with magnetic field strengths ranging from 0.05 to 2 Tesla are currently in clinical use; however, studies that compare the image quality of these scanners with different magnetic field strengths are scarce. One study compared images from two different scanners obtained with equal acquisition time and demonstrated significantly better image quality with the high-field system (Fig. 18-29).[90] Although the lower image quality of the 0.3 Tesla scanner could be somewhat compensated for by increasing the acquisition time (the number of excitations) by a factor of about 4, in clinical work this increases the risk of motion artifact.[90]

Some principal advantages and disadvantages of MR imaging compared with CT are outlined in Box 18-3. Contraindications for MR imaging are outlined in Box 18-4.

Surface Coil and Scanning Technique

The oblique sagittal and oblique coronal planes are standard for MR imaging of the TMJ (Fig. 18-30). A standard imaging protocol is shown in Table 18-1. The use of the dual surface coil technique for imaging of the left and

Copyright © 2003, Mosby, Inc. All rights reserved.

right TMJs at the same time has been of great value because the time on the scanner can be significantly shortened for bilateral TMJ imaging.[91, 92] Bilateral abnormalities are seen in up to 60% of patients with pain and dysfunction who initially present with unilateral symptoms.[93, 94]

MR imaging is performed using the body coil as the transmitter and the two surface coils as the receivers. Surface coils are essential for good image quality, and a diameter between 6 and 12 cm provides an optimal signal-to-noise ratio in most patients. The standard imaging protocol obtains oblique sagittal and oblique coronal images perpendicular and parallel to the long axis of the mandibular condylar head (Fig.18-30).[95] Sagittal images should be obtained in both closed- and open-mouth positions to determine the function of the disk. Coronal images are usually obtained only in the closed-mouth position. The protocol shown in Table 18-1 may need to be adjusted, depending on the performance of the scanner and the type of surface coils used.

Proton density images are preferable to T1-weighted images for outlining morphology because of the ''greater latitude'' and better visualization of disk tissue relative to the surrounding joint capsule and cortical bone. T2-weighted images are obtained routinely to document the presence of joint effusion and inflammatory changes in the joint capsule. Because of the arthrographic effect created by the high signal intensity of the joint effusion on T2-weighted images, these images also may be useful for outlining perforations. T2-weighted images obtained in both sagittal and coronal planes frequently help outline the joint effusion.

Fast spin-echo T2-weighted images provide a better signal-to-noise ratio than standard T2-weighted images.

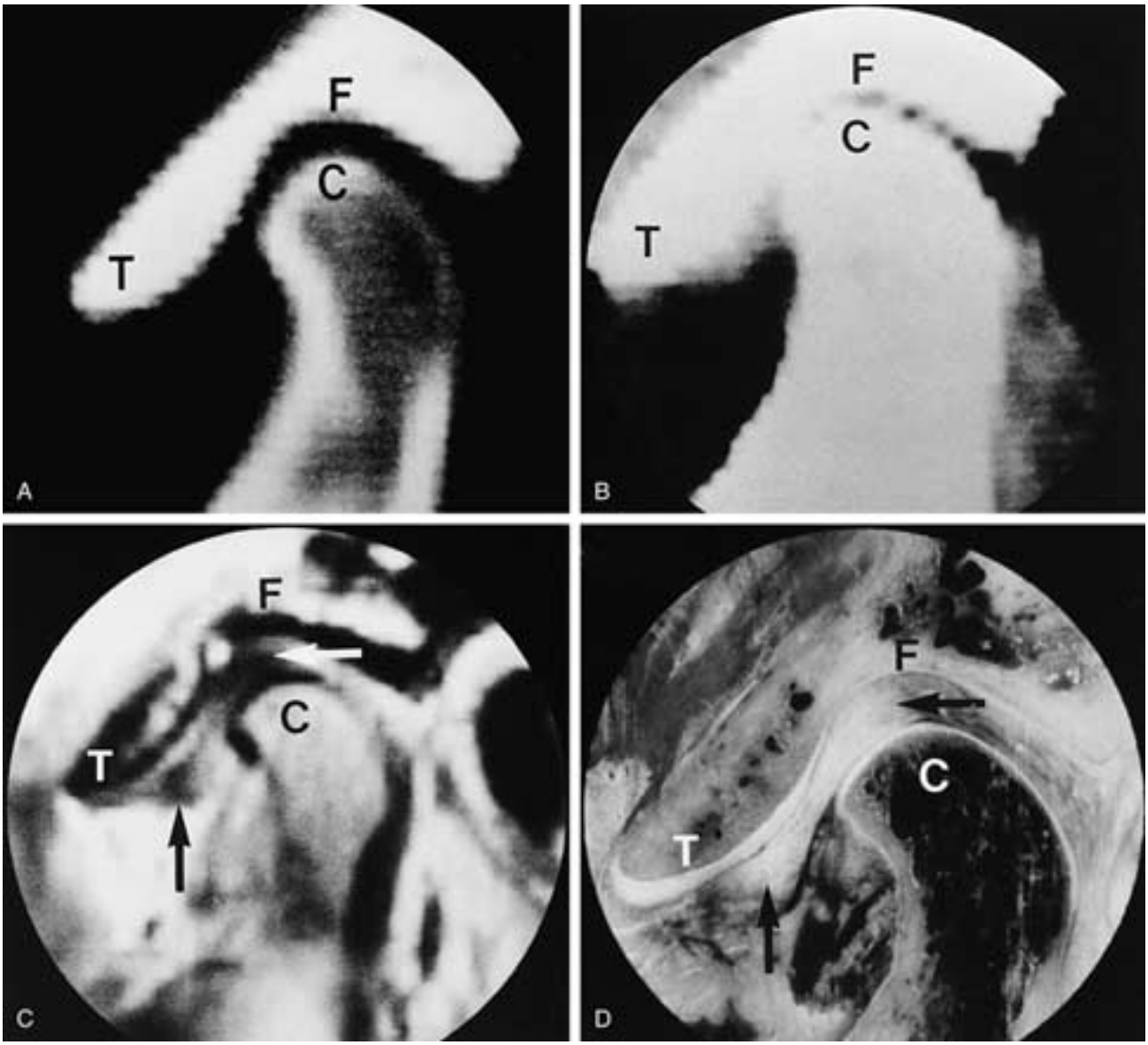

FIGURE 18-25 CT in hard-tissue (**A**) and soft-tissue (**B**) settings, MR imaging (**C**), and corresponding cryosection (**D**) of a TMJ with the normal superior disk position. The tubercle (*T*), fossa (*F*), and condyle (*C*) are indicated. The anterior and posterior bands of the disk are indicated by arrows.

VIEW IMAGE

Copyright © 2003, Mosby, Inc. All rights reserved.

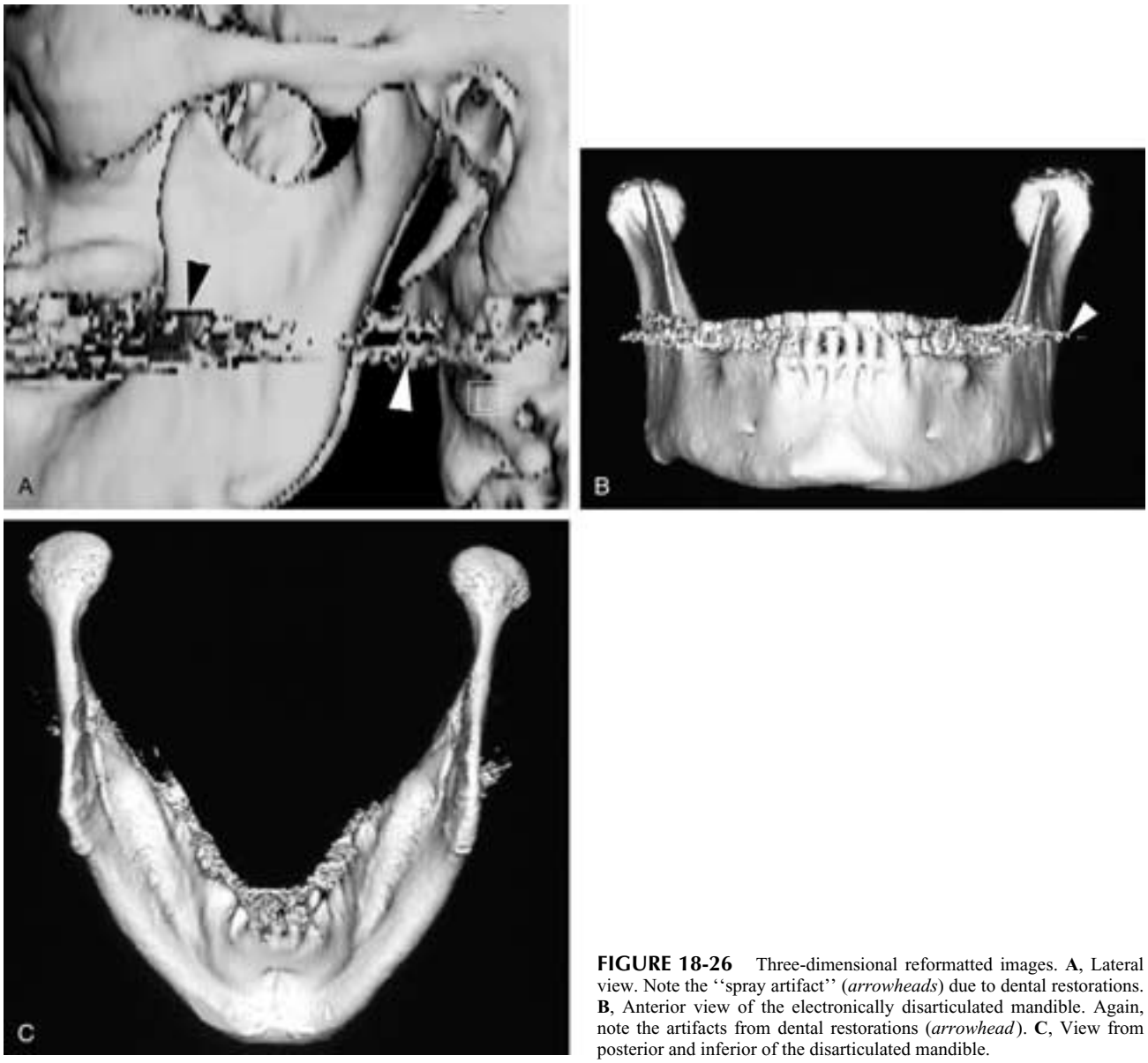

FIGURE 18-26 Three-dimensional reformatted images. **A**, Lateral view. Note the ''spray artifact'' (*arrowheads*) due to dental restorations. **B**, Anterior view of the electronically disarticulated mandible. Again, note the artifacts from dental restorations (*arrowhead*). **C**, View from posterior and inferior of the disarticulated mandible.

VIEW IMAGE

However, the standard proton density images provide superior soft-tissue separation, and many imagers prefer standard spin-echo images because they are sharper than fast spin-echo images. Open-mouth images are obtained to determine the function of the disk. Syringes of various sizes or commercially available bite block devices are used to stabilize the patient's jaw in the open-mouth position (Fig. 18-31). Slice thickness should be 3 mm or less. The gap or interval between slices should be 0.5 to 1.5 mm for the sagittal images; for the coronal images it should be reduced to about 0.3 mm to obtain at least one good image through the center of the condyle. The anteroposterior dimension of the condyle is usually about 8 to 10 mm, and volume averaging is a greater problem for coronal images than for sagittal images. By angling the coronal images along the horizontal long axis of the condyle, images of both left and right joints can be obtained simultaneously. In the rare instance in which the slices of the left and right joints interfere with each other, separate scans of the left and right joints should be obtained.

The coronal images are valuable in identifying medial and lateral displacements of the disk. Additionally, the osseous anatomy of the condyle can sometimes be better appreciated in the coronal plane.

If the patient's oral splint is to be assessed, additional oblique sagittal images are obtained with the splint in place. The same scanning parameters are used for the closed-mouth sagittal images.

MR Imaging Findings of the Normal TMJ

MR imaging nicely shows the normal TMJ anatomy in the sagittal and coronal planes (Figs. 18-32 and 18-33). In the sagittal plane the disk is biconcave, with the posterior band (posterior thick part) lying over the condyle. The central thin zone articulates against the anterior prominence of the condyle. Because the fibrous connective tissue of the

Copyright © 2003, Mosby, Inc. All rights reserved.

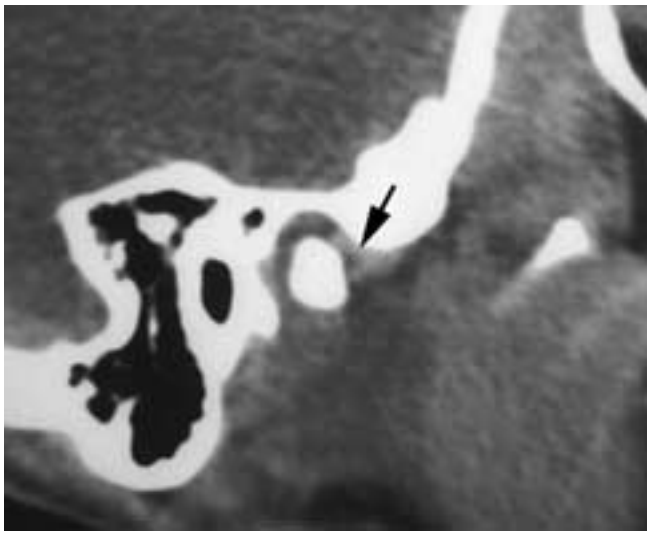

VIEW IMAGE

FIGURE 18-27 Direct sagittal CT scan with a soft-tissue setting depicting an anteriorly displaced disk. The image of the disk has a relatively high CT attenuation contrasted against the fat close to the lateral pterygoid muscle. The arrow points to the thin portion of the disk.

disk has low signal intensity, the disk usually can be distinguished from the surrounding tissues, which have higher signal intensity. The cortices of both the condylar and temporal bone components of the joint have low signal intensity, but the articular coverings of the joint have higher signal intensity. This makes the outline of the osseous components easily visible. The posterior disk attachment has relatively high signal intensity compared with the posterior portion of the disk itself because of the fatty tissue in the posterior disk attachment. MR imaging is the only modality that consistently allows the disk to be distinguished from its posterior attachment.

The upper and lower heads (or bellies) of the lateral pterygoid muscle are seen extending anteriorly from the TMJ. The upper belly can be followed into the anterior margin of the disk. The lower belly attaches to the anterior surface of the condylar neck. There is a thin, fibrous band at the junction of the upper and lower heads at the point where the muscles reach their attachments to the disk and condyle. This fibrous band is seen as a linear low-signal structure just inferior to the position of the disk, and it should not be mistaken for the disk. This is a particular problem when the disk is medially or laterally displaced and the fibrous band of the lateral pterygoid muscle is the only low-signal structure anterior to the condylar head.

In MR imaging scans obtained at maximum mouth opening, the central thin zone of the disk is visualized between the condyle and the tubercle (Fig. 18-33B). The posterior band of the disk articulates against the posterior surface of the condyle, as has been demonstrated in anatomic specimens (Fig. 18-3).

In the coronal plane (Fig. 18-33C), the normal disk has a crescent shape. The medial aspect of the disk attaches just inferior to the medial pole of the condyle and to the medial capsule. Similarly, the lateral part of the disk attaches just inferior to the lateral pole of the condyle and to the lateral capsule (Fig. 18-2). Normally, the lateral and medial capsules are visualized and do not bulge outward.

Disk Displacement

Displacements of the disk in the anterior (Fig. 18-34), anteromedial, or anterolateral direction are the most common findings observed when interpreting MR images of patients with clinical signs and symptoms of internal derangement.[43] In the sagittal plane the disk is noted to be displaced when its posterior band is anterior to the condyle (Fig. 18-34).

Disk displacement may be complete or partial. In complete disk displacement, the entire mediolateral dimension of the disk is displaced anterior to the condyle. In partial disk displacement, only the medial or lateral part of the disk is displaced anterior to the condyle. Most frequently, the lateral part is displaced anteriorly and the more medial part of the disk is still in a normal superior position. Partial disk displacement is frequently seen in joints with disk displacement with reduction (Fig. 18-35); the disk is displaced anteriorly in the lateral part of the joint (Fig. 18-35A) and is in a normal position in the medial part of the joint (Fig. 18-35B). This is probably because the displaced part of the disk, being anchored by the normally positioned medial

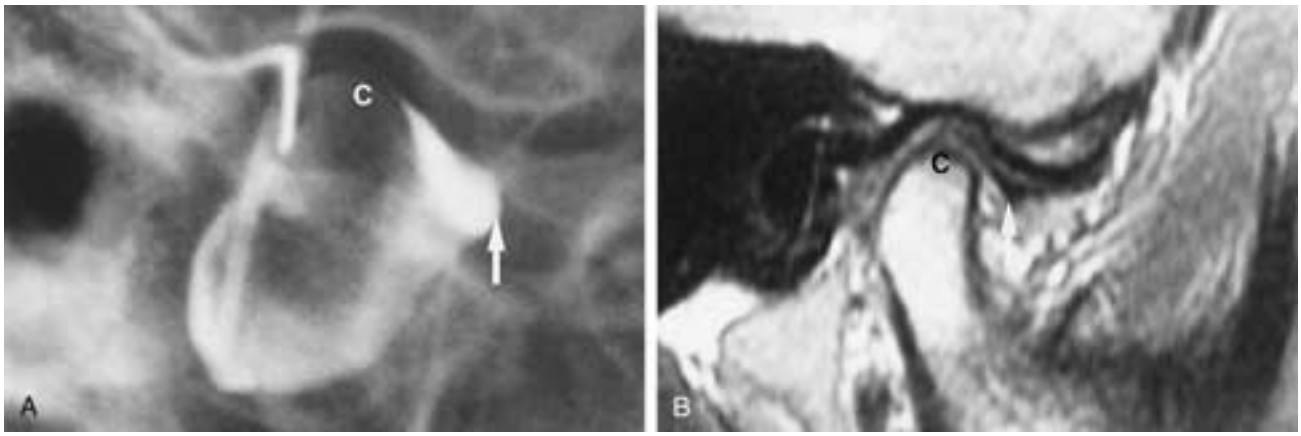

VIEW IMAGE

FIGURE 18-28 **A**, Arthrogram. **B**, MR image of the same TMJ showing the normal superior disk position. The anterior recess of the lower joint compartment is indicated by an arrow in the arthrogram. In the MR image the disk is located superior to the condyle. The condyle (*C*) is noted in both studies.

Copyright © 2003, Mosby, Inc. All rights reserved.

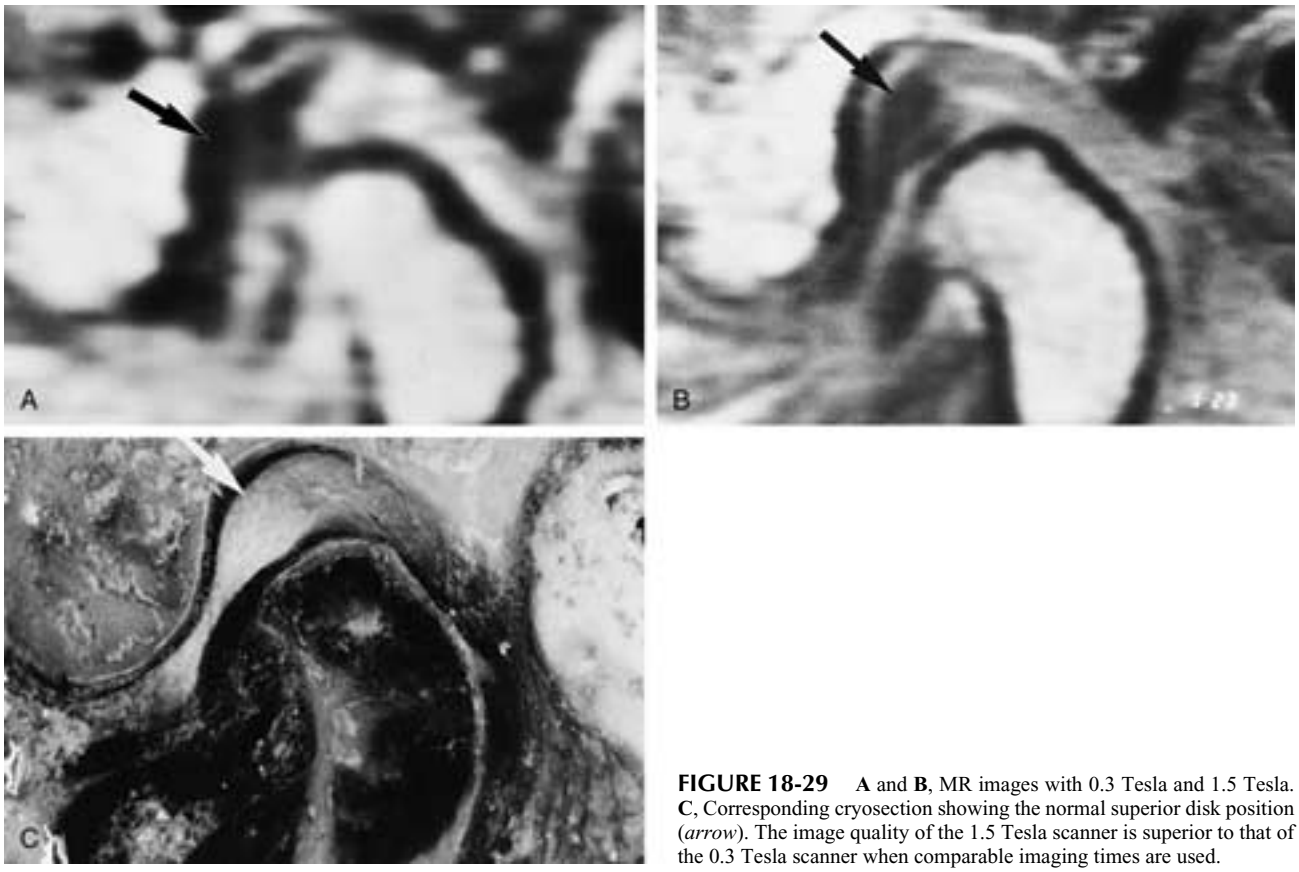

FIGURE 18-29 **A** and **B**, MR images with 0.3 Tesla and 1.5 Tesla. **C**, Corresponding cryosection showing the normal superior disk position (*arrow*). The image quality of the 1.5 Tesla scanner is superior to that of the 0.3 Tesla scanner when comparable imaging times are used.

VIEW IMAGE

portion of the disk, is allowed to revert to its normal position on opening without being squeezed between the two joint components as much as in cases with a complete anterior disk displacement.

Frequently, the anterior disk displacement is combined with either medial or lateral displacement. Initially, when MR imaging was done in the true coronal plane, medial displacements were considered more prevalent than lateral displacements. This was probably the result of the scanning technique rather than pathologic changes because, with oblique coronal images parallel to the horizontal long axis of the condylar head, medial and lateral displacements are seen with approximately the same frequency. In most cases, the sagittal images show the anterior component of the displacement, and the coronal images show the medial or lateral component. In approximately 10% of patients

BOX 18-3

ADVANTAGES AND DISADVANTAGES OF MR IMAGING COMPARED WITH CT

Advantages	No ionizing radiation
	Fewer artifacts from dense bone and metal clips
	Imaging possible in several planes without moving the patient
	Superior anatomic detail of soft tissues
Disadvantages	High initial cost of the scanner Special site planning and shielding
	Patient claustrophobia in magnet
	Inferior images of bone

BOX 18-4

CONTRAINDICATIONS TO MR IMAGING

Absolute	Patients with cerebral aneurysm clips
	Patients with cardiac pacemakers
Relative	Ferromagnetic foreign bodies in critical locations (e.g., eyes)
	Metallic prosthetic heart valves
	Claustrophobic or uncooperative patients
	Implanted stimulator wires for pain control
Not contraindications	Metallic prostheses
	Orthodontic fixed appliances

Copyright © 2003, Mosby, Inc. All rights reserved.

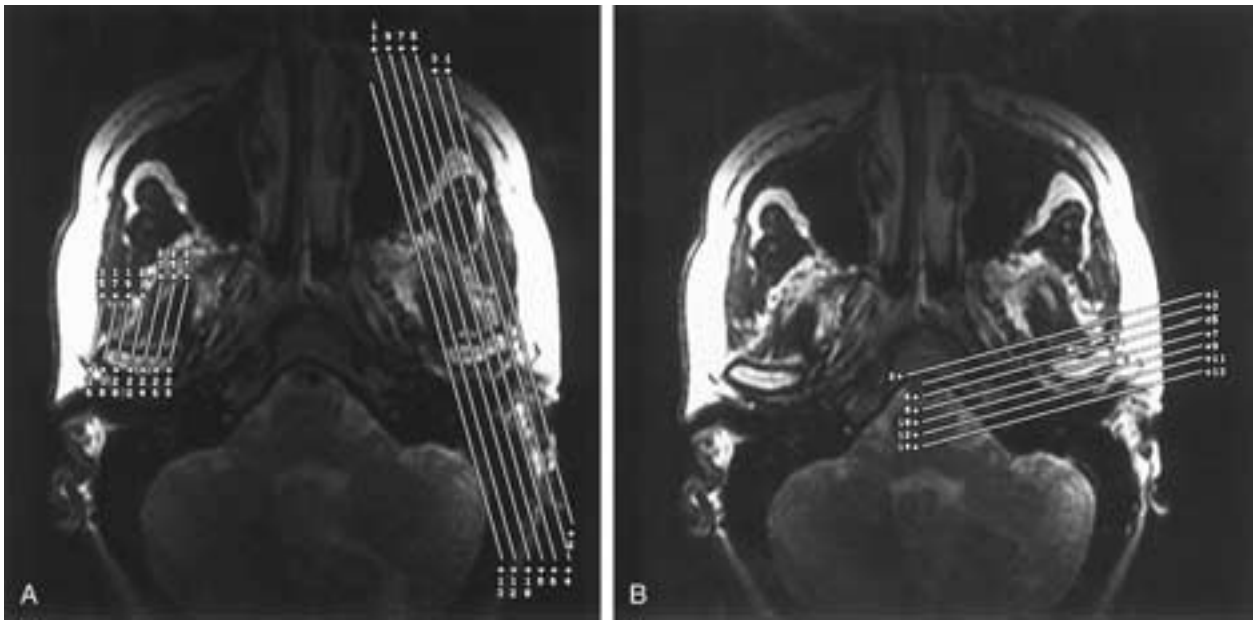

VIEW IMAGE

FIGURE 18-30 Axial scout images for sagittal (**A**) and coronal (**B**) MR images. The orientations of the sagittal and coronal images are outlined. It is important to cover the area of the lateral and medial poles of the condyle with the sagittal images. For the coronal images, one image should be through the center of the condyle.

presenting with TMJ pain and dysfunction, there is a pure lateral or pure medial disk displacement that is not detected on sagittal images (Fig. 18-36).[10] The displacement can be dramatic in both the lateral (Fig. 18-36) and medial (Fig. 18-37) directions. When the disk is displaced medially or laterally in combination with anterior displacement, it is called rotational disk displacement (Box 18-1).

The empty fossa sign seen in the sagittal images (Fig. 18-38) is an indication of a medial or lateral disk displacement. When the disk displaces in a medial direction, the lateral capsular tissue is pulled between the condyle and glenoid fossa and gives the appearance of an ''empty'' fossa. Thus, when the disk is not clearly seen in the glenoid fossa in the closed-mouth position (Fig. 18-38), medial or lateral disk displacement should be suspected. The coronal images are examined for verification. Medial and lateral disk displacement may or may not (Fig. 18-38) reduce on

Table 18-1
SCANNING PARAMETERS FOR MR IMAGING

Image	Scanning Time
Axial Localizer TR/TE = 300 ms; 16 ms NEX = 0.5 FOV = 18 cm Slice thickness = 3 mm Matrix = 256 × 128	25 sec
Sagittal, Closed Mouth TR/TE = 2000 ms; 1⅞₀ ms NEX = 0.5–0.75 FOV = 10–12 cm Slice thickness = 3 mm Matrix = 256 × 192	3 min, 52 sec
Sagittal, Open Mouth TR/TE = 1500 ms; 1⅞₀ ms NEX = 0.75 FOV = 10–12 cm Slice thickness = 3 mm Matrix = 256 × 128	2 min, 42 sec
Coronal, Closed Mouth TR/TE = 2000 ms; 1⅞₀ ms NEX = 0.5–0.75 FOV = 10–12 cm Slice thickness = 3 mm Matrix = 256 × 192	3 min, 52 sec

FOV, field of view; *NEX*, number of excitations.

FIGURE 18-31 Clinical positioning with dual surface coils and a syringe between upper and lower teeth used as a bite block.

VIEW IMAGE

Copyright © 2003, Mosby, Inc. All rights reserved.

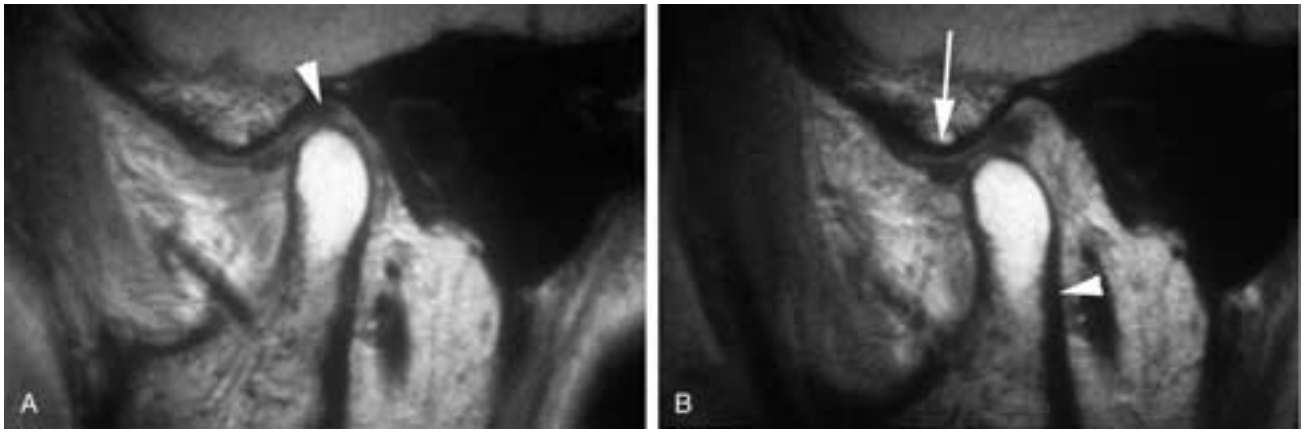

VIEW IMAGE

FIGURE 18-32 Normal MR imaging, Normal TMJ. **A**, The posterior thick band (*arrowhead*) is located immediately superior to the condylar head. Just anterior to this band is the central thin region. The low signal just anterior to the condylar head is the anterior thick band. The disk gives a ''bowtie'' appearance due to the anterior and posterior thick bands. **B**, Open-mouth position. The mouth is slightly open. The disk has translated down anteriorly so that the anterior thick band of the disk is immediately inferior to the articular eminence (*arrow*). The condylar head has rotated with respect to the disk. Note how the posterior edge of the mandible has rotated posteriorly (*arrowhead*) compared to **A**.

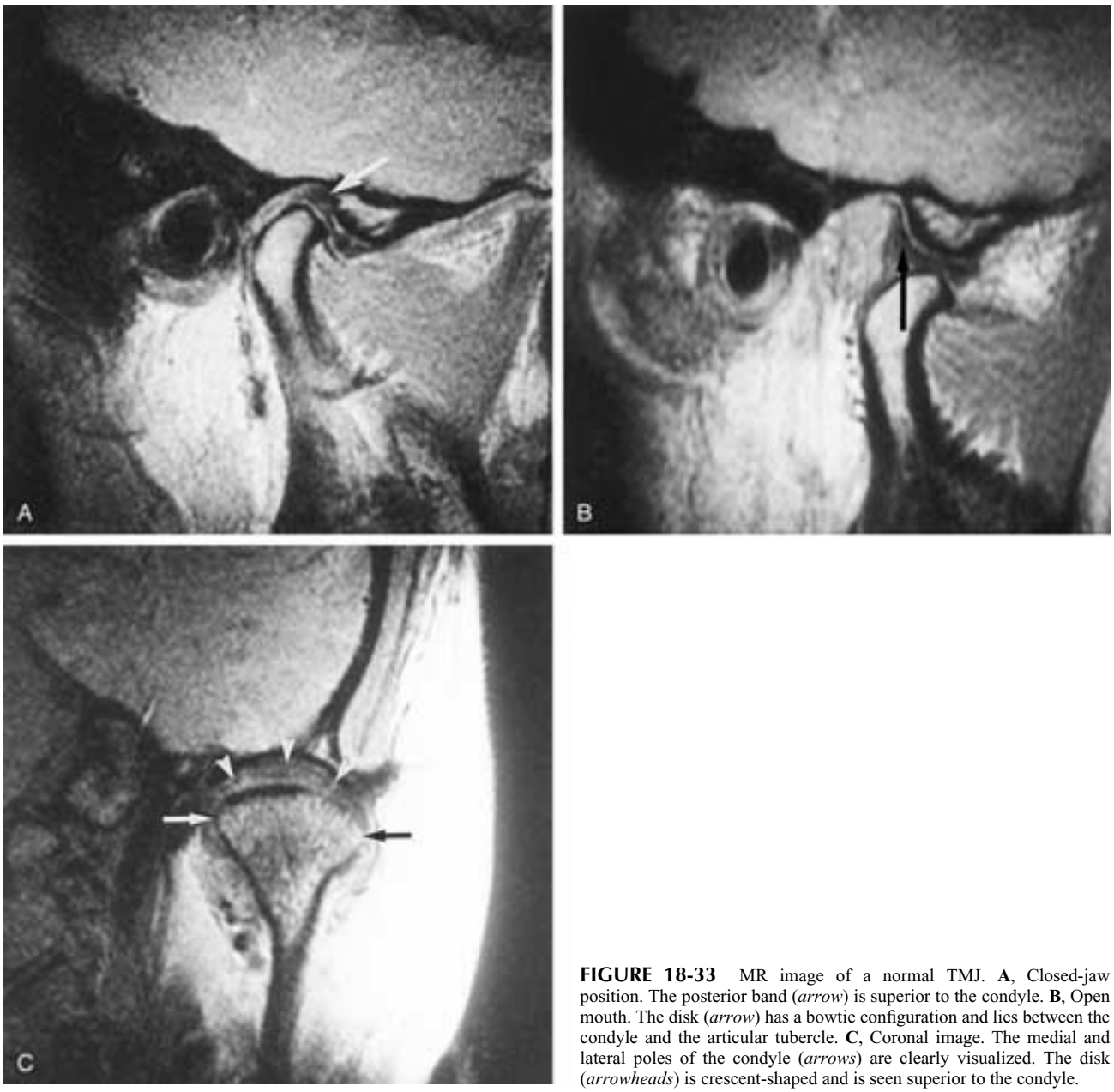

FIGURE 18-33 MR image of a normal TMJ. **A**, Closed-jaw position. The posterior band (*arrow*) is superior to the condyle. **B**, Open mouth. The disk (*arrow*) has a bowtie configuration and lies between the condyle and the articular tubercle. **C**, Coronal image. The medial and lateral poles of the condyle (*arrows*) are clearly visualized. The disk (*arrowheads*) is crescent-shaped and is seen superior to the condyle.

VIEW IMAGE

Copyright © 2003, Mosby, Inc. All rights reserved.

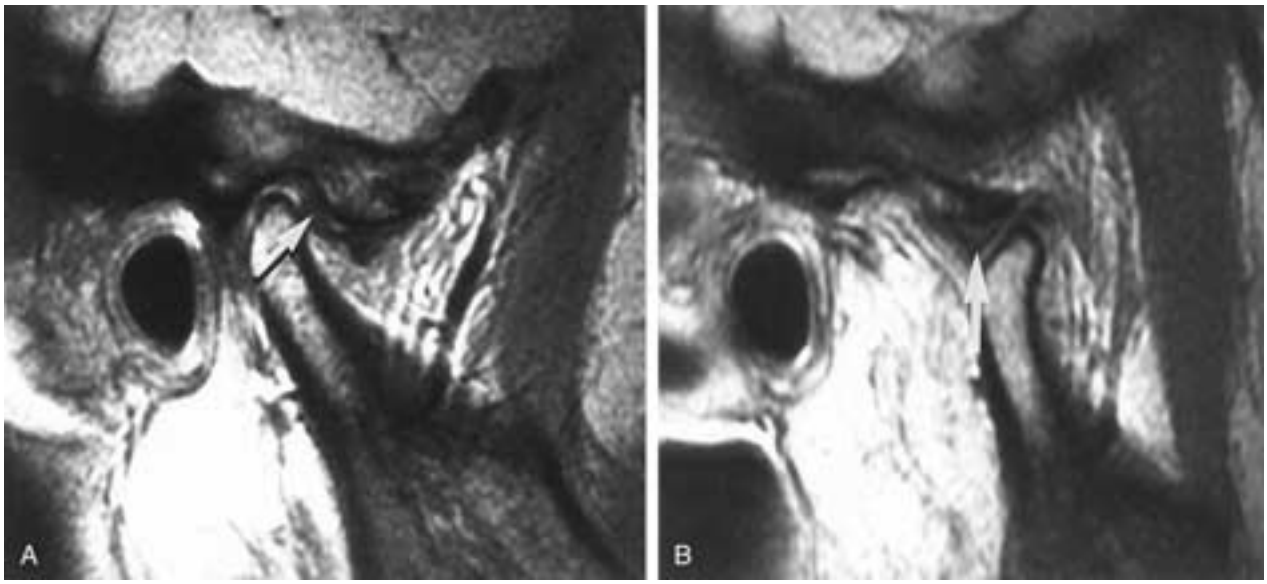

VIEW IMAGE

FIGURE 18-34 Disk displacement with reduction. **A**, A posterior band of the displaced disk (*arrow*) is anterior to the condyle. **B**, Open-mouth image shows the posterior band (*arrow*) in a normal relationship posterior to the condyle. This indicates reduction on opening.

opening. The function of the disk with sideways displacement is more difficult to evaluate than with anterior displacement because the location of the disk is best seen in the coronal plane in the closed position and the sagittal plane in the open position.

MR images obtained at maximum mouth opening determine whether the disk displacement reduces. In displacement with reduction (Fig. 18-34) the disk position normalizes during jaw opening. In disk displacement without reduction (Fig. 18-39) the disk remains anterior to the condyle in all mandibular positions. Disk displacement with reduction practically always precedes late-stage disk displacement without reduction.

Disk Deformity

Deformity of the disk (Fig. 18-9) resulting from chronic displacement can usually be demonstrated by MR imaging (Fig. 18-40). Initial deformity includes thickening of the

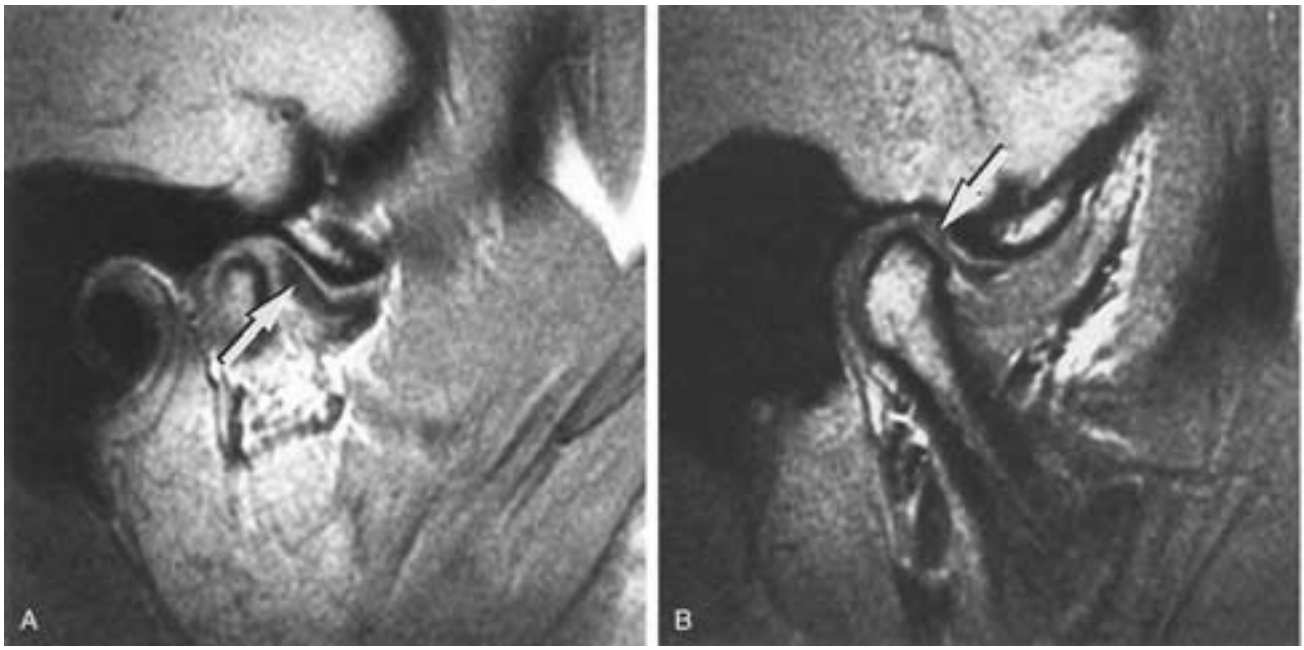

VIEW IMAGE

FIGURE 18-35 Partial anterior disk displacement. **A**, In the lateral part of the joint, the disk (*arrow*) is anteriorly displaced. **B**, In the medial part of the joint, the disk (*arrow*) is located in a normal superior position. This indicates partial anterior disk displacement.

Copyright © 2003, Mosby, Inc. All rights reserved.

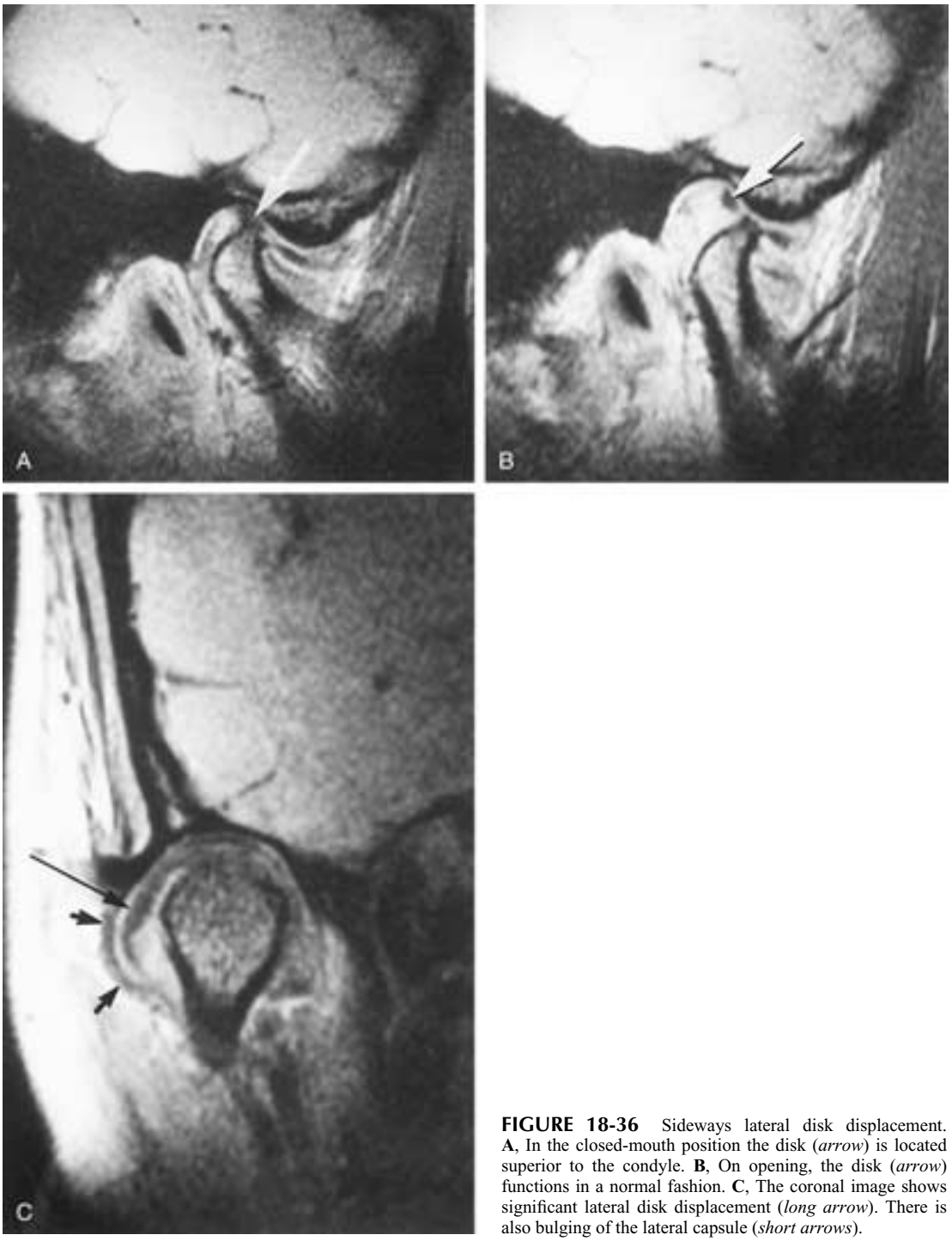

FIGURE 18-36 Sideways lateral disk displacement. **A**, In the closed-mouth position the disk (*arrow*) is located superior to the condyle. **B**, On opening, the disk (*arrow*) functions in a normal fashion. **C**, The coronal image shows significant lateral disk displacement (*long arrow*). There is also bulging of the lateral capsule (*short arrows*).

VIEW IMAGE

posterior band. Late-stage deformity may include a rounder, biconvex disk or a severely diminished amount of disk tissue. Disk deformation is significant in the clinical management of patients because a deformed disk usually cannot be repositioned surgically, and more aggressive surgical treatment with diskectomy may be necessary. It is therefore important to evaluate the degree of disk deformity and communicate this information to the referring clinician.

Another form of tissue alteration secondary to disk displacement is the formation of the so-called pseudodisk (Fig. 18-41). A pseudodisk appears as a band-like structure of low signal intensity replacing the normally bright signal from the posterior disk attachment. Histologically, it is thought to represent the fibrotic change that occurs in the posterior disk attachment in response to pressure from the condyle against the loose tissue of the posterior disk attachment (bilaminar zone). It has been suggested that this fibrotic change in the posterior disk attachment is associated with decreasing pain, but this has not been confirmed in systematic studies.[96, 97]

Copyright © 2003, Mosby, Inc. All rights reserved.

Other Findings and Conditions Related to Internal Derangement

Joint Effusion

An assessment of the amount of joint fluid is essential because small amounts of fluid are seen outlining the articular surfaces in both normal and abnormal individuals (Fig. 18-42).[98] Large accumulations of joint fluid (Fig. 18-43) are seen only in symptomatic patients. Such effusions are best seen in T2-weighted MR imaging.

Joint fluid is significantly more prevalent in painful joints than in nonpainful joints.[98] Not all individuals with pain have joint effusion, but a significant accumulation of joint effusion is likely to be associated with pain and the status of the disk.[99–101] Joint effusion may also have some diagnostic value, as the fluid outlines the morphology of the disk and may outline a perforation in the posterior disk attachment (Fig. 18-44).

Osteoarthritis

Osteoarthritis is frequently seen in joints with long-standing disk displacement without reduction.[18, 26] Disk displacement seems to be a precursor of osteoarthritis. Osteoarthritis is infrequently seen in joints with a normal superior disk position, occasionally in disk displacement with reduction, and more frequently when disk displacement without reduction has been present for some time. Imaging evidence of osteoarthritis can be seen in teenagers with disk displacement without reduction. Disk displacement and internal derangement are, however, only one cause of osteoarthritis, the common final pathway for a multitude of primary joint lesions.

Osteoarthritis is characterized radiographically by flattening and irregularities of the articular surfaces, osteophytosis, and erosion (Figs. 18-45 and 18-46). There may be irregularity of the glenoid fossa, particularly when there is bone-to-bone contact because of a tear in the disk or retrodiskal tissues. The distinction between early arthritis and advanced remodeling on MR imaging, as well as on other imaging modalities, is difficult to define, and overlap will exist.

Osteoarthritis has been suggested as a source of pain. However, osteoarthritis is present in a large proportion of older individuals and is usually completely asymptomatic. It is well recognized that symptoms related to TMJ dysfunction decrease with age, and are often remitting and self-limited.[102–105] The discrepancy between imaging findings and patient symptoms indicates the need for a good clinical examination to determine which imaging findings are significant.

FIGURE 18-37 Medial disk displacement. Coronal MR image shows the disk (*arrows*) displaced medial to the condyle.

VIEW IMAGE

Marrow Abnormalities of the Mandibular Condyle

Claims have been made, based on comparison with other joints, that areas within the bone marrow of the condyle having low signal intensity on T1-weighted images (variable signal on T2-weighted images) represent osteonecrosis (avascular or aseptic necrosis) (Figs. 18-47 to 18-50).[89, 106] However, based on this MR imaging appearance, other etiologies such as sclerosis or fibrosis of the bone marrow cannot be ruled out.

Multiple MR imaging studies have described abnormalities of the mandibular condyle similar to the appearance of osteonecrosis (aseptic necrosis) in the femoral head.[107–111] One study used core biopsy to document that edema and osteonecrosis may occur in the marrow of the mandibular condyle.[112] Histologic evidence of bone marrow edema was also found without evidence of osteonecrosis, suggesting that edema may be a precursor to osteonecrosis, as is known from investigation of other joints.[112] MR findings suggesting bone marrow edema include intermediate signal intensity on T1-weighted and proton density images and increased signal intensity on T2-weighted image (Fig. 18-48).

Osteoarthritis may develop secondary to osteonecrosis in the TMJ (Fig. 18-50).[112, 113] However, edema and osteonecrosis are separate entities from osteoarthritis and do occur without osteoarthritis.[113]

Avascular necrosis is best characterized in the hip. Predisposing factors include sickle cell disease, alcoholism, and steroid therapy. Avascular necrosis in the mandibular condyle probably has a different etiology and has not been associated with the same systemic factors but rather with local trauma from internal derangement.[89] Disk displacement may be one factor that leads to bone marrow changes.[109–111, 113, 114]

Abnormal bone marrow of the mandibular condyle may be seen in less than 10% of joints with TMJ disease.[113, 115] A study has shown markedly greater pain in joints that have bone marrow alterations in the mandibular condyle compared to joints with normal bone marrow.[116] Increased intraarticular pressure in conditions such as synovitis and hemophilia has also been suggested as an etiology of osteonecrosis.[117] A relationship between osteonecrosis and larger amounts of joint fluid has also been described.[111, 112]

Copyright © 2003, Mosby, Inc. All rights reserved.

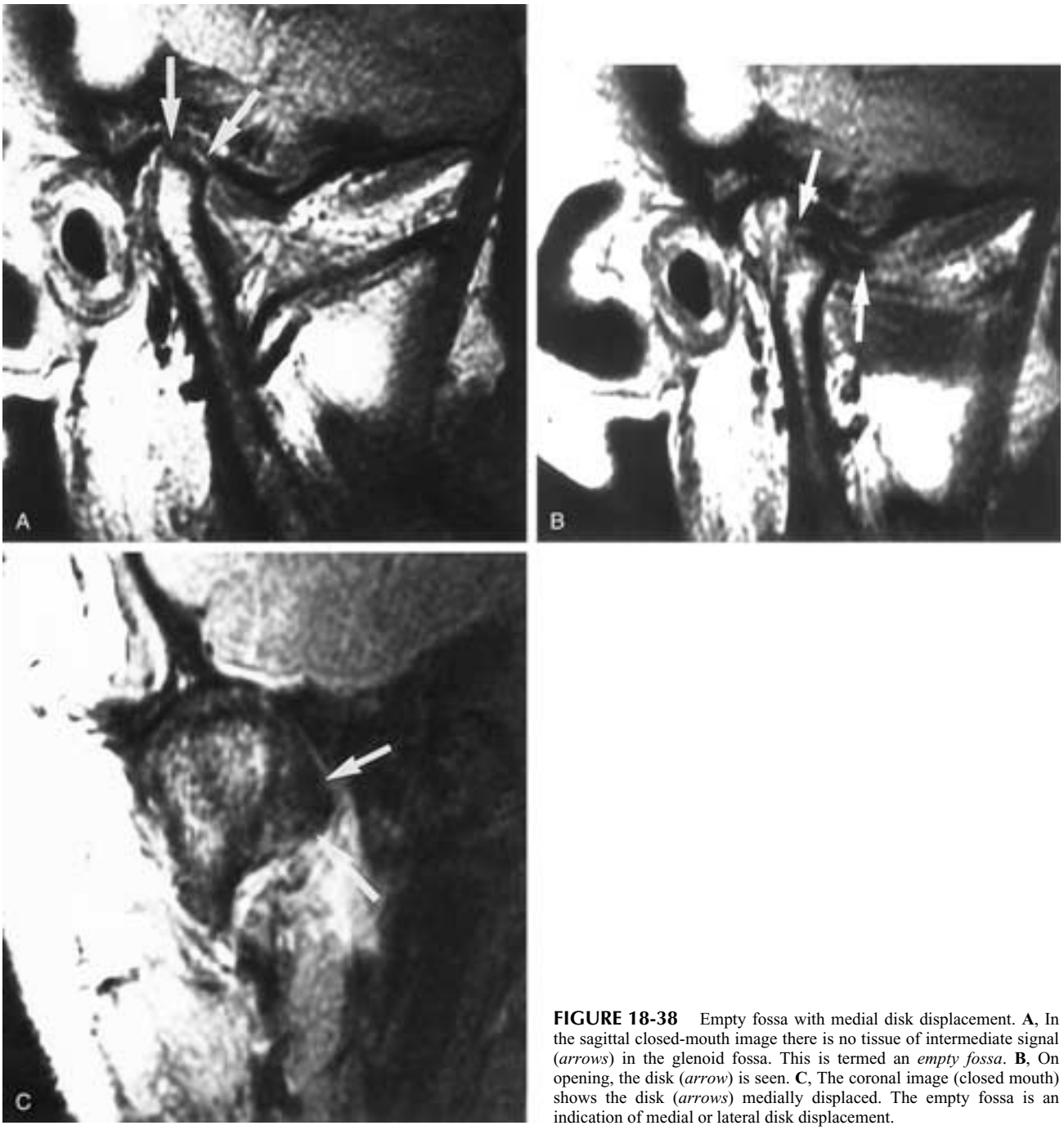

FIGURE 18-38 Empty fossa with medial disk displacement. **A**, In the sagittal closed-mouth image there is no tissue of intermediate signal (*arrows*) in the glenoid fossa. This is termed an *empty fossa*. **B**, On opening, the disk (*arrow*) is seen. **C**, The coronal image (closed mouth) shows the disk (*arrows*) medially displaced. The empty fossa is an indication of medial or lateral disk displacement.

VIEW IMAGE

Osteochondritis Dissecans

Loose bodies are seldom found in the TMJ. One loose body in the joint space associated with a defect in the condyle of the same size can be characterized as osteochondritis dissecans.[89] In this condition, a small part of the condyle is dislodged into the joint space and acts as a small, loose body (Fig. 18-51). The condition has been described as being associated with avascular necrosis, although the relationship between the two conditions is not fully understood.[89] Osteochondritis dissecans has been demonstrated in a cadaver joint (Fig. 18-52). Multiple loose bodies are discussed in the section on Synovial Chondromatosis.

Stuck Disk

In the normal opening sequence, the disk moves relative to both the condyle and the temporal bone component of the joint. Most of the movement in the upper joint compartment represents translation. The disk slides or translates relative to the glenoid. In the lower joint compartment the predominant motion is rotation. The condyle rotates within the concavity of the disk. Translation or sliding of the condyle relative to the disk is normally minimal. It has been suggested in the arthroscopic literature that inability of the disk to move, relative to the glenoid fossa, is a significant cause of pain and dysfunction.[28] This observation has not been extensively and systematically documented, but there

Copyright © 2003, Mosby, Inc. All rights reserved.

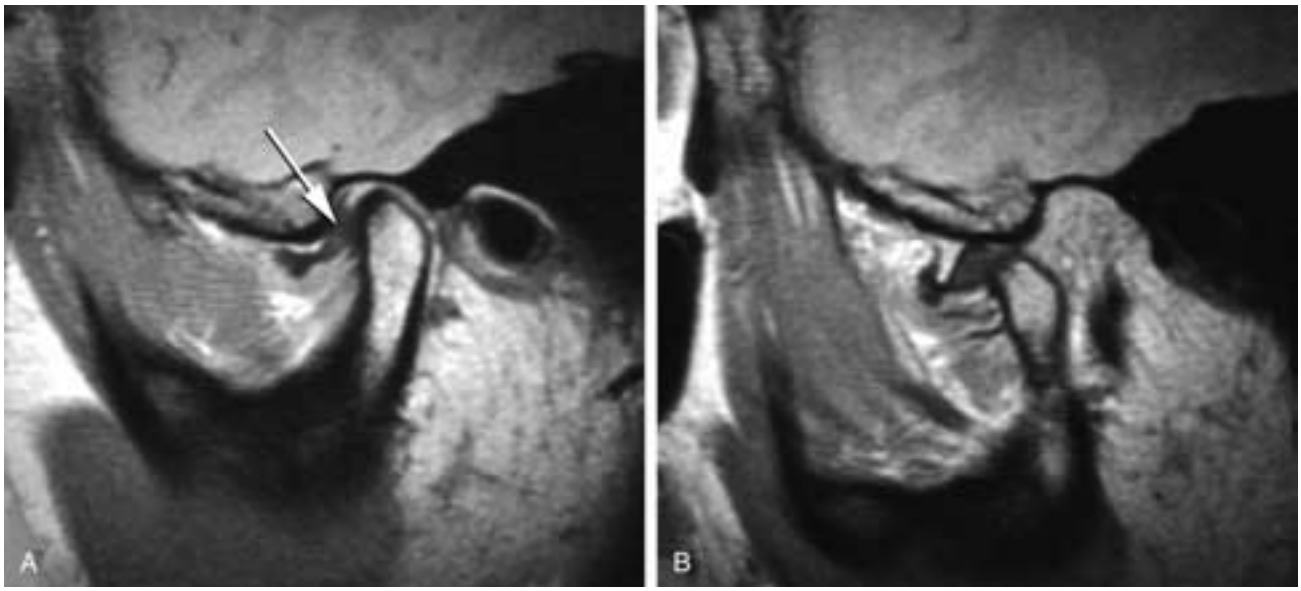

VIEW IMAGE

FIGURE 18-39 Anterior displacement without reduction (closed lock). **A**, The head of the condyle is posteriorly positioned in the glenoid fossa. The posterior thick band of the disk (*arrow*) is completely anterior to the condylar head. **B**, Upon opening of the mouth, the condyle moves to a point just inferior to the articular eminence. Rather than recapturing the disk, it pushes the disk anteriorly and does not regain the normal relationship.

are indications that MR definition of a stuck disk (Figs. 18-53 and 18-54) may be associated with pain and dysfunction.[118] As the patient opens the mouth, the disk maintains a constant relationship to the glenoid while the condyle rotates and may translate relative to the disk.

Lock

The most frequent situation with locking of the TMJ is the inability of the patient to open the mouth completely. This is most frequently caused by anterior disk displacement without reduction.

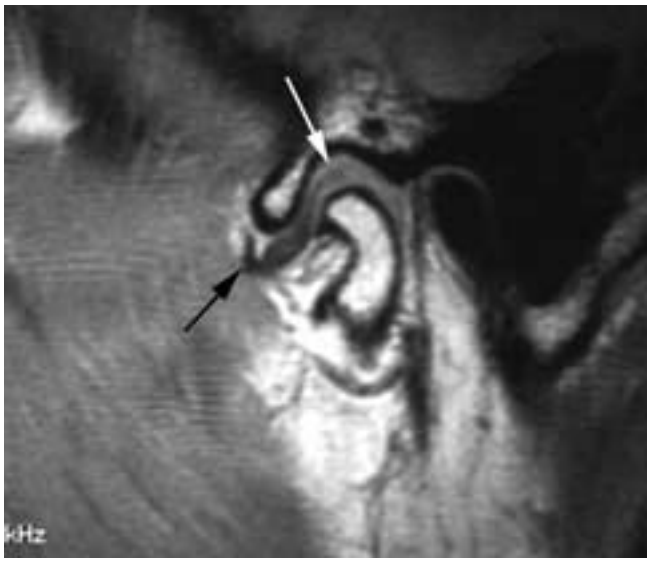

VIEW IMAGE

FIGURE 18-40 Disk deformation. The disk is anteriorly displaced. There is thickening of the posterior band (*black arrow*) and folding of the disk. The lack of signal from the retrodiskal attachments (*white arrow*) suggests fibrosis secondary to the chronic trauma of the dislocation.

The open lock condition is encountered more infrequently. In this condition, the patient can open the mouth widely but is temporarily or permanently unable to close the mouth. This condition sometimes requires manipulation of the jaw by the patient or a health care professional to move the mandible into place. These patients frequently present in the emergency room but rarely for imaging assessment.

There are two different causes of the open lock condition.

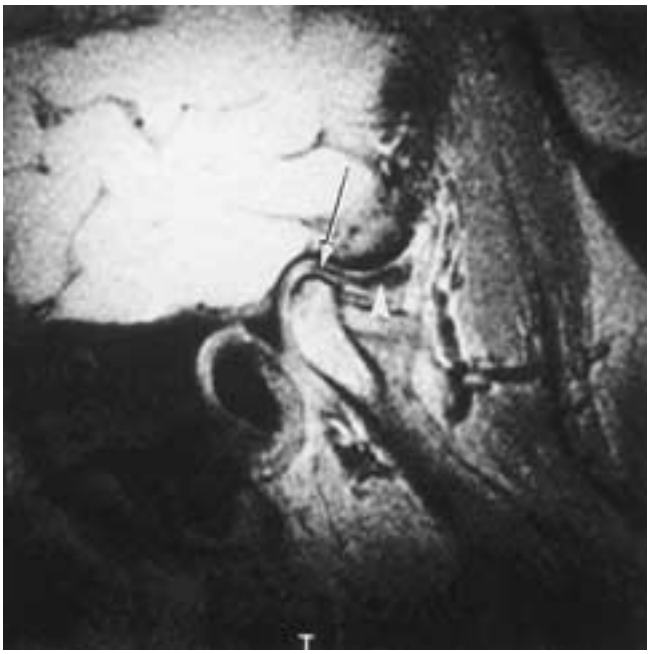

FIGURE 18-41 Fibrosis of the posterior disk attachment. The disk (*arrowhead*) is anteriorly displaced. There is an area of low signal in the posterior disk attachment (*long arrows*), which indicates fibrosis.

VIEW IMAGE

Copyright © 2003, Mosby, Inc. All rights reserved.

In the classic situation, the condyle is luxated (subluxed or dislocated) in front of the articular eminence, and the articular eminence prevents the condyle from retruding back into the glenoid fossa. In the other situation, the condyle translates anteriorly to the anterior band of the disk, and the disk prevents the condyle from retruding back into the glenoid fossa (Fig. 18-55). Characteristically, in this situation the disk is folded behind the condyle (Fig. 18-55). It is usually not possible to differentiate between the two causes on physical examination. Although acute management with reduction of the subluxation is similar in both situations, if definitive surgery is necessary, it differs depending on the cause of the subluxation. If the disk is blocking the reversion of the condyle, surgery has to be directed to the disk. If the articular eminence is the cause of the patient's inability to close the mouth, surgery must focus on the bone.

Accuracy of TMJ Imaging

Knowing the diagnostic accuracy of an imaging modality is essential for its clinical use. The accuracy of tomography, arthrography, CT, and MR imaging has been investigated in several studies on fresh autopsy material (Tables 18-2 and 18-3 on p. 1029).[81, 119–122] All techniques have demonstrated relatively high accuracy in determining osseous conditions and disk position; however, MR imaging has the highest accuracy and demonstrates both joint structures and the soft tissues surrounding the joint.

The accuracies noted in Tables 18-2 and 18-3 are from investigations performed without the biases of clinical work. The figures are relevant for the comparison between the different techniques because the studies were performed under the same conditions. In a clinical situation, however, additional information about the patient is available that

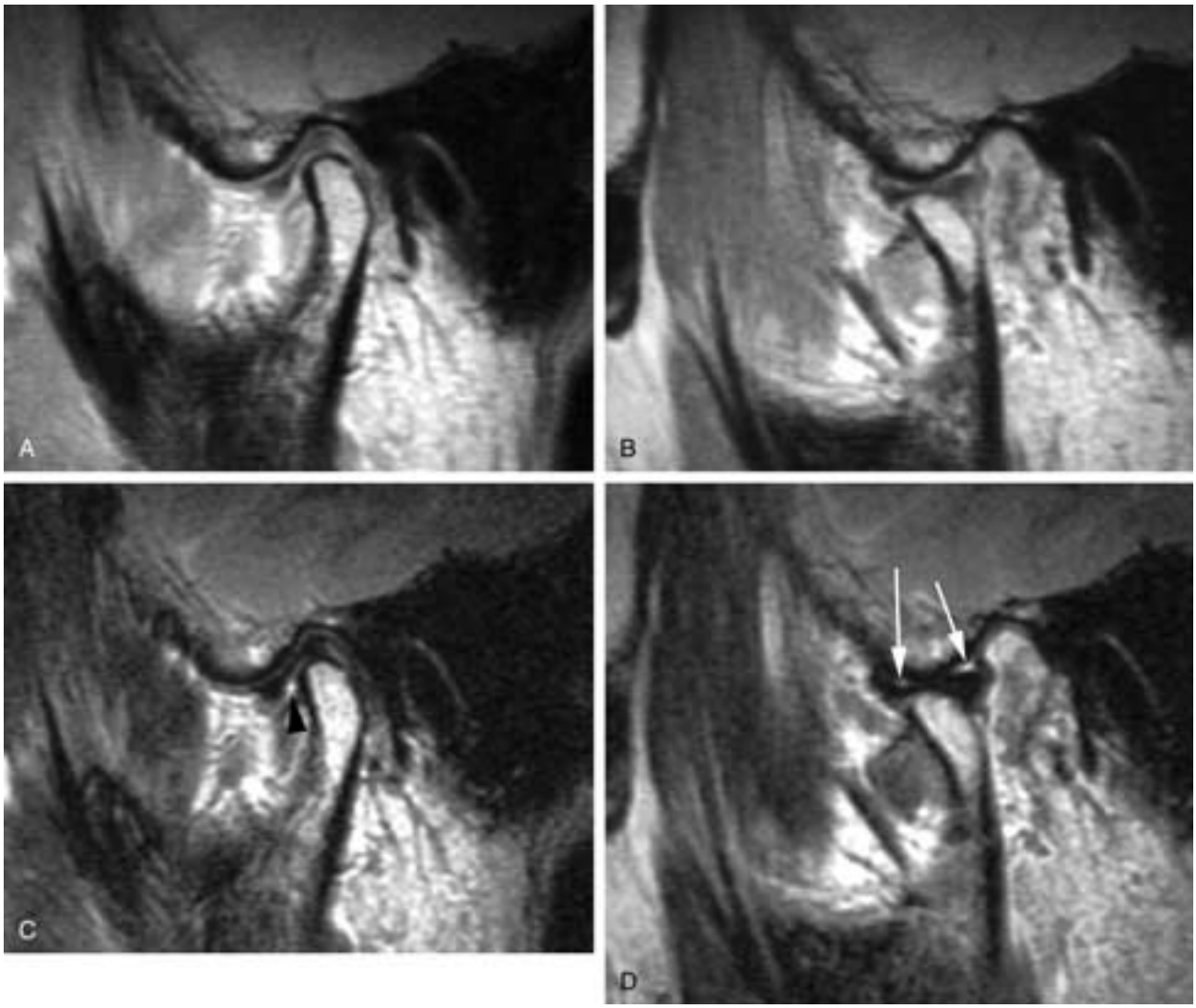

VIEW IMAGE

FIGURE 18-42 Normal TMJ with minimal joint fluid. **A**, Proton density image, closed-mouth position. The disk is seen in the normal location. The condyle is in the normal position relative to the glenoid fossa. **B**, Open-mouth position. The disk and condyle have translated downward beneath the articular eminence. **C**, T2-weighted image, closed-mouth position. A very small amount of high signal (*arrowhead*), which may represent a small amount of fluid in the anterior recess of the inferior joint space. **D**, T2-weighted image, open-mouth position, shows a small amount of fluid (*arrows*) in the superior joint space.

Copyright © 2003, Mosby, Inc. All rights reserved.

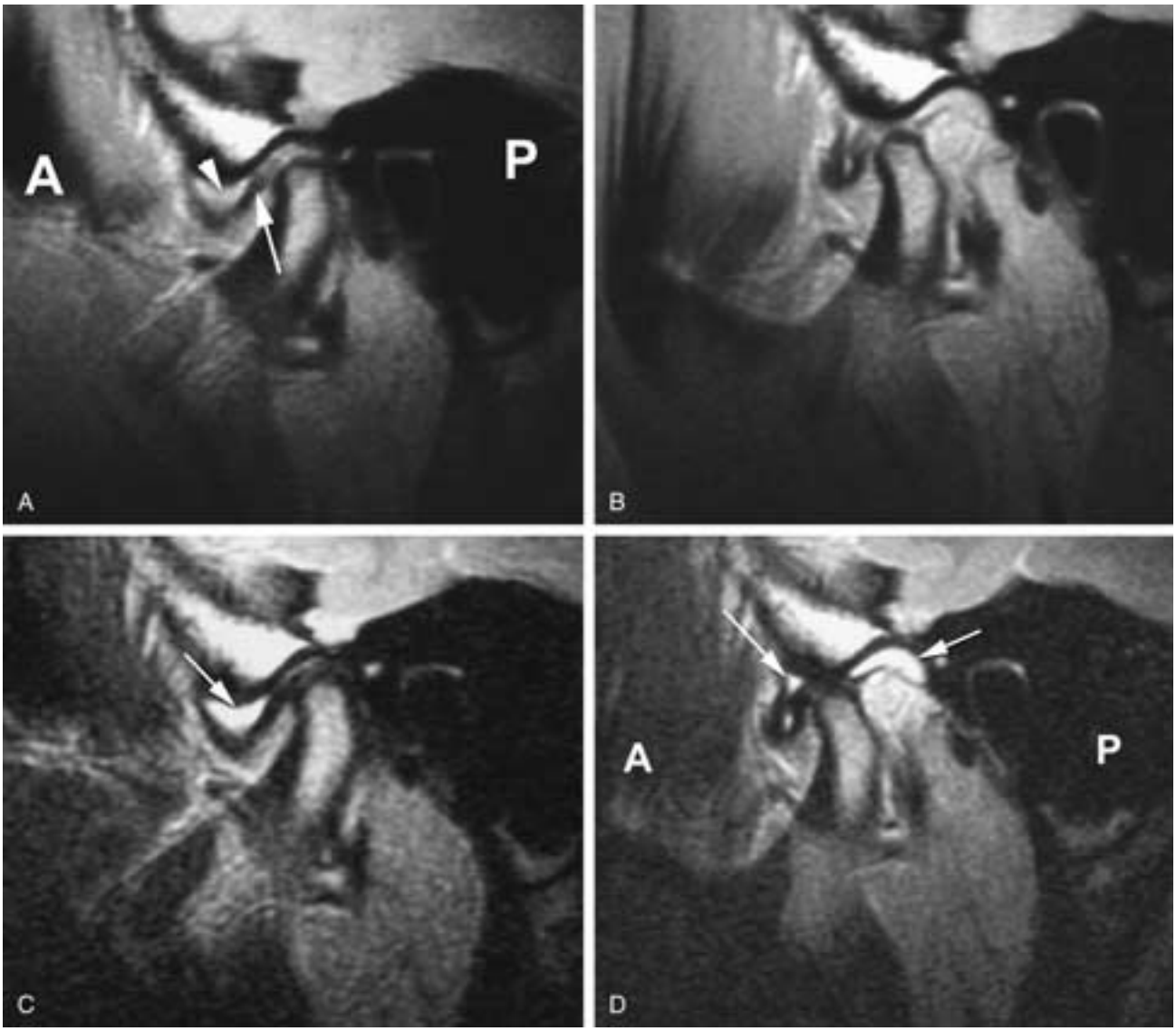

VIEW IMAGE

FIGURE 18-43 Large amount of joint fluid (effusion) in a painful joint. Closed lock (anterior displacement without recapture). **A**, Proton density image. The disk is completely dislocated anteriorly in the closed-mouth position. The fluid (*arrowhead*) in the upper joint compartment can be appreciated even on the proton density image. Posterior thick band (*arrow*). **B**, Open-mouth position, proton density image. The condyle pushes the disk anteriorly but does not recapture. The disk is deformed. **C**, T2-weighted image, closed-mouth position. The bright fluid (*arrow*) in the upper compartment of the joint is easily appreciated. **D**, Open-mouth position. The fluid in the joint (*arrows*) is more clearly seen on the T2-weighted image. Anteriorly, the fluid outlines the upper contour of the disk. Posteriorly, the fluid outlines the superior surface of the bilaminar folds (retrodiskal tissues). *A*, anterior; *P*, posterior.

might help further improve interpretation of the image. In addition, by detecting medially or laterally displaced disks, the multiplanar imaging capability of MR imaging may provide even greater accuracy (Fig. 18-56). A recent study demonstrated the accuracy of MR imaging in determining disk position and configuration to be more than 90%.[123]

Imaging After Treatment

Imaging after surgical treatment is indicated in patients who continue to have symptoms that might be related to intraarticular pathology such as recurrence of disk displacement, intraarticular adhesions, or inflammatory changes. Although surgery is performed for a variety of pathologies of the jaw and TMJ, most surgery is done for patients with internal derangements. For this reason, imaging of the postoperative joint is discussed in this section.

The primary goal of treatment of TMJ disorders is to eliminate pain and dysfunction. Secondary goals are restoration of normal anatomy and prevention of disease progression. If a patient continues to have symptoms after treatment, imaging is frequently helpful in determining the etiology of the problem.

Copyright © 2003, Mosby, Inc. All rights reserved.

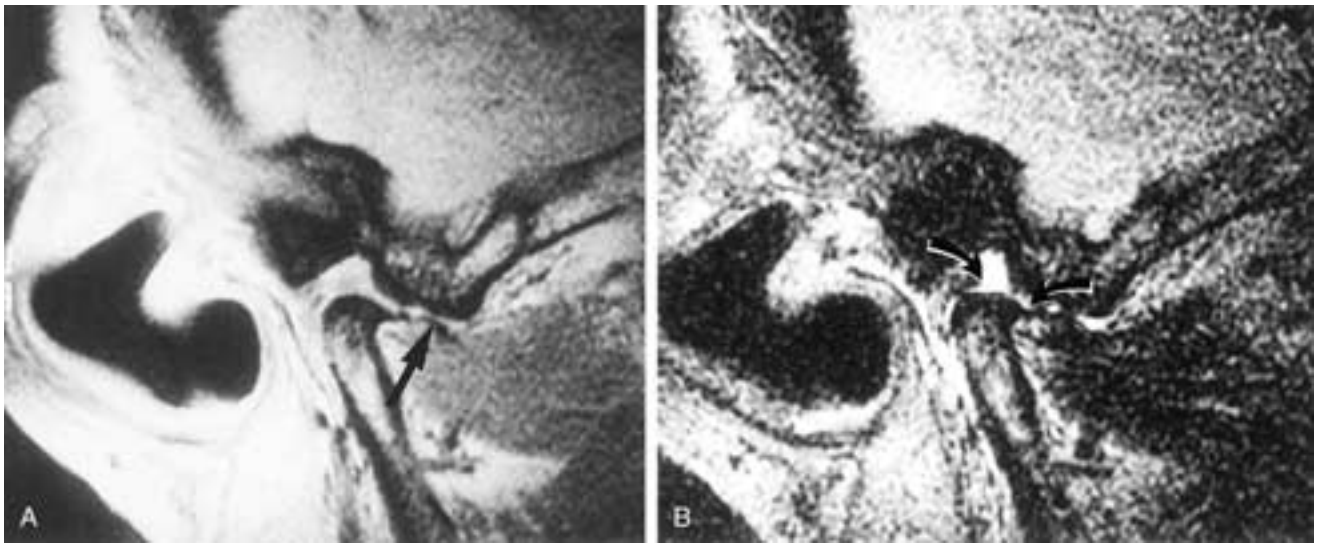

VIEW IMAGE

FIGURE 18-44 Disk perforation demonstrated with proton density. **A**, The disk (*arrow*) is anteriorly displaced and extensively deformed. There is an anterior osteophyte of the condyle indicating degenerative changes. Also, the component is flattened. **B**, In the T2-weighted image the defect in the posterior disk attachment (*arrows*) is well outlined by the joint effusion.

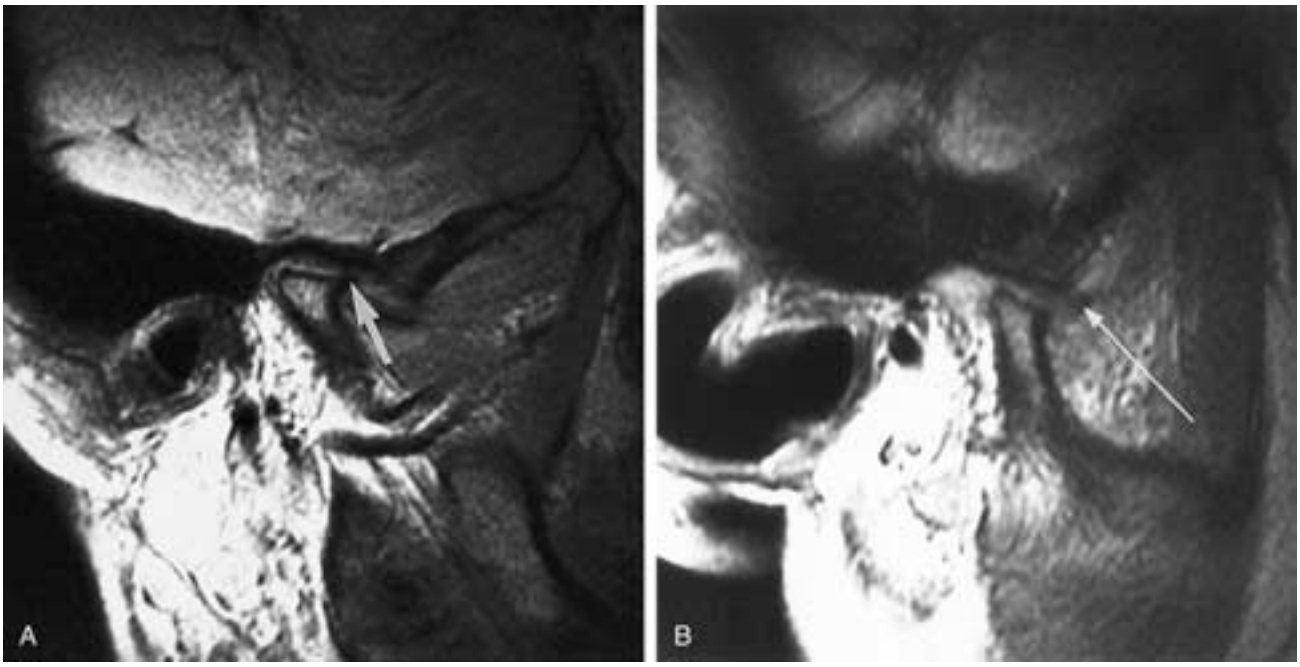

VIEW IMAGE

FIGURE 18-45 Osteoarthritis. **A**, Proton density closed-mouth image shows an anterior osteophyte of the condyle (*arrow*) and superior flattening. The glenoid fossa is widened, and the articular tubercle is flattened. These changes are consistent with degenerative joint disease. **B**, On opening, the two flat articular surfaces slide against each other and a small part of the disk remains anterior (*arrow*).

Copyright © 2003, Mosby, Inc. All rights reserved.

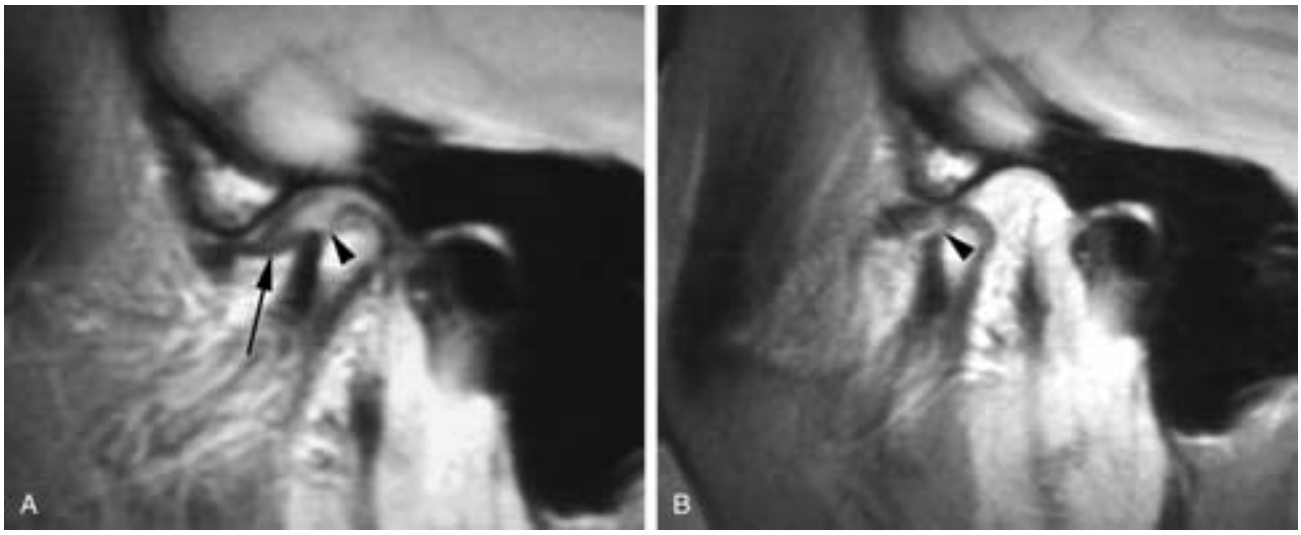

VIEW IMAGE

FIGURE 18-46 Osteoarthritis with erosion of the condylar head. **A**, Proton density MR image shows a defect (*arrowhead*) in the head of the condyle. The disk is completely dislocated anteriorly, with the posterior thick band (*arrow*) completely anterior to the condylar head. **B**, Open-mouth position. The condyle pushes the disk anteriorly but does not recapture. Note how the posterior thick band fits into the cortical defect (*arrowhead*) and the head of the condyle.

Treatment Modalities for TMJ Internal Derangement

Conservative treatment of TMJ internal derangement includes reassurance, observation, occlusal adjustment, bite splints, nonsteroidal antiinflammatory medications, muscle relaxants, and physical therapy. Arthroscopic surgery includes lysis and lavage of adhesions and disk repositioning. Open joint surgery includes disk repositioning, diskectomy without replacement, diskectomy with autologous implant, and joint reconstruction with rib grafts. The use of alloplastic disk replacement implants has been discontinued.

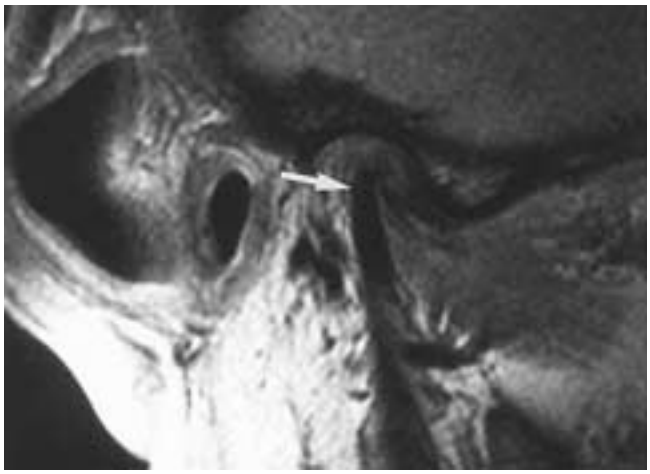

VIEW IMAGE

FIGURE 18-47 Sclerosis of the condyle and condyle neck. A proton density image shows decreased signal from the entire condyle head and condyle neck (*arrow*). This may indicate sclerosis, fibrosis, or possibly avascular necrosis. No histologic proof was available in this case.

Imaging Techniques after Surgical Treatment

Before the availability of MR imaging, plain films (Fig. 18-57), tomography, and arthrography were used to evaluate patients after surgery. Plain films and tomography show only the osseous structures, and there is often a need for soft-tissue evaluation as well. Arthrography can be difficult to perform once surgery has been done because the anatomy is altered and the joint spaces are narrowed as a result of peripheral and intraarticular adhesions (Fig. 18-58). For this reason, MR imaging is a preferable method of examination in most postoperative patients.[1, 82, 83]

Postoperative MR imaging is helpful in confirming whether surgical treatment has corrected the position of the displaced disk. Frequently, however, the disk remains anteriorly displaced after disk-repositioning surgery. This is seen in both symptomatic and asymptomatic individuals, and less emphasis should be placed on the position of the disk after surgery because symptoms may be associated more with peripheral adhesions than with disk position per se.

In patients who have undergone diskectomy, there is a soft-tissue interface between the condyle and the glenoid fossa (Fig. 18-59), which is a natural replacement for the extirpated disk.[124] This is a normal postsurgical development. On MR imaging this soft tissue has intermediate to high signal intensity compared to fibrous adhesions, which have low signal intensity (Fig. 18-60). The most important imaging assessment in these patients is to evaluate for peripheral or intraarticular adhesions following diskectomy, because such adhesions (Fig. 18-60) frequently are the cause of the patient's limited opening and pain. Thickening of the lateral joint capsule is also frequently seen after surgery (Fig. 18-61) in both symptomatic and asymptomatic individuals and is probably of limited clinical significance as long as the scar tissue does not extend into the joint space. The amount of scar tissue in the lateral capsule wall varies

Copyright © 2003, Mosby, Inc. All rights reserved.

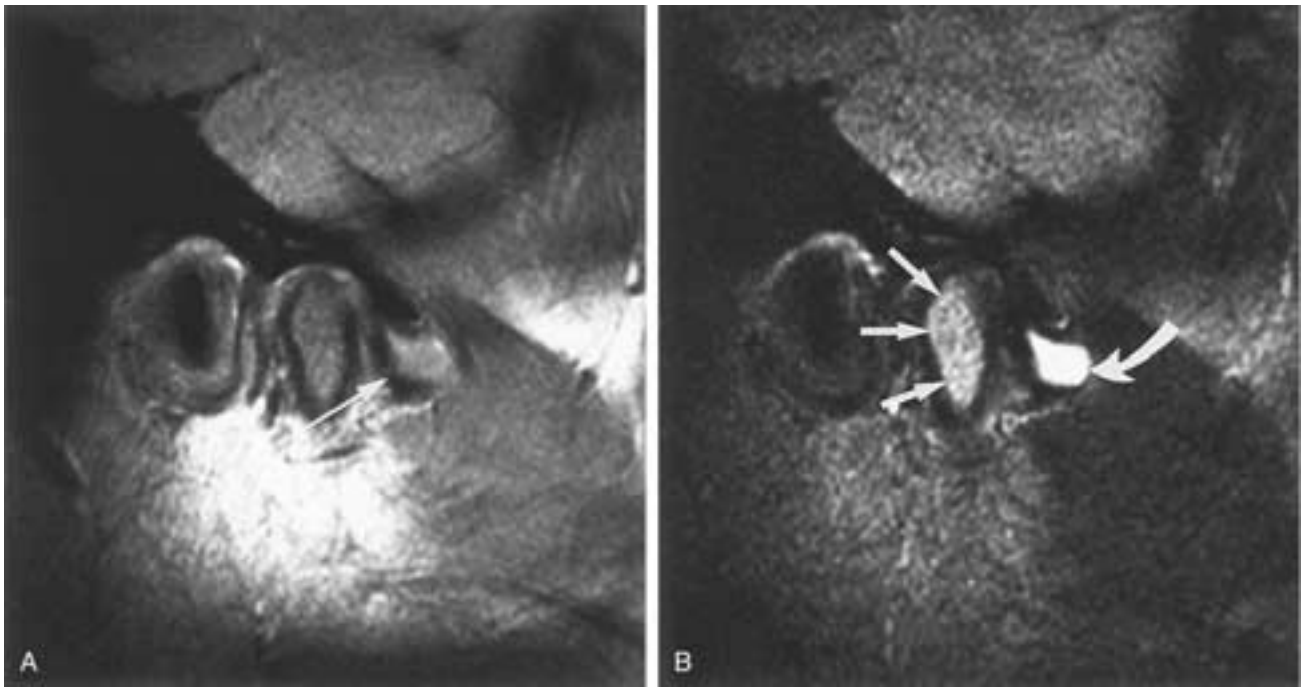

VIEW IMAGE

FIGURE 18-48 Bone marrow edema. **A**, Proton density sagittal MR image shows anterior displacement of the disk (*arrow*). **B**, T2-weighted image shows increased signal in the bone marrow of the condyle (*arrows*). There is also a large effusion (*curved arrow*) in the upper joint space. The increased signal in the bone marrow indicates bone marrow edema.

significantly among patients; some scar tissue in asymptomatic patients is quite large but does not extend into the joint space (Fig. 18-61).

Complete fibrous (Fig. 18-60) or bony ankylosis may occur after surgery in a few instances. Jaw motion is severely restricted, but opening can be up to about 10 mm, even with a heavy fibrous ankylosis. In bony ankylosis there is no motion. CT or tomography is preferred over MR imaging for demonstration of these bony changes.

Alloplastic Implants

During the 1980s and early 1990s, alloplastic implants were used to replace the disk. Two types of implants, Proplast Teflon (Figs. 18-62 and 18-63) and silicone rubber material (Silastic) were mainly used. The Proplast implants were intended to be permanent, whereas the silicon implants were used either on a temporary or a permanent basis. The initial results were favorable and these surgical techniques

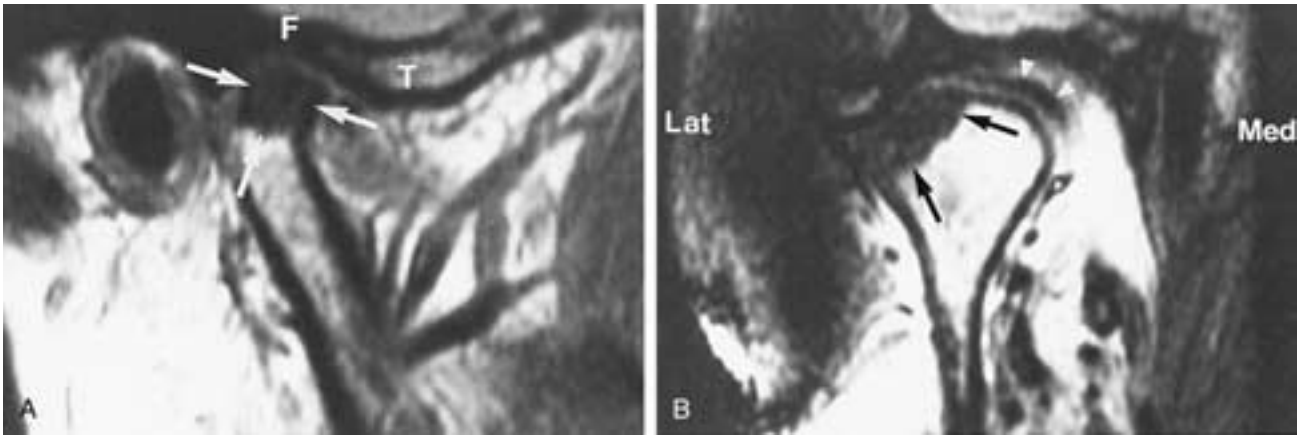

VIEW IMAGE

FIGURE 18-49 Probable aseptic necrosis. **A**, Sagittal MR image showing decreased signal from the bone marrow in the upper part of the mandibular condyle (*arrows*). The fossa (*F*) and tubercle (*T*) are indicated. **B**, Coronal MR image of the same joint as in **A** showing the low signal intensity area (*arrows*) in the lateral part of the joint. In the medial part of the condyle, the disk is seen superior to the condyle (*arrowheads*) and laterally the disk is absent, suggesting perforation.

Copyright © 2003, Mosby, Inc. All rights reserved.

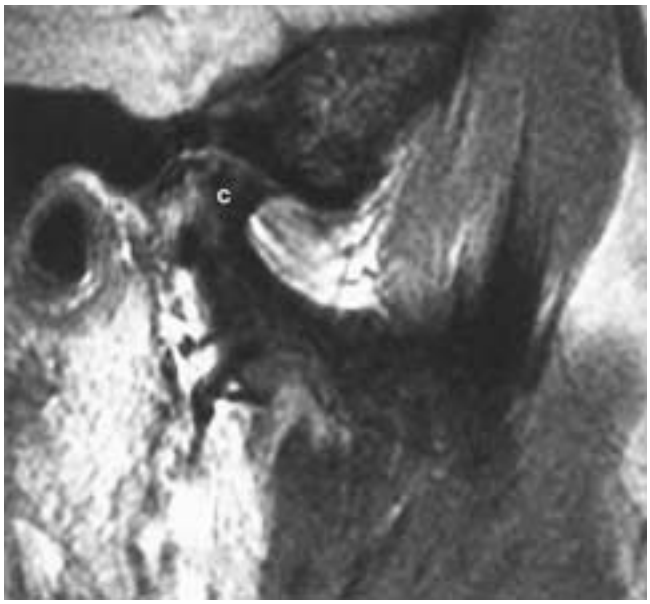

VIEW IMAGE

FIGURE 18-50 Sagittal proton density MR image showing degenerative changes of the mandibular condyle (*C*). A core biopsy of this condyle showed avascular necrosis.

quickly gained popularity, although clinical studies to support long-term success were lacking. After about 2 to 4 years, patients frequently developed gradually increasing pain. This was later shown to be due to fragmentation of the implant material and a foreign body giant cell reaction to this material. Although the reaction to the particulated material was similar with both Silastic and Proplast, it seemed more aggressive with Proplast. Clinically, the patient presented with pain, and radiographically erosive changes of the bone have been observed (Fig. 18-64). The long-term prognosis for TMJ alloplastic implants is poor, and probably all implants eventually have to be removed.

While the implants are still in place, imaging evaluation is frequently necessary. The principal findings relate to the extent of erosive change of the glenoid fossa and the mandibular condyle. The integrity of the glenoid fossa is critical since erosions can extend into the middle cranial fossa (Fig. 18-63). For the initial evaluation of a patient with a TMJ alloplastic implant, both MR imaging (Fig. 18-62) and CT (Figs. 18-63 and 18-65) may be necessary. MR imaging shows the extent of the soft-tissue alteration (Fig. 18-62), fragmentation of the implant material, and expansion of the joint capsule. CT is valuable for assessment of bones, especially the integrity of the glenoid fossa (Fig. 18-63B). For follow-up examination, CT with coronal or sagittal images is the optimal imaging modality. Irregularity of the implant is best appreciated on CT. Sagittal or coronal CT images best demonstrate the implant and show erosive changes of the condyle most clearly. The status of the condyle following the temporary use of Silastic is best appreciated on CT, as is the bony ankylosis that may occur between the condyle and the glenoid fossa (Fig. 18-64).

FIGURE 18-51 Osteochondritis dissecans. Sagittal MR image shows a defect in the upper part of the condyle (*arrowheads*) and a corresponding structure in the glenoid fossa, which was interpreted as a loose body (*long arrow*). This condition is consistent with osteochondritis dissecans.

VIEW IMAGE

Copyright © 2003, Mosby, Inc. All rights reserved.

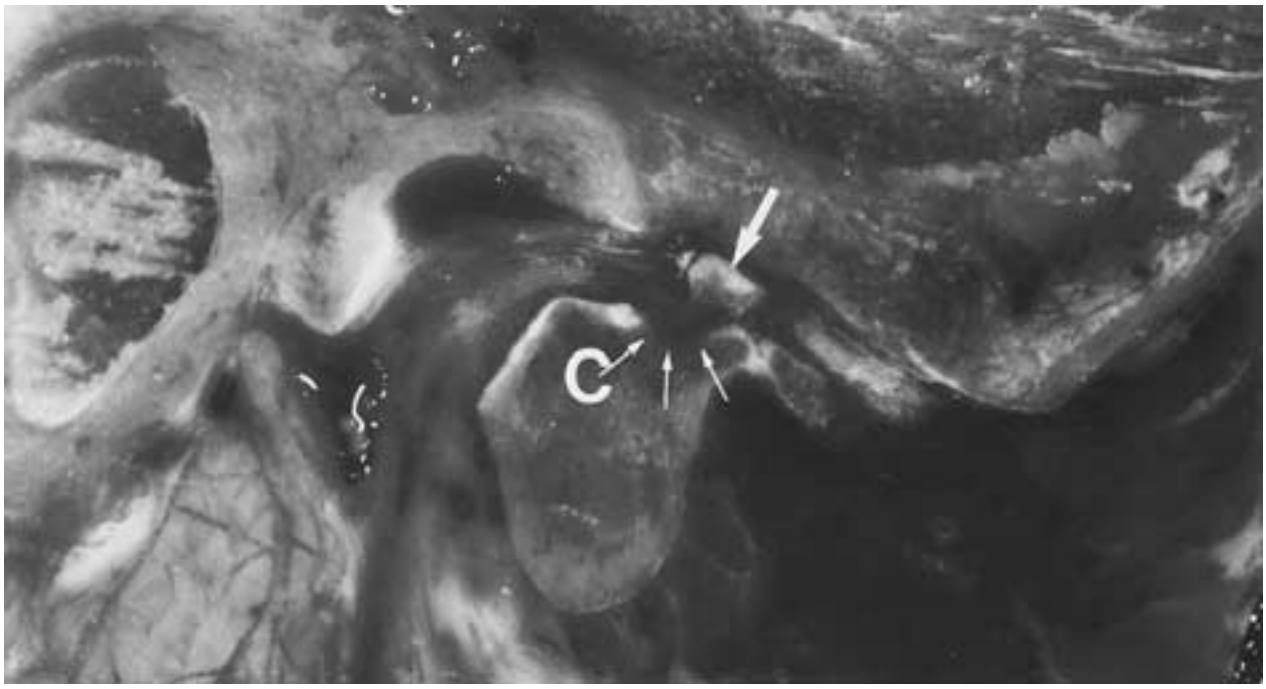

VIEW IMAGE

FIGURE 18-52 Osteochondritis dissecans. Cadaver specimen with advanced degenerative changes and a loose body (*thick arrow*) in the joint space with a corresponding defect in the mandibular condyle (*thin arrows*). Condyle (*C*).

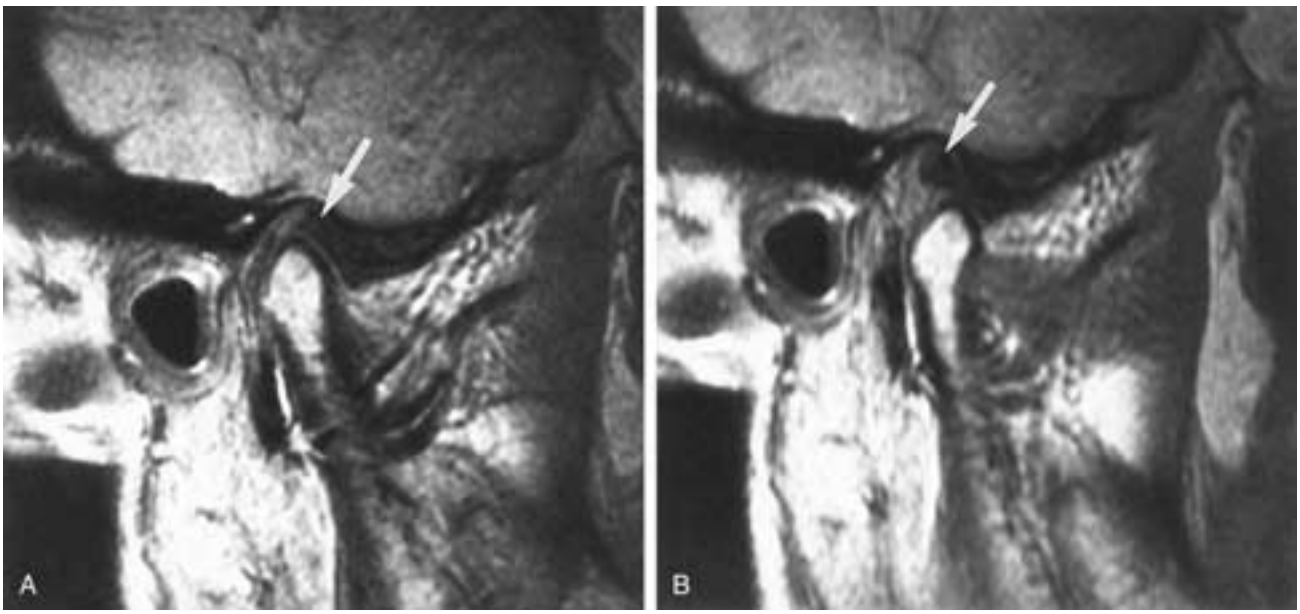

VIEW IMAGE

FIGURE 18-53 Stuck disk. Sagittal proton density MR images with a closed mouth (**A**) and maximal mouth opening (**B**) in a patient with limitation of mouth opening. The disk (*arrow*) is located in the normal superior position with a closed mouth. On opening, the disk does not move out of the glenoid fossa and the condyle does not translate all the way down to the articular eminence. This is consistent with a stuck disk condition.

Copyright © 2003, Mosby, Inc. All rights reserved.

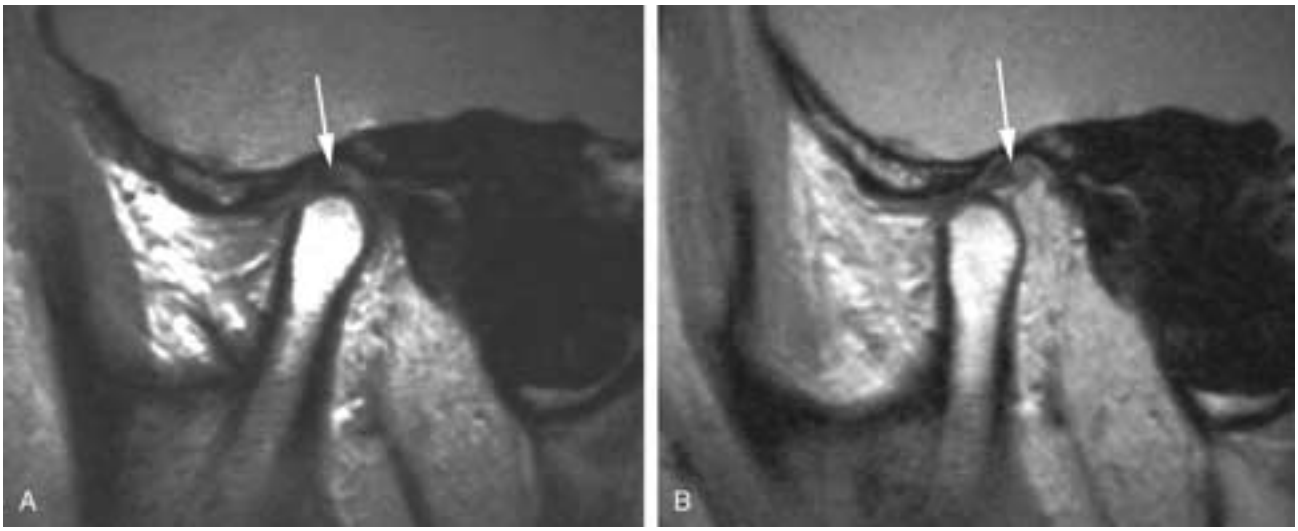

VIEW IMAGE

FIGURE 18-54 Stuck disk. **A**, In the closed-mouth position, the condyle has a normal relationship to the disk. The posterior edge of the posterior thick band (*arrow*) is located immediately superior to the condylar head. **B**, In the open-mouth position, the condyle has translated anteriorly and now is seated on the thick anterior portion of the disk. The disk has not moved relative to the glenoid and the articular eminence. Note that the posterior edge of the disk (*arrow*) remains at the same point as in the closed-mouth image.

Total Joint Replacement

Total replacement of the TMJ has been attempted for many years.[125, 126] There continue to be problems with stabilization of both the glenoid and condyle parts of the prosthesis, and these patients frequently present for imaging evaluation. In a situation where there are large metallic implants, neither CT nor MR imaging is feasible because of degradation artifacts. Plain films and tomography are the only imaging modalities available (Fig. 18-66). The assessment should concentrate on motion between the implant and the underlying bone, osteolytic changes of the bone, and evidence of loosening of the implant.

Costochondral Grafts

Costochondral grafts were formerly used for reconstruction of the TMJ and have recently regained popularity since the alloplastic joint prostheses have essentially been abandoned.[127] Imaging of costochondral grafts can be done with plain films, tomography, CT, and MR imaging. MR imaging gives good images of the cartilaginous part of the graft. CT shows the osseous part of the graft but does not show the cartilaginous segment as well (Figs. 18-67 and 18-68). The size and orientation of the cartilaginous segment are represented by the apparent gap between the osseous part of the graft and the skull base, and the cartilage itself can

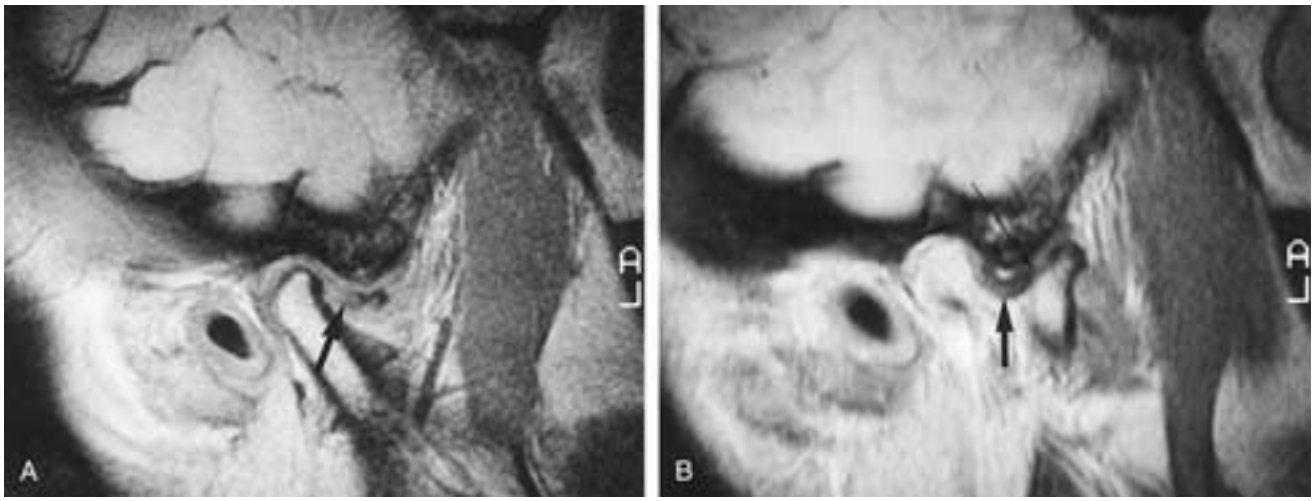

VIEW IMAGE

FIGURE 18-55 Subluxation in front of the disk. **A**, Proton density sagittal MR image shows the disk (*arrow*) anterior to the condyle. The disk is deformed. **B**, On maximal mouth opening the condyle is in front of the disk (*arrow*), and the disk is preventing the condyle from reverting back into the glenoid fossa. The long arrow indicates the anterior edge of the disk.

Copyright © 2003, Mosby, Inc. All rights reserved.

Table 18-2
ACCURACY OF TMJ IMAGING OSSEOUS CHANGES

Imaging	Accuracy (%)	Sensitivity	Specificity
Tomography	63–85	0.47	0.94
CT	66–87	0.28–0.75	0.91–1.0
MR imaging	60–100	0.50–0.87	0.71–1.0

Modified from Lindvall AM, et al. Radiographic examination of the temporomandibular joint. Dentomaxillofac Radiology 1976;5:24–32; Bean LR, et al. Comparison between radiologic observations and macroscopic tissue changes in temporomandibular joint. Dentomaxillofac Radiol 1977;6:90–106; Rohlin M, et al. Tomography as an aid to detect microscopic changes of the temporomandibular joint. Acta Odontol Scand 1986;44:131–140; Tanimoto K et al. Comparison of computed tomography with conventional tomography in the evaluation of temporomandibular joint disease: a study of autopsy specimens. Dentomaxillofac Radiol 1990;19:21–27; Westesson P-L, et al. CT and MRI of the temporomandibular joint: comparison using autopsy specimens. AJR 1987;148:1165–1171; Westesson P-L et al. Temporomandibular joint: comparison of MR images with cryosectional anatomy. Radiology 1987;164: 59–64; Hansson L-G et al. MR imaging of the temporomandibular joint: comparisons of images of specimens made at 0.3T and 1.5T with cryosections. AJR 1989;152:1241–1244; and Tasaki MM, Westesson P-L. Temporomandibular joint: diagnostic accuracy with sagittal and coronal MR imaging. Radiology 1993;186: 723–729.

Table 18-3
ACCURACY OF TMJ IMAGING FOR DISK POSITION

Imaging	Accuracy (%)	Sensitivity	Specificity
Lower space, single-contrast arthrography	84–100	0.95	0.76
CT	40–67	0.45–0.85	0.50–0.87
MR imaging	73–95	0.86–0.90	0.63–1.0

Modified from Westesson P-L et al. Temporomandibular joint: Correlation between single-contrast videoarthrography and post mortem morphology. Radiology 1986;160:767–771; Schellhas KP et al. The diagnosis of temporomandibular joint disease: two-compartment arthrography and MR. AJNR 1988;51:341–350; Tanimoto K et al. Computed tomography versus single-contrast arthrotomography in evaluation of the temporomandibular joint disc. A study of autopsy specimens. Int J Oral Maxillofac Surg 1989;18:354–358; Westesson P-L et al. Temporomandibular joint: Comparison of MR images with cryosectional anatomy. Radiology 1987;164:59–64; Hansson L-G et al. MR imaging of the temporomandibular joint: comparisons of images of specimens made at 0.3T and 1.5T with cryosections. AJR 1989;152:1241–1244; Westesson P-L et al. CT and MRI of the temporomandibular joint: comparison using autopsy specimens. AJR 1987;148:1165–1171; and Tasaki MM, Westesson P-L. Temporomandibular joint: diagnostic accuracy with sagittal and coronal MR imaging. Radiology 1993;186:723–729.

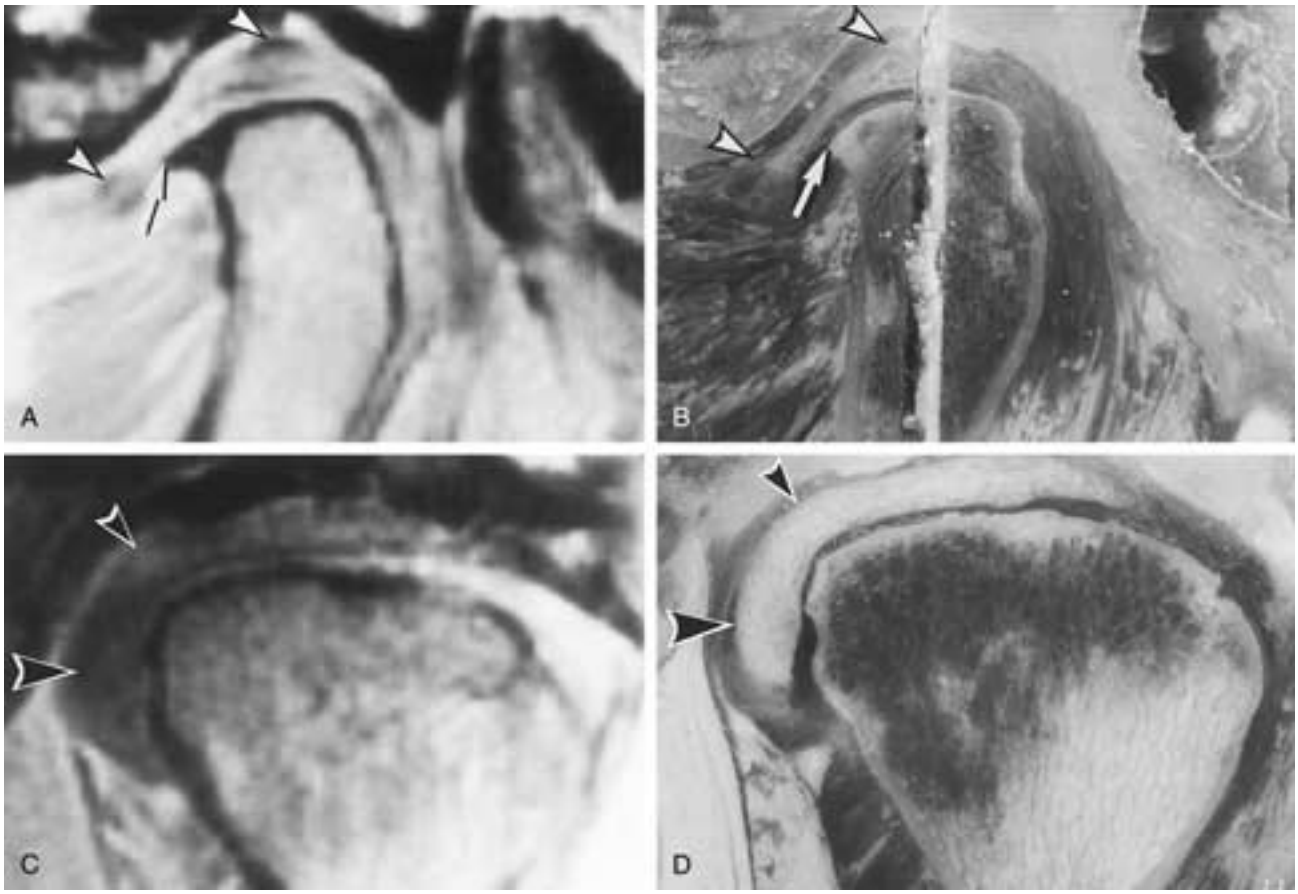

FIGURE 18-56 Correlation between MR image and cryosection. **A** and **C**, Sagittal and coronal MR images show the disk (*arrowheads*) superior to the condyle in the sagittal view (**A**) but medially displaced in the coronal view (**C**). **B** and **D**, The corresponding cryosections confirm the MR images. The condyle also demonstrates an anterior osteophyte (*arrow* in **A**).

VIEW IMAGE

Copyright © 2003, Mosby, Inc. All rights reserved.

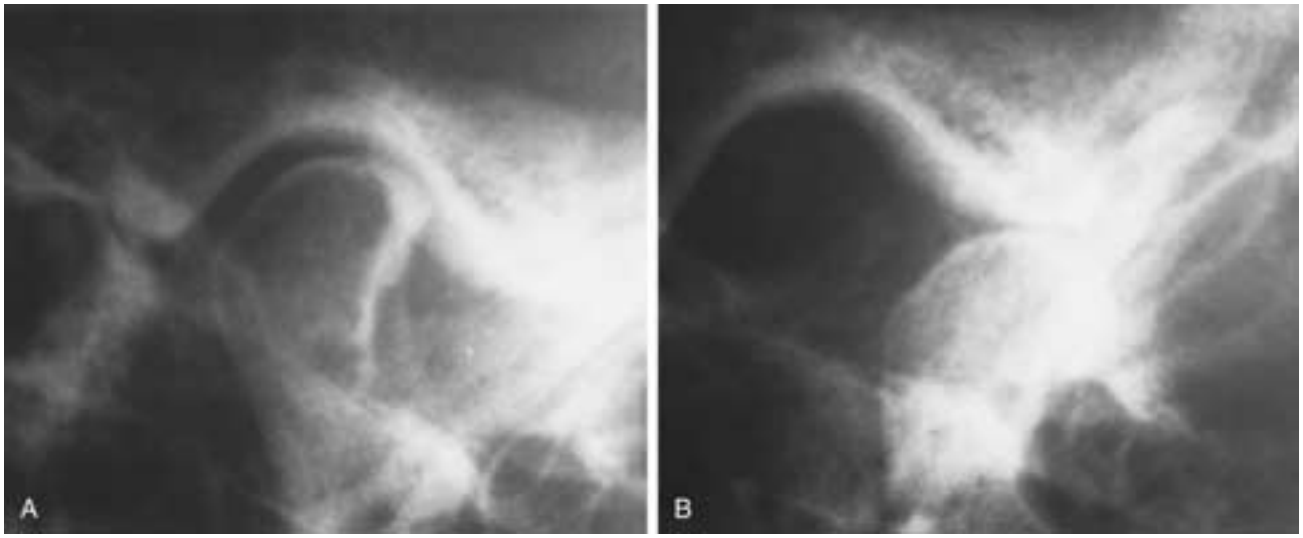

VIEW IMAGE

FIGURE 18-57 Transcranial plain film in the closed-mouth (**A**) and open-mouth (**B**) positions 29 years after diskectomy. The osseous structures are relatively normal, with only a decreased joint space. The outline of the condyle and temporal joint components is smooth, without evidence of degenerative joint disease.

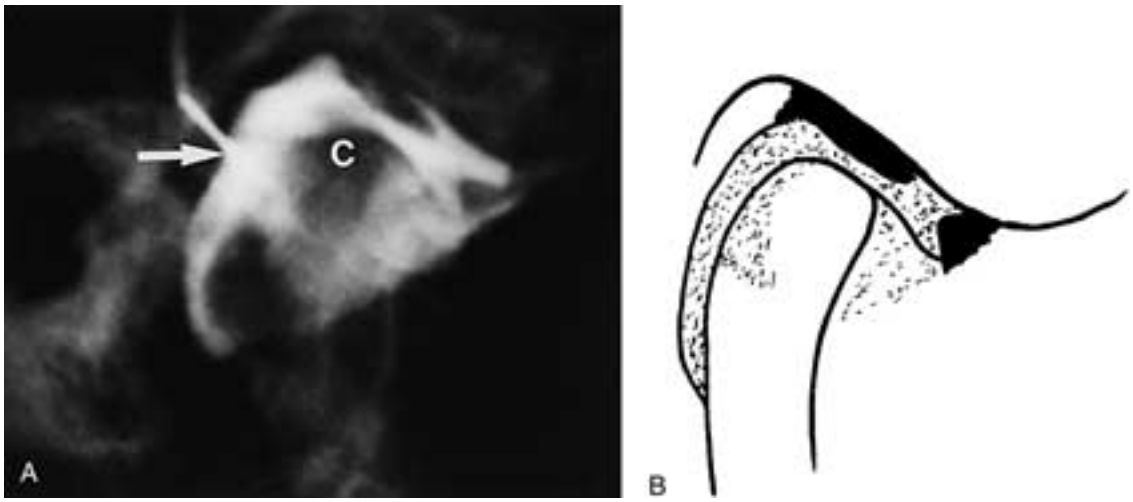

VIEW IMAGE

FIGURE 18-58 **A** and **B**, Postsurgical arthrogram and schematic drawing. Contrast medium was injected into the lower joint space (*arrow*), and there is a perforation to the upper joint space. Peripheral adhesions make the joint space smaller than normal. A disk plication had been performed 2 years before this arthrogram was obtained.

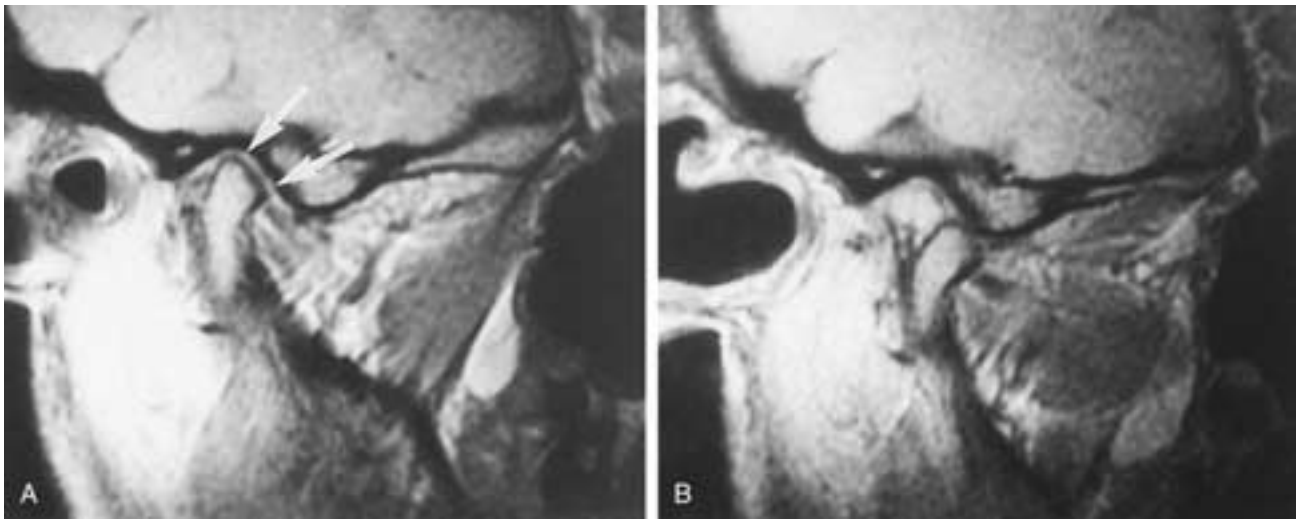

VIEW IMAGE

FIGURE 18-59 Successful diskectomy. **A**, Closed-mouth MR image shows an area of intermediate to high signal (*arrows*) in the joint space. This is the normal appearance after a successful diskectomy. **B**, On opening, the condyle translates anteriorly and inferiorly, and there is no evidence of fibrous ankylosis.

Copyright © 2003, Mosby, Inc. All rights reserved.

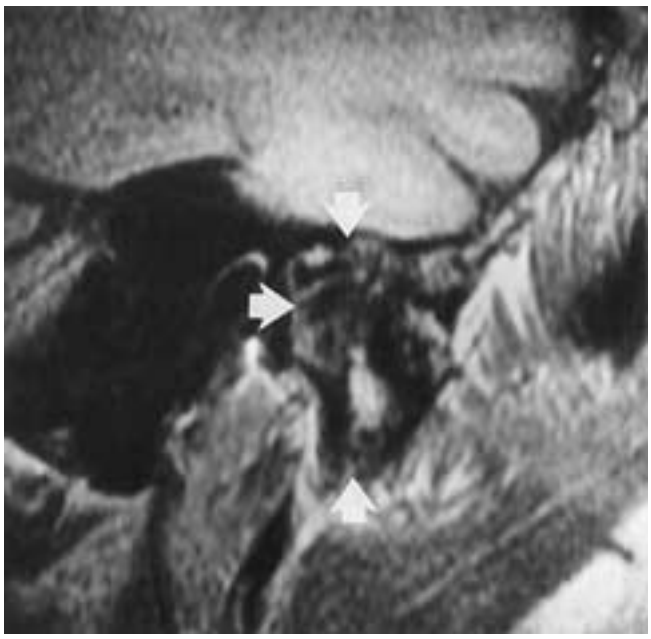

VIEW IMAGE

FIGURE 18-60 Intraarticular adhesions following diskectomy. Sagittal MR image 2 years after diskectomy. There is an irregular area of low signal intensity in the entire joint region (*arrows*). This is indicative of extensive fibrous adhesions.

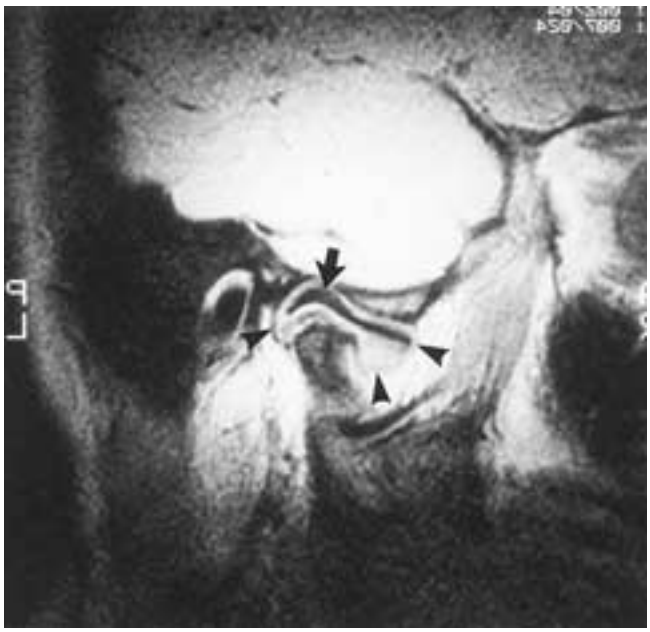

VIEW IMAGE

FIGURE 18-62 Alloplastic TMJ implant. Sagittal proton density MR image shows an alloplastic TMJ implant (*arrow*). The implant has been in place for 3 years, and there is an expanded capsule (*arrowheads*) surrounding it. Degenerative changes of the condyle with an anterior osteophyte are seen.

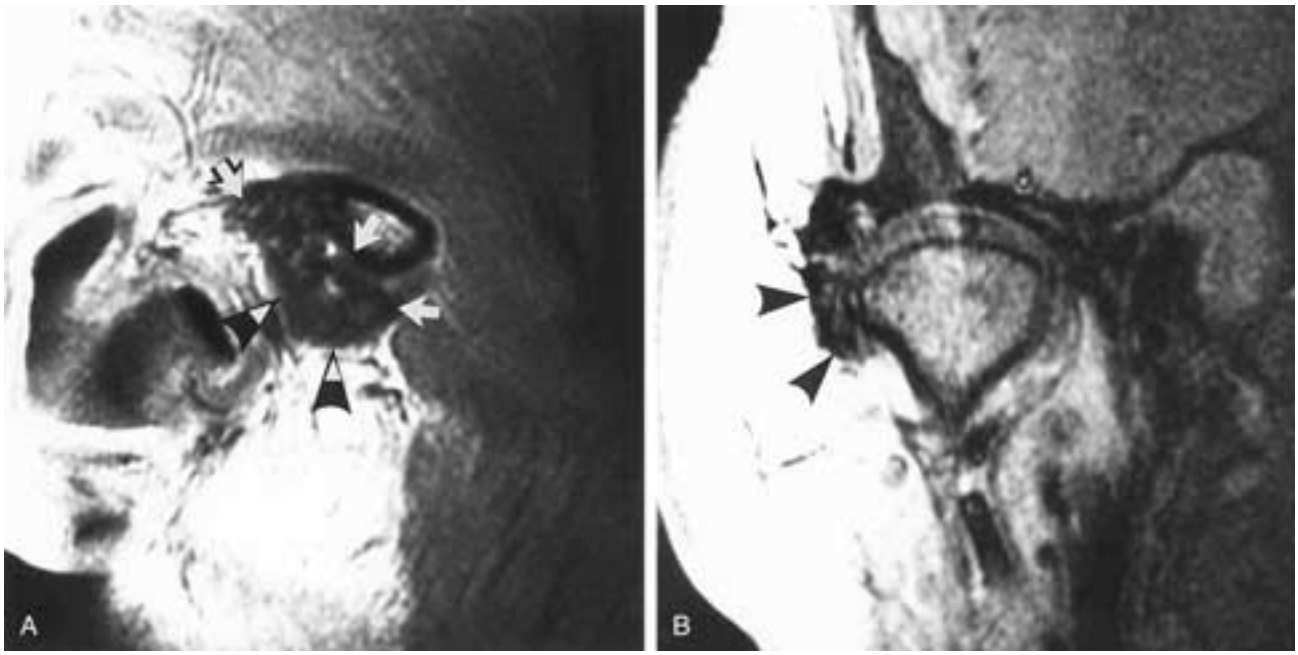

VIEW IMAGE

FIGURE 18-61 Scar tissue in the lateral capsule. Sagittal (**A**) and coronal (**B**) MR images after diskectomy. There is an irregular area of decreased signal in the lateral capsule wall (*arrows*) indicative of scar tissue. Coronal image (**B**) shows the area confined to the capsule wall. This fibrous tissue (*arrowheads*) does not extend into the joint space.

Copyright © 2003, Mosby, Inc. All rights reserved.

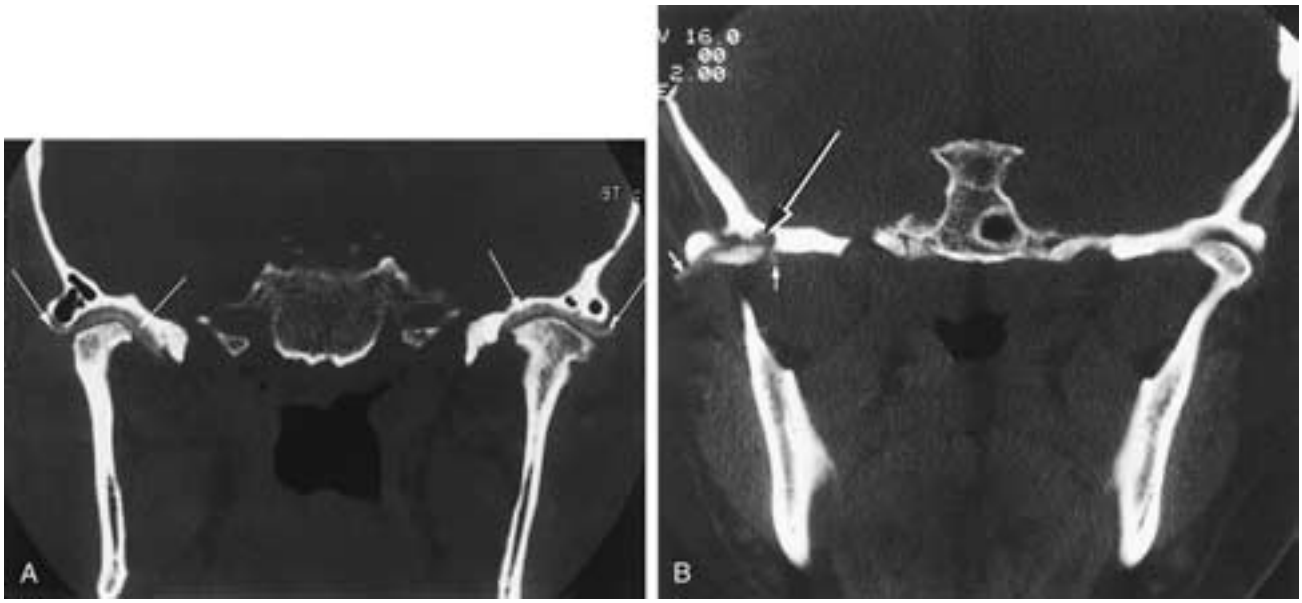

VIEW IMAGE

FIGURE 18-63 **A**, Coronal CT scan of a patient with bilateral Proplast Teflon implants (*arrows*) in good condition. There is no evidence of erosions into the middle cranial fossa, and the implants appear intact and with a good relationship to the condyle and glenoid fossa. **B**, Erosions of the glenoid fossa secondary to an alloplastic implant. Coronal CT scan of another patient with a Proplast Teflon implant (*short arrows*) and erosions of the glenoid fossa (*long arrow*). Also note that the implant is difficult to outline due to partial fragmentation.

sometimes be demonstrated. Points of contact between the osseous part of the graft and the skull base can be demonstrated, and sclerosis of the bone may be present. Fusion can occur, causing progressive limitation of opening. CT imaging with 3D reconstructions allows for a more graphic demonstration of the relationship between the joint components; however, portions of the cartilaginous graft are still not visualized (Fig. 18-69).

Metallic Artifacts

Metallic artifacts are frequently seen in MR imaging of postoperative osseous structures. The metallic artifact appears as an area of signal void bordered by areas of high signal intensity (Fig. 18-70). Even very small metallic particles can cause significant areas of loss of signal, and thus minuscule pieces shredded from metallic instruments used to scrape the bone could be sufficient to create a significant artifact. These small artifacts are seen in both symptomatic and asymptomatic patients after surgery, and they are probably of no clinical significance.[124] The most important aspect of the metallic artifact is that it may prevent further MR imaging.

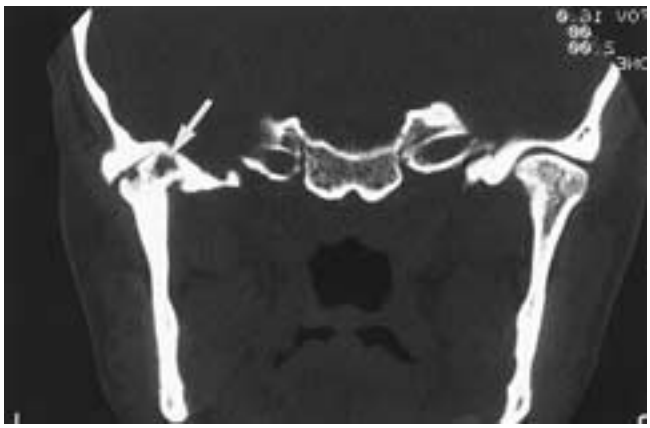

VIEW IMAGE

FIGURE 18-64 Erosions and bony ankylosis following temporary Silastic implant. Coronal CT scans through the TMJ show extensive erosive changes of the right condyle. There is bony ankylosis between the condyle and the glenoid fossa and the medial part of the joint. The patient used a temporary Silastic implant for a few months. These extensive radiographic changes are the sequelae from the use of the implant.

MISCELLANEOUS CONDITIONS INVOLVING THE TMJ

Though most imaging evaluations are done for possible internal derangements and their sequelae, many other types of pathology occasionally affect the TMJ. Tumors, systemic arthritides, and congenital anomalies may be found during an evaluation of the TMJ or during assessment for suspected pathology in the adjacent head and neck region.

Tumors and Tumor-Like Conditions of the TMJ

Synovial Chondromatosis

The TMJ is infrequently affected by tumors. The most common neoplastic lesion affecting the TMJ is probably synovial chondromatosis.[128, 129] This tumor can be locally aggressive, and cases with intracranial extension have been described.[130, 131] It is a benign lesion characterized by formation of multiple small ''pearls'' of cartilage, usually within the joint space. MR imaging can show synovial chondromatosis primarily affecting the upper joint space

Copyright © 2003, Mosby, Inc. All rights reserved.

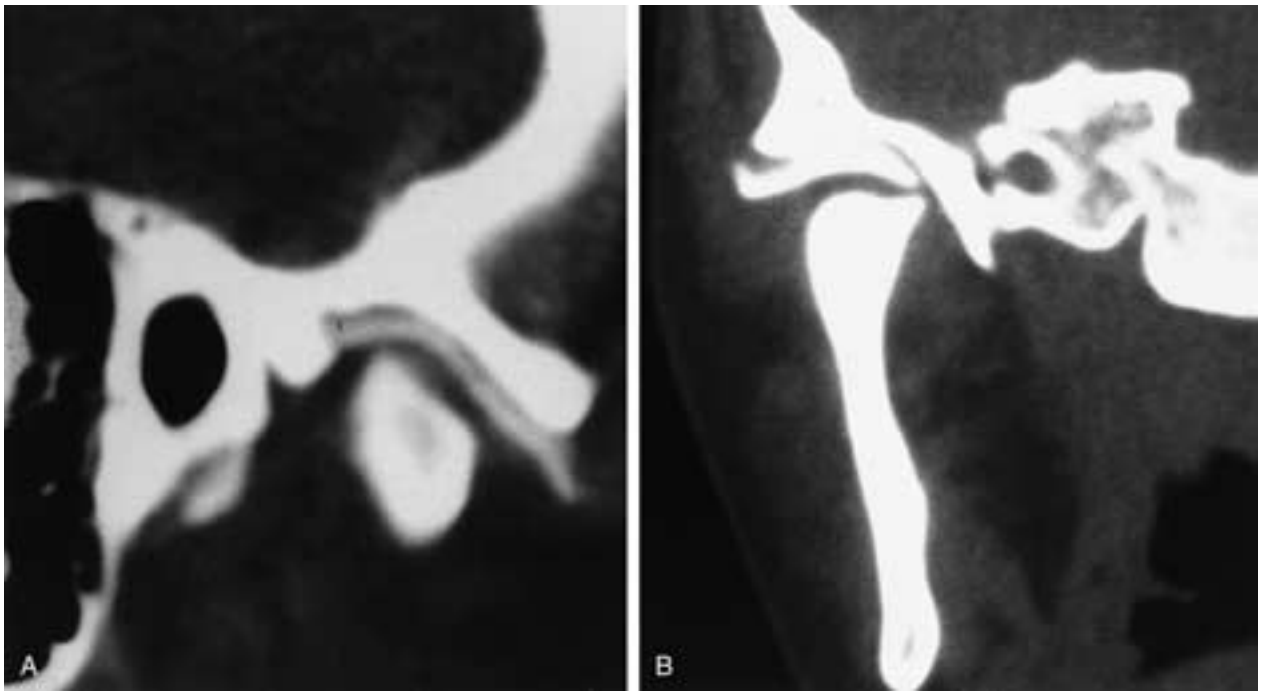

VIEW IMAGE

FIGURE 18-65 CT scan in the sagittal (**A**) and coronal (**B**) planes showing an implant in a good position.

(Fig. 18-71) or both the upper and lower joint spaces (Fig. 18-72). There is often significant joint expansion, and there may be multiple areas of low signal intensity that represent the pearls (Fig. 18-72). The clinical presentation of patients with synovial chondromatosis is similar to the general presentation of TMJ pain and dysfunction, and the findings are usually detected with imaging studies or at surgery. Evaluation can be done with both MR imaging and CT.[132–134]

Pigmented Villonodular Synovitis

Pigmented villonodular synovitis is a benign proliferative disease or tumor affecting the synovial lining of joints as well as tendons. There is nodular synovial proliferation and hemarthrosis. Pathology shows a mixture of histiocytes, giant cells, and spindle cells. There is evidence of hemorrhage with intracellular hemosiderin. The condition rarely involves the TMJ.[135–141] An enlarging mass is centered in the TMJ or the lesion may seem to extend away from the joint. The lesion tends to be dense on CT.

VIEW IMAGE

FIGURE 18-66 Bilateral total joints. Anterior posterior plain film shows bilateral total replacement. The condyle fragments are attached to the ramus of the mandible. Proplast Teflon fossa implants are attached to the articular eminence and the zygomatic arch with screws. Also note the osteosynthesis in the left symphysis region from an old mandibular fracture.

FIGURE 18-67 Bilateral costochondral grafts. Coronal CT scan of an asymptomatic patient with bilateral costochondral grafts. Note how the grafts are integrated into the ramus of the mandible. The most superior cartilaginous parts of the grafts are not well visualized on CT.

VIEW IMAGE

Copyright © 2003, Mosby, Inc. All rights reserved.

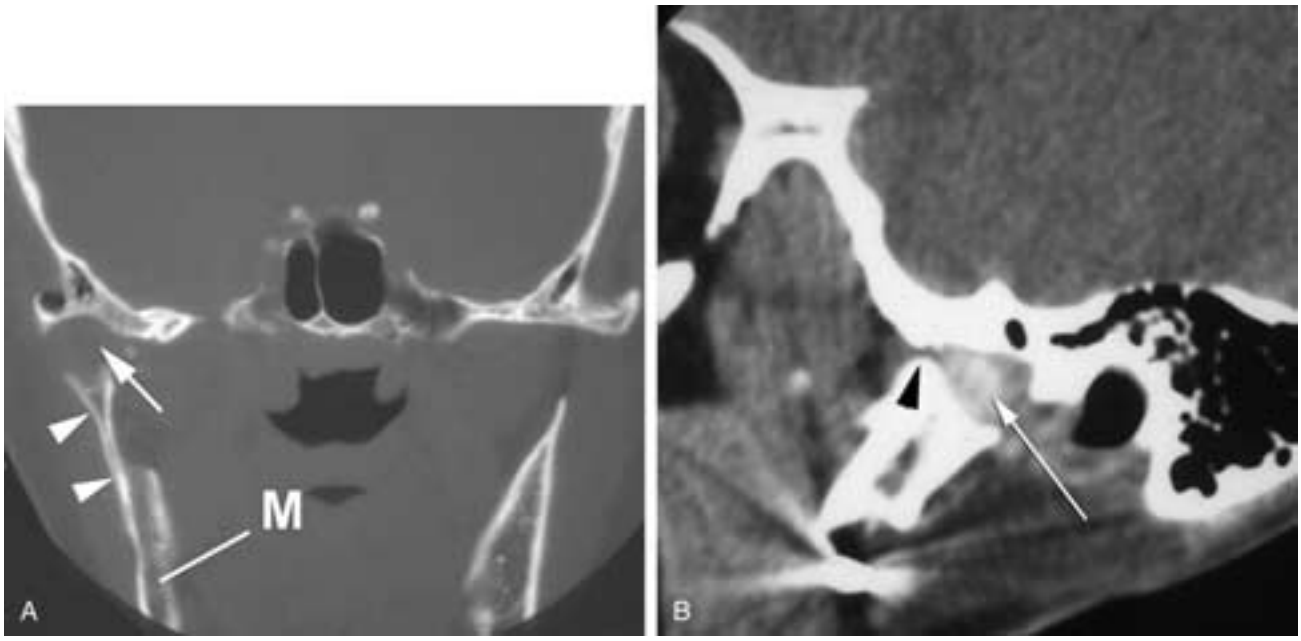

VIEW IMAGE

FIGURE 18-68 Costochondral graft CT. **A**, Coronal CT scan shows the osseous portion of the costochondral graft (*arrowheads*) attached to the lateral aspect of the native mandible (*M*). The chondral part of the graft (*arrow*) is seen as a lucency separating the osseous part of the graft from the glenoid. **B**, The cartilage portion of the graft (*arrow*) is seen more clearly on the sagittal reformatted image. Note that the edge of the osseous portion of the graft (*arrowhead*) is very close to the articular eminence.

The head of the condyle is usually eroded, and in more extensive cases the skull base may also be involved. The hemorrhage by-products give the lesion low signal on both T1- and T2- weighted images (Fig. 18-73). Indeed, the extensive iron deposition can give a pronounced susceptibility artifact, particularly on T2-weighted MR images.

Osteochondroma

Osteochondroma is probably the second most common neoplastic lesion affecting the TMJ. Osteochondroma (Fig. 18-74), osteoma, and condyle hyperplasia are difficult to differentiate clinically and on imaging studies. MR imaging can define these conditions in both the sagittal and coronal planes, but CT may delineate more precisely the extension of the tumor and its relationship to anatomic structures medial to the TMJ region.

VIEW IMAGE

FIGURE 18-69 Three-dimensional right-sided costochondral graft in an asymptomatic patient. Note that the graft is integrated into the mandible. The superior cartilaginous portion of the graft is not well visualized on the CT scan. The image was obtained in a partial mouth-open position.

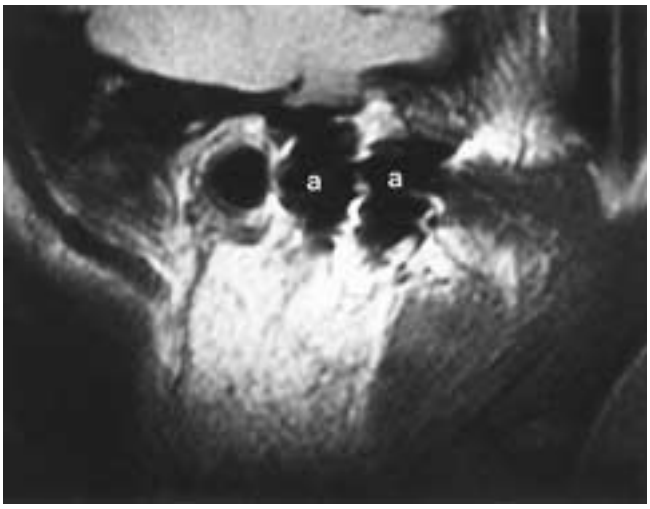

FIGURE 18-70 Metal artifact. MR proton density image of a joint with metallic wires. These artifacts (*a*) are characterized by irregular areas of signal void bordered by areas of high signal.

VIEW IMAGE

Copyright © 2003, Mosby, Inc. All rights reserved.

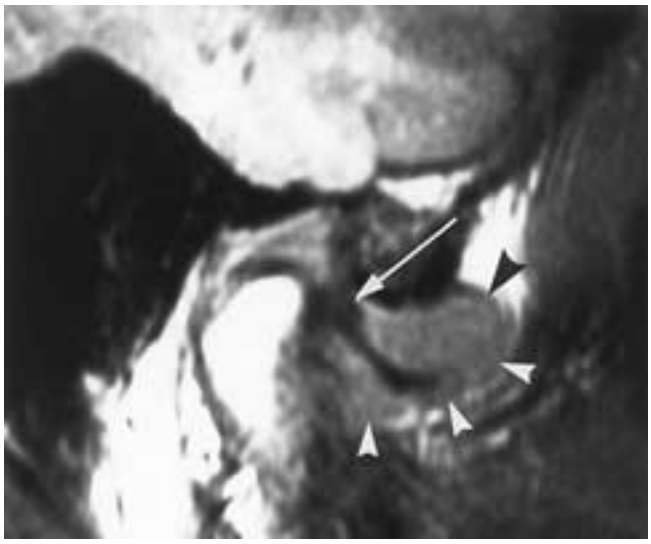

VIEW IMAGE

FIGURE 18-71 Synovial chondromatosis. Sagittal MR image showing expansion of the upper and lower joint spaces (*arrowheads*). The disk (*arrow*) is anteriorly displaced.

Calcium Pyrophosphate Arthropathy (Pseudogout)

Calcium pyrophosphate dihydrate (CPPD) deposition disease, or pseudogout, infrequently affects the TMJ. Involvement can be mild or quite severe. Mild cases of this condition have been described with subtle calcifications in the disk and in the joint space (Fig. 18-75).[142–144] Clinically, the patient presents with pain and dysfunction similar to the symptoms of other TMJ patients. There can be associated swelling and degenerative changes in the joint. CT is the best imaging modality for demonstration of the minute intraarticular calcifications. More extensive cases present with enlarging masses.[143, 145–147] Calcification can be demonstrated on a CT scan. There can be significant erosion of the contiguous skull base as well as the condyle. Malignancy may be suspected because of the apparent aggressiveness and bone ''destruction'' shown at imaging (Fig. 18-76). The pathology can also suggest sarcoma, and thus the importance of considering this benign diagnosis so that aggressive therapy inappropriate for this benign disease can be avoided.[145, 146, 148, 149]

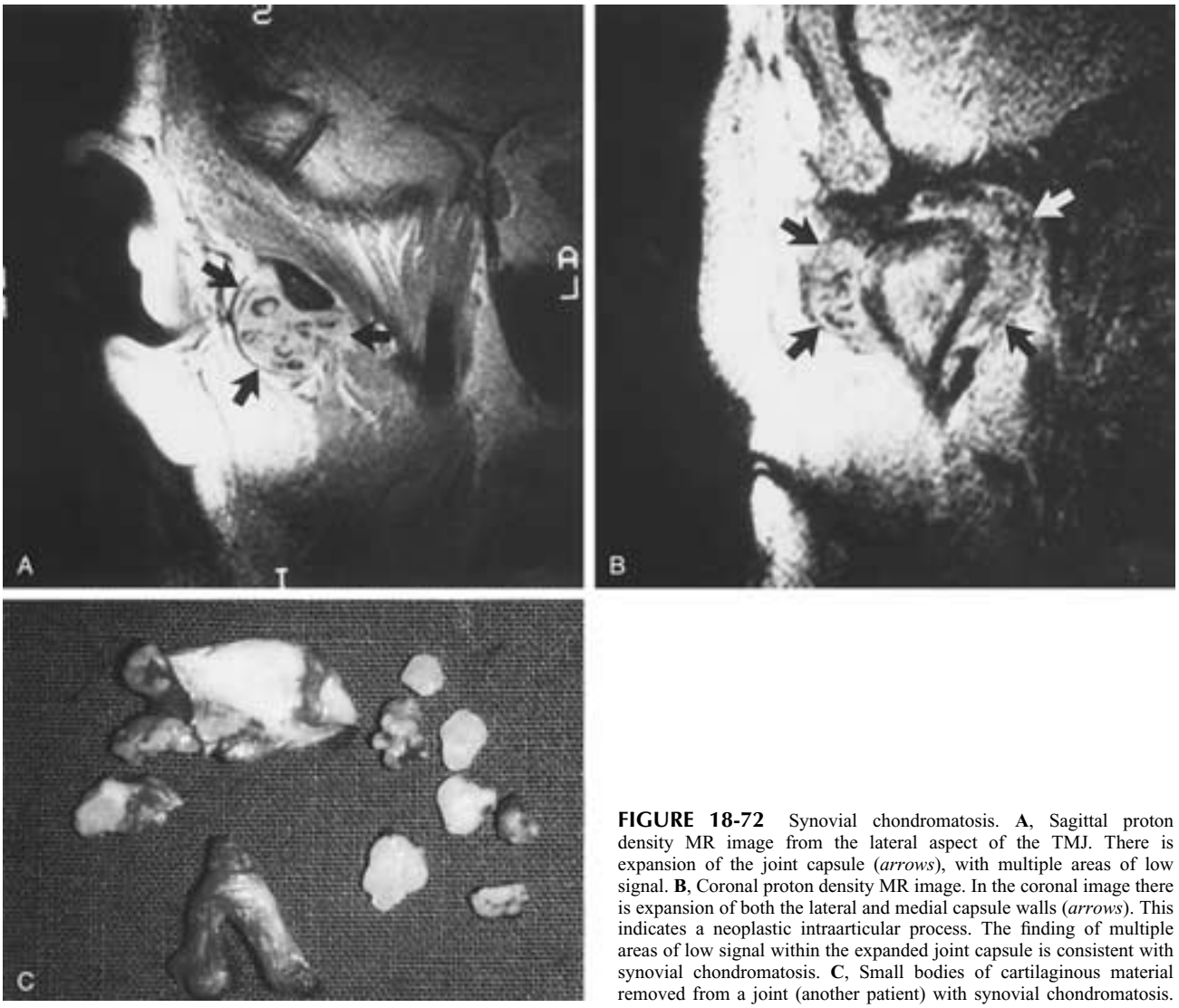

VIEW IMAGE

FIGURE 18-72 Synovial chondromatosis. **A**, Sagittal proton density MR image from the lateral aspect of the TMJ. There is expansion of the joint capsule (*arrows*), with multiple areas of low signal. **B**, Coronal proton density MR image. In the coronal image there is expansion of both the lateral and medial capsule walls (*arrows*). This indicates a neoplastic intraarticular process. The finding of multiple areas of low signal within the expanded joint capsule is consistent with synovial chondromatosis. **C**, Small bodies of cartilaginous material removed from a joint (another patient) with synovial chondromatosis.

Copyright © 2003, Mosby, Inc. All rights reserved.

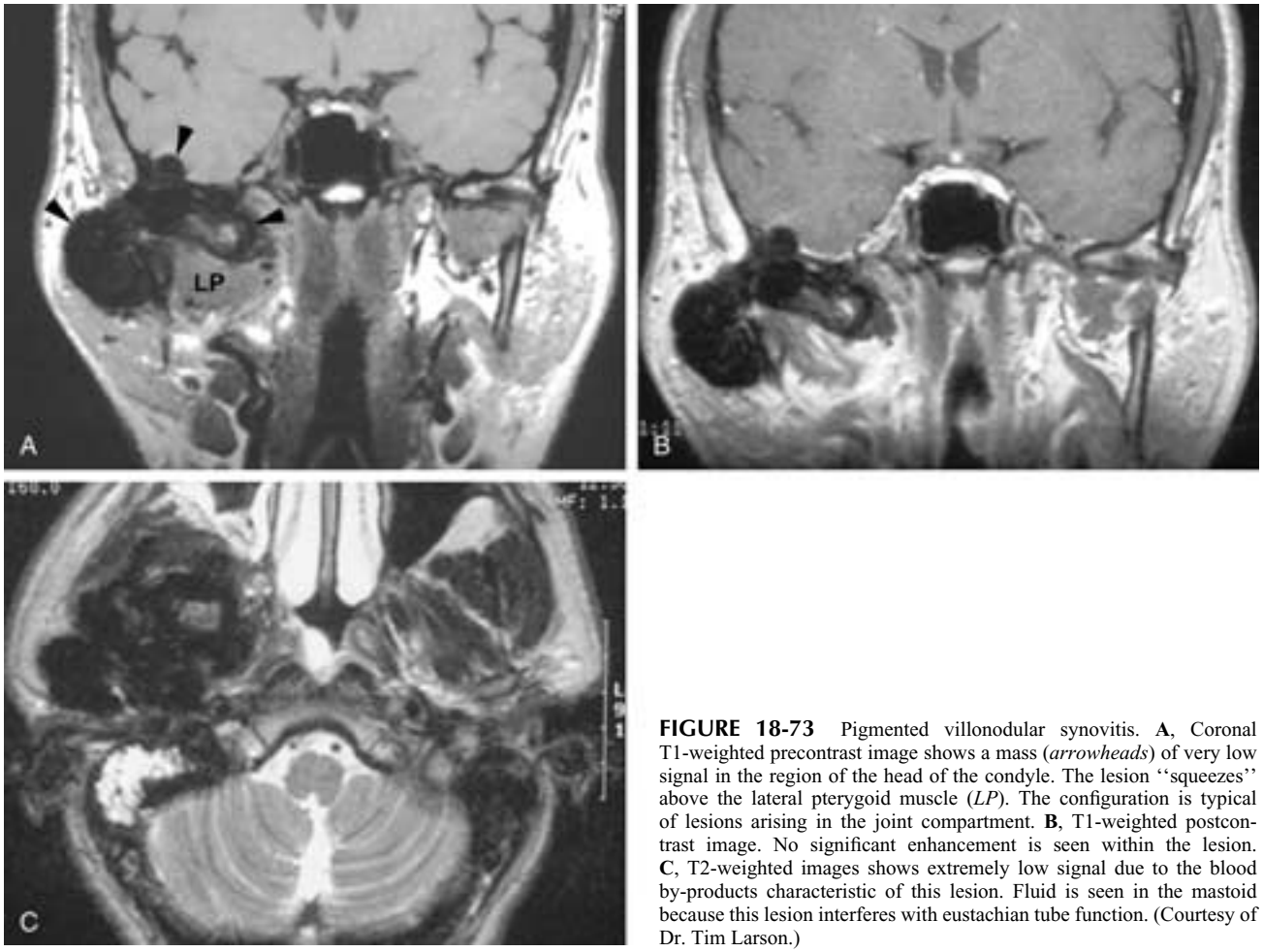

FIGURE 18-73 Pigmented villonodular synovitis. **A**, Coronal T1-weighted precontrast image shows a mass (*arrowheads*) of very low signal in the region of the head of the condyle. The lesion ''squeezes'' above the lateral pterygoid muscle (*LP*). The configuration is typical of lesions arising in the joint compartment. **B**, T1-weighted postcontrast image. No significant enhancement is seen within the lesion. **C**, T2-weighted images shows extremely low signal due to the blood by-products characteristic of this lesion. Fluid is seen in the mastoid because this lesion interferes with eustachian tube function. (Courtesy of Dr. Tim Larson.)

VIEW IMAGE

Synovial Cysts and Simple Bone Cysts

Synovial cysts of the TMJ have been reported but are rare (Fig. 18-77).[150, 151] They present with unilateral pain and possible enlargement of the condyle head, and there can be associated swelling.

Simple bone cysts are most frequently located in the body of the mandible. However, they may occur in the condyle head (Fig. 18-78), and often the remaining joint components are normal.

Rare Lesions and Tumors

Eosinophilic granuloma may also present as a lytic lesion involving the mandibular condyle and ramus (Fig. 18-79). Rarely, tumoral calcinosis has been described involving the joint and contiguous muscles.[152] The calcified lesions are best defined on CT scan.

Chondrosarcoma and synovial cell sarcoma, as well as other sarcomas, can occasionally involve the TMJ. Meningiomas, chondroblastomas, and a variety of other tumors may extend into the joint from the contiguous bone, as can malignancies of the external ear and parotid gland.

Metastatic Disease in the TMJ Region

Fewer than 1% of all tumors metastasize to the maxillofacial area.[153-155] Adenocarcinoma is the most common of all metastatic tumors in the jaw, accounting for 70% of the cases. A review of 115 cases of mandibular metastasis found that 30% were metastases from breast carcinoma, 16% from kidney, 15% from lung, 8% from colon and rectum, 7% from prostate, 6% from thyroid, 5% from stomach, 4% from skin, 3% from testes, and other sites represented less than 1% each. Most metastases are found in the molar and premolar regions of the mandible, and only a few cases of metastasis to the mandibular condyle have been reported. Most cases with metastasis to the TMJ region have presented with TMJ-related symptoms.[154] Lymphoma can also rarely involve the TMJ (Fig. 18-80), and bone regeneration may occur after chemotherapy (Fig. 18-80B).[156]

Arthritides

The TMJ is involved in approximately 50% of patients with rheumatoid diseases such as rheumatoid arthritis, ankylosing spondylitis, and psoriatic arthritis. Imaging is an important adjunct to the clinical diagnosis and is particularly valuable for follow-up of patients with these diseases. Plain films and panoramic images are standard, but MR imaging may be indicated to evaluate the soft-tissue involvement of these diseases.[157] Morphologically, inflammatory arthritis is characterized by synovial proliferation and secondary erosive changes of the bone (Fig. 18-81). Studies with MR

Copyright © 2003, Mosby, Inc. All rights reserved.

imaging have shown potential for accurate evaluation of the soft-tissue components of the joint (Fig. 18-82).[85, 86] A study indicated the additional value of contrast-enhanced images for defining the area of inflammatory change within the joint and in the periarticular soft tissue (Fig. 18-82B).[157] Only limited experience is available with MR imaging of other inflammatory arthritides such as psoriatic arthritis and ankylosing spondylitis. Gout rarely involves the TMJ.[158] There can be erosion of the condyle and swelling of the tissues contiguous to an acutely painful joint. Rarely, the skull base can be eroded.

Acute Trauma

Plain films, panoramic examinations, or CT may be done for acute trauma to the mandible. Most patients do not come to imaging specifically for the TMJ, but in many patients with condylar neck and mandibular fractures there is also injury to the TMJ. Such TMJ trauma is frequently not recognized until after the acute clinical course. MR imaging may occasionally show fractures and effusions not seen on other imaging studies (Fig. 18-83), and thus MR imaging could be helpful in evaluating patients with acute pain following trauma to the face and jaw despite other negative examinations. The external auditory canal should also be closely examined when a jaw fracture is suspected.

Both CT and MR imaging may be helpful in cases with intracapsular fractures (Fig. 18-84). Although CT may show the positional relationship of the osseous fragments, MR imaging (Fig. 18-84) shows any associated disk abnormality. In a situation where reconstructive surgery is contemplated, 3D reconstructions (Fig. 18-84D) may be helpful to evaluate the positional relationships between the joint components.

Penetrating trauma to the TMJ is relatively rare, but it warrants imaging evaluation. It can cause fracture, hematoma, and dislocations. CT is the preferred method of examination, and it is important to obtain both axial and coronal images (Fig. 18-85).

FIGURE 18-74 Osteochondroma of the mandibular condyle. **A** and **B**, Axial and reconstructed sagittal CT scans show the right condyle (*arrows*) to be two to three times larger than the left condyle. There is also irregular mineralization in this condyle. **C** and **D**, Sagittal and coronal MR images of the same joints show mixed low and high signal from the enlarged parts of the condyle (*curved arrows*). The temporal component is normal. The disk (*arrowheads*) is biconcave and located in a normal superior position. (Courtesy of Dr. Donald Macher, Rochester, New York.)

VIEW IMAGE

Copyright © 2003, Mosby, Inc. All rights reserved.

VIEW IMAGE

FIGURE 18-75 Pseudogout. Coronal CT scan of a patient with chronic TMJ pain and normal disk position on an MR image (not shown). There are subtle calcifications in the joint space (*arrows*). Aspiration showed pyrophosphate crystals.

Coronoid Hyperplasia

Hyperplasia or elongation of the coronoid process of the mandible can mimic symptoms of TMJ internal derangement with limitation of jaw opening. This condition has been extensively described, and a study has indicated that elongation of the coronoid process may occur in up to 5% of patients with TMJ symptoms and limitation of jaw opening.[159–161] If the coronoid process is significantly elongated, it can impact on the zygomatic process of the maxilla, causing limitation of jaw opening. CT scans in the axial or sagittal plane, performed in the closed- and open-mouth positions, are valuable in the imaging assessment of patients with a clinical suspicion of coronoid hyperplasia because they can demonstrate the coronoid impaction on the maxilla (Fig. 18-86). Surgical treatment with removal of the coronoid process usually yields good results.

Congenital Anomalies

Bifid Condyle

Congenital anomalies of the TMJ are relatively rare. The most common congenital anomaly is probably the so-called bifid condyle. This implies a partial or complete separation of the condyle into a lateral and a medial half (Fig. 18-87). This is usually of no clinical significance other than in the rare situation in which surgery should be performed and preoperative knowledge of the morphology is important. The picture of a bifid condyle is characteristic on coronal imaging and should be distinguished from acquired pathologic conditions with remodeling and degenerative joint disease.

Hemifacial Microsomia

The TMJ is affected in other conditions such as hemifacial microsomia with underdevelopment of the TMJ. Frequently, there is a flat articular eminence and a small mandibular condyle (Fig. 18-88). The mastoid typically is underdeveloped, with no aeration. The disk is usually in a normal location in hemifacial microsomia. In advanced cases the entire ramus, condyle, and coronoid process of the mandible are not developed (Fig. 18-89).

Asymmetry of the Mandible

Asymmetry of the mandible is a frequent clinical presentation. The most prominent facial features include a shift of the chin to the short side and prominence of the mandibular angle on the long side. There are several obvious causes of mandibular asymmetry such as trauma with fractures, tumors, and congenital anomalies. In many cases, however, the cause of mandibular asymmetry leading to facial deformities is unclear on physical examination, and imaging assessment may be warranted.[162, 163]

Mandibular asymmetry can result principally from enlargement of the condylar head (condylar hyperplasia) on the long side (Fig. 18-90) or from decreased condyle growth (condylar hypolasia) (Fig. 18-91) or degenerative joint disease on the short side (Fig. 18-92).[163–165] Imaging studies are done to determine the cause of mandibular asymmetry and for treatment planning. The imaging evaluation of mandibular asymmetry is outlined in Box 18-5 on page 1049. Soft-tissue imaging is important, and MR imaging may be performed as well as CT. Condylar hypoplasia is most frequently caused by regressive remodeling secondary to long-standing internal derangement; however, the condyle may have a relatively normal appearance, without evidence of degenerative joint disease. The joint appears to be more sensitive to regressive remodeling if the internal derangement occurs during the growth and development phase. However, mandibular asymmetry and change in occlusion have also been described in adults.

Atrophy of the Muscles of Mastication

Atrophy of the muscles of mastication is occasionally seen in patients who are unable to open their mouths. These atrophic changes in the muscles are most frequently secondary to trauma or orthognathic surgery.[88, 166] Less often, they may occur secondary to a tumor (or tumor surgery) affecting the mandidular nerve at the skull base. On MR imaging the atrophic changes of the muscles of mastication are usually reflected as fatty replacement.

Following orthognathic surgery, there is frequently asymptomatic muscle atrophy.[166] Occasionally, this is associated with chewing difficulties and fatigue in the jaw

Text continued on page 1046

Copyright © 2003, Mosby, Inc. All rights reserved.

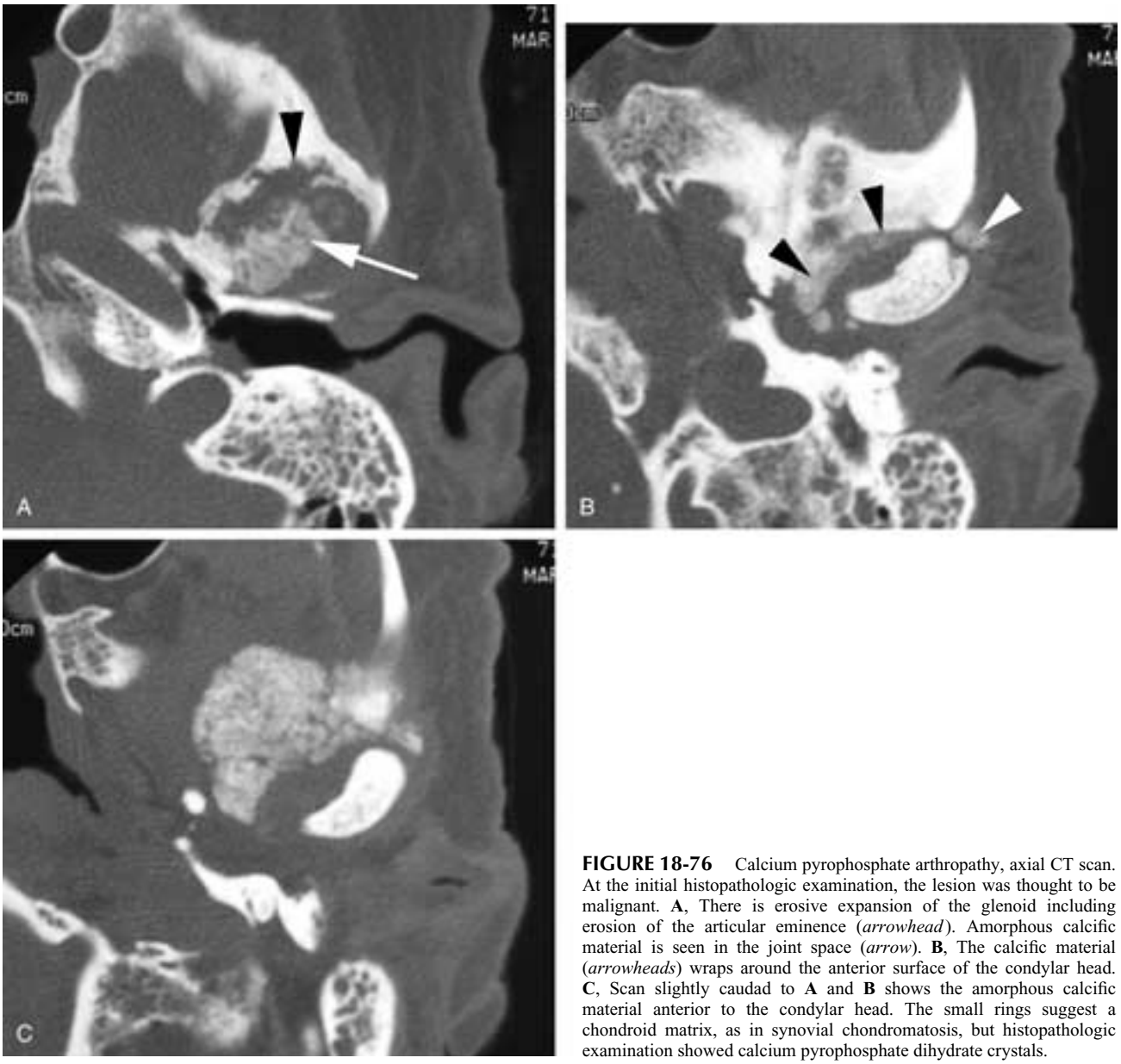

FIGURE 18-76 Calcium pyrophosphate arthropathy, axial CT scan. At the initial histopathologic examination, the lesion was thought to be malignant. **A**, There is erosive expansion of the glenoid including erosion of the articular eminence (*arrowhead*). Amorphous calcific material is seen in the joint space (*arrow*). **B**, The calcific material (*arrowheads*) wraps around the anterior surface of the condylar head. **C**, Scan slightly caudad to **A** and **B** shows the amorphous calcific material anterior to the condylar head. The small rings suggest a chondroid matrix, as in synovial chondromatosis, but histopathologic examination showed calcium pyrophosphate dihydrate crystals.

VIEW IMAGE

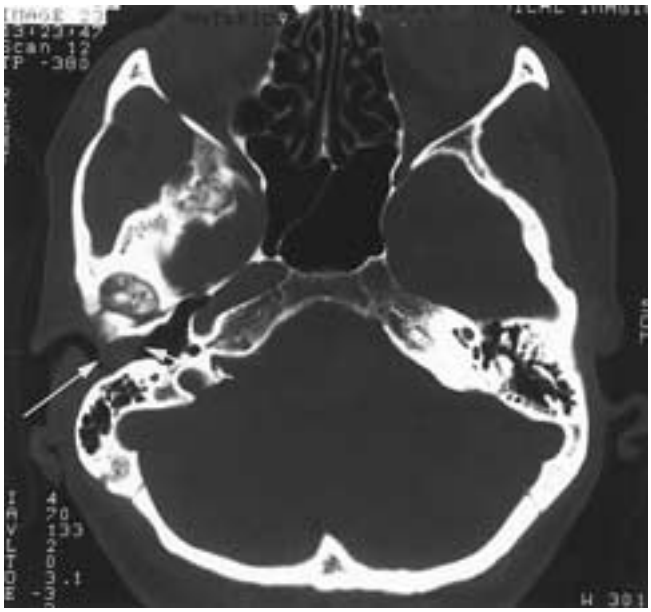

FIGURE 18-77 Synovial cyst. Axial CT scan of a patient with a 1 cm synovial cyst (*arrows*) extending into the external auditory canal. There are extensive degenerative changes of the condyle head. At surgery the cyst was found to extend into the joint through the bony fissure.

VIEW IMAGE

Copyright © 2003, Mosby, Inc. All rights reserved.

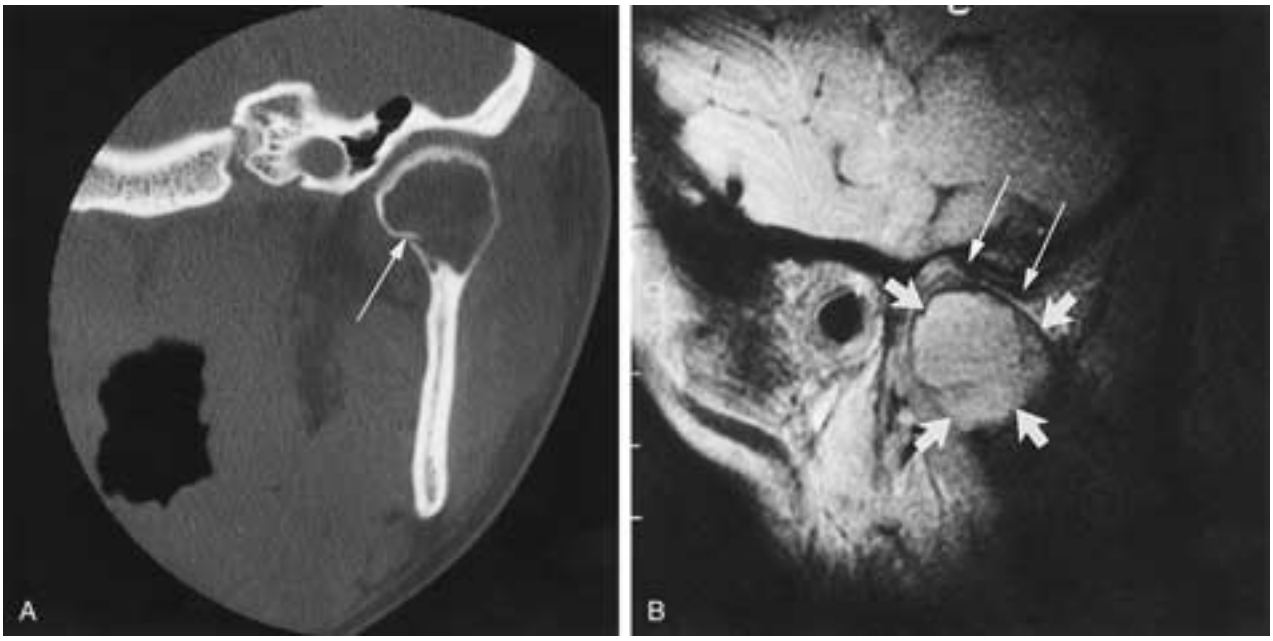

VIEW IMAGE

FIGURE 18-78 Simple bone cyst. **A**, Coronal CT scan shows a large cystic lesion involving the entire condyle head. There is expansion and enlargement of the condyle and thinning of the cortex. Medially and inferiorly (*arrow*) there is a small pathologic fracture. **B**, Sagittal proton density MR image shows intermediate signal of the expanded bone marrow of the condyle (*thick arrows*). The disk (*long arrows*) is in the normal location.

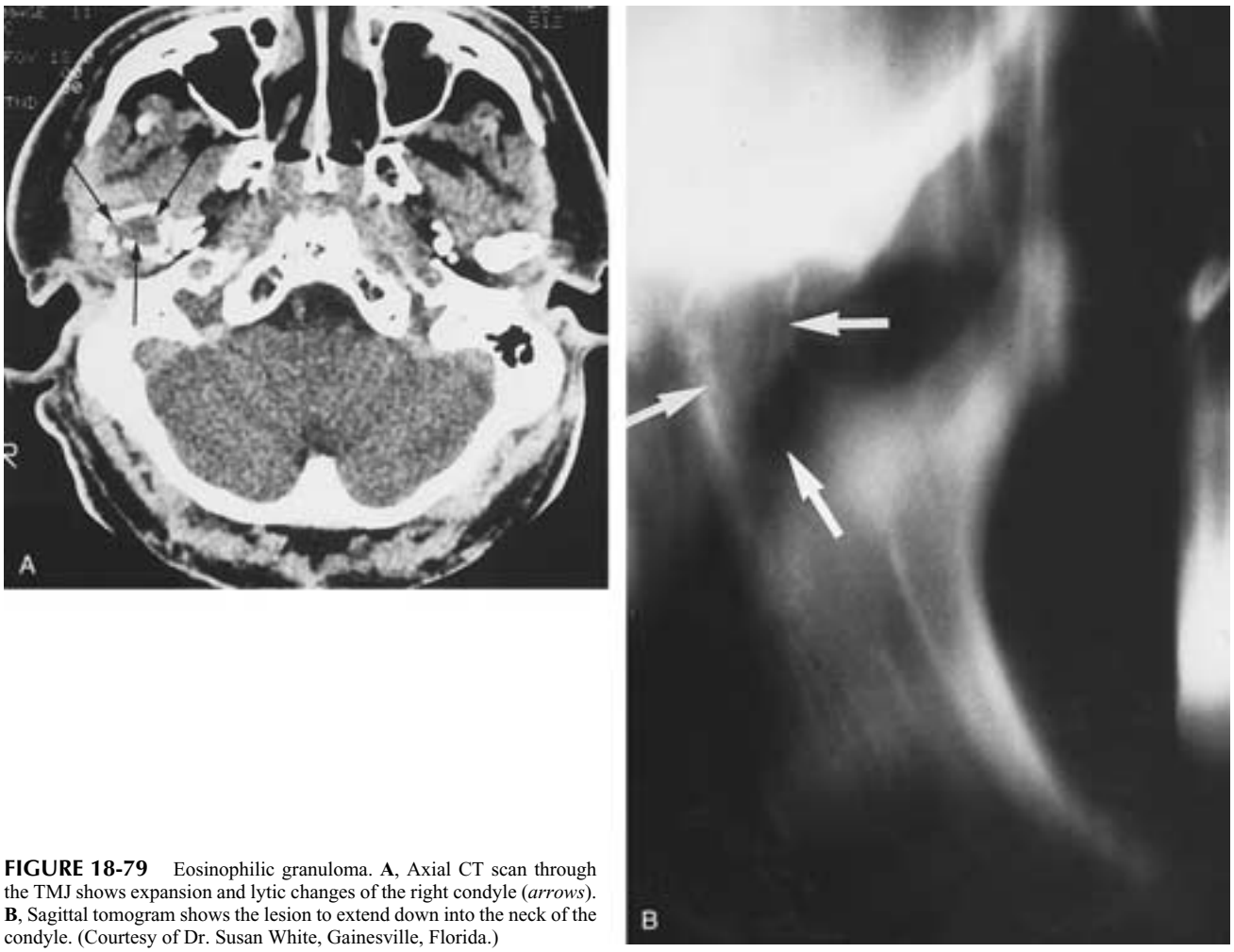

VIEW IMAGE

FIGURE 18-79 Eosinophilic granuloma. **A**, Axial CT scan through the TMJ shows expansion and lytic changes of the right condyle (*arrows*). **B**, Sagittal tomogram shows the lesion to extend down into the neck of the condyle. (Courtesy of Dr. Susan White, Gainesville, Florida.)

Copyright © 2003, Mosby, Inc. All rights reserved.

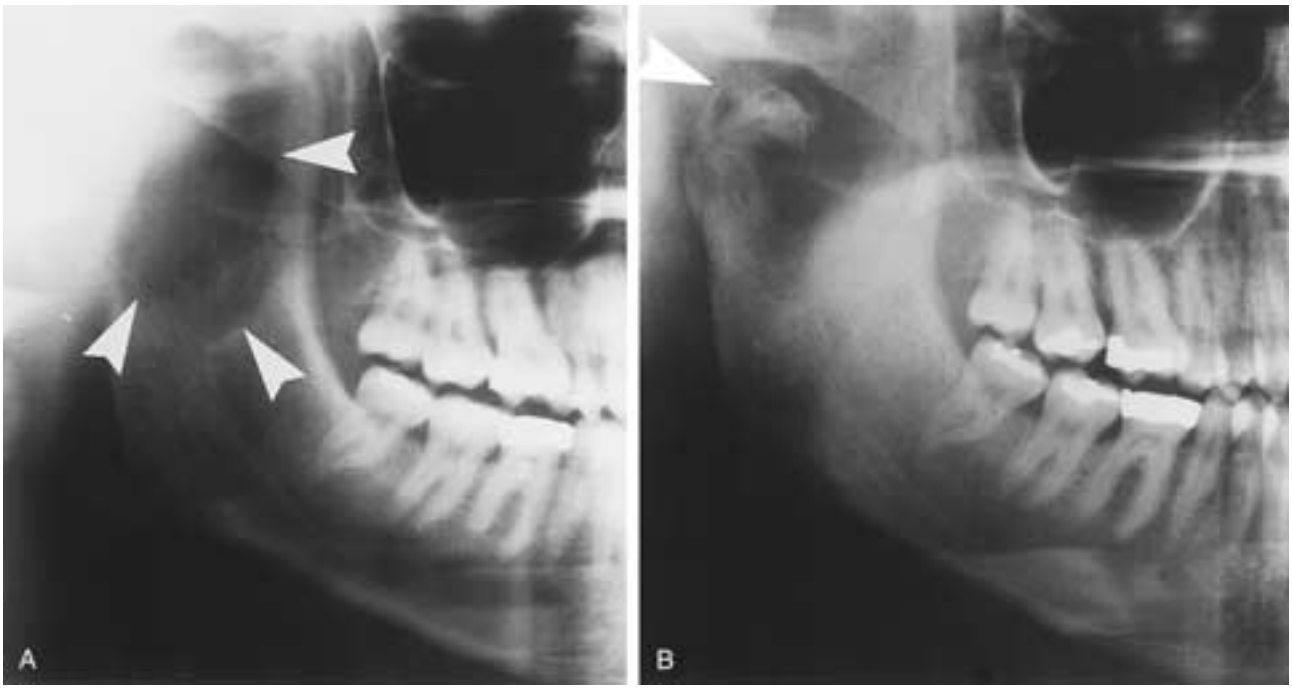

VIEW IMAGE

FIGURE 18-80 Metastatic lymphoma to the TMJ. **A**, Large osteolytic defect involving the condyle, condyle neck, coronoid process, and upper half of the ascending ramus (*arrowheads*). **B**, Following chemotherapy, there was regeneration of the condyle neck and condyle (*arrowhead*). The patient died 1 year later from intracranial and generalized metastasis.

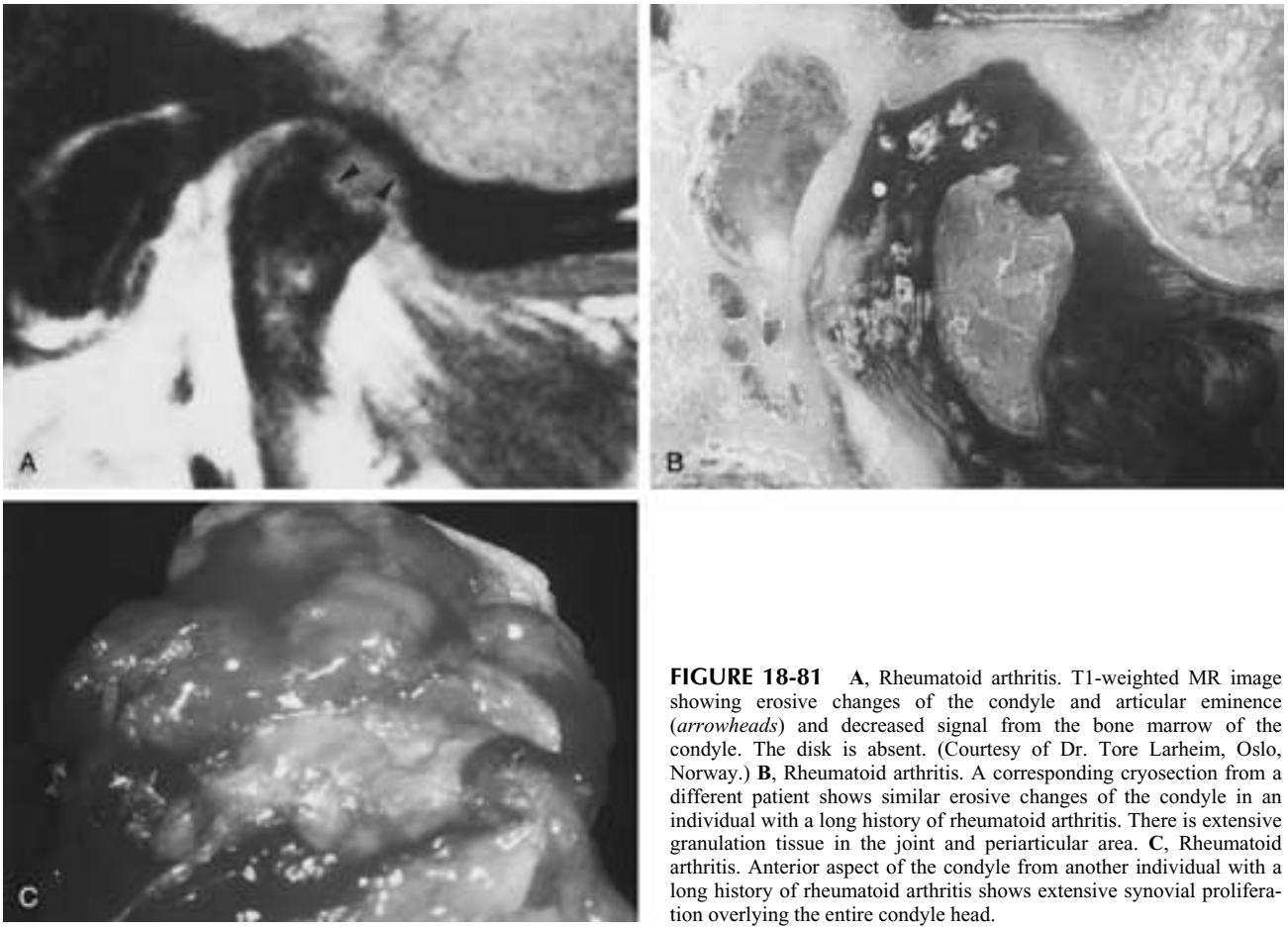

VIEW IMAGE

FIGURE 18-81 **A**, Rheumatoid arthritis. T1-weighted MR image showing erosive changes of the condyle and articular eminence (*arrowheads*) and decreased signal from the bone marrow of the condyle. The disk is absent. (Courtesy of Dr. Tore Larheim, Oslo, Norway.) **B**, Rheumatoid arthritis. A corresponding cryosection from a different patient shows similar erosive changes of the condyle in an individual with a long history of rheumatoid arthritis. There is extensive granulation tissue in the joint and periarticular area. **C**, Rheumatoid arthritis. Anterior aspect of the condyle from another individual with a long history of rheumatoid arthritis shows extensive synovial proliferation overlying the entire condyle head.

Copyright © 2003, Mosby, Inc. All rights reserved.

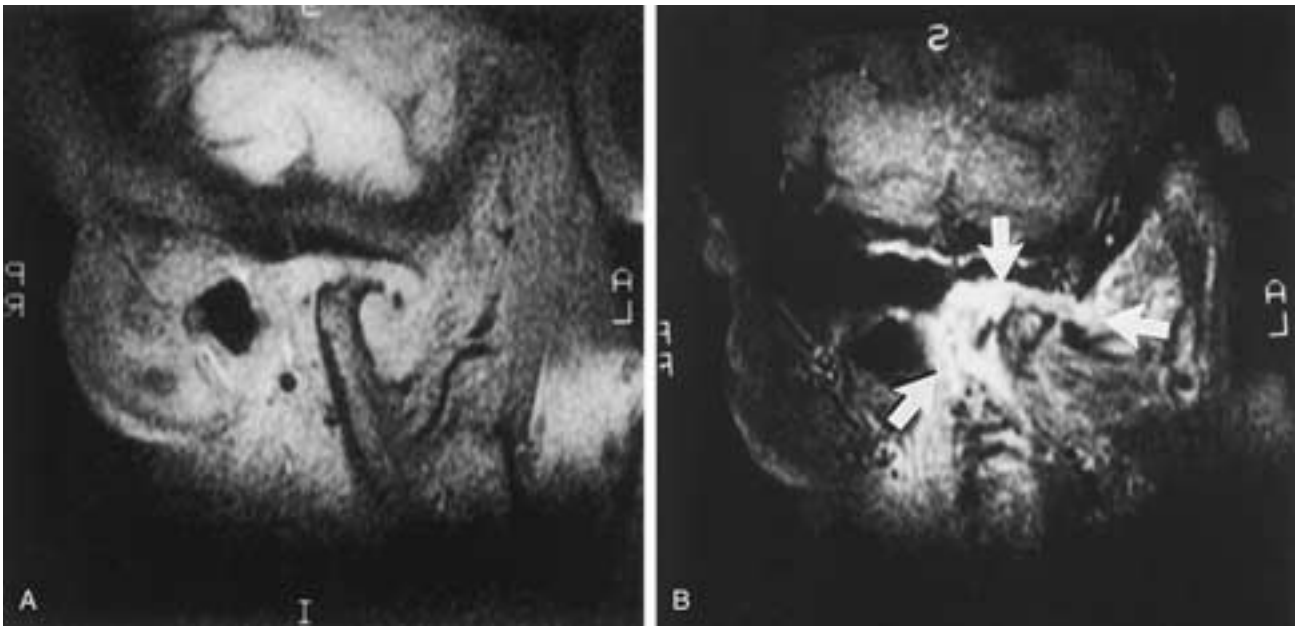

VIEW IMAGE

FIGURE 18-82 Rheumatoid arthritis with contrast enhancement. **A**, Sagittal proton density image shows advanced degenerative disease of both the condyle and the temporal joint component. **B**, With contrast enhancement there is significant enhancement in the joint and the periarticular area (*arrows*). This indicates the area of synovial proliferation. There is also a small area of meningeal enhancement of unclear clinical significance.

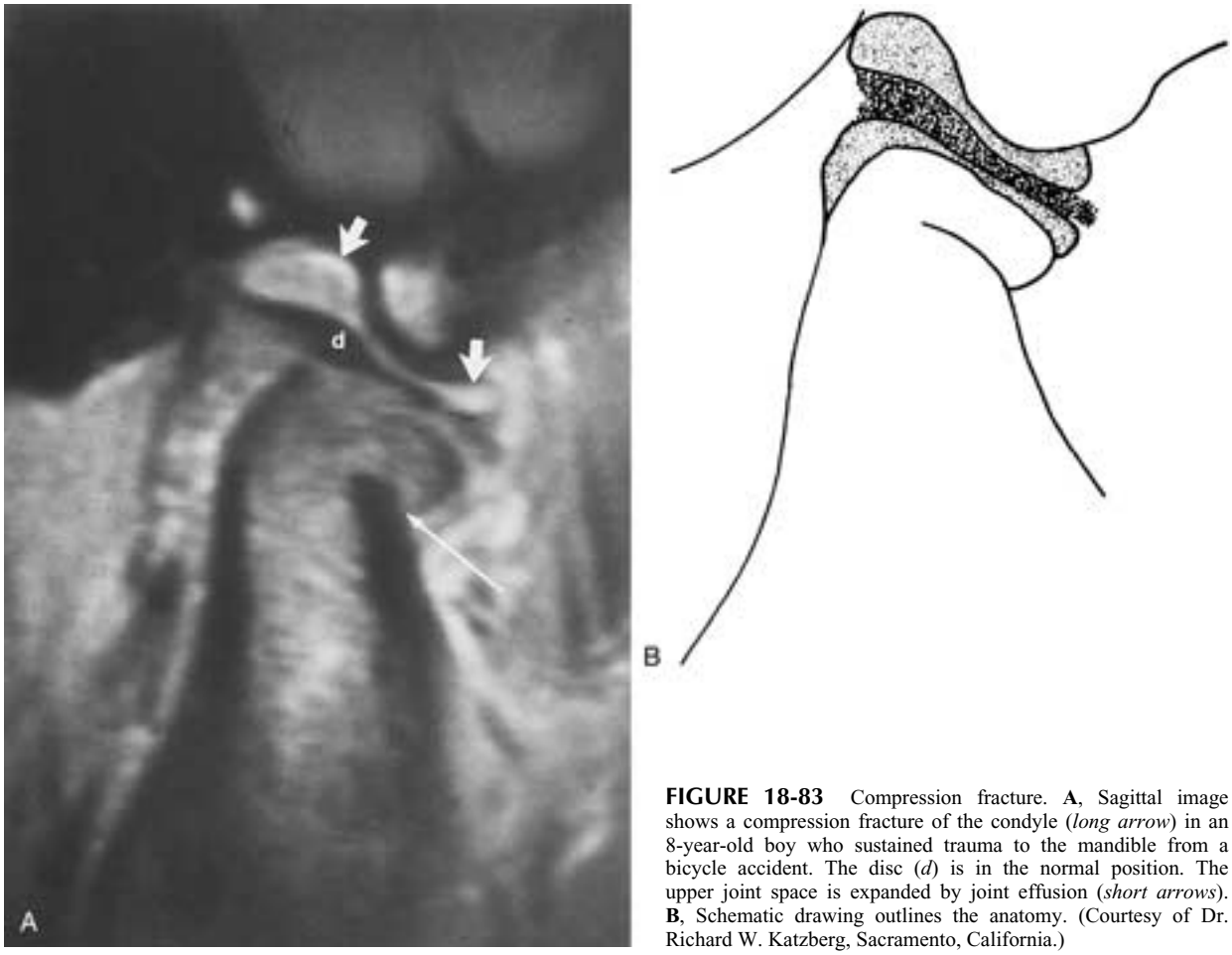

FIGURE 18-83 Compression fracture. **A**, Sagittal image shows a compression fracture of the condyle (*long arrow*) in an 8-year-old boy who sustained trauma to the mandible from a bicycle accident. The disc (*d*) is in the normal position. The upper joint space is expanded by joint effusion (*short arrows*). **B**, Schematic drawing outlines the anatomy. (Courtesy of Dr. Richard W. Katzberg, Sacramento, California.)

VIEW IMAGE

Copyright © 2003, Mosby, Inc. All rights reserved.

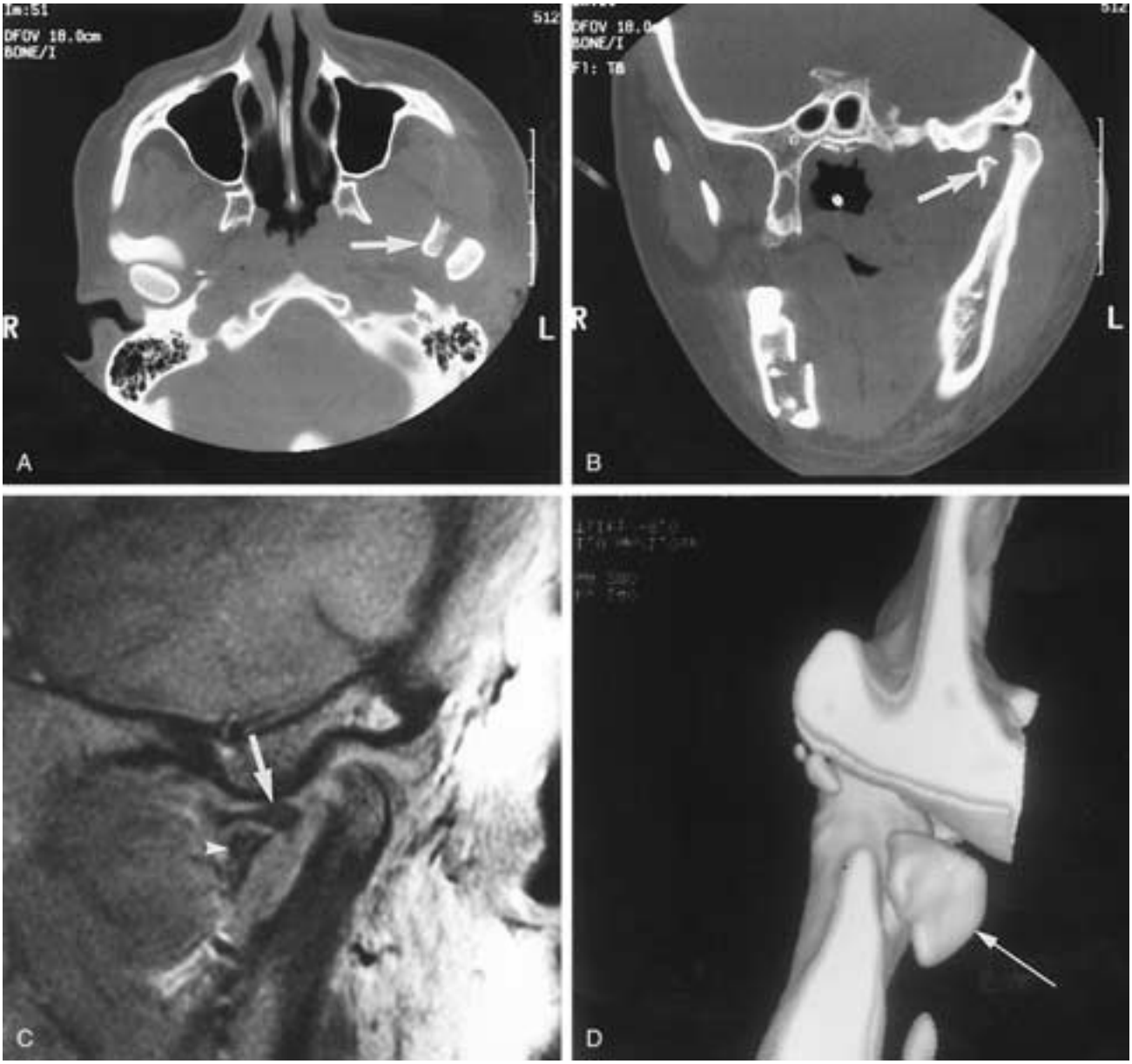

VIEW IMAGE

FIGURE 18-84 Intracapsular fracture with displacement of a condyle fragment and disk. **A**, Axial CT scan shows fracture of the medial part of the condyle (*arrow*) with anterior and medial displacement. **B**, Coronal CT scan confirms the inferior medial displacement of the condyle fragment (*arrow*) and shows small intraarticular air collections. Note the contralateral mandibular body fracture. **C**, Sagittal proton density MR image shows the condyle fragment (*arrowhead*) anteriorly and inferiorly displaced. The disk (*arrow*) is located superior to the fragment but is anteriorly and inferiorly displaced relative to the remaining condyle. **D**, Coronal three-dimensional reconstruction of CT image demonstrates the inferior medial location of the displaced fragment (*arrow*).

Copyright © 2003, Mosby, Inc. All rights reserved.

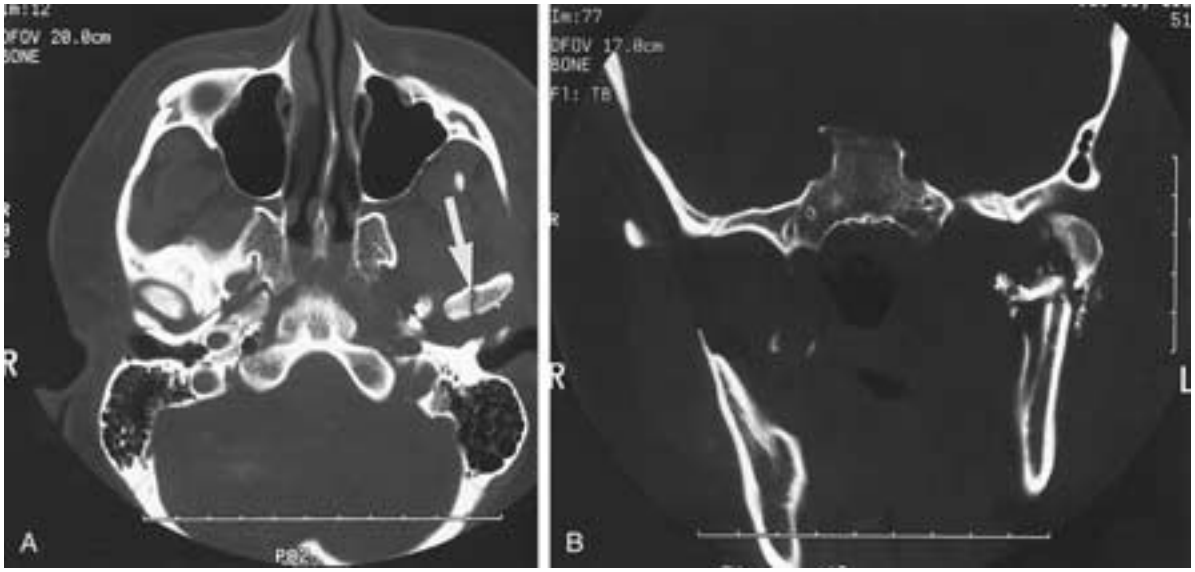

VIEW IMAGE

FIGURE 18-85 Penetrating trauma to the TMJ. **A**, Axial CT scan through the condyle shows a sagittal fracture in the center of the condyle head. **B**, Coronal image through the joint shows comminuted fractures with displacement of the medial fragment. Axial and coronal views are supplementary because the displacement was not well appreciated on the axial image.

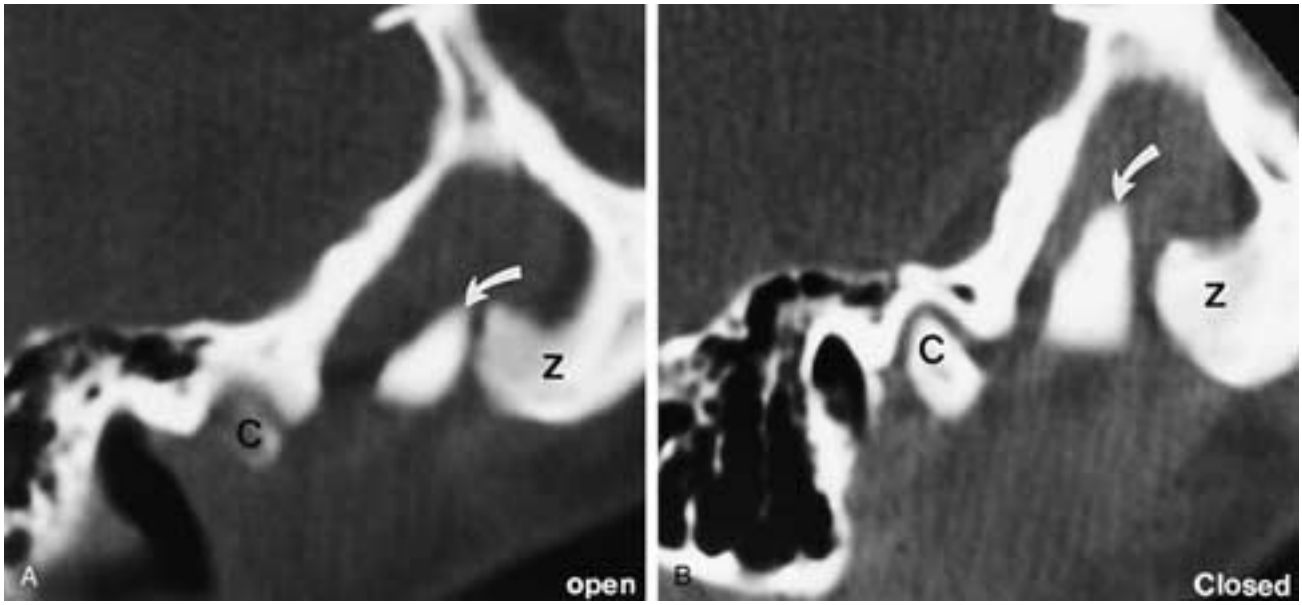

VIEW IMAGE

FIGURE 18-86 Coronoid hyperplasia restricting mouth opening. **A** and **B**, Direct sagittal CT scans in the open-mouth and closed-mouth positions showing the elongated coronoid process (*arrows*) interfering with the zygomatic process (*z*) of the maxilla at the open-mouth position. The condyle (*C*) is in the glenoid fossa.

Copyright © 2003, Mosby, Inc. All rights reserved.

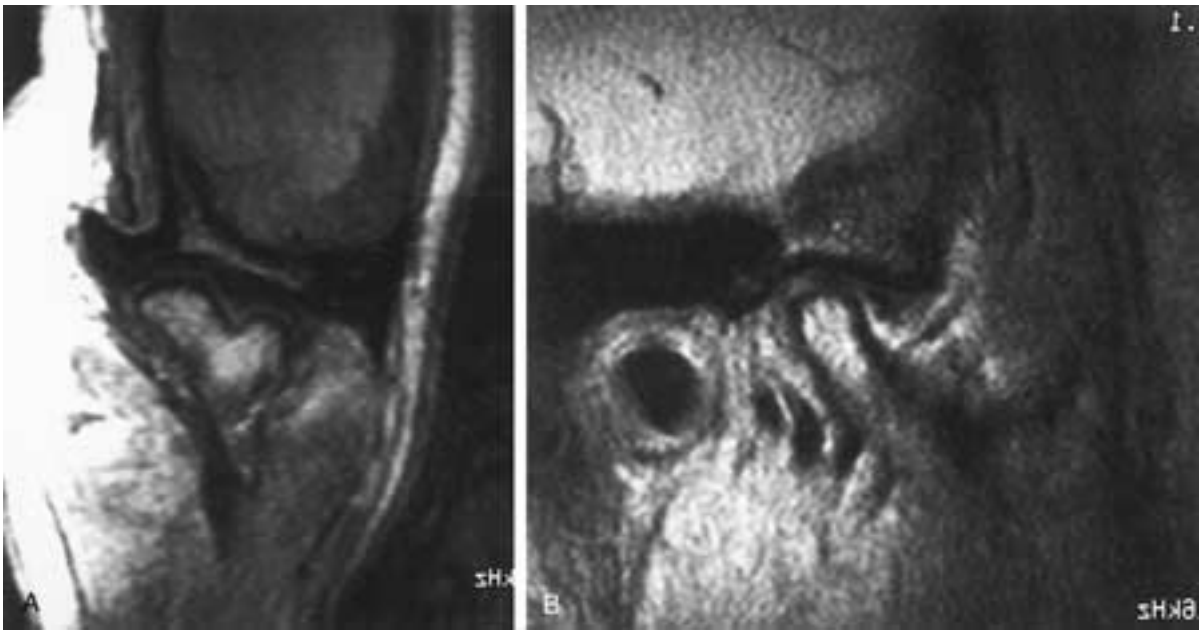

VIEW IMAGE

FIGURE 18-87 Bifid condyle. **A**, Coronal MR image shows the characteristic appearance of a bifid condyle. **B**, Sagittal MR image shows a normal appearance of the condyle and disk.

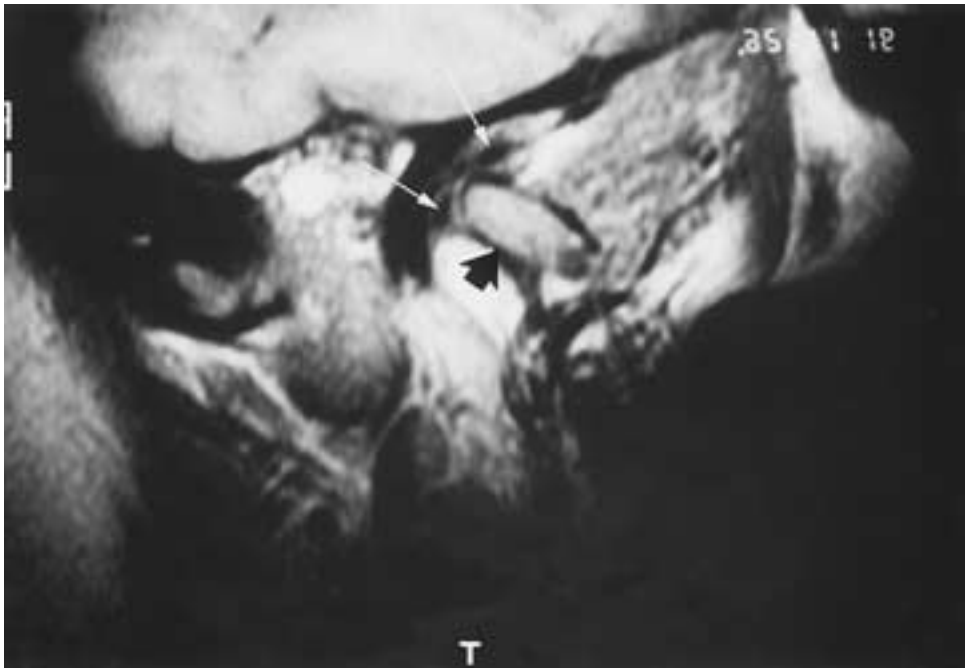

VIEW IMAGE

FIGURE 18-88 Hemifacial microsomia. Sagittal MR image of a young patient with hemifacial microsomia. The temporal bone is underdeveloped. The mastoid is not aerated; instead, there is fat filling the mastoid air cells. The mandibular condyle (*thick arrow*) is underdeveloped, with a curvature posteriorly. The disk (*thin arrows*) is in a normal relationship with the condyle. The articular eminence is absent, and the condyle is essentially articulating against the flat skull base. The lateral pterygoid muscle appears normal.

Copyright © 2003, Mosby, Inc. All rights reserved.

muscles; in these cases, MR imaging is the best imaging modality. Electromyography may be of some value when asymmetric recordings of the left and right sides can be documented.

MISCELLANEOUS IMAGING

Radionuclide Imaging

Studies have suggested that radionuclide imaging of the TMJ (Fig. 18-93), using conventional skeletal imaging techniques, may be a valuable screening test for osseous disease.[167, 168] The technique can be performed easily, and the radiation dose to the patient is low.[1] An advantage of the technique is that conditions outside the joint also may be easily detected. Radionuclide imaging has not gained popularity for TMJ imaging. This is probably because it is nonspecific, and frequently a second imaging modality is needed to determine the nature of the problem and to form a treatment plan.

Thin-Section MR Imaging

There is continuous ongoing development in MR imaging technology. The signal-to-noise ratio and soft-tissue and spatial resolution are improved each time MR scanners are upgraded. This means that the image quality can be expected to continue to improve, and experimental MR images with improved spatial and soft-tissue resolution (Fig. 18-94) may soon be available commercially. Figure 18-94 was obtained on an autopsy TMJ specimen. It shows significantly improved spatial and soft-tissue resolution because of thinner slice thickness and a smaller field of view. In this image the trabecular pattern of the condyle can be clearly identified, and the perforation of the disk and the osteophyte of the condyle, protruding into the perforation, can be seen with exquisite detail.

Dynamic MR Imaging

The time needed to acquire an image is also rapidly decreasing, and within the next few years, one may be able

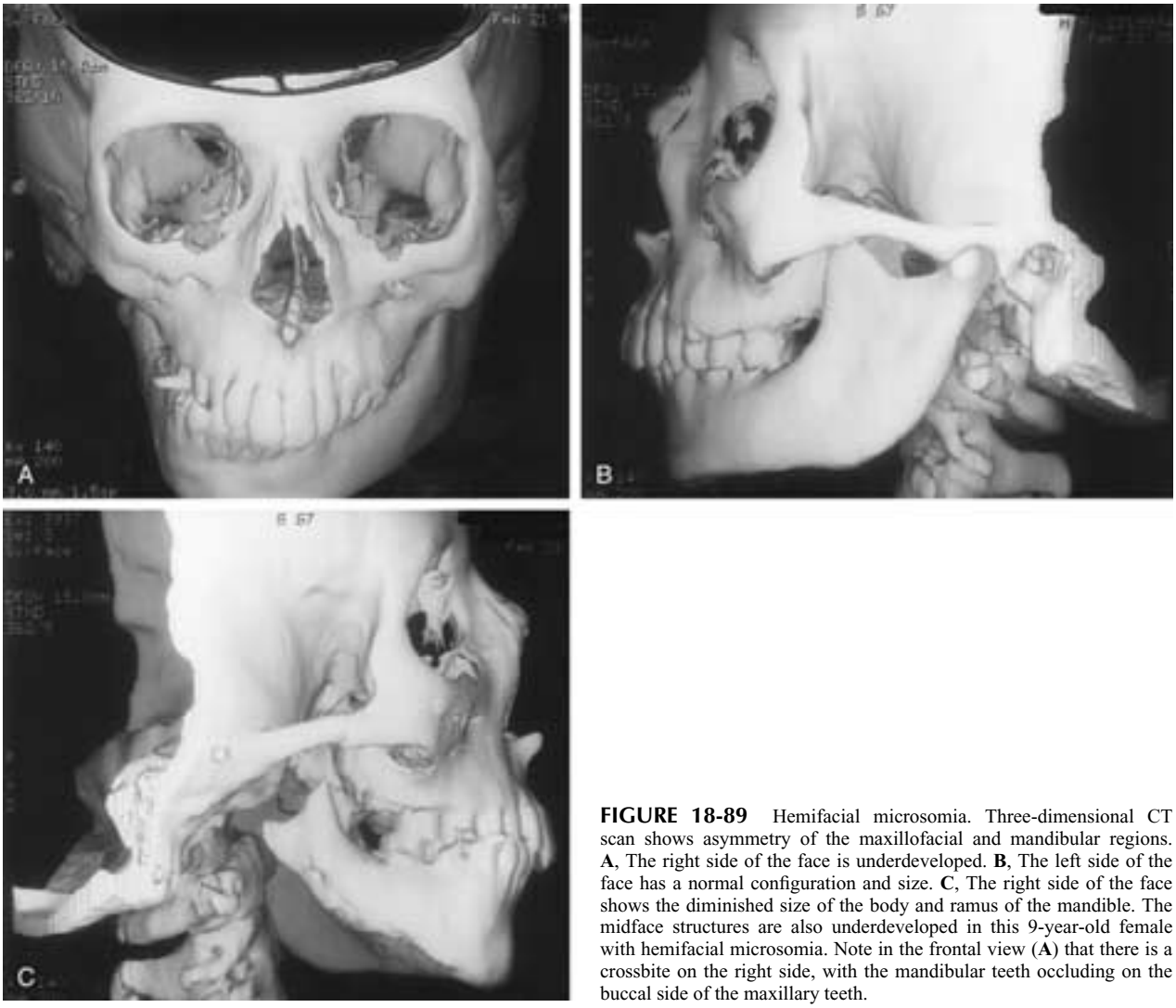

FIGURE 18-89 Hemifacial microsomia. Three-dimensional CT scan shows asymmetry of the maxillofacial and mandibular regions. **A**, The right side of the face is underdeveloped. **B**, The left side of the face has a normal configuration and size. **C**, The right side of the face shows the diminished size of the body and ramus of the mandible. The midface structures are also underdeveloped in this 9-year-old female with hemifacial microsomia. Note in the frontal view (**A**) that there is a crossbite on the right side, with the mandibular teeth occluding on the buccal side of the maxillary teeth.

VIEW IMAGE

Copyright © 2003, Mosby, Inc. All rights reserved.

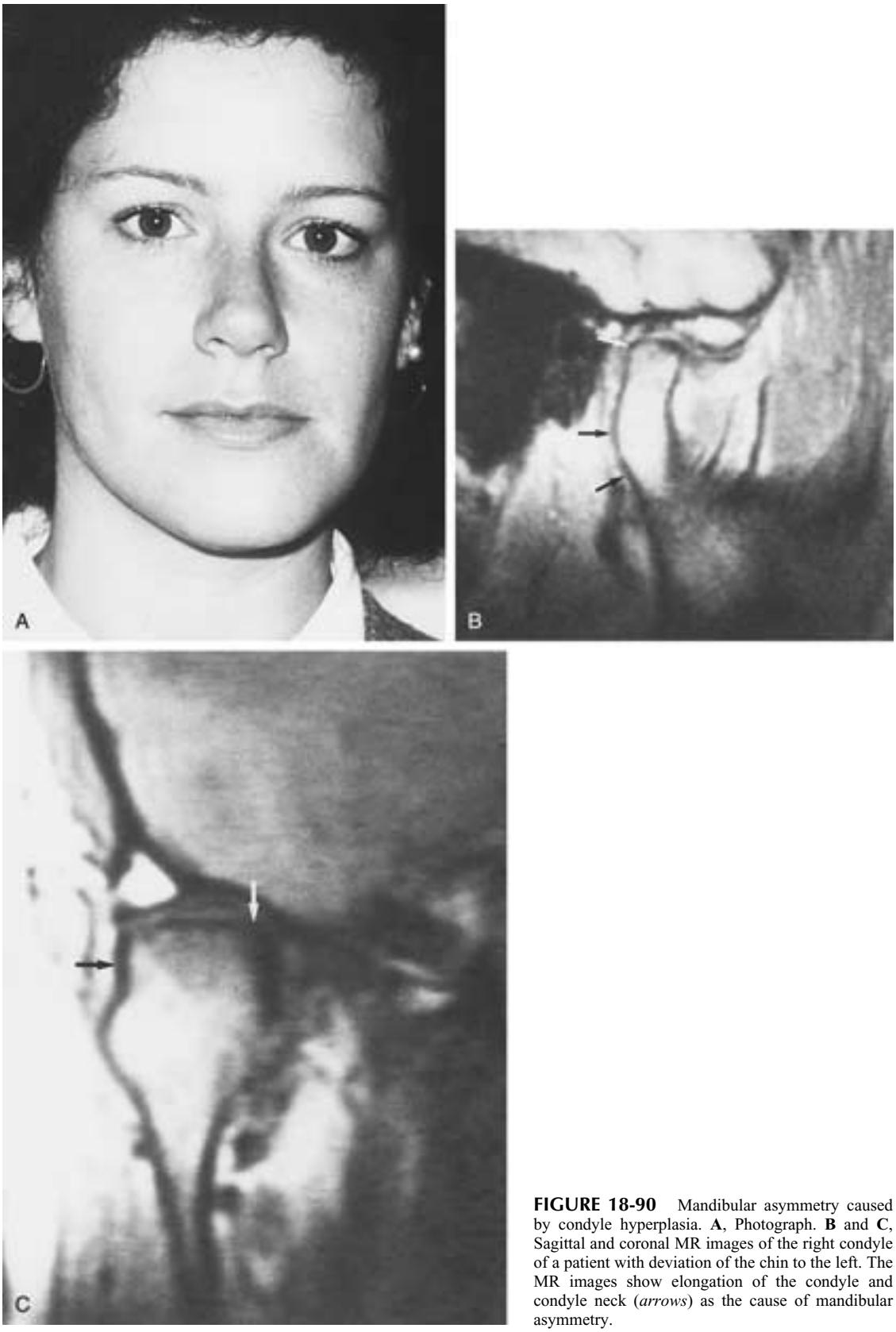

FIGURE 18-90 Mandibular asymmetry caused by condyle hyperplasia. **A**, Photograph. **B** and **C**, Sagittal and coronal MR images of the right condyle of a patient with deviation of the chin to the left. The MR images show elongation of the condyle and condyle neck (*arrows*) as the cause of mandibular asymmetry.

VIEW IMAGE

Copyright © 2003, Mosby, Inc. All rights reserved.

VIEW IMAGE

FIGURE 18-91 Mandibular asymmetry secondary to condyle hypoplasia. **A**, Photograph. **B**, Panoramic image. **C**, Sagittal MR image. **D**, Coronal MR image. There is deviation of the chin to the left. Panoramic view (**B**) shows a normal configuration on the right side of the mandible. The left side shows shortening of the ramus and regressive remodeling of the left condyle. MR images (**C** and **D**) show erosive changes of the condyle (*arrowheads*) and anterior disk displacement (*arrow*). The diminished size of the left condyle was the cause of the asymmetry in this patient.

Copyright © 2003, Mosby, Inc. All rights reserved.

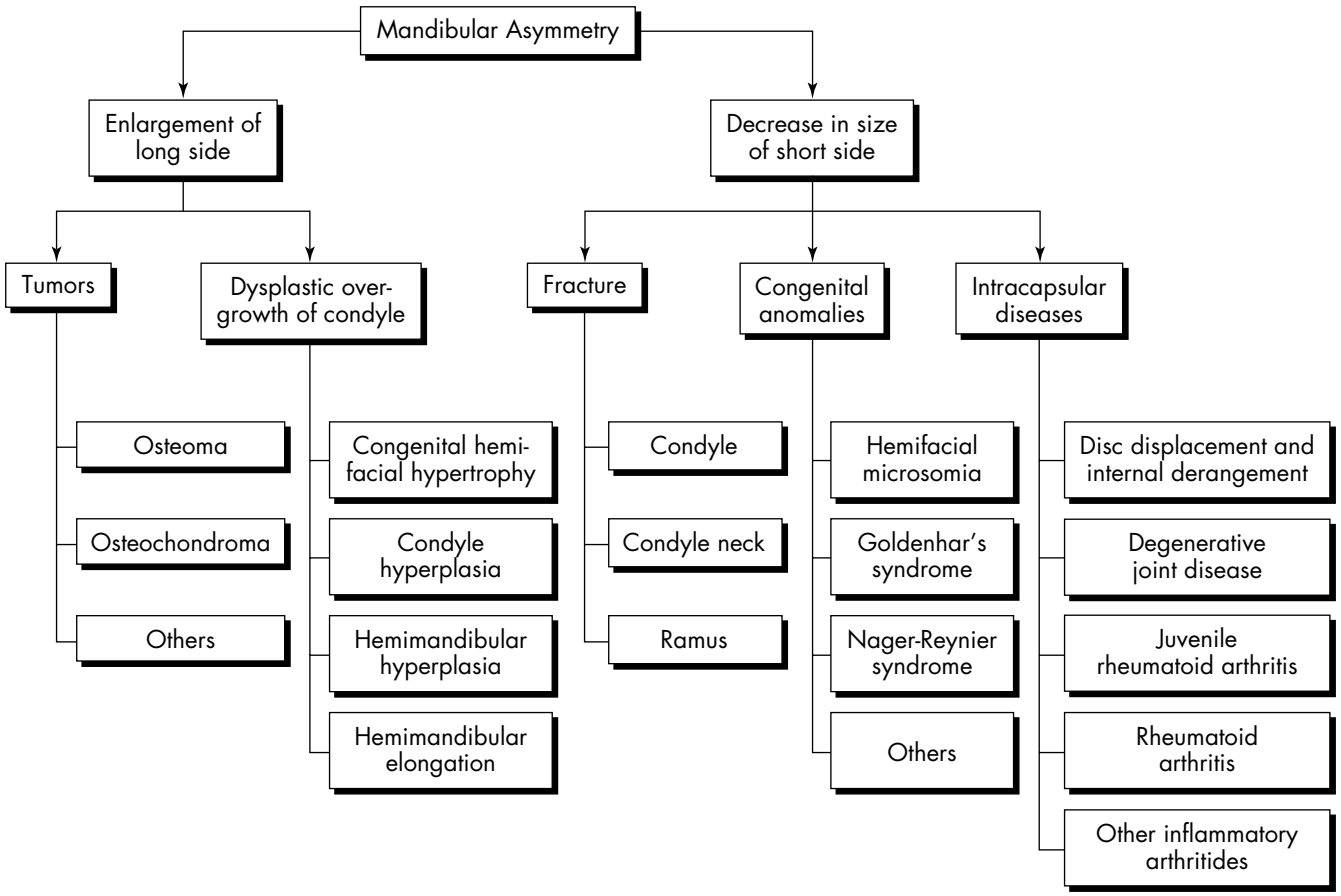

VIEW IMAGE

FIGURE 18-92 Etiologies of mandibular asymmetry.

to obtain real-time dynamic MR images. This will make possible the study of joint dynamics without injection of contrast medium or a local anesthetic. Pseudodynamic imaging with magnetic resonance is possible today, but its value for diagnostic work is not fully understood.[169] Multiple images are collected with the mouth opened to different widths, and the images are rapidly viewed on a *cine loop*. This creates the illusion of a real-time examination even though the images were acquired at separate points in time. However, the position of the disk can be followed, and the snapping of the condyle over the back of the disk can be appreciated.

BOX 18-5

IMAGING STRATEGY FOR PATIENTS WITH MANDIBULAR ASYMMETRY

1. Lateral and anterior posterior cephalograms
2. Lateral tomograms of TMJs, including entire mandibular ramus
3. MR imaging or arthrography of both left and right TMJs

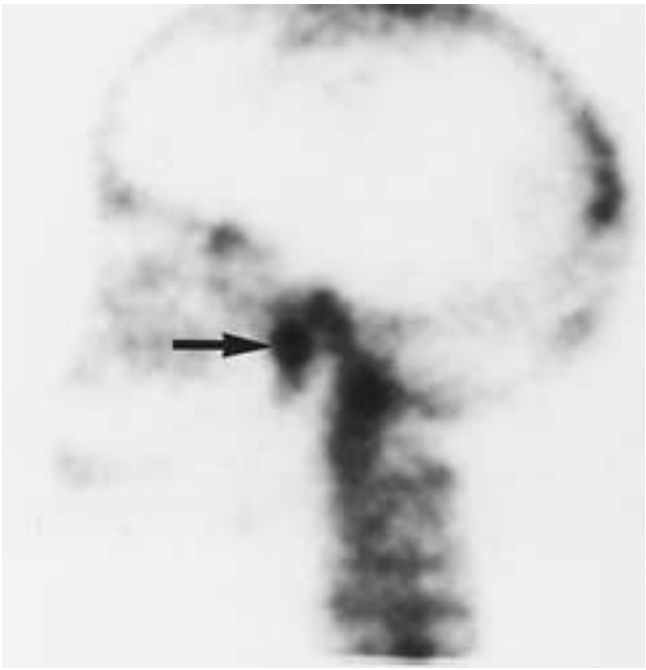

FIGURE 18-93 Radionuclide imaging of a patient with condylar hyperplasia of the left TMJ (*arrow*).

VIEW IMAGE

Copyright © 2003, Mosby, Inc. All rights reserved.

VIEW IMAGE

FIGURE 18-94 High-resolution MR image. This experimental MR image was obtained with a slice thickness of 1.5 mm and a field of view of 4 cm. The perforation of the disk (between the *long arrows*) and the osteophyte of the condyle filling the perforation are well visualized. The disk (*d*) is indicated for orientation.

MR Spectroscopy

The third area that will probably develop into a more useful clinical tool is MR spectroscopy. This may be helpful in evaluating metabolic and biochemical changes in the joints and muscles. Previous reports have suggested abnormalities of lactate accumulation in the intervertebral peridiskal tissues of the spine in the presence of degeneration and herniation.[170] MR spectroscopy has also been applied to experimental situations and appears capable of showing changes in areas of inflammation.[171]

REFERENCES

1. Katzberg RW. Temporomandibular joint imaging. Radiology 1989; 170:297–307.
2. Rees LA. The structure and function of the mandibular joint. Br Dent J 1954;96:125–133.
3. Adams JC, Hamblen DL. Outline of Orthopedics, 13th ed., London: Churchill Livingstone, 2001;135.
4. Eriksson L, Westesson PL. Clinical and radiological study of patients with anterior disc displacement of the temporomandibular joint. Swed Dent J 1983;7:55–64.
5. Katzberg RW, Dolwick MF, Helms CA, et al. Arthrotomography of the temporomandibular joint. AJR 1980;134:995–1003.
6. Westesson PL. Double-contrast arthrography and internal derangement of the temporomandibular joint. Swed Dent J Suppl 1982;13:1–57.
7. Wilkes CH. Arthrography of the temporomandibular joint in patients with the TMJ pain-dysfunction syndrome. Minn Med 1978;61:645–652.
8. Wilkes CH. Structural and functional alterations of the temporomandibular joint. Northwest Dent 1978;57:287–294.
9. Wilkes CH. Internal derangements of the temporomandibular joint. Arch Otolaryngol 1989;115:469–477.
10. Brooks SL, Westesson PL. Temporomandibular joint: value of coronal MR images. Radiology 1993;188:317–321.
11. Katzberg RW, Westesson PL, Tallents RH, et al. Temporomandibular joint: magnetic resonance assessment of rotational and sideways disc displacements. Radiology 1988;169:741–748.
12. Liedberg J, Westesson PL. Sideways position of the temporomandibular joint disk: coronal cryosectioning of fresh autopsy specimens. Oral Surg Oral Med Oral Pathol 1988;66:644–649.
13. Liedberg J, Westesson PL, Kurita K. Sideways and rotational displacement of the temporomandibular joint disk: diagnosis by arthrography and correlation to cryosectional morphology. Oral Surg Oral Med Oral Pathol 1990;69:757–763.
14. Ireland VE. The problem of the ''clicking jaw.'' Proc R Soc Med 1951;44:363–372.
15. Isberg-Holm AM, Westesson PL. Movement of disc and condyle in temporomandibular joints with clicking: an arthrographic and cineradiographic study on autopsy specimens. Acta Odontol Scand 1982;40:151–164.
16. Isberg-Holm AM, Westesson PL. Movement of disc and condyle in temporomandibular joints with and without clicking: a high speed cinematographic and dissection study on autopsy specimens. Acta Odontol Scand 1982;40:165–177.
17. Westesson PL. Arthrography of the temporomandibular joint. J Prosthet Dent 1984;51:534–543.
18. Westesson PL, Rohlin M. Internal derangement related to osteoarthritis in temporomandibular joint autopsy specimens. Oral Surg Oral Med Oral Pathol 1984;57:17–22.
19. Westesson PL, Bronstein SL, Liedberg J. Internal derangement of the temporomandibular joint: morphologic description with correlation to function. Oral Surg Oral Med Oral Pathol 1985;59: 323–331.
20. Bessette RW, Katzberg RW, Natiella JR, et al. Diagnosis and reconstruction of the human temporomandibular joint after trauma or internal derangement. Plast Reconstr Surg 1985;75:192–205.
21. Kurita K, Westesson PL, Sternby NH, et al. Histologic features of the temporomandibular joint disk and posterior disk attachment: comparison of symptom-free persons with normally positioned disks and patients with internal derangement. Oral Surg Oral Med Oral Pathol 1989;67:635–643.
22. Blaustein DI, Scapino RP. Remodelling of the temporomandibular joint disk and posterior attachment in disk displacement specimens in relation to glycosaminoglycan content. Oral Surg Oral Med Oral Pathol 1986;78:756–764.
23. Isberg AM, Isacsson G. Tissue reactions associated with internal derangement of the temporomandibular joint: a radiographic, cryomorphologic, and histologic study. Acta Odontol Scand 1986;44:160–164.
24. Pereira FJ Jr, Lundh H, Eriksson L, et al. Histologic characterization of the TMJ in patients and asymptomatic persons. Manuscript in preparation.
25. Westesson PL. Double-contrast arthrotomography of the temporomandibular joint: introduction of an arthrographic technique for visualization of the disc and articular surfaces. J Oral Maxillofac Surg 1983;41:163–172.
26. Westesson PL. Structural hard-tissue changes in temporomandibular joints with internal derangement. Oral Surg Oral Med Oral Pathol 1985;59:220–224.
27. Paesani D, Westesson PL, Hatala MP, et al. Accuracy of clinical diagnosis for TMJ internal derangement and arthrosis. Oral Surg Oral Med Oral Pathol 1992;73:360–363.
28. Roberts D, Schenck J, Joseph P, et al. Temporomandibular joint: magnetic resonance imaging. Radiology 1985;155:829–830.
29. Roberts CA, Tallents RH, Espeland MA, et al. Mandibular range of motion versus arthrographic diagnosis of the temporomandibular joint. Oral Surg Oral Med Oral Pathol 1985;60:244–251.
30. Roberts CA, Tallents RH, Katzberg RW, et al. Clinical and arthrographic evaluation of temporomandibular joint sounds. Oral Surg Oral Med Oral Pathol 1986;62:373–376.
31. Roberts CA, Tallents RH, Katzberg RW, et al. Comparison of internal derangements of the TMJ to occlusal findings. Oral Surg Oral Med Oral Pathol 1987;63:645–650.

Copyright © 2003, Mosby, Inc. All rights reserved.

32. Roberts CA, Tallents RH, Katzberg RW, et al. Clinical and arthrographic evaluation of the location of TMJ pain. Oral Surg Oral Med Oral Pathol 1987;64:6–8.
33. Roberts CA, Tallents RH, Katzberg RW, et al. Comparison of arthrographic findings of the temporomandibular joint with palpation of the muscles of mastication. Oral Surg Oral Med Oral Pathol 1987;64:275–277.
34. Anderson GC, Schiffman EL, Schellhas KP, et al. Clinical vs. arthrographic diagnosis of TMJ internal derangement. J Dent Res 1989;68:826–829.
35. Drace JE, Enzmann DR. Defining the normal temporomandibular joint: closed-, partially open-, and open-mouth MR imaging of asymptomatic subjects. Radiology 1990;177:67–71.
36. Kircos LT, Ortendahl DA, Mark AS, et al. Magnetic resonance imaging of the TMJ disk in asymptomatic volunteers. J Oral Maxillofac Surg 1987;45:852–854.
37. Westesson PL, Eriksson L, Kurita K. Temporomandibular joint: variation of normal arthrographic anatomy. Oral Surg Oral Med Oral Pathol 1990;69(4):514–519.
38. Boden SD, Davis DO, Dina TS, et al. Abnormal magnetic resonance scans of the lumbar spine in asymptomatic subjects. A prospective investigation. J Bone Joint Surg (Am) 1990;72: 403–408.
39. Boden SD, Davis DO, Dina TS, et al. A prospective and blinded investigation of magnetic resonance imaging of the knee. Abnormal findings in asymptomatic subjects. Clin Orthop 1992;282: 177–185.
40. Kornick J, Trefelner NE, McCarty S, et al. Meniscal abnormalities in the asymptomatic population in MR imaging. Radiology 1990;177: 463–465.
41. Nagendak WG, Fernandez FR, Halbrun LK, et al. Magnetic resonance imaging of meniscal degeneration in asymptomatic knees. J Orthop Res 1990;8:311–320.
42. Shellock FG, Morris E, Deutsch AL, et al. Hematopoietic bone marrow hyperplasia: high prevalence on MR images of the knee in asymptomatic marathon runners. AJR 1992;158:335–338.
43. Paesani D, Westesson PL, Hatala M, et al. Prevalence of internal derangement in patients with craniomandibular disorders. Am J Orthod Dentofacial Orthop 1992;101:41–47.
44. Tasaki MM, Westesson PL, Isberg AM, Tallents RH, Ren YF. Classification and prevalence of temporomandibular joint disk displacement in patients and asymptomatic volunteers. Am J Orthod Dentofac Orthop 1996;109:249–262.
45. Katzberg RW, Westesson PL, Tallents RH, Drake CM. Orthodontics and temporomandibular joint internal derangement. Am J Orthod Dentofac Orthop 1996;109:515–520.
46. Katzberg RW, Westesson PL, Tallents RH, Drake CM. Anatomic disorders of the temporomandibular joint disc in asymptomatic subjects. J Oral Maxillofac Surg 1996;54:147–153.
47. Larheim TA, Westesson P, Sano T. Temporomandibular joint disk displacement: comparison in asymptomatic volunteers and patients. Radiology 2001;218:428–432.
48. Widmalm S-E, Westesson PL, Kim I-K, et al. Temporomandibular joint pathosis related to sex, age, and dentition in autopsy material. Oral Surg Oral Med Oral Pathol 1994;78:416–425.
49. Oberg T, Carlsson GE, Fajers CM. The temporomandibular joint: a morphologic study of human autopsy material. Acta Odontal Scand 1971;29:349–384.
50. McCabe JB, Keller SE, Moffet BC. A new radiographic technique for diagnosing temporomandibular joint disorders. J Dent Res 1959;38: 663.
51. Omnell K-A, Peterson A. Radiography of the temporomandibular joint utilizing oblique lateral transcranial projections: comparison of information obtained with standardized technique and individualized technique. Odontol Rev 1976;26:77–92.
52. Nørgaard F. Artografi av kaebeleddet. Preliminary report. Acta Radiol 1944;25:679–685.
53. Nørgaard F. Temporomandibular Arthrography. Thesis. Copenhagen: Munksgaard, 1947.
54. Farrar WB, McCarty WL Jr. Inferior joint space arthrography and characteristics of condylar paths in internal derangements of the TMJ. J Prosthet Dent 1979;41:548–555.
55. Katzberg RW, Dolwick MF, Bales DJ, et al. Arthrotomography of the temporomandibular joint: new technique and preliminary observations. AJR 1979;132:949–955.
56. Westesson PL, Omnell K-Å, Rohlin M. Double-contrast tomography of the temporomandibular joint. A new technique based on autopsy examinations. Acta Radiol (Diagn) (Stockh) 1980;21: 777–784.
57. Annadale T. Displacement of the inter-articular cartilage of the lower jaw and its treatment by operation. Lancet 1987;1:411.
58. Burman M, Sinberg SE. Condylar movement in the study of internal derangement of the temporomandibular joint. J Bone Joint Surg (Br) 1946;28:351–373.
59. Farrar WB. Diagnosis and treatment of anterior dislocation of the articular disc. NY J Dent 1971;41:348–351.
60. Pringle JH. Displacement of the mandibular meniscus and its treatment. Br J Surg 1918;6:385–389.
61. Silver CM, Simon SD, Savastano AA. Meniscus injuries of the temporomandibular joint. J Bone Joint Surg (Am) 1956;38A: 541–552.
62. Bell KA, Walters PJ. Videofluoroscopy during arthrography of the temporomandibular joint. Radiology 1983;147:879.
63. Dolwick MF, Riggs RR. Diagnosis and treatment of internal derangements of the temporomandibular joint. Dent Clin North Am 1983;27:561–572.
64. Lundh H, Westesson PL, Kopp S, et al. Anterior repositioning splint in the treatment of temporomandibular joints with reciprocal clicking: comparison with a flat occlusal splint and an untreated control group. Oral Surg Oral Med Oral Pathol 1985;60: 131–136.
65. McCarty WL, Farrar WB. Surgery for internal derangements of the temporomandibular joint. J Prosthet Dent 1979;42:191–196.
66. McCarty WL. Surgery. In: Farrar WB, McCarthy WL, eds. A Clinical Outline of Temporomandibular Joint Diagnosis and Treatment, 7th ed. Montgomery, Ala: Normandie Publications, 1982.
67. Arnaudow M, Haage H, Pflaum I. Die Doppelkontrastarthrographie des Kiefergelenkes. Dtsch Zahnarztl Z 1968;23:390–393.
68. Arnaudow M, Pflaum I. Neue Erkenntnisse in der beurteilung bei der Kiefergelenktomographie. Dtsch Zahnarztl Z 1974;29:554–556.
69. Tallents RH, Katzberg RW, Macher DJ, et al. Arthrographically assisted splint therapy: 6-month follow-up. J Prosthet Dent 1986;56:224–226.
70. Ross JB. The intracapsular therapeutic modalities in conjunction with arthrography: case reports. J Craniomandib Disord 1989;3: 35–43.
71. Katzberg RW, Westesson PL. Temporomandibular Joint Arthrography, Section I. Single Contrast Arthrography. In: Diagnosis of the temporomandibular joint. Philadelphia: WB Saunders, 1993; 101–142.
72. Katzberg RW, Westesson PL. Double Contrast Arthrography. In: Diagnosis of the Temporomandibular Joint. Philadelphia: WB Saunders, 1993;143–165.
73. Westesson PL, Eriksson L, Kurita K. Reliability of a negative clinical temporomandibular joint examination: prevalence of disk displacement in asymptomatic temporomandibular joints. Oral Surg Oral Med Oral Pathol 1989;68:551–554.
74. Anderson QN, Katzberg RW. Loose bodies of the temporomandibular joint: arthrographic diagnosis. Skeletal Radiol 1984;11:42–46.
75. Manzione JV, Seltzer SE, Katzberg RW, et al. Direct sagittal computed tomography of the temporomandibular joint. AJNR 1982;3:677–679.
76. Manzione JV, Katzberg RW, Brodsky GI, et al. Internal derangement of the temporomandibular joint: diagnosis by direct sagittal computed tomography. Radiology 1984;150:111–115.
77. Helms CA, Morrish RB Jr, Kircos LT, et al. Computed tomography of the meniscus of the temporomandibular joint: preliminary observations. Radiology 1982;145:719–722.
78. Manco LG, Messing SG, Busino LJ, et al. Internal derangements of the temporomandibular joint evaluated with direct sagittal CT: a prospective study. Radiology 1985;157:407–412.
79. Sartoris DJ, Neumann CH, Riley RW. The temporomandibular joint: true sagittal computed tomography with meniscus visualization. Radiology 1984;150:250–254.
80. Thompson JR, Christiansen EL, Hasso AN, et al. The temporomandibular joint: high resolution computed tomographic evaluation. Radiology 1984;150:105–110.
81. Westesson PL, Katzberg RW, Tallents RH, et al. CT and MRI of the temporomandibular joint: comparison with autopsy specimens. AJR 1987;148:1165–1171.

Copyright © 2003, Mosby, Inc. All rights reserved.

82. Harms SE, Wilk RM, Wolford LM, et al. The temporomandibular joint: magnetic resonance imaging using surface coils. Radiology 1985;157:133–136.
83. Katzberg RW, Schenck J, Roberts D, et al. Magnetic resonance imaging of the temporomandibular joint meniscus. Oral Surg Oral Med Oral Pathol 1985;59:332–335.
84. Katzberg RW, Besettte RW, et al. Normal and abnormal temporomandibular joint: MR imaging with surface coil. Radiology 1986;158:183–189.
85. Larheim TA. Imaging of the temporomandibular joint in rheumatic disease. In: Westesson PL, Katzberg RW, eds. Imaging of the Temporomandibular Joint, Vol. 1. Cranio Clinics International. Baltimore: Williams & Wilkins, 1991;133–153.
86. Larheim TA. Imaging of the temporomandibular joint in juvenile rheumatoid arthritis. In: Westesson PL, Katzberg RW, eds. Imaging of the Temporomandibular Joint, Vol. 1. Cranio Clinics International. Baltimore: Williams & Wilkins, 1991;155–172.
87. Manzione JV, Katzberg RW, Tallents RH, et al. Magnetic resonance imaging of the temporomandibular joint. J Am Dent Assoc 1986;113:398–402.
88. Schellhas KP. MR imaging of muscles of mastication. AJR 1989;153:847–855.
89. Schellhas KP, Wilkes CH, Fritts HM, et al. MR of osteochondritis dissecans and avascular necrosis of the mandibular condyle. AJNR 1989;10:3–12.
90. Hansson L-G, Westesson PL, Katzberg RW, et al. MR imaging of the temporomandibular joint: comparison of images of autopsy specimens made at 0.3 T and 1.5 T with anatomic cryosections. AJR 1989;152:1241–1244.
91. Hardy CJ, Katzberg RW, Frey RL, et al. Switched surface coil system for bilateral MR imaging. Radiology 1988;167:835–838.
92. Shellock FG, Pressman BD. Dual-surface-coil MR imaging of bilateral temporomandibular joints: improvements in imaging protocol. AJNR 1989;10:595–598.
93. Isberg A, Stenstrom B, Isacsson G. Frequency of bilateral temporomandibular joint disc displacement in patients with unilateral symptoms: a 5-year follow-up of the asymptomatic joint. A clinical and arthrotomographic study. Dentomaxillofac Radiol 1991;20:73-76.
94. Sanchez-Woodworth RE, Tallents RH, Katzberg RW, et al. Bilateral internal derangements of temporomandibular joint: evaluation by magnetic resonance imaging. Oral Surg Oral Med Oral Pathol 1988;65:281–285.
95. Musgrave MT, Westesson PL, Tallents RH, et al. Improved magnetic resonance imaging of the temporomandibular joint by oblique scanning planes. Oral Surg Oral Med Oral Pathol 1991;71:525–528.
96. Manzione JV, Tallents RH. ''Pseudomeniscus'' sign: potential indicator of repair or remodeling in temporomandibular joints with internal derangements. Presented at Radiologic Society of North America. Radiology 1992;185(suppl):175.
97. Paesani D, Westesson PL. MR imaging of the TMJ: decreased signal from the retrodiscal tissue. Oral Surg Oral Med Oral Pathol 1993;76:631–635.
98. Westesson PL, Brooks SL. Temporomandibular joint: relation between MR evidence of effusion and the presence of pain and disk displacement. AJR 1992;159:559–563.
99. Larheim TA, Westesson PL, Sano T. MR grading of temporomandibular joint fluid: association with disk displacement categories, condyle marrow abnormalities and pain. Int J Oral Maxillofac Surg 2001;30:104–112.
100. Rudisch A, Innerhofer K, Bertram S, Emshoff R. Magnetic resonance imaging findings of internal derangement and effusion in patients with unilateral temporomandibular joint pain. Oral Surg Oral Med Oral Pathol Oral Radiol Endod 2001;92:566–571.
101. Larheim TA, Katzberg RW, Westesson PL, Tallents RH, Moss ME. MR evidence of temporomandibular joint fluid and condyle marrow alterations: occurence in asymptomatic volunteers and symptomatic patients. Int J Oral Maxillofac Surg 2001;30:113–117.
102. Pereira FJ Jr, Lundh H, Westesson PL, Carlsson LE. Clinical findings related to morphologic changes in TMJ autopsy specimens. Oral Surg Oral Med Oral Pathol 1994;78:288–295.
103. Lundh H, Westesson PL, Kopp S. A three year follow-up of patients with reciprocal temporomandibular joint clicking. Oral Surg Oral Med Oral Pathol 1987;63:530–533.
104. Rasmussen OC. Description of population and progress of symptoms in a longitudinal study of temporomandibular arthropathy. Scand J Dent Res 1981;89:196–203.
105. Randolph CS, Greene CS, Moretti R, Forbes D, Perry HT. Conservative management of temporomandibular disorders: a posttreatment comparison between patients from a university clinic and from private practice. Am J Orthod Dentofacial Orthop 1990;98:77–82.
106. Schellhas KP, Wilkes CH. Temporomandibular joint inflammation: comparison of MR fast scanning with T1-and T2-weighted imaging techniques. AJR 1989;153:93–98.
107. Schellhas KP, Wilkes CH, Omlie MR, Peterson CM, Johnson SD, Keck RJ, Block JC, Fritts HM, Heithoff KB. The diagnosis of temporomandibular joint disease: two-compartment arthrography and MR. AJR 1988;151:341–350.
108. Schellhas KP. Internal derangement of the temporomandibular joint: radiologic staging with clinical, surgical, and pathologic correlation. Magn Reson Imaging 1989;7:495–515.
109. Schellhas KP, Wilkes CH. Temporomandibular joint inflammation: comparison of MR fast scanning with T1- and T2-weighted imaging techniques. AJR 1989;153:93–98.
110. Schellhas KP, Wilkes CH, Fritts HM, Omlie MR, Lagrotteria LB. MR of osteochondritis dissecans and avascular necrosis of the mandibular condyle. AJR 1989;152:551–560.
111. Schellhas KP. Temporomandibular joint injuries. Radiology 1989; 173:211–216.
112. Larheim TA, Westesson PL, Hicks DG, Eriksson L, Brown D. Osteonecrosis of the temporomandibular joint: correlation of magnetic resonance imaging and histology. J Oral Maxillofac Surg 1999;57:888–898.
113. Sano T, Westesson PL, Larheim TA, Rubin SJ, Tallents RH. Osteoarthritis and abnormal bone marrow of the mandibular condyle. Oral Surg Oral Med Oral Pathol Oral Radiol Endod 1999;87:243–252.
114. Reiskin AB. Aseptic necrosis of the mandibular condyle: a common problem? Quintessence Int 1979;2:85–89.
115. Lieberman JM, Gardner CL, Motta AO, Schwartz RD. Prevalence of bone marrow signal abnormalities observed in the temporomandibular joint using magnetic resonance imaging. J Oral Maxillofac Surg 1996;54:434–439.
116. Sano T, Westesson PL, Larheim TA, Takagi R. The association of temporomandibular joint pain with abnormal bone marrow of the mandibular condyle. J Oral Maxillofac Surg 2000;58: 254–257.
117. Resnick D, Sweet DE, Madewell JE. Osteonecrosis and osteochondrosis. In: Resnick D, ed. Bone and Joint Imaging, 2nd ed. Philadelphia: WB Saunders, 1996;941–959.
118. Rao VM, Lliem MD, Farole A, et al. Elusive ''stuck'' disk in the temporomandibular joint: diagnosis with MR imaging. Radiology 1993;189:823–827.
119. Westesson PL, Rohlin M. Diagnostic accuracy of double-contrast arthrotomography of the temporomandibular joint: correlation with postmortem morphology. AJR 1984;143:655–660.
120. Westesson PL, Bronstein SL, Liedberg J. Temporomandibular joint: correlation between single-contrast videoarthrography and postmortem morphology. Radiology 1986;160:767–771.
121. Westesson PL, Katzberg RW, Tallents RH, et al. Temporomandibular joint: comparison of MR images with cryosectional anatomy. Radiology 1987;164:59–64.
122. Westesson PL, Bronstein SL. Temporomandibular joint: comparison of single- and double-contrast arthrography. Radiology 1987; 164:65–70.
123. Tasaki M, Westesson PL. Temporomandibular joint: diagnostic accuracy with sagittal and coronal MR imaging. Radiology 1993;186:723–729.
124. Hansson L-G, Eriksson L, Westesson PL. Temporomandibular joint: magnetic resonance evaluation after diskectomy. Oral Surg Med Oral Pathol 1992;74:801–810.
125. Kent JN, Misiek DJ, Akin RK, et al. Temporomandibular joint condylar prosthesis: a ten-year report. J Oral Maxillofac Surg 1983;41:245–254.
126. Kent JN, Block MS, Homsey CA, et al. Experience with a polymer glenoid fossa prosthesis for partial or total temporomandibular joint reconstruction. J Oral Maxillofac Surg 1986;44: 520–533.

Copyright © 2003, Mosby, Inc. All rights reserved.

127. Lindqvist C, Jokinen J, Paukku P, et al. Adaptation of autogenous costochondral grafts used for temporomandibular joint reconstruction: a long-term clinical and radiologic follow-up. J Oral Maxillofac Surg 1988;46(6):465–470.
128. Heffez LB. Imaging of internal derangements and synovial chondromatosis of the temporomandibular joint. Radiol Clin North Am 1993;31:149–162.
129. Nomoto M, Nagao K, Numata T, et al. Synovial osteochondromatosis of the temporomandibular joint. J Laryngol Otol 1993;107:742–745.
130. Quinn PD, Stanton DC, Foote JW. Synovial chondromatosis with cranial extension. Oral Surg Oral Med Oral Pathol 1992;73:398–402.
131. Sun S, Helmy E, Bays R. Synovial chondromatosis with intracranial extension: a case report. Oral Surg Oral Med Oral Pathol 1990;70:5–9.
132. Boccardi A. CT evaluation of chondromatosis of the temporomandibular joint. J Comput Assist Tomogr 1991;15:826–828.
133. Herzog S, Mafee M. Synovial chondromatosis of the TMJ: MR and CT findings. Am J Neuroradiol 1990;11:742–745.
134. van Ingen JM, de Man K, Bakri I. CT diagnosis of synovial chondromatosis of the temporomandibular joint. Br J Oral Maxillofac Surg 1990;28:164–167.
135. Rickert RR, Shapiro MJ. Pigmented villonodular synovitis of the temporomandibular joint. Otolaryngol Head Neck Surg 1982;90(5): 668–670.
136. Lapayowker MS, Miller WT, Levy WM, Harwick RD. Pigmented villonodular synovitis of the temperomandibular joint. Radiology 1973;108(2):313–316.
137. Curtin HD, Williams R, Gallia L, Meyers EN. Pigmented villonodular synovitis of the temporomandibular joint. Comput Radiol 1983;7(4):257–260.
138. O'Sullivan TJ, Alport EC, Whiston HG. Pigmented villonodular synovitis of the temporomandibular joint. J Otolaryngol 1984;13(2): 123–126.
139. Song MY, Heo MS, Lee SS, et al. Diagnostic imaging of pigmented villonodular synovitis of the temporomandibular joint associated with condylar expansion. Dentomaxillofac Radiol 1999;28(6):386–390.
140. Bemporad JA, Chaloupka JC, Putman CM, et al. Pigmented villonodular synovitis of the temporomandibular joint: diagnostic imaging and endovascular therapeutic embolization of a rare head and neck tumor. AJNR 1999;20(1):159–162.
141. Klenoff JR, Lowlicht RA, Lesnik T, Sasaki CT. Mandibular and temporomandibular joint arthropathy in the differential diagnosis of the parotid mass. Laryngoscope 2001;111(12):2162–2165.
142. Dijkgraaf LC, Liem RS, de Bont LG. Temporomandibular joint osteoarthritis and crystal deposition diseases: a study of crystals in synovial fluid lavages in osteoarthritic temporomandibular joints. Int J Oral Maxillofac Surg 1998;27(4):268–273.
143. Goudot P, Jaquinet A, Gilles R, Richter M. A destructive calcium pyrophosphate dihydrate deposition disease of the temporomandibular joint. J Craniofac Surg 1999;10(5):385–388.
144. Jibiki M, Shimoda S, Nakagawa Y, Kawasaki K, Asada K, Ishibashi K. Calcifications of the disc of the temporomandibular joint. J Oral Pathol Med 1999;28(9):413–419.
145. Olin HB, Pedersen K, Francis D, Hansen H, Poulsen FW. A very rare benign tumour in the parotid region: calcium pyrophosphate dihydrate crystal deposition disease. J Laryngol Otol 2001;115(6): 504–506.
146. Jordan JA, Roland P, Lindberg G, Mendelsohn D. Calcium pyrophosphate deposition disease of the temporal bone. Ann Otol Rhinol Laryngol 1998;107(11 Pt 1):912–916.
147. Vargas A, Teruel J, Trull J, Lopez E, Pont J, Velayos A. Calcium pyrophosphate dihydrate crystal deposition disease presenting as a pseudotumor of the temporomandibular joint. Eur Radiol 1997;7(9): 1452–1453.
148. Kurihara K, Mizuseki K, Saiki T, Wakisaka H, Maruyama S, Sonobe J. Tophaceous pseudogout of the temporomandibular joint: report of a case. Pathol Int 1997;47(8):578–580.
149. Slater LJ. Distinguishing calcium pyrophosphate dihydrate deposition disease from synovial chondrosarcoma. J Oral Maxillofac Surg 1998;56(5):693–694.
150. Lopes V, Jones JAH, Sloan P, et al. Temporomandibular ganglion or synovial cyst? Oral Surg Oral Med Oral Pathol 1994;77:627–630.
151. McGuirt WF, Myers EN. Ganglion of the temporomandibular joint. Presentation as a parotid mass. Otolaryngol Head Neck Surg 1993;109:950–953.
152. Noffke C, Raubenheimer E, Fischer E. Tumoral calcinosis of the temporomandibular joint region. Dentomaxillofac Radiol 2000;29(2): 128–130.
153. Bhaskar SN. Synopsis of Oral Pathology. St. Louis: CV Mosby, 1977;304–324.
154. Ruben MM, Jui B, Cozzi GM. Metastatic carcinoma of the mandibular condyle presenting as temporomandibular joint syndrome. J Oral Maxillofac Surg 1989;47:511–513.
155. Zachariades N. Neoplasms metastatic to the mouth, jaws and surrounding tissues. J Craniomaxillofac Surg 1989;17:283–291.
156. Ruggiero SL, Donoff RB. Bone regeneration after mandibular resection: report of two cases. J Oral Maxillofac Surg 1991;49: 647–651.
157. Smith HJ, Larheim TA, Aspestrand F. Rheumatic and nonrheumatic disease in the temporomandibular joint: gadolinium-enhanced MR imaging. Radiology 1992;185:229–234.
158. Barthelemy I, Karanas Y, Sannajust JP, Emering C, Mondie JM. Gout of the temporomandibular joint: pitfalls in diagnosis. J Craniomaxillofac Surg 2001;29(5):307–310.
159. Isberg A, Isacsson G, Nah KS. Mandibular coronoid process locking: a prospective study of frequency and association with internal derangement of the temporomandibular joint. Oral Surg Oral Med Oral Pathol 1987;63:275–279.
160. Langenbeck B. Augeborene kleinheit des unterkiefers; kiefersperre verbunden, geheilt durch resection der processus coronoidei. Archiv Klin Chir 1860;1:30.
161. Munk PL, Helms CA. Coronoid process hyperplasia: CT studies. Radiology 1989;171:783–784.
162. Markey RJ, Potter BE, Moffett BC. Condylar trauma and facial asymmetry: an experimental study. J Maxillofac Surg 1980;8:38–51.
163. Wang-Norderud R, Ragab RR. Unilateral condylar hyperplasia and the associated deformity of facial asymmetry. Scand J Plast Reconstr Surg Hand Surg 1977;11:91–96.
164. Lineaweaver W, Vargervik K, Tomer BS, et al. Posttraumatic condylar hyperplasia. Ann Plast Surg 1989;22:163–171.
165. Katzberg RW, Tallents RH, Hayakawa K, et al. Internal derangements of the temporomandibular joint: findings in the pediatric age group. Radiology 1985;154:125–127.
166. Westesson PL, Dahlberg G, Hansson L-G, et al. Osseous and muscular changes after vertical ramus osteotomy. An MRI study. Oral Surg Oral Med Oral Pathol 1991;72:139–145.
167. Collier DB, Carrera GF, Messer EJ, et al. Internal derangement of the temporomandibular joint: detection by single-photon emission computed tomography. Radiology 1983;149:557–561.
168. Katzberg RW, O'Mara RE, Tallents RH, et al. Radionuclide skeletal imaging and single photon emission computed tomography in suspected internal derangements of the temporomandibular joint. J Oral Maxillofac Surg 1984;42:782–787.
169. Bell KA, Jones JP, Miller KD, et al. The added gradient echo pulse sequence technique: application to imaging of fluid in the temporomandibular joint. AJNR 1993;14:375–381.
170. Diamant B, Karlsson J, Nachemson A. Correlation between lactate levels and pH in disks in patients with lumbar rhizopathies. Experientia 1969;24:1195–1196.
171. Alder ME, Dove SB, Murrah VA, et al. Magnetic resonance spectroscopy of inflammation associated with the temporomandibular joint. Oral Surg Oral Med Oral Pathol 1992;74:515–523.

Copyright © 2003, Mosby, Inc. All rights reserved.

Copyright © 2003, Mosby, Inc. All rights reserved.

Section V

Temporal Bone

Copyright © 2003, Mosby, Inc. All rights reserved.

Copyright © 2003, Mosby, Inc. All rights reserved.

19

Temporal Bone: Embryology and Anatomy

Hugh D. Curtin, Pina C. Sanelli, and Peter M. Som

SECTION ONE: EMBRYOLOGY AND ANATOMY
EMBRYOLOGY AND DEVELOPMENTAL ANATOMY
- Inner Ear
  - Endolymphatic Labyrinth
  - Perilymphatic (Periotic) Labyrinth
  - Bony Labyrinth
- Outer and Middle Ear
- Pneumatic Cells of the Temporal Bone
- Neonatal Temporal Bone
- Formation of the Mastoid Process

NORMAL ANATOMY
- Temporal Bone
  - Squamous Portion
  - Mastoid Portion
  - Petrous Portion
  - Tympanic Portion
  - Styloid Process
- External Auditory Canal
  - Vessels and Nerves
  - Tympanic Membrane
- Middle Ear
  - Roof or Tegmental Wall
  - Floor or Jugular Wall
  - Mastoid or Posterior Wall
  - Carotid or Anterior Wall
  - Eustachian Tube
  - Lateral or Membranous Wall
  - Medial or Labyrinthine Wall
  - Epitympanic Recess
  - Contents of the Tympanic Cavity
    - *Auditory Ossicles*
    - *Ligaments*
    - *Muscles*
    - *Nerves and Vessels*
- Route of the Facial Nerve (Cranial Nerve VII)
  - Bony Dehiscences
  - Anomalous Course in Petrous Bone
- Inner Ear
  - Bony Labyrinth
    - *Vestibule*
    - *Semicircular Canals*
    - *Cochlea*
  - Membranous Labyrinth
    - *Cochlear Duct*
    - *Vestibular Sense Organs*
    - *Endolymphatic Duct and Sac*
    - *Round Window Membrane*
    - *Vascular System*
  - Perilymphatic Spaces and Fluid Systems

HOW THE EAR AMPLIFIES SOUND
SECTION TWO: SECTIONAL ANATOMY

Copyright © 2003, Mosby, Inc. All rights reserved.

SECTION ONE

EMBRYOLOGY AND ANATOMY*

EMBRYOLOGY AND DEVELOPMENTAL ANATOMY

Each of the organs of special sense has a fascinating phylogeny. However, none surpasses the ear in demonstrating the resourcefulness and richness of invention of a biologic system in making adaptive modifications to deal successfully with a changing environment. The ear began as an organ of balance. In the fish of 350 million years ago it existed as a fluid-filled pocket, sunk beneath the surface of the skin on either side of the head. The pocket communicated directly with the ocean water in which the ancient fish swam, providing a mechanism whereby the fish could sense its orientation in the sea. It is physically possible for such a structure to be sensitive to low-frequency vibrations transmitted through the water, and indeed such was likely the case. Hearing nonetheless was incidental, if not accidental, to a structure primarily developed to provide balance.

By the time evolution produced creatures that existed on land, the vestibular system had become much more highly developed. But in so doing, it lost its continuity with the external environment, becoming deeply encased and sealed off within the base of the skull. However, for the creatures to become successful land dwellers, perception of sound had become important to survival. The economy of nature prevailed. Connection between the external environment and the inner ear was reestablished, and the middle and external ears evolved. Concurrently, the hearing portion of the inner ear structure became much more highly specialized (Fig. 19-1).

The following is the story of the development of the ear as we know it. It bears great relevance to the understanding of congenital anomalies, malformations, anatomic variations, and the normal state of the ear.

Streeter provides the definitive account of the embryologic development of the inner ear.[1, 2] Numerous other investigators also studied the development of the ear in the twentieth and previous centuries, but the most complete single source of information relating to development of all portions of the temporal bone remains in Bast and Anson's *The Temporal Bone and Ear*.[3] Shambaugh and Glasscock present the essence of their work in abbreviated form in *Surgery of the Ear*.[4] Iurato presents an even more concise precis in *Submicroscopic Structure of the Inner Ear*.[5]

Inner Ear

The development of the inner ear may be considered in terms of the following three structures: (1) endolymphatic (otic or membranous) labyrinth, (2) perilymphatic (periotic) labyrinth, and (3) bony labyrinth.

Endolymphatic Labyrinth

Inner ear formation commences when the embryo is only about 2 mm in length (crown to rump). A plate-like thickening of neuroectoderm on either side of the head forms midway alongside the hindbrain; this is called the otic placode. It quickly invaginates to form the otic pit. Soon the pit has deepened and narrowed, its lips have fused to form the otocyst (otic vesicle), and it has descended away from its surface ectodermal origin.

The otocyst is fluid-filled and ectoderm-lined and constitutes the primitive endolymphatic (otic), or membranous, labyrinth. The otocyst comes to lie opposite the fifth neuromere and is in contact rostrally with the facial-acoustic primordium, the precursor of the seventh and eighth nerves. Accompanied by these neural cells, the cyst then migrates to the developing skull base.

By the time the embryo is 6 to 7 mm long, the otocyst has elongated and started to divide into two main sections, the longer utriculosaccular portion and the smaller endolymphatic portion that arises at the point on the otocyst wall that originally joined the neuroectoderm. The utricle and semicircular canals differentiate from the posterolateral aspect of the otocyst, and the saccule and cochlear duct and the communication between the two, the ductus reuniens, arise anteromedially.

By the 9 mm stage, two flattened pouch-like diverticuli project from the otocyst. The superior and posterior semicircular ducts will eventually arise from the pouch at the dorsal margin of the otocyst, while the lateral semicircular duct differentiates from the more lateral outpouching. In the 12 to 15 mm stages, the central portions of the walls of these pouches pinch inward and fuse. Thus each disk-like pouch changes into a ring. Initially, a thin plate representing the pinched-in epithelium crosses the central portion, and the canal lumen remains at the periphery of each pouch. The central epithelial plates eventually break down, leaving only the semicircular canals. The region where these canals join the otocyst becomes the utricle.

The saccule originates from the anteromedial portion of the otocyst. By the 7 to 8 mm stage (3½ to 4 weeks' gestation) the future cochlea is appearing in the form of the primordial cochlear pouch, which develops as an evagination of the saccule (Fig. 19-2). By the 9 mm stage the duct is elongated and beginning to coil; by about 10 weeks (30 mm), it has formed two and a half turns.

Later, the communication between the cochlear duct and the saccule narrows, forming the ductus reuniens. Similarly, parts of the utricle and saccule become constricted to form the utricular duct and the shorter saccular duct, which contribute to the final form of the endolymphatic duct. The major portion of the endolymphatic duct also forms as folds pinch off a portion of the otocyst.

The membranous labyrinth is surrounded by mesenchyme, which differentiates into cartilage that envelops the entire labyrinth. The membranous labyrinth enlarges within its cartilaginous encasement until midterm, by which time it has reached its complicated adult form.

The surrounding cartilaginous otic capsule then ossifies.

*Revised from Bergeron, R. Thomas. Introduction to the temporal bone. In Som PM, Bergeron RT. Head and Neck Imaging. St. Louis: Mosby, 1991, pp. 927–934.

Copyright © 2003, Mosby, Inc. All rights reserved.

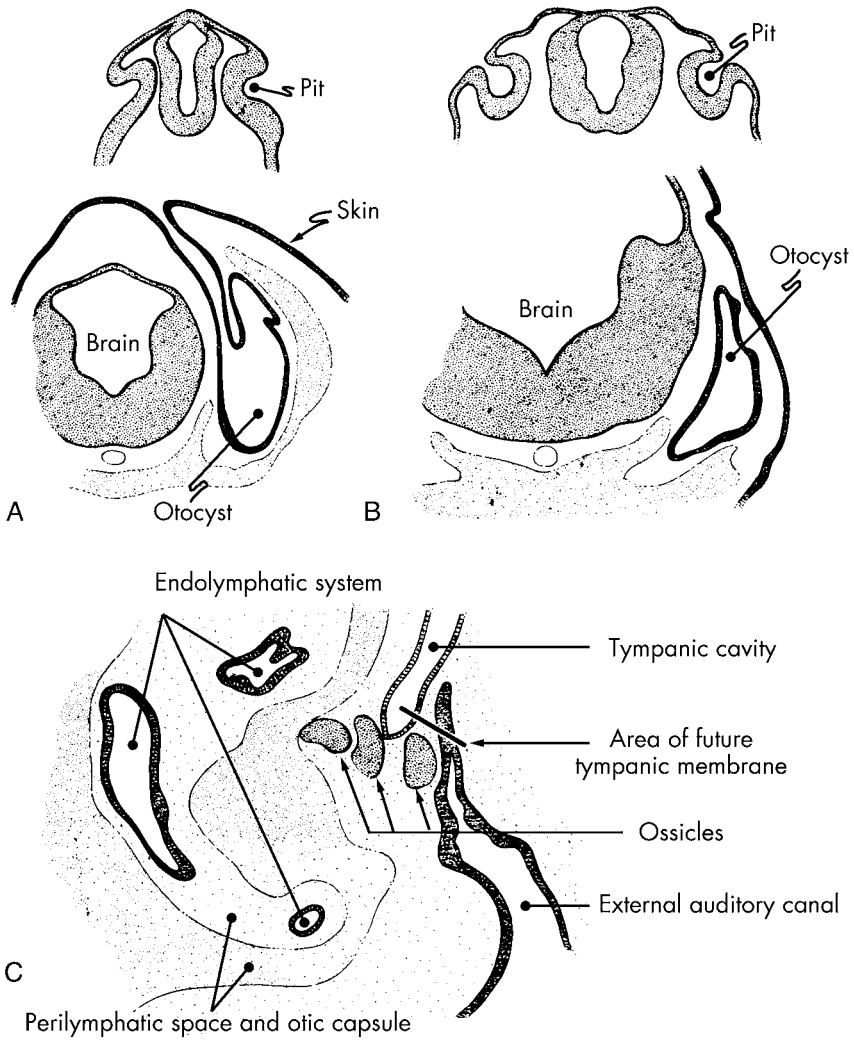

VIEW IMAGE

FIGURE 19-1 Comparative embryology of the ear. **A**, In a shark the otocyst is in communication with circumambient water. **B**, Human endolymph contained within the membranous labyrinth is surrounded by another fluid, perilymph. The aqueous system of human progenitors is restored in this way, and the equilibratory function of the inner ear is maintained. **C**, The auditory function, which is subserved by a wave-transmitting system, is brought about in humans by conversion of the branchial arch apparatus of sharks. (Modified from Anson B, Harper D, Winch T. The vestibular and cochlear aqueducts: developmental and adult anatomy of their contents and parietes. Third Symposium on the Role of the Vestibular Organs in Space Exploration. NASA SP 1967;152:125.)

With the exception of the endolymphatic duct and sac, no further growth of these structures occurs during the lifetime of the individual. The endolymphatic duct and sac are the earliest appendages of the otic vesicle to appear. However, unlike the rest of the membranous labyrinth, which reaches adult shape and size by midterm, the duct and sac continue to change throughout infancy and childhood, achieving their adult configuration after puberty. At full adulthood, the endolymphatic sac is three times larger than it is at birth. Its function is discussed later.

The labyrinth reaches its mature anatomic configuration by approximately 6 to 7 months of fetal age, when the membranous labyrinth is completely developed. The formation of its sensory end organs parallels this development and appears in the utricle and saccule first, then within the semicircular ducts, and finally within the cochlea. Differentiation in the cochlear duct goes on at the slowest rate, not being completed until after midterm. It is noteworthy that the cochlea is the last part of the labyrinth to differentiate, and is less stable and more subject to developmental malformations than are the phylogenetically older vestibular end organs.

Perilymphatic (Periotic) Labyrinth

The development of the mesenchyme surrounding the membranous labyrinth is complex.[1, 2] By 6 to 7 weeks (around 20 mm) of fetal age it has become precartilage. At 8 weeks the precartilage changes to an outer zone of true cartilage that forms the otic capsule. The inner zone begins to loosen and vacuolize and forms the perilymphatic space. Fluid-filled cavities appear around the vestibule and cochlear duct and finally surround the semicircular ducts. These spaces all eventually fuse and become confluent, forming a continuous perilymphatic labyrinth containing a delicate matrix composed of arachnoid-like connective tissue. The perilymph circulates within the interstices of the

Copyright © 2003, Mosby, Inc. All rights reserved.

filaments as they traverse the distance between the membranous labyrinth and the endosteum of the otic capsule. This filamentous matrix is present to some degree in all portions of the perilymphatic space except within the scala tympani and scala vestibuli of the cochlea. The absence of filaments within the scalae permits undampened though slight pulsatile movement of the perilymph between the oval and round windows. The kinetic energy of the sound waves is absorbed by the membranes of the cochlear duct and the secondary tympanic membrane of the round window.

The perilymphatic space has three prolongations into the surrounding osseous otic capsule: the cochlear aqueduct (perilymphatic duct), the small fissula ante fenestram, and the fossula postfenestram. The latter two structures are of only remote radiologic interest; however, either or both of them may be involved as a focus of diseased bone in otosclerosis.

The cochlear aqueduct extends from the scala tympani near the round window to the subarachnoid space near the emergence of the glossopharyngeal nerve on the inferior surface of the petrous pyramid. It is described in further detail in the section on Normal Anatomy.

Bony Labyrinth

Ossification of the otic capsule commences only when the cartilage has attained maximum growth and maturity. Once the membranous labyrinth has become encased by enchondral bone, all growth of the inner ear structures ceases and there is no possibility for future expansion of this rigid structure. The enchondral bone formed in the cartilage of the otic capsule is never removed and replaced by haversion bone, that is, there is no remodeling. Along with the ossicles, the otic capsule is unique within the human body. They remain as a primitive, relatively avascular type of bone that is exceptionally hard and poor in its osteogenic response.[6]

Ossification occurs between weeks 16 and 23 of fetal life. Fourteen separate centers are identifiable. No suture lines are visible because ossification begins only after all growth has ceased. The bony otic capsule is complete except for an area over the lateral semicircular canal, a narrow rim of cartilage that remains around the oval window, and the fissula ante fenestram.

The otic capsule is made up of concentric layers of dense enchondral bone, with a thin, uniform layer of endosteal bone being laid down against the endosteal membrane that lines the labyrinth. Outside the enchondral layer, periosteal bone is laid down in parallel lamellae.

The endosteal layer and the thick middle enchondral layer of the capsule remain relatively inert and unchanged throughout life. In response to infection or trauma the endosteal membrane lining the labyrinth may proliferate, obliterating the lumen of the labyrinth.

The enchondral layer has very limited capability for osteogenic repair, so fractures of the labyrinth may remain completely unhealed except by fibrous union. However, there are also advantages to this poor bone repair. The poor osteogenic response made possible the construction of labyrinthine fenestra that remained permanently open in early operations for stapedial otosclerosis. One of the conditions that prompted the development of stapes prosthesis implantation surgery following stapes mobilization procedures in early otosclerosis surgery was the failure of fractured stapedial crura or footplates to heal.

The periosteal bone of the labyrinthine capsule (i.e., the bone that lies peripheral to the dense middle endochondral bone) continues to be added to by apposition during infancy and up to early adult life. In due course this periosteal bone is removed and replaced by haversian bone. Eventually, pneumatic cells invade most of the periosteal layer of the capsule along with much of the remainder of the temporal bone. As with other periosteal bone, the periosteal layer of the otic capsule reacts readily to infection or trauma with osteogenesis.

As noted, ossification about the entire otic capsule is relatively uniform and complete, with the exception of the following three areas: the area around the oval window, the area of the fissula ante fenestram, and an area over the lateralmost bulge of the lateral semicircular canal.

Ossification in this last region is unique because in early stages it is the same as in the remainder of the otic capsule, with the production of three layers of bone; however, at approximately midterm, the portion covering the lateralmost sweep of the lateral semicircular canal undergoes dissolution. By the thirteenth week, the periosteal layer and varying amounts of the middle enchondral layer have been removed. Eventually there is reconstitution with a varying thickness of the periosteal bone. In some circumstances this reconstitution is (normally) very thin, and for that reason it can appear radiographically as a site of bony dehiscence; this can be misinterpreted as a sign of labyrinthine fistula when it occurs in the presence of cholesteatoma. One should therefore be circumspect and not overinterpret this finding on imaging.

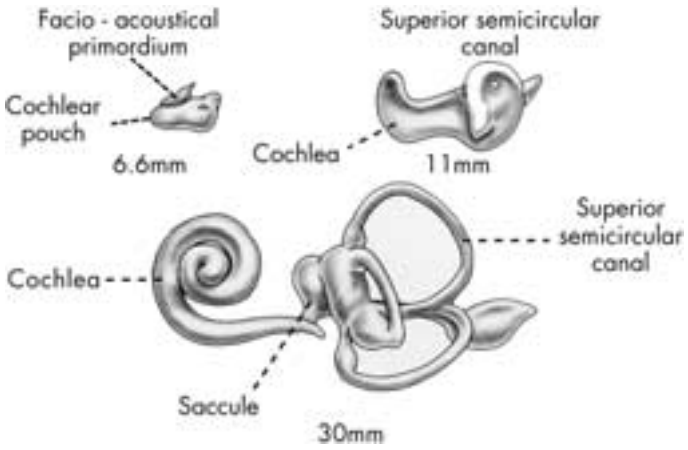

VIEW IMAGE

FIGURE 19-2 Drawing of the developing membranous labyrinth. The 6.6 mm stage shows the beginning of differentiation of the cochlear pouch. The facioacoustical primordium represents the combined seventh and eighth nerves. This primordium separates into individual nerves at the 10 to 11 mm stage. The 11 mm stage shows the cochlear primordium beginning to curl. The shape of the semicircular canals can be identified posteriorly. (Modified from Streeter GL. On the development of the membranous labyrinth and the acoustic and facial nerves in the human embryo. Am J Anat 1907;6:139–167; and Curtin HD, Vignaud J, Bar D. Anomaly of the facial canal in a Mondini malformation with recurrent meningitis. Radiology 1982;144:335–341.)

Copyright © 2003, Mosby, Inc. All rights reserved.

Outer and Middle Ear

Although it is apparent that the sound-perceiving neurosensory apparatus of the inner ear comes from the neuroectodermal otocyst, the sound-conducting mechanism arises from totally different and widely separated anlages. The sound-conducting mechanisms of the outer and middle ear are derived from the branchial or gill apparatus of the embryo.

By about 4 weeks (6 to 7 mm) of fetal age, several branchial arches separated by external branchial grooves have developed on either side of the head. The first branchial groove deepens to become the primitive external auditory meatus, and the corresponding evagination from the pharynx, the first pharyngeal pouch, grows outward and upward toward it, forming the primitive eustachian tube. For a brief moment in embryologic time, the epithelium of the first branchial groove touches the endoderm of the first pharyngeal pouch at the site of the future tympanic membrane. However, mesoderm soon grows between and separates these two layers, so that the mature tympanic membrane is formed by all three germinal layers.

Over the next 5 fetal months, the first branchial groove contributes to the development of the mature configuration of the external acoustic meatus, the outer, cuticular layer of the tympanic membrane, and the tympanic ring.

The auricle develops from around the first branchial groove from six knob-like outgrowths or hillocks arising from the first and second branchial arches, appearing at the sixth week of embryonic life and fusing by the third month.

The first pharyngeal pouch becomes the eustachian tube and middle ear cavity and its epithelial lining. The cartilages of the first and second branchial arches form the ossicles. The first branchial arch forms the bodies of the malleus and incus; the second branchial arch forms the crura of the stapes, the lenticular process and long crus of the incus, and the manubrium of the malleus. The footplate of the stapes comes from the otic capsule. With further development, the ossicles separate from the remainder of the arch cartilages and join.

The ossicles, similar to the otic capsule and labyrinth, grow only throughout the first half of uterine life and then ossify. Each of these bones ossifies from a single center; the incus appears at 16 weeks, the malleus at 16½ weeks, and the stapes at 18 weeks. The ossicles are formed of enchondral bone that persists for the rest of the individual's life, as does the enchondral layer of the labyrinthine capsule. The malleus and incus remain solid and relatively constant in size and shape. The stapes, however, undergoes a process of erosion and thinning soon after it ossifies. The adult stapes is less bulky and considerably more delicate and fragile than in midfetal life. With this diminution in bulk and weight, exceptional variations in the size, shape, and strength of the adult crura and footplate occur. A normal adult footplate varies from thick and uniform to thin and irregular. It even may be dehiscent in its central portion.

As the ossicles differentiate and ossify, the surrounding mesenchymal connective tissue becomes less dense and less cellular. By 18 to 21 weeks, the tissue filling the space of what is to become the middle ear is very loose, somewhat vacuolated, and mucoid in character. By 22 weeks this vacuolated, mucoid connective tissue gives way to the upward-expanding tympanic epithelium of the first pharyngeal pouch. The latter envelops the ossicles and their tendons and ligaments, investing them with epithelial tissue derived from endoderm. Communication between the pharynx and middle ear is thus established. At maturity, the eustachian tube remains as an anatomic reminder of the upward migration of the first pharyngeal pouch in the formation of the tympanic cavity and communicating spaces.

By 30 weeks, pneumatization of the tympanum proper is almost complete. Pneumatization of the mastoid antrum soon follows and progresses rapidly from weeks 34 to 35, but in the epitympanum it lags and is not completed until the last month of fetal life.

The use of the term *pneumatization* at this stage of development does not imply the actual presence of air in the ear; used in this context, it refers rather to the process of focal dissolution and displacement of mesenchymal connective tissue, with eventual formation of the space that comes to be lined by an advancing layer of endodermal (respiratory) epithelium arising from the first pharyngeal pouch. This space will become the aerated cavities of the eustachian tube, the middle ear, the antrum, and so on at term. Pneumatization thus comes to refer to the creation of an epithelium-lined space to be aerated later.

Pneumatic Cells of the Temporal Bone

The air cells of the temporal bone develop as outpouchings of the antrum, epitympanum, tympanic cavity, and eustachian tube. Despite tentative epithelial evaginations appearing from the antrum as early as 34 weeks, no significant pneumatic cellular expansion into the remainder of the temporal bone occurs until after birth, with the stimulation caused by the presence of air within the middle ear. The pneumatizing process then goes into a period of high activity, proceeding over several years. The petrous apex frequently shows continued progression of pneumatization into early adult life.

Pneumatization occurs as a result of epithelium-lined projections arising from the lining of the middle ear and its extensions. These evaginations probe the spaces between spicules of new bone that are forming and the spaces created by the degeneration of bone marrow into a loose connective tissue stroma. The air cells will invade bone only after the marrow has been converted into a loose mesenchymal tissue. Wittmaack suggests that the presence of middle ear infections in infancy causes the embryonic subepithelial connective tissue to fibrose; this prevents its condensation and thinning and impedes the progress of the advancing fingers of evaginating pneumatic cells.[7] This would explain pneumatization arrest following otitis media in infants and children.

Neonatal Temporal Bone

At birth the anatomic portions of the hearing and vestibular system are virtually fully developed, with the exception of the formation of the osseous portion of the external acoustic canal. Even the internal acoustic canal

Copyright © 2003, Mosby, Inc. All rights reserved.

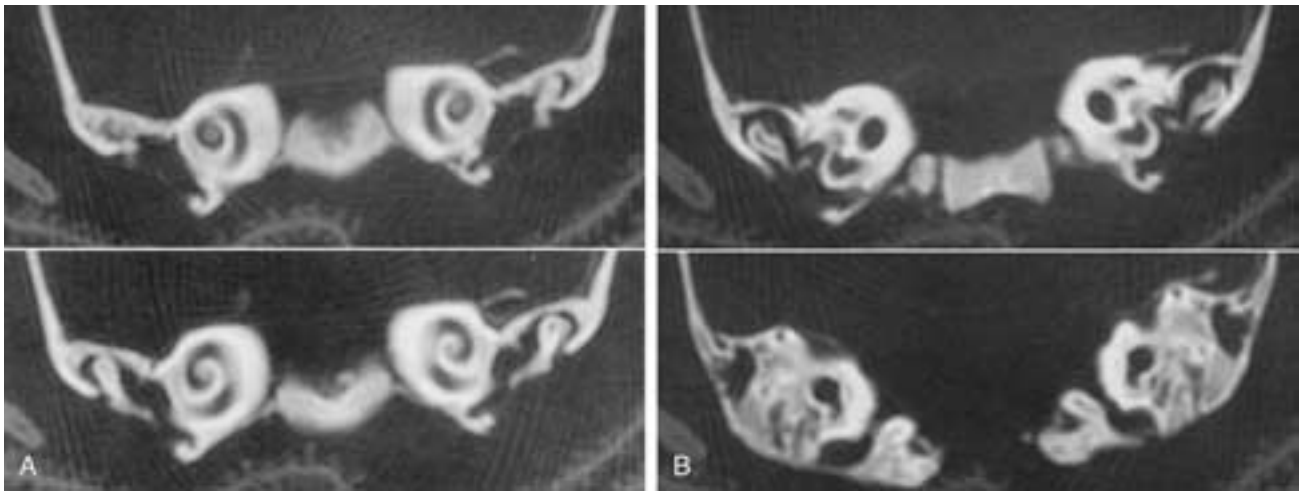

VIEW IMAGE

FIGURE 19-3 Coronal CT scan, late fetal stage. **A**, The position of the temporal bone in the inferolateral part of the skull is identified. Although the malleus and cochlea are well formed, there is no bony external auditory canal. The tympanic membrane faces inferolaterally the undersurface of the skull. **B**, The ossicular chain is well formed and has achieved its adult size and shape. No significant mastoid process is identified. (Courtesy of the Louis E. Etter Collection.)

(which is not part of the bony labyrinth but is by common clinical practice considered part of the inner ear because of its juxtaposition and functional relationship to the labyrinth) has a nearly adult vertical dimension and will grow probably no more than 1 mm in height during the remainder of the individual's life. (The length of the internal acoustic canal, however, will increase substantially during childhood.)

Shambaugh and Glasscock emphasize that the remainder of the neonatal temporal bone, however, is small and differs from the adult bone both in shape and in position, occupying the inferolateral surface of the skull rather than the lateral aspect, as in mature individuals (Fig. 19-3).[4] They note that, as viewed from the side, the infant temporal bone consists of a large squamous portion, a diminutive tympanic portion, and virtually no mastoid. Whereas in the adult the mastoid lies posterior to the tympanic ring, in the child the petrous portion lies behind the tympanic ring and below the squamous portion.

Formation of the Mastoid Process

The mastoid process begins to develop during the second year of life, with downward growth of the squamous portion and partially as a result of extensions of the petrous portion. These two parts of the mastoid process come together at the petrosquamous suture line. Air cells grow down from the antrum vertically toward the mastoid tip and laterally and radially into the squamous portion. A dividing bridge of bone separating these two cell tracks (at the junction of the petrous and mastoid ossifications) is known as Koerner's septum. This is visible radiographically as a pointed, bony spicule originating from the antral roof and directed obliquely downward.

With further maturation of the mastoid, the thin, incomplete infantile ring that constitutes the tympanic portion of the bone grows laterally and inferiorly to form the osseous portion of the previously completely cartilaginous external auditory canal. Two suture lines are formed: the tympanosquamous suture arising in the anterosuperior meatal wall and the posteriorly positioned tympanomastoid suture.

NORMAL ANATOMY

The anatomy of the temporal bone is complex and in many circumstances confusing (Figs. 19-4 and 19-5; see also the figures in Section Two of this chapter). Part of the complexity has to do with 350 million years of evolutionary modification of this organ, and part has to do with unfortunate anatomic terminology, ambiguity, imprecision, and redundancy that have become fixed in scientific nomenclature. The following section is a compendium gathered from many anatomic sources.[3, 5, 6, 8–13]

Temporal Bone

The temporal bones are situated at the sides and base of the skull. Each consists of the following five parts: squamous, mastoid, petrous, tympanic, and styloid process.

Squamous Portion

The squamous portion forms the anterolateral and upper part of the bone; it is shell-like and thin. The external surface is smooth and convex, giving attachment to the temporalis muscle; it forms part of the wall of the temporal fossa. A gently arching zygomatic process arises from the lower portion of the squama and is directed anteriorly. Its lateral surface is convex and lies directly beneath the skin and subcutaneous tissue. The medial surface of the zygomatic process is concave and serves as the origin of the masseter muscle. The anterior end of the zygomatic process articulates with the zygomatic bone. The posterior portion of the zygomatic process is divided into an anterior and a

Copyright © 2003, Mosby, Inc. All rights reserved.

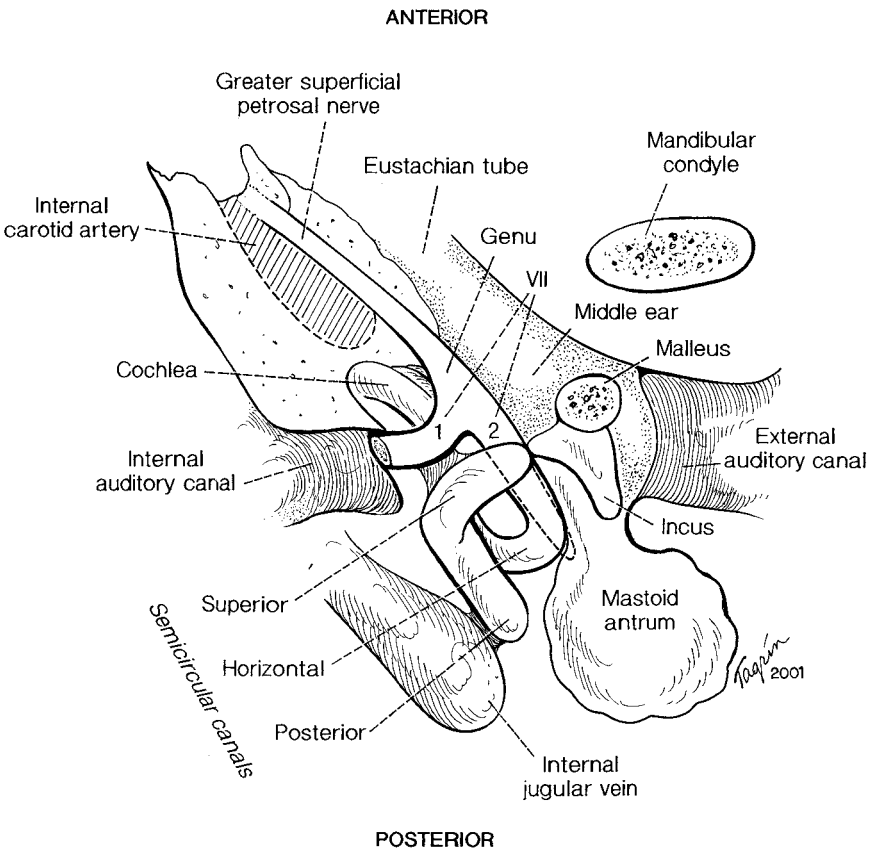

VIEW IMAGE

FIGURE 19-4 Diagram of the right temporal bone as viewed from superiorly showing the gross relationships of the key structures to one another. The axis of the temporal bone would run from the upper left-hand corner to the lower right. Note that the first segment (1) of the seventh nerve, the axis of the cochlea, and the superior semicircular canal are perpendicular to this plane, while the second segment (2) of the facial nerve and the posterior semicircular canal are parallel to this plane.

posterior root. The posterior root lies above the external auditory canal and becomes continuous with the temporal line posterior to the external auditory canal. The anterior root becomes the articular tubercle of the condylar (glenoid or mandibular) fossa. The condylar fossa is bound posteriorly to the anterior surface of the tympanic bone.

The mandibular fossa is cleaved in the coronal plane by the tympanosquamous suture laterally and by that suture's inward extension, the petrotympanic (Glaserian) fissure, medially. The portion of the condylar fossa anterior to the fissure is the articular portion of the joint; the portion posterior to the Glaserian fissure is the nonarticular portion.

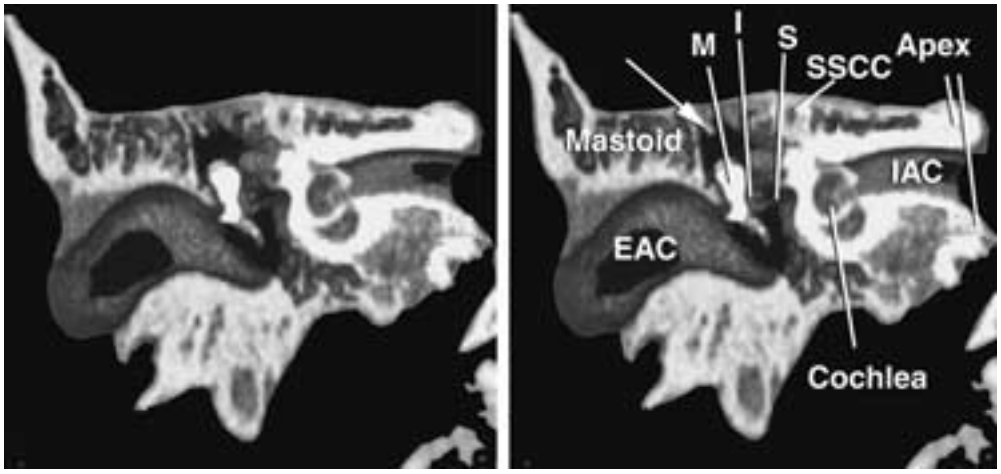

VIEW IMAGE

FIGURE 19-5 Thick coronal CT image (frontal view) showing the relationship of the structures within the temporal bone. The external ear including the external auditory canal (*EAC*) forms the lateral part of the ear. The middle ear contains the ossicles (*M* = malleus; *I* = incus; *S* = stapes). The labyrinth, situated central to the middle ear, includes the cochlea, vestibule, and semicircular canals (*SSCC* = superior semicircular canal). The more medial portion of the temporal bone includes the petrous apex and the transiting internal auditory canal (*IAC*). The mastoid is an extension from the antrum, which is an extension from the middle ear. The mastoid air cells can extend to the most lateral plate of the temporal bone. Koerner's septum (*arrow*).

Copyright © 2003, Mosby, Inc. All rights reserved.

The internal surface of the squama is concave and irregular. Meningeal vessels groove the inner surface. The superior border articulates with the parietal bone, and the anteroinferior border articulates with the greater wing of the sphenoid.

Mastoid Portion

The mastoid portion has a rough outer surface and serves as the origin of a portion of the occipital and posterior auricular muscles. In the adult the mastoid portion is continued inferiorly into a conical projection, the mastoid process. This process gives attachment to the sternocleidomastoid, splenius capitis, and longissimus capitis muscles. On the medial side of the process is a deep groove, the mastoid notch or digastric groove, for the attachment of the posterior belly of the digastric muscle. Medial to this is a shallow furrow, the occipital groove, that lodges the occipital artery.

The inner or intracranial surface of the mastoid presents a deeper groove, the sigmoid sulcus, that lodges part of the transverse sinus.

The posterior superior border is serrated and articulates with the parietal bone. The posterior border, similarly serrated, articulates with the inferior border of the occipital bone. Anteriorly and above, the mastoid portion is fused with the descending process of the temporal squama; below, it enters into the formation of the external acoustic meatus and the tympanic cavity.

The mastoid process is hollowed to form a number of spaces, the mastoid cells, that vary greatly in size and number. In the upper and anterior part of the process, these cells are large and irregular, toward the middle part they diminish in size, and those in the apex of the process frequently are small. In addition to these cells a large, irregular cavity, the tympanic antrum, occurs and is situated at the upper and anterior part of the mastoid portion of the bone. The antrum communicates with the epitympanum (attic), situated anteroinferiorly and medially by way of the narrow channel, the additus ad antrum.

Petrous Portion

The petrous pyramid is wedged in at the base of the skull between the sphenoid bone anteriorly and the occipital bone posteriorly. Its apex is directed medially, forward, and slightly upward. It contains the inner ear.

The petrous portion resembles a toppled three-sided pyramid lying on the flat surface of one of its sides. The base of this pyramid is laterally positioned and fused with the internal surfaces of the squamous and mastoid portions of the temporal bone. The apex points medially and forward (at approximately a 45° angle with the coronal and sagittal planes) and is inserted into the angular interval between the posterior border of the greater wing of the sphenoid bone and the basilar part of the occipital bone. The anterior (middle fossa) face of the petrous pyramid has a more horizontal orientation and is ''longer'' than the posterior surface, which is relatively vertical and ''shorter.''

The surface of the petrous portion often considered the superior surface actually faces somewhat anteriorly and so is more accurately called the anterior face. This anterior face forms the posterior limit of the floor of the middle cranial fossa and is continuous laterally with the inner surface of the squamous portion; it is united at these edges by the petrosquamous suture. Its surfaces are somewhat irregular and marked by depressions for convolutions of the brain and by a shallow depression medially for the reception of the semilunar ganglion (Meckel's cave) of the fifth cranial nerve. The arcuate eminence, which marks the approximate site of the underlying superior semicircular canal, is near its midportion. Anterior and slightly lateral to this eminence is a depression that marks the position of the tympanic cavity. The layer of bone that separates the tympanic and cranial cavities is usually very thin and is known as the tegmen tympani. Two small grooves cross this surface of the temporal bone, passing from the area of the foramen spinosum and foramen lacerum laterally and posteriorly to a small opening called the facial hiatus. The facial hiatus is a small opening or defect that transmits the greater superficial petrosal nerve and the petrosal branch of the middle meningeal artery. This small opening marks the location of the geniculate ganglion and first genu or turn of the facial nerve. The amount of bone ''closing'' the facial hiatus is variable. In some cases, the facial nerve and geniculate ganglion are positioned just below the dura of the middle fossa and lack a significant bony covering.

The posterior face (surface) of the petrous pyramid forms the anterior bony limit of the posterior fossa and is continuous with the inner surface of the mastoid portion of the temporal bone at the petromastoid suture. To reiterate, this face has a more vertical orientation than the anterior surface. Near the center of this surface is the opening to the internal auditory (acoustic) canal (meatus), which transmits the seventh and eighth cranial nerves, the nervus intermedius, and the internal auditory artery. The opening of the internal auditory canal is known as the porus acusticus. The lateral end of the internal auditory canal is closed by a vertical plate of bone that separates the fundus of the canal from the vestibule. This bony separation has many perforations allowing passage of nerve filaments. These regions are called the cribriform areas. The fundus is divided by a transverse (axially oriented) crest of bone, the crista falciformis, into a smaller upper and a larger lower compartment. The crista, which arises anteriorly, continues for a variable distance along the anterior wall of the internal auditory canal. The upper compartment occupies about 40% and the lower about 60% of the vertical dimension of the canal. In the upper compartment the facial nerve (VII) lies anteriorly, and the superior vestibular division of cranial nerve VIII lies posteriorly. The branches of the latter go to the utricle and the superior and lateral semicircular canals. A thin vertical crest of bone separates the lateral portion of this upper compartment into its anterior and posterior portions. This crest is referred to as Bill's bar. The bony bar separates the aperture for the exit of the facial nerve anteriorly from the small openings for the branches of the superior vestibular nerve posteriorly. A small channel along the posterolateral aspect of the vertical crest may be seen carrying a small branch of the vestibular nerve passing toward the ampulated end of the superior semicircular canal. In the compartment beneath the crista falciformis there are three sets of foramina. Anteriorly, a set of perforations is arranged spirally to accommodate the cochlear division of the eighth cranial nerve. Posteriorly, branches of the inferior division of the vestibular nerve take their exit, one set of

Copyright © 2003, Mosby, Inc. All rights reserved.

foramina leading to the saccule and the remainder leading to the posterior semicircular canal. The nerve to the posterior semicircular canal follows a small channel called the singular or singulate canal.

On the posterior surface of the petrous bone, slightly posteroinferior to the internal acoustic meatus, is a small slit that leads to the vestibular aqueduct. The aqueduct transmits the endolymphatic duct and sac. The endolymphatic sac fills most of the bony aqueduct and protrudes beneath its lower margin. Thus the sac has an intraosseous part, within the aqueduct, and an extraosseous part lying between the layers of the dura of the posterior fossa. The sac is not a single cavity but rather a system of connected channels.

The inferior face (surface) of the petrous pyramid is a rough, irregular surface and forms part of the exterior of the base of the skull. It furnishes partial attachment for the levator veli palatini and the cartilaginous portion of the eustachian tube. It is pierced anteriorly by the aperture of the carotid canal. Posterior to the entrance of the carotid canal lies the jugular foramen. This aperture has an anteromedial and a posterolateral part. Cranial nerves IX, X, and XI transit the anteromedial part in close association with the inferior petrosal sinus. The sigmoid sinus curves into the posterolateral part. The cochlear aqueduct, which communicates with the basal turn of the cochlea, arcs superiorly and laterally from the notch-like anteromedial portion of the jugular foramen.

Thus, near the midportion of the posterior surface of the petrous portion of the temporal bone, extending roughly in a straight line from cranially to caudally, are the internal auditory canal, the aperture of the cochlear aqueduct, and the jugular fossa.

There are two minute canals that perforate the inferior surface of the petrous portion within or near the jugular fossa. The inferior tympanic canaliculus, which accommodates the tympanic branch of the glossopharyngeal nerve (Jacobson's nerve) and the inferior tympanic artery (from the ascending pharyngeal), lies between the carotid canal and the jugular fossa. The mastoid canaliculus, which serves as entrance for the auricular branch of the vagus nerve (Arnold's nerve), is located within the lateral part of the jugular fossa.

The styloid process originates from the inferior face of the pyramid. The stylomastoid foramen is situated between the downward projections of the mastoid process and the styloid process. This foramen constitutes the terminus of the bony facial nerve canal.

The superior angle (border) of the petrous portion of the temporal bone is grooved for the superior petrosal sinus and gives attachment to the tentorium cerebelli. This superior angle, commonly referred to as the petrous ridge, represents the line of the intersection between the anterior and posterior surfaces of the pyramid. The anteromedial extremity of the ridge is notched or scalloped for the reception of the roots of the trigeminal nerve. A small notch marks the position of Dorello's canal, a small dural reflection through which the sixth cranial nerve transits into the cavernous sinus.

The posterior angle of the pyramid is defined by the junction of the lower aspect of the posterior surface with the posterior limits of the inferior surface. From the perspective of the inner surface of the skull within the posterior fossa, the posterior angle is marked by a sulcus on the petrous portion that, along with a corresponding sulcus on the occipital bone, forms the channel for the inferior petrosal sinus. An excavation on the inferior and medial aspect of the posterior surface of the pyramid, in continuity with this sulcus, is known as the jugular fossa. The corresponding depression, in continuity with the sulcus arising from the anterolateral surface of the occipital bone, is known as the jugular notch. These semilunar cavities face one another and together form the jugular foramen. Within the temporal bone, the jugular vein has a dilated portion called the jugular bulb. The jugular bulb rises variably toward the labyrinth and middle ear.

The anterior angle of the pyramid marks the junction between the pyramid and the bones of the anterior floor of the middle cranial fossa. The anterior border is divided into two parts: the medial part, which articulates with the greater wing of the sphenoid, and the lateral portion, which adjoins the squamous part at the petrosquamous suture.

At the angle of the junction of the petrous and squamous portions along the anteromedial margin of the middle ear cavity, there are two (semi) canals placed one above the other, which are separated by a thin plate of bone. This septum is known as the septum canalis musculotubarii (cochleariform process). The upper canal contains the tensor tympani muscle, and the lower canal is the bony portion of the eustachian tube.

Tympanic Portion

The tympanic portion of the temporal bone is a curved plate lying below the squamous portion and in front of the mastoid process. Its posterior surface is somewhat C-shaped and forms the anterior wall, the floor, and the posteroinferior aspect of the bony external auditory canal. At the medial end of the canal is a narrow furrow, the tympanic sulcus, for the attachment of the tympanic membrane. The lateral border of the tympanic portion of the temporal bone is roughened, forming a large part of the margin of the opening of the external auditory canal; this is continuous with the cartilaginous part of the canal. The lateral part of the upper border is fused with the back of the postglenoid tubercle. Its medial extension forms the posterior boundary of the petrotympanic fissure.

There is considerable ambiguity in anatomic descriptions regarding the terms *petrotympanic fissure*, *tympanosquamous fissure*, and *Glaserian fissure*. Many anatomic depictions point unassailably to a junction between the squamous and tympanic portions, labeling the area the *petrotympanic fissure*. This is more easily understood if one recognizes that the tympanosquamous fissure (squamotympanic) is merely the lateral extension of the petrotympanic fissure, and the Glaserian fissure is the medial extension of the petrotympanic fissure. This serves as a passageway for the anterior tympanic branch of the internal maxillary artery. In the most medial extreme portion of the petrotympanic fissure is the small canal for the chorda tympani, the iter chordae anterius (anterior tympanic aperture, canal of Huguier).

The lower border of the tympanic bone encloses the root of the styloid process. Posteriorly the tympanic portion blends with the squamous and mastoid portions, forming the anterior boundary of the tympanomastoid fissure.

Copyright © 2003, Mosby, Inc. All rights reserved.

Styloid Process

The styloid process of the temporal bone averages about 2.5 cm in length and projects downward and forward from the undersurface immediately anterior to the stylomastoid foramen. It gives origin to the stylohyoid ligament and the stylohyoid, stylopharyngeus, and styloglossus muscles.

External Auditory Canal

The walls of the external auditory canal (meatus) are formed laterally of fibrocartilage and medially of bone, and both parts are lined by skin reflected inward. The osseous portion of the meatus, which makes up slightly more than half of the canal, is a tunnel through the temporal bone. The bony canal is about 16 mm long and is directed inward, forward, and downward. On a sagittal scan the canal is oval or elliptical in shape, with its long axis directed downward and slightly backward. The anterior wall, floor, and lower part of the posterior wall are formed by the tympanic component of the temporal bone; the remainder of the posterior wall and the roof arise from the squamous portion of the temporal bone.[11]

The tympanic membrane makes a compound angle with the external acoustic meatus. The inferior border of the tympanic membrane lies closer to the midsagittal plane of the head than does the superior border. Additionally, the anterior border lies closer to the midsagittal plane than does the posterior border. This means that the tympanic membrane is sloping both downward and inward. The posterosuperior wall of the external auditory meatus is about 25 mm long in the adult, and the anteroinferior wall is more than 30 mm.

Vessels and Nerves

The arteries of the external auditory meatus are derived from the external carotid artery through branches from the posterior auricular, superficial temporal, and internal maxillary arteries. The veins and lymphatics connect with those of the auricle. The veins ultimately empty into the internal and external jugular veins and occasionally into the sigmoid sinus by way of mastoid emissary veins.

The lymphatics of the external acoustic canal and auricle empty into all adjacent regional nodes, including the parotid, superficial cervical, and retroauricular groups.

Because the development of the external ear is embryologically complex, the cutaneous innervation is similarly complex and subject to considerable variation. Innervation is derived from the auriculotemporal branch of the mandibular division of the trigeminal nerve and from cutaneous branches of the cervical plexus, primarily the greater auricular nerve from C2 and C3. There are also contributions from sensory fibers originating in the seventh, ninth, and tenth cranial nerves.

Tympanic Membrane

The tympanic membrane is the medial boundary of the external auditory canal, separating the canal from the middle ear. This thin, transparent membrane is somewhat oval in shape. It is slightly broader above than below. Its greatest diameter is approximately 9 to 10 mm. The manubrium or handle of the malleus is attached to the membrane along a line from just caudad to the midpoint of the membrane to a point just inferior to the upper margin. The most caudad point of attachment is pulled slightly medially toward the middle ear. This point is readily identified using an otoscope and is called the umbo. The periphery of the tympanic membrane is a fibrocartilaginous ring that attaches to the tympanic sulcus at the medial end of the external auditory canal. The ring is incomplete superiorly and anteriorly, corresponding to a similar gap in the superior aspect of the tympanic ring called the notch of Rivinus. From the anterior and posterior magins of this notch, thin folds called the anterior and posterior mallear (malleolar) folds extend to the lateral process of the malleus. These two folds in the membrane along with the superior rim of the canal create a triangular, thin, lax zone, the pars flaccida, in the superior-anterior portion of the tympanic membrane. This lies immediately under the scutum, the most medial point of the roof of the external auditory canal (see below). The remaining tympanic membrane is taut and is referred to as the pars tensa.

Middle Ear

The middle ear, or tympanic cavity, is an irregular, laterally compressed space within the temporal bone. It is filled with air conveyed to it from the nasopharynx via the eustachian tube. The middle ear is traversed by the ossicular chain connecting the lateral and medial walls. The ossicles both transmit and amplify the vibrations incident on the tympanic membrane across the cavity to the inner ear.

The tympanic cavity consists of three parts: the tympanic cavity proper (or mesotympanum) opposite the tympanic membrane, the attic (or epitympanic recess or epitympanum) above (cranial to) the level of the membrane, and the hypotympanum, a variable inferior and medial extension occurring below (caudal to) the level of the tympanic membrane.

Shaped more like a cleft than a box, the vertical dimension (including the attic) and the anteroposterior dimension of the cavity are each about 15 mm. The transverse dimensions measure about 6 mm superiorly and 4 mm inferiorly. Opposite the center of the tympanic membrane the transverse dimension may be only about 2 mm. The lateral extent of the cavity is defined by the tympanic membrane or membranous wall, and the medial or labyrinthine wall is formed by the otic capsule. The roof is known as the tegmental wall, and the floor, separated from the jugular fossa by a thin plate of bone, is known as the jugular wall. Anteriorly the space is delimited by the carotid wall and posteriorly by the mastoid wall.

Roof or Tegmental Wall

The tegmen tympani is a plate of bone that arises from the petrous portion of the temporal bone. Its forward prolongation becomes the roof of the canal for the tensor tympani muscle, and its backward continuation forms the roof of the mastoid antrum. The tegmen tympani separates the middle ear cavity from the middle cranial fossa. The lateral margin of the tegmen interdigitates with the squamous portion of the temporal bone at the petrosquamous suture. In children this may be unossified and may allow direct passage of infection

Copyright © 2003, Mosby, Inc. All rights reserved.

from the middle ear to the epidural space of the middle cranial fossa. In adults, veins from the middle ear perforate this suture to end in the petrosquamous sinus (present in about 50% of cases) and the superior petrosal sinus. They may transmit infection directly to the cranial venous sinuses.[10]

Floor or Jugular Wall

The floor or jugular wall of the middle ear cavity lies either at or slightly below the level of the floor of the external auditory meatus and is usually a very thin plate of cortical bone that separates the cavity from the internal jugular vein. If the jugular bulb is particularly small, the floor may be correspondingly thick (occasionally up to 1 cm), and it may contain air cells intervening between the middle ear cavity and the internal jugular vein. The inferior extent of the tympanic cavity below the level of the inferior attachment of the tympanic membrane, along with its medial extension, is known as the hypotympanum.

If the jugular bulb is very large, it may bulge upward into the floor of the tympanic cavity, giving it a convex margin. This bulging reduces the potential size of the hypotympanum. Occasionally the bone may be dehiscent with the jugular bulb present within the hypotympanum.

A small aperture for the passage of the tympanic branch of the glossopharyngeal nerve (Jacobson's nerve) is present between the carotid canal and the jugular plate near the labyrinthine wall.

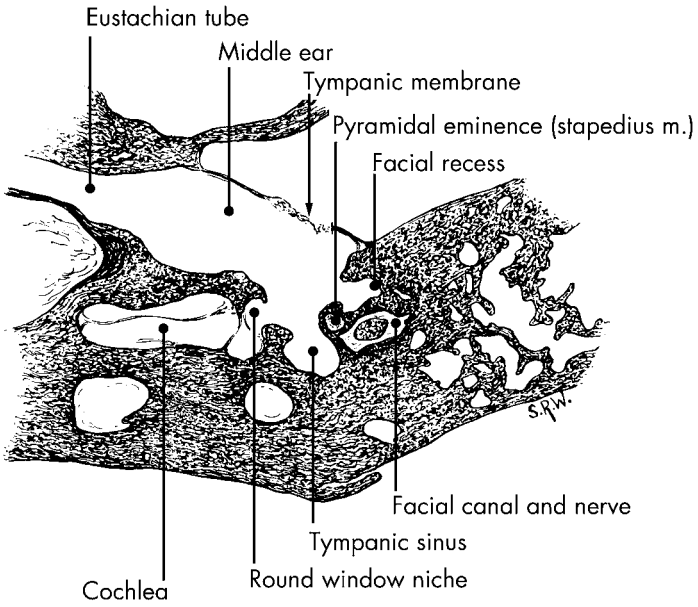

FIGURE 19-6 Relationships of the sinus tympani, facial recess, and facial canal within the posterior wall of the middle ear. Axial section through the temporal bone at the level of the round window niche. These relationships are of paramount importance to the operating surgeon because they affect the surgeon's ability to gain access to diseased tissue. The tympanic sinus may be the site of occult disease. Primary facial nerve pathologic processes may also obliterate these spaces. This minute anatomy is exquisitely defined on axial CT.

VIEW IMAGE

Mastoid or Posterior Wall

The mastoid or posterior wall is wide above and below and presents the additus ad antrum (entrance to the tympanic antrum), the pyramidal eminence, and the incudal fossa. The additus ad antrum is a large, irregular aperture that leads posteriorly from the epitympanic recess to the mastoid antrum. The pyramidal eminence is situated immediately behind (dorsolateral to) the oval window and in front of (ventral or medial to) the vertical (mastoid) portion of the facial canal; it is hollow and contains the origin and belly of the stapedius muscle. Its summit projects forward toward the stapes and is pierced by a small aperture that transmits the tendon of the muscle. The cavity of the pyramidal eminence is prolonged downward and backward in front of or slightly medial to the facial canal and communicates with it by a minute aperture that transmits a twig from the facial nerve to the stapedius muscle.

There are two important recesses in the posterior wall, the sinus tympani and the facial recess (Fig. 19-6). They may be the sites of occult extension of disease within the middle ear, and they are demonstrated well on axial CT scans.

The tympanic sinus is a space that is bounded by the labyrinthine wall medially and by the pyramidal eminence laterally.

The facial recess is bounded by the pyramidal eminence, styloid complex, and facial canal medially and by the bony tympanic annulus laterally. The facial recess is an important surgical landmark when the middle ear cavity is entered via the mastoid approach. Entrance is initially gained into the mesotympanum by enlarging this recess using the facial nerve and chorda tympani as landmarks.

The incudal fossa is a small depression in the lower and posterior portion of the epitympanum. This recess contains the short process of the incus and is the attachment, the posterior ligament of the short process of the incus.

Just lateral and usually slightly inferior to the aperture transmitting the tendon of the stapedius muscle is the aperture for the chorda tympani nerve that is separated from the mastoid portion of the facial nerve by part of the facial recess. The chorda tympani leaves the mastoid part of the facial nerve usually in the lower part of that portion of the facial canal and then turns superiorly to travel up through the canaliculus of the chorda (iter tympani posteriorus). The nerve enters the middle ear cavity, runs lateral to the long process of the incus, medial to the manubrium of the malleus, and then exits the middle ear cavity.

Carotid or Anterior Wall

The carotid or anterior wall is wider above than below and corresponds to the carotid canal, from which it is separated by a thin plate of cortical bone that is perforated by the tympanic branch of the internal carotid artery and by the caroticotympanic nerve. At the upper part of the anterior wall are the orifice of the semicanal for the tensor tympani muscle and the tympanic orifice of the eustachian tube, separated from each other by the septum canalis musculotubarii. These structures run from the tympanic cavity forward and downward to the angle between the squamous and petrous portions of the temporal bone. These channels lie one above the other rather than side by side.

The semicanal for the tensor tympani is the superior and smaller of the two structures; it is cylindrical and lies beneath the tegmen tympani. It extends to the labyrinthine wall of the tympanic cavity and ends immediately above the

Copyright © 2003, Mosby, Inc. All rights reserved.

oval window. In current usage the septum canalis musculotubarii is more commonly known as the cochleariform process (processus cochleariformis). This bony structure forms the lateral wall and floor of the semicanal for the tensor tympani.

Eustachian Tube

The eustachian tube is the lower of the two channels and the one through which the tympanic cavity communicates with the nasopharynx. Its length is about 3.5 cm, and its direction is downward, forward, and medial. It forms an angle of about 45° with the sagittal plane and one of about 30° to 40° with the horizontal plane. Part of the eustachian tube is composed of bone, and part is composed of fibrous tissue and cartilage. The osseous portion is a little more than 1 cm in length. It begins in the carotid wall below the process cochleariformis and, tapering slowly, ends at the angle of the junction of the squamous and petrous portions of the temporal bone. Its most distal end has a serrated margin for the attachment of the cartilaginous portion. The cartilaginous portion is about 2.5 cm in length. The cartilage lies in a groove between the petrous part of the temporal bone and the greater wing of the sphenoid. This groove ends opposite the upper posterior margin of the medial pterygoid plate.

The tube is not of uniform diameter; its narrowest portion (the isthmus) lies at the junction of the bony and cartilaginous portions. It is at its widest diameter at the pharyngeal orifice. The cartilaginous and bony portions of the tube are not in the same vertical plane, the cartilaginous portion being slightly more steeply inclined than the bony portion. The pharyngeal opening of the cartilaginous portion of the eustachian tube is C-shaped, so that the tensor veli palatini, levator veli palatini, and salpingopharyngeus muscles (by attaching to both the medial and lateral sides of the cartilage) can open its lumen maximally during swallowing. This helps ensure that the middle ear and pharyngeal air pressures are equilibrated during swallowing.

Lateral or Membranous Wall

The tympanic cavity extends above the level of the tympanic membrane as the epitympanic recess. The lateral boundary of the tympanic cavity proper therefore is the tympanic membrane, together with the small rim of the temporal bone to which it is attached. The osseous tympanic ring is incomplete superiorly at the notch of Rivinus. Close to this notch are three small apertures: the petrotympanic (Glaserian) fissure and the anterior and posterior tympanic apertures (iter chordae anterius and posterius).

The petrotympanic fissure transmits the anterior tympanic branch of the internal maxillary artery and houses the anterior process of the malleus and its anterior ligament.

The chorda tympani nerve gains entrance to and finds egress from the tympanic cavity by way of the posterior and anterior tympanic apertures, respectively. As the chorda tympani traverses the tympanic cavity, it gives off no branches.

The tympanic membrane is directed obliquely downward and inward, forming an angle of about 50° with the floor of the external acoustic canal and about 15° with the midsagittal plane. The manubrium of the malleus is attached to the medial aspect of the tympanic membrane at its center and pulls the membrane inward; the lateral surface of the membrane therefore appears concave.

Medial or Labyrinthine Wall

The medial wall of the tympanic cavity is the part of the petrous portion of the temporal bone that surrounds the inner ear and separates it from the middle ear cavity.[10] Several bulges and depressions are apparent, reflecting the various contours of the inner ear structures.

Posteriorly and superiorly, in what is the medial wall in the region of the additus, is the prominence produced by the anterior limb of the lateral semicircular canal. Below this and extending more anteriorly is the prominence of the facial canal produced by the bone overlying the intratympanic portion of the facial nerve. Anterior to the prominence of the facial canal is the curving terminus of the septum canalis musculotubarii; this also serves as a landmark for the position of the geniculum of the facial nerve (geniculate ganglion), which lies immediately anterior to the first knee (genu) of the facial nerve.

Immediately below the mesotympanic facial canal is the laterally directed oval window niche, which contains the oval window at its medial terminus. Below the oval window lies the promontory, a convexity that bulges into the tympanic cavity and represents a portion of the otic capsule over the basal turn of the cochlea. Below and behind the back part of the promontory is the round window niche, leading to the round window. Posterior to the promontory is a smooth, bony projection, the subiculum promontorii, which forms the inferior border of the deep depression known as the tympanic sinus. Anterior and inferior to the subiculum lies the round window niche. The opening of the tympanic sinus approximates the junction of the medial and posterior walls of the tympanic cavity. The superior border of the sinus tympani is bounded by another smooth, bony ridge, the ponticulus. The oval window niche lies anterior and superior to the ponticulus.

Epitympanic Recess

That portion of the tympanic cavity extending above the level of the tympanic membrane is known as the epitympanic recess, or attic. This is a chamber having a height about one third that of the entire tympanic cavity; the attic projects slightly more superiorly than does the tympanic membrane. This small portion of the tympanic cavity has as its lateral wall a part of the squamous portion of the temporal bone. The inferior, medially directed, pointed terminus of the lateral attic wall is known as the lateral attic spur or scutum, which is directly above the tympanic membrane.

The attic contains the head of the malleus and the body and short process of the incus. Superiorly the epitympanic recess is bounded by the tegmen tympani; medially by the prominence of the lateral semicircular canal and the prominence of the facial nerve; laterally by the scutum and lateral wall of the attic; and inferiorly by the incudal fossa and the bony surface just behind it. The boundary line between the tympanic cavity proper and the epitympanic recess is marked by the prominence of the facial canal medially, the inferior limit of the incudal fossa inferiorly, and the scutum laterally. The additus ad antrum originates from the posterosuperior aspect of the epitympanic recess.

Copyright © 2003, Mosby, Inc. All rights reserved.

A small recess extends anteriorly from the part of the epitympanum containing the head of the malleus. This anterior epitympanic recess is located just beneath the floor of the middle cranial fossa, lateral to the geniculate turn of the facial nerve and just superior to the cochleariform process and the entrance to the eustachian tube. A small ridge of bone called the cog may partially separate the anterior tympanic recess from the remainder of the epitympanum.

Contents of the Tympanic Cavity

Auditory Ossicles

Three small bones or ossicles span the width of the tympanic cavity: the malleus, the incus, and the stapes. The malleus consists of a head, a neck, the manubrium, and the anterior and lateral processes. The head lies within the epitympanum. The manubrium is attached to the tympanic membrane. The lateral process abuts the tympanic membrane immediately below the pars flaccida. The anterior process is a slender spicule of bone that passes forward and downward into the petrotympanic fissure.

The incus is shaped somewhat like a premolar tooth, with two widely diverging roots that differ in length. The body is somewhat cuboid but compressed transversely. On its anterior surface is a deeply concavoconvex facet that articulates with the head of the malleus. The body of the incus and the head of the malleus are bound to one another by a thin capsular ligament, forming a diarthrodial joint known as the incudomalleolar articulation. The two processes of the incus diverge from one another at nearly right angles. The short crus (short process) projects almost horizontally backward and is attached to the incudal fossa in the lower and posterior portion of the epitympanic recess. The long crus (long process) descends nearly vertically behind and parallel to the manubrium of the malleus and bends medially to end in a rounded projection, the lenticular process, which is tipped with cartilage and articulates with the head of the stapes. This is also a diarthrodial joint and is called the incudostapedial articulation.

From its articulation with the incus, the stapes passes almost horizontally (but slightly cephalad) across the tympanic cavity to meet the wall of the labyrinth at the oval window. The stapes resembles a stirrup and consists of a head, a neck, two crura, and a base. The head has a depression covered by cartilage that articulates with the lenticular process of the incus. The neck is the constricted part of the bone succeeding the head, and its posterior aspect gives insertion to the tendon of the stapedius muscle. The anterior and posterior crura diverge from the neck and are connected at their ends to the flattened oval plate known as the *base*, which forms the footplate of the stapes and is fixed to the margin of the oval window by the annular ligament. The anterior crus is shorter and less curved than the posterior one. The edge of the stapedial base is covered with cartilage, as is the rim of the oval window; the junction thereof constitutes the tympanostapedial syndesmosis.

In summary, the head of the malleus and the body and short process of the incus lie above the level of the scutum, or lateral attic spur, in the epitympanum or attic. The neck of the malleus and the junction of the body and the long process of the incus lie at the level of the scutum, or the junction of the epitympanum and mesotympanum. The manubrium of the malleus and the long process of the incus lie opposite the tympanic membrane in the mesotympanum or main middle ear cavity.

Ligaments

The ossicles are connected with the walls of the tympanic cavity by ligaments, three for the malleus and one each for the incus and stapes.

The anterior ligament goes from the neck of the malleus just above the anterior process to the carotid wall near the petrotympanic fissure. The superior ligament descends from the roof of the epitympanic recess to the head of the malleus. The lateral ligament goes from the posterior part of the notch of Rivinus to the head of the malleus.

The posterior ligament of the incus is a short, thick band connecting the neck and end of the short crus to the posterior wall of the incudal fossa.

The annular ligament of the base of the stapes was described previously. It represents the fibrous ring that encircles the base of the stapes and attaches to the margin of the oval window.

Muscles

The muscles of the tympanic cavity already have been alluded to; one each arises from the anterior and posterior walls.

The tensor tympani, the larger muscle, is contained in the bony canal above the osseous portion of the eustachian tube, from which it is separated by the processus cochleariformis. It passes backward through the canal and ends in a slender tendon that enters the tympanic cavity; it makes a sharp bend around the terminus of the process cochleariformis and is inserted into the neck of the malleus. The tensor tympani is supplied by a branch of the mandibular nerve that passes through the otic ganglion.

The stapedius muscle rises from the walls of the conical cavity hollowed out of the interior of the pyramidal eminence. Its tendon emerges from the orifice at the apex of the pyramidal eminence, extends forward, and inserts into the posterior surface of the neck of the stapes. It is supplied by a branch of the facial nerve.

By their actions, both the tensor tympani and stapedius muscles reduce the efficiency of the sound-conducting mechanism. Both dampen the vibration of the ossicular chain. The tensor tympani accomplishes this by increasing the tension of the tympanic membrane and thereby diminishing the amplitude of excursion of the malleus. The stapedius muscle exerts its action by pulling the head of the stapes backward, which causes the base of the bone to rotate on a vertical axis drawn through its own center. The posterior part of the base is pressed inward toward the vestibule, and the forward portion is withdrawn from it. This reduces the amount of area effectively transmitting the vibration at the footplate and diminishes the mechanical advantage of the lever mechanism. Both of these muscles therefore serve to protect the inner ear from excessive amplitude oscillations of the footplate of the stapes when there is a loud noise. This protective reflex is invoked with low-frequency vibration only and is most effective at frequencies under 5000 Hz.

Copyright © 2003, Mosby, Inc. All rights reserved.

Nerves and Vessels

The nerves of the middle ear cavity are represented by the tympanic plexus, which lies on the cochlear promontory under the mucosa, within grooves or canals in the bone. This plexus is formed chiefly by the tympanic branch (nerve of Jacobson) of the ninth cranial nerve, but is reinforced by one or more caroticotympanic nerves derived from the internal carotid sympathetic plexus. The facial nerve also makes a minor contribution to the tympanic plexus. These fibers are mostly parasympathetic secretomotor fibers. The tympanic branch of cranial nerve IX supplies sensory innervation to the mucosa of the middle ear. Along the branches of the tympanic plexus are paraganglionic cells, and the glomus tympanicum tumor arises from these cell groups associated with the tympanic plexus.

The chorda tympani arising from cranial nerve VII traverses the middle ear cavity but is not a source of innervation to the cavity.

The tympanic cavity derives its arterial supply from a number of vessels. Most are branches of the external carotid artery. The anterior tympanic artery arises from the internal maxillary artery; the inferior tympanic artery arises from the ascending pharyngeal artery. The stylomastoid artery arises from either the posterior auricular or the occipital artery and gives off the posterior tympanic artery. The superior tympanic and the petrosal artery arise from the middle meningeal artery, and the caroticotympanic branches arise from the internal carotid artery.

The veins roughly parallel the arteries and empty into the superior petrosal sinus and pterygoid plexus. The lymphatics begin as a network in the mucous membrane and end chiefly in the retropharyngeal lymph nodes.

Route of the Facial Nerve (Cranial Nerve VII)

The facial or seventh cranial nerve emerges from the brainstem as two roots, motor and sensory. The motor root is the larger one. It leaves the medulla oblongata at the inferior border of the pons, medial to the acoustic nerve. The smaller sensory root or nervus intermedius (of Wrisberg) contains efferent and visceral efferent fibers. It emerges from the medulla between the motor root of the facial nerve and the acoustic nerve.

As the motor root leaves the medulla, it pierces the pia mater and receives its sheath. The bundle then continues forward and laterally in the posterior fossa to the internal auditory meatus. The facial nerve enters the canal in conjunction with the nervus intermedius and acoustic nerve. As it spans the distance between the medulla and the porus acousticus, the motor root aligns itself in a groove on the superior surface of the cochlear division of the eighth nerve. This intracranial segment is 23 to 24 mm in length.

The internal auditory canal segment is 7 to 8 mm in length and is superior to the cochlear nerve, passing above the crista falciformis in the anterior upper portion of the canal. While within the canal, the motor root is separated from the acoustic bundle by the nervus intermedius, but the three nerve bundles are all surrounded by one sheath of arachnoid and dura and by continuations of the subarachnoid and subdural spaces. While still within the canal, the motor root and the nervus intermedius unite to form the combined nerve trunk.

The labyrinthine segment of the nerve measures 3 to 4 mm in length and passes forward and laterally within its own bony channel, the fallopian canal. This segment of the facial nerve canal travels anterolaterally, roughly perpendicular to the longitudinal axis of the petrous bone. The labyrinthine segment of the facial canal describes a subtle curve just superior to the cochlea and anterior to the semicircular canals. At the end of the labyrinthine segment is the geniculate ganglion. The ganglion represents only a small part of the nerve at this location. Only the cell bodies of the somatosensory and taste fibers are located in the ganglion. At approximately the position of the ganglion, the direction of the nerve reverses itself, executing a hairpin turn so that it runs posteriorly. This is the so-called anterior knee or first genu of the facial nerve. At this point the facial nerve is lying just above the base of the cochlea, that is, above and medial to the promontory. Here the nerve is very close to the cochleariform process.

The first genu of the facial nerve, in the limb distal to the geniculate ganglion, delineates the most anterior extent of the tympanic segment of the nerve. This tympanic segment is about 12 mm in length and passes posteriorly and laterally, in the long axis of the petrous bone and along the medial wall of the tympanic cavity. The nerve is contained within the tympanic segment of the facial nerve canal and courses just above the oval window and below the lateral semicircular canal. At the level of the sinus tympani, the nerve changes direction at the second genu. At this point the nerve assumes a vertical position, dropping down along the posterior wall of the tympanic cavity and passing through the anterior mastoid to exit at the base of the skull from the stylomastoid foramen. This mastoid segment is about 15 to 20 mm in length.[12]

There are three primary branches of the facial nerve: the greater superficial petrosal nerve, the nerve to the stapedius muscle, and the chorda tympani.

The greater superficial petrosal nerve leaves the facial nerve at the geniculate ganglion and exits the petrous bone and facial canal just anterior to the geniculate ganglion by way of the facial hiatus along the anterior aspect of the petrous pyramid. The greater superficial petrosal nerve is a mixed nerve, containing both parasympathetic fibers (from the nervus intermedius) and a few motor fibers. This nerve receives sympathetic fibers from the deep petrosal nerve, at which point it becomes the Vidian nerve.

The nerve to the stapedius muscle is a small twig given off from the facial nerve as it descends in the mastoid segment behind the pyramidal eminence.

The chorda tympani originates about 5 mm above the stylomastoid foramen. The chorda is composed mainly of sensory fibers but also contains a few parasympathetic fibers. As it leaves the trunk of the facial canal, it pursues a recurrent course upward and forward in the canaliculis chorda tympani (iter chordae posterius), a narrow canal in the posterior wall of the tympanic cavity. It enters the tympanic cavity close to the border of the tympanic membrane. It then crosses the cavity, running along the medial surface of the tympanic membrane at the junction of

Copyright © 2003, Mosby, Inc. All rights reserved.

its upper and middle thirds. It is covered by the mucous membrane lining of the tympanic cavity and passes lateral to the long process of the incus and then medial to the manubrium of the malleus above the tendon of the tensor tympani. It passes between the malleus and the incus. The chorda tympani leaves the tympanic cavity by way of a small canal in the medial petrotympanic fissure to pass to the base of the skull through a small foramen, the iter chordae anterius (anterior tympanic aperture). It eventually joins the lingual nerve to supply taste sensation to the anterior two thirds of the tongue.

Bony Dehiscences

It is customary to consider the facial canal a closed bony tube except where branches make their exit. Such is not invariably the case. Baxter reported dehiscence in more than half of over 500 temporal bones studied microscopically.[14] Dehiscences in the canal were most common in the tympanic portion near the oval window region and were occasionally present in the mastoid segment and near the region of the geniculate ganglion. The average dimension of these dehiscences was less than 1 mm. The radiologic demonstration of a substantial loss of bone in any region of the facial canal therefore should be considered abnormal. However, it should be remembered that the tympanic segment of the facial nerve canal is at about a 45° angle relative to the coronal plane. Because the angle of slice is oblique to the canal, partial volume effects can make the thin, bony cortex of the canal very difficult to visualize.

Anomalous Course in Petrous Bone

Although the course of the facial nerve through the temporal bone is one of the most constant anatomic relationships, anomalous courses do occur. Such a circumstance may be extremely treacherous for a surgeon, and everyone involved in the interpretation of temporal bone images must be alert to the possibility of such an anomaly.

An anomalous course of the mastoid portion is to be expected in the presence of atresia of the external acoustic canal (discussed later), but numerous such courses have been reported in the absence of any other significant developmental abnormality.

Most of the anomalous courses reported are involved in the part of the nerve peripheral to the geniculate ganglion. The interested reader is referred to the work of Basek, Schuknecht, Shambaugh, Dunkin et al., and Wright et al.[6, 12, 15–17]

The main trunk of the facial nerve in its tympanic portion may take an anomalous course along the medial wall of the tympanic cavity. If there is a delay in the formation of the bony covering of the tympanic segment, the nerve will appear to ''migrate'' inferiorly. The nerve can be slightly displaced and come to lie on the stapes. This migration tends to occur just as the crura of the stapes are forming and growing to meet the footplate of the stapes. The nerve can pass through this region and come to lie on the promontory of the cochlea. Rarely, the crura can actually attach to the nerve that passes directly across the oval window. In this instance the position of the nerve obviously limits the movement of the stapes, and a conductive hearing loss results.

The nerve may divide into two or more branches at any position along its course, and these branches may either parallel one another or diverge.

An anomalous course of the facial nerve within the tympanic cavity is difficult to diagnosis at imaging. The radiologist should confirm that the facial nerve is in the normal position in every case. The canal is usually seen as a small oval or ''notch'' just beneath the lateral semicircular canal. Lack of visualization of the notch should raise suspicion of an abnormal course of the facial nerve. The abnormally positioned nerve may be directly visible, passing along the promontory or even across the oval window. Preoperative identification of such an anomalous course can be very helpful to the surgeon and can help avoid an inadvertent iatrogenic facial nerve paralysis.

Inner Ear

Bony Labyrinth

The bony labyrinth consists of the vestibule, semicircular canals, and cochlea (Fig. 19-7).

Vestibule

The central portion of the cavity of the bony labyrinth is the vestibule. The vestibule is a relatively large ovoid perilymphatic space measuring approximately 4 mm in diameter. The vestibule is continuous anteriorly with the cochlea and posteriorly with the semicircular canals. There are cribrose areas, minute openings for the entrance of the nerve branches from the vestibular nerve on the medial wall and floor of the vestibule, where the vestibule abuts the lateral end of the internal acoustic canal. The vestibule has two other openings, the oval window (for the footplate of the stapes) and the vestibular aqueduct.

Semicircular Canals

The three semicircular canals are continuous with the vestibule. Each of the canals makes about two thirds of a circle and measures about 1 mm in cross-sectional diameter. Each canal is enlarged anteriorly by an ampulla. The nonampulated ends of the superior and posterior semicircular canals join to form the bony common crus.

A portion of the superior semicircular canal is closely related to a ridge (arcuate eminence) on the anterior surface of the petrous bone (the posterior delimitation of the middle cranial fossa). The lateral (horizontal) semicircular canal projects as a ridge on the medial wall of the attic.

The perilymphatic space of each semicircular canal opens into and communicates freely with the vestibule at both ends.

The superior and posterior semicircular canals are both arranged in a vertical orientation at approximately right angles to one another. The superior canal is directed anterolaterally at an angle of about 45° to the midsagittal plane, and the posterior canal is directed posterolaterally at a corresponding angle. It should be noted therefore that the angles of the vertical canals are oriented within both temporal bones so that the superior semicircular canal of one side has the same orientation as the posterior canal of the opposite side.

Copyright © 2003, Mosby, Inc. All rights reserved.

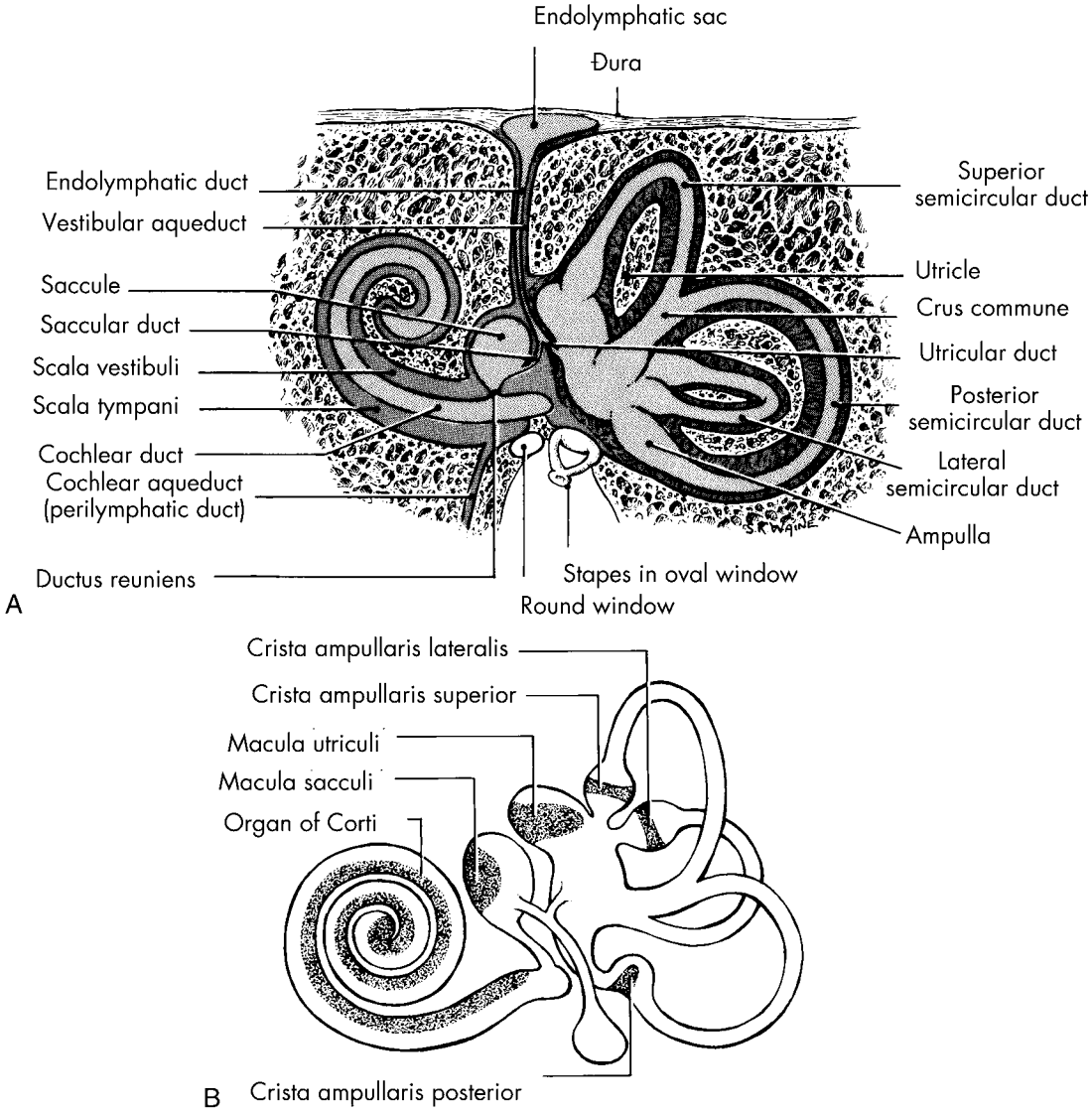

FIGURE 19-7 **A**, Inner ear, schematic drawing. The membranous labyrinth is enclosed within the bony labyrinth and separated from it by the perilymphatic space. The cochlear and vestibular portions of the membranous labyrinth are surrounded by perilymph. The vestibule and semicircular canals tend to be suspended from the walls of the bony labyrinth by myriad tiny arachnoid-like filaments. No such filaments exist around the cochlear duct. The membranous labyrinth encloses the endolymphatic space and is filled with endolymph. The endolymphatic sac and duct are in continuity with the endolymphatic space. The cochlear aqueduct communicates with the subarachnoid space and is in continuity with the perilymphatic space. The oval window abuts against the vestibule; the round window is located at the commencement of the basilar turn of the cochlea. The perilymphatic space is dark gray. **B**, Specialized sensory areas of the membranous labyrinth. Sensory cells mediating hearing are located in the organ of Corti within the cochlear duct. Sensory organs of the vestibular labyrinth are located in the maculae of the utricle and saccule and within the ampullae of the semicircular canals. The macula of the utricle mediates most of the sensations related to linear acceleration of the head; the ampullary cristae are sensitive to changes in angular acceleration of the head.

VIEW IMAGE

Copyright © 2003, Mosby, Inc. All rights reserved.

The lateral semicircular canal does not occupy a horizontal plane, and for this reason the older terminology (*horizontal*) has been discarded. The anterior limb of the lateral semicircular canal lies in the plane higher than the posterior limb, making an angle of about 30° with the horizonal. In the erect position therefore the neck would have to be flexed about 30° for the lateral semicircular canal to be ''horizontal.''

Cochlea

The perilymphatic cavity of the vestibule is also continuous with the cochlea anteriorly (Fig. 19-8 and see the figures in the next section). The cochlea is a conical structure, its base facing the internal auditory canal and its apex or cupola directed anteriorly, laterally, and slightly downward. The base measures around 9 mm, and its axis height is about 5 mm. The base is perforated by numerous apertures for the passage of the cochlear nerve. The cochlea consists of a bony canal wound around a conical central core called the modiolus. The canal winds through slightly more than 2½ turns. The thin osseous spiral lamina projects from the modiolus into the canal and partially divides it. The division of the canal is completed by the basilar membrane, stretching from the free border of the osseous spiral lamina to the outer wall of the bony cochlea. The two passages into which the cochlear canal is thus divided communicate with each other at the apex of the modiolus by a small opening, the helicotrema.

The modiolus is the conical central pillar of the cochlea. Its base is broad and appears at the lateral end of the internal acoustic canal, where it corresponds with the cochlear exit of the corresponding part of the eighth cranial nerve. It is perforated by numerous orifices for the transmission of the branches of the nerve.

The bony cochlear canal takes between 2½ and 2¾ turns around the modiolus. The first turn bulges toward the tympanic cavity, and this elevation on the medial wall of the tympanic cavity is known as the promontory. The bony cochlear canal is about 30 mm long and diminishes gradually in diameter from the base to the summit, where it ends in the cupola, which forms the apex of the cochlea. The cross-sectional diameter of the beginning of the canal is about 3 mm. The openings in or near the first portion of the cochlear canal include the round window, which is covered by the secondary tympanic membrane; the oval window (actually an opening of the vestibule), which is covered by the footplate of the stapes; and the cochlear canaliculus, which leads via a small canal to the subarachnoid space, opening on the inferior surface of the petrous portion of the temporal bone. The cochlear canaliculus, also known as the cochlear aqueduct or perilymphatic duct, allows at least theoretical equilibration between the perilymphatic space and the subarachnoid space; however, it is usually completely filled with arachnoid and fibrous tissue.

The bone separating one turn of the cochlea from the next is called the interscalar septum.

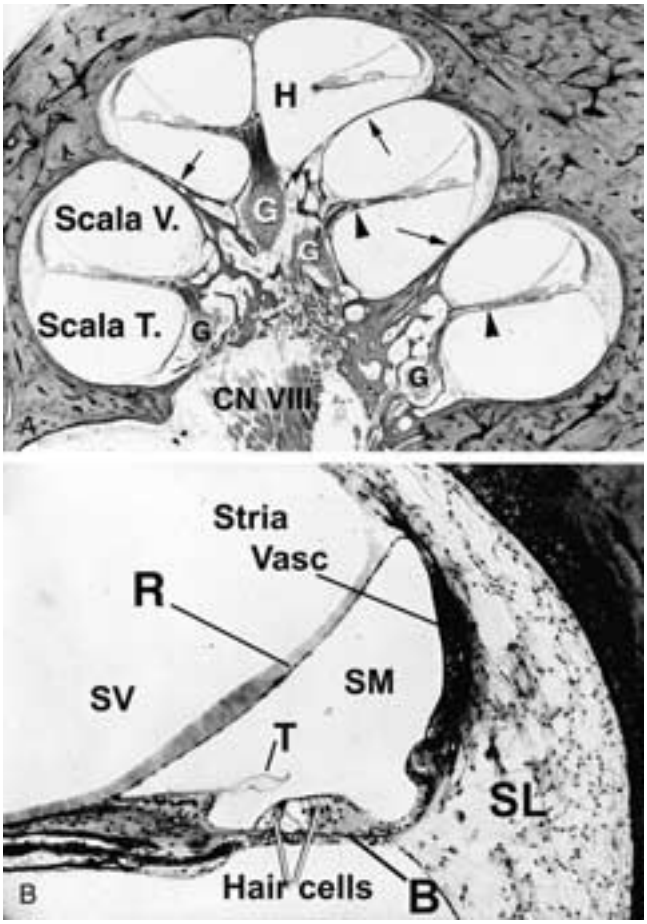

VIEW IMAGE

FIGURE 19-8 **A**, Photomicrograph of a normal cochlea. The eighth cranial nerve (*CN VIII*) can be seen entering the modiolus. The modiolus forms the core or axis in the center portion of the cochlea. The modiolus contains the cells of the spiral ganglion (*G*) seen in several turns in this photomicrograph. Note that much of the bulk of the upper modiolus is composed of nerve rather than bone. The spiral lamina (*arrowheads*) projects from the modiolus into the turns of the cochlea. This partially separates the lumen of the cochlea into the scala vestibuli (*Scala V.*) and scala tympani (*Scala T.*). The scala vestibuli and scala tympani communicate at the helicotrema (*H*). The interscalar septum (*arrows*) is seen at several levels. **B**, The basilar membrane (*B*) extends from the spiral lamina to the spiral ligament (*SL*). The hair cells are seen in the organ of Corti. Small projections from the hair cells are stimulated by the tectorial membrane (*T*). Reissner's membrane (*R*) closes the cochlear duct and separates the scala media (*SM*) from the scala vestibuli (*SV*). Stria vasculare (*Stria Vasc.*)

Membranous Labyrinth

The interconnecting spaces actually within the membranous labyrinth (see Fig. 19-7) constitute the endolymphatic cavity. The membranous labyrinth consists of the cochlear duct, the vestibular sense organs, the endolymphatic duct and sac, the round window membrane, and the vascular system.

Cochlear Duct

The cochlear duct is a spiral tube lying within the cochlea and attached to its outer wall. The cochlear duct is a blind pouch; it cleaves the perilymphatic space within the bony labyrinth, dividing it into two portions, the scala vestibuli and the scala tympani (see Fig. 19-8). The cochlear duct is triangular, its roof being formed by Reisner's membrane, its outer wall by the endosteum lining the bony canal, and its floor by the basilar membrane and the outer part of the

Copyright © 2003, Mosby, Inc. All rights reserved.

osseous spiral lamina. It contains the organ of Corti, which is the site of placement of the supporting and sensory (hair) cells that mediate hearing.

Vestibular Sense Organs

The sensory organs of the vestibular labyrinth are located in the maculae of both the utricle and saccule and within the ampullae of the semicircular canals. The epithelium consists of supporting cells and hair cells (sensory cells) covered by a gelatinous layer into which the cilia project.

Vestibular physiology is complex. The maculae are referred to as organs of static balance because the otoliths, under the influence of gravity (they have a specific gravity of 2.71), exert traction on the cilia of the hair cells in varying positions of the head. The macula of the utricle mediates most of the sensations that have to do with linear acceleration of the head. The ampullary crests located within the semicircular canals are called organs of kinetic balance because they are stimulated by the movement of or pressure changes in the endolymph caused by the angular acceleration of the head; this produces deviation of the cupulae.

The utricle resides within the elliptical recess of the vestibule. The sensory cells of the utricle lie within the macula. The membranous semicircular ducts all open into the utricle. From the anteromedial part of the utricle the ductus utriculosaccularis takes its origin and opens into the endolymphatic duct.

The saccule lies in the spherical recess near the opening of the scala vestibuli of the cochlea. The macula of the saccule is located along its anterior wall. The saccule communicates with the sinus of the endolymphatic duct by way of the saccular duct, and from the lower part of the saccule the ductus reuniens communicates with the basal end of the cochlear duct.

The membranous semicircular ducts are about one quarter of the diameter of the osseous semicircular canals. Each duct has an ampulla at one end that lies within the ampulla of the corresponding bony canal. The semicircular ducts open by five orifices into the utricle, the common crus being a single opening for the junction of the medial end of the superior and the upper end of the posterior semicircular ducts. A crestlike septum, the ampullary crest, crosses the base of each ampulla and is made up of sensory epithelium distributed on a mound of connective tissue and covered by a gelatinous cupula.

Endolymphatic Duct and Sac

The endolymphatic duct begins within the vestibule as a dilated portion, the endolymphatic sinus. It arises at the confluence of the utricular and saccular ducts. As it leaves the vestibule, it narrows into an isthmus and passes into the vestibular aqueduct, located near the crus common. As the aqueduct turns caudally to approach the dural opening of the vestibular aqueduct, the membranous duct (within the bony aqueduct) widens again into the flat endolymphatic sac. The intraosseous part of the sac fills most of the vestibular aqueduct. The remainder of the sac protrudes from the inferior aperture of the aqueduct and lies between the periosteum of the petrous bone and the dura mater. The sac is not one compartment but rather a complex system of connecting channels.

Round Window Membrane

The round window membrane (secondary tympanic membrane) measures about 3 mm in its horizontal axis and about 1.5 mm in its transverse axis. The round window membrane is of particular importance in acoustic energy transfer within the inner ear, where it performs as a yielding area of the bony labyrinth to permit movement of the perilymph in association with excursions of the stapedial footplate. Typically, movements of these two diaphragms should be 180° out of phase with one another.

Vascular System

The arterial blood supply to the membranous labyrinth originates within the cranial cavity and effectively is distinct from the vessels that supply the otic capsule and the tympanic cavity, although there are a few terminal branches that penetrate the endosteal layer. In a study of 100 human specimens, Mazzoni reported finding a consistent arterial loop in the region of the internal auditory canal.[18] This loop is either the main trunk or a branch of the anterior inferior cerebellar artery in 80% of cases, of the accessory anterior cerebellar artery in 17%, or a branch of the posterior inferior cerebellar artery in 3%. The loop was found inside the internal auditory canal in 40%, at the porus in 37%, and within the cerebellopontine angle cistern in 33% of cases.

The anterior inferior cerebellar artery (AICA) arterial loop gives rise to the internal auditory artery (labyrinthine artery) and also frequently to the subarcuate artery. The AICA then takes a recurrent course to the cerebellum. The internal auditory artery distributes to the dura and nerves in the internal auditory canal, to adjacent bone of the canal, and to the medial aspect of the inner ear before dividing into the common cochlear artery.[18] The further ramifications of these arteries to the membranous labyrinth are discussed by Hawkins and are further elaborated on by Schuknecht.[12, 19]

The main venous channels of the cochlea are the posterior and anterior spiral veins. These join together near the base of the cochlea to form the common modiolar vein. The common modiolar vein is joined by the vestibulocochlear vein to become the vein of the cochlear aqueduct. This main channel enters a bony canal near (but not within) the cochlear aqueduct to empty into the inferior petrosal sinus.

The semicircular canals are drained by vessels that pass toward the utricular end to form the vein of the vestibular aqueduct, which accompanies the endolymphatic duct and drains into the lateral venous sinus.

Bast and Anson describe an internal auditory vein that traverses the internal auditory canal and drains into the inferior petrosal sinus, but this is an inconstant vessel.[3]

Perilymphatic Spaces and Fluid Systems

The perilymphatic space (see Fig. 19-7) of each semicircular canal is continuous at both ends with the perilymphatic space of the vestibule, and this space is in turn continuous widely with that of the scala vestibuli. The scala vestibuli is continuous with the scala tympani at the helicotrema. All the perilymphatic spaces therefore open widely into each other.

The total volume of fluid contained within the develop-

Copyright © 2003, Mosby, Inc. All rights reserved.

mentally mature periotic space is estimated to be approximately 0.2 ml or about three drops. Without those three drops of fluid, the transmission of sound waves from the oval window to Reissner's membrane in the cochlea could not be mediated.

There are several actual or potential dehiscences in the compact bone of the petrous portion of the temporal bone that could theoretically permit abnormal communication between the perilymphatic space and the bordering structures.[10] These include (1) the oval window, normally sealed off from the middle ear cavity by the footplate of the stapes and its annular ligament; (2) the round window, normally sealed off from the middle ear by the secondary tympanic membrane; (3) the fissula ante fenestram and the fossula postfenestram, two small extensions of the perilymphatic space extending from the vestibule toward the middle ear cavity that are usually obliterated by connective tissue; and (4) the vestibular aqueduct, a channel that extends through the otic capsule from the vestibule to the posterior cranial fossa and transmits the endolymphatic duct and accompanying vein. The duct, vein, and connective tissue surrounding them so fill the aqueduct that there is no perilymphatic space and therefore no actual communication between the perilymphatic space of the vestibule and the epidural space. The fifth actual or potential dehiscence is the cochlear aqueduct (perilymphatic duct, cochlear canaliculus), a normally minute canal that opens on the inferior surface of the petrous part of the temporal bone and permits communication between the subarachnoid space and the scala tympani. Occasionally the cochlear aqueduct is very patulous, although filled with arachnoid and fibrous tissue, and this provides at least a theoretical possibility of free communication of the perilymphatic space with the subarachnoid space. Whether this is physiologically important in the transport of potentially noxious substances to the inner ear from the violated subarachnoid space is unproved.

HOW THE EAR AMPLIFIES SOUND

Once the inner ear becomes sequestered within the base of the skull, it becomes necessary in the evolutionary sense to reestablish continuity with the external environment so as to provide a suitable apparatus for the reception of sound. Evolution elegantly fashioned a solution based on the simplest of mechanical and hydraulic principles. The ossicular chain acts as a simple lever mechanism attached to the large-area diaphragm (tympanic membrane) on one side and the small-area diaphragm (stapes footplate) on the fluid side.

Sound waves are amplified by three different mechanisms by the time the vibrations in the air of the external acoustic canal are changed to fluid pulsations of the perilymph within the membranous labyrinth.

The first mechanism is the ''organ pipe'' resonance of the external canal. The resonant frequency of the column of air enclosed within the external acoustic canal accounts for approximate doubling of the pressure at the tympanic membrane compared to that at the entrance to the canal for frequencies between 2000 and 5400 Hz.

Secondly, the area of the tympanic membrane varies between 15 and 30 times the area of the oval window. This concentration of force at the stapes footplate amplifies the incoming vibrations of sound approximately 15 to 30 times.

Finally, the lever mechanism of the ossicular chain reduces the amplitude of the excursion of the bone at the footplate of the stapes in comparison to the long handle of the malleus and thereby increases the force by a factor of 2 to 3.

The sound waves therefore may be amplified by a factor of up to 180 by the time they encounter the perilymph.[20]

REFERENCES

1. Streeter GL. The development of the scala tympani, scala vestibuli and perioticular system in the human embryo. Am J Anat 1917;21:299–320.
2. Streeter GL. The histogenesis and growth of the otic capsule and its contained periotic tissue spaces in the human embryo. Contrib Embryol 1918;20:5–55.
3. Bast TH, Anson BJ. The Temporal Bone and Ear. Springfield, Ill: Charles C Thomas, 1949.
4. Shambaugh GE, Glasscock ME. Surgery of the Ear, 3rd ed. Philadelphia: WB Saunders, 1980;5–29.
5. Iurato S. Submicroscopic Structure of the Inner Ear. New York: Pergamon Press, 1967.
6. Shambaugh GE, Glasscock ME. Surgery of the Ear, 3rd ed. Philadelphia: WB Saunders, 1980;14.
7. Wittmaack K. Uber die normale und die pathologische. Pneumatisation des Schlafenbeines. Jena, Germany: Fischer, 1918.
8. Anson BJ, Donaldson JA. Surgical Anatomy of the Temporal Bone. 3rd ed. Philadelphia: WB Saunders, 1981.
9. Goss CC, ed. Gray's Anatomy. Philadelphia: Lea & Febiger, 1959.
10. Schaeffer JP, ed. Morris' Human Anatomy. Philadelphia: Blakiston, 1942.
11. Hollinshead WH. Anatomy for Surgeons. Vol 1. The Head and Neck. 2nd ed. New York: Harper & Row, 1968.
12. Schuknecht HF. Pathology of the Ear. Cambridge, Mass: Harvard University Press, 1974.
13. Warwick R, Williams PL, eds. Gray's Anatomy. 35th British ed. Philadelphia: WB Saunders, 1973.
14. Baxter A. Dehiscence of the fallopian canal. J Laryngol Otol 1971;85:587–594.
15. Basek M. Anomalies of the facial nerve in normal temporal bones. Ann Otol Rhinol Laryngol 1962;71:392.
16. Durcan DJ, Shea JJ, Sleeckx JP, et al. Bifurcation of the facial nerve. Arch Otolaryngol 1967;86:619–631.
17. Wright J Jr, Taylor C, McKay D. Variations in the course of the facial nerve as illustrated by tomography. Laryngoscope 1967;77:717–733.
18. Mazzoni A. Internal auditory artery supply to the petrous bone. Ann Otol Rhinol Laryngol 1972;81:13–21.
19. Hawkins J. Vascular patterns of the membranous labyrinth. Third symposium on the role of the vestibular organs in space exploration. NASA SP 1967;152:241.
20. Stevens SS, Warshowsky F. Sound and Hearing. New York: Time-Life Books, 1965.

OTHER READINGS

Caparosa RJ. An Atlas of Surgical Anatomy and Techniques of the Temporal Bone. Springfield, Ill: Charles C Thomas, 1972.

Donaldson JA, Anson BJ. Surgical Anatomy of the Temporal Bone, 4th ed. New York: Raven Press, 1992.

Glasscock ME, Shambaugh GE, Johnson GD. Surgery of the Ear, 4th ed. Philadelphia: WB Saunders, 1990.

Gulya AJ, Schuknecht HF. Anatomy of the Temporal Bone with Surgical Implications, 2nd ed. New York: Parthenon, 1995.

Schuknecht HF, Gulya AJ. Anatomy of the Temporal Bone with Surgical Implications. Philadelphia: Lea & Febiger, 1986.

Vignaud J, Dulac GL, Francois J, et al. Temporal, Fosses Nasales, Cavites Accessoires, Vol. 17-1. (Fischgold H, ed. Traite de Radiodiagnostic.) Paris: Masson, 1974.

Copyright © 2003, Mosby, Inc. All rights reserved.

SECTION TWO

SECTIONAL ANATOMY

Hugh D. Curtin and Pina Sanelli

The radiologist is presented with the anatomy of the temporal bone as planar sectional images.[1–7] The axial and coronal planes are currently considered standard in modern imaging only because these planes were most conveniently achieved by the typical CT scanner of the 1980s and 1990s. The patient was positioned routinely on the back, with the head comfortably placed in a neutral position for axial images. For coronal images, the patient was placed in either the supine or prone position, and the neck was extended as far as possible. Although oblique planes were occasionally attempted, patient positioning was uncomfortable and these planes were never widely accepted. MR imaging is capable of oblique planar imaging but lacks the ability to define the fine cortical bony anatomy of the temporal bone.

Prior to the advent of CT, multiplanar imaging using pluridirectional tomography was routine. Many different obliquities were used to generate a perfect cross-sectional image through a particular part of the temporal bone anatomy. Indeed, coronal and sagittal images were routine. Axial images were more difficult to achieve because of the awkward patient position needed for the basal view. Oblique planes carried names such as Poschl, Guillen, Stenvers, and so on, named after the people who described them. Each plane was designed to optimize visualization of a certain structure. The design of the planes was based on the principle that the optimal plane for visualization of a plate of bone or a relatively linear structure is in a plane perpendicular to the structure. Subtle angles were measured and precise obliquities were generated.

Now, with the introduction of multidetector spiral CT scanners, an entire volume of the temporal bone is examined with one pass of the scanner in one plane. The volume is organized based on the *isotropic voxel* and spatial resolution is the same in any plane, be it the plane of acquisition or a reconstructed plane. The data set can be sectioned in virtually any plane. The plane of the reformatted image is not governed by ease of patient positioning, but rather by the optimal plane for visualizing a structure.

As the plane of the final image is not dependent on the original scan angle, the scan can be performed while avoiding direct irradiation of the lens of the eye (Fig. 19-9). The ideal orientation for even the axial plane can then be generated as a reformatted image. Most of the images in this section are reformatted images rather than direct scans.

The following images detail the anatomy of the temporal bone in various planes of section. Images are provided in the routine axial and coronal planes with several gross anatomic cross sections for comparison (see Figs. 19-10 to 19-14). Other planes are shown for imaging of particular anatomic structures (see Figs. 19-15 to 19-17).

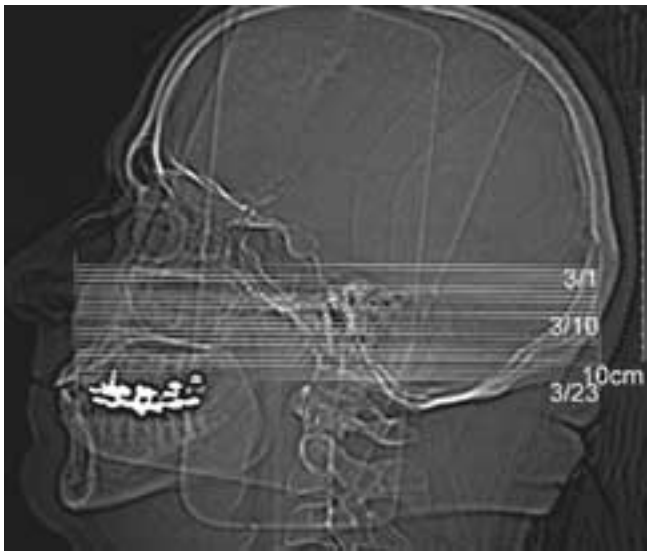

FIGURE 19-9 Original plane of sections. The scan angle is chosen to cover the temporal bone but to avoid the eye, in particular the lens of the eye.

VIEW IMAGE

Copyright © 2003, Mosby, Inc. All rights reserved.

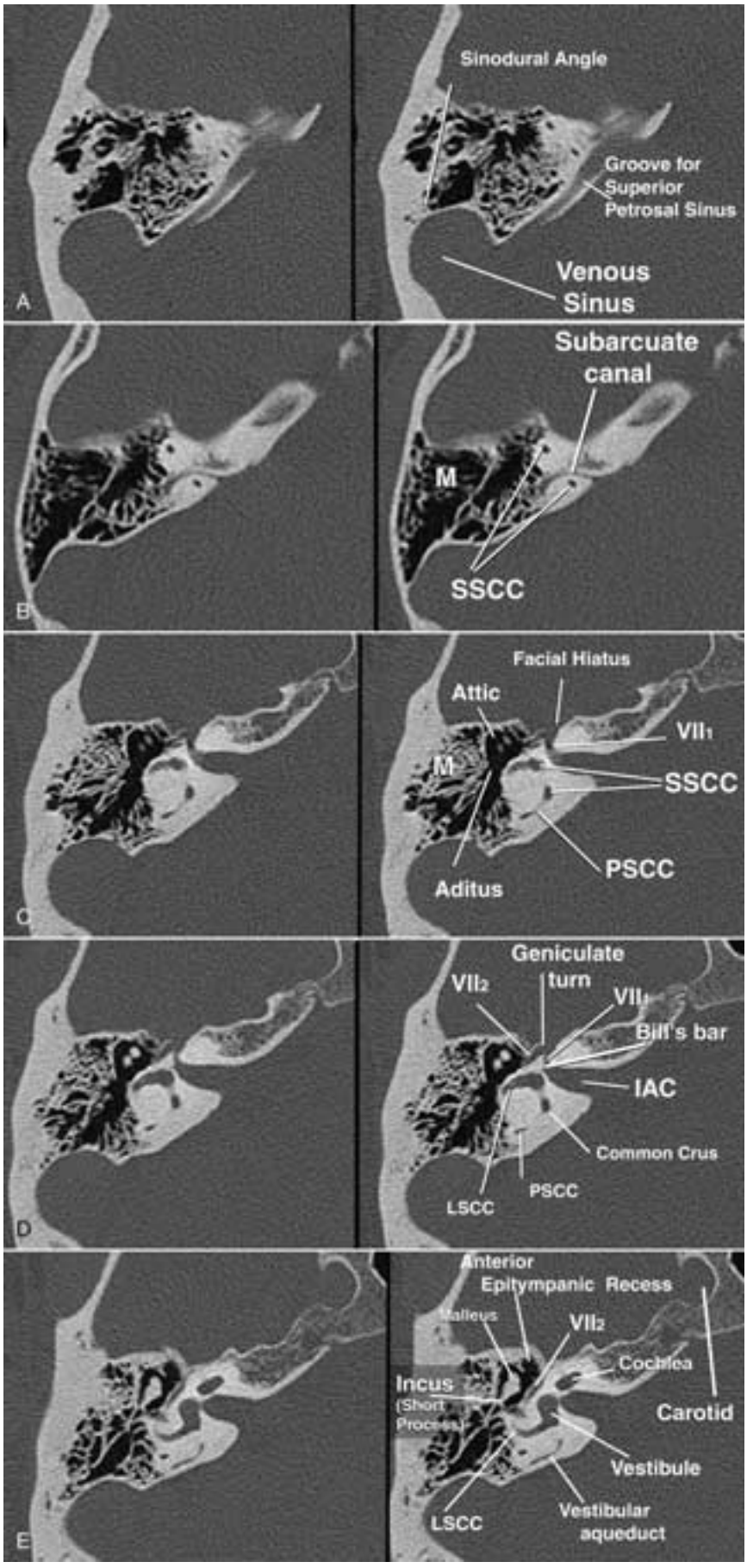

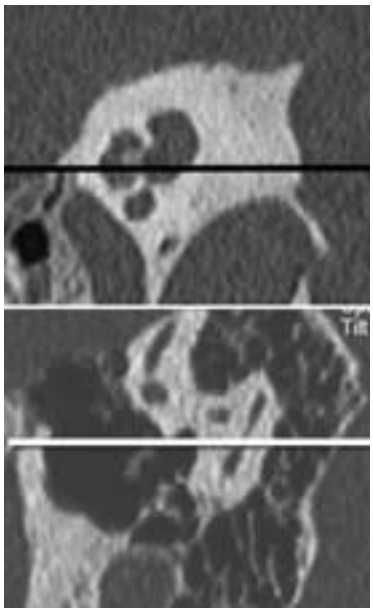

Scout

FIGURE 19-10 **A** to **L**, Axial images taken approximately along the anthropomorphic baseline. These are approximately parallel to the original scan angle. However, the scans were prescribed from a sagittal plane preliminary view, reformatted along the axis of the cochlea (*see inset*). These scans correspond approximately to the gross section shown in Figure 3. At level **D**, the labyrinthine segment of the facial nerve canal courses from the internal auditory canal toward the geniculate turn of the facial nerve. The tympanic segment then passes posteriorly along the medial wall of the middle ear. At level **E** the tympanic segment of the facial nerve passes beneath the horizontal semicircular canal. The ''ice cream cone'' configuration of the malleus head (the ice cream) and the incus (the cone) is appreciated at this level.

Illustration continued on following page

Copyright © 2003, Mosby, Inc. All rights reserved.

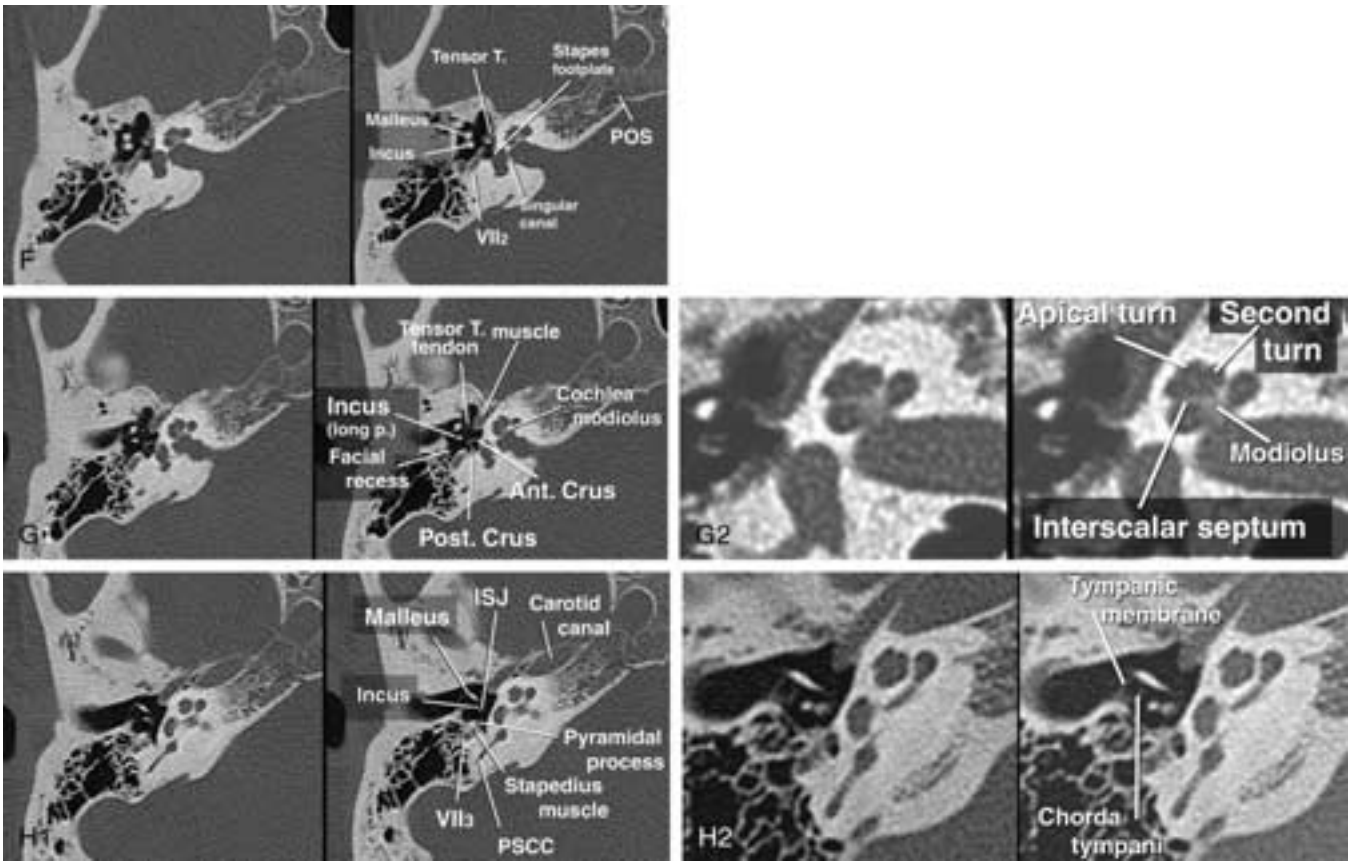

VIEW IMAGE

FIGURE 19-10 *Continued.* When the neck of the malleus and the lower portion of the body of the incus (and/or the uppermost portion of the long process of the incus) are seen as two ''dots'' (section **F**), the scan plane is just above the level of the scutum, which lies immediately lateral to this portion of the ossicles. The next most caudal scan will start to go through the external auditory canal. When the manubrium of the malleus and the long process of the incus are seen as two roughly parallel lines (level **H**), the scan plane is in the mesotympanum. At level **G**, both crura of the stapes are seen, and the inner architecture of the cochlea can be appreciated.

Copyright © 2003, Mosby, Inc. All rights reserved.

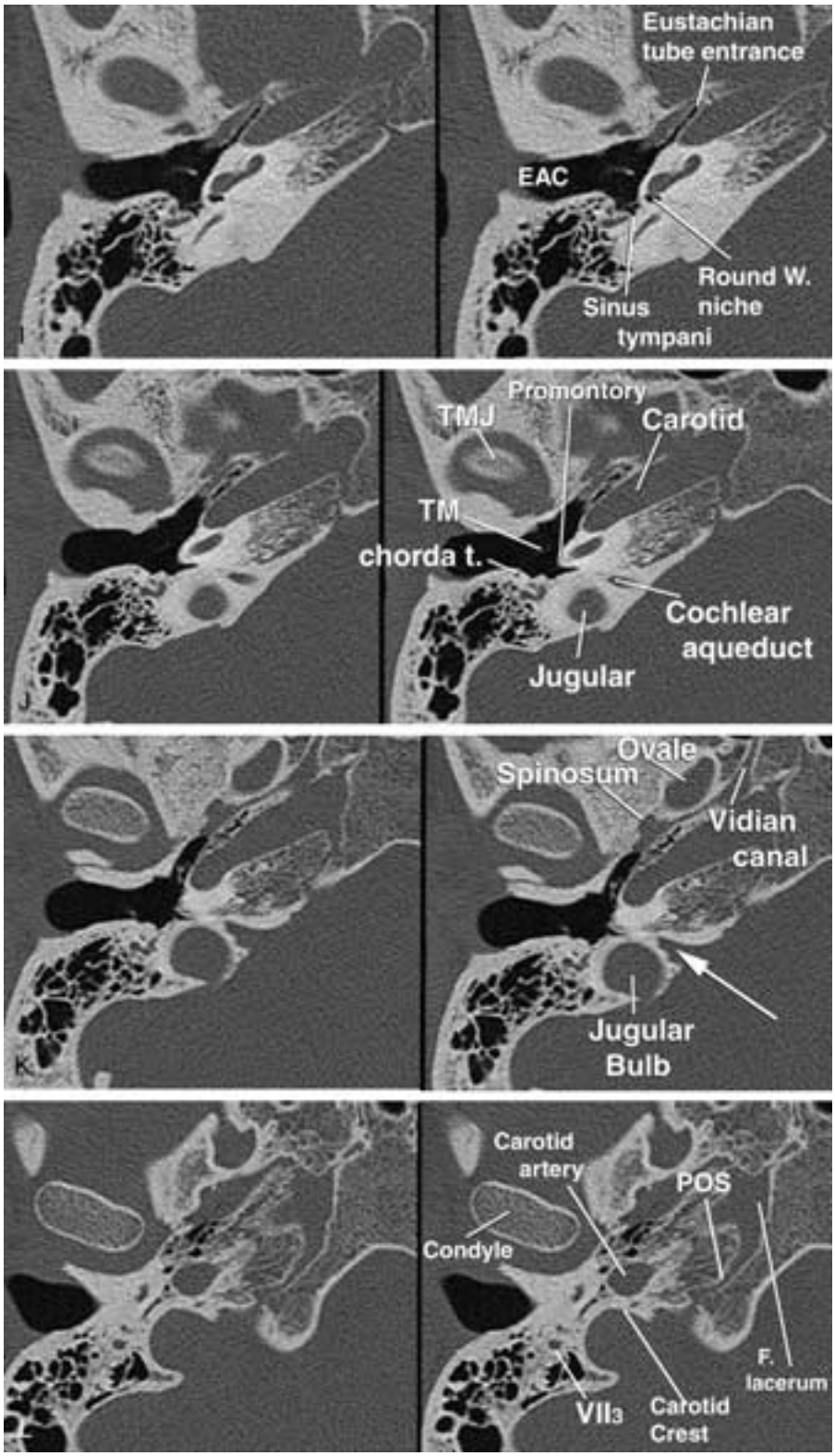

VIEW IMAGE

FIGURE 19-10 *Continued.* At level **K** there is visualization of the lateral cortical plates of the carotid canal and the jugular foramen. The arrow shows the aperture of the cochlear aqueduct opening into the jugular foramen. In **H** through **L** the vertical or mastoid section of the facial nerve is seen in cross section. *M*, mastoid; *SSCC*, superior semicircular canal; *LSCC*, lateral semicircular canal; *PSCC*, posterior semicircular canal; *IAC*, internal auditory canal; *EAC*, external auditory canal; *POS*, petrooccipital synchondrosis (petroclival synchondrosis); *Tensor T*, tensor tympani; *p*, process; *Ant.*, anterior; *Post.*, posterior; *ISJ*, incudostapedial joint; *W*, window; *TM*, tympanic membrane; *TMJ*, temporomandibular joint; *chorda t.*, chorda tympani; *VII*, the seventh nerve (subscripts: 1—labyrinthine segment, 2—tympanic segment, 3—mastoid segment). Blowup views in the region of **G** and **H**. Compare to Figure 19-11B and C.

Copyright © 2003, Mosby, Inc. All rights reserved.

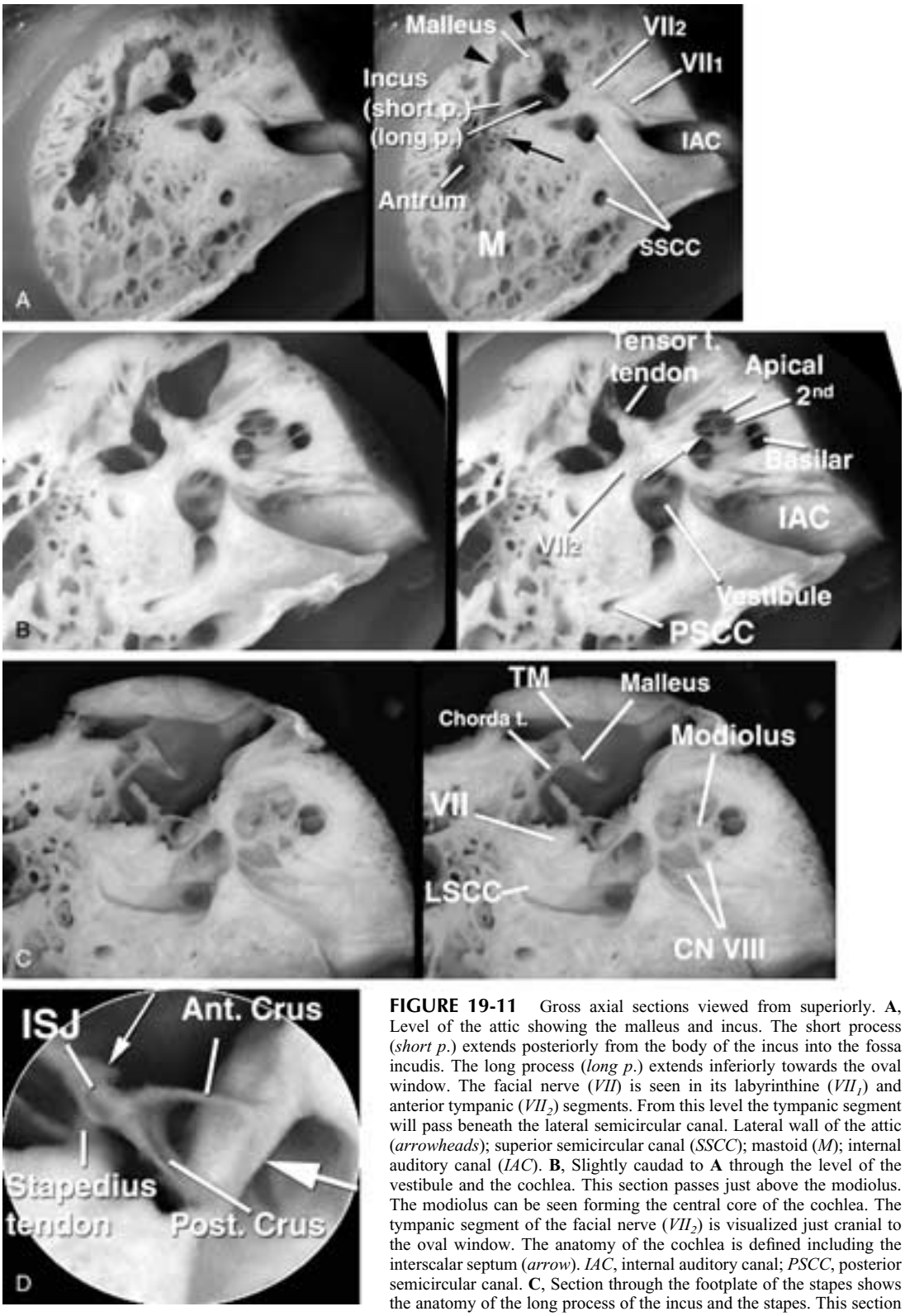

FIGURE 19-11 Gross axial sections viewed from superiorly. **A**, Level of the attic showing the malleus and incus. The short process (*short p.*) extends posteriorly from the body of the incus into the fossa incudis. The long process (*long p.*) extends inferiorly towards the oval window. The facial nerve (*VII*) is seen in its labyrinthine (VII_1) and anterior tympanic (VII_2) segments. From this level the tympanic segment will pass beneath the lateral semicircular canal. Lateral wall of the attic (*arrowheads*); superior semicircular canal (*SSCC*); mastoid (*M*); internal auditory canal (*IAC*). **B**, Slightly caudad to **A** through the level of the vestibule and the cochlea. This section passes just above the modiolus. The modiolus can be seen forming the central core of the cochlea. The tympanic segment of the facial nerve (VII_2) is visualized just cranial to the oval window. The anatomy of the cochlea is defined including the interscalar septum (*arrow*). *IAC*, internal auditory canal; *PSCC*, posterior semicircular canal. **C**, Section through the footplate of the stapes shows the anatomy of the long process of the incus and the stapes. This section passes through the modiolus of the cochlea. The chorda tympani (*Chorda t.*) can be seen crossing through the middle ear. The branches of the eighth cranial nerve (*CN VIII*) are seen within the internal auditory canal. The cochlear branches are seen anterior to the vestibular branches. *TM*, tympanic membrane; *LSCC*, lateral semicircular canal. **D**, Blown-up view through the incudostapedial joint shows the terminus of the lenticular process of the incus (*small arrow*), the incudostapedial joint (*ISJ*), and the anterior crus (*Ant. Crus*) and posterior crus (*Post. Crus*) of the stapes. The posterior crux can have a curved cross section. Footplate of the stapes (*large arrow*).

VIEW IMAGE

Copyright © 2003, Mosby, Inc. All rights reserved.

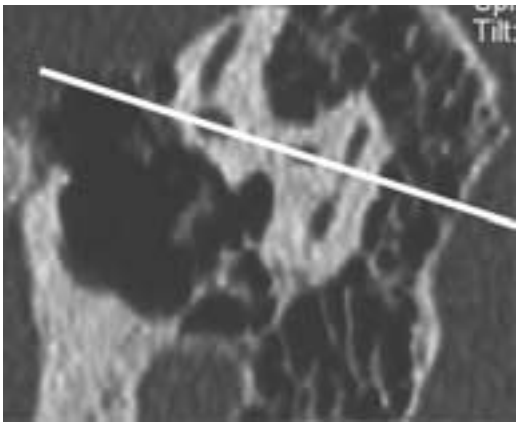

Scout

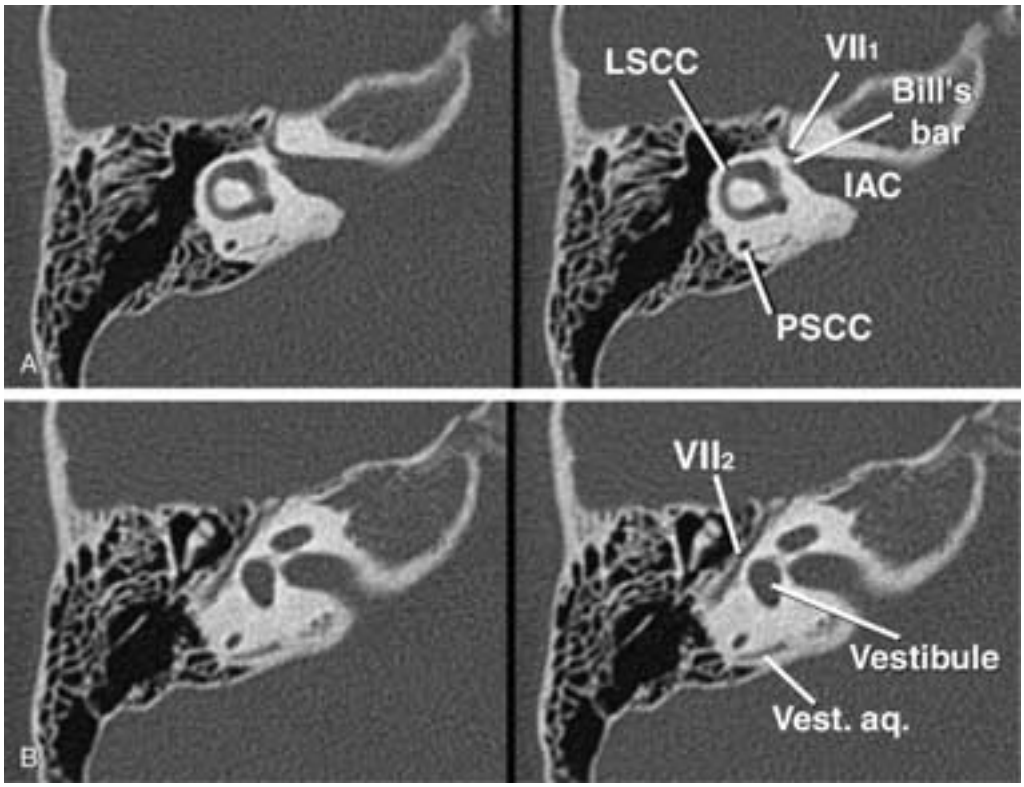

FIGURE 19-12 Axial section reformatted parallel to the lateral semicircular canal. These reformatted images are prescribed from a sagittal scout preliminary image. Connecting the anterior and posterior limbs of the lateral semicircular canal (*see inset*) allows the plane to pass directly along the arc of the canal. **A**, This allows visualization of the cortical plate of bone along the outer curve of the canal. **B**, Most of the tympanic segment of the seventh nerve (VII_2) is seen just inferior to the lateral semicircular canal (*LSCC*). *PSCC*, posterior semicircular canal; *IAC*, internal auditory canal; *Vest. aq*., vestibular aqueduct.

Copyright © 2003, Mosby, Inc. All rights reserved.

VIEW IMAGE

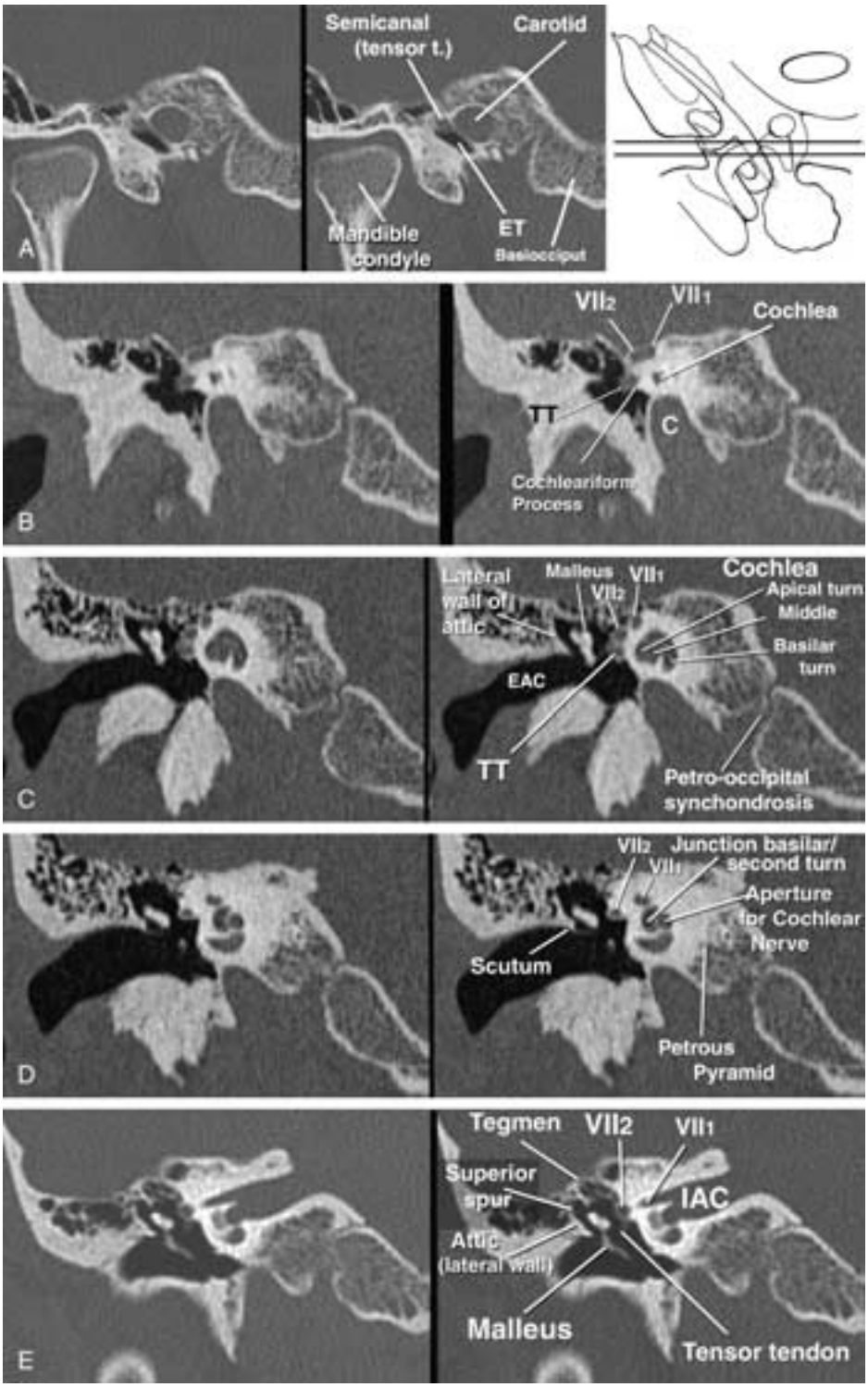

VIEW IMAGE

FIGURE 19-13 Coronal plane images through the temporal bone from anteriorly to posteriorly (compare to Fig. 6). Most of the images are reformatted from a single case. However, several are direct scans emphasizing certain parts of the anatomy. The images are taken in the plane shown in the inset. Level **C** shows the relationship of the labyrinthine and anterior tympanic segments of the facial nerve canal to the cochlea. The malleus is visualized well at level **E** just anterior to the incus and stapes, seen in level **F**. The tympanic segment of the facial nerve canal courses under the lateral semicircular canal and over the stapes and oval window (levels **B** through **I**) before turning inferiorly. The entire course of the mastoid (vertical) segment of the facial nerve canal is seen at level **J**. *Tensor t*., tensor tympani; *ET*, eustachian tube; *TT*, tensor tympani; *VII*, seventh nerve (subscripts 1, 2, and 3 indicate the labyrinthine, tympanic, and mastoid segments of the canal, respectively); *C*, carotid artery within the carotid canal; *EAC*, external auditory canal; *IAC*, internal auditory canal; *SSCC*, superior semicircular canal; *LSCC*, lateral semicircular canal; *PSCC*, posterior semicircular canal; *p*, process; *F*, foramen; xii, twelfth nerve; *M*, mastoid; *J*, jugular fossa.

FIGURE I Blown-up view through the sinus tympani showing the relationship to the seventh nerve and the stapedius muscle within the pyramidal process.

Copyright © 2003, Mosby, Inc. All rights reserved.

VIEW IMAGE

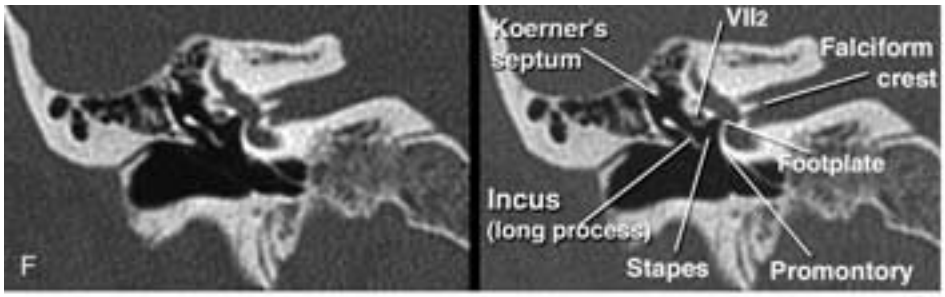

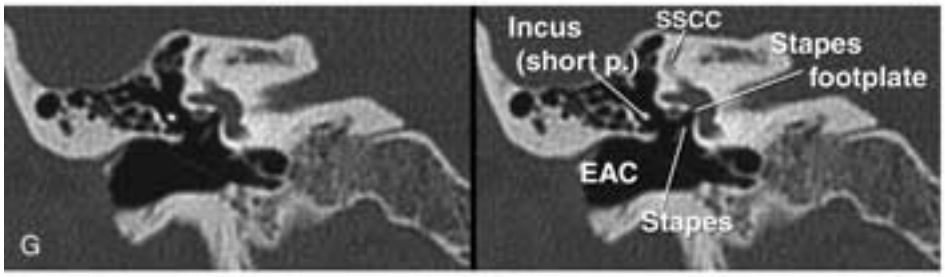

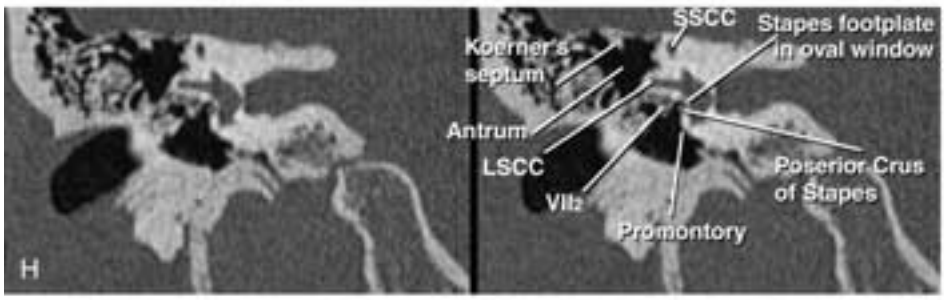

VIEW IMAGE

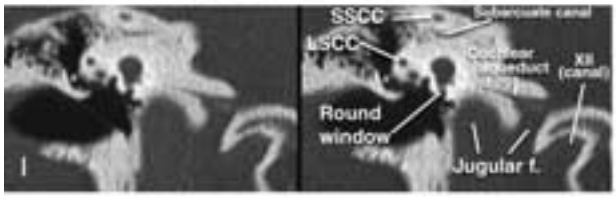

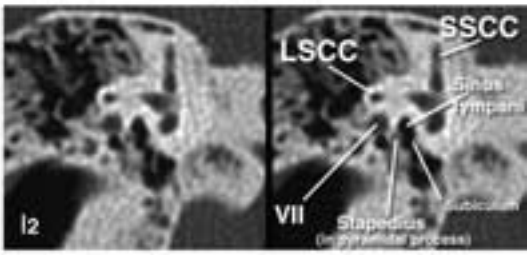

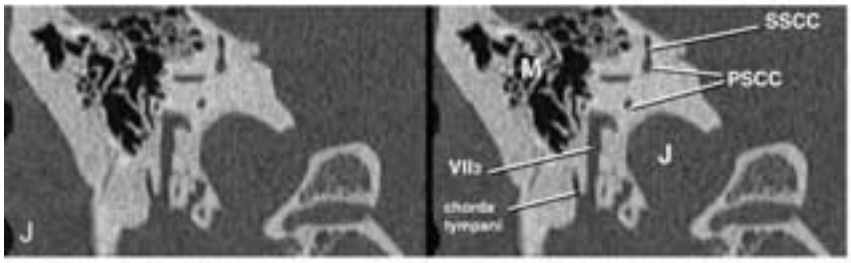

FIGURE 19-13 *Continued.* For legend see previous page.

Copyright © 2003, Mosby, Inc. All rights reserved.

VIEW IMAGE

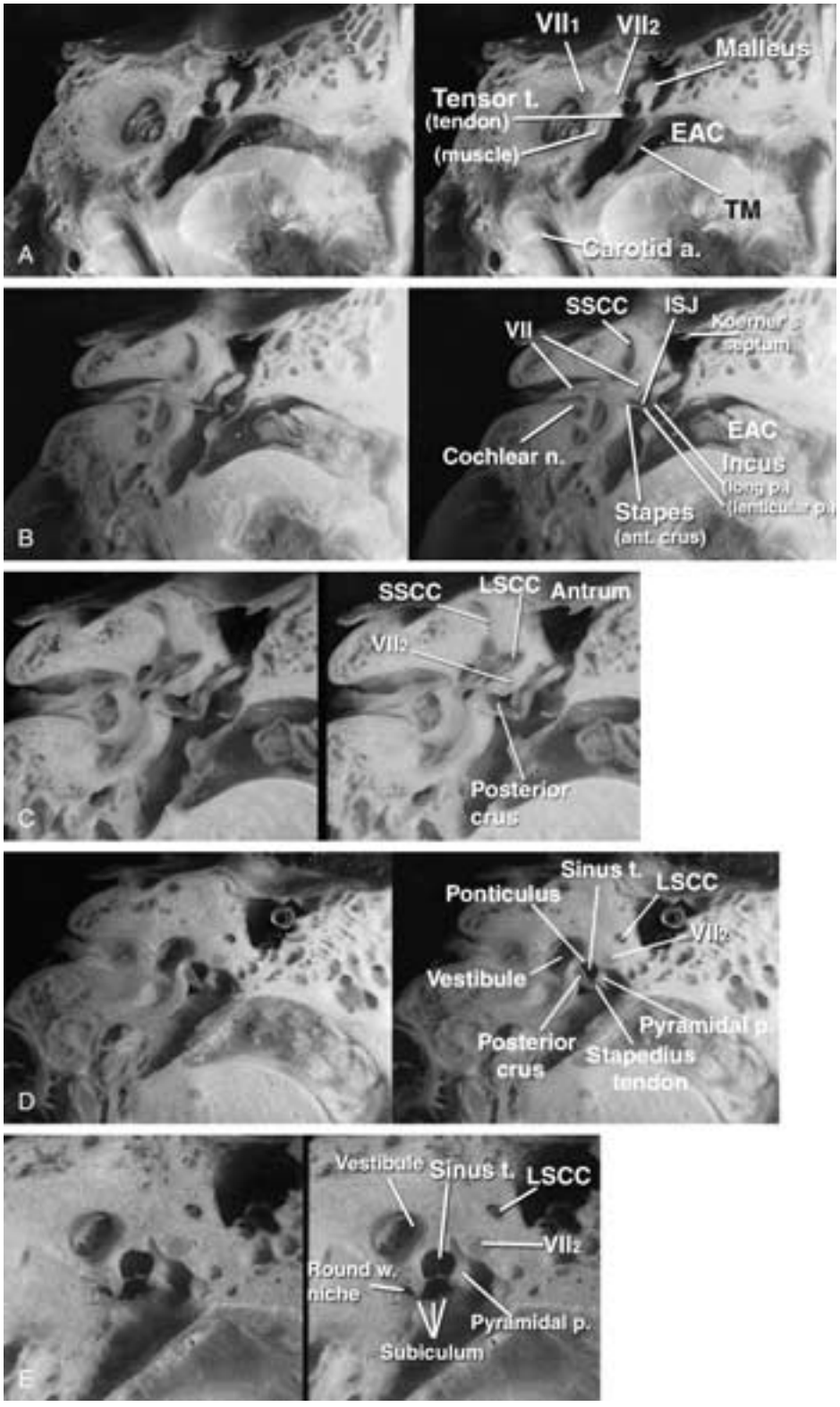

VIEW IMAGE

FIGURE 19-14 Coronal gross sections of the temporal bone from anteriorly to posteriorly. **A**, Section through the cochlea. The spiral lamina can be seen bisecting part of the basilar turn. The tensor tympani (*tensor t.*) is seen in the region of the cochleariform process just inferior to the seventh nerve (VII_1, VII_2). The tensor tympani tendon can be seen crossing the middle ear. This image shows the malleus and its relationship to the tympanic membrane. *EAC*, external auditory canal; *TM*, tympanic membrane; *carotid a.*, carotid artery. **B**, Section just posterior to **A** shows cranial nerve VII within both the internal auditory canal and the tympanic segment passing along the medial wall of the middle ear. The cochlear nerve can be seen entering its aperture into the cochlea. *ISJ*, incudostapedial joint; *SSCC*, superior semicircular canal. This section shows the incus and stapes well. **C**, Slightly posterior to **B**. There is good demonstration of the stapes and the incudostapedial joint. Cranial nerve seven (VII_2) passes just beneath the lateral semicircular canal (*LSCC*). The important relationship with the seventh nerve just above the stapes is clearly demonstrated. The posterior crux of the stapes can be curved or C-shaped in cross section, giving its appearance in this section. Note the nerves in the internal auditory canal above and below the falciform crest. **D**, Section slightly posterior to **C**. This section has removed the anterior crux of the stapes to show the characteristic shape of the posterior crux. This image shows the stapedius tendon extending from the pyramidal process to the superstructure of the stapes. **E**, Section slightly posterior to **D** through the level of the round window niche shows the entrance into the sinus tympani. The pyramidal process and facial nerve are clearly seen.

Copyright © 2003, Mosby, Inc. All rights reserved.

VIEW IMAGE

Scout

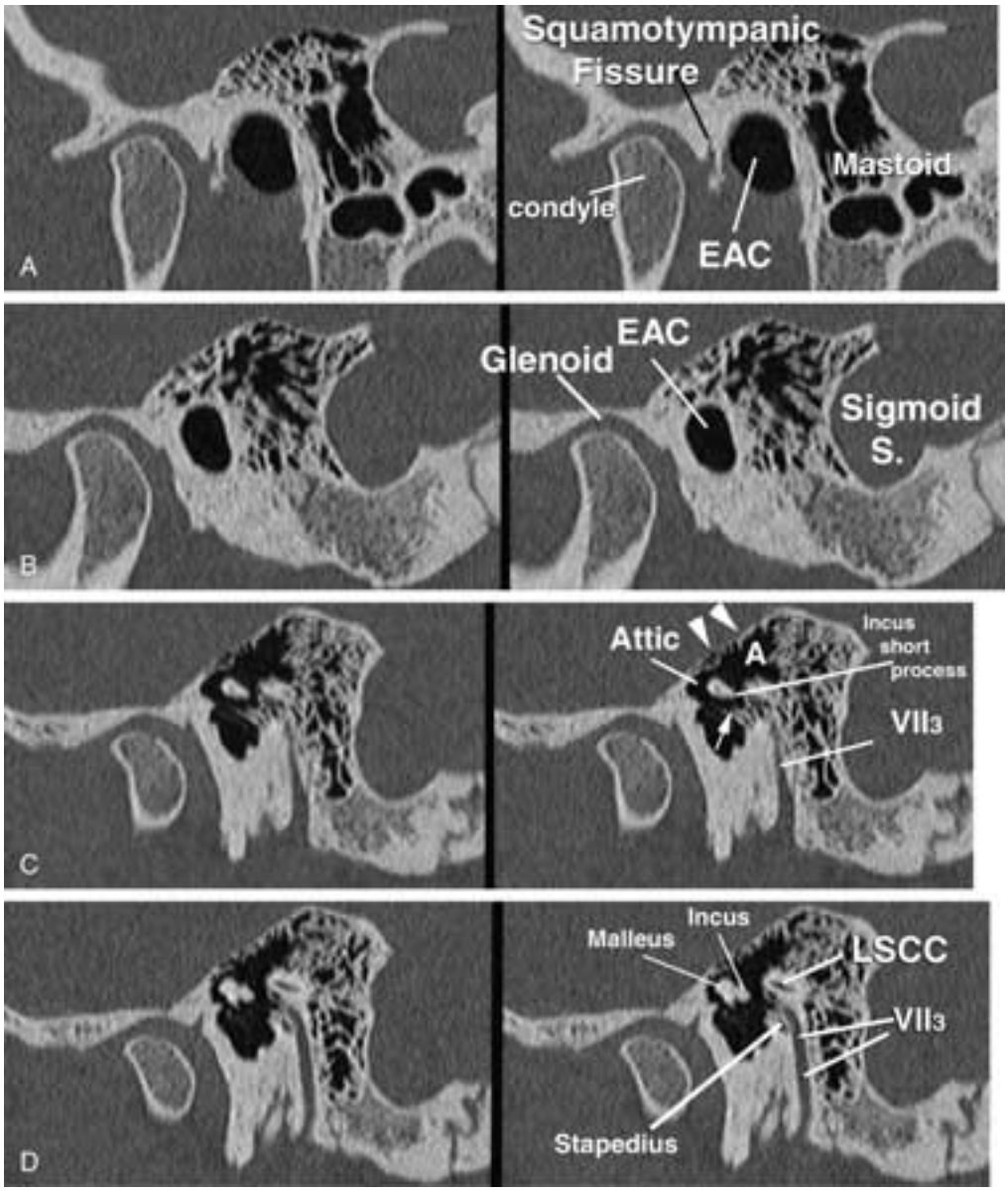

VIEW IMAGE

FIGURE 19-15 Sagittal plane images through the temporal bone. (**A-J**) The images are reformatted along the plane indicated in the inset diagram. The images are done sequentially from laterally to medially. They are taken through the left temporal bone. The external auditory canal is seen in cross section in the most lateral images (**A** and **B**), and the internal auditory canal is seen in cross section in the most medial images (**I** and **J**). The facial nerve canal mastoid (vertical) segment is seen in **D**. The stapedius muscle is seen within the pyramidal process at the same level.

Illustration continued on following page

Copyright © 2003, Mosby, Inc. All rights reserved.

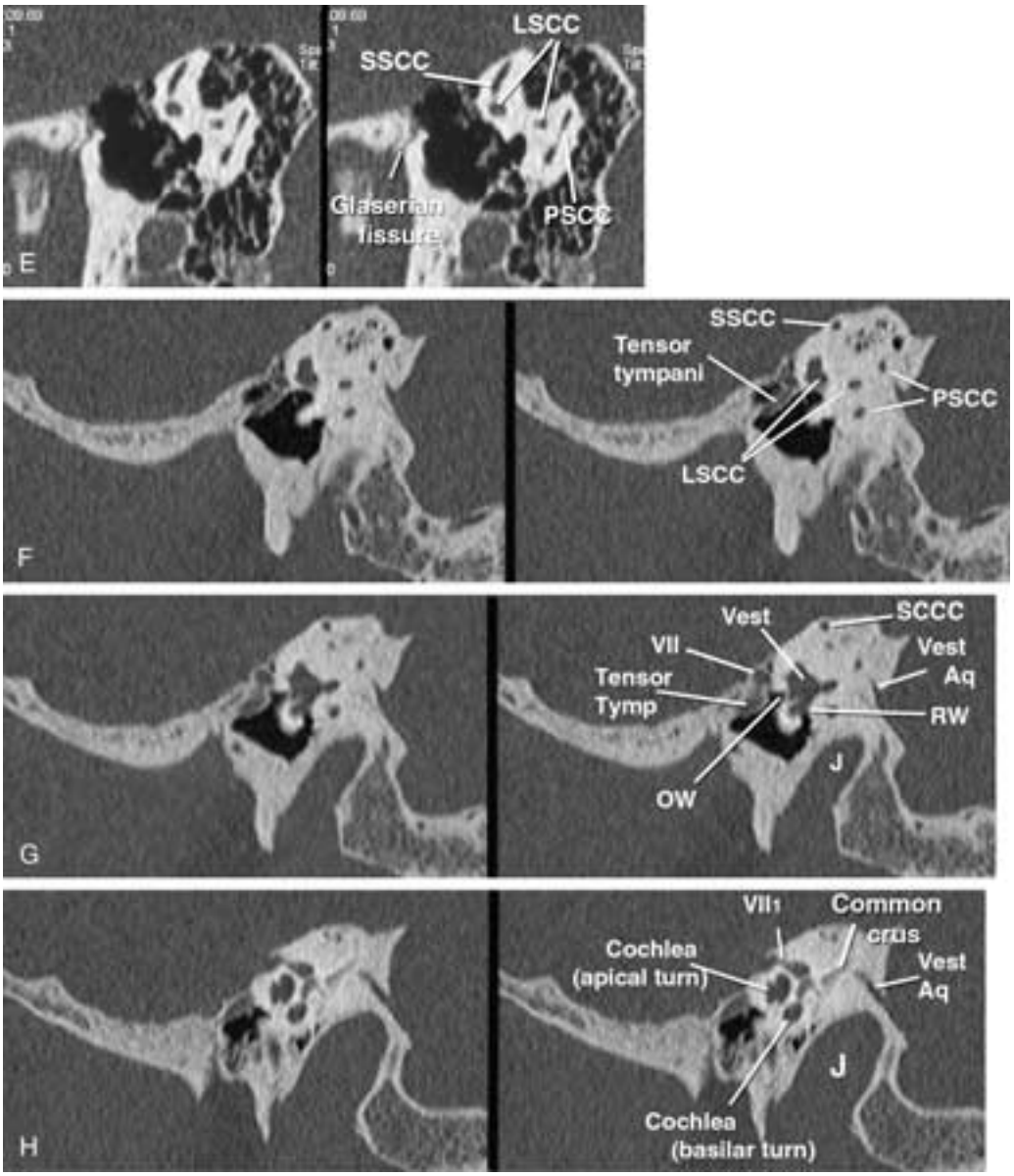

FIGURE 19-15 *Continued.* The oval and round windows are seen in **G**. The vestibular aqueduct and cochlea are seen well in section **H**. *EAC*, external auditory canal; *S*, sinus. The arrow in **C** represents the iter tympani posterior. The chorda tympani leaves from this point to traverse the middle ear. *Arrowheads*, the tegmen; *A*, antrum; *LSCC*, lateral semicircular canal; *SSCC*, superior semicircular canal; *PSCC*, posterior semicircular canal; *IAC*, internal auditory canal; *OW*, oval window; *RW*, round window; *J*, jugular vein; *Vest. aq*., vestibular aqueduct; *Vest*., vestibule; *Tensor tymp*., tensor tympani; *Crista f*., crista falciformis; VII_3, mastoid segment of facial nerve. Image **E** is slightly more magnified than the others and was taken at a slightly different angle. (Inset diagram modified from Vignaud J, Dulac GL, François J, et al: Temporal, Fosses Nasales, Cavities Accessoires, Vol. 17-1. (Fischgold H, ed. Traite de Radiodiagnostic.) Paris: Masson, 1974.)

VIEW IMAGE

Copyright © 2003, Mosby, Inc. All rights reserved.

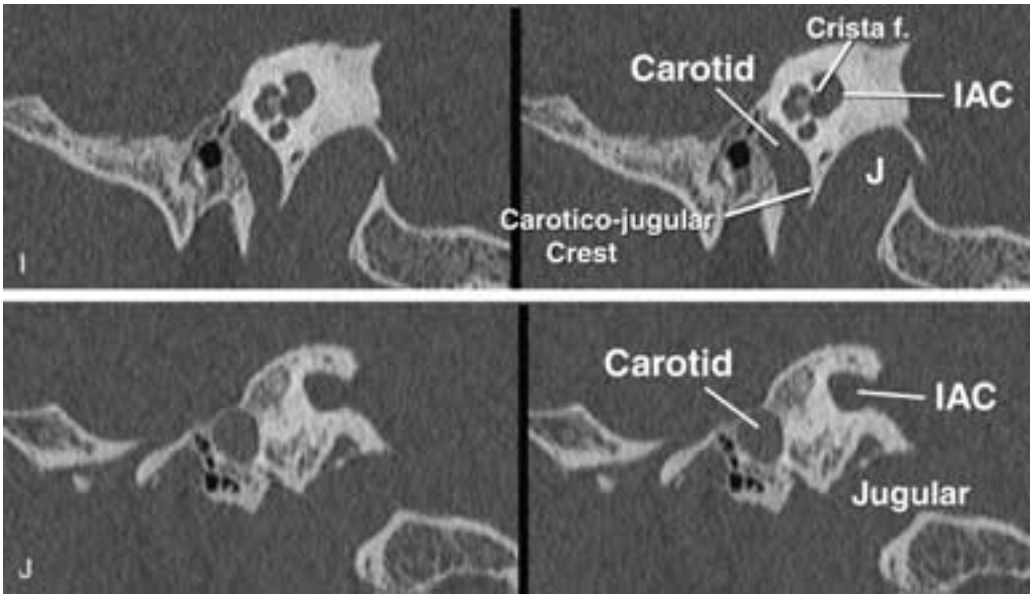

FIGURE 19-15 *Continued.* For legend see previous pages.

VIEW IMAGE

Copyright © 2003, Mosby, Inc. All rights reserved.

VIEW IMAGE

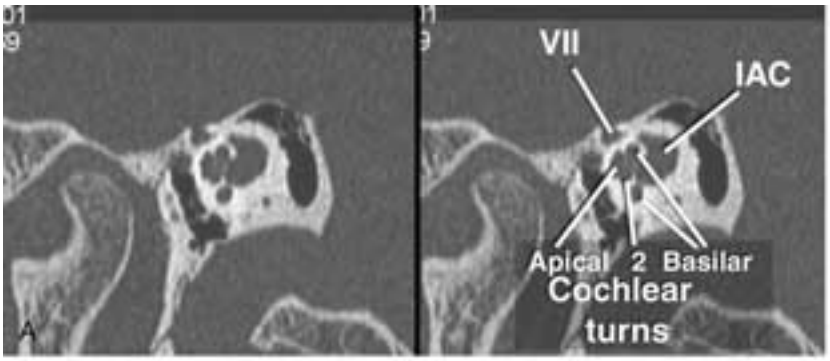

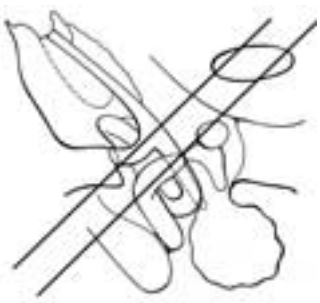

Inset

VIEW IMAGE

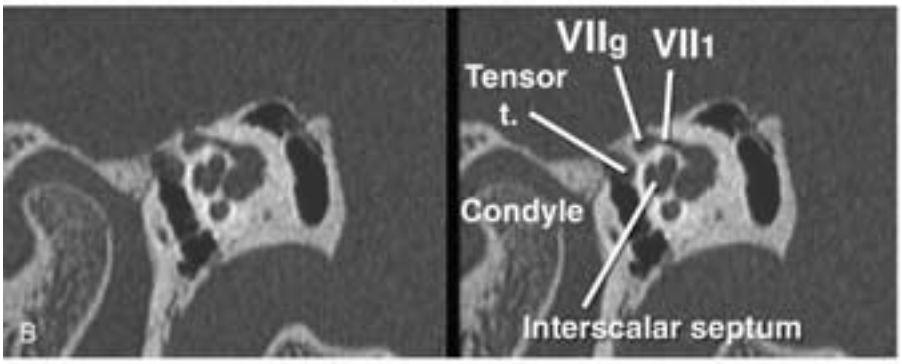

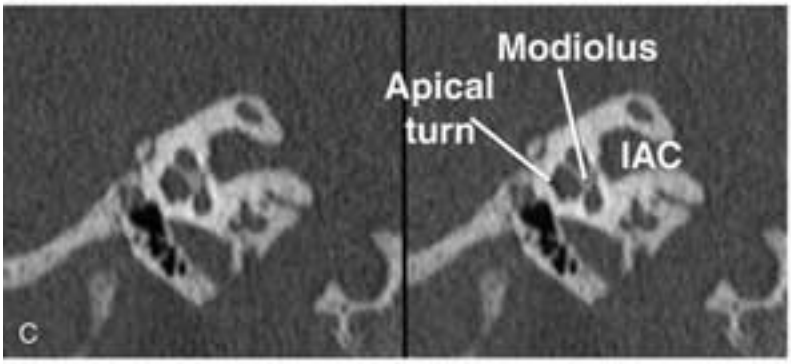

VIEW IMAGE

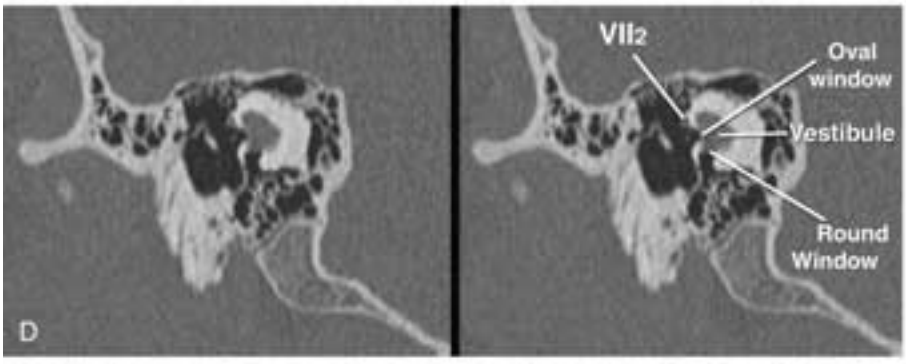

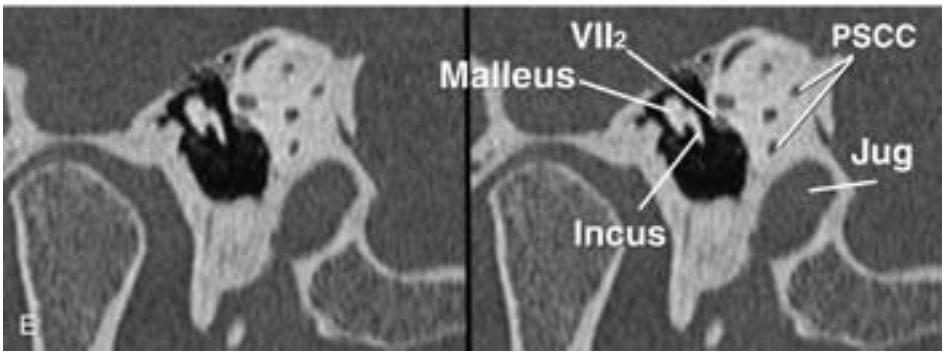

FIGURE 19-16 **A** to **G**, Poschl plane (approximately). This plane is perpendicular to the axis of the pyramid (see the lines in the inset). This plane is parallel to the plane of the axis (modiolus) of the cochlea, the plane of the superior semicircular canal and the labyrinthine segment of the facial nerve canal. This plane is perpendicular to the plane of the posterior semicircular canal and the tympanic segment of the facial nerve canal. It is also an excellent plane for visualization of the vestibular aqueduct. Note that the superior semicircular canal is seen through its entire course, and the bone separating it from the middle cranial fossa is clearly defined. This plane also gives a perfect cross section through much of the tympanic segment of the facial nerve canal (VII_2). The images are taken from anteromedially to posterolaterally. Figure **C** is at a slightly different angle than the plane of the other images relative to the axial plane. *VII*, seventh nerve; VII_1, labyrinthine segment, facial nerve; $VIII_3$, mastoid segment, facial nerve; *IAC*, internal auditory canal; VII_g: geniculate turn; *Tensor t.*, tensor tympani; *PSCC*, posterior semicircular canal; *LSCC*, lateral semicircular canal; *SSCC*, superior semicircular canal; *Jug.*, jugular vein, *Chorda t.*, chorda tympani. (Inset diagram modified from Vignaud J, Dulac GL, François J, et al: Temporal, Fosses Nasales, Cavities Accessoires, Vol. 17-1. (Fischgold H, ed. Traite de Radiodiagnostic.) Paris: Masson, 1974.)

Copyright © 2003, Mosby, Inc. All rights reserved.

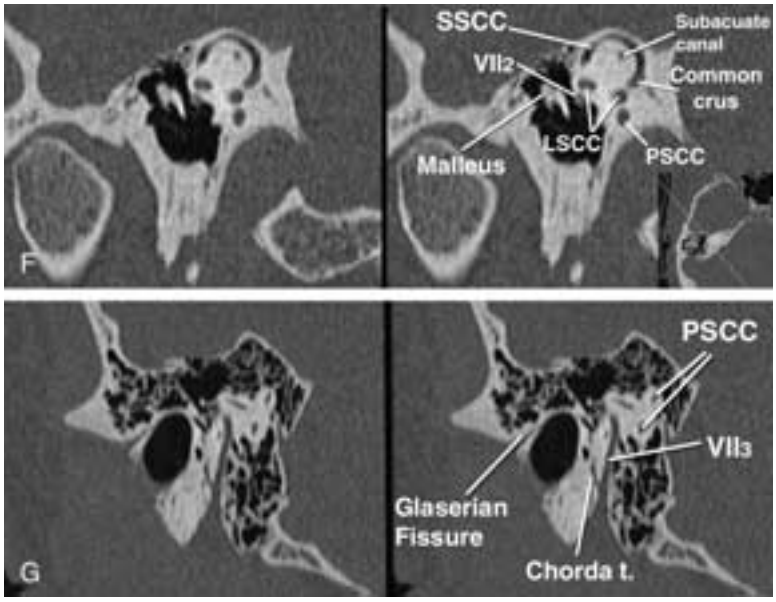

VIEW IMAGE

FIGURE 19-16 *Continued.* For legend see previous page.

Copyright © 2003, Mosby, Inc. All rights reserved.

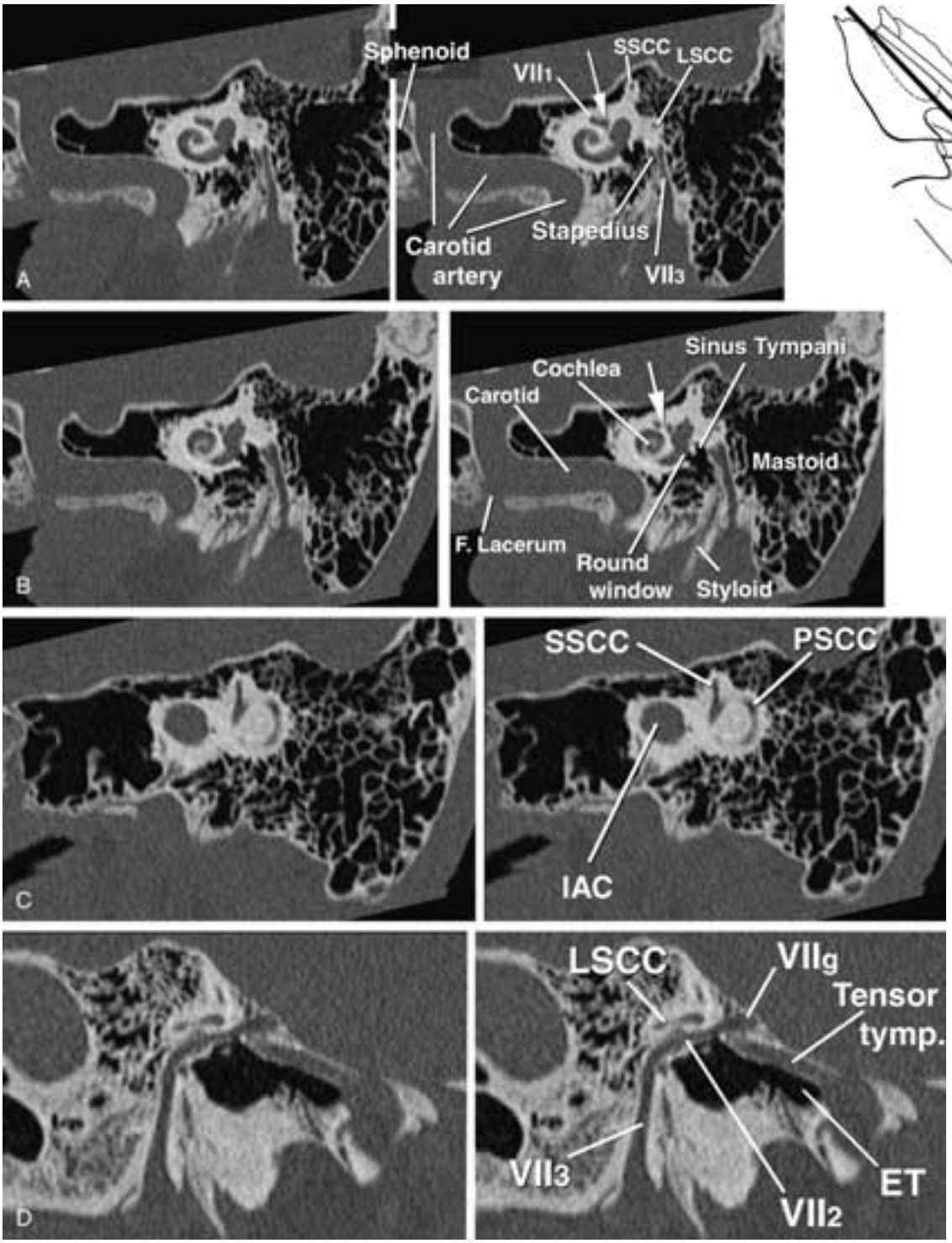

VIEW IMAGE

VIEW IMAGE

FIGURE 19-17 Stenvers plane (approximately). Sections along the axis of the temporal bone (petrous pyramid). **A**, **B**, and **C** are taken from the left temporal bone; **D** is taken from the right. This plane (Stenvers plane) passes along the axis of the temporal bone. It is parallel to the plane of the posterior semicircular canal and perpendicular to the plane of the superior semicircular canal. It is perpendicular to the labyrinthine segment of the facial nerve canal and parallels the tympanic segment of the facial nerve canal. Note how the superior semicircular canal is seen in cross section in **A**. **D** shows the tympanic segment of the facial nerve canal from the geniculate to the pyramidal turns and the tensor tympani in its course extending along the eustachian tube. The arrow in **A** shows the small canal for a portion of the superior vestibular nerve. The arrow in **B** indicates Bill's bar. *SSCC*, superior semicircular canal; *PSCC*, posterior semicircular canal; *LSCC*, lateral semicircular canal; *F*, foramen; *IAC*, internal auditory canal; *ET*, eustachian tube; *F. Lacerum*, VII_2—tympanic segment, facial nerve VII_3—mastoid segment, facial nerve. (Inset diagram modified from Vignaud J, Dulac GL, François J, et al: Temporal, Fosses Nasales, Cavities Accessoires, Vol. 17-1. (Fischgold H, ed. Traite de Radiodiagnostic.) Paris: Masson, 1974.)

Copyright © 2003, Mosby, Inc. All rights reserved.

REFERENCES

1. Caparosa RJ. An Atlas of Surgical Anatomy and Techniques of the Temporal Bone. Springfield, Ill, Charles C Thomas, 1972.
2. Gulya AJ, Schuknecht HF. Anatomy of the Temporal Bone with Surgical Implications, 2nd ed. New York: Parthenon, 1995.
3. Schuknecht HF, Gulya AJ. Anatomy of the Temporal Bone with Surgical Implications. Philadelphia: Lea & Febiger, 1986.
4. Swartz JD, Harnsberger HR. Imaging of the Temporal Bone, 3rd ed. New York: Thieme, 1998.
5. Valvassori GE, Buckingham RA. Tomography and Cross Sections of the Ear. Stuttgart: Thieme, 1975.
6. Vignaud J, Dulac GL, François J, et al: Temporal, Fosses Nasales, Cavites Accessoires, Vol. 17-1. (Fischgold H, ed. Traite de Radiodiagnostic.) Paris: Masson, 1974.
7. Vignaud J, Jardin C, Rosen L. The Ear, Diagnostic Imaging: CT Scanner, Tomography, and Magnetic Resonance. New York: Masson, 1986.

Copyright © 2003, Mosby, Inc. All rights reserved.

Copyright © 2003, Mosby, Inc. All rights reserved.

20

Temporal Bone: Imaging

Donald W. Chakeres and Mark A. Augustyn

COMPUTED TOMOGRAPHY: TECHNICAL CONSIDERATIONS
MR IMAGING TECHNIQUES
FOUR BASIC MR IMAGING PROTOCOLS
ROUTINE BRAIN SURVEY
HIGH-RESOLUTION T2-WEIGHTED IMAGING
HIGH-RESOLUTION T1-WEIGHTED CONTRAST IMAGES
MAGNETIC RESONANCE ANGIOGRAPHY
CONCLUSION

Temporal bone imaging is extremely challenging, as the normal anatomy includes many small but clinically important structures, and a significant abnormality in this area may be less than 1 mm in size. The wide range of tissues existing in the area must be evaluated simultaneously, making it impossible to develop a single optimal imaging technique for studying all potential pathology. One must use both computed tomography (CT) and magnetic resonance (MR) imaging techniques of the highest possible resolution to precisely characterize the bone, air spaces, and the wide variety of soft tissues present in the temporal bone region. Often it is necessary to use both CT and MR imaging for satisfactory tissue characterization and identification of pathology or confident exclusion of abnormalities. This chapter reviews CT and MR imaging techniques appropriate for evaluation of the temporal bone. A more complete atlas using multiplanar CT is provided in Chapter 19.

CT excels in the evaluation of disorders that primarily affect air spaces or cortical bone.[1–8] Although the wide differences in the density of the temporal bone structures produce excellent inherent image contrast on CT, soft-tissue characterization is much more limited than with MR imaging. Thus, with CT, the individual cranial nerves cannot be seen without the use of intrathecal cisternography, a technique no longer commonly used and currently replaced by high-resolution MR imaging. In contrast, MR imaging provides poor information about the air spaces and cortical bone but excellent soft-tissue contrast resolution. In addition, MR is more sensitive to the effects of gadolinium as a contrast agent than is CT to iodinated contrast agents. In fact, CT contrast enhancement may be difficult to visualize within the temporal bone itself due to the high density of the bone. For example, enhancement of the vestibule in inflammatory pathology is quite conspicuous on MR (since the surrounding bone is a signal void), while the same enhancement is impossible to recognize using CT. Although one may not be able to visualize the architecture of the normal bone and air spaces, MR imaging can still provide useful information about these structures in diseased states, as there is signal due to fluid or a mass where normally there should be a signal void from either cortical bone or air.

These techniques can be complementary. For example, in the case of paragangliomas, CT can best demonstrate pathologic bone destruction, while MR more clearly displays vascular invasion or intracranial extension. Fast CT imaging can be used to create postprocessed angiographic studies, but the dense bone often presents difficulties in the reconstructions. MR imaging can also be used to generate excellent angiographic information; however, routine catheter angiography remains important for vascular imaging and is still the gold standard for analyzing the most challenging vascular pathology. Catheter angiography is also used to direct interventional procedures. Catheter angiography will not be discussed in this chapter.

COMPUTED TOMOGRAPHY: TECHNICAL CONSIDERATIONS

If the goal of a temporal bone CT study is to focus on the otic capsule, cortical plates, ossicles, and the air spaces alone, such as when studying a temporal bone fracture, then high-resolution bone algorithm techniques may be adequate.[1–8] However, if it is also important to evaluate the soft tissues, as in the case of a patient with cancer of the external auditory canal (EAC), then it may be necessary to use intravenous contrast and techniques similar to those used for a brain or soft-tissue neck study. The main disadvantages of CT are poor soft-tissue definition within the bony labyrinth and internal auditory canal (IAC) and radiation exposure for the patient. Although in the past it was essential to position the patient for axial and/or coronal images (Figs. 20-1 to

Copyright © 2003, Mosby, Inc. All rights reserved.

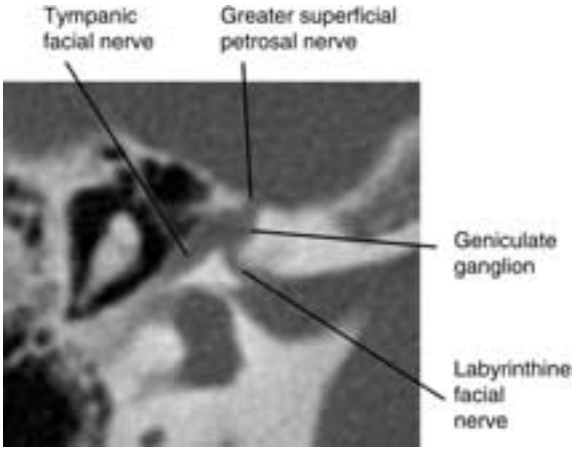

VIEW IMAGE

FIGURE 20-1 This axial CT section through the geniculate ganglion demonstrates the facial hiatus for the greater superficial petrosal nerve. The thin, bony margin between the lateral margin of the horizontal facial nerve and the middle ear is seen.

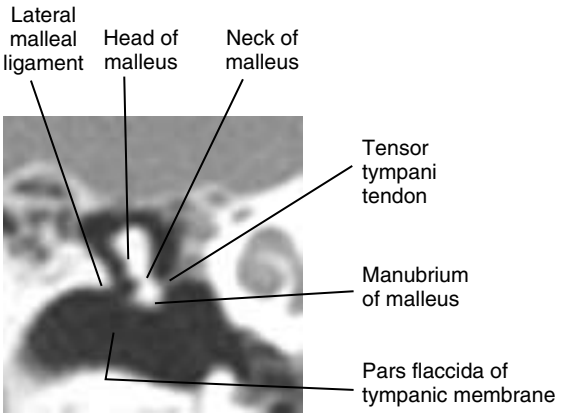

VIEW IMAGE

FIGURE 20-3 Coronal CT, malleus level. Prussak's space lies between the lateral malleal ligament and the pars flaccida of the tympanic membrane.

20-3), newer high-resolution multidetector spiral imaging systems can generate nearly isotropic voxels for multiplanar reconstructions, making the need for multiple series with direct imaging in several planes unnecessary. Postprocessing software has also improved, allowing multiplanar cross sections (Figs. 20-4 to 20-6), as well as transparent and surface volume image presentations (Figs. 20-7 to 20-12). A nearly perfect ''solid model'' of the temporal bone can be created from routine clinical CT data acquisitions.

Typically, a high-resolution matrix should be used (512 × 512), with thin sections (0.6 to 1.5 mm) and a field of view of 15 to 20 cm. CT images can be rapidly acquired, either sequentially or using a spiral technique. The exact technique, including collimation and reconstruction algorithms of spiral imaging, depends on the specifications of a particular piece of equipment. The faster the data acquisition, the less likely it is that the examination will be degraded by motion artifact. A low-mA (70 mA) technique is adequate for most of the bony structures, but higher mA (250 to 400 mA) techniques, thicker slices (3 to 5 mm), and contrast enhancement are necessary for the evaluation of the brain and other soft tissues.

CT images are usually acquired or displayed in axial and coronal planes. For axial imaging, sections are made in a plane rotated 30° superior to the anthropologic base line (the line intersecting the inferior orbital rim and the EAC). Scans produced in this plane display the temporal bone structures to good advantage.[3] This plane allows separation of the individual components of the temporal bone so that they are better visualized in their entirety, with less overlap and fewer partial volume imaging artifacts.[2] Direct coronal images are usually obtained at an angle of approximately 120° from the anthropologic baseline, while reconstruction coronal images are usually oriented 90° from the anthropologic baseline. Sagittal images can be very helpful in selected situations, and postprocessing can create multiple oblique or curved projections. For example, a plane rotated approximately 45° between the coronal and sagittal planes approximates Stenver's view and produces an image section plane parallel to the long axis of the temporal bone (see Chapter 19). Curved sections parallel to structures of interest (such as segments of the facial nerve canal) can be individually created, as can three-dimensional (3D) surface

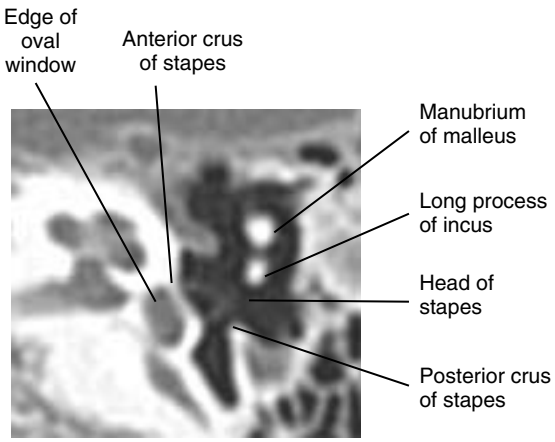

VIEW IMAGE

FIGURE 20-2 Axial CT, stapes level. The incus and malleus are seen lateral and anterior to the stapes. The annular ligament and footplate of the stapes cannot be seen due to volume averaging with the adjacent rim of the oval window.

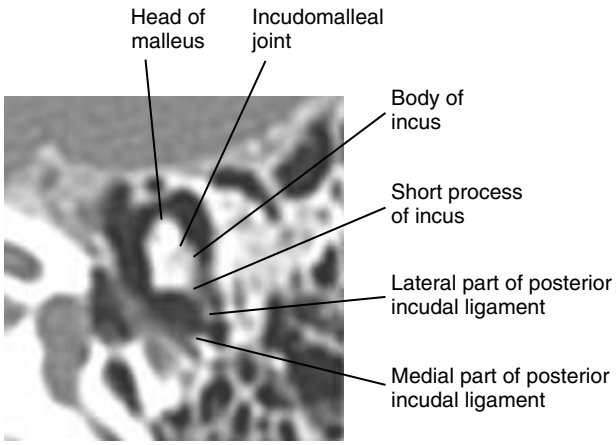

FIGURE 20-4 Axial CT, incudomalleal joint. The articulation of the malleus with the incus is seen in the epitympanum.

VIEW IMAGE

Copyright © 2003, Mosby, Inc. All rights reserved.

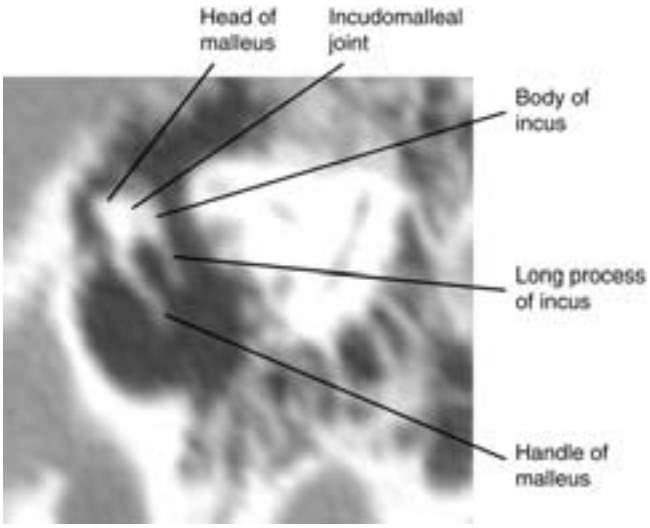

VIEW IMAGE

FIGURE 20-5 Oblique CT, incus and malleus. This view approximates the otoscopic view from the EAC.

reconstructions, allowing physical models to be created from the imaging data (Figs. 20-7 to 20-12).

MR IMAGING TECHNIQUES

The MR images in this chapter were obtained with a 1.5 Tesla General Electric Signa LX CDI Horizon imaging system. MR imaging has become the primary imaging modality for evaluation of the nonosseous components of the temporal bone region, including the major blood vessels, fluid spaces (cerebrospinal fluid, endolymph, perilymph), nerves, muscle, cartilage, brain, salivary glands, and fat (Figs. 20-13 to 20-22).[9–36] The spatial resolution currently available with MR has progressed to a point where it is comparable to and can even exceed that of CT.[12, 21]

As spatial resolution increases, the images become noisier as a result of an inherently decreased signal-to-noise ratio within any given voxel. This produces poorer-quality images when larger matrices are used, despite better spatial resolution. There are a number of strategies to deal with the potential low signal-to-noise ratio and poor image quality. Three-dimensional Fourier transform imaging (3DFT) uses radio frequency (RF) signal from an entire imaging volume during the entire acquisition rather than a single slice, thus increasing the signal-to-noise ratio. Therefore, very thin sections can be obtained for high-resolution 3DFT T1- and T2-weighted images.[9] Both gradient and spin-echo 3DFT techniques are possible.[10, 20, 22, 24, 28] If short TE times are available and the sequences are optimized, the quality of the examination using a gradient echo technique can rival or surpass spin-echo alternatives. For T1 weighting, spoiled gradient echo imaging with short TR (50 ms) and TE (4 ms), and with flip angles of 30°, generate images similar to routine spin-echo images but can also demonstrate the vessels to advantage.[36] Caution must be exercised, as high signal of vessels may be mistaken for enhancement in a tumor. For this reason, some radiologists prefer standard high-resolution, thin-slice postcontrast 2D spin-echo sequences for evaluation of the IAC. Steady-state T2-weighted gradient echo images using constructive interference techniques also have excellent quality and are not marred by increased magnetic susceptibility artifacts because of their short TE times.[11, 12, 20, 22, 29] One can also utilize a T2-weighted 3DFT gradient echo technique called SIMCAST (segment-interleaved motion-compensated acquisition in a steady state).[29] Two-dimensional Fourier transform and 3DFT T2-weighted spin-echo imaging techniques are also possible.[28] The resulting images using the gradient and spin-echo 3DFT techniques are comparable and have similar acquisition times.

The signal-to-noise ratio can be improved by using dedicated phased-array surface coils specifically designed for temporal bone imaging.[30, 31] Such phased array coils are more effective than those obtained by simply combining a series of routine coils to a single input. Each phased-array coil is composed of two or more separate but overlapping

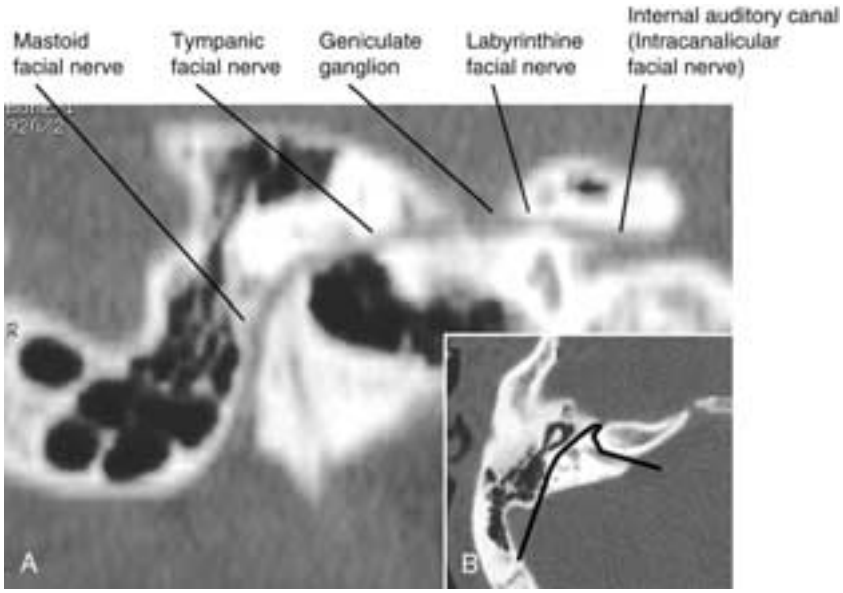

VIEW IMAGE

FIGURE 20-6 Curved coronal-sagittal CT reconstruction of the facial nerve. **A**, The facial nerve is seen from the IAC to the point where it exits the temporal bone at the stylomastoid foramen. **B**, The dark line represents the course of the curved surface in **A**.

Copyright © 2003, Mosby, Inc. All rights reserved.

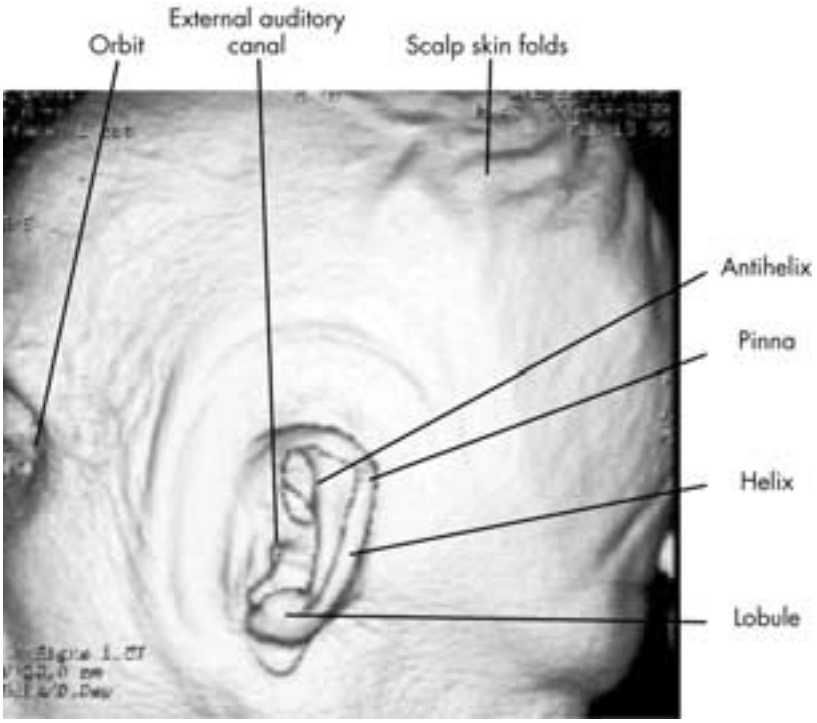

FIGURE 20-7 Surface MR imaging, reconstruction of the pinna. This is a surface volume reconstruction of an axial MR imaging 3DFT data set of 60 images. The head is viewed from laterally. The image suggests that the patient is bald, but this is due to the lack of signal from hair. Many of the details of the surface anatomy are accurately displayed. All of the deep anatomy is also available for analysis.

VIEW IMAGE

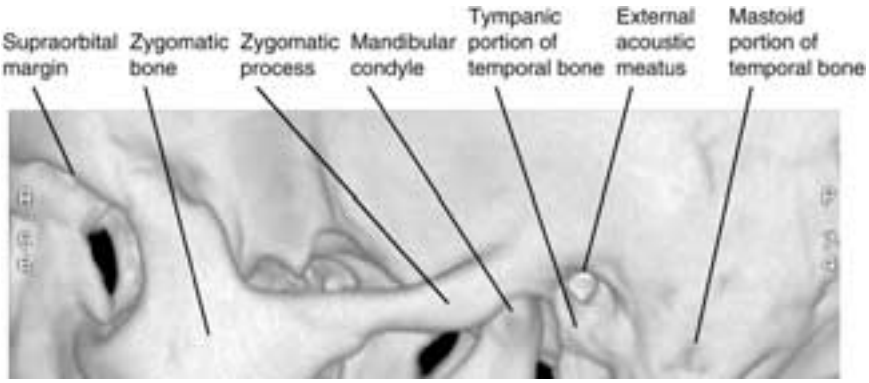

VIEW IMAGE

FIGURE 20-8 Three-dimensional CT surface reconstruction, lateral view. This surface reconstruction mimics a skull model and demonstrates the surface of the lateral mastoid; the tympanic bone, which makes up most of the EAC; the zygomatic arch; and the squamous portion of the tympanic bone (not labeled).

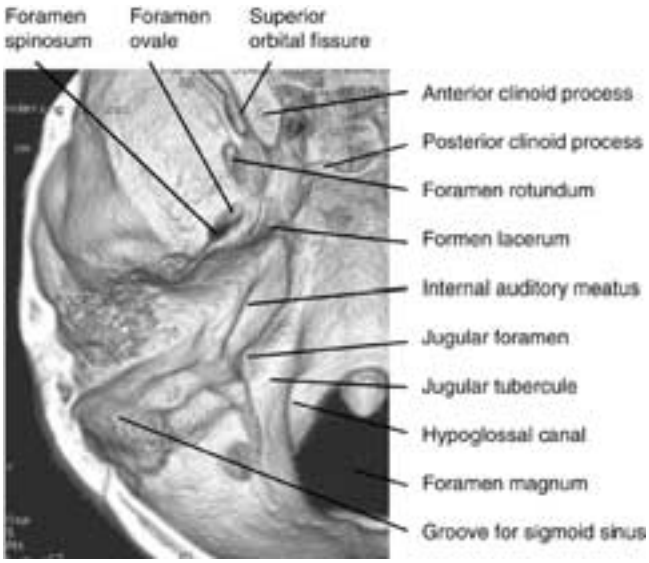

VIEW IMAGE

FIGURE 20-9 Three-dimensional CT surface reconstruction, superior view. This is a view into the posterior and middle cranial fossas from above. The temporal bone is well seen. The petrous apex is outlined by the foramen lacerum and the clivus (not labeled). The impressions for the IAC, jugular fossa, hypoglossal canal, and sigmoid sinuses are all well demonstrated.

Copyright © 2003, Mosby, Inc. All rights reserved.

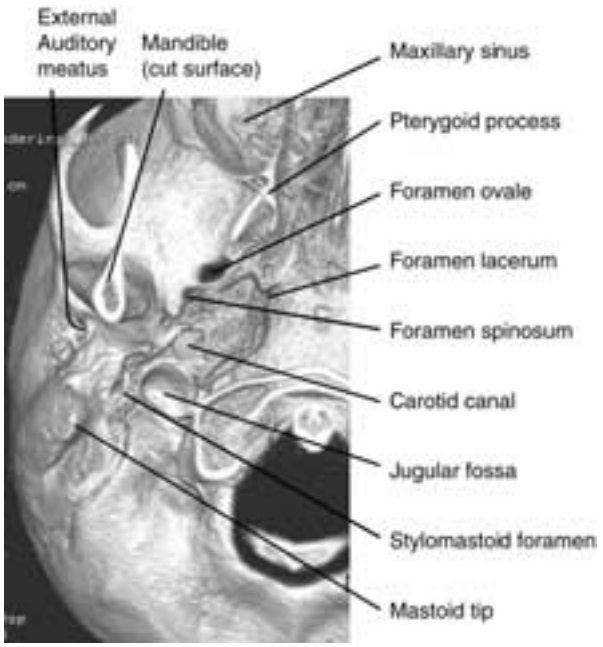

VIEW IMAGE

FIGURE 20-10 Three-dimensional CT surface reconstruction, inferior view. The oval-shaped jugular fossa is just posterior to the carotid canal. The stylomastoid foramen and the mastoid tip are lateral to the jugular fossa. The foramen spinosum and ovale are just anterior to the petrous apex (not labeled).

coil loops. Phased-array coils also allow shorter imaging times. The disadvantage of using these coils is that the images are not homogeneous in signal intensity, and the coils are more cumbersome for the technologist to position. Using surface coils to study the superficial structures can increase the signal-to-noise ratio approximately three to five times compared with that of a routine head coil.

Gradient echo imaging is more sensitive to a number of factors, including T2* signal loss from magnetic susceptibility artifacts, and magnetic susceptibility between water and air can result in a distortion of MR images somewhat similar to chemical shift artifact. These local magnetic field distortions are exaggerated with high-resolution imaging, narrow bandwidth, and high magnetic field strength. Magnetic susceptibility artifacts may be seen as regions of high and low signal in locations near the oval and round windows not corresponding to anatomic structures (see Fig. 20-13D).[20] Gradient echo techniques have been developed that use short TE times to specifically suppress these artifacts since they are more pronounced with increasing TE. Though spin-echo images are not immune to these artifacts, they are less sensitive. Short TE times increase the signal-to-noise ratio by diminishing the effects of T2* decay, and short TE times limit the effects of magnetic susceptibility artifacts that occur at the air-water interfaces of the oval and round windows.[22] A short TE time allows fat and water to be in phase, thus diminishing the artifacts associated with intravoxel fat-water subtraction seen with gradient-echo high-resolution imaging.[36] The ideal TE time varies with field strength.

Contrast-enhanced studies are of value in many situations.[32–36] An enhanced study can be acquired as 2DFT T1-weighted axial or coronal series of the whole brain. A 3DFT T1-weighted axial MR series can also be acquired.

FOUR BASIC MR IMAGING PROTOCOLS

Four basic MR imaging protocol techniques are used to address specific goals: whole brain/head imaging, high-resolution fluid space imaging, high-resolution T1-weighted, contrast-enhanced imaging, and MR angiography (MRA) techniques (Table 20-1). The actual sequences used vary from institution to institution and with the specific MR scanner utilized.

Some radiologists feel that the demonstration of high signal in blood vessels on T1-weighted images is helpful. Others feel that signal of the small vessels in the IAC can be confusing when looking for subtle enhancement of a small eighth nerve tumor, and they therefore prefer spin echo T1-weighted images with contrast enhancement for evaluation of sensorineural hearing loss. The lack of any high signal within the canal on this sequence is a reliable

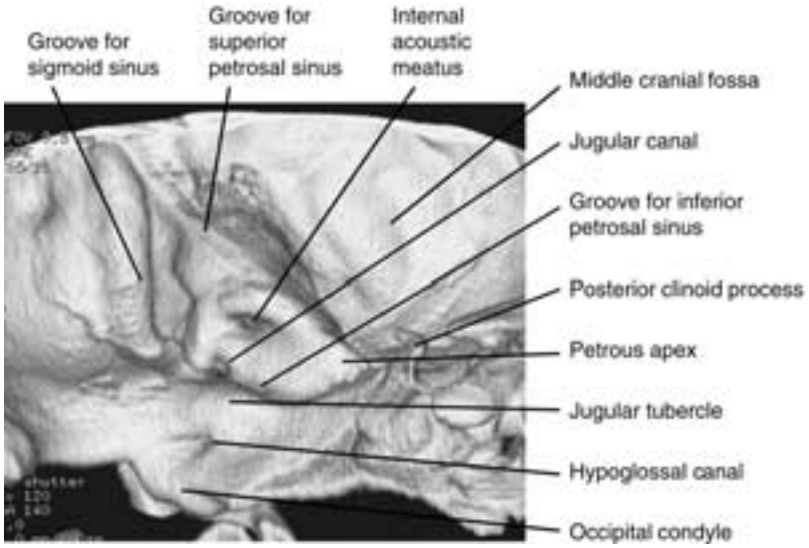

VIEW IMAGE

FIGURE 20-11 Three-dimensional CT surface reconstruction, from medially and slightly superiorly. This is a view of the medial surface of the temporal bone. The hypoglossal canal is seen interposed between the occipital condyle and the jugular tubercle. The IAC is seen in the midportion of the temporal bone. The vascular grooves for the sigmoid sinus and the superior petrosal sinus are well seen.

Copyright © 2003, Mosby, Inc. All rights reserved.

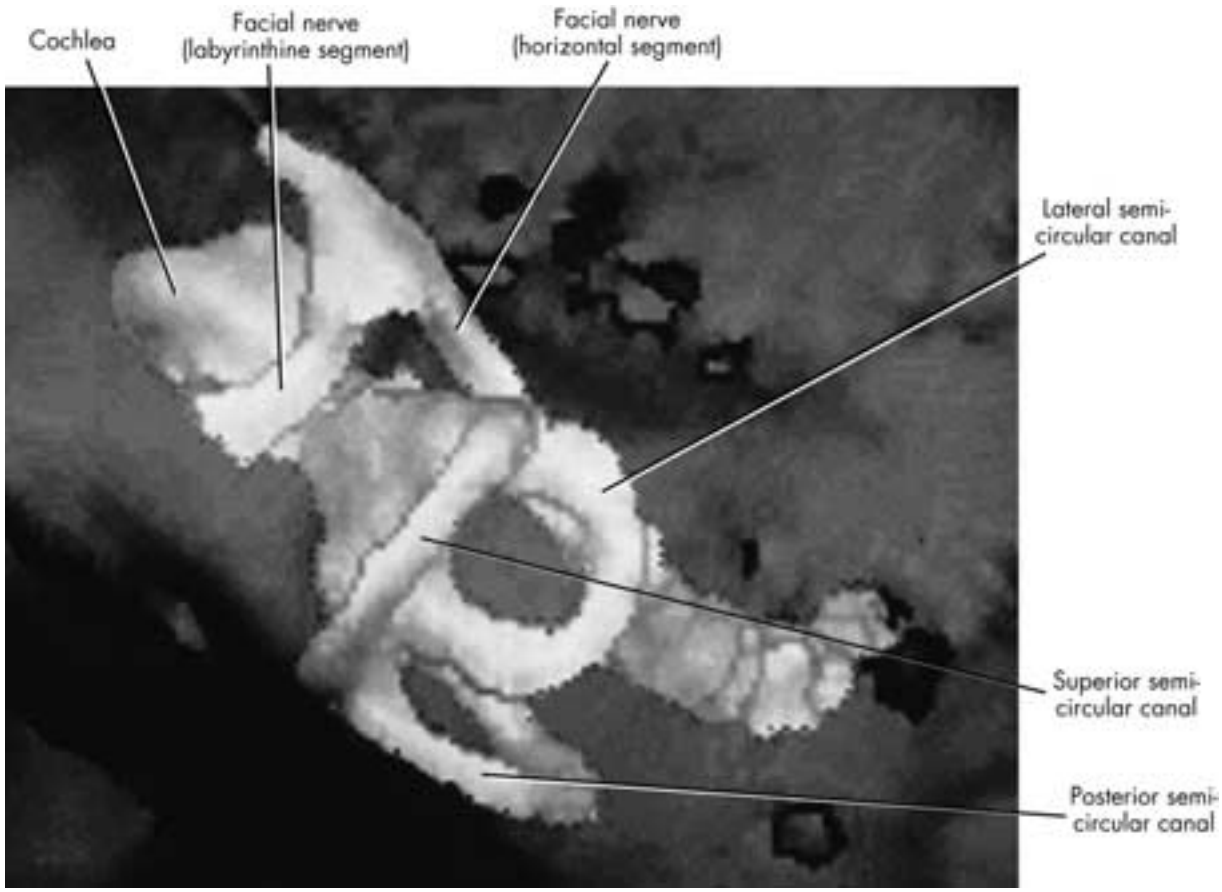

VIEW IMAGE

FIGURE 20-12 Surface reconstruction from CT data. The structures are viewed from superiorly. The geniculate ganglion region of the facial nerve is well demonstrated. Note that both CT and MR imaging data can be used for this type of image display.

indicator that no eighth nerve tumor is present. A thin section 2DFT spin-echo T1-weighted sequence is obtained in the axial plane after intravenous gadolinium administration. Typical parameters include TR of 450, TE of 15, three acquisitions, a field of view of 170 mm, and a matrix of 192 × 256. Some radiologists add fat suppression to eliminate potentially confusing high signal from the fat in the petrous apex.

ROUTINE BRAIN SURVEY

Routine head imaging is important to evaluate brain or other soft-tissue pathology. For example, a patient who presents with symptoms of dizziness could have pathology that results from brainstem demyelination or a tumor. For this reason, images of the whole brain are routinely obtained. Acquisition of a noncontrast T1-weighted sequence is of value to help characterize high-signal regions on contrast studies, since without a noncontrast examination, it may be difficult to differentiate fat or subacute hemorrhage. T1-weighted, contrast-enhanced studies are routinely acquired. In general, lower-resolution 2DFT T1-weighted images are acquired to evaluate the brain and adjacent soft-tissue structures, while fat saturation and contrast enhancement may be of value if the suspected pathology involves the fat spaces.

Low- to high-resolution axial (256 × 256 matrix, 4 to 5 mm thick) fluid-attenuated inversion recovery (FLAIR) and T2-weighted fast spin-echo (FSE) images are also used to evaluate the brain. The FLAIR images are particularly sensitive to brain pathology such as demyelination or infarcts, and they are also helpful in differentiating hemorrhage from fat.

HIGH-RESOLUTION T2-WEIGHTED IMAGING

Fluid-sensitive high-resolution images are noncontrast enhanced and demonstrate the CSF and endolymphatic spaces as high signal intensity regions. The cisternal cranial nerves can be visualized without contrast using this technique since the nerves are surrounded by the higher signal intensity fluid. Fluid in the otic capsule structures is best visualized utilizing this technique, making it possible to evaluate cochlear or vestibular pathology. This technique has been used as a screening technique to rule out vestibular schwannomas.[36]

T2-weighted high-resolution images can be acquired

Copyright © 2003, Mosby, Inc. All rights reserved.

with short TR, low flip angle gradient-echo 3DFT imaging. This is achieved by preserving rather than spoiling transverse magnetization using an appropriate selection of rephasing gradients, a short TR (20 to 30 ms) and a moderate flip angle (30° to 50°). Such images are referred to as steady-state or steady-state-free-precession images. Stationary fluid with long T2 relaxation time yields high signal intensity similar to that seen on standard T2-weighted spin-echo images. However, for fluid in motion (such as CSF in the cerebellopontine angle), the transverse magnetization is spoiled due to the motion, and the fluid gives very low signal intensity. Other differences between steady-state

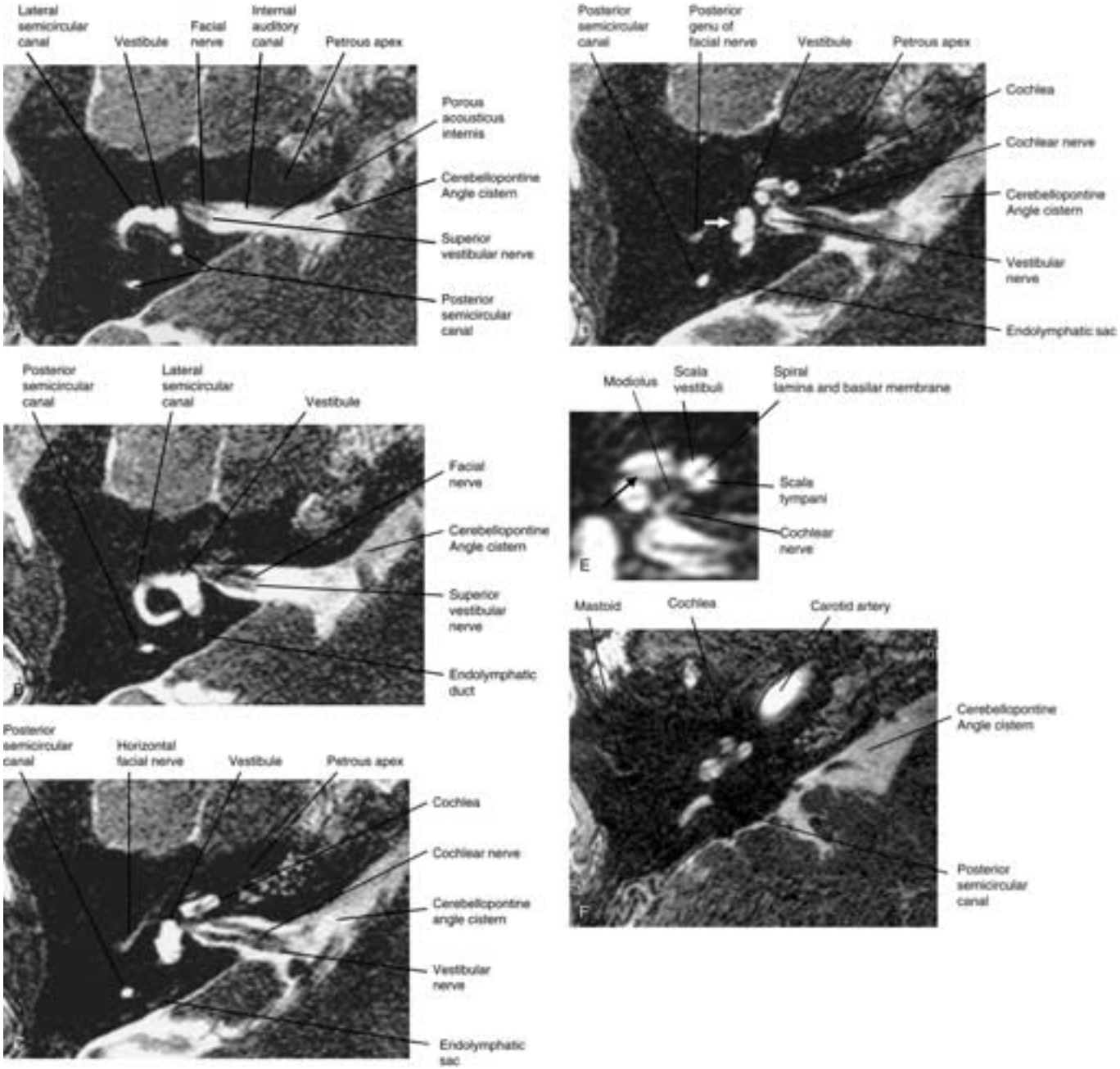

FIGURE 20-13 **A** to **F**, Axial MR imaging, IAC level. Each axial image is a gradient echo steady-state SIMCAST 0.7 mm thick, 1024 × 1024 matrix axial section of the right temporal bone. The images appear to be T2-weighted, although the origin of the contrast is more complicated. The CSF and other fluid spaces demonstrate high signal intensity. The brain is intermediate in signal intensity, and the bone and pneumatized air spaces are signal voids. The IAC contains the seventh and eighth nerves. They are seen as thin, linear low signal intensity structures in the canal. The cochlea, vestibule, and semicircular canals are well seen. This section is not made 30° from the anthropologic baseline, so the complete lateral semicircular canal is not seen. The endolymphatic sac is seen posterior and medial to the posterior semicircular canal. In **D** the apparent notch (*arrow*) in the margin of the vestibule is susceptibility artifact. **E** is a magnified view of the cochlea at approximately the same level as **D**. Note the interscalar septum (*arrow*). Compare to the image provided by CT in Figures 19-10 and 19-11.

VIEW IMAGE

Copyright © 2003, Mosby, Inc. All rights reserved.

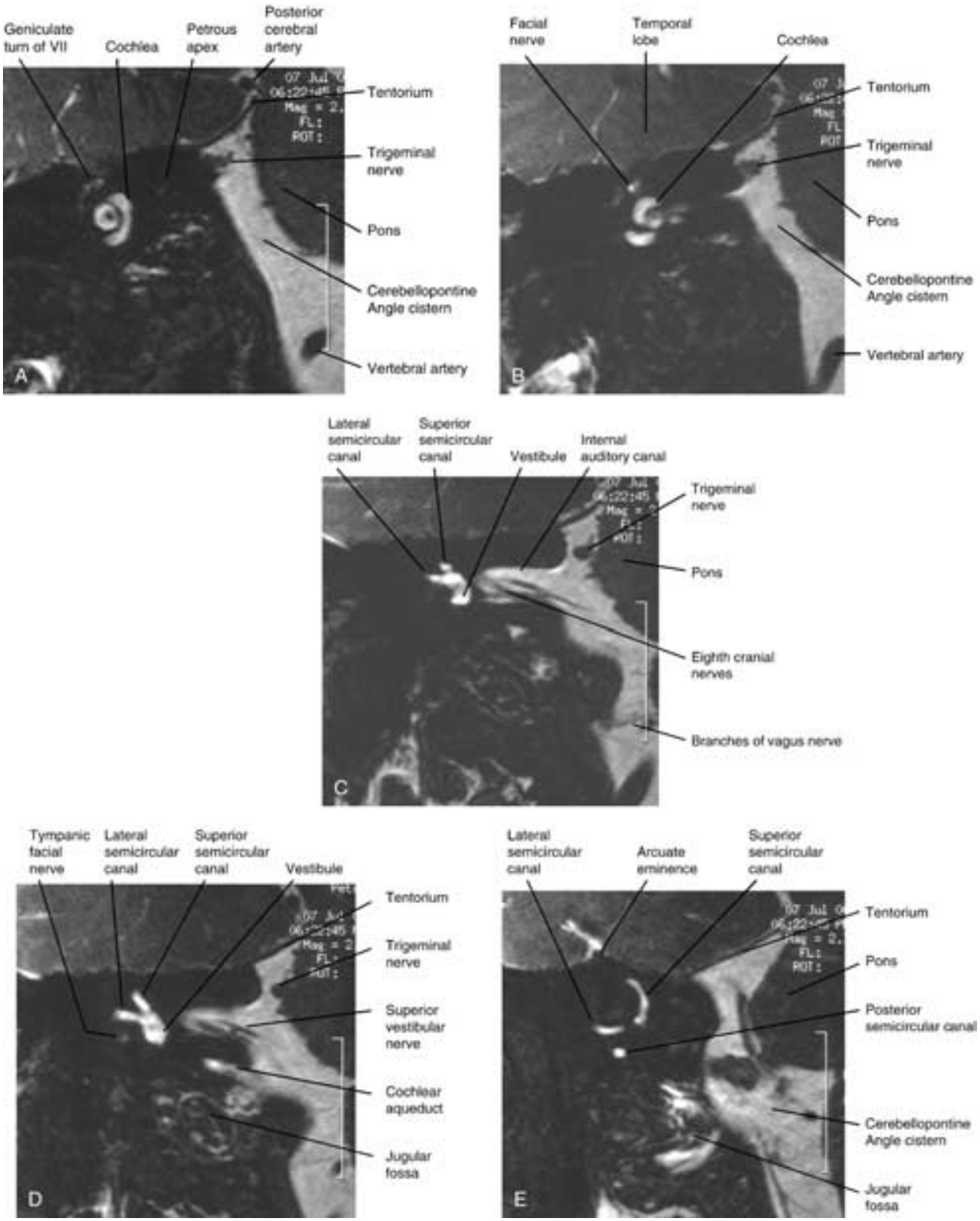

FIGURE 20-14 **A** to **E**, Coronal MR imaging from anterior to posterior. As in Figure 20-13, the fluid spaces are visualized as high signal. Nerves are seen crossing the bright signal of the CSF within the IAC.

VIEW IMAGE

Copyright © 2003, Mosby, Inc. All rights reserved.

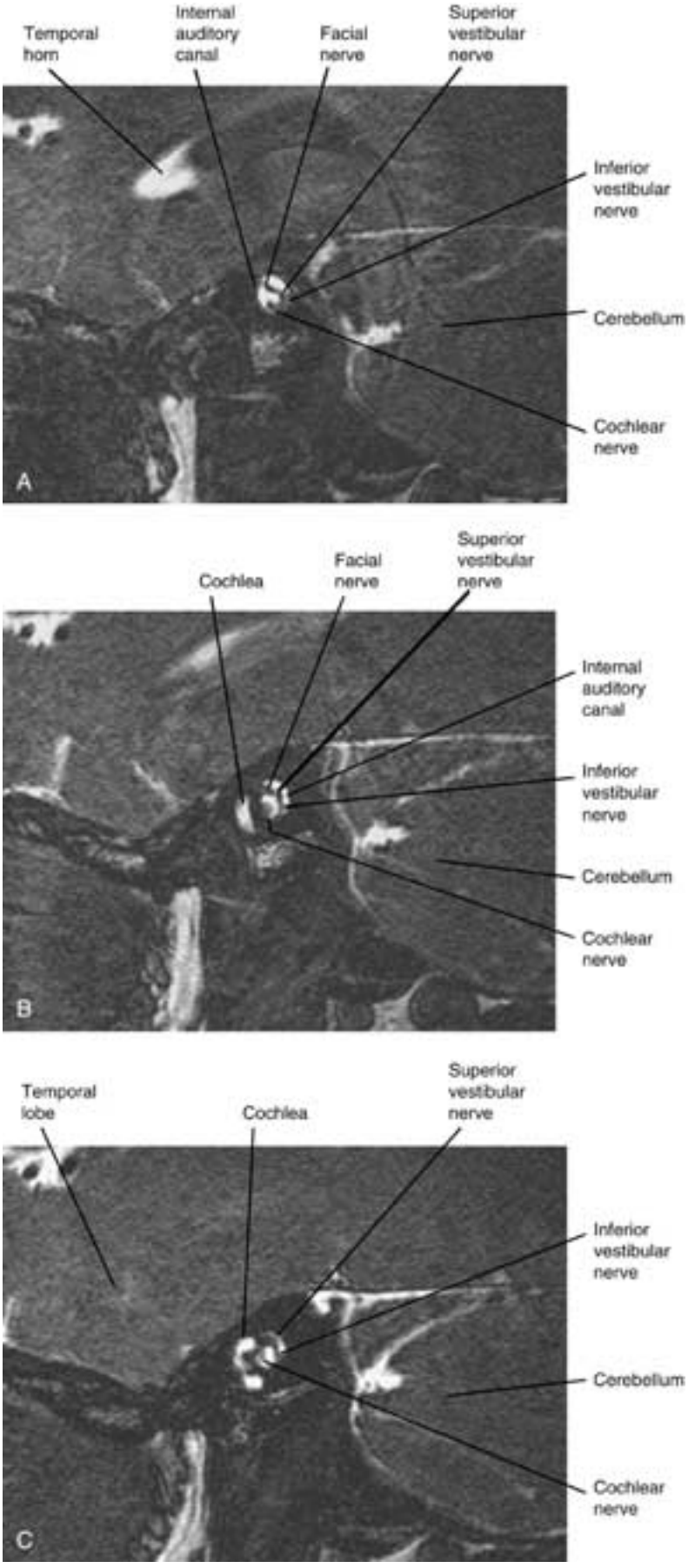

VIEW IMAGE

FIGURE 20-15 **A** to **G**, Sagittal MR imaging from medial to lateral. The facial nerve and the branches of the vestibulocochlear nerve are seen in the IAC in the medial images. The facial nerve travels in the anterior superior aspect of the canal. The cochlear nerve lies in the anterior inferior portion of the canal. The superior and inferior vestibular nerves lie in their respective portions of the posterior canal. More laterally, fluid is seen in the vestibule and the semicircular canals.

Illustration continued on following page

Copyright © 2003, Mosby, Inc. All rights reserved.

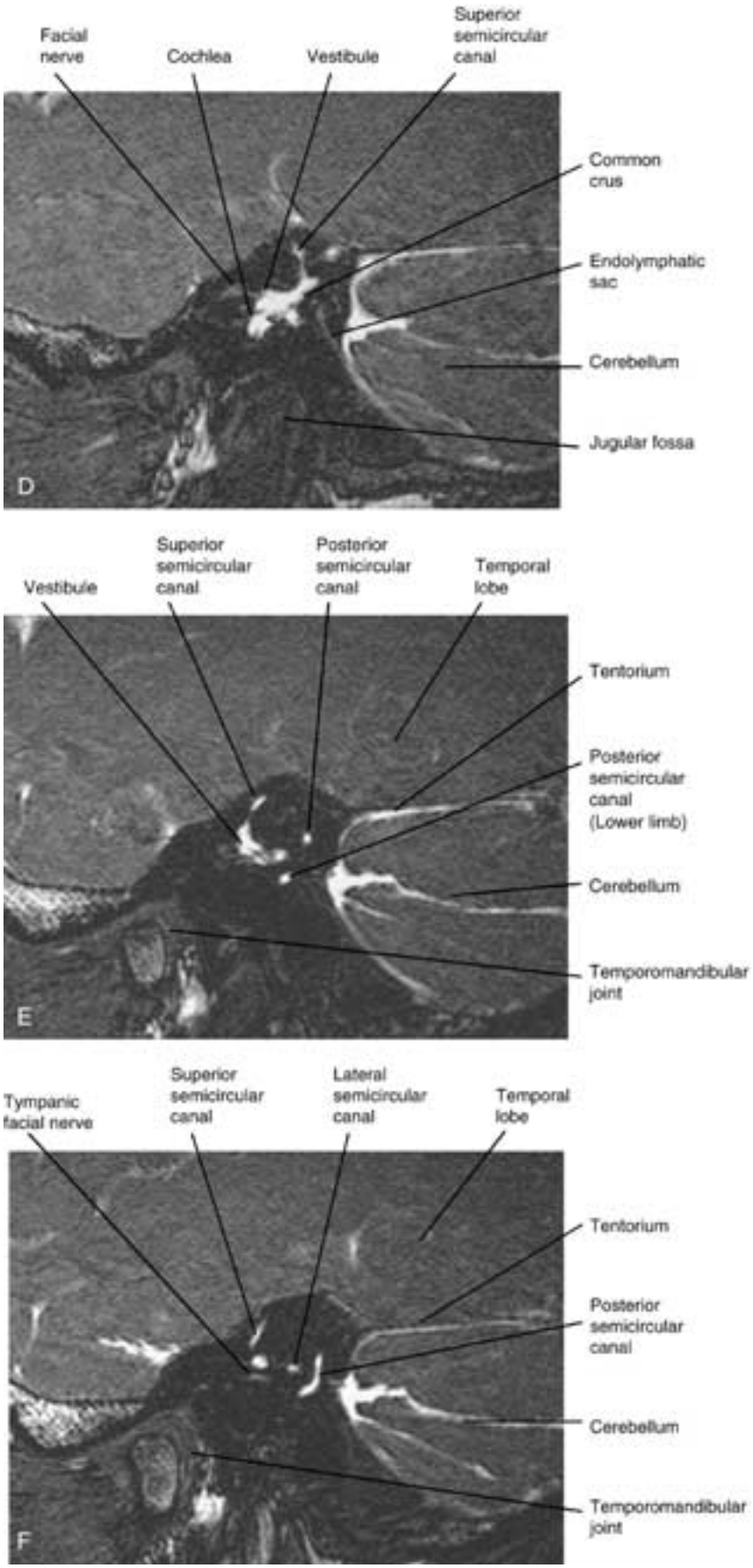

FIGURE 20-15 *Continued.* For legend see previous page.

VIEW IMAGE

Copyright © 2003, Mosby, Inc. All rights reserved.

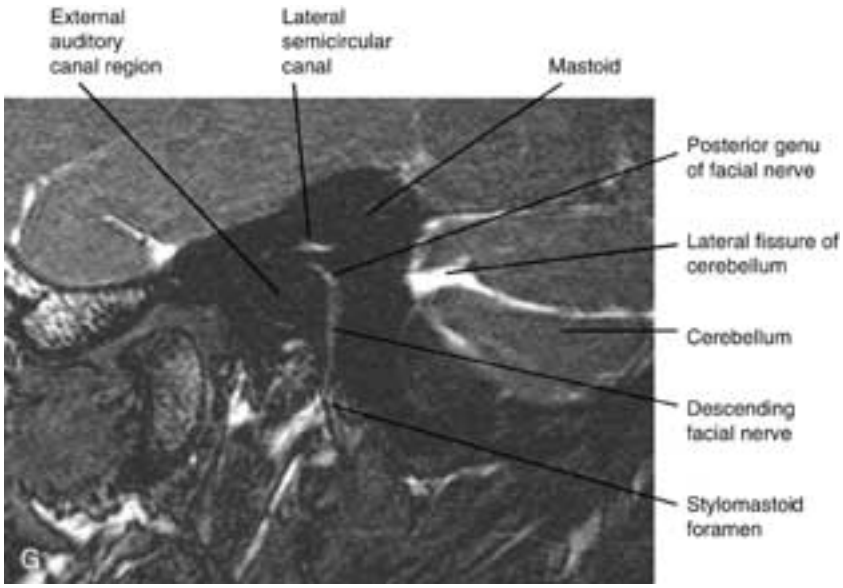

VIEW IMAGE

FIGURE 20-15 *Continued.* In **G** the facial nerve is seen as a thin line of signal. Although not fluid, there is enough signal from the soft tissue of the nerve to be contrasted against the signal void of the bone and air in the mastoid.

and standard T2-weighted spin-echo images include high signal for fatty tissue (with a short T1 relaxation time) and low signal intensity for all other tissues (gray matter, white matter, and muscle). Typical parameters of an unspoiled 3DFT axial series include 0.8 mm thick sections, a 512 × 288 matrix, 60 slices, TR of 17, TE of 4, flip angle of 30, NEX 1.[36] Postprocessing of the image data can create any specific projection or surface desired.

A common spin-echo alternative to this type of T2-weighted sequence is a 3DFT FSE technique that utilizes a TR of 5000, TE of 100, echo train of 16, matrix of 512 × 384, and a small field of view. Fat and spatial saturation pulses may be needed to suppress chemical shift and blood flow artifacts.

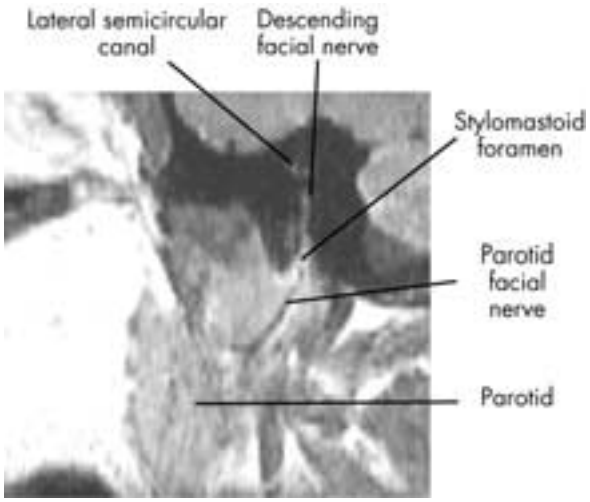

VIEW IMAGE

FIGURE 20-16 Sagittal MR imaging, descending facial nerve level. At the posterior genu, the facial nerve turns inferiorly, exiting the temporal bone through the stylomastoid foramen.

HIGH-RESOLUTION T1-WEIGHTED CONTRAST IMAGES

A high-resolution, contrast-enhanced T1-weighted technique similar to the T2-weighted studies can be acquired using a 3DFT technique to evaluate the temporal bone, but in this case the fluid spaces have low signal intensity and the nerves have higher signal intensity. This technique is also used to generate MRA images. Intravenous contrast enhancement is commonly used in conjunction with this type of technique. This sequence is ideal for identification of subtle changes, like those seen with vestibulitis or small vestibular tumors. T1-weighted gradient-echo images can be acquired by using a moderate TR (30 to 50 ms) and flip angle (30° to 50°) and by spoiling (destroying residual transverse magnetization). Spoiling is achieved by using spoiler gradients or, more efficiently, by utilizing RF spoiling (i.e., by randomizing the RF excitation pulse phase). Spoiling is needed to eliminate T2 contrast components from the acquired signal, thus yielding T1-weighted images that can be used to increase the visualization of the gray-white matter interfaces and create other section planes using postprocessing of the volume data sets. Routine spin-echo T1-weighted images can be utilized, but the resolution is significantly lower.

As vessels can be bright with 3D gradient echo sequences, some radiologists prefer the standard 2DFT FSE sequences. Although the images are slightly thicker, the in-plane resolution is high and the images depict the anatomy very well. Flow-related signal is less likely to be confused with subtle enhancement.

MAGNETIC RESONANCE ANGIOGRAPHY

Finally, a dedicated MRA acquisition may be of value in specific instances (Figs. 20-21 and 20-22). Different

Copyright © 2003, Mosby, Inc. All rights reserved.

VIEW IMAGE

FIGURE 20-17 Curved MR imaging reconstruction of the facial nerve. **A**, Axial T1-weighted image of the left parotid region from a 60 image 3DFT data set. The curved white line represents the course of a curved reconstruction following the facial nerve from the brainstem into the parotid. Note the geniculate ganglion bend. **B**, Curved surface reconstruction. Note that the facial nerve can be followed in continuity from the brainstem into the parotid. The internal auditory canal (*IAC*) demonstrates high signal intensity because these are not spoiled images. Therefore, the stationary CSF in the IAC generates a high signal. This novel presentation simplifies the interpretation because the nerve is visible over a long segment.

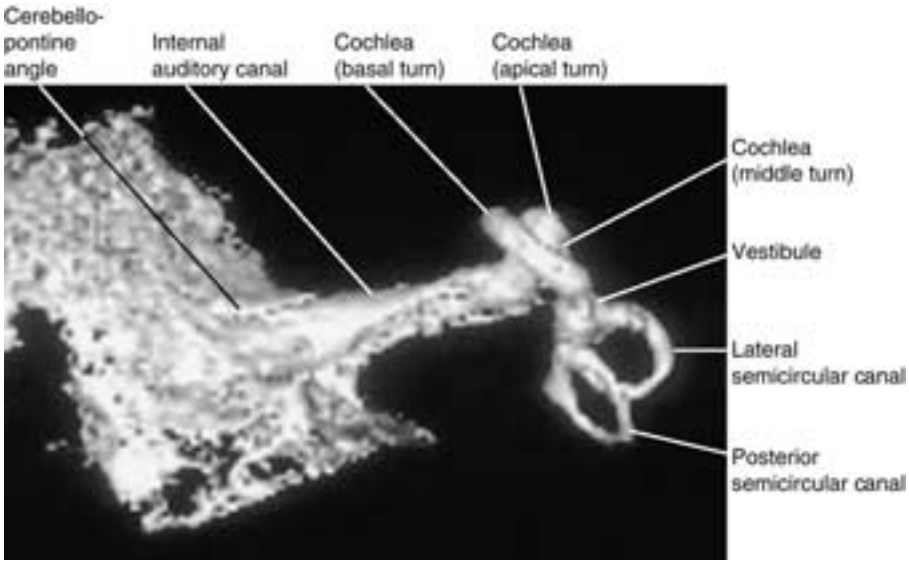

FIGURE 20-18 Three-dimensional reconstruction of MR imaging data. The data set is a 3D volume acquisition. The thresholds are set to include the fluid of the IAC and labyrinth.

VIEW IMAGE

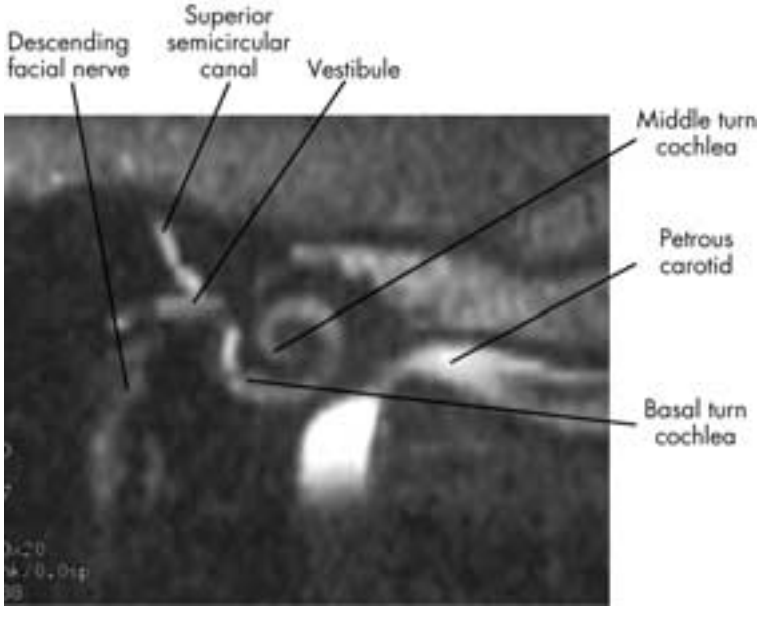

VIEW IMAGE

FIGURE 20-19 Oblique MR imaging of the cochlea. This is an oblique MR imaging reconstruction of the right temporal bone. The original data set was a 60 slice free precession high-resolution series. The section plane is obliqued to parallel the long axis of the temporal bone. The plane is a steep sagittal section intersecting the descending facial nerve posteriorly and the carotid canal anteriorly. A long segment of the cochlear spiral is seen, with the appearance of a spring.

Copyright © 2003, Mosby, Inc. All rights reserved.

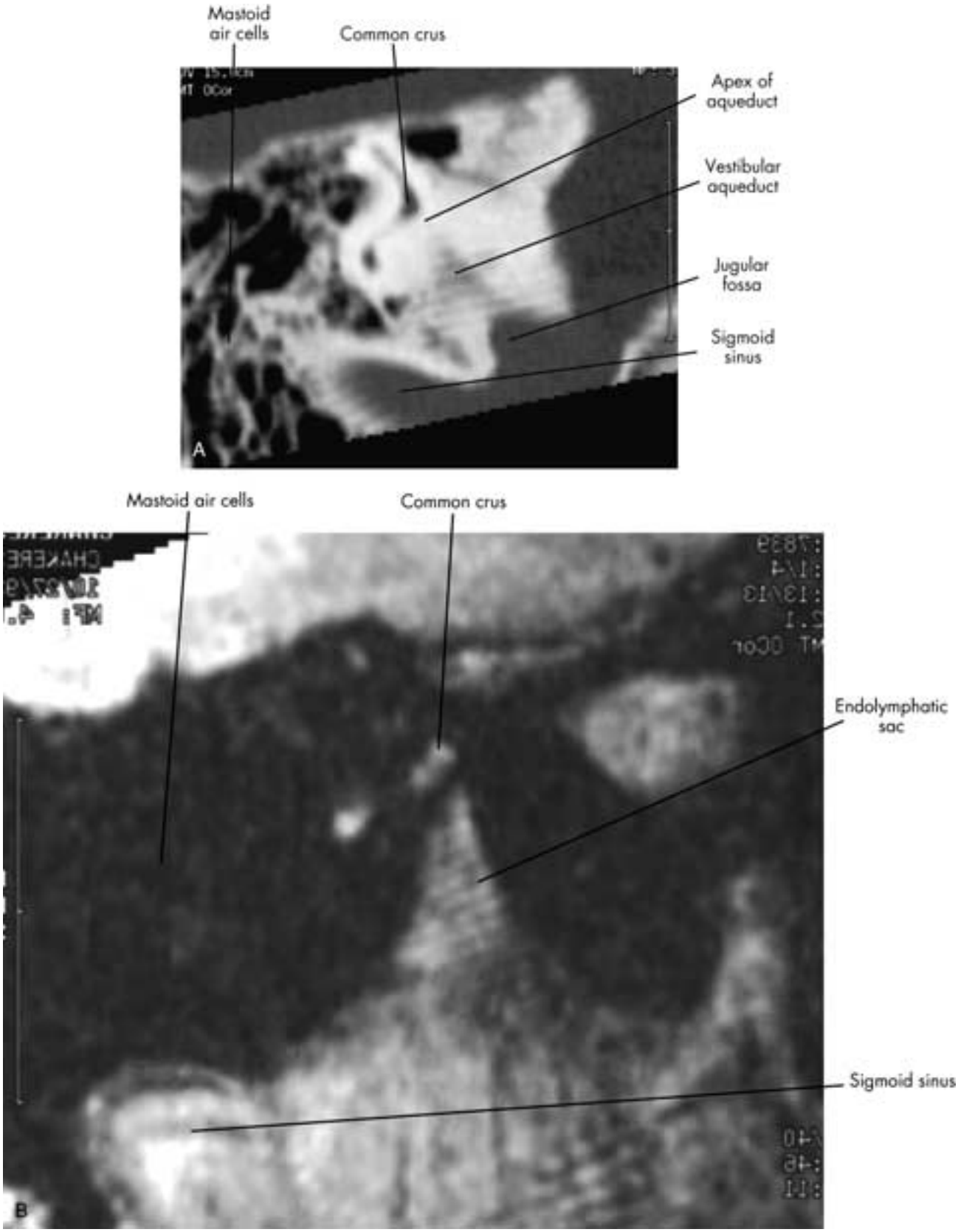

FIGURE 20-20 Double oblique MR imaging and CT, endolymphatic sac. **A**, Reconstruction of axial CT images. This is a double oblique section completely paralleling the flat plane of the endolymphatic sac. The sac is triangular in shape, similar to a Christmas tree, with the apex pointing at the common crus. The base of the sac broadens inferiorly. **B**, The identical projection on a different patient generated from 60 free precession 3DFT MR image series. This type of presentation of the endolymphatic sac is easier to analyze than the multiple short segments seen on routine imaging.

VIEW IMAGE

Copyright © 2003, Mosby, Inc. All rights reserved.

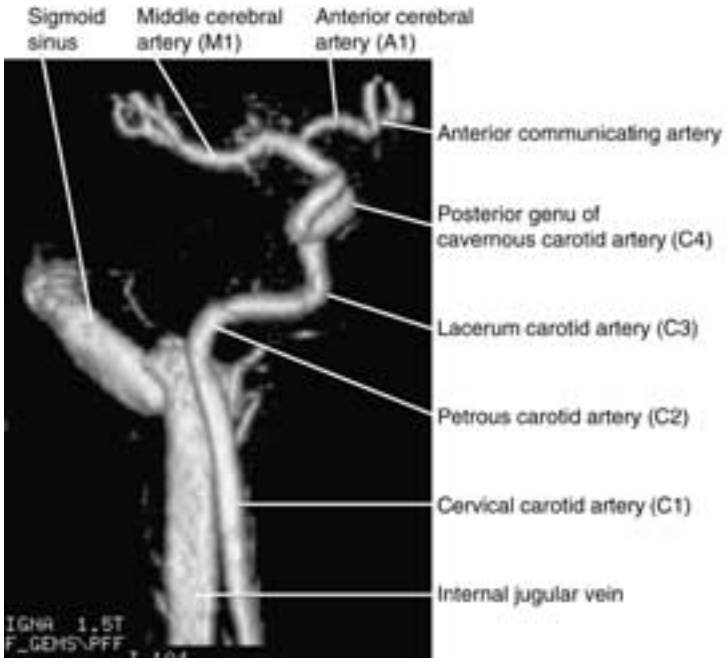

FIGURE 20-21 Two-dimensional time-of-flight MR image. Anterior surface reconstruction MRA. This is a surface reconstruction of a 2D MR angiogram acquisition obtained without any saturation pulses or contrast enhancment. It allows visualization of both the arterial and venous systems. The carotid and jugular vessels in the neck are parallel to each other. As they enter the temporal bone, they separate, with the carotid artery turning medially and the jugular vein laterally. The carotid is anterior to the jugular system.

VIEW IMAGE

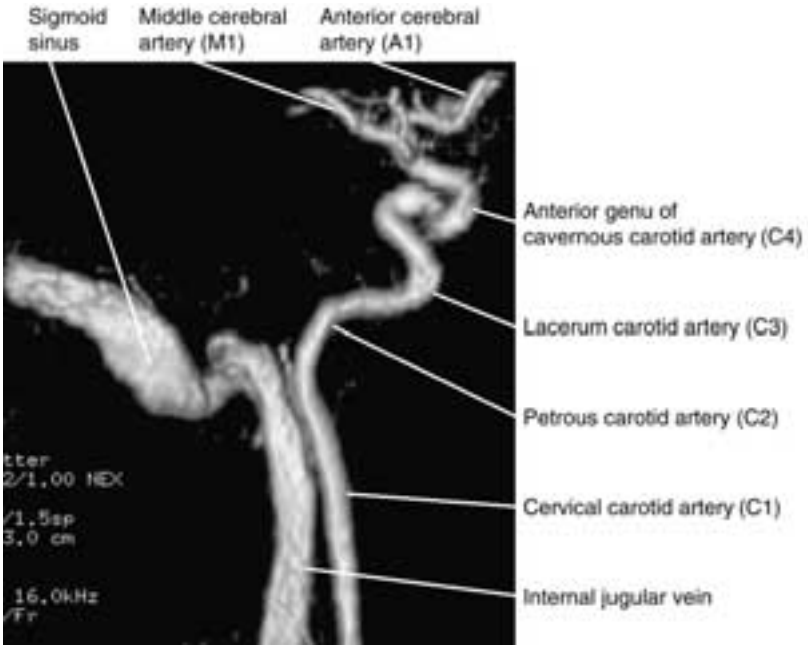

VIEW IMAGE

FIGURE 20-22 Two-dimensional time-of-flight MR imaging, lateral projection. The perspective is from the medial to lateral. The diverging carotid artery and jugular vein are well demonstrated. The jugular vein turns enter the sigmoid sinus.

Table 20-1
MR IMAGING PROTOCOLS

Sequence	Plane	TR	TE	NEX/Echoes	Matrix	Flip Angle
T2 FSE C–	Axial	5000	100	1/16	384 × 256	90/180
T1 SE C–	Coronal	500	12	1/1	384 × 256	90/180
3DFT-GE T2 C–	Axial	30	4	1/1	512 × 256	30
3DFT-FSE T2 C–	Axial	5000	100	1/16	512 × 384	90/180
3D GE T1 C+	Axial	17	4.2	1/1	512 × 288	30
3DFT-MRA C–	Axial	48	7	1/1	512 × 192	20
2DFT-MRV C–	Axial	26	7	1/1	256 × 192	60

Copyright © 2003, Mosby, Inc. All rights reserved.

techniques must be utilized for visualization of arterial versus venous anatomy. For arterial studies, 3DFT sequences generate the best detail and are usually not acquired with contrast enhancement. The 3DFT T1-weighted high-resolution technique previously described can be used as an excellent MRA technique as well. MRA sequences are designed to minimize stationary tissue signal by using a TE for which fat and water are out of phase or by using magnetization transfer. Flow compensation decreases signal from the moving CSF and thereby increases the contrast-to-noise-ratio between the blood vessels and the CSF in MRA; therefore, the soft-tissue detail may be poor. Although current MRA can provide high-quality images, they cannot substitute for traditional catheter angiography in many cases.

Venous anatomy must be studied using a different technique since the venous structures are much more sensitive to saturation because of slower flow rates. For venous anatomy, a technique employing a series of contiguous 2DFT coronal or axial images without saturation pulses is commonly used. Both the arteries and veins are seen, but there is usually little confusion. Common parameters include a TR of 26, a TE of 7, a flip angle of 60°, a matrix 256 × 192, no spatial saturation pulses, and a field of view of 24 cm. If saturation pulses are used, there is potential for demonstration of an artificial ''thrombosis,'' caused by low signal intensity resulting from saturation of inflowing spins. This is a *time of flight* technique, so coronal and axial images have different advantages to avoid saturation effects. Postprocessing of these volume data sets can be used to create detailed 3D projections in different planes and perspectives.

CONCLUSION

Temporal bone imaging remains at the forefront of the development of high-resolution imaging techniques of the body. The improved detection and understanding of temporal bone pathology provided by modern imaging methods allows for a very precise assessment of most pathologic entities. A thorough understanding of the anatomy is very important in correctly assessing pathology. The myriad formats in which the same anatomic region is presented continue to challenge radiologists.

REFERENCES

1. Bagger-Sjoback D, Jansson B, Friberg U, et al. Three dimensional anatomy of the human endolymphatic sac. Arch Otolaryngol Head Neck Surg 1990;116:345–349.
2. Chakeres DW. Clinical significance of partial volume averaging of the temporal bone. AJNR 1984;5:297-302.
3. Chakeres DW, Spiegel PK. A systematic method for comprehensive evaluation of the temporal bone by computed tomography. Radiology 1983;146:97–106.
4. Green JD, Marion MS, Erickson BJ, et al. Three dimensional reconstruction of the temporal bone. Laryngoscope 1990;100:1–4.
5. Jackler RK, Dillon WP. Computed tomography and magnetic resonance imaging of the inner ear. Otolaryngol Head Neck Surg 1988;99:494–504.
6. Mori K, Naito Y, Hirono Y, et al. Three dimensional computer graphics of the eustachian tube. Acta Otolaryngol 1987;8: 211–213.
7. Stahle J, Wilbrand H. The vestibular aqueduct in patients with Meniere's disease: a tomographic and clinical investigation. Acta Otolaryngol 1974;78:36–48.
8. Yamamoto E, Mizukami C, Isono M, et al. Observation of the external aperture of the vestibular aqueduct using three dimensional surface reconstruction imaging. Laryngoscope 1991;101: 480–483.
9. Brogan M, Chakeres D, Schmalbrock P. High resolution 3DFT MR imaging of the endolymphatic duct and soft tissues of the otic capsule. AJNR 1991;12:1–11.
10. Brogan M, Chakeres D. Computed tomography and magnetic resonance imaging of the normal anatomy of the temporal bone. Semin Ultrasound CT MR 1989;10:178–194.
11. Casselman CW, Kuhweide R, Dehaene I, et al. Magnetic resonance examination of the inner ear and cerebellopontine angle in patients with vertigo and/or abnormal findings at vestibular testing. Acta Otolaryngol Suppl (Stockh) 1994;513:15–27.
12. Casselman JW, Kuhweide R, Deimling M, et al. Constructive interference in steady state 3DFT MRI of the inner ear and CP angle. AJNR 1993;14:47–57.
13. Casselman JW, Kuhweide R, Ampe W, et al. Pathology of the membranous labyrinth: comparison of T1 and T2 weighted and gadolinium-enhanced spin-echo and 3DFT-CISS images. AJNR 1993;14:59–69.
14. Cohen TI, Powers SK, Williams DW III, et al. MR appearance of intracanalicular 8th nerve lipoma. AJNR 1992;13:1188–1190.
15. Henson MM, Henson OW, Gewalt SL, et al. Imaging of the cochlea by MRI. Hear Res 1994;74:75–80.
16. Jackler RK, DeLaCruz A. The large vestibular aqueduct syndrome. Laryngoscope 1989;99:1238–1242.
17. Mafee MF, Charletta D, Kumar A, et al. Large vestibular aqueduct and congenital sensorineural hearing loss. AJNR 1992;13:805–819.
18. McGhee R, Chakeres DW, Schmalbrock P, et al. The extracranial facial nerve: high resolution three dimensional Fourier transform MR imaging. AJNR 1993;14:464–472.
19. Oehler MC, Chakeres DW, Schmalbrock P. Reformatted planar ''Christmas tree'' magnetic resonance imaging appearance of the endolymphatic sac. AJNR 1995;16:1525–1528.
20. Oehler M, Schmalbrock P, Chakeres DW, et al. Magnetic susceptibility artifacts on high resolution MR of the temporal bone. AJNR 1995;16:1135–1143.
21. Schmalbrock P, Brogan M, Chakeres DW, et al. Optimization of submillimeter resolution MR imaging methods for the inner ear. J Magn Reson Imaging 1993;3:451–459.
22. Schmalbrock P, Yuan C, Chakeres DW, et al. Methods to achieve very short echo times for volume magnetic resonance angiography. Radiology 1990;175:861–865.
23. Tanioka H, Shirakawa T, Machida T, et al. Three dimensional reconstructed MR imaging of the inner ear. Radiology 1991;178: 141–144.
24. Tien R, Felsberg G. Fast spin echo high resolution MR imaging of the inner ear. AJR 1992;159:395–398.
25. Tien RD, Felsberg GJ, MacFall J. 3D MR gradient recalled echo imaging of the inner ear: comparison of FID and echo imaging. Magn Reson Imaging 1993;11:429–435.
26. Tien RD, Bernstein M, MacFall J. Pulsatile motion artifact reduction in 3D steady state free precession echo brain imaging. Magn Reson Imaging 1993;11:175–181.
27. Ying K, Schmalbrock P, Clymer BD. Echo-time reduction for submillimeter resolution imaging with a 3D phase encode time reduced acquisition method. Magn Reson Med 1995;33:82–87.
28. Schmalbrock P. Comparison of three-dimensional fast spin echo and gradient echo sequences for high-resolution temporal bone imaging, J Magn Reson Imaging 2000;12(6):814–825.
29. Kurucay S, Schmalbrock P, Chakeres DW, Keller PJ. A segment-interleaved motion-compensated acquisition in the steady state (SIMCAST) technique for high resolution imaging of the inner ear. J Magn Reson Imaging 1997;7(6):1060–1068.
30. Schmalbrock P, Pruski J, Sun L, Rao A, Monroe JW. Phased array RF coils for high-resolution MRI of the inner ear and brain stem. J Comput Assist Tomogr 1995;19(1):8–14.

Copyright © 2003, Mosby, Inc. All rights reserved.

31. Hayes H, Tsaruda J. Temporal lobes: surface MR coil phased array imaging. Radiology 1993;189:918–920.
32. Mark AS, Seltzer S. Labyrinthine enhancement on Gd MRI in sudden deafness and vertigo: correlation with audiologic and electronystagmographic studies. Ann Otol Rhinol Laryngol 1992;101: 459–464.
33. Mark AS, Seltzer S, Harnsberger HR. Sensorineural hearing loss: more than meets the eye? AJNR 1993;13:37–45.
34. Seltzer S, Mark AS. Contrast enhancement of the labyrinth on MR scans in patients with sudden hearing loss and vertigo: evidence of labyrinthine disease. AJNR 1991;12:13–16.
35. Weisman JL, Curtin HD, Hirsch BE, et al. High signal from the otic labyrinth on unenhanced MRI. AJNR 1992;13:1183–1187.
36. Schmalbrock P, Chakeres DW, Monroe JW, Saraswat A, Miles BA, Welling DB. Assessment of internal auditory canal tumors: a comparison of contrast-enhanced T1-weighted and steady-state T2-weighted gradient-echo MR imaging. AJNR 1999;20(7):1207–1213.

Copyright © 2003, Mosby, Inc. All rights reserved.

21

Temporal Bone: Congenital Anomalies

Laura V. Romo, Jan W. Casselman, and Caroline D. Robson

INTRODUCTION
ANOMALIES OF THE OUTER EAR
- Associated Middle Ear and Ossicular Abnormalities
- Other Associated Abnormalities
- Surgical Considerations

ANOMALIES OF THE MIDDLE EAR
ANOMALIES OF THE INNER EAR
- Imaging Techniques
- Membranous and Bony Labyrinthine Anomalies
  - Semicircular Canals
  - Vestibule/Utriculosaccular Structures
  - Cochlea
- Other Anomalies
  - Internal Auditory Canal and the Vestibulocochlear and Facial Nerves
  - Vestibular Aqueduct

VASCULAR ANOMALIES
- Internal Carotid and Stapedial Arteries
  - Partial Absence and Aberrant (Lateral) Course
  - Agenesis
- Jugular Vein
  - High Jugular Bulb
    - *Protruding/Dehiscent Jugular Bulb*
    - *Jugular Diverticulum*
    - *Agenesis and Stenosis*

MALFORMATIONS OF THE PETROUS BONE ASSOCIATED WITH MENINGITIS
- Perilabyrinthine Fistulas
  - Dehiscence of the Tegmen Tympani
  - Hyrtl's Fissure
  - Fissula Antefenestram
  - Giant Apical Air Cell and Apical Meningocele
  - Petromastoid Canal
  - Widened Labyrinthine Segment of the Facial Nerve Canal
- Translabyrinthine Fistulas

CONGENITAL SYNDROMES INVOLVING THE EAR

INTRODUCTION

The temporal bone develops from two separate precursors. The pars branchialis radiates from the first and second branchial arches, the first branchial groove, and the adjacent mesenchyme. The pars otica develops from the auditory vesicle and the adjacent mesenchyme. The development of the external ear and the middle ear is therefore independent of the development of the inner ear. One portion of the ear may be normal, while another portion may be grossly malformed.[1–4] Because the development of the external and middle ears is closely linked, significant malformations of the external auditory canal are usually accompanied by middle ear deformities and vice versa. Inner ear anomalies usually occur independently. However, compared to the normal population, inner ear anomalies do occur more frequently in patients with anomalies of the other compartments.

Mesenchyme is involved in the development of all portions of the ear, so there are certain situations in which combined malformations characteristically occur. The toxic embryopathy subsequent to maternal ingestion of thalidomide is an example of such a situation, and some of the otocranio-facial dysplasias show similar combined malformations (Table 21-1).

Text continued on page 1113

Revised from: Hasso, A., J. Casselman, and R. Broadwell, ''Temporal bone congenital anomalies,'' in *Head and Neck Imaging*, P. Som and H. Curtin, editors. 1996, Mosby: St. Louis, pp. 1351–1390.

Copyright © 2003, Mosby, Inc. All rights reserved.

Table 21-1
SYNDROMES WITH CONGENITAL ABNORMALITIES OF THE EAR

Syndrome	Ear Abnormalities (Outer)	Ear Abnormalities (Middle)	Ear Abnormalities (Inner)	Major Associated Anomalies
Achondroplasia (chondrodystrophia fetalis) **(Otoskeletal or AD)**	None	Ossicular fusion; dense, thick trabeculae without islands of cartilage in the enchondral bone and periosteal bone	Deformed cochlea; thickened intercochlear partitions	Dwarfism
Alagille syndrome (arteriohepatic dysplasia) **(AD)**	Large ears; incompletely folded helices	Bulky incus/stapes; immature interossicular joints	Dysplastic cochlea; partial or total absence of posterior and anterior SCCs; absence or stenosis of ICA	Intrahepatic cholestasis secondary to decreased intrahepatic ducts; peripheral pulmonary artery stenosis
Apert's syndrome (acrocephalosyndactyly) **(Otocraniofacial)**	None	Fixation of the stapes footplate	Patent cochlear aqueduct; enlarged IAC; unusually large subarcuate fossa that connects to middle fossa dura	Craniosynotosis, midface hypoplasia; exophthalmos; high palatal arch; syndactyly of hands and feet; hypertelorism; antimongoloid slant; crowded teeth
Branchio-otorenal dysplasia (Melnick-Fraser syndrome) **(Otocraniofacial or AD)**	Preauricular pits or fistulas; small ears; low-set ears; cup-shaped anteverted pinnae	Shortened manubrium of malleus or long process of incus; bulky malleus or incus; absent stapes; fixation of malleus or incus to attic; dysplasia or fixation of stapedial footplate; lateral ossicular displacement; small middle ear cavity; absent oval window or stapedial tendon; large or deep OW; hypoplastic facial nerve with dehiscent canal	Dilated vestibule; small SCCs; saccular LSCC; cochlear hypoplasia; enlarged endolymphatic duct (ELD)	Cervical fistulas or cysts; renal abnormalities; long, narrow facies; stenosis/atresia of nasolacrimal duct; retrognathia
CHARGE association (coloboma, heart anomaly, choanal atresia; retardation; and genital and ear anomalies) **(Unknown Mode of Inheritance)**	Small ears; cup-shaped lop ears; low-set short and wide, cup-shaped ears with triangular concha; small or absent ear lobes; ''snipped-off'' helical folds	Absent stapes suprastructure; foreshortened incus with missing long process; misshapen stapes footplate; absent stapedial tendon and pyramidal process, absent OW and RW	Mondini dysplasia of pars inferior; absent pars superior; short cochlea; hypoplasia of vestibular sense organs and nerves	Colobomas of eye; congenital heart anomalies (tetralogy of fallot, ASD, VSD, PDA); choanal atresia; short stature secondary to growth retardation developmental delay; mental retardation; CNS anomalies; genital hypoplasia
Chromosome 18 deletion syndrome **(Chromosomal)**	Low-set auricles, stenosis or atresia of EAC	Ossicular abnormalities	None	Hypertelorism; hypoplasia of midface; epicanthic folds; carp-shaped mouth; foot anomalies; mental retardation; congenital heart disease
Cleidocranial dyostosis **(Otocervical and AD)**	Atresia/narrowed EAC; small pinna	Marked sclerosis of mastoid; small ossicles; absent manubrium and long process of incus; fixation of stapes footplate; small tympanic cavity	Marked sclerosis of petrous bone	Large brachycephalic head; large fontanelles with wide sutures; partial or total aplasia of clavicles; spinal abnormalities; and small, poorly developed facial bones
Craniometaplyseal dysplasia (Pyle's syndrome) **(Otoskeletal and AD or AR)**	Sclerosis of canal	Enlargement of chorda tympani nerve; osseous proliferation within tympanic cavity; encasement of malleus in bone; deformed incus fixed by bone to promontory; stapes head in OW filled with bone; constriction of facial canal; obliteration of the mastoids	Constriction/sclerosis of IAC/meatus	Flask-shaped enlargement of the metaphysis of the long bones; overgrowth of the craniofacial skeleton; obliteration of the sinuses

Copyright © 2003, Mosby, Inc. All rights reserved.

Table 21-1
SYNDROMES WITH CONGENITAL ABNORMALITIES OF THE EAR *Continued*

Syndrome	Ear Abnormalities (Outer)	Ear Abnormalities (Middle)	Ear Abnormalities (Inner)	Major Associated Anomalies
Crouzon's disease (craniofacial dysostosis) **(Otocraniofacial or AD)**	Stenosis or atresia of EAC; rotated ears; low-set ears; microtia	Absent TM; distortion/narrowing of middle ear cavity; narrowing RW; narrow tympanic cavity; ossicular chain fixation via ankylosis of malleus to attic or of stapes to promontory	None	Ocular proptosis; hypertelorism; hypoplasia of the maxilla; parrot-like nose; craniosynotosis
DiGeorge syndrome **(AR)**	Malformed low-set ears; low-set pinna; atresia of EAC	Partial atresia of tympanic cavity; absent OW; absent stapedius muscle; absent or deformed ossicles; small facial nerve	High incidence of Mondini malformation; varying degrees of aplasia/dysplasia of cochlea; absent LSCC; hypoplastic seventh and eighth nerves	Congenital absence of parathyroid and thymus gland; heart and kidney abnormalities
Frontometaphyseal dysplasia (Gorlin-Holt syndrome) **(Otoskeletal)**	None	Deformed ossicles	Osseous infiltration around cochlea	Large supraorbital ridge; absent pneumatization of the frontal sinuses; micrognathia; metaphyseal splaying of the tubular bones; wide nasal bridge; flaring of the iliac wings
Goldenhar's syndrome (oculoauriculovertebral dysplasia) **(Otocervical or Multifactorial Disorder)**	Preauricular appendages; deformed auricle, atresia of canal	Severe dysplasia with narrow cavity; absent ossicles; straightened tensor tympani muscle running past an absent cochleariform process; poor development of stapedius muscle; absent chorda tympani nerve; hypoplasia OW and facial nerve	Hypoplastic cochlea and petrous ridge; short IAC with acute upward inclination; shortened LSCC and SSCC	Epibulbar dermoids; hemi- or block vertebrae; unilateral hypoplasia of maxilla/mandible; coloboma of upper lid; pharyngeal anomalies
Hemifacial microsomia **(Otocraniofacial or Multifactorial Disorder)**	Microtia; atresia/stenosis of EAC; vertically oriented EAC	Descent of tegmen; ossicles deformed or absent	None	Unilateral mandibular/maxillary hypoplasia; macrostomia; hypoplastic TMJ; hemivertebrae or hypoplasia; coloboma of upper lid
Klippel-Feil syndrome **(Otocervical or AR)**	Low-set ears; microtia; atresia/vertical orientation of EAC	Absent ossicles; thickening and fixation of stapes; bony obliteration of tympanic cavity	High incidence of Mondini malformation; range from hypoplasia of cochlea and SCCs to a simple otocyst; stenotic IAC	Short neck; fusion of two or more cervical vertebrae; low occipital hairline
Mixed deafness with perilymph gusher during stapes surgery (or X-linked progressive mixed hearing loss) **(X-Linked Recessive)**	None	Congenital fixation of stapedial footplate	Dilation of lateral part of IAC; thin osseous separation between lateral end of IAC and vestibule/basal turn of cochlea	Widening of labyrinthine facial nerve canal; abnormal cochlear size
Moebius syndrome (congenital facial diplegia) **(AR)**	Auricular malformation; microtia; slight EAC atresia	Facial canal absent, with no enlargement at geniculate ganglion; ossicular mass without identifiable stapes, OW or RW	SCC and vestibule dilated; hypoplastic cochlea, which may be a cystic cavity	Facial and abducens nerve palsies; possible additional cranial nerve involvement
Osteogenesis imperfecta (van der Hoeve's syndrome) **(Otoskeletal or AD, with Variable Expressivity and Incomplete Penetrance)**	None	Stapes abnormalities	Loss of otic capsule (changes identical to those of cochlear otosclerosis)	Deformity and bending of extremities; short stature; hyperextensibility of ligaments; dental defects; blue sclera; fine hair; thin cornea

Table continued on following page

Copyright © 2003, Mosby, Inc. All rights reserved.

Table 21-1
SYNDROMES WITH CONGENITAL ABNORMALITIES OF THE EAR *Continued*

Syndrome	Ear Abnormalities (Outer)*	Ear Abnormalities (Middle)*	Ear Abnormalities (Inner)*	Major Associated Anomalies
Osteopetrosis (Albers-Schonberg disease) **(Otoskeletal or AD, AR, or Sporadic)**	Narrowed canal	Persistent stapedial artery; fetal form of stapes; abnormal malleus/incus; sclerotic bone with narrowing of the facial canal and typanic cavity and covering of the OW and RW; obliteration of mastoid air cells	IAC narrowed	Generalized increase in bone density with narrowed neural foramina; obliterated paranasal sinuses and mastoid air cells; fractures; anemia; facial paralysis
Pendred's syndrome **(AR)**	None	None	High incidence of Mondini malformation; incompletely developed cochlea with hypoplasia; flattening of promontory	Triad of goiter, malformed inner ear vs. congenital SNHL, and pathologic perchlorate test
Pierre Robin syndrome (cleft palate, micrognathia, and glossoptosis) **(Otocraniofacial or AD)**	Cup ears; low-set ears	Thickened stapes, crura and footplate; small facial nerve; dehiscent facial canal; absent middle ear	Scala communis between apical and middle cochlear turns; small modiolus; small IAC	MR; hydrocephalus; microcephaly-microphthalmia; myopia—congenital cataracts; esotropia; retinal detachment; sixth nerve palsy; Moebius syndrome; cleft palate—hypoplastic mandible; congenital heart disease; spina bifida; syndactyly
Refsum syndrome (heredopathia atactica polyneuritiformis) **(AR)**	None	None	Cochleosaccular atrophy reported; thickening about peripheral nerves by concentrically arranged lamellae of connective tissue; no known radiographic abnormality	Hearing loss; retinitis pigmentosa; cerebellar ataxia; peripheral neuropathy; cardiac myopathy; congenital ichthyosis
Thalidomide embryopathy **(Teratogen; Iatrogenic Ototoxicity)**	Complete absence of auricle; atresia of canal	Forwardly displaced mastoid process; contracted tympanic cavity; absent, fixed, or abnormally situated ossicles	Range from saccular dilation of LSCC to severe dysplasia of the otic cystic remnant	Varying degrees of limb reduction defects; cardiac anomalies; deafness; gastrointestinal malformations; hemangiomas; cranial nerve palsies
Treacher-Collins syndrome (mandibulofacial dyostosis) **(Otocraniofacial or AD)**	Deformed, low-set auricles; varying degrees of stenosis or atresia of EAC	Deformed or absent ossicles; decreased size of middle ear cavity; underdeveloped mastoids; abnormal course of the facial nerve (usually anteriorly displaced)	Occasional abnormal vestibule with a short, wide LSCC; large CA	Antimongoloid slant of palpebral fissures; coloboma of internal third of lower lid; malar/mandibular hypoplasia; scalp hair projecting onto side of face
Trisomy 13–15 (Patau syndrome) **(Chromosomal)**	Low-set, malformed ears; stenotic EAC; small TM	Thick manubrium; distorted incudostapedial joint; deformed stapes; small facial nerve; wide angle of facial genu; absent stapedial muscle and tendon; absent pyramidal eminence; absent or small antrum; small mastoids	Distorted/shortened cochlea; absent cochlear hook; malformed apical cochlear turn; absent or underdeveloped modiolus; large/patent cochlear duct; widened LSCC; narrowed PSCC; short/straight ELD; shallow/wide IAC; scala communis between apical and middle and between middle and basal cochlear turns	Microcephaly and arrhinencephaly; multiple eye anomalies; hypertelorism, cleft lip and palate; VSD/abnormal palm print; simian creases/hyperconvex nails
Trisomy 18 syndrome (Edwards syndrome) **(Chromosomal)**	Low-set/deformed ears; atretic EAC	Deformed malleus/ incus; columella type or fetal form of stapes; split tensor tympani muscle; exposed stapedial muscle; absent stapedial tenon; hypoplastic facial nerve; abnormal course of facial and chorda tympani nerves; absent pyramidal eminence	Hypoplastic modiolus; scala communis betweem apical and middle turns; ELD increased; double singular nerve; absent lateral limb of SSCC and crista and lateral limb of LSCC	Ptosis of eyelids; high-arched palate; micrognathia; flexion deformities; hypertrophic pancreas

Copyright © 2003, Mosby, Inc. All rights reserved.

Table 21-1
SYNDROMES WITH CONGENITAL ABNORMALITIES OF THE EAR *Continued*

Syndromes	Ear Abnormalities (Outer)*	Ear Abnormalities (Middle)*	Ear Abnormalities (Inner)*	Major Associated Anomalies
Trisomy 21 (Down syndrome) **(Chromosomal)**	Small, malformed, low-set pinnae; EAC stenosis	Mesenchymal remnants; wide angle of facial nerve genu; bulky malleus/incus with bone marrow; deformed stapes and distorted crura; underdeveloped pyramidal eminence; high jugular bulb; poorly developed mastoids	Shortened cochlea; wide utricle and SCCs; wide CA; small PSCC; enlarged bony posterior canal ampulla	Hypertelorism; epicanthic fold; slanting eyes; strabismus; narrowed nasal space; hypoplastic paranasal sinuses; protruding tongue; high palate; flattened skull; VSD/ASD, PDAs, situs inversus; MR
Usher's syndrome **(AD, AR, or X-Linked Recessive)**	None	None	Atrophic changes of the organ of Corti and spiral ganglia in the basal turn; milder degrees of atrophy of stria vascularis, limbus, tectorial membrane, and Reissner's membrane reported; no known radiographic abnormality	Hearing loss; retinitis pigmentosa; vestibulocerebellar ataxia; mental retardation
VATER (vertebral defects; anal atresia; tracheoesophageal fistula; renal anomalies **(Unknown Mode of Inheritance)**	None	Hypoplasia of facial nerve, chorda tympani nerve, and greater superficial petrosal nerve; decreased geniculate ganglion secondary to decreased number of cells; anterior curvature of stapes superstructure; hypertrophic anterior annular ligament	Irregular course of LSCC; superior utricle; superior saccule; enlarged ELD and ELS	Vertebral defects; anal atresia; Tracheoesophageal fistula; esophageal atresia; renal defects; radial limb hypoplasia; large fontanelles; cardiac defects; single umbilical artery; genital anomalies
Waardenburg syndrome **(AD)**	None	None	PSCC absent; LSCC slightly dilated; vestibule slightly irregular in shape	Hypertelorism; broad, high nasal root; white forelock; pigmentary disorders of the eye
Wildervanck syndrome (cervicooculoacoustic syndrome) **(Otocervical or Sex-Linked Disorder)**	Preauricular tags; posteriorly displaced pinnae; small, deformed ears; hypoplasia and absence of EAC	Rudimentary ossicles; fusion of malleus/incus; absent stapes and OW; fixation of stapes; ossified stapedius tendon	Aplasia or hypoplasia of various structures; abnormal SCCs; bony septum in IAC	Manifestation of Klippel-Feil syndrome plus deafness; abducens palsy; and retraction of the orbits

AD, autosomal dominant; *AR,* autosomal recessive; *ASD,* atrial septal defect; *CA,* cochlear aqueduct; *EAC*, external auditory canal; *ELD,* endolymphatic duct; *ELS,* endolymphatic sac; *IAC*, internal auditory canal; *LSCC*, lateral semicircular canal; *OW,* oval window; *PDA,* patent ductus arteriosus; *PSCC*, posterior semicircular canal; *RW,* round window; *SCC*, semicircular canal; *SSCC,* superior semicircular canal; *TC,* tympanic cavity; *TM,* tympanic membrane; *TMJ*, temporomandibular joint; *VSD,* ventricular septal defect.

The internal auditory canal (IAC) may be normal in the presence of a grossly deformed inner ear. Conversely, cases of dysplasia or aplasia of the IAC may occur in the presence of a normal labyrinth. However, extreme hypoplasia or aplasia of the IAC is associated more commonly with significant bony malformations of the inner ear. The development of the IAC is distinct from that of the labyrinth, and the underlying mechanism explaining the coexistence of these congenital deformities is not apparent.

Anatomic variations include a range of dimensions, contours, and spatial orientations of the structures within the temporal bone region encountered in a normal population with neither functional impairment nor anatomic substrate carrying the potential for imperiling the well-being of the individual. These two criteria provide the crucial distinction between a variation and an anomaly.[1]

Complete descriptions of the embryology and anatomy of the various parts of the ear are presented in Chapter 19. Concepts important to this discussion are briefly summarized in the appropriate sections.

ANOMALIES OF THE OUTER EAR

The outer ear is composed of the auricle and the external auditory canal (EAC). The auricle develops from tissues of both the first (mandibular) and second (hyoid) branchial arches. The EAC develops from the first branchial cleft, which forms between the first and second branchial arches. In the sixth fetal week, the cleft invaginates. The tympanic cavity is formed in the fourth fetal week from invagination of the first pharyngeal pouch. The meeting of these two invaginations results in formation of the primitive tympanic membrane. These two invaginations are temporarily separated by a core of epithelial cells that is later canalized in the twenty-sixth fetal week. Partial or complete failure of this

Copyright © 2003, Mosby, Inc. All rights reserved.

canalization results in stenosis or atresia of the EAC, respectively.[5]

Malformations of the outer ear are referred to as congenital aural dysplasias (CAD). A malformation of the auricle alone is referred to as microtia. CAD has been estimated to occur in 1 of 3300 to 10,000 births, with a higher incidence of 1 in 900 reported in the era of thalidomide embryopathy. CAD is most commonly isolated, without known cause, and unilateral. The right ear is more commonly affected, and in up to one third of cases, CAD may be bilateral.[6] CAD may also occur in conjunction with other organ abnormalities due to genetic disorders, chromosomal aberrations, intrauterine infections, and environmental teratogens.[7]

A classification system developed by Weerda et al. divides the deformites into first, second, and third degrees. The third degree is the most pronounced deformity and is defined as either absence of normal auricular structure (anotia) or severe dysplasia of the auricular soft tissues, with possible inferior displacement due to incomplete ascension from the neck. With first or second degree dysplasias, the EAC is commonly stenotic. With third degree auricular dysplasias, the EAC is commonly atretic.[7]

EAC malformations may be fibrous, bony, or both (Fig. 21-1). In the fibrous type, there is a soft-tissue plug where the tympanic membrane (TM) should be. In the bony type, there is a bony plate where the TM should be.[6, 7] The thickness of the bony plate is variable and reaches 31 mm.[7] Stenotic EACs often have a more superiorly angulated course than normal, extending from inferolaterally to superomedially (Fig. 21-2). With stenosis or atresia, there is an increased incidence of both primary (congenital) and secondary (acquired) cholesteatomas or epidermoids (Figs. 21-3 and Fig. 21-4). These may occur in the stenosed EAC or deep to the atretic plate in the middle ear cavity.

Associated Middle Ear and Ossicular Abnormalities

Middle ear abnormalities tend to occur concomitantly with CAD because of the common embryologic origins of the EAC and middle ear. The ossicular chain, with the exception of the footplate of the stapes, develops from the first and second branchial arches. The tympanic cavity develops from the first pharyngeal pouch.[5] Ossicular deformities include dysplasia, decreased size, abnormal rotation, and absence of the malleus and incus. There can be deformity of the malleoincudal and incudostapedial articulations, as well as fusion of the malleus and incus to the attic wall. More severe CADs tend to have more severe ossicular abnormalities. Abnormalities of the stapes are less common and do not directly correlate with the degree of CAD because of the dual origin of the stapes from the second branchial arch and the otic capsule.[6]

Pneumatization of the middle ear cavity is often reduced in CAD, with the extent of reduction correlating directly with the severity of the dysplasia. Although pneumatization of the entire middle ear can be affected, the hypotympanum is usually most severely reduced.[7]

Other Associated Abnormalities

Other osseous abnormalities may occur with CAD including aplasia or hypoplasia of the tympanic part or

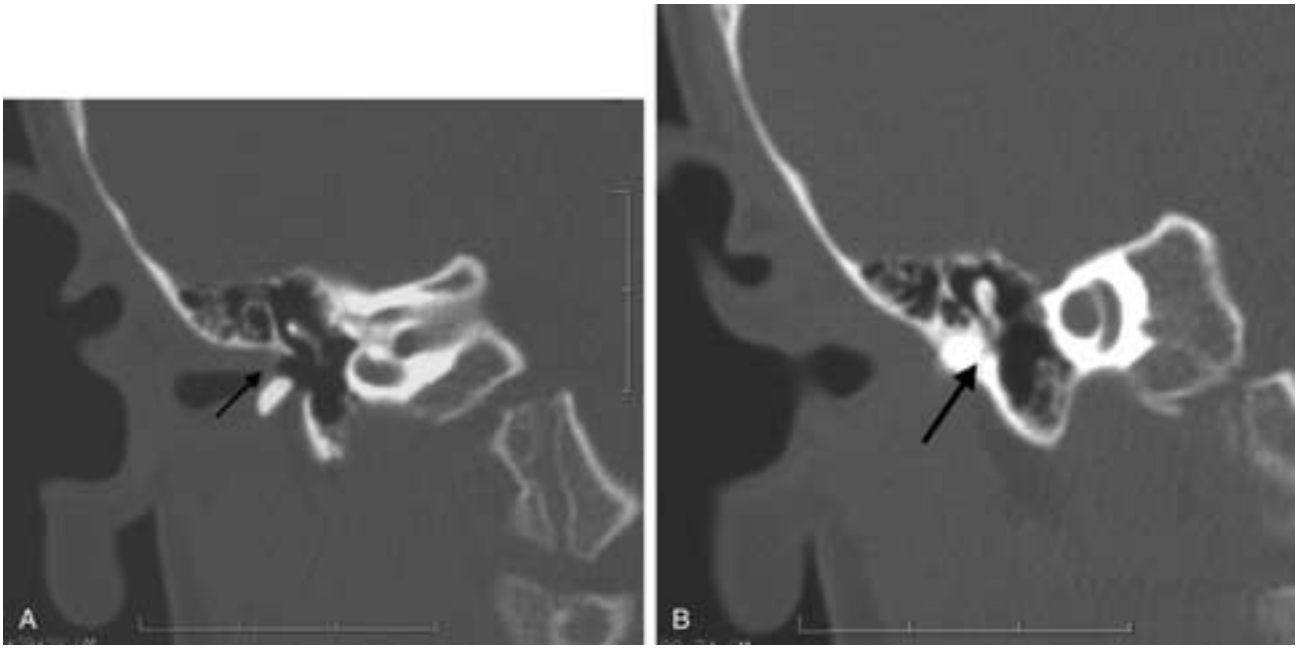

VIEW IMAGE

FIGURE 21-1 EAC stenosis. **A**, Coronal CT image at the level of the incudostapedial joint and oval window showing stenosis of the EAC with membranous apposition of the superior and inferior walls (*black arrow*). **B**, Coronal CT image of the same patient more anteriorly showing a bony atretic plate (*black arrow*) with fusion of the handle of the malleus to the plate.

Copyright © 2003, Mosby, Inc. All rights reserved.

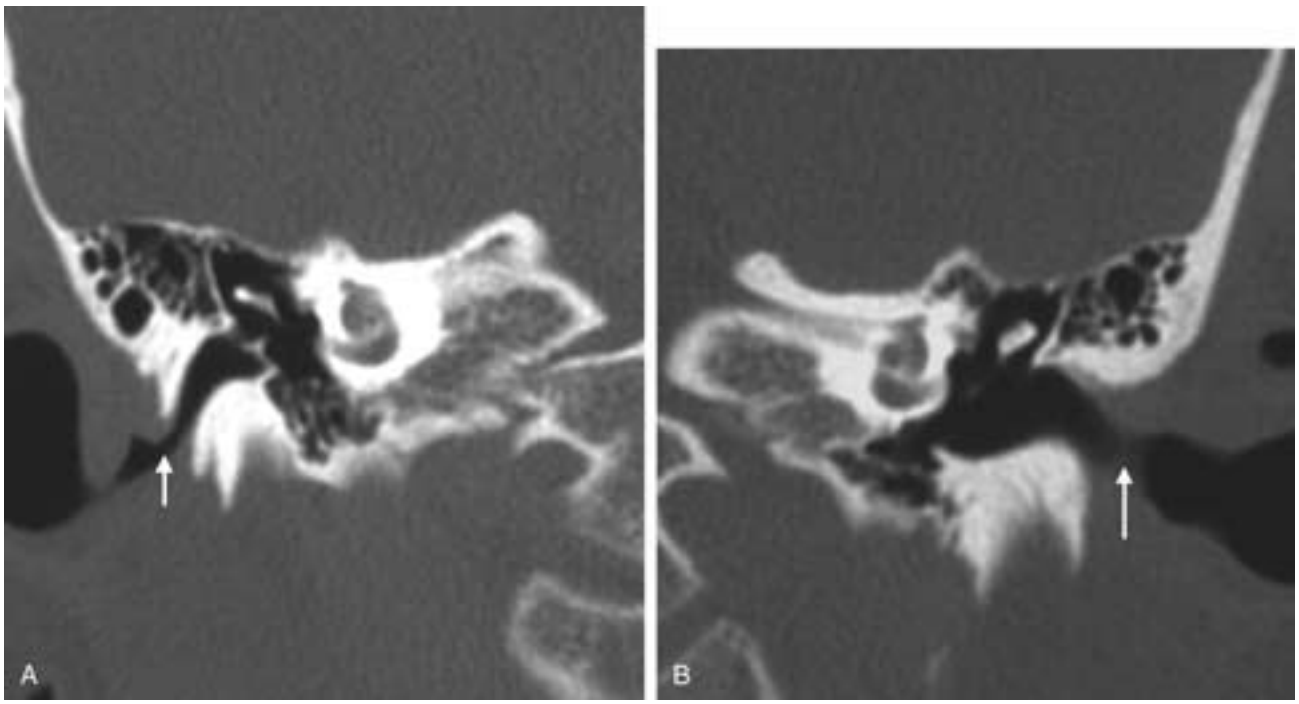

VIEW IMAGE

FIGURE 21-2 EAC stenosis. **A**, Coronal CT image at the level of the body of the incus showing stenosis of the right EAC. **B**, Coronal CT image at the same level as **A** on the opposite side showing a normal EAC without stenosis.

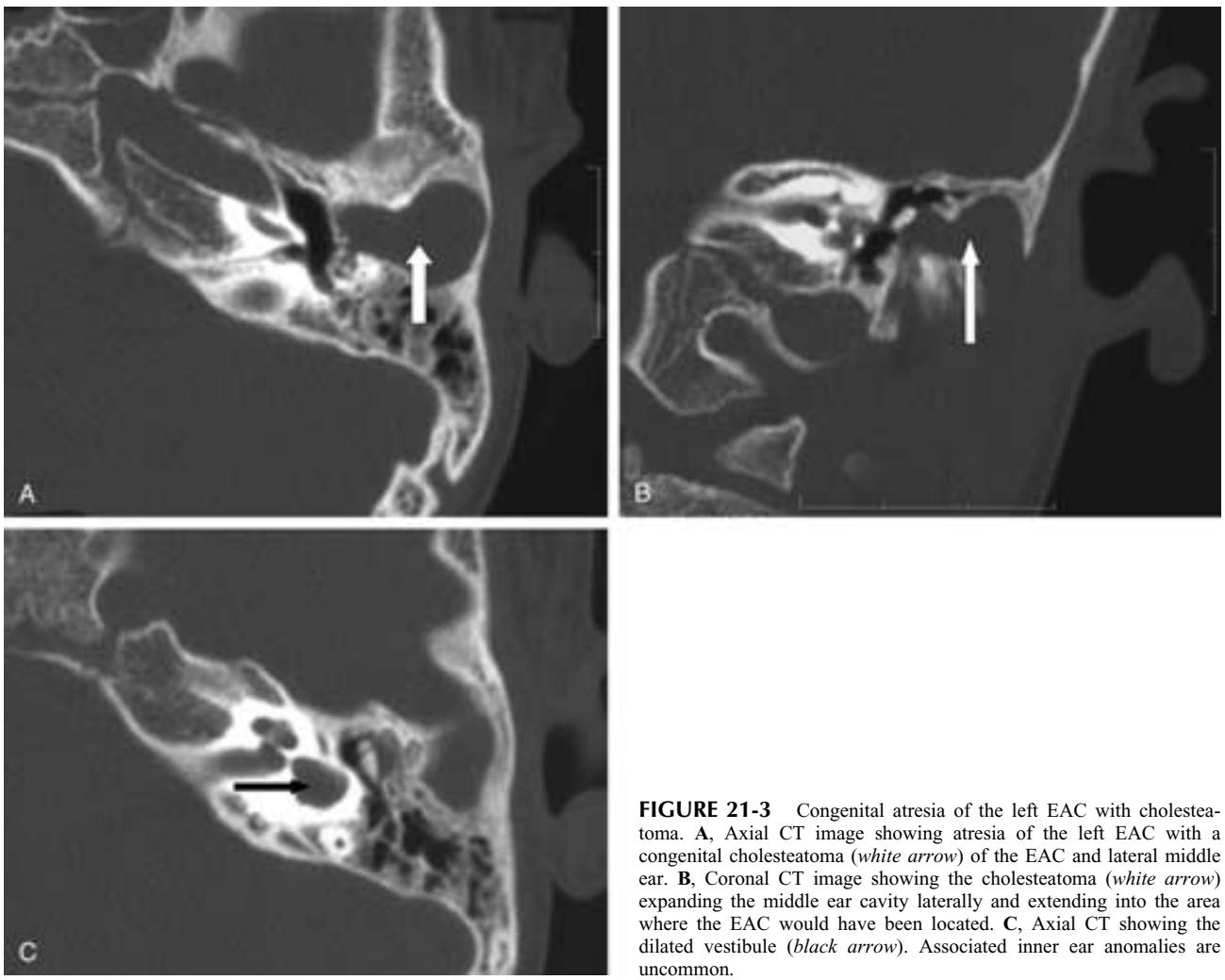

VIEW IMAGE

FIGURE 21-3 Congenital atresia of the left EAC with cholesteatoma. **A**, Axial CT image showing atresia of the left EAC with a congenital cholesteatoma (*white arrow*) of the EAC and lateral middle ear. **B**, Coronal CT image showing the cholesteatoma (*white arrow*) expanding the middle ear cavity laterally and extending into the area where the EAC would have been located. **C**, Axial CT showing the dilated vestibule (*black arrow*). Associated inner ear anomalies are uncommon.

Copyright © 2003, Mosby, Inc. All rights reserved.

mastoid process of the temporal bone, deformity of the temporomandibular joint (TMJ), and defects in the zygomatic arch. The severity of hypoplasia of the tympanic part or mastoid process of the temporal bone correlates with the degree of auricular dysplasia. Pneumatization of the mastoid is often reduced, in turn affecting the position of the sigmoid sinus.[7] The mandibular condyle is frequently dysplastic, and the joint space is often shallow.[8] The temporal squama may be pushed down and the glenoid fossa may be markedly flattened or even absent.[9] The joint position is frequently abnormal, being relatively higher and more posterior in relation to the middle ear. Rotation or elevation of the carotid canal, as well as hypoplasia or aplasia of the internal carotid artery, may also occur.[7]

The facial nerve canal frequently has an anomalous course in patients with CAD. The tympanic and mastoid segments are most commonly affected, with rare involvement of the labyrinthine segment. The tympanic segment is typically displaced caudally, extending as inferiorly as the round window. It may also be dehiscent and medially displaced, overlying the oval window and/or passing between the crura of the stapes. The mastoid segment is usually displaced anterolaterally, with the facial nerve exiting the temporal bone at the level of the round window.[6, 7] In some cases, the nerve may exit the skull base in a narrow space between the glenoid fossa and the mastoid process.

The oval and round windows may be absent in CAD, although isolated absence of the oval window is more common. Absence of either window does not correlate directly with the degree of dysplasia.[7] When there is CAD or underdevelopment of the first arch structures, there is compensatory anterior shifting of the second arch structures including the stapes superstructure. As a result, the stapes does not make appropriate contact with the otic capsule. Such contact is thought necessary for induction of formation of the oval window.[10]

Anomalies of the inner ear and IAC are rarely associated with CAD. In one study of atretic patients, 12% (8 of 66) had a radiographically detectable inner ear abnormality.[11] Inner ear anomalies include hypoplastic cochleas (5%), hypoplasia or enlargement of the lateral semicircular canal (most common, 10%), and/or enlargement of the vestibule and vestibular aqueduct. The IAC may have an anomalous orientation extending from superomedially to inferolaterally and may be hypoplastic.[7]

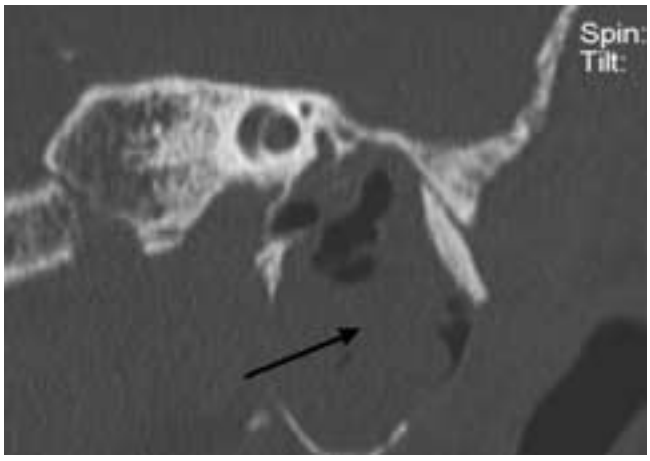

VIEW IMAGE

FIGURE 21-4 EAC atresia with cholesteatoma. Coronal CT image showing a large cholesteatoma expanding the EAC and middle ear cavity (*black arrows*) in a patient with EAC atresia. A spontaneous fistula formed between the cholesteatoma and the skin (not shown).

Surgical Considerations

The surgical approach for correction of aural atresia, as defined by Jahrsdoerfer et al., is an anterior approach that involves drilling through bone in close proximity to the TMJ anteriorly, the middle cranial fossa superiorly and the mastoid posteriorly.[12] Yeakley and Jahrsdoerfer[13] devised a 10-point CT preoperative evaluation of aural atresia to help estimate the likelihood of a favorable surgical outcome. In this system, the EAC, malleus, incus, and their respective joints; the oval and round windows; the middle ear and mastoid pneumatization; and the facial nerve course are evaluated.

The presence of the stapes is given most importance. The course of the facial nerve is also critical, as marked anterior migration of the mastoid segment would likely result in injury at the time of surgical repair. The presence and width of the mastoid antrum and the middle ear are important for surgical accessibility. Patients with scores of 5 or less are not considered for surgery, and patients with scores of 8 or more have an 80% chance of having their hearing restored to almost normal levels. Cochlear function must be intact, as assessed clinically, and CT must show a normal inner ear to qualify for surgery. A deformed cochlea associated with CAD is more vulnerable to injury from vibratory trauma at surgery, with an increased risk of inducing sensorineural hearing loss.[14] The optimal timing of surgical correction, as agreed on by most authors, is between 5 and 8 years of age since mastoid development is complete by that time.

ANOMALIES OF THE MIDDLE EAR

Isolated anomalies of the ossicles and middle ear without EAC stenosis or atresia do occur but are much less common than those of the outer ear. Autosomal dominant inheritance has been reported in some cases. These anomalies may also be found in association with a variety of syndromes, the more common of which are Goldenhar and Treacher-Collins syndromes.[15] Depending on the source, either the incus or stapes are the ossicles most frequently malformed or absent.[15, 16] Anomalies of the incus include aplasia, fusion of the short process to the lateral semicircular canal, shortening or malformation of the long process, absent incudostapedial joint, and fibrous union of the joint. Stapes anomalies include aplasia, absence of the head and crura, hypoplasia or a fetal form, a columnar-type deformity, fusion of the head to the promontory, and footplate fixation. Anomalies of the malleus include aplasia, deformed head, triple bony union of the handle (manubrium) with the long process of the incus and stapes head, and fusion of the incudomalleal joint. A rare anomaly of the malleus is congenital fixation of the head to the lateral epitympanic wall called the malleus bar (Figs. 21-5 and 21-6).[17, 18] This

Copyright © 2003, Mosby, Inc. All rights reserved.

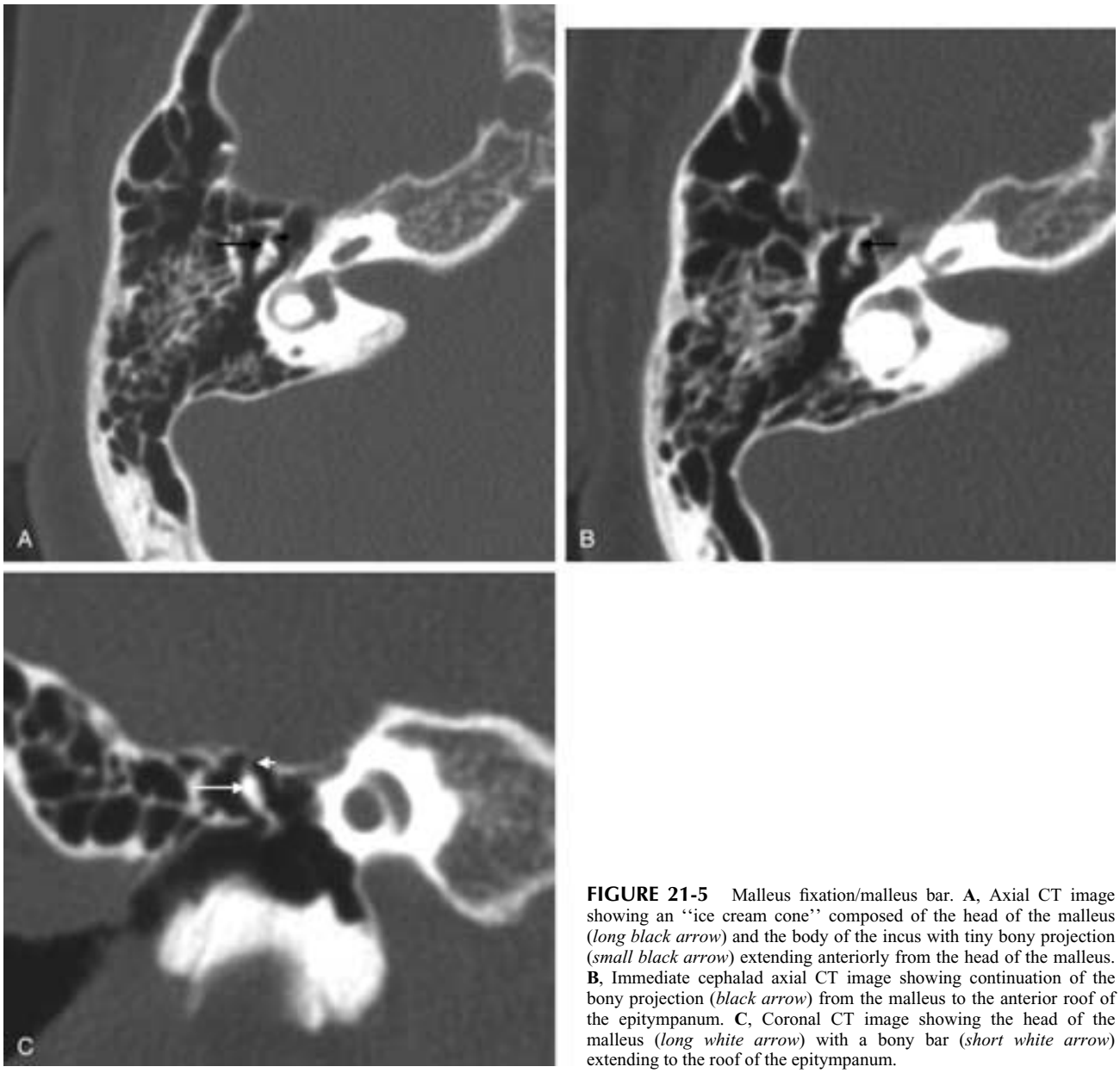

FIGURE 21-5 Malleus fixation/malleus bar. **A**, Axial CT image showing an ''ice cream cone'' composed of the head of the malleus (*long black arrow*) and the body of the incus with tiny bony projection (*small black arrow*) extending anteriorly from the head of the malleus. **B**, Immediate cephalad axial CT image showing continuation of the bony projection (*black arrow*) from the malleus to the anterior roof of the epitympanum. **C**, Coronal CT image showing the head of the malleus (*long white arrow*) with a bony bar (*short white arrow*) extending to the roof of the epitympanum.

VIEW IMAGE

may also involve fixation of the incus body.[17] Isolated fixation of the incus to the scutum has been reported and is likely an even rarer phenomenon.[16]

The ossicles and the ossicular chain may not only be absent or malformed, but may also have anomalies classified as those of ''delayed disappearance.''[15] These anomalies include preservation of embryologic structures such as bone marrow and mesenchymal tissue within the ossicles beyond 25 months of age. Normally, bone marrow is present in the head of the malleus and the body of the incus at birth and persists up to 25 months of age. It is gradually converted to bone and vascular channels. The marrow may have a role as hematogenous tissue in infancy. After 25 months, the presence of marrow is no longer normal.[19] The most frequently reported abnormalities of this kind are a large bone marrow cavity in the incus or malleus and an incus largely composed of mesenchymal tissue. These anomalies may occur with Treacher-Collins syndrome and trisomy 13.[15]

The facial nerve course is often anomalous in the presence of ossicular chain anomalies as the ossicles develop from the first and second branchial arches and the nerve develops from the second arch. The most common facial nerve anomalies noted to occur in patients with congenital middle ear malformations without stenosis or atresia of the EAC are displacement and wide bony dehiscence of the tympanic segment (Fig. 21-7).[15, 20] The nerve is typically displaced inferiorly and medially, and often either crosses the oval window, lies inferior to it, or is in apposition to the stapes. Less commonly, the tympanic and mastoid segments may be laterally displaced.[15] The tympanic segment has also been described in cases of dehiscence as being freely suspended in the aerated middle ear cavity.[20] More proximally, the first genu of the nerve

Copyright © 2003, Mosby, Inc. All rights reserved.

may have an abnormally wide (obtuse) angle.[15] Anomalies of the chorda tympani and greater superficial petrosal nerve may occur in conjunction with facial nerve anomalies and include an enlarged chorda tympani nerve.[15, 20]

Often associated with a dehiscent facial nerve that overlies the oval window and/or stapes is congenital absence of the oval window (Fig. 21-8). Many authors feel that the anomalous position of the facial nerve acts as a mechanical barrier to the stapes, preventing it from making appropriate contact with the developing otic capsule at the future oval window site. As such, oval window development is not induced. Theoretically, less interference by the facial nerve would result in partial absence or hypoplasia of the oval window. This theory is supported by the fact that other anomalies of the inner ear are extremely rare in cases of congenital absence of the oval window, a derivative of the inner ear.[10, 21, 22] Of note, isolated atresia of the oval window may also occur in the absence of facial nerve dehiscence (Fig. 21-9).

Lastly, other anomalies that may occur within the middle ear include an absent stapedius muscle and/or tendon, absence or elongation of the pyramidal eminence, and hypoplasia of the tympanic cavity.[23] Cholesteatomas may also occur as congenital lesions within the middle ear cavity without associated stenosis or atresia of the EAC (Fig. 21-10).

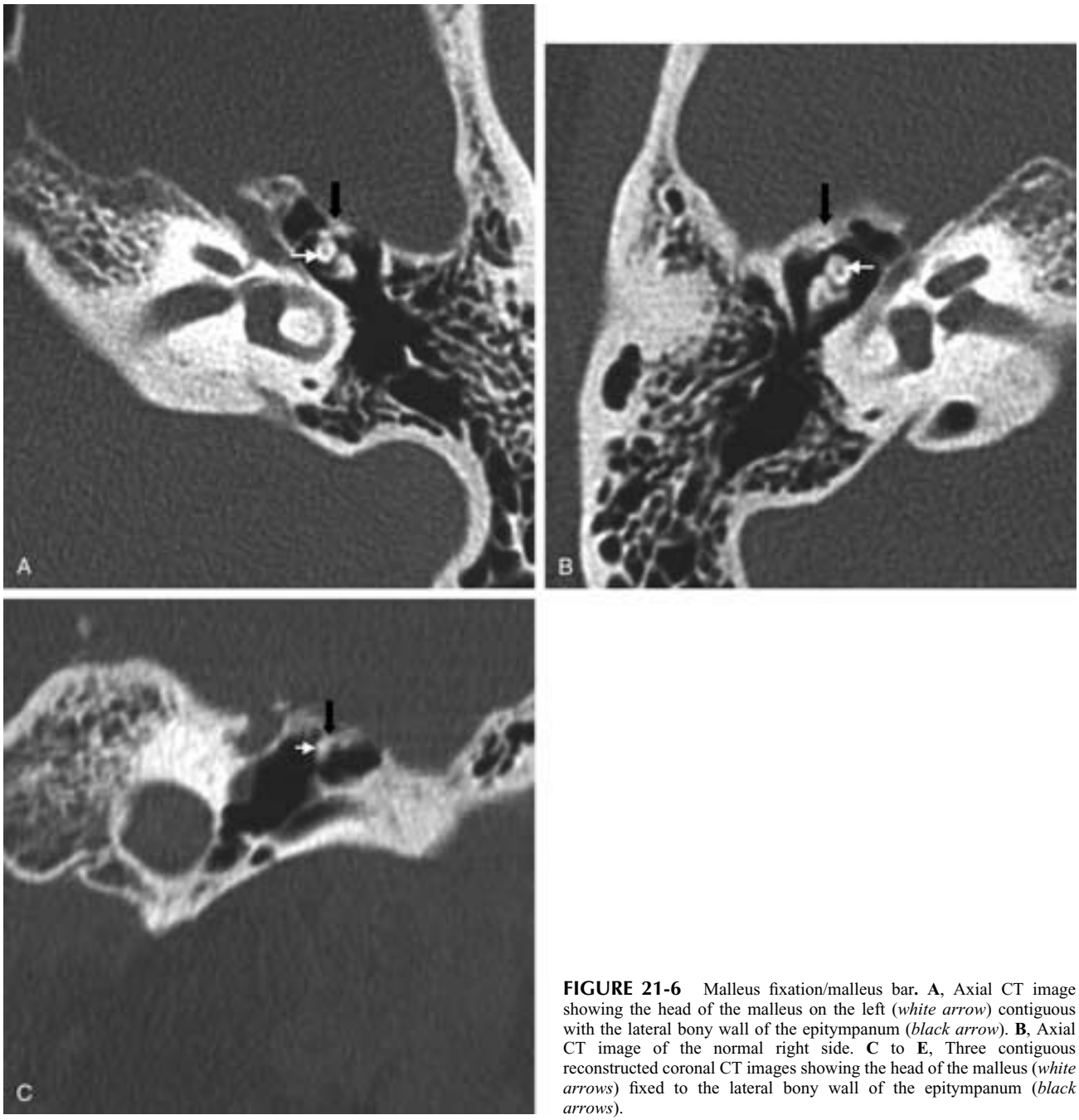

FIGURE 21-6 Malleus fixation/malleus bar**. A**, Axial CT image showing the head of the malleus on the left (*white arrow*) contiguous with the lateral bony wall of the epitympanum (*black arrow*). **B**, Axial CT image of the normal right side. **C** to **E**, Three contiguous reconstructed coronal CT images showing the head of the malleus (*white arrows*) fixed to the lateral bony wall of the epitympanum (*black arrows*).

VIEW IMAGE

Copyright © 2003, Mosby, Inc. All rights reserved.

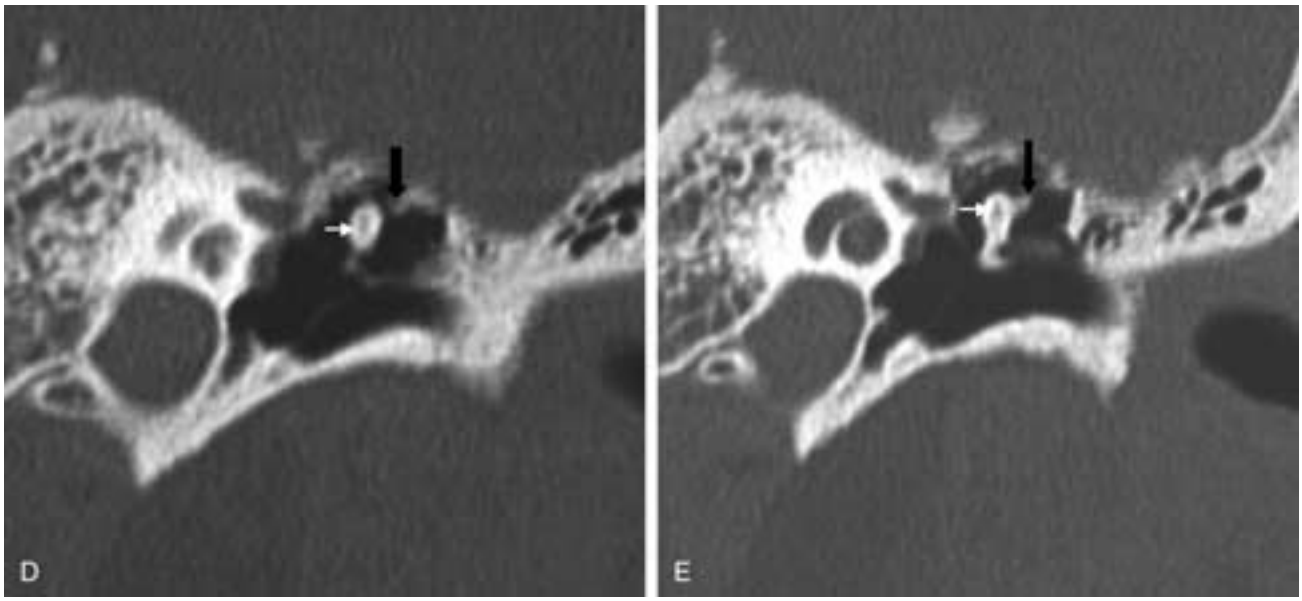

VIEW IMAGE

FIGURE 21-6 *Continued.* For legend see previous page.

ANOMALIES OF THE INNER EAR

Congenital inner ear anomalies represent a wide range of pathologies that have had variable classifications over the years. The original classification of these anomalies was by discrete patterns of histopathologic change described by various investigators.[24] These included the Bing-Siebenmann (BS), Scheibe, Mondini, Alexander, and Michel-type dysplasias. BS dysplasia is characterized by anomalies of the cochlear and vestibular components of the membranous labyrinth. In the cochlea, a rudimentary mound of undifferentiated cells replaces the organ of Corti, against which Reisner's membrane is collapsed. In Scheibe's dysplasia, abnormalities are limited to the saccule and cochlea and include stria vascularis atrophy, a deformed tectorial membrane, and a poorly differentiated organ of Corti, against which Reisner's membrane is collapsed. Scheibe's dysplasia is the most commonly observed temporal bone dysplasia in cases of profound congenital sensorineural hearing loss.[25] Mondini dysplasia is characterized by a normal basilar turn but a decreased number of upper turns, with modiolar hypoplasia and absence of the interscalar septum. The upper turns are represented by a sac-like remnant. Alexander's deafness is characterized by underdevelopment of the basilar turn. Michel dysplasia is complete absence of the labyrinth including absence of the sensorineural structures of the inner ear. Other authors[3] have simply classified inner ear anomalies into Scheibe and Mondini dysplasias and anomalies associated with chromosomal disorders, stating that the BS and Alexander types have been inadequately documented and that the Michel type is too rare to be of any clinical significance. Jackler proposed a classification system based on the hypothesis that the various inner ear anomalies result from an arrest of maturation during different stages of inner ear embryogenesis.[32]

None of these classification systems, however, is all-inclusive. There are anomalies that have been and continue to be documented with thin-section, high-resolution CT and MR imaging that do not fit neatly into any particular system. Therefore, in this section, the various inner ear anomalies that have been documented radiographically will be presented and related to a particular classification system when possible.

Imaging Techniques

In many institutions, CT of the temporal bone remains the method of choice for the evaluation of congenital inner ear malformations. CT is readily able to define the bony labyrinth and give information regarding concomitant middle and external ear anomalies. Alternatively, thin-section, high-resolution MR imaging of the inner ear, which can be achieved with both gradient-echo and fast spin-echo T2-weighted techniques, gives exquisite detail of the membranous labyrinth, in which there may be anomalies not necessarily associated with anomalies of the bony labyrinth. For example, MR imaging allows differentiation between the scala tympani and scala vestibuli. In patients with congenital inner ear malformations requiring cochlear implantations, fibrous obliteration of the scala tympani and scala vestibuli has been shown with T2-weighted gradient echo imaging. Scalar asymmetry with enlargement of the scala vestibuli and media has been shown with fast spin echo T2-weighted techniques.[26] MR imaging also provides the ability to diagnose aplasia or hypoplasia of the vestibulocochlear nerves. With high-resolution imaging in the sagittal plane, the cochlear nerve may be defined separately from the superior and inferior vestibular nerves and from the facial nerve within the IAC. Malformations of Reisner's membrane and the organ of Corti are too small to be detected, and the complete membranous labyrinth dysplasia occuring in BS dysplasia remains below the resolving capabilities of MR imaging. To date, MR imaging has been unable to identify the abnormalities in patients with Scheibe dysplasia.

Copyright © 2003, Mosby, Inc. All rights reserved.

Similarly, in Usher's, Refsum's, and Cockayne's syndromes, the abnormality is considered membranous and imaging is not likely to be abnormal. However, these patients have coexistent eye pathology such as retinitis pigmentosa (Usher's and Refsum's syndromes) or retinal degeneration (Cockayne's syndrome), so imaging is not crucial to making the diagnosis. However, very few of these patients have been examined with MR imaging, and it is possible that some abnormalities might be documented if MR imaging were used routinely (Fig. 21-11).

Imaging of the temporal bone with CT can be performed with both nonspiral and spiral techniques. With nonspiral techniques, a slice thickness of 1 mm is acceptable for images acquired in both the axial and coronal planes. Alternatively, with spiral techniques, images may be acquired using 0.5 mm collimation. The images can be

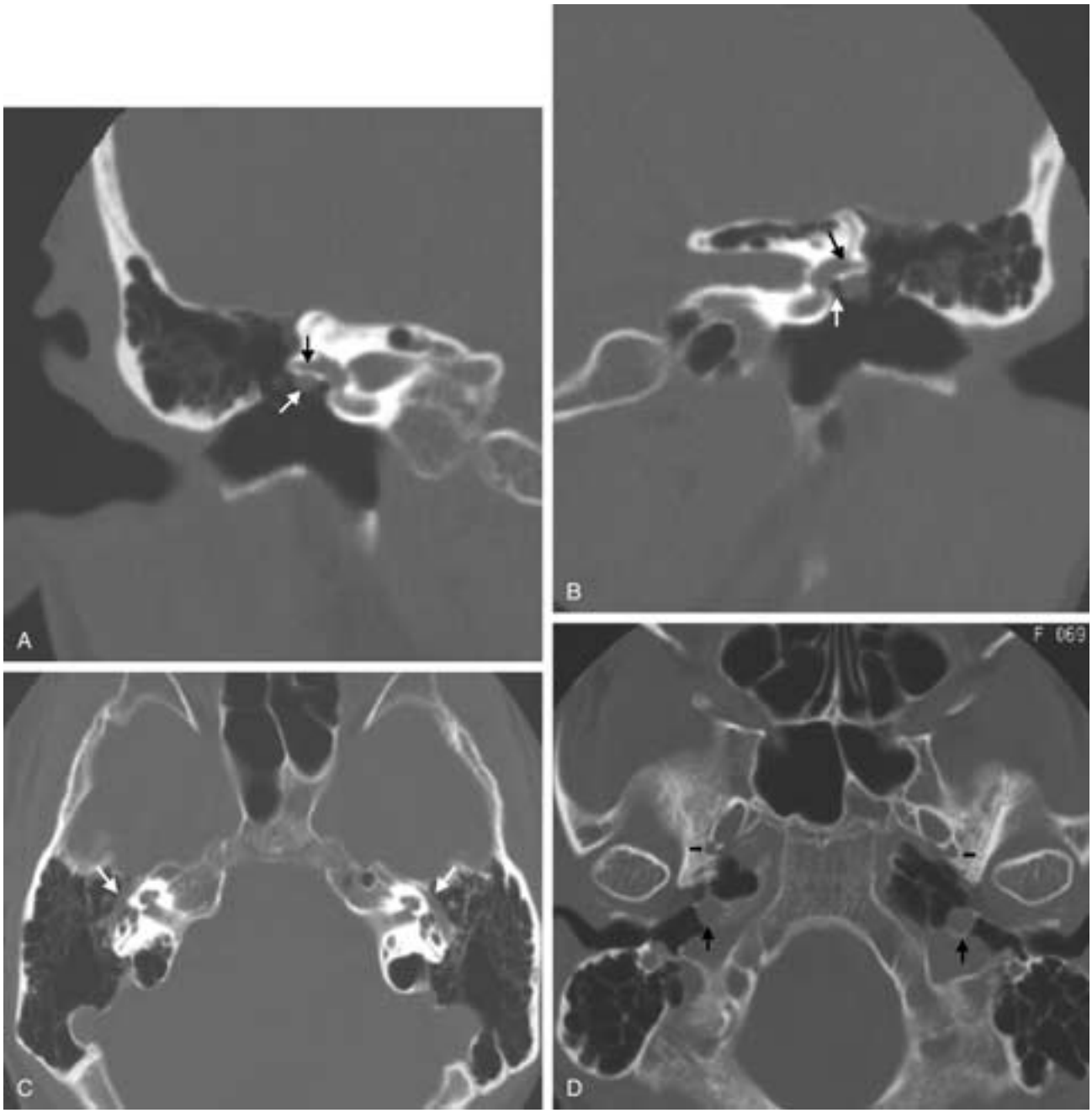

FIGURE 21-7 Dehiscent facial nerve. **A** and **B**, Right and left coronal CT images showing soft-tissue prominence in the middle ear cavity immediately inferior to the lateral semicircular canal (*black arrows*) in the expected location of the tympanic segment of the facial nerve (*white arrows*). No bony canal for tympanic segments consistent with dehiscence is identified. **C**, Axial CT image showing bilateral facial nerve dehiscence (*white arrows*). **D**, Axial CT image showing normal carotid canals (*long black arrows*) and presence of the foramen spinosum (*short black arrows*), indicating that the prominent soft tissue at the expected location of the tympanic facial nerve is not a persistent stapedial artery.

VIEW IMAGE

Copyright © 2003, Mosby, Inc. All rights reserved.

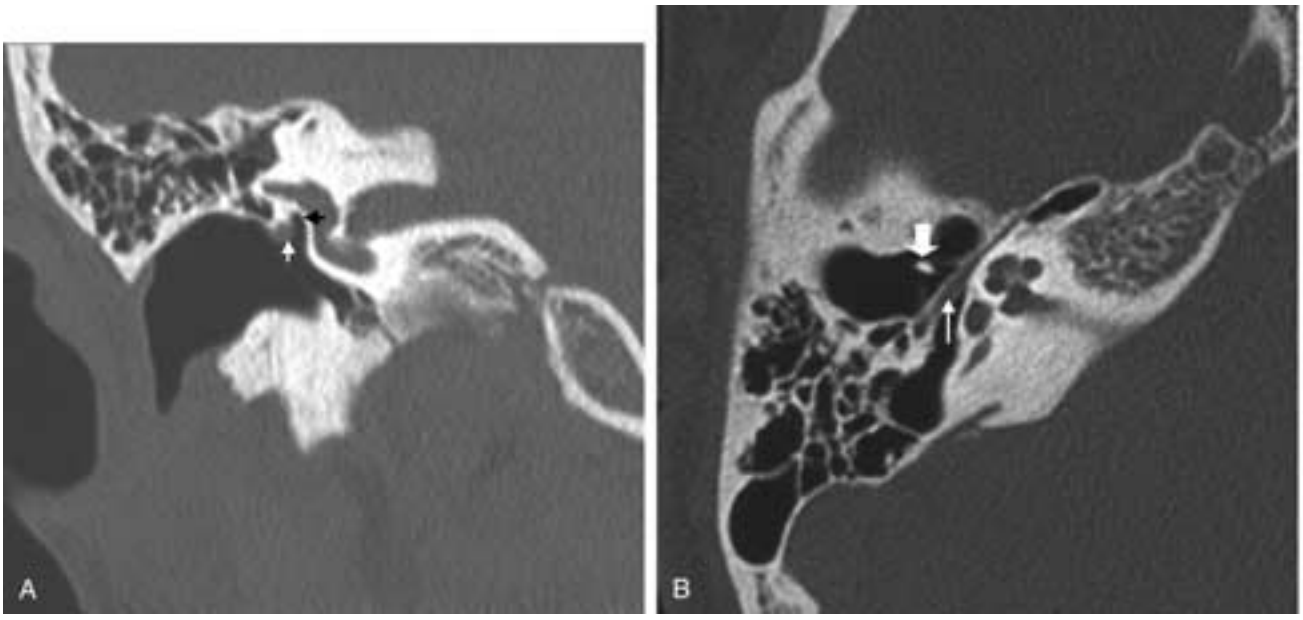

VIEW IMAGE

FIGURE 21-8 Inferior migration of the facial nerve, absent stapes, and stenotic oval window. **A**, Coronal CT image showing inferior migration of tympanic segments of the facial nerve (*white arrow*) approaching the stenotic oval window (*black arrow*). The stapes is absent. **B**, Axial CT image showing a low-lying tympanic segment of the facial nerve (*white arrow*) in the middle ear cavity. Note the handle of the malleus (*white block arrow*) on the tympanic membrane.

reconstructed with a slice thickness of less than 1 mm. This technique also provides submillimeter coronal reformatted images, which may obviate the need for direct coronal scanning. With these images, greater anatomic detail can be achieved and, as a result, more subtle anomalies may be revealed. The coronal reformatted images are true coronal images exactly perpendicular to the axial plane of acquisition so that the petrous ridge is viewed tangentially rather than obliquely. This may be useful, for example, when assessing the integrity of the tegmen tympani and when evaluating for possible dehiscence of the superior semicircular canals.

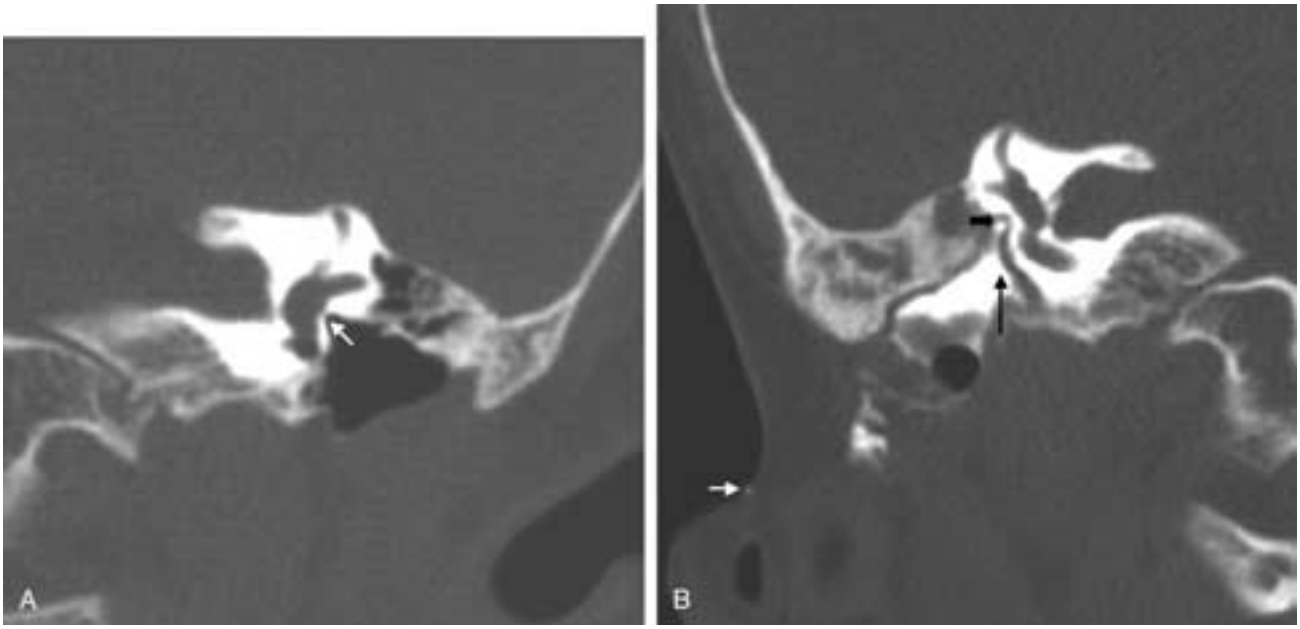

VIEW IMAGE

FIGURE 21-9 Bilateral stenoses/atresias of the oval windows and associated first branchial cleft fistula. **A**, Coronal CT image showing stenotis/atresia of the left oval window (*white arrow*) and possible absence of the stapes. **B**, Coronal CT image showing a right-sided first branchial cleft abnormality, with contrast injected from a periauricular skin opening (*white arrow*) and tracking into a stenotic middle ear cavity (*long black arrow*) up to the atretic oval window. Again, note the absence of the stapes (*short black arrow*).

Copyright © 2003, Mosby, Inc. All rights reserved.

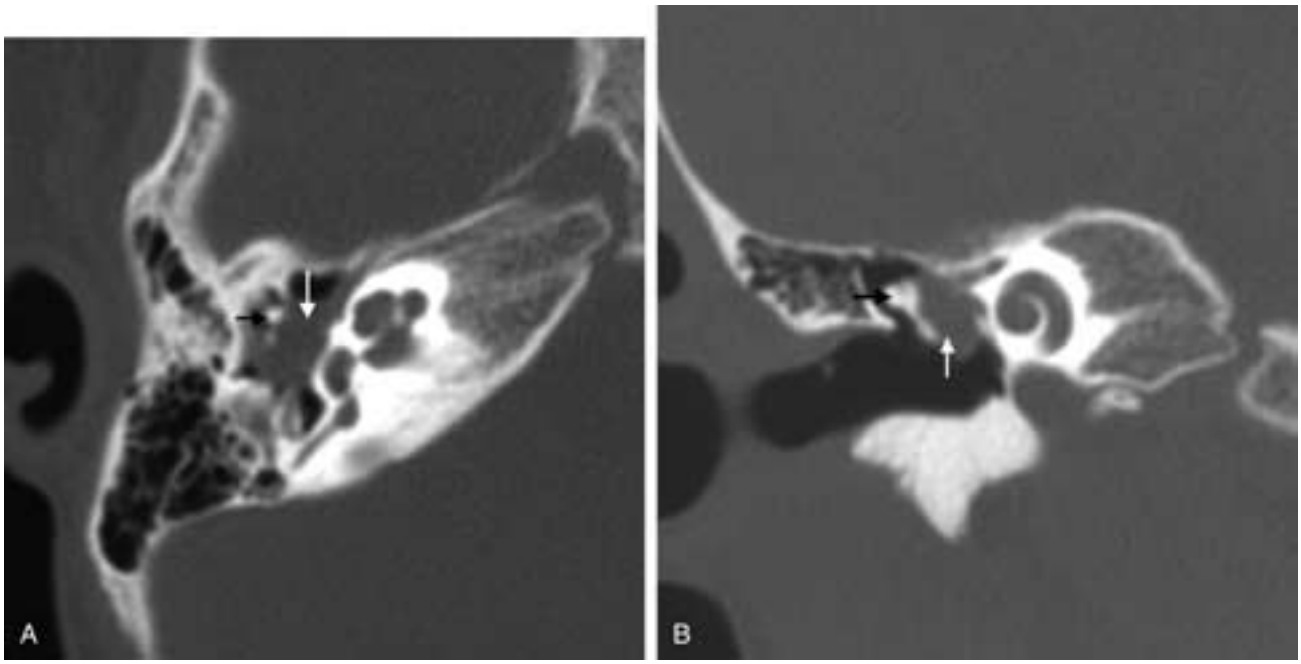

VIEW IMAGE

FIGURE 21-10 Congenital cholesteatoma of the middle ear without EAC atresia. Axial CT (**A**) and coronal CT (**B**) images showing a lobulated soft-tissue mass (*white arrows*) within the middle ear cavity medial to the ossicular chain (*black arrows*) consistent with congenital cholesteatoma.

With MR imaging, routine 2 to 3 mm thick contiguous T1-weighted spin-echo images before and after intravenous gadolinium contrast administration may detect some congenital inner ear malformations. Thin T2-weighted gradient echo or spin echo images are more sensitive and may detect other congenital inner ear malformations. In one study, the T1-weighted images showed only portions of the congenital malformations, and the malformations were not visible in 40% of the patients. Nearly all anomalies were recognized on the thin gradient echo images.[27] Since the whole membranous labyrinth is only approximately 12 mm high and 10 mm wide, sections less than 1 mm thick must be used to study this small structure. Good in-plane spatial resolution and optimal contrast between the intralabyrinthine fluid and surrounding bone and nerves are required. Heavily T2-weighted gradient echo or spin echo images can provide such images with bright intralabyrinthine fluid and dark surrounding bone and nerves. Several gradient echo techniques including three-dimensional Fourier transform fast imaging with steady precession (3DFT-FISP), 3D-gradient-recalled acquisition in the steady state (GRASS), and constructive interference in the steady state (3DFT-CISS) have proven valuable in the study of the membranous labyrinth and IAC.[28, 29] The parameters may vary with the technique. However, by using small fields of view of 95 to 100 mm, high matrices of 256 × 512, and slice thicknesses of less than 1 mm, the acquisition of images with very high spatial resolution of, for example, 0.49 × 0.37 mm may be achieved. The ability to acquire MR images in multiple planes, and the use of multiplanar reconstructions and 3D maximum intensity projections (MIP), further facilitate the detection and detailed evaluations of inner ear malformations. Davidson et al.[26] have obtained high-resolution images of the membranous labyrinth by employing a surface coil placed over the EAC and a fast spin echo T2-weighted technique with a slice thickness of 2 mm. Their protocol consists of a small field of view of 20 × 10 cm, triple interleaved acquisition, and a matrix of 512 × 512.

Membranous and Bony Labyrinthine Anomalies

Semicircular Canals

Malformation of the lateral semicircular canal is one of the most common inner ear anomalies.[30–32] Malformation of the superior and posterior semicircular canals without involvement of the lateral canal is unusual, as the lateral semicircular canal is the last to form embryologically. The malformed canals are either narrow or, more commonly, are short and wide. In extensive malformations, the vestibule is dilated and forms a common lumen with the lateral canal. This anomaly may be called a lateral semicircular duct–vestibule dysplasia or a common utriculosaccular–lateral semicircular duct cavity. In some cases, it may not be possible to identify the canals because the lumen is obliterated or the canal is absent. When the canal is absent, there is a typical flattening of the corresponding portion of the otic capsule.[31]

The correct diagnosis can be made with thin-section CT of the temporal bone and with thin-section, T2-weighted gradient echo or fast spin echo MR imaging. The correct diagnosis can be missed on routine T1-weighted images because of poor contrast resolution and volume-averaging artifacts. The deformity has a variable appearance, and imaging may reveal a common utriculosaccular-lateral semicircular duct or short, wide semicircular ducts or

Copyright © 2003, Mosby, Inc. All rights reserved.

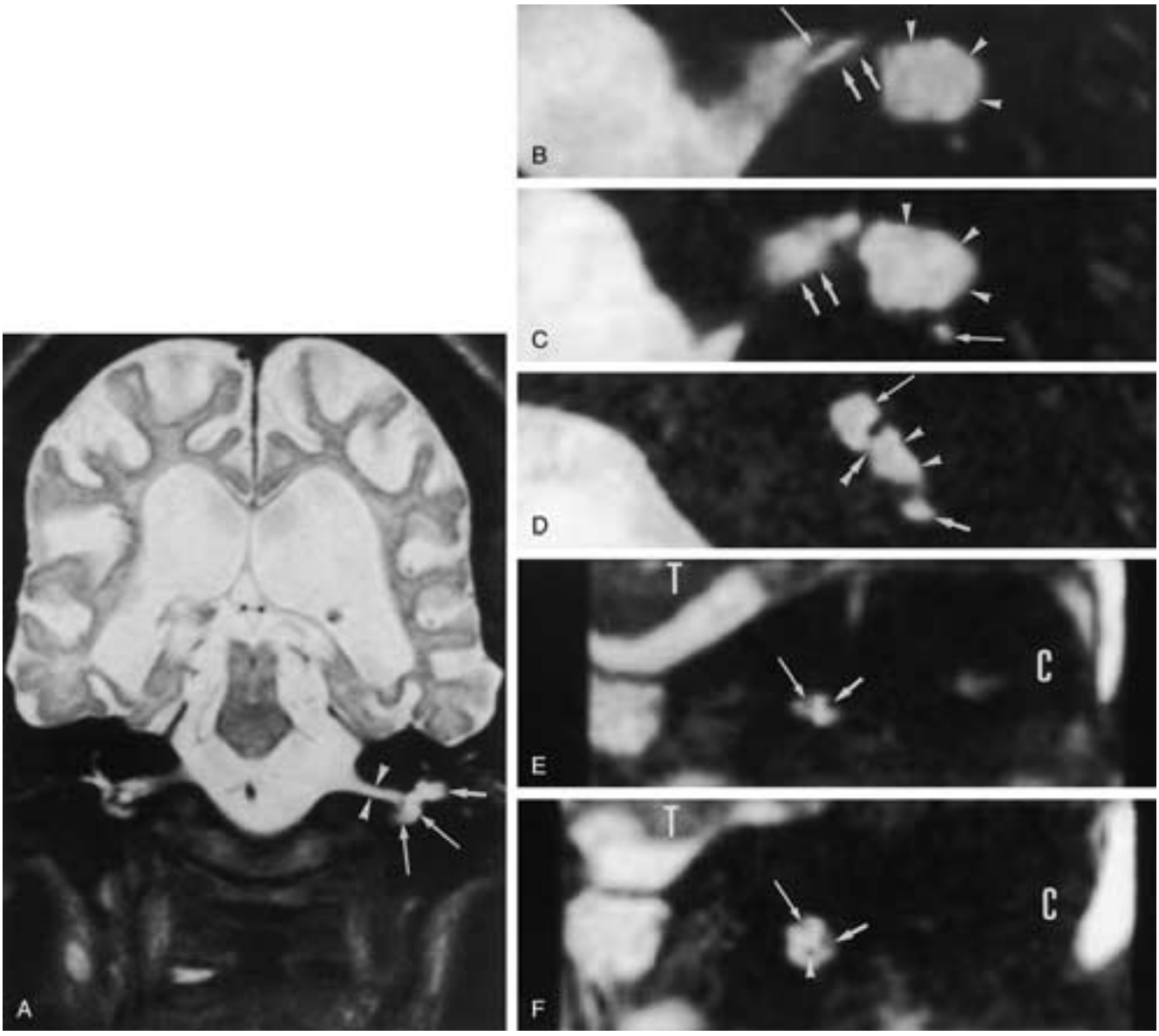

VIEW IMAGE

FIGURE 21-11 Cockayne's syndrome in a 20-year-old girl with atrophic appearance of the brain, severe dysplasia of the left inner ear, and malformation of the VCN. **A**, Coronal Turbo-SE T2-weighted image through the brain and inner ears. The ventricles and sulci are enlarged, and there is severe brain atrophy for a patient of this age, a typical finding in Cockayne syndrome. The left IAC is stenotic (*white arrowheads*), and the lateral semicircular canal (*small white arrow*) and cochlea (*long white arrows*) are enlarged in comparison with the normal right side. **B** to **D**, Axial 3DFT-CISS image through the upper part (**B**) and inferior part (**C**) of the IAC and through the inferior part of the abnormal membranous labyrinth (**D**). **B**, A fluid-filled ''cystic vestibule/lateral semicircular duct'' structure can be recognized (*white arrowheads*). The facial nerve (*long white arrow*) and a common VCN (*small white arrows*) can be seen near the fundus of the IAC. **C**, The cystic inner ear structure can again be depicted (*white arrowheads*), and the posterior semicircular duct has a normal appearance (*long white arrow*). The IAC contains CSF only at the level where normally a cochlear and inferior vestibular branch of the eighth nerve are found (*small white arrows*). **D**, A dysplastic cochlea (*long white arrow*) and vestibule (*white arrowheads*) can be found, and these structures are linked with one another (*double arrowhead*). Posterior semicircular duct (*small white arrow*). **E** and **F**, Parasagittal 3DFT-CISS reconstructions made perpendicular to the nerves in the middle one third of the left (**E**) and right (**F**) IAC. **E**, The facial nerve *(long white arrow*) and an undividing common VCN (*small white arrow*) can be seen in a narrowed IAC. **F**, Compare this with the normal size of the right IAC. A normal facial nerve (*long white arrow*), cochlear branch (*white arrowhead*), and common undivided vestibular branch (*small white arrow*) of the eighth nerve can be seen on the normal right side. Cerebellum (*C*), temporal lobe (*T*).

Copyright © 2003, Mosby, Inc. All rights reserved.

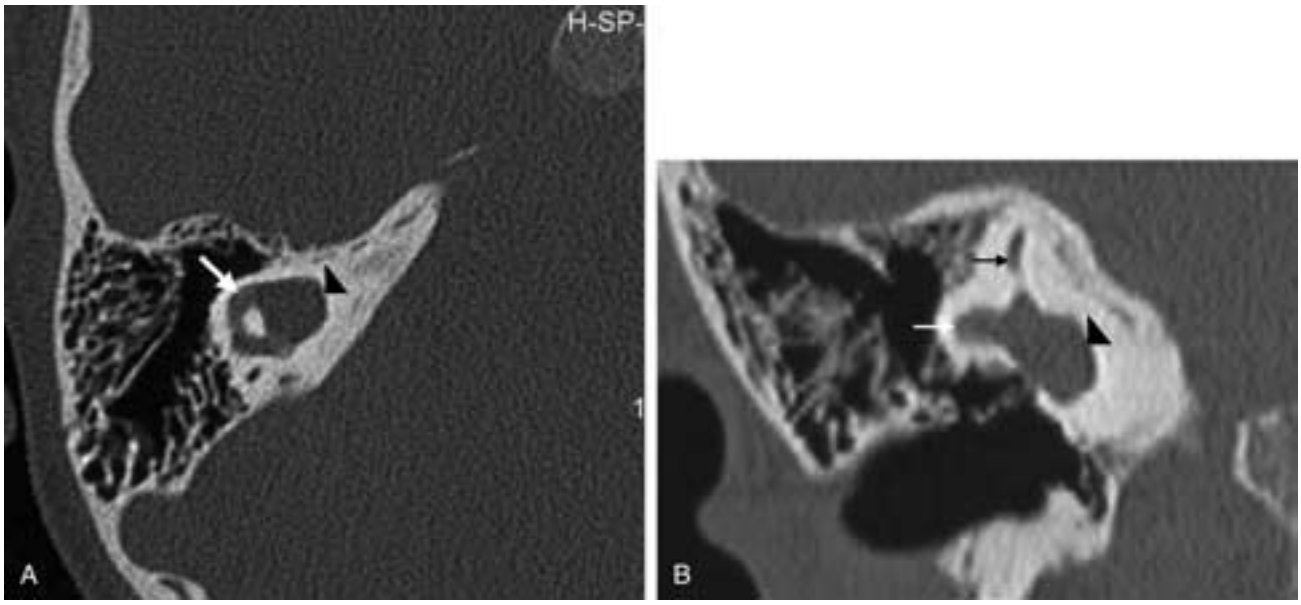

VIEW IMAGE

FIGURE 21-12 Enlarged vestibule. **A,** Axial CT image showing enlarged vestibule (*black arrowhead*) and partial incorporation of a widened lateral semicircular canal (*white arrow*). **B**, Coronal CT image of the same patient showing the same condition as in **A** (*black arrow* = normal superior semicircular canal, *white arrow* = widened lateral semicircular canal, *black arrowhead* = enlarged vestibule).

narrowing of the semicircular ducts (Figs. 21-12 to 21-19). This deformity may be bilateral and may be associated with other inner ear malformations (Fig. 21-16).

Semicircular duct aplasia is far less common than dysplasia. The deformity may be bilateral and may occur in combination with a normal or near-normal cochlea. The first cases of this entity were reported by Parnes and Chernoff.[33] If such an anomaly were caused by arrested development, the cochlea should also be malformed. Thus, occasionally, a specific aberration may occur, halting further development at a confined level.[30] Absence of all semicircular ducts is known to occur frequently in patients with CHARGE syndrome (Fig. 21-20 and Table 21-1). Isolated aplasia of the posterior semicircular duct has been described in patients

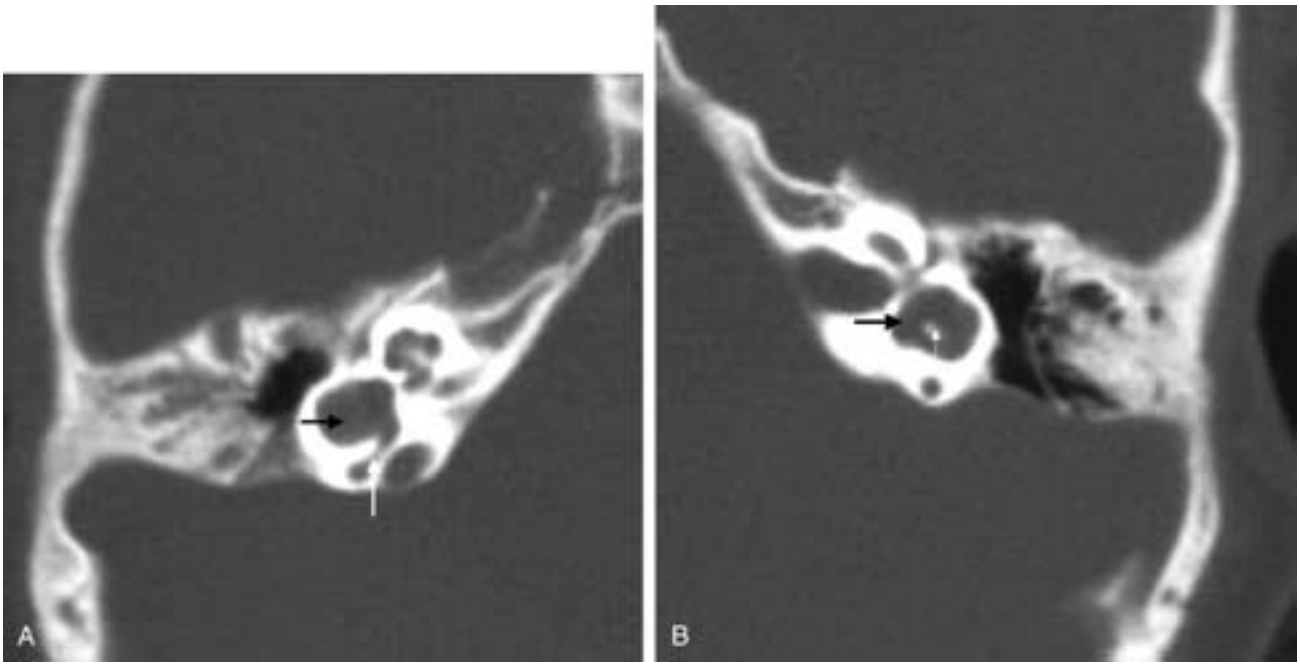

VIEW IMAGE

FIGURE 21-13 Enlarged vestibules. **A**, Axial CT image showing complete assimilation of the right lateral semicircular canal into the vestibule (*black arrow*). Note the normal posterior semicircular canal (*white arrow*). **B**, Axial CT image showing nearly complete assimilation of the left lateral semicircular canal into the vestibule (*black arrow*). Note the small central bony core (*white arrow*).

Copyright © 2003, Mosby, Inc. All rights reserved.

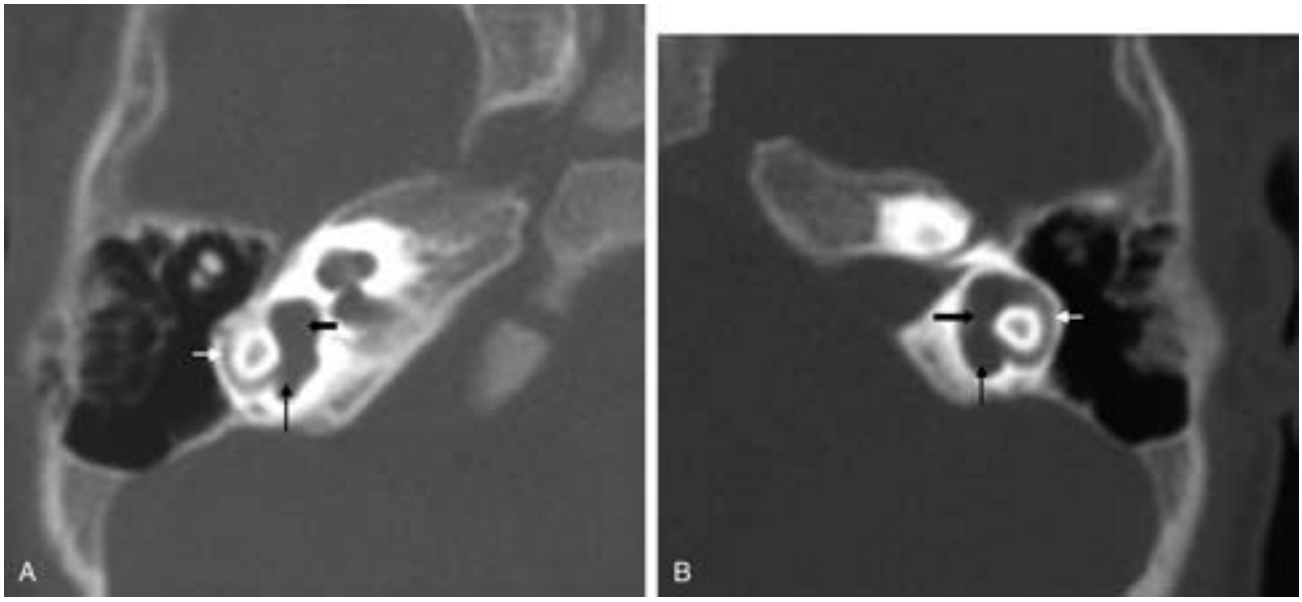

VIEW IMAGE

FIGURE 21-14 Anomalies of the lateral and posterior semicircular canals. **A** and **B**, Axial CT images of the right and left sides showing dilatation of the posterior semicircular canals (*black arrows*) and the relatively small lateral semicircular canals (*white arrows*). Note the enlarged vestibules (*black block arrows*).

VIEW IMAGE

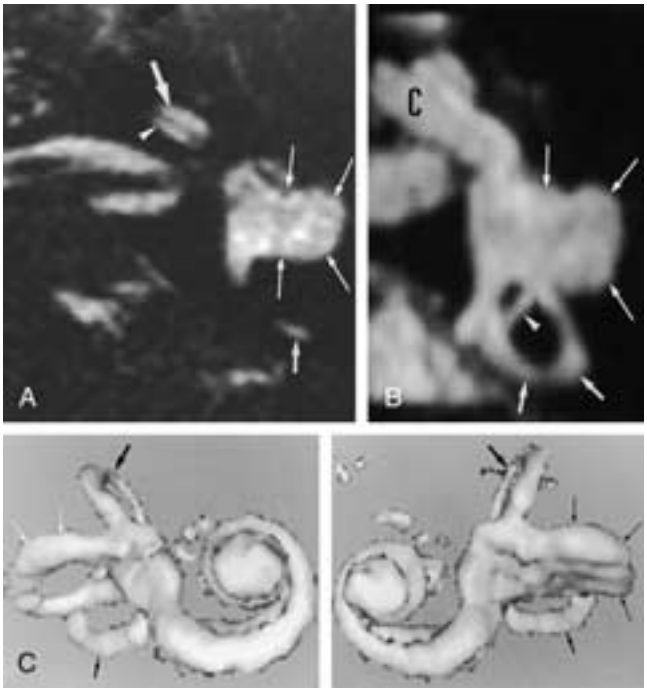

FIGURE 21-15 Lateral semicircular canal-vestibule dysplasia (LCVD) of the left inner ear. **A**, Axial 1 mm thick 3DFT-CISS gradient-echo image. Normal fluid is recognized in the scala vestibuli/media (*large white arrow*) and scala tympani (*white arrowhead*) of the cochlea. The fluid in the vestibule cannot be separated from the fluid in the lateral semicircular canal, and both structures form a fluid-filled cystic or saccular cavity (*long white arrows*). There is fluid in the posterior semicircular duct (*small white arrow*). **B**, Three-dimensional maximum intensity projection of the 3DFT-CISS images viewed from above. A normal amount of fluid can be detected in the cochlea (*C*). The LCVD deformity can be appreciated on this reconstructed image (*long white arrows*). Normal posterior (*small white arrows*) and superior (*white arrowhead*) semicircular ducts can be recognized. **C** and **D**, Three-dimensional virtual images of the right (**C**) and left (**D**) membranous labyrinths, made by using 0.7 mm thick T2-weighted gradient-echo images. The superior (*large black arrows*) and posterior (*small black arrows*) semicircular ducts have a normal shape on both sides. The vestibule and the basal, second, and apical turns of the cochlea also appear normal on both sides. A normal lateral semicircular duct can be seen on the right side (*long white arrows*), while a saccular lateral semicircular duct or LCVD can be depicted on the left side (*long black arrows*).

Copyright © 2003, Mosby, Inc. All rights reserved.

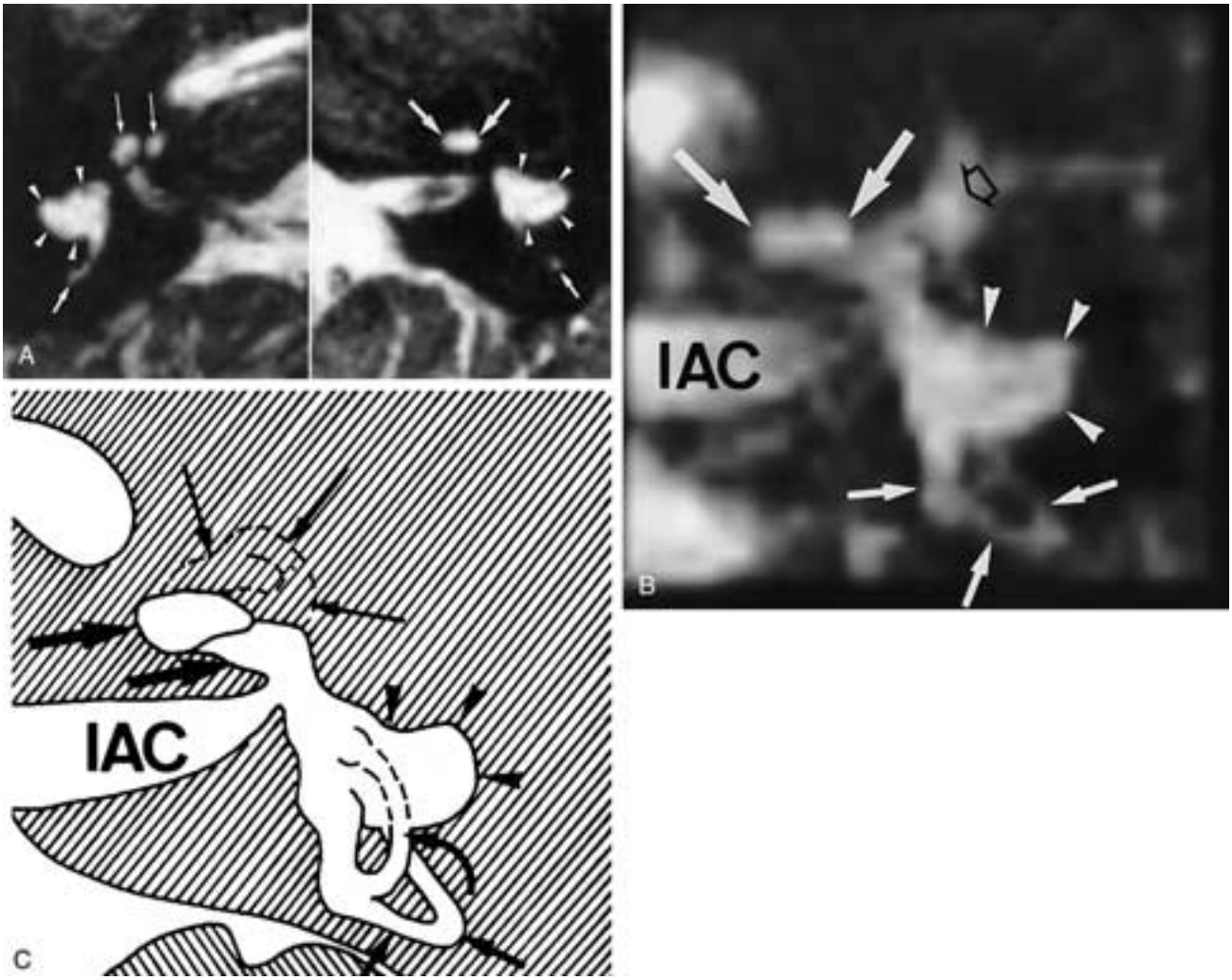

VIEW IMAGE

FIGURE 21-16 Bilateral common lateral semicircular duct–utriculosaccular cavity associated with cochlear hypoplasia on the left side. **A**, Axial 0.7 mm thick gradient-echo images through both inner ears. The lateral semicircular duct is seen as a cystic structure, and it cannot be separated from the fluid inside the vestibule (*white arrowheads*) on either side. A normal fluid-filled posterior semicircular duct is seen (*small white arrows*). Fluid can be detected in the basal turn and second turn of the normal cochlea of the right inner ear (*long white arrows*). The left cochlea is hypoplastic, and only three quarters of the basal turn is present, resulting in a reduction of the maximal dimension of the basal turn (*large white arrows*). **B** and **C**, Gradient-echo image, 3D reconstruction of the left inner ear with corresponding diagram. The fluid-filled saccular semicircular canal (*arrowheads*), the normal posterior semicircular duct (*small arrows*), and the hypoplastic cochlea represented by a rudimentary basal turn (*large arrows*) can all be recognized. (See Fig. 21-15B for comparison with a normal cochlea.) *Long black arrows,* absent part of the cochlea; *open arrow*, superposition of venous structures; *curved arrow*, superior semicircular duct; *IAC*, internal auditory canal.

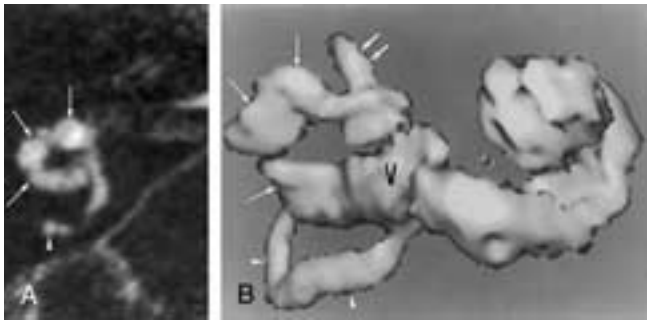

VIEW IMAGE

FIGURE 21-17 Enlarged lateral semicircular duct. **A**, Axial 0.7 mm thick T2-weighted gradient echo image through the right inner ear. A fluid-filled thickened lateral semicircular duct can be seen (*long white arrows*). Compare this with the normal thickness of the posterior semicircular duct (*white arrowhead*). **B**, Three-dimensional virtual image of the right membranous labyrinth, made by using 0.7 mm thick T2-weighted gradient-echo images. The irregular and enlarged lateral semicircular duct can be recognized (*long white arrows*). The superior (*small white arrows*) and posterior (*white arrowheads*) semicircular ducts have a normal size. *V*, vestibule.

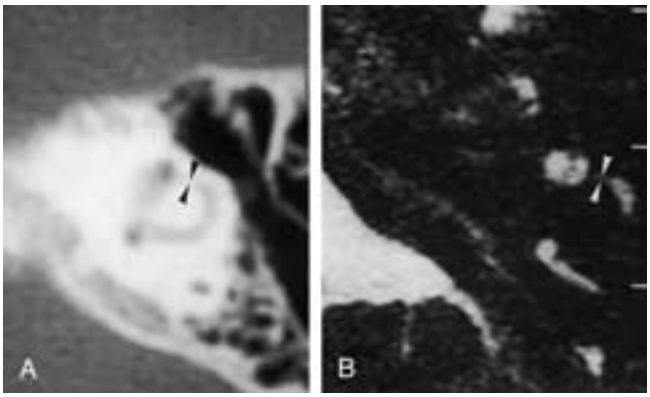

VIEW IMAGE

FIGURE 21-18 Stenosis of the ampulla of the lateral semicircular duct in a patient with the branchio-oto-renal syndrome. **A**, Axial CT image through the left lateral semicircular canal. The lateral semicircular canal is narrowed at the site where the ampulla normally is found (*black arrowheads*). **B**, Corresponding axial T2-weighted gradient-echo image through the left lateral semicircular duct. The fluid-filled ampulla of the lateral semicircular duct is stenotic (*white arrowheads*).

Copyright © 2003, Mosby, Inc. All rights reserved.

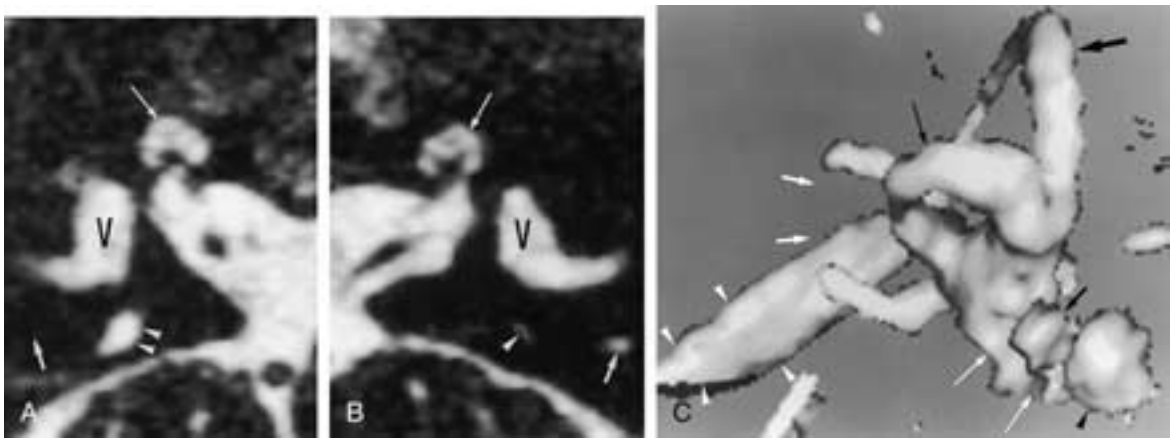

VIEW IMAGE

FIGURE 21-19 Partial absence of the posterior semicircular canal. **A**, Axial T2-weighted gradient-echo image through the right inner ear. A normal vestibule (*V*) can be seen. The cochlea is too small; the apical and second turns (*long white arrow*) are developed but are too small. A large endolymphatic duct/sac can be recognized (*white arrowheads*). The posterior semicircular duct cannot be seen; there is no high signal intensity at the site where the duct should be (*small white arrow*). **B**, Axial T2-weighted gradient-echo image through the left inner ear. Hypoplasia of the apical and second turns of the cochlea can again be appreciated (*long white arrow*). High signal intensity fluid can be seen in the posterior semicircular duct on the left side (*small white arrow*), and the endolymphatic duct has a normal size (*white arrowhead*). Normal vestibule (*V*). **C**, Three-dimensional virtual image of the right membranous labyrinth, made by using 0.7 mm thick T2-weighted gradient-echo images. The interruption of the posterior semicircular duct can be recognized (*small white arrows*). The large endolymphatic duct/sac can be seen (*white arrowheads*). The apical turn (*black arrowhead*) and the second turn of the cochlea (*small black arrow*) are slightly hypoplastic, but the basal turn (*long white arrows*) is severely hypoplastic (compare this with the normal cochlea in Figs. 21-15C, D and 21-17B, and especially with the same view in Fig. 21-51F). Normal lateral (*long black arrow*) and superior (*large black arrow*) semicircular ducts. The middle part of the posterior semicircular canal also cannot be seen on CT (not shown). This excludes fibrous obliteration of this segment of the canal. Labyrinthitis ossificans involving the posterior semicircular canal cannot be excluded. However, the association with several other congenital malformations, the absence of other obliterations or calcifications of the membranous labyrinth, and the normal aeration of the adjacent middle ear and mastoid all support the diagnosis of congenital absence of the middle part of the posterior semicircular duct.

with Waardenburg's and Alagille's syndromes.[34] Patients with semicircular duct aplasia may present with vertigo or abnormal findings during vestibular testing, and there is absence of fluid-filled semicircular ducts on MR imaging (Fig. 21-19). Occasionally, the lumen of a semicircular duct may be partially or completely obliterated with fibrous or calcified tissue, which may give the impression of aplasia on MR imaging. Therefore, confirmation of the absence of the semicircular canals with CT may be necessary for differentiation between aplasia and fibrous or calcified obliteration of the canals, as can be seen with labyrinthitis ossificans (Fig. 21-21).

Another presumed anomaly of the semicircular canals that has been described only recently with high-resolution CT of the temporal bone is dehiscence of the roof of the superior semicircular canal (SSCC).[35, 36] This defect can be best appreciated on coronal images through the temporal bone (Fig. 21-22). This anomaly may be associated with a clinical entity known as Tullio's phenomenon, which consists of sound-induced vertigo, nystagmus, or both. Normally, sound is transmitted from the stapes through the oval window into the cochlea, where the hair cells are activated, causing neural stimulation. The round window allows the sound pressure to dissipate and transmits it back to the middle ear. The semicircular canals do not normally have a window to dissipate pressure. Therefore, the pressure in the canals remains constant, without vibration of the related hair cells. However, the dehiscence of the roof of the superior semicircular canal acts as a ''mobile'' window and allows the sound pressure to be transmitted into the vestibular apparatus, stimulating the hair cells and producing vertigo.[37]

Vestibule/Utriculosaccular Structures

Anomalies of the vestibule or utriculosaccular structures rarely occur as an isolated event. More frequently, they are present in association with other inner ear anomalies.[38] As previously discussed, the vestibular/utriculosaccular anomalies often consist of complete (Fig. 21-15) or partial (Fig. 21-23) assimilation of the semicircular canals (usually the lateral semicircular canal) into the vestibule.[32] Occasionally, subtle enlargement or malformation of the vestibule (Figs. 21-23 and 21-24) and semicircular ducts can be detected on CT or MR imaging. Rarely, an enlarged globular vestibule may be found without assimilation of the semicircular canals. This anomaly of the inner ear has been associated with thalidomide-induced deafness.[38]

Cochlea

Jackler et al. proposed a classification system of cochlear anomalies based on their experience with radiographs (CT and polytomograms). In this system, each anomaly was proposed to be the result of an arrest of maturation or development of the cochlea at different stages of organogenesis.[32] Many of these cochlear anomalies, first identified radiographically with polytomography and then CT, have

Copyright © 2003, Mosby, Inc. All rights reserved.

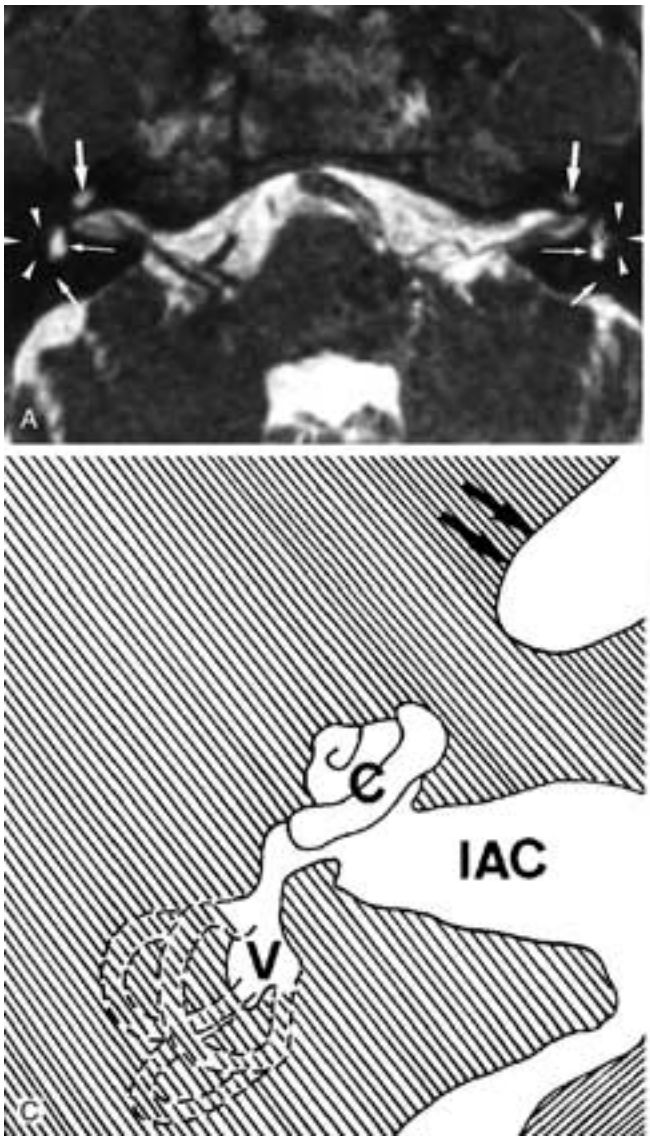

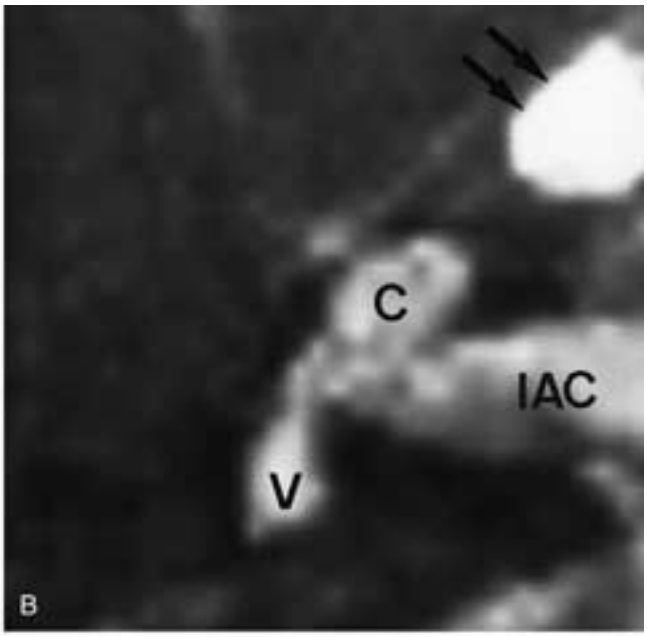

FIGURE 21-20 Bilateral complete semicircular duct aplasia. **A**, Axial gradient-echo image through both inner ears. Normal fluid is seen in the cochlea (*large white arrows*) and vestibule (*long white arrows*). No fluid is seen at the sites where the lateral semicircular ducts (*white arrowheads*) and posterior limbs of the posterior semicircular ducts (*small white arrows*) are normally situated. **B**, and **C**, Gradient-echo image, 3D reconstruction of the right inner ear and corresponding diagram. High signal CSF and intralabyrinthine fluid are seen in the internal auditory canal (*IAC),* cochlea (*C*), and vestibule (*V*), respectively. The semicircular canals are absent (*dotted lines* on drawing), and no intralabyrinthine fluid is seen lateral and posterior to the vestibule. (*Large black arrows*, ICA.)

VIEW IMAGE

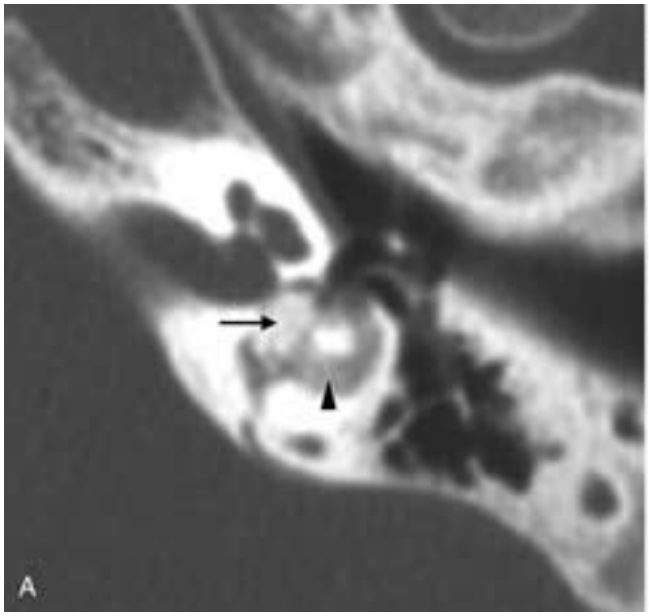

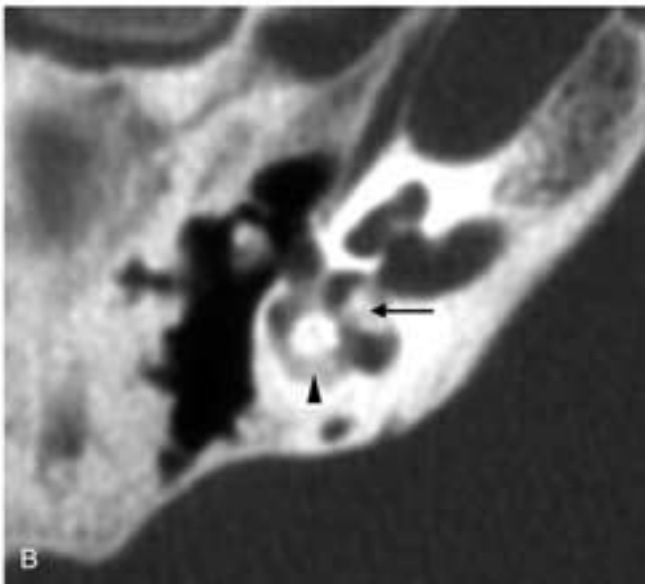

FIGURE 21-21 Labyrinthitis ossificans. **A** and **B**, Axial CT images showing ossification of the labyrinth bilaterally, consistent with labyrinthitis ossificans (*black arrows*, vestibules; *black arrowheads*, lateral semicircular canals).

VIEW IMAGE

Copyright © 2003, Mosby, Inc. All rights reserved.

also been identified with MR imaging. While many cochlear anomalies fit into this classification system, there are some that do not. These include cochleas with extra turns, cochlear duplications, and small ''dwarf''-type cochleas that are small or hypoplastic but do possess the normal number of turns.[24] These anomalies may result from ''aberrant'' rather than ''arrested'' development, according to Jackler et al. As well, since their classification system was based on anomalies detected by polytomography and/or CT, some of the cochlear anomalies recently described with MR imaging are difficult to place. For example, defects between the scala vestibuli/media and scala tympani can sometimes be the only detectable deformities in an otherwise normal bony labyrinth and cochlea. These changes may not be seen on CT and may be detectable only on high-resolution, T2-weighted gradient echo or fast spin echo images (Fig. 21-25).

The spectrum of cochlear anomalies as described by Jackler et al. ranged from early arrest of development, cochlear aplasia, to late arrest of development, cochlear partition defects (Figs. 21-26 to 21-28). At imaging these abnormalities can be classified approximately following Jackler et al.'s classification of cochlear anomalies:

- *Complete Labyrinthine Aplasia (Michel's Deformity).* In complete labyrinthine aplasia there is no inner ear development. In place of the normal inner ear structures, a small, single cystic cavity or several small cavities are present. This description corresponds to the histopathology classically described by Michel and represents an early failure in development correlating with the third gestational week. It is essentially an aplasia of the inner ear and is very rare.[3]
- *Common Cavity*. Arrested growth during the fourth fetal week results in a common cavity for the cochlea and vestibule. There is a large cystic cavity with no internal architecture. One fourth of all cochlear anomalies are common cavity malformations. The semicircular canals may be normal or malformed (Figs. 21-27 and 21-28).
- *Cochlear Aplasia*. Arrested development during the fifth week of embryogenesis produces aplasia of the

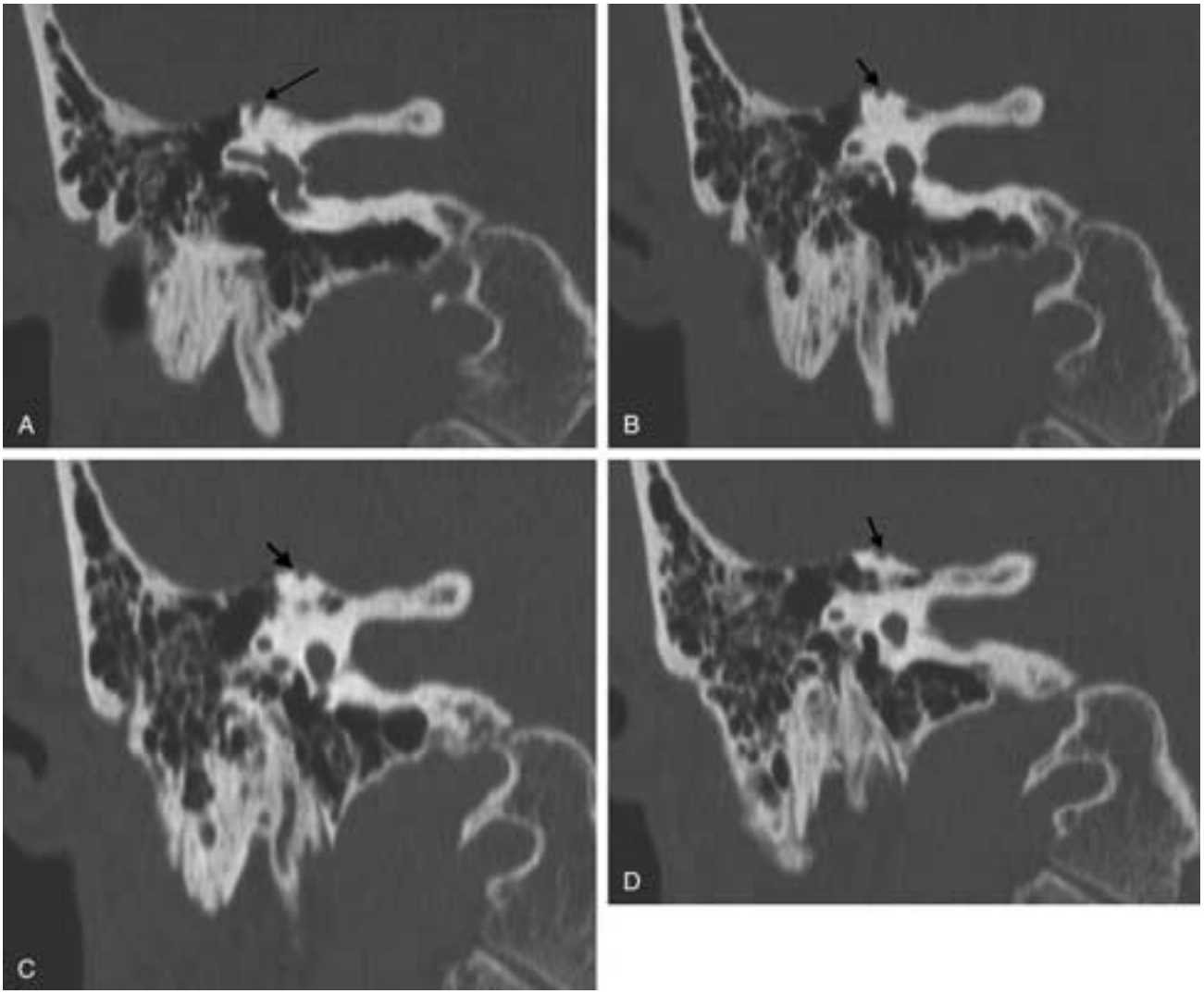

FIGURE 21-22 Tullio's phenomenon: pressure- or sound-induced vertigo. **A** to **D**, four contiguous coronal CT images showing dehiscence of the right superior semicircular canal (*black arrows*).

Illustration continued on following page

VIEW IMAGE

Copyright © 2003, Mosby, Inc. All rights reserved.

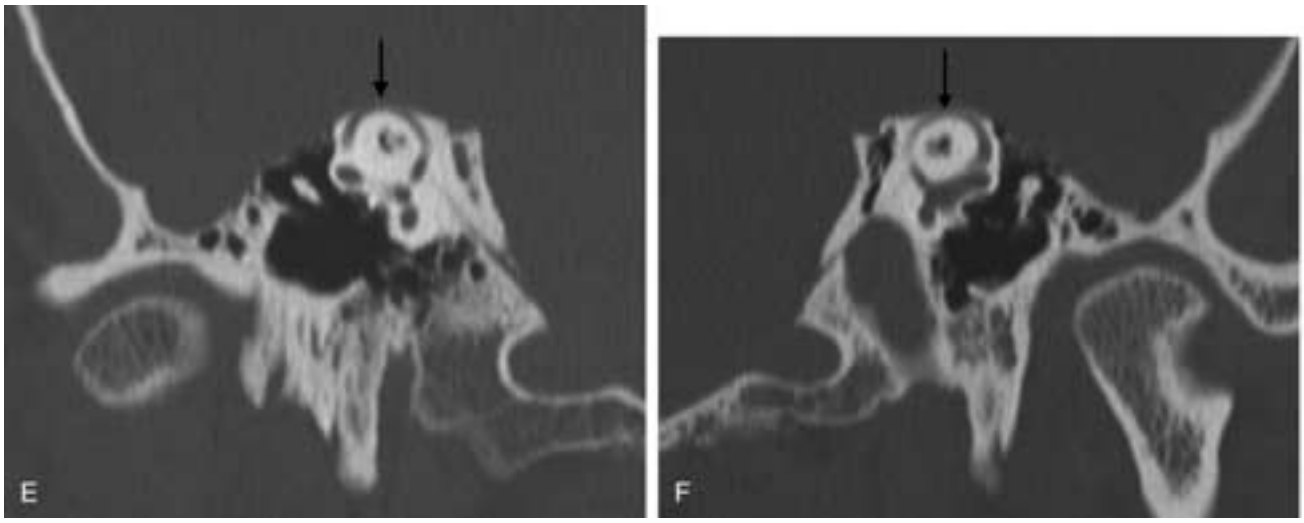

VIEW IMAGE

FIGURE 21-22 *Continued.* **E** and **F**, Oblique coronal reconstruction showing both the right and left superior semicircular canals in full with dehiscence of the roofs, greater on the right than on the left.

cochlea. The cochlea fails to form. The other elements of the inner ear (i.e., the vestibule and semicircular canals) may be normal or malformed.

- *Cochlear Hypoplasia*. Cochlear hypoplasia displays a small rudimentary cochlear bud associated with a normal or malformed vestibule and semicircular canals. Cessation of cochlear development during the sixth week of intrauterine life is the probable cause of this defect (Figs. 21-16, 21-19).
- *Incomplete Partition and Dilatational Defects (Including Classic Mondini's Dysplasia*). This entity represents a small cochlea with an incomplete partitioning of or absent interscalar septum. There is a basilar cochlear turn and a common cloaca or cavity where the middle and apical turns would normally occur. The abnormalities of the bony labyrinth in this anomaly can readily be identified on CT (Fig. 21-29), and the membranous abnormalities can be identified with T2-weighted gradient echo (Fig. 21-30) or fast spin echo MR images. Since the scala tympani and vestibuli can normally be shown as distinct structures on MR imaging,[29] the interscalar septal defects and the absence of the osseous spiral lamina of the middle and apical turns that result in a scala communis cochleae can be identified (Figs. 21-31 and 21-32). Anomalies of the remaining inner ear, such as dilatation of the vestibular aqueduct, may also be present. The vestibule and semicircular canals may be normal or malformed. Arrest of maturation at the seventh week of intrauterine life may result in this type of incomplete partition defect. Incomplete partition of the cochlea characterizes a classic histologic malformation first described by Mondini in 1791. Mondini documented a flat cochlea having 1½ turns instead of the normal 2½ to 2¾ turns. He also described a large vestibule.[39] Aside from Scheibe's deafness, Mondini's malformation is probably the most common form of genetic deafness.[40] A Mondini malformation is frequently present in patients with the branchio-oto-renal syndrome (Fig. 21-31).

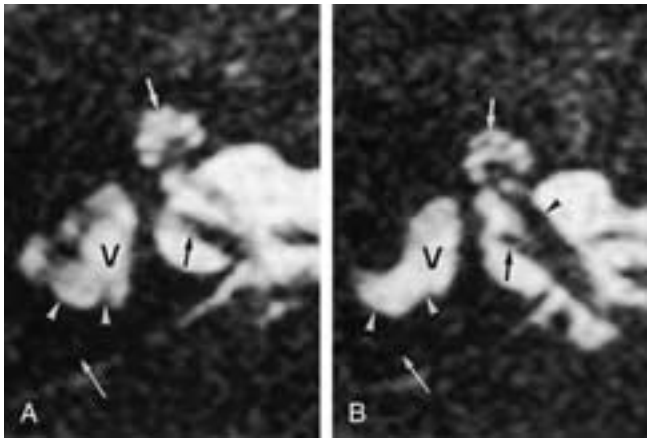

VIEW IMAGE

FIGURE 21-23 Globular enlargement of the utriculosaccular structures in association with semicircular duct malformations. **A**, Axial 0.7 mm thick T2-weighted gradient-echo (3DFT-CISS) images through the upper part of the right utriculosaccular structures. Enlarged fluid-filled utriculosaccular structures can be seen inside the vestibule (*V*). The lateral semicircular duct (*white arrowheads*) is irregular and too thick and is partially incorporated in the large vestibule. The posterior semicircular duct is absent (*long white arrow*). Normal cochlea (*small white arrow*) and inferior vestibular branch of the VCN (*small black arrow*). **B**, Axial T2-weighted gradient-echo image through the inferior part of the utriculosaccular structures. The posterior part of the lateral semicircular duct is too large (*white arrowheads*). The posterior semicircular duct is absent (*long white arrow*), and the utriculosaccular structures inside the vestibule (*V*) are still a little too large. Normal cochlea (*small white arrow*), inferior vestibular (*small black arrow*), and cochlear (*black arrowhead*) branch of the VCN.

More subtle partition defects than the Mondini malformation have been described since the Jackler et al. classification system was first proposed. Included in this group are modiolar and interscalar septal defects. Lemmerling et al.[41] described the normal modiolus on high-resolution, thin-section CT as an ''hourglass-shaped, rectangular, triangular, or trapezoidal bony structure located along the central axis of the basal and middle turns of the cochlea.'' They described four distinct parts of the modiolus, which were best appreciated on the ''midmodiolar'' view. On this view, the medial and lateral portions of the modiolar base were

Copyright © 2003, Mosby, Inc. All rights reserved.

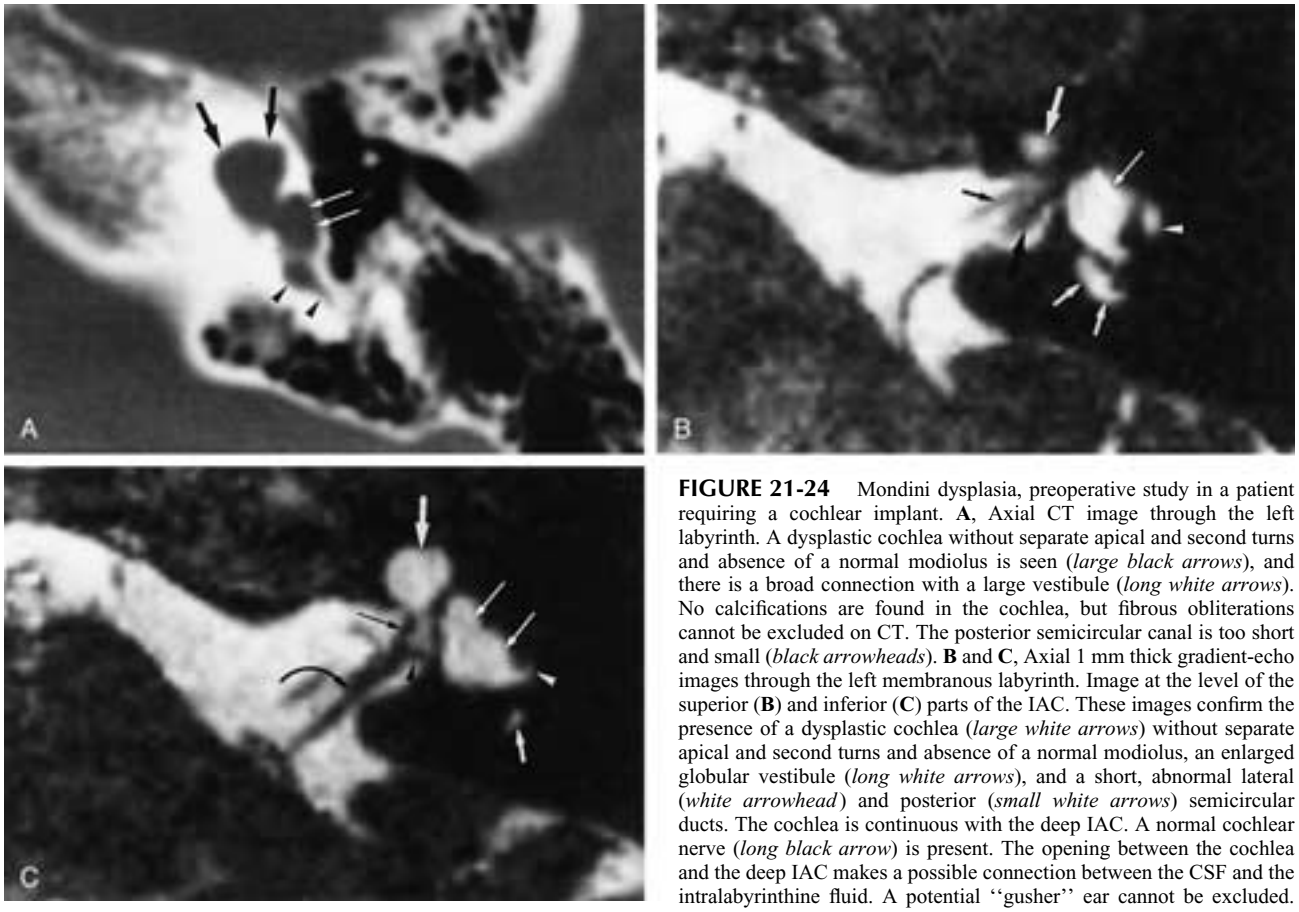

VIEW IMAGE

FIGURE 21-24 Mondini dysplasia, preoperative study in a patient requiring a cochlear implant. **A**, Axial CT image through the left labyrinth. A dysplastic cochlea without separate apical and second turns and absence of a normal modiolus is seen (*large black arrows*), and there is a broad connection with a large vestibule (*long white arrows*). No calcifications are found in the cochlea, but fibrous obliterations cannot be excluded on CT. The posterior semicircular canal is too short and small (*black arrowheads*). **B** and **C**, Axial 1 mm thick gradient-echo images through the left membranous labyrinth. Image at the level of the superior (**B**) and inferior (**C**) parts of the IAC. These images confirm the presence of a dysplastic cochlea (*large white arrows*) without separate apical and second turns and absence of a normal modiolus, an enlarged globular vestibule (*long white arrows*), and a short, abnormal lateral (*white arrowhead*) and posterior (*small white arrows*) semicircular ducts. The cochlea is continuous with the deep IAC. A normal cochlear nerve (*long black arrow*) is present. The opening between the cochlea and the deep IAC makes a possible connection between the CSF and the intralabyrinthine fluid. A potential ''gusher'' ear cannot be excluded. *Short black arrow,* facial nerve; *large black arrow*, superior vestibular branch; *black arrowhead*, inferior vestibular branch; *curved black arrow*, vestibulocochlear nerve.

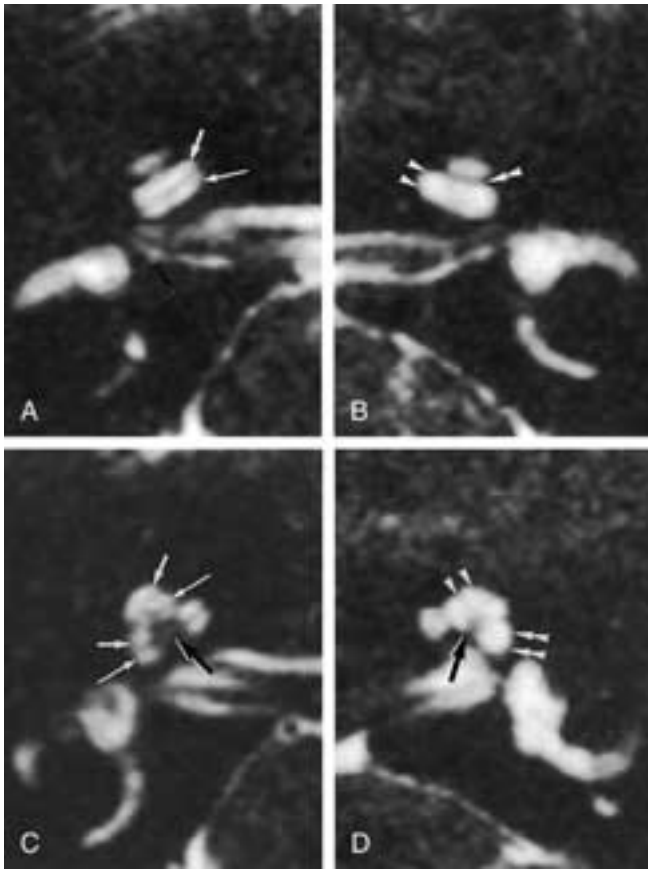

VIEW IMAGE

FIGURE 21-25 Absence of the barrier between the scala tympani and vestibuli in the left cochlea in a patient with congenital deafness on the left side. **A** and **B**, Axial 0.7 mm thick, T2-weighted gradient-echo images through the upper part of the right (**A**) and left (**B**) cochleas. A clear separation can be seen between the scala vestibuli/media (*small white arrow*) and scala tympani (*long white arrow*) of the second turn of the right cochlea. On the left side, only a bony separation can be seen between the apical and second turns (*double arrowhead*); there is no separation between the scala vestibuli/media and scala tympani (*white arrowheads*). The intrascalar defect was the only visible lesion in an otherwise normal-appearing cochlea on CT and MR imaging. **C** and **D**, Similar images at the level of the right (**C**) and left (**D**) modioli. The scala vestibuli/media (*small white arrows*) and tympani (*long white arrows*) can be separated from one another in the second and basal turns of the right cochlea. The modiolus has a normal appearance and can be seen as a low signal intensity structure at the base of the cochlea (*large black arrow*). The scala vestibuli/media and scala vestibuli form a single fluid-containing cavity in both the second (*white arrowheads*) and basal turns (*double arrowheads*) of the left cochlea. Moreover, the modiolus on the left side is hypoplastic (*large black arrow*) in comparison with the modiolus on the right side.

Copyright © 2003, Mosby, Inc. All rights reserved.

seen posteriorly within the center of the basal turn and between the basal and middle turns. The medial and lateral parts of the interscalar septum then radiated from the modiolus to the bony capsule of the cochlea anteriorly between the basal and middle cochlear turns (Fig. 21-33). Lemmerling et al. defined modiolar defects as nonvisualization of all or part of the modiolus or interscalar septum on the midmodiolar view, which was then classified as a cochlear dysplasia of the incomplete partition variety, according to Jackler et al.'s scheme (Fig. 21-34).

Other Anomalies

There is another entity that also may qualify as a partition defect and modiolar deficiency that has a known pattern of inheritance: X-linked progressive mixed hearing loss or X-linked congenital mixed deafness. This entity was originally described by Olson and Lehman in 1968 in two half-brothers.[42] In this entity, there is dilatation of the lateral part of the IAC, absence or severe hypoplasia of the bony modiolus (with a normal number of cochlear turns) and hypoplasia of the cochlear base, with or without widening of the labyrinthine segment of the facial nerve canal and dilatation of the vestibular aqueduct (Figs. 21-35 and 21-36). There is also fixation of the stapes footplate, which is not readily apparent radiographically.[43, 44] In this condition, the absence or hypoplasia of the modiolus and cochlear base is thought to result in an abnormal fistulous communication between the cerebrospinal fluid (CSF) within the IAC and the perilymphatic fluid in the scala vestibuli. This fistulous communication results in increased pressure within the cochlea and at the oval window at the stapes insertion. This increased pressure causes both a sensorineural and a conductive hearing loss and predisposes to a stapes ''gusher'' (an outpouring of fluid from the inner ear through the oval window into the middle ear cavity) at surgery for the fixed footplate.

Another cochlear anomaly not otherwise classified is scalar asymmetry within the cochlea. This anomaly has only

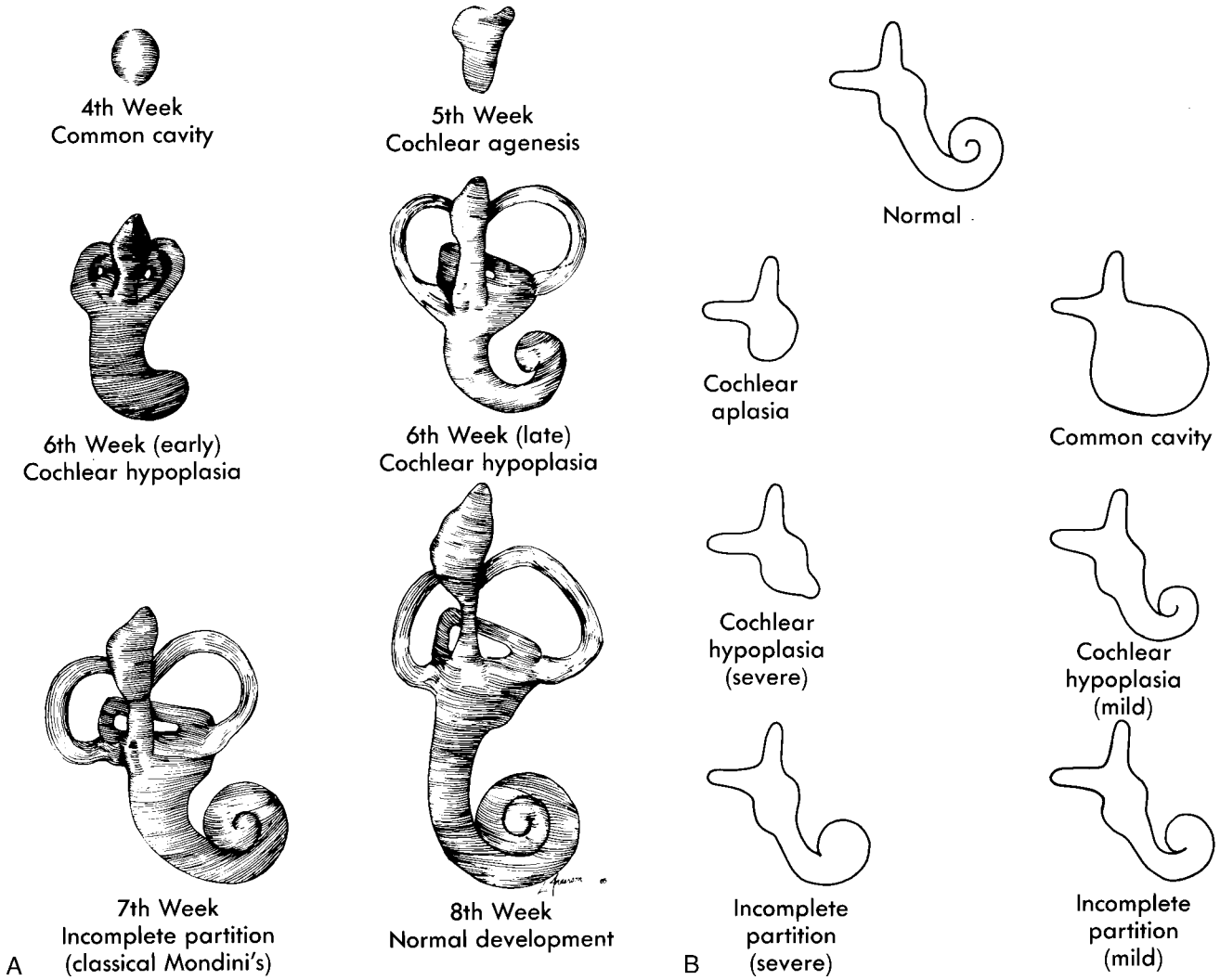

FIGURE 21-26 **A**, Schematic representation of labyrinthine malformations. Anomalies are depicted as a result of arrests during various stages of embryogenesis. **B**, Schematic representation of the radiographic appearance of the continuum of labyrinthine malformations. (From Jackler RK, Luxford WM, House WF. Congenital malformations of the inner ear. Laryngoscope 1987;97:2–14.)

VIEW IMAGE

Copyright © 2003, Mosby, Inc. All rights reserved.

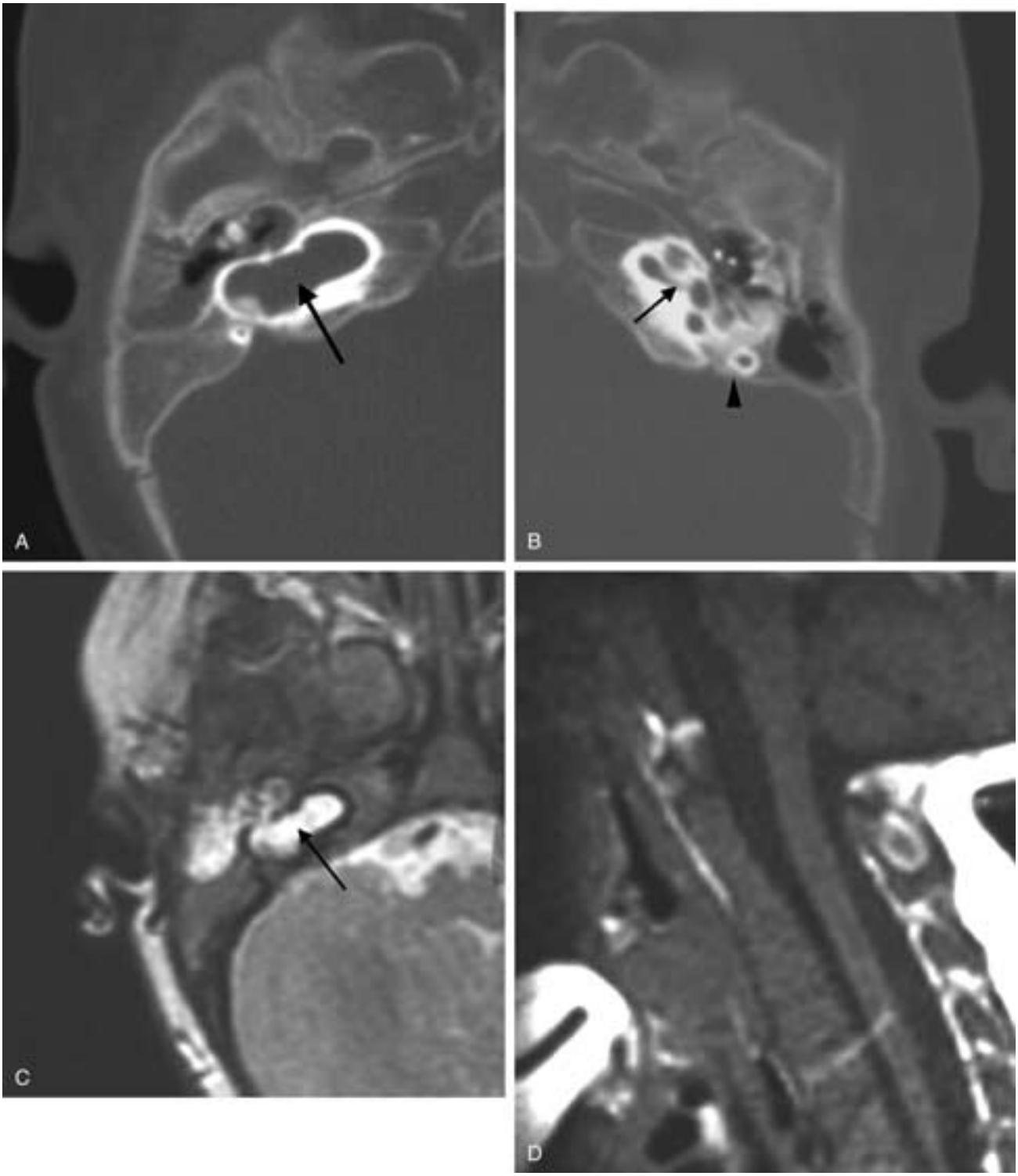

VIEW IMAGE

FIGURE 21-27 Klippel-Feil syndrome/common cavity. **A**, Axial CT image showing no distinct cochlea, vestibule, or semicircular canals and large common cavity (*black arrow*) on the right. **B**, Axial CT image of normal inner structures on the left: normal cochlea (*black arrow*) and normal posterior semicircular canal (*black arrowhead*). **C**, Axial T2-weighted MR image showing the fluid signal intensity in the common cavity (*black arrow*). **D**, Sagittal T1-weighted MR image showing fusion of multiple cervical vertebral bodies.

Copyright © 2003, Mosby, Inc. All rights reserved.

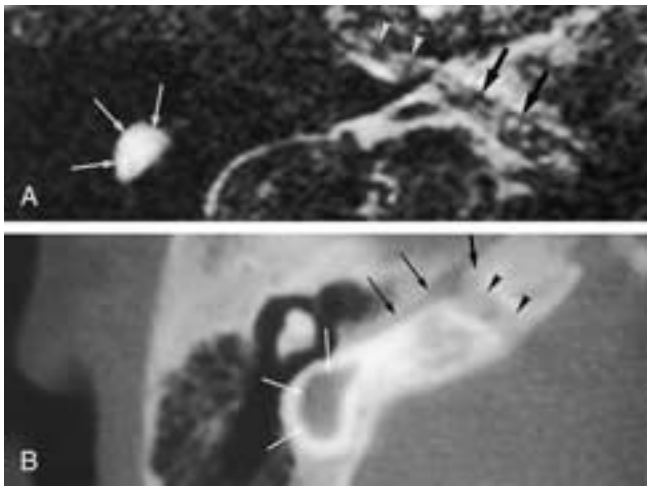

VIEW IMAGE

FIGURE 21-28 Common cavity type of cochlear-vestibular malformation. **A**, Axial 0.7 mm thick gradient-echo image through the left inner ear. Only a single fluid-filled cavity (*long white arrows*) can be seen in the right inner ear. The neurovascular bundle, however, is present in the cerebellopontine angle (*large black arrows*) and the IAC (*white arrowheads*). **B**, Axial CT image through the right inner ear. The single inner ear cavity can again be seen (*long white arrows*). The IAC (*black arrowheads*) and the tympanic segment of the facial nerve canal (*long black arrows*) can be seen. No cochlear structure is visible at the site anterior to the IAC, the site where the cochlea is normally situated (*small black arrow*).

recently been documented with high-resolution, T2-weighted MR imaging. The anterior scalar chamber contains the scala vestibuli and scala media, and the posterior scalar chamber contains the scala tympani. Normally, the anterior and posterior chambers are fairly equal in size. However, in an abnormal setting, the anterior chamber may be larger than the posterior chamber, with a ratio as high as 1.45 to 1.[26] This finding is thought to be a manifestation of cochlear dysplasia, which is often coexistent with an enlarged vestibular aqueduct. The precise relationship of the anomalies is unknown. In cases of enlargement of the anterior chamber, the scala vestibuli has been shown to be enlarged. However, the scala vestibuli contains perilymph and is *not* in direct communication with the endolymphatic system. Rather, the scala media comprises the endolymphatic cochlear duct in continuity with the remainder of the endolymphatic system including the duct and sac. Therefore, the relationship of the aqueduct and the scalar asymmetry is unclear. The scala media has not been shown to be enlarged. Future improvements in resolution may allow better definition of the structure of this anomaly.

The ''dwarf'' cochlea has been mentioned.[24] At CT the cochlea appears to be relatively normal, with a normal number of turns. However, the dimensions of the cochlea are significantly smaller than normal. The diameter of the lumen of the turns of the cochlea is also diminished. This anomaly is considered to be quite rare. The position of the facial nerve in association with this anomaly can be abnormal. The labyrinthine segment can be anteriorly positioned (see the next section).

Internal Auditory Canal and the Vestibulocochlear and Facial Nerves

The normal range of the IAC's diameter is 2 to 8 mm, with an average of 4 mm.[45] Canals smaller than 2 mm are generally considered stenotic. The IAC may also be atretic or may have a bony septum that partitions the canal into two or more separate canals.

CT may readily demonstrate either stenosis or atresia of the IAC by defining the bony margins of the canal (Fig. 21-37). On high-resolution, T2-weighted gradient echo or fast spin echo MR images, the absence of CSF between the

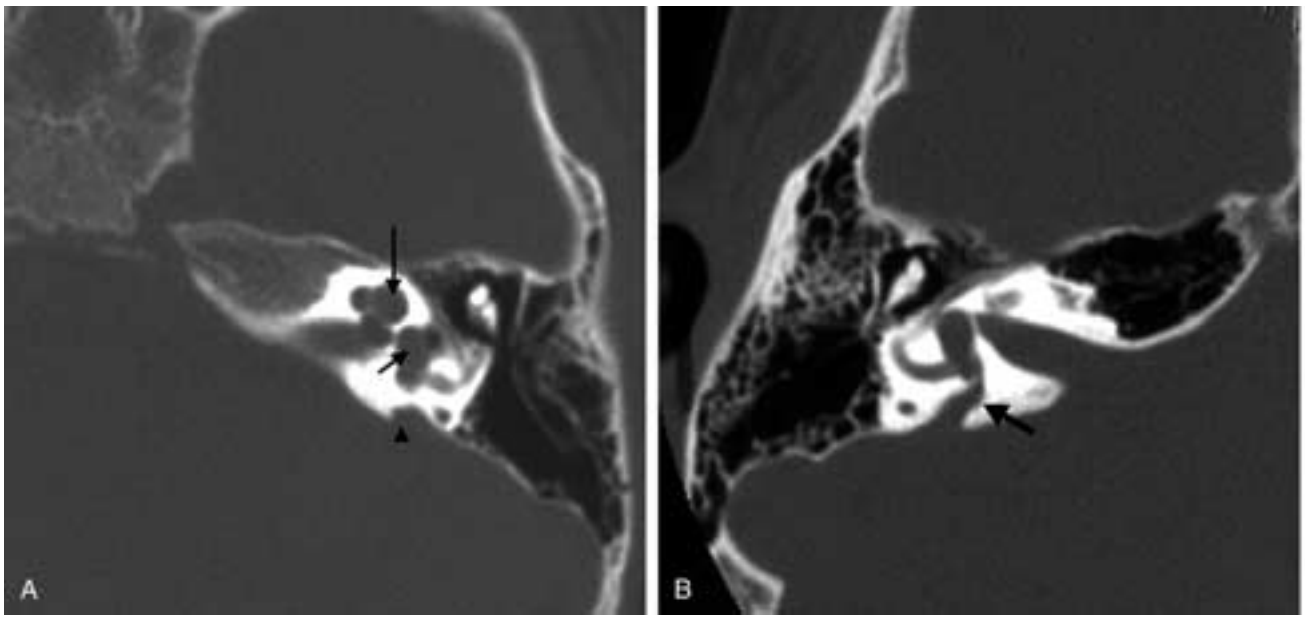

VIEW IMAGE

FIGURE 21-29 Mondini malformation. **A**, Axial CT image showing the sac-like representation of the second and third cochlear turns (*long arrow*), dilated vestibular aqueduct (*arrowhead*), and dilated vestibule (*short arrow*). **B**, Axial CT image of another patient with the Mondini malformation with an enlarged vestibular aqueduct (*black arrow*) extending to the vestibule.

Copyright © 2003, Mosby, Inc. All rights reserved.

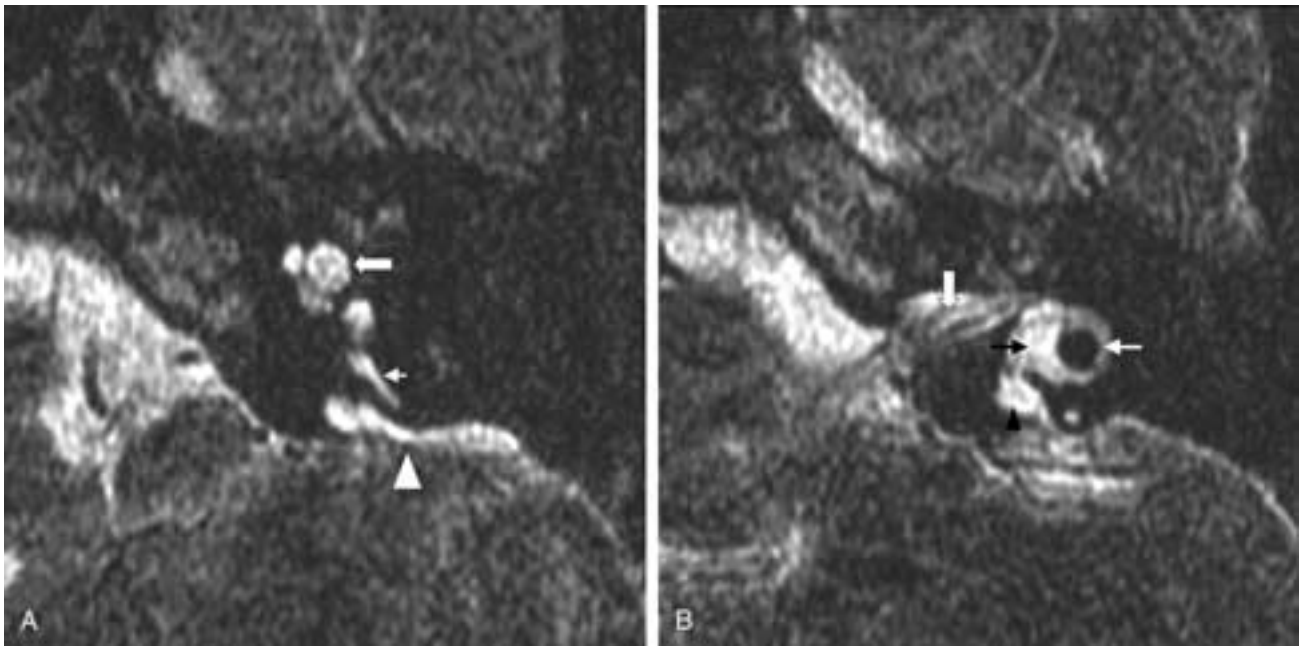

VIEW IMAGE

FIGURE 21-30 Mondini malformation. **A**, High-resolution axial T2-weighted MR image showing dilated endolymphatic sac (*white arrowhead*) and sac-like representation of the second and third cochlear turns (*white block arrow*) and normal posterior semicircular canal (*small white arrow*). **B**, More cephalad image showing the dilated endolymphatic duct (*black arrowhead*) extending to the dilated vestibule (*black arrow*). Also note the normal lateral semicircular canal (*white arrow*) and IAC (*white block arrow*).

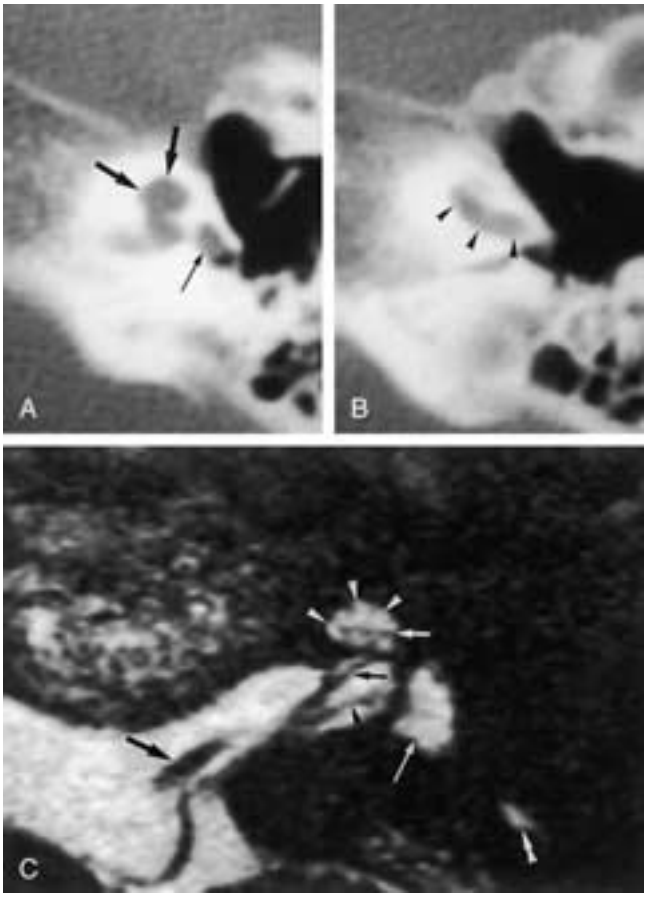

VIEW IMAGE

FIGURE 21-31 Mondini malformation and hypoplasia of the cochlear branch of the VCN in a patient with the branchio-oto-renal syndrome. **A** and **B**, Axial CT image through the apical and second turns of the left cochlea (**A**) and through the basal turn (**B**). The apical and second turns of the cochlea cannot be separated from one another on CT (*large black arrows*). The basal turn, however, has a normal shape and appearance (*black arrowheads*). Normal vestibule (*long black arrow*). **C**, Axial 0.7 mm thick T2-weighted gradient-echo image through the left IAC. An incomplete and obliquely orientated septum (*small white arrow*) is seen between the apical and second turns of the cochlea (*white arrowheads*). The cochlear branch of the VCN (*small black arrow*) is much smaller in diameter than the facial nerve (*large black arrow*). Normally these nerves have a more equal size. Normal vestibule (*long white arrow*), posterior semicircular duct (*double white arrowhead*), and inferior vestibular branch of the eighth nerve (*black arrowhead*).

Illustration continued on following page

Copyright © 2003, Mosby, Inc. All rights reserved.

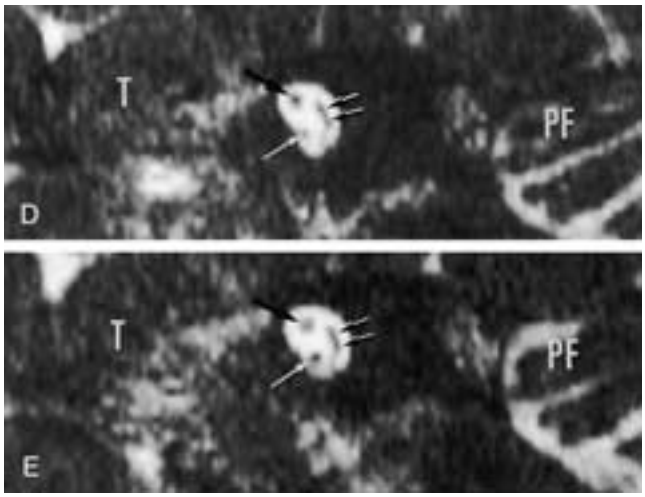

VIEW IMAGE

FIGURE 21-31 *Continued.* **D**, Gradient-echo T2-weighted parasagittal reconstructed image through the lateral part of the left internal auditory canal. On this 3DFT-CISS image the facial nerve (*large black arrow*) has a much larger diameter than the cochlear branch of the VCN (*long white arrow*). The common vestibular branch of the eighth nerve has a normal size (*small black arrows*). **E**, Gradient-echo T2-weighted parasagittal reconstructed image through the lateral part of the normal right IAC for comparison. The facial nerve (*large black arrow*) and cochlear branch of the VCN (*long white arrow*) have a similar diameter, which is a normal finding. The common vestibular branch of the VCN is normal in size (*small black arrows*). *PF*, posterior fossa; *T*, temporal lobe.

cerebellopontine angle and the intralabyrinthine fluid is a reliable sign of atresia. A thin layer of CSF may be seen in the IAC in cases of stenosis (Fig. 21-38).

The relationship of IAC stenosis/atresia to congenital sensorineural hearing loss (SNHL) is unclear. Some patients with unilateral IAC stenosis have normal hearing bilaterally, and others have hearing loss in the ear without stenosis.[46] When there is SNHL in the ear with IAC stenosis, it is unclear whether the bony deformity causes the hearing loss by compressive effects upon the vestibulocochlear nerves (VCN) or whether a membranous deformity of the cochlea or vestibule, not radiographically detectable, results in failure of neural growth induction for the VCN, with subsequent canal hypoplasia.[11, 46–48] In either case, evaluation for hypoplasia or aplasia of the VCN and/or facial nerve within the IAC may be accomplished with MR imaging.

Normally, the vestibulocochlear nerves and facial nerve can be identified when thin-section, high-resolution MR images through the IAC are obtained with any of the various techniques previously discussed. Evaluation for hypoplasia or aplasia of the nerves is best done with direct sagittal images or reconstructions perpendicular to the long axis of the IAC (Fig. 21-39) such that the nerves are visualized in cross section and an accurate assessment of their diameters can be made. In very stenotic IACs, the diagnosis may be difficult due to inability to separate the nerves.

Three types of vestibulocochlear nerve hypoplasia and aplasia can be distinguished.[49] In Type 1, the IAC is stenotic and the VCN is absent (Fig. 21-38). In cochlear implant candidates, it is important to recognize this type of aplasia because the cochlear implantation will not be successful on the side of aplasia and will not be possible when the aplasia is bilateral. In Type 2A, a common VCN is found with aplasia or hypoplasia of its cochlear branch in the presence of a labyrinthine malformation (Figs. 21-39 and 21-40). When the labyrinthine structures are normal, it is a Type 2B malformation (Fig. 21-41). Patients with Type 2 malformations often have residual hearing or only one ear is affected. Therefore, in this group, patients are not necessarily cochlear implant candidates.

Like the VCN, the facial nerve may also be congenitally hypoplastic or aplastic (Figs. 21-42 and 21-43). This anomaly may occur in isolation or as part of Moebius syndrome, also known as congenital facial diplegia, congenital oculofacial paralysis, or congenital abducens–facial paralysis. These patients not only have facial diplegia, but also bilateral lateral rectus muscle paralysis.[50] In patients with isolated congenital facial nerve palsy, the VCN and cochlea are usually normal. However, in Types 1, 2A, and 2B malformations of the VCN, an abnormal course of the facial nerve frequently can be found. The nerve can leave the IAC in its middle third and then continue in a separate facial nerve canal (Fig. 21-44). The nerve can also be situated in a completely separate canal parallel to the IAC (Figs. 21-45 and 21-46). Finally, the nerve can also pass between the temporal bone and temporal lobe.

Duplication of the facial nerve, also referred to as a bifid facial nerve, is another anomaly that, although usually associated with other congenital anomalies, can occur in isolation. Most commonly, the facial nerve will bifurcate along the proximal aspect of the tympanic segment inferior to the lateral semicircular canal into a larger lateral branch and a smaller medial branch. These two branches usually reunite at the stylomastoid foramen (Fig. 21-47). Rarely, the facial nerve may bifurcate proximal to the geniculate

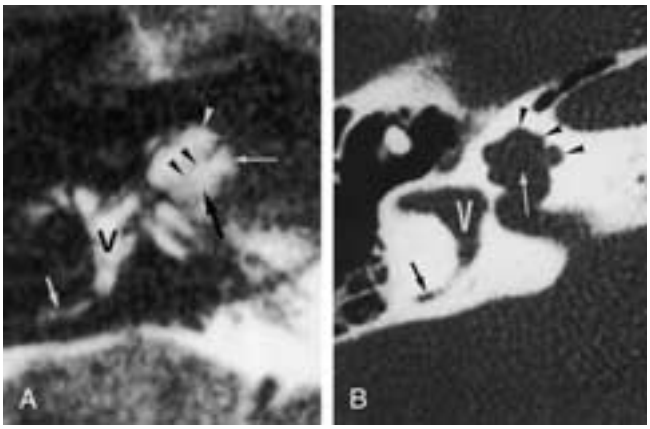

VIEW IMAGE

FIGURE 21-32 Mondini malformation. **A**, Axial 0.7 mm thick gradient-echo T2-weighted image (3DFT-CISS) through the apical and second turns of the right cochlea. There is a defect (*black arrowheads*) in the bony wall between the apical turn (*white arrowhead*) and second turn (*long white arrow*) of the cochlea. The bony wall between the cochlea and IAC is absent (*large black arrow*). Common crus (*small white arrow*), vestibule (*V*). **B**, Corresponding axial CT image through the right cochlea. The modiolus is absent (*long white arrow*), and the bony barrier between the IAC and the cochlea is absent. The apical and second turns of the cochlea can still be outlined on the surface of the cochlea (*black arrowheads*), but the separation between the two turns inside the cochlea cannot be recognized. Absence of the osseous spiral lamina of the middle and apical turns results in a scala communis cochleae. Posterior semicirucular canal (*small black arrow*), vestibule (*V*).

Copyright © 2003, Mosby, Inc. All rights reserved.

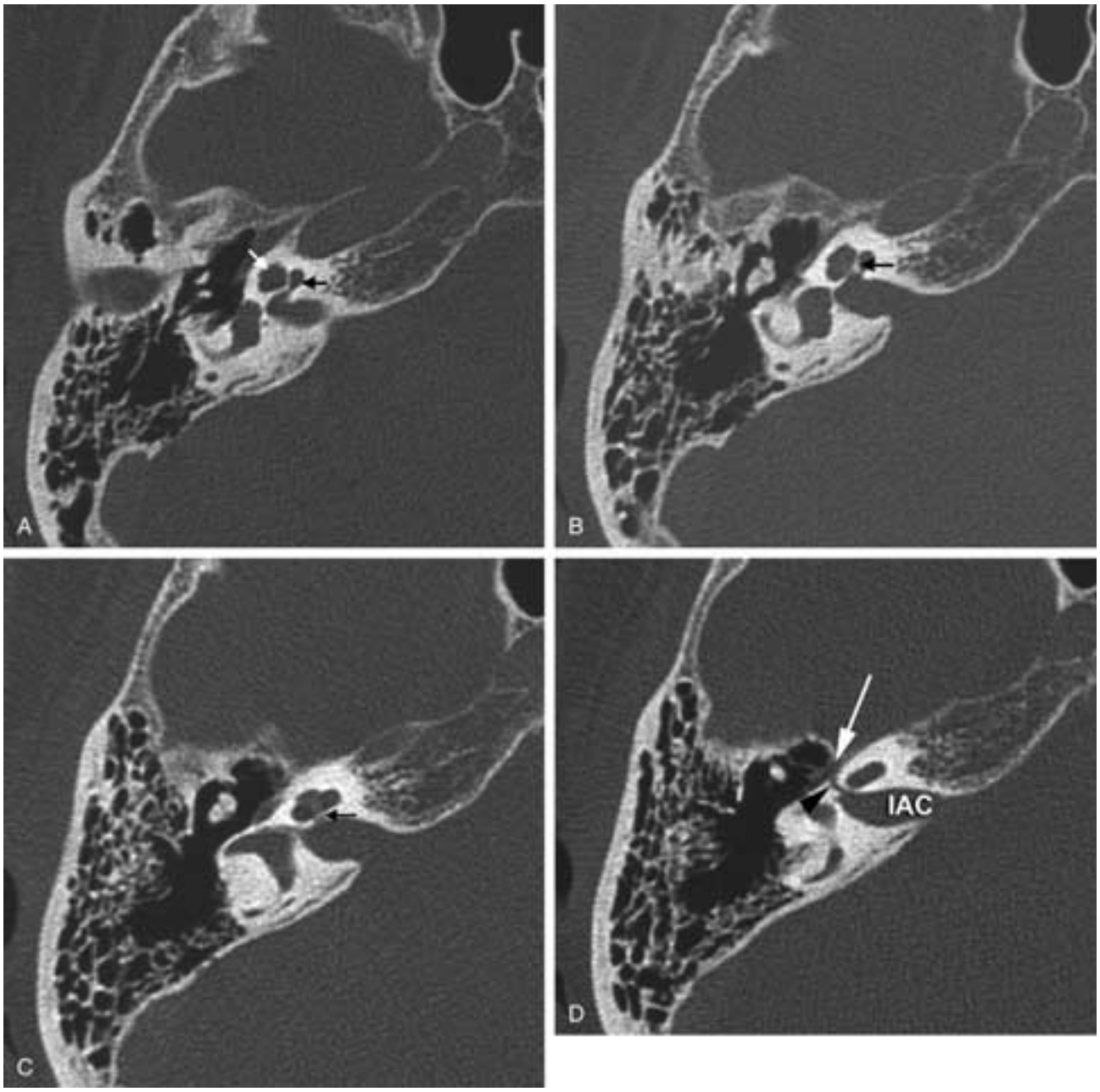

VIEW IMAGE

FIGURE 21-33 Normal cochlea/modiolus and facial nerve. **A** to **C**, Three contiguous 0.5 mm axial CT images through the cochlea from inferior to superior showing a normal basilar turn (*black arrow* in **A**), normal second and third turns (*white arrow* in **A**); normal modiolus (*black arrow* in **B**), and normal cochlear fossette (*black arrow* in **C**). **D**, Axial CT image showing the normal origin of the right facial nerve from the IAC. Labyrinthine segment of the facial nerve canal (*black arrowhead*); geniculate ganglion region of the facial nerve (*white arrow*).

ganglion (Fig. 21-48). In this variation, there may also be duplication of the IAC.[51]

Anterior migration of the facial nerve has been described with certain cochlear malformations.[52] It has been proposed that because of the intimate relationship between the development of the cochlea and the facial nerve, cochlear development or lack thereof may influence the position of the proximal or labyrinthine segment of the facial nerve canal. In some types of malformations, such as cochlear hypoplasia, common cavity malformations, and ''dwarf'' cochlea, lack of a significant cochlear mass results in anterior migration of the proximal or labyrinthine segment of the facial nerve as it attempts to take a more direct course to the pterygopalatine fossa and ganglion (Figs. 21-49 and 21-50). The nerve can exit the IAC more medially closer to the porus.

The tympanic and mastoid segments of the facial nerve can also be in an abnormal position. This is most commonly seen in association with EAC and ossicular abnormalities. This has been described in the section on middle ear anomalies. However, facial nerve abnormalities can be found in isolation. The tympanic segment of the facial canal

Copyright © 2003, Mosby, Inc. All rights reserved.

can be dehiscent, with the nerve bulging into the middle ear. The facial nerve can migrate inferiorly to abut the stapes or cross the promontory. Identification of the position of the facial nerve is always a crucial part of preoperative planning.

Vestibular Aqueduct

Valvassori and Clemis were the first to report an association between SNHL and a dilated vestibular aqueduct, as identified on polytomograms in 1978.[53] In their study of 3700 consecutive patients, 50 (1.4%) showed an enlarged vestibular aqueduct (more than 1.5 mm in diameter). Of the 50 patients, 60% had radiographically identifiable anomalies of the vestibule, semicircular canals, and cochlea. The malformed cochleas were classified into the Mondini or Mondini-Alexander types. However, only 8 of the 50 patients (16%) had identifiable cochlear anomalies on polytomography. This association of vestibular aqueductal dilatation and incomplete partitioning of the cochlea (classic Mondini's deformity) was thought to be likely given the embryology of these structures. The vestibular aqueduct and partitioning of the cochlea were known to be the last-developing entities of the inner ear, and a teratogen exerting its effects in this late stage of development might easily interfere with the normal development of both of these structures simultaneously. The remaining 40% of the patients showed no other identifiable anomalies of the inner ear and may have had associated pathology of the membranous labyrinth, which was not visible with polytomography. The authors coined the term *large vestibular aqueduct syndrome*, implying that this anomaly could exist in isolation. The clinical findings in these patients with enlargement of the vestibular aqueduct included vestibular symptoms in five patients. The remaining 45 patients demonstrated either pure SNHL or mixed hearing loss.

Since Valvassori and Clemis's original polytomographic study, there have been many studies using both CT and MR imaging for the evaluation of the large vestibular aqueduct syndrome.[53–58] On CT, the bony confines of the enlarged aqueduct can easily be demonstrated. The vestibular aqueduct is considered enlarged if it is more than 1.5 mm and is therefore larger than the normal posterior semicircular canal, which runs anterior and parallel to the aqueduct. On T2-weighted gradient echo or fast spin echo MR imaging, the fluid-filled endolymphatic duct and the sac within the bony vestibular aqueduct are hyperintense and surrounded by hypointense bony structures (Figs. 21-19, 21-36, 21-51 to 21-53). Multiplanar imaging and 3D reconstructions provide further detail of the enlarged endolymphatic duct and sac (Figs. 21-51 and 21-53). Also, the 3DFT gradient echo images and other T2-weighted sequences show the full extension of the endolymphatic sac into the posterior fossa (often invisible on CT). This extraosseous sac is a major component of the enlarged endolymphatic structure (Fig. 21-51). Usually the endolymph is slightly more hyperintense than CSF because of differing flow and pulsation rates. The MR images may show a thin dural lining between the endolymphatic sac and CSF, which makes it possible to follow the endolymphatic sac from the vestibule into the posterior fossa (Figs. 21-51 to 21-53). Sometimes on MR imaging, a portion of the endolymphatic duct and sac has a lower signal intensity than CSF or intralabyrinthine fluid. This is seen most frequently at the posterior edge of the sac, near the sigmoid sinus, but is occasionally seen in the entire endolymphatic duct and sac

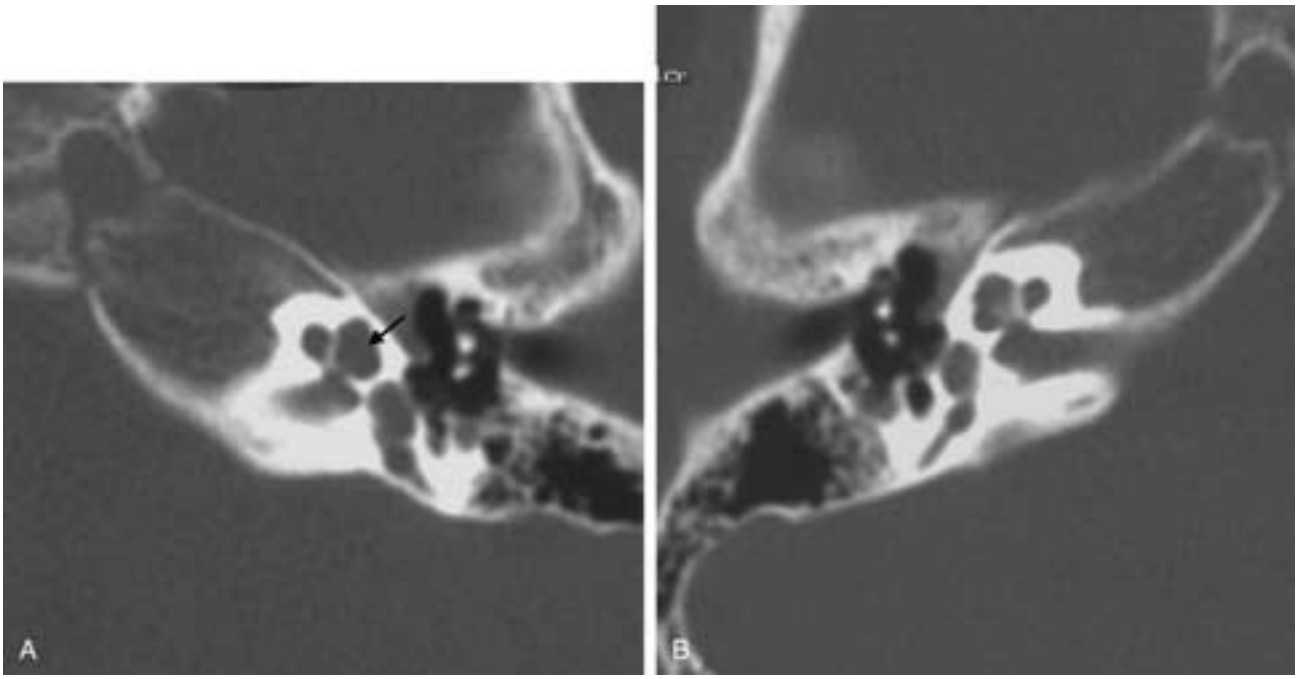

VIEW IMAGE

FIGURE 21-34 Modiolar deficiency. **A**, Axial CT image showing a deficient modiolus with incomplete separation of the second and third cochlear turns on the left (*black arrow*). **B**, Axial CT image of the right ear showing a normal bony modiolus with normal separation of the cochlear turns.

Copyright © 2003, Mosby, Inc. All rights reserved.

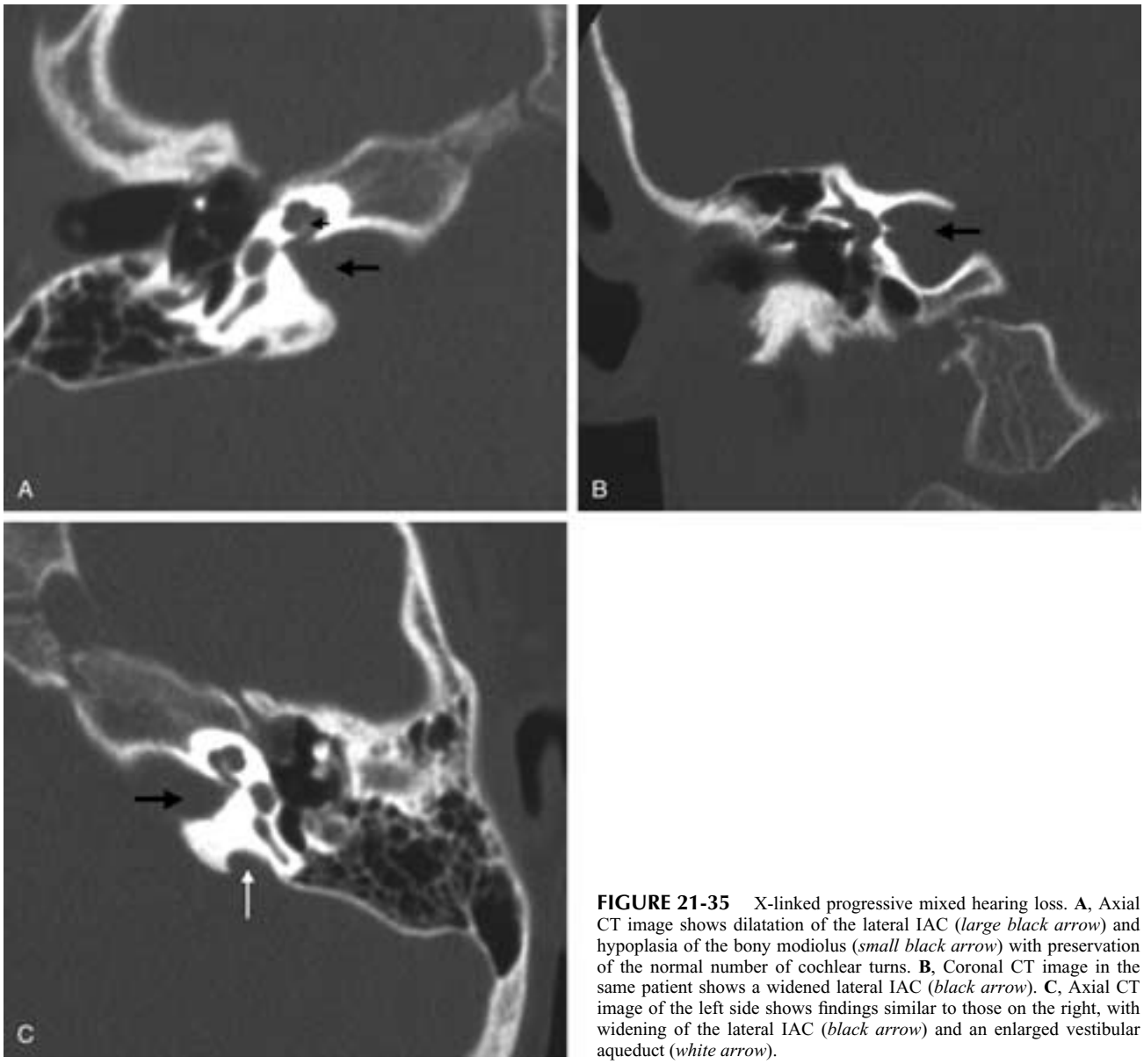

FIGURE 21-35 X-linked progressive mixed hearing loss. **A**, Axial CT image shows dilatation of the lateral IAC (*large black arrow*) and hypoplasia of the bony modiolus (*small black arrow*) with preservation of the normal number of cochlear turns. **B**, Coronal CT image in the same patient shows a widened lateral IAC (*black arrow*). **C**, Axial CT image of the left side shows findings similar to those on the right, with widening of the lateral IAC (*black arrow*) and an enlarged vestibular aqueduct (*white arrow*).

VIEW IMAGE

(Fig. 21-53).[59] This low signal may represent fibrous tissue. Endoymph is not the only component of the normal endolymphatic sac and duct. Histologically, these structures also contain rugosity, loose vascular subepithelial connective tissue and cuboidal or columnar epithelial cells, and it may be that the low signal intensity corresponds to these rugose portions.[60]

Many of the older studies using polytomography or older CT scanners with thicker sections implied that enlargement of the vestibular aqueduct frequently exists without a cochlear anomaly. More recent studies using either high-resolution CT or MR imaging have shown vestibular aqueduct enlargement or a large endolymphatic duct and sac (LEDS) to coexist frequently with cochlear anomalies.[61] In a study by Lemmerling et al. in 1997 using high-resolution CT,[41] modiolar deficiencies of the cochlea were detected in all patients with enlarged vestibular aqueducts. Another study using high-resolution, fast spin echo, T2-weighted MR imaging showed 76% of patients with LEDS to have cochlear anomalies including modiolar deficiency (94%), gross dysmorphism (71%), and scalar asymmetry (65%).[26] Another study using MR imaging measured the modiolus in normal subjects and in patients with LEDS and found a high association between a smaller than normal modiolus and LEDS, but also found cases of LEDS with a normal modiolus.[62]

Most patients with enlarged vestibular aqueducts have progressive SNHL that begins in infancy and childhood. The mechanism by which hearing loss is induced is still unknown. Various theories have been proposed. Transmission of hyperosmolar proteins in the enlarged endolymph sac through the enlarged endolymphatic duct and eventually into the cochlear duct (scala media) may cause damage to the neuroepithelium.[56, 61] In patients with a modiolar deficiency, elevations in CSF pressure associated with certain activites [56, 57] may be transmitted into the cochlea via

Copyright © 2003, Mosby, Inc. All rights reserved.

a relatively incompetent lateral wall of the IAC, potentially injuring the membranous labyrinth and hair cells within the organ of Corti.[41] Some of these theories have originated from studies showing either greater SNHL with greater degrees of endolymphatic duct enlargement[56, 61] or greater SNHL with more extensive modiolar deficiencies.[41] However, others have shown no positive correlation between the degree of SNHL and the degree of endolymphatic duct enlargement or modiolar abnormalities.[63]

VASCULAR ANOMALIES

Internal Carotid and Stapedial Arteries

Partial Absence and Aberrant (Lateral) Course

An aberrant course of the internal carotid artery (ICA) through the middle ear is rare, with approximately 45 cases reported in the English language literature. Most of these cases occurred in females, with the majority occurring on the right side.[64, 65] No convincing explanation for the female or the right-sided predominance has been presented.

Absence of the normal vertical petrous portion of the ICA leads to the development of an aberrant or lateral-coursing carotid artery. The vertical petrous portion is replaced by the more lateral-coursing and enlarged inferior tympanic and caroticotympanic arteries. These arteries normally form part of the tympanic arterial plexus. The inferior tympanic artery normally originates from the ascending pharyngeal artery and extends through the inferior tympanic canaliculus into the middle ear. The caroticotympanic artery normally originates from the vertical petrous segment of the ICA and extends into the middle ear (Fig. 21-54A). When the vertical petrous segment of the ICA is absent, the inferior tympanic artery enlarges and forms the proximal portion of the ICA, which anastomoses more distally through an enlarged inferior tympanic canaliculus with an enlarged caroticotympanic artery (Fig. 21-54A). The caroticotympanic artery carries blood flow to the transverse petrous segment of the carotid artery. The flow through the enlarged caroticotym-

VIEW IMAGE

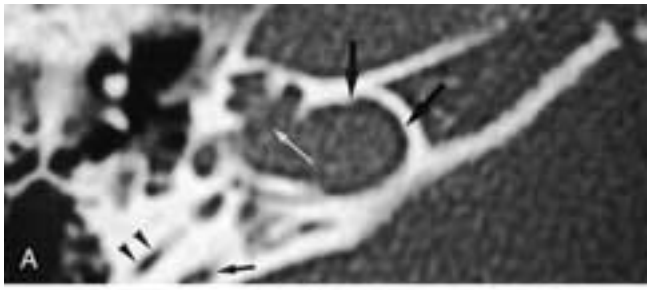

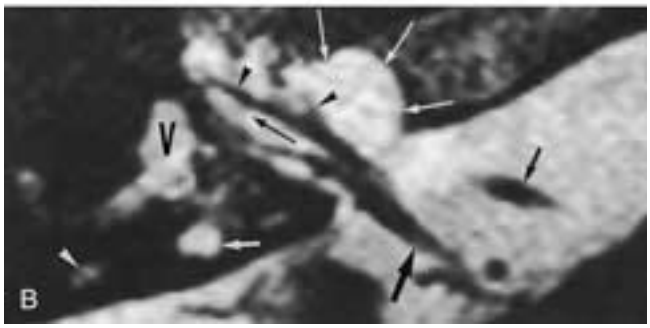

VIEW IMAGE

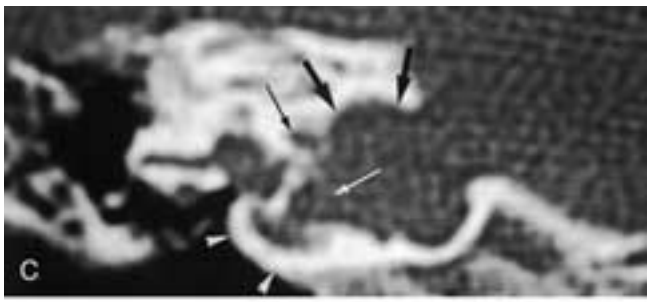

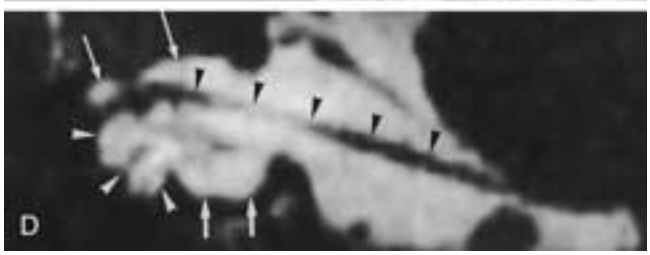

FIGURE 21-36 X-linked deafness/gusher ear in a patient with congenital deafness. **A**, Axial CT image through the right inner ear. There is no bony barrier between the IAC canal and the basal turn of the cochlea (*long white arrow*), and the modiolus is absent. There is a bulbous enlargement of the IAC (*large black arrows*), which is another typical finding in patients with X-linked deafness. The diameter of the vestibular aqueduct (*small black arrow*) is larger than the diameter of the posterior semicircular canal (*black arrowheads*). Therefore, a large vestibular aqueduct is present. **B**, Axial T2-weighted gradient-echo image through the right inner ear. The bulbous IAC can again be seen (*long white arrows*). The bony separation between the fluid inside the IAC and the basal turn of the cochlea is absent (*long black arrow*), as is the modiolus. Therefore, the cochlear branch of the VCN can be followed from the IAC into the cochlea, and even the separation in some of the distal branches (spiral ganglia) can be seen (*black arrowheads*). The enlarged endolymphatic duct (*small white arrow*) can be recognized and has a larger diameter than the posterior semicircular duct (*white arrowhead*). Normal facial nerve (*small black arrow*) and VCN (*large black arrow*) in the right cerebellopontine angle. Vestibule (*V*). **C**, Coronal CT image through the right inner ear. The bulbous enlargement of the right IAC can again be seen (*large black arrows*), and the fluid inside the IAC continues, without any barrier (*long white arrow*), into the cochlea (*white arrowheads*). The labyrinthine segment of the facial nerve canal is enlarged (*long black arrow*). **D**, Coronal T2-weighted gradient-echo image through the right inner ear. The IAC is wide and has a bulbous shape (*small white arrows*), and the CSF in the IAC cannot be separated from the fluid inside the cochlea (*white arrowheads*). The facial nerve can be followed in the cerebellopontine angle and IAC (*black arrowheads*) and continues in the enlarged labyrinthine segment of the facial nerve canal. Normally, this segment of the facial nerve canal is very small, and there is no space left between the nerve and the walls of the canal. However, in gusher ears the canal enlarges, and fluid can be found between the nerve and the canal walls (*long white arrows*).

Copyright © 2003, Mosby, Inc. All rights reserved.

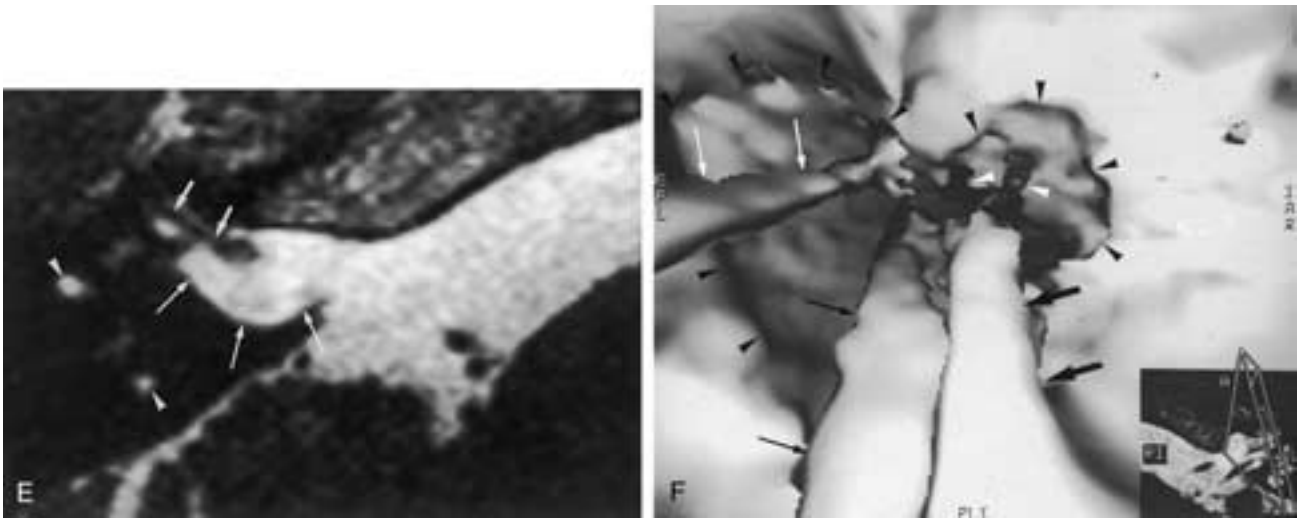

VIEW IMAGE

FIGURE 21-36 *Continued.* **E**, Axial gradient-echo T2-weighted image through the enlarged labyrinthine segment of the facial nerve canal, confirming the presence of fluid surrounding the labyrinthine segment of the facial nerve (*small white arrows*). Wide, bulbous IAC (*long white arrows*) and fluid in the anterior and posterior branches of the superior semicircular duct (*white arrowheads*). **F**, Three-dimensional virtual images of the fundus of the right IAC, made by using 0.7 mm thick T2-weighted gradient-echo images. The facial nerve (*long white arrows*) can be seen inside the lateral part of the IAC and disappears in the facial nerve canal. The common vestibular branch (*long black arrows*) and cochlear branch (*large black arrows*) of the VCN can be followed in the IAC, and branches (spiral ganglia) of the latter nerve can be followed inside the cochlea (*white arrowheads*). One can look inside the abnormal cochlea, as no bony barrier exists between the IAC and the lumen of the cochlea. Defect in the base of the cochlea (*black arrowheads*).

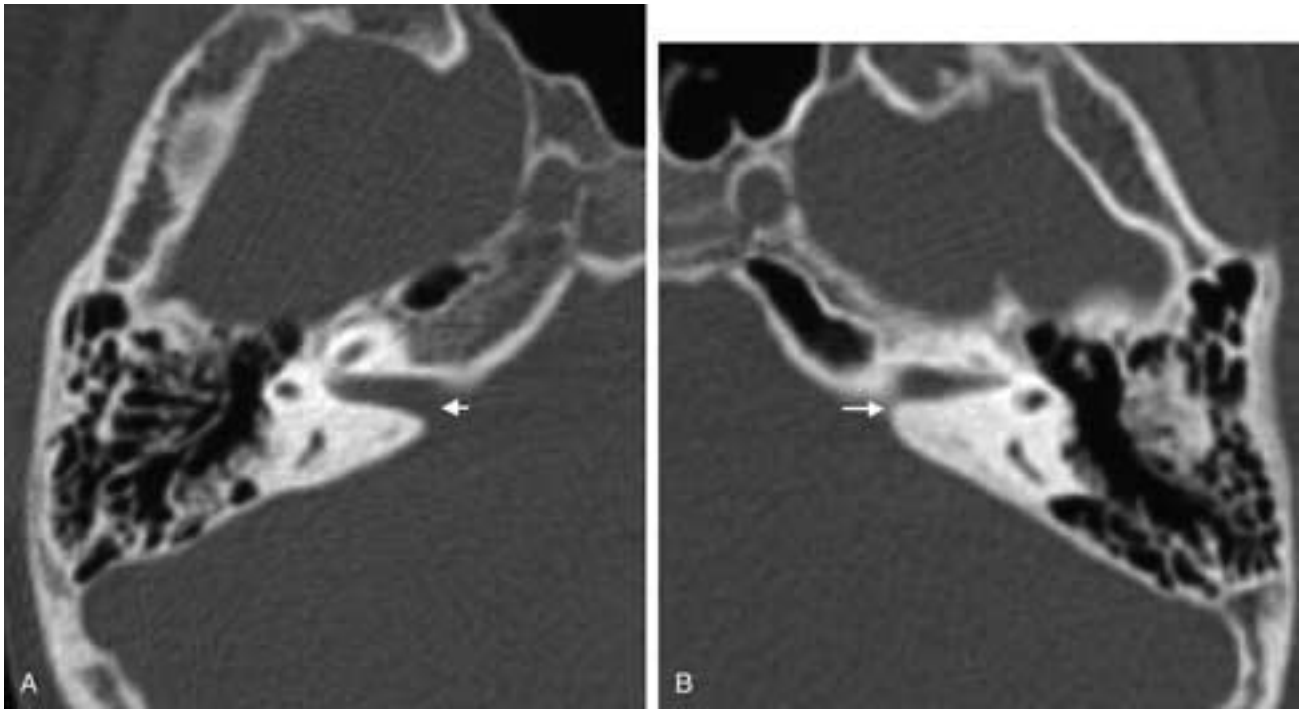

VIEW IMAGE

FIGURE 21-37 Stenosis of the IAC. **A**, Axial CT image showing a normal right-sided IAC (*white arrow*). **B,** Axial CT image showing a stenosed left-sided IAC (*white arrow*).

Copyright © 2003, Mosby, Inc. All rights reserved.

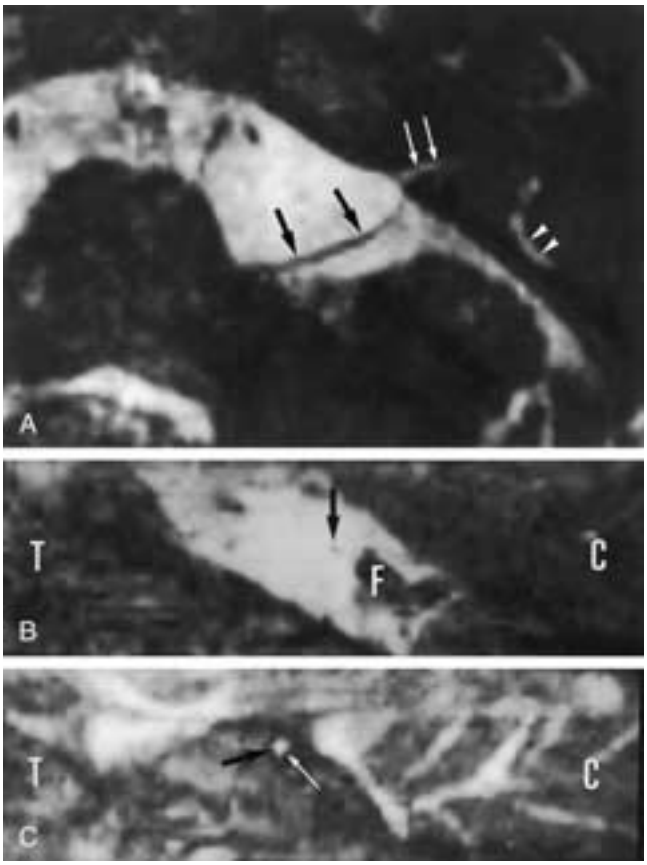

VIEW IMAGE

FIGURE 21-38 Type 1 malformation, aplasia of the VCN with a stenotic IAC in a patient presenting with complete congenital deafness. **A**, Axial 0.7 mm thick T2-weighted gradient-echo image through the left inner ear. A very narrow fluid-filled IAC can be seen (*long white arrows*). On the axial images only a single nerve, the facial nerve, can be found in the left cerebellopontine angle (*large black arrows*). Normal fluid in the common crus (*white arrowheads*). **B** and **C**, Parasagittal T2-weighted gradient-echo images perpendicular to the course of the nerves at the level of the left cerebellopontine angle (**B**) and IAC (**C**). **B**, In the cerebellopontine angle, only the facial nerve (*large black arrow*) can be seen anterosuperior to the floccule (*F*). **C**, Only a little CSF can be visualized inside the very narrow IAC (*large black arrow*). Nerves are difficult to visualize in such a narrow IAC. Here the facial nerve can be depicted lying against the posteroinferior wall of the IAC (*long white arrow*). The VCN is absent. *C*, Cerebellum; *T*, temporal lobe.

panic segment is reversed from the normal direction, carrying blood back into the ICA rather than away from it into the middle ear region.

A persistent stapedial artery (PSA) is often found in association with an aberrant ICA. The PSA leaves the aberrant ICA through a small canaliculus to enter the middle ear cavity, where it courses along the cochlear promontory. It then passes through the crura of the stapes and either enters the canal for the tympanic portion of the facial nerve or runs parallel to it in a separate canal. The PSA continues superiorly to supply the middle meningeal artery through enlargement of the superior tympanic or superficial petrosal artery. The foramen spinosum, through which the middle meningeal artery normally travels after originating from the internal maxillary artery, is absent. The PSA may also occur without an aberrant ICA. In this situation, the vertical petrous segment of the ICA is present and the PSA is formed by enlargement of the more distal caroticotympanic artery arising from the vertical petrous ICA (Figs. 21-54B, 21-55 and 21-56).[66, 67]

There is no universally accepted etiology for the aberrant carotid artery.[68] Among the proposed mechanisms is a congenital failure of ossification of the bony limiting wall of the petrous carotid canal. Some authors have reported that the bony plate is frequently less than 0.5 mm thick, and with age, as the vessel elongates and becomes tortuous, it may protrude through the defect into the tympanic cavity.[64, 69] Persistence of embryonic vessels also may produce sufficient traction to pull the artery into the middle ear.[64]

Signs and symptoms of an aberrant ICA include tinnitus, hearing loss (mostly conductive), a red-blue pulsatile mass behind the tympanic membrane, vertigo, and a sensation of fullness in the ear.[64, 69] In some cases, otalgia has been reported as one of the initial symptoms. The tinnitus may be caused either by the direct mechanical transmission of the vessel's pulsations to the tympanic membrane and ossicles or by the audible sound produced by arterial blood flow emanating from the abnormal vessel within the middle ear. Pulsatile tinnitus has also been reported to occur with erosion of the bone separating the aberrant ICA and basal turn of the cochlea, allowing direct transmission of pulse vibration to the cochlea. As well, in this scenario, although the aberrant ICA is a congenital vascular malformation, the tinnitus may not occur until the erosion of the bone separating the vessel from the cochlea occurs.[70] Hearing loss may result from dampening of the tympanic membrane vibrations or from encroachment or erosion of the ossicles.[64] Still, many patients are asymptomatic.

Not infrequently, the red-blue mass behind the tympanic membrane has been inadvertently ruptured during therapeutic myringotomies, biopsy for suspected glomus tumors, or both. This has resulted in catastrophic hemorrhage from the middle ear, emergently treated by ear packing.

CT of an aberrant ICA shows an enhancing soft-tissue mass in the hypotympanum extending toward the oval window area, indenting the promontory and displacing the tympanic membrane laterally (Fig. 21-57).[64] The aberrant ICA may be detectable on MR imaging with flow-sensitive techniques, MR angiography (MRA) or fast spin echo, T-2 weighted images as a laterally positioned vascular structure (Fig. 21-57). Grooving of the apical, middle, and basilar turns of the cochlea by the artery also may be seen on CT.[68] The lateral bony wall of the carotid canal is dehiscent, a finding best appreciated on CT. If there is an associated PSA, the foramen spinosum is absent and there is enlargement of the anterior tympanic facial nerve canal or a canal parallel to it.

Asymptomatic aberrant arteries require no treatment. Therapy usually is reserved for patients with pulsatile tinnitus, hemorrhage, or cranial nerve palsies. Intervention includes the interposition of synthetic material between the artery and ossicles, disarticulation of the ossicular chain, or ligation of the ICA in cases of hemorrhage.[64]

Agenesis

The etiology of congenital absence of the ICA is unknown. Keen has suggested that unilateral absence of the ICA may result from mechanical stresses in early development such as pressure effects, excessive bending of the

Copyright © 2003, Mosby, Inc. All rights reserved.

cephalic end of the embryo from side to side, or the effects of amniotic adhesions.[71] No explanation has been offered for bilateral absence of the ICA, which is extremely rare.

Symptoms may or may not lead to the discovery of an absent ICA. The agenesis may be discovered as an incidental finding during workup for an unrelated problem[72] or, more commonly, during the workup for neurologic symptoms. In 42 reported cases of congenital absence of the ICA, 12 patients initially had subarachnoid hemorrhage caused by a ruptured intracranial aneurysm. Other clinical presentations include multiple cranial nerve palsies caused by compression by a dilated loop of the basilar artery, hemiparesis after minor head trauma, and various other neurologic signs and symptoms resulting from major head injuries.

CT usually shows unilateral absence of the carotid canal in the petrous part of the temporal bone or a small vertical cleft, possibly representing an abortive carotid canal (Fig. 21-58). Internal carotid angiography demonstrates unilateral absence of the ICA. Angiography also shows the frequent occurrence of associated anomalies of the remaining vasculature (i.e., dilated basilar artery collaterals, ipsilateral dilation of the posterior communicating artery filling the

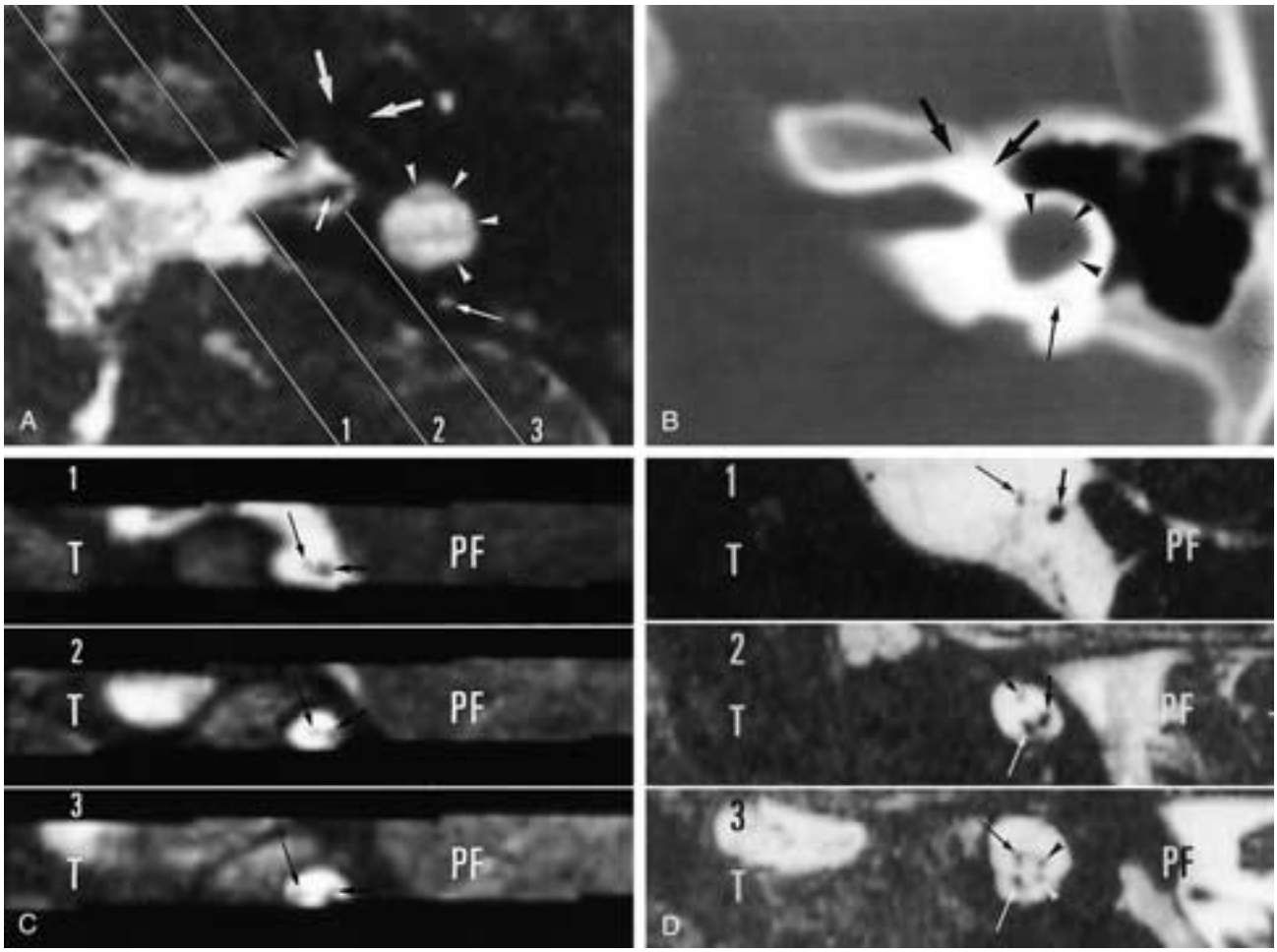

VIEW IMAGE

FIGURE 21-39 Common cavity-type cochlear-vestibular malformation with associated aplasia of the cochlear branch of the VCN, Type 2A malformation. **A**, Axial 0.7 mm thick gradient-echo image through the left inner ear. A fluid-filled cavity (*white arrowheads*) is seen posterior and lateral to the fundus of the IAC. No fluid can be seen at the site where the cochlea is expected to be located (*large white arrows*). A normal posterior semicircular duct can be recognized (*long white arrow*). Only two nerves are seen passing through the IAC—the facial nerve (*small black arrow*) and a common VCN or vestibular nerve (*small white arrow*). **B**, Axial CT image through the left inner ear. Confirmation of the absence of a separate cochlear structure (*black arrows*) and the presence of a common cavity (*black arrowheads*) and normal posterior semicircular canal (*long black arrow*). **C**, Gradient-echo images, oblique sagittal reconstructions of the left inner ear at the level of the cerebellopontine angle (*1*), and porus (*2*) and fundus (*3*) of the IAC; see the levels on **A**. A smaller facial nerve (*long black arrows*) and a thicker common, or rudimentary, VCN (*small black arrows*) can be followed from the cerebellopontine angle (*1*) to the fundus of the IAC (*3*). A separate cochlear branch normally situated in the anterior and inferior parts of the IAC cannot be recognized, and there is no bifurcation into a superior and inferior vestibular branch. **D**, Gradient-echo images, oblique sagittal reconstructions of a normal inner ear for comparison. The facial nerve again can be depicted as a smaller nerve (*long black arrows*). The common VCN (*small black arrows*) gives off its cochlear branch (*long white arrows*) when it reaches the porus (*2*) and divides into a superior (*black arrowhead*) and inferior (*white arrowhead*) vestibular branch deeper in the IAC (*3*). *PF*, posterior fossa; *T*, temporal lobe. A cochlear implant was installed, and the results were moderate to satisfactory. This case proves that cochlear implantation can be of benefit once a fluid-filled inner ear cavity is found and the presence of a nerve, which is not the facial nerve, can be demonstrated.

Copyright © 2003, Mosby, Inc. All rights reserved.

corresponding anterior or middle cerebral arteries or both, ipsilateral ophthalmic or anterior cerebral arteries arising from the middle cerebral artery, or aneursyms). Congenital absence of both ICAs has also been reported. Their absence was compensated for by a hypertrophied accessory meningeal artery through an enlarged foramen ovale on one side and a trigeminal artery on the other.[73] Spin-echo T1- and T2-weighted MR images show absence of the normal ICA flow void at the skull base, and MRA shows lack of flow-related enhancement.[72]

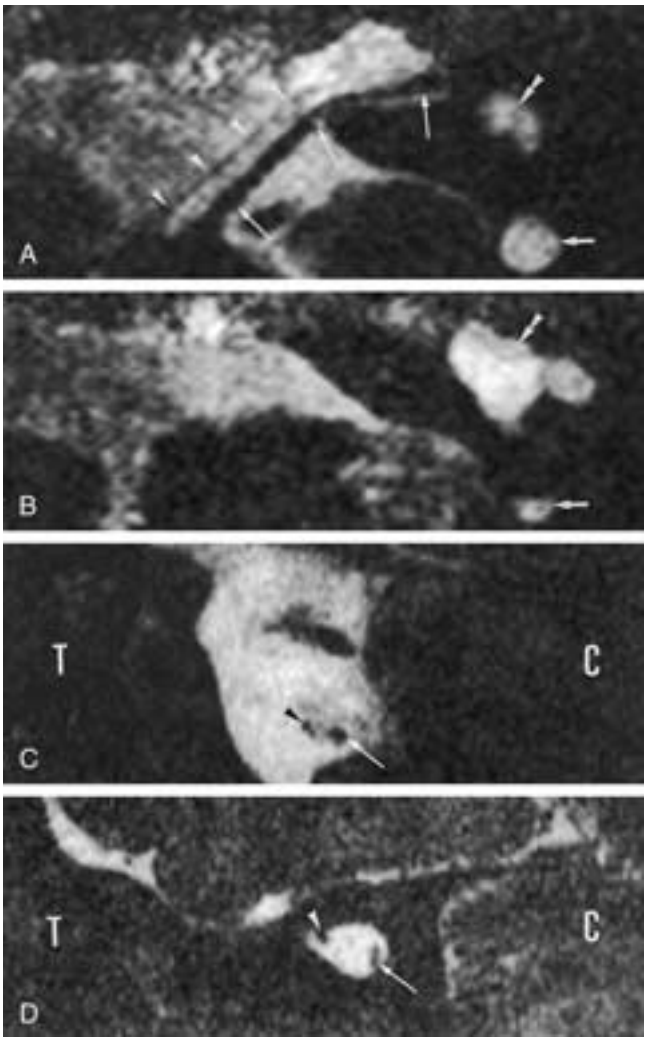

VIEW IMAGE

FIGURE 21-40 Type 2A malformation, aplasia of the cochlear branch of the VCN in the presence of an abnormal membranous labyrinth. **A** and **B**, Axial 0.7 mm thick gradient-echo T2-weighted images through the left inner ear at the level of the IAC (**A**) and below the level of the IAC (**B**). **A**, Fluid can be seen in an abnormal vestibule (*double arrowhead*) and in an enlarged posterior semicircular duct (*small white arrow*). The facial nerve (*white arrowheads*) and a common undividing VCN (*long white arrows*) can be followed to the fundus of the IAC and the region of the abnormal inner ear. **B**, The abnormal shape and enlargement of the vestibule (*double arrowhead*) are depicted on this image. The shape of the posterior semicircular duct is abnormal (*small white arrow*). **C** and **D**, Parasagittal 3DFT-CISS reconstruction perpendicular to the nerves at the level of the cerebellopontine angle (**C**) and IAC (**D**). **C**, Both the facial nerve (*black arrowhead*) and the VCN (*long white arrow*) can be seen in the CSF of the cerebellopontine angle. **D**, The facial nerve can be seen in its normal position anterior and high in the IAC (*white arrowhead*). The VCN, however, is not dividing into cochlear and vestibular branches and can be followed as a single nerve to the fundus of the IAC (*long white arrow*). *C*, Cerebellum; *T*, temporal lobe.

Jugular Vein

High Jugular Bulb

Protruding/Dehiscent Jugular Bulb

The dome of the jugular bulb normally lies beneath the floor of the tympanic cavity. When it is higher, it is referred to as a high jugular bulb. Various definitions of a high jugular bulb are found in the literature. Anatomic studies have defined it as lying above the level of the inferior tympanic rim or bony annulus of the temporal bone, as well as a bulb that abuts the round window or lies less than 2 mm under the inferior edge of the internal acoustic meatus. Some CT studies have defined a high bulb as one that lies at the level of the basal turn of the cochlea (Figs. 21-59 and 21-60).[74–76] Because of its high position, the bony covering of the jugular bulb may be thin or *dehiscent*, rendering the bulb vulnerable to trauma (Fig. 21-61). A high jugular bulb has been reported in up to 6% of temporal bones examined histologically, making it the most common vascular anomaly of the petrous portion of the temporal bone.[75] The anomaly is more common on the right side, as the dural sinuses and jugular vein are larger on the right in 75% of individuals.[77]

This entity bears some relation to the degree of pneumatization of the mastoid air cells. In poorly pneumatized mastoid air cells, the sigmoid sinus is more anterior, the jugular fossa tends to be deep, and the jugular bulb has a correspondingly high dome.[78] The height of the bulb is significant because of the risk of inadvertently entering the vein during myringotomy or middle ear procedures. The high position of the bulb can be appreciated on both CT and MR imaging. The thin or dehiscent hypotympanic bony wall can be appreciated with CT (Figs. 21-59 to 21-61).

The high jugular bulb is usually an incidental finding on clinical examination. It is seen as a bluish discoloration in the posteroinferior quadrant of the tympanic membrane and on radiographic examination.[79] However, conductive hearing loss, pulsatile tinnitus, and Meniere's disease have all been reported to occur with this vascular anomaly.[74, 77] Conductive hearing loss and pulsatile tinnitus have been attributed to a high *lateral* jugular bulb and to one of three mechanisms: obstruction of the round window niche, contact with the tympanic membrane, or ossicular chain interference. The first two mechanisms are considered more common than ossicular chain interference, which requires an extremely high jugular bulb reaching as far as the incudostapedial joint.[77] A high *medial* jugular bulb has been proposed to induce Meniere's disease by contacting and compressing the distal portion of the vestibular aqueduct and endolymphatic duct and/or sac. The compression of the endolymphatic duct and/or sac could result in a decrease in endolymph resorption or disruption of the venous drainage of the duct and/or sac, and thereby inducing Meniere's disease.[74] Surgical lowering of a high medial jugular bulb has been proposed as a treatment option in symptomatic patients and has shown some efficacy.[74]

Jugular Diverticulum

A jugular diverticulum (JD) is a smooth outpouching of the jugular bulb that extends superiorly, medially, and

Copyright © 2003, Mosby, Inc. All rights reserved.

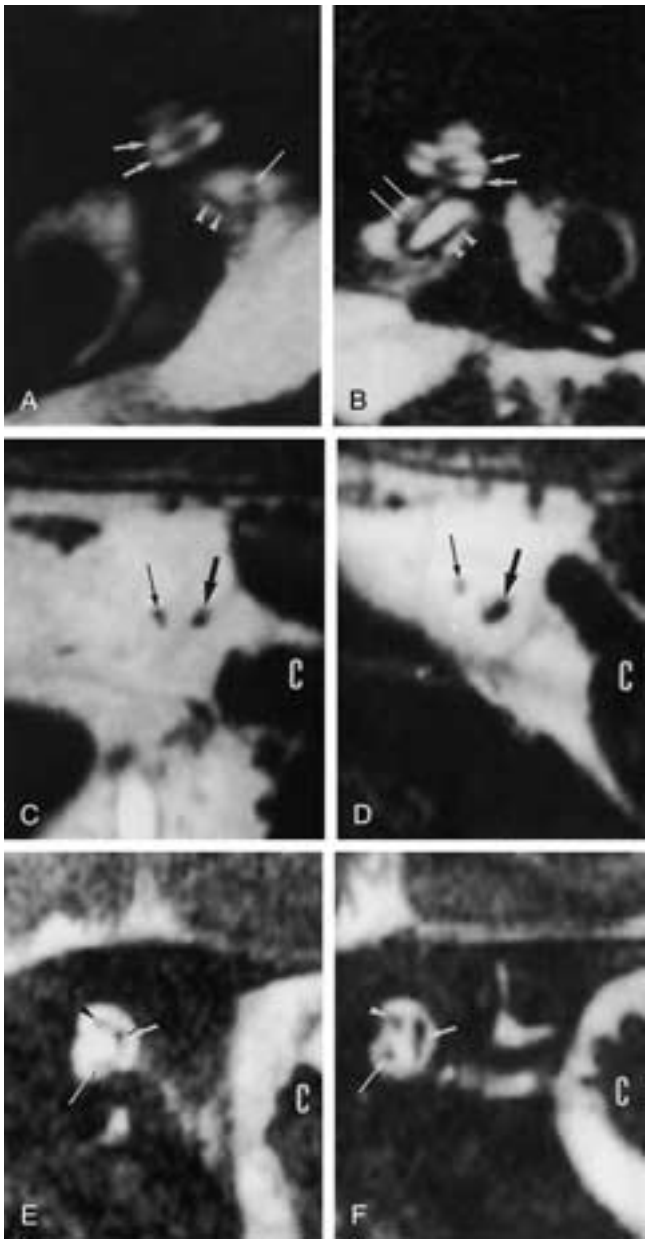

VIEW IMAGE

FIGURE 21-41 Type 2B malformation, hypoplasia of the cochlear branch of the right VCN in the presence of a normal labyrinth in a patient with severe but not complete congenital deafness on the right side. **A** and **B**, Axial T2-weighted gradient-echo images through the right (**A**) and left (**B**) IACs. **A**, A normal cochlea with distinguishable scala vestibuli/media and scala tympani can be seen (*small white arrows*). A normal-sized inferior vestibular branch (*white arrowheads*) can be seen, but the cochlear branch (*long white arrow*) of the VCN is hypoplastic. **B**, On the left side, both the cochlear (*long white arrows*) and inferior vestibular branches (*white arrowheads*) are normal in size. The scala vestibuli/media and scala tympani can again be distinguished in a normal-appearing cochlea (*small white arrows*). **C** to **F**, Parasagittal 3DFT-CISS reconstruction through the right (**C**) and left (**D**) cerebellopontine angles and through the right (**E**) and left (**F**) fundi of the IAC. **C**, The sizes of the facial nerve (*long black arrow*) and the VCN (*large black arrow*) are similar. Normally the VCN is one and a half to two times larger in diameter. The small diameter of the VCN corresponds with a smaller number of neuronal fibers in the ''hypoplastic'' nerve. **D**, On the normal left side, the VCN (*large black arrow*) is at least twice as large as the facial nerve (*long black arrow*). **E**, A hardly visible cochlear branch (*long white arrow*) and common undividing vestibular branch (*small white arrow*) of the VCN can be seen. The VCN therefore is hypoplastic. The facial nerve has a normal size (*black arrowhead*). **F**, On the left side, a normal facial nerve (*white arrowhead*) and a normal-sized cochlear branch (*long white arrow*) and dividing common vestibular branch (*small white arrow*) of the VCN can be seen. *C*, Cerebellum.

posteriorly in the temporal bone. This venous anomaly is thought to be rare, with only 21 cases reported in the English language literature. However, the apparent rarity may, in part, be due to the fact that many patients with this entity are asymptomatic.[80–82] There are characteristic differences between a JD and a protruding (high) jugular bulb. A JD is situated more medially and posteriorly in the petrous bone than is a high jugular bulb. A JD does not protrude into the middle ear, is not visible on inspection, and is not exposed to surgical trauma from a myringotomy or tympanotomy. The diagnosis of a JD is made only radiographically. A high jugular bulb can be diagnosed by both radiologic and otoscopic examinations.[78] In addition, a JD, unlike a high or protruding jugular bulb, is more common on the left side and has been reported to be more common in women.[80, 82]

Symptoms produced by a JD are controversial but would presumably be related to its size and extent. The structures with which a JD may come in contact with include the cochlear aqueduct, vestibular aqueduct/endolymphatic duct and/or sac, the posterior semicircular canal (PSCC), and the IAC. Hearing loss from a JD has been described as sensorineural and may theoretically result from encroachment on either the IAC or the PSCC. Tinnitus has been proposed to be the result of turbulent blood flow within the JD. Vertigo, SNHL, tinnitus, and aural fullness, mimicking Meniere's disease, could result from compression of the endolymphatic duct and/or sac (Fig. 21-62).[82]

CT demonstrates the JD in continuity with the jugular bulb, extending superiorly into the petrous pyramid (Fig. 21-62). The bony margins are smooth, consistent with slow remodeling without evidence of permeative destruction. The JD may encroach upon the IAC, the vestibular aqueduct, or the PSCC.[81] The most superior extension of the JD lies in a plane higher than the level of a protruding jugular bulb, often reaching the cranial margin of the petrous pyramid. Documentation of a JD with MR imaging may not be as straightforward as with CT. Contrast-enhanced, T1-weighted images may highlight the jugular bulb and JD if there is slow enough flow. MR venography, utilizing either 2D time-of-flight or phase contrast techniques may also demonstrate the JD.

Agenesis and Stenosis

Agenesis of the jugular bulb and sigmoid sinus is extremely rare. In these cases, the absent sigmoid sinus redirects the flow from the transverse sinus into a canal posterior and superior to the petrous pyramid. This canal then drains directly through transmastoidian venous channels into adjacent scalp veins. CT and MR imaging of the temporal bone and skull base will document the absent sigmoid sinus and jugular bulb, along with the aberrant venous drainage system. Aberrant venous drainage may also result from congenital stenosis of the jugular foramen, in which the jugular vein is present but small (Fig. 21-63).[83]

MALFORMATIONS OF THE PETROUS BONE ASSOCIATED WITH MENINGITIS

CSF leakage via the temporal bone structures is a rare but potentially life-threatening condition. Most CSF fistulas of the temporal bone are acquired and are a result of either

Copyright © 2003, Mosby, Inc. All rights reserved.

trauma or infection. Congenital abnormalities of the temporal bone are a much rarer cause of CSF fistulas and should always be suspected in cases of recurrent meningitis in the absence of an inciting event. Congenital CSF fistulas of the temporal bone have been traditionally classified as perilabyrinthine or translabyrinthine (Figs. 21-64A,B).[84] Perilabyrinthine fistulas are rare and occur through defects close to but not involving the labyrinth. Translabyrinthine fistulas, which are far more common, are usually associated with anacusis, severe labyrinthine dysplasia, and a route via the IAC.

Both the translabyrinthine and perilabyrinthine fistulas tend to present in the first 5 to 10 years of life. The various presentations include CSF rhinorrhea with an intact tympanic membrane as CSF passes from the middle ear down into the eustachian tube, nasopharynx, and nasal cavity, resulting in nasal discharge; CSF otorrhea in a child with a perforated tympanic membrane or with a myringotomy tube for presumed serous otitis media; or recurrent meningitis.

Perilabyrinthine Fistulas

Several different routes for the development of perilymphatic fistulas have been proposed, and some have been confirmed pathologically (Fig. 21-64A).

Dehiscence of the Tegmen Tympani

A CSF fistula may arise from congenital absence of a portion of the tegmen tympani.[85–87] The tegmen tympani is normally formed by the joining of the superior aspect of the petrous part of the temoral bone with the caudal squamous portion of the temporal bone.[88, 89] Fusion of the petrosquamosal suture is usually complete by 1 year of age but can be delayed by growth abnormalities. Small bony dehiscences have been reported to occur in up to 34% of the population, although actual meningoceles, meningoencephaloceles, and fistulas are rare. This is likely secondary to the fact that dural weakening, which is not as common as bony dehiscence, is necessary for such communication.[90–92] CSF fistulas through a dehiscence in the tegmen tympani usually present

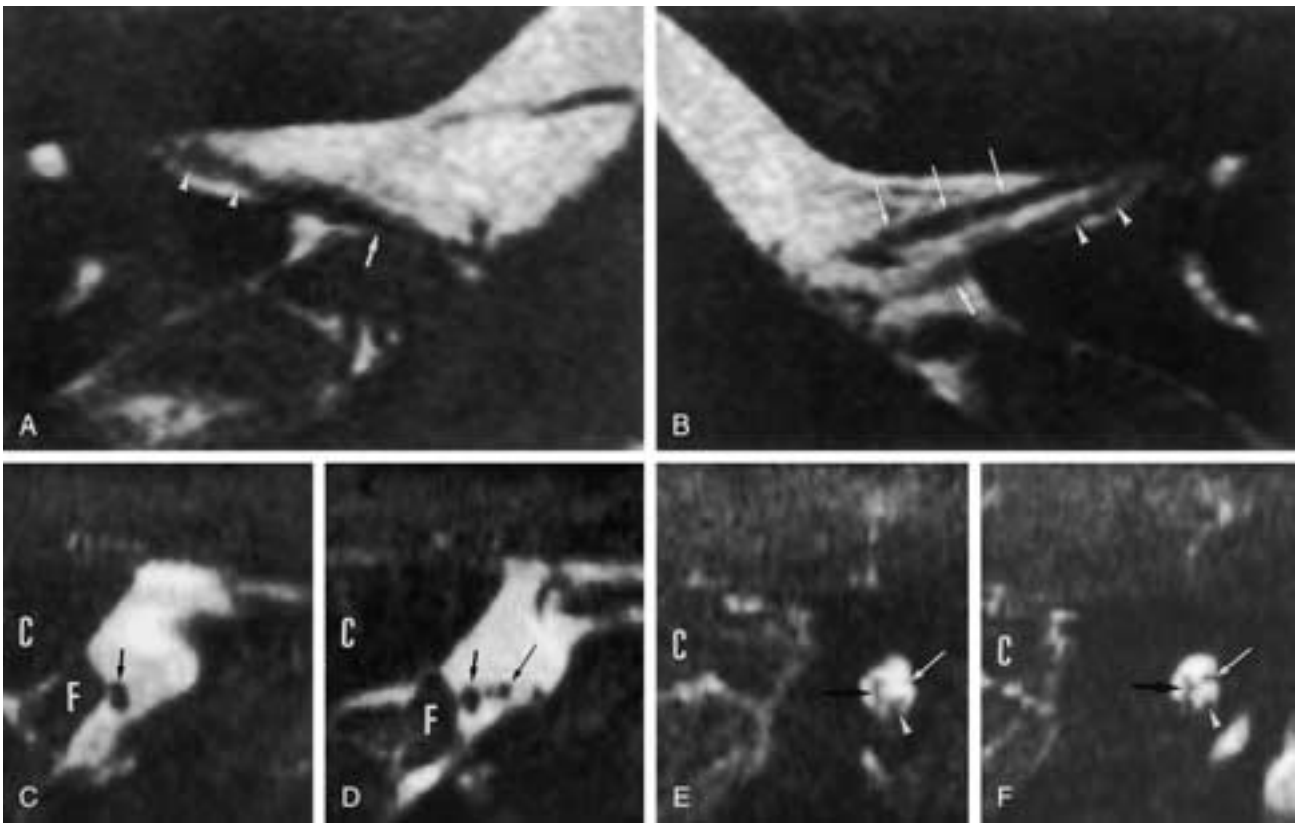

VIEW IMAGE

FIGURE 21-42 Aplasia of the right facial nerve in a patient with congenital facial nerve palsy. **A** and **B**, Axial 0.7 mm thick gradient-echo T2-weighted images through the right (**A**) and left (**B**) IACs. **A**, Only one nerve, the VCN, can be seen in the right cerebellopontine angle (*small white arrow*) and IAC (*white arrowheads*). **B**, The VCN can again be seen in the cerebellopontine angle (*small white arrow*) and IAC (*white arrowheads*). The facial nerve can be seen anterior to the VCN (*long white arrows*). **C** to **F**, Parasagittal 3DFT-CISS reconstructions perpendicular to the course of the nerves at the level of the right (**C**) and left (**D**) cerebellopontine angles and the right (**E**) and left (**F**) IACs. **C**, A large nerve, the VCN (*small black arrow*), can be seen in the right cerebellopontine angle, situated just anterior to the floccule. **D**, The facial nerve (*long black arrow*) and a larger VCN (*small black arrow*) can be seen anterior to the floccule on the left side. **E**, The common vestibular branch (*large black arrow*) and cochlear branch (*white arrowhead*) of the VCN have a normal appearance. The facial nerve cannot be found in the anterosuperior segment of the IAC (*long white arrow*). **F**, The cochlear (*white arrowhead*) and common vestibular (*large black arrow*) branches of the VCN can be distinguished in the middle one third of the IAC. The facial nerve also has a normal size (*long white arrow*). *C*, Cerebellum; *F*, floccule.

Copyright © 2003, Mosby, Inc. All rights reserved.

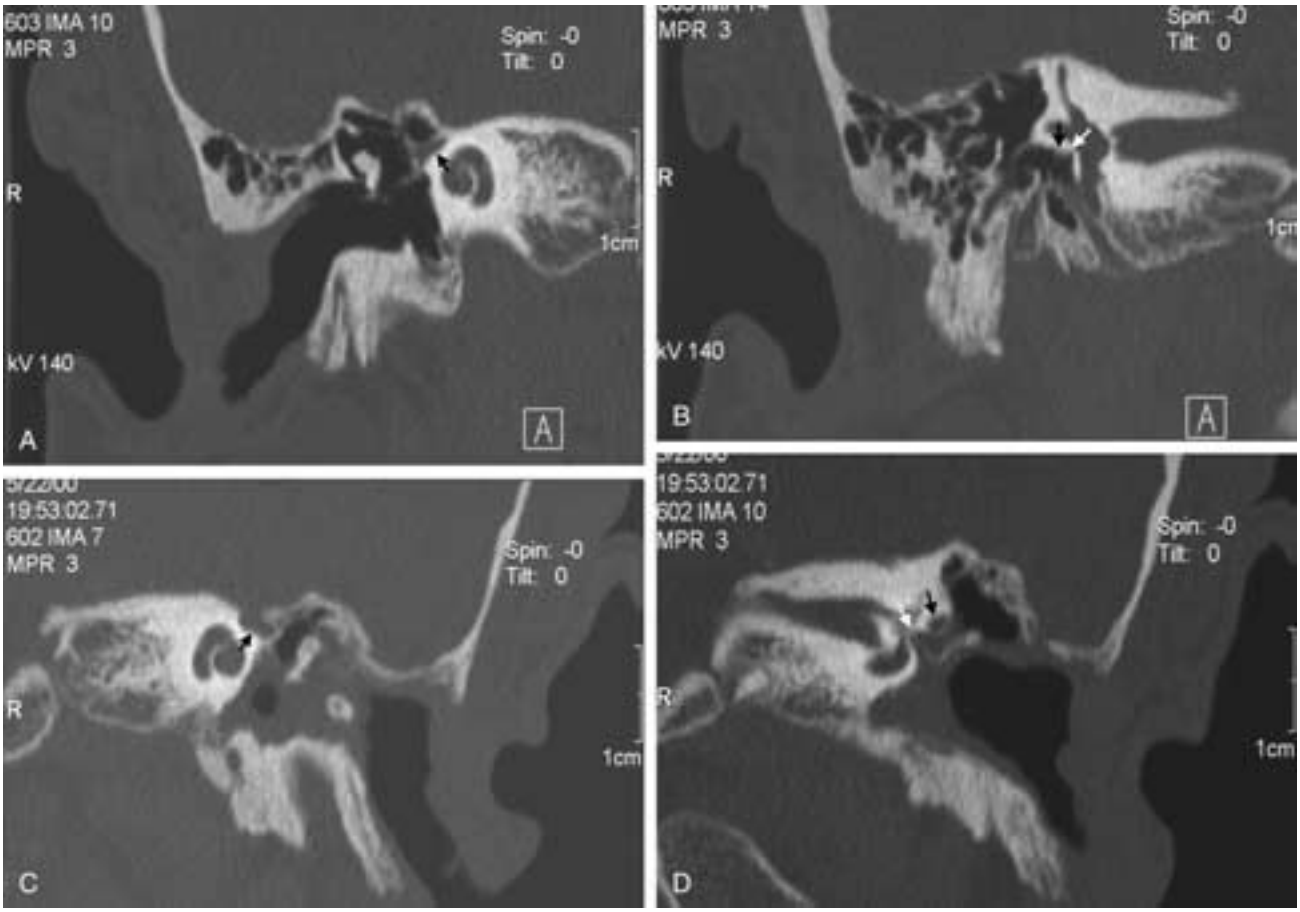

VIEW IMAGE

FIGURE 21-43 Moebius syndrome (congenital facial diplegia). **A** and **B**, Two coronal CT images from anterior to posterior showing a small right geniculate ganglion (*black arrow* in **A**) and a small tympanic segment of the right facial nerve (*black arrow* in **B**). Also note the stenotic oval window (*white arrow* in **B**). **C** and **D,** One mm coronal CT images from anterior to posterior showing a normal left geniculate ganglion (*black arrow* in **C**) and a normal tympanic segment of the left facial nerve (*black arrow* in **D**) and a normal left oval window (*white arrow* in **D**). The soft tissue in the left EAC is postoperative.

in adults. Coronal CT of the petrous pyramid typically demonstrates incomplete development of the tegmen tympani, and there may be an associated meningocele or meningoencephalocele protruding into the middle ear. Treatment consists of neurosurgical repair of the bone and meningeal defects.

Small arachnoid granulations can occur not only in the tegemen but in any plate of bone separating the mastoid or petrous air cells from the CSF. Rarely, CSF can ''break through'' into the air-containing structures.

Hyrtl's Fissure

Hyrtl's fissure is an embryonic remnant that can rarely remain patent and, when present, opens inferior to the round window niche. It runs parallel to the cochlear aqueduct and extends along the inferior aspect of the cochlea connecting the hypotympanum with the posterior fossa at the jugular fossa. Gacek and Leipzig[93] described a large meningocele of the middle ear that extended through Hyrtl's fissure in a patient presenting with CSF otorrhea following a myrigotomy for serous otitis media. Phelps described two similar cases.[84]

Fissula Antefenestram

The fissula antefenestram is a microfissure like Hyrtl's fissure. It is an appendage of the perilymphatic labyrinth. It consists of periotic connective tissue that extends from the vestibule anterior to the oval window through a slit-like space in the otic capsule into the middle ear near the cochleariform process. In a large series of 331 temporal bones, 25% were found to have microfissures near the round window, and Hyrtl's fissure and the fissula antefenestram were among those most commonly seen.[94]

Giant Apical Air Cell and Apical Meningocele

Kraus and McCabe[95] described a dehiscence in the medial wall of the middle ear anterior to the cochlea. The defect contained ruptured pulsating arachnoid, and there was a copious CSF leak into the middle ear cavity and eustachian tube resulting in CSF rhinorrhea. A large air cell in the petrous apex can have very thin bone separating the air space from the CSF. An arachnoid granulation may potentially perforate into this air space, allowing it to fill with CSF. Dilated or giant air cells can be seen in the petrous bone as an isolated finding without CSF leak as well.

Copyright © 2003, Mosby, Inc. All rights reserved.

An apical meningocele is a CSF-filled space in the apex of the petrous bone. Usually it communicates with the CSF space in Meckel's cave. Such a collection may be seen as an incidental finding or it may communicate with the middle ear, resulting in a CSF leak. The cavity may be rounded and apparently slightly expanded, mimicking a cholesterol cyst on CT. The density is characteristic of CSF and is low. On MR imaging, the fluid follows a signal pattern of CSF rather than having the high signal on T1-weighted images characteristic of cholesterol granuloma (cyst). These abnormalities are usually seen in the elderly and are not truly congenital. They may be the result of softening of the thin bone.

Petromastoid Canal

The petromastoid canal is a canal parallel and superior to the IAC that carries the subarcuate vessels beneath the superior semicircular canal to the periantral mastoid air cells. It has been proposed but not proven to be a potential route for fistulas or meningitis.[3, 84]

Widened Labyrinthine Segment of the Facial Nerve Canal

There have been a few case reports of CSF fistulas occurring through abnormal lateral extension of the subarachnoid space following the labyrinthine segment of the facial nerve to the geniculate turn, thereby producing a potential CSF fistula directly into the middle ear cavity (Fig. 21-65).[84, 93, 96, 97] These cases have been reported in patients with normal labyrinths, although, CSF fistulas of this type may also occur in patients with anomalies of the labyrinth.[84]

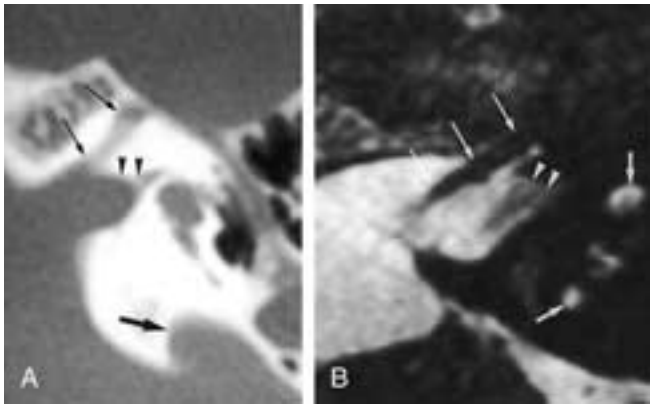

VIEW IMAGE

FIGURE 21-44 Facial nerve leaving the IAC in its middle one third in a patient with bilateral congenital deafness. **A**, Axial CT image through the right IAC. The labyrinthine segment of the facial nerve canal (*long black arrows*) leaves the IAC in its middle one third. Fundus of the IAC (*black arrowheads*), large vestibular aqueduct (*large black arrow*). **B**, Axial T2-weighted gradient-echo image through the right IAC. The facial nerve (*long white arrows*) can be followed from the IAC into the long labyrinthine segment of the facial nerve canal. Fluid in the fundus of the IAC (*white arrowheads*) and fluid in the branches of the superior semicircular duct (*small white arrows*). The presence of CSF between the facial nerve and the walls of the labyrinthine segment of the facial nerve canal, together with the presence of a large vestibular aqueduct on CT, are findings that should alert the examiner to the presence of a gusher ear.

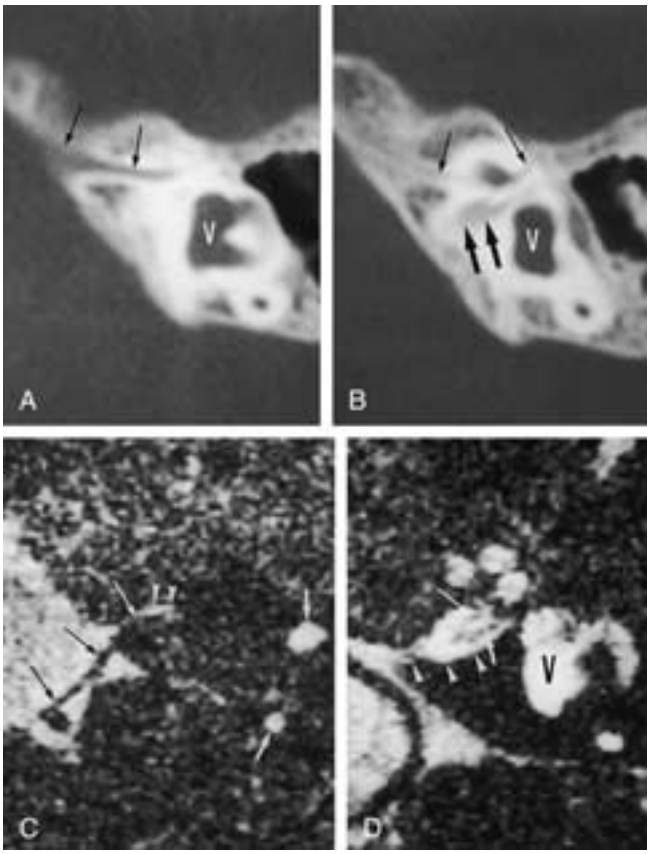

VIEW IMAGE

FIGURE 21-45 Facial nerve running in a separate canal parallel to the IAC. **A** and **B**, Axial CT image made above the left cochlea (**A**) and at the level of the upper part of the left cochlea and through the IAC (**B**). **A**, A separate canal for the facial nerve can be seen high and anteriorly in the left temporal bone (*long black arrows*). *V*, vestibule. **B**, The facial nerve canal can be followed posterior to the upper part of the cochlea (*long black arrows*). The IAC can now also be seen (*large black arrows*). *V*, vestibule. **C** and **D**, Axial 0.7 mm thick 3DFT-CISS images made at the level of the superior semicircular duct (**C**) and IAC (**D**). **C**, In the cerebellopontine angle, the facial nerve can be found in a high and anterior position (*long black arrows*) and continues its course in a separate facial nerve canal (*long white arrow*). Fluid in the labyrinthine segment of the facial nerve canal (*white arrowheads*) and fluid in the branches of the superior semicircular duct (*small white arrows*). **D**, The cochlear branch (*long white arrow*) and inferior vestibular branch (*small white arrow*) of the eighth nerve can be seen in the CSF-filled IAC (*white arrowheads*). *V,* Vestibule.

Translabyrinthine Fistulas

Translabyrinthine fistulas may occur through deficiencies in the lamina cribrosa, a thin, bony layer separating the apex of the IAC from the vestibule, or through deficiencies in the cochlear modiolus (Fig. 21-64B). These deficiencies allow a communication between the CSF in the IAC with the perilymph in the vestibule or cochlea, resulting in increased hydrostatic pressure within the inner ear, a condition known as *perilymphatic hydrops*.[4, 85] Perilymphatic hydrops may result in displacement and/or perforation of the stapes footplate, allowing CSF and perilymph to enter the middle ear cavity through the oval window. This transmission of CSF and perilymph into the middle ear cavity may occur spontaneously. In the past, surgical manipulation of the stapes for presumed fixation resulted in an acute outpouring of fluid known as the *stapes gusher*. Although fistulous

Copyright © 2003, Mosby, Inc. All rights reserved.

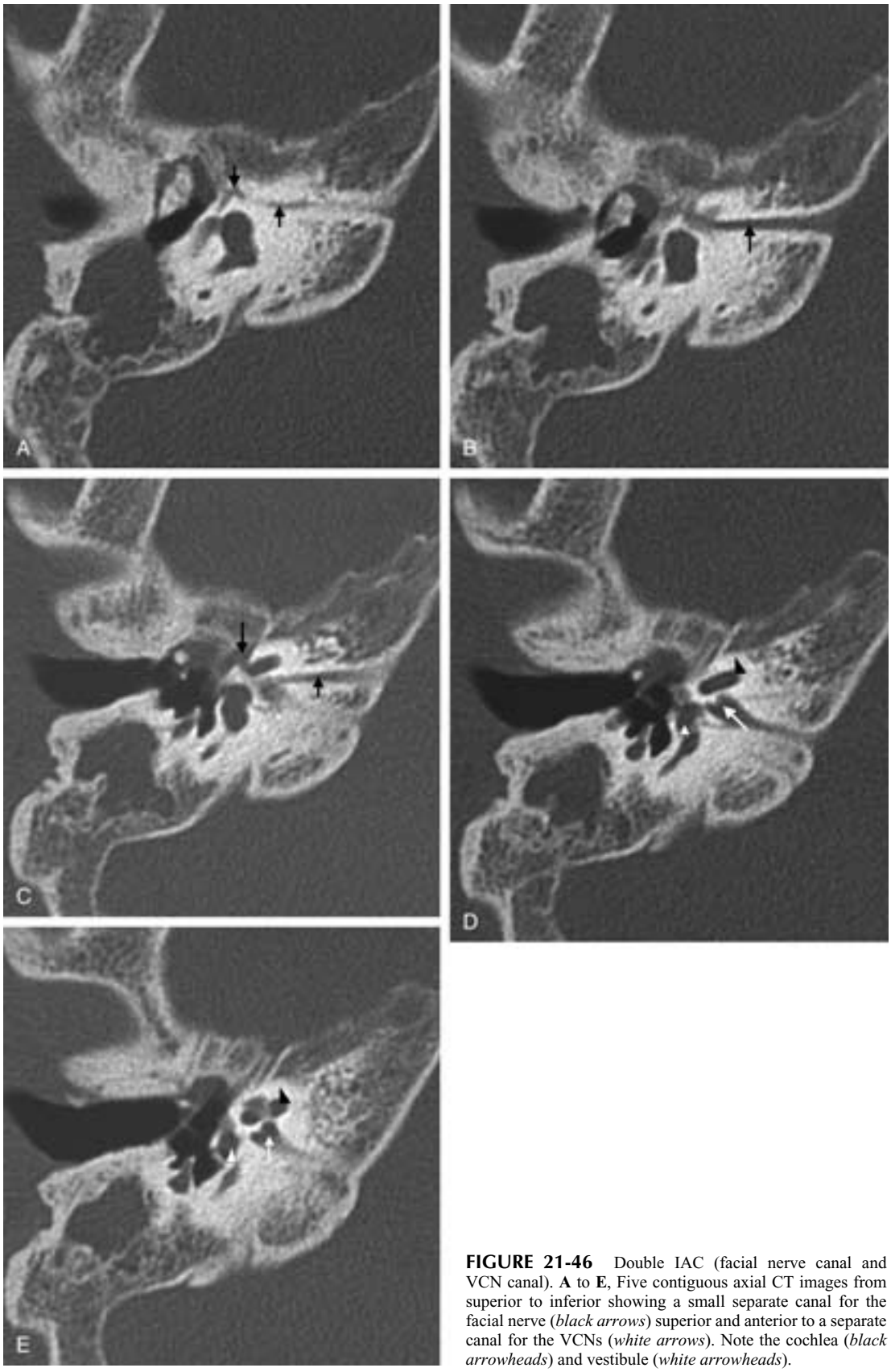

FIGURE 21-46 Double IAC (facial nerve canal and VCN canal). **A** to **E**, Five contiguous axial CT images from superior to inferior showing a small separate canal for the facial nerve (*black arrows*) superior and anterior to a separate canal for the VCNs (*white arrows*). Note the cochlea (*black arrowheads*) and vestibule (*white arrowheads*).

VIEW IMAGE

Copyright © 2003, Mosby, Inc. All rights reserved.

communication through the round window is also possible, it is much less common. Of note, not all cochlear dysplasias are associated with translabyrinthine fistulas. Mondini dysplasias were previously thought to be associated with these fistulas, but in fact, the intact modiolar base in Mondini dysplasias may prevent a fistulous communication between CSF in the IAC and perilymph in the cochlea.[84, 98]

Another route that has been proposed for translabyrinthine fistulas is the wide cochlear aqueduct. The cochlear aqueduct extends from the subarachnoid space medially, where the orifice lies between the IAC superiorly and the jugular foramen posteriorly, to the cochlea, opening laterally close to the round window membrane. It is a bony channel that houses the perilymphatic duct. Many anatomists believe that there is not a true open lumen, but rather that loose connective tissue fills the aqueduct, and thus that there is only a potential communication between the perilymph and the CSF.[99] It is generally accepted that the cochlear aqueduct is functionally patent in animals and young children, but there is controversy regarding its patency in adult life.[100] Persistent patency or enlargement of the aqueduct or a deficiency in the connective tissue within the duct might allow for the development of perilymphatic hydrops and a translabyrinthine fistula. However, this theory has been called into question.[84] This proposed route has not been documented with contrast or radiolabeled isotopes,[101] and cochlear aqueduct ablation in patients with presumed fistulas via an enlarged aqueduct has not succeeded in obliterating the fistula.[102]

What defines an enlarged cochlear aqueduct is not clear. In a study by Jackler and Hwang,[100] the cochlear aqueduct was divided into four parts, which were, from medial to lateral, a medial aperture into the posterior fossa; a petrous apex segment; an otic capsule segment; and a lateral orifice into the cochlea. They found great variability in the medial aperture ranging from 0 to 11 mm in normal subjects, with a mean of 4.5 mm. The measurements called into question previous reports of enlarged medial apertures.[102, 103] In contrast, the otic capsule segment was very narrow in every case, not visualized in some and never exceeding 2 mm in diameter. The authors stated that the narrowest segment should dictate whether or not CSF flow through the duct was possible, not the widest segment, which is usually the medial aperture. They therefore recommended that the radiographic criterion for cochlear aqueduct enlargement be established as the duct's exceeding 2 mm in diameter through its course from the posterior fossa to the inner ear. In fact, the otic segment of the duct actually averages less than 0.2 mm,

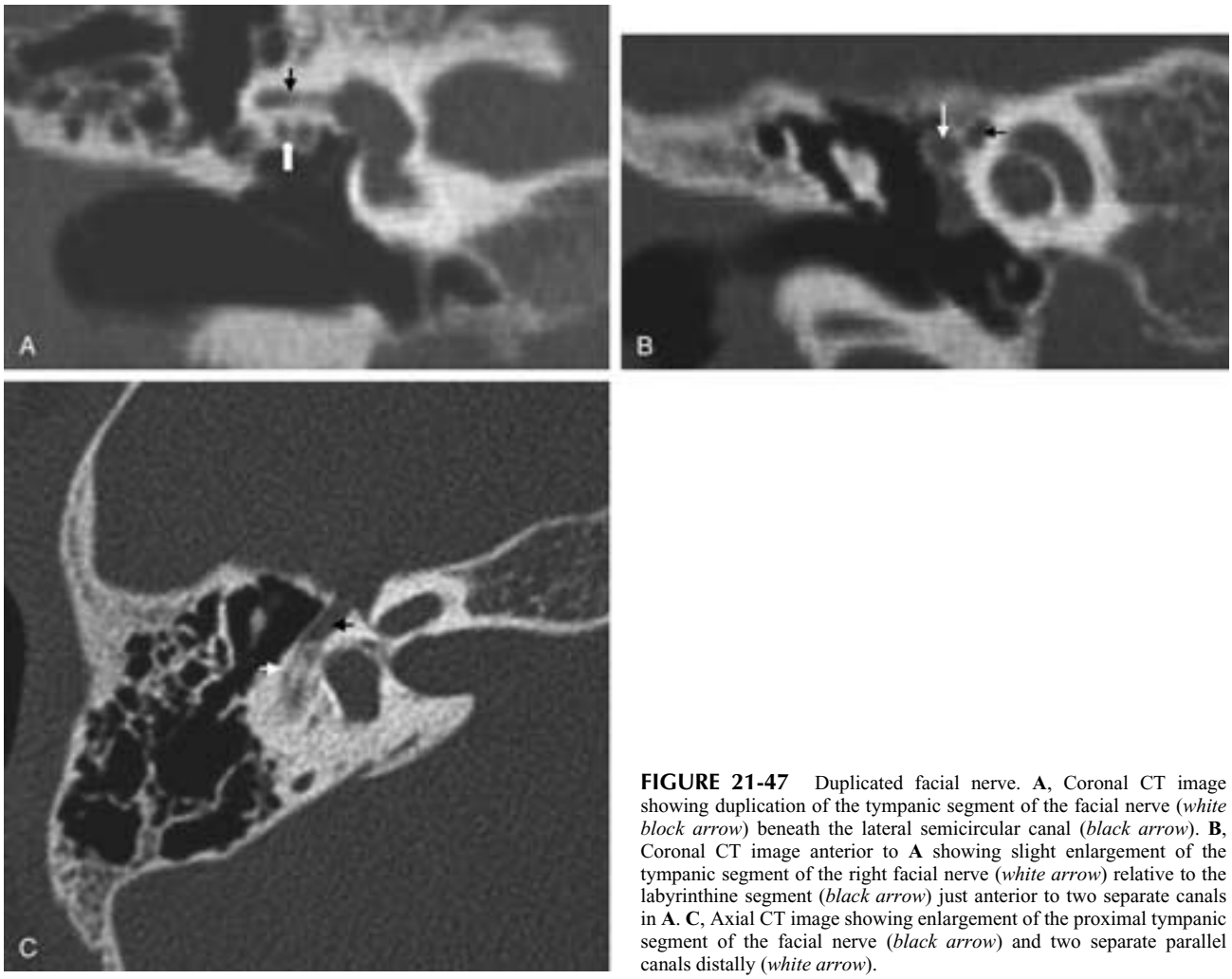

FIGURE 21-47 Duplicated facial nerve. **A**, Coronal CT image showing duplication of the tympanic segment of the facial nerve (*white block arrow*) beneath the lateral semicircular canal (*black arrow*). **B**, Coronal CT image anterior to **A** showing slight enlargement of the tympanic segment of the right facial nerve (*white arrow*) relative to the labyrinthine segment (*black arrow*) just anterior to two separate canals in **A**. **C**, Axial CT image showing enlargement of the proximal tympanic segment of the facial nerve (*black arrow*) and two separate parallel canals distally (*white arrow*).

VIEW IMAGE

Copyright © 2003, Mosby, Inc. All rights reserved.

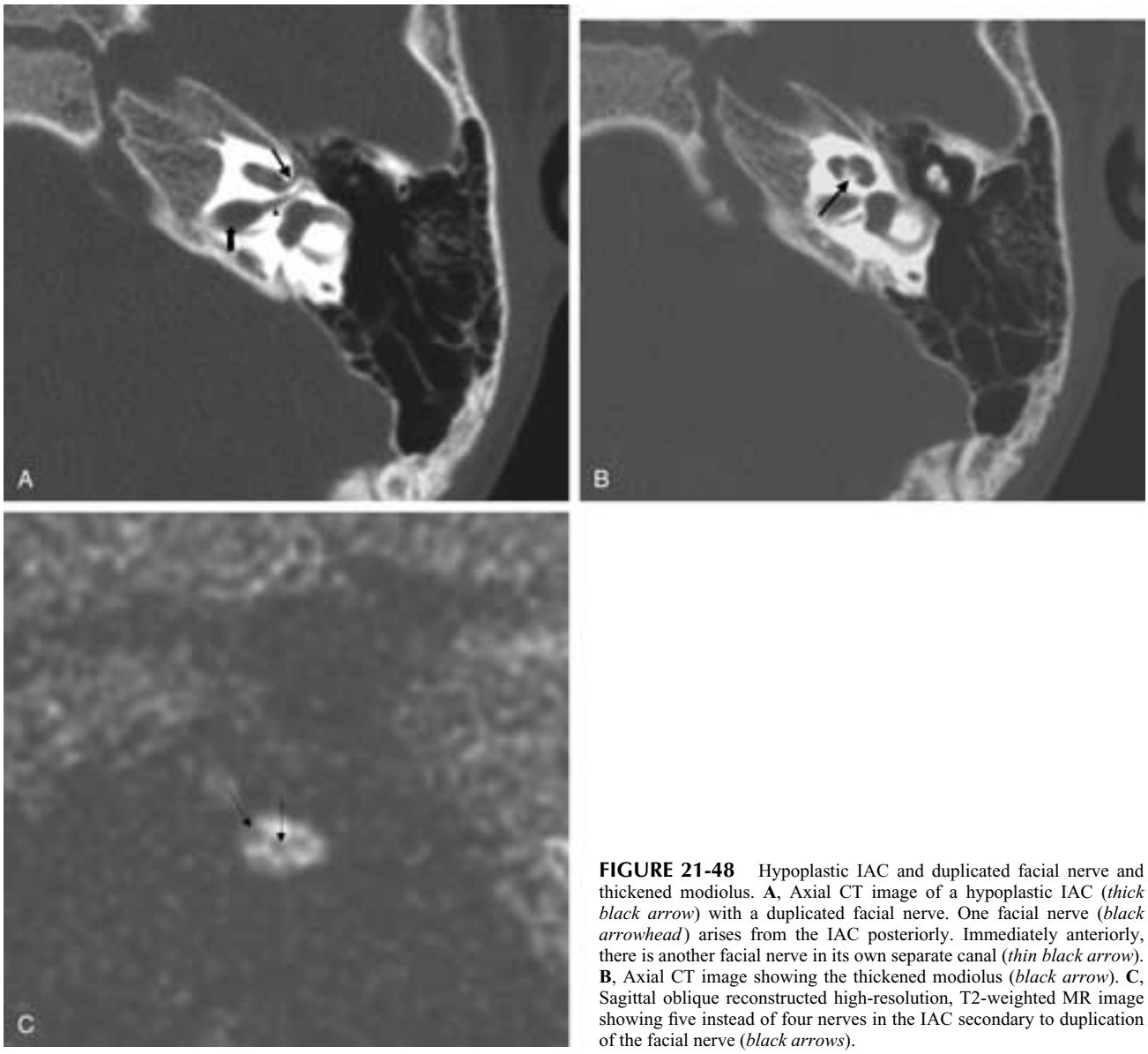

FIGURE 21-48 Hypoplastic IAC and duplicated facial nerve and thickened modiolus. **A**, Axial CT image of a hypoplastic IAC (*thick black arrow*) with a duplicated facial nerve. One facial nerve (*black arrowhead*) arises from the IAC posteriorly. Immediately anteriorly, there is another facial nerve in its own separate canal (*thin black arrow*). **B**, Axial CT image showing the thickened modiolus (*black arrow*). **C**, Sagittal oblique reconstructed high-resolution, T2-weighted MR image showing five instead of four nerves in the IAC secondary to duplication of the facial nerve (*black arrows*).

VIEW IMAGE

currently below the limit of resolution with CT. Jackler et al.'s recommendation for an enlarged aqueduct is limited by the fact that submillimeter increments in duct diameter may be significant and again below the limit of resolution with CT, and by the fact that deficiencies in the connective tissue within the canal would not likely be manifested as canal enlargement.

CONGENITAL SYNDROMES INVOLVING THE EAR

Syndromes associated with congential anomalies of the ear are often the result of an inherited disorder, although substrate damage in utero as a result of an external teratogen may also occur. The hearing loss associated with these syndromes tends to be severe and is less responsive to correction because the onset is early and significant architectural anomalies are present.

These syndromes may be classified and organized in a variety of ways. They may be organized according to their Mendelian inheritance pattern: autosomal dominant, autosomal recessive, or sex-linked. Some syndromes are the result of a chromosomal aberration, either augmentation or deletion. In utero exposure to certain drugs or teratogens may result in specific anomalies. Still other syndromes are the result of an interaction of genetic factors with environmental influences and can be categorized as ''multifactorial genetic disorders.''[104] Others may be classified according to common clinical and radiologic features. For example, certain syndromes that involve the ear may also have associated craniofacial, cervical, or skeletal anomalies.[105] In the otocraniofacial group, the syndromes may share anomalies of the ear, skull, and face. Many of these are of autosomal dominant inheritance and have anomalies primarily of the outer ear and middle ears or anomalies of structures derived from the first and second branchial arches, with only occasional inner ear anomalies. In the otocervical

Text continued on page 1161

Copyright © 2003, Mosby, Inc. All rights reserved.

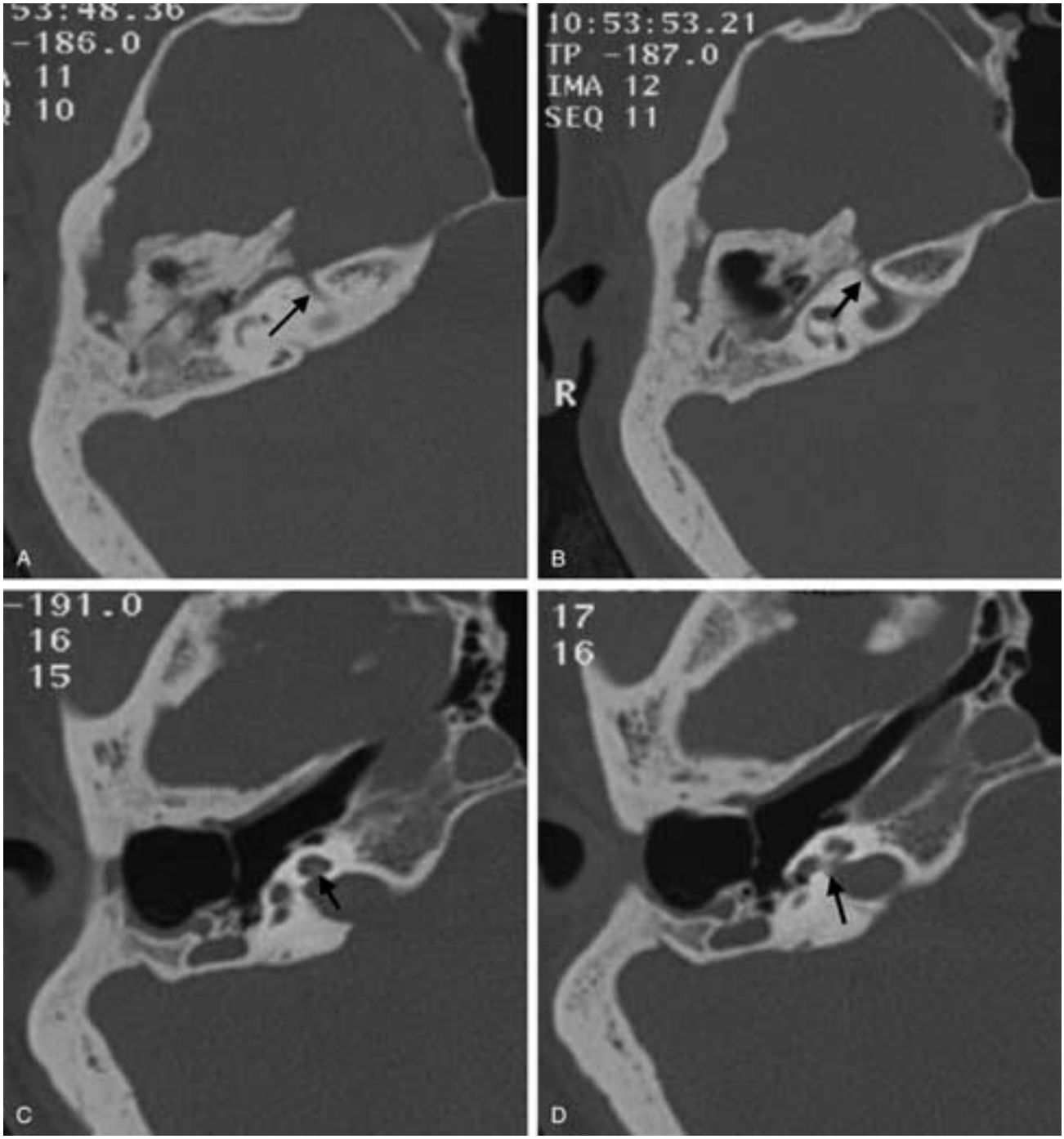

VIEW IMAGE

FIGURE 21-49 Hypoplastic (''dwarf'') cochlea and anterior migration of the facial nerve. **A** and **B**, Two contiguous 1 mm axial CT images showing anterior migration of the facial nerve canal (*black arrow*). **C** and **D**, Two contiguous axial CT images showing a hypoplastic cochlea (*black arrow*) with all three cochlear turns present but small: a dwarf cochlea.

Copyright © 2003, Mosby, Inc. All rights reserved.

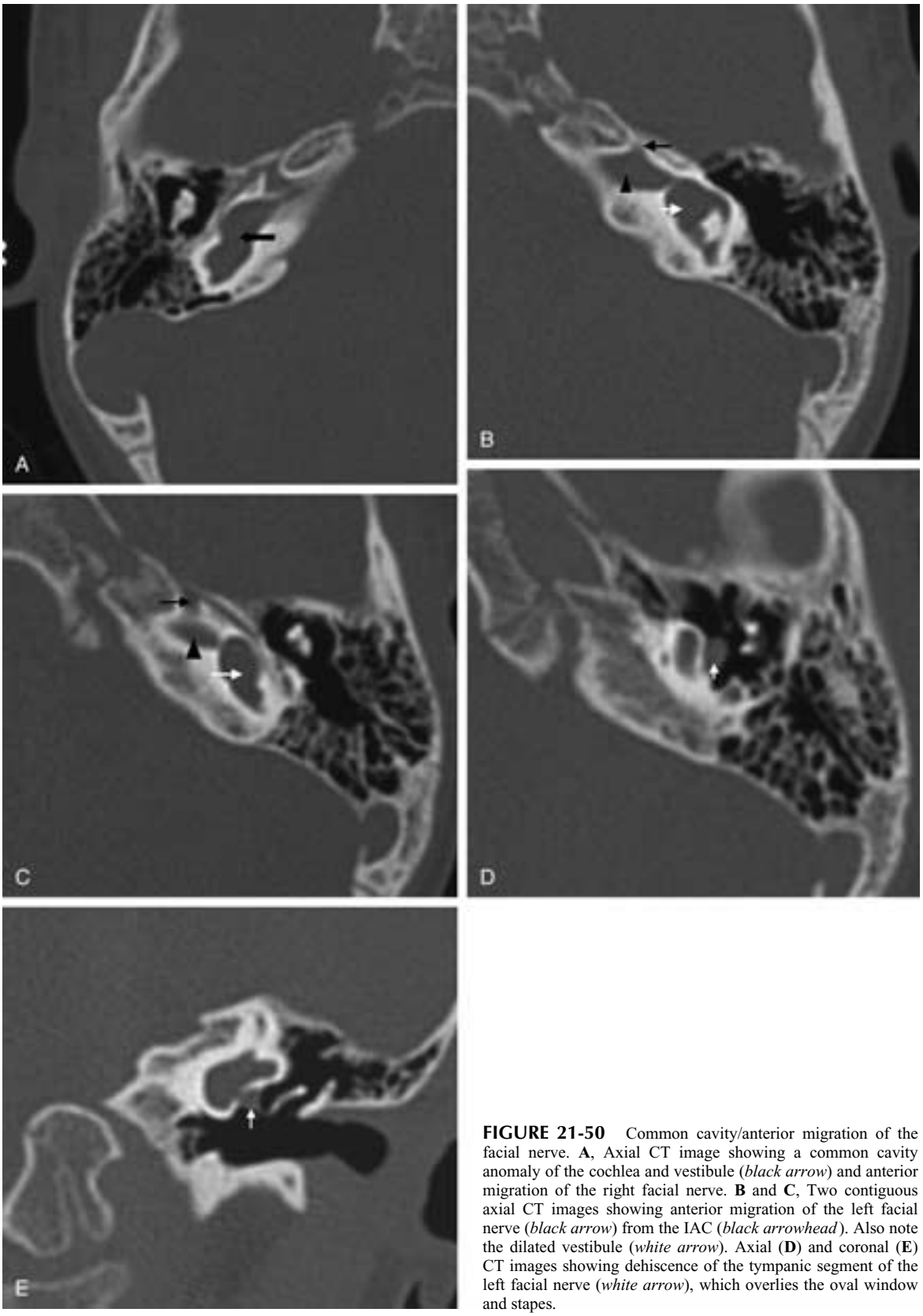

FIGURE 21-50 Common cavity/anterior migration of the facial nerve. **A**, Axial CT image showing a common cavity anomaly of the cochlea and vestibule (*black arrow*) and anterior migration of the right facial nerve. **B** and **C**, Two contiguous axial CT images showing anterior migration of the left facial nerve (*black arrow*) from the IAC (*black arrowhead*). Also note the dilated vestibule (*white arrow*). Axial (**D**) and coronal (**E**) CT images showing dehiscence of the tympanic segment of the left facial nerve (*white arrow*), which overlies the oval window and stapes.

VIEW IMAGE

Copyright © 2003, Mosby, Inc. All rights reserved.

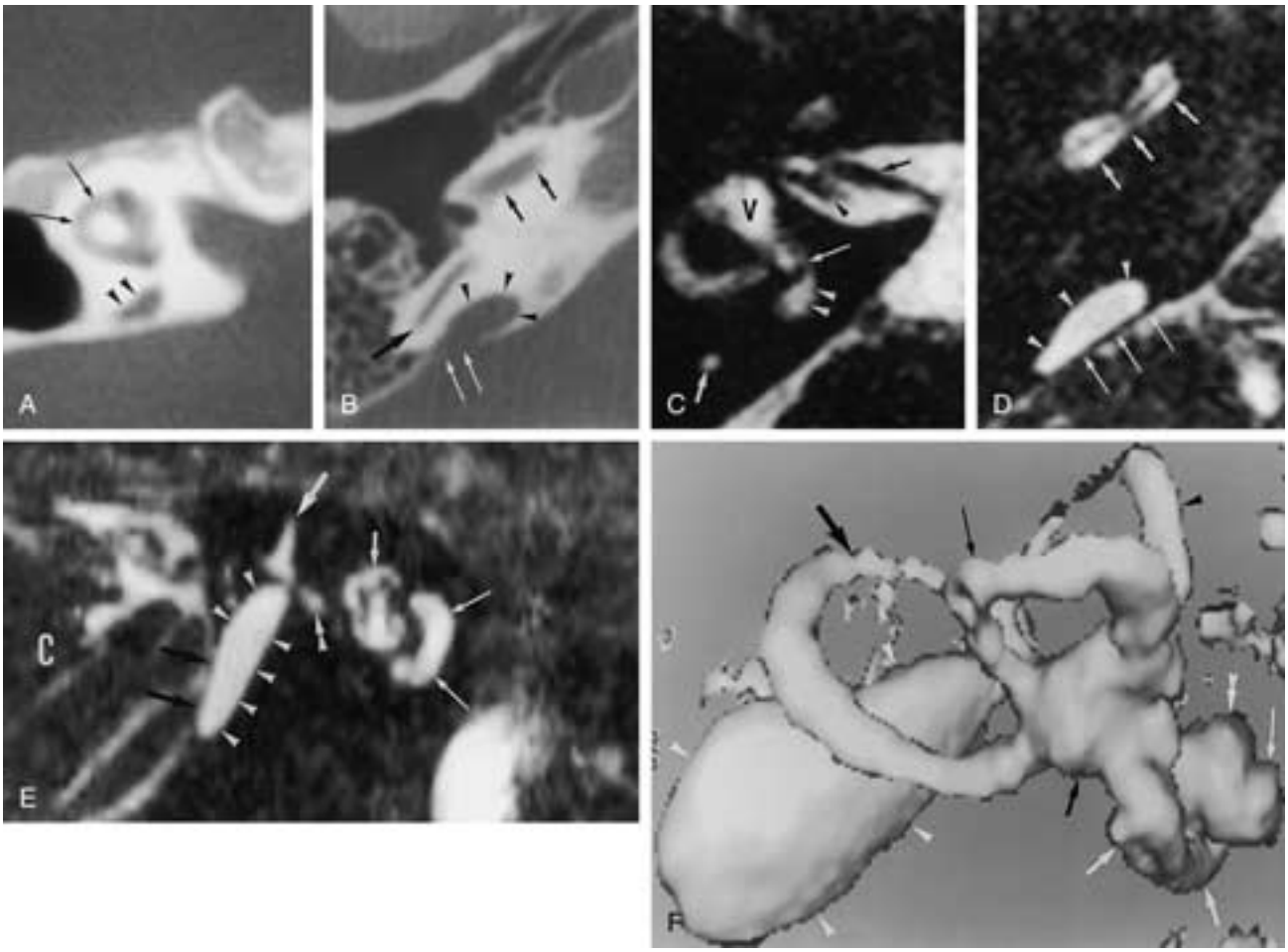

VIEW IMAGE

FIGURE 21-51 Large vestibular aqueduct/duct and sac. **A**, Axial CT image at the level of the right lateral semicircular canal. The diameter of the vestibular aqueduct is more than 1.5 mm (*black arrowheads*) and is therefore enlarged. Normal lateral semicircular canal (*long black arrows*). Normally, the diameter of the vestibular aqueduct never exceeds the diameter of the semicircular canals. **B**, Axial CT image at the level of the basal turn of the right cochlea. The enlarged vestibular aqueduct (*black arrowheads*) opens in the posterior fossa, but the sac inside the aqueduct cannot be distinguished from the posterior fossa structures (*long white arrows*). Normal posterior semicircular canal (*large black arrow*) and basal turn of the cochlea (*small black arrows*). **C**, Axial T2-weighted gradient-echo image through the right endolymphatic duct. The connection (*long white arrow*) between the enlarged endolymphatic duct (*white arrowheads*) and the vestibule (*V*) can be recognized. The endolymphatic duct is enlarged, as its diameter is more than 1.5 mm or because it is larger than the diameter of the posterior semicircular canal (*small white arrow*). Facial nerve (*small black arrow*) and superior vestibular branch of the VCN (*black arrowhead*). **D**, Axial T2-weighted gradient-echo image through the enlarged endolymphatic sac. The large fluid-filled endolymphatic sac (*white arrowheads*) can be separated from the CSF in the posterior fossa because the dura mater between the two fluid-filled spaces can be depicted on MR imaging (*long white arrows*). Note that the signal intensity of the fluid inside the endolymphatic sac is higher than the signal intensity of the CSF. The lower signal intensity of CSF is caused by CSF flow. Normal basal turn of the cochlea (*small white arrows*). **E**, T2-weighted gradient-echo images, parasagittal reconstruction through the right inner ear and large endolymphatic duct and sac. The enlarged endolymphatic duct and sac (*white arrowheads*) can be followed from the labyrinth to the posterior fossa. The endolymphatic sac can be distinguished from the posterior fossa structures (*large black arrows*). Superior semicircular duct (*large white arrow*), vestibule (*double white arrowhead*), IAC (*small white arrow*), cochlea (*long white arrows*), cerebellum (*C*). **F**, Three-dimensional virtual image of the right inner ear, made by using 0.7 mm thick T2-weighted gradient-echo images. The large endolymphatic duct and sac can be visualized in their full extent on this *image* (*white arrowheads*). Normal lateral (*long black arrow*), superior (*black arrowhead*), and posterior (*large black arrow*) semicircular ducts; normal *basal* (*small white arrows*), second (*double white arrowhead*), and apical *turns* (*long white arrow*) of the cochlea; and normal vestibule (*small black arrow*).

Copyright © 2003, Mosby, Inc. All rights reserved.

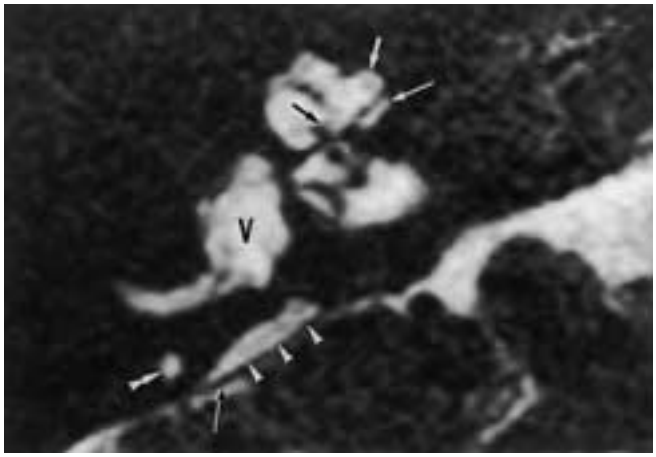

VIEW IMAGE

FIGURE 21-52 Large endolymphatic duct and sac with asymmetry of the cochlear scalar chambers. Axial T2-weighted gradient-echo image through the right cochlea and vestibule. The large endolymphatic sac (*white arrowheads*) can be separated from the CSF in the posterior fossa because the dura mater (*long black arrow*) can be distinguished on MR imaging. The scala vestibuli/media (*small white arrow*) is two to three times larger than the scala tympani (*long white arrow*), which is abnormal. Normally, both scalas have the same size (see Figs. 21-25A,C and 21-51D). The modiolus is dysplastic and small (*small black arrow*), another frequent finding in patients with large endolymphatic sacs and ducts. Normal posterior semicircular duct (*double arrowhead*) and vestibule (*V*).

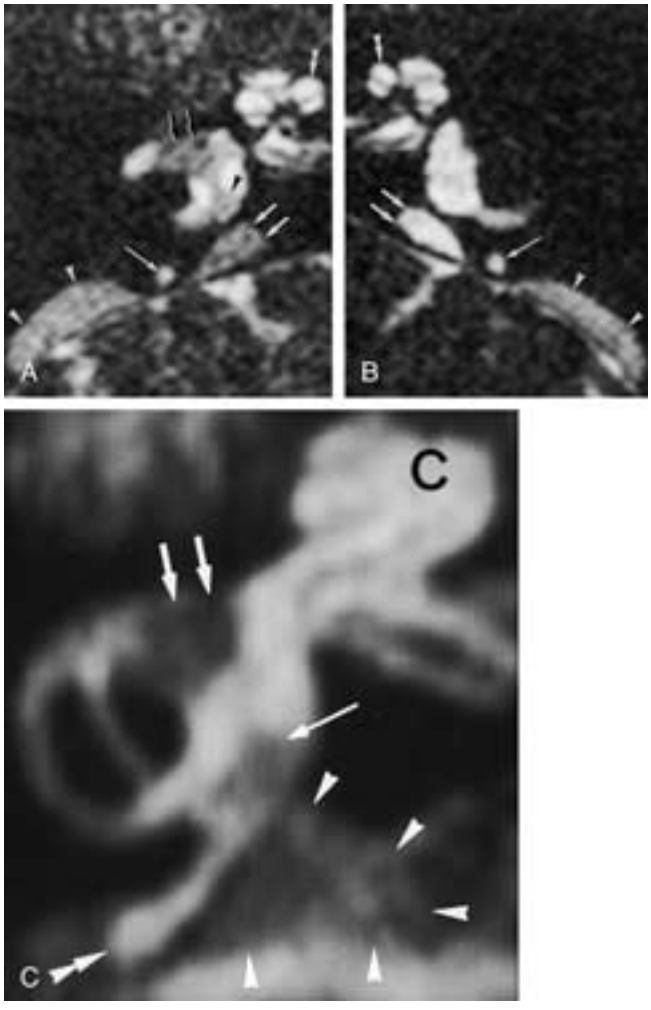

VIEW IMAGE

FIGURE 21-53 Pendred syndrome: bilateral large endolymphatic sac and duct, with loss of normal fluid in the endolymphatic sac on both sides and in the endolymphatic duct and vestibule on the right side. **A**, Axial 0.7 mm gradient-echo T2-weighted image through the right inner ear. The endolymphatic duct (*small white arrows*) and sac (*white arrowheads*) are enlarged, and the fluid in these enlarged structures is replaced by low signal intensity soft tissues. Similar signal changes occurred in the ampulla of the lateral semicircular duct (*small black arrows*) and in the posterior part of the vestibule (*black arrowhead*). This lower signal can represent fibrous tissue or loose vascular subepithelial connective tissue and cuboidal to columnar epithelial cells, also called the *rugose* portion. Note that the scala vestibuli/media (*double arrowhead*) is again larger than the scala vestibuli. The asymmetry of the cochlear chambers is, however, less pronounced than in Figure 21-52. Normal fluid inside the posterior semicircular duct (*long white arrow*). **B**, Axial 0.7 mm gradient-echo T2-weighted image through the left inner ear. The enlarged endolymphatic duct contains normal fluid (*small white arrows*), while the normal fluid in the endolymphatic sac is replaced by soft tissues (*white arrowheads*). Normal fluid can be seen inside the posterior semicircular duct (*long white arrow*). The scala vestibuli/media (*double arrowhead*) is again larger than the scala vestibuli. **C**, Three-dimensional 3DFT-CISS reconstruction of the inner ear, viewed from above. The fluid-filled cochlea (*C*) and posterior semicircular duct (*double arrowhead*) can be seen. The triangular endolymphatic duct and sac are difficult to recognize because the normal fluid has been replaced by low signal intensity tissue (*white arrowheads*). Low signal intensity can be seen in the ampulla of the lateral semicircular duct (*small white arrows*) and in the posterior part of the vestibule (*long white arrow*).

Copyright © 2003, Mosby, Inc. All rights reserved.

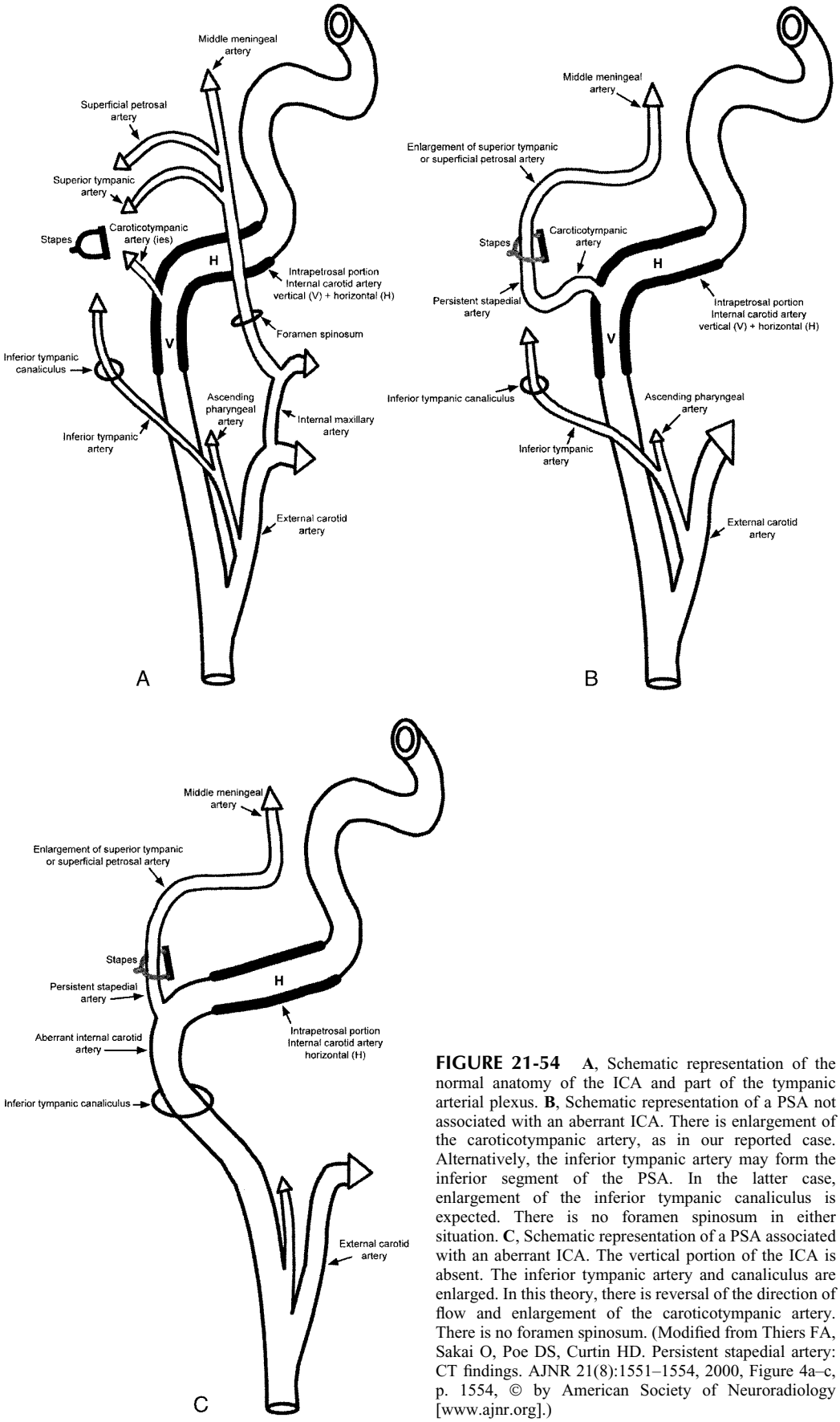

FIGURE 21-54 **A**, Schematic representation of the normal anatomy of the ICA and part of the tympanic arterial plexus. **B**, Schematic representation of a PSA not associated with an aberrant ICA. There is enlargement of the caroticotympanic artery, as in our reported case. Alternatively, the inferior tympanic artery may form the inferior segment of the PSA. In the latter case, enlargement of the inferior tympanic canaliculus is expected. There is no foramen spinosum in either situation. **C**, Schematic representation of a PSA associated with an aberrant ICA. The vertical portion of the ICA is absent. The inferior tympanic artery and canaliculus are enlarged. In this theory, there is reversal of the direction of flow and enlargement of the caroticotympanic artery. There is no foramen spinosum. (Modified from Thiers FA, Sakai O, Poe DS, Curtin HD. Persistent stapedial artery: CT findings. AJNR 21(8):1551–1554, 2000, Figure 4a–c, p. 1554, © by American Society of Neuroradiology [www.ajnr.org].)

Copyright © 2003, Mosby, Inc. All rights reserved.

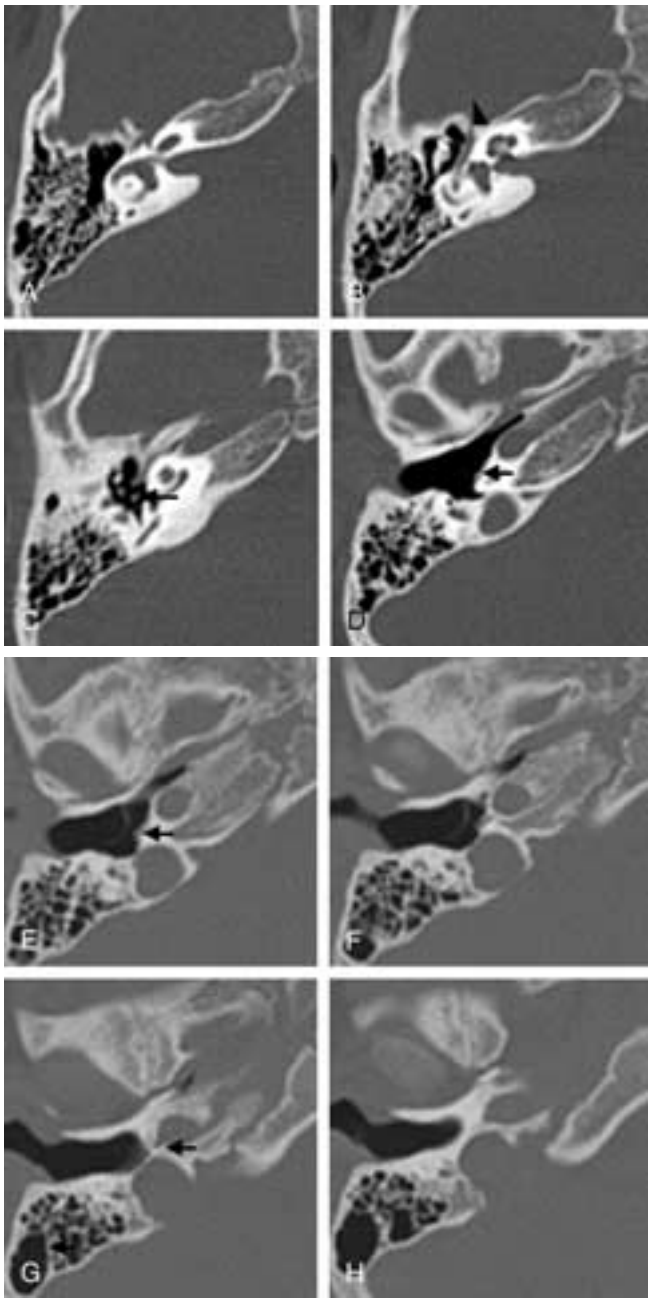

VIEW IMAGE

VIEW IMAGE

FIGURE 21-55 PSA. **A** to **H**, Axial CT images from superior to inferior. The small vascular channel can be seen leaving the vertical carotid at G (*arrow*) and can be followed along the lower medial wall of the middle ear (**D** to **F**) (*arrows*). Level **C** is at the plane of the stapedial crura. The vessel cannot be clearly separated from the anterior crus of the stapes. After following the facial nerve canal, the small vascular channel reaches the middle cranial fossa at level **B** (*arrowhead*). Level **A** represents the position of the geniculate ganglion turn of the facial nerve canal. (Modified from Thiers FA, Sakai O, Poe DS, Curtin HD. Persistent stapedial artery: CT findings. AJNR 21(8):1551–1554, 2000, Figure 2, p. 1553, © American Society of Neuroradiology [www.ajnr.org].)

Copyright © 2003, Mosby, Inc. All rights reserved.

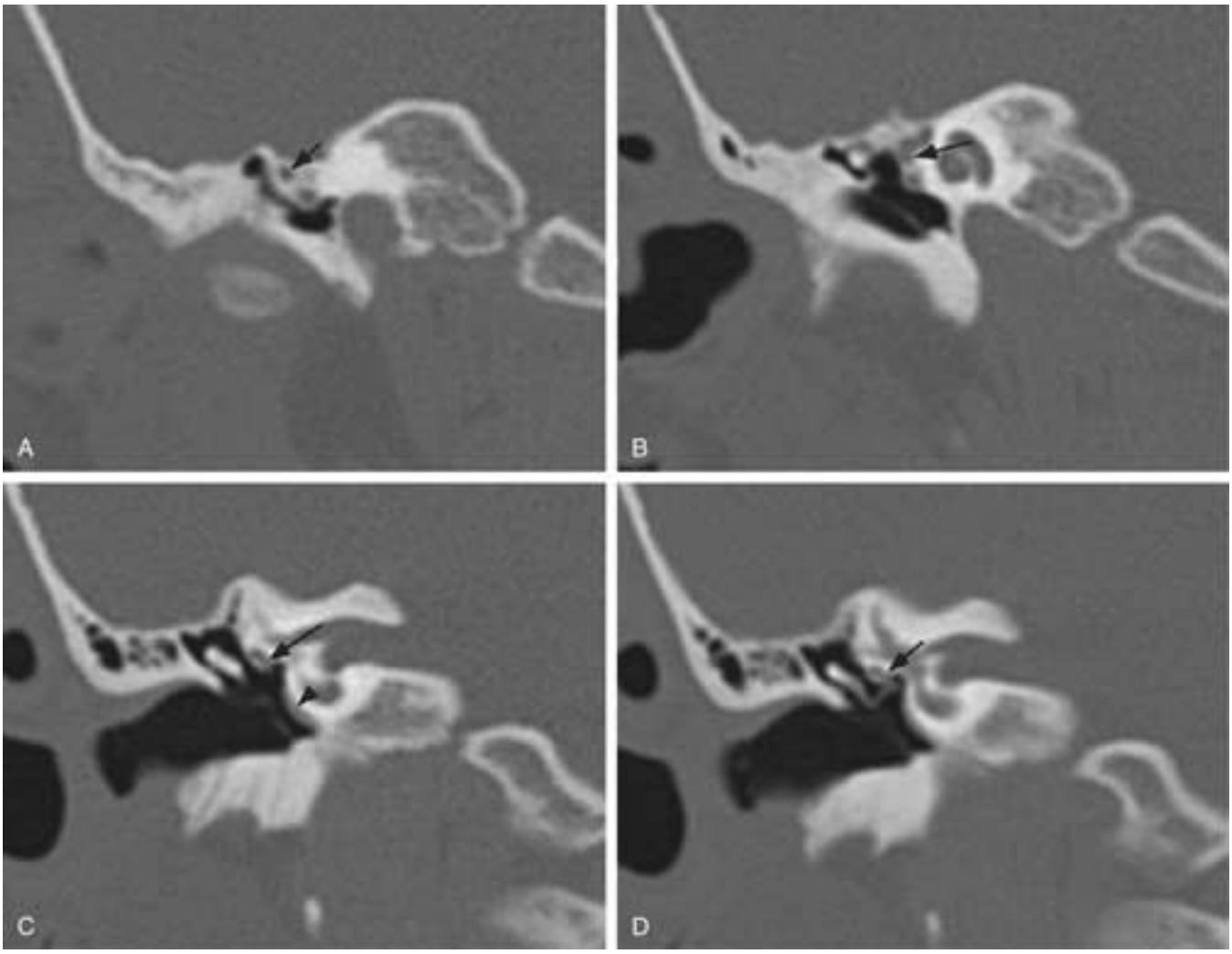

VIEW IMAGE

FIGURE 21-56 PSA. **A** to **D**, Coronal CT images from anterior to posterior. The narrow presumed vascular structure is seen at level **C** (*arrowhead*), coursing along the promontory. At level **D**, the small vascular structure crosses the oval window niche, to end in the lower inferomedial aspect of the tympanic segment of the facial nerve canal (*arrow*). This small channel is also seen at level **C** (*arrow*). More anteriorly (**A** and **B**), the small canal (*arrows*) courses just inferior to the tympanic segment of the facial nerve canal in a separate channel as it passes toward the floor of the middle cranial fossa. The small soft-tissue structure immediately inferior to this canal is the tensor tympani muscle within its semicanal.

Copyright © 2003, Mosby, Inc. All rights reserved.

VIEW IMAGE

FIGURE 21-57 Aberrant ICA. **A**, Axial CT image showing an aberrant left ICA projecting into the left middle ear cavity (*black arrow*). Petrous carotid canal (*white arrow*). **B**, Axial CT image showing a normal right carotid canal (*black arrow*). **C**, Conventional digital subtraction angiography showing far lateral displacement of the left ICA (*black arrow*). **D**, MRA showing far lateral displacement of the left ICA (*white arrow*) and normal placement of the right ICA (*black arrowhead*).

Copyright © 2003, Mosby, Inc. All rights reserved.

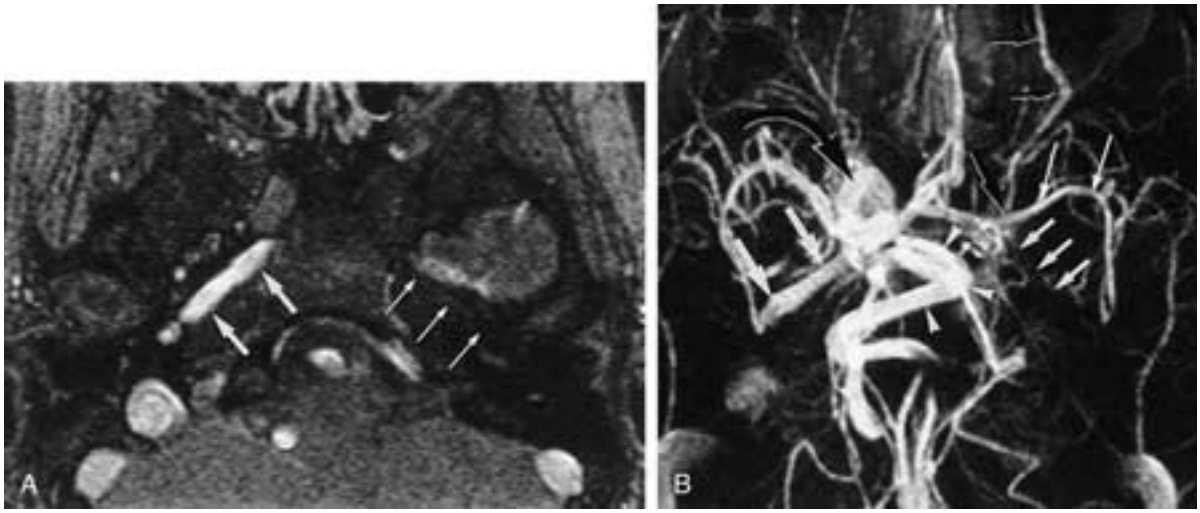

VIEW IMAGE

FIGURE 21-58 Agenesis or congenital absence of the left ICA. **A**, Axial high-resolution 3D-Flash time-of-flight MRA image at the level of the petrous apex. Normal flow can be seen in the ICA inside the right petrous carotid canal (*large white arrows*). No blood flow is evident inside the left petrous carotid canal (*long white arrows*). **B**, MIP reconstruction of the intracerebral vessels showing a normal ICA inside the petrous bone (*large white arrows*) and in the parasellar region (*curved black arrow*) on the right side. The left ICA is absent (*small white arrows*), and a tortuous large basilar artery can be recognized (*white arrowheads*). A slightly hypertrophic ophthalmic artery (*small black arrows*) arises beneath (*large black arrow*) the middle cerebral artery (*long white arrows*) from the internal carotid remnant.

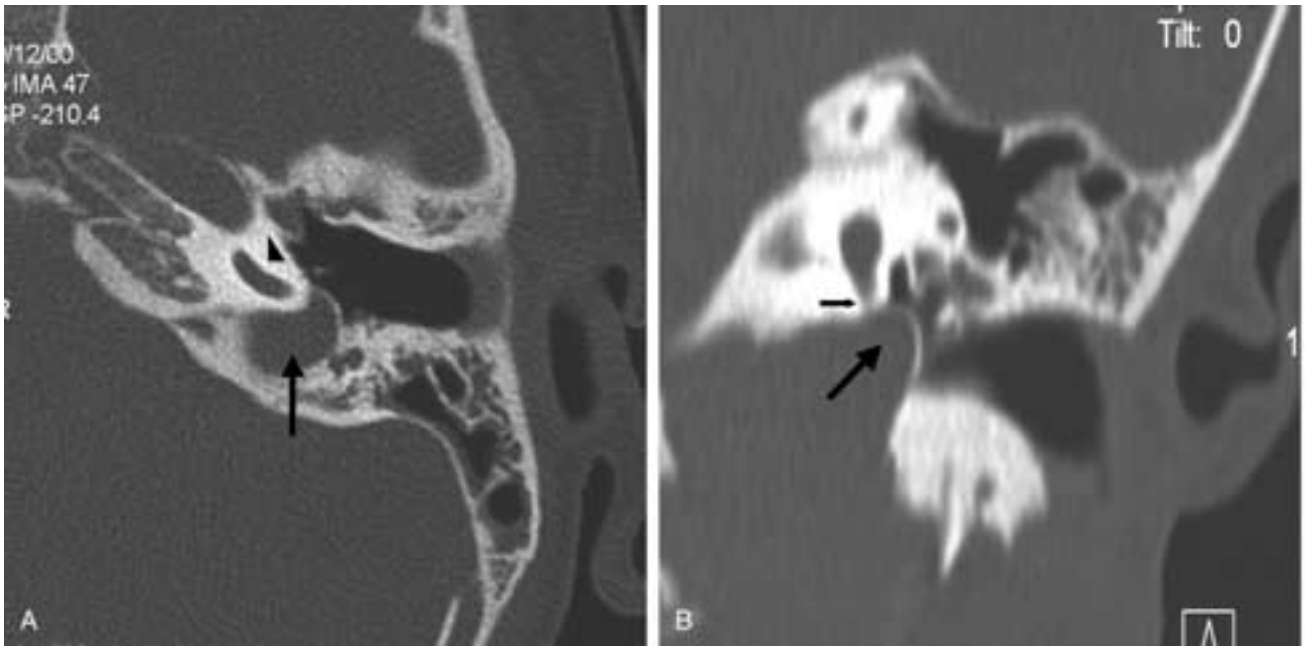

VIEW IMAGE

FIGURE 21-59 High-riding jugular bulb. **A**, Axial CT image showing the jugular bulb (*black arrow*) covering the basal turn of the cochlea (*black arrowhead*). **B**, Coronal CT image showing the jugular bulb (*large black arrow*) covering the round window (*small black arrow*).

Copyright © 2003, Mosby, Inc. All rights reserved.

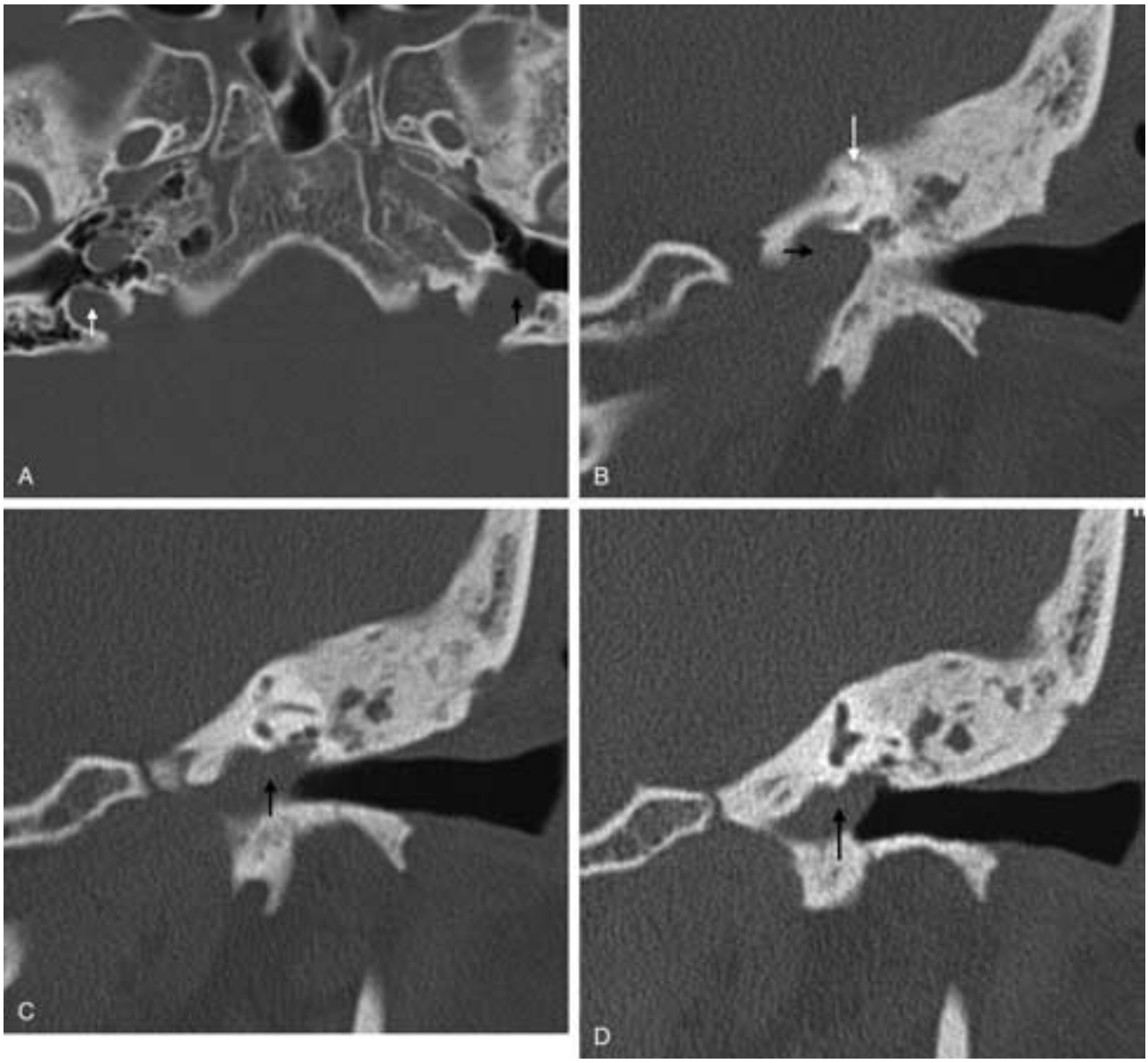

VIEW IMAGE

FIGURE 21-60 High-riding jugular bulb. **A**, Axial CT image showing a normal right jugular bulb (*white arrow*) and a high-riding left jugular bulb (*black arrow*) projecting into the left hypotympanum. **B** to **D**, Three contiguous coronal CT images, from posterior to anterior, showing a high-riding left jugular bulb (*black arrow*) abutting the PSCC (*white arrow* in **B**) and extending into the middle ear cavity in **C** and **D**.

group, the syndromes may share anomalies of the ear, neck, and shoulder, with the most common shared anomaly being fusion of two or more cervical vertebral bodies. In this group, inner ear anomalies are more common than outer or middle ear anomalies. In the otoskeletal group, the syndromes may share anomalies of the ear, face, and limbs, with the otic manifestations usually related to anomalies of osseous development, growth, or proliferation. Some syndromes fall into an ''other'' category, not having features common to other syndromes and not having a known cause or pattern of inheritance. A list of the more common or well-known syndromes can be found in Table 21-1, and Figures 21-66 to 21-71 show a few examples of the temporal bone findings on CT in some of these syndromes. The syndromes are listed alphabetically, and for many of them, note is made of one or more groups into which they may be classified or assigned. It must be emphasized that Table 21-1 represents only a partial list of syndromes that may involve the ear. There are many other textbooks dedicated to this subject alone.

Text continued on page 1169

Copyright © 2003, Mosby, Inc. All rights reserved.

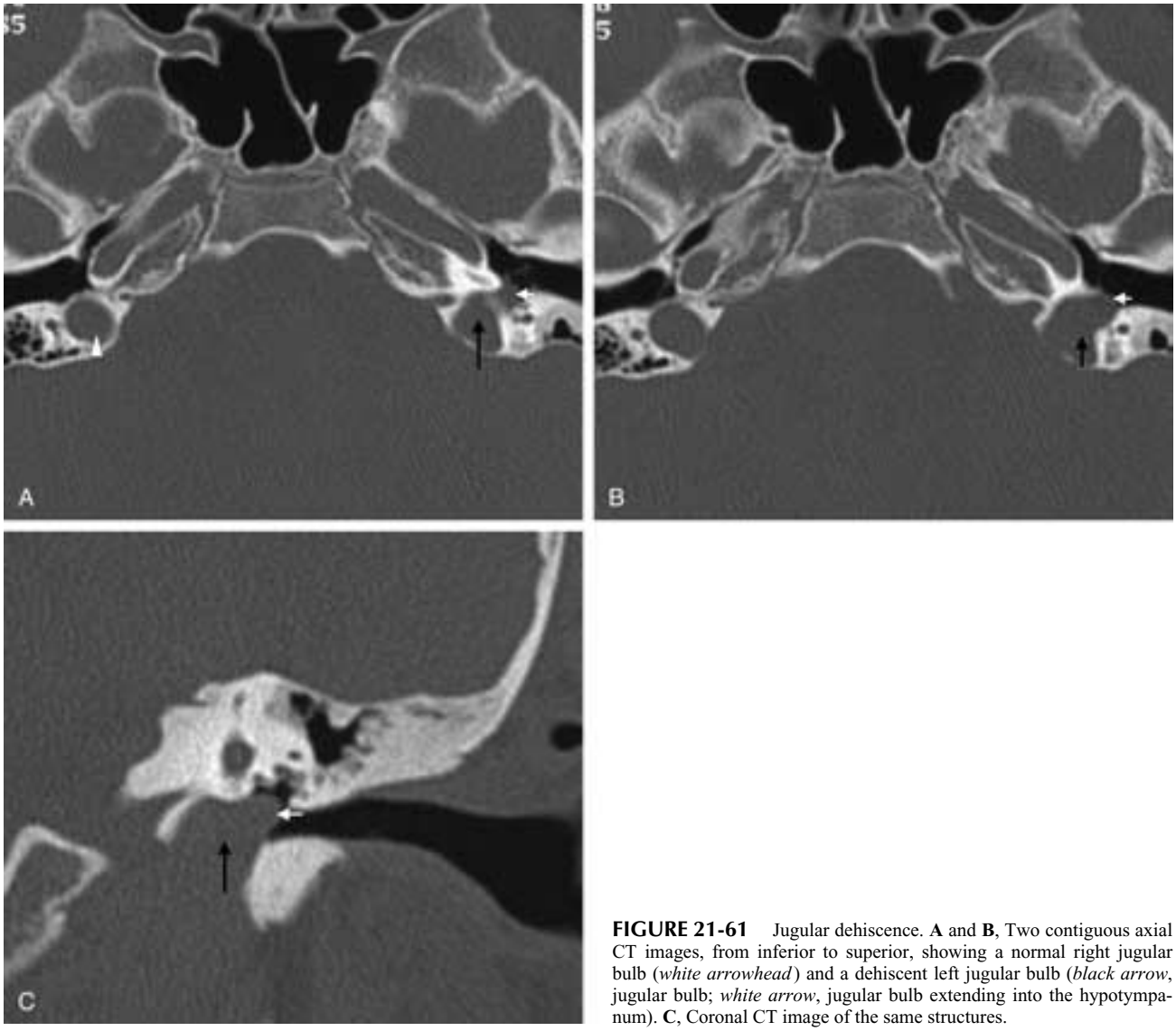

FIGURE 21-61 Jugular dehiscence. **A** and **B**, Two contiguous axial CT images, from inferior to superior, showing a normal right jugular bulb (*white arrowhead*) and a dehiscent left jugular bulb (*black arrow*, jugular bulb; *white arrow*, jugular bulb extending into the hypotympanum). **C**, Coronal CT image of the same structures.

VIEW IMAGE

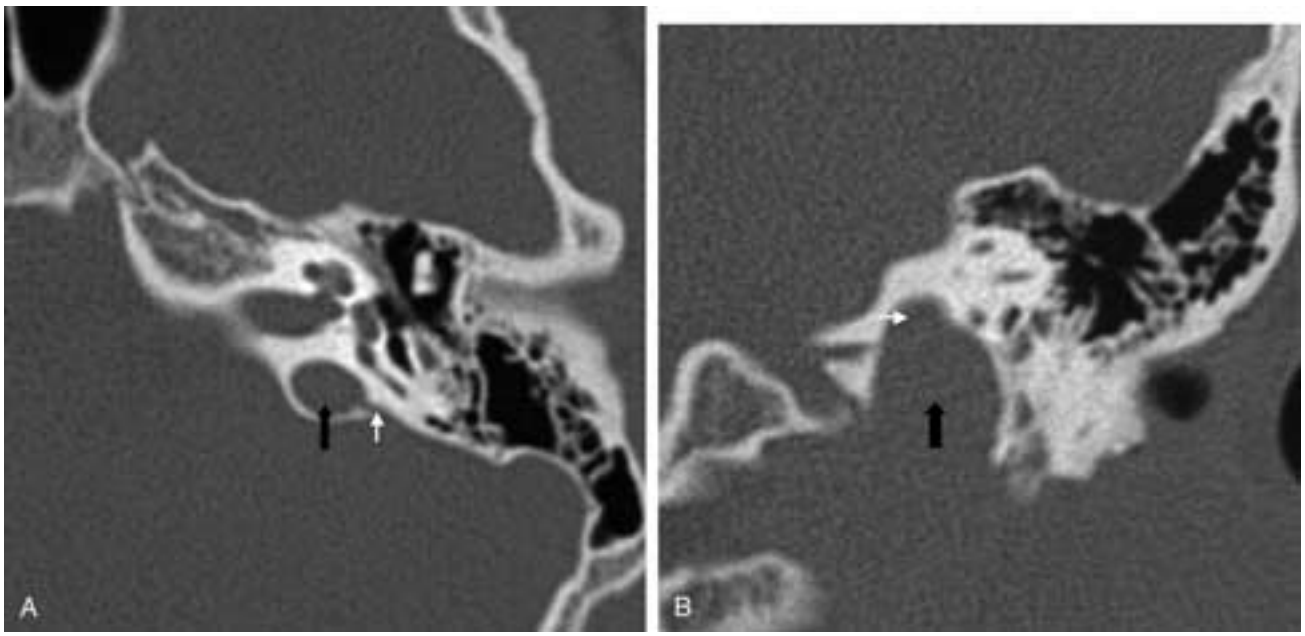

FIGURE 21-62 JD. **A**, Axial CT image of a JD (*black block arrow*) abutting the vestibular aqueduct (*white arrow*). **B**, Coronal CT image showing a jugular bulb (*black block arrow*) and a small diverticulum (*white arrow*) projecting superiorly toward the semicircular canals.

VIEW IMAGE

Copyright © 2003, Mosby, Inc. All rights reserved.

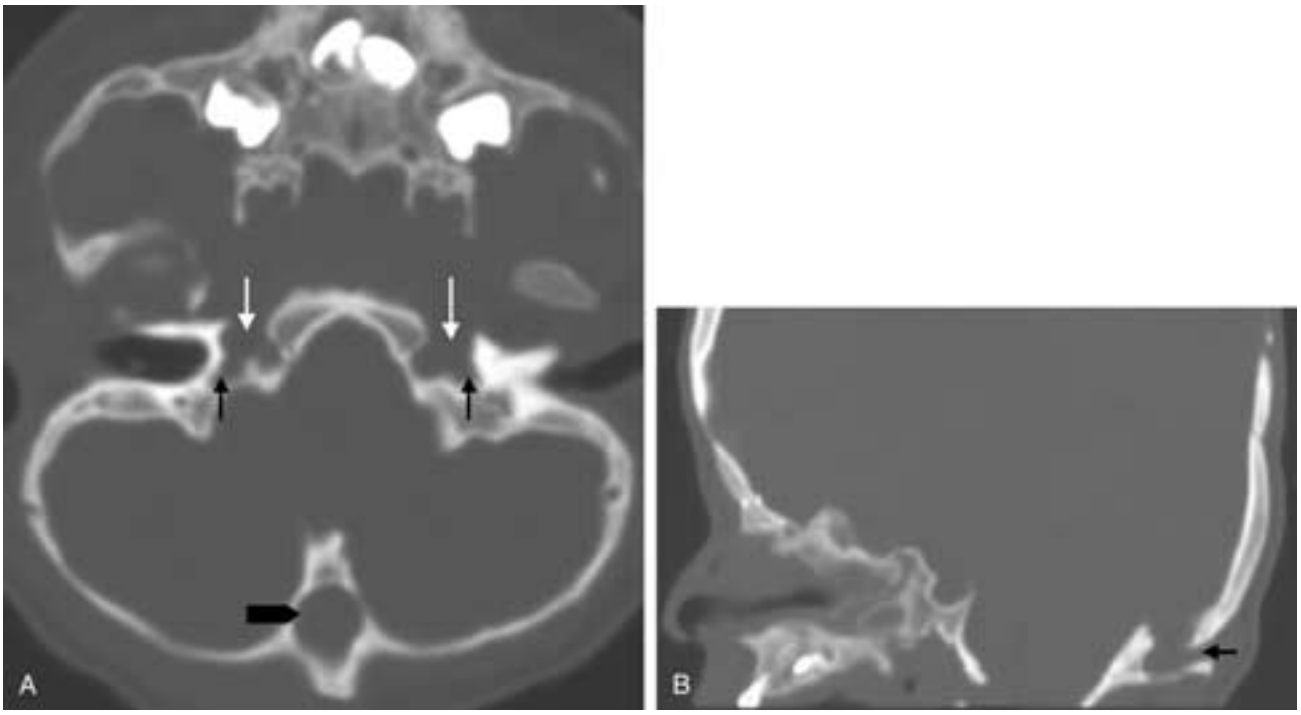

VIEW IMAGE

FIGURE 21-63 Jugular foramen stenosis. **A**, Axial CT image showing normal-sized carotid canals bilaterally (*white arrows*) with marked stenosis of the jugular foramina bilaterally (*black arrows*) and expansion of the occipital bone in the region of the torcula (*black arrowhead*), with a defect through which an enlarged emissary vein passes because of severe jugular stenosis. **B**, Sagittal reconstructed CT image showing a defect (*black arrow*) in the occipital bone at the site of the confluence of the dural sinuses for the emissary vein to drain.

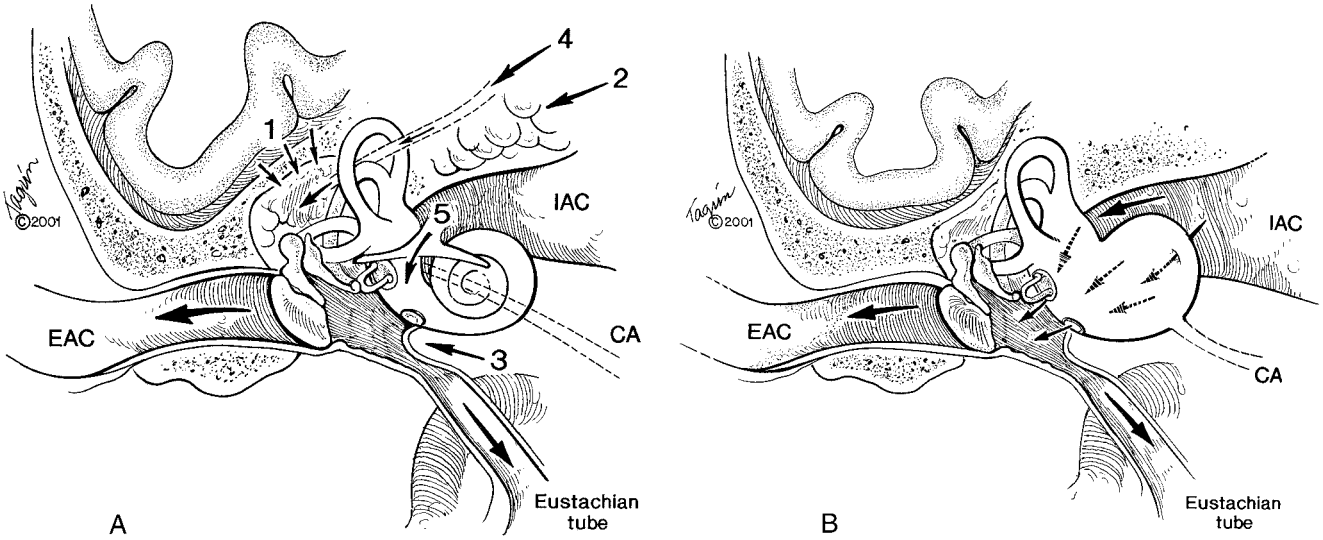

VIEW IMAGE

FIGURE 21-64 Illustration of perilabyrinthine and translabyrinthine fistulas. **A**, Perilabyrinthine fistulas: coronal diagram through the temporal bone showing five potential routes for fistulas: (1) through the tegmen tympani; (2) through large apical air cells; (3) through Hyrtl's fissure; (4) through the petromastoid or subarcuate canal; (5) through the facial nerve canal. *IAC*, Internal auditory canal; *CA*, cochlear aqueduct; *EAC*, external auditory canal. **B**, Translabyrinthine fistulas: coronal diagram through the temporal bone showing potential communication between the CSF within the internal auditory canal (*IAC*) with the perilymph in the vestibule or cochlea. The labyrinth is shown as dysplastic. The upper arrow in the apex of the IAC extends into the vestibule through a deficiency in the lamina cribrosa, a thin bony layer separating the apex of the IAC from the vestibule. The lower arrow in the apex of the IAC extends into the cochlea through a deficiency in the modiolus. The abnormal communication of CSF and perilymph could potentially lead to increased pressure within the vestibule and/or cochlea and allow for potential extension of fluid into the middle ear cavity through the oval or round windows (*upper and lower arrows*), respectively, extending from the vestibule and cochlea into the middle ear cavity. *EAC*, External auditory canal; *CA*, cochlear aqueduct.

Copyright © 2003, Mosby, Inc. All rights reserved.

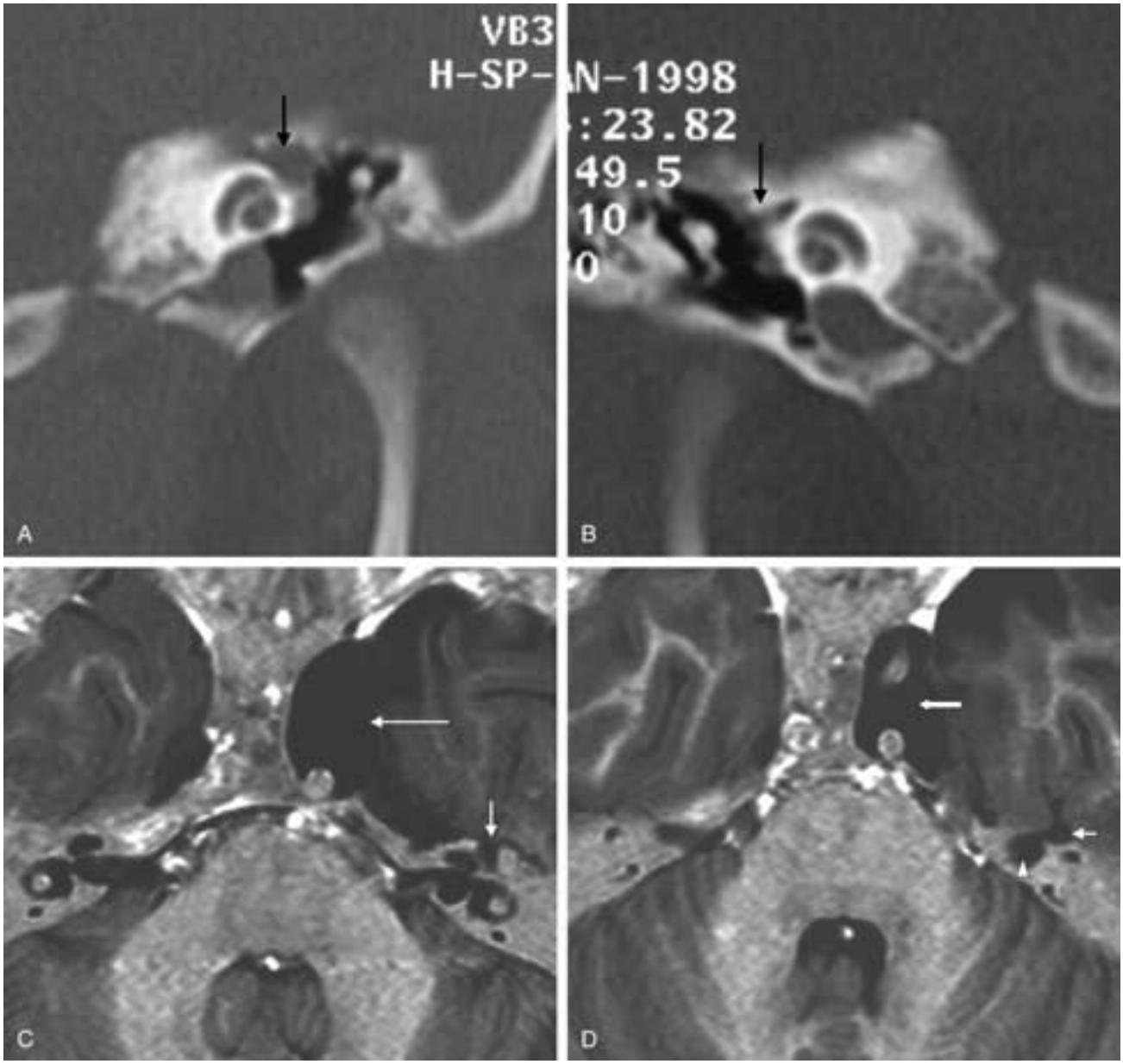

VIEW IMAGE

FIGURE 21-65 Possible perilabyrinthine fistula: lateral extension of the subarachnoid space surrounding the facial nerve within the IAC extending into the labyrinthine segment and geniculate ganglion region (*GG*) of the facial nerve canal, with a coexisting middle cranial fossa meningocele. **A**, Coronal CT image showing enlarged left GG (*black arrow*). **B**, Coronal CT image of the normal right side and normal right GG (*black arrow*). **C**, Axial MR image showing an enlarged left GG (*vertical white arrow*). Note also the large congenital meningocele of the central skull base/middle cranial fossa (*horizontal white arrow*). **D**, Axial MR image showing a prominent left GG (*small white arrow*) and a widened IAC (*white arrowhead*). Again, note the meningocele (*large white arrow*).

Copyright © 2003, Mosby, Inc. All rights reserved.

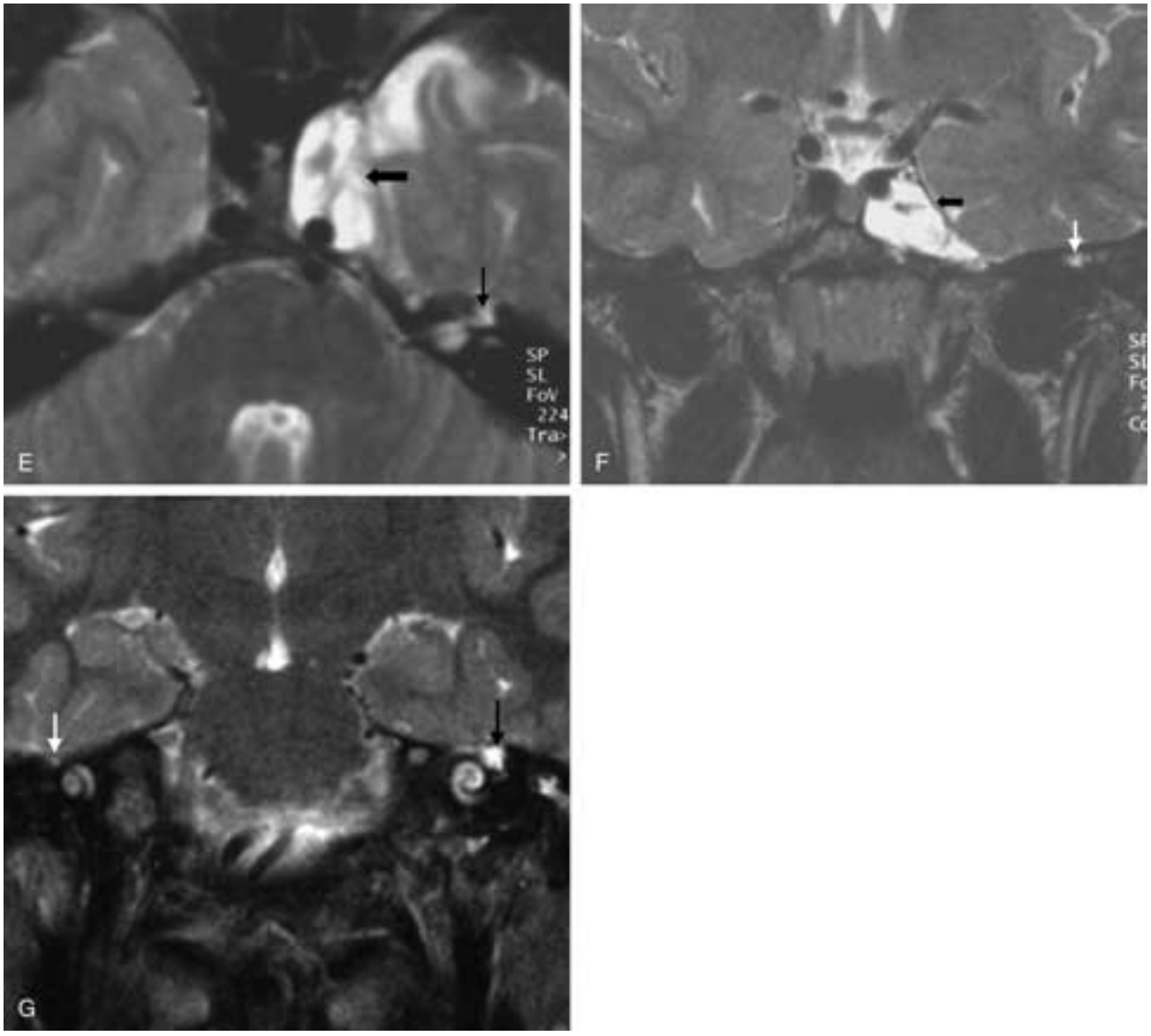

VIEW IMAGE

FIGURE 21-65 *Continued.* **E**, Axial T2-weighted MR image with an enlarged left GG (*small black arrow*) and meningocele (*large black arrow*). **F**, Coronal T2-weighted MR image with an enlarged GG (*white arrow*) and a meningocele (*black arrow*). **G**, Coronal T2-weighted MR image posterior to **F** showing an enlarged left GG (*black arrow*) over the cochlea compared to the normal right GG (*white arrow*).

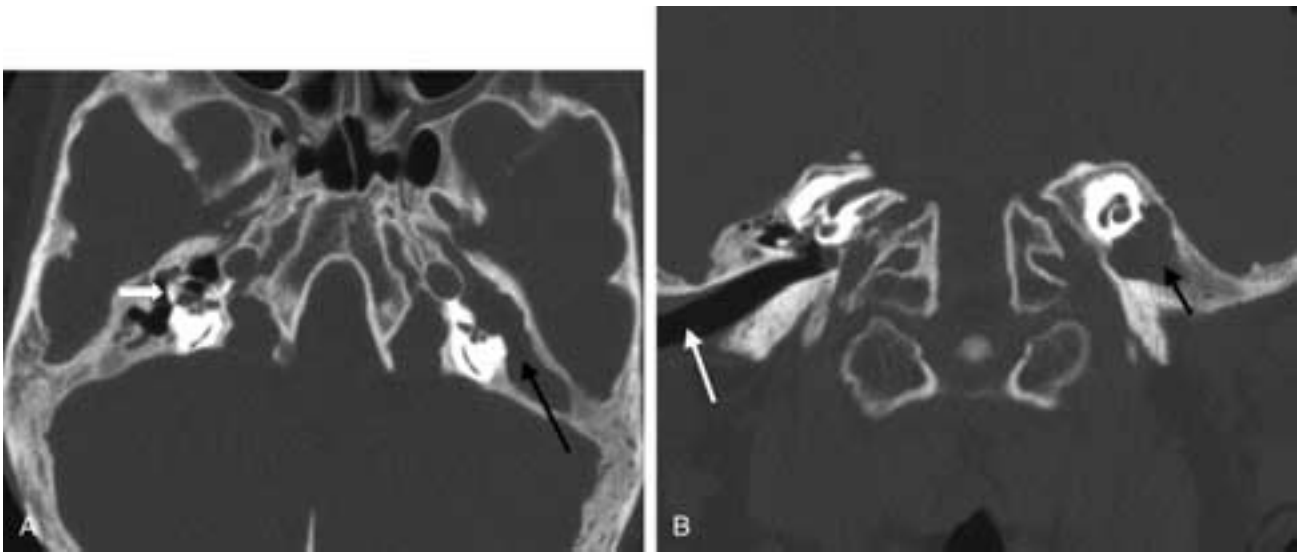

VIEW IMAGE

FIGURE 21-66 Achondroplasia. **A**, Axial CT image showing a congenital cholesteatoma on the left side (*black arrow*) and fused ossicles on the right (*white arrow*). **B**, Coronal CT image showing vertically oriented EACs (*white arrow*) secondary to hypoplasia of the central skull base and a left-sided cholesteatoma (*black arrow*).

Copyright © 2003, Mosby, Inc. All rights reserved.

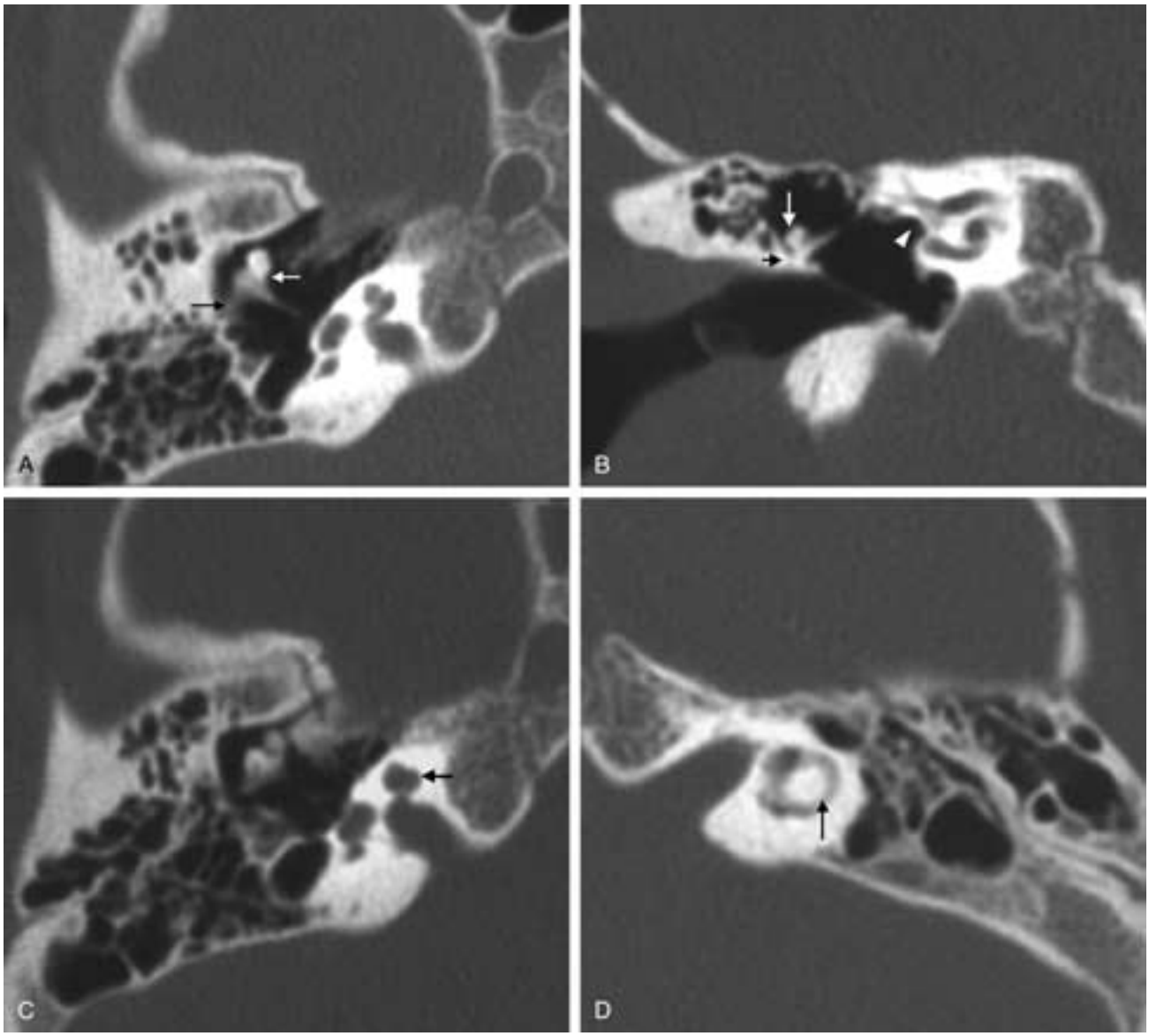

VIEW IMAGE

FIGURE 21-67 Branchio-otorenal dysplasia. **A** and **B**, Axial and coronal CT images showing a dysplastic malleus and incus (*white arrow*) with fusion to the lateral attic wall (*black arrow*). In **B**, note the large, deep oval window niche (*white arrowhead*). **C**, Axial CT image showing a hypoplastic cochlea (*black arrow*). **D**, Axial CT image showing a small lateral semicircular canal (*black arrow*).

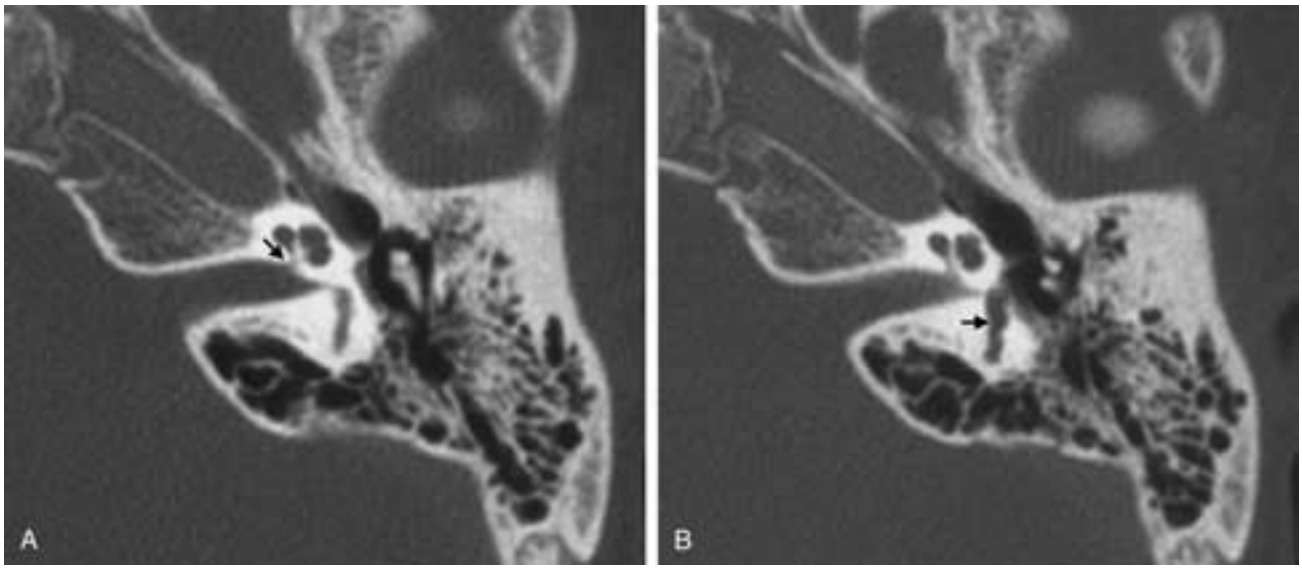

VIEW IMAGE

FIGURE 21-68 CHARGE association. **A** and **B**, Two contiguous axial CT images showing hypoplasia of the cochlear nerve fossette (*black arrow* in **A**) and a dysplastic vestibule (*black arrow* in **B**), with absence of the semicircular canals.

Copyright © 2003, Mosby, Inc. All rights reserved.

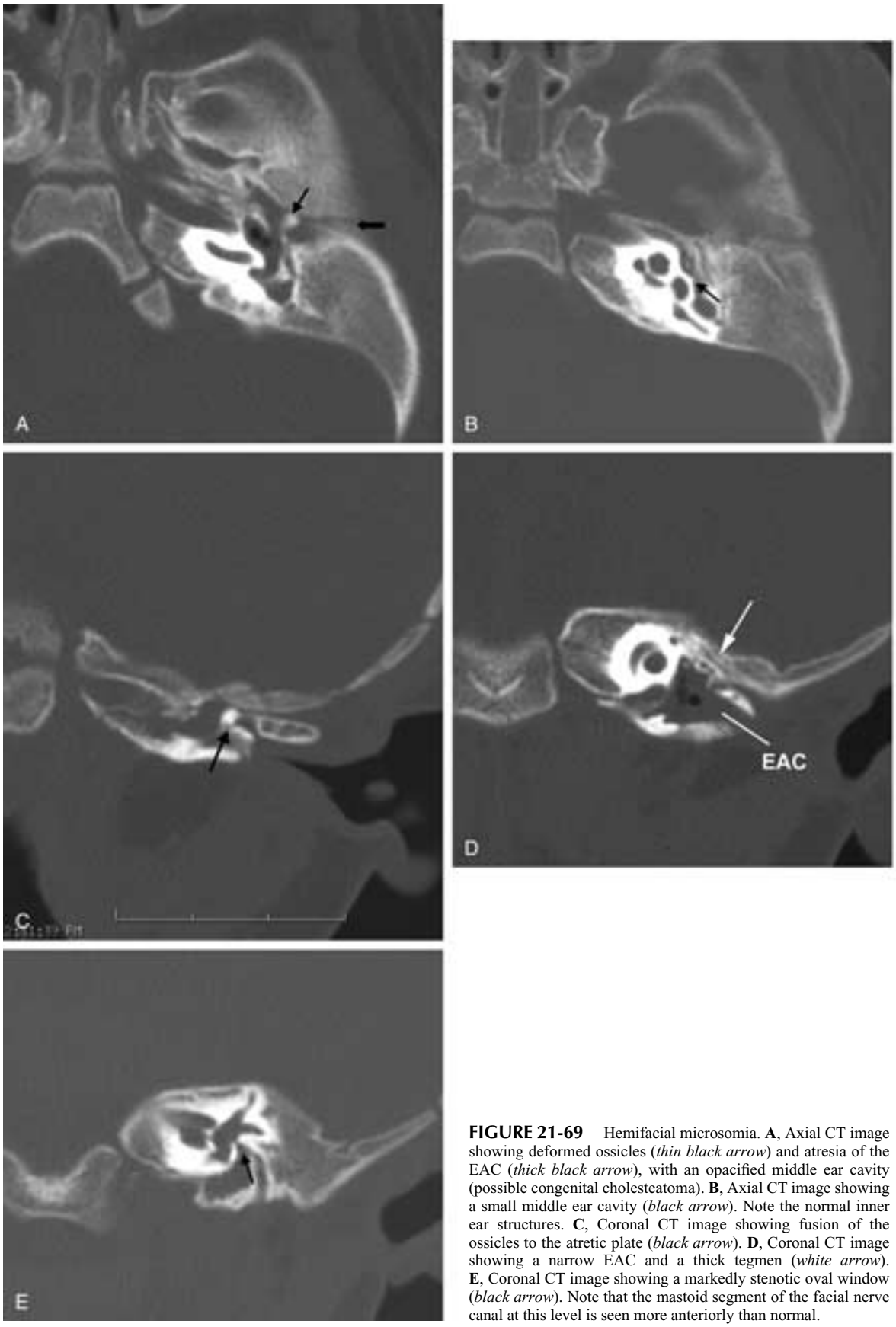

FIGURE 21-69 Hemifacial microsomia. **A**, Axial CT image showing deformed ossicles (*thin black arrow*) and atresia of the EAC (*thick black arrow*), with an opacified middle ear cavity (possible congenital cholesteatoma). **B**, Axial CT image showing a small middle ear cavity (*black arrow*). Note the normal inner ear structures. **C**, Coronal CT image showing fusion of the ossicles to the atretic plate (*black arrow*). **D**, Coronal CT image showing a narrow EAC and a thick tegmen (*white arrow*). **E**, Coronal CT image showing a markedly stenotic oval window (*black arrow*). Note that the mastoid segment of the facial nerve canal at this level is seen more anteriorly than normal.

VIEW IMAGE

Copyright © 2003, Mosby, Inc. All rights reserved.

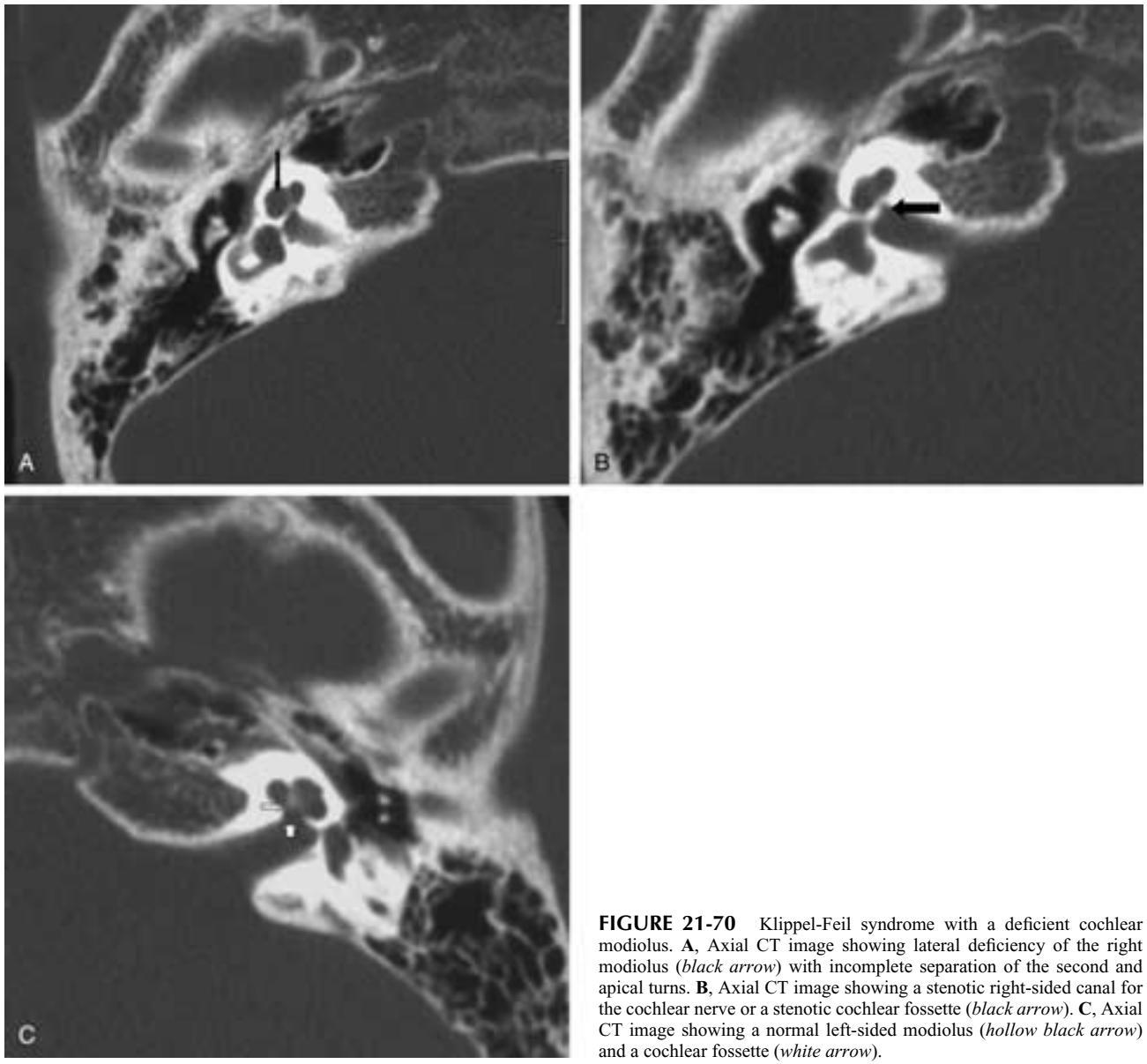

FIGURE 21-70 Klippel-Feil syndrome with a deficient cochlear modiolus. **A**, Axial CT image showing lateral deficiency of the right modiolus (*black arrow*) with incomplete separation of the second and apical turns. **B**, Axial CT image showing a stenotic right-sided canal for the cochlear nerve or a stenotic cochlear fossette (*black arrow*). **C**, Axial CT image showing a normal left-sided modiolus (*hollow black arrow*) and a cochlear fossette (*white arrow*).

VIEW IMAGE

Copyright © 2003, Mosby, Inc. All rights reserved.

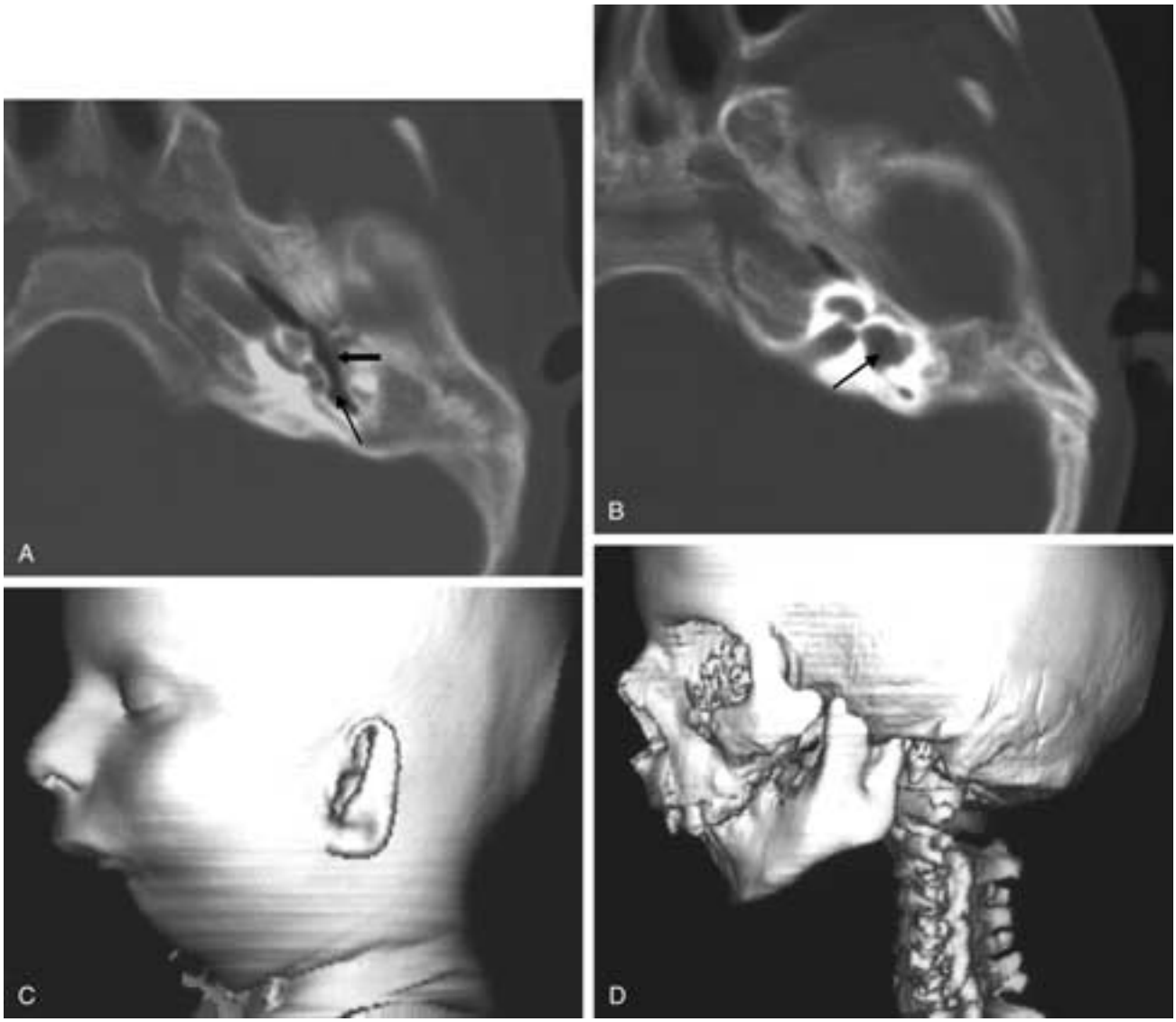

VIEW IMAGE

FIGURE 21-71 Treacher-Collins syndrome (mandibulo-facial dysostosis). **A**, Axial CT image showing atresia of the right EAC with a thick osseous atretic plate, a hypoplastic middle ear cavity (*thick black arrow*) and mastoids, and absence of the ossicular chain. Sinus tympani (*thin black arrow*). **B**, Axial CT image showing a dysplastic, enlarged vestibule (*black arrow*). **C** and **D**, Soft-tissue and bony 3D reconstructions showing a hypoplastic mandible and low-set ears, as well as malocclusion of the teeth and hypoplasia of the malar bones.

REFERENCES

1. Wright T, ed. Diseases of the Ear, 6th ed. London: Arnold, 1998.
2. Bergeron RT, Som PM, eds. Head and Neck Imaging: Excluding the Brain. St. Louis: Mosby, 1984.
3. Schucknecht H, ed. Pathology of the Ear, 2nd ed. Philadelphia: Lea and Febiger, 1993.
4. Jorgen, J. Congenital anomalies of the inner ear. Radiol Clin North Am 1974;12:473.
5. Fisher NA, Curtin HD. Radiology of congenital hearing loss. Otolaryngol Clin North Am 1994;27(3):511–531.
6. Robson CD, Robertson RL, Barnes PD. Imaging of pediatric temporal bone abnormalities. Neuroimag Clin North Am 1999;9(1): 133–155.
7. Mayer TE et al. High-resolution CT of the temporal bone in dysplasia of the auricle and external auditory canal. AJNR 1997;18(1): 53–65.
8. Lapayowker MS. Congenital anomalies of the middle ear. Radiol Clin North Am 1974;12(3):463–471.
9. Wright JJ. Polytomography and congenital external and middle ear anomalies. Laryngoscope 1981;91:1806–1811.
10. Booth TN et al. Imaging and clinical evaluation of isolated atresia of the oval window. AJNR 2000;21(1):171–174.
11. Naunton R, Valvassori GE. Inner ear anomalies: their association with atresia. Laryngoscope 1968;78:1041.
12. Alexander AE Jr, Caldemeyer KS, Rigby P. Clinical and surgical application of reformatted high-resolution CT of the temporal bone. Neuroimag Clin North Am 1998;8(3):631–650.
13. Yeakley JW, Jahrsdoerfer RA. CT evaluation of congenital aural atresia: what the radiologist and surgeon need to know. J Comput Assist Tomogr 1996;20(5):724–731.
14. Cummings C et al, eds. Otolaryngology: Head and Neck Surgery, 3rd ed. St. Louis: Mosby, 1998;418–438.
15. Sando I et al. Frequency and localization of congenital anomalies of the middle and inner ears: a human temporal bone histopathological study. Int J Pediatr Otorhinolaryngol 1988;16(1):1–22.
16. Staecker H, Merchant SN. Temporal bone pathology case of the month. Congenital fixation of the incus. Am J Otol 2000;21(1): 137–138.

Copyright © 2003, Mosby, Inc. All rights reserved.

17. Kurosaki Y, Tanaka YO, Itai Y. Malleus bar as a rare cause of congenital malleus fixation: CT demonstration. AJNR 1998;19(7): 1229–1230.
18. Subotic R, Mladina R, Risavi R. Congenital bony fixation of the malleus. Acta Otolaryngol 1998;118(6):833–836.
19. Yokoyama T et al. Human temporal bone study on the postnatal ossification process of auditory ossicles. Laryngoscope 1999;109(6): 927–930.
20. Jahrsdoerfer RA. The facial nerve in congenital middle ear malformations. Laryngoscope 1981;91(8):1217–1225.
21. Zeifer B, Sabini P, Sonne J. Congenital absence of the oval window: radiologic diagnosis and associated anomalies. AJNR 2000;21(2): 322–327.
22. Jahrsdoerfer R. Embryology of the facial nerve. Am J Otol 1988;9:423–426.
23. Bluestone C, Stool S, Kenna M, eds. Pediatric Otolaryngology. Vol 1, 3rd ed. WB Saunders, Philadelphia, 1996;333–370.
24. Valvassori GE, Naunton RF, Lindsay JR. Inner ear anomalies: clinical and histopathological considerations. Ann Otol Rhinol Laryngol 1969;78(5):929–938.
25. Bluestone C, Stool S, Kenna M, eds. Pediatric Otolaryngology. Vol. 1, 3rd ed. Philadelphia: WB Saunders, 1996, 649–670.
26. Davidson HC et al. MR evaluation of vestibulocochlear anomalies associated with large endolymphatic duct and sac. AJNR 1999;20(8): 1435–1441.
27. Casselman JW et al. Inner ear malformations in patients with sensorineural hearing loss: detection with gradient-echo (3DFT-CISS) MR imaging. Neuroradiology 1996;38:278–286.
28. Schmalbrock P, Brogan MA, Chakeres DW, et al. Optimization of submillimeter-resolution MR imaging methods for the inner ear. J Magn Reson Imag 1993;3:451–459.
29. Casselman JW, Kuhweide R, Deimling M, et al. Constructive interference in steady state-3DFT MR imaging of the inner ear and cerebellopontine angle. Am J Neuroradiol 1993;14:47–57.
30. Sando I, Takahara T, Ogawa A. Congenital anomalies of the inner ear. Ann Otol Rhinol Laryngol 1984;93(Suppl 112):110–118.
31. Petasnick J. Congenital malformations of the ear. Otolaryngol Clin North Am 1973;6:413–428.
32. Jackler R, Luxford WM, House WF. Congenital malformations of the inner ear. Laryngoscope 1987;97:2–14.
33. Parnes L, Chernoff W. Bilateral semicircular canal aplasia with near normal cochlear development. Ann Rhinol Laryngol 1990;99:957–959.
34. Okuno T et al. Temporal bone histopathologic findings in Alagille's syndrome. Arch Otolaryngol Head Neck Surg 1990;116;217–220.
35. Mong A et al. Sound- and pressure-induced vertigo associated with dehiscence of the roof of the superior semicircular canal. AJNR 1999;20(10):1973–1975.
36. Minor LB et al. Sound- and/or pressure-induced vertigo due to bone dehiscence of the superior semicircular canal. Arch Otolaryngol Head Neck Surg 1998;124(3):249–258.
37. Baloh R, Halmagyi G. Perilymphatic Fistula. In: Disorders of the vestibular system. New York: Oxford University Press, 1996; 396–406.
38. Lagundoye S, Martinson F, Fajemisin A. The syndrome of enlarged vestibule and dysplasia of the lateral semicircular canal in congenital deafness. Radiology 1974;115:377–378.
39. Mondini C. Anatomia surdi nedi sectio. De Bonofiensi Scientiarium et Artium Instituto Atque Academia Commentarri. Boniensi 1791;7:28, 419.
40. Paparella MM. Mondini's deafness. A review of histopathology. Ann Otol Rhinol Laryngol Suppl 1980;89(2 Pt 3):1–10.
41. Lemmerling MM et al. Normal modiolus: CT appearance in patients with a large vestibular aqueduct. Radiology 1997;204(1): 213–219.
42. Olson NR, Lehman RH. Cerebrospinal fluid otorrhea and the congenitally fixed stapes. Laryngoscope 1968;78(3):352–360.
43. Talbot JM, Wilson DF. Computed tomographic diagnosis of X-linked congenital mixed deafness, fixation of the stapedial footplate, and perilymphatic gusher. Am J Otol 1994;15(2):177–182.
44. Tang A, Parnes L. X-linked progressive mixed hearing loss: computed tomographic findings. Ann Otol Rhinol Laryngol 1994; 103:655–657.
45. Valvassori G, Pierce R. The normal internal auditory canal. AJR 1964;92:1232–1241.
46. Rothschild MA et al. Isolated primary unilateral stenosis of the internal auditory canal. Int J Pediatr Otorhinolaryngol 1999;50(3): 219–224.
47. Shelton C et al. The narrow internal auditory canal in children: a contraindication to cochlear implants. Otolaryngol Head Neck Surg 1989;100(3):227–231.
48. Van de Water T, Ruben R. Neurotrophic interactions during in vitro development of the inner ear. Ann Otol Rhinol Laryngol 1984;93: 558–564.
49. Casselman JW. Aplasia and hypoplasia of the vestibulocochlear nerve: diagnosis with MR imaging. Radiology 1997;202(3):773–781.
50. Taybi H, Lachman R, eds. Radiology of Syndromes, Metabolic Disorders, and Skeletal Dysplasias, 3rd ed. Chicago: Year Book Medical, 1990;307–308.
51. May M, ed. The Facial Nerve. New York: Thieme, 1986;284–286.
52. Romo LV, Curtin HD. Anomalous facial nerve canal with cochlear malformations. AJNR 2001;22(5):838–844.
53. Valvassori GE, Clemis JD. The large vestibular aqueduct syndrome. Laryngoscope 1978;88(5):723–728.
54. Okumura T et al. Sensorineural hearing loss in patients with large vestibular aqueduct. Laryngoscope 1995;105(3 Pt 1):289–293; discussion 293–294.
55. Mafee MF et al. Large vestibular aqueduct and congenital sensorineural hearing loss. AJNR 1992;13:805–819.
56. Levenson MJ et al. The large vestibular aqueduct syndrome in children. A review of 12 cases and the description of a new clinical entity. Arch Otolaryngol Head Neck Surg 1989;115(1):54–58.
57. Jackler R, De la Cruz A. The large vestibular aqueduct syndrome. Laryngoscope 1989;99:1238–1243.
58. Dahlen RT et al. Overlapping thin-section fast spin-echo MR of the vestibular aqueduct syndrome. AJNR 1997;18:67–75.
59. Phelps P et al. Radiologic manifestations of the ear in Pendred syndrome. Clin Radiol 1998;53:268–273.
60. Kodoma A, Sando I. Postnatal development of the vestibular aqueduct and endolymphatic sac. Ann Otol Rhinol Laryngol 1982;91(Suppl 96):3–12.
61. Okamoto K et al. MRI of enlarged endolymphatic sacs in the large vestibular aqueduct syndrome. Neuroradiology 1998;40(3): 167–172.
62. Naganawa S et al. MR imaging of the cochlear modiolus: area measurement in healthy subjects and in patients with a large endolymphatic duct and sac. Radiology 1999;213:819–823.
63. Naganawa S et al. MR imaging of the enlarged endolymphatic duct and sac syndrome by use of a 3D fast asymmetric spin-echo sequence: volume and signal-intensity measurement of the endolymphatic duct and sac and area measurement of the cochlear modiolus. AJNR 2000;21:1664–1669.
64. Sinnreich A, Parisier S, Cohen N. Arterial malformations of the middle ear. Otolaryngol Head Neck Surg 1984;92:194–206.
65. Tian Q, Linthicum FH Jr. Temporal bone histopathology of aberrant carotid artery. Otolaryngol Head Neck Surg 1998;119(5): 506–507.
66. Lasjaunias P et al. Arterial anomalies at the base of the skull. Neuroradiology 1977;13(5):267–272.
67. Thiers F et al. Persistent stapedial artery: CT findings. AJNR 2000;21:1551–1554.
68. Swartz JD et al. Aberrant internal carotid artery lying within the middle ear. High resolution CT diagnosis and differential diagnosis. Neuroradiology 1985;27(4):322–326.
69. Glasscock ME 3rd, Seshul M, Seshul MB. Bilateral aberrant internal carotid artery case presentation. Arch Otolaryngol Head Neck Surg 1993;119(3):335–339.
70. Yao W, Benjamin LC, Korzec K. Aberrant internal carotid artery causing erosion of the otic capsule: an unusual cause of pulsatile tinnitus. Otolaryngol Head Neck Surg 1998;118(5):678–679.
71. Keen J. Absence of both internal carotid arteries. Clin Proc 1946;4:588–594.
72. Martinez-Granero M et al. Unilateral agenesis of the internal carotid artery in childhood: a description of a case. Rev Neurol 1997;25(144):1207–1209.
73. Dilenge D. Bilateral agenesis of internal carotid artery. J Can Assoc Radiol 1975;26(2):91–94.
74. Couloigner V et al. Surgical treatment of the high jugular bulb in patients with Meniere's disease and pulsatile tinnitus. Eur Arch Otorhinolaryngol 1999;256:224–229.

Copyright © 2003, Mosby, Inc. All rights reserved.

75. Overton SB, Ritter FN. A high placed jugular bulb in the middle ear: a clinical and temporal bone study. Laryngoscope 1973;83(12):1986–1991.
76. Caldemeyer K et al. The jugular foramen: a review of anatomy, masses, and imaging characteristics. Radiographics 1997;17:1123–1139.
77. Weiss RL et al. High jugular bulb and conductive hearing loss. Laryngoscope 1997;107(3):321–327.
78. Jahrsdoerfer RA, Cail WS, Cantrell RW. Endolymphatic duct obstruction from a jugular bulb diverticulum. Ann Otol Rhinol Laryngol 1981;90(6 Pt 1):619–623.
79. Halvorson DJ, Porubsky ES. Asymptomatic high jugular bulb in the pediatric population. Am J Otolaryngol 1997;18(1):69–71.
80. Pappas D Jr et al. Petrous jugular malposition (diverticulum). Otolaryngol Head Neck Surg 1993;109:847–852.
81. el-Kashlan HK, Gebarski SS. Imaging case of the month: jugular diverticulum. Am J Otol 1998;19(4):525–526.
82. El-Kashlan H. Arts A, Gebarski S., Jugular diverticulum: clinical significance. Otolaryngol Head Neck Surg, 2000;122:575–576.
83. Robson CD et al. Prominent basal emissary foramina in syndromic craniosynostosis: correlation with phenotypic and molecular diagnoses. AJNR 2000;21(9):1707–1717.
84. Phelps PD. Congenital cerebrospinal fluid fistulae of the petrous temporal bone. Clin Otolaryngol Allied Sci 1986;11(2):79–92.
85. Pimontel-Appel B, Vignaud J. Liquorrhea in congenital malformation of the petrous bone. J Belg Radiol 1980;63:283–289.
86. Kaufman B et al. Acquired spontaneous nontraumatic normal-pressure cerebrospinal fluid fistulas originating from the middle fossa. Radiology 1977;122:379–387.
87. Gavilan J, Trujillo M, Gavilan C. Spontaneous encephalocele of the middle ear. Arch Otolaryngol 1984;110:206–207.
88. Gottlieb MBC, Blaugrund JE, Niparko JK. Imaging quiz case 1. Tegmental encephalocele. Arch Otolaryngol Head Neck Surg 1998;124:1274–1277.
89. Proctor B, Neisen E, Proctor C. Petrosquamosal suture and lamina. Otolaryngol Head Neck Surg 1981;89:482–495.
90. Kemink JL, Graham MD, Kartush JM. Spontaneous encephalocele of the temporal bone. Arch Otolaryngol Head Neck Surg 1986;112:558–561.
91. Kapur TR, Bangash W. Tegmental and petromastoid defects in the temporal bone. J Laryngol Otol 1986;100:1129–1132.
92. Lang DV. Macroscopic bony deficiency of the tegmen tympani in adult temporal bones. J Laryngol Otol 1983;97:685–688.
93. Gacek RR, Leipzig B. Congenital cerebrospinal fluid otorrhea. Ann Otol 1979;88:358–365.
94. Roman S, Bouriliere-Najean B, Triglia JM. Fistola perilinfatica congenita e acquisita: revisione della letteratura. Acta Otorhinolaryngol Ital Suppl 1998;59:28–32.
95. Kraus EM, McCabe BF. The giant apical air cell syndrome. A new entity. Ann Otol Rhinol Laryngol 1982;91:237–239.
96. Petrus LV, Lo WWM. Spontaneous CSF otorrhea caused by abnormal development of the facial nerve canal. AJNR 1999;20:275–277.
97. May JS et al. Spontaneous cerebrospinal fluid otorrhea from defects of the temporal bone: a rare entity? Am J Otol 1995;16:765–771.
98. Phelps PD, Lloyd GAS. Mondini dysplasia is not associated with meningitis and cerebrospinal fluid fistula (letter). Arch Otolaryngol Head Neck Surg 1991;117:931.
99. Anson B. The endolymphatic and perilymphatic aqueducts of the human ear: developmental and adult anatomy of their varieties and contents in relation to otologic surgery. Acta Otolaryngol 1965;59:140–151.
100. Jackler RK, Hwang PH. Enlargement of the cochlear aqueduct: fact or fiction? Otolaryngol Head Neck Surg 1993;109(1):14–25.
101. Ritter F, Lawrence M. A histological and experimental study of cochlear aqueduct patency in the adult human. Laryngoscope 1965;75:1224–1233.
102. Weider D, Saunders R, Musiek F. Repair of a cerebrospinal fluid perilymph fistula primarily through the middle ear and secondarily by occluding the cochlear aqueduct. Otolaryngol Head Neck Surg 1991;105:35–39.
103. Dorph S, Jensen J, Oigaard A. Visualization of canaliculus cochleae by multidirectional tomography. Arch Otolaryngol 1973;98:121–123.
104. Sakashita T, Sando I, Kamerer D. Congenital anomalies of the external and middle ears. In: Bluestone C, Stool S, Kenna M, eds. Pediatric Otolaryngology. Philadelphia: WB Saunders, 2000;333–370.
105. Hasso A, Casselman J, Broadwell R. Temporal bone congenital anomalies. In: Som P, Curtin H, eds. Head and Neck Imaging. St. Louis: CV Mosby, 1996;1351–1390.

Copyright © 2003, Mosby, Inc. All rights reserved.

Copyright © 2003, Mosby, Inc. All rights reserved.

22

Temporal Bone: Inflammatory Disease

William R. Nemzek and Joel D. Swartz

INTRODUCTION
MIDDLE EAR AND MASTOID
- Eustachian Tube Function
- Otitis Media and Mastoiditis
- Complications of Acute Otitis Media and Mastoiditis
  - Coalescent Mastoiditis
  - Facial Nerve Palsy
  - Dural Sinus Thrombosis
  - Venous Infarction
  - Abscess/Meningitis
  - Otitic Hydrocephalus
  - Labyrinthitis
  - Chronic Otitis Media with Effusion
- Sequelae of Chronic Otitis
  - Granulation Tissue
  - Cholesteatoma
  - Ossicular Erosions and Ossicular Fixation
  - Tympanosclerosis
- Miscellaneous
  - Tuberculosis
  - Mycotic Infections

PETROUS APEX
- Abnormalities of Aeration of the Petrous Apex
- Petrous Apex Effusion
- Acute Petrositis
- Cholesterol Granuloma, Mucocele, and Cholesteatoma

INNER EAR
- Labyrinthitis
- Bacterial Labyrinthitis
- Viral Labyrinthitis
  - Perinatal Conditions
  - Cytomegalovirus Infection
  - Rubella
  - Mumps
  - Varicella Zoster Virus
  - Measles
- Labyrinthitis Ossificans
- Otosyphilis
- Lyme Disease
- Autoimmune Inner Ear Disease
  - Polyarteritis Nodosa
  - Wegener's Granulomatosis
  - Relapsing Polychondritis
  - Systemic Lupus Erythematosus
  - Rheumatoid Arthritis
  - Cogan's Syndrome
- Perilymph Fistula

EXTERNAL EAR
- External Otitis
- Necrotizing External Otitis (Malignant External Otitis)
- Differential Diagnosis and Other Lesions
  - Osteoradionecrosis
  - Malignancy
  - Tumors of Ceruminous Gland Origin
  - Exostosis and Osteoma
  - Cholesteatoma and Keratosis Obturans

POSTOPERATIVE TEMPORAL BONE
- Mastoidectomy
- Ossiculoplasty and Ossicular Reconstruction
- Cochlear Implantation

INTRODUCTION

Infections of the temporal bone are usually considered based on anatomic regions: (1) the external ear, (2) middle ear and mastoid, (3) the inner ear, and (4) the petrous apex. The tissues and anatomic structure of each region have a strong influence on the types of infections occurring in that part of the temporal bone.

The external ear consists of the auricle and the external auditory canal. The external auditory canal is closed

Copyright © 2003, Mosby, Inc. All rights reserved.

medially by the tympanic membrane, thus isolating it from the middle ear, and the external canal is separated from the mastoid by a thick, bony wall lined by skin.

The middle ear contains the tympanic cavity that communicates with the nasopharynx via the eustachian tube. The tympanic cavity, its contents, and communicating air spaces, which include the air cells of the petrous apex, are completely covered with mucous membrane. Thus, infections and inflammations of the middle ear, mastoid, and petrous apex share some characteristics.

The inner ear consists of the membranous labyrinth enclosed in the osseous labyrinth, contained in the petrous bone.[1, 2]

Discussion of inflammation in the temporal bone will follow this anatomic organization. As infections of the middle ear are most often imaged, the discussion begins in that region, followed by the related petrous apex and then the inner and external ear. Much temporal bone surgery is done for infections of the ear, so postoperative findings are included in this chapter.

MIDDLE EAR AND MASTOID

Eustachian Tube Function

Understanding middle ear and mastoid disease requires knowledge of eustachian tube function. In addition, because all the pneumatized regions of the temporal bone are contiguous, inflammation of the middle ear may involve the other pneumatized spaces (mastoid, petrous apex, and perilabyrinthine air cells).[3–5] The formation of the mastoid antrum and mastoid air cells begins late in fetal life and continues during infancy and childhood.[1] The cavity and lining mucous membrane of the middle ear and eustachian tube arise from the expanding first pharyngeal pouch, and epithelium-lined projections emanating from the lining of the middle ear infiltrate the new bone.[1] Bone marrow is converted into a loose connective tissue stroma prior to pneumatization, and the pneumatized mastoid cavity develops after birth and grows to almost adult size by the age of 5 years.[6, 7] Primary pneumatization of the middle ear depends on numerous factors, including nutrition, heredity, and environment.[8–10] Aeration of existing cells is a dynamic process dependent on a normally functioning eustachian tube, and atticoantral aeration is further dependent on the patency of the anterior and posterior tympanic isthmi, which provide communication between the middle ear and attic.[11, 12] It is eustachian tube compromise (dysfunction or obstruction), with resultant decreased intratympanic pressure (ITP), that has been widely accepted as the primary cause of most of the subsequently discussed varieties of chronic inflammatory disease of the middle ear and mastoid (Table 22-1).[8, 13–16]

Middle ear infection in infancy and the inflammatory changes of the pneumatic space mucosa cause the subepithelial connective tissue to fibrose. Thus, growth of the pneumatic space is impaired and pneumatization is interrupted.[6, 17, 18] That is, recurrent tympanomastoid infections occurring in early childhood lead to arrest of mastoid pneumatization and result in a small mastoid cavity with sclerotic, bony walls. The additional presence of cholesteatoma may exacerbate the inflammatory response of middle ear infection and further suppress mastoid pneumatization.[19]

Table 22-1
COMPLICATIONS OF OTITIS MEDIA AND MASTOIDITIS

Extracranial
Intratemporal
Sequelae of Acute Otomastoiditis
Coalescent mastoiditis
Facial paralysis
SNHL (chemical toxins invade labyrinth via round window)
Labyrinthine fistula (usually result from cholesteatoma)
Labyrinthitis
Petrous apicitis
Sequelae of Chronic Otomastoiditis
Chronic otitis media with effusion
Tympanic membrane retraction
Tympanosclerosis
Acquired cholesteatoma
Granulation tissue
Cholesterol granuloma
Postinflammatory ossicular fixation
Noncholesteatomatous erosion of the ossicles (portion of the incus or stapes)
Conductive hearing loss
Osteoneogenesis
Extratemporal
Postauricular abscess
Bezold's abscess
Zygomatic abscess
Cervical/postauricular fistula
Extramastoid cholesteatoma
Intracranial
Epidural, subdural abscess
Cerebral abscess
Dural sinus thrombosis
Venous infarction
Otitic meningitis
Otitic hydrocephalus
Brain herniation

The eustachian tube (ET) connects the middle ear-mastoid complex with the nasopharynx. The ET has three functions with respect to the middle ear: (1) pressure regulation to equilibrate gas pressure in the middle ear with atmospheric pressure (this is a discontinuous process, as the middle ear is not constantly ventilated), (2) clearance of middle ear secretions into the nasopharynx, and (3) protection of the middle ear from nasopharyngeal secretions and sound pressure.[4]

The ET complex consists of a mucosal-lined lumen, a bony portion, a cartilaginous portion, and surrounding peritubal muscles (i.e., tensor veli palatini, levator veli palatini, salpingopharyngeus, and tensor tympani).[4] Overall, the ET is about 36 mm long and descends from the middle ear at an angle of about 45° with the midsagittal plane and 30° with the horizontal plane. The bony portion is about 12 mm long and is a tapered tube whose narrowest portion is near the pharynx. The cartilaginous portion of the ET is about 24 mm long and slightly flexible, being an incomplete tube along its lower and lateral margin, where it is completed by fibrous tissue. This configuration allows the opposing muscles attached to the cartilaginous portion of the ET immediately below the skull base to widen the tubal diameter and assist in maximizing the possibility of

Copyright © 2003, Mosby, Inc. All rights reserved.

equalizing pharyngeal and middle ear pressure. The narrowest portion of the entire ET system is at the bony-cartilaginous junction (isthmus), a location virtually inaccessible to therapeutic intervention.

Most anatomic and physiologic evidence supports the conclusion that cartilaginous tubal dilation is caused solely by the tensor veli palatini muscle, which originates along the lateral wall of the ET and the scaphoid fossa. This muscle converges to a tendon that wraps around the hamulus of the medial pterygoid muscle and inserts into the posterior border of the horizontal process of the palatine bone and the palatine aponeurosis of the anterior portion of the velum.

The bony ET (protympanum) lies within the petrous portion of the temporal bone and communicates with the anterior superior portion of the middle ear. The osseous portion normally remains open at all times. The fibrocartilaginous portion is closed at rest and opens during swallowing, yawning, sneezing, or a Valsalva maneuver. The ET opens for approximately 0.2 second once every 1 to 2 minutes, that is, for a total of 3 to 4 minutes every 24 hours.[7] There is an inherent tendency for gas to leave the middle ear by diffusion into the surrounding mucosa and circulation. This loss is compensated for by the ET admitting just enough air to maintain near-atmospheric pressure in the middle ear. If this system fails, negative pressure develops in the middle ear.[7]

Otitis Media and Mastoiditis

Otitis media is the second most common disease of childhood after upper respiratory tract infection. Two-thirds of children have at least one episode of otitis media by 3 years of age.[3] Acute otitis media with effusion (OME) is an infection of the middle ear, associated with pain and an effusion behind an intact tympanic membrane (Fig. 22-1).

Risk factors contributing to otitis media include low socioeconomic status and repeated exposure to many other children, either at home or in a day-care setting. Associated disease states include cleft palate, immunodeficiency, ciliary dyskinesia, trisomy 21, and cystic fibrosis. The protective effect of breast-feeding and the detrimental effect of secondhand smoke are significant in the first year of life.[20]

The middle ear, mastoid, and pneumatized petrous bone are extensions of the upper respiratory tract, and bacteria can enter the middle ear from reflux of infected secretions from the nasopharynx through the ET. Facilitating factors include bacterial colonization of the nasopharynx, incompetence of the protective function of the ET, and negative pressure in the middle ear relative to the nasopharynx.[21] Acute otitis media is often the sequel of a viral upper respiratory infection in which the mucosal barrier is disrupted, allowing adherence and growth of bacteria in the nose and nasopharynx. *Streptococcus pneumoniae, Haemophilus influenzae,* and *Moxarella catarrhalis* are common pathogens.[20, 21]

The vast majority of patients with acute otomastoiditis are cured after a course of antibiotics, and no imaging is required.[8, 9] However, should computed tomography (CT) or magnetic resonance imaging (MRI) be performed at this time, nonspecific debris within the middle ear and mastoid is seen, possibly with several fluid levels (Fig. 22-2). Importantly, the integrity of the mastoid septae, ossicular chain, and external and internal mastoid cortices is preserved. As fluid may be found in the mastoids of asymptomatic individuals, the diagnosis of acute mastoiditis with air-fluid levels in the mastoid is a clinical diagnosis.

Acute otitis media may go on to a more chronic involvement of the middle ear and mastoid. Current terminology describes acute otitis media as the rapid onset of inflammatory signs and symptoms related to the middle ear. Fluid is usually seen behind the tympanic membrane. If fluid persists for 3 months, the disease is considered chronic.[3] Chronic

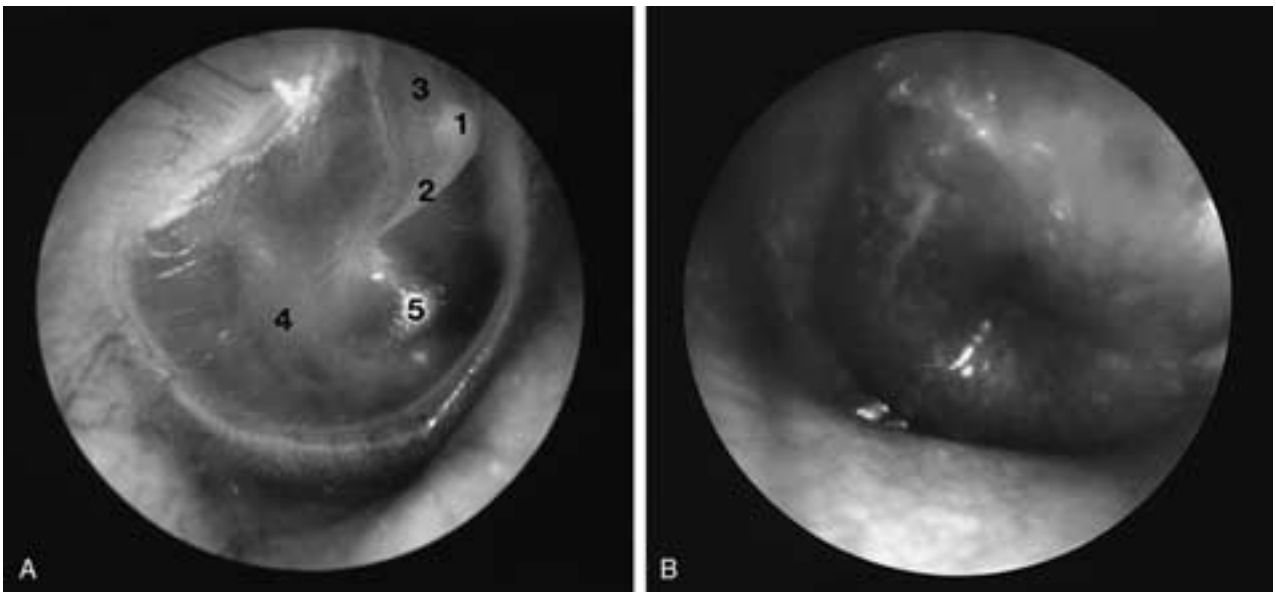

FIGURE 22-1 **A**, Otoscopy: Normal right tympanic membrane. (*1*) Lateral (short) process of malleus. (*2*) Manubrium of malleus. (*3*) Small upper pars flaccida. (*4*) Lower pars tensa. (*5*) Light reflex seen in the anterior inferior quadrant. **B**, Acute otitis media. Tympanic membrane is bulging, and middle ear is filled with purulent material.

VIEW IMAGE

Copyright © 2003, Mosby, Inc. All rights reserved.

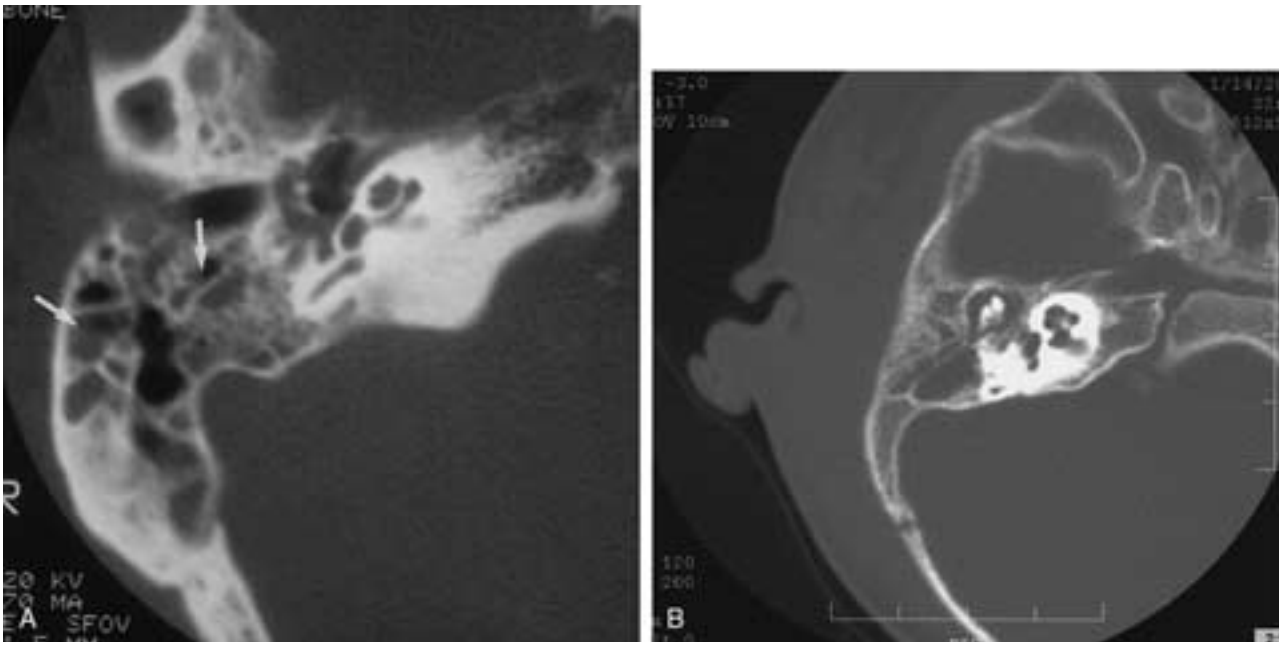

VIEW IMAGE

FIGURE 22-2 **A**, Acute otitis media and mastoiditis. Opacified air cells and fluid levels (*arrows*) are identified in the axial projection in the middle ear and mastoid. Note that the mastoid septae are clearly defined and intact. **B**, Acute otitis media and mastoiditis with superficial soft tissue edema with an intact mastoid cortex. The middle ear and mastoid are opacified. Infection spreads through foramina carrying mastoid emissary veins.

suppurative otitis media indicates that otorrhea has existed for at least 6 weeks. Otorrhea, defined as drainage from the ear, occurs through a nonintact tympanic membrane, either via placement of a tympanostomy tube or through a tympanic membrane (drum) perforation. A cholesteatoma may or may not be present.

Complications of Acute Otitis Media and Mastoiditis

Coalescent Mastoiditis

The clinical turning point for these patients occurs when mucoperiosteal disease extends into the bone. This results in the development of coalescent mastoiditis, defined as the erosion of mastoid septae with the associated development of an intramastoid empyema (Fig. 22-3, Table 22-1).[10, 22] As detection of subtle bony changes is required for diagnosis, high-resolution CT is the best imaging modality during this interval.[22] The radiologist must painstakingly seek subtle evidence of alteration of these mastoid septations, often comparing the affected side to the opposite side. Although some asymmetry between the two sides can occur normally (thereby potentially confusing the issue), usually the findings are not subtle and the diagnosis is obvious.

Importantly, in addition to the mastoid septae, the inner and outer mastoid cortices must be carefully studied. By direct extension, the mastoid disease may spread via a defect or thinning of the outer mastoid cortex to form a subperiosteal abscess that is generally postauricular in location (Macewen's triangle) (Figs. 22-4 and 22-5).[8] Perimastoid edema and cellulitis may occur, without a cortical defect, due to thrombosis of the mastoid emissary veins (Griesinger's sign) and spread of infection through foramina carrying emissary veins (Fig. 22-3).[23] Preauricular abscess formation is possible if the infection preferentially spreads along the zygomatic root. Necrosis of the mastoid tip (Fig. 22-6) allows infection to spread inferiorly into the neck deep to the fascial planes that surround the sternocleidomastoid and trapezius muscles. The result is a Bezold abscess. An untreated Bezold abscess can spread caudally to the larynx and mediastinum.[24, 25]

Facial Nerve Palsy

Facial nerve palsy is a rare complication of acute otitis media and is reported to occur in only about 5% of cases. Complete recovery is the rule.

Dural Sinus Thrombosis

Defects in the inner mastoid cortex, when present, place inflammatory debris in contact with the sigmoid sinus and adjacent dura (Figs. 22-7 and 22-8). The result may be dural thrombophlebitis and dural sinus thrombosis. Diagnosis is made by contrast-enhanced CT or MR and MR venography. A clot is seen as a filling defect within the dural sinus (''empty delta sign'') on contrast-enhanced CT or MR images obtained perpendicular to the dural sinus (Fig. 22-9).[26] Evaluation of the venous sinus on CT at appropriate window levels is crucial if one is to visualize a clot. MR is ideal for diagnosis and follow-up of dural venous sinus thrombosis.[27] The radiologist must scrutinize the images for the expected normal flow void in the venous sinuses on spin-echo sequences and flow-related enhancement on gradient-echo sequences. The absence of these normal venous signal intensities should arouse the suspicion of thrombosis. On occasion, signal characteristics allow for direct visualization of the clot within the lumen of the sinus (Fig. 22-9). Despite MR, the imaging diagnosis of dural

Copyright © 2003, Mosby, Inc. All rights reserved.

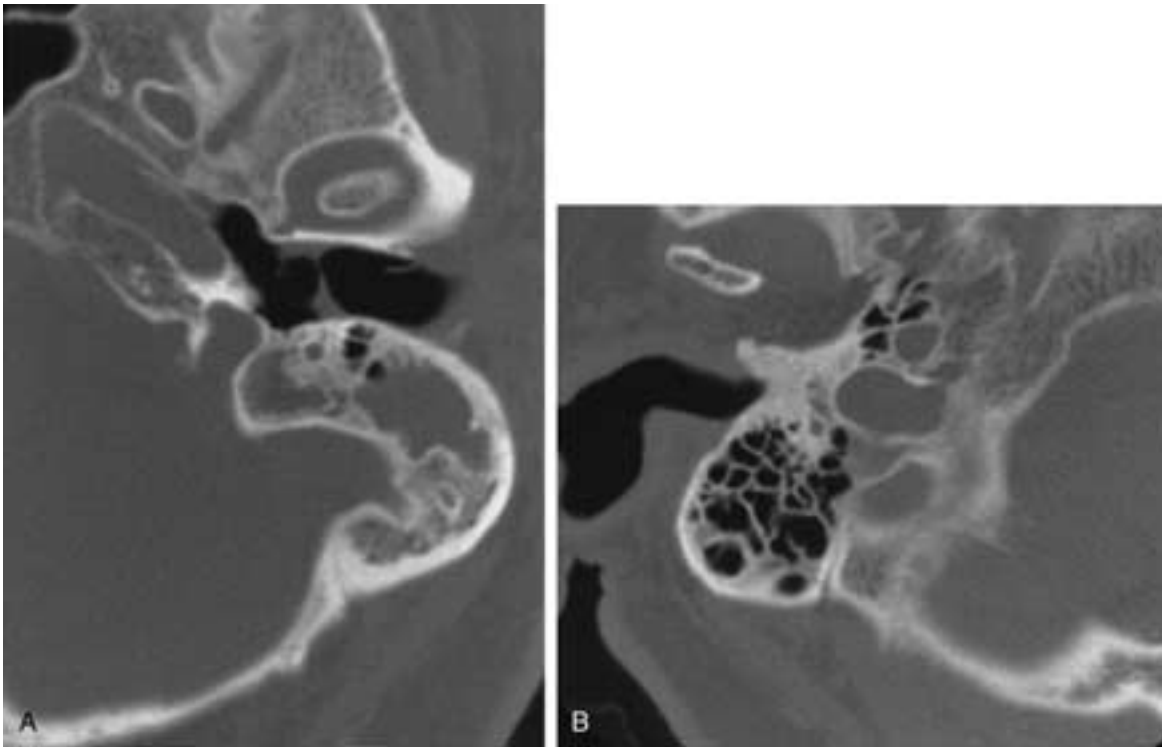

VIEW IMAGE

FIGURE 22-3 **A**, Coalescent mastoiditis. Debris fills the mastoid, and there is poor definition and destruction of mastoid septa. **B**, Normal opposite mastoid for comparison.

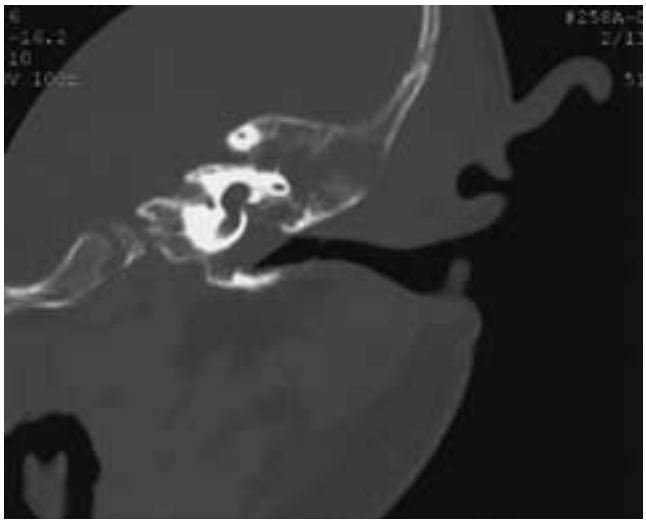

VIEW IMAGE

FIGURE 22-4 Coalescent mastoiditis. There is opacification of the mastoid, destruction of mastoid septae, and a defect in the external cortex with perimastoid cellulitis.

Copyright © 2003, Mosby, Inc. All rights reserved.

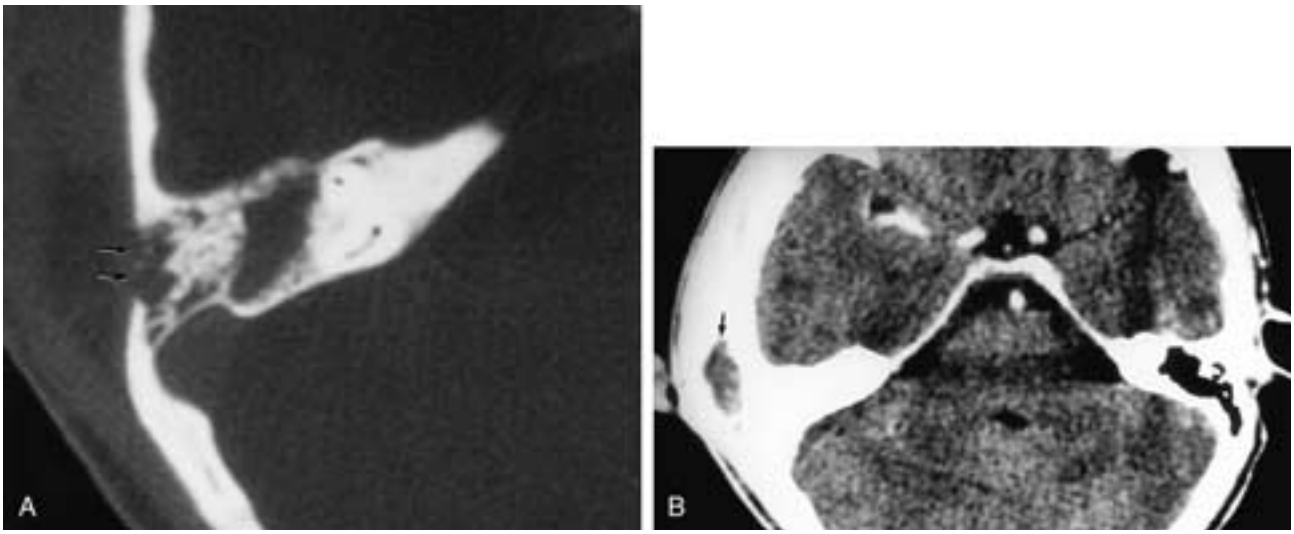

VIEW IMAGE

FIGURE 22-5 Coalescent mastoiditis with subperiosteal abscess. **A**, Axial CT, right ear. Poor definition of mastoid septae, with a large defect in the external mastoid cortex (*arrows*). **B**, Palpable postauricular mass of low CT density (*arrow*). At surgery, an abscess pocket was found emanating from this site. (Courtesy of Dr. Roy A. Holliday).

sinus thrombosis remains difficult because of the vagaries in flow phenomena and the varying signal intensity of blood products.[28] Thus, the hyperintense signal of normal flow-related enhancement may be confused with methemoglobin, and enhancement may occur in normal venous sinuses due to physiologic slow flow.[29] Artifactual flow gaps occur in about one-third of normal nondominant transverse sinuses because of signal loss secondary to in-plane vascular flow.[30] Subacute thrombus, composed of extracellular methemoglobin, may appear hypointense on T2-weighted images simulating a normal flow void. Subacute clot that is hyperintense on T1-weighted MR images due to methemoglobin may be confused with flow on time-of-flight MR venography, which utilizes T1-weighted gradient-echo techniques.[26] Organizing thrombus may enhance due to conversion of clot into vascularized connective tissue.[31]

VIEW IMAGE

FIGURE 22-6 Mastoiditis (coronal CT) with erosion of the medial mastoid tip (*arrow*). This defect could allow infection to spread inferiorly into the neck, causing a Bezold abscess.

Phase contrast or time-of-flight magnetic resonance angiography (MRA) may be done for the evaluation and follow-up of patients with suspected dural sinus thrombosis (Fig. 22-9).[31] An inferior presaturation pulse is applied to reduce the signal of arterial flow, and low-velocity encoding (VENC) gradients of 20 cm/sec should be collected.[29] The postcontrast 3D gradient-echo technique may offer the best sensitivity in the detection of abnormal dural venous sinus flow and thrombus.[32]

Identification of thrombus in the dural sinus is the definitive diagnostic imaging sign. However, caution must be used when evaluating magnetic resonance venographic studies. Firstly, the observer must be aware of variations in the size of the dural sinuses. Secondly, and more importantly, arachnoid granulations can appear as filling defects in the sinus and simulate clot on CT or MR, which may lead to a false-positive diagnosis of dural sinus thrombosis.[24, 33–37]

A CT scan with contrast and CT venography can also be used to evaluate the dural sinuses. Contrast is injected and a rapid scan done, catching the bolus passing through the vein. A thrombus is seen as a filling defect, and normal opacification of the vein is good evidence that the vein is patent. Organizing thrombus can enhance, but this is not considered a problem during the acute phase.

Dural sinus thrombophlebitis is preceded by epidural abscess in more than 50% of cases. Infected thrombus forms within the sinus and may break down to form an intrasinus abscess that is excluded from circulation by occlusive thrombi. Progression of infection and propagation of clot

Copyright © 2003, Mosby, Inc. All rights reserved.

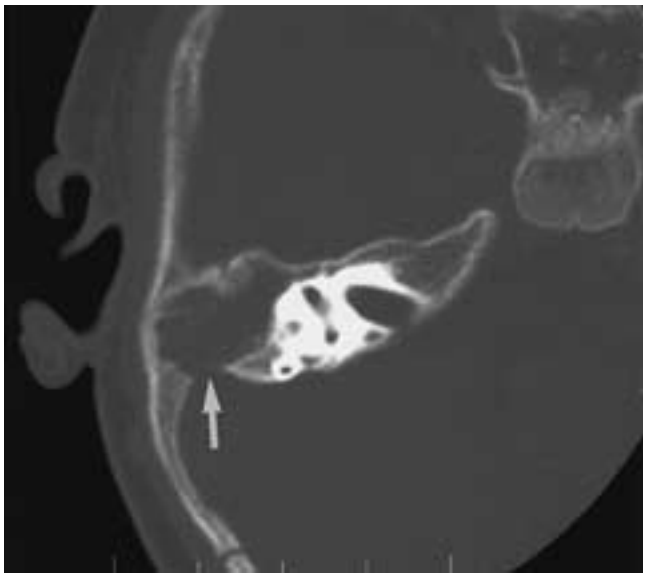

VIEW IMAGE

FIGURE 22-7 Coalescent mastoiditis. There is destruction of mastoid septae and erosion of cortical bone overlying the sigmoid sinus (*arrow*).

may lead to thrombosis of the superior petrosal sinus and the cavernous sinus anteriorly and the jugular bulb and the internal jugular vein inferiorly. Meningitis and brain abscess may also occur and dominate the clinical picture, obscuring the signs of thrombophlebitis.

Venous Infarction

Thrombophlebitis of the sigmoid and transverse sinus may propagate retrograde into the superior sagittal sinus, causing venous outflow obstruction, and venous hypertension can lead to cerebral edema, infarction, and hemorrhage. Venous infarcts are characteristically subcortical (Fig. 22-9G) and do not conform to major arterial vascular territories. Infarctions due to superior sagittal sinus thrombosis are usually bilateral in the frontal, parietal, and occipital lobes. Infarctions of the thalamus occur with thrombosis of the internal cerebral veins and straight sinus. Transverse sinus thrombosis may result in temporal lobe infarction.[26]

Treatment is controversial. Some advocate endovascular approaches using direct infusion of thrombolytic drugs into the occluded sinuses to produce recanalization.[38, 39] Others promote ligation of the jugular vein to prevent dissemination of infected thrombotic material.[40–43]

Diffusion- and perfusion-weighted MR studies provide more information than conventional MR imaging about the

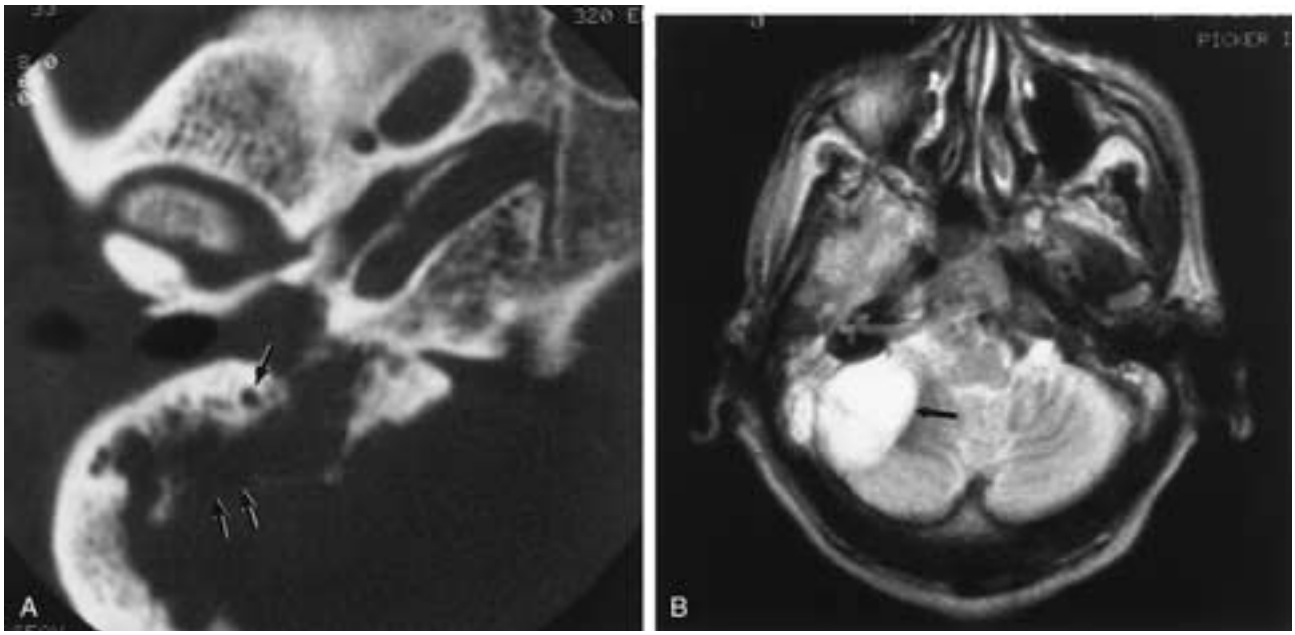

VIEW IMAGE

FIGURE 22-8 Tuberculous otomastoiditis with cerebellar abscess. **A**, Axial CT, right ear. Diffuse destruction of internal mastoid cortex (*double arrows*) associated with middle ear and mastoid debris. Single arrow, facial nerve. **B**, Large, hyperintense mass seen on T2-weighted MR image. Abscess confirmed at surgery.

Copyright © 2003, Mosby, Inc. All rights reserved.

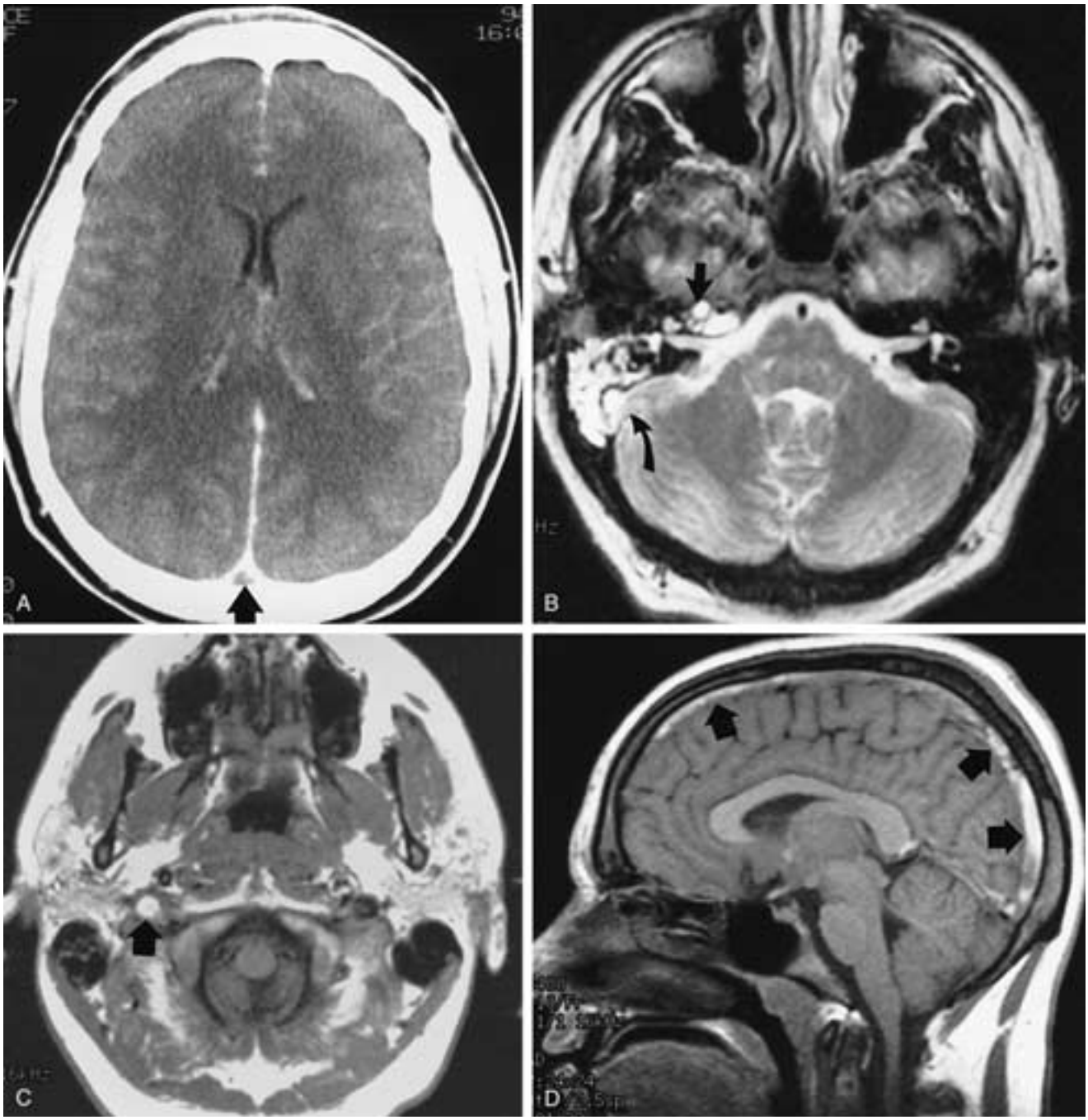

VIEW IMAGE

FIGURE 22-9 Mastoiditis with venous sinus thrombosis and venous infarction. This is a 19-year-old man who presented with headache and transient left-sided weakness. **A**, Contrast-enhanced CT image shows clot in the superior sagittal sinus (*arrow*) (''empty delta sign''). **B**, T2-weighted image shows hyperintense fluid in the mastoid and the petrous apex (*arrow*). Note the abnormal high signal caused by thrombus in the right sigmoid sinus (*curved arrow*). **C**, T1-weighted image. The normal flow void in the jugular vein has been replaced by the bright signal of methemoglobin in the thrombosed jugular vein (*arrow*). **D**, T1-weighted midline sagittal MR image shows hyperintense thrombus in the superior sagittal sinus (*arrows*).

Copyright © 2003, Mosby, Inc. All rights reserved.

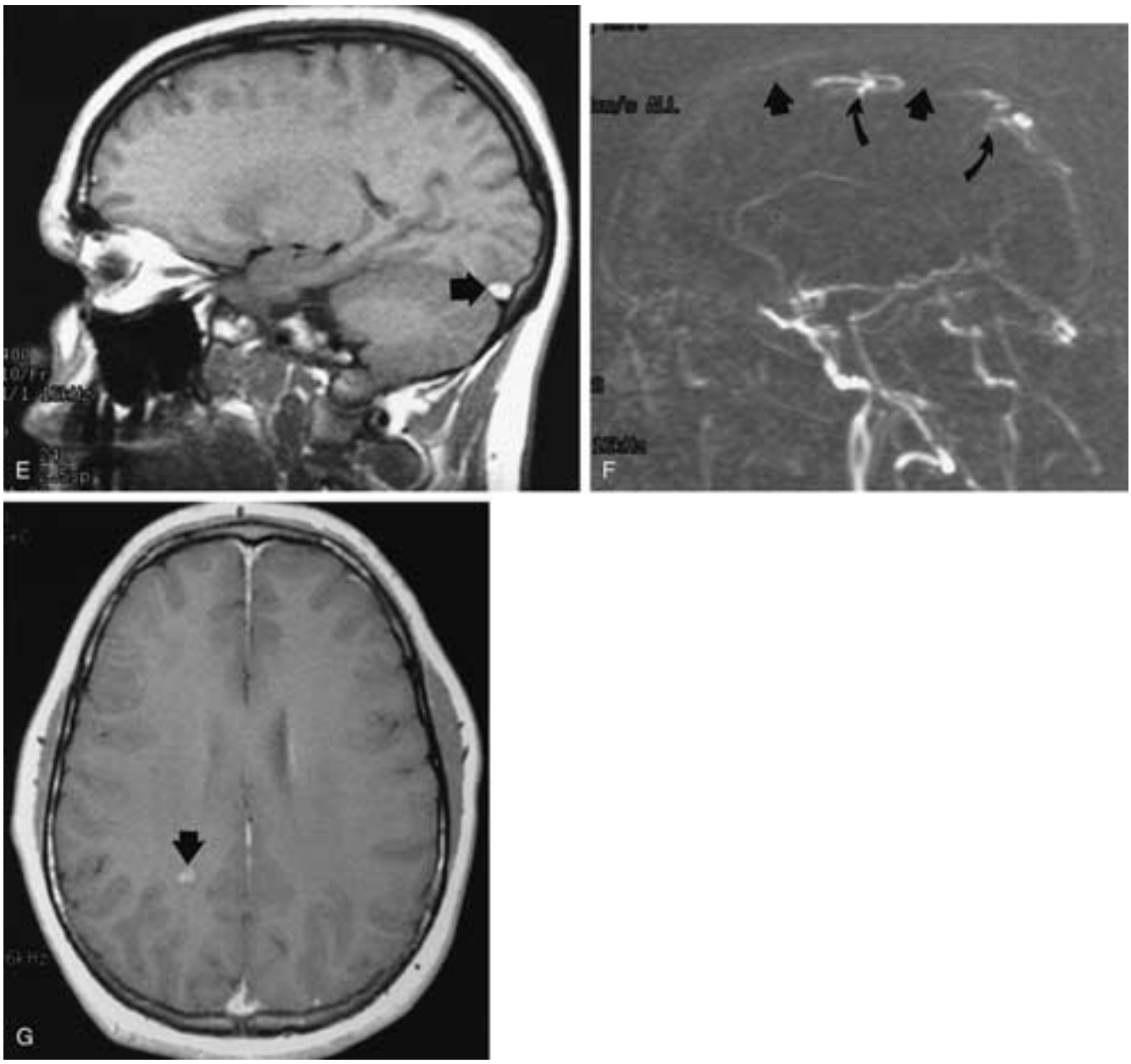

VIEW IMAGE

FIGURE 22-9 *Continued* **E**, T1-weighted parasagittal image reveals clot (*arrow*) in the transverse sinus (*arrow*). **F**, 2D phase contrast MR venogram (sagittal) shows nearly complete absence of flow in the superior sagittal sinus (*arrows*), with minimal flow in the cortical veins. **G**, T1-weighted image after gadolinium enhancement reveals an area of enhancement (*arrow*) in white matter compatible with venous infarction.

Copyright © 2003, Mosby, Inc. All rights reserved.

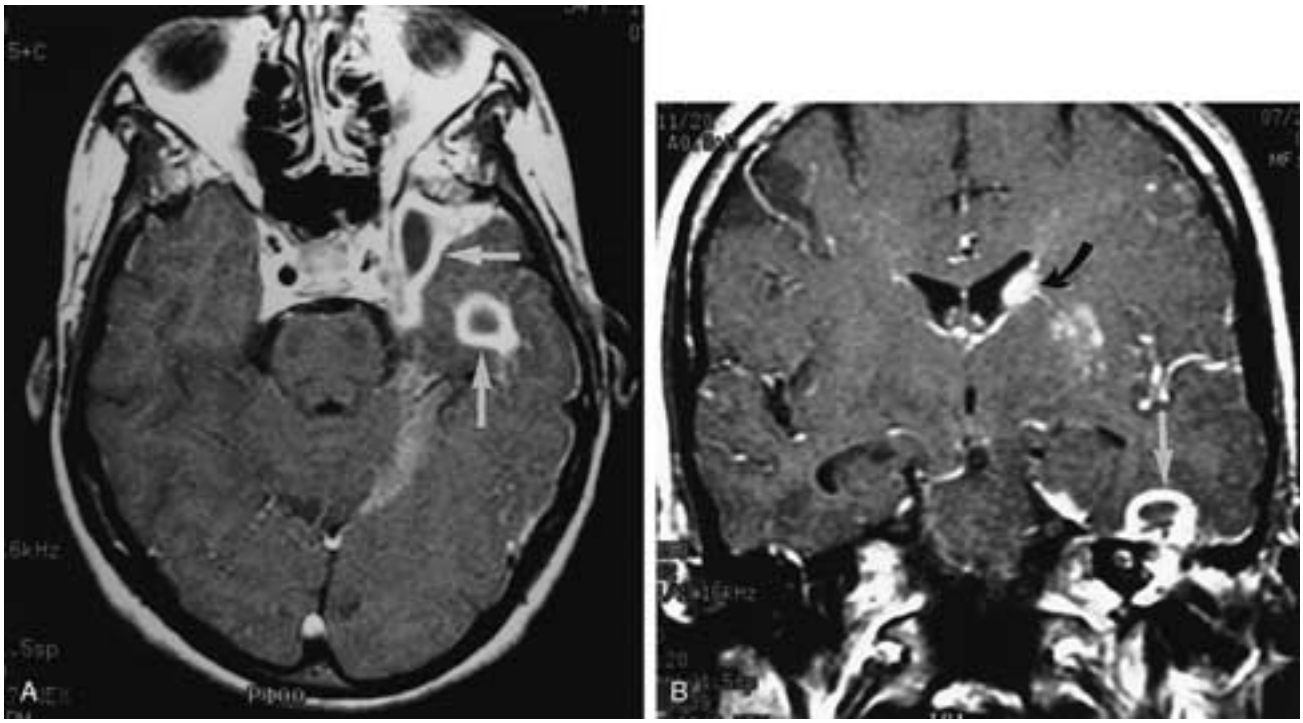

VIEW IMAGE

FIGURE 22-10 **A** and **B**, Otomastoiditis with epidural abscesses. T1-weighted, contrast-enhanced images show epidural abscesses (*arrows*). There was associated meningitis with involvement of the lenticulostriate arteries and the recurrent artery of Huebner, producing infarction in the basal ganglia and head of the caudate (*arrow*).

physiologic state of the brain after dural sinus thrombosis. These techniques may allow triage of patients between conservative therapy with heparin and microcatheter-directed thrombolysis.[44]

Abscess/Meningitis

Other dangerous intracranial complications include epidural, subdural, and intracerebral abscess formation (Figs. 22-8, 22-10, and 22-11). Meningitis and other intracranial inflammatory complications can occur via direct extension of disease from the mastoid through a cortical defect or can be secondary to retrograde thrombophlebitis, in which case the bone appears to be intact.[10] When a brain abscess develops, it usually occurs in the temporal lobe and cerebellum (2:1). Almost all otogenic brain abscesses have chronic suppurative otorrhea, and more than half have a cholesteatoma.[10]

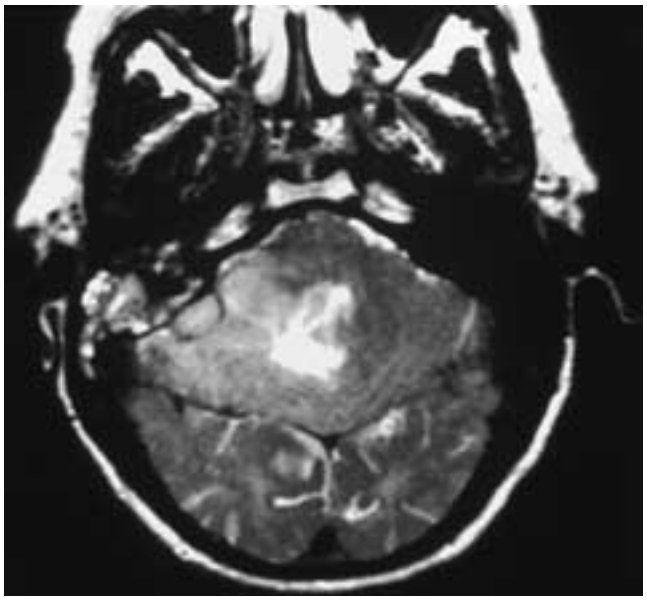

VIEW IMAGE

FIGURE 22-11 Acute otomastoiditis with meningitis and ''cerebellitis.'' (Courtesy of Dr. David Yousem.)

Episodes of meningitis, particularly when they occur in children, should provoke a search for a parameningeal focus. When there is a history of otitis media, careful CT investigation of the margins of the temporal bone should ensue, with special attention to the tegmen, sinus plate, and lamina cribrosa. In this context, congenital fistulas, often associated with inner ear malformation, also must be sought.

Aberrant arachnoid granulations in the temporal bone should be sought for patients with persistent serous otitis media or septic meningitis following acute otitis media.[33] Anomalous arachnoid granulations appear as characteristic bone defects in the posterior or middle fossa surfaces of the temporal bone (Fig. 22-12), and the dural defect of an arachnoid granulation may permit intracranial extension of mastoid disease.

Otitic Hydrocephalus

Individuals with sigmoid sinus thrombosis are often gravely ill. Otitic hydrocephalus (otitic intracranial hypertension) is secondary to dural sinus thrombosis and is believed to result from impaired intracranial venous drainage. Further increased intracranial pressure may be caused by obstruction of arachnoid granulations along the

Copyright © 2003, Mosby, Inc. All rights reserved.

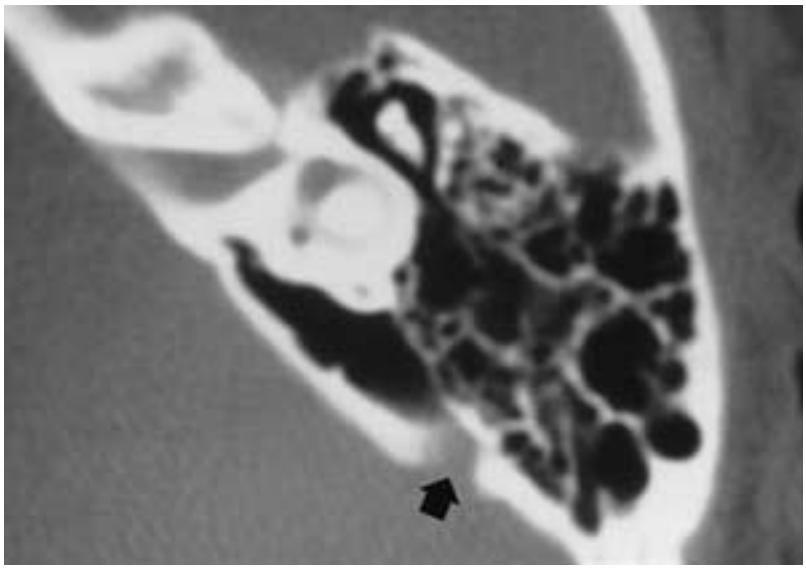

VIEW IMAGE

FIGURE 22-12 Anomalous arachnoid granulation. Note the defect in the mastoid cortex (*arrow*).

superior sagittal sinus, and alterations of posture can be catastrophic for those patients.[8–10] Changes in mentation and high spiking fevers (''picket fence'' fever pattern) are among the classic clinical findings associated with this disorder. Mastoid exploration with surgical decompression of the adjacent dural sinuses is often curative.[10, 26]

Labyrinthitis

Labyrinthitis is also a potential complication of acute otomastoiditis, and access to the labyrinth is usually via the round or oval window.[8–10] Exotoxins also have been implicated in the development of labyrinthitis, suggesting hematogenous dissemination. Imaging reveals pathologic contrast enhancement within the membranous labyrinth on T1-weighted, contrast-enhanced studies. This phenomenon will be considered again in the section on the inner ear.

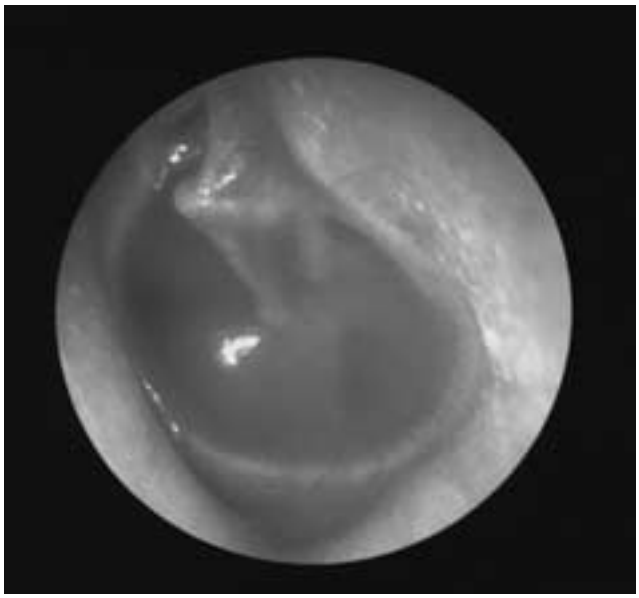

VIEW IMAGE

FIGURE 22-13 Chronic otitis media with effusion. Otoscopy.

Chronic Otitis Media with Effusion

Chronic otitis media with effusion (COME) is an accumulation of inflammatory effusion in the middle ear and a frequent sequela of acute otitis media.[21] Otitis media with effusion is also known as *serous otitis* (Fig. 22-13). Middle ear effusion results from decreased intratympanic pressure and may occur as an isolated phenomenon or in association with other manifestations of chronic otitis media.[14, 16, 45] Serous otitis media is associated with malfunction or obstruction of the ET. The etiology includes abnormal development of the temporal bone and obstruction of the ET by bone dysplasia, trauma, adenoid hyperplasia, tumor, or surgery. Tubal patency may be compromised by mucosal edema secondary to rhinopharyngitis, allergy, or neoplasm.[46]

Occlusion of the ET causes a decrease in intratympanic pressure and impaired air exchange in the middle ear. Negative intratympanic pressure results from resorption of oxygen by the mucoperiosteum of the middle ear, and the negative pressure causes collapse of the tubal wall and occlusion of the tubal isthmus. There is then extravasation of fluid from the vascular bed into the intercellular spaces and air spaces of the middle ear.[46]

Persistent ET dysfunction may lead to a succession of events. There may be atrophy of the drum, with or without attic retraction pockets. There is greater risk of tympanic membrane (TM) perforation due to trauma or acute otitis. Poor TM healing results in an increased chance of perforation.[5] Long-standing ET dysfunction may result in middle ear atelectasis. The TM becomes retracted onto the promontory and ossicles of the middle ear (Figs. 22-14 and 22-15).[47] These retractions may be associated with ossicular defects (long process of incus) and, when exaggerated, may result in an ossicular discontinuity whereby the TM is placed in direct apposition to the stapes capitulum (''nature's

Copyright © 2003, Mosby, Inc. All rights reserved.

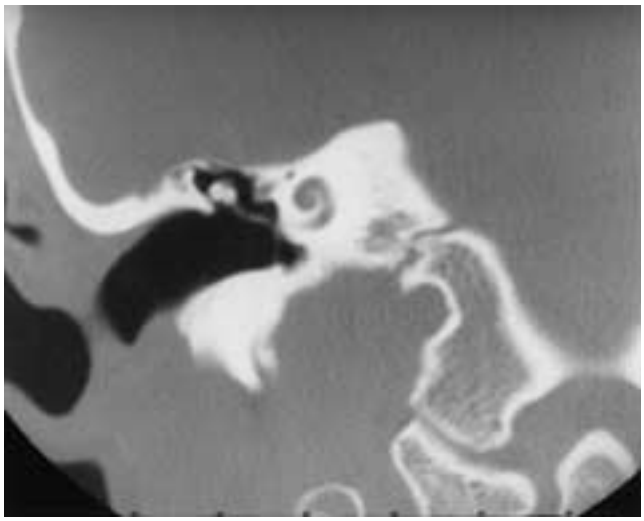

VIEW IMAGE

FIGURE 22-14 TM retraction. Coronal CT image demonstrates retraction of the pars tensa (*arrow*) to the level of the promontory.

myringostapediopexy'') (Fig. 22-15). These patients often have normal conductive hearing.[10, 45]

Osteoneogenesis may be caused by chronic healed otitis media and mastoiditis. Osteoneogenesis is unusual in the middle ear but is a common sequela to infection in other pneumatized areas of the temporal bone. The thickened bony trabeculae coalesce and progressively obliterate the intervening air spaces.[10]

Middle ear effusions occurring in infants and children are usually treated without the aid of radiologic intervention.[16] However, middle ear effusions occurring spontaneously in an adult should be investigated with imaging and should include examination of the nasopharynx to exclude a neoplasm obstructing the ET (Fig. 22-16). Nasopharyngeal imaging should be performed routinely at the time of temporal bone examination.

Another cause of middle ear effusion is trigeminal motor dysfunction. The mandibular branch of the trigeminal nerve provides innervation to the tensor veli palatini muscle, which regulates ET patency. Tensor veli palatini dysfunction secondary to V3 denervation will compromise ET function and cause middle ear and mastoid fluid to accumulate. The etiology is usually a tumor in the cavernous sinus region or perineural spread of malignancy.[48]

Effusions may occur anywhere in the middle ear cleft (tympanic cavity proper) or within the attic, antrum, or mastoid air cell system. The imaging diagnosis is made by demonstration of an air-fluid level, preferably in two orthogonal planes.[45] Unfortunately, the diagnosis of an effusion in the completely opacified middle ear often is not possible because no fluid levels are seen, and CT attenuation numbers are unreliable because of the diversity of the components of the collection. Tympanostomy tubes (pressure-equalization tubes) are used in these patients both for drainage and for normalization of intratympanic pressure (Fig. 22-17).[14, 49, 50] These tubes are made of various plastics and metals, including stainless steel. They are of widely varying shapes and are consistently visible at CT, except when obscured by adjacent soft-tissue debris.[51–53] Ventilation tubes tend to be spontaneously extruded from the TM after 3 to 6 months.

Sequelae of Chronic Otitis

Granulation Tissue

Granulation tissue is probably the most common cause of debris in the middle ear. On CT, a soft-tissue density is seen, with no ossicular displacement or bone erosion. The distinction between granulation tissue and cholesteatoma can be made with contrast-enhanced MR imaging. Granulation tissue is usually quite vascular and enhances intensely on contrast-enhanced, T1-weighted images, while cholesteatoma does not enhance (Fig. 22-18).[11, 23, 24, 54] Hearing loss and aural drainage are variable findings with granulation tissue, and one must be aware that such granulation tissue often occurs concurrently with other manifestations of chronic otitis, including cholesteatoma.[11, 45, 53, 55, 56]

Cholesteatoma

A cholesteatoma is simply skin growing in the wrong place and consists of a sac lined with stratified squamous epithelium filled with exfoliated keratin debris. A cholesteatoma may be classified as either acquired or congenital in origin.[10, 15, 24, 56, 57] An acquired middle ear cholesteatoma is the most common type (98%) and occurs in the context of chronic otitis media and/or a perforated TM.[24, 58] This type of cholesteatoma has also been called a secondary-acquired cholesteatoma, a Prussak's cholesteatoma, or an attic cholesteatoma. Cholesteatomas arising from retraction pockets in the absence of infection are known as primary acquired cholesteatomas and may be the result of extension of squamous epithelium from the pars flaccida into the unresolved mesenchyme of the epitympanum in early life[59] (Table 22-2).

Congenital (primary) cholesteatomas of the temporal bone are due to epithelial rests of embryonal origin. Congenital cholesteatomas (epidermoids) within the tempo-

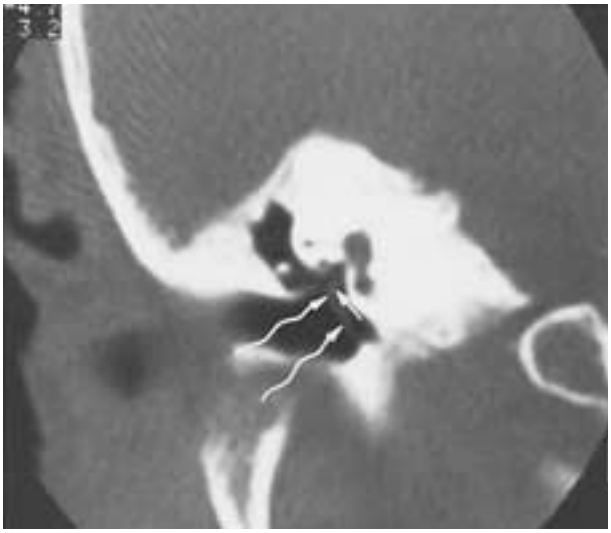

FIGURE 22-15 Myringostapediopexy. Coronal image demonstrates retraction (*long white arrows*) articulating with the head of the stapes (*small arrow*).

VIEW IMAGE

Copyright © 2003, Mosby, Inc. All rights reserved.

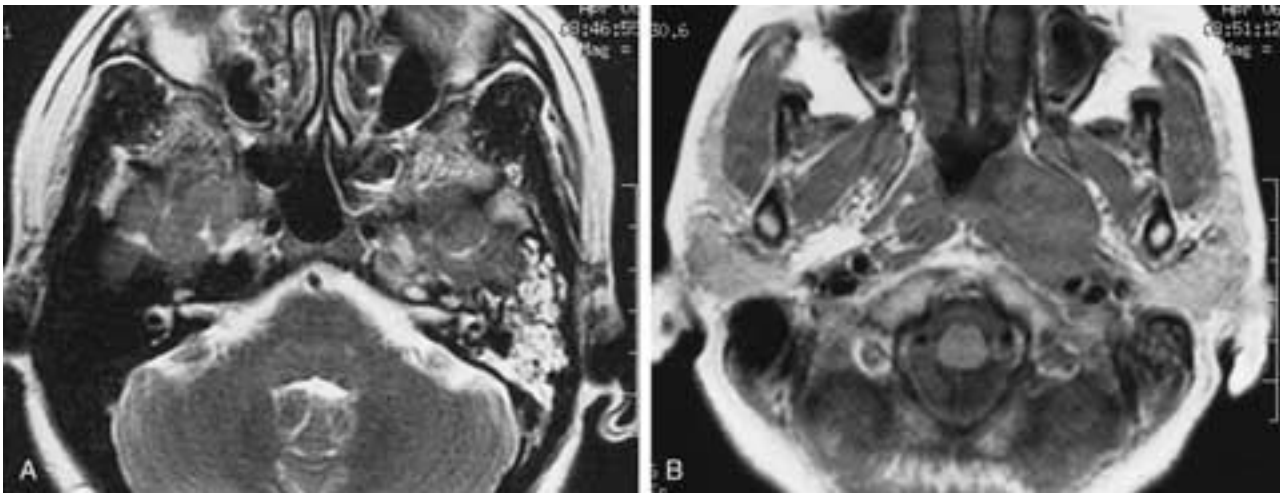

VIEW IMAGE

FIGURE 22-16 Nasopharyngeal carcinoma, middle ear and mastoid effusion. **A**, Axial T2-weighted MR image shows fluid in the left mastoid and middle ear. **B**, Axial T1-weighted image demonstrates a large left nasopharyngeal mass.

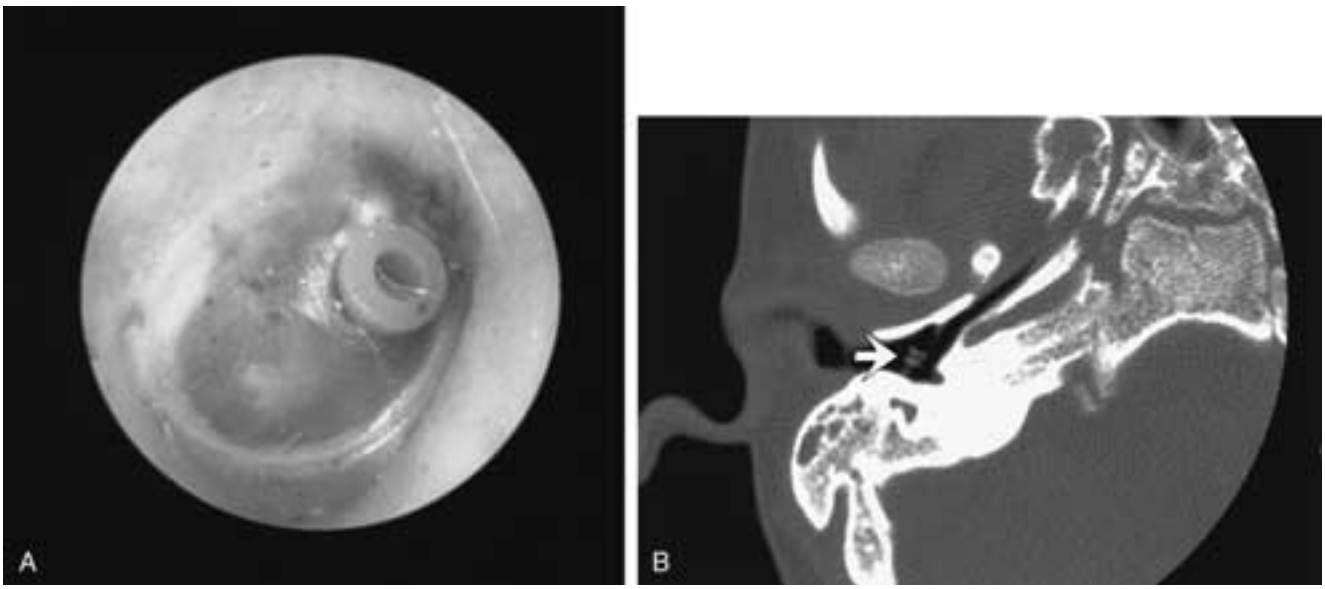

VIEW IMAGE

FIGURE 22-17 Tympanostomy tube. **A**, Otoscopy. A myringotomy tube is seen anterior to the malleus in the right TM. **B**, Axial CT (*arrow*).

Copyright © 2003, Mosby, Inc. All rights reserved.

VIEW IMAGE

FIGURE 22-18 Bilateral granulation tissue. Coronal contrast-enhanced, T1-weighted image demonstrates enhancing debris bilaterally (*arrows*). CT revealed a diffuse, non-space-occupying abnormality without alteration and the contour of the TM.

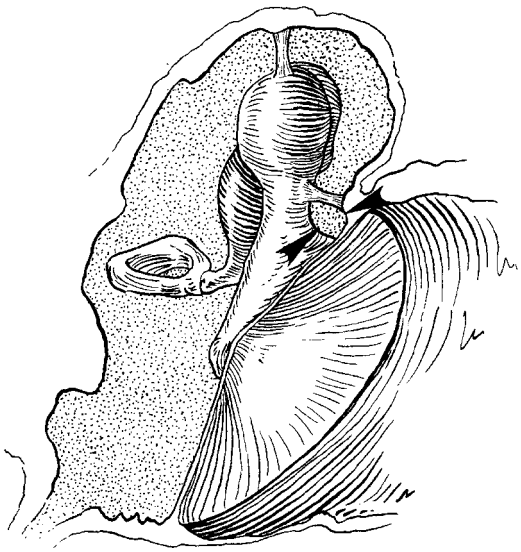

FIGURE 22-19 Prussak's space (*arrowheads*) is subtended by the lateral mallear ligament, the neck of the malleus, and the pars flaccida of the TM. (Reprinted with permission from Swartz JD, Harnsberger HR. Imaging of the Temporal Bone. 3rd ed. New York and Stuttgart: Thieme, 1998.)

VIEW IMAGE

ral bone have been reported in the middle ear, mastoid, middle ear and mastoid, petrous portion of the temporal bone, temporal squama, and within the TM. Intradural (cisternal) congenital cholesteatoma is another type of cholesteatoma that usually involves the cerebellopontine angle (CPA) and may cause varying degrees of cochlear and vestibular symptoms and signs.[58, 60, 61] A cholesteatoma in the diploic space is in the differential diagnosis of a solitary lytic calvarial lesion. Although congenital cholesteatomas of the middle ear may occur anywhere, they tend to occur in the anterior tympanic cavity near the ET or stapes.[23]

The acquired cholesteatoma is unique to the middle ear, and its etiology is related to the anatomy and embryology of the TM.[15, 62] The TM contains all three germinal layers; an external epidermal layer contiguous with the skin (ectoderm), an inner layer continuous with the mucosa of the middle ear (endoderm), and a middle fibrous layer (mesoderm). The skin on the outer surface of the TM grows quite rapidly, desquamates, and then normally migrates outward from the external auditory canal with cerumen, which develops in the lateral cartilaginous third of the external auditory canal.[15, 63]

Most acquired cholesteatomas arise in the superior pars flaccida portion of the TM and extend into Prussak's space (Fig. 22-19). Prussak's space is limited laterally by the pars flaccida (Shrapnell's membrane), which is attached superiorly to the tympanic ring near the scutum, inferiorly by the lateral (short) process of the malleus, and medially by the neck of the malleus. The superior and anterior walls are formed by the lateral mallear ligament, which radiates from its site of origin on the neck of the malleus to the scutum and from the anterior and posterior malleal folds.[10, 12, 23, 64–66]

There are four major theories concerning the etiology of acquired cholesteatoma (Table 22-3). Perhaps the most widely accepted theory suggests that cholesteatoma arises from retraction pockets (Figs. 22-20 to 22-22). If negative pressure develops in the middle ear, atmospheric pressure compresses the TM from the outside, causing the weakest portion to retract. Thus, the pars flaccida, lacking a well-defined middle fibrous layer, retracts more easily due to its elasticity.[7, 67] Healing perforations of the pars tensa may also be predisposed to retract. As the retraction pocket forms and deepens, due to negative middle ear pressure and possibly repeated inflammation, the TM retraction pocket disrupts the normal physiologic desquamation of the external epidermal layer of the TM. This allows debris to become trapped within the pocket, accumulate, expand, and form a keratin plug.[47, 68–70] A cholesteatoma is formed.

Table 22-2
CLASSIFICATION OF MIDDLE EAR CHOLESTEATOMA

Congenital cholesteatoma	2%
Acquired cholesteatoma	98%
Pars flaccida (usually primary acquired)	82%
Pars tensa (usually secondary acquired)	18%
Posterosuperior	78%
Anterior and inferior	22%

Source: Modified from Swartz JD, Harnsberger HR. Imaging of the Temporal Bone. 3rd ed. New York and Stuttgart: Thieme, 1998.

Table 22-3
THEORY OF ACQUIRED MIDDLE EAR CHOLESTEATOMA PATHOGENESIS

Retraction pocket (invagination) theory
Epithelial invasion through TM perforation
Squamous metaplasia of middle ear epithelium
Basal cell hyperplasia

Source: Modified from Swartz JD, Harnsberger HR. Imaging of the Temporal Bone. 3rd ed. New York and Stuttgart: Thieme, 1998.

Copyright © 2003, Mosby, Inc. All rights reserved.

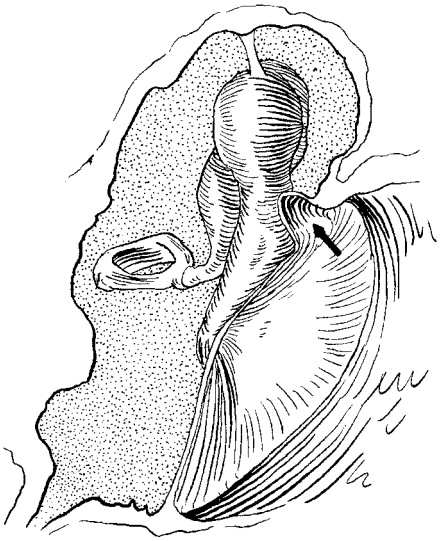

VIEW IMAGE

FIGURE 22-20 Prussak's space cholesteatoma, invagination theory. Coronal diagram. Retraction of the pars flaccida (*arrow*). (Reprinted with permission from Swartz JD, Harnsberger HR. Imaging of the Temporal Bone. 3rd ed. New York and Stuttgart: Thieme, 1998.)

Other etiologies of secondary acquired cholesteatoma include epithelial invasion or implantation of skin into the middle ear through a perforation in the TM secondary to otitis media, surgery with placement of ventilating tubes, or tympanoplasty.

Other pathogenic theories involve metaplasia of the simple squamous or cuboidal epithelium of the middle ear into keratinized stratified squamous epithelium secondary to chronic or recurrent otitis media. Proponents of basal cell hyperplasia theorize that epithelial cells, via proliferating columns of cells, invade the intact TM through microscopic defects.[47] Such epithelial migration is facilitated by infection that destroys the normal middle ear mucosa.[68, 70] Epithelial breaks are also commonly observed in the middle ear in association with otitis media. These dehiscenses leave areas of connective tissue from the mucoperiosteum in direct contact with a middle ear effusion. As the effusion becomes organized, it serves as a bridge for granulation tissue. In later stages, these areas become totally or partially covered with epithelium, and these epithelial breaks become connected to each other through the organized effusion. The cholesteatomas seem to spread by using the connective tissue as scaffolding.[71] Because the TM appears to be normal, these cholesteatomas are impossible to differentiate from the congenital type.

By virtue of their location in Prussak's space, acquired cholesteatomas generally displace the malleus head (and incus body) medially and erode the adjacent bony scutum (junction of the lateral attic wall and external auditory canal at the lateral attic spur) (Figs. 22-23 and 22-24).[56, 66, 72, 73] Prussak's space opens posteriorly into the epitympanum. From there, the mass easily extends posteriorly in the superior incudal space to the posterolateral attic and then via the aditus ad antrum to the antrum and mastoid air cells. Widening of the aditus is often an important imaging diagnostic finding.[74] Larger lesions may extend from the attic inferiorly into the posterior tympanic recesses.

Cholesteatomas arising from the pars tensa are much less common than those arising from the pars flaccida. Most pars tensa cholesteatomas arise from posterosuperior retractions and often involve the recesses of the posterior tympanum, initially the facial recess laterally and then the more medial sinus tympani (Fig. 22-25).[62] Superior extension of these lesions into the attic generally displace the ossicular mass (malleus head and incus body) laterally. Thus, the pars tensa cholesteatoma tends to extend initially toward the medial wall of the middle ear and comes into contact early with the ottic capsule over the lateral semicircular canal. As a result, fistulous formation to the lateral semicircular canal is more commonly seen than in the pars flaccida cholesteatoma. The pars tensa cholesteatoma is easiest to diagnose on axial CT, in contrast to the early Prussak's-type cholesteatoma, which is best seen on coronal images.

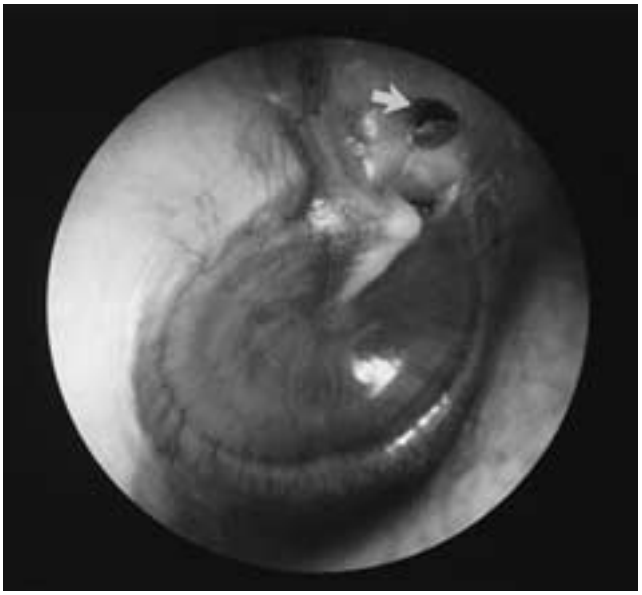

VIEW IMAGE

FIGURE 22-21 Otoscopic view of the pars flaccida retraction pocket (*arrow*) in the right TM.

Copyright © 2003, Mosby, Inc. All rights reserved.

FIGURE 22-22 **A**, Coronal diagram. Cholesteatomatous debris in sac (*arrow*). **B**, Attic cholesteatoma. Otoscopy. **C**, Congenital cholesteatoma (*arrow*) seen at otoscopy. **D**, Cholesteatoma seen in the mastoid at surgery (*arrow*).

VIEW IMAGE

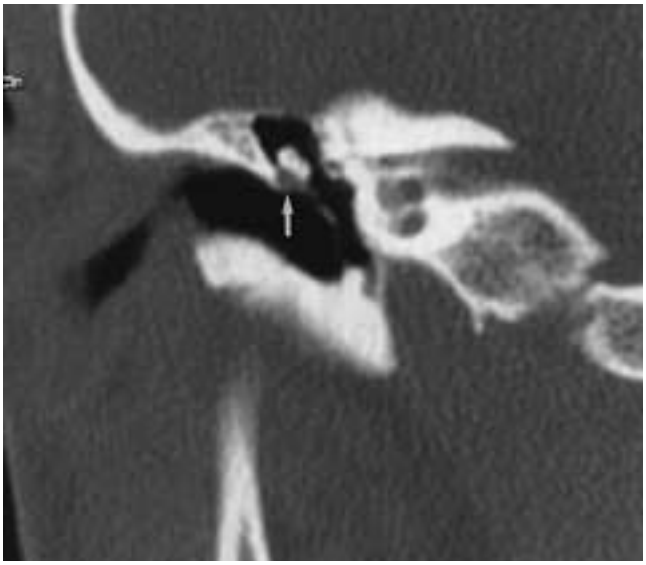

FIGURE 22-23 Pars flaccida retraction pocket with small cholesteatoma (*arrow*).

VIEW IMAGE

Copyright © 2003, Mosby, Inc. All rights reserved.

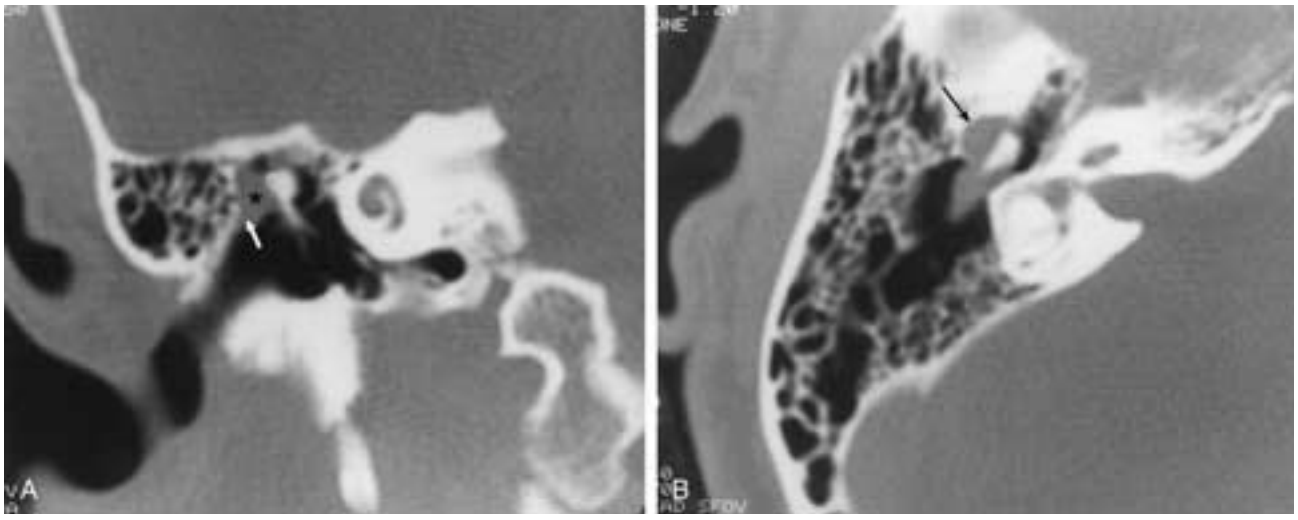

VIEW IMAGE

FIGURE 22-24 Acquired cholesteatoma, Prussak's space. **A**, Coronal CT image demonstrates a soft-tissue mass (*asterisk*) interposed between the lateral attic wall and the malleus head. Note the blunted scutum (*arrow*). **B**, Axial CT image again demonstrates a soft-tissue mass with remodeling of the lateral attic wall (*arrow*). The mass extends posteriorly through the aditus into the mastoid antrum.

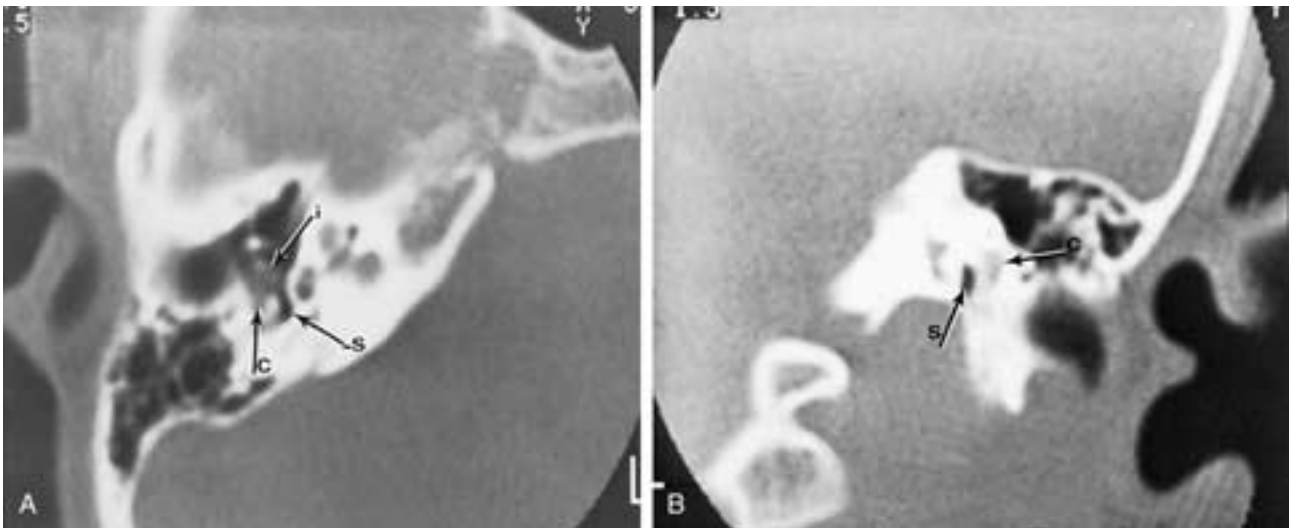

VIEW IMAGE

FIGURE 22-25 Facial recess cholesteatoma. **A**, Axial image demonstrates a soft-tissue mass (*C, arrow*) within the facial recess. The mass does not extend medially into the clear sinus tympani (*S, arrow*). The incudostapedial articulation (*i, arrow*) is intact. **B**, Coronal image demonstrates a mass (*C, arrow*) in a more laterally positioned facial recess. Again, more medial sinus tympani (*S, arrow*) is clear.

Copyright © 2003, Mosby, Inc. All rights reserved.

Middle ear opacification, associated with TM retraction, is a helpful diagnostic clue that indicates the absence of a mass lesion (cholesteatoma, paraganglioma, etc.) in the middle ear.

The most medial extension of the anterior epitympanic space is known as the anterior epitympanic recess or supratubal recess. The supratubal recess is separated from the main epitympanic space by an incomplete bony or fibrous partition attached to the tegmen anterior to the malleus. This bony ridge has been named the *cog* by Dr. William House (Fig. 22-26A). This recess is in intimate contact with the proximal tympanic segment of the facial nerve and the geniculate ganglion. If the cog is absent, cholesteatomatous masses may spread anteriorly and jeopardize the facial nerve in the region of the geniculate ganglion (Fig. 22-26B,C).[75] Other conditions leading to the development of an anterior epitympanic cholesteatoma are a canal wall down mastoidectomy or blockage of the aditus ad antrum.[75]

The imaging signature of cholesteatoma is bone erosion associated with a nonenhancing soft-tissue mass, and it is the bone destruction that makes these lesions particularly dangerous[57] (Table 22-4). Cholesteatomas may erode the scutum, ossicles, tegmen tympani, and bony labyrinth.

Erosion of the scutum is the classic finding in attic cholesteatoma.[23] Ossicular destruction occurs in 75% of pars flaccida cholesteatomas and in as many as 90% of pars tensa cholesteatomas.[76–79] The long process of the incus, by virtue of its limited ligamentous support and poor blood supply, is the most common segment of the ossicular

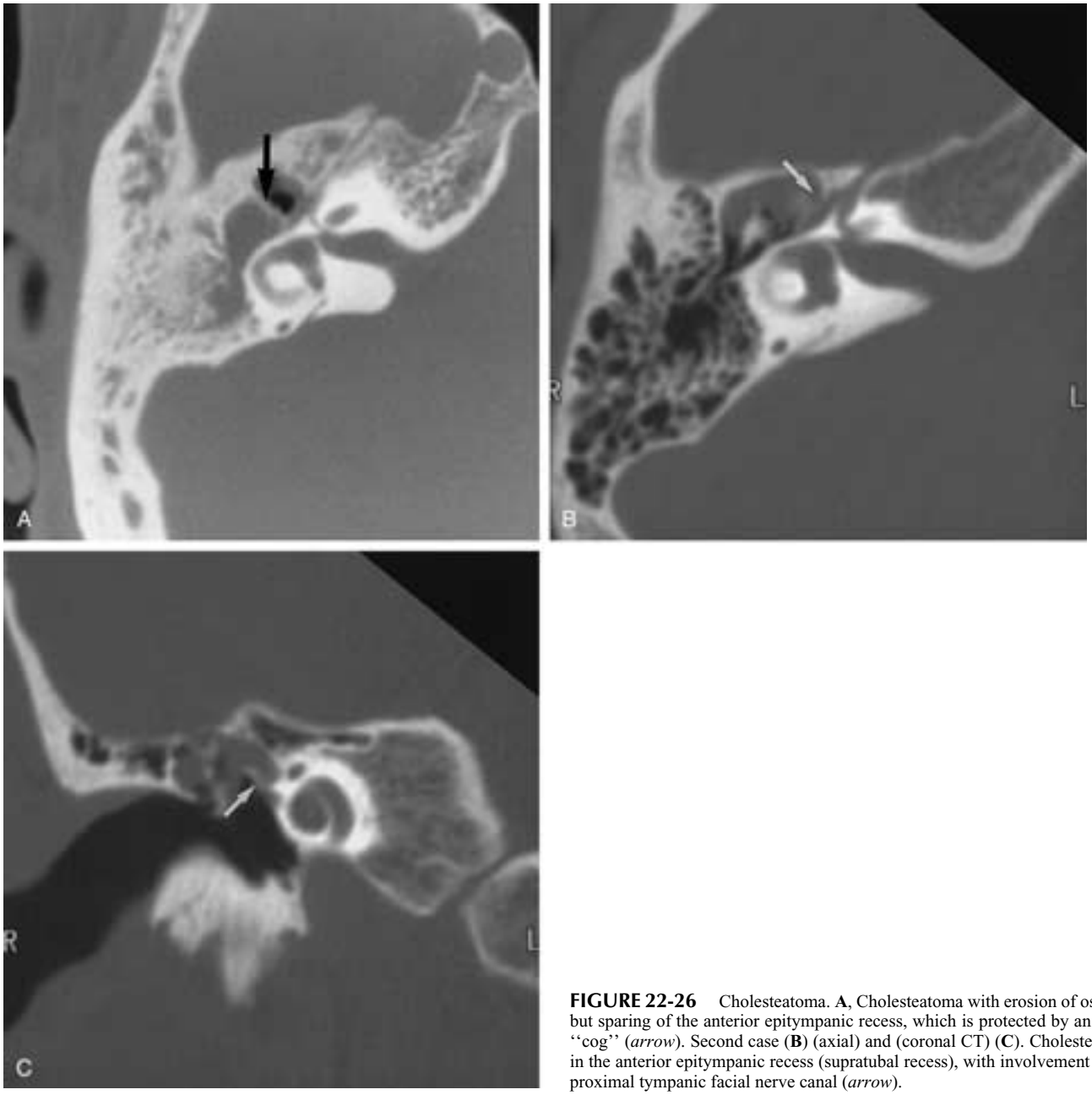

FIGURE 22-26 Cholesteatoma. **A**, Cholesteatoma with erosion of ossicles but sparing of the anterior epitympanic recess, which is protected by an intact ''cog'' (*arrow*). Second case (**B**) (axial) and (coronal CT) (**C**). Cholesteatoma in the anterior epitympanic recess (supratubal recess), with involvement of the proximal tympanic facial nerve canal (*arrow*).

VIEW IMAGE

Copyright © 2003, Mosby, Inc. All rights reserved.

Table 22-4
ACQUIRED CHOLESTEATOMA: COMPLICATIONS

Ossicular erosion Pars flaccida (75%) Pars tensa (90%)
Labyrinthine fistula (especially of the lateral semicircular canal)
Facial nerve canal invasion (tympanic segment, particularly of the first and second genu)
Tegmen disruption*
Sinus plate disruption*
Superinfection (potential for intracranial complication)

*MR imaging recommended.

chain eroded by both varieties of acquired cholesteatoma. The stapes also must be carefully evaluated when the lesion involves the oval window niche. Amputation of the malleus head and incus body occurs classically in far-advanced lesions, particularly those arising in Prussak's space (Fig. 22-27).

Labyrinthine fistula is a potentially serious complication of cholesteatoma, with an incidence of 5% to 10%. In order of decreasing frequency, fistulas occur in the lateral semicircular canal, superior ampulla, posterior canal, and promontory of the cochlea.[10] By far the most commonly compromised region is the lateral semicircular canal (Fig. 22-28). In all patients with middle ear disease, this area should be carefully evaluated on both coronal and axial images for evidence of cortical thinning. The diagnosis of fistula can be made when the mass is in direct apposition to the lumen of the labyrinth. The patient usually has symptoms of vertigo intermittently complicating long-standing chronic otitis. Classically, the patient has an acute vertiginous episode during otoscopic manipulation of the lesion. Identification of bony erosion in the absence of a gross fistula is also important to note because surgical removal of the adjacent mass may cause an acute fistula. Complications of fistula formation include the potential for total hearing loss and persistent, unremitting vertigo.[63] The latter complication may necessitate labyrinthectomy.

The facial nerve canal can be eroded; thus, it must be carefully evaluated on imaging.[80] Even if there is erosion, however, facial nerve function may be normal. Facial nerve dysfunction occurs in approximately 1% of patients with cholesteatoma.[23] The most common site of facial nerve compression is the tympanic segment, which lies inferior to the lateral semicircular canal in the middle ear. When a complete bony canal is present, erosion of the canal wall is easily seen on imaging (Fig. 22-29B). Unfortunately, the tympanic facial nerve segment may be covered by a very thin layer of bone or may be an uncovered canal with the nerve exposed to the middle ear. In such cases, subtle erosion is difficult, if not impossible, to demonstrate. However, gross invasion of the facial nerve canal in these regions is quite demonstrable.[53, 56, 81]

Bony erosion may also occur at several other strategic locations. Especially ominous is involvement of the tegmen tympani and sigmoid sinus plate (Fig. 22-29). MR imaging is recommended when defects occur at these sites because there could be associated epidural invasion by cholesteatoma, increasing the potential for development of meningitis, cerebritis, or abscess should the lesion become infected. MR imaging also is useful to define an encephalocele extending through the eroded tegmen (Fig. 22-30).

The precise etiology of the bone destruction that occurs secondary to cholesteatoma has not been identified. However, there has been excellent documentation that stratified squamous epithelium, in the absence of associated granulation tissue, does not erode bone.[15, 76, 77, 82]

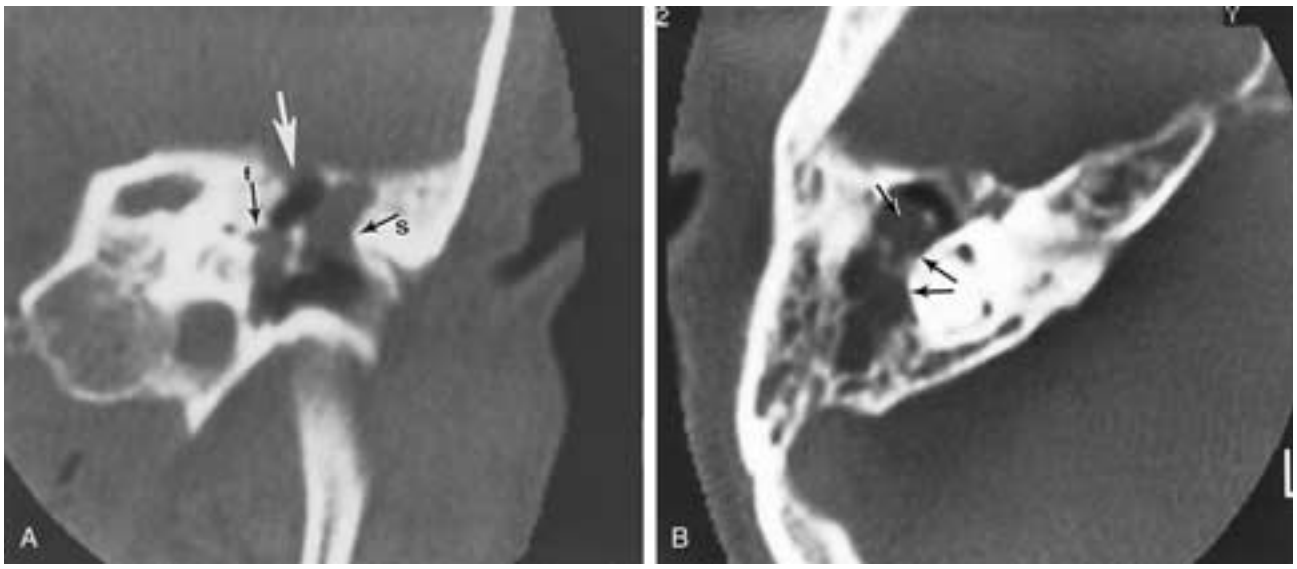

VIEW IMAGE

FIGURE 22-27 Aggressive acquired cholesteatoma. **A**, Coronal image demonstrates a mass displacing the malleus head medially. There is striking erosion of the scutum (*S, arrow*). This image also demonstrates a tegmen defect (*white arrow*). The mass has extended medially and is in direct apposition to the proximal tympanic segment of the facial nerve canal (*f, arrow*). **B**, Axial image demonstrates that the ossicular mass in the attic essentially has been destroyed (*single arrow*). The lateral semicircular canal (*double arrows*) is intact, indicating absence of a fistula.

Copyright © 2003, Mosby, Inc. All rights reserved.

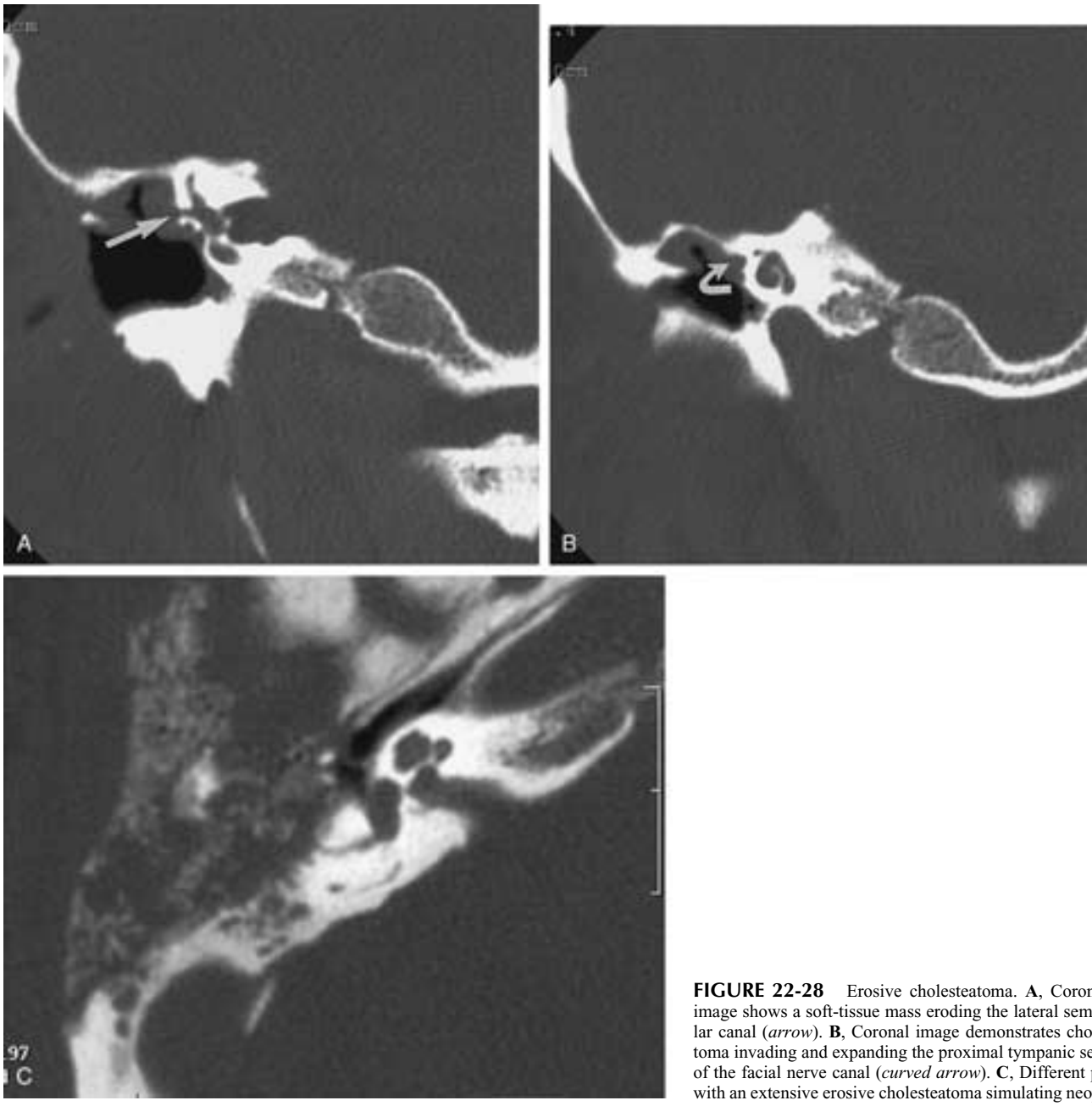

FIGURE 22-28 Erosive cholesteatoma. **A**, Coronal CT image shows a soft-tissue mass eroding the lateral semicircular canal (*arrow*). **B**, Coronal image demonstrates cholesteatoma invading and expanding the proximal tympanic segment of the facial nerve canal (*curved arrow*). **C**, Different patient with an extensive erosive cholesteatoma simulating neoplasm.

VIEW IMAGE

Copyright © 2003, Mosby, Inc. All rights reserved.

VIEW IMAGE

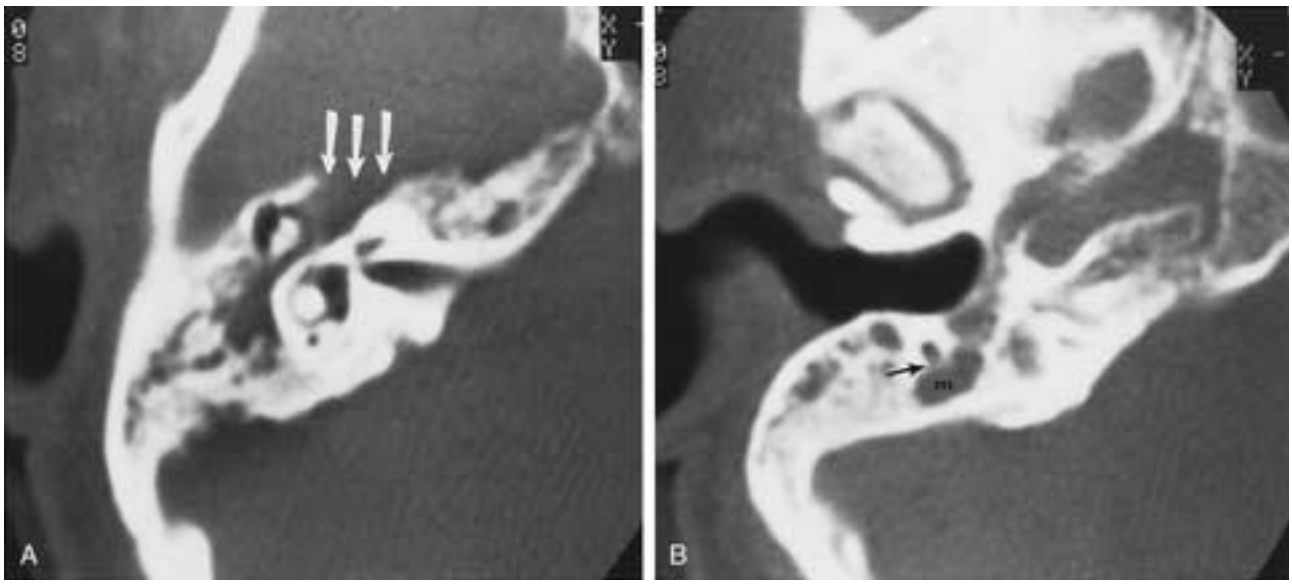

VIEW IMAGE

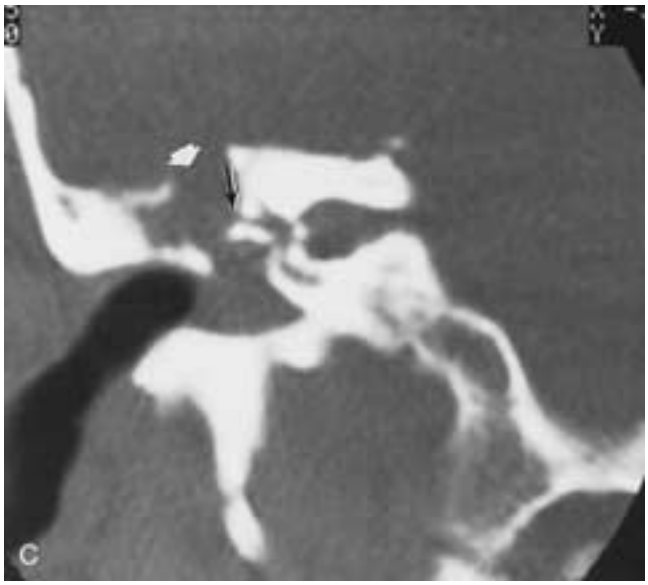

FIGURE 22-29 Erosive cholesteatoma. **A**, Axial image demonstrates soft-tissue density throughout the attic and antrum. There is a large defect anteriorly, indicating that the mass may be in direct apposition to the middle cranial fossa dura (*white arrows*). **B**, The mass (*m*) has eroded the sinus tympani and has extended posterolaterally to come in direct contact with the mastoid segment of the facial nerve canal. There is erosion in the posterior margin of this structure (*arrow*). **C**, Coronal image on a different patient demonstrates a large mass throughout the middle ear. There is a large tegmen defect (*white arrow*) and an obvious labyrinthine fistula (*black arrow*).

Illustration continued on following page

Copyright © 2003, Mosby, Inc. All rights reserved.

VIEW IMAGE

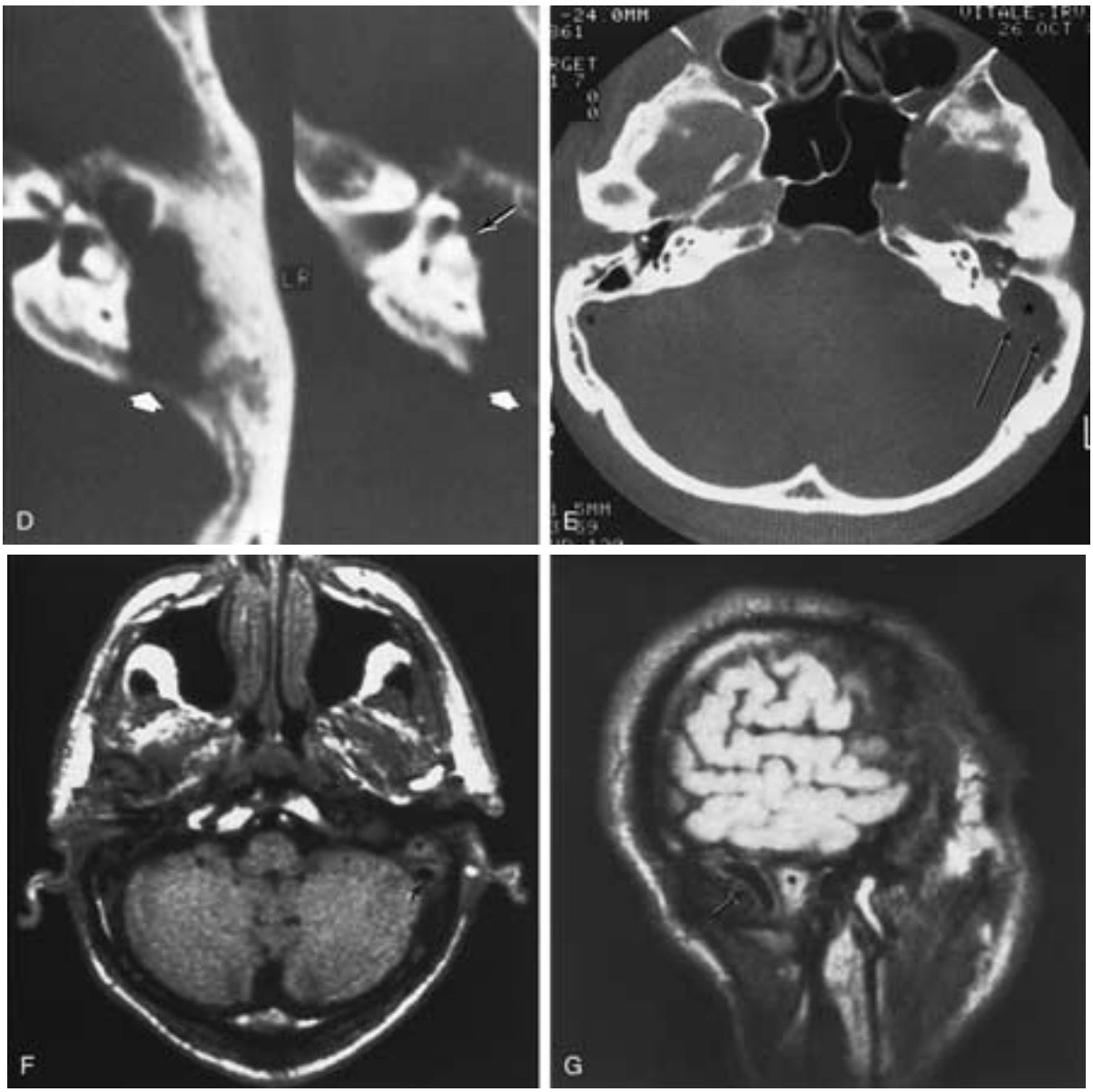

VIEW IMAGE

FIGURE 22-29 *Continued* **D**, In addition to the large fistula (*black arrow*), contiguous axial images demonstrate the presence of a defect in the sigmoid sinus plate (*white arrowhead*). **E**, Axial CT image on a different patient. Asterisk, Mastoid mass; arrows, sigmoid sinus plate defect. **F**, Axial T1-weighted MR image on another patient. Asterisk, Mastoid mass; arrows, patent sigmoid sinus, flow void. **G**, Sagittal T1-weighted MR image. Asterisk, Mastoid mass; arrow, patent sigmoid sinus, flow void.

Copyright © 2003, Mosby, Inc. All rights reserved.

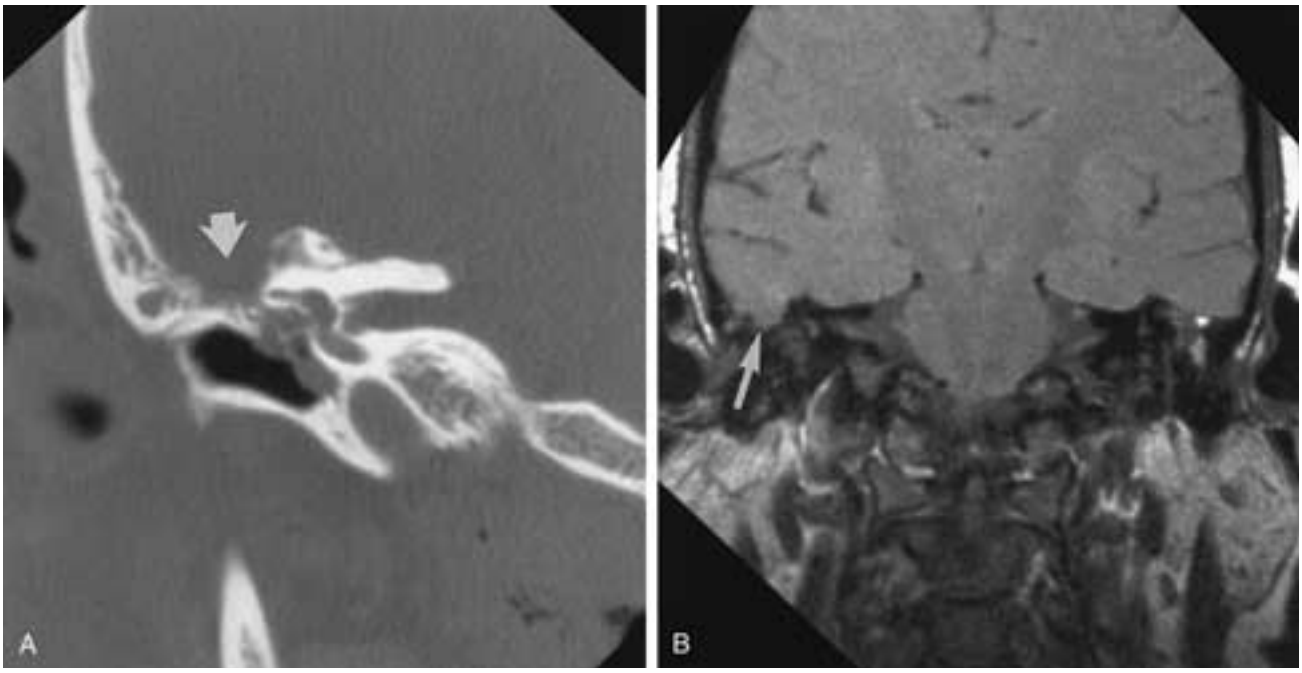

VIEW IMAGE

FIGURE 22-30 Erosive cholesteatoma with encephalocele. **A**, Coronal CT shows a mass in the middle ear with erosion of the tegmen (*arrow*). **B**, MR demonstrates herniation of brain through a defect in the tegmen (*arrow*).

Simple mechanical pressure is a doubtful cause because it is unlikely that a cholesteatoma could exert pressure exceeding capillary perfusion pressure (approximately 25 mm Hg). Chole and Choo have shown that bone resorption is primarily caused by multinucleated osteoclasts that activate or produce enzymes such as acid phosphatase, collagenase, and acid proteases.[47]

Cholesteatomas provide an excellent culture medium, and there is always potential for infection. In the preantibiotic era, such infection was responsible for most life-threatening intracranial complications such as meningitis, abscess, and sinovenous thrombosis. Fortunately, today these complications are rare.[56, 82–85] Individuals with clinical evidence of one of these intracranial complications should probably undergo MR imaging before CT.

The differential diagnosis of a destructive middle ear mass includes cholesteatoma, rhabdomyosarcoma, Langerhan's cell histiocytosis, squamous cell carcinoma, metastasis, giant cell tumor, and xanthoma.

The CT density of middle ear debris is not histologically specific.[86] The observer must rely on secondary factors to arrive at an appropriate diagnosis. Such factors include age, location, distribution, calcification or ossification, TM status (bulge or retraction), bony erosion, degree of mastoid pneumatization, and amount of conductive hearing deficit. Bony alteration is commonly associated with attic cholesteatoma, and this diagnosis should be questioned if such changes are not present. Typical findings associated with cholesteatoma include scutum blunting, attic expansion (lateral wall remodeling), and erosion of the anterior tympanic spine. The latter structure (inferior border of the Glaserian fissure) is best appreciated in the sagittal plane.[87]

Holotympanic debris in the absence of TM alteration or significant conductive hearing deficit quite likely represents granulation tissue or fluid.[88] In the presence of TM retraction and conductive deficit, the possibility of inflammatory ossicular fixation should be considered, especially when there is associated calcification or ossification. It should be remembered that granulation tissue may accompany cholesteatoma. Contrast-enhanced, T1-weighted MR images are highly accurate in separating typical granulation tissue, which enhances, from cholesteatoma, which does not (Fig. 22-31). The MR signal (nonenhanced) characteristics of cholesteatomas of the middle ear are nonspecific, and ordinarily both T1 and T2 relaxation times are relatively long.[89, 90] If bone destruction is excessive, neoplasm must be considered (Fig. 22-28C). Such neoplasms, fortunately, are quite unusual and often are accompanied by sclerosis and bloody discharge.[91] When these lesions are large, the exact site of origin may be difficult to discern. In children, rhabdomyosarcoma is notorious for its propensity to masquerade as benign middle ear disease.[92]

A cholesteatoma can evacuate spontaneously through the external canal, leaving a cavity that has an appearance similar to that of a mastoidectomy. The resulting defect is called an automastoidectomy (Fig. 22-32) and is discussed later in this chapter.

Ossicular Erosions and Ossicular Fixation

The high incidence of conductive hearing deficit (CHD) in individuals with congenital and acquired cholesteatoma is well known, and ossicular erosions are the predominant cause. Less well described is the commonplace occurrence of CHD due to ossicular resorption as a complication of chronic otitis media (Fig. 22-33), or ossicular fixation. These patients could possibly have a healed TM, and fenestral otosclerosis may be suspected clinically.

Copyright © 2003, Mosby, Inc. All rights reserved.

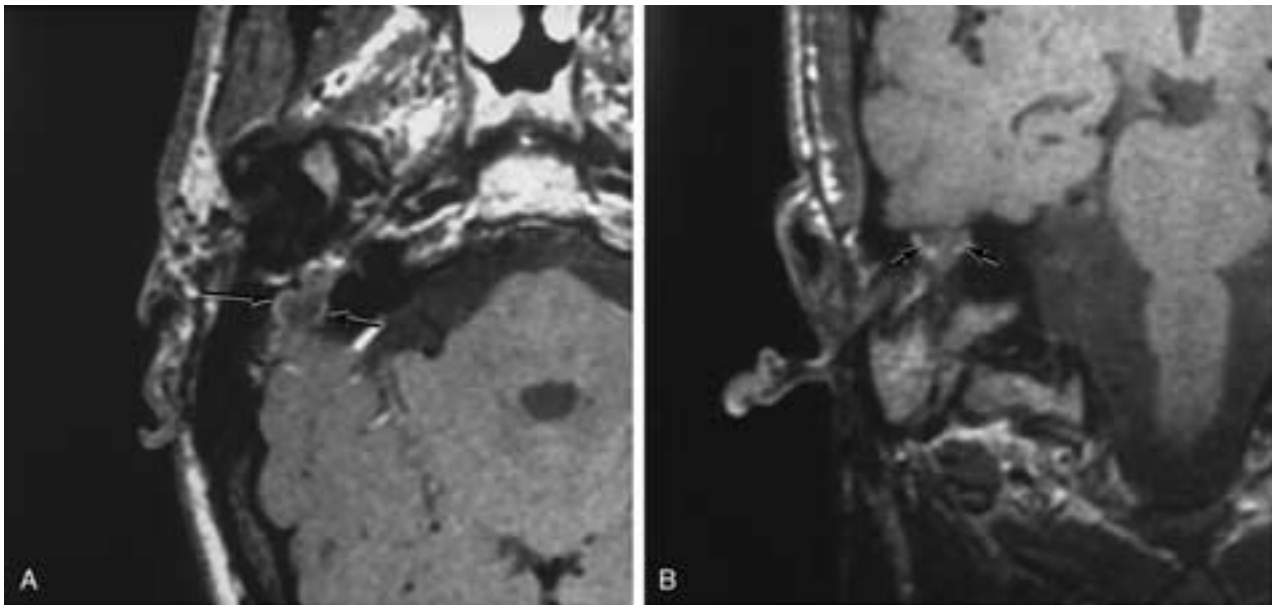

VIEW IMAGE

FIGURE 22-31 Cholesteatoma—granulation tissue. **A** and **B**, Axial and coronal contrast-enhanced, T1-weighted image demonstrates enhancing granulation tissue (*arrows*) surrounding a nonenhancing cholesteatoma.

Erosive changes occur, in order of decreasing frequency, in the long process incus, crura of stapes, body of the incus, and manubrium.[77] Attic changes (malleus head or incus body) are less common but occur on occasion (Fig. 22-34). Both axial and coronal images must be carefully studied to make a specific anatomic diagnosis.[93] The coronal images yield the best information regarding the status of the vertically oriented long process. The remainder of the chain is best visualized on axial CT scans; on images obtained just inferior to the oval window, two parallel ''lines'' representing the stapes crura should be seen.[53, 93] Anteriorly, the tensor tympani tendon and malleus neck are identified, and more posteriorly and more importantly, the lenticular process of the incus and the stapes superstructure are identified with the intervening incudostapedial joint (ISJ) (Fig. 22-35). This region should be carefully scrutinized because a widened ISJ could be secondary to erosive changes and is associated with fibrous replacement.[94] Ossicular defects are seen to best advantage in the nonopaque ''dry ear.''

Ossicular fixation also may be responsible for postinflammatory CHD.[95–98] At CT, fibrous tissue has a nonspecific appearance (Fig. 22-36). The observer should be alerted to this diagnosis in the presence of nonerosive and

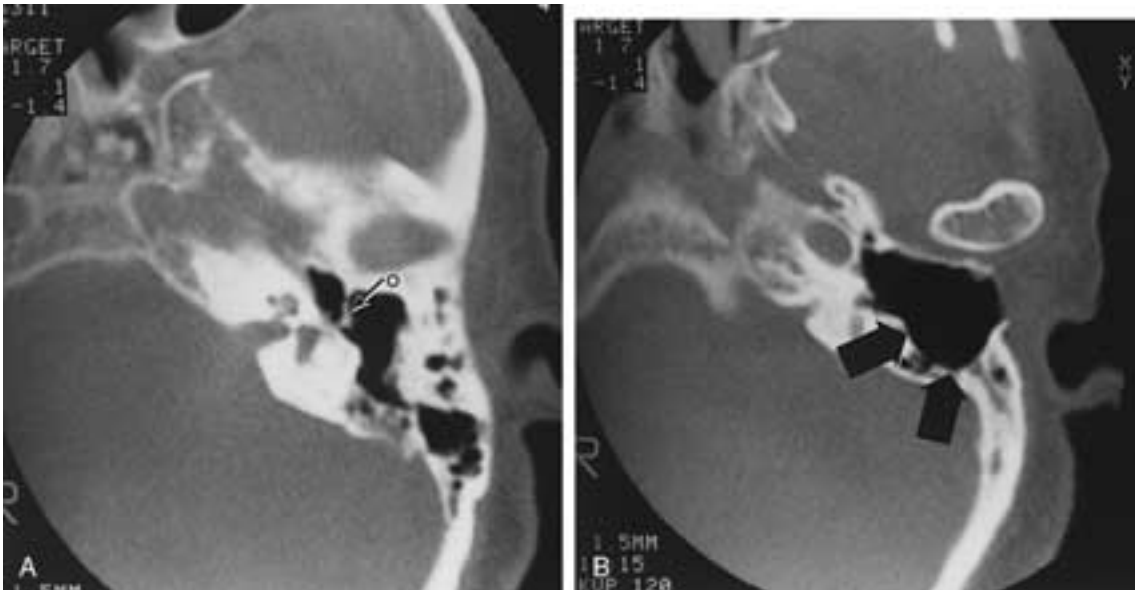

VIEW IMAGE

FIGURE 22-32 **A** and **B**, Automastoidectomy. Axial sections, left ear. This patient has had no surgery. Note the extensive remodeling caused by the aggressive cholesteatoma membrane (*arrows*). *O*, residual ossicular chain.

Copyright © 2003, Mosby, Inc. All rights reserved.

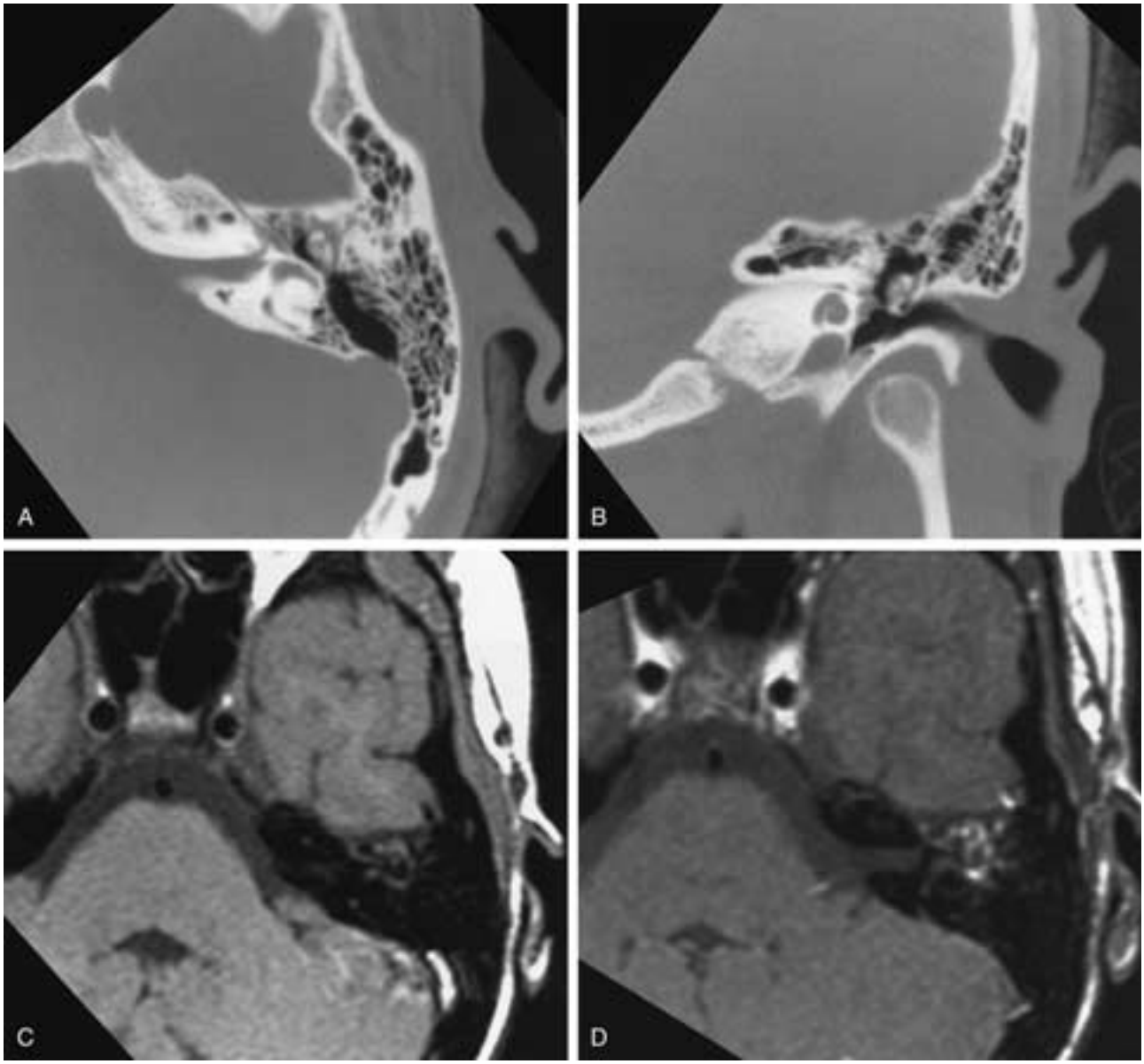

VIEW IMAGE

FIGURE 22-33 Noncholesteatomatous erosion of ossicles. **A** and **B**, Axial and coronal CT images show erosion of ossicles surrounded by soft tissue debris. **C** and **D**, Axial T1-weighted MR images before and after gadolinium enhancement demonstrate only enhancing tissue surrounding the ossicles. At surgery, only granulation tissue was found.

Copyright © 2003, Mosby, Inc. All rights reserved.

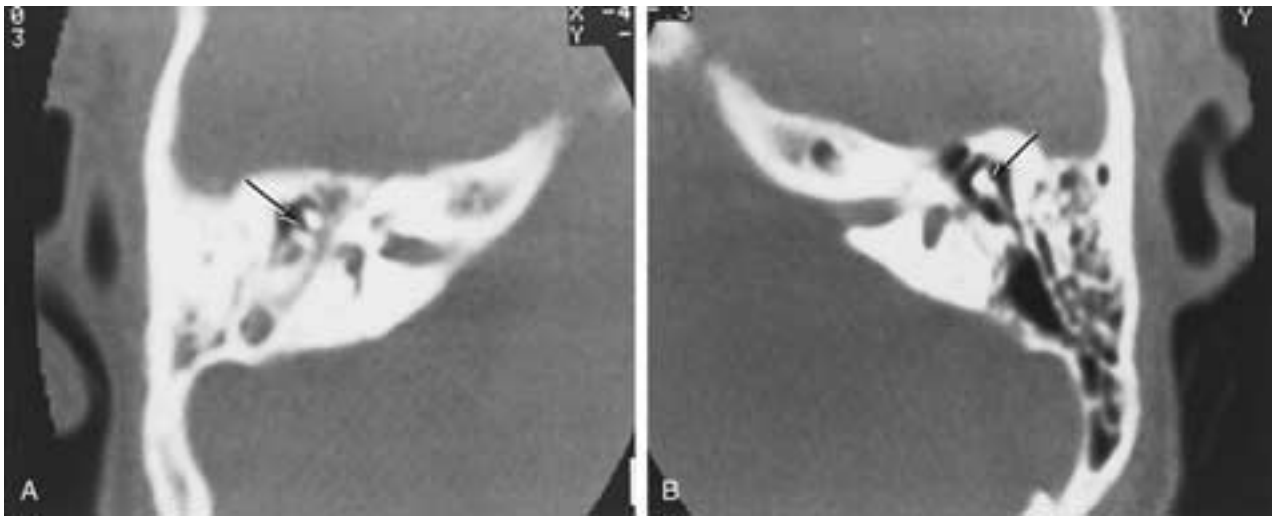

VIEW IMAGE

FIGURE 22-34 Noncholesteatomatous erosion. **A**, There is an erosion of the head of the malleus and body of the incus in the vicinity of the malleoincudal articulation (*arrow*). **B**, Normal axial section for comparison (malleoincudal articulation indicated) (*arrow*).

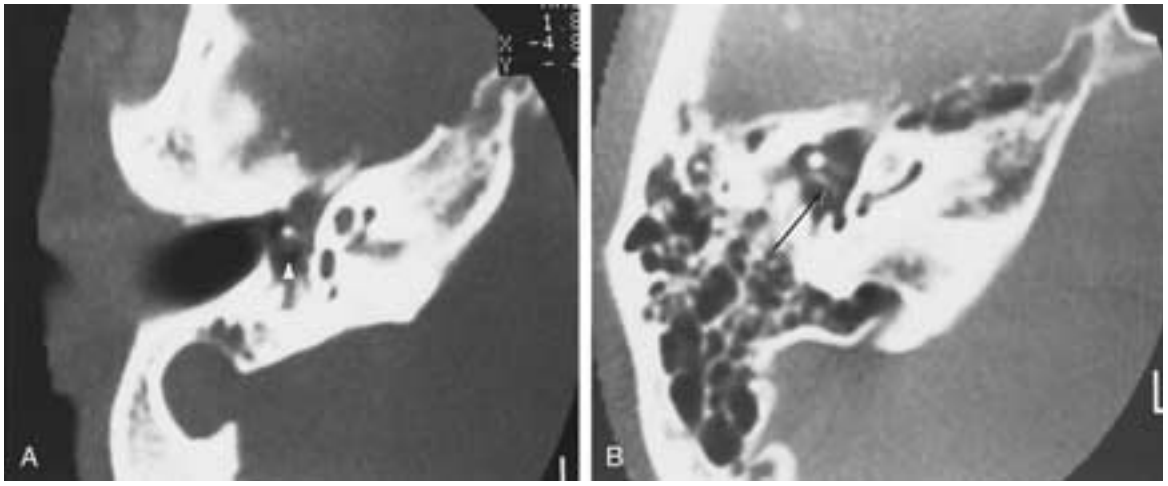

VIEW IMAGE

FIGURE 22-35 Noncholesteatomatous erosion. **A**, Axial image (right ear) indicates an absent lenticular process (*white arrowhead*). **B**, Normal patient for comparison (right ear). Normal lenticular process and stapes head are present. The incudostapedial articulation is indicated (*arrow*). More anteriorly, one can see the malleus head and the tensor tympani tendon.

Copyright © 2003, Mosby, Inc. All rights reserved.

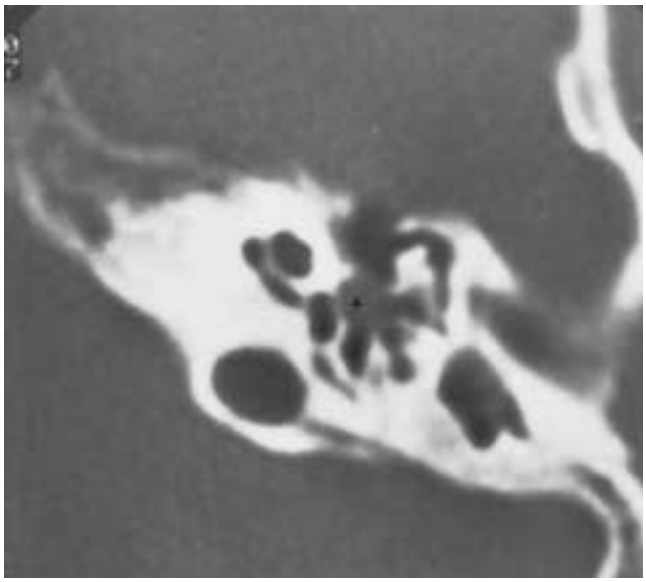

VIEW IMAGE

FIGURE 22-36 Fibrous tissue fixation. Axial section reveals nonspecific soft tissue (*asterisk*) in the oval window niche. The patient had a maximal conductive deficit.

nonexpansile changes in the middle ear of a patient with a wide audiometric air-bone gap (CHD). The TM is often retracted. The fibrous tissue may be generalized or focal. If it is focal, there is a propensity for involvement in the region of the oval window (peristapedial tent) and Prussak's space.

Tympanosclerosis

Tympanosclerosis (or dystrophic calcification) is caused by chronic otitis media followed by healing. The result is fibroblastic invasion of the submucosa, with resultant thickening and fusion of collagenous fibers to form a homogeneous mass in the tympanic cavity, with deposition of intra- and extracellular calcium and phosphate crystals.[10, 95, 99–101]

Involvement of the TM is common but often is asymptomatic (Fig. 22-37). CHD results when the process involves or encases the ossicles or their suspensory ligaments and tendons.[102] The CT appearance consists of punctate or web-like calcific density(s) (Fig. 22-38). Peristapedial tympanosclerosis may be treated with prosthetic stapedectomy, a procedure with an increased incidence of poor results in this clinical setting.[103]

New bone formation (fibroosseous sclerosis) is the least common histologic type of postinflammatory ossicular fixation.[95] This is most likely to occur in the attic and to cause encasement of the ossicular chain (Fig. 22-39).[102]

Miscellaneous

Tuberculosis

The incidence of tuberculosis and the number of drug-resistant strains of *Mycobacterium tuberculosis* have been increasing with the rise of HIV-infected patients. *M. tuberculosis* can involve multiple head and neck sites, including the larynx, pharynx, oral cavity, nasal cavity, salivary glands, cervical spine, middle ear, and mastoid. The eighth cranial nerve is very frequently affected. Tuberculous otitis media and mastoiditis have an insidious painless onset and a chronic course[23] (Fig. 22-8). TM involvement leads to early perforation and aural discharge, allowing release of the purulent exudate before there is sufficient accumulation of pus to cause pain. The portal of entry of tuberculous otitis media may be the ET or hematogenous spread of a casseous focus.

Mycotic Infections

Mycotic infections are more common in immunocompromised hosts, diabetics, and patients with lymphoma or burns. Candidiasis, aspergillosis, phycomyosis (mucormycosis), noncardiosis, and cryptococcosis are typical examples of these opportunistic infections.

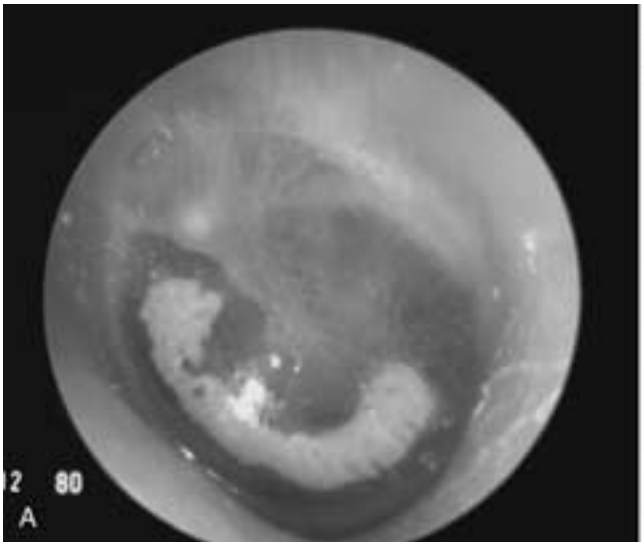

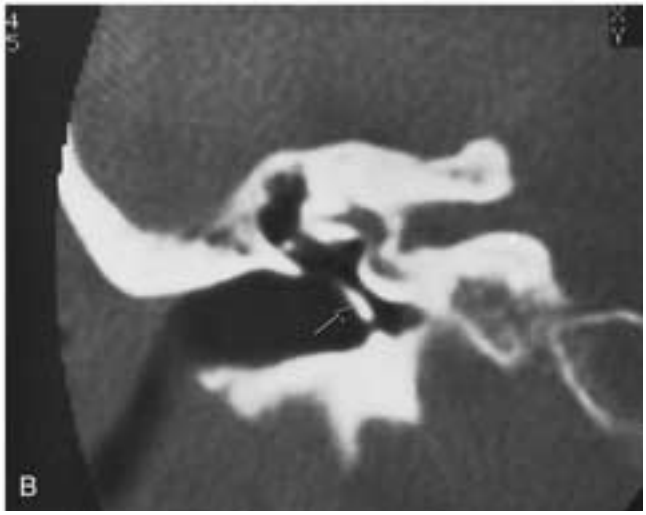

VIEW IMAGE

FIGURE 22-37 Tympanosclerosis. **A**, Otoscopy. Crescentic chalky white deposit of tympanosclerosis seen in the left tympanic membrane. **B**, Tympanosclerosis. Coronal image demonstrates tympanosclerosis (*arrow*) involving the TM. This was asymptomatic.

Copyright © 2003, Mosby, Inc. All rights reserved.

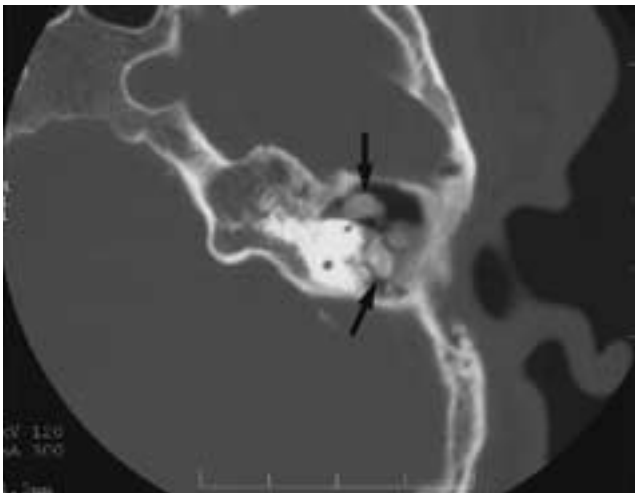

VIEW IMAGE

FIGURE 22-38 Tympanosclerosis. Note the patchy calcification (*arrows*) in the attic and mastoid on this axial image.

PETROUS APEX

Abnormalities of Aeration of the Petrous Apex

The petrous apex may be pneumatized (filled with mucosa-lined air cells) (33%), filled with marrow (60%), or sclerotic (7%).[104–106] Air cells extend into the petrous apex from the middle ear following tracts above and below the cochlea.[107, 108] Pneumatization is asymmetrical in 4–7%.[105, 106] Because the petrous apex contains mucosa-lined air cells, middle ear infection can lead to obstruction and inflammation of these apex cells and a spectrum of clinical problems, including effusion, apicitis, mucocele, and cholesterol granuloma.

Petrous Apex Effusion

Simple effusion is often an incidental finding and probably the most common radiographically identified abnormality of the petrous apex.[109] Fluid in the petrous apex usually has a bright signal on T2-weighted images but can have variable signal intensity, depending on the protein content. However, CT is necessary for definitive evaluation of these cells to exclude expansion and destruction and to define intact intercellular bone septations (Fig. 22-40).[105, 108]

Acute Petrositis

Apical petrositis is caused by spread of infection from the middle ear to the pneumatized areas of perilabyrinthine and apical regions of the temporal bone. Petrous apicitis has been considered synonymous with the complex of symptoms described by Guiseppi Gradenigo in 1904. Gradenigo's syndrome results from a suppurative otitis media that spreads to the petrous apex and then extends further to affect adjacent intracranial structures. The syndrome includes a middle ear infection with otorrhea, pain in the orbit or behind the eye (trigeminal ganglionitis), and lateral rectus palsy secondary to involvement of the sixth nerve as it follows Dorello's canal across the tip of the petrous apex.[110, 111]

The classic Gradenigo triad is rarely present, and cranial nerves II, III, VII, VIII, IX, and X may also be involved.[11, 22, 112, 113] Petrous apicitis should be suspected whenever a chronic suppurative ear infection is associated with deep ipsilateral pain.[111]

The pathogenesis of petrous apicitis is assumed to be extension of infection from the middle ear and mastoid air cells into the pneumatized petrous apex via the perilabyrinthine air tracts. The trigeminal ganglion is affected in Meckel's cave, located on the petrous apex. Meckel's cave

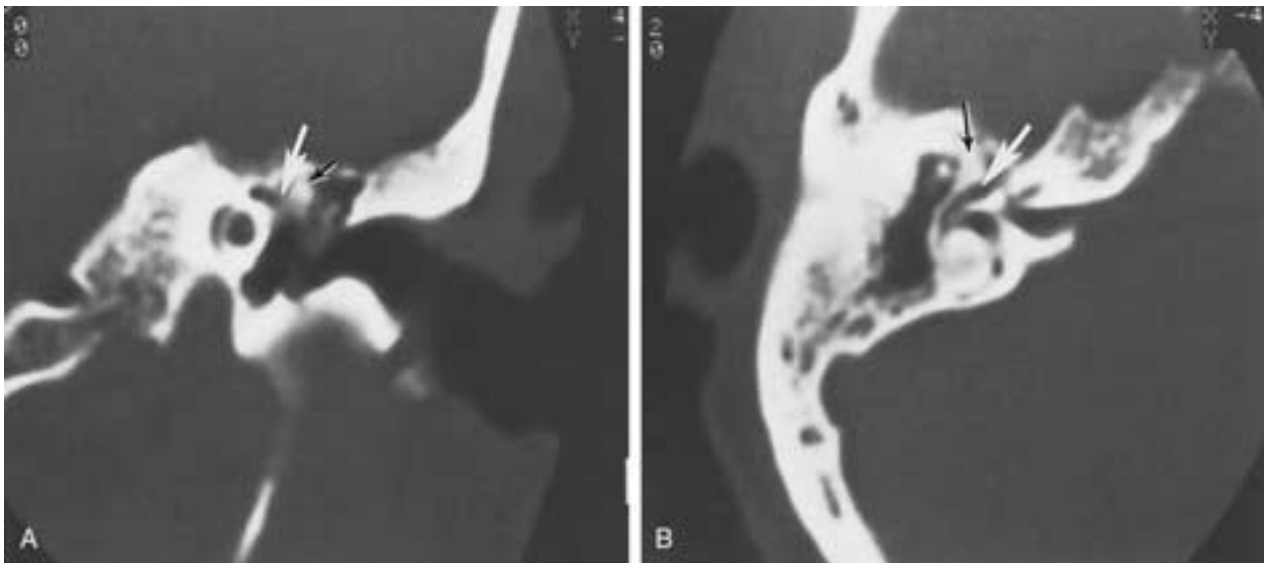

VIEW IMAGE

FIGURE 22-39 Tympanosclerosis. New bone formation. Coronal (**A**) and axial (**B**) images demonstrate new bone formation (*black arrow*) in the medial aspect of the attic in direct apposition to the proximal tympanic segment of the facial nerve canal (*white arrow*).

Copyright © 2003, Mosby, Inc. All rights reserved.

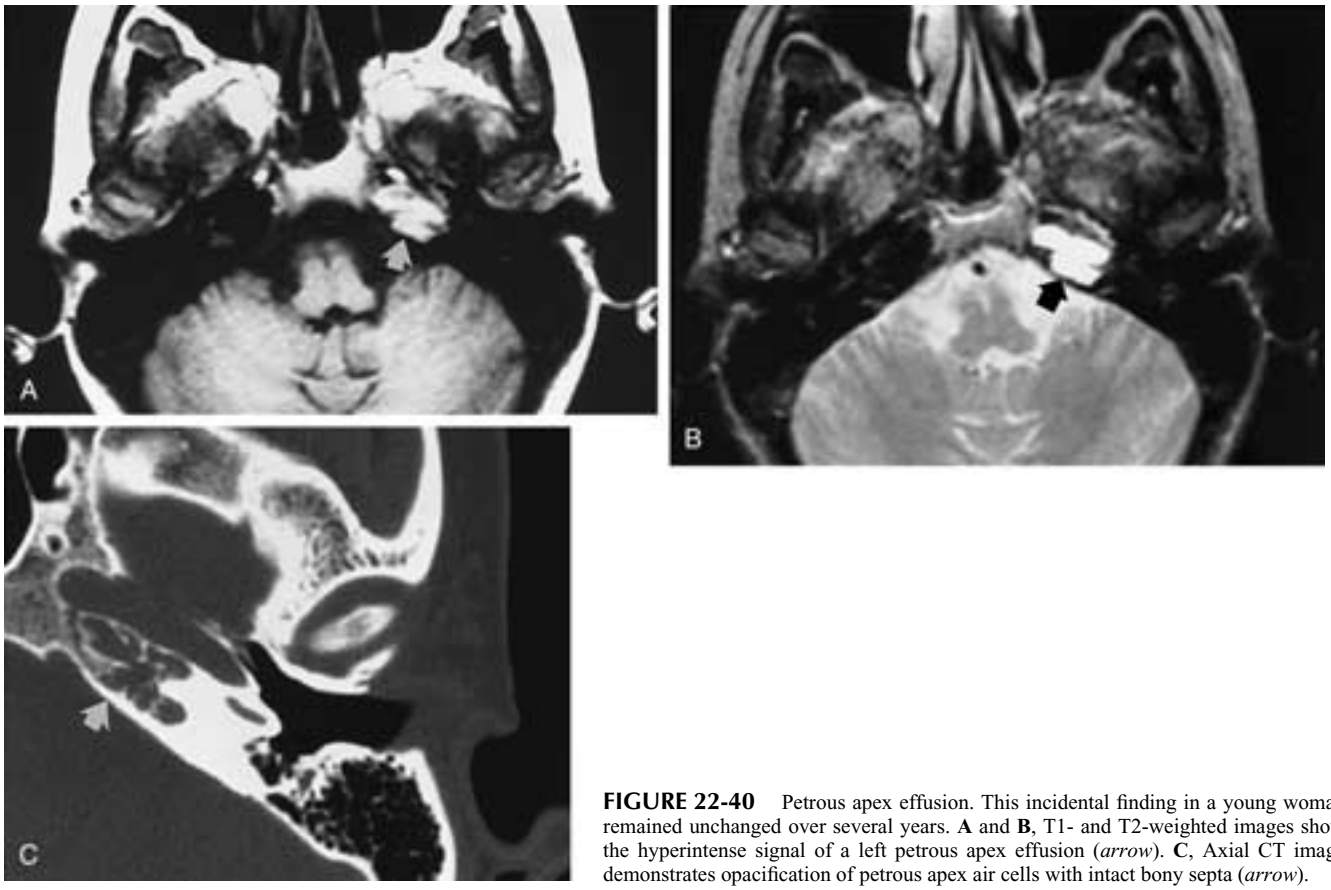

FIGURE 22-40 Petrous apex effusion. This incidental finding in a young woman remained unchanged over several years. **A** and **B**, T1- and T2-weighted images show the hyperintense signal of a left petrous apex effusion (*arrow*). **C**, Axial CT image demonstrates opacification of petrous apex air cells with intact bony septa (*arrow*).

VIEW IMAGE

lies near Dorello's canal. The abducens nerve exits the pontomedullary junction, ascends in the subarachnoid space, and pierces the dura on the back of the clivus to enter a petroclival venous confluence located between two layers of dura. This petroclival venous confluence contains the inferior petrosal sinus, which drains into the jugular bulb. The petroclival venous confluence communicates with the cavernous sinus anterosuperiorly, the superior petrosal sinus laterally, and the basal sinus of the clivus medially. At the level of the petrous apex, the sixth nerve penetrates an osteofibrous conduit (Dorello's canal) that is formed by the petrous apex and the petrosphenoidal ligament (Gruber's ligament). The sixth nerve then enters the cavernous sinus and runs along the lateral aspect of the internal carotid artery.[114–116]

Whether petrous apicitis always occurs in a pneumatized petrous apex is a matter of dispute. Petrositis has been described in the nonpneumatized apex presumably due to hematogenous spread of infection. Suppuration in the petrous apex may be a true osteomyelitis of the medullary bone of the petrous apex or the result of coalescent osteitis within the pneumatized spaces of the petrous apex.[111, 117] Most researchers consider the development of petrous apicitis to be a complication of acute purulent otitis media, paralleling the occurrence of coalescent mastoiditis as a complication of acute otitis media.

CT scans reveal debris within petrous apex air cells. Lysis of bony septae and disruption of the adjacent bony cortex may also occur. Occasionally, petrositis presents only with fluid in the petrous apex, without bone destruction. The MR findings include pathologic enhancement at the periphery of the defect, presumably within meninges, with possible extension to the gasserian ganglion (Meckel's cave) (Figs. 22-41 and 22-42).

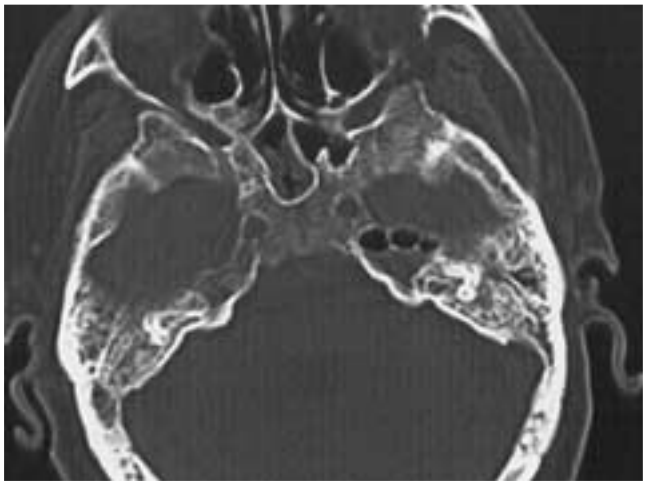

FIGURE 22-41 Petrous apex effusion. CT image shows bilateral mastoid fluid, with an air-fluid level in the left petrous apex and intact bony septa. Serous otitis was found at surgery, and petrous apex fluid was an incidental finding in an asymptomatic patient.

VIEW IMAGE

Copyright © 2003, Mosby, Inc. All rights reserved.

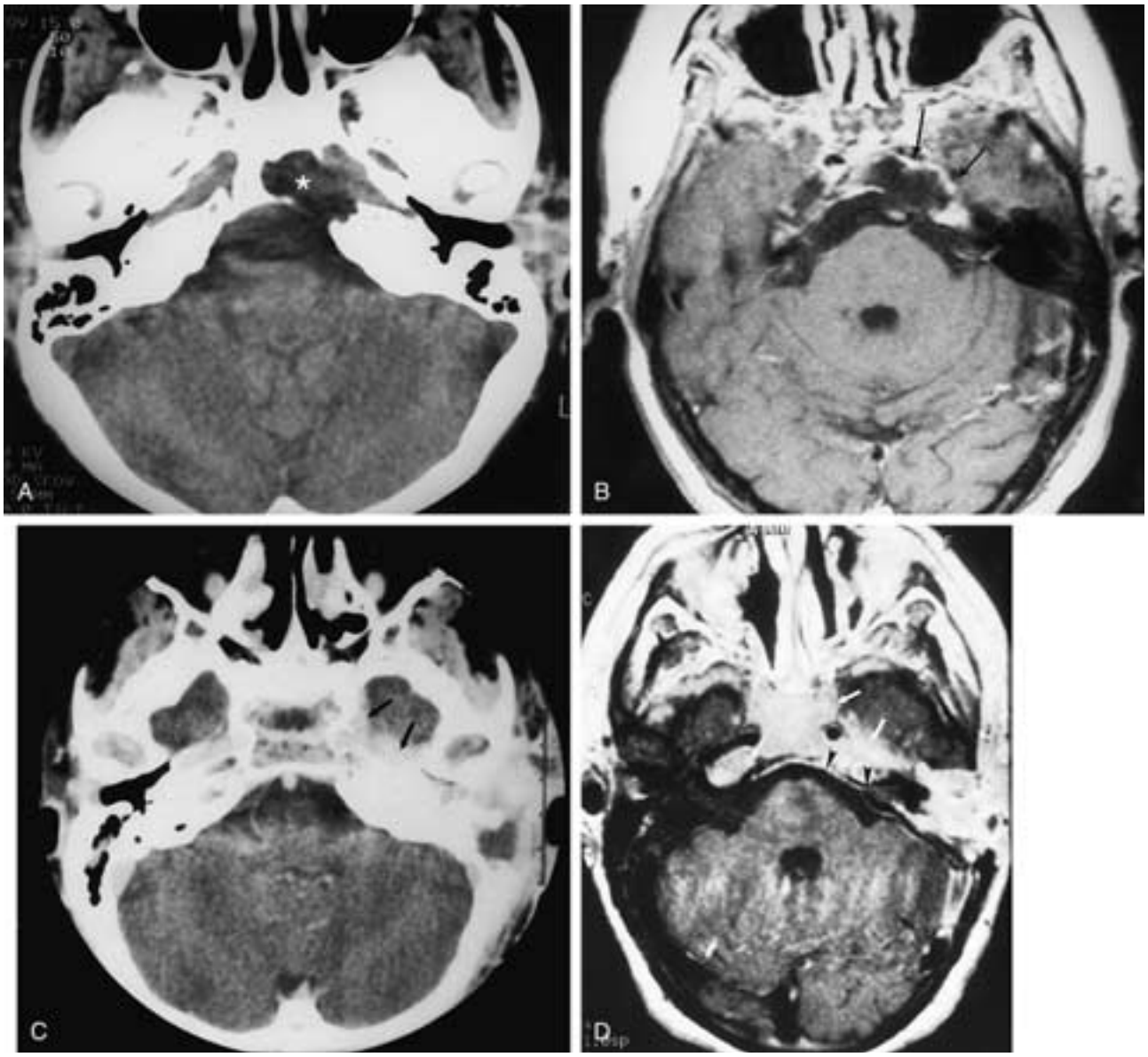

VIEW IMAGE

FIGURE 22-42 Petrous apicitis. **A**, Axial CT image, soft-tissue window. Debris is of low CT density (*asterisk*). **B**, Contrast-enhanced, T1-weighted axial image demonstrates contrast enhancement (*arrows*) along the periphery of the lesion, which is indicative of its inflammatory etiology. **C**, Different patient. Axial CT postcontrast scan shows enhancement (*arrows*) along the petrous apex extending to the cavernous sinus. The patient has had a mastoidectomy. **D**, T1-weighted postgadolinium image. Again, the enhancement (*arrows*) is seen extending along the petrous apex toward the cavernous sinus. There is enhancement (*arrowheads*) along the posterior fossa extending into the internal auditory canal. Comparison with the precontrast examination (not shown) showed that the high signal in the petrous apex represented enhancement. The opposite apex showed fat rather than enhancement.

Copyright © 2003, Mosby, Inc. All rights reserved.

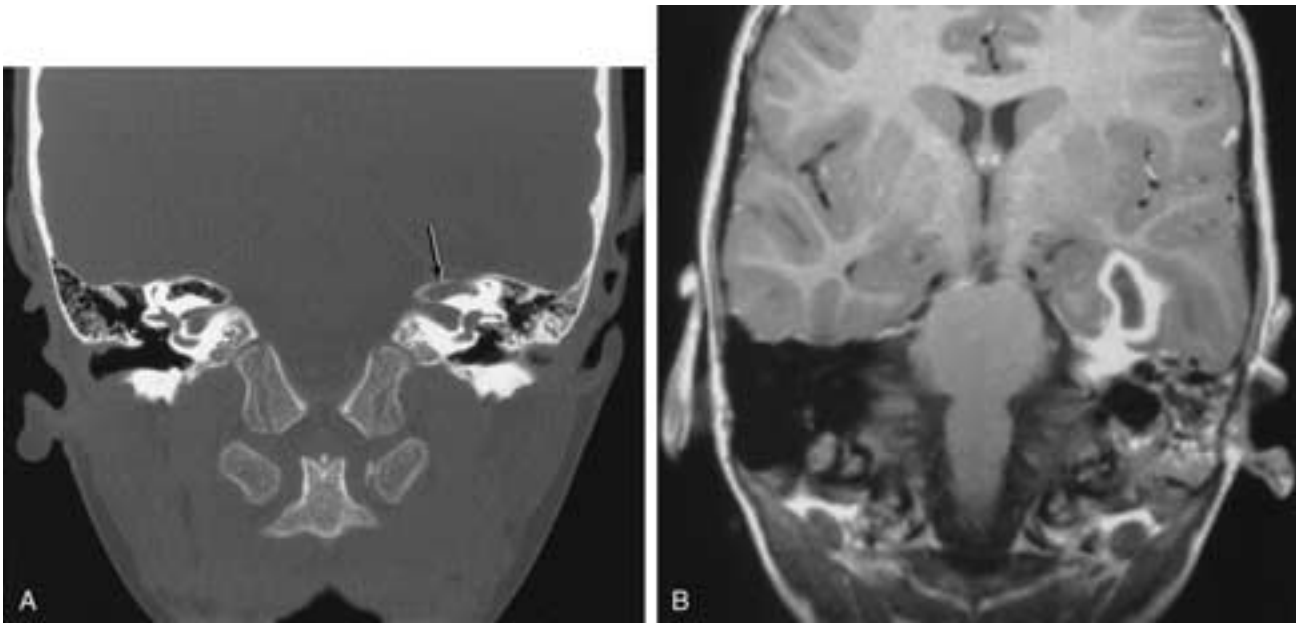

VIEW IMAGE

FIGURE 22-43 Petrous apicitis with intracranial abscess. **A**, Coronal CT image shows opacification of the left petrous apex with cortical erosion (*arrow*). **B**, T1-weighted, contrast-enhanced MR image reveals enhancement of the petrous apex and an adjacent temporal lobe abscess.

Complications of petrositis include meningitis, epidural abscess, brain abscess, and venous sinus thrombosis (Fig. 22-43). The sigmoid sinus, cavernous sinus, and jugular vein are at risk because of their proximity to the petrous apex.[108]

Cholesterol Granuloma, Mucocele, and Cholesteatoma

The three most common expansile lesions to arise within the petrous apex are the cholesterol granuloma (cholesterol cyst), the cholesteatoma, and the rare mucocele. The cholesterol granuloma is six times more common than the cholesteatoma.[118, 119]

Mucoceles of the petrous apex and paranasal sinus have a similar pathophysiology. Obstruction of air cells occurs while there is continued mucosal secretion of mucus. As a result, the involved sinus, or air cells, become remodeled and expanded. This is an unusual lesion of the petrous apex, probably because there are so few mucous glands.

Cholesterol granuloma (CG) (or cholesterol cyst) is an expansile, erosive lesion that occurs in the middle ear, mastoid, or petrous apex.[10] It develops as a result of obstruction that leads to a repetitive cycle of hemorrhage and granulation tissue formation.[120]

Patients with CG often have a history of purulent or serous otitis media and allergies, and there is impairment of ventilation in the petrous air cells. CG is a foreign body giant cell reaction to cholesterol deposits that occur in obstructed, fluid-filled air cells in the temporal bone. Microscopically, the CG contains numerous clefts of cholesterol crystals surrounded by histiocytes, round cells, macrophages, and many small, often pathologic blood vessels. These fragile blood vessels are prone to rupture, producing contiguous areas of new and old hemorrhage.[10, 46] CG can be thought of as a hemorrhagic mucocele. CGs are lined by fibrous connective tissue and not keratinized stratified squamous epithelium, as are cholesteatomas.[121]

It is believed that the obstruction of the petrous air cells leads to negative intraluminal pressure, which in turn causes rupture of the fragile vessels that line the air cells. The resulting hemorrhage and blood products, and the reaction to them, are the pathophysiologic basis of the CG.

CG occurring within a mastoidectomy cavity has been variously referred to as a chocolate cyst or a blue-domed cyst. If the TM has healed and a history of chronic otitis media is not elicited, otoscopically a CG in the middle ear may mimic a vascular mass such as an aberrant internal carotid artery, an exposed dehiscent jugular bulb, or a paraganglioma.[46, 122] The CT appearance is that of a nonspecific soft-tissue density. The MR appearance of high signal intensity on all sequences, secondary to the presence of extracellular methemoglobin, is diagnostic (Fig. 22-44).[123, 124] Frequently, there are areas of low signal as well, representing hemosiderin.

Petrous apex effusions with high T1 signal intensity may be confused with CG. CT is necessary to demonstrate the nonexpansile air cell opacification with intact bone septation.

Cholesteatoma of the petrous apex may be primary, arising from epithelial rests, or acquired.[119] The histologic findings are identical, and most of these lesions are primary in etiology.[108]

On occasion, aggressive middle ear cholesteatomas can spread from the middle ear into the pneumatized petrous apex. They do so by detouring around the bony labyrinth, following pathways of least resistance: infralabyrinthine, anterosuperior, and posterosuperior air tracts (Fig. 22-45).[89,124] They may also expand and extend along the facial nerve canal.[108]

Copyright © 2003, Mosby, Inc. All rights reserved.

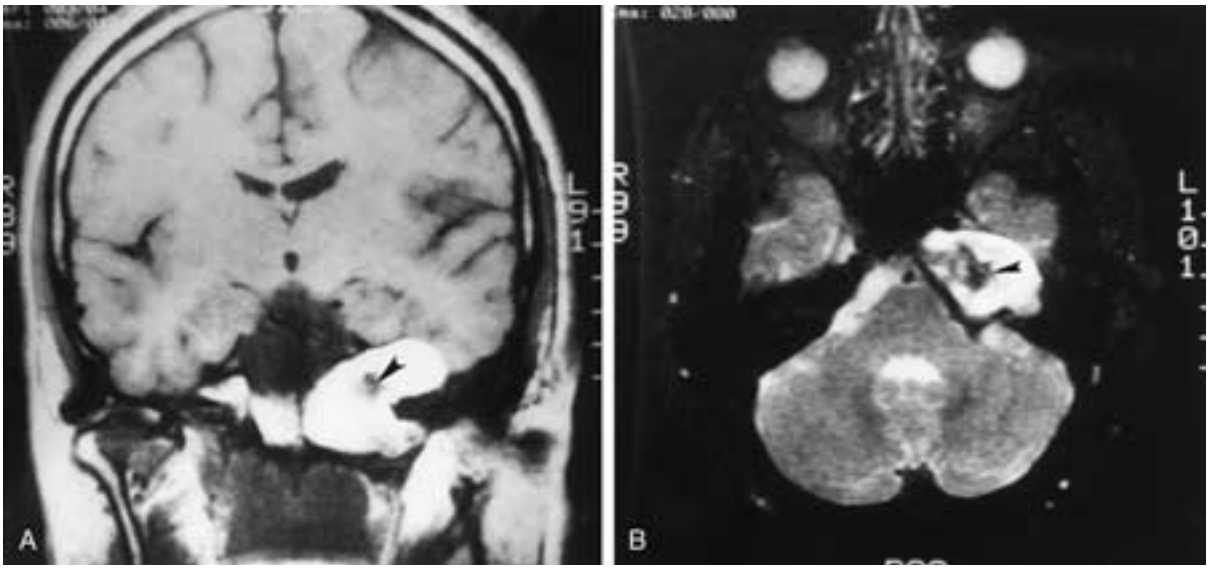

VIEW IMAGE

FIGURE 22-44 Cholesterol granuloma. **A**, Coronal T1-weighted image without contrast shows the high signal expansile lesion in the petrous apex. An area of low signal (*arrowhead*) within the abnormality is believed to represent hemosiderin. **B**, Axial T2-weighted image shows the high signal of the cholesterol cyst. Again, the low signal (*arrowhead*) represented hemosiderin.

On CT, a cholesteatoma is a smooth-walled, expansile lesion with a density slightly lower than that of brain. On MR, the lesion has a similar signal intensity to brain (low to intermediate signal intensity on T1-weighted images and higher signal intensity on T2-weighted images). This pattern distinguishes cholesteatoma from CG, which is bright on both T1- and T2-weighted images.[108] The differential diagnosis of a smooth-walled, expansile lesion of the petrous apex includes a petrous carotid aneurysm and a meningocele (Fig. 22-46). Apex meningoceles are seen as fluid-filled cavities in the petrous apex. There may be slight expansion. On CT a meningocele can mimic a cholesterol

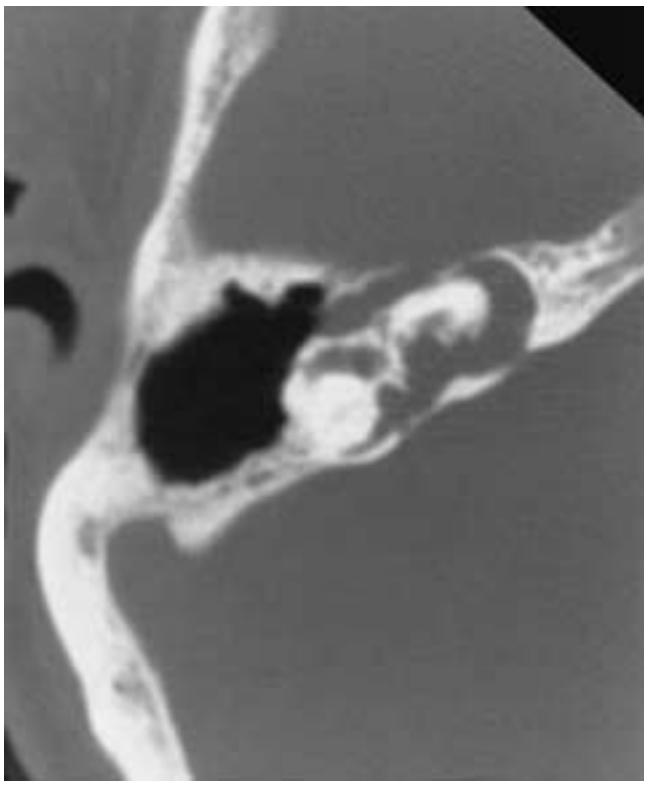

FIGURE 22-45 Cholesteatoma of the petrous apex. Mastoidectomy with recurrent cholesteatoma that has extended into the petrous apex from the middle ear.

VIEW IMAGE

Copyright © 2003, Mosby, Inc. All rights reserved.

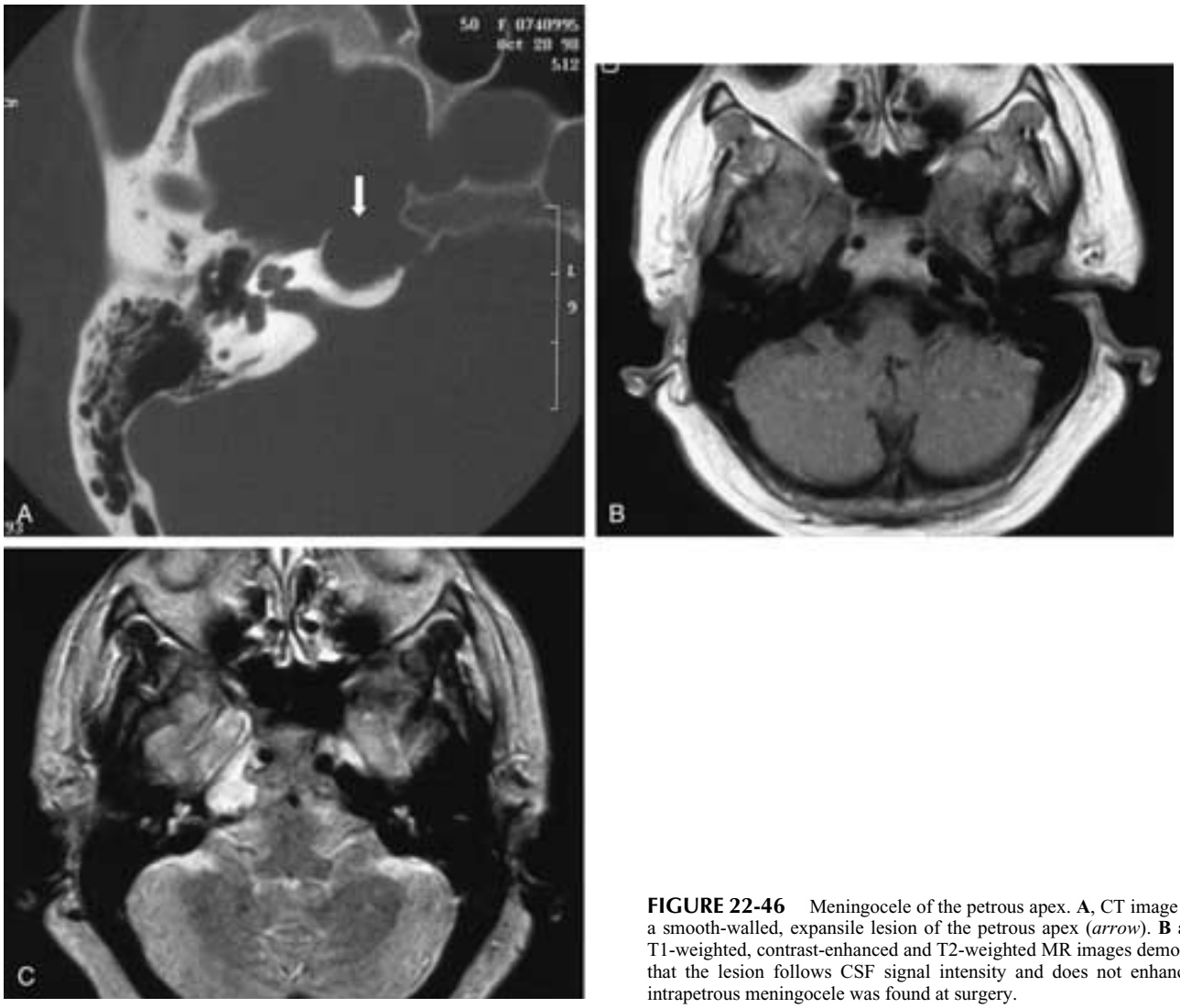

FIGURE 22-46 Meningocele of the petrous apex. **A**, CT image shows a smooth-walled, expansile lesion of the petrous apex (*arrow*). **B** and **C**, T1-weighted, contrast-enhanced and T2-weighted MR images demonstrate that the lesion follows CSF signal intensity and does not enhance. An intrapetrous meningocele was found at surgery.

VIEW IMAGE

granuloma but with MR imaging signal follows CSF exactly. T1-weighted images show low signal rather than the high signal characteristic of a cholesterol granuloma or cyst. These meningoceles often connect to Meckel's cave and will fill with contrast injected intrathecally.

INNER EAR

Labyrinthitis

Labyrinthitis implies an inflammatory process involving the membranous labyrinth.[10, 125–127] The labyrinth may be involved as part of a systemic disease or as the primary target of an invading agent.[128] Labyrinthitis may be classified according to its etiology as viral, bacterial, luetic, posttraumatic, or autoimmune[129, 130] (Table 22-5). Another classification is based on the portal of entry of the offending agent and subdivides labyrinthitis into tympanogenic, meningogenic, hematogenic, and posttraumatic categories.[10] Labyrinthitis is most commonly the result of a viral infection.[23, 109]

Bacterial Labyrinthitis

Bacterial labyrinthitis is an unusual complication of acute infection of the middle ear (tympanogenic labyrinthitis). The labyrinth connects with the middle ear via the oval and round windows, and breaching of the round window membrane is often implicated as the course of spread of middle ear infections. Labyrinthitis also may occur secondary to a labyrinthine fistula, which most commonly occurs at the level of the lateral semicircular canal and is usually the result of a cholesteatoma. Most often, labyrinth involvement is a reaction to bacterial endotoxins rather than bacterial invasion.

Table 22-5
LABYRINTHITIS CLASSIFICATION

Viral
Bacterial
Luetic
Posttraumatic
Autoimmune

Copyright © 2003, Mosby, Inc. All rights reserved.

Bacteria may reach the cochlea from the subarachnoid space (meningogenic labyrinthitis), and meningogenic labyrinthitis is often bilateral.[10] Bacterial labyrinthitis with profound hearing deficit occurs in about 10% of patients with bacterial meningitis. Vestibular neuritis, producing intense vertigo, is commonly thought to also have an infectious origin.[131]

Medially the labyrinth potentially communicates with the CSF spaces via the cochlear aqueduct and the IAC. The cochlear aqueduct arises in the basal turn of the scala tympani near the round window, and ends caudal to the porus acousticus and medial and cranial to the jugular fossa.[128] Bacterial meningitis invasion is believed to occur via either the cochlear aqueduct or the small perforations in the fundus of the IAC (lamina cribrosa) that transmit the cranial nerves. Pathogens include *Haemophilus influenzae*, *Neisseria menigitidis*, *Streptococcus pnemonniae*, *Escherichia coli*, *Proteus*, *Listeria moncytogenes*, and *M. tuberculosis*.[128] Ototoxic antibiotics used to manage infection may also contribute to auditory and vestibular symptoms.

Infectious processes also can be transmitted to the membranous labyrinth via a hematogenous route through the cochlear vasculature. This is referred to as hematogenous labyrinthitis.[10] These cases are usually viral in nature, and mumps and measles often have been implicated. Syphilis, tuberculosis, and other bacterial infections also can cause hematogenic labyrinthitis.

Posttraumatic labyrinthitis occurs in the context of previous injury, especially when a fracture is present. Iatrogenic tympanogenic labyrinthitis can occur after middle ear surgery. Clinically, there is sensorineural hearing loss and vertigo.

Regardless of the etiology, the MR imaging finding in labyrinthitis is contrast enhancement of the normally nonenhancing, fluid-filled spaces of the labyrinth[23, 24, 125, 132] (Fig. 22-47). There also is an excellent correlation between such enhancement and the presence of clinical symptoms.[132]

A precontrast T1-weighted image should be obtained because of the importance of distinguishing enhancement of labyrinthitis from intralabyrinthine hemorrhage. In cases of hemorrhage, the normal low labyrinthine T1-weighted signal intensity is replaced by a high signal intensity due to the presence of methemoglobin.[133] Such hemorrhage may be due to labyrinthitis but more commonly results from coagulopathy, neoplasm, or trauma. Intralabyrinthine hemorrhage is also associated with barotrauma, sickle cell disease, and tumor fistulization.[134, 135] T1 shortening may also be produced by proteinaceous fluid.

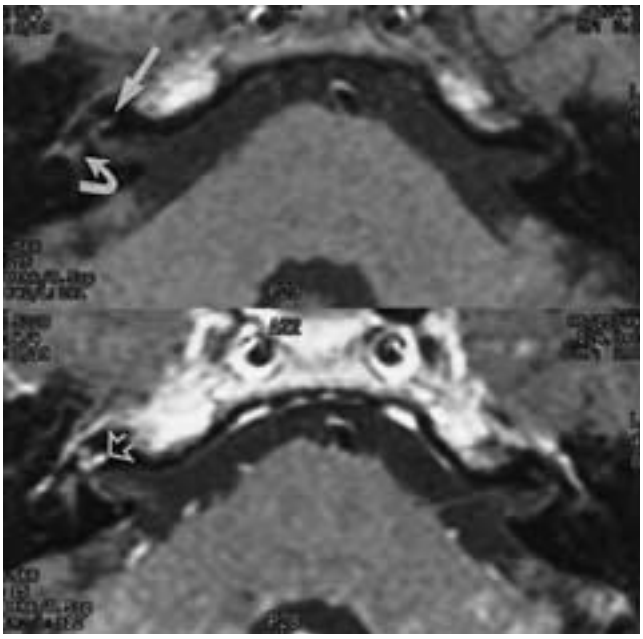

FIGURE 22-47 Labyrinthitis. T1-weighted images before (top) and after (bottom) gadolinium enhancement. Four weeks after trauma, this 21-year-old man had persistent hearing loss in the right ear. Note the mild hyperintensity of the right cochlea (*arrow*) and vestibule (*curved arrow*) on the unenhanced image. There is marked contrast enhancement of the cochlea (*open arrow*). There is normal bilateral enhancement of the tympanic segment of the facial nerve.

VIEW IMAGE

Viral Labyrinthitis

Viral infection of the labyrinth may be a cause of sudden sensorineural hearing loss (SNHL), and damage to the inner ear involves the organ of Corti and the vestibular labyrinth. There is contrast enhancement on MR images caused by breakdown of the normal blood-endolymph barrier.[130] Viral labyrinthitis may be due to a direct viral insult or may be associated with an immune response to the invading pathogen.[136]

Viral labyrinthitis is the most common cause of delayed hydrops syndrome. Meniere's disease is considered a form of delayed endolymphatic hydrops occurring in a normal ear that perhaps has suffered a prior subclinical viral insult. Vestibular atelectasis and idiopathic sudden deafness may also have a viral etiology.

Perinatal Conditions

Every year, several thousand infants are born with impaired hearing or deafness. At least 18% of these cases are caused by a proven congenital viral infection, and a greater number are suspected of having an infectious etiology.[131] Congenital cytomegalovirus (CMV) and rubella are the most widely recognized prenatal viral infections associated with perinatal complications including hearing loss.

Cytomegalovirus Infection

CMV is the most common congenital infection in the United States, occurring in 1% to 2% of live births. More than 95% of these infections are clinically silent. CMV is also the leading cause of human congenital viral infection and hearing loss, and it causes progressive hearing loss in children and sudden deafness in adults. Between 1% and 5% of infants infected with CMV develop cytomegalic inclusion disease, which damages the liver, spleen, brain, eye, and inner ear.[131]

Rubella

Maternal rubella during the first trimester places the fetus at the greatest risk of hearing loss and congenital infection. Rubella is responsible for multiple congenital malformations, including cardiac anomalies, vision loss, and developmental delay.[131]

Copyright © 2003, Mosby, Inc. All rights reserved.

Mumps

Mumps is caused by a paramyxovirus and is transmitted by saliva via the respiratory tract. Clinical manifestations include parotitis, salivary adenitis, pancreatitis, thyroiditis, polyarthritis, and myocarditis. Complications include epididymoorchitis in postpubertal males, prostatitis, nephritis, and meningoencephalitis. Hearing loss is usually unilateral (80%) and develops toward the end of the parotitis.[131] The hearing loss is usually permanent. Vestibular symptoms also occur and tend to resolve over several weeks.

Varicella Zoster Virus

Varicella zoster is an exclusively human virus of the herpes family that produces chickenpox (varicella). The virus can become latent in cranial nerves and dorsal root ganglia, and reactivates decades later to cause herpes zoster (shingles) and postherpetic neuralgia.[137]

Herpes zoster oticus, or Ramsay-Hunt syndrome, results from reactivation of latent virus within the geniculate ganglion of the facial nerve. The latent virus lingers in dorsal roots and can be reactivated by systemic disease, immunosuppressed states induced by therapy, or aging. The first symptom is burning pain in the ear, followed 1 to 4 days later by vesicular eruption on the auricle and external auditory canal in the area of sensory innervation of the facial nerve. Facial paralysis, hearing loss, and vertigo may occur singly or in combination. About one-half of patients have a persistent deficit with facial motor disturbance, and a few sustain complete paralysis. Vestibular symptoms include mild unsteadiness to severe vertigo with nausea and vomiting. Auditory symptoms consist of tinnitus and SNHL.

Enhancement on imaging of the seventh and eighth cranial nerves, the membranous labyrinth, and the pontine facial nerve nucleus may occur in this condition (Fig. 22-48).[138–141] There can also be slight enlargement of the nerve in the lateral aspect of the internal auditory canal.

Measles

Rubeola is a paramyxovirus that causes the clinical syndrome of measles with rash, conjunctivitis, and buccal mucosal lesions called Koplik spots. SNHL is abrupt in onset, is usually bilateral, and occurs at the same time as the macular skin rash. Hearing loss is permanent, and 70% of affected patients have abnormal vestibular responses. Prior to the introduction of measles vaccine, rubeola accounted for 3% to 10% of acquired deafness in children.[131] Pathologic findings include severe degeneration of the organ of Corti, the spiral ganglia, and the vestibular sense organs.

Measles encephalitis occurs once in every 600 to 1000 cases. Subacute sclerosing panencephalitis is a progressive neurologic disorder that is usually fatal. Typically, onset occurs months to years after an attack of measles.

Otosclerosis is also associated with measles. It has been demonstrated that the lytic phase of otosclerosis (otospongiosis) is related to the host's ongoing immunologic response to measles. Under influences that are not yet well understood (e.g., estrogens), the osteolytic process is arrested and changed to osteoblast activity accompanied by new bone formation. If the process takes place within the area of the oval window, it results in fixation of the stapes and conductive hearing loss. When the otosclerotic process is restricted to the cochlea, clinical signs are not as well defined.[142–146]

Labyrinthitis Ossificans

Labyrinthitis ossificans (sclerosing labyrinthitis) is the pathologic ossification of the bony labyrinth and cochlea that occurs as the final product of the repair process following a destructive or inflammatory insult. The most common cause of labyrinthitis ossificans is suppurative bacterial labyrinthitis.[147, 148] Other causes of labyrinthitis ossificans include viral labyrinthitis, advanced otosclerosis, trauma, autoimmune inner ear disease, occlusion of the labyrinthine artery, leukemia, and tumors of the temporal bone.[149]

The progression of suppurative labyrinthitis to labyrinthitis ossificans is divided into three stages. The acute phase is characterized by purulence and a serofibronous exudate in the perilymphatic spaces. In the second stage, there is fibroblastic proliferation, resulting in fibrosis. The third stage includes osteoid deposition and osteoneogenesis.[147]

The most common location for fibrosis and new bone formation in the cochlea is the basal turn region of the scala tympani near the round window.[149] Ossification generally progresses from the basal turn to the cochlear apical turn[150] (Fig. 22-49).

As the membranous labyrinth is replaced by fibrous tissue, CT findings are minimal and consist of an ill-defined

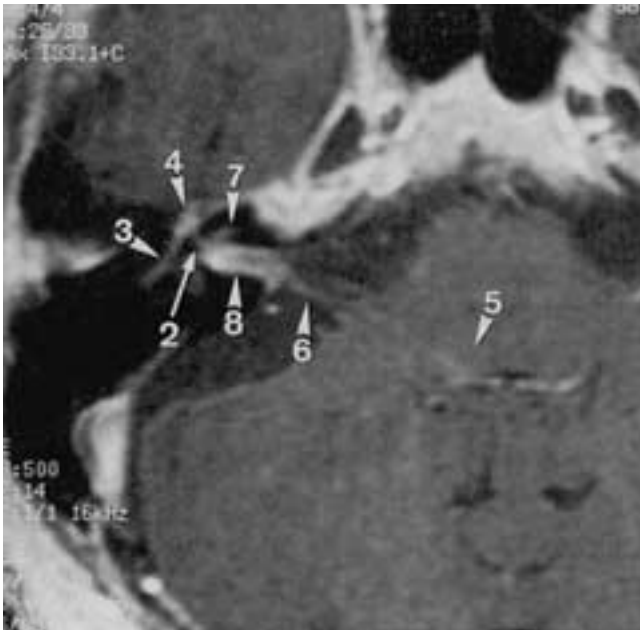

FIGURE 22-48 Ramsay-Hunt syndrome (herpes zoster oticus). A 58-year-old man with acute onset of complete peripheral facial nerve palsy, hearing loss, and vertigo for 28 hours. Postcontrast axial T1-weighted image shows abnormal enhancement of the right facial nerve in the labyrinthine (*2*) segment and normal enhancement of the tympanic (*3*) segment. There is abnormal enhancement of the geniculate ganglion (*4*), the pontine facial colliculus (*5*), the vestibulocochlear nerve (*6*), and the basal turn of the cochlea (*7*). There is also abnormal enhancement of the meninges in the internal auditory canal (*8*). (Reprinted with permission from Sartoretti-Schefer S, Kollias S, Valavanis A. Ramsay-Hunt syndrome associated with brain stem enhancement. AJNR 1999;20(2):278–280.)

VIEW IMAGE

Copyright © 2003, Mosby, Inc. All rights reserved.

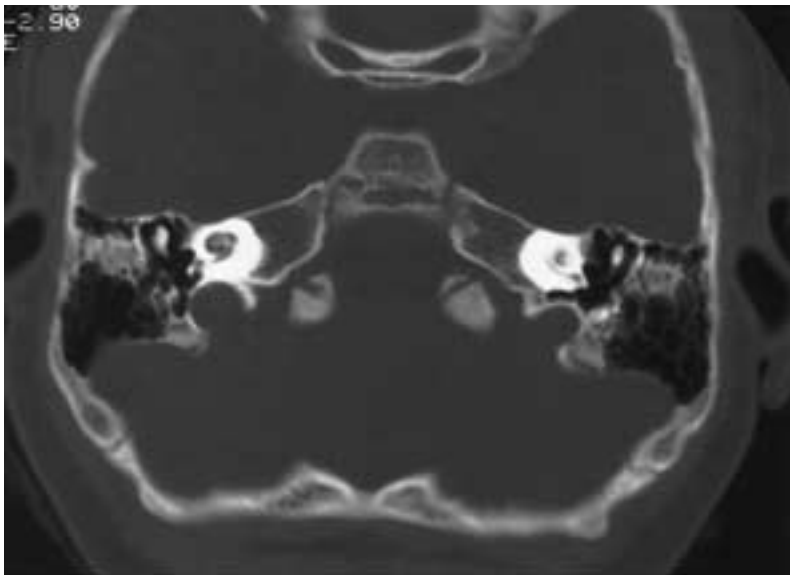

FIGURE 22-49 Labyrinthitis ossificans. Axial CT shows new bone formation partially obliterating left cochlea.

VIEW IMAGE

haziness of the membranous labyrinth. However, high-resolution, T2-weighted, fast spin-echo images show loss of normal hyperintensity of the fluid in the membranous labyrinth[151] (Fig. 22-50). The end result is labyrinthine ossification that is easily demonstrated by CT. This process of replacement of fibrous tissue with bone takes place over a period of months to years.[152, 153] Severe labyrinthitis ossificans results in total ''white-out'' of the membranous labyrinth (Fig. 22-51) and the presence of signal void in the labyrinth on T2-weighted images. This appearance may be confused with that of congenital otic dysplasias. The key imaging differential point is the contour of the otic capsule, which is reduced in congenital deformity and maintained in labyrinthitis ossificans[24, 151, 154, 155] (Fig. 22-52). The identification of fibroosseous replacement of the cochlea is of paramount importance when cochlear implantation is contemplated.

Otosyphilis

Syphilis is caused by the spirochete *Treponema pallidum*. Primary acquired syphilis is manifest clinically by a chancre. Secondary acquired syphilis is marked by a cutaneous rash, mucocutaneous lesions, lymphadenopathy, and fever. Tertiary syphilis begins 3 to 10 years after the original infection. Skin, bone, visceral, heart, and central nervous system involvement can occur.

Congenital syphilis, caused by intrauterine infection, is associated with hearing loss in 25% to 38% of patients.

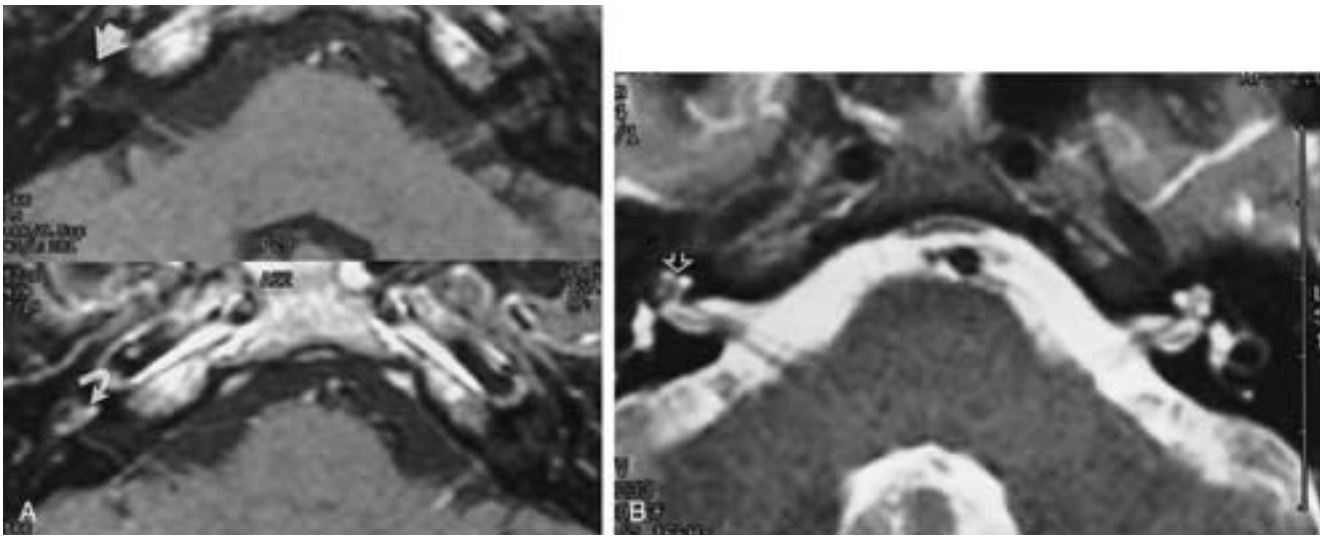

VIEW IMAGE

FIGURE 22-50 Labyrinthitis ossificans. **A**, T1-weighted axial images before (top) and after (bottom) gadolinium enhancement show mild hyperintensity of the cochlea on the unenhanced image (*arrow*), with intense enhancement after gadolinium enhancement (*curved arrow*). **B**, T2-weighted axial MR image demonstrates replacement of the normal bright signal of the membranous labyrinth (*open arrow*).

Copyright © 2003, Mosby, Inc. All rights reserved.

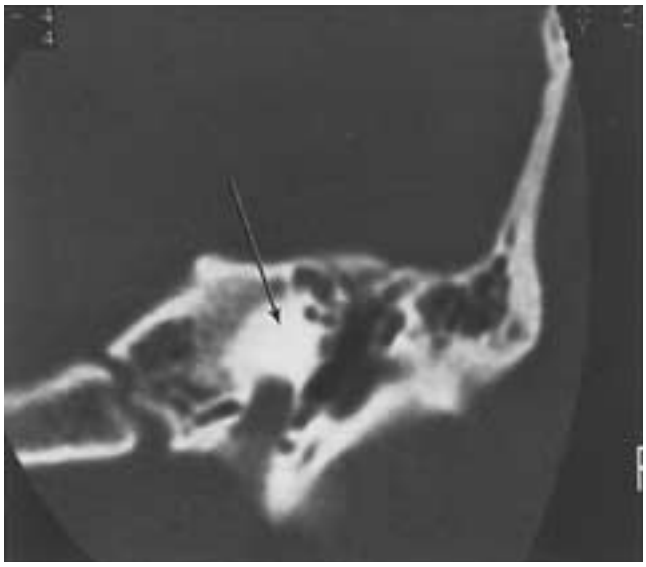

VIEW IMAGE

FIGURE 22-51 Labyrinthine ossification. Coronal image demonstrates complete ossification of the membranous labyrinth, with resultant absence of delineation of the cochlear turns.

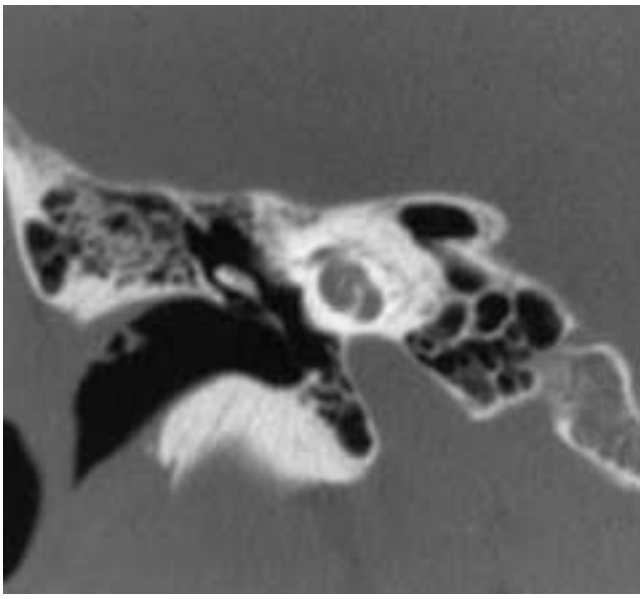

FIGURE 22-53 Otosyphilis. Note the bone destruction and new bone formation surrounding the cochlea.

VIEW IMAGE

Clinical manifestations include destructive lesions of the nose (saddle nose), tibial periostitis (saber shins), interstitial keratitis, and dental injury (Hutchinson's teeth). Labyrinthine involvement can occur in congenital syphilis or in the secondary or tertiary stages of acquired infection.

On histopathology, a meningo-neuro-labyrinthitis is found in early infantile congenital syphilis and in the acute meningitides of secondary and tertiary syphilis. Osteitis of the temporal bone with secondary involvement of the membranous labyrinth occurs in late congenital, late latent, secondary, and tertiary acquired syphilis.[131]

Both Meniere's disease and congenital syphilis are known to produce progressive endolymphatic hydrops and have similar clinical expressions. Clinical findings include (1) severe episodic vertigo, (2) fluctuating hearing loss temporally related to vertiginous attacks, (3) low-frequency hearing loss in the initial stages, and (4) flat audiometric patterns in later stages of disease.

The assumption is that these symptoms are the result of overaccumulation of endolymph, with episodic features caused by rupture of the walls of the membranous labyrinth.[10] Vertigo and nystagmus provoked by exposure to high-intensity sound, known as Tullio's phenomenon, can occur in association with congenital syphilis.[10] Tullio's phenomenon may be caused by the development of a third mobile window within the bony labyrinth that permits transmission of vibration to the vestibular apparatus. The first two mobile windows are the oval and round windows. Under normal physiologic conditions, sound pressure is transmitted to the stapes through the oval window and is dissipated at the round window. Dehiscence of bone in the labyrinth creates an alternative path for dissipation of sound through the vestibular apparatus and this allows motion within the perilymph of the semicircular canals, producing the sensation of vertigo.[156]

The osteitis of luetic otosyphilis is characterized by a permeative, or ''moth-eaten,'' demineralization seen on CT (Fig. 22-53). The differential diagnosis of demineralization of the cochlea includes otosyphilis, otosclerosis, Paget's disease, and osteogenesis imperfecta. The bone destruction of Paget's disease is usually diffuse and homogeneous. Bone involvement in otosclerosis and osteogenesis imperfecta is more plaque-like.[23]

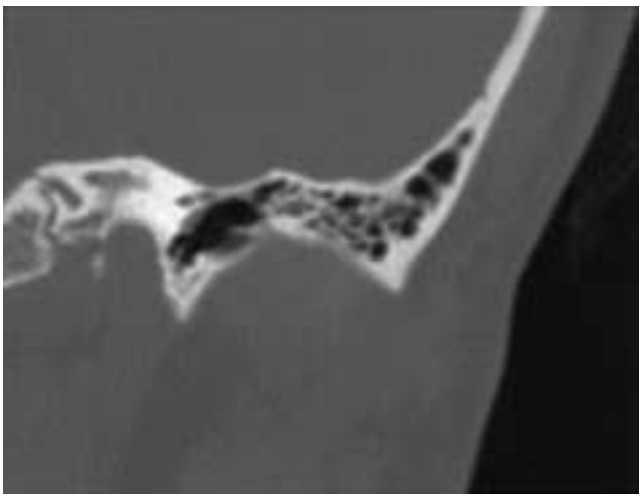

VIEW IMAGE

FIGURE 22-52 Cochlear aplasia. Note the absence of the cochlea in its expected location inferior to the facial nerve canal.

Lyme Disease

Lyme disease is caused by the spirochete *Borrelia burgdorferi*, which is transmitted by deer ticks. The initial manifestation is a rash, erythema migrans. Later symptoms include arthritis and myocarditis. Late CNS manifestations

Copyright © 2003, Mosby, Inc. All rights reserved.

consist of multiple neuropathies, including SNHL, and meningitis.[157, 158] Lyme disease is a common cause of facial paralysis, responsible for 50% of cases of acute facial paralysis in children.

Autoimmune Inner Ear Disease

The brain and labyrinth possess blood-brain and blood-labyrinthine barriers that isolate them from most systemic immune responses. Both the brain and the inner ear lack lymphatic drainage.[159, 160] The immuno-isolation of the inner ear can be violated because of the existence of resident lymphocytes around the endolymphatic sac or by entry of circulating leukocytes through the spiral modiolar vein.[159] Autoimmune disease of the ear may be the result of organ-specific disease, or the cochlea may be an innocent bystander of the immune response to other systemic autoimmune diseases, such as systemic lupus erythematosus, polyarteritis nodosa, rheumatoid arthritis, Cogan's syndrome, or polymyositis.[136, 159–161]

The inner ear is more commonly affected in women than in men and, when involved, there is a rapidly progressive SNHL that occurs over a period of several weeks. The hearing loss is usually bilateral (79%).

Autoimmune inner ear disease is characterized by fluctuating, progressive SNHL that responds to immunosuppressive drugs. Antigen-nonspecific screening tests include elevated erythrocyte sedimentation rate, positive autoantibodies (rheumatoid factors, anti-nuclear and anti-thyroglobulin antibodies), circulating immune complexes (IgG, IgM, IgA), and complement levels. Antigen-specific tests include the lymphocyte transformation test and the lymphocyte migration inhibition test. The Western blot analysis for cochlear antigens is also a promising test.[126, 161]

The following pathologic features characterize autoimmune inner ear disease: (1) acute labyrinthitis resulting in atrophy of inner ear tissues, including the sense organs and their supporting structures; (2) endolymphatic hydrops; (3) focal and diffuse proliferation of fibrous tissue and bone in the labyrinth; and (4) retrograde neuronal degeneration of the vestibular and cochlear branches of the eighth nerve.[151, 154, 162, 163]

Polyarteritis Nodosa

Polyarteritis nodosa is a systemic disorder affecting small and medium-sized arteries. The cochlea is rarely affected; SNHL may be the only presenting symptom. Arteritis involving the internal auditory artery, with ischemic changes in the vestibule and cochlea, has been reported, with fibrous tissue and osteoneogenesis in the basilar turns.[159]

Wegener's Granulomatosis

The clinical triad of Wegener's granulomatosis consists of necrotizing granulomas with vasculitis of the upper and lower respiratory tracts, focal necrotizing glomerulonephritis, and systemic vasculitis of the small arteries and veins. The disease is found almost exclusively in Caucasians, with a peak incidence in the fifth and sixth decades.

Wegener's granulomatosis frequently first presents with otologic symptoms that often involve the middle ear and mastoid. Otitis media and conductive hearing loss may result from obstruction of the ET, and SNHL is also common. Histopathologic studies suggest vasculitis involving the cochlear arteries and endolymphatic sac.[159, 161, 164]

Relapsing Polychondritis

Relapsing polychondritis is a disease of unknown etiology characterized by episodic inflammatory necrosis affecting the cartilaginous structures of the ears, nose, upper respiratory tract, and peripheral joints.[159] Airway obstruction may result from loss of cartilaginous support of the trachea. The pinna is red, tender, and edematous, with sparing of the external auditory canal. Vestibuloauditory symptoms point toward an immune-related disease.[161]

Systemic Lupus Erythematosus

Systemic lupus erythematosus has protean manifestations including polyarthralgia, arthritis, pleuritis, pericarditis, pneumonitis, myocarditis, nephritis, cranial nerve palsies, stroke, retinal degeneration caused by vasculitis, and inflammatory bowel disease. The otologic abnormalities include chronic otitis media with necrotizing vasculitis, progressive dysequilibrium, and SNHL.[159, 161]

Rheumatoid Arthritis

In patients with rheumatoid arthritis, both conductive hearing loss and SNHL can occur. The SNHL is probably related to circulating immune complexes.[161] The conductive hearing loss can be explained by middle-ear stiffness secondary to involvement of the synovial joints of the ossicles.

Cogan's Syndrome

Cogan's syndrome is a rare disease of young adults characterized by interstitial keratitis and audiovestibular dysfunction. The median age of onset is 22 years, and there is no gender predilection. Ocular symptoms include photophobia, lacrimation, and eye pain.[160] Vestibuloauditory symptoms are similar to those of Meniere's disease and are progressive.[161] Symptoms include vertigo, ataxia, tinnitus, nausea, vomiting, and hearing loss. Cogan's syndrome may be accompanied by a systemic vasculitis of large and medium-sized vessels, and aortitis usually leads to aortic insufficiency. Involvement of the major vessels arising from the aorta causes stenosis, occlusion, and aneurysm formation. Occlusion of the coronary arteries also can occur.[162]

Immunologic mechanisms play a role in the pathogenesis of this disease, and corticosteroids are the mainstay of therapy.[161] Patients with bilateral deafness may benefit from cochlear implants.

The temporal bone pathology in Cogan's syndrome shows changes that are similar to those observed in other autoimmune disorders (including polyarteritis nodosa, relapsing polychondritis, and autoimmune inner ear disease) associated with audiovestibular dysfunction. Formation of intralabyrinthine fibrous tissue is more frequent and precedes new bone formation. CT scans will detect bony obliteration, but MR will show soft-tissue replacement of the membranous labyrinth. On T2-weighted images, there is loss of the normal high signal intensity of the fluid-filled labyrinth. T1-weighted hyperintensity is attributed to hemorrhage, and contrast enhancement has been reported.[154]

Copyright © 2003, Mosby, Inc. All rights reserved.

VIEW IMAGE

FIGURE 22-54 Air in the vestibule. Axial image demonstrates a collection of air within the vestibule (*arrow*). This is of profound significance because it indicates a direct communication between the middle and inner ear.

Perilymph Fistula

Perilymph fistula, an abnormal communication between the inner ear and middle ear, can cause vertigo and hearing loss.[165] Though not an infection or inflammation, it is mentioned here because of its relationship to potential movement of infection from the middle ear to the inner ear and potentially to the CSF. The leakage of perilymph should be considered a type of CSF otorrhea and can result in meningitis.[166] Perilymph fistulas may be the result of trauma, surgery, or congenital anomalies. Common sites include the oval and round windows. These fistulas have also been called perilymphatic gushers and oozers, depending on the size of the defect. Patent cochlear aqueducts or small defects in the fundus of the IAC have been implicated as the cause of oozers, a milder welling type of flow. A gusher, a jet-like flow, is probably the result of a larger defect in the fundus of the IAC.[10, 167]

Clinically, a perilymph fistula should be suspected when a patient complains of sudden onset of vertigo after stress, such as barotrauma, head injury, exertion, or air bag trauma. Barotrauma occurring during descent while flying, forced Valsalva maneuver, nose blowing, or suppressed sneezing produces an implosive force on the labyrinthine windows. Lifting, straining, coughing, and sneezing can cause a dramatic increase in CSF pressure that is transmitted via the vestibule to the oval window annulus and the round window membrane. Fracture of the stapes footplate, producing a perilymph fistula, has been reported following suppressed sneezing and childbirth. Also implicated are postoperative complications of stapes surgery for otosclerosis.

There may be a congenital defect in the stapes footplate that occurs alone or in association with other anomalies such as Mondini's dysplasia. The perilymph fistula in Mondini's dysplasia is caused by congenital defects in the modiolus and oval window. The diagnosis of postoperative perilymph fistula is crucial to the surgeon, because repair must be planned to prevent labyrinthitis and possible meningitis. The CT diagnosis is difficult and depends on fluid dynamics within the vestibule. Unexplained dependent middle ear or mastoid fluid collections emanating from the oval window should be viewed with suspicion, and a pneumolabyrinth is obviously highly suggestive in this context (Figs. 22-54 and 22-55). Unfortunately, there may be no CT findings in these cases. Enhanced T1-weighted MR images may demonstrate diffuse enhancement of the membranous labyrinth, suggesting labyrinthitis. Segmental enhancement has also been identified at the site of the perilymph fistula, presumably within granulation tissue.[125, 129, 132]

Intralabyrinthine enhancement also may be secondary to a schwannoma.[168, 169] A schwannoma occurs most commonly in the vestibule and such enhancement is ordinarily quite intense, in contrast to the relatively faint contrast enhancement noted in patients with labyrinthitis. Neoplastic

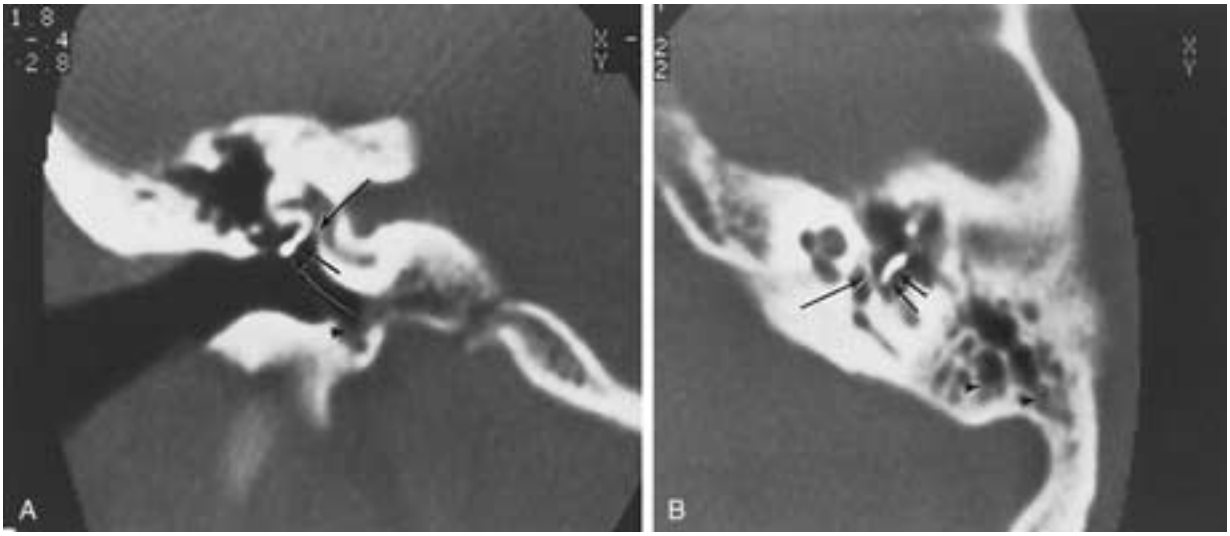

VIEW IMAGE

FIGURE 22-55 Perilymph fistula. Prosthesis (*double arrows*) is located superosuperficially to the otosclerotic oval window (*arrow*). Several fluid levels (*arrowheads*) are identified on both the coronal (**A**) and axial (**B**) images.

Copyright © 2003, Mosby, Inc. All rights reserved.

enhancement persists, and the symptoms are typically nonremitting.[126]

EXTERNAL EAR

External Otitis

External otitis is a common condition also known as swimmer's ear. The condition is caused by many pathogens, and when associated with fungal growth, the condition is called otomycosis. Rarely, first branchial cleft anomalies are the cause of chronic external otitis. First branchial cleft anomalies may appear as a parotid cyst or sinus tract that drains into the external auditory canal.[23, 170] Branchial cleft cysts are discussed further in Chapter 35.

The CT identification of abnormal soft-tissue debris in the external auditory canal (EAC) is not uncommon, is of variable clinical significance, and in most cases is histologically nonspecific. On CT, cerumen is often seen within the EAC as isolated areas of soft-tissue-density material. Simple otoscopic manipulation can cause transient mucosal thickening within the canal, which may cause imaging confusion unless such a history is available. Although the clinician can visualize granulation tissue or fibrous tissue, the medial extent of such debris is usually not apparent otoscopically. In these cases, CT may demonstrate continuity of the EAC disease with the middle ear.

Necrotizing External Otitis

Necrotizing external otitis (malignant external otitis) is an aggressive, resorptive osteomyelitis of the temporal bone (Fig. 22-56).[171–175] This is a disease of elderly diabetics with poor control of diabetes. Culture classically reveals *Pseudomonas aeruginosa*, although *Staphylococcus epidermidis* has also been implicated.[176] Necrotizing external otitis in patients with AIDS occurs in a significantly younger and nondiabetic population. *P. aeruginosa* is not the predominant pathologic organism. Other pathogens, such as *Aspergillus*, are found, and the outcome in AIDS patients is significantly worse than in immunocompetent patients.[177–179]

The term *malignant external otitis* was first coined by Chandler in 1968.[180] The word malignant was chosen to describe the high mortality associated with this disease prior to the availability of effective antibiotic therapy. Because this is an infection and not a malignant process, more appropriate pathophysiologic terms include *necrotizing external otitis* or the more inclusive description *skull base osteomyelitis*.[181] Patients often experience exquisite otalgia or deep pain, and symptoms may begin after irrigation of the external canal with tap water for impacted cerumen.[182]

P. aeruginosa is a gram-negative, motile aerobic rod that tends to proliferate in moist, devitalized tissue, particularly when host defenses are impaired.[183] The exact cause is obscure, although excessive moisture, hyperglycemia, and ischemic perichondritis all have been postulated. This organism produces a variety of endotoxins, exotoxins, neurotoxins, and destructive enzymes. Among the last, elastase and collagenase are the most significant because they allow invasion across fascial planes. The increased severity of this process in diabetic patients is presumably related to poor tissue microcirculation and defective chemotaxis of leukocytes.[182]

Necrotizing external otitis often begins in an insidious fashion at the osseous-cartilaginous junction as a focal area of ulceration and osteitis of the EAC. The TM is resistant to the infectious process, but the disease extends inferiorly via tiny clefts in the cartilaginous portion of the EAC, the fissures of Santorini, allowing access to the soft tissues beneath the temporal bone around the stylomastoid foramen and the infratemporal fossa. The infection may extend into the parotid gland, TMJ, soft tissues of the neck, and skull base.[181, 182] Involvement of the mastoid, middle ear, and petrous apex may also occur.

Facial palsy is a grave prognostic sign and may occur as a

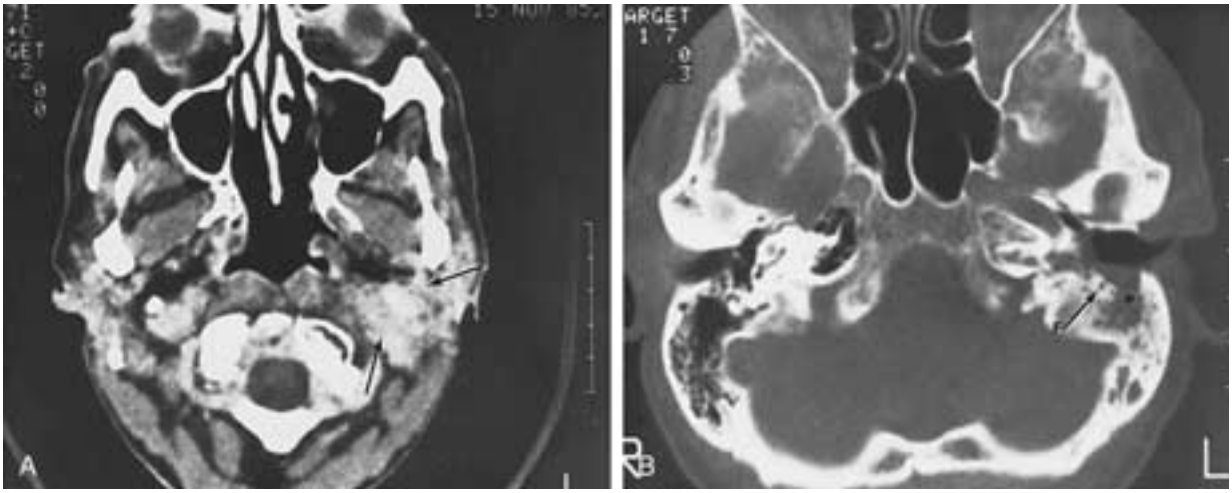

FIGURE 22-56 Malignant external otitis. **A**, Contrast-enhanced axial image demonstrates enhancing debris (*arrows*) in subtemporal regions surrounding the styloid process. **B**, More superior axial image targeted for bone demonstrates debris eroding into the mastoid (*asterisk*). The mastoid segment of the facial nerve canal (*arrow*) is intact.

VIEW IMAGE

Copyright © 2003, Mosby, Inc. All rights reserved.

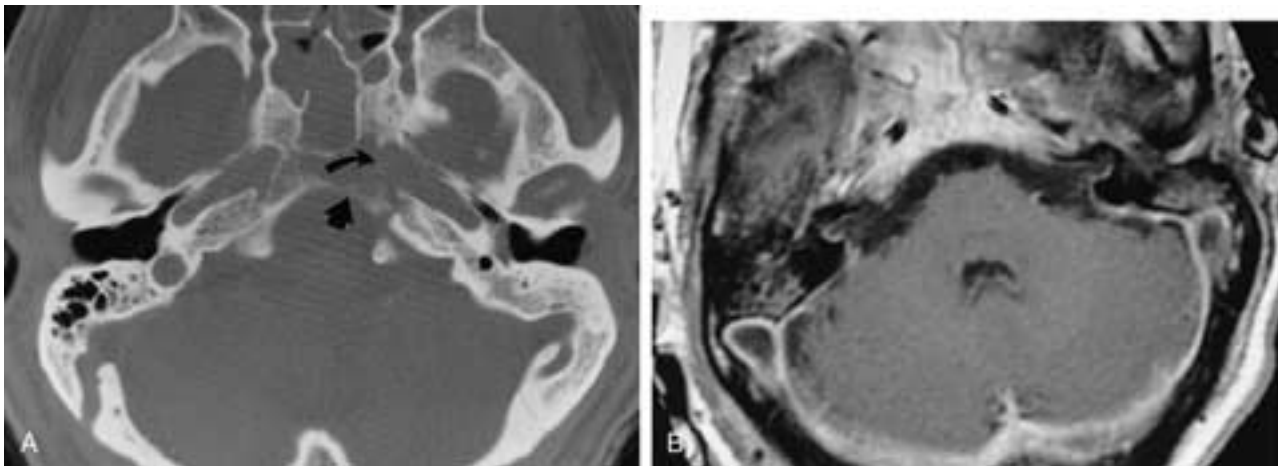

VIEW IMAGE

FIGURE 22-57 Skull base osteomyelitis secondary to sphenoid sinusitis. **A**, Axial CT image. There is opacification of the sphenoid sinus, thinning of the posterior wall of the sinus, and destruction of the clivus (*arrow*) and the petrous apex, with erosion extending into the internal carotid artery canal (*curved arrow*). **B**, T1-weighted axial postcontrast MR image shows enhancement of the clivus, petrous apices, and diffuse dural enhancement extending into the IACs.

result of mastoid destruction or, more commonly, as a result of subtemporal spread of infection to the stylomastoid foramen. Further medial extension can involve the nerves exiting the jugular foramen as well as the hypoglossal nerve. Intracranial involvement can result from extension through the petrooccipital (petroclival) synchondrosis and may be a preterminal event leading to the development of meningitis, abscess formation, infarcts, or sinus thrombosis.

Both CT and MR imaging provide excellent delineation of soft-tissue invasion in the subtemporal region and give accurate information about the status of the stylomastoid foramen. CT is needed for the evaluation of cortical bone and details regarding involvement of the middle ear, mastoid, and intratemporal bony facial nerve canal.[184–186] Because the soft tissues inferior to the external auditory canal are most often involved, CT or MR imaging in the coronal plane is advantageous to show alteration of the normal fat surrounding the canal as well as the fat planes beneath the more medial skull base. When intracranial pathology is suspected, MR imaging is superior to CT, and dural enhancement and abnormalities of the skull base medullary bone are best appreciated on MR images.[182] Because of its high sensitivity, radionuclide evaluation has a role in the initial diagnosis of this disease.[171]

Pathologically, there is a combination of osteoclastic bone resorption, active new bone formation, and bone necrosis. The differential diagnosis includes malignancy and osteoradionecrosis.

Osteomyelitis of the skull base is usually secondary to inadequately treated necrotizing otitis externa in diabetic or immunocompromised patients. Skull base osteomyelitis may also occur after surgical drainage of a mastoid infection, and rarely as a complication of a sinonasal infection, and there is an increased incidence associated with AIDS.[181, 187–191] Infection extending to the skull base foramina results in cranial nerve palsies, and these patients usually present with unremitting headache in the temporal region. A conductive hearing loss is another common symptom due to middle ear fluid secondary to ET dysfunction. A change in voice quality and dysphagia are usually the initial symptoms of vagal nerve involvement. In descending order of occurrence, abnormalities of cranial nerves 12, 11, and 9 follow, with associated difficulty with speech and swallowing and weakness of the shoulder.[189] Intense inflammation around the jugular fossa may also produce jugular vein and sigmoid sinus thrombosis.[190]

Although *Pseudomonas* is the usual pathogen in skull base osteomyelitis, *Aspergillus*, *Staphylococcus aureus*, *S. epidermidis*, *Proteus*, and *Salmonella* have also been implicated.

A technetium bone scan can identify osteomyelitis before bone destruction is identified on CT scans. Because bone repair may continue long after the infection has resolved, the technetium bone scan has limitations for therapeutic monitoring, as it will remain positive long after the osteomyelitis has cleared.[181]

More advanced cases demonstrate bone destruction and bone sequestration on CT (Fig. 22-57). Soft-tissue edema and abscess formation in the parapharyngeal space and nasopharynx can also occur. CT is of little use in determining resolution of the bone infection, as remineralization is a slow process and the destroyed bone may never return to a normal appearance.[181]

Although MR is superior to CT in the detection of marrow abnormalities and soft-tissue changes, MR is not useful in evaluating the response to therapy, as the marrow changes caused by inflammation may take up to 6 months to return to normal. Similarly, gallium-67 studies may also take up to 6 months to return to normal after successful therapy. Currently, CT and bone SPECT scintigraphy are the best methods for detecting osteomyelitis in areas of the skull that have little or no bone marrow. Indium (In-111) 111 WBC and Tc-99m MDP bone SPECT are best for detecting osteomyelitis in patients with cranial base alterations resulting from changes such as surgery.[187, 188] A combination of In-111 WBC and Tc-99m SPECT may be the best imaging approach to assess the posttherapeutic response, as abnormal findings revert to normal sooner with In-111 WBC

Copyright © 2003, Mosby, Inc. All rights reserved.

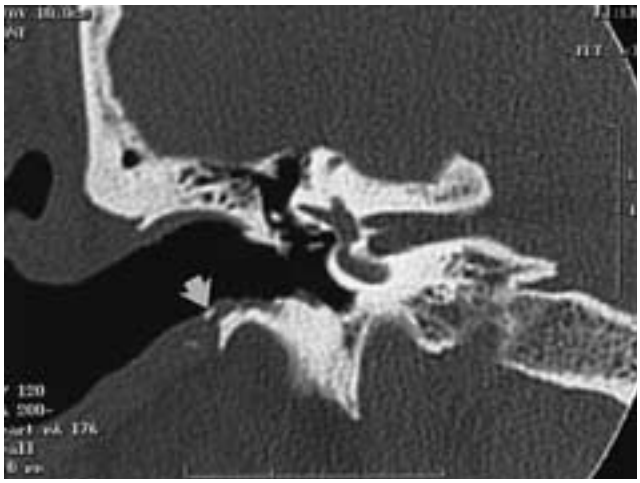

VIEW IMAGE

FIGURE 22-58 Osteoradionecrosis. There is destruction of bone in the EAC with a sequestrum (*arrow*).

scanning than they do with gallium, MR, or CT in successfully treated patients.[187] In-111 WBC scintigraphy may become normal while the patient is being treated with antibiotics, and a follow-up scan 4 weeks after completion of therapy may provide the most reliable assessment of the therapeutic outcome.[23]

Differential Diagnosis and Other Lesions

Osteoradionecrosis

SNHL and osteoradionecrosis are late sequelae of irradiation of the temporal bone. SNHL is due to atrophy of the membranous labyrinth and spiral ligament, with degeneration of the organ of Corti. Osteoradionecrosis is a slowly destructive process that may be confused with malignancy, osteomyelitis, or necrotizing external otitis. There is destruction of bone with sequestration[192] (Fig. 22-58). Symptoms of otalgia and persistent otorrhea begin as early as several months to as late as many years after radiation therapy.[193–196]

Malignancy

The pathology most commonly confused with necrotizing external otitis is malignancy. The malignancies involving the EAC may arise within the canal or extend to it from surrounding structures. The most common histologies are squamous cell and basal cell carcinomas and minor salivary gland carcinomas.[100, 197, 198] Melanomas, metastases, and gliomas are rare.

Squamous cell carcinoma, a disease primarily of the elderly, may originate in the canal or extend to it from the middle ear. In the latter circumstance, there usually is a long-standing history of chronic otitis media. Squamous cell carcinoma may simulate necrotizing external otitis with regard to symptoms of pain and ear drainage, otoscopic findings, and bone destruction on CT. Histologic examination is therefore mandatory in all patients with suspected malignant external otitis.[199]

Basal cell carcinoma invading the external auditory canal often originates in the postauricular sulcus. Neoplasms of salivary origin (i.e., mucoepidermoid carcinoma, adenoid cystic carcinoma) may originate in the parotid gland or may arise from minor salivary gland rests within the external canal or middle ear.

Tumors of Ceruminous Gland Origin

There are two types of sweat glands in the body: eccrine (which have a generalized distribution) and apocrine (which have a limited distribution). The apocrine glands located within the EAC are referred to as ceruminous glands. The normal cerumen produced in the EAC is a mixture of secretions from both ceruminous and sebaceous glands, and

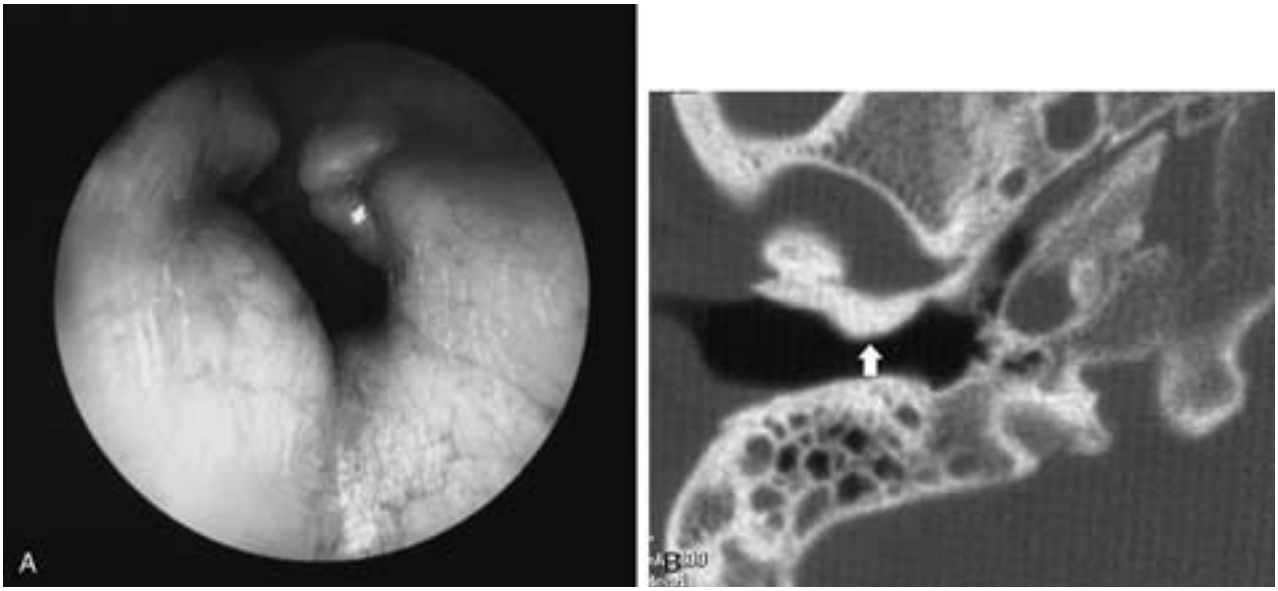

VIEW IMAGE

FIGURE 22-59 Exostosis in the EAC. **A**, Otoscopy. The EAC is nearly obliterated by multiple sessile exostoses. **B**, Axial CT image. Exostosis is a broad-based mass (*arrow*) in the EAC.

Copyright © 2003, Mosby, Inc. All rights reserved.

its acidic and chemical composition is thought to aid in avoiding infections.

The tumors of ceruminous gland origin include ceruminous adenoma, pleomorphic adenoma, adenoid cystic carcinoma, mucoepidermoid carcinoma, and ceruminous adenocarcinoma. Adenomas and pleomorphic adenomas are rare tumors of the EAC, with adenoma being more common. Both tumors occur in the fourth to sixth decades of life and can develop anywhere in the EAC. The CT findings of a soft-tissue mass in the EAC without bone destruction are nonspecific. Adenoid cystic carcinoma and adenocarcinoma are much more aggressive lesions.[23]

Exostosis and Osteoma

The most common benign ''neoplasm'' of the external canal is the exostosis.[200, 201] (Fig. 22-59). This lesion arises in the medial aspect of the osseous portion of the EAC, near the tympanic annulus, usually in patients with prolonged exposure to cold sea water or swimming pool water. As such, vasodilation is believed to play a causative role. Bilateral exostoses are common, the lesions are often broad based, and they usually arise along the tympanomastoid or tympanosquamous suture lines. Interestingly, they do not occur in African Americans.

Although clinically similar, the exostosis is distinct from an osteoma, which is much less common and usually unilateral. Osteomas are pedunculated bony growths, usually found lateral to the isthmus of the IAC (Fig. 22-60). Other temporal bone sites occur, in particular the mastoid.[23, 202] Although the mass is readily apparent on otoscopic examination, CT can define the entire extent of the lesion and evaluate middle ear disease.

Cholesteatoma and Keratosis Obturans

Keratosis obturans (KO) and external auditory canal cholesteatoma (EACC) both represent accumulations of exfoliated keratin within the EAC. Although there is controversy about the exact definitions, many believe that they are entirely different clinical and pathologic processes.[174, 175, 203]

FIGURE 22-60 Otoscopy. Osteoma is a pedunculated mass in the EAC.

VIEW IMAGE

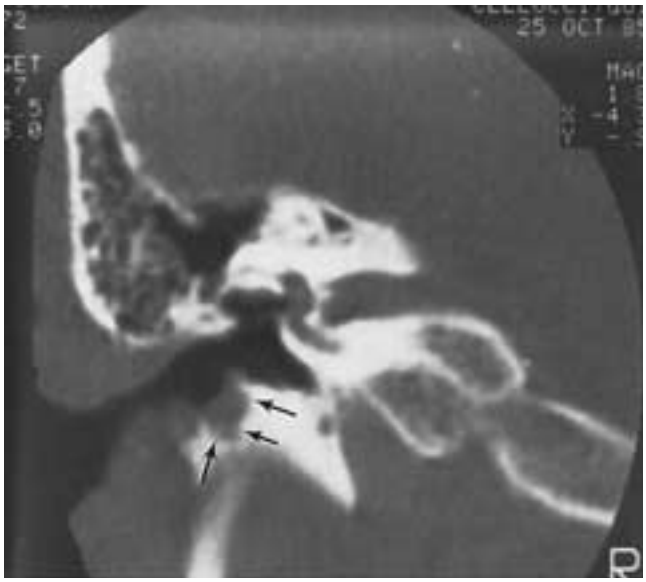

FIGURE 22-61 EAC cholesteatoma. There is a soft-tissue mass in the EAC. ''Punched-out'' erosions in the floor of the EAC are demonstrated on this coronal image (*arrows*).

VIEW IMAGE

Cholesteatomas occur almost exclusively in the middle ear and mastoid. However, cholesteatomas occasionally arise in the EAC in 0.1% to 0.5% of otologic patients.[204] Patients typically present between the ages of 40 and 75 with a history of persistent otorrhea and chronic dull otalgia. Otoscopic findings show erosion of the osseous EAC with squamous debris, granulation tissue associated with periostitis, and necrotic bone (Fig. 22-61). Sequestra may occur. The process is usually unilateral. Although the cause of cholesteatoma of the EAC is unknown, a periostitis of the bone of the canal is frequently implicated as the initial abnormality. Invasion of the squamous epithelium follows, and the cholesteatoma is formed. The location is typically along the posterior inferior wall of the canal just lateral to the TM. There may be an accumulation of keratin, giving a mass appearance with erosion of the canal wall, or the lesion may have the appearance of an ulcerated cavity lined by squamous epithelium. The cholesteatoma is considered to be a more localized lesion than the KO, which fills the entire canal with debris.

KO usually is diagnosed in patients under the age of 40 years who have a history of sinusitis or bronchiectasis. There often is severe pain and conductive deficit, but otorrhea rarely occurs. KO is often bilateral, associated with an abnormal TM, and heralded by a keratin plug and smooth widening of the canal on otoscopic inspection (Fig. 22-62). By comparison to the cholesteatoma, the keratin plug of KO fills the canal rather than extending into the wall of the canal, and the bony wall is expanded outward rather than destroyed. The pathogenesis of KO is unknown. One theory proposes that bronchiectasis may produce sympathetic reflex stimulation of ceruminous glands in the EAC, leading to hyperemia and the formation of the epidermal plug. Another theory suggests that abnormal pathways of epithelial migration are responsible.[205]

Copyright © 2003, Mosby, Inc. All rights reserved.

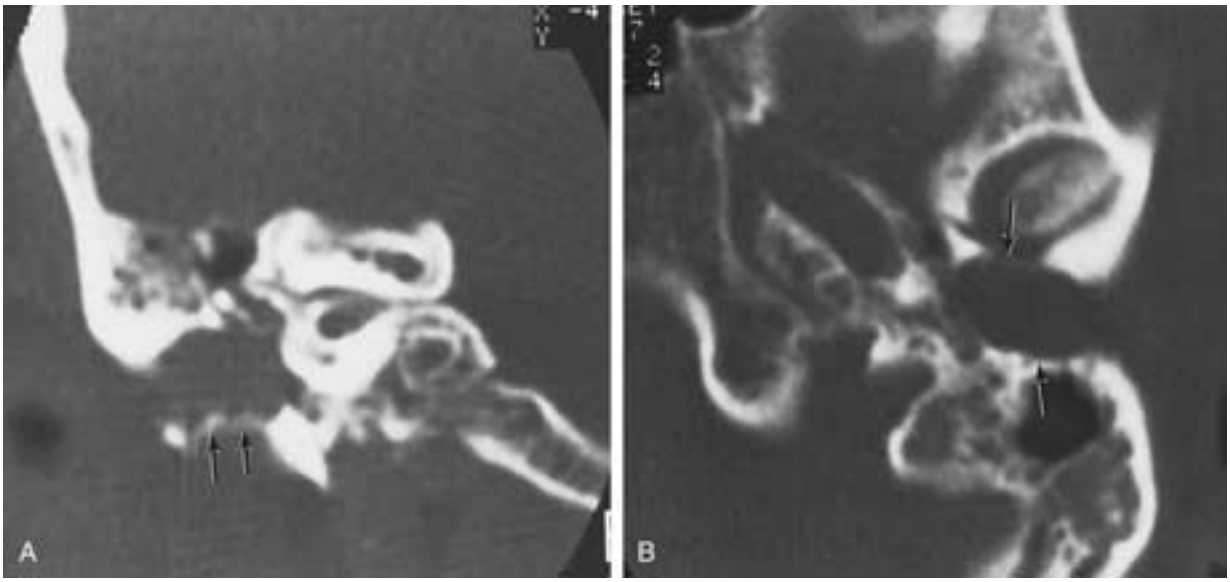

VIEW IMAGE

FIGURE 22-62 KO. Coronal (**A**) and axial (**B**) scans reveal smooth expansion and erosion of the canal wall (*arrows*).

CT is of value for determining the extent of disease and for aiding in the differentiation of these entities, as patients with KO may show gradual widening of the EAC with an intact smooth cortex, while patients with cholesteatoma tend to have an irregular invasion of bone. Because the mastoid segment of the facial nerve canal is located immediately adjacent to the posterior tympanic annulus, axial CT is well suited for determining the proximity of disease to this crucial structure.

POSTOPERATIVE TEMPORAL BONE

CT has become an indispensable tool for evaluating the postoperative middle ear and mastoid.[52, 53, 206, 207] This examination is especially helpful when the surgery was performed many years ago or by a surgeon other than the one referring the study. CT should be routinely recommended in the evaluation of the symptomatic postmastoidectomy patient. It is also wise to recommend that a baseline CT scan be obtained (with which future studies can be compared) in the recently operated asymptomatic patient. CT is also informative for evaluating the prosthetic stapedectomy and other forms of ossiculoplasty.[53, 103, 208]

Mastoidectomy

Regardless of the exact surgical approach (postauricular, endaural, transcanal), the object of surgery for chronic otitis media and cholesteatoma is to remove all diseased tissue while sparing as many normal structures as possible.[209]

A structured CT evaluation of the postmastoidectomy patient should include (1) categorization of the surgical defect (Table 22-6), (2) evaluation of the cavity for residual debris, (3) careful study of the margins of the cavity for bony defects, (4) observation of the status of the ossicular chain, (5) evaluation of the inner ear structures to exclude fistula formation, and (6) careful study of the margins of the facial nerve canal. Removal of air cells with maintenance of the EAC wall and ossicular chain (OC) constitutes a simple (cortical) mastoidectomy (Fig. 22-63A). The simple (cortical) mastoidectomy has fallen into disrepute.

Removal of all mastoid air cells with sparing of the EAC wall and OC is termed an intact canal wall mastoidectomy (ICWM) or canal wall up mastoidectomy (Fig. 22-63B).[210, 211] In this procedure Koerner's septum is removed, providing access to the attic and antrum. This procedure is used for cholesteatoma in children with well-pneumatized mastoids.[24] It avoids the tympanomastoid cavity; however, published recurrence rates are unacceptably high. These procedures are categorized as closed-cavity mastoidectomies.

The open-cavity procedures (radical mastoidectomy, modified radical mastoidectomy) are encountered much more commonly.[210, 212, 213] The EAC wall is removed with a canal wall down (open cavity) mastoidectomy. Resection of the scutum allows access to the attic. Thus, there is

Table 22-6
MASTOIDECTOMY CLASSIFICATION

Closed cavity (canal wall up) EAC intact
Simple (cortical) mastoidectomy (limited removal of mastoid air cells)
Intact canal wall mastoidectomy (removal of all mastoid air cells)
Open cavity (canal wall down): resection EAC
Modified radical mastoidectomy (ossicular chain preserved)
Radical mastoidectomy (ossicles removed but stapes preserved)
To access IAC
Translabyrinthine approach (canal wall up mastoidectomy, removal of semicircular canals and of bone over sigmoid sinus)
Retrosigmoid approach (subocciptial craniotomy, removal of posterior wall IAC)

Copyright © 2003, Mosby, Inc. All rights reserved.

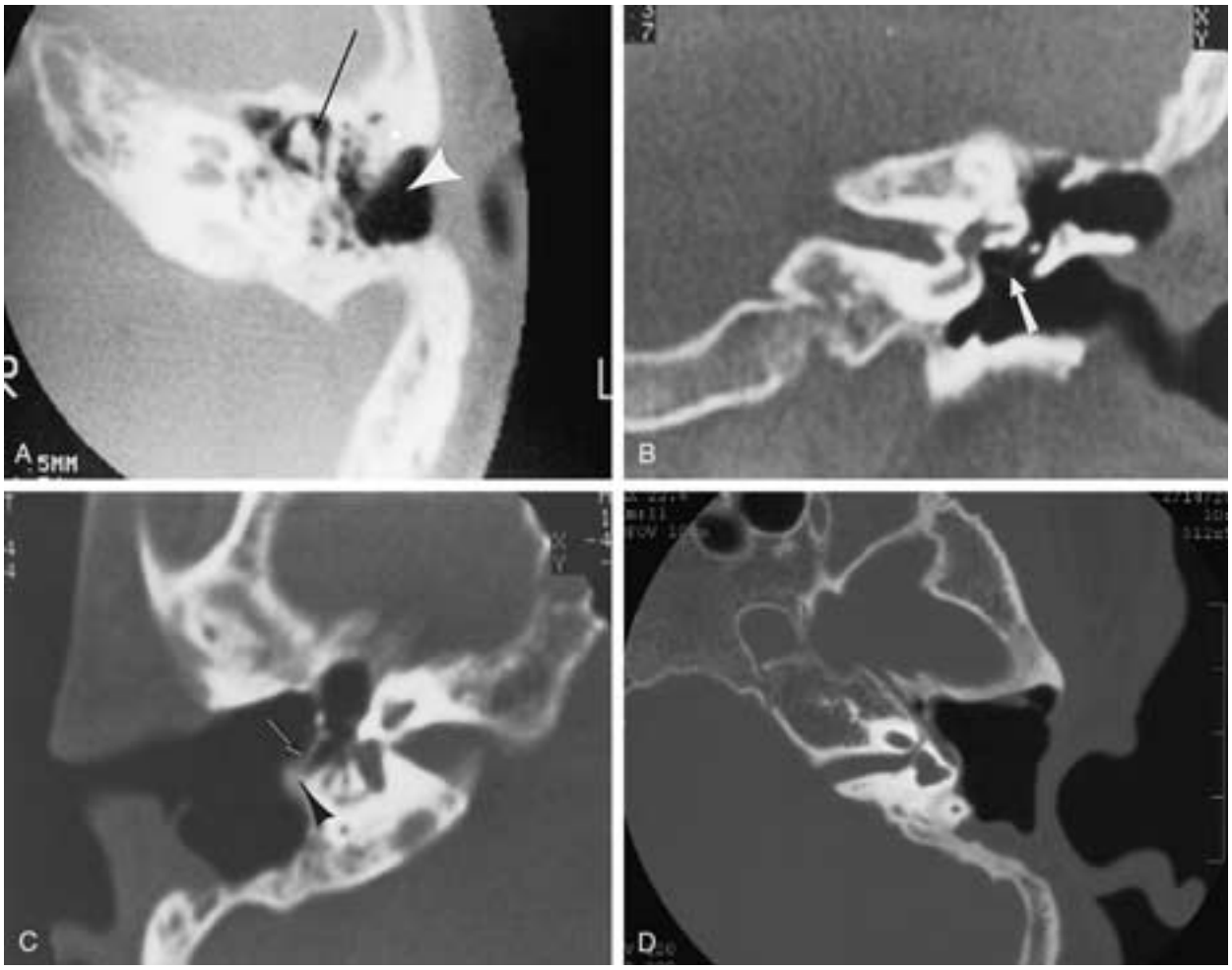

VIEW IMAGE

FIGURE 22-63 Mastoidectomy. **A**, Cortical mastoidectomy. Several mastoid air cells have been removed (*white arrowhead*). The OC is entirely intact (*arrow*). **B**, Intact canal wall mastoidectomy. Mastoid air cells have been removed. The EAC is intact. The OC (*white arrow*) is preserved. **C**, Modified radical mastoidectomy. Mastoid air cells and the EAC have been removed. The OC is intact. In this patient, the short process of the incus (*arrow*) was fixed within residual fibrous tissue (*arrowhead*) adjacent to the lateral semicircular canal. **D**, Radical mastoidectomy. Axial image demonstrates absence of mastoid air cells, the EAC wall, and the OC.

communication between the mastoid cavity and the EAC. In the modified radical mastoidectomy (Bondy procedure), which is performed primarily for atticoantral cholesteatoma, the OC is meticulously preserved and reconstructed (Fig. 22-63C). For this reason, both preoperative and postoperative CT evaluation should include an investigation of the status of the stapes superstructure.

A radical mastoidectomy is necessary for more extensive disease. It includes removal of most of the OC, with preservation of the stapes (Fig. 22-63D).

Access to the IAC also can be via a mastoidectomy. In the translabyrinthine approach, a canal wall up mastoidectomy is performed, and the facial nerve is skeletonized and preserved. The semicircular canals are resected, along with the bone covering the sigmoid sinus and adjacent dura of the middle and posterior cranial fossa. This approach allows access to the posterior aspect of the IAC and is used to remove acoustic schwannomas in patients with irreversible hearing loss (Fig. 22-64).[214]

In the retrosigmoid approach, a suboccipital craniotomy is performed and the posterior wall of the IAC is removed, allowing access to the intracanalicular seventh and eighth nerves and the cerebellopontine angle. Hearing may be preserved with this approach, as the middle and inner ear structures are not involved in the procedure.[214]

It is virtually impossible to make a histologic diagnosis of debris in a tympanomastoid cavity based on the CT appearance (Fig. 22-65). On CT, recurrent cholesteatoma, granulation tissue, and even simple redundant mucosa or surgical packing may appear identical. However, granulation tissue will enhance intensely on contrast-enhanced MR imaging. As mentioned, a cholesteatoma does not enhance. Fortunately, such a specific diagnosis is not important and the surgeon is much more concerned about associated clinical and imaging findings. Regardless of the histopathology, most debris is identified in the posterosuperior aspect of the cavity, and an attempt should be made to distinguish debris in the mastoid bowl from that in the middle ear or attic proper (deep to or superficial to a tympanoplasty, if present).

Before reoperation, the surgeon will want to ensure that the margins of the cavity are intact. In this regard, focal bony

Copyright © 2003, Mosby, Inc. All rights reserved.

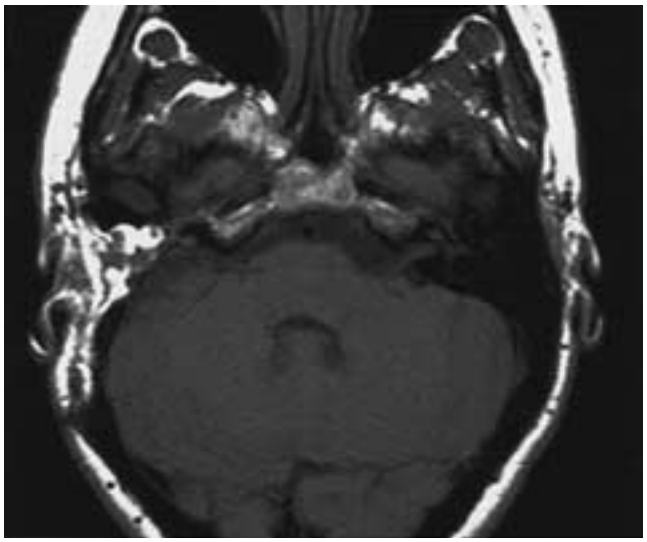

VIEW IMAGE

FIGURE 22-64 Translabyrinthine approach to the IAC. Axial T1-weighted MR image shows a right canal mastoidectomy with removal of the labyrinth and the posterior wall of the EAC. There is high signal intensity fat packing in the surgical defect.

defects, especially in the region of the tegmen or sigmoid sinus plate, can be especially significant (Fig. 22-65B). Individuals with defects adjacent to the sigmoid sinus plate are at risk for the development of sigmoid sinus thrombosis should complications arise. A mass protruding downward through a defect in the tegmen may represent a cephalocele, and the presence or absence of brain within the mass is easily identified with MR imaging.[24] In the presence of bony defects, MR imaging is strongly recommended to evaluate the adjacent cerebellum and sigmoid sinus.[215]

The margins of the OC must be carefully studied, particularly if the surgeon plans a definitive procedure that may include tympanoplasty and ossiculoplasty. In this regard, the distal incus is especially vulnerable in the preoperative patient with a long history of chronic otitis media. The otic capsule, particularly over the lateral semicircular canal, should be carefully evaluated for thinning that suggests fistula formation. The facial nerve canal, particularly in the mastoid segment, may be dangerously close to the surgical defect, and the referring physician should be cautioned. Occasionally, a defect in the canal may be seen along the lateral aspect.

Under unusual circumstances, the contents of a nonoperated acquired cholesteatoma may drain externally, leaving only the aggressive peripheral microscopic membrane, which consists of keratinizing stratified squamous epithelium. The CT appearance in these patients simulates a mastoidectomy because no soft-tissue mass is seen. As previously mentioned, this is variously referred to as automastoidectomy, mural cholesteatoma, and cholesteatoma ''shell'' (Fig. 22-32A,B).[216] The smooth outline of the defect follows the original wall of the cholesteatoma. There is a continuity of the cavity with the EAC. The term autoatticotomy has been used to describe smaller defects where only the scutum and lower lateral attic wall are absent.

Ossiculoplasty and Ossicular Reconstruction

The purpose of ossiculoplasty is to rebuild the sound-conducting mechanism of the middle ear. Damage to this mechanism most likely is caused by chronic otitis media, cholesteatoma, trauma, or congenital ossicular malformation.[217–219] This reconstruction consists of medialization of the TM or creation of a prosthesis to reestablish continuity between the TM and the remaining OC or oval window. Autograft prostheses are tissues harvested from the patient and include rib cartilage, tragal cartilage, and incus. Homograft prostheses are obtained from human donor tissue. Examples include TM, ossicles, and total or partial cartilaginous ossicular reconstruction prostheses. Allograft protheses are biocompatible synthetic materials. A number

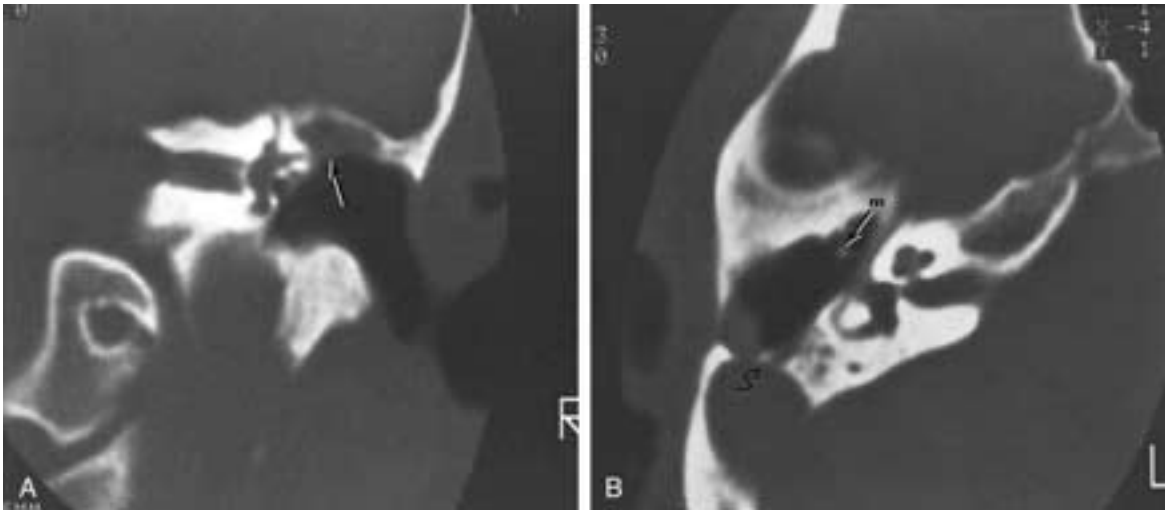

VIEW IMAGE

FIGURE 22-65 Radical mastoidectomy, recurrent debris. **A**, Coronal section. There is residual soft-tissue debris representing residual cholesteatoma (*arrow*) in the mastoid bowl. **B**, Axial image demonstrates a residuum of the malleus neck (*m, arrow*). There is an anterolaterally placed sigmoid sinus (*S*) with an overlying focal bony defect. The surgeon should be cautioned if reoperation is planned.

Copyright © 2003, Mosby, Inc. All rights reserved.

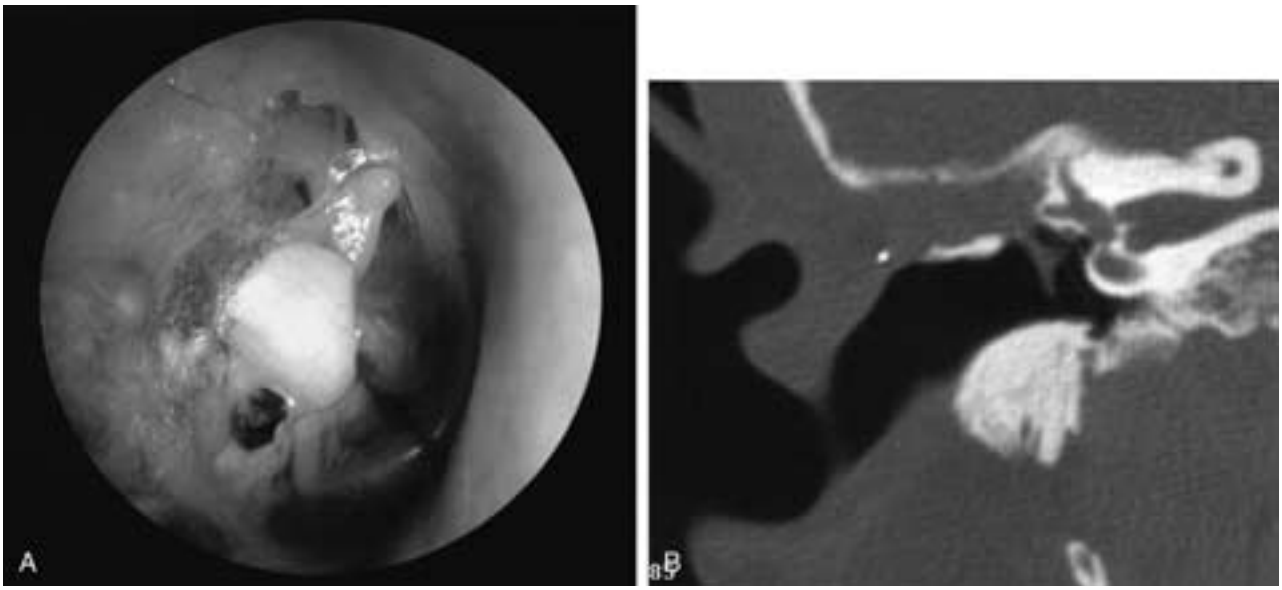

VIEW IMAGE

FIGURE 22-66 Cartilage PORP. **A**, Otoscopy. **B**, Coronal CT shows PORP articulating with the tympanoplasty and extending toward the oval window. The stapes is often difficult to visualize.

of materials are used, including high-density polyethylene sponge (Plastipore), aluminum oxide ceramic, and hydroxyapatite, as well as various other products.[220–222] Most of these devices are nonferromagnetic and are not a contraindication to MR imaging.[223]

The most common sites of ossicular discontinuity are the incudostapedial joint and the lenticular process of the incus. If the incus is missing or unsalvageable, ossicular reconstruction prostheses (ORP) may be employed. If the stapes is intact, with a mobile footplate, a partial ossicular reconstruction prostheses (PORP) (Fig. 22-66) is used. Incus interposition involves removal of the incus (or its remnants), then sculpting and drilling it so that the redesigned incus can be interposed between the TM and the intact stapes superstructure (Fig. 22-67). The absence of both incus and stapes requires a total ossicular replacement prosthesis (TORP). The TORP is interposed between the TM and the oval window (Fig. 22-68).

A stapes prosthesis is the most common ossicular reconstruction and is performed to restore conductive hearing loss in individuals with fenestral otosclerosis or congenital abnormalities.[219, 224] Many different types are in use, including Teflon, wire, Silastic (silicone), and stainless steel piston devices.[23]

Protheses made of 35-gauge wire are especially difficult to see on CT, although usually the tip of the wire can be

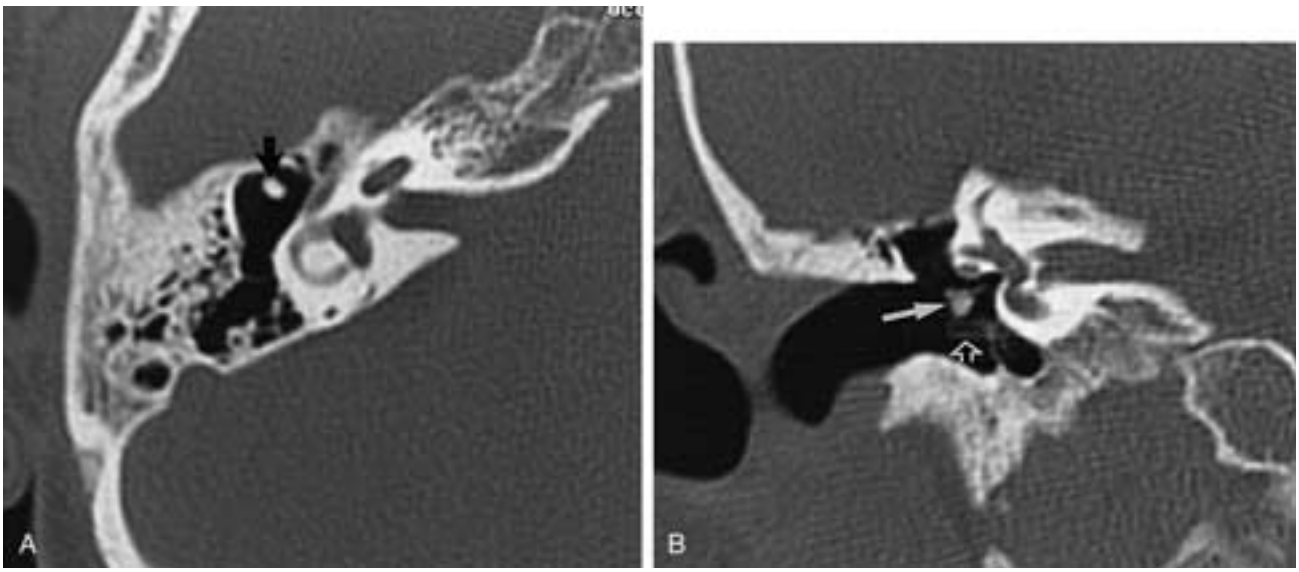

VIEW IMAGE

FIGURE 22-67 Incus interposition. **A**, Axial CT image shows the malleus head (*arrow*) in its normal position and absence of the incus from the attic. **B**, Coronal CT image demonstrates resculpted incus (*arrow*) extending toward the oval window. The stapes is not visualized on this image. Note the tympanostomy tube (*open arrow*).

Copyright © 2003, Mosby, Inc. All rights reserved.

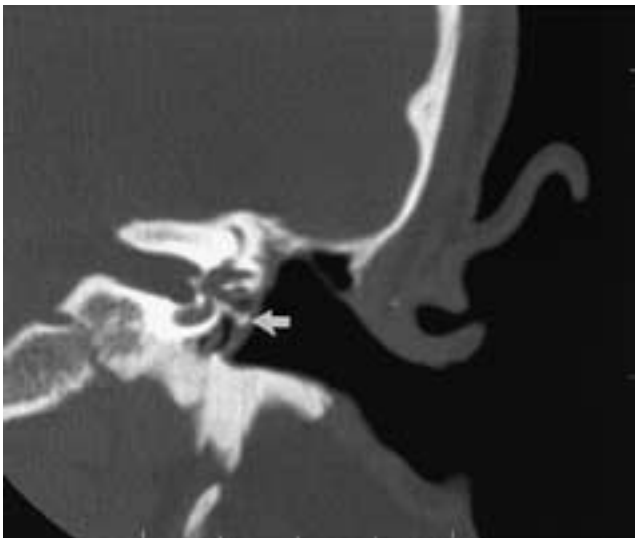

VIEW IMAGE

FIGURE 22-68 Hydroxyapatite TORP. Coronal CT image shows the TORP (*arrow*) displaced inferiorly from the oval window.

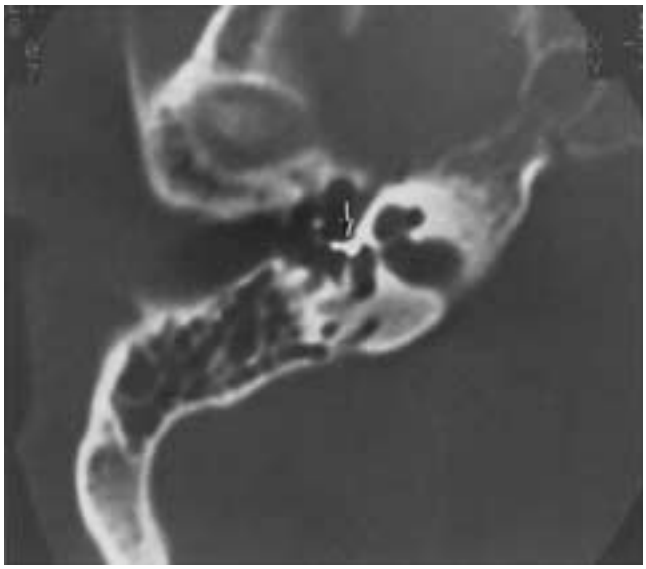

VIEW IMAGE

FIGURE 22-70 Stapes prosthesis, metallic piston, anteriorly placed. Axial image demonstrates the metallic prosthesis (*arrow*) within the oval window anteriorly. This was a normally functioning device.

identified with overlapping, thin axial scans (Fig. 22-69).[103] The metallic piston prosthesis is easily seen in all projections (Figs. 22-70 to 22-72). Identification of the Teflon and Silastic devices is intermediate in difficulty (Fig. 22-73).

Causes of postoperative hearing loss include prosthesis subluxation, incus necrosis, granuloma or fibrous tissue formation, or recurrent growth of otosclerosis and incus dislocation. The prosthesis need not be located centrally in the oval window to be effective. The normally functioning prosthesis may be located in the anterior, central, or posterior portion of the oval window (Fig. 22-70). By comparison, displacement of the prosthesis superficial to the oval window or into the vestibule implies malposition (Fig. 22-71). Audiometric evaluation is much more sensitive in this regard.[24]

The most common cause of correctable prosthetic failure is subluxation or dislocation, which is seen in 50% to 60% of patients with postoperative hearing loss.[219] The CT finding in cases of prosthesis subluxation is a ''vacant'' oval window. Careful evaluation of the posterior recesses and ridges in the axial projection usually yields evidence of the dislocated prosthesis itself (Figs. 22-74 and 22-75).

Incus necrosis may occur at the attachment of the wire to the long process.[184, 225] The CT diagnosis is difficult and depends on careful evaluation of high-quality overlapping

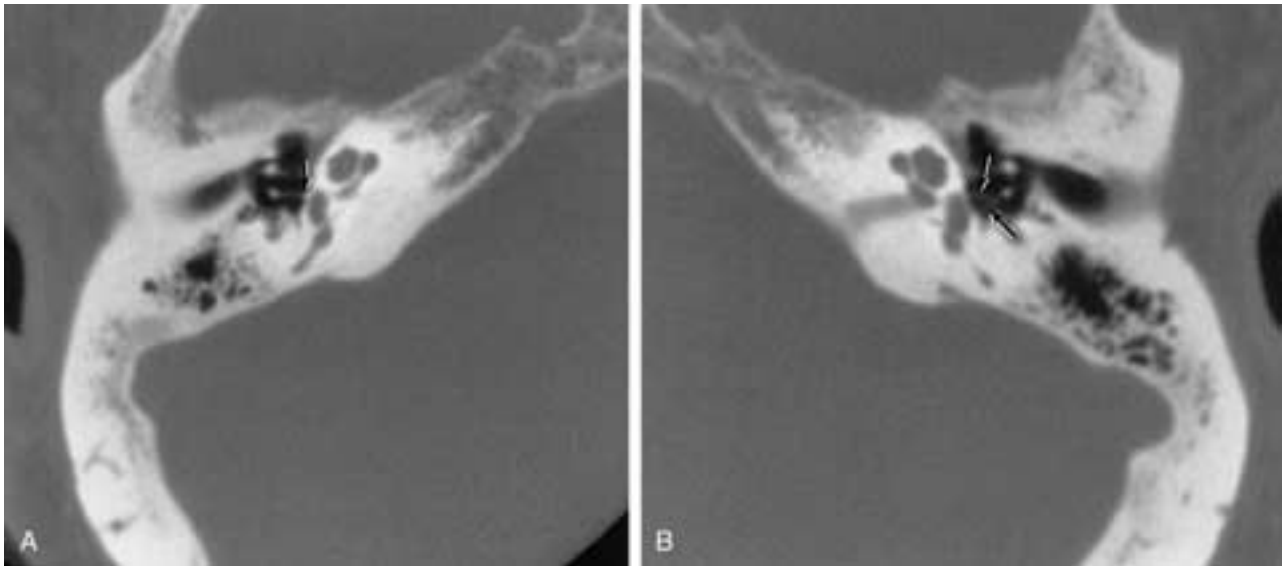

VIEW IMAGE

FIGURE 22-69 Normal wire stapes prosthesis. **A**, Axial CT image shows wire stapes prosthesis (*arrow*) in the oval window. **B**, Axial CT image of the normal left ear with intact stapes (*arrows*).

Copyright © 2003, Mosby, Inc. All rights reserved.

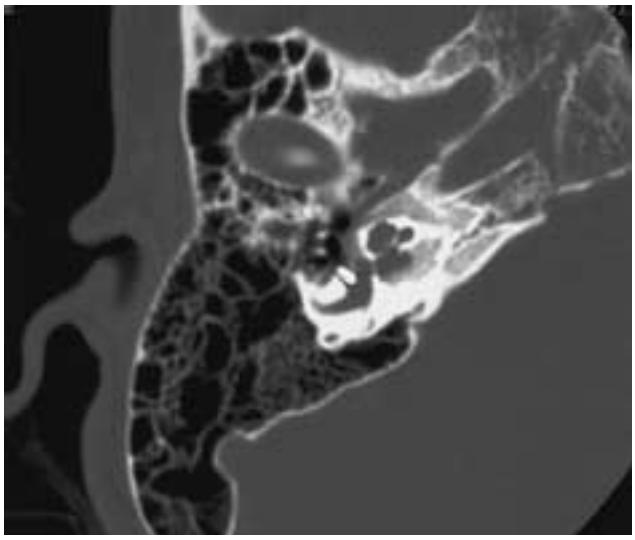

VIEW IMAGE

FIGURE 22-71 Stapes prosthesis. Axial CT image. Note the malposition of the stapes prosthesis, which is displaced medially through the oval window. The patient has severe fenestral and cochlear otosclerosis.

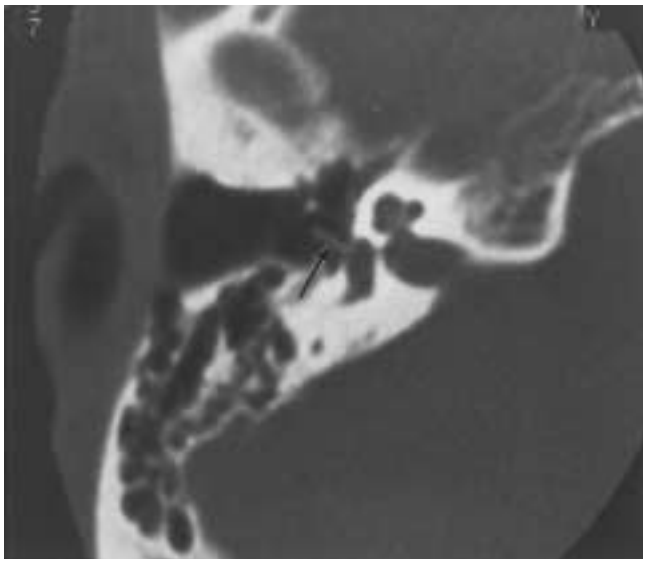

FIGURE 22-73 Stapes prosthesis, Teflon. Axial image demonstrates a nonmetallic prosthesis (*arrow*) seen in its entirety.

VIEW IMAGE

coronal images (Fig. 22-76).[53] Any defects in the long process should be viewed with intense scrutiny.

Possible complications of ossicular reconstruction include dislocation or postinflammatory fixation (or both) by granuloma or fibrous tissue formation. CT is quite valuable in the postoperative evaluation of these patients.[52, 218, 226] Postoperative debris found near the oval window more than 4 to 6 weeks after surgery in the presence of persistent or recurrent conductive hearing loss must be regarded with suspicion for granuloma formation or tympanic fibrosis.[23]

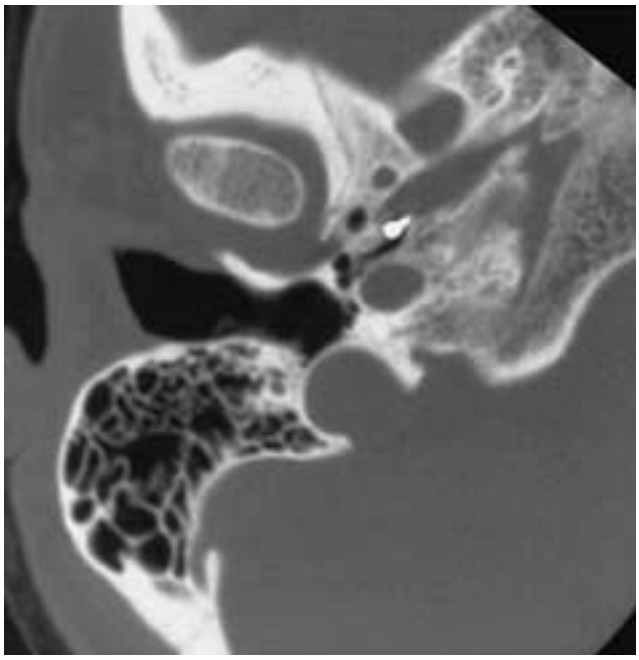

VIEW IMAGE

FIGURE 22-72 Stapes prosthesis. Dislocated metallic piston stapes prosthesis in the ET.

Such tissue may also develop more laterally at the incal attachment and is especially likely to occur in individuals with preexistent chronic otitis (prosthetic stapedectomy in individuals with tympanosclerosis has a much higher incidence of poor surgical results).[53]

Continued growth of otosclerotic plaques can cause further narrowing of the oval window and thus compromise function of the prosthesis. Although a specific diagnosis often can be inferred when this occurs, in the absence of preoperative images it is quite difficult to make a CT diagnosis. CT is often requested for evaluation of recurrent conductive deficit, vertigo, and SNHL in the poststapedectomy patient.[211, 224, 225] Vertigo and SNHL are common in the immediate postoperative period and are usually self-limited. However, persistent or recurrent and fluctuating symptoms of this type may have significant implications, such as the presence of a perilymphatic fistula. Perilymphatic fistula may be difficult to identify on CT but is suspected in the presence of pneumolabyrinth or a new, unexplained middle ear effusion.[219]

SNHL loss or vertigo also may result from abnormal penetration of the prosthesis into the vestibule with compromise of the utriculosaccular organ. The CT diagnosis may be simple, but it depends on the type of prosthesis used.

Acute labyrinthitis, endolymphatic hydrops, and intravestibular fibrous adhesions are additional causes of poststapedectomy dizziness, vertigo, and SNHL.[227] There are no known CT manifestations. Enhancement of the membranous labyrinth in individuals with labyrinthitis may occur in subacute cases on T1-weighted MR images, and enhancement of the endolymphatic sac has been described in individuals with endolymphatic hydrops.[126] Ossification of the membranous labyrinth may develop in long-standing chronic labyrinthitis.[53] In such a circumstance, the CT findings are quite obvious (Fig. 22-51).

Simple tympanoplasty is performed in individuals with an unhealed perforation of the TM, and CT usually plays no

Copyright © 2003, Mosby, Inc. All rights reserved.

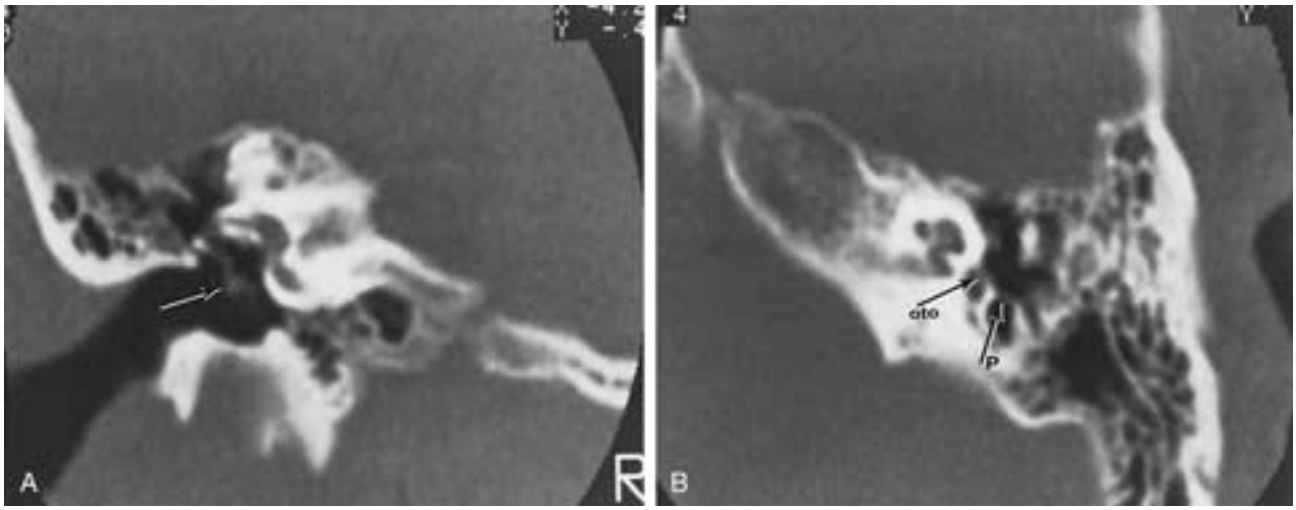

VIEW IMAGE

FIGURE 22-74 Stapes prosthesis, dislocation. **A**, Coronal image demonstrates lateralization of the graft (*arrow*). **B**, Axial image. The oval window niche is vacant. The stapes footplate is abnormally thickened by otosclerosis (*oto, arrow*). The dislocated prosthesis (*p, arrow*) is identified posteriorly.

role in the evaluation of this procedure. Both the homograft and synthetic replacements referred to in the previous paragraphs require tympanoplasty.

Cochlear Implantation

For individuals with severe to profound sensorineural deafness, cochlear implantation has become increasingly available and both single-channel and multichannel devices are in clinical use.[228–230] The electrodes are introduced by making an opening in the basal turn of the cochlea anterior to the round window. The electrodes are usually inserted into the scala tympani for a variable distance to stimulate the cochlear nerve.

Temporal bone imaging has been used for both preoperative and postoperative evaluation. In the postoperative patient in whom placement was technically difficult, CT can be helpful in identifying the site of the electrode tip. However, preoperative evaluation is generally more critical, particularly for the multichannel device, which must be inserted 22 to 26 mm into the middle cochlear turn (Fig. 22-77). Obstruction of the labyrinth by ectopic bone or fibrous tissue is a common consequence of meningitis or labyrinthitis. Absolute contraindications to implantation include bilateral acoustic neuromas, severe fractures, obliterative labyrinthine (cochlear) ossification, and, of course, congenital absence of the cochlear nerve. Relative contraindications include diffuse otosclerosis, obliterative labyrinthitis, hypoplasia of the IAC, congenital cochlear malformations, and uncontrolled otitis media or mastoiditis.[214, 231] Fibrous changes within the membranous labyrinth, which are also a source of surgical difficulty, are not demonstrable by CT. However, thin section MR imaging, utilizing

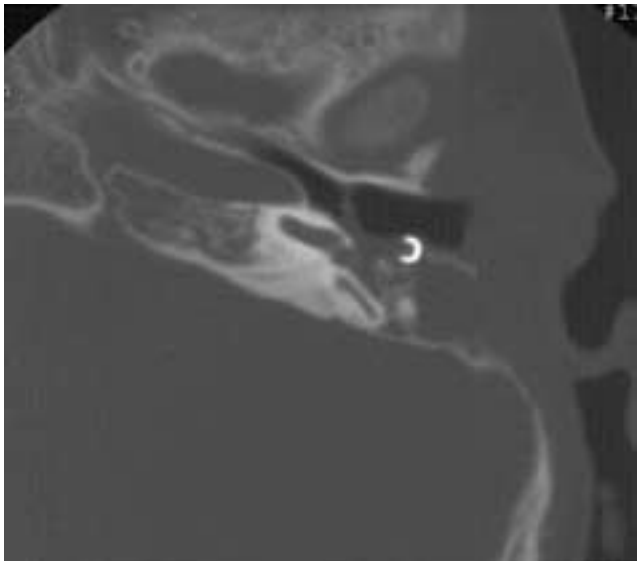

FIGURE 22-75 Dislocated Black prosthesis. CT shows dislocation of the egg-shaped hydroxyapatite head of the prosthesis into the external auditory canal.

VIEW IMAGE

Copyright © 2003, Mosby, Inc. All rights reserved.

VIEW IMAGE

FIGURE 22-76 Incus necrosis. Coronal image demonstrates a focal defect (*arrow*) in the long process of the incus. The patient had recurrent conductive deficit several months after stapedectomy and prosthesis insertion.

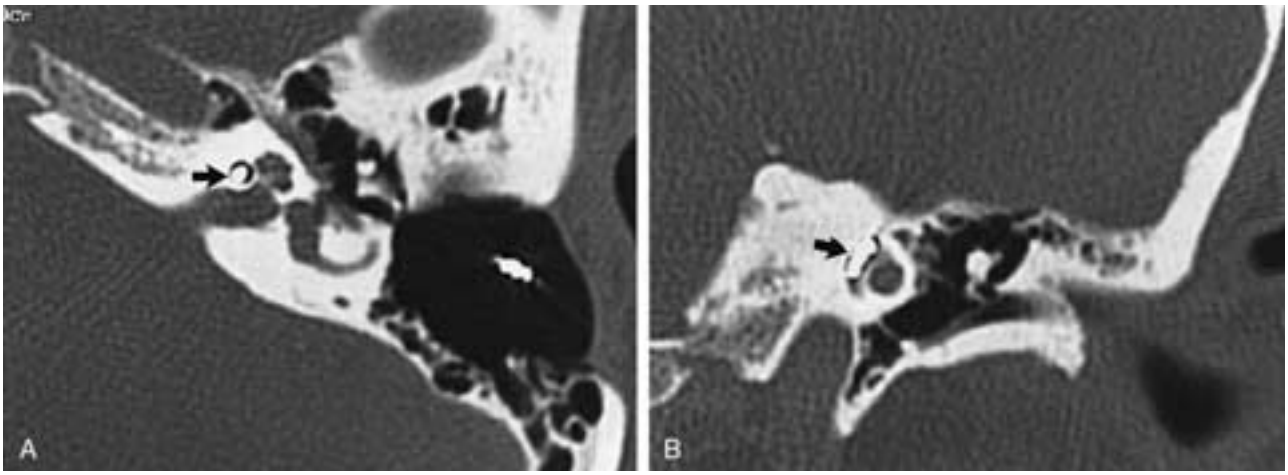

VIEW IMAGE

FIGURE 22-77 Multichannel cochlear implant. Axial (**A**) and coronal CT (**B**) images show a metallic device (*arrow*) in the basal turn of the cochlea.

Copyright © 2003, Mosby, Inc. All rights reserved.

thin sections and T2-weighting, may be quite informative.[151, 154, 155, 229, 231–233]

IDIOPATHIC FACIAL PARALYSIS (BELL'S PALSY)

The term *Bell's Palsy* refers to a facial paralysis or paresis that has no identifiable cause and therefore is considered to be idiopathic. As inflammation related to a viral infection is the most likely mechanism for the palsy, idiopathic facial paralysis is included in this chapter.

Bell's or idiopathic facial paralysis has a very typical presentation. The weakness is of very rapid onset. Frequently, the patient will wake up with the paralysis, which may progress for several hours or, rarely, up to three weeks. Continued progression beyond that time, however, is distinctly unusual and should suggest another cause of the problem. The paralysis is peripheral and all branches are involved. Almost all patients show some recovery. The Bell's palsy will almost always begin to improve and more than 80% of patients have improvement to a satisfactory level within six months.[234] There are various electrophysiological tests used to follow the progression and look for early or disordered recovery, allowing for a more accurate documentation of the course than does simple physical examination.[234, 235]

Most investigation suggests a viral or viral inflammatory immune mechanism. Many studies point toward the herpes simplex virus but findings are not definitive. A virus may cause swelling of the nerve as the initial insult. The swelling causes compression of the blood supply within the very narrow confines of the bony facial nerve canal. This vascular compromise gives further injury to the nerve and paralysis results.

The narrowest point in the canal is the labyrinthine segment. Thus, insult to the nerve in this region has been suggested as the most likely cause of paralysis.[236] Swelling in the labyrinthine segment extending into the internal auditory canal has been documented during surgical decompression.[236]

Bell's is a diagnosis of exclusion. If a specific cause is determined then the term *Bell's* or *idiopathic* should not be used. Trauma (including birth trauma), various neurologic diseases, specific infections, metabolic diseases, toxins, and tumors can all cause facial paralysis.[235] Tumor is the most important etiology to be excluded. A tumor can occur anywhere along the course of the facial nerve from the brainstem to the peripheral face. The most common locations of tumors presenting as facial paralysis are in the temporal bone and in the parotid gland region, and these are the areas usually examined by imaging in ambiguous cases. Specific viral agents have been identified as causing facial paralysis. For instance, Herpes oticus (Ramsey Hunt syndrome) is caused by herpes varicella zoster virus. This virus produces a very specific presentation (discussed earlier in this chapter) and is not included as a Bell's palsy. If further investigation determines that a specific virus is the responsible etiologic agent for some group of patients carrying the Bell's designation then this group of patients would presumably be taken out of the Bell's category.

Imaging

Many clinicians consider imaging unnecessary in a patient with the typical presentation of Bell's palsy. If the patient has a rapid onset of paralysis and has the typical clinical course, no imaging may be done. It should be remembered, however, that tumors can mimic Bell's palsy so that the classic Bell's presentation does not exclude tumor or other central pathologies. Factors that more strongly suggest tumor include slow onset of weakness and progression beyond a short interval. Failure to have significant improvement by six months or recurrence of an improved paralysis should suggest tumor. Bilateral paralysis should also be considered suggestive of a more central pathology.

MR imaging with gadolinium is the usual choice for evaluation of suspicious cases. High-resolution imaging should focus on the temporal bone but should be continued through the parotid gland. Imaging includes the brain—particularly the brainstem.

The findings in Bell's, or idiopathic facial paralysis, are typical.[234, 237–242] With gadolinium, there is increased enhancement of the facial nerve (Fig. 22-78). Any segment can be involved, but typically there is pronounced enhancement in the region of the geniculate ganglion and in the labyrinthine and anterior tympanic segments of the nerve. There is usually some enhancement in this region normally, but with Bell's the enhancement is increased. The nerve should not be enlarged within the facial nerve canal itself. Enlargement of the segments within the temporal bone suggests tumor. The enhancement continues into the most lateral part of the internal auditory canal. Here the nerve just proximal (medial) to the entrance into the facial canal from the IAC will actually swell and enhance (see Fig. 22-78). This focal enlargement and enhancement can be appreciated on MR imaging and should not be mistaken for tumor. However, in questionable cases a follow-up study is done to ensure that the finding reverts to normal. Recently, high-resolution T2-weighted imaging has also visualized the slight enlargement of the facial nerve in the lateral part of the IAC.[243]

Most specialists consider MR imaging to be the study of choice in facial paralysis. Resolutioin of modern machines allows documentation of the normal size of the nerve. MR imaging is more sensitive than CT in detecting more central pathologies and therefore can more reliably exclude them. The parotid gland is easily evaluated. CT gives high-resolution imaging of the bony canal within the temporal bone. Documentation of a normal canal without expansion and with no eroding lesion is strong evidence that there is no tumor. Small lesions within the IAC can be missed and central pathology is not well evaluated. If CT is done the study should be carried down through the parotid gland to exclude a tumor. CT is also used to clarify an ambiguous finding on MR imaging. Definition of the fine bony detail of the facial nerve canal and surrounding temporal bone may help exclude a tumor if the enhancement seems atypical on MR imaging.

Attempts have been made to use the degree of enhancement as an indicator of prognosis but so far studies have been inconclusive.[239, 241]

Copyright © 2003, Mosby, Inc. All rights reserved.

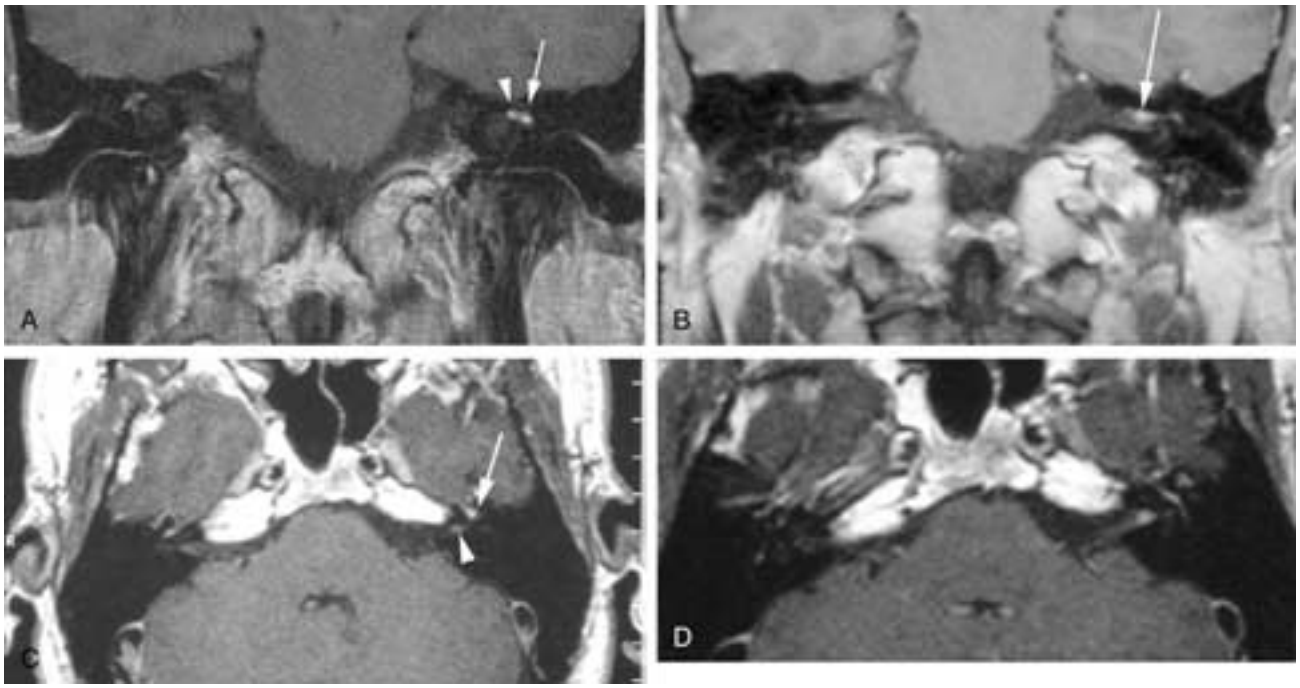

VIEW IMAGE

FIGURE 22-78 Bell's palsy (idiopathic facial paralylsis). Post gadolinium T1-weighted MR imaging. **A**, The coronal plane shows the enhancing facial nerve. Both the labyrinthine segment (*arrowhead*) and the anterior tympanic segment (*arrow*) enhance compared to the opposite side. **B**, Slightly posterior to **A**. There is enhancement and enlargement of the facial nerve in the fundus of the internal auditory canal (*arrow*). This is typical of Bell's palsy and should not be considered evidence of a tumor. **C**, Axial image shows the enhancement in the region of the geniculate ganglion (*arrow*) and in the internal auditory canal (*arrowhead*). **D**, Slightly inferiorly to **C**. There is enhancement of the anterior tympanic segment (*arrow*). Note also the enhancement of the enlarged nerve within the internal auditory canal (*arrowhead*).

REFERENCES

1. Bast T, Anson B. The Temporal Bone and Ear. Springfield, Ill: Charles C. Thomas, 1949.
2. Donaldson J, et al. Surgical Anatomy of the Temporal Bone. 4th ed. New York: Raven Press, 1992;143–177.
3. Kenna M. Otitis media with effusion. In: Bailey B, ed. Head and Neck Surgery—Otolaryngology. Philadelphia: Lippincott-Raven, 1998;1297–1310.
4. Bluestone C. Anatomy and physiology of the eustachian tube. In Bailey B, ed. Head and Neck Surgery—Otolaryngology. Philadelphia: Lippincott-Raven, 1998;1285–1295.
5. Tos M. Importance of eustachian tube function in middle ear surgery. Ear Nose Throat J 1998;77(9):744–747.
6. Curtin H, Som P, Bergeron R. Temporal bone embryology and anatomy. In: Som P, Curtin H, eds. Head and Neck Imaging. St. Louis, CV Mosby. 1996;1300–1318.
7. Sade J, Ar A. The eustachian tube. In: Ludman H, Wright T, eds. Diseases of the Ear. London: Arnold, 1998;334–351.
8. Cummings CW, et al. Otolaryngology—Head and Neck Surgery. St. Louis: Mosby-Year Book, 1986.
9. Holliday RA. Inflammatory diseases of the temporal bone: evaluation with CT and MR. Semin Ultrasound CT MR 1989;10(3):213–235.
10. Schuknecht HF. Pathology of the Ear. 2nd ed. Philadelphia: Lea & Febiger, 1993.
11. Mafee MF, Aimi K, Kahen HL, et al. Chronic otomastoiditis: a conceptual understanding of CT findings. Radiology 1986;160(1): 193–200.
12. Proctor B. Chronic otitis media and mastoiditis. In: Paparella MM, Schumrick DA, eds. Otolaryngology—The Ear. Philadelphia: WB Saunders, 1980;1465–1489.
13. Beaumont GD. Radiology and the management of chronic suppurative otitis media. Australas Radiol 1980;24:238–245.
14. Bluestone CD, Cantekin EI. Eustachian tube dysfunction. In: English GM, ed. Otolaryngology. New York: Harper & Row, 1979.
15. Moran WB Jr. Cholesteatoma. In: English GM, ed. Otolaryngology. New York: Harper & Row, 1980.
16. Paparella MM. The middle ear effusions. In: Paparella MM, Shumrick DA, eds. Otolaryngology—The Ear. Philadelphia: WB Saunders, 1980;1422–1444.
17. Aoki K, et al. Relationship between middle ear pressure, mucosal lesion, and mastoid pneumatization. Laryngoscope 1998;108(12): 1840–1845.
18. Caye-Thomasen P, et al. Bone modeling dynamics in acute otitis media. Laryngoscope 1999;109(5):723–729.
19. Iino Y, et al. Mastoid pneumatization in children with congenital cholesteatoma: an aspect of the formation of open-type and closed-type cholesteatoma. Laryngoscope 1998;108(7):1071–1076.
20. Jung TT, Hanson JB. Classification of otitis media and surgical principles. Otolaryngol Clin North Am 1999;32(3):369–383.
21. Gates G. Otitis media with effusion. In: Hughes G, Pensak M, eds. Clinical Otology. New York: Thieme, 1997;205–214.
22. Mafee MF, Singleton EL, Valvassori GE, et al. Acute otomastoiditis and its complications: role of CT. Radiology 1985;155:391.
23. Swartz J, Harnsberger H. Imaging of the Temporal Bone. 3rd ed. New York and Stuttgart: Thieme, 1998.
24. Swartz JD, Harnsberger MR, Mukherji SK. The temporal bone. Contemporary diagnostic dilemmas. Radiol Clin North Am 1998; 36(5):819–853, vi.
25. Castillo M, et al. Imaging of Bezold's abscess. AJR 1998;171(6): 1491–1495.
26. Davison SP, et al. Use of magnetic resonance imaging and magnetic resonance angiography in diagnosis of sigmoid sinus thrombosis. Ear Nose Throat J 1997;76(7):436–441.
27. Vogl TJ, et al. Dural sinus thrombosis: value of venous MR angiography for diagnosis and follow-up. AJR 1994;162(5):1191–1198.

Copyright © 2003, Mosby, Inc. All rights reserved.

28. Kelley KE, Jackler RIC, Dillon WP. Diagnosis of septic sinus thrombosis resonance imaging. Otolaryngol Head Neck Surg 1991;105(4):617–624.
29. Laine FJ. What pulse sequences should be used when the clinical question is ''rule out superior sagittal sinus thrombosis''? AJR 1995;164(3):763.
30. Ayanzen RH, et al. Cerebral MR venography: normal anatomy and potential diagnostic pitfalls [in process citation]. AJNR 2000;21(1): 74–78.
31. Dormont D, et al. Gadolinium-enhanced MR of chronic dural sinus thrombosis. AJNR 1995;16(6):1347–1352.
32. Ikushima I, et al. Evaluation of dural sinus invasion and extension of extra-axial intracranial tumors. The advantages of a high-resolution postcontrast 3D gradient-echo technique [in process citation]. Acta Radiol 2000;41(1):8–12.
33. Gacek RR. Evaluation and management of temporal bone arachnoid granulations. Arch Otolaryngol Head Neck Surg 1992;118(3): 327–332.
34. Mamourian AC, Towfighi J. MR of giant arachnoid granulation, a normal variant presenting as a mass within the dural venous sinus. AJNR 1995;16(Suppl4):901–904.
35. Roche J, Warner D. Arachnoid granulations in the transverse and sigmoid sinuses: CT, MR, and MR angiographic appearance of a normal anatomic variation [see comments]. AJNR 1996;17(4): 677–683.
36. Chin SC, et al. Giant arachnoid granulation mimicking dural sinus thrombosis in a boy with headache: MRI. Neuroradiology 1998; 40(3):181–183.
37. Leach JL, et al. Normal appearance of arachnoid granulations on contrast-enhanced CT and MR of the brain: differentiation from dural sinus disease [see comments]. AJNR 1996;17(8):1523–1532.
38. Hsu FP, et al. Dural sinus thrombosis endovascular therapy. Crit Care Clin 1999;15(4):743–753, vi.
39. Kim SY, Suh JH. Direct endovascular thrombolytic therapy for dural sinus thrombosis: infusion of alteplase. AJNR 1997;18(4):639–645.
40. Dallari S, et al. Acute mastoiditis with complications: a report of two cases. Acta Otorhinolaryngol Belg 1997;51(2):113–118.
41. Grafstein E, Fernandes CM, Samoyloff S. Lateral sinus thrombosis complicating mastoiditis. Ann Emerg Med 1995;25(3):420–423.
42. Oyarzabal MF, Patal KS, Tolley NS. Bilateral acute mastoiditis complicated by lateral sinus thrombosis. J Laryngol Otol 1992; 106(6): 535–537.
43. Tovi F, Hirsch M. Computed tomographic diagnosis of septic lateral sinus thrombosis. Ann Otol Rhinol Laryngol 1991;100(1):79–81.
44. Manzione J, et al. Diffusion- and perfusion-weighted MR imaging of dural sinus thrombosis [in process citation]. AJNR 2000;21(1): 68–73.
45. Swartz JD, Goodman RS, Russell KBEA. High resolution computed tomography of the middle ear and mastoid: tubotympanic disease. Radiology 1983;148:455–459.
46. Nager G. Pathology of the Ear and Temporal Bone. Baltimore: Williams & Wilkins, 1992.
47. Chole R, Choo M-J. Chronic otitis media, mastoiditis, and petrositis. In Cummings C et al, eds. Otolaryngology—Head and Neck Surgery. St. Louis: CV Mosby, 1998;3026–3046.
48. Russo CP, Smoker WR, Weissman JL. MR appearance of trigeminal and hypoglossal motor denervation. AJNR 1997;18(7):1375–1383.
49. Buckingham RA. Cholesteatoma in chronic otitis media following middle ear intubation. Laryngoscope 1981;91:1415–1456.
50. Pratt LL, Murray J. The placement of middle ear ventilation tubes: some indications and complications. Laryngoscope 1973;83:1022–1026.
51. Klein MA, Kelly JK, Eggleston D. Recognizing tympanostomy tubes on temporal bone CT: typical and atypical appearances. AJR 1988;150:1411–1414.
52. Swartz JD, Goodman RS, Russell KB, et al. High resolution computed tomography of the middle ear and mastoid. III. Surgically altered anatomy and pathology. Radiology 1983;148:461–464.
53. Swartz JD, Harnsberger HR. Imaging of the Temporal Bone. 2nd ed. New York: Thieme, 1992.
54. Martin N, Sterkers O, Nahum H. Chronic inflammatory disease of the middle ear cavities: Gd-DTPA-enhanced MR imaging. Radiology 1990;176(2):399–405.
55. Paparella MM, Meyerhoff WC. Clinical significance of granulation tissue of chronic otitis media. In: Sade J, ed. Cholesteatoma and Mastoid Surgery. Amsterdam: Kugler, 1982;387–395.
56. Swartz JD. Cholesteatomas of the middle ear: diagnosis, etiology and complications. Radiol Clin North Am 1984;22(1):15–35.
57. Strunk C. Cholesteatoma. In: Bailey B, ed. Head and Neck Surgery—Otolaryngology. Philadelphia: Lippincott-Raven, 1998; 2041–2051.
58. Swartz JD, Glazer AV, Faerber EN, et al. Congenital middle ear deafness: CT study. Radiology 1986;159:187.
59. Linthicum F, Schwartzman J. An Atlas of Micropathology of the Temporal Bone. San Diego, Ca: Singular Publishing Group, 1994.
60. Mafee MF. MRI and CT in the evaluation of acquired and congenital cholesteatomas of the temporal bone. J Otolaryngol 1993;22(4):239–248.
61. Nager GT. Epidermoids (congenital cholesteatomas) involving the temporal bone. In: Sade J, ed. Cholesteatoma and Mastoid Surgery. Amsterdam: Kugler, 1982;41–60.
62. Nager GT. Cholesteatoma of middle ear: pathogenesis and surgical indication. In: McCabe BS, Sade J, Abramson M, eds. Cholesteatoma. Birmingham, Ala: Aesculapius,1977;191–203.
63. Sade J. Pathogenesis of attic cholesteatoma. J R Soc Med 1978;71:716–732.
64. Proctor B. Epitympanic mucosal folds. Arch Otolaryngol 1971; 94(6):578.
65. Proctor B. Alexander Prussak. Ann Otol Rhinol Laryngol 1968; 77(2):344–349.
66. Buckingham RA, Valvassori GE. Tomographic evaluation of cholesteatomas of the middle ear and mastoid. Otolaryngol Clin North Am 1973;6(2):363.
67. Swartz JD, Varghese S. Pars flaccida cholesteatoma as demonstrated by computed tomography. Arch Otolaryngol 1984;110:515–517.
68. Cody DTR. The definition of cholesteatoma. In: McCabe BS, Sade J, Abramson M, eds. Cholesteatoma. Birmingham, Ala: Aesculapius, 1977;6–9.
69. Ruedi L. Acquired cholesteatoma. Arch Otolaryngol 1983;78:252.
70. Sade J. Pathogenesis of attic cholesteatoma: the metaplasia theory. In: McCabe BS, Sade J, Abramson M, eds. Cholesteatoma. Birmingham, Ala: Aesculapius, 1977;212–232.
71. Goycoolea MV, et al. The theory of the trigger, the bridge and the transmigration in the pathogenesis of acquired cholesteatoma. Acta Otolaryngol (Stockh) 1999;119(2):244–248.
72. Mafee MF, Kumar A, Yannias DA, et al. CT of the middle ear in evaluation of cholesteatoma and other soft tissue masses. Radiology 1983;148:465–472.
73. Phelps PD, Lloyd GAS. The radiology of cholesteatoma. Clin Radiol 1980;31:501–512.
74. Kikuchi S, Yamasoba T, Iinuma T. An analysis of bone destruction in cholesteatomas by high resolution computed tomography. Auris Nasus Larynx 1993;20(1):11–7.
75. Chu FW, Jackler RK. Anterior epitympanic cholesteatoma with facial paralysis: a characteristic growth pattern. Laryngoscope 1988;98(3): 274–279.
76. Sade J, Berco E, Buyanover, D. Ossicular damage in chronic middle ear inflammation. In: Sade J, ed. Cholesteatoma and Mastoid Surgery. Amsterdam: Kugler, 1982;347–358.
77. Sade J, Berco E, Halevy A. Bone resorption in chronic otitis media with and without cholesteatoma. In: McCabe BS, Sade J, Abramson M, eds. Cholesteatoma. Birmingham, Ala: Aesculapius, 1977;128–135.
78. Nager GT. Theories on the origin of attic retraction cholesteatoma. In: Shambaugh GE and Shea JJ, eds. Proceedings of the Shambaugh 5th International Workshop on Microsurgery and Fluctuant Hearing Loss. Huntsville, Ala: Strode, 1977.
79. Tos M. Can cholesteatoma be prevented?, In: Sade J, ed. Cholesteatoma and Mastoid Surgery. Amsterdam: Kugler, 1982; 591–598.
80. Silver AJ, Janecka I, Wazen J, et al. Complicated cholesteatomas: CT findings in inner ear complications of middle ear cholesteatomas. Radiology 1987;164:47.
81. Swartz JD. Facial nerve canal: CT analysis of the protruding tympanic segment. Radiology 1984;153:443–447.
82. Ritter FN. Complications of cholesteatoma. In: McCabe BS, Sade J, Abramson M, eds. Cholesteatoma. Birmingham, Ala: Aesculapius, 1977;430–437.
83. Fisch U. Intracranial complications of cholesteatoma. In: Sade J, ed. Cholesteatoma and Mastoid Surgery. Amsterdam: Kugler, 1982; 369–382.

Copyright © 2003, Mosby, Inc. All rights reserved.

84. Mathews TJ, Marcus G. Otogenic intradural complications: a review of 37 patients. J Otolaryngol 1988;102(2):121–124.
85. Sheehy JL, Brackman N, Graham MN. Complications of cholesteatoma: a report of 1024 cases. In: McCabe BS, Sade J, Abramson M, eds. Cholesteatoma. Birmingham, Ala: Aesculpius, 1977;420–429.
86. Phelps PD, Lloyd GA. Vascular masses in middle ear. Clin Radiol 1986;37(4):359–364.
87. Manzione JV, Rumbaugh GL, Katzberg RW. Direct sagittal computed tomography of the temporal bone. J Comput Assist Tomogr 1985;9:417–419.
88. O'Donoghue GM, Bates GJ, Anslow P et al. The predictive value of high resolution computerized tomography in chronic suppurative ear disease. Clin Otolaryngol 1987;12(2):89.
89. Ishii K, et al. Middle ear cholesteatoma extending into the petrous apex: evaluation by CT and MR imaging. AJNR 1991;12(4):719–724.
90. Ishii K, et al. MR imaging of middle ear cholesteatomas. J Comput Assist Tomogr 1991;15(6):934–937.
91. Friedman DP, Rao VM. MR and CT of squamous carcinoma of the middle ear and mastoid complex. AJNR 1991;12:878–879.
92. Castillo M, Pillsburg HC. Rhabdo-myosarcoma of the middle ear: imaging features in two children. AJNR 1993;14:730–733.
93. Swartz JD, Berger AS, Zwillenberg S, et al. Ossicular erosions of the dry ear: CT diagnosis. Radiology 1987;163:763–765.
94. Swartz JD, Zwillenberg S, Berger AS, et al. Acquired disruptions of the incudostapedial joint. Radiology 1989;171:779–781.
95. Kinney SE. Post-inflammatory ossicular fixation in tympanoplasty. Laryngoscope 1978;88:821–838.
96. Lumio JS. Contribution to the knowledge of chronic adhesive otitis: the diagnosis. Acta Otolaryngol 1981;39:196.
97. Swartz JD, Wolfson RJ, et al. Post-inflammatory ossicular fixation: CT analysis with surgical correlation. Radiology 1985;154: 697–700.
98. VanBaarle PW, Huygen PL, Brickman WF. Findings in surgery for chronic otitis media: a retrospective data analysis of 2225 cases followed for two years. Clin Otolaryngol 1983;8:151.
99. Gibb AG. Tympanosclerosis. Ear Nose Throat J 1981;60:565–570.
100. Goodwin WJ, Jesse RH. Malignant neoplasms of the external auditory canal and temporal bone. Arch Otolaryngol 1980;106: 675–679.
101. Zollner F. Tympanosclerosis. J Laryngol Otol 1956;70:77–85.
102. Tos M. Bony fixation of the malleus and incus. Acta Otolaryngol 1970;70:95.
103. Swartz JD, Lansman AK, Berger AS, et al. Stapes prosthesis: evaluation with CT. Radiology 1986;158:179.
104. Chole R. Petrous apicitis—surgical anatomy. Ann Otol Rhinol Laryngol 1985;94:251–257.
105. Moore KR, et al. ''Leave me alone'' lesions of the petrous apex. AJNR 1998;19(4):733–738.
106. Virapongse C, et al. Computed tomography of temporal bone pneumatization: 1. Normal pattern and morphology. AJR 1985; 145(3):473–481.
107. Proctor B. Surgical Anatomy of the Ear and Temporal Bone. New York: Thieme, 1989.
108. Curtin HD, Som PM. The petrous apex. Otolaryngol Clin North Am 1995;28(3):473–496.
109. Davidson H, Harnsberger H. The temporal bone. In: Orrison W, ed. Neuroimaging. Philadelphia: WB Saunders, 2000;947–984.
110. Graamans K. Neurological disorders of the head and neck. In: Jones A, Phillips D, Hilgers F, eds. Disease of the Head and Neck, Nose and Throat. London: Arnold, 1998;616–627.
111. Chole RA, Donald PJ. Petrous apicitis. Clinical considerations. Ann Otol Rhinol Laryngol 1983;92(6 Pt 1):544–551.
112. Holliday RA, Reede DL. MRI of mastoid and middle ear disease. Radiol Clin North Am 1989;27(2):283–299.
113. Swartz JD. Current imaging approach to the temporal bone. Radiology 1989;171:309–317.
114. Lemmerling M, et al. Imaging of the normal pontine cisternal segment of the abducens nerve, using three-dimensional constructive interference in the steady state MRI. Neuroradiology 1999;41(5): 384–386.
115. Destrieux C, et al. A new concept in Dorello's canal microanatomy: the petroclival venous confluence. J Neurosurg 1997;87(1):67–72.
116. Umansky F, Elidan J, Valarezo A. Dorello's canal: a microanatomical study. J Neurosurg 1991;75(2):294–298.
117. Horn KL, Erasmus MD, Akiya FI. Suppurative petrous apicitis: osteitis or osteomyelitis? an imaging case report. Am J Otolaryngol 1996;17(1):54–57.
118. Chang P, et al. Imaging destructive lesions of the petrous apex. Laryngoscope 1998;108(4 Pt 1):599–604.
119. Muckle RP, De la Cruz A, Lo WM. Petrous apex lesions. Am J Otol 1998;19(2):219–225.
120. Palacios E, Valvassori G. Petrous apex lesions: cholesterol granuloma. Ear Nose Throat J 1999;78(4):234.
121. Lo WWM, Solti-Bohman LG, Brackman DE, et al. Cholesterol granuloma of the petrous apex: CT diagnosis. Radiology 1984;153: 705–711.
122. Eby TL, Guthrie BL. Bilateral cholesterol granulomas of the temporal bone. ORL J Otorhinolaryngol Relat Spec 1998;60(6):318–321.
123. Gomori JM, Grossman RI. Mechanisms responsible for the MR appearance and evolution of intracranial hemorrhage. Radiographics 1988;8:427.
124. Chole R, Brodie H. Surgery of the mastoid and petrosa. In: Bailey B, ed. Head and Neck Surgery—Otolaryngology. 2nd ed. Philadelphia: Lippincott-Raven, 1998;2053–2072.
125. Seltzer S, Mark AS. Contrast enhancement of the labyrinth on MR scans in patients with sudden hearing loss and vertigo: evidence of labyrinthine disease. AJNR 1991;12:13–16.
126. Mark A. Contrast enhanced magnetic resonance imaging of the temporal bone. Neuroimaging Clin North Am 1994;4(1):117–131.
127. Schleuning A, Andersen P, Morrissey D. Otologic manifestations of systemic disease. In: Bailey B, ed. Head and Neck Surgery—Otolaryngology. 2nd ed. Philadelphia: Lippincott-Raven, 1998;2125–2135.
128. Gulya A. Infections of the labyrinth. In: Bailey B, ed. Head and Neck Surgery—Otolaryngology. 2nd ed. Philadelphia: Lippincott-Raven, 1998;2137–2151.
129. Mark AS, Fitzgerald D. Segmental enhancement of the cochlea on contrast-enhanced MR: correlation with the frequency of hearing loss and possible sign of perilymphatic fistula and autoimmune labyrinthitis. AJNR 1993;14(4):991–996.
130. Fitzgerald DC, Mark AS. Viral cochleitis with gadolinium enhancement of the cochlea on magnetic resonance imaging scan. Otolaryngol Head Neck Surg 1999;121(1):130–132.
131. Davis L. Infections of the labyrinth. In: Cummings C, et al, eds. Otolaryngology—Head and Neck Surgery. St. Louis: CV Mosby, 1998;3139–3151.
132. Mark AS, Seltzer S, Nelson-Drake J, et al. Labyrinthine enhancement on GD MRI in patients with sudden hearing loss and vertigo. Ann Otol Rhinol Laryngol 1992;101:459–464.
133. Weissman JR, Cumin HD, Hirsch B, et al. High signal from the otic labyrinth on unenhanced magnetic resonance imaging. AJNR 1992;13:1183–1187.
134. Sheridan MF, Hetherington HH, Hull JJ. Inner ear barotrauma from scuba diving. Ear Nose Throat J 1999;78(3):181, 184, 186–187 passim.
135. Whitehead RE, et al. Spontaneous labyrinthine hemorrhage in sickle cell disease. AJNR 1998;19(8):1437–1440.
136. Harris JP, et al. Immunopathology of the inner ear: an update. Ann NY Acad Sci 1997;830:166–178.
137. Gilden D, et al. Neurologic complications of the reactivation of varicella-zoster virus. N Engl J Med 2000;342:635–645.
138. Canellas AR, Torres CS, Isern EJ, et al. Ramsay-Hunt syndrome and high-resolution 3D FT MRI. J Comput Assist Tomogr 1993;17(3): 495–497.
139. Osumi A, Tien RD. MR findings in a patient with Ramsay-Hunt syndrome. J Comput Assist Tomogr 1990;14:991–993.
140. Li J, Xiong L, Jinkins JR. Gadolinium enhanced MRI in a patient with AIDS and the Ramsay-Hunt syndrome. Neuroradiology 1993; 35:269.
141. Sartoretti-Schefer S, Kollias S, Valavanis A. Ramsay-Hunt syndrome associated with brain stem enhancement. AJNR 1999;20(2):278–280.
142. Arnold W, Kau R, Schwaiger M. [Clinical aspects of the osteolytic (inflammatory) phase of cochlear otosclerosis]. Laryngorhinootologie 1999;78(1):20–23.
143. Arnold W, et al. Measles virus in otosclerosis and the specific immune response of the inner ear. Acta Otolaryngol (Stockh) 1996;116(5):705–709.
144. Niedermeyer HP, Arnold W. Otosclerosis: a measles virus associated inflammatory disease. Acta Otolaryngol (Stockh) 1995;115(2): 300–303.

Copyright © 2003, Mosby, Inc. All rights reserved.

145. Niedermeyer H, et al. Evidence of measles virus RNA in otosclerotic tissue. ORL J Otorhinolaryngol Relat Spec 1994;56(3): 130–132.
146. Harris JP, Keithley EM. Inner ear inflammation and round window otosclerosis. Am J Otol 1993;14(2):109–112.
147. DeSautel M, Brodie H. Effects of depletion of complement in the development of labyrinthitis ossificans. Laryngoscope 1999;109: 1674–1678.
148. Suga F, Lindsay J. Labyrinthitis ossificans. Ann Otol 1977;86:17–29.
149. Green J, Marion M, Hinojosa R. Labyrinthitis ossificans: histopathologic consideration for cochlear implantation. Otolaryngol Head Neck Surg 1991;104:320–326.
150. Jackler RK, Dillon WP, Schindler RA. Computed tomography in suppurative ear disease: a correlation of surgical and radiographic findings. Laryngoscope 1984;94(6):746–752.
151. Casselman JW, et al. Pathology of the membranous labyrinth: comparison of T1- and T2-weighted and gadolinium-enhanced spin-echo and 3DFT-CISS imaging. AJNR 1993;14(1):59–69.
152. Weissman JL, Kamerer DB. Labyrinthitis ossificans. Am J Otolaryngol 1993;14(5):363–365.
153. Swartz JD, et al. Labyrinthine ossification: etiologies and CT findings. Radiology 1985;157(2):395–398.
154. Casselman JW, Majoor MH, Albers FW. MR of the inner ear in patients with Cogan syndrome. AJNR 1994;15(1):131–138.
155. Casselman JW, Kuhweide R, Deimling M. Constructive interference in the steady state (CISS)-3DFT MR imaging of the inner ear and cerebellopontine angle. AJNR 1993;14:47–57.
156. Mong A, et al. Sound- and pressure-induced vertigo associated with dehiscence of the roof of the superior semicircular canal [in process citation]. AJNR 1999;20(10):1973–1975.
157. Quinn SJ, Boucher BJ, Booth JB. Reversible sensorineural hearing loss in Lyme disease. J Laryngol Otol 1997;111(6):562–564.
158. Bertholon P, et al. Bilateral sensorineural hearing loss and spastic paraparesis in Lyme disease [in process citation]. Otolaryngol Head Neck Surg 2000;122(3):458–460.
159. Harris JP, Ryan AF. Fundamental immune mechanisms of the brain and inner ear. Otolaryngol Head Neck Surg 1995;112(6): 639–653.
160. Harris J. Immunologic disorders affecting the ear. In: Cummings C, et al, eds. Otolaryngology—Head and Neck Surgery. St. Louis: CV Mosby, 1998;3172–3185.
161. Dornhoffer JL, et al. Pathophysiological mechanisms in immune inner ear disease. Acta Otolaryngol Suppl 1997;526:30–36.
162. St Clair EW, McCallum RM. Cogan's syndrome. Curr Opin Rheumatol 1999;11(1):47–52.
163. Schuknecht HF, Nadol JB Jr. Temporal bone pathology in a case of Cogan's syndrome. Laryngoscope 1994;104(9):1135–1142.
164. Dagum P, Roberson JB Jr. Otologic Wegener's granulomatosis with facial nerve palsy. Ann Otol Rhinol Laryngol 1998;107(7):555–559.
165. Dawes JD, Watson RT. Perilymph fistula. Clin Otolaryngol 1979;4:291–302.
166. Nomura Y. Perilymph fistula: concept, diagnosis and management. Acta Otolaryngol Suppl (Stockh) 1994;514:52–54.
167. Stevenson DS, Proops DW, Phelps PD. Severe cochlear dysplasia causing recurrent meningitis: a surgical lesion. J Laryngol Otol 1993;107(8):726–729.
168. Brogan M, Chakeres DW. GD DTPA enhanced MR imaging of cochlear schwannoma. AJNR 1990;11:407–408.
169. Saeed SR, Birzgalis AR, Ramsden RT. Intralabyrinthine schwannoma shown by magnetic resonance imaging. Neuroradiology 1994;36:63–64.
170. Mukherji SK, et al. Evaluation of first branchial anomalies by CT and MR. Tomogr 1993;17(4):576–581.
171. Mendelson DS, Som PM, Mendelson MH, et al. Malignant external otitis: the role of computed tomography and radionuclides in evaluation. Radiology 1983;149:745–749.
172. Ostfeld E, Aviel A, Pelet D. Malignant external otitis: diagnostic value of bone scintigraphy. Laryngoscope 1981;91:960–964.
173. Bergeron RT, Osborn AG, Som PM. Head and Neck Imaging: Excluding the Brain. St. Louis: Mosby-Year Book, 1984;728–846.
174. Biber JJ. The so-called primary cholesteatoma of the external auditory meatus. Laryngol Otolaryngol 1953;67:474.
175. Piepergerdes MC, Kramer BM, Behnke EE. Keratosis obturans and external auditory canal cholesteatoma. Laryngoscope 1980;90: 383–391.
176. Barrow HN, Levenson MJ. Necrotizing ''malignant'' external otitis caused by *Staphylococcus epidermidis*. Arch Otolaryngol Head Neck Surg 1992;118(1):94–96.
177. Ress BD, et al. Necrotizing external otitis in patients with AIDS. Laryngoscope 1997;107(4):456–460.
178. Weinroth SE, Schessel D, Tuazon CU. Malignant otitis externa in AIDS patients: case report and review of the literature. Ear Nose Throat J 1994;73(10):772–774, 777–778.
179. Hern JD, et al. Malignant otitis externa in HIV and AIDS. J Laryngol Otol 1996;110(8):770–775.
180. Chandler J. Malignant external otitis. Laryngoscope 1968;78:1257.
181. Slattery WH 3rd, Brackmann DE. Skull base osteomyelitis. Malignant external otitis. Otolaryngol Clin North Am 1996;29(5): 795–806.
182. Grandis JR, Curtin HD, Yu VL. Necrotizing (malignant) external otitis: prospective comparison of CT and MR imaging in diagnosis and follow-up. Radiology 1995;196(2):499–504.
183. Myerhoff W, Gates G, Montalbo P. Pseudomonas mastoiditis. Laryngoscope 1977;87:483–492.
184. Crabtree JA, Britton BH, Powers WH. An evaluation of recent stapes surgery. Laryngoscope 1980;90:224–227.
185. Curtin HD, Wolfe P, Snyderman N. Facial nerve between the stylomastoid foramen and the parotid. Radiology 1983;149:165–169.
186. Gherini SG, Brackmann DE, Bradley WG. Magnetic resonance imaging and computerized tomography in malignant external otitis. Laryngoscope 1986;96(5):542–548.
187. Seabold JE, et al. Cranial osteomyelitis: diagnosis and follow-up with In-111 white blood cell and Tc-99m methylene diphosphonate bone SPECT, CT, and MR imaging. Radiology 1995;196(3):779–788.
188. Murray ME, Britton J. Osteomyelitis of the skull base: the role of high resolution CT in diagnosis. Clin Radiol 1994;49(6):408–411.
189. Chandler JR. Malignant external otitis and osteomyelitis of the base of the skull. Am J Otol 1989;10(2):108–110.
190. Chandler JR, et al. Osteomyelitis of the base of the skull. Laryngoscope 1986;96(3):245–251.
191. Chan LL, et al. Imaging of mucormycosis skull base osteomyelitis [in process citation]. AJNR 2000;21(5):828–831.
192. Adler M, et al. Radiation effects on the external auditory canal. J Otolaryngol 1985;14(4):226–232.
193. Meiteles L, et al. Osteoradionecrosis of the temporal bone. Ear Nose Throat J 1998;77(1):56–57.
194. Nishimura R, et al. MR evaluation of radiation otomastoiditis. Int J Radiat Oncol Biol Phys 1997;39(1):155–160.
195. Leonetti JP, et al. Intracranial complications of temporal bone osteoradionecrosis. Am J Otol 1997;18(2):223–228; discussion 228–229.
196. Guida RA, et al. Radiation injury to the temporal bone. Am J Otol 1990;11(1):6–11.
197. Crabtree JA, Britton BH, Pierce MK. Carcinoma of the external auditory canal. Laryngoscope 1976;86:405–415.
198. Hicks GW. Tumors arising from glandular structures of the external auditory canal. Laryngoscope 1983;93:326–340.
199. Grandis JR, Hirsch BE, Yu VL. Simultaneous presentation of malignant external otitis and temporal bone cancer. Arch Otolaryngol Head Neck Surg 1993;119(6):687–689.
200. DiBartolomeo JR. Exostosis of the external auditory canal. Ann Otolaryngol 1979;88(suppl 61):2–20.
201. Turetsky DB, Vines FS, Cayman DA. Surfer's ear: exostosis of the external auditory canal. AJNR 1990;11:1217–1218.
202. Denia A, Perez F, Canalis RR, et al. Extracanalicular osteomas of the temporal bone. Arch Otolaryngol 1979;105:706.
203. Bunting WP. Ear canal cholesteatoma and bony resorption. Trans Am Acad Ophthalmol Otolaryngol 1968;72:161–172.
204. Anthony PF, Anthony WP. Surgical treatment of external auditory canal cholesteatoma. Laryngoscope 1982;92(1):70–75.
205. Corbridge RJ, Michaels L, Wright T. Epithelial migration in keratosis obturans. Am J Otolaryngol 1996;17(6):411–414.
206. Hasso AN, Vignaud J, Bird CH. Pathology of the temporal bone and mastoid. In: Newton TH, Hasso AN, Dillon WP, eds. Computed Tomography of the Head and Neck, Vol. 3, Modern Neuroradiology. New York: Raven Press, 1988;1–45.
207. Johnson DW. CT of the postsurgical ear. Radiol Clin North Am 1984;22:67–75.
208. Swartz JD, Berger AS, Zwillenberg S, et al. Synthetic ossicular replacements: normal and abnormal CT appearance. Radiology 1987;163:766–768.

Copyright © 2003, Mosby, Inc. All rights reserved.

209. Shambaugh GE, Glasscock MD. Surgery of the ear. Philadelphia: WB Saunders, 1980;251–287.
210. Cody DTR, Taylor WF. Mastoidectomy for acquired cholesteatoma: long term results. In: McCabe BS, Sade J, Abramson M, eds. Cholesteatoma. Birmingham, Ala: Aesculapius, 1977;337–351.
211. Sheehy JL. Intact canal wall tympanoplasty with mastoidectomy. In: Snow JB, ed. Controversy in Otolaryngology. Philadelphia: WB Saunders, 1980;213–222.
212. Paparella MM, Meyerhoff W. Mastoidectomy and tympanoplasty. In: Paparella MM, Shumrick DA, eds. Otolaryngology—The Ear. Philadelphia: WB Saunders, 1980;1510–1547.
213. Kohut RI. Cholesteatoma: the advantages of modified radical and radical mastoidectomy. In: Snow JB, ed. Controversy in Otolaryngology. Philadelphia: WB Saunders, 1980;223–227.
214. Mukherji SK, et al. CT of the temporal bone: findings after mastoidectomy, ossicular reconstruction, and cochlear implantation. AJR 1994;163(6):1467–1471.
215. Martin N, Sterkers O, Murat M, et al. Brain herniation into the middle ear cavity: MR imaging. Neuroradiology 1989;31:184–186.
216. Nardis PF, Teramo M, Guinta S, et al. Unusual cholesteatoma shell: CT findings. J Comput Assist Tomogr 1988;12:1084.
217. Hilding DA, et al. Reconstruction of the ossicular chain. In Snow JB, ed. Controversy in Otolaryngology. Philadelphia: WB Saunders, 1980;57–83.
218. Torizuka T, Hayakawa K, Satoh Y, et al. Evaluation of high resolution CT after tympanoplasty. J Comput Assist Tomogr 1992;16(5):779–783.
219. Stone JA, et al. CT evaluation of prosthetic ossicular reconstruction procedures: what the otologist needs to know. Radiographics 2000;20(3):593–605.
220. Brackmann DE, Sheehy JL, Luxford WM. TORPS and PORPS in tympanoplasty: A review of 1042 operations. Otolaryngol Head Neck Surg 1984;92:337.
221. Jackson CG, Glasscock MEI, Schwaber MK, et al. Ossicular chain reconstructions: the TORP and PORP in chronic ear disease. Laryngoscope 1983;93:981–988.
222. Chole RA, Skarada DJ. Middle ear reconstructive techniques [in process citation]. Otolaryngol Clin North Am 1999;32(3): 489–503.
223. Shellock FG, Schatz CJ. Metallic otologic implants: in vitro assessment of ferromagnetism at 1.5 T. AJNR 1991;12(2):279–281.
224. Sheehy JL, Nelson RA, House HP. Revision stapedectomy: review of 258 cases. Laryngoscope 1981;91:43–56.
225. Gibbin KT. The histopathology of the incus after stapedectomy. Clin Otolaryngol 1979;4:343.
226. Swartz JD, Laucks RL, Berger AS, et al. Computed tomography of the disarticulated incus. Laryngoscope 1986;96:1207–1210.
227. Belal A Jr, Ylikoski J. Post stapedectomy dizziness: a histopathologic agent. J Otol 1982;3:187–191.
228. Ball JBJ, Miller GW, Hepfner ST. Computed tomography of single channel cochlear implants. AJNR 1986;7:41–47.
229. Harnsberger HR, et al. Cochlear implant candidates: assessment with CT and MR imaging. Radiology 1987;164(1):53–57.
230. Mueller DP, Dolan KD, Gantz BJ, et al. Temporal bone computed tomography in the preoperative evaluation for cochlear implantation. Ann Otol Rhinol Laryngol 1989;98:346–349.
231. Nair SB, Abou-Elhamd KA, Hawthorne M. A retrospective analysis of high resolution computed tomography in the assessment of cochlear implant patients. Clin Otolaryngol 2000;25(1):55–61.
232. Murugasu E, et al. The application of three-dimensional magnetic resonance imaging rendering of the inner ear in assessment for cochlear implantation. Am J Otol 1999;20(6):752–757.
233. Weber BP, et al. Pediatric cochlear implantation in cochlear malformations. Am J Otol 1998;19(6):747–753.
234. Schaitkin BM, May M, Podvinec M, Ulrich J, Peitersen E, Klein SR: Idiopathic (Bell's) Palsy, Herpes Zoster Cephalicus, and other Facial Nerve Disorders of Viral Origin. In: May M, Schaitkin BM, eds. The facial nerve, May's 2nd ed. New York: Thieme, 2000;319–338.
235. Schaitkin BM, May M, Klein SR: Office Evaluation of the Patient with Facial Paralysis. In: May M, Schaitkin BM, eds. The facial nerve, May's 2nd ed. New York: Thieme, 2000;179–212.
236. Fisch U, Esslen E: Total intratemporal exposure of the facial nerve. Pathologic findings in Bell's palsy. Arch Otolaryngol 1972;95(4): 335–341.
237. Daniels DL, Czervionke LF, Millen SJ, et al.: MR imaging of facial nerve enhancement in Bell's palsy or after temporal bone surgery. Radiology 1989;171(3):807–809.
238. LaBagnara J, Jr., Jahn AF, Habif DV, Jr., Solomon EM: MRI findings in two cases of acute facial paralysis. Otolaryngol Head Neck Surg 1989;101(5):562–565.
239. Korzec K, Sobol SM, Kubal W, Mester SJ, Winzelberg G, May M: Gadolinium-enhanced magnetic resonance imaging of the facial nerve in herpes zoster oticus and Bell's palsy: clinical implications. Am J Otol 1991;12(3):163–168.
240. Sartoretti-Schefer S, Wichmann W, Valavanis A: Idiopathic, herpetic, and HIV-associated facial nerve palsies: abnormal MR enhancement patterns. AJNR Am J Neuroradiol 1994;15(3):479–485.
241. Sartoretti-Schefer S, Brandle P, Wichmann W, Valavanis A: Intensity of MR contrast enhancement does not correspond to clinical and electroneurographic findings in acute inflammatory facial nerve palsy. AJNR Am J Neuroradiol 1996;17(7):1229–1236.
242. Tien R, Dillon WP, Jackler RK: Contrast-enhanced MR imaging of the facial nerve in 11 patients with Bell's palsy. AJNR Am J Neuroradiol 1990;11(4):735–741.
243. Sartoretti-Schefer S, Kollias S, Wichmann W, Valavanis A: T2-weighted three-dimensional fast spin-echo MR in inflammatory peripheral facial nerve palsy. AJNR Am J Neuroradiol 1998;19(3): 491–495.

Copyright © 2003, Mosby, Inc. All rights reserved.

23

Temporal Bone: Trauma

Joel D. Swartz and Hugh D. Curtin

INTRODUCTION
FRACTURES AND PSEUDOFRACTURES
- Longitudinal Fractures
- Transverse Fractures
- Pseudofractures

OSSICULAR DISLOCATION AND FRACTURE
COMPLICATIONS OF TEMPORAL BONE TRAUMA
- Fistulous Communications
- Hearing Loss
- Facial Nerve Dysfunction

INTRODUCTION

Temporal bone trauma usually results from blunt head injury.[1, 2] The discussion in this chapter will be subdivided into the topics of fractures and pseudofractures, ossicular dislocations, and complications of temporal bone trauma. This chapter will also emphasize that in the imaging evaluation of the posttraumatic patient with a possible temporal bone fracture, CT and MR imaging are complementary studies.

FRACTURES AND PSEUDOFRACTURES

Temporal bone fractures follow the paths of least resistance, usually connecting natural fissures and foramina. These fractures are classified by their orientation relative to the long axis of the petrous bone.[2–6] Overall, these fractures are best imaged, especially in the critically injured patient, in the axial CT study.[7] Up until recently, the axial examination was the only plane available for imaging the severely injured patient. However, recent advances such as multidetector spiral CT have made possible multiplanar reformatting from axial image data. These reformatted images approach the resolution of the original image acquisition and allow assessment in various planes without repositioning an unstable patient (Fig. 23-1).

Most observers continue to believe that longitudinal fractures are by far the most common type of temporal bone fracture, followed by transverse, oblique, and mixed-type fractures. There is, however, some dispute on this subject, as some recent investigators have concluded that most of these fractures are actually oblique in alignment.[8] Nonetheless, for the purposes of this discussion, the well-accepted concept that the longitudinal variety is indeed the most common fracture will be used. More severe fractures frequently have components extending both along and perpendicular to the axis of the temporal bone. Fractures associated with gunshot wounds are typically quite complex, and the quality of evaluation may be limited by metallic artifact. Chin-dashboard trauma is associated with less common injuries including tympanic ring fracture and TMJ injury. Styloid process fractures are rare and difficult to diagnose. They often have nonspecific clinical manifestations including headache and upper neck pain.[9]

Longitudinal Fractures

Longitudinal fractures of the petrous temporal bone are parallel to the long axis of the petrous pyramid and are typically associated with a blunt temporoparietal blow[10, 11] (Figs. 23-2 to 23-5). Approximately 10% are associated with a visible ecchymosis over the mastoid process (‘‘Battle’s sign’’). These fractures cross the middle ear and are very frequently associated with ossicular dislocation (see below). As longitudinal fractures follow the paths of least resistance, they are usually extralabyrinthine, most commonly deflecting anteriorly toward the eustachian tube and middle cranial fossa.[2, 12–14] Less commonly, the fracture can deflect posteriorly relative to the labyrinth, exiting the temporal bone through the jugular foramen and extending into the posterior fossa.

Involvement of the external auditory canal (EAC), tegmen tympani, and squamous temporal bone is common, and occlusion of the EAC by bony fracture fragments or soft-tissue debris may preclude otoscopic inspection. Sensorineural hearing loss is unusual unless there is a so-called cochlear concussion or perilymphatic fistula. Perilymphatic

Copyright © 2003, Mosby, Inc. All rights reserved.

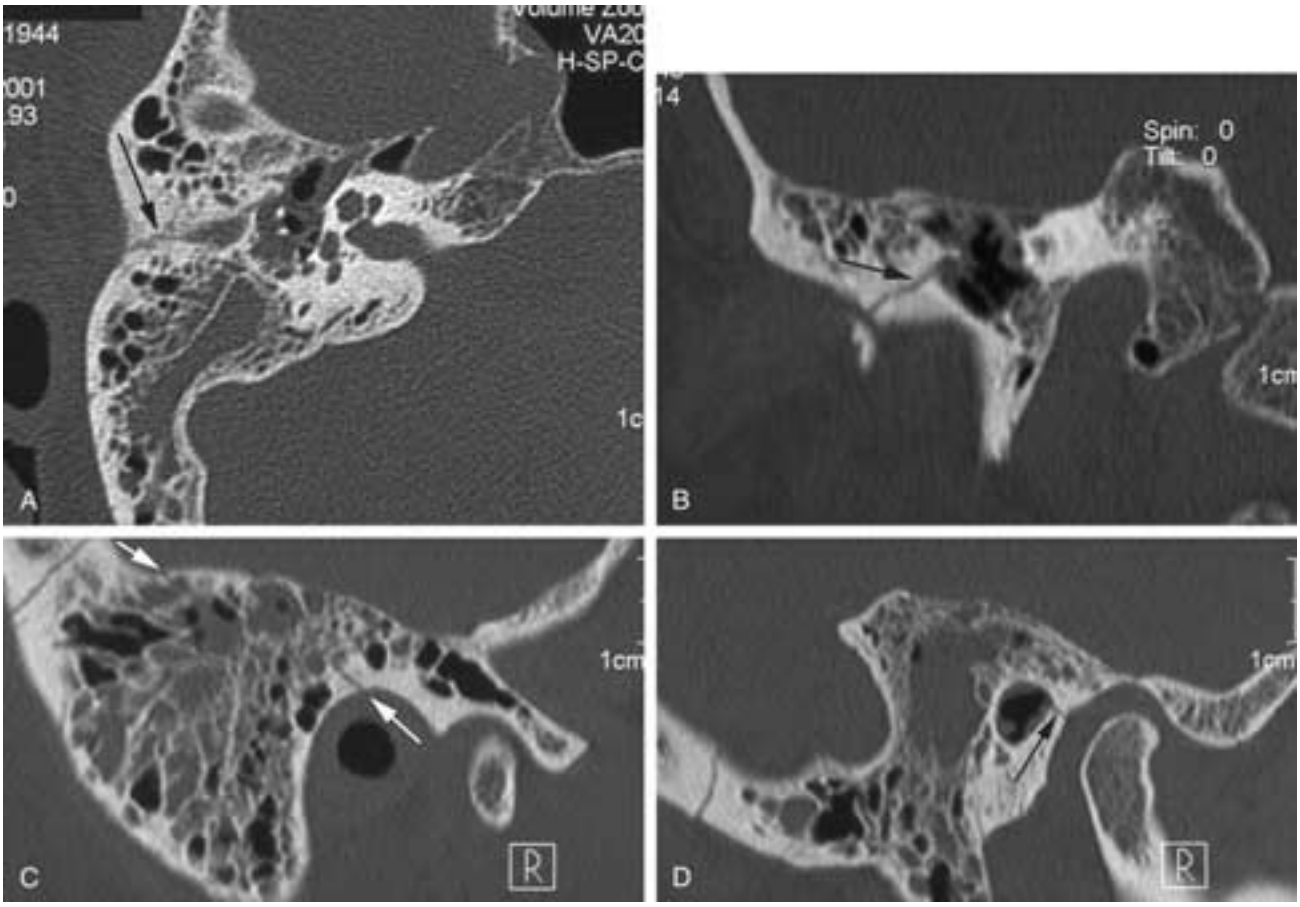

VIEW IMAGE

FIGURE 23-1 Longitudinal fracture with multidetector CT and multiplanar reformatting. **A**, Axial plane. The fracture (*arrow*) is oblique to this plane but is seen passing along the roof of the EAC. There is fluid (blood) in the mastoid and middle ear. **B**, Coronal reformat shows the fracture (*arrow*) extending into the middle ear. **C**, Sagittal plane reformat is perpendicular to the fracture line and shows the fracture crossing the tegmen and extending into the external canal (*arrows*). **D**, Sagittal reformat medial to **C** shows fracture *(arrow)* extending into the temporomandibular joint.

fistula may result from implosion or displacement of the stapes footplate or from rupture of the round window membrane. Conductive hearing loss is quite common and is often due to ossicular disruption.

As mentioned, fractures crossing anterior to the labyrinth can pass along the eustachian tube. They can, however, also fracture the thin cortical plate of the carotid canal, be multiple, and continue to extend across the foramen lacerum and reach the sphenoid bone. Rarely, the fracture can cross through the opposite side of the sphenoid, becoming bilateral.[11] Commonly, the sphenoid bone fractures where the carotid artery causes an impression on the lateral sphenoid sinus wall. Thus, the carotid artery is at risk for damage in both the petrous and sphenoid portions of its canal. There is the risk of an arterial tear, a pseudoaneurysm, or a carotid cavernous sinus fistula. Dissection or complete occlusion of the artery can also occur.[12] If CT demonstrates a fracture involving the carotid canal, angiography should be considered. MR angiography and CT angiography are less invasive alternatives to conventional angiography. The artery is placed at significantly increased risk if there is displacement of a bone fragment into the canal or if there is substantial dislocation of the petrous apex.[11]

Longitudinal fractures have been described as having posterior and anterior subtypes, based primarily on the site of origin.[15, 16] The posterior subtype often originates in the mastoid process or posterior aspect of the squamosal portion of the temporal bone and terminates in the foramen lacerum. This fracture usually does not involve the glenoid fossa. The anterior subtype originates in the anterior portion of the squamosal portion of the temporal bone and traverses the tegmen tympani to terminate at the petrous apex or pass again along the eustachian tube to the foramen lacerum. This anterior subtype may result in disruption of the middle meningeal artery with development of an epidural hematoma. The glenoid fossa is typically involved in the anterior subtype.

Both the posterior and anterior subtypes tend to involve the first genu or proximal tympanic segment of the facial nerve, but facial palsy is less common and less severe than palsies associated with transverse fracture (see later in the chapter). Rather than extending across the nerve, the longitudinal fracture may extend along the neural canal itself. Because this fracture does not directly cross the canal, it is unlikely to transect the nerve. Rather, the glancing or shearing effect of the fracture can cause swelling or a

Copyright © 2003, Mosby, Inc. All rights reserved.

FIGURE 23-2 Drawing of the longitudinal fracture. Note that the fracture line is parallel to the long axis of the petrous bone. (From Swartz JD, Harnsberger HR. Imaging of the Temporal Bone, 3rd ed. New York: Thieme, 1998.)

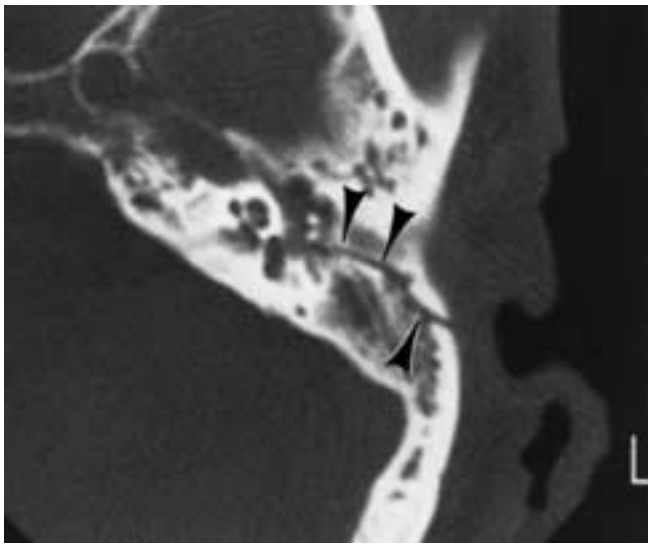

FIGURE 23-4 Longitudinal fracture. Fracture line is demonstrated through the mastoid (*arrowheads*), extending to but not disrupting the ossicular chain. (From Swartz JD, Harnsberger HR. Imaging of the Temporal Bone. New York: Thieme, 1992.)

hematoma in the nerve. Lastly, a fracture fragment may impale the nerve, causing further injury.

In traumatic facial paralysis, the relationship of the time of onset of the paralysis to the trauma is important. A paralysis of immediate onset, coinciding with the moment of injury, may represent a severed nerve, while a delayed onset implies that the nerve is intact. In the latter case, it is the swelling or developing hematoma that causes the delayed paralysis. The prognosis is better if the patient has demonstrated some posttraumatic facial function, as this ensures that there is gross integrity of the nerve.

Fractures passing posterior to the labyrinth also may put the facial nerve at risk, as the fracture, while passing into the

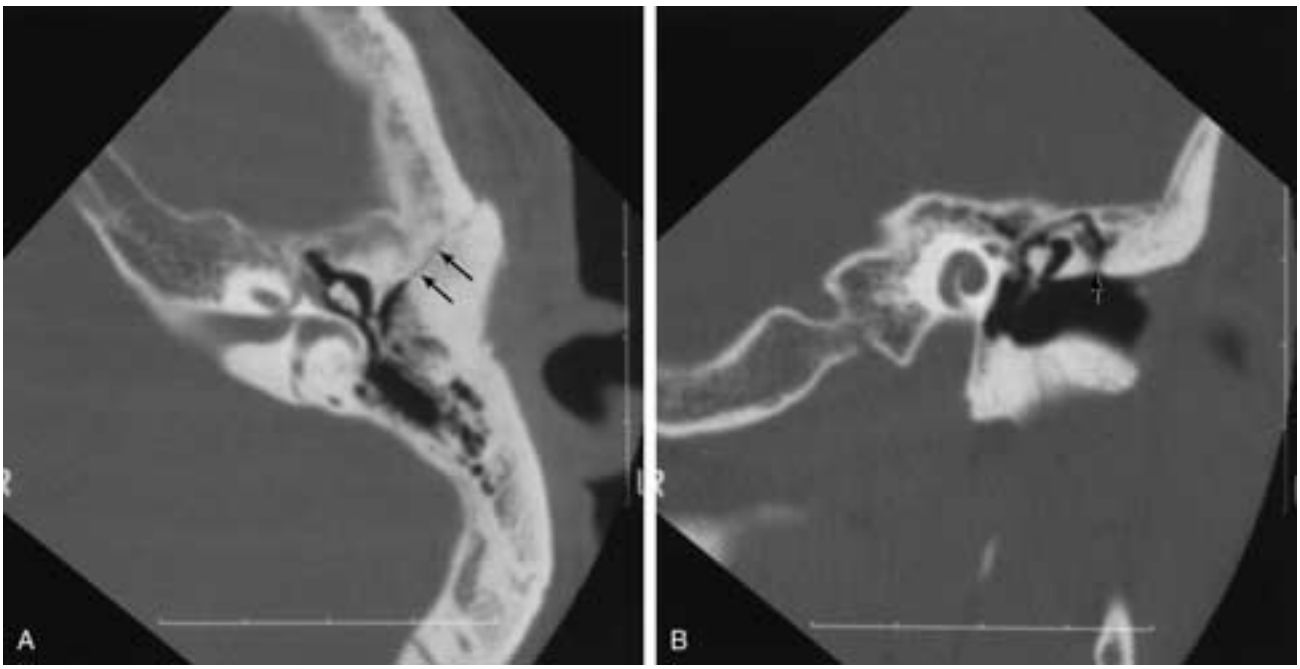

FIGURE 23-3 Longitudinal fracture. **A**, Axial CT image, left ear. Fracture line (*arrows*) is actually somewhat oblique to the long axis of the petrous bone. **B**, Coronal CT, left ear. Involvement of the EAC/tegmental air cell system (*arrow*).

Copyright © 2003, Mosby, Inc. All rights reserved.

jugular fossa or posterior wall of the temporal bone, usually passes through the vertical or mastoid portion of the facial nerve. These uncommon fractures are prone to transect the nerve.

Rarely, a fracture can pass both posterior and anterior to the otic capsule. The anterior fracture passes into the foramen lacerum and then can pass posteriorly along the petrooccipital synchondrosis to the posterior fossa. The posterior fracture enters the posterior fossa more laterally, in or near the jugular foramen, or perhaps through the posterior mastoid. This combination of fractures can result in a freely moving fragment including the otic capsule and petrous apex and has been referred to as a floating petrous bone.[17] The petrous apex can rotate slightly, putting pressure on or pinching the sixth nerve passing through Dorello's canal at the apex of the bone (Fig. 23-6). This can happen without injury to the eighth nerve, as no fracture line crosses its path. However, the posterior component of the fracture will likely cross the vertical facial nerve canal in the mastoid, causing facial paralysis.

Temporal bone fractures have little ability to form a ''callus.'' There is therefore a tendency for squamous invasion at the fracture site, and acquired cholesteatoma is a potential delayed complication[18, 19] (Fig. 23-5). These cholesteatomas have a tendency to become large and extensive, as most of these patients lack a history of chronic otitis media and therefore have well-pneumatized mastoids.

Longitudinal fractures are best diagnosed with CT. The MR imaging manifestations of this type of fracture include dural enhancement, believed to correlate with ''microfractures.''[20, 21]

Transverse Fractures

Transverse fractures are perpendicular to the long axis of the petrous pyramid and typically result from a blunt occipital or occipitomastoid impact[22–24] (Figs. 23-7 to 23-10). There are medial and lateral subtypes defined by their position relative to the arcuate eminence (a landmark along the superior petrous surface corresponding roughly to the position of the apex of the curve of the superior semicircular canal). The temporal bone's entry point for both fractures is usually near the vestibular aqueduct.[15, 16] The medial subtype of transverse fracture traverses the fundus (lateralmost aspect) of the internal auditory canal (IAC). Sensorineural hearing loss is secondary to cochlear nerve transection, and therefore is often complete and permanent. The lateral subtype of transverse fracture traverses the bony labyrinth rather than the IAC (Fig. 23-8). This results in sensorineural hearing loss, and there is frequently an associated perilymphatic fistula due to the communication between the middle ear and the inner ear as a result of the fracture.[25] Air can follow a fracture line from the middle ear into the labyrinth, causing a pneumolabyrinth. Carotid canal involvement is associated with catastrophic complications.[26]

Pseudofractures

Temporal bone pseudofractures can be subdivided into extrinsic sutures/fissures, intrinsic fissures, and intrinsic channels.[27]

Extrinsic sutures/fissures separate the temporal bone from adjacent bones. Examples include petrooccipital, temporooccipital, and occipitomastoid sutures.[27] The petrooccipital fissure, consistently appreciated between the clivus and the petrous apex, contains the inferior petrosal sinus coursing inferiorly from the cavernous sinus to exit the skull base via the anteromedial aspect of the jugular foramen (pars nervosa). The occipitomastoid suture is a constant structure visible on both axial and coronal CT images (Fig. 23-11). Its appearance varies from smooth and well corticated to irregular, coarse, and relatively wide. The observer should keep in

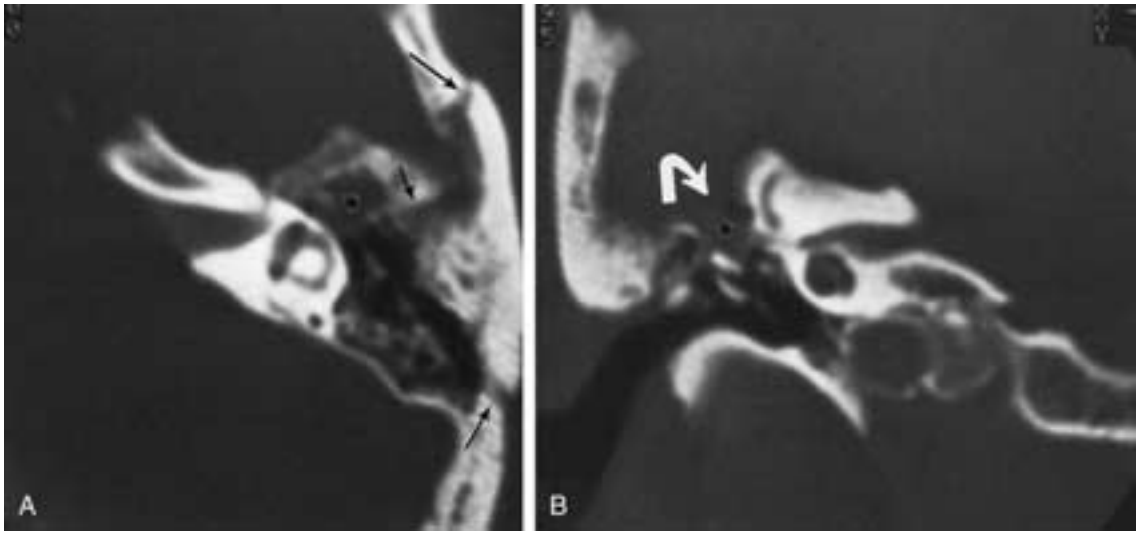

FIGURE 23-5 Complicated mixed fracture. **A**, Axial section. Fracture lines are demonstrated (*arrows*). A soft-tissue mass is identified in the attic (*). **B**, Coronal image. A large tegmen defect is present (*curved white arrow*). A soft-tissue mass is identified in the attic (*). This mass could represent encephalocele or cholesteatoma invading the fracture line. MR imaging was recommended.

VIEW IMAGE

Copyright © 2003, Mosby, Inc. All rights reserved.

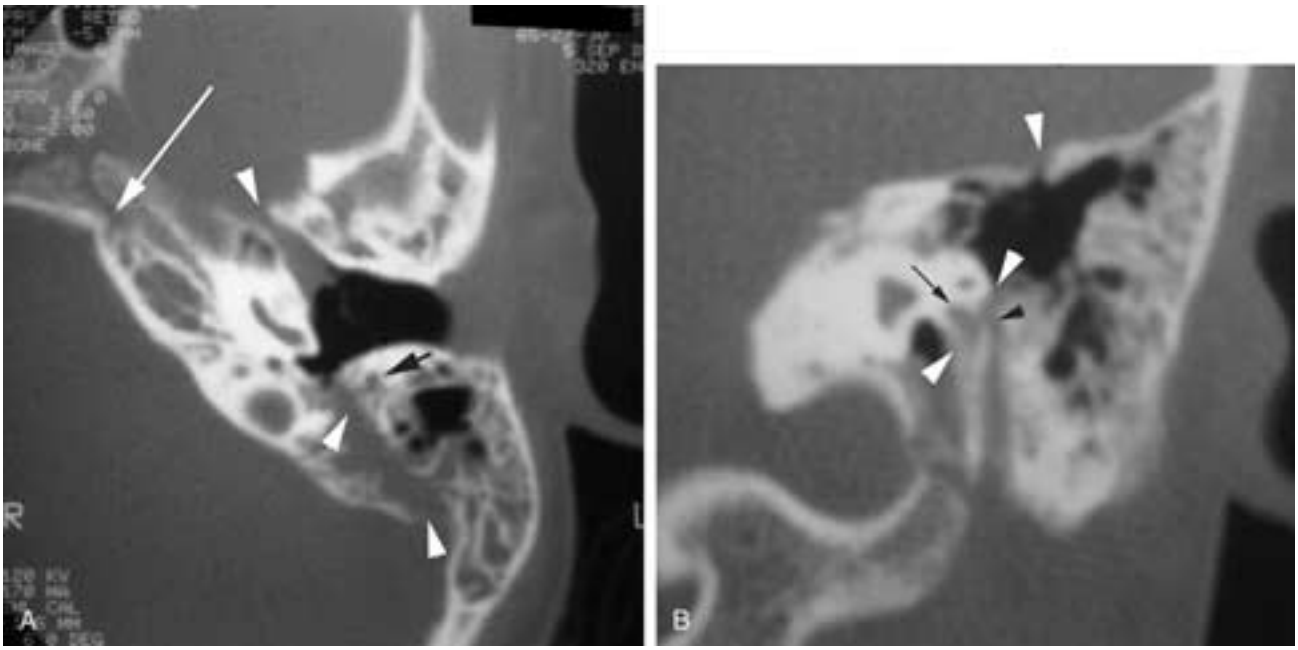

VIEW IMAGE

FIGURE 23-6 Fracture dislocation of the temporal bone apex (floating petrous bone). CT. This child had a compression from laterally and presents with facial paralysis and sixth nerve palsy. **A**, Axial scan shows the fracture (*arrowheads*) crossing from the posterior plate of the mastoid anteriorly through the middle ear, exiting by the anterior genu of the facial nerve. The medial portion of the temporal bone (including the labyrinth) is a single movable fragment. This part of the bone has rotated slightly, impacting the tip against the clivus. This pinches into Dorrello's canal (*white arrow*), explaining the sixth nerve palsy. The fracture separates the mastoid segment (*black arrow*) of the facial nerve from the tympanic segment, explaining the facial paralysis. **B**, Coronal image shows the fracture line (*white arrowheads*) passing through the tegmen, then crossing the facial nerve into the middle ear. Note that the fracture separates the facial canal mastoid section (*black arrowhead*) from the tympanic section (*black arrow*).

mind that the transversely oriented sphenooccipital synchondrosis, consistently visualized on axial CT images, generally closes at approximately age 10.

The temporal bone has five parts: squamous, petrous, mastoid, tympanic, and styloid. Examples of intrinsic fissures include the tympanosquamous, tympanomastoid, and petrotympanic fissures. The tympanomastoid suture is longitudinally oriented along the posterior bony cortex of the EAC (Fig. 23-10). The tympanosquamous suture is typically oriented along the anterior surface of the EAC. EAC fractures cannot be consistently diagnosed unless the observer has a working knowledge of these normal variations. The petrotympanic fissure, containing the chorda tympani nerve and the anterior tympanic branch of the maxillary artery, is best seen on images obtained in the sagittal plane. The anterior tympanic spine forms the inferior boundary of this fissure and may be injured due to the retropulsive effects of chin-dashboard trauma.

There are numerous intrinsic channels. The cochlear aqueduct is a potential communication between the CSF in the pars nervosa of the jugular fossa and the perilymph of the basilar turn of the cochlea. In the coronal plane, the aqueduct is obliquely oriented, curving superiorly and tapering laterally toward the junction of the basilar turn of the cochlea and vestibule (Fig. 23-12). The aqueduct roughly parallels the long axis of the IAC. This is a consistently narrow channel identified on axial and coronal CT images. The vestibular aqueduct contains the endolymphatic duct and part of the endolymphatic sac. On axial images, the

FIGURE 23-7 Drawing of the transverse fracture. The fracture line is perpendicular to the long axis of the petrous bone. (From Swartz JD, Harnsberger HR. Imaging of the Temporal Bone, 3rd ed. New York: Thieme, 1998.)

VIEW IMAGE

Copyright © 2003, Mosby, Inc. All rights reserved.

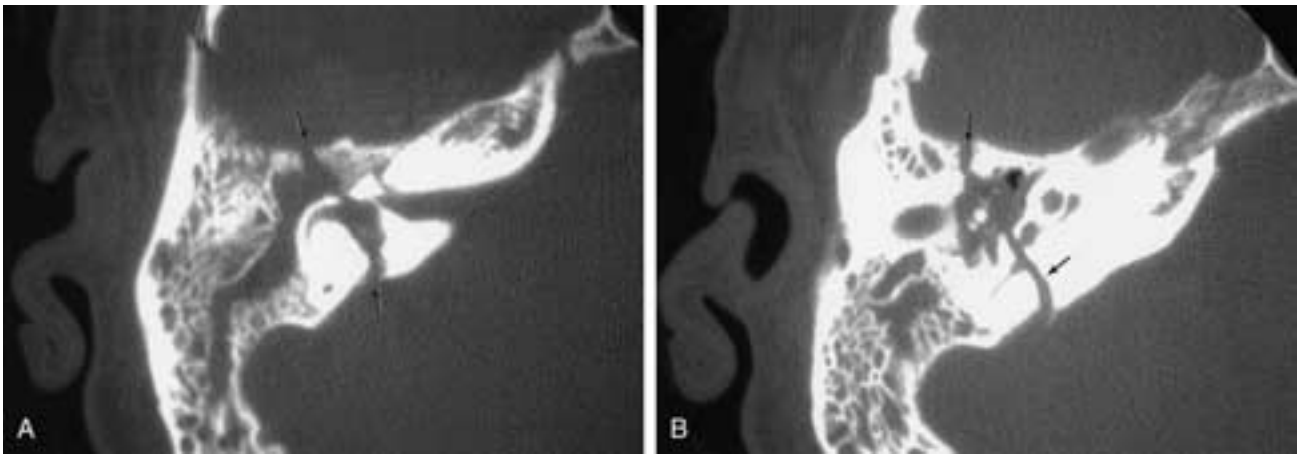

VIEW IMAGE

FIGURE 23-8 Transverse fracture, lateral subtype. **A**, Axial CT image, right ear. Fracture (*arrows*) begins at the posterior petrous surface in the vicinity of the vestibular aqueduct and disrupts the anterior portion of the tegmen tympani, as well as the squamous portion of the petrous bone. **B**, Axial CT image, right ear, more inferior, also reveals disruption of the promontory fracture (*arrows*). Note the diffuse hematotympanum.

vestibular aqueduct is seen in cross section as an intrusion or channel into the posterior cortex of the petrous bone, oriented along the long axis of the petrous pyramid parallel to the posterior semicircular canal close to common crus of the labyrinth (Fig. 23-13). The vestibular aqueduct is obliquely oriented from superior to inferior and is therefore also well seen on sagittal imaging. The petromastoid (subarcuate) canal containing the subarcuate artery/vein is consistently seen at the petrous apex on axial CT images, appearing as a curvilinear lucency at the level of the superior semicircular canal passing between the anterior and posterior limbs of this canal (Fig. 23-14). The petromastoid canal is a remnant of the voluminous subarcuate fossa seen consistently in the newborn.[28]

The singular canal exits the posterior inferior part of the IAC and then runs parallel to the IAC to reach the labyrinth.[1] The singular canal contains the singular nerve, a branch of the inferior vestibular nerve supplying the posterior semicircular canal (Fig. 23-15). The mastoid canaliculus contains the nerve of Arnold, a branch of the vagus nerve, and can be seen in either the axial or coronal plane as a lucency connecting the jugular foramen with the mastoid segment of the facial nerve canal (Fig. 23-16). The inferior tympanic canaliculus (ITC) is oriented vertically and is consistently seen on coronal CT images between the carotid canal and the jugular fossa (Fig. 23-17). The ITC contains the inferior tympanic branch of the glossopharyngeal nerve, also known as the nerve of Jacobsen, and the

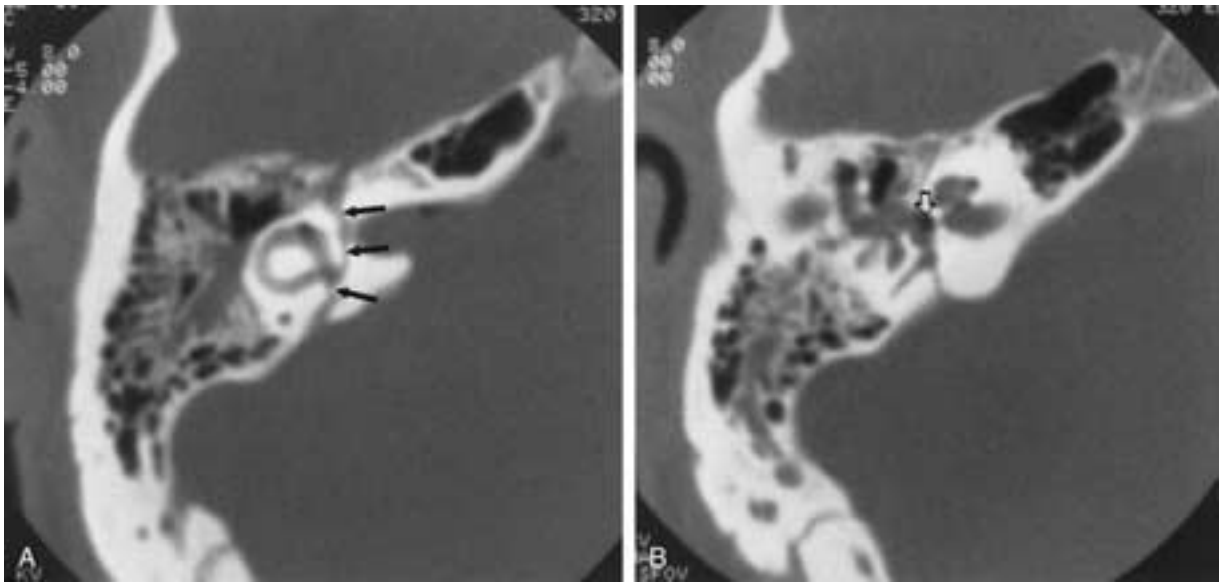

VIEW IMAGE

FIGURE 23-9 Transverse fracture, medial subtype. **A**, Fracture line (*arrows*) begins at the posterior petrous surface in the vicinity of the vestibular aqueduct and extends through the fundus of the IAC toward the first genu of the facial nerve canal. **B**, Pneumovestibule (*arrow*).

Copyright © 2003, Mosby, Inc. All rights reserved.

FIGURE 23-10 Transverse fracture, medial subtype. Axial CT, right ear. Fracture (*arrows*) extends from the posterior petrous surface through the fundus of the IAC. (From Swartz JD, Harnsberger HR. Imaging of the Temporal Bone, 3rd ed. New York: Thieme, 1998).

inferior tympanic artery. Interestingly, this is also the point of entry of the rare aberrant internal carotid artery, as the vertical portion of the carotid canal does not develop in this circumstance. This lucent channel should not be confused with a fracture.

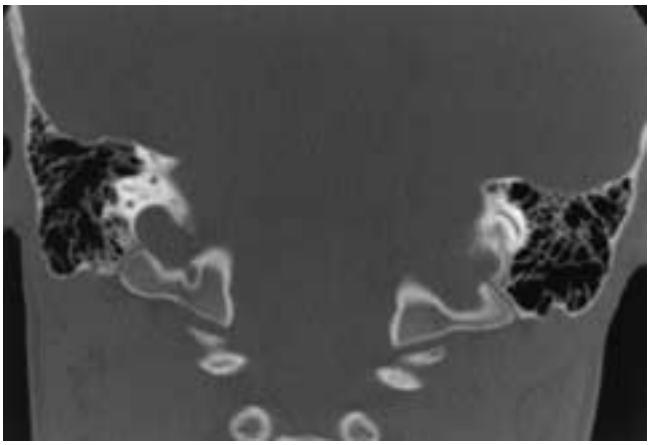

FIGURE 23-11 Pseudofracture, occipitomastoid sutures. This magnified coronal CT image of the left ear demonstrates normal occipitomastoid sutures (*arrows*). They are symmetric and smoothly corticated in this example, but may be irregular and asymmetric and still be within the range of normal.

OSSICULAR DISLOCATION AND FRACTURE

Ossicular injury can occur either in association with fractures of the temporal bone or as an isolated event. Longitudinal fractures are more commonly associated with ossicular dislocations than are transverse fractures, as the shearing force of a longitudinal fracture passes through the middle ear, putting the continuity of the ossicular chain at risk. Dislocations can occur without fracture and may result either from a penetrating injury or from blunt local trauma to the tympanic membrane. Blasts, which cause a rapid, wide pressure change in the EAC, can result in ossicular dislocation, as can a blow to the ear with a cupped hand.

In order to understand the pathophysiology of ossicular dislocation and posttraumatic conductive hearing loss, the

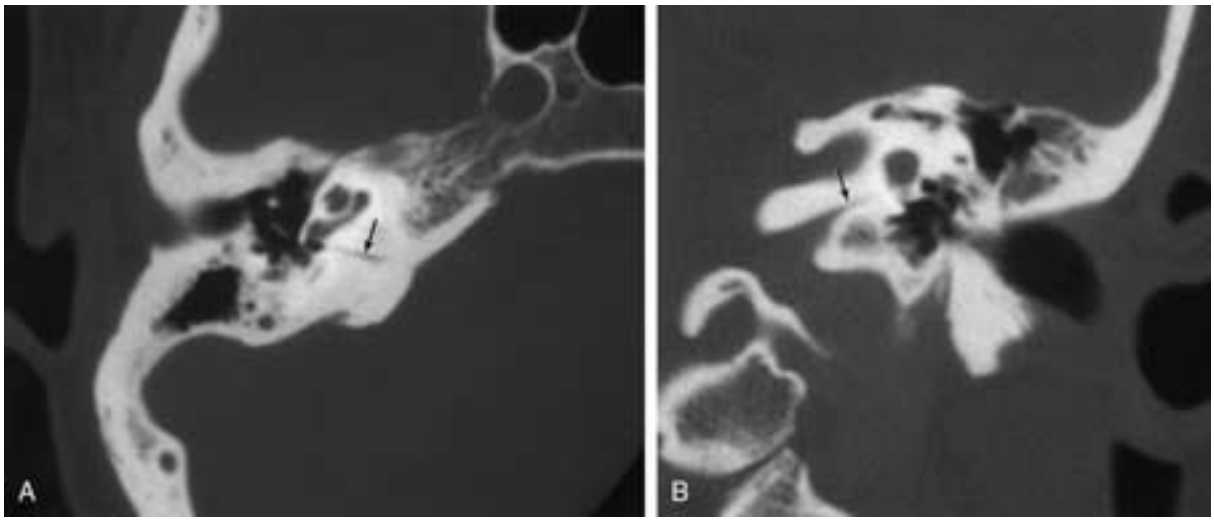

FIGURE 23-12 Pseudofracture, cochlear aqueduct. **A**, Axial CT image. **B**, Coronal CT image. These magnified CT images clearly demonstrate a normal-appearing cochlear aqueduct (*arrows*), which should not be confused with a fracture.

Copyright © 2003, Mosby, Inc. All rights reserved.

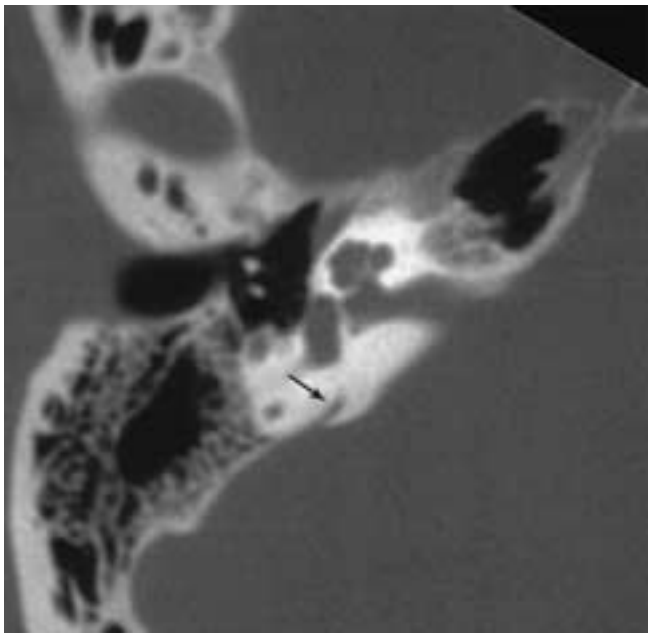

FIGURE 23-13 Pseudofracture, vestibular aqueduct. Note the focal intrusion into the posterior cortex of the petrous bone (*arrow*) at this location on this magnified axial CT image of the right ear. This is the normal appearance of the vestibular aqueduct in the axial plane.

observer must appreciate the anatomy pertaining to the ossicular support[29] (Fig. 23-18). The malleus is well supported by the anterior, lateral, and superior malleal ligaments. In addition, both the short process and the manubrium are embedded within the tympanic membrane. The stapes is well supported by the stapediovestibular articulation (footplate/annular ligament) as well as by the

FIGURE 23-14 Pseudofracture, petromastoid canal. This is a magnified axial CT image of the left ear demonstrating a curvilinear lucency at the petrous apex (*arrow*) consistent with the petromastoid canal. (Modified from Swartz JD, Harnsberger HR. Imaging of the Temporal Bone, 3rd ed. New York: Thieme, 1998.)

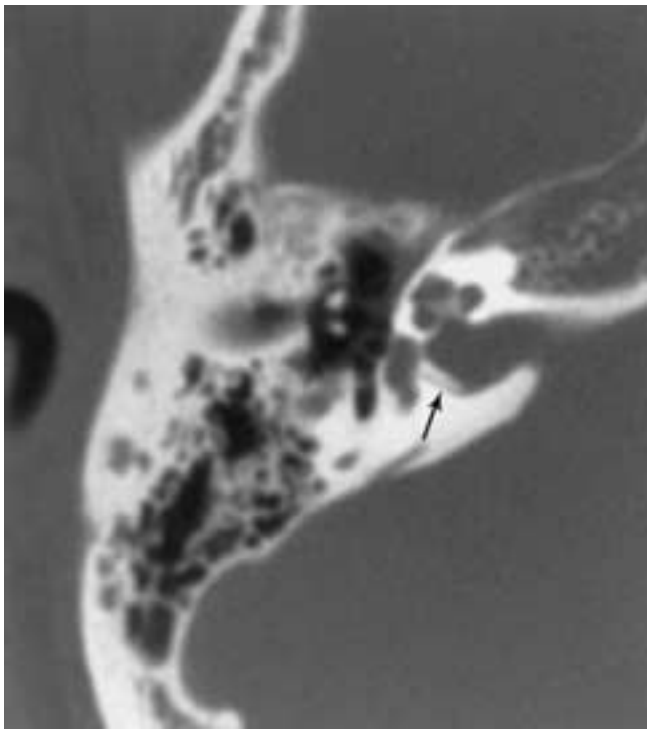

FIGURE 23-15 Pseudofracture, singular canal. Magnified axial CT image obtained through the IAC demonstrates a tiny channel parallel and posterior to the IAC fundus (*arrow*). (From Swartz JD, Harnsberger HR. Imaging of the Temporal Bone, 3rd ed. New York: Thieme, 1998.)

stapedius tendon and the articulation with the incus. The incus, however, is relatively heavy (25 mg) and is provided only minor ligamentous support by the posterior incudal ligament. Therefore, the incus is clearly the most vulnerable

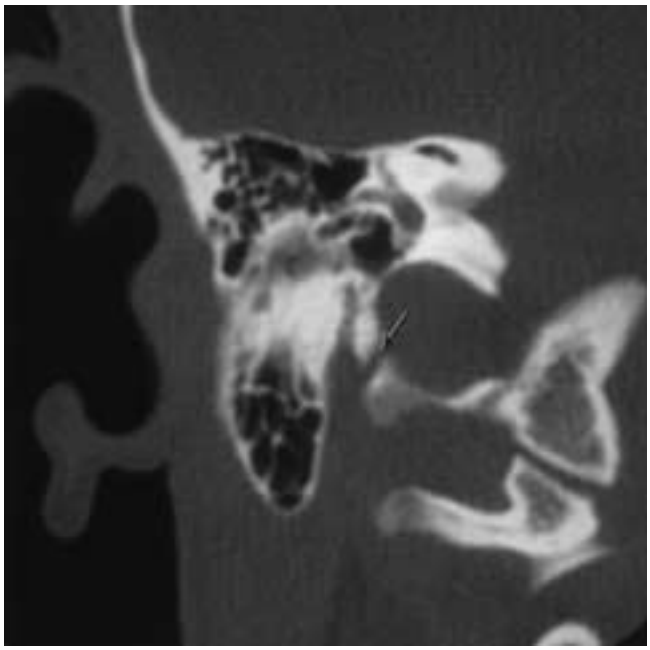

FIGURE 23-16 Pseudofracture, mastoid canaliculus. Coronal CT image of the right ear demonstrates the communication between the jugular foramen and the mastoid segment of the facial nerve canal (*arrow*). (From Swartz JD, Harnsberger HR. Imaging of the Temporal Bone, 3rd ed. New York: Thieme, 1998.)

Copyright © 2003, Mosby, Inc. All rights reserved.

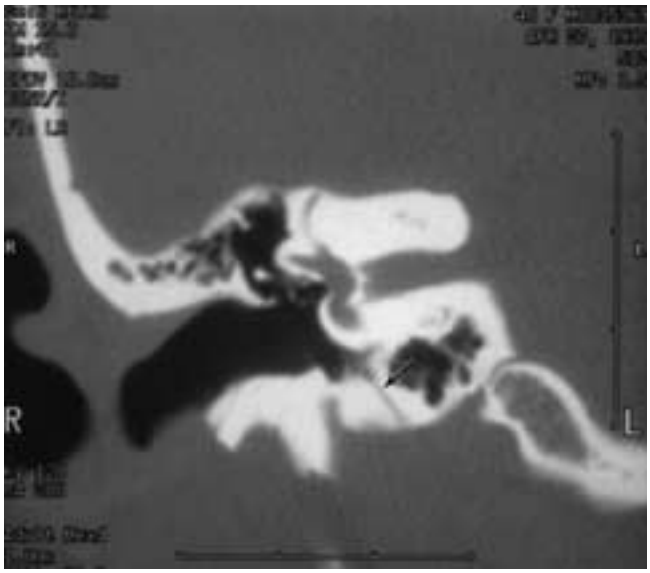

VIEW IMAGE

FIGURE 23-17 Pseudofracture, inferior tympanic canaliculus. Coronal CT image of the right ear demonstrates this vertically oriented structure (*arrow*).

ossicle, and most ossicular discontinuities involve the incus.[30]

The various types of ossicular discontinuity include incudostapedial subluxation, malleoincudal subluxation, incus dislocation, stapes fracture and dislocation, and the rare malleus fracture.[31–34] Dislocation of the entire malleoincudal complex has also been reported.

The incudostapedial joint is a fragile enarthrosis. A well-accepted theory for the cause of incudostapedial subluxation is tetanic contraction of the tensor tympani and stapedius tendons that results in a medial thrust of the incus and a posterior thrust of the stapes.[2, 34] Most observers believe this to be the most common variety of posttraumatic ossicular disruption. In order to diagnose such a disruption, a sound knowledge of the normal anatomy is needed. This anatomy is best appreciated on axial images. The lenticular process of the incus is well seen in the axial plane, as is the stapes superstructure, including the stapes head (capitulum) and the anterior and posterior crura. The footplate is seen as a thin cortical bony line crossing the oval window. The supporting stapedius tendon is also appreciated in this plane emanating from the pyramidal eminence of the posterior tympanum. More anteriorly lies the tensor tendon attaching to the malleus neck. Incudostapedial subluxation may be manifest by either an anterior or a posterior position of the lenticular process relative to the stapes head (Figs. 23-19 and 23-20).

The malleoincudal articulation is a true diarthrodial joint well protected within the attic (epitympanic recess). This joint has a capsule as well as medial and lateral ligamentous support.[35] The pathophysiology of malleoincudal subluxation is similar to that of the incudostapedial joint subluxation. These are also best seen on axial images as separation of the malleus head from the incus body (the ice cream from the cone) (Figs. 23-21 and 23-22).

The diagnosis of incus dislocation requires demonstration of complete separation of the incus from its incudosta-

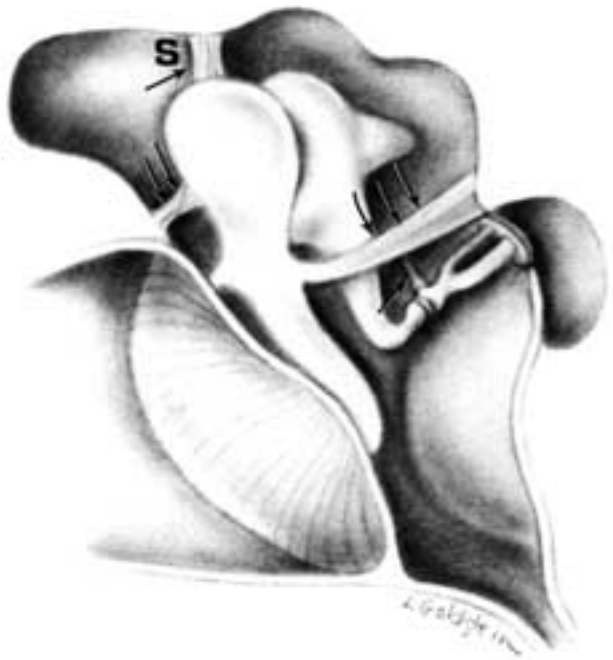

FIGURE 23-18 The ossicles and their supporting structures. Lateral mallear ligament (*double arrow*). Tensor tympani tendon (*triple arrows*). Stapedius tendon (*long thin arrow*). Superior mallear ligament (*S, arrow*). (From Swartz JD, Harnsberger HR. Imaging of the Temporal Bone, 3rd ed. New York: Thieme, 1998.)

VIEW IMAGE

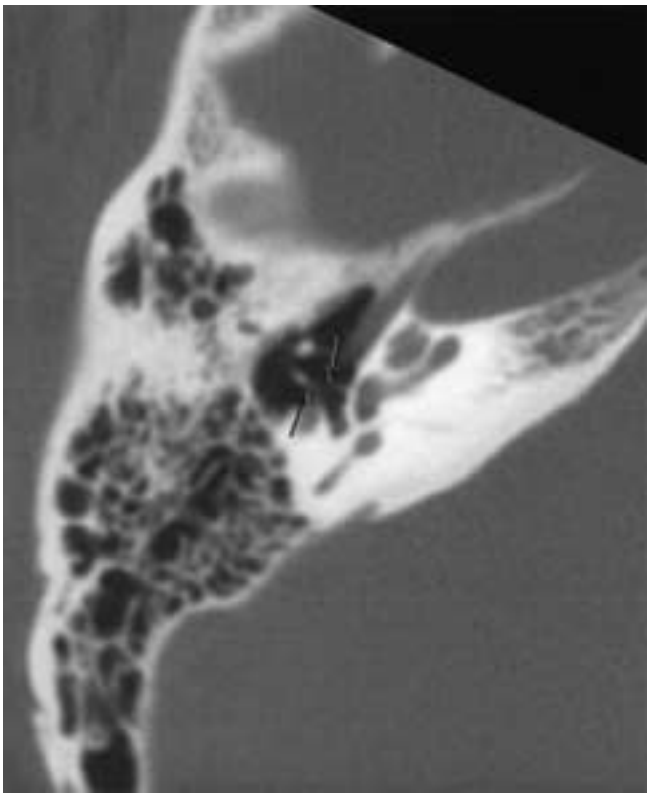

FIGURE 23-19 Incudostapedial subluxation. Axial CT image, right ear. The lenticular process is posteriorly positioned (*arrows*) relative to the stapes head.

VIEW IMAGE

Copyright © 2003, Mosby, Inc. All rights reserved.

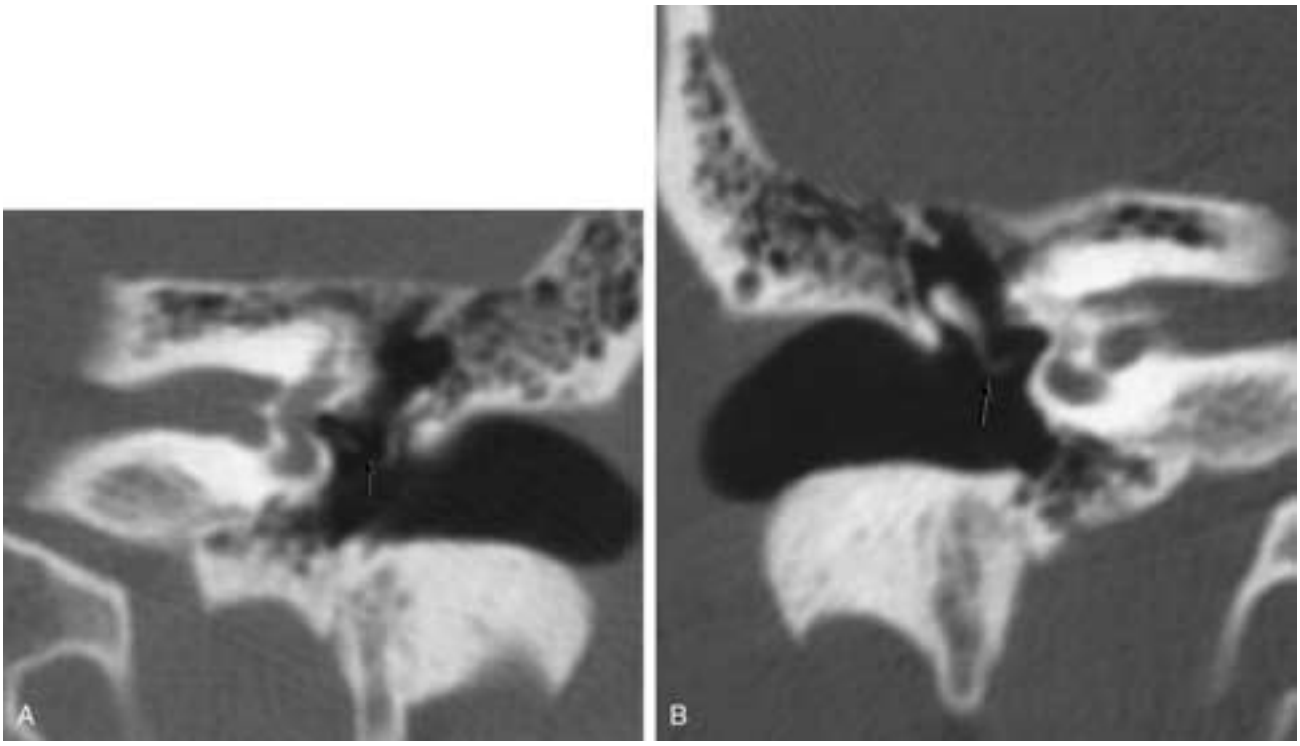

VIEW IMAGE

FIGURE 23-20 Incudostapedial subluxation. **A**, Coronal CT image, left ear. Note the separation between the distal incus and the stapes on this coronal image (*arrow*). Diagnosis in this plane is ordinarily quite difficult. **B**, Coronal CT image, right ear. Normal side for comparison. Note the relationship of incus to stapes (*arrow*).

pedial and the malleoincudal attachments.[32] This may be partial or complete. If the incus dislocation is complete, the incus may reside in the attic, middle ear, or EAC, or may be completely absent, presumably resorbed over time (Figs. 23-23 and 23-24). The diagnosis is best made using axial CT images; however, coronal CT images may demonstrates the incus lateral to the malleus, referred to as a Y configuration[30] (Fig. 23-23).

VIEW IMAGE

FIGURE 23-21 Malleoincudal articulation, normal anatomy. This is a magnified axial CT image of the left ear demonstrating the normal ice cream cone within the attic, with the malleus anteriorly (*arrow*) and the incus posteriorly.

Stapes arch fractures are believed to be due to twisting torsion of the incus, while stapes footplate fractures are often associated with the lateral subtype of transverse fracture.[36] Stapes dislocation into the vestibule is often the result of overaggressive use of cotton-tipped cleansing devices[36, 37] (Fig. 23-25). The normal stapes superstructure should be visible in the axial plane in every patient, provided that appropriate technique is utilized. The diagnosis of stapes injury is more difficult than the diagnosis of most of the other varieties of ossicular injury, but it should be suspected if the stapes is not visualized in the axial plane in the appropriate clinical context. Recall that there is an association of stapes fractures with perilymphatic fistula.

COMPLICATIONS OF TEMPORAL BONE TRAUMA

Clinical complications associated with temporal bone fractures include fistulous communications, vertigo, hearing loss and facial nerve dysfunction.

Fistulous Communications

Fistulous communications include CSF leak and perilymphatic fistula.[38, 39] Traumatic CSF leak is usually secondary

Copyright © 2003, Mosby, Inc. All rights reserved.

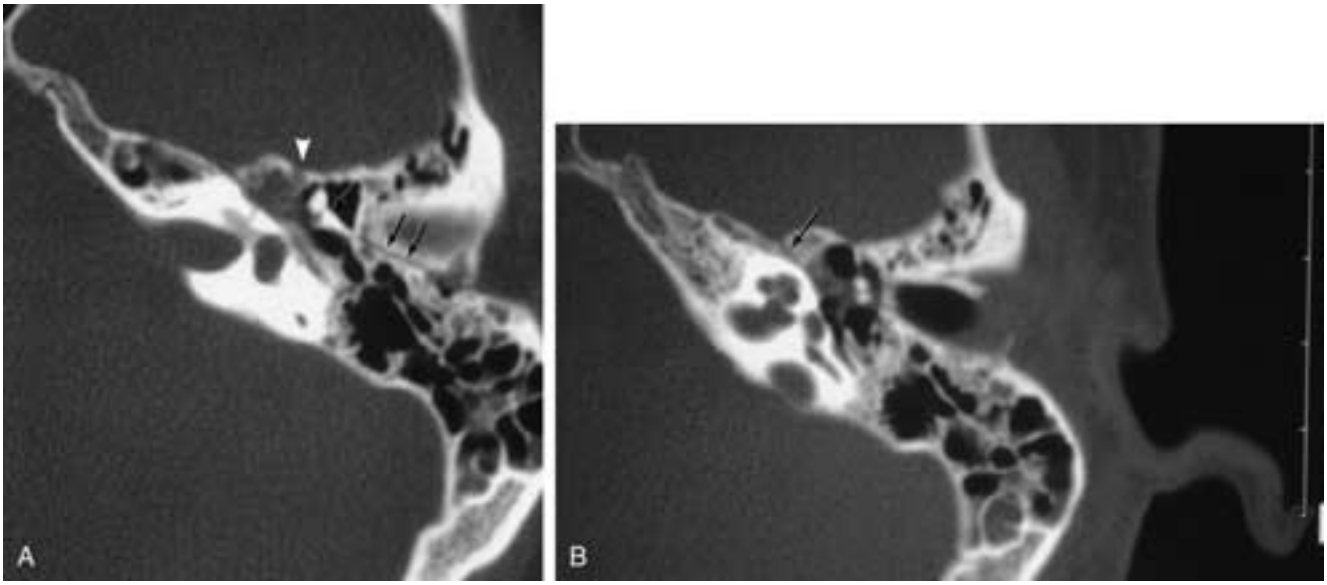

VIEW IMAGE

FIGURE 23-22 Malleoincudal subluxation. **A**, Magnified axial CT image, left ear. There is clearly definable pathologic rotation of the incus body (*arrow*) relative to the malleus head. Note the fracture (*double arrows*), as well as the patchy debris along the proximal tympanic segment of the facial nerve canal (*arrow*). **B**, Magnified axial CT image, left ear, more inferior. The stapes is normal. Debris tracks along the tensor tympani tendon. Subtle extension of the fracture line (*arrow*). (From Swartz JD, Harnsberger HR. Imaging of the Temporal Bone, 3rd ed. New York: Thieme, 1998.)

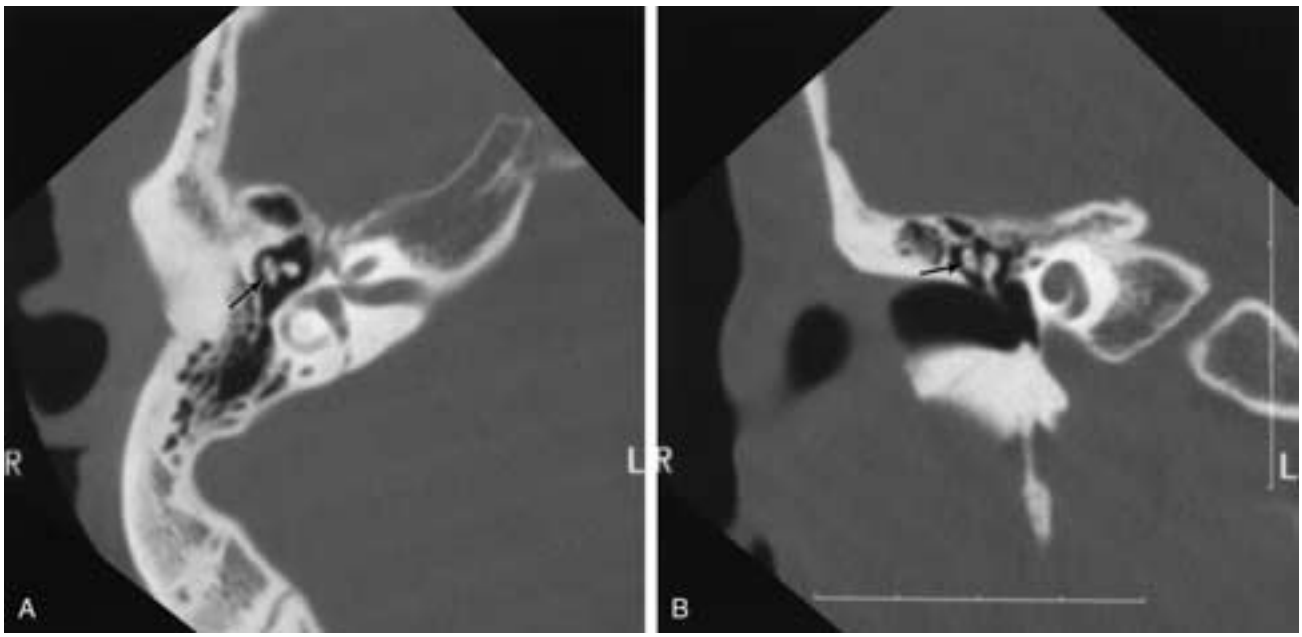

VIEW IMAGE

FIGURE 23-23 Incus dislocation. **A**, Magnified axial CT image, right ear. The incus (*arrow*) is dislocated and positioned lateral to the malleus head. **B**, Magnified coronal CT image, right ear. The anterolaterally dislocated incus (*arrow*) is not normally seen at the level of the malleus, creating a so-called Y configuration. See the text. (Courtesy of Dr. F. Veillon)

Copyright © 2003, Mosby, Inc. All rights reserved.

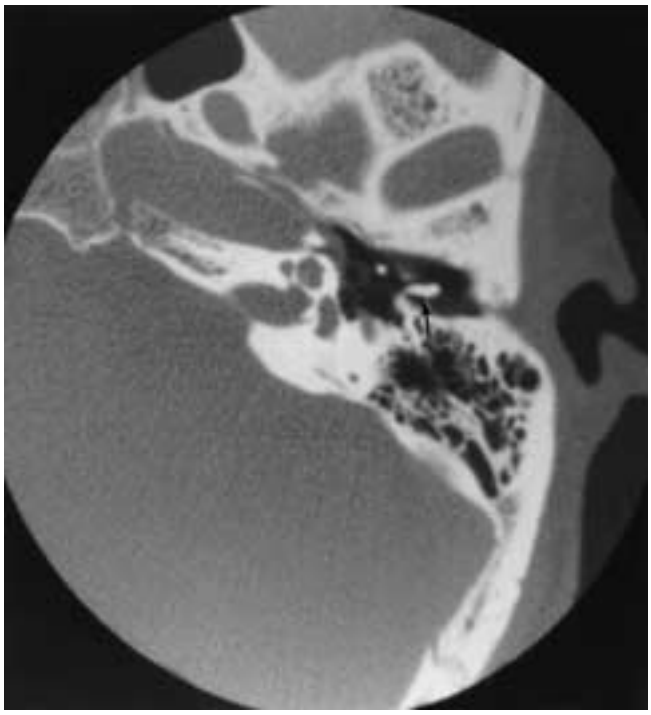

FIGURE 23-24 Incus dislocation. Magnified axial CT image, left ear. The incus (*arrow*) is dislocated into the external auditory canal. (Courtesy of Dr. F.Veillon)

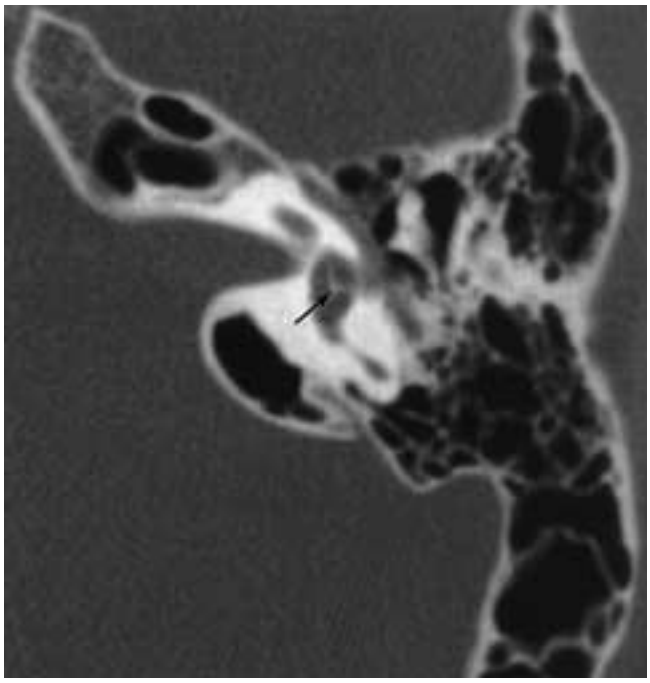

FIGURE 23-25 Stapes fracture. Magnified axial image, left ear. Subluxation of the entire stapes superstructure (*arrows*) into the vestibule. (Courtesy of Dr. F.Veillon)

to disruption of the tegmen tympani or roof of the middle ear. Because endochondral bone heals by fibrous union, there is an increased likelihood of CSF leak due to a fracture in this location.[38] If there is a CSF leak and there is also disruption of the tympanic membrane, there will be CSF *otorrhea*. If there is an intact tympanic membrane, the CSF drains via the eustachian tube into the nasopharynx and nasal cavity, resulting in CSF *rhinorrhea*. CSF leaks may resolve spontaneously, but surgical intervention is required when the leak persists for more than 7 to 10 days due to the risk of developing meningitis.[3] Larger tegmen defects may result in a meningoencephalocele[40–42] (Fig. 23-26).

Perilymphatic fistula is an abnormal communication between the inner ear perilymph and the middle ear space.[42–45] Classic corresponding clinical symptoms include fluctuating sensorineural hearing loss, tinnitus, vertigo, and possibly nystagmus. Although nystagmus may be either neoplastic or idiopathic in origin, trauma is the most

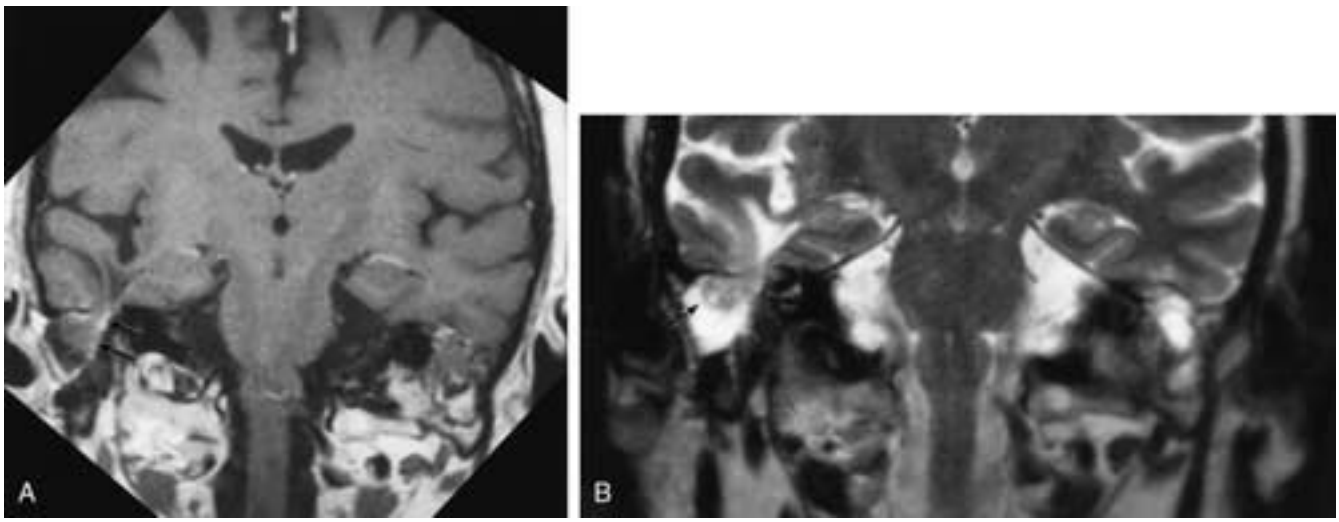

FIGURE 23-26 Posttraumatic meningoencephalocele. **A**, Coronal T1-weighted postcontrast image. **B**, Coronal T2-weighted fast spin-echo image. There is tegmen disruption on the right side. Note the herniation not only of the meninges into the attic but also of a portion of the inferior temporal gyrus (*arrows*). There is debris within the left middle ear cleft as well.

Copyright © 2003, Mosby, Inc. All rights reserved.

common cause. Perilymphatic fistula can be associated with congenital inner ear anomalies. The etiology of perilymphatic fistula may be a sudden increase in CSF pressure transmitted to the perilymph, the so-called *explosive* etiology, or tympanic membrane trauma, the so-called *implosive* etiology. The oval window and round window are the most common sites of perilymphatic fistula. Sudden gross movement of the tympanic membrane is transmitted, via the ossicular chain, to the stapes, which may be dislodged, and pronounced pressure changes may tear the round window membrane. In some centers, suspected perilymphatic fistula is an indication for surgical exploration and repair.

The imaging diagnosis of perilymphatic fistula may be quite elusive. The diagnosis can be suggested in the presence of labyrinthine fracture, stapes fracture/nonvisualization of the stapes, unexplained middle ear effusion, or pneumolabyrinth[46–48] (Fig. 23-27). The symptoms of perilymphatic fistula overlap with those of Meniere's disease, another elusive imaging diagnosis.[49]

Hearing Loss

Posttraumatic hearing loss may be sensorineural or conductive. Sensorineural hearing loss can be caused by fracture through the IAC, by fracture through the labyrinth, and by the so-called cochlear concussion, which is a disruption of the membranous labyrinth, typically without imaging manifestations.[4, 6, 23] Sensorineural hearing loss can also be caused by intralabyrinthine hemorrhage, brainstem injury (specifically to the cochlear nuclei or inferior colliculi), and perilymphatic fistula (Fig. 23-27). Shearing injury at the root entry zone of the vestibulocochlear nerve has been reported on numerous occasions, and impaction of the tentorium against the tectum secondary to acceleration-deceleration forces is the presumed cause of damage to the inferior colliculi in this context. Intralabyrinthine hemorrhage can occur secondary to blunt trauma or result from a coagulopathy or sickle cell disease.[50] This is best appreciated on axial T1-weighted noncontrast thin-section images[51] (Fig. 23-28).

Conductive hearing loss is common in this context and is particularly interesting to evaluate with CT due to the high incidence of important positive findings. Causes include hemotympanum, tympanic membrane damage, and ossicular discontinuity (see above). A conductive hearing loss that persists after blood is resorbed and the tympanic membrane is healed/repaired is presumably due to ossicular damage.[35–37, 52] Ossicular injuries are far more commonly the result of longitudinal rather than transverse fracture and, as mentioned, there are numerous reports of ossicular injury resulting from the aggressive use of cotton-tipped ear-cleansing devices.

Facial Nerve Dysfunction

Excluding Bell's palsy, trauma is the most common cause of facial nerve dysfunction.[53–55] Possible etiologies

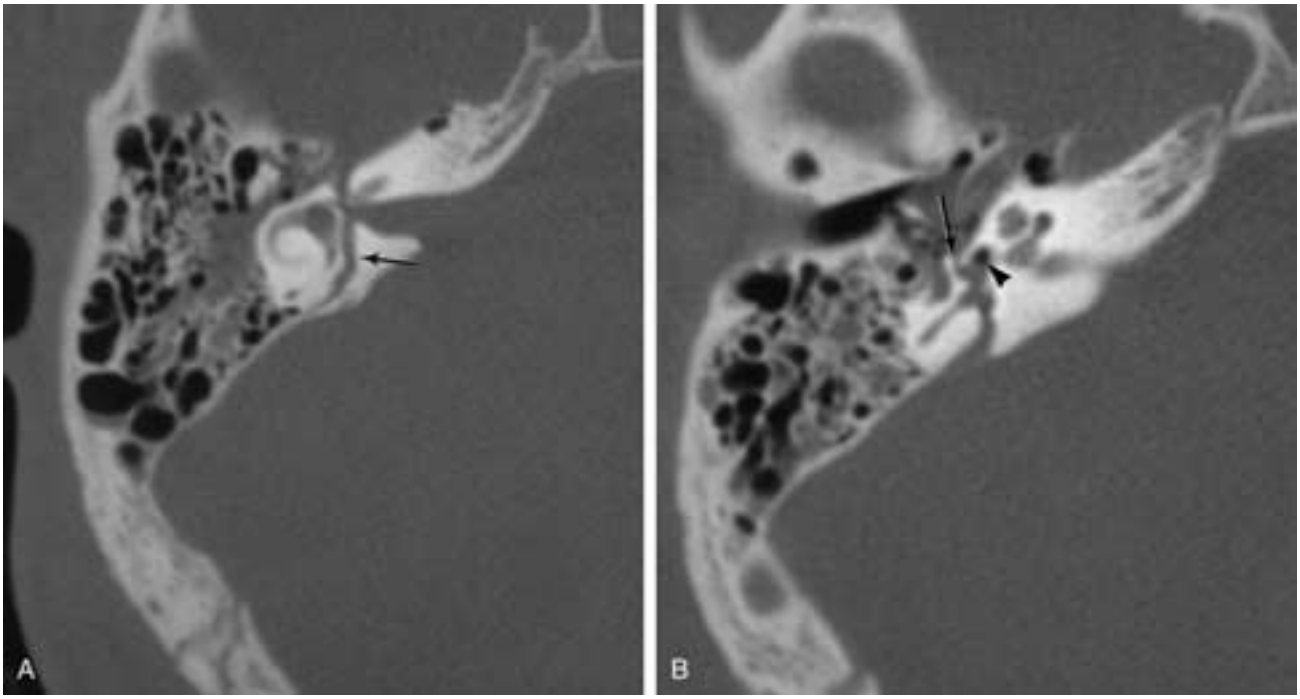

VIEW IMAGE

FIGURE 23-27 Perilymphatic fistulas, complex transverse fracture. **A**, Axial CT image, right ear transverse fracture (*arrow*) extends from the posterior petrous surface through the fundus of the IAC. There is hematotympanum. **B**, Axial CT image, right ear, more inferior. Oblique component of the fracture (*arrow*) traverses the promontory. There is a pneumovestibule (*arrowhead*). At surgery, disruption at the oval window was found and a perilymphatic fistula was diagnosed. (From Swartz JD, Harnsberger HR. Imaging of the Temporal Bone, 3rd ed. New York: Thieme, 1998.)

Copyright © 2003, Mosby, Inc. All rights reserved.

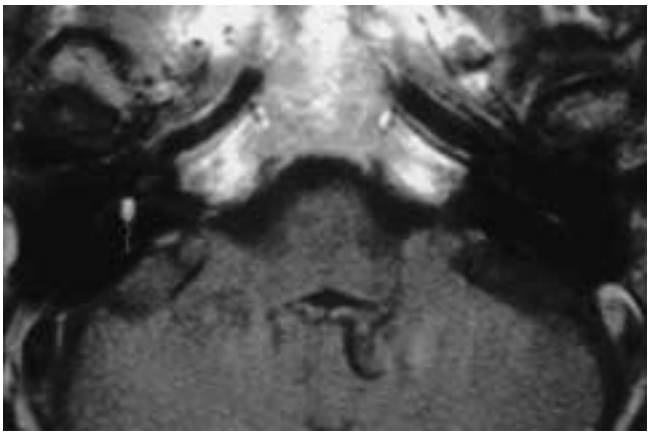

VIEW IMAGE

FIGURE 23-28 Intralabyrinthine hemorrhage. There is a region of hypersignal within the vestibule on these noncontrast T1-weighted images (*arrow*).

include intraneuronal hematoma, impingement by fracture fragments, and complete transection. Complete transection may result in complete, permanent facial palsy. Surgical intervention is a controversial topic but appears more valuable when the palsy is of delayed onset, as the etiology is more likely edema, swelling, or hematoma rather than complete transection. Delayed-onset paralysis is more common than that of immediate onset. When indicated, surgical decompression is generally most helpful if performed within 72 hours of onset of facial nerve dysfunction, prior to the development of Wallerian degeneration.[3, 53]

As indicated previously, facial nerve compromise is more common with transverse than with longitudinal fractures. The medial subtype (see above) is especially notorious in this regard, as the path of the fracture line extends through the region of the junction of the labyrinthine segment of the nerve canal with the fundus of the IAC. This region is considered to be the most vulnerable segment of the nerve by most observers. The lateral subtype of transverse fracture typically disrupts the nerve at the first genu. In a recent series, facial nerve injury was noted in 48% of fractures involving the otic capsule and in 10% to 18% of fractures sparing the otic capsule.[2] Facial paralysis associated with longitudinal fracture occurs less commonly (10% to 20%) and is often delayed, and the involvement is usually within the proximal tympanic segment of the nerve. Hematoma can affect the midtympanic segment of the nerve near the oval window, and spontaneous resolution of the facial paralysis is the rule in this circumstance. There is a general consensus that facial nerve injury is much less common in pediatric patients.[41]

MR imaging may play a crucial role in the evaluation of the traumatized facial nerve, as pathologic enhancement of the nerve may occur secondary to disruption of the blood-nerve barrier. This finding correlates especially well with traction and stretching of the greater superficial petrosal nerve leading to hematoma, edema, and nerve degeneration.[19] Demonstration of hematoma formation requires the use of thin-section noncontrast T_1-weighted images.

REFERENCES

1. Swartz JD, Harnsberger HR. Imaging of the Temporal Bone. 3rd ed. New York: Thieme, 1998; 318–344.
2. Kelly KE, Tami TA. Temporal bone and skull base trauma. In: Jackler RK, Brackmann DE, eds. Neurotology. St. Louis: Mosby Year Book 1994;1127–1155.
3. Cannon CR, Jahrsdoerfer RA. Temporal bone fractures: review of 90 cases. Arch Otolaryngol 1983;109:285–288.
4. Goodwin WJ. Temporal bone fractures. Radiol Clin North Am 1983;16:651–659.
5. Harvey FH, Jones AM. ''Typical'' basal skull fracture of both petrous bones: an unreliable indicator of head impact site. J Forensic Sci 1980;25:280–286.
6. Lindeman RC. Temporal bone trauma in facial paralysis. Otolaryngol Clin North Am 1979;12:403–413.
7. Swartz JD, Swartz NG, Korsvik H, et al. CT evaluation of the middle ear and mastoid for post-traumatic hearing loss. Ann Otol Rhinol Laryngol 1985;94:263–266.
8. Ghorayeb BY, Yeakley JW, Hall JW, Jones BE. Unusual complications of temporal bone fractures. Arch Otolaryngol Head Neck Surg 1987;113:749–753.
9. Wong E, Lee G, Mason DT. Temporal headaches and associated symptoms related to the styloid process and its attachments. Ann Head Med Singapore 1995;24:124–128.
10. Avrahami E, Chen Z, Solomon A. Modern HRCT diagnosis of longitudinal fractures of the temporal bone. Neuroradiology 1988;30: 166–168.
11. Griffin JE, Altenau MM, Schaefer SD. Bilateral longitudinal temporal bone: a retrospective review of 17 cases. Laryngoscope 1979;89:1432–1435.
12. Patay Z, Louryan S, Baleriaux D. Early complications of petrous bone fractures. Riv Neuroradiol 1995;8:855–866.
13. Brodie HA, Thompson TC. Management of complications from 820 temporal bone fractures. Am J Otol 1997;18:188–197.
14. Yeakley JW. Temporal bone fractures. Curr Probl Diagn Radiol 1999;28:65–98.
15. Bonafe A, Laval C, Arrue P, Manelfe C. Temporal bone fractures. Riv Neuroradiol 1995;8:847–854.
16. Gentry LR. Temporal bone trauma: current perspectives for diagnostic evaluation. Neuroimaging Clin North Am 1991;1(2): 319–340.
17. Merwin W, May M, Curtin HD. Floating petrous bone fracture. Otolaryngol Head Neck Surg 1989;100(1):69–73.
18. Freeman J. Temporal bone fractures and cholesteatoma. Ann Otol Rhinol Laryngol 1983;92:558–560.
19. McKennan KX, Chole RA. Posttraumatic cholesteatoma. Laryngoscope 1989;99:779–782.
20. Sartoretti-Schefer S, Scherler M, Wichmann W, et al. Contrast-enhanced MRI of the facial nerve in patients with post-traumatic peripheral facial nerve palsy. AJNR 1997;18:1115–1122.
21. Zimmerman RA, Bilaniuk LT, Hackney DB, et al. Magnetic resonance imaging in temporal bone fractures. Neuroradiology 1987;29: 246–251.
22. Hasso AN. Traumatic injuries of the temporal bone. Otolaryngol Clin North Am 1988;21:295–316.
23. Hasso AN, Vignaud J, Bird CH. Pathology of the temporal bone and mastoid. In: Newton TH, Hasso AN, Dillon WP, eds. Computed Tomography of the Head and Neck. Vol. 3, Modern Neuroradiology. New York: Raven Press, 1988;Chapter 5.
24. Schuknecht HF. Pathology of the Ear. 2nd ed. Philadelphia: Lea & Febiger, 1993.
25. Liebetrau R, Draf W, Kahle G. Temporal bone fractures: high-resolution CT. J Otolaryngol 1993;22:249–252.
26. Pollanen MS, Deck JH, Blenkinsop B. Fracture of temporal bone with exsanguination. Can J Neurol Sci 1992;19:196–200.
27. Leproux F, Aubry JC, Louryan S, et al. Temporal bone pseudofractures of children on CT. Riv Neuroradiol 1995;8:869–879.
28. Proctor B. Surgical Anatomy of the Ear and Temporal Bone. New York: Thieme, 1989;121.
29. Lemmerling MM, Stambuck HE, Mancuso AA, et al. CT of the normal suspensory ligaments of the ossicles in the middle ear. AJNR 1997;18:471–477.
30. Lourenco MTC, Yeakley JW, Ghorayeb BY. The ''Y'' sign of lateral dislocation of the incus. Am J Otol 1995;16:387–392.

Copyright © 2003, Mosby, Inc. All rights reserved.

31. Lyos AT, Marsh MA, Jenkins HA, et al. Progressive hearing loss after temporal bone fracture. Arch Otolaryngol Head Neck Surg 1995;121: 795–799.
32. Swartz JD, Laucks RL, Berger AS, et al. Computed tomography of the disarticulated incus. Laryngoscope 1986;96:1207–1210.
33. Swartz JD, Zwillenberg S, Berger AS. Acquired disruptions of the incudostapedial articulation: diagnosis with CT. Radiology 1989;171: 779–781.
34. Swartz JD. Current imaging approach to the temporal bone. Radiology 1989;171:309–317.
35. Stephan AL, Isaacson JE. Incudomalleolar joint separation. Am J Otol 2000;21:284–285.
36. Herman P, Guichard JP, Van den Abbeele T, et al. Traumatic luxation of the stapes evidenced by high-resolution CT. AJNR 1996;17:1242–1244.
37. Meriot P, Veillon F, Garcia JF, et al. CT appearance of ossicular injuries. RadioGraphics 1997;17:1445–1454.
38. Lundy LB, Graham MD, Kartush JM, LaRouere MJ. Temporal bone encephalocele and cerebrospinal fluid leaks. Am J Otol 1996;17: 461–469.
39. Neely JG, Neblett CR, Rose JE. Diagnosis and treatment of spontaneous cerebrospinal fluid otorrhea. Laryngoscope 1982;92:609–612.
40. Martin N, Sterkers O, Murat M, Hahum N. Brain herniation into the middle ear cavity: MR imaging. Neuroradiology 1989;31:184–186.
41. McGuirt WF, Stool SE. Temporal bone fractures in children: a review with emphasis on long-term sequelae. Clin Pediatr 1992;31: 12–18.
42. Nageris B, Hanson MC, Lavelle WG, VanPelt FA. Temporal bone fractures. Am J Emerg Med 1995;13: 211–214.
43. Fitzgerald DC. Head trauma: hearing loss and dizziness. J Trauma 1996;40:488–496.
44. Fitzgerald DC. Persistent dizziness following head trauma and perilymphatic fistula. Arch Phys Med Rehabil 1995;76:1017–1020.
45. Hough JVD. Otologic trauma. In: Paparella MM, Shumrick DA, eds. Otolaryngology. Vol. 2, The Ear. Philadelphia: WB Saunders, 1980;1656–1679.
46. Lipkin AF, Bryan RN, Jenkins HA. Pneumolabyrinth after temporal bone fracture: documentation by high resolution CT. AJNR 1985;6:294–297.
47. Nurre JW, Miller GW, Ball JB. Pneumolabyrinth as a late sequela of temporal bone fracture. Am J Otol 1988;9:489–493.
48. Weissman JL, Curtin HD. Pneumolabyrinth: A computed tomographic sign of temporal bone fracture. Am J Otolaryngol 1992;13: 113–114.
49. Shea JJ, Ge X, Orchik DJ. Traumatic endolymphatic hydrops. Am J Otol 1995;16:235–240.
50. Whitehead RE, MacDonald CB, Melhem ER, McMahon L. Spontaneous labyrinthine hemorrhage in sickle cell disease. AJNR 1998;19:1437–1440.
51. Jane NN, Laureno R, Mark AS, et al. Deafness after bilateral midbrain contusion: a correlation of magnetic resonance imaging with auditory brainstem evoked responses. Neurosurgery 1991;29:1101.
52. Iurato S, Quaranta A. Malleus-handle fracture: historical review and three new cases. Am J Otol 1999;20:19–25.
53. May M. Trauma to the facial nerve. In: May M, ed. The Facial Nerve. New York: Thieme, 1986;421–440.
54. McCabe BF. Injuries to the facial nerve. Laryngoscope 1972;82:1891–1896.
55. McKennan KX, Chole RA. Facial paralysis in temporal bone trauma. Am J Otol 1992;13:167–172.

Copyright © 2003, Mosby, Inc. All rights reserved.

24

Otosclerosis and Dysplasias of the Temporal Bone

Osamu Sakai, Hugh D. Curtin, Anton N. Hasso, and Joel D. Swartz

OTOSCLEROSIS
- **Oval Window Involvement (Fenestral)**
- **Cochlear Otosclerosis (Retrofenestral)**
- **Differential Diagnosis**

FIBROUS DYSPLASIA
- **Differential Diagnosis**

PAGET'S DISEASE (OSTEITIS DEFORMANS)
- **Differential Diagnosis**

OSTEOGENESIS IMPERFECTA
- **Differential Diagnosis**

OSTEOPETROSIS
- **Differential Diagnosis**

PROGRESSIVE DIAPHYSEAL DYSPLASIA (CAMURATI-ENGELMANN-RIBBING SYNDROME)
- **Differential Diagnosis**

OTHER DYSPLASIAS AND DISORDERS CAUSING OSTEOSCLEROSIS OF THE TEMPORAL BONE
- **Endosteal Hyperostosis**
- **Craniometaphyseal Dysplasia and Craniodiaphyseal Dysplasia**
- **Oculo-Dento-Osseous Dysplasia (Oculodentodigital Syndrome)**
- **Dysosteosclerosis**
- **Pyle's Disease (Metaphyseal Dysplasia)**
- **Hereditary Hyperphosphatasia (Juvenile Paget's Disease)**
- **Pyknodysostosis**
- **Osteopathia Striata (Voorhoeve Syndrome)**
- **Hyperparathyroidism**

Various diseases and dysplasias can affect the temporal bone and impair audiovestibular function. Some, such as otosclerosis, involve only the temporal bone, while others are more generalized, involving the temporal bone as well as other portions of the skeletal system. Some conditions cause demineralization of the otic capsule, and these are frequently genetically determined.[1–3] Both ears are often affected, and the impact on the quality of life can be devastating.[1] Patients with these lesions may present with conductive, sensorineural, or mixed hearing loss, depending on the location and extent of the lesions. Dysplastic bone can compress nerves, resulting in cranial neuropathies, or can limit ossicular chain movement. Because high-resolution computed tomography (CT) can depict very subtle bone findings, it is the modality of choice for evaluating osseous changes in the temporal bone. Magnetic resonance (MR) imaging can be used to evaluate the lumen of the labyrinth and the bone marrow, but depicting definitive bone changes is often difficult. However, contrast-enhanced MR imaging can help predict the vascularity or activity of certain lesions.

OTOSCLEROSIS

Otosclerosis is a disorder of the bony labyrinth and stapes affecting only humans.[1] It has an autosomal dominant inheritance with varying degrees of expressivity.[4] This slowly progressive disorder has a 65% to 72.5% female predominance, with a peak incidence in the second or third decade.[1, 5–8] The disease is bilateral in 80% of patients, and although tinnitus may be the presenting symptom, hearing loss will always develop. Although a conductive component is almost always present, there may be a sensorineural or mixed hearing loss.[5, 9]

The temporal bone is unique in that there normally is persistence of primary endochondral bone as the middle

Copyright © 2003, Mosby, Inc. All rights reserved.

layer of the cochlear or otic capsule. This middle layer is between the thin inner endosteal layer (bordering the lumen of the labyrinth) and the outer periosteal layer. Resorption of this middle endochondral layer, with deposition of spongy vascular new bone, is referred to as otosclerosis or otospongiosis.[8, 10, 11] This abnormal bone is usually less dense than the surrounding normal bone, but it can be sclerotic, presumably representing a mature or inactive form of otosclerosis. Imaging studies can confirm the clinical assumption of otosclerosis and can play a role in excluding some of the other causes of hearing loss.[11] In this regard, high-resolution CT is the modality of choice for evaluating the labyrinthine windows, stapes footplate, cochlear capsule, and other inner ear structures.[11–14] (Figs. 24-1 and 24-2).

The lesions of otosclerosis may be isolated to the oval window or may involve the labyrinth more extensively. The terminology used to refer to this disease is variable, with some otologists simply referring to otosclerosis and then subclassifying it depending on the type of hearing loss present. Other otologists refer to either fenestral or retrofenestral (cochlear) otosclerosis.[1–14] The fenestral type refers to lesions involving only the oval window region, while the retrofenestral type refers to otosclerosis that more extensively affects the cochlea. The retrofenestral type seldom occurs without a fenestral component.

Oval Window Involvement (Fenestral)

Radiologic evaluation may not be necessary in patients who present with a conductive hearing loss and disease limited to the oval window (fenestral otosclerosis).[15, 16] The clinical findings are quite characteristic, as patients present with a progressive conductive loss, a normal tympanic membrane, and no evidence of middle ear inflammation. Seen through the tympanic membrane, the promontory may have a faint pink tinge reflecting the vascularity of the lesion. This coloration has been referred to as the Schwartze sign. Some patients with a sensorineural hearing loss require imaging to confirm the diagnosis of retrofenestral otosclerosis or to exclude retrocochlear lesions.[16–18] A conductive hearing loss is almost always secondary to impingement of abnormal bone on the stapes footplate, and it is this oval window involvement that is the basis of the name fenestral otosclerosis. The most common lesion of otosclerosis occurs

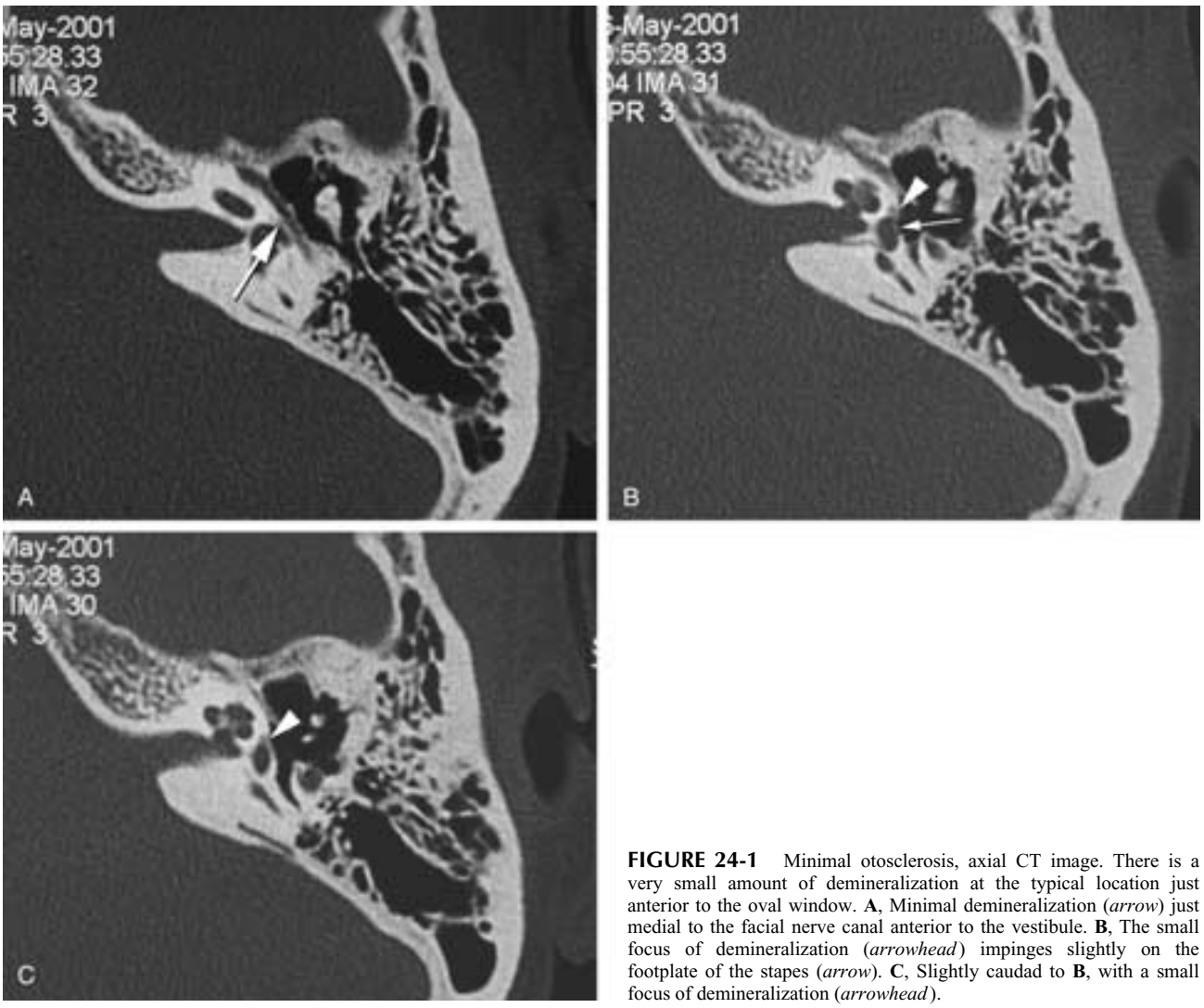

FIGURE 24-1 Minimal otosclerosis, axial CT image. There is a very small amount of demineralization at the typical location just anterior to the oval window. **A**, Minimal demineralization (*arrow*) just medial to the facial nerve canal anterior to the vestibule. **B**, The small focus of demineralization (*arrowhead*) impinges slightly on the footplate of the stapes (*arrow*). **C**, Slightly caudad to **B**, with a small focus of demineralization (*arrowhead*).

VIEW IMAGE

Copyright © 2003, Mosby, Inc. All rights reserved.

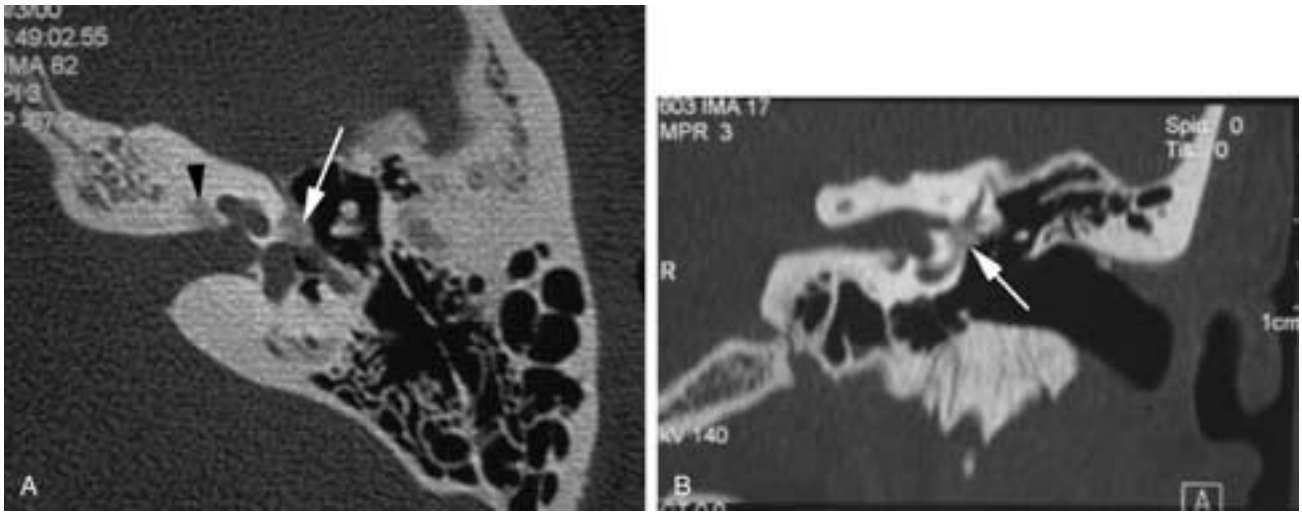

VIEW IMAGE

FIGURE 24-2 Otosclerosis, CT scan. **A**, Axial slice through the labyrinth shows a demineralization (*arrow*) just anterior to the footplate of the stapes. Note that the small area of demineralized bone has actually increased in volume. This patient had a component of cochlear otosclerosis. Note the area of demineralization (*arrowhead*) just medial to the cochlea. **B**, Coronal image shows the demineralized bone (*arrow*). This slice is just anterior to the oval window.

in the bone just anterior to the oval window, at the location of the embryologic fissula ante fenestram[9–11, 19] (Figs. 24-1 to 24-3). The fissula is a thin fold of connective tissue extending through the endochondral layer, approximately between the oval window and the cochleariform process, where the tensor tympani tendon turns laterally toward the malleus. To diagnose fenestral otosclerosis with CT, assessment of patients with a noninflammatory conductive hearing loss must include careful evaluation of the oval window for either subtle lucent areas or otosclerotic foci.[20, 21] This is best accomplished by using high-resolution CT with a 1-mm (or less) slice thickness. Early disease is visualized as a small, demineralized focus anterior to the oval window (Fig. 24-1). This represents the abnormal ''spongiotic'' bone replacing the normal dense otic capsule, and this imaging finding confirms the diagnosis. Other foci of demineralization should be sought in both ears, as the incidence of bilateral involvement is high even when the audiogram shows no measurable air-bone gap in the other ear. With more pronounced disease, the demineralized bone enlarges, protrudes slightly into the middle ear cavity, and further impinges on the anterior margin of the oval window (Fig. 24-2). CT may demonstrate narrowing of the oval window, thickening of the footplate of the stapes, and small decreased density lesions in the lateral wall of the labyrinth. Rarely, the lesion is dense, approaching the same density as

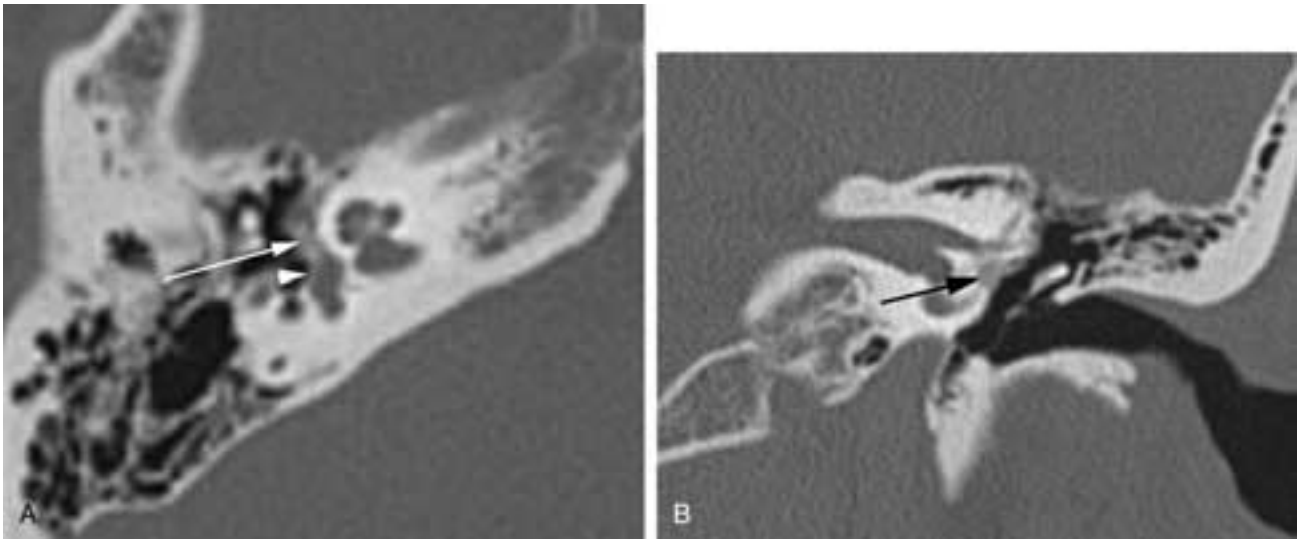

VIEW IMAGE

FIGURE 24-3 Otosclerosis impinging on the footplate of the stapes. **A**, Axial CT image shows the intermediate density bone (*arrow*) just anterior to the oval window impinging on the footplate of the stapes (*arrowhead*). **B**, The focus of demineralization (*arrow*) just anterior to the oval window. Note that the focus of demineralization abuts the medial aspect of the facial nerve canal.

Copyright © 2003, Mosby, Inc. All rights reserved.

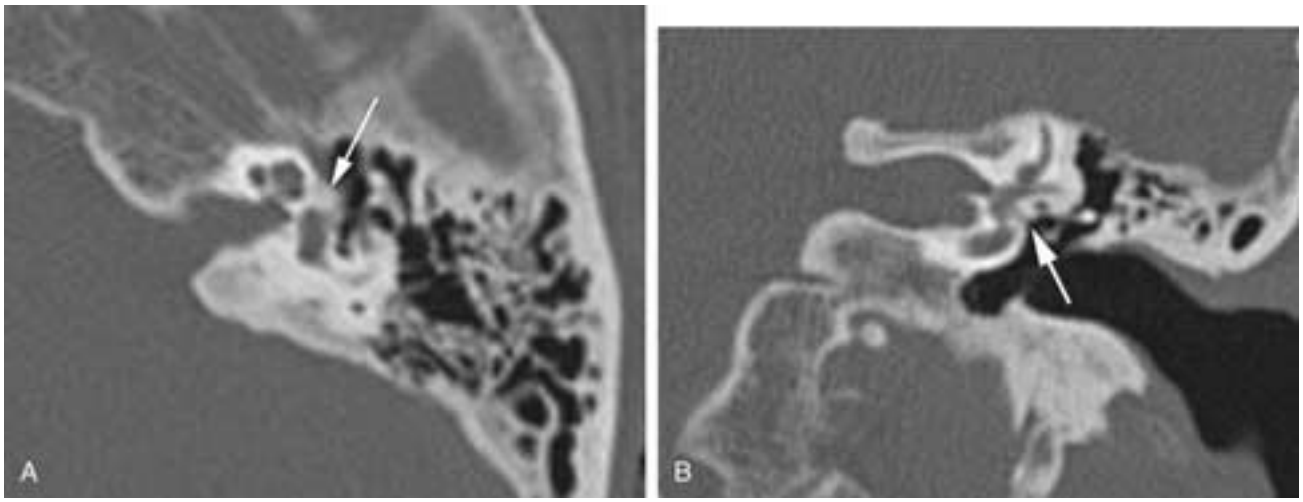

VIEW IMAGE

FIGURE 24-4 Sclerotic phase of otosclerosis, CT scan. **A**, The focus of abnormal bone (*arrow*) just anterior to the footplate of the stapes. Note that the bone has almost the same density as the otic capsule. It is also enlarged in size. **B**, The overgrowth of bone impinges on the oval window (*arrow*) causing significant narrowing. The bone has approximately the same density as the otic capsule.

the otic capsule (Fig. 24-4). In these circumstances, the disease is identified by showing thickening of the bone at the anterior margin of the oval window. This may reflect the later, inactive phase of otosclerosis.[8]

Complete obliteration of the oval window, obliterative fenestral otosclerosis, occurs in approximately 2% of cases and is classified into three types: (1) massive thickening of the footplate that almost fills the oval window niche; (2) massive overgrowth of the margins of the oval window, obliterating the niche and obscuring the footplate; and (3) a combination of footplate thickening and marginal overgrowth.[5, 8, 22] Occasionally, patients have only subtle thickening of the stapes footplate/annular ligament complex. This appearance may also occur as a result of previous inflammatory disease with the development of tympanosclerosis.[23]

When an oval window lesion is not appreciated on imaging, the ossicular chain must be carefully evaluated for evidence of a congenital anomaly or perhaps for an indication of an inflammatory cause of the conductive hearing loss. On occasion, although no abnormality is apparent despite an intensive imaging evaluation, at surgery congenital stapes fixation may be identified.[10]

Careful evaluation of the round window, facial nerve canal, jugular foramen, and cochlear aqueduct is necessary as part of the preoperative imaging assessment.[21] Round window obliteration secondary to otosclerosis is rare, occurring with retrofenestral disease (Figs. 24-5 and 24-6). If this occurs, stapes surgery is less likely to be successful and hearing improvement will be minimal.[22] A small percentage of patients with fenestral otosclerosis also have lateral ossicular fixation, usually manifested by a bony web interposed between the malleus or incus and the lateral attic wall. Dehiscence of the facial nerve may also be appreciated on CT, and the preoperative demonstration of this anomaly can help the surgeon avoid facial nerve injury.[8, 24]

Treatment of the fenestral component of otosclerosis is surgical, and various procedures have been designed to reestablish the conductive pathway from middle to inner ear. The stapes is either removed or a hole is drilled through the footplate and a prosthesis inserted (Figs. 24-7 and 24-8). Other procedures have included stapes mobilization and fenestration of the horizontal semicircular canal.[25] Currently, the most common procedure involves drilling a small hole in the stapes (stapedotomy), with the placement of a small-diameter Teflon-wire piston through this small fenestra in the footplate (Fig. 24-9). This procedure has lessened complications including postoperative vertigo, granuloma formation, and fibrous fixation of the lenticular process to the promontory.[22] CT is useful to evaluate the precise location of the prosthesis and to assess postoperative complications.[25, 26] It should be noted that because of volume averaging effects, a thin wire prosthesis may not be

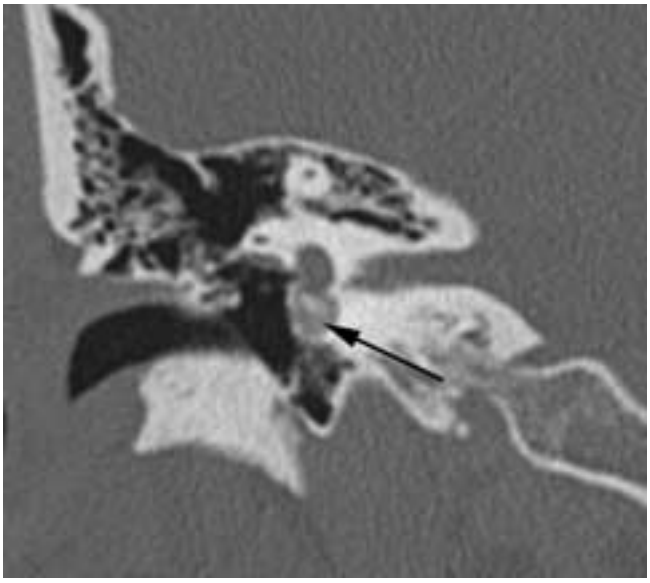

FIGURE 24-5 Otosclerosis, round window obliteration. Coronal CT image demonstrates prominent overgrowth of the demineralized, otosclerotic plaque obstructing the round window (*arrow*).

VIEW IMAGE

Copyright © 2003, Mosby, Inc. All rights reserved.

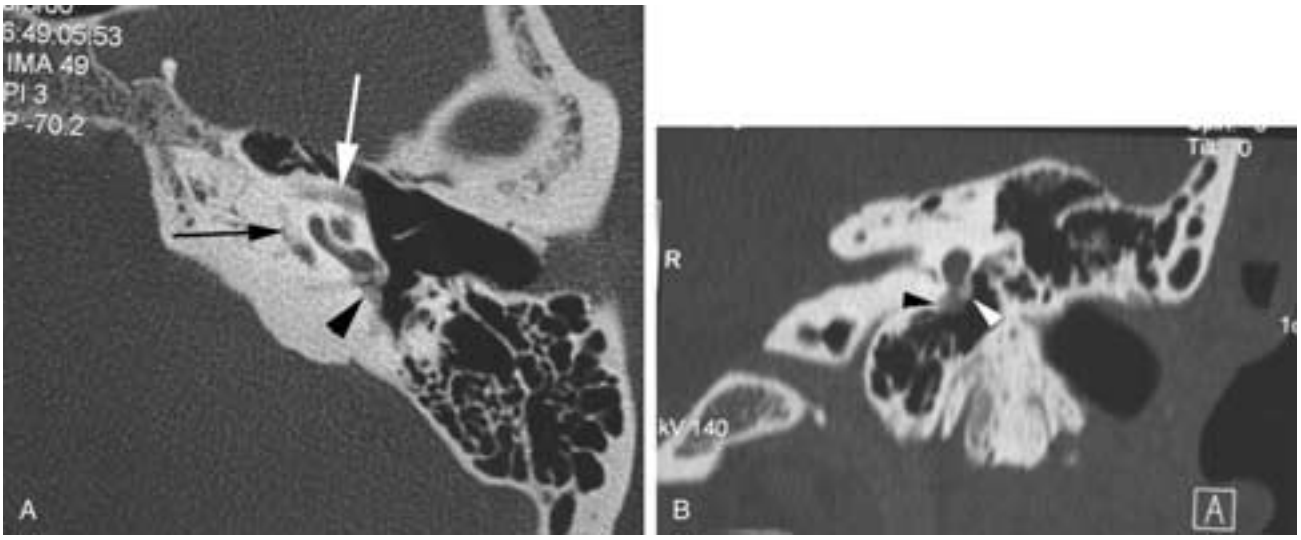

VIEW IMAGE

FIGURE 24-6 Fenestral and cochlear otosclerosis, CT scan. **A**, There is demineralization (*arrows*) around the cochlea. The demineralization seen just medial to the basilar turn is referred to as the fourth turn of the cochlea (double ring sign). Note the demineralized bone (*arrowhead*) impinging on the round window niche. **B**, Coronal image shows the demineralized bone both lateral (*white arrowhead*) and medial (*black arrowhead*) to the round window, causing narrowing.

visualized, whereas thicker pistons may appear wider than their actual size.[11]

With oval window manipulation, a pouring, jet-like outflow (gusher) or milder welling-like flow (oozer) of cerebrospinal fluid (CSF) may occur in patients with a defect either in the modiolus or in the bone at the fundus of the internal auditory canal, giving a communication between the CSF and the perilymph.[22] Some authors have suggested a communicating pathway through an enlarged cochlear aqueduct; however, there is considerable controversy in the otolaryngologic literature on this subject. Enlargement or flaring of the cochlear duct aperture seen on imaging is of very doubtful significance.[27]

Cochlear Otosclerosis (Retrofenestral)

Cochlear (retrofenestral or labyrinthine) otosclerosis presents with combined sensorineural and conductive hearing loss. Isolated sensorineural loss is considered to be extremely rare. A few patients present with vestibular symptoms.[28–30] The cause of the sensorineural hearing loss

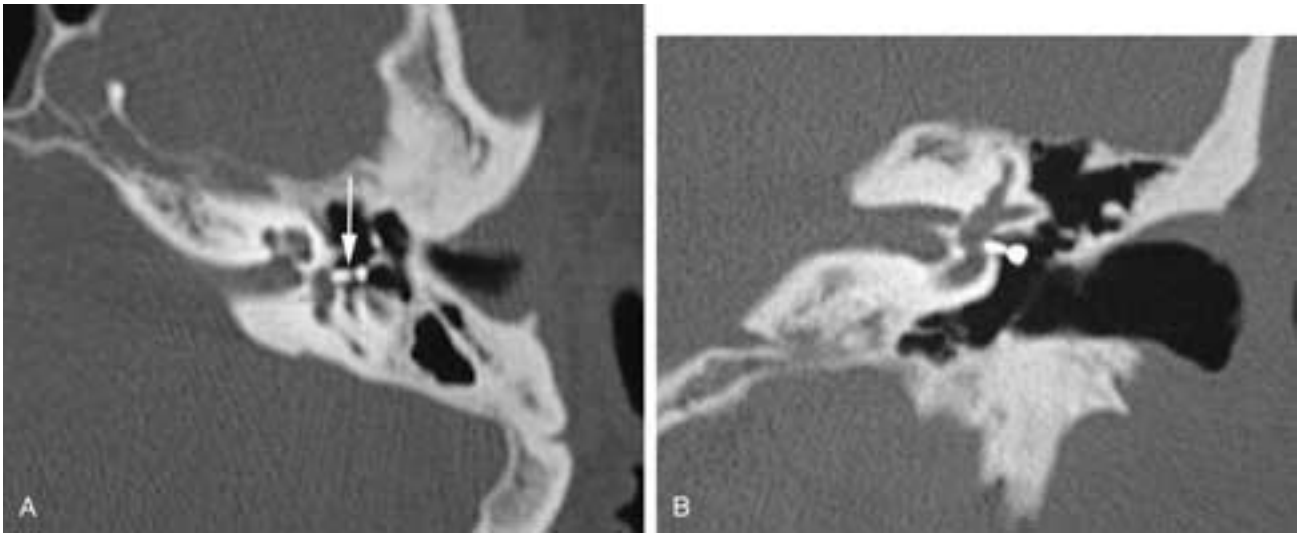

VIEW IMAGE

FIGURE 24-7 Fenestral otosclerosis after stapedotomy. **A**, Axial CT image of the left ear shows a prosthesis (*arrow*) inserted into the oval window. Otosclerotic plaque is noted anterior to the oval window. **B**, Coronal CT image of the left ear demonstrates the prosthesis. Note that the end of the prosthesis protrudes minimally into the vestibule.

Copyright © 2003, Mosby, Inc. All rights reserved.

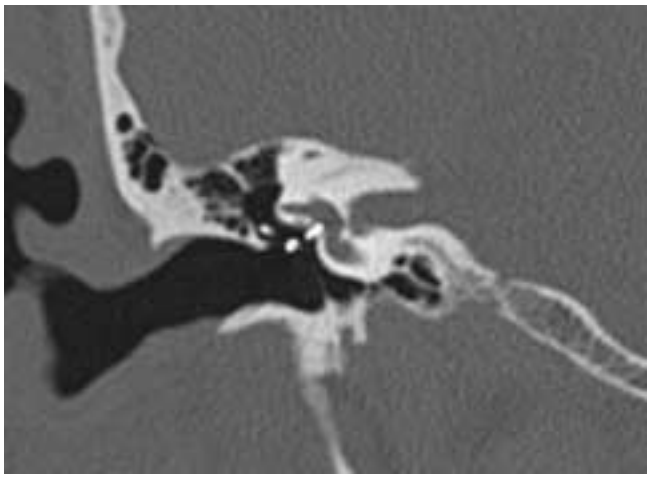

VIEW IMAGE

FIGURE 24-8 Coronal fenestral otosclerosis after stapedotomy and insertion of the prosthesis. Coronal CT image of the right ear demonstrates the prosthesis inserted into the oval window.

in otosclerosis is controversial, and cytotoxic enzymes have been implicated.[31, 32] Diffusion of these enzymes into the cochlear fluid is theorized to be responsible for hyalinization of the spiral ligament and subsequent hearing loss.

The basilar membrane forms the boundary between the cochlear duct and the scala tympani, and this membrane thickens as it approaches the apical turn. Low-frequency tones have a maximum effective amplitude toward the apical turn, while high-frequency tones have a maximum effective amplitude at the basilar turn, where the basilar membrane is relatively thin. Areas of demineralization at various locations within the cochlear capsule can be appreciated on CT, and attempts have been made to correlate the type of frequency loss in sensorineural hearing loss with the location of demineralized foci seen on CT.[33, 34]

In cochlear or retrofenestral otosclerosis, demineralization of the cochlear capsule is greater than that seen in fenestral otosclerosis, and the area just anterior to the oval window is almost always involved. In addition, the so-called double ring or fourth turn sign refers to a low-density demineralized enchondral defect around the cochlea[11, 12, 33–35] (Figs. 24-6 and 24-9). These lucent lesions of cochlear otosclerosis may abut the lumen of the labyrinth or may be separated from it by denser bone. These areas of demineralization represent otospongiosis in the cochlear capsule (Figs. 24-10 and 24-11). In the chronic or sclerotic phase of the disease, these lesions can undergo remineralization and become indistinguishable from the normal dense cochlear capsule. In this case, there may be no CT manifestations other than subtle periosteal thickening, and this may explain the relatively high incidence of otherwise asymptomatic sensorineural hearing loss occurring in young patients with normal CT scans.[11, 12]

There is a strong tendency for the findings in cochlear

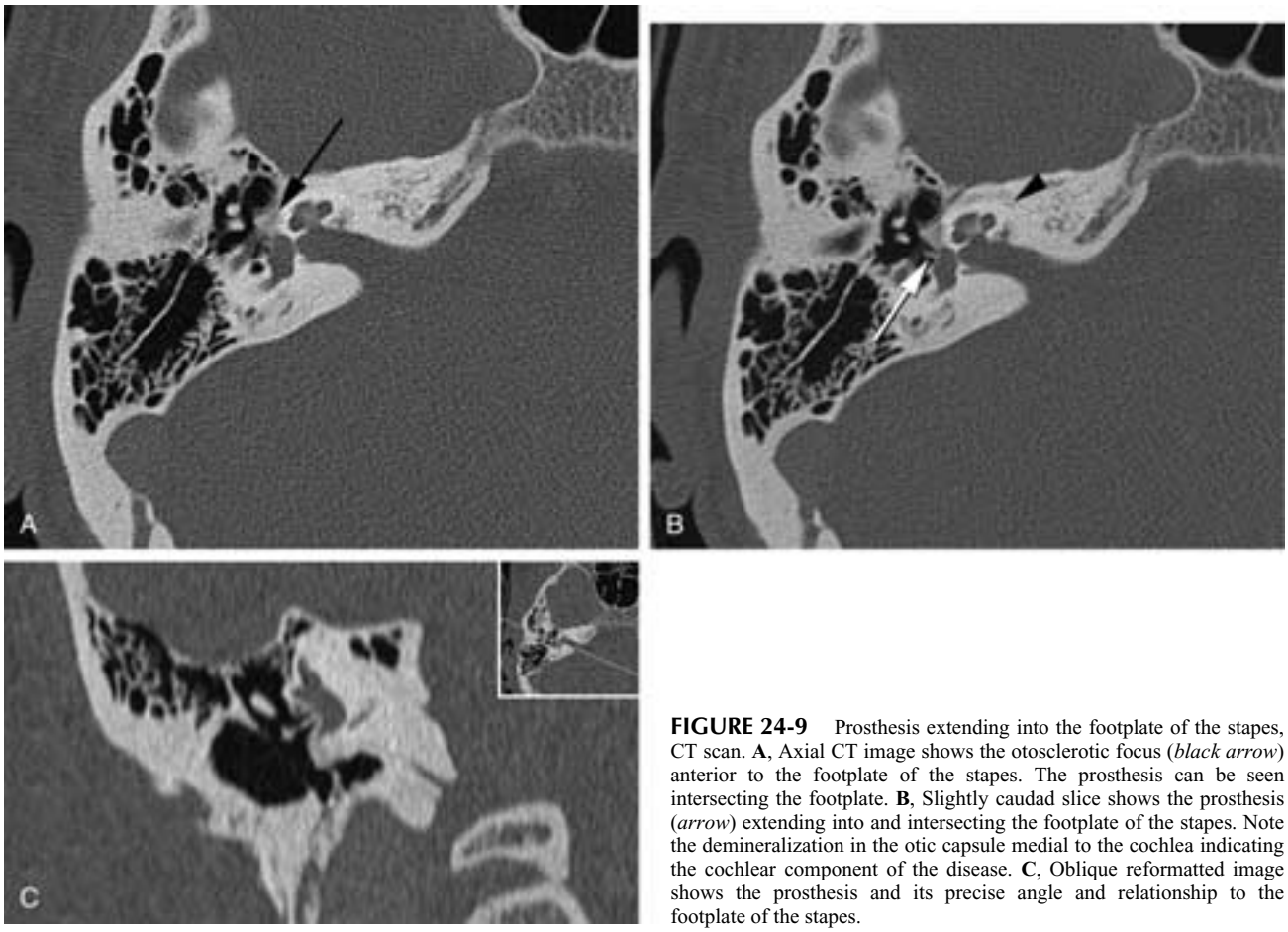

FIGURE 24-9 Prosthesis extending into the footplate of the stapes, CT scan. **A**, Axial CT image shows the otosclerotic focus (*black arrow*) anterior to the footplate of the stapes. The prosthesis can be seen intersecting the footplate. **B**, Slightly caudad slice shows the prosthesis (*arrow*) extending into and intersecting the footplate of the stapes. Note the demineralization in the otic capsule medial to the cochlea indicating the cochlear component of the disease. **C**, Oblique reformatted image shows the prosthesis and its precise angle and relationship to the footplate of the stapes.

VIEW IMAGE

Copyright © 2003, Mosby, Inc. All rights reserved.

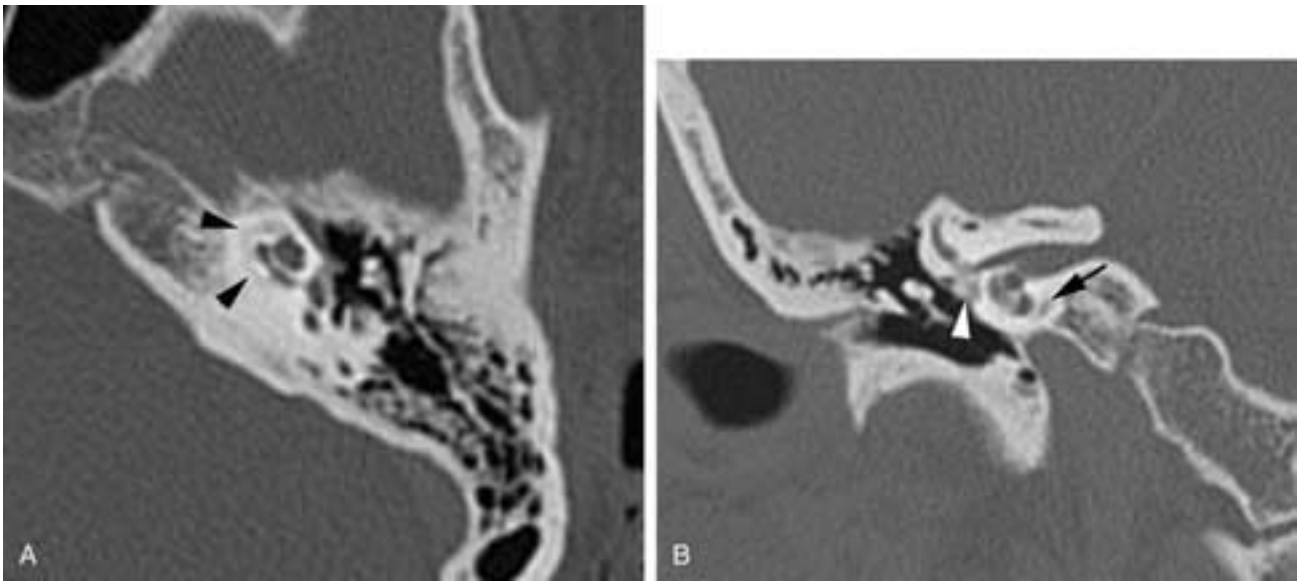

VIEW IMAGE

FIGURE 24-10 Cochlear (retrofenestral) otosclerosis. **A**, Axial CT image shows typical demineralization (*black arrowheads*) around the cochlea. Overgrowth of the demineralized, otosclerotic plaque anterior to the oval window is also visible. **B**, The demineralization of the otic capsule (*black arrow*) and the demineralization just anterior to the oval window (*arrowhead*).

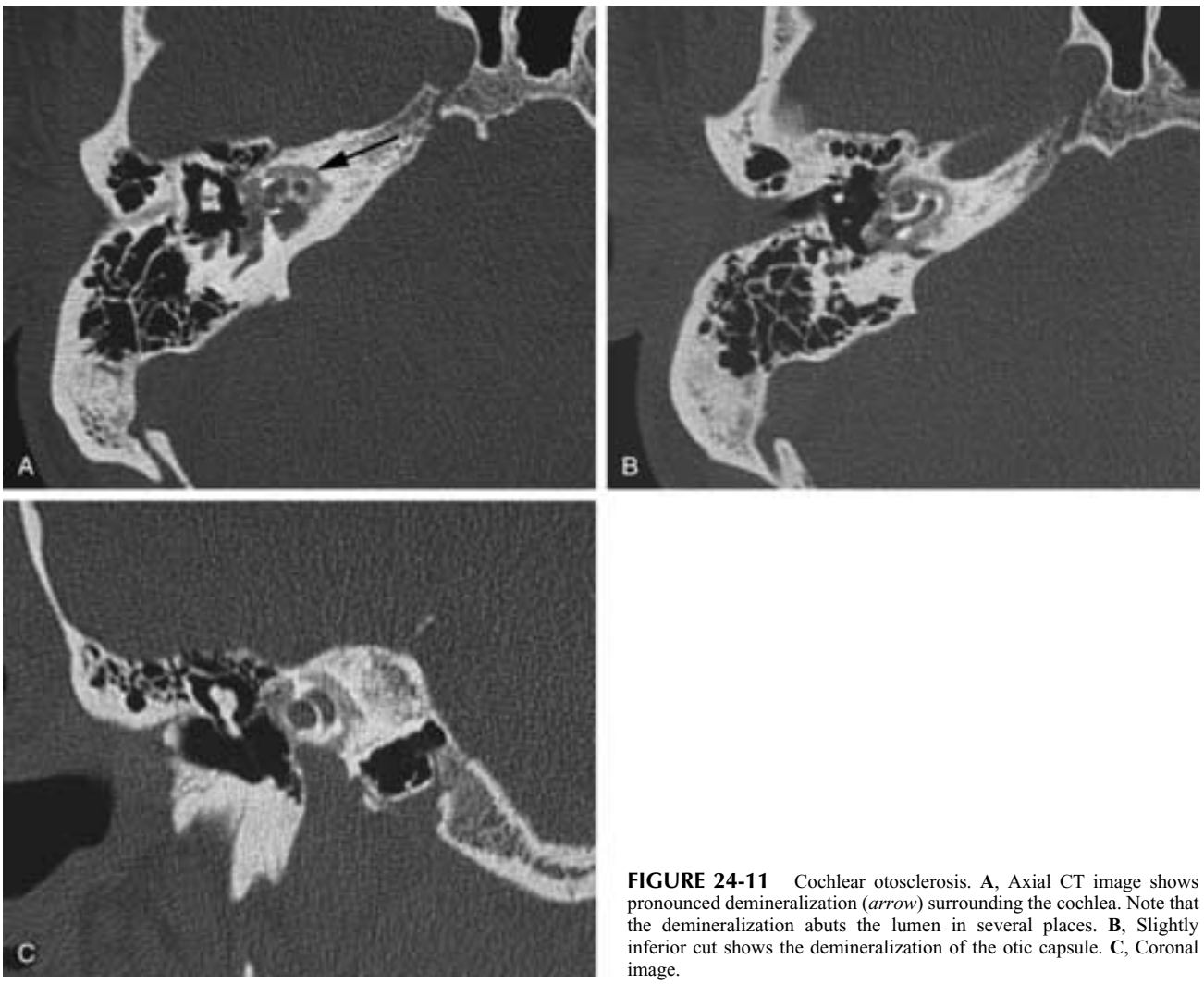

FIGURE 24-11 Cochlear otosclerosis. **A**, Axial CT image shows pronounced demineralization (*arrow*) surrounding the cochlea. Note that the demineralization abuts the lumen in several places. **B**, Slightly inferior cut shows the demineralization of the otic capsule. **C**, Coronal image.

VIEW IMAGE

Copyright © 2003, Mosby, Inc. All rights reserved.

otosclerosis to be symmetric, and CT scans obtained in both the axial and coronal planes should be carefully evaluated for otospongiotic foci. CT densitometry has been proposed as an objective method of assessing otospongiosic foci, and this technique may provide an opportunity to monitor the effectiveness of therapy before and after medical treatment.[36, 37]

MR imaging has had limited applications for evaluation of the cochlear capsule. The normal cochlear or otic capsule is seen as a complete loss of signal because of its dense bony structure. Both T1- and T2-weighted images may show very subtle signal changes in a demineralized cochlear capsule, but the T2-weighted images are considered relatively less sensitive.[15, 16, 35] On the other hand, in the assessment of the membranous labyrinth prior to cochlear implant surgery in patients with profound bilateral hearing loss, T2-weighted imaging is very useful. The fluid of the membranous labyrinth gives high signal on T2-weighted images, and obliteration of the signal indicates fibrosis or bone deposition within the labyrinthine lumen.[15, 18, 35]

Contrast-enhanced T1-weighted imaging is presumed to give information concerning activity of the lesions, as linear enhancement is noted in the bony labyrinth in the active phase of the disease. Enhancement is presumed to be due to contrast medium pooling in the numerous blood vessels of the otospongiotic foci[11, 15, 16, 35, 38] (Fig. 24-12).

Retrofenestral or cochlear otosclerosis has been considered a relative contraindication to cochlear implant surgery.[10, 18, 33, 34, 39–41] However, end-stage otosclerosis and profound sensorineural hearing loss may still be managed with multichannel cochlear implantation. Temporal bone histopathology studies indicate relatively good spiral ganglion populations, and these patients are frequently cited as ''good responders'' after cochlear implantation[42–44] (Fig. 24-13). Preoperative CT and MR imaging evaluation for assessment of the intracochlear space is necessary.[18, 44, 45]

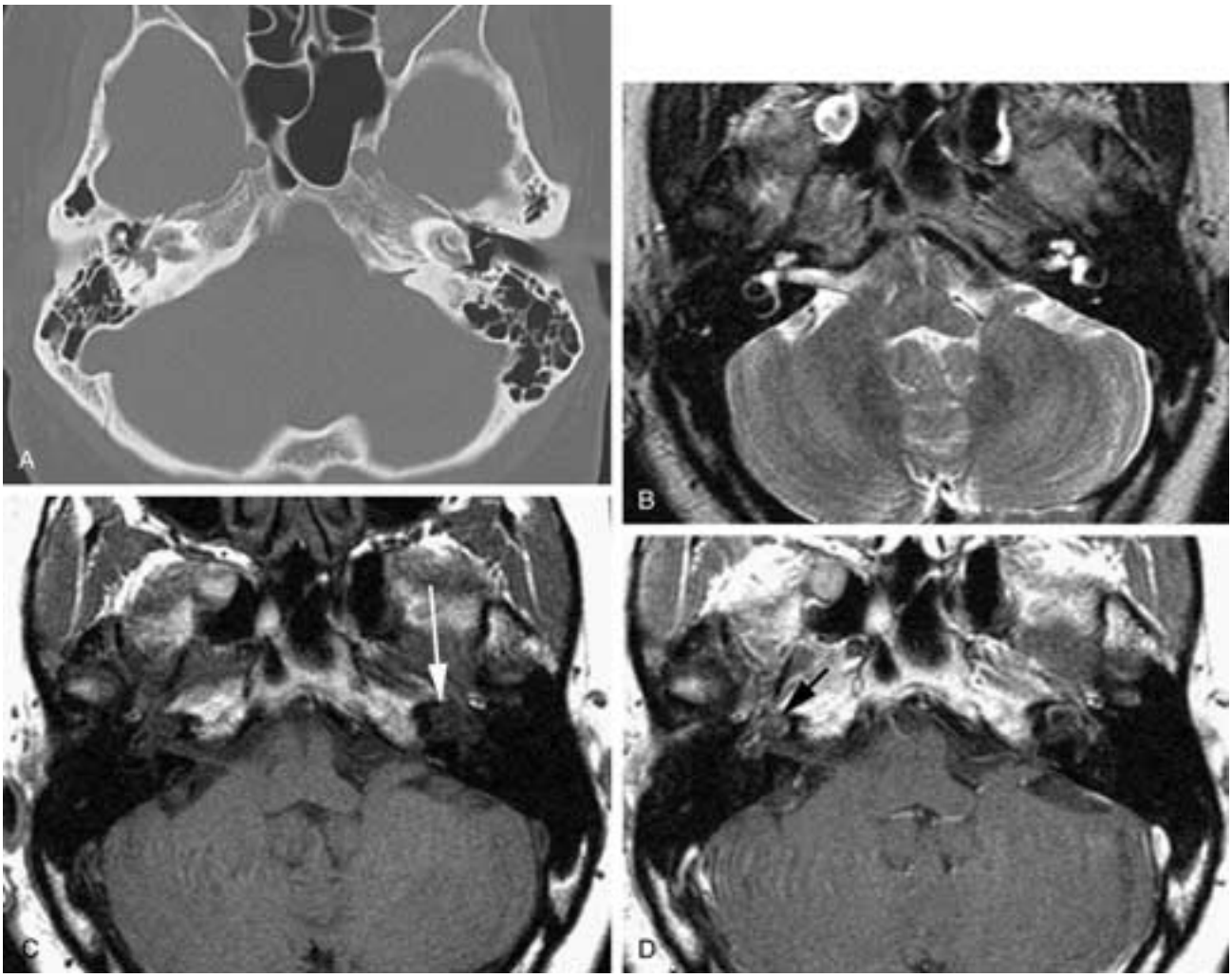

FIGURE 24-12 Cochlear otosclerosis, CT and MR scans. **A**, Axial image shows the demineralization around the cochlea on either side. This gives the appearance of the double ring or fourth turn of the cochlea. **B**, MR T2-weighted image shows the lumen of the cochlea but only a very faint hint of demineralization on the left side. **C**, Axial T1-weighted image shows the indistinctness of the outline of the labyrinth because of the demineralized bone (*arrow*) surrounding the lumen of the cochlea. **D**, Enhancement of the demineralized bone (*arrow*). (From Sakai O, Curtin HD, Fujita A, et al. Otosclerosis: CT and MR finding. Am J Otolaryngol 2000;21(2):116–118.)

VIEW IMAGE

Copyright © 2003, Mosby, Inc. All rights reserved.

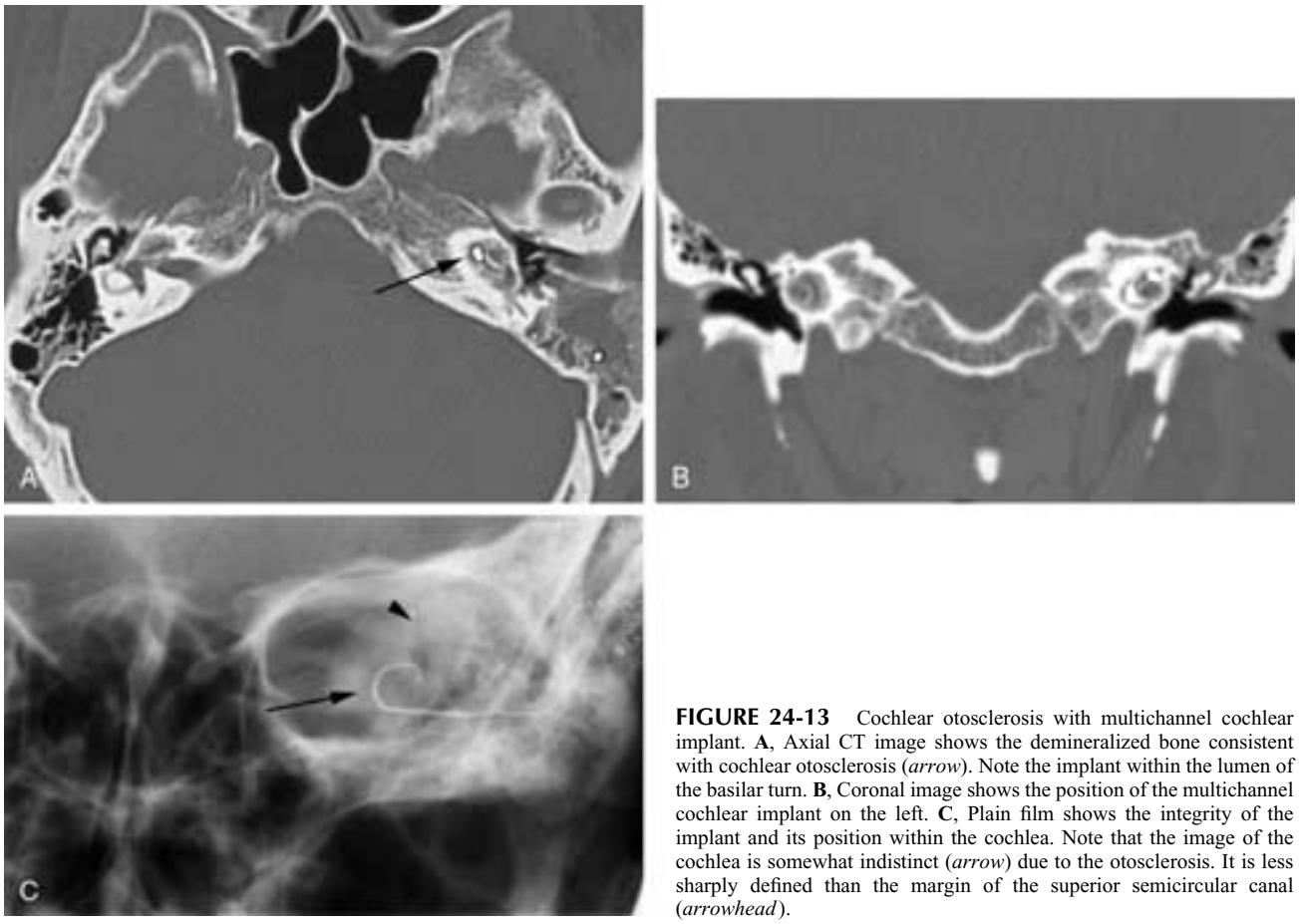

FIGURE 24-13 Cochlear otosclerosis with multichannel cochlear implant. **A**, Axial CT image shows the demineralized bone consistent with cochlear otosclerosis (*arrow*). Note the implant within the lumen of the basilar turn. **B**, Coronal image shows the position of the multichannel cochlear implant on the left. **C**, Plain film shows the integrity of the implant and its position within the cochlea. Note that the image of the cochlea is somewhat indistinct (*arrow*) due to the otosclerosis. It is less sharply defined than the margin of the superior semicircular canal (*arrowhead*).

VIEW IMAGE

Postoperative evaluation of cochlear implants can be performed with CT; however, assessment of the insertion depth of the device can also be achieved with plain films[10, 46] (Fig. 24-13).

Differential Diagnosis

The differential diagnosis of fenestral otosclerosis is quite limited, while that of cochlear (retrofenestral) otosclerosis includes various diseases that demineralize the cochlear capsule. Such diseases include osteogenesis imperfecta and Paget's disease. Ankylosing rheumatoid arthritis and inflammatory/infectious diseases such as syphilis have also been mentioned as mimicking some aspects of otosclerosis.[8, 10, 28] These diseases have systemic manifestations, in contrast to otosclerosis. Diffuse labyrinthine ossification, labyrinthitis ossificans, is a different entity and is not considered a consequence of otosclerosis unless inflammation complicates stapes surgery[47] (Fig. 24-14). Ossification of the membranous labyrinth may occur as a result of a previous inflammatory process such as meningitis, blood-borne septic emboli, middle ear infection, trauma, or surgery such as labyrinthectomy.[8, 47] Labyrinthine ossification may be localized and limited to the basilar turn of the cochlea or the round window niche, and such a limited manifestation is usually of a tympanogenic etiology.[10]

FIBROUS DYSPLASIA

Fibrous dysplasia is a disorder of unknown etiology characterized by slowly progressive replacement of normal bone by dysplastic fibroosseous tissue. The ability to form normal mature lamellar bone is defective, resulting in a developmental arrest at the level of immature woven bone. The abnormal trabeculae of woven bone form a disordered whorled pattern and spicules of bone undergo resorption and reformation, with active but disordered osteoblastic activity. The replaced tissue may be relatively acellular, with predominance of collagenous ground substance, or it may be extremely cellular. There may be a whorled arrangement resembling that of osteogenic sarcoma, and scattered islands of cartilage may be present.[1, 48, 49]

This proliferative process may give rise to expansion, distortion, and structural weakness of the bone. Because fibrous dysplasia primarily involves the cancellous bone and rarely involves the cortical bone, this lesion usually widens the bone by replacing the normal medullary space. The abnormal dysplastic bone is often covered by a thin normal cortical margin.[8, 48–51] Females are affected twice as often as males.

Fibrous dysplasia may affect one, a few, or many bones and can be grossly divided into monostotic, oligostotic, and polyostotic forms. The polyostotic lesions tend to be distributed unilaterally. The monostotic form may arrest at

Copyright © 2003, Mosby, Inc. All rights reserved.

puberty, whereas the polyostotic form may progress beyond the third and even later decades. The McCune-Albright syndrome is a special form of polyostotic fibrous dysplasia, representing about 3% of the cases, and is associated with endocrine disorders.[48, 49] Malignant transformation of fibrous dysplasia is rare (0.5%), and although several forms of sarcoma may develop, osteosarcoma is the most common.[48, 52]

The radiologic findings of fibrous dysplasia can be grossly divided into three patterns: pagetoid, sclerotic, and cyst-like. Throughout the entire skeletal system the pagetoid form of fibrous dysplasia is most common, occurring in about 53% of cases; the patient is usually over 30 years of age. The pagetoid form has regions of bony expansion and mixed areas of radiopacity and radiolucency (Fig. 24-15). The sclerotic form, which occurs in 23% of cases, is usually seen in younger patients and consists radiographically of more homogeneous ''ground-glass'' opacities and bone expansion (Figs. 24-16 and 24-17). The cyst-like form, which occurs in 21% of cases, also occurs in younger patients and is characterized by round or oval ''cystic'' lesions with sclerotic borders. In some cases, the sclerotic and cyst-like forms are precursors of the pagetoid form. In the temporal bone, fibrous dysplasia is almost always of the predominantly sclerotic form, and the cyst-like form is uncommon.[50, 53]

The most common presenting symptoms relating to fibrous dysplasia in the temporal bone are progressive hearing loss (characteristically conductive), an increase in the size of the temporal bone or a postauricular deformity, and obstruction of the external auditory canal (Fig. 24-15C). Stenosis or obstruction of the external auditory canal may result in infection and lead to external canal cholesteatoma and keratosis obturans medial to the narrowing.[50, 54, 55] Facial weakness or hearing loss, or both, may occur as a result of entrapment and compression of the seventh and eighth cranial nerves.[55–57]

High-resolution CT of the temporal bone depicts details of the lesions of fibrous dysplasia. The most common CT findings include an increase in bone thickness, a homogeneous radiodensity, and a loss of the trabecular pattern.[50] There may be varying degrees of obliteration of the mastoid air cells and external auditory canal. Primary involvement of the tympanic cavity is relatively uncommon. Secondary pathology such as cholesteatoma with erosion of the canal and ossicles is shown superimposed on the primary pathology.[55] Bony impingement on the internal auditory canal or facial nerve may explain the corresponding symptoms. The cochlear capsule may be involved, though it is characteristically spared.[50, 53, 56, 57]

Although CT demonstrates lesions of fibrous dysplasia best, MR imaging also can depict the abnormalities. On both T1- and T2-weighted images, low to intermediate signal intensity is usually seen in the largest part of the lesions. Smaller regions of high signal intensity perhaps representing cysts may be also observed. Following administration of contrast material, the lesions demonstrate moderate to marked enhancement (Fig. 24-18). The cellularity and activity of the lesions do not correlate well with signal intensity and enhancement degree or pattern.[58] MR imaging is also useful for evaluating the cranial nerves, including the seventh and eighth, the brainstem, and other soft tissue structures adjacent to the lesions.[56]

Differential Diagnosis

The differential diagnosis of fibrous dysplasia of the temporal bone includes other *benign fibroosseous lesions*

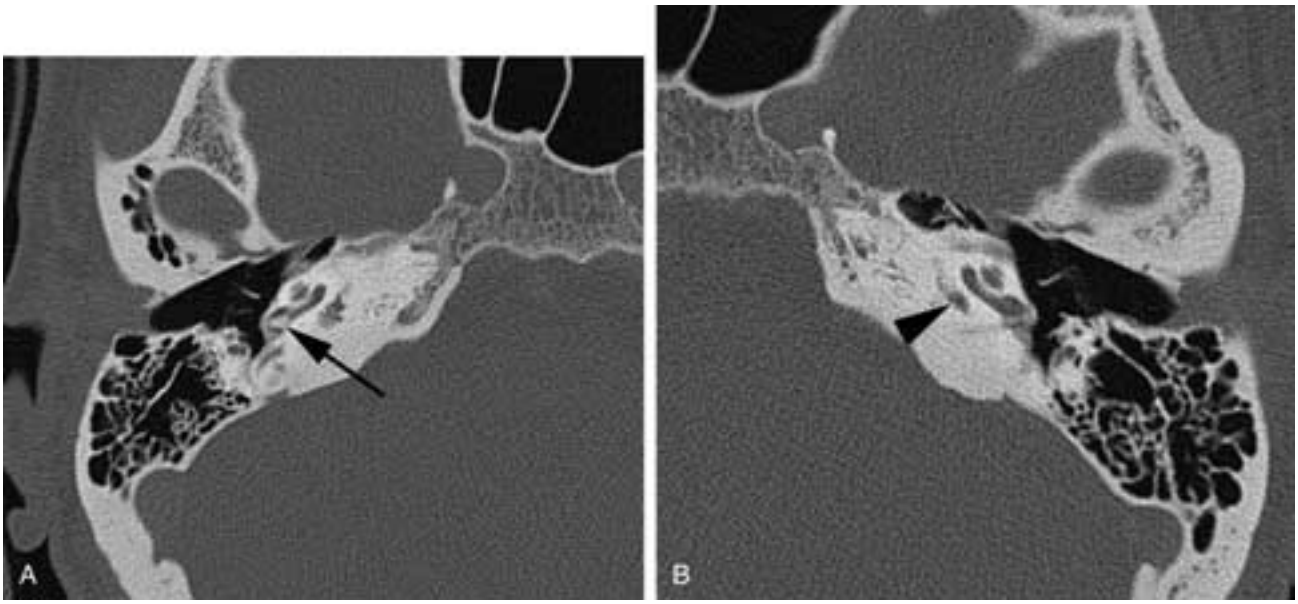

VIEW IMAGE

FIGURE 24-14 Labyrinthitis ossificans superimposed on otosclerosis. The patient has bilateral otosclerosis and has had a prosthesis placed on the right. **A**, Right side. Note the focus of bone density within the lumen of the basilar turn (*black arrow*) compared to the opposite side, seen in **B**. This focus of bone does not represent otosclerosis but rather is a secondary labyrinthitis ossificans superimposed on the primary disease. **B**, Left side. Note the demineralization of the otic capsule (fourth turn of the cochlea) on the left side (*arrowhead*).

Copyright © 2003, Mosby, Inc. All rights reserved.

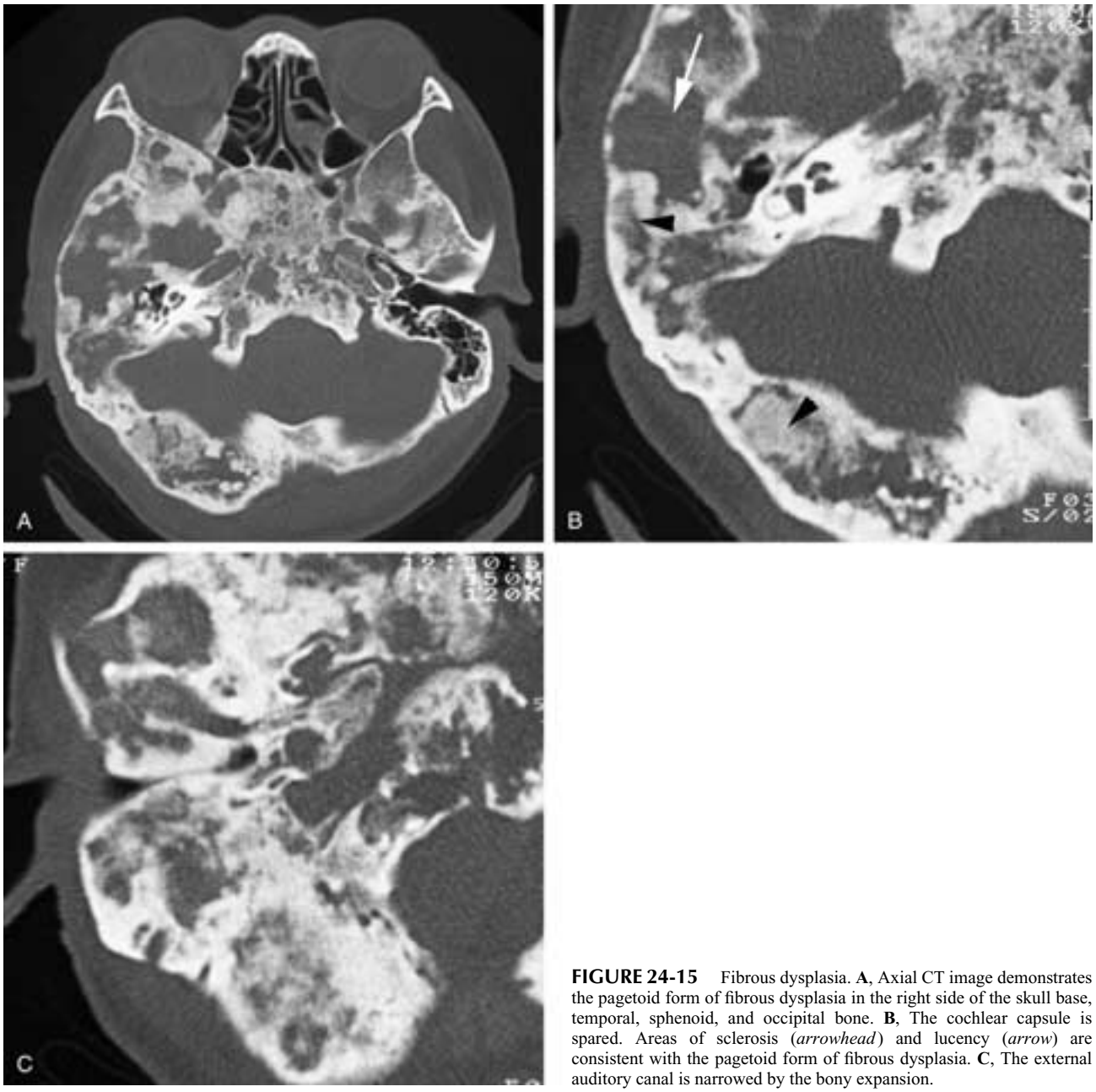

FIGURE 24-15 Fibrous dysplasia. **A**, Axial CT image demonstrates the pagetoid form of fibrous dysplasia in the right side of the skull base, temporal, sphenoid, and occipital bone. **B**, The cochlear capsule is spared. Areas of sclerosis (*arrowhead*) and lucency (*arrow*) are consistent with the pagetoid form of fibrous dysplasia. **C**, The external auditory canal is narrowed by the bony expansion.

VIEW IMAGE

such as *ossifying fibroma*. The imaging findings of these lesions are very similar, but ossifying fibroma tends to be more localized, appearing as more of a mass-like lesion. However, it is often impossible to differentiate by imaging alone, and the histopathologic findings of these two lesions are also quite similar. *Paget's disease* is one of the major differential diagnoses of temporal bone fibrous dysplasia. It is usually bilateral and exhibits osteopenia with a small number of sclerotic foci, and the patients are usually older than those with fibrous dysplasia.[59, 60] In Paget's disease, there usually is not the same degree of osseous thickening seen with fibrous dysplasia, and the outer margin of the otic capsule is more frequently demineralized. *Hyperparathyroidism* may also cause ground-glass, sclerotic bone, particularly with the secondary form of this disease. Usually, the skeletal manifestations are symmetrically evident throughout the entire skeletal system, and there is systemic hypercalcemia.[61, 62] *Sclerosteosis* (*endosteal hyperostosis*) is an autosomal recessive disease first appearing in infancy or early childhood. There is overgrowth of the skull, vertebrae, and mandible, with gigantism and syndactyly. Cranial nerve palsies are common. The long bones have sclerotic changes, which can be differentiated from those of fibrous dysplasia.[63, 64] *Neurofibromatosis* may simulate fibrous dysplasia, particularly when a neurofibroma erodes into or originates within the temporal bone. However, the additional clinical features and other skeletal manifestations are different from those of fibrous dysplasia. *Chondroblastoma* is rare in the temporal bone. However, it can present as an expansile soft-tissue density mass with bony erosion and may simulate fibrous dysplasia. Spotty calcification may be seen, and the lesion enhances with contrast material.[65, 66] An

Copyright © 2003, Mosby, Inc. All rights reserved.

aneurysmal bone cyst may occur in the temporal bone. Although this cyst is expansile, it is usually accompanied by pain and tenderness, symptoms uncommonly associated with fibrous dysplasia.[8, 48, 57, 67–69] *Chondrosarcoma* may mimic the pagetoid form of fibrous dysplasia, with spotty calcification often being seen on CT and arc-like or curvilinear enhancement often being seen on contrast-enhanced MR[70, 71] (Fig. 24-19). *Metastatic bone tumors* may present a sclerotic, almost ground-glass appearance and may simulate fibrous dysplasia or other benign fibroosseous lesions, particularly metastases from prostate or breast cancers.

PAGET'S DISEASE (OSTEITIS DEFORMANS)

A well-known English surgeon, Sir James Paget (1877, 1882), described the clinical and pathologic features of this disease, although it was Czerny (1873) who named this disorder osteitis deformans.[1, 60] Paget's disease is quite common, affecting 3% of the population over 40 years of age and up to 10% of patients over 80 years of age. There is an ill-defined genetic factor suggested by familial and geographic clustering. The disease is a chronic, sometimes progressive condition that may present as a solitary monostotic form that remains asymptomatic, only to be discovered as an incidental finding. Alternatively, the disease may develop into a clinically apparent entity. In its disseminated polyostotic form, many bones in different regions are affected, with the pelvis being most commonly involved, followed by the femur, skull, tibia, and spine. Progressive involvement of the temporal bone results in an increase in size and changes in the architecture and position of the petrous pyramid, external auditory canal, middle ear, and otic capsule.[59, 60, 72, 73] The ossicles are rarely involved in the pagetic process.[1]

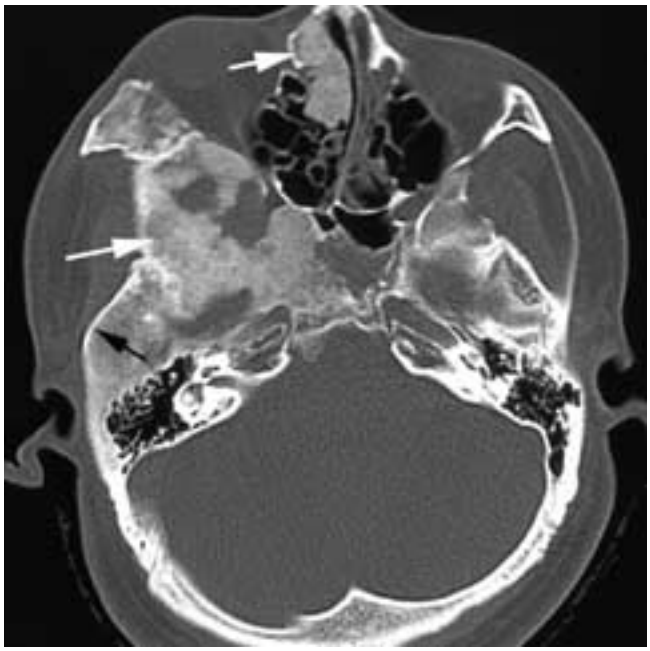

VIEW IMAGE

FIGURE 24-16 Fibrous dysplasia. Axial CT image demonstrates diffusely increased ground-glass density (*white arrows*). Note the involvement of the sphenoid bone. There is also involvement of parts of the ethmoid bone anteriorly. Note that the cortex (*black arrow*) is intact.

The histopathology of Paget's disease in the temporal bone can be divided into four phases: (1) osteolytic, (2) mixed, (3) osteoblastic, and (4) remodeled phases.[1] The osteolytic phase begins with increased vascularity and cellularity in the adjacent bone marrow spaces. Osteoclastic resorption of trabeculae of the spongiosa or walls of the Haversian canals of the compacta can be seen. Heightened bone formation leads to an increase in vascularity, with blood flow as much as 20 times that of normal.[1] In the calvarium, the outer cortical table becomes thin and may even disappear. This results in *osteoporosis circumscripta*, sharply demarcated areas of ''washed-out'' radiolucency, which are typically seen in the skull base or calvarium[8, 72] (Fig. 24-20).

Eventually, the osteolytic areas may be replaced by new bone. This process is associated with an increase in bone density and thickness and represents the mixed phase, with new bone formation predominating over bone resorption. A mixture of phases results in a ''cotton-wool'' appearance caused by simultaneous osteolysis, and sclerosis and a prominent mosaic pattern is seen. A ''burn-out'' or osteoblastic phase follows. The involved bone is replaced by densely packed, narrow trabeculae of lamellar, coarse-fibered bone. The medullary cavity may be filled by avascular, fibrous connective tissue. This sclerotic form of the disease is much less common in the temporal bone. A pagetoid lesion in the sclerotic phase has an ''ivory'' appearance, which distinguishes it from the adjacent bone. Bone expansion continues until resorption occurs. Although the mass of the bone is increased, it is structurally unstable and weak, probably because of the failure of the collagen fibers to align along stress lines in each spicule of bone.[1] Like other normal bones, the inactive osteoblastic pagetic bone may undergo remodeling into normal-appearing lamellar bone with distinct Haversian canals. Malignant transformation is seen in about 1% of patients.[1, 8, 59, 72, 74]

Hearing impairment is the most common manifestation in patients with the temporal bone involvement of this disease. The loss may be conductive, sensorineural, or mixed. Less common symptoms include tinnitus, vertigo, and unsteadiness.[59, 72, 74] High-resolution CT of the temporal bone shows the decreased density typically seen when demineralization is progressing. Areas may show a mixed appearance of bone thickening and sclerosis[60, 75, 76] (Figs. 24-21 to 24-23).

In the temporal bone, the disease begins at the petrous apex, the site of the greatest marrow deposition, and progresses inferolaterally. Demineralization of the otic capsule may occur as a later manifestation. Areas of resorption tend to advance from the periphery of the otic capsule toward the central regions. The stapedial footplate may be thickened, contributing to hearing loss. The mastoid process may show bone thickening, demineralization, or a mosaic pattern.[73] Frequently, the central skull base is also involved. With progression, basilar invagination occurs and the petrous apex tilts upward as the softening bone responds to the various forces placed on the skull base and the cervical spine protrudes into the foramen magnum (Fig. 24-22). Hearing impairment, from direct involvement of the temporal bone, may be further accentuated by stretching of

Copyright © 2003, Mosby, Inc. All rights reserved.

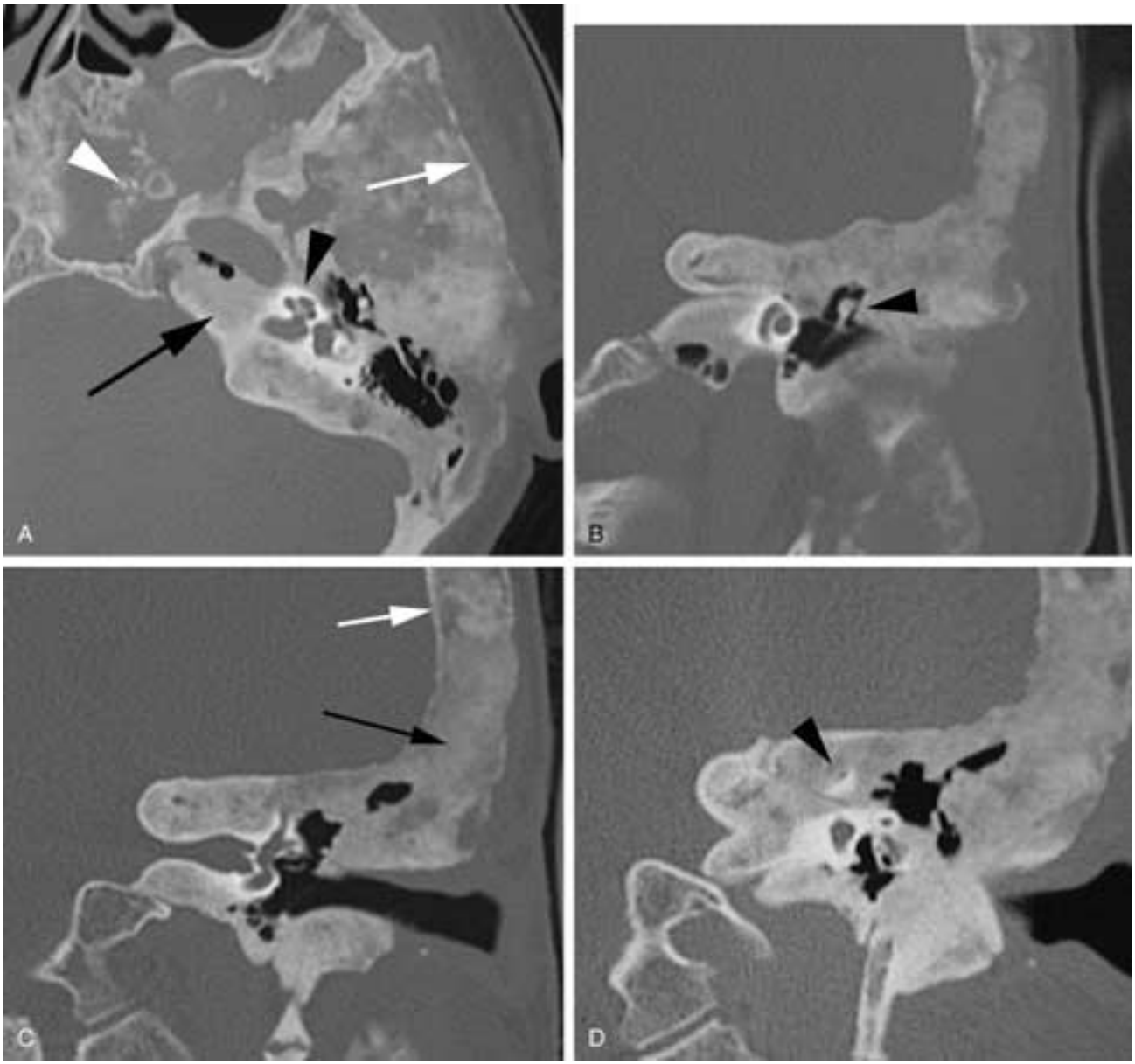

VIEW IMAGE

FIGURE 24-17 Fibrous dysplasia demonstrating a mixed appearance of pagetoid and sclerotic, ground-glass forms of fibrous dysplasia in the left temporal bone. The cochlear capsule is spared. **A**, Diffuse involvement of the petrous apex (*black arrow*). Note that the cortex is partially defined (*white arrow*). Some chondroid matrix (*arrowhead*) is noted in the region of the sphenoid. **B**, There is enlargement of the bone. The lateral wall of the attic (*arrowhead*) impinges slightly on the head of the malleus. **C**, Coronal image shows the ground-glass appearance (*black arrow*) and the intact cortex (*white arrow*) characteristic of fibrous dysplasia. **D**, There is some demineralization of the peripheral portion of the otic capsule, with subtle demineralization (*arrowhead*) of the superior semicircular canal.

the eighth cranial nerve that results from the basilar invagination.[8]

MR findings of Paget's disease are variable. Marrow replacement by fibrous tissue results in decreased signal intensity on T1-weighted images; however, patchy, heterogeneous high signal intensities may occur secondary to hemorrhage or slow flow in vascular channels. Contrast enhancement reflects the hypervascular nature of this process.[77] Diffuse meningeal enhancement may be noted, presumably reflecting increased metabolism and blood flow of the lesions (Fig. 24-21).

Differential Diagnosis

The variety of findings in Paget's disease leads to an extensive differential diagnosis. *Fibrous dysplasia* results in widening of the diploic spaces as the medullary region becomes filled with fibrous material. Often there is a ground-glass appearance, and the corticomedullary junction tends to be preserved. Patients with fibrous dysplasia are usually younger and have greater marrow involvement than patients with Paget's disease.[76] The manifestations of *hyperparathyroidism* are usually seen throughout the skele-

Copyright © 2003, Mosby, Inc. All rights reserved.

ton and may be accompanied by other clinical and or laboratory manifestations. Hyperparathyroidism may cause diffusely sclerotic bone changes, particularly secondary hyperparathyroidism and renal osteodystrophy. A progressive form of osteitis fibrosa cystica, osteofibrosis associated with localized cysts, rarefied and thinned cortex, distorted and blurred cancellous trabeculae, and deformity can be observed.[61, 62] *Osteogenesis imperfecta* may have some similarities to the findings in Paget's disease, but the clinical and radiologic findings are different. *Hereditary hyperphosphatasia* (juvenile Paget's disease) is a rare autosomal recessive disease seen in infancy and childhood. It is characterized by generalized cortical thickening and sustained elevation of serum alkaline phosphatase and urinary hydroxyprolamine. Thickening and deossification of the skull base with bowing of tubular bones are observed.[67, 68, 78] *Progressive diaphyseal dysplasia* (Camurati-Engelmann-Ribbing disease or syndrome) is an autosomal dominant disease usually diagnosed in childhood. It consists of typical hyperostosis of the long bones that can be easily differentiated from Paget's disease.[68, 79] The skull base thickening and sclerosis seen in *pyknodysostosis* is also

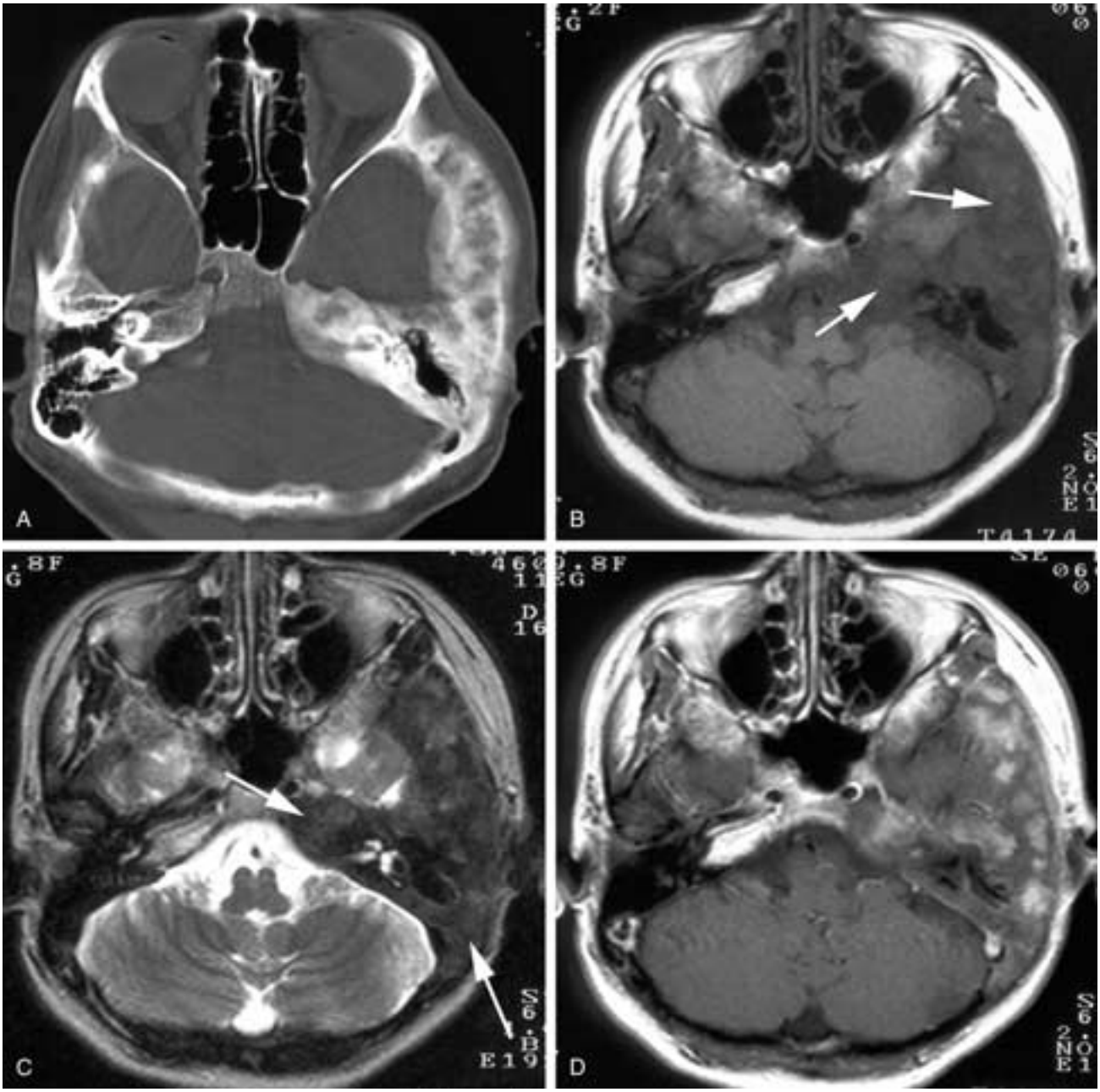

FIGURE 24-18 Fibrous dysplasia. **A**, Axial CT image shows the expansile pagetoid form of fibrous dysplasia of the left temporal bone. **B**, Axial T1-weighted image shows the intermediate signal intensity (*arrows*) of the bony enlargement. **C**, T2-weighted image shows relatively low signal intensity with expansion of the bone (*arrows*). **D**, After contrast there is patchy enhancement of the abnormal bone.

VIEW IMAGE

Copyright © 2003, Mosby, Inc. All rights reserved.

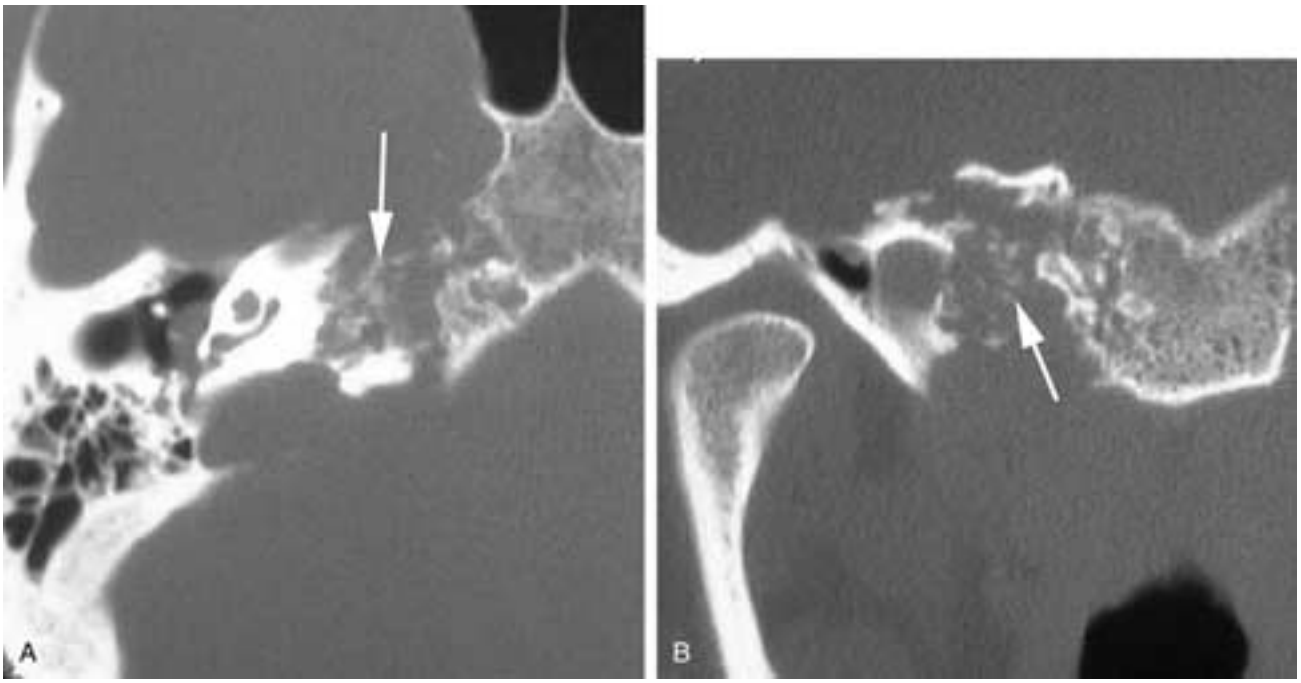

VIEW IMAGE

FIGURE 24-19 Maffucci's syndrome with chondrosarcoma arising in the petroclival synchondrosis. **A**, Axial image shows the abnormal bone involving the petrous apex (*arrow*) but crossing the petroclival synchondrosis. The density of the bone might be mistaken for fibrous dysplasia. **B**, Coronal image shows the small ring-like calcifications characteristic of chondrosarcoma (*arrow*). Chondroid matrix can be seen in fibrous dysplasia.

uniformly present throughout the skeleton, unlike the patchy lesions of Paget's disease.[80] *Meningiomas* are usually sharply demarcated and tend to show inward growth from the inner table of the skull, which differentiate them from Paget's disease.[8, 69] *Metastatic osseous lesions* may also mimic Paget's disease, particularly when originating from prostate or breast cancers. Clinical information is important to differentiate these diseases.

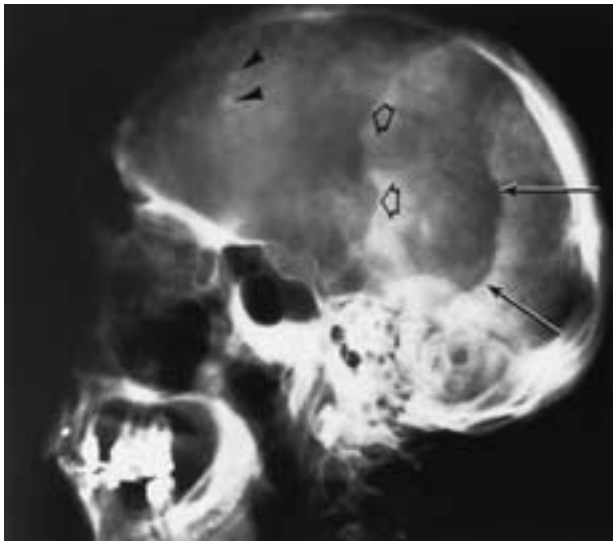

VIEW IMAGE

FIGURE 24-20 Paget's disease. Lateral skull film demonstrates classic changes of osteoporosis circumscripta. Posterior margins on each side (*advancing edge*) are demonstrated (*arrows and open arrows*). Countless dense foci (*black arrowheads*) are noted.

OSTEOGENESIS IMPERFECTA

Osteogenesis imperfecta (Van der Hoeve's syndrome) is a genetic disorder of connective tissue caused by an error in type I collagen formation manifested as a deficiency in fibroblastic and osteoblastic activity.[1, 81] The classic description of osteogenesis imperfecta includes fragile bones, blue sclerae, and deafness. The fragile bones lead to recurring fractures and skeletal deformity. Additional clinical manifestations are abnormal dentinogenesis, hyperextensible joints, and wormian bones. The genetic defects leave patients with decreased amounts of type I collagen, and this form of collagen is not only predominant in bones but is also present in skin, connective tissue, and dentin.[67, 82]

Four major types of osteogenesis imperfecta have been described with several subtypes, based on relatively distinct syndromes that reflect different defects in type I collagen synthesis.[83–85] Type I, previously called osteogenesis imperfecta tarda, is the most common and mildest form and reflects decreased production of type I collagen. Patients usually present with a bone fracture following minimal or no trauma. Blue sclerae are always present, and deafness is common after childhood. These patients can have joint dislocations and hyperflexibility, as well as easy bruisability. Dentin production may be normal or abnormal. Type II, previously known as osteogenesis imperfecta congenita, is the most severe form of this disease. Death in utero or shortly after birth is common due to multiple fractures of the skull, vertebrae, or chest wall. Type III osteogenesis imperfecta presents with marked bony deformity and frequent early fractures of the long bones. Short stature is common, as is abnormal production of dentin or *dentinogen-*

Copyright © 2003, Mosby, Inc. All rights reserved.

esis imperfecta. The sclerae originally are blue but turn white as the patient grows. The genetic defect is not well understood. Type IV osteogenesis imperfecta has variable severity, with a defect in one subunit of collagen. Some patients exhibit normal sclera and dentin with minimal bone fragility.[67, 84, 85]

Radiologic findings of the skull include generalized osteopenia with diminished trabeculae and a thin cortex and wormian bones; occasionally, basilar invagination is noted. The extremities show marked bowing and deformity as a result of multiple fractures. The ribs are thin and notched and may also show evidence of fractures. The vertebrae are usually biconvex because the soft endplates mold around the intervertebral disk, and sclerosis of the vertebral bodies may occur.[75, 84, 85]

CT of the temporal bone may show proliferation of undermineralized, thickened bone around the otic capsule (Fig. 24-24). As this thickened bone extends from the labyrinth, the middle ear cavity may be narrowed; the oval window may become obstructed, with the stapedial crura embedded in a dysplastic osseous mass; and the facial canal may be narrowed, with corresponding damage to the facial nerve.[75, 76, 86, 87] The CT appearance is very similar to that of retrofenestral or cochlear otosclerosis but is much more extensive. In osteogenesis imperfecta, the demineralization can reach the level of the superior semicircular canal.

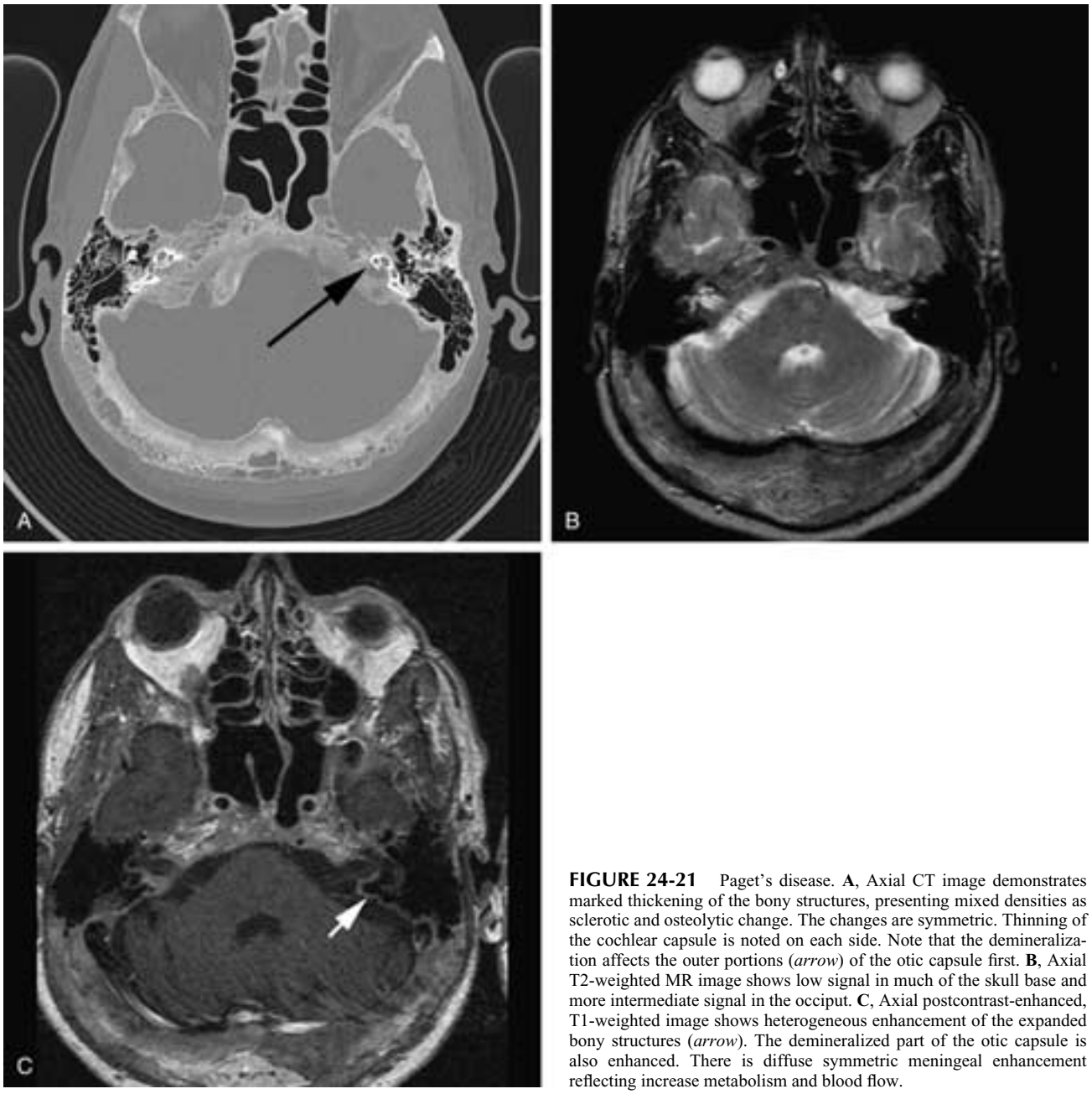

FIGURE 24-21 Paget's disease. **A**, Axial CT image demonstrates marked thickening of the bony structures, presenting mixed densities as sclerotic and osteolytic change. The changes are symmetric. Thinning of the cochlear capsule is noted on each side. Note that the demineralization affects the outer portions (*arrow*) of the otic capsule first. **B**, Axial T2-weighted MR image shows low signal in much of the skull base and more intermediate signal in the occiput. **C**, Axial postcontrast-enhanced, T1-weighted image shows heterogeneous enhancement of the expanded bony structures (*arrow*). The demineralized part of the otic capsule is also enhanced. There is diffuse symmetric meningeal enhancement reflecting increase metabolism and blood flow.

VIEW IMAGE

Copyright © 2003, Mosby, Inc. All rights reserved.

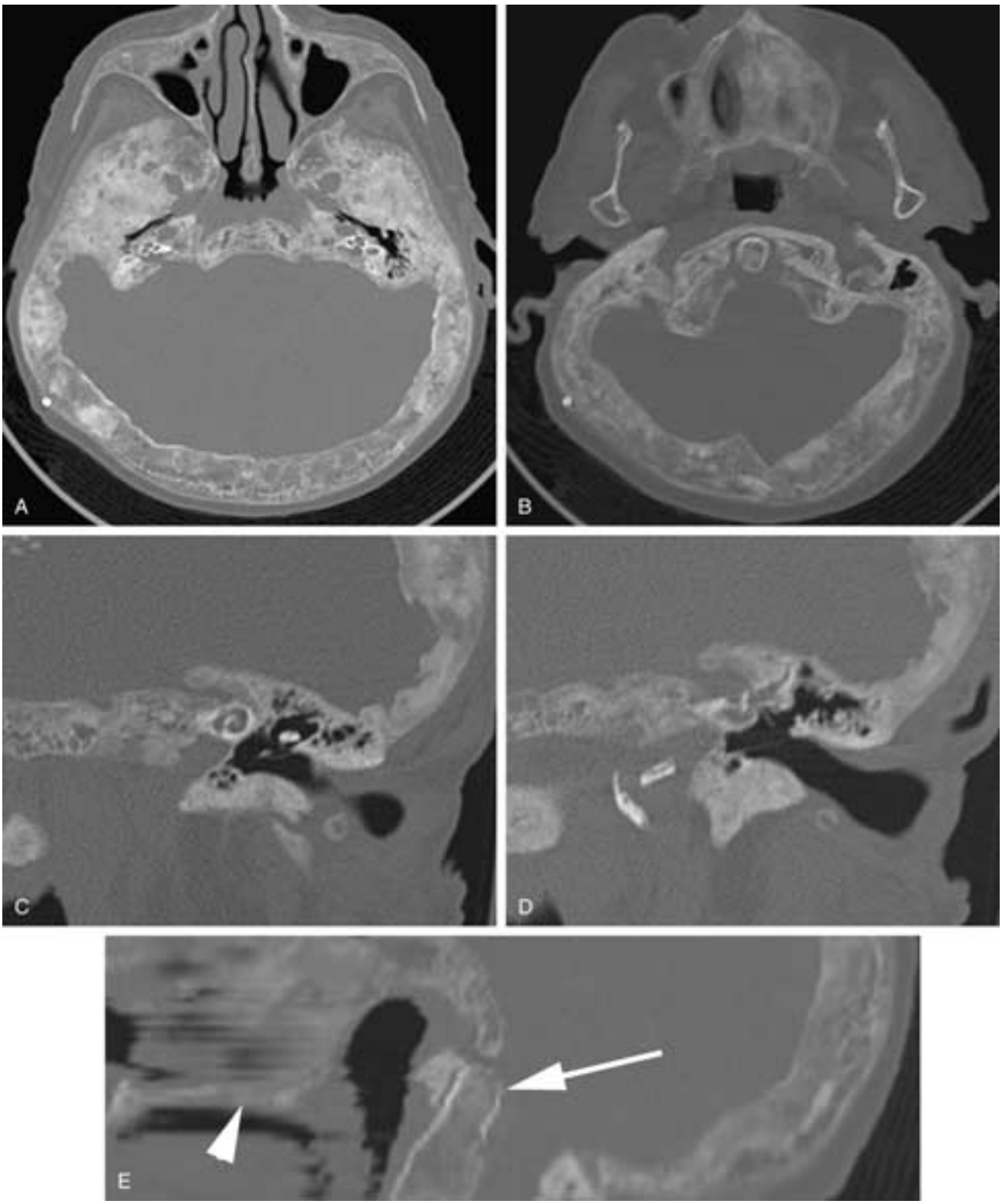

VIEW IMAGE

FIGURE 24-22 Paget's disease. **A** and **B**, Axial CT images demonstrate marked thickening of the bony structures with mixed densities of osteosclerosis and osteolysis. The changes are symmetric. Thinning of the cochlear capsule is noted bilaterally. The odontoid process protrudes above the foramen magnum to the level of the clivus. **C** and **D**, Coronal CT images show thickening of the bony structure and loss of the normal density of the otic capsule. **E**, Sagittal reformatted image shows a protrusion of the odontoid process (*arrow*) into the foramen magnum. Note that the tip of the odontoid is significantly higher than the hard palate (*arrowhead*). This represents basilar invagination.

Copyright © 2003, Mosby, Inc. All rights reserved.

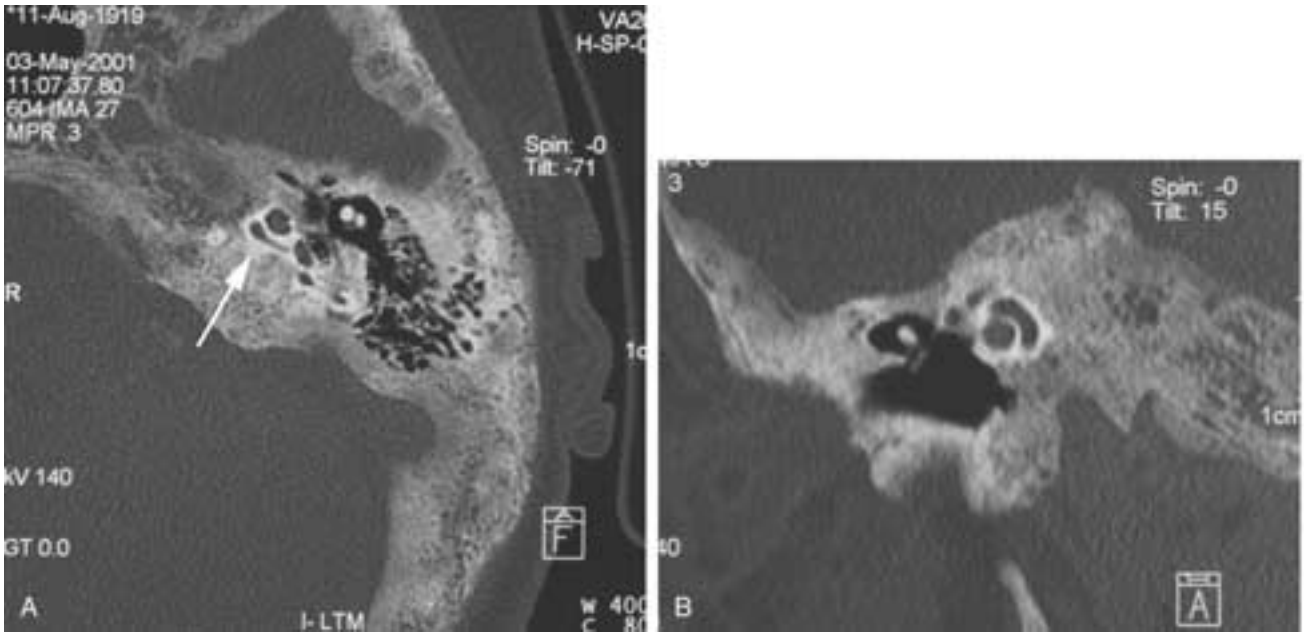

FIGURE 24-23 Paget's disease, CT scan. **A**, The bone has increased in size. There is demineralization and thinning of the otic capsule (*arrow*). **B**, Coronal image showing thinning of the otic capsule.

VIEW IMAGE

The histologic appearance of these two disorders is very similar.[1]

Differential Diagnosis

The differential diagnosis of osteogenesis imperfecta includes *otosclerosis* (Fig. 24-25), *Paget's disease*, and *hyperparathyroidism*. Retrofenestral or cochlear otosclerosis causes a zone of decreased density around the otic capsule similar to that of osteogenesis imperfecta. Also, otosclerosis can have focal areas of sclerosis, and the abnormal bone may involve the stapedial footplate and oval window. It is virtually impossible to differentiate otosclerosis from osteogenesis imperfecta in some cases, but usually the extensive nature of osteogenesis imperfecta will suggest the diagnosis. Obliteration of the oval and round windows and sensorineural hearing loss may be encountered and may

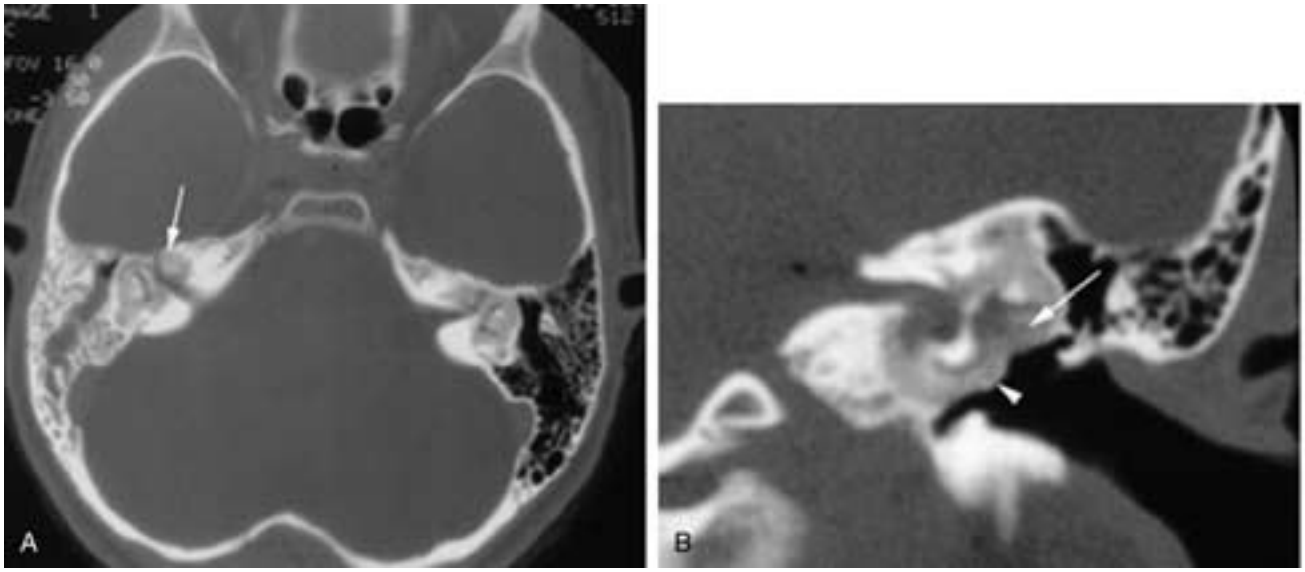

FIGURE 24-24 Osteogenesis imperfecta. **A**, Axial CT image shows the gross demineralization of the otic capsule (*arrow*). **B**, Coronal image shows thickening of the bone as well as the demineralization. Note the thickness of the bone over the promontory (*arrowhead*) and in the region of the tympanic segment of the facial nerve canal (*arrow*). The patient presented with a conductive hearing loss and facial paralysis.

VIEW IMAGE

Copyright © 2003, Mosby, Inc. All rights reserved.

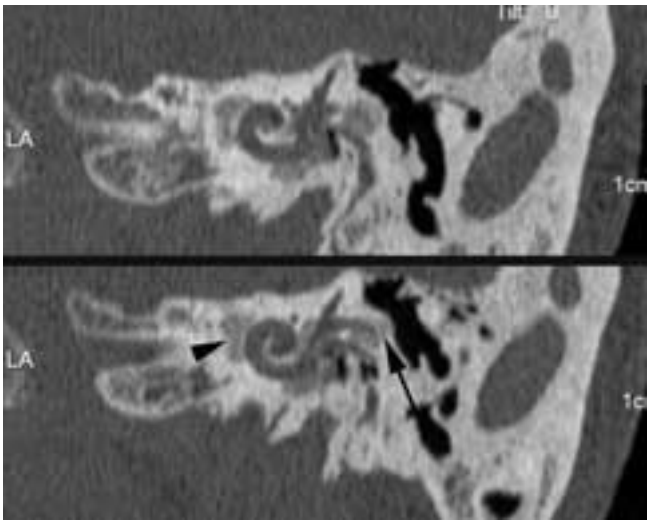

VIEW IMAGE

FIGURE 24-25 Osteogenesis imperfecta versus diffuse cochlear otosclerosis. The image is a 45° oblique reformat showing the gross demineralization along the basilar turn of the cochlea (*arrowhead*) as well as along the horizontal semicircular canal (*arrow*).

compromise the success of stapedial surgery.[87] Typically, patients with Paget's disease are older and do not have prominent hypertrophic bone around the stapes and oval window. Usually, the manifestations of hyperparathyroidism are seen throughout the skeletal system. These patients have cortical bone cysts, with local tenderness and systemic hypercalcemia. Hyperparathyroidism may also cause sclerotic bone changes, particularly with the secondary form of this disease.[61, 62, 75]

OSTEOPETROSIS

Osteopetrosis (Albers-Schonberg disease) is a rare hereditary disorder in which there is a defect in the mechanism of bone remodeling. Failure of osteoclastic function is the most likely etiology, along with defective absorption of the primary spongiosa. This results in thick, dense, but fragile bones giving rise to the suitable terminology *chalk bones* and *marble bone disease*.[1, 2, 10, 88–90] Overproduction of immature bone causes thickening of the cortex and narrowing or obliteration of the medullary cavity, and may cause neutropenia and anemia.[88–90]

There are two modes of inheritance in osteopetrosis: autosomal recessive (malignant) and autosomal dominant (benign). There may be severe and mild forms of the less common autosomal recessive type.[91] There is frequent stillbirth, and those surviving birth rarely survive childhood. The clinical features may be severe, as compromise of the marrow cavity, obliterated by the immature bone, can lead to pancytopenia and extramedullary hematopoiesis. There may be multiple cranial nerve palsies due to foraminal stenosis. Hydrocephalus, hepatosplenomegaly, improper dental development, and deafness may also be present.[88]

The autosomal dominant type of osteopetrosis is separated into type I and type II, both of which may be asymptomatic. Type I patients may experience bone pain or have symptoms of foraminal stenosis. These patients may have normal fracture rates. Type II patients often have long bone fractures with minimal trauma and may show delayed healing. There is an intermediate recessive type that is less severe than the typical autosomal recessive type in its manifestations of anemia, hepatosplenomegaly, and frequent fractures. An autosomal recessive type with renal tubular acidosis has also been described. Affected patients have renal tubular acidosis, cerebral calcifications, hypotonia, mental retardation, and easy fracturing that improves with increasing age.[67, 87, 92]

The radiographic findings differ among the various types of osteopetrosis. The autosomal recessive form shows generalized dense bone and flaring of the metaphyses from defective tubular modeling. Transverse striations are often seen as a result of alternating areas of mature and sclerotic bone.[67] In the autosomal dominant type I disease, sclerosis of the skull is pronounced and thickening of the cranial vault is evident, without involvement of the spine. The long bone may have ''Erlenmeyer flask'' deformity of the metaphyseal region from overproduction and faulty resorption of bone.[93] Autosomal dominant type II disease shows endplate thickening of the vertebrae resulting in a ''rugger jersey'' appearance of the spine. The base of the skull shows sclerosis, but the calvarium has little involvement[94–96] (Fig. 24-26). The intermediate recessive type gives rise to marked thickening and sclerosis of the base of the skull. The autosomal recessive type with renal tubular acidosis demonstrates intracranial calcifications, most commonly centered in the basal ganglia. Metaphyseal expansion and endobones (bone within bone) may also be present.[67]

In patients with the autosomal recessive form of osteopetrosis, temporal bone CT shows increased mastoid density and a lack of pneumatization of the mastoid air cells, which may be filled with osteoporotic bone (Fig. 24-27). The internal auditory canals are shortened and trumpet-shaped. The subarcuate fossae are enlarged, resulting in a fetal appearance of the bone that persists past infancy. The ossicles may be thickened and enlarged.[91, 97] MR imaging shows obliteration of the mastoid and generalized thickening of the bone (Figs. 24-26 and 24-28).

Differential Diagnosis

When diagnosing osteopetrosis, it is important to consider inheritance, age of manifestation, and radiologic findings in the skeletal system. Paget's disease is characterized by recurrent bone resorption and formation. The temporal bone characteristically shows bony resorption, with occasional sclerosis of specific portions. The age and systemic manifestations of Paget's disease differ from those of osteopetrosis. Fibrous dysplasia is a disorder of proliferating fibroosseous tissues that results in widening of the diploic spaces. Patients with fibrous dysplasia have greater marrow involvement than patients with osteopetrosis. Hyperparathyroidism may also cause sclerotic bone changes, particularly with the secondary form.[62] It can be differentiated from osteopetrosis by clinical information or laboratory tests. Pyknodysostosis is an autosomal recessive disease first evident in infancy and early childhood and

Copyright © 2003, Mosby, Inc. All rights reserved.

characterized by short stature, frequent fractures, and a large cranium with frontal and occipital bossing. Thickening of the base of the skull with sclerosis is often seen. Osteosclerosis in patients with pyknodysostosis is uniform, and the long bones retain their normal external shape, unlike the autosomal recessive type of osteopetrosis.[80] Sclerosteosis (endosteal hyperostosis) is a rare, potentially lethal, autosomal recessive disorder with characteristic facial and skeletal features. Overgrowth of the skull, vertebrae, and mandible with giantism and syndactyly are noted. The temporal bone changes include a marked increase in overall size and extensive sclerosis. Cranial nerve palsies are common in this condition because of attenuation of their bony canals.[63, 64, 67, 98] Progressive diaphyseal dysplasia (Camurati-Engelmann-Ribbing syndrome) is an autosomal dominant disease usually diagnosed in childhood. It is characterized by muscle weakness, bone pain, and difficulty in walking. The unusual hyperostosis of the long bones in progressive diaphyseal dysplasia gives a thick, irregular cortex rather than the more uniformly dense bone seen with osteopetrosis.[67, 68, 78–80] Osteopathia striata (Voorhoeve syndrome) is an autosomal dominant disease, that may result in generalized temporal bone sclerosis and conductive hearing loss.[99]

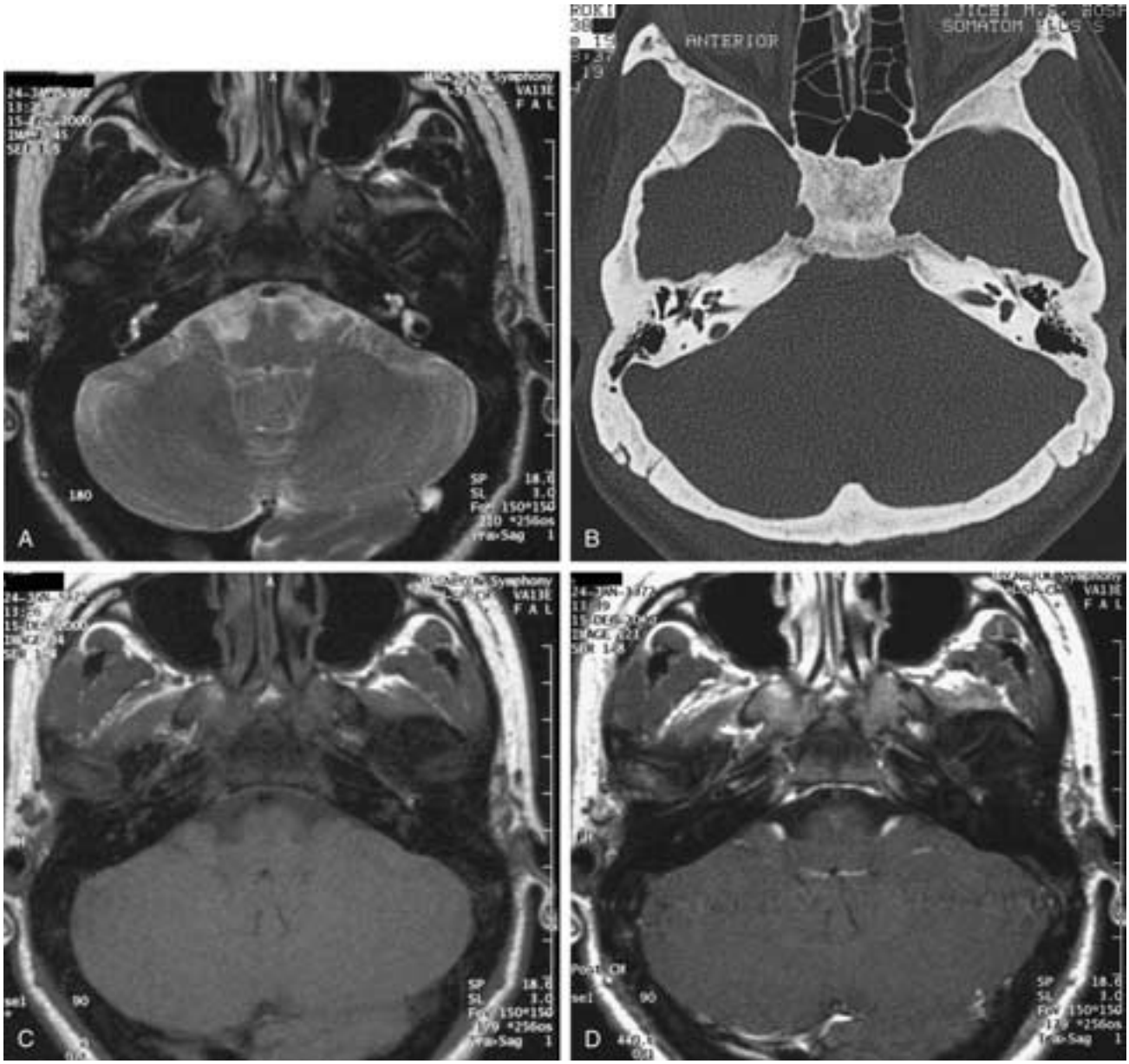

FIGURE 24-26 Osteopetrosis. **A**, Axial CT image demonstrates diffuse sclerotic change in the skull base including the temporal bone. **B**, Axial T1-weighted MR image shows absence of the high signal usually seen in the normal fatty marrow of the skull base. **C**, Axial T2-weighted MR image shows diffuse low signal from the skull base. The normal high signal of the membranous labyrinth is preserved. **D**, Axial postcontrast-enhanced, T1-weighted image shows minimal enhancement of the residual marrow in the clivus.

VIEW IMAGE

Copyright © 2003, Mosby, Inc. All rights reserved.

FIGURE 24-27 Osteopetrosis, autosomal dominant form. **A** and **B**, Frontal and lateral skull films demonstrate diffuse thickening and sclerotic change at the cranial facial bones. **C**, Axial CT image of the right temporal bone shows diffuse sclerotic change. There is narrowing of the middle ear and the internal auditory canal. (Courtesy of Dr. Shigeru Ehara, Morioka, Japan.)

VIEW IMAGE

PROGRESSIVE DIAPHYSEAL DYSPLASIA (CAMURATI-ENGELMANN-RIBBING SYNDROME)

Progressive diaphyseal dysplasia (Camurati-Engelmann-Ribbing syndrome) is a rare autosomal dominant disease initially described in 1922 by Camurati.[100] This was followed by a similar report by Engelmann in 1929.[101] Neuhauser and his colleagues named this disease progressive diaphyseal dysplasia in 1948.[102] Patients with this disorder are usually diagnosed in childhood and show a variety of symptoms such as headache, poor appetite, muscle weakness, bone pain, easy fatigability, difficulty in walking, and exophthalmos. Vestibular nerve dysfunction may rarely occur.[103] This disease represents a slowly progressive and unpredictable hyperostotic process characterized by new bone formation along both the periosteal and endosteal surfaces of the long bones. The calvarium and other membranous bones are commonly affected in severe cases.[67, 68, 76, 78, 79, 87]

The radiologic findings in this disease are usually symmetric, with the upper extremities less often affected than the lower extremities. In mild cases there is only minimal middiaphyseal thickening of the cortex. Patients

Copyright © 2003, Mosby, Inc. All rights reserved.

with more advanced conditions exhibit more pronounced sclerosis that has spread to the metaphyseal regions, with narrowing of the medullary cavities. In some severe cases, both the skull base and calvarium show the characteristic sclerosis, and the vertebral column, shoulder girdles, and metacarpal and metatarsal bones can also be affected.

The CT examination documents mild to moderate thickening of the skull base with hyperostosis and sclerosis. The middle ear may be completely encased by sclerotic bone, along with widespread foraminal narrowing (Figs. 24-29 and 24-30; see also Fig. 12-103). MR imaging of the skull base shows a signal void around the base of the skull and calvaria on both the T1-weighted and T2-weighted images. Hyperostotic bone may be seen encasing the otic capsule, middle ear, and external ear.[67, 68, 104–106]

The diagnosis of progressive diaphyseal dysplasia should be established as early as possible, since treatment determines the severity and progression of the disease. Treatment options include alternate-day administration of corticosteroids, which may yield significant relief of pain and symptoms. Calcitonin injections have also been shown to relieve symptoms. Surgery may be indicated to relieve pain and decompress the affected cranial nerves.[79, 103, 104, 106]

Differential Diagnosis

The differential diagnosis of progressive diaphyseal dysplasia includes various rare diseases involving sclerotic changes in the temporal bone: generalized cortical hyperostosis (van Buchem's disease), sclerosteosis (endosteal hyperostosis), craniotubular sclerosis, craniometaphyseal dysplasia, craniodiaphyeal dysplasia, pyknodystosis, osteopetrosis, and Paget's disease.[8, 102]

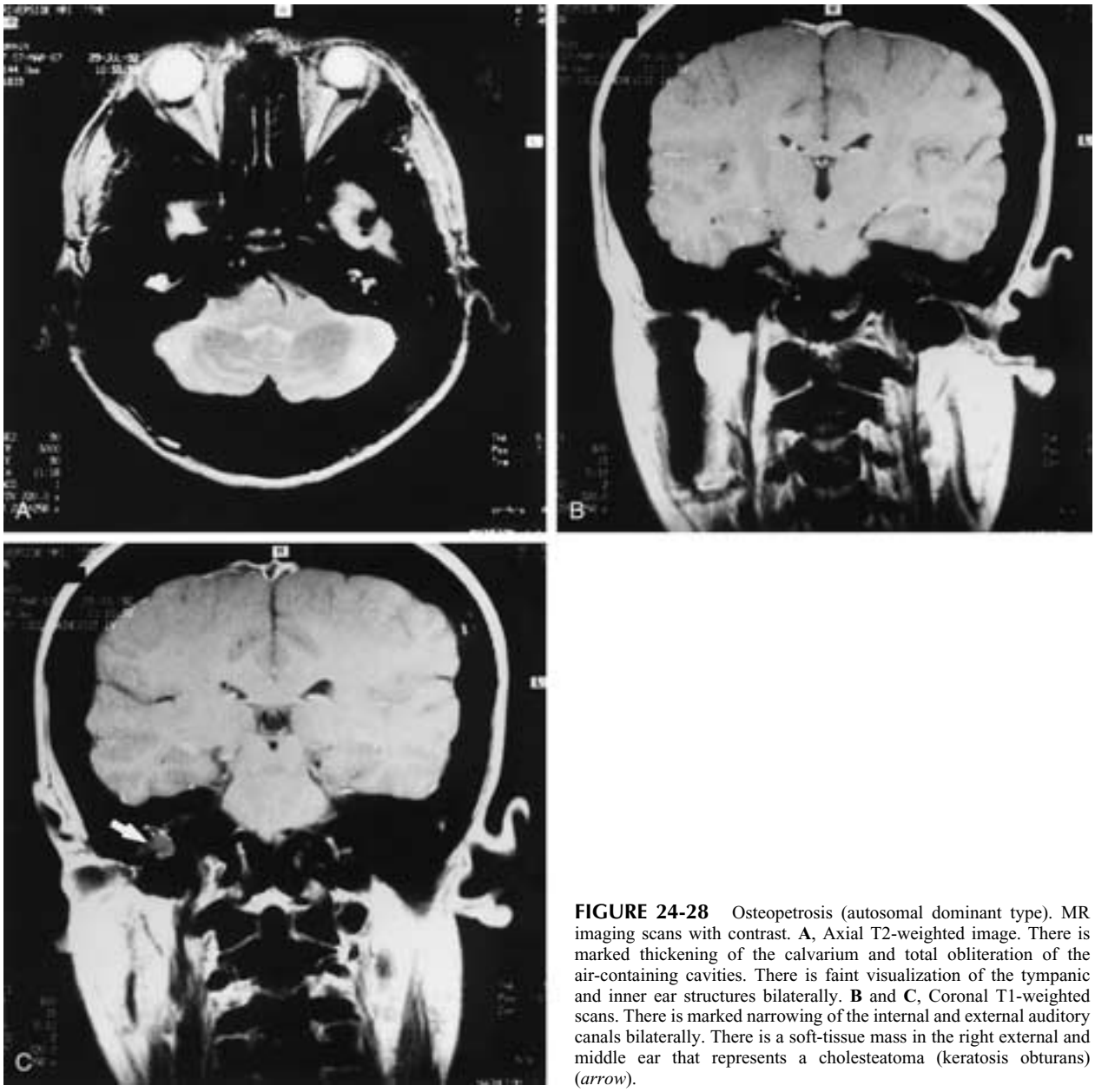

FIGURE 24-28 Osteopetrosis (autosomal dominant type). MR imaging scans with contrast. **A**, Axial T2-weighted image. There is marked thickening of the calvarium and total obliteration of the air-containing cavities. There is faint visualization of the tympanic and inner ear structures bilaterally. **B** and **C**, Coronal T1-weighted scans. There is marked narrowing of the internal and external auditory canals bilaterally. There is a soft-tissue mass in the right external and middle ear that represents a cholesteatoma (keratosis obturans) (*arrow*).

VIEW IMAGE

Copyright © 2003, Mosby, Inc. All rights reserved.

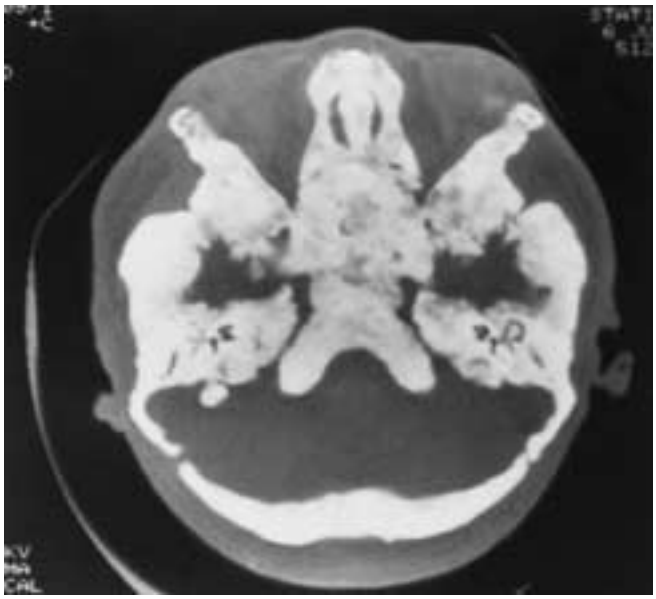

VIEW IMAGE

FIGURE 24-29 Progressive diaphyseal dysplasia (Engelmann's disease). Remarkable bony density involving the entire cranial base, including the temporal bones, is demonstrated. (From Swartz JD, Harnsberger HR. Imaging of the Temporal Bone. New York: Thieme, 1992.)

OTHER DYSPLASIAS AND DISORDERS CAUSING OSTEOSCLEROSIS OF THE TEMPORAL BONE

Other entities of dysplasias or diseases present diffusely or focally increased density lesions with or without cystic or decreased densities in the temporal bone. When diagnosing diseases described before in this chapter, such diseases must be considered as their differential diagnoses. Many have overlapping imaging findings in the skull base. The distribution of the abnormality in the peripheral skeleton is frequently more characteristic and is helpful in separating these various rare entities.

Endosteal Hyperostosis

Generalized Cortical Hyperostosis (van Buchem's Disease) is an autosomal recessive form of endosteal hyperostosis. It is characterized by osteosclerosis of the skull base and calvarium, mandible, and long and short bones (Fig. 24-31). Enlargement of the mandible is first noted in childhood, usually at puberty. Signs and symptoms of van Buchem's disease become apparent earlier than in the autosomal dominant form of endosteal hyperostosis, *Worth's syndrome*.[67] Narrowing of the neural foramina and neurologic impairment can occur in patients with both autosomal recessive and dominant forms of endosteal hyperostosis, and an elevated level of alkaline phosphatase is typically present.[107–109] Other types of autosomal dominant endosteal hyperostosis have been reported, showing unusual manifestations of sclerosis of the jaw bones but sparing the mandibular ramus.[110]

Sclerosteosis is a rare, potentially lethal, very severe form of endosteal hyperostosis with autosomal recessive inheritance. The disease begins in infancy or early childhood, causing overgrowth of the skull, vertebrae, and mandible with giantism and syndactyly. The temporal bone changes include a marked increase in overall size, extensive sclerosis, narrowing of the external auditory canal, and severe constriction of the internal auditory canal, fallopian canal, eustachian tube, and middle ear cleft. Cranial nerve palsies are common in this condition because of attenuation of their bony canals. Reduction in the size of the internal carotid artery, and severe obliteration of the sigmoid sinus and jugular bulb, also occur. Loss of hearing, generally bilateral, is a frequent symptom and often manifests in early childhood initially as sound conduction impairment. Later, sensorineural hearing loss and vestibular nerve dysfunction often develop.[63, 64, 67, 98]

Craniometaphyseal Dysplasia and Craniodiaphyseal Dysplasia

The *craniotubular dysplasias* have been divided into *Pyle's disease* (*metaphyseal dysplasia*), autosomal dominant and recessive craniometaphyseal dysplasia, craniodiaphyseal dysplasia, frontometaphyseal dysplasia (Fig. 24-32), Schwarz-Lèlek syndrome, dysosteosclerosis, and oculo-dento-osseous dysplasia.[78, 111] Craniometaphyseal dysplasia is characterized by metaphyseal widening of the tubular bones and bony overgrowth of the facial and skull bones (leontiasis ossea), which results in facial deformity from the early sclerosis of the skull and facial bones[112] (Fig. 24-33). Craniodiaphyseal dysplasia is characterized by massive craniofacial hyperostosis and sclerosis associated with the tubular bones. In both dysplasias, the cranial nerves may be affected due to stenosis and narrowing of the foramina.[78, 112] The genetic basis of both craniometaphyseal and craniodiaphyseal dysplasias has not yet been identified. Craniometaphyseal dysplasia is more often inherited as an autosomal dominant trait rather than by recessive transmission, while craniodiaphyseal dysplasia is likely to be transmitted as an autosomal recessive trait.[111–113]

Oculo-Dento-Osseous Dysplasia (Oculodentodigital Syndrome)

Oculo-dento-osseous dysplasia is presumed to be transmitted as an autosomal dominant trait; however, other patterns of inheritance are possible. Osteosclerosis of the skull, especially in the basal area, and enlargement of the mandible can be noted, although the coronoid process may be hypoplastic. Calcification in the basal ganglia and eyes may be present.[78] Enamel dysplasia, hypocalcification of the dentin, and other dental abnormalities are also present.

Dysosteosclerosis

Dysosteosclerosis has autosomal recessive inheritance. In early childhood, small stature, dental anomalies, and increased bone fragility can be noted. Thickening and sclerotic

Copyright © 2003, Mosby, Inc. All rights reserved.

changes in the cranial vault, skull base, and tubular bones may resemble osteopetrosis. However, this disorder can be differentiated by the presence of platyspondyly and lucency about expanded diametaphyseal segments of long bones.[78]

Pyle's Disease (Metaphyseal Dysplasia)

Pyle's disease (metaphyseal dysplasia) is a rare disorder with autosomal recessive or dominant inheritance. Marked expansion of the metaphyseal segments of tubular bones is noted, especially in the lower extremities. Changes in the skull are relatively subtle, and mild sclerosis of the cranial vault and skull base may be noted.[78]

Hereditary Hyperphosphatasia (Juvenile Paget's Disease)

Hereditary hyperphosphatasia (juvenile Paget's disease) is a rare autosomal recessive disease seen in infancy and childhood. It is characterized by generalized cortical thickening and by sustained elevation of serum alkaline phosphatase and urinary hydroxyprolamine. Thickening and

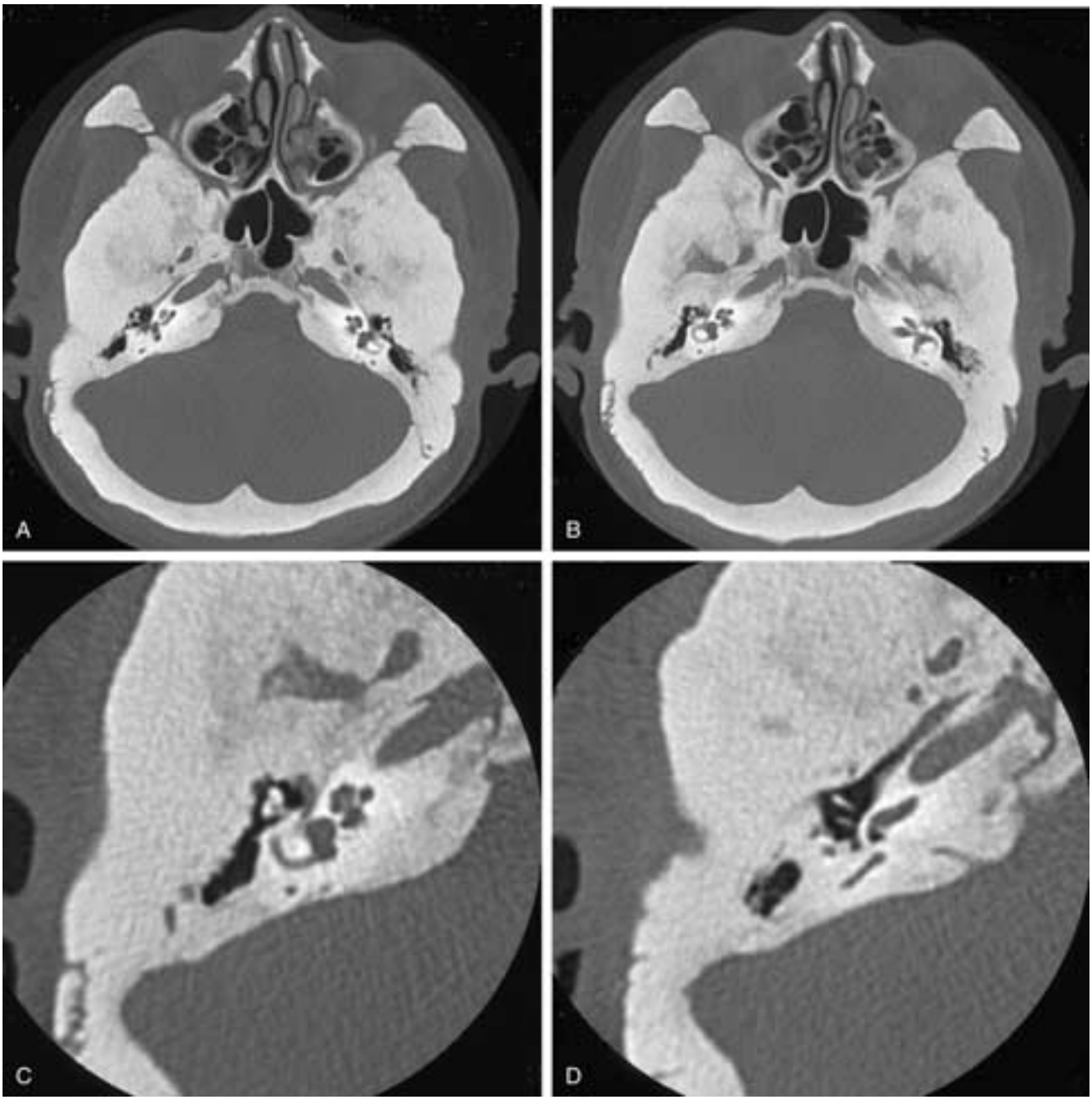

FIGURE 24-30 Progressive diaphyseal dysplasia (Engelmann's disease). **A** and **B**, Axial CT images demonstrate marked thickening and sclerosis of the entire bony structure of the skull base, including the temporal bones. **C** and **D**, Axial images of the right ear demonstrate narrowed middle ear cavity, while the lumen of the labyrinth is preserved. (Courtesy of Dr. Kenichi Nagasawa, Asahikawa, Japan.)

VIEW IMAGE

Copyright © 2003, Mosby, Inc. All rights reserved.

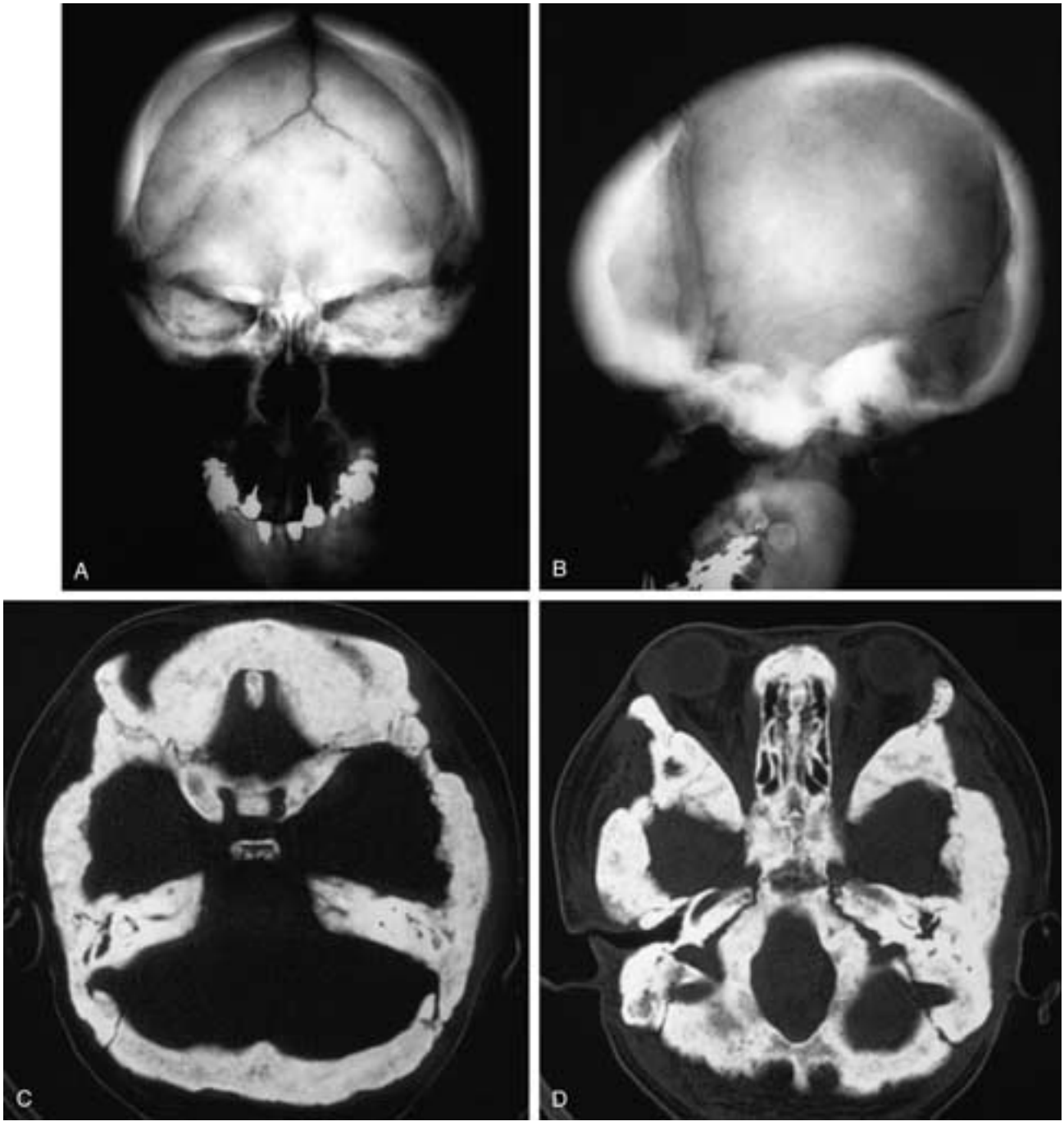

FIGURE 24-31 Generalized cortical hyperostosis (van Buchem's disease). Frontal (**A**) and lateral (**B**) skull films demonstrate marked thickening and sclerotic change of the calvarium and the skull base. **C** and **D**, Axial CT images show marked sclerotic change, with thickening of the skull base including the temporal bone. The middle ear cavity is narrow, as is the right internal auditory canal. (Courtesy of Dr. Shoki Takahashi, Sendai, Japan.)

VIEW IMAGE

Copyright © 2003, Mosby, Inc. All rights reserved.

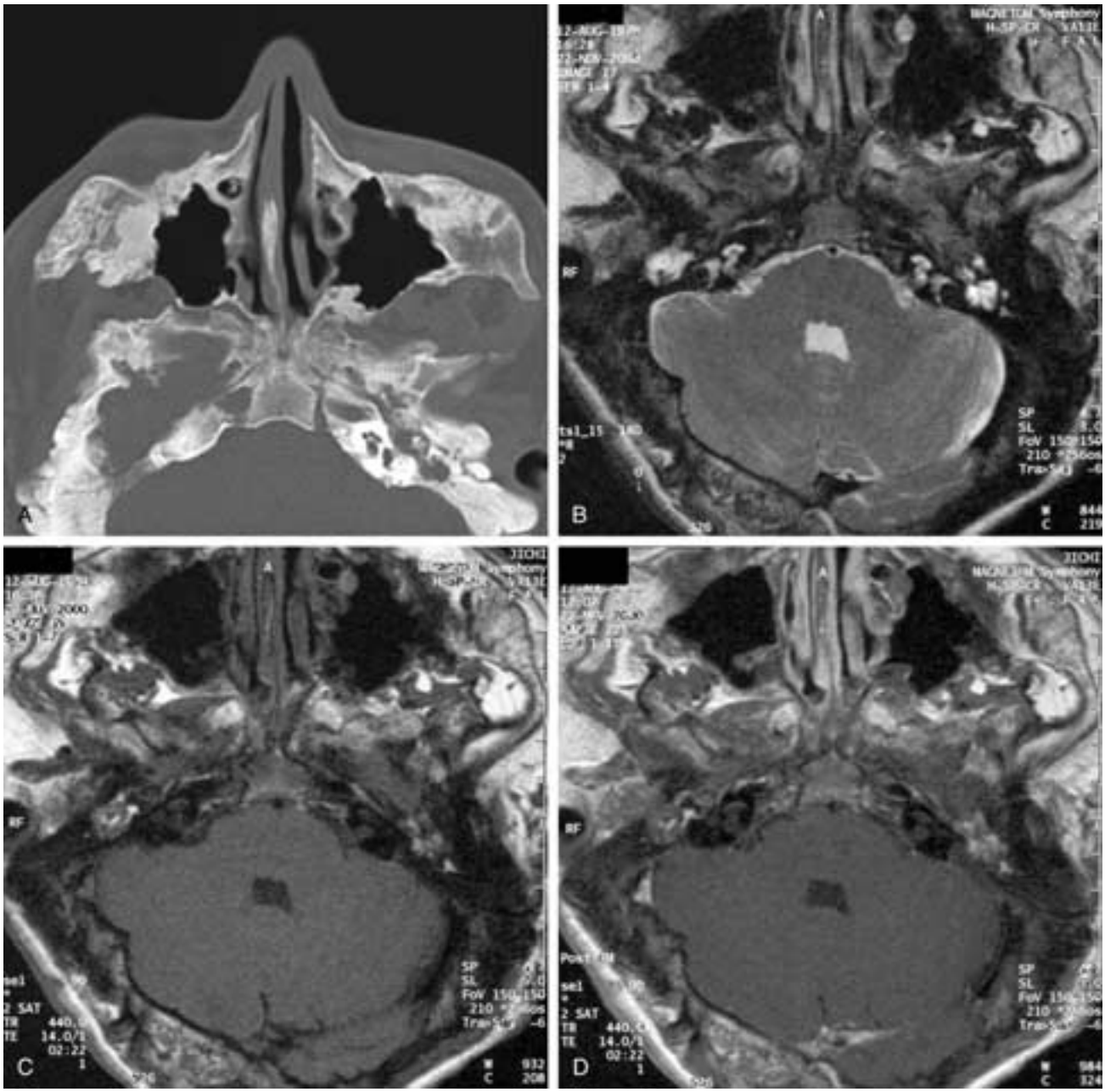

VIEW IMAGE

FIGURE 24-32 Frontometaphyseal dysplasia. **A**, Axial CT image demonstrates marked thickening and sclerotic change in the bony structures of the skull base including the temporal bone. **B**, Axial T2-weighted MR image shows fluid in the narrowed middle ear cavity on each side. The normal high signal of the labyrinth is preserved. **C**, Axial T1-weighted MR image shows a deformity and marked thickening of the bony structure in the inhomogeneous signal intensity of the bone marrow. **D**, Axial postcontrast-enhanced, T1-weighted MR image shows slight heterogeneous enhancement of the bony structures.

deossification of the skull base with bowing of tubular bones are observed.[67, 68, 78]

Pyknodysostosis

Pyknodysostosis is an autosomal recessive disease first evident in infancy and early childhood and characterized by short stature, small face and jaw, short hands and feet, hypoplasia of the nails, and a large cranium with frontal and occipital bossing.[66] Thickening of the base of the skull with sclerosis is often seen. The osteosclerotic change in patients with pyknodysostosis is uniform, and the long bones retain their normal external shape. Frequent fractures can be seen.[80]

Copyright © 2003, Mosby, Inc. All rights reserved.

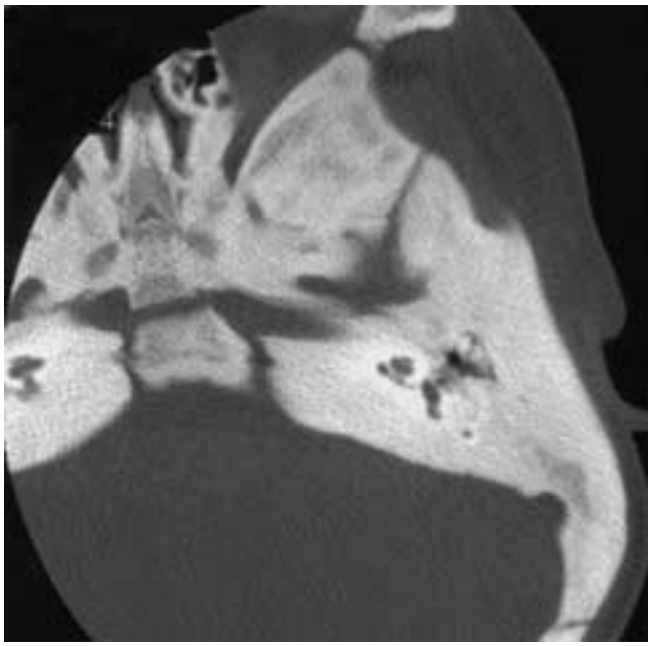

VIEW IMAGE

FIGURE 24-33 Craniometaphyseal dysplasia. Axial CT image through the left temporal bone demonstrates marked thickening and sclerotic change in the bony structure. The middle ear is significantly narrowed, with impingement on the malleus and incus. The findings were symmetric. (Courtesy of Dr. Noriko Aida, Yokohama, Japan.)

Osteopathia Striata (Voorhoeve Syndrome)

Osteopathia striata (Voorhoeve syndrome) is a rare disorder with autosomal dominant inheritance with complete penetrance and variable expressivity.[114] The syndrome may result in generalized temporal bone sclerosis. Conductive hearing loss, especially at low frequencies, or mixed deafness can be present. Bony atresia or stenosis of the external auditory canals, middle ear cavities, and internal auditory canals, as well as abnormal ossicular chain fixation, may be observed.[99]

Hyperparathyroidism

Hyperparathyroidism may cause diffusely sclerotic bone changes, particularly with the secondary hyperparathyroidism, renal osteodystrophy. A progressive form of osteitis fibrosa cystica, osteofibrosis associated with localized cysts, rarefied and thinned cortex, distorted and blurred cancellous trabeculae, and deformity can be observed[61, 62] (Fig. 24-34). The manifestations of hyperparathyroidism are seen throughout the skeleton and are accompanied by other clinical and or laboratory manifestations.

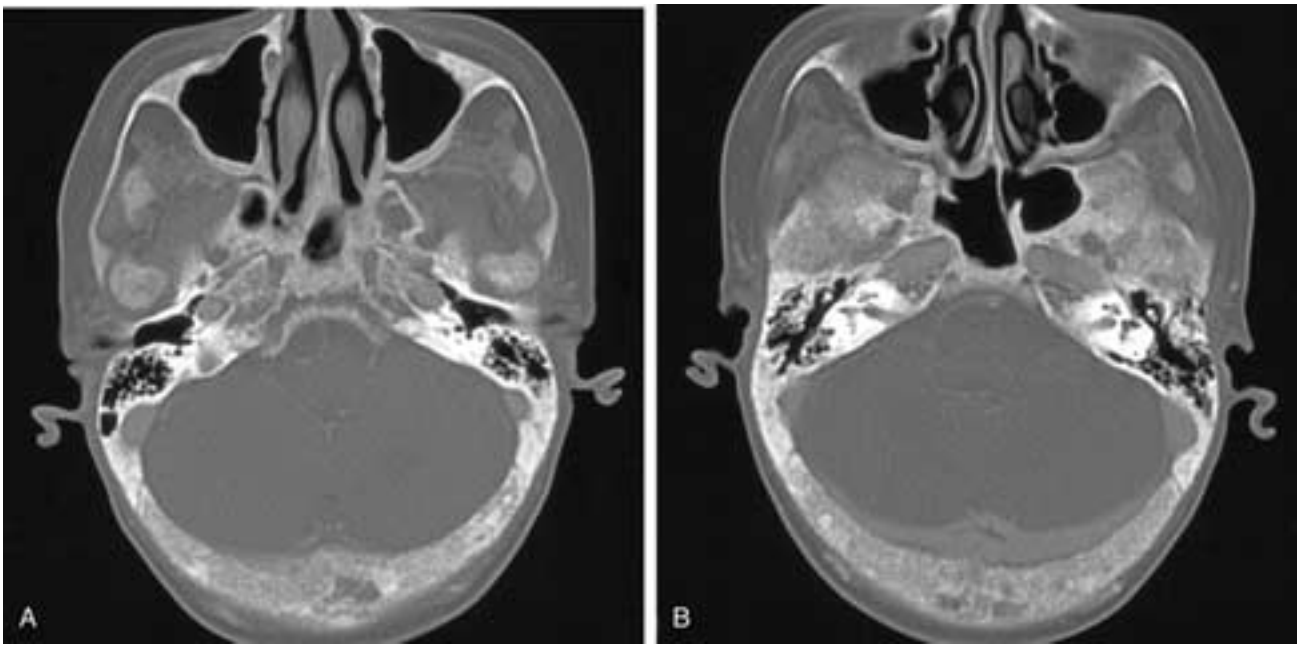

VIEW IMAGE

FIGURE 24-34 Hyperparathyroidism. **A** and **B**, Axial CT images show diffuse sclerotic change in the skull base. The cancellous trabeculae of the involved bones are blurred. Changes are also noted in the mandibular condyle and coronoid processes on each side.

Copyright © 2003, Mosby, Inc. All rights reserved.

REFERENCES

1. Schuknecht HF. Disorders of bone. In: Schuknecht HF. Pathology of the Ear. 2nd ed. Malvern, Pa: Lea & Febiger, 1993;365–414.
2. Valvassori GE. Otodystrophies. In: Barrett A, Brunner S, Valvassori GE, eds. Modern Thin Section Tomography. Springfield, Ill: Thomas, 1973;109–117.
3. Valvassori GE. Otosclerosis. Otolaryngol Clin North Am 1973;6(2): 379–389.
4. Morrison AW. Genetic factors in otosclerosis. Ann R Coll Surg Engl 1967;41(2):202–237.
5. Nager GT. Otosclerosis. In: Nager GT. Pathology of the Ear and Temporal Bone. Baltimore: Williams & Wilkins, 1993;943–1010.
6. Lindsay JR. Otosclerosis. In: Paparella MM, Shumrick DA, eds. Otolaryngology. Vol 2, The Ear. 2nd ed. Philadelphia: WB Saunders, 1980;1617–1644.
7. Ruedi L. Pathogenesis of otosclerosis. Arch Otolaryngol 1963;78: 469–477.
8. Hasso AN, Opp RL, Swartz JD. Otosclerosis and dysplasias of the temporal bone. In: Som PM, Curtin HD, eds. Head and Neck Imaging. 3rd ed. St. Louis: Mosby Year Book, 1996;1432–1448.
9. Rovsing H. Otosclerosis: fenestral and cochlear. Radiol Clin North Am 1974;12:505–515.
10. Swartz JD, Harnsberger HR. The otic capsule and otodystrophies. In: Imaging of the Temporal Bone. 3rd ed. New York: Thieme, 1998;240–317.
11. Valvassori GE. Imaging of otosclerosis. Otolaryngol Clin North Am 1993;26:359–371.
12. Mafee MF, Valvassori GE, Deitch RL, et al. Use of CT in the evaluation of cochlear otosclerosis. Radiology 1985;156:703–708.
13. Vartiainen E, Saari T. Value of computed tomography (CT) in the diagnosis of cochlear otosclerosis. Clin Otolaryngol 1993;18:462–464.
14. Damsma H, de Groot JAM, Zonneveld FW, et al. CT of cochlear otosclerosis (otospongiosis). Radiol Clin North Am 1984;22:37–43.
15. Ziyeh S, Berlis A, Ross UH, et al. MRI of active otosclerosis. Neuroradiology 1997;39:453–457.
16. Saunders JE, Derebery MJ, Lo WW. Magnetic resonance imaging of cochlear otosclerosis. Ann Otol Rhinol Laryngol 1995;104:826–829.
17. Clemis JD, Toriumi DM, Gavron JP. Otosclerosis masking coexistent acoustic neuroma. Am J Otol 1988;9:117–121.
18. Harnsberger HR, Dart DJ, Parkin JL, et al. Cochlear implant candidates: assessment with CT and MR imaging. Radiology 1987;164:53–57.
19. Bretlau P. Relation of the otosclerotic focus to the fissula ante-fenestram. J Laryngol Otol 1969;83(12):1185–1193.
20. Mafee MF, Henrikson GC, Deitch RL, et al. Use of CT in stapedial otosclerosis. Radiology 1985;156:709–714.
21. Swartz JD, Faerber EN, Wolfson RJ, et al. Fenestral otosclerosis: significance of preoperative CT evaluation. Radiology 1984;151: 703–707.
22. Schuknect HF. Otosclerotic surgery. In: Nadol JB, Schuknect HF, eds. Surgery of the Ear and Temporal Bone. New York: Raven Press, 1993;223–244.
23. Gussen R. Early Paget's disease of the labyrinthine capsule. Case report and bone study. Arch Otolaryngol 1970;91:341–345.
24. Swartz JD. The facial nerve canal: CT analysis of the protruding tympanic segment. Radiology 1984;153:443–447.
25. Swartz JD, Lansman AK, Berger AS, et al. Stapes prosthesis: evaluation with CT. Radiology 1986;158:179–182.
26. Williams MT, Ayache D, Elmaleh M, et al. Helical CT findings in patients who have undergone stapes surgery for otosclerosis. Am J Roentgenol 2000;174(2):387–392.
27. Jackler RK, Hwang PH. Enlargement of the cochlear aqueduct: fact or fiction? Otolaryngol Head Neck Surg 1993;109:14–25.
28. Emmett JR. Physical examination and clinical evaluation of the patient with otosclerosis. Otolaryngol Clin North Am 1993;26(3): 353–357.
29. Hannley MT. Audiologic characteristics of the patient with otosclerosis. Otolaryngol Clin North Am 1993;26(3):373–387.
30. Sando I, Hemenway WG, Miller DR, et al. Vestibular pathology in otosclerosis: temporal bone histopathological report. Laryngoscope 1974;84:593–605.
31. Antoli-Candela F Jr, McGill T, Peron D. Histopathological observations on the cochlear changes in otosclerosis. Ann Otol Rhinol Laryngol 1977;86:813–820.
32. Parahy C, Linthicum FH. Otosclerosis: relationship of spiral ligament hyalinization to sensorineural hearing loss. Laryngoscope 1983;93: 717–720.
33. Swartz JD, Mandell DW, Berman SE, et al. Cochlear otosclerosis (otospongiosis): CT analysis with audiometric correlation. Radiology 1985;155:147–150.
34. Swartz JD, Mandell DW, Wolfson RJ, et al. Fenestral and cochlear otosclerosis: CT evaluation. Am J Otol 1985;6(6):476–481.
35. Sakai O, Curtin HD, Fujita A, et al. Otosclerosis: CT and MR findings. Am J Otolaryngol 2000;21(2):116–118.
36. Valvassori GE, Dobben GD. CT densitometry of the cochlear capsule in otosclerosis. AJNR 1985;6:661–667.
37. Valvassori GE. CT densitometry in otosclerosis. Adv Otorhinolaryngol 1987;37:47–49.
38. Mark AS, Seltzer S, Harnsberger HR. Sensorineural hearing loss: more than meets the eye? AJNR 1993;14:37–45.
39. Balkany TJ, Dreisbach JN, Seibert CE. Radiographic imaging of the cochlear implant candidate: preliminary results. Otolaryngol Head Neck Surg 1986;95(5):592–597.
40. Ball JB Jr, Miller GW, Hepfner ST. Computed tomography of single channel cochlear implants.
41. O'Donoghue GM, Jackler RK, Jenkins WM, et al. Cochlear implantation in children: the problem of head growth. Otolaryngol Head Neck Surg 1986;94(1):78–81.
42. Callanan V, O'Connor AF. Cochlear implantation for children and adults. Lancet. 1996;347:412–414.
43. Cohen NL, Waltzman SB, Fisher SG. A prospective, randomized study of cochlear implants. N Engl J Med 1993;328:233–237.
44. Phelps PD, Proops DW. Imaging for cochlear implants. J Laryngol Otol Suppl 1999;24:21–23.
45. Huang TS, Yen PT, Liu SY. Cochlear implantation in a patient with osteogenesis imperfecta and otospongiosis. Am J Otolaryngol 1998;19(3):209–212.
46. Shpizner BA, Holliday RA, Roland JT, et al. Postoperative imaging of the multichannel cochlear implant. AJNR 1995;16:1517–1524.
47. Swartz JD, Mandell DW, Faerber EN, et al. Labyrinthine ossification: CT appearance and possible etiology. Radiology 1985;157:395–398.
48. Nager GT, Kennedy DW, Kopstein E. Fibrous dysplasia: a review of the disease and its manifestation in the temporal bone. Ann Otol Rhinol Laryngol Suppl 1982;92:1–52.
49. Nager GT. Fibrous dysplasia. In: Nager GT. Pathology of the Ear and Temporal Bone. Baltimore: Williams & Wilkins, 1993;1082–1148.
50. Lambert PR, Brackmann DE. Fibrous dysplasia of the temporal bone: the use of computerized tomography. Otolaryngol Head Neck Surg 1984;92:461–467.
51. Kransdorf MJ, Moser RP, Gilkey FW. Fibrous dysplasia. RadioGraphics 1990;10:519–537.
52. Schwartz DT, Alpert M. The malignant transformation of fibrous dysplasia. Am J Med Sci 1964;247:35–74.
53. Daffner RH, Kirks DR, Gehweiler JA, et al. Computed tomography of fibrous dysplasia. Am J Roentgenol 1982;139:943–948.
54. Barrionuevo CE, Marcallo FA, Coelho A, et al. Fibrous dysplasia and the temporal bone. Arch Otolaryngol 1980;106:298–301.
55. Smouha EE, Edelstein DR, Parisier SC. Fibrous dysplasia involving the temporal bone: report of three new cases. Am J Otol 1987;8(2):103–107.
56. Brown EW, Megerian CA, McKenna, MJ, et al. Fibrous dysplasia of the temporal bone: imaging findings. AJR 1995;164:679–682.
57. Megerian CA, Sofferman RA, McKenna MJ, et al. Fibrous dysplasia of the temporal bone: ten new cases demonstrating the spectrum of otologic sequelae. Am J Otol 1995;16(4):408–419.
58. Casselman JW, DeJonge I, Neyt L, et al. MRI in craniofacial fibrous dysplasia. Neuroradiology 1993;35:234–237.
59. Nager GT. Paget's disease of the temporal bone. Ann Otol Rhinol Laryngol 1975;84(suppl 22):1–32.
60. Nager GT. Osteitis deformans Paget. In: Nager GT. Pathology of the Ear and Temporal Bone. Baltimore: Williams & Wilkins, 1993; 1011–1050.
61. Potts JT. Diseases of the parathyroid gland and other hyper- and hypocalcemic disorders. In: Isselbacher KJ, Braunwald E, Wilson JD, et al, eds. Harrison's Principles of Internal Medicine. 13th ed. New York: McGraw-Hill, 1994;2151–2171.
62. Resnick D, Niwayama G. Parathyroid disorders and renal osteodystrophy. In: Resnick D, Niwayama G., eds. Diagnosis of Bone and Joint Disorders. 2nd ed. Philadelphia: WB Saunders, 1988;2219–2285.

Copyright © 2003, Mosby, Inc. All rights reserved.

63. Nager GT, Hamersma H. Sclerosteosis involving the temporal bone: histopathologic aspects. Am J Otolaryngol 1986;7(1):1–16.
64. Nager GT. Sclerosteosis. In: Nager GT. Pathology of the Ear and Temporal Bone. Baltimore: Williams & Wilkins, 1993;1149–1174.
65. Tanohata K, Noda M, Katoh H, et al. Chondroblastoma of temporal bone. Neuroradiology 1986;28:367–370.
66. Muntane A, Valls C, Angeles de Miquel MA, et al. Chondroblastoma of the temporal bone: CT and MR appearance. AJNR 1993;14:70–71.
67. Herman TE, McAlister WH. Inherited diseases of bone density in children. Radiol Clin North Am 1991;29:149–164.
68. Kaftori JK, Kleinhaus U, Naveh Y. Progressive diaphyseal dysplasia (Camurati-Engelmann): radiographic follow-up and CT findings. Radiology 1987;164:777–782.
69. Leeds N, Seaman WB. Fibrous dysplasia of the skull and its differential diagnosis. A clinical and roentgenographic study of 46 cases. Radiology 1962;78:570–582.
70. Watters GW, Brookes GB. Chondrosarcoma of the temporal bone. Clin Otolaryngol 1995;20(1):53–58.
71. Ramirez-Camacho R, Pinilla M, Ramon y Cajal S, et al. Chondrosarcoma of the temporal bone and otosclerosis. J Otorhinolaryngol Relat Spec 1998;60(1):58–60.
72. Krane SM. Paget's disease of bone. In: Isselbacher KJ, Braunwald E, Wilson JD, et al, eds. Harrison's Principles of Internal Medicine. 13th ed. New York: McGraw-Hill, 1994;2190–2193.
73. Kelly JK, Denier JE, Wilner HI, et al. MR imaging of lytic changes in Paget disease of the calvarium. J Computed Assist Tomogr 1989; 13:27–29.
74. Swartz JD, Vanderslice RB, Korsvik H, et al. High resolution computed tomography. Part 6. Craniofacial Paget's disease and fibrous dysplasia. Head Neck Surg 1985;8:40–47.
75. Jardin C, Ghenassia M, Vignaud J. Tomographic and CT features of the petrous bone in Lobstein's disease. J Neuroradiol 1985;12:317–326.
76. d'Arhchambeau O, Parizel PM, Koekelkoren E, et al. CT diagnosis and differential diagnosis of otodystrophic lesions of the temporal bone. Eur J Radiol 1990;11:22–30.
77. Ginsberg LE, Elster AD, Moody DM. MRI of Paget's disease with temporal bone involvement pre-existing with sensorineural hearing loss. J Comput Assist Tomogr 1992;162(2):314–316.
78. McAlister WH. Osteochondrodysplasias, dysostoses, chromosomal aberrations, mucopolysaccharidoses, and mucolipidoses. In: Resnick D, Niwayama G, eds. Diagnosis of Bone and Joint Disorders. 2nd ed. Philadelphia: WB Saunders, 1988;3442–3515.
79. Naveh Y, Kaftori JK, Alon U, et al. Progressive diaphyseal dysplasia: genetics and clinial and radiologic manifestations. Pediatrics 1984;74:399–405.
80. Whyte MP. Metabolic and dysplastic bone diseases. Endocrinol Metab Clin North Am 1990;19:133–173.
81. Nager GT. Osteogenesis imperfecta. In: Nager GT. Pathology of the Ear and Temporal Bone. Baltimore: Williams & Wilkins, 1993; 1051–1081.
82. Kocher MS, Shapiro F. Osteogenesis imperfecta. J Am Acad Orthop Surg 1998;6:225–236.
83. Sillence DO, Senn A, Danks DM. Genetic heterogeneity in osteogenesis imperfecta. J Med Genet 1979;16:101–106.
84. Ablin DS, Greenspan A, Reinhart M, Grix A. Differentiation of child abuse from osteogenesis imperfecta: medical and legal implications. Am J Roentgenol 1990;154:1035–1046.
85. Ablin DS. Osteogenesis imperfecta: a review. Can Assoc Radiol J 1998;49:110–123.
86. Tabor EK, Curtin HD, Hirsch BE, et al. Osteogenesis imperfecta tarda: appearance of the temporal bones at CT. Radiology 1990;175: 181–183.
87. Garretsen TJTM, Cremers CWRJ. Stapes surgery in osteogenesis imperfecta: analysis of postoperative hearing loss. Ann Otol Rhinol Laryngol 1991;100:120–130.
88. Hawke M, Jahn AF, Baily D. Osteopetrosis of the temporal bone. Arch Otolaryngol 1981;107:278–282.
89. Greenspan A. Sclerosing bone dysplasias: a target-site approach. Radiology 1991;20:561–583.
90. Nager GT. Osteopetrosis. In: Nager GT. Pathology of the Ear and Temporal Bone. Baltimore: Williams & Wilkins, 1993;1175–1179.
91. Bartynski WS. Cranial CT of autosomal recessive osteopetrosis. AJNR 1989;10:543–550.
92. Milroy CM, Michales L. Temporal bone pathology of adult-type osteopetrosis. Arch Otolaryngol Head Neck Surg 1990;116:79–84.
93. Jackson WPU, Albright F, Drewry G, et al. Metaphyseal dysplasia, epiphyseal dysplasia, diaphyseal dysplasia, and related conditions. Arch Intern Med 1954;94:871–885.
94. Anderson PE, Bollerslev J. Heterogeneity of autosomal dominant osteopetrosis. Radiology 1987;164:223–225.
95. Bollerslev J, Anderson PE. Radiological, biochemical, and hereditary evidence of two types of autosomal dominant osteopetrosis. Bone 1988;9:7–13.
96. Bollerslev J, Mosekilde L. Autosomal dominant osteopetrosis. Clinical Orthop 1993;294:45–51.
97. Elster AD, Theros EG, Key LL, et al. Cranial imaging in autosomal recessive osteopetrosis. Part II. Skull base and brain. Radiology 1992;183:137–144.
98. Nager GT. Craniotubular sclerosis. In: Nager GT. Pathology of the Ear and Temporal Bone. Baltimore: Williams & Wilkins, 1993; 1198–1209.
99. Odrezin GT, Krasikov N. CT of the temporal bone in a patient with osteopathic striata with cranial sclerosis. AJNR 1993;14:72–75.
100. Camurati M. Di un raro caso di osteite simmetrica ereditaria degli arti inferiori. Chir Organi Mov 1922;6:662.
101. Engelmann G. Ein Fall von osteopathia hyperostotica (scleroticans) multiplex infantilis. Fortschr Rontgenstr 1929;39:1101.
102. Neuhauser EB, Schwachman H, Wittenborg M, Cohen J. Progressive diaphyseal dysplasia. Radiology 1948;51:11.
103. Hellier WP, Brookes GB. Vestibular nerve dysfunction and decompression in Engelmann's disease. J Laryngol Otol 1996; 110(5):462–465.
104. Applegate LJ, Applegate GR, Kemp SS. MR of multiple cranial neuropathies in a patient with Camurati-Engelmann disease: case report. AJNR 1991;12:557–559.
105. Dannenmaier B, Weber B. Observations on the Camurati-Engelmann syndrome. Demonstration of changes of the petrous bone using high-resolution computed tomography. Rofo Fortschr Geb Rontgenstr Neuen Bildgeb Verfahr 1989;151(2):175–178.
106. Higashi K, Matsuki C. Hearing impairment in Engelmann disease. Am J Otol 1996;17:26–29.
107. Owen RH. Van Buchem's disease. Br J Radiol 1976;49(578): 126–132.
108. Eastman JR, Bixler D. Generalized cortical hyperostosis (Van Buchem disease): nosologic considerations. Radiology 1977; 125(2):297–304.
109. Ades LC, Morris LL, Burns R, Haan EA. Neurological involvement in Worth type endosteal hyperostosis: report of a family. Am J Med Genet 1994;51(1):46–50.
110. Nakamura T, Yamada N, Nonaka R, Sasaki M. Autosomal dominant type of endosteal hyperostosis with unusual manifestations of sclerosis of the jaw bones. Skeletal Radiol 1987;16(1):48–51.
111. Gorlin RJ, Spranger J, Koszalka MF. Genetic craniotubular bone dysplasias and hyperostoses. A critical analysis. Birth Defects 1969;5(4):79–95.
112. Richards A, Brian C, Dillon MJ, Bailey CM. Craniometaphyseal and craniodiaphyseal dysplasia, head and neck manifestations and management. J Laryngol Otol 1996;110:328–338.
113. Gorlin RJ, Cohen NM, Levin LS. Syndromes of the Head and Neck: Craniotubular Bone Disorders. 3rd ed. New York: Oxford University Press, 1990.
114. Robinow M, Unger F. Syndrome of osteopathia striata, macrocephaly, and cranial sclerosis. Am J Dis Child 1984;138:821–823.

Copyright © 2003, Mosby, Inc. All rights reserved.

Copyright © 2003, Mosby, Inc. All rights reserved.

25

Temporal Bone Tumors and Cerebellopontine Angle Lesions

M. Marcel Maya, William W.M. Lo, and Ilhami Kovanlikaya

CLINICAL OVERVIEW
IMAGING OVERVIEW
ACOUSTIC SCHWANNOMAS (NEUROMAS)
- Incidence and Terms
- Pathology
- Bilateral Acoustic Schwannomas
- Clinical Evaluation
- Treatment
- CT and MR Imaging Appearance
  - Size, Location, and Configuration
  - CT Density
  - MR Imaging Intensity
  - Secondary Changes

DIFFERENTIAL DIAGNOSIS OF TUMORS OF THE INTERNAL AUDITORY CANAL AND THE CEREBELLOPONTINE ANGLE
- Statistics and Categorization
- Meningiomas and Simulants
- Epidermoid and Other Cysts
- Nonacoustic Posterior Fossa Schwannomas
- Vascular Lesions
- Petrous Bone Lesions
- Paragangliomas
- Intraaxial Tumors
- Intracanalicular Lesions
- Summary

PARAGANGLIOMAS AND JUGULAR FORAMEN TUMORS
- Incidence, Origin, and Terms
- Clinical Features
- Growth Pattern and CT Findings
- Angiographic Features
- MR Imaging Appearance
- Radionuclide Scintigraphy
- Treatment and Surgical Classification

DIFFERENTIAL DIAGNOSIS
- Retrotympanic or Intratympanic Masses
- Pulsatile Masses
- Other Benign Lesions
- Jugular Foramen Masses
- Jugular Foramen Schwannomas
- Hypoglossal Schwannomas
- Meningiomas
- Malignant Tumors
- Chondrosarcomas
- Nasopharyngeal Carcinoma
- Miscellaneous

TUMORS INVOLVING THE FACIAL NERVE
- Manifestations of Facial Nerve Dysfunction and Lesion Localization
- Tumors
- Facial Schwannomas
- Benign Vascular Tumors
- Epidermoid Cysts
- Miscellaneous Tumors

OTHER TUMORS AND CYSTS OF THE TEMPORAL BONE

EXTERNAL AUDITORY CANAL
- Benign Tumors
- Malignant Tumors

MIDDLE EAR TUMORS
- Benign Tumors
- Malignant Tumors

MASTOID
- Histiocytosis

Copyright © 2003, Mosby, Inc. All rights reserved.

THE PETROUS APEX
Cholesterol Granuloma (Cysts)
Epidermoid Cysts
Mucoceles
Carotid Artery Aneurysms
Chondrosarcomas
Endolymphatic Sac Tumors
Miscellaneous

CLINICAL OVERVIEW

A discussion of tumors of the temporal bone is not complete without a discussion of tumors that involve the cerebellopontine angle (CPA). Because the fifth through twelfth cranial nerves exit the posterior cranial fossa either through the temporal bone or immediately adjacent to it, the clinical presentation of tumors of the temporal bone and the CPA is often similar. The temporal bone and the CPA also form the junctional region where neurosurgery and otologic surgery (neurootology) overlap.[1, 2] The most common clinical problems that warrant an imaging evaluation for a possible tumor include the investigation of the following: (1) sensorineural hearing loss, tinnitus, disequilibrium, or other symptoms of the CPA syndrome in search of an acoustic schwannoma (vestibular schwannoma) or one of the other tumors of this region; (2) pulsatile tinnitus or the jugular foramen syndrome in search of a paraganglioma or one of the other tumors or vascular lesions of the region; (3) peripheral facial nerve dysfunction in search of a tumor; and (4) a previously clinically identified tumor of the external canal. Each of these clinical settings has a different differential diagnosis, and the following discussion is organized with these settings in mind.

IMAGING OVERVIEW

Historically the investigation of acoustic schwannomas (neuromas, vestibular schwannomas) and other tumors of the CPA and the temporal bone has progressed through the use of plain films, tomography, pneumoencephalography, positive contrast meatocisternography, and angiography.[2–7] With each of these modalities, diagnosis was based on indirect signs of a mass such as erosion or displacement of either vessels or contrast material. Modern imaging uses predominantly either magnetic resonance (MR) imaging or computed tomography (CT). Both of these modalities image the lesion directly. These modalities have been indispensable allies to the recent advances in surgical management of temporal bone tumors, and the discussions of imaging in this section are directed almost completely to them.[8]

Before clinical availability of paramagnetic contrast agents, Gentry, Jacoby, Turski, and others, comparing the diagnosis of 75 CPA and petromastoid masses by MR imaging and CT, found that both modalities were accurate and had similar capabilities for detecting lesions of neoplastic, nonneoplastic, or vascular origin.[9] However, since the introduction of paramagnetic contrast agents, the capability of MR imaging has greatly improved. At present, when a retrocochlear lesion is the suspected cause of vestibulocochlear symptoms, gadolinium-enhanced MR (Gd-MR) imaging is considered to be the most reliable study.[10] When a labyrinthine or cochlear lesion is suspected, high-resolution CT with bone detail is usually the initial study.[11] MR imaging is preferred over CT for the investigation of cranial nerve dysfunctions, and in most cases, if the MR imaging examination is normal, no other imaging studies are performed. A comprehensive examination typically includes thin-section (1–3 mm) T1-weighted (short TE, short TR) images through the posterior cranial fossa, before gadolinium, fat-suppressed corresponding T1-weighted images after gadolinium, and thicker (5–6 mm) T2-weighted (long TE, long TR) and/or FLAIR (fluid attenuated inversion recovery) images surveying the brain. Supplementary sequences, such as diffusion-weighted images, gradient echo sequence, and MR angiography may be added.[12–15] Recently developed constructive interference steady state (CISS) and fast spin echo techniques use heavily T2-weighted images without gadolinium.[16, 17] Both of these sequences have succeeded in consistently outlining the facial nerve, the cochlear and both vestibular divisions of the acoustic nerve, the anterior inferior cerebellar artery (AICA), and the tumors in the CPA and internal auditory canal (IAC).

On the other hand, CT is still preferred over MR imaging as the initial imaging modality to investigate pulsatile tinnitus, conductive hearing loss, or a retrotympanic mass that suggests the presence of a paraganglioma or a vascular anomaly. If a mass is found localized within the tympanic cavity or if a vascular anomaly is recognized, no other imaging is usually needed. MR imaging and CT, however, must not be considered mutually exclusive, and when diagnostically indicated, each may be employed to supplement the other. In fact, both MR imaging and CT are usually required for full assessment of skull base lesions.[18] Today, angiography is reserved for the detection of arterial stenotic lesions and arteriovenous fistulae, for the evaluation of tumor vascularity, and for preoperative embolization.

ACOUSTIC SCHWANNOMAS (NEUROMAS)

Incidence and Terms

Acoustic schwannomas account for about 8% to 10% of all intracranial tumors and about 60% to 90% of all CPA tumors (Table 25-1).[19–21] They are slightly more common in women than in men. Most of the tumors appear in patients between 30 and 70 years of age, with the majority of lesions occurring in those between 40 and 60 years of age.[22] Occasionally these tumors appear in young adults or children without any of the stigmata of neurofibromatosis.[23, 24] Although more than 25 names, including those commonly used

Copyright © 2003, Mosby, Inc. All rights reserved.

Table 25-1
CLASSIFICATION AND FREQUENCY OF CPA LESIONS

	Revilla (1947)		Brackmann (1980)		Valavanis (1987)	
	No.	%	No.	%	No.	%
Primary Tumors of the CPA						
Acoustic schwannoma	154	75.1	1236	91.3	275	60.5
Meningioma	13	6.3	42	3.1	31	6.8
Epidermoid	13	6.3	32	2.4	17	3.7
Arachnoid cyst	—	—	7	0.5	9	2.0
Schwannoma of the fifth, seventh, ninth, tenth, and eleventh nerves	10	4.9	19	1.4	18	4.0
Primary melanoma	1	0.5	—	—	1	0.2
Hemangioma	—	—	4	0.3	3	0.7
Lipoma, dermoid, teratoma	—	—	5	0.4	—	—
Secondary Tumors of the CPA						
Paraganglioma	1	0.5	—	—	47	10.3
Ceruminoma	—	—	—	—	1	0.2
Chondroma-chondrosarcoma	—	—	1	0.1	2	0.4
Chordoma	—	—	—	—	8	1.8
Extension of cerebellar and petrous bone tumors	13	6.4	5	0.4	6	1.3
Metastases	—	—	3	0.2	12	2.6
Vascular Lesions						
Aneurysm	—	—	—	—	4	0.9
Arteriovenous malformation	—	—	—	—	4	0.9
Vertebrobasilar dolichoectasia	—	—	—	—	17	3.7

such as neurinoma, neurilemmoma, and neuroma, have been applied to the acoustic nerve tumor, most authorities regard schwannoma as the most appropriate term.[19, 25–28] As most of these lesions arise from the vestibular nerve, the term *vestibular schwannoma* is often used as the most accurate term.

Pathology

A schwannoma is a benign, slowly growing, encapsulated neoplasm that originates in the nerve sheath and is composed of Schwann cells in a collagenous matrix.[26, 27] By comparison, a neurofibroma is a benign, relatively circumscribed, nonencapsulated neoplasm that consists of proliferating axons and Schwann cells. The absence of a capsule, Verocay bodies, hyaline thickening of vascular walls, and Antoni A and B growth patterns (see the following discussion) are features that distinguish a neurofibroma from a schwannoma. However, in some cases these two benign nerve sheath tumors cannot be differentiated pathologically.

For unexplained reasons, schwannomas arise from the acoustic nerve (CN VIII) much more often than from any other cranial nerve, and the vestibular division is far more commonly involved than the cochlear division.[25, 29, 30] Hence the Consensus Development Panel recommended that acoustic schwannomas be termed *vestibular schwannomas*.[31] Because the glial–Schwann cell junction of the acoustic nerve lies (with some variation) near the internal acoustic porus, and because schwannomas may arise from any portion of the nerve between this zone of transition and the fundus of the IAC, these tumors arise within the IAC, at the porus, or occasionally in the CPA cistern.[19, 32] A schwannoma is typically composed of Antoni type A and type B tissue. Type A tissue is compact, with elongated spindle cells in irregular streams, often having a tendency to form palisades. Type B tissue, often intermingled with type A, is characterized by a loose texture, often with cyst formation. Microcystic and, less commonly, macrocystic changes and hemorrhage characteristically develop in type B tissue.[19, 25] Most acoustic schwannomas consist predominantly of type A tissue. With increasing size of the lesion, there is a tendency for tumor cellularity to decrease and degenerative changes and vascularity to increase.[22] Kasantikul, Netsky, Glasscock, and others have also noted that a hemangiomatous component is often present.[22] Most tumors grow at a slow (0.02 cm per year) or medium rate (0.2 cm per year), but a small percentage grows as much as 1 cm or more per year.[33] Larger tumors are found in younger patients, in females, and in patients with no intracanalicular component.[34] Acoustic schwannomas are more common in women and tend to be larger and more vascular. Pregnancy has been noted to accelerate symptoms and tumor growth.[35] On the other hand, intracanalicular tumors may be more common in men.[36]

Malignant schwannomas are extremely rare and usually are seen in patients with neurofibromatosis 1.[25, 37, 38] An astrocytoma arising in the glial portion of the acoustic nerve also has been reported.[39]

Bilateral Acoustic Schwannomas

The neurofibromatoses consist of at least two distinct disorders, the genes for which are located on separate chromosomes.[40–42] Von Recklinghausen's neurofibromatosis, which manifests primarily peripherally and is now called neurofibromatosis 1 (NF1), affects approximately 100,000 people in the United States. Bilateral acoustic neurofibromatosis, which manifests primarily centrally and is now called neurofibromatosis 2 (NF2), affects several thousand Americans. Both of these disorders may be inherited as an

Copyright © 2003, Mosby, Inc. All rights reserved.

autosomal dominant trait or acquired by spontaneous mutation.

Patients with NF1 have multiple brown skin macules (café au lait spots), intertriginous freckling, iris hamartomas (Lisch nodules), multiple neurofibromas (especially plexiform neurofibromas), optic gliomas, and distinctive osseous lesions.[37, 38] They may have Schwann cell tumors on any nerve, but an estimated 5% or fewer have acoustic tumors.[38, 43, 44]

Patients with NF2 (Fig. 25-1) have bilateral acoustic schwannomas (96%) commonly accompanied by other Schwann cell tumors and multiple meningiomas, neurofibromas, and glial tumors.[37, 45] They are not associated with optic gliomas or malignant tumor degeneration, which occur in NF1.[44, 46] Members of some kindreds also develop ependymomas, usually in the cervical cord.[47] In NF2 patients with concurrent meningiomas, the growth of the schwannomas accelerates 10-fold, with infiltration from the adjacent meningiomas.[48] A rare case of schwannoma and meningioma coexisting within the same tumor has also been reported in an NF2 patient.[49]

Compared with unilateral schwannomas, bilateral acoustic schwannomas tend to develop early, with many appearing before the patient is 21 years of age; about half of these individuals are symptomatic by the age of 25 years.[40] These schwannomas are more liable to infiltrate the facial and cochlear nerves than are unilateral types and present a formidable challenge to surgical management.[50] Early detection and resection appear to offer the best hope of hearing preservation.[40, 44, 46, 51, 52] MR imaging screening at an early age (10 to 12 years) in all children with an appropriate family history has been recommended regardless of the auditory-brainstem response.[37, 52] Careful evaluation of the contralateral ear of young patients (under 30 years of age) with unilateral acoustic schwannoma is advised, as is routine imaging of the cervical spine.[37] First-generation relatives of patients with either bilateral acoustic schwannomas or unilateral tumors of early onset also should be counseled and, if found appropriate, screened with imaging.[50, 53] Prenatal diagnosis, however, is not yet feasible.[33]

With regard to treatment, direct placement of acoustic brainstem implants (ABI) adjacent to the cochlear nuclei in patients deafened by bilateral tumor removal is now FDA approved for clinical use. The majority of recipients report daily use of their devices and satisfaction with the decision to receive the ABI.[54–58]

Clinical Evaluation

The most common symptoms associated with acoustic schwannomas are those caused by pressure on the cochlear and vestibular divisions of the acoustic nerve, namely, sensorineural hearing loss, tinnitus, and disequilibrium.[59, 60] Frequently, patients with acoustic schwannoma have difficulty understanding speech in the affected ear. This condition is referred to as decreased speech discrimination.

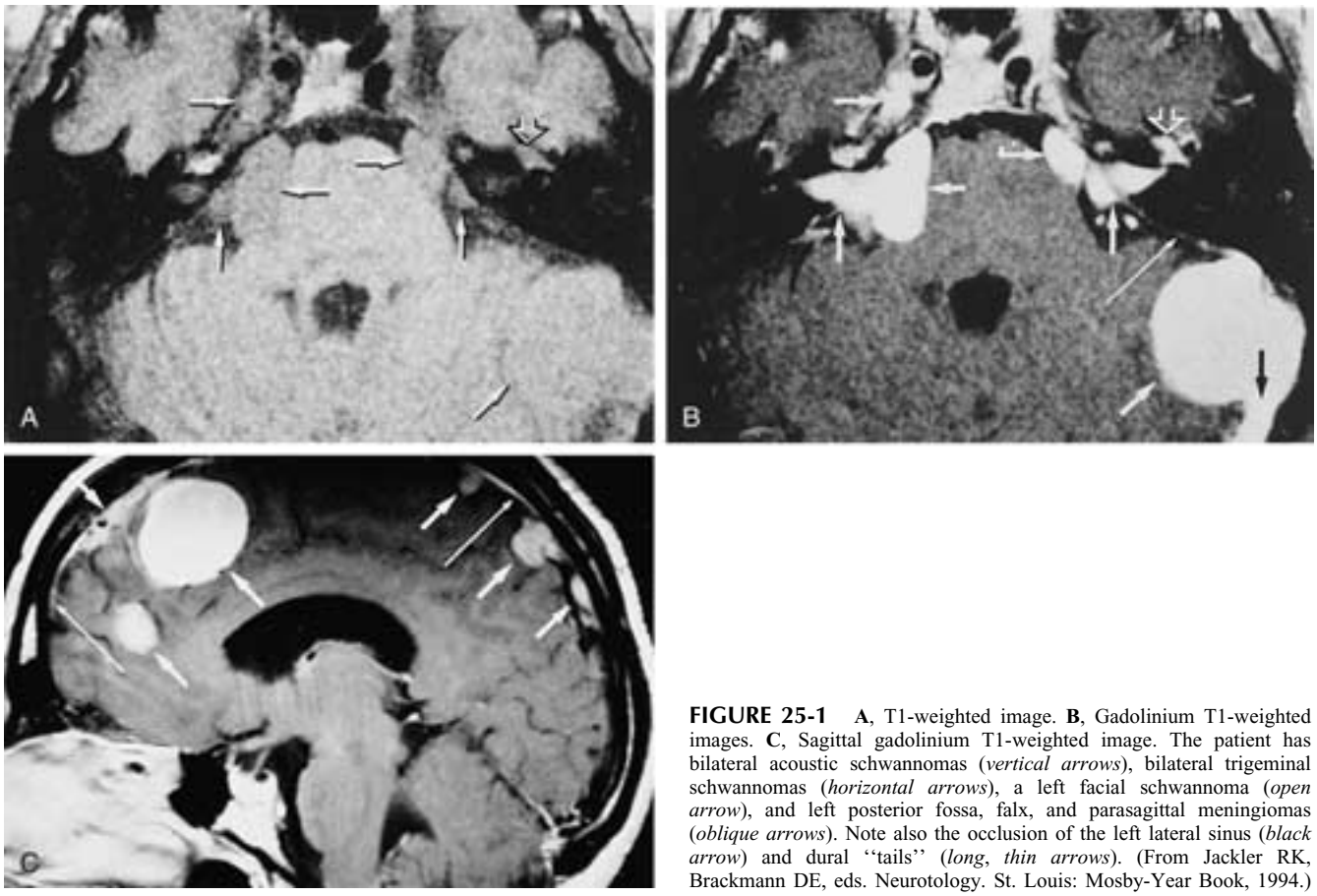

FIGURE 25-1 **A**, T1-weighted image. **B**, Gadolinium T1-weighted images. **C**, Sagittal gadolinium T1-weighted image. The patient has bilateral acoustic schwannomas (*vertical arrows*), bilateral trigeminal schwannomas (*horizontal arrows*), a left facial schwannoma (*open arrow*), and left posterior fossa, falx, and parasagittal meningiomas (*oblique arrows*). Note also the occlusion of the left lateral sinus (*black arrow*) and dural ''tails'' (*long, thin arrows*). (From Jackler RK, Brackmann DE, eds. Neurotology. St. Louis: Mosby-Year Book, 1994.)

VIEW IMAGE

Copyright © 2003, Mosby, Inc. All rights reserved.

The problem may not be evident to the patient during conversation because of the normal hearing in the contralateral ear. However, when using the abnormal ear, the patient may complain of difficulty in understanding speech on the telephone. The symptoms are usually slowly progressive, evolving over months or years; in one series, the median duration was about 2 years.[22] The duration of symptoms is not necessarily correlated with tumor size. Some authors have noted an inverse correlation, with up to 10% of patients with acoustic schwannomas having only tinnitus as a presenting symptom.[22]

Facial nerve manifestations such as twitching or weakness are relatively uncommon.[60, 61] Instead, larger tumors are more likely to cause trigeminal manifestations such as facial numbness and loss of the corneal reflex.[59, 60] Still larger tumors may cause deficits of the lower cranial nerves, cerebellar signs and symptoms, or signs and symptoms of hydrocephalus.[60, 61] Rarely, an acoustic schwannoma, usually a large one, can present as a subarachnoid hemorrhage.[62–65]

Among the commonly employed clinical laboratory tests, brainstem electric response audiometry (BERA) is considered the most sensitive preimaging test for acoustic schwannoma.[54] The ability to understand speech is measured as a ''speech discrimination'' score, and a low score suggests an acoustic schwannoma. Until MR imaging became widely available, the diagnostic steps typically included a history and physical examination, an audiogram, a brainstem-evoked response, CT with contrast, and then, if necessary, a gas-CT cisternogram.[66, 67] MR imaging is now clearly the imaging method of choice.[10, 68] Some groups even advise Gd-MR imaging for all patients with unilateral sensorineural hearing loss or unexplained tinnitus, without performing BERA.[60, 69] Schmidt and colleagues have concluded that BERA cannot be relied on for detection of small acoustic neuromas and should not be used to determine whether MR imaging should be performed when an acoustic neuroma is suspected clinically.[70] Newly developed noncontrast, thin-section, T2-weighted imaging sequences may become a screening modality (Fig. 25-2).[71] These techniques are less expensive than comprehensive studies for screening; however, the true goal of imaging remains exclusion of acoustic tumor. The contrast-enhanced, T1-weighted sequence remains the easiest examination to do and interpret, with the highest negative predictive value in exclusion of vestibular schwannoma as a cause of sensorineural hearing loss.[72] Contrast-enhanced examinations are also of value in demonstrating inflammatory conditions of the nerve, which would be enhanced by the gadolinium but show little swelling.[73]

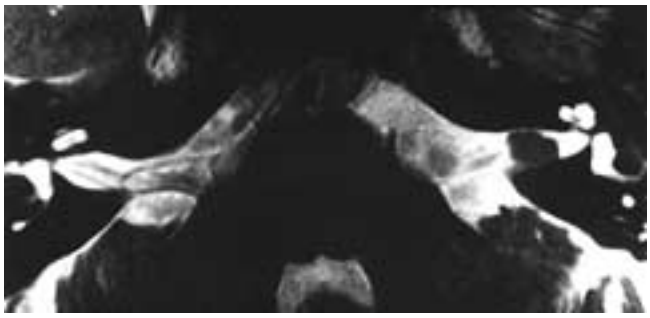

FIGURE 25-2 Thin-section (2 mm) T2-weighted image of the IAC. Note the loop of the AICA in the right CPA and the porous acousticus, a segment of the right facial and superior vestibular nerves in the right IAC, and an intracanalicular tumor in the left IAC. (Courtesy of Dr. H.R. Harnsberger.)

VIEW IMAGE

Treatment

Whenever feasible, the accepted treatment for acoustic schwannoma is surgical resection.[31] With microsurgery, total tumor removal and functional preservation of the facial nerve, with low morbidity and mortality, is now the rule.[74, 75] In the 1990s, attention focused on hearing preservation, and it is generally agreed that hearing preservation is more successful with removal of small tumors.[52, 76] Early detection therefore continues to be emphasized, and high-quality MR imaging contributes immeasurably to these goals. New MR techniques provide the surgeon with more useful information when an intracanalicular tumor is detected.[14] It is often possible to determine if the tumor is located in the facial nerve or in one of the three branches of the vestibulocochlear nerve.[77] Sartoretti-Schefer and colleagues have identified the entire course of the facial nerve and nerve tumor relationships in small vestibular schwannomas utilizing 3D T2-weighted sequences.[78] While this preoperative information may not change the surgical approach in vestibular schwannomas, it can influence the surgical technique and approach in other CPA masses.[79] MR imaging can also be used to predict hearing preservation, which is found to be four times more likely when the labyrinthine signal is normal on 3D-CISS images.[80] Other investigators found that the absence of cochlear contrast enhancement ipsilateral to tumor correlates well with preservation of hearing following surgery.[81]

For the treatment of acoustic tumors, there are basically three surgical approaches—translabyrinthine, suboccipital, and middle (cranial) fossa—and a number of variations and combinations thereof.[2, 82–85] There is considerable variation in the surgical approach used, but in general, small tumors with preservation of hearing are operated on using the middle fossa or the suboccipital approach.[85, 86] In general, the middle fossa is favored for small tumors involving the lateral IAC, and the suboccipital retrosigmoid approach is preferred for small tumors in the CPA and the medial IAC. The translabyrinthine approach is used for patients with poor hearing or large tumors. However, some surgeons prefer the translabyrinthine approach for tumors of all sizes, and others prefer the suboccipital approach in most cases.

No consensus exists for grading the size of acoustic tumors. However, one might consider tumors that are either intracanalicular or those that extend up to 0.5 cm into the CPA as small tumors; lesions with 0.5 to 2 cm cisternal components as medium-sized tumors; lesions with 2 to 4 cm cisternal components as large tumors; and lesions with greater than 4 cm cisternal components as giant tumors.[22, 84, 87, 88]

Acoustic tumors in elderly or high-risk patients are followed by annual CT or MR imaging until their growth rates can be determined.[89, 90] Vestibular schwannomas can be managed safely in the elderly patient by serial MR

Copyright © 2003, Mosby, Inc. All rights reserved.

scanning. When significant tumor growth or neurologic deterioration is demonstrated, early surgical intervention may be required to avoid complications.[53, 91–98] In one series of 41 patients over 65 years of age, who were followed for an average of 3.5 years, 21 patients demonstrated tumor growth at an average rate of 0.322 cm per year.[99] Only five patients required intervention. No patients developed significant complications. No correlation could be found between initial tumor size and subsequent tumor growth. In a series of 116 patients over 65 years of age who had acoustic tumor surgery, with all but 10 having total tumor removal, the operative mortality rate was less than 1%.[100] Alternatively, acoustic tumors, especially in high-risk patients and those with bilateral tumors, may be treated by stereotactic radiosurgery using sharply collimated and focused cobalt-60 sources (gamma knife).[101] In a study of 86 patients with vestibular schwannomas, low-dose gamma knife radiotherapy was found to be effective for both small and large tumors up to 4 cm in size.[102] The tumor control rate was 81%. An increase in tumor size up to 2 years after radiotherapy is likely to be followed by regression. Dynamic changes in the enhancement pattern and T2 abnormalities of the adjacent brain are expected in serial MR imaging following radiotherapy.[102] Although the surgical results are excellent in preserving hearing in patients with small intracanalicular schwannomas, radiotherapy has results comparable to those of surgery in patients with small and mid-sized tumors.[102, 103] Patients with medical contraindications to surgery and residual tumors are good candidates for radiotherapy.

CT and MR Imaging Appearance

Size, Location, and Configuration

Acoustic schwannomas range in size from a few millimeters to 5 to 6 cm (Figs. 25-2 to 25-8), and tumors as large as 8 cm have been encountered.[104] A small percentage of acoustic schwannomas are entirely intracanalicular, in which case they are usually cylindrical in shape, are less than 1 cm in length, fill the IAC, and have a convex medial margin (Figs. 25-2 to 25-4).[105] The majority of medium-sized schwannomas have a spherical cisternal component up to 2 cm in diameter centered at the acoustic porus and a stem of tumor that extends into the IAC and expands the porus to a funnel shape. The overall appearance of the tumor resembles an ice-cream cone or a mushroom (Fig. 25-4). Tumors between 2 and 4 cm may be considered large, and usually are ovoid or slightly lobulated. Their petrous surface remains centered on the acoustic porus, and their long axis lies parallel to the petrous surface (Fig. 25-5). The very large or ''giant'' tumors often arise from the cisternal portion of the nerve and possess little or no canalicular component. The majority (85%) of schwannomas show acute angles at the bone–tumor interface (Figs. 25-4, 25-5, 25-7 and 25-8), in contrast to meningiomas, which tend to show obtuse angles (75%) (Fig. 25-9).[106] Acoustic schwannomas seldom if ever herniate through the tentorium.[32]

CT Density

On noncontrast-enhanced CT, the majority (64%) of acoustic schwannomas are isodense with the adjacent

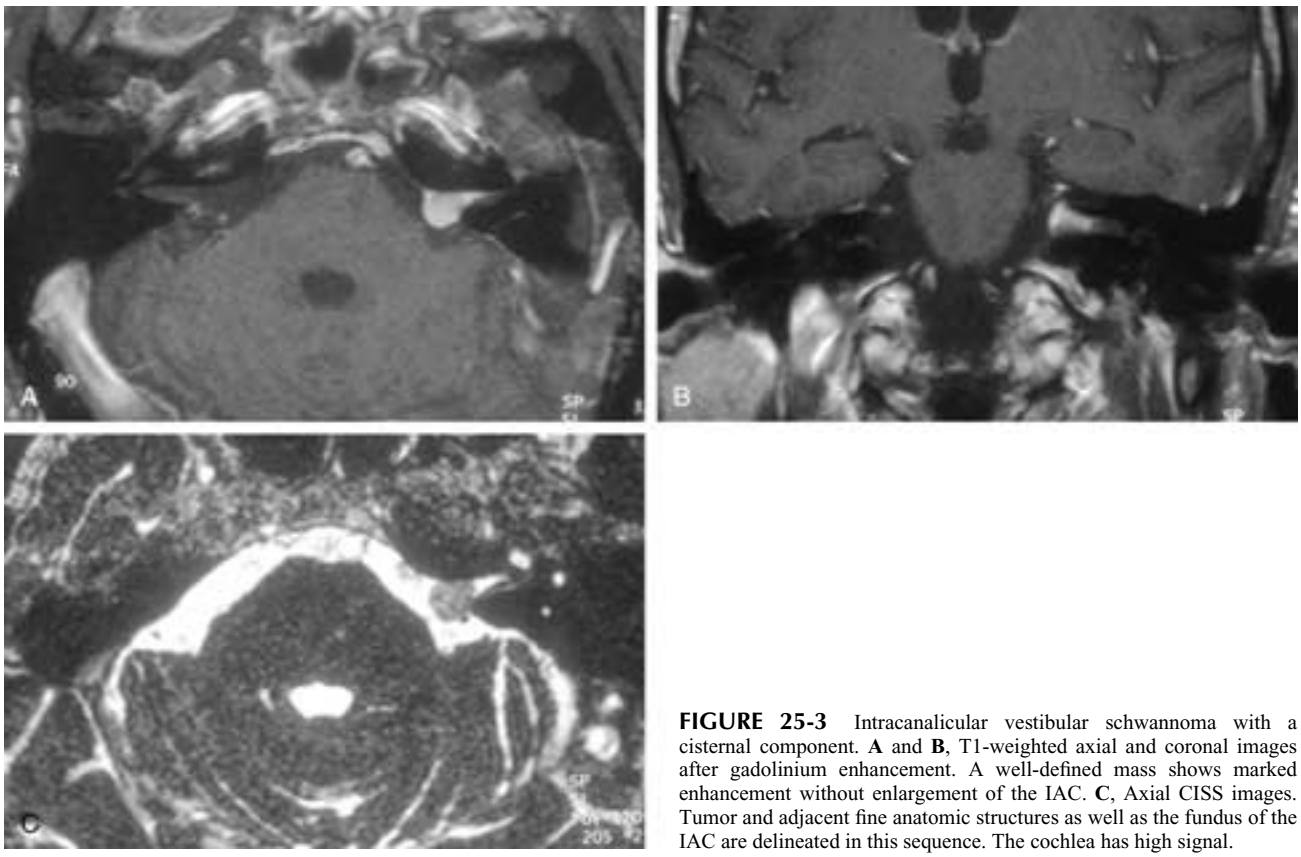

FIGURE 25-3 Intracanalicular vestibular schwannoma with a cisternal component. **A** and **B**, T1-weighted axial and coronal images after gadolinium enhancement. A well-defined mass shows marked enhancement without enlargement of the IAC. **C**, Axial CISS images. Tumor and adjacent fine anatomic structures as well as the fundus of the IAC are delineated in this sequence. The cochlea has high signal.

VIEW IMAGE

Copyright © 2003, Mosby, Inc. All rights reserved.

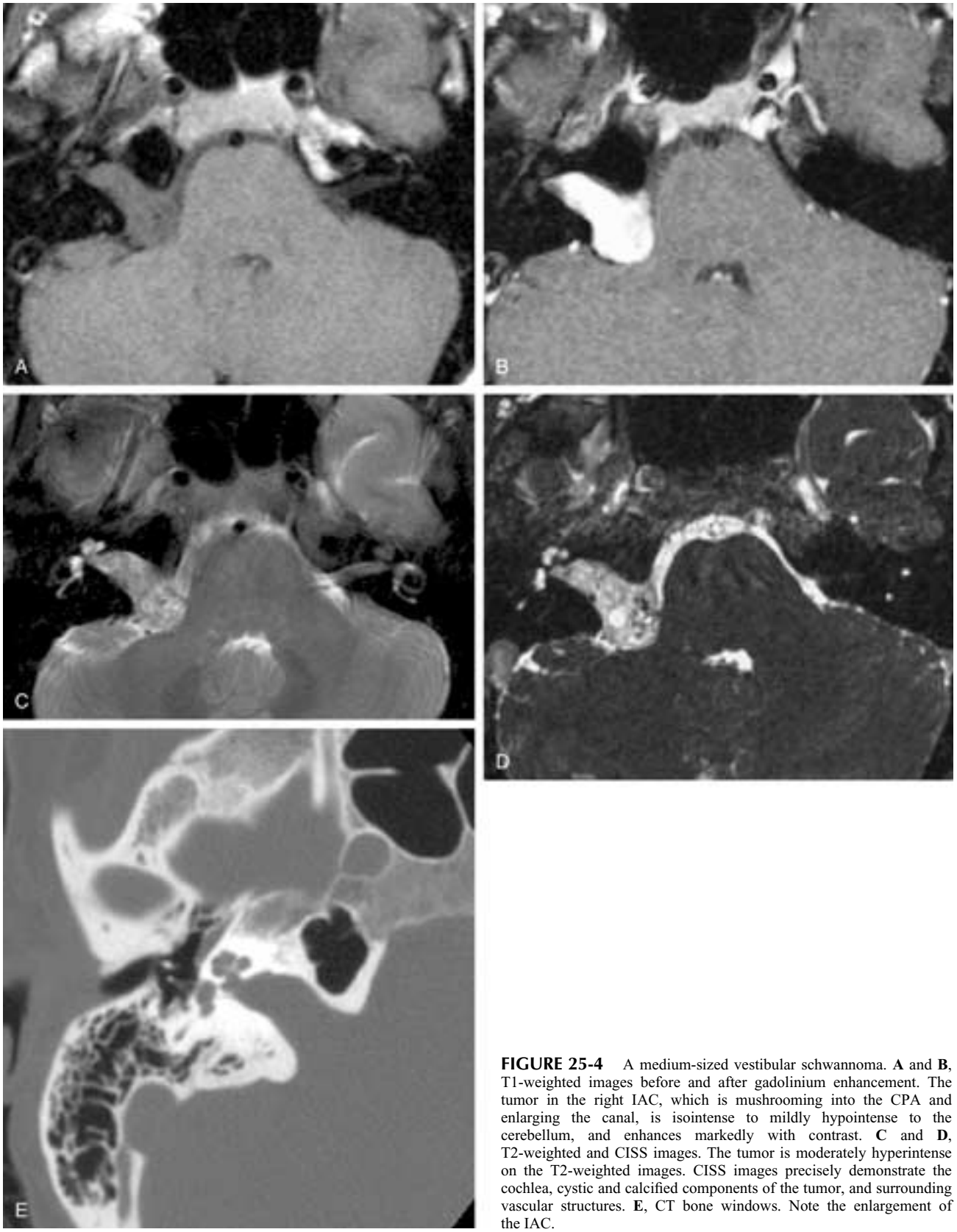

FIGURE 25-4 A medium-sized vestibular schwannoma. **A** and **B**, T1-weighted images before and after gadolinium enhancement. The tumor in the right IAC, which is mushrooming into the CPA and enlarging the canal, is isointense to mildly hypointense to the cerebellum, and enhances markedly with contrast. **C** and **D**, T2-weighted and CISS images. The tumor is moderately hyperintense on the T2-weighted images. CISS images precisely demonstrate the cochlea, cystic and calcified components of the tumor, and surrounding vascular structures. **E**, CT bone windows. Note the enlargement of the IAC.

VIEW IMAGE

Copyright © 2003, Mosby, Inc. All rights reserved.

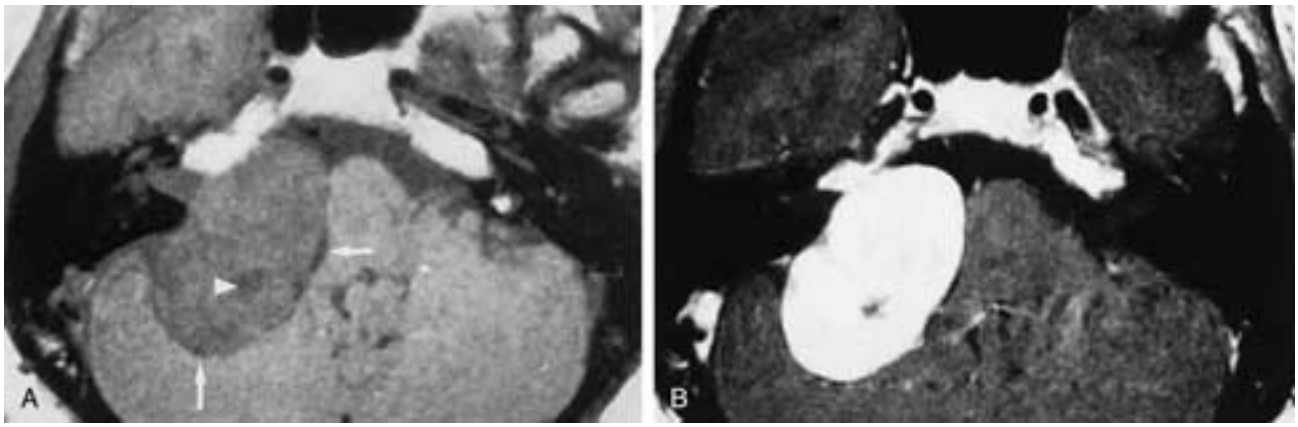

VIEW IMAGE

FIGURE 25-5 Giant cisternal acoustic schwannoma. The tumor (*arrows*) is extraaxial, smoothly marginated, ovoid, and centered over the porous acousticus, and it deforms the pons, cerebellum, and fourth ventricle. **A**, T1-weighted image. The tumor is mildly hypointense to brain and hyperintense to CSF and is nearly homogeneous except for the cystic component (*arrowhead*). **B**, Gadolinium T1-weighted image. The tumor shows marked contrast enhancement except for the cystic component. Giant tumors are often entirely extracanalicular, as in this case. (From Jackler RK, Brackmann DE, eds. Neurotology. St. Louis: Mosby-Year Book, 1994.)

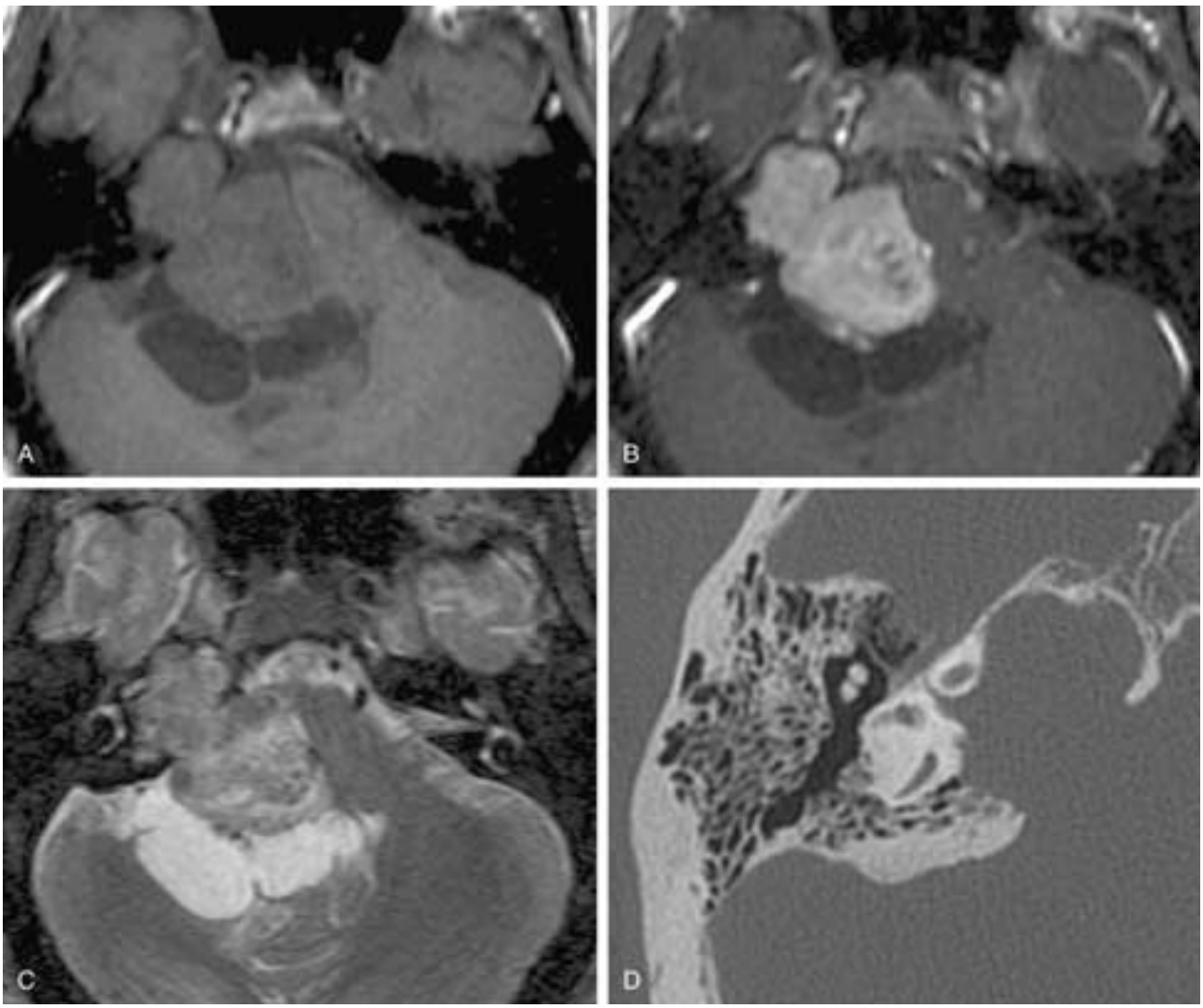

VIEW IMAGE

FIGURE 25-6 Giant cystic vestibular schwannoma with accompanying arachnoid cysts. **A** and **B**, T1-weighted images before and after gadolinium enhancement. Note the superficial arachnoid cysts. The tumor is invading to the petrous apex and compressing the brainstem and the fourth ventricle, causing hydrocephalus. **C**, T2-weighted image. The tumor is heterogeneously hyperintense and is surrounded by vascular structures and hyperintense cysts. **D**, CT bone windows. Note the smooth osseous expansion of the petrous apex and IAC.

Copyright © 2003, Mosby, Inc. All rights reserved.

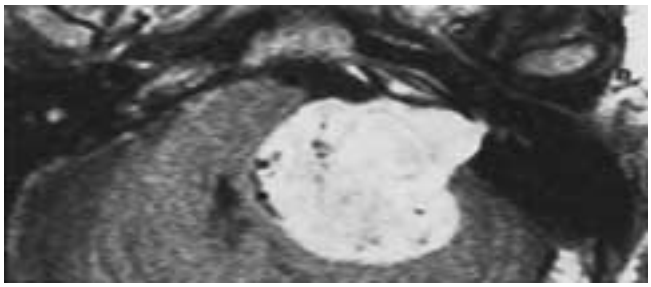

VIEW IMAGE

FIGURE 25-7 Large acoustic schwannoma, T1-weighted postgadolinium image. Note the serpentine flow voids of the vessels in this relatively vascular tumor and the displaced tributaries of the petrosal and capsular veins on the surface of the tumor.

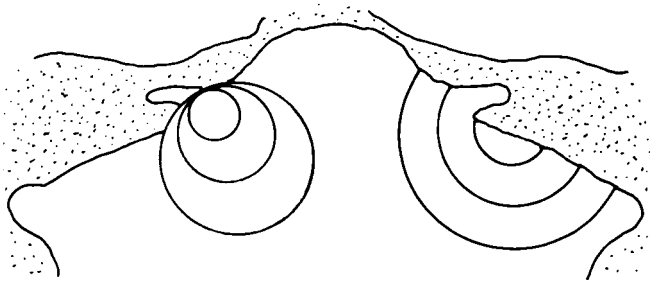

VIEW IMAGE

FIGURE 25-9 Diagrammatic representation of typical configurations of acoustic schwannoma versus CPA meningioma. Schwannoma: a spherical mass centered at the porous acousticus, making an acute angle with the petrous bone. Meningioma: hemispheric mass eccentric to the porous acousticus, making an obtuse angle with the petrous bone. (From House JW, O'Conner AF. Handbook of Neurotological Diagnosis. New York: Marcel Dekker, 1987;296.)

cerebellum and are not discernible without IV contrast.[20] The remaining tumors are either slightly hypodense, hyperdense, or of mixed density. Calcification or detectable hemorrhage is rare in untreated tumors.[64, 104]

CT contrast enhancement occurs in nearly 90% of untreated tumors, and the enhancement is usually homogeneous and dense.[104] Most acoustic schwannomas rapidly enhance. The enhancement declines rapidly within 15 minutes after completion of contrast infusion, then less rapidly within the next 45 minutes, and residual enhancement may remain for hours.[107] Some investigators, however, indicate that maximum enhancement occurs about one half hour after infusion, and some researchers recommend a slight delay between infusion and scanning because the tumor enhancement may not be as obvious during the ''vascular'' phase.[108] The contrast must be given time to move from the intravascular compartment to the extravascular tissue.

Some tumors show irregular central lucencies or inhomogeneous enhancement. The initially unenhanced portions of the schwannoma may take many minutes to attain full enhancement, and tumors with such an appearance contain prominent cystic components at surgery. Loss of contrast enhancement is common after stereotactic radiotherapy.[101]

Rarely, an arachnoid cyst may develop around a tumor and become the dominant lesion.[109]

MR Imaging Intensity

On MR imaging, as on CT, small and medium-sized acoustic schwannomas are most likely to be homogeneous, and large tumors are most likely to contain internal zones of inhomogeneity (Figs. 25-6 to 25-8).[20] Cysts may be intra- or extramural and single or multiple.[110]

On T1-weighted images, schwannomas are usually isointense or mildly hypointense relative to the pons and are hyperintense to CSF. On T2-weighted images they are mildly hyperintense to the pons and iso- to hypointense to CSF (Fig. 25-4).[68, 111, 112] With very long TR and TE, the CSF gives a very high signal, and almost all acoustic schwannomas, particularly those limited to the IAC, have a lower signal than the CSF when these imaging parameters are used. Thus the CSF becomes a natural contrast for detecting the tumor. Previously, such sequences took too long to perform, and patient motion limited their usefulness. Recently, fast spin-echo technology has allowed such imaging in a reasonable time interval (see Fig. 25-2).

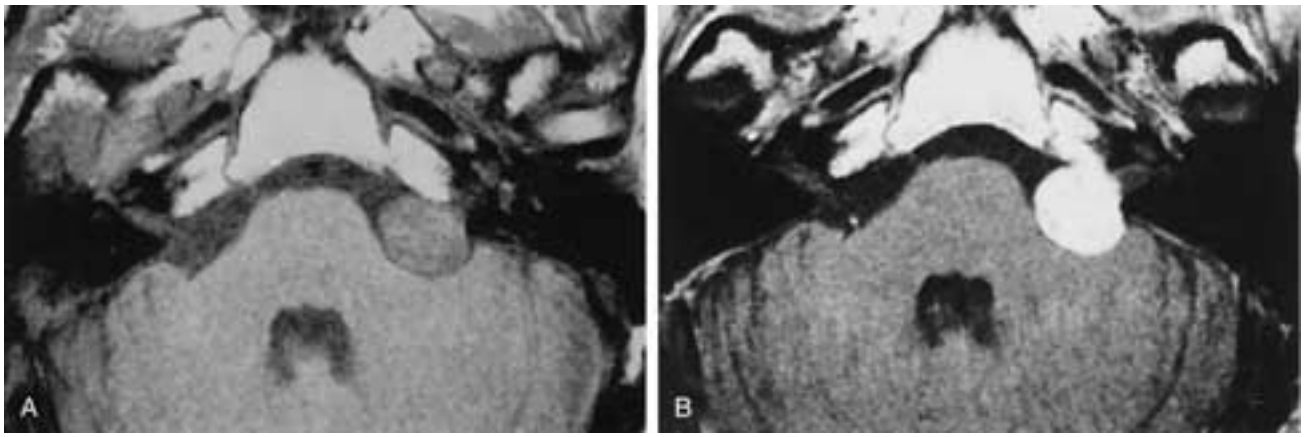

VIEW IMAGE

FIGURE 25-8 Medium-sized cisternal acoustic schwannoma. The tumor is extraaxial, smoothly marginated, rounded, and centered at the porous acousticus. **A**, T1-weighted image. The tumor is mildly hypointense to brain, hyperintense to CSF, and slightly granular in texture. **B**, Gadolinium T1-weighted image. The tumor shows marked, nearly homogeneous enhancement. (Compare with Fig. 25-30.) (From Jackler RK, Brackmann DE, eds. Neurotology. St. Louis: Mosby-Year Book, 1994.)

Copyright © 2003, Mosby, Inc. All rights reserved.

Tumors large enough to deform the pons are readily recognizable on both T1-weighted and T2-weighted images. Tumors too small to deform the pons stand out well against the hypointense CSF on T1-weighted images (Fig. 25-3), but they may be obscured by the nearly isointense CSF on T2-weighted images.[68, 112, 113]

Displaced tributaries of petrosal and capsular veins, which are difficult if not impossible to see on CT, are often recognizable on MR imaging in medium-sized and large tumors (Fig. 25-7).[68] Intratumoral hemorrhage, at various stages of hemoglobin breakdown, may also be detected on MR imaging.[114]

Acoustic schwannomas enhance intensely after intravenous administration of a gadolinium contrast agent on T1-weighted images (Figs. 25-1, 25-3 to 25-8).[115] The sensitivity of contrast-enhanced, T1-weighted MR imaging can approach 100% in detecting schwannomas.[73] With a small field of view, the voxel size can be decreased to 0.7 × 0.4 × 0.3 mm.[116] In a recent series, both contrast T1-weighted and high-resolution T2-weighted images detected tumors ranging from 0.06 to 3.0 cm^3.[117]

As a group, acoustic schwannomas enhance substantially more than meningiomas, neurofibromas, and paragangliomas on T1-weighted, contrast-enhanced spin-echo images.[118] However, enhancement varies greatly in tumors of the same type and overlaps among different tumor types. Unless enhancement is marked, it is of limited value in differentiating schwannomas from other extraaxial tumors.[118] In contrast to meningiomas, schwannomas rarely show dural ''tails'' (Fig. 25-10).[119]

Secondary Changes

Because acoustic schwannomas are extraaxial, as they grow they enlarge toward the cerebellopontine junction and displace the brainstem to the contralateral side. Indirect signs of an extraaxial mass (such as widening of the ipsilateral CPA and the quadrigeminal cisterns, narrowing of the contralateral cisterns, and displacement and compression of the fourth ventricle) accompany the larger tumors (Figs. 25-5 to 25-7). Acoustic schwannomas, however, do not extend anterosuperiorly above the dorsum and, unlike meningiomas, extremely rarely herniate into the middle fossa.[32] The incidence of hydrocephalus correlates roughly with tumor size, and one report noted hydrocephalus in 17 of 44 patients in whom a tumor measuring 3 cm or more was present.[120] Edema of the adjacent brain also may be associated with large acoustic schwannomas.[20, 121]

Bone changes associated with acoustic schwannomas are limited to the IAC (Figs. 25-1, 25-4 to 25-7 and 25-10). By comparing the normal IAC to the abnormal side and using the criteria of a difference in canal height of more than 2 mm, a shortening of the posterior wall of the canal of more than 3 mm, a downward displacement of the crista falciformis, and the presence of focal erosion, Valvassori found abnormal IACs on polytomography in 78% of surgically verified tumors.[6] On high-resolution CT the incidence of bone changes is probably comparable or higher. Tumors arising from the intracanalicular portion of the nerve typically cause flaring of the porus acousticus as they enlarge (Figs. 25-1, 25-4 to 25-7 and 25-10), whereas those arising from the cisternal portion may cause little or no erosion (Fig. 25-8). Regarding canal size, bilateral enlargement of the IAC in the absence of intracanalicular tumors may be seen in neurofibromatosis, and unilateral asymmetry also may be seen on rare occasions.[1, 109, 122, 123]

In a series of 86 patients treated with stereotactic radiotherapy, three patterns of enhancement were seen: (1) transient loss of contrast enhancement (84%), (2) continuous increase in contrast enhancement (5%), and (3) no change in contrast enhancement (11%). There was no significant correlation between changes in tumor volume and tumor enhancement.[102] The same investigators found T2 abnormalities in the adjacent brain parenchyma in 19 patients (31%). These changes disappeared or improved in 14 patients. There was no correlation between dose, tumor size, and the T2 signal changes. A series of 89 tumors treated with stereotactic radiotherapy showed that, on evaluation approximately 12 months after treatment, most vestibular schwannomas remained stable (73%), some shrank (22%), and a few grew (3%).[101] By contrast, most untreated tumors remained stable (59%), many grew (38%), and a few shrank (3%) (Fig. 25-11).[101] About 5 to 15 months after radiation

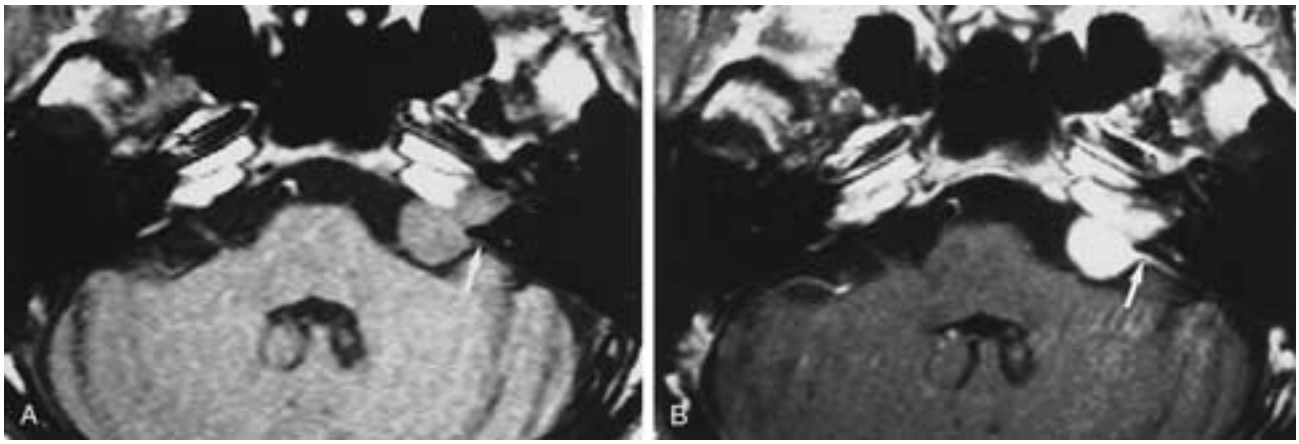

VIEW IMAGE

FIGURE 25-10 Acoustic schwannoma with dural tail. **A**, T1-weighted image. **B**, Gadolinium T1-weighted image. This otherwise typical-appearing IAC-CPA acoustic schwannoma shows an enhancing dural tail (*arrow*) extending to the posterior petrous surface. This finding was present in only 1 of 100 acoustic schwannomas in an unpublished series. (From Jackler RK, Brackmann DE, eds. Neurotology. St. Louis: Mosby-Year Book, 1994.)

Copyright © 2003, Mosby, Inc. All rights reserved.

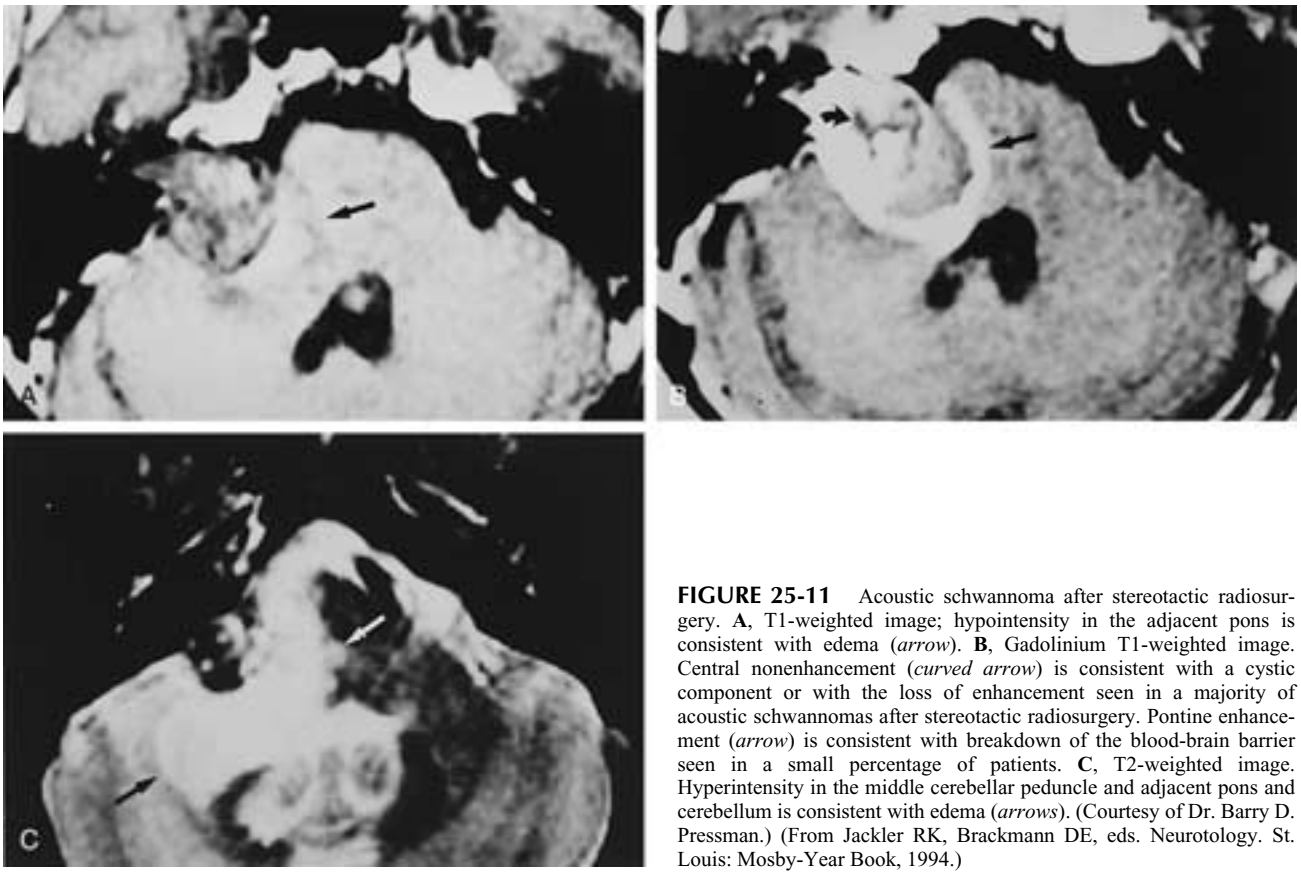

FIGURE 25-11 Acoustic schwannoma after stereotactic radiosurgery. **A**, T1-weighted image; hypointensity in the adjacent pons is consistent with edema (*arrow*). **B**, Gadolinium T1-weighted image. Central nonenhancement (*curved arrow*) is consistent with a cystic component or with the loss of enhancement seen in a majority of acoustic schwannomas after stereotactic radiosurgery. Pontine enhancement (*arrow*) is consistent with breakdown of the blood-brain barrier seen in a small percentage of patients. **C**, T2-weighted image. Hyperintensity in the middle cerebellar peduncle and adjacent pons and cerebellum is consistent with edema (*arrows*). (Courtesy of Dr. Barry D. Pressman.) (From Jackler RK, Brackmann DE, eds. Neurotology. St. Louis: Mosby-Year Book, 1994.)

VIEW IMAGE

therapy, the tumors frequently lost central enhancement (79%), which in some cases returned with time. In the adjacent pons and cerebellar peduncle, contrast enhancement on T1-weighted images may develop. Hyperintensity on T2-weighted images, which did not closely correspond to neurologic symptoms, appeared in 9% of patients. Delayed trigeminal nerve enhancement and development of hydrocephalus were also observed in some patients.[101, 124] Some tumors may continue to grow and require resection.[97, 121]

DIFFERENTIAL DIAGNOSIS OF TUMORS OF THE INTERNAL AUDITORY CANAL AND THE CEREBELLOPONTINE ANGLE

Statistics and Categorization

Although by far the most common tumor associated with the CPA syndrome is the acoustic schwannoma, many other neoplastic and nonneoplastic mass lesions occur in the region (Table 25-1).

Brackmann and Bartels, reviewing 1354 CPA tumors, excluding paragangliomas, found 91.3% acoustic schwannomas, 3.1% meningiomas, 2.4% primary cholesteatomas (epidermoid cysts), 1.2% facial nerve schwannomas, and 0.2% schwannomas of other posterior fossa cranial nerves. There were 25 rare tumors, including 7 arachnoid cysts, 4 hemangiomas, 1 hemangioblastoma, 2 astrocytomas, 2 medulloblastomas, 3 metastatic tumors, 2 dermoids, 2 lipomas, 1 malignant teratoma, and 1 chondrosarcoma.[21]

Similarly, Valavanis et al., analyzing 455 CPA lesions, found the following among the primary tumors: 60.5% acoustic schwannomas; 6.8% meningiomas; 3.7% epidermoid cysts; 2% arachnoid cysts; 4% schwannomas of the fifth, seventh, ninth, tenth, and eleventh cranial nerves; 0.2% primary melanomas; and 0.7% hemangiomas. Among secondary tumors of the CPA, the following were found: 10.3% paragangliomas (chemodectomas), 0.2% germinomas, 0.4% chondromas, 1.8% chordomas, and 1.3% cerebellar and bone tumors; among vascular lesions: 0.9% aneurysms, 0.9% arteriovenous malformations, and 3.7% megadolichobasilar anomalies. There were also 2.6% metastases.[20]

Both of the above series are in substantial agreement with the often-cited series of 205 CPA tumors of Gonzalez Revilla, which consisted of 75.1% acoustic schwannomas, 6.3% meningiomas, 6.3% epidermoids, 4.9% nonacoustic schwannomas, 0.5% primary melanomas, 0.5% paragangliomas, and 6.4% cerebellar and petrous bone tumors infiltrating the CPA.[125]

Thus the four most common tumors are the same in all three series: acoustic schwannoma, meningioma, epidermoid cyst, and nonacoustic posterior fossa schwannoma. Together they account for 75% to 98% of all CPA mass lesions.

Although the probability of a CPA mass being an acoustic schwannoma is 60% to 90%, the remaining possibilities are diverse and numerous. In practice, the imaging differential diagnosis of a CPA lesion may be simplified by classifying the possible lesions into groups by their imaging appearance (Table 25-2). Essentially there are

Copyright © 2003, Mosby, Inc. All rights reserved.

Table 25-2
CT/MR IMAGING DIFFERENTIAL DIAGNOSIS CATEGORIES OF CPA LESIONS

	Location	Incidence	Type
I	Extraaxial	Most common	Acoustic schwannoma
II	Extraaxial	Common	Meningioma
III	Extraaxial	Common	Epidermoid (and other cysts: arachnoid cysticeral, lipoma)
IV	Extraaxial	Rare	Nonacoustic posterior fossa schwannomas (V, VII, IX, X, XI, XII)
V	Extraaxial	Rare	Vascular lesions (VBD,* aneurysm, AVM,† hemangioma, AICA‡ loop, siderosis)
VI	Extraaxial	Common	Paraganglioma
VII	Extraaxial	Rare	Bone lesion (benign or malignant: primary or metastatic)
VIII	Intraaxial	Rare	Astrocytoma, ependymona, papilloma, hemangioblastoma, metastasis, etc.

**VBD,* Vertebrobasilar dolichoesctasia.
†*AVM,* Arteriovenous malformation.
‡*AICA,* Anterior inferior cerebellar artery.

three common extraaxial tumors (acoustic schwannoma, meningioma, and epidermoid cyst) (Table 25-3), two groups of rare extraaxial lesions (nonacoustic posterior fossa schwannomas and vascular masses), two groups of extradural masses (paragangliomas and bone lesions), and finally, the intraaxial lesions. For simplicity, rare nonenhancing masses such as lipomas, dermoids, and arachnoid and cysticercal cysts may be placed in the same group as epidermoid cysts.

The three most common lesions in adults—acoustic schwannoma, meningioma, and epidermoid cyst—are the same in older teenagers. However, in younger children, acoustic schwannomas are extremely rare, and gliomas, which are capable of enlarging the internal acoustic canal, are the most common cause of CPA tumors.[126]

Meningiomas and Simulants

Meningioma arises from the meningothelial arachnoid cell and accounts for 13% to 18% of all primary intracranial tumors.[27] In the CPA, it is a distant second to acoustic schwannoma in incidence, and it is the lesion offering the most difficulty in the differential diagnosis of acoustic schwannoma (Figs. 25-13 to 25-16).[20, 21, 106] Like acoustic schwannomas, meningiomas are extraaxial. However, unlike acoustic schwannomas, they are usually eccentric to the porus.[127] Also unlike acoustic schwannomas, which seldom if ever herniate into the middle fossa, meningiomas frequently do (56%).[106, 127, 128] Meningiomas also may extend into the middle fossa by growth through the tentorium (19%) or temporal bone (Fig. 25-15).[106, 128] In size they are usually moderate to large compared with acoustic schwannomas.[9]

Meningiomas are almost always broad-based against a dural surface such as the posterior petrous wall. Their configurations generally fall into three groups. Unlike acoustic schwannomas, which are by and large spherical or ovoid, most meningiomas are hemispherical (Figs. 25-12 to 25-15).[127] Consequently, most meningiomas (75%) show obtuse bone tumor angles, while schwannomas tend to show acute angles (85%) (Fig. 25-9).[106] Some meningiomas are plaquelike (en plaque) and often deeply infiltrate the underlying bone (Fig. 25-16). A few meningiomas appear nearly rounded and by configuration are more difficult to distinguish from schwannomas.

Meningiomas are either isodense (31%) or, more often, hyperdense (69%) on noncontrast CT.[106] Unlike schwannomas, they are often calcified (25%), usually homogeneously and sometimes densely.[104, 106] More than 90% show homogeneous enhancement inversely proportional to their precontrast density.[106] CPA meningiomas are isointense or slightly hypointense to gray matter on T1-weighted images but are extremely variable in intensity on T2-weighted

Table 25-3
COMPARISON OF SALIENT CT AND MR IMAGING FEATURES OF THE THREE MOST COMMON CPA LESIONS

	Acoustic Schwannoma	Meningioma	Epidermoid Tumor
Location	Centered to IAC	Posterior petrous wall most eccentric to IAC	Anterolateral or posterolateral to brainstem
Bone changes	Most enlarging IAC	Occasional hyperostosis	Occasional erosion
Shape	Spherical or ovoid, occasionally lobulated, acute bone tumor angle	Hemispherical, rarely plaque-like, may herniate, obtuse bone tumor angle	Variable with tendency to dumbell into middle fossa or contralateral CPA
Density	Mostly isodense, a few slightly hypodense or hyperdense	Isodense or mostly slightly hyperdense, some calcified	Mostly about CSF density, rarely denser than brain, occasional peripheral calcification
CT enhancement	Moderate to marked, often with inhomogeneous enhancement	Marked and homogeneous	Nonenhancing
Intensity T_1W image	CSF < M ≤ Gr	CSF < M ≤ Gr	CSF ≤ M < Gr
Intensity T_2W image	≤CSF	Variable	≤CSF
MR enhanced	Marked, some ''cystic''	Moderate	Nonenhancing

T_1W, T1-weighted; *T_2W,* T2-weighted; *CSF,* cerebrospinal fluid; *M,* mass; *IAC,* internal auditory canal; *CPA,* cerebellopontine angle; *GR,* gray matter.

Copyright © 2003, Mosby, Inc. All rights reserved.

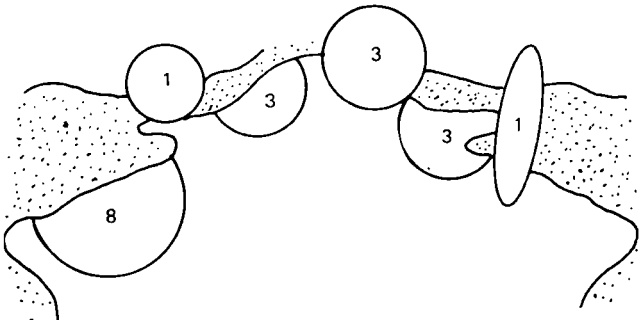

VIEW IMAGE

FIGURE 25-12 Diagrammatic representation of the locations of 19 meningiomas producing CPA symptoms (left and right sides combined). (From House JW, O'Conner AF. Handbook of Neurotological Diagnosis. New York: Marcel Dekker, 1987;290.)

images, more so than any other CPA mass lesion (Figs. 25-14 to 25-16).[9] When the intensity of a CPA mass is equal to or less than that of gray matter on T2-weighted images, meningioma is the most likely diagnosis.[9] Otherwise, signal intensity as a diagnostic criterion for meningioma is far less helpful than location and configuration. The wide variation in signal intensity among meningiomas appears to reflect the diversity of histopathology in meningiomas. Tumors significantly hypointense to brain cortex tend to be composed primarily of fibrous or transitional elements. Tumors significantly hyperintense to brain cortex tend to be composed primarily of syncytial or angioblastic elements.[129, 130] Nevertheless, accurate prediction of the histology and behavior of meningioma by imaging is not possible.[131–133] The metabolic rate, as revealed by positron emission tomography (PET), may be a better prognosticator of tumor aggressiveness and recurrence.[134]

Other MR imaging findings in meningioma include marginal pial blood vessels manifesting as surface flow voids, surface CSF spaces or clefts, and arterial feeders to the tumor, which are seen as arborizing flow voids (Fig. 25-15).[9, 135, 136] These findings are less commonly seen in infratentorial than in supratentorial meningiomas.[9]

Heterogeneity in meningiomas may be caused by calcifications and cystic foci, and perifocal edema is occasionally discernible on both CT and MR imaging.[9, 104, 135] Marked peritumoral edema, absence of visible calcium aggregates, nonhomogeneous contrast enhancement with nonenhancing ''cystic'' components, and poorly defined irregular borders suggest aggressive or invasive characteristics more commonly found in the angioblastic and syncytial variants.[137]

Dural thickening surrounding a meningioma (''dural tail,'' ''meningeal sign,'' or ''flare sign'') is best seen on Gd-MR imaging and is found in 52% to 72% of the cases (Figs. 25-14 to 25-16).[138–140] In most cases, ''dural tails'' represent reactive rather than neoplastic changes.[139, 141–143] Much less frequently, peritumoral dural thickening also has been found in other tumors, including oligodendroglioma, schwannoma, glioblastoma, and metastases.[119, 140, 142] Dural thickening bordering a meningioma extending into the

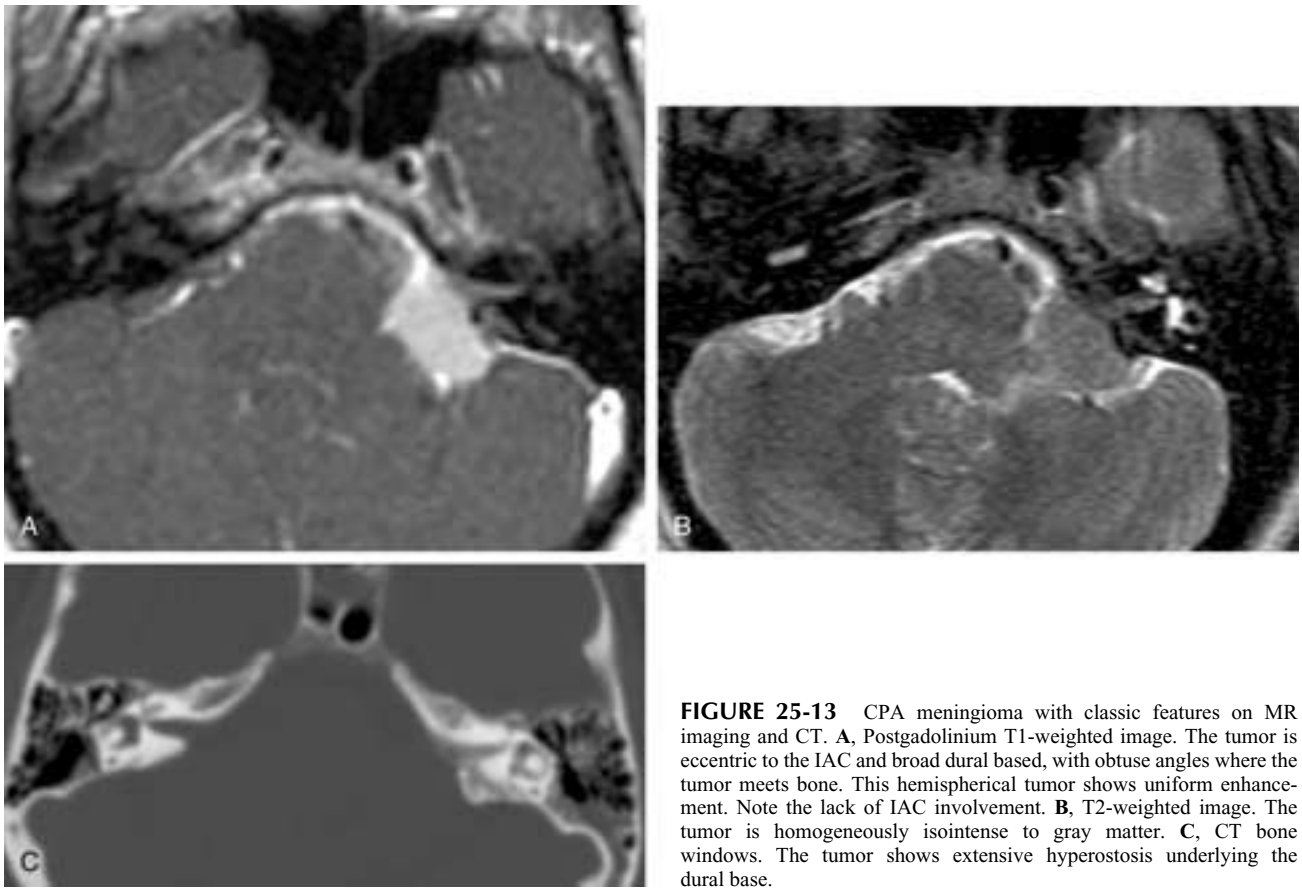

VIEW IMAGE

FIGURE 25-13 CPA meningioma with classic features on MR imaging and CT. **A**, Postgadolinium T1-weighted image. The tumor is eccentric to the IAC and broad dural based, with obtuse angles where the tumor meets bone. This hemispherical tumor shows uniform enhancement. Note the lack of IAC involvement. **B**, T2-weighted image. The tumor is homogeneously isointense to gray matter. **C**, CT bone windows. The tumor shows extensive hyperostosis underlying the dural base.

Copyright © 2003, Mosby, Inc. All rights reserved.

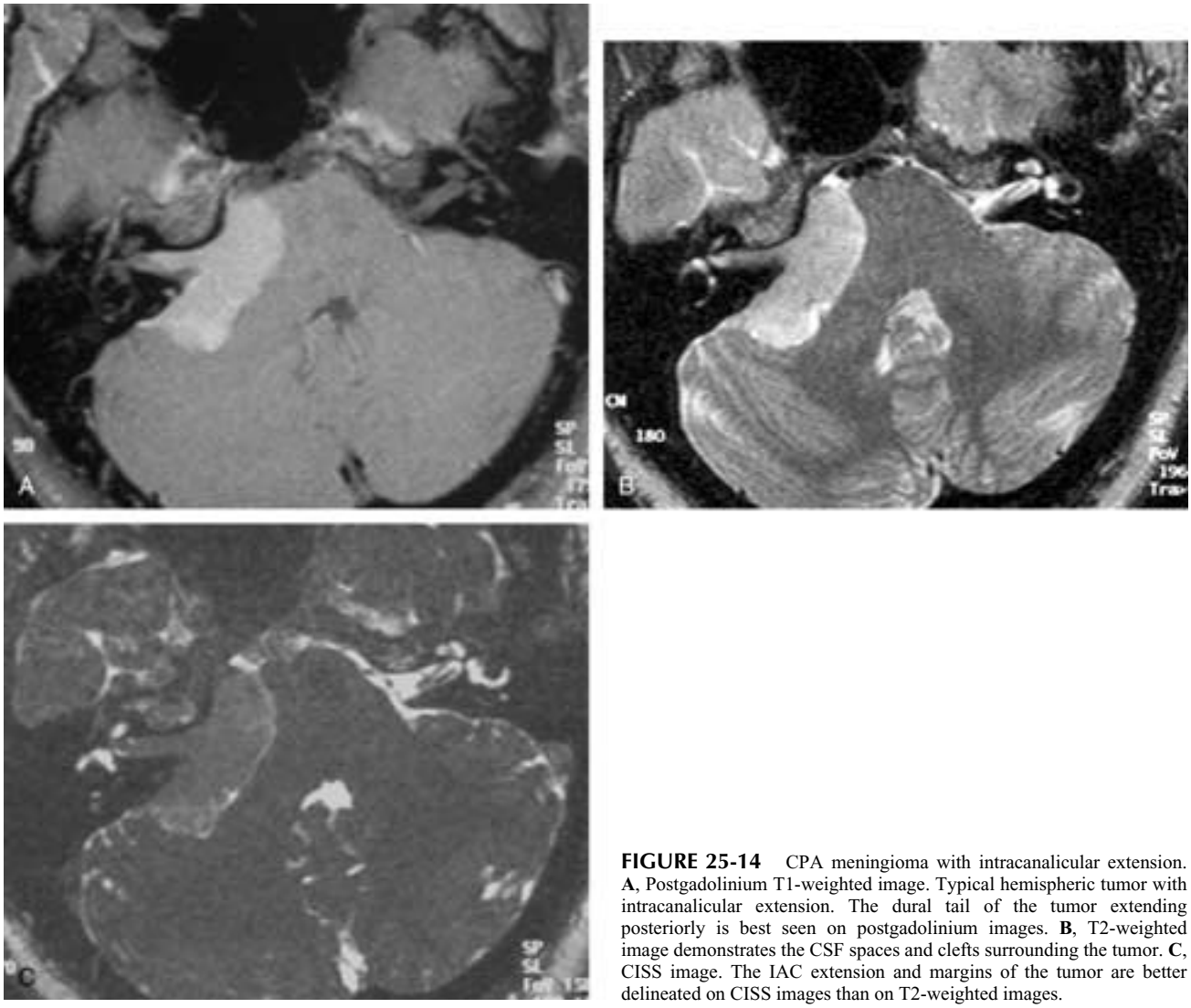

FIGURE 25-14 CPA meningioma with intracanalicular extension. **A**, Postgadolinium T1-weighted image. Typical hemispheric tumor with intracanalicular extension. The dural tail of the tumor extending posteriorly is best seen on postgadolinium images. **B**, T2-weighted image demonstrates the CSF spaces and clefts surrounding the tumor. **C**, CISS image. The IAC extension and margins of the tumor are better delineated on CISS images than on T2-weighted images.

VIEW IMAGE

IAC may simulate the stem of an acoustic schwannoma.[138] Underlying hyperostosis is seen infrequently but is highly characteristic when present (Figs. 25-13C).[20, 106] The IAC is rarely enlarged. The treatment for meningioma is surgical, and local recurrences are not uncommon.[27, 144] In a series of 134 CPA meningiomas, complete tumor removal was accomplished in 95%.[145] Since complete surgical removal of skull base meningiomas has a high morbidity rate, radiotherapy should be considered as an adjunctive or alternative method of therapy.[146]

Several rare neoplastic and inflammatory processes involving the meninges may simulate meningiomas on CT or MR imaging and should be suspected when the presenting symptoms or imaging features of the lesions are not entirely typical of meningioma. Among the neoplasms are leptomeningeal metastasis (meningeal carcinomatosis) (Figs. 25-17 and 25-18), primary meningeal lymphoma, and primary malignant melanoma.[147–153] Among the inflammatory diseases are meningeal sarcoidosis, Lyme disease, tuberculosis, syphilis, and idiopathic hypertrophic cranial pachymeningitis (Fig. 25-19).[154–156] All of these processes may appear as diffuse dural thickening simulating en plaque meningiomas or localized dural-based masses simulating sessile meningiomas. However, they are not expected to elicit underlying hyperostosis, produce intratumoral calcification, or possess discernible feeding or draining meningeal vessels.

Epidermoid and Other Cysts

Also called primary cholesteatomas or pearly tumors, congenital intradural epidermoid cysts (or tumors) are the third most common tumor in the CPA (Figs. 25-20 to 25-22).[20, 21] Although congenital, they do not present clinically until young or middle adulthood. Originating from ectodermal cell rests, they consist of stratified squamous epithelial linings surrounding desquamated keratin.[27] As the contents slowly accumulate, the lesions often reach considerable size and yet cause only minimal symptoms.[157] The duration of symptoms is usually long, more than 4 years in one series.[158] The CSF protein is usually normal unless associated meningitis is present.[157, 158]

Epidermoid cysts may be located anterolateral or posterolateral to the brainstem. They tend to expand where

Copyright © 2003, Mosby, Inc. All rights reserved.

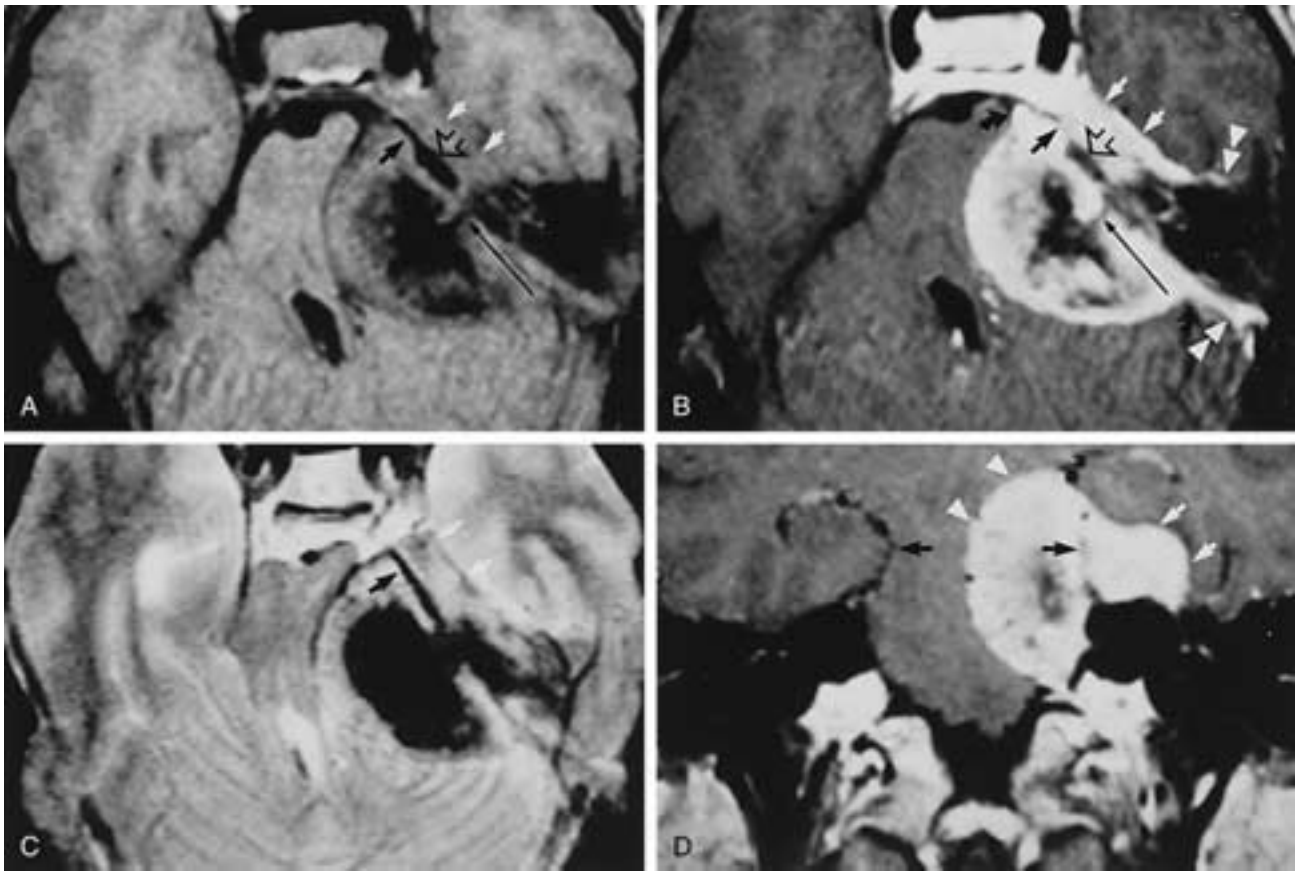

VIEW IMAGE

FIGURE 25-15 CPA meningioma with classic features. **A**, T1-weighted images. **B**, Gadolinium T1-weighted images. **C**, T2-weighted images. **D**, Coronal gadolinium T1-weighted images. The tumor is an extraaxial hemispherical mass with its broad base against the posterior petrous wall, obtuse bone–tumor angle, underlying focal hyperostosis (*open arrow*), central vascular pedicle (*long*, *thin arrow*), and transincisural (*arrowheads*) and transtentorial (*paired white arrows*) middle fossa extensions. The tentorium is indicated by black arrows. Central hypointensity is consistent with fibrosis and calcification. Note the dural tails (*tandem arrowheads*) in **B**. (From Jackler RK, Brackmann DE, eds. Neurotology. St. Louis: Mosby-Year Book, 1994.)

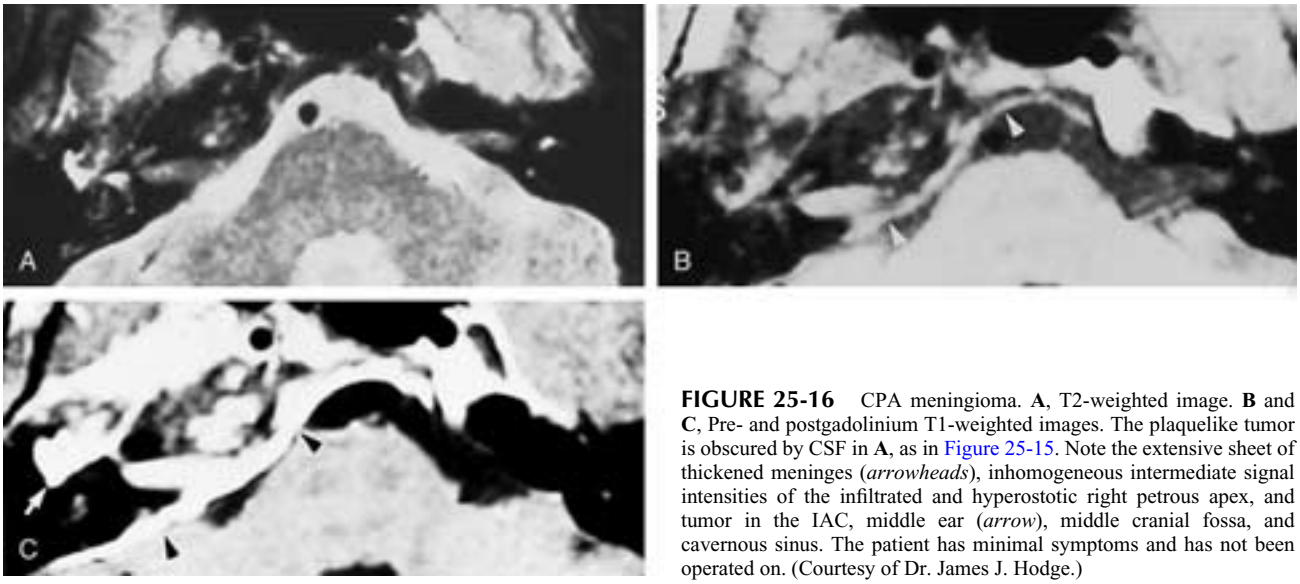

VIEW IMAGE

FIGURE 25-16 CPA meningioma. **A**, T2-weighted image. **B** and **C**, Pre- and postgadolinium T1-weighted images. The plaquelike tumor is obscured by CSF in **A**, as in Figure 25-15. Note the extensive sheet of thickened meninges (*arrowheads*), inhomogeneous intermediate signal intensities of the infiltrated and hyperostotic right petrous apex, and tumor in the IAC, middle ear (*arrow*), middle cranial fossa, and cavernous sinus. The patient has minimal symptoms and has not been operated on. (Courtesy of Dr. James J. Hodge.)

Copyright © 2003, Mosby, Inc. All rights reserved.

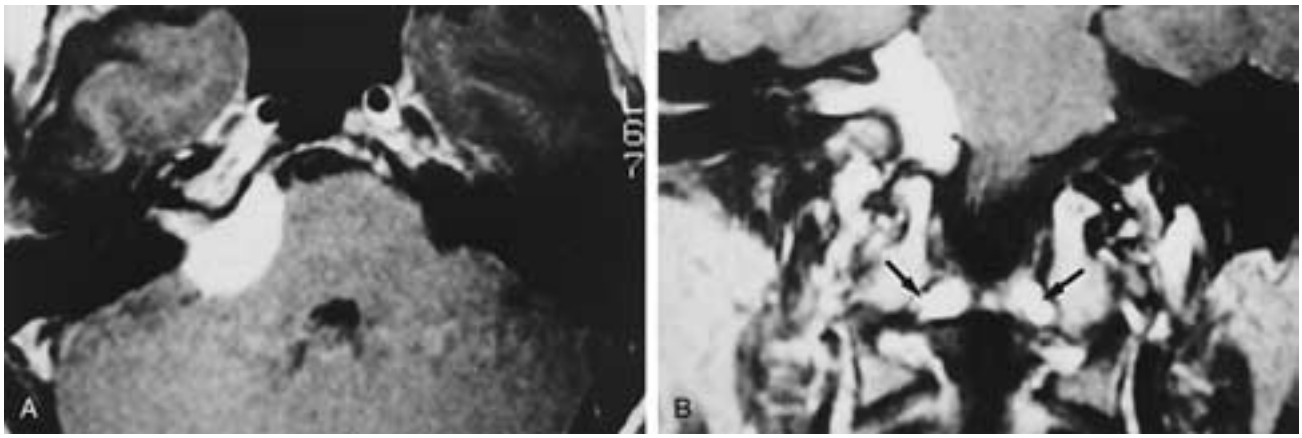

VIEW IMAGE

FIGURE 25-17 Loculated leptomeningeal metastasis simulating meningioma. The patient had right hearing loss for only 2 weeks, an unusually short duration of symptoms for a meningioma, and had previously had a malignant melanoma removed from her trunk. Metastatic melanoma was surgically confirmed. **A**, Gadolinium T1-weighted image. Hemispherical, homogeneously enhancing extraaxial mass eccentric to the porous acousticus with extension into the IAC, entirely consistent with a meningioma. **B**, Coronal gadolinium T1-weighted image. Subtle symmetric additional metastases within the foramen magnum are seen (*arrows*). (Courtesy of Dr. Peter W. Joyce.) (From Jackler RK, Brackmann DE, eds. Neurotology. St. Louis: Mosby-Year Book, 1994.)

physical resistance is low and often burrow into crevices on the surface of the brain, ''dumbbell'' into the middle fossa (Fig. 25-20), or extend around the brainstem into the contralateral cistern. Their shapes are thus quite variable, and their surfaces tend to show fine cauliflower-like irregularity (Figs. 25-20 to 25-22).[158]

On CT, epidermoid cysts approximate CSF in density, and they are usually nonenhancing masses. However, hyperdense epidermoid cysts have been reported, as have enhancing borders, and small amounts of calcification are sometimes found in the periphery of the tumors.[159–163] Squamous cell carcinoma arising from an epidermoid cyst has been reported, and an enhancing component in an epidermoid cyst may suggest an associated malignancy.[164, 165] Perifocal edema is rarely observed in association with epidermoid tumors, and pressure erosion of the petrous apex is sometimes encountered.[20, 158, 159]

On MR imaging, epidermoid cysts tend to be relatively homogeneous. They are usually isointense or slightly hyperintense to CSF on T1-weighted images and are hyperintense to CSF on T2-weighted images (Fig. 25-21).[9, 166] Steady-state free precession images (FISP) improve the visibility of epidermoid cysts over conventional spin-echo images.[167] A thin capsule or fine tissue strands may be seen in some of the tumors.[168] Epidermoid cysts may resemble schwannomas, meningiomas, or chondromas by signal intensity criteria, but unlike the other tumors, they are nonenhancing. Their CT density also may help in the differentiation. Rarely, epidermoid tumors show reversed signal intensities and are hyperintense on T1-weighted images and hypointense on T2-weighted images (white epidermoids) (Fig. 25-22).[160, 169, 170]

An arachnoid cyst, also of CSF density and intensity, is difficult to differentiate from an epidermoid on both CT and MR imaging (Fig. 25-23).[171] An attempt to differentiate the two may be worthwhile because the symptoms of arachnoid cysts may be controlled by diuretics alone.[172] Arachnoid cysts, usually large masses, possess smoother surfaces than epidermoids, and on CT, intrathecal contrast may be used to differentiate their surface characteristics (Fig. 25-24).[145] CISS, FLAIR, and diffusion-weighted MR imaging sequences are of critical value in differentiating arachnoid cysts from epidermoids.[173–177] These new MR imaging techniques usually obviate the need for intrathecal contrast administration.

Cysticercosis is another diagnostic consideration in endemic areas (Fig. 25-25). In contrast to parenchymal and intraventricular cysts, which are separate from one another, cisternal cysticercal cysts are usually racemose, several centimeters in size, and lacking a scolex.[178] Such cysts in the CPA may cause symptoms suggestive of acoustic schwannoma. Because their fluid may be identical to CSF on CT and MR imaging, the presence of cysticercal cysts is sometimes suggested only

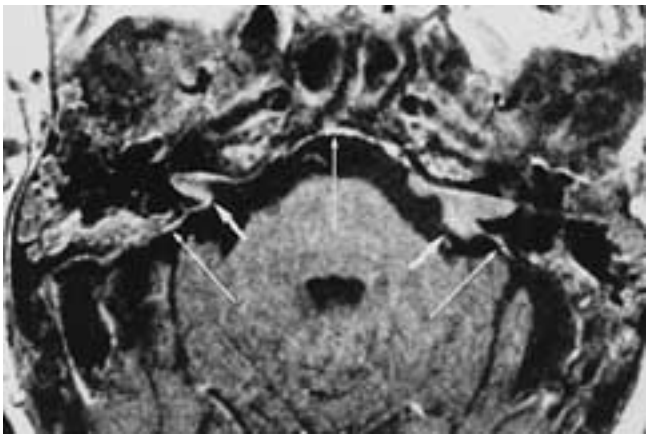

VIEW IMAGE

FIGURE 25-18 Meningeal metastases from prostate carcinoma, gadolinium T1-weighted image. Localized metastases are present in both IACs (*arrows*), and diffuse dural metastases (*long*, *thin arrows*) similar to a dural tail are noted. Differential diagnosis: meningeal lymphoma, melanoma, sarcoidosis, tuberculosis, Lyme disease, syphilis, idiopathic hypertrophic pachymeningitis. (From Jackler RK, Brackmann DE, eds. Neurotology. St. Louis: Mosby-Year Book, 1994.)

Copyright © 2003, Mosby, Inc. All rights reserved.

by focal cisternal widening.[178] They are seen better on MR imaging than on CT. The majority are detectable only on T1-weighted images, but T2-weighted images demonstrate the surrounding tissue reaction to greater advantage.[179]

Rarely, congenital cysts such as an epithelial cyst, a neurenteric cyst, or a craniopharyngioma, found in the CPA may show CT densities and MR signal intensities atypical of uncomplicated cysts.[180–187] Very rarely, a totally cystic schwannoma may also simulate an epidermoid cyst.[187]

Lipomas, more likely in the midline than in the CPA, show negative Hounsfield unit numbers on CT and isointensity to fat on MR imaging (Figs. 25-26 and 25-27).[27, 188, 189] Dermoid cysts show fatty density or signal intensity and may also contain teeth and peripheral calcifications.[157, 188] Fat-suppression techniques may be used for confirmation.[12] Because most authors recommend conservative management of CPA and IAC lipomas, a correct preoperative diagnosis is important.[190, 191]

Nonacoustic Posterior Fossa Schwannomas

The nonacoustic schwannomas resemble acoustic schwannomas in appearance but not in location.[192] Thus it is important to note the precise location of a schwannoma-appearing tumor and to search carefully for any associated foraminal changes in the skull base. Acoustic schwannomas account for 95% of all intracranial schwannomas, and trigeminal schwannomas are in a distant second place.[130, 192]

Trigeminal schwannomas may arise intradurally from the nerve root in the CPA and Meckel's cave or extradurally from the gasserian ganglion in the middle cranial fossa.[193–196] They also may involve both the posterior and the middle fossa (Figs. 25-28 and 25-29).[193, 195–197] The tumor is centered anteromedial to the IAC, and careful study often shows that a portion of the tumor extends through the porus trigeminus into Meckel's cave.[20, 195] The foramen ovale or the foramen rotundum also may be enlarged. Compared with acoustic schwannomas, trigeminal schwannomas are more likely to contain cystic components and are

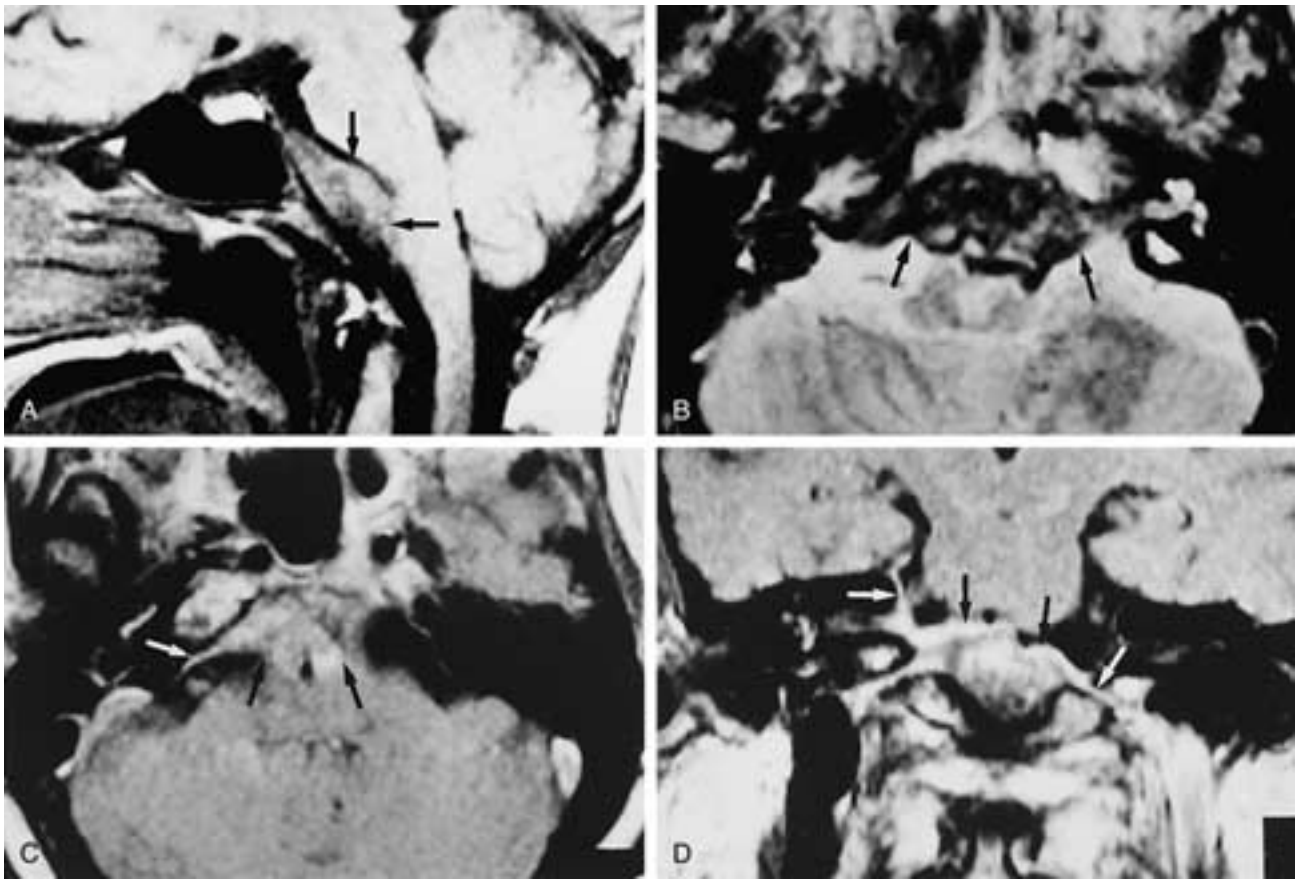

FIGURE 25-19 Idiopathic hypertrophic pachymeningitis. **A**, Sagittal T1-weighted image. **B**, T2-weighted image. **C**, Gadolinium T1-weighted image. **D**, Coronal gadolinium T1-weighted image. The mass (*black arrows*) is extraaxial and dural-based on the clivus and posterior petrous surface. It is slightly inhomogeneous and hypointense on T1-weighted images (**A**) and inhomogeneous in intensity on T2-weighted images (**B**), with mild inhomogeneous enhancement after contrast administration (**C** and **D**), except for dural tails (*white arrow*), where enhancement is more intense. The patient is a 50-year-old woman who was found to have a rubbery, hypovascular prepontine mass on transtemporal exploration, and had well-formed granulomas and chronic inflammation on histopathologic examination. No organisms were found on stains and cultures. (Courtesy of Dr. Robert K. Jackler.) (From Jackler RK, Brackmann DE, eds. Neurotology. St. Louis: Mosby-Year Book, 1994.)

VIEW IMAGE

Copyright © 2003, Mosby, Inc. All rights reserved.

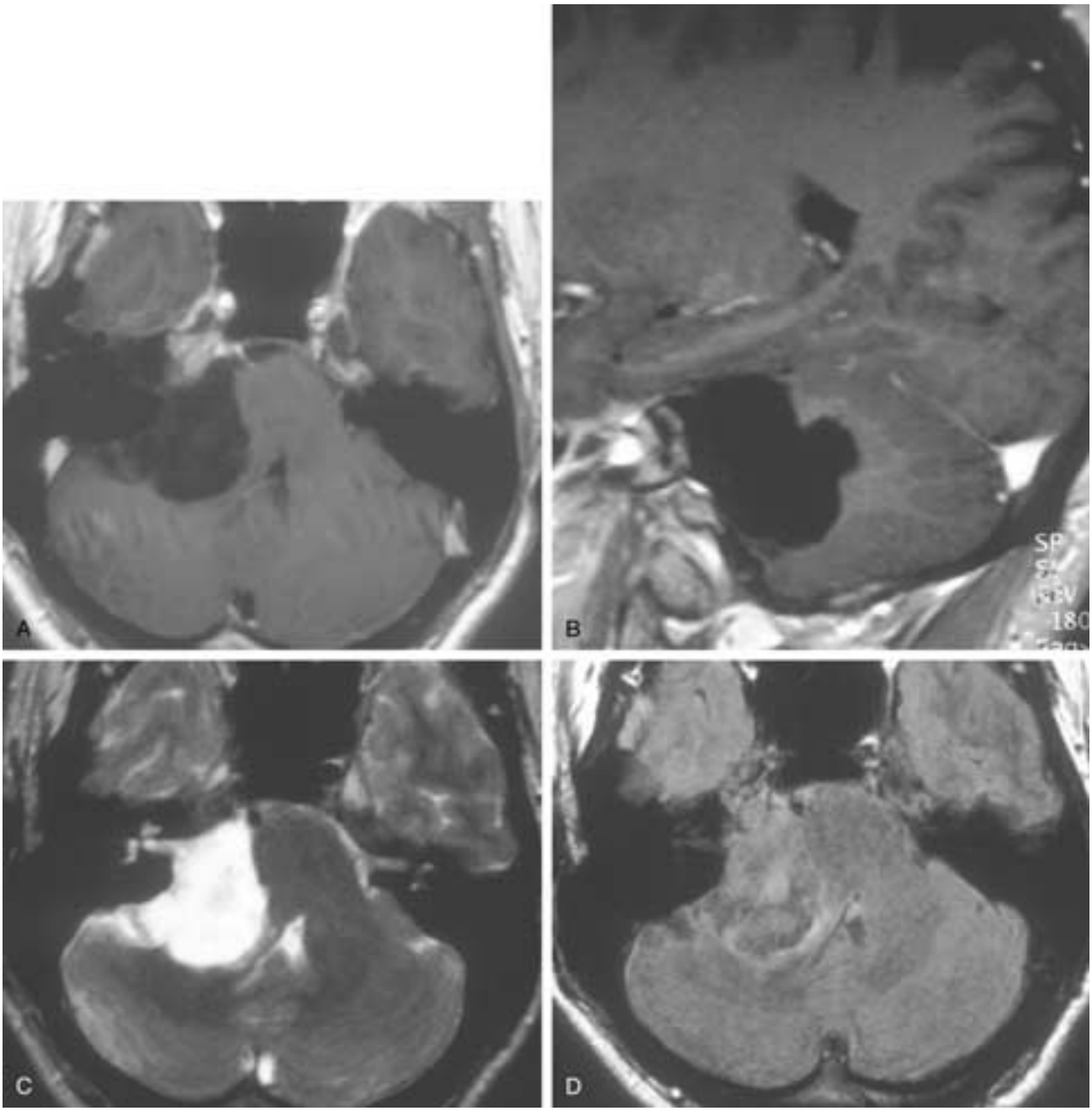

VIEW IMAGE

FIGURE 25-20 CPA epidermoid. **A** and **B**, T1-weighted axial and sagittal images after gadolinium administration. The CPA mass extending to the prepontine cistern is isointense to CSF and shows no enhancement. **C**, T2-weighted image. The tumor, with irregular, cauliflower-like margins, is isointense to CSF, as in T1-weighted images, and is compressing the fourth ventricle. The IAC is normal. **D**, FLAIR image. In this sequence the epidermoid has heterogeneous hyperintense foci, enabling differentiation of an epidermoid from an arachnoid cyst in this case.

thus more varied in appearance (Fig. 25-29).[20, 197] On CT they may be isodense or slightly hypodense or show mixed iso-hypodensity. They exhibit well-circumscribed enhancement that may or may not be homogeneous.[197] On MR imaging, their signal intensities are similar to those of acoustic schwannomas.[9, 194, 197] In most cases they are better localized and characterized on MR imaging than on CT.[9]

Facial nerve schwannomas are rare tumors that may arise from any segment of the facial nerve. When arising in the CPA or the IAC, they usually first cause sensorineural hearing loss rather than facial palsy, and thus may be both clinically and radiologically indistinguishable from acoustic schwannomas (Figs. 25-30 to 25-32).[198–200]

Similarly, glossopharyngeal, vagus, and spinal accessory schwannomas cause specific neural deficits only when they occur within the jugular foramen (Figs. 25-33 and 25-34).[201, 202] When arising within the posterior fossa, they may attain considerable size and first appear instead with

Copyright © 2003, Mosby, Inc. All rights reserved.

predominantly acoustic or cerebellar signs and symptoms.[202, 203] Hence they also should be considered in the differential diagnosis of acoustic schwannomas. Foraminal widening, if present, aids immensely in the diagnosis.[203] A correct preoperative diagnosis averts the use of the translabyrinthine approach, which would destroy residual hearing.[204]

Vascular Lesions

Vascular lesions of the CPA are rare, but a number of them may clinically mimic neoplasms and thus assume differential diagnostic importance on CT and MR imaging. Vertebrobasilar dolichoectasia (VDB), or elongation and dilatation of the vertebrobasilar artery, is probably the most common vascular lesion associated with compressive symptoms of the posterior fossa cranial nerves. Elongation of the basilar artery is considered present if any portion of it extends lateral to the margin of the clivus or the dorsum sellae or if the artery bifurcates above the plane of the suprasellar cistern (Figs. 25-35 and 25-36). Ectasia is diagnosed if the diameter of the basilar artery is greater than 4.5 mm on CT.[205] If angiography is necessary in a patient with a basilar artery more than 1.5 cm in diameter, a nonselective digital subtraction study is advised.[206] The larger volume of the vessel prevents adequate washout of the contrast, and stagnation can occur with layering along the posterior wall of the vessel. The contrast may cover the exit points of small arteries supplying the pons and limit flow to these important vessels. An infarct can result.

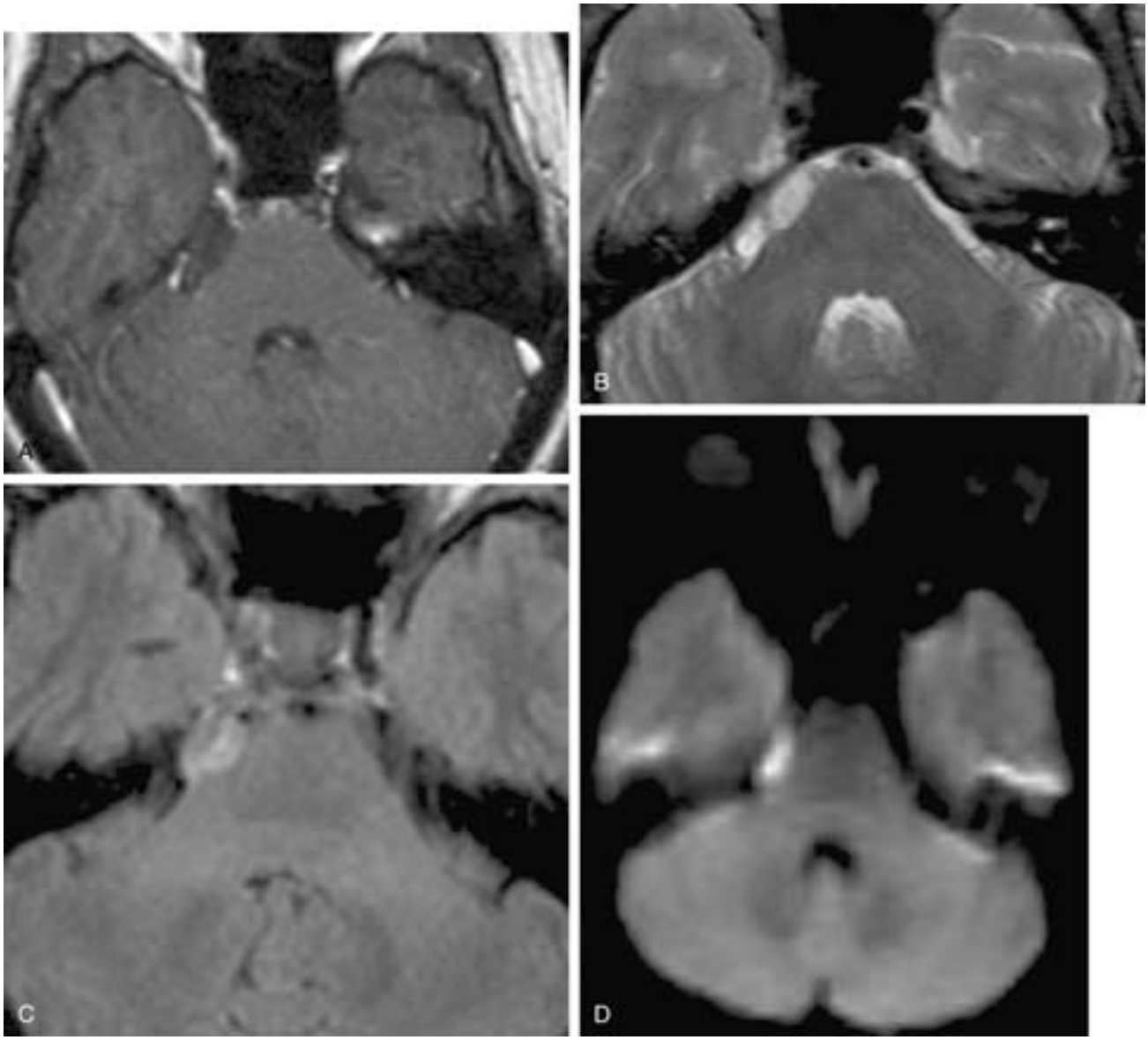

VIEW IMAGE

FIGURE 25-21 Epidermoid. **A** and **B**, T1-weighted postgadolinium and T2-weighted images. A small mass is seen adjacent and anterior to the right fifth nerve. The lesion is isointense to CSF in spin echo sequences and does not enhance. **C**, FLAIR image shows hyperintensity relative to CSF. **D**, Diffusion-weighted image. The epidermoid has hyperintense signal due to restricted proton motion, differentiating it from an arachnoid cyst.

Copyright © 2003, Mosby, Inc. All rights reserved.

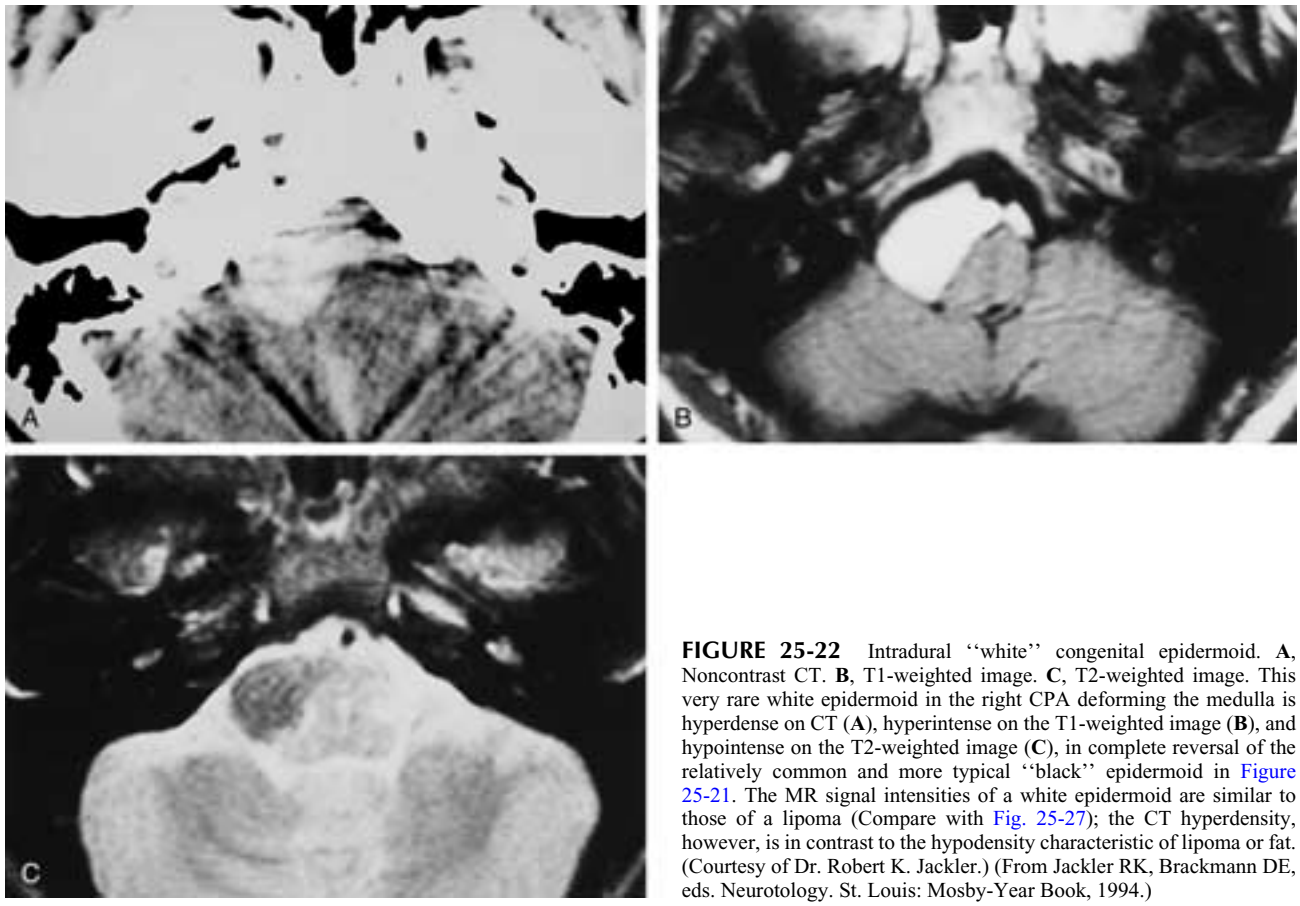

FIGURE 25-22 Intradural ''white'' congenital epidermoid. **A**, Noncontrast CT. **B**, T1-weighted image. **C**, T2-weighted image. This very rare white epidermoid in the right CPA deforming the medulla is hyperdense on CT (**A**), hyperintense on the T1-weighted image (**B**), and hypointense on the T2-weighted image (**C**), in complete reversal of the relatively common and more typical ''black'' epidermoid in Figure 25-21. The MR signal intensities of a white epidermoid are similar to those of a lipoma (Compare with Fig. 25-27); the CT hyperdensity, however, is in contrast to the hypodensity characteristic of lipoma or fat. (Courtesy of Dr. Robert K. Jackler.) (From Jackler RK, Brackmann DE, eds. Neurotology. St. Louis: Mosby-Year Book, 1994.)

VIEW IMAGE

The vertebrobasilar artery is superbly demonstrated on MR imaging by its signal void, and magnetic resonance angiography (MRA) gives an even more graphic depiction (Fig. 25-37). However, the CSF flow phenomenon may mimic a basilar artery aneurysm, and a thrombosed or partially thrombosed dolichoectatic basilar artery may simulate an extraaxial tumor.[207, 208]

The most common symptoms reported are those associated with the facial nerve, such as hemifacial spasm and facial paresis.[206, 209] The second most common symptom is trigeminal neuralgia.[206] Other cranial nerves that have been affected include the oculomotor, abducens, acoustic, glossopharyngeal, and vagus.[206, 210, 211] Disabling positional vertigo resulting from vascular compression of the acoustic nerve has been described in a series of patients without specific reference to VBD.[212]

Patients with VBD may or may not be symptomatic, but the incidence of symptoms does appear to correlate with the degree of tortuosity.[213, 214] In general, symptomatic patients with elongated but undilated vertebrobasilar arteries are much more likely to have single cranial nerve involvement (Figs. 25-35, 25-37); those with elongated and dilated arteries are much more likely to have combinations of multiple compressive cranial nerve deficits, compressive and ischemic central nervous system deficits, and hydrocephalus (Fig. 25-36).[206] The compressive symptoms can in some cases be relieved by microvascular decompression.[215–217] Preoperative angiography may be of predictive value, but because of its invasive nature it has generally been replaced by MR imaging or MRA.[218–220] Neurovascular conflict imaging protocols have evolved and include high-resolution 3D time-of-flight (TOF), 3D-CISS, and T2-weighted sequences. These volume-acquired sequences allow for reconstructions and reformation in multiple planes and facilitate identification of nerve vessel conflicts in most cases.[221–227]

Vascular loop, a loop of the AICA, has been implicated in acoustic nerve symptoms, in particular, vertigo.[210, 212, 228] On its normal course from the basilar artery to the cerebellum, the AICA forms a loop under, over, or between the facial and acoustic nerves as it gives rise to the auditory artery.[229] The loop may be located in the cistern or at the porus, or it may be found, in up to 19% by microdissection and in 22% by gas-CT cisternography, in the IAC.[229, 230] Thus the mere finding of an AICA loop, intracanalicular or otherwise, does not establish it as the cause of symptoms. Furthermore, vascular compression of a nerve, even to the point of grooving it, may fail to cause symptoms in some patients.[231] To produce symptoms, the cross-compression may have to coincide with the glial–Schwann cell junction.[229] Thin-section T2-weighted (Fig. 25-38) and CISS images have proven to be very sensitive and are utilized as a noninvasive replacement for gas-CT cisternography.[221–227, 232]

Berry aneurysms of the AICA are quite rare, representing less than 1% of intracranial aneurysms (Fig. 25-39).[233] They have often carried a preoperative diagnosis of acoustic tumor, and of 22 reported patients, 16 had acoustic and 14

Copyright © 2003, Mosby, Inc. All rights reserved.

had facial nerve signs and symptoms, and 14 had subarachnoid hemorrhage.[233] Dense homogeneous enhancement may be a clue, and dynamic CT may contribute by showing rapid opacification. MR imaging is diagnostic if a signal void from rapidly flowing blood is demonstrated in the aneurysm. MRA may be useful, but angiography is definitive.

Giant aneurysms are those exceeding 2.5 cm in diameter (Fig. 25-40).[20] They may originate from the vertebrobasilar artery or from one of its branches and extend into the CPA as a mass lesion. They rarely cause subarachnoid hemorrhage, and most commonly they are partially thrombosed.[20, 234] On CT a partially thrombosed aneurysm shows an enhancing rim with an isodense, nonenhancing mural thrombus and an enhancing lumen. A calcific rim may be present. A nonthrombosed aneurysm shows homogeneous enhancement, and a thrombosed one shows an enhancing rim with an isodense, nonenhancing center.[20] MR imaging demonstrates a flow void in the patent lumen, laminated thrombus of varying signal intensities, and sometimes a low signal intensity rim.[235–237]

Superficial siderosis (SS) of the acoustic nerves, or pial siderosis, is not a vascular lesion per se but instead is the result of chronic capillary or venous subarachnoid hemorrhage such as may be caused by an ependymoma.[238, 239] It is a long-recognized, rare pathologic entity, the antemortem noninvasive diagnosis of which has become possible with the advent of high-field MR imaging (Fig. 25-41).[238, 239] It consists of intracellular and extracellular deposition of hemosiderin in the leptomeninges, subpial tissue, spinal cord, and cranial nerves. The acoustic nerve, with its long glial-lined segment, is especially vulnerable to the toxic effects of hemoglobin and hemosiderin deposition. The clinical findings include hearing loss, cerebellar dysfunction, pyramidal tract signs, and, at times, progressive mental deterioration. The CSF is xanthochromic and rich in protein.

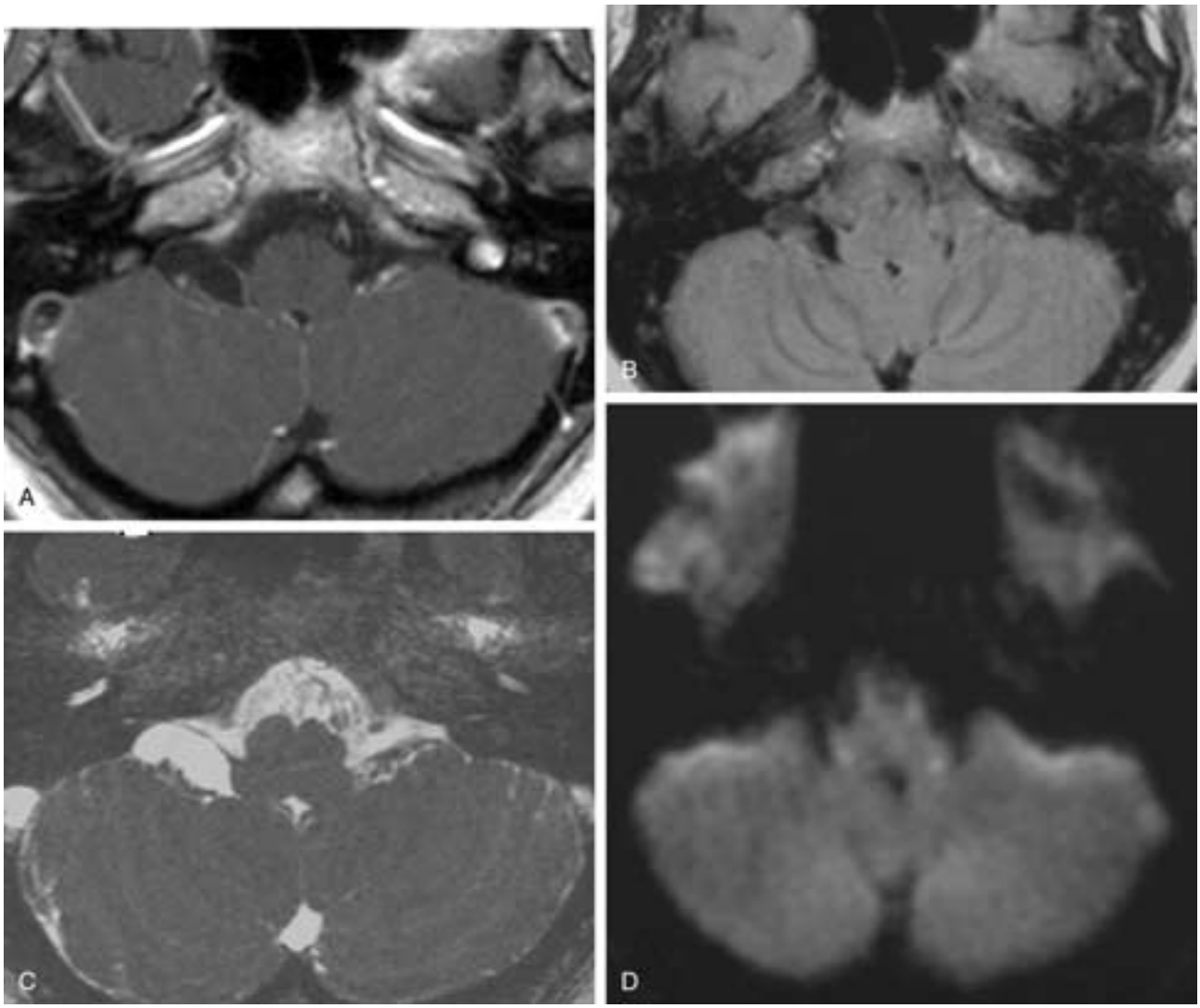

VIEW IMAGE

FIGURE 25-23 CPA arachnoid cyst. **A**, T1-weighted postgadolinium image. **B**, Proton density image and **C**, T2-weighted image. There is a cyst in the right CPA with a moderate mass effect on cranial nerve IX and the cerebellum. The nonenhancing cyst has a smooth surface, its signal tracking with CSF. **D**, Diffusion-weighted image. The low signal intensity of the cyst, similar to that of CSF, confirms the pure fluid contents, differentiating it from epidermoid.

Copyright © 2003, Mosby, Inc. All rights reserved.

VIEW IMAGE

FIGURE 25-24 CPA arachnoid cyst. **A**, T1-weighted image. **B**, T2-weighted image. **C** and **D**, T1-weighted coronal and axial images, respectively. The cyst is isointense to CSF on all sequences. It is homogeneous, with a smooth surface that can be helpful in differentiating it from an epidermoid.

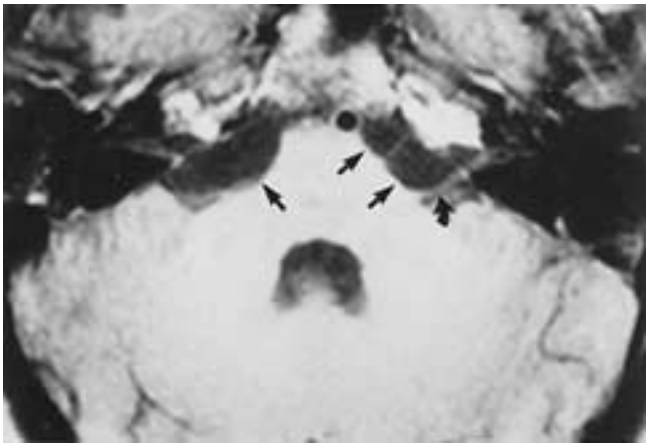

FIGURE 25-25 CPA cysticercal cysts, T1-weighted image. Bilateral cisternal cysts (*arrows*) isointense with CSF indent the pons and slightly bow the left facioacoustic nerves (*curved arrow*). (From Jackler RK, Brackmann DE, eds. Neurotology. St. Louis: Mosby-Year Book, 1994.)

VIEW IMAGE

Copyright © 2003, Mosby, Inc. All rights reserved.

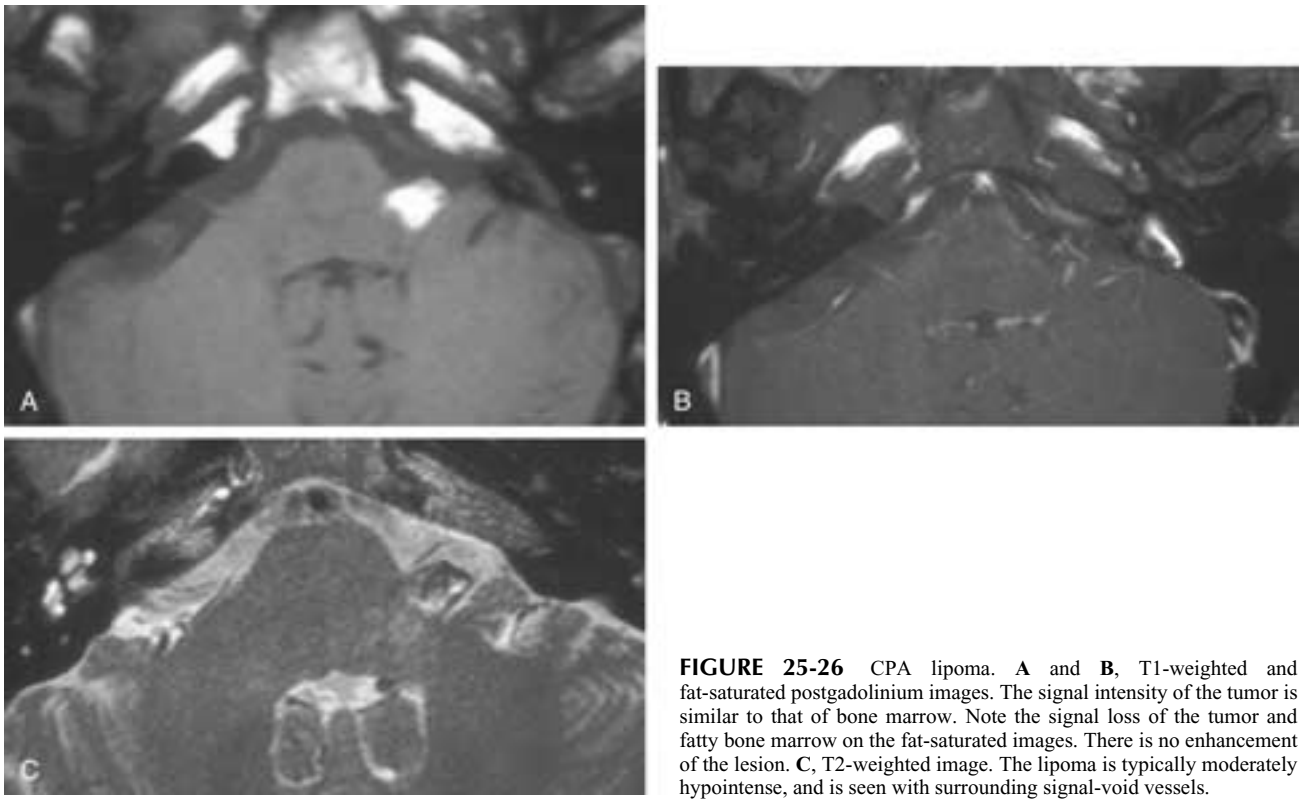

FIGURE 25-26 CPA lipoma. **A** and **B**, T1-weighted and fat-saturated postgadolinium images. The signal intensity of the tumor is similar to that of bone marrow. Note the signal loss of the tumor and fatty bone marrow on the fat-saturated images. There is no enhancement of the lesion. **C**, T2-weighted image. The lipoma is typically moderately hypointense, and is seen with surrounding signal-void vessels.

VIEW IMAGE

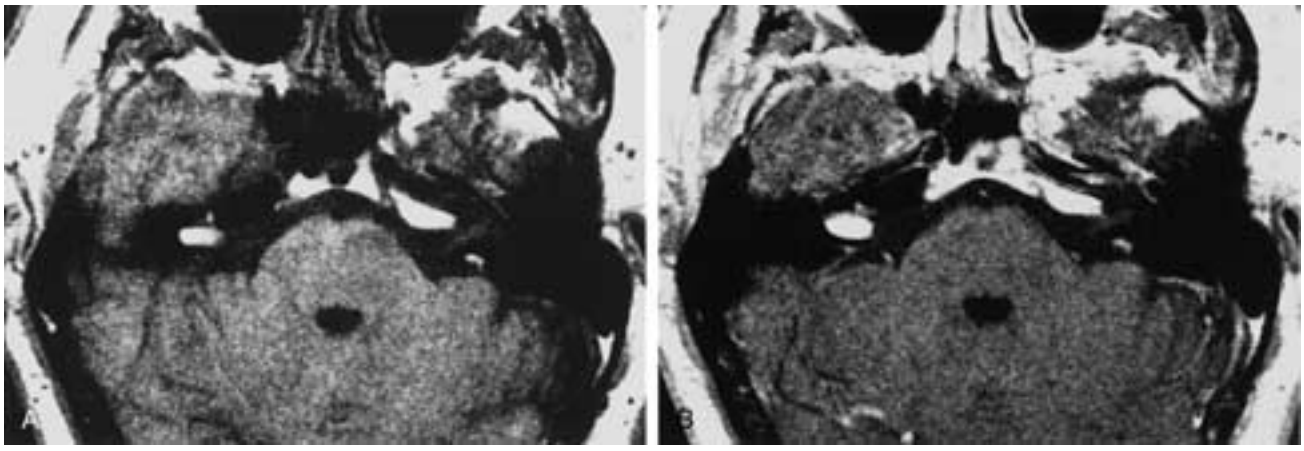

VIEW IMAGE

FIGURE 25-27 Lipoma of the right IAC. **A**, T1-weighted image without gadolinium enhancement. **B**, Gadolinium-enhanced T1-weighted image. The lipoma has high signal without gadolinium and does not change after contrast enhancement.

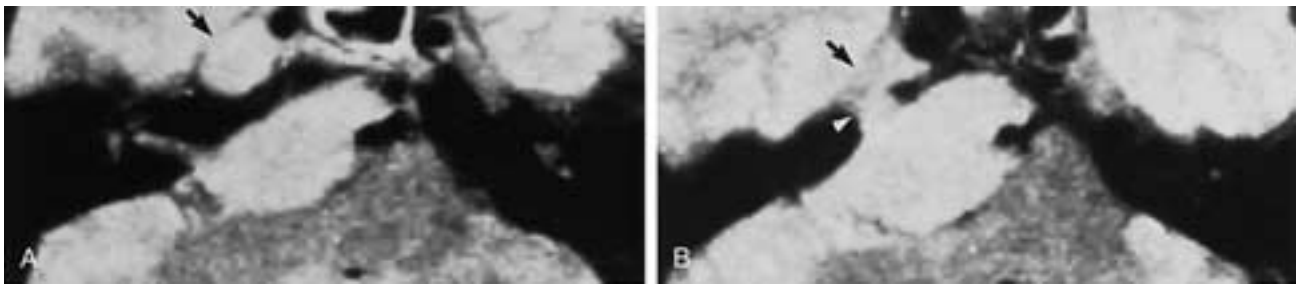

VIEW IMAGE

FIGURE 25-28 Bilobed trigeminal schwannoma. **A** and **B**, Proton density images. Tumor ''dumbbells'' from the posterior fossa through the porus trigeminus (*arrowhead*) into Meckel's cave (*arrow*). (Courtesy of Dr. Jerald V. Robinson.)

Copyright © 2003, Mosby, Inc. All rights reserved.

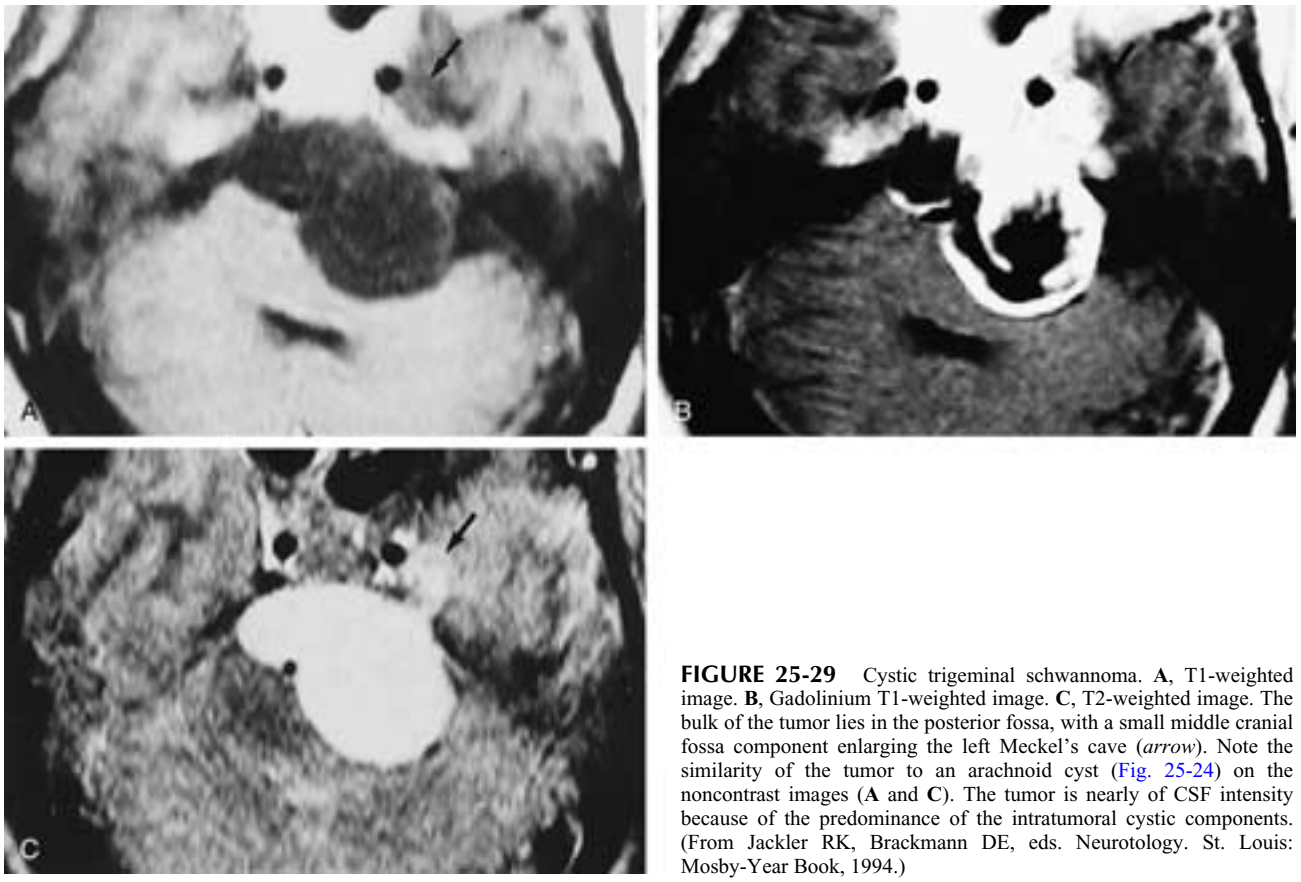

FIGURE 25-29 Cystic trigeminal schwannoma. **A**, T1-weighted image. **B**, Gadolinium T1-weighted image. **C**, T2-weighted image. The bulk of the tumor lies in the posterior fossa, with a small middle cranial fossa component enlarging the left Meckel's cave (*arrow*). Note the similarity of the tumor to an arachnoid cyst (Fig. 25-24) on the noncontrast images (**A** and **C**). The tumor is nearly of CSF intensity because of the predominance of the intratumoral cystic components. (From Jackler RK, Brackmann DE, eds. Neurotology. St. Louis: Mosby-Year Book, 1994.)

VIEW IMAGE

On high-field MR imaging, the T2-weighted images show marked hypointensity of the pial and arachnoid membranes and the acoustic nerves (Fig. 25-41).[240]

A hemangioma or vascular malformation of the acoustic or facial nerves appears as an intracanalicular tumor. Some may contain intratumoral bone spicules best seen on high-resolution CT with bone algorithm (Figs. 25-42 and 25-43).[241] On MR imaging they tend to be more hyperintense on T2-weighted images than are acoustic schwannomas (Fig. 25-44), and they may invade the adjacent temporal bone.[241, 242]

Arteriovenous malformations (AVMs) in the CPA are exceedingly rare, but extracerebral AVMs, predisposed to subarachnoid bleeding, may occur in this location.[243] Dilated enhancing vessels may be seen on CT, and serpentine hypointense loops are found on MR imaging.[20] Angiography provides definitive visualization of the feeding arteries and draining veins. AVMs, which are congenital, should be distinguished from dural arteriovenous fistulas (DAVFs), which are acquired (Fig. 25-45).

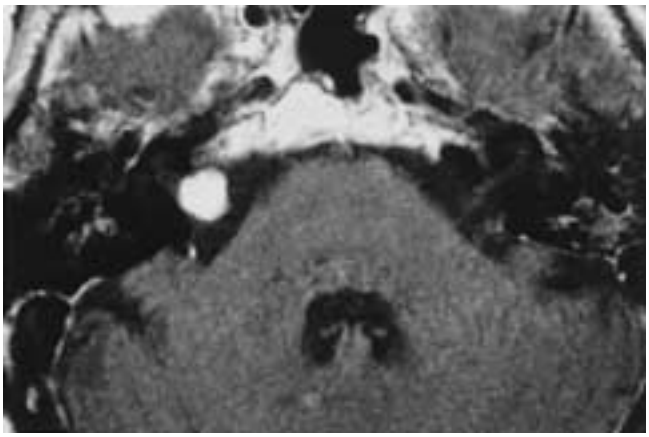

VIEW IMAGE

FIGURE 25-30 CPA facial schwannoma. Gadolinium T1-weighted image. This isointense, rounded, extraaxial tumor is centered at the porus acousticus. The lesion enhances intensely and is indistinguishable from acoustic schwannoma (Fig. 25-9). (From Jackler RK, Brackmann DE, eds. Neurotology. St. Louis: Mosby-Year Book, 1994.)

Petrous Bone Lesions

These are quite numerous and will be discussed in greater detail in a following section of this chapter. However, they should be considered in the differential diagnosis of CPA masses; for example, an exophytic growth from a chondrosarcoma may be mistaken for a meningioma (see Fig. 25-83).[244]

Paragangliomas

These tumors, discussed in greater detail in a following section, have a different presenting symptom complex and are not usually confused clinically with acoustic schwannomas. However, they may have intracranial extradural or

Copyright © 2003, Mosby, Inc. All rights reserved.

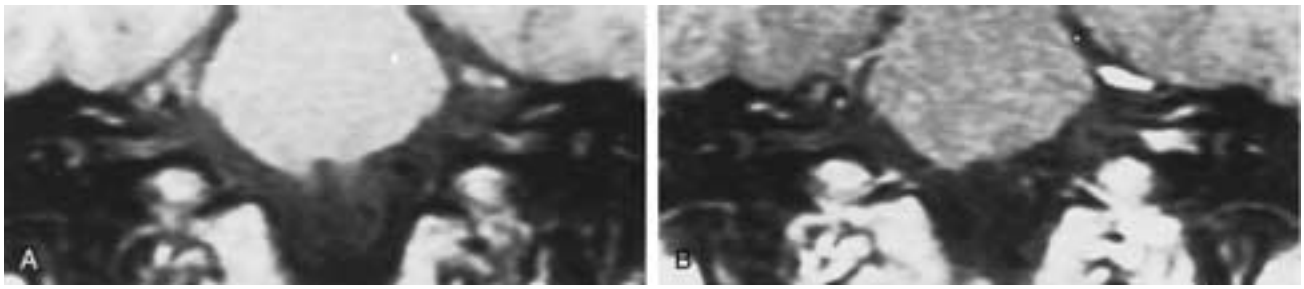

VIEW IMAGE

FIGURE 25-31 IAC facial schwannoma. **A** and **B**, Coronal pre- and postgadolinium T1-weighted images. The patient presented with progressive sensorineural hearing loss and no facial palsy. The 3 × 5 mm enhancing intracanalicular tumor is indistinguishable from an acoustic schwannoma. The tumor was exposed by the middle fossa approach but was not resected or biopsied. (Courtesy of Dr. Joseph R. Scalley and Mark R. Laussade.)

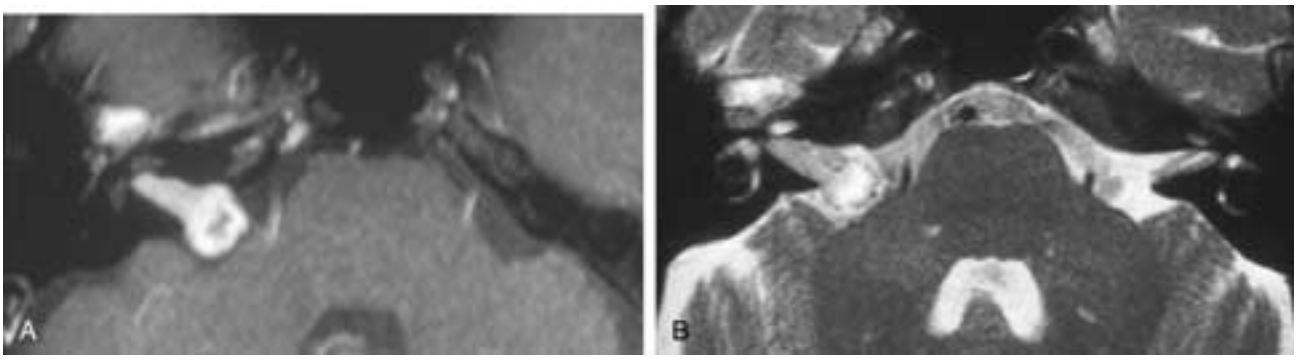

VIEW IMAGE

FIGURE 25-32 IAC facial schwannoma. **A** and **B**, postgadolinium T1-weighted and T2-weighted images. This patient presented with progressive sensorineural hearing loss and later developed facial palsy. The enhancing intracanalicular tumor is indistinguishable from an acoustic schwannoma. Note also the extension of the tumor to the geniculate ganglion.

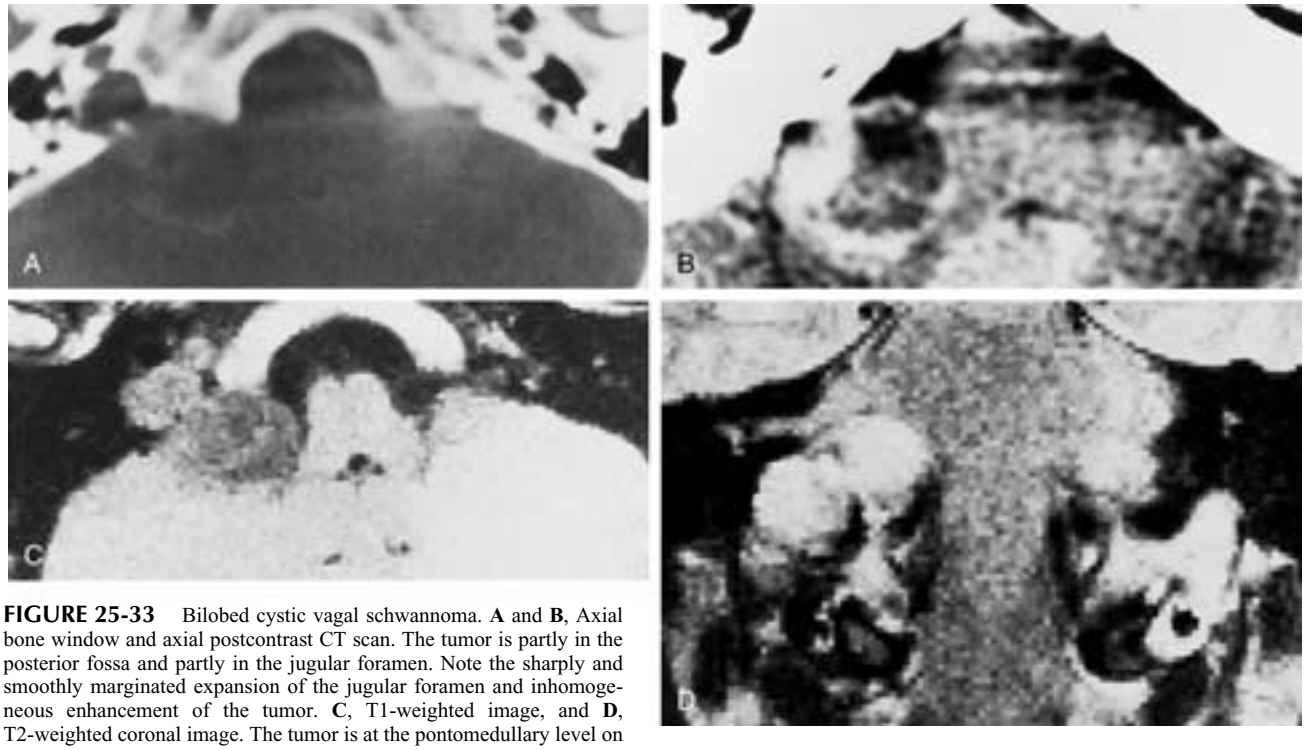

VIEW IMAGE

FIGURE 25-33 Bilobed cystic vagal schwannoma. **A** and **B**, Axial bone window and axial postcontrast CT scan. The tumor is partly in the posterior fossa and partly in the jugular foramen. Note the sharply and smoothly marginated expansion of the jugular foramen and inhomogeneous enhancement of the tumor. **C**, T1-weighted image, and **D**, T2-weighted coronal image. The tumor is at the pontomedullary level on the coronal image.

Copyright © 2003, Mosby, Inc. All rights reserved.

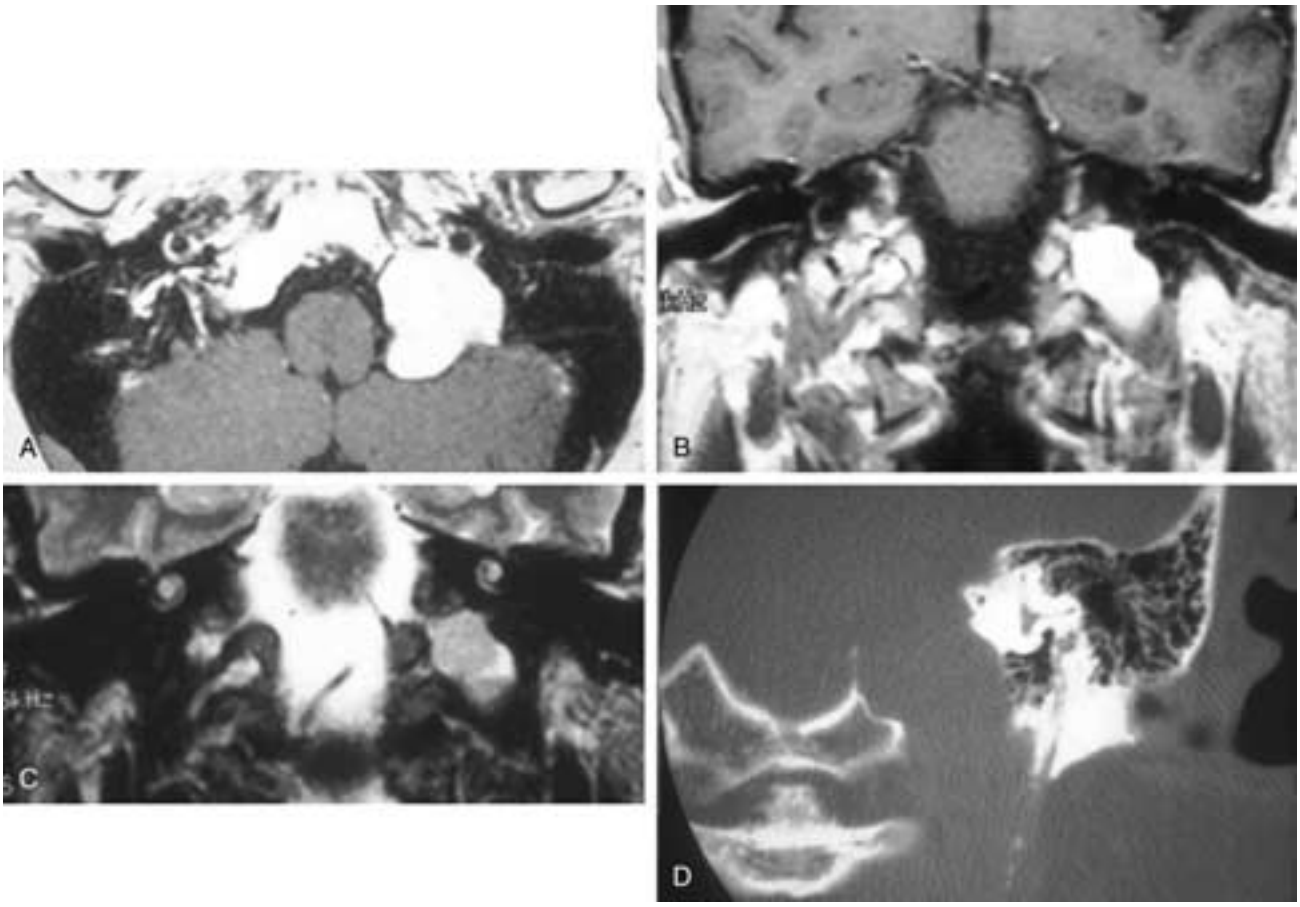

VIEW IMAGE

FIGURE 25-34 Jugular foramen schwannoma. **A** and **B**, Axial and coronal T1-weighted postgadolinium images. The large tumor in the left jugular fossa is extending inferiorly. It shows avid enhancement. **C**, T2-weighted coronal image depicts the extracranial portion of the tumor, which is hyperintense to gray matter. **D**, CT bone windows, coronal image. Expansion of the jugular foramen is symmetric, and the margins are well defined. (Contrast with Figs. 25-66, 25-67, 25-68, and 25-69.)

transdural extensions in the posterior fossa, which on CT or MR imaging mimic schwannomas or meningiomas. Identifying their precise location and associated bone changes should help avoid misdiagnoses.

Intraaxial Tumors

A detailed description of these and other primary lesions of the brain is beyond the scope of this section. Some intraaxial tumors occasionally occur in the CPA and must be considered in the differential diagnosis. Intraaxial posterior fossa tumors may arise from the brainstem, the cerebellum, or the fourth ventricle. Tumors of the brainstem include those from the medulla, the pons, the midbrain, and the cerebellar peduncles, and they are mainly astrocytomas occurring in children or young adults (Fig. 25-46).[245–247] On CT they are isodense or hypodense, and on MR they are hypointense on T1-weighted images and hyperintense on T2-weighted images.[246] They show little enhancement.[126] The brainstem is usually enlarged, the fourth ventricle is posteriorly displaced, and there may be exophytic growth extending into the cistern.[245] The diffuse fibrillary high-grade astrocytomas carry a poor prognosis, and the smaller and more localized pilocystic astrocytomas carry a better prognosis.[246]

Tumors of the cerebellum may arise from the vermis or the hemisphere. Vermian tumors, principally medulloblastomas (an embryonal tumor) in childhood, rarely may extend to the CPA. They are hyperdense and enhancing. Hemispheric tumors are most commonly hemangioblastomas and

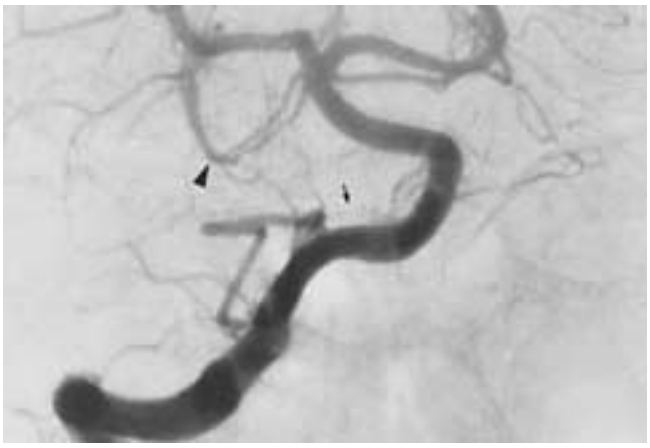

FIGURE 25-35 VBD. Selective vertebral angiogram. The superior cerebellar (*arrowhead*) and anteroinferior cerebellar (*arrow*) arteries are also tortuous.

VIEW IMAGE

Copyright © 2003, Mosby, Inc. All rights reserved.

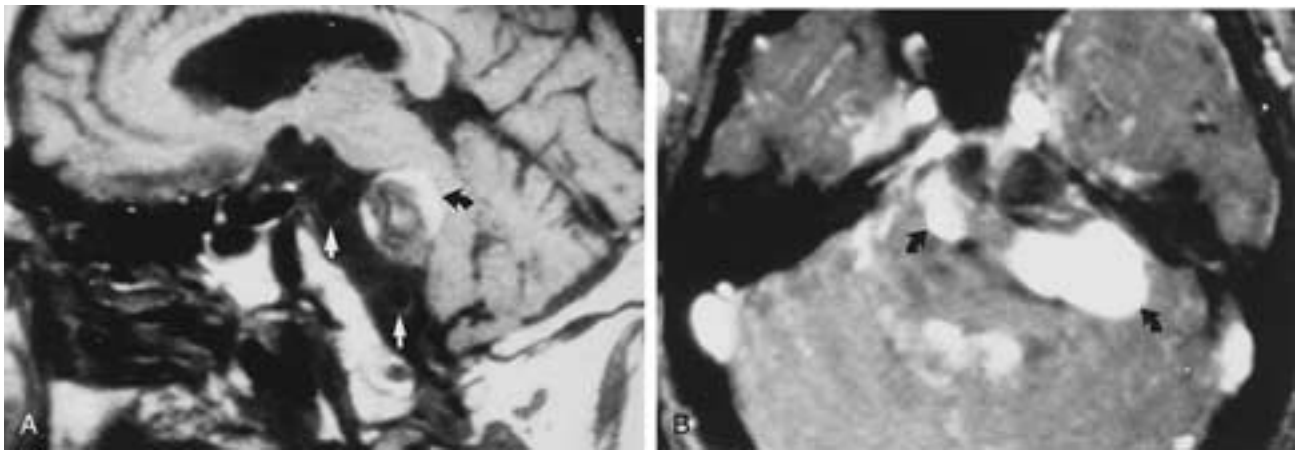

VIEW IMAGE

FIGURE 25-36 VDB. **A**, Sagittal T1-weighted image. The dilated, tortuous basilar artery (*curved arrow*) shows peripheral laminar hyperintensity caused by very slow flow or thrombi and central moderate intensities resulting from moderately slow flow within the patent lumen. A normal flow void is seen in the undilated proximal and distal arteries (*straight arrows*). **B**, Gradient-echo image. Flowing blood appears hyperintense on such images. The basilar artery (*curved arrows*) shows marked fusiform dilatation and marked tortuosity. Signal intensities in such dilated arteries are often complex because of the presence of thrombi of varying age and flow of varying velocity. Similarly complex intensity patterns also may be found in giant aneurysms, although the latter lesions are rounded or ovoid rather than fusiform. (Courtesy of Dr. William P. Dillon.) (From Jackler RK, Brackmann DE, eds. Neurotology. St. Louis: Mosby-Year Book, 1994.)

metastases in adults and astrocytomas in young adults or children. All three lesions may be either enhancing solid masses or cystic masses with solid components. Hemangioblastomas may be multiple and associated with von Hippel-Lindau disease. Their solid components are characteristically hypervascular on angiography or MR imaging.[248, 249]

From the fourth ventricle arise the ependymoma and choroid plexus papilloma (Figs. 25-47 to 25-49). They may cause CPA symptoms when growing through the foramen of Luschka.[250–254] Naidich et al. found extension to the CPA in 7 of 12 ependymomas, 2 of 6 in a group of medulloblastomas and a cerebellar sarcoma, 1 of 23 astrocytomas, and 1 of 8 hemangioblastomas.[128]

Ependymomas tend to calcify. The calcified portions are variable in density and enhancement.[126] Papillomas are well-defined lesions, slightly hyperdense, and moderately enhancing.[126] Both tumors are nearly isointense to brain on T1-weighted images and mildly hyperintense on T2-weighted images (Figs. 25-47 and 25-49).[252–255] The intraaxial tumors are generally nearly isointense on T1-weighted images and hyperintense on T2-weighted images, and except for any calcifications, they are better demonstrated on MR imaging than on CT.[256, 257] Lym-

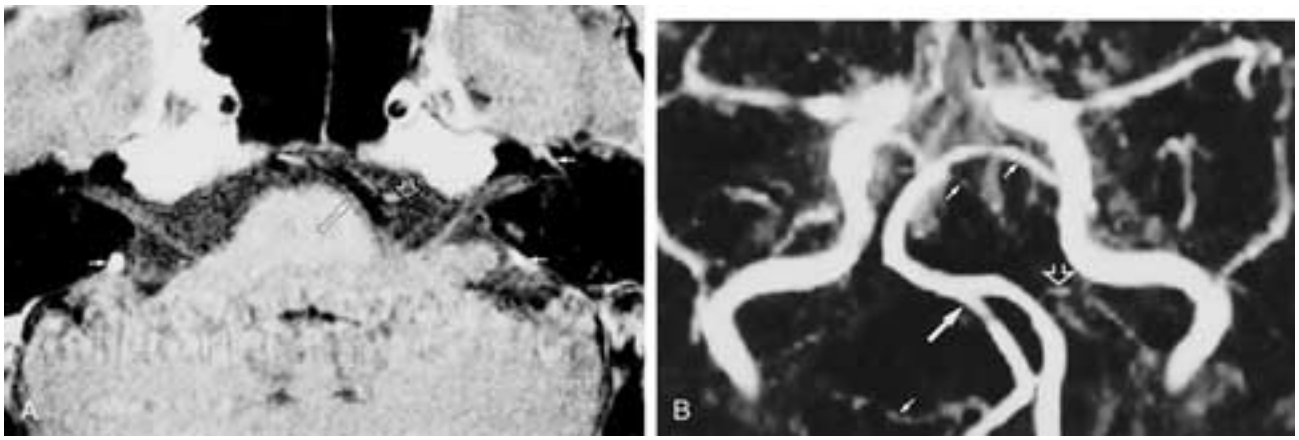

VIEW IMAGE

FIGURE 25-37 VBD. **A**, Axial gadolinium T1-weighted image. The tortuous left vertebrobasilar artery (*arrow*) crosses from left to right anterior to the pons. The small arterial branch (*open arrow*) coursing toward the left CPA probably represents the left AICA. Note the normal enhancement of the geniculate ganglion and proximal tympanic facial nerve and posterior fossa veins (*small arrows*). Serration across the cerebellum between the sigmoid sinuses is caused by pulsating flow of blood in the sigmoid sinuses. **B**, Coronal MRA, 3D TOF technique, maximum intensity projection. Same vertebrobasilar artery (*arrow*) and probable left AICA (*open arrow*) as in **A**. Superior cerebellar, posterior cerebral, and right posteroinferior cerebellar arteries (*small arrows*) also are seen. No contrast injection is necessary for MRA. (From Jackler RK, Brackmann DE, eds. Neurotology. St. Louis: Mosby-Year Book, 1994.)

Copyright © 2003, Mosby, Inc. All rights reserved.

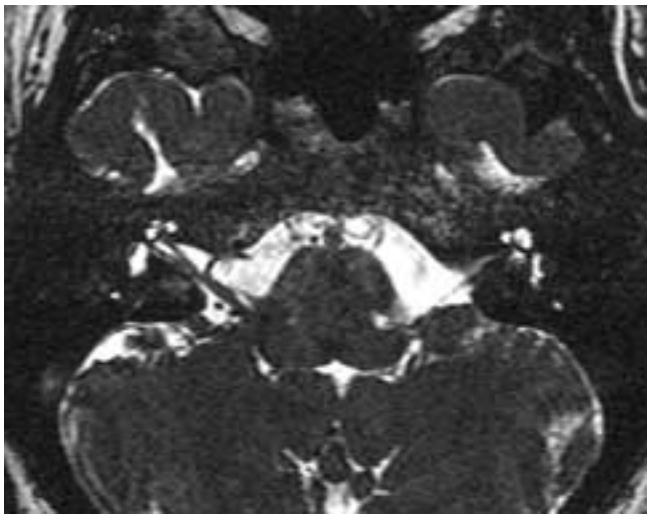

FIGURE 25-38 AICA loops. CISS image.

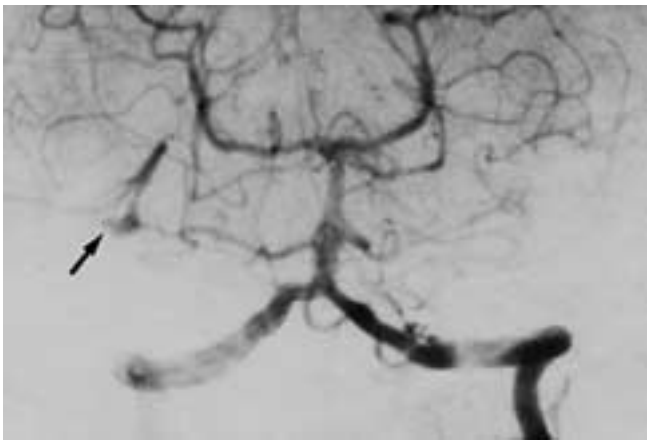

FIGURE 25-39 AICA berry aneurysm. Selective vertebral angiogram. The patient had subarachnoid hemorrhage and hearing loss. The aneurysm (*arrow*) shows a nipple-like configuration suggestive of recent bleeding. (From Jackler RK, Brackmann DE, eds. Neurotology. St. Louis: Mosby-Year Book, 1994.)

phoma, much more common in the 1990s in both immunosuppressed and immunocompetent patients, also may occur in the CPA (Fig. 25-50).[150, 258–260] Nonneoplastic brain lesions such as multiple sclerosis (Fig. 25-51) and infarct (Fig. 25-52), of course, may be occasionally encountered in the investigation of CPA symptoms. Primitive neuroepithelial tumors (PNETs) can be seen in the CPA and should be part of the differential diagnosis. These are densely cellular tumors with imaging characteristics similar to those of PNETs in other sites. They exhibit hypointense signal on T1-weighted images and iso- to hypointense signal on T2-weighted images with moderately intense heterogeneous contrast enhancement (Fig. 25-53).[261]

FIGURE 25-40 Giant AICA aneurysm. **A**, T1-weighted image. Large aneurysm with mixed signal from turbulent flow in the vortex. Note the mural thrombus, seen as a layer of high signal clot. **B**, T2-weighted image. Well-demarcated, round, hypointense mass with surrounding edema. **C**, Selective vertebral angiogram. Broad-necked giant aneurysm of the AICA basilar artery junction.

Copyright © 2003, Mosby, Inc. All rights reserved.

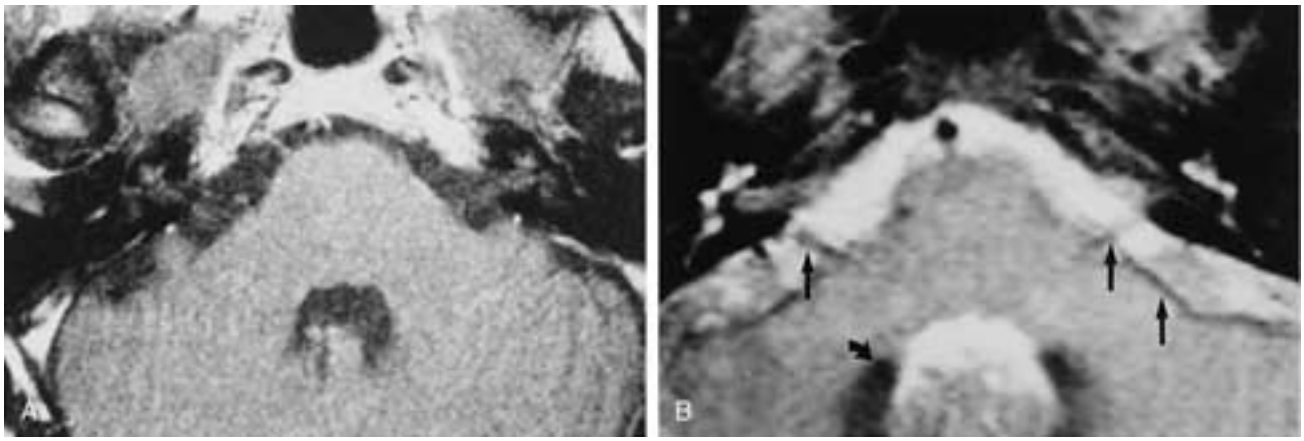

VIEW IMAGE

FIGURE 25-41 Superficial siderosis. The patient had bilateral progressive sensorineural hearing loss several years after surgical resection of a left inferior frontal AVM. **A**, T1-weighted image. No abnormality is apparent. **B**, T2-weighted image. A thin layer of hypointensity from pial and subpial deposition of hemosiderin is visible on the pons, cerebellum, and acoustic nerves (*arrows*). A thin layer of hypointensity is also present on the inferior surfaces of the cerebral hemisphere (not illustrated). Hypointensity of the dentate nuclei (*curved arrow*) may be physiologic. (From Jackler RK, Brackmann DE, eds. Neurotology. St. Louis: Mosby-Year Book, 1994.)

Intracanalicular Lesions

The differential diagnoses of intracanalicular lesions differ slightly from those of CPA masses (Box 25-1) as follows:

1. Acoustic schwannomas are by far the most common lesions, representing over 90% of the intracanalicular lesions (Figs. 25-3 and 25-4).[36, 105]
2. Facial schwannomas (Fig. 25-31) are often clinically and radiologically identical to acoustic schwannomas, and they may extend into the labyrinthine facial nerve canal.[200, 262]
3. Meningiomas are often cited but seldom are fully documented.[263] An intracanalicular meningioma may be indistinguishable from a schwannoma unless accompanied by hyperostosis or a dural tail.
4. Intracanalicular vascular tumors tend to cause a greater degree of nerve deficits and more commonly result in facial nerve symptoms than do acoustic schwannomas of comparable size.[264, 265] Some of them contain intratumoral bone spicules discernible on high-resolution CT with a bone algorithm (Figs. 25-42 and 25-43). On MR imaging they tend to be slightly more hyperintense than the typical schwannoma (Fig. 25-44), and they may invade the adjacent petrous bone.[241, 242]
5. Intracanalicular metastases are rare but may be suspected from a short duration of symptoms, facial weakness, a known history of malignancy, and a rapid growth rate on serial studies (Figs. 25-18, 25-54 and 25-55).[266–268] They may be bilateral.[268]
6. Lipomas show fatty CT density and MR intensities (Figs. 25-26, 25-27) and may be confirmed by fat suppression techniques.[189, 190, 269]
7. Lymphomas may be neural or leptomeningeal, primary (Fig. 25-56) or systemic (Fig. 25-57).[259]
8. Osteoma (Fig. 25-58).
9. Melanoma, typically hyperintense on T1-weighted images and hypointense on T2-weighted images when intraocular, may not follow such a pattern when intracranial (Figs. 25-17 and 25-55).[153, 270]
10. Glioma.[24, 39]

    Note: Melanoma and glioma are very rare IAC neoplasms.

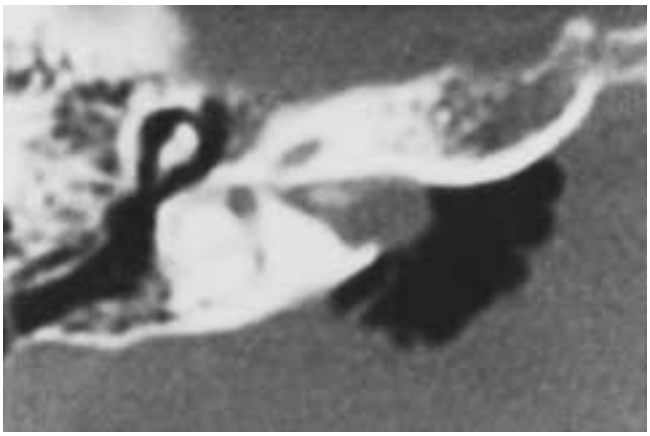

VIEW IMAGE

FIGURE 25-42 IAC vascular tumor. Gas CT cisternogram. Note the intratumoral bone spicule seen in some vascular tumors. (From Lo WWM, Horn HR, Carberry JN, et al. Intratemporal vascular tumors: evaluation with CT. Radiology 1986;159:181–185.)

Rarely, a hamartoma of the acoustic nerve has been found at autopsy or encountered in clinical practice.[271, 272] Other nonneoplastic conditions include (1) intracanalicular loop of the AICA (Fig. 25-38), (2) aneurysm arising from the AICA (Fig. 25-39), (3) arachnoid adhesions, (4) neuritis (Fig. 25-59), and (5) chronic inflammation (Fig. 25-60).[79, 191, 193–195, 234–237] Focal neuritis (Fig. 25-59) can have an appearance treacherously similar to that of an intracanalicular schwannoma (Fig. 25-3). A rare cause of nonneoplastic hypertrophic neuropathy, Dejerine-Sottas disease, can also result in thickening and abnormal contrast enhancement of multiple cranial nerves including the facial and vestibulocochlear nerves (Fig. 25-61).[273, 274]

Copyright © 2003, Mosby, Inc. All rights reserved.

FIGURE 25-43 IAC hemangioma. **A**, T1-weighted image. **B**, Gadolinium T1-weighted image. **C**, T2-weighted image. **D** and **E**, CT. The tumor (*white arrow*) extending slightly anteroinferiorly beyond the IAC is nearly isointense on the T1-weighted image (**A**), strongly enhancing after contrast administration (**B**), and hyperintense on the T2-weighted image (**C**), similar to schwannomas. CT reveals the characteristic intratumoral bone spicule (*black arrow*) in **D**. **E** shows ''honeycomb'' bone (*black arrow*) in the IAC. (Courtesy of Dr. Malcolm D. Graham.) (From Jackler RK, Brackmann DE, eds. Neurotology. St. Louis: Mosby-Year Book, 1994.)

VIEW IMAGE

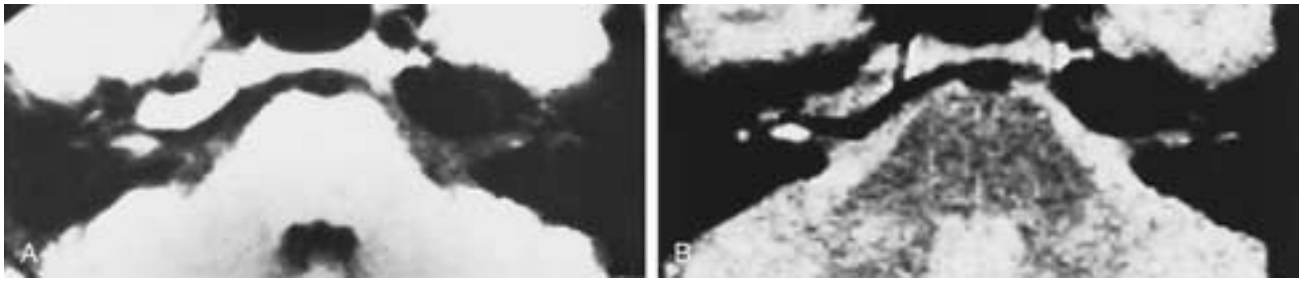

FIGURE 25-44 IAC, intratemporal vascular tumor. **A** and **B**, T1-weighted and T2-weighted images, respectively. The tumor is more hyperintense on T2-weighted images than is the typical schwannoma. (Courtesy of Dr. Michael Anselmo.) (**B** From Lo WWM, Shelton C, Waluch V, et al. Intratemporal vascular tumors: detection with CT and MR. Radiology 1989;171:443–448.)

VIEW IMAGE

Copyright © 2003, Mosby, Inc. All rights reserved.

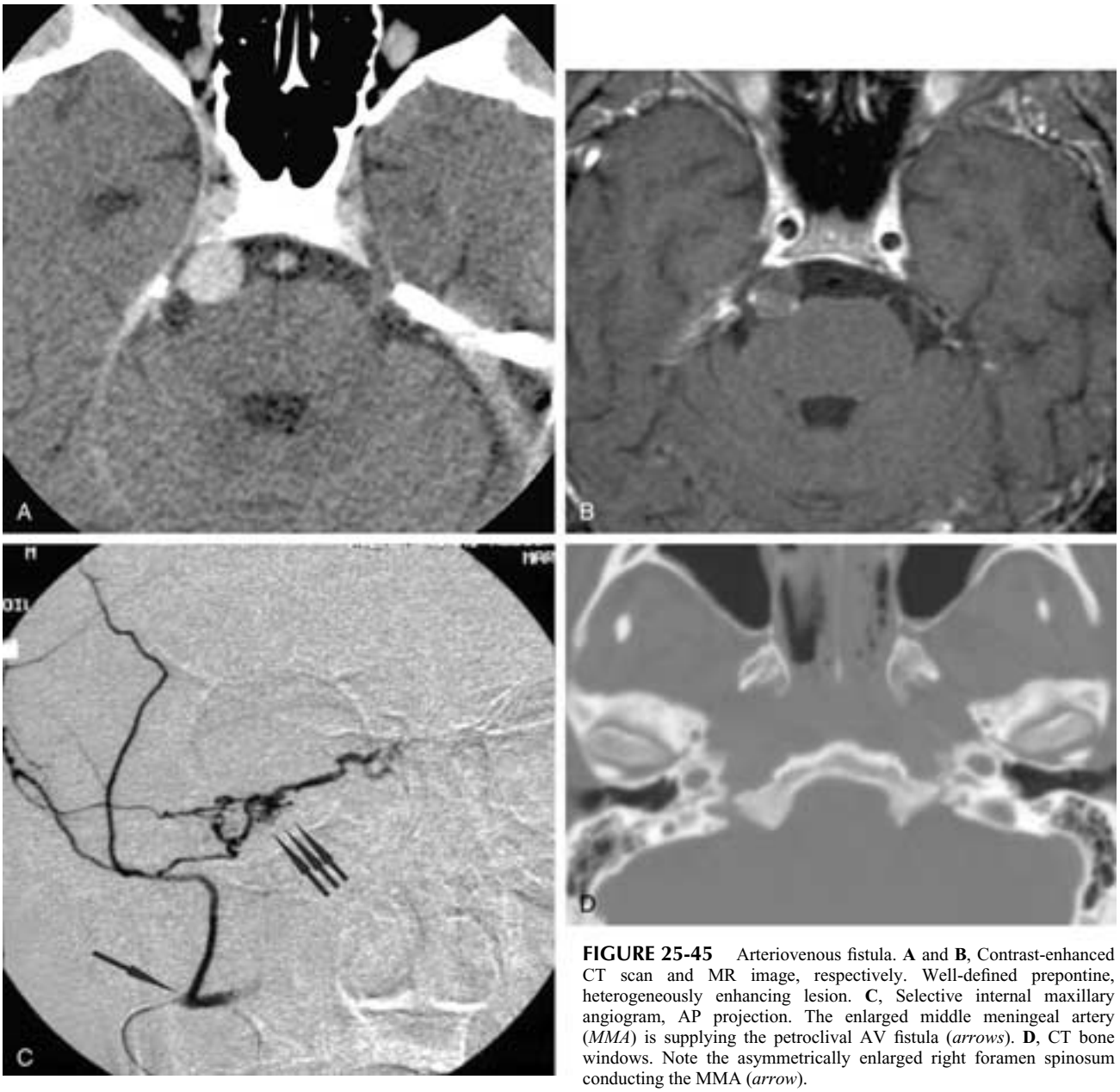

FIGURE 25-45 Arteriovenous fistula. **A** and **B**, Contrast-enhanced CT scan and MR image, respectively. Well-defined prepontine, heterogeneously enhancing lesion. **C**, Selective internal maxillary angiogram, AP projection. The enlarged middle meningeal artery (*MMA*) is supplying the petroclival AV fistula (*arrows*). **D**, CT bone windows. Note the asymmetrically enlarged right foramen spinosum conducting the MMA (*arrow*).

VIEW IMAGE

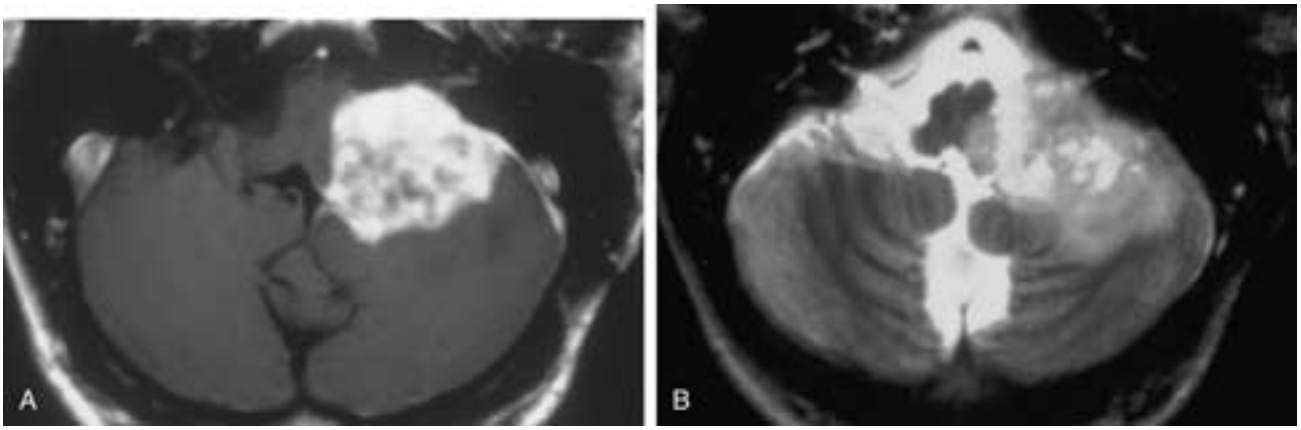

VIEW IMAGE

FIGURE 25-46 Pontine glioblastoma multiforme. **A**, T1-weighted postgadolinium image and **B**, T2-weighted image. The well-marginated intraaxial tumor involving the middle cerebellar peduncle and the cerebellar hemisphere shows heterogeneous enhancement and a mass effect on the fourth ventricle. The tumor is hyperintense on T2-weighted images. Exophytic growth of the tumor fills the cerebellopontine cistern.

Copyright © 2003, Mosby, Inc. All rights reserved.

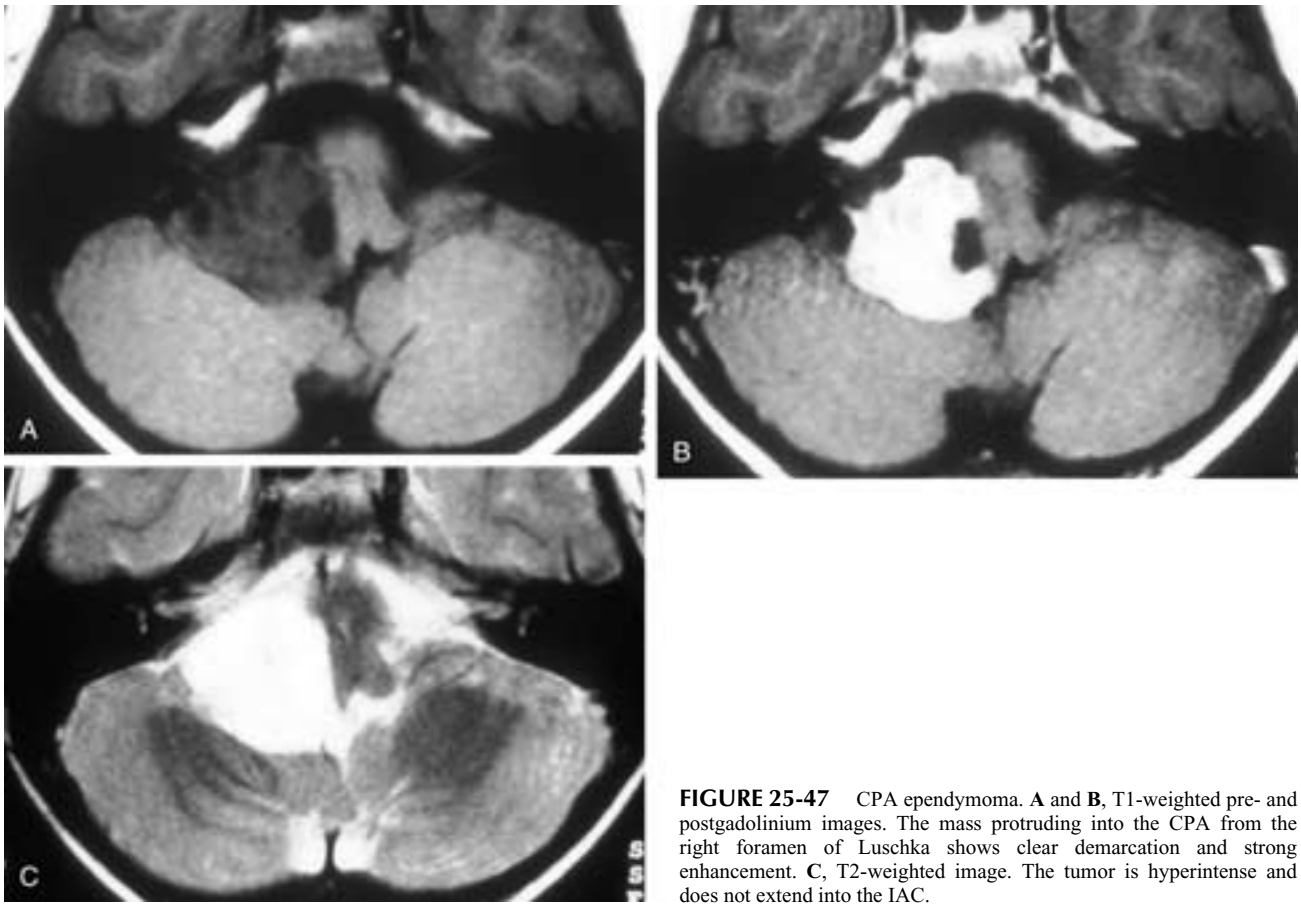

FIGURE 25-47 CPA ependymoma. **A** and **B**, T1-weighted pre- and postgadolinium images. The mass protruding into the CPA from the right foramen of Luschka shows clear demarcation and strong enhancement. **C**, T2-weighted image. The tumor is hyperintense and does not extend into the IAC.

VIEW IMAGE

Because intracanalicular lesions are frequently only 3 or 4 mm in size, excellent technique is required for their demonstration. At MR imaging, this requires T1-weighted contiguous 2 mm sections and the use of intravenous gadolinium. Images less than 1 mm can be obtained with the use of 3D gradient-echo sequences.[85] High-resolution, thin-section, T2-weighted, 3D-CISS MR imaging, by outlining the contours of the cranial nerves surrounded by CSF, has detected small tumors without the use of intravenous paramagnetic contrast (Fig. 25-2).[17, 275]

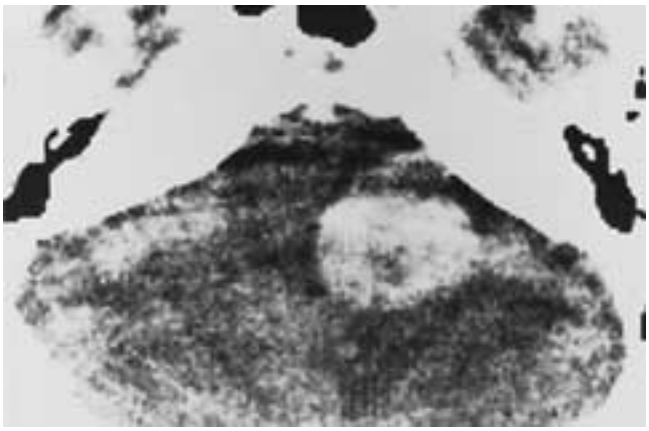

VIEW IMAGE

FIGURE 25-48 CPA choroid plexus papilloma. Postcontrast CT scan. The tumor is located at the foramen of Luschka. It is more sharply defined than an ependymoma. Like a giant aneurysm, it is detached from the petrous bone, in contrast to schwannomas and meningiomas.

Summary

In summary, the three most common extraaxial masses in the CPA are acoustic schwannoma, meningioma, and congenital epidermoid cyst. They are relatively consistent in location, configuration, CT density, MR intensity, and enhancement patterns (Table 25-3). The same may be said for the rarer nonacoustic posterior fossa schwannomas and the various vascular lesions. If one analyzes each lesion systematically, takes into consideration the clinical information, and avoids the traps set by the occasional extradural or intraaxial lesions intruding into the CPA, a correct preoperative diagnosis can be reached in an overwhelmingly large percentage of the cases.

PARAGANGLIOMAS AND JUGULAR FORAMEN TUMORS

Incidence, Origin, and Terms

Paraganglioma is the second most common tumor involving the temporal bone and is the most common in the middle ear.[20, 276] In the branchiomeric family of paraganglia, two groups are by location closely related to the jugular

Copyright © 2003, Mosby, Inc. All rights reserved.

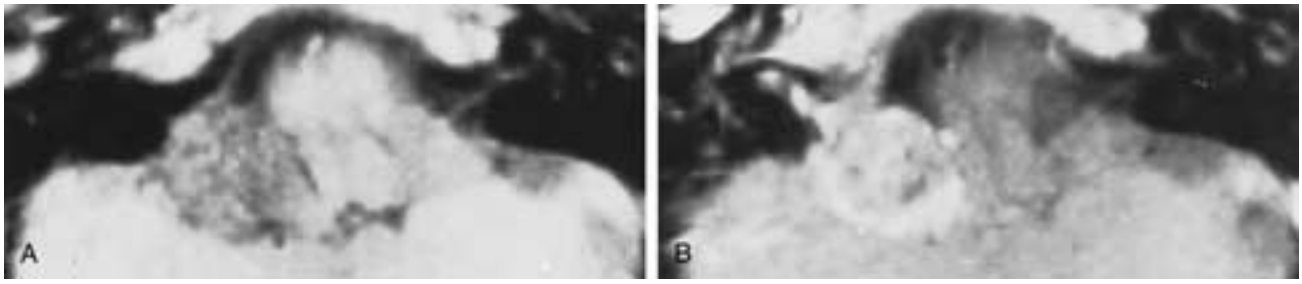

VIEW IMAGE

FIGURE 25-49 CPA choroid plexus papilloma. **A** and **B**, T1-weighted pre- and postgadolinium images. The tumor is located at the foramen of Luschka, as in Figure 25-50. It is well demarcated from the brain. Enhancement is mild and inhomogeneous. The specks, which are hypointense on both images, suggest calcifications. (Courtesy of Dr. Val M. Runge.)

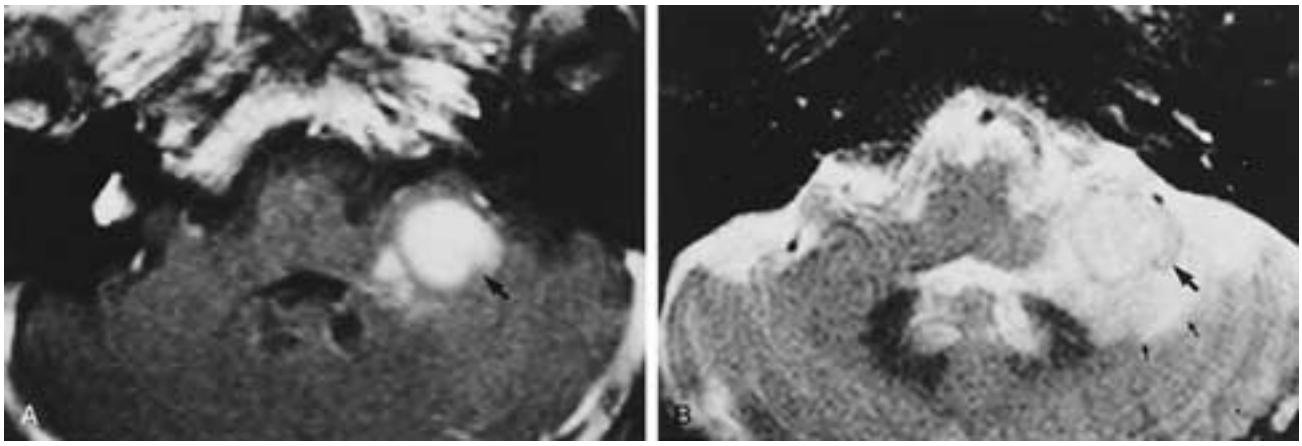

VIEW IMAGE

FIGURE 25-50 Primary cerebellar lymphoma. **A**, Gadolinium T1-weighted image. **B**, T2-weighted image. A moderately enhancing intraaxial tumor in the region of the flocculus (*arrow*), mildly hyperintense on the T2-weighted image (**B**), with peritumoral edema (*small arrows*) not apparent on the gadolinium T1-weighted image (**A**). Differential diagnosis: solid astrocytoma, hemangioblastoma, and metastasis. (From Jackler RK, Brackmann DE, eds. Neurotology. St. Louis: Mosby-Year Book, 1994.)

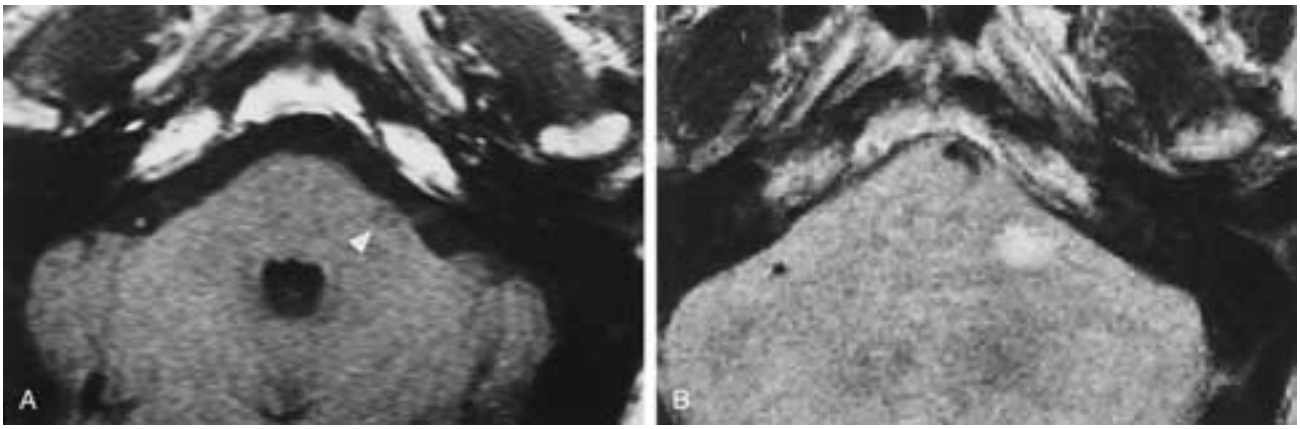

VIEW IMAGE

FIGURE 25-51 Multiple sclerosis. **A**, T1-weighted image. The subtle pontine lesion (*arrowhead*) shows easily overlooked minimal hypointensity. **B**, T2-weighted image. Hyperintensity of the lesion is obvious. (From Jackler RK, Brackmann DE, eds. Neurotology. St. Louis: Mosby-Year Book, 1994.)

Copyright © 2003, Mosby, Inc. All rights reserved.

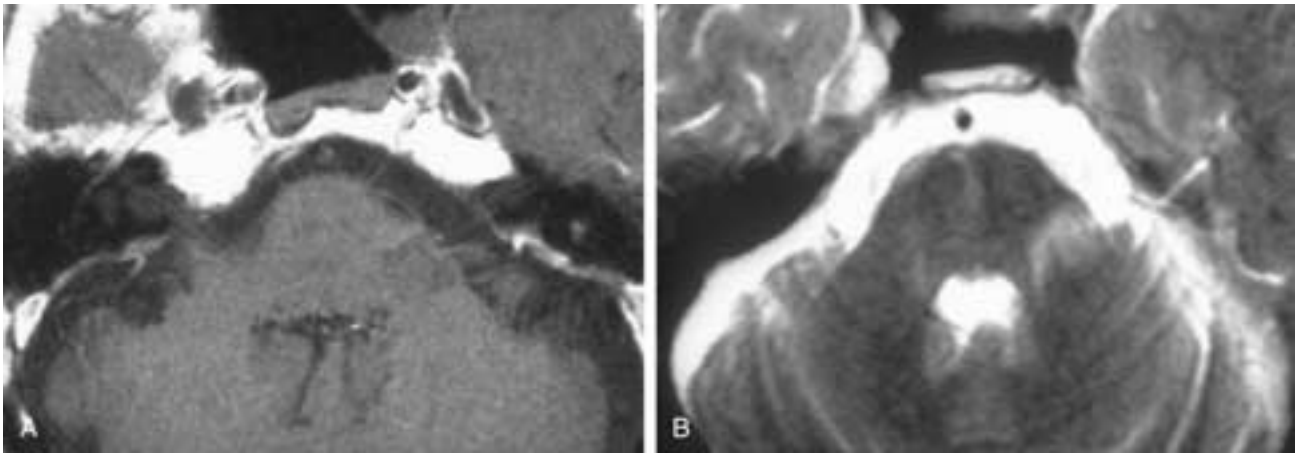

VIEW IMAGE

FIGURE 25-52 AICA infarct. **A**, T1-weighted image. A hypointense, nonexpansile pontocerebellar lesion is seen in the territory of the AICA. **B**, T2-weighted image. The infarct is seen as a hyperintense lesion without mass effect.

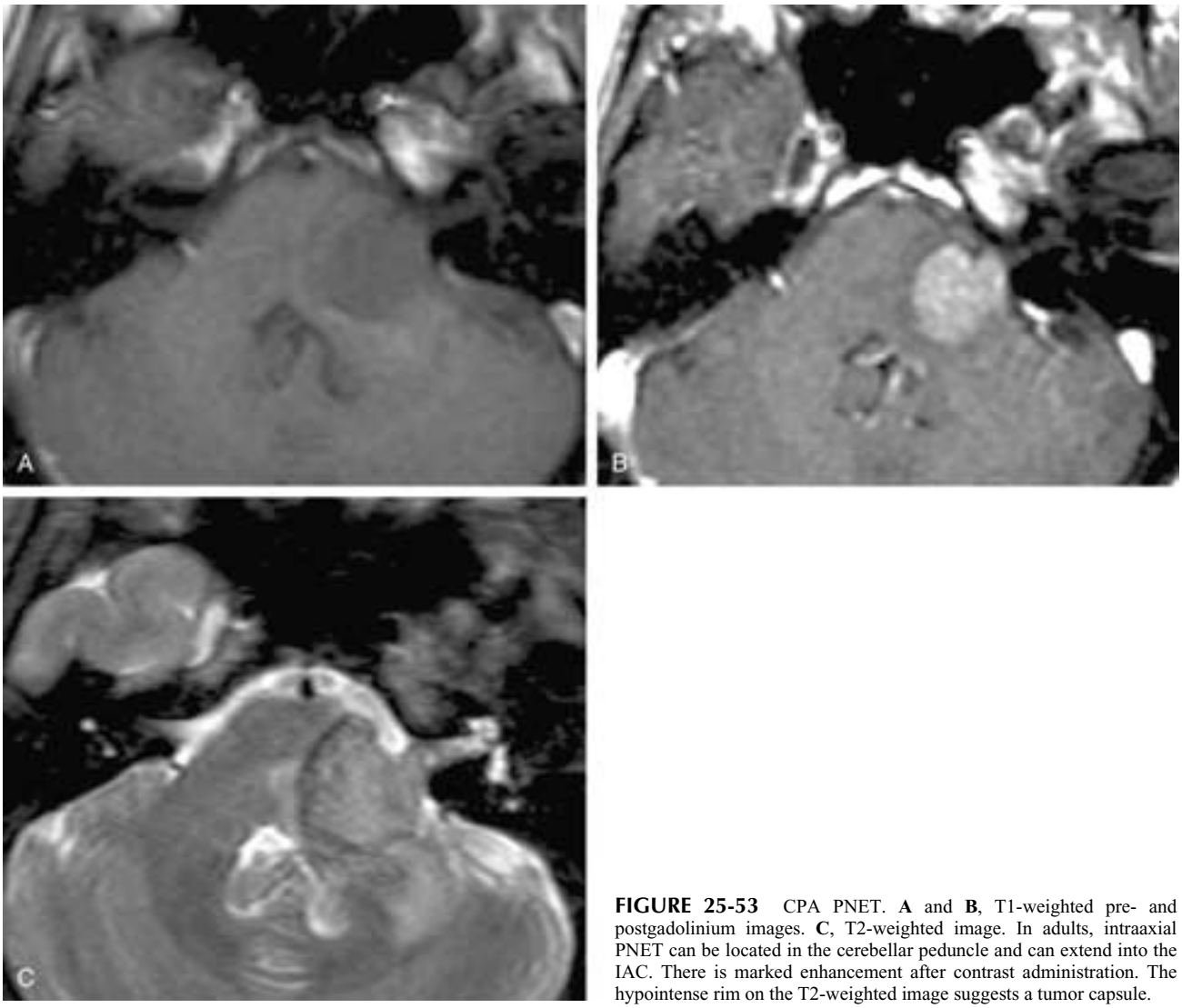

FIGURE 25-53 CPA PNET. **A** and **B**, T1-weighted pre- and postgadolinium images. **C**, T2-weighted image. In adults, intraaxial PNET can be located in the cerebellar peduncle and can extend into the IAC. There is marked enhancement after contrast administration. The hypointense rim on the T2-weighted image suggests a tumor capsule.

VIEW IMAGE

Copyright © 2003, Mosby, Inc. All rights reserved.

BOX 25-1
INTRACANALICULAR LESIONS

Neoplastic
Acoustic schwannoma
Facial schwannoma
Hemangioma
Meningioma
Metastasis
Glioma
Lipoma
Osteoma
Lymphoma
Melanoma

Nonneoplastic
AICA* loop
AICA aneurysm
Arachnoiditis
Hamartoma
Neuritis

*AICA, Anterior inferior cerebellar artery.

foramen: the jugulotympanic paraganglia along the tympanic branch of the glossopharyngeal nerve and the auricular branch of the vagus nerve (the nerves of Jacobson and Arnold, respectively) and the intravagal paraganglia inferior to the foramen.[277] Paraganglia are organelles 0.1 to 1.5 mm in length. Those distributed along the nerves of Jacobson and Arnold lie (1) in the adventitia of the jugular bulb, (2) in the inferior tympanic canaliculus, (3) on the cochlea promontory, and (4) in the mastoid canaliculus and the descending facial nerve canal (Fig. 25-62).[278] According to Glenner and Grimley, tumors from the paraganglia are more appropriately called paragangliomas than chemodectomas or glomus tumors.[277]

The term *glomus jugulare tumor* has been used among clinicians since Guild named the paraganglia glomus

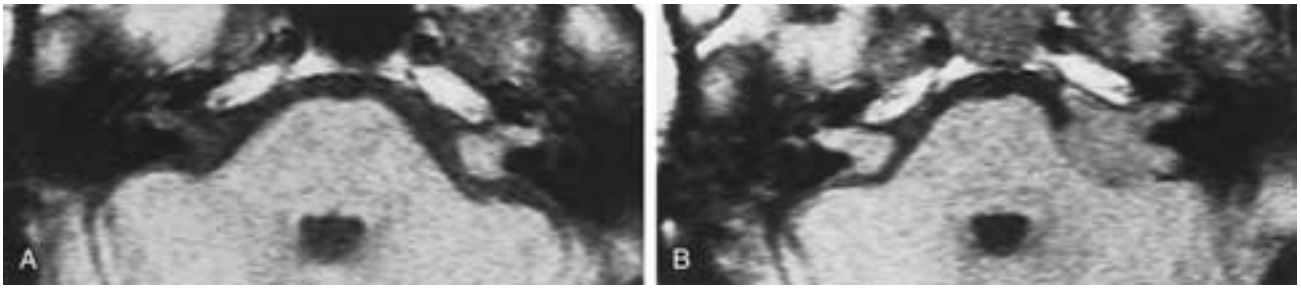

VIEW IMAGE

FIGURE 25-54 Metastases from carcinoma of the bladder. **A** and **B**, Postcontrast T1-weighted images obtained 1 month apart. The patient developed rapidly progressive hearing loss and facial palsy on the left side, followed by similar symptoms on the right.

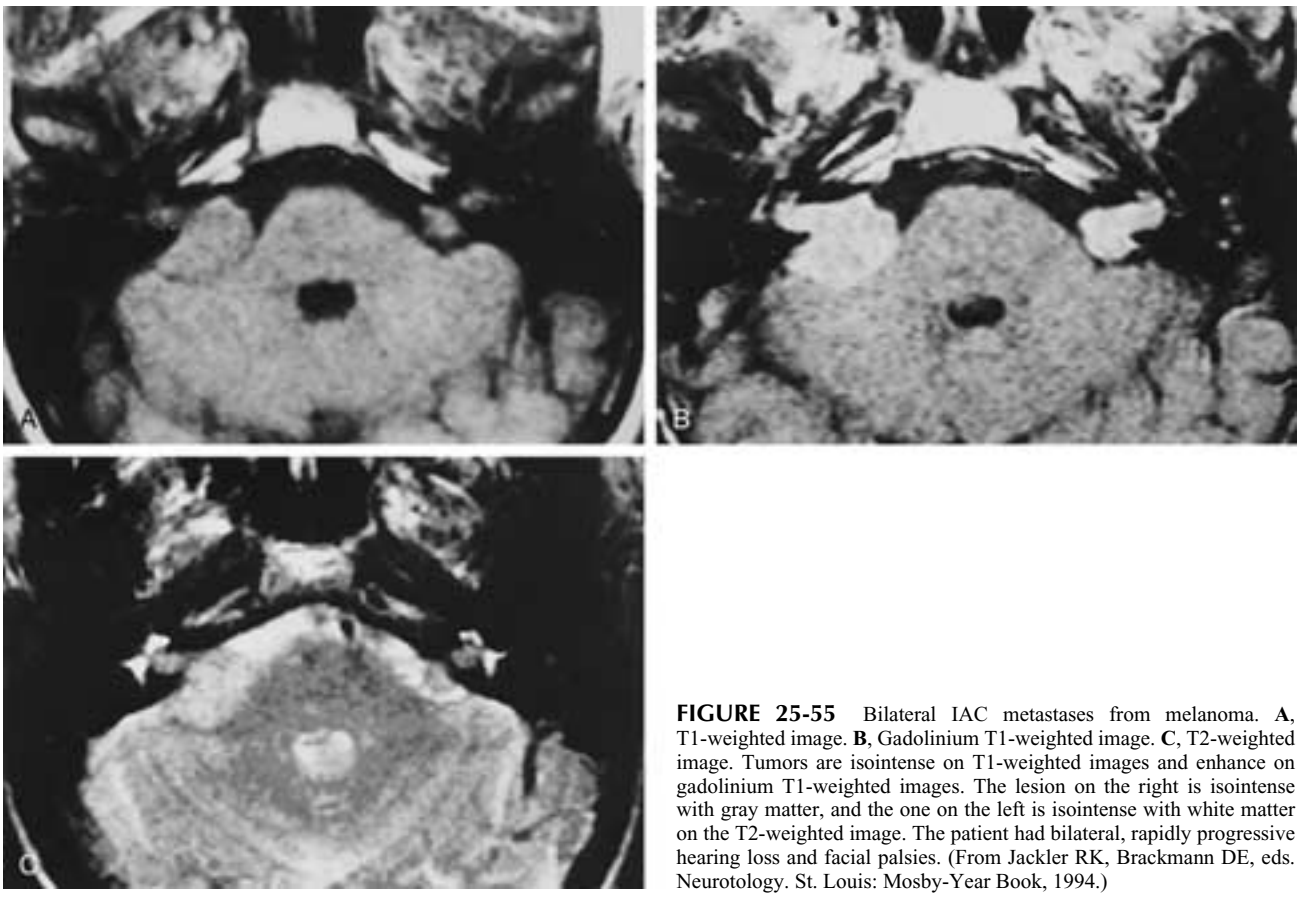

FIGURE 25-55 Bilateral IAC metastases from melanoma. **A**, T1-weighted image. **B**, Gadolinium T1-weighted image. **C**, T2-weighted image. Tumors are isointense on T1-weighted images and enhance on gadolinium T1-weighted images. The lesion on the right is isointense with gray matter, and the one on the left is isointense with white matter on the T2-weighted image. The patient had bilateral, rapidly progressive hearing loss and facial palsies. (From Jackler RK, Brackmann DE, eds. Neurotology. St. Louis: Mosby-Year Book, 1994.)

VIEW IMAGE

Copyright © 2003, Mosby, Inc. All rights reserved.

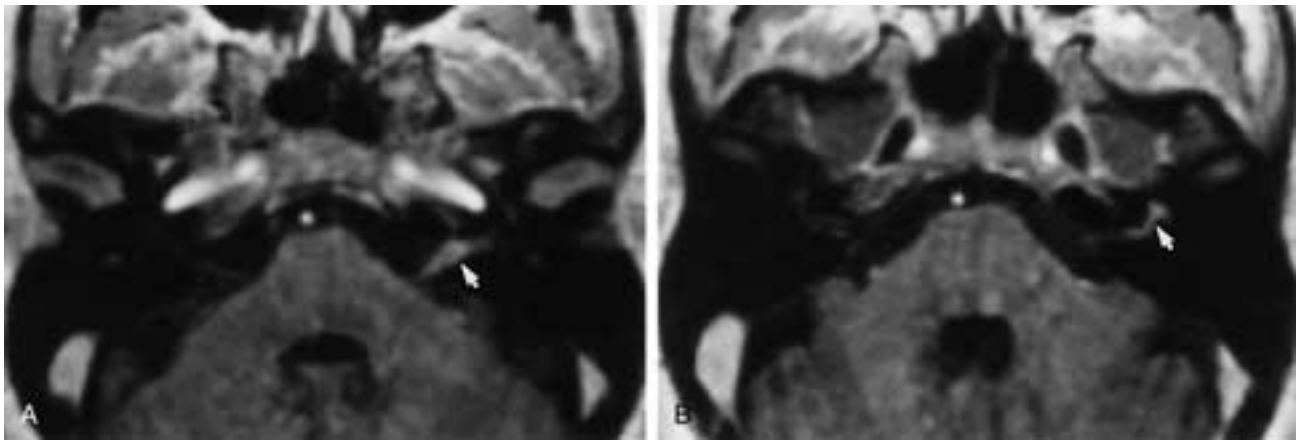

VIEW IMAGE

FIGURE 25-56 Primary left facioacoustic nerve lymphoma. **A**, Gadolinium T1-weighted image shows a moderately enhancing fusiform tumor (*arrow*) along the left facioacoustic nerves in the IAC extending into the CPA. The pointed medial extension is atypical of schwannomas. **B**, Gadolinium T1-weighted image shows marked enhancement (*arrow*) along the labyrinthine facial nerve and in the geniculate region. The patient had hearing loss and facial palsy.

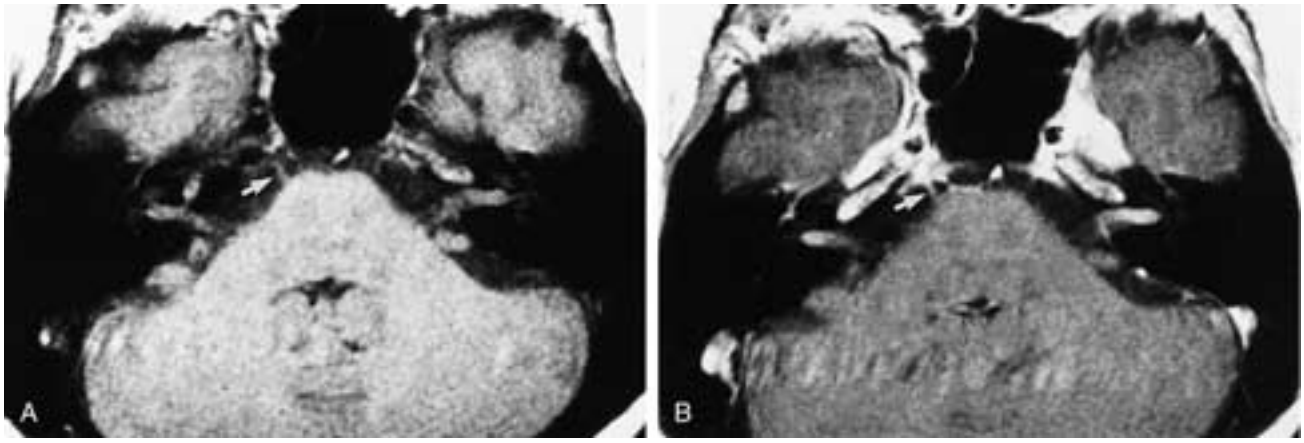

VIEW IMAGE

FIGURE 25-57 Bilateral IAC lymphoma. **A**, T1-weighted image shows IAC tumors isointense to the pons. **B**, Gadolinium T1-weighted image shows moderate to marked enhancement of the tumors. The patient also had similar involvement of the trigeminal nerves (not shown) and the abducens nerves (*arrows*), partly shown on this section.

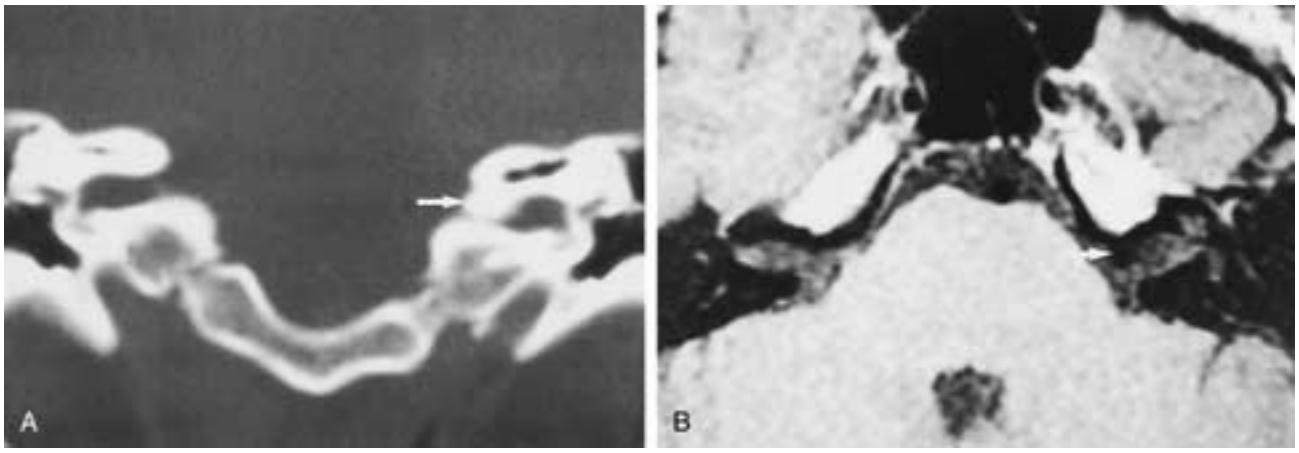

VIEW IMAGE

FIGURE 25-58 IAC osteoma. **A**, Coronal CT. Osteoma (*arrow*) consisting entirely of cortical bone arising from the anterosuperior wall of the porous acousticus caused sensorineural hearing loss relieved by resection. **B**, Gadolinium T1-weighted image. The tumor (*arrow*) is hypointense in all sequences and nonenhancing after contrast administration. A marrow-containing osteoma would have shown central hyperintensity on the T1-weighted image similar to that of marrow in petrous apices. (Courtesy of Dr. Derald E. Brackmann.) (From Jackler RK, Brackmann DE, eds. Neurotology. St. Louis: Mosby-Year Book, 1994.)

Copyright © 2003, Mosby, Inc. All rights reserved.

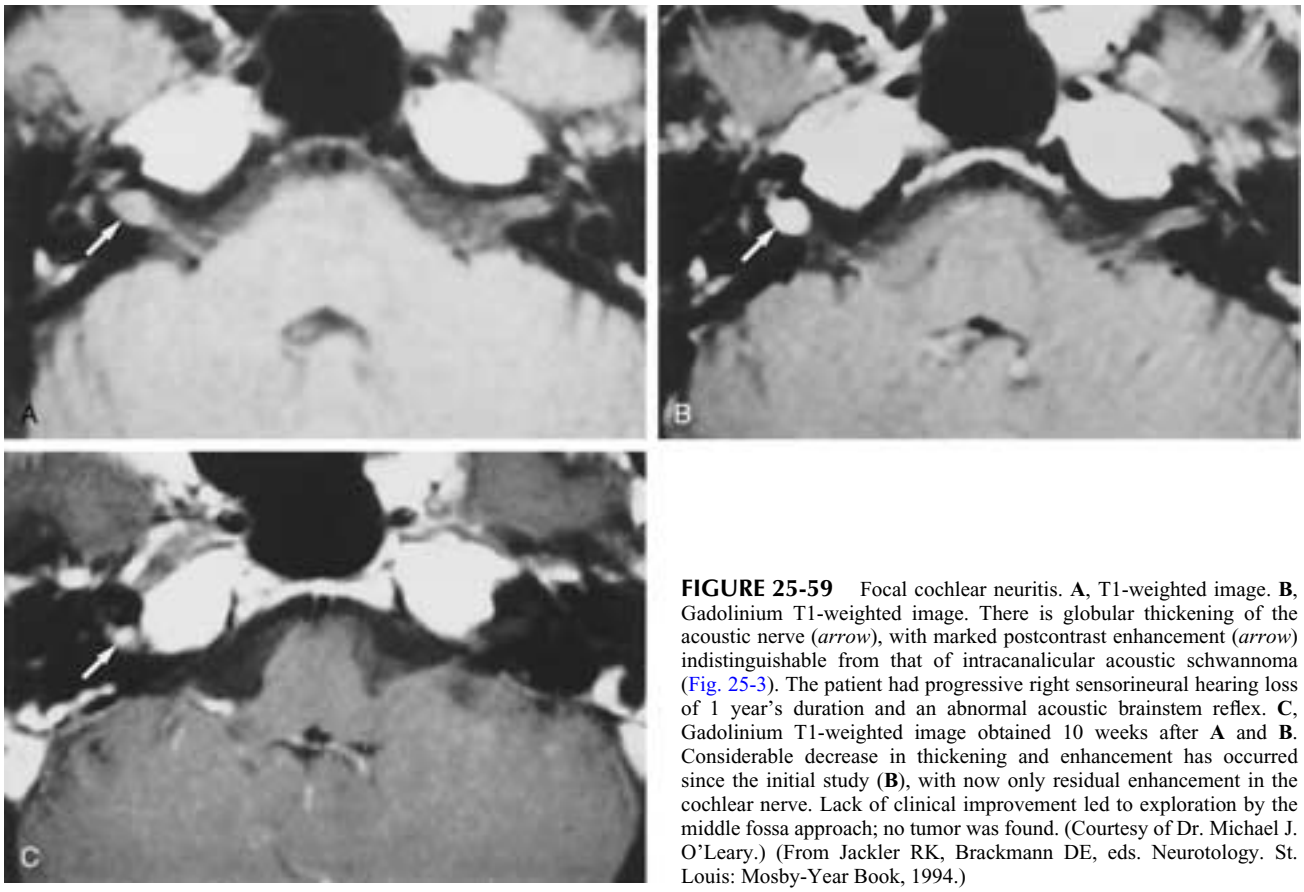

FIGURE 25-59 Focal cochlear neuritis. **A**, T1-weighted image. **B**, Gadolinium T1-weighted image. There is globular thickening of the acoustic nerve (*arrow*), with marked postcontrast enhancement (*arrow*) indistinguishable from that of intracanalicular acoustic schwannoma (Fig. 25-3). The patient had progressive right sensorineural hearing loss of 1 year's duration and an abnormal acoustic brainstem reflex. **C**, Gadolinium T1-weighted image obtained 10 weeks after **A** and **B**. Considerable decrease in thickening and enhancement has occurred since the initial study (**B**), with now only residual enhancement in the cochlear nerve. Lack of clinical improvement led to exploration by the middle fossa approach; no tumor was found. (Courtesy of Dr. Michael J. O'Leary.) (From Jackler RK, Brackmann DE, eds. Neurotology. St. Louis: Mosby-Year Book, 1994.)

VIEW IMAGE

jugulare.[278, 279] The term *glomus tympanicum tumor* was introduced by Alford and Guilford when they noted that those arising ''away from the jugular bulb, in the middle ear, along the course of Jacobson's nerve'' had a better prognosis than those arising ''in the area of the jugular bulb.''[280, 281] Glasscock et al. clarified the definition so that glomus tympanicum tumors include those in the tympanic cavity and the mastoid, and glomus jugulare tumors include those involving the jugular bulb and the base of the skull.[282] Glomus vagale tumors (vagal paragangliomas) arise from the intravagal paraganglia at or below the skull base and are primarily parapharyngeal masses (see Chapter 38).

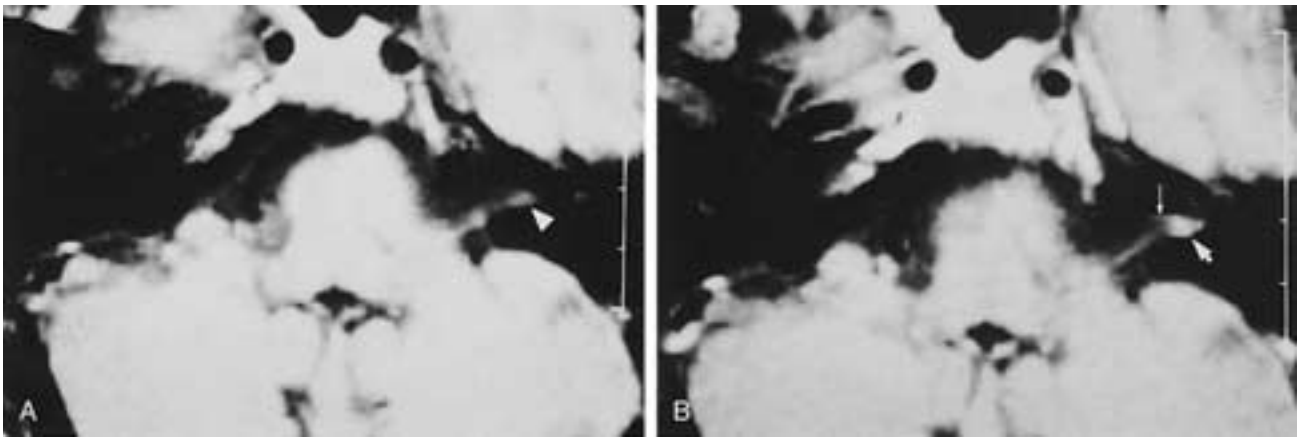

VIEW IMAGE

FIGURE 25-60 Chronic inflammation. **A**, T1-weighted image. **B**, Gadolinium T1-weighted image. Isointense soft tissue in the fundus of the IAC (*arrowhead*) enhanced after contrast administration (*arrow*), indistinguishable from a small acoustic schwannoma except perhaps for the presence of a small dural tail (*small arrow*). Compare with Figures 25-3 and 25-59. The patient had progressive left sensorineural hearing loss of 3 years' duration. The mass in the fundus of the left IAC adherent to the dura and involving the acoustic nerve was completely removed. Pathologic diagnosis: nongranulomatous active chronic nonspecific inflammation. (Courtesy of Dr. Robert D. Sostrin.) (From Jackler RK, Brackmann DE, eds. Neurotology. St. Louis: Mosby-Year Book, 1994.)

Copyright © 2003, Mosby, Inc. All rights reserved.

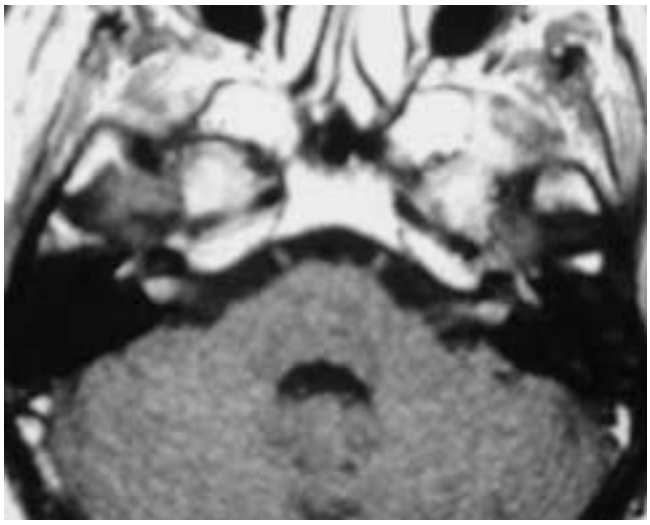

VIEW IMAGE

FIGURE 25-61 Dejerine-Sottas disease. T1-weighted postgadolinium image. This is a rare case of intracranial nerve involvement in Dejerine-Sottas disease demonstrating bilateral intracanalicular acoustic nerve hypertrophies, which show intense enhancement. This pattern may not be distinguishable from that of bilateral vestibular schwannomas seen in NF2. The same patient also has bilateral trigeminal nerve hypertrophies in Meckel's cave, with marked enhancement (not shown).

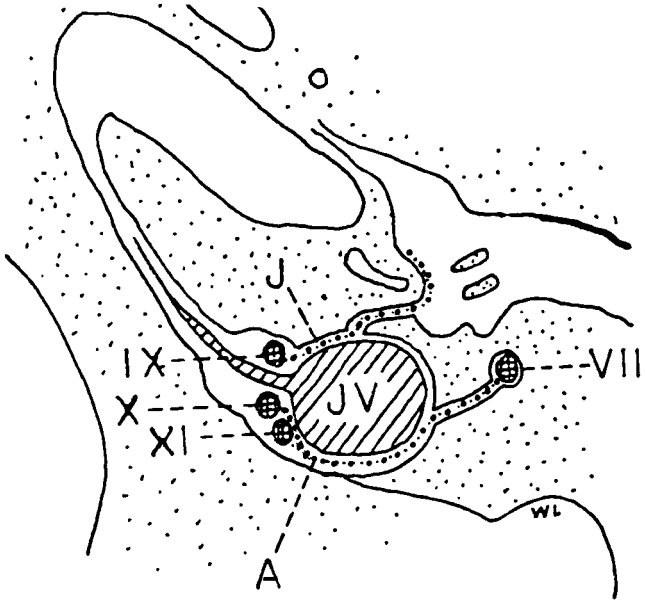

FIGURE 25-62 Schematic representation of important contents of the jugular foramen. The inferior petrosal sinus (unlabeled) and the glossopharyngeal nerve (*IX*) traverse the pars nervosa. The vagus (*X*) and spinal accessory (*XI*) nerves and internal jugular vein (*JV*) traverse the pars vascularis. The inferior tympanic branch of the glossopharyngeal (*J*) and the mastoid branch of the vagus (*A*) are represented by dotted lines. Approximately half of paragangliomas are distributed along each of the two branches. (Modified from Lo WWM, Solti-Bohman LG. High-resolution CT of the jugular foramen: anatomy and vascular variants and anomalies. Radiology 1984;150:743–747.)

VIEW IMAGE

Clinical Features

Paragangliomas occur in women three times as often as in men. When first seen, two thirds of the patients are in their fourth and fifth decades of life. The tumors may be bilateral, and other tumors such as carotid body tumors may coexist. Up to 10% of the patients may have multiple tumors.[283] Normally locally infiltrating, these tumors rarely may metastasize. Up to 10% are accompanied by malignant tumors in other organ systems. Very rarely, larger paragangliomas may secrete norepinephrine (as in pheochromocytomas) or, less often, ACTH, serotonin, calcitonin, and dopamine.[284] Occasionally, paragangliomas have been found to be familial.[285]

Paragangliomas can grow laterally, producing otologic symptoms (conductive hearing loss, pulsatile tinnitus, or a retrotympanic mass), and medially, resulting in the jugular foramen (or Vernet's) syndrome, consisting of glossopharyngeal, vagus, and spinal accessory deficits.[286, 287] However, in both tympanicum and jugulare tumors, otologic symptoms predominate and cranial nerve palsies appear only in a minority of the patients.[286] Clinical differentiation between the two groups is therefore impossible in the majority of cases unless a small tympanicum tumor is circumferentially visible.

In addition to involvement of the ninth through eleventh cranial nerves as the tumor enlarges, the hypoglossal nerve may be compromised in the region of the hypoglossal canal (Collet-Sicard's syndrome) and the facial nerve in its mastoid segment.[287, 288] Involvement of the carotid canal may cause Horner's syndrome, extension to the cavernous sinus will cause a cavernous sinus syndrome, and extension to the posterior fossa may cause brainstem and cerebellar signs and symptoms and hydrocephalus.[286, 287]

Vagal paragangliomas (glomus vagale tumors) develop inferior to the skull base, usually appearing as masses in the neck or the pharynx, and often involve the cranial nerves. They do not cause pulsatile tinnitus or conductive hearing loss, and they may or may not involve the temporal bone.[289]

High-resolution CT with bone detail is the most helpful imaging study for relating tumor extent to surgical landmarks and determining the surgical approach (Figs. 25-63 to 25-68). Angiography can be valuable in the differential diagnosis when the identity of a tumor is not obvious at sectional imaging, and angiography is frequently done to provide ac-

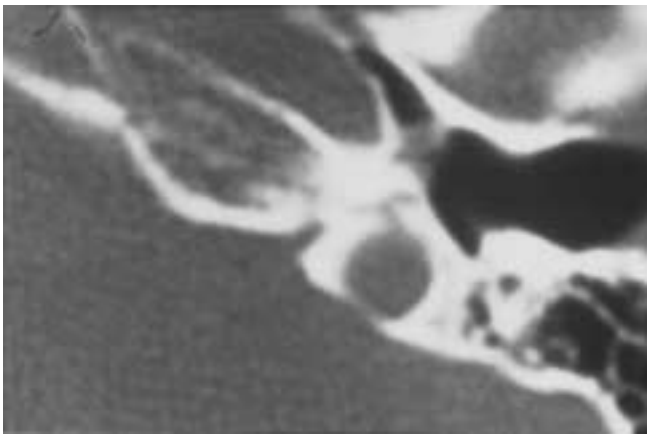

FIGURE 25-63 Small glomus tympanicum tumor. Axial CT. This otoscopically circumferentially visible tumor, corresponding to Fisch type A, is removable by the transmeatal approach. Angiography is not necessary.

VIEW IMAGE

Copyright © 2003, Mosby, Inc. All rights reserved.

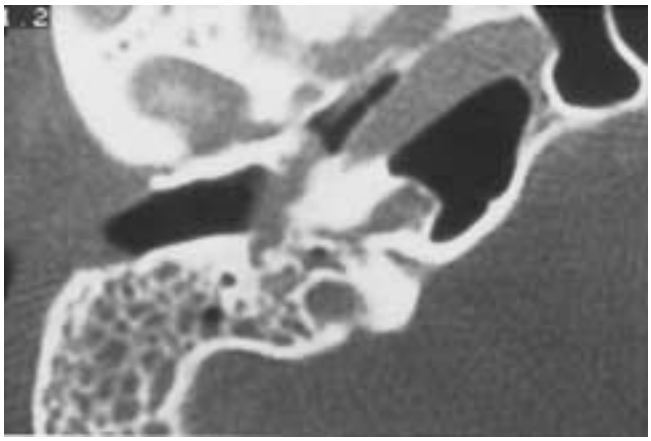

VIEW IMAGE

FIGURE 25-64 Large glomus tympanicum tumor. Axial CT. Fisch type A tumor too large to be differentiated from glomus jugulare tumor by otoscopy. CT, showing an intact jugular plate, definitely excludes a glomus jugulare tumor. The tumor, extending to the protympanum and obstructing mastoid drainage, is not distinguishable from other benign middle ear tumors by CT. All such tumors can be resected by the transmastoid approach. Angiography is not necessary.

cess for preoperative embolization (Figs. 25-69 and 25-70). MR imaging is helpful in soft-tissue localization and characterization of the tumor (Figs. 25-71 to 25-75).[8, 290, 291]

Growth Pattern and CT Findings

Paragangliomas grow slowly and rarely metastasize.[283] Although localized bone destruction around the jugular foramen is common, extensive destruction by expansion occurs relatively late. Paragangliomas tend to grow along the planes of least resistance by following preexisting pathways in the temporal bone (i.e., fissures, air cell tracts, vascular channels, and foramina) (Figs. 25-71 and 25-74).[292, 293] Tumors commonly descend through the jugular vein (Fig. 25-76), and central nervous system invasion may ultimately cause death.[292]

When first diagnosed, a paraganglioma may vary from a few millimeters in diameter and easily resectable to 10 cm or larger and life-threatening (Figs. 25-63 and 25-77). The CT appearance of paragangliomas is therefore highly variable. Because paraganglia are located along the nerves of Jacobson and Arnold, the earliest findings of jugulotympanic paragangliomas are along the course of these two nerves (Figs. 25-62 to 25-65 and 25-74).[294]

Glomus tympanicum tumors tend to produce symptoms early, so that when first seen, they are often well-defined intratympanic soft-tissue masses without bone involvement (Fig. 25-63).[295, 296] They may extend into the external auditory canal, but often even when filling the tympanic cavity they leave the ossicles intact.[296]

Because of the proximity of the hypotympanum to the jugular fossa, a large percentage of paragangliomas involve both regions by extending through the jugular plate (Figs. 25-65 to 25-68 and 25-74).[294, 297] Early irregular demineralization is thus often first found in the jugular plate or in the lateral portion of the caroticojugular spine (Figs. 25-65 and 25-66). The jugular plate may be involved early by tumors originating from paraganglia located in the inferior tympanic canaliculus. More extensive destruction extends from around the pars vascularis and beyond (Fig. 25-66). The bone changes are irregular, and the margins are indistinct and may be described as ''moth-eaten.''[298] Further destruction extends medially to the pars nervosa and the petrooccipital fissure, anteriorly to the vertical and then the horizontal carotid canal, and posteriorly along the sigmoid sulcus to the transverse sulcus. The infralabyrinthine compartment is frequently destroyed, but superior tumor extension is often slowed by the dense bone of the otic capsule (Figs. 25-66 and 25-67). An intratympanic tumor may spread into the mastoid, and vice versa, the protympanum, and less often into the epitympanum (Fig. 25-64).

An infralabyrinthine soft-tissue mass is common, extending either intraluminally down the internal jugular vein or along the carotid sheath, frequently to the C2-3 level or even lower, appearing as an enhancing mass on CT (Fig. 25-76). Further posterior extension of tumor may displace the dura inward or grow through the dura to involve the cerebellum (Figs. 25-68 and 25-77). Very large tumors may also destroy

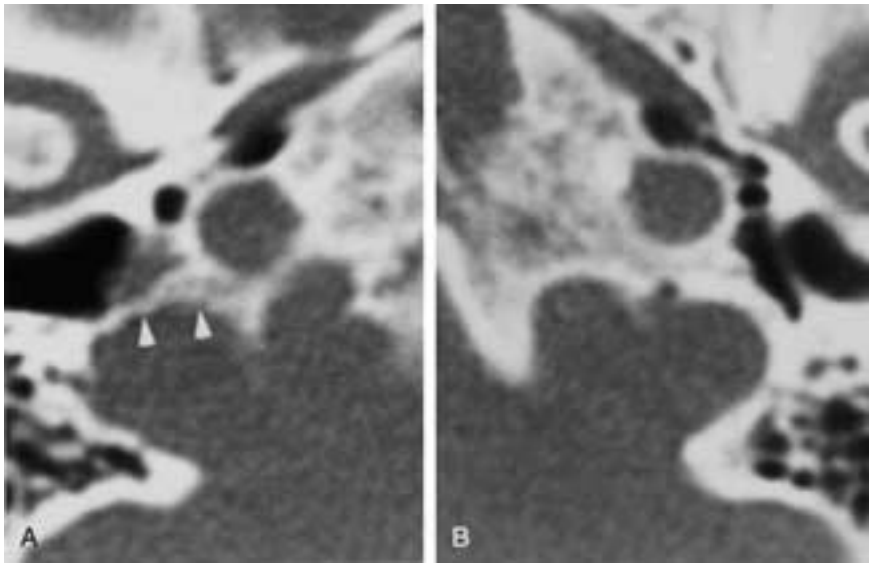

VIEW IMAGE

FIGURE 25-65 Small glomus jugulare tumor. **A** and **B**, Axial CT. Fisch type C1 tumor similar to the glomus tympanicum tumor in otoscopic appearance. Cortical demineralization of the jugular plate (*arrowheads*) on CT, however, indicates involvement of the jugular bulb (**A**). Compare with the normal contralateral side (**B**). Angiography is indicated, with possible preoperative embolization.

Copyright © 2003, Mosby, Inc. All rights reserved.

VIEW IMAGE

FIGURE 25-66 Glomus jugulare tumor. CT. **A**, Axial image shows demineralization of the bony margins of the jugular foramen on the right side (*black arrows*). There is demineralization of the fine cortical line usually demonstrated along the lateral aspect of the vascular portion of the jugular foramen. Compare with the intact cortical plate on the opposite side (*white arrow*). Note the demineralization of the bony wall separating the carotid canal from the jugular foramen. **B**, Blown-up axial image shows the demineralization of the lateral cortical plate (*arrowhead*), as well as slight demineralization of the bony plate between the carotid canal and the jugular foramen (*white arrow*). Note the proximity of the demineralized bone to the vertical section of the facial nerve canal (*black arrow*). **C**, Axial image enlarged through the normal side shows the intact white cortical line (*arrow*) along the lateral aspect of the jugular foramen. The integrity of this line essentially excludes a glomus jugulotympanicum tumor. **D**, Coronal image shows demineralization of the margins (*arrowheads*) as well as the soft tissue of the intratympanic portion of the tumor (*arrow*). (Courtesy of Dr. H.D. Curtin.)

the jugular tubercle, the hypoglossal canal, and portions of the foramen magnum and the clivus. Anterosuperior extension of tumor may involve the cavernous sinus (Fig. 25-77).

Angiographic Features

Paragangliomas are characteristically hypervascular (Figs. 25-69 and 25-70).[299, 300] There are enlarged feeding arteries and rapidly draining veins, and the tumor blush is coarser than in meningiomas but less so than in AVMs. The blush is not as prolonged as in meningiomas. The most common feeders are branches of the ascending pharyngeal artery, which supplies the inferomedial compartment of the tumor around the jugular foramen and the medial tympanic cavity (Figs. 25-70 and 25-71).[262] Other common feeders are the posterior auricular, stylomastoid, and occipital arteries, which supply the posterolateral compartment in the

Copyright © 2003, Mosby, Inc. All rights reserved.

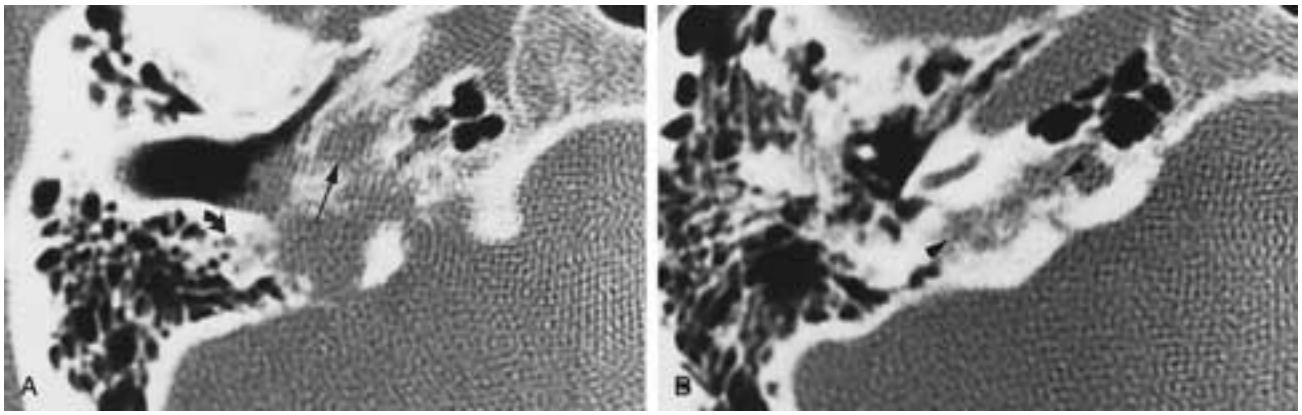

VIEW IMAGE

FIGURE 25-67 Medium-sized glomus jugulare tumor. **A** and **B**, Axial CT. Fisch type C2 tumor destroying the fossa-infiltrating vertical carotid canal (*arrow*) and infralabyrinthine compartment (*arrowheads*), bypassing the dense bone of the otic capsule. The tumor is resectable by the infratemporal fossa approach, with anterior rerouting of the facial nerve (*curved arrow*).

mastoid region. Larger tumors derive their blood supply anteriorly from the internal maxillary (anterior tympanic branch) and superiorly from the internal carotid (carotico-tympanic and lateral clival branches).[299, 300] Even larger tumors receive an additional blood supply from the contralateral carotid artery or the vertebral artery from its meningeal and even pial branches. A pial arterial supply signifies transdural involvement.[301] The angiographic vascularity is sufficiently characteristic that some authors believe it is diagnostic and that biopsy is not necessary.[283] Exceptions that should be considered include metastatic pheochromocytoma, metastatic hypernephroma, metastatic thyroid carcinoma, and hemangiopericytoma.[302] Retrograde jugular venography is now seldom indicated because intravenous tumor extension in itself does not determine the surgical approach (Fig. 25-76).

MR Imaging Appearance

In paragangliomas larger than 2 cm, an apparently unique salt-and-pepper pattern of hyperintensity and hypointensity on T1-weighted and T2-weighted images has been described (Figs. 25-71 and 25-72).[303] Also identified are the serpentine and arborizing flow voids of the hypertrophic medium-sized and larger tumor vessels (Fig. 25-73). These findings, reflecting hypervascularity, are highly suggestive of paragangliomas. The signal intensities from the tumor should be carefully distinguished from those of bone marrow and from mastoid secretions accumulated by virtue of tumor obstruction of the tympanic cavity or eustachian tube (Fig. 25-73). High intensity from stagnant blood in the jugular bulb must not be mistaken for a jugular foramen tumor (Fig. 25-75).

The tumor signal intensity is generally more than that of cortical bone, aerated air cells, and flowing blood but less than that of bone marrow. A dropout effect in the early enhancement pattern of paraganglioma may distinguish this lesion from other tumors.[291] Demonstration of this phenomenon requires ''dynamic'' MR scanning and takes advantage of the fact that if the concentration of gadolinium is sufficiently high, there is actually a signal decrease. Multiple images are taken at the same level as the gadolinium is administered and passes through the tumor. The signal coming from the tumor first rises as the bolus reaches the tumor. However, because of the large volume of blood within the tumor, the gadolinium transiently reaches a high enough concentration that there is actually a signal drop. As the gadolinium concentration of the initial bolus is diluted, the signal increases once again. Tumor types other than paraganglioma do not show this phenomenon.[291]

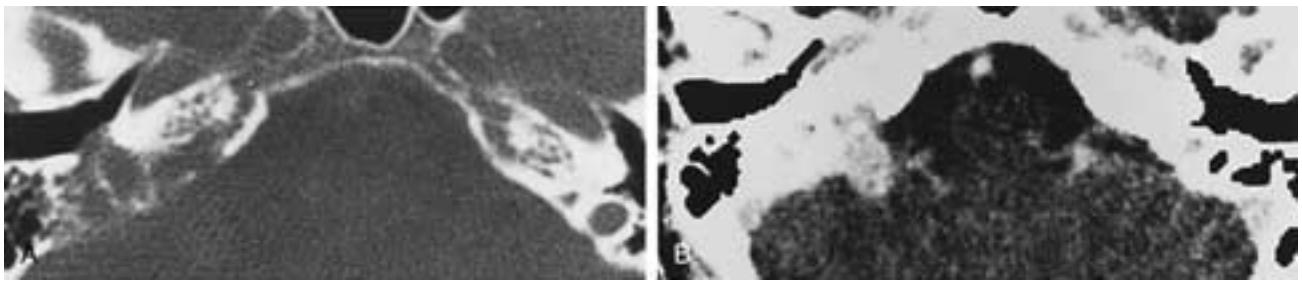

VIEW IMAGE

FIGURE 25-68 Medium-sized glomus jugulare tumor. **A** and **B**, Axial bone algorithm and soft tissue algorithm postcontrast CT. Fisch type D tumor with small intracranial extension. For resection, a combined otologic and neurosurgical approach is required.

Copyright © 2003, Mosby, Inc. All rights reserved.

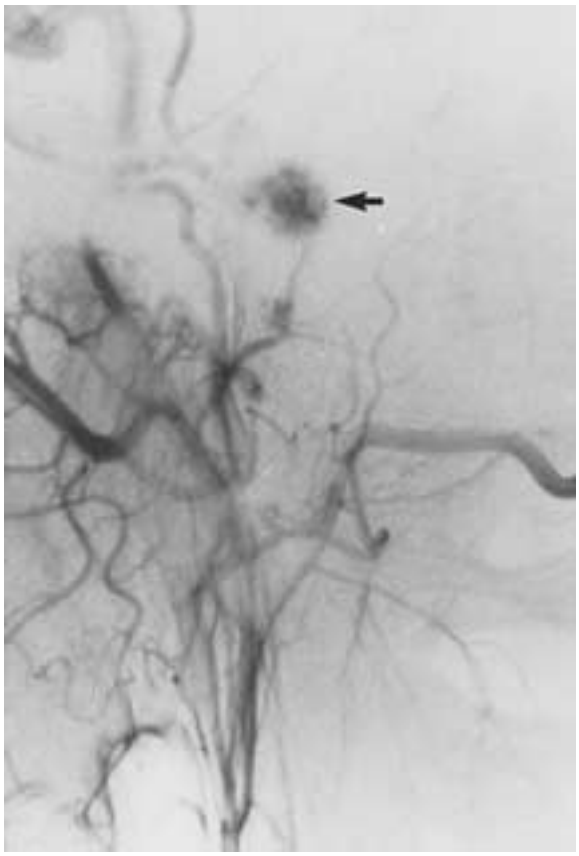

VIEW IMAGE

FIGURE 25-69 Glomus tympanicum tumor. Selective external carotid angiogram. Characteristic hypervascularity (*arrow*) is seen.

VIEW IMAGE

FIGURE 25-70 Glomus jugulare tumor. Selective external carotid angiogram. The characteristically hypervascular tumor is supplied by the hypertrophic ascending pharyngeal artery (*arrow*). Note the early draining vein (*arrowhead*) seen during the midarterial phase. The differential diagnosis includes other hypervascular tumors such as metastatic hypernephroma, metastatic pheochromocytomas, myeloma, and so on (see Fig. 25-122).

Although MR imaging does not show the bone changes or the tumor relationships to the bony landmarks as well as high-resolution CT, it defines the infralabyrinthine soft tissue extension better than CT (Fig. 25-72). Thus the two procedures are sometimes of complementary value (Fig. 25-74).

MRA has not reliably demonstrated the characteristic tumor vascularity invariably seen on catheter angiography, and postcontrast enhancement in the jugular vein may be difficult to differentiate paraganglioma from a true jugular tumor. Vogl et al. found MR venography helpful in such cases (Fig. 25-74E,F).[290]

After radiation therapy, stabilization or reduction in tumor size, decreased enhancement, diminished flow voids, and reduced T2-weighted signal intensity indicate local control.[304] Bone demineralization and erosion, however, may persist. Rarely does the actual tumor mass resolve completely after irradiation.

Radionuclide Scintigraphy

Indium-111-octreotide, recently made available commercially, shows greater sensitivity than iodine-123-metaiodobenzyl-guanidine (MIBG) to paragangliomas and appears useful in detecting multicentric, metastatic, or recurrent tumors.[305–307]

Treatment and Surgical Classification

Paragangliomas can be lethal if left untreated.[283] Current treatment includes mainly resection for cure or radiation for long-term control.[308–311] Using the infratemporal fossa approach advanced by Fisch, the entire petrous bone can be resected, including a portion of the clivus.[307, 308, 312]

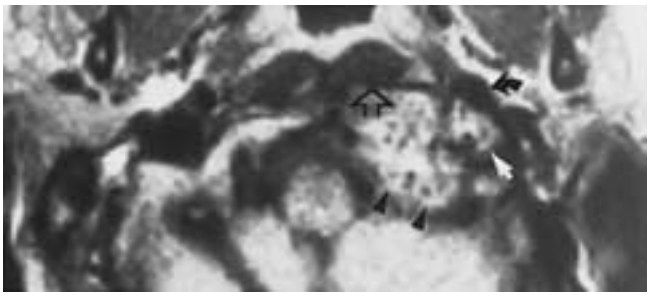

VIEW IMAGE

FIGURE 25-71 Glomus jugulare tumor. Proton density image. Heterogeneous hyper- and hypointensity are characteristically seen in larger paragangliomas. This tumor has only a small component in the jugular fossa (*arrow*) posterior to the carotid (*curved arrow*) but has a large component in the infralabyrinthine skull base (*arrowheads*) displacing the longus colli muscle anteriorly (*open arrow*).

Copyright © 2003, Mosby, Inc. All rights reserved.

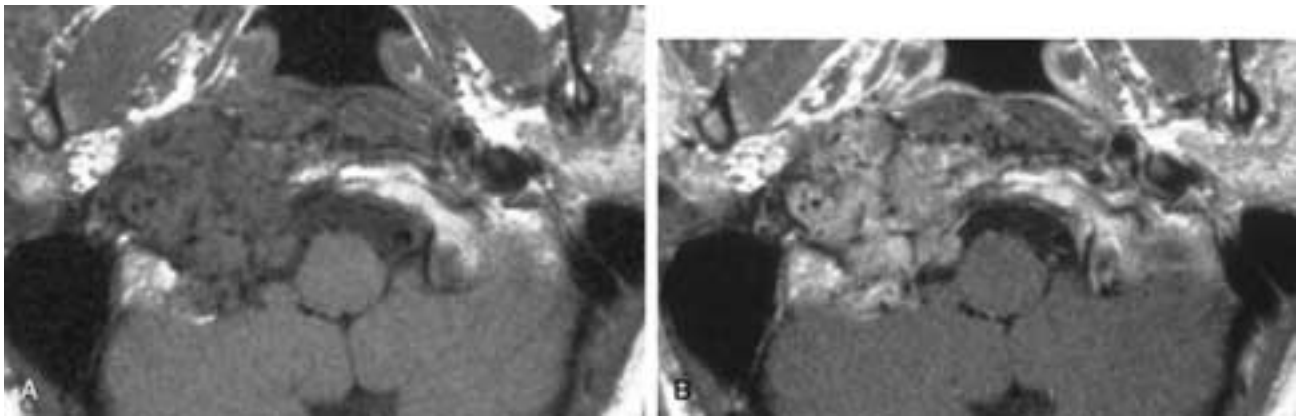

VIEW IMAGE

FIGURE 25-72 Glomus jugulare tumor. **A** and **B**, T1-weighted pre- and postgadolinium images. The heterogeneously hypointense tumor is located in the jugular fossa, extending into the parapharyngeal space and foramen magnum, with temporal bone and clivus invasion. Areas of signal void within the tumor are related to hypertrophic neoplastic vessels. The tumor shows strong enhancement after gadolinium administration.

Elaborate classifications have been devised matching tumor extent to surgical procedure (Tables 25-4 and 25-5).[309, 313] The details are pertinent only to those frequently involved in such cases, but the principles behind the classifications are of practical importance to those consulted even only occasionally.

1. A tumor that is intratympanic, intramastoid, or both is resectable by a transmeatal or transmastoid approach, which can be performed by most otologists (Fig. 25-64).
2. A tumor that involves the jugular bulb requires expertise in neck surgery in addition to mastoid surgery.
3. A tumor involving the carotid canal or the infralabyrinthine compartment requires the infratemporal fossa approach used only at neurotologic or skull base centers (Fig. 25-67).
4. A tumor with a transdural component calls for neurosurgical in addition to neurotologic expertise (Fig. 25-68).
5. Cavernous sinus or massive foramen magnum tumors may be unresectable (Fig. 25-77). Modern imaging techniques are thus indispensable in helping to decide the necessity of referral and the choice of proper management.

In tympanicum tumors the surgical blood loss is small, and preoperative embolization is not indicated.[314] In jugulare tumors, the blood loss is at least 1 or 1.5 L and often much more.[314, 315] Preoperative embolization reduces the blood loss by 1 L or more and is now commonly performed.[300, 301, 314–317]

DIFFERENTIAL DIAGNOSIS

The differential diagnosis of paragangliomas and the appropriate imaging choices depend on the clinical presentation, which may be either (1) a retrotympanic or intratympanic mass with or without pulsatile tinnitus or (2) deficits of

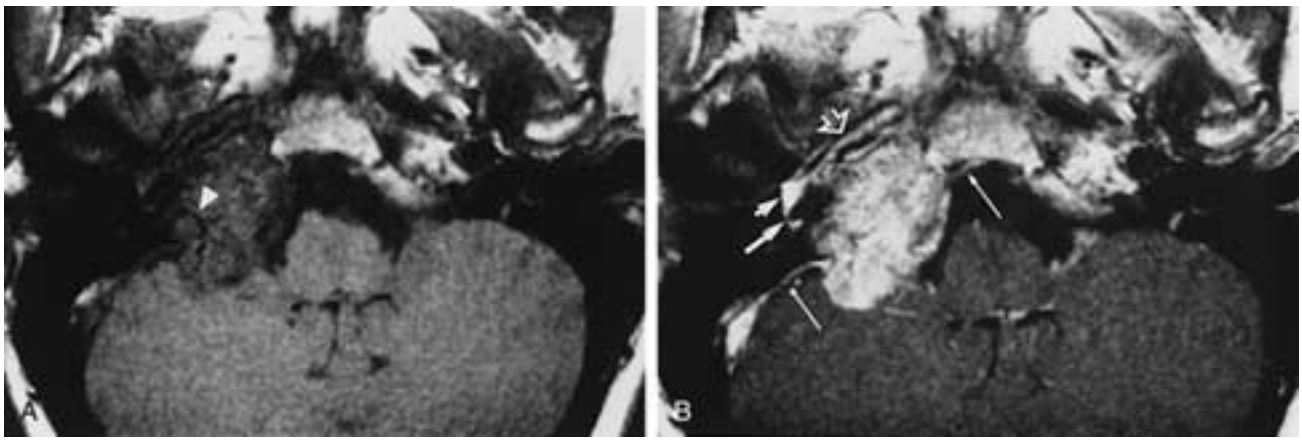

VIEW IMAGE

FIGURE 25-73 Jugular paraganglioma (glomus jugulare tumor) with posterior fossa extension. **A**, T1-weighted image. **B**, Gadolinium T1-weighted image. Note the loss of natural contrast between the tumor and the clivus marrow after Gd-DTPA administration and the importance of precontrast images to serve as a baseline. The tumor circumferentially narrows the intrapetrous carotid (*open arrow*) and extends to the protympanum (*short arrow*) to surround the cochlea (*arrow*). Note the dural tails (*long*, *thin arrows*) and arterial branch (*arrowheads*) supplying the tumor. Note also the intracranial extension. (From Jackler RK, Brackmann DE, eds. Neurotology. St. Louis: Mosby-Year Book, 1994.)

Copyright © 2003, Mosby, Inc. All rights reserved.

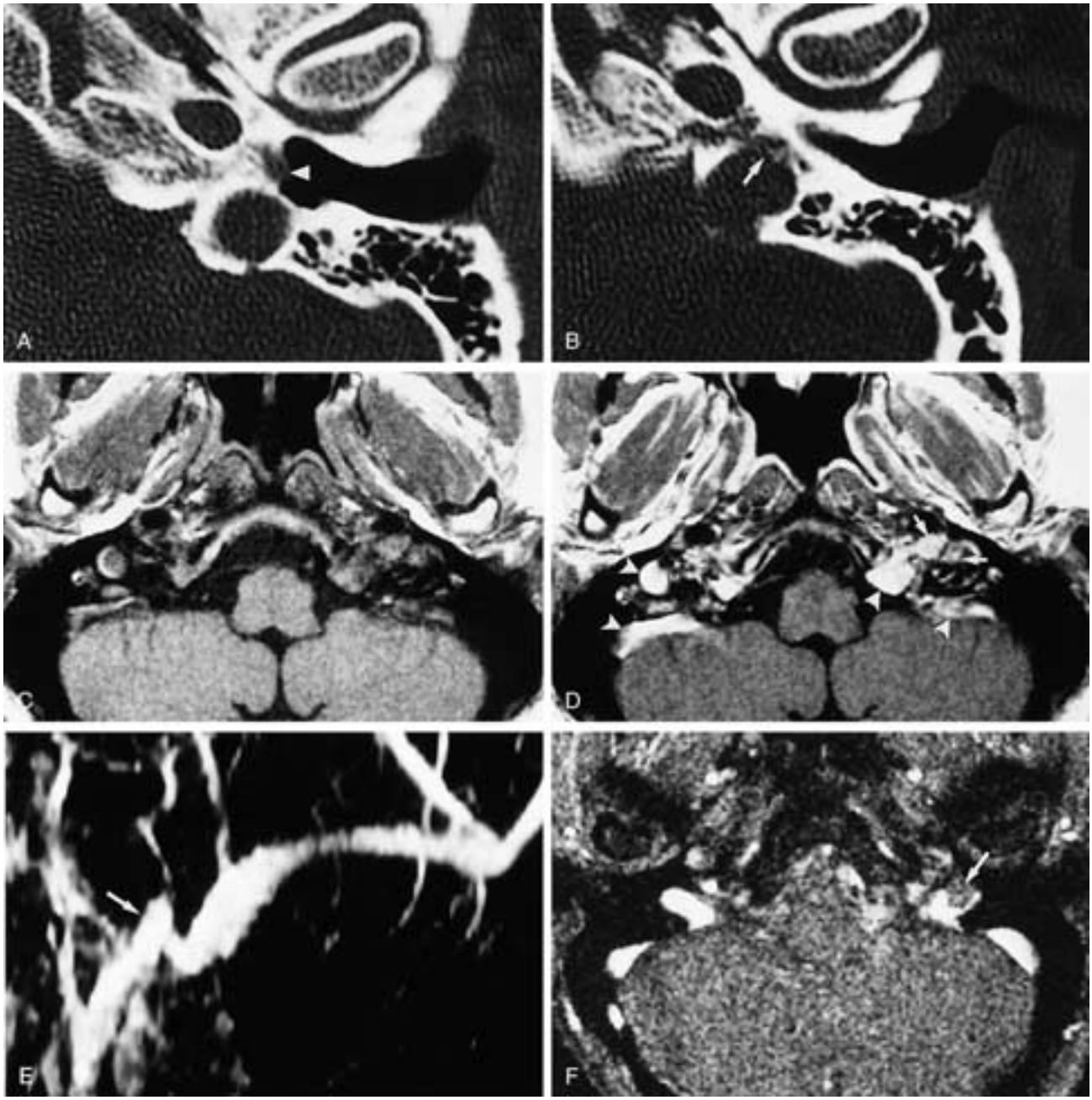

VIEW IMAGE

FIGURE 25-74 Small right jugulotympanic paraganglioma (glomus jugulare) requiring CT, MR imaging, and MRV for full delineation. **A**, CT shows a small otoscopically visible intratympanic pulsatile mass apparently confined to the tympanic cavity (*arrowhead*). **B**, CT, 2 mm below **A**, shows subtle tumor extension down the caroticojugular spine to the anterior wall of the inferior portion of the jugular fossa (*arrow*). **C**, Gadolinium T1-weighted image. **C** and **D** show multiple sites of enhancement. It is difficult to differentiate between slow flow enhancement (*arrowheads*) and true tumor (*arrows*). **E**, MRV (2D TOF, maximum-intensity projection) shows questionable indentation of the jugular bulb (*arrow*). **F**, MRV (2D TOF, individual partition) shows unequivocal tumor invasion (*arrow*) of the jugular bulb that is not apparent on **A** through **E**. The presence or absence of jugular bulb invasion is critical for selection of the surgical approach to the jugulotympanic paraganglioma.

Copyright © 2003, Mosby, Inc. All rights reserved.

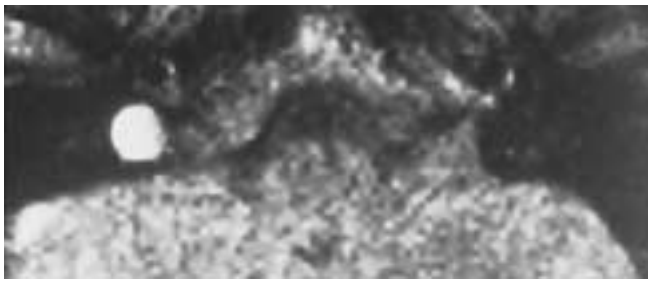

VIEW IMAGE

FIGURE 25-75 High jugular bulb. T2-weighted image. Flow-related enhancement must not be mistaken for a jugular foramen tumor. Note the smooth, perfectly rounded outline of hyperintensity filling the jugular bulb.

the caudal cranial nerves. When the clinical presentation is a retrotympanic or intratympanic mass, high-resolution CT is the modality of choice for the initial imaging modality. MR imaging may follow, if necessary. When a patient presents with deficits of the caudal cranial nerves, MR imaging is the imaging modality of choice. CT may be used as a supplement.

Retrotympanic or Intratympanic Masses

For a list of intratympanic masses, see Box 25-2.

Pulsatile Masses

Although paraganglioma is the most common cause of a pulsatile mass with conductive hearing loss, the otologist is confronted with the following important differential considerations in such a clinical setting: (1) glomus tympanicum tumor confined to the middle ear, (2) glomus jugulare tumor involving the jugular bulb, (3) aberrant carotid artery, and (4) exposed jugular bulb.[318, 319]

An experienced otologist can usually, but not always, distinguish these conditions by their appearance (Table 25-6). Ill-advised biopsies performed on aberrant carotid arteries or exposed jugular bulbs have resulted in massive hemorrhage or hemiplegia.[320, 321] To prevent inappropriate intervention, the radiologist must identify the characteristic findings of the aberrant carotid artery or the exposed jugular bulb on CT[319, 322] (see Chapter 26). MRA may serve to confirm the diagnosis. Angiography usually is not necessary.[319] CT also distinguishes glomus tympanicum tumor, which requires no angiography and limited surgery, from glomus jugulare tumor, which requires angiography, preoperative embolization, and extensive surgery (Figs. 25-64 to 25-69).[294, 319]

Two rarer arterial anomalies may clinically resemble the aberrant carotid artery. Both lesions are associated with dehiscence of the carotid plate: the laterally displaced internal carotid artery herniating into the middle ear and an aneurysm of the internal carotid artery from the junction between its vertical and horizontal intrapetrous segments located in the middle ear.[323–325] MRA may be used to confirm the diagnosis. The persistent stapedial artery may

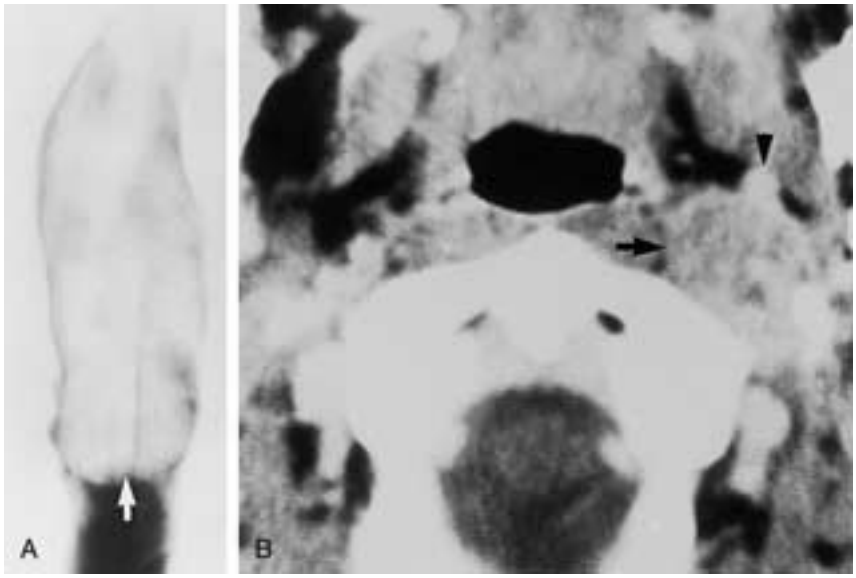

VIEW IMAGE

FIGURE 25-76 Intravenous extension of a glomus jugulare tumor. **A**, Retrograde jugular venogram. **B**, Postcontrast CT. An intravenous tumor (*arrow*) in the descending jugular vein is the common growth pattern of jugular paraganglioma. The ICA is displaced anteriorly (*arrowhead*).

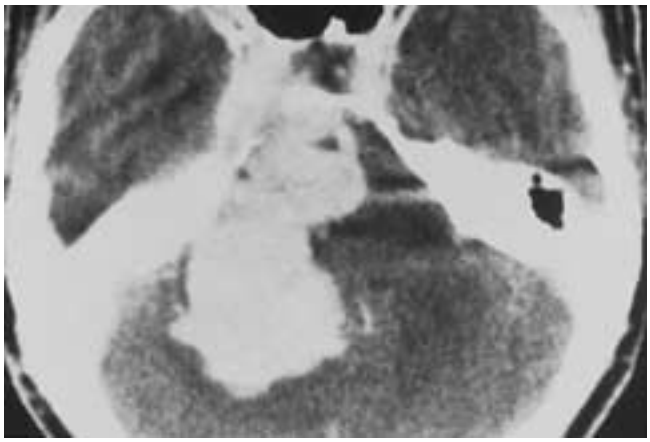

VIEW IMAGE

FIGURE 25-77 Large glomus jugulare tumor. Postcontrast CT. Fisch type D tumor with large intracranial tumor and cavernous sinus extension, usually considered incapable of resection.

Copyright © 2003, Mosby, Inc. All rights reserved.

Table 25-4
GLASSCOCK-JACKSON CLASSIFICATION OF PARAGANGLIOMAS

Tumor Type	Anatomic Extent	Surgical Procedure
Glomus Tympancium		
I	Small mass limited to promontory	Transcanal
II	Completely filling middle ear space	Extended facial recess
III	Filling middle ear and extending into mastoid	Extended facial recess
IV	Filling middle ear, extending into mastoid or through tympanic membrane to fill external auditory canal; may extend anterior to carotid	Extended facial recess
Glomus Jugulare		
I	Small; involving jugular bulb, middle ear, and mastoid	Traditional skull base dissection
II	Extending under internal auditory canal, may have intracranial extension	Traditional skull base dissection
III	Extending into petrous apex; may have intracranial extension	Modified infratemporal fossa approach
IV	Extending beyond petrous apex into clivus or infratemporal fossa; may have intracranial extension	Modified intratemporal fossa approach

or may not be visible on otoscopy, but it can be seen enlarging the anterior portion of the tympanic facial nerve canal on CT.[326]

Other Benign Lesions

Other intratympanic masses may be encountered from time to time and may be indistinguishable from glomus tympanicum tumors on CT, especially when they fill the tympanic cavity and obscure their precise origin. However, all of these lesions are rare and benign. The surgical approach for them is similar as long as the lesions are confined to the middle ear.[295] These lesions are discussed later along with malignant tumors of the middle ear.

Jugular Foramen Masses

For a description of jugular foramen masses, see Table 25-7. About 10% of the tumors involving the jugular foramen are not paragangliomas. These lesions include schwannoma of the caudal cranial nerves, meningioma, carcinomas (primary and metastatic), chondrosarcoma, and extension from nasopharyngeal carcinoma.

Jugular Foramen Schwannomas

Schwannomas of the caudal cranial nerves are rare.[20, 21] Jugular schwannomas, which include schwannomas from the glossopharyngeal, vagus, and spinal accessory nerves, are not always distinguishable from one another (Figs. 25-33 and 25-34). They have been classified into three types according to their location: (1) type A tumors grow predominantly intracranially, (2) type B tumors grow predominantly at the jugular foramen, and (3) type C tumors grow predominantly extracranially.[201] Type A tumors (Fig. 25-33) tend to cause acoustic or cerebellar symptoms, and type B and C tumors (Fig. 25-34) tend to be associated with the jugular foramen syndrome.[201, 202]

Schwannomas expand the jugular foramen symmetrically in contrast to paragangliomas, which often extend along dural sinuses and fissures and infiltrate the bone (Figs. 25-33 and 25-34).[20, 202, 298] Their angiographic hypervascularity is much less than that of paragangliomas, and small

Table 25-5
FISCH CLASSIFICATION OF PARAGANGLIOMAS

Tumor Type	Anatomic Extent	Surgical Procedure
A	Localized to middle ear cleft	Transmeatal
B	Limited to tympanomastoid area, with no infralabyrinthine compartment involvement	Combined transmeatal and transmastoid approach
C	Involving infralabyrinthine compartment and extending into petrous apex	Infratemporal fossa approach
C_1	Destroying jugular foramen and bulb, with limited involvement of vertical carotid canal	Usually sacrificing CN IX
C_2	Destroying infralabyrinthine compartment and invading vertical carotid canal	Usually sacrificing CN IX and X
C_3	Involving infralabyrinthine and apical compartments, with invasion of horizontal carotid canal	Usually sacrificing CN IX, X, and XI
D	With intradural extension	
D_1	Intradural extension less than 2 cm in diameter	Infratemporal fossa approach
D_2	Intradural extension greater than 2 cm in diameter	Two-stage neurosurgical-otologic removal
D_3	Inoperable intradural invasion	

Copyright © 2003, Mosby, Inc. All rights reserved.

BOX 25-2
INTRATYMPANIC MASSES

Vascular
Aberrant carotid artery
Laterally placed carotid
Carotid artery aneurysm
Persistent stapedial artery
Exposed jugular bulb

Nonneoplastic
Acquired cholesteatoma—common
Cholesterol granuloma (cyst)
Temporal lobe herniation
Choristoma

Benign Neoplasm
Paraganglioma—common
Facial schwannoma
Chorda tympani schwannoma
Hemangioma
Meningioma
Adenoma

Malignant Neoplasm
Squamous carcinoma
Adenocarcinoma
Rhabdomyosarcoma
Malignant melanoma
Lymphoma
Metastasis

scattered ''puddles'' of contrast medium are seen in the midarterial, capillary, and venous phases, with no arteriovenous shunting.[201, 203, 327, 328]

The CT and MR imaging appearances of jugular schwannomas are similar to those of acoustic schwannomas, varying with the proportion of cellular and cystic components of the tumor. The tumor itself, especially its extracranial component along the carotid sheath, is best demonstrated on MR imaging, and coronal and sagittal imaging has been another advantage of MR imaging over CT (Fig. 25-34). More recently, multidetector CT has produced excellent multiplanar images as well. CT with bone detail best demonstrates the foraminal changes and is most helpful in differentiating schwannomas from paragangliomas and jugular from hypoglossal schwannomas. Glossopharyngeal schwannomas can be suggested when there is selective enlargement of the pars nervosa. Vagus and spinal accessory schwannomas tend to arise slightly more laterally at the junction of the pars nervosa and vascularis.

Table 25-6
OTOSCOPIC DIFFERENTIAL DIAGNOSIS OF PULSATILE INTRATYMPANIC MASSES

Lesion	Color	Location
Aberrant carotid artery	Pink	Anteroinferior quadrant
Exposed jugular bulb	Blue	Posteroinferior quadrant
Glomus tympanicum tumor	Reddish purple	Posteroinferior quadrant
Glomus jugulare tumor	Reddish purple	Posteroinferior quadrant

Hypoglossal Schwannomas

Much of what has been said about jugular foramen schwannomas also applies to hypoglossal schwannomas. These tumors may be intracranial or extracranial or may be dumbbell-shaped, extending into both spaces (Fig. 25-78). In addition, because of the proximity of the hypoglossal canal to the foramen magnum, caudal intraspinal extension has been observed.[20]

Besides ipsilateral hemiatrophy of the tongue, other caudal cranial nerve deficits may develop as the tumor enlarges, and medullary and cerebellar compression and hydrocephalus may follow.[329, 330] In fact, many patients with intracranial hypoglossal schwannomas initially present with cerebellar symptoms or hydrocephalus rather than tongue dysfunction.[330]

Well-defined erosion of the hypoglossal canal is characteristic, although not invariably present.[331] After eroding the hypoglossal canal, the tumor may also erode the jugular foramen, the jugular tubercle, and the clivus, making differentiation from schwannomas of the jugular foramen difficult.[329]

Meningiomas

In addition to their common site of origin on the posterior petrous surface, meningiomas may rarely arise from within the temporal bone. Nager et al. list four such sites: (1) the internal acoustic meatus, (2) the jugular foramen, (3) the region of the geniculate ganglion, and (4) the sulcus of the greater and lesser superficial petrosal nerves.[332] Jugular foramen meningiomas show some of the behavior patterns

Table 25-7
DIFFERENTIAL DIAGNOSIS OF JUGULAR FORAMEN TUMORS

Tumor	CT Margin	Angiographic Vascularity	Typical MR Imaging Appearance
Schwannoma	Well-defined	Minimal to moderate	Homogeneous or cystic
Paraganglioma	Ill-defined	Marked	Salt-and-pepper
Meningioma	Subtly ill-defined	Minimal	Homogeneous
Malignant tumors (carcinomas, metastases)	Ill-defined	Minimal to marked	Homogeneous
Chondrosarcoma	Ill-defined	Minimal	Inhomogeneous T2
Nasopharyngeal carcinoma	Medial	Minimal	Infiltrative

Copyright © 2003, Mosby, Inc. All rights reserved.

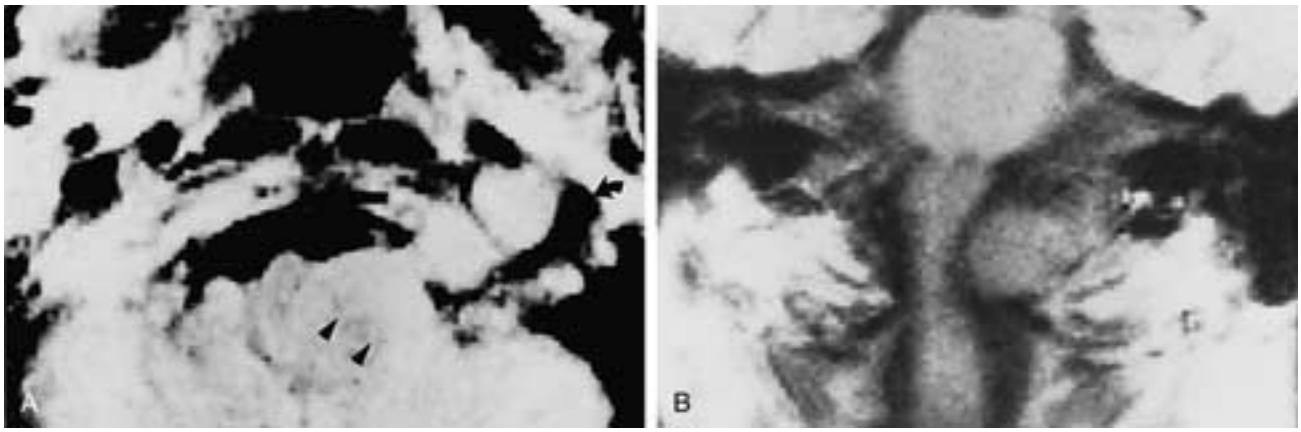

VIEW IMAGE

FIGURE 25-78 Trilobed hypoglossal schwannoma. **A** and **B**, T1-weighted images. The tumor is difficult to distinguish from jugular foramen schwannoma on transverse images, but its more caudal position at the medullocord junction is quite apparent on the coronal image (**B**). (Compare with Fig. 25-33D). The intracranial component of the tumor deforms the medulla (*arrowheads*), and the parapharyngeal component displaces the jugular vein (*curved arrows*).

of paragangliomas. Locally invasive around the jugular foramen, they grow through the jugular plate into the hypotympanum, descend through and along the jugular vein, and may show a small extension into the posterior fossa (Fig. 25-79).[333, 334]

On CT, their soft tissue components are indistinguishable from those of paragangliomas. Their bone margins, however, are better defined than those of paragangliomas but less well defined than those of schwannomas (Fig. 25-79F). Subtle sclerosis may be present in the infiltrated bone.

On MR imaging, they appear as other meningiomas do and lack the salt-and-pepper pattern of paragangliomas (Fig. 25-79A,B).[129, 135, 136, 303] On angiography, they show minimal vascularity, less than that of schwannomas, and do not have the prolonged cloudlike blush commonly seen in supratentorial meningiomas.

Malignant Tumors

Carcinoma, sarcoma, myeloma, metastasis, and other malignancies may be indistinguishable from paragangliomas on CT if they happen to destroy the jugular fossa (Figs. 25-80 to 25-82).[335] They usually lack the salt-and-pepper appearance of paragangliomas on MR imaging.[303] On angiography, most of them are much less vascular than paragangliomas. Exceptions to be considered include metastatic hypernephroma, metastatic pheochromocytoma, metastatic thyroid carcinoma, and hemangiopericytoma.[302, 336]

Chondrosarcomas

Occurring along the petrooccipital fissure, chondrosarcomas may involve the jugular foramen from its medial aspect and may contain calcifications (Figs. 25-83 and 25-84).[337]

Nasopharyngeal Carcinoma

Direct extension from nasopharyngeal carcinoma also may involve the jugular foramen, usually involving the medial aspect along with the petrooccipital fissure (Fig. 25-85).

Miscellaneous

An amyloidoma has been reported in the CPA and the jugular foramen, appearing as a patchy hyperdense mass with slight contrast enhancement and angiographic avascularity.[338] Skull base osteomyelitis can involve the jugular foramen as well as the rest of the temporal bone (Fig. 25-86). The clinical presentation helps differentiate osteomyelitis from tumors but the imaging appearances can overlap.

TUMORS INVOLVING THE FACIAL NERVE

Of the 1575 cases of facial nerve disorders managed over a 20-year period by May, only 91, or 6%, were caused by tumors; 895, or 57%, were caused by idiopathic or Bell's palsy, which classically begins abruptly and resolves or at least improves spontaneously within a few weeks.[287, 339] Thus the majority of facial nerve palsies do not require a radiologic workup.

The other causes of facial nerve disease in May's series were herpes zoster oticus (7%), trauma (17%), infection (4%), congenital (3%), hemifacial spasm (2%), central nervous system disease (1%), other (2%), and unknown (1%). However, May pointed out that 46 of the 91 tumors in his series were initially misdiagnosed as Bell's palsy.[339] Hence slow progression of paralysis beyond 3 weeks, absence of recovery after 6 months, ipsilateral recurrence, and other signs such as hemifacial spasm atypical of Bell's palsy demand a thorough radiologic investigation for

Copyright © 2003, Mosby, Inc. All rights reserved.

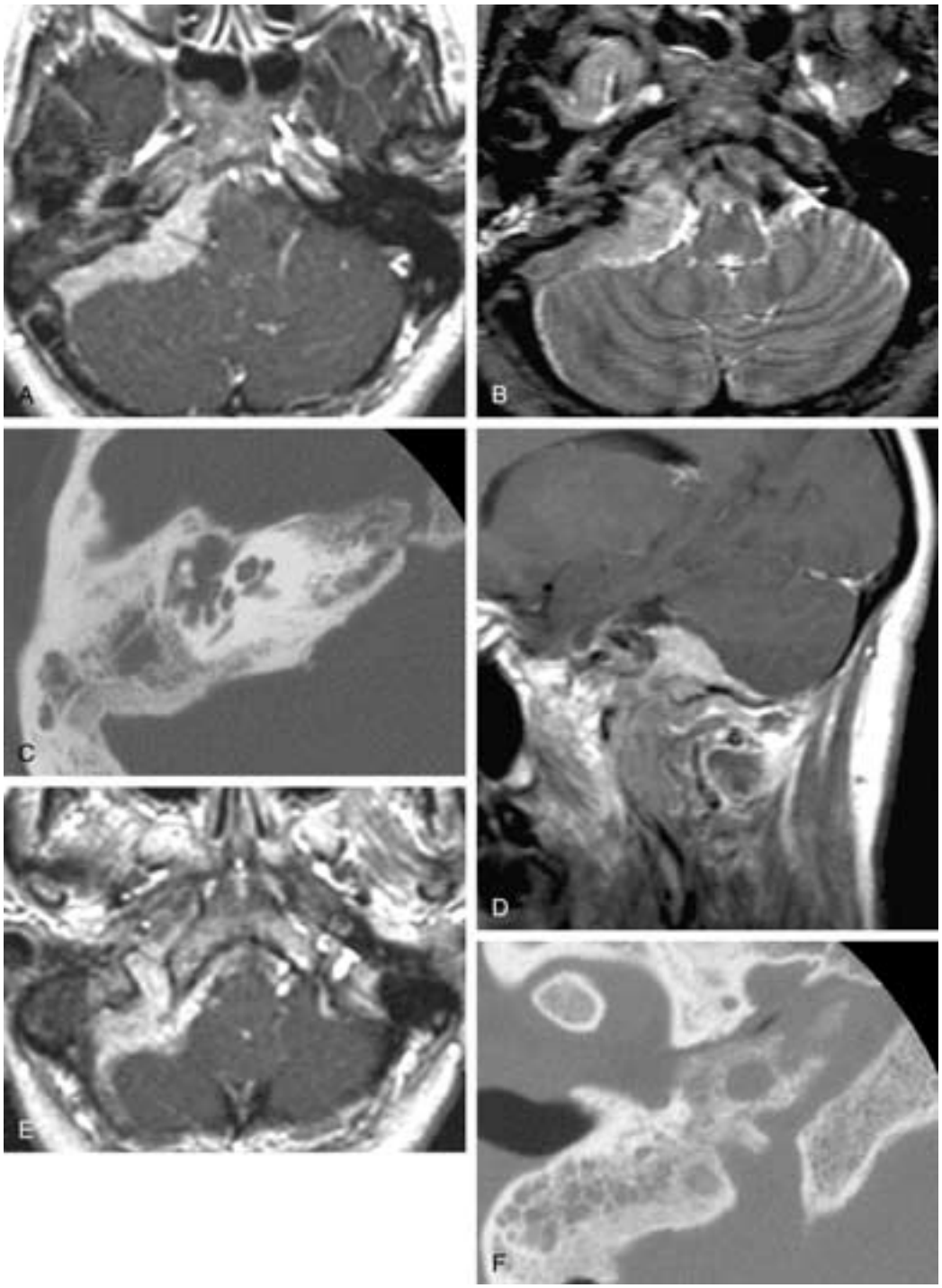

VIEW IMAGE

FIGURE 25-79 Jugular fossa meningioma. **A**, T1-weighted postgadolinium image. The broad dural-based tumor occupies the CPA cistern. Mastoid cell aeration is obliterated, and some enhancement is seen in the temporal bone as well. **B**, T2-weighted image at the same level. The tumor is isointense with gray matter. Note the signal changes in the temporal bone. **C**, CT bone window. Note the loss of sharpness of the cortex and sclerosis of the infiltrated bone. **D** and **E**, T1-weighted postgadolinium images. The meningioma extends through the jugular foramen. **F**, CT bone windows. Hyperostosis, new bone formation in the jugular foramen.

Copyright © 2003, Mosby, Inc. All rights reserved.

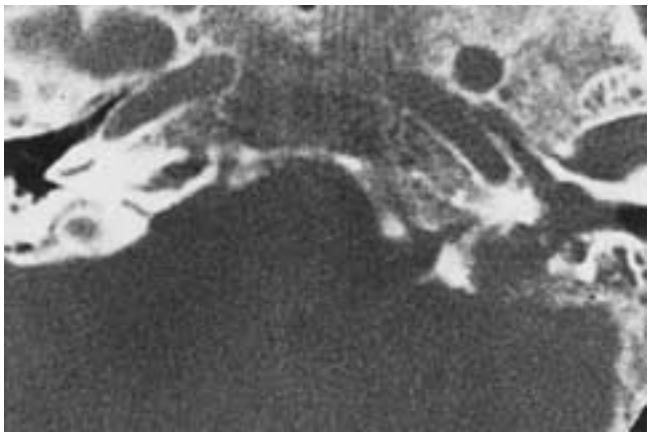

VIEW IMAGE

FIGURE 25-80 Anaplastic carcinoma of the jugular foramen. CT. Irregular, ill-defined destruction of the left jugular fossa is indistinguishable from that of glomus jugulare tumor. A selective external carotid angiogram (not shown) showed no tumor vascularity.

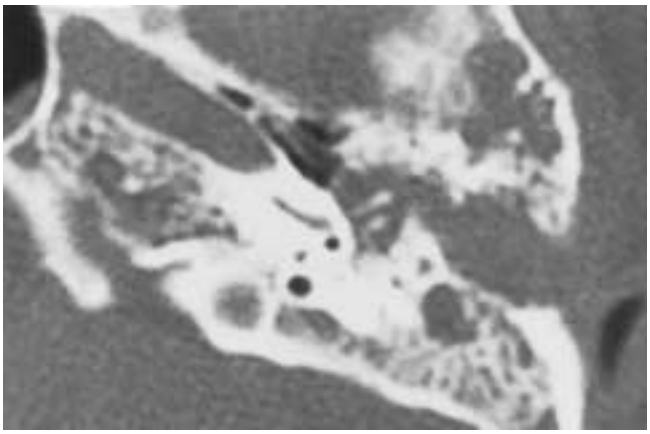

VIEW IMAGE

FIGURE 25-82 EAC and middle ear squamous cell carcinoma. Axial CT. There is ill-defined destruction of the anterior and posterior walls of the EAC and the lateral wall of the protympanum. The tumor is indistinguishable from adenoid cystic carcinoma or adenocarcinoma.

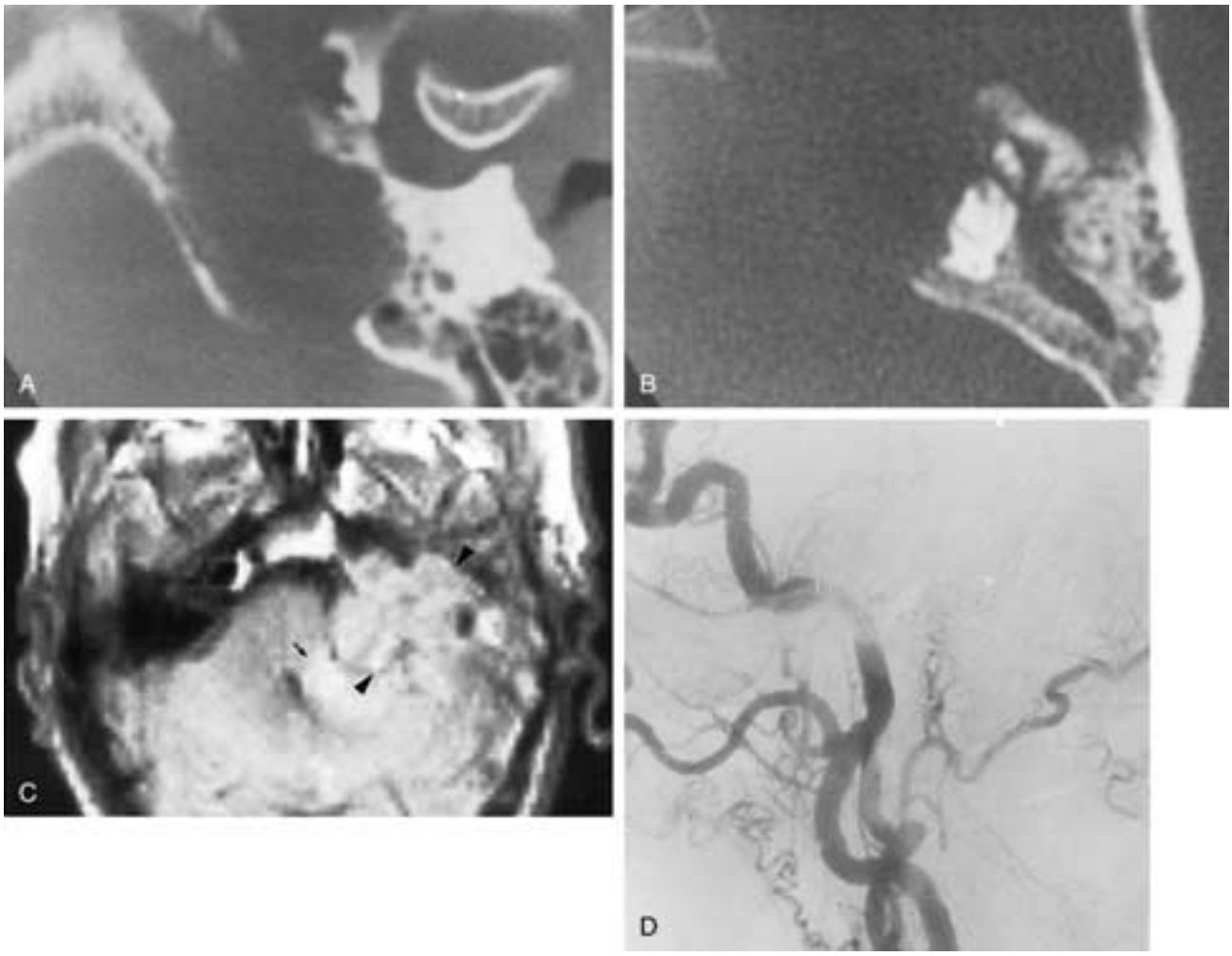

VIEW IMAGE

FIGURE 25-81 Malignant giant cell tumor. **A** and **B**, Axial CT. Ill-defined geographic borders suggest a moderately aggressive lesion. Destruction of the otic capsule is atypical of paraganglioma. **C**, Proton density image. The tumor is inhomogeneous on T2-weighted images but lacks the salt-and-pepper heterogeneity seen in medium-sized or large paragangliomas on T1-weighted images (tumor, *arrowheads*; compare with Fig. 25-71). There is adjacent edema (*arrow*). **D**, Selective carotid angiogram. As in most malignant tumors, tumor vascularity is much less than in a paraganglioma. (Compare with Fig. 25-70.)

Copyright © 2003, Mosby, Inc. All rights reserved.

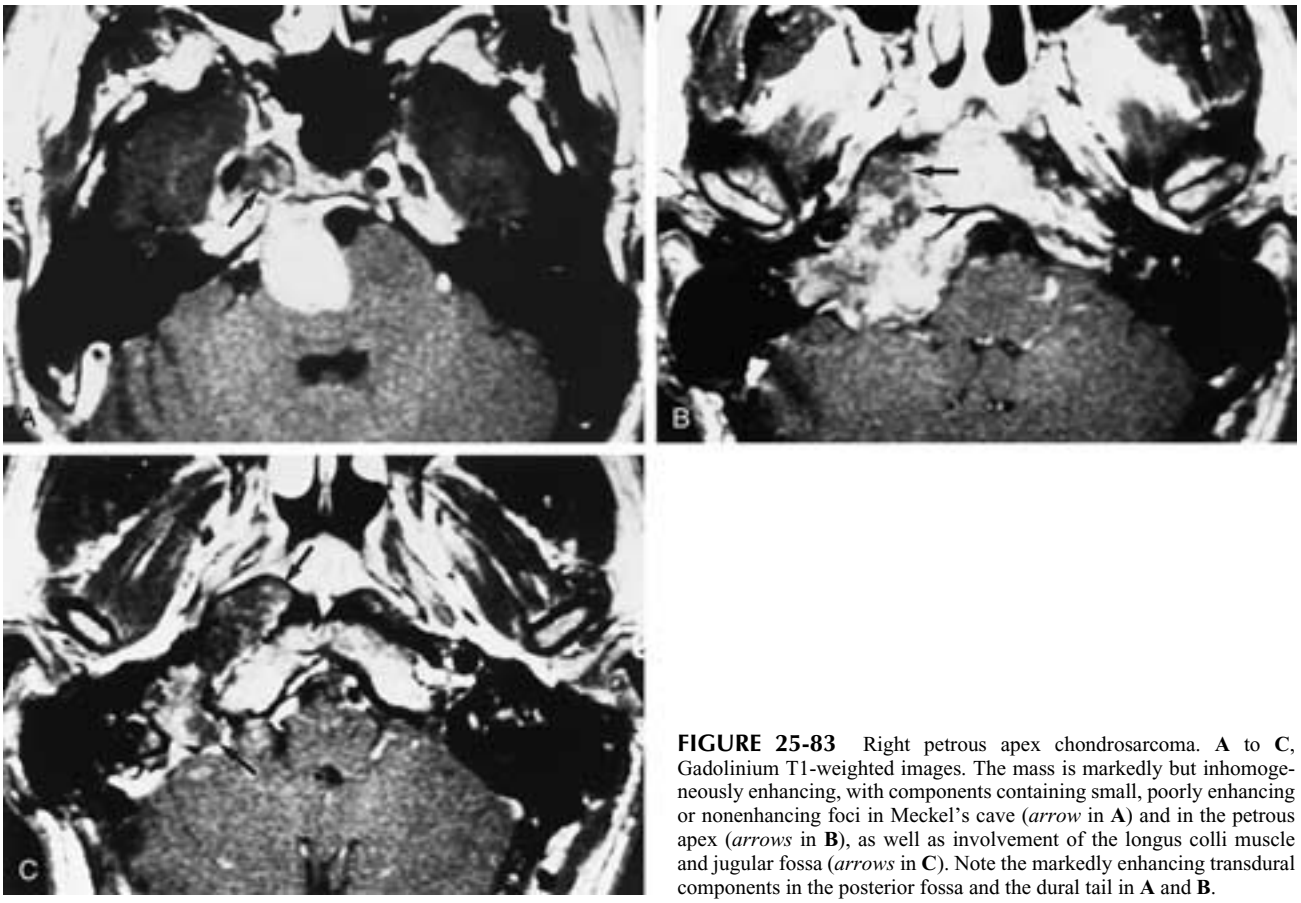

FIGURE 25-83 Right petrous apex chondrosarcoma. **A** to **C**, Gadolinium T1-weighted images. The mass is markedly but inhomogeneously enhancing, with components containing small, poorly enhancing or nonenhancing foci in Meckel's cave (*arrow* in **A**) and in the petrous apex (*arrows* in **B**), as well as involvement of the longus colli muscle and jugular fossa (*arrows* in **C**). Note the markedly enhancing transdural components in the posterior fossa and the dural tail in **A** and **B**.

VIEW IMAGE

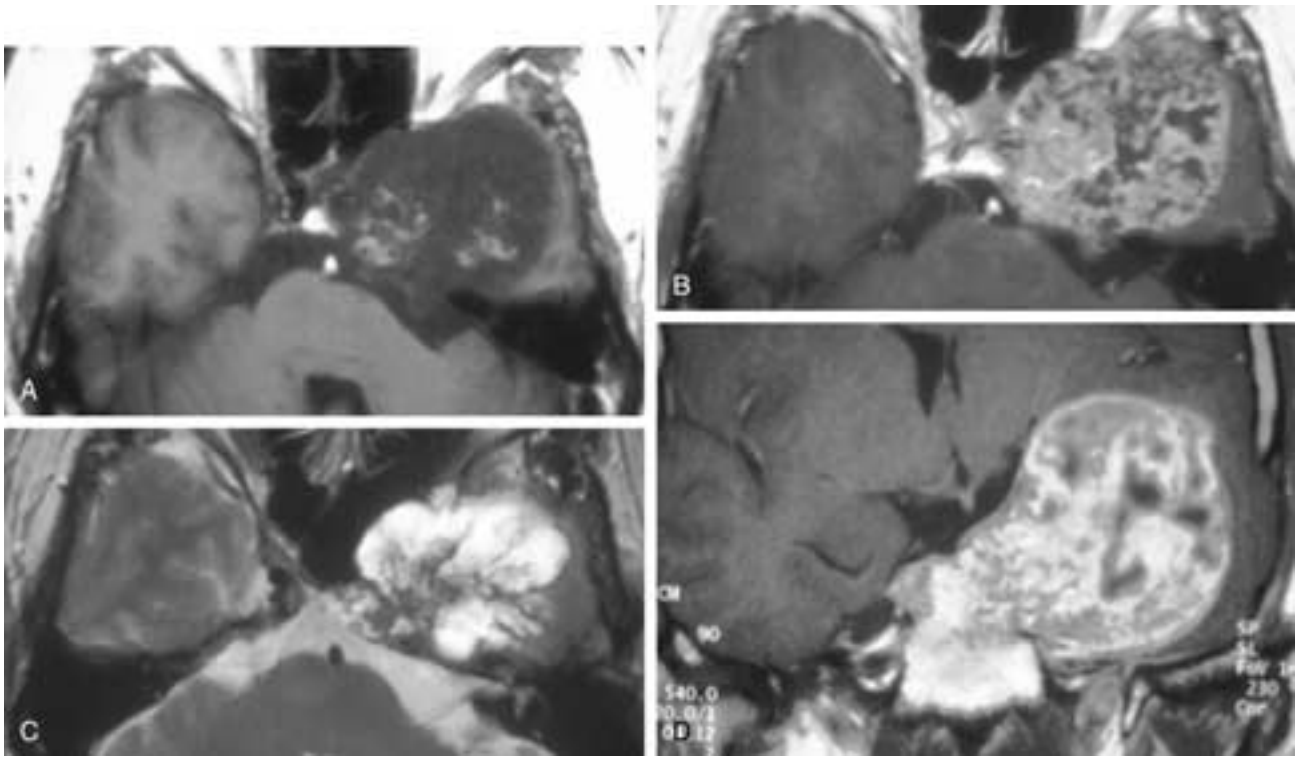

FIGURE 25-84 Skull base chondrosarcoma. **A** and **B**, T1-weighted pre- and postgadolinium images. **C**, Axial T2-weighted image. **D**, Coronal T1-weighted image after gadolinium enhancement.

VIEW IMAGE

Copyright © 2003, Mosby, Inc. All rights reserved.

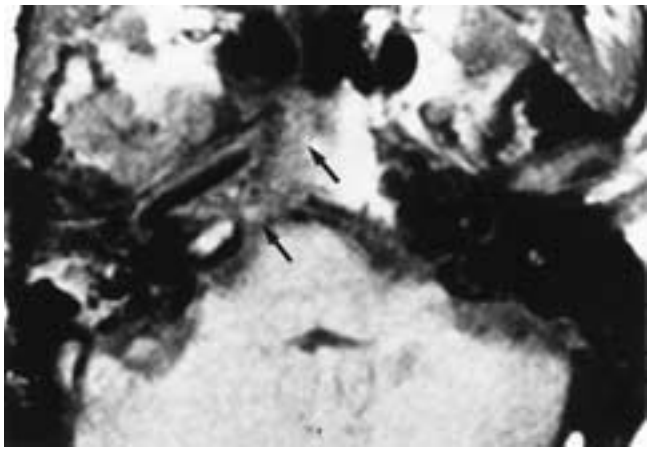

VIEW IMAGE

FIGURE 25-85 Nasopharyngeal carcinoma invading the right petrous apex bone and clivus. The image shows hypointense tumor (*arrows*) infiltrating the right petrous apex and right half of the clivus.

tumor.[339] Abrupt onset alone is no assurance that the palsy is not caused by tumor.[340, 341]

Manifestations of Facial Nerve Dysfunction and Lesion Localization

The facial nerve, in its long course from the pons through the CPA, IAC, and facial nerve canal (FNC) to its arborization in the parotid gland, is subject to involvement by tumors of many types at different locations, and unfocused or misdirected imaging studies have often delayed diagnosis.[310, 311] Awareness of clinical localization is of great assistance to the radiologic investigation.

Facial nerve paralysis is classically divided into central and peripheral categories. Central lesions are located above the motor nucleus in the brainstem and result in contralateral motor weakness of the lower part of the face. Peripheral nerve lesions cause ipsilateral motor weakness of both the upper and lower parts of the face. Hemifacial spasm is an irritative phenomenon of the facial nerve. Myokymia is a fine fibrillary activity of all muscles on one side of the face and is most often seen in patients with multiple sclerosis or brainstem glioma.[287]

Facial nerve compromise in the brainstem is likely to be accompanied by palsy of other cranial nerves and perhaps contralateral long tract signs. In the CPA and the IAC, it is likely to be accompanied or preceded by symptoms involving the acoustic nerve.[342, 343]

A facial nerve lesion within the temporal bone can be further localized according to the presence or absence of involvement of (1) the greater superficial petrosal nerve (lacrimation), (2) the nerve of the stapedius muscle (stapes reflex), and (3) the chorda tympani nerve (taste and salivation). Thus a lesion may be described as suprageniculate if all three are affected, suprastapedial if (2) and (3) are affected, infrastapedial if only (3) is affected, and infrachordal if all three are intact.[344] However, in the case of tumors, the accuracy of ''topognosis'' has been questioned because tumors may spare some of the fibers in the involved segment of the nerve. Thus, for instance, a tumor of the geniculate ganglion may leave the stapedial reflex intact. However, a positive finding is considered accurate. If, for instance, lacrimation is affected, then the lesion must be at the geniculate or more central.

If the origin of a peripheral facial palsy is clinically unlocalized or is localized to the pons, the CPA, or the IAC, MR imaging including the pons and the parotid gland is the preferred imaging modality. If a lesion is clinically localized to the FNC, MR imaging and high-resolution CT with maximum bone detail may both be used. For acute facial palsy, Gd-MR imaging is clearly the modality of choice.[345, 346]

It should be noted that tumor destruction of the FNC does not necessarily cause facial nerve palsy if there is no invasion of the facial nerve.[347] Conversely, perineural and intraneural tumor spread (notably from adenoid cystic carcinoma of the parotid gland) can extend along a considerable length of the facial nerve within the FNC, causing facial palsy but little if any bone change (Fig. 25-87).[347, 348] In such a case, Gd-MR imaging may show the abnormality more readily than CT (Fig. 25-88).

There are other important caveats when imaging facial

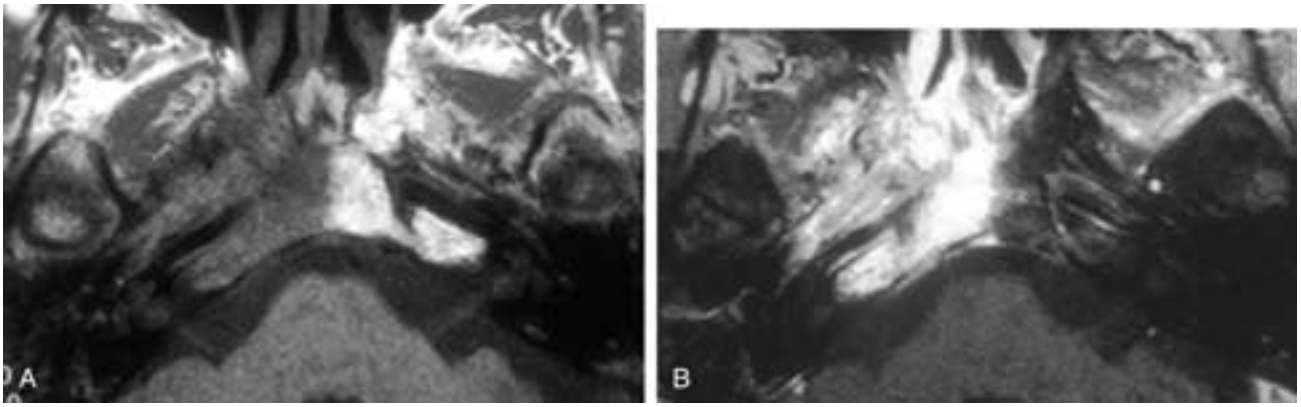

VIEW IMAGE

FIGURE 25-86 Skull base osteomyelitis. **A** and **B**, T1-weighted pre- and postgadolinium fat-saturated images. The petrous apex and right side of the clivus are hypointense, with soft-tissue involvement. The fat-saturated image after gadolinium administration shows strong enhancement of the involved soft tissue and bones. (Compare with Fig. 25-85.)

Copyright © 2003, Mosby, Inc. All rights reserved.

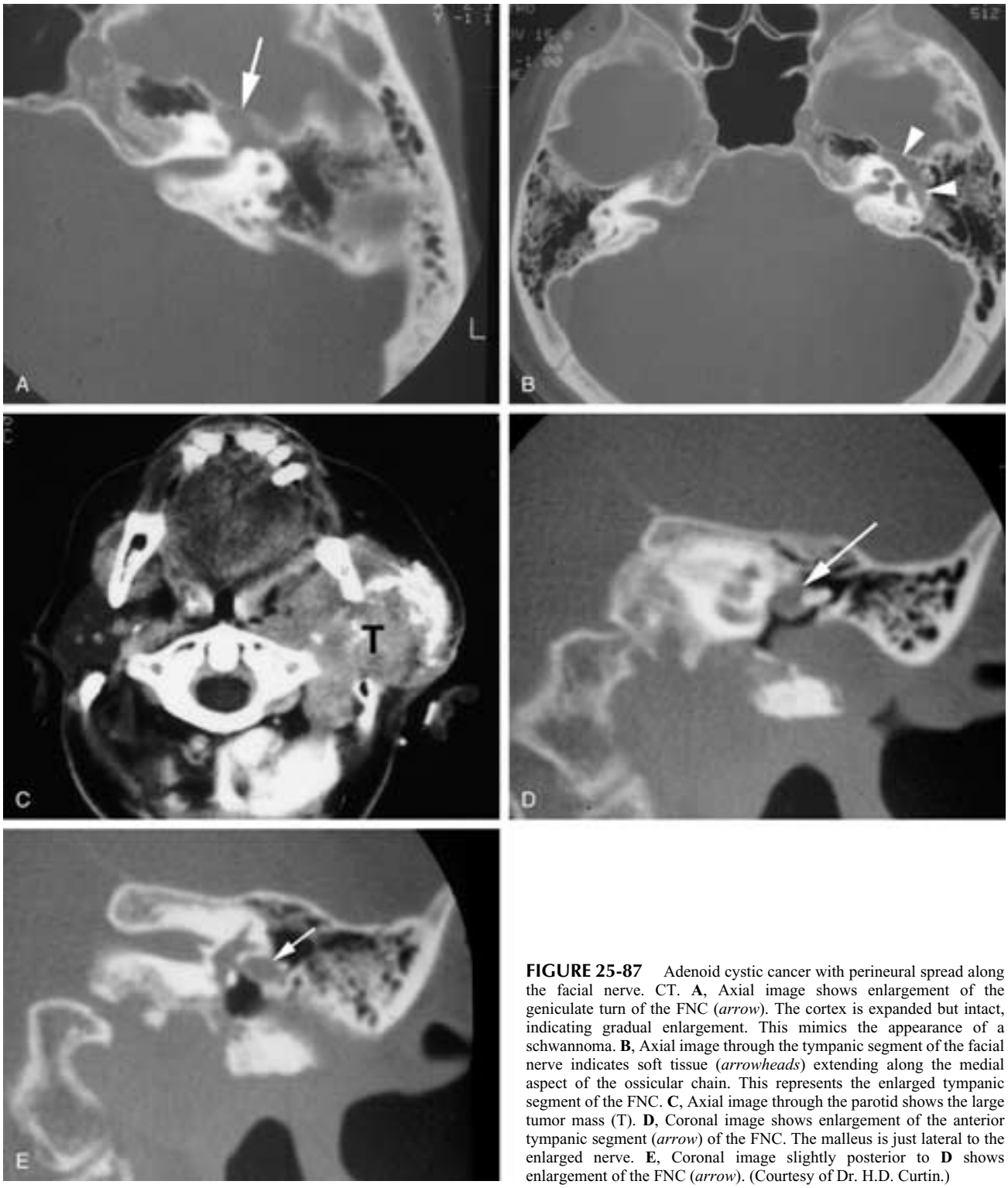

FIGURE 25-87 Adenoid cystic cancer with perineural spread along the facial nerve. CT. **A**, Axial image shows enlargement of the geniculate turn of the FNC (*arrow*). The cortex is expanded but intact, indicating gradual enlargement. This mimics the appearance of a schwannoma. **B**, Axial image through the tympanic segment of the facial nerve indicates soft tissue (*arrowheads*) extending along the medial aspect of the ossicular chain. This represents the enlarged tympanic segment of the FNC. **C**, Axial image through the parotid shows the large tumor mass (T). **D**, Coronal image shows enlargement of the anterior tympanic segment (*arrow*) of the FNC. The malleus is just lateral to the enlarged nerve. **E**, Coronal image slightly posterior to **D** shows enlargement of the FNC (*arrow*). (Courtesy of Dr. H.D. Curtin.)

VIEW IMAGE

nerve palsy. On Gd-MR imaging, mild to moderate enhancement of the facial nerve, because of the presence of the perineural venous plexus, is seen in the facial nerve canal in the majority of normal subjects.[349] Such physiologic enhancement is usually symmetric in intensity. Thus, in a patient with unilateral symptoms, it is only when there is asymmetric facial nerve enhancement or apparent enlargement of the nerve that pathology should be suspected. Intense enhancement along the nerve, with or without discernible swelling, is found in idiopathic Bell's palsy and herpes zoster oticus (Ramsay-Hunt syndrome).[345, 350–353] In these inflammations the neural enhancement occurs not only along the facial nerve canal, including the labyrinthine segments, but also in the fundus of the IAC. These

Copyright © 2003, Mosby, Inc. All rights reserved.

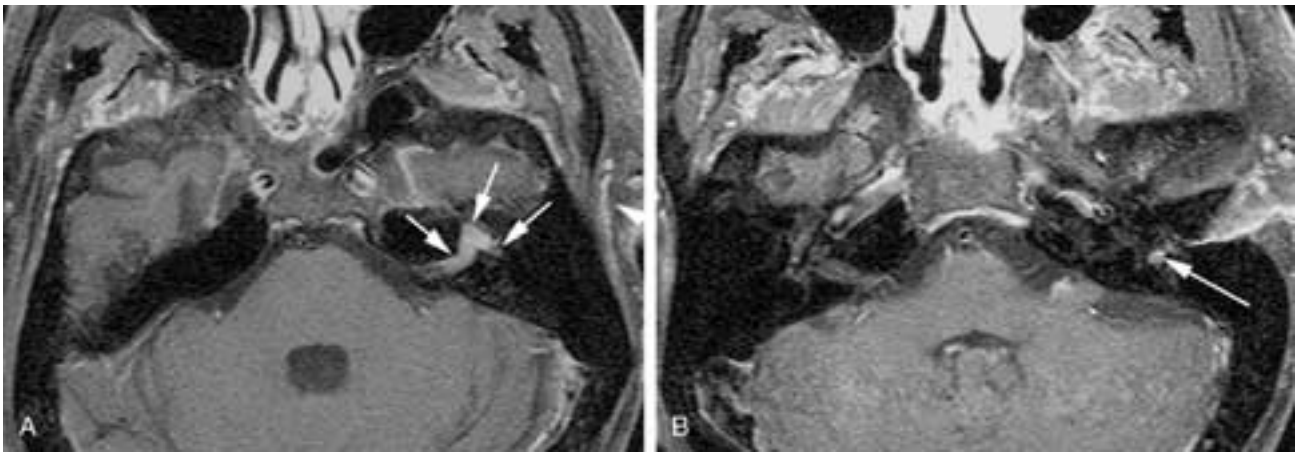

VIEW IMAGE

FIGURE 25-88 MR imaging of perineural spread from adenoid cystic cancer of the parotid gland (not shown). **A**, Postgadolinium T1-weighted MR image with fat suppression. There is enlargement of the anterior tympanic segment (*lateral arrow*) and the geniculate turn (*middle arrow*), as well as the labyrinthine segment of the FNC. There is an enhancing mass (*medial arrow*) extending into the IAC. **B**, Caudad slice shows the enlarged, enhancing facial nerve (*arrow*) at the region of the pyramidal turn. (Courtesy of Dr. Peter Som.)

enhancements should not be mistaken for tumors. Also not to be confused with a facial nerve tumor is enlargement of the tympanic facial nerve canal by a persistent stapedial artery, best seen on CT (Chapter 26) and enlargement of the geniculate fossa by an arachnoid diverticulum.[354]

Tumors

Tables 25-8 and 25-9 show the gamut of benign and malignant tumors, respectively, in May's experience of 91 tumors causing facial palsy.[339] In Fisch and Rüttner's series of 43 intratemporal tumors involving the facial nerve, there were 12 congenital cholesteatomas (10 supralabyrinthine and 2 apex), 9 schwannomas (neuromas), and 9 hemangiomas (4 cavernous and 5 ossifying). Less common benign tumors included three meningiomas, three glomus jugular tumors, and one arachnoid cyst.[341, 355] Malignant tumors included four squamous carcinomas and two rhabdomyosarcomas. Although the majority of Fisch and Rüttner's patients had slowly progressive facial palsy, six had facial palsy of sudden onset. This group included three of the five patients with ossifying hemangiomas.[341]

Facial nerve tumors in the CPA and IAC share the same differential diagnosis as acoustic schwannomas, and those in the tympanic cavity share the same differential diagnosis as intratympanic paragangliomas. These differential diagnoses have been discussed in the sections on Acoustic Schwannomas (Neuromas) and Paragangliomas and Jugular Foramen Tumors, respectively. The three most common tumors in Fisch and Rüttner's series—schwannoma, hemangioma, and congenital cholesteatoma—are described in detail in the following three sections. All three tend to occur in the region of the geniculate ganglion (Table 25-10).[341]

Facial Schwannomas

Facial schwannomas can occur along any segment of the nerve (Figs. 25-31 and 25-32, 25-89 to 25-97).[356] The

Table 25-8
BENIGN TUMORS CAUSING FACIAL PALSY IN 44 PATIENTS

Cell Type	Tumor Location	Patients (No.)	Total
Schwannoma	Acoustic nerve		12
	CPA*	6	
	IAC†	6	
	Facial nerve		12
	Labyrinthine segment	3‡	
	Geniculate ganglion	1	
	Tympanic segment	2	
	Mastoid segment	5	
	Chorda tympani nerve	1	
Vascular			6
Meningioma	CPA	3	
	Geniculate ganglion	3	
Hemangioma			3
Osseous	Geniculate ganglion	1	
Capillary	Geniculate ganglion	1	
	Parotid	1	
AV Malformation			1
	Geniculate ganglion	1	
Glomus Jugulare			3
	Skull base	3	
Congenital Cholesteatoma			3
	IAC	2	
	Tympanic segment	1	
Others			4
Inflammatory mass	Vertical segment	1	
Granular cell myoblastoma	Vertical segment	1	
Giant cell tumor	Sphenoid	1	
Branchial cleft cyst	Skull base	1	
			44

From May M. The Facial Nerve. New York: Thieme, 1986.
**CPA,* Cerebellopontine angle.
†*IAC,* Internal auditory canal.
‡Facial nerve schwannoma extended from labyrinthine segment to extracranial segment.

Copyright © 2003, Mosby, Inc. All rights reserved.

Table 25-9
MALIGNANT TUMORS CAUSING FACIAL PALSY IN 47 PATIENTS

Location	Type	Patients (No.)	Total
Temporal bone			19
	Primary (epidermoid)	2	
	Leukemia	5	
	Lymphoma	3	
	Reticular sarcoma	1	
	Metastatic (breast)	3	
	Lung	3	
	Prostate	2	
Parotid			14
	Adenoid cystic carcinoma	5	
	Mucoepidermoid carcinoma	3	
	Epidermoid carcinoma	3	
	Undifferentiated carcinoma	2	
	Anaplastic carcinoma	1	
Submandibular gland			1
	Adenoid cystic carcinoma	1	
Skin			5
	Epidermoid carcinoma	2	
	Basal cell carcinoma	2	
	Fibrous histiocytoma	1	
Other			8
	Tonsil (epidermoid)	2	
	Nasopharyngeal (epidermoid)	2	
	Orohypopharyngeal (epidermoid)	2	
	Hodgkins' (neck)	1	
	Unconfirmed	1	
			47

From May M. The Facial Nerve. New York: Thieme, 1986.

geniculate ganglion is frequently involved and is often affected whether the tumor extends primarily proximally or distally.[199]

The clinical presentations of facial schwannomas depend on the segment of the nerve involved.[262] Interestingly, fewer than half of the facial schwannomas initially appear with facial palsy.[198, 199] Many have no facial nerve symptoms at all. In one series, only two of eight cases had facial palsy as a presenting symptom, and only two of the eight had hemifacial spasm.[199] This may result partly from the fact that some schwannomas compress but do not invade the nerve. Consequently, nerve deficits result only where high pressure can be exerted on the nerve. However, even when the tumor exerts enough pressure to enlarge the facial nerve canal, paralysis is not universally present, and some investigators have indicated that a facial paralysis occurs only after a substantial percentage of the nerve fibers have been destroyed.

In general, facial schwannomas in the CPA and the IAC are characterized by sensorineural hearing loss, apparently because the more thinly myelinated sensory fibers of the acoustic nerve are more vulnerable to compression than are the more thickly myelinated motor fibers of the facial nerve (Figs. 25-32 and 25-33).[199] Schwannomas straddling the posterior and middle cranial fossae may cause both acoustic and facial nerve symptoms (Fig. 25-90). Schwannomas in the geniculate region grow silently into the middle cranial fossa, reaching several centimeters in diameter before hearing loss or facial nerve symptoms appear (Fig. 25-91).[357] Those in the tympanic segment tend to first cause conductive hearing loss by ossicular interference (Figs. 25-92 and 25-93). Those in the mastoid segment are likely to have facial palsy as the presenting symptom (Figs. 25-94 and 25-96).[199] Finally, those tumors distal to the stylomastoid foramen appear as painless neck masses.[358] Multisegment tumors (Figs. 25-94 and 25-95) are usually accompanied by facial nerve symptoms.[359]

Excision of a facial schwannoma almost always requires segmental resection of the facial nerve. Tumor removal is usually postponed in patients without facial weakness, but it should be performed before substantial loss of neural function occurs. In most cases, it is best to resect the tumor and restore continuity of the nerve with an end-to-end anastomosis or a ''cable'' nerve graft.[360]

Facial schwannomas are often sausage-shaped, expanding long segments of the FNC (Figs. 25-89, 25-94 and 25-95). There may be more than one ''link,'' for example, a component in the IAC and a component in the middle cranial fossa connected via a narrow waist through the labyrinthine FNC (Figs. 25-90 and 25-97). Their CT density and enhancement and MR imaging intensity are similar to those of acoustic schwannomas.

When facial schwannomas occur in the CPA or in the IAC, they may be clinically and radiologically indistinguishable from acoustic schwannomas (Figs. 25-31 to 25-33).[200, 361] Eccentricity of tumor mass to the axis of the IAC may be a diagnostic clue.[362] The differential diagnoses in these two regions are identical to those of acoustic schwannomas (Tables 25-2 and 25-4).

For differential diagnosis in the geniculate ganglion

Table 25-10
DIFFERENTIAL FEATURES OF COMMON GENICULATE GANGLION TUMORS ON CT

Feature	Facial Schwannoma	Benign Vascular Tumor	Epidermoid
Size	Quite variable	Very small	Small
Shape	Round or sausage shaped	Irregular	Unilocular or multilocular
Margins	Well defined	Ill-defined	Extremely well defined
Location	Along IAC,* FNC,† or in MF‡	IAC, GG§ or posterior genu	Supralabyrinthine
Density	Nearly isodense	Intratumoral bone	Hypodensity
Enhancement	Yes	Yes	No

**IAC,* Internal auditory canal.
†*FNC,* Facial nerve canal.
‡*MF,* Middle fossa.
§*GG,* Geniculate ganglion.

Copyright © 2003, Mosby, Inc. All rights reserved.

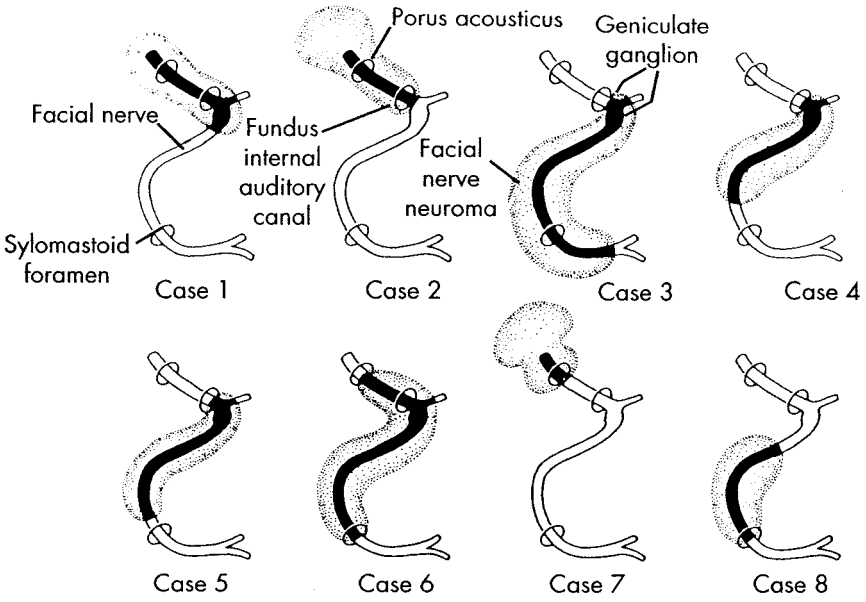

FIGURE 25-89 Diagrammatic representation of eight facial schwannomas. The shaded area represents segments of nerve involved by tumor. Most facial schwannomas involve long segments of nerve. (From Latack JT, Gabrielson TO, Knake JE, et al. Facial nerve neuromas. Radiologic evaluation. Radiology 1983;149:731–739.)

VIEW IMAGE

region, other tumors prevalent in that location, namely, epidermoid cyst, hemangioma, and meningioma, are the primary considerations (Figs. 25-98 to 25-100). The changes seen on high-resolution CT are helpful: the borders of hemangiomas are not sharp (Figs. 25-98 and 25-99), those of epidermoids are extremely sharp (Fig. 25-101), and those of schwannomas are moderately sharp (Figs. 25-90 to 25-96). Hemangiomas and epidermoids are usually small, and schwannomas are variable in size and may be quite large (Figs. 25-90, 25-91, 25-94, 25-98 and 25-100). Hemangiomas may contain intratumoral bone (ossifying hemangioma) (Figs. 25-42, 25-43, 25-98 and 25-99).[241, 242] Epidermoids are isodense or hypodense and are nonenhancing.[363] The CT and MR imaging features of meningioma at this location may be expected to resemble those in the CPA.

Facial schwannomas straddling the posterior and middle fossae transgress the petrous bone through its midsection

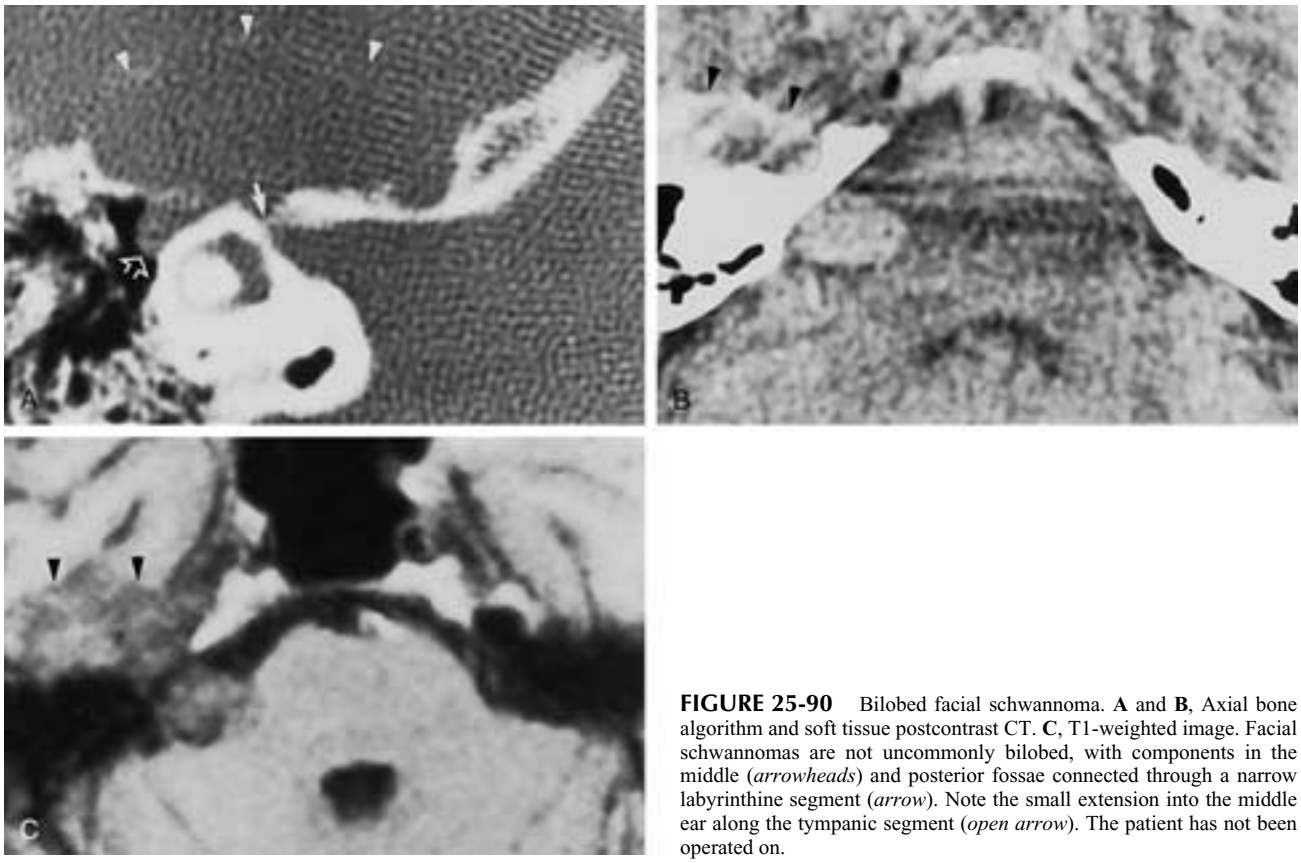

FIGURE 25-90 Bilobed facial schwannoma. **A** and **B**, Axial bone algorithm and soft tissue postcontrast CT. **C**, T1-weighted image. Facial schwannomas are not uncommonly bilobed, with components in the middle (*arrowheads*) and posterior fossae connected through a narrow labyrinthine segment (*arrow*). Note the small extension into the middle ear along the tympanic segment (*open arrow*). The patient has not been operated on.

VIEW IMAGE

Copyright © 2003, Mosby, Inc. All rights reserved.

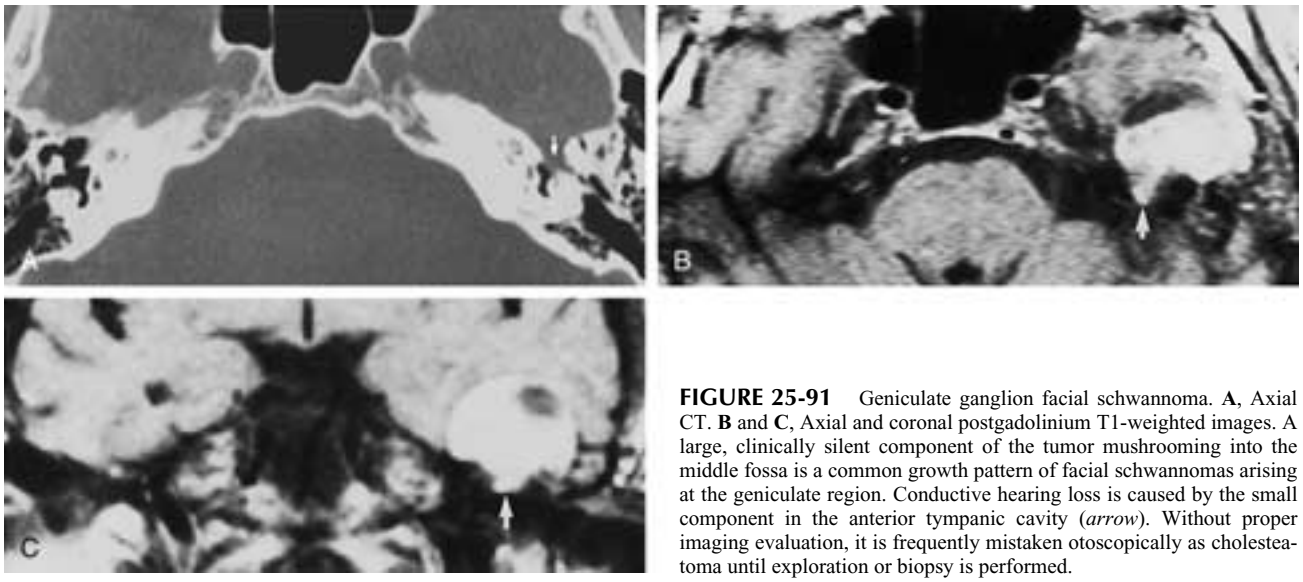

FIGURE 25-91 Geniculate ganglion facial schwannoma. **A**, Axial CT. **B** and **C**, Axial and coronal postgadolinium T1-weighted images. A large, clinically silent component of the tumor mushrooming into the middle fossa is a common growth pattern of facial schwannomas arising at the geniculate region. Conductive hearing loss is caused by the small component in the anterior tympanic cavity (*arrow*). Without proper imaging evaluation, it is frequently mistaken otoscopically as cholesteatoma until exploration or biopsy is performed.

VIEW IMAGE

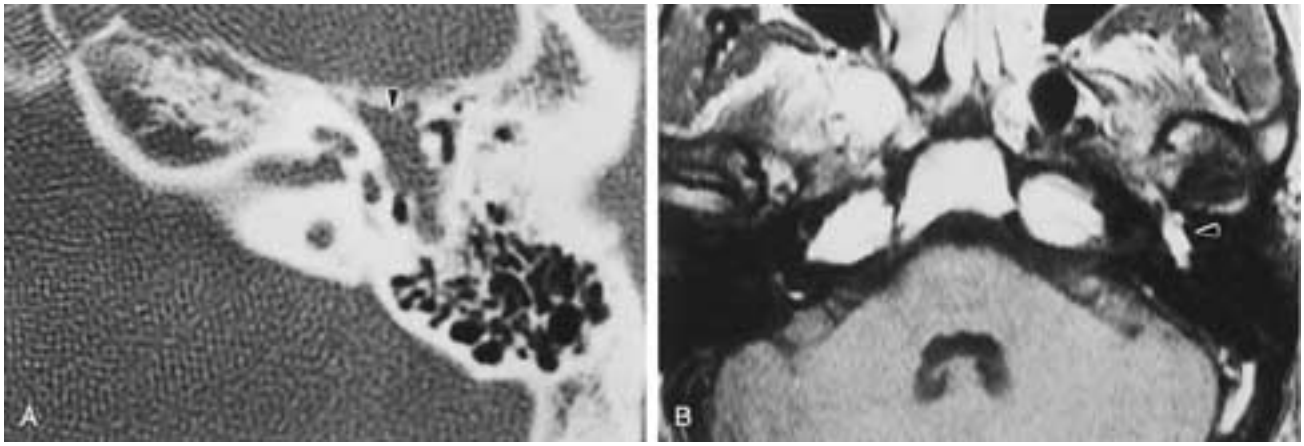

FIGURE 25-92 Tympanic facial nerve schwannoma, left. **A**, Axial CT. The arrowhead points to a soft-tissue mass in the middle ear, medial to the ossicles, lying along the tympanic FNC. **B**, Axial T1-weighted postcontrast MR image. The arrowhead shows an enhancing mass along the tympanic facial nerve. (From Jackler RK, Brackmann DE, eds. Neurotology. St. Louis: Mosby-Year Book, 1994.)

VIEW IMAGE

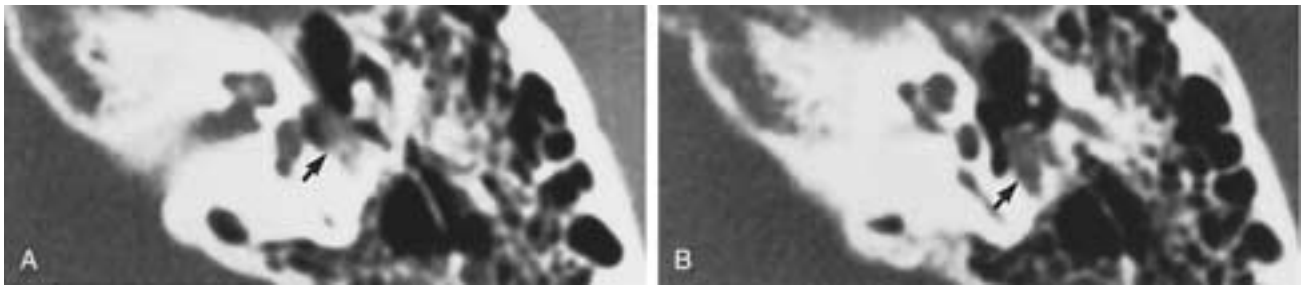

FIGURE 25-93 Tympanic segment facial schwannoma. **A** and **B**, Axial CT. Tumor (*arrow*) arising from the posterior genu region caused conductive hearing loss. Other tumors that may be similar in appearance include intratemporal cholesteatoma. (See also Fig. 25-89.) (Courtesy of Dr. Lyle Wendling.)

VIEW IMAGE

Copyright © 2003, Mosby, Inc. All rights reserved.

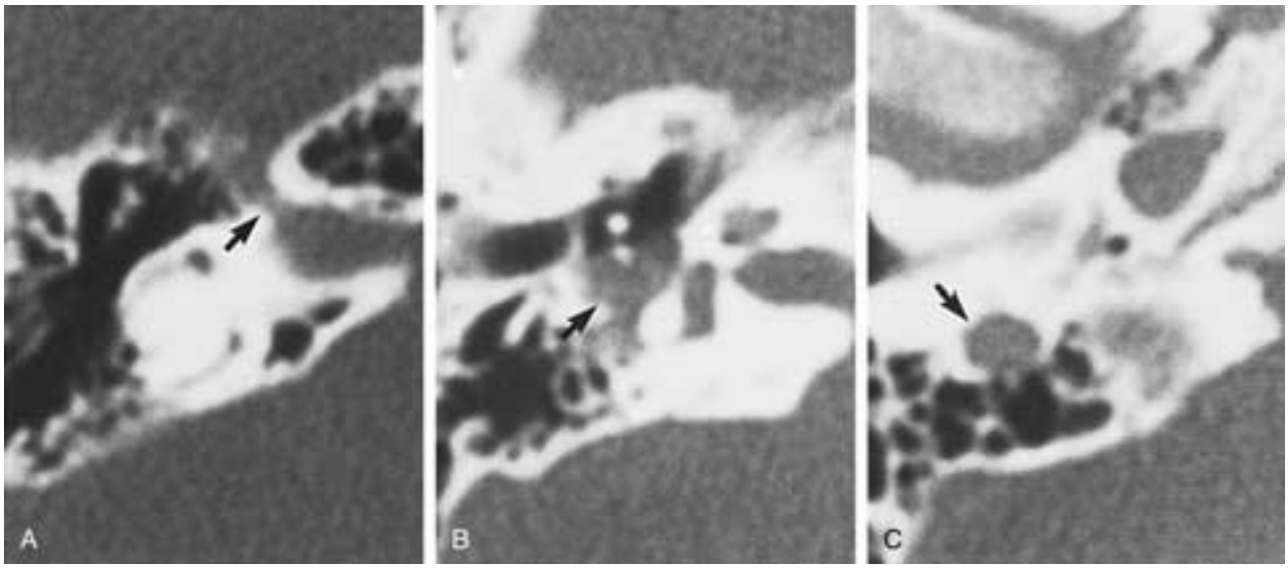

VIEW IMAGE

FIGURE 25-94 FNC facial schwannoma. **A** to **C**, Axial CT. To varying degrees, the tumor has expanded along the entire length of the FNC (*arrows*).

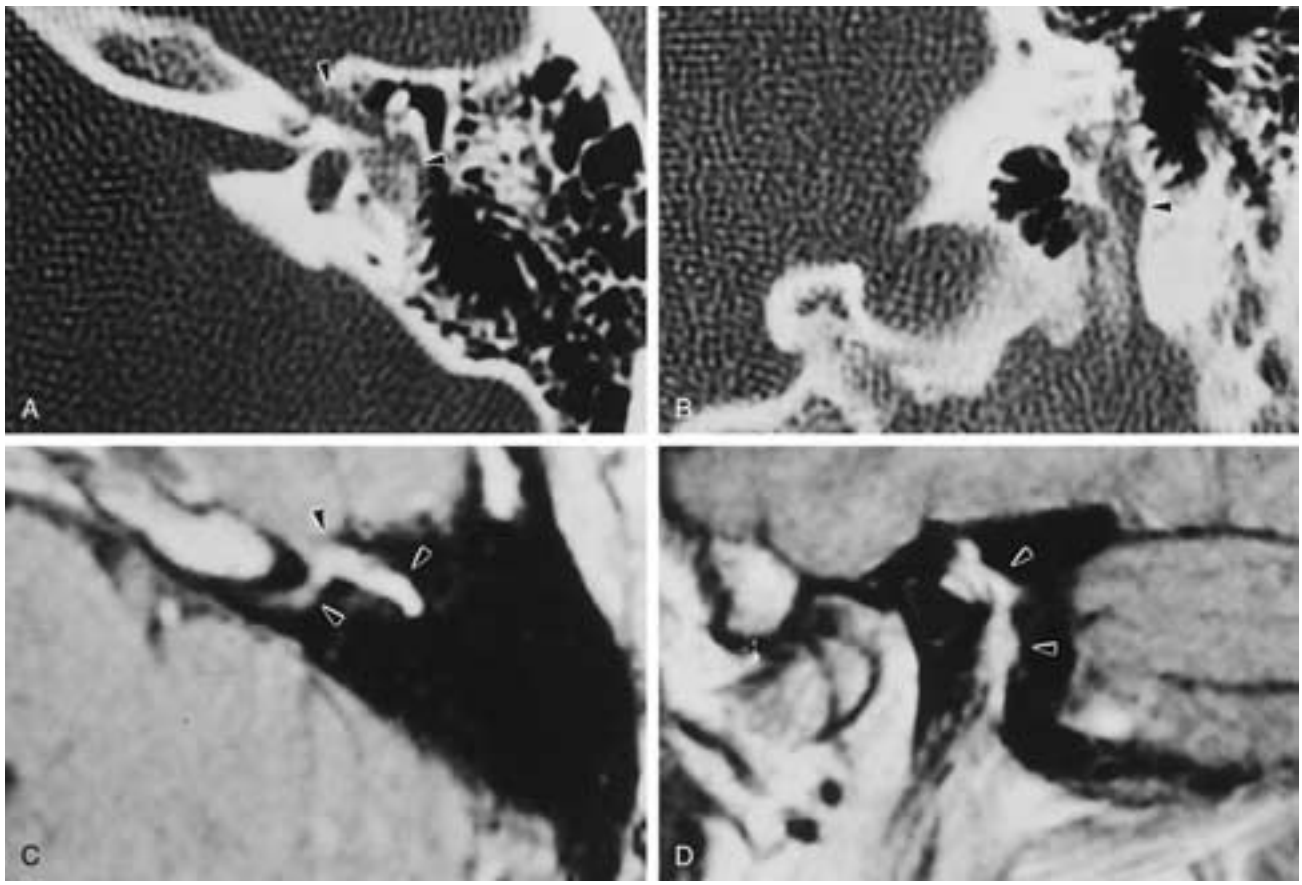

VIEW IMAGE

FIGURE 25-95 Facial nerve schwannoma, left, extending from the IAC through the descending (mastoid) segment. **A**, Axial CT. Arrowheads at the schwannoma in the geniculate and tympanic segments. **B**, Coronal CT. Tumor in the mastoid segment (*arrowhead*). **C**, Axial T1-weighted postcontrast MR image. Tumor in the IAC, geniculate, and tympanic segments (*arrowheads*). **D**, Sagittal T1-weighted postcontrast MR image. Tumor in the tympanic and mastoid segments (*arrowheads*). (From Jackler RK, Brackmann DE, eds. Neurotology. St. Louis: Mosby-Year Book, 1994.)

Copyright © 2003, Mosby, Inc. All rights reserved.

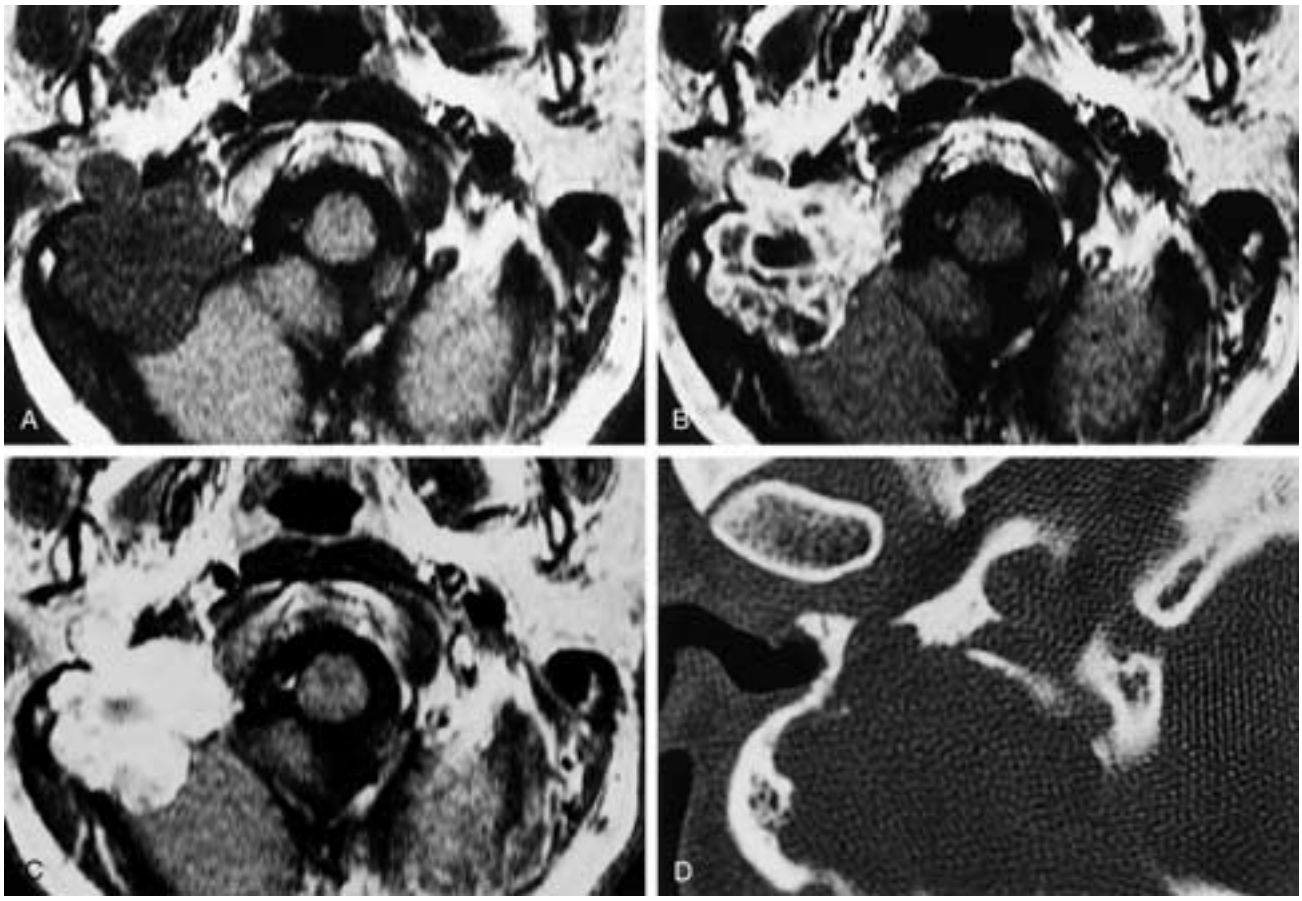

VIEW IMAGE

FIGURE 25-96 Large cystic mastoid segment facial schwannoma. **A**, T1-weighted image. **B**, Gadolinium T1-weighted image. **C**, Gadolinium T1-weighted image delayed 20 minutes. The images show a multilobulated, multicystic tumor protruding beyond the right mastoid cortex anteriorly, posteriorly, and medially. The cystic appearance is common in large schwannomas. **D**, Axial CT shows sharply and smoothly defined bone margins reflecting the slow growth rate of the tumor. (Compare with Figs. 25-115 and 25-118.)

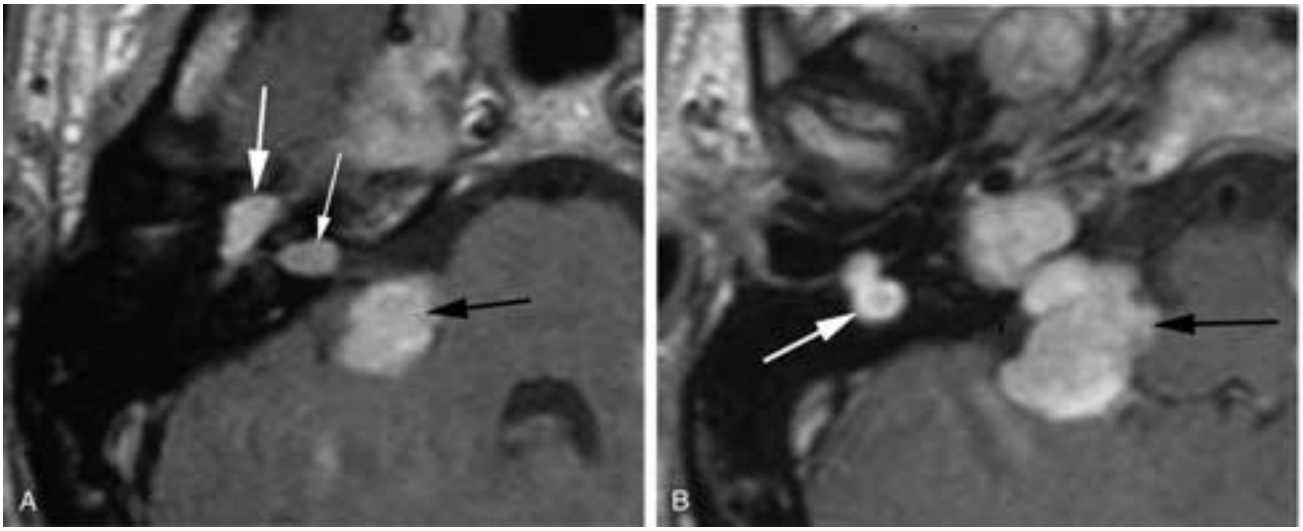

VIEW IMAGE

FIGURE 25-97 Patient with neurofibromatosis and multiple peripheral nerve tumors. **A**, T1-weighted postgadolinium axial MR image. There is involvement of the IAC (*small white arrow*) and the geniculate turn/anterior tympanic segment (*large white arrow*) of the FNC. The enhancement (*black arrow*) in the posterior fossa is the upper edge of a tumor extending through the jugular foramen. **B**, Caudad to **A** is the enlarging lesion in the vertical (mastoid) FNC (*white arrow*). Note the small protuberance of tumor just anterior to the vertical FNC. This tumor is following the chorda tympani nerve. Jugular foramen tumor (*black arrow*). (Courtesy of Dr. H.D. Curtin.)

Copyright © 2003, Mosby, Inc. All rights reserved.

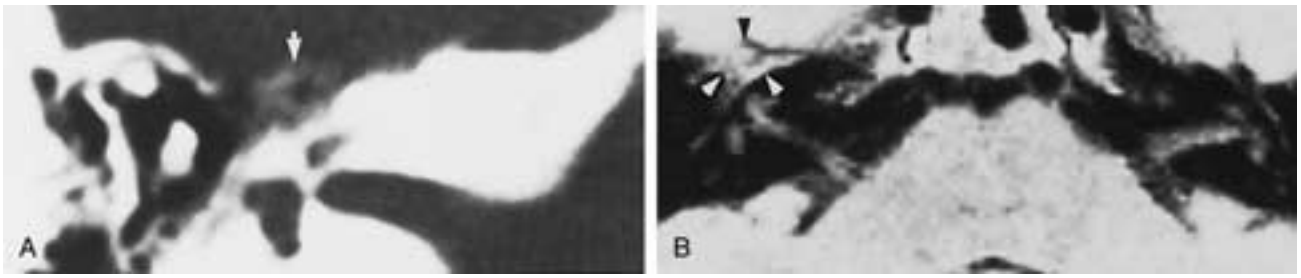

VIEW IMAGE

FIGURE 25-98 Geniculate intratemporal vascular tumor. **A**, Axial CT. Note the characteristic ''honeycomb'' bone (*arrow*). Bone interspersed within the tumor tissue is less dense than adjacent normal bone. **B**, Proton density image. Note the heterogeneous hyperintensity in the geniculate fossa and the surrounding region (*arrowheads*) adjacent to the temporal lobe. (From Lo WWM, Shelton C, Waluch V, et al. Intratemporal vascular tumors: detection with CT and MR. Radiology 1989;171:443–448.)

(Fig. 25-90), in contrast to trigeminal schwannomas, which are located at the petrous apex (Fig. 25-28).[364]

Geniculate region schwannomas, when sufficiently large, may be mistaken for temporal lobe gliomas or metastases (Fig. 25-91).[357, 365] Coronal images are helpful in the evaluation of tumors in this region, and smooth enlargement of the facial nerve canal should be a distinguishing feature in favor of a facial schwannoma. Multisegment facial schwannomas may need to be differentiated from perineural spread of malignant tumor (Fig. 25-87).

Enlargement of the proximal tympanic segment of the FNC by a persistent stapedial artery must not be mistaken for a facial nerve schwannoma.[326] In addition, developmental dehiscence of the FNC, present in about half of the temporal bones, most often near the oval window, should not be mistaken for an area of localized destruction.[366]

Gd-MR imaging rivals CT with bone algorithm in the early detection of intratemporal facial nerve tumors (Figs. 25-31, 25-91 and 25-92).[367] However, for precise correlation with bony landmarks, CT with bone detail remains invaluable (Figs. 25-90 to 25-94).

Benign Vascular Tumors

Hemangiomas or vascular malformations along the intratemporal course of the facial nerve were once thought to be rare.[368, 369] More recently, however, they have been found in some series at least as often as the much better-known schwannomas.[241, 341, 370] Hemangiomas are composed of thin-walled vascular spaces. Vascular malformations are composed of thick-walled vascular spaces lined by a single layer of endothelium surrounded by fibroblasts and collagen. The latter histologic type is the more common of the two. Because the two histologic variations may coexist in a single mass, they have been grouped together under intratemporal benign vascular tumors (IBVT), and the terms are sometimes loosely interchanged.[241, 371]

Hemangiomas may be further categorized into cavernous and capillary types by the predominant size of their vascular spaces. Vascular tumors often grow among bone trabeculae and may form bone (Figs. 25-42, 25-43, 25-98 and 25-99). In the latter case they have been called ossifying hemangiomas.[341, 370] All of these tumors are benign.[241]

IBVT cause nerve deficits by invasion rather than compression. Therefore, unlike schwannomas, they cause hemifacial spasm and facial palsy early; and if located in the IAC, they also cause sensorineural hearing loss to a greater degree than would be expected based solely on their size (Figs. 25-42 and 25-44).[241, 264, 272, 372] Although facial nerve resection and grafting may be necessary in many cases, in contrast with schwannomas, IBVT, being of extraneural origin, if operated on early, can at times be removed, with preservation of facial nerve continuity. Early detection is therefore extremely important.

Early detection of IBVT requires excellent imaging techniques and meticulous scrutiny. Although many of these tumors are missed initially because of inadequate technique, some are missed even with excellent technique because of their small size and subtle findings.[241, 242, 370]

IBVT occur most often at the geniculate ganglion region, next most often in the IAC, and least often at the posterior genu. They are usually less than 1 cm in diameter.

These lesions may contain intratumoral bone spicules, best seen on CT (Figs. 25-42, 25-43 and 25-99).[241] In the labryinthine FNC and at the geniculate ganglion, they show subtle findings that may include irregular and indistinct bone margins and reticular or ''honeycomb'' bone (Figs. 25-43 and 25-98).[241, 370] At the posterior genu they are focal, in contrast to schwannomas, which tend to be segmental (Fig. 25-93). Although the IBVT enhances with contrast, enhancement does not play a significant role in detection because such density changes in a small intratemporal lesion, contiguous to bone, are difficult to discern.

On MR imaging, vascular tumors are extremely well demonstrated when located in the IAC (Fig. 25-44).[242] They are isointense to mildly hyperintense on T1-weighted images and are markedly hyperintense on T2-weighted images, more so than the typical schwannoma. When located in the geniculate ganglion region, they are less reliably demonstrated by MR imaging without gadolinium than by CT with bone detail. When they are identifiable on MR imaging, they show nonhomogeneous signal intensities, which may be the MR imaging correlate of the CT ''honeycomb'' bone (Fig. 25-98). Thin sections, high matrices, close slice spacing, and the use of gadolinium may improve the MR imaging results.

Copyright © 2003, Mosby, Inc. All rights reserved.

Epidermoid Cysts

Besides arising intradurally from the CPA, epidermoid cysts, also called congenital or primary cholesteatomas, may arise extradurally from the petrous apex, the supralabyrinthine temporal bone, or the tympanic cavity. From the petrous apex they attain considerable size before involving the facial and acoustic nerves in the CPA or the IAC, and thus clinically they appear late (Fig. 25-101). From the supralabyrinthine region they readily erode the proximal FNC and tend to be discovered early, while still small (Fig. 25-100). Of the epidermoids causing

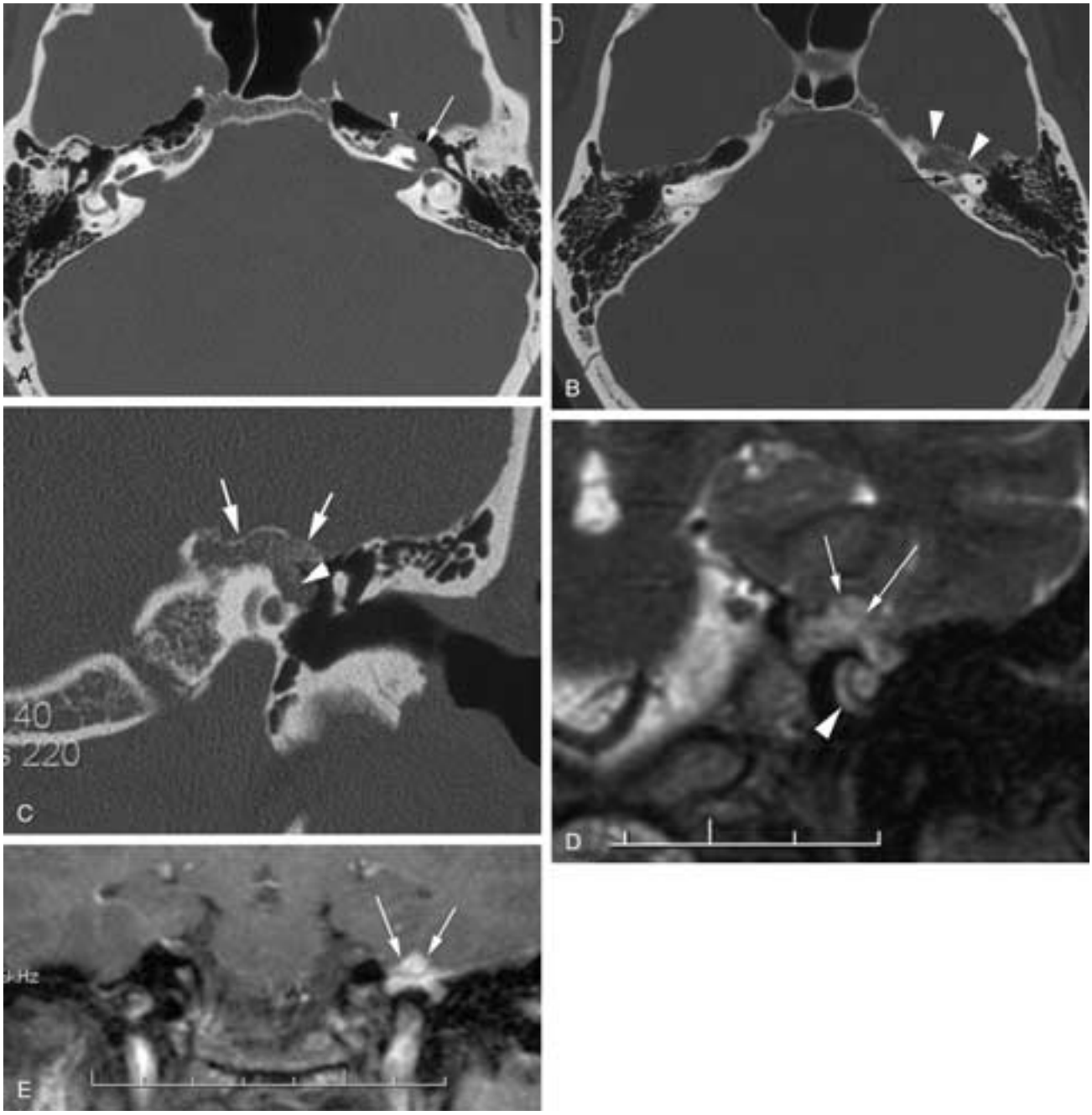

FIGURE 25-99 Intratemporal vascular tumor in the region of the geniculate ganglion. **A**, Axial CT image through the geniculate ganglion shows expansion of the facial nerve (*arrow*). There is irregular bone extending medially toward the petrous apex (*arrowhead*). **B**, Slightly superior to **A**, there is demineralization in the region of the labyrinthine segment of the canal (*black arrow*). Note that the lesion (*arrowheads*) contains small spicules of bone. **C**, Coronal CT image shows the demineralized bone (*arrows*). The abnormality extends inferiorly to enlarge the FNC (*arrowhead*) and involve the facial nerve. **D**, Coronal T2-weighted MR image shows the relatively high signal (*arrows*) of the vascular lesion. The fluid within the cochlea (*arrowhead*) is noted for comparison and orientation. **E**, Coronal postcontrast gadolinium T1-weighted image shows the enhancement (*arrows*) of the lesion. (Courtesy of Dr. H.D. Curtin.)

VIEW IMAGE

Copyright © 2003, Mosby, Inc. All rights reserved.

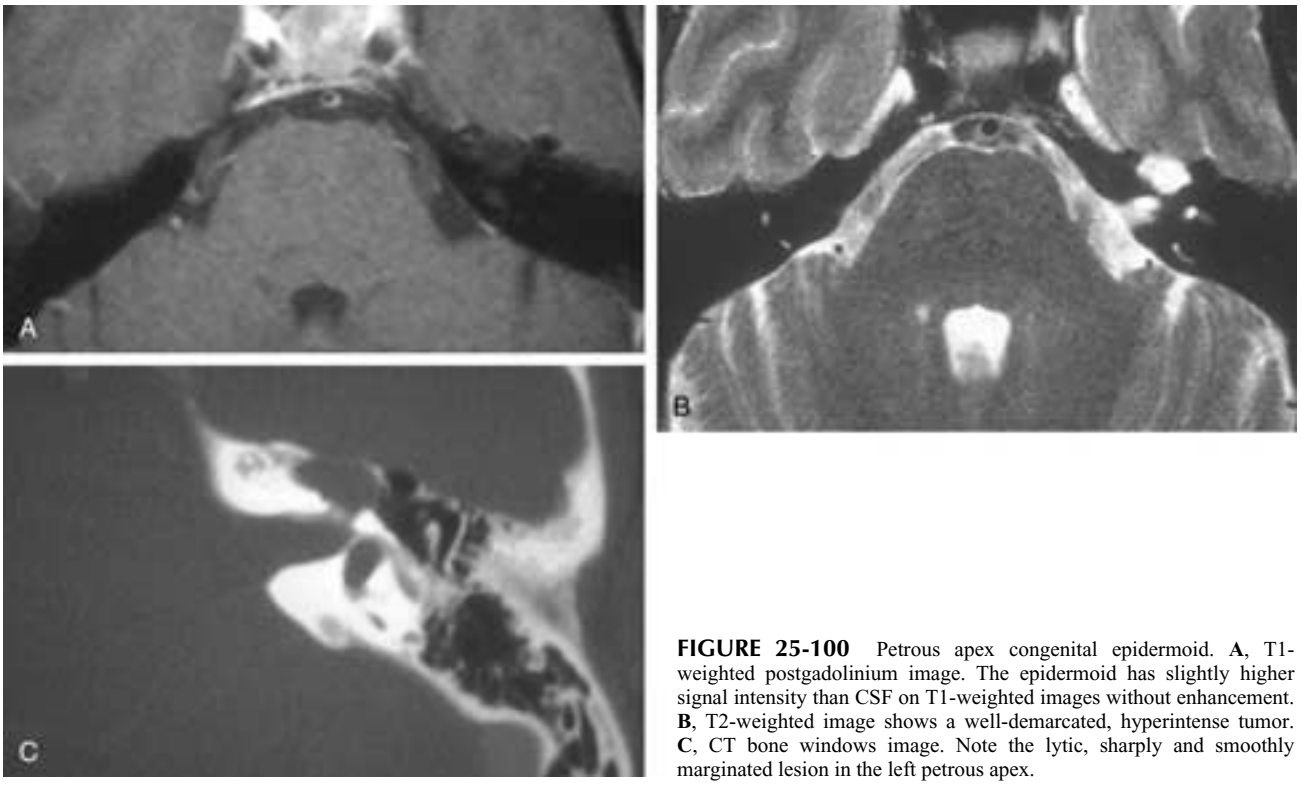

FIGURE 25-100 Petrous apex congenital epidermoid. **A**, T1-weighted postgadolinium image. The epidermoid has slightly higher signal intensity than CSF on T1-weighted images without enhancement. **B**, T2-weighted image shows a well-demarcated, hyperintense tumor. **C**, CT bone windows image. Note the lytic, sharply and smoothly marginated lesion in the left petrous apex.

VIEW IMAGE

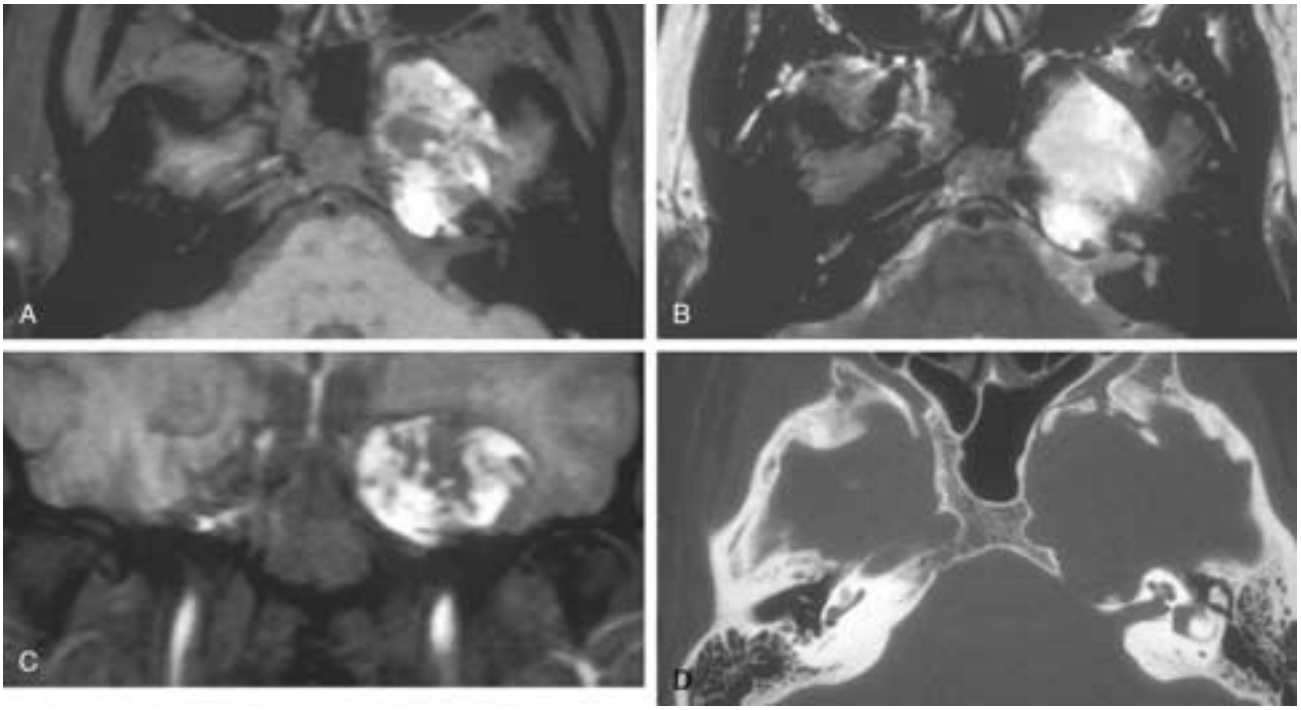

VIEW IMAGE

FIGURE 25-101 Skull base epidermoid. **A** to **C**, T1-weighted, T2-weighted, and T1-weighted coronal postgadolinium images, respectively. Extensive epidermoid tumor invading the skull base shows heterogeneous high signal intensity on both T1- and T2-weighted images without enhancement. **D**, Bone algorithm CT scan. Note the sharp margin of the lesion.

Copyright © 2003, Mosby, Inc. All rights reserved.

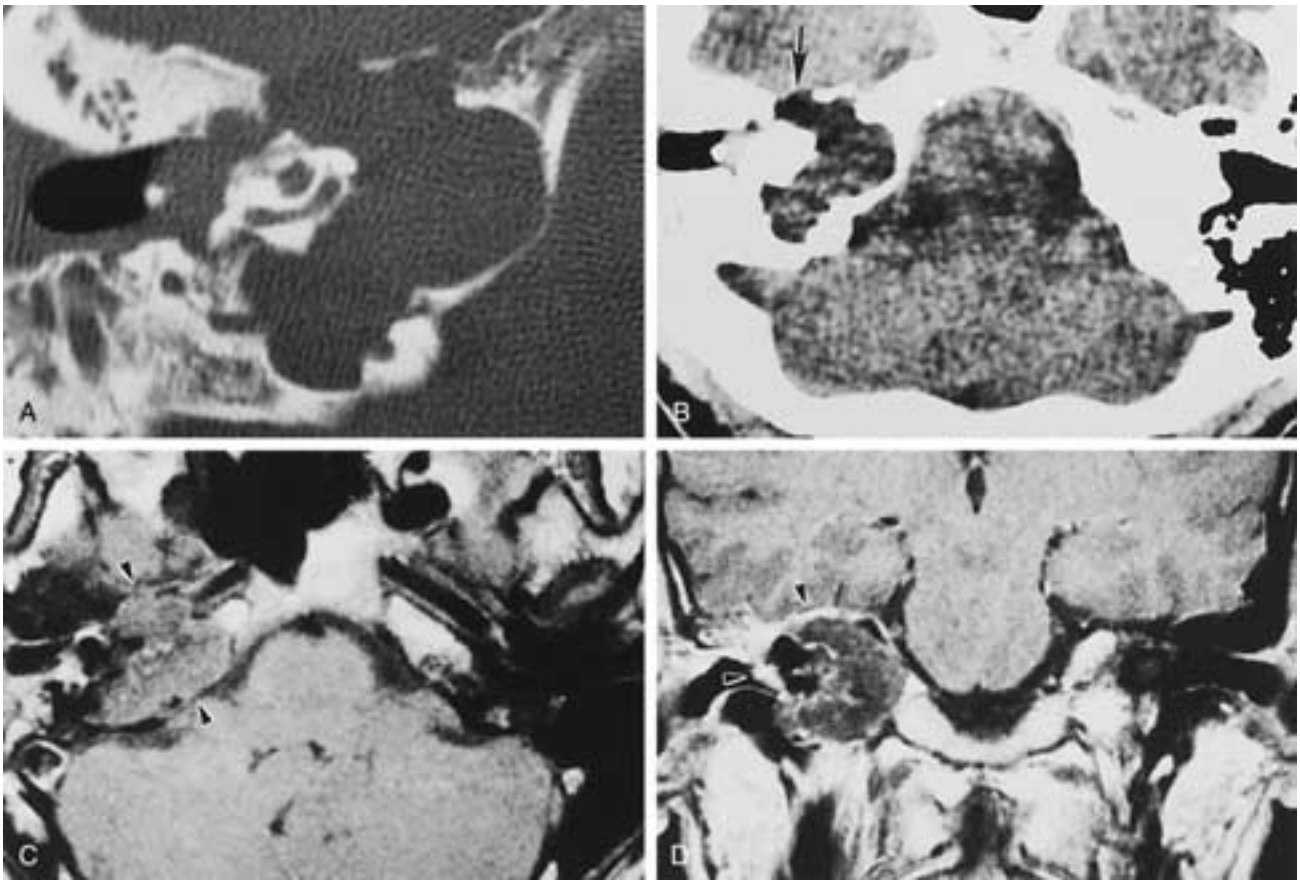

VIEW IMAGE

FIGURE 25-102 Acquired epidermoid of the temporal bone, right ear. **A**, Axial CT shows a sharply and smoothly marginated lobular mass extending from the middle ear cavity, anterior to the cochlea to expand the petrous apex, eroding portions of the cochlear capsule. **B**, Axial CT with a soft-tissue algorithm shows the mass to be mildly hypodense relative to brain. The patient's facial weakness was due to erosion in the geniculate ganglion region (*arrow*). **C**, Axial T1-weighted MR image shows that the mass is mildly hypointense, with a thin, isointense capsule (*arrowheads*). **D**, Coronal T1-weighted MR postcontrast image. The cholesteatomatous material shows no enhancement; there is enhancement of tissue in the middle and surrounding the capsule (*arrowheads*) as a result of reactive inflammation. (From Jackler RK, Brackmann DE, eds. Neurotology. St. Louis: Mosby-Year Book, 1994.)

facial nerve palsy in Fisch and Rüttner's series, 10 of 12 occurred in this region. From this point of origin they often reach around the superior semicircular canal and extend superomedially to the IAC or laterally into the epitympanum (Fig. 25-100).[363] They may erode the superior surface of the cochlear capsule or the ampullary limb of the superior semicircular canal to the point of fistulization (Fig. 25-100).[341]

On CT their bone margins are characteristically extremely sharp.[341, 363] Their general configuration may be either unilocular or multilocular. Hypodensity compared with brain may or may not be seen.[363] On MR imaging they are hypointense with brain on T1-weighted images but hyperintense on T2-weighted images (Fig. 25-100), and only their capsule enhances.

The petrous apex epidermoid cysts are discussed further in the section on Other Tumors and Cysts of the Temporal Bone. They may involve the facial nerve by expansion toward the IAC. Congenital epidermoid cysts in the tympanic cavity cause conductive hearing loss but rarely cause facial palsy. By comparison, acquired cholesteatomas involve the geniculate ganglion as they grow from the anterior epitympanic space into the petrous apex. (Fig. 25-102).[373]

Miscellaneous Tumors

Two rare lesions may originate along the facial nerve canal. Choristoma, usually consisting of ectopic salivary tissue, arises along the tympanic segment and causes conductive hearing loss. It may be associated with facial nerve and incudostapedial abnormality.[374] Primary paraganglioma, arising in the descending facial nerve canal from paraganglia along the distal Arnold's nerve, should be included in the differential diagnosis of pulsatile tinnitus and facial palsy (Fig. 25-103).[375]

Tumors from adjacent anatomic structures may involve the facial nerve by direct extension, and of these tumors the jugular foramen paraganglioma is perhaps the most common.[288] Papillary cystadenomatous tumor from the endolymphatic sac is rare, but when present it often involves the facial nerve in the medial mastoid bone (Fig. 25-104).[376] Carcinomas of the parotid gland, principally adenoid cystic

Copyright © 2003, Mosby, Inc. All rights reserved.

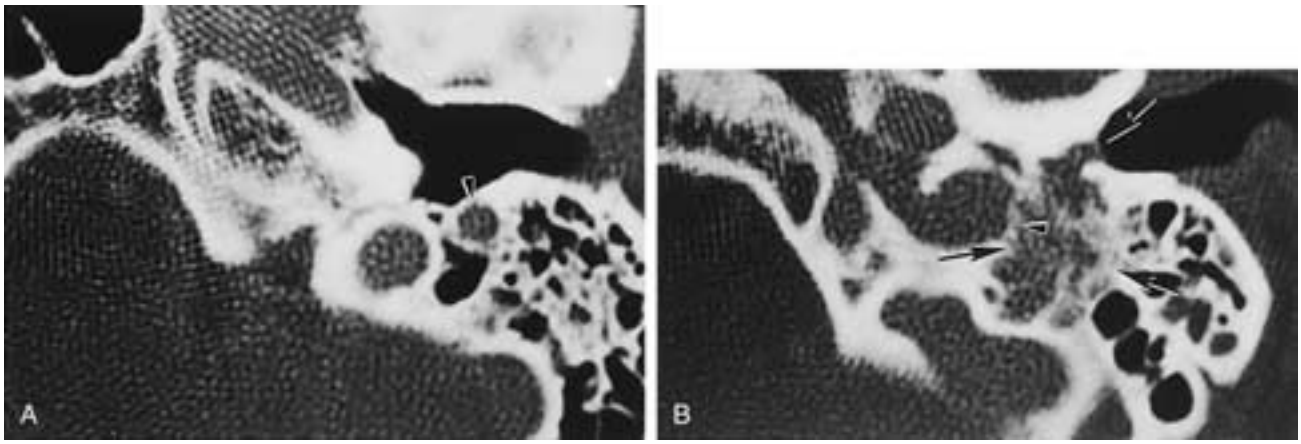

VIEW IMAGE

FIGURE 25-103 Facial canal paraganglioma (glomus faciale), left ear, axial CT. **A**, Expansion of the vertical FNC (*arrowhead*). **B**, Arrows show extension of tumor beyond the FNC to the adjacent mastoid and EAC, encroaching on the jugular fossa (*arrowhead*). (From Jackler RK, Brackmann DE, eds. Neurotology. St. Louis: Mosby-Year Book, 1994.)

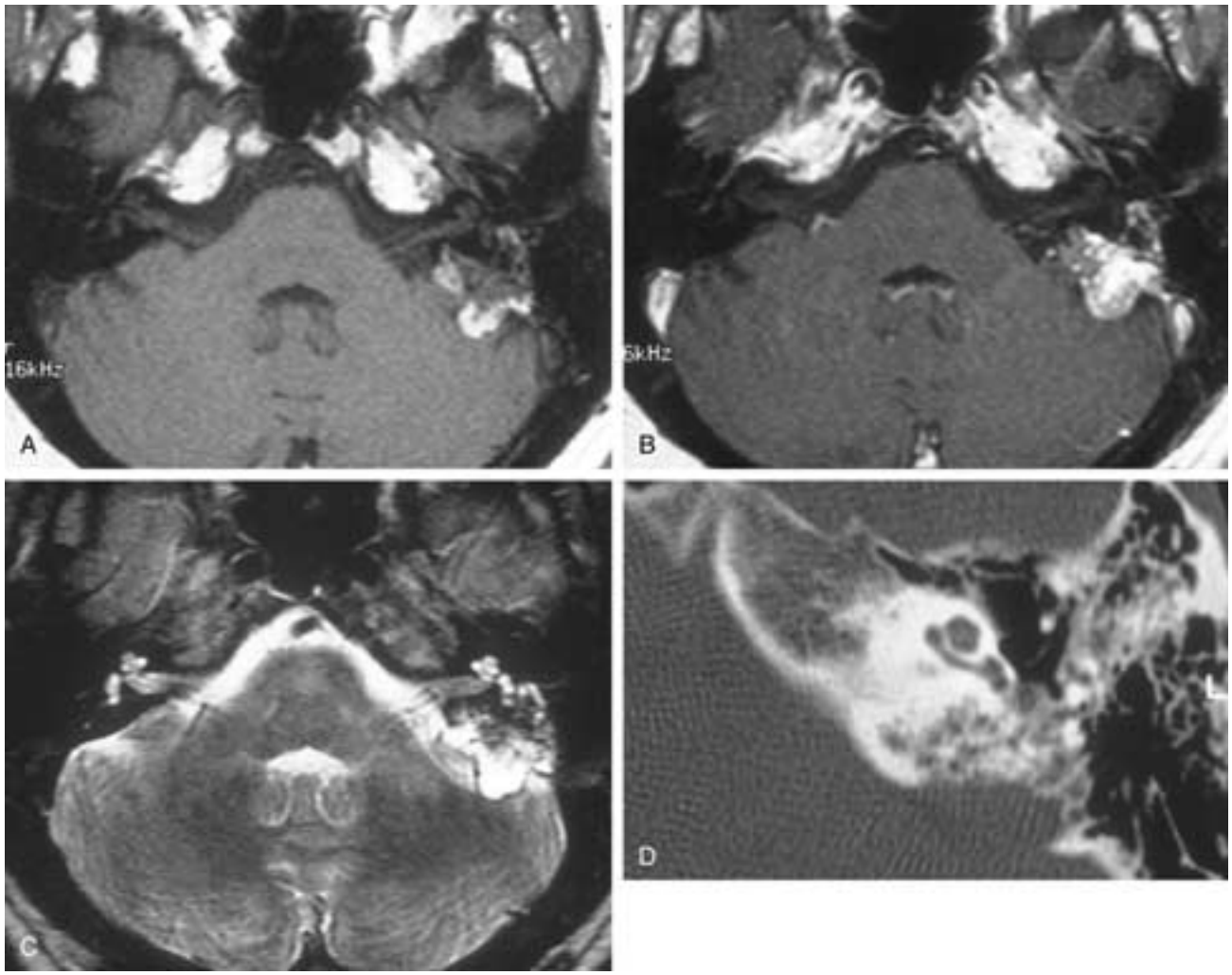

VIEW IMAGE

FIGURE 25-104 Papillary adenomatous tumor of the endolymphatic sac. **A** and **B**, T1-weighted pre- and postgadolinium images. **C**, T2-weighted image. The tumor has focal heterogeneous signal intensity on both T1-weighted and T2-weighted images due to blood product and calcification. It shows heterogeneous enhancement after gadolinium administration. **D**, CT bone window image shows a destructive lesion with irregular, moth-eaten bone margins extending to the medial mastoid.

Copyright © 2003, Mosby, Inc. All rights reserved.

and mucoepidermoid, are notorious for perineural extension along the facial nerve, and advanced squamous carcinoma of the external auditory canal may involve the mastoid segment of the facial nerve (Fig. 25-105).[377, 378] On rare occasions, systemic malignancies occurring in the mastoid region may involve the facial nerve. These include embryonal rhabdomyosarcoma in young children, Langerhans cell histiocytosis in children and young adults, lymphoma, and metastases (see the sections on External Auditory Canal and Mastoid).[377, 378]

OTHER TUMORS AND CYSTS OF THE TEMPORAL BONE

Many other tumors and cysts occurring in the temporal bone have not been specifically discussed thus far. These are lesions mainly in the external auditory canal (EAC), the middle ear, the mastoid, and the petrous apex. In the differential diagnosis of an osteolytic lesion of the temporal bone, Chasin and Goodman discussed 25 diseases under eight categories: carcinomas, sarcomas, metastases, benign epithelial lesions, benign nonepithelial lesions, hematologic malignancies, infections and inflammatory lesions, and histiocytosis.[379] Exhaustive as their list was, it was incomplete. For example, one may add mucocele, cholesterol granuloma or cyst (Fig. 25-106), giant cell tumor (Figs. 25-81 and 25-107), intrapetrous carotid aneurysm, xanthoma (Fig. 25-108), and so on.[380–391] The number of possible lesions is indeed enormous (Box 25-3).

On the other hand, the nonspecificity of the bone changes, the CT density, the MR imaging signal intensities, and the degree and pattern of enhancement limit one's ability to provide a specific diagnosis in the vast majority of these lesions. The internal margins of a bone lesion, whether ''geographic,'' ''moth-eaten,'' or ''permeative,'' are reflections of increasing growth rates and not of histologic types.[392] Geographic borders, whether sclerotic-rimmed, well defined, or ill defined, likewise reflect growth rates in ascending order. Rapidly spreading lesions such as osteomyelitis or Ewing's sarcoma may show no visible internal margin. In the temporal bone, the varying degrees of resistance offered by capsular, cortical, diploic, and pneumatized bones may further modify the appearance of the margin of a lesion. Nevertheless, the internal margins do provide a guide to the growth rate of a lesion.

The location of a lesion may alter the differential diagnosis. For example, a destructive lesion with a moth-eaten border around the EAC is probably a squamous carcinoma, but one around the jugular fossa is probably a paraganglioma. The patient's age group also may be helpful in making a diagnosis. For example, carcinoma is more likely in an adult, and embryonal rhabdomyosarcoma is much more probable in a young child. A history of malignancy favors metastasis, and the presence of calcifications suggests meningioma, chordoma, chondrosarcoma, and epidermoid.

Thus the radiologist's principal task is to localize a lesion accurately and to suggest its growth rate rather than to provide a specific diagnosis, at least for those laterally placed lesions that are readily available to inspection and biopsy.[393] In the petrous apex, where a lesion is beyond direct inspection and its surgical access is difficult, the case is different. Besides detection, localization, and characterization, every effort should be made to arrive at a specific preoperative diagnosis. Fortunately, in this location, diagnosis in many cases is possible.

EXTERNAL AUDITORY CANAL

Benign Tumors

Several benign tumor or tumor-like conditions are specific to the EAC. Some of them are not true neoplasms but may be confused with them. Two such soft-tissue lesions are keratosis obturans and EAC cholesteatoma.[394] Keratosis obturans usually occurs in individuals under 40 years of age with a history of sinusitis or bronchiectasis. The condition is usually bilateral, acute, and painful. Keratin plugs occlude the medial portion of the EAC (Fig. 25-109), and the

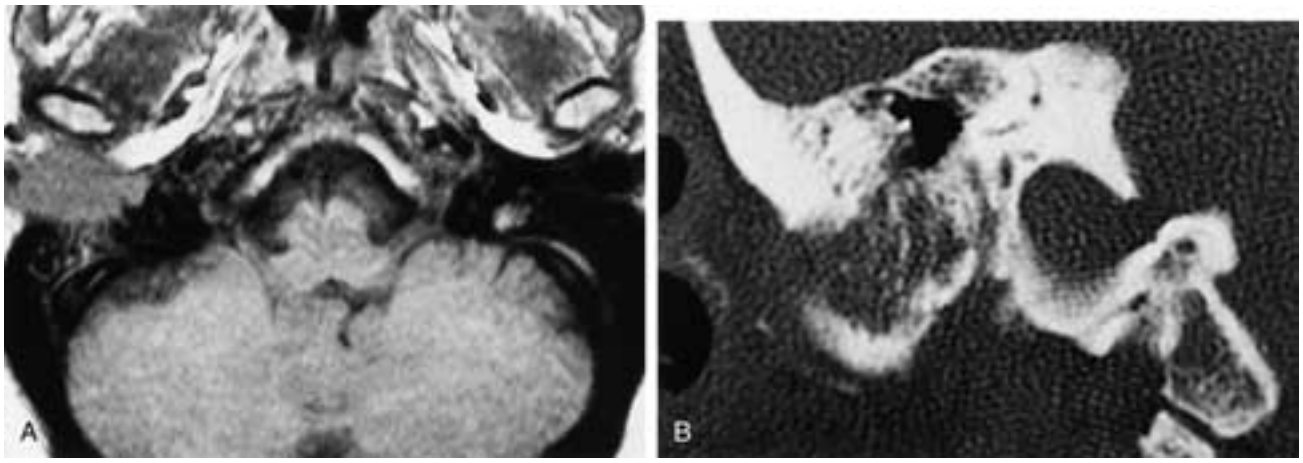

VIEW IMAGE

FIGURE 25-105 EAC squamous cell carcinoma. **A**, T1-weighted image shows destruction of the canal wall and extension into the tympanic cavity. **B**, CT, coronal section, shows extension of tumor into the mastoid process and invasion of the descending nerve canal. (Compare with Fig. 25-115.)

Copyright © 2003, Mosby, Inc. All rights reserved.

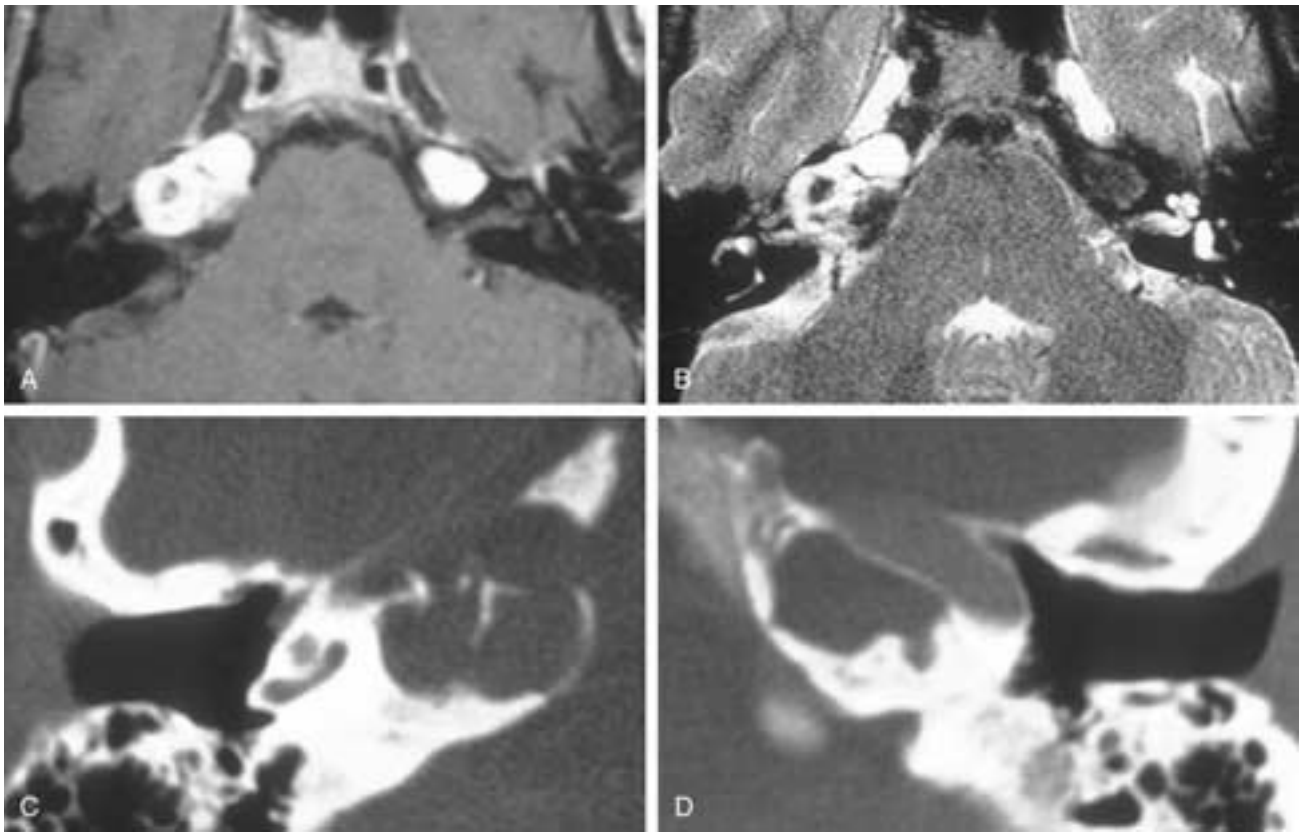

VIEW IMAGE

FIGURE 25-106 Bilateral petrous apex cholesterol granuloma. **A**, T1-weighted image shows ovoid, smoothly marginated, expansile (especially on the right side) lesions of both petrous apices with typical high signal intensity. **B**, T2-weighted image. The granulomas have heterogeneous signal intensity with a peripheral hypointense rim due to expanded cortical bone. **C** and **D**, CT bone window images. Cystic, lobulated lesions are seen bilaterally. Granuloma on the right side is more expansile and also has eroded the medial wall of the carotid canal.

adjacent bony canal may be diffusely widened. Reflex hyperemia has been theorized as the mechanism, and treatment consists of removing the plug and treating the granulations.[394]

EAC cholesteatoma occurs in individuals over 40 years of age. Usually unilateral, chronic, and associated with otorrhea, it causes localized erosion of the canal wall and elevation of the epidermis by cholesteatoma embedded in the bony wall (Fig. 25-110). Sequestration of bone and formation of sinus tracts may be present. Circumscribed periostitis is the probable cause. Complete surgical removal of the cholesteatoma sac and the necrotic bone is usually necessary for successful treatment.[394]

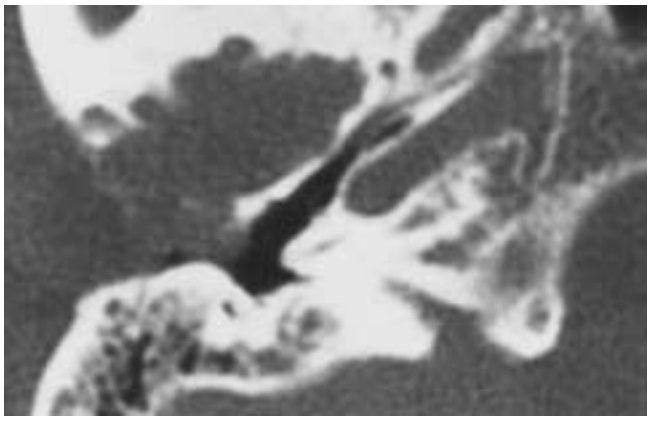

VIEW IMAGE

FIGURE 25-107 Benign giant cell tumor. Axial CT. Tumor partially occludes the EAC. Well-defined scalloped borders suggest a benign lesion.

Exostoses of the EAC are sessile multinodular bony masses arising deep in the EAC (Figs. 25-111 and 25-112). They are thought to be caused by prolonged physical, chemical, or thermal irritation—for example, frequent excessive contact with cold sea water for many years. In the case of aquatic exposure, the exostoses are usually asymptomatic until after the tenth year; then pain, infection, and hearing loss may appear. Total canal occlusion is rare.[395, 396]

Osteomas are sporadic, solitary, unilateral, pedunculated growths of mature bone located in the outer portion of the bony EAC (Fig. 25-113). They are much less common than exostoses, and the mastoid is the most prevalent extracanalicular site.[395, 397]

To the clinician, fibrous dysplasia may mimic an osteoma, but differentiation between the two is quite apparent on imaging (Fig. 25-114).[398]

Malignant Tumors

Squamous cell carcinoma is by far the most common malignant tumor of the ear (Figs. 25-82, 25-105 and 25-

Copyright © 2003, Mosby, Inc. All rights reserved.

115).[19, 399] Squamous cell carcinoma may arise in the EAC and spread to the middle ear or arise in the middle ear.[400] Unlike auricular basal cell carcinomas, which are uniformly associated with actinic damage to the epidermis, nearly always are found in men, and are rarely fatal, EAC squamous carcinomas are not associated with such damage, are more common in women, and have a 5-year mortality rate of about 50%.[401] Such carcinoma is frequently preceded by a long history of chronic ear infection. The tumor destroys the adjacent bone in the EAC and middle ear and invades the surrounding soft tissues. Extradural growth into the middle cranial fossa is common, as are mastoid involvement and extension into the soft tissues beneath the temporal bone.[402, 403] The temporomandibular joint, the parotid gland, and the carotid canal can be involved; however, the otic capsule is relatively resistant to erosion.[403, 404] CT accurately predicts tumor extent.[378] Middle ear extension of EAC squamous cell carcinoma reduces the 5-year survival from 56% to 27% (Fig. 25-82).[405] Other predictors of a poor outcome are extensive tumor, facial nerve paralysis, and cervical or periparotid adenopathy.[406] Initial complete resection followed by irradiation is the most effective treatment,[401, 405] except for tumors confined to the EAC without bone involvement, in which case resection alone may suffice.[407] Careful preoperative mapping of the entire tumor must be stressed.

The term *ceruminoma* is used by some authors to include all glandular tumors arising from the apocrine, seromucinous, or salivary glands of the EAC and middle ear.[19] This practice, however, is opposed by other authors who stress the divergent behaviors of the various tumors that are included in this general classification.[408] Adenoid cystic carcinoma is the most common tumor in the group. It is to be distinguished from ceruminous adenoma and pleomorphic adenoma, which are benign lesions, and from ceruminous adenocarcinoma, which has variable malignant potential. Adenoid cystic carcinoma, which histologically and pathologically resembles similar tumors of the salivary gland, is locally invasive and is treated best by radical en bloc resection.[408, 409]

Metastases, basal cell carcinoma, malignant melanoma, chondrosarcoma, osteosarcoma, lymphoma, and myeloma also may occur in the EAC, although much less frequently. Giant cell tumors (Fig. 25-107) and benign chondroblastomas likewise may cause bone destruction.[389, 410, 411] Chronic infections and inflammatory diseases such as malignant external otitis tuberculosis, Wegener's granulo-

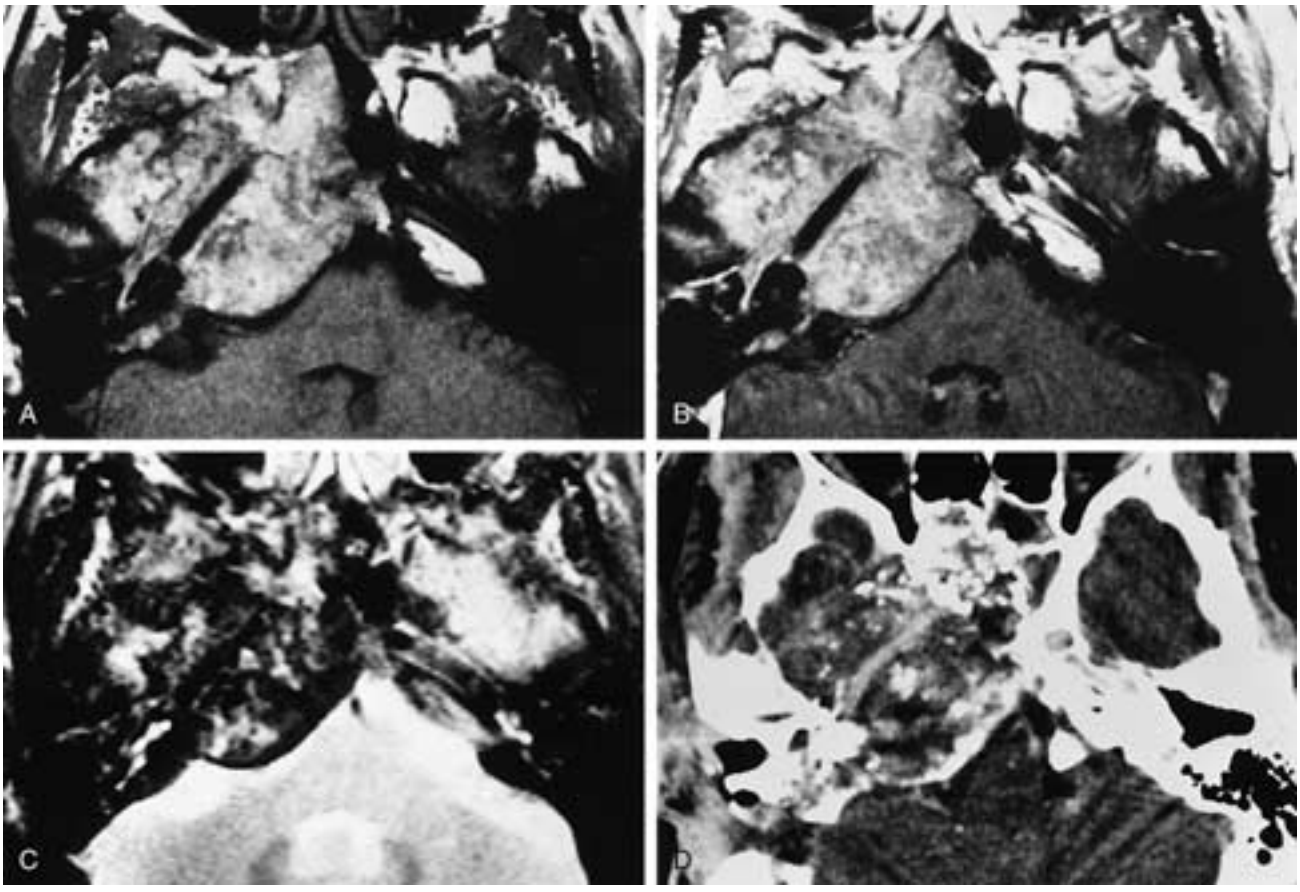

VIEW IMAGE

FIGURE 25-108 Xanthoma of the right petrous bone. **A**, T1-weighted image shows heterogeneous moderate hyperintensity. **B**, Gadolinium T1-weighted image shows no enhancement of the tumor. **C**, T2-weighted image shows marked heterogeneity of tumor intensity. The tumor could have been mistaken for a chondrosarcoma (see Fig. 25-86) on **B** and **C**. **D**, Postcontrast CT shows many small bony or calcific foci in a completely nonenhancing tumor. Note the enhancing horizontal intrapetrous carotid artery. The CT appearance is also similar to that of a chondrosarcoma except for the lack of enhancement.

Copyright © 2003, Mosby, Inc. All rights reserved.

BOX 25-3 EXAMPLES OF DESTRUCTIVE LESIONS OF TEMPORAL BONE

Primary carcinomas	Squamous cell carcinoma
	Adenoid cystic carcinoma
	Adenocarcinoma
Primary sarcomas	Embryonal rhabdomyosarcoma
	Chondrosarcoma
	Osteosarcoma
	Giant cell tumor
Metastases	Breast
	Kidney
	Lung
Benign epithelial lesions	Mixed adenoma
	Papillary adenoma
	Congenital epidermoid
	Mucocele
Benign nonepithelial lesions	Paraganglioma
	Hemangioma
	Facial schwannoma
	Acoustic schwannoma
	Meningioma
	Chondroblastoma
	Cholesterol granuloma
	Xanthoma
Hematologic malignancies	Myeloma
	Lymphoma
Infection and inflammatory lesions	Malignant external otitis
	Tuberculosis
	Wegener's granulomatosis
	Acquired cholesteatoma
Histiocytosis	Eosinophilic granuloma
Vascular	Carotid aneurysm

matosis, and histiocytosis (Figs. 25-116 and 25-117) should also be considered.

MIDDLE EAR TUMORS

Benign Tumors

The most common middle ear tumor, paraganglioma (glomus tympanicum tumor), is discussed in detail earlier in the chapter. Other benign middle ear tumors include cholesterol granuloma, hemangioma, facial nerve or chorda tympani schwannoma, congenital cholesteatoma, meningioma, adenomatous tumor of the mixed

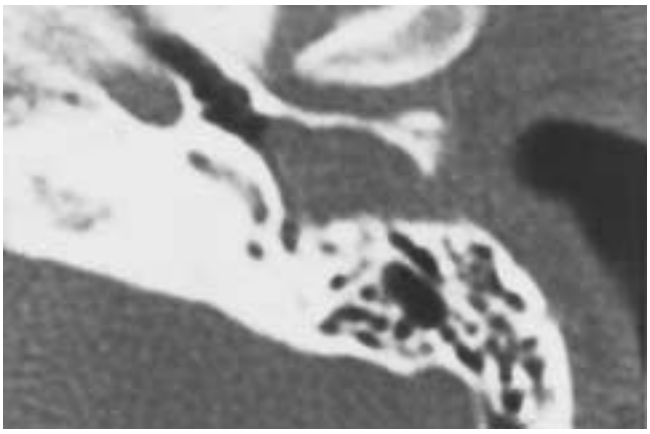

FIGURE 25-109 Keratosis obturans. Axial CT. A soft-tissue plug by itself is not a specific finding. There is mild diffuse thinning of the cortex of the EAC. The tympanic membrane is displaced medially, but the middle ear is normal.

VIEW IMAGE

pattern type (Fig. 25-118), and choristoma (ectopic salivary tissue).

Adenomatous tumor of the mixed pattern type is a benign lesion occurring in the middle ear.[362, 412] Bone invasion is not characteristic, and therefore CT of the lesion gives an appearance that cannot be distinguished from that of chronic ear disease. The only finding at CT may be opacification of the middle ear space. Previously, adenomatous tumors of the middle ear were separated into two subtypes, the mixed pattern and the papillary pattern. The papillary pattern was considered much more aggressive, showing significant bone destruction. Many of these papillary tumors are now considered low-grade malignant adenomatous tumors arising from the endolymphatic sac. These tumors secondarily invaded the middle ear, and this component of the tumor caused the patient to seek medical help, hence the confusion with the less aggressive nonpapillary mixed pattern type. The more aggressive papillary low-grade malignant adenomatous tumors arising from the endolymphatic sac are discussed later in this chapter. Those with the mixed pl
can have variable histology. Most have a glandular

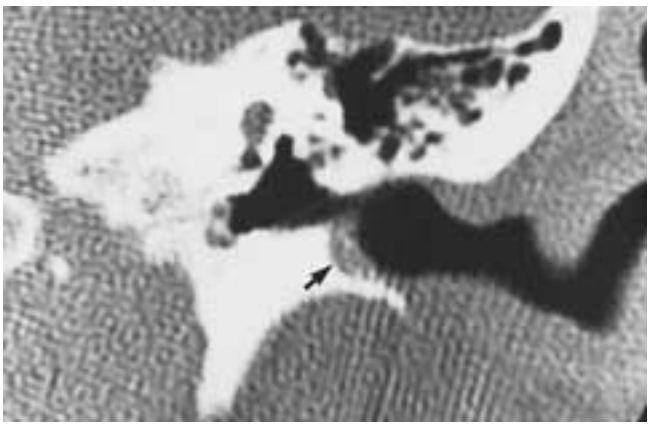

FIGURE 25-110 EAC cholesteatoma. Coronal CT. There is well-defined localized erosion of the inferior canal wall (*arrow*) lateral to the isthmus.

VIEW IMAGE

Copyright © 2003, Mosby, Inc. All rights reserved.

appearance, but sections frequently lose the glandular pattern, and neuroendocrine differentiation suggesting carcinoid tumor has occasionally been identified. The benign mixed pattern lesions do not have a papillary pattern, as do the more aggressive tumors arising in this region.

Most choristomas in the middle ear consist of salivary gland tissue, but neural sebaceous tissue or, rarely, odontogenic remnants also may be found.[413, 414] Salivary choristomas may be accompanied by an incudostapedial or tympanic facial nerve abnormality.[374] A cholesteatoma found behind an intact ear drum without a history of otitis media is considered by some to be congenital in origin.[399, 415] Whether congenital or not, these cholesteatomas account for 2% of all middle ear cholesteatomas.[416] Their most common middle ear sites are the epitympanum and the vicinity of the incudostapedial joint.[415, 417] By comparison, an acquired cholesteatoma is accompanied by evidence of chronic infection.

If discovered early, certain intratympanic tumors may be recognized by their locations. For example, small tympanic paragangliomas can be identified on the promontory (Fig. 25-63); small facial schwannomas (Figs. 25-92 and 25-93), hemangiomas, and choristomas are along the facial nerve canal (FNC); and small chorda tympani schwannomas are on the lateral tympanic wall.[374]

Malignant Tumors

There are several malignant tumors of the middle ear, all of which are rare. Among these lesions, squamous carcinoma is the most common.[400] It is thought to arise secondary to metaplasia of the normal cuboidal or ciliated columnar epithelium.[404] Twenty-three patients treated with mastoidectomy and radiation therapy had a 5-year survival rate of 39%, and death is usually by intracranial extension.[404]

Rhabdomyosarcoma occurs in early childhood.[418] Although rare, embryonal rhabdomyosarcoma is the most common middle ear neoplasm in that age group. Initially the tumor appears as chronic otitis media, and a superficial biopsy often yields only inflammatory granulation tissue. Destruction then rapidly extends beyond the middle ear, and facial nerve palsy is common.[418–420] The MR findings are nonspecific.[421] Although the disease is highly malignant and is usually fatal, multiple-drug chemotherapy and radiation therapy after a mastoidectomy have resulted in several long-term survivals.[419, 422]

Adenocarcinoma and metastases can also occur in the middle ear cleft.[348, 399, 412, 423] In addition, the primary presentation of malignant lymphoma in the middle ear and primary melanoma have been reported.[424, 425]

MASTOID

Tumors of the mastoid are often malignant. These include squamous cell carcinomas, adenocarcinomas, undifferentiated carcinomas (Fig. 25-119), myeloma, lymphoma, and metastases in adults, embryonal rhabdomyosarcoma in young children, and Langerhans cell histiocytosis in children, adolescents, and young adults (Figs. 25-116 and 25-117). Malignant tumors of the mastoid are often large and also may involve the EAC or the middle ear.[400] Their imaging findings are usually nonspecific, and their diagnoses are established by biopsy.

Benign processes principally include osteoma, fibrous dysplasia (Fig. 25-114), descending facial nerve schwannoma, and primary facial nerve canal paraganglioma (Fig. 25-103). Because of its clearer delineation of the bone margins, CT may be more helpful than MR imaging in distinguishing benign from malignant tumors. Contrast, for example, the well-defined sclerotic margins of a large mastoid segment facial nerve schwannoma (Fig. 25-96D) with the infiltrated, moth-eaten margins of an undifferentiated carcinoma (Fig. 25-119C). On CT, note also that despite the extensive bone changes of fibrous dysplasia, the bone margins, including the facial nerve canal, are well preserved (Fig. 25-114).

Histiocytosis

Langerhans cell histiocytosis, formerly known as histiocytosis X, is a rare disease, probably a clonal neoplastic disorder, occurring primarily in the pediatric age group.[426, 427] Occasionally a less severe form occurs in adults. It includes a spectrum of disorders with histiocytic proliferation involving bone or soft tissues, namely, eosinophilic granuloma, Hand-Schüller-Christian's syndrome, and Letterer-Siwe disease, in order of prognosis from best to worst. In general, the patients with late-onset, unifocal bone lesions and without soft-tissue involvement have the best prognosis. Patients with eosinophilic granuloma, by definition, have only one or at most several bone

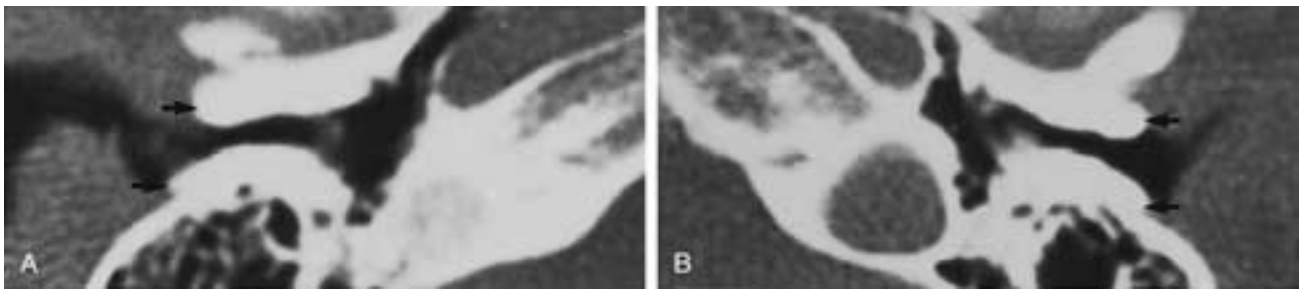

VIEW IMAGE

FIGURE 25-111 Bilateral EAC exostoses. **A** and **B**, CT. Sclerotic bone (*arrows*) layered on the anterior and posterior walls of the tympanic bone has diffusely narrowed EACs. (Compare with Fig. 25-112; courtesy of Dr. Anton N. Hasso.)

Copyright © 2003, Mosby, Inc. All rights reserved.

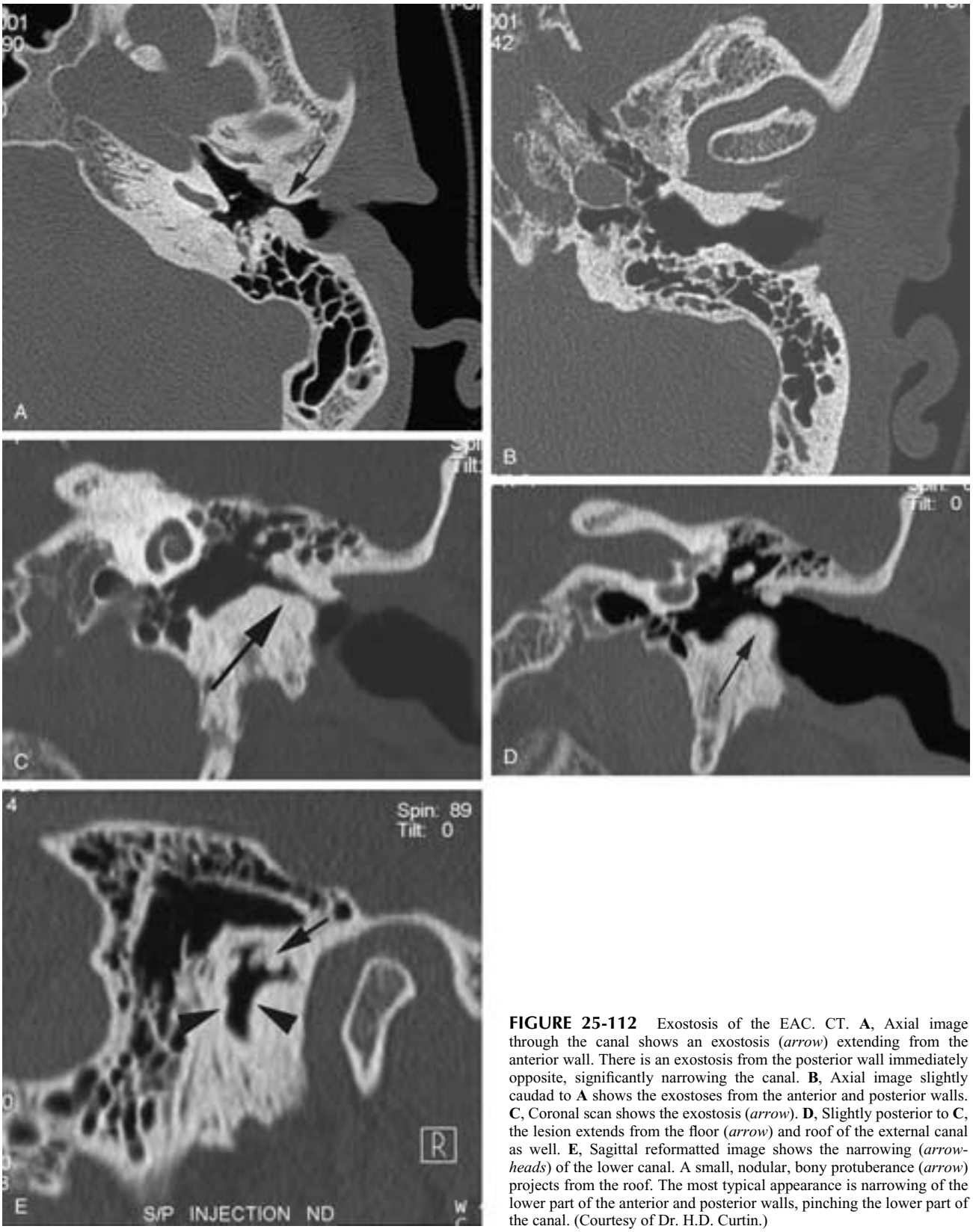

FIGURE 25-112 Exostosis of the EAC. CT. **A**, Axial image through the canal shows an exostosis (*arrow*) extending from the anterior wall. There is an exostosis from the posterior wall immediately opposite, significantly narrowing the canal. **B**, Axial image slightly caudad to **A** shows the exostoses from the anterior and posterior walls. **C**, Coronal scan shows the exostosis (*arrow*). **D**, Slightly posterior to **C**, the lesion extends from the floor (*arrow*) and roof of the external canal as well. **E**, Sagittal reformatted image shows the narrowing (*arrowheads*) of the lower canal. A small, nodular, bony protuberance (*arrow*) projects from the roof. The most typical appearance is narrowing of the lower part of the anterior and posterior walls, pinching the lower part of the canal. (Courtesy of Dr. H.D. Curtin.)

VIEW IMAGE

Copyright © 2003, Mosby, Inc. All rights reserved.

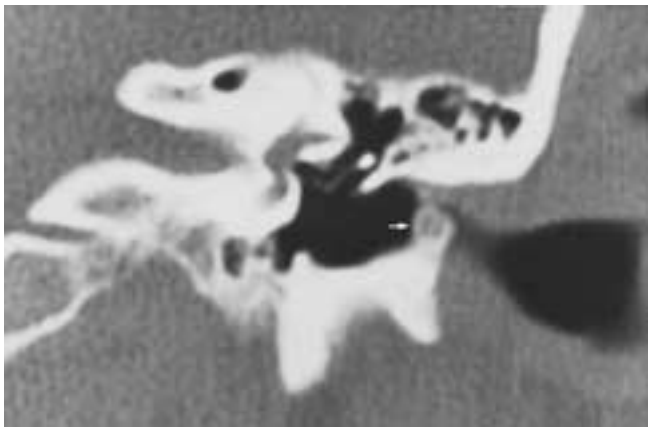

VIEW IMAGE

FIGURE 25-113 EAC osteoma. CT. Tumor typically arises at the tympanomastoid or tympanosquamosal suture (*arrow*). (Compare with Fig. 25-111.) (Courtesy of Dr. Anton N. Hasso.)

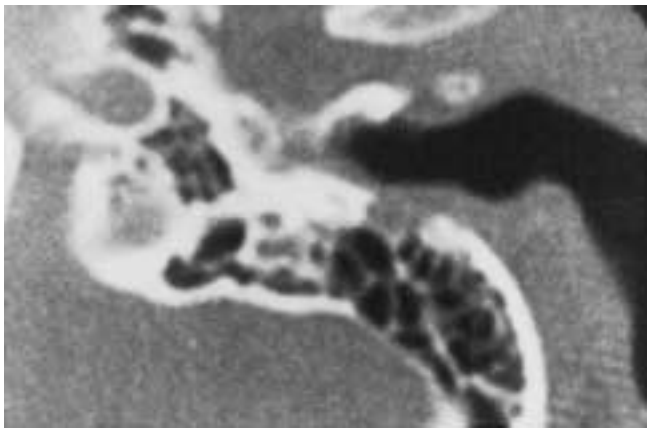

VIEW IMAGE

FIGURE 25-115 Early EAC squamous cell carcinoma. CT. Note the ill-defined localized cortical destruction on the posterior wall of the bony EAC. (Compare with Figs. 25-105 and 25-110.)

lesions, and the disease is generally benign, although progressive dissemination can occur (Figs. 25-116 and 25-117).[428] The treatment consists of surgery, irradiation, or chemotherapy (alone or in combination).[428]

In one series of 50 patients with disseminated histiocytosis, 18 had otomastoid involvement.[429] When the temporal bone is involved, the region of the EAC and mastoid appears to be a common location.[420, 428] Histiocytosis affects the petrous apex less frequently. Patients with middle ear and mastoid involvement present with symptoms such as otalgia and draining ear. Frequently, cases are diagnosed only after treatment with antibiotics fails to cure a suspected middle ear or mastoid infection. Early imaging findings also mimic inflammatory disease. In several reported cases, the bone margins were geographic and moderately well defined. ''Punched-out'' borders and beveled edges also may be found, and more irregular margins can be present especially after treatment.[430] On CT, enhancement within the lesion may be homogeneous or may occur only in the periphery.[430] On MR imaging, similar enhancement may be seen.[431]

THE PETROUS APEX

Petrous apex mass lesions are principally those that arise from within the petrous bone and expand the bone (e.g., cholesterol granuloma, intrapetrous epidermoid cyst, and intrapetrous carotid aneurysm) and those that arise in the immediate vicinity of the petrous apex and secondarily erode or invade the apex (e.g., chondrosarcoma from the petroclival junction, meningioma, trigeminal schwannoma, and intradural epidermoid).

Chondrosarcoma (Fig. 25-84), meningioma (Figs. 25-15 and 25-16), trigeminal schwannoma (Figs. 25-28 and 25-29), and intradural epidermoid cyst (Fig. 25-20) all can possess components in both the posterior and middle cranial fossae, straddling the petrous tip.[244] Frequently the posterior fossa component is intradural, and the middle fossa component may be either intradural, on the medial floor of the middle cranial fossa or in Meckel's cave, or extradural, extending into the cavernous sinus and sphenoid. These primarily CPA tumors are important considerations in the differential

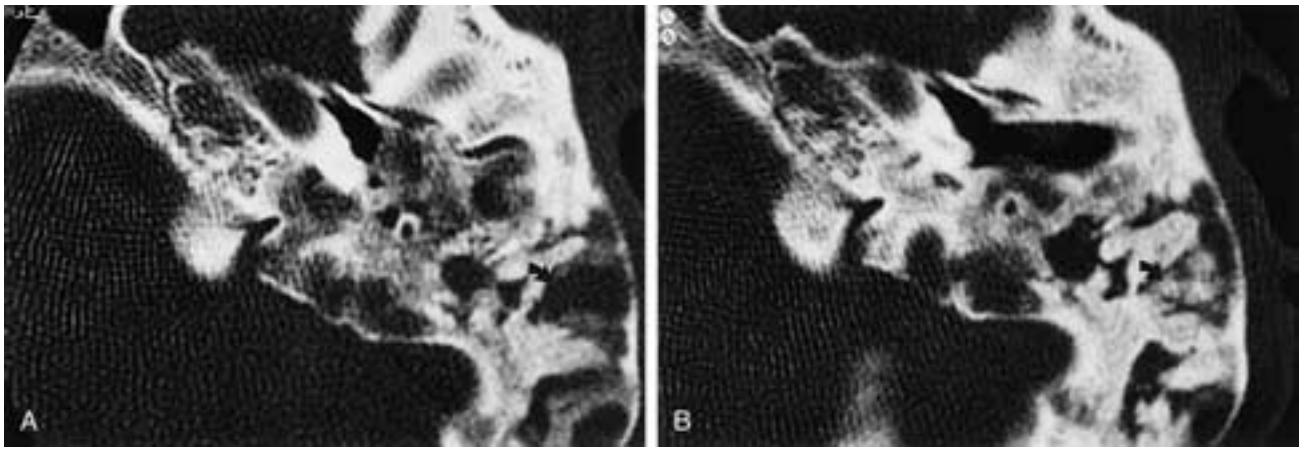

VIEW IMAGE

FIGURE 25-114 Monostotic fibrous dysplasia of the left mastoid. **A**, Axial CT shows a large, inhomogeneous mass with an intact cortex occluding the EAC and the tympanic cavity. The facial nerve canal is well preserved. **B**, CT 1 year after canaloplasty shows partial ossification of a previously unossified component (*curved arrow*).

Copyright © 2003, Mosby, Inc. All rights reserved.

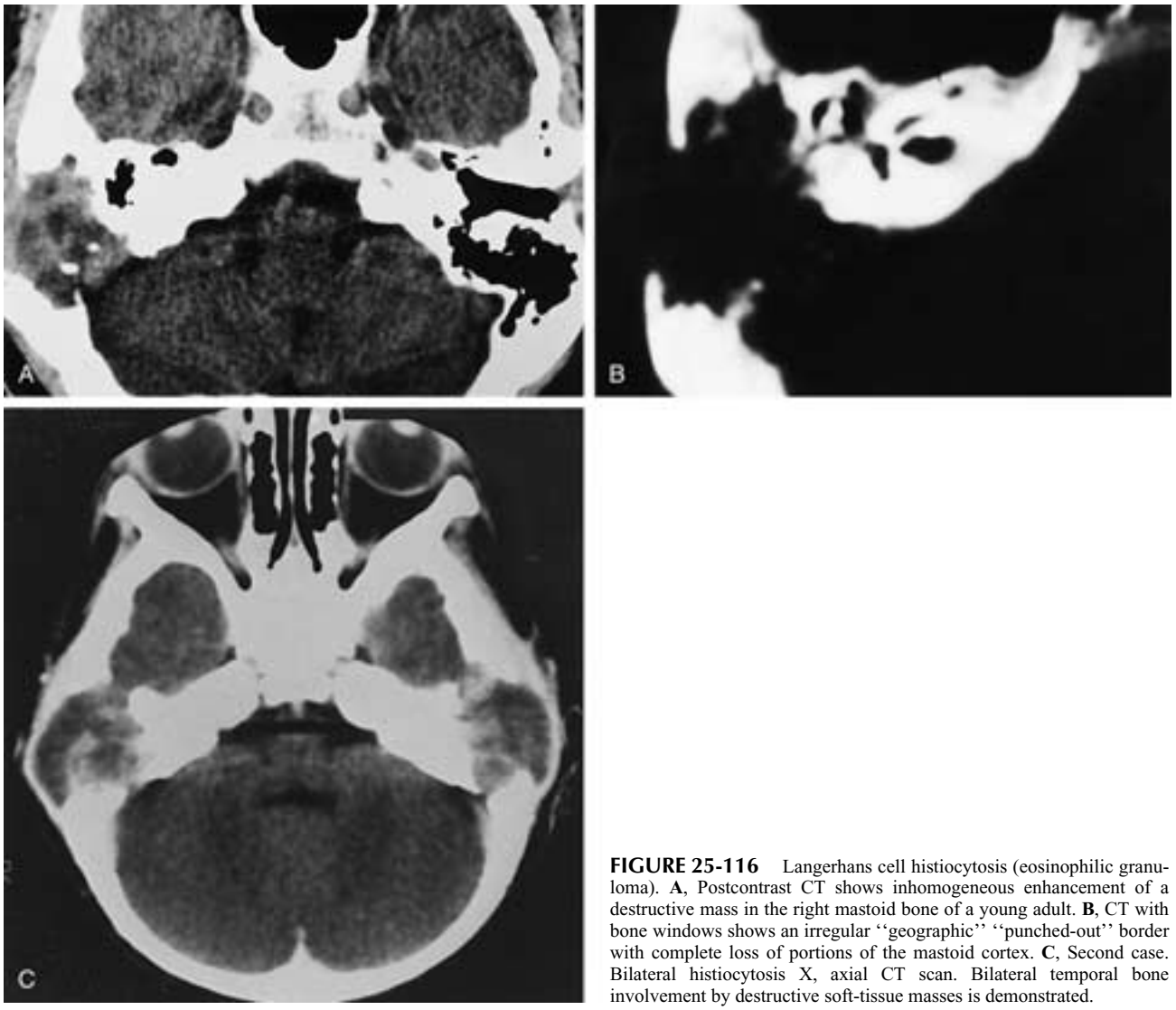

FIGURE 25-116 Langerhans cell histiocytosis (eosinophilic granuloma). **A**, Postcontrast CT shows inhomogeneous enhancement of a destructive mass in the right mastoid bone of a young adult. **B**, CT with bone windows shows an irregular ''geographic'' ''punched-out'' border with complete loss of portions of the mastoid cortex. **C**, Second case. Bilateral histiocytosis X, axial CT scan. Bilateral temporal bone involvement by destructive soft-tissue masses is demonstrated.

VIEW IMAGE

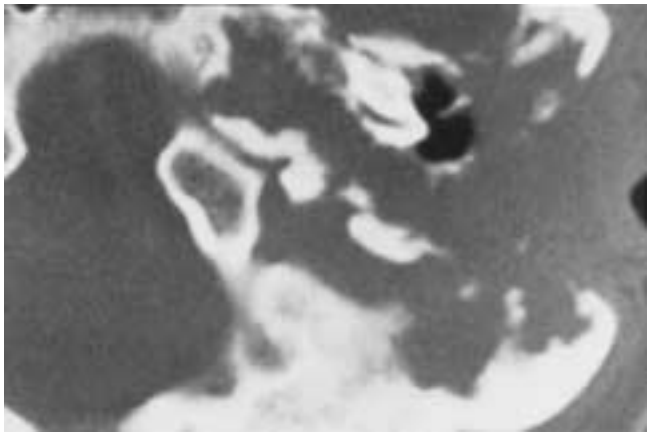

VIEW IMAGE

FIGURE 25-117 Eosinophilic granuloma. CT. The lesion is generally poorly defined, suggesting a moderately rapid growth rate. There is erosion of the otic capsule. (Courtesy of Dr. Roy A. Holliday.)

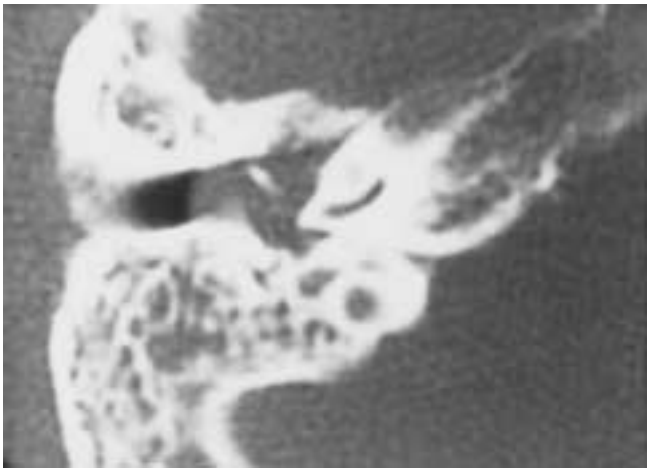

FIGURE 25-118 Adenomatous tumor, mixed pattern type. CT. The tumor filling the tympanic cavity and medial EAC, without destruction of the middle ear ossicles, is identical in appearance to the glomus tympanicum tumor. (Compare with Fig. 25-64.) Dynamic contrast CT may help make the differentiation. Because the surgical approach is basically the same for both tumors, angiography for the differential diagnosis is not warranted.

VIEW IMAGE

Copyright © 2003, Mosby, Inc. All rights reserved.

diagnosis of petrous apex masses, but all except chondrosarcoma have been described at some length in the section Differential Diagnosis of Tumors of the Internal Auditory Canal and the Cerebellopontine Angle and therefore are not discussed further in this section.

The petrous apex also may be invaded by direct extension of jugular paragangliomas (Figs. 25-73 and 25-77) and nasopharyngeal carcinomas (Fig. 25-85), usually along the petrooccipital fissure, which is immediately superior to the fossa of Rosenmüller. For a complete differential diagnosis, systemic diseases and malignancies also need to be considered.

Two pitfalls have trapped the unwary, primarily on MR imaging: (1) asymmetric pneumatization of the petrous apex and (2) unilateral retention of secretions in apical air cells.[432] In the first instance, there is unilateral hyperintensity on T1-weighted images, from marrow of the nonpneumatized petrous apex, which fades in signal intensity on T2-weighted images, paralleling the signal intensity of fat. The use of fast spin-echo sequences leaves fat with significant signal on the T2-weighted images. This can confuse the issue, but the addition of a fat-suppression pulse clarifies the situation. In the second instance, there is unilateral hyperintensity on T2-weighted images from retained secretions that are usually hypointense on T1-weighted images, paralleling the signal intensity of fluid or mucus. Both of these conditions have been mistaken for tumors on MR imaging. CT usually resolves the question. Unlike true cysts or tumors, neither of these conditions shows bone erosion or expansion.

In contrast with lesions in the IAC, the geniculate fossa, or the tympanic cavity, which are frequently small when first seen, lesions in the petrous apex usually attain considerable size before causing cranial nerve symptoms. They are thus readily apparent on CT or MR imaging. However, besides localization and characterization, an important task for the radiologist is the preoperative differentiation between cystic and solid lesions (Table 25-11). Whereas solid lesions of the petrous apex require biopsy to determine appropriate treatment and extensive surgery if resection is indicated, cysts can be simply and definitively treated by drainage and permanent fistulization if a proper preoperative diagnosis is made.[385, 433, 434] MR imaging is generally used for the initial detection of such lesions, and CT with bone detail is used for surgical planning.

Cholesterol Granuloma (Cysts)

Cholesterol granuloma of the petrous apex has also come to be known as cholesterol cyst or giant cholesterol cyst (Fig. 25-106 and Table 25-11).[383–387, 435] *Cholesterol granuloma* is a term that emphasizes the histopathologic features of the lesion, and *cholesterol cyst* is a term that better describes the gross appearance of the lesion. Cholesterol cyst is the most common primary petrous apex lesion.[383, 384]

Cholesterol cysts possess a fibrous lining that may or may not be complete. The lining contains multinucleated giant cells with cholesterol crystals in acicular (needle-shaped)

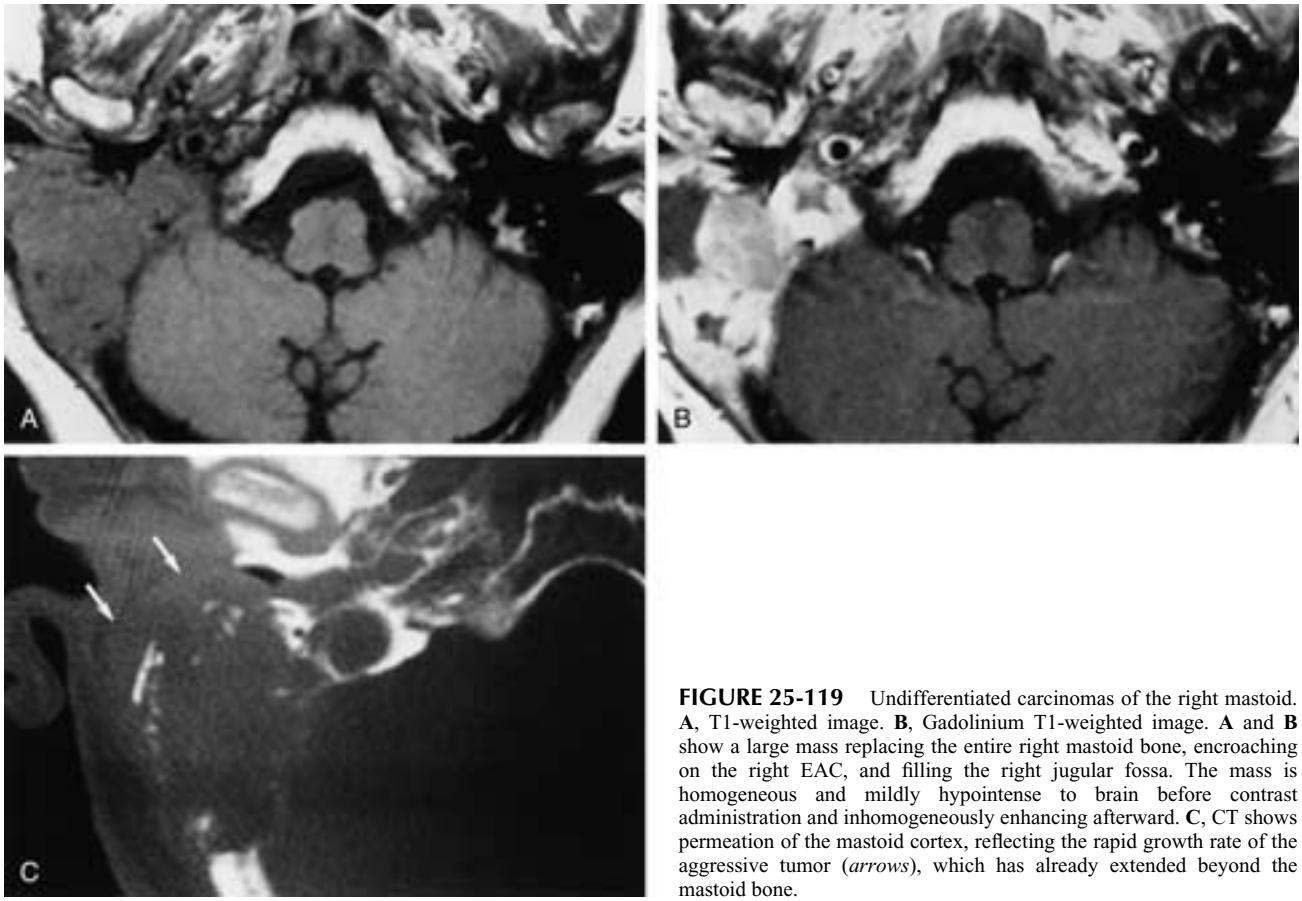

FIGURE 25-119 Undifferentiated carcinomas of the right mastoid. **A**, T1-weighted image. **B**, Gadolinium T1-weighted image. **A** and **B** show a large mass replacing the entire right mastoid bone, encroaching on the right EAC, and filling the right jugular fossa. The mass is homogeneous and mildly hypointense to brain before contrast administration and inhomogeneously enhancing afterward. **C**, CT shows permeation of the mastoid cortex, reflecting the rapid growth rate of the aggressive tumor (*arrows*), which has already extended beyond the mastoid bone.

VIEW IMAGE

Copyright © 2003, Mosby, Inc. All rights reserved.

Table 25-11
DIFFERENTIAL FEATURES OF PETROUS APEX "CYSTIC" LESIONS

	Cholesterol Granuloma (Cholesterol Cyst)	Epidermoid (Congenital Cholesteatoma)	Mucocele
CT density	= brain	≤ Brain	< Brain
T1W* image intensity	> brain	≤ Brain	≤ Brain
T2W† image intensity	> brain	> Brain	> Brain
Content arrangement	Homogeneous or with hypointense, irregular debris	Lamination on T1W images	Homogeneous

**T1W,* T1-weighted.
†*T2W,* T2-weighted.

clefts, blood vessels, fibrous tissues, red blood cells, hemosiderin, and chronic inflammatory cells. The content of the cyst is a brownish liquid glistening with cholesterol crystals and containing a brownish sediment.[382, 384] The contralateral petrous apex is usually well pneumatized, suggesting that these cysts arise in pneumatized apices (Fig. 25-106). Obstruction of the ventilation outlet has been theorized as the initiating cause of repetitive cycles of hemorrhage and granulomatous reaction.[436]

Cholesterol cysts occur in young and middle-aged adults of both sexes. Most of the patients have had symptoms for about 2 years.[382] Hearing loss, tinnitus, and hemifacial spasm are the most common complaints, but deficits of cranial nerves V, VI, IX, X, XI, and XII have all been encountered.[382, 384] Many of these deficits have been relieved by surgical decompression.[384, 437] Cholesterol cysts arise from within the petrous apex, posterior to the horizontal portion of the carotid canal, and they usually range from 2 to 4 cm in length at the time of their initial diagnosis.[382] On CT, they are sharply and smoothly marginated (Fig. 25-106). Generally ovoid in configuration, they expand the petrous apex, especially posteriorly, where the overlying bone is often paper thin or absent. Where bone is still present, the internal margin of the lesion is often sclerotic. The abutting portions of the carotid and jugular walls may be absent, the horizontal carotid canal is often bowed, and the adjacent occipital and sphenoid bones are commonly remodeled.[382] The lesions are approximately isodense with brain, and are homogeneous and free of calcium. They show no contrast enhancement except for a thin, smooth peripheral rim, which has variously been interpreted as representing either the capsule or the overlying dura.[382, 383]

On MR imaging, these lesions are strongly hyperintense on both T1-weighted and T2-weighted images. They frequently contain nonhomogeneous hypointense substances most likely representing hemosiderin from previous hemorrhage (Fig. 25-120).[386, 387] Some of them show a

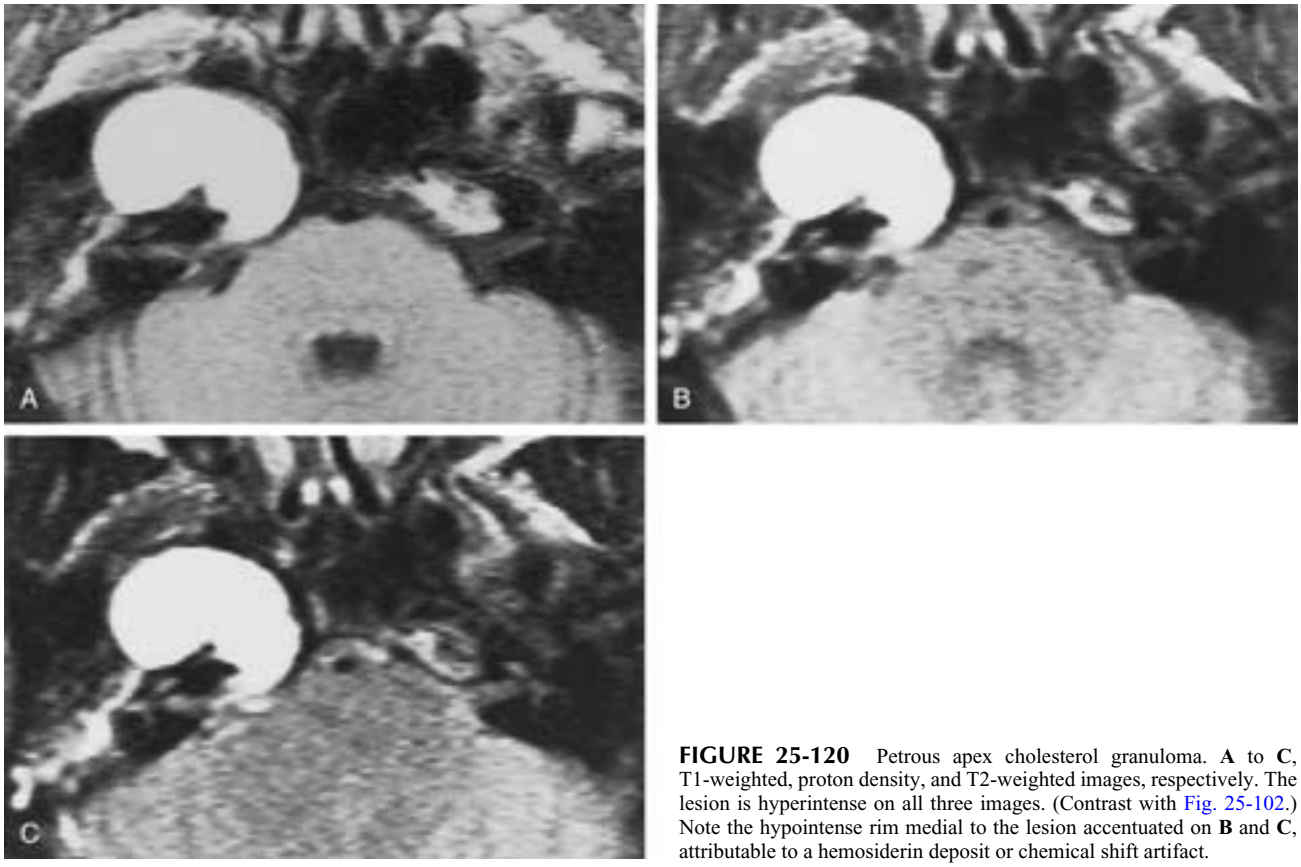

FIGURE 25-120 Petrous apex cholesterol granuloma. **A** to **C**, T1-weighted, proton density, and T2-weighted images, respectively. The lesion is hyperintense on all three images. (Contrast with Fig. 25-102.) Note the hypointense rim medial to the lesion accentuated on **B** and **C**, attributable to a hemosiderin deposit or chemical shift artifact.

VIEW IMAGE

Copyright © 2003, Mosby, Inc. All rights reserved.

hypointense rim on both T1-weighted and T2-weighted images.[387] Peripheral magnetic susceptibility on gradient-recalled echo sequences and central evidence of aliphatic protons on chemical shift imaging add specificity to the diagnosis.[387]

Epidermoid Cysts

Epidermoid cysts (or tumors) are also called primary cholesteatomas. They are less common in the petrous apex than in the supralabyrinthine region.[341, 363] Congenital intrapetrous epidermoid cyst is much rarer than cholesterol cyst. They are ''cysts,'' but they contain solid material and are usually treated by complete surgical resection with removal of the entire cyst wall to prevent recurrence, rather than by simple drainage and fistulization. Their preoperative differentiation from cholesterol granulomas (cysts) is therefore important.

Epidermoid cysts possess a capsule of stratified squamous lining and contain desquamated keratin, which appears grossly to be whitish friable material. As the desquamated keratin accumulates, the mass slowly expands. Thus, on CT, they appear as homogeneous, nonenhancing, sharply defined, ovoid expansile lesions (Fig. 25-101), like cholesterol cysts (Fig. 25-106).[19, 363, 438] Some epidermoid cysts appear hypodense and some isodense to brain. Hence, on CT, they may or may not be distinguishable from cholesterol cysts, which are isodense to brain.

Because of the rarity of intrapetrous epidermoid cysts, limited information exists in the literature on their MR imaging findings.[363] However, in two cases they were between CSF and brain in intensity on T1-weighted images, with a capsule isointense to brain (Fig. 25-101). A layered appearance may be present in the periphery on off-center sections. On T2-weighted images, they are strongly hyperintense to brain, but perhaps less so than cholesterol cysts.

Mucoceles

Mucoceles are lined with cuboidal or columnar epithelium and contain mucus. Petrous apex mucoceles are even rarer than petrous apex epidermoid cysts, and their CT and MR imaging appearances rarely have been documented in the literature.[380, 381, 439] They are also sharply defined, ovoid, expansile, nonenhancing masses. MR imaging of a single case shows hypointensity on T1-weighted images with a thin enhancing rim and hyperintensity on T2-weighted images (Fig. 25-121).[381] Thus it appears very similar to a congenital epidermoid cyst (Fig. 25-101).

Carotid Artery Aneurysms

Giant aneurysms from the intrapetrous horizontal carotid canal are extremely rare, but for obvious reasons they are extremely important in the differential diagnosis of petrous lesions.[237, 440] They also appear as well-defined ovoid, expanding masses. However, as with the intracranial giant aneurysms described earlier, their internal appearances vary considerably according to the extent of mural thrombus formation.[234]

On CT, a mural thrombus is isodense and nonenhancing, and the patent lumen shows a rapid rise and decline in enhancement. On MR imaging, a laminated mural thrombus shows varying signal intensities and the patent lumen appears as a signal void.[235–237] Flow-related enhancement may present confusing signals. Carotid artery aneurysms may be treated surgically or with transvascular techniques.[441, 442]

Chondrosarcomas

Primary intracranial cartilaginous tumors are rare.[18, 443, 444] Yet, chondrosarcoma is probably the most common primary malignant neoplasm in the region of the petrous apex. Affected patients range from children to the elderly.[445]Among its histologic subtypes, conventional is the most common.[217] The much rarer mesenchymal and dedifferentiated subtypes are more vascular, more aggressive, and less favorable in prognosis.[217]

Arising from embryonal rests in the skull base, chondrosarcomas tend to occur off midline, along synchondroses in the parasellar or the CPA region, but occasionally they may overlap in location and radiologic appearance with chordomas, which arise from notochordal remnants and typically occupy the midline.[446, 447] Since the time Heffelfinger et al. introduced the concept of a chondroid subtype of chordoma, pathologists often had difficulty differentiating it from the myxoid variant of chondrosarcoma.[130, 448] Over the years, controversy raged as to whether the two entities may not in fact be one.[130, 449] However, recent evidence such as results from cytokeratin stains seems to indicate that chondroid chordoma indeed exists and differs from myxoid chondrosarcoma, although over the years errors in diagnosis appear to have been made.[450] The entity of laterally placed chordoma probably has been overdiagnosed, or perhaps it never truly existed.[451] Hence before accepting a diagnosis of chondrosarcoma or chordoma, one should be aware of the criteria on which the diagnosis is based.

Most chondrosarcomas are centered more along the petrosphenoidal and petrooccipital fissures than within the petrous apex itself. Both chondrosarcoma and chordoma cause bone destruction and enhance mildly to moderately on CT, and both may contain calcifications.[443, 446, 452] On MR imaging, both are usually low to intermediate in signal intensity on T1-weighted images and hyperintense on T2-weighted images (Fig. 25-84).[445, 446, 452] Typically they are relatively homogeneous on T1-weighted images but heterogeneous on T2-weighted images (Fig. 25-84).[445] Their postcontrast enhancement is marked but may be heterogeneous (Fig. 25-84). The marked hyperintensity and heterogeneity on T2-weighted images, if present, may help to distinguish chondrosarcoma from other malignancies in the region such as myeloma (Fig. 25-122) and nasopharyngeal carcinoma (Fig. 25-85), which are less hyperintense and more homogeneous.

Compared with meningiomas, chondrosarcomas enhance less on CT and cause bone destruction rather than sclerosis or hyperostosis (Fig. 25-13).[443] However, very rarely, intradural chondrosarcoma overlying the petrous apex may extend into the posterior and middle cranial fossae, with CT

Copyright © 2003, Mosby, Inc. All rights reserved.

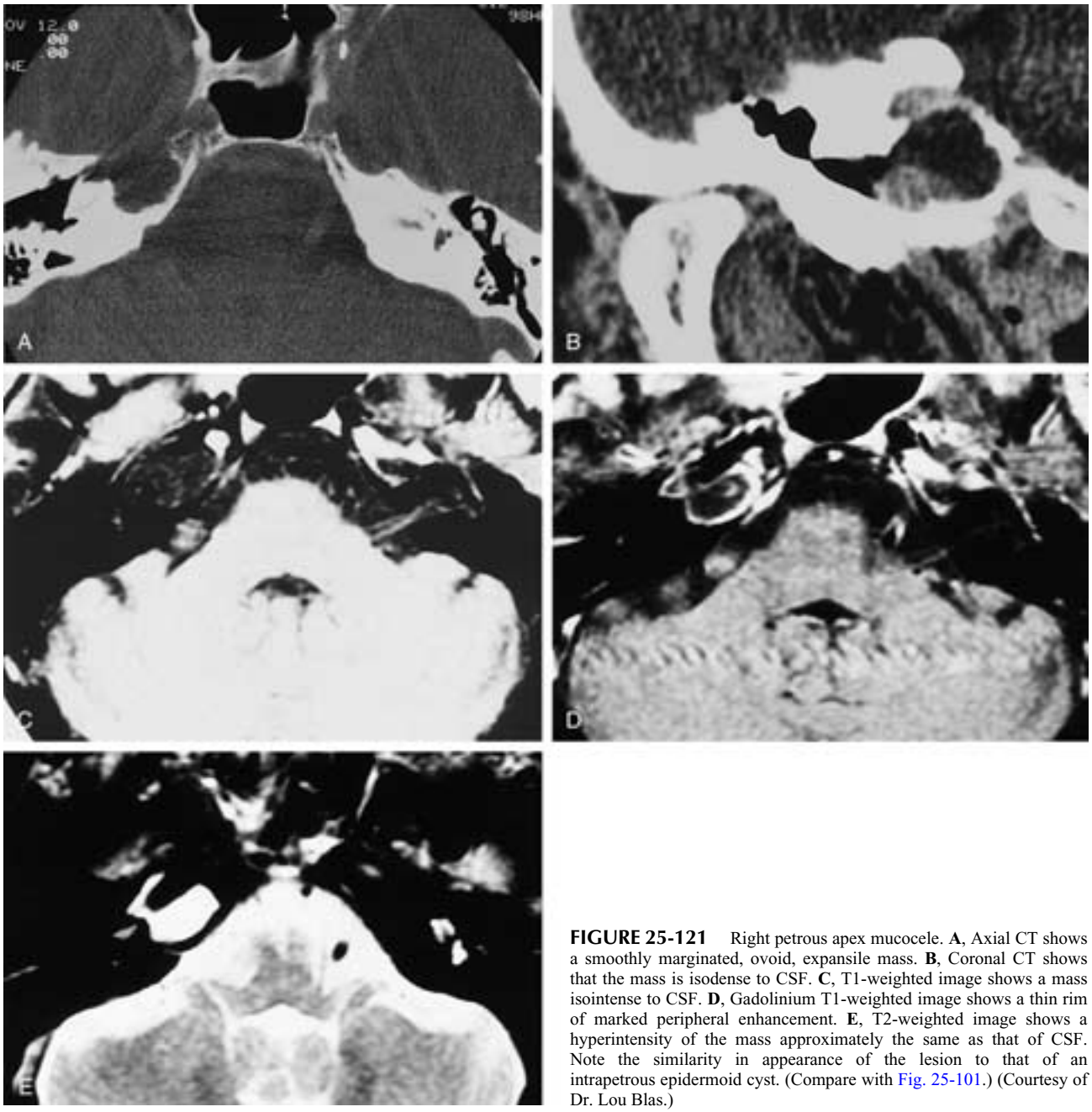

FIGURE 25-121 Right petrous apex mucocele. **A**, Axial CT shows a smoothly marginated, ovoid, expansile mass. **B**, Coronal CT shows that the mass is isodense to CSF. **C**, T1-weighted image shows a mass isointense to CSF. **D**, Gadolinium T1-weighted image shows a thin rim of marked peripheral enhancement. **E**, T2-weighted image shows a hyperintensity of the mass approximately the same as that of CSF. Note the similarity in appearance of the lesion to that of an intrapetrous epidermoid cyst. (Compare with Fig. 25-101.) (Courtesy of Dr. Lou Blas.)

VIEW IMAGE

and MR imaging appearances suggestive of a meningioma.[244] Locally invasive chondrosarcomas may be treated with surgery using the infratemporal fossa approach or with radiation therapy.[8, 301, 446, 453–455]

A chondroblastoma, an uncommon benign tumor, may be indistinguishable from a chondrosarcoma on CT or MR imaging.[411]

Endolymphatic Sac Tumors

Endolymphatic sac tumors (ELST) are rare, locally invasive papillary cystadenomatous tumors causing sensorineural hearing loss and at times facial palsy.[412, 456, 457] Until pinpointed recently to the endolymphatic sac, they were often misdiagnosed as ceruminous neoplasms, metastatic thyroid and renal carcinomas, or choroid plexus papillomas.[458–461] ELST affect adults sporadically and are more common in patients with von Hippel-Lindau disease (vHL), an autosomal dominant multisystem disorder.[462, 463] In the latter case the tumors may be bilateral.[457, 462, 463] In the French registry of vHL, of 180 patients with cranial CT or MR imaging, 12 had findings of ELST, and 4 of the 12 had ELST as their initial manifestation of vHL (K. Marsot-Dupuch, personal communication).

ELST cause local destruction in the retrolabyrinthine petrous bone but may extend into the medial mastoid to invade the facial nerve or transdurally into the posterior cranial fossa (Fig. 25-104).[457, 462, 463] On CT, the bone margins are irregular, and intratumoral bone spicules are

Copyright © 2003, Mosby, Inc. All rights reserved.

commonly present.[376] On MR imaging, foci of hyperintensity are often found on precontrast T1-weighted images.[376, 464, 465] The treatment is wide local resection.[412]

Miscellaneous

Nasopharyngeal carcinoma is a frequent invader of the skull base.[217] Its posterior fossa extension tends to involve the petrous and occipital bones along the petrooccipital fissure.[466] In contrast to chondrosarcoma, nasopharyngeal carcinoma is likely to be more infiltrative, less bulky, and more homogeneous in its bone involvement (Fig. 25-85).

Xanthomas are specialized granulomas composed of lipid-laden, ''foamy'' histiocytes associated with cholesterol clefts and inflammation, usually associated with disorders of lipid metabolism such as hyperlipoproteinemia.[391] More commonly seen in the olecranon and Achilles tendon regions, they occasionally occur in the temporal bone. On CT, they appear as lytic masses containing many small calcific foci.[391] On MR imaging, xanthomas show an inhomogeneous, hyperintense mass with small, hypointense

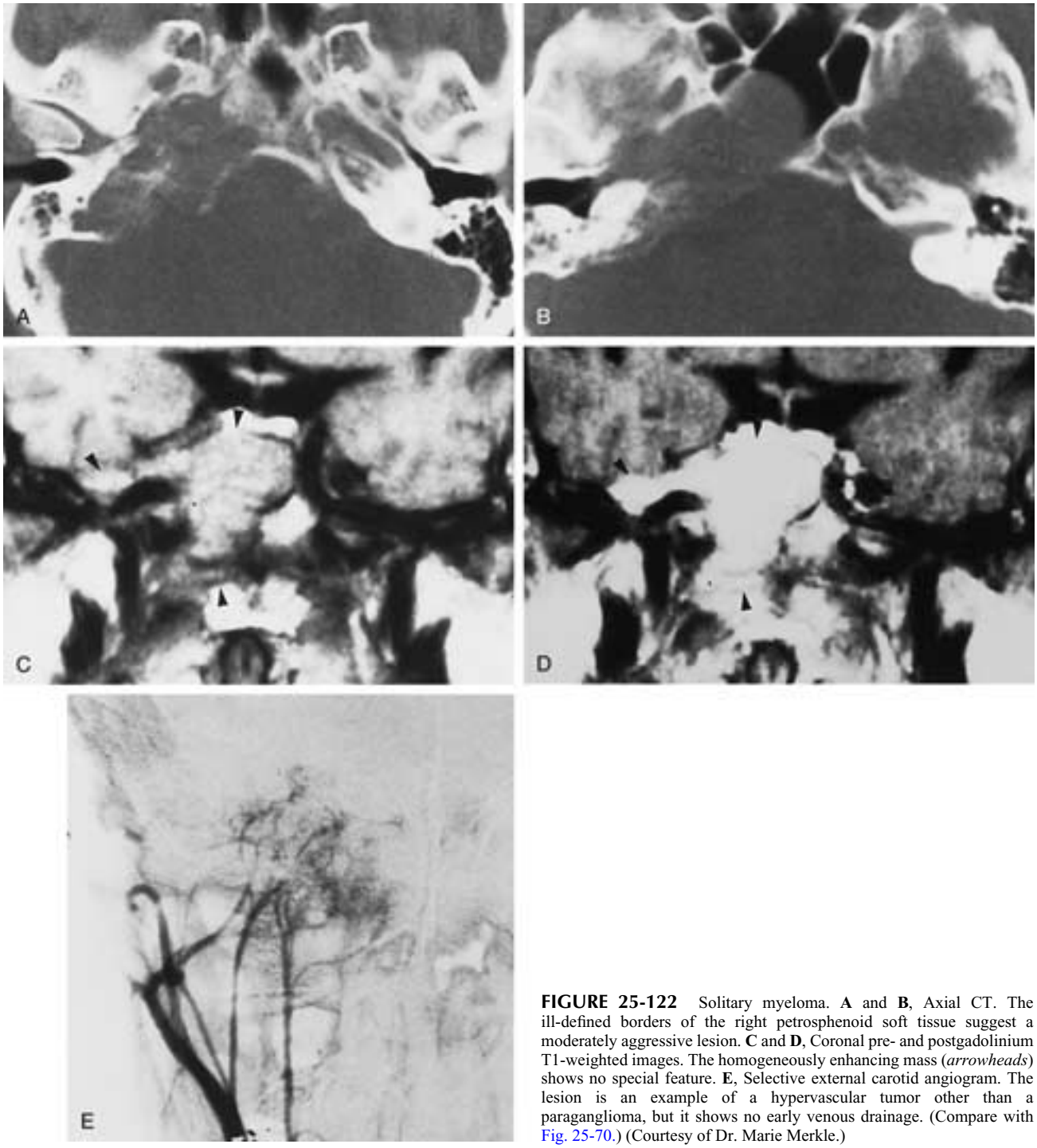

FIGURE 25-122 Solitary myeloma. **A** and **B**, Axial CT. The ill-defined borders of the right petrosphenoid soft tissue suggest a moderately aggressive lesion. **C** and **D**, Coronal pre- and postgadolinium T1-weighted images. The homogeneously enhancing mass (*arrowheads*) shows no special feature. **E**, Selective external carotid angiogram. The lesion is an example of a hypervascular tumor other than a paraganglioma, but it shows no early venous drainage. (Compare with Fig. 25-70.) (Courtesy of Dr. Marie Merkle.)

VIEW IMAGE

Copyright © 2003, Mosby, Inc. All rights reserved.

foci on T1-weighted images and no appreciable contrast enhancement. On T2-weighted images, they are generally hypointense, with some hyperintense foci (Fig. 25-108).[467]

Myeloma (Fig. 25-122), lymphoma, metastases, giant cell tumors (Figs. 25-81 and 25-107), and other malignant tumors occasionally involve the petrous bone. The findings are nonspecific. Petrous apex abscess and skull base osteomyelitis (malignant external otitis) may also enter the differential diagnosis. Meningoceles can extend into the petrous apex usually from Meckel's cave. They can mimic expansile lesions of the apex. They follow CSF on various MR sequences (see Chapter 21).

REFERENCES

1. Jackler R, Brackmann D. Neurotology. St. Louis: Mosby-Year Book, 1994.
2. Cohen NL, Hammerschlag P, Berg H, Ransohoff J. Acoustic neuroma surgery: an eclectic approach with emphasis on preservation of hearing. The New York University-Bellevue experience. Ann Otol Rhinol Laryngol 1986;95(1 Pt 1):21–27.
3. Amundsen P, Newton T. Subarachnoid cisterns. In: Newton T, Potts D, eds. Radiology of the Skull and Brain. Vol 4 Ventricles and Cisterns. St. Louis: Mosby, 1978:3588–3711.
4. Camp J, Cilley E. Significance of asymmetry of pori acustici as an aid in diagnosis of eighth nerve tumors. Am J Roentgenol 1939;41:713–719.
5. Takahashi M, Okudera T, Tomanaga M, Kitamura K. Angiographic diagnosis of acoustic neurinomas: analysis of 30 lesions. Neuroradiology. 1971;2(4):191–200.
6. Valvassori GE. The abnormal internal auditory canal: the diagnosis of acoustic neuroma. Radiology 1969;92(3):449–459.
7. Scanlon R. Positive contrast medium (Iophendylate) in diagnosis of acoustic neuroma. Arch Otolaryngol 1964;80:698–706.
8. Fisch U, Mattox D. Microsurgery of the Skull Base. New York: Thieme, 1988.
9. Gentry LR, Jacoby CG, Turski PA, Houston LW, Strother CM, Sackett JF. Cerebellopontine angle-petromastoid mass lesions: comparative study of diagnosis with MR imaging and CT. Radiology 1987;162(2):513–520.
10. Jackler RK, Shapiro MS, Dillon WP, Pitts L, Lanser MJ. Gadolinium-DTPA enhanced magnetic resonance imaging in acoustic neuroma diagnosis and management. Otolaryngol Head Neck Surg 1990;102(6):670–677.
11. Mafee M. Acoustic neuroma and other acoustic nerve disorders: role of MRI and CT: an analysis of 238 cases. Semin Ultrasound CT MR 1987;8:256–261.
12. Tien RD. Fat-suppression MR imaging in neuroradiology: techniques and clinical application. AJR 1992;158(2):369–379.
13. Masaryk T, Lewin J, Laub G. Magnetic resonance angiography. In: Stark D, Bradley WJ, eds. Magnetic Resonance Imaging. 2nd ed. St. Louis: Mosby-Year Book, 1992;273–312.
14. Casselman JW. Advanced sequences improve evaluation of temporal bone disease. Diagn Imaging (San Franc) 2000;22(11):172–177.
15. Phelps PD. Fast spin echo MRI in otology. J Laryngol Otol 1994;108(5):383–394.
16. Hermans R, Van der Goten A, De Foer B, Baert AL. MRI screening for acoustic neuroma without gadolinium: value of 3DFT-CISS sequence. Neuroradiology 1997;39(8):593–598.
17. Casselman JW, Kuhweide R, Deimling M, Ampe W, Dehaene I, Meeus L. Constructive interference in steady state-3DFT MR imaging of the inner ear and cerebellopontine angle. AJNR 1993;14(1):47–57.
18. Brown E, Hug EB, Weber AL. Chondrosarcoma of the skull base. Neuroimaging Clin North Am 1994;4(3):529–541.
19. Schuknecht H. Pathology of the Ear. Cambridge, Mass: Harvard University Press, 1974.
20. Valavanis A, Schubiger O, Naidich T. Clinical Imaging of the Cerebellopontine Angle. Berlin: Springer-Verlag, 1986.
21. Brackmann DE, Bartels LJ. Rare tumors of the cerebellopontine angle. Otolaryngol Head Neck Surg 1980;88(5):555–559.
22. Kasantikul V, Netsky MG, Glasscock ME 3rd, Hays JW. Acoustic neurilemmoma. Clinicoanatomical study of 103 patients. J Neurosurg 1980;52(1):28–35.
23. Graham MD, Sataloff RT. Acoustic tumors in the young adult. Arch Otolaryngol 1984;110(6):405–407.
24. Krause CJ, McCabe BF. Acoustic neuroma in a 7-year-old girl. Report of a case. Arch Otolaryngol 1971;94(4):359–363.
25. Gruskin P, Carberry J. Pathology of Acoustic Tumors. Vol I. Diagnosis. Baltimore: University Park Press, 1979.
26. Harkin J, Reed R. Tumors of the Peripheral Nervous System. Vol 3. Washington, DC: Armed Forces Institute of Pathology, 1969.
27. Rubenstein L. Tumors of the Central Nervous System. Vol 6. Washington, DC: Armed Forces Institute of Pathology, 1972.
28. Woodruff J, Horten B, Erlandson R. Pathology of Peripheral Nerves and Paragangliomas. New York: Churchill-Livingstone, 1990.
29. Clemis JD, Ballad WJ, Baggot PJ, Lyon ST. Relative frequency of inferior vestibular schwannoma. Arch Otolaryngol Head Neck Surg 1986;112(2):190–194.
30. Komatsuzaki A, Tsunoda A. Nerve origin of the acoustic neuroma. J Laryngol Otol 2001;115(5):376–379.
31. National Institutes of Health Consensus Development Conference Statement on Acoustic Neuroma, December 11–13, 1991. The Consensus Development Panel. Arch Neurol 1994;51(2):201–207.
32. Bebin J. Pathophysiology of Acoustic Tumors. Vol I. Diagnosis. Baltimore: University Park Press, 1979.
33. Lanser MJ, Sussman SA, Frazer K. Epidemiology, pathogenesis, and genetics of acoustic tumors. Otolaryngol Clin North Am 1992;25(3):499–520.
34. Nutik SL, Babb MJ. Determinants of tumor size and growth in vestibular schwannomas. J Neurosurg 2001;94(6):922–926.
35. Kasantikul V, Brown WJ. Estrogen receptors in acoustic neurilemmomas. Surg Neurol 1981;15(2):105–109.
36. Kasantikul V, Netsky MG, Glasscock ME 3rd, Hayes JW. Intracanalicular neurilemmomas: clinicopathologic study. Ann Otol Rhinol Laryngol 1980;89(1 Pt 1):29–32.
37. Martuza RL, Eldridge R. Neurofibromatosis 2 (bilateral acoustic neurofibromatosis). N Engl J Med 1988;318(11):684–688.
38. Riccardi VM. Von Recklinghausen neurofibromatosis. N Engl J Med 1981;305(27):1617–1627.
39. Kasantikul V, Palmer JO, Netsky MG, Glasscock ME 3rd, Hays JW. Glioma of the acoustic nerve. Arch Otolaryngol 1980;106(8):456–459.
40. Martuza RL, Ojemann RG. Bilateral acoustic neuromas: clinical aspects, pathogenesis, and treatment. Neurosurgery 1982;10(1):1–12.
41. Barker D, Wright E, Nguyen K, et al. Gene for von Recklinghausen neurofibromatosis is in the pericentromeric region of chromosome 17. Science 1987;236(4805):1100–1102.
42. Rouleau GA, Wertelecki W, Haines JL, et al. Genetic linkage of bilateral acoustic neurofibromatosis to a DNA marker on chromosome 22. Nature 1987;329(6136):246–248.
43. Kanter WR, Eldridge R, Fabricant R, Allen JC, Koerber T. Central neurofibromatosis with bilateral acoustic neuroma: genetic, clinical and biochemical distinctions from peripheral neurofibromatosis. Neurology 1980;30(8):851–859.
44. Eldridge R. Central neurofibromatosis with bilateral acoustic neuroma. Adv Neurol 1981;29:57–65.
45. Wertelecki W, Rouleau GA, Superneau DW, et al. Neurofibromatosis 2: clinical and DNA linkage studies of a large kindred. N Engl J Med 1988;319(5):278–283.
46. Glasscock ME 3rd, Hart MJ, Vrabec JT. Management of bilateral acoustic neuroma. Otolaryngol Clin North Am 1992;25(2):449–469.
47. Bognanno JR, Edwards MK, Lee TA, Dunn DW, Roos KL, Klatte EC. Cranial MR imaging in neurofibromatosis. AJR 1988;151(2):381–388.
48. Pallini R, Tancredi A, Casalbore P, et al. Neurofibromatosis type 2: growth stimulation of mixed acoustic schwannoma by concurrent adjacent meningioma: possible role of growth factors. Case report. J Neurosurg 1998;89(1):149–154.
49. Kim DG, Paek SH, Chi JG, Chun YK, Han DH. Mixed tumour of schwannoma and meningioma components in a patient with NF-2. Acta Neurochir (Wien) 1997;139(11):1061–1064; discussion 1064–1065.
50. Kishore A, O'Reilly B. A clinical study of vestibular schwannomas in type 2 neurofibromatosis. Clin Otolaryngol 2000;25(6):561–565.

Copyright © 2003, Mosby, Inc. All rights reserved.

51. Hughes GB, Sismanis A, Glasscock ME 3rd, Hays JW, Jackson CG. Management of bilateral acoustic tumors. Laryngoscope 1982; 92(12):1351–1359.
52. Dutcher PO Jr, House WF, Hitselberger WE. Early detection of small bilateral acoustic tumors. Am J Otol 1987;8(1):35–38.
53. Glasscock ME 3rd, Pappas DG Jr, Manolidis S, Von Doersten PG, Jackson CG, Storper IS. Management of acoustic neuroma in the elderly population. Am J Otol 1997;18(2):236–241; discussion 241–242.
54. Brackmann D, Selters W. Auditory Brainstem Response Audiometry in Acoustic Tumor Detection. New York: Raven Press, 1982.
55. Shannon RV, Fayad J, Moore J, et al. Auditory brainstem implant: II. Postsurgical issues and performance. Otolaryngol Head Neck Surg 1993;108(6):634–642.
56. Gebarski SS, Tucci DL, Telian SA. The cochlear nuclear complex: MR location and abnormalities. AJNR 1993;14(6):1311–1318.
57. Lo WW, Tasaka A, Zink B, Harris O. A simple CT method for location of auditory brain stem implant electrodes. AJNR 1995;16(3): 599–601.
58. Ebinger K, Otto S, Arcaroli JSS, Arndt P. Multichannel auditory brainstem implant: US clinical trial results. J Laryngol Otol Suppl 2000;27:50–53.
59. Brow R. Pre- and Postoperative Management of the Acoustic Tumor Patient. Vol 2. Management. Baltimore: University Park Press, 1979.
60. Selesnick SH, Jackler RK. Clinical manifestations and audiologic diagnosis of acoustic neuromas. Otolaryngol Clin North Am 1992;25(3):521–551.
61. Hart RG, Gardner DP, Howieson J. Acoustic tumors: atypical features and recent diagnostic tests. Neurology 1983;33(2):211–221.
62. McCoyd K, Barron KD, Cassidy RJ. Acoustic neurinoma presenting as subarachnoid hemorrhage. Case report. J Neurosurg 1974;41(3): 391–393.
63. Gleeson RK, Butzer JF, Grin OD Jr. Acoustic neurinoma presenting as subarachnoid hemorrhage. Case report. J Neurosurg 1978;49(4): 602–604.
64. Castillo R, Watts C, Pulliam M. Sudden hemorrhage in an acoustic neuroma. Case report. J Neurosurg 1982;56(3):417–419.
65. Yonemitsu T, Niizuma H, Kodama N, Fujiwara S, Suzuki J. Acoustic neurinoma presenting as subarachnoid hemorrhage. Surg Neurol 1983;20(2):125–130.
66. Cohn AI, Le Liever WC, Hokanson JA, Quinn FB Jr. Acoustic neurinoma diagnostic model evaluation using decision support systems. Arch Otolaryngol Head Neck Surg 1986;112(8):830–835.
67. Hart RG, Davenport J. Diagnosis of acoustic neuroma. Neurosurgery 1981;9(4):450–463.
68. Press GA, Hesselink JR. MR imaging of cerebellopontine angle and internal auditory canal lesions at 1.5 T. AJR 1988;150(6):1371–1381.
69. Welling DB, Glasscock ME 3rd, Woods CI, Jackson CG. Acoustic neuroma: a cost-effective approach. Otolaryngol Head Neck Surg 1990;103(3):364–370.
70. Schmidt RJ, Sataloff RT, Newman J, Spiegel JR, Myers DL. The sensitivity of auditory brainstem response testing for the diagnosis of acoustic neuromas. Arch Otolaryngol Head Neck Surg 2001;127(1): 19–22.
71. Annesley-Williams DJ, Laitt RD, Jenkins JP, Ramsden RT, Gillespie JE. Magnetic resonance imaging in the investigation of sensorineural hearing loss: is contrast enhancement still necessary? J Laryngol Otol 2001;115(1):14–21.
72. Zealley IA, Cooper RC, Clifford KM, et al. MRI screening for acoustic neuroma: a comparison of fast spin echo and contrast enhanced imaging in 1233 patients. Br J Radiol 2000;73(867): 242–247.
73. Curtin HD. Rule out eighth nerve tumor: contrast-enhanced T1-weighted or high-resolution T2-weighted MR? AJNR 1997; 18(10):1834–1838.
74. Glasscock MI, Steenerson R. History of Acoustic Tumor Surgery, 1961-Present. Vol I. Diagnosis. Baltimore: University Park Press, 1979.
75. House W. Translabyrinthine Approach. Vol 2. Management. Baltimore: University Park Press, 1979.
76. Shelton C. Hearing preservation in acoustic tumor surgery. Otolaryngol Clin North Am 1992;25(3):609–621.
77. Kim HS, Kim DI, Chung IH, Lee WS, Kim KY. Topographical relationship of the facial and vestibulocochlear nerves in the subarachnoid space and internal auditory canal. AJNR 1998;19(6): 1155–1161.
78. Sartoretti-Schefer S, Kollias S, Valavanis A. Spatial relationship between vestibular schwannoma and facial nerve on three-dimensional T2-weighted fast spin-echo MR images. AJNR 2000;21(5):810–816.
79. Shelton C. Preoperative identification of the facial nerve achieved using fast spin-echo MR imaging: can it help the surgeon? AJNR 2000;21(5):805.
80. Somers T, Casselman J, de Ceulaer G, Govaerts P, Offeciers E. Prognostic value of magnetic resonance imaging findings in hearing preservation surgery for vestibular schwannoma. Otol Neurotol 2001;22(1):87–94.
81. Dubrulle F, Ernst O, Vincent C, Vaneecloo FM, Lejeune JP, Lemaitre L. Cochlear fossa enhancement at MR evaluation of vestibular schwannoma: correlation with success at hearing-preservation surgery. Radiology 2000;215(2):458–462.
82. Harner SG, Ebersold MJ. Management of acoustic neuromas, 1978–1983. J Neurosurg 1985;63(2):175–179.
83. Glasscock ME 3rd, Kveton JF, Jackson CG, Levine SC, McKennan KX. A systematic approach to the surgical management of acoustic neuroma. Laryngoscope 1986;96(10):1088–1094.
84. Tator CH. Acoustic neuromas: management of 204 cases. Can J Neurol Sci 1985;12(4):353–357.
85. Jackler RK, Pitts LH. Selection of surgical approach to acoustic neuroma. Otolaryngol Clin North Am 1992;25(2):361–387.
86. House WF, Shelton C. Middle fossa approach for acoustic tumor removal. Otolaryngol Clin North Am 1992;25(2):347–359.
87. Glasscock ME 3rd, Gulya AJ, Pensak ML. Surgery of the posterior fossa. Otolaryngol Clin North Am 1984;17(3):483–497.
88. Wiet RJ, Kazan RP, Raslan W, Herzon GD. Complications in the approach to acoustic tumor surgery. Ann Otol Rhinol Laryngol 1986;95(1 Pt 1):28–31.
89. Wazen J, Silverstein H, Norrell H, Besse B. Preoperative and postoperative growth rates in acoustic neuromas documented with CT scanning. Otolaryngol Head Neck Surg 1985;93(2): 151–155.
90. Nedzelski JM, Canter RJ, Kassel EE, Rowed DW, Tator CH. Is no treatment good treatment in the management of acoustic neuromas in the elderly? Laryngoscope 1986;96(8):825–829.
91. Gillespie JE. MRI screening for acoustic neuroma. Br J Radiol 2000;73(874):1129–1130.
92. Charabi S, Tos M, Thomsen J, Charabi B, Mantoni M. Vestibular schwannoma growth—long-term results. Acta Otolaryngol Suppl 2000;543:7–10.
93. Tschudi DC, Linder TE, Fisch U. Conservative management of unilateral acoustic neuromas. Am J Otol 2000;21(5):722–728.
94. Walsh RM, Bath AP, Bance ML, Keller A, Tator CH, Rutka JA. The natural history of untreated vestibular schwannomas. Is there a role for conservative management? Rev Laryngol Otol Rhinol (Bord) 2000;121(1):21–26.
95. Walsh RM, Bath AP, Bance ML, Keller A, Tator CH, Rutka JA. The role of conservative management of vestibular schwannomas. Clin Otolaryngol 2000;25(1):28–39.
96. O'Reilly B, Murray CD, Hadley DM. The conservative management of acoustic neuroma: a review of forty-four patients with magnetic resonance imaging. Clin Otolaryngol 2000;25(2):93–97.
97. Rosenberg SI. Natural history of acoustic neuromas. Laryngoscope 2000;110(4):497–508.
98. Fucci MJ, Buchman CA, Brackmann DE, Berliner KI. Acoustic tumor growth: implications for treatment choices. Am J Otol 1999;20(4):495–499.
99. Perry BP, Gantz BJ, Rubinstein JT. Acoustic neuromas in the elderly. Otol Neurotol 2001;22(3):389–391.
100. House JW, Nissen RL, Hitselberger WE. Acoustic tumor management in senior citizens. Laryngoscope 1987;97(2):129–130.
101. Noren G, Arndt J, Hindmarsh T. Stereotactic radiosurgery in cases of acoustic neurinoma: further experiences. Neurosurgery 1983;13(1): 12–22.
102. Nakamura H, Jokura H, Takahashi K, Boku N, Akabane A, Yoshimoto T. Serial follow-up MR imaging after gamma knife radiosurgery for vestibular schwannoma. AJNR 2000;21(8):1540–1546.
103. Moller P, Myrseth E, Pedersen PH, Larsen JL, Krakenes J, Moen G. Acoustic neuroma—treatment modalities. Surgery, gamma-knife or observation? Acta Otolaryngol Suppl 2000;543:34–37.
104. Moller A, Hatam A, Olivecrona H. Diagnosis of acoustic neuroma with computed tomography. Neuroradiology 1978;17(1):25–30.

Copyright © 2003, Mosby, Inc. All rights reserved.

105. Solti-Bohman LG, Magaram DL, Lo WW, et al. Gas-CT cisternography for detection of small acoustic nerve tumors. Radiology 1984;150(2):403–407.
106. Valavanis A, Schubiger O, Hayek J, Pouliadis G. CT of meningiomas on the posterior surface of the petrous bone. Neuroradiology 1981;22(3):111–121.
107. Hatam A, Bergstrom M, Moller A, Olivecrona H. Early contrast enhancement of acoustic neuroma. Neuroradiology 1978;17(1): 31–33.
108. Valvassori G, Buckingham R. Internal Auditory Canal and Acoustic Neuroma. New York: Thieme, 1995.
109. Krassanakis K, Sourtsis E, Karvounis P. Unusual appearance of an acoustic neuroma on computed tomography. Neuroradiology 1981; 21(1):51–53.
110. Tali ET, Yuh WT, Nguyen HD, et al. Cystic acoustic schwannomas: MR characteristics. AJNR 1993;14(5):1241–1247.
111. Valvassori GE, Garcia Morales F, Palacios E, Dobben GE. MR of the normal and abnormal internal auditory canal. AJNR 1988;9(1):115–119.
112. Daniels DL, Millen SJ, Meyer GA, et al. MR detection of tumor in the internal auditory canal. AJR 1987;148(6):1219–1222.
113. Enzmann DR, O'Donohue J. Optimizing MR imaging for detecting small tumors in the cerebellopontine angle and internal auditory canal. AJNR 1987;8(1):99–106.
114. Gomori JM, Grossman RI, Goldberg HI, Zimmerman RA, Bilaniuk LT. Intracranial hematomas: imaging by high-field MR. Radiology 1985;157(1):87–93.
115. Curati WL, Graif M, Kingsley DP, Niendorf HP, Young IR. Acoustic neuromas: Gd-DTPA enhancement in MR imaging. Radiology 1986;158(2):447–451.
116. Held P, Fellner C, Seitz J, Graf S, Fellner F, Strutz J. The value of T2(*)-weighted MR images for the diagnosis of acoustic neuromas. Eur J Radiol 1999;30(3):237–244.
117. Schmalbrock P, Chakeres DW, Monroe JW, Saraswat A, Miles BA, Welling DB. Assessment of internal auditory canal tumors: a comparison of contrast-enhanced T1-weighted and steady-state T2-weighted gradient-echo MR imaging. AJNR 1999;20(7):1207–1213.
118. Breger RK, Papke RA, Pojunas KW, Haughton VM, Williams AL, Daniels DL. Benign extraaxial tumors: contrast enhancement with Gd-DTPA. Radiology 1987;163(2):427–429.
119. Paz-Fumagalli R, Daniels DL, Millen SJ, Meyer GA, Thieu TM. Dural ''tail'' associated with an acoustic schwannoma in MR imaging with gadopentetate dimeglumine. AJNR 1991;12(6):1206.
120. Witten R, Wade C. Computed Tomography in Acoustic Tumors Diagnosis. Vol I. Diagnosis. Baltimore: University Park Press, 1979.
121. Noren G. Stereotactic Treatment of Acoustic Neuromas. Boston: Martinus Nijhoff, 1988.
122. Hill MC, Oh KS, Hodges FJ. Internal auditory canal enlargement in neurofibromatosis without acoustic neuroma. Radiology 1977; 122(3):730.
123. Sarwar M, Swischuk LE. Bilateral internal auditory canal enlargement due to dural ectasia in neurofibromatosis. AJR 1977;129(5): 935–936.
124. Thomsen J, Tos M, Borgesen SE. Gamma knife: hydrocephalus as a complication of stereotactic radiosurgical treatment of an acoustic neuroma. Am J Otol 1990;11(5):330–333.
125. Gonzalez-Revilla A. Differential diagnosis of tumors at cerebellopontine recess. Johns Hopkins Hosp Bull 1948(83):187–189.
126. Segall HD, Zee CS, Naidich TP, Ahmadi J, Becker TS. Computed tomography in neoplasms of the posterior fossa in children. Radiol Clin North Am 1982;20(1):237–253.
127. Lo W, Solti-Bohman L. Computed Tomography of the Petrous Bone and Posterior Fossa. New York: Marcel Dekker, 1987.
128. Naidich TP, Lin JP, Leeds NE, Pudlowski RM, Naidich JB. Primary tumors and other masses of the cerebellum and fourth ventricle: differential diagnosis by computed tomography. Neuroradiology 1977;14(4):153–174.
129. Elster AD, Challa VR, Gilbert TH, Richardson DN, Contento JC. Meningiomas: MR and histopathologic features. Radiology 1989; 170(3 Pt 1):857–862.
130. Russell D, Rubenstein L. Pathology of Tumours of the Nervous System. 4th ed. Baltimore: Williams & Wilkins, 1977.
131. Demaerel P, Wilms G, Lammens M, et al. Intracranial meningiomas: correlation between MR imaging and histology in fifty patients. J Comput Assist Tomogr 1991;15(1):45–51.
132. Kepes JJ. Presidential address: the histopathology of meningiomas. A reflection of origins and expected behavior? J Neuropathol Exp Neurol 1986;45(2):95–107.
133. Servo A, Porras M, Jaaskelainen J, Paetau A, Haltia M. Computed tomography and angiography do not reliably discriminate malignant meningiomas from benign ones. Neuroradiology 1990; 32(2):94–97.
134. Di Chiro G, Hatazawa J, Katz DA, Rizzoli HV, De Michele DJ. Glucose utilization by intracranial meningiomas as an index of tumor aggressivity and probability of recurrence: a PET study. Radiology 1987;164(2):521–526.
135. Spagnoli MV, Goldberg HI, Grossman RI, et al. Intracranial meningiomas: high-field MR imaging. Radiology 1986;161(2): 369–375.
136. Zimmerman RD, Fleming CA, Saint-Louis LA, Lee BC, Manning JJ, Deck MD. Magnetic resonance imaging of meningiomas. AJNR 1985;6(2):149–157.
137. Vassilouthis J, Ambrose J. Computerized tomography scanning appearances of intracranial meningiomas. An attempt to predict the histological features. J Neurosurg 1979;50(3):320–327.
138. Aoki S, Sasaki Y, Machida T, Tanioka H. Contrast-enhanced MR images in patients with meningioma: importance of enhancement of the dura adjacent to the tumor. AJNR 1990;11(5):935–938.
139. Goldsher D, Litt AW, Pinto RS, Bannon KR, Kricheff II. Dural ''tail'' associated with meningiomas on Gd-DTPA-enhanced MR images: characteristics, differential diagnostic value, and possible implications for treatment. Radiology 1990;176(2):447–450.
140. Schorner W, Schubeus P, Henkes H, Lanksch W, Felix R. ''Meningeal sign'': a characteristic finding of meningiomas on contrast-enhanced MR images. Neuroradiology 1990;32(2):90–93.
141. Tokumaru A, O'Uchi T, Eguchi T, et al. Prominent meningeal enhancement adjacent to meningioma on Gd-DTPA-enhanced MR images: histopathologic correlation. Radiology 1990;175(2): 431–433.
142. Wilms G, Lammens M, Marchal G, et al. Prominent dural enhancement adjacent to nonmeningiomatous malignant lesions on contrast-enhanced MR images. AJNR 1991;12(4):761–764.
143. Wilms G, Lammens M, Marchal G, et al. Thickening of dura surrounding meningiomas: MR features. J Comput Assist Tomogr 1989;13(5):763–768.
144. Saleh E, Taibah A, Achilli V, et al. Postfossa meningioma: surgical strategy. Skull Base Surg 1994;4:202–212.
145. Matthies C, Carvalho G, Tatagiba M, Lima M, Sami M. Meningiomas of the cerebellopontine angle. Acta Neurochir (Wien) Suppl 1996;65:86–91.
146. Iwai Y, Yamanaka K, Yasui T, Komiyama M, Nakajima H, Kishi H. Gamma knife surgery for skull base meningiomas. The effectiveness of low dose treatment. Surg Neurol 1999;52(1):40–44.
147. Flickinger FW, Yuh WT, Nichols RD 2nd, Kemp JD. Solitary prostatic metastasis to the cerebellopontine angle: MR and CT findings. J Comput Assist Tomogr 1989;13(6):1088–1090.
148. Lee YY, Tien RD, Bruner JM, De Pena CA, Van Tassel P. Loculated intracranial leptomeningeal metastases: CT and MR characteristics. AJNR 1989;10(6):1171–1179.
149. Phillips ME, Ryals TJ, Kambhu SA, Yuh WT. Neoplastic vs. inflammatory meningeal enhancement with Gd-DTPA. J Comput Assist Tomogr 1990;14(4):536–541.
150. Yang PJ, Seeger JF, Carmody RF, Mehta BA. Cerebellopontine angle lymphoma. AJNR 1987;8(2):368–369.
151. Jazy FK, Shehata WM, Tew JM, Meyer RL, Boss HH. Primary intracranial lymphoma of the dura. Arch Neurol 1980;37(8): 528–529.
152. Prabhu SS, Lynch PG, Keogh AJ, Parekh HC. Intracranial meningeal melanocytoma: a report of two cases and a review of the literature. Surg Neurol 1993;40(6):516–521.
153. Vasdev A, David P, Villemot D, et al. Apparently primary malignant melanoma of the cerebellopontine angle. One case. J Neuroradiol 1990;17(2):152–156.
154. Hayes WS, Sherman JL, Stern BJ, Citrin CM, Pulaski PD. MR and CT evaluation of intracranial sarcoidosis. AJR 1987;149(5):1043–1049.
155. Martin N, Masson C, Henin D, Mompoint D, Marsault C, Nahum H. Hypertrophic cranial pachymeningitis: assessment with CT and MR imaging. AJNR 1989;10(3):477–484.
156. Seltzer S, Mark AS, Atlas SW. CNS sarcoidosis: evaluation with contrast-enhanced MR imaging. AJNR 1991;12(6):1227–1233.

Copyright © 2003, Mosby, Inc. All rights reserved.

157. Brackmann D, Anderson R. Cholesteatomas of the Cerebellopontine Angle. Vol 2. Birmingham, Ala: Aesculapius, 1979.
158. Berger MS, Wilson CB. Epidermoid cysts of the posterior fossa. J Neurosurg 1985;62(2):214–219.
159. Braun IF, Naidich TP, Leeds NE, Koslow M, Zimmerman HM, Chase NE. Dense intracranial epidermoid tumors. Computed tomographic observations. Radiology 1977;122(3):717–719.
160. Gualdi GF, Di Biasi C, Trasimeni G, Pingi A, Vignati A, Maira G. Unusual MR and CT appearance of an epidermoid tumor. AJNR 1991;12(4):771–772.
161. Mikhael M, Mattu A. Intracranial pearly tumors: The roles of computed tomography, angiography and pneumoencephalography. J Comput Assist Tomogr 1978(2):421–426.
162. Nagashima C, Takahama M, Sakaguchi A. Dense cerebellopontine epidermoid cyst. Surg Neurol 1982;17(3):172–177.
163. Gao PY, Osborn AG, Smirniotopoulos JG, Harris CP. Radiologic-pathologic correlation. Epidermoid tumor of the cerebellopontine angle. AJNR 1992;13(3):863–872.
164. Garcia CA, McGarry PA, Rodriguez F. Primary intracranial squamous cell carcinoma of the right cerebellopontine angle. J Neurosurg 1981;54(6):824–828.
165. Nosaka Y, Nagao S, Tabuchi K, Nishimoto A. Primary intracranial epidermoid carcinoma. Case report. J Neurosurg 1979;50(6): 830–833.
166. Davidson HD, Ouchi T, Steiner RE. NMR imaging of congenital intracranial germinal layer neoplasms. Neuroradiology 1985;27(4): 301–303.
167. Sakamoto Y, Takahashi M, Ushio Y, Korogi Y. Visibility of epidermoid tumors on steady-state free precession images. AJNR 1994;15(9):1737–1744.
168. Tampieri D, Melanson D, Ethier R. MR imaging of epidermoid cysts. AJNR 1989;10(2):351–356.
169. Horowitz BL, Chari MV, James R, Bryan RN. MR of intracranial epidermoid tumors: correlation of in vivo imaging with in vitro 13C spectroscopy. AJNR 1990;11(2):299–302.
170. Li F, et al. Short T1/T2 epidermoids: lipid or water signal. Paper presented at the 28th annual meeting of the American Society of Neuroradiology, March 19–23, 1990, Los Angeles.
171. Gardner W, McCormack L, Dohn D. Embrional atresia of the fourth ventricle: the cause of ''arachnoid cyst'' of the cerebellopontine angle. J Neurosurg 1960;17:226–231.
172. Haberkamp TJ, Monsell EM, House WF, Levine SC, Piazza L. Diagnosis and treatment of arachnoid cysts of the posterior fossa. Otolaryngol Head Neck Surg 1990;103(4):610–614.
173. Tsuruda JS, Chew WM, Moseley ME, Norman D. Diffusion-weighted MR imaging of the brain: value of differentiating between extraaxial cysts and epidermoid tumors. AJR 1990;155(5):1059–1065; discussion 1066–1068.
174. Kawamura N, Uesaka T, Inamura T, et al. [Small epidermoid induced trigeminal neuralgia unrecognized by conventional CT and MRI for over 25 years]. No To Shinkei 2000;52(12):1113–1116.
175. Murakami N, Matsushima T, Kuba H, et al. Combining steady-state constructive interference and diffusion-weighted magnetic resonance imaging in the surgical treatment of epidermoid tumors. Neurosurg Rev 1999;22(2–3):159–162.
176. Dechambre S, Duprez T, Lecouvet F, Raftopoulos C, Gosnard G. Diffusion-weighted MRI postoperative assessment of an epidermoid tumour in the cerebellopontine angle. Neuroradiology 1999;42(11): 829–831.
177. Gizewski E. [Epidermoid or arachnoid cyst: CISS, FLAIR and difusion images as solution of the diagnostic dilemma]. Rofo Fortschr Geb Rontgenstr Neuen Bildgeb Verfahr 2001;173(1):77–78.
178. Suss RA, Maravilla KR, Thompson J. MR imaging of intracranial cysticercosis: comparison with CT and anatomopathologic features. AJNR 1986;7(2):235–242.
179. Zee CS, Segall HD, Boswell W, Ahmadi J, Nelson M, Colletti P. MR imaging of neurocysticercosis. J Comput Assist Tomogr 1988;12(6): 927–934.
180. Leung SY, Ng TH, Fung CF, Fan YW. An epithelial cyst in the cerebellopontine angle. Case report. J Neurosurg 1991;74(2): 278–282.
181. Lee ST, Huang CC. Respiratory epithelial cyst in the cerebellopontine angle. Surg Neurol 1989;32(6):418–420.
182. Schwartz AM, Jensen ME, Saks DA, Ghatak NR. Epithelial cyst in cerebellopontine angle with xanthogranulomatous changes simulating cholesterol granuloma. Surg Neurol 1989;31(6):454–458.
183. Urasaki E, Fukumura A, Ito Y, et al. Choroidal epithelial cyst in the cerebellopontine angle associated with trigeminal neuralgia—case report. Neurol Med Chir (Tokyo) 1989;29(5):424–428.
184. Malcolm GP, Symon L, Kendall B, Pires M. Intracranial neurenteric cysts. Report of two cases. J Neurosurg 1991;75(1):115–120.
185. Gokalp HZ, Mertol T. Cerebellopontine angle craniopharyngioma. Neurochirurgia (Stuttg) 1990;33(1):20–21.
186. Shimada M, Tsugane R, Shibuya N, Sato O. Craniopharyngioma with extension into the cerebellopontine angle. Case report. Tokai J Exp Clin Med 1989;14(2):113–116.
187. Kawamura Y, Sze G. Totally cystic schwannoma of the tenth cranial nerve mimicking an epidermoid. AJNR 1992;13(5):1333–1334.
188. Zimmerman RA, Bilaniuk LT, Dolinskas C. Cranial computed tomography of epidermoid and congenital fatty tumors of maldevelopmental origin. J Comput Tomogr 1979;3(1):40–50.
189. Dalley RW, Robertson WD, Lapointe JS, Durity FA. Computed tomography of a cerebellopontine angle lipoma. J Comput Assist Tomogr 1986;10(4):704–706.
190. Wong ML, Larson TI, Brackmann DE, Lo WW. Lipoma of internal auditory canal. Otolaryngol Head Neck Surg 1992;107(3):374–376.
191. Saunders JE, Kwartler JA, Wolf HK, Brackmann DE, McElveen JT Jr. Lipomas of the internal auditory canal. Laryngoscope 1991; 101(10):1031–1037.
192. Pinto RS, Kricheff II. Neuroradiology of intracranial neuromas. Semin Roentgenol 1984;19(1):44–52.
193. McCormick PC, Bello JA, Post KD. Trigeminal schwannoma. Surgical series of 14 cases with review of the literature. J Neurosurg 1988;69(6):850–860.
194. Daniels DL, Pech P, Pojunas KW, Kilgore DP, Williams AL, Haughton VM. Trigeminal nerve: anatomic correlation with MR imaging. Radiology 1986;159(3):577–583.
195. Kapila A, Chakeres DW, Blanco E. The Meckel cave: computed tomographic study. Part I: normal anatomy; Part II: pathology. Radiology 1984;152(2):425–433.
196. Pollack IF, Sekhar LN, Jannetta PJ, Janecka IP. Neurilemomas of the trigeminal nerve. J Neurosurg 1989;70(5):737–745.
197. Goldberg R, Byrd S, Winter J, Takahashi M, Joyce P. Varied appearance of trigeminal neuroma on CT. AJR 1980;134(1):57–60.
198. Nelson R, House W. Facial nerve neuroma of the posterior fossa: surgical consideration. Paper presented at Proceedings of the Fourth International Symposium on Facial Nerve Surgery, New York, 1982.
199. Latack JT, Gabrielsen TO, Knake JE, et al. Facial nerve neuromas: radiologic evaluation. Radiology 1983;149(3):731–739.
200. Dort J, Fisch U. Facial nerve schwannomas. Skull Base Surg 1991;1:51–57.
201. Kaye AH, Hahn JF, Kinney SE, Hardy RW Jr, Bay JW. Jugular foramen schwannomas. J Neurosurg 1984;60(5):1045–1053.
202. Horn KL, House WF, Hitselberger WE. Schwannomas of the jugular foramen. Laryngoscope 1985;95(7 Pt 1):761–765.
203. Sasaki T, Takamura K. Twelve cases of jugular foramen neurinoma. Skull Base Surg 1991;1:152–160.
204. Neely JG. Reversible compression neuropathy of the eighth cranial nerve from a large jugular foramen schwannoma. Arch Otolaryngol 1979;105(9):555–560.
205. Smoker WR, Price MJ, Keyes WD, Corbett JJ, Gentry LR. High-resolution computed tomography of the basilar artery: 1. Normal size and position. AJNR 1986;7(1):55–60.
206. Smoker WR, Corbett JJ, Gentry LR, Keyes WD, Price MJ, McKusker S. High-resolution computed tomography of the basilar artery: 2. Vertebrobasilar dolichoectasia: clinical-pathologic correlation and review. AJNR 1986;7(1):61–72.
207. Burt TB. MR of CSF flow phenomenon mimicking basilar artery aneurysm. AJNR 1987;8(1):55–58.
208. Han JS, Bonstelle CT, Kaufman B, et al. Magnetic resonance imaging in the evaluation of the brainstem. Radiology 1984;150(3): 705–712.
209. Jannetta PJ, Abbasy M, Maroon JC, Ramos FM, Albin MS. Etiology and definitive microsurgical treatment of hemifacial spasm. Operative techniques and results in 47 patients. J Neurosurg 1977;47(3): 321–328.
210. Janetta P. Neurovascular cross compression in patient with hyperactive dysfunction symptoms of the eighth cranial nerve. Surg Forum 1975;26:467–469.
211. Morales F, Albert P, Alberca R, de Valle B, Narros A. Glossopharyngeal and vagal neuralgia secondary to vascular compression of the nerves. Surg Neurol 1977;8(6):431–433.

Copyright © 2003, Mosby, Inc. All rights reserved.

212. Janetta PJ, Moller MB, Moller AR. Disabling positional vertigo. N Engl J Med 1984;310(26):1700–1705.
213. Brichaux JC, Gense D, Greselle JF, Jasek F, Bouin H, Caille JM. Radioclinical problems raised by megalodolichobasilar artery. 17 cases and a review of the literature. J Neuroradiol 1989;16(1): 11–24.
214. Resta M, Gentile MA, Di Cuonzo F, Vinjau E, Brindicci D, Carella A. Clinical-angiographic correlations in 132 patients with megadolichovertebrobasilar anomaly. Neuroradiology 1984;26(3):213–216.
215. Schwaber M. Vascular compression syndromes. In: Jackler R, ed. Neurotology. St. Louis: Mosby, 1994;881–903.
216. Janetta P. Microvascular decompression in trigeminal neuralgia and hemifacial spasm. In: Brachmann D, ed. Neurological Surgery of the Ear and Skull Base. New York: Raven Press, 1982;49–54.
217. Barnes L. Pathobiology of selected tumors of base of skull. Skull Base Surg 1991(1):207–216.
218. Carlos R, Fukui M, Hasuo K, et al. Radiological analysis of hemifacial spasm with special reference to angiographic manifestations. Neuroradiology 1986;28(4):288–295.
219. de Lange EE, Vielvoye GJ, Voormolen JH. Arterial compression of the fifth cranial nerve causing trigeminal neuralgia: angiographic findings. Radiology 1986;158(3):721–727.
220. Meaney JF, Miles JB, Nixon TE, Whitehouse GH, Ballantyne ES, Eldridge PR. Vascular contact with the fifth cranial nerve at the pons in patients with trigeminal neuralgia: detection with 3D FISP imaging. AJR 1994;163(6):1447–1452.
221. Palacios E, Valvassori G. Vascular loop and hemifacial spasm. Ear Nose Throat J 1999;78(7):470.
222. Tan EK, Chan LL, Lim SH, Lim WE, Khoo JB, Tan KP. Role of magnetic resonance imaging and magnetic resonance angiography in patients with hemifacial spasm. Ann Acad Med Singapore 1999;28(2):169–173.
223. Wiet RJ, Harvey SA, Jin CZ, Dobben G. Hemifacial spasm: evaluation and management options. Eur Arch Otorhinolaryngol Suppl 1994:S337–342.
224. Tan EK, Chan LL. A case-controlled MRI/MRA study of neurovascular contact in hemifacial spasm. Neurology 2000;55(1): 155–156.
225. Yamamoto S, Ryu H, Tanaka T, Takehara Y. Usefulness of high-resolution magnetic resonance cisternography in patients with hemifacial spasm. Acta Otolaryngol Suppl 2000;542:54–57.
226. Chung SS, Chang JW, Kim SH, Chang JH, Park YG, Kim DI. Microvascular decompression of the facial nerve for the treatment of hemifacial spasm: preoperative magnetic resonance imaging related to clinical outcomes. Acta Neurochir (Wien) 2000;142(8):901–906; discussion 907.
227. Yamakami I, Kobayashi E, Hirai S, Yamaura A. Preoperative assessment of trigeminal neuralgia and hemifacial spasm using constructive interference in steady state-three-dimensional Fourier transformation magnetic resonance imaging. Neurol Med Chir (Tokyo) 2000;40(11):545–555; discussion 555–556.
228. Esfahani F, Dolan KD. Air CT cisternography in the diagnosis of vascular loop causing vestibular nerve dysfunction. AJNR 1989; 10(5):1045–1049.
229. Quaknine G. Microsurgical anatomy of the arterial loops in the pontocerebellar angle and the internal acoustic meatus. In: Samii M, Janetta P, eds. The Cranial Nerves. New York: Springer-Verlag, 1981;378–390.
230. Bird CR, Hasso AN, Drayer BP, Hinshaw DB Jr, Thompson JR. The cerebellopontine angle and internal auditory canal: neurovascular anatomy on gas CT cisternograms. Radiology 1985;154(3): 667–670.
231. Reisser C, Schuknecht HF. The anterior inferior cerebellar artery in the internal auditory canal. Laryngoscope 1991;101(7 Pt 1): 761–766.
232. Barzo P, Voros E, Klivenyi P, Krizsan L, Bodosi M. [Results of surgical treatment in hemifacial spasm—the role of MR-angiography in detecting microvascular compression]. Orv Hetil 2001;142(18): 953–956.
233. Dalley RW, Robertson WD, Nugent RA, Durity FA. Computed tomography of anterior inferior cerebellar artery aneurysm mimicking an acoustic neuroma. J Comput Assist Tomogr 1986;10(5): 881–884.
234. Pinto RS, Kricheff II, Butler AR, Murali R. Correlation of computed tomographic, angiographic, and neuropathological changes in giant cerebral aneurysms. Radiology 1979;132(1):85–92.
235. Atlas SW, Grossman RI, Goldberg HI, Hackney DB, Bilaniuk LT, Zimmerman RA. Partially thrombosed giant intracranial aneurysms: correlation of MR and pathologic findings. Radiology 1987;162(1 Pt 1):111–114.
236. Olsen WL, Brant-Zawadzki M, Hodes J, Norman D, Newton TH. Giant intracranial aneurysms: MR imaging. Radiology 1987;163(2): 431–435.
237. Tsuruda JS, Halbach VV, Higashida RT, Mark AS, Hieshima GB, Norman D. MR evaluation of large intracranial aneurysms using cine low flip angle gradient-refocused imaging. AJR 1988;151(1):153–162.
238. Zimmerman R. Bilateral pial sclerosis and hearing loss. Paper presented at the Eleventh International Congress of Head and Neck Radiology, June 9–10, 1988, Uppsala, Sweden.
239. Gomori JM, Grossman RI, Bilaniuk LT, Zimmerman RA, Goldberg HI. High-field MR imaging of superficial siderosis of the central nervous system. J Comput Assist Tomogr 1985;9(5):972–975.
240. Kwartler JA, De La Cruz A, Lo WW. Superficial siderosis of the central nervous system. Ann Otol Rhinol Laryngol 1991;100(3): 249–250.
241. Lo WW, Horn KL, Carberry JN, et al. Intratemporal vascular tumors: evaluation with CT. Radiology 1986;159(1):181–185.
242. Lo WW, Shelton C, Waluch V, et al. Intratemporal vascular tumors: detection with CT and MR imaging. Radiology 1989;171(2): 445–448.
243. Lownie S. Intracranial hemorrhage in aneurysms and vascular malformation. Neuroimaging Clin North Am 1992(2):195–201.
244. Lee YY, Van Tassel P, Raymond AK. Intracranial dural chondrosarcoma. AJNR 1988;9(6):1189–1193.
245. Hasso A, Fahmy J, Hinshaw D. Tumors of the posterior fossa. In: Stark D, Bradley WJ, eds. Magnetic Resonance Imaging. St. Louis: Mosby-Year Book, 1988;425–450.
246. Vezina LG, Packer RJ. Infratentorial brain tumors of childhood. Neuroimaging Clin North Am 1994;4(2):423–436.
247. Swaroop GR, Whittle IR. Exophytic pontine glioblastoma mimicking acoustic neuroma. J Neurosurg Sci 1997;41(4):409–411.
248. Cornell SH, Hibri NS, Menezes AH, Graf CJ. The complementary nature of computed tomography and angiography in the diagnosis of cerebellar hemangioblastoma. Neuroradiology 1979;17(4):201–205.
249. Lee SR, Sanches J, Mark AS, Dillon WP, Norman D, Newton TH. Posterior fossa hemangioblastomas: MR imaging. Radiology 1989; 171(2):463–468.
250. Morello G, Migliavacca F. Primary choroid papillomas in the cerebellopontine angle. J Neurol Neurosurg Psych 1964;27:445–452.
251. McGirr SJ, Ebersold MJ, Scheithauer BW, Quast LM, Shaw EG. Choroid plexus papillomas: long-term follow-up results in a surgically treated series. J Neurosurg 1988;69(6):843–849.
252. Ken JG, Sobel DF, Copeland B, Davis J 3rd, Kortman KE. Choroid plexus papillomas of the foramen of Luschka: MR appearance. AJNR 1991;12(6):1201–1203.
253. Martin N, Pierot L, Sterkers O, Mompoint D, Nahum H. Primary choroid plexus papilloma of the cerebellopontine angle: MR imaging. Neuroradiology 1990;31(6):541–543.
254. Spoto GP, Press GA, Hesselink JR, Solomon M. Intracranial ependymoma and subependymoma: MR manifestations. AJNR 1990;11(1):83–91.
255. Ford WJ, Brooks BS, el Gammal T, Massey CE, Beveridge WD. Adult cerebellopontine angle choroid plexus papilloma: MR evaluation. AJNR 1988;9(3):611.
256. Lee BC, Kneeland JB, Walker RW, Posner JB, Cahill PT, Deck MD. MR imaging of brainstem tumors. AJNR 1985;6(2):159–163.
257. Kucharczyk W, Brant-Zawadzki M, Sobel D, et al. Central nervous system tumors in children: detection by magnetic resonance imaging. Radiology 1985;155(1):131–136.
258. Fine HA, Mayer RJ. Primary central nervous system lymphoma. Ann Intern Med 1993;119(11):1093–1104.
259. Ierokomos A, Goin DW. Primary CNS lymphoma in the cerebellopontine angle. Report of a case. Arch Otolaryngol 1985;111(1): 50–52.
260. Schwaighofer BW, Hesselink JR, Press GA, Wolf RL, Healy ME, Berthoty DP. Primary intracranial CNS lymphoma: MR manifestations. AJNR 1989;10(4):725–729.
261. Kalamarides M, Dewolf E, Couvelard A, et al. Extraaxial primitive neuroectodermal tumor mimicking a vestibular schwannoma: diagnostic and therapeutic difficulties. Report of two cases. J Neurosurg 2001;94(4):612–616.

Copyright © 2003, Mosby, Inc. All rights reserved.

262. Neely JG, Alford BR. Facial nerve neuromas. Arch Otolaryngol 1974;100(4):298–301.
263. Langman AW, Jackler RK, Althaus SR. Meningioma of the internal auditory canal. Am J Otol 1990;11(3):201–204.
264. Sundaresan N, Eller T, Ciric I. Hemangiomas of the internal auditory canal. Surg Neurol 1976;6(2):119–121.
265. Bird CR, Drayer BP, Yeates AE. Gas CT cisternography of an intracanalicular vascular malformation. AJNR 1985;6(6):969–970.
266. Jung TT, Jun BH, Shea D, Paparella MM. Primary and secondary tumors of the facial nerve. A temporal bone study. Arch Otolaryngol Head Neck Surg 1986;112(12):1269–1273.
267. Nelson DR, Dolan KD. Cerebellopontine angle metastatic lung carcinoma resembling an acoustic neuroma. Ann Otol Rhinol Laryngol 1991;100(8):685–686.
268. Yuh WT, Mayr-Yuh NA, Koci TM, et al. Metastatic lesions involving the cerebellopontine angle. AJNR 1993;14(1):99–106.
269. Cohen TI, Powers SK, Williams DW 3rd. MR appearance of intracanalicular eighth nerve lipoma. AJNR 1992;13(4):1188–1190.
270. Marx HF, Colletti PM, Raval JK, Boswell WD Jr, Zee CS. Magnetic resonance imaging features in melanoma. Magn Reson Imaging 1990;8(3):223–229.
271. Babin RW, Fratkin JD, Cancilla PA. Hamartomas of the cerebellopontine angle and internal auditory canal: report of two cases. Arch Otolaryngol 1980;106(8):500–502.
272. Neely JG, Neblett CR. Differential facial nerve function in tumors of the internal auditory meatus. Ann Otol Rhinol Laryngol 1983;92(1 Pt 1):39–41.
273. Maki D, Yousem D, Corcoran C, Galetta S. MR imaging of Dejerine-Sottas disease. AJNR 1999;20:378–380.
274. Yener G, Guiochon-Mantel A, Obuz F, et al. Phe 84 deletion of the *PMP22* gene associated with hereditary motor and sensory neuropathy HMSN III with multiple cranial neuropathy: clinical, neuropsychological and magnetic resonance imaging findings. J Neurol 2001;248(3):193–196.
275. Tien RD, Felsberg GJ, MacFall J. Three dimensional MR gradient recalled echo imaging of the inner ear: comparison of FID and echo imaging techniques. Magn Reson Imaging 1993;11(3):429–435.
276. Batsakis J, ed. Tumors of the Head and Neck: Clinical and Pathological Considerations. 2nd ed. Baltimore: Williams & Wilkins, 1979.
277. Glenner G, Grimley P. Tumors of the extraadrenal paraganglion system (including chemoreceptors). In: Firminger H, ed. Atlas of Tumor Pathology. Vol 9. Washington, DC: Armed Forces Institute of Pathology, 1974;13–75.
278. Guild S. A hitherto unrecognized structure, the glomus jugularis, in man. Anat Rec 1941;79(suppl 2):28–34.
279. Guild S. The glomus jugulare, a nonchromaffin paraganglioma, in man. Ann Otol Rhinol Laryngol 1953(62):1045–1071.
280. Alford B, Guilford F. A comprehensive study of the tumors of the glomus jugulare. Laryngoscope 1962;72:765–805.
281. Britton BH. Glomus tympanicum and glomus jugulare tumors. Radiol Clin North Am 1974;12(3):543–551.
282. Glassock ME 3rd, Jackson CG, Dickins JR, Wiet RJ. Panel discussion: glomus jugulare tumors of the temporal bone. The surgical management of glomus tumors. Laryngoscope 1979;89(10 Pt 1):1640–1654.
283. Spector GJ, Sobol S, Thawley SE, Maisel RH, Ogura JH. Panel discussion: glomus jugulare tumors of the temporal bone. Patterns of invasion in the temporal bone. Laryngoscope 1979;89(10 Pt 1):1628–1639.
284. Nelson MD, Kendall BE. Intracranial catecholamine secreting paragangliomas. Neuroradiology 1987;29(3):277–282.
285. Zak F, Lawson W. Paraganglionic Chemoreceptor System: Physiology, Pathology, and Clinical Medicine. New York: Springer-Verlag, 1982.
286. Spector GJ, Druck NS, Gado M. Neurologic manifestations of glomus tumors in the head and neck. Arch Neurol 1976;33(4):270–274.
287. Adams R, Victor M. Principles of Neurology. 3rd ed. New York: McGraw-Hill, 1985.
288. Makek M, Franklin DJ, Zhao JC, Fisch U. Neural infiltration of glomus temporale tumors. Am J Otol 1990;11(1):1–5.
289. Ogura JH, Spector GJ, Gado M. Glomus jugulare and vagale. Ann Otol Rhinol Laryngol 1978;87(5 Pt 1):622–629.
290. Vogl TJ, Juergens M, Balzer JO, et al. Glomus tumors of the skull base: combined use of MR angiography and spin-echo imaging. Radiology 1994;192(1):103–110.
291. Vogl TJ, Mack MG, Juergens M, et al. Skull base tumors: gadodiamide injection—enhanced MR imaging—drop-out effect in the early enhancement pattern of paragangliomas versus different tumors. Radiology 1993;188(2):339–346.
292. Spector GJ, Maisel RH, Ogura JH. Glomus tumors in the middle ear. I. An analysis of 46 patients. Laryngoscope 1973;83(10):1652–1672.
293. Chakeres DW, LaMasters DL. Paragangliomas of the temporal bone: high-resolution CT studies. Radiology 1984;150(3):749–753.
294. Lo WW, Solti-Bohman LG. High-resolution CT of the jugular foramen: anatomy and vascular variants and anomalies. Radiology 1984;150(3):743–747.
295. Som PM, Reede DL, Bergeron RT, Parisier SC, Shugar JM, Cohen NL. Computed tomography of glomus tympanicum tumors. J Comput Assist Tomogr 1983;7(1):14–17.
296. Larson TC 3rd, Reese DF, Baker HL Jr, McDonald TJ. Glomus tympanicum chemodectomas: radiographic and clinical characteristics. Radiology 1987;163(3):801–806.
297. Lo WW, Solti-Bohman LG, Lambert PR. High-resolution CT in the evaluation of glomus tumors of the temporal bone. Radiology 1984;150(3):737–742.
298. Di Chiro G, Fisher R, Nelson K. The jugular foramen. J Neurosurg 1964;(21):447–460.
299. Hesselink JR, Davis KR, Taveras JM. Selective arteriography of glomus tympanicum and jugulare tumors: techniques, normal and pathologic arterial anatomy. AJNR 1981;2(4):289–297.
300. Moret J, Delvert JC, Bretonneau CH, Lasjaunias P, de Bicetre CH. Vascularization of the ear: normal-variations-glomus tumors. J Neuroradiol 1982;9(3):209–260.
301. Fisch U, Fagan P, Valavanis A. The infratemporal fossa approach for the lateral skull base. Otolaryngol Clin North Am 1984;17(3):513–552.
302. Weber AL, McKenna MJ. Radiologic evaluation of the jugular foramen. Anatomy, vascular variants, anomalies, and tumors. Neuroimaging Clin North Am 1994;4(3):579–598.
303. Olsen WL, Dillon WP, Kelly WM, Norman D, Brant-Zawadzki M, Newton TH. MR imaging of paragangliomas. AJR 1987;148(1):201–204.
304. Mukherji SK, Kasper ME, Tart RP, Mancuso AA. Irradiated paragangliomas of the head and neck: CT and MR appearance. AJNR 1994;15(2):357–363.
305. van Gils AP, van der Mey AG, Hoogma RP, et al. Iodine-123-metaiodobenzylguanidine scintigraphy in patients with chemodectomas of the head and neck region. J Nucl Med 1990;31(7):1147–1155.
306. Kwekkeboom DJ, van Urk H, Pauw BK, et al. Octreotide scintigraphy for the detection of paragangliomas. J Nucl Med 1993;34(6):873–878.
307. Krenning EP, Kwekkeboom DJ, Bakker WH, et al. Somatostatin receptor scintigraphy with [111In-DTPA-D-Phe1]- and [123I-Tyr3]-octreotide: the Rotterdam experience with more than 1000 patients. Eur J Nucl Med 1993;20(8):716–731.
308. Oldring D, Fisch U. Glomus tumors of the temporal region: surgical therapy. Am J Otol 1979;1(1):7–18.
309. Jackson CG, Glasscock ME 3rd, Harris PF. Glomus tumors. Diagnosis, classification, and management of large lesions. Arch Otolaryngol 1982;108(7):401–410.
310. Simko TG, Griffin TW, Gerdes AJ, et al. The role of radiation therapy in the treatment of glomus jugulare tumors. Cancer 1978;42(1):104–106.
311. Dickens WJ, Million RR, Cassisi NJ, Singleton GT. Chemodectomas arising in temporal bone structures. Laryngoscope 1982;92(2):188–191.
312. Fisch U. Infratemporal fossa approach for glomus tumors of the temporal bone. Ann Otol Rhinol Laryngol 1982;91(5 Pt 1):474–479.
313. Valavanis A, Schubiger O, Oguz M. High-resolution CT investigation of nonchromaffin paragangliomas of the temporal bone. AJNR 1983;4(3):516–519.
314. Simpson GT 2nd, Konrad HR, Takahashi M, House J. Immediate postembolization excision of glomus jugulare tumors: advantages of new combined techniques. Arch Otolaryngol 1979;105(11):639–643.
315. LaRouere MJ, Zappia JJ, Wilner H, et al. Selective embolisation of glomus jugulare tumors. Skull Base Surg 1994;4:21–25.

Copyright © 2003, Mosby, Inc. All rights reserved.

316. Lasjaunias P, Berenstein A. Surgical Neuroangiography. II. Endovascular Treatment of Craniofacial Lesions. New York: Springer-Verlag, 1987.
317. Young NM, Wiet RJ, Russell EJ, Monsell EM. Superselective embolization of glomus jugulare tumors. Ann Otol Rhinol Laryngol 1988;97(6 Pt 1):613–620.
318. Valvassori GE, Buckingham RA. Middle ear masses mimicking glomus tumors: radiographic and otoscopic recognition. Ann Otol Rhinol Laryngol 1974;83(5):606–612.
319. Lo WW, Solti-Bohman LG, McElveen JT Jr. Aberrant carotid artery: radiologic diagnosis with emphasis on high-resolution computed tomography. Radiographics 1985;5(6):985–993.
320. Reilly JJ Jr, Caparosa RJ, Latchaw RE, Sheptak PE. Aberrant carotid artery injured at myringotomy. Control of hemorrhage by a balloon catheter. JAMA 1983;249(11):1473–1475.
321. Anderson JM, Stevens JC, Sundt TM Jr, Stockard JJ, Pearson BW. Ectopic internal carotid artery seen initially as middle ear tumor. JAMA 1983;249(16):2228–2230.
322. Curtin HD. Radiologic approach to paragangliomas of the temporal bone. Radiology 1984;150(3):837–838.
323. Goodman RS, Cohen NL. Aberrant internal carotid artery in the middle ear. Ann Otol Rhinol Laryngol 1981;90(1 Pt 1):67–69.
324. Sinnreich AI, Parisier SC, Cohen NL, Berreby M. Arterial malformations of the middle ear. Otolaryngol Head Neck Surg 1984;92(2):194–206.
325. Stallings JO, McCabe BF. Congenital middle ear aneurysm of internal carotid. Arch Otolaryngol 1969;90(1):39–43.
326. Guinto FC Jr, Garrabrant EC, Radcliffe WB. Radiology of the persistent stapedial artery. Radiology 1972;105(2):365–369.
327. Crumley RL, Wilson C. Schwannomas of the jugular foramen. Laryngoscope 1984;94(6):772–778.
328. Abramowitz J, Dion JE, Jensen ME, et al. Angiographic diagnosis and management of head and neck schwannomas. AJNR 1991;12(5): 977–984.
329. Dolan EJ, Tucker WS, Rotenberg D, Chui M. Intracranial hypoglossal schwannoma as an unusual cause of facial nerve palsy. Case report. J Neurosurg 1982;56(3):420–423.
330. Fujiwara S, Hachisuga S, Numaguchi Y. Intracranial hypoglossal neurinoma: report of a case. Neuroradiology 1980;20(2):87–90.
331. Valvassori GE, Kirdani MA. The abnormal hypoglossal canal. Am J Roentgenol Rad Ther Nucl Med 1967;99(3):705–711.
332. Nager GT, Heroy J, Hoeplinger M. Meningiomas invading the temporal bone with extension to the neck. Am J Otolaryngol 1983;4(5):297–324.
333. Molony TB, Brackmann DE, Lo WW. Meningiomas of the jugular foramen. Otolaryngol Head Neck Surg 1992;106(2):128–136.
334. Watanabe A, Lo W. The jugular foramen meningioma: imaging findings. In preparation.
335. Miyachi S, Negoro M, Saito K, Nehashi K, Sugita K. Myeloma manifesting as a large jugular tumor: case report. Neurosurgery 1990;27(6):971–977.
336. Sehitoglu MA, Uneri C, Celikoyar MM, Tutkun A, Kullu S. Hemangiopericytoma as the cause of Collet-Sicard syndrome. ORL 1990;52(2):133–136.
337. Harvey SA, Wiet RJ, Kazan R. Chondrosarcoma of the jugular foramen. Am J Otol 1994;15(2):257–263.
338. Matsumoto T, Tani E, Maeda Y, Natsume S. Amyloidomas in the cerebellopontine angle and jugular foramen. Case report. J Neurosurg 1985;62(4):592–596.
339. May M. Tumors involving the facial nerve. In: May M, ed. The Facial Nerve. New York: Thieme, 1986;455–467.
340. Wiet RJ, Lotan AN, Monsell EM, Shambaugh GE Jr. Tumor involvement of the facial nerve. Laryngoscope 1983;93(10):1301–1309.
341. Fisch U, Rüttner J. Pathology of intratemporal tumors involving the facial nerve. In: Fisch U, ed. Facial Nerve Surgery. Birmingham, Ala: Aesculapius, 1997;448–456.
342. Chakeres DW, Kapila A. Normal and pathologic radiographic anatomy of the motor innervation of the face. AJNR 1984;5(5):591–597.
343. Disbro MA, Harnsberger HR, Osborn AG. Peripheral facial nerve dysfunction: CT evaluation. Radiology 1985;155(3):659–663.
344. May M. Anatomy of the facial nerve for the clinician. In: May M, ed. The Facial Nerve. New York: Thieme, 1986;21–62.
345. Korzec K, Sobol SM, Kubal W, Mester SJ, Winzelberg G, May M. Gadolinium-enhanced magnetic resonance imaging of the facial nerve in herpes zoster oticus and Bell's palsy: clinical implications. Am J Otol 1991;12(3):163–168.
346. Sartoretti-Schefer S, Wichmann W, Valavanis A. Idiopathic, herpetic, and HIV-associated facial nerve palsies: abnormal MR enhancement patterns. AJNR 1994;15(3):479–485.
347. Saito H. Tumoral invasion of the facial nerve: a study of eighth temporal bones. Paper presented at the Proceedings of the Fourth International Symposium on Facial Nerve Surgery, New York, 1982.
348. Adam W, Johnson JC, Paul DJ, Clausen K, Schuller DE. Primary adenocarcinoma of the middle ear. AJNR 1982;3(6):674–676.
349. Gebarski SS, Telian SA, Niparko JK. Enhancement along the normal facial nerve in the facial canal: MR imaging and anatomic correlation. Radiology 1992;183(2):391–394.
350. Anderson RE, Laskoff JM. Ramsay Hunt syndrome mimicking intracanalicular acoustic neuroma on contrast-enhanced MR. AJNR 1990;11(2):409.
351. Daniels DL, Czervionke LF, Millen SJ. MR findings in the Ramsay-Hunt syndrome. AJNR 1988;9(3):609.
352. Osumi A, Tien RD. MR findings in a patient with Ramsay-Hunt syndrome. J Comput Assist Tomogr 1990;14(6):991–993.
353. Tien R. Inflammatory disease of the cranial nerves. Neuroimaging Clin North Am 1991(1):89–103.
354. Petrus LV, Lo WW. Spontaneous CSF otorrhea caused by abnormal development of the facial nerve canal. AJNR 1999;20(2):275–277.
355. Dutcher PO Jr, Brackmann DE. Glomus tumor of the facial canal. A case report. Arch Otolaryngol Head Neck Surg 1986;112(9): 986–987.
356. Pulec JL. Facial nerve neuroma. Laryngoscope 1972;82(7):1160–1176.
357. Kienzle GD, Goldenberg MH, Just NW, Arbit E. Facial nerve neurinoma presenting as middle cranial fossa mass: CT appearance. J Comput Assist Tomogr 1986;10(3):391–394.
358. Conley J, Janecka I. Schwann cell tumors of the facial nerve. Laryngoscope 1974;84(6):958–962.
359. Lo W, Slattery WI, Chandrashekar S. Facial nerve schwannomas: radiologic patterns and clinical presentations. In preparation.
360. Bailey CM, Graham MD. Intratemporal facial nerve neuroma: a discussion of five cases. J Laryngol Otol 1983;97(1):65–72.
361. McMenomey SO, Glasscock ME 3rd, Minor LB, Jackson CG, Strasnick B. Facial nerve neuromas presenting as acoustic tumors. Am J Otol 1994;15(3):307–312.
362. Fagan PA, Misra SN, Doust B. Facial neuroma of the cerebellopontine angle and the internal auditory canal. Laryngoscope 1993;103(4 Pt 1):442–446.
363. Latack JT, Kartush JM, Kemink JL, Graham MD, Knake JE. Epidermoidomas of the cerebellopontine angle and temporal bone: CT and MR aspects. Radiology 1985;157(2):361–366.
364. Inoue Y, Tabuchi T, Hakuba A, et al. Facial nerve neuromas: CT findings. J Comput Assist Tomogr 1987;11(6):942–947.
365. Tew JM Jr, Yeh HS, Miller GW, Shahbabian S. Intratemporal schwannoma of the facial nerve. Neurosurgery 1983;13(2):186–188.
366. Baxter A. Dehiscence of the fallopian canal. An anatomical study. J Laryngol Otol 1971;85(6):587–594.
367. Daniels DL, Czervionke LF, Pojunas KW, et al. Facial nerve enhancement in MR imaging. AJNR 1987;8(4):605–607.
368. Pulec JL. Facial nerve tumors. Ann Otol Rhinol Laryngol 1969;78(5):962–982.
369. Glasscock ME 3rd, Smith PG, Schwaber MK, Nissen AJ. Clinical aspects of osseous hemangiomas of the skull base. Laryngoscope 1984;94(7):869–873.
370. Curtin HD, Jensen JE, Barnes L Jr, May M. ''Ossifying'' hemangiomas of the temporal bone: evaluation with CT. Radiology 1987;164(3):831–835.
371. Lo WW, Brackmann DE, Shelton C. Facial nerve hemangioma. Ann Otol Rhinol Laryngol 1989;98(2):160–161.
372. Mangham CA, Carberry JN, Brackmann DE. Management of intratemporal vascular tumors. Laryngoscope 1981;91(6):867–876.
373. Ishii K, Takahashi S, Matsumoto K, et al. Middle ear cholesteatoma extending into the petrous apex: evaluation by CT and MR imaging. AJNR 1991;12(4):719–724.
374. Bottrill ID, Chawla OP, Ramsay AD. Salivary gland choristoma of the middle ear. J Laryngol Otol 1992;106(7):630–632.
375. Petrus LV, Lo WM. Primary paraganglioma of the facial nerve canal. AJNR 1996;17(1):171–174.
376. Lo WW, Applegate LJ, Carberry JN, et al. Endolymphatic sac tumors: radiologic appearance. Radiology 1993;189(1):199–204.

Copyright © 2003, Mosby, Inc. All rights reserved.

377. Parker GD, Harnsberger HR. Clinical-radiologic issues in perineural tumor spread of malignant diseases of the extracranial head and neck. Radiographics 1991;11(3):383–399.
378. Arriaga M, Curtin HD, Takahashi H, Kamerer DB. The role of preoperative CT scans in staging external auditory meatus carcinoma: radiologic-pathologic correlation study. Otolaryngol Head Neck Surg 1991;105(1):6–11.
379. Chasin W, Goodman M. Case records of the Massachusetts General Hospital: case 7-1080. N Engl J Med 1980(302):456–462.
380. Osborn AG, Parkin JL. Mucocele of the petrous temporal bone. AJR 1979;132(4):680–681.
381. Larson TL, Wong ML. Primary mucocele of the petrous apex: MR appearance. AJNR 1992;13(1):203–204.
382. Lo WW, Solti-Bohman LG, Brackmann DE, Gruskin P. Cholesterol granuloma of the petrous apex: CT diagnosis. Radiology 1984; 153(3):705–711.
383. Latack JT, Graham MD, Kemink JL, Knake JE. Giant cholesterol cysts of the petrous apex: radiologic features. AJNR 1985;6(3):409–413.
384. Graham MD, Kemink JL, Latack JT, Kartush JM. The giant cholesterol cyst of the petrous apex: a distinct clinical entity. Laryngoscope 1985;95(11):1401–1406.
385. Palva T, Lehto VP, Johnsson LG, Virtanen I, Makinen J. Large cholesterol granuloma cysts in the mastoid. Clinical and histopathologic findings. Arch Otolaryngol 1985;111(12):786–791.
386. Griffin C, DeLaPaz R, Enzmann D. MR and CT correlation of cholesterol cysts of the petrous bone. AJNR 1987;8(5):825–829.
387. Greenberg JJ, Oot RF, Wismer GL, et al. Cholesterol granuloma of the petrous apex: MR and CT evaluation. AJNR 1988;9(6):1205–1214.
388. Livingston PA. Differential diagnosis of radiolucent lesions of the temporal bone. Radiol Clin North Am 1974;12(3):571–583.
389. Glasscock ME 3rd, Hunt WE. Giant-cell tumor of the sphenoid and temporal bones. Laryngoscope 1974;84(7):1181–1187.
390. Anderson RD, Liebeskind A, Schechter MM, Zingesser LH. Aneurysms of the internal carotid artery in the carotid canal of the petrous temporal bone. Radiology 1972;102(3):639–642.
391. Jackler RK, Brackmann DE. Xanthoma of the temporal bone and skull base. Am J Otol 1987;8(2):111–115.
392. Madewell JE, Ragsdale BD, Sweet DE. Radiologic and pathologic analysis of solitary bone lesions. Part I: internal margins. Radiol Clin North Am 1981;19(4):715–748.
393. Yousem DM. Dashed hopes for MR imaging of the head and neck: the power of the needle. Radiology 1992;184(1):25–26.
394. Naiberg J, Berger G, Hawke M. The pathologic features of keratosis obturans and cholesteatoma of the external auditory canal. Arch Otolaryngol 1984;110(10):690–693.
395. Di Bartelomeo J. Exostosis of the external auditory canal. Ann Otol Rhinol Laryngol 1979(88 suppl 61):2–20.
396. Sheehy JL. Diffuse exostoses and osteomata of the external auditory canal: a report of 100 operations. Otolaryngol Head Neck Surg 1982;90(3 Pt 1):337–342.
397. Denia A, Perez F, Canalis RR, Graham MD. Extracanalicular osteomas of the temporal bone. Arch Otolaryngol 1979;105(12):706–709.
398. Kessler A, Wolf M, Ben-Shoshan J. Fibrous dysplasia of the temporal bone presenting as an osteoma of the external auditory canal. Ear Nose Throat J 1990;69(3):197–199.
399. Friedman I. The ear. In: Silverberg S, ed. Principles and Practice of Surgical Pathology. New York: Wiley, 1983;1521–1545.
400. Friedman D, Rao V. MR and CT of squamous carcinoma of the middle ear and mastoid complex. Am J Neuroradiol 1991(12):872–874.
401. Chen KT, Dehner LP. Primary tumors of the external and middle ear. II. A clinicopathologic study of 14 paragangliomas and three meningiomas. Arch Otolaryngol 1978;104(5):253–259.
402. Wilson JS, Blake GB, Richardson AE, Westbury G. Malignant tumours of the ear and their treatment. II. Tumours of the external auditory meatus, middle ear cleft and temporal bone. Br J Plast Surg 1974;27(1):77–91.
403. Bird CR, Hasso AN, Stewart CE, Hinshaw DB Jr, Thompson JR. Malignant primary neoplasms of the ear and temporal bone studied by high-resolution computed tomography. Radiology 1983;149(1): 171–174.
404. Michaels L, Wells M. Squamous cell carcinoma of the middle ear. Clin Otolaryngol 1980;5(4):235–248.
405. Goodwin WJ, Jesse RH. Malignant neoplasms of the external auditory canal and temporal bone. Arch Otolaryngol 1980;106(11): 675–679.
406. Arriaga M, Curtin H, Takahashi H, Hirsch BE, Kamerer DB. Staging proposal for external auditory meatus carcinoma based on preoperative clinical examination and computed tomography findings. Ann Otol Rhinol Laryngol 1990;99(9 Pt 1):714–721.
407. Moody SA, Hirsch BE, Myers EN. Squamous cell carcinoma of the external auditory canal: an evaluation of a staging system. Am J Otol 2000;21(4):582–588.
408. Hicks GW. Tumors arising from the glandular structures of the external auditory canal. Laryngoscope 1983;93(3):326–340.
409. Pulec JL. Glandular tumors of the external auditory canal. Laryngoscope 1977;87(10 Pt 1):1601–1612.
410. Harner SG, Cody DT, Dahlin DC. Benign chondroblastoma of the temporal bone. Otolaryngol Head Neck Surg 1979;87(2):229–236.
411. Muntane A, Valls C, Angeles de Miquel MA, Pons LC. Chondroblastoma of the temporal bone: CT and MR appearance. AJNR 1993;14(1):70–71.
412. Benecke JE Jr, Noel FL, Carberry JN, House JW, Patterson M. Adenomatous tumors of the middle ear and mastoid. Am J Otol 1990;11(1):20–26.
413. Gulya AJ, Glasscock ME 3rd, Pensak ML. Neural choristoma of the middle ear. Otolaryngol Head Neck Surg 1987;97(1):52–56.
414. Nelson EG, Kratz RC. Sebaceous choristoma of the middle ear. Otolaryngol Head Neck Surg 1993;108(4):372–373.
415. Peron DL, Schuknecht HF. Congenital cholesteatomata with other anomalies. Arch Otolaryngol 1975;101(8):498–505.
416. Cody D. The definition of cholesteatoma. Paper presented at the Cholesteatoma First International Conference, Birmingham, Ala, 1977.
417. Sanna M, Zinni C. Congenital cholesteatoma of the middle ear. In: Sade J, ed., Cholesteatoma and Mastoid Surgery. Amsterdam: Kugler, 1982;29–36.
418. Schwartz RH, Movassaghi N, Marion ED. Rhabdomyosarcoma of the middle ear: a wolf in sheep's clothing. Pediatrics 1980;65(6):1131–1133.
419. Goepfert H, Cangir A, Lindberg R, Ayala A. Rhabdomyosarcoma of the temporal bone. Is surgical resection necessary? Arch Otolaryngol 1979;105(6):310–313.
420. Curtin HD. CT of acoustic neuroma and other tumors of the ear. Radiol Clin North Am 1984;22(1):77–105.
421. Yousem DM, Lexa FJ, Bilaniuk LT, Zimmerman RI. Rhabdomyosarcomas in the head and neck: MR imaging evaluation. Radiology 1990;177(3):683–686.
422. Wiatrak BJ, Pensak ML. Rhabdomyosarcoma of the ear and temporal bone. Laryngoscope 1989;99(11):1188–1192.
423. Paulus W, Romstock J, Weidenbecher M, Huk WJ, Fahlbusch R. Middle ear adenocarcinoma with intracranial extension. Case report. J Neurosurg 1999;90(3):555–558.
424. Gapany-Gapanavicius B, Chisin R, Weshler Z. Primary presentation of malignant lymphoma in middle ear cleft. Ann Otol Rhinol Laryngol 1980;89(2 Pt 1):180–183.
425. McKenna EL Jr, Holmes WF, Harwick R. Primary melanoma of the middle ear. Laryngoscope 1984;94(11 Pt 1):1459–1460.
426. Willman CL, Busque L, Griffith BB, et al. Langerhans'-cell histiocytosis (histiocytosis X)—a clonal proliferative disease. N Engl J Med 1994;331(3):154–160.
427. Stool S, Goodman M. A 13-year-old boy with a destructive lesion of the left mastoid bone. N Engl J Med 1991(324):1489–1495.
428. Shelby JH, Sweet RM. Eosinophilic granuloma of the temporal bone: medical and surgical management in the pediatric patient. S Med J 1983;76(1):65–70.
429. Nezelof C, Frileux-Herbet F, Cronier-Sachot J. Disseminated histiocytosis X: analysis of prognostic factors based on a retrospective study of 50 cases. Cancer 1979;44(5):1824–1838.
430. Cunningham MJ, Curtin HD, Butkiewicz BL. Histiocytosis X of the temporal bone: CT findings. J Comput Assist Tomogr 1988;12(1): 70–74.
431. Bonafe A, Joomye H, Jaeger P, Fraysse B, Manelfe C. Histiocytosis X of the petrous bone in the adult: MRI. Neuroradiology 1994;36(4):330–333.
432. Haynes RC, Amy JR. Asymmetric temporal bone pneumatization: an MR imaging pitfall. AJNR 1988;9(4):803.
433. House JL, Brackmann DE. Cholesterol granuloma of the cerebellopontine angle. Arch Otolaryngol 1982;108(8):504–506.

Copyright © 2003, Mosby, Inc. All rights reserved.

434. Flood LM, Kemink JL, Graham MD. The investigation and management of petrous apex erosion. J Laryngol Otol 1985;99(5): 439–450.
435. Wyler AR, Leech RW, Reynolds AF, Ojemann GA, Mead C. Cholesterol granuloma of the petrous apex. Case report. J Neurosurg 1974;41(6):765–768.
436. Nager GT, Vanderveen TS. Cholesterol granuloma involving the temporal bone. Ann Otol Rhinol Laryngol 1976;85(2 Pt 1):204–209.
437. Gherini SG, Brackmann DE, Lo WW, Solti-Bohman LG. Cholesterol granuloma of the petrous apex. Laryngoscope 1985;95(6):659–664.
438. Phelps PD, Lloyd GA. The radiology of cholesteatoma. Clin Radiol 1980;31(5):501–512.
439. DeLozier HL, Parkins CW, Gacek RR. Mucocele of the petrous apex. J Laryngol Otol 1979;93(2):177–180.
440. Kudo S, Colley DP. Multiple intrapetrous aneurysms of the internal carotid artery. AJNR 1983;4(5):1119–1121.
441. Fisch UP, Oldring DJ, Senning A. Surgical therapy of internal carotid artery lesions of the skull base and temporal bone. Otolaryngol Head Neck Surg 1980;88(5):548–554.
442. Berenstein A, Ransohoff J, Kupersmith M, Flamm E, Graeb D. Transvascular treatment of giant aneurysms of the cavernous carotid and vertebral arteries. Functional investigation and embolization. Surg Neurol 1984;21(1):3–12.
443. Grossman RI, Davis KR. Cranial computed tomographic appearance of chondrosarcoma of the base of the skull. Radiology 1981;141(2): 403–408.
444. Sekhar L. Letter. Neurosurgery 1993(32):355–356.
445. Meyers SP, Hirsch WL Jr, Curtin HD, Barnes L, Sekhar LN, Sen C. Chondrosarcomas of the skull base: MR imaging features. Radiology 1992;184(1):103–108.
446. Oot RF, Melville GE, New PF, et al. The role of MR and CT in evaluating clival chordomas and chondrosarcomas. AJR 1988; 151(3):567–575.
447. Meyers SP, Hirsch WL Jr, Curtin HD, Barnes L, Sekhar LN, Sen C. Chordomas of the skull base: MR features. AJNR 1992;13(6):1627–1636.
448. Heffelfinger MJ, Dahlin DC, MacCarty CS, Beabout JW. Chordomas and cartilaginous tumors at the skull base. Cancer 1973;32(2):410–420.
449. Brooks JJ, LiVolsi VA, Trojanowski JQ. Does chondroid chordoma exist? Acta Neuropathol (Berl) 1987;72(3):229–235.
450. Rosenberg AE, Brown GA, Bhan AK, Lee JM. Chondroid chordoma—a variant of chordoma. A morphologic and immunohistochemical study. Am J Clin Pathol 1994;101(1):36–41.
451. Reid CB, Fagan PA, Turner J. Low-grade myxoid chondrosarcoma of the temporal bone: differential diagnosis and report of two cases. Am J Otol 1994;15(3):419–422.
452. Bourgouin PM, Tampieri D, Robitaille Y, et al. Low-grade myxoid chondrosarcoma of the base of the skull: CT, MR, and histopathology. J Comput Assist Tomogr 1992;16(2):268–273.
453. Sen CN, Sekhar LN, Schramm VL, Janecka IP. Chordoma and chondrosarcoma of the cranial base: an 8-year experience. Neurosurgery 1989;25(6):931–940; discussion 940–941.
454. Stapleton SR, Wilkins PR, Archer DJ, Uttley D. Chondrosarcoma of the skull base: a series of eight cases. Neurosurgery 1993;32(3):348–355; discussion 355–356.
455. Suit HD, Goitein M, Munzenrider J, et al. Definitive radiation therapy for chordoma and chondrosarcoma of base of skull and cervical spine. J Neurosurg 1982;56(3):377–385.
456. Batsakis JG, el-Naggar AK. Papillary neoplasms (Heffner's tumors) of the endolymphatic sac. Ann Otol Rhinol Laryngol 1993;102(8 Pt 1):648–651.
457. Megerian CA, McKenna MJ, Nuss RC, et al. Endolymphatic sac tumors: histopathologic confirmation, clinical characterization, and implication in von Hippel-Lindau disease. Laryngoscope 1995;105(8 Pt 1):801–808.
458. Hassard AD, Boudreau SF, Cron CC. Adenoma of the endolymphatic sac. J Otolaryngol 1984;13(4):213–216.
459. Michaels L. Ear, Nose and Throat Histopathology. New York: Springer-Verlag, 1987.
460. MacDougall A, Sangalang V, Huetis S. A previously unrecognised papillary endolymphatic sac tumor presenting as a cerebellopontine angle lesion. Can J Neurol Sci 1985(189):203–204.
461. Heffner DK. Low-grade adenocarcinoma of probable endolymphatic sac origin. A clinicopathologic study of 20 cases. Cancer 1989;64(11):2292–2302.
462. Lo W. Endolymphatic sac tumor: more than a curiosity. Am J Neuroradiol 1993(14):1322–1323.
463. Palmer JM, Coker NJ, Harper RL. Papillary adenoma of the temporal bone in von Hippel-Lindau disease. Otolaryngol Head Neck Surg 1989;100(1):64–68.
464. Meyer JR, Gebarski SS, Blaivas M. Cerebellopontine angle invasive papillary cystadenoma of endolymphatic sac origin with temporal bone involvement. AJNR 1993;14(6):1319–1321; discussion 1322–1323.
465. Mukherji SK, Albernaz VS, Lo WW, et al. Papillary endolymphatic sac tumors: CT, MR imaging, and angiographic findings in 20 patients. Radiology 1997;202(3):801–808.
466. Sham JS, Cheung YK, Choy D, Chan FL, Leong L. Nasopharyngeal carcinoma: CT evaluation of patterns of tumor spread. AJNR 1991;12(2):265–270.
467. Bonhomme GR, Loevner LA, Yen DM, Deems DA, Bigelow DC, Mirza N. Extensive intracranial xanthoma associated with type II hyperlipidemia. AJNR 2000;21(2):353–355.

Copyright © 2003, Mosby, Inc. All rights reserved.

26

Temporal Bone: Vascular Tinnitus

William W.M. Lo and M. Marcel Maya

ARTERIAL CAUSES
- Atherosclerosis
- Fibromuscular Dysplasia
- Dissection of the Carotid or Vertebral Artery
- Styloid Carotid Compression
- Petrous Carotid Aneurysm
- Aberrant Carotid Artery
- Laterally Displaced Carotid Artery
- Persistent Stapedial Artery
- Miscellaneous Arterial Anomalies

ARTERIOVENOUS CAUSES
- Paraganglioma
- Miscellaneous Vascular Head and Neck Tumors
- Paget's Disease
- Otosclerosis or Otospongiosis
- Cerebral Head and Neck Arteriovenous Malformation
- Dural Arteriovenous Fistula
- Direct Arteriovenous Fistula

VENOUS CAUSES
- Venous Tinnitus in Systemic Conditions
- Venous Tinnitis in Intracranial Hypertension
- Venous Tinnitus Caused by Transverse Sinus Stenosis
- Venous Tinnitus Associated with a Large or Exposed Jugular Bulb or Large Emissary Veins
- Idiopathic Venous Tinnitus

RADIOLOGIC INVESTIGATION

Tinnitus is a broad and complex subject concerning a symptom, rather than a syndrome or a disease.[1] The following discussion is confined to tinnitus from vascular causes.

Tinnitus may be caused by an intrinsic process such as vestibulocochlear disease, or it may have an extrinsic muscular or vascular cause.[1] Intrinsic tinnitus is subjective, being audible only to the patient, and extrinsic tinnitus is often objective, being potentially although not always audible to the examiner as well as to the patient. Although muscular tinnitus such as myoclonus of the palatal muscles or of the tensor tympani muscle can be pulsatile, it is not usually pulse-synchronous. By comparison, vascular tinnitus is always pulse-synchronous, and it is often a recordable sound audible to the examiner as a bruit.[1] However, whether a vascular tinnitus can be classified as objective may depend on the thoroughness of the search, the equipment used, and the level of ambient noise.[2, 3]

Tinnitus is a common complaint affecting some 30 to 40 million Americans.[4] In the majority of cases, it is subjective and may be associated with numerous conditions including conductive or sensorineural hearing loss and brainstem and cortical lesions.[1] When tumor, anomaly, or trauma is the suspected cause, the patient usually receives a radiologic evaluation. However, the majority of tinnitus cases are caused by Meniere's disease or syndrome, viropathies, drugs, allergy, noise, or systemic diseases, and the patients do not come to the attention of the radiologist.[5] Unfortunately, the cause of subjective tinnitus is often unclear, and effective treatment is lacking.

By contrast, although it is far rarer, objective tinnitus can usually be traced to a specific cause. In the case of vascular tinnitus, the radiologist tends to have a more active role in the diagnosis and treatment of this entity.

The causes of vascular tinnitus may be arterial, arteriovenous, or venous (Box 26-1). Some authors believe that paragangliomas are the most common cause of vascular tinnitus, but others cite dural arteriovenous fistula (AVF), idiopathic venous tinnitus, or idiopathic intracranial hypertension as being the most common causes.[3, 6–10] The experience of different authors likely reflects their individual expertise and referral patterns. Interestingly, in Remley et al.'s series of 107 patients with pulsatile tinnitus and a vascular retrotympanic mass, paraganglioma was the most common cause of subjective tinnitus, while dural and extracranial AVFs were the most common causes of objective tinnitus.[11]

Copyright © 2003, Mosby, Inc. All rights reserved.

BOX 26-1
VASCULAR TINNITUS: CAUSES

Arterial
Atherosclerosis
Fibromuscular dysplasia
Arterial dissection
Styloid carotid compression
Petrous carotid aneurysm
Aberrant carotid artery
Laterally displaced carotid artery
Persistent stapedial artery
Miscellaneous arterial anomalies
Arteriovenous (AV)
Paraganglioma (tympanicum, jugulare)
Miscellaneous vascular tumors
Paget's disease of bone
Otosclerosis or spongiosis
Cerebral AV malformation
Dural sinus AV fistula
Direct AV fistula
Venous
Chronic anemia
Pregnancy
Thyrotoxicosis
Hypertensive patients on vasodilators
Intracranial hypertension
Transverse sinus stenosis
Idiopathic venous tinnitus with or without large or exposed jugular bulb or large emissary vein

ARTERIAL CAUSES

The arterial causes of tinnitus include abnormalities in the lumen and abnormalities in the course. Aberrant arteries are rare but exceedingly important because of the hazards of mistreatment they invite when mistaken for tumors. They are discussed in greater detail in Chapter 21.

Atherosclerosis

Atherosclerotic plaques may produce turbulence of carotid flow and occasionally cause pulsatile tinnitus. However, in proportion to its high prevalence as a cause of asymptomatic carotid bruit, atherosclerosis is not a common cause of symptomatic pulsatile tinnitus.[12] This may be because the stenosis or luminal irregularity usually lies at the origin of the internal or external carotid artery, distant from the petrous bone.[13] Nonetheless, some cases have been reported.[14–17] In a report of eight patients with objective tinnitus caused by atherosclerotic carotid artery disease, tinnitus was the presenting symptom in five; however, no patient in the series required surgery or angioplasty for relief of symptoms.[15] On rare occasions, contralateral carotid artery stenosis or occlusion, or stenosis in the proximal brachiocephalic arteries, have also been reported as causes of pulsatile tinnitus.[18–21] Transluminal angioplasty and stenting may be performed on those lesions that are not readily accessible to surgical endarterectomy.[22, 23] Transmitted cardiac murmurs have also been implicated.[3]

Fibromuscular Dysplasia

Among the stenotic arteries, fibromuscular dysplasia (FMD), a segmental nonatheromatous, noninflammatory angiopathy of unknown etiology, is probably the most important cause of pulsatile tinnitus.[24–30] FMD, seen in 0.5% to 0.6% of carotid angiograms and autopsies, is the second most common cause of extracranial carotid narrowing.[12, 25] It is due to a fibroblastlike transformation of the smooth muscle cells of the arterial wall in medium-sized muscular arteries.[26] The vertebral and renal arteries may also be involved, bilaterality is common, and some patients may have intracranial berry aneurysms.[27, 31] Genetic predisposition may be a factor in this disease.[26, 32]

Often an incidental angiographic finding, FMD occurs predominantly in middle-aged women, many of whom are asymptomatic.[25] FMD appears to be more common than atherosclerosis as a cause of pulsatile tinnitus. This may be due to the fact that the stenosis in FMD is usually high in the cervical internal carotid artery at the level of the first and second cervical vertebrae, and the resultant turbulence is readily transmitted into the petrous bone.[13] Next to cerebral ischemic or hemorrhagic symptoms (such as headache, transient ischemic attack, stroke, and subarachnoid hemorrhage), pulsatile tinnitus is the most common complaint.[33] Among patients with symptoms of carotid FMDs, one third or more name pulsatile tinnitus as a presenting symptom, and in some patients this may be the primary complaint (Fig. 26-1).[24, 26, 33] Spontaneous dissection (Fig. 26-2B) or arteriovenous fistulization superimposed on carotid FMD may also precipitate pulsatile tinnitus, and rarely, vertebral FMD has caused pulsatile tinnitus.[29, 34, 35]

The classic angiographic appearance of FMD is the ''string of beads'' pattern, which is found in 85% of carotid FMD (Fig. 26-2A).[36] The less common patterns are tubular stenosis and semicircumferential narrowing. The accuracy of magnetic resonance angiography (MRA) in detecting FMD (Fig. 26-2) is unclear.[7, 37] However, magnetic resonance (MR) imaging has been shown to help distinguish tubular FMD from arterial dissection and arterial hypoplasia.[38]

Besides surgery and antiplatelet therapy, transluminal angioplasty has been successful in treating FMD.[28, 32, 33, 39–42] However, because most patients follow a benign course, treatment should not be instituted in the absence of progressive cerebral ischemia unless the patient feels that the noise is incapacitating.[13, 25] A survey for possible intracranial aneurysm with MRA is strongly advisable because an associated aneurysm may pose a greater hazard to the patient than the FMD itself.[43] The differential diagnosis of FMD includes Ehlers-Danlos syndrome type IV and giant cell and Takayasu's arteritides.[44]

Dissection of the Carotid or Vertebral Artery

Dissection of the cervicocephalic arteries may be spontaneous or traumatic.[45] Spontaneous dissections, sometimes after trivial trauma, usually affect one or both of the cervical internal carotid arteries of a young to middle-aged adult, and the vertebral artery is occasionally involved.[46–49] The etiology of spontaneous dissection is unknown;

Copyright © 2003, Mosby, Inc. All rights reserved.

however, angiographic FMD is present in 10% to 15% of the patients.[46]

The majority of the patients complain of ipsilateral headache.[46, 49] Other common manifestations are focal cerebral ischemic symptoms (transient ischemic attack or stroke), oculosympathetic paresis (partial Horner's syndrome), and bruit.[49] Bruits, subjective or objective, are found in about 40% of the patients (Fig. 26-3).[50]

The angiographic findings include luminal stenosis, abrupt reconstitution of the lumen, dissecting aneurysm, intimal flap, slow flow, occlusion, and distal emboli.[51] MR imaging may show loss of flow void in occlusion and hyperintense signal from intraluminal hemorrhage.[52, 53] MRA, dynamic computed tomography (CT), and ultrasonography have all been used for evaluation of cervicocephalic arterial dissection.[54–61]

Though the efficacy of medical and surgical therapy is unclear, anticoagulant followed by antiplatelet therapy is commonly prescribed.[49, 53] A persistent dissecting aneurysm discharging emboli may be resected. Nearly all of the stenoses resolve, but many occlusions do not recanalize, and further dissections may occur in other cervicocephalic arteries.[48, 49, 51]

Styloid Carotid Compression

An elongated styloid process compressing a tortuous carotid artery has been reported as a cause of pulsatile tinnitus, but this appears to be a unique case.[6]

Petrous Carotid Aneurysm

Bruit may be the main complaint of patients with petrous carotid aneurysms.[62, 63] These aneurysms have been successfully treated with percutaneous transarterial embolization using detachable balloons or with surgical resection.[62, 64]

Aberrant Carotid Artery

The aberrant carotid artery is a rare anomaly, and patients who have one may be seen at almost any age.[65] Some of the patients experience pulsatile tinnitus and some have conductive hearing loss, but most have relatively mild symptoms that do not require treatment.[65] The aberrant carotid artery is extremely important in that clinically it simulates a paraganglioma in the middle ear.[65, 66] Many of the cases first reported were diagnosed after myringotomy or biopsy, often with disastrous consequences such as massive hemorrhage and hemiplegia.[67, 68] The aberrant artery enters the tympanic cavity through an enlarged inferior tympanic canaliculus and then undulates through the middle ear to enter the horizontal carotid canal through a dehiscence in the carotid plate.[65, 69] The ipsilateral ascending carotid canal is absent. CT is diagnostic (Figs. 26-4A and 26-5A). MRA may be used for confirmation (Fig. 26-4B) or for detection of a suspected associated aneurysm (Fig. 26-5B). Angiography is not necessary.[70]

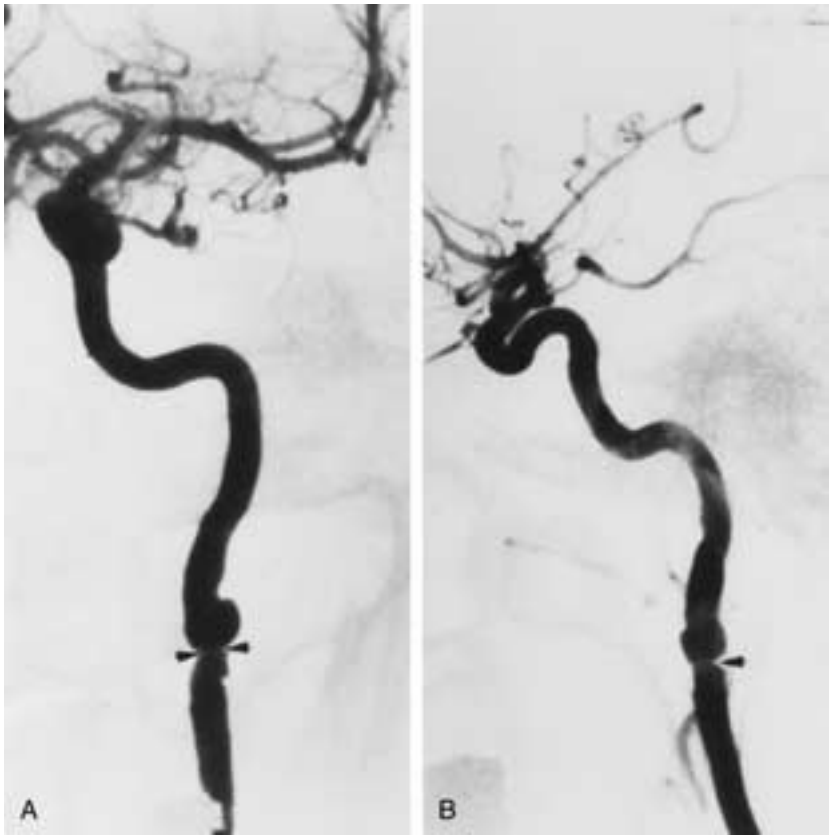

VIEW IMAGE

FIGURE 26-1 Fibromuscular dysplasia of the internal carotid artery. Selective left internal carotid angiogram. **A**, Anteroposterior projection. **B**, Lateral projection. Critical noncircumferential web-like stenosis (*arrowheads*) immediately proximal to an eccentric diverticulum. The patient's major complaint was pulsatile tinnitus in the left ear aggravated by exercise and sufficient to cause sleeplessness. Symptoms were promptly relieved by percutaneous transluminal angioplasty. (From Hasso AN, Bird CR, Zinke DE, et al. Fibromuscular dysplasia of the internal carotid artery: percutaneous transluminal angioplasty. AJNR 1981;2: 175–180.)

Copyright © 2003, Mosby, Inc. All rights reserved.

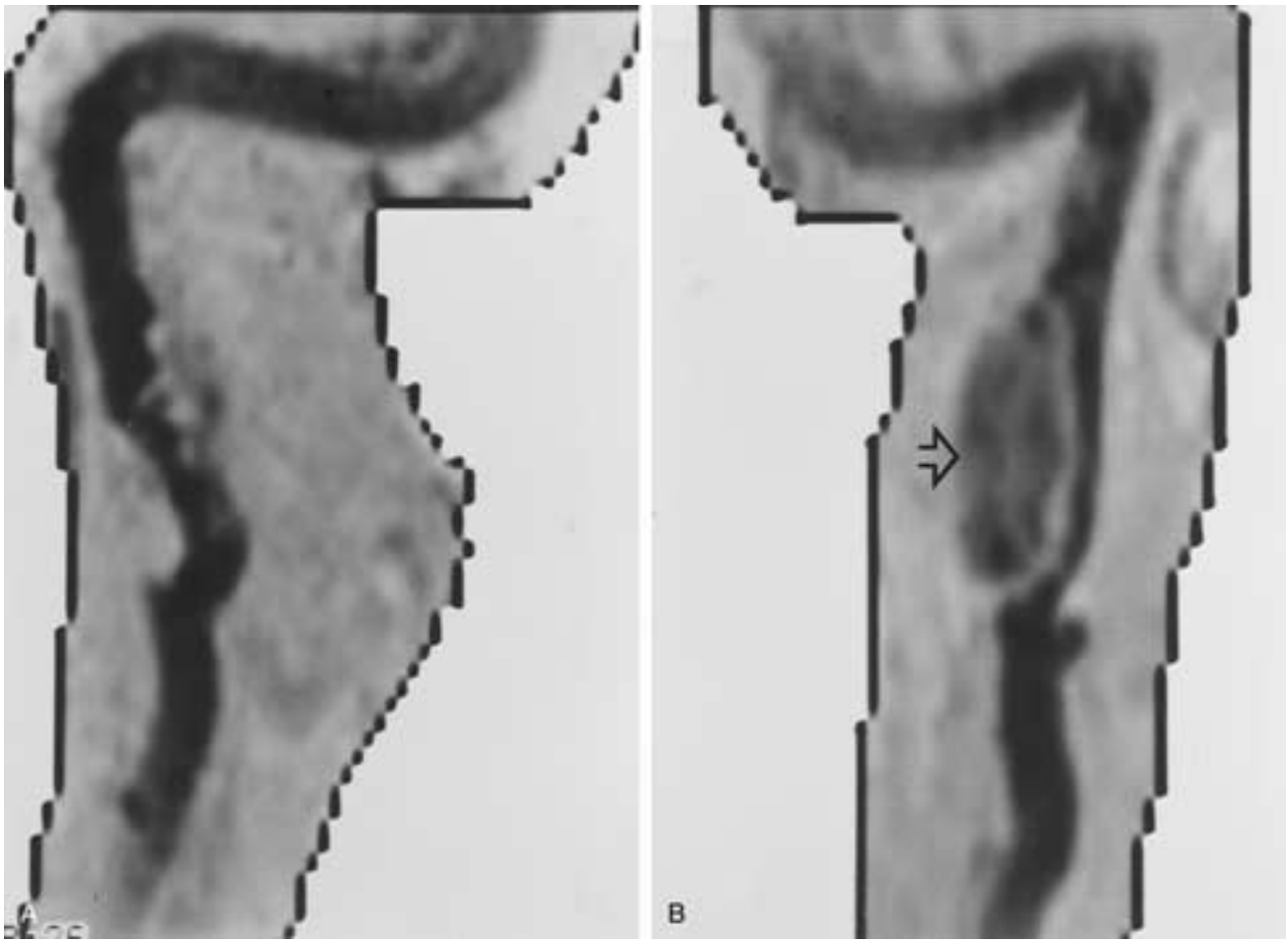

VIEW IMAGE

FIGURE 26-2 Bilateral carotid fibromuscular dysplasia. MRA 3D time-of-flight technique, maximum intensity projection. **A**, Right internal carotid artery shows segmental corrugation at the first and second cervical levels. **B**, Left internal carotid artery shows similar irregularity with a superimposed spontaneous carotid dissection (*open arrow*). The patient had intermittent right pulsatile tinnitus of gradual onset but no symptoms on the left side. Cranial MRA also showed an internal carotid bifurcation berry aneurysm. The findings were confirmed by angiography. (Courtesy of Dr. Fred Steinberg.)

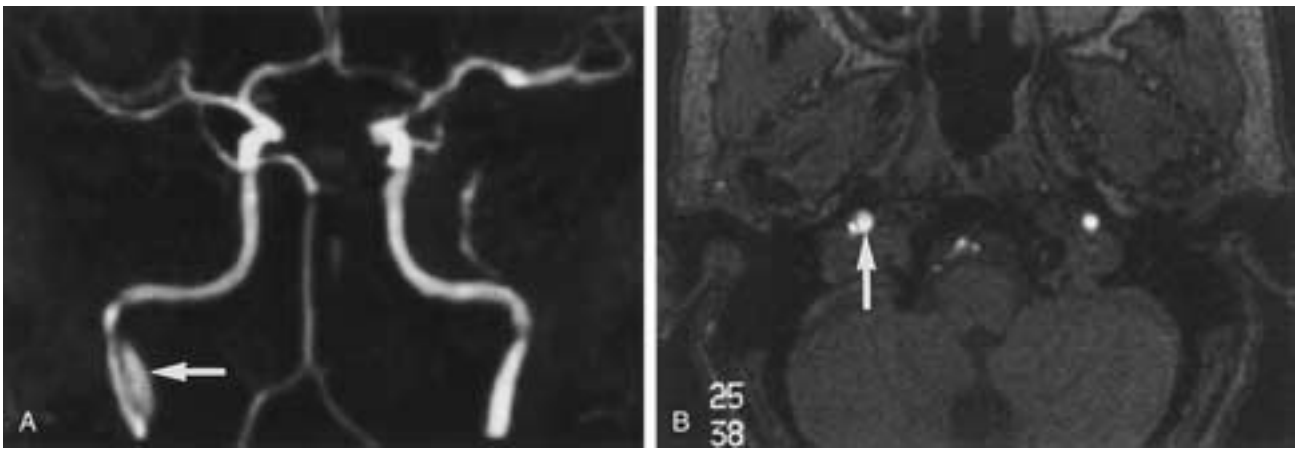

VIEW IMAGE

FIGURE 26-3 Spontaneous dissection of a right internal carotid artery. The patient abruptly developed right pulsatile tinnitus without headache, ischemic symptoms, or Horner's syndrome. **A**, MRA 3D time-of-flight technique, maximum intensity projection. **B**, MRA individual partition. Arrows point to a false lumen or a dissecting aneurysm, which contains flowing blood or subacute thrombus.

Copyright © 2003, Mosby, Inc. All rights reserved.

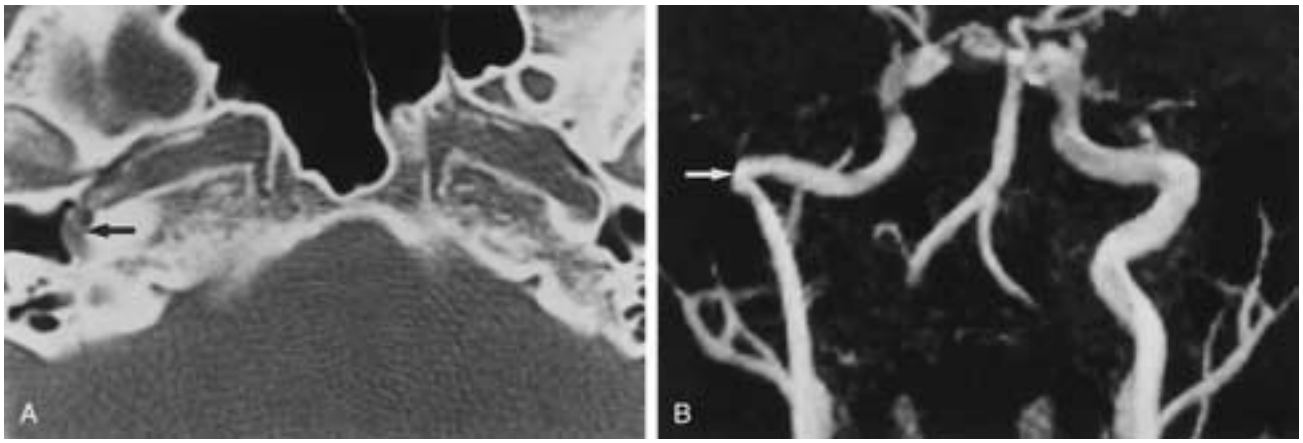

VIEW IMAGE

FIGURE 26-4 Right aberrant carotid artery. **A**, High-resolution CT. The arrow indicates an aberrant artery coursing through the right tympanic cavity to enter the horizontal carotid canal through a dehiscence in the carotid plate. **B**, MRA 3D time-of-flight technique, maximum intensity projection, shows the typical sharp bend of a narrow aberrant artery (*arrow*) through the tympanic cavity.

Laterally Displaced Carotid Artery

The laterally displaced carotid artery is one that knuckles into the tympanic cavity through a dehiscence of the bony carotid canal at the junction between the canal's vertical and horizontal segments.[71, 72] The artery does not take the long, narrow detour of an aberrant carotid artery, and it may be accompanied by an aneurysm. Although even rarer than the aberrant carotid artery and embryologically different, it does present the same hazards.

Persistent Stapedial Artery

A persistent stapedial artery large enough to be symptomatic is extremely rare. The artery courses from the infracochlear carotid through the stapedial obturator foramen and then enlarges the tympanic facial nerve canal en route to the middle cranial fossa to terminate as the middle meningeal artery.[69, 73, 74] The facial canal enlargement must not be mistakenly attributed to a facial nerve tumor. Characteristically, the ipsilateral foramen spinosum is absent.[73] CT is diagnostic (Fig. 26-6). The persistent stapedial artery may also accompany an aberrant carotid artery or a laterally displaced carotid artery, or it may originate from an ascending pharyngeal artery.[69, 72, 75]

Miscellaneous Arterial Anomalies

An anomalous artery 0.5 mm in diameter was encountered in the stria vascularis of the apex of the cochlea at postmortem histopathology. This anomaly appeared to be the cause of the patient's low-tone pulsatile tinnitus.[76] Such a vessel may be detectable with the recently available high-resolution, heavily T2-weighted, fast spin-echo or constructive interference steady-state MR imaging. Cross-compression of the eighth nerve in the cerebellopontine

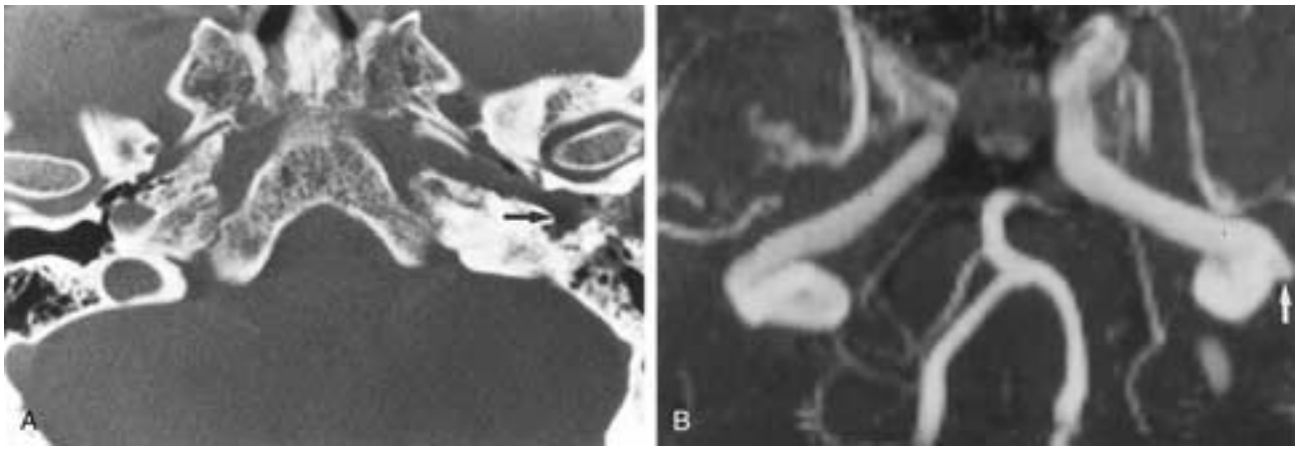

VIEW IMAGE

FIGURE 26-5 Left aberrant carotid artery after needling. **A**, High-resolution CT shows an aberrant artery (*arrow*) coursing through the left tympanic cavity to enter horizontal carotid canal through a dehiscence in the carotid plate. Note the packing material in the external auditory canal for hemostasis. **B**, MRA 3D time-of-flight technique, maximum intensity projection, shows a false aneurysm (*arrow*) in its intratympanic segment, confirmed by selective catheter angiography.

Copyright © 2003, Mosby, Inc. All rights reserved.

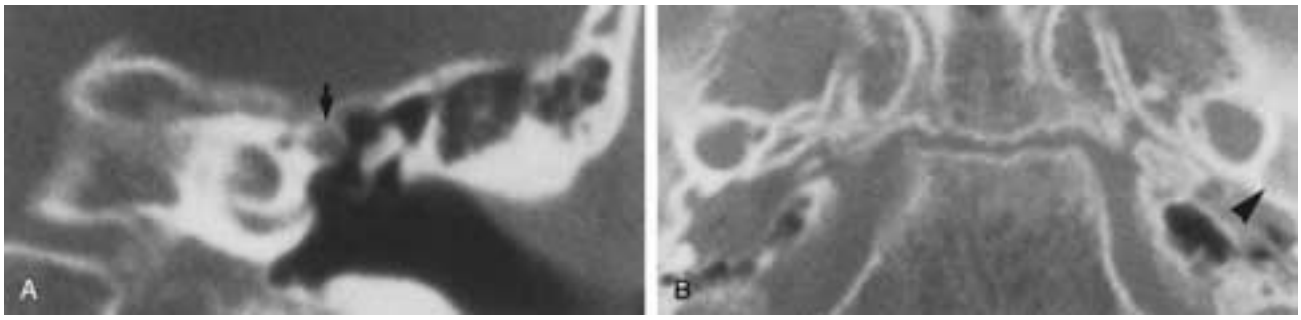

VIEW IMAGE

FIGURE 26-6 Persistent stapedial artery. **A**, **B**, High-resolution CT. The artery in the tympanic cavity through the stapes is not visualized, but the anterior portion of the tympanic segment of the facial nerve canal is enlarged (*arrow*) and the ipsilateral foramen spinosum is absent (*arrowhead*). (Courtesy of Dr. David Sobel.)

angle by a persistent trigeminal artery was suggested as a cause of pulsatile tinnitus, although the evidence was circumstantial and venous tinnitus was not clearly excluded in the cases described.[77] Anterior communicating artery berry aneurysm has also been implicated in pulsatile tinnitus.[78] However, in view of the common coexistence of intracranial berry aneurysms with cervical internal carotid FMD, unless the latter has been specifically excluded, a causal relationship should not be assumed.[31]

ARTERIOVENOUS CAUSES

Arteriovenous (AV) causes include hypervascular tumors, hypervascular bone diseases, and high-flow shunts.

Paraganglioma

Paraganglioma is the second most common tumor of the temporal bone and the most common in the middle ear.[79] Characteristically hypervascular, it is one of the most common causes of pulsatile tinnitus. Whether involving the jugular bulb (glomus jugulare or jugulotympanicum) or confined to the middle ear or mastoid (glomus tympanicum), the majority of the paragangliomas first appear with pulsatile tinnitus (see Chapter 25).[80] The clinical differentiation between tympanicum and jugulare tumors is often difficult; however, CT with bone detail can be used to define the tumor and differentiate the tympanicum tumors, which require no angiography and only simple surgery, from the jugulare tumors, which require MR imaging, angiography, preoperative embolization, and extensive surgery.[81] An MR venogram (MRV) may also help detect jugular vein invasion.[82] MRA has not been shown to be reliable for assessment of tumor vascularity.

Miscellaneous Vascular Head and Neck Tumors

Other vascular tumors in the head and neck, both inside and outside the temporal bone, have been sporadically reported as causes of pulsatile tinnitus. These include, among others, AV malformation, capillary hemangioma, cavernous hemangioma, histiocytosis, jugular meningioma, adenoma, and cholesterol granuloma.[6, 11, 83–87]

Paget's Disease

Paget's disease affects 3% of the population over 40 years of age, men more often than women. The majority of cases are discovered incidentally.[88] Three histologic phases are recognized: (1) osteoclastic resorption, (2) osteoblastic regeneration, and (3) ''mosaic'' bone replacing the original bone.[88] Increase in the size and number of blood vessels and extensive AV shunting are frequently present.[88] In a series of 165 patients with skull involvement, 31 had tinnitus, 20 of whom had pulsatile tinnitus.[89] Two of the patients in the series had common carotid flow measurements determined, and values twice the normal rate were found. Proximal ligation of the hypertrophic arteries gives only temporary relief, but experience with transarterial embolization of the distal vessels does not appear to have been reported.[90]

Otosclerosis or Otospongiosis

Pulsatile tinnitus has been encountered in a small number of otosclerotic patients and is attributed to neovascularization and arteriovenous microfistulas.[3]

Cerebral and Head and Neck Arteriovenous Malformation

Cerebral AV malformations are congenital lesions consisting of a cluster of nonneoplastic dilated, tortuous arteries and veins without an intervening arteriole-capillary bed. Cerebral blood flow through large AV malformations may be markedly increased.[91, 92] The majority of the patients are young adults who most commonly have headache, subarachnoid hemorrhage, and seizures.[93] Although in one series as many as one third of the patients had cranial bruit on auscultation, few had pulsatile tinnitus as a complaint.[93] Rarely, cerebral AV malformations may cause a symptomatic bruit, and in at least one case pulsatile tinnitus was the primary complaint.[94, 95] Because the symptoms presumably result from high flow through the

Copyright © 2003, Mosby, Inc. All rights reserved.

sigmoid and petrosal sinuses, the malformation itself does not need to be in close proximity to the temporal bone. The same applies to large extracranial AV malformation in the head and neck.

Dural Arteriovenous Fistula

Most if not all dural arteriovenous fistulas (DAVFs) are acquired.[96] The pathogenesis is unclear, but some arise because of recanalization of a thrombosed dural sinus, with the transverse, sigmoid, and cavernous sinuses being the most common sites.[97–99] The blood supply may come from any of the meningeal branches of the external or even of the internal carotid arteries (Figs. 26-7 to 26-9). Delayed postoperative DAVFs have been reported after suboccipital craniotomy.[100–102]

Accounting for 10% to 15% of all intracranial AV malformations, DAVFs are rare.[103] However, they are a much more common cause of pulsatile tinnitus than are cerebral AV malformations, and in the experience of some clinicians they are the most common cause.[6, 10]

Nearly all patients with lateral or sigmoid sinus DAVFs, and some patients with cavernous sinus DAVFs, have pulsatile tinnitus and an audible bruit.[98, 101] In more than half of the patients in a Mayo Clinic series, the tinnitus stabilized or regressed, and spontaneous closures, usually of small fistulas, also were reported.[104–107] On the other hand, aggressive lesions may cause cerebral ischemic or hemorrhagic events or chronic increased intracranial pressure.[108, 109] The presence of veno-occlusive disease is a major determinant of the aggressiveness of a fistula.[42, 101, 104, 108]

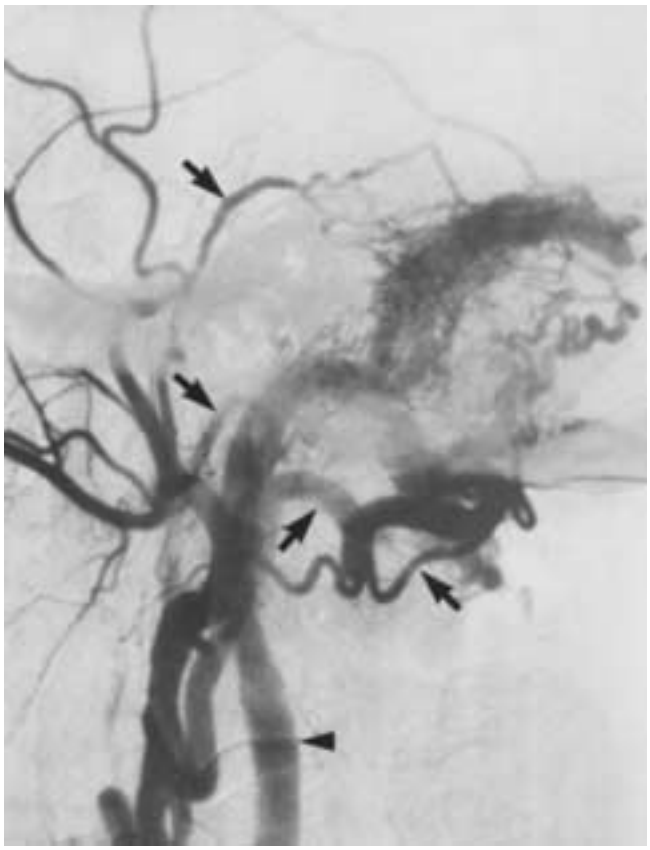

FIGURE 26-8 Large DAVF. Selective left external carotid angiogram. An extensive lesion along the transverse and sigmoid sinuses supplied by several hypertrophic external carotid branches (*arrows*) with rapid drainage down the internal jugular vein (*arrowhead*). The patient had temporary relief of pulsatile tinnitus after surgical ligation and, subsequently, partial relief of recurrent symptoms after transcatheter occlusive procedures.

VIEW IMAGE

FIGURE 26-7 Small DAVF. Selective left external carotid angiogram. A small lesion in the region of the inferior petrosal sinus (*arrow*) supplied by the ascending pharyngeal artery. The patient's pulsatile tinnitus diminished after a program of self-administered compression.

VIEW IMAGE

Although selective catheter angiography remains definitive in the evaluation of DAVF, three-dimensional (3D) time-of-flight MRA, which successfully demonstrated the fistula site in a series of six of seven cases, is a capable screening tool.[110] Nevertheless, while MR imaging effectively identifies infarct and hemorrhage in patients with veno-occlusive disease, neither MRA nor MR imaging is completely reliable in excluding dilated cortical veins, which is an important determinant for management.[110, 111]

A variety of treatment methods have been employed successfully.[98, 99, 112] In one series, self-administered external compression benefited about half of the patients without causing complications.[99] Patients who gain no relief from external compression can be treated by embolization with either isobutyl cyanoacrylate or polyvinyl alcohol sponges. The most problematic cases can be treated with a combination of embolization and surgery. In a series of 28 patients treated with these various methods, there were three strokes but no deaths, and transvenous embolization at the

Copyright © 2003, Mosby, Inc. All rights reserved.

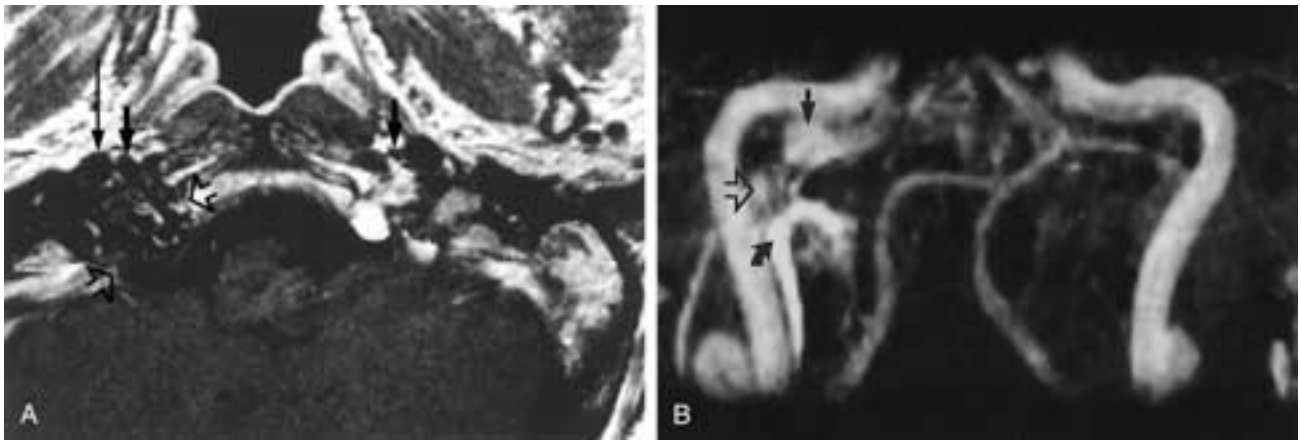

VIEW IMAGE

FIGURE 26-9 DAVF. The patient developed increasing right pulsatile tinnitus of gradual onset over a 2-year period after head trauma. No basal skull fracture was found on high-resolution CT. **A**, Gadolinium T1-weighted image. The long arrow points to the right internal carotid artery; short arrows point to the enlarged right and normal left ascending pharyngeal arteries. A cluster of serpentine ''flow voids'' without an associated soft-tissue mass lies posterior to the right internal carotid and ascending pharyngeal arteries and between the open arrows. **B**, MRA 3D time-of-flight technique, maximum intensity projection. The hypertrophic right ascending pharyngeal artery (*curved arrow*) and a cluster of dilated vessels (*open arrow*) lie immediately medial, and a dilated inferior petrosal sinus (*arrow*) lies inferior to the right internal carotid artery.

fistula site may be indicated in some patients.[42, 99, 112] Surgical excision with packing of the sinus, now out of favor, also produced excellent results in most of the patients, but in a series of 27 patients there were two deaths by exsanguination.[98]

An analysis of 205 patients with DAVFs by Cognard et al. has shown that five angiographic patterns of venous drainage are highly predictive of the clinical course of the fistulas.[113] These patterns, with subtypes, form valuable guidelines for management. In essence, in the presence of antegrade dural sinus flow, only 1 of 84 patients developed intracranial hypertension and none experienced aggressive symptoms. Thus, such fistulas may be considered benign, and the patients should be treated only if incapacitated by their tinnitus. They may be monitored annually with Doppler studies for flow and should be reevaluated upon change of symptoms. In the presence of retrograde dural sinus flow, 8 of 27 patients developed intracranial hypertension; arterial embolization should be done in these patients to reduce flow and venous hypertension. With the development of retrograde leptomeningeal venous drainage (Fig. 26-10), hemorrhage and focal neurologic deficits occur; thus, occlusion or at least suppression of the leptomeningeal drainage by arterial embolization becomes mandatory. If necessary, transvenous occlusion or surgical resection of the sinus should be considered. Direct drainage of a fistula into the cortical veins carries an extremely high risk of hemorrhage and demands complete occlusion by any and all means.[113] Based on similar observations, Borden et al. proposed a simpler classification of three drainage patterns.[114, 115]

Recently, Davies et al. validated the value of both the Cognard and Borden classifications for predicting development of symptoms. They also confirmed that low-grade lesions tended to remain benign or resolve, while high-grade lesions tended to result in poor outcomes without therapeutic embolization and/or surgery.[116–118] Surgical disconnection yielded better results with far less mortality than excision.[118] Some groups, however, maintain that the variability in degrees of sinus occlusion is a progressive process in DAVFs, and hence that all such lesions should be treated.[119]

Direct Arteriovenous Fistula

Direct AV fistulas (AVFs) occur most often in the vertebral artery, but they may also involve the internal carotid artery or a branch of the external carotid artery. In the experience of some clinicians they are usually due to trauma, but in the experience of others they are more often spontaneous.[42, 120] The vertebral artery in its course through the foramen transversarum from C6 through C2 is closely

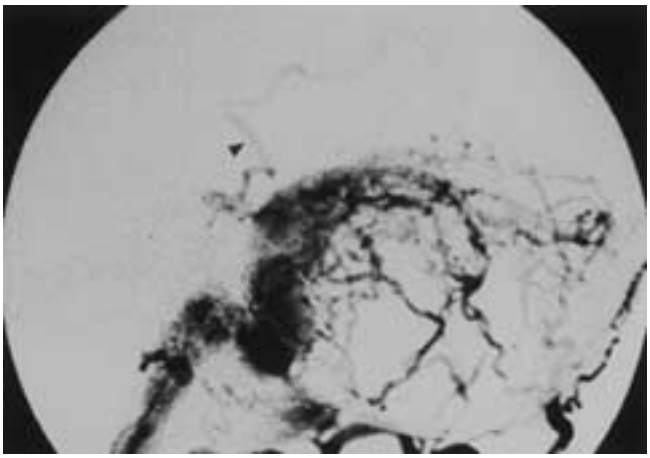

FIGURE 26-10 Large DAVF. Superselective occipital angiogram shows rapid antegrade drainage into the sigmoid sinus and down the internal jugular vein, and retrograde leptomeningeal reflux into the anastomotic lateral mesencephalic vein (*arrowhead*), a risk factor for intracranial hemorrhage not apparent on MRA.

VIEW IMAGE

Copyright © 2003, Mosby, Inc. All rights reserved.

surrounded by a venous plexus and is thus prone to develop AVFs when subjected to penetrating trauma (Fig. 26-11). Stab and bullet wounds are the most common causes.[121] Iatrogenic causes include direct vertebral puncture for angiography and anterior cervical discectomy.[122, 123] Spontaneous development occurs in neurofibromatosis 1 and FMD, as well as without specific underlying disease.[124–126] Tinnitus is the usual complaint in patients with vertebral AVF, and endovascular occlusion is the treatment of choice.[120, 127]

Traumatic AVF of the internal carotid artery usually develops in the cavernous sinus, where it is closely surrounded by a venous plexus.[128] Spontaneous carotico-cavernous fistulas may occur in fibromuscular dysplasia, Ehlers-Danlos syndrome, or neurofibromatosis.[1, 35, 42, 129] Ophthalmic symptoms and signs and pulsatile tinnitus are present in most of the patients. For vertebral AVFs, transarterial balloon embolization is the treatment of choice. Scalp AVFs also may cause pulsatile tinnitus.[42, 130, 131]

VENOUS CAUSES

Laminar flow is silent, and turbulent flow creates noise. When the noise exceeds the masking capability of the ear, it becomes venous tinnitus to the patient and may be audible to the examiner as a continuous bruit.[132] A venous bruit is usually heard around the ear. It should be distinguished from a venous hum, which can be elicited over the lower jugular vein in about half of normal subjects and in 80% of pregnant women.[133]

Venous tinnitus is invariably heard on the side of the dominant jugular vein.[8, 134, 135] Because the jugular fossa is larger on the right twice as often as it is on the left, it follows that the majority of venous tinnitus is heard on the right.[8, 134, 136]

Venous tinnitus is heard as a continuous murmur accentuated in systole. It is abolished by light pressure on the ipsilateral jugular vein and is accentuated by pressure on the contralateral vein. The symptom decreases when the head is rotated toward the involved side, and it increases when the head is turned away. Depending on its severity, venous tinnitus may or may not be audible to the examiner.[8]

Venous Tinnitus in Systemic Conditions

Venous tinnitus may be heard in conditions of hyperdynamic systemic circulation such as chronic anemia, pregnancy, and thyrotoxicosis.[132, 134, 137, 138] Hypertensive patients taking an angiotensin-converting enzyme inhibitor or a calcium channel blocker to reduce peripheral vascular resistance may rarely experience pulsatile tinnitus as a side effect.[15] Venous tinnitus in systemic conditions disappears as the underlying condition resolves.

Venous Tinnitus in Intracranial Hypertension

Headaches and blurring of vision are the predominant symptoms of intracranial hypertension, but venous tinnitus may also be a symptom.[139, 140] The pathogenesis of tinnitus in intracranial hypertension is unknown, but it is clearly and directly related to cerebrospinal fluid (CSF) pressure, and compression of dural sinuses by transmitted intracranial arterial pulsations has been postulated to be the mechanism.[15] Drainage of CSF by lumbar puncture promptly relieves the tinnitus.

Occasionally, pulsatile tinnitus can be a prominent symptom of intracranial hypertension resulting from a variety of causes.[42, 141, 142] These include aqueductal stenosis, Chiari I malformation and pneumocephalus.[143, 144] In some cases of idiopathic intracranial hypertension (IIH), also called benign intracranial hypertension and pseudotumor cerebri syndrome, it can be the presenting symptom or even the only symptom.[140, 142, 145, 146]

IIH is a syndrome characterized by increased intracranial pressure without focal neurologic signs, except for an occasional sixth nerve palsy.[139] The diagnosis is made by exclusion of lesions such as hydrocephalus, mass, chronic meningitis, dural sinus thrombosis, and hypertensive and pulmonary encephalopathy.

Patients suffering from pulsatile tinnitus from IIH tend to be young, obese women.[139, 141] In Sismanis et al.'s series of 31 patients, tinnitus was unilateral in 27 and bilateral in 4 and was also objective in 27 and subjective in 4.[141] On the CT and MR imaging scans performed to rule out

VIEW IMAGE

FIGURE 26-11 Vertebral AV fistula. Selective innominate angiogram (right posterior oblique projection). The right vertebral artery (*arrow*) is larger than the right carotid (*curved arrow*). A fistula (*open arrow*) at the C3-4 level drains promptly into the surrounding venous plexus. The patient developed pulsatile tinnitus 3 months after suffering a stab wound in the neck. Symptoms were promptly relieved by transcatheter ballon occlusion.

Copyright © 2003, Mosby, Inc. All rights reserved.

other causes of intracranial hypertension, more than half of the patients showed an empty sella or small ventricles.[141, 144, 147] A subsequent report by Sismanis and Smoker noted that papilledema was present in only 16 of 42 patients with CSF pressure over 200 mm Hg.[3]

The treatment must be directed to the underlying cause of the intracranial hypertension. In the case of IIH, acetazolamide, furosemide, and weight reduction are usually effective. Cases refractory to medical management may necessitate subarachnoid peritoneal shunting.[139–142]

Venous Tinnitus Caused by Transverse Sinus Stenosis

Venous tinnitus resulting from transverse sinus stenosis independent of DAVF is a diagnosis thus far seldom made.[7, 148, 149] Little information exists in the literature with regard to its etiology, natural history, or treatment. When warranted by incapacitating symptoms, transvenous stenting has been successfully performed.[149] True stenosis should be differentiated from arachnoid granulations in a dural sinus.[150] When there is unilateral transverse sinus thrombosis, the shifting of all of the blood flow to the contralateral side appears to be the cause of the contralateral pulsatile tinnitus.

Venous Tinnitus Associated with a Large or Exposed Jugular Bulb or Large Emissary Veins

Venous tinnitus has often been encountered in association with a large, high, or exposed jugular bulb.[134, 135, 137, 151] In view of the fact that the jugular bulb rises above the inferior tympanic annulus in 6% of the population and rises above the inferior border of the round window in 25%, and that venous tinnitus is much rarer, a high or large bulb in itself is not likely to be the cause of venous tinnitus.[152, 153] However, a large, high, or exposed bulb may indeed provide an environment conducive to the production of venous tinnitus. Furthermore, if a high bulb is exposed by dehiscence of the jugular plate and becomes visible as a bluish retrotympanic mass, it may be mistaken for a tumor.[65, 154, 155]

A laterally placed sigmoid sinus has been reported to be associated with pulsatile tinnitus.[156] Large emissary veins, probably of an incidental nature, may be seen in patients with venous tinnitus.[157, 158]

Venous tinnitus associated with a large, high, or exposed jugular bulb or a large emissary vein is essentially idiopathic venous tinnitus and can be managed similarly. Venous tinnitus associated with an exposed bulb has been successfully treated using a septal cartilage homograft over the dehiscent plate, but most patients do not require treatment.[159] Surgical lowering of the jugular bulb has been performed for high bulbs thought to be causing Meniere's disease and pulsatile tinnitus.[160]

Below the skull base, venous tinnitus can occur with an enlarged retromandibular vein and other vascular malformations in the periauricular region.

Idiopathic Venous Tinnitus

After exclusion of all specific causes, some cases of venous tinnitus remain unexplained and hence idiopathic. These cases usually involve women who are otherwise healthy, most of whom require only explanation and reassurance.[8, 135] The symptoms often resolve spontaneously.[14]

If the noise is truly intolerable, an external prosthetic clamp may be tried, and ligation of the vein under local anesthesia promptly relieves the symptom.[6, 132, 134] As an option, the optimal level of ligation may be tested by transvenous balloon occlusion; however, recurrences after ligation have been reported on the same or the contralateral side.[14, 134]

Moreover, jugular ligation risks causing intracranial hypertension. If it is to be attempted at all, IIH must first be excluded by lumbar puncture, contralateral venous drainage must be established and transverse sinus stenosis excluded by angiography or MRV, and an exposed jugular bulb must be excluded by otoscopy or high-resolution CT. In the absence of adequate contralateral drainage, jugular ligation may cause intracranial hypertension.[161] In the presence of dehiscence of the jugular plate, jugular ligation may cause herniation of the bulb into the middle ear. In such rare cases, a sigmoid-jugular bypass may be applied with or without jugular ligation.[8]

RADIOLOGIC INVESTIGATION

It is clear from the foregoing discussion that the causes of vascular tinnitus are diverse and numerous. To some patients, the symptom may be a mere nuisance; to others, it may herald a life-threatening disease. The natural history of the disease in different patients with the same diagnosis can vary widely. Management can also be complex, with some conditions requiring medical treatment, some requiring surgical treatment, some requiring endovascular treatment, some requiring a combination of treatments, and some requiring only explanation and reassurance with no other treatment.

The proper choice of imaging procedures is best tailored to the clinical findings of the patient.[3] Reliance on imaging procedures alone may cause failure to reach a diagnosis in some 40% of cases.[7] Direct communication with the referring clinician should be established, and, if necessary, the patient should be examined by the radiologist. The following imaging guidelines are suggested:

1. In the presence of a visible intratympanic or retrotympanic mass, noncontrast high-resolution CT is clearly the first examination of choice.[162] If an arterial anomaly, exposed jugular bulb, or intratympanic tumor is found, usually no further imaging is necessary. If destruction of the jugular plate suggests a glomus jugulare (jugulotympanicum) tumor, MR imaging or postcontrast CT may be done, followed by angiography, and, if indicated, a balloon occlusion test and preoperative embolization. An MRV with source images may be used in cases in which jugular vein invasion is questionable (see Fig. 25-74).[82]

Copyright © 2003, Mosby, Inc. All rights reserved.

2. When the tinnitus can be abolished by light pressure over the ipsilateral internal jugular vein, it is presumably of venous origin.[3] Systemic diseases, intracranial hypertension, and lateral sinus stenosis become the major considerations. Noncontrast MR imaging (to survey the brain) and an MRV (to define the posterior fossa dural sinuses, to confirm ipsilateral dominance, and to establish contralateral drainage in case of intervention) should suffice in most cases. Unless dural sinus angioplasty or stenting is indicated, patients in this group will rarely need angiography.
3. When a systolic bruit or machinery murmur is audible over the head or neck, indicating the presence of a stenotic artery or an arteriovenous shunt, MRA of the neck and head and noncontrast MR imaging of the head (to evaluate ischemic and hemorrhagic changes) will most likely yield a diagnosis.[7] If MRA fails to show a small fistula, gadolinium-enhanced MRA may be attempted.[110] Although MRA is less definitive than catheter angiography, the information that it provides can be most helpful for discussion and planning with the patients. If indicated, conventional angiography may then follow.

   As currently performed, MRA appears to be at least as accurate as ultrasonography in the evaluation of carotid bifurcation stenosis.[163] In addition, it allows evaluation of the upper cervical arteries and surveying for possible intracranial aneurysm in the same procedure.[164] CT angiography based on helical CT may be used for patients unable to undogo MR imaging.
4. If none of the aforementioned findings is present, the search is likely to be more difficult and the yield from imaging is likely to be low.[7] Nevertheless, significant lesions may still be detected by imaging.[7] Thus, MR imaging/MRA/MRV should be done to exclude intracranial abnormalities, high and deep-seated carotid stenosis or aneurysm, and dural sinus stenosis. Still, mild changes of FMD and small DAVFs may escape detection. High-resolution CT should be used to detect Paget's disease of the temporal bone, cochlear otospongiosis, and deep-seated tumors in the temporal bone. If these studies show no abnormality, the probability of significant disease becomes minimal. The benefit and risks of angiography must then be weighed carefully against the severity of the patient's symptoms.

REFERENCES

1. Goodhill V. Ear: Disease, Deafness and Dizziness. Hagerstown, Md.: Harper & Row, 1979;731–739.
2. Sismanis A, Williams GH, King MD. A new electronic device for evaluation of objective tinnitus. Otolaryngol Head Neck Surg 1989;100:644–645.
3. Sismanis A, Smoker WRK. Pulsatile tinnitus: recent advances in diagnosis. Laryngoscope 1994;104:681–688.
4. American Academy of Otolaryngology Head and Neck Surgery. Doctor, What Causes the Noise in My Ear? Washington, DC: The Academy, 1981.
5. Schleuning A. Neurotologic evaluation of subjective idiopathic tinnitus. J Laryngol Otol 1981;4(suppl):99–101.
6. Ward PHG, Babin R, Calcaterra TC, et al. Operative treatment of surgical lesions with objective tinnitus. Ann Otol 1975;84:473–482.
7. Dietz RR, Davis WL, Harnsberger HR, et al. MR imaging and MR angiography in the evaluation of pulsatile tinnitus. AJNR 1994;15:879–889.
8. George B, Reizine D, Laurian C, et al. Tinnitus of venous origin: surgical treatment by the ligation of the jugular vein and lateral sinus jugular vein anastomosis. J Neuroradiol 1983;10:23–30.
9. Sismanis A. Pulsatile tinnitus: a 15-year experience. Am J Otol 1998;19:472–477.
10. Waldvogel D, Mattle HP, Sturzenegger M, Schroth G. Pulsatile tinnitus—a review of 84 patients. J Neurol 1998;245:137–142.
11. Remley KB, Coit WE, Harnsberger HR, et al. Pulsatile tinnitus and the vascular tympanic membrane: CT, MR, and angiographic findings. Radiology 1990;174:383–389.
12. Sandok BA, Whisnant JP, Furlan AJ, et al. Carotid artery bruits: prevalence survey and differential diagnosis. Mayo Clin Proc 1982;57:227–230.
13. Sundt TM Jr. Carotid bruit audible to patient. JAMA 1991;265:121.
14. Hentzer E. Objective tinnitus of the vascular type: a followup study. Acta Otolaryngol (Stockh) 1968;66:273–281.
15. Sismanis A, Stamm MA, Sobel M. Objective tinnitus in patients with atherosclerotic carotid artery disease. Am J Otol 1994;15:404–407.
16. Sila CA, Furlan AJ, Little JR. Pulsatile tinnitus. Stroke 1987;18:252–256.
17. Louwrens HD, Botha J, Van der Merve DM. Subjective pulsatile tinnitus cured by carotid endarterectomy: a case report. S Afr Med J 1989;75:497.
18. Norman LKV, West POB, Perry PM. Unilateral pulsatile tinnitus relieved by contralateral carotid endarterectomy. J R Soc Med 1999;92:406–407.
19. Nishikawa M, Handon H, Hirai O, et al. Intolerable pulse-synchronous tinnitus caused by occlusion of the contralateral common carotid artery. Acta Neurochir 1989;101:80–83.
20. Campbell JB, Simons RM. Brachiocephalic artery stenosis presenting with objective tinnitus. J Laryngol Otol 1987;101:718–720.
21. Donald JJ, Raphael MJ. Case report: pulsatile tinnitus relieved by angioplasty. Clin Radiol 1991;43:132–134.
22. Tsai FY, Matovich V, Hieshima G, et al. Percutaneous transluminal angioplasty of the carotid artery. AJNR 1986;7:349–358.
23. Emery DJ, Ferguson RDG, Williams JS. Pulsatile tinnitus cured by angioplasty and stenting of petrous carotid artery stenosis. Arch Otolaryngol Head Neck Surg 1998;124:460–461.
24. Wells RP, Smith RR. Fibromuscular dysplasia of the internal carotid artery: a long term follow-up. Neurosurgery 1982;10:39–43.
25. Corrin LS, Sandok BA, Houser OW. Cerebral ischemic events in patients with carotid artery fibromuscular dysplasia. Arch Neurol 1981;38:616–618.
26. Mettinger KL, Ericson K. Fibromuscular dysplasia and the brain: observations on angiographic, clinical and genetic characteristics. Stroke 1982;13:46–52.
27. Sandok BA. Fibromuscular dysplasia of the internal carotid artery. Neurol Clin 1983;1:17–26.
28. Moreau P, Albat B, Thevenet A. Fibromuscular dysplasia of the internal carotid artery: long term surgical results. J Cardiovasc Surg 1993;34:465–472.
29. Gruber B, Hemmati M. Fibromuscular dysplasia of the vertebral artery: an unusual cause of pulsatile tinnitus. Otolaryngol Head Neck Surg 1991;105:113–114.
30. So EL, Toole JF, Dalal P, et al. Cephalic fibromuscular dysplasia in 32 patients: clinical findings and radiologic features. Arch Neurol 1981;38:619–622.
31. George B, Mourrier KL, Gelbert F, et al. Vascular abnormalities in the neck associated with intracranial aneurysms. Neurosurgery 1989;24:499–508.
32. Mettinger KL. Fibromuscular dysplasia and the brain, II. Current concept of the disease. Stroke 1982;13:53–58.
33. Dufour JJ, Lavigne F, Plante R, et al. Pulsatile tinnitus and fibromuscular dysplasia of the internal carotid. J Otolaryngol 1985;14:293–295.
34. Nevins MA, Lyon LJ, Kim JM. Multiple arterial abnormalities presenting as pulsatile tinnitus. J Med Soc NJ 1978;75:467–470.
35. Hieshima GB, Cahan LD, Mehringer CM, et al. Spontaneous arteriovenous fistulas of cerebral vessels in association with fibromuscular dysplasia. Neurosurgery 1986;18:454–458.
36. Osborn AG, Anderson RE. Angiographic spectrum of cervical and intracranial fibromuscular dysplasia. Stroke 1977;8:617–626.

Copyright © 2003, Mosby, Inc. All rights reserved.

37. Heiserman JE, Drayer BP, Fram EK, et al. MR angiography of cervical fibromuscular dysplasia. AJNR 1992;13:1454–1457.
38. Furie DM, Tien RD. Fibromuscular dysplasia of arteries of the head and neck: imaging findings. AJR 1994;162:1205–1209.
39. Hasso AN, Bird CR, Zinke DE, et al. Fibromuscular dysplasia of the internal carotid artery: percutaneous transluminal angioplasty. AJR 1981;136:955–960.
40. Balagura S, Carter JB, Gossett DL. Surgical approach to the high subcranial internal carotid artery. Neurosurgery 1985;16:402–405.
41. Smith LL, Smith DC, Killeen JD, et al. Operative balloon angioplasty in the treatment of internal carotid artery fibromusculaar dysplasia. J Vasc Surg 1987;6:482–487.
42. Dowd CF et al. Diagnostic and therapeutic angiography. In: Jackler RK, Brackmann DE, eds. Neurotology. St. Louis, Mo.: Mosby Year Book, 1994;399–436.
43. Juvela S, Porras M, Heiskanen O. Natural history of unruptured intracranial aneurysms: a long-term follow-up study. J Neurosurg 1993;79:174–182.
44. Schievink WI, Limburg M. Angiographic abnormalities mimicking fibromuscular dysplasia in a patient with Ehlers-Danlos syndrome, Type IV. Neurosurgery 1989;l25:482–483.
45. Mokri B. Traumatic and spontaneous extracranial internal carotid artery dissection. J Neurol 1990;237:356–361.
46. Mokri B, Sundt TM Jr, Houser OW, et al. Spontaneous dissection of the cervical internal carotid artery. Ann Neurol 1986;19:126–138.
47. Saeed SR, Hinton AE, Ramsden RT. Spontaneous dissection of the intrapetrous internal carotid artery. J Laryngol Otol 1990;104: 491–493.
48. Schievink WI, Mokri B, O'Fallon WM. Recurrent spontaneous cervical-artery dissection. N Engl J Med 1994;330:393–397.
49. Schievink WI. Spontaneous dissection of the carotid and vertebral arteries. N Engl J Med 2001;344:898–906.
50. Vories A, Liening D. Spontaneous dissection of the internal carotid artery presenting with pulsatile tinnitus. Am J Otolaryngol 1998;19:213–215.
51. Houser OW, Mokri B, Sundt TM Jr, et al. Spontaneous cervical cephalic arterial dissection and its residuum: angiographic spectrum. AJNR 1984;5:27–34.
52. Gelbert F, Assouline E, Hodes JE, et al. MRI in spontaneous dissection of vertebral and carotid arteries: 15 cases studied at 0.5 Tesla. Neuroradiology 1991;33:111–113.
53. Rothrock JF, Lim V, Press G, et al. Serial magnetic resonance and carotid duplex examinations in the management of carotid dissection. Neurology 1989;39:686.
54. Klufas RA, Hsu L, Barnes PD, et al. Dissection of the carotid and vertebral arteries imaging with MR angiography. Am J Roentgenol 1995;164:673–677.
55. Zuber M, Meary E, Meder JF, et al. Magnetic resonance imaging and dynamic CT scan in cervical artery dissections. Stroke 1994;25:576–581.
56. Kasner SE, Hankins LL, Bratina P, Morgenstern LB. Magnetic resonance angiography demonstrates vascular healing of carotid and vertebral artery dissections. Stroke 1997;28:1993–1997.
57. Kirsch E, Kaim A, Engelster S, et al. MR angiography in internal carotid artery dissection: improvement of diagnosis by selective demonstration of the intramural haematoma. Neuroradiology 1998; 40:704–709.
58. Leclerc X, Lucas C, Godefroy O, et al. Helical CT for the follow-up of cervical internal carotid artery dissection. AJNR 1998;19:831–837.
59. Leclerc X, Lucas C, Godefroy O, et al. Preliminary experience using contrast-enhanced MR angiography to assess vertebral artery structure for the follow-up of suspected dissection. AJNR 1999;20: 1482–1490.
60. Lu C-J, Sun Y, Jeng J-S, et al. Imaging in the diagnosis and follow-up evaluation of vertebral artery dissection. J Ultrasound Med 2000;19:263–270.
61. Djouhri H, Guillon B, Brunereau L, et al. MR angiography for the long-term follow-up of dissecting aneurysm of the extracranial internal carotid artery. AJR 2000;174:1134–1140.
62. Berenstein A, Ransohoff J, Kupersmith M, et al. Transvascular treatment of giant aneurysms of the cavernous carotid and vertebral arteries: functional investigation and embolization. Surg Neurol 1984;21:3–12.
63. Kudo S, Colley DP. Multiple intrapetrous aneurysms of the internal carotid artery. AJNR 1983;4:1119–1121.
64. Fisch U, Oldring D, Senning A. Surgical therapy of internal carotid lesions of the skull base and temporal bone. Otolaryngol Head Neck Surg 1980;88:548–554.
65. Lo WWM, SoltiBohman LG, McElveen JT. Aberrant carotid artery: radiologic diagnosis with emphasis on high resolution computed tomography. Radiographics 1985;5:985–993.
66. Valvassori GE, Buckingham RA. Middle ear masses mimicking glomus tumors: radiographic and otoscopic recognition. Ann Otol Rhinol Laryngol 1974;83:606–612.
67. Reilly JJ, Caprosa RJ, Latchaw RE, et al. Aberrant carotid artery injured at myringotomy: control of hemorrhage by a balloon catheter. JAMA 1983;249:1473–1475.
68. Anderson JM, Stevens JL, Sundt TM Jr, et al. Ectopic internal carotid artery seen initially as middle ear tumor. JAMA 1983;249:2228–2230.
69. Moret J, Delvert JC, Lasjaunias P. Vascularization of the ear: normal, variations, glomus tumors. J Neuroradiol 1982;9:209–260.
70. Davis WL, Harnsberger HR. MR angiography of an aberrant internal carotid artery. AJNR 1991;12:1225.
71. Goodman RS, Cohen NL. Aberrant internal carotid artery in the middle ear. Ann Otol Rhinol Laryngol 1981;90:67–69.
72. Sinnreich AI, Parisier SC, Cohen NL, et al. Arterial malformations of the middle ear. Otolaryngol Head Neck Surg 1984;92:194–206.
73. Guinto FC Jr, Garrabrant EC, Radcliffe WB. Radiology of the persistent stapedial artery. Radiology 1972;105:365–369.
74. Mitchell M, Hinojosa R, Khan AA. Persistence of the stapedial artery: a histopathologic study. Otolaryngol Head Neck Surg 1985;93:298–312.
75. Lasjaunias P, Moret J, Manelfe L, et al. Arterial anomalies at the base of the skull. Neuroradiology 1977;13:267–272.
76. Gulya AJ, Schuknecht HF. To the editor. Am J Otol 1984;5:262.
77. Lesinski SG, Chambers AA, Komray R, et al. Why not the eighth nerve? Neurovascular compression—probable cause for pulsatile tinnitus. Otolaryngol Head Neck Surg 1979;87:89–94.
78. Austin JR, Maceri DR. Anterior communicating artery aneurysm presenting as pulsatile tinnitus. ORL 1993;55:54–57.
79. Batsakis JG. Tumors of the Head and Neck: Clinical and Pathological Considerations. 2nd ed. Baltimore: Williams & Wilkins, 1979; 369–380.
80. Spector GJ, Druck NS, Gado M. Neurologic manifestations of glomus tumors in the head and neck. Arch Neurol 1976;33:270–274.
81. Lo WWM, Solti Bohman LG, Lambert PR. High resolution CT in the evaluation of glomus tumors of the temporal bone. Radiology 1984;150:737–742.
82. Vogl T, Jurgens M, Balzer JO, et al. Glomus tumors of the skull base: combined use of MR angiography and spin echo imaging. Radiology 1994;192:103–110.
83. Taber JR. Cavernous hemangioma of the middle ear and mastoid. Laryngoscope 1965;75:673–677.
84. Bonaf A, Joomye H, Jaeger P, et al. Histiocytosis X of the petrous bone in the adult: MRI. Neuroradiology 1994;36:330–333.
85. Levine SB, Snow JB Jr. Pulsatile tinnitus. Laryngoscope 1987;97: 401–406.
86. Molony TB, Brackmann DE, Lo WWM. Meningiomas of the jugular foramen. Otolaryngol Head Neck Surg 1992;106:128–136.
87. Martin N, Sterkers O, Mompoint D, et al. Cholesterol granulomas of the middle ear cavities: MR imaging. Radiology 1989;172:521–525.
88. Nager GT. Paget's disease of the temporal bone, Ann Otol Rhinol Laryngol 1975;84(suppl 22):1–32.
89. Davies DG. Paget's disease of the temporal bone: a clinical histopathological survey. Acta Otolaryngol (Stockh) 1968;242(suppl):1–47.
90. Gibson R. Tinnitus in Paget's disease with external carotid ligation. J Laryngol Otol 1973;87:299–301.
91. Parkinson D, Bachers G. Arteriovenous malformations: summary of 100 consecutive supratentorial cases. J Neurosurg 1980;53:285–299.
92. McCormick WF. Pathology of vascular malformations of the brain. In: Wilson CB, Stein BM, eds. Intracranial Arteriovenous Malformations. Baltimore: Williams & Wilkins, 1984;44–63.
93. Paterson JH, McKissock W. Clinical survey of intracranial angiomas with special reference to their mode of progression and surgical treatment: report of 110 cases. Brain 1956;79:233–266.
94. Hardison JE. Cervical venous hum: a clue to the diagnosis of intracranial arteriovenous malformations. N Engl J Med 1968;278: 587–590.
95. Tewfik S. Phonocephalography and pulsatile tinnitus in a surface cerebral angioma: report of a case. J Laryngol Otol 1983;97:959–962.

Copyright © 2003, Mosby, Inc. All rights reserved.

96. Houser OW, Campbell JK, Campbell RJ, et al. Arteriovenous malformation affecting the transverse dural venous sinus—an acquired lesion. Mayo Clin Proc 1979;54:651–661.
97. Mullan S. Reflections upon the nature and management of intracranial and intraspinal vascular malformations and fistulae. J Neurosurg 1994;80:606–616.
98. Sundt TM, Piepgras DG. The surgical approach to arteriovenous malformations of the lateral and sigmoid dural sinuses. J Neurosurg 1983;59:32–39.
99. Halbach VV, Higashida RT, Hieshima GB, et al. Dural fistulas involving the transverse and sigmoid sinuses: results of treatment in 28 patients. Radiology 1987;163:443–447.
100. Holgate RC, Wortzman G, Noyek AM, et al. Pulsatile tinnitus: the role of angiography. J Otolaryngol 1977;3(suppl 3):49–62.
101. Fermand M, Reizne D, Melki JP, et al. Long term followup of 43 pure dural arteriovenous fistulae (AVF) of the lateral sinus. Neuroradiology 1987;29:348–353.
102. Nabors MW, Azzam CJ, Albanna FJ, et al. Delayed postoperative dural arteriovenous malformations: report of two cases. J Neurosurg 1987;66:768–772.
103. Newton TH, Cronqvist S. Involvement of the dural arteries in intracranial arteriovenous malformations. Radiology 1969;93:1071–1078.
104. Brown RD Jr, Wiebers DO, Nichols DA. Intracranial dural arteriovenous fistulae: angiographic predictors of intracranial hemorrhage and clinical outcome in nonsurgical patients. J Neurosurg 1994;81:531–538.
105. Magidson MA, Weinberg DE. Spontaneous closure of a dural arteriovenous malformation. Surg Neurol 1976;6:107–110.
106. Bitoh S, Sakaki S. Spontaneous cure of dural arteriovenous malformations in the posterior fossa. Surg Neurol 1979;12:111–114.
107. Landman JA, Braun IF. Spontaneous closure of a dural arteriovenous fistula associated with acute hearing loss. AJNR 1985;6:448–449.
108. Vinuela F, Fox AJ, Pelz DM, et al. Unusual clinical manifestations of dural arteriovenous malformations. J Neurosurg 1986;64:554–558.
109. Lasjaunias P, Chiu M, ter Brugge K, et al. Neurological manifestations of intracranial dural arteriovenous malformations. J Neurosurg 1986;64:724–730.
110. Chen J-C, Tsuruda JS, Halbach W. Suspected dural arteriovenous fistula: results with screening MR angiography in seven patients. Radiology 1992;183:265–271.
111. DeMarco JK, Dillion WP, Halbach VV, et al. Dural arteriovenous fistulas: evaluation with MR imaging. Radiology 1990;175:193–199.
112. Halbach VV, et al. Treatment of dural arteriovenous fistulas involving the transverse and sigmoid sinuses by transvenous embolization: results in 20 patients. Neuroradiology 1991;33(suppl):550–552.
113. Cognard C, Gobin YP, Pierot L, et al. Cerebral dural arteriovenous fistulas: clinical and angiographic correlation with a revised classification of venous drainage. Neuroradiology 1995;194:671–680.
114. Borden JA, Wu JK, Shucart WA. A proposed classification for spinal and cranial dural arteriovenous fistulous malformations and implications for treatment. J Neurosurg 1995;82:166–179.
115. Borden JA, Wu JK, Shucart WA. Correction: dural arteriovenous fistulous malformations. J Neurosurg 1995;82:705–706.
116. Davies MA, TerBrugge K, Willinsky R, et al. The validity of classification for the clinical presentation of intracranial dural arteriovenous fistulas. J Neurosurg 1996;85:830–837.
117. Davies MA, Saleh J, TerBrugge K, Willinsky R, Wallace MC. The natural history and management of intradural arteriovenous fistulae. Part 1: benign lesions. Intervent Neuroradiol 1997;3:295–302.
118. Davies MA, TerBrugge K, Willinsky R, Wallace MC. The natural history and management of intracranial dural arterial arteriovenous fistulae. Part 2: aggressive lesions. Intervent Neuroradiol 1997;3:303–311.
119. Shah SB, Lalwani AK, Dowd CF. Transverse/sigmoid sinus dural arteriovenous fistulas presenting as pulsatile tinnitus. Laryngoscope 1999;109:54–58.
120. Beaujeux RL, Reizine DL, Casasco A, et al. Endovascular treatment of vertebral arteriovenous fistula. Radiology 1992;183:361–367.
121. Chou SN, French LA. Arteriovenous fistula of vertebral vessels in the neck. J Neurosurg 1965;22:77–80.
122. Bergquist E, Bergstorm K, Hugosson R, et al. Complicated arteriovenous fistula after vertebral angiography. Neuroradiology 1971;2:170–175.
123. Cosgrove GR, Theron J. Vertebral arteriovenous fistula following anterior cervical spine surgery: report of two cases. J Neurosurg 1987;66:297–299.
124. Markham JW. Spontaneous arteriovenous fistula of the vertebral artery and vein (case report). J Neurosurgery 1969;31:220–223.
125. Halbach VV, Higashida RT, Hieshima GB. Treatment of vertebral arteriovenous fistulas. AJNR 1987;8:1121–1128.
126. Deans WR, Bloch S, Leibrock L, et al. Arteriovenous fistula in patients with neurofibromatosis. Radiology 1982;144:103–107.
127. Debrun G, Legre J, Kasbarian M, et al. Endovascular occlusion of vertebral fistulae by detachable balloons with conservation of the vertebral blood flow. Radiology 1979;130:141–147.
128. Debrun G, et al. Traumatic carotid-cavernous fistulas: etiology, clinical presentation, diagnosis, treatment, results. Semin Interventional Radiol 1987;4:242–248.
129. Halbach VV, Higashida RT, Dowd CF, et al. Treatment of carotid-cavernous fistulas associated with Ehlers-Danlos syndrome. Neurosurgery 1990;26:1021–1027.
130. Barnwell SL, Hallbach VV, Dowd CF, et al. Endovascular treatment of scalp arteriovenous fistulas associated with a large varix. Radiology 1989;173:533–539.
131. Agrawal R, Flood LM, Bradey N. Iatrogenic pulsatile tinnitus. J Laryngol Otol 1993;107:445–447.
132. Carey FH. Symptomatic venous hum: report of a case. N Engl J Med 1961;264:869.
133. Cutforth R, Wiseman J, Sutherland RD. The genesis of the cervical venous hum. Am Heart J 1970;80:488–492.
134. Buckwalter JA, Sasaki CT, Virapongse C, et al. Pulsatile tinnitus arising from jugular megabulb deformity: a treatment rationale. Laryngoscope 1983;93:1534–1539.
135. Adler JR, Ropper AH. Self-audible venous bruits and high jugular bulb. Arch Neurol 1986;43:257–259.
136. Di Chiro G, Fisher RL, Nelson KB. The jugular foramen. J Neurosurg 1964;21:447–460.
137. Cochran JH, Kosmicki PW. Tinnitus as a presenting symptom in pernicious anemia. Ann Otol Rhinol Laryngol 1979;88:297.
138. Hardison JE, Smith RB, Crawley IS, et al. Self-heard venous hum. JAMA 1981;245:1146–1147.
139. Soelberg Sorensen P, Krogsaa B, Gjerris F. Clinical course and prognosis of pseudotumor cerebri: a prospective study of 24 patients. Acta Neurol Scand 1988;77:164–172.
140. Sismanis A, Hughes GB, Abedi E, et al. Otologic symptoms and findings of the pseudotumor cerebri syndrome: a preliminary report. Otolaryngol Head Neck Surg 1985;93:398–402.
141. Sismanis A, Butts FM, Hughes GB. Objective tinnitus in benign intracranial hypertension: an update. Laryngoscope 1990;100:33–36.
142. Meador KJ, Swift TR. Tinnitus from intracranial hypertension. Neurology 1984;34:1258–1261.
143. Wiggs WJ Jr, Sismanis A, Laine FJ. Pulsatile tinnitus associated with congenital central nervous system malformations. Am J Otol 1996;17:242–244.
144. Saitoh Y, Takeda N, Yagi R, et al. Pneumocephalus causing pulsatile tinnitus. J Neurosurg 2000;92:505.
145. Marcelis J, Silberstein SD. Idiopathic intracranial hypertension without papilledema. Arch Neurol 1991;48:392–399.
146. Biousse V, Newman NJ, Lessell S. Audible pulsatile tinnitus in idiopathic intracranial hypertension. Neurology 1998;50:1185–1186.
147. Silbergleit R, Junck L, Gebarski SS, et al. Idiopathic intracranial hypertension (pseudotumor cerebri): MR imaging. Radiology 1989;170:207–209.
148. Russell EJ, Kim KS, Mulopoulos G. Segmentation of the lateral/sigmoid sinus junction: an etiology of objective tinnitus of venous origin. Presented at the 28th Meeting of the American Society of Neuroradiology, Los Angeles, March 1990.
149. Marks MP, Dake MD, Steinberg GK, et al. Stent placement for arterial and venous cerebrovascular disease: preliminary experience. Radiology 1994;191:441–446.
150. Leach JL, Jones BV, Tomsick TA, Stewart CA, Balko MG. Normal appearance of arachnoid granulations on contrast-enhanced CT and MR of the brain: differentiation from dural sinus disease. AJNR 1996;17:1523–1532.
151. Willinsky RA, Nezelski JM, et al. A dehiscent jugular megabulb associated with a dominant occipital sinus. Neuroradiology 1987;19:408.

Copyright © 2003, Mosby, Inc. All rights reserved.

152. Overton SB, Ritter FN. A high placed jugular bulb in the middle ear: a clinical and temporal bone study. Laryngoscope 1973;83:1986–1991.
153. Wadin K, Wilbrand H. The topographic relationship of the high jugular fossa to the inner ear: a radioanatomic investigation. Acta Radiol Diagn 1986;27:315–324.
154. Lloyd TV, Van Aman MV, Johnson JC. Aberrant jugular bulb presenting as a middle ear mass. Radiology 1979;131:139–141.
155. Farrel FW, Hantz O. Protruding jugular bulb presenting as a middle ear mass: case report and brief review. AJR 1979;128:685–687.
156. Mehall CJ, Wilner HI, La Rouere MJ. Pulsatile tinnitus associated with a laterally placed sigmoid sinus. AJNR 1995;16:905–907.
157. Lambert PR, Cantrell RW. Objective tinnitus in association with abnormal posterior condylar emissary vein. Am J Otolaryngol 1986;7:204–207.
158. Forte V, Turner A, Liu P. Objective tinnitus associated with abnormal emissary vein. Otolaryngol 1989;18:232–235.
159. Rouillard R, Leclerc J, Savary P. Pulsatile tinnitus: a dehiscent jugular vein. Laryngoscope 1985;95:188–189.
160. Couloigner V, Grayeli AB, Boucarra D, Julian N, Sterkers O. Surgical treatment of the high jugular bulb in patients with Meniere's disease and pulsatile tinnitus. Eur Arch Otorhinolaryngol 1999;256: 224–229.
161. Lam BL, Schatz NJ, Glaser JS, et al. Pseudotumor cerebri from cranial venous obstruction. Ophthalmology 1992;99:706–712.
162. Hasso AN. Imaging of pulsatile tinnitus: basic examination versus comprehensive examination package. AJNR 1994;15:890–892.
163. Mittl RL Jr, Broderick M, Carpenter JP, et al. Blinded-reader comparison of magnetic resonance angiography and duplex ultrasonography for carotid artery bifunction stenosis. Stroke 1994;25:4–10.
164. Schievink WI, Mokri B, Piepgras DG. Angiographic frequency of saccular intracranial aneurysms in patients with spontaneous cervical artery dissection. J Neurosurg 1992;76:62–66.

Copyright © 2003, Mosby, Inc. All rights reserved.

Section VI

Upper Aerodigestive Tract

Copyright © 2003, Mosby, Inc. All rights reserved.

Copyright © 2003, Mosby, Inc. All rights reserved.

27

The Oral Cavity

Wendy R.K. Smoker

NORMAL ANATOMY
- The Oral Tongue
  - Intrinsic Muscles of the Tongue
  - Extrinsic Muscles of the Tongue
    - *The Genioglossus Muscles*
    - *The Hyoglossus Muscles*
    - *The Styloglossus Muscle*
    - *The Palatoglossus Muscle*
  - Motor and Sensory Innervation of the Tongue
- Floor of the Mouth
  - The Mylohyoid Muscle
  - The Digastric Muscle
  - The Geniohyoid Muscle
  - The Sublingual Region
- Submandibular Space
- Lips and Gingivobuccal Region
- Buccomasseteric Region

PATHOLOGY
- Congenital Anomalies
  - Congenital Absence of the Tongue
  - Accessory Parotid Tissue
  - Digastric Muscle Anomalies
  - Vascular Lesions
- Hemangiomas
- Vascular Malformations
  - Capillary Malformations
  - Venous Malformations
  - Arterial Malformations
  - Lymphatic Malformations (Lymphangiomas)
  - Dermoid Cysts
  - Thyroglossal Duct Cysts
  - Lingual Thyroid
  - Lingual Artery Aneurysms
  - Heterotopic Tissues of the Tongue
- Infections and Inflammatory Lesions
  - Abscess, Cellulitis, and Sialoliths
  - Ludwig's Angina
  - HIV Involvement of the Oral Cavity
  - Ranulas

Benign Lesions
- Pleomorphic Adenomas
- Aggressive Fibromatosis
- Rhabdomyomas
- Lipomas
- Nerve Sheath Tumors
  - *Schwannomas*
  - *Neurofibromas*
  - *Granular Cell Myoblastomas*
- Exostoses
- Fibroosseous Lesions
  - *Fibrous Dysplasia*
  - *(Central) Cementifying Fibroma*
  - *Osteomas*
  - *Giant Cell Lesions*
- Benign Odontogenic Lesions
- Miscellaneous Benign Lesions
  - *Incisive Canal (Nasopalatine Duct) Cysts*
  - *Osteochondroma (Osteocartilaginous Exostosis)*
  - *Chondroma*
  - *Epithelioid Hemangioendothelioma*
  - *Asymmetric Maxillary Sinus Pneumatization*

Malignant Lesions
- Squamous Cell Carcinoma
  - *SCCa of the Lip*
  - *SCCa of the Floor of the Mouth*
  - *SCCa of the Oral Tongue*
  - *SCCa of the Gingiva/Buccal Mucosa*
  - *SCCa of the Hard Palate*
  - *SCCa of the Retromolar Trigone*
- Lymphoma
- Adenoid Cystic Carcinoma
- Mucoepidermoid Carcinoma
- Liposarcoma
- Rhabdomyosarcoma
- Miscellaneous Malignancies

Miscellaneous Pathology
- Ossification of the Stylohyoid Ligament

Copyright © 2003, Mosby, Inc. All rights reserved.

Denervation Muscle Atrophy
Mandibular Division of the Trigeminal Nerve (V3)
Facial Nerve (VII)
Hypoglossal Nerve (XII)
Benign Masseteric Hypertrophy
Macroglossia

The oral cavity is the most ventral portion of the aerodigestive tract and is separated from the oropharynx by a ring of structures that includes the circumvallate papillae, the anterior tonsillar pillars, and the soft palate. From a clinical standpoint this anatomic subdivision is useful because malignancies, especially squamous cell carcinomas, in these two regions differ in their presentations, prognoses, and histologic grades.[1, 2] This chapter is primarily confined to the oral cavity, including the oral tongue (anterior two thirds of the tongue), floor of the mouth, lips, gingivobuccal and buccomasseteric regions, and the adjacent maxilla and mandible. The posterior one third of the tongue (base of the tongue) is discussed in Chapter 28. The muscles described in the following sections are summarized in Table 27-1.

NORMAL ANATOMY

The Oral Tongue

The tongue consists of symmetric halves separated from each other by a midline septum. The ''supporting skeleton'' of the tongue is composed of the lingual septum and the hyoglossus membrane, a thin, broad sheet suspended between the two minor tubercles of the hyoid bone. The fibrous lingual septum arises from the midline of the hyoglossus membrane and the middle of the hyoid bone, and because it is seen as a hypodense midline structure on CT scans through the tongue, it has also been referred to as the *midline low-density plane* (Figs. 27-1 and 27-2).[3, 4] Each half of the tongue is composed of muscular fibers arranged in various directions, which can be divided into extrinsic and intrinsic muscles. There are four interdigitating intrinsic muscles—the superior and inferior longitudinal, the transverse, and the vertical or oblique muscles—which make up the bulk of the tongue. The extrinsic muscles are those that have their origins external to the tongue itself, yet their more distal fibers interdigitate within the substance of the tongue. The extrinsic muscles provide attachment of the tongue to the hyoid bone, mandible, and styloid process of the skull base. The main extrinsic tongue muscles are the genioglossus, hyoglossus, and styloglossus muscles.[5, 6] Some authors also include the palatoglossus and superior pharyngeal constrictor muscles in their discussion of extrinsic tongue muscles.[7]

Intrinsic Muscles of the Tongue

The superior longitudinal muscle consists of a thin layer of oblique and longitudinal fibers that arise from the hyoglossus membrane and the fibrous lingual septum. The fibers fan out into a broad sheet, passing forward and outward to the edges of the tongue, just under the mucosa of the dorsum of the tongue.

The inferior longitudinal muscle has the same origin as the superior longitudinal muscle, but it is divided into two halves by the genioglossus muscle situated in the undersurface of the tongue. The inferior longitudinal muscle extends from the base to the tip of the tongue, lying medial to the hyoglossus and lateral to the genioglossus muscles.

The transverse muscles originate from the fibrous septum and fan outward to insert into the submucosal fibrous layer at the sides of the tongue. Intersecting with these transverse fibers are fibers from the vertical (oblique) muscles that extend from the upper surface to the undersurface of the tongue. These vertical fibers are encountered only at the borders of the anterior portion of the tongue.[7]

The intrinsic muscles are difficult to identify on CT, and fibers of the superior longitudinal muscle have, on occasion, been mistaken for a tumor.[4] However, these muscle bundles are easily appreciated on MR imaging because the low signal intensity muscle fibers are surrounded by the higher signal intensity of the fibrofatty supporting tissues (Fig. 27-3).[8] In particular, sagittal MR imaging demonstrates the full extent of the longitudinal muscles (Fig. 27-3C).[9]

The complex arrangement of the tongue musculature enables enunciation of various consonants. The superior longitudinal muscle tends to shorten the tongue and turn its tip and sides upward to render the dorsum concave. The inferior longitudinal muscle also shortens the tongue but pulls the tip down to render the dorsum convex. The transverse muscle fibers narrow and elongate the tongue, and the vertical fibers flatten and broaden the tongue. The intrinsic muscles of the tongue receive motor innervation from the hypoglossal nerve (XII).

Extrinsic Muscles of the Tongue

The Genioglossus Muscles

The paired genioglossus muscles originate via a short tendon from the superior genial tubercle on the inner surface of the mandible, just above the origin of the geniohyoid muscles. The fibers quickly fan out, the inferior fibers attaching via a thin aponeurosis to the body of the hyoid bone, the middle fibers coursing posteriorly, and the superior fibers directed upward and dorsally to insert into the entire length of the undersurface of the tongue from its base to its apex. Posteriorly, the genioglossus muscles are quite distinct from each other, separated by the midline lingual septum and fatty tissue, easily identified on both axial and coronal CT and MR images (Figs. 27-1 to 27-3). The two muscles are quite symmetric, measuring 9 to 11 mm in the transverse dimension at their intersection with the hyoglossus muscle.[10] More anteriorly, however, the fibers from the two muscles are less distinct and somewhat blended together as

Copyright © 2003, Mosby, Inc. All rights reserved.

Table 27-1
MUSCLES ASSOCIATED WITH THE ORAL CAVITY

Muscle Innervation	Action	Origin	Insertion	Motor
Superior longitudinal constrictor muscles	Hyglossal membrane and fibrous lingual septum	Edges of the tongue under dorsum mucosa, fanning out to a broad sheet	Hypoglossal nerve (XII)	Shortens the tongue and turns the lip and sides up to render the dorsum concave
Inferior longitudinal constrictor muscles	Hyglossal membrane and fibrous lingual septum but divided by genioglossus muscles and situated on undersurface of the tongue	From base to tip of the tongue medial to hyoglossus and lateral to genioglossus muscles	Hypoglossal nerve (XII)	Shortens the tongue but pulls tip downward to render the dorsum convex
Transverse muscles	Fibrous lingual septum	Fan out to insert into the submucosal fibrous layer at the sides of tongue	Hypoglossal nerve (XII)	Narrows and elongates the tongue
Vertical/oblique muscles	Upper surface of the tongue	Undersurface of the tongue	Hypoglossal nerve (XII)	Flattens and broadens the tongue
Genioglossus muscle	From the upper mental spines of the genial tubercles	Contacts its counterpart in the median plane and fans vertically into the tongue, inserted throughout its length; some inferior fibers reach the hyoid bone	Hypoglossal nerve (XII)	Acting together, the two muscles protrude the tongue; if one muscle is paralyzed, the tip of the tongue deviates toward the inactive side
Hyoglossus muscle	Body and greater horn of hyoid bone	Posterior one half of the side of the tongue	Hypoglossal nerve (XII)	Depresses the sides of the tongue and enlarges the cavity of the mouth
Styloglossus muscle	From tip of styloid process of temporal bone and adjacent part of stylohyoid ligament	Entire length of the side of the tongue, interdigitating with fibers of the hyoglossus muscle	Hypoglossal nerve (XII)	Pulls the tongue posterosuperiorly during swallowing
Mylohyoid muscle	Entire length of the mylohyoid line on inner surface of the mandible	Into a fibrous median raphe extending from the symphysis of the mandible to the body of the hyoid bone	Mylohyoid nerve branch of the inferior alveolar branch of the mandibular division of the trigeminal nerve (V3)	Raises the hyoid bone and tongue during swallowing and forms the muscular floor of the mouth
Anterior belly of the digastric muscle	Digastric fossa of the mandible just below the genial tubercles	United by an intermediate tendon with the posterior belly; bound to the upper border of the hyoid bone by a loop of fibrous tissue	Mylohyoid nerve branch of the inferior alveolar branch of the mandibular division of trigeminal nerve (V3). (*Note*: The posterior belly is innervated by the facial nerve [VII].)	Acting with its posterior belly, it raises the hyoid bone during swallowing; acting with the infrahyoid strap muscles, it fixes the hyoid bone to form a stable base on which the tongue can move
Geniohyoid muscle	From the lower mental spines of the genial tubercles, on the inner surface of mandible near the midline	The paired muscles course side by side on the superior surface of the mylohyoid muscle to insert onto the anterior body of the hyoid bone	Fibers from C1	Pulls the hyoid bone anterosuperiorly
Buccinator muscle	Outer surface of the alveolar processes of the mandible and maxilla corresponding to the three molar teeth; anterior margin of the pterygomandibular raphe	Fibers coverage toward the angle of the mouth where central fibers intersect each other, being continuous with the orbicularis oris, and upper- and lowermost fibers continuing into corresponding segments of the lip without decussation	Facial nerve (VII)	Used during mastication to press cheek against the teeth, thus preventing food from escaping into vestibule of the mouth
Masseter muscle	Inferior margin and deep surface of the zygomatic arch from the tubercle at its root posteriorly to the junction with the zygomatic process of the maxilla anteriorly	Lateral surface of the ramus and coronoid process of the mandible	Branch of the mandibular division of the trigeminal nerve (V3)	Raises the mandible and clenches the teeth; superficial fibers help protract the mandible

Table continued on following page

Copyright © 2003, Mosby, Inc. All rights reserved.

Table 27-1
MUSCLES ASSOCIATED WITH THE ORAL CAVITY *Continued*

Muscle Innervation	Action	Origin	Insertion	Motor
Medial pterygoid muscle	Superficial head arises from maxillary tuberosity; deep head arises from medial surface of the lateral pterygoid plate, deep to the lateral pterygoid muscle	Rough area between the mandibular foramen and angle of the mandible; its fibers essentially parallel those of the anterior masseter fibers	Branch of the mandibular division of the trigeminal nerve (V3)	Raises the mandible, assists in its protrusion, and slews the chin to the opposite side; acting alternately, the muscles produce a grinding movement
Lateral pterygoid muscle	Upper head arises from infratemporal ridge and infratemporal surface of greater wing of sphenoid bone; lower head arises from lateral surface of lateral pterygoid plate	Into front of the neck of the mandible and the articular disk through the capsule of the temporomandibular joint	Branch of the mandibular division of the trigeminal nerve (V3)	Together, the two muscles protrude the mandible and depress the chin, drawing the head of the mandible and the disk forward onto the articular tubercle; when one acts alone, the head of the mandible on that side is drawn forward, the mandible pivots around the joint, and the chin is slewed to the opposite side
Temporalis muscle	Floor of the temporal fossa and from temporal fascia	Summit and anterior margin of coronoid process and anterior margin of ramus; medial side of coronoid process down to junction of ramus with body of mandible behind the third molar tooth	Deep temporal branches of the mandibular division of the trigeminal nerve (V3)	Raises the mandible; posterior fibers retract the mandible after protraction

fascicles from one muscle cross the midline to interdigitate with those of the contralateral muscle.[7]

The Hyoglossus Muscles

The hyoglossus muscles are thin, flat quadrilateral muscles forming the lateral borders of the tongue. They arise from the greater cornua of the hyoid bone and course vertically, lateral to the genioglossus muscles, to insert into the sides of the tongue. In their posterosuperior aspect, fibers of the hyoglossus interdigitate with fibers of the styloglossus muscle (see the next section). The hyoglossus muscles are best seen on CT or MR imaging in the axial plane (Figs. 27-1 and 27-3A).[3] The normal transverse diameter of each muscle, measured in the axial plane, is 5 to 7 mm.[10]

The Styloglossus Muscle

The styloglossus muscle arises from the anterolateral surface of the styloid process of the temporal bone, near its apex, and from portions of the stylomandibular ligament. Passing downward and forward between the internal and external carotid arteries, it divides at the side of the tongue into two sets of fibers. The longitudinal fibers enter the side of the tongue near its dorsal surface, anterior to the hyoglossus fibers, and the more posterior oblique fibers interdigitate with fibers of the hyoglossus muscle.

The Palatoglossus Muscle

The palatoglossus muscle with its overlying mucosa forms the palatoglossal arch (anterior tonsillar pillar). The muscle arises from the oral surface of the palatal aponeurosis and the soft palate and extends laterally, forward, and downward to the palatine tonsil to insert on the dorsum and side of the tongue, its fibers blending with those of the styloglossus and transverse lingual muscles.

Motor and Sensory Innervation of the Tongue

The intrinsic and extrinsic muscles of the tongue all receive motor innervation from the hypoglossal nerve (XII), which courses between the mylohyoid and hyoglossus muscles. The palatoglossus muscle is innervated by the pharyngeal plexus. Adjacent to the hypoglossal nerve is the lingual nerve, a branch of the trigeminal nerve that carries sensory fibers from the anterior portion of the tongue. Special sensory taste fibers from the anterior two thirds of the tongue course with the lingual nerve over a short distance before they coalesce to form the chorda tympani nerve, which extends to the lateral skull base, traverses the middle ear, and joins the facial nerve. Special sensory taste fibers from the posterior one third of the tongue are supplied by the glossopharyngeal nerve (IX).

Floor of the Mouth

The floor of the mouth is a U-shaped structure covered by squamous mucosa. The primary muscles comprising the floor of the mouth are the mylohyoid muscles and their fibrous median raphe. Additional support is provided by the paired anterior bellies of the digastric muscles and the geniohyoid muscles (Figs. 27-2 and 27-3B). Surgically, the floor of the mouth is considered that space between

Copyright © 2003, Mosby, Inc. All rights reserved.

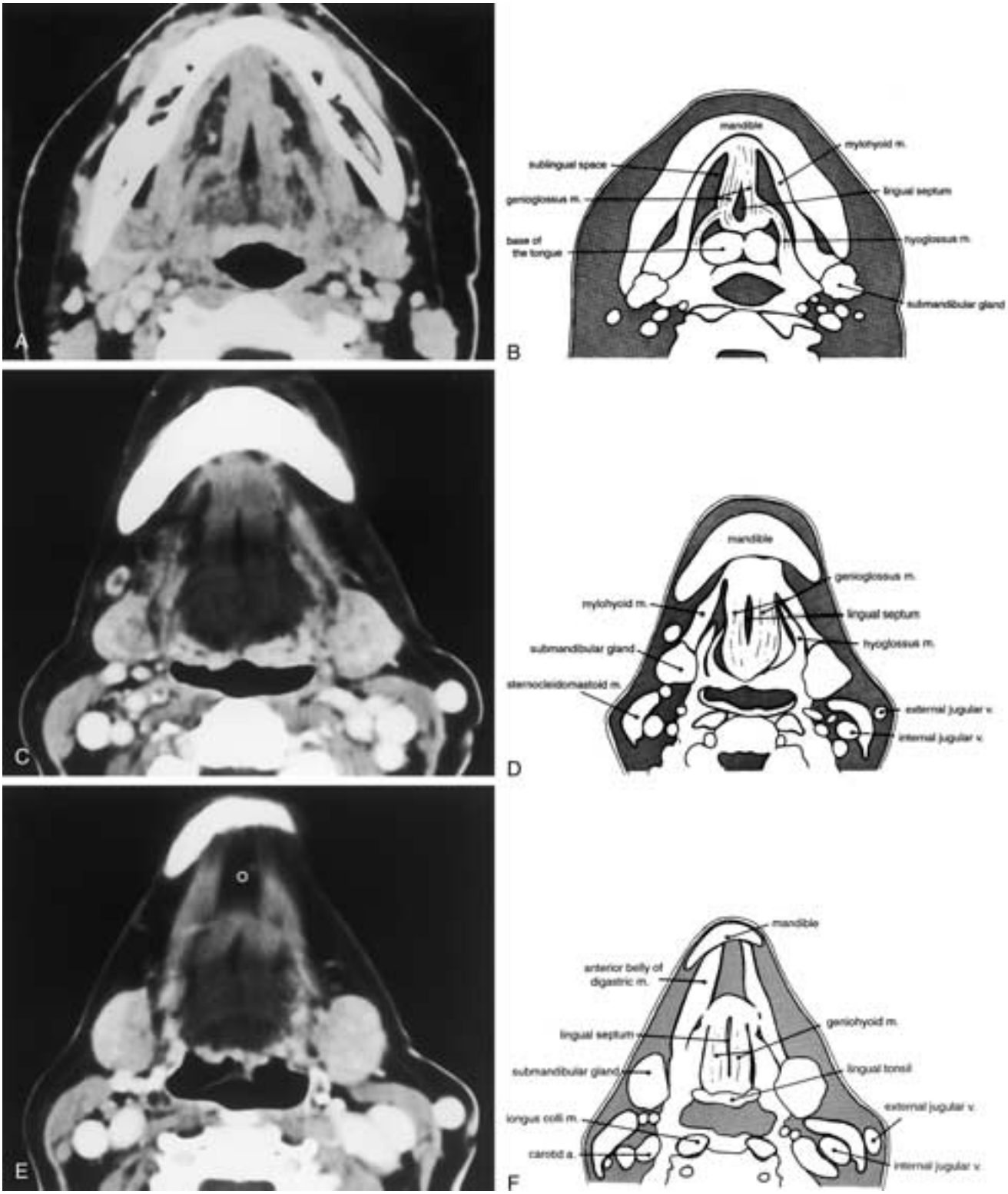

FIGURE 27-1 Normal anatomy. Axial CT scans and corresponding line diagrams through the high (**A** and **B**), middle (**C** and **D**), and low (**E** and **F**) floor of the mouth. (*White circle* in **E** represents the fat-filled midline submental space.)

VIEW IMAGE

Copyright © 2003, Mosby, Inc. All rights reserved.

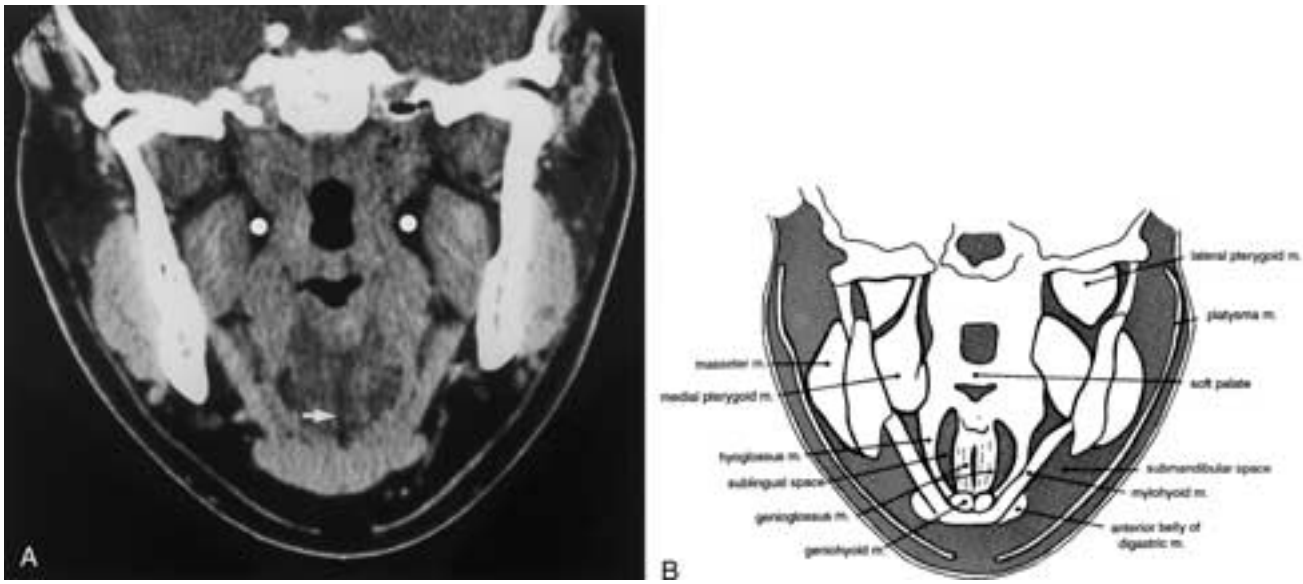

FIGURE 27-2 Normal anatomy. Coronal CT scan (**A**) and corresponding diagram (**B**) through the floor of the mouth, buccomasseteric regions, and masticator spaces. *Arrow* in **A**, Lingual septum; *dots*, parapharyngeal space fat.

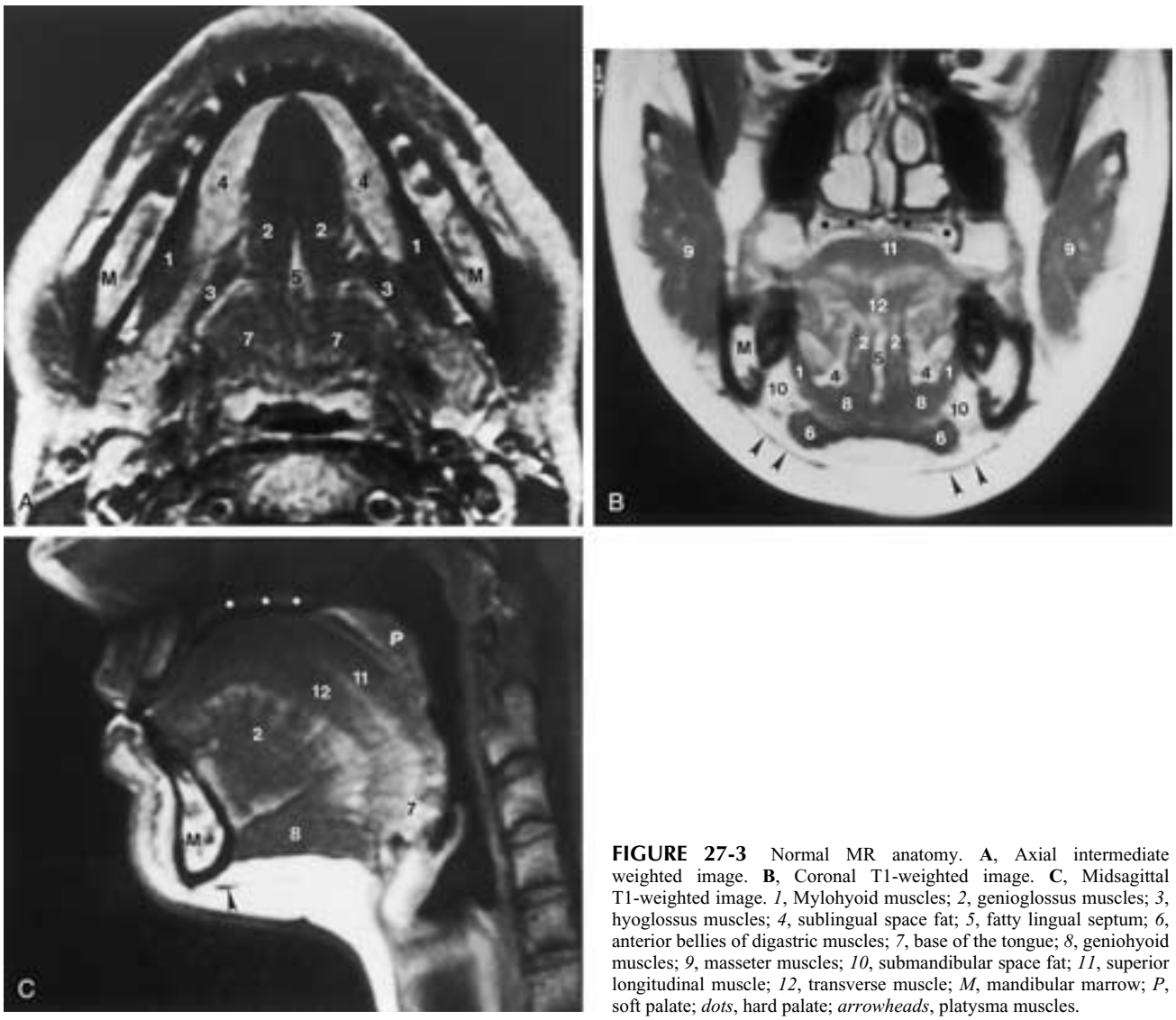

FIGURE 27-3 Normal MR anatomy. **A**, Axial intermediate weighted image. **B**, Coronal T1-weighted image. **C**, Midsagittal T1-weighted image. *1*, Mylohyoid muscles; *2*, genioglossus muscles; *3*, hyoglossus muscles; *4*, sublingual space fat; *5*, fatty lingual septum; *6*, anterior bellies of digastric muscles; *7*, base of the tongue; *8*, geniohyoid muscles; *9*, masseter muscles; *10*, submandibular space fat; *11*, superior longitudinal muscle; *12*, transverse muscle; *M*, mandibular marrow; *P*, soft palate; *dots*, hard palate; *arrowheads*, platysma muscles.

Copyright © 2003, Mosby, Inc. All rights reserved.

the mucosa of the floor of the mouth and the mylohyoid muscle sling. Caudal to this muscle but above the hyoid bone, the space is considered the suprahyoid neck.

The Mylohyoid Muscle

The mylohyoid muscle is a flat, triangular muscle that arises from the entire length of the mylohyoid ridge on the inner surface of the mandible and extends from the mandibular symphysis anteriorly to the last molar tooth posteriorly.[7] Posterior fibers course inferiorly to insert onto the body of the hyoid bone. The remaining middle and anterior fibers insert into the fibrous median raphe that runs between the mandibular symphysis and the hyoid bone, thus joining with fibers from the opposite side to form the U-shaped muscular floor of the mouth. The mylohyoid muscle sling is best demonstrated by CT and MR imaging in the coronal plane (Figs. 27-2 and 27-3B). The mylohyoid branch of the inferior alveolar nerve (a branch of the mandibular division of the trigeminal nerve [V3]) provides motor innervation to the mylohyoid muscle. Just before entering the mandibular foramen, the inferior alveolar nerve gives off the small mylohyoid nerve, which descends in a groove on the inner surface of the mandible, held in position by a fibrous membrane.[7]

There is a gap at the free posterior border of the mylohyoid muscle, between it and the hyoglossus muscle. It is via this gap that the submandibular gland wraps around the dorsal aspect of the mylohyoid muscle, with the deep lobe of the gland lying cranial to the muscle fibers and the superficial lobe lying on its external (caudal) surface.

The Digastric Muscle

The digastric muscle consists of two bellies. The anterior belly arises from the digastric fossa on the inner surface of the mandible, just below the genial tubercles. The posterior belly arises from the digastric fossa on the inner surface of the mastoid process of the temporal bone. The two bellies terminate in a central tendon that pierces the stylohyoid muscle and runs through a fibrous loop (lined with a synovial membrane) that is attached to the body and greater cornua of the hyoid bone. The two paramedian anterior digastric muscles lie just below (caudal to) the mylohyoid muscle sling and thus contribute to the muscular floor of the mouth. They are best seen on CT and MR imaging in the coronal plane. Like the mylohyoid muscle, the anterior belly of the digastric muscle is innervated by the mylohyoid branch of the mandibular nerve (V3). The posterior belly receives its innervation from the facial nerve (VII).

The Geniohyoid Muscle

Each geniohyoid muscle is a slender muscle that arises from the inferior genial tubercle on the inner surface of the mandible. It passes inferiorly to insert onto the anterior surface of the body of the hyoid bone. Closely approximated, the geniohyoid muscles lie just above the mylohyoid sling; this is best appreciated on CT scans and MR images obtained in the coronal plane. Because the geniohyoid muscles do not have interspersed fibrofatty tissue, as do the extrinsic muscles of the tongue, they may occasionally appear denser than the genioglossus muscles on CT. Motor innervation to the geniohyoid muscles is variably described to be from the hypoglossal nerve (XII), by the few fibers from C1 that course with the hypoglossal nerve until it crosses the internal carotid artery, or by motor fibers from both C1 and C2.[5–7, 11]

The Sublingual Region

Superomedial to the mylohyoid muscle, lateral to the genioglossus-geniohyoid muscles, and below the mucosa of the floor of the mouth is the primarily fat-filled sublingual area known as the *sublingual space* or *sublingual compartment of the submandibular space.* Based on its CT appearance, it is also referred to by some authors as the *lateral low-density plane* (see also Chapters 34 and 39).[3, 4, 12] This region is continuous with the submandibular region at the posterior margin of the mylohyoid muscle (Fig. 27-4A). Contents of this sublingual ''space'' include the deep portion and hilum of the submandibular gland, Wharton's duct, the anterior fibers of the hyoglossus muscle, and the lingual nerve, artery, and vein. On either side, the hyoglossus, styloglossus, and palatoglossus muscles form a slightly curved lateral muscular bundle in the sublingual space. Together these muscles are an important surgical

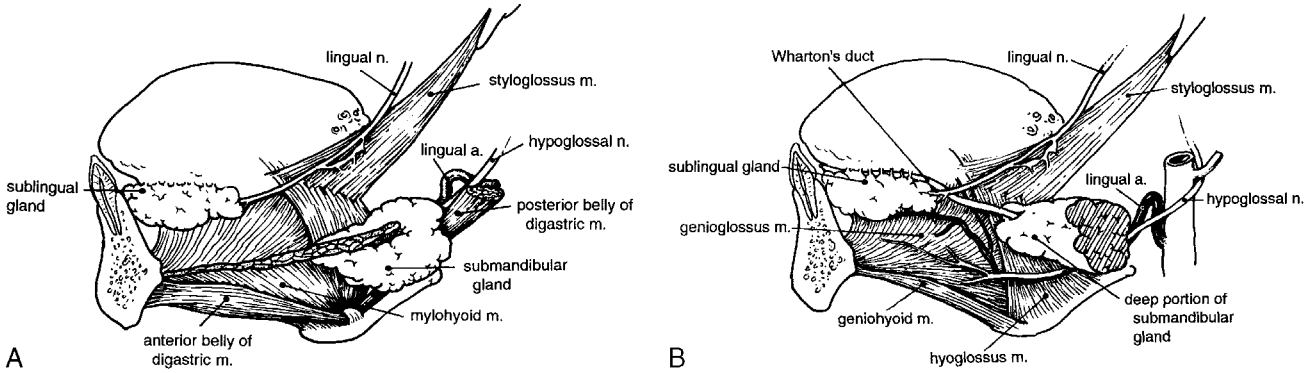

FIGURE 27-4 Diagram demonstrating normal structural relationships. **A**, Lateral view with the mylohyoid muscle in place. The mylohyoid muscle separates the anterior belly of the digastric muscle, which lies superficial, from the geniohyoid muscle, which lies on a deeper plane. The submandibular gland wraps around the posterior margin of the mylohyoid muscle, and its deep lobe enters the posterior aspect of the sublingual space. Note the fibrous loop that anchors the common digastric tendon to the hyoid bone. **B**, Lateral view of the oral cavity with the mylohyoid and digastric muscles removed. Note that Wharton's duct, along with the hypoglossal and lingual nerves, lies superficial to the hyoglossus muscle and the facial vessels lie on a plane deep to the muscle.

VIEW IMAGE

Copyright © 2003, Mosby, Inc. All rights reserved.

landmark to the anatomy of the sublingual region, as they separate Wharton's duct and the hypoglossal and lingual nerves, which lie laterally, from the lingual artery and vein, which course medially (Fig. 27-4B).[3] Wharton's duct arises from the deep portion of the gland and runs anteriorly, in contact with the hypoglossal and lingual nerves. Initially, it lies between the hyoglossus and mylohyoid muscles, and more anteriorly it lies between the genioglossus and mylohyoid muscles. The duct drains into the floor of the mouth, just lateral to the frenulum of the tongue.

Submandibular Space

Inferior to the mylohyoid muscle lies the submandibular space (also see Chapter 34). It is a fascially defined space except at the posterior margin of the mylohyoid muscle, where it is in continuity with the posterior aspect of the sublingual space and the anterior aspect of the parapharyngeal space (Fig. 27-4A). This communication permits easy spread of pathology among these spaces. The primary contents of the submandibular space are fat and the larger superficial portion of the submandibular gland. On either side, the anterior belly of the digastric muscle lies within the fat in a paramedian location, and the region between these two muscle bellies is referred to as the *submental portion of the submandibular space* or the *submental space* (Figs. 27-1E,F, 27-2 and 27-3B). This is a small triangular midline area in which the submental lymph nodes (level IA) reside. Submandibular lymph nodes (level IB) and branches of the facial artery and vein lie lateral to the anterior digastric muscle in the fat surrounding the superficial portion of the submandibular gland. The artery courses deep to the gland, while the vein runs superficially, just beneath the investing fascia. The vein is a useful landmark when evaluating submandibular region masses. Primary disease of the submandibular gland is never separated from the gland by the vein but displaces the vein laterally. However, lymphadenopathy and other soft-tissue masses that lie lateral to the gland are separated from the gland by the interposed vein.[13]

On CT, the normal submandibular gland is fairly homogeneous in appearance and may be of either a relatively fatty or soft-tissue attenuation. The density and enhancement of the two glands should be symmetric. If not, one gland is abnormal. On MR imaging, the normal submandibular gland has either a homogeneous or heterogeneous MR signal intensity, which is higher than that of surrounding muscle on both T1-weighted and T2-weighted images.[14]

Lips and Gingivobuccal Region

The lips are composed primarily of the orbicularis oris muscle, which is not a sphincter muscle but rather is composed of muscle fibers derived from multiple facial muscles that insert into the lips and some additional fibers proper to the lips themselves. Muscles that contribute to the orbicularis oris include the levator labii superioris alaeque nasi, levator labii superioris, levator anguli oris, zygomaticus major, depressor anguli oris, platysma, risorius, and buccinator muscles.[7] Motor innervation to the lips is supplied by branches of the facial (VII) nerve, and lymphatic drainage is primarily to the submental and submandibular lymph nodes (level I). The external surface of the lips is covered by keratinizing stratified squamous epithelium, and the internal surface is lined by nonkeratinizing stratified squamous mucosa.

The vestibule of the mouth separates the lips and cheeks, which are lined by buccal mucosa, from the teeth and gums. It is essentially a cleft into which drain the ducts of the parotid glands and the mucous glands of the lips and cheeks. The vestibule is bounded superiorly and inferiorly by reflections of the buccal mucosa onto the maxilla and mandible, respectively. The vestibule is continuous posteriorly with the oral cavity proper through an interval between the last molar tooth and the ramus of the mandible.

The gingiva is the mucosal covering and overlies both the medial (lingual) and lateral (buccal) aspects of the alveolar processes of the mandible and maxilla. The junction of the gingiva with the buccal mucosa is termed the *gingivobuccal sulcus* and is a common location for squamous cell carcinoma of the oral cavity. At times it may be difficult to determine if a lesion originates from the gingival or buccal mucosa. On imaging, instructing patients to ''puff'' their cheeks, thereby dilating the vestibule with air and separating these mucosal surfaces, is a useful maneuver for visualizing lesions in this area (Fig. 27-5). There is also a triangular area of mucosa posterior to the last mandibular molar tooth termed the *retromolar trigone.* This region covers the lower ascending ramus of the mandible, and it is another area in which squamous cell carcinomas commonly arise.

Buccomasseteric Region

The term *buccomasseteric region* refers to the masseter and buccinator muscles, the buccal space, and the inferior body of the mandible (Fig. 27-6).[15]

The masseter muscle is one of the muscles of mastication and is innervated by the masticator nerve, a branch of the mandibular division of the trigeminal nerve. Posteriorly, the muscle is largely covered by the superficial lobe of the parotid gland, and buccomasseteric pathology is often initially mistaken for parotid disease.

The buccinator (*buccina*, a trumpet) muscle, the major muscle of the cheek, is located external to the buccal mucosa. It is a deep muscle of facial expression that is innervated by a branch of the facial (VII) nerve. Its main function is to compress the cheeks (i.e., during mastication, playing the trumpet, etc.). The origin of this muscle is from the alveolar processes of both the maxilla and the mandible, opposite the sockets of the molar teeth, and the anterior border of the pterygomandibular raphe. The fibers of the buccinator muscle converge toward the angle of the mouth, where they blend and insert into the orbicularis oris muscle. The pterygomandibular raphe is a thick fascial band that extends between the hamulus of the medial pterygoid plate and the posterior border of the mylohyoid ridge of the mandible. Forming the line of attachment for the buccinator and superior pharyngeal constrictor muscles, the pterygomandibular raphe is the junction of the oropharynx and oral cavity, lying between the anterior tonsillar pillar and the retromolar trigone.[16] Malignancies in the retromolar trigone

Copyright © 2003, Mosby, Inc. All rights reserved.

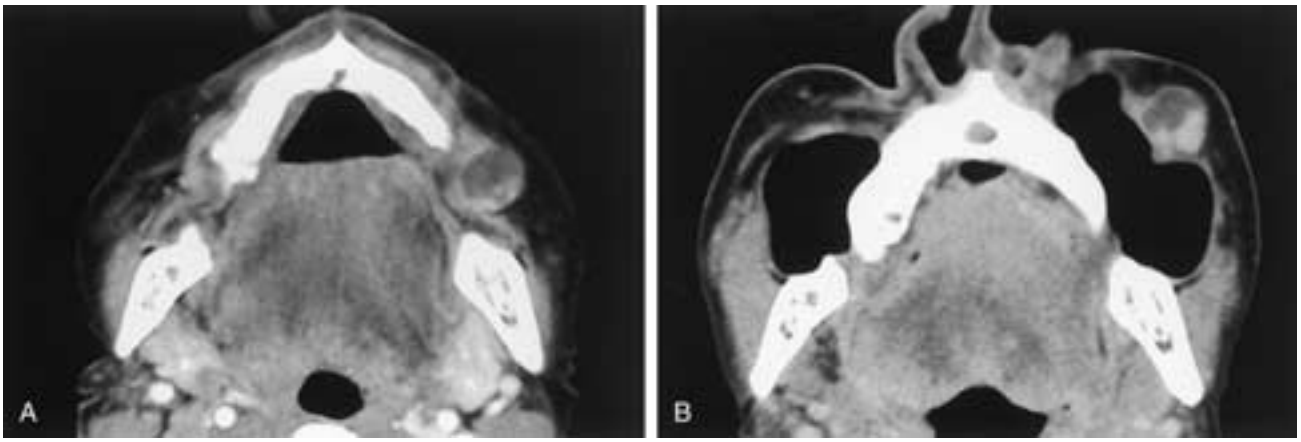

VIEW IMAGE

FIGURE 27-5 Value of the ''puffed cheek'' maneuver. **A**, Axial CT scan with the patient breathing normally. A mass has been identified, but it is difficult to determine if the mass arises from the gingival or buccal mucosa. **B**, Axial CT scan with puffed cheeks places air in the vestibule and confirms that the mass arises from the buccal mucosa. Pathologic examination revealed monomorphic adenoma.

may extend cephalad along this raphe into the upper buccomasseteric region or the suprazygomatic portion of the masticator space, or they may extend caudally to the mylohyoid muscle and along the floor of the mouth. The pterygomandibular raphe also is the anterior boundary of the prestyloid compartment of the parapharyngeal space and the masticator space (see Chapter 38). The lingual and inferior alveolar branches of the trigeminal nerve traverse the parapharyngeal space.

The buccal space, limited by the superior and inferior attachments of the buccinator muscle, is located lateral to the buccinator muscle, deep to the zygomaticus major muscle, and anterior to the mandibular ramus and masseter muscle (Fig. 27-6). It primarily contains the buccal fat pad, the major portion of which lies lateral to the buccinator, with prolongations that may extend between the muscles of mastication.[17] Four projections of fat may be identified extending peripherally from the more central fat pad. Laterally the fat follows the course of the parotid duct posteriorly to lie adjacent to the anterolateral portion of the superficial lobe of the parotid gland. Medially the buccal fat pad extends between the mandible and maxillary sinus and

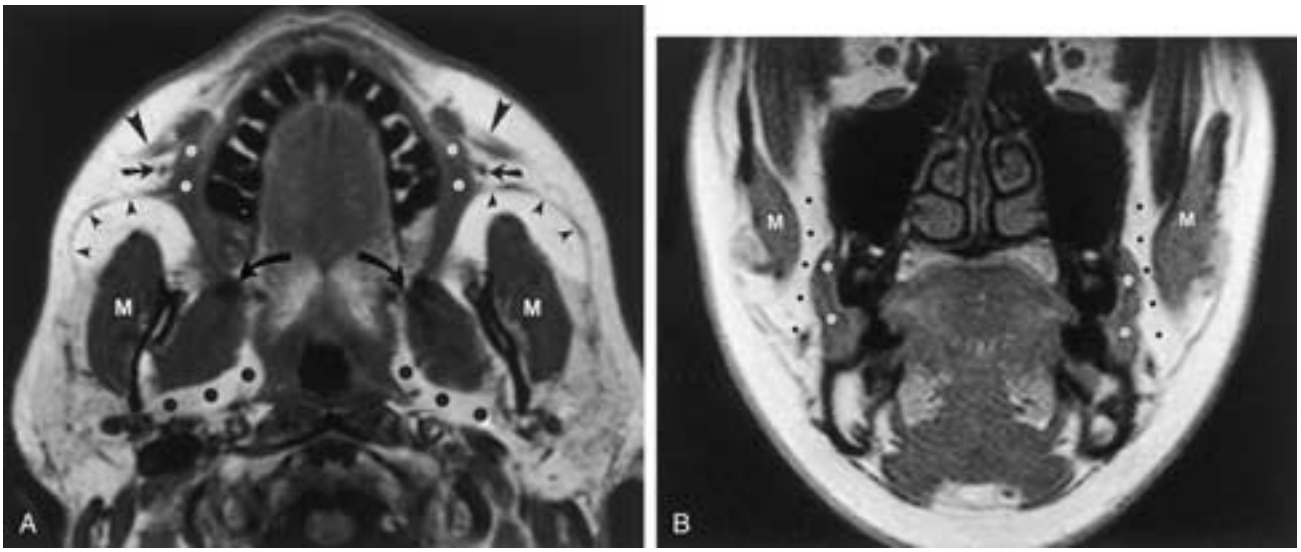

VIEW IMAGE

FIGURE 27-6 Buccomasseteric region, normal anatomy. (**A**) Axial and (**B**) coronal T1-weighted MR images demonstrate the anatomy of the buccal spaces. These fat-filled spaces lie posterior to the zygomaticus major muscles (*large arrowheads*), anterior and medial to the masseter muscles (*M*), and lateral to the buccinator muscles (*white dots*). The parotid gland ducts are well visualized on the axial image (*small arrowheads*) as they cross the buccal fat pads to pierce the buccinator muscles and open into the vestibule of the mouth opposite the second maxillary molars. The facial veins (*straight arrows* in **A**) are visualized anterior to the parotid ducts, posterior to the zygomaticus major muscles, and lateral to the buccinator muscles. The parapharyngeal space fat (*large black dots* in **A**) is also well seen, medial to the mandible and medial pterygoid muscles and lateral to the pharyngeal constrictor muscles. The region of the pterygomandibular raphe is indicated by the curved arrows in **A**. The buccal space fat is indicated by the small black dots in **B**.

Copyright © 2003, Mosby, Inc. All rights reserved.

frequently communicates with fat in the masticator space. Superiorly the temporal extensions of the buccal fat are divided into deep and superficial portions based upon their relationship to the temporalis muscle. The anterior extension of the fat pad is located superficial to the parotid duct.[18, 19] The main duct of the parotid gland (Stensen's duct) crosses the masseter muscle, courses transversely through the buccal fat pad, pierces the buccinator muscle opposite the second maxillary molar, and drains into the vestibule of the mouth (Fig. 27-6A).

The parotid duct separates the buccal space into fairly equal-sized anterior and posterior compartments. Fat in the posterior compartment reportedly differs from that in the anterior compartment, being composed of a special type of adipose tissue known as *syssarcosis* that may represent the remnants of the succatory fat pad of infants.[20] This specialized adipose tissue aids in muscular motion such as that required for opening and closing the mouth.[20] The CT attenuation of this specialized adipose tissue is reported to be less than that of fat in adjacent spaces, including the fat within the anterior compartment of the buccal space.[21]

Within the buccal space, the angular segment of the facial artery, originating from the external carotid artery, and the buccal artery, originating from the internal maxillary artery, may be identified. The angular artery extends through the buccal space to reach the nasolabial region. The buccal artery courses to the posteromedial portion of the buccal space between the medial border of the masseter muscle and the lateral border of the buccinator muscle. The facial vein is typically identified on cross-sectional images along the lateral margin of the buccinator muscle, anterior to Stenson's duct. It courses through the buccal space from the nasolabial region to the external jugular venous system and averages 3.5 mm in the transverse dimension.[21] Nerves within the buccal space, not routinely identified on cross-sectional images, include the buccal division of the facial nerve, which primarily innervates the buccinator muscle, and the buccal branch of the mandibular nerve, which innervates the mucosa deep to the buccinator muscle and the skin overlying the buccal space.

When involved by tumor or infection, the buccal space may serve as a route of spread between the mouth and the parotid gland.[22] The lack of fascial compartmentalization superiorly, inferiorly, and posteriorly permits spread of pathology (especially infections) both to and from the buccal space.[21] The buccomasseteric region is commonly affected by disease involving the masticator space, a fascially defined region that contains the muscles of mastication, portions of the mandible, the maxillary artery, and branches of the mandibular division of the trigeminal nerve (Fig. 27-7).[23, 24] Pathology of the masticator space most commonly results from dental infections involving the second and third mandibular molars (see Chapter 38).

PATHOLOGY

Congenital Anomalies

Congenital Absence of the Tongue

Extremely rare, approximately 60 cases of congenital absence of the tongue have been reported.[25, 26] Most reported cases have associated limb defects, micrognathia, and oral synechiae.[27] Reports of associated conductive hearing loss also exist, which have prompted some to suggest that audiologic examinations should be performed in all patients with aglossia/hypoglossia syndromes.[26]

Accessory Parotid Tissue

In approximately 20% of the population, accessory parotid tissue is present, usually just anterior to the parotid gland hilum and almost always above the parotid duct in the

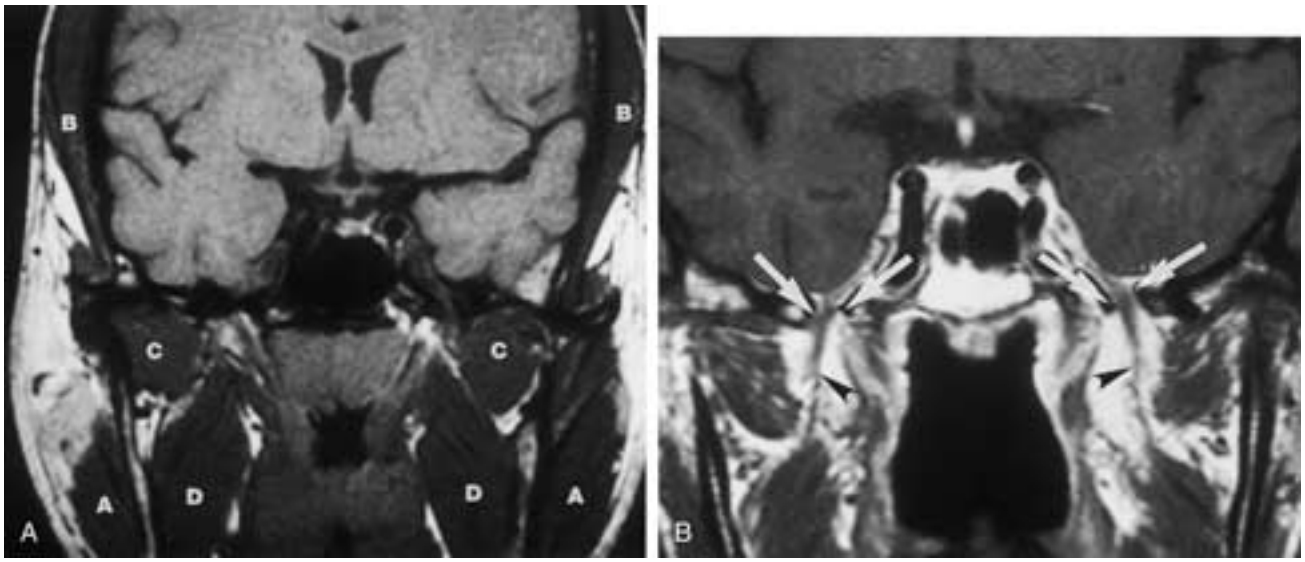

FIGURE 27-7 Masticator space, normal anatomy. **A**, Coronal T1-weighted MR image demonstrates normal muscles of mastication bilaterally. *A*, Masseter muscles; *B*, temporalis muscles; *C*, lateral pterygoid muscles; *D*, medial pterygoid muscles. **B**, Coronal T1-weighted MR image following contrast administration optimally demonstrates the mandibular nerves bilaterally (*arrowheads*) as they traverse the foramen ovale bilaterally (*arrows*).

VIEW IMAGE

Copyright © 2003, Mosby, Inc. All rights reserved.

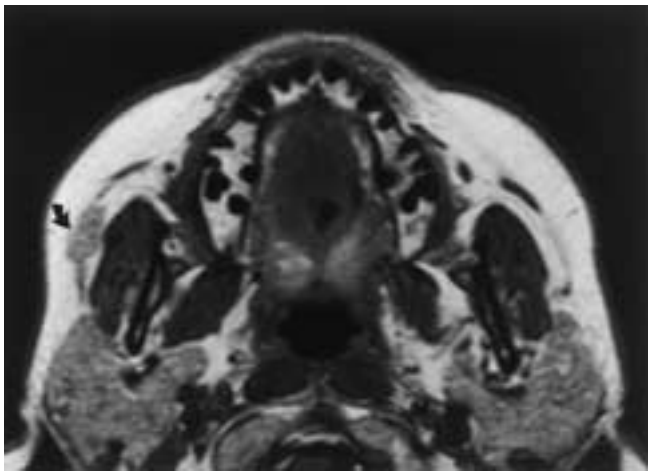

VIEW IMAGE

FIGURE 27-8 Accessory parotid tissue. Axial T1-weighted MR image. Unilateral accessory parotid tissue (*arrow*) is demonstrated overlying the masseter muscle. This tissue has the same signal intensity as tissue in the main parotid gland.

buccal space, overlying the anterior margin of the masseter muscle (Fig. 27-8). Accessory parotid tissue may be unilateral or bilateral, it drains into Stenson's duct, it is histologically and physiologically identical to tissue in the main parotid gland, and it is affected by the same pathology.[28–30] Accessory parotid tissue is reportedly identified by CT more often than by MR imaging.[21] The topic of pathology affecting parotid tissue is discussed in Chapter 39.

Digastric Muscle Anomalies

Anomalies of the anterior belly of the digastric muscle are uncommon, ranging from interdigitating fibers between the two anterior digastric muscles or between the anterior digastric and mylohyoid muscles to four separate digastric muscle bundles.[31, 32] Both bilateral and unilateral accessory anterior digastric muscles have been described, with a unilateral accessory muscle being more common.[31, 32] Hypoplasia or aplasia of one anterior belly of the digastric muscle has also been reported (Fig. 27-9).[32, 33] The importance of being familiar with various anterior digastric muscle anomalies was highlighted in Larsson and Lufkin's paper, which emphasized the risk of confusing these anomalies with masses in the floor of the mouth or enlarged submental lymph nodes.[31] Hypoplasia or aplasia may also be mistaken for denervation atrophy associated with injury to the mylohyoid nerve; however, the identification of a normal ipsilateral mylohyoid muscle bundle makes a distal V3 injury highly unlikely.[34]

Vascular Lesions

The nomenclature concerning vascular lesions of the head and neck has been a source of confusion, based neither on their cellular kinetics nor on their clinical behavior. Historically, these lesions were named for the size of the channels within the lesions and the type of fluid they contained. In an attempt to address these issues, Mulliken and Glowacki proposed a biological classification for these endothelial malformations based upon their natural history, cellular turnover, histology, and management.[35] Two major types of lesions are recognized: hemangiomas and vascular malformations. Vascular malformations are further subdivided into capillary, venous, arterial, and lymphatic malformations. Although imaging has been used to classify vascular lesions into one of these categories, the more pertinent issue from a treatment standpoint is their classification as either high-flow or low-flow lesions. Malformations with an arterial component are considered high-flow lesions, while those lacking an arterial component are considered low-flow lesions.[36] This topic is discussed further in Chapter 35.

Hemangiomas

Hemangiomas are neoplastic and exhibit increased proliferation and turnover of endothelial cells, mast cells, fibroblasts, and macrophages.[37] They are the most common tumors of the head and neck in infancy and childhood, accounting for 7% to 12% of all benign soft-tissue tumors.[38, 39] Using the classification proposed by Mulliken and Glowacki, the term *hemangioma* should be reserved for those lesions that present in early infancy, enlarge rapidly, and involute by adolescence.[35, 40, 41]

During their proliferative phase, hemangiomas are classified as high-flow lesions that are well circumscribed and angiographically exhibit a lobular pattern of intense persistent tissue staining.[42] The frequent arteriovenous shunting and high flow in these lesions may not permit distinction from high-flow vascular malformations. On MR imaging, the solid component of the hemangioma demonstrates signal intensity isointense or slightly hyperintense to muscle on T1-weighted images and higher signal intensity on progressively more heavily weighted T2-weighted images (Fig. 27-10). Enhancement following contrast administration is typical.[43]

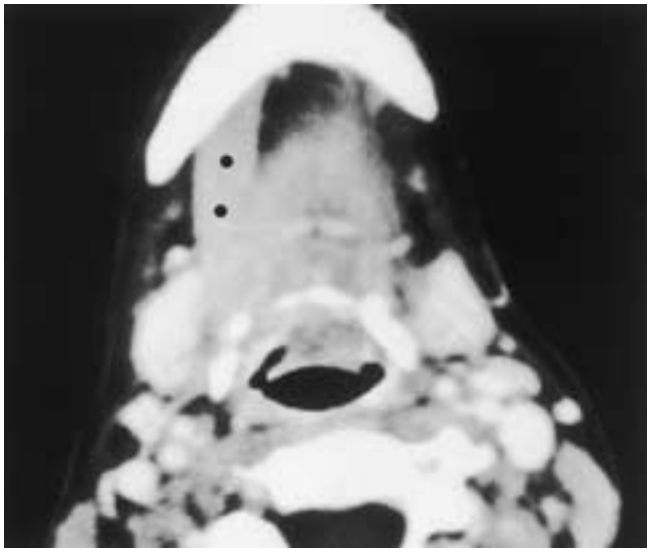

FIGURE 27-9 Digastric muscle aplasia. Axial CT scan demonstrates aplasia of the left anterior belly of the digastric muscle. The right digastric muscle is indicated by the dots.

VIEW IMAGE

Copyright © 2003, Mosby, Inc. All rights reserved.

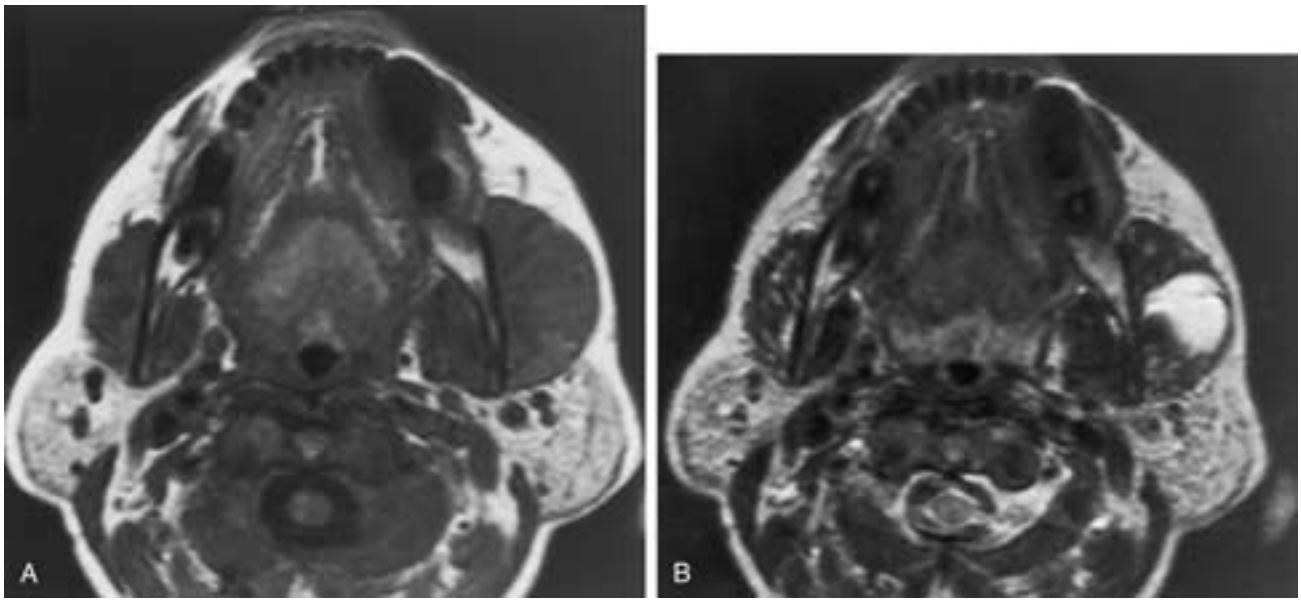

VIEW IMAGE

FIGURE 27-10 Hemangioma. (**A**) Axial T1-weighted and (**B**) axial T2-weighted MR images. Enlargement of the left masseter muscle without definition of the isointense mass is demonstrated on the T1-weighted MR image in **A**. The hemangioma becomes hyperintense on the T2-weighted image in **B**.

Vascular Malformations

In contrast to hemangiomas, vascular malformations are not tumors, but rather true congenital vascular anomalies that are always present at birth, although they may not manifest clinically until late infancy or early childhood. The proliferation and turnover characteristics of the endothelial cells are normal. These lesions demonstrate slow, steady growth commensurate with the growth of the child, and they neither regress nor involute. Skeletal changes are more commonly associated with vascular malformations (35%) than with hemangiomas.[44] Rapid enlargement of these lesions is reported to occur in association with trauma, infection, or endocrine changes (i.e., in puberty and pregnancy).[45]

Vascular malformations are classified, based upon the predominant type of anomalous vessel involved, into capillary, venous, arterial, and lymphatic malformations.[37, 40] A variety of therapies have been employed for the treatment of vascular malformations and rapidly enlarging hemangiomas, with varying degrees of success. These include steroid administration, laser photocoagulation, sclerotherapy, embolization, subcutaneous interferon, and surgical resection.[46–60]

Capillary Malformations

These lesions were previously referred to as port-wine stains, capillary hemangiomas, and nevus flammeus.[61] They are low-flow lesions and may be associated with the distribution of the trigeminal nerve as one component of the Sturge-Weber syndrome, which also involves an underlying vascular anomaly of the choroid plexus and leptomeninges. The underlying cheek, lip, and gingiva may be affected, and gingival hypertrophy or chronic hemorrhage may be associated with these capillary malformations.

Venous Malformations

These lesions, occasionally termed *cavernous hemangiomas*, unlike true hemangiomas, may involve bone and do not involute.[61] They are the most common ones to affect the oral cavity and share many imaging features with subcutaneous hemangiomas. Venous malformations may attain enormous size and cause airway compromise when located in the extracranial head and neck, and although they are predominantly soft-tissue masses, they may infiltrate deeply along fascial planes and rarely may be entirely intramuscular.[62, 63] Of all the skeletal muscle hemangiomas-venous malformations, approximately 14% occur in the head and neck region, with the masseter muscle being most commonly affected, followed by the trapezius and sternocleidomastoid muscles.[64, 65] These lesions typically present as muscle-density masses on CT and manifest variable patterns of enhancement.[22] Like their capillary counterparts, venous malformations are low-flow lesions supplied by small arteries. On CT they may not demonstrate sufficient enhancement to enable separation of their margins from surrounding muscles, while angiographically one may not be able to identify their arterial supply.[66] On MR imaging, these lesions may appear very similar to deep hemangiomas because they are isointense or hyperintense to muscle on T1-weighted images, hyperintense on T2-weighted images, and typically enhance following the administration of contrast (Fig. 27-11). The identification of discrete areas of homogeneous high signal intensity, representing venous lakes, or the presence of phleboliths may be extremely helpful in suggesting the diagnosis of a venous malformation (Fig. 27-12).[39, 66, 67] Venous malformations are encountered in the blue rubber bleb nevus syndrome and are also associated with multiple enchondromas in Maffucci's syndrome.[68]

Arterial Malformations

These lesions are high-flow malformations that result from abnormal blood vessel morphogenesis. Arteriovenous malformations and fistulae are included in this category (Fig. 27-13). The head and neck region is considered one of

Copyright © 2003, Mosby, Inc. All rights reserved.

the more common sites for congenital arterial malformations, although they are uncommonly encountered within the oral cavity proper.[1] Angiographically, arterial malformations are characterized by rapid flow and enlarged, tortuous arteries and draining veins. Parenchymal staining is unusual. On MR imaging, the enlarged arterial components appear as flow voids on T1-weighted and T2-weighted images.

A subgroup of patients demonstrates combined vascular malformations that share features of both high-flow and low-flow lesions.[41] Capillary-venous, veno-lymphatic, and arteriovenous malformations have all been described. These lesions may be highly invasive, become enormous in size, and may be resistant to all forms of therapy, tending to involve the deep musculature and subcutaneous tissues.[40] On MR imaging these lesions demonstrate serpiginous flow voids, characteristic of an arterial malformation, as well as a soft-tissue infiltrating component typical of a venous malformation (Fig. 27-14).[40]

Lymphatic Malformations (Lymphangiomas)

Although the vast majority of lymphatic malformations are congenital in origin, some acquired lesions, presenting later in life, have been reported in association with tumors, trauma, infection, or previous surgical procedures (iatrogenic).[69, 70] Lymphatic malformations are classified, based on their clinical and histologic characteristics, into four categories: (1) capillary lymphangiomas, (2) cavernous lymphangiomas, (3) cystic lymphangiomas (hygromas), and (4) lymphangioma-hemangiomas.[69, 71] This topic is discussed further in Chapter 35.

Capillary lymphangiomas are cutaneous lesions that commonly affect the oral region, appearing as small, wart-like excrescences on the skin or mucous membranes. The simplex variety is confined to the epidermis and superficial dermis, although the circumscriptum variety can extend into deeper layers of the dermis.[69, 71]

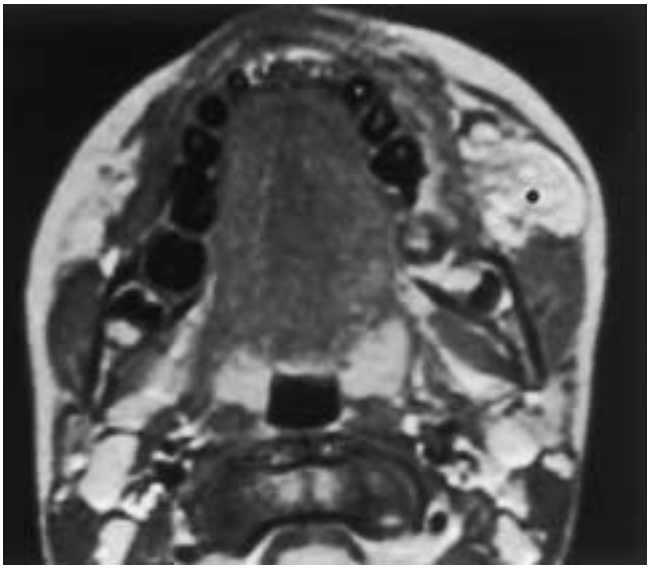

VIEW IMAGE

FIGURE 27-11 Venous malformation. Proton density MR image demonstrates a discrete, mildly heterogeneous, high signal intensity mass (*dot*) within the left buccal space immediately anterior to the left masseter muscle.

Cavernous lymphangiomas affect the subcutaneous tissues and may extend deeply into underlying muscles. They are usually diagnosed within the first months of life and commonly affect the oral cavity, neck, and tongue.[69, 71] These lesions may be subclassified into loose and compact forms. The loose variety is most often encountered in the mucous membranes of the lips, cheeks, and floor of the mouth, and the compact form more commonly affects the tongue, where the surrounding structures are more muscular.[69] There are isolated reports of lymphangiomas, probably of the cavernous variety, involving the masseter muscle.[72] Diffuse lymphangiomas of the tongue are usually bilateral (Fig. 27-15), may produce macroglossia, and lead to a variety of dentoalveolar complications, although respiratory problems seem to be rare.[73]

Cystic lymphangiomas (hygromas) are the lesions that most often present for imaging. The vast majority of these lesions are encountered in the cervical region, with a predilection for the left posterior neck.[69] When they extend to involve the floor of the mouth, sublingual and submandibular regions, or the tongue, cystic hygromas may displace the soft tissues sufficiently posteriorly into the oropharynx to obstruct both breathing and swallowing.[69] Although these lesions tend to enlarge slowly, they may suddenly increase in size secondary to trauma or hemorrhage or in association with a viral infection when large quantities of lymphatic fluid are produced from lymphoid follicles in the cyst wall.[74]

On imaging studies, cystic hygromas appear as large, single, or multiseptated, heterogeneous fluid-filled masses. They are of low density on CT, are usually poorly circumscribed, and demonstrate variable enhancement of the septations following contrast administration (Fig. 27-16).[75] At times it may be difficult to separate these lesions from surrounding soft-tissue structures of similar attenuation on CT examinations.[76] Multiple fluid-fluid levels may occur in the presence of hemorrhage.[77] On MR imaging, cystic hygromas typically manifest a signal intensity that is hypointense or isointense to muscle on T1-weighted images and a high signal intensity, greater than that of fat, on T2-weighted images (Fig. 27-17).[76, 78] Occasionally, T1-weighted hyperintensity may be present in association with clotted blood, and most cystic hygromas have a signal intensity greater than that of CSF on both T1-weighted and T2-weighted sequences, suggesting the presence of proteinaceous fluid that may contain subacute blood or lipid components.[78, 79] Focal inhomogeneities, corresponding to fibrous septae, are identified in many patients (Fig. 27-18). Contrast-enhanced MR imaging usually demonstrates enhancement of the cyst wall and septae, providing clearer definition of the capsule and septae than do the noncontrast images.[78]

Lymphangioma–hemangiomas (diffuse systemic lymphangiomas) are rare and not well described in discussions of lymphatic malformations.[69] They have not been reported in the oral cavity.

Dermoid Cysts

Dermoid cysts are the least common of the congenital neck lesions, accounting for only 7% of all cysts in this location.[80] Despite Meyer's detailed classification of these lesions into epidermoid, dermoid, and teratoid forms, the term *dermoid cyst* is commonly used in reference to all three types of lesions without regard to their differing histolo-

Copyright © 2003, Mosby, Inc. All rights reserved.

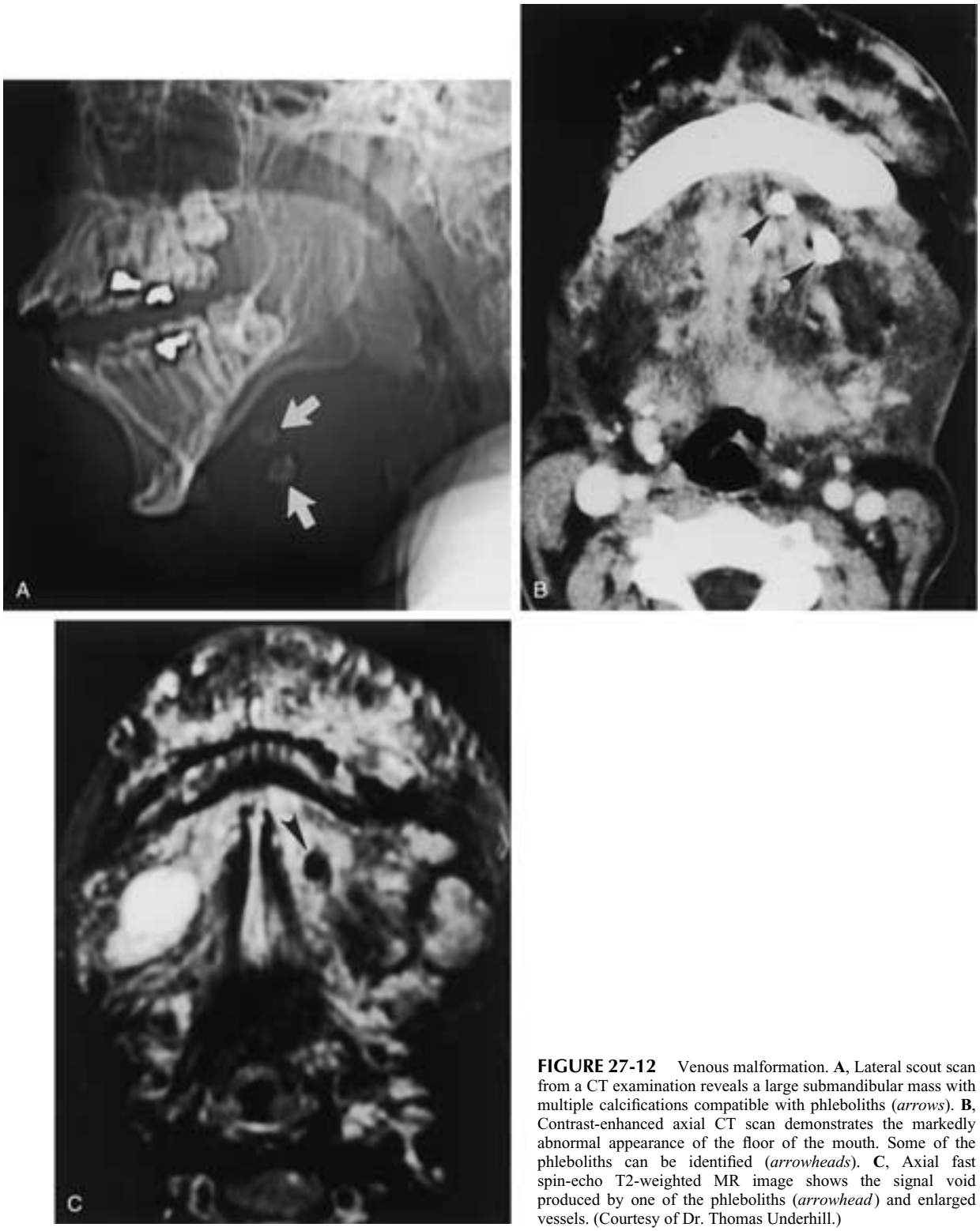

FIGURE 27-12 Venous malformation. **A**, Lateral scout scan from a CT examination reveals a large submandibular mass with multiple calcifications compatible with phleboliths (*arrows*). **B**, Contrast-enhanced axial CT scan demonstrates the markedly abnormal appearance of the floor of the mouth. Some of the phleboliths can be identified (*arrowheads*). **C**, Axial fast spin-echo T2-weighted MR image shows the signal void produced by one of the phleboliths (*arrowhead*) and enlarged vessels. (Courtesy of Dr. Thomas Underhill.)

VIEW IMAGE

gies.[81] This topic is discussed further in Chapter 35. A histologic distinction should be made between epidermoid cysts and dermoid/teratoid cysts because the latter two cysts have malignant potential, whereas epidermoid cysts do not.[82]

The most popular theory regarding the etiology of these lesions suggests that they are derived from epithelial rests that become enclaved during midline closure of the first (mandibular) and second (hyoid) branchial arches.[83] This theory may help to explain the simultaneous occurrence of sublingual and submental cysts. A case of a dermoid cyst of the floor of the mouth and a coexisting gastric choristoma has also been reported.[84]

When they occur in the oral cavity, dermoid cysts most

Copyright © 2003, Mosby, Inc. All rights reserved.

commonly involve the floor of the mouth (sublingual, submental, or submandibular regions), although other sites also have been reported including the lips, tongue, and buccal mucosa.[83, 85–90] The sublingual location is reported to be the most common (52%), followed by the submental (26%) and submandibular (6%) regions. The remaining 16% involve more than one location.[82] Extracapsular excision of oral cavity cysts is performed by either an intraoral or an external approach, depending upon the relationship of the cyst to the mylohyoid muscle.[82, 91] For those cysts that lie above the mylohyoid muscle (sublingual), an intraoral approach is preferable because it avoids a conspicuous scar, preserves the mylohyoid muscle, and is associated with a shorter recovery time. Those lesions that lie inferior to the mylohyoid muscle (submental and submandibular cysts) must usually be removed via an external approach. Therefore, imaging localization of the cyst in relation to the mylohyoid muscle is extremely helpful for appropriate surgical planning. Sagittal and especially coronal imaging are useful in this regard.[91] These lesions can occur either in the midline or just off the midline.

On CT, simple (epidermoid) dermoid cysts typically appear as low-density, well-circumscribed, thin-walled, unilocular masses that are less dense than muscle (Fig.

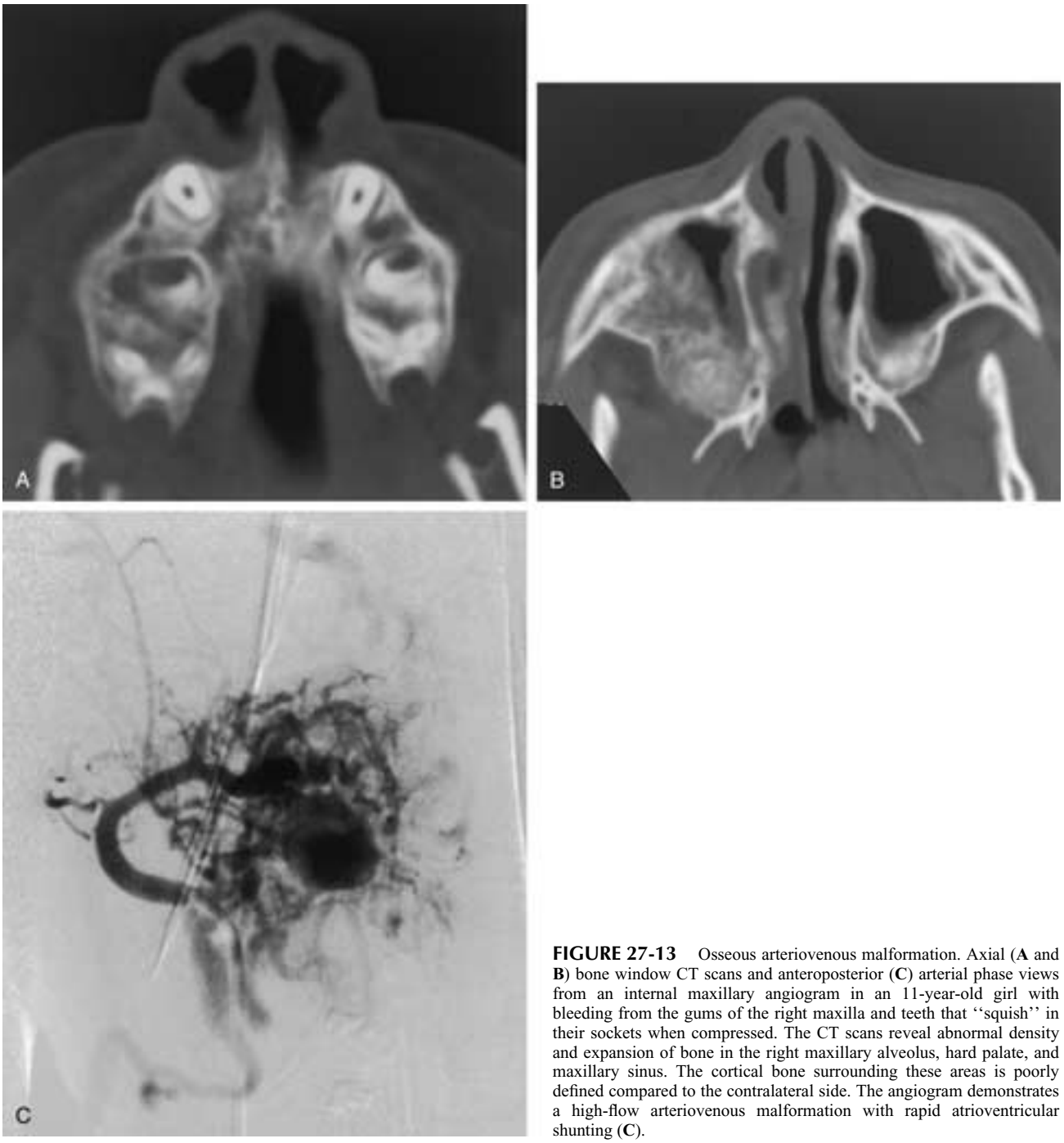

FIGURE 27-13 Osseous arteriovenous malformation. Axial (**A** and **B**) bone window CT scans and anteroposterior (**C**) arterial phase views from an internal maxillary angiogram in an 11-year-old girl with bleeding from the gums of the right maxilla and teeth that ''squish'' in their sockets when compressed. The CT scans reveal abnormal density and expansion of bone in the right maxillary alveolus, hard palate, and maxillary sinus. The cortical bone surrounding these areas is poorly defined compared to the contralateral side. The angiogram demonstrates a high-flow arteriovenous malformation with rapid atrioventricular shunting (**C**).

VIEW IMAGE

Copyright © 2003, Mosby, Inc. All rights reserved.

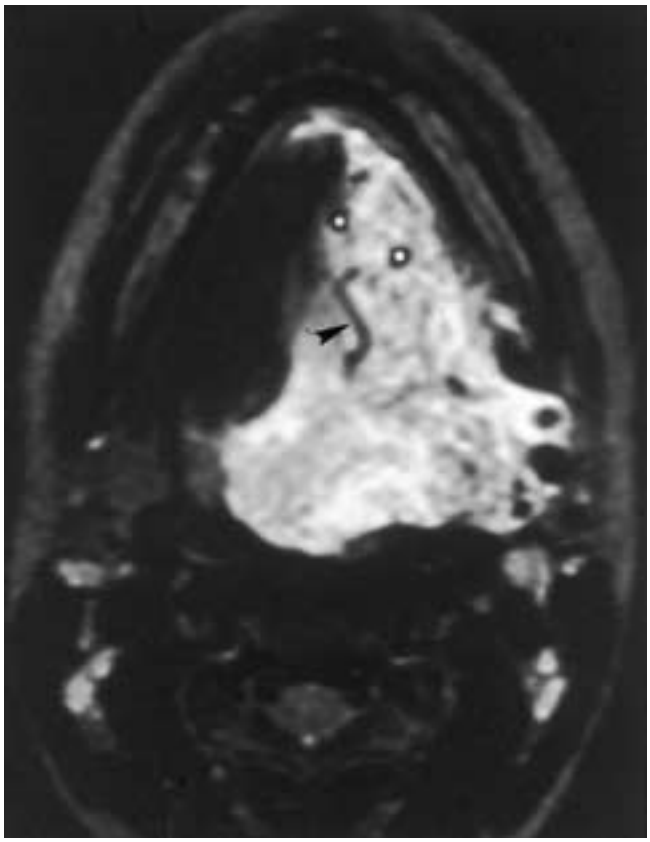

VIEW IMAGE

FIGURE 27-14 Combined vascular malformation. Axial proton density MR image demonstrates a large, invasive vascular malformation possessing features consistent with both arterial and venous components. Vessels are seen as serpiginous signal voids (*arrowhead*). Circular signal voids (*white dots*) may represent vessels or phleboliths. A large, solid mass component demonstrates high signal intensity and marked heterogeneity involving the left half of the tongue, crossing the midline. (Courtesy of Dr. Edward Kassel.)

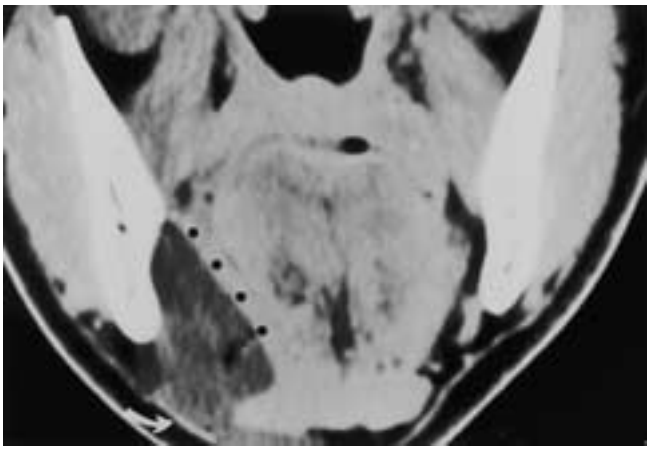

VIEW IMAGE

FIGURE 27-16 Lymphangioma. Coronal contrast-enhanced CT scan demonstrates a lymphangioma in the right submandibular space elevating and displacing the right mylohyoid muscle (*black dots*). The lesion is contained by fibers of the platysma muscle (*white arrow*).

27-19). The wall of the cyst usually enhances following contrast administration, and in the absence of fat globules, epidermoid and dermoid cysts are indistinguishable.[92] On MR imaging, epidermoid cysts are of low signal intensity on T1-weighted images and of high signal intensity on T2-weighted images, reflecting their fluid content. When located within the sublingual space, these lesions may be impossible to distinguish from other cystic lesions, such as a simple ranula, on the basis of imaging criteria alone.

Compound dermoid cysts have a more variable appearance, depending upon their fat content. On CT they may appear filled with homogeneous low-attenuation (0 to 18 HU) material or the central cavity may demonstrate a fat-fluid level or a single fat globule (Figs. 27-20 and 27-21). The identification of multiple discernible low-attenuation

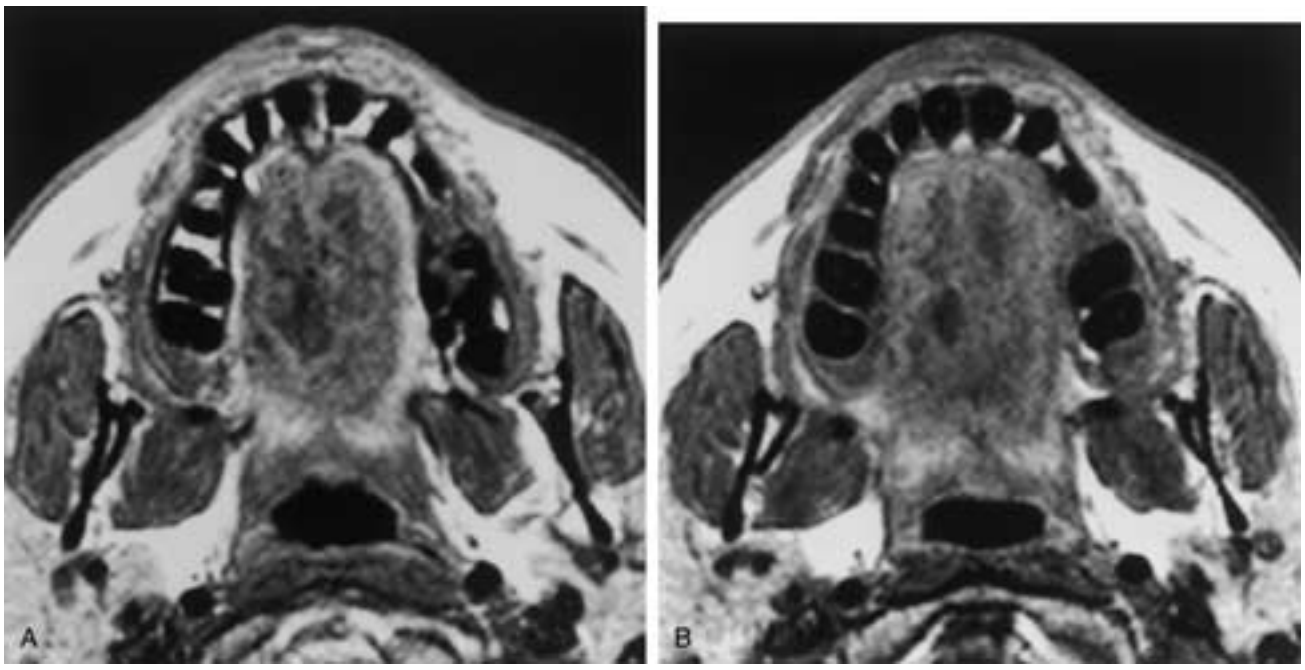

VIEW IMAGE

FIGURE 27-15 Diffuse lymphangioma of the tongue. **A** and **B**, Axial T1-weighted MR images demonstrate poorly defined multiple areas of hypointensity bilaterally within the tongue.

Copyright © 2003, Mosby, Inc. All rights reserved.

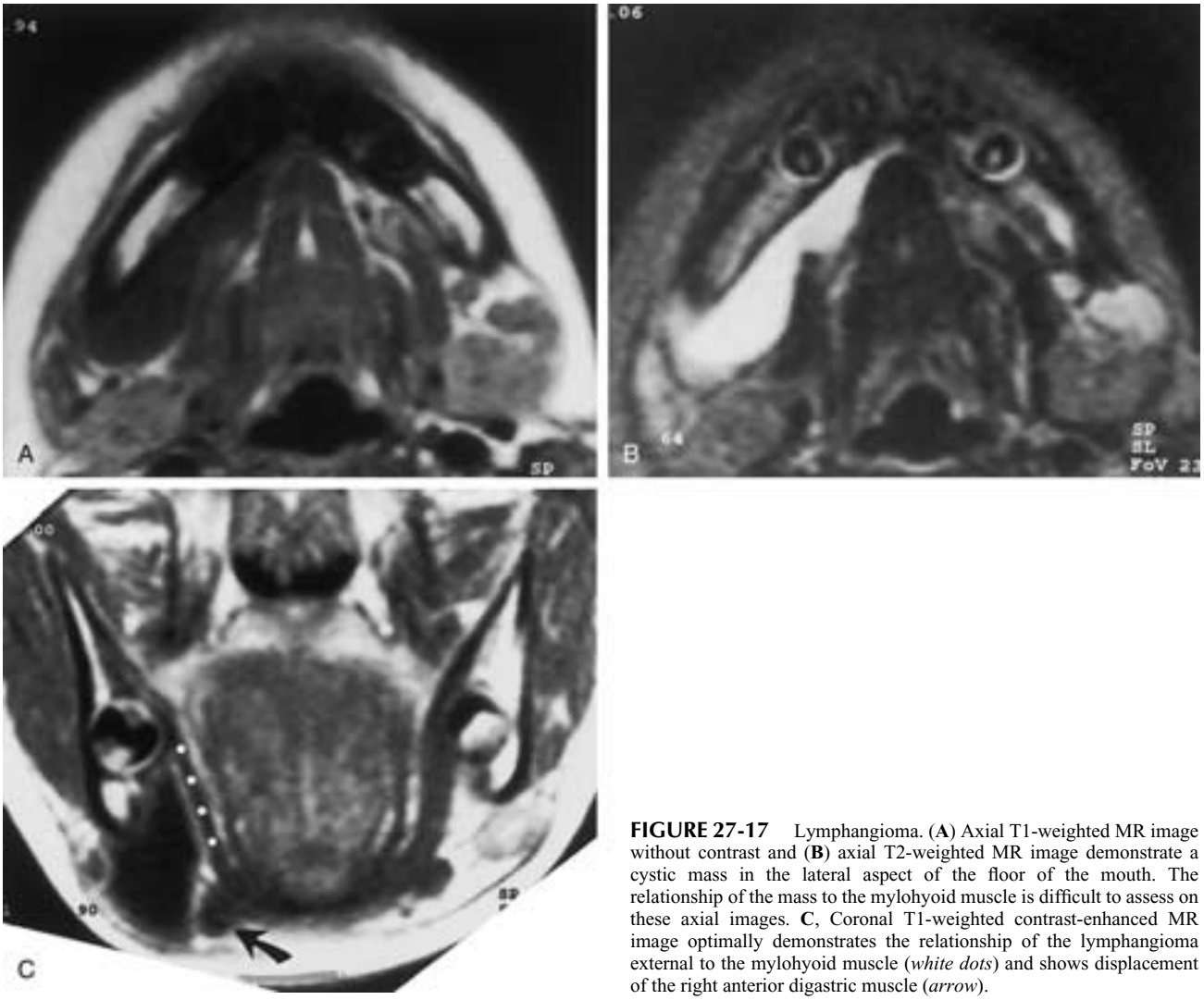

FIGURE 27-17 Lymphangioma. (**A**) Axial T1-weighted MR image without contrast and (**B**) axial T2-weighted MR image demonstrate a cystic mass in the lateral aspect of the floor of the mouth. The relationship of the mass to the mylohyoid muscle is difficult to assess on these axial images. **C**, Coronal T1-weighted contrast-enhanced MR image optimally demonstrates the relationship of the lymphangioma external to the mylohyoid muscle (*white dots*) and shows displacement of the right anterior digastric muscle (*arrow*).

VIEW IMAGE

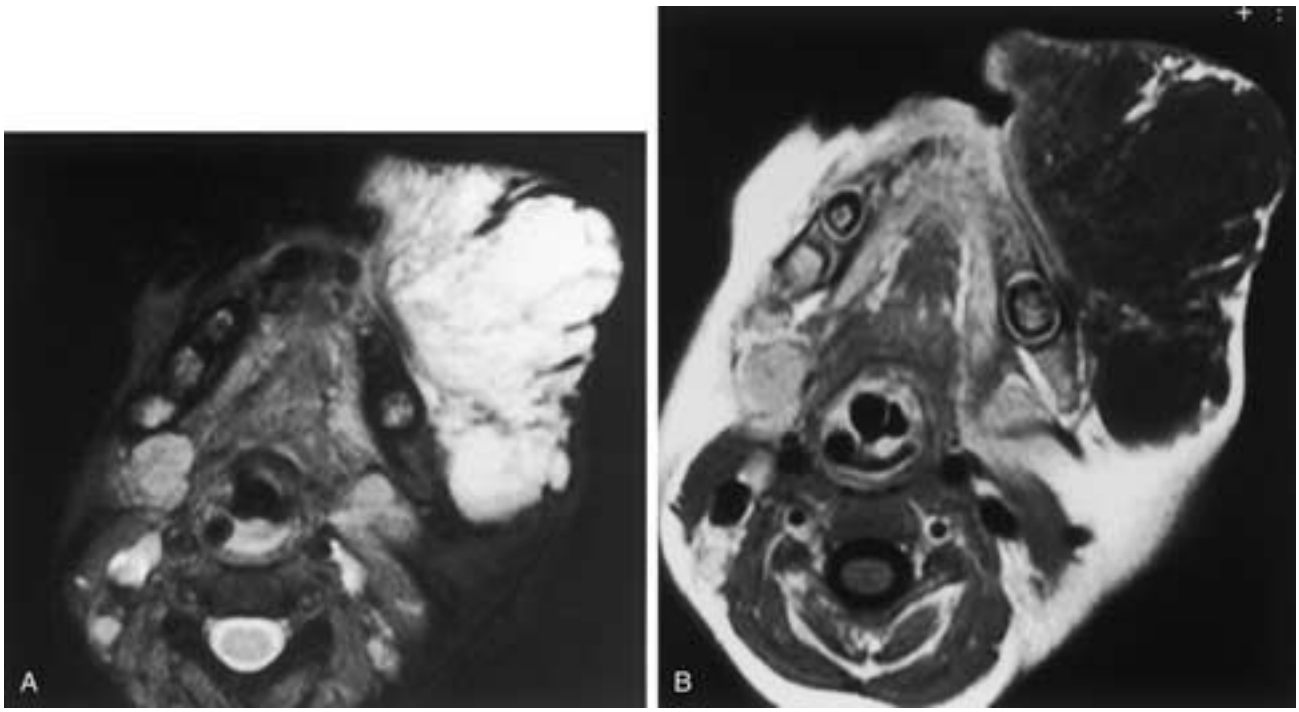

FIGURE 27-18 Lymphangioma. Axial T2-weighted (**A**) and T1-weighted (**B**) images following contrast enhancement. These images demonstrate a large subcutaneous lymphangioma involving the left buccal region. The lesion is isointense to muscle on the T1-weighted image (**B**), is markedly hyperintense on the T2-weighted image (**A**), and demonstrates no enhancement following contrast administration.

VIEW IMAGE

Copyright © 2003, Mosby, Inc. All rights reserved.

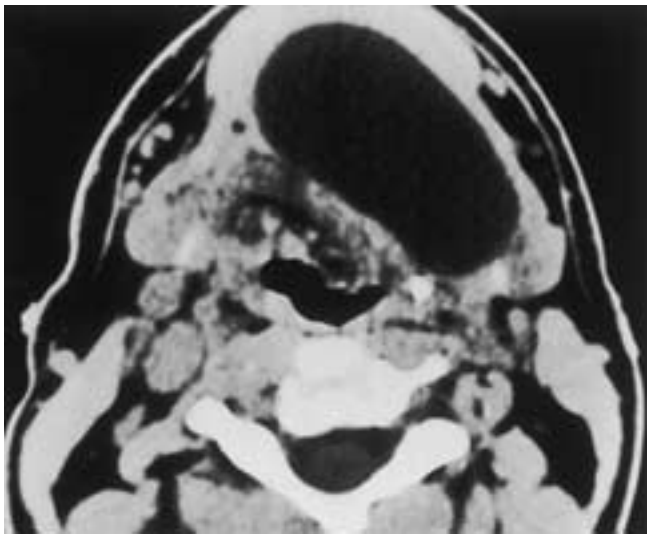

VIEW IMAGE

FIGURE 27-19 Epidermoid cyst. Axial CT scan reveals a large, unilocular, hypodense cystic lesion in the floor of the mouth. From an imaging standpoint, this appearance is consistent with either an epidermoid or a dermoid cyst.

nodules, due to coalescence of fat globules within the fluid matrix, has a ''sack-of-marbles'' appearance and is virtually pathognomonic for a compound dermoid cyst in this location (Fig. 27-22).[79] On MR studies, compound dermoid cysts may be either isointense or hyperintense to muscle on T1-weighted images, depending upon their lipid content (Figs. 27-23 and 27-24).[91] They are typically hyperintense on T2-weighted sequences, and the use of contrast permits determination of the thickness of the cyst wall, typically 2 to 6 mm.[91]

Thyroglossal Duct Cysts

Thyroglossal duct cysts (TGDCs) are the most common nonodontogenic cysts occurring in the neck, and they account for 70% of congenital neck abnormalities.[1, 93] This

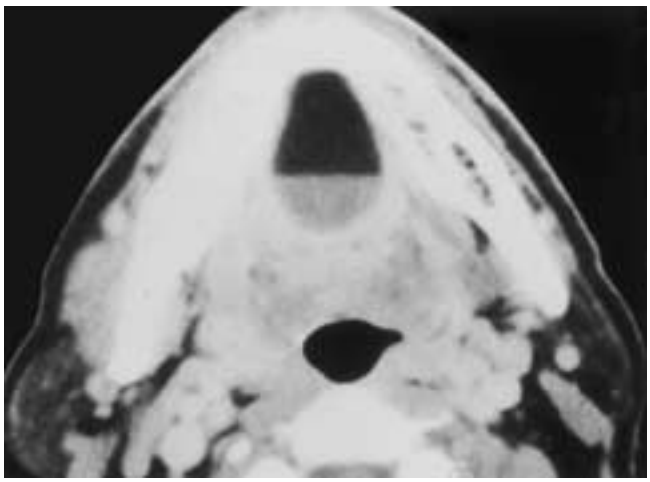

VIEW IMAGE

FIGURE 27-20 Dermoid cyst. Axial contrast-enhanced CT scan demonstrates a midline cystic lesion with a fat-fluid level and peripheral rim enhancement. The presence of fat is virtually pathognomonic for a true dermoid cyst.

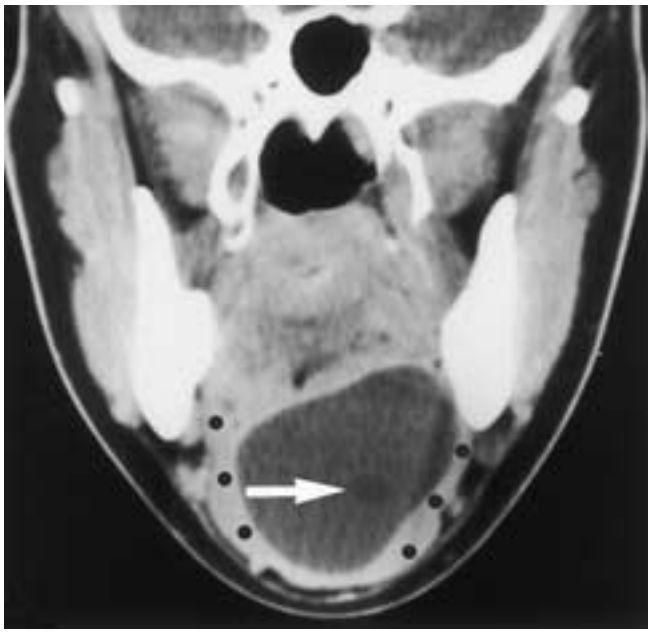

FIGURE 27-21 Dermoid cyst. Contrast-enhanced coronal CT image demonstrates a hypoattenuating mass in the floor of the mouth. A fat globule (*arrow*) is demonstrated, ensuring the diagnosis of a dermoid cyst. The relationship of the cyst to the mylohyoid muscles (*dots*) is well seen.

VIEW IMAGE

topic is discussed further in Chapter 35. These lesions may occur anywhere along the course of the thyroglossal duct or they may involve the entire length of the duct, from the base of the tongue (foramen cecum) to the thyroid gland (Figs.

FIGURE 27-22 Dermoid cyst. Contrast-enhanced axial CT scans demonstrate a large lesion in the floor of the mouth that is well circumscribed and exhibits peripheral enhancement. Multiple fat globules are identified, producing a ''sack-of-marbles'' appearance.

VIEW IMAGE

Copyright © 2003, Mosby, Inc. All rights reserved.

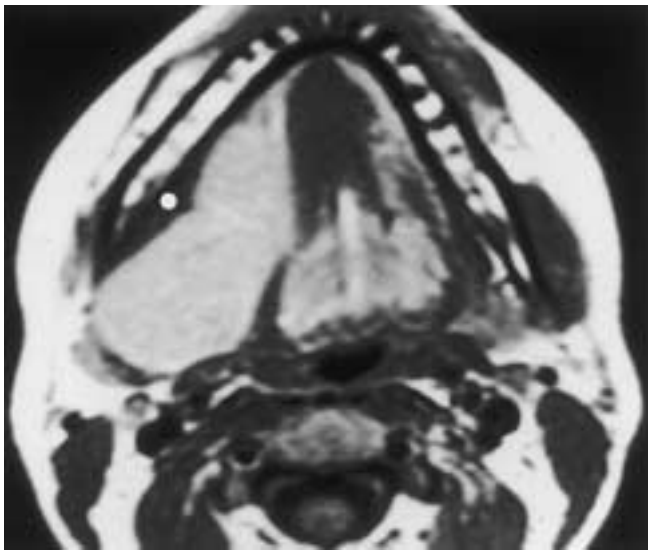

VIEW IMAGE

FIGURE 27-23 Dermoid cyst. Axial T1-weighted MR image reveals the lesion to be of high signal intensity but of slightly less intensity than that of the subcutaneous fat. The relationship of this lesion to the right mylohyoid muscle (*white dot*) is clearly established. The fatty lingual septum is displaced slightly to the left of midline. This lesion involves much of the right sublingual space, dissecting posteriorly to involve the deep aspect of the right submandibular space.

27-25 and 27-26). If any portion of the thyroglossal duct persists, secretions from the epithelial lining (likely secondary to repeated local trauma or inflammation) may give rise to a TGDC. One diagnostic pearl for the clinical identification of these lesions is their upward movement when the tongue is protruded, a reflection of the duct origin at the foramen cecum.[79] Approximately 65% of TGDCs are infrahyoid in location, in the region of the thyrohyoid membrane, 15% are at the level of the hyoid bone, and the remaining 20% are suprahyoid.[1] In contrast to the typically paramedian infrahyoid TGDC, suprahyoid TGDCs are commonly midline, located between the bellies of the anterior digastric muscles (Fig. 27-25). They are frequently embedded within or lie below the mylohyoid sling in the submental region, and rarely they may present as masses within the floor of the mouth.[94] From 1% to 2% of TGDCs are reported to be intralingual.[95]

On CT, TGDCs are usually thin-walled, well-circumscribed, unilocular cystic lesions, 2 to 4 cm in diameter, that exhibit capsular enhancement (Fig. 27-25).[96] Occasionally, a TGDC may be septated, and this should be viewed with some caution. Figure 27-27 demonstrates what appears to be a simple septated TGDC just below the level of the hyoid bone on CT. However, MR imaging reveals differing signal intensities in the two compartments, with a solid tumor in the posterior compartment that proved to be papillary carcinoma.

On MR imaging, TGDCs exhibit low to intermediate signal intensity on T1-weighted images, depending on the protein content of the cyst, and are of high signal intensity on T2-weighted images. The adjacent soft tissues and fascial planes are normal unless infection, which is reported in approximately 60% of patients, is present.[97] In the presence of infection, thickening of the overlying skin and/or platysma muscle and induration of subcutaneous fat may be demonstrated, making it extremely difficult to differentiate the infected TGDC from malignant submental adenopathy.[96] In this regard, close attention to the appearance of the cyst wall and clinical information may be very helpful (Fig. 27-28).

Less than 1% of thyroglossal duct abnormalities are associated with coexisting carcinoma, papillary carcinoma being the most common (80%). Approximately 95% of TGD carcinomas are thyrogenic and 5% are squamous in nature, appearing more aggressive and occurring in an older age group.[98] Virtually every type of thyroid malignancy has been reported in association with these cysts, which arise from ectopic rests of thyroid tissue within the duct walls, not from the duct itself. Only medullary carcinoma has not been reported within a TGDC, as these carcinomas are unique in that they develop from the ultimobranchial bodies and not from the thyroid anlage.[99–104] Most of these thyroid carcinomas are rarely suspected preoperatively.[105]

Lingual Thyroid

Failure of the thyroid gland to descend from the foramen cecum to the lower neck results in residual thyroid tissue along the thyroglossal duct tract. In autopsy studies, ectopic thyroid tissue less than 3 mm in size has been reported in 10% of the normal population.[1] Ectopic thyroid tissue, which may or may not be functioning, has a high female/male ratio (7:1), which is attributed to hormonal disturbances in females during puberty and pregnancy.[106] The tongue is the most common location, accounting for 90% of ectopic thyroid tissue, most of which occurs in the midline dorsum of the tongue, although rare cases of involvement of the entire tongue have been reported.[107, 108] Ectopic thyroid tissue is typically asymptomatic and is discovered incidentally; however, symptoms of dysphagia, dysphonia, stridor, dyspnea, hemorrhage, and hoarseness may occur.[109–112] Hypothyroidism and cretinism have both been reported in patients with lingual thyroid tissue.[113, 114] Malignancy in lingual thyroid tissue is rare.[115] In a large percentage of patients (70% to 80%), no other functioning thyroid tissue is present, and surgical excision would render the patient permanently hypothyroid. For this reason, if surgery is contemplated, iodine-123 radionuclide scanning should be performed to establish the presence or absence or normal functioning thyroid tissue within the neck. This study will also serve to establish the presence of functioning lingual thyroid tissue.

On noncontrast CT, lingual thyroid tissue usually presents as a hyperdense mass within the intrinsic musculature of the tongue and enhances avidly, typically in a homogeneous fashion (Fig. 27-29).[3, 112] Markedly heterogeneous contrast enhancement has been reported in a patient with goitrous changes and thyroiditis affecting the lingual thyroid tissue.[111] On MR imaging, lingual thyroid tissue is isointense or hyperintense to the tongue musculature on both T1-weighted and T2-weighted sequences and strongly enhances following contrast administration.[110] The imaging characteristics of pathologic lingual thyroid tissue are similar to those of pathology involving the thyroid gland (multinodular goiter, thyroiditis, carcinoma, etc.) (Fig. 27-30).

Copyright © 2003, Mosby, Inc. All rights reserved.

Lingual Artery Aneurysms

Aneurysms of the external carotid artery branches are distinctly uncommon, with the superficial temporal artery being most often affected as a result of trauma.[116] Aneurysms of the lingual artery, on the other hand, are uncommon.[117–120] Rare reports of presumed congenital lingual artery aneurysms (absence of previous trauma) exist.[118] In one report, a patient with bilateral lingual artery aneurysms presented with ecchymosis of the neck following spontaneous rupture of one of the aneurysms.[120] Batten and Heeneman reported a case of a 2 × 3 cm traumatic facial artery (mandibular branch) aneurysm presenting as a pulsatile mass in the submental region following uncomplicated mandibular alveoplasty.[121] CT may suggest the diagnosis but may not be able to distinguish an aneurysm from other vascular lesions, and the aneurysm's appearance is variable, depending upon the degree of thrombosis (Fig. 27-31).[120] Although the use of MR imaging has not been reported, its ability to demonstrate vascular structures as flow voids may prove useful in the evaluation of these lesions, as might MR angiography.

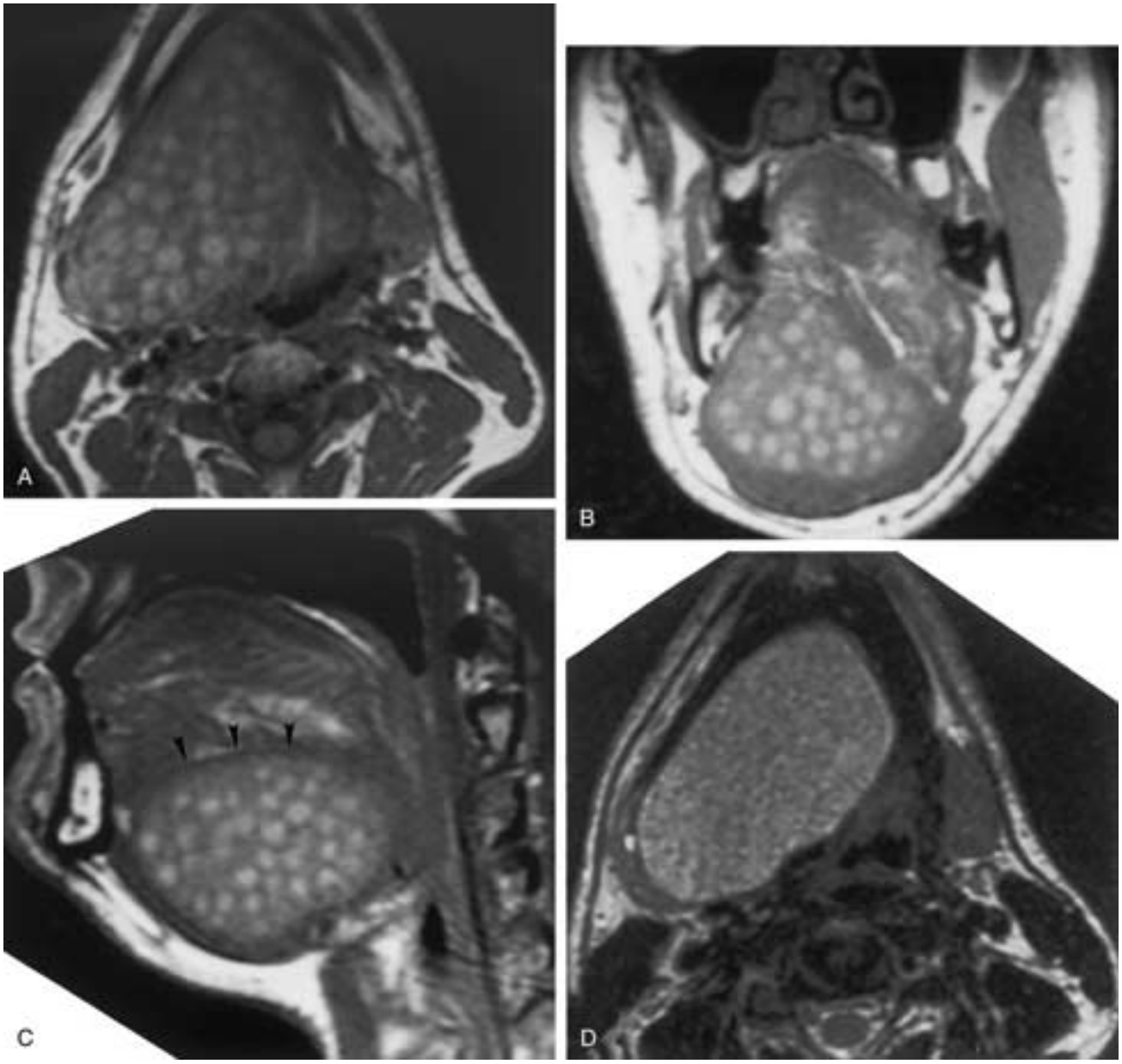

VIEW IMAGE

FIGURE 27-24 Dermoid cyst. T1-weighted MR images in the axial (**A**), coronal (**B**), and sagittal (**C**) planes demonstrate a large sublingual dermoid cyst characterized by multiple fat globules, which are easily identified by their high signal intensity. The relationship of this lesion to the floor of the mouth musculature is well demonstrated on the sagittal image (**C**), on which it lies between the fibers of the mylohyoid muscle inferiorly and those of the geniohyoid muscle (*arrowheads*) superiorly. Axial T2-weighted MR image (**D**) reveals a very heterogeneous signal to the contents of this dermoid cyst, without definition of the individual fat globules so easily visualized on the T1-weighted images. (Courtesy of Dr. Walter Rose.)

Copyright © 2003, Mosby, Inc. All rights reserved.

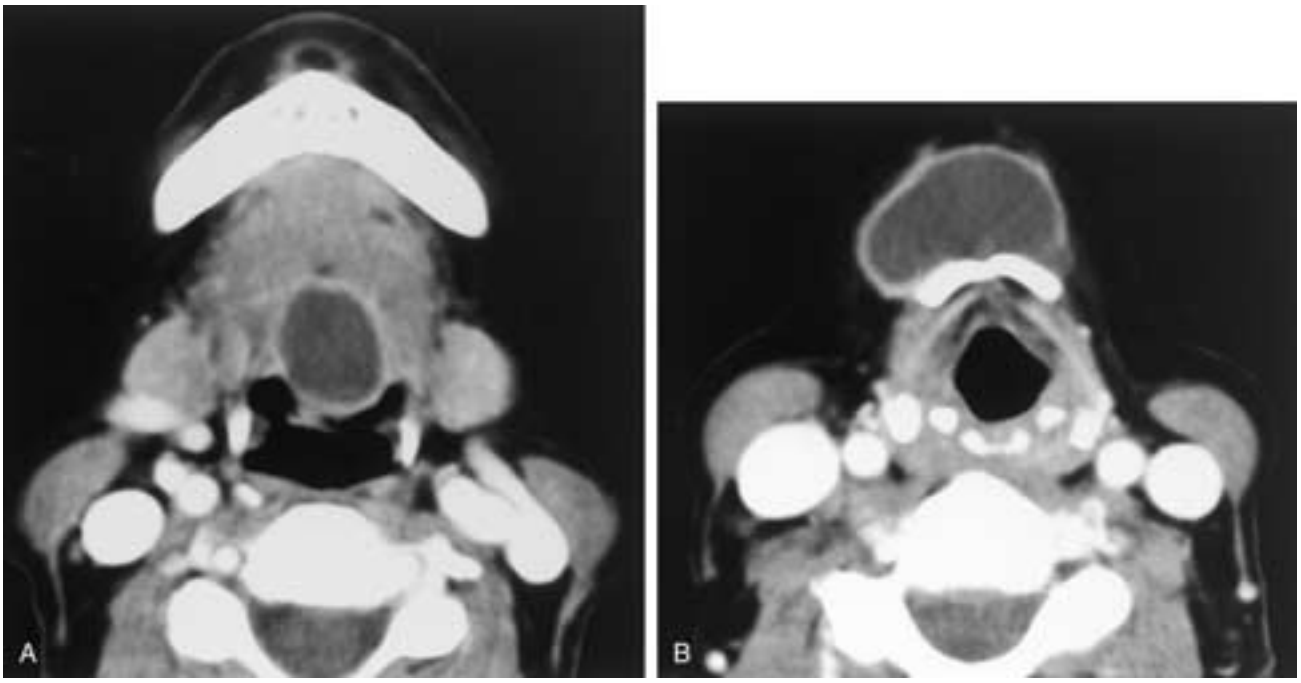

VIEW IMAGE

FIGURE 27-25 Thyroglossal duct cyst. **A** and **B**, Contrast-enhanced axial CT scans reveal a well-circumscribed, rim-enhancing cystic mass along the entire path of the thyroglossal duct from the foramen cecum (**A**) into the infrahyoid neck.

Heterotopic Tissues of the Tongue

Rare reports of heterotopic central nervous system tissue involving the dorsum of the tongue exist in the literature.[122, 123] Bras et al. suggested that glial tissue in the tongue may occur by dislocation of neuroectodermal cells that accompany migrating muscle-forming cells into the tongue.[124] In the few reported cases, newborns, young infants, and females were more often affected.

Approximately 30 cases of heterotopic intralingual cysts of foregut origin have been described in the oral cavity, 97% involving the tongue and floor of the mouth. The nomenclature regarding these cysts is confusing, and these lesions

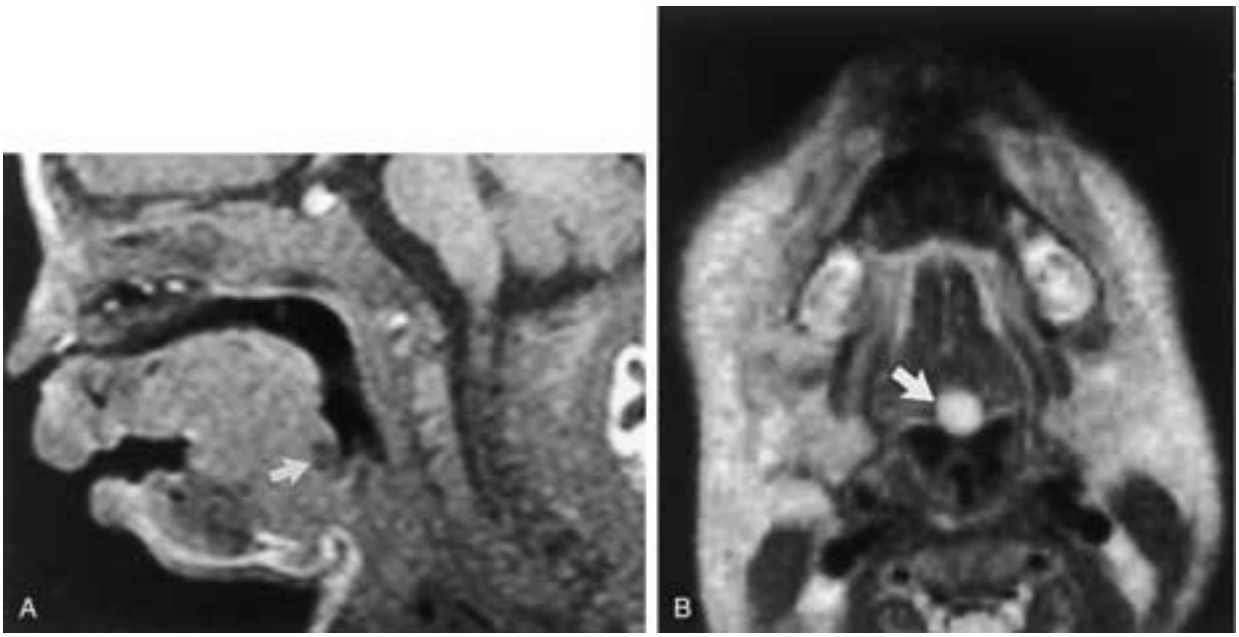

VIEW IMAGE

FIGURE 27-26 Thyroglossal duct cyst at the foramen cecum in a neonate. (**A**) Sagittal T1-weighted and (**B**) axial T2-weighted MR images demonstrate a small lesion with cystic characteristics in the midline of the tongue base at the site of the foramen cecum (*arrows*).

Copyright © 2003, Mosby, Inc. All rights reserved.

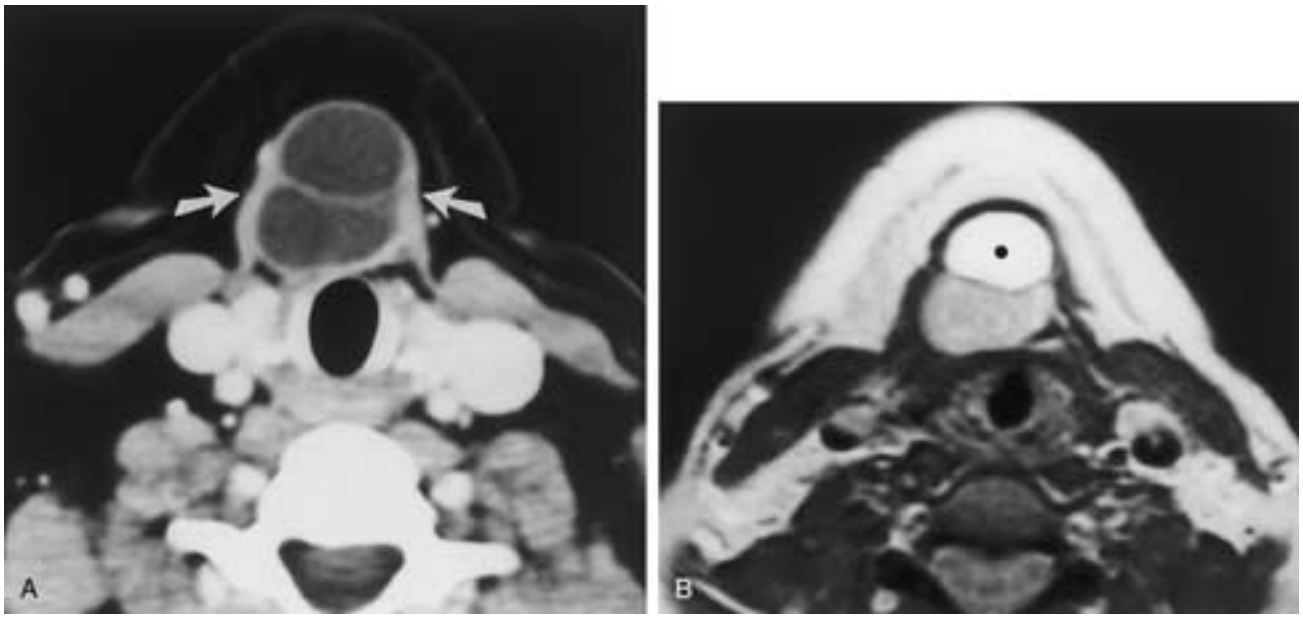

VIEW IMAGE

FIGURE 27-27 Papillary carcinoma in an infrahyoid thyroglossal duct cyst. **A**, Axial CT scan demonstrates a septated midline infrahyoid thyroglossal duct cyst lying deep to the infrahyoid strap muscles (*arrows*). **B**, Axial proton density (intermediate) MR image demonstrates high signal intensity fluid within the anterior compartment (*dot*) but heterogeneous solid tissue within the posterior compartment.

have been variously termed *mucus cysts*,[125] *glossoceles*,[126] *retention cysts of the tongue*,[127] *lingual cysts*,[128] *median lingual cysts*,[129] *gastrointestinal mucosal cysts*,[130] and *choristomas*.[131, 132] In 1982, Constantinides et al. suggested that any cyst containing ciliated epithelium, with or without other types of epithelia, should be regarded as a cyst of foregut origin because ciliated epithelium was considered the hallmark of the primitive foregut.[133] The occurrence of these lesions is probably related to entrapment of undifferentiated, noncommitted endoderm at the junction of the oral tongue, originating from portions of the second and third branchial arches, during the third to fourth weeks of fetal life. These cysts typically occur in infants and young children, and approximately 80% of affected individuals are male (Fig. 27-32). Most cysts are 1 to 3 cm in size, although a 9 cm cyst has been reported. Thirty percent of affected infants may have symptoms related to difficulty with feeding, swallowing, and breathing. The CT appearance of a single lesion is described as ''a relatively well defined cystic structure without loculation or septation.''[134]

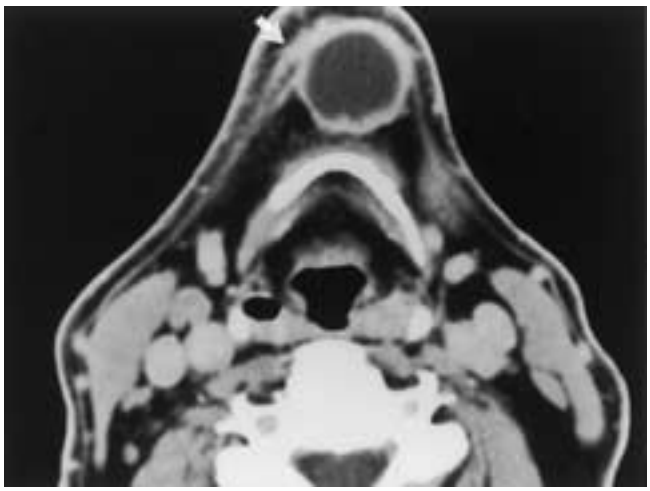

VIEW IMAGE

FIGURE 27-28 Malignant submental adenopathy in a 63-year-old male with a history of squamous cell carcinoma of the left external auditory canal 7 years earlier. Axial CT image with contrast enhancement demonstrates a midline submental cystic-appearing lesion interpreted initially as a thyroglossal duct cyst. The enhancing margin, however, has irregular thickness and is ''stranded'' (*arrow*), the overlying fat is ''dirty'' in appearance, and the skin is thickened. Contrast this appearance with that of the thyroglossal duct cyst in Figure 27-25.

Infections and Inflammatory Lesions

Abscess, Cellulitis, and Sialoliths

Infections within the oral cavity, including the sublingual and submandibular regions, most commonly result from either stenosis or calculi within the salivary gland ductal systems or from dental infections or manipulation. In many cases, infections may primarily involve the masticator space and secondarily spread to involve the oral cavity. The relationship of the apices of the mandibular teeth to the mylohyoid ridge may determine which region is primarily involved by dental infections. The roots of the second and third molars lie below the mylohyoid ridge, and apical infections of these teeth directly involve the submandibular space. By comparison, the apices of the first molar and premolar roots are located above the mylohyoid ridge, and infections of these teeth preferentially involve the sublingual region.[135]

For evaluation of oral cavity infections in adults, CT with contrast enhancement is preferred to MR imaging because CT is superior for demonstrating small calculi and is usually superior for assessing the integrity of the mandibular cortex

Copyright © 2003, Mosby, Inc. All rights reserved.

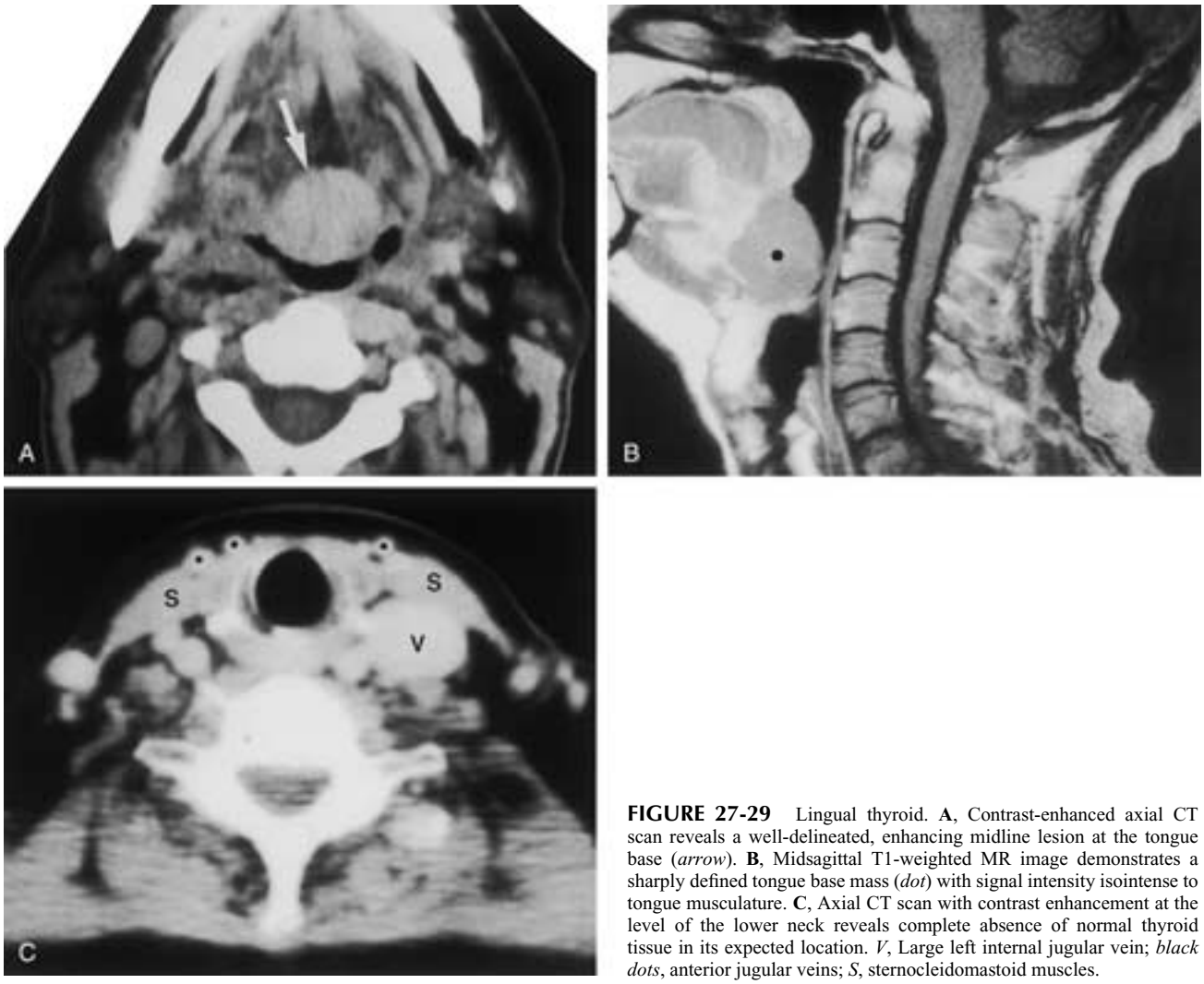

FIGURE 27-29 Lingual thyroid. **A**, Contrast-enhanced axial CT scan reveals a well-delineated, enhancing midline lesion at the tongue base (*arrow*). **B**, Midsagittal T1-weighted MR image demonstrates a sharply defined tongue base mass (*dot*) with signal intensity isointense to tongue musculature. **C**, Axial CT scan with contrast enhancement at the level of the lower neck reveals complete absence of normal thyroid tissue in its expected location. *V*, Large left internal jugular vein; *black dots*, anterior jugular veins; *S*, sternocleidomastoid muscles.

VIEW IMAGE

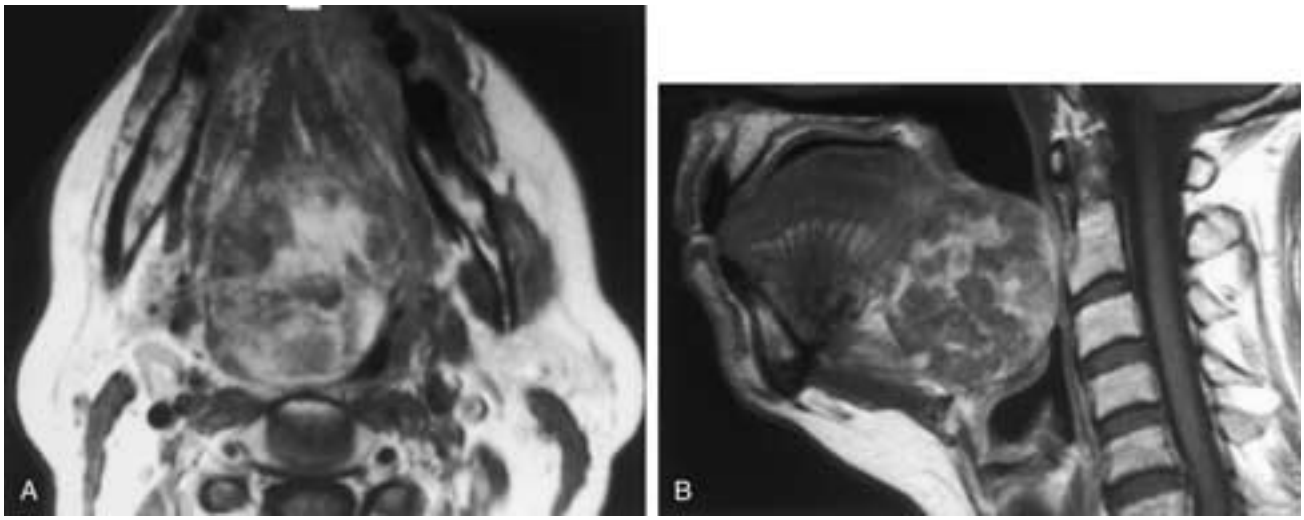

FIGURE 27-30 Lingual thyroid with goiter. **A** and **B**, Axial and midsagittal T1-weighted MR images following contrast administration reveal markedly heterogeneous enhancement of this multinodular goiter affecting lingual thyroid tissue. Note the severe compromise of the oropharyngeal airway on both images. (Courtesy of Dr. Jan Casselman.)

VIEW IMAGE

Copyright © 2003, Mosby, Inc. All rights reserved.

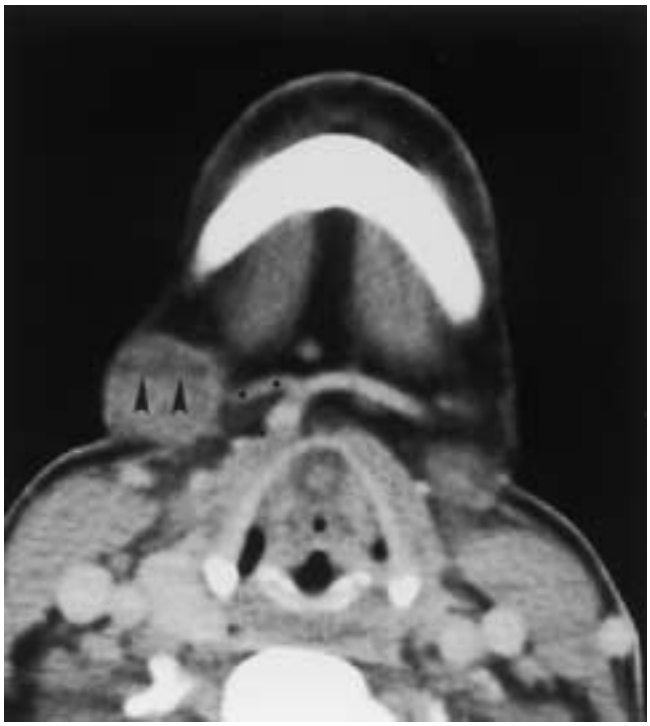

VIEW IMAGE

FIGURE 27-31 Lingual artery aneurysm. Axial contrast-enhanced CT scan in a 23-year-old female with a right submandibular region mass clinically demonstrates a well-circumscribed lesion on the right. A fluid level is visible within the lesion (*arrowheads*), and a branch of the right lingual artery can be seen entering this lesion (*black dots*).

and evaluating for associated osteomyelitis. In addition, total examination times are typically shorter, an important consideration for the acutely ill patient.[136] For patients in the pediatric age group and for adults in whom the use of iodinated contrast is contraindicated, MR imaging may be a preferable modality. The ability of MR to image in multiple planes and the decreased susceptibility to artifacts from dental amalgams are distinct advantages over CT. Every effort must be made to identify associated osteomyelitis in these patients to ensure that appropriate long-term antibiotic treatment is provided. If dental amalgams prevent this assessment, nuclear scintigraphy or MR imaging should be performed.

On CT, an abscess appears as a single or multiloculated low-density area, with or without gas collections, that usually conforms to fascial spaces and demonstrates peripheral rim enhancement (Figs. 27-33 to 27-36). On MR imaging, an abscess typically has low T1-weighted and high T2-weighted signal intensities. Rim enhancement following contrast administration is identified in mature abscesses (Fig. 27-37). In addition to the abscess cavity, cutaneous and subcutaneous manifestations of infection are typically present, including myositis (adjacent muscle enlargement), thickening of the overlying skin, ''dirty'' edematous fat, and enhancement of fascial planes (Figs. 27-38 to 27-40). These cutaneous manifestations are not as obvious on MR imaging as they are on CT, which is one limitation of MR imaging when scanning for infections.[136] The presence of these cutaneous and subcutaneous manifestations, without a definite low-density collection, is consistent with cellulitis.

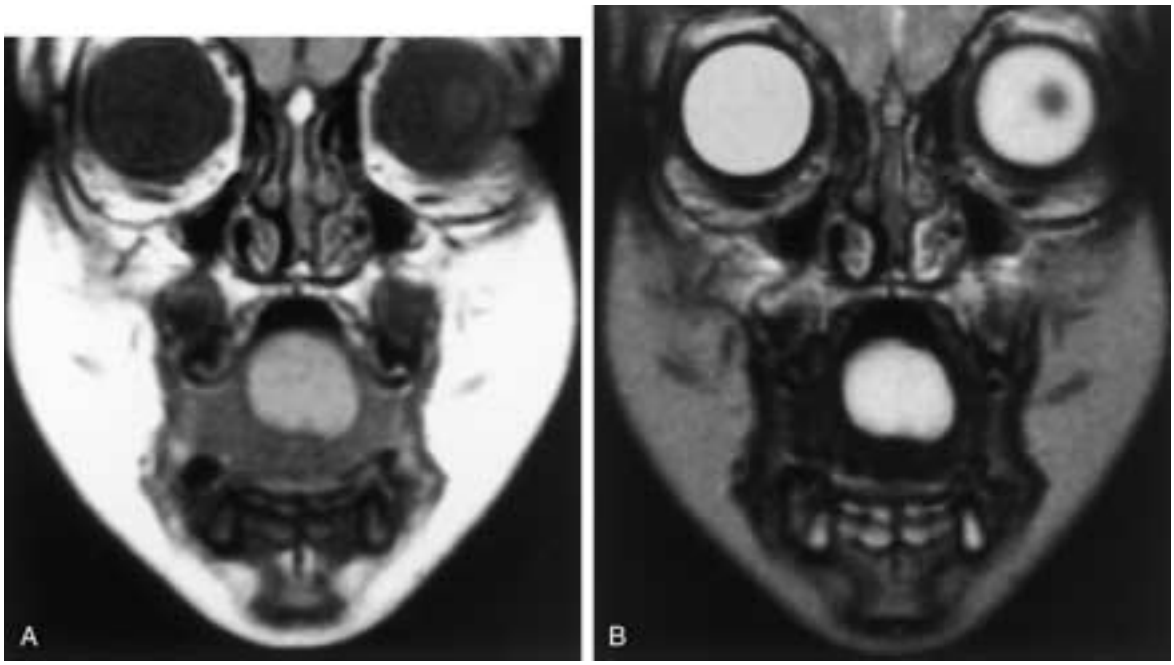

VIEW IMAGE

FIGURE 27-32 Intralingual cyst of foregut origin in a 3-year-old male. (**A**) Coronal T1-weighted and (**B**) T2-weighted MR images demonstrate a well-defined lesion in the dorsum of the tongue. The mild hyperintensity on the T1-weighted image is due to the mucoid content of the cyst.

Copyright © 2003, Mosby, Inc. All rights reserved.

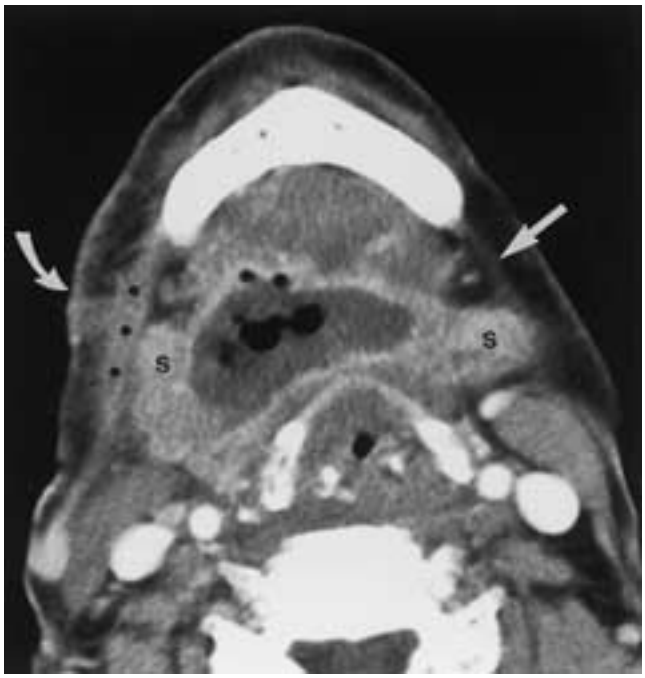

VIEW IMAGE

FIGURE 27-33 Floor of the mouth abscess. Contrast-enhanced axial CT scan through the floor of the mouth reveals a large abscess containing gas. The margins of the abscess exhibit peripheral rim enhancement. Both submandibular glands (*s*) are identified on this plane. In addition to the abscess, marked cellulitis of surrounding soft tissues is identified; this is manifested by thickening of the right platysma muscle (*black dots*) compared with the left platysma muscle (*straight arrow*). There is thickening of the skin on the right (*curved arrow*) and ''dirty,'' edematous fat in the subcutaneous soft tissues between the thickened skin and thickened platysma muscle on the right.

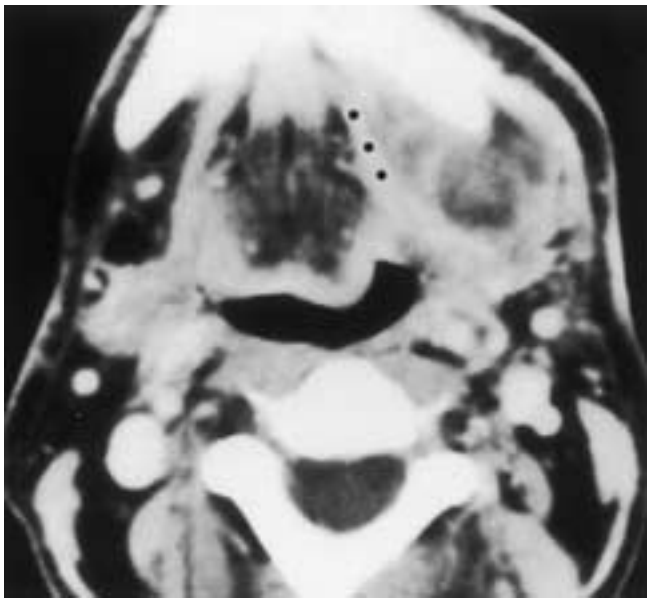

FIGURE 27-34 Submandibular space abscess. Axial CT scan demonstrates a large submandibular space abscess on the left, limited externally by the fibers of the platysma muscle. The abscess displaces the left mylohyoid muscle (*black dots*) medially and superiorly. (Courtesy of Dr. Deborah Reede.)

VIEW IMAGE

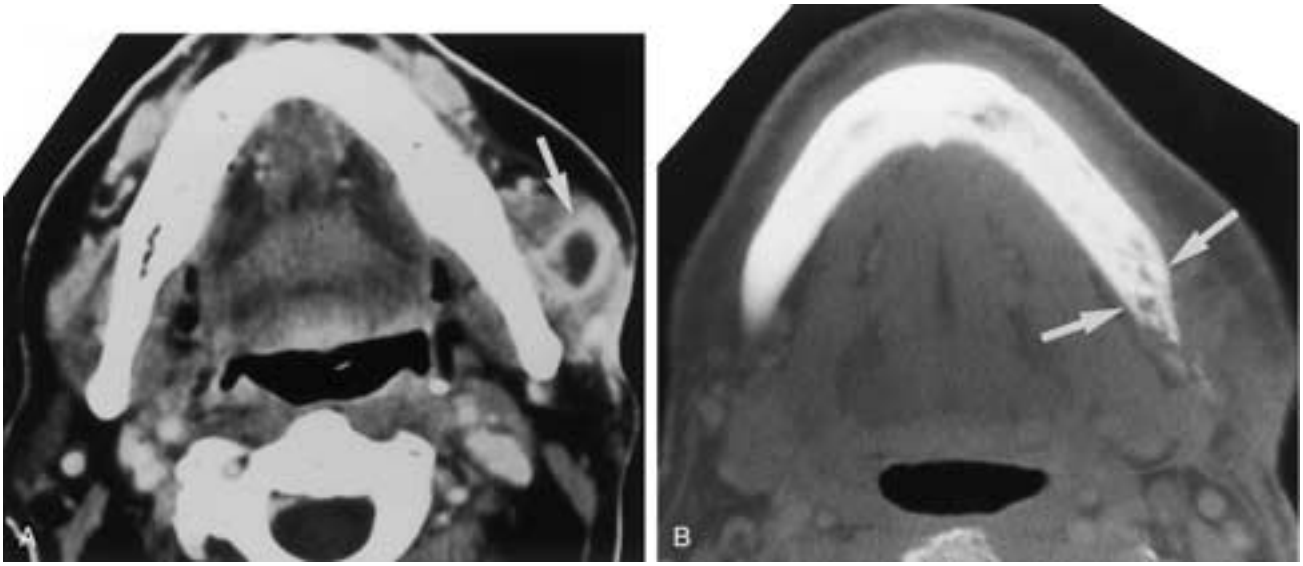

VIEW IMAGE

FIGURE 27-35 Masticator space abscess in a 75-year-old male with recurrent facial infections. **A**, Axial contrast-enhanced CT scan demonstrates an abscess within the left masseter muscle (*arrow*). **B**, CT scan with bone window settings on a slightly different plane reveals a permeated appearance of the mandible consistent with osteomyelitis (*arrows*).

Copyright © 2003, Mosby, Inc. All rights reserved.

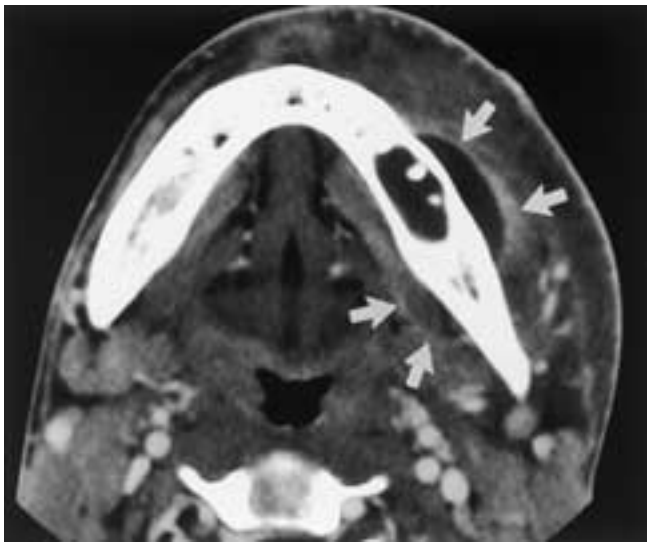

VIEW IMAGE

FIGURE 27-36 Periapical abscess in a 16-year-old male with tooth pain and left facial swelling. Contrast-enhanced axial CT scan shows an abscess cavity within the mandible in the region of the first molar. Rim-enhancing abscesses also involve both the buccal and lingual gingiva (*arrows*).

Primary abscesses of the tongue are rare.[137, 138] Most lingual abscesses originate via direct invasion from trauma (i.e., jagged teeth, bite injury, foreign body penetration) or local infection (apical infections from molar teeth, infected lingual tonsils or TGDCs). The imaging features of tongue abscesses are similar to those of nonlingual lesions.

Inflammatory processes involving the submandibular gland most often result from obstructing intraductal calculi. The inflamed gland is enlarged and painful, and purulent material may be expressed from the duct in most bacterial infections. Salivary pathology is discussed further in Chapter 39.

Obstruction of Wharton's duct by stricture or a calculus may lead to proximal dilation of the duct and, if protracted, may result in submandibular sialadenitis or gland abscess (Figs. 27-41 and 27-42). When sialolithiasis is suspected, the examination of choice is a nonenhanced CT scan (Fig. 27-43). Reconstructed images may be useful in the detection of multiple sialoliths.[139] Contrast should not be used initially because blood vessels in this region may simulate small sialoliths (if infection is suspected, a contrast-enhanced scan may be obtained following the nonenhanced study). Visualization of submandibular gland ducts is common on both CT and MR imaging. However, a duct more than 3 mm

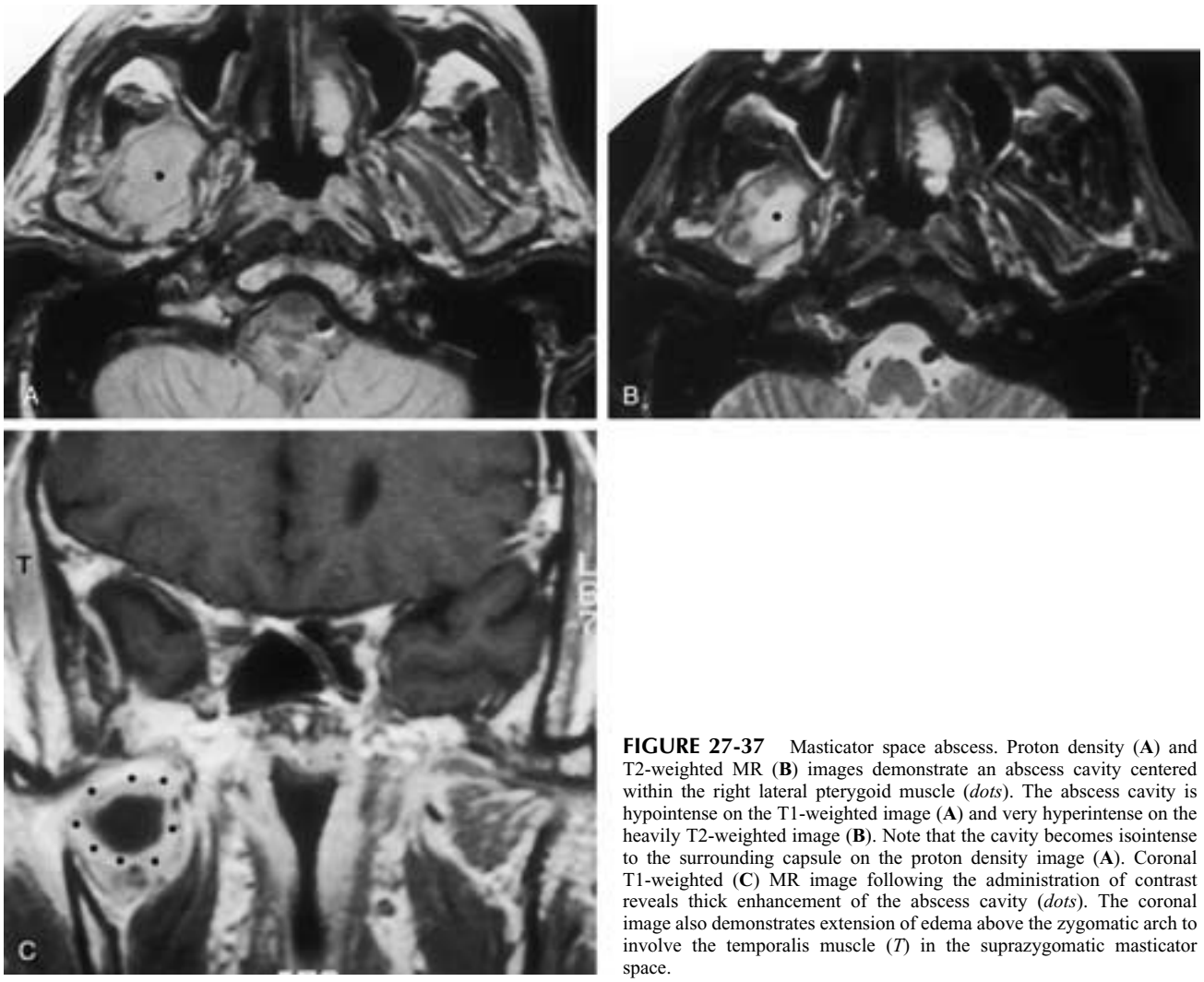

VIEW IMAGE

FIGURE 27-37 Masticator space abscess. Proton density (**A**) and T2-weighted MR (**B**) images demonstrate an abscess cavity centered within the right lateral pterygoid muscle (*dots*). The abscess cavity is hypointense on the T1-weighted image (**A**) and very hyperintense on the heavily T2-weighted image (**B**). Note that the cavity becomes isointense to the surrounding capsule on the proton density image (**A**). Coronal T1-weighted (**C**) MR image following the administration of contrast reveals thick enhancement of the abscess cavity (*dots*). The coronal image also demonstrates extension of edema above the zygomatic arch to involve the temporalis muscle (*T*) in the suprazygomatic masticator space.

Copyright © 2003, Mosby, Inc. All rights reserved.

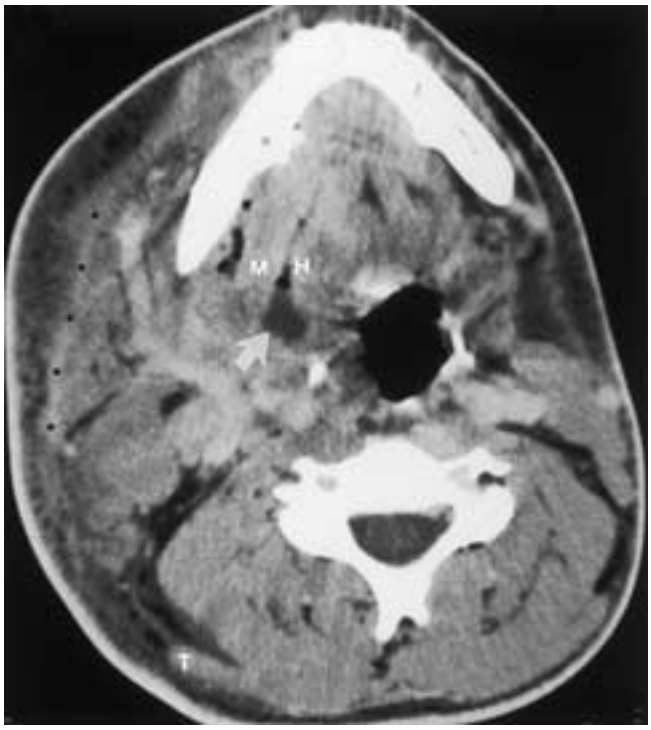

VIEW IMAGE

FIGURE 27-38 Abscess or cellulitis. Axial contrast-enhanced CT scan demonstrates a small abscess cavity (*arrow*) at the posterior aspect of the right tongue, between the mylohyoid (*M*) and hyoglossus (*H*) muscles, both of which are enlarged due to associated myositis. Small collections of gas can be seen to dissect between the muscle fibers. Marked cellulitis involving multiple fascial spaces is identified. The right platysma muscle (*black dots*) is markedly thickened, and the left muscle is much less affected. There is marked edema and a ''dirty'' appearance of the subcutaneous fat involving the right side of the face. The skin overlying this edematous fat is slightly thickened as well. This edema and cutaneous thickening extend posteriorly in the superficial space to at least the margin of the right trapezius muscle (*T*).

VIEW IMAGE

FIGURE 27-39 Abscess or cellulitis. Axial contrast-enhanced CT scan demonstrates a large, heterogeneous, multiloculated abscess involving the left submandibular space. Associated with this abscess is marked thickening of the overlying skin (*white arrows*), thickening of the left platysma muscle (*black dots*), and a ''dirty'' stranded appearance to the subcutaneous fat. Note that there is significantly more cellulitis associated with this abscess than with the abscess illustrated in Figure 27-34.

in diameter, whether intraglandular or extraglandular, indicates possible obstruction, and there should be a thorough evaluation to exclude calculi or obstructing floor-of-mouth tumors (Figs. 27-44 and 27-45).[140] This holds true for the parotid gland and Stenson's duct as well (Fig. 27-46). When large, calculi may be visualized on MR imaging as well as CT (Fig. 27-47), but MR imaging should be reserved for patients with demonstrated sialoliths in whom glandular parenchymal changes require assessment or for patients in whom a sialolith is not demonstrated by CT.[141, 142] MR sialography has recently become possible and is reported to be superior to ultrasound for the detection of sialoliths, but it is currently less sensitive than CT (Fig. 27-48).[141, 143–145]

Ludwig's Angina

Ludwig's angina is a term used to refer to an extensive infection of the floor of the mouth, typically caused by oral

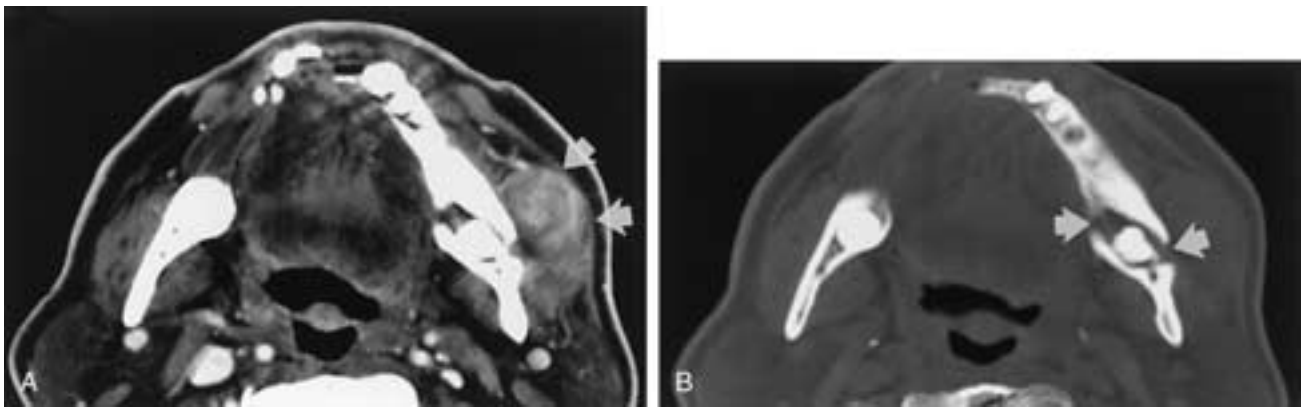

VIEW IMAGE

FIGURE 27-40 Masseter muscle myositis. **A**, Contrast-enhanced axial CT scan demonstrates enlargement and enhancement of the left masseter muscle, which causes bulging of the platysma muscle laterally (*arrows*). **B**, Same image viewed at bone window settings shows evidence of osteomyelitis (*arrows*).

Copyright © 2003, Mosby, Inc. All rights reserved.

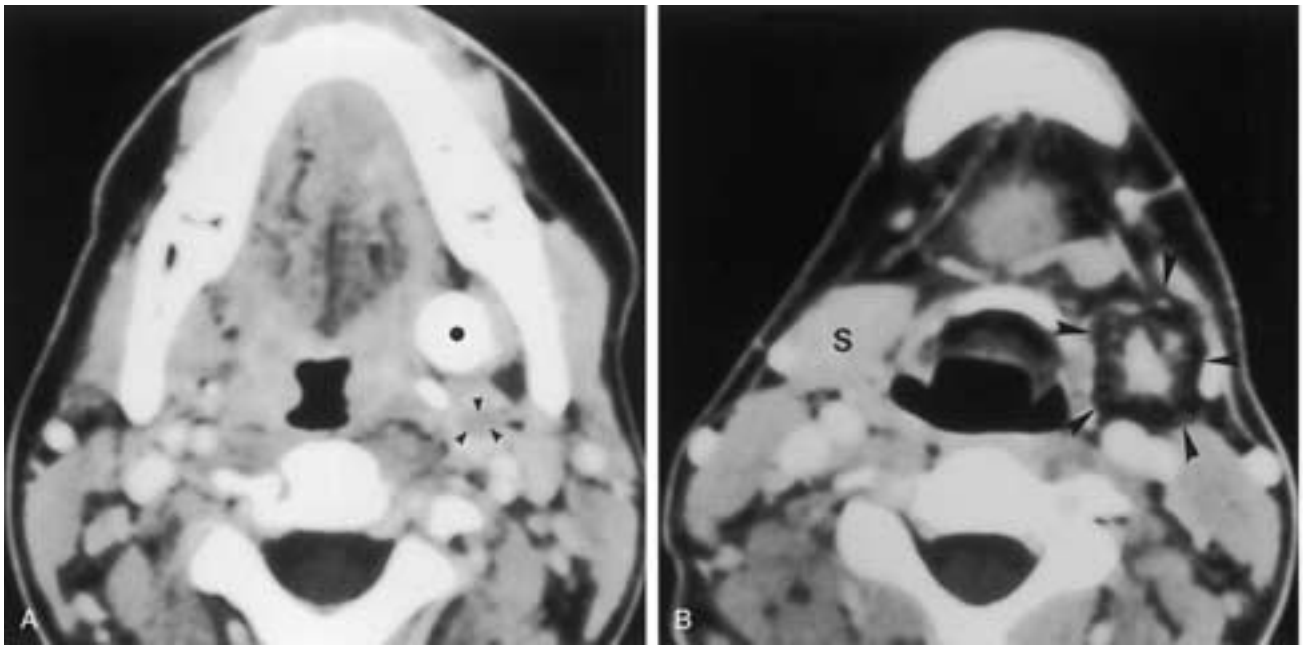

VIEW IMAGE

FIGURE 27-41 Submandibular gland duct calculus with submandibular gland abscess. Axial CT scan (**A**) with contrast enhancement demonstrates a large calculus (*black dot*) along the course of the submandibular gland duct. The most superior extent of the resulting abscess involving the left submandibular gland may be identified on this image (*arrowheads*). **B**, Axial CT scan with contrast enhancement at a lower level reveals a normal right submandibular gland (*S*). An extensive abscess involves the majority of the left submandibular gland (*arrowheads*).

flora (especially streptococcal and staphylococcal bacteria). Specifically, infections of the mandibular molars account for up to 90% of reported cases.[146] Before the antibiotic era, infections in this region dissected inferiorly along fascial planes into the mediastinum, and the patient presented with angina-like chest pain. As early as 1939, Grodinsky established strict clinical criteria to diagnose this entity.[147] Ludwig's angina is a cellulitis, not a focal abscess, that always involves both the sublingual and submandibular spaces and is frequently bilateral; produces gangrene or serosanguinous phlegmon, but little or no frank pus;

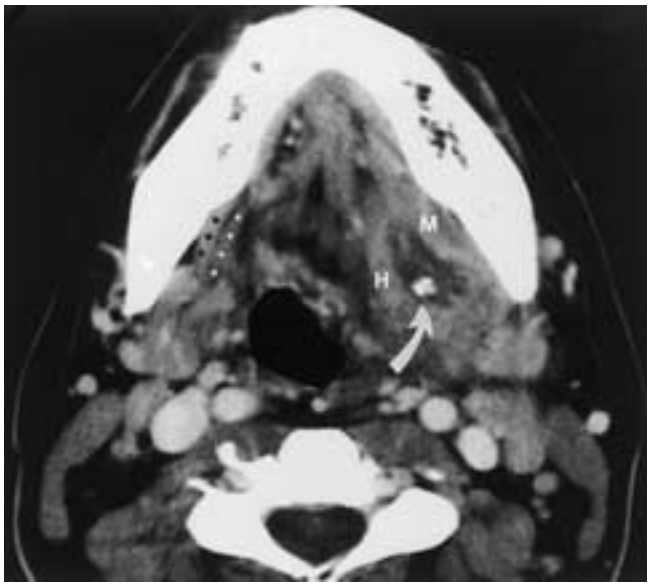

VIEW IMAGE

FIGURE 27-42 Submandibular gland duct calculus with abscess and duct obstruction. Axial contrast-enhanced CT scan demonstrates a calculus with surrounding hypoattenuating fluid density material (pus) (*arrow*). There is significant surrounding edema and a mass effect. Myositis of the left hyoglossus (*H*) and mylohyoid (*M*) muscles is identified compared to the normal contralateral mylohyoid (*black dots*) and hyoglossus (*white dots*) muscles.

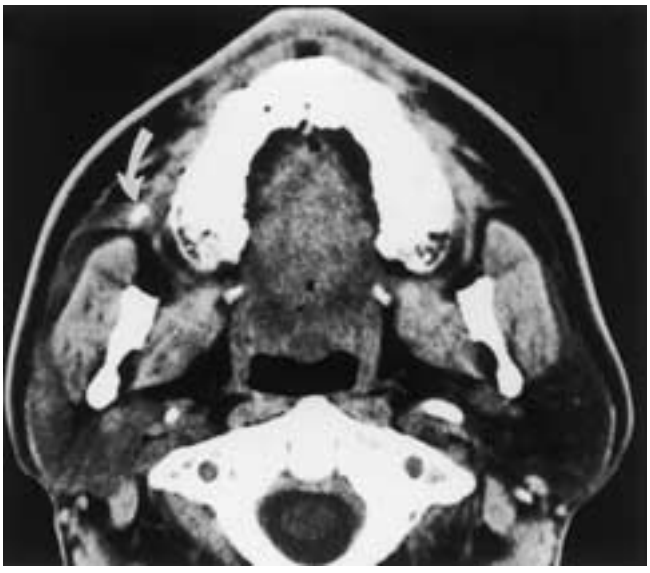

FIGURE 27-43 Calculus in the right parotid duct. Axial noncontrast-enhanced CT scan demonstrates a small calculus in the distal portion of Stensen's duct (*arrow*). Dilated intraglandular ducts are not identified on this image. However, the attenuation of the right parotid gland is higher than that of the normal left parotid gland. This reflects congestion, edema, and/or infection. (Courtesy of Dr. Deborah Reede.)

VIEW IMAGE

Copyright © 2003, Mosby, Inc. All rights reserved.

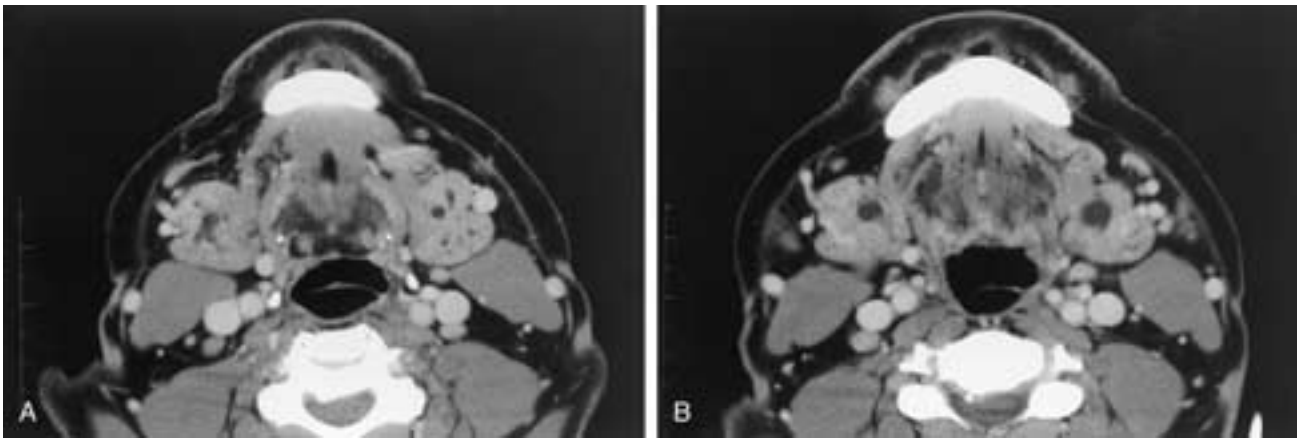

VIEW IMAGE

FIGURE 27-44 Bilateral intraglandular duct dilatation. **A** and **B**, Adjacent contrast-enhanced axial CT scans in a 33-year-old male with recurrent painful enlargement of both submandibular glands. Scans demonstrate marked enlargement of intraglandular ducts bilaterally, with no enlargement of the main duct and no calcified calculi identified.

involves connective tissue, fascia, and muscle but not glandular structures; and is spread by contiguity, not lymphatics. The main role of imaging is to evaluate the integrity of the airway and document the presence of gas-forming organisms, underlying dental infection, and possibly drainable neck abscesses (Fig. 27-49).[146]

Reactive or suppurative adenopathy involving the submandibular and submental lymph nodes is commonly seen in association with oral cavity infections or as part of a more systemic process involving multiple lymph node chains. Submandibular and submental lymph node chains receive drainage from the chin, lips, cheeks, floor of the mouth, and oral tongue, and foci of infection within these regions should be sought.

HIV Involvement of the Oral Cavity

Among the protean manifestations of HIV infections in the extracranial head and neck, parotid gland lymphoepithelial cysts with associated diffuse cervical adenopathy has been shown to be a reliable predictor of HIV infection.[148, 149] More recently, cases of these cysts involving the submandibular glands have also been reported (see Chapter 39).[150–152] In some of these reported cases, parotid cysts were present, either synchronously or preceding the development of submandibular cysts, but in other reports, the presence or absence of associated parotid cysts was not noted.

A wide variety of opportunistic infections affecting the oral cavity occur in association with AIDS.[153] Oral candidiasis, a superficial fungal infection (*Candida albicans*), also termed *thrush* in its most common form, is one of the most frequent infections in this population. Hairy leukoplakia, a manifestation of the Epstein-Barr virus, typically appears as an isolated white plaque on the lateral margin of the oral tongue. Herpes simplex viral infections may produce deep, painful ulcerations. All of these oral infections are usually readily diagnosed by visual inspection. Imaging is reserved for those patients in whom there is a suspicion of disease spread to deeper tissues of the face or to assess the integrity of the mandible and maxilla.

Bacillary epithelioid angiomatosis, although most often occurring on the skin, has also been reported to affect the oral cavity.[154, 155] The causative organism is *Bartonella henselae*, a rickettsia-like organism. The lesion may resemble Kaposi's sarcoma, both clinically and microscopically, and is composed of areas of prominent vascular proliferation. It most often presents as a cutaneous lesion similar to a pyogenic granuloma.

Ranulas

Ranulas, also termed *mucoceles* or *mucous retention cysts* of the floor of the mouth, are of two varieties. The simple variety occurs in the floor of the mouth above the mylohyoid muscle in the region of the sublingual gland and is a true epithelium-lined cyst. These simple ranulas are usually due to obstruction of a minor salivary gland or of the

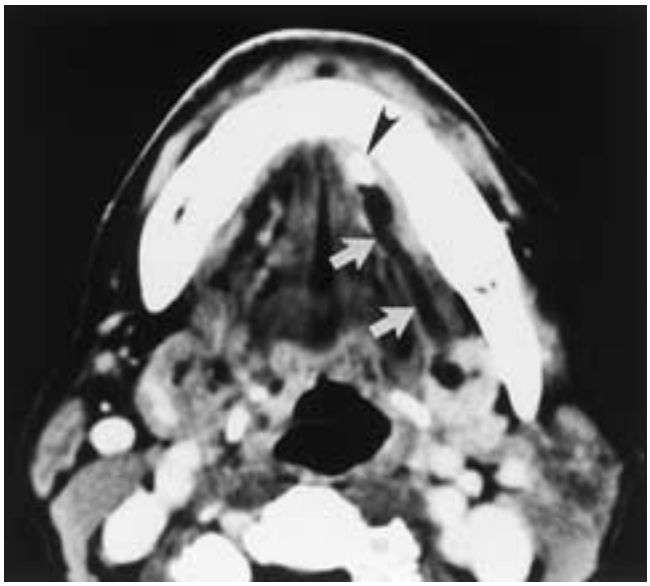

FIGURE 27-45 Distal submandibular duct calculus with marked duct dilatation. Contrast-enhanced axial CT scan demonstrates a distal calculus in Wharton's duct (*arrowhead*) and marked dilatation of the entire duct (*arrows*).

VIEW IMAGE

Copyright © 2003, Mosby, Inc. All rights reserved.

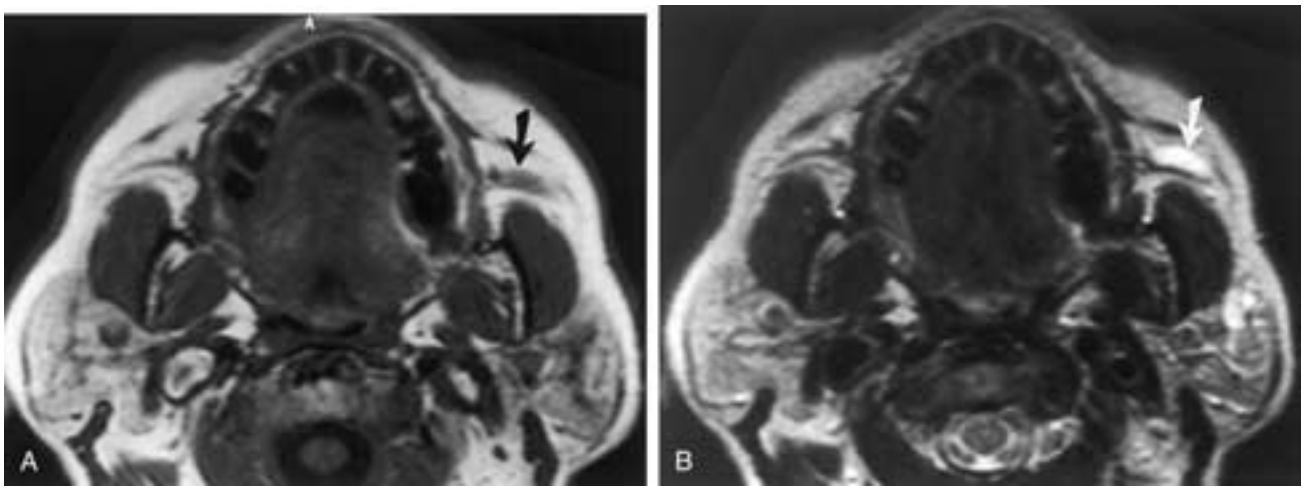

VIEW IMAGE

FIGURE 27-46 Dilated left parotid duct in the left buccal space. (**A**) Axial T1-weighted and (**B**) axial T2-weighted MR images demonstrate marked dilatation of the left parotid duct, hypointense on **A** and hyperintense on **B**, compatible with fluid (*arrows*). Only portions of the duct are visible on these images. There is also ductal dilatation within the left parotid gland best seen in (**B**).

sublingual gland. A ''diving'' or ''plunging'' ranula follows rupture of the simple ranula's wall. As such, these ranulas are not true epithelium-lined retention cysts but are pseudocysts lined by dense connective or granulation tissue.[156, 157] The extravasated mucus is most often directed posteriorly into the submandibular region, but occasionally it may dissect into the adjacent upper cervical soft tissues. These lesions may, therefore, present as masses in either the submental or submandibular regions. Ranulas are discussed further in Chapter 39.

On CT, ranulas are usually thin-walled unilocular, well-defined, nonenhancing, cystic-appearing lesions of low attenuation (Fig. 27-50).[158, 159] They have homogeneously low T1-weighted and high T2-weighted MR signal intensities (Fig. 27-51).[160, 161] When simple, they are confined to the sublingual region. When diving, the bulk of the ranula is typically identified in the submandibular region, although a portion of the lesion is usually identified in the sublingual region, suggesting the diagnosis (Fig. 27-52).[158] Rarely, ranulas may dissect across the midline between the mylohyoid and geniohyoid muscles, and present clinically as bilateral masses (Fig. 27-53).[162, 163] A completely intralingual ranula has also been reported (Fig. 27-54).[161]

Occasionally, the distinction between a plunging ranula in the submandibular space, with little or no visible sublingual component, and a second branchial cleft cyst may be problematic. Careful evaluation of the location of the cystic mass in relation to the submandibular gland may be helpful in making this distinction. Whereas the bulk of a plunging ranula typically lies medial to the submandibular gland and displaces it laterally (Fig. 27-55A), second branchial cleft cysts are usually located posterior to the gland, displacing it anteriorly (Fig. 27-55B).

Rarely, sialolithiasis, trauma, or tumoral obstruction of the submandibular gland duct system may lead to disruption of the duct, with extravasation of mucus into adjacent tissues. This incites an inflammatory reaction and is eventually lined with granulation tissue, forming a pseudocyst (Figs. 27-56 and 27-57). These have been termed *mucoceles of the extravasation type*, with imaging and histologic characteristics paralleling those of plunging ranulas of sublingual origin.[164] The epicenter of these mucoceles is usually not the same as that of the plunging ranula, which is typically at the posterior border of the mylohyoid muscle, displacing the submandibular gland laterally. These extravasation mucoceles are more commonly identified lateral and/or inferior to the gland, in the

VIEW IMAGE

FIGURE 27-47 Submandibular gland duct calculus with obstruction. T1-weighted right parasagittal MR image demonstrates a large signal void (*arrowheads*) produced by a submandibular gland duct calculus.

Copyright © 2003, Mosby, Inc. All rights reserved.

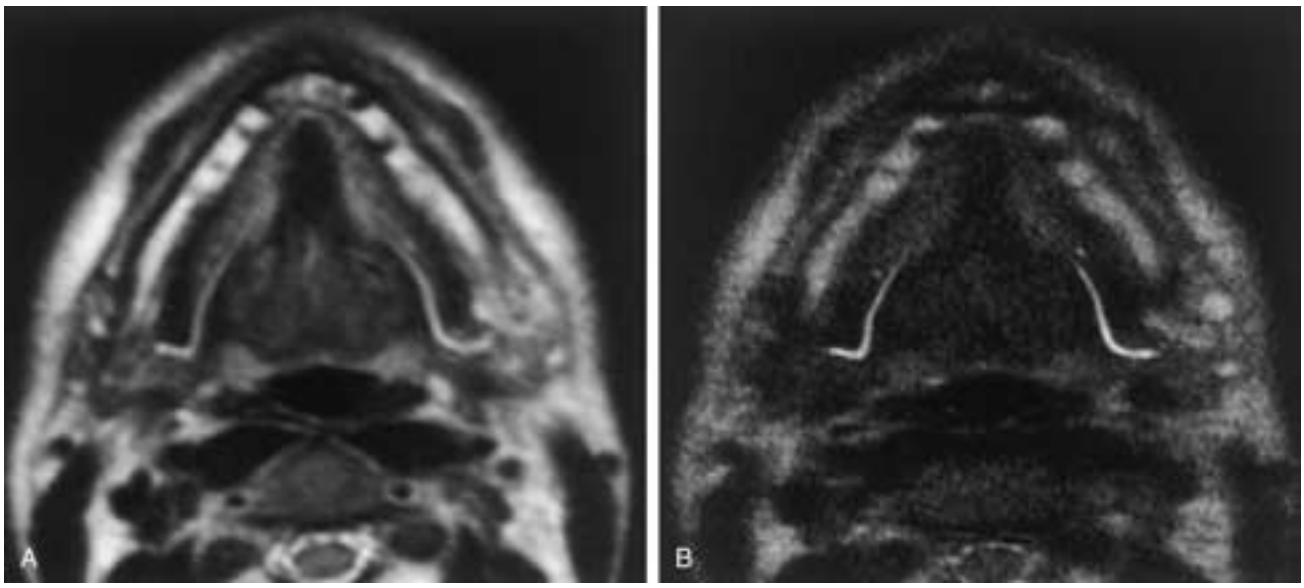

VIEW IMAGE

FIGURE 27-48 MR sialography of the submandibular gland ducts. **A**, Axial MR image with TR = 4.3, TE = 100, 1 NEX. **B**, Axial MR image with TR = 10.9, TE = 87, and 1 NEX.

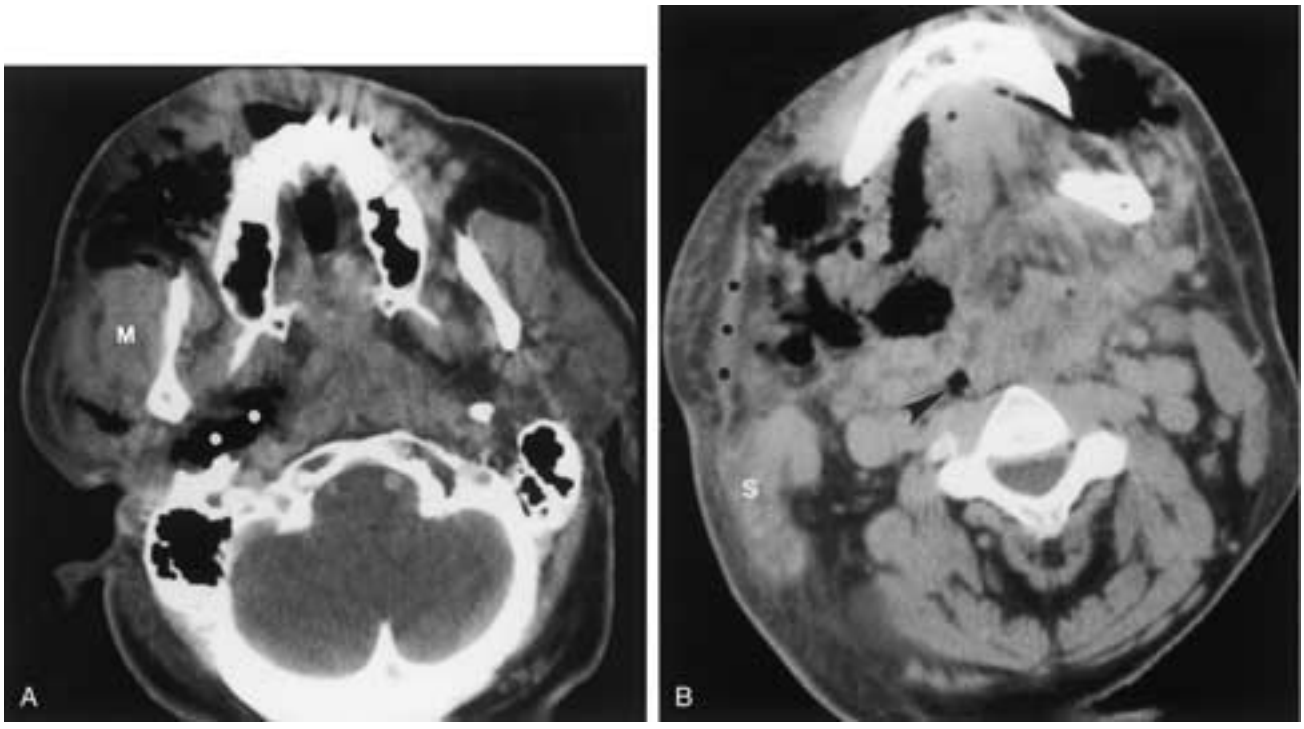

VIEW IMAGE

FIGURE 27-49 Gas-forming infection. **A**, Axial contrast-enhanced CT scan at the level of the maxilla reveals extensive infection with gas collections involving multiple spaces of the suprahyoid neck. These include the buccal spaces bilaterally and the right parapharyngeal space (*white dots*). Myositis involving the right masseter muscle (*M*) is easily appreciated. Involvement of the subcutaneous fat on the right is also identified at this level. **B**, Axial CT scan at a lower level demonstrates gas collections within the right sublingual space, the submandibular spaces bilaterally, the right parapharyngeal space, and the right retropharyngeal space (*arrowhead*). Note the myositis involving the right sternocleidomastoid (*S*) and platysma (*black dots*) muscles. Extensive subcutaneous infection is manifested by edema and a ''dirty'' appearance of the fat. Although this is most prominent on the right, it is also identified anteriorly on the left. Note the absence of a patent airway at this level.

Copyright © 2003, Mosby, Inc. All rights reserved.

FIGURE 27-50 Simple ranula. **A**, Axial contrast-enhanced CT scan demonstrates a low-density lesion in the right floor of the mouth producing a significant midline shift. **B**, On a slightly more inferior plane, the full extent of this large lesion is better appreciated. **C**, Reconstructed sagittal image permits accurate localization of the ranula to the sublingual space lying above the stretched mylohyoid muscles (*white dots*).

VIEW IMAGE

submandibular and submental regions. Differential considerations of cystic-appearing lesions in the sublingual and submandibular regions include dermoid cysts, thyroglossal duct cysts, and cystic lymphangiomas.

Benign Lesions

Pleomorphic Adenomas

Pleomorphic adenomas (benign mixed tumors) are the most common benign glandular tumors of the oral cavity and are characterized by the presence of both mesodermal and glandular tissue. Although the majority of pleomorphic adenomas occur in the parotid gland, 8% arise within the submandibular gland, 0.5% involve the sublingual gland, and 6.5% occur in minor salivary glands situated throughout the upper aerodigestive tract. Only the gingiva and the most anterior portion of the hard palate are relatively devoid of these glands.

On CT, pleomorphic adenomas are usually well demarcated, homogeneous, and slightly hyperdense to muscle on noncontrast images (Fig. 27-58). Typically, there is no significant enhancement. Occasionally, the medial margin of a submandibular or sublingual pleomorphic adenoma may be poorly defined, suggesting a more aggressive lesion (Fig. 27-58).[165] When the hard palate is involved, there is usually a surrounding rim of well-defined cortical bone produced by the slow tumor growth and adjacent bone remodeling (Fig. 27-59). Large lesions may be inhomogeneous and have areas of necrosis, cystic changes, and amorphous calcification.

On MR imaging, pleomorphic adenomas are usually

Copyright © 2003, Mosby, Inc. All rights reserved.

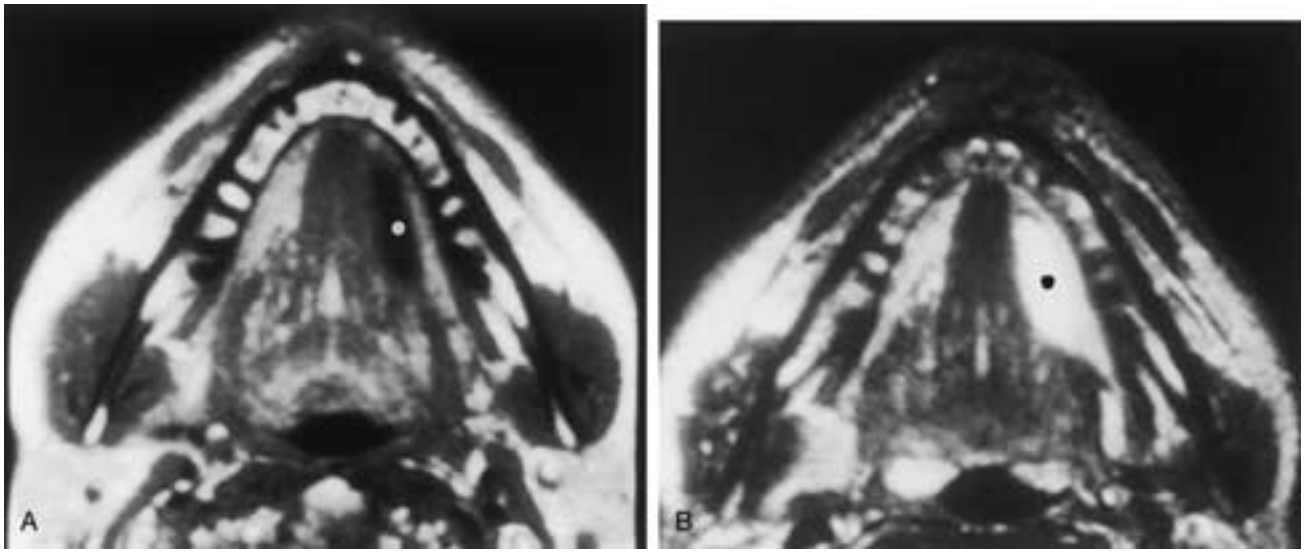

VIEW IMAGE

FIGURE 27-51 Simple ranula. (**A**) T1-weighted and axial (**B**) T2-weighted MR images reveal a small lesion in the left sublingual space (*dots*) hypointense on **A** and hyperintense on **B**, compatible with the presence of fluid.

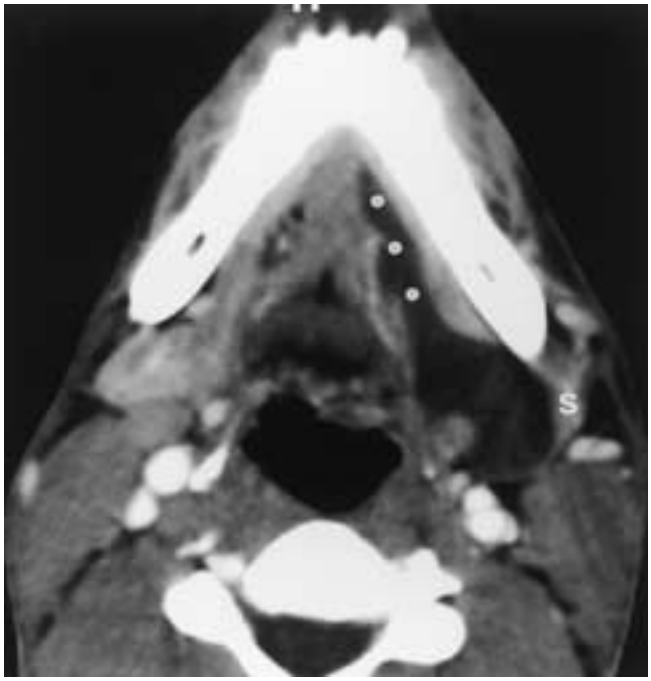

VIEW IMAGE

FIGURE 27-52 Plunging ranula. Axial contrast-enhanced CT scan reveals a cystic lesion in the left submandibular region with a visible ''tail'' in the left sublingual space (*dots*). The left submandibular gland (*S*) is compressed and displaced laterally.

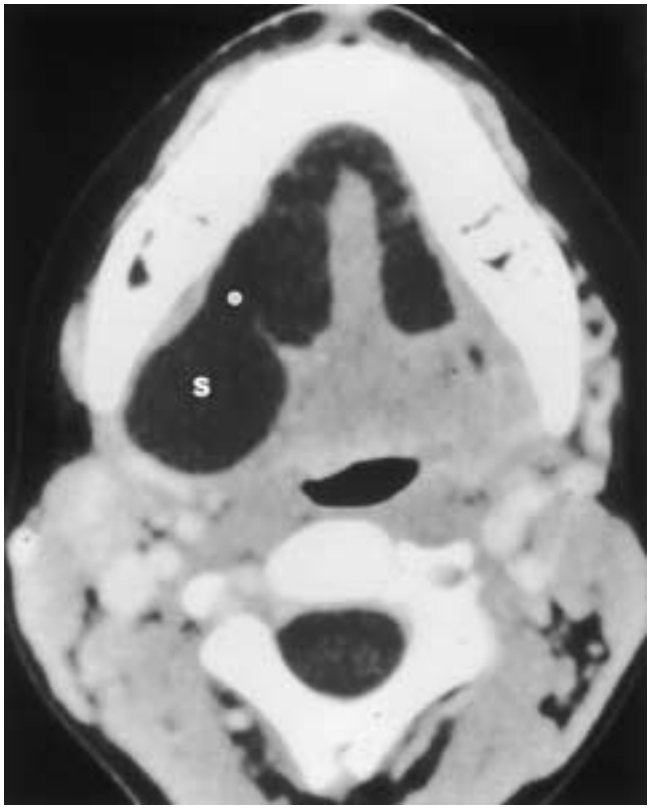

FIGURE 27-53 Diving ranula. Axial CT scan performed with contrast enhancement demonstrates a diving ranula on the right; the bulk of the ranula is centered within the deep aspect of the right submandibular space (*S*), with a ''tail'' extending anteriorly into the right sublingual space (*dot*). The ranula has dissected across the midline, between the fibers of the mylohyoid and geniohyoid muscles, to be visualized within the left sublingual space.

VIEW IMAGE

Copyright © 2003, Mosby, Inc. All rights reserved.

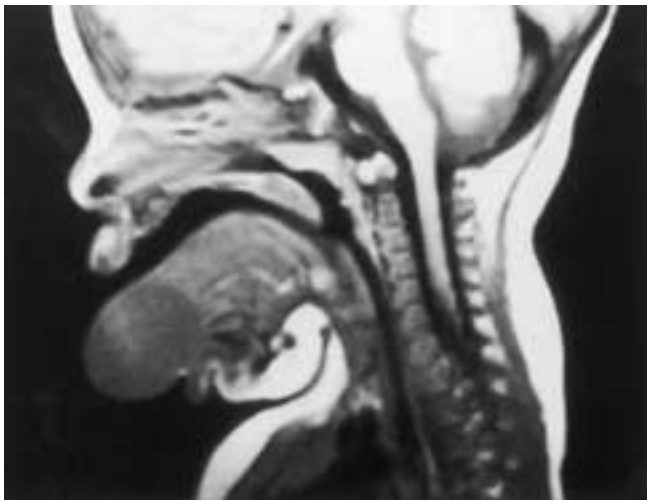

VIEW IMAGE

FIGURE 27-54 Intralingual ranula. Midsagittal T1-weighted image demonstrates a cystic lesion replacing the distal half of the oral tongue. The lesion is hypointense on T1-weighted images, and it became markedly hyperintense in a very homogeneous fashion on the heavily T2-weighted image (not shown), suggesting the fluid nature of the mass. (From Silverstein MI, Castillo M, Hudgins PA, et al. MR imaging of intralingual ranula in a child. J Comput Assist Tomogr 1990;14:672–673.)

isointense to muscle on T1-weighted images and become hyperintense on progressively more T2-weighted sequences.[165] Varying signal intensities within these tumors reflect their heterogeneous composition, and cystic change, necrosis, and hemorrhage may all be encountered. Excisional biopsy and incomplete resection are not advocated for treatment of these lesions, as they increase the likelihood of recurrence (Fig. 27-60). These lesions are discussed in greater detail in Chapter 39.

Aggressive Fibromatosis

Tumors of fibrous origin include a variety of histologies ranging from simple keloids at the benign end of the spectrum to fibrosarcomas at the malignant end. Between these extremes is aggressive fibromatosis, an extraabdominal desmoid ''tumor.''[166, 167] Termed *juvenile fibromatosis* by Stout and *aggressive infantile fibromatosis* by Enzinger, this entity represents one of the most complex problems in the classification of fibrous lesions. Several patterns are identified microscopically that essentially reflect progressive stages of fibroblast differentiation. Distinction between the more cellular varieties of fibromatosis and well-differentiated infantile fibrosarcoma may be extremely difficult, perhaps impossible.[168] Terms including *aggressive fibromatosis*, *differentiated fibrosarcoma*, and *fibrosarcoma-like fibromatosis* have all been applied to these lesions.[168] This topic is discussed further in Chapter 41.

Approximately 11% of infantile fibromatosis cases occur in the extracranial head and neck, primarily in young children, during the first or second year of life. There is a slightly higher prevalence in boys than in girls. The neck and supraclavicular regions are most commonly affected.[169] The oral cavity, nasal cavity, paranasal sinuses, nasopharynx,

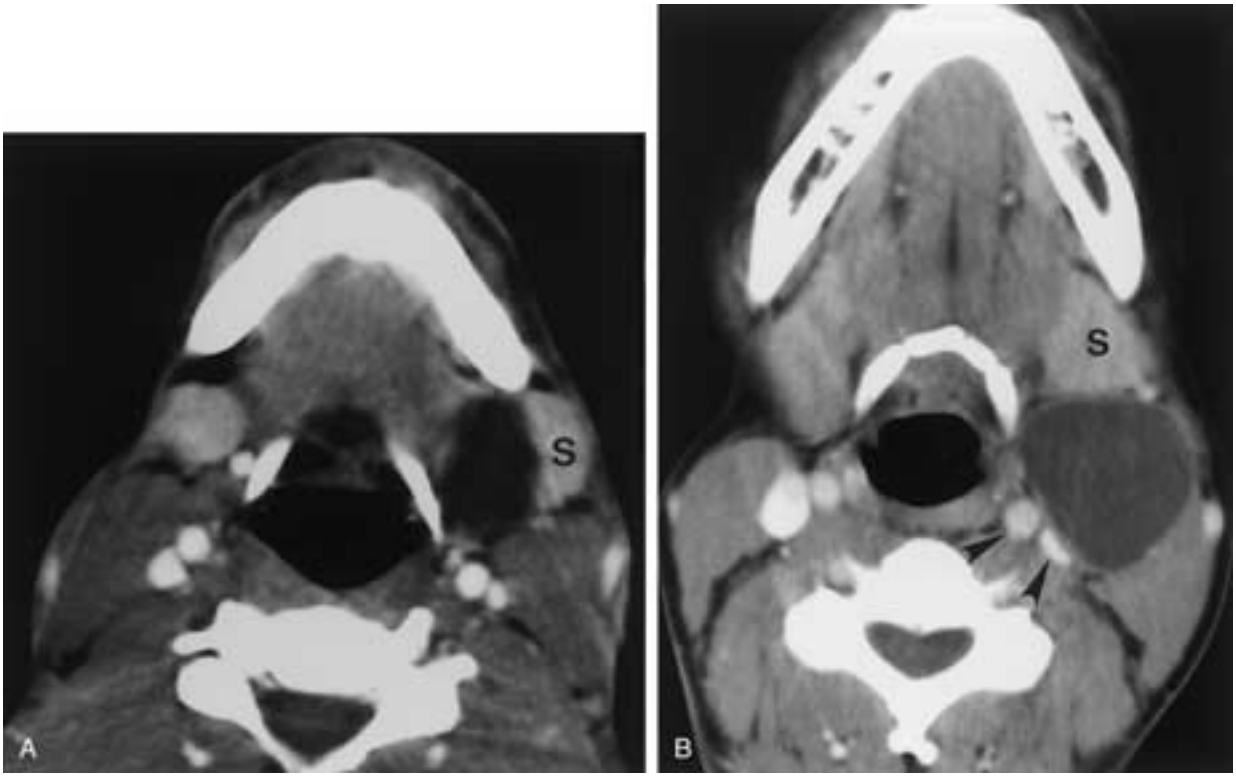

VIEW IMAGE

FIGURE 27-55 Ranula versus second branchial cleft cyst. Axial contrast-enhanced CT scans demonstrate characteristic displacements by a ranula (**A**) and a second branchial cleft cyst (**B**). The ranula displaces the submandibular gland (*S*) laterally, while the typical second branchial cleft cyst displaces it anteriorly. Both may produce a mass effect on the sternocleidomastoid muscle if large enough, but the second branchial cleft cyst will often displace the carotid space structures posteromedially (*arrowheads* in **B**).

Copyright © 2003, Mosby, Inc. All rights reserved.

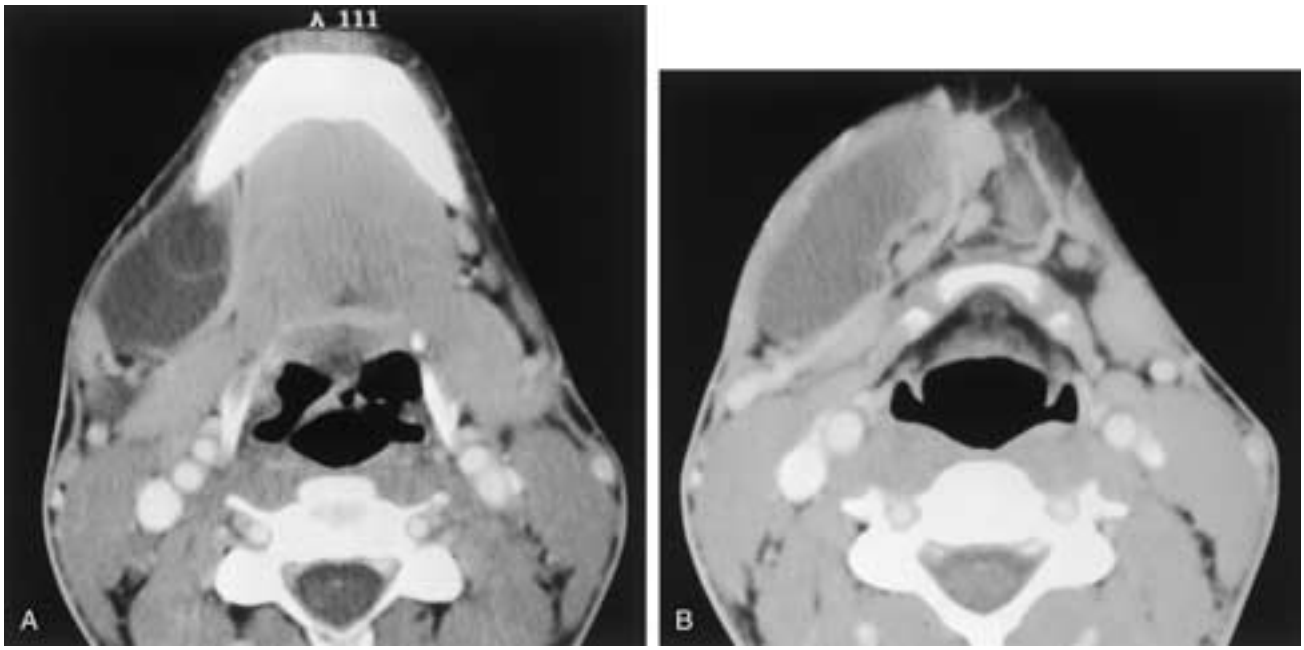

VIEW IMAGE

FIGURE 27-56 Extravasation mucocele. Serial contrast-enhanced CT images (**A** and **B**) demonstrate a cystic lesion in the right submandibular space, clearly lateral and inferior to the mylohyoid muscle. The mucocele wraps around the posterior margin of the mandible. The bulk of the mucocele is at the level of the hyoid bone.

and larynx are involved much less frequently.[170] Rare reports of fibromatosis involving the tongue also exist.[171–173] As a group, these lesions tend to manifest much more aggressive behavior than those that originate from the anterior abdominal wall because they infiltrate muscles and encase adjacent nerves and vessels.[1] Cases of head and neck fibromatosis extending into the epidural space and even intracranially have been reported.[174–176] Although aggressive fibromatosis has no malignant potential and does not metastasize, it manifests innate local aggressiveness and a high rate of recurrence after incomplete surgical resection. Recurrences after a delay of many years have also been reported.[177]

Aggressive fibromatosis arises as a solitary mass within

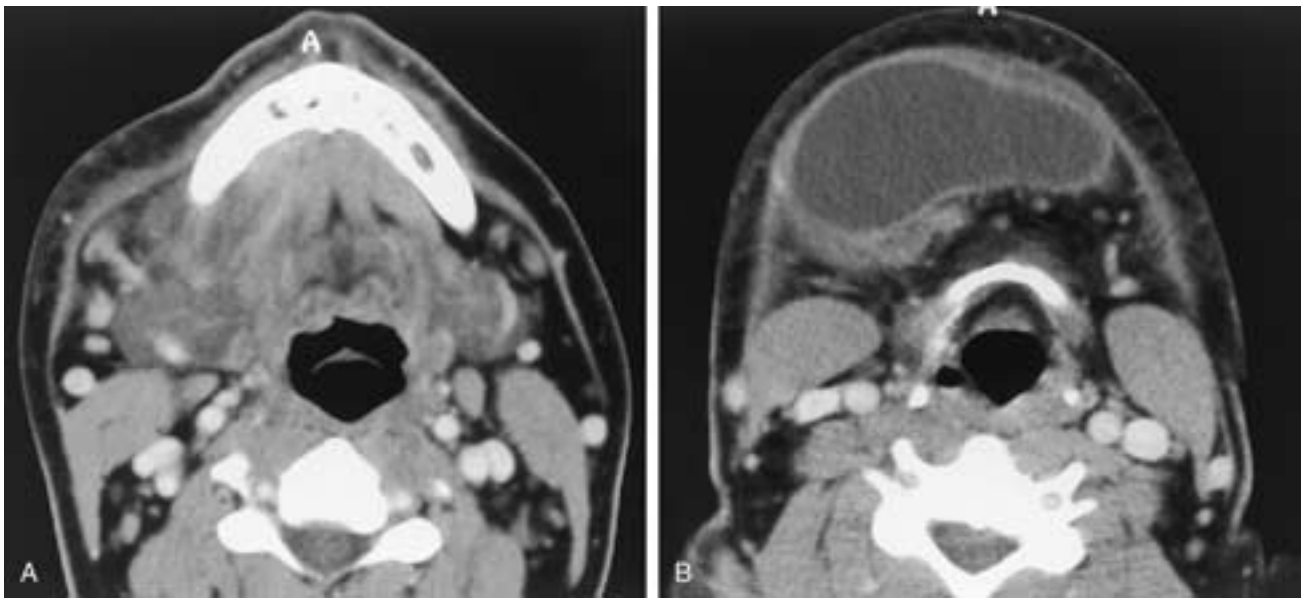

VIEW IMAGE

FIGURE 27-57 Extravasation mucocele in a 23-year-old male with a rapidly enlarging mass under his chin. Serial contrast-enhanced CT scans (**A** and **B**) demonstrate a cystic-appearing right submandibular space mass associated with extensive changes of infection. There is marked thickening of the platysma muscle and a ''dirty'' stranded appearance to the subcutaneous fat. As in Figure 27-56, the bulk of this extravasation mucocele lies at the level of the hyoid bone.

Copyright © 2003, Mosby, Inc. All rights reserved.

VIEW IMAGE

FIGURE 27-58 Pleomorphic adenoma. Contrast-enhanced axial CT scan demonstrates a large mass anterior to the left submandibular gland (*S*), displacing the gland slightly posteriorly. Although (because of the size of this lesion) the exact epicenter is difficult to ascertain, the fact that the anterior aspect of the left sublingual space (*white dot*) is widened suggests that the lesion arises within this space. Pathologically, this proved to be a pleomorphic adenoma of the left sublingual gland. Note that the lesion is extremely homogeneous in appearance, as well as being very well circumscribed, although the medial margin seems to blend with the genioglossus muscle and is not as well defined. The lesion abuts the cortex of the mandible; however, the mandible appears intact on this soft-tissue window scan. (Courtesy of Dr. Patricia Hudgins.)

VIEW IMAGE

FIGURE 27-59 Pleomorphic adenoma. Coronal CT scan demonstrates a well-defined soft-tissue mass replacing much of the right aspect of the hard palate. The mass has characteristics of a benign lesion because the hard palate is remodeled and well marginated rather than being destroyed. (Courtesy of Dr. Nicole Freling.)

skeletal muscle or in the adjacent fascia, aponeurosis, or periosteum. It has a fairly homogeneous, low to intermediate attentuation relative to surrounding muscles on unenhanced CT, enhances to a variable degree after contrast administration, and may be inseparable from adjacent muscles (Fig. 27-61).[23, 174, 175, 178, 179] On MR imaging, aggressive fibromatosis has variable signal intensity, typically isointense or slightly hypointense to muscle on T1-weighted sequences and hypointense to hyperintense on T2-weighted sequences (Figs. 27-62 and 27-63).[171, 180, 181] Linear and curvilinear

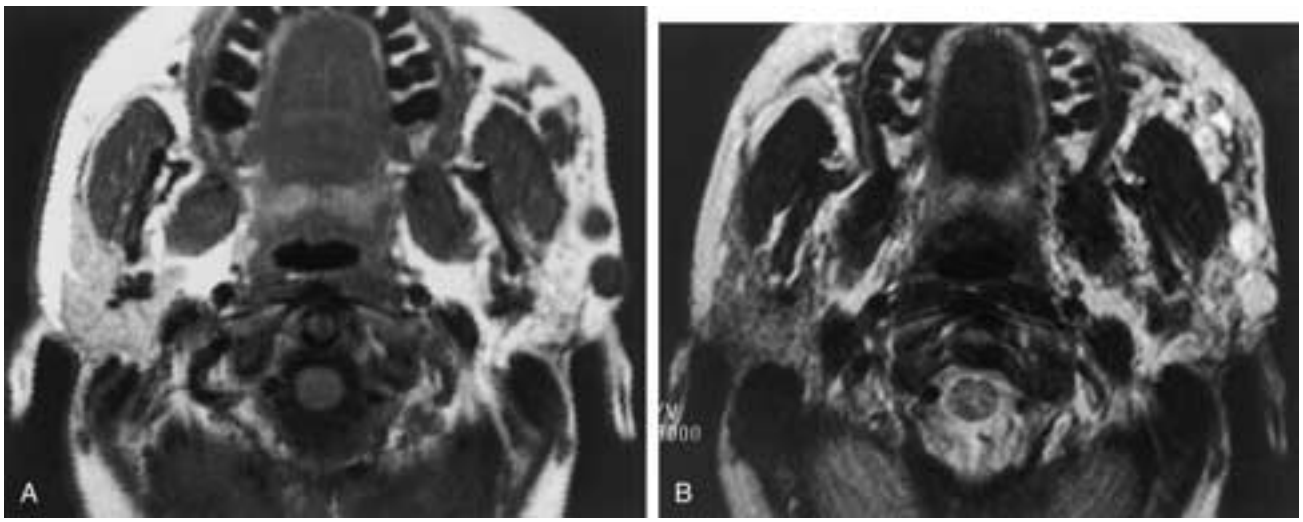

VIEW IMAGE

FIGURE 27-60 Seeding of the left buccal space from a partially resected parotid pleomorphic adenoma. **A**, Axial T1-weighted MR image demonstrates multiple nodules in the left buccal space. These lesions become very hyperintense on the T2-weighted image (**B**). Note the heavy seeding anterior to the masseter muscle and posterior to the parotid duct.

Copyright © 2003, Mosby, Inc. All rights reserved.

FIGURE 27-61 Aggressive fibromatosis (extraabdominal desmoid). **A**, Axial contrast-enhanced CT scan demonstrates a nonenhancing mass involving the right masticator space centered within the pterygoid musculature. The lesion encroaches upon the right parapharyngeal space fat (*arrowheads*). It also slightly encroaches upon the nasopharyngeal air shadow on the right (*white curved arrow*), producing an abnormal contour compared with the left. The pterygoid plates, well visualized on the left (*black dots*), have been eroded by this lesion and are absent on the right. Coronal T1-weighted MR noncontrast image (**B**) demonstrates that the lesion is slightly hyperintense to muscle. Mild enhancement was noted following contrast administration as seen on this axial T2-weighted image (**C**). This desmoid tumor became progressively more hyperintense on the proton density and heavily T2-weighted MR images.

VIEW IMAGE

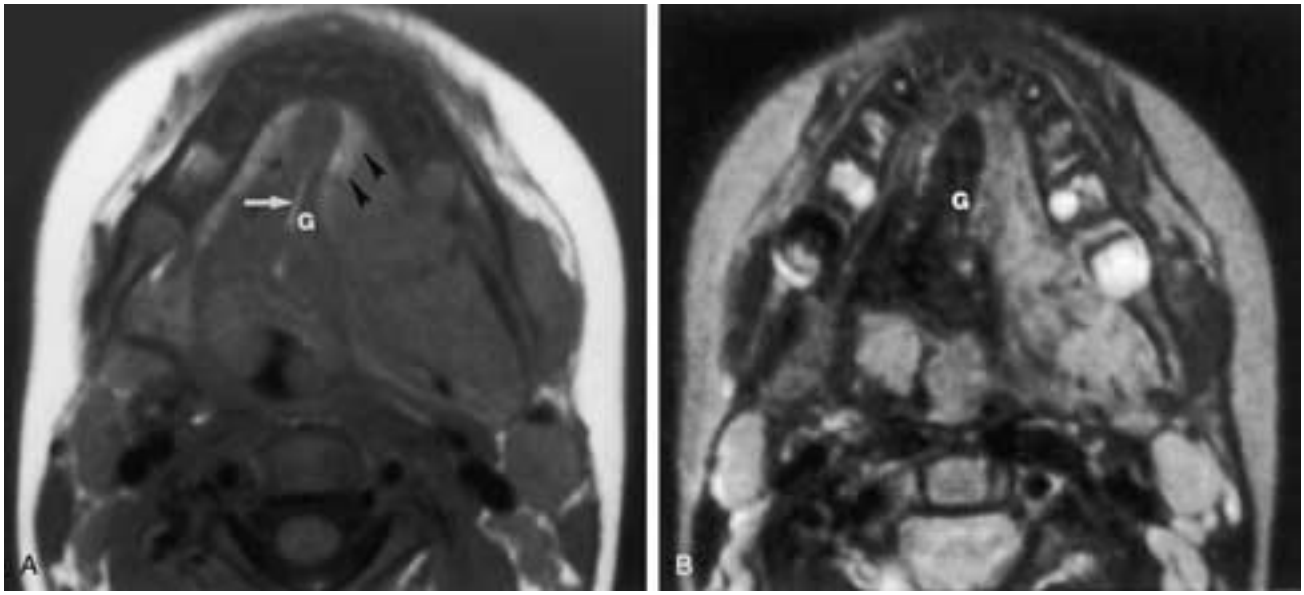

VIEW IMAGE

FIGURE 27-62 Aggressive fibromatosis. Axial T1-weighted (**A**) and T2-weighted (**B**) MR images demonstrate a left submandibular space lesion that is minimally hyperintense to muscle on **A** becoming progressively more hyperintense on **B**. Although the lesion can be separated anteriorly from the fat-filled sublingual space on the T1-weighted image (*arrowheads* in **A**), separation on the T2-weighted image is not possible. Note the compression of the left genioglossus muscle (*G*) and displacement of the midline lingual septum to the right (*arrow*). (Courtesy of Dr. Jan Casselman.)

Copyright © 2003, Mosby, Inc. All rights reserved.

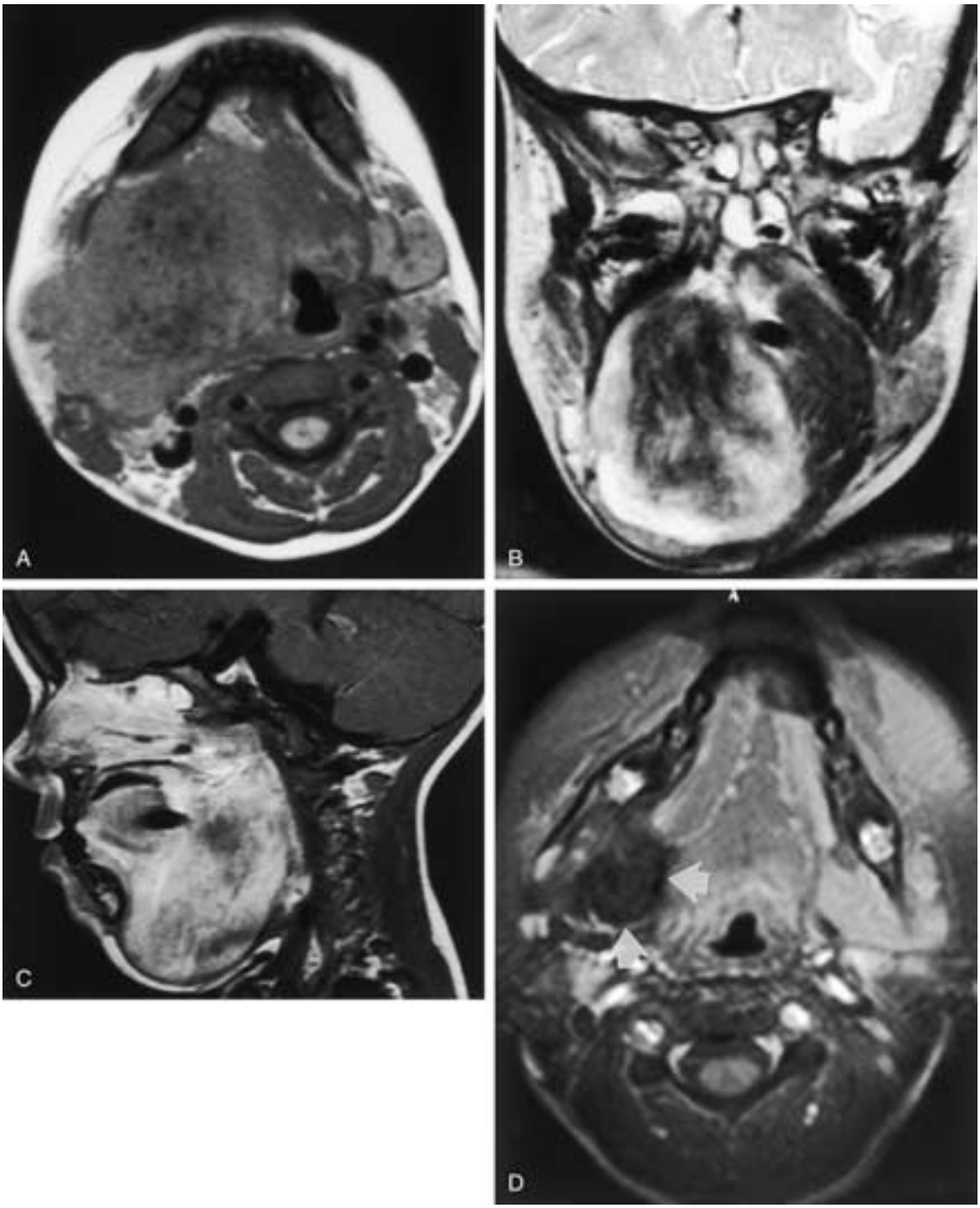

VIEW IMAGE

FIGURE 27-63 Aggressive fibromatosis. (**A**) Axial T1-weighted MR image demonstrates more heterogeneity in this lesion than that seen in Figure 27-62, reflecting its dense fibrous content. This is impressive on the coronal T2-weighted image (**B**), as a significant portion of the lesion is markedly hypointense. T1-weighted image after contrast enhancement in the sagittal plane (**C**) demonstrates very heterogeneous enhancement. The true craniocaudad extent of the lesion is best appreciated on the sagittal image (**C**), which demonstrates involvement up to the skull base. Imaging 3 years later (after extensive treatment) with contrast-enhanced, fat-suppressed, T1-weighted imaging in the axial (**D**) plane reveals a remarkable decrease in the size of the lesion, with only an area of residual dense fibrous tissue remaining (*arrows*).

Copyright © 2003, Mosby, Inc. All rights reserved.

areas of signal void that may be identified on both T1-weighted and T2-weighted images, probably reflecting dense collagen, are considered the hallmark of this entity (Fig. 27-63).[182] There is usually some degree of enhancement following contrast administration. It is probable that the spectrum of appearances on MR imaging is related to the relative amounts of fibroblast proliferation, fibrosis, and collagen contained within the lesion.[183]

Rhabdomyomas

Rhabdomyomas are rare benign tumors of striated muscle, most of which occur in the extracranial head and neck. In contrast to cardiac rhabdomyomas, considered to be hamartomatous lesions and often associated with tuberous sclerosis, extracardiac rhabdomyomas have no association with this syndrome. Extracardiac rhabdomyomas are subdivided clinically and morphologically into two histologic types: adult and fetal.[184] Adult rhabdomyomas occur predominantly in middle-aged men and have a predilection for the base of the tongue, floor of the mouth, larynx, and pharynx. For this reason, it has been suggested that these lesions arise from the striated muscles of the third and fourth branchial arches.[185] Fetal rhabdomyomas usually occur in children under the age of 3 years and also have a predilection for the extracranial head and neck. These fetal lesions may actually be hamartomatous malformations rather than true neoplasms. The preferred treatment for rhabdomyomas is complete surgical excision, which is often easily accomplished because these lesions tend to be well encapsulated.[186]

Rhabdomyomas are of muscle density on unenhanced CT and demonstrate enhancement following the administration of contrast.[187] On MR imaging, rhabdomyomas are isointense or slightly hyperintense to muscle on T1-weighted images, hyperintense on T2-weighted images, and enhance slightly following contrast administration (Fig. 27-64).

Lipomas

The ordinary lipoma is the most common tumor of mesenchymal origin. Only 13% arise in the extracranial head and neck; most are located in the posterior cervical region.[188] The remaining lesions, as a group, are rare, occurring primarily in the oral cavity, pharynx, parotid gland, and larynx. Within the oral cavity, lipomas represent only 1% to 4% of benign oral tumors and 1% of benign tongue tumors. These lesions are composed of mature fat cells arranged in lobules, separated by fibrous tissue septae, usually surrounded by a thin, fibrous capsule.[189] Some variants have been classified histologically, according to the kind and amount of tissue, other than fat, that may also be present.[190] Most common is the fibrolipoma, containing an increased amount of fibrous connective tissue between the fat cells. Other variants include angiolipoma, containing an excess of capillaries; myxolipoma, with wide areas of myxoid change; and chondrolipoma, the most uncommon of the variant lipomas, with osseous or cartilaginous change.[189]

Lipomas are more common in overweight individuals and tend to increase in size during periods of rapid weight gain, being most common below the clavicle in obese women over 40 years of age. In contrast, lipomas in men tend to occur after the seventh decade, primarily in the head and neck region.

Within the oral cavity, lipomas, in decreasing order of frequency, are encountered in the cheek, tongue, floor of the mouth, buccal sulcus, palate, lip, and gingiva, with one third to one half occurring in the cheek.[168, 190] Of those lesions that occur within the tongue, most arise within the oral tongue, as opposed to the tongue base. A huge oral tongue lipoma measuring $10 \times 9 \times 6$ cm, extending to involve the submandibular and sublingual regions, has been reported.[191]

These lesions have a virtually pathognomic, homogeneous, nonenhancing, low CT attenuation ranging from –65 to –125 HU (Figs. 27-65 and 27-66). The most common

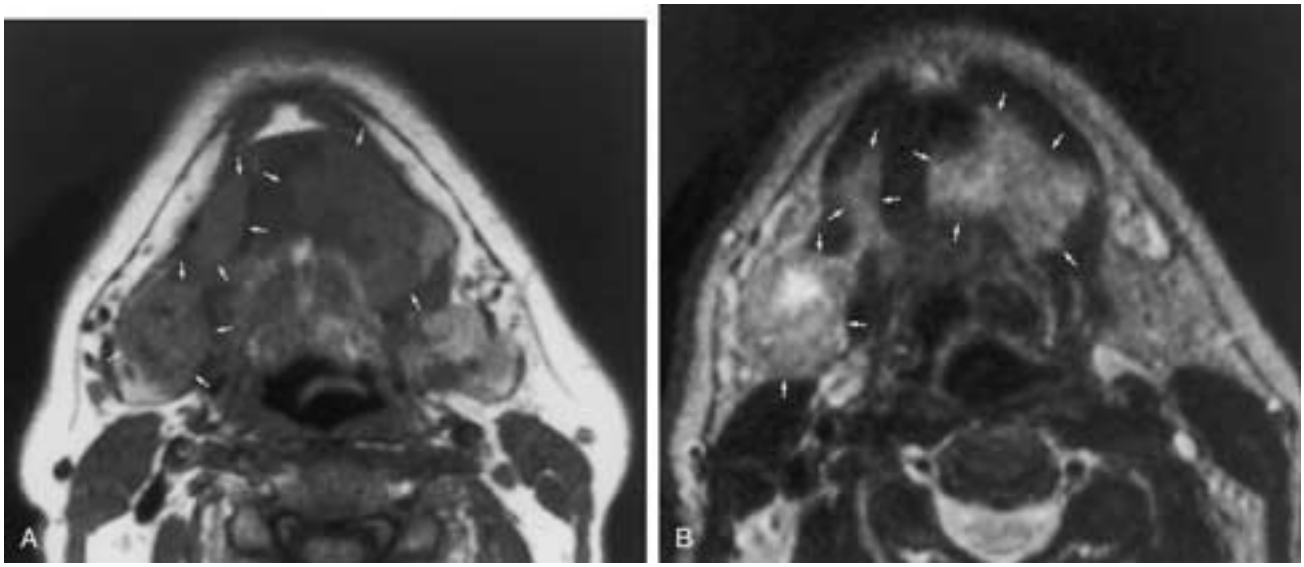

VIEW IMAGE

FIGURE 27-64 Rhabdomyomas. (**A**) Axial T1-weighted and (**B**) axial T2-weighted MR images demonstrate multiple rhabdomyomas involving the oral tongue on the left, the right sublingual space, and the right submandibular region (*arrows*). The lesions are slightly hyperintense to muscle on **A**, becoming more hyperintense to muscle on **B**. Following the administration of contrast, there was faint enhancement of these lesions. The lesions are indicated by the arrows. (Courtesy of Dr. Jan Casselman.)

Copyright © 2003, Mosby, Inc. All rights reserved.

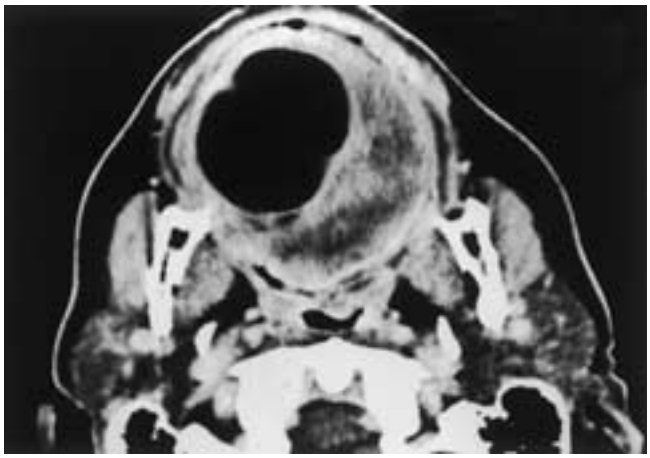

VIEW IMAGE

FIGURE 27-65 Lipoma. Axial contrast-enhanced CT scan demonstrates a very hypodense lesion compatible with fat in the tongue that is virtually indistinguishable from subcutaneous fat.

differential diagnosis includes suprahyoid thyroglossal duct cysts, ranulas, and dermoid lesions, none of which have the typical low fat attenuation. Lipomas often displace and compress adjacent structures but rarely infiltrate them.[192] MR imaging of a typical lipoma demonstrates high signal intensity, consistent with fat, on T1-weighted images and lower T2-weighted signal intensity.

Nerve Sheath Tumors

The terminology used to classify nerve sheath tumors has been somewhat confusing. Schwannomas have been variously termed *neurolemmomas, neuromas, neurinomas,* and *perineural fibroblastomas*.[1] Additionally, some have applied the term *schwannoma* to encompass both neurolemmoma and neurofibroma, while others include schwannomas and neuromas in discussions of neurolemmoma.[193] However, schwannomas (neurolemmoma) and neurofibromas can be distinguished on a histologic basis.[1] Neither should be confused with neuromas, which represent an exaggerated repair response to neuronal injury in which a tangle of regenerating axons, fibrous tissue, and Schwann cells forms at the site of a severed nerve.[194]

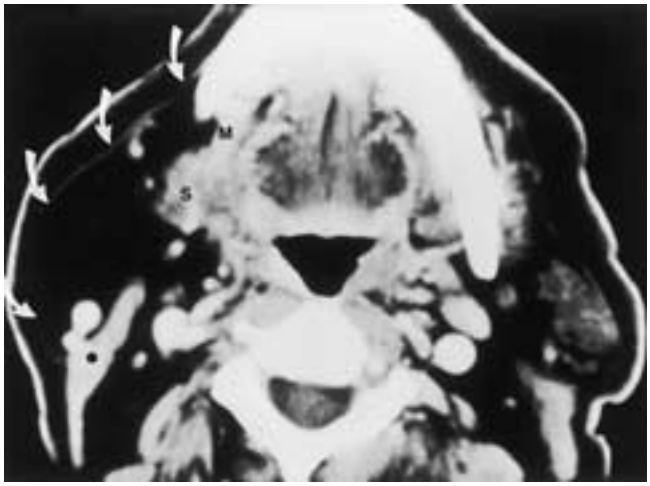

VIEW IMAGE

FIGURE 27-66 Lipoma. Contrast-enhanced CT scan reveals a large lipoma within the right submandibular space. The fat-density lesion is virtually impossible to distinguish from the subcutaneous fat, although it is separated by thin fibers of the platysma muscle (*arrows*). The lesion insinuates among the normal structures of this region. *S*, Submandibular gland; *black dot*, sternocleidomastoid muscle; *M*, mylohyoid muscle.

Schwannomas

Approximately 13% of schwannomas occur in the extracranial head and neck; most are encountered in the lateral cervical region, with the sympathetic chain being the most common site of origin.[195, 196] In 1977, Gallo et al. reported 152 cases of oral schwannomas, 71 of them lingual.[197] In general, schwannomas tend to be somewhat more common in women and typically occur in the 30- to 40-year-old age group.[195] Most schwannomas appear as well-circumscribed, homogeneous, soft-tissue density masses on unenhanced CT and exhibit contrast enhancement. Larger lesions may contain one or more cystic areas and present a more variable CT appearance.[198] Schwannomas tend to be isointense to muscle on T1-weighted images and hyperintense on T2-weighted images.[193] The cystic components of larger schwannomas may be difficult to distinguish from the solid components on T2-weighted MR images because both manifest high signal intensity.[198] Enhancement following administration of contrast is the rule (Fig. 27-67).

Angiographically, schwannomas demonstrate a pattern of moderate hypervascularity, tortuous tumor vessels, and scattered contrast puddles without arteriovenous shunting or vascular encasement. Embolization has been shown to be a useful presurgical adjunct.[199]

Neurofibromas

Neurofibromas involving the oral cavity are rare, and most are associated with neurofibromatosis. Oral manifestations of neurofibromatosis are reported in only 4% to 5% of affected individuals, the tongue being the most common site of involvement.[200] Within the tongue, these rare lesions have been reported to involve either the lingual or the hypoglossal nerves or both.[201] Neurofibromas have a density similar to that of muscle on unenhanced CT studies and enhance following contrast administration. They are typically isointense to muscle on T1-weighted images and hyperintense on T2-weighted images.

Granular Cell Myoblastomas

Granular cell myoblastomas are considered to be of neurogenic origin, although they also contain skeletal muscle and histiocytes. Of these tumors, 50% involve the tongue or floor of the mouth, occurring primarily in young adults. The lateral tip or dorsum of the tongue is most often affected, with infiltration of surrounding tissues being common. The CT appearance is nonspecific, similar to that of squamous cell carcinoma. The MR imaging features, however, may be somewhat more specific because these lesions tend to exhibit low signal intensity on both T1-weighted and T2-weighted images, most likely reflecting their fibrous or skeletal components.[202]

Congenital epulides of the newborn are rare gingival tumors that most often occur along the alveolar ridge of the maxilla in newborn girls. Occasionally, these tumors may involve the mandible or may be multiple. Although the term *congenital gingival granular cell tumor* has been used in

Copyright © 2003, Mosby, Inc. All rights reserved.

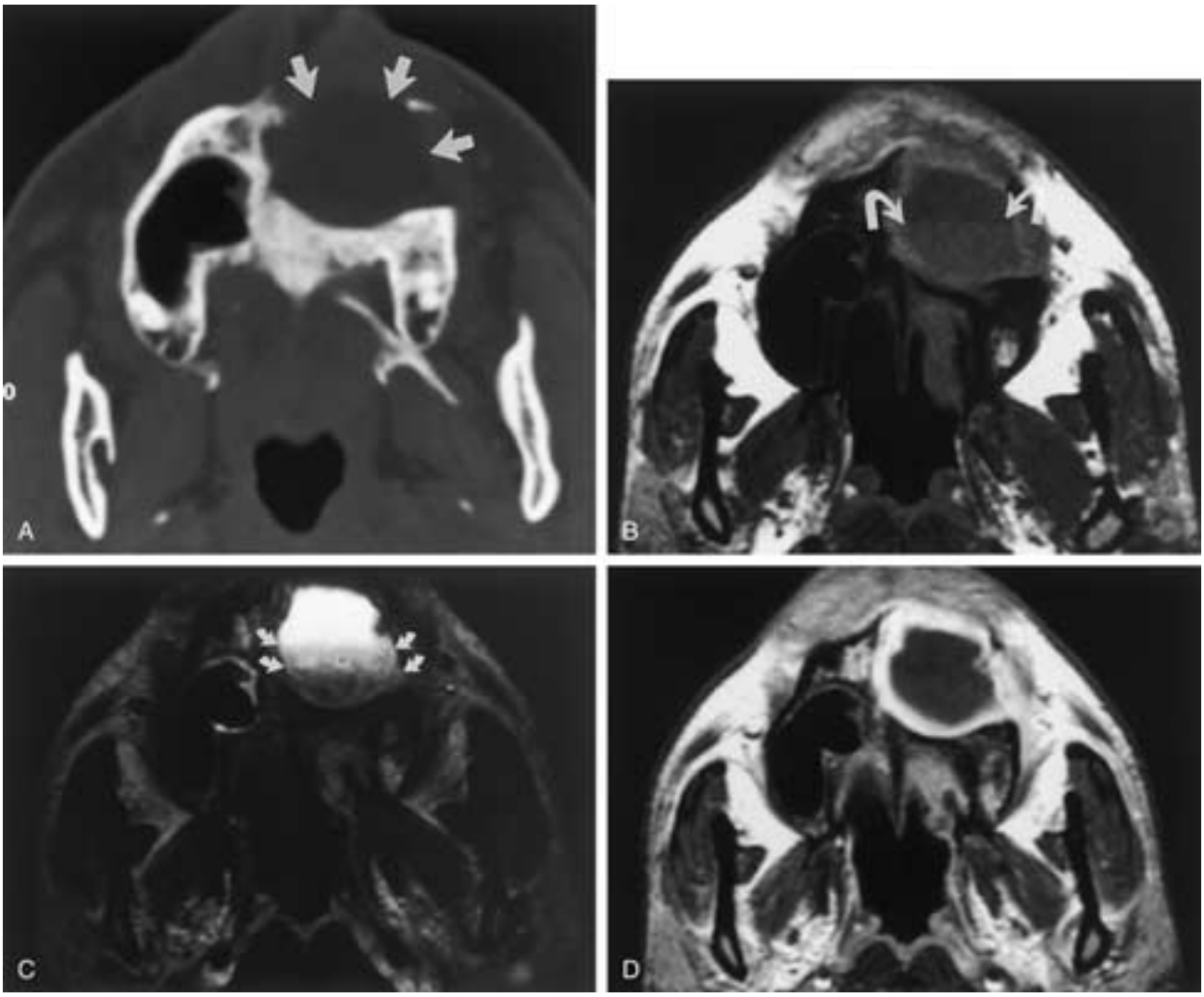

VIEW IMAGE

FIGURE 27-67 Schwannoma in a patient with neurofibromatosis type 2 (probably of the incisive canal). **A**, Axial CT scan at a bone window setting demonstrates a cystic-appearing mass that has destroyed much of the left hard palate and portions of the left maxillary alveolus (*arrows*). Axial T1-weighted (**B**) and T2-weighted (**C**) MR images confirm the cystic nature of this lesion and demonstrate a fluid level within it (*arrows*). The T2-weighted image (**C**) actually shows three definite different density levels. Following contrast administration, an axial (**D**) image reveals well-defined rim enhancement.

reference to these legions, congenital epulides are more vascular, contain less conspicuous nerve bundles, occur exclusively in the pediatric population, and do not involve other organs, in contrast to granular cell myoblastomas.[203, 204] A single report by Koch et al. described the MR imaging appearance of a congenital epulis as heterogeneous, smooth, and well defined, with a signal intensity slightly greater than that of muscle on both T1-weighted and T2-weighted imaging.[205] Complete surgical excision is curative.

Exostoses

Torus palatinus is a benign thickening of the cortical and medullary bone on the oral surface of the hard palate. The nasal portion of the hard palate is unaffected. The exact etiology of this lesion is not known, but it may represent downward misdirection of underused growth potential of the palatal shelf.[206] Heredity appears to be a definite factor in the development of palatal tori. These lesions typically occur in the middle of the hard palate and extend to either side, approximately symmetrically, sparing the region of the greater palatine foramen. Tori grow as the patient grows until maturity at 20 to 30 years of age, although some may continue to grow in later decades of life. Females are affected twice as often as males after the newborn period.

Palatal tori have been subclassified by shape into flat, spindle, nodular, and lobulated varieties, flat and spindle shapes being the most common (86%).[206] Their size is extremely variable, ranging from flat lesions measuring only a few millimeters to large, lobulated lesions that may be 15 mm or larger. On CT, smaller lesions appear as dense cortical bone protruding inferiorly from the oral aspect of the hard palate, optimally demonstrated on scans obtained in the coronal plane (Fig. 27-68), whereas larger tori may

Copyright © 2003, Mosby, Inc. All rights reserved.

VIEW IMAGE

FIGURE 27-68 Torus palatinus. Coronal CT scan at a bone window setting shows a palatal torus composed only of dense cortical bone (*arrow*).

demonstrate cortical bone surrounding areas of cancellous bone, often with a midline fissure (Fig. 27-69).

Most tori remain asymptomatic, tending to be flat or spindle-shaped. Larger lesions, however, may promote food impaction within the grooves and lead to halitosis. Large palatal tori may restrict tongue motion and distort the oral airway, leading to speech disturbances, or may require resection prior to dental prosthesis placement to avoid poor adhesion or rocking of the prosthesis.[206]

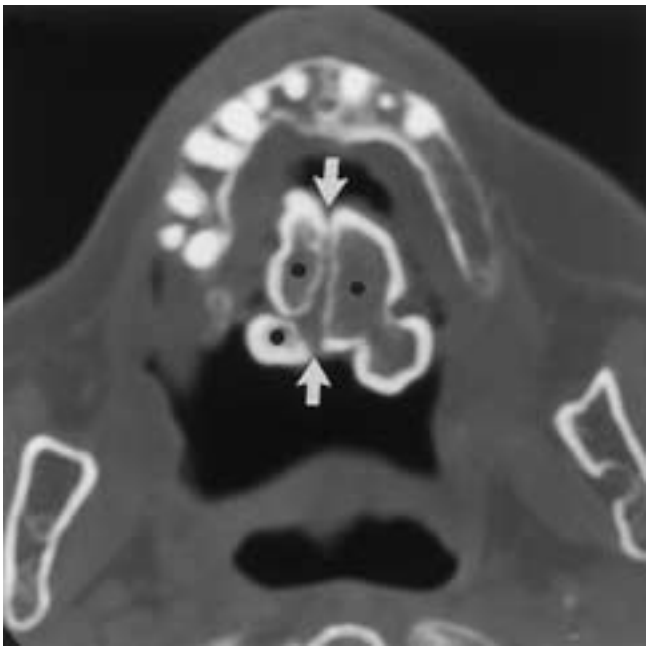

VIEW IMAGE

FIGURE 27-69 Torus palatinus. Axial CT scan obtained at a bone window setting demonstrates a very large torus palatinus projecting into the upper aspect of the oral cavity. The torus is multilobulated, with multiple areas of well-corticated cancellous bone (*dots*). A midline fissure is also present (*arrows*). (Courtesy of Dr. Deborah Reede.)

Tori maxillaris and mandibularis occur more often in patients who have palatal tori than in the general population.[206] Torus maxillaris refers to unilateral or bilateral exostoses that may occur on either the buccal (torus maxillaris externa) or lingual (torus maxillaris interna) aspect of the maxilla (Fig. 27-70). Torus mandibularis occurs exclusively on the lingual aspect of the mandible, typically opposite the root of the second premolar in the region of the mental foramen (Fig. 27-70).[206]

Fibroosseous Lesions

Fibroosseous lesions are a challenging and diverse group of pathologic conditions that are difficult to classify and treat. There are no universally accepted criteria to distinguish these lesions absolutely from one another either clinically, radiographically, or histopathologically.[207, 208]

Many of these lesions are addressed elsewhere in this book but, given the high rate of involvement, if not exclusive involvement, of the maxilla and mandible by some of these entities, a brief discussion of fibroosseous lesions in this chapter on the oral cavity (including the maxilla and mandible) seems warranted.

The common denominator to all of the fibroosseous lesions is the replacement of bone with benign fibrous tissue containing varying amounts of (calcified) mineralized material. These lesions are basically divided into two main groups: fibrous dysplasia, a developmental lesion due to idiopathic arrest in the normal maturation of bone at the woven bone stage, and those lesions that have been postulated to originate from the periodontal ligament. Included in the latter group are central cementifying fibromas and periapical, focal, or florid cemento-osseous dysplasias.[207, 209] Some authors also include lesions such as osteomas, giant cell lesions, and osteoblastomas in discussions of fibroosseous lesions.[207, 210, 211]

Fibrous Dysplasia

Fibrous dysplasia is an idiopathic disorder in which there is an arrest of primitive fibrous stroma at the woven bone stage such that the normal replacement of immature woven bone by lamellar bone does not occur.[212] Osteoblasts are conspicuously absent. The medullary bone is replaced by poorly organized and loosely woven bone, which is manifest radiographically as obliteration of the medullary canal of involved bone associated with bone expansion and thinning of the overlying cortex. The disease may be monostotic (70%) (Figs. 27-71 and 27-72) or polyostotic (30%); the latter tends to occur at an earlier age and may be associated with the McCune-Albright syndrome.[212] Of the monostotic form, approximately 25% of cases involve the head and neck, the maxilla and mandible being the most common sites, while 40% to 60% of patients with the polyostotic form have involvement of the skull and facial bones (Fig. 27-73). Malignant transformation occurs following craniofacial irradiation in approximately 0.5% of cases, predominantly in the polyostotic form. The classic ''ground glass'' or ''frosted glass'' appearance of fibrous dysplasia on plain radiographs and CT is due to the myriad dispersed minute

Copyright © 2003, Mosby, Inc. All rights reserved.

spicules of bone within the lesion, which, as it is not encapsulated, blends imperceptibly into normal cortical bone.[210] The plain radiographic features have been classified into three patterns: pagetoid (56%), sclerotic (23%), and radiolucent or cystic (21%).[213] Fibrous dysplasia is typically hypointense on T1-weighted MR images and of variable signal intensity on T2-weighted images, ranging from low to intermediate to high.[214–216] In a study by Jee et al., 75% of lesions demonstrated central enhancement following contrast administration.[217]

FIGURE 27-70 Maxillary and mandibular tori in a patient with torus palatinus. Coronal (**A**) and axial (**B** and **C**) CT scans obtained at bone window settings demonstrate tori maxillaris interna (*straight arrows* in **A**), tori maxillaris externa (*curved arrows* in **A** and **B**), and tori mandibularis (*dots* in **A** and **C**).

VIEW IMAGE

Copyright © 2003, Mosby, Inc. All rights reserved.

VIEW IMAGE

FIGURE 27-71 Mandibular monostotic fibrous dysplasia. Axial CT scan obtained at a bone window setting demonstrates marked right mandibular expansion and the typical ''ground glass'' appearance of fibrous dysplasia.

(Central) Cementifying Fibroma

At one time the World Health Organization (WHO) separated central ossifying fibromas (COFs), considered to be tumors of osseous origin, from central cementifying fibromas (CCFs), considered to represent tumors of odontogenic origin. However, today there is general agreement that these two lesions merely represent histologic variants of the same lesion, and the 1992 WHO classification now groups them under a single designation as central cemento-ossifying fibroma (CCOF).[218] If the stroma consists primarily of osteoid tissue, the lesions are labeled *ossifying fibromas*. Lesions with connective tissue stroma consisting primarily of foci of basophilic masses of cementum-like tissue are termed *cementifying fibromas*, and those with a combination of osteoid formation and cementum-like tissue within the stroma are termed *cemento-ossifying fibromas*.[219] CCOFs occur almost exclusively in the facial bones of the skull. Seventy percent or more occur in the mandibular molar/premolar area, and there is a definite female predominance (5:1).[209] There is convincing evidence that these lesions originate from elements of the periodontal ligament.[209] CCOFs tend to occur in an older age group (the third and fourth decades) than fibrous dysplasia and are more invasive. Histologic differentiation between CCOFs and fibrous dysplasia is often difficult, and many overlapping features exist. However, two features are noted as distinguishing CCOF from fibrous dysplasia: most of the disorganized bony spicules in CCOFs are composed of lamellar bone rather than immature woven bone, as in fibrous dysplasia, and osteoblasts rim the trabeculae in CCOFs, whereas they are absent in fibrous dysplasia.[210] On CT, CCOFs are usually well-circumscribed, expansile, unilocular lesions with discrete areas of calcification and ossification. Their MR imaging appearance is variable, but most reported lesions are iso- or hypointense to muscle on T1-weighted images and very hypointense on T2-weighted images secondary to the calcific and fibrous nature of the lesions and resulting low free water content (Fig. 27-74).[220]

There is a juvenile aggressive form of CCOF that presents in childhood (approximately 80% of patients are under 15 years of age), more commonly involves the maxilla rather than the mandible, and is more aggressive clinically, exhibiting rapid growth.[209, 221, 222] Pathologically, these lesions tend to be more vascular than the typical CCOF.

VIEW IMAGE

FIGURE 27-72 Maxillary monostotic fibrous dysplasia. Coronal CT scan at a bone window setting reveals enlargement of the right maxillary alveolus and hard palate with distortion of dentition. The right maxilla is almost double the size of the left. A very large intrasinus component is present, the appearance of which differs from that in the alveolar bone.

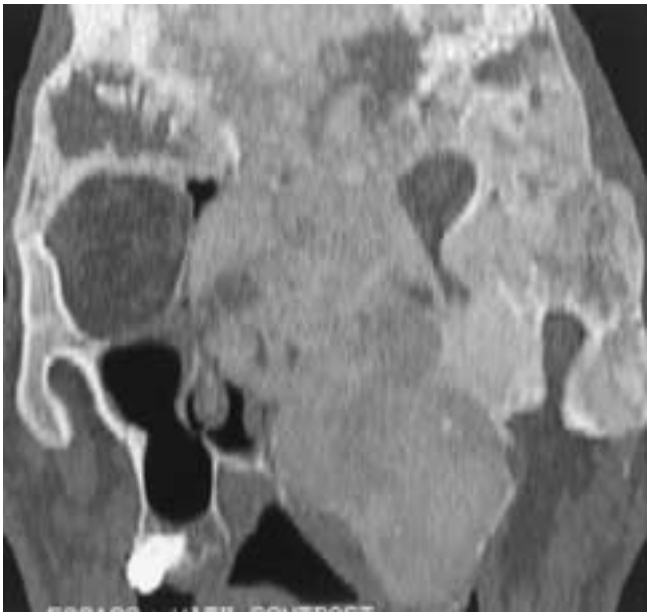

FIGURE 27-73 Diffuse skull and facial fibrous dysplasia. This coronal CT scan reveals the extensive involvement of the midface and left facial bones with obliteration of the left maxillary sinus, most of the nasal cavity, ethmoid, and frontal air cells, and severe left orbital encroachment. This pattern of severe facial bone involvement is termed *leontitis ostea*.

VIEW IMAGE

Copyright © 2003, Mosby, Inc. All rights reserved.

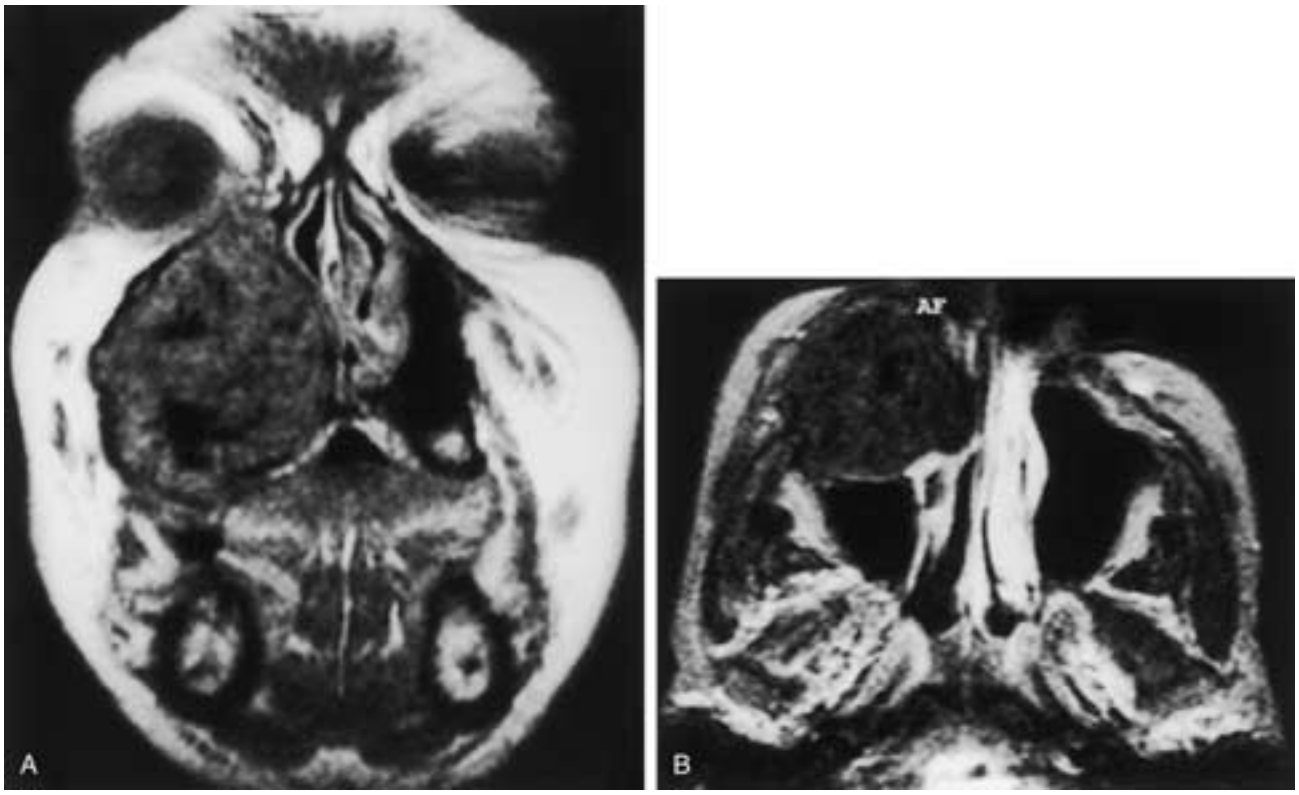

VIEW IMAGE

FIGURE 27-74 Central cementifying ossifying fibroma. **A**, Coronal T1-weighted MR image reveals heterogeneous hypointensity and the lesion became even more hypointense on the T2-weighted image (**B**).

Osteomas

Osteomas are well-differentiated benign tumors consisting predominantly of cancellous or compact bone that increase in size by continuous formation of bone.[223, 224] They are most commonly encountered within or on the periphery of membranous bones of the skull, face, and jaws. Their pathogenesis is obscure, although the combination of trauma and muscle traction has been proposed.[225] Solitary osteomas of the mandible and maxilla are uncommon and occur more often in the mandible.[225] Multiple osteomas are encountered in association with Gardner's syndrome. Most lesions are very slow-growing and are identified after the age of 25 years.

Osteomas are rare within the soft tissues of the extracranial head and neck, especially the tongue. In a review of the English-language literature in 1989, Nash et al. reviewed 31 previously reported cases of lingual osteomas and added one of their own.[226] These lesions predominate in the third decade, and 75% occur in females. The majority of reported lingual osteomas occur at the junction of the anterior two thirds and the posterior one third of the tongue, in the region of the circumvallate papillae or foramen cecum (Fig. 27-75). Because of its location, a lingual osteoma may be mistaken clinically for lingual thyroid tissue.[227]

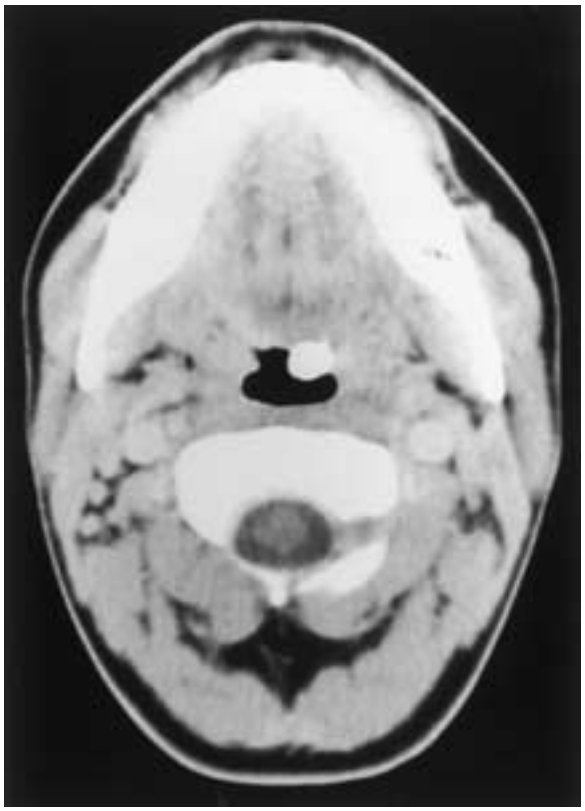

FIGURE 27-75 Lingual osteoma. Axial CT scan shows a bone density mass near the midline of the base of the tongue.

VIEW IMAGE

Giant Cell Lesions

Much controversy exists regarding the terminology and nature of central giant cell lesions of the jaws. The histologic differentiation between central giant cell granulomas (CGCGs) and central giant cell tumors (CGCTs) is rather

Copyright © 2003, Mosby, Inc. All rights reserved.

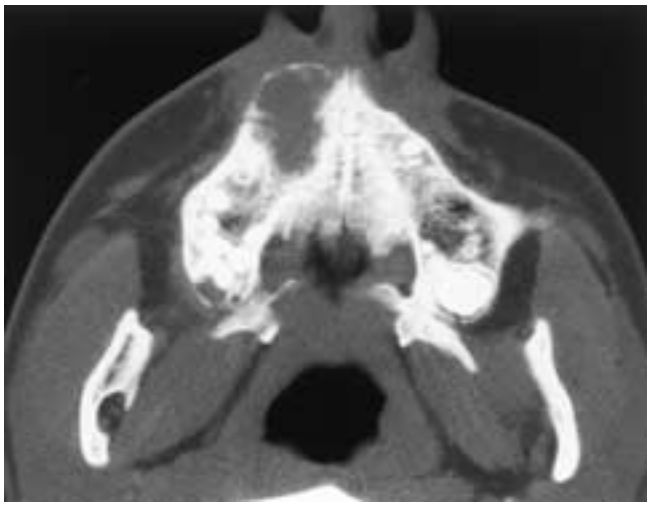

VIEW IMAGE

FIGURE 27-76 Central giant cell granuloma (nonaggressive). Axial CT scan obtained with bone window settings reveals destruction of the right hard palate by a somewhat poorly defined lesion. The margins are somewhat indistinct and the lesion is not well corticated, which may suggest a more ominous histology. (Courtesy of Dr. Thomas Underhill.)

obscure as there are only gradual differences and no absolute criteria for differentiation.[228] These two entities probably represent a continuum of a single disease process.[229] Although the term *granuloma* is still often used, some have suggested the designations of nonaggressive and aggressive forms, the aggressive form behaving more like the classically described CGCT. In the jaws, CGCG may arise in association with Paget's disease, whereas in the skeleton, CGCT is associated with this disease.[230]

CGCG, as it has been classically described, is an uncommon nonneoplastic fibroosseous lesion, accounting for less than 7% of all benign jaw lesions. It is found almost exclusively in the mandible, maxilla, or associated structures, is most common in the anterior mandible, and often crosses the midline.[231, 232] This lesion occurs most frequently in young adults (50% occur prior to age 30), and there is a definite female predilection. The CT features of these lesions in 10 children reported by Bodner and Bar-Zin fell into two distinct patterns: a unilocular osteolytic lesion (Fig. 27-76) or multilocular with septations coursing through the lesion (Fig. 27-77).[232] The MR imaging features are relatively nonspecific and do not allow differentiation from other benign lesions of the jaw such as Langerhans' histiocytosis (Figs. 27-78 and 27-79).

Benign Odontogenic Lesions

A variety of cysts and benign neoplasms arising from various components of dental structures are encountered in the mandible, the maxillary alveolus, and the hard palate. The *radicular cyst* (periodontal, periapical cyst) is the most common odontogenic cyst. It arises at the apical end of an erupted, devitalized, infected tooth in a preexisting periapical granuloma.[233] The *dentigerous cyst* represents 95% of follicular cysts and develops from the enamel organ of an unerupted tooth after the crown has developed.[233, 234] These are also usually well-defined, corticated, round, unilocular cystic lesions, and the tooth crown is typically identified within the cyst (Fig. 27-80), although large cysts may be multilocular. The *primordial cyst* represents the remaining 5% of follicular cysts and results from degeneration of the enamel organ with absence of the tooth crown. This cyst is also typically unilocular and well circumscribed. *Odontogenic keratocysts,* representing 5% to 15% of all jaw cysts, are most often of the parakeratotic variety. They are rapidly growing, aggressive lesions that contain keratin, occur two to four times more often in the mandible (usually the body and ramus) than in the maxilla, and are associated with basal cell nevus (Gorlin's syndrome) and Marfan's syndrome. These lesions have the highest rate of recurrence of any odontogenic cyst after excision (12% to 63%).[234, 235] Squamous cell carcinomas arising in odontogenic keratocysts have been reported.[236] Keratocysts tend to be unilocular and expansile radiolucent lesions with sclerotic, sharply defined smooth or scalloped margins (Fig. 27-81). When they occur in the maxilla, keratocysts may elevate the floor of the maxillary sinus, similar to dentigerous cysts.[237] On MR imaging, keratocysts demonstrate variable signal intensity, usually intermediate or high on T1-weighted images, depending upon the amounts of contained epithelial debris and blood degradation products. These lesions typically brighten and demonstrate heterogeneous intermediate signal intensity on T2-weighted images.[235, 237] Their walls are thin and usually demonstrate weak enhancement, features that allow their distinction from ameloblastomas.[235]

Ameloblastomas are benign, locally aggressive, nonencapsulated, infiltrating neoplasms of odontogenic origin. They are thought to originate from enamel organ-like tissue composed of epithelial elements, but these lesions do not differentiate sufficiently to form enamel and may not even contain ameloblasts.[238] They occur in the mandible about 85% of the time, usually present in the fourth or fifth decade, and show no definite sex predilection.[233, 234, 239, 240] A variety of benign histologic variants have been described, as has a metastasizing malignant form (ameloblastic carcinoma), discussions of which are beyond the scope of this chapter.[240] On CT, ameloblastomas may be unilocular, well circumscribed, and radiolucent in younger patients (average age, 26 years), but they grow to become multiloculated, expansile neoplasms as the patient ages (average age, 38 years). The locules may be only 1 cm in size, producing an overall honeycomb appearance, typically nonenhancing and inhomogeneous. Lesions with larger locules have been described as having a ''soap bubble'' appearance (Fig. 27-82).[233, 238] On MR imaging, these lesions are usually of slightly inhomogeneous intermediate signal intensity on T1-weighted images, largely isointense with muscle, and of inhomogeneous higher signal intensity on T2-weighted images with lower signal intensity septations.[238] Areas of signal void, corresponding to areas of calcification, may be present, and the solid portions of the tumor enhance markedly.[235]

Miscellaneous Benign Lesions

Incisive Canal (Nasopalatine Duct) Cysts

These lesions are one of a group of fissural cysts that develop from trapped epithelium in fusion lines during facial development. Incisive foramen/canal cysts are the most common developmental cysts of the maxilla.[233] The size of the normal incisive foramen varies greatly, averaging 3 by 3 mm.[241] The majority of the time, the incisive foramen does not have a cortical margin. However, when a cyst is present,

Copyright © 2003, Mosby, Inc. All rights reserved.

the incisive foramen or canal will appear enlarged, often with a sclerotic margin on CT. This is best appreciated on axial images (Fig. 27-83). The cysts develop from proliferation of epithelial or mucous cells within the nasopalatine canal.[233] This permits secretion of mucoid material and explains the signal characteristics noted within these cysts on MR images (Fig. 27-84). The signal is typically hyperintense on T1-weighted images and falls off somewhat on T2-weighted images, but this is variable and reflective of the mucoid content of the cysts. These lesions are located within the midline of the hard palate when they involve the incisive canal rather than the incisive foramen, expanding the palate, usually with a well-defined margin, and are easily identified on MR imaging.

Osteochondroma (Osteocartilaginous Exostosis)

Osteochondromas are the most common benign tumors of bone, representing 35% to 50% of all benign bone tumors.[225] In the craniofacial region, however, these lesions are quite rare, reported in the skull base, maxillary sinus, zygomatic arch, and mandible.[242] Mandibular osteochondromas are most often located on the coronoid process, followed by the condyle, but have also been reported to occur in the ramus, body, and symphyseal regions.[243–246] These exophytic lesions arise from the cortex of bone and are covered by a cartilaginous cap.

Chondroma

Chondromas are benign tumors of cartilage. Uncommon within the oral cavity, most chondromas occur in the hard palate and alveolar ridge or involve the condyle or coronoid process of the mandible. Only a few extraskeletal oral chondromas have been reported, the tongue being the most common site.[247] These lesions most often affect the lateral borders or dorsum of the oral tongue and occur equally in both sexes; the mean age at presentation is 31 years.[247] The etiology of these cartilaginous lesions in the tongue is not yet clearly established.

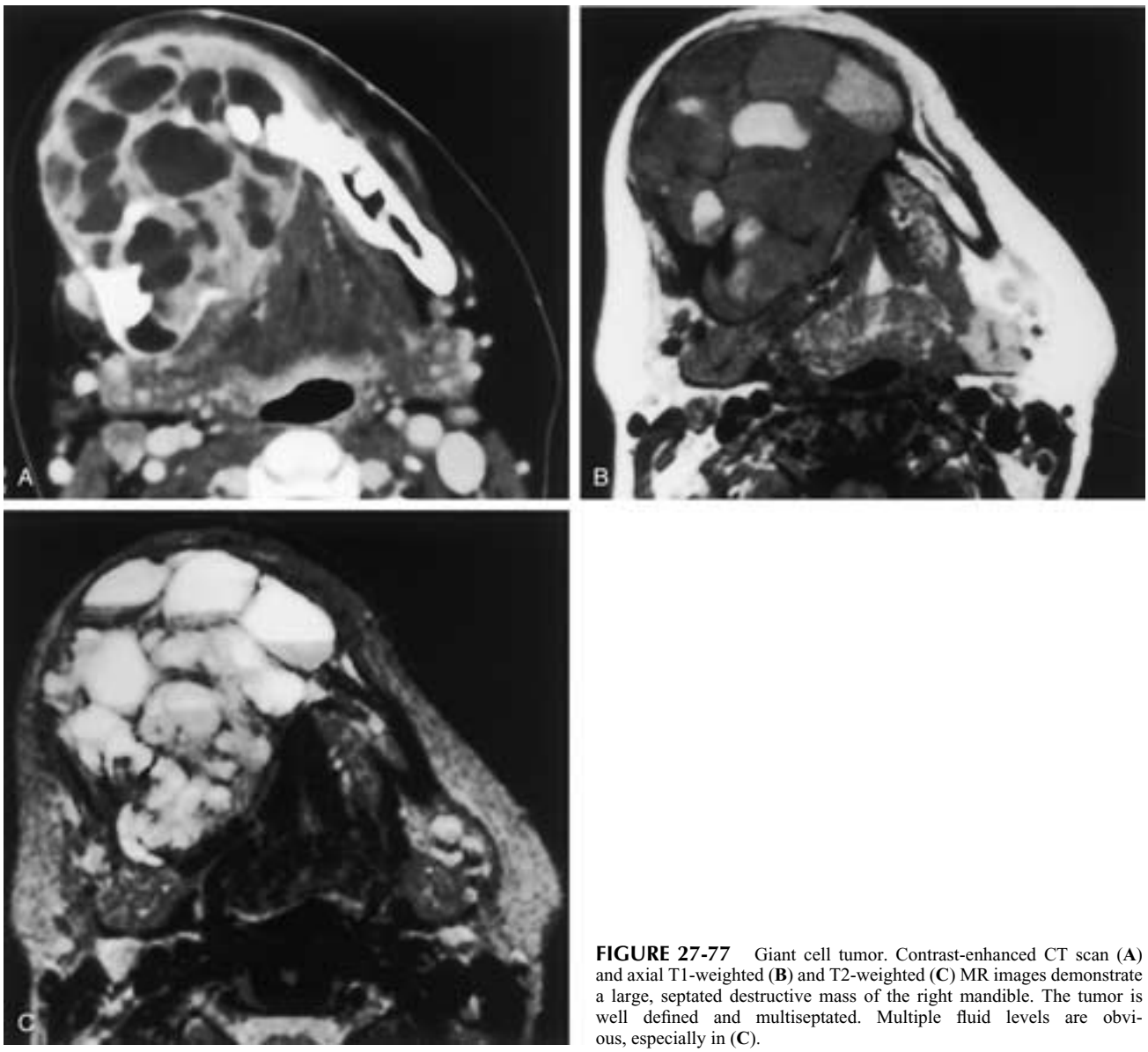

FIGURE 27-77 Giant cell tumor. Contrast-enhanced CT scan (**A**) and axial T1-weighted (**B**) and T2-weighted (**C**) MR images demonstrate a large, septated destructive mass of the right mandible. The tumor is well defined and multiseptated. Multiple fluid levels are obvious, especially in (**C**).

VIEW IMAGE

Copyright © 2003, Mosby, Inc. All rights reserved.

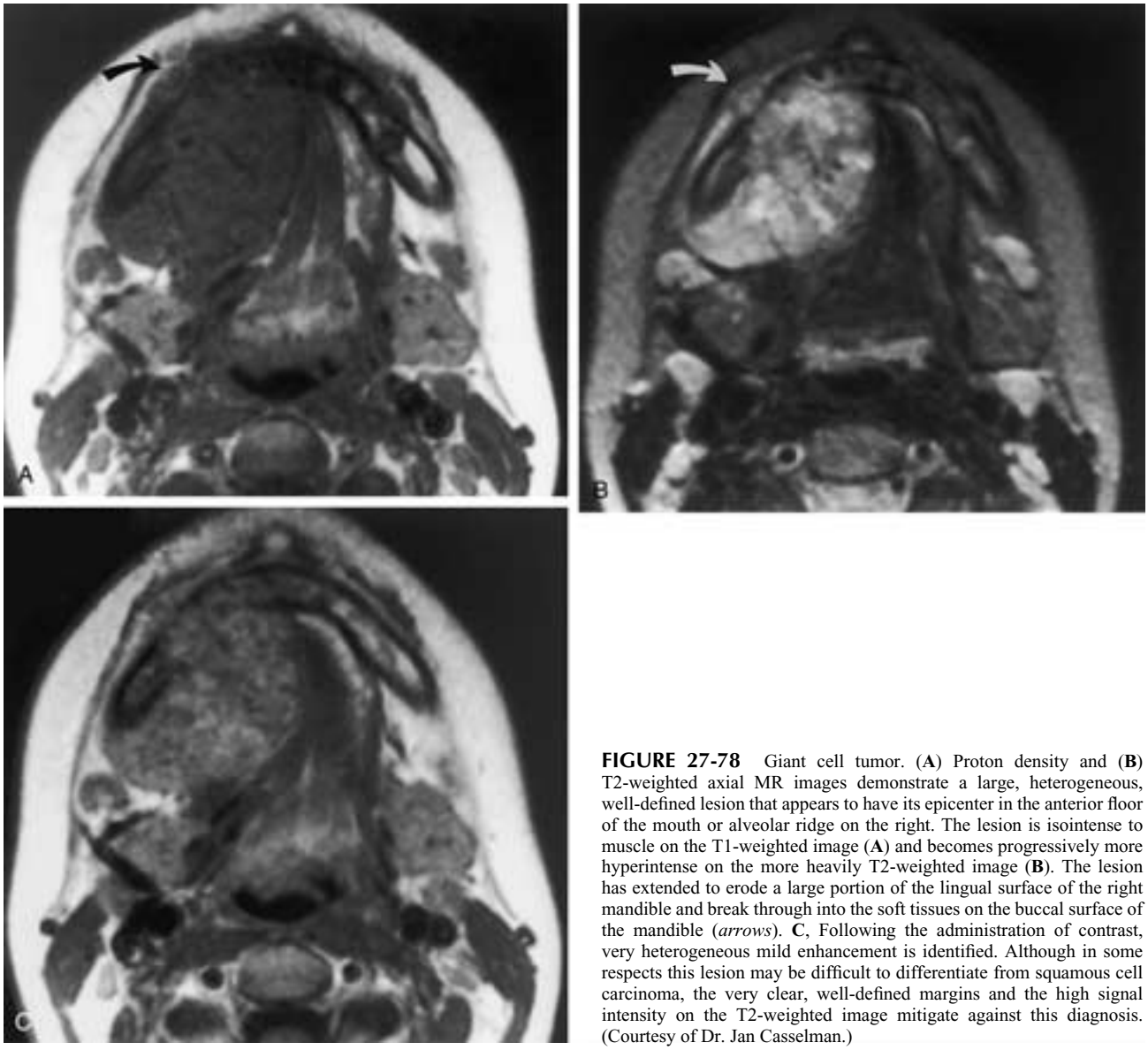

FIGURE 27-78 Giant cell tumor. (**A**) Proton density and (**B**) T2-weighted axial MR images demonstrate a large, heterogeneous, well-defined lesion that appears to have its epicenter in the anterior floor of the mouth or alveolar ridge on the right. The lesion is isointense to muscle on the T1-weighted image (**A**) and becomes progressively more hyperintense on the more heavily T2-weighted image (**B**). The lesion has extended to erode a large portion of the lingual surface of the right mandible and break through into the soft tissues on the buccal surface of the mandible (*arrows*). **C**, Following the administration of contrast, very heterogeneous mild enhancement is identified. Although in some respects this lesion may be difficult to differentiate from squamous cell carcinoma, the very clear, well-defined margins and the high signal intensity on the T2-weighted image mitigate against this diagnosis. (Courtesy of Dr. Jan Casselman.)

VIEW IMAGE

Epithelioid Hemangioendothelioma

Only five cases of these rare lesions involving the oral cavity have been reported.[248–251] Three tumors involved the gingiva, one involved the tongue, and one involved the palate. These lesions are soft-tissue vascular neoplasms characterized by proliferation of endothelial cells with an epithelioid morphology. Their biologic behavior is considered borderline in that they have an indolent course with a potential for recurrence but rarely metastasize.

Asymmetric Maxillary Sinus Pneumatization

Pneumatization of the maxillary sinus is quite variable, and patients have been examined for asymmetry of the hard palate on physical examination produced by extensive asymmetric maxillary sinus pneumatization. Figure 27-85 is of a 43-year-old man referred for CT by his dentist to exclude a mass on the left aspect of the hard palate because the contour of the palate was extremely asymmetric.

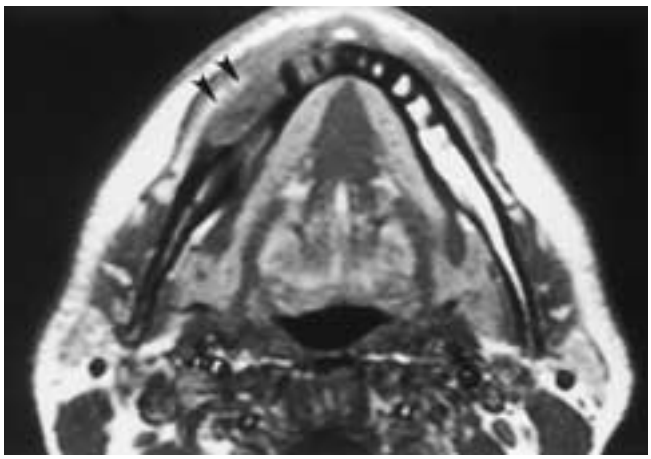

FIGURE 27-79 Eosinophilic granuloma. Axial T1-weighted MR image demonstrates a destructive lesion involving much of the buccal cortex of the mandible on the right and extending into the soft tissues anteriorly (*arrowheads*).

VIEW IMAGE

Copyright © 2003, Mosby, Inc. All rights reserved.

VIEW IMAGE

FIGURE 27-80 Dentigerous cyst. Coronal CT scan obtained at bone window settings reveals a unilocular cyst lesion that replaces much of the right maxillary alveolus and fills the right maxillary sinus. The crown of an unerupted tooth is seen in the superior aspect of the cyst (*arrow*).

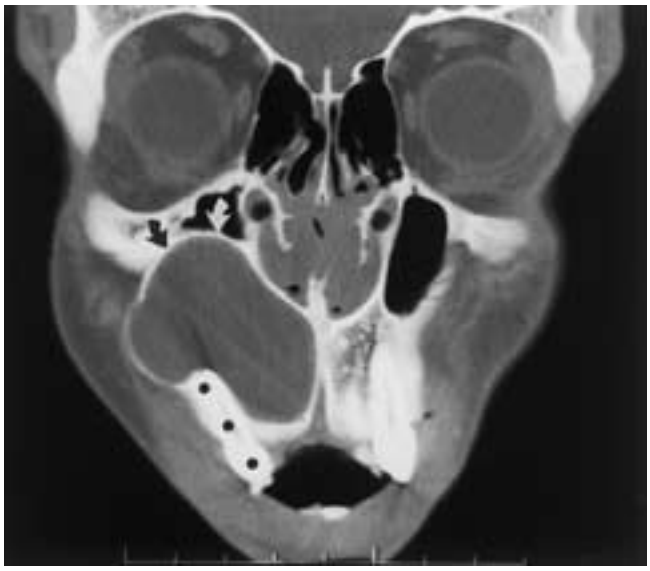

VIEW IMAGE

FIGURE 27-81 Odontogenic keratocyst. Coronal CT scan at bone window settings demonstrates a right maxillary/hard palate cystic-appearing lesion. Note the very well defined sclerotic margins compared to the margins of the dentigerous cysts of Figure 27-80. Located in a more anterior position, this keratocyst replaces much of the hard palate on the right and elevates the maxillary sinus floor (*arrows*) but does not fill the entire sinus. No associated unerupted tooth crown is seen, but there is a fully erupted canine tooth that is significantly malpositioned by the cyst (*dots*). (Courtesy of Dr. Thomas Underhill.)

Malignant Lesions

Only 7% of oral cavity lesions are malignant, but of these lesions, squamous cell carcinoma accounts for 90%.[252] Other malignancies encountered in this region include minor salivary gland tumors (adenoid cystic carcinoma, adenocarcinoma, and mucoepidermoid carcinoma), lymphomas, other rare tumors including sarcomas (liposarcoma, rhabdomyosarcoma), and a variety of common and uncommon neoplasms of the mandible. Most masses within the oral cavity, both benign and malignant, are amenable to direct clinical examination, which is the best means by which to detect mu-

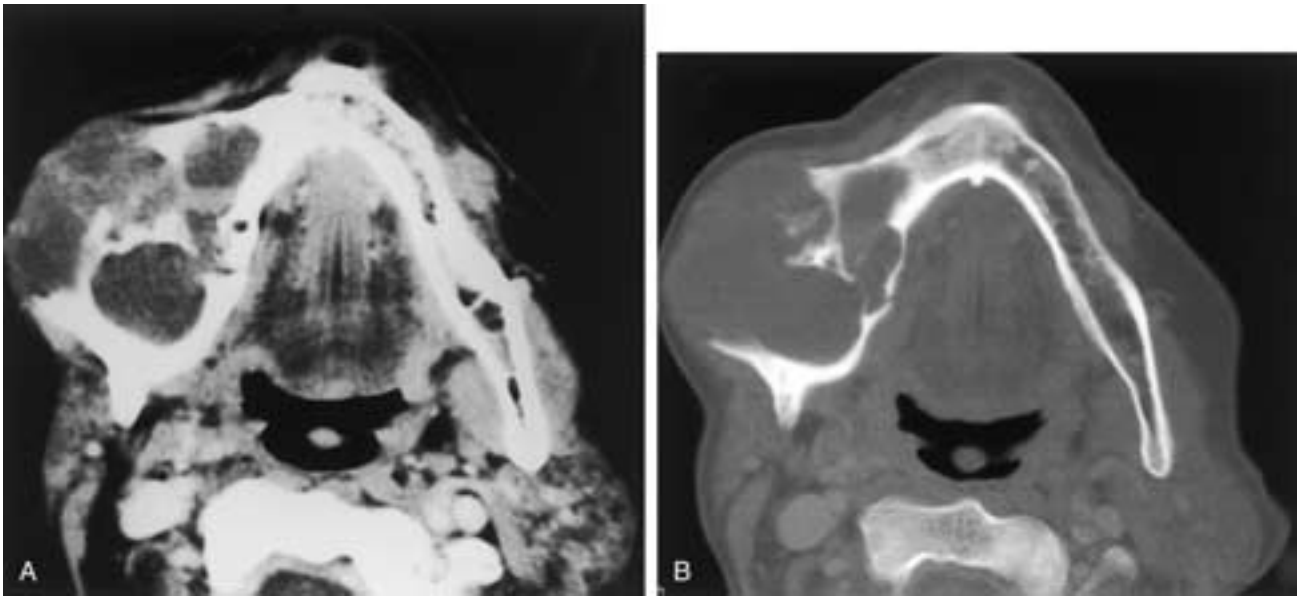

VIEW IMAGE

FIGURE 27-82 Ameloblastoma. Axial contrast-enhanced CT scans filmed at (**A**) soft-tissue and (**B**) bone window settings demonstrate a large, poorly circumscribed, destructive lesion of the right mandible. The tumor is enlarging at the expense of the buccal aspect of the mandible. There is an overall ''soap-bubble'' appearance to this lesion, which appears to contain both solid and cystic components. (Courtesy of Dr. Thomas Underhill.)

Copyright © 2003, Mosby, Inc. All rights reserved.

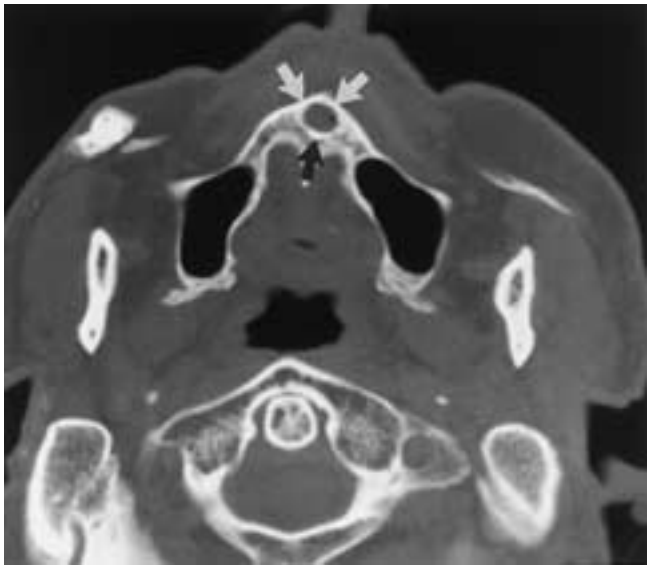

FIGURE 27-83 Incisive foramen cyst. Axial CT scan demonstrates an incisive foramen cyst. It is a benign-appearing, well-corticated lesion (*arrows*).

VIEW IMAGE

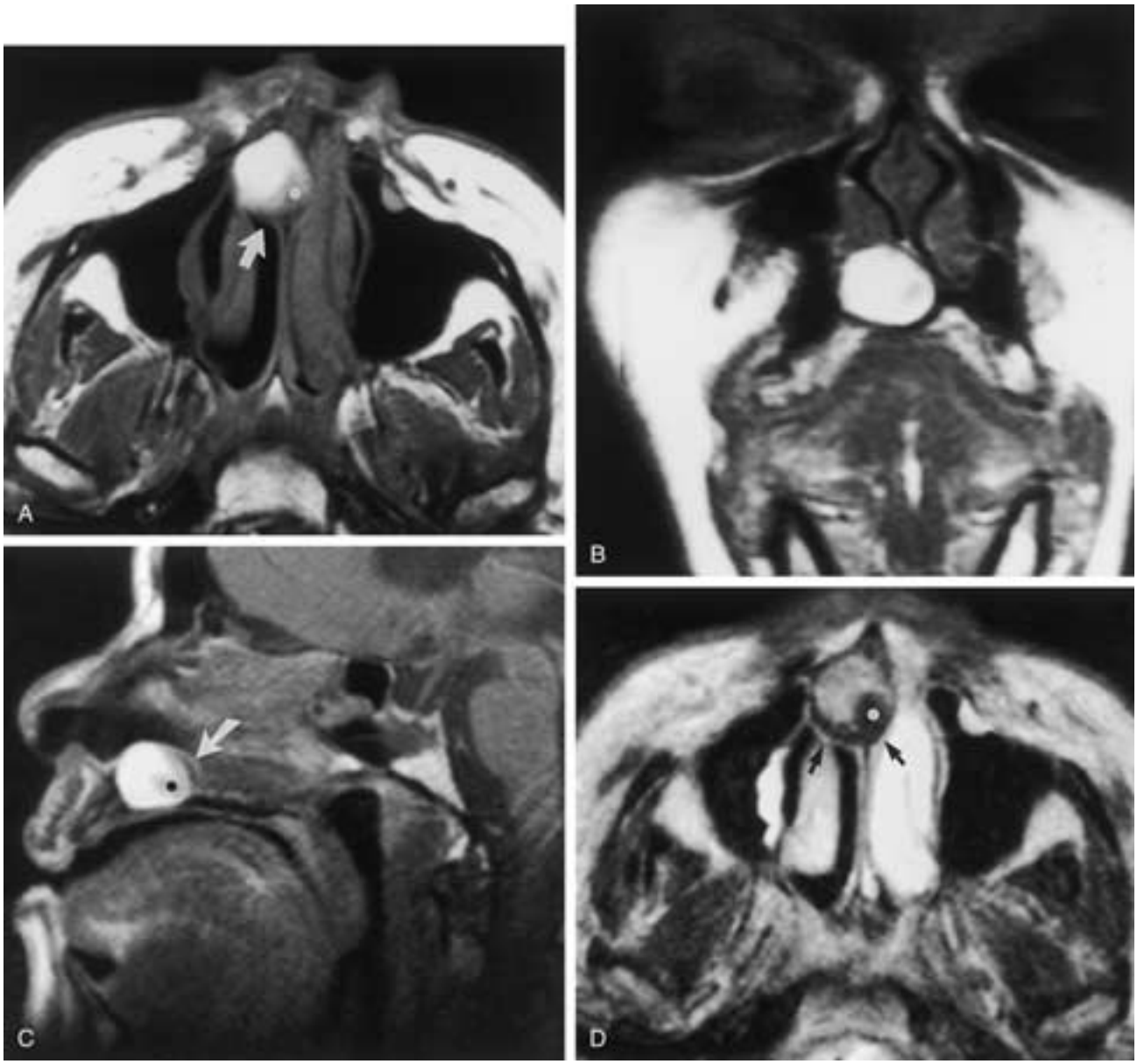

VIEW IMAGE

FIGURE 27-84 Incisive canal cyst. Axial T1-weighted MR images in the (**A**) axial, (**B**) coronal, and (**C**) sagittal planes demonstrate a unilocular lesion of high signal intensity in the midline of the hard palate. There is a small area of low signal intensity in the posterior aspect of this lesion (*dots*). Bony expansion can be appreciated (*arrows*). **D**, Axial T2-weighted MR image reveals relatively intermediate signal in the lesion. The solid component (*dot*) and bony expansion (*arrows*) are better defined.

Copyright © 2003, Mosby, Inc. All rights reserved.

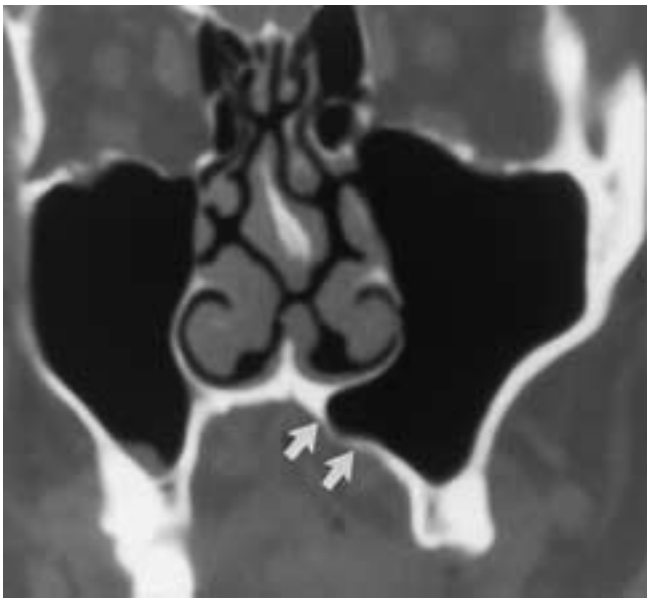

VIEW IMAGE

FIGURE 27-85 Asymmetric maxillary sinus pneumatization. Coronal CT scan obtained with bone window settings demonstrates extensive left maxillary sinus pneumatization. Extension to involve the hard palate has produced a mass effect and depression of the palate on the left (*arrows*), which are responsible for the asymmetry palpated by the patient's dentist.

Table 27-2
ORAL CAVITY: OROPHARYNGEAL SCCa: TNM STAGING

TX	Primary tumor cannot be evaluated	
T0	No evidence of primary tumor	
Tis	Carcinoma in situ	
T1	Tumor 2 cm or less in greatest diameter	
T2	Tumor more than 2 cm but less than 4 cm in greatest diameter	
T4	Tumor invades adjacent structures (skin, cortical bone, etc.)	
NX	Regional lymph node metastases	
N0	No regional lymph node metastases	
N1	Metastasis to a single ipsilateral lymph node less than 3 cm in greatest diameter	
N2a	Metastasis to a single ipsilateral lymph node more than 3 cm but less than 6 cm in greatest diameter	
N2b	Metastases to multiple ipsilateral lymph nodes, all less than 6 cm in greatest diameter	
N2c	Metastases to bilateral or contralateral lymph nodes, all less than 6 cm in greatest diameter	
N3	Metastases to any lymph nodes more than 6 cm in greatest diameter	
MX	Presence of distant metastases cannot be measured	
M0	No distant metastases	
M1	Distant metastases present	
	Stage 0	Tis N0 M0
	Stage 1	T1 N0 M0
	Stage 2	T2 N0 M0
	Stage 3	T3 N0 M0 T1, 2, 3 N1 M0
	Stage 4	All T4 lesions All N2, N3 lesions All M1 lesions

cosal involvement. The primary purpose of imaging these lesions is to detect their deep or submucosal extent. Staging of primary malignancies of the oral cavity is uniformly based on the TNM system developed by the American Joint Commission on Cancer Staging (Table 27-2).[252]

Squamous Cell Carcinoma

Squamous cell carcinoma (SCCa) typically affects men aged 50 to 70 years with a long history of alcohol and tobacco abuse.[253, 254] Heavy-drinking smokers have a risk of developing SCCa 6 to 15 times greater than that of abstainers.[254] Approximately two thirds of the tumors are moderately or far advanced at the time of initial presentation. The behavior of SCCa of the oral cavity differs somewhat from that of SCCa of the oropharynx. The mucosa of the oropharynx, posterior to the circumvallate papillae, is derived from endoderm and has a tendency to be affected by less well-differentiated, aggressive carcinomas. The squamous epithelium within the oral cavity, however, is derived from ectodermal elements and tends to be affected by less aggressive lesions.[1, 255] Differences in lymphatic drainage also exist.

Although SCCa may arise from any mucosal surface, it has a tendency to affect three specific intraoral areas: the floor of the mouth, the ventrolateral tongue, and the soft palate complex (soft palate proper, retromolar trigone, anterior tonsillar pillar).[254, 256] Of 222 asymptomatic SCCa in 161 drinking smokers (excluding 15 involving the lip), 201 (97%) were identified in these three locations: 101 (50%) in the floor of the mouth, 64 (32%) in the soft palate complex, and 6 (18%) on the ventrolateral tongue.[257] Only 6 of the 222 lesions were not located in one of these three high-risk areas (excluding the lip). Frequency according to site of occurrence, as reported by Lederman from a study of 14,253 patients, is listed in Table 27-3.[258] The observation that the vast majority of oral cavity SCCa arise from the relatively limited most dependent portions of the oral cavity mucosa may be due to a variety of factors. Two of these dependent regions (floor of the mouth and oral tongue) are continuously bathed in a pool of saliva, which may serve as a reservoir of exogenous carcinogens, primarily derived from the irritating effects of alcoholic beverages and tobacco. Individuals with SCCa of the oral tongue and floor of the mouth have the highest rates of alcohol consumption. Although the soft palate complex is not a dependent reservoir, it is possible that inhaled tobacco smoke is concentrated in this area and exerts a direct carcinogenic

Table 27-3
FREQUENCY OF ORAL CAVITY CANCER BY LOCATION

Location	Frequency (%)
Lower lip	38
Oral tongue	22
Floor of the mouth	17
Gingiva	6
Palate (hard/soft)	5.5
Upper lip	4
Buccal mucosa	2
Other	5.5

From Lederman M. The anatomy of cancer. J Laryngol Otol 1964;78:181–208.

Copyright © 2003, Mosby, Inc. All rights reserved.

effect.[254] In addition, in contrast to the relatively thick layer of squamous cell epithelium, containing well-developed rete pegs and a prominent superficial keratin layer that lines most of the oral cavity, these high-risk areas are lined by thin, relatively atrophic mucosa with shallow or nonexistent rete pegs and little surface keratin.[147, 254, 256]

Primary floor of the mouth SCCa, or extension from adjacent SCCa into the floor of the mouth, carries a potential for involvement of nerves and vessels within the neurovascular bundles. Vascular and perineural invasion have adverse effects on overall patient survival due to reduced local and regional tumor control.[259, 260] Vascular invasion is associated with an increased likelihood of cervical nodal metastases, which in turn is the most reliable prognostic indicator for patients with SCCa.[261] Perineural invasion is often clinically silent and permits tumor extension beyond the expected tumor margins, often resulting in positive margins at surgical resection and a greater likelihood of recurrence.[262] Most authors believe that neurovascular invasion is indicative of tumors with aggressive biological behavior and greater metastatic potential.[260, 263] Elective neck dissection, radiation therapy of cervical nodes, or both is therefore recommended.[264]

It has been shown that CT can reliably predict neurovascular invasion by SCCa in this region.[261] Aggressive tumor margins, invasion of the sublingual space, and lesion location adjacent to neurovascular structures are all highly suggestive findings of neurovascular invasion. There is also a strong correlation between tumor size and neurovascular invasion such that tumors with a mean diameter of at least 2 cm on CT are more likely to be associated with neurovascular invasion.[261]

It is estimated that 30% to 65% of patients with oral cavity SCCa have nodal involvement at the time of initial presentation, the presence or absence of which is the single most important prognostic indicator in this patient population.[2, 265–268] For this reason, all of the cervical lymph node chains should be imaged at the same time that the primary tumor is imaged.[269] This may be accomplished by either CT or MR imaging, although currently, MR imaging is not as accurate as CT in its ability to demonstrate either extranodal tumor spread or central necrosis.[270, 271]

On CT, SCCa has a density similar to that of muscle and enhances, usually moderately, following administration of contrast. These tumors are also identified by their distortion of the normal structures and surrounding fat planes. Squamous cell carcinomas possess MR signal intensities similar to those of muscle on T1-weighted images and inhomogeneous increased signal intensity on T2-weighted images. Tumors enhance to some degree with gadolinium.[272, 273] Nonenhanced T1-weighted MR imaging appears to provide the most useful sequence for delineation of tumor margins and for assessing the extent of tumor, as some lesions are poorly seen on T2-weighted fast spin-echo (FSE) sequences. If margins are not clearly defined on the T1-weighted sequences, the recommendation is to proceed with T2-weighted FSE and contrast-enhanced T1-weighted imaging.[273]

SCCa of the Lip

SCCa of the lip typically arises from the vermillion border and spreads to involve the orbicularis oris muscle and adjacent skin. Small lesions are very difficult to distinguish from normal orbicularis oris muscle fibers. More advanced lesions may extend to directly involve the buccal mucosa and mandible, and rarely the mental nerve, permitting access to the mandibular marrow and potential perineural extension along the inferior alveolar nerve. The presence of osseous involvement classifies a lesion as stage T4 and is a contraindication for treatment with wide local excision.[274] The lymphatic drainage of these tumors is to submental, submandibular, and internal jugular nodes.

SCCa of the Floor of the Mouth

Ninety percent of tumors in this location originate within 2 cm of the anterior midline of the floor of the mouth. Three basic types of information must be provided when evaluating SCCa of the floor of the mouth: (1) the presence and extent of mandibular involvement; (2) the degree of submucosal extension; and (3) the status of regional lymph nodes.[274] Contrast-enhanced CT is the preferred modality for assessment of these lesions due to its availability, its better demonstration of cortical bone invasion, and its superior detection of lymph node metastases.[270] MR imaging, however, is more sensitive than CT for evaluation of bone marrow involvement and perineural tumor spread.[4, 275–277] T1-weighted images, in particular, which normally display mandibular marrow fat as high signal intensity, easily demonstrate marrow replacement, even in the absence of cortical destruction (Figs. 27-86 and 27-87). SCCa of the floor of the mouth is free to spread in virtually any direction. There can be medial spread across the midline, which may occur either directly across the genioglossus muscle and lingual septum or via the potential space between the genioglossus and geniohyoid muscles

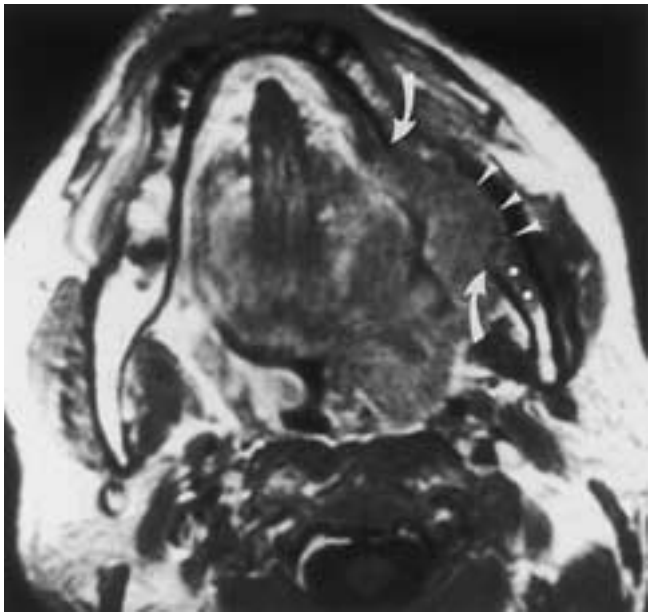

FIGURE 27-86 Squamous cell carcinoma invading the left mandible. Axial T1-weighted image demonstrates a large mass centered in the region on the tongue base and left tonsillar fossa with obvious erosion of a large portion of the lingual surface of the left mandible (*curved white arrows*). The tumor is visualized extending to the buccal cortex of the mandible (*arrowheads*). In addition, however, there is tumor extension into the posterior aspect of the mandible, replacing the normal high-signal fat, in an area where no lingual cortical mandibular destruction is identified (*white dots*).

VIEW IMAGE

Copyright © 2003, Mosby, Inc. All rights reserved.

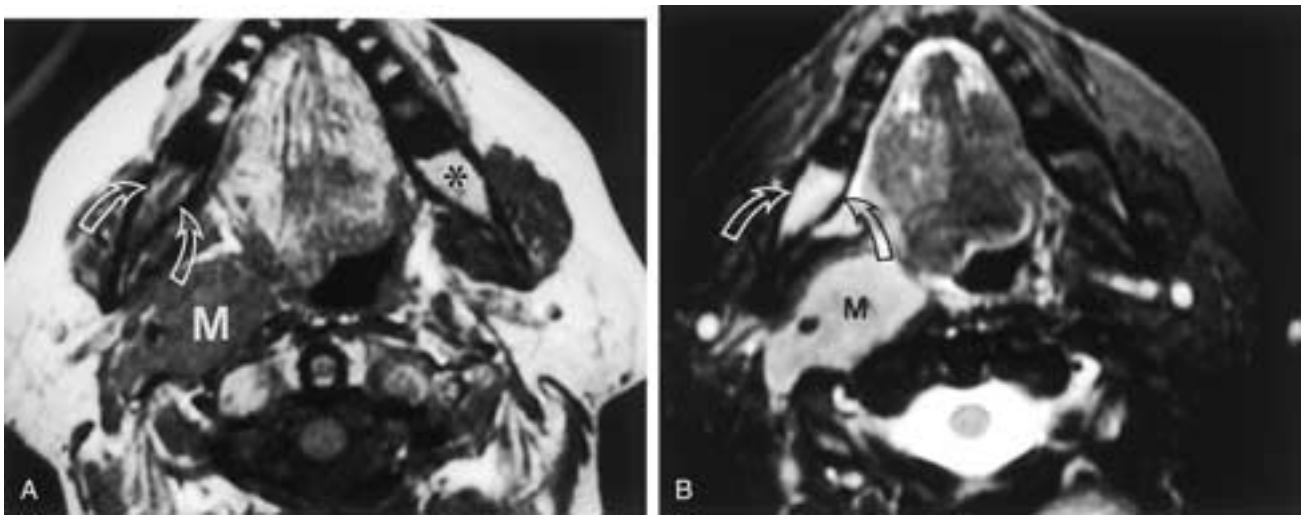

VIEW IMAGE

FIGURE 27-87 Marrow invasion in the absence of cortical destruction. Axial T1-weighted (**A**) and T2-weighted (**B**) MR images demonstrate normal high signal intensity marrow on the T1-weighted image in the left aspect of the mandible (*asterisk*) and lack of normal marrow signal in the right mandible (*arrows* in **A**). The pathologic marrow demonstrates high signal intensity on the T2-weighted image (*arrows* in **B**). No evidence of cortical bone erosion is identified. Also note the nearby large myelomatous mass (*M*), as well as the fatty replacement and prolapse of the right hemitongue from denervation atrophy in this patient with myeloma. (Courtesy of Dr. Thomas Underhill.)

(Fig. 27-88). The relationship of the tumor to the lingual septum, as well as to the ipsilateral and contralateral neurovascular bundles, is essential to assess in order to provide appropriate clinical therapeutic counseling. There can be lateral spread, typically contained by the mylohyoid muscle, that involves the periosteum of the mandible. Although the periosteum is an effective barrier against mandibular invasion, in partially or completely edentulous patients (who represent the majority of patients with SCCa), the route of entry is often along the occlusal surface.

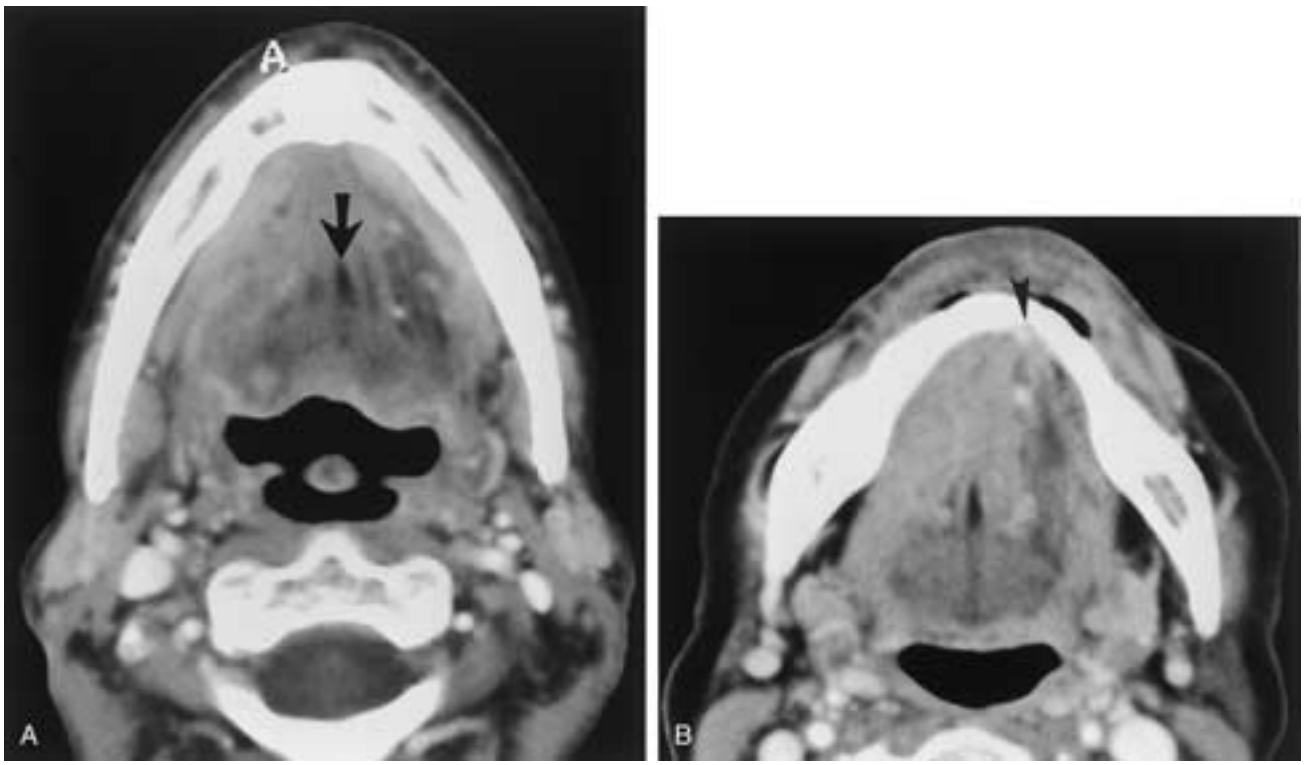

VIEW IMAGE

FIGURE 27-88 Squamous cell carcinoma of the floor of the mouth in two different patients. Axial contrast-enhanced CT scans in patients 1 (**A**) and 2 (**B**) demonstrate poorly defined masses in the right floor of the mouth obliterating the right sublingual space fat. In **A** there appears to be involvement of the right genioglossus muscle with midline displacement (*arrow*), while in **B** there is involvement of both genioglossus muscles as well as cortical mandibular erosion (*arrowhead*).

Copyright © 2003, Mosby, Inc. All rights reserved.

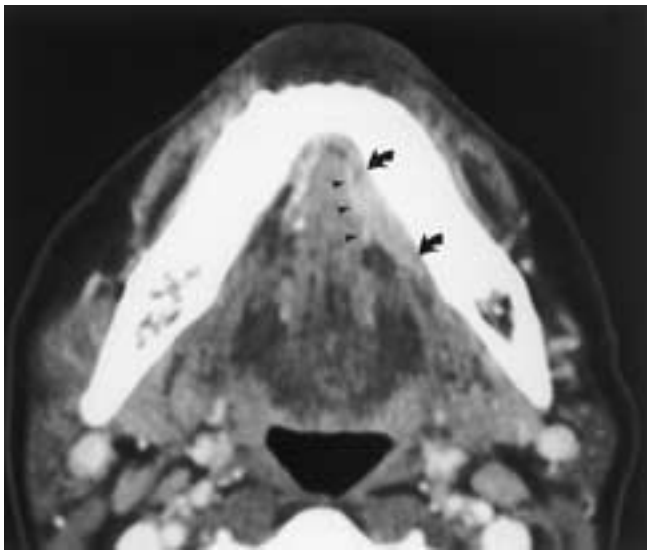

VIEW IMAGE

FIGURE 27-89 Small squamous cell carcinoma of the floor of the mouth. Axial contrast-enhanced CT scan reveals a small lesion on the left extending along the mylohyoid muscle (*arrows*). There is subtle asymmetry to the sublingual space fat, and the tumor appears to remain lateral to the left neurovascular structures (*arrowheads*). There are no midline displacements. This lesion was initially overlooked.

Subsequent spread occurs along the horizontal body and ramus of the mandible.[278] Identification of bone erosion immediately places the tumor at the T4 stage. There can be posterior spread along the mylohyoid muscle, usually within the sublingual space (Fig. 27-89), which may extend over the free margin of the mylohyoid muscle into the deep fascial spaces of the upper neck. This spread typically involves the ipsilateral neurovascular bundle. These lesions are T4 lesions that will require mandibulotomy, in addition to a combined transoral and cervical approach.[274] There can be inferior spread along the mylohyoid and hyoglossus muscles within the upper cervical neck to their inferior attachments on the hyoid bone. There can be posteroinferior spread that involves the base of the tongue. Lastly, there can be superior spread that may directly involve the oral tongue.

The ostia of the submandibular ducts may become obstructed by floor-of-the-mouth SCCa, resulting in duct dilatation or obstructive inflammatory enlargement of the submandibular gland (Fig. 27-90). Similarly, obstruction or inflammatory involvement of the sublingual salivary glands may also occur. Encasement of the lingual artery is common, but life-threatening hemorrhage is infrequent. The major lymph node drainage from SCCa of the floor of the mouth is to submental, submandibular, and internal jugular nodes (levels I and II).[2] The depth of tumor invasion in the floor of the mouth is more closely related to the presence of cervical lymph node metastases than is the surface size of the tumor. Thus, careful attention should be given to identify the tumor's depth on imaging.

SCCa of the Oral Tongue

Nearly all SCCa of the oral tongue occur on the ventrolateral surface of the tongue, and most of the lateral lesions arise from the middle and posterior one third of the lateral oral tongue (Fig. 27-91).[279] These tumors typically invade the tongue musculature, spreading easily along the bundles of the intrinsic muscles deeper into the oral tongue or along extrinsic muscles to their sites of attachment (hyoid bone, mandible, styloid process, etc.). These tumors may also extend submucosally to involve the floor of the mouth, tonsils, mandible, and pharyngeal walls (Figs. 27-92 and 27-93).[2] Middle third lateral lesions tend to invade the lateral floor of the mouth and mandible. Posterior third

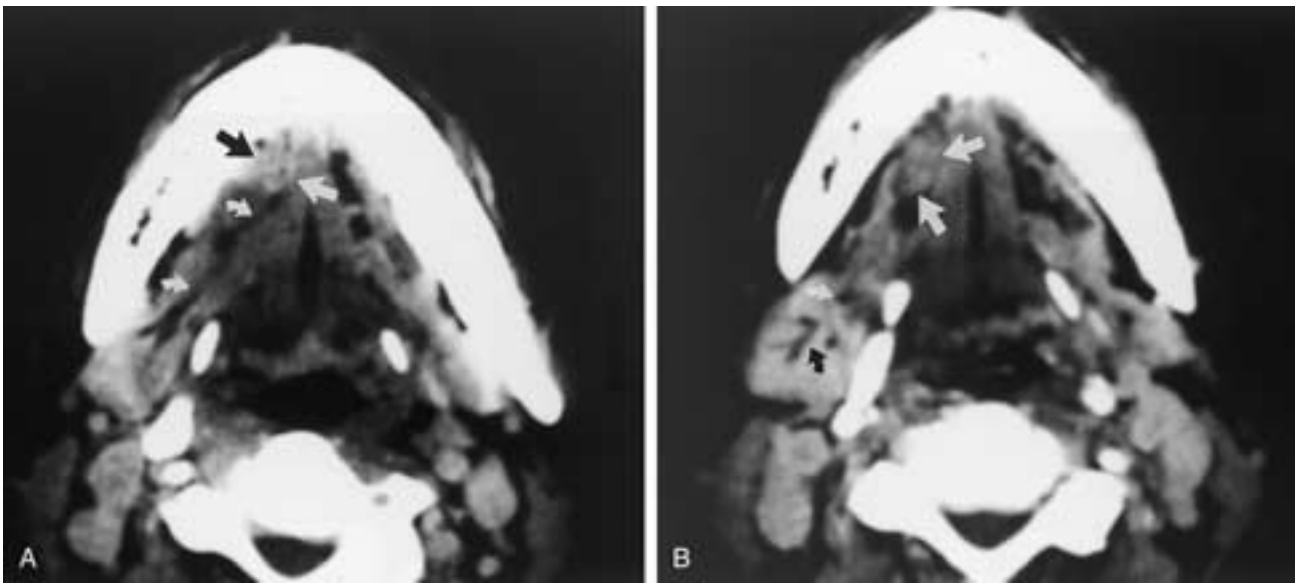

VIEW IMAGE

FIGURE 27-90 Right squamous cell carcinoma of the floor of the mouth with obstruction of the submandibular gland duct. **A** and **B**, Axial contrast-enhanced CT images demonstrate a tumor in the right floor of the mouth (*straight arrows*), which is best identified by noting the asymmetry of the sublingual space fat between the two sides. The tumor has obstructed the submandibular duct distally, and main duct dilatation (*curved arrows* in **A**) as well as dilated intraglandular ducts (*curved arrows* in **B**) are noted.

Copyright © 2003, Mosby, Inc. All rights reserved.

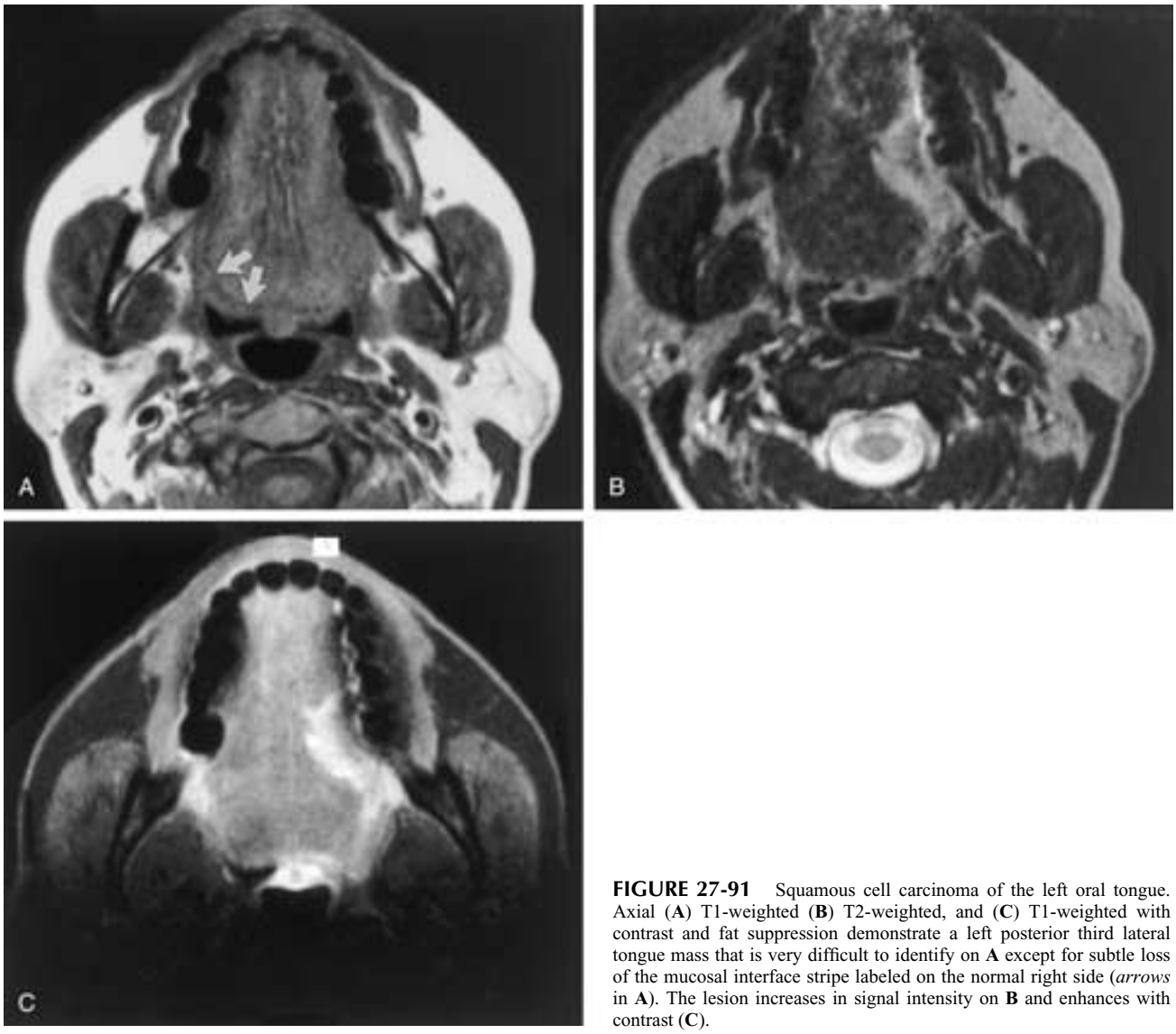

FIGURE 27-91 Squamous cell carcinoma of the left oral tongue. Axial (**A**) T1-weighted (**B**) T2-weighted, and (**C**) T1-weighted with contrast and fat suppression demonstrate a left posterior third lateral tongue mass that is very difficult to identify on **A** except for subtle loss of the mucosal interface stripe labeled on the normal right side (*arrows* in **A**). The lesion increases in signal intensity on **B** and enhances with contrast (**C**).

VIEW IMAGE

lateral lesions grow into the floor of the mouth and glossotonsillar sulcus, the oropharyngeal tonsil, and the underlying deep spaces.[272] Lesions may extend superiorly to the soft palate via the palatoglossus muscle and from the soft palate to the nasopharynx via the veli palatini muscles.[272] When evaluating oral tongue SCCa, it is extremely important to assess the extent of the tumor in relation to the midline (Figs. 27-94 and 27-95). In addition, findings indicative of contralateral lingual neurovascular bundle invasion indicate that total glossectomy is necessary for curative resection or that nonsurgical organ preservation therapy is required. Total glossectomy, although technically possible, is rarely performed because it is poorly tolerated, and demonstration of tumor extension across the midline essentially contraindicates hemiglossectomy. Only recently have partial hemiglossectomies been performed, usually with a free flap reconstruction, and there is promise that these more advanced procedures may be better tolerated by patients. The lymphatic drainage of oral tongue SCCa is primarily to submandibular and internal jugular nodes (levels I and II), often with bilateral involvement.

SCCa of the Gingiva/Buccal Mucosa

Buccal mucosa covers the lips and cheeks and is continuous with the gingival covering on the buccal surface of the maxillary and mandibular alveolar ridges and the retromolar trigone. Overall, SCCa affecting these regions requires an approach to evaluation and management similar to that of carcinomas in the floor of the mouth and oral tongue. Buccal mucosa SCCa most commonly originates along the lateral walls, and lateral submucosal extension along the buccinator muscle to the pterygomandibular raphe with erosion of the underlying bone is the most common method of spread (Figs. 27-96 and 27-97). Mandibular invasion is of special concern for tumors arising in the lower gingiva that may erode the lingual cortex and spread by perineural or intramedullary extension (Figs. 27-98 and 27-99). These lesions mandate extensive resection with segmental mandibulectomy or partial maxillectomy.[279]

SCCa of the Hard Palate

Primary SCCa of the hard palate is rare and usually represents extension from primary gingival SCCa. When

Copyright © 2003, Mosby, Inc. All rights reserved.

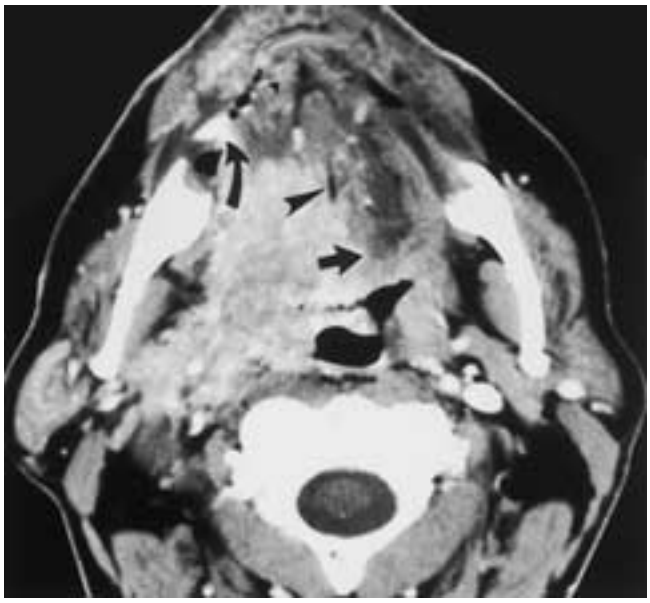

VIEW IMAGE

FIGURE 27-92 Squamous cell carcinoma. Axial CT scan with contrast demonstrates a large tumor involving the oral tongue and tongue base extending to involve the oropharynx, tonsillar fossa, carotid, and parapharyngeal spaces. The tumor clearly crosses the midline to involve the left tongue base (*straight arrows*). Extension anteriorly along the mylohyoid muscle and lateral floor of the mouth is present (*curved arrow*). The lingual septum is well visualized (*arrowhead*).

evaluating the uncommon primary SCCa of the hard palate, it is important to assess possible osseous erosion into the floor of the nasal cavity and the maxillary sinus or extension into the soft palate (Fig. 27-100). Perineural tumor extension is of special concern, as tumor may extend along the greater and lesser palatine nerves back to the pterygopalatine fossa and involve the maxillary division of the trigeminal nerve.[274] Perineural tumor extension is best evaluated by MR imaging, especially in the coronal plane.

SCCa of the Retromolar Trigone

Retromolar trigone lesions may extend superiorly deep to the maxillary tuberosity and invade the buccal space fat posterolateral to the maxillary antrum (Fig. 27-101). These lesions may also extend anteriorly along the orbicularis oris and buccinator muscles or posteriorly to involve the superior pharyngeal constrictor muscle, as these muscles arise from the pterygomandibular raphe, which lies beneath the mucosal surface of the retromolar trigone (Fig. 27-102).[274] This spread, not detected clinically, is seen on imaging studies as obliteration of the normal fat planes (Fig. 27-103). The pterygomandibular raphe attaches superiorly to the hamulus of the medial pterygoid plate and inferiorly to the mylohyoid line of the mandible. Involvement of the pterygopalatine fossa, buccal space, and masticator spaces may also occur, allowing invasion of neurovascular bundles and permitting continued cephalad extension to involve the

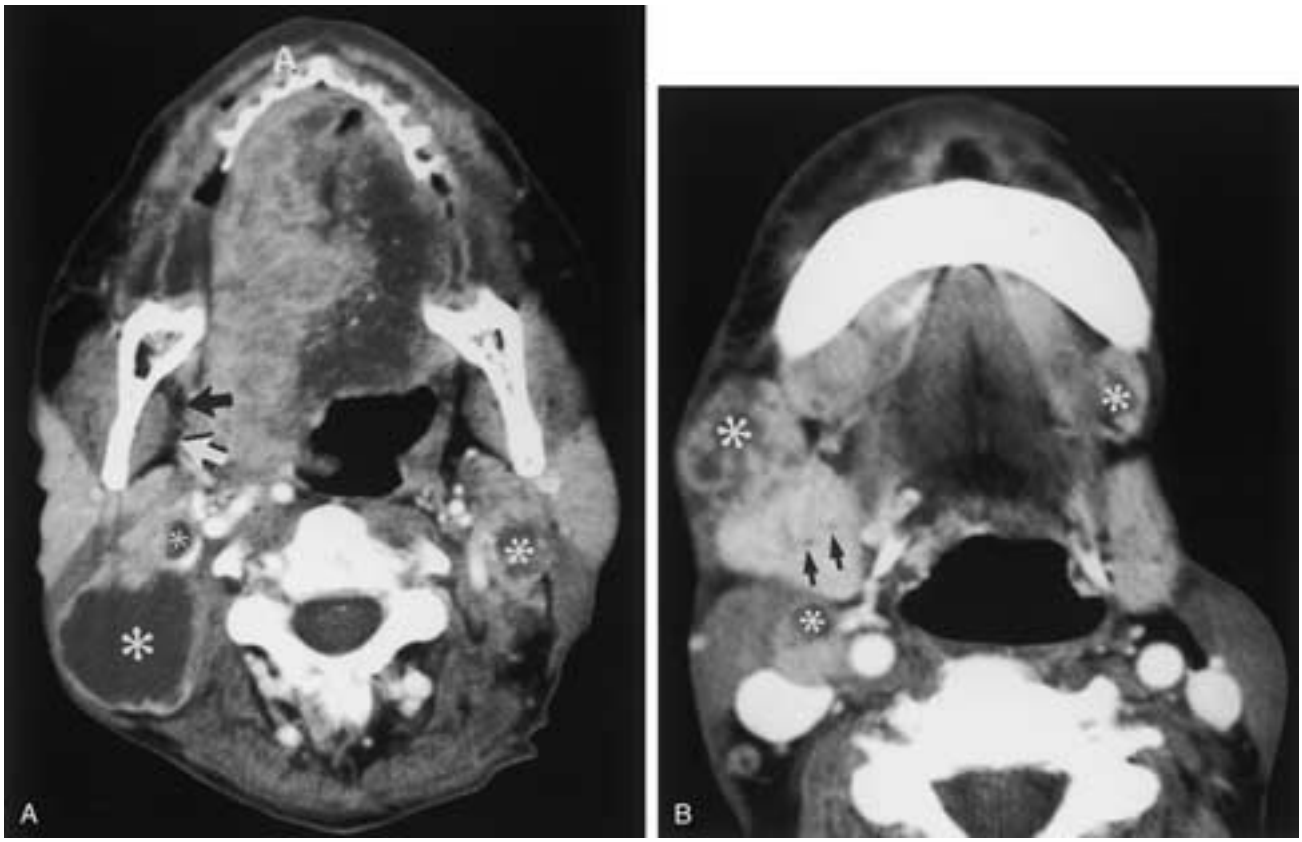

VIEW IMAGE

FIGURE 27-93 Squamous cell carcinoma. **A** and **B**, Axial contrast-enhanced CT scans demonstrate a large lateral oral tongue tumor that extends to involve the entire right oral tongue and extends posteriorly to the tongue base/oropharynx. The right parapharyngeal space fat is different in density from that on the left, with a ''dirty,'' stranded appearance most likely representing tumor infiltration (*arrows* in **A**). Tumor extension across the midline is obvious in **A**. Large, malignant-appearing, necrotic lymph nodes are present bilaterally (*asterisks*). Obstruction of Wharton's duct is suggested by identification of intraglandular duct dilatation in the right submandibular gland (*arrows* in **B**).

Copyright © 2003, Mosby, Inc. All rights reserved.

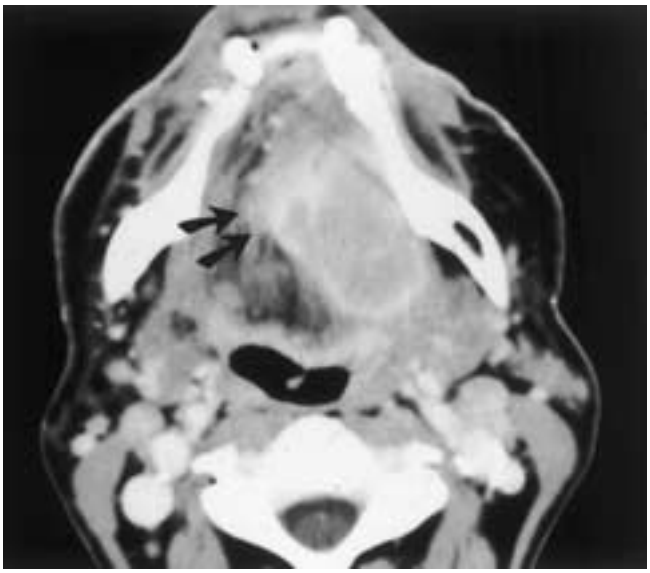

VIEW IMAGE

FIGURE 27-94 Oral tongue squamous cell carcinoma. Contrast-enhanced axial CT scan demonstrates a tumor of the left lateral oral tongue with medial extension across the midline to involve the right oral tongue (*arrows*). Although the tumor is fairly well defined posteriorly, it is poorly defined in its anterior extent and its margins are indistinct.

cavernous sinus via the maxillary and mandibular nerves (Fig. 27-104).[274] Posterior extension may involve the superior pharyngeal constrictor muscle and the tonsil, while posteromedial extension may occur along the pterygomandibular raphe, typically affecting the medial pterygoid muscle; in this case, trismus will almost always be associated. Invasion into the mandibular ramus must also be assessed. Inferomedial spread along the raphe may reach the mylohyoid muscle and the posterior aspect of the floor of the mouth.

Lymphoma

Both Hodgkin's and non-Hodgkin's lymphomas occur in the head and neck region, with lymph node enlargement being the most common presenting symptom for both types of lymphoma. Although Hodgkin's lymphoma tends to be predominantly nodal, with extranodal involvement uncommonly encountered, non-Hodgkin's lymphoma frequently involves extranodal sites.[280, 281]

Although the internal jugular (deep cervical) chain nodes are most often affected, involvement of submandibular nodes occasionally occurs. Involved lymph nodes range in size from 1 cm to several centimeters, and some have been reported to exceed 10 cm.[281] These nodes exhibit striking homogeneity and may manifest peripheral rim enhancement, but central necrosis is distinctly uncommon, reported to occur only after the patient has undergone treatment.[280] It is not possible to differentiate lymph nodes involved by Hodgkin's lymphoma from those affected by non-Hodgkin's lymphoma or metastatic disease solely on the basis of CT or MR imaging. Imaging of lymph nodes is discussed in Chapter 36.

Adenoid Cystic Carcinoma

Adenoid cystic carcinoma (ACCa) accounts for only 5% of major salivary gland neoplasms, but it comprises more than 25% of the malignancies occurring in the minor salivary glands.[282] More than 1000 minor salivary glands are distributed throughout the upper aerodigestive tract. They are concentrated especially in the buccal, labial, palatal, and lingual regions. Only the gingiva and anterior hard palate have few or none of these glands. ACCa has been reported to involve the minor salivary glands in the maxillary sinuses and nasal cavity, the hard and soft palates, buccal mucosa, floor of the mouth, tongue, lip, and retromolar trigone.[283] These lesions typically occur in the fifth or sixth decade of life, and although some authors report a male predominance, others report a female predominance or no sexual predominance.[284–287]

Three histologic subtypes of ACCa exist: tubular, cribriform, and solid. The degree of cellularity increases from the tubular to the solid form, and in general, the greater the cellularity, the worse the prognosis.[288] Most tumors manifest more than one subtype, making accurate staging difficult. In addition, transformation from one subtype to another suggests that this malignancy may represent a morphologic continuum.

ACCa is characterized by slow, relentless growth and a tendency toward extensive local invasion. A particular feature of this tumor is its propensity for perineural tumor extension. For primary lesions that occur within the oral cavity, this extension mainly affects the maxillary and mandibular branches of the trigeminal nerve due to involvement of the masticator space or the pterygomaxillary fissure. Regional lymph node metastases, however, are uncommon and are primarily associated with more poorly differentiated lesions (solid subtype).[289] ACCa is reported to have a worse prognosis when it involves minor salivary glands compared with major salivary glands.[285, 290] This may be due to the fact that minor salivary gland tumors have a greater opportunity to infiltrate and invade the surrounding soft tissues and bone.[284] In one large series, the median relapse-free interval for patients with major salivary gland ACCa was 83 months compared with 52 months for patients with minor salivary gland tumors.[284] Overall, ACCa carries a grave prognosis, regardless of treatment, as evidenced by the decline in survival of all patients from 58% at 5 years to 16% at 15 years.[291]

On CT and MR imaging, ACCa cannot be distinguished from SCCa or other malignancies on the basis of density or signal intensity (Figs. 27-105 and 27-106). However, signal intensity on T2-weighted images has been shown to correlate well with the degree of tumor cellularity.[292] Lesions with higher signal intensities correspond to tumors with low cellularity and the best prognosis, while tumors with low signal intensity on T2-weighted images have dense cellularity and a poor prognosis (Fig. 27-107).

Among patients with extracranial head and neck malignancies, those with ACCa are at greater risk for perineural tumor extension. Although perineural tumor spread has been reported equally or more often in association with SCCa in some literature, this is most likely a reflection of the more frequent overall occurrence of SCCa.[293–295]

Although CT and MR imaging are reported to be virtually identical in demonstrating perineural tumor below the skull base (provided that direct coronal thin-section CT scans are obtained), MR imaging is superior to CT in demonstrating involvement of the cisternal segments and cavernous sinus portions of the cranial nerves.[295, 296] The topic of perineural

Text continued on page 1438

Copyright © 2003, Mosby, Inc. All rights reserved.

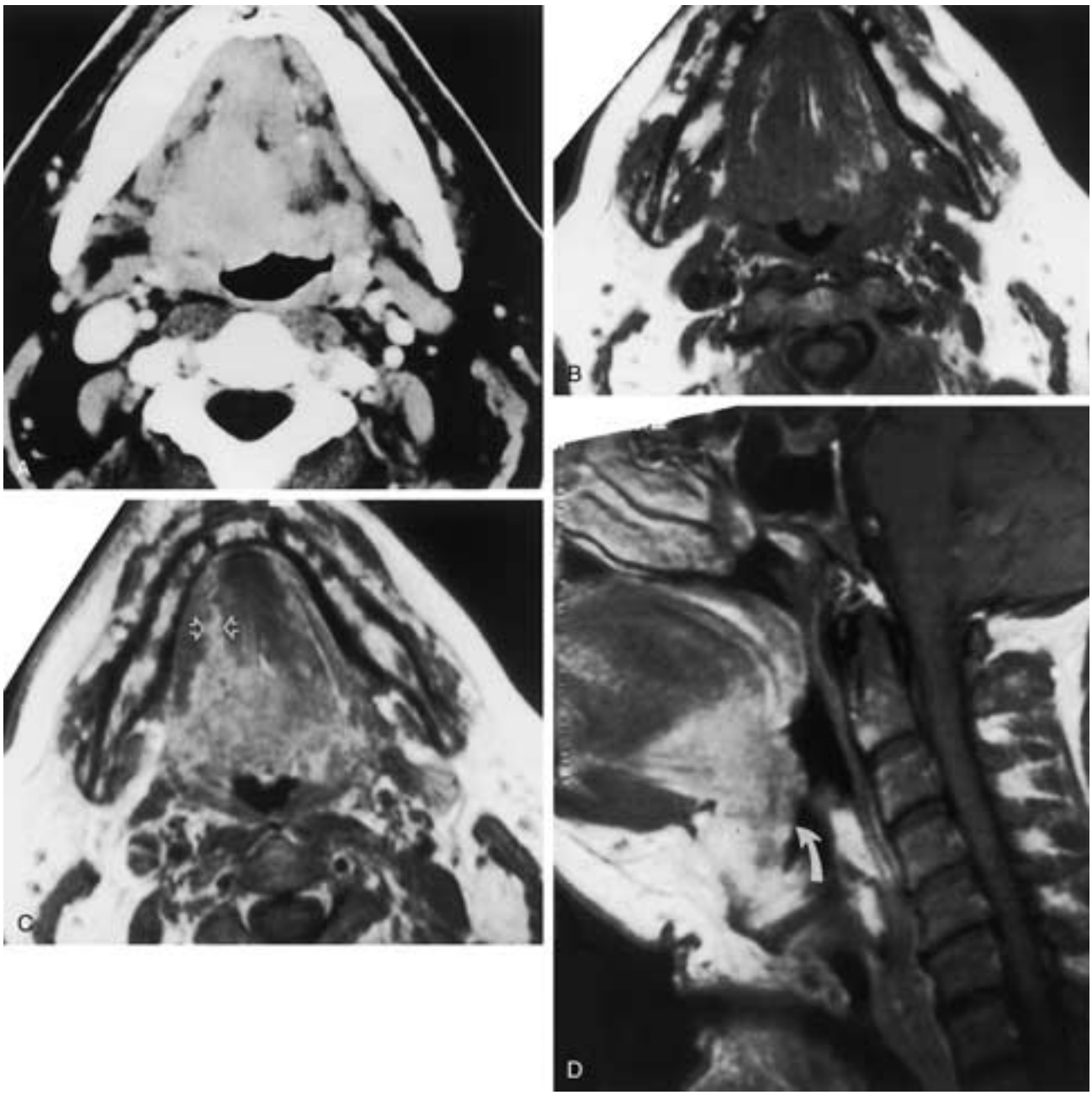

VIEW IMAGE

FIGURE 27-95 Squamous cell carcinoma of the oral tongue/tongue base. **A**, Contrast-enhanced axial CT scan demonstrates a large, fairly well defined tumor centered in the region of the circumvallate papillae crossing the midline. **B**, T1-weighted MR image without contrast enhancement demonstrates the tumor to be isointense to muscle and very difficult to define. Axial (**C**) and sagittal (**D**) T1-weighted MR images with contrast enhancement more clearly demonstrate the tumor extension to involve virtually the entire tongue base and the right sublingual region far anteriorly between the medial margin of the mylohyoid muscle and the lateral margin of the genioglossus muscle (*arrows* in **C**). The oropharyngeal extension inferiorly to the epiglottis is best appreciated on the sagittal image (*arrow* in **D**), as is the anterior extension along the floor of the mouth.

Copyright © 2003, Mosby, Inc. All rights reserved.

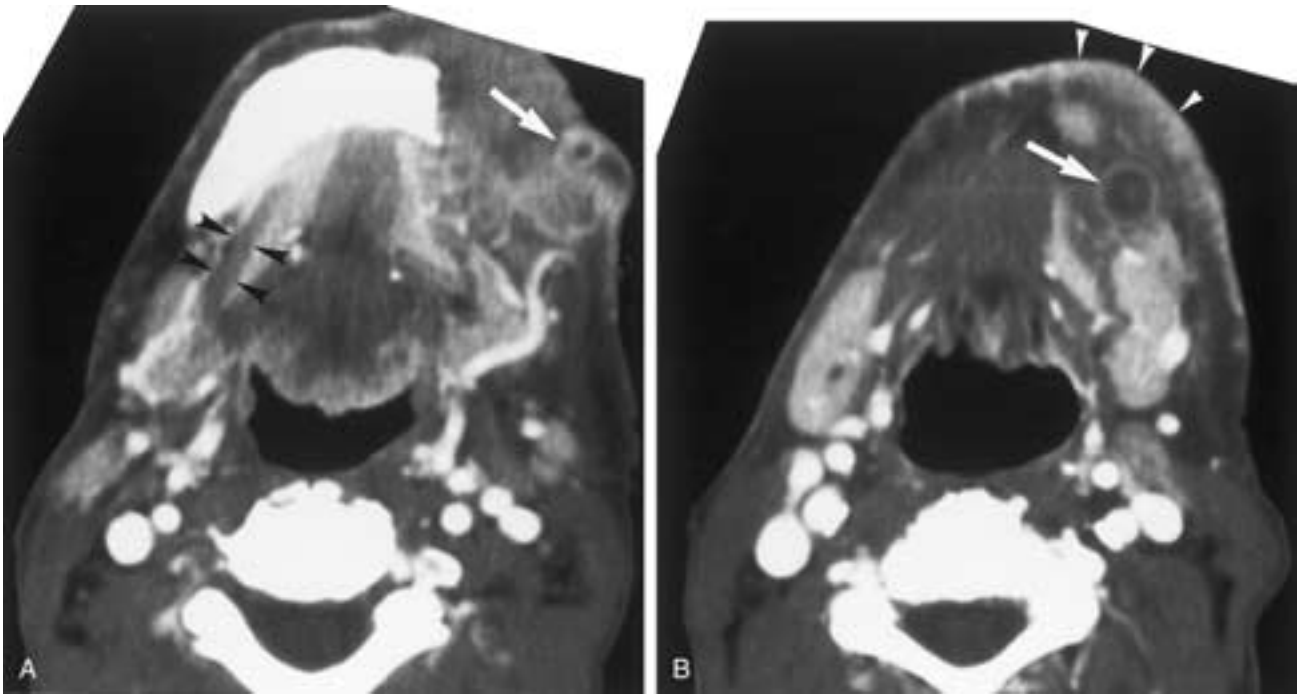

VIEW IMAGE

FIGURE 27-96 Squamous cell carcinoma probably arising from the gingiva-buccal mucosa. **A**, and **B**, Axial contrast-enhanced CT scans reveal a large tumor on the left, extending to the skin, destroying the left portion of the mandible, and invading the left mylohyoid muscle. Fibers of the right mylohyoid muscle are well defined (*black arrowheads* in **A**). Metastatic disease to the left submandibular nodes is also identified (*white arrows* in **A** and **B**). Thickening and involvement of the skin are easily seen (*white arrowheads* in **B**).

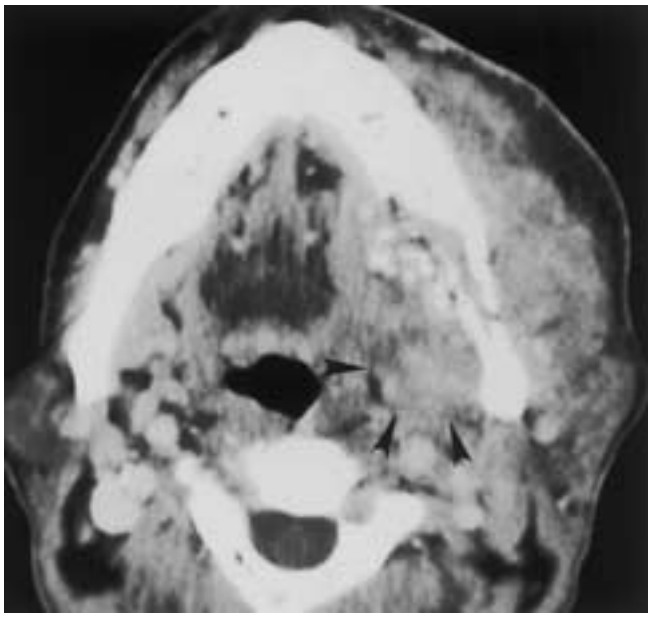

VIEW IMAGE

FIGURE 27-97 Squamous cell carcinoma of the buccal mucosa. Axial contrast-enhanced CT scan demonstrates a large mass on the left, with its epicenter located in the left gingiva-buccal mucosa. There is obvious destruction of the posterior aspect of the left mandible. Medial to the mandible, the tumor appears to be extending along the mylohyoid muscle to involve the deep aspect of the submandibular space (*arrowheads*).

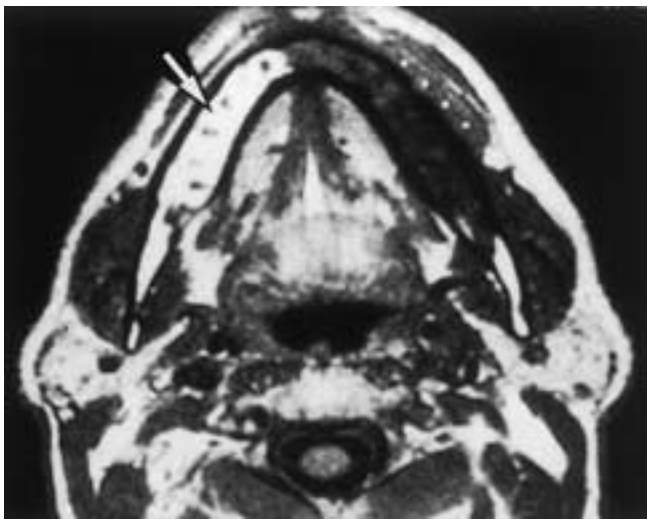

FIGURE 27-98 Squamous cell carcinoma of the gingiva-buccal mucosa. Axial T1-weighted MR image demonstrates a soft-tissue mass lateral to the mandible on the left (*white dots*). Although both the buccal and lingual aspects of the mandibular cortex appear intact, there is replacement of a large portion of the marrow within the mandible, manifested as replacement of the normal high signal intensity fat. Normal fat in the right aspect of the mandible is indicated by the arrow. This has probably resulted from perineural tumor extension via the mental nerve with retrograde involvement of the inferior alveolar nerve. Notice the similar appearance of this carcinoma compared with the eosinophilic granuloma presented in Figure 27-79. (Courtesy of Dr. Edward Kassel.)

VIEW IMAGE

Copyright © 2003, Mosby, Inc. All rights reserved.

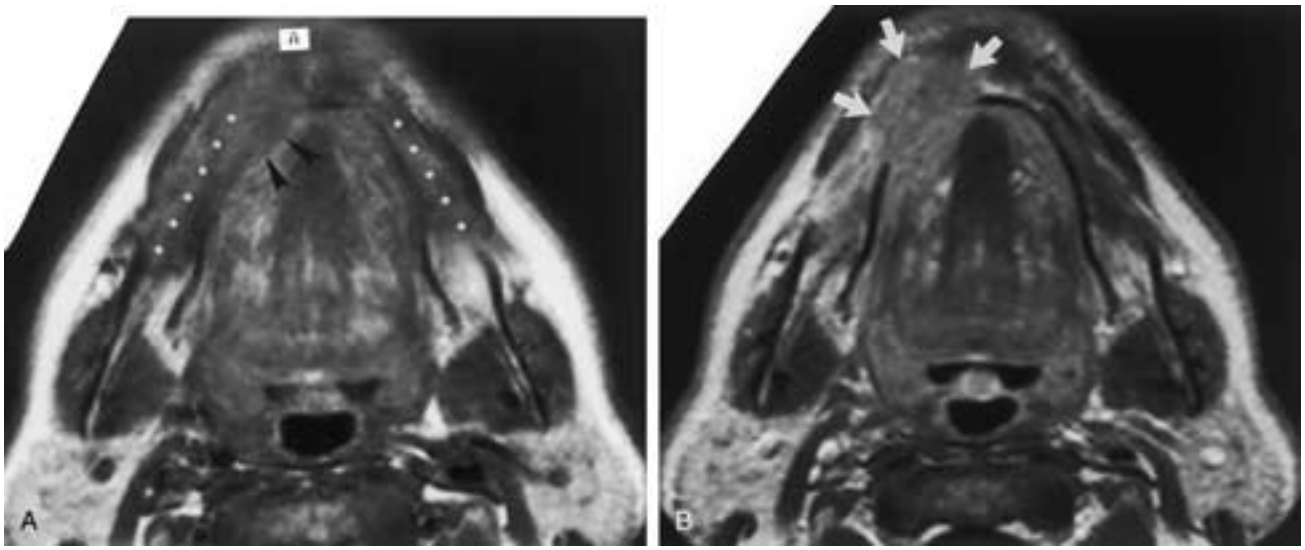

VIEW IMAGE

FIGURE 27-99 Squamous cell carcinoma of the gingiva-buccal mucosa. Axial T1-weighted MR images without (**A**) and with (**B**) contrast enhancement demonstrate a mass involving the anterior aspect of the right mandible. Both the buccal and lingual cortices are destroyed, and tumor extends into the soft tissues of the face anteriorly and into the anterior aspect of the oral tongue posteriorly (*black arrowheads* in **A**). The anterior extension is somewhat better defined of the postcontrast image (*arrows* in **B**). Separation from the heterogeneous sublingual space is better appreciated on the noncontrast image (*arrowheads* in **A**). Extensive replacement of the high-signal marrow within the mandible is best appreciated on the noncontrast image (*white dots* in **A**), because the lesion enhances slightly after contrast administration, somewhat obscuring this separation.

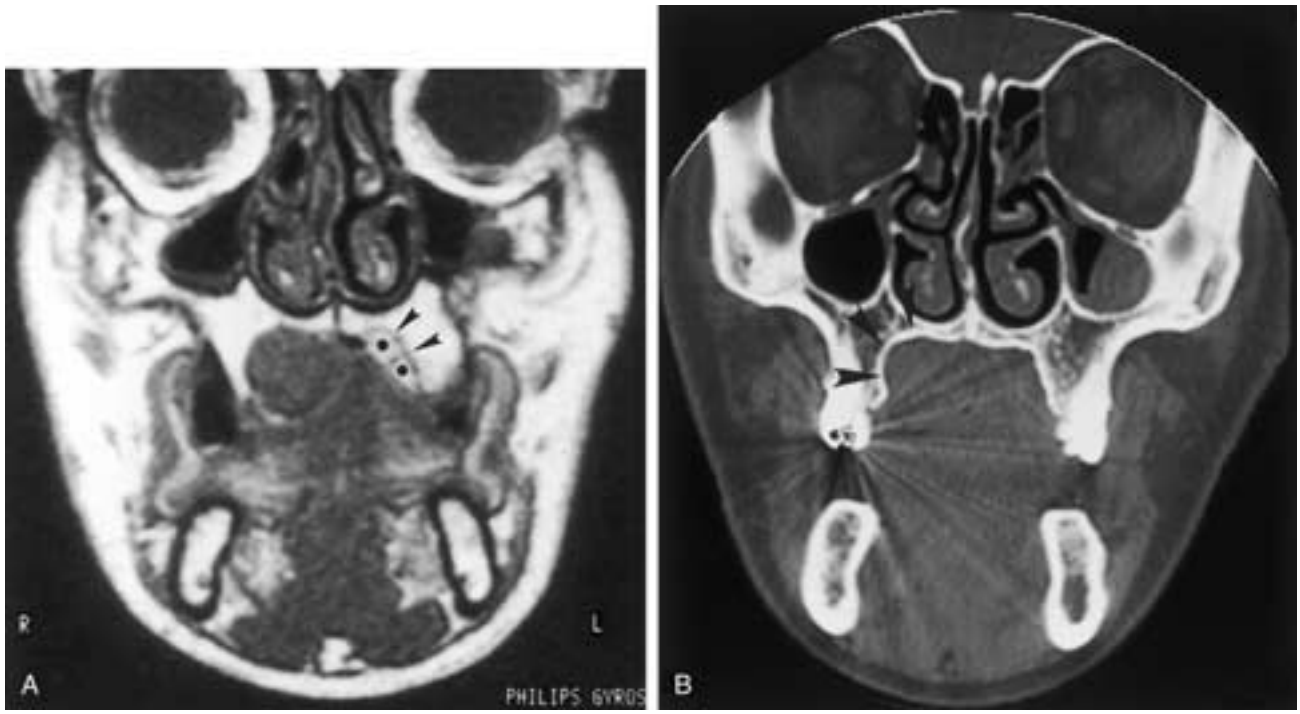

VIEW IMAGE

FIGURE 27-100 Squamous cell carcinoma of the hard palate. **A**, Coronal T1-weighted MR image demonstrates a fairly well defined lesion involving the right hard palate, which appears to be centered within the minor salivary glands. The glandular tissue of the left hard palate is indicated by the dots. A good cortical margin to the left hard palate can be identified (*arrowheads*). The cortical margin on the right is not, however, appreciated. There is no apparent infiltration or replacement of the marrow. There is no evidence of extension to involve the maxillary sinus or nasal cavity. **B**, Coronal CT scan obtained at bone window levels demonstrates an intact cortical margin of the hard palate on the right (*arrowheads*). There is slight fossa formation compared with the hard palate on the left. From an imaging standpoint, this SCCa exhibits features of a relatively benign process. (Courtesy of Dr. Nicole Freling.)

Copyright © 2003, Mosby, Inc. All rights reserved.

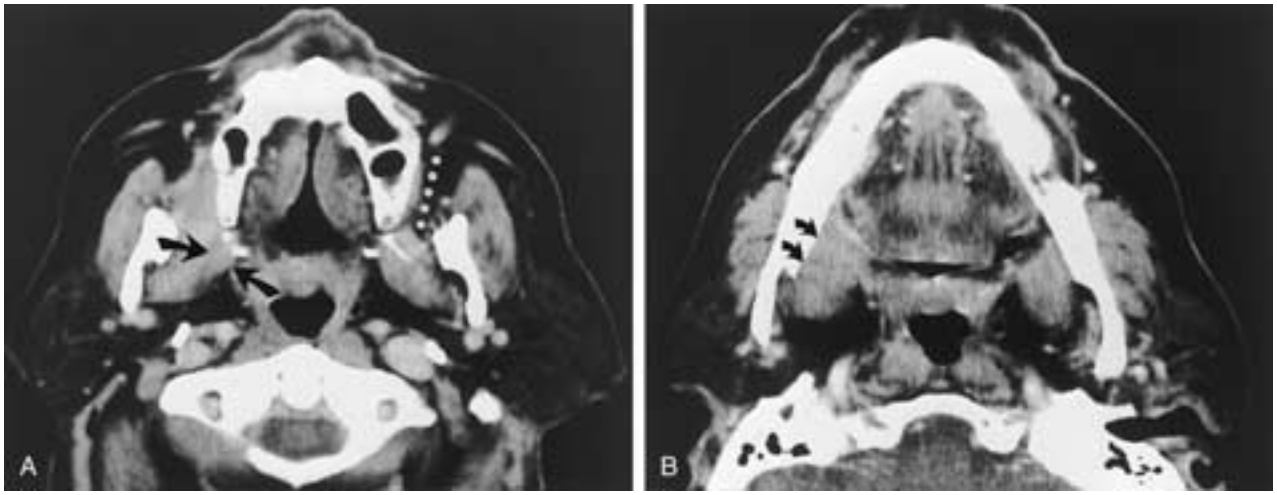

VIEW IMAGE

FIGURE 27-101 Retromolar trigone squamous cell carcinoma. **A** and **B**, Axial contrast-enhanced CT scans demonstrate a right retromolar trigone tumor invading the buccal space fat. The normal fat in this region on the left is indicated by the dots in **A**. Tumor also extends medial to the medial pterygoid muscle and obliterates the most anterior extension of the parapharyngeal space fat (*arrows* in **A**). The tumor extends along the pterygomandibular raphe to the mylohyoid line on the inner surface of the mandible (*arrows* in **B**).

VIEW IMAGE

FIGURE 27-102 Retromolar trigone squamous cell carcinoma in a 39-year-old male presenting to his dentist with trismus. He underwent a right third molar extraction, and carcinoma was found at the base of the tooth socket. His outside CT scan was interpreted as normal, but no bone windows were reviewed. **A**, T2-weighted axial MR image reveals a retromolar trigone mass on the right that extends into the pterygomaxillary fissure (*curved black arrow*). There is also asymmetry of the superior pharyngeal constrictor muscles, with poor definition of the lateral margin on the right suggesting tumor involvement. The normal lateral margin is indicated on the left (*white arrows*). Note the apparent loss of posterior cortical bone of the right maxilla. This lesion extends anterolaterally along the buccinator muscle fibers (*straight black arrow*). **B**, Axial contrast-enhanced T1-weighted MR image. It is much more difficult to appreciate the pathology in this image, as the tumor enhances to relative isointensity with muscle. The superior pharyngeal constrictor muscle bundles appear relatively symmetric in signal and contour. **C**, Coronal contrast-enhanced T1-weighted MR image nicely demonstrates involvement of the right buccinator muscle, with tumor filling the buccal fat space between the maxilla and mandible (*asterisk*). Also, note the loss of the cortical bone of the lateral maxillary alveolus compared with the normal left side (*arrow*).

Copyright © 2003, Mosby, Inc. All rights reserved.

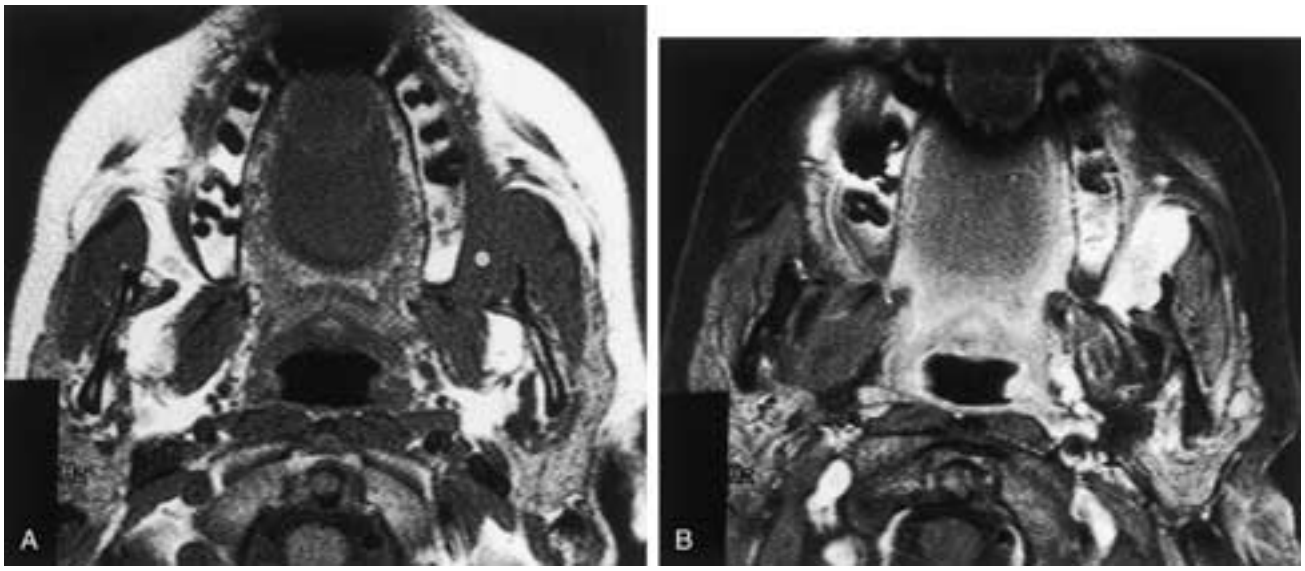

VIEW IMAGE

FIGURE 27-103 Left retromolar trigone squamous cell carcinoma. **A**, Axial T1-weighted MR images reveals obliteration of the left buccal space fat between the maxilla and mandible by a soft-tissue mass (*dot*). The signal intensity is such that separation from adjacent muscle tissue and definition of tumor margins are not possible. **B**, Contrast-enhanced T1-weighted axial MR image obtained with the fat suppression technique optimally demonstrates the presence and extent of the tumor margins. Compare this image with the postcontrast images in Figure 27-102 that were not obtained with the fat suppression technique. (Courtesy of Dr. Deborah Reede.)

tumor spread is discussed in Chapter 14. In summary, perineural tumor is demonstrated on CT by identifying enlargement of skull base foramina and fissures such as the foramen ovale (V3), the foramen rotundum (V2), and the pterygomaxillary fissure (and pterygopalatine fossa) (V2). Only rarely can a diffusely enlarged nerve be seen on CT. MR imaging may demonstrate increased thickness of the affected nerve(s) (Fig. 27-108) and diffuse or marginal enhancement following administration of contrast. Unfortunately, neither enlargement nor enhancement is pathognomonic for perineural tumor, as it may also be caused by edema, neuritis, primary neural tumor, and, in the cisternal segments, by meningeal inflammatory conditions.[292, 295] False-positive perineural tumor spread in patients with ACCa has been reported, producing an erroneous overestimation of the severity of the disease.[292]

Mucoepidermoid Carcinoma

Mucoepidermoid carcinomas arise from glandular ductal epithelium, and approximately 30% of these tumors arise from the minor salivary glands located primarily in the buccal mucosa and palate. These tumors may be classified as low-, intermediate-, or high-grade lesions. The low-grade lesions tend to behave similarly to benign lesions, with an overall 5-year patient survival rate of 90%. They have a benign imaging appearance with fairly well-delineated, smooth margins. Cystic areas may be present and, rarely, calcifications may be encountered (Figs. 27-109 and 27-110). High-grade lesions are poorly circumscribed, with indistinct infiltrating margins and an overall 5-year patient survival rate of only 42%. These tumors tend to be solid and demonstrate low to intermediate signal intensities on both T1-weighted and T2-weighted MR images (Fig. 27-111).[297] These lesions are discussed further in Chapter 39.

Liposarcoma

Liposarcomas are rare in the extracranial head and neck, although they are common in the retroperitoneum and peripheral soft tissues. Within the oral cavity, these lesions have been reported in the cheek, lip, palate, floor of the mouth, and submental regions.[298, 299] They originate from lipoblasts, within or adjacent to fascia, and do not originate from preexisting lipomas.[1] They are more common in males than in females and occur predominantly in the fourth to sixth decades of life.[298] The histologic tumor type correlates closely with the clinical behavior. The 5-year survival rate for patients with myxoid and well-differentiated tumors is 77% and 85%, respectively, while for round-cell and pleomorphic lesions it is 18% and 21%, respectively.[300]

On CT, liposarcomas are inhomogeneous, demonstrating a combination of fat and soft-tissue elements. The density of the fat is greater than that of subcutaneous fat, and these lesions tend to infiltrate adjacent structures (Fig. 27-112). On MR imaging, liposarcomas appear primarily as fatty lesions but display signal intensities lower than those of subcutaneous fat on short TR sequences.[301]

Rhabdomyosarcoma

Rhabdomyosarcomas are rare malignant mesenchymal tumors, 36% of which involve the head and neck.[302] In spite of a head and neck predilection, rhabdomyosarcoma involving the tongue is rare, representing only 0.34% of cases reported by the Intergroup Rhabdomyosarcoma Studies.[303] These tumors most often involve the base of the

Copyright © 2003, Mosby, Inc. All rights reserved.

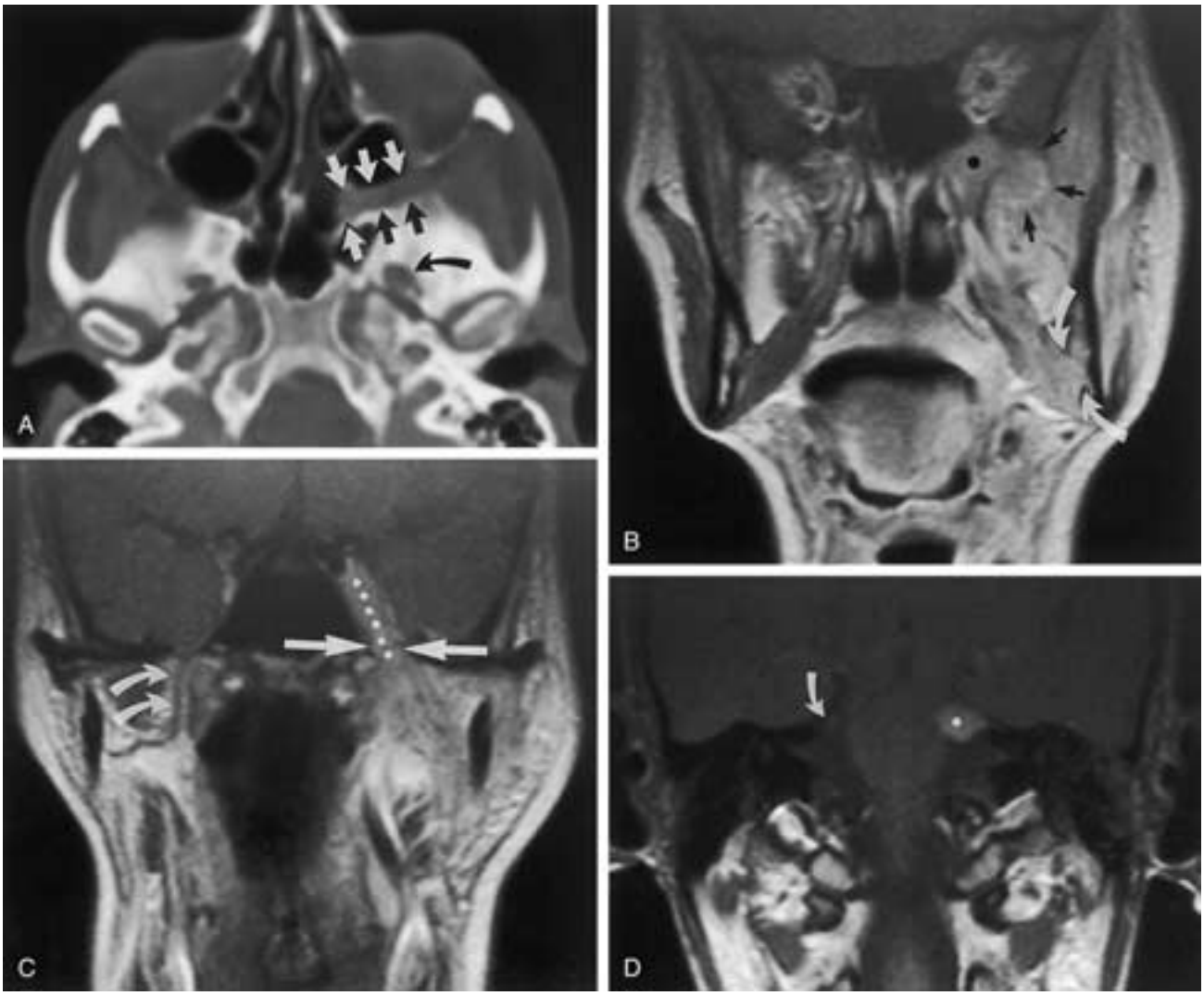

VIEW IMAGE

FIGURE 27-104 Left retromolar trigone squamous cell carcinoma, now with new left trismus and decreased sensation in the V2 distribution. **A**, Bone window axial CT scan reveals enlargement of the left foramen ovale (*curved arrow*) and widening of the left pterygopalatine fossa (*straight arrows*). **B**, Coronal T1-weighted MR image with contrast enhancement demonstrates tumor in the pterygoid fossa (*dot*) and lateral extension into the fat between the lateral pterygoid plate and the medial margin of the infiltrated and enhancing temporalis muscle (*straight arrows*). Also note the infiltration of the medial pterygoid and masseter muscles on the left, identified by their slight enlargement and enhancement. Tumor has also gained access to the mandibular marrow cavity by extension along the inferior alveolar nerve, widening the entrance to the canal on the medial border of the mandible (*curved arrows*). **C** and **D**, Coronal T1-weighted MR images following contrast administration. Perineural tumor extension along the left mandibular nerve (V3), widening the left foramen ovale (*arrows* in **C**) and extending into the cavernous sinus (*dots* in **C**) is identified. The normal, nonenhancing right mandibular nerve (V3) is indicated by the curved arrows in **C**. Extension of tumor all the way back to the brainstem is present, identified by marked enlargement and enhancement of the trigeminal nerve at its root entry zone (*dot* in **D**). The normal right trigeminal nerve in the peripontine cistern is indicated in **D** by the arrow.

Copyright © 2003, Mosby, Inc. All rights reserved.

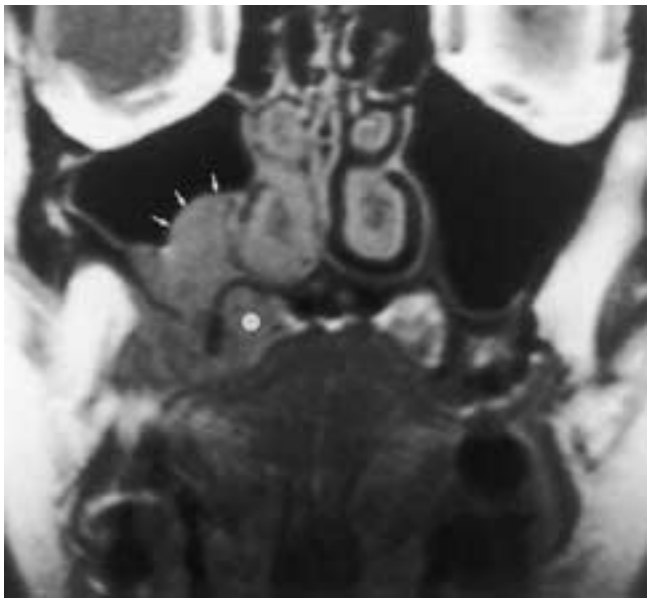

VIEW IMAGE

FIGURE 27-105 Adenoid cystic carcinoma of the hard palate. Coronal T1-weighted MR image demonstrates replacement of the normal high signal intensity of the minor salivary gland tissue in the right aspect of the hard palate (*white dot*). Normal salivary glands are identified on the left. This tumor has eroded the inferior aspect of the right maxillary sinus and has an intrasinus component (*arrows*).

tongue but have also been reported within the oral tongue.[304] Oral rhabdomyosarcomas are more common in males and predominate within the first two decades of life.[305]

Rhabdomyosarcomas appear as muscle density masses on CT and as muscle signal intensity masses on MR imaging, although they often have higher T2-weighted signal intensity than normal muscle. These tumors tend to infiltrate the surrounding structures. They may exhibit a variable amount of enhancement following contrast administration.

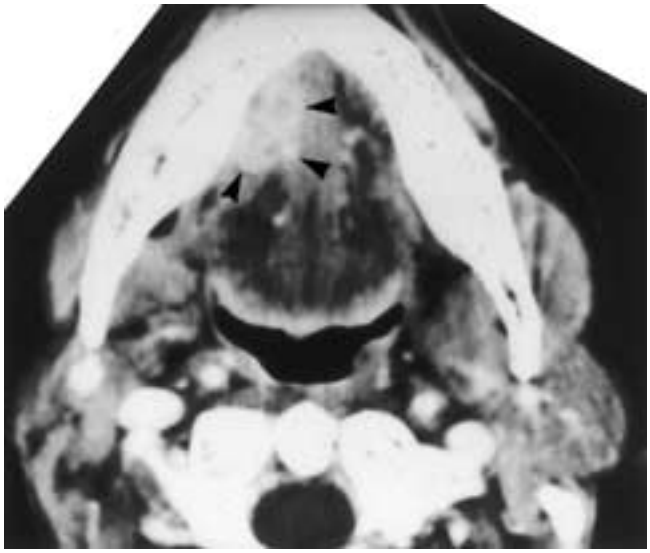

VIEW IMAGE

FIGURE 27-106 Adenoid cystic carcinoma of the right sublingual gland. Axial contrast-enhanced CT scan reveals an enhancing mass in the anterior aspect of the right tongue obliterating the normally fat-filled right sublingual space (*arrowheads*). On the basis of imaging characteristics, this lesion cannot be distinguished from SCCa originating within the floor of the mouth.

Miscellaneous Malignancies

Cases of other, less common malignancies involving portions of the oral cavity may be found in isolated reports. These include adenocarcinomas (Fig. 27-113), fibrosarcomas, angiosarcomas, myosarcomas, and leiomyosarcomas.[168, 306] Because the buccal space is in intimate contact with the mandible and is fascially contained within the masticator space, malignant lesions involving these regions of the oral cavity not infrequently secondarily involve the mandible and structures within the masticator space. Similarly, lesions of the jaw such as Ewing's sarcoma, chondrosarcoma (Fig. 27-114), osteosarcoma (Figs. 27-115 and 27-116), metastases (Figs. 27-117 and 27-118), and malignant schwannomas of the inferior alveolar nerve (Fig. 27-119), may extend to involve other regions of the oral cavity. Among metastatic lesions, the most common primary tumors in order of frequency are those of the breast, kidney, lung, colon, prostate, and thyroid. Mandibular pathology is discussed in Chapter 17.

Miscellaneous Pathology

Ossification of the Stylohyoid Ligament

The stylohyoid ligament obliquely traverses the neck, extending from the tip of the styloid process of the temporal bone to its attachment on the lesser cornua of the hyoid bone. Medial to the ligament, in close association, are the internal carotid artery, internal jugular vein, and cranial nerves IX to XII. The external carotid artery lies lateral to the ligament.[307] The ligament lies posterior to the tonsillar fossa and lateral to the pharyngeal wall. Ossification of this ligament and elongation of the styloid process have been associated with Eagle's syndrome, with symptoms primarily related to dysphagia (80%), pharyngeal foreign body sensation (55%), and a constantly aching throat (40%).[308] Other symptoms include otalgia, headache, pain on neck rotation, and facial pain.[309] Neck pain along the distribution of the carotid artery has been reported in cases for which surgical or angiographic confirmation of arterial compression by the ossified ligament was demonstrated.[310, 311]

Ossification of the stylohyoid ligament is reported in only 1.4% of the population, with no sex predilection, but very few of these individuals are symptomatic. The syndrome is rare in persons under 30 years of age and is most frequent in the 40- to 80-year-old age range; women tend to be symptomatic more often than men.[312, 313] A case of Eagle's syndrome secondary to fracture of the styloid process has also been reported.[314]

The radiographic identification of stylohyoid ligament ossification is readily apparent on plain radiographs and coronal CT images (Fig. 27-120A,B) and is also identified by observation of persistent small calcifications along the course of the ligament on axial CT images. Reformatted CT is visually impressive (Fig. 27-120C) but not necessary for the diagnosis.

Text continued on page 1448

Copyright © 2003, Mosby, Inc. All rights reserved.

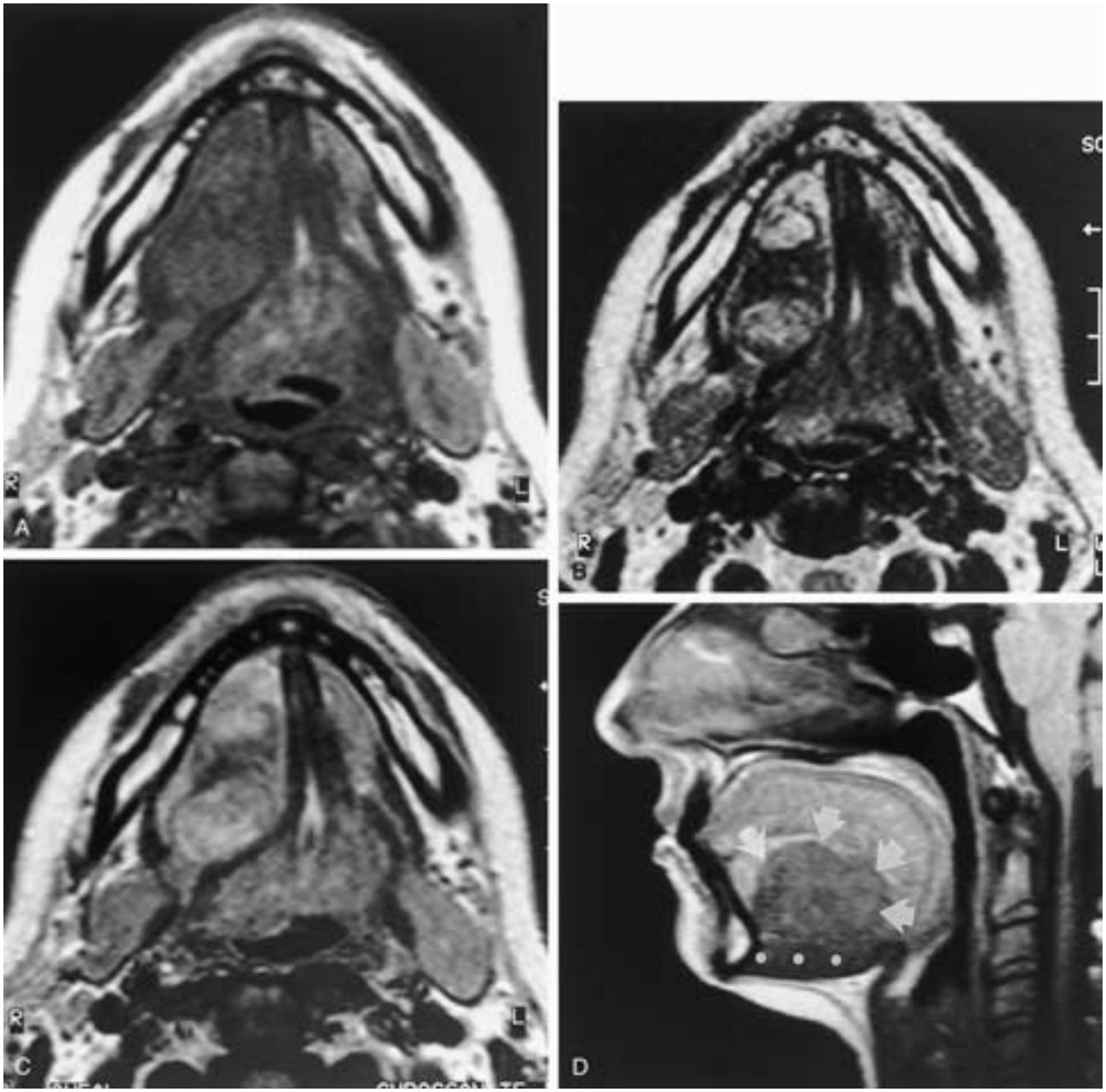

VIEW IMAGE

FIGURE 27-107 Adenoid cystic carcinoma of the right sublingual gland (cribriform and solid components). **A**, Axial T1-weighted MR image demonstrates a right sublingual space mass with signal intensity almost isointense to muscle, making definition difficult. **B**, The T2-weighted image reveals areas of moderate and low signal intensity corresponding to the areas of cribriform and solid components, respectively. **C**, Axial T1-weighted MR image after contrast administration reveals enhancement of the cribriform areas, but the solid central component demonstrates significantly less enhancement. **D**, Sagittal T1-weighted image optimally demonstrates the tumor location cephalad to the mylohyoid muscle fibers (*dots*) and the tumor size (*arrows*).

Copyright © 2003, Mosby, Inc. All rights reserved.

FIGURE 27-108 Adenoid cystic carcinoma of the hard palate. **A** and **B**, Axial and coronal contrast-enhanced CT scans demonstrate a destructive lesion of the right hard palate. There is erosion of the medial wall of the right maxillary sinus with extension of tumor into the sinus, as well as destruction of the posterior aspect of the nasal septum with involvement of the nasal cavity bilaterally. There is widening of the pterygomaxillary fissure on the right (*arrowheads* in **A**) and the inferior orbital fissure (*arrowheads* in **B**), which is highly suggestive of perineural tumor involvement. Involvement of the right masticator space musculature is probable, on the basis of enlargement of the right medial pterygoid muscle, when compared with the normal appearance on the left (*white dots* in **A**). The normal configuration of the parapharyngeal space fat is lost on the right side compared with the normal left. Extension of the tumor along the pharyngeal constrictor muscle on the right is identified by enlargement and poor definition of this muscle. The normal contour of the left pharyngeal constrictor muscle is indicated by the white arrows in **A**. **C**, Coronal T1-weighted MR image demonstrates perineural tumor extension along the right mandibular nerve as it courses through an enlarged right foramen ovale (*white arrows*) into the inferior aspect of the right cavernous sinus.

VIEW IMAGE

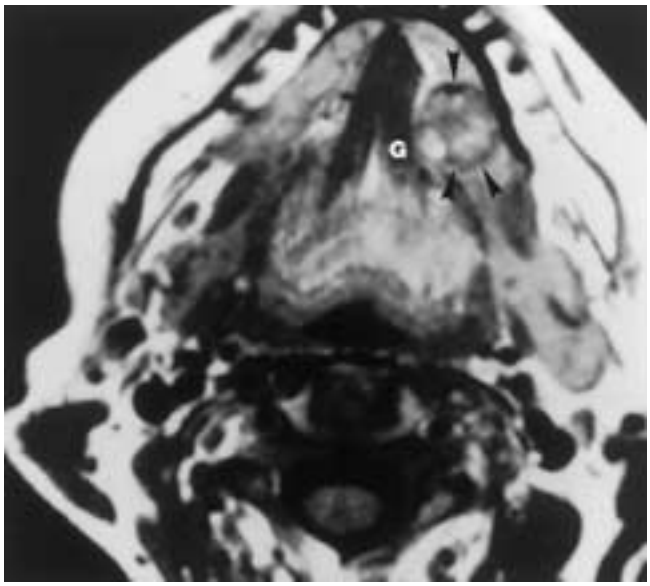

FIGURE 27-109 Mucoepidermoid carcinoma of the left sublingual gland. Axial T1-weighted MR image demonstrates a fairly well circumscribed heterogeneous lesion centered within the left sublingual space (*arrowheads*). The lingual aspect of the adjacent mandibular cortex appears intact, as does the lateral margin of the left genioglossus muscle (*G*).

VIEW IMAGE

Copyright © 2003, Mosby, Inc. All rights reserved.

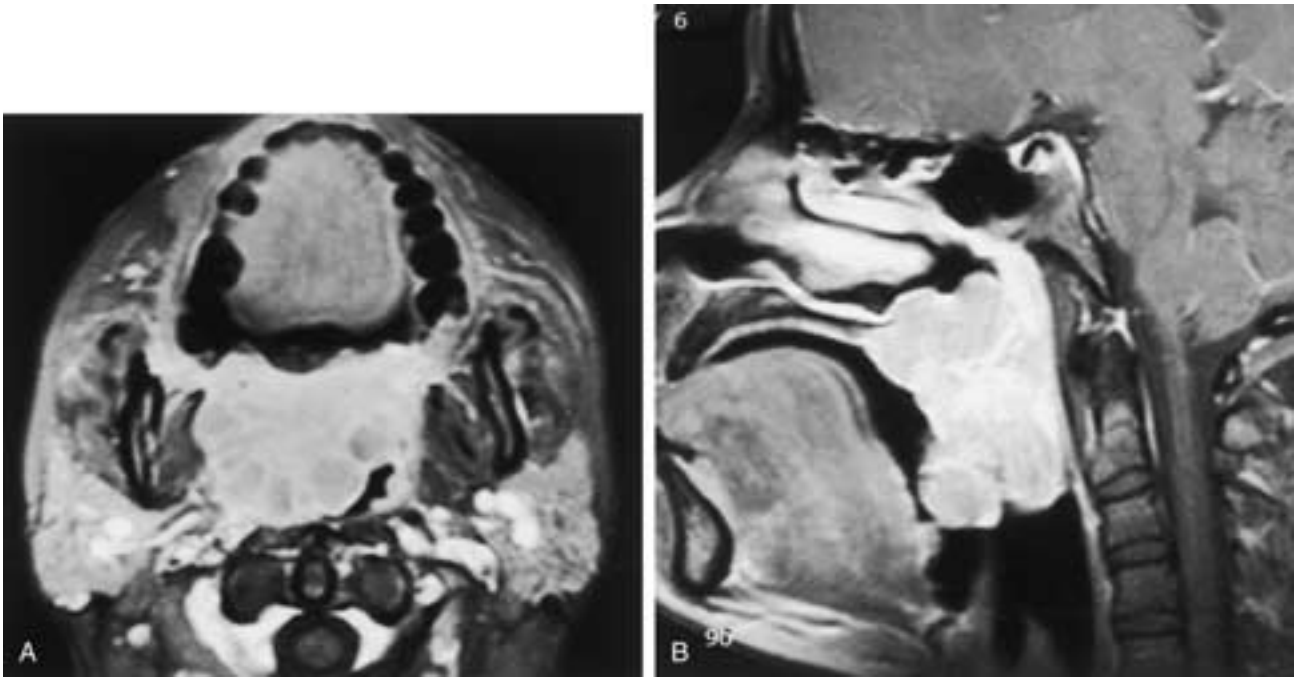

VIEW IMAGE

FIGURE 27-110 Mucoepidermoid carcinoma of the soft palate (low grade). Contrast-enhanced, fat-suppressed T1-weighted MR images in the (**A**) axial and (**B**) sagittal planes demonstrate a large, lobulated, overall benign-appearing lesion. Multiple nests of cells are present, rather than sheets of solid neoplastic cells. Note the significant airway compromise.

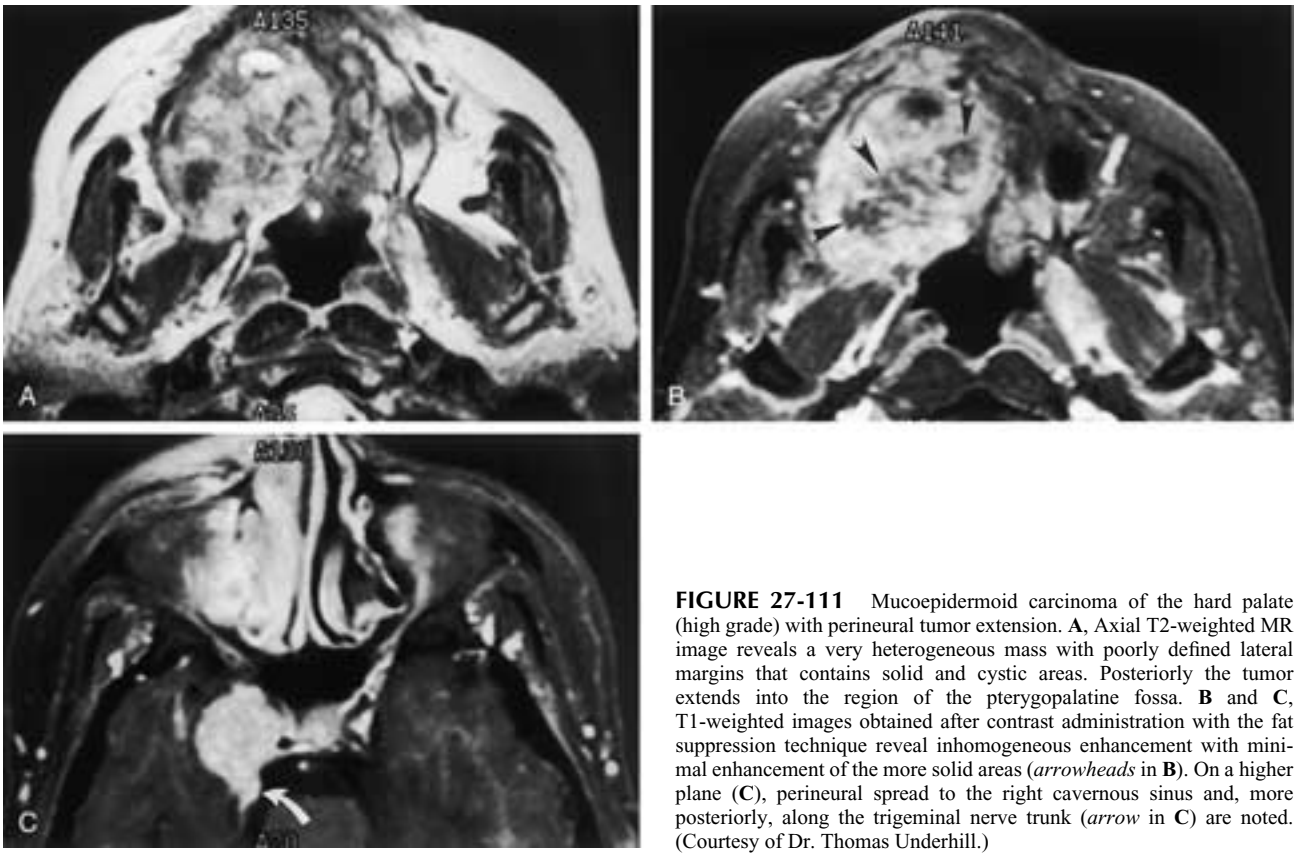

FIGURE 27-111 Mucoepidermoid carcinoma of the hard palate (high grade) with perineural tumor extension. **A**, Axial T2-weighted MR image reveals a very heterogeneous mass with poorly defined lateral margins that contains solid and cystic areas. Posteriorly the tumor extends into the region of the pterygopalatine fossa. **B** and **C**, T1-weighted images obtained after contrast administration with the fat suppression technique reveal inhomogeneous enhancement with minimal enhancement of the more solid areas (*arrowheads* in **B**). On a higher plane (**C**), perineural spread to the right cavernous sinus and, more posteriorly, along the trigeminal nerve trunk (*arrow* in **C**) are noted. (Courtesy of Dr. Thomas Underhill.)

VIEW IMAGE

Copyright © 2003, Mosby, Inc. All rights reserved.

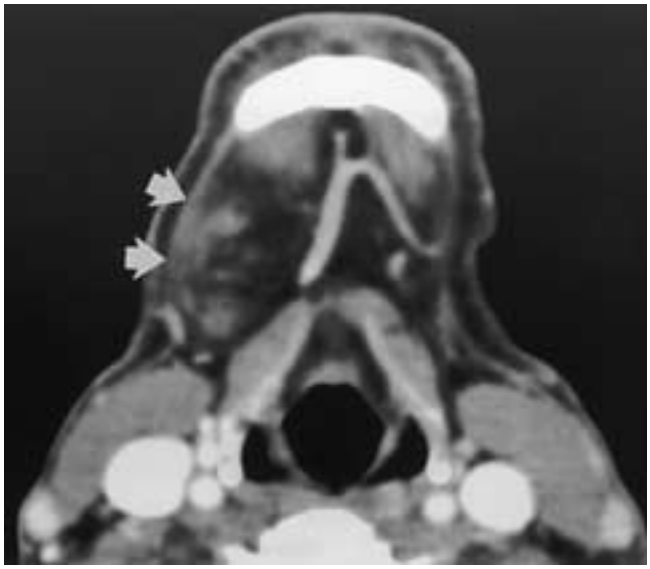

FIGURE 27-112 Liposarcoma in the right submandibular space. Axial contrast-enhanced CT scan reveals a poorly defined tumor in the right submandibular space fat. Soft-tissue density material as well as dirty-appearing fat is present in this lesion, which bulges the right platysma muscle laterally (*arrows*).

VIEW IMAGE

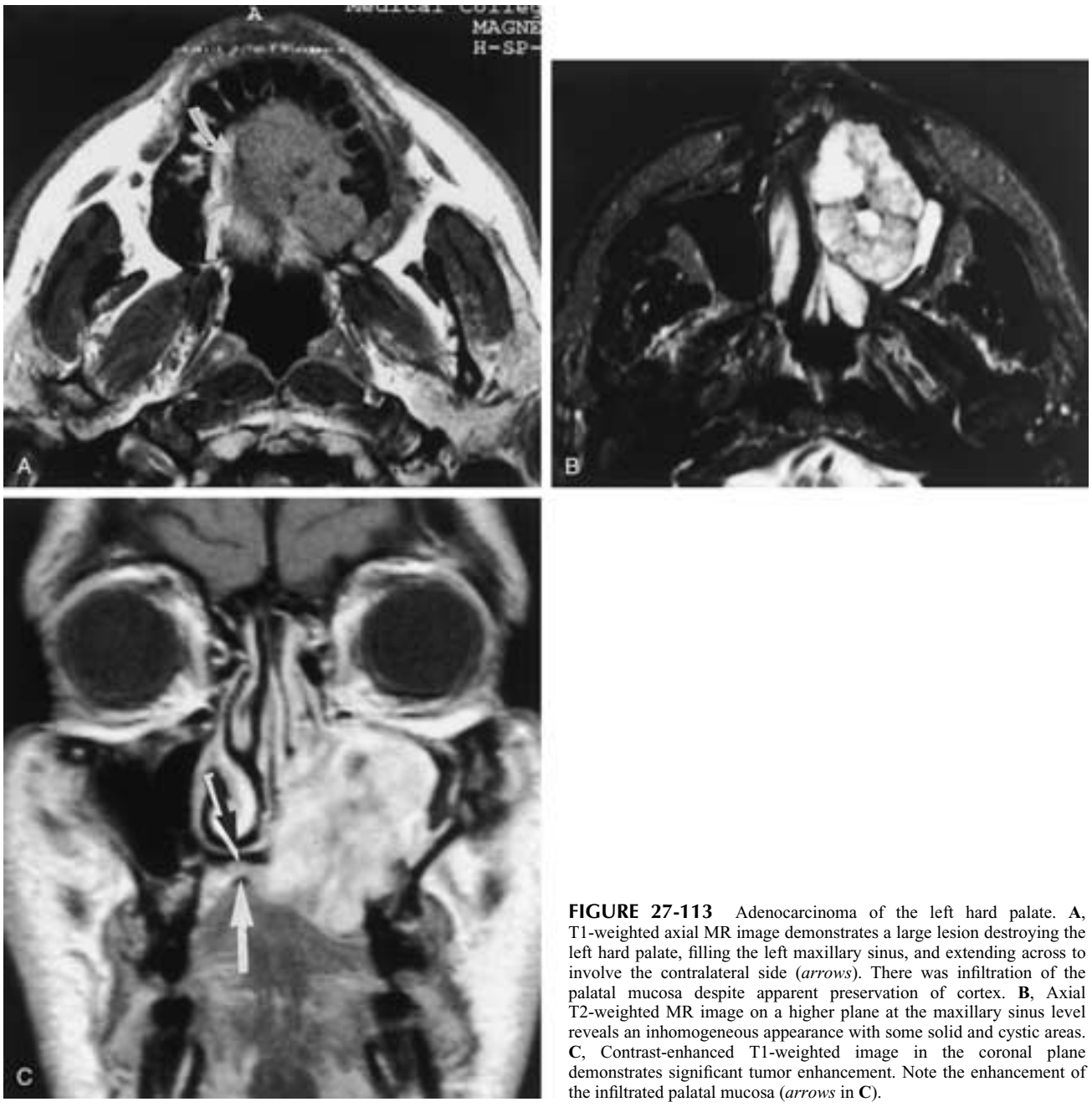

FIGURE 27-113 Adenocarcinoma of the left hard palate. **A**, T1-weighted axial MR image demonstrates a large lesion destroying the left hard palate, filling the left maxillary sinus, and extending across to involve the contralateral side (*arrows*). There was infiltration of the palatal mucosa despite apparent preservation of cortex. **B**, Axial T2-weighted MR image on a higher plane at the maxillary sinus level reveals an inhomogeneous appearance with some solid and cystic areas. **C**, Contrast-enhanced T1-weighted image in the coronal plane demonstrates significant tumor enhancement. Note the enhancement of the infiltrated palatal mucosa (*arrows* in **C**).

VIEW IMAGE

Copyright © 2003, Mosby, Inc. All rights reserved.

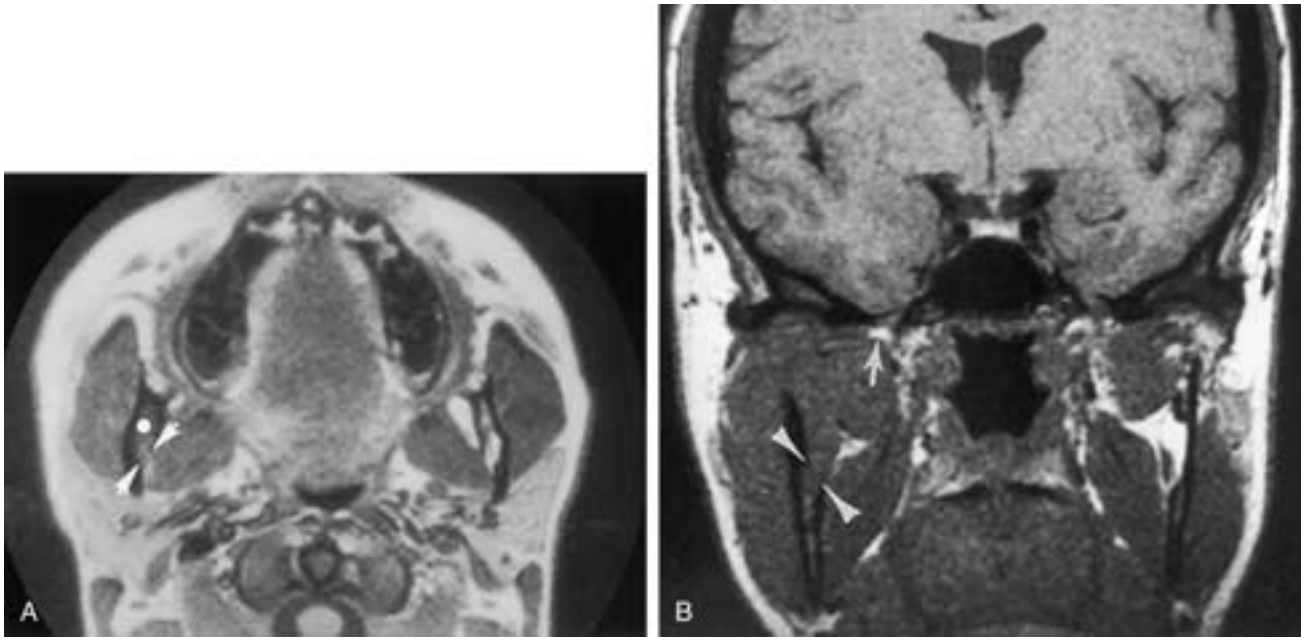

VIEW IMAGE

FIGURE 27-114 Mandibular chondrosarcoma. **A** and **B**, Axial and coronal T1-weighted MR images demonstrate a right masticator space mass with involvement of the lateral pterygoid, medial pterygoid, and masseter muscles. There is antegrade perineural tumor extension along the inferior alveolar nerve with widening of the inferior alveolar foramen (*white arrowheads*). Replacement of the normal high signal fatty marrow is best appreciated on the axial image (*white dot*). At this time, there is no evidence of retrograde perineural tumor because the margins of the right foramen ovale are intact and normal fat is identified just inferior to the foramen (*white arrow* in **B**). (From Tryhus MR, Smoker WRK, Harnsberger HR. The normal and diseased masticator space. Semin Ultrasound CT MR 1990;11:476–485.)

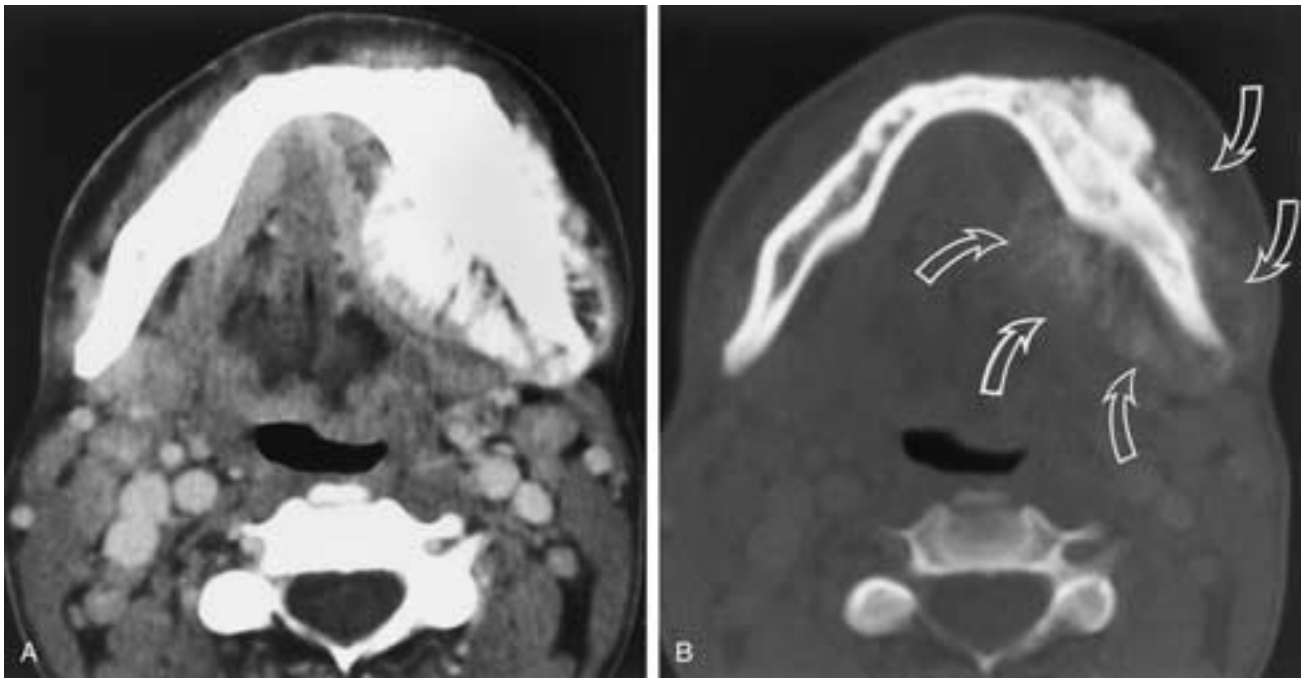

VIEW IMAGE

FIGURE 27-115 Mandibular osteogenic sarcomas in two different patients. Contrast-enhanced axial CT scans in soft-tissue (**A**) and bone (**B**) windows reveal masses arising from the mandible and involving both the buccal and lingual surfaces. The characteristic spiculated periosteal reaction is noted in both tumors, more prominently on the bone window image (*arrows* in **B**).

Copyright © 2003, Mosby, Inc. All rights reserved.

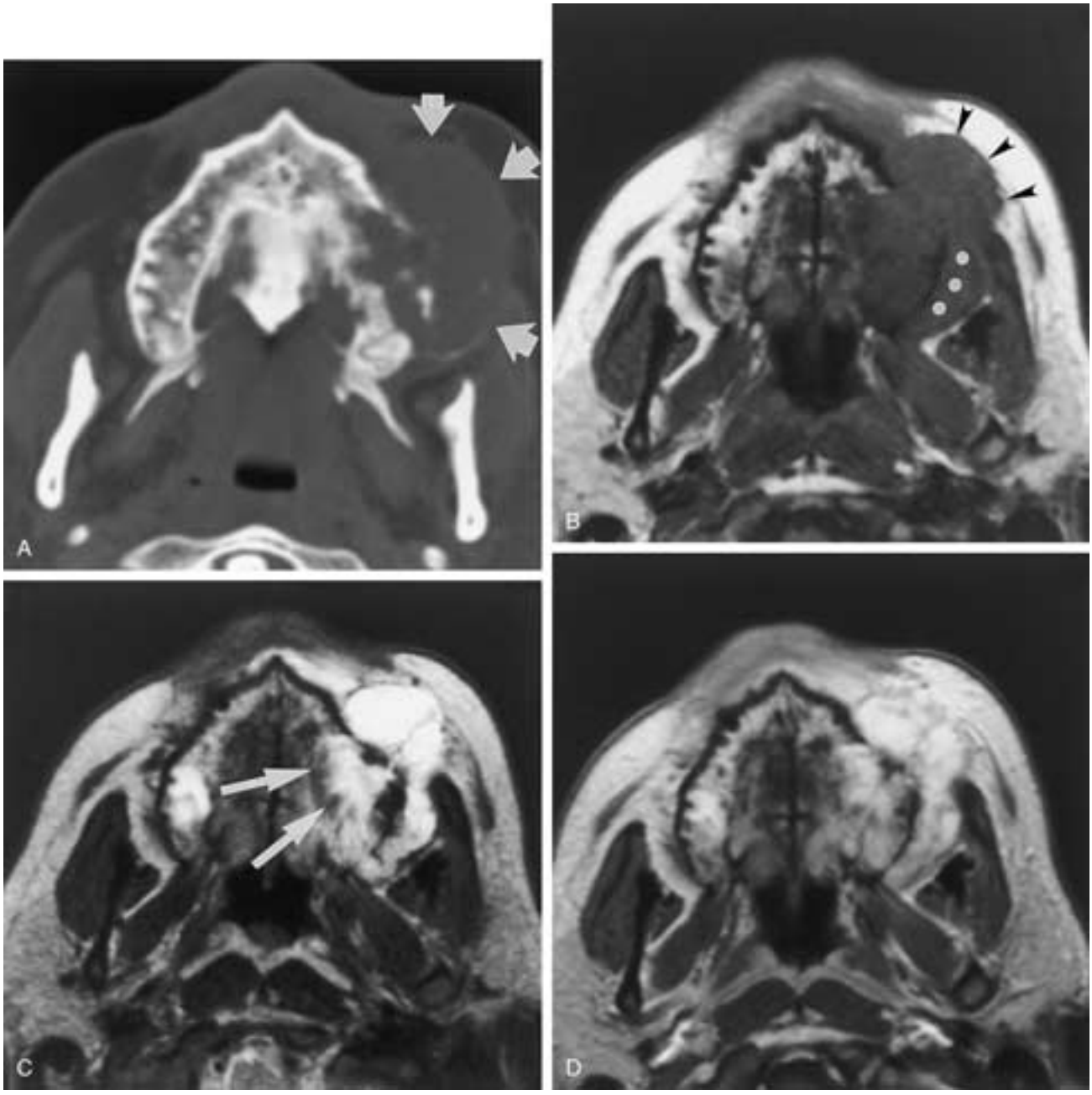

VIEW IMAGE

FIGURE 27-116 Maxillary osteogenic sarcoma with involvement of the hard palate. **A**, Axial CT scan with bone window settings reveals a destructive lesion of the left maxillary alveolus extending laterally into the malar soft tissues (*arrows*). The characteristic periosteal reaction, well seen in the tumors in Figure 27-115, is not appreciated in this lesion, making it very difficult to suggest the correct histology. **B**, The T1-weighted MR image better demonstrates the tumor extension into the soft tissues of the cheek (*arrowheads*) and reveals tumor in the left medial buccal space (*white dots*). **C**, T2-weighted MR image predominantly shows signal hyperintensity throughout the tumor with very stranded medial margins (*arrows*). **D**, Contrast-enhanced axial T1-weighted MR image with fat suppression reveals heterogeneous enhancement, and the margins remain somewhat poorly defined. How much of the left hard palate is involved remains difficult to assess even with the various imaging sequences. However, it is possible to say that there is no evidence of right hard palate involvement.

Copyright © 2003, Mosby, Inc. All rights reserved.

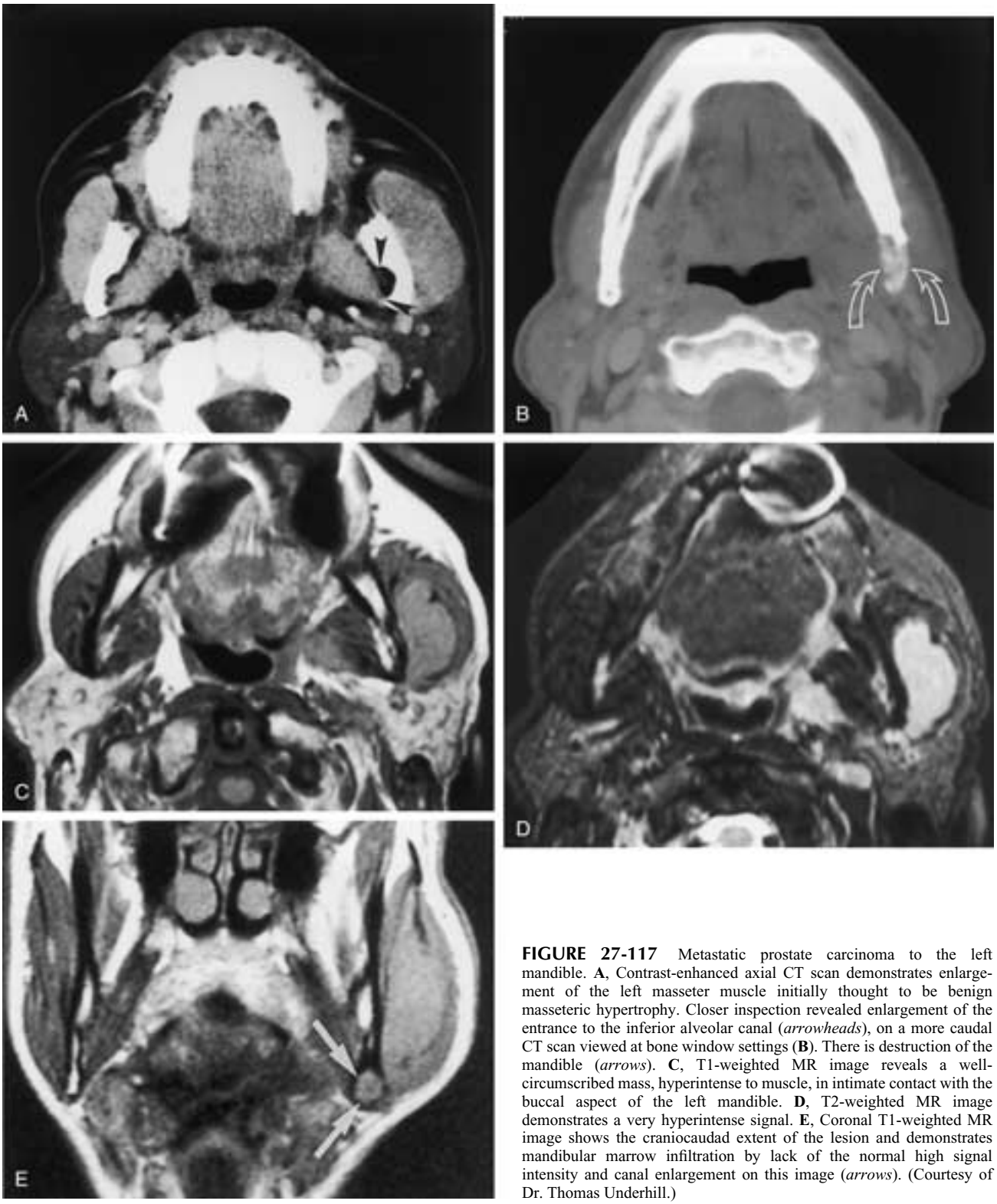

FIGURE 27-117 Metastatic prostate carcinoma to the left mandible. **A**, Contrast-enhanced axial CT scan demonstrates enlargement of the left masseter muscle initially thought to be benign masseteric hypertrophy. Closer inspection revealed enlargement of the entrance to the inferior alveolar canal (*arrowheads*), on a more caudal CT scan viewed at bone window settings (**B**). There is destruction of the mandible (*arrows*). **C**, T1-weighted MR image reveals a well-circumscribed mass, hyperintense to muscle, in intimate contact with the buccal aspect of the left mandible. **D**, T2-weighted MR image demonstrates a very hyperintense signal. **E**, Coronal T1-weighted MR image shows the craniocaudad extent of the lesion and demonstrates mandibular marrow infiltration by lack of the normal high signal intensity and canal enlargement on this image (*arrows*). (Courtesy of Dr. Thomas Underhill.)

VIEW IMAGE

Copyright © 2003, Mosby, Inc. All rights reserved.

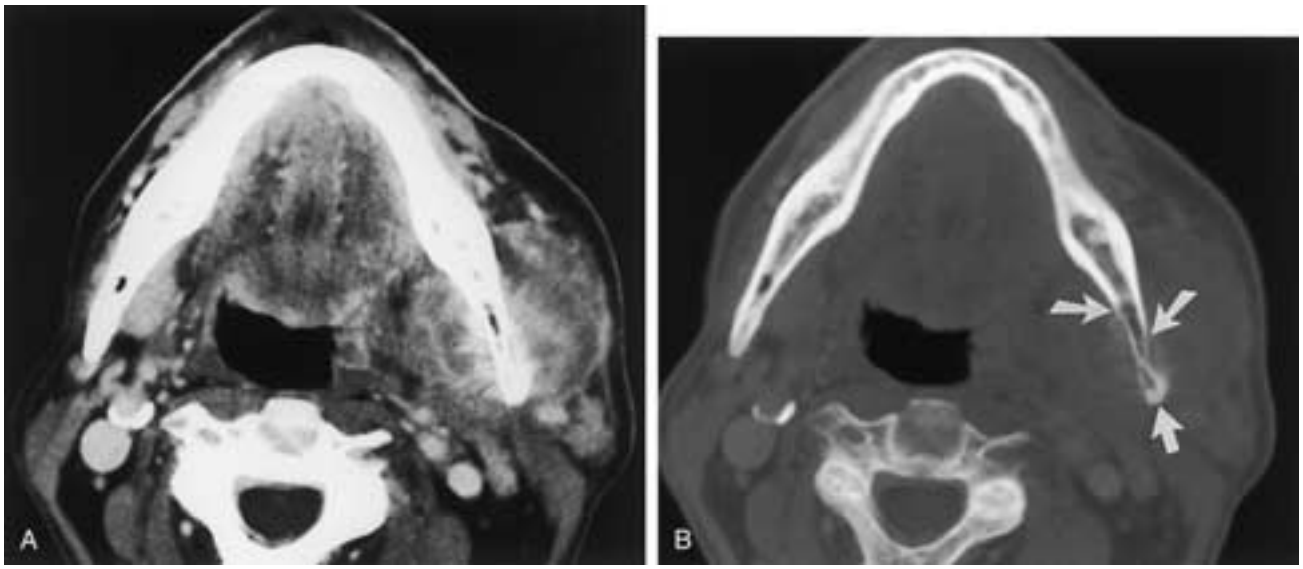

VIEW IMAGE

FIGURE 27-118 Metastatic rectal carcinoma to the left mandible. Axial contrast-enhanced CT scans in (**A**) soft-tissue and (**B**) bone windows reveal a destructive lesion of the left mandible extending through both the lingual and buccal cortices to involve the medial pterygoid and masseter muscles. There is a spiculated appearance that is very similar to that of the osteosarcomas demonstrated in Figures 27-116B and 27-116D. The cortical destruction is best appreciated on the bone window image (*arrows* in **B**), but the spiculation is very faint. (Courtesy of Dr. Deborah Reede.)

Denervation Muscle Atrophy

Motor innervation to the musculature of the oral cavity and masticator space is primarily derived from the mandibular division of the trigeminal nerve (V3), the facial nerve (VII), and the hypoglossal nerve (XII). Damage to these nerves anywhere along their course may lead to denervation and subsequent muscle atrophy with fatty replacement.[315, 316] Various patterns of motor denervation of V3 and XII are presented in Figure 27-121.

The identification of these patterns on CT is based primarily upon the presence of atrophy and fatty replacement of certain muscle groups, which are not appreciated until the chronic stages of denervation occur. On MR imaging, however, abnormalities may be appreciated much earlier in the denervation process if the muscle bundles are of sufficient size.

In the acute/subacute phase of muscle denervation, there is T2 prolongation of denervated muscle secondary to an

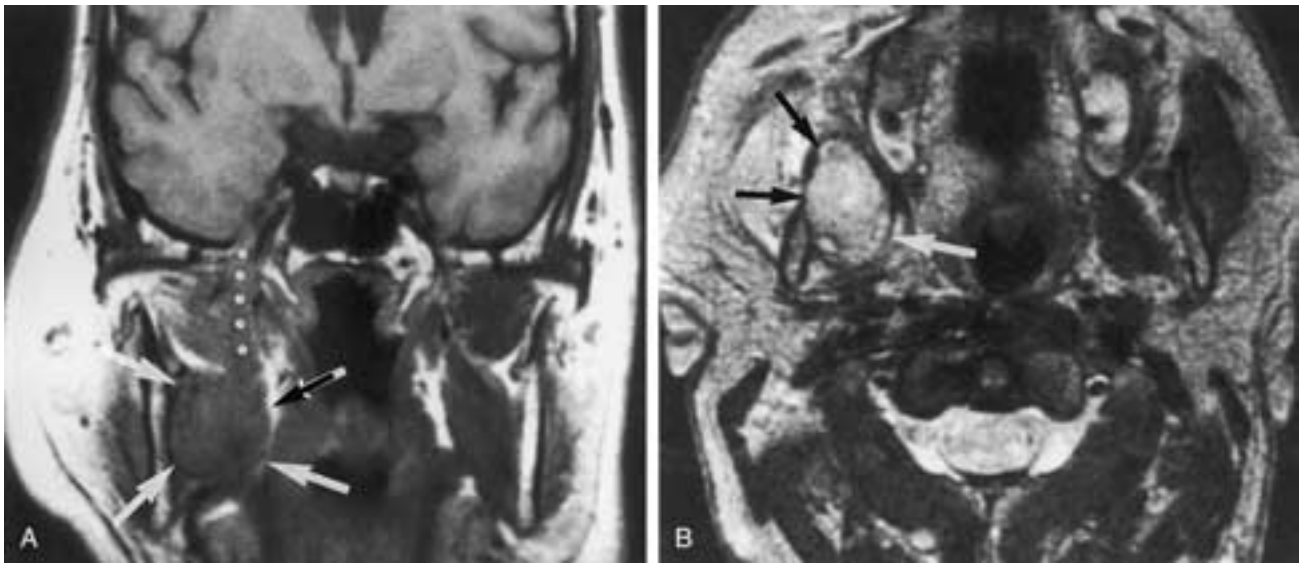

VIEW IMAGE

FIGURE 27-119 Malignant schwannoma of the right mandibular nerve. **A**, Coronal T1-weighted MR image demonstrates a mass centered within the right medial pterygoid muscle (*arrows*), extending along the masticator nerve through the foramen ovale and into the cavernous sinus (*dots*). **B**, Axial T2-weighted MR image demonstrates that the mass is hyperintense to muscle on **B** (*arrows*).

Copyright © 2003, Mosby, Inc. All rights reserved.

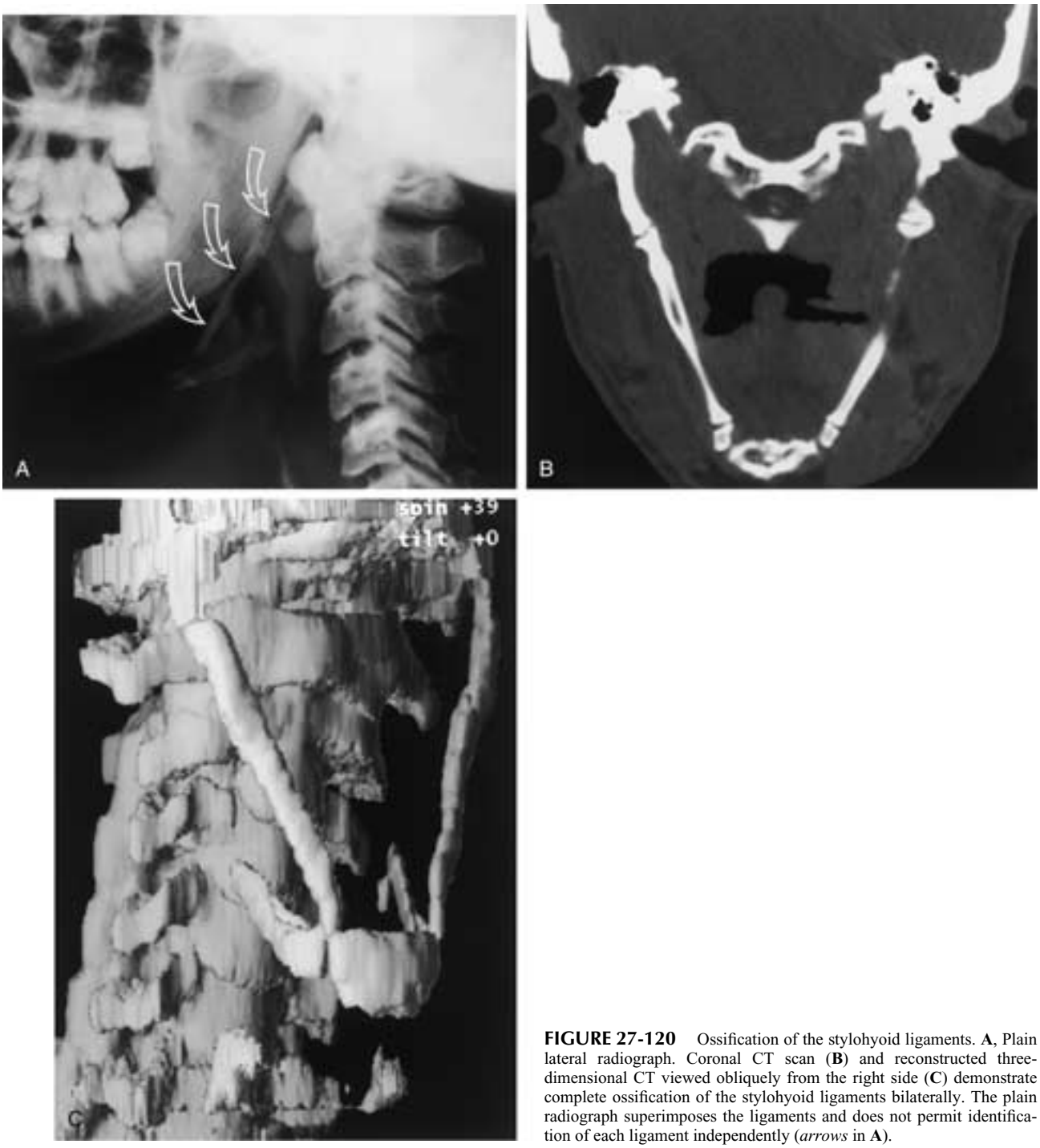

FIGURE 27-120 Ossification of the stylohyoid ligaments. **A**, Plain lateral radiograph. Coronal CT scan (**B**) and reconstructed three-dimensional CT viewed obliquely from the right side (**C**) demonstrate complete ossification of the stylohyoid ligaments bilaterally. The plain radiograph superimposes the ligaments and does not permit identification of each ligament independently (*arrows* in **A**).

VIEW IMAGE

Copyright © 2003, Mosby, Inc. All rights reserved.

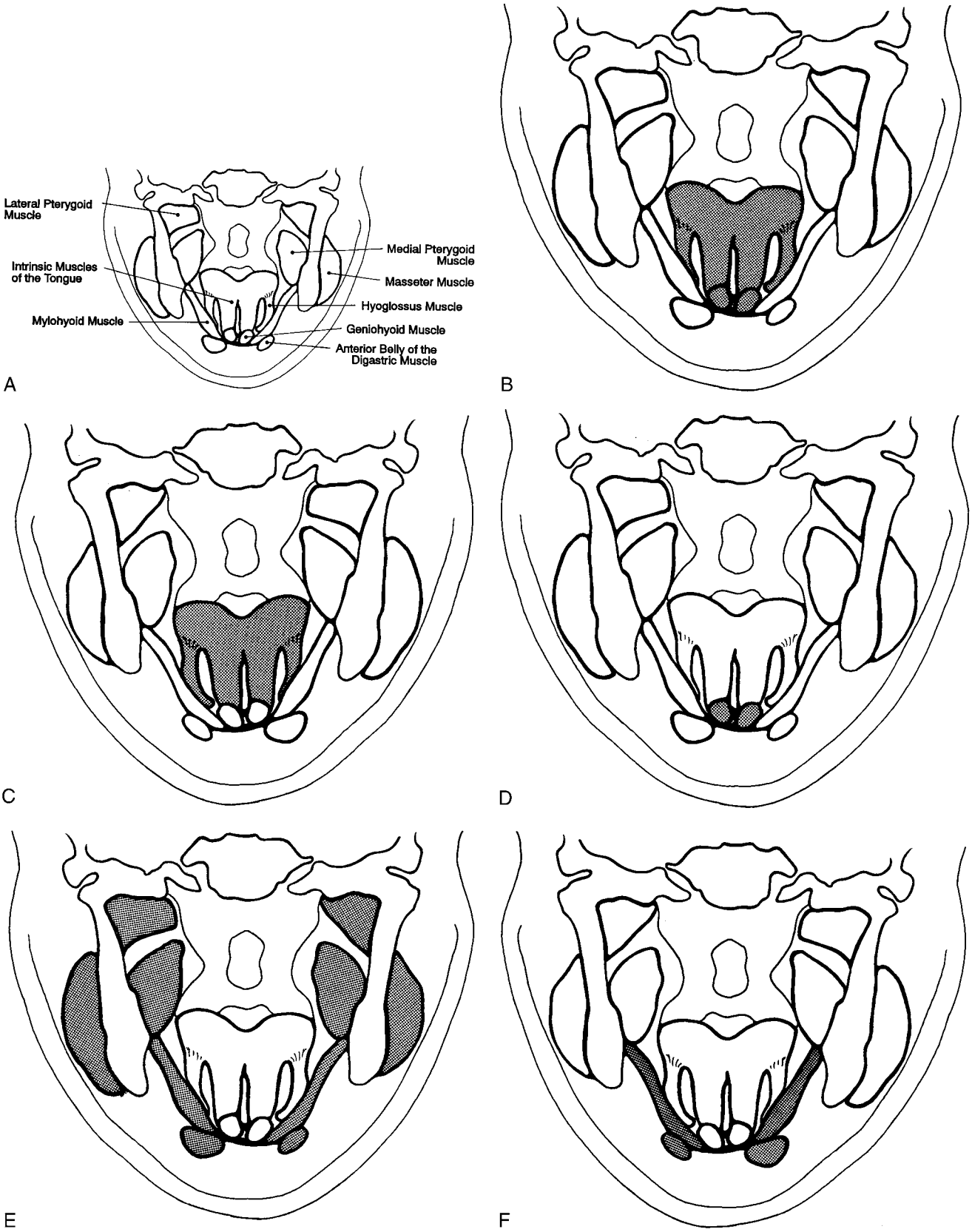

FIGURE 27-121 Denervation atrophy patterns. **A**, Diagram illustrating the muscles of the masticator space, oral tongue, and floor of the mouth. **B** to **F**, Diagrams illustrating muscles affected by denervation atrophy from injury to (**B**) the hypoglossal nerve and fibers from C1; (**C**) the hypoglossal nerve proper, without C1 fiber involvement; (**D**) selective involvement of C1 fibers, distal to the exit of the main hypoglossal nerve fibers; (**E**) the mandibular division of the trigeminal nerve, involving both the masticator and mylohyoid nerves; (**F**) selective involvement of the mylohyoid nerve (arising from the inferior alveolar nerve).

VIEW IMAGE

Copyright © 2003, Mosby, Inc. All rights reserved.

Table 27-4
STAGES OF MOTOR DENERVATION

	Acute	Subacute	Early Chronic	Late Chronic
Muscle volume	+	+	—	↓
T2 prolongation	+	+	—	—
Fatty infiltration	—	+	+	++
Abnormal enhancement	+	+	—	—

+ Finding present
— Finding normal or not present
↓ Muscle volume decreased

increase in extracellular water, which may be associated with increased muscle volume.[34] Abnormal enhancement may also be present secondary to the expanded extracellular space and relatively increased vascularity per cubic millimeter. It is important to become familiar with these acute/subacute changes of denervation (abnormal enhancement and edema-like appearance) because neoplastic and inflammatory processes may have a very similar imaging appearance.[34]

Early chronic denervation changes include visible fatty muscle replacement but no increase in muscle mass, no pathologic enhancement, and no edema-like changes on T2-weighted MR images. Long-standing chronic denervation manifests as substantial muscle volume loss and fatty replacement. In these cases, one must take special care not to diagnose a mass in the larger (normal) muscles. The MR characteristics of denervation are summarized in Table 27-4.

Mandibular Division of the Trigeminal Nerve (V3)

The mandibular division of the trigeminal nerve supplies motor innervation to the muscles of mastication (via the masticator branch), the tensor tympani muscles, and, via the mylohyoid branch of the inferior alveolar nerve, the mylohyoid and anterior belly of the digastric muscles (Fig. 27-122). Proximal injury to the nerve, which is most often affected by perineural spread of tumor or retrogasserian rhizotomy,[294, 295] results in denervation and atrophy of all of these muscles (Figs. 27-123 to 27-125). If the injury occurs more distally, affecting the inferior alveolar nerve after it arises from the main motor trunk, selective atrophy of the mylohyoid and anterior belly of the digastric muscle will result (Fig. 27-126). Identification of denervation atrophy should prompt an exhaustive search along the entire course of the nerve back to the brainstem in an attempt to localize an offending lesion.

Facial Nerve (VII)

The facial nerve supplies motor innervation to a large number of muscles, including the mimetic muscles of facial expression, most of them quite diminutive. For the purposes of this discussion, only those muscles that may be identified on cross-sectional imaging are of interest and include the zygomaticus major, buccinator, and platysma muscles (Fig. 27-127). Acute/subacute and early chronic changes of denervation are very difficult to identify within these muscles due to their small size, and it is not until substantial atrophy and fatty infiltration occur that atrophic changes can be identified. Fibers of the buccinator are easily recognized on MR images that demonstrate the parotid gland duct as it pierces the muscle. The widths of the muscles on the two sides can readily be compared and atrophic changes appreciated (Fig. 27-128). Atrophic changes of the zygomaticus muscle bundle may also be identified, but one must be certain that the patient is centered and not rotated on the images. Platysma atrophy usually manifests as failure to identify muscle fibers on the affected side.

The facial nerve is often damaged during parotid gland surgery but is also affected by neoplasms. As with the mandibular nerve, the entire course of the facial nerve must be examined when denervation atrophy is identified.

Hypoglossal Nerve (XII)

The hypoglossal nerve supplies motor innervation to intrinsic and extrinsic tongue musculature from its nucleus within the medulla (Fig. 27-129). Chronic atrophic changes are easily identified on both CT and MR imaging, but as the tongue represents a large muscle bundle, acute/subacute changes may also be identified on MR imaging. Acute denervation atrophy of the hypoglossal nerve produces initial enlargement and enhancement of the affected hemitongue, as described previously, and if imaging is performed at this time, the affected side of the tongue may be mistakenly diagnosed as harboring a mass (Figs. 27-130

Text continued on page 1456

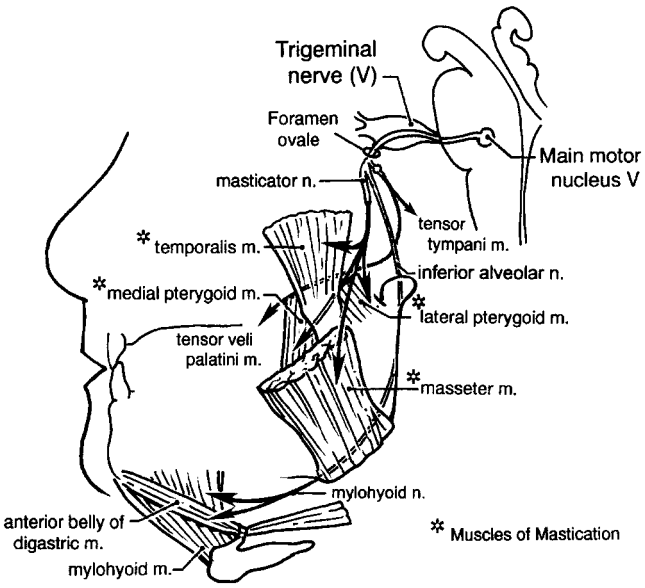

FIGURE 27-122 Motor fibers of the mandibular division of the trigeminal nerve (V3). The motor nucleus of the trigeminal nerve is located in the middle pons. The nerve root exits the brainstem at the lateral pons, courses through the prepontine cistern (preganglionic segment), and passes into the gasserian ganglion within Meckel's cave, just lateral to the cavernous sinus. The postganglionic segment trifurcates just distal to the ganglion, and V3 passes inferiorly to exit the skull base via the foramen ovale. V3 enters the masticator space; the motor component divides into two branches: the masticator nerve and the mylohyoid nerve. The masticator nerve supplies the muscles of mastication, and the mylohyoid nerve supplies the anterior belly of the digastric and the mylohyoid muscles.

VIEW IMAGE

Copyright © 2003, Mosby, Inc. All rights reserved.

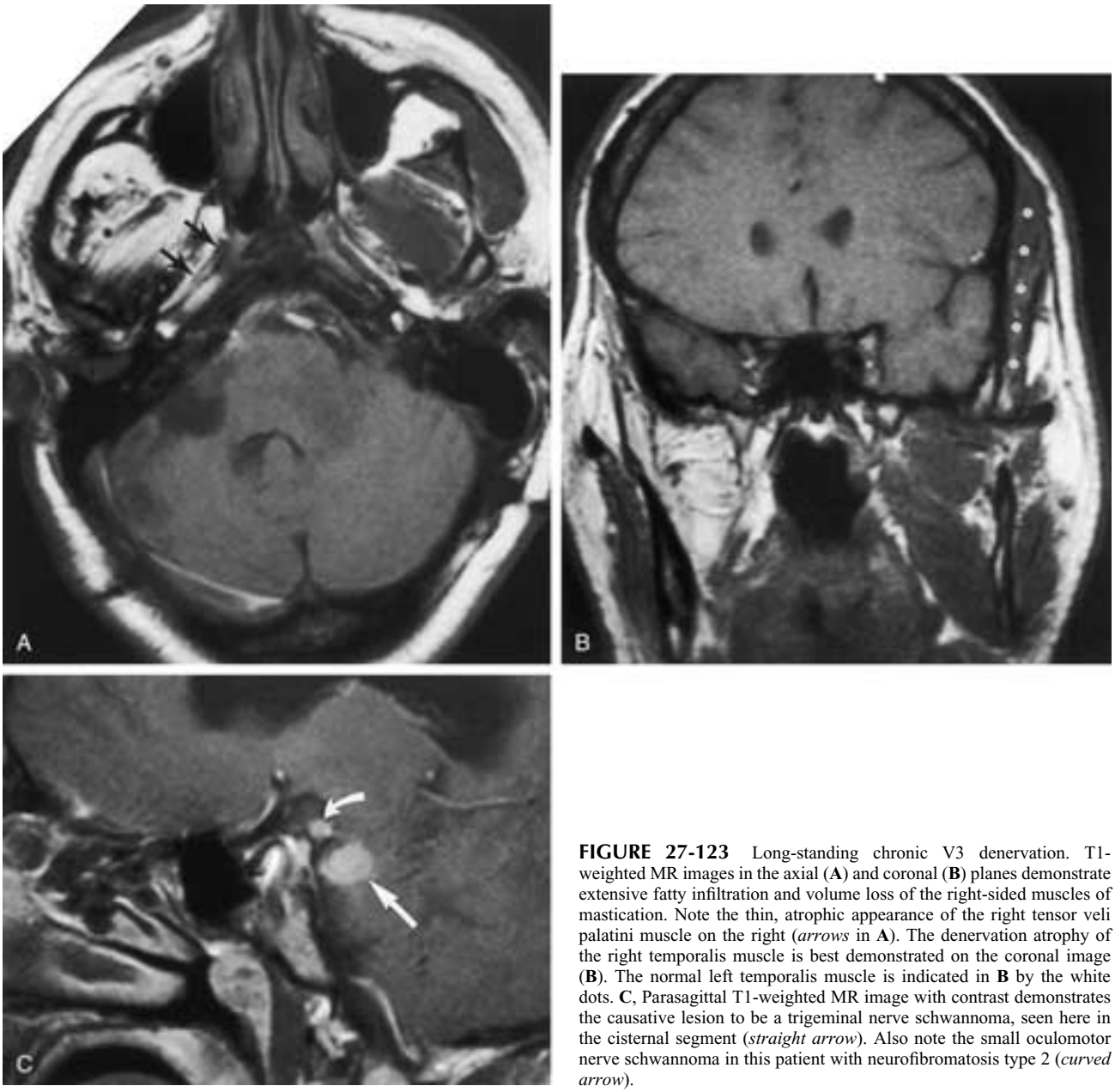

FIGURE 27-123 Long-standing chronic V3 denervation. T1-weighted MR images in the axial (**A**) and coronal (**B**) planes demonstrate extensive fatty infiltration and volume loss of the right-sided muscles of mastication. Note the thin, atrophic appearance of the right tensor veli palatini muscle on the right (*arrows* in **A**). The denervation atrophy of the right temporalis muscle is best demonstrated on the coronal image (**B**). The normal left temporalis muscle is indicated in **B** by the white dots. **C**, Parasagittal T1-weighted MR image with contrast demonstrates the causative lesion to be a trigeminal nerve schwannoma, seen here in the cisternal segment (*straight arrow*). Also note the small oculomotor nerve schwannoma in this patient with neurofibromatosis type 2 (*curved arrow*).

VIEW IMAGE

Copyright © 2003, Mosby, Inc. All rights reserved.

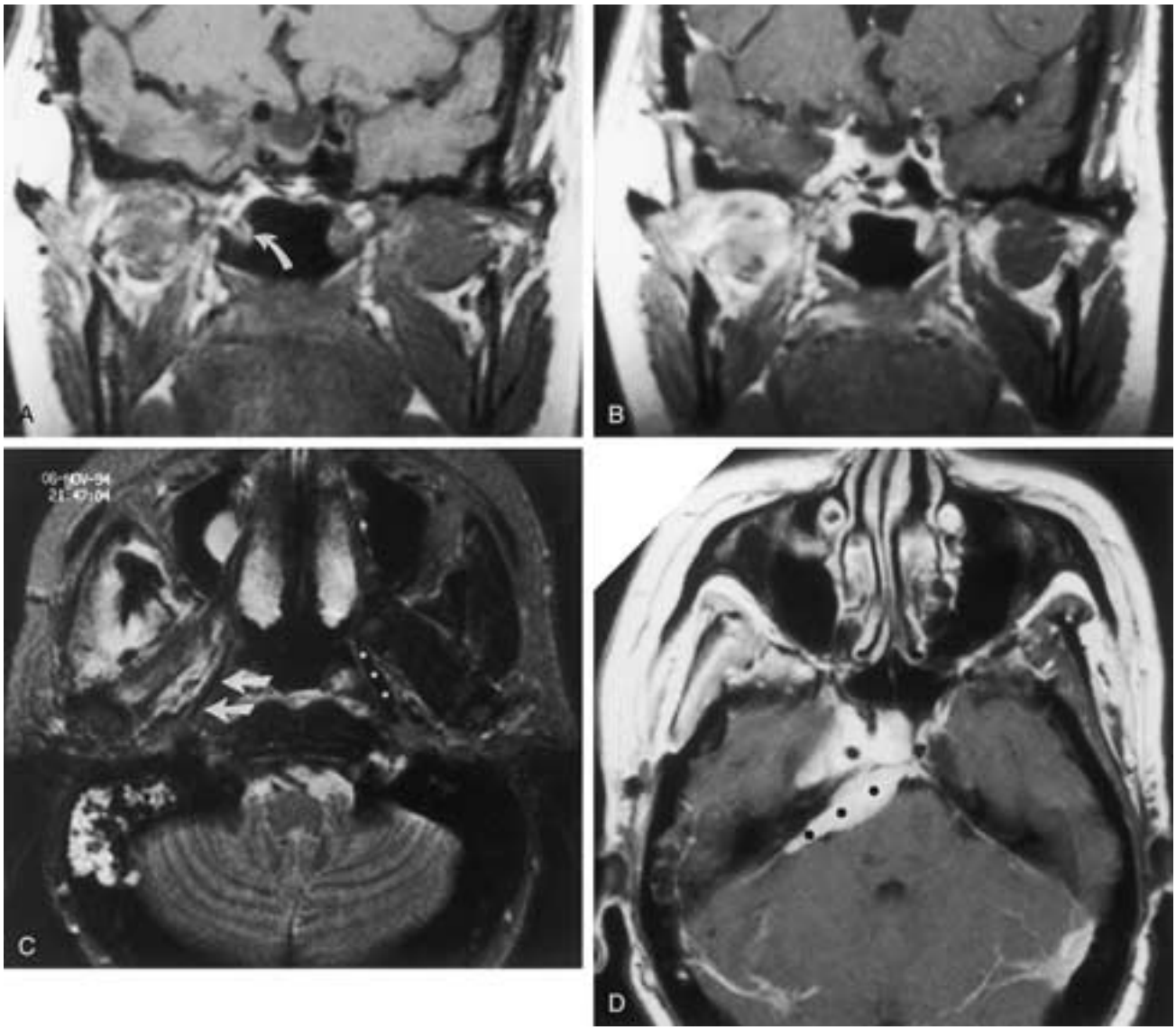

VIEW IMAGE

FIGURE 27-124 Subacute V3 denervation. **A**, Coronal T1-weighted MR image demonstrates some fatty infiltration and mild volume loss of the right muscles of mastication. Note the diminutive right torus tubarius, which may be related to tensor veli palatini dysfunction (*arrow*). **B**, Coronal contrast-enhanced T1-weighted MR image demonstrates enhancement of the right muscles of mastication. **C**, Axial T2-weighted MR image reveals significant fluid within the right mastoid air cells due to tensor veli palatini dysfunction. Note the diminutive size of the right tensor veli palatini muscle (*arrows*) compared to the normal muscle on the left (*dots*). **D**, Axial contrast-enhanced T1-weighted MR image demonstrates the causative lesion to be meningioma affecting the trigeminal nerve in its cisternal and cavernous sinus segments (*dots*).

Copyright © 2003, Mosby, Inc. All rights reserved.

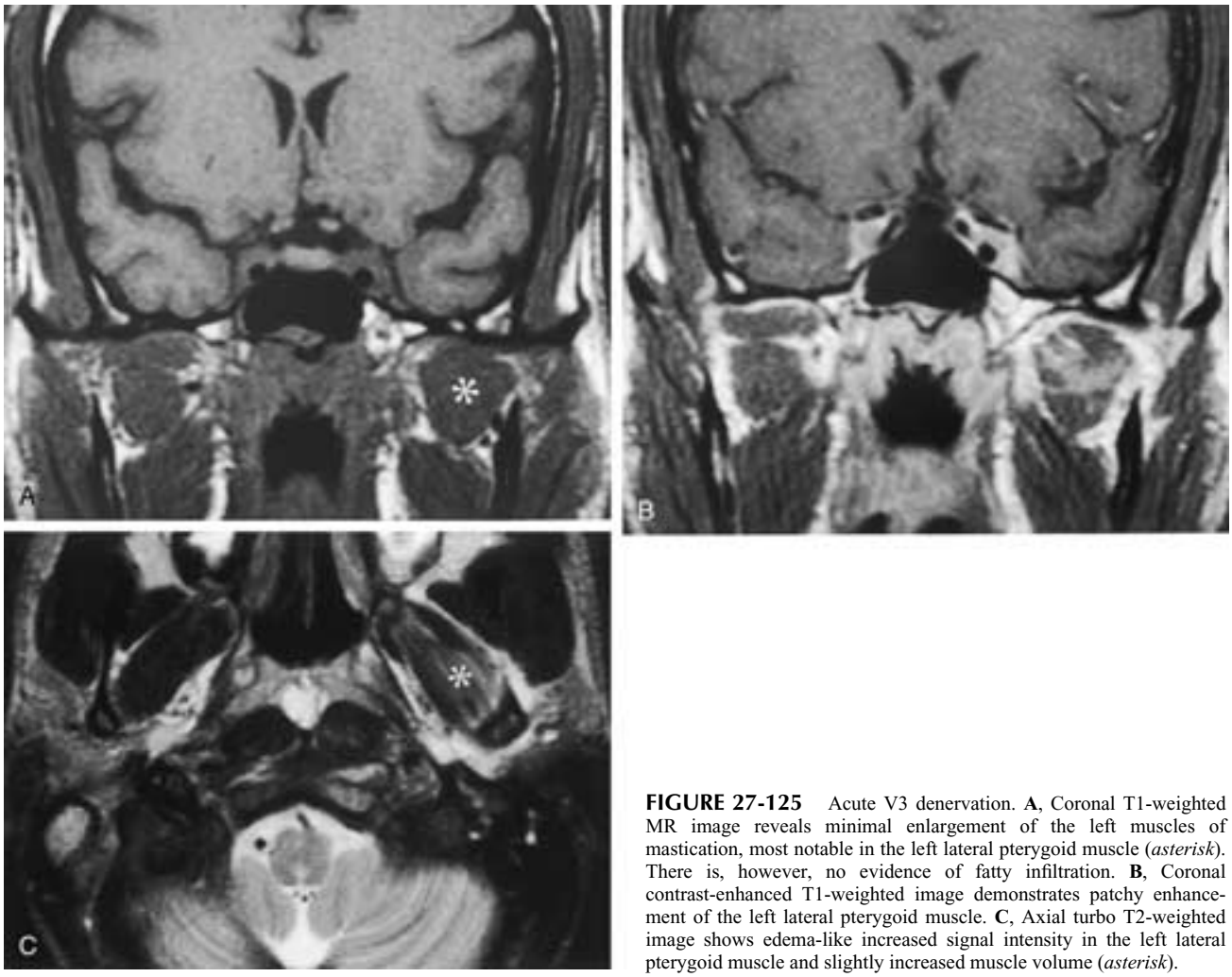

FIGURE 27-125 Acute V3 denervation. **A**, Coronal T1-weighted MR image reveals minimal enlargement of the left muscles of mastication, most notable in the left lateral pterygoid muscle (*asterisk*). There is, however, no evidence of fatty infiltration. **B**, Coronal contrast-enhanced T1-weighted image demonstrates patchy enhancement of the left lateral pterygoid muscle. **C**, Axial turbo T2-weighted image shows edema-like increased signal intensity in the left lateral pterygoid muscle and slightly increased muscle volume (*asterisk*).

VIEW IMAGE

FIGURE 27-126 Chronic V3 denervation atrophy. Coronal T1-weighted MR image demonstrates marked atrophy of the left mylohyoid muscle (*arrowhead*) and the anterior belly of the digastric (*arrow*) muscle. The normal right-sided digastric (*large dot*) and mylohyoid (*small dots*) muscles are indicated.

VIEW IMAGE

Copyright © 2003, Mosby, Inc. All rights reserved.

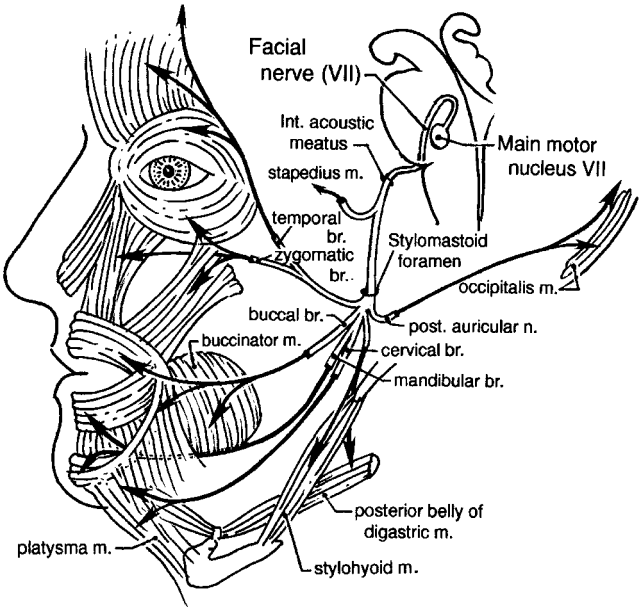

FIGURE 27-127 The facial nerve nucleus is at the level of the pons. This complex nerve provides small branches to the posterior belly of the digastric and stylohyoid muscles just after it exits the skull base through the stylomastoid foramen. Within the substance of the parotid gland, the facial nerve divides into its five terminal branches supplying motor innervation to the small muscles of facial expression, as well as to the buccinator and platysma muscles.

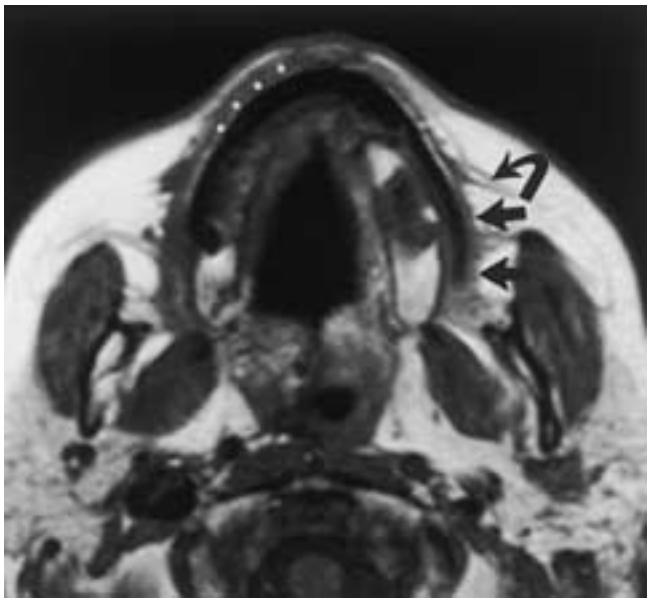

FIGURE 27-128 Early chronic facial nerve denervation in a woman who had undergone left parotid gland surgery. Axial T1-weighted MR image reveals fatty replacement and volume loss involving the left buccinator (*straight arrows*) and zygomaticus (*curved arrow*) muscles. Also note the involvement of other small mimetic facial muscles on the left compared to the normal muscle mass on the right (*dots*).

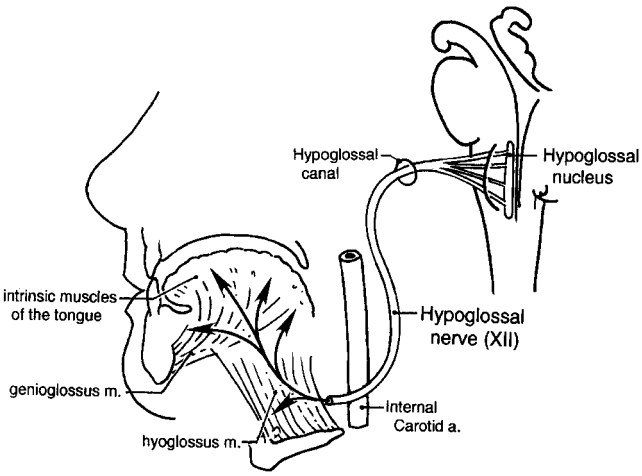

FIGURE 27-129 In this diagram, the hypoglossal nuclei are situated in the medulla, just deep to the floor of the fourth ventricle. Multiple XII nerve rootlets exit the medulla at the preolivary sulcus, in proximity to the vertebral artery, and cross the premedullary cistern to enter the hypoglossal canal. After emerging from the hypoglossal canal, nerve XII passes into the carotid space and loops caudally to the level of the hyoid bone. The nerve then courses upward to the sublingual space, where it ramifies to supply motor branches to the intrinsic and extrinsic muscles of the tongue.

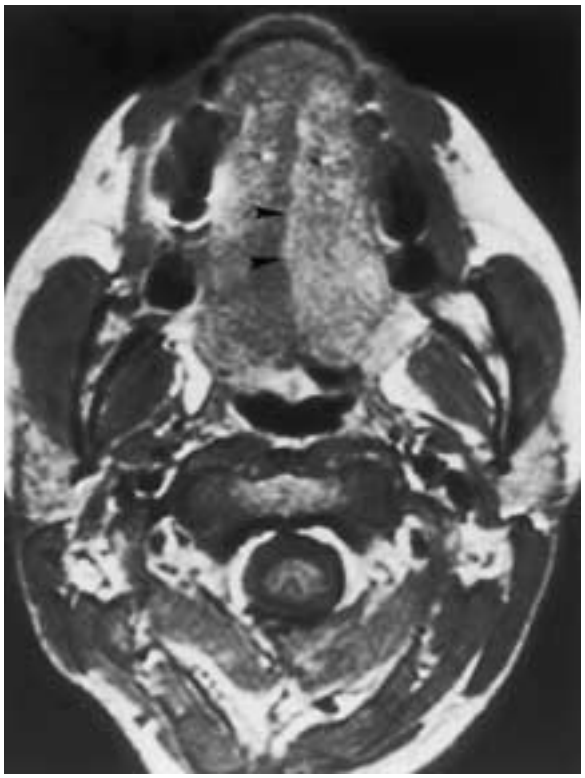

FIGURE 27-130 Acute hypoglossal nerve denervation. Axial T1-weighted MR image in a 17-year-old female after left tonsillectomy 2 weeks earlier. The examination reveals the earliest changes of denervation atrophy of the left hemitongue, which, because it is imaged relatively acutely, demonstrates a positive mass effect (*arrowheads*). Early fatty infiltration is identified by high-signal replacement of the intrinsic tongue musculature. (From Smoker WRK. The hypoglossal nerve. Neuroimag Clin North Am 1993;3:193–206.)

Copyright © 2003, Mosby, Inc. All rights reserved.

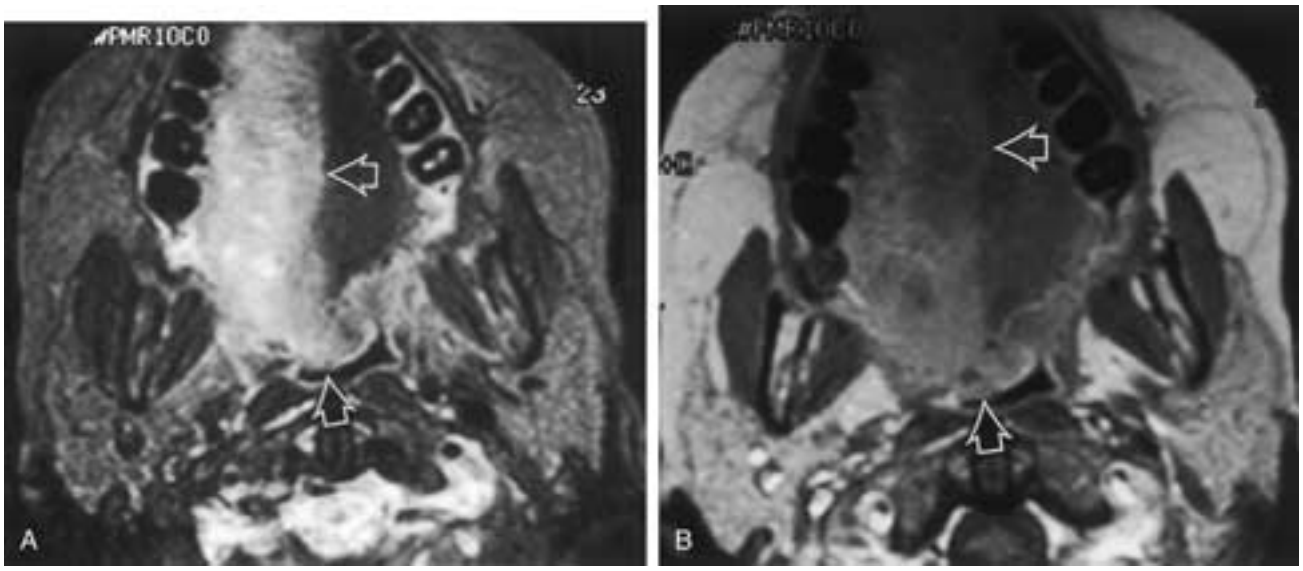

VIEW IMAGE

FIGURE 27-131 Acute hypoglossal nerve denervation. (**A**) Axial T2-weighted and (**B**) axial T1-weighted images with contrast enhancement and fat suppression reveal edema-like increased signal intensity in the right hemitongue on **A** that demonstrates enhancement (**B**). Note the protrusion of the hemitongue across the midline and posteriorly into the oropharynx (*arrows*).

and 27-131).[34] The first clinical sign of peripheral XII palsy is deviation of the tongue toward the side of pathology, primarily the result of paralysis of the genioglossus muscle, which controls protrusion of the tongue. More often, however, imaging is not performed until the paralysis has become permanent, at which time the affected hemitongue is replaced by variable amounts of fat (Fig. 27-132). With long-standing denervation, the muscle bundles will no longer be recognizable and only the arteries and veins remain intact. At this time, the atrophic hemitongue prolapses back into the oropharynx (Figs. 27-133 and 27-134). As with all denervated muscles, the entire course of the nerve must be evaluated in the search for an offending lesion.

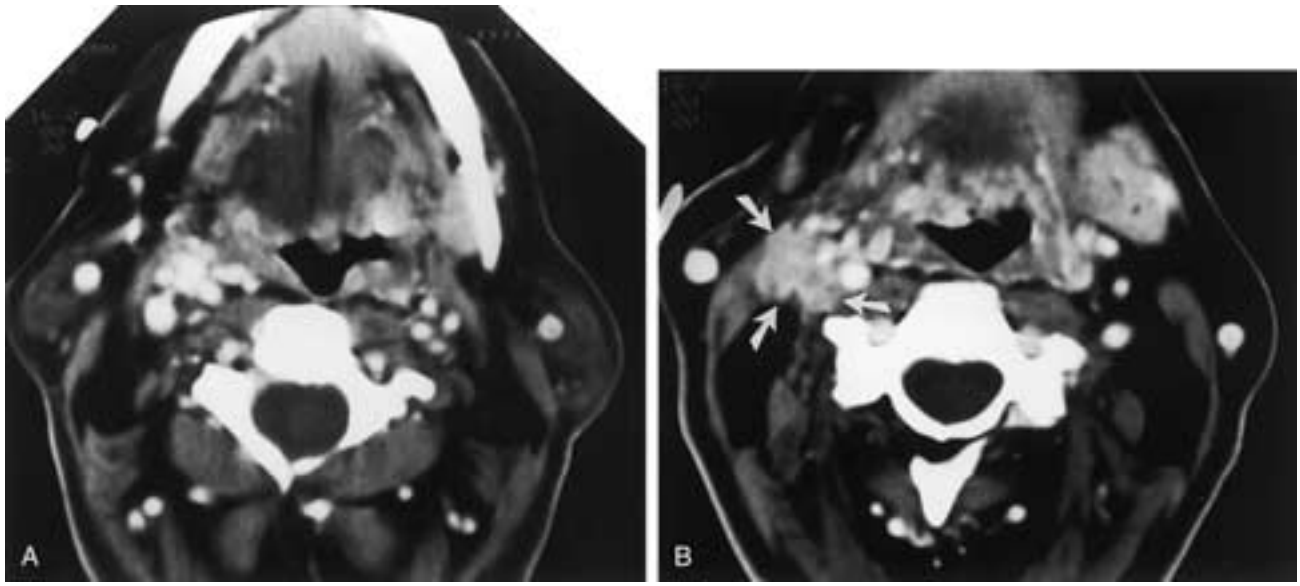

VIEW IMAGE

FIGURE 27-132 Early chronic hypoglossal nerve denervation. **A** and **B**, Axial CT scans in a 46-year-old woman 8 years after mastectomy for breast carcinoma who now presents with right cranial nerve XII palsy. At the level of the mandible (**A**), fatty replacement and loss of muscle fibers involving the intrinsic musculature and genioglossus muscles of the right hemitongue are identified by its lower density compared with the left hemitongue. On a more inferior plane (**B**) an extranodal mass is visible adjacent to the right carotid sheath (*arrows*), which proved to be metastatic breast carcinoma. This case highlights the importance of imaging the most inferior loop of the hypoglossal nerve, inferior to the mandible, so as to visualize nerve XII fibers coursing in the low oropharyngeal carotid space.

Copyright © 2003, Mosby, Inc. All rights reserved.

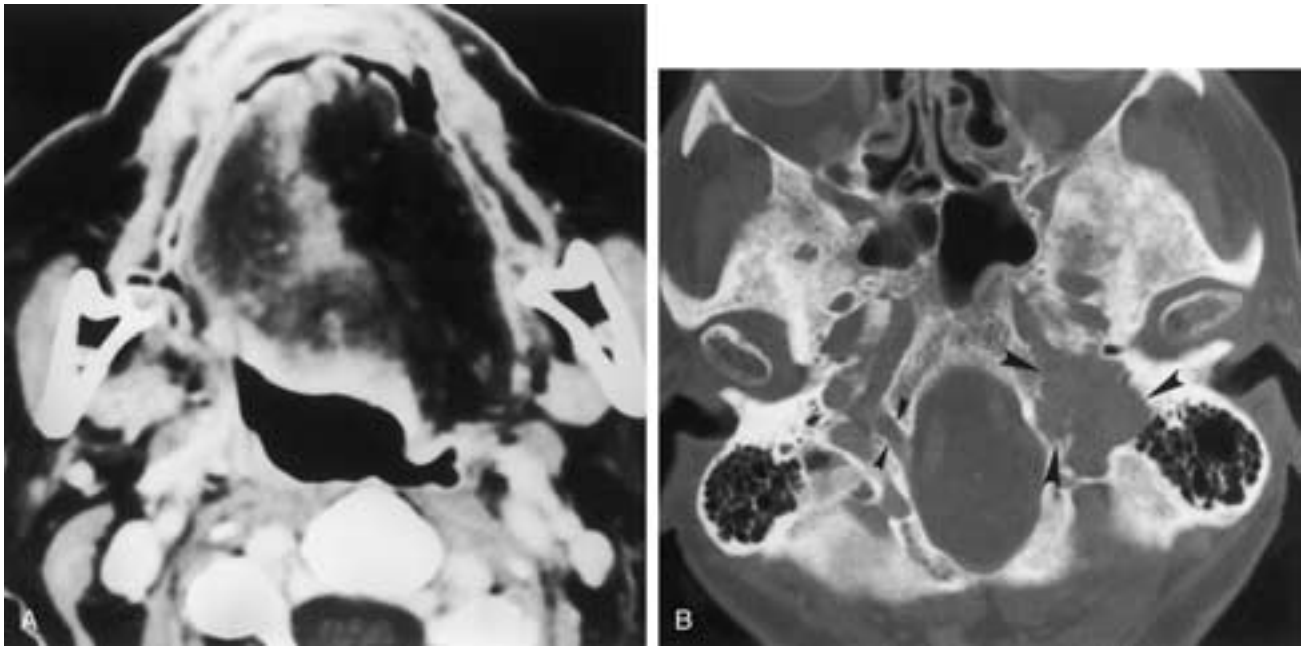

VIEW IMAGE

FIGURE 27-133 Long-standing chronic hypoglossal nerve denervation atrophy. **A**, Axial contrast-enhanced CT scan of the oral tongue reveals complete atrophy and fatty replacement of all of the left hemitongue muscular structures, both intrinsic and extrinsic. There is prolapse of the left hemitongue into the oropharynx, producing contour abnormality. **B**, Axial CT scan at the level of the hypoglossal canal with a bone window setting reveals extensive skull base destruction on the left (*large arrowheads*). The cortical margins of the normal right hypoglossal canal are well identified (*small arrowheads*). The large area of skull base destruction on the left (*large arrowheads*) clearly involves the region of the left hypoglossal canal. (From Smoker WRK. The hypoglossal nerve. Neuroimag Clin North Am 1993;3:193–206.)

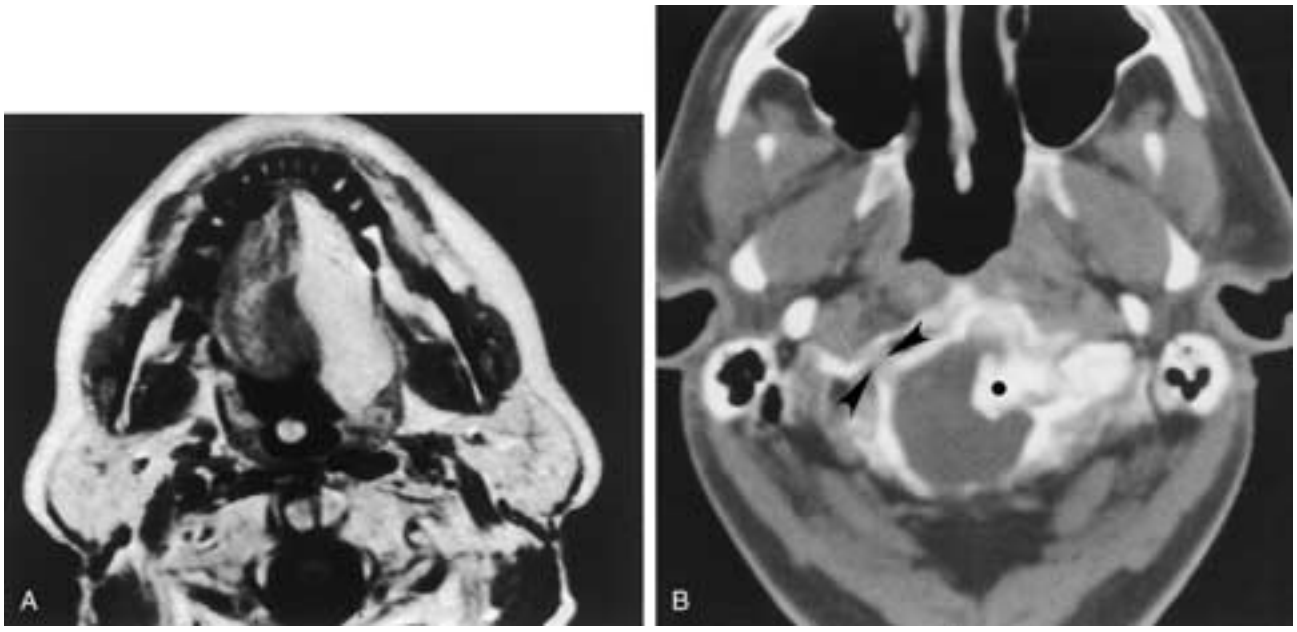

VIEW IMAGE

FIGURE 27-134 Long-standing chronic hypoglossal nerve denervation atrophy. **A**, Axial T1-weighted MR image demonstrates complete fatty replacement of the entire left hemitongue. There is marked prolapse of the left hemitongue back into the oropharynx. **B**, Axial CT scan at bone windows reveals the causative lesion to be a small meningioma centered at the level of the left hypoglossal canal (*dot*). The margins of the normal right hypoglossal canal are indicated by the arrowheads.

Copyright © 2003, Mosby, Inc. All rights reserved.

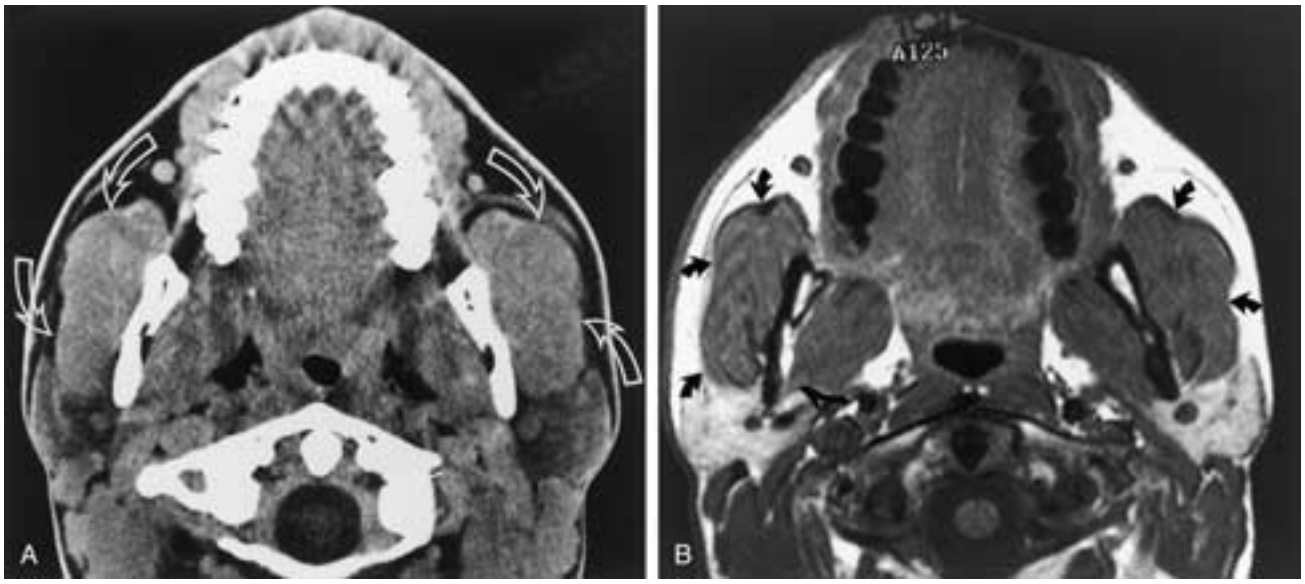

VIEW IMAGE

FIGURE 27-135 Benign masseteric hypertrophy. (**A**) Axial CT scan without contrast enhancement and (**B**) T1-weighted MR image reveal marked bilateral enlargement of the masseter muscles, which are otherwise normal in density/signal intensity and contour (*arrows*). (Courtesy of Dr. Deborah Reede.)

Benign Masseteric Hypertrophy

Benign masseteric hypertrophy (BMH) refers to idiopathic enlargement of the masseter muscle. Although uncommon, this condition is important because it must be considered in the differential diagnosis of masses in the parotid region.[22] Males are affected twice as often as females, and approximately 50% of the cases are bilateral. The etiology of BMH is uncertain, although a variety of theories have been proposed. Both familial and acquired forms are likely, with the acquired form most often associated with dental malocclusion or bruxism (teeth grinding).[24] CT and MR imaging demonstrate enlargement of the involved muscle(s) with preservation of muscle margins and surrounding fascial planes; otherwise, the hypertrophic muscle(s) look the same as the noninvolved normal muscles (Fig. 27-135). In some patients, an area of hyperostosis is present at the mandibular insertion of the masseter muscle, probably representing a secondary manifestation of muscle hypertrophy. In addition to isolated BMH, diffuse hypertrophy involving all muscles of mastication in patients with bruxism may occur (Fig. 27-136).[24, 317]

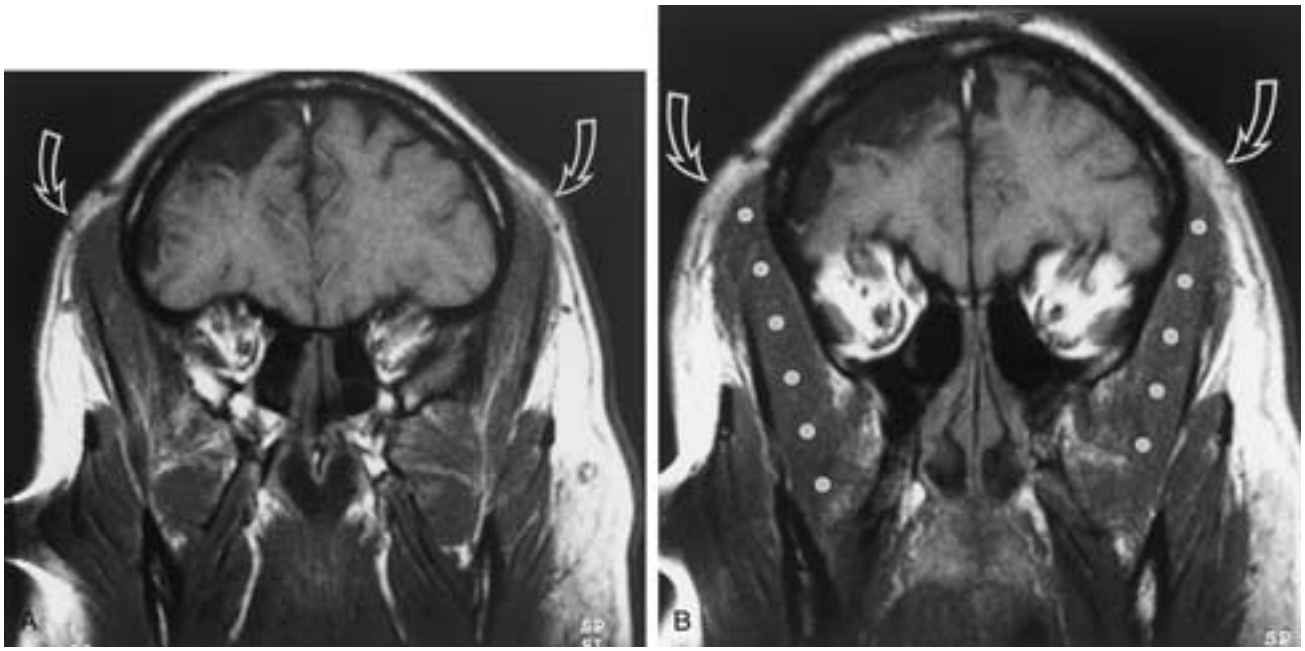

VIEW IMAGE

FIGURE 27-136 Hypertrophy of all muscles of mastication. **A** and **B**, Coronal T1-weighted MR images demonstrate marked enlargement of all muscles of mastication bilaterally. Note especially the temporalis muscle hypertrophy (*dots* in **B**) in the suprazygomatic masticator spaces, which causes the contour of the overlying scalp to bulge (*arrows*).

Copyright © 2003, Mosby, Inc. All rights reserved.

Table 27-5
CONDITIONS ASSOCIATED WITH TONGUE ENLARGEMENT

Congenital disorders
Beckwith-Wiedermann syndrome
Down's syndrome
Robinow's syndrome
Endocrine and metabolic disorders
Mucopolysaccharidosis
Acromegaly
Cretinism and myxedema
Amyloidosis
Lipoid proteinosis
Tumor-like disorders
Hemangioma
Lymphangioma
Lymphangioendotheliomatosis

Macroglossia

Macroglossia, or tongue enlargement, is for the most part a clinical diagnosis. In addition to occurring in any number of tumoral conditions, macroglossia may occur in a variety of congenital, endocrine, and metabolic conditions (Table 27-5). From their study of 40 normal persons and 12 patients with systemic primary amyloidosis involving the tongue, Larsson et al. suggested that macroglossia can be suspected if (1) the base of the tongue is more than 50 mm in the transverse diameter, (2) the genioglossus muscle is more than 11 mm in the transverse diameter, (3) the surface of the tongue base has a midline cleft, and (4) despite being normal in size, the submandibular glands are displaced laterally, producing an outward bulging of the overlying platysma muscles.[10]

With regard to amyloidosis of the tongue, scattered CT reports indicate symmetric enlargement of both the extrinsic and intrinsic tongue musculature. Obliteration of the normal fascial planes, caused by increased muscle bulk, is typically present, without identification of any focal mass.[10, 12] This is in sharp contrast to tumors, which, until well advanced, usually present as focal masses that do not typically involve both the intrinsic and extrinsic tongue muscles but do displace the normal fascial planes. In amyloidosis the abnormally enlarged, infiltrated musculature does not exhibit pathologic enhancement. Usually the T1-weighted and T2-weighted signal intensities are similar to those of normal skeletal muscle.

REFERENCES

1. Batsakis JG. Tumors of the Head and Neck: Clinical and Pathological Considerations, 2nd ed. Baltimore: Williams & Wilkins, 1979.
2. Million RR, Cassisi NJ. Management of Head and Neck Cancer, 2nd ed. Philadelphia: JB Lippincott, 1994.
3. Larsson SG, Mancuso A, Hanafee W. Computed tomography of the tongue and floor of the mouth. Radiology 1982;143:493–500.
4. Muraki AS, Mancuso AA, et al. CT of the oropharynx, tongue base, and floor of the mouth: normal anatomy and range of variations, and applications in staging of carcinoma. Radiology 1983;148:725–731.
5. Hollinshead W. Anatomy for Surgeons. Vol 1. The Head and Neck, 3rd ed. Hagerstown, NJ: Harper & Row, 1982.
6. Last RJ. Anatomy: Regional and Applied, 6th ed. Edinburgh, London, and New York: Churchill Livingstone, 1978.
7. Gray H. Anatomy, descriptive and surgical. In: Pick TP, Howden R, eds. Philadelphia: Running Press, 1974.
8. Lufkin RB, et al. Tongue and oropharynx: findings on MR imaging. Radiology 1986;161:69–75.
9. Lufkin RB, Larsson SG, Hanafee WN. NMR anatomy of the larynx and tongue base. Radiology 1983;148:173–175.
10. Larsson SG, Benson L, Westermark P. Computed tomography of the tongue in primary amyloidosis. J Comput Assist Tomogr 1986;10: 836–840.
11. Smoker WRK. The hypoglossal nerve. Neuroimag Clin North Am 1993;3:193–206.
12. Manco LG, Hanafee WN. Computed tomography of macroglossia secondary to amyloidosis. J Comput Assist Tomogr 1984;8:659–661.
13. Weissman JL, Carrau RL. Anterior facial vein submandibular gland together: predicting the histology of submandibular masses with CT or MR imaging. Radiology 1998;208:441–446.
14. Kaneda T, Minami M, Ozawa K, et al. MR of the submandibular gland: normal and pathologic states. AJNR 1996;17:1575–1581.
15. Braun IF, Hoffman JC. Computed tomography of the buccomasseteric region. I. Anatomy. AJNR 1984;5:605–610.
16. Mancuso AA, Harnsberger HR, Dillon WP. Workbook for MRI and CT of the Head and Neck, 2nd ed. Baltimore: Williams & Wilkins, 1989;163.
17. Paonessa DB, Goldstein JC. Anatomy and physiology of head and neck infections (with emphasis on the fascia of the face and neck). Otolaryngol Clin North Am 1976;3:562–580.
18. Stuzin JM, Baker TJ. Discussion of anatomy of the buccal fat pad and its significance. Plast Reconstr Surg 1989;83:263–264.
19. Dubin B, Jackson IT, Halim A, et al. The anatomy of the buccal fat pad and its significance. Plast Reconstr Surg 1989;83:257–262.
20. DuBrul EL. Oral Anatomy, 8th ed. St. Louis: Ishiyaku EuroAmerica, 1988;162–165, 301–304.
21. Tart RP, Kotzur IM, Mancuso AA, Glantz MS, Mukherji SK. CT and MR imaging of the buccal space and buccal space masses. RadioGraphics 1995;15:531–550.
22. Braun IF, Hoffman JC Jr, Reede D, et al. Computed tomography of the buccomasseteric region. II. Pathology. AJNR 1984;5:611–616.
23. Hardin CW, Harnsberger HR, Osborn AG, et al. Infection and tumor of the masticator space: CT evaluation. Radiology 1985;157: 413–417.
24. Tryhus MR, Smoker WRK, Harnsberger HR. The normal and diseased masticator space. Semin Ultrasound CT MR 1990;11: 476–485.
25. Ardran GM. Becket JM. Kemp FH. Aglossia congenita. Arch Dis Childhood 1964;39:389–391.
26. Higashi K, Edo M. Conductive deafness in aglossia. J Laryngol Otol 1996;110:1057–1059.
27. Weingarten RT, Walner DL, Holinger DL. Tongue hypoplasia in a newborn. Int J Pediatr Otolaryngol 1993;25:235–241.
28. Frommer J. The human accessory parotid gland: its incidence, nature, and significance. Oral Surg 1977;43:671–676.
29. Johnson FE, Spiro RH. Tumors arising in accessory parotid tissue. Am J Surg 1979;138:576–579.
30. Kakulas EG, Smith AC, Sormann G. Pleomorphic adenoma of the accessory parotid gland: case report. J Oral Maxillofac Surg 1994;52:867–870.
31. Larsson SG, Lufkin RB. Anomalies of digastric muscles: CT and MR demonstration. J Comput Assist Tomogr 1987;11:422–425.
32. Traini M. Bilateral accessory digastric muscles. Anat Clin 1983;5: 199–201.
33. Norton MR. Bilateral accessory digastric muscles. Br J Oral Maxillofac Surg 1991;29:167–168.
34. Russo CP, Smoker WRK, Weissman JL. MR appearance of trigeminal and hypoglossal motor denervation. AJNR 1997;18:1375–1383.
35. Mulliken JB, Glowacki J. Hemangiomas and vascular malformations in infants and children: a classification based on endothelial characteristics. Plast Reconstr Surg 1982;69:412–420.
36. Donnelly LF, Adams DM, Bisset GS. Vascular malformations and hemangiomas: a practical approach in a multidisciplinary clinic. AJR 2000;174:597–608.
37. Chen JW, et al. Hemangiomas and vascular malformations. BNI Quart 1994;10:19–25.
38. Watson WL, McCarthy WD. Blood and lymphatic vessel tumors: report of 1056 cases. Surg Gynecol Obstet 1940;71:569–588.

Copyright © 2003, Mosby, Inc. All rights reserved.

39. Bowers RE, Graham EA, Tomlinson KM. The natural history of the strawberry nevus. Arch Dermatol 1960;82:667–673.
40. Baker LL, Dillion WP, Hieshima GB, et al. Hemangiomas and vascular malformations of the head and neck: MR characterization. AJNR 1993;14:307–314.
41. Kaban L, Mulliken JB. Vascular anomalies of the maxillofacial region. J Oral Maxillofac Surg 1986;44:201–213.
42. Burrows PE, Mulliken JB, Fellowes KE, et al. Childhood hemangiomas and vascular malformations: angiographic differentiation. AJR 1983;141:483–488.
43. Meyer JS, Hoffer FA, Barnes PD, et al. Biological classification of soft-tissue vascular anomalies: MR correlation. AJR 1991;157: 559–564.
44. Boyd JB, Mulliken JB, Kaban LB, et al. Skeletal changes associated with vascular malformations. Plast Reconstr Surg 1984;74:789–795.
45. Mulliken JB. Vascular malformations of the head and neck. In: Mulliken JB. Young AE, eds. Vascular Birthmarks, Hemangiomas and Malformations. Philadelphia: WB Saunders, 1988;301–342.
46. Bartlett JA, Riding KH, Salkeld LJ. Management of hemangiomas of the head and neck in children. J Otolaryngol 1988;17:111–120.
47. Edgerton MT. The treatment of hemangiomas. Ann Surg 1976;183: 517–530.
48. Sasaki GH, Pang CY, Wittliff L. Pathogenesis and treatment of infant skin strawberry hemangiomas: clinical and in vitro studies of hormonal effects. Plast Reconstr Surg 1984;73:359–368.
49. Apfelberg DB, Maser MR, White DN, et al. A preliminary study of the combined effect of Neodymium:YAG laser photocoagulation and direct steroid instillation in the treatment of capillary/cavernous hemangiomas of infancy. Ann Plast Surg 1989;22:94–104.
50. Waner M, Suen JY, Dinehart S. Treatment of hemangiomas of the head and neck. Laryngoscope 1992;102:1123–1132.
51. Berthelsen B, Fogdestam I, Svendsen P. Venous malformations in the face and neck: radiologic diagnosis and treatment with absolute ethanol. Acta Radiol 1986;27:149–155.
52. Yakes WF, Haas DK, Parker SH, et al. Symptomatic vascular malformations: ethanol embolotherapy. Radiology 1989;170:1059–1066.
53. Forbes G, Earnest F, Jackson IT, et al. Therapeutic embolization angiography for extra-axial lesions in the head. Mayo Clin Proc 1986;61:427–441.
54. Leikensohn JR. Epstein LI, Vasconez LO. Superselective embolization and surgery of noninvoluting hemangiomas and A-V malformations. Plast Reconstr Surg 1981;68:143–152.
55. Biller HF, Krespi YP, Som PM. Combined therapy of vascular lesions of the head and neck with intra-arterial embolization and surgical excision. Otolaryngol Head Neck Surg 1982;90:37–47.
56. Persky MS. Congenital vascular lesions of the head and neck. Laryngoscope 1986;96:1002–1015.
57. Dubois J, Garel L, Abela A, Laberge L, Yazbeck S. Lymphangiomas in children: percutaneous sclerotherapy with an alcohol solution of Zein. Radiology 1997;204:651–654.
58. Lewin JS, Merkle EM, Duerk JL, Tarr RW. Low-flow vascular malformations in the head and neck: safety and feasibility of MR imaging-guided sclerotherapy—preliminary experience with 14 procedures in three patients. Radiology 1999;211:566–570.
59. Molitch HI, Unger EC, Witte CL, von Sonnenberg E. Percutaneous sclerotherapy of lymphangiomas. Radiology 1995;194:343–347.
60. Bauman NM, Burke DK, Smith RJ. Treatment of massive or life-threatening hemangiomas with recombinant alpha 2a-interferon. Otolaryngol Head Neck Surg 1997;117:99–110.
61. Mulliken JB. Classification of vascular birthmarks. In: Mulliken JB, Young AE, eds. Vascular Birthmarks, Hemangiomas and Malformations. Philadelphia: WB Saunders, 1988;24–37.
62. Elahi MM, Parnes L, Fox A. Hemangioma of the masseter muscle. J Otolaryngol 1992;21:177–179.
63. Ott JES: Hemangiomata in skeletal muscle. Br J Surg 1957;44: 496–501.
64. lngalls GK, Bonnington GJ, Sisk AL. Intramuscular hemangioma of the mentalis muscle. Oral Surg Oral Med Oral Pathol 1986;60: 476–481.
65. Wolf GT, Daniel F, Krause CJ, et al. Intramuscular hemangioma of the head and neck. Laryngoscope 1985;95:210–213.
66. Itoh K, Nishimura K, Togashi K, et al. MR imaging of cavernous hemangiomas of the face and neck. J Comput Assist Tomogr 1986;10:831–835.
67. Gelbert F, Riche MC, Reizine D, et al. MR imaging of head and neck vascular malformations. J MRI 1991;1:579–584.
68. Burrows PE, Laor T, Paltiel H, Robertson RL. Diagnostic imaging in the evaluation of vascular birthmarks. Dermatol Clin 1998;16: 455–488.
69. Kennedy TL. Cystic hygroma-lymphangioma: a rare and still unclear entity. Laryngoscope 1989;99:1–10.
70. Yuh WTC, Gleason TJ, Tali ET, et al. Traumatic cervical cystic lymphangioma in an adult. Ann Otol Rhinol Laryngol 1993;102: 564–566.
71. Stal S, Hamilton S, Spira M. Hemangiomas, lymphangiomas, and vascular malformations of the head and neck. Otolaryngol Clin North Am 1986;19:769–796.
72. Chisin R, Fabian R, Weber AL, et al. MR imaging of a lymphangioma involving the masseter muscle. J Comput Assist Tomogr 1988;12:690–692.
73. Postlethwaite KR. Lymphangiomas of the tongue. Br J Oral Maxillofac Surg 1986;24:63–68.
74. Emery P, Bailey C, Evans J. Cystic hygroma of the head and neck. J Laryngol Otol 1984;98:613–619.
75. Caro PA, Mahboubi S, Fearber EN. Computed tomography in the diagnosis of lymphangiomas in infants and children. Clin Imag 1991;15:41–46.
76. Siegel MJ, Glazer HS, St Amour TE, et al. Lymphangiomas in children: MR imaging. Radiology 1989;170:467–470.
77. Zadvinski DP, Benson MT, Kerr HH, et al. Congenital malformations of the cerviothoracic lymphatic system: embryology and pathogenesis. RadioGraphics 1992;12:1175–1189.
78. Yuh WTC, Buehner LS, Kao SC, et al. Magnetic resonance imaging of pediatric head and neck cystic hygromas. Ann Otol Rhinol Laryngol 1991;100:737–742.
79. Koeller KK, Alamo L, Adair CF, Smirniotopoulos JG. Congenital cystic masses of the neck: radiologic–pathologic correlation. RadioGraphics 1999;19:121–146.
80. New GB. Congenital cysts of the tongue, the floor of the mouth, the pharynx and the larynx. Arch Otolaryngol 1947;45:145–158.
81. Meyer I. Dermoid cysts (dermoids) of the floor of the mouth. Oral Surg Oral Med Oral Pathol 1955;8:1149–1164.
82. King RC, Smith BR, Burk JL. Dermoid cysts in the floor of the mouth. Oral Surg Oral Med Oral Pathol 1994;78:567–576.
83. Worley CM, Laskin DM. Coincidental sublingual and submental epidermoid cysts. J Oral Maxillofac Surg 1993;51:787–790.
84. Arcand P, Granger J, Brochu P. Congenital dermoid cyst of the oral cavity with gastric choristoma. J Otolaryngol 1988;15:219–222.
85. Black EE, Leathers RD, Youngblood D. Dermoid cyst of the floor of the mouth. Oral Surg Oral Med Oral Pathol 1992;75:556–558.
86. Mathur SK, Menon PR. Dermoid cyst of the tongue: report of a case. Oral Surg Oral Med Oral Pathol 1980;50:217–219.
87. Quinn JH. Congenital epidermoid cyst of anterior half of tongue. Oral Surg Oral Med Oral Pathol 1960;13:1283–1285.
88. Rajayogeswaran V, Eveson JW. Epidermoid cyst of the buccal mucosa. Oral Surg Oral Med Oral Pathol 1989;67:181–183.
89. Ruggieri M, Tine A, Rizzo R, et al. Lateral dermoid cyst of the tongue: case report. Int J Pediatr Otorhinolaryngol 1994;30:79–84.
90. Rule DC. Dermoid cyst of the lower lip: a case report. Br J Oral Surg 1976;131:543–545.
91. Vogl TJ, Steger W, Ihrer S, et al. Cystic masses in the floor of the mouth: value of MR imaging in planning surgery. AJR 1993:161: 183–186.
92. Hardin CW, et al. CT in the evaluation of the normal and diseased oral cavity and oropharynx. Semin Ultrasound CT MR 1986;7: 131–153.
93. Thomas JR. Thyroglossal duct cysts. Ear Nose Throat J 1979;58: 512–514.
94. Dolata J. Thyroglossal duct cyst in the mouth floor: an unusual location. Otolaryngol Head Neck Surg 1994;110:580–583.
95. Allard RHB. The thyroglossal cyst. Head Neck Surg 1982;5: 134–146.
96. Reede DL, Bergeron RT. CT of thyroglossal duct cysts. Radiology 1985;157:121–125.
97. Nachlas NE. Thyroglossal duct cysts. Ann Otol Rhinol Laryngol 1950;59:381–390.
98. Yanagisawa K, Eisen RN, Sasaki CT. Squamous cell carcinoma arising in a thyroglossal duct cyst. Arch Otolaryngol Head Neck Surg 1992;118:538–541.

Copyright © 2003, Mosby, Inc. All rights reserved.

99. Gardner DJ. Unusual CT appearance of a thyroglossal duct cyst carcinoma. J Otolaryngol 1989;18:258–259.
100. Lustmann J, Benoliel R, Zeltser R. Squamous cell carcinoma arising in a thyroglossal duct cyst in the tongue. J Oral Maxillofac Surg 1989;47:81–85.
101. McNicoll MP, Hawkins DB, England K, et al. Papillary carcinoma arising in a thyroglossal duct cyst. Otolaryngol Head Neck Surg 1988;99:50–54.
102. Silverman PM, Degesys GE, Ferguson BJ, et al. Papillary carcinoma in a thyroglossal duct cyst: CT findings. J Comput Assist Tomogr 1985;9:806–808.
103. Yildiz K, Koksal H, Ozoran Y, et al. Papillary carcinoma in a thyroglossal duct remnant with normal thyroid gland. J Laryngol Otol 1993;107:1174–1176.
104. Kennedy TL, Whitaker M, Wadih G. Thyroglossal duct carcinoma: a rational approach to management. Laryngoscope 1998;108:1154–1158.
105. Allard R. The thyroglossal cyst. Head Neck Surg 1982;5:135–146.
106. Elprana D, Manni JJ, Smals AGH. Lingual thyroid: case report and review of the literature. Otorhinolaryngol Relat Spec 1984;46:147–152.
107. Douglas PS, Baker AW. Lingual thyroid. Br J Oral Maxillofac Surg 1994;32:123–124.
108. Wertz ML. Management of undescended lingual and subhyoid thyroid glands. Laryngoscope 1974;84:507–521.
109. Chan FL, Low LC, Yeung HW, et al. Case report: lingual thyroid, a cause of neonatal stridor. Br J Radiol 1993;66:462–464.
110. Johnson JC, Coleman LL. Magnetic resonance imaging of a lingual thyroid gland. Pediatr Radiol 1989;19:461–462.
111. Shah HR, Boyd CM, Williamson M, et al. Lingual thyroid: unusual appearance on computed tomography. Comput Med Imag Graphics 1988;12:263–266.
112. Willinsky RA, Kassell EE, et al. Computed tomography of lingual thyroid. J Comput Assist Tomogr 1987;11:182–183.
113. Liauba R, Kennedy TL. Lingual thyroid. Trans Pa Acad Ophthalmol Otolaryngol 1983;36:204–208.
114. Little B, et al. Cryptothyroidism: the major cause of sporadic ''athyreotic'' cretinism. J Clin Endocrinol Metab 1965;25:1529–1536.
115. Okstad S, Mair IW, Sundsfjord JA, et al. Ectopic thyroid tissue in the head and neck. J Otolaryngol 1986;15:52–55.
116. Peick AL, Nichols WK, Curtis JJ, et al. Aneurysms and pseudoaneurysms of the superficial temporal artery caused by trauma. J Vasc Surg 1988;8:606–610.
117. DiStefano JF, Maimon W, Mandel MA. False aneurysm of the lingual artery. J Oral Surg 1977;35:918–920.
118. Gomori JM, Dermer R, Shifrin E. Aneurysm of the lingual artery. Neuroradiology 1983;25:111–112.
119. Orron DE, Greenberg JJ, Kim D, et al. Pseudoaneurysm of the lingual artery. Comput Med Imag Graphics 1988;12:349–352.
120. Adib A, Gluckman JL, Mendelson D. Bilateral idiopathic aneurysms of the lingual arteries. Otolaryngol Head Neck Surg 1993;108:87–90.
121. Batten TF, Heeneman H. Traumatic pseudoaneurysm of floor of mouth treated with selective embolization. J Otolaryngol 1994;23:423–425.
122. Morita N, Harada M, Sakamoto T. Congenital tumors of heterotopic central nervous system tissue in the oral cavity. J Oral Maxillofac Surg 1993;51:1030–1033.
123. Zalzal GH, Patterson K, Cotton RT. Congenital tumors of the dorsum of the tongue. Int J Pediatr Otolaryngol 1994;28:219–227.
124. Bras G, Butts D, Hoyte DA. Gilomatous teratoma of the tongue. Cancer 1969;24:1045–1050.
125. Lloyd EI. Mucus cyst of the tongue. Br J Surg 1926;13:568–570.
126. Fink HA. Retention cyst of the tongue (glossocele). Oral Surg Oral Med Oral Pathol 1963;16:1290–1293.
127. Samuel J, Raz S, Schindel J. A retention cyst in the body of the tongue: a report of a case. J Oral Surg 1970;28:918–921.
128. Velcek FT, Klotz DH, Hill CH, et al. Tongue lesions in children. J Pediatr Surg 1979;14:238–246.
129. Naidoo LCD. Median lingual cyst: review of the literature and report of a case. J Oral Maxillofac Surg 1997;55:172–175.
130. Kinoshita Y, Honma Y, Otuka T, Shimura K. Gastrointestinal mucosal cyst of the oral cavity. J Oral Maxillofac Surg 1994;52:1203–1205.
131. Chou L, Hansen LS, Daniels TE. Choriostomas of the oral cavity: a review. Oral Surg Oral Med Oral Pathol 1991;72:584–593.
132. Batsakis JG, El-Nagger AK, Hicks MJ. Epithelial choriostomas and teratomas of the tongue. Ann Otol Rhinol Laryngol 1993;102:567–569.
133. Constantinides CG, Davis MRQ, Cywes S. Intralingual cysts of foregut origin. S Afr J Surg 1982;20:227–232.
134. Morgan WE, Jones JK, Flaitz CM, Hicks MJ. Congenital heterotopic gastrointestinal cyst of the oral cavity in a neonate: case report and review of the literature. Int J Pediatr Otolaryngol 1996;36:69–77.
135. Tschiassny K. Ludwig's angina: an anatomic study of the lower molar teeth in its pathogenesis. Arch Otolaryngol 1943;38:485–496.
136. Holliday RA, Prendergast NC. Imaging inflammatory processes of the oral cavity and suprahyoid neck. Oral Maxillofac Surg Clin North Am 1992;4:215–240.
137. Ozturk M, Durak AC, Ozcan N, Yigitbasi OG. Abscess of the tongue: findings on MR imaging. AJR 1998;170:797–798.
138. Munoz A, Ballesteros AI, Castelo JAB. Primary lingual abscess presenting as acute swelling of the tongue obstructing the upper airway: diagnosis with MR. AJNR 1998;194:496–498.
139. Avrahami E, Englender M, Chen E, Shabtay D, Katz R, Harell M. CT of submandibular gland sialolithiasis. Neuroradiology 1996;38:287–290.
140. Aasen S, Kolbenstvedt A. CT appearances of normal and obstructed submandibular gland duct. Acta Radiol 1992;33:414–419.
141. Yousem DM, Kraut MA, Chalian AA. Major salivary gland imaging. Radiology 2000;216:19–29.
142. Sumi M, Izumi M, Yonetsu K, Nakamura T. The MR imaging assessment of submandibular gland sialoadenitis secondary to sialolithiasis: correlation with CT and histopathologic findings. AJNR 1999;20:1737–1743.
143. Varghese JC, Thornton F, Lucey BC, Walsh M, Farrell MA, Lee MJ. A prospective comparative study of MR sialography and conventional sialography of salivary duct disease. AJR 1999;173:1497–1503.
144. Jager L, Menauer F, Holzknecht N, Scholz V, Grevers G, Reiser M. Sialolithiasis: MR sialography of the submandibular duct: an alternative to conventional sialography and US? Radiology 2000;216:665–671.
145. Murakami R, Baba Y, Nishimura R, et al. MR sialography using half-fourier acquisition single-shot turbo spin-echo (HASTE) sequences. AJNR 1998;19:959–961.
146. Nguyen VD, Potter JL, Hersh-Schick MR. Ludwig angina: an uncommon and potentially lethal neck infection. AJNR 1992;13:215–219.
147. Grodinsky MD. Ludwig's angina: an anatomical and clinical study with review of the literature. Surgery 1939;5:678–696.
148. Holliday RA, Cohen WA, Schinella RA, et al. Benign lymphoepithelial parotid cysts and hyperplastic cervical adenopathy in AIDS-risk patients: a new CT appearance. Radiology 1988;168:439–441.
149. Gottesman RI, Som PM, Mester J, Silvers R. Observations on two cases of apparent submandibular gland cysts in HIV positive patients: MR and CT findings. J Comput Assist Tomogr 1996;20:444–447.
150. Chapnik JS, Noyek AM, Berris B, et al. Parotid gland enlargement in HIV infection: clinical/imaging findings. J Otolaryngol 1990;19:189–194.
151. Elliot JN, Aortal YC. Lymphoepithelial cysts of the salivary glands. Histologic and cytologic features. Am J Clin Pathol 1990;93:39–43.
152. Reiderer A, Zietz C, Ihrler S, Vogl T. Cystic lymphoepithelial lesions in the head and neck area in HIV-infected patients. Laryngol Rhinol Otol 1994;73:209–214.
153. Phelan JA. Oral manifestations of human immunodeficiency virus infection. Med Clin North Am 1997;81:511–531.
154. Levell NJ, Bewley AP, Chopra S. Bacillary angiomatosis with cutaneous and oral lesions in an HIV-infected patient from the UK. Br J Dermatol 1995;132:113–115.
155. Lozada F, Silverman S Jr, Migliorati CA, et al. Oral manifestations of tumor and opportunistic infections in the acquired immunodeficiency syndrome (AIDS): findings in 53 homosexual men with Kaposi's sarcoma. Oral Surg Oral Med Oral Pathol 1983;56:491–498.
156. Crysdale WS, Mendelsohn JD, Conley S. Ranulas—mucoceles of the oral cavity: experience in 26 children. Laryngoscope 1988;98:296–298.
157. Galloway RH, et al. Pathogenesis and treatment of ranula: report of three cases. J Oral Maxillofac Surg 1989;47:299–302.

Copyright © 2003, Mosby, Inc. All rights reserved.

158. Charnoff SK, Carter BL. Plunging ranula: CT diagnosis. Radiology 1986;158:467–468.
159. Coit WE, et al. Ranulas and their mimics: CT evaluation. Radiology 1987;263:211–216.
160. Matt BH, Crockett DM. Plunging ranula in an infant. Otolaryngol Head Neck Surg 1988;99:330–333.
161. Silverstein MI, Castillo M, Hudgins PA, et al. MR imaging of intralingual ranula in a child. J Comput Assist Tomogr 1990;14: 672–674.
162. Barnard NA. Plunging ranula: a bilateral presentation. Br J Oral Maxillofac Surg 1991;29:112–113.
163. Horiguchi H, Kakuta S, Nagumo M. Bilateral plunging ranula. Int J Oral Maxillofac Surg 1995;24:174–175.
164. Van der Goten A, Hermans R, Smet MH, Baert AL. Submandibular gland mucocele of the extravasation type. Pediatr Radiol 1995;25: 366–368.
165. Mirich DR, McArdle CB, Kulkarni MV. Benign pleomorphic adenomas of the salivary glands: surface coil MR imaging versus CT. J Comput Assist Tomogr 1987;11:620–623.
166. Enzinger FM. Fibrous tumors of infancy. In: Tumors of Bone and Soft Tissue: A Collection of Papers. Eighth Clinical Conference on Cancer. Chicago: Year Book Medical, 1965;375–396.
167. Stout AP. Juvenile fibromatosis. Cancer 1954;7:953–978.
168. Enzinger FM, Weiss SW. Soft Tissue Tumors. St. Louis: CV Mosby, 1983.
169. Das Gupta TK, Brasfield RD, O'Hara J. Extra-abdominal desmoids: a clinicopathological study. Ann Surg 1969;170:109–121.
170. Fu YS, Perzin KH. Nonepithelial tumors of the nasal cavity, paranasal sinuses, and nasopharynx: a clinicopathological study. VI. Fibrous tissue tumors (fibroma, fibromatosis, fibrosarcoma). Cancer 1976;37:2912–2928.
171. Chen PC, Ball WS, Towbin RB. Aggressive fibromatosis of the tongue: MR demonstration. J Comput Assist Tomogr 1989;13: 343–345.
172. Shah AC, Katz RL. Infantile aggressive fibromatosis of the base of the tongue. Otolaryngol Head Neck Surg 1988;98:346–349.
173. Swartz HE, Ward PH. Aggressive fibromatosis of the tongue. Am J Otol 1979;88:12–15.
174. Smoker WRK, Lusk RP, Menezes AH. Supraclavicular fibromatosis with intraspinal extension. Ann Otol Rhinol Laryngol 1986;95: 319–320.
175. Lidov MW, Stollman AL, Wolfe D, Rothman A, Sacher M, Som PM. Fibromatosis involving the epidural space. AJNR 1995;16:885–888.
176. Flacke S, Pauleit D, Keller E, et al. Infantile fibromatosis of the neck with intracranial involvement: MR and CT findings. AJNR 1999;20:923–925.
177. Masson JK, Soule EH. Desmoid tumors of the head and neck. Am J Surg 1966;112:615–627.
178. El-Sayed Y. Fibromatosis of the head and neck. J Laryngol Otol 1992;106:459–462.
179. Yang WC, Shah V, Mussbaum M, et al. Desmoid tumor of the neck: CT and angiographic findings. AJNR 1984;5:478–480.
180. Aisen AM, Martel W, Braunstein EM, et al. MRI and CT evaluation of primary bone and soft tissue tumors. AJR 1986;146:49–56.
181. Lewin JS, Lavertu P. Aggressive fibromatosis of the prevertebral and retropharyngeal spaces: MR and CT characteristics. AJNR 1995;16: 897–900.
182. Kransdorf MJ, Jelinek JS, Mose RP, et al. Magnetic resonance appearance of fibromatosis. Skeletal Radiol 1990;19:495–499.
183. Sundaram M, McGuire MH, Schajowicz F. Soft-tissue masses: histologic basis for decreased signal (short T2) on T2W MR images. AJR 1987;148:1247–1250.
184. Di Sant' Agnese PA, Knowles DM. Extracardiac rhabdomyoma: a clinicopathological study and review of the literature. Cancer 1980;46:780–789.
185. Batsakis JG, Manning JT. Soft tissue tumors: unusual forms. Otolaryngol Clin North Am 1986;19:664–673.
186. Balatsouras DG, Eliopoulos PN, Economou CN. Adult-type rhabdomyoma of the submandibular region. J Otolaryngol 1993;22: 14–17.
187. Boysen M, et al. Rhabdomyoma of the tongue: report of a case with light microscopic, ultrastructural and immunohistochemical observations. J Laryngol Otol 1988;102:1185–1188.
188. Som PM, et al. Rare presentations of ordinary lipomas of the head and neck: a review. AJNR 1986;7:657–664.
189. Fujimura N, Enomoto S. Lipoma of the tongue with cartilaginous changes: a case report and review of the literature. J Oral Maxillofac Surg 1992;50:1015–1017.
190. Hatziotis JC. Lipomas of the oral cavity. Oral Surg 1971;31:511–524.
191. Dattilo DJ, Ige JT, Nwana EJC. Intraoral lipoma of the tongue and submandibular space. J Oral Maxilloc Surg 1996;54:915–917.
192. Reede DL, Bergeron RT. The CT evaluation of the normal and diseased neck. Semin Ultrasound CT MR 1986;7:181–201.
193. Flickinger FW, et al. Neurilemmoma of the tongue: MR findings. J Comput Assist Tomogr 1989;13:886–888.
194. Abramowitz J, et al. Angiographic diagnosis and management of head and neck schwannomas. AJNR 1991;12:977–984.
195. Al-Ghamdi S, Black MJ, Lafond G. Extracranial head and neck schwannomas. J Otolaryngol 1992;21:186–188.
196. Gore DO, Rankow R, Hanford JM. Parapharyngeal neurilemmoma. Surg Gynecol Obstet 1956;103:193–199.
197. Gallo WJ, Moss M, Shapiro DN, et al. Neurilemmoma: review of the literature and report of five cases. J Oral Surg 1977;35:235–236.
198. Sutay S, Tekinsoy B, Ceryan K, et al. Submaxillary hypoglossal neurilemmoma. J Laryngol Otol 1993;107:953–954.
199. Abramowitz J, Dion JE, Jensen ME, et al. Angiographic diagnosis and management of head and neck schwannomas. AJNR 1991;12: 977–984.
200. Gray P, Kapadia R. Neurofibroma of the tongue. J Otolaryngol Otol 1972;80:275–279.
201. Sahota JS, Viswanathan A, Nayak DR, Hazarika P. Giant neurofibroma of the tongue. Int J Pediatr Otolaryngol 1996;34: 153–157.
202. Dillon WP. The pharynx and oral cavity. In: Som PM, Bergeron RT, eds. Head and Neck Imaging, 2nd ed. St. Louis: Mosby-Year Book, 1991; 407–466.
203. Damm DD, Cibull ML, Geissler RH, et al. Investigation into histogenesis of congenital epulis of the newborn. Oral Surg Oral Med Oral Pathol 1993;76:205–212.
204. Batsakis JG. Tumors of the peripheral nervous system. In: Tumors of the Head and Neck, Clinical and Pathological Correlations, 2nd ed. Baltimore: Williams & Wilkins, 1979;313–333.
205. Koch BL, Myer C, Egelhoff JC. Congenital epulis. AJNR 1997;18:739–741.
206. Naidich TP, Valente M, Abrams K, Spreitzer JJ, Doundoulakis SH. Torus palatinus. Int J Neuroradiol 1997;3:229–243.
207. Mohammadi-Araghi H, Haery C. Fibro-osseous lesions of cranio-facial bones. Radiol Clin North Am 1993;31:121–134.
208. Waldron CA, Giansanti JS. Benign fibro-osseous lesions of the jaws: a clinical-radiologic-histologic review of sixty-five cases. Oral Surg 1973;35:340–350.
209. Waldron CA. Fibro-osseous lesions of the jaws. J Oral Maxillofac Surg 1993;51:828–835.
210. Mafee MF. Fibro-osseous lesions. Proceedings of the American Society of Head and Neck Radiology's annual meeting, 1996;95–99.
211. Laine FJ. Diagnostic imaging of the maxillary sinus. Oral Maxillofac Surg Clin North Am 1999;11:45–67.
212. Jaffe T, Castillo M, Naidich TP, et al. Facies to remember: fibrous dysplasia. Int J Neuroradiol 1998;4:112–120.
213. Fries JW. The roentgen features of fibrous dysplasia of skull and facial bones. A critical analysis of 39 pathologically proved cases. AJR 1957;77:71–80.
214. Casselman JW, DeJonge I, DeClercq C, D'Hont G. MRI in craniofacial fibrous dysplasia. Neuroradiology 1993;35:234–237.
215. Norris MA, Kaplan PA, Pathria M, Greenway G. Fibrous dysplasia: magnetic resonance imaging appearance at 1.5 Tesla. Clin Imaging 1990;14:211–215.
216. Utz JA, Kransdorf MJ, Jelink JS, Moser RP, Berrey BH. MR appearance of fibrous dysplasia. J Comput Assist Tomogr 1989;13: 845–851.
217. Jee WH, Choi KH, Choe BY, Park JM, Shinn KS. Fibrous dysplasia: MR imaging characteristics with radiopathologic correlation. AJR 1996;167:1523–1527.
218. Eversole LR, Leider AS, Nelson K. Ossifying fibroma. A clinicopathologic study of sixty-four cases in San Francisco, CA. Oral Surg Oral Med Oral Pathol 1985;60:505–511.
219. Kreutziger KL, Weiss LS. Cementifying fibroma. Resection of recurrent mandibular lesion with microsurgical preservation of inferior alveolar nerve and immediate reconstruction. South Med J 1994;87:653–658.

Copyright © 2003, Mosby, Inc. All rights reserved.

220. Kuta AJ, Worley CM, Kaugers GE. Central cementoossifying fibroma of the maxillary sinus. A review of six cases. AJNR 1995;16:1282–1286.
221. Halkias LE, Larson PE, Allen CM, Steinberg MJ. Rapidly growing, expansile mass of the mandible in a 6-year old boy. J Oral Maxillofac Surg 1998;56:866–871.
222. Bertrand B, Eloy PH, Cornelis J, et al. Juvenile aggressive ossifying fibromas: case report and review of the literature. Laryngoscope 1993;103:1385–1390.
223. Kaplan I, Calderon S, Buchner A. Peripheral osteoma of the mandible: a study of ten new cases and analysis of the literature. J Oral Maxillofac Surg 1994;52:467–470.
224. Schneider LC, Dolinsky HB, Grodjesk JE. Solitary peripheral osteoma of the jaws. Report of case and reviews of literature. J Oral Surg 1980;38:452–455.
225. Huvos AG. Bone Tumors, 2nd ed. Philadelphia: WB Saunders, 1991;2–5.
226. Nash M, Harrison T, Lin PT, et al. Osteoma of the tongue. Ear Nose Throat J 1989;68:63–69.
227. Lutcavage GJ, Fulbright DK. Osteoma of the tongue. J Oral Maxillofac Surg 1993;51:697–699.
228. Van Damme Ph A, Mooren RECM. Central giant cell granulomas of the jaws. Letter to the editor. Br J Oral Maxillofac Surg 1995;33:266.
229. Auclair PL, Cuenin P, Kratochvil FJ, Slater LJ, Ellis GL. A clinical and histomorphologic comparison of the central giant cell granuloma and giant cell tumor. Oral Surg Oral Med Oral Pathol 1988;66:197–208.
230. Hoffman CD, Huntley TA, Wiesenfeld D, Kleid S, Kung ITM. Maxillary giant cell tumor associated with Paget's disease of bone. Br J Oral Maxillofac Surg 1994;23:161–164.
231. Fotos PG, Pikos MA, Rose MW. Multiple enlargements of the premaxilla and mandible. J Oral Maxillofac Surg 1985;43:822–826.
232. Bodner L, Bar-Zin J. Radiographic features of central giant cell granuloma of the jaws in children. Pediatr Radiol 1996;26:148–151.
233. DelBalso AM. Lesions of the jaws. Semin Ultrasound CT MR 1995;16:487–512.
234. Scholl RJ, Kellet HM, Neumann DP, Lurie AG. Cysts and cystic lesions of the mandible: clinical and radiologic-histopathologic reviews. RadioGraphics 1999;19:1107–1124.
235. Minami M, Kaneda T, Ozawa K, et al. Cystic lesions of the maxillomandibular region: MR imaging distinction of odontogenic keratocysts and ameloblastomas from other cysts. AJR 1996;166: 943–949.
236. Dabbs DJ, Schweitzer RJ, Schweitzer ME, Mantz F. Squamous cell carcinoma arising in recurrent odontogenic keratocysts: case report and literature review. Head Neck 1994;16:375–378.
237. LaTona A, Arino A, Manfre L. Odontogenic keratocysts of the maxillary sinus: CT and MR findings. Rev Neuroradiol 1997;10: 475–478.
238. Weissman JL, Snyderman CH, Yousem SA, Curtin HD. Ameloblastoma of the maxilla: CT and MR appearance. AJNR 1993;14: 223–226.
239. Dunn JL, Olan WJ, Bank WO, Narang AK, Schwartz AM. Giant ameloblastoma: radiologic diagnosis and treatment. RadioGraphics 1997;17:531–536.
240. Brenenkamp JK, Zimmerman MC, Mickel RA. Maxillary ameloblastoma. Arch Otolaryngol Head Neck Surg 1989;15:99–104.
241. Langlais RP, Langland OE, Nortje CJ. Diagnostic Imaging of the Jaws. Baltimore: Williams & Wilkins, 1995;34.
242. Karras SC, Wolford LM, Cottrell DA. Concurrent osteochondroma of the mandibular condyle and ipsilateral cranial base resulting in temporomandibular joint ankylosis. J Oral Maxillofac Surg 1996;54: 640–646.
243. Brady FA, Sapp JP, Christensen RE. Extracondylar osteochondromas of the jaws. Oral Surg Oral Med Oral Pathol 1978;46:658–660.
244. Gaines RE, Lee MB, Crocker DJ. Osteochondroma of the mandibular condyle. Case report and review of the literature. J Oral Maxillofac Surg 1992;50:899–903.
245. Goyal M, Sidhu SS. A massive osteochondroma of the mandibular condyle. Br J Oral Maxillofac Surg 1992;30:66–71.
246. Henry CH, Granite EL, Rafetto LK. Osteochondroma of the mandibular condyle: report of a case and review of the literature. J Oral Maxillofac Surg 1992;50:1002–1008.
247. Tani Y, Azuma I, Nagayama M. Chondroma of the tongue. J Oral Maxillofac Surg 1989;47:91–92.
248. De Araujo VC, Marcucci G, Sesso A, et al. Epithelioid hemangioendothelioma of the gingiva, case report and ultrastructural study. Oral Surg Oral Med Oral Pathol 1987;63:472–477.
249. Ellis CL, Kratochvil FJ. Epithelioid hemangioendothelioma of the head and neck, a clinicopathologic report of twelve cases. Oral Surg Oral Med Oral Pathol 1986;61:61–68.
250. Marrogi AJ, Boyd D, el-Mofty S, et al. Epithelioid hemangioendothelioma of the oral cavity: report of two cases and review of the literature. J Oral Maxillofac Surg 1991;49:633–638.
251. Moran WJ, Dobleman TJ, Bostwick DC. Epithelioid hemangioendothelioma (histoid hemangioma) of the palate. Laryngoscope 1987;97: 1299–1302.
252. Yarington CT. Pathology of the oral cavity. In: Paparella MM, Shumrick M, eds. Otolaryngology. Philadelphia: WB Saunders, 1980;
253. American Joint Commission on Cancer. Beahrs OH et al, eds. Manual for Staging of Cancer, 3rd ed. Philadelphia: JB Lippincott, 1988.
254. Mashberg A, Samit A. Early diagnosis of asymptomatic oral and oropharyngeal squamous cancers. CA Cancer J Clin 1995;45: 328–351.
255. Paparella MM, Shumrick DA. Otolaryngology, Vol. 3. Head and Neck. Philadelphia: WB Saunders, 1980.
256. Crissman JD, Gluckman J, Whiteley J, et al. Squamous-cell carcinoma of the floor of the mouth. Head Neck Surg 1980;3:2–7.
257. Mashberg A, Myers H. Anatomical site and size of 222 early asymptomatic oral squamous cell carcinomas. Cancer 1976;37:2149–2157.
258. Lederman M. The anatomy of cancer. J Laryngol Otol 1964;78: 181–208.
259. Close LG, Burns DK, Reisch J, Schaefer SD. Microvascular invasion in cancer of the oral cavity and oropharynx. Arch Otolaryngol Head Neck Surg 1987;113:1191–1195.
260. Close LG, Brown PM, Vuitch MF, Reisch J, Schaefer SD. Microvascular invasion of the oral cavity and oropharynx. Arch Otolaryngol Head Neck Surg 1989;115:1304–1309.
261. Mukherji SK, Weeks SM, Castillo M, Yankaskas BC, Krishnan LAG, Schiro S. Squamous cell carcinomas that arise in the oral cavity and tongue base: Can CT help predict perineural or vascular invasion? Radiology 1996;198:157–162.
262. Brown B, Barnes L, Mazariegos J, Taylor F, Johnson J, Wagner RI. Prognostic factors in mobile tongue and floor of mouth carcinoma. Cancer 1989;64:1195–1202.
263. Conte CC, Ergin MT, Ricci A, Deckers PJ. Clinical and pathologic prognostic variables in oropharyngeal squamous cell carcinoma. Am J Surg 1989;157:582–584.
264. Scholl P, Byers RM, Batsakis JG, Wolf O, Santini H. Microscopic cut-through of cancer in the surgical treatment of squamous cell carcinoma of the tongue: prognostic and therapeutic implications. Am J Surg 1986;152:354–360.
265. Harnsberger HR. Head and Neck Imaging. Chicago: Year Book Medical, 1990.
266. Johnson JT. A surgeon looks at cervical lymph nodes. Radiology 1990;175:607–610.
267. Lindberg R. Distribution of cervical lymph node metastases from squamous cell carcinoma of the upper respiratory and digestive tracts. Cancer 1972;29:1446–1449.
268. Som PM. Lymph nodes of the neck. Radiology 1987;165:593–600.
269. Madison MT. Radiologic diagnosis and staging of head and neck squamous cell carcinoma. Radiol Clin North Am 1994;32: 163–181.
270. Som PM. Detection of metastases in cervical lymph nodes: CT and MR criteria and differential diagnosis. AJR 1992;158:961–969.
271. Yousem DM, Som PM, Hackney DB, et al. Central nodal necrosis and extracapsular neoplastic spread in cervical lymph nodes: MR imaging versus CT. Radiology 1992;182:753–759.
272. Sigal R, Zagdanski A, Schwaab G, et al. CT and MR imaging of squamous cell carcinoma of the tongue and floor of the mouth. RadioGraphics 1996;16:787–810.
273. Yasumoto M, Shibuya H, Takida M, Korenaga T. Squamous cell carcinoma of the oral cavity: MR findings and value of T1- versus T2-weighted fast spin-echo images. AJR 1995;164:981–987.
274. Mukherji SK, Pillsbury HR, Castillo M. Imaging squamous cell carcinomas of the upper aerodigestive tract: what clinicians need to know. Radiology 1997;205:629–646.

Copyright © 2003, Mosby, Inc. All rights reserved.

275. Mancuso AA. The oropharynx and oral cavity. Proceedings of the 26th Annual Conference and Postgraduate Course of the American Society of Head and Neck Radiology 1993;5:1–60.
276. Takashima S, Ikezo J, Harada K, et al. Tongue cancer: correlation of MR imaging and sonography with pathology. AJNR 1989;10: 419–424.
277. Chung TS, Yousem DM, Siegerman H, Schlakman BN, Weinstein GS, Hayden RR. MR of mandibular invasion in patients with oral and oropharyngeal malignant neoplasms. AJNR 1994;15:1949–1955.
278. McGregor AD, MacDonald DG. Routes of entry of squamous cell carcinoma to the mandible. Head Neck 1988;10:294–301.
279. Million RR, Cassisi NJ, Mancuso AA. Oral cavity. In: Million RR, Cassisi NJ, eds. Management of Head and Neck Cancer: A Multidisciplinary Approach, 2nd ed. Philadelphia: JB Lippincott, 1994;321–400, 599–626.
280. Harnsberger HR, Bragg DG, Osborn AG, et al. Non-Hodgkin's lymphoma of the head and neck: CT evaluation of nodal and extranodal sites. AJNR 1987;8:673–679.
281. Lee YY, Van Tassel P, Nauert C, et al. Lymphomas of the head and neck: CT findings at initial presentation. AJNR 1987;8:665–671.
282. Lucas RB. Pathology of Tumors of the Oral Tissues, 3rd ed. London: Churchill Livingstone, 1976;329–334.
283. Suej Y, Tanimoto K, Taguchi A, et al. Radiographic evaluation of bone invasion of adenoid cystic carcinoma in the oral and maxillofacial region. J Oral Maxillofac Surg 1994;52:821–826.
284. Kim KH, Sung MW, Chung PS, et al. Adenoid cystic carcinoma of the head and neck. Arch Otolaryngol Head Neck Surg 1994;120: 721–726.
285. Nascimento AG, Amaral AI, Prado LA, et al. Adenoid cystic carcinoma of salivary glands: a study of 61 cases with clinicopathologic correlation. Cancer 1986;57:312–319.
286. Spiro RH, Huvos AG, Strong EW. Adenoid cystic carcinoma: factors influencing survival. Am J Clin Pathol 1979;138:579–583.
287. Waldron CA, El-Mofty SK, Gnepp DR. Tumors of the intraoral minor salivary glands: a demographic and histologic study of 426 cases. Oral Surg Oral Med Oral Pathol 1988;66:323–330.
288. Perzin K, Gullane P, Clairmont A. Adenoid cystic carcinoma arising in salivary glands: a correlation of histologic features and clinical courses. Cancer 1978;42:265–282.
289. Stell PM, et al. Lymph node metastases in adenoid cystic carcinoma. Am J Otol 1985;6:433–436.
290. Maso MD, Lippi L. Adenoid cystic carcinoma of the head and neck: a clinical study of 37 cases. Laryngoscope 1985;95:177–181.
291. Friedman M, Levin B, Grybauskas V, et al. Malignant tumors of the major salivary glands. Otolaryngol Clin North Am 1986;19:625–636.
292. Sigal R, et al. Adenoid cystic carcinoma of the head and neck: evaluation with MR imaging and clinical–pathologic correlation in 27 patients. Radiology 1992;184:95–101.
293. Castillo M. MRI of perineural tumor spread along the trigeminal nerves. Imag Decisions 1994;
294. Laine FJ, Braun IF, Jensen ME, et al. Perineural tumor extension through the foramen ovale: evaluation with MR imaging. Radiology 1990;174:65–71.
295. Parker GD, Harnsberger HR. Clinical-radiologic issues in perineural tumor spread of malignant diseases of the extracranial head and neck. RadioGraphics 1991;11:383–399.
296. Laccourreye O, Bely N, Guimaraes R, Halmi P, Brasnu D. Cavernous sinus involvement from recurrent adenoid cystic carcinoma. Ann Otol Rhinol Laryngol 1994;103–822–825.
297. Som PM. Salivary glands. In: Som PM, Bergeron RT, eds. Head and Neck Imaging, 2nd ed. St. Louis: Mosby-Year Book, 1991;334–335.
298. McCulloch TM, Makielski KH, McNutt MA. Head and neck liposarcoma: a histopathologic reevaluation of reported cases. Arch Otolaryngol Head Neck Surg 1992;118:1045–1049.
299. Nakahara H, Sirasuna K, Teradak K. Liposarcoma of the floor of the mouth. J Oral Maxillofac Surg 1994;35:555–560.
300. Enzinger FM, Winslow DJ. Liposarcoma: a study of 103 cases. Virchows Arch 1962;335:367–388.
301. Dooms GC, Hricak H, Sollitto RA, et al. Lipomatous tumors and tumors with fatty component: MR imaging potential and comparison of MR and CT results. Radiology 1985;157:479–482.
302. Maurer HM, Moon T, Donaldson M, et al. The Intergroup Rhabdomyosarcoma Study: a preliminary report. Cancer 1977;40: 2015–2026.
303. Kodet R, Fajstavr I, Kabelka Z, et al. Is fetal cellular rhabdomyosarcoma an entity or a differentiated rhabdomyosarcoma? A study of patients with rhabdomyoma of the tongue and sarcoma of the tongue enrolled in the Intergroup Rhabdomyosarcoma Studies I, II and III. Cancer 1991;67:2907–2913.
304. Doval DC, Kannan V, Acharya RS, et al. Rhabdomyosarcoma of the tongue. Br J Oral Maxillofac Surg 1994;32:183–186.
305. Peters E, Cohen M, Altini M, et al. Rhabdomyosarcoma of the oral and paraoral region. Cancer 1989;63:963–966.
306. Schwetschke O, Heppt W, Born JA. Leiomyosarkom von mundboden und oropharynx. HNO 1992;40:277–279.
307. Lorman JG, Biggs JR. The eagle syndrome. AJR 1983;140:881–882.
308. Lavine MH, Stoopack JC, Jerrold TL. Calcification of the stylohyoid ligament. Oral Surg Oral Med Oral Pathol 1968;25:55–58.
309. Gossman JR, Tarsitano JJ. The styloid-stylohyoid syndrome. J Oral Surg 1977;35:555–560.
310. Eagle WW. Symptomatic elongated styloid process. Arch Otolaryngol 1949;49:490–503.
311. Messer EJ, Abramson AM. The stylohyoid syndrome. J Oral Surg 1975;33:664–667.
312. Correll RW, Jensen JL, Taylor JB, Rhyne RR. Mineralization of the stylohyoid-stylomandibular ligament complex: a radiographic incidence study. Oral Surg 1979;48:286–291.
313. Keur JJ, Campbell JP, McCarthy JF, Ralph WJ. The clinical significance of the elongated styloid process. Oral Surg Oral Med Oral Pathol 1986;61:399–404.
314. Smith RG, Cherry JE. Traumatic Eagle's syndrome: report of a case and review of the literature. J Oral Maxillofac Surg 1988;46: 606–609.
315. Harnsberger HR, Dillon WP. Major motor atrophic patterns in the face and neck: CT evaluation. Radiology 1985;155:665–670.
316. Larsson SG. Hemiatrophy of the tongue and floor of the mouth demonstrated by computed tomography. J Comput Assist Tomogr 1985;9:914–917.
317. Schellhas KP. MR imaging of muscles of mastication. AJR 1989;153:847–855.

Copyright © 2003, Mosby, Inc. All rights reserved.

28

Pharynx

Suresh K. Mukherji

INTRODUCTION
GENERAL ANATOMY
EMBRYOLOGY
SPECIFIC ANATOMY
- Nasopharynx
- Oropharynx
- Hypopharynx

IMAGING TECHNIQUES
- Barium Studies
- Computed Tomography
- Magnetic Resonance Imaging
- Tissue Differentiation

NEOPLASMS
- General Considerations
- Nasopharyngeal Carcinomas
- Imaging Features
- Oropharyngeal Carcinomas
  - Anterior Tonsillar Pillar
  - Posterior Tonsillar Pillar
  - Tonsillar Fossa
  - Soft Palate
  - Base of the Tongue

HYPOPHARYNGEAL CANCERS
LYMPHOMAS
- Imaging Findings

MINOR SALIVARY GLAND TUMORS
- Imaging Features

RHABDOMYOSARCOMAS
- Imaging Features

GRANULAR CELL TUMORS
- Imaging Features

OTHER TUMORS
- Rhabdomyomas
- Fibromatoses
- Schwannomas and Neurofibromas
- Hemangiomas
- Lipomas

UNKNOWN PRIMARY TUMORS
- Imaging Findings

NONNEOPLASTIC PROCESSES
- Retropharyngeal Infections
  - Imaging Features
- Peritonsillar Abscesses
- Acute Calcific Prevertebral Tendinitis (Tendinitis of the Longus Colli)
- Tornwaldt's Cysts
  - Imaging Features
- Adenoidal Hypertrophies
- Acquired Immunodeficiency Syndrome

TRAUMA
MISCELLANEOUS LESIONS
POSTTREATMENT PHARYNX
- Radiation Therapy
- Surgery

INTRODUCTION

Behind the oral cavity, and extending from the skull base to the level of the caudal cricoid cartilage, is the mucosa-lined musculomembranous tube known as the *pharynx*.[1, 2] Historically, the pharynx has been subdivided into three sections: the nasopharynx, which extends from the skull base to the level of the hard palate; the oropharynx, which extends from the level of the hard palate to the level of the hyoid bone; and the hypopharynx, which extends from the level of the hyoid bone to the caudal margin of the cricoid cartilage or the top of the cricopharyngeus.

GENERAL ANATOMY

There are three overlapping constrictor muscles that comprise the primary pharyngeal musculature.[1] All of these muscles insert posteriorly in the midline on a median raphe that is attached to the skull base at the pharyngeal tubercle.

Copyright © 2003, Mosby, Inc. All rights reserved.

The superior constrictor muscle has its origin from the lower third of the posterior edge of the medial pterygoid plate, the pterygomandibular raphe, the alveolar process of the mandible, and the lateral aspect of the tongue. The middle constrictor muscle has its origin along the stylohyoid ligament and the greater and lesser cornua of the hyoid bone. The inferior constrictor muscle has its origin from the oblique line of the thyroid cartilage, the lateral cricoid cartilage, and the posterior border of the cricothyroid muscle. Structurally, the inferior constrictor muscle encircles the lower middle constrictor muscle, which in turn encircles the lower superior constrictor muscle.

The cricopharyngeus sphincter muscle is composed of parallel, nonraphed horizontal fibers that extend from one side of the cricoid cartilage to the other. This sphincter separates the hypopharynx from the cervical esophagus.[1] As a functioning unit, the pharyngeal constrictor muscles increase intrapharyngeal pressure as they contract in an organized, peristaltic manner from superiorly to inferiorly. There are no major pharyngeal dilator muscles, and the pharynx is primarily passively dilated by increasing intrapharyngeal pressure. The pharyngeal constrictor muscles are supplied by the pharyngeal plexus, formed primarily by branches of cranial nerves IX and X, with branches from cranial nerve XI and branches from the sympathetic plexus.

The salpingopharyngeus, stylopharyngeus, palatopharyngeus, and tensor and levator veli palatini muscles also contribute to the pharynx and its function. The salpingopharyngeus extends from the eustachian tube cartilage to interdigitate with posterior fascicles of the palatopharyngeus. This muscle is supplied by the pharyngeal plexus, and helps raise the pharynx and open the eustachian tube orifice during swallowing.

The stylopharyngeus extends from the styloid process caudally, passing between the external and internal carotid arteries, to insert on the superior and posterior borders of the thyroid cartilage, with some fibers intermingling with the constrictor muscles. This muscle raises, and to a minimal degree dilates, the pharynx. It is supplied by cranial nerve IX.

The palatopharyngeus extends from the soft palate and the pharyngeal wall to the posterior border of the thyroid cartilage, forming the substance of the posterior tonsillar pillar. This muscle narrows the oropharyngeal isthmus, elevates the pharynx, and helps close off the nasopharynx. It is supplied by the pharyngeal plexus.

The tensor veli palatini extends from the scaphoid fossa, sphenoid spine, and lateral side of the eustachian tube, around the hamulus of the pterygoid process, to the soft palate and part of the palatine bone. The tensor runs primarily outside of the pharynx and is considered part of the deglutitory musculature. It is innervated by the third division of the trigeminal nerve.

The levator veli palatini muscle has its origin from the undersurface of the petrous portion of the temporal bone and the medial side of the eustachian tube. It runs through the sinus of Morgagni, along the upper posterior edge of the medial pterygoid plate, and caudally within the pharynx to insert in the soft palate. As such, it is considered a pharyngeal muscle and it is innervated by the pharyngeal plexus.

The levator veli palatini and tensor velli palatini muscles function together to elevate and firm the soft palate, effectively closing off the nasopharynx during swallowing. These palatini muscle and the salpingopharyngeus also function together to maximize the patency of the eustachian tube orifice during swallowing.

The arterial supply of the pharynx is from the major branches of the external carotid artery, including the ascending pharyngeal artery, tonsillar branches of the facial artery, and palatine branches of the maxillary artery.[1, 2] The primary venous drainage is via the pharyngeal veins, which communicate with the pharyngeal plexus located in the lateral aspect of the pterygopalatine fossa and which then drain inferiorly into the internal jugular vein.

EMBRYOLOGY

The embryology of the branchial apparatus is discussed in detail in Chapter 33. Briefly, those derivatives that pertain to the pharynx include the muscles of mastication, the tensor veli palatini muscle, and the anterior belly of the digastric muscle, all of which come from the first branchial arch. All of these muscles are innervated by the mandibular division of the trigeminal nerve. The first pharyngeal pouch is the precursor to the eustachian tube.[3]

The ventral second branchial arch forms the lesser cornu and superior portion of the hyoid bone, while the dorsal second arch gives rise to the styloid process and the stylohyoid ligament. The muscles derived from the second arch mesoderm, and thus innervated by the facial nerve, include the posterior belly of the digastric and the stylohyoid muscle.[3] The ventral portion of the second pharyngeal pouch is largely obliterated by the development of the palatine tonsil. The dorsal portion of the second pouch gives rise to the tonsillar fossa. The endoderm proliferates and forms the surface epithelium and the lining of the palatine tonsillar crypts. The second arch mesenchyme forms the lymphatic tissue of the palatine tonsils.

The third branchial arch forms the lower body and greater cornu of the hyoid bone. The third branchial arch forms the stylopharyngeus, which is supplied by the glossopharyngeal nerve. Some authors claim that the palatopharyngeus muscle is also a third arch derivitive.[4] The mucosa covering the posterior third of the tongue (base of the tongue) is a derivative of the third arch.

SPECIFIC ANATOMY

Nasopharynx

The nasopharynx is an epithelium-lined cavity situated in the uppermost aerodigestive tract. It is approximately 2 cm in anteroposterior diameter and 4 cm in height. The roof is downward sloping and is formed from cranially to caudally by the basisphenoid, the basiocciput, and the anterior aspect of the first two cervical vertebrae.[1,5] The inferior margin of the nasopharynx is the level of the hard palate and Passavant's muscle. This muscle is composed of fibers that arise laterally from the palatopharyngeus muscle and the lateral aspect of the posterior border of the hard palate. The

Copyright © 2003, Mosby, Inc. All rights reserved.

fibers encircle the pharynx inside the superior constrictor muscle. When they contract they raise a ridge, Passavant's ridge, which opposes the soft palate when it is elevated. The ridge meeting the elevating soft palate closes off the nasopharynx during swallowing.

The lateral nasopharyngeal walls are formed and supported by the margins of the superior constrictor muscle and the pharyngobasilar fascia. The nasopharynx is fairly rigid, having its shape maintained by the strong pharyngobasilar fascia. This fascia is considered the cranial extension of the upper edge of the superior pharyngeal muscle and extends from this muscle to the skull base. Anteriorly, the nasopharynx is in direct continuity with the nasal cavity via the posterior choanae.[1, 5]

The nasopharynx communicates with the middle ear cavity via the eustachian tubes. As mentioned, these tubes gain access to the nasopharynx through the sinus of Morgagni, a defect in the anterior portion of the pharyngobasilar fascia, which is above the superior pharyngeal constrictor muscle and along the upper posterior border of the medial pterygoid plate (Figs. 28-1 and 28-2). The sinus of Morgagni is also the route of entry into the pharynx for the levator velli palatini muscle, and this pathway may provide access for advanced nasopharyngeal cancer to spread to the parapharyngeal region and central skull base.[5, 6]

The opening of each eustachian tube is located along the upper posterolateral wall of the nasopharynx, and with the cartilaginous eustachian tube, the levator veli palatini muscle, and the overlying mucosa, it forms the torus tubarius. The opening of the eustachian tube is about 1 cm behind and slightly below the posterior end of the inferior turbinate. Because of their location, the eustachian tubes are prone to obstruction by nasopharyngeal masses. It is estimated that such obstruction, which results in serous otitis, occurs in 50% of patients with a nasopharyngeal mass.[5–7]

Located just behind and above the torus tubarius is the fossa of Rosenmüller, a mucosa-lined recess that is the most cranial and superior aspect of the lateral recess of the nasopharynx. This fossa lies immediately lateral to the flexor muscles of the neck, the longus capitus and coli muscles (Fig. 28-3), and is a common site of origin of nasopharyngeal cancer.[8, 9] When tumors arise in this fossa, they are often clinically occult.[5, 6] Mucosal folds are also present in the nasopharynx, covering the salpingopharyngeus and levator veli palatini muscles. During a normal swallow, the palatini muscles and the salpingopharyngeus muscle pull the margins of the cartilaginous end of the eustachian tube in opposing directions, thereby maximizing the opening of this tube and allowing equalization of pressure between the pharynx and the middle ear.

The mucosa of the nasopharynx is composed of both stratified squamous and columnar epithelium. The latter predominates during the first 10 years of life, whereas stratified squamous epithelium becomes more common with advancing age. The adenoids, or pharyngeal tonsils, are lymphatic tissue located in the midline roof of the nasopharynx. Prominent adenoids are typically present in children, and if such adenoids are not identified, the patient is either in an immune deficiency state or has an immune deficiency syndrome. The maximal size of the adenoids occurs at about 5 years of age; around the time of puberty, gradual adenoidal involution normally begins. The majority of individuals have lost most of this adenoidal tissue by 30 years of age.[8, 10] Nonetheless, normal adenoidal tissue may occasionally be seen in adults in their fourth, fifth, and even sixth decade of life. After the first decade of life, it is unusual for the adenoidal mass to extend up to the posterior margin of the medial pterygoid plate. If such a nasopharyngeal mass is seen in an older patient, clinical correlation should be sought.

The visceral (buccopharyngeal) fascia surrounds the nasopharyngeal mucosa and the constrictor muscles. This

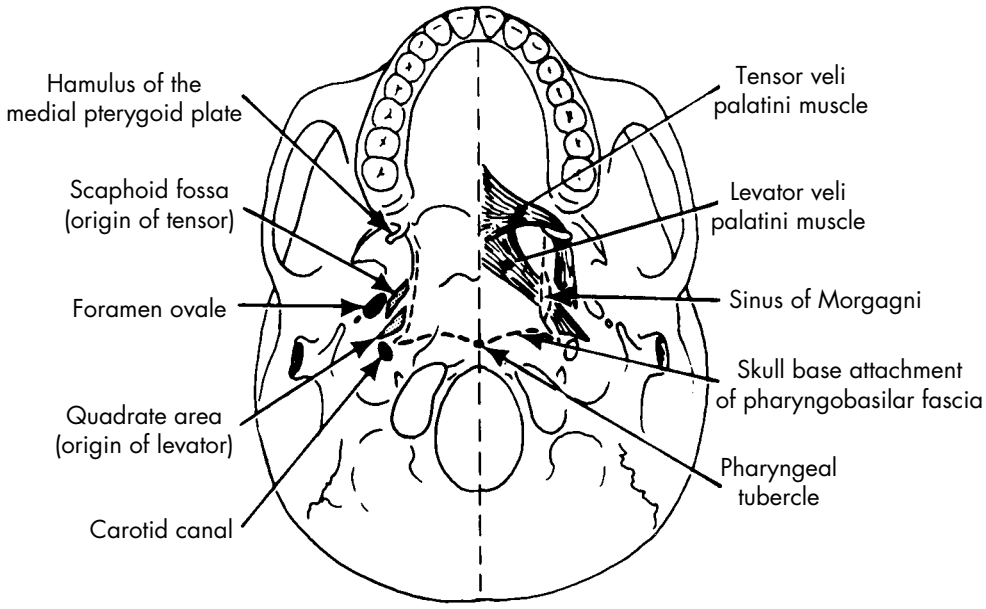

FIGURE 28-1 Axial schematic of skull base demonstrates attachment of levator and tensor veli palatini muscles and pharyngobasilar fascia. (Courtesy of Dr. Wendy Smoker, University of Utah.)

VIEW IMAGE

Copyright © 2003, Mosby, Inc. All rights reserved.

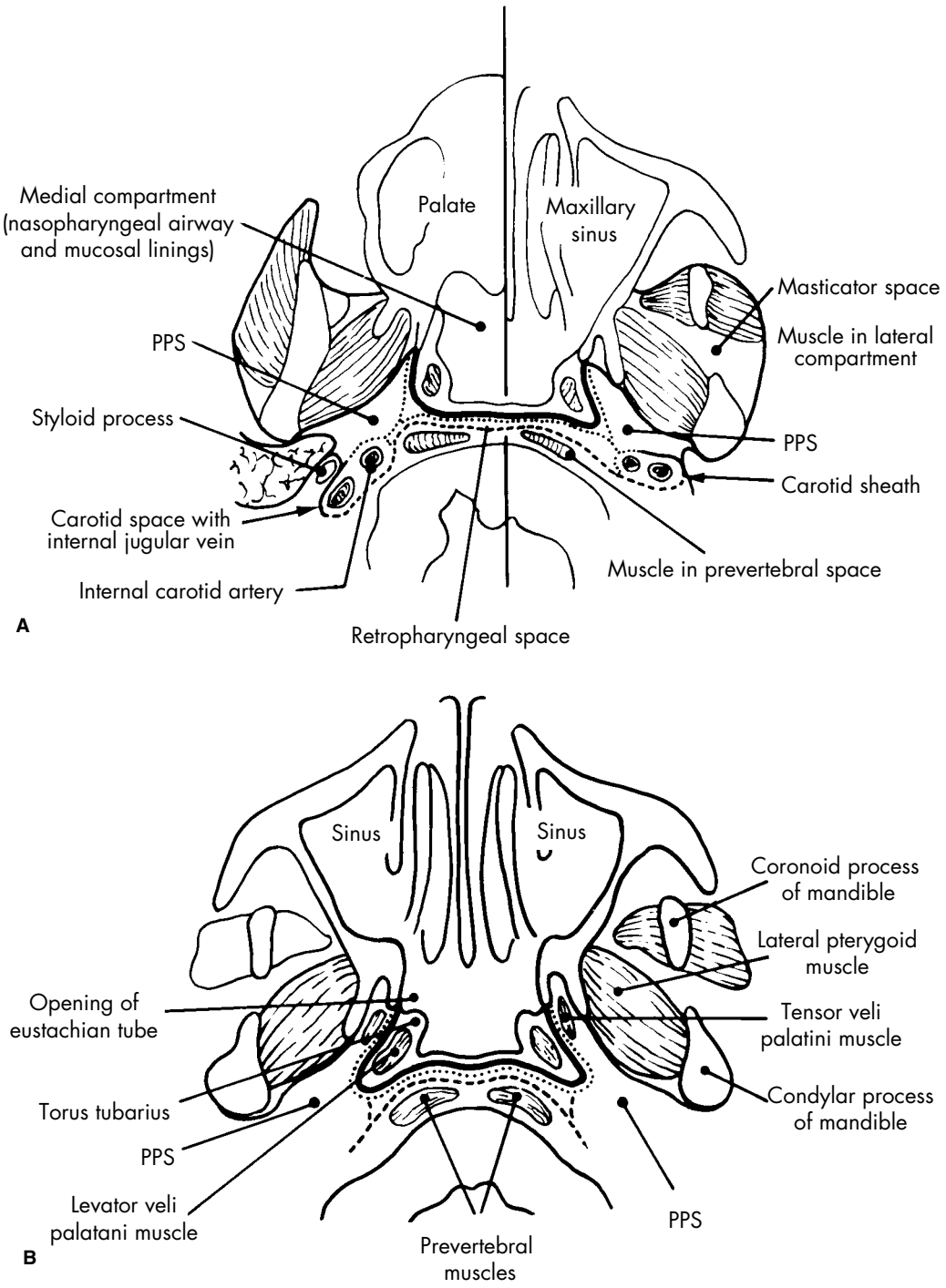

FIGURE 28-2 **A**, Axial schematic of upper nasopharynx. The left side of the image is at a lower level than the right side of the image. Various deep spaces of the head and neck include the masticator space, parapharyngeal space (*PPS*), carotid space, and retropharyngeal and prevertebral spaces. Dense heavy line represents pharyngobasilar fascia; thin dotted line represents buccopharyngeal fascia. Note that the carotid sheath is made up of components of all fascial layers. **B**, Axial schematic through the midnasopharynx demonstrating the relationship of the levator and tensor palatini muscles to the pharyngobasilar fascia and torus tubarius. (Courtesy of Dr. Wendy Smoker, University of Utah.)

fascia separates the nasopharynx from the deep fascial spaces and is thought to be a barrier to deep spread of infection and early malignancy (see also Chapter 34) (Fig. 28-4).[5–8, 11] An extensive lymphatic plexus drains the nasopharynx, and this explains the high incidence of cervical nodal metastases associated with nasopharyngeal carcinomas.[5, 7, 12] Primary nodal drainage is to the retropharyngeal nodes. However, the lymphatic pathways to these

Copyright © 2003, Mosby, Inc. All rights reserved.

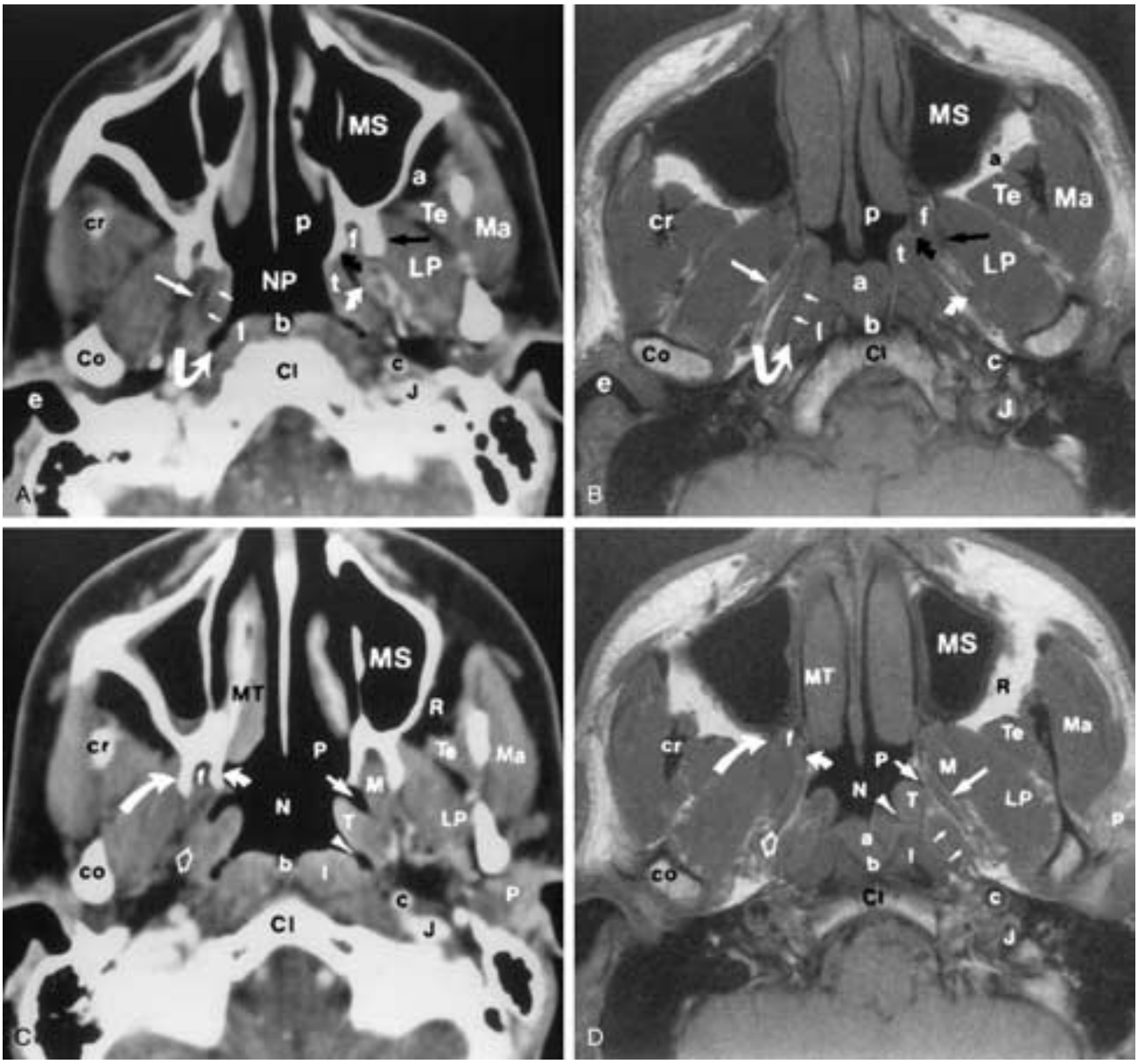

VIEW IMAGE

FIGURE 28-3 Normal anatomy of the nasopharynx. *Normal anatomy of the superior portion of the nasopharynx*. **A, *CT***: *MS*, Maxillary sinus; *p*, posterior choana; *NP*, nasopharyngeal airway; *a*, retroantral fat; *straight black arrow*, lateral pterygoid plate; *curved black arrow*, medial pterygoid plate; *f*, pterygoid fossa; *LP*, lateral pterygoid muscle; *small curved white arrow*, third division of cranial nerve V; *Ma*, masseter muscle; *Te*, deep head of the temporalis muscle; *t*, superior aspect of the torus tubarius; *large curved white arrow*, fossa of Rosenmüller (lateral pharyngeal recess); *l*, longus colli muscle; *b*, pharyngeal bursa; *large straight arrow*, tensor veli palatini muscle; *small straight arrows*, levator veli palatini muscle; *cr*, coronoid process of the mandible; *Co*, condyle of the mandible; *Cl*, clivus; *c*, internal carotid artery; *J*, internal jugular vein. **B, *MR***: MS, maxillary sinus; *p*, posterior choana; white *a*, adenoidal tissue in nasopharynx; black *a*, retroantral fat; *straight black arrow*, lateral pterygoid plate; *curved black arrow*, medial pterygoid plate; *f*, pterygoid fossa; *LP*, lateral pterygoid muscle; *small curved white arrow*, third division of cranial nerve V; *Ma*, masseter muscle; *Te*, deep head of the temporalis muscle; *t*, superior aspect of the torus tubarius; *large curved white arrow*, fossa of Rosenmüller (lateral pharyngeal recess); *l*, longus colli muscle; *b*, pharyngeal bursa; *large straight arrow*, tensor veli palatini muscle; *small straight arrows*, levator veli palatini muscle; *cr*, coronoid process of the mandible; *Co*, condyle of the mandible; *Cl*, clivus; *c*, internal carotid artery; *J*, internal jugular vein. *Normal anatomy of the midnasopharynx*. **C, *CT***: *MS*, maxillary sinus; *MT*, middle turbinate; *P*, posterior choana; *N*, nasopharyngeal airway; *large curved arrow*, lateral pterygoid plate; *small curved arrow*, medial pterygoid plate; *f*, pterygoid fossa; *LP*, lateral pterygoid muscle; *M*, medial pterygoid muscle; *open white arrow*, third division of cranial nerve V; *Ma*, masseter muscle; *Te*, deep head of the temporalis muscle; *straight arrow*, eustachian tube opening; *T*, torus tubarius; *arrowhead*, fossa of Rosenmüller (lateral pharyngeal recess); *l*, longus colli muscle; *b*, pharyngeal bursa; *P*, parotid gland; *cr*, coronoid process of the mandible; *co*, condylar neck of the mandible; *c*, internal carotid artery; *J*, internal jugular vein; *Cl*, clivus. **D, *MR***: *MS*, Maxillary sinus; *MT*, middle turbinate; *P*, posterior choana; *N*, nasopharyngeal airway; *large curved arrow*, lateral pterygoid plate; *small curved arrow*, medial pterygoid plate; *f*, pterygoid fossa; *LP*, lateral pterygoid muscle; *M*, medial pterygoid muscle; *open white arrow*, third division of cranial nerve V; *Ma*, masseter muscle; *Te*, deep head of the temporalis muscle; *medium straight arrow*, eustachian tube opening; *T*, torus tubarius; *arrowhead*, fossa of Rosenmüller (lateral pharyngeal recess); *large straight arrow*, tensor veli palatini muscle; *small straight arrows*, levator veli palatini muscle; *l*, longus colli muscle; *a*, adenoid tissue; *b*, pharyngeal bursa; *P*, parotid gland; *cr*, coronoid process of the mandible; *co*, condylar neck of the mandible; *c*, internal carotid artery; *J*, internal jugular vein; *Cl*, clivus. (Reprinted with permission from Mukherji SK, Castillo M. Normal cross-sectional anatomy of the nasopharynx, oropharynx, and oral cavity. Neuroimaging Clin North Am 1998;8:211-218, Figs. 1 and 2.)

Copyright © 2003, Mosby, Inc. All rights reserved.

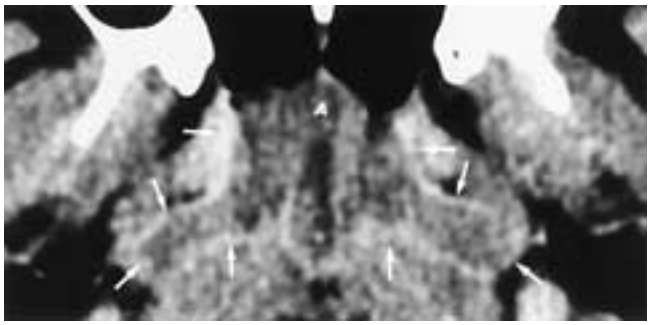

VIEW IMAGE

FIGURE 28-4 Axial contrast-enhanced CT scan through the nasopharynx of a 4-year-old child shows normal enhancement of the venous plexus and pharyngobasilar fascia (*arrows*). Note the adenoidal tissue normally seen in this age group (*A*).

nodes are thought to become obliterated by adulthood secondary to the numerous pharyngeal infections that occur in childhood. As such, nasopharyngeal cancers often drain to the second-order nodes in levels II, III, and occasionally in level V.[5, 12]

Oropharynx

The oropharynx is the region of the pharynx posterior to the oral cavity (see Chapter 27) and includes the posterior one third of the tongue (tongue base), the palatine tonsils, the soft palate, and the oropharyngeal mucosa and constrictor muscles. The posterior oropharyngeal wall is related to the second and third cervical vertebrae. Laterally are two faucial arches. The anterior arch is formed by mucosa over the palatoglossus muscle, and the posterior arch is formed by mucosa over the palatopharyngeus muscle. Between these arches is the tonsillar fossa containing the palatine tonsil (Figs. 28-5 and 28-6). The visceral fascia surrounding the mucosa and musculature of the pharynx often acts as a barrier to contain tumor. However, if this fascia is violated, tumor can invade posteriorly into the longus capitis and colli muscles and the vertebrae.[13] Lateral tumor extension on either side is into the lower parapharyngeal space. The palatine tonsils rapidly increase in size over the first 5 to 6 years of life, and reach maximal size at puberty (20–25 mm in vertical diameter and 10–15 mm in transverse diameter).

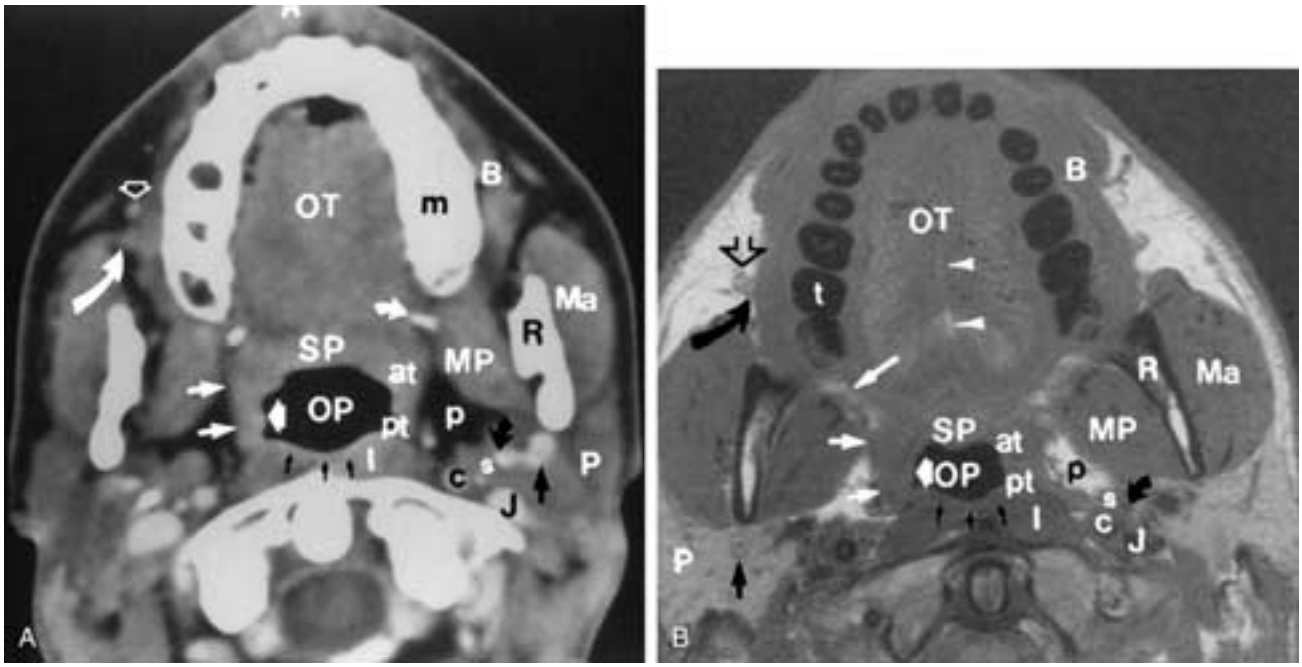

VIEW IMAGE

FIGURE 28-5 Normal anatomy of the oropharynx and surrounding structures. **A**, ***CT***: *B*, Buccinator muscle; *OT*, oral tongue; *m*, maxillary alveolar ridge; *white curved arrow*, hook of the hamulus; *SP*, soft palate; *Ma*, masseter muscle; *R*, ramus of the mandible; *MP*, medial pterygoid muscle; *open arrow*, angular vein; *large curved arrow*, parotid duct; *OP*, airway of the oropharynx; *at*, region of the anterior tonsillar pillar (palatoglossus muscle); *pt*, region of the posterior tonsillar pillar (palatopharyngeus muscle); *fat white arrow*, tonsillar fossa (palatine, faucial tonsil); *small black arrows*, posterior wall of the oropharynx; *l*, longus colli muscle; *p*, fat within the prestyloid parapharyngeal space; *curved black arrow*, styloid process; *s*, origin of the styloid musculature; *P*, parotid gland; *straight black arrow*, retromandibular vein; *c*, internal carotid artery; *J*, internal jugular vein. **B, *MR***: *B*, Buccinator muscle; *OT*, oral tongue; *t*, tooth arising from the maxillary alveolar ridge; *large straight white arrow*, location of the pterygomandibular raphe, which is attached above to the hook of the hamulus; *SP*, soft palate; *Ma*, masseter muscle; *R*, ramus of the mandible; *MP*, medial pterygoid muscle; *open arrow*, angular vein; *large curved arrow*, parotid duct; *OP*, airway of the oropharynx; *at*, region of the anterior tonsillar pillar (palatoglossus muscle); *pt*, region of the posterior tonsillar pillar (palatopharyngeus muscle); *fat white arrow*, tonsillar fossa (palatine, faucial tonsil); *small black arrows*, posterior wall of the oropharynx; *l*, longus colli muscle; *p*, fat within the prestyloid parapharyngeal space; *curved black arrow*, styloid process; *s*, origin of the styloid musculature; *P*, parotid gland, retromandibular vein; *c*, internal carotid artery; *J*, internal jugular vein. (Reprinted with permission from Mukherji SK, Castillo M. Normal cross-sectional anatomy of the nasopharynx, oropharynx, and oral cavity. Neuroimaging Clin North Am 1998;8:211–218, Fig. 3.)

Copyright © 2003, Mosby, Inc. All rights reserved.

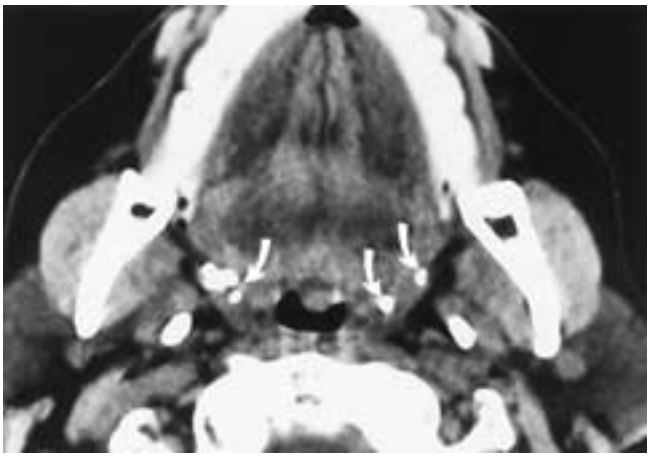

VIEW IMAGE

FIGURE 28-6 Axial CT scan demonstrates the characteristic appearance of benign tonsillar calcifications (*curved arrows*).

The lingual tonsil, which can be quite variable in size, lies at the base of the tongue. It is usually more prominent laterally, often with a midline groove. Although this tonsillar tissue can normally extend down to the anterior wall of the vallecula, it will not extend into the floor or posterior vallecular wall. Thus, any contiguous mass with the lingual tonsil that does extend into the vallecular floor or posterior wall should be considered a tumor until proven otherwise.

The major arterial supply to the oropharynx is from the tonsillar branch of the facial artery, the ascending pharyngeal artery, the dorsal lingual arteries, and the internal maxillary and facial arteries. The majority of venous drainage is through the peritonsillar veins, which pierce the constrictor musculature and drain into the common facial vein and the pharyngeal plexus.[1, 2] The primary lymphatic drainage is to level II and III nodes, the retropharyngeal nodes, and less often to level V nodes. The palatine tonsil can also drain to the parotid nodes (see Chapter 36).[12]

Hypopharynx

The hypopharynx, or laryngopharynx, is the most caudal portion of the pharynx that extends from the level of the hyoid bone to the cricopharyngeus.[14, 15] On imaging, this caudal margin can be approximated by the lower level of the cricoid cartilage. Below this level, the gullet becomes the cervical esophagus (Fig. 28-7). Most authors divide the hypopharynx into the following three regions: the pyriform sinuses, the posterior wall, and the postcricoid region (Fig. 28-7).[14–16] Some authors also refer to a fourth or ''marginal'' area, the hypopharyngeal (lateral) surface of each aryepiglottic fold (Fig. 28-7).[17]

The pyriform (pear-shaped) sinus is an anterolateral recess of the hypopharynx situated on either side of the pharynx between the inner surface of the thyrohyoid membrane and thyroid cartilage and the lateral surface of the aryepiglottic fold. The anterior pyriform sinus mucosa abuts on the posterior paraglottic space of the larynx.[14] The most caudal portion, or apex, of each pyriform sinus lies at the level of the true vocal cord (Figs. 28-8 and 28-9). As mentioned, the lateral wall of the pyriform sinus is formed above by the thyrohyoid membrane and below by the thyroid cartilage. These two areas have been referred to

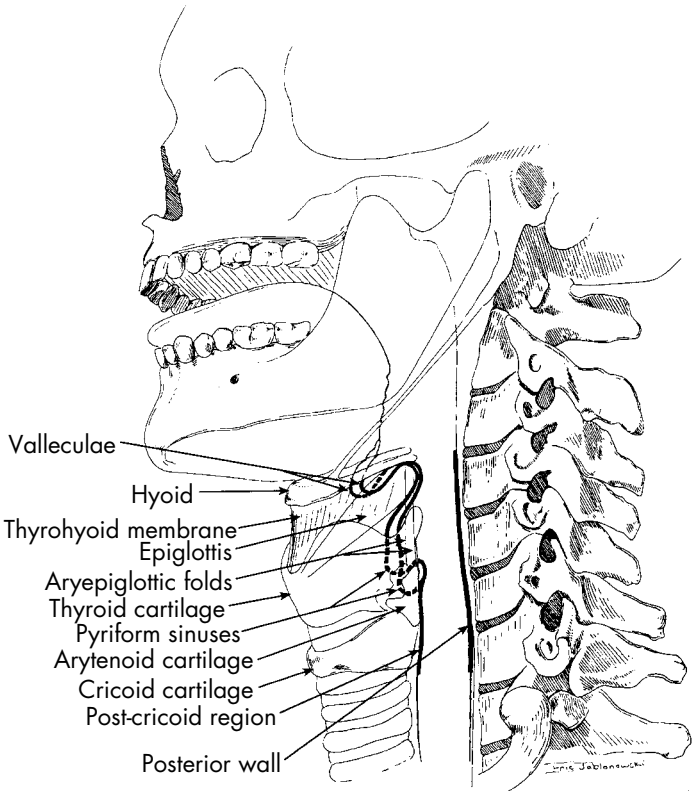

VIEW IMAGE

FIGURE 28-7 Diagram of the hypopharynx. The heavy black lines indicate the region of the hypopharynx.

Copyright © 2003, Mosby, Inc. All rights reserved.

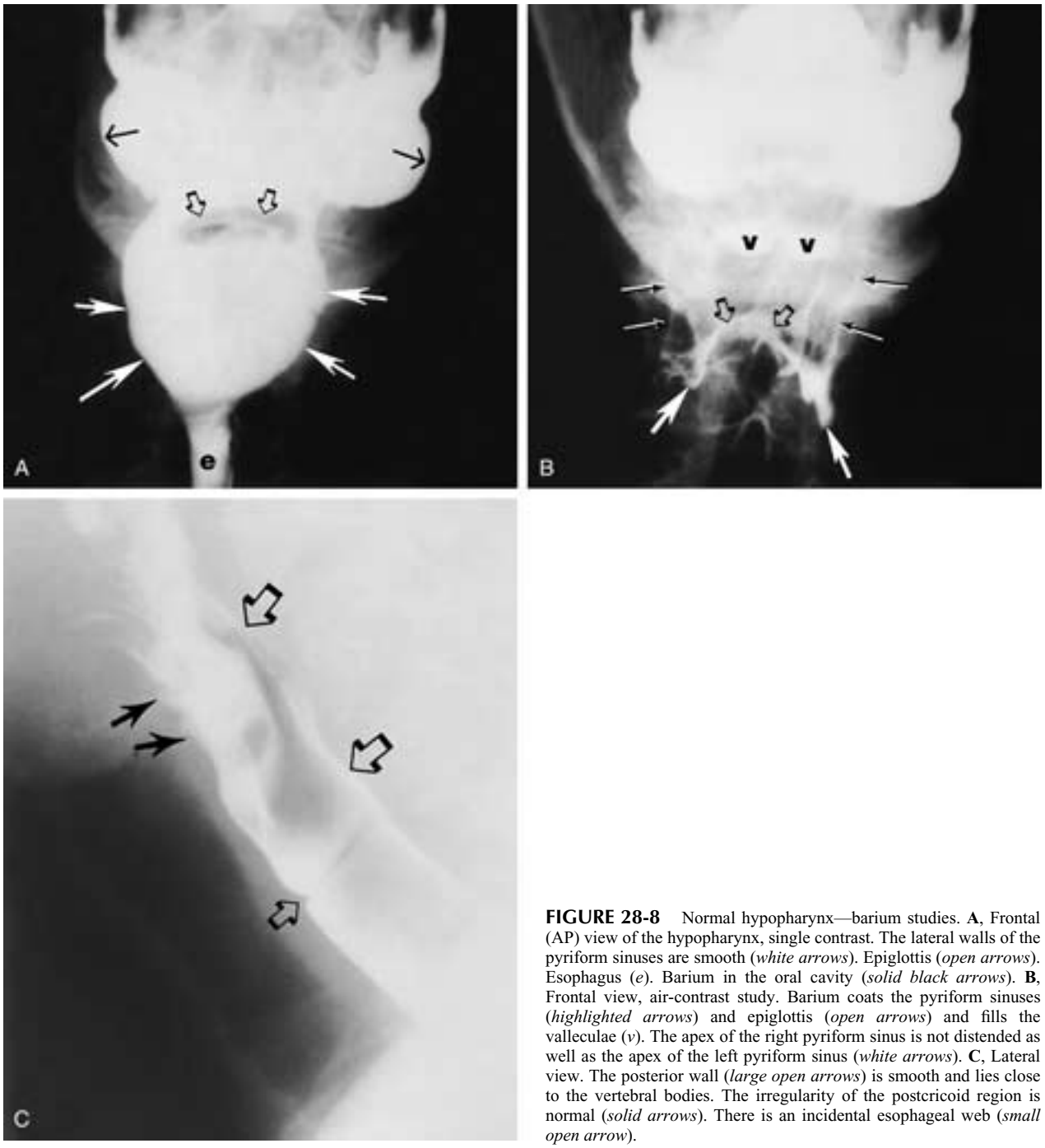

FIGURE 28-8 Normal hypopharynx—barium studies. **A**, Frontal (AP) view of the hypopharynx, single contrast. The lateral walls of the pyriform sinuses are smooth (*white arrows*). Epiglottis (*open arrows*). Esophagus (*e*). Barium in the oral cavity (*solid black arrows*). **B**, Frontal view, air-contrast study. Barium coats the pyriform sinuses (*highlighted arrows*) and epiglottis (*open arrows*) and fills the valleculae (*v*). The apex of the right pyriform sinus is not distended as well as the apex of the left pyriform sinus (*white arrows*). **C**, Lateral view. The posterior wall (*large open arrows*) is smooth and lies close to the vertebral bodies. The irregularity of the postcricoid region is normal (*solid arrows*). There is an incidental esophageal web (*small open arrow*).

VIEW IMAGE

respectively as the membranous and cartilaginous portions of this lateral pyriform sinus wall.[14–16]

The medial wall of the pyriform sinus is formed by the lateral surface of the aryepiglottic fold and is often considered a marginal zone. Although the aryepiglottic fold is part of the supraglottic larynx, it can also be considered part of the hypopharynx. An aryepiglottic fold tumor confined to the laryngeal surface behaves clinically like a supraglottic tumor. However, a tumor involving the lateral wall of the aryepiglottic fold usually behaves more aggressively, more consistent with the behavior of hypopharyngeal tumors.

The posterior wall of the hypopharynx is the inferior continuation of the posterior wall of the oropharynx. The hypopharynx is considered to start at the level of the hyoid bone (and valleculae) (Fig. 28-10). Caudally, the posterior and lateral walls of the hypopharynx merge with the cricopharyngeus, which in turn merges with the cervical esophagus. The visceral fascia surrounds the inferior pharyngeal constrictor muscles, and the retropharyngeal space lies behind the posterior pharyngeal wall (see Chapter 36).

The postcricoid region is the anterior wall of the lower hypopharynx. This area is the interface between the hypopharynx and the anteriorly located larynx (Fig. 28-11).

Copyright © 2003, Mosby, Inc. All rights reserved.

The postcricoid portion of the hypopharynx extends from the level of the cricoarytenoid joints down to the lower edge of the cricoid cartilage. Thus, the postcricoid regions abuts the dorsal surface of the cricoid lamina.[14–16]

The inferior pharyngeal constrictor muscle has two components. The upper fibers arise from the posterior midline pharyngeal raphe and insert on the thyroid cartilage. These fibers are obliquely oriented, being highest in the posterior midline.[18] The inferior pharyngeal oblique fibers overlap and interdigitate with the oblique muscle fibers of the middle pharyngeal constrictor muscle.[19] The lowermost portion of the inferior pharyngeal constrictor, the cricopharyngeus, is composed of horizontally oriented, parallel, nonraphed muscle fibers that arise from either side of the cricoid cartilage. These fibers become continuous with the circular muscles of the cervical esophagus.[18, 19] Between the upper border of the cricopharyngeus and the lowermost margin of the oblique fibers of the inferior pharyngeal constrictor muscle on either side of the raphe is a small triangular, mucosa-covered space called Killian's dehiscence. It is through this area that Zenker's diverticulum arises.

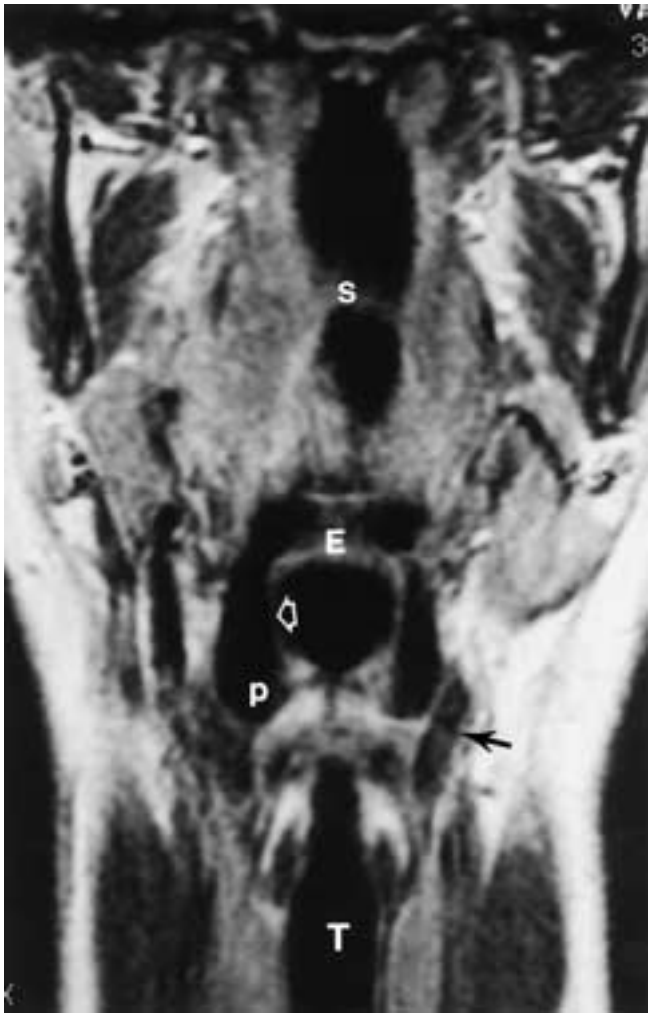

VIEW IMAGE

FIGURE 28-9 Coronal T1-weighted MR image after gadolinium administration shows the pyriform sinuses (*p*), epiglottis (*E*), aryepiglottic folds (*open arrow*), thyroid cartilage (*solid arrow*), soft palate (*s*), and trachea (*T*).

The superior, middle, and inferior pharyngeal constrictors contract in a coordinated peristaltic manner with each swallow. This contraction increases intrapharyngeal pressure, creating a pressure head that assists in moving a bolus from the hypopharynx into the cervical esophagus. The cricopharyngeus, or superior esophageal sphincter, is normally closed in its resting state. In response to a minimum specific volume and pressure in the hypopharynx, the cricopharyngeus relaxes, allowing the hypopharyngeal bolus to enter the cervical esophagus. Equally important, the cricopharyngeus then closes to prevent esophagopharyngeal reflux (see Chapter 32).[19]

The pharyngeal plexus of nerves receives contributions primarily from the glossopharyngeal and vagus nerves. Lesser contributions come from the spinal accessory nerve and the sympathetic plexus. It is the vagus that primarily supplies motor innervation to the constrictor muscles.[19] Sensory information from the hypopharynx travels along the glossopharyngeal nerve and the internal laryngeal branch of the superior laryngeal nerve, a branch of the vagus nerve.[14] Pain from a hypopharyngeal tumor may be transmitted up from the pyriform sinus along the internal branch of the superior laryngeal nerve. The impulses may then continue along the vagus nerve to the auricular nerve, a branch of the vagus nerve. Since the auricular nerve (Arnold's nerve) supplies sensory innervation to the external auditory canal and pinna via this referred pathway, a hypopharyngeal tumor may present with otalgia.[14]

The pyriform sinuses are drained by a network of lymphatics, most of which are directed to levels II and III nodes and secondarily to level V nodes.[14, 16] The lymphatics of the posterior wall of the hypopharynx drain to the level II and III nodes, as well as to the retropharyngeal nodes.[16] The postcricoid lymphatics drain to level III and IV nodes as well as to level VI nodes (see Chapter 36).[20]

Branches of the superior and inferior thyroid arteries supply most of the lower pharynx.[1] The venous drainage more superiorly is into the pharyngeal plexus, while the drainage inferiorly is into the superior and inferior thyroid veins and into individual pharyngeal veins that drain directly into the internal jugular veins.[1]

IMAGING TECHNIQUES

Barium Studies

Barium studies allow both anatomic and dynamic assessment of the upper aerodigestive tract. These studies provide information regarding the integrity of the mucosa and can determine if the pharyngeal wall is pliable or fixed. A barium swallow is usually the first radiographic study performed in the evaluation of a patient with dysphagia and/or odynophagia (see Chapter 32) (Fig. 28-12). Barium studies can detect small mucosal abnormalities that are not apparent on either CT or MR imaging, and barium studies are helpful for detecting traumatic or iatrogenic perforations and postoperative fistulae. Because there is about a 10% incidence of second primary tumor in a patient with squamous cell carcinoma of the upper aerodigestive tract,

Copyright © 2003, Mosby, Inc. All rights reserved.

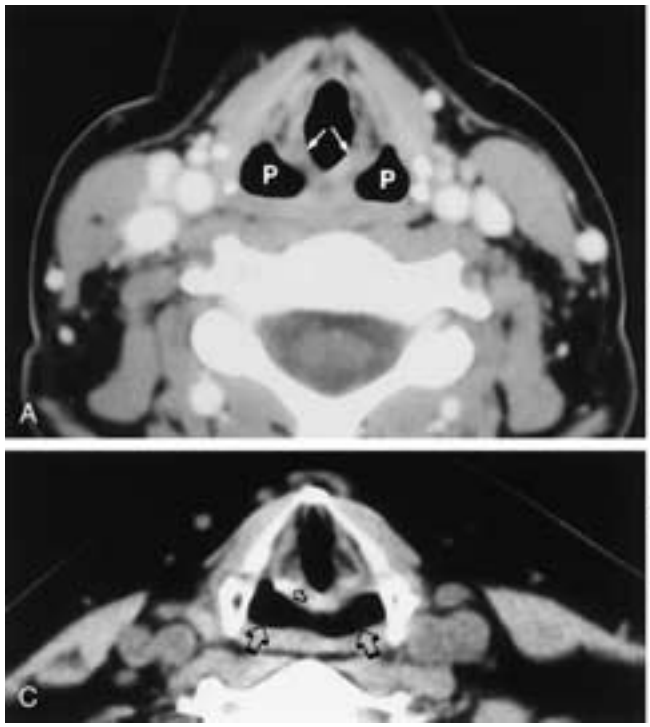

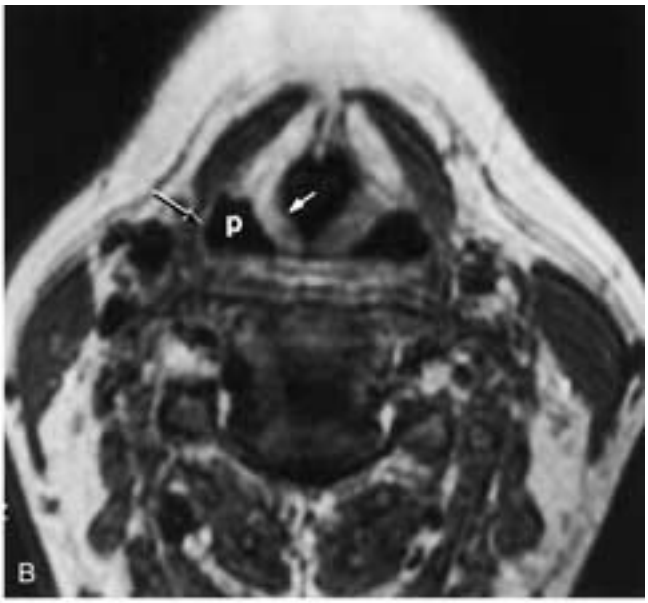

FIGURE 28-10 Normal hypopharynx—axial CT and MR studies. **A**, Axial CT scan through the pyriform sinuses (*P*) and aryepiglottic folds (*arrows*). **B**, T1-weighted MR image after gadolinium administration shows normal enhancement of the mucosa of the aryepiglottic folds (*white arrow*). The thin, smooth mucosa (*highlighted arrow*) of the pyriform sinuses (*p*) also enhances. **C**, Normal axial CT scan of another patient shows air distending the hypopharynx (*large open arrows*). Arytenoid cartilage (*small open arrow*).

VIEW IMAGE

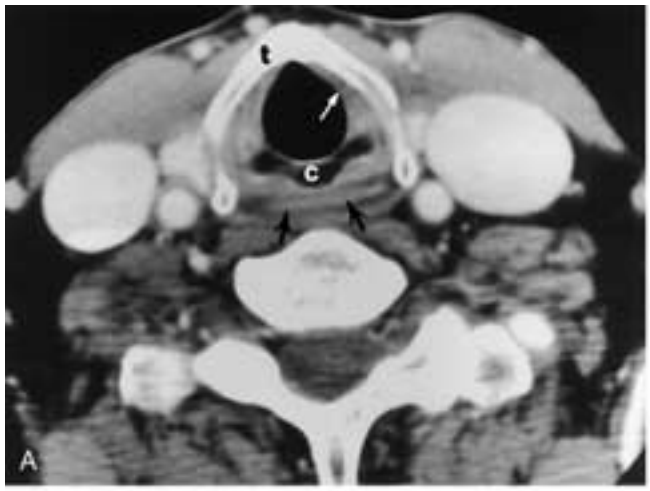

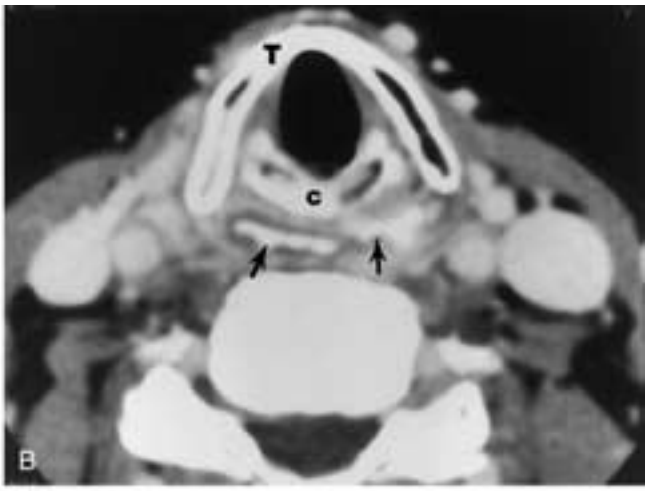

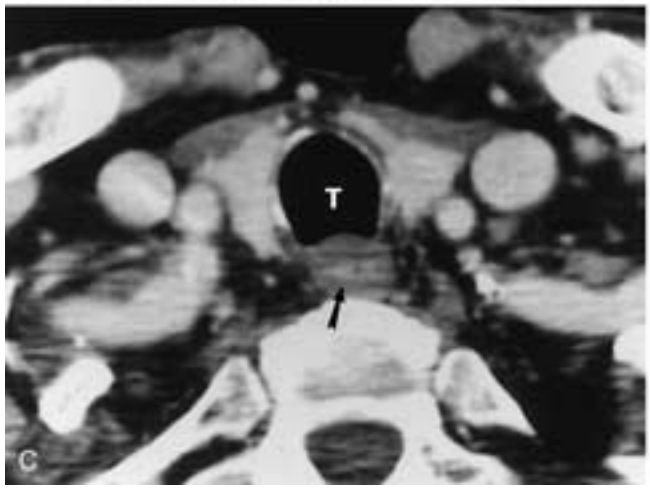

FIGURE 28-11 Axial CT scans through the normal postcricoid region. **A**, The postcricoid mucosa (*black arrows*) is slightly more dense than the wall. This image is at the level of the cricoid cartilage (*c*), thyroid cartilage (*t*), and inferior surface of the true vocal cords (*white arrow*). **B**, Barium shows the location of the lumen of the postcricoid hypopharynx (*arrows*). Cricoid cartilage (*c*). Thyroid cartilage (*T*). When not distended by air, the shape of the postcricoid hypopharynx is a flattened oval. **C**, Axial CT scan through the upper cervical esophagus for comparison. Instead of the flattened oval of the hypopharynx, the cervical esophagus is round (*arrow*) and indents the membranous posterior wall of the trachea (*T*).

VIEW IMAGE

Copyright © 2003, Mosby, Inc. All rights reserved.

VIEW IMAGE

FIGURE 28-12 Pyriform sinus carcinoma—barium studies. **A**, The lateral wall of the right pyriform sinus (*black arrows*) is irregular with tumor on this frontal air-contrast study. The tumor spares the apex of the pyriform sinus (*curved arrow*). The lateral pharyngeal wall on the left is normal (*open arrows*). **B**, In another patient, a frontal view from a single-contrast barium study shows irregularities and filling defects (*solid arrows*) along the lateral wall of the left pyriform sinus. The right pyriform sinus wall is normal (*open arrows*).

virtually all of these patients should be followed with either periodic endoscopy or a barium swallow. These second cancers most often arise in the upper aerodigestive tract or the lung.[16]

Although barium is the contrast agent of choice for the routine evaluation of patients with dysphagia, a water-soluble iodinated medium is preferable when evaluating for a perforation, as these agents (diatrizoate meglumine and diatrizoate sodium) are readily absorbed from the soft tissues of the neck. However, these contrast agents are quite hypertonic (1900 mosm/kg water) and are contraindicated in a patient who may have significant aspiration.[21] Such aspirated hypertonic contrast media draw fluid into the lungs and can result in pulmonary edema. For such patients, the best contrast agents are low-osmolality, iodinated, water-soluble contrast media such as metrizamide and iohexol.[21] If a perforation to the tracheobronchial tree is suspected, either barium or a low-osmolality contrast agent is recommended.

Computed Tomography

The best CT evaluation of the pharynx is achieved on axial images with the patient supine. The head should be carefully aligned in the cephalocaudad axis, usually with the hard palate perpendicular to the table top and a scan plane parallel to the inferior orbital meatal plane. Poor positioning may result in an appearance that either simulates pathology or occasionally makes pathology difficult to see. Coronal imaging (either direct or reformatted) should also be performed in any patient suspected of having a nasopharyngeal, palatal, or skull base carcinoma, as early erosion of the

Copyright © 2003, Mosby, Inc. All rights reserved.

skull base and hard palate is best seen in the coronal plane. If the patient has dental amalgams or other oral cavity metal products that cause severe artifacts, additional scans should be performed through the region of degraded images with a gantry angulation along the plane of the mandible. All studies should be reconstructed in both soft-tissue and bone algorithms.

Spiral and multidetector CT are fast becoming the preferred techniques.[22–24] Due to their short imaging times, imaging of the pharynx can be performed in a single short breath hold or even with the patient breathing normally. Patient movement artifact is virtually eliminated. The optimal field of view (FOV) varies between 14 and 18 cm, with the final FOV dependent on the size of the patient. The preferred slice thickness is between 2 and 3 mm, and images are made contiguously through the neck.

If intravenous contrast is not contraindicated, such contrast is recommended for all CT studies of the neck. Intravenous contrast not only increases the conspicuity of pathology but is essential for evaluating the cervical lymph nodes (see Chapter 36). The use of a power injector is preferred, with an initial bolus injection of 50 cc followed by a continuous infusion to a total contrast volume of between 100 and 150 cc.

Magnetic Resonance Imaging

MR images of the nasopharynx and oropharynx can be performed with a head coil, while images to evaluate the hypopharynx and cervical lymph nodes must utilize a dedicated neck coil sufficient in size to cover the patient from the level of the floor of the mouth to the supraclavicular region. In order to obtain high-quality images, the patient must be instructed not to talk or move and, if possible, to minimize swallowing. If possible, the patient should not fall asleep, as snoring often degrades image quality.

For the routine MR examination, sagittal T1-weighted, spin-echo localizer images are obtained. Axial T1-weighted and fast spin-echo, T2-weighted images are then obtained through the field of interest. A coronal T1-weighted sequence also provides an additional orthogonal view of the skull base and superior nasopharynx.

The use of intravenous paramagnetic contrast is essential when evaluating patients with malignancies of the pharynx. The initial noncontrast T1-weighted images will have covered the primary region of interest. These important images allow areas of high T1-weighted signal intensity (i.e., fat, high protein content, methemoglobin) to be identified and thus not confused with areas of enhancement of the contrast-enhanced, T1-weighted images.

When studying lesions of the tongue base, sagittal images are helpful to assess the caudal and ventral extent of disease. Coronal scans of the oropharynx are generally not essential, but they can give a good assessment of the craniocaudal extent of disease. In addition, level V nodes are often better seen on coronal than on axial images.

Sections 4 or 5 mm thick, with a 1-mm interslice gap, are mandatory to prevent volume averaging. Proper acquisition parameters and filming are also essential for optimal imaging of the pharynx. An 18- to 20-cm FOV with a 512×256 matrix can be used in the nasopharynx and oropharynx in most patients without a phase wrap artifact. A smaller matrix (256×256) is recommended for the hypopharynx, as this will help increase the signal-to-noise ratio of this smaller region. Presaturation pulses are also helpful to reduce the often troublesome phase-encoding flow artifact.

Tissue Differentiation

In the pharynx, the three primary soft tissues that are imaged are muscle, lymphoid tissue, and fat, each with different CT and MR imaging characteristics.[25] The primary task of the radiologist is to differentiate these normal tissues from tumor and infection. On CT, muscle and lymphoid tissues are often difficult to distinguish from neoplastic tissues but are easily differentiated from fat (Fig. 28-13). On MR imaging, muscle has an intermediate T1-weighted and a low T2-weighted signal intensity. Lymphoid tissue has a signal intensity similar to that of muscle and of most tumors on T1-weighted images[25–28] (Fig. 28-13). However, lymphoid tissue has a relatively high T2-weighted signal intensity. Most cellular tumors have an intermediate T1-weighted and a slightly higher intermediate T2-weighted signal intensity, also allowing their distinction from muscle.

The T1-weighted images afford the best contrast between fat and muscle, whereas the T2-weighted images best demonstrate the contrast between muscle and tumor and lymphoid tissue.[25, 27, 28] Because of similar signal intensities, most tumors and lymphoid tissue cannot be reliably differentiated from each other on MR imaging.

The dominant fat plane on either side of the pharynx is the parapharyngeal space, which is best defined on T1-weighted images. In cases of pharyngeal tumor, infiltration of the parapharyngeal space fat usually indicates deep invasion of the neoplasm.

The tonsils and faucial pillars usually appear as bilaterally symmetric soft-tissue masses on either side of the oropharyngeal airway.[29–31] Any asymmetry in the size or configuration of these tonsils may indicate the presence of a tumor or infection in the larger side. A large cystic area within a palatine tonsil may indicate a lymphoma, a necrotic tumor, or an abscess. The presence of a well-defined enhancing rim around such an area suggests an abscess; however, because some tumors can also have this imaging appearance, the history in such cases is essential. The presence of infection is virtually always associated with pain and malaise. Tumor usually causes little, if any, pain. Dystrophic calcifications from prior infections are commonly seen within the tonsillar crypts (Fig. 28-6), and a benign minor salivary gland retention cyst may occur, usually either within the nasopharynx or palatine tonsils or in the hypopharyngeal mucosa (Figs. 28-14 and 28-15).

NEOPLASMS

General Considerations

The mucosa of the entire upper aerodigestive tract is potentially exposed to the same carcinogenic agents and risk factors. Thus, it is not surprising that multiple primary

Copyright © 2003, Mosby, Inc. All rights reserved.

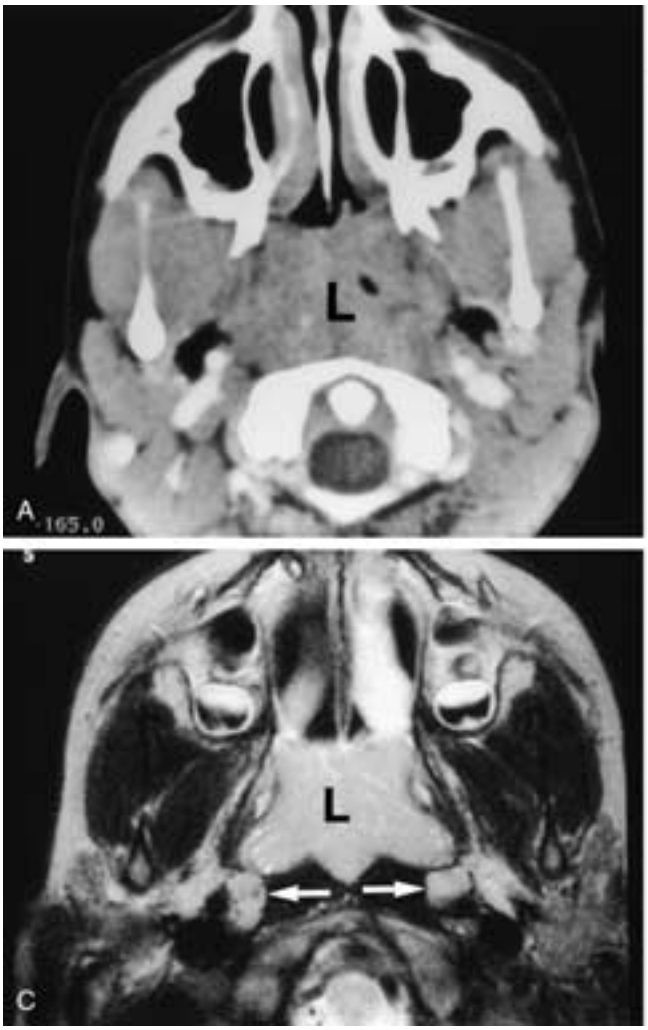

FIGURE 28-13 Normal appearance of nasopharyngeal lymphoid tissue in a 10-year-old child**. A**, Axial contrast-enhanced CT scan of the nasopharynx shows a large amount of soft tissue (*L*) replacing the airway of the nasopharynx. Note that the attenuation of the lymphoid tissue is similar to that of the surrounding muscle. **B**, Noncontrast T1-weighted MR imaging scan performed in the same patient illustrated in **A** shows the normal appearance of lymphoid tissue in the nasopharynx (*L*). The T1-weighted signal of the lymphoid tissue is slightly higher than that of the surrounding muscle. **C**, Axial T2-weighted sequence obtained in the same patient illustrated in **B** shows increased signal within the adenoidal tissue. Note the appearance of normal retropharyngeal lymph nodes that can be seen in children (*arrows*). Retropharyngeal lymph nodes are most easily identified on T2-weighted sequences.

VIEW IMAGE

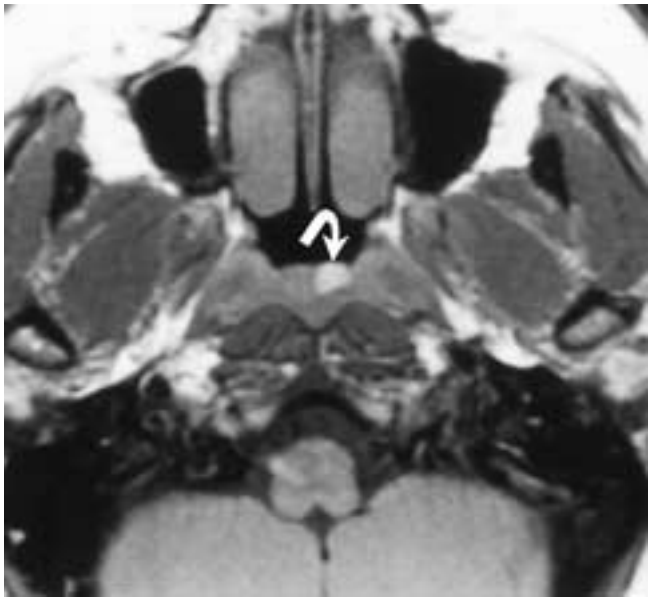

VIEW IMAGE

FIGURE 28-14 Noncontrast axial T1-weighted MR image demonstrates a high signal intensity, round lesion (*arrow*), with well-defined margins, located just at and deep to the mucosa of the nasopharynx. This was a retention cyst, and the increased signal was due to the high protein content of the cyst fluid.

Copyright © 2003, Mosby, Inc. All rights reserved.

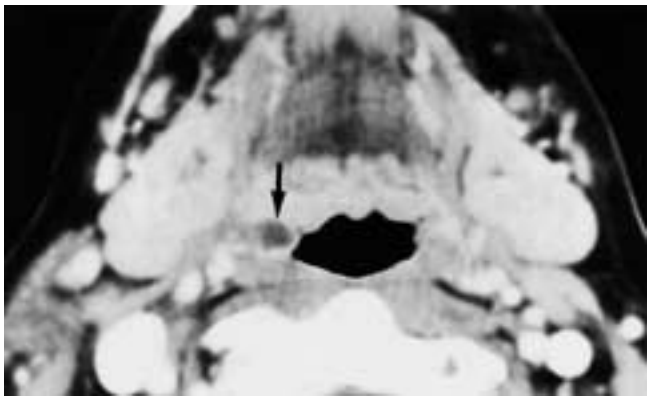

FIGURE 28-15 Axial CT scan shows a well-delineated low-attenuation lesion in the right palatine tonsil (*arrow*). The patient had no symptoms referable to this lesion, which has an incidental tonsillar retention cyst.

VIEW IMAGE

tumors may develop, with an incidence of 10% to 35%. The second tumor is considered a synchronous lesion if it is discovered either at the same time or within 6 months of the diagnosis of the primary tumor. The second tumor is considered metachronous if it is diagnosed more than 6 months after the primary tumor. If, at the same time, two apparent tumors are identified in the upper aerodigestive tract, there must be normal mucosa separating them in order for them to qualify as synchronous cancers. Otherwise, they are considered one tumor. In general, most second tumors are metachronous. Second cancers are most often seen when the initial tumor is located in the oral cavity, oropharynx, or hypopharynx.[32] Nasopharyngeal carcinoma does not share the same associations.

Compared to patients with a single cancer, there is decreased survival in patients who have a second cancer. The best strategy to improve survival in these patients appears to be early detection of the second cancer. This is best accomplished by constant and regular vigilance, including serial imaging studies.

The most important epidemiologic factors in the development of upper aerodigestive tract cancers are tobacco use and alcohol use. Other risk factors include prior irradiation; work in the hardwood furniture, asbestos, or nickel industries; poor oral hygiene; Epstein-Barr virus infection; and betel nut chewing.[32] As a general statement, p53 overexpression has been reported to be a predictor of shorter survival due to the associated development of tumor recurrence and the appearance of a second primary tumor (see Chapter 45).

Several syndromes and diseases are associated with the development of cancers of the upper aerodigestive tract. These include Bloom's syndrome, Lynch-II syndrome, Fanconi's anemia, xeroderma pigmentosum, ataxia-telangiectasia, Li-Fraumani syndrome, and an immunocompromised state.[32]

Nasopharyngeal Carcinomas

Squamous cell carcinoma (SCCA) accounts for about 70% of the malignancies arising in the nasopharynx in adults.[5,6] Lymphomas account for approximately 20% of the cases. The remaining 10% are caused by a variety of lesions including adenocarcinoma, adenoid cystic carcinoma, rhabdomyosarcoma, melanoma, extramedullary plasmacytoma, fibrosarcoma, and carcinosarcoma.[6] SCCA of the nasopharynx is a relatively rare cancer that accounts for only 0.25% of all malignancies in North America. However, this tumor has a high incidence in Asia, where it is the most common cancer in males and the third most common cancer in females, accounting for 18% of all cancers in China.[33] In the United States, SCCA is more common in males than in females, with the majority of cases being diagnosed during the sixth decade of life.[6] The biologic behavior of nasopharyngeal carcinomas is the same, regardless of ethnic origin. The staging of nasopharyngeal cancer (NPC) is presented in Table 28-1.[15]

Several factors have been linked to an increased likelihood of developing NPC. IGA antibodies against Epstein-Barr virus have been associated with the undifferentiated form of this tumor, while HLA-A2 and HLA-B-Sin histocompatibility loci have been identified as possible markers for genetic susceptibility to SCCA among the Chinese population.[34] The incidence of this tumor decreases among Chinese born in North America, although the rate is still seven times higher than that in native Americans.[35] Other potential risk factors include nitrosamines (present in dry, salted fish), polycyclic hydrocarbons, poor living conditions, and chronic sinonasal infections.[6] Recent studies have also identified associations between genetic alterations involving specific loci on chromosomes 11q, 9q, and 3p.[36–39]

The World Health Organization (WHO) histologic classification for NPC has recently been updated and

Table 28-1
1997 AMERICAN JOINT COMMITTEE ON CANCER STAGING FOR EPITHELIAL TUMORS OF THE NASOPHARYNX

T1	Tumor confined to the nasopharynx
T2	Tumor extends to soft tissues of oropharynx and/or nasal fossa
T2a	Without parapharyngeal extension
T2b	With parapharyngeal extension
T3	Tumor invades bony structures and/or paranasal sinuses
T4	Tumor with intracranial extension and/or involvement of cranial nerves, infratemporal fossa, hypopharynx, or orbit

Copyright © 2003, Mosby, Inc. All rights reserved.

recognizes two major subtypes of NPC: squamous cell carcinoma (1) and nonkeratinizing carcinoma (2).[40] The squamous cell type is similar to other SCCA found in the remainder of the upper aerodigestive tract. The nonkeratinizing subtype is further subdivided into differentiated (2a) and undifferentiated (2b) forms.[40] Because NPC is often heavily infiltrated by lymphocytes, the term *lymphepithelioma* has been used to describe the nonkeratinizing subtypes (2a and 2b). It should be noted that subtypes 2a and 2b correspond with the original WHO types 2 and 3, respectively.[40]

The clinical presentation depends on the size and location of the lesion, with most small lesions being asymptomatic. The most common presenting complaint is level II to V lymphadenopathy. NPC carcinoma is one of the few head and neck primary tumors with no relationship between primary tumor size and the presence of nodal disease. Large tumors may have no nodal metastasis, while small tumors may present with diffuse, bilateral cervical metastases. Serous otitis media, caused by eustachian tube obstruction, may also be a presenting complaint. Other symptoms include headaches, nasal obstruction, epistaxis, sore throat, trismus, and proptosis. Advanced lesions may spread to the adjacent cranial nerves and present with neurologic symptoms. Thus, tumor extension into the cavernous sinus may result in palsies of cranial nerves III to VI, while tumor in the poststyloid parapharyngeal space may involve cranial nerves IX to XII and the sympathetic chain.[5, 6]

The standard treatment of NPC is external beam supervoltage irradiation, with brachytherapy being of some benefit in selected individuals.[5, 6, 41] For more advanced tumors, combined chemotherapy and radiation therapy is now gaining acceptance as the alternative treatment of choice.[42, 43] Surgery plays a very limited role in the treatment of NPC because adequate surgical margins are difficult to obtain. However, if neck disease persists or recurs after radiotherapy, a neck dissection is usually performed to control the disease.[5, 6] The reported 5-year survival rates for patients treated with radiation therapy at M.D. Anderson Hospital vary with the histologic type and are as follows: SCCA (42%), lymphoepithelioma (65%), and unclassified carcinomas (14%).[44] However, the overall prognosis is dependent on other factors including the size of the primary lesion, extent of disease, duration and extent of symptoms, presence of skull base erosion, and nodal involvement at multiple levels.

Table 28-2
IMAGING CHECKLIST FOR NASOPHARYNGEAL CARCINOMA

- Detailed assessment of the spread pattern of tumor, with an emphasis on deep and superior extension
- Skull base erosion
- Involvement of the mandibular division of the fifth cranial nerve
- Cavernous sinus involvement

Imaging Features

CT and MR imaging play essential and complementary roles in the staging and treatment of patients with NPC (Table 28-2) (Fig 28-16). As imaging studies usually are unable to differentiate between SCCA and other malignancies, the primary role of imaging is accurate tumor mapping. The most reliable imaging finding of a malignancy is that of an aggressive, often enhancing mass that infiltrates the deep fascial planes and spaces about the nasopharynx[7] (Figs. 28-17 and 28-18). A noninfiltrating, homogeneously enhancing mass situated on the mucosal surface may either be a low-grade tumor or prominent adenoidal tissue, and clinical correlation should be requested (Fig. 28-13). MR imaging provides excellent visualization of the soft-tissue planes of the nasopharynx and is superior to CT for detecting perineural spread of tumor (Fig. 28-19).[45, 46] Both CT and MR may be used for identifying skull base invasion. CT is superior to MR for identifying early cortical invasion, while MR is superior to CT for detecting marrow involvement [47] (Figs. 28-20 to 28-23).

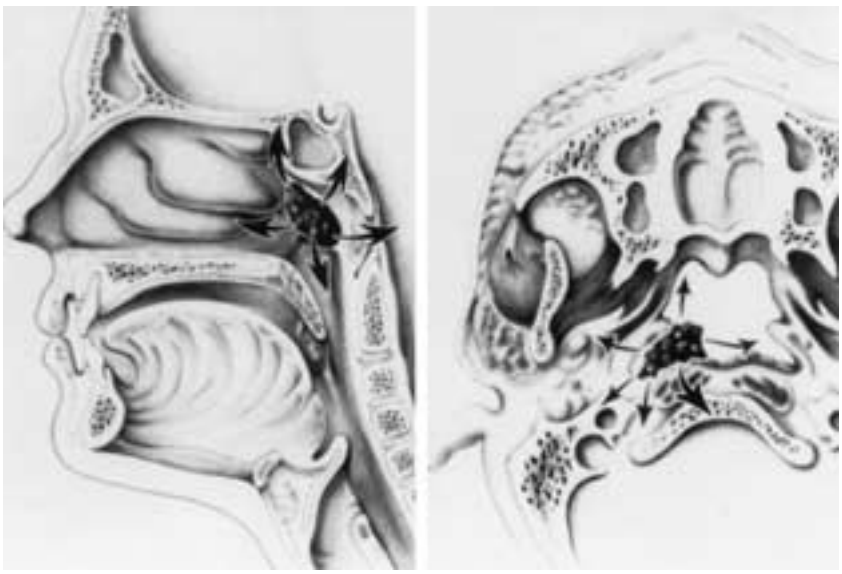

VIEW IMAGE

FIGURE 28-16 Schematic illustrations demonstrate the potential pathways of spread (*arrows*) for nasopharyngeal carcinomas. (From Mukherji SK, Pillsbury H, Castillo M. Imaging squamous cell carcinomas of the upper aerodigestive tract: what the clinicians need to know. Radiology 1997;205:629–646.)

Copyright © 2003, Mosby, Inc. All rights reserved.

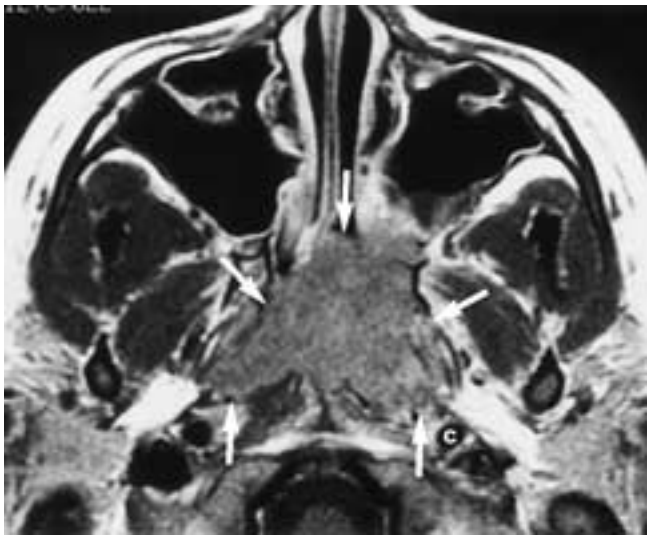

FIGURE 28-17 Axial T1-weighted, contrast-enhanced MR image better demonstrates the full extent of this lymphoepithioma (*arrows*). Note the proximity of the tumor to the left carotid artery (*C*).

VIEW IMAGE

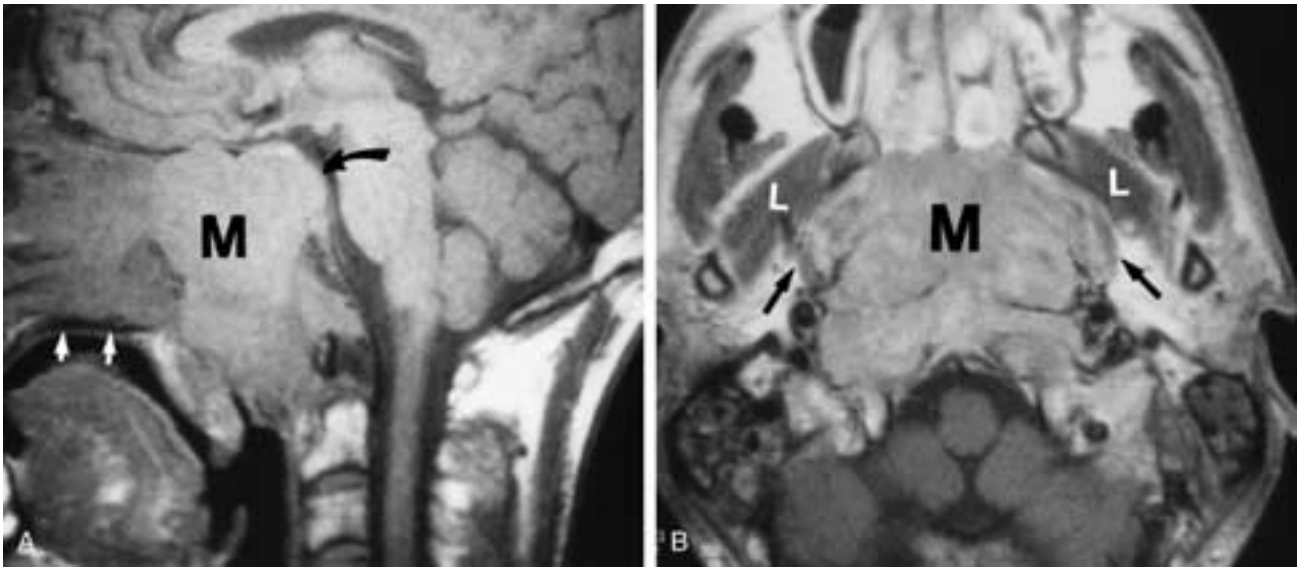

VIEW IMAGE

FIGURE 28-18 Nasopharyngeal carcinoma**. A**, Noncontrast sagittal T1-weighted image shows an aggressive soft-tissue mass (*M*) arising in the nasopharynx that erodes the clivus (*curved arrow*). The mass extends inferiorly below the level of the hard palate (*straight arrows*). **B**, Axial T1-weighted, contrast-enhanced study shows extension of the mass (*M*) into the superior aspect of the parapharyngeal space bilaterally (*arrows*). Note the lateral displacement of the lateral pterygoid muscles (*L*).

Copyright © 2003, Mosby, Inc. All rights reserved.

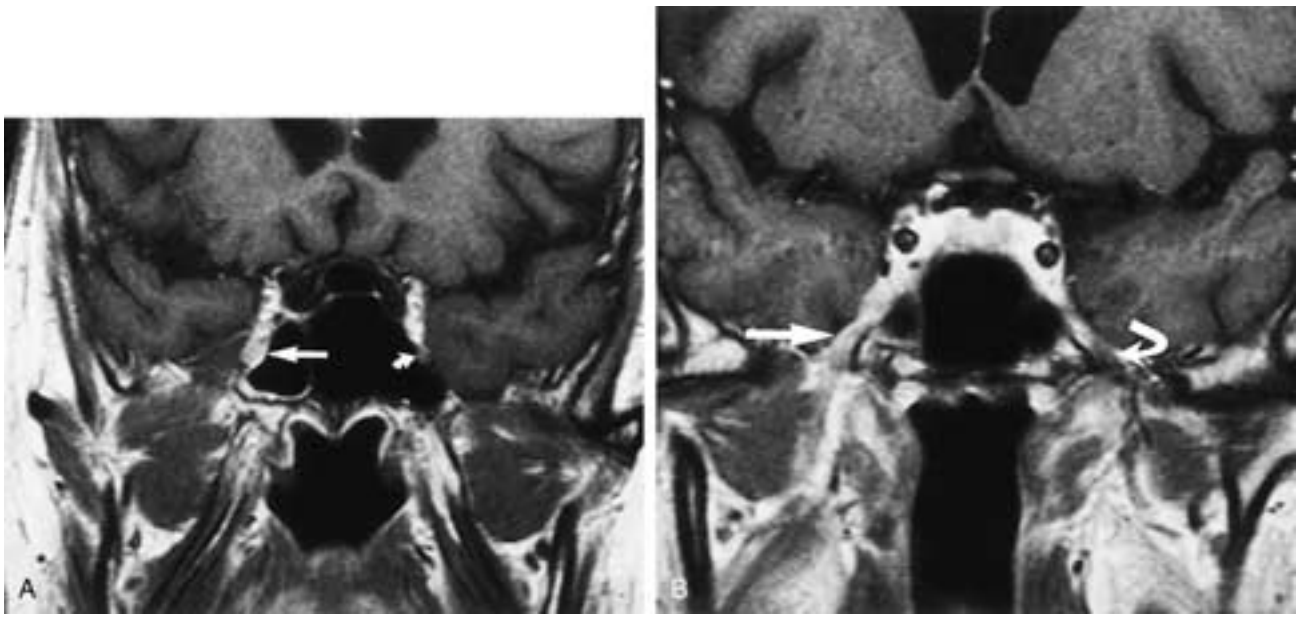

VIEW IMAGE

FIGURE 28-19 **A**, Coronal-enhanced T1-weighted MR image shows enlargement and enhancement of the second division of the trigeminal nerve (*straight arrow*) caused by perineural spread of squamous cell carcinoma. Note the normal appearance of V2 on the opposite side (*curved arrow*). **B**, Postgadolinium coronal T1-weighted MR image shows perineural spread of tumor along the third division of the trigeminal nerve (*straight arrow*). Note the normal appearance of V3 on the opposite side (*curved arrow*).

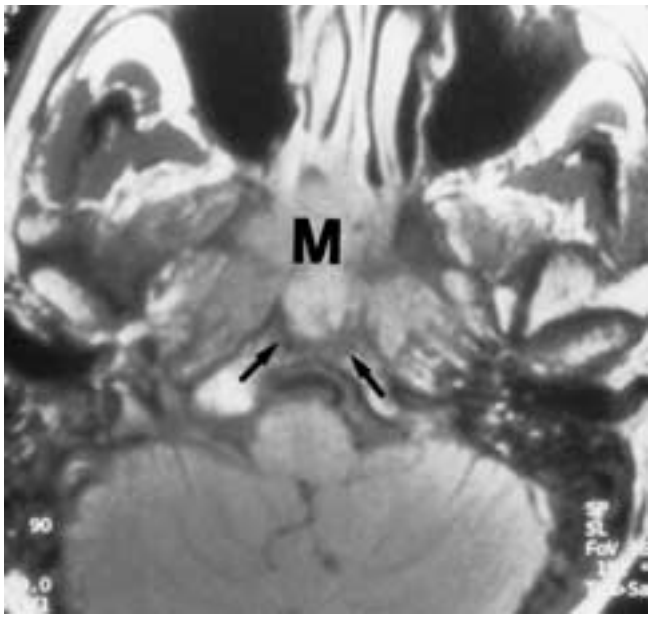

VIEW IMAGE

FIGURE 28-20 Axial noncontrast, T1-weighted image shows a nasopharyngeal carcinoma (*M*) extending into the clivus and replacing the normal increased T1-weighted signal (*arrows*). These findings are indicative of skull base erosion on MR imaging.

Copyright © 2003, Mosby, Inc. All rights reserved.

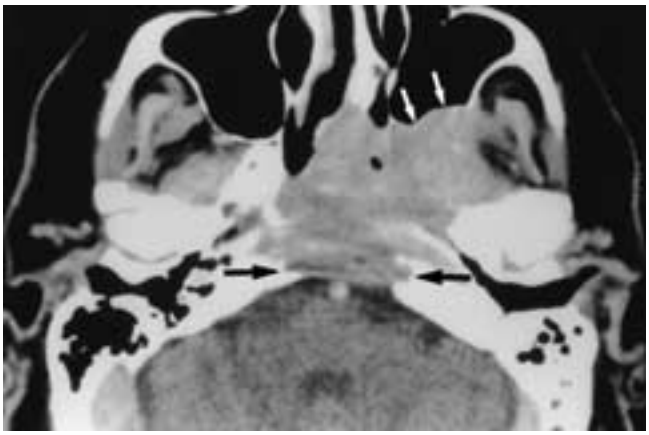

VIEW IMAGE

FIGURE 28-21 Axial contrast-enhanced CT scan shows an extensive nasopharyngeal carcinoma eroding the clivus (*black arrows*). Note the anterolateral extension into the left pterygopalatine fossa (*white arrows*).

NPC tend to grow along the path of least resistance. Potential pathways of tumor extension include growth along muscle bundles, neurovascular bundles, fascial planes, and within the mucosa and submucosa. However, the natural spread of tumor may be altered by certain normal structures that are relatively resistant to tumor invasion. In the nasopharynx, such structures are the cartilaginous portion of the eustachian tube and the pharyngobasilar fascia [7, 11, 48, 49] (Fig. 28-16).

As mentioned, small lesions are often limited by the surrounding pharyngobasilar fascia[45] (Fig. 28-24). However, once this barrier is breached, the tumor may directly invade the skull base; the most common sites of intrusion are the region of the petroclival fissure and the foramen lacerum. Aggressive lesions may extend into the foramen lacerum, encase the internal carotid artery, and gain access to the cavernous sinus (Fig. 28-25). Skull base erosion is also likely to occur at sites of musculature attachments, and the levator and tensor veli palatini muscles provide common pathways for cranial tumor spread.[7, 11, 48, 49]

As previously mentioned, the upper anterior portion of the lateral wall of the nasopharynx (pharyngobasilar fascia) is incomplete due to the sinus of Morgagni, through which passes the cartilaginous portion of the eustachian tube and the levator veli palatini muscle.[5] However, this natural defect also allows passage of tumor into the parapharyngeal region and retrograde perineural spread along V_3 into the cavernous sinus (Fig. 28-26). Such nerve or perineural invasion should be suspected when there is enlargement and abnormal enhancement of the nerve with obliteration of the surrounding fat planes. Tumors may also directly invade the skull base at the foramen ovale, and CT and MR imaging can help determine whether tumor has invaded the sphenoid sinus.[46, 47]

Tumor extension may also involve the pterygopalatine fossa and/or posterior aspect of the nasal cavity; however, invasion of the posterior ethmoids, orbit, and maxillary antrum is unusual (Fig. 28-27). Caudal tumor extension along the lateral pharyngeal walls and the anterior and posterior tonsillar pillars is seen in nearly 33% of patients.[5] This form of spread is often submucosal and may be clinically occult.

Imaging of all of the cervical lymph nodes is essential because 85% to 90% of patients have nodal spread at the time of initial diagnosis, and nearly 50% of patients have bilateral disease.[5, 44, 50, 51] The retropharyngeal nodes are usually the first nodes to be affected; however, level II nodes may be involved without imaging evidence of retropharyngeal nodal disease.[51–53] Level I nodes and occipital nodes typically become affected only after alteration of the primary lymphatic drainage, as found following radiation therapy.[5]

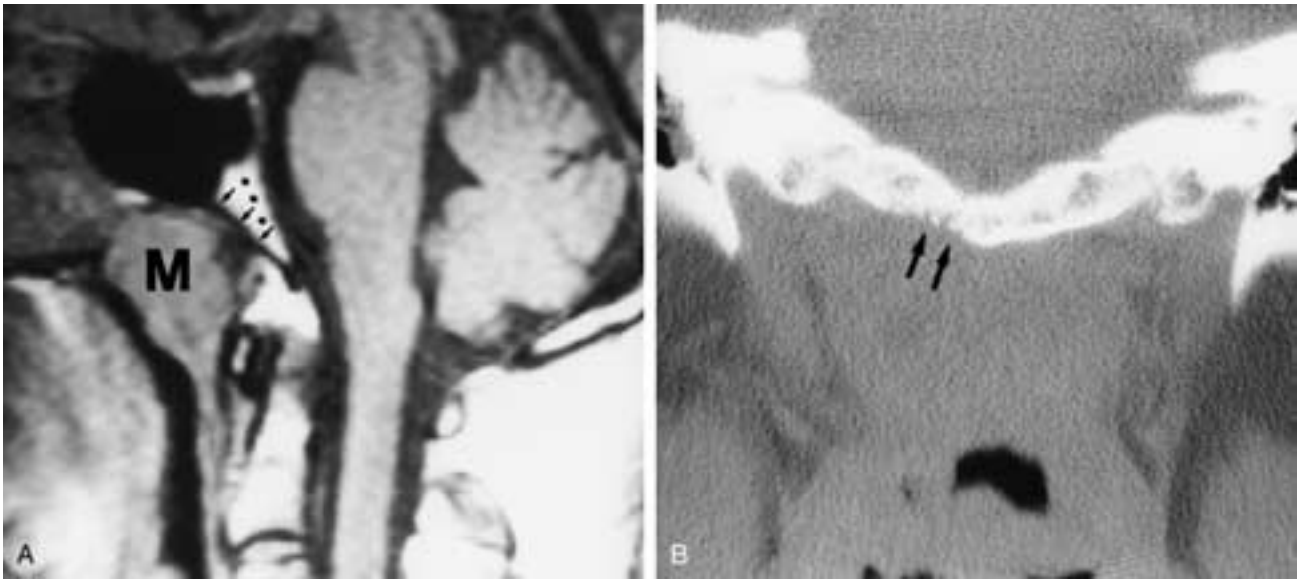

VIEW IMAGE

FIGURE 28-22 Skull base erosion identified on CT but not present on MR imaging. **A**, Sagittal noncontrast, T1-weighted MR image shows a nasopharyngeal carcinoma (*M*) associated with normal signal in the clivus (***) and an apparently intact cortex (*arrows*). **B**, Coronal CT scan of the clivus reconstructed in a bone algorithm obtained in the same patient illustrated in **A** shows cortical irregularity (*arrows*) suspicious for early cortical erosion.

Copyright © 2003, Mosby, Inc. All rights reserved.

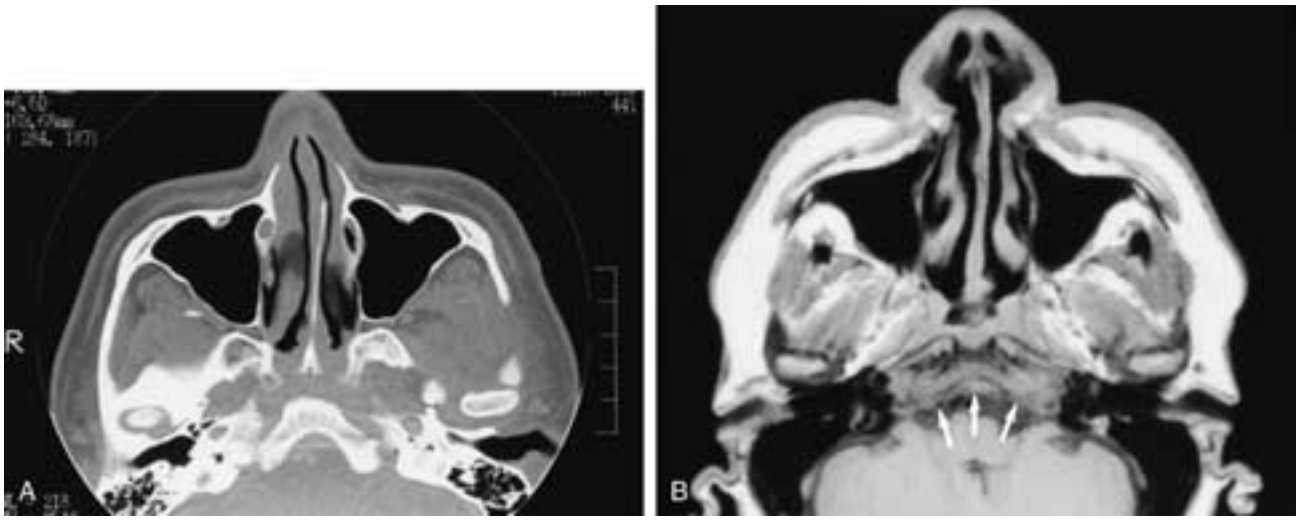

VIEW IMAGE

FIGURE 28-23 Skull base erosion identified on MR imaging but not present on CT. **A**, Axial CT scan of the central skull base reconstructed in a bone algorithm in a patient with nasopharyngeal carcinoma shows no evidence of skull base erosion. **B**, Axial noncontrast, T1-weighted image obtained in the same patient illustrated in **A** shows replacement of the increased T1-weighted signal that is normally present in the clivus. The replacement of the signal may be due to direct tumor invasion or replacement of the marrow by peritumoral inflammation. (Courtesy of Dr. Vincent Chong, Singapore General Hospital.)

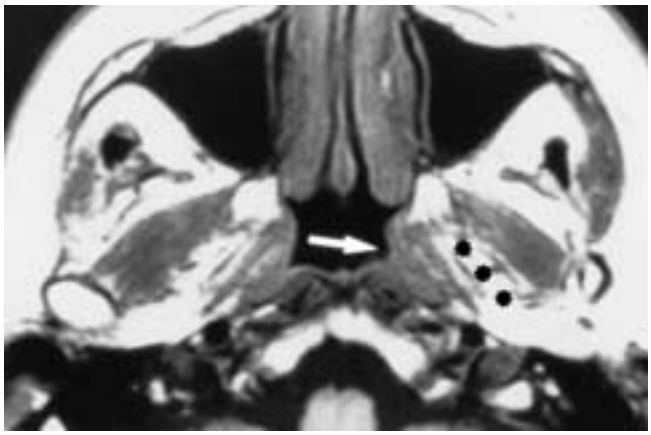

VIEW IMAGE

FIGURE 28-24 T1-weighted nasopharyngeal carcinoma. Axial noncontrast T1-weighted image shows an early tumor in the left fossa of Rosenmüller (*arrow*). Note the normal appearance of the parapharyngeal space (***), thereby staging this tumor as T1. (From Chong VFH, Fan YF, Mukherji SK. Carcinoma of the nasopharynx. Semin Comput Tomogr Ultrasound MRI 1998;19:449–462.)

Copyright © 2003, Mosby, Inc. All rights reserved.

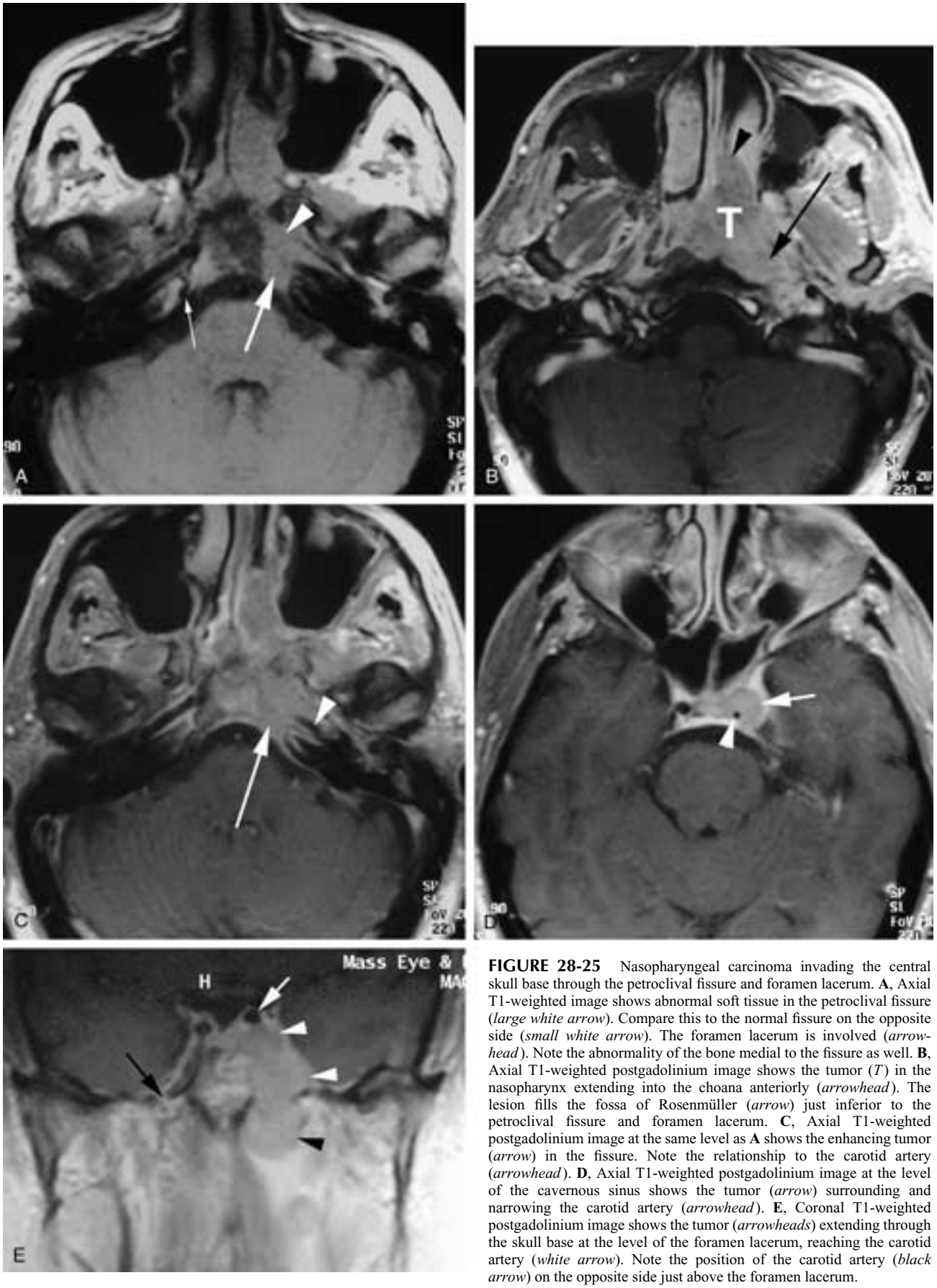

FIGURE 28-25 Nasopharyngeal carcinoma invading the central skull base through the petroclival fissure and foramen lacerum. **A**, Axial T1-weighted image shows abnormal soft tissue in the petroclival fissure (*large white arrow*). Compare this to the normal fissure on the opposite side (*small white arrow*). The foramen lacerum is involved (*arrowhead*). Note the abnormality of the bone medial to the fissure as well. **B**, Axial T1-weighted postgadolinium image shows the tumor (*T*) in the nasopharynx extending into the choana anteriorly (*arrowhead*). The lesion fills the fossa of Rosenmüller (*arrow*) just inferior to the petroclival fissure and foramen lacerum. **C**, Axial T1-weighted postgadolinium image at the same level as **A** shows the enhancing tumor (*arrow*) in the fissure. Note the relationship to the carotid artery (*arrowhead*). **D**, Axial T1-weighted postgadolinium image at the level of the cavernous sinus shows the tumor (*arrow*) surrounding and narrowing the carotid artery (*arrowhead*). **E**, Coronal T1-weighted postgadolinium image shows the tumor (*arrowheads*) extending through the skull base at the level of the foramen lacerum, reaching the carotid artery (*white arrow*). Note the position of the carotid artery (*black arrow*) on the opposite side just above the foramen lacerum.

VIEW IMAGE

Copyright © 2003, Mosby, Inc. All rights reserved.

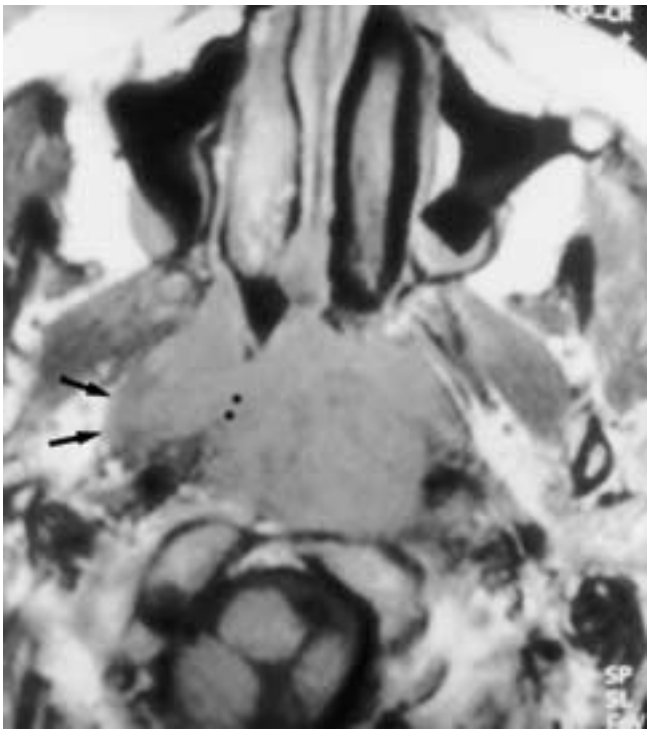

VIEW IMAGE

FIGURE 28-26 Axial noncontrast, T1-weighted image shows lateral extension of a nasopharyngeal cancer into the superior portion of the parapharyngeal space (*arrows*) though the expected location of the sinus of Morgagni (*).

Oropharyngeal Carcinomas

The majority of tumors involving the oropharynx are SCCA, followed by other, less common neoplasms such as lymphoma, minor salivary gland tumors, and other rare mesenchymal lesions. The incidence of SCCA of the oropharynx increases in patients with a history of tobacco or alcohol abuse. The staging system for these tumors is presented in Table 28-3.[15] Because the spread patterns and lymphatic drainage vary with the site of origin, tumors arising in the anterior tonsillar pillar, posterior tonsillar pillar, tonsillar fossa, soft palate, and tongue base will be discussed separately.

Anterior Tonsillar Pillar

The anterior tonsillar pillar (ATP) is a mucosal fold over the palatoglossus muscle, and tumors arising on the ATP tend to spread along this muscle and its fascial attachments. Thus, tumors may extend superiorly to involve both the soft and hard palates. From the palate, the tumor may continue to extend superiorly along the tensor and levator veli palatini muscles and the pterygoid muscles to the skull base[54, 55] (Fig. 28-28). Such an advanced tumor spread pattern may be confused with that of a large NPC that has spread inferiorly. However, extensive ATP lesions tend to invade and extend into the ipsilateral nasopharynx and masticator space, whereas large NPCs tend to involve the nasopharynx bilaterally.

Anteriorly and medially, ATP lesions may also spread along the superior constrictor muscle to the pterygomandibular raphe and from there to the buccinator muscle. This spread pattern mimics that of a tumor arising in the retromolar trigone region. Tongue base invasion may also be present in large lesions and is most likely a result of inferior tumor growth along the palatoglossus muscle[54–56] (Table 28-4).[22]

Table 28-3
1997 AMERICAN JOINT COMMITTEE ON CANCER STAGING FOR EPITHELIAL TUMORS OF THE OROPHARYNX

TIS	Carcinoma in situ
T1	Tumor 2 cm or less in greatest dimension
T2	Tumor more than 2 cm but not more than 4 cm in greatest dimension
T3	Tumor more than 4 cm in greatest dimension
T4	Tumor invades adjacent structures (e.g., pterygoid muscle(s), mandible, hard palate, deep muscle of tongue, larynx)

The lymphatic drainage of ATP tumors is primarily to level I, II, and III nodes. However, because the lymphatic drainage is determined by the site of the tumor, a lesion spreading to the soft palate and above will acquire the drainage pattern of this area. The overall likelihood of positive nodes with ATP carcinomas at presentation is 45%, although the incidence is dependent on the stage of the disease as follows: T_1, 11%; T_2, 38%; T_3, 54%; and T_4, 68%.[54, 58] The likelihood of nodal involvement in a clinically negative neck (N0) is 10%; contralateral nodal involvement has been reported to occur in 5% of cases.[54]

Posterior Tonsillar Pillar

The posterior tonsillar pillar (PTP) is a mucosal fold over the palatopharyngeus muscle. Isolated PTP lesions are rare, and when present are usually small. PTP lesions may spread along the course of the palatopharyngeus muscle, and superior extension may involve the soft palate, while inferior growth may involve the posterior aspect of the thyroid cartilage, the middle pharyngeal constrictor, and the pharyngoepiglottic fold[54] (Table 28-4).[22]

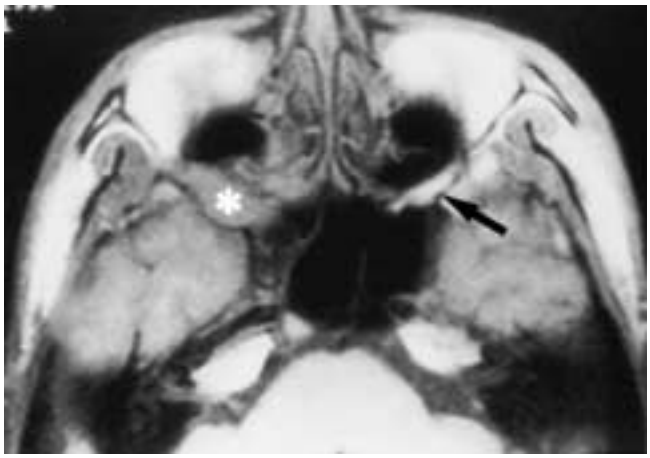

FIGURE 28-27 Axial noncontrast T1-weighted MR image shows enlargement of the right pterygopalatine fossa (*). Compare this to the normal fat-filled pterygopalatine fossa on the contralateral uninvolved side (*arrow*). (From Chong VFH, Fan YF, Mukherji SK. Carcinoma of the nasopharynx. Semin Comput Tomogr Ultrasound MRI 1998;19:449–462.)

VIEW IMAGE

Copyright © 2003, Mosby, Inc. All rights reserved.

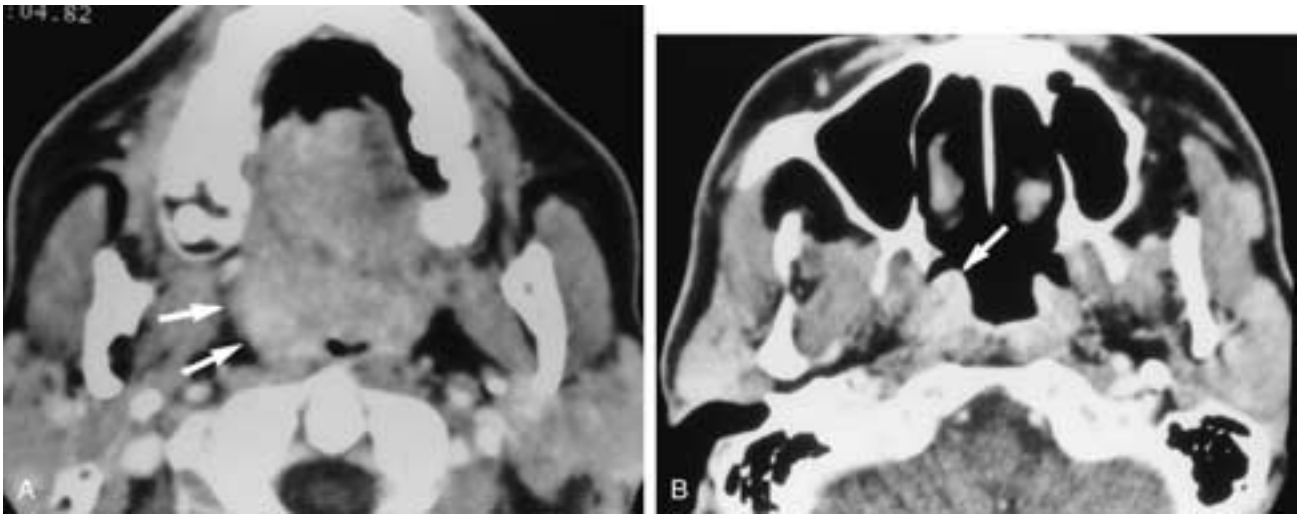

VIEW IMAGE

FIGURE 28-28 Superior extension into the nasopharynx from tonsil carcinoma. **A**, Axial contrast-enhanced CT scan through the oropharynx demonstrates a right tonsil carcinoma (*arrows*). **B**, Axial scan obtained through the nasopharynx in the same patient illustrated in **A** shows asymmetric enlargement of the right torus tubarius (*arrow*). These findings are indicative of superior extension of the tumor. Based on these findings, the patient was treated nonsurgically.

Although the primary lymphatic drainage is to the level II nodes, if these tumors spread posteriorly, they can involve the posterior pharyngeal wall and place the retropharyngeal and level V nodes at risk.[54]

Tonsillar Fossa

Malignancies of the tonsillar fossa are believed to arise from the mucosa lining the niche between the ATP and PTP or from remnants of the palatine tonsil.[54] Tumors in this location often are clinically occult and present with cervical nodal metastases without an obvious primary tumor. Given their location, these lesions may spread anteriorly or posteriorly to involve the adjacent tonsillar pillars, thereby acquiring the potential spread patterns associated with these sites (Fig. 28-29). These lesions may also extend deeply and invade the superior constrictor muscle, thus gaining access to the parapharyngeal space and skull base[22,54–56] (Table 28-4)[22] (Fig. 28-30).

The primary lymphatic drainage for the tonsillar fossa is to level I to IV nodes and occasionally to level V and the parotid nodes. Tumors arising within the tonsillar fossa have an overall 76% chance of having clinically positive nodal metastases. Specifically, the likelihood of having clinically positive nodes for tonsillar fossa tumors is as follows: T_1, 71%; T_2, 68%; T_3, 70%; and T_4, 89%.[57] The incidence of involved contralateral nodes is 11% and increases if the lesion invades the tongue base or spreads across the midline of the soft palate.[24, 25]

Table 28-4
IMAGING CHECKLIST FOR OROPHARYNGEAL CARCINOMA

Tonsil, Soft Palate, or Posterior Pharyngeal Wall Carcinoma
• Detailed evaluation of submucosal extension into the soft tissues of the neck (pre- and poststyloid parapharyngeal space, nasopharynx)
• Tongue base invasion
• Encasement of carotid artery
• Bone erosion
• Prevertebral muscle invasion
Tongue Base Carcinoma
• Extension to floor of mouth and surrounding structures
• Relationship to ipsilateral lingual neurovascular bundle
• Extension across midline and relationship to contralateral neurovascular bundle

Soft Palate

The majority of soft palate malignancies are SCCA; however, minor salivary gland cancers also have their highest frequency in the posterior hard palate and soft palate. Carcinomas of the palate usually affect the oral aspect, tend to be well differentiated, and have the best prognosis of all of the oropharyngeal carcinomas. The nasopharyngeal side of the soft palate is rarely involved, even when the tumors are extensive. Although tumor extension of palatal cancer can occur in any direction, the tonsillar pillars and hard palate are usually affected first. Deep lateral invasion occurs along the levator or tensor veli palatini muscles and into the parapharyngeal space, nasopharynx, and base of the skull[22] (Fig. 28-31).

At the time of diagnosis, lymphatic spread is present in 60% of patients. The incidence of cervical node metastases depends on the size of the primary lesion, with T_1 carcinomas having an 8% incidence and T_4 tumors having a 70% incidence. Palatal carcinomas drain to level II nodes first, and then to the level III and retropharyngeal nodes. Tumor extension up the greater and lesser palatine nerves can also occur, allowing spread into the pterygopalatine fossa and then via the foramen rotundum to the cavernous sinus.

The treatment of palatal lesions depends on the stage of the disease. Advanced lesions such as T_2 and T_3 carcinomas are usually treated with both surgery and radiation to the primary tumor and cervical lymph nodes. However, because surgery requires wide excision, there may be a significant

Copyright © 2003, Mosby, Inc. All rights reserved.

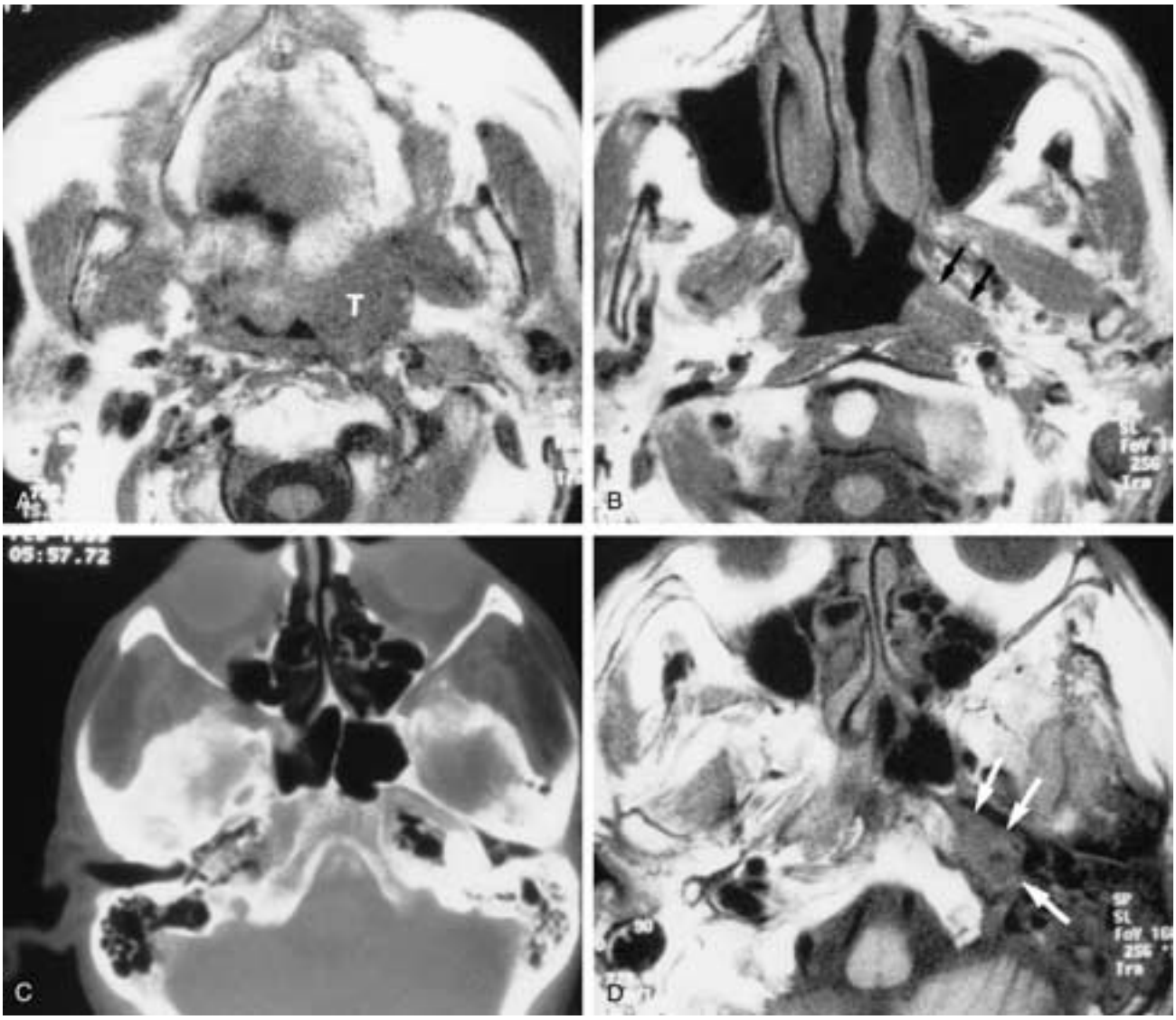

VIEW IMAGE

FIGURE 28-29 **A**, Noncontrast T1-weighted image demonstrates a left tonsillar carcinoma (*T*). Based on the clinical examination, the tumor was believed to be resectable. **B**, Axial noncontrast MR image through the nasopharynx performed in the same patient illustrated in **A** shows a mass deep to the left torus tubarius that was suspicious for superior extension into the nasopharynx (*arrows*). **C**, Axial CT scan through the skull base (same patient illustrated in **B**) reconstructed in bone algorithm shows no evidence of skull base invasion. **D**, However, axial noncontrast T1-weighted image through the skull base (same patient illustrated in **C**) shows replacement of the normal signal in the petrous bone by intermediate signal (*arrows*). These findings were suspicious for skull base invasion. Based on these findings, the patient was believed to be inoperable and died 3 weeks after these studies.

postoperative defect causing difficulty with phonation and swallowing (nasal regurgitation).[58]

The CT findings of soft palate carcinomas vary with the size of the lesion. Small oral surface lesions are best seen on direct clinical examination. Larger lesions may cause unilateral fullness in the region of the soft palate and tonsil, and there may be invasion of the parapharyngeal space.[59] Direct coronal imaging must be used to evaluate the soft and hard palates because these structures lie in the axial plane and thus are often poorly seen (Fig. 28-32). MR imaging is ideally suited to evaluate the palate in both the sagittal and coronal planes[60] (Fig. 28-33). In general, T1-weighted images suffice, as the palate has a high concentration of mucous glands and normally has a high signal intensity. The tumor is usually well seen as an area of lower signal intensity. T2-weighted images and contrast-enhanced images often provide little additional information (Table 28-4).[22]

Base of the Tongue

The tongue base is defined as the area posterior to the circumvallate papilla, and it extends inferiorly to the vallecula[22] (Fig. 28-34). The tongue base contains varying amounts of lingual tonsil; for this reason, it is often difficult to diagnose small tumors with either CT or MR imaging. Superficial lesions detected by direct visualization may not be seen on imaging studies. In addition, the fat planes that are normally seen in areas such as the floor of the mouth and

Copyright © 2003, Mosby, Inc. All rights reserved.

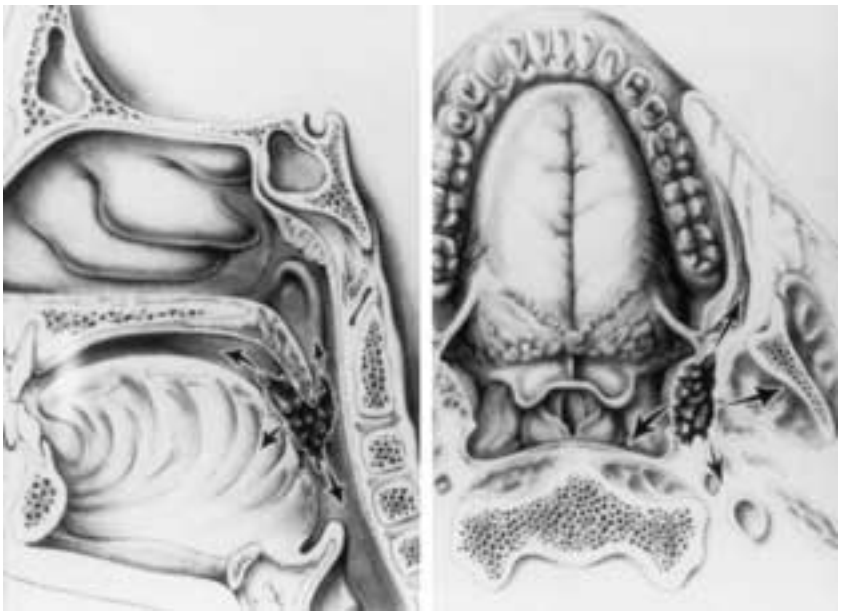

FIGURE 28-30 Schematic illustrations demonstrate the potential spread patterns of a tonsillar carcinoma (*arrows*). (From Mukherji SK, Pillsbury H, Castillo M. Imaging squamous cell carcinomas of the upper aerodigestive tract: what the clinicians need to know. Radiology 1997;205:629-646.)

VIEW IMAGE

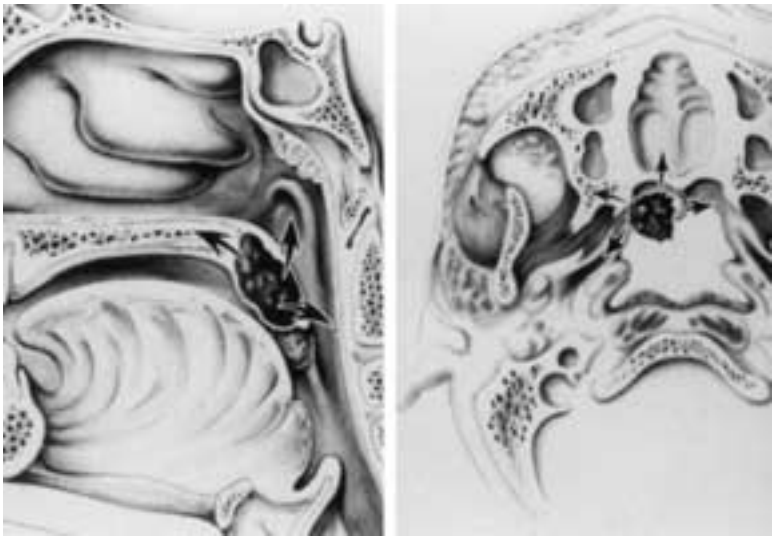

VIEW IMAGE

FIGURE 28-31 Schematic illustrations demonstrate the potential spread patterns of a soft palate carcinoma (*arrows*). (From Mukherji SK, Pillsbury H, Castillo M. Imaging squamous cell carcinomas of the upper aerodigestive tract: what the clinicians need to know. Radiology 1997;205:629-646.)

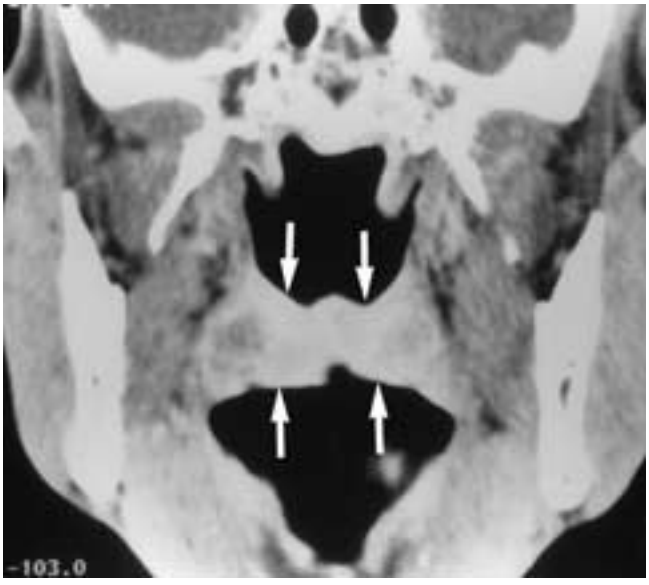

FIGURE 28-32 Coronal CT scan of a soft palate carcinoma demonstrates diffuse enlargement of the soft palate due to an infiltrating carcinoma (*arrows*).

VIEW IMAGE

Copyright © 2003, Mosby, Inc. All rights reserved.

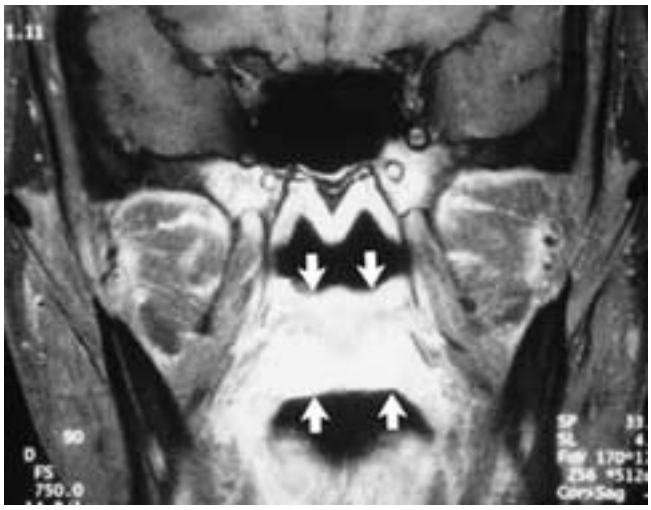

VIEW IMAGE

FIGURE 28-33 Coronal postcontrast T1-weighted image performed following fat saturation shows diffuse enlargement and enhancement of the soft palate (*arrows*) due to an infiltrating carcinoma.

masticator space, and that allow detection of subtle lesions, are not as evident in the base of the tongue. Rather, this area consists mostly of the dense tongue musculature.

Tongue base carcinomas are often clinically silent, and the tongue base is a common location of ''occult'' malignancies originating in the upper aerodigestive tract. Because of this, these lesions often have progressed to an advanced stage at the time of initial presentation[54, 55] (Fig. 28-35).

On MR imaging, noncontrast T1-weighted images are often most helpful to visualize the full extent of these lesions and specifically to help determine whether the tumor has crossed the midline. This is especially important if the patient is a candidate for partial glossectomy.

Malignancies of the tongue base often are limited to one side of the tongue, crossing the midline only when the tumor becomes large. These tumors may also spread to the tonsillar pillar, pharyngeal wall, anteriorly into the sublingual space, and submucosally under the valleculae into the supraglottic larynx[54] (Fig. 28-36). If surgery is the treatment, this latter spread is critical to identify, as it determines if a partial or total laryngectomy is required. The hyoepiglottic ligament can usually be seen on imaging (see Chapter 30), and tumor extension below this structure indicates spread into the preepiglottic space of the larynx. Lesions may also grow inferiorly and laterally to spread into the deep soft tissues of the neck, eventually involving the styloid musculature and the internal carotid artery[54, 55] (Table 28-4).[22]

The tongue base has a rich lymphatic network with a significant amount of cross-drainage, explaining why nearly 30% of patients have bilateral cervical metastases at initial presentation.[24, 57] The primary lymphatic drainage is to level II to IV nodes, with occasional involvement of level V nodes. Tumor spread to the floor of the mouth may also involve level I nodes. Overall, 75% of patients have positive nodes on clinical examination. When nodes are analyzed by tumor stage, the incidence of clinically positive nodes is as follows: T_1, 70%; T_2, 70%; T_3, 75%; and T_4, 84%.[57] Presumably because of the rich lingual lymphatic network and the often advanced stage at which these tumors are discovered, there is a high incidence (nearly 60%) of nodal metastases in clinically negative necks.[53, 54, 61] In these cases, the cervical nodes must be carefully scrutinized on CT or MR imaging, as identification of clinically occult nodal disease will alter treatment.

HYPOPHARYNGEAL CANCERS

Over 95% of all hypopharyngeal tumors are SCCA[14] (Table 28-5). Risk factors include alcohol abuse, smoking, and previous radiation therapy.[14] Hypopharyngeal tumors can remain asymptomatic for a long time.[14] Occasionally, patients with hypopharyngeal carcinomas may present with referred pain. This referred pain travels up from the pyriform sinus along the internal laryngeal nerve of the vagus nerve and then along the auricular nerve (Arnold's nerve) of the vagus to the external auditory canal and pinna.[19] Tumors originating from the hypopharynx, in addition to those

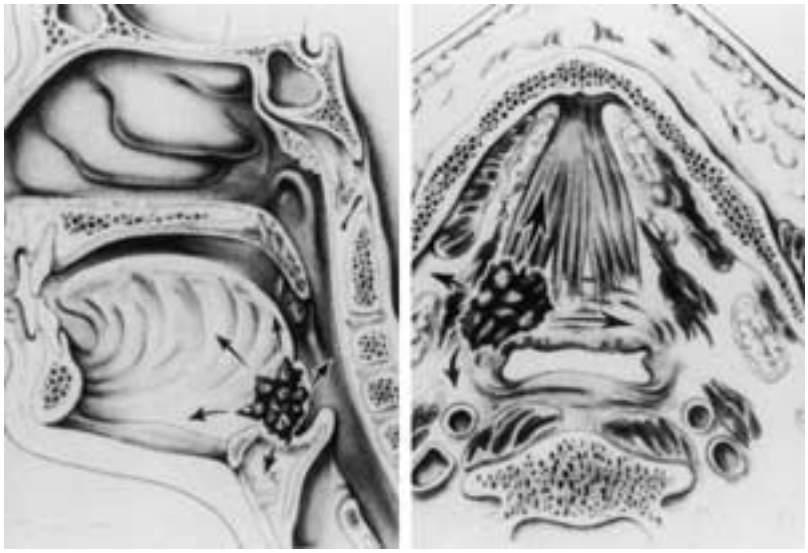

VIEW IMAGE

FIGURE 28-34 Schematic illustrations demonstrate the potential spread patterns of a tongue base carcinoma (*arrows*). (From Mukherji SK, Pillsbury H, Castillo M. Imaging squamous cell carcinomas of the upper aerodigestive tract: what the clinicians need to know. Radiology 1997;205:629-646.)

Copyright © 2003, Mosby, Inc. All rights reserved.

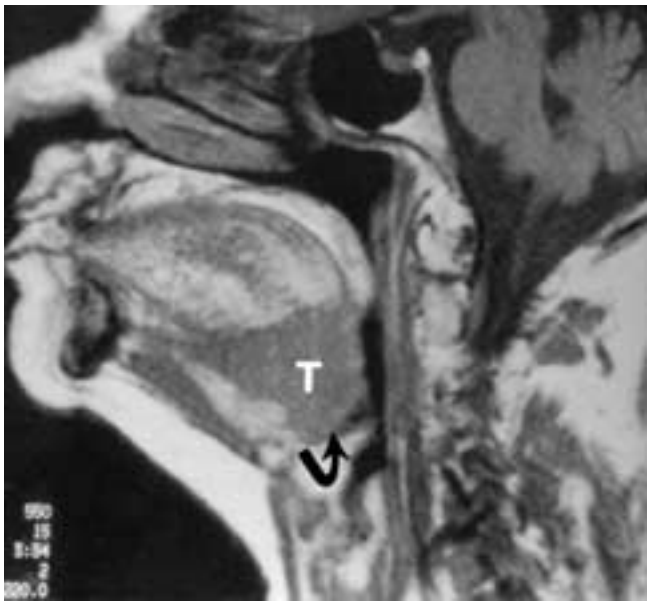

FIGURE 28-35 Sagittal T1-weighted (550/15/2) sequence demonstrates a squamous cell carcinoma involving the tongue base (*T*). The lesion extends inferiorly to the root of the tongue and involves the vallecula (*curved arrow*). The surgical management of a tumor with this pattern of spread would require total glossectomy. This patient was treated with RT and concomitant chemotherapy. (From Mukherji SK, Pillsbury H, Castillo M. Imaging squamous cell carcinomas of the upper aerodigestive tract: what the clinicians need to know. Radiology 1997;205:629-646.)

VIEW IMAGE

arising from the tongue base, tonsil, and nasopharynx, must be included in the differential diagnosis of patients who present with otalgia.[14] Up to 75% of patients with hypopharyngeal tumors have metastases to cervical lymph nodes at the time of initial diagnosis.[14] Up to 15% of patients with SCCA of the hypopharynx have a synchronous (25%) or metachronous (40%) second primary tumor.[14]

Superficial mucosal lesions in the pyriform sinus are best evaluated by direct clinical observation and by barium studies. On CT and MR studies, a collapsed (nondistended) pyriform sinus can mimic a tumor. Conversely, it is not always possible to exclude a tumor when the pyriform sinus is not normally distended.[14] Submucosal spread may not be apparent on direct clinical inspection but usually is well seen on CT and MR imaging. As the apex of the pyriform sinus is located at the level of the true vocal cords, and as the anterior wall of the pyriform sinus is the posterior surface of the paraglottic space, tumor spread into the larynx may occur; this is well seen on imaging[8, 22] (Figs. 28-37 to 28-40) (Table 28-6).

Pyriform sinus carcinomas may spread submucosally into the posterior wall of the hypopharynx, along the anterior wall in the postcricoid region, or along the medial wall (the aryepiglottic fold).[8] Large tumors may extend into the paraglottic and preepiglottic fat and the base of the tongue (Fig. 28-39).[8, 14] Tumors arising from the lateral wall or apex of the pyriform sinus often have already invaded the thyroid cartilage at the time of diagnosis.[8, 14] Lesions involving the aryepiglottic fold may spread into the false vocal cord and arytenoid cartilage.[8, 14] Involvement of the hypopharynx may lead to tumor spread to the contralateral pyriform sinus.

Tumors confined to the postcricoid region are rare [14] (Fig. 28-41). Tumors can invade the posterior larynx (arytenoid and posterior cricoid cartilage), causing vocal cord paralysis

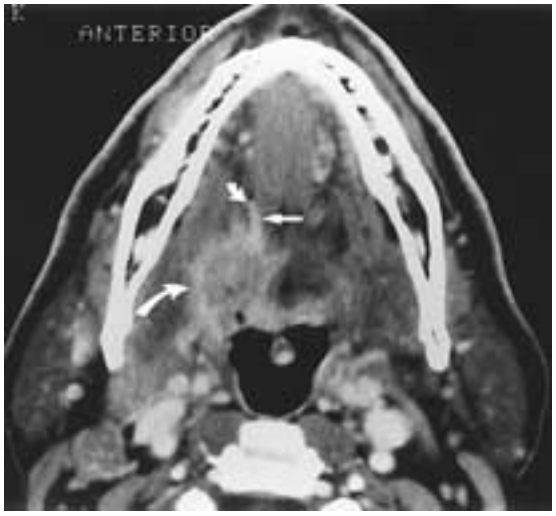

VIEW IMAGE

FIGURE 28-36 Axial contrast-enhanced CT scan shows the characteristic appearance of a tongue base carcinoma (*large curved arrow*). There is extension into the floor of the mouth (*small straight arrow*), with infiltration and obliteration of the fat surrounding the lingual vessels (*small curved arrow*), suggesting perineural or perivascular invasion of tumor. This was confirmed at histologic examination of the resected specimen.

Table 28-5
1997 AMERICAN JOINT COMMITTEE ON CANCER STAGING FOR EPITHELIAL TUMORS OF THE HYPOPHARYNX

TIS	Carcinoma in situ
T1	Tumor limited to one subsite of hypopharynx and 2 cm or less in greatest dimension
T2	Tumor involves more than one subsite of hypopharynx or an adjacent site, or measures more than 2 cm but not more than 4 cm in greatest diameter without fixation of hemilarynx
T3	Tumor measures more than 4 cm in greatest dimension or with fixation of hemilarynx
T4	Tumor invades adjacent structures (e.g., thyroid/cricoid cartilage, carotid artery, soft tissues of neck, prevertebral facial muscles, thyroid, and/or esophagus)

Copyright © 2003, Mosby, Inc. All rights reserved.

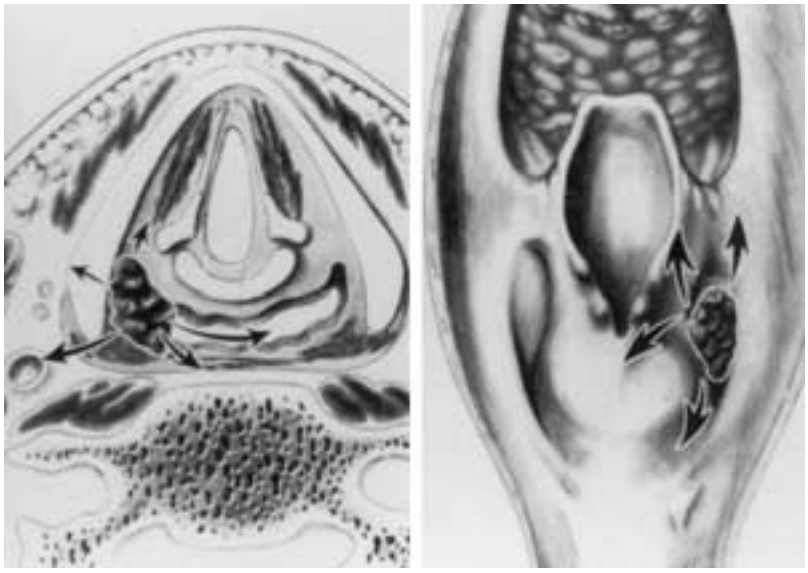

VIEW IMAGE

FIGURE 28-37 Schematic illustrations demonstrate the potential spread patterns of a pyriform sinus carcinoma (*arrows*). (From Mukherji SK, Pillsbury H, Castillo M. Imaging squamous cell carcinomas of the upper aerodigestive tract: what the clinicians need to know. Radiology 1997;205:629-646.)

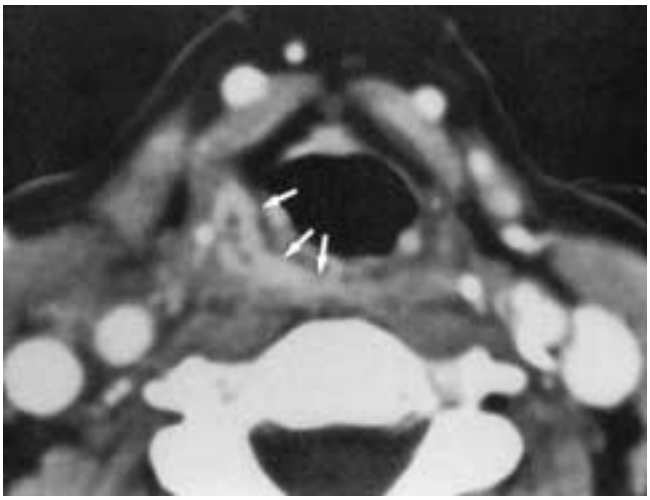

FIGURE 28-38 Contrast-enhanced CT scan performed in a patient with a low volume (<6 cc) pyriform sinus carcinoma arising from the right pyriform sinus (*arrows*). The tumor extends to the midline, thereby precluding treatment with wide local excision or partial pharyngectomy. (From Mukherji SK, Pillsbury H, Castillo M. Imaging squamous cell carcinomas of the upper aerodigestive tract: what the clinicians need to know. Radiology 1997;205:629-646.)

VIEW IMAGE

Copyright © 2003, Mosby, Inc. All rights reserved.

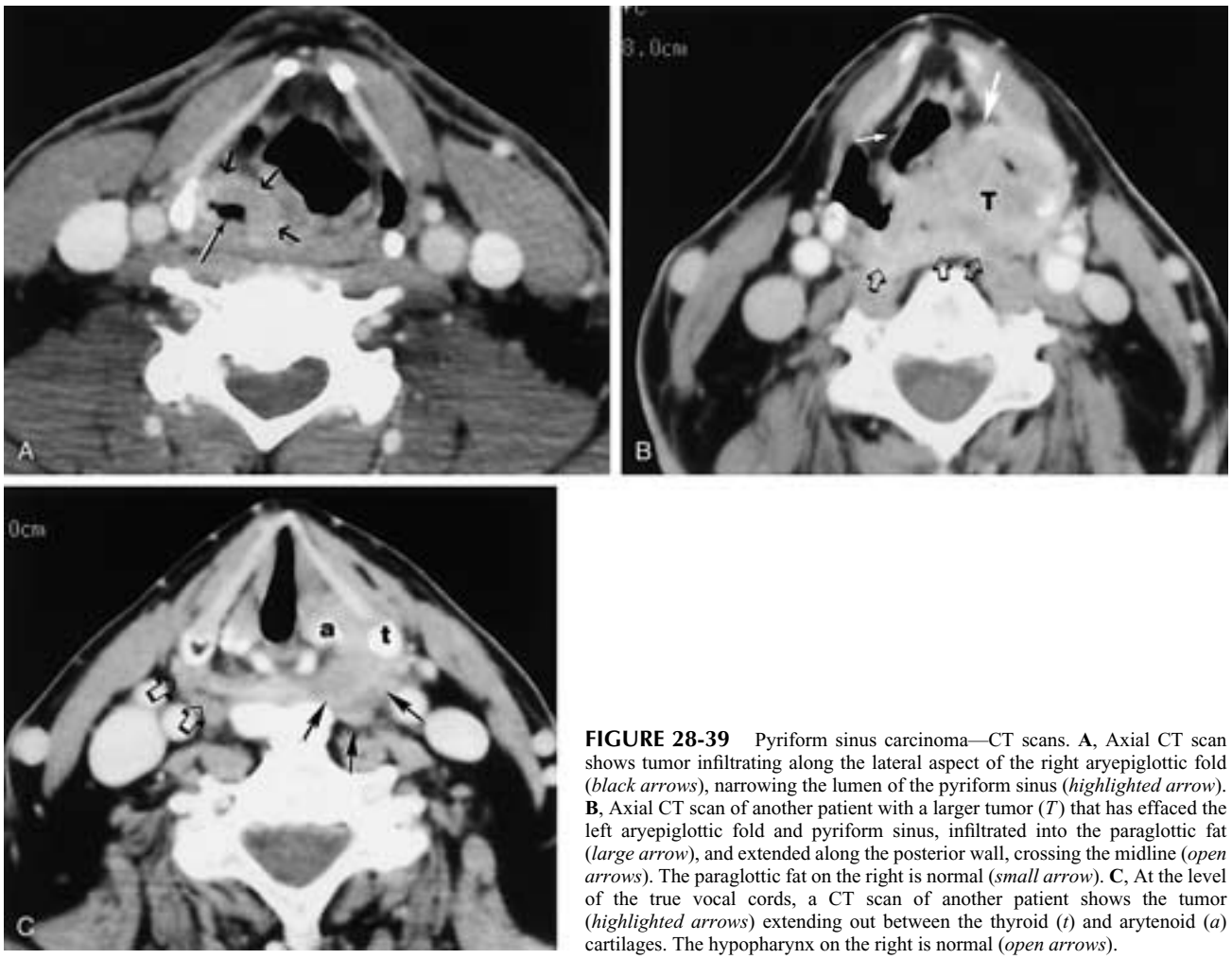

FIGURE 28-39 Pyriform sinus carcinoma—CT scans. **A**, Axial CT scan shows tumor infiltrating along the lateral aspect of the right aryepiglottic fold (*black arrows*), narrowing the lumen of the pyriform sinus (*highlighted arrow*). **B**, Axial CT scan of another patient with a larger tumor (*T*) that has effaced the left aryepiglottic fold and pyriform sinus, infiltrated into the paraglottic fat (*large arrow*), and extended along the posterior wall, crossing the midline (*open arrows*). The paraglottic fat on the right is normal (*small arrow*). **C**, At the level of the true vocal cords, a CT scan of another patient shows the tumor (*highlighted arrows*) extending out between the thyroid (*t*) and arytenoid (*a*) cartilages. The hypopharynx on the right is normal (*open arrows*).

VIEW IMAGE

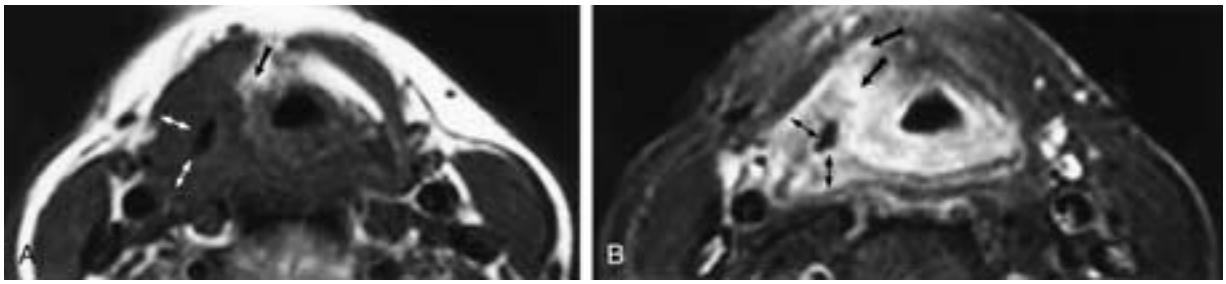

FIGURE 28-40 Pyriform sinus carcinoma—MR images. **A**, Axial T1-weighted image of a carcinoma infiltrating the right pyriform sinus (*double-headed arrows*) and the paraglottic (paralaryngeal) fat (*black arrow*). **B**, Axial T1-weighted image after gadolinium enhancement and fat suppression shows the pyriform sinus tumor (*double-headed arrows*). The anterior extent of the tumor is apparent (*single black arrows*), but the infiltration of the paraglottic fat is not seen well.

VIEW IMAGE

Copyright © 2003, Mosby, Inc. All rights reserved.

Table 28-6
IMAGING CHECKLIST FOR HYPOPHARYNGEAL CARCINOMA

Surgery
• Midline extension
• Apical involvement
• Extension into esophageal inlet
• Cartilage invasion
• Anterior extension into paraglottic space
• Exolaryngeal spread
• Prevertebral muscle invasion
Radiation Therapy
• Tumor size
• Apical involvement
• Cartilage invasion

and hoarseness (Figs. 28-42 and 28-43). Large tumors concentrically infiltrate and narrow the lumen of the hypopharynx and may extend through the cricopharyngeus to the inlet of the cervical esophagus (esophageal verge).[14] Inferior tumor extension to involve the esophageal verge and cervical esophagus may alter the surgical treatment and, if undetected preoperatively, may result in a positive surgical margin.

A well-known risk factor for developing cancer of the postcricoid hypopharynx is the Plummer-Vinson syndrome (also known as the Paterson-Brown syndrome).[8] This syndrome is more common in women than men. Its four components are dysphagia, iron-deficiency anemia, weight loss, and webs in the hypopharynx and cervical esophagus.[14] The associated carcinomas are usually in the postcricoid region, perhaps related to stasis above the webs.

Carcinomas of the posterior wall of the hypopharynx spread cranially and caudally along the posterior wall. These tumors may spread submucosally and be quite bulky at initial presentation.[8,14] Tumor may extend up into the posterior wall of the oropharynx and even infiltrate the posterior aspect of the tonsillar pillars.[8, 14] Invasive posterior wall tumors may extend into the prevertebral muscles and may even invade the vertebrae. Obliteration of the prevertebral fat planes by tumor on CT and MR imaging should raise the suspicion of tumor fixation to the longus coli muscles[8] (Fig. 28-43). Such muscle invasion is best seen on T2-weighted MR imaging, where the normal low signal intensity of the muscle is replaced by the intermediate signal intensity of tumor. However, in nearly half of the cases with such MR findings at surgery, the muscles are not invaded. The altered signal intensity in these cases reflects inflammation of the muscles. Nonetheless, such an MR finding should be considered to reflect muscle invasion until proven otherwise.

LYMPHOMAS

Lymphoma is the most common lymphoproliferative disorder occurring in the extracranial head and neck.[62] Hodgkin's disease (HD) is a malignancy of the hematopoietic system that predominantly affects adolescents and young adults, with males being affected more frequently than females (2:1). The diagnosis of HD is strongly suggested by the presence of Reed-Sternberg cells on nodal biopsy. Extranodal disease in the head and neck is rare. Overall, the most common extranodal site is the spleen, often associated with liver involvement. Bone marrow involvement is believed to result from hematogenous spread, whereas pulmonary involvement is thought to be secondary to direct extension from hilar and mediastinal lymph nodes.[62, 63]

Non-Hodgkin's lymphoma (NHL) is most commonly seen in older patients than those affected by HD. Males are more commonly affected than females, and predisposing conditions include various congenital and acquired immunodeficiency states. The most commonly used classifications of NHL are those of Rappaport and of Lukes and Collins. The Rappaport system is based on the resemblance of the various malignant cells to their benign counterparts, whereas the Lukes and Collins system is based on immunologic markers that separate the tumor cells into B-cell, T-cell, and histiocytic types.

Unfortunately, the majority of patients with NHL have advanced disease at the time of presentation. Whereas 98% of HD patients present with nodal disease, 60% of NHL patients present with disease in extranodal sites, and 60% of all extranodal presentations occur in the head and neck.[64] The extranodal areas predisposed to develop lymphoma are those areas normally rich in lymphoid tissue such as Waldeyer's ring. Other primary sites in the extracranial head and neck include the parotid gland (15% of these patients

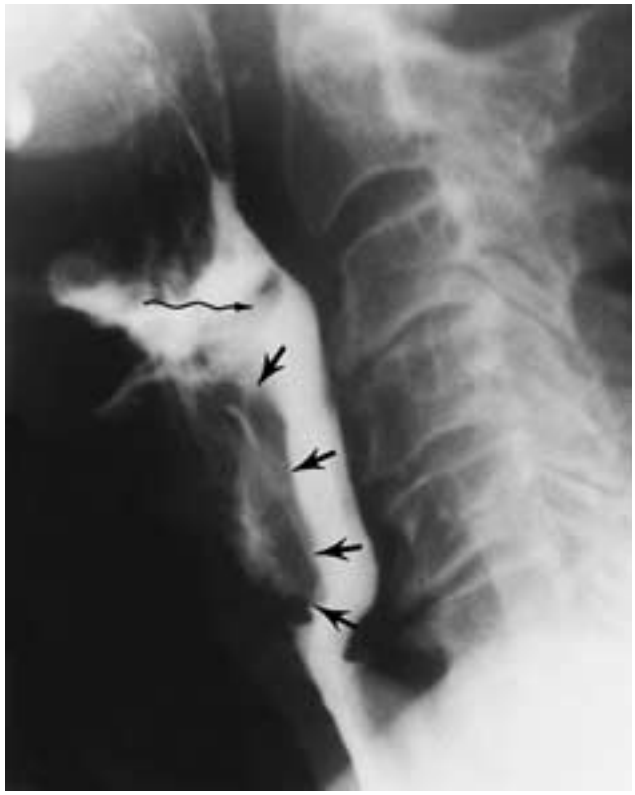

FIGURE 28-41 Postcricoid carcinoma. Lateral view from a barium study shows postcricoid irregularity (*straight arrows*) that is much more pronounced and extensive than normal. At fluoroscopy, the irregularity was fixed and not pliable. Epiglottis (*wavy arrow*).

VIEW IMAGE

Copyright © 2003, Mosby, Inc. All rights reserved.

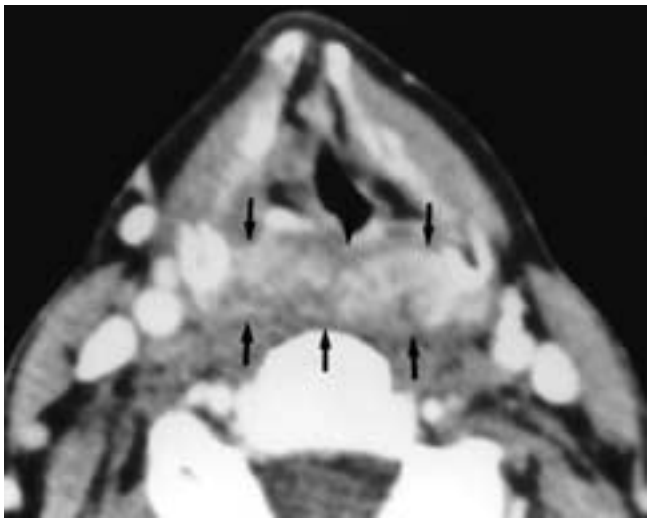

VIEW IMAGE

FIGURE 28-42 Axial contrast-enhanced CT scan shows a squamous cell carcinoma involving the posterior pharyngeal wall (*arrows*).

have a prior history of Sjögren's syndrome), palate, gingiva, lacrimal gland, eyelid, conjunctiva, and paranasal sinuses.[62]

Typically, patients with HD present with a painless mass or complain of systemic symptoms such as night sweats, fever, and weight loss. The clinical symptoms of patients with extranodal NHL often mimic those of patients with SCCA arising at the same site. Thus, patients with NHL arising in the nasopharynx may present with nasal obstruction or unilateral serous otitis media, whereas patients with tonsillar or tongue base NHL complain of unilateral sore throat, dysphagia, or other obstructive symptoms. Nodal involvement is present in 80% of patients with NHL who present with extranodal primary lesions.[62]

The treatment of HD and NHL must be individualized, and depends on the stage of disease and the histologic type. Potential treatment modalities include radiation therapy, chemotherapy, and occasionally surgery for a localized extranodal NHL site.[62]

Imaging Findings

The imaging findings of extranodal head and neck lymphomas are essentially indistinguishable from those of the more common SCCA (Figs. 28-44 and 28-45). The diagnosis may be suggested if the primary lesion is associated with large, homogeneously enhancing lymph nodes that do not have central necrosis. However, this combination of findings may also be seen in poorly differentiated SCCA. As mentioned, the high concentration of lymphoid tissue in the tongue base and palatine tonsil makes these areas likely sites for the development of lymphoma (Figs. 28-44 to 28-46). Lymphoma should be suggested in the differential diagnosis, especially in tumors that occur in the region of Waldeyer's ring. Large lesions may infiltrate the deep spaces and mimic advanced SCCA radiographically. Primary nasopharyngeal lymphoma may invade the skull base and spread along nerves in a manner similar to that of SCCA. In other cases, the diagnosis of a nasopharyngeal lymphoma may be suggested by the imaging appearance of a bulky mucosa-based mass that has not violated the deep fascial planes about the pharynx. Ultimately, the diagnosis of lymphoma and the other lymphoproliferative disorders is based on histologic examination of tissue.

MINOR SALIVARY GLAND TUMORS

The minor salivary glands are distributed within the mucosa of the upper aerodigestive tract. Their greatest concentration is in the oral cavity and oropharynx, where it has been estimated that there are between 500 and 1000 minor salivary glands. They are also found throughout the pharynx, larynx, trachea, and major bronchi. For the most part, the same tumors arise in the minor salivary glands that arise in the major salivary glands.

Minor salivary gland tumors (MSGT) account for 2% to 3% of all malignancies of the extracranial head and neck.[65] These tumors most commonly occur in adults, and there is no reported sex predilection. The most common MSGT include adenoid cystic carcinoma, mucoepidermoid carcinoma, adenocarcinoma, malignant mixed tumor, acinic cell carcinoma, and pleomorphic adenoma (Figs. 28-47 and 28-48). Depending on the series, benign tumors comprise approximately one half of MSGT versus about 70% to 80% of parotid tumors.

The soft palate is the most common site of MSGT, where their incidence is almost equal to that of SCCA. These tumors are usually off midline, in the posterolateral portion of the soft palate, and they are not typically found anterior to a line drawn between the first upper molar teeth.[65] These lesions may spread directly anteriorly to invade the hard

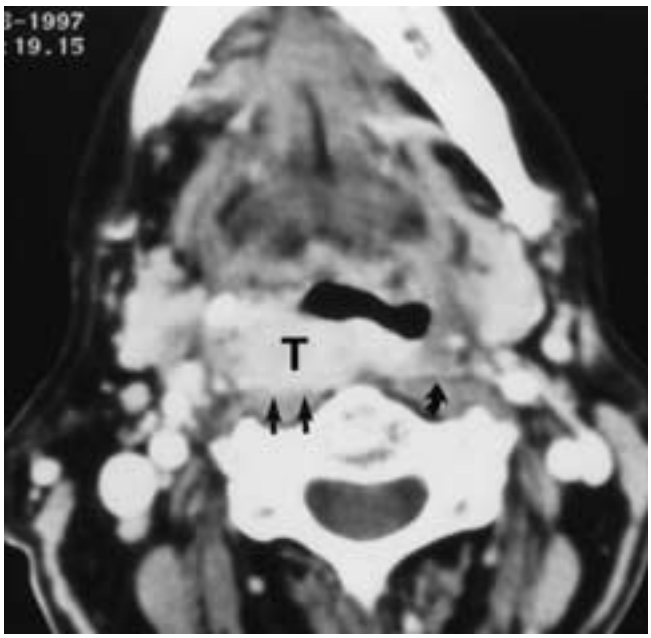

FIGURE 28-43 Axial contrast-enhanced CT scan demonstrates a posterior pharyngeal wall carcinoma situated at the level of the oropharynx (*T*). Note the obliteration of the fat plane between the tumor and the underlying right longus colli muscle (*straight arrows*). Compare this to the normal appearance on the left side (*curved arrow*).

VIEW IMAGE

Copyright © 2003, Mosby, Inc. All rights reserved.

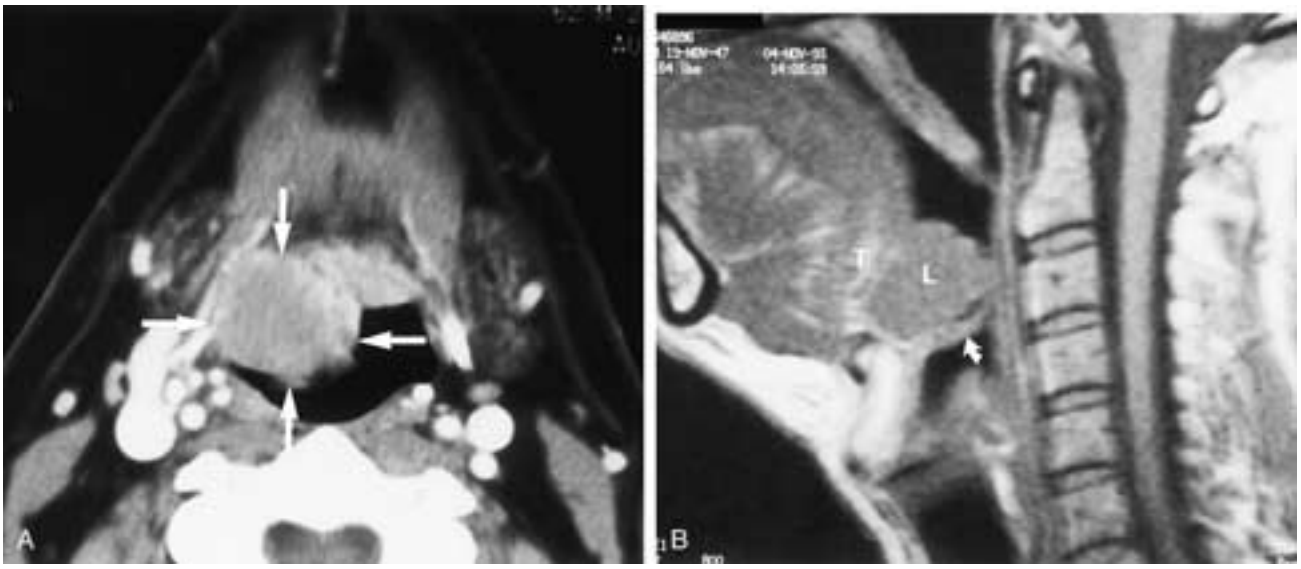

VIEW IMAGE

FIGURE 28-44 **A**, Axial contrast-enhanced CT scan obtained through the base of tongue shows an exophytic soft-tissue mass (*arrows*) bulging into the right valeculla. Histologic examination showed non-Hodgkin's lymphoma. **B**, Sagittal T1-weighted MR image demonstrates a primary lymphoma (*L*) arising within the lingual tonsil. Note how the mass is situated anterior to the epiglottis (*curved arrow*) and posterior to the tongue base (*T*).

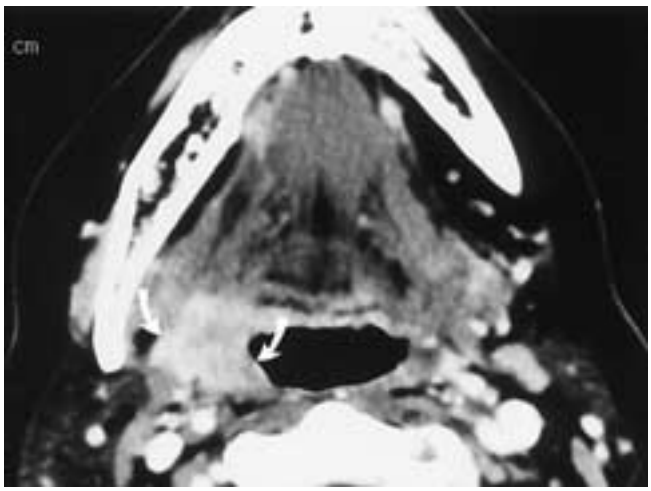

VIEW IMAGE

FIGURE 28-45 Axial contrast-enhanced CT scan shows an enhancing mass centered within the right palatine tonsil (*arrows*). Histologic examination of this lesion was consistent with pseudotumor.

Copyright © 2003, Mosby, Inc. All rights reserved.

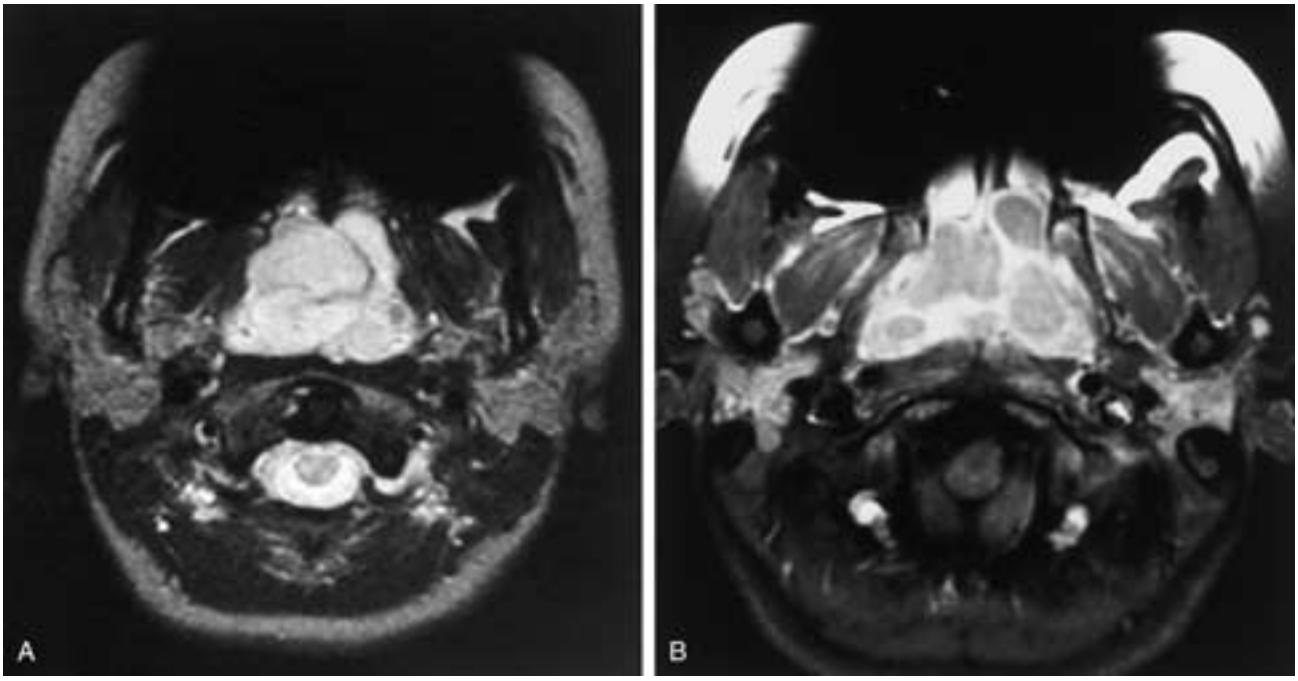

VIEW IMAGE

FIGURE 28-46 Non-Hodgkin's lymphoma involving the nasopharynx in 14-year-old female with nasal stuffiness and bilateral conductive hearing loss. **A**, Axial T2-weighted MR sequence. A bulky mucosal mass of increased signal intensity is seen filling the nasopharyngeal lumen. Note that there is no deep invasion of soft-tissue structures. **B**, T1-weighted MR sequence following gadolinium-DTPA. Peripheral enhancement is noted within the mass. There is a homogeneous appearance to the mass without evidence of necrosis. Diagnosis is non-Hodgkin's lymphoma.

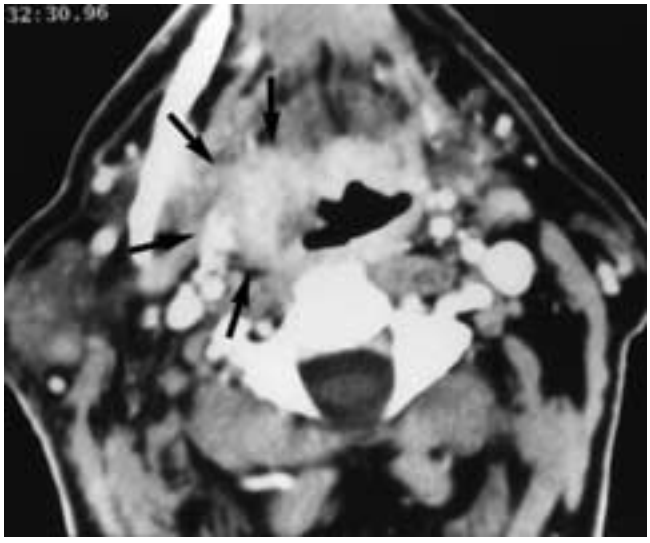

FIGURE 28-47 Axial contrast-enhanced CT scan shows the nonspecific CT appearance of an adenoid cystic carcinoma arising from the tongue base (*arrows*).

VIEW IMAGE

Copyright © 2003, Mosby, Inc. All rights reserved.

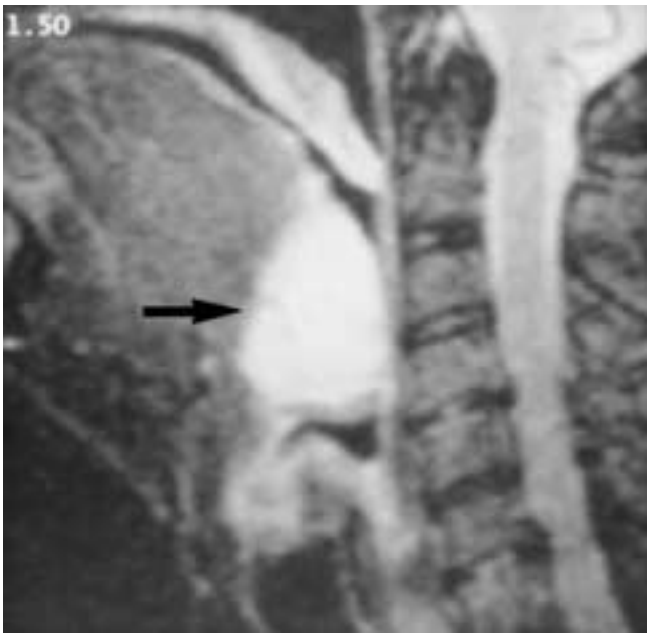

VIEW IMAGE

FIGURE 28-48 Sagittal T2-weighted image demonstrates increased signal in a pleomorphic adenoma arising from the tongue base (*arrow*).

palate (Fig. 28-49). Other extracranial sites include the lips, gingiva, buccal mucosa, tongue base, floor of the mouth, paranasal sinuses, nasal cavity, nasopharynx, hypopharynx, larynx, and trachea (Figs. 28-27 and 28-28).

Imaging Features

The radiographic findings of these tumors are nonspecific, and the diagnosis is based on endoscopy and biopsy. Although CT and MR imaging play complementary roles in evaluating patients with malignant MSGT, the full extent of the tumor and any perineural spread is best evaluated with MR imaging. Bone invasion is best seen on CT, and both axial and coronal contrast-enhanced images (no greater than 3-mm contiguous sections) should be taken through the palate. Intraoral films or DentaScan-type CT images are also recommended for evaluating early bone erosion, especially if the lesion is adjacent to the lingual surface of the maxillary alveolar ridge.

Adenoid cystic carcinoma has a strong predilection to spread along perineural pathways, with such disease being diagnosed histologically in approximately 50% of cases. Continued tumor growth may eventually extend into the skull base and cavernous sinus and, if unrecognized, may be a cause of treatment failure (see Chapter 13). To further complicate matters, perineural spread may occur with skip areas of intervening normal nerve. Some investigators have suggested that this propensity for perineural spread may be due to the production of a substance that promotes adhesion to neural elements (neural cell adhesion molecule [NCAM]).[66] The role of mutations in the genome that normally produces the suppressor protein p53 and their relationship to the recurrence of adenoid cystic carcinoma are also currently being investigated.[67] Perineural spread can be identified with MR imaging; however, the extent of perineural spread is often underestimated.[68] This is especially true of lesions that arise in the soft palate because of their proximity to the pterygopalatine fossa. Obliteration of the fat in this fossa, or erosion or asymmetric enlargement of the greater and lesser palatine foramina, are findings highly suggestive of perineural tumor spread (Fig. 28-29) (see Chapter 13).

In the oropharynx, the risk of nodal involvement is directly related to the size, grade, and location of the primary lesion. The likelihood of cervical metastasis increases in sites that are rich in lymphatic drainage, and the chance of nodal metastasis for nasopharyngeal and oropharyngeal tumors is nearly eight times greater (59% vs. 7%) than that for tumors arising in the paranasal sinuses.[65] Thus, imaging should always include the entire neck if such potential nodal metastases are to be identified.

RHABDOMYOSARCOMAS

Rhabdomyosarcomas are uncommon mesenchymal malignant tumors found throughout the body.[69, 70] About 30% of these tumors involve the head and neck, with the orbit and nasopharynx being the most frequently involved sites, followed by the paranasal sinuses and the middle ear. These tumors occur primarily in young children, but they may occur in adolescents and rarely in adults.[71] The initial symptoms may be abrupt or insidious, depending on the location of the tumor. Nasopharyngeal rhabdomyosarcomas usually present with rhinorrhea, sore throat, and serous otitis media. Invasion of the skull base is common and often produces a cavernous sinus syndrome. Local recurrence and distant metastases are also common. Combined therapeutic regimens with chemotherapy, radiation therapy, and surgery have improved response rates to more than 60% to 70%.[72] The 5-year survival rate after recurrence is less than 5%.

Imaging Features

On CT, nasopharyngeal rhabdomyosarcoma appears as an aggressive infiltrating soft-tissue mass that destroys the skull base and posterior maxillary sinus.[73] The MR imaging features of rhabdomyosarcoma are also similar to those of SCCA (Fig. 28-50); however, rhabdomyosarcomas are primarily submucosal tumors. They show a variable amount of enhancement following contrast administration. In children, malignant tumors that may mimic rhabdomyosarcomas of the nasopharynx include neuroblastoma and rhabdoid tumor (Fig. 28-51).

GRANULAR CELL TUMORS

Granular cell tumors (GCT) are unusual benign neoplasms that can be found throughout the body.[74] They occur most often in the fourth decade of life, and they are more common in females than in males (2:1) and in African Americans than in Caucasians (5:1). Multiple GCT occur in approximately 4% to 10% of patients.

About 50% of GCT occur within the tongue, and approximately 30% arise in the skin. The remaining GCT

Copyright © 2003, Mosby, Inc. All rights reserved.

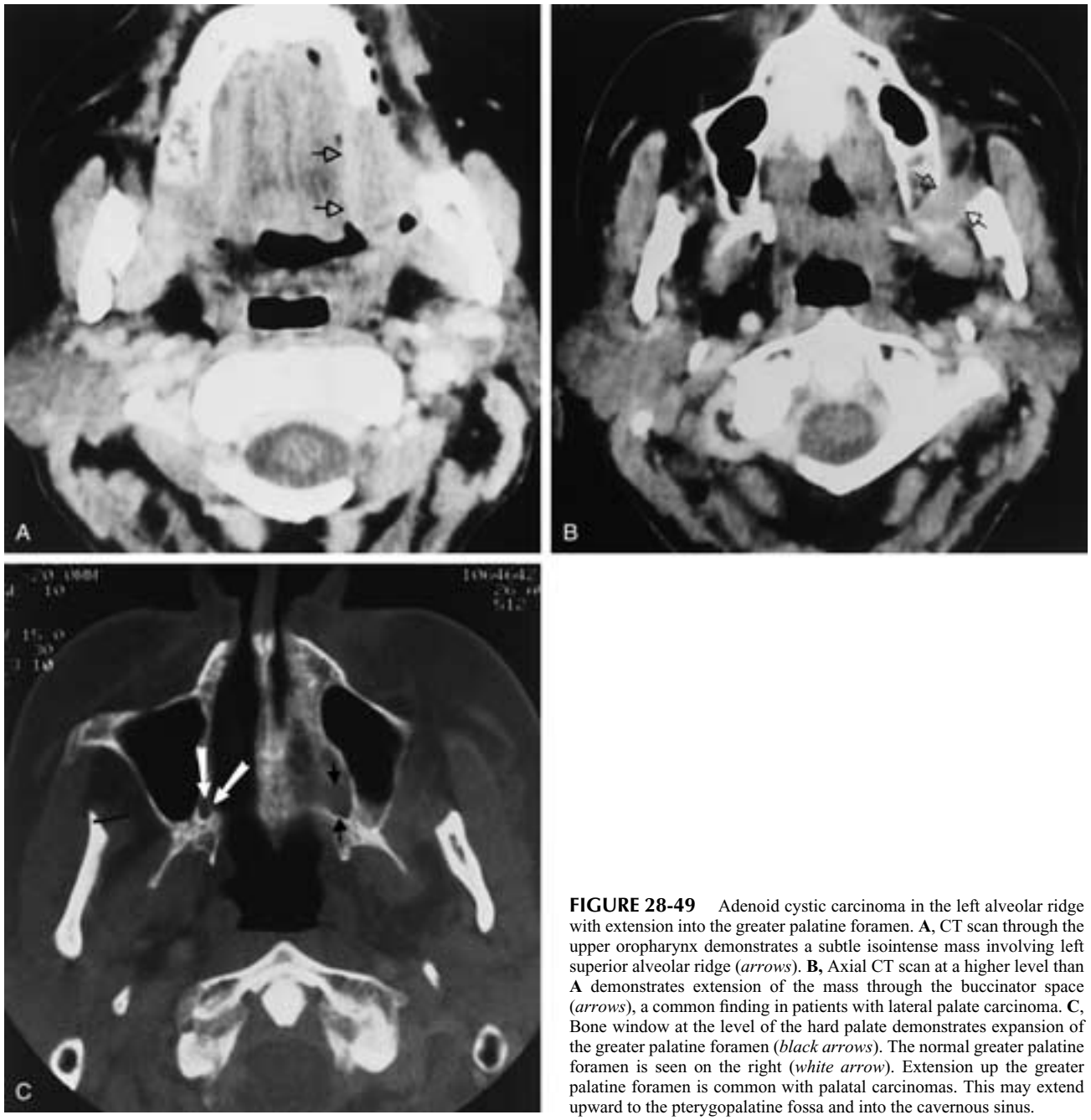

FIGURE 28-49 Adenoid cystic carcinoma in the left alveolar ridge with extension into the greater palatine foramen. **A**, CT scan through the upper oropharynx demonstrates a subtle isointense mass involving left superior alveolar ridge (*arrows*). **B,** Axial CT scan at a higher level than **A** demonstrates extension of the mass through the buccinator space (*arrows*), a common finding in patients with lateral palate carcinoma. **C**, Bone window at the level of the hard palate demonstrates expansion of the greater palatine foramen (*black arrows*). The normal greater palatine foramen is seen on the right (*white arrow*). Extension up the greater palatine foramen is common with palatal carcinomas. This may extend upward to the pterygopalatine fossa and into the cavernous sinus.

VIEW IMAGE

are seen in the breast, muscle, bronchi, temporal bone, and other areas of the upper respiratory and digestive tracts.[74] Most of the GCT found in the upper aerodigestive tract are intraluminal and solitary; however, synchronous lesions do occur and, when present, tend to behave more aggressively.[75] When these lesions occur in the larynx, the most common location is the posterior aspect of the true vocal cords, although GCT have been reported in the subglottic and supraglottic larynx.[75]

GCT of the upper aerodigestive tract occur in two forms. One type occurs in the gingiva of newborns and has been termed *congenital epulis*. The second type occurs later in life, arises predominantly within the submucosa of the upper respiratory and digestive tracts, and is referred to as *granular cell tumor*. Although these lesions are similar histologically, they are considered to be separate diagnostic entities because of their respective locations and the ages of the patients.

The histogenesis of GCT is controversial, and this has led to a variety of terms including Abrikosov's tumor, congenital epulis, nonchromaffin paraganglioma, granular cell myoblastoma, granular cell neurofibroma, myoblastic myoma, uniform myoblastoma, and embryonal rhabdomyoblastoma.[75] GCT is now believed to be of primitive neuroectodermal origin, and the term *granular cell tumor* is thought to be most appropriate.

Copyright © 2003, Mosby, Inc. All rights reserved.

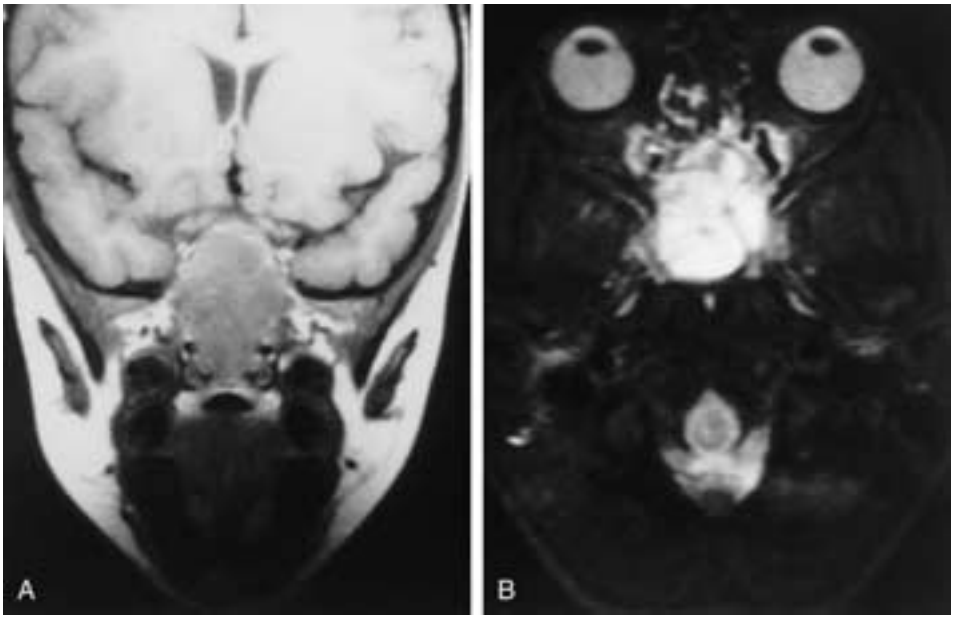

VIEW IMAGE

FIGURE 28-50 Six-year-old female with rhabdomyosarcoma of the nasopharynx invading the skull base and sphenoid sinus. **A**, Coronal T1-weighted MR image demonstrates a mass extending into the sphenoid sinus and posterior ethmoid air cells. The mass extends upward to involve the planum sphenoidale. **B**, Axial T2-weighted MR sequence demonstrates diffuse homogeneous increased signal intensity. Intensity is nonspecific. Rhabdomyosarcoma must be included in the differential diagnosis along with nasopharyngeal lymphoma and squamous carcinoma in a young patient with a nasopharyngeal mass.

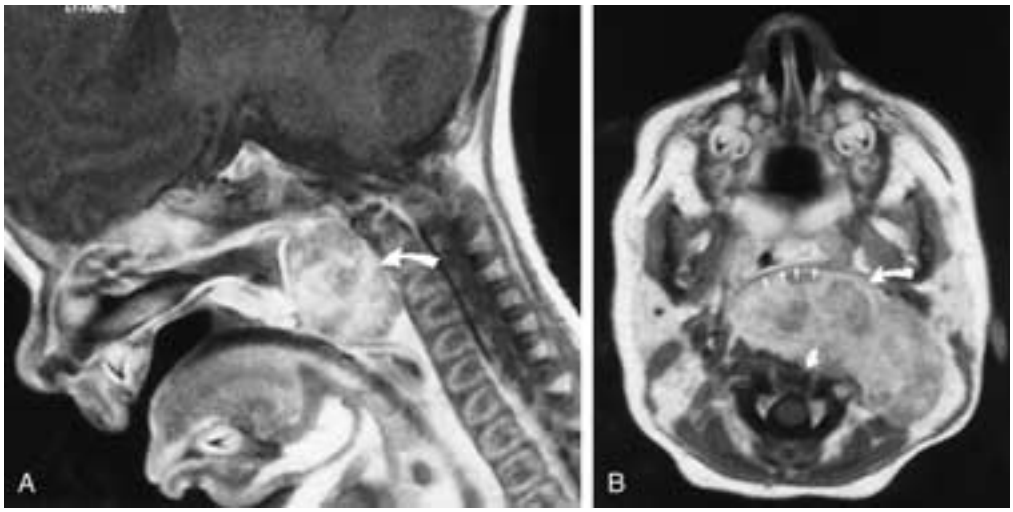

VIEW IMAGE

FIGURE 28-51 **A**, Contrast-enhanced T1-weighted MR image demonstrates a large, heterogeneous mass (*curved arrow*) in the posterior aspect of the nasopharynx. Biopsy showed a rhabdoid tumor. **B**, Axial image shows that the mass (*large curved arrow*) extends into the lateral compartment of the neck. There is erosion of the anterior portion of the vertebral body (*small curved arrow*) and anterior displacement of the posterior pharyngeal wall (*small straight arrows*).

Copyright © 2003, Mosby, Inc. All rights reserved.

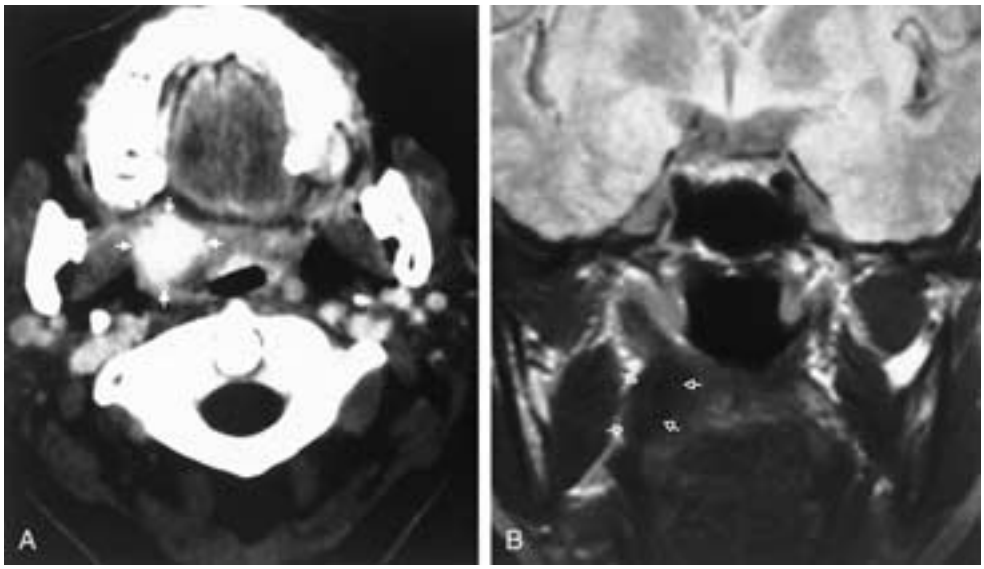

VIEW IMAGE

FIGURE 28-52 Granular cell of the right tonsillar pillar. **A**, Contrast-enhanced axial CT scan demonstrates an enhancing mass that involves the right tonsil (*arrows*). **B**, Coronal proton density MR. The mass has decreased signal intensity (*arrows*). This is typical for carcinoma. Low signal is a reflection of fibrotic elements within granular cell myoblastoma. (**A** and **B** courtesy of Dr. H. Ric Harnsberger, University of Utah.)

Histologically, this tumor has a characteristic appearance. Its cells are polymorphic, ranging from a definite polyhedral shape to a bizarre spindle form, and mitoses are uncommon.[76] The tumor cells are embedded in variable amounts of connective or reticular tissue, and they may extend into the adjacent fibrous stroma. GCT are often circumscribed but not encapsulated.

Imaging Features

The imaging features of a laryngeal lesion are thought to be typical of this lesion, which occurs anywhere in the upper aerodigestive tract. On MR imaging, GCT have a slightly low T1-weighted signal intensity, and they homogeneously enhance. On T2-weighted images they may have either increased or decreased signal intensity. On CT these lesions are solid and relatively homogeneously enhancing (Fig. 28-52). Radiographically, GCT may mimic a primary SCCA.

OTHER TUMORS

Rhabdomyomas

Rhabdomyomas are rare benign skeletal tumors that have a predilection for the head and neck. Whereas cardiac rhabdomyomas affect patients with tuberous sclerosis, extracardiac rhabdomyomas have no relationship to this syndrome. Affected regions include the oropharynx, nasopharynx, larynx, and submandibular triangle. On CT and MR imaging the tumors are well circumscribed, with a density or signal intensity similar to that of muscle. A subgroup of rhabdomyomas occur in newborns and children less than 3 years of age. These so-called fetal rhabdomyomas may actually be hamartomatous malformations rather than true neoplasms (Fig. 28-53).[77]

Fibromatoses

Fibrous lesions of the head and neck vary in their biologic activity and histologic appearance. Even though in some cases their histologic appearance is benign, they may be so locally aggressive that they are considered to be low-grade fibrosarcomas. The term *desmoid* has also been applied to a subgroup of these lesions, which present as well-differentiated but locally infiltrating fibrous masses near the musculoaponeurotic junctions. Of desmoids, 12% involve

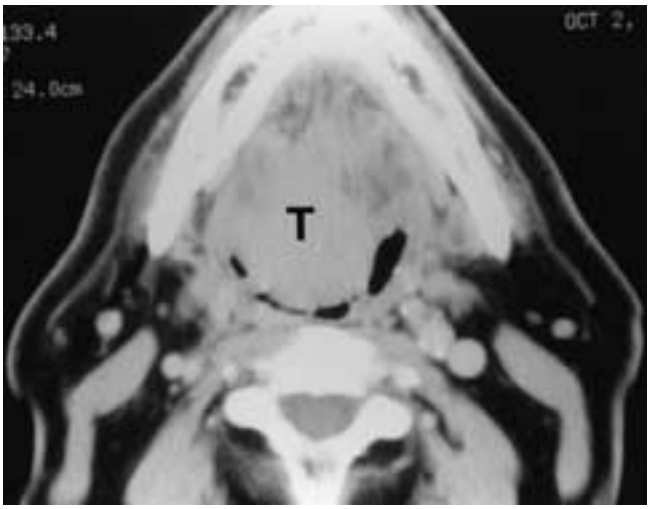

FIGURE 28-53 Axial contrast-enhanced CT scan shows a soft-tissue mass arising from the tongue base (*T*). Biopsy revealed a rhabdomyoma.

VIEW IMAGE

Copyright © 2003, Mosby, Inc. All rights reserved.

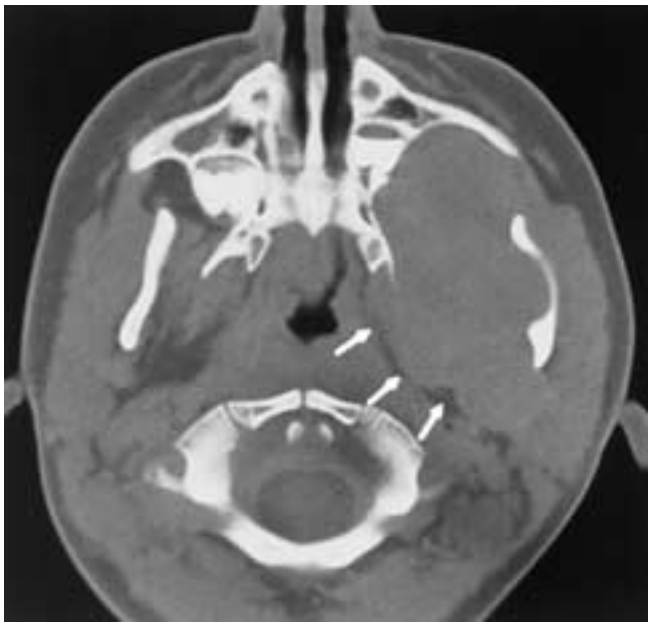

VIEW IMAGE

FIGURE 28-54 Axial CT scan shows a masticator space mass in a 6-year-old patient with aggressive fibromatosis of the masticator space with deviation of the left mandible and left maxillary sinuses. This mass compresses the parapharyngeal space posteriorly and medially (*arrows*). This deviation is typical of masticator space masses.

the region of the head and neck, most commonly the soft tissues of the supraclavicular region and face.[78] Involvement of the oral cavity or nasopharynx is rare in adults, and the CT findings of the fibromatoses are nonspecific. Desmoids involving the head and neck usually encase and infiltrate the musculature of the supraclavicular region. They may infiltrate fat planes, and on CT they cannot be differentiated from malignant lesions (Fig. 28-54).

Schwannomas and Neurofibromas

Of all schwannomas, 25% are located in the head and neck region, and most involve the cranial nerves. The tongue, palate, and floor of the mouth are the most frequent sites in the oral cavity. Most schwannomas are diagnosed in the second and third decades of life as asymptomatic enlarging masses. On CT they are solitary, ovoid, well-encapsulated masses.[79] Small lesions are usually homogeneous, whereas focal cystic areas are often present in larger masses. These tumors enhance, despite the fact that they are relatively hypovascular.[79] On MR imaging, schwannomas have low T1-weighted and high T2-weighted signal intensity, and they enhance with contrast (Figs. 28-55 and 28-56). Neurofibromas of the oral cavity are rare lesions that are usually associated with von Recklinghausen's syndrome.[80] The tongue is the most frequent oral region affected, and unilateral macroglossia is a characteristic finding (Figs. 28-55 and 28-56).

Hemangiomas

In children, hemangiomas are the most common tumor in the cervical region. They may involve the oropharynx or face, usually as a sessile reddish submucosal mass near the base of the tongue. The cavernous type is most common. CT demonstrates a mass of muscle density that may or may not enhance. If present, phleboliths are diagnostic. MR imaging demonstrates an infiltrative mass of low T1-weighted and high T2-weighted signal intensity (Fig. 28-57).[81]

Lipomas

Lipomas often occur in the posterior neck, but they are rare in the pharynx.[82] When these arise in the pharynx, the

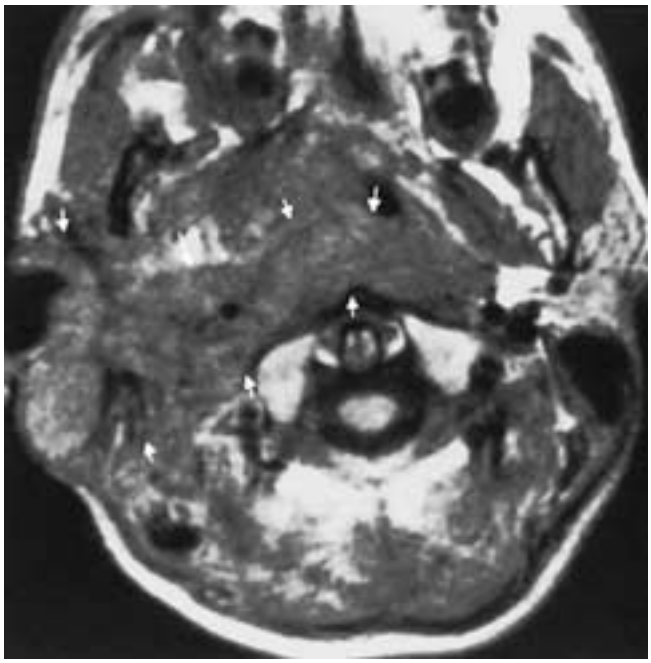

VIEW IMAGE

FIGURE 28-55 A patient with neurofibromatosis involving nasopharynx. Axial T1-weighted MR image through nasopharynx of 16-year-old demonstrates invasive mass that diffusely involves nasopharynx, retropharyngeal space, and carotid space. Mass is homogeneous and infiltrates throughout these spaces, as well as throughout subcutaneous tissue (*arrows*).

Copyright © 2003, Mosby, Inc. All rights reserved.

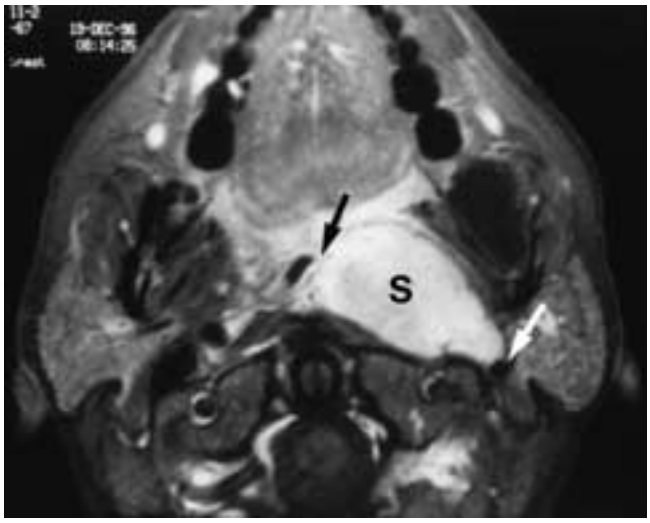

VIEW IMAGE

FIGURE 28-56 Axial postcontrast T1-weighted image performed after fat saturation shows a schwannoma (*S*) arising from the carotid space that extends anteromedially to involve the parapharyngeal space and medially to displace the lateral pharyngeal wall (*black arrow*). Note the posterior displacement of the carotid artery (*white arrow*), which suggests that the mass is arising from the carotid space.

most common location is the aryepiglottic fold.[83] They are smooth, compressible, painless masses, although bulky ones may cause dysphagia or dyspnea and large retropharyngeal lipomas may compress the hypopharynx.[82, 83] Rare hibernomas have also been reported in the retropharyngeal region. On imaging, all of these fatty tumors can be diagnosed by their low CT density and their fatty MR signal characteristics.

UNKNOWN PRIMARY TUMORS

Patients with SCCA of the upper aerodigestive tract frequently present with cervical metastases.[84] The majority of these patients have an identifiable primary tumor. However, about 10% of patients have no visible lesion even after careful endoscopy and multiple blind biopsies. The diagnosis of metastatic SCCA is established by needle biopsy of the cervical adenopathy. These patients are considered to have an unknown primary tumor of the upper aerodigestive tract.

Treatment of patients believed to have an occult malignancy of the upper digestive tract varies from institution to institution. Most physicians favor wide-field external beam radiation to the nasopharynx, tonsil, tongue base, and pyriform sinus.[84, 85] Other physicians favor a more conservative approach consisting of a unilateral neck dissection and close observation to eventually identify a primary site.[86]

Identifying a primary cancer in a patient thought to have an occult or unknown tumor will alter the treatment plan. If the patient is to be treated with primary radiation, a wide-field radiation plan becomes more focused by applying a shrinking-field technique to the primary site. This change potentially increases the total dose delivered to the primary tumor from 5500 to 7440 cGy.[84] The concomitant reduction of the volume of tissue irradiated may decrease both the acute and chronic complications associated with radiation therapy. Thus, identification of a primary tumor site results in a higher and more localized tumor dose, reduces treatment morbidity, may increase local tumor control, and may lead to an increase in patient survival.

Detection of a clinically occult lesion is difficult for the otolaryngologist, radiation therapist, and radiologist. ''Blind'' endoscopic biopsies are often performed in locations known to be at high risk. Some centers perform an ipsilateral tonsillectomy, given the high incidence of occult lesions present in the palatine tonsil. Despite these efforts, the likelihood of detecting an occult lesion is only 20%.[84] One thing that has become clear in recent years is that if imaging is to help identify such an unknown tumor, it must be performed before any scoping or biopsy. If the imaging is performed before these clinical manipulations, any site of mucosal thickening is suspected of being a primary tumor and directed biopsies can be performed. If imaging is performed after scoping, hemorrhage and edema in the pharyngeal wall lessen the sensitivity of the study.

Imaging Findings

CT has been shown to be useful for detecting an unknown primary tumor and in experienced hands has a sensitivity of 37%.[87, 88] To obtain the maximum information from CT, the study must be of high quality and must be performed with 3-mm contiguous sections from the nasopharynx into the thoracic inlet. Metastases to level V nodes should suggest a nasopharyngeal lesion.[87] Historically the presence of large necrotic nodes has been associated with clinically occult tonsillar tumors.[84] Bilateral upper cervical lymph nodes suggest a lesion within the nasopharynx, tongue base, soft palate, supraglottic larynx, or pyriform sinus.[84] The main role of CT is to focus the endoscopic evaluation and guide the otolaryngologist so that a larger biopsy specimen can be

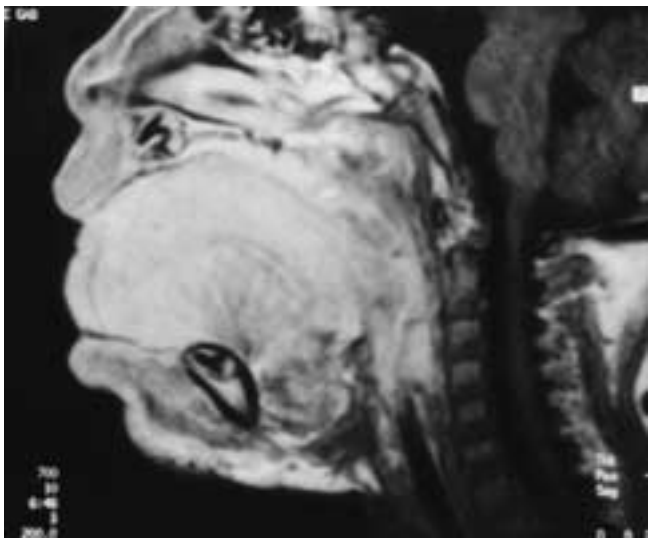

FIGURE 28-57 Sagittal postcontrast T1-weighted image shows diffuse enhancement and enlargement of the tongue due to a vascular malformation.

VIEW IMAGE

Copyright © 2003, Mosby, Inc. All rights reserved.

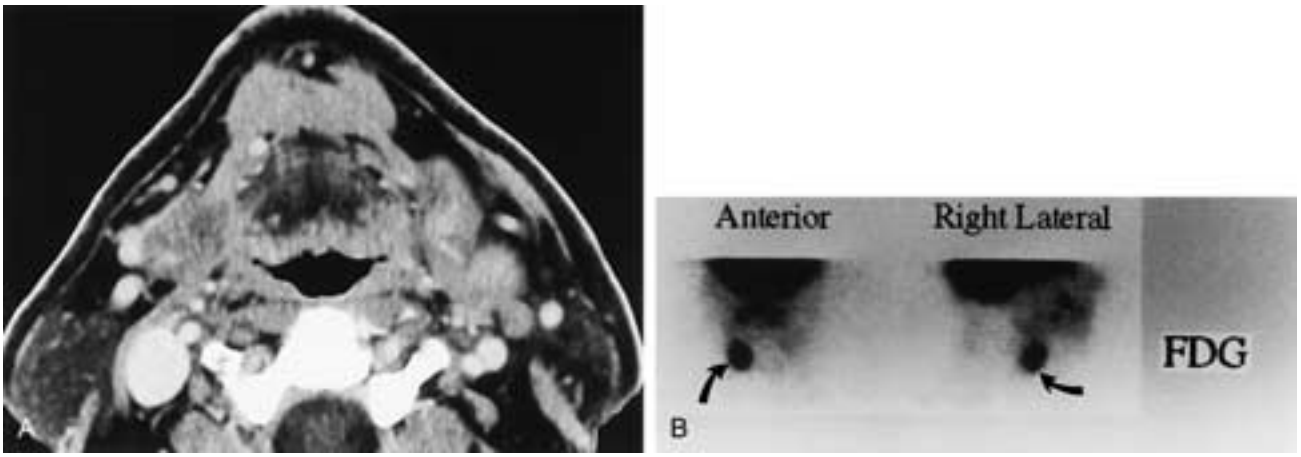

VIEW IMAGE

FIGURE 28-58 **A**, Axial CT scan from a contrast-enhanced study demonstrates a normal-appearing tongue base. **B**, FDG images show a focus of abnormal uptake in the tongue base (*arrows*). Biopsies of this area showed squamous cell carcinoma.

obtained from suspicious areas, thus potentially increasing the diagnostic yield over that of the limited and ''undirected'' speculative biopsies. Special attention should be paid to areas of asymmetric fullness ipsilateral to the side of nodal involvement. The precise role of MR imaging in detecting occult lesions has not yet been determined.

Recently, imaging with 2[F18] fluoro-2-deoxy-D-glucose (FDG) has shown promise in detecting occult primary lesions of the upper aerodigestive tract[87] (Fig. 28-58) (see Chapter 45).

NONNEOPLASTIC PROCESSES

Retropharyngeal Infections

A retropharyngeal space infection is a potentially life-threatening disease whose incidence has decreased in the antibiotic era. Historically, these infections were believed to occur almost exclusively in children less than 6 years of age.[89] However, with the increase in the immunocompromised patient population, these infections have become more frequent in adults, being more common in males than in females (2:1). Infections involving the retropharyngeal space usually result from an infection at a site whose primary lymphatic drainage is to the retropharyngeal lymph nodes. These sites include the sinonasal tract, throat, tonsil, oral cavity, and middle ear. Retropharyngeal infections also can result from a direct traumatic inoculation.[90, 91]

The anatomy of the retropharyngeal space is discussed in Chapter 34. This space extends from the skull base to the level of the carina, and its contents include fat and lymph nodes. The retropharyngeal lymph nodes are subdivided into lateral and medial groups.[12, 92, 93] The lateral group consists of one to three nodes situated just medial to the carotid sheath on the longus colli and longus capitus muscles, behind the posterior pharyngeal wall. These lymph nodes usually extend from the skull base to the level of C3. The medial group is inconstant and is located near the midline. When present, these nodes are usually found at the level of C2, although they may extend inferiorly as low as the vertebral body of C6. Most of the involved retropharyngeal nodes lie within 2 cm of the skull base. The afferent drainage of the retropharyngeal lymph nodes is from the nasopharynx, oropharynx, palate, nasal cavity, paranasal sinuses, middle ear, and eustachian tube, and the efferent drainage is to the level II nodes.

The danger space is situated dorsal to the retropharyngeal space between the alar and prevertebral fascia.[93] This space extends from the skull base to the level of the posterior diaphragm, and it is discussed in Chapter 34. Infections that involve the retropharyngeal space may enter the danger space and thus extend into the mediastinum.[93]

Patients with retropharyngeal space infections often present with fever, chills, odynophagia, sore throat, dysphagia, nausea, vomiting, respiratory distress, and neck pain and stiffness; these symptoms may suggest meningitis. On physical examination the patient may be drooling and diaphoretic, with bulging of the posterior nasopharyngeal/oropharyngeal wall.

Historically, a retropharyngeal space abscess was believed to be the ultimate result of efferent spread of infection to the retropharyngeal lymph nodes.[90] These nodes enlarged and underwent suppuration, eventually rupturing into the retropharyngeal space and creating an abscess. With the development of broad-spectrum antibiotics, the evolution of this disease has been slowed so that it is diagnosed and treated at an earlier stage, often before the development of a frank retropharyngeal abscess. That is, the treatment is directed to a suppurative (abscessed) node rather than to a retropharyngeal space abscess.

Today, a true retropharyngeal abscess is often the result of penetrating trauma to the oropharynx or nasopharynx. These abscesses also develop from a cervical spine osteomyelitis or diskitis or as a complication of spinal surgery.[89] The treatment is surgical drainage, either by an intraoral or open procedure, depending on the size of the lesion and the clinical stability of the patient.

As mentioned, currently retropharyngeal infections are often diagnosed before the formation of a true retropharyngeal abscess. Recent experience suggests that a retropharyn-

Copyright © 2003, Mosby, Inc. All rights reserved.

geal suppurative adenitis, diagnosed on either CT or MR imaging, may be successfully managed with antibiotics, without the need for surgical exploration and drainage.[94]

The ability to medically manage a retropharyngeal abscess successfully appears to be the result of both early sectional imaging and the use of effective antibiotic therapy. Historically, no more than 10% to 15% of these infections resolved with medical therapy alone. Recent reports suggest that 40% to 50% of patients can be successfully treated without surgical drainage.[89]

Imaging Features

The initial diagnostic imaging evaluation of a patient suspected of having a retropharyngeal space infection usually consists of a lateral plain film of the neck, taken during quiet breathing with the head in a neutral position. The presence of prevertebral swelling (in adults, usually more than one half of the AP diameter of C4), the loss of the normal cervical lordosis, and air in the prevertebral soft tissues are all findings suggestive of an underlying infection. However, plain films alone usually cannot determine the exact location and the extent of the process.

CT and MR imaging permit accurate localization of infections involving the deep neck and help distinguish between suppurative retropharyngeal adenitis with associated retropharyngeal space edema and a true retropharyngeal abscess. CT is the preferred modality because of its high resolution, shorter scan times, lower costs, and overall better evaluation of nodal disease. The reduction in scan time with CT is especially advantageous in the pediatric population and may reduce or eliminate the need for sedation in infants and young children.

A retropharyngeal abscess appears as a low-attenuation region expanding the retropharyngeal space, with enhancement along the margins of the space. There often is an associated significant mass effect, and the posterior pharyngeal wall may be quite displaced ventrally[93] (Fig. 28-59). Air may occasionally be seen within the abscess (Fig. 28-60). Abscesses resulting from an adjacent diskitis are contiguous with the adjacent disk space and are associated with erosion of the neighboring vertebral body endplates (Fig. 28-61).

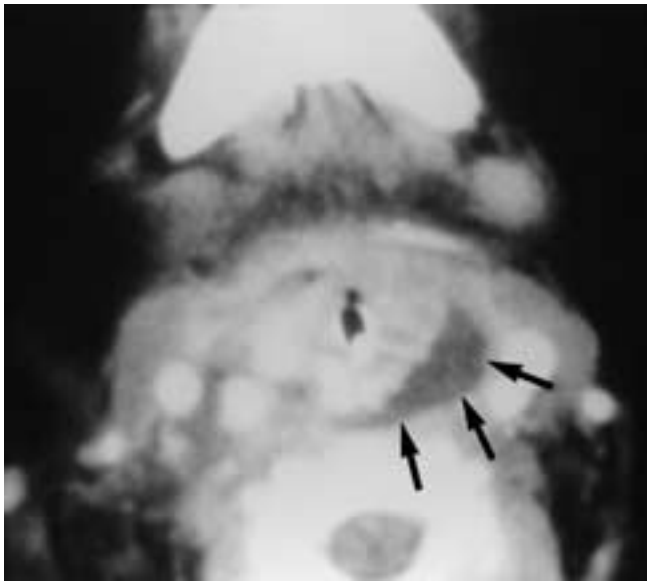

VIEW IMAGE

FIGURE 28-59 Axial contrast-enhanced CT scan shows a fluid collection in the retropharyngeal space (*arrows*). The lack of a thick, enhancing wall does not exclude a retropharyngeal abscess and, in our experience, an enhancing wall is rarely present in a retropharyngeal space abscess.

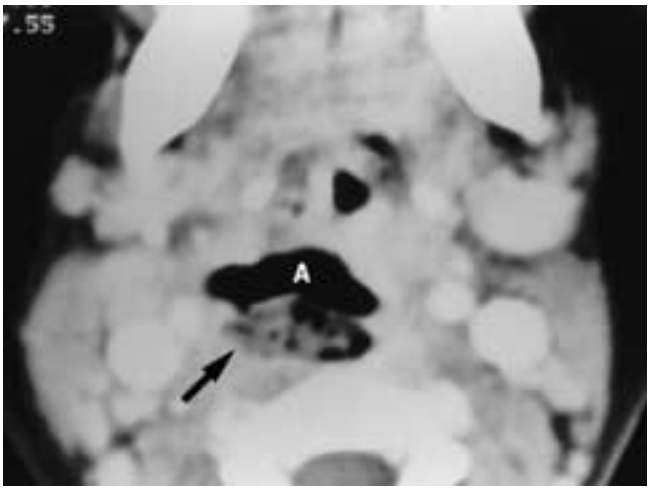

FIGURE 28-60 Axial contrast-enhanced CT scan shows a retropharyngeal abscess containing fluid and air (*arrow*). *A*, Normal airway of the oropharynx.

VIEW IMAGE

Suppurative retropharyngeal adenitis is characterized by an enlarged retropharyngeal lymph node that contains a low-attenuation center with an enhancing rim (Fig. 28-62).[93, 94] The low-attenuation center does not necessarily imply the presence of actual pus, as the same CT appearance is present in lymph nodes containing early liquefaction (presuppurative phase) and in those that have undergone complete liquefaction necrosis (suppurative phase). Suppurative retropharyngeal adenitis is often associated with edema, which is characterized by a smooth expansion of the retropharyngeal space with ''mucoid'' density material (10 to 25 HU). However, there is no enhancement of the margins of the retropharyngeal space, which differentiates a suppurative adenitis from a retropharyngeal abscess.

Previous reports have shown that ultrasound may be used to differentiate solid lesions from complex fluid collections located within the retropharyngeal region.[95] However, ultrasound is often unable to determine whether these collections are within enlarged lymph nodes or involve the entire retropharyngeal space. For this reason, if ultrasound is the only imaging modality, surgical intervention has been recommended in all of these cases. CT and MR imaging permit localization of areas of liquefaction and in most cases allow accurate differentiation between suppurative adenitis and retropharyngeal abscess.

Peritonsillar Abscesses

Acute tonsillitis is usually a self-limited febrile disease of adolescents or young adults. The most common offending bacterial organisms include beta-hemolytic streptococcus,

Copyright © 2003, Mosby, Inc. All rights reserved.

staphylococcus, pneumococcus, and hemophilus. Suppurative uncontrolled infection of the tonsils may result in a peritonsillar abscess (quinsy) or, rarely, in a tonsillar abscess. A peritonsillar abscess is an accumulation of pus around the palatine tonsils, and if this abscess extends outside the tonsillar fossa, it may involve the lateral retropharyngeal or parapharyngeal spaces. A severe sore throat and pharyngeal edema that progress despite antibiotic therapy are the usual clinical presentations of such an abscess. Trismus develops if the medial pterygoid muscle is involved.

On CT, the appearance of acute or chronic tonsillitis is nonspecific, and the focal homogeneous swelling of the palatine tonsil may simulate a tumor[93] (Fig. 28-63). The inflammatory process may extend laterally into the parapharyngeal space, medial pterygoid muscle and masticator space, and soft palate. If a frank abscess is present, there is a low-attenuation central region surrounded by an enhanced rim in the peritonsillar or tonsillar region (Figs. 28-64 and 28-65). The abscess may also extend from the tonsillar bed into the retropharyngeal and submandibular spaces.[96]

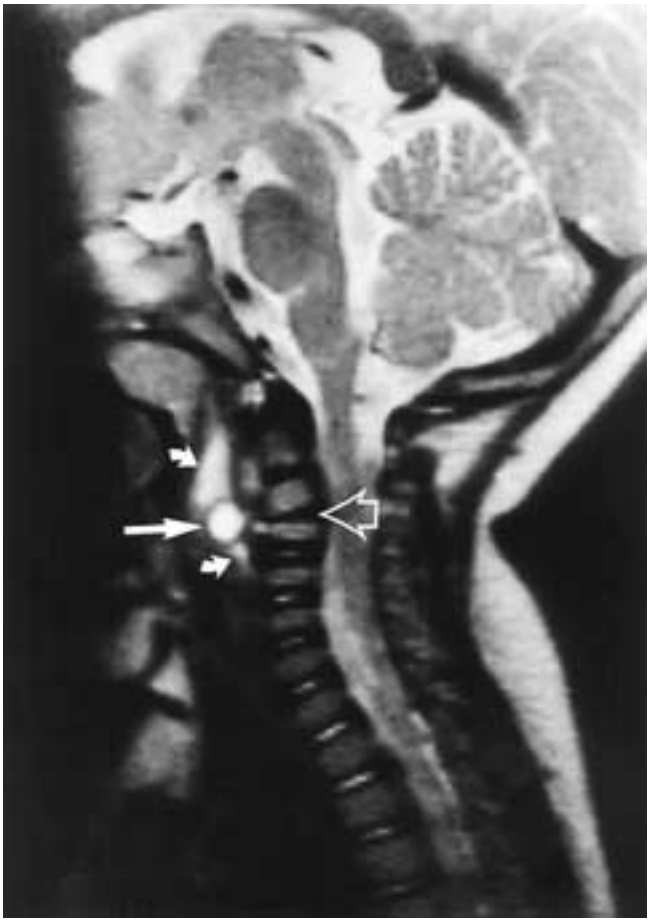

VIEW IMAGE

FIGURE 28-61 Sagittal T2-weighted MR image shows a fluid-containing mass (*solid straight arrow*) located within the retropharyngeal space with surrounding edema (*curved arrows*) consistent with a retropharyngeal space abscess. The abscess was secondary to a diskitis seen as a loss of height of the adjacent disk space (*open arrow*). There was erosion of the endplates of the adjacent vertebral bodies on CT (not shown).

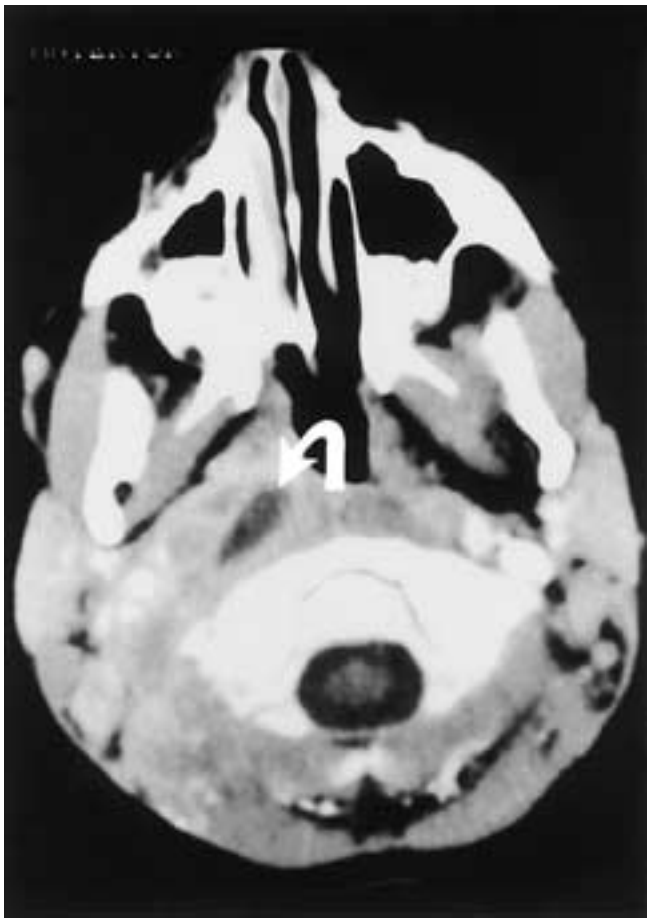

FIGURE 28-62 Axial contrast-enhanced CT scan demonstrates an oval-shaped, low-attenuation lesion (*arrow*) in the expected location of a lateral retropharyngeal lymph node. This is the typical finding of a suppurative retropharyngeal adenitis.

VIEW IMAGE

Acute Calcific Prevertebral Tendinitis (Tendinitis of the Longus Colli)

Acute calcific prevertebral tendinitis is an idiopathic noninfectious inflammation that can be confused with retropharyngeal abscess.[97] Other names for this uncommon disease include tendinitis of the longus colli and retropharyngeal calcific tendinitis. There is inflammation of the tendinous insertion of the longus colli muscle with deposition of calcium hydroxyapatite crystals. The oblique fibers of the muscle are involved. An effusion can extend from the prevertebral space into the retropharyngeal space. The presentation can mimic that of retropharyngeal abscess, but the patient is less febrile and may have a normal white blood cell count.

CT shows calcific density in the region of the insertion of the longus colli muscle just anterior to the upper cervical spine (Fig. 28-66). An effusion extends into the retropharyngeal space and is seen in a typical pattern extending from C1 down to the level of C5 or C6. The abnormality begins in the prevertebral space rather than in the retropharyngeal space, so the edema or fluid collection may surround part of the muscle, particularly superiorly.

MR imaging shows the extent of the disease and the tapering of the effusion. The calcification is less obvious, but

Copyright © 2003, Mosby, Inc. All rights reserved.

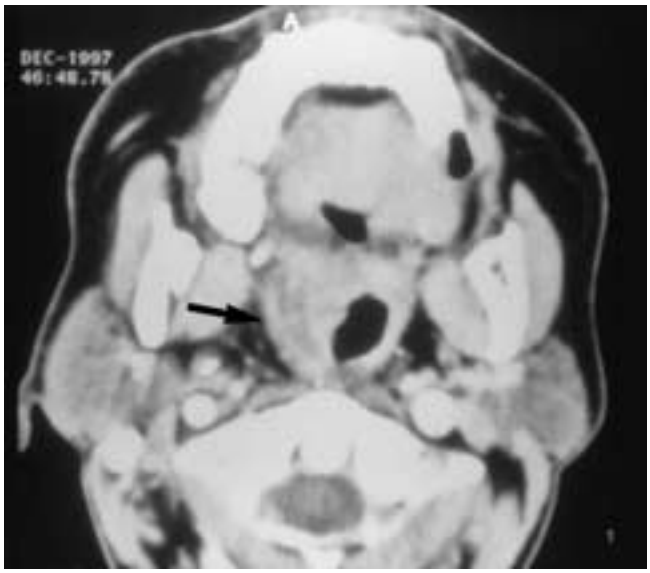

FIGURE 28-63 Axial contrast-enhanced CT scan shows diffuse thickening of the right tonsil consistent with inflammation (*arrow*). There is no evidence of a tonsillar or peritonsillar abscess.

VIEW IMAGE

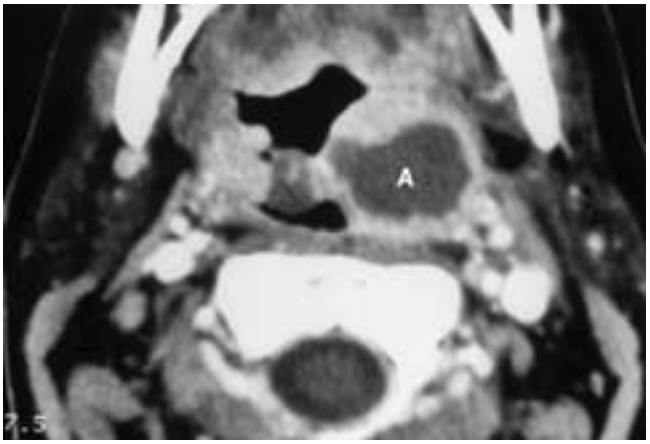

VIEW IMAGE

FIGURE 28-64 Axial contrast-enhanced CT scan shows the typical appearance of a large left tonsillar abscess (*A*).

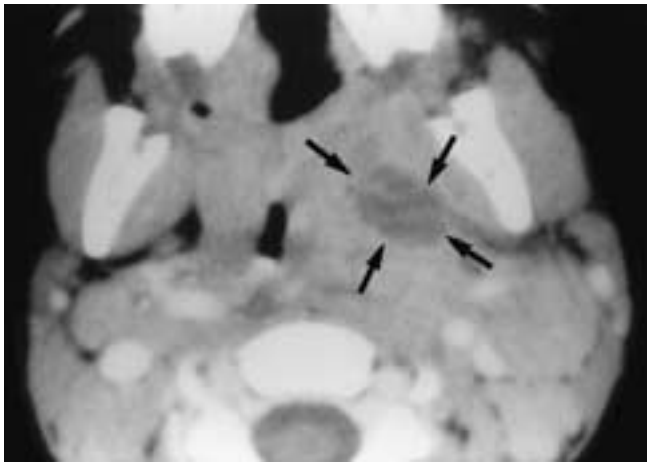

FIGURE 28-65 Axial contrast-enhanced CT scan shows a left peritonsillar abscess extending into the left parapharyngeal space (*arrows*). Note that it is located lateral to the left tonsil. Based on its location, it was drained by a cervical approach rather than by intraoral drainage, as would normally be performed for a tonsillar abscess.

VIEW IMAGE

Copyright © 2003, Mosby, Inc. All rights reserved.

the relationship of the fluid collection to the muscle may be easier to appreciate, particularly on T2-weighted images.

Recognition of the imaging appearance is important, as this illness is self-limited and responds to either steroids or nonsteroidal anti-inflammatory drugs. It is not an infection, and surgery to drain the collection is of no benefit.

Tornwaldt's Cysts

Tornwaldt's cyst is a benign developmental lesion within the midline nasopharynx. Its incidence at autopsy is 4%, the peak age of presentation is 15 to 30 years, and there is no sex predilection. The development of Tornwaldt's cyst is related to the embryogenesis of the notochord. In the early embryo, before the notochord reaches the prechordal plate, it comes into contact with the endoderm of the primitive pharynx. At this level, a small outpouching of the pharyngeal mucosa develops, directed toward the brain. Some believe that this outpouching is related to Seessel's pouch, which contributes to the preoral gut.[3] If a focal adhesion develops between the notochord and this endoderm, when the notochord ascends back to the level of the developing skull base, a small portion of the nasopharyngeal mucosa is carried along it. This results in the creation of a midline diverticulum that in the adult is lined by normal pharyngeal mucosa. When the patient develops a pharyngitis, the orifice of this diverticulum swells and closes, and a cyst is formed. The cyst contents typically have a high protein content and are infected with anaerobic bacteria. In this state, Tornwaldt's cysts are usually asymptomatic, incidental imaging findings. Periodically, the pressure within the cysts increases and overcomes the relative stenosis at the orifice. This releases anaerobic secretions into the nasopharynx, and the patient complains of periodic halitosis. Asymptomatic cysts require no treatment, but symptomatic lesions are drained via an intraoral approach.

Imaging Features

On MR imaging, a Tornwaldt's cyst appears as a well-delineated, thin-walled, midline cystic lesion that usually varies between 2 and 10 mm in diameter. The signal

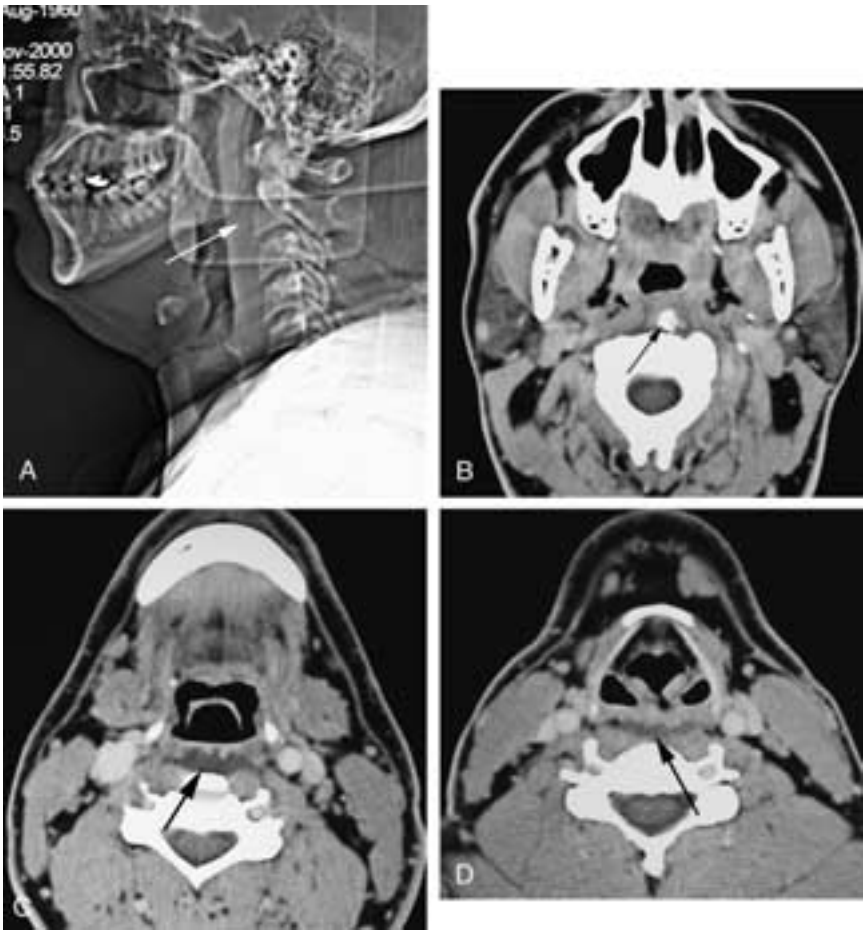

FIGURE 28-66 Acute calcific prevertebral tendinitis. **A**, Scout topogram prior to CT. There is widening of the prevertebral stripe (*arrow*). **B**, Axial CT scan at the upper cervical level shows a calcific density (*arrow*) in the region of the tendon of the longus colli muscle. Note the position of the prevertebral muscle on the opposite side (*arrowhead*). This relationship indicates that the abnormality is in the prevertebral space. **C**, Image slightly caudad to **B** shows fluid (*arrow*). From this image, one could not know if it is located in the prevertebral or retropharyngeal space. **D**, More caudad the effusion (*arrow*) tapers.

Illustration continued on following page

VIEW IMAGE

Copyright © 2003, Mosby, Inc. All rights reserved.

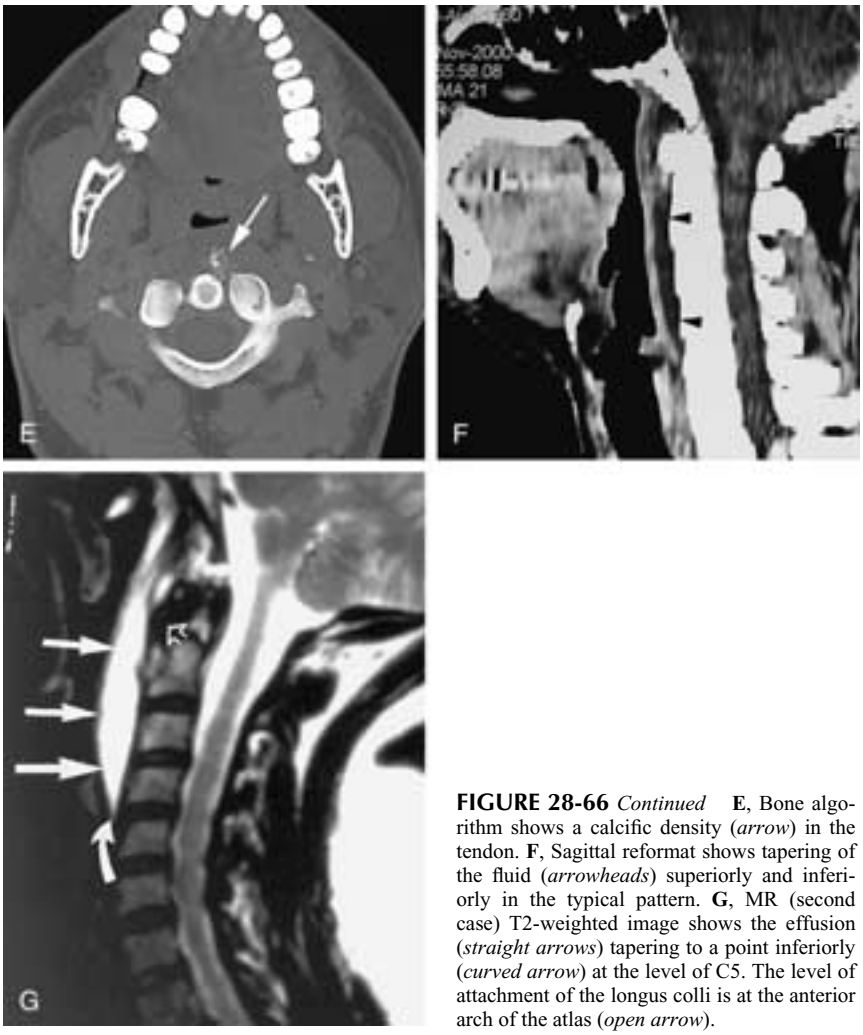

FIGURE 28-66 *Continued* **E**, Bone algorithm shows a calcific density (*arrow*) in the tendon. **F**, Sagittal reformat shows tapering of the fluid (*arrowheads*) superiorly and inferiorly in the typical pattern. **G**, MR (second case) T2-weighted image shows the effusion (*straight arrows*) tapering to a point inferiorly (*curved arrow*) at the level of C5. The level of attachment of the longus colli is at the anterior arch of the atlas (*open arrow*).

VIEW IMAGE

characteristics vary, as does the protein content of the cyst. The T1-weighted signal intensity can be either low or high, and the T2-weighted signal intensity is high (Figs. 28-67 and 28-68). There usually is no enhancement with contrast. On CT, these cysts present as midline nasopharyngeal cysts with mucoid attenuation located between the longus colli muscles. If the cyst contains a high protein content, the resulting increased density may on occasion mimic a soft-tissue mass (Fig. 28-68). In patients with prominent adenoids, these cysts may be difficult to identify.

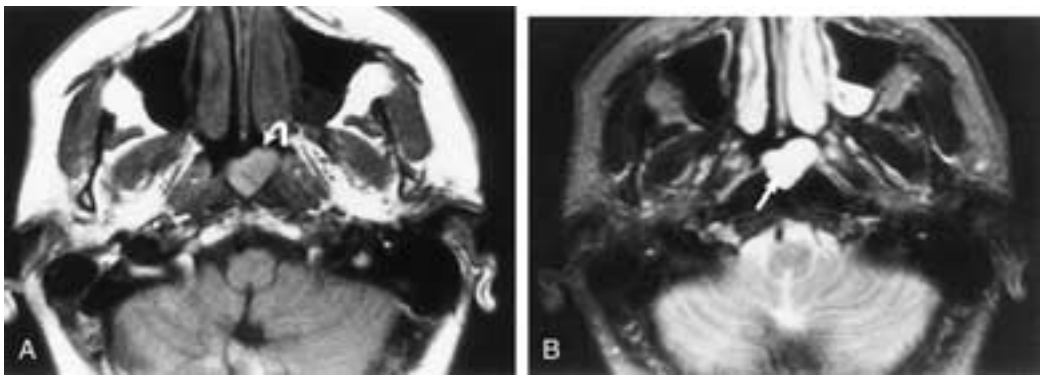

FIGURE 28-67 **A**, Axial T1-weighted noncontrast MR image shows a well-delineated lesion (*arrow*) with increased signal intensity located within the nasopharynx. This was a Tornwaldt's cyst. **B**, There is increased signal within the lesion on the T2-weighted sequence, which is consistent with the cystic nature of the mass. Note the internal septation present within the lesion (*arrow*).

VIEW IMAGE

Copyright © 2003, Mosby, Inc. All rights reserved.

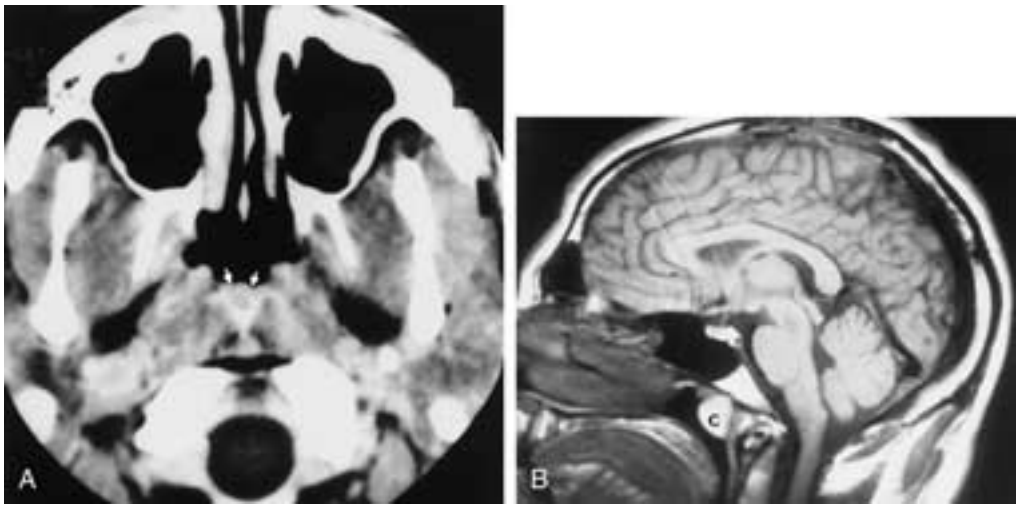

VIEW IMAGE

FIGURE 28-68 Tornwaldt's cyst. **A**, CT scan through the upper nasopharynx demonstrates a midline Tornwaldt's cyst (*arrows*). Note that its density is similar to that of the surrounding muscle. The high density of this cyst is probably related to its high protein concentration. **B**, Sagittal T1-weighted MR scan through the upper nasopharynx demonstrates a high signal intensity Tornwaldt's cyst (*c*). The high intensity is due to the high protein concentration within the cyst. This shortens the T1 relaxation time sufficiently to produce increase in intensity on T1-weighted images.

Adenoidal Hypertrophies

Adenoids, or nasopharyngeal tonsils, are located in the roof of the nasopharynx. They start to become prominent by age 2 to 3 years, often filling the entire nasopharynx and extending into the posterior choanae. Regression starts in early adolescence and continues into later life. Most people have little if any identifiable adenoidal tissue by age 30 to 40 years. However, normal adenoids can occasionally be identified in patients 50 to 60 years old. Conversely, if no adenoidal tissue is seen in a young child, the possibility of an immune deficiency syndrome should be considered. Prominent adenoidal tissue in adults should raise the possibility of HIV disease.[10]

On CT, adenoids appear as homogeneous, superficial soft tissue filling the superior and upper lateral recesses of the nasopharynx. The adenoids have an attenuation similar to that of muscle, and small superficial cysts and calcifications are often present. After contrast administration, a thin, enhancing line is often seen along the deep surface of the adenoids. This mucosal venous and pharyngobasilar enhancement should be present and intact, as violation of this line indicates the presence of an aggressive mass in the nasopharyngeal roof. On MR imaging, the adenoids have a T1-weighted signal intensity similar to that of muscle; however, they have a high T2-weighted signal intensity, which distinguishes them from muscle (Fig. 28-69). Unfortunately, the signal intensities of the adenoids are similar to those of lymphoma and most cellular tumors, and distinction between normal lymphoid tissue and tumor may be impossible on CT and MR imaging.[98] Endoscopy with biopsy is the only way to definitively make this distinction. Reactive cervical adenopathy often accompanies prominent adenoidal tissue in children, but it can also be seen in HIV-infected patients and in patients with nasopharyngeal lymphoma.

Acquired Immunodeficiency Syndrome

Acquired immunodeficiency syndrome (AIDS) is caused by human T-cell lymphotrophic virus type III (HTLVIII) and is a potentially devastating disease of childhood and adulthood.[99] Opportunistic infections and certain malignancies have been identified in up to 50% of patients with AIDS.[99–101] A variety of infections involving the oral cavity and oropharynx have been described in AIDS patients, including fungal diseases such as oral candidiasis, cryptococcosis, and histoplasmosis; bacterial infections, including those caused by *Streptococcus pneumoniae*, *Staphylococcus aureus*, and *Haemophilus influenzae*; and herpes simplex infections, which require treatment with oral acyclovir or intravenous foscarnet (Fig. 28-70).[101, 102] Hairy cell leukoplakia is a manifestation of Epstein-Barr virus and presents as a white plaque most often seen on the lateral margin of the tongue.

The typical immunocompetent patient with a pharyngitis usually does not undergo CT or MR imaging. The diagnosis is established clinically and by cultures. However, the immunocompromised patient with pharyngitis may have an opportunistic infection such as candida or cytomegalic virus, with involvement of the hypopharynx and esophagus. In these patients, occasional imaging is performed with the goal of mapping the disease and establishing the presence or absence of an associated abscess.

A variety of neoplasms have been reported to have a tendency to occur in AIDS patients. Because of their rarity in the general population, in the proper clinical setting these neoplasms are considered AIDS-defining malignancies.[99] These malignancies include Kaposi's sarcoma and small noncleaved B-cell (Burkitt's, non-Burkitt's) and large B-cell (immunoblastic) NHL (Fig. 28-71). Involvement of the oropharynx has been reported in up to 20% of patients with cutaneous Kaposi's sarcoma, although any portion of the upper

Copyright © 2003, Mosby, Inc. All rights reserved.

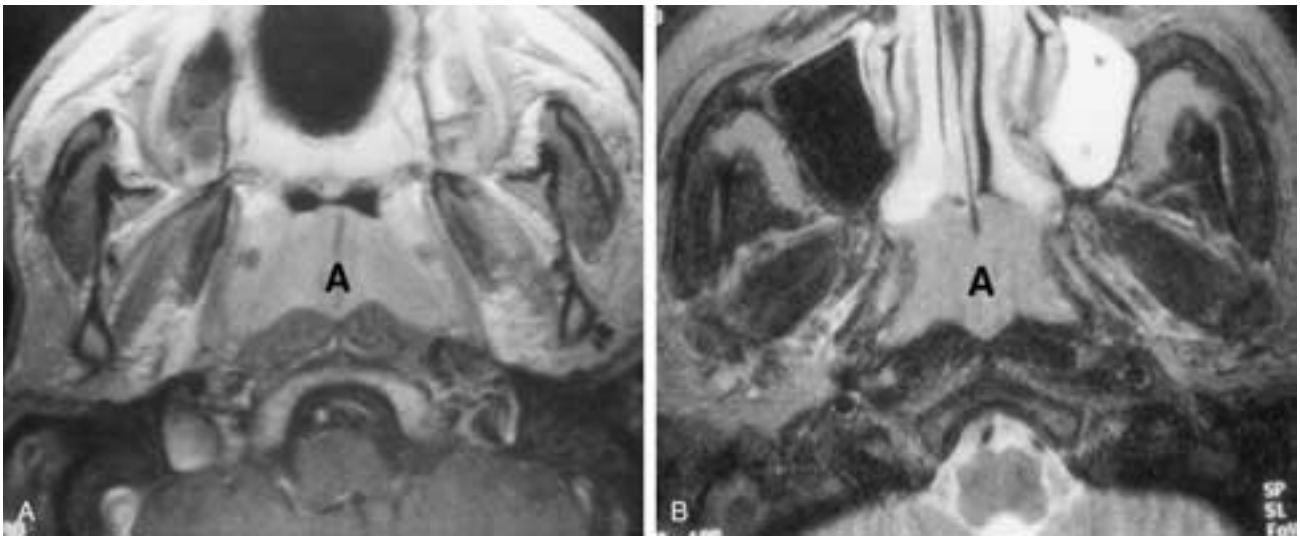

VIEW IMAGE

FIGURE 28-69 **A**, Axial contrast-enhanced, T1-weighted image shows the nonspecific appearance of prominent adenoidal tissue in the nasopharynx (*A*). This appearance may be seen in nasopharyngeal carcinoma or lymphoma. The lack of invasion of the adjacent soft-tissue structure is suggestive of benign adenoidal tissue. **B**, Axial T2-weighted image obtained in the same patient illustrated in **A** shows increased signal within the visceral space mass (*A*). These signal characteristics are suggestive of nonmalignant lymphoid tissue.

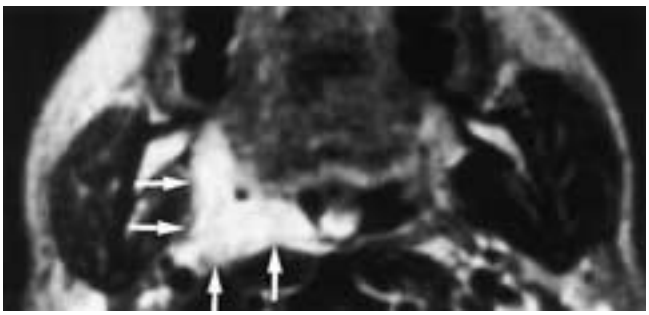

FIGURE 28-70 Axial T2-weighted MR image shows thickening and increased signal intensity of the posterior and lateral oropharyngeal walls (*arrows*) consistent with a clinical diagnosis of herpes pharyngitis.

VIEW IMAGE

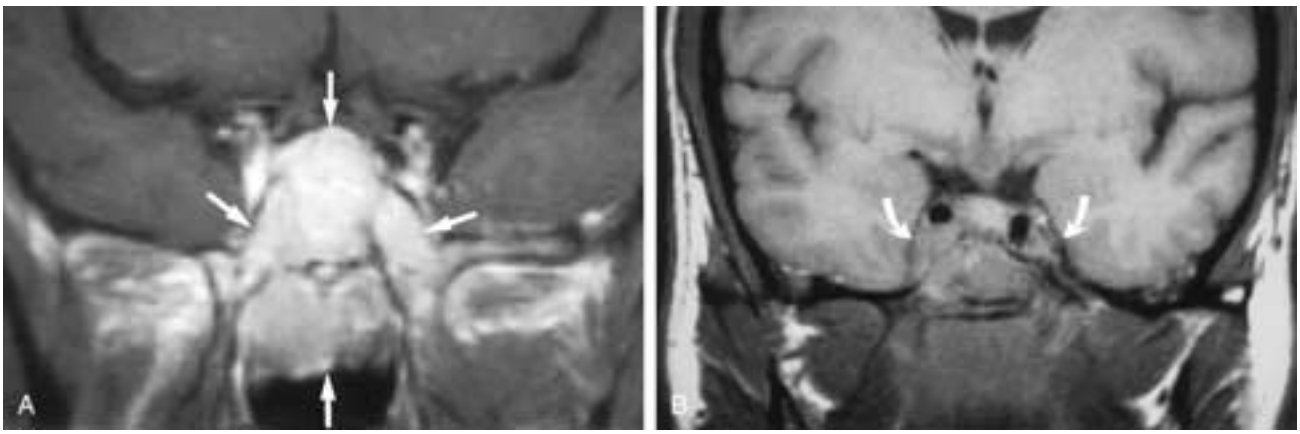

VIEW IMAGE

FIGURE 28-71 **A**, Coronal-enhanced T1-weighted MR scan performed with fat saturation shows a large nasopharyngeal mass (*arrows*) that has invaded the sphenoid sinus in this patient who was HIV positive. Biopsy showed immunoblastic lymphoma. **B**, Coronal T1-weighted noncontrast MR scan shows that abnormal soft tissue is present within the cavernous sinuses (*arrows* in **B**). This disease enhances homogeneously with contrast.

Copyright © 2003, Mosby, Inc. All rights reserved.

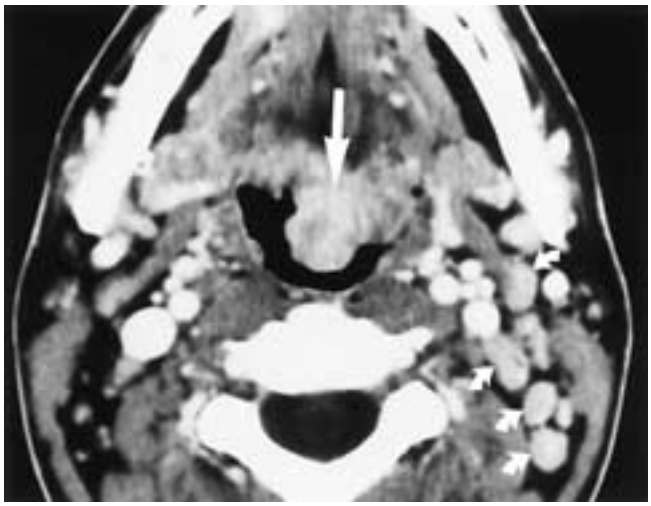

VIEW IMAGE

FIGURE 28-72 Axial contrast-enhanced CT scan shows an enhancing mass (*arrow*) in the tongue base and multiple enhancing cervical lymph nodes (*curved arrows*). Biopsy showed Kaposi's sarcoma.

aerodigestive tract may be involved (Fig. 28-72).[103, 104] Clinically, these tumors may present as either small, violaceous nodules or lobulated masses that measure several centimeters in diameter. Lymphoma preferentially involves the adenoidal and palatine tonsillar lymphoid tissues, and early nasopharyngeal lesions may mimic the diffuse adenoidal hypertrophy typically seen in immunocompromised hosts.[105, 106] Large lymphomas may extend into the cavernous sinus, usually along neurovascular channels. On imaging, skull base erosion is rarely demonstrated[99] (Fig. 28-73). The clinical symptoms often reflect the location of the tumor and include dysphagia and airway obstruction.

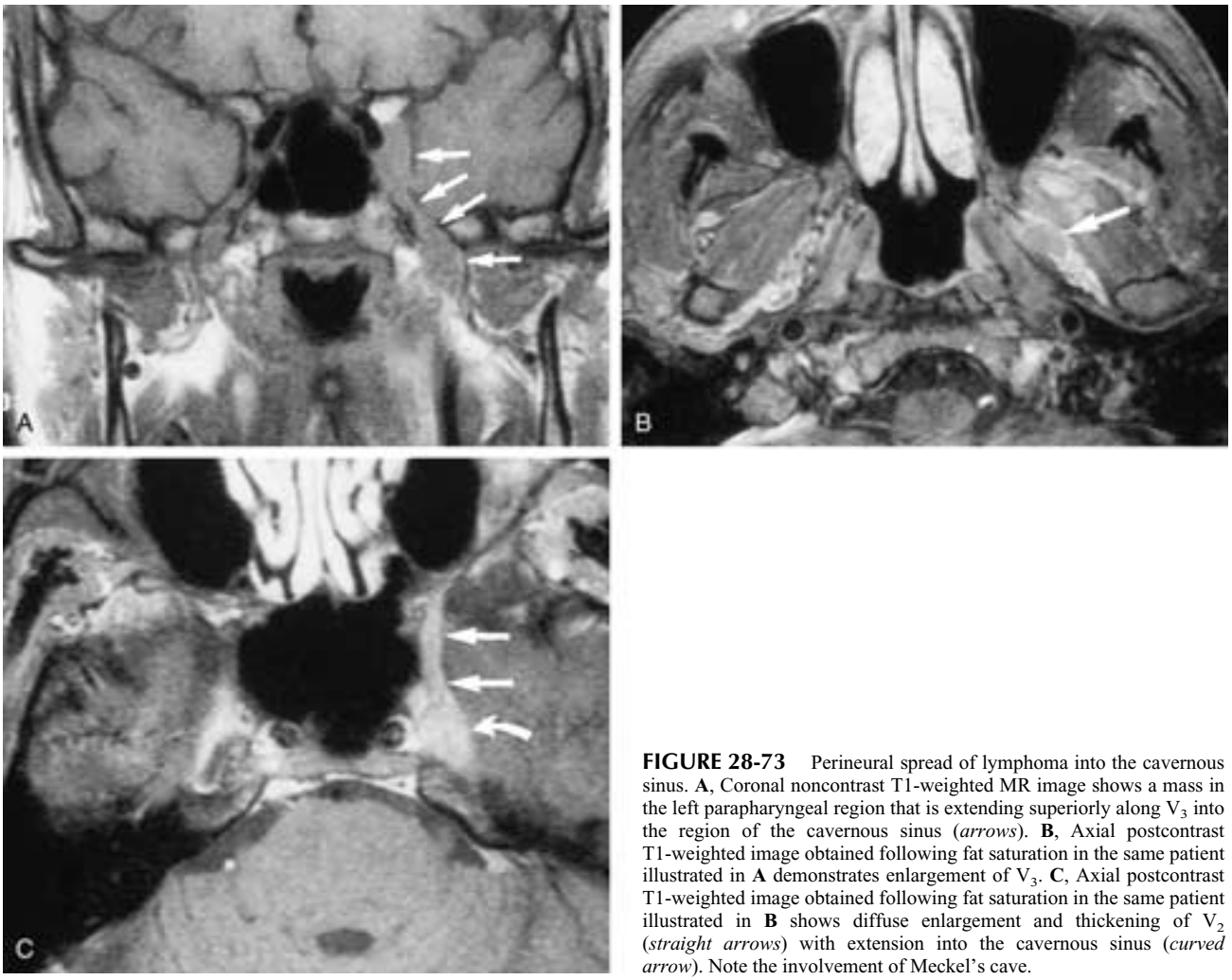

FIGURE 28-73 Perineural spread of lymphoma into the cavernous sinus. **A**, Coronal noncontrast T1-weighted MR image shows a mass in the left parapharyngeal region that is extending superiorly along V_3 into the region of the cavernous sinus (*arrows*). **B**, Axial postcontrast T1-weighted image obtained following fat saturation in the same patient illustrated in **A** demonstrates enlargement of V_3. **C**, Axial postcontrast T1-weighted image obtained following fat saturation in the same patient illustrated in **B** shows diffuse enlargement and thickening of V_2 (*straight arrows*) with extension into the cavernous sinus (*curved arrow*). Note the involvement of Meckel's cave.

VIEW IMAGE

Copyright © 2003, Mosby, Inc. All rights reserved.

VIEW IMAGE

FIGURE 28-74 Axial contrast-enhanced CT scan demonstrates a soft-tissue mass situated in the left tonsil (*straight arrows*) associated with edema in the retropharyngeal space (*curved arrows*). The patient was involved in a motor vehicle accident, and the lesion was due to a hematoma located within the tonsillar fossa.

In an adult, the triad of increased adenoidal tissue, parotid cysts (lymphoepithelial cysts), and diffuse cervical lymph adenopathy is highly suggestive of HIV infection. However, since the advent of effective chemotherapy, the prominent adenoids and cervical adenopathy need not be present in these patients.

Advanced SCCA have recently been reported in patients under the age of 45 years. In many of these patients, the typical risk factors of smoking and alcohol abuse were not present. It is unclear whether there is an increased incidence of SCCA in patients with HIV infection. However, it appears that these tumors are more aggressive, and the prognosis of these patients tends to be worse.[107]

TRAUMA

Pharyngeal trauma may be due to blunt trauma, such as that experienced in a motor vehicle accident, and may result in mucosal and retropharyngeal hematomas (Fig. 28-74). Hematoma of the hypopharynx may also be iatrogenic, either from instrumentation (Fig. 28-75) or from a foreign body such as a chicken bone. Rarely, retropharyngeal hematomas have occurred after minor trauma in hemophiliac patients. The high CT attenuation of a hematoma usually allows the diagnosis to be suggested (Fig. 28-75A).

Penetrating trauma can cause perforation of the pharyngeal wall, resulting in a direct communication between the oral cavity and the retropharyngeal space. Persistent communication results in large amounts of air tracking throughout the deep fascial planes (Fig. 28-76). This communication provides a direct route for spread of organisms that normally colonize the oral cavity, allowing them to enter the deep neck and place the patient at high risk of developing a retropharyngeal abscess, fasciitis, and even mediastinitis.

VIEW IMAGE

FIGURE 28-75 **A**, Axial CT scan without contrast shows a large, hyperdense intramural hematoma of the hypopharynx. The patient had been anticoagulated and then required emergency intubation. The nasogastric tube (*n*) is in the right hypopharynx. **B**, Axial CT scan shows a large postcricoid mass (*m*) thought to be carcinoma clinically and radiographically. Biopsy showed acute and chronic inflammation and granulation tissue in a patient who had been intubated for long periods of time. There is a small amount of air in the appendix of the left laryngeal ventricle (*arrow*). **C**, Axial CT scan with contrast shows diffuse edema secondary to radiation therapy. The aryepiglottic folds are thick (*a*), the subcutaneous fat is streaky (*thin, straight arrows*), and the platysma muscle (*curved arrow*) and the skin (*open arrows*) are thick.

Copyright © 2003, Mosby, Inc. All rights reserved.

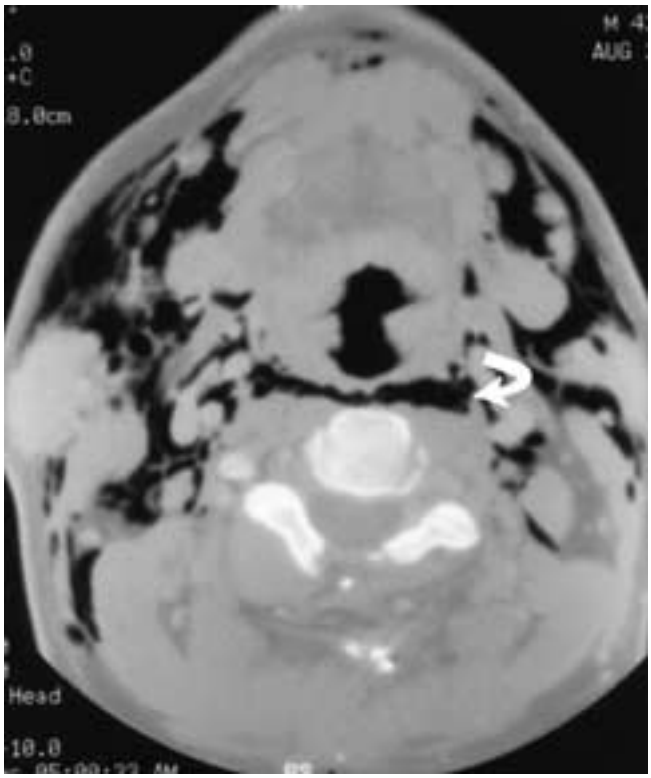

VIEW IMAGE

FIGURE 28-76 Axial CT scan obtained following penetrating trauma shows air dissecting along the fascial planes. Note the air extending along the retropharyngeal space (*arrow*).

MISCELLANEOUS LESIONS

A tortuous internal carotid artery and/or common carotid artery may swing behind the posterior wall of the oropharynx and hypopharynx, respectively, causing a pulsating submucosal bulge that is apparent on clinical inspection. Before the CT and MR imaging era, this abnormality was considered rare. However, presently this abnormality is considered relatively common, often occurring as an incidental finding on scans. Imaging is important to identify the etiology of this diagnosis, thus stopping an unnecessary and dangerous biopsy.

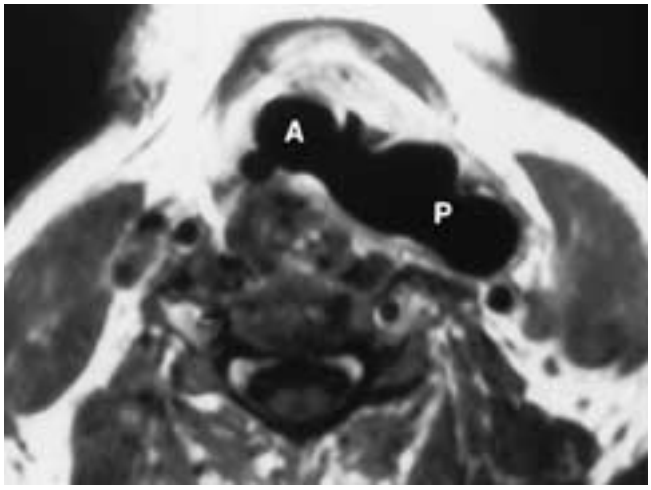

VIEW IMAGE

FIGURE 28-77 Axial noncontrast T1-weighted MR image shows marked dilatation of the lateral wall of the pharynx which is characteristic of a pharyngocele (*P*). Note the normal appearance of the airway (*A*).

A pharyngocele is a benign outpouching of the pharyngeal mucosa of the upper pyriform sinus. A frontal barium swallow film best shows the pharyngocele, which fills with barium as a broad-based outpouching (Fig. 28-77). These pharyngoceles distend on phonation and with Valsalva maneuvers. An air-filled pharyngocele can occasionally be seen on CT or MR imaging as an incidental finding (Fig. 28-77). Zenker's diverticulum is a mucosa-lined outpouching of the hypopharynx (Figs. 28-78 and 28-79). Dyssynergy of the cricopharyngeus muscle seems to play a role in the formation of this pulsion diverticulum.[18] Because this muscle fails to relax as a bolus passes, a high ''upstream'' pressure is created, thus contributing to the development of this diverticulum. Zenker's diverticulum protrudes through Killian's dehiscence and extends posteriorly and often laterally, usually to the left side.[18]

On a barium swallow, during maximum relaxation of the cricopharyngeus, normally no posterior submucosal mass should be seen that identifies the level of the cricopharyngeus. If such an impression is identified, it suggests dyssynergy or cricopharyngeal spasm (Fig. 28-80).

Posterior submucosal impressions on the barium column can result from osteophytes or rare anterior bulging of intervertebral disks. Interestingly, even exuberant anterior osteophytes rarely cause dysphagia unless there is a concomitant reason to limit the range of motion of the larynx (prior surgery, irradiation, etc.). A prominent lobe of the thyroid gland may occasionally cause an extrinsic mass on the anterolateral pharyngeal barium column, especially in older patients. It must be also noted that often symptoms of dysphagia reflect a hiatal hernia with reflux.

A retention cyst of a minor salivary gland is a small, superficial mass that can occur virtually anywhere in the pharynx and supraglottic larynx. Its CT fluid density and MR signal intensities are fairly diagnostic. The appearance is similar to that of retention cysts elsewhere in the pharynx.

''Crack'' cocaine burns of the larynx and hypopharynx may result in granulation tissue. The imaging findings may mimic those of carcinoma, both clinically and radiographically, and the patient may not volunteer the history that would help establish the correct diagnosis.[108] Biopsy is usually necessary to differentiate between granulation tissue and carcinoma.

In a patient with a paralyzed vocal cord or unilateral vagal paralysis, the ipsilateral pyriform sinus may be large. This appearance is described in Chapter 30.

POSTTREATMENT PHARYNX

Radiation Therapy

Radiation therapy (RT) has proven to be an effective modality for the treatment of a variety of laryngeal and pharyngeal carcinomas, with local control rates similar to those achieved with surgery.[109–114] RT is being given to patients as the preferred treatment, as well as to patients who

Copyright © 2003, Mosby, Inc. All rights reserved.

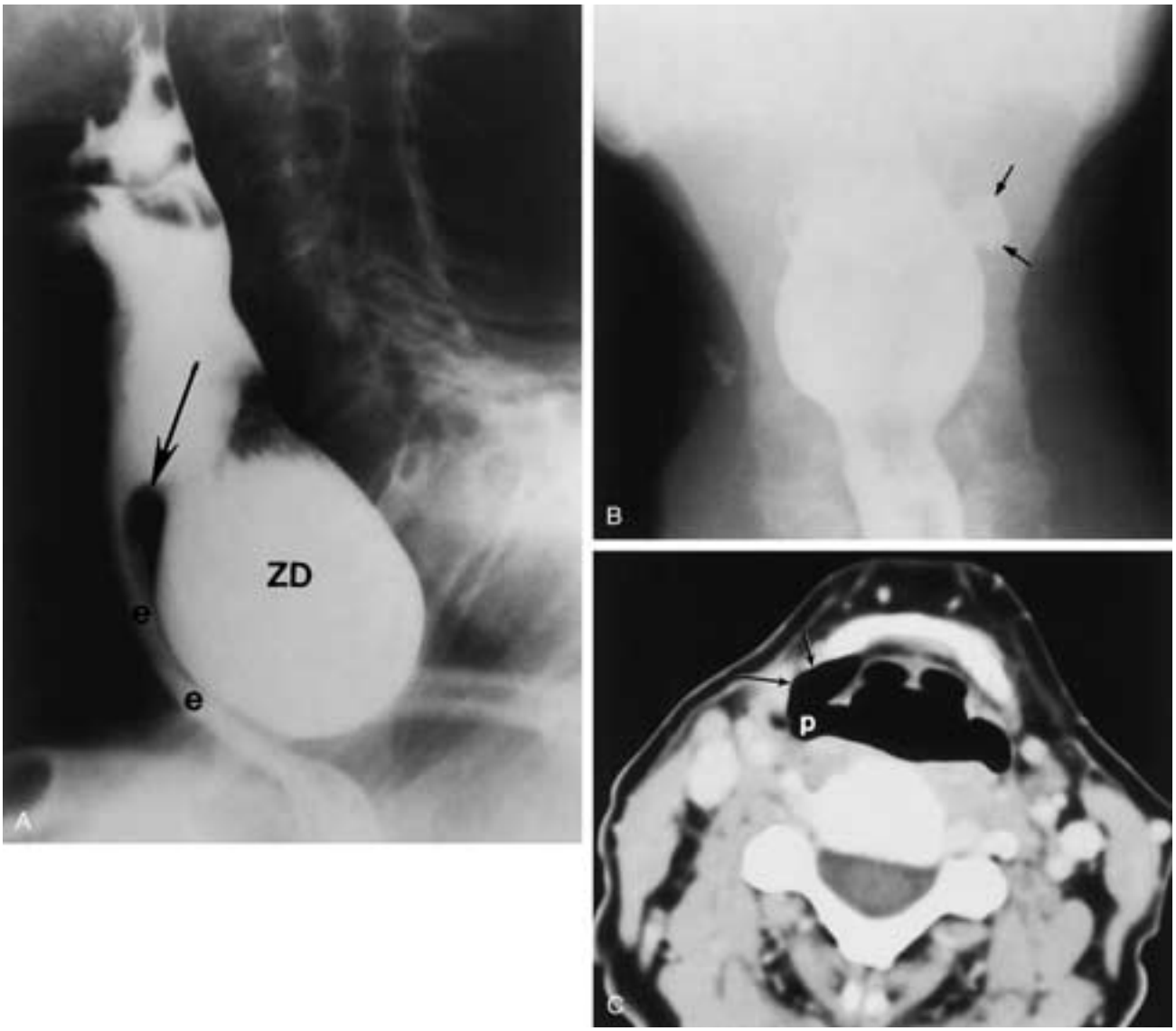

VIEW IMAGE

FIGURE 28-78 **A**, Oblique view of a barium swallow shows a large Zenker's diverticulum (*ZD*) extending from the hypopharynx above the cricopharyngeus muscle (*arrow*) and extending down into the upper chest behind the cervical esophagus (*e*). **B**, Frontal view of a barium swallow shows a small pharyngocele (*arrows*) arising from the left pyriform sinus. **C**, Axial CT scan shows an air-filled pharyngocele (*arrows*) arising from the right pyriform sinus (*p*).

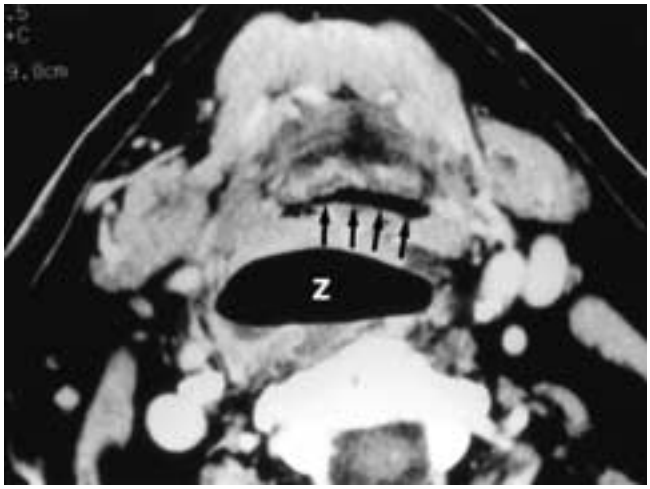

FIGURE 28-79 Axial contrast-enhanced CT scan shows a large air-containing cavity posterior to the airway (*arrows*) in a patient with a large Zenker's diverticulum (*Z*).

VIEW IMAGE

Copyright © 2003, Mosby, Inc. All rights reserved.

VIEW IMAGE

FIGURE 28-80 Extrinsic impressions on the hypopharynx. Lateral view of a barium swallow of a patient with dysphagia shows a prominent cricopharyngeus muscle (*black arrow*) that fails to relax as the bolus passes. The irregularity of the postcricoid region is normal (*white arrow*).

refuse surgery or who are poor surgical candidates because of underlying medical conditions.

Histologically, RT results early on in an acute inflammatory reaction within the deep connective tissues characterized by leukocytic infiltration, histiocyte formation, necrosis, and hemorrhage.[114–119] Detachment of the endothelial cells lining small arteries, veins, and lymphatics causes increased permeability, resulting in interstitial edema. Within 1 to 4 months after RT, there is deposition of rich collagenous fibers, with sclerosis and hyalinosis of the connective tissues. This inflammatory process eventually results in the obstruction of small arteries, veins, and lymphatics. By 8 months, there is advanced sclerosis, hyalinosis, and fragmentation of the collagen fibers within the connective tissues. Eventually there may be a reduction in interstitial fluid resulting from the formation of collateral neocapillary and lymphatic channels.[115, 118] The extent of the observed changes in the area included within the radiation port is mainly dependent on the total dose; however, more advanced and persistent changes may be seen in patients who continue to smoke after RT.

The pharynx is subjected to a high dose of radiation during definitive treatment of cancers and subsequently undergoes predictable changes that should not be confused with those of tumor. Pharyngeal changes resulting from RT include increased enhancement of the pharyngeal mucosa, which is thought to be due to the formation of telangiectatic vessels that may arise as a sequela of the radiation-induced mucositis.[118] The posterior pharyngeal wall typically thickens from a normal 2 to 3 mm to 6 to 7 mm in the post-RT patient. Additionally, patients typically develop 3 to 5 mm of edema in the retropharyngeal space (Fig. 28-81). These reactive changes may persist for many months or years.[118]

As has been previously reported for laryngeal tumors, successfully treated pharyngeal tumors result in a reduction in primary lesion size (Fig. 28-82).[119] However, the diffuse

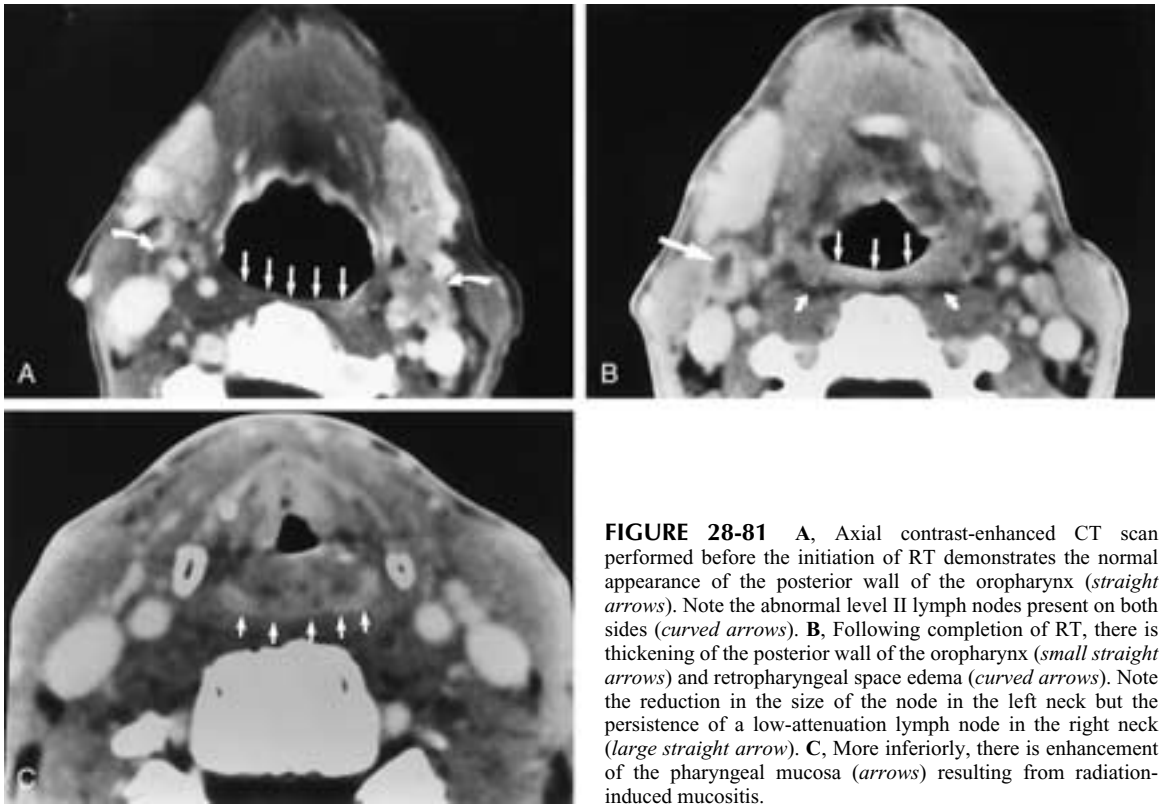

VIEW IMAGE

FIGURE 28-81 **A**, Axial contrast-enhanced CT scan performed before the initiation of RT demonstrates the normal appearance of the posterior wall of the oropharynx (*straight arrows*). Note the abnormal level II lymph nodes present on both sides (*curved arrows*). **B**, Following completion of RT, there is thickening of the posterior wall of the oropharynx (*small straight arrows*) and retropharyngeal space edema (*curved arrows*). Note the reduction in the size of the node in the left neck but the persistence of a low-attenuation lymph node in the right neck (*large straight arrow*). **C**, More inferiorly, there is enhancement of the pharyngeal mucosa (*arrows*) resulting from radiation-induced mucositis.

Copyright © 2003, Mosby, Inc. All rights reserved.

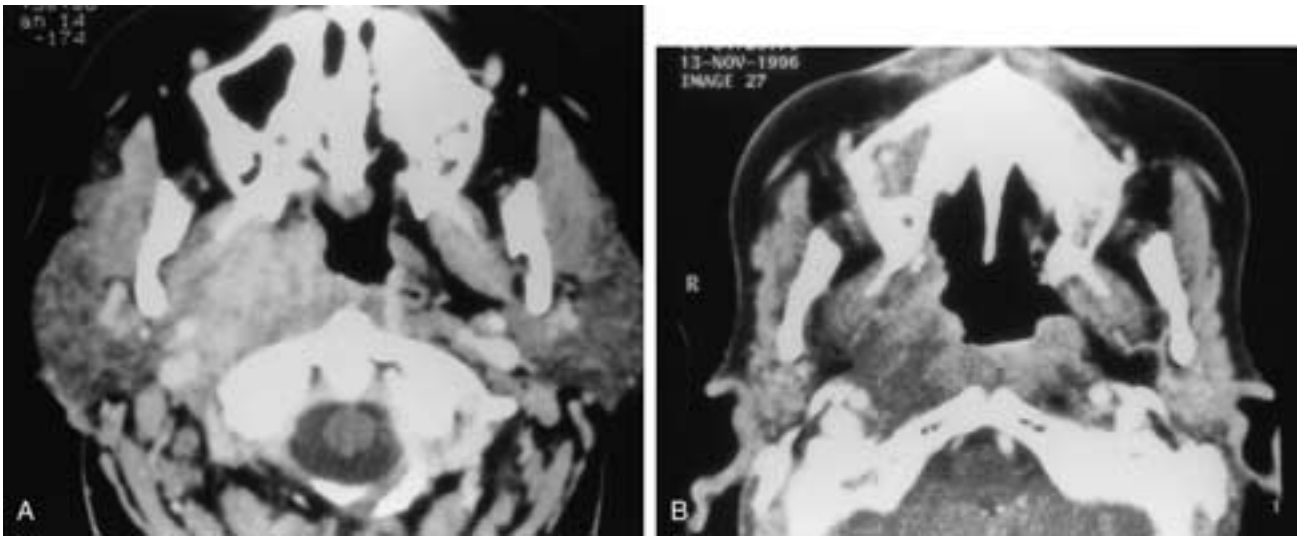

VIEW IMAGE

FIGURE 28-82 **A**, Axial pretreatment, contrast-enhanced CT scan demonstrates a large right tonsillar carcinoma. The mass extends laterally to involve the parapharyngeal space and invades the medial pterygoid muscle. The mass extends posteriorly to involve the carotid space. **B**, Following combined chemotherapy and RT, there is a marked reduction in the size and enhancement of the mass. This patient had no evidence of recurrent disease 2 years following completion of treatment.

and residual changes occurring in the pharynx should not be confused with residual tumor (Figs. 28-82 and 28-83). Comparing a present imaging study with a prior examination is the best method for making this distinction. Soft-tissue thickening caused by RT will not progressively enlarge, and any such progressive change should be suspected of representing tumor. In addition, the edematous changes tend to have an attenuation less than that of muscle, whereas tumor has a similar attenuation to that of muscle. Potential pharyngeal and laryngeal complications following RT

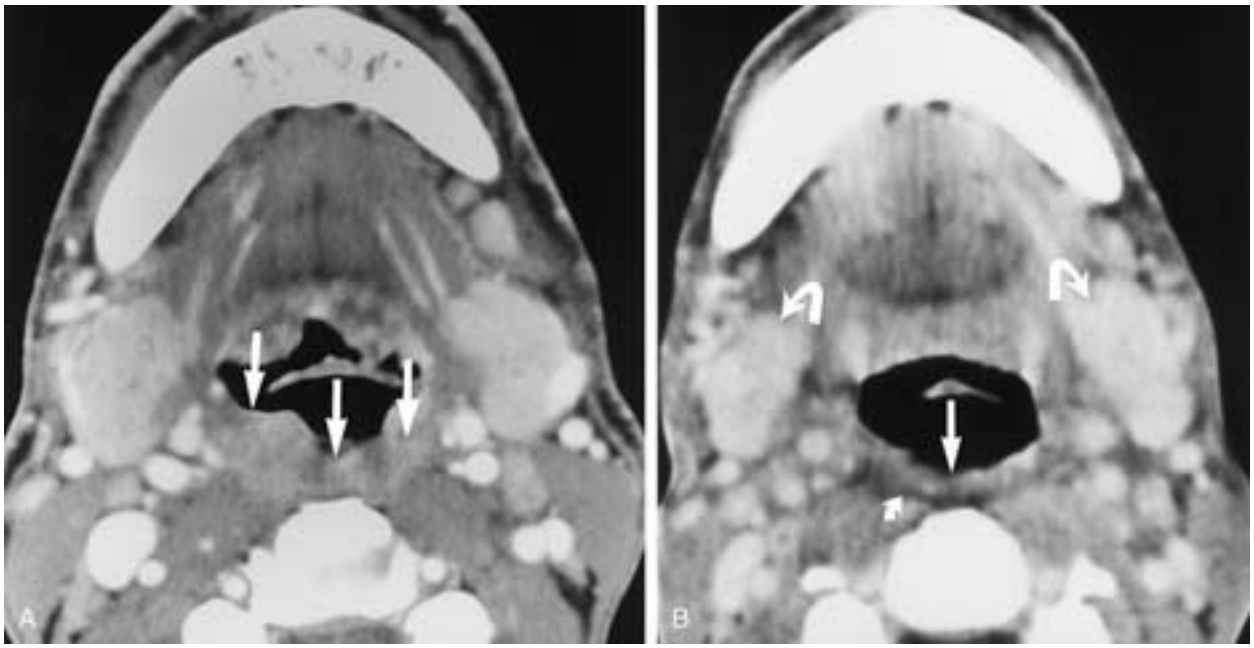

VIEW IMAGE

FIGURE 28-83 **A**, Axial contrast-enhanced CT scan demonstrates a tumor involving the posterior wall of the oropharynx (*arrows*) with bilateral nodal disease. **B**, Following RT, there is a marked reduction in the size of the tumor, with residual thickening of the posterior wall of the oropharynx (*straight arrow*). Retropharyngeal space edema (*small curved arrow*) and mild atrophy of the submandibular glands (*large curved arrows*) are normal changes resulting from RT.

Copyright © 2003, Mosby, Inc. All rights reserved.

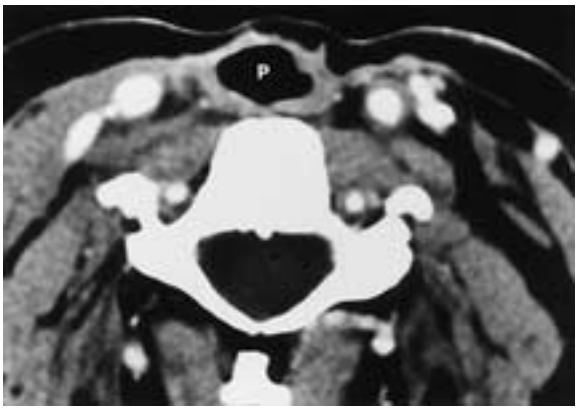

VIEW IMAGE

FIGURE 28-84 Axial CT scan shows the normal appearance of the pharynx (*P*) following a total laryngectomy. Because the larynx has been removed, the pharynx is in a more anterior position and is typically situated just deep to the subcutaneous fat.

include laryngeal necrosis, pharyngocutaneous fistula, pharyngeal stenosis, and peripheral nerve paralysis.[120]

Surgery

A variety of surgical procedures are available for treatment of malignancies involving the upper aerodigestive tract. However, resection results in marked distortion of the underlying anatomy, making interpretation of postoperative imaging studies difficult. The postoperative pharyngeal wall is typically thin and smooth (Fig. 28-84).

A variety of reconstruction procedures have been developed that utilize either myocutaneous flaps or free flaps.[121] This topic is discussed further in Chapter 43. When a myocutaneous flap is used, the resulting imaging picture characteristically shows the thin, rotated mucosal surface overlying the fatty bulk of the flap (Fig. 28-85).

The postsurgical neck is difficult to evaluate because of the extensive anatomic alterations caused by the resection. Because granulation and scar tissue normally enhance, the presence of contrast enhancement on CT or MR imaging does not help differentiate tumor from postoperative change. However, if an area that has reduced T1-weighted signal intensity progressively loses signal intensity on proton density and T2-weighted images, it is likely to be fibrosis rather than tumor.

As mentioned, comparison with a baseline posttreatment CT or MR study is often the best way to evaluate recurrent disease. Recurrent tumor should be considered when there is progressive enlargement of a node or a mass within the original primary site or along the margins of the surgical resection.[122–124] If prior studies are unavailable, the most reliable signs of recurrent disease are the presence of an obvious enhancing mass at the primary site or an obviously positive lymph node, as seen on CT. Tumor invasion of the internal carotid artery is difficult to diagnose on CT and MR imaging unless there is obvious narrowing of the vessel caliber (Fig. 28-52). This topic is discussed in Chapters 36 and 43.

Because tumors are more metabolically active than nontumorous surrounding tissue, measurement of the metabolic activity of a potential tumor recurrence may be more beneficial than pure morphologic analysis. Modalities

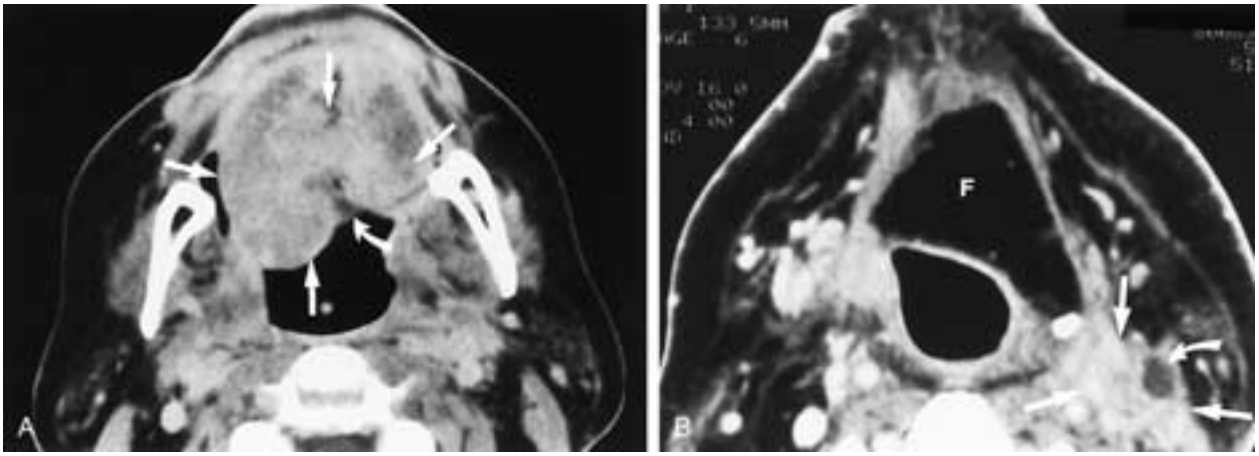

VIEW IMAGE

FIGURE 28-85 **A**, Axial CT scan obtained through the tongue base shows a large, ulcerated mass invading and replacing the tongue base (*straight arrows*, tumor; *curved arrow*, ulceration. **B**, This patient underwent a total glossectomy and myocutaneous flap reconstruction. The flap (*F*) fills in the operative defect and provides a mucosal surface to the pharynx. Note the low-attenuation lymph node (*curved arrow*) and the surrounding soft-tissue mass (*straight arrows*) indicating recurrent disease.

Copyright © 2003, Mosby, Inc. All rights reserved.

that can evaluate metabolic activity such as FDG and thallium-201, as well as MR spectroscopy, are currently being investigated (Fig. 28-53).[125–128] These topics are discussed in Chapter 45.

REFERENCES

1. Moore KL. The neck. In: Moore KL. Clinically Oriented Anatomy. 2nd ed. Baltimore: Williams & Wilkins, 1985;1033–1050.
2. Wenig BM, Kornblut AD. Pharyngitis. In: Baily BJ, ed. Head and Neck Surgery Otolaryngology. Philadelphia: JB Lippincott, 1993; 551–553.
3. Moore KL. The branchial apparatus and the head and neck. In: Moore KL, ed. The Developing Human: Clinically Oriented Embryology. 4th ed. Philadelphia: WB Saunders, 1988;170–194.
4. Batsakis JG. Cysts, sinuses and ''coeles.'' In: Batsakis JG. Tumors of the Head and Neck. 2nd ed. Baltimore: Williams & Wilkins; 1979;514–520.
5. Mendenhall WM, Million RR, Mancuso AA, et al. Nasopharynx. In: Million RR, Cassisi NJ, eds. Management of Head and Neck Cancer: A Multidisciplinary Approach. Philadelphia: JB Lippincott, 1994; 599–626.
6. Neel HB, Slavitt DH. Nasopharyngeal cancer. In: Baily BJ, ed. Head and Neck Surgery Otolaryngology. Philadelphia: JB Lippincott, 1993;1257–1260.
7. Mancuso AA, Hanafee WN. Nasopharynx and parapharyngeal space. In: Computed Tomography and Magnetic Resonance Imaging of the Head and Neck. 2nd ed. Baltimore: Williams & Wilkins, 1985;428–498.
8. Mukherji SK, Weissman JL, Holliday R. The pharynx. In: Som PM, Curtin H, eds. Head and Neck Imaging. 3rd ed. New York: CV Mosby, 1996;437–488.
9. Mukherji SK, Castillo M. Normal cross-sectional anatomy of the nasopharynx, oropharynx, and oral cavity. Neuroimaging Clin North Am 1998;8:211–218.
10. Youssem DM, Loevner LA, Tobey JD, et al. Adenoidal width and HIV factors. AJNR 1997;18:1721–1725.
11. Lederman M. Cancer of the Nasopharynx: Its Natural History and Treatment. Springfield, Ill: Charles C Thomas, 1961;150.
12. Rouvierre H. Anatomy of the Human Lymphatic System. Tobias MJ, trans. Ann Arbor, Mich: Edwards Brothers, 1938;1–76.
13. Louvner LA, Ott IL, Youssem DM, et al. Neoplastic fixation to the prevertebral compartment by squamous cell carcinoma of the head and neck. AJR 1998;170:1389–1394.
14. Million RR, Cassisi NJ, Mancuso AA. Hypopharynx: pharyngeal walls, pyriform sinus, postcricoid pharynx. In: Million RR, Cassisi NJ, eds. Management of Head and Neck Cancer: A Multidisciplinary Approach. Philadelphia: JB Lippincott, 1994;505–532.
15. Fleming ID, Cooper JS, Henson DE, et al, eds. American Joint Committee on Cancer, Manual for Staging of Cancer. 5th ed. Philadelphia: Lippincott-Raven, 1992;24–40.
16. Barnes L, Gnepp DR. Diseases of the larynx, hypopharynx, and esophagus. In: Barnes L, ed. Surgical Pathology of the Head and Neck. New York: Marcel Dekker, 1985;141–226.
17. Muntz H, Sessions DG. Surgery of laryngopharyngeal and subglottic cancer. In: Bailey BT, Hiller HF, eds. Surgery of the Larynx. Philadelphia: WB Saunders, 1985;293–315.
18. Graney DO, Marsh B. Trachea/bronchus/esophagus: anatomy. In: Cummings CW, Fredrickson JM, Harker LA, et al, eds. Otolaryngology—Head and Neck Surgery. St. Louis, Mo: Mosby Year Book, 1993;2207–2216.
19. Hollinshead WH. Textbook of Anatomy. Hagerstown, Md: Harper & Row, 1974;928–948.
20. Robbins KT. Pocket Guide to Neck Dissection: Classification and TNM Staging of Head and Neck Cancer. Alexandria, Va: American Academy of Otolaryngology-Head and Neck Surgery Foundation, 1991.
21. Brick SB, Caroline DF, Lev-Toaff AS, et al. Esophageal disruption: evaluation with Iohexol esophagography. Radiology 1988;169: 141–143.
22. Mukherji SK, Pillsbury H, Castillo M. Imaging squamous cell carcinomas of the upper aerodigestive tract: what the clinicians need to know. Radiology 1997;205:629–646.
23. Suojanen JS, Mukherji SK, Whippold FJ. Spiral CT of the larynx. AJNR 1994;15:1579–1582.
24. Mukherji SK, Castillo M, Huda W, et al. Comparison of dynamic and spiral CT for imaging of the glottic larynx. J Comput Assist Tomogr 1995;19:899–904.
25. Dillon WP, Mill CM, Kjos B, et al. Magnetic resonance image of the nasopharynx. Radiology 1984;152:731–735.
26. Unger JM. The oral cavity and tongue: magnetic resonance imaging. Radiology 1986;155:151–153.
27. Lufkin RB, Larsson SG, Hanafee WN. Work in progress: NMR anatomy of the larynx and tongue base. Radiology 1983;148:173–175.
28. Lufkin R, Wortham DG, Dietrich RB, et al. Tongue and oropharynx: findings on MR imaging. Radiology 1986;161:69–75.
29. Larsson SG, Mancuso AA, Hanafee WN. Computed tomography of the tongue and floor of the mouth. Radiology 1982;143:493–500.
30. Byrd SE, Schoen PJ, Gill G, et al. Computed tomography of palatine tonsillar carcinoma, J Comput Assist Tomogr 1983;7:976–982.
31. Muraki AS, Mancuso AA, Harnsberger HR. CT of the oropharynx, tongue base and floor of the mouth: normal anatomy and range of variations and applications in staging carcinoma. Radiology 1983;148:725–731.
32. Slootweg PJ, Richardson M. Squamous cell carcinoma of the upper aerodigestive system. In: Gnepp DR, ed. Diagnostic Surgical Pathology of the Head and Neck. Philadelphia: WB Saunders, 2000;19–78.
33. Hsu MM, Huang SC, Lynn TC, et al. The survival of patients with nasopharyngeal carcinoma. Otolaryngol Head Neck Surg 1982;90: 289–290.
34. Simons MJ, Wee GB, Day NE, et al. Immunogenetic aspects of nasopharyngeal carcinoma. I. Differences in HLA antigen profiles between patients and control groups. Int J Cancer 1974;13:122–124.
35. Dickson RI. Nasopharyngeal carcinomas: an evaluation of 209 patients. Laryngoscope 1981;91:333–334.
36. Huang DP, Ho JHC, Chan WK, et al. Cytogenetics of undifferentiated nasopharyngeal carcinoma xenografts from southern Chinese. Int J Cancer 1989;43:936–939.
37. Huang DP, Lo KW, Choi PHK, et al. Loss of heterozygosity on the short arm of chromosome 3 in nasopharyngeal carcinoma. Cancer Genet Cytogenet 1991;54:91–99.
38. Huang DP, Lo KW, van Hasselt CA, et al. A region of homozygous deletion on chromosome 9p21-22 in primary nasopharyngeal carcinoma. Cancer Res 1994;54:4003–4006.
39. Hui ABY, Lo KW, Leung SF, et al. Loss of heterozygosity on the long arm of chromosome 11 in nasopharyngeal carcinoma. Cancer Res 1996;56:3225–3229.
40. Shanmugaratnam K. Histological typing of tumors of the upper respiratory tract and ear. WHO International Histologic Classification of Tumors. 2nd ed. Berlin and Heidelberg: Springer-Verlag, 1991;32–33.
41. Sanguineti G, Geara FB, Garden AS, et al. Carcinoma of the nasopharynx treated by radiotherapy alone: determinants of local and regional control. Int J Radiat Oncol Biol Phys 1997;37:985–996.
42. Garden AS, Lippman SM, Morrison WH, et al. Does induction chemotherapy have a role in the management of nasopharyngeal carcinoma? Results of treatment in the era of computerized tomography. Int J Radiat Oncol Biol Phys 1996;36:1005–1012.
43. Chua DTT, Sham JST, Kwong DLW, et al. Volumetric analysis of tumor extent in nasopharyngeal carcinoma and correlation with treatment outcome. Int J Radiat Oncol Biol Phys 1997;39:711–719.
44. Mesic JB, Fletcher GH, Goepfert H. Megavoltage irradiation of epithelial tumors of the nasopharynx. Int J Radiat Oncol Biol Phys 1981;7:447–453.
45. Chong VFH, Fan YF, Mukherji SK. Carcinoma of the nasopharynx. Semin Ultrasound CT MRI 1998;19:449–462.
46. Chong VFH, Mukherji SK, Ng SHH, et al. Nasopharyngeal carcinoma: review of how imaging affects staging. J Comput Assist Tomogr 1999;23:984–993.
47. Chong VFH, Fan YF. Skull base erosion in nasopharyngeal carcinoma: detection by CT and MRI. Clin Radiol 1996;51:625–631.
48. Chong VFH, Fan YF, Khoo JBK. Nasopharyngeal carcinoma with intracranial spread: CT and MRI characteristics. J Comput Assist Tomogr 1996;20:563–639.
49. Sham JST, Cheung YK, Choy D, et al. Cranial nerve involvement and base of skull erosion in nasopharyngeal carcinoma. Cancer 1991;68:422–426.

Copyright © 2003, Mosby, Inc. All rights reserved.

50. Fletcher GH, Million RR. Malignant tumors of the nasopharynx. Am J Roentgenol Radium Ther Nucl Med 1965;93:44–45.
51. Sham JST, Choy D, Wei W. Nasopharyngeal carcinoma: orderly neck node spread. Int J Radiat Oncol Biol Phys 1990;19:929–933.
52. McLaughlin MP, Mendenhall WM, Mancuso AA, et al. Retropharyngeal adenopathy as a predictor of outcome in squamous cell carcinoma of the head and neck. Head Neck 1995;17:190–198.
53. Chong VFH, Fan YF, Khoo JBK. Retropharyngeal lymphadenopathy in nasopharyngeal carcinoma. Eur J Radiol 1995;21:100–105.
54. Million RR, Cassisi, NJ, Mancuso AA. The oropharynx. In: Million RR, Cassisi NJ, eds. Management of Head and Neck Cancer: A Multidisciniplinary Approach. Philadelphia: JB Lippincott, 1994; 402–431.
55. Mancuso AA, Hanafee WN. Oral cavity and oropharynx including tongue base, floor of mouth and mandible. In: Mancuso AA, Hanafee WN. Computed Tomography and Magnetic Resonance Imaging of the Head and Neck. 2nd ed. Baltimore: Williams & Wilkins; 1985;358–427.
56. Batsakis JG. Tumors of the Head and Neck: Clinical and Pathologic Considerations. 2nd ed. Baltimore: Williams & Wilkins, 1979;144–176.
57. Lindberg RD. Distribution of cervical lymph node metastases from squamous cell carcinoma of the upper respiratory and digestive tracts. Cancer 1972;29:1448–1449.
58. Russ JE, Applebaum EL, Sisson CA. Squamous cell carcinoma of the soft palate. Laryngoscope 1977;87:1151–1156.
59. Byrd SE, Schoen PJ, Gill G, et al. Computed tomography of palatine tonsillar carcinoma. J Comput Assist Tomogr 1983;7:976–982.
60. Schaefer SD, Marvilla KR, Suss RA, et al. Magnetic resonance imaging versus computed tomography: comparison in imaging oral cavity and pharyngeal carcinomas. Arch Otolaryngol Head Neck Surg 1985;111:730–734.
61. Byers RM, Wolf PF, Ballantyne AJ. Rationale for elective modified neck dissection. Head Neck Surg 1988;10:106–167.
62. Mendenhall NP. Lymphomas and related diseases presenting in the head and neck. In: Million RR, Cassisi NJ, eds. Management of Head and Neck Cancer: A Multidisciplinary Approach. Philadelphia: JB Lippincott, 1994;857–878.
63. Myers EN, Cunningham MJ. Tumors of the neck. In: Bluestone CD, Stool SE, Scheetz MD, eds. Pediatric Otolaryngology. Vol 2. Philadelphia: WB Saunders, 1990;1339–1363.
64. Wong DS, Fuller LM, Butler JJ, et al. Extranodal non-Hodgkin's lymphomas of the head and neck. Am J Radiol 1975;123: 471–481.
65. Million RR, Cassisi, NJ. Minor salivary gland tumors. In: Million RR, Cassisi NJ, eds. Management of Head and Neck Cancer: A Multidisciplinary Approach. Philadelphia: JB Lippincott, 1994; 737–750.
66. Gandour-Edwards R, Kapadia SB, Barnes L, et al. Neural cell adhesion molecule (NCAM) in adenoid cystic carcinoma of the skull base (abstract). Presented at the meeting of the North American Skull Base Society, 1995.
67. Papadaki H, Finkelstein SD, Kounelis S, et al. The role of p53 mutation and protein expression in primary and recurrent adenoid cystic carcinoma. Hum Pathol 1996;27:567–572.
68. Nemzek WR, Hecht S, Gandour-Edwards R, et al. Perineural spread of head and neck tumors: how accurate is MR imaging? AJNR 1998;19:701–706.
69. Lee FA. Rhabdomyosarcoma. In: Parker BR, Castellano RA, eds. Pediatric Oncologic Radiology. St. Louis: CV Mosby, 1977;33–55.
70. Canalis RF, Jenkens HA, Hemenway WG, et al. Nasopharyngeal rhabdomyosarcoma: a clinical perspective. Arch Otolaryngol Head Neck Surg 1978;104:122–126.
71. Dito WR, Batsakis JG. Intraoral, pharyngeal and nasopharyngeal rhabdomyosarcoma. Arch Otolaryngol Head Neck Surg 1963;77: 123–129.
72. McGill T. Rhabdomyosarcoma of the head and neck: an update. Otolaryngol Clin North Am 1989;22(3):631–636.
73. Scotti G, Harwood-Nash DC. Computed tomography of rhabdomyosarcomas of the skull base in children. J Comput Assist Tomogr 1982;6(1):33–39.
74. Robb PJ, Girling A. Granular cell myoblastoma of the supraglottis. J Laryngol Otol 1989;103:328–330.
75. Cree IA, Bingham BJG, Ramesar KCRB. View from beneath: pathology in focus: granular cell tumour of the larynx. J Laryngol Otol 1990;104:159–161.
76. Batsakis JG. Tumors of the Head and Neck: Clinical and Pathological Considerations. 2nd ed. Baltimore: Williams & Wilkins, 1979;313–333.
77. Batsakis JG. Tumors of the Head and Neck. 2nd ed. Baltimore: Williams & Wilkins, 1979;228–289.
78. Masson JK, Soule EH. Desmoid tumor of the head and neck. Am J Surg 1966;112:615–622.
79. Som PM, Lanzieri CF, Sacher M, et al. Extracranial tumor vascularity: determination by dynamic CT scanning. Radiology 1985;154:401–412.
80. Das Gupta TK. Tumors of the peripheral nerves. In: Das Gupta TK, ed. Tumors of the Soft Tissues. East Norwalk, Conn: Appleton-Century-Crofts, 1983;89–95.
81. Itoh K, Nishimura K, Togashi K, et al. MR imaging of cavernous hemangioma of the face and neck. J Comput Assist Tomogr 1986;10: 831–835.
82. Barnes L. Tumors and tumorlike lesions of the soft tissues. In: Barnes L, ed. Surgical Pathology of the Head and Neck. New York: Marcel Dekker, 1985;725–880.
83. Johnson JT, Curtin HD. Deep neck lipoma. Ann Otol Rhinol Laryngol 1987;96:472–473.
84. Million RR, Cassisi NJ, Mancuso AA. The unknown primary. In: Million RR, Cassisi NJ, eds. Management of Head and Neck Cancer: A Multidisciplinary Approach. 2nd ed. Philadelphia: JB Lippincott, 1994;311–321.
85. Harper CS, Mendenhall WM, Parsons JT, et al. Cancer in neck nodes with unknown primary site: role of mucosal radiotherapy. Head Neck 1990;12:463–469.
86. Templer J, Perry MC, Davis WE. Metastatic cervical adenopathy from an unknown primary tumor: treatment dilemma. Arch Otolaryngol 1981;107:45–47.
87. Mukherji SK, Drane WE, Mancuso AA, et al. Occult primary tumors of the head and neck. Detection with 2-[F-18] fluoro-2-deoxy-D-glucose SPECT Radiology 1996;199:761–766.
88. Johnson JT, Newman RK. The anatomic location of neck metastases from occult squamous cell carcinoma. Otol Head Neck Surg 1981;89:54–58.
89. Gianoli GJ, Espinola TE, Guarisco JL, et al. Retropharyngeal space infection: changing trends. Otol Head Neck Surg 1991;105:92–100.
90. Grodinsky M. Retropharyngeal and lateral pharyngeal space abscesses: an anatomical and clinical study with review of the literature. Am J Surg 1979;110:179–199.
91. Batsakis JG, Sneige N. Parapharyngeal and retropharyngeal space disease. Ann Otol Rhinol Laryngol 1989;98:320–321.
92. Davis WL, Harnsberger HR, Smoker WRK, et al. Retropharyngeal space: evaluation of normal anatomy and disease with CT and MR imaging. Radiology 1990;174:59–64.
93. Mukherji SK, Castillo M. A simplified approach to the spaces of the extracranial head & neck. Radiol Clin North Am 1998;36:761–780.
94. Mukherji SK, Mancuso AA, Shook J. Retropharyngeal suppurative lymphadenitis: differentiation from retropharyngeal abcess and treatment implications (abstract). Presented at the meeting of the Radiological Society of North America, 1994.
95. Glasier CM, Stark JE, Jacobs RF, et al. CT and ultrasound imaging of retropharyngeal abscesses in children. AJNR 1992;13:1191–1195.
96. Kornbutt AD. Infections of the pharyngeal spaces. In: Paparilla M, Shumrick M, eds. Otolaryngology. Vol. 3. Philadelphia: WB Saunders, 1980.
97. Eastwood JD, Hudgins PA, Malone D: Retropharyngeal effusion in acute calcific prevertebral tendinitis: diagnosis with CT and MR imaging. AJNR 1988;19(9):1789–1792.
98. Dillon WP, Mills CM, Kjos B, et al. Magnetic resonance image of the nasopharynx. Radiology 1984;152:731–735.
99. Holliday RA. Manifestations of AIDS in the oromaxillofacial region: the role of imaging. Radiol Clin North Am 1993;31:45–60.
100. Marcusen DC, Sooy CD. Otolaryngologic and head and neck manifestations of acquired immunodeficiency syndrome (AIDS). Laryngoscope 1985;95:401–405.
101. Rosenberg RA, Schneider KL, Cohen NL. Head and presentations of acquired immunodeficiency syndrome. Otolaryngol Head Neck Surg 1985;93:700–705.
102. Grepp DR, Chandler W, Hyams V. Primary Kaposi's sarcoma of the head and neck. Ann Intern Med 1984;100:107–114.
103. MacPhail LA, Greenspan D, Schiodt M, et al. Acyclovir-resistant, foscarnet-sensitive oral herpes simplex type 2 lesion in a patient with AIDS. Oral Surg Oral Med Oral Pathol 1989;67:427–432.

Copyright © 2003, Mosby, Inc. All rights reserved.

104. Abeymayor E, Calcaterra T. Kaposi's sarcoma and community acquired immunodeficiency syndrome: an update with emphasis on its head and neck manifestations. Arch Otolaryngol 1983;109: 536–542.
105. Grepp DR, Chandler W, Hyams V. Primary Kaposi's sarcoma of the head and neck. Ann Intern Med 1984;100:107–114.
106. Stern JC, Lin PT, Lucente FE. Benign nasopharyngeal masses and HIV infection. Arch Otolaryngol Head Neck Surg 1990;116: 206–208.
107. Roland JT, Rothstein SG, Khushbakhat RM, et al. Squamous cell carcinoma in HIV-positive patients under age 45. Laryngoscope 1993;103:509–511.
108. Snyderman CH, Weissman JL, Tabor ET, et al. Crack cocaine burns of the larynx. Arch Otolaryngol Head Neck Surg 1991;117:792–795.
109. Fein DA, Mendenhall WM, Parsons JT, et al. T1T2 squamous cell carcinoma of the glottic larynx treated with radiotherapy: a multivariate analysis of variables potentially influencing local control. Int J Radiat Oncol Biol Phys 1993;25:605–611.
110. Lee WR, Mancuso AA, Saleh EM, et al. Can pretreatment computed tomography findings predict local control in T3 squamous cell carcinoma of the glottic larynx treated with radiotherapy alone? Int J Radiat Oncol Biol Phys 1993;25:683–687.
111. Freeman DE, Mancuso AA, Parsons JT, et al. Irradiation alone for supraglottic carcinoma: can CT findings predict treatment results? I Int J Radiat Oncol Biol Phys 1990;19:485–490.
112. Amdur RJ, Parsons JT, Mendenhall WM, et al. Postoperative irradiation for squamous cell carcinoma of the head and neck: an analysis of treatment results and complications. Int J Radiat Oncol Biol Phys 1989;16:25–36.
113. Mukherji SK, Mancuso AA, Mendenhall W, et al. Can pretreatment computed tomography predict local control in T2 glottic carcinomas treated with radiation therapy alone? AJNR 1995;16:655–662.
114. Mancuso AA, Mukherji SK, Kotzur I, et al. Preradiotherapy-computed tomography as a predictor of local control in supraglottic carcinoma. J Clin Oncol 1999;17:631–636.
115. Manara M. Histological changes of the human larynx irradiated with various technical therapeutic methods. Arch Ital Otol 1966;79: 596–635.
116. Goldman JL, Cheren RV, Zak FG, et al. Histopathology of larynges and radical neck specimens in a combined radiation and surgery for advanced carcinoma of the larynx and hypopharynx. Ann Otol 1966;75:313–321.
117. Calcaterra TC, Stern F, Ward PH. Dilemma of delayed radiation injury of the larynx. Ann Otol Rhinol Laryngol 1972;81:501–507.
118. Mukherji SK, Mancuso AA, Kotzur IM, et al. Radiographic appearance of the irradiated larynx. Part I, expected changes. Radiology 1994;193:141–148.
119. Mukherji SK, Mancuso AA, Kotzur IM, et al. Radiographic appearance of the irradiated larynx. Part II, primary site response. Radiology 1994;193:149–154.
120. Becker M, Schroth G, Zbaren P, et al. Long-term changes induced by high-dose irradiation of the head and neck region: imaging findings. RadioGraphics 1997;17:5–26.
121. Tiwari R, Snow GB. Role of myocutaneous flaps in reconstruction of the head and neck. J Laryngol Otol 1983;97:441–458.
122. Hudgins PA, Burson JG, Gussak GS, et al. CT and MR appearance of recurrent malignant head and neck neoplasms after resection and flap reconstruction. AJNR 1994;15:1689–1694.
123. Som PM, Urken ML, Biller H, et al. Imaging of the postoperative neck. Radiology 1993;187:593–603.
124. Som PM, Biller F. Computed tomography of the neck in the postoperative patient: radical neck dissection and the myocutaneous flap. Radiology 1983;148:157–160.
125. Mukherji SK, Drane WE, Tart RP, et al. Comparison of SPECT FDG and SPECT thallium 201 for imaging of squamous cell carcinoma of the head and neck. AJNR 1994;15:1837–1842.
126. Fischbein NJ, Assar SA, Caputo GR, et al. Clinical utility of positron emission tomography with F-18 fluorodeoxyglucose in detecting residual/recurrent squamous cell carcinoma of the head and neck. AJNR 1998;19:1189–1196.
127. Mukherji SK, Gapany M, Phillips D, et al. Squamous cell carcinoma of the upper aerodigestive tract: the ability of thallium-201 SPECT to detect recurrent tumor. Am J Neuroradiol 1999;20:1215–1220.
128. Mukherji SK, Schiro S, Castillo M, et al. MR proton spectroscopy of squamous cell carcinoma of extracranial head and neck: in vitro and in vivo studies. Am J Neuroradiol 1997;18:1057–1072.

Copyright © 2003, Mosby, Inc. All rights reserved.

29

Pediatric Airway Disease

Caroline D. Robson and Patricia A. Hudgins

SECTION ONE: EMBRYOLOGY
FACE AND NASOLACRIMAL DUCTS
PALATE
NASAL CAVITIES
PHARYNX, LARYNX, AND TRACHEA
GREAT VESSELS
SECTION TWO: CLINICAL EVALUATION
STRIDOR
OBSTRUCTIVE SLEEP APNEA
SECTION THREE: RADIOGRAPHIC TECHNIQUES
PLAIN FILMS
FLUOROSCOPY
COMPUTED TOMOGRAPHY
MAGNETIC RESONANCE IMAGING
SECTION FOUR: NORMAL ANATOMY
NASAL CAVITY
NASOPHARYNX AND OROPHARYNX
HYPOPHARYNX
LARYNX AND TRACHEA
SECTION FIVE: CONGENITAL AIRWAY DISEASES
NASAL OBSTRUCTION
- Choanal Atresia
- Nasolacrimal Duct Cysts
- Pyriform Aperture Stenosis
- Other Forms of Nasal Stenosis and Nasal Agenesis
- Nasopharyngeal Atresia
- Meningocele, Encephalocele, Nasal Dermoid, and Neuroglial Heterotopia

CRANIOFACIAL MALFORMATIONS
OROPHARYNGEAL OBSTRUCTION
- Thyroglossal Duct Cyst and Ectopic Thyroid
- Lingual Cysts
- Macroglossia and Glossoptosis
- Micrognathia and Retrognathia

LARYNGEAL OBSTRUCTION
- Laryngomalacia
- Vocal Cord Paralysis
- Laryngoceles and Laryngeal Cysts
- Anomalies of the Epiglottis
- Laryngeal Webs, Clefts, and Atresia

SUBGLOTTIC OBSTRUCTION
- Congenital Subglottic Stenosis

TRACHEAL OBSTRUCTION
- Tracheomalacia
- Intrinsic Tracheal Stenosis
- Vascular Compression of the Airway

VASCULAR ANOMALIES
- Hemangioma
- Lymphatic Malformation
- Venous Malformation

SECTION SIX: INFECTIOUS AND INFLAMMATORY DISORDERS
VIRAL ADENOTONSILLITIS AND LYMPHADENOPATHY
- Nonspecific Viral Infection
- Infectious Mononucleosis (Epstein-Barr Virus)

BACTERIAL ADENOTONSILLITIS, LYMPHADENOPATHY, CELLULITIS, AND ABSCESS
- Acute Bacterial Infection
- Granulomatous Infection

SUPRAGLOTTITIS (EPIGLOTTITIS)
LARYNGOTRACHEOBRONCHITIS (CROUP)
BACTERIAL TRACHEITIS
MISCELLANEOUS CONDITIONS
SECTION SEVEN: TRAUMA
FACIAL TRAUMA
OROPHARYNGEAL TRAUMA
LARYNGEAL AND TRACHEAL TRAUMA
THERMAL TRAUMA AND CAUSTIC INGESTION

Copyright © 2003, Mosby, Inc. All rights reserved.

INTUBATION TRAUMA
INGESTED OR ASPIRATED FOREIGN BODY
MISCELLANEOUS CONDITIONS
SECTION EIGHT: BENIGN TUMORS AND TUMOR-LIKE CONDITIONS
ADENOIDAL AND TONSILLAR HYPERTROPHY
RECURRENT RESPIRATORY PAPILLOMATOSIS
JUVENILE NASOPHARYNGEAL ANGIOFIBROMA
MISCELLANEOUS CONDITIONS
SECTION NINE: MALIGNANT TUMORS
LYMPHOMA
RHABDOMYOSARCOMA
NASOPHARYNGEAL CARCINOMA
MISCELLANEOUS CONDITIONS

SECTION ONE

EMBRYOLOGY

The face and neck are formed primarily by the paired pharyngeal or branchial arches. A detailed discussion of facial embryology is given in Chapter 1, and a thorough review of neck embryology is presented in Chapter 33. The reader is referred to these chapters for information on these subjects. With specific reference to lesions or abnormalities that can encroach upon the airway, the following areas are briefly reviewed.

FACE AND NASOLACRIMAL DUCTS

The facial prominences appear at the end of the fourth week of fetal development, and these structures are derived mainly from the first pair of pharyngeal arches (Fig. 29-1). The stomodeum forms the center of the developing face and, relative to the stomodeum, the mandibular prominences are caudal, the maxillary prominences are lateral, and the frontonasal prominence is cranial. The nasal placodes originate lateral to the frontonasal prominence under inductive influence from the ventral portion of the forebrain.[1, 2] During the fifth week the nasal placodes invaginate to form nasal pits, which are surrounded by ridges of tissue called the medial and lateral nasal prominences. Medial growth of the maxillary processes compresses the medial nasal prominences toward the midline. These structures fuse to form the upper lip. The four upper incisor teeth, the medial superior alveolar ridge, and the primary palate originate as the *intermaxillary segment* from the medial nasal prominences.[2] The mandibular prominences form the lower lip and jaw.

The nasolacrimal groove is a deep furrow between the maxillary and lateral nasal prominences. This groove detaches from the overlying ectoderm and ultimately canalizes to form the nasolacrimal duct and sac. The nasolacrimal duct runs from the medial canthus of the orbit to the inferior meatus of the nasal cavity. The maxillary prominences form the cheeks and maxillae and fuse with the lateral nasal prominences over the developing nasolacrimal duct. The nose is formed from the frontal prominence (bridge), the medial nasal prominences (crest and tip), and the lateral nasal prominences (alae).

PALATE

The triangular primary palate develops from the intermaxillary segment and is located anterior to the midline incisive foramen. The secondary palate (hard and soft palates) arises as two palatal shelves from the maxillary prominences (Fig. 29-2).

NASAL CAVITIES

The formation of the nasal cavity depends mainly on the inferior migration of the primitive nasal septum and the

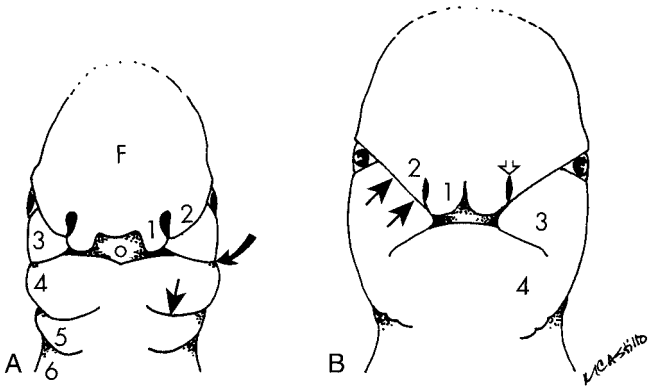

FIGURE 29-1 Development of the face. **A**, Frontal drawing of a 5-week-old fetus shows the oral placode (*o*), which divides the face into superior and inferior compartments. Superiorly and centrally is the massive frontal eminence (*F*). The medial nasal prominence (*1*) is separated from the lateral nasal prominence (*2*) by the nasal pit. The nasooptic groove separates the lateral nasal prominence from the maxillary process (*3*). The inferior compartment of the face is formed by the mandibular arch (*4*) which is separated from the lower hyoid arch (*5*) by the hypomandibular cleft (*arrow*). The third branchial arch (*6*) is present inferiorly. The curved arrow indicates the position of the ear tubercules. **B**, Frontal drawing of a 7-week-old fetus shows that the face has acquired a more recognizable pattern. The medial nasal (*1*) and lateral nasal (*2*) processes are separated by the rudimentary nostril (*open arrow*) and are delineated laterally by the nasal ala. The midface consists mainly of the maxillary process (*3*) on either side. The inferior face is formed by the two mandibular processes (*4*). The orbits are better developed and have migrated inferiorly and medially to a more midline position. The nasooptic grooves (*small arrows*) deepen and eventually canalize to form the nasolacrimal ducts.

VIEW IMAGE

Copyright © 2003, Mosby, Inc. All rights reserved.

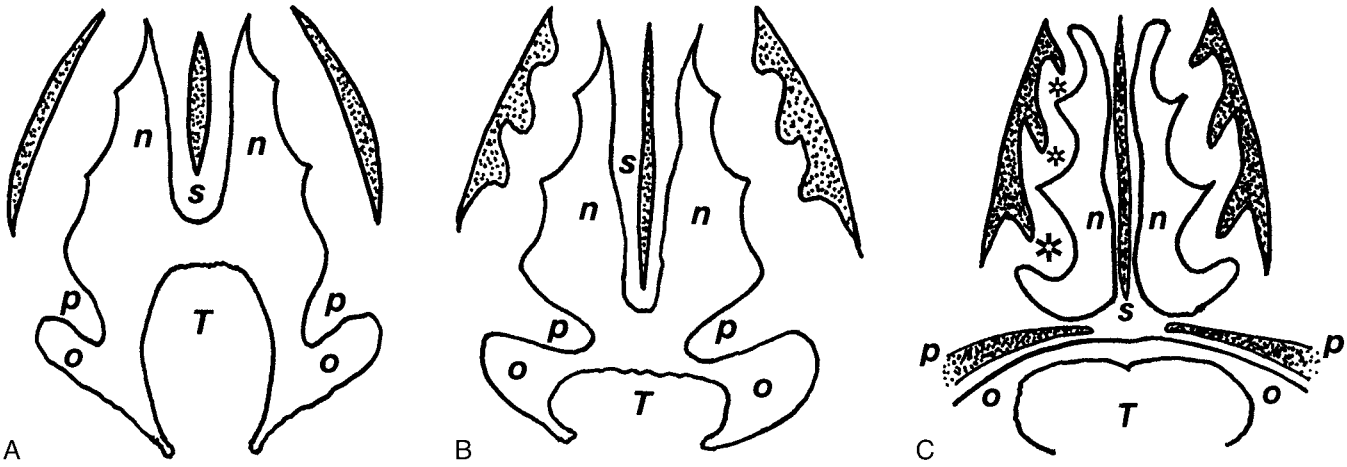

VIEW IMAGE

FIGURE 29-2 Development of the palate and nasal cavity. **A**, Drawing of a coronal view of a 6-week-old fetus shows that the oral (*o*) and nasal (*n*) cavities communicate with each other. The superior nasal cavity is divided by the midline septum (*s*), which contains cartilage (*shaded area*). The palatal shelves (*p*) are short and are located posterior to the primary palate. The palatal shelves are separated by a space that contains a relatively large tongue (*T*). **B**, Drawing of a coronal view of an 8-week-old fetus shows that the nasal septum (*s*) has elongated and extended inferiorly. The rudimentary nasal (*n*) and oral (*o*) cavities remain joined. The palatal shelves (*p*) are larger and begin to migrate medially. The tongue (*T*) is relatively smaller. **C**, Drawing of a coronal view of a 10-week-old fetus shows that the palatal shelves (*p*) and the inferior border of the nasal septum (*s*) have fused, creating a separation between both nasal cavities (*n*) and the oral (*o*) cavity. The tongue (*T*) is now confined to the oral cavity. Rudimentary nasal conchae (*) are present. The configuration of this region now approximates that of the adult.

medial migration of the palatal shelves (Fig. 29-2). Development of the nasal cavity progresses with deepening of the nasal pits. The oronasal membrane separates the pits from the primitive oral cavity. The primitive choanae are foramina in the oronasal membrane located on either side of the midline immediately behind the primary palate. With the subsequent formation of the secondary palate, the definitive choanae form at the junction of the nasal cavity with the pharynx.

PHARYNX, LARYNX, AND TRACHEA

The respiratory primordium begins at about the fourth week of gestation with the formation of the laryngotracheal groove. As this groove evaginates, it forms a pouch-like laryngotracheal diverticulum located ventral to the caudal part of the developing foregut. Longitudinal folds develop from caudal to rostral on either side of the diverticulum and ultimately fuse to form the tracheoesophageal septum that separates the respiratory system from the esophagus (Fig. 29-3). Abnormalities in partitioning of the esophagus and trachea result in esophageal atresia, with or without tracheoesophageal fistula. The primitive laryngotracheal tube arises from gradual elongation of the diverticulum. The distal end of the tube eventually develops into the lung buds, and the proximal end forms the primitive laryngeal aditus.[1]

The larynx develops from the proximal end of the laryngotracheal tube. The arytenoid swellings develop at the cranial end of the laryngotracheal tube, and these two lateral swellings grow cranially and medially to produce the T-shaped slit of the laryngeal aditus (Fig. 29-4).[1] The laryngeal lumen becomes temporarily occluded at 8 weeks of gestation as a result of epithelial proliferation. If normal recanalization does not occur during the tenth gestational week, a laryngeal web results. The laryngeal ventricles form during recanalization of the larynx. These recesses are bounded by folds of mucous membrane that become the vocal folds (cords) and vestibular folds (false cords).[3] Failure of separation of the vocal folds results in congenital atresia of the larynx. This rare anomaly results in the congenital high airway obstruction syndrome (CHAOS).[4]

The thyroid cartilage develops from the fourth arch as two lateral plates that fuse in the midline. This process is nearly complete by the ninth gestational week. The cricoid

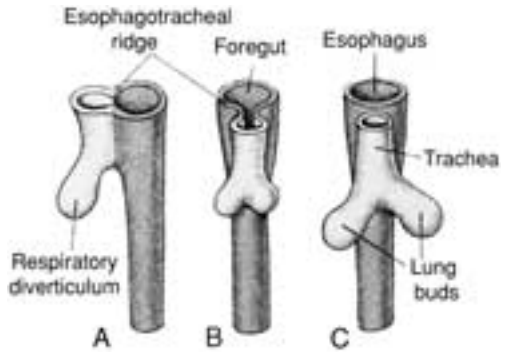

VIEW IMAGE

FIGURE 29-3 Development of the respiratory system. **A–C**, Successive stages in the development of the respiratory diverticulum. The tracheoesophageal ridges form a septum that separates the developing trachea and lung buds from the esophagus. A tracheoesophageal fistula is an abnormal persistence of the original communication between the trachea and the esophagus. (From Langman's Medical Embryology, 7th ed. Baltimore: Williams & Wilkins, 1995;233.)

Copyright © 2003, Mosby, Inc. All rights reserved.

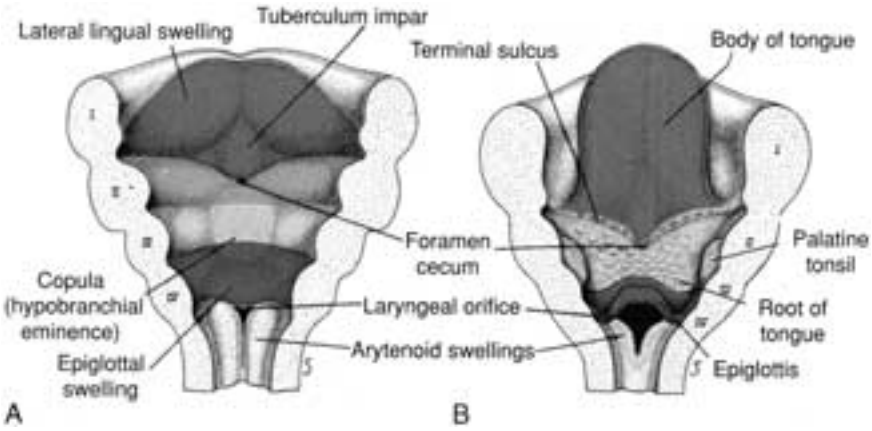

FIGURE 29-4 Development of the larynx. Drawings show the laryngeal orifice and surrounding swellings at successive stages of development. **A**, 6 weeks. **B**, 12 weeks. (From Langman's Medical Embryology, 7th ed. Baltimore: Williams & Wilkins, 1995;234.)

VIEW IMAGE

cartilage begins as two cartilaginous centers of the sixth arch. First, the centers grow and unite in the ventral midline; then, by the seventh gestational week, they fuse dorsally. The rostral advancement of the tracheoesophageal septum results in the fusion of the dorsal cricoid lamina. At first the cricoid lumen is slit-like in shape, but eventually the ventral and lateral walls of the cricoid cartilage condense, and there is progressive enlargement of the lumen. Failure of this condensation process results in congenital subglottic stenosis. The arytenoid cartilages are initially fused to the cricoid cartilage but eventually separate from it and form the cricoarytenoid joints.

GREAT VESSELS

The embryology of the great vessels is reviewed in Chapter 33. Errors in this embryologic process may result in aberrant vessels that can cause impressions on the trachea (Fig. 29-5). Of particular note are the following two situations: the persistence of the entire right dorsal aorta, which results in a double aortic arch forming a complete vascular ring, and incomplete obliteration of the proximal right dorsal aortic arch with persistence of the distal portion, which results in an aberrant retroesophageal subclavian artery.

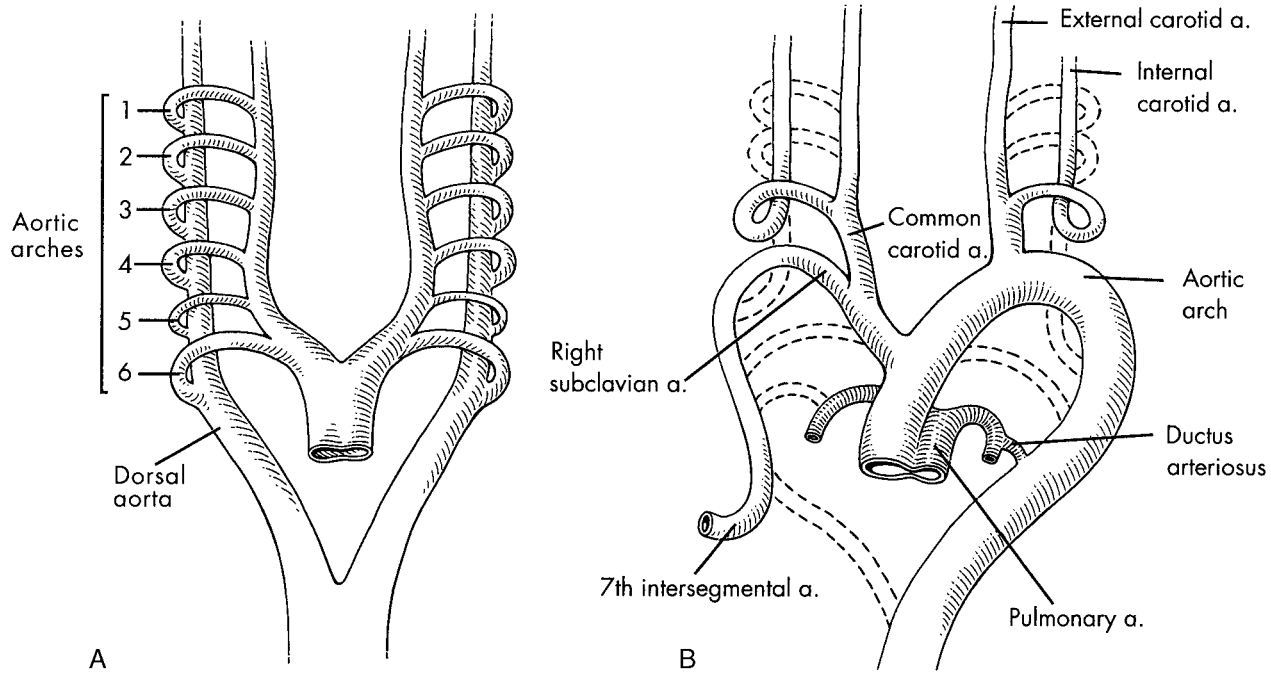

FIGURE 29-5 Development of the great vessels. **A**, Diagram of the paired dorsal and ventral aortas, which are connected by six pairs of aortic arches. Each of the six paired aortic arches is the arterial component of a branchial arch. **B**, Diagram at a later stage of development shows that the first, second, and fifth arches have disappeared (*broken lines*). Errors in the obliterative process result in vascular rings. (From Langman's Medical Embryology, 7th ed. Baltimore: Williams & Wilkins, 1995;214.)

VIEW IMAGE

Copyright © 2003, Mosby, Inc. All rights reserved.

SECTION TWO

CLINICAL EVALUATION

Assessment of airway problems in pediatric patients begins with a comprehensive history and physical examination. Information should be elicited about congenital, inflammatory, traumatic, or other conditions that may adversely affect the airway. The history should also include a review of any prior anesthetic records, as an increased risk of airway abnormalities may result from prior surgery, intubation, or radiation treatment to the face or neck.

The airways in infants and children are small, and slight narrowing produces signs of respiratory obstruction.[5] Pertinent signs or symptoms include snoring, apnea, daytime somnolence, stridor, and a hoarse voice. Respiratory obstruction is indicated by flaring of the nasal alae, retractions of the neck, intercostal muscles, and abdominal muscles, restlessness, and cyanosis.[5] On physical examination the presence of craniofacial or spinal malformation, obesity, abnormalities of dentition, enlargement of the tongue, and neck or facial masses should be noted.

STRIDOR

Stridor, which is defined as noisy breathing, is the audible result of turbulent airflow. Stridor may be either acute or chronic and may result from obstruction anywhere in the airway from the nasal cavity to the distal bronchi. Acute stridor is commonly caused by acquired conditions such as infection, trauma, or a foreign body.[6] The most common causes of chronic stridor in the infant are congenital laryngeal or tracheal anomalies such as laryngomalacia or tracheomalacia and vocal cord paralysis. Stridor may be associated with respiratory distress, the degree of distress dictating the urgency of the situation and the need for immediate clinical intervention. Significant respiratory compromise is an indication for endoscopy or intubation. In infants and young children, conventional emergency airway techniques, such as cricothyrotomy and transtracheal jet ventilation, are problematic because of limited surface landmarks and the relatively small larynx and trachea. Therefore, direct cannulation of the trachea by rigid bronchoscopy or emergent tracheotomy should be considered early in the management of the emergency airway in pediatric patients.[7]

The phase of respiration in which stridor occurs is the most important characteristic for localizing the site of airway obstruction. Stridor during inspiration usually indicates obstruction at or above the glottis. Biphasic stridor suggests subglottic or high tracheal obstruction, and expiratory stridor is characteristic of lower tracheal or bronchial obstruction.[6] Low-pitched stridor indicates nasal or oropharyngeal obstruction. High-pitched sounds usually indicate laryngeal obstruction.

There are other clinical characteristics that may suggest the etiology of the stridor. If stridor has been present since birth, then the most likely causes are congenital laryngomalacia, subglottic stenosis, vocal cord paralysis, or a vascular ring.[8] Laryngomalacia causes stridor that is more pronounced in the supine position and diminishes if the child is resting and in the prone position. Patients with significant vascular compression of the airway present with symptoms such as stridor, cough, recurrent lower respiratory tract infections, difficulty feeding, and reflex apnea.[9] Bilateral vocal cord paralysis is most often seen in children with neurologic abnormalities. Fever or cough suggests croup, and drooling or odynophagia is often a sign of epiglottitis. A history of prematurity and prior intubation in a child with stridor suggests the possibility of acquired subglottic stenosis. The relationship of stridor to feeding and the possibility of reflux and/or aspiration may indicate the need for gastrointestinal evaluation.[5]

Depending on the clinical situation and the severity of stridor, plain films may be obtained. However, if the diagnosis is uncertain or if immediate intervention is required, endoscopy should be performed. Flexible fiberoptic laryngoscopy has become the technique of choice to evaluate the pediatric larynx, especially when airway dynamics are of concern. Rigid direct laryngoscopy remains the preferred technique when laryngeal/tracheal surgery is planned or establishment and protection of the airway with intubation or bronchoscopy is required.[10] Manipulations such as extraction of foreign bodies can be performed only through the rigid endoscope. Endoscopy is more sensitive than radiographic examination in detecting airway lesions caused by laryngomalacia, subglottic stenosis, and tracheal stenosis, but the two methods are comparable for evaluating other common pediatric airway lesions.[11]

OBSTRUCTIVE SLEEP APNEA

Obstructive sleep apnea (OSA) in children results from airway obstruction and cessation of airflow for a finite period of time during sleep. Snoring, laborious breathing, and profuse sweating characterize OSA. When awake, children may have breath-holding spells and, during feeding, difficulty with breathing and coordinating swallowing. Daytime symptoms also include excessive sleepiness, with poor performance and behavior problems. Severe forms may be associated with failure to thrive or death.[12]

The most common cause of OSA in children is adenotonsillar hypertrophy, which is treated by tonsillectomy and adenoidectomy.[13] Less common causes of OSA in children include neuromuscular disorders, macroglossia, nasopharyngeal masses, craniofacial syndromes, obesity, and pharyngeal flaps following cleft palate repair.[13] OSA is also a feature of some genetic syndromes such as Down syndrome and Prader-Willi syndrome (short stature, obesity, and gonadal hypodevelopment). In many of these children OSA is multifactorial, and obstruction of the airway can potentially occur at multiple sites from fixed anatomic abnormalities as well as dynamic changes such as posterior displacement of the tongue during sleep (glossop-

Copyright © 2003, Mosby, Inc. All rights reserved.

tosis) and hypotonia of the hypopharyngeal and glossal musculature.[14]

The diagnosis of OSA is usually established by the clinical history alone. Most parents can vividly describe loud snoring, obstructive pauses, retractions, and mouth breathing. When the diagnosis is uncertain, studies such as polysomnography (sleep studies), sleep sonography, physical examination, and radiographs may confirm the diagnosis of OSA. Lateral plain films are useful for evaluating the size of the adenoids and tonsils and for excluding the presence of other obstructing lesions. If the diagnosis remains uncertain after the physical examination and plain films, airway fluoroscopy may determine the actual site of obstruction during quiet respiration or sleep.[15] Dynamic sleep fluoroscopy has been advocated as an adjunct to endoscopy in the identification and management of pediatric upper airway obstruction when hypopharyngeal collapse or multiple levels of obstruction are suspected.[16] This technique requires the administration of sedation to induce sleep followed by periodic lateral fluoroscopy in order to correlate anatomic changes in the airway with episodes of oxygen desaturation. Using dynamic sleep fluoroscopy, glossoptosis has been identified in 25% of pediatric patients referred for fluoroscopic sleep studies.[14]

Helical CT or CT with the capacity to scan during several respiratory cycles is also useful in diagnosing the site of obstruction in children with a questionable diagnosis of OSA. Multidetector CT with inspiratory-expiratory imaging may also be useful in the evaluation of patients with dynamic airway collapse.[17]

Ultrafast MR imaging is useful for localizing the sites of pharyngeal airway obstruction in patients with OSA. Multiple images are obtained using ultrafast pulse sequences at different anatomic levels.

SECTION THREE

RADIOGRAPHIC TECHNIQUES

PLAIN FILMS

When investigating a possible upper airway obstruction, the imaging modality of choice depends on the suspected location of the lesion and whether the airway compromise is acute or chronic. Impending or progressive airway obstruction necessitates rapid, efficient workup, often including same-day operative endoscopy. Commonly, the first examinations obtained are plain soft-tissue film radiographs of the sinuses, neck, and chest. Tightly coned, high-kilovoltage (to optimize soft-tissue detail and thus maintain resolution of the airway), magnified views of the airway are obtained in the lateral projection, and frontal airway films should be obtained when the symptoms are not emergent or life-threatening. The radiographic appearance of the pediatric airway is affected by patient position, crying, swallowing, and the phase of respiration. The lateral film should be obtained with the child upright when possible, with the neck in a neutral position or slightly extended, during deep inspiration. If the neck is flexed or the film is obtained during expiration or crying, the retropharyngeal soft tissues may appear abnormally prominent, simulating retropharyngeal pathology (Fig. 29-6). Sometimes the impression of a neck or mediastinal mass is created by the normal buckling of the trachea to the right on the anteroposterior (AP) examination.

When life-threatening airway obstruction is suspected, as in acute epiglottitis, some clinicians believe that a plain film is not initially needed because the time spent obtaining it

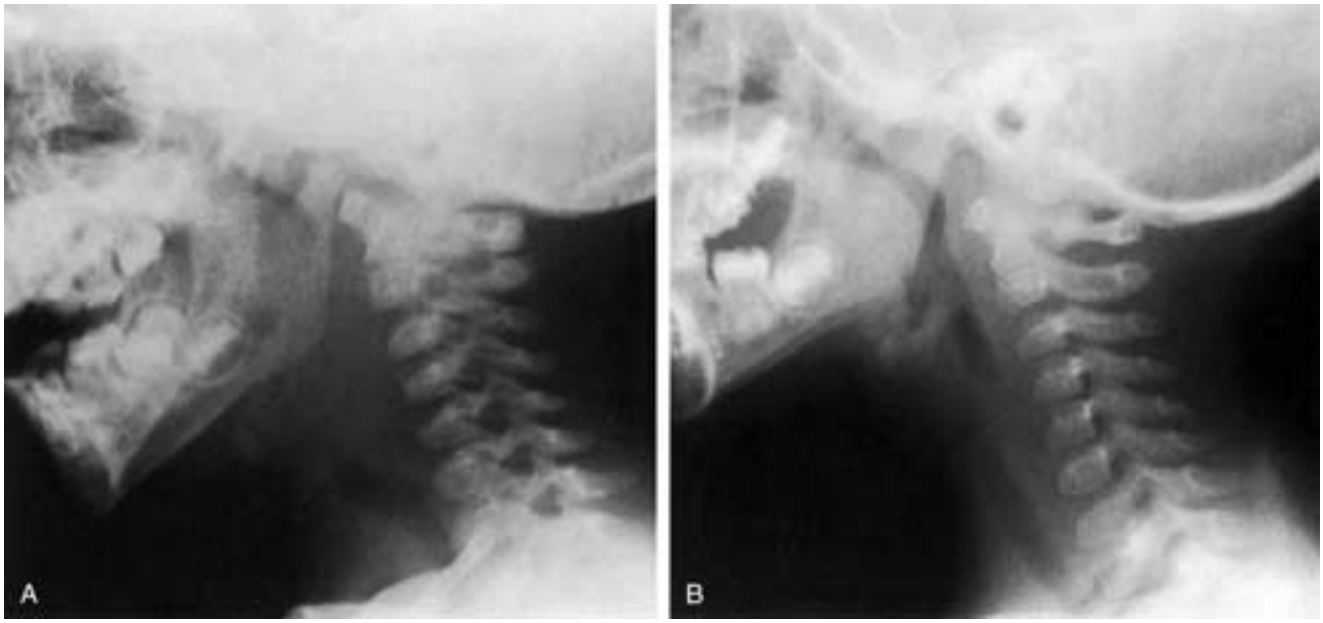

FIGURE 29-6 Importance of radiographic technique. Child with fever and drooling. **A**, Lateral plain film of the neck obtained while the child is swallowing shows retropharyngeal soft-tissue thickening simulating an abscess or a mass in the retropharynx. **B**, Repeat film 5 minutes later while the child is quiet shows normal retropharyngeal soft tissues. (**A** and **B**, From Gay B, Radiology for Anesthesia and Critical Care. New York: Churchill Livingstone, 1987; Chapter 11.)

VIEW IMAGE

Copyright © 2003, Mosby, Inc. All rights reserved.

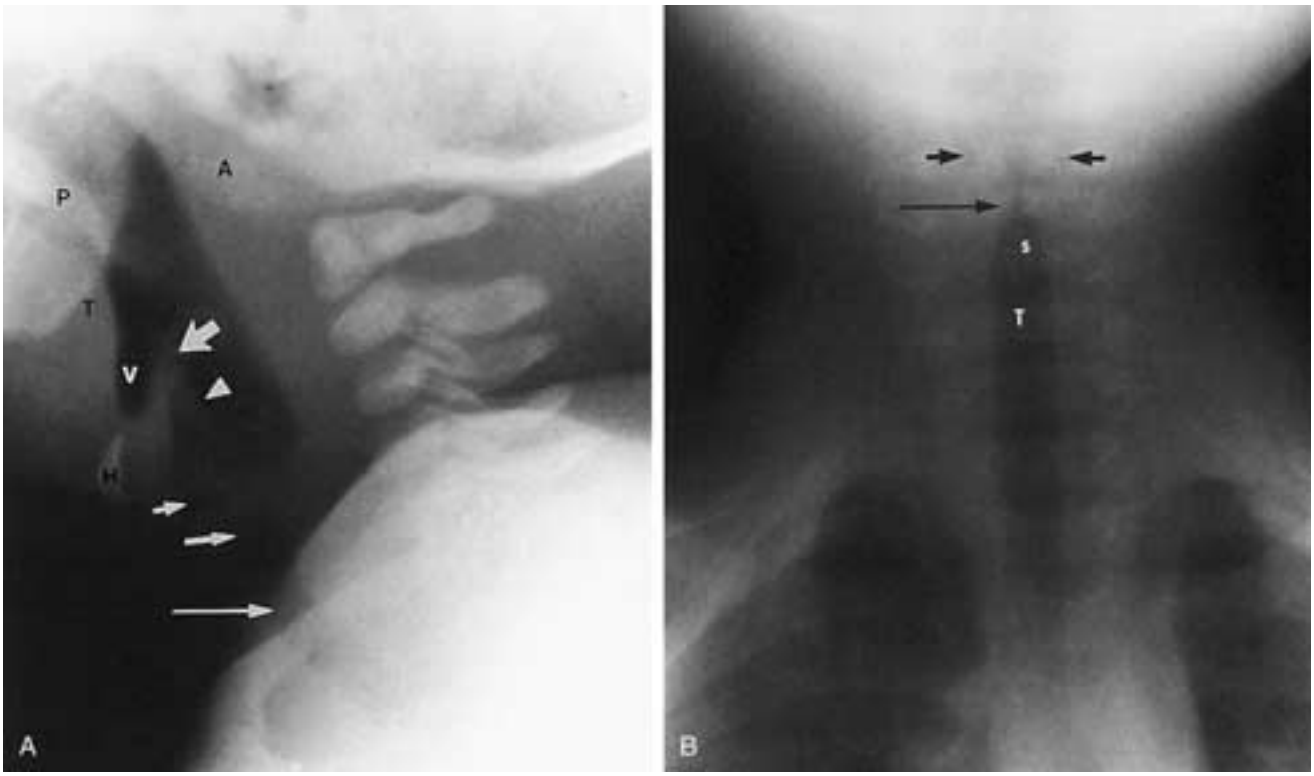

VIEW IMAGE

FIGURE 29-7 Normal lateral and AP radiographs in a 2-month-old infant. **A**, Lateral film obtained during inspiration, with the neck in the neutral position. Normal soft-tissue structures include adenoidal tissue (*A*), the free edge of the epiglottis (*thick white arrow*), aryepiglottic fold (*white arrowhead*), soft palate (*P*), tongue base (*T*), and calcified hyoid bone (*H*). Air-filled structures include the vallecula (*V*), laryngeal ventricle (*short white arrow*), subglottic airway (*white arrow*), and trachea (*long white arrow*). **B**, Normal AP radiograph shows air-filled pyriform sinuses (*short arrows*), true vocal cord (*long arrow*), subglottic airway (*s*), and trachea (*T*).

delays initiation of treatment. However, if a film is to be obtained, a single lateral film of the airway is usually all that is necessary to confirm the diagnosis. Additional frontal views only delay the workup and treatment and typically contribute little new information. A clinician should accompany the child to the radiology suite, and the radiologist should supervise the appropriate examinations, remaining in the department until the radiographic portion of the workup is completed. The child with acute airway obstruction should not be placed in the supine position or immobilized because these manuevers may exacerbate airway compromise.

Normal air-filled structures seen on the lateral plain film are the nasopharyngeal, oropharyngeal, hypopharyngeal, and supraglottic airways, as well as the valleculae, laryngeal ventricle, and infraglottic trachea (Fig. 29-7). Soft-tissue structures routinely visualized on the lateral examination are the palate, base of the tongue, adenoids, epiglottis, aryepiglottic folds, and retropharyngeal and prevertebral soft tissues (Fig. 29-7). The AP film displays the laryngeal and tracheal airway. Specifically, the false and true vocal cords, the laryngeal ventricles, the subglottic region, and the trachea can be identified.

On plain films, standard measurements for normal soft-tissue structures have been determined, and soft tissues exceeding the normal values may indicate an airway lesion. However, all measurements should be used with caution because tremendous variability is seen in the normal pediatric airway, especially with dynamic structures such as the epiglottis, pharyngeal soft tissues, and trachea. The retropharyngeal and prevertebral soft-tissue thickness is one of the most commonly measured regions, and the most frequently used measurement is the distance between the posterior pharyngeal air column and the anterior portion of the third or fourth cervical vertebral body. Normally in children, on a properly positioned film this distance should not exceed one half to three fourths the diameter of the vertebral body.[18]

Chest radiographs often are obtained when evaluating the child with airway obstruction. The entire trachea to the level of the bifurcation should be evaluated with respect to diameter, position, and patency.

FLUOROSCOPY

Fluoroscopy of the airway provides dynamic information not available with plain films. Video fluoroscopy with 105 mm spot films or digital images obtained at a rate of three to four frames per second allows fast imaging and is useful for evaluating the child with chronic airway obstruction. Changes in airway caliber during inspiration and expiration can be assessed over several respiratory cycles. The tracheal diameter increases during inspiration and decreases during expiration, and any paradoxical changes can be appreciated with dynamic fluoroscopy.[19] Dynamic examination of vocal

Copyright © 2003, Mosby, Inc. All rights reserved.

cord movement during quiet breathing and phonation (crying in the infant) can also be performed using fluoroscopy. The cords should abduct symmetrically during inspiration and adduct with phonation. On such a study, an unsuspected vocal cord paralysis can be diagnosed. However, fluoroscopy is limited by its inability to image the soft-tissue structures surrounding the airway. For example, narrowing of the tracheal airway by a neck mass can be seen, but the characteristics of the mass are determined better on cross-sectional imaging.

Barium esophagography, performed under fluoroscopic control, is often part of the workup of the pediatric patient with an airway problem, and this study is usually performed in conjunction with airway fluoroscopy. Lesions that may be detected on barium swallow studies include esophageal foreign bodies, congenital vascular rings and slings, mediastinal masses, and bronchopulmonary foregut anomalies. Patient aspiration may also be detected.

COMPUTED TOMOGRAPHY

CT adds important information about the soft tissues surrounding the airway. However, children often require sedation for these studies, and sedation routinely results in a decrease of the AP diameter of the pharynx at the level of the palatine tonsils and soft palate and at the level of the epiglottis.[20] When general anesthesia is used, there is distortion of the airway as a result of the endotracheal tube.

Lesions within the airway or involving the function of the airway, such as subglottic stenosis or tracheomalacia, are often best evaluated by fluoroscopy or endoscopy. Conversely, extraluminal disease is best studied with CT or MR imaging. Because the region of interest is limited, scans should be obtained using axial thin-slice collimation, usually 3 mm contiguous or helical images. Direct coronal MR imaging or direct or reformatted coronal CT is recommended for lesions of the skull base and nasopharynx, as well as those of the larynx and trachea, for assessment of the craniocaudal extent of disease. When a focal mass or an inflammatory lesion is suspected, intravenous nonionic iodinated CT contrast should be used.

Older children who cooperate can be scanned with conventional CT using a breath-hold technique. This helps ensure that the serial scans are performed during the same phase of respiration with similar lung volumes, thus decreasing the potential for respiratory misregistration artifacts. In younger or sedated children who cannot voluntarily suspend respiration, scanning is performed during quiet respiration. Early experience with airway measurements on cine or ultrafast CT suggested that cross-sectional airway areas were reduced in patients with obstructive sleep apnea and tracheomalacia, and that dynamic CT could show changes in these areas during different phases of the respiratory cycle.[21–23] However, the cine CT technique is not widely available clinically, and most radiologists have little or no experience with this technique.

Current spiral and multidetector CT technology, allowing volume scanning at a rapid speed, is now widely available. In older children, this technique allows the neck to be scanned during a single breath-hold. In infants, the entire airway can be scanned during a single 10 to 15 second or shorter acquisition period, often obviating the need for sedation. Sections that are 1 mm thin can be obtained routinely with the spiral technique, and these thin sections are necessary when evaluating a newborn or infant with a suspected small subglottic web, cyst, stenosis, hemangioma, or papilloma. To further aid the clinician, the region of narrowing should be described with reference to its distance from a fixed anatomic landmark such as the glottis, inferior cricoid, or carina. Dynamic imaging can also be performed, if necessary, through a specific level of airway obstruction. In this way, using static and dynamic airway imaging, lesions that change diameter with the respiratory cycle may be studied, complementing airway fluoroscopy. However, especially in pediatric patients, it is important to take the radiation dose into consideration when using these techniques. This limits the utilization of dynamic CT scanning.

MAGNETIC RESONANCE IMAGING

Most children under the age of 5 years require some form of sedation in order to undergo MR imaging. Where compromise of the airway is suspected, an anesthesiology consultation should be obtained, as a general anesthetic may be indicated to avoid the risk of sedating a child with a tenuous airway. The choice of coil and pulse sequence for MR imaging of the pediatric neck and airway will depend on the clinical indication for the examination. Surface coils may be of use if the region of interest is superficial and small (e.g., subglottic hemangioma). Multiplanar imaging should be acquired with T1-weighted, T2-weighted, and fat-suppressed, T2-weighted or fast spin-echo inversion recovery (FSEIR) imaging. Cardiac gating and respiratory compensation are useful if the airway lesion is in the thoracic trachea. Coronal T1-weighted images are especially useful to display a paratracheal mass that is causing extrinsic tracheal compression. Narrowing in any region of the airway should be confirmed with a second acquisition in an orthogonal plane. A sequence sensitive to flow-related enhancement (e.g., spoiled gradient recalled acquisition) is useful in evaluating suspected vascular anomalies. When imaging neck masses, gadolinium should be used with fat-suppressed, T1-weighted images.

SECTION FOUR

NORMAL ANATOMY

NASAL CAVITY

Because neonates are obligate nasal breathers, the nasal cavity is an important component of the pediatric airway. The air-filled nasal cavity extends from the nostrils to the posterior choanae. The lateral nasal walls should be straight or slightly concave medially (Fig. 29-8). The nasal septum consists of the vomer, the perpendicular plate of the ethmoid, and cartilage. The normal nasal septum is midline,

Copyright © 2003, Mosby, Inc. All rights reserved.

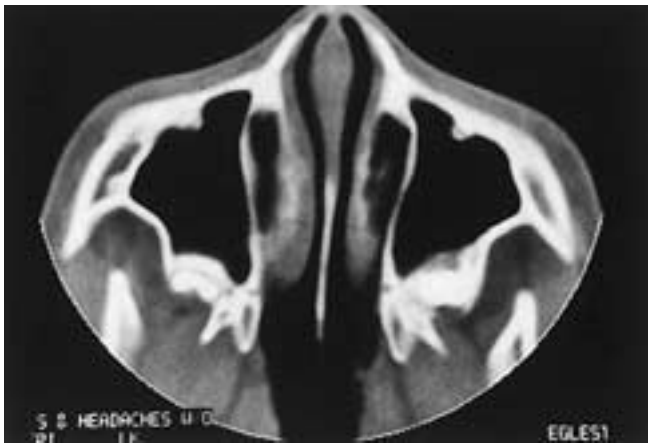

VIEW IMAGE

FIGURE 29-8 Normal nasal cavity in a 13-year-old child. Axial CT scan of a normal nasal cavity in a child is similar in appearance to that in an adult, with the nasal septum wider at its anterior portion, slightly concave lateral nasal walls, and a patent posterior choanae.

thicker anteriorly, and is separated from the turbinates by air. The anterior thickening is diamond-shaped and should not be mistaken for a mass. The mean width of the posterior choanal airspace in the newborn is 0.67 cm, increasing to 0.86 cm at 6 years and to 1.13 cm by 16 years of age.[24] In children less than 8 years of age, the vomer generally measures less than 0.23 cm in width and should not exceed 0.34 cm. In those over 8 years of age, the mean vomer width should not exceed 0.55 cm.[24]

NASOPHARYNX AND OROPHARYNX

The plane of the hard palate separates the nasopharynx from the oropharynx. On CT and MR imaging, the marrow within the bony hard palate is usually clearly identified. By comparison, the soft palate is primarily muscular. The junction between the soft and hard palates is well seen on CT and MR imaging (Fig. 29-9). The soft palate in the infant and child is a prominent structure on plain radiographs, separating the nasopharyngeal airway from the oropharyngeal airway. During quiet breathing the soft palate moves down, opposing the tongue base. However, during swallowing and phonation, the soft palate elevates and moves posteriorly, closing the nasopharynx and opening the oropharynx, which prevents nasal regurgitation.

The nasopharynx and oropharynx of the child differ from those of the adult in that they are smaller and normally have more lymphoid tissue within the mucosa and extending into the airway. The vertical height and depth of the nasopharynx increase during childhood, but the width, or distance between the eustachian tubes, does not significantly increase.[25] The primary lymphoid tissue of Waldeyer's ring consists of the adenoids (pharyngeal tonsils), the palatine (faucial) tonsils, and the lingual tonsils. The adenoids are situated in the posterior nasopharyngeal roof and upper posterior wall. On plain films and fluoroscopy they appear confluent with the prevertebral soft tissues, and are separated from the upper surface of the soft palate by the nasopharyngeal airway (Fig. 29-7A). The adenoids are not routinely seen at birth but are 1 to 5 mm thick in the normal 3-month-old. If no adenoidal soft tissue is seen by 6 months of age, hypogammaglobulinemia or an immune deficiency syndrome should be suspected. The adenoids normally begin to regress in adolescence, and in most people they have completely involuted by middle age. However, occasionally the adenoids can be identified in the fifth and sixth decades of life.

On CT, adenoidal tissue fills the posterior nasopharynx, is isodense to muscle on noncontrast CT, and enhances with iodinated contrast. A thin line of enhancement, probably indicating the submucosal veins, is usually seen between the adenoids and the nasopharyngeal wall (Fig. 29-10). Ventrally the adenoidal tissue is usually flat, but it can appear asymmetrically lobular or thickened. Occasional small calcifications, due to concretions in small lymphoid clefts, can be seen within the adenoids on CT. On T1-weighted MR images, the adenoids are isointense to slightly hyperintense with respect to muscle and are of lower signal intensity than fat. On T2-weighted images they are homogeneously hyperintense with respect to muscle (Fig. 29-11). Sometimes, focal round or oval foci of signal abnormality within the adenoids are seen on MR imaging. These probably represent small mucous retention cysts. The adenoidal tissue enhances slightly with gadolinium contrast agents (Fig. 29-11C).

The paired palatine tonsils can be identified radiographically by about 1 year of age, are greatest in size at about 4 years of age, and begin to involute after the age of 10 years.[26] The palatine tonsils may normally be obscured by the tongue base and mandibular angle on a lateral plain film. However, if the airway is distended (as occurs when the

FIGURE 29-9 Normal palate and nasooropharyngeal airway in a 4-year-old child. T1-weighted sagittal image shows the junction of the hard and soft palates (*small arrow*). The soft palate separates the nasopharyngeal (*arrowhead*) from the oropharyngeal (*large arrow*) airway. During quiet breathing, the soft palate opposes the tongue base.

VIEW IMAGE

Copyright © 2003, Mosby, Inc. All rights reserved.

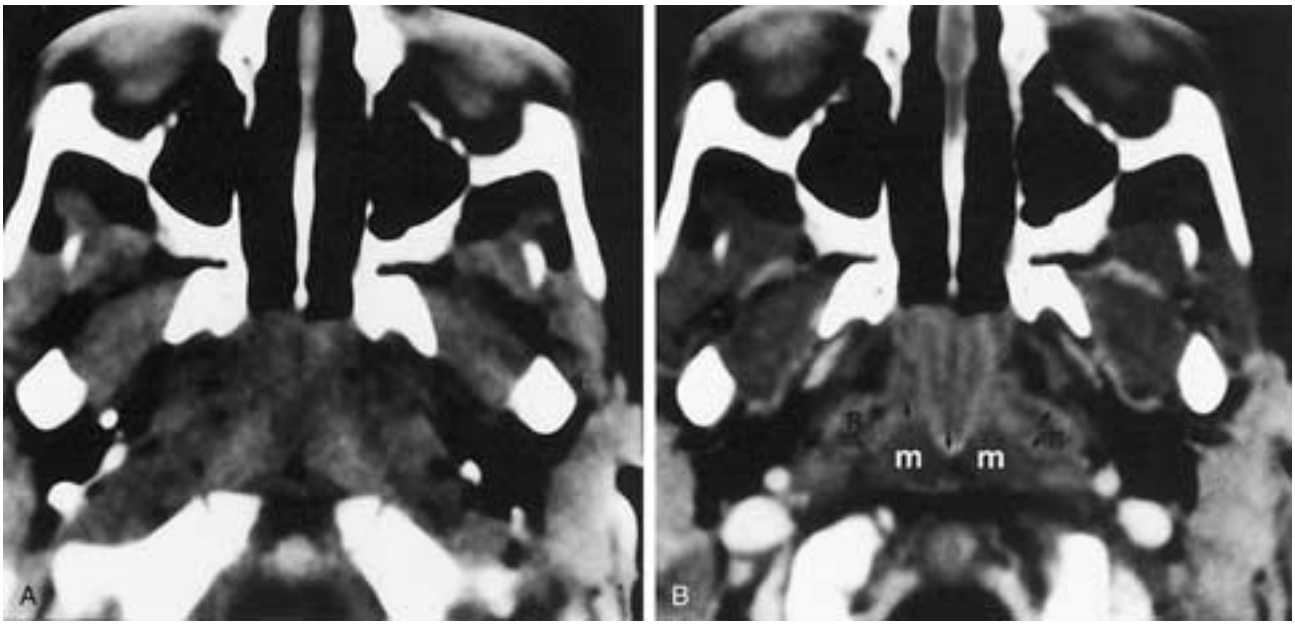

VIEW IMAGE

FIGURE 29-10 Normal adenoids on CT in a 14-month-old child. **A**, Axial noncontrast CT shows adenoidal tissue, nearly isodense to prevertebral muscles, filling the nasopharynx. **B**, Same child scanned following intravenous iodinated contrast administration using a spiral technique. The adenoidal tissue enhances, but prevertebral muscles (*m*) do not. Notice the thin linear enhancement at the interface between the adenoids and muscle (*black arrows*). The adenoidal tissue characteristically fills the lateral pharyngeal recesses (*R*), is flat ventrally, and does not extend into the deep pharyngeal spaces. (Courtesy of Dr. John J. Alarcon, Scottish Rite Children's Medical Center, Atlanta, Georgia.)

child cries) or if there is significant tonsillar hypertrophy, these tonsils can be identified on a lateral plain film (Fig. 29-12). The lingual tonsils are located at the base of the tongue, usually just above the valleculae. The CT density and MR signal intensity of lingual and palatine lymphatic tissue is similar to those of the adenoids (Figs. 29-13 and 29-14).

The median and lateral retropharyngeal lymph nodes provide lymphatic drainage for the sinonasal cavities and pharynx. These nodes are seen on MR imaging in most infants and children (Figs. 29-14 and 29-15). Because they are isodense to muscle on CT, they are appreciated only when enlarged or necrotic. However, because of the numerous normal childhood infections, the efferent lymph vessels to these nodes usually become obstructed by the second decade of life, and these nodes are not commonly seen in the normal adult.

HYPOPHARYNX

The hypopharynx lies between the tip of the epiglottis and the cricopharyngeus, extending posterior to the larynx from the level of the hyoid bone to the lower cricoid bone. The middle and inferior constrictor muscles support the posterior and lateral walls of the hypopharynx. The anterior wall is bordered by the laryngeal cartilages and laryngeal inlet and anterolaterally by the aryepiglottic folds. The hypopharynx has two recesses, known as the pyriform sinuses, that are bounded medially by the lateral surfaces of the aryepiglottic folds and laterally by the thyroid cartilages and thyrohyoid membrane. At the inferior extent of the pharynx, the oblique fibers of the inferior constrictor end and the horizontal fibers of the cricopharyngeus muscle begin.[27] Between the lower edge of the oblique fibers and the upper edge of the horizonal fibers is Killian's dehiscence, the site of formation of Zenker's diverticulae. The cricopharyngealo muscle fibers serve as a pharyngoesophageal sphincter, remaining closed apart from deglutition, severe gastroesophageal reflux, and vomiting.

LARYNX AND TRACHEA

The pediatric larynx and trachea differ in appearance from their adult counterparts. Compared with the larynx of an adult, the pediatric larynx is smaller relative to the overall body size. Thin contiguous sections, no greater than 3 mm, are required to adequately image the pediatric larynx. The small size of the pediatric laryngeal airway explains why, with only minimal mucosal edema or swelling such as occurs with laryngotracheobronchitis, symptoms such as stridor and respiratory distress may occur. The newborn glottis is only 7 mm in the anteroposterior dimension. The newborn subglottis, the smallest area of the pediatric airway, measures only 4 to 5 mm in diameter.[28]

The larynx rapidly increases in size during the first 6 years of life and then gradually slows its growth until adolescence, when it reaches adult proportions. In the adult, only the male thyroid cartilage continues to change shape and grow on its external anterior aspect.[29] The change in voice character normally noted during puberty is secondary to growth of the vocal cords, histologic changes in the vocal folds (as the fibers change in density), and a change in the

Copyright © 2003, Mosby, Inc. All rights reserved.

angle of the thyroid cartilage.[29] Of these, the most important change appears to be the thyroid cartilage angle, which until puberty is 100° to 120° open posteriorly. The angle of the thyroid laminae decreases to approximately 90° in both sexes as the anteroposterior length of the glottis increases, but the male thyroid eminence becomes much more prominent.[28]

The pediatric larynx also changes significantly in shape during early life. In adults the glottis is the narrowest portion of the airway. However, in the infant the larynx has a characteristic funnel shape, which results in the subglottic region being the narrowest portion of the larynx and upper airway, as described earlier in this chapter. Below the subglottis, the pediatric airway again widens to a fairly uniform diameter that is maintained down to the level of the carina.

When viewed from above, the epiglottis is omega-shaped and is more angular in the infant than in the adult. This contour may be exaggerated in infants who have congenital laryngeal stridor. This characteristic shape and the resultant stridor disappear in most cases by the second year of life.[30] The glottic airway is elliptical in shape, with the greatest diameter in the anteroposterior dimension, the subglottis is round, and the trachea is ovoid and slightly flattened posteriorly (Fig. 29-16C–E). The tracheal shape is consistent between girls and boys.[31]

During the first several years of life, the pediatric larynx changes its position in the neck. Thus, the normal radiographic landmarks are different from those in the adult. The superior free edge of the epiglottis in the neonate is found at or near the C1 level, and the cricoid cartilage, representing the most caudal portion of the larynx, is at the C4-C5 level. The epiglottis can be visualized in the oral cavity in most infants, and because of the early rostral position of the larynx, the infant is an obligate nasal breather. By adolescence the epiglottis is found at the C2-C3

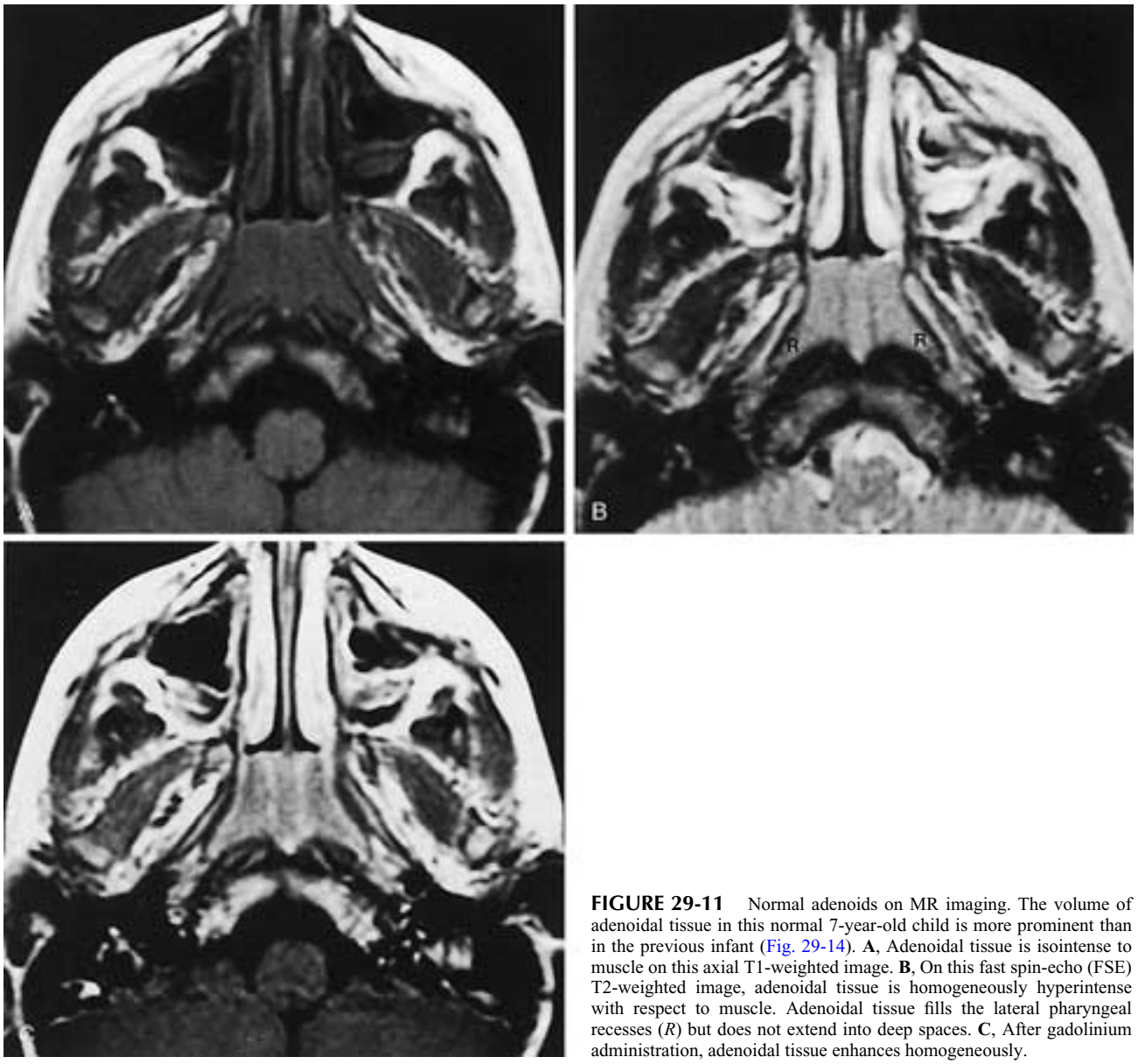

FIGURE 29-11 Normal adenoids on MR imaging. The volume of adenoidal tissue in this normal 7-year-old child is more prominent than in the previous infant (Fig. 29-14). **A**, Adenoidal tissue is isointense to muscle on this axial T1-weighted image. **B**, On this fast spin-echo (FSE) T2-weighted image, adenoidal tissue is homogeneously hyperintense with respect to muscle. Adenoidal tissue fills the lateral pharyngeal recesses (*R*) but does not extend into deep spaces. **C**, After gadolinium administration, adenoidal tissue enhances homogeneously.

VIEW IMAGE

Copyright © 2003, Mosby, Inc. All rights reserved.

VIEW IMAGE

FIGURE 29-12 Palatine tonsillar hypertrophy in a 5-year-old child. Lateral plain film reveals prominent palatine tonsils (*black arrows*) and adenoidal tissue (*A*) in this child with obstructive sleep apnea.

FIGURE 29-13 Lingual tonsillar hypertrophy. Young child with obstructive sleep apnea. Axial CT shows prominent symmetric soft tissue at the tongue base (*arrows*) filling the valleculae bilaterally. There was surgically proven hypertrophy of the lingual lymphoid tissue.

VIEW IMAGE

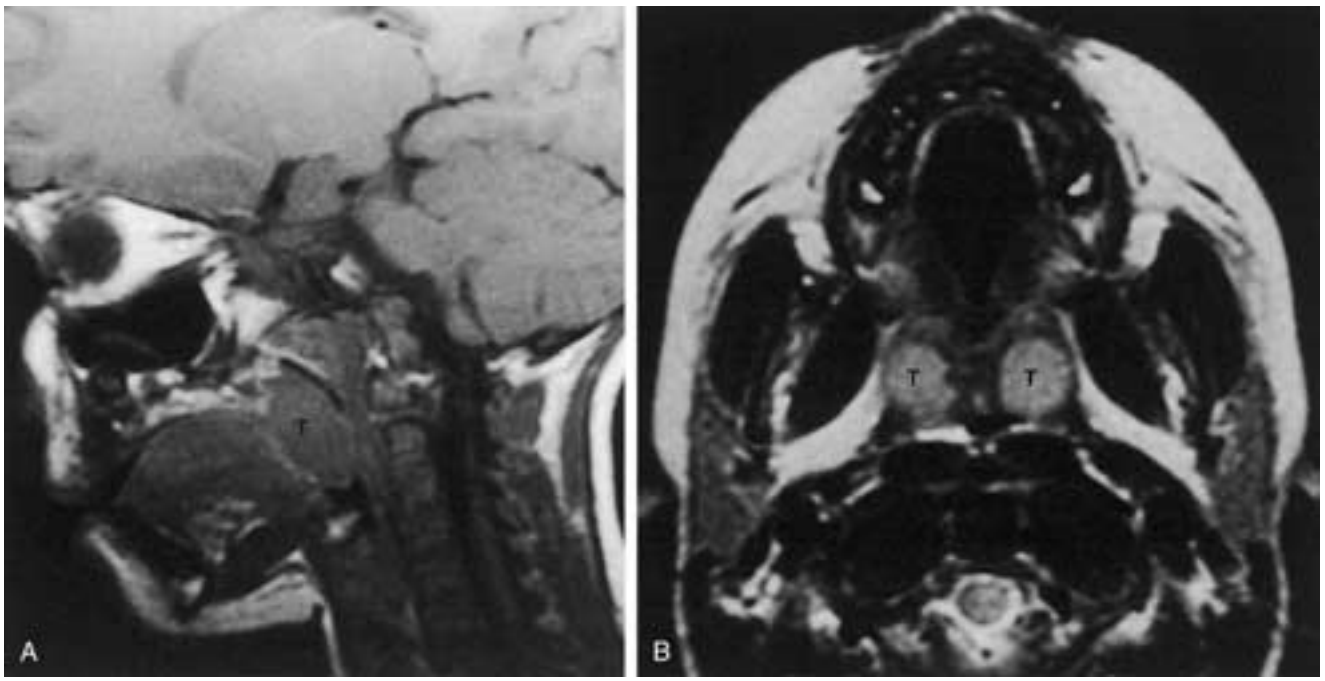

VIEW IMAGE

FIGURE 29-14 Palatine tonsillar hypertrophy in a 4-year-old child without airway symptoms who received oral sedation. **A**, T1-weighted sagittal image shows a prominent palatine tonsil with airway narrowing caused by the tonsillar hypertrophy. **B**, Same child, T2-weighted FSE image shows that the palatine tonsils are prominent, symmetric, contained within the tonsillar fossae, and nearly touching in the midline.

Copyright © 2003, Mosby, Inc. All rights reserved.

VIEW IMAGE

FIGURE 29-15 Retropharyngeal lymph nodes. FSE T2-weighted axial image shows normal retropharyngeal lymph nodes (*N*) medial to the internal carotid arteries (*black arrows*) and lateral to the longus capitus muscles (*white arrows*). These nodes are a normal finding in the asymptomatic pediatric patient.

level, and the cricoid is at the C6 level. The adult epiglottis is usually seen at the C3 level, with the cricoid at the C6-C7 level. The arytenoid cartilage, a radiologic landmark that helps localize the true vocal cord, is found at the C4-C5 level in children.

Although the cartilaginous framework for the larynx is established in the infant, the structures are not calcified at birth. The larynx is softer and the ligaments have greater laxity than they do in the adult larynx. The hyoid bone is the first laryngeal structure to ossify. Ossification of the hyoid bone is seen after 30 weeks' gestation. The body of the hyoid is ossified in infants older than 4 months, and the greater cornua is ossified in those older than 6 months. Ossification of the lesser cornua does not appear in children less than 15 years of age.[32] Premature calcification of the laryngeal cartilages in infancy is abnormal and may be associated with stridor.[33]

The cricoid cartilage is a complete cartilaginous ring, and it is the narrowest portion of the infantile larynx (Fig. 29-17). The anterior and lateral portions of the cricoid cartilage arch are narrow, and the posterior portion forms a thick lamina. The cricothyroid articulation is on the superolateral portion of the cricoid arch. This small depression articulates with the inferior horn of the thyroid cartilage. The cricothyroid ligament spans the gap between the cricoid and thyroid cartilages anteriorly.

The paired arytenoid cartilages sit on the superior rounded surface of the posterior lamina of the cricoid cartilage (Fig. 29-17B). The vocal ligament is attached to the anterior vocal process of the arytenoid cartilage, which is at the level of the cricoarytenoid joint.

The CT appearance of the pediatric larynx reflects the anatomic characteristics discussed. Children under the age of about 7 years may require sedation, so scans are obtained during quiet respiration, without breath-hold maneuvers. Therefore, respiratory motion artifact is common. The hyoid bone and the free edge of the epiglottis are seen at a higher level than in the adult, usually at the C1-C2 level or just at

space is fat density and only several millimeters thick, and the paraglottic fat is not as prominent as it is in the adult larynx. The aryepiglottic folds are thin, and the pyriform sinuses are usually air-filled. The thyroid cartilage is occasionally seen as a thin linear high-density structure, despite the fact that calcification is not seen on plain radiographs until the third decade (Fig. 29-16B,C). The ossified, or calcified, arytenoid cartilages, landmarks for the true vocal cords on CT of the adult larynx, are not seen in the pediatric larynx as discrete structures. Therefore, the level of the true vocal cords is determined primarily by the contour of the glottis, which has a characteristic oval shape (rather than the adult anteriorly narrowed, thin triangular shape). The glottis also can be localized by the location of the air-containing laryngeal ventricle. The ventricle is immediately cranial to the true cord, at the C3 level in the pediatric larynx, and can often be seen on lateral scout or plain films.[26] Most of the endolaryngeal structures, including the true vocal cords and intrinsic laryngeal muscles, are otherwise featureless on imaging (Figs. 29-16, 29-18, and 29-19). In the subglottis, a circumferential rim of soft tissue surrounds the airway. This is the noncalcified cricoid cartilage. The CT appearance of the pediatric larynx also differs from that of the adult because the cartilaginous structures, although fully formed, are not calcified, or ossified (Fig. 29-20).

High-resolution MR imaging of the pediatric larynx is difficult to perform because of the infant's relatively short, fat neck, the high position of the larynx, and respiratory artifact. On MR imaging there is little paraglottic fat. (Fig. 29-21). The nonossified cartilaginous laryngeal structures are hyperintense on T2-weighted images. On T1-weighted images, except for the thyroid cartilage, which is hyperintense to muscle, the cartilaginous structures of the larynx are isointense to soft tissue and are featureless. High-resolution MR imaging of the cadaveric larynx shows that the laryngeal cartilages are hyperintense to muscle on T2-weighted images, with a thin rim of low signal intensity around the cartilage (Fig. 29-21). However, such high-resolution imaging often is not clinically possible or necessary. As with CT, the airway contour indicates the airway level.

The cartilaginous trachea in children is uncalcified, smooth, and featureless on CT. Cartilaginous detail is, however, seen well on T2-weighted MR imaging. The tracheal contour is round anteriorly and flat posteriorly, at the membranous portion of the tracheal wall. Generally, the diameter of the normal infant trachea is slightly larger than that of the subglottis. The anteroposterior

Copyright © 2003, Mosby, Inc. All rights reserved.

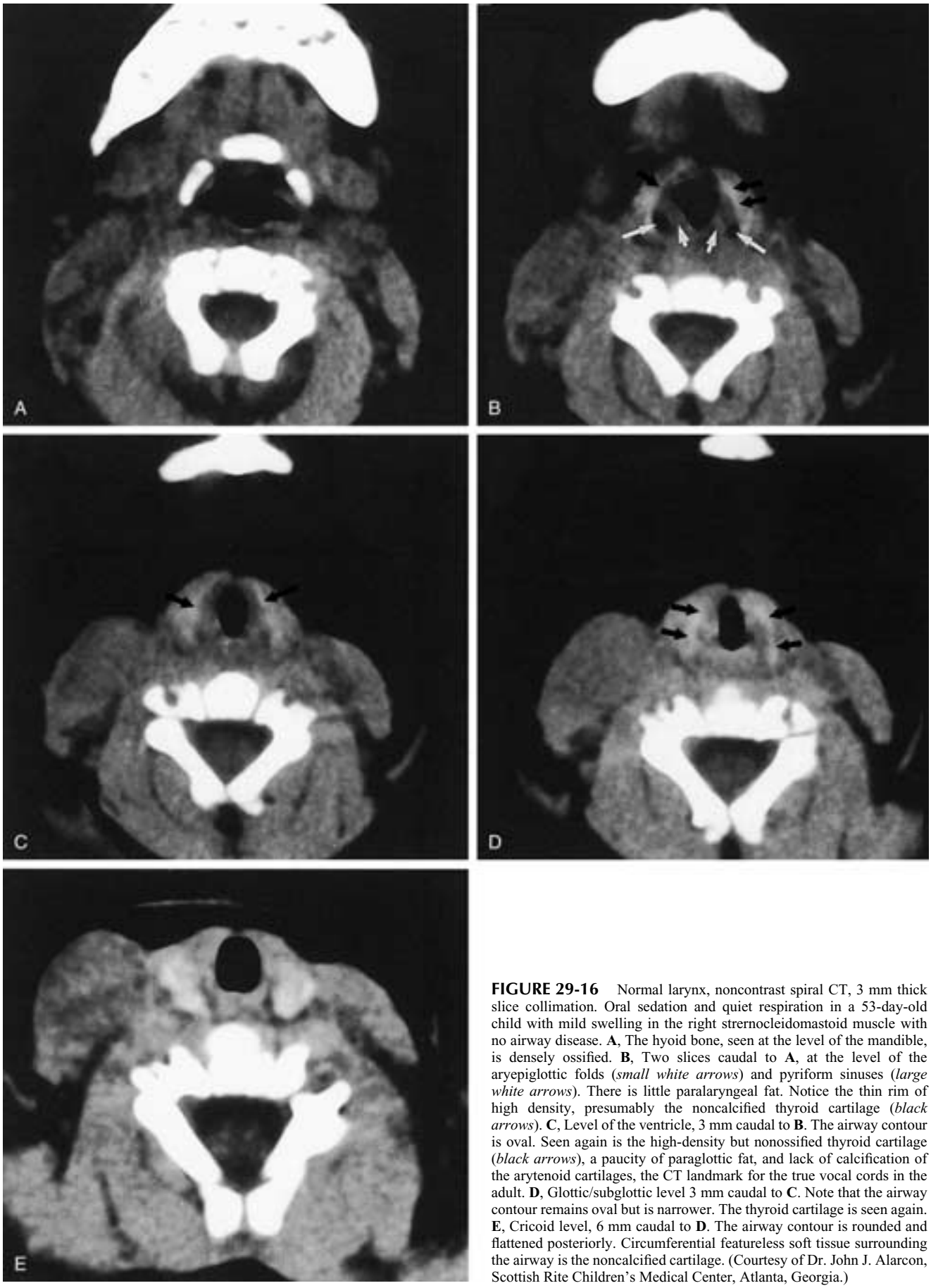

FIGURE 29-16 Normal larynx, noncontrast spiral CT, 3 mm thick slice collimation. Oral sedation and quiet respiration in a 53-day-old child with mild swelling in the right strernocleidomastoid muscle with no airway disease. **A**, The hyoid bone, seen at the level of the mandible, is densely ossified. **B**, Two slices caudal to **A**, at the level of the aryepiglottic folds (*small white arrows*) and pyriform sinuses (*large white arrows*). There is little paralaryngeal fat. Notice the thin rim of high density, presumably the noncalcified thyroid cartilage (*black arrows*). **C**, Level of the ventricle, 3 mm caudal to **B**. The airway contour is oval. Seen again is the high-density but nonossified thyroid cartilage (*black arrows*), a paucity of paraglottic fat, and lack of calcification of the arytenoid cartilages, the CT landmark for the true vocal cords in the adult. **D**, Glottic/subglottic level 3 mm caudal to **C**. Note that the airway contour remains oval but is narrower. The thyroid cartilage is seen again. **E**, Cricoid level, 6 mm caudal to **D**. The airway contour is rounded and flattened posteriorly. Circumferential featureless soft tissue surrounding the airway is the noncalcified cartilage. (Courtesy of Dr. John J. Alarcon, Scottish Rite Children's Medical Center, Atlanta, Georgia.)

VIEW IMAGE

Copyright © 2003, Mosby, Inc. All rights reserved.

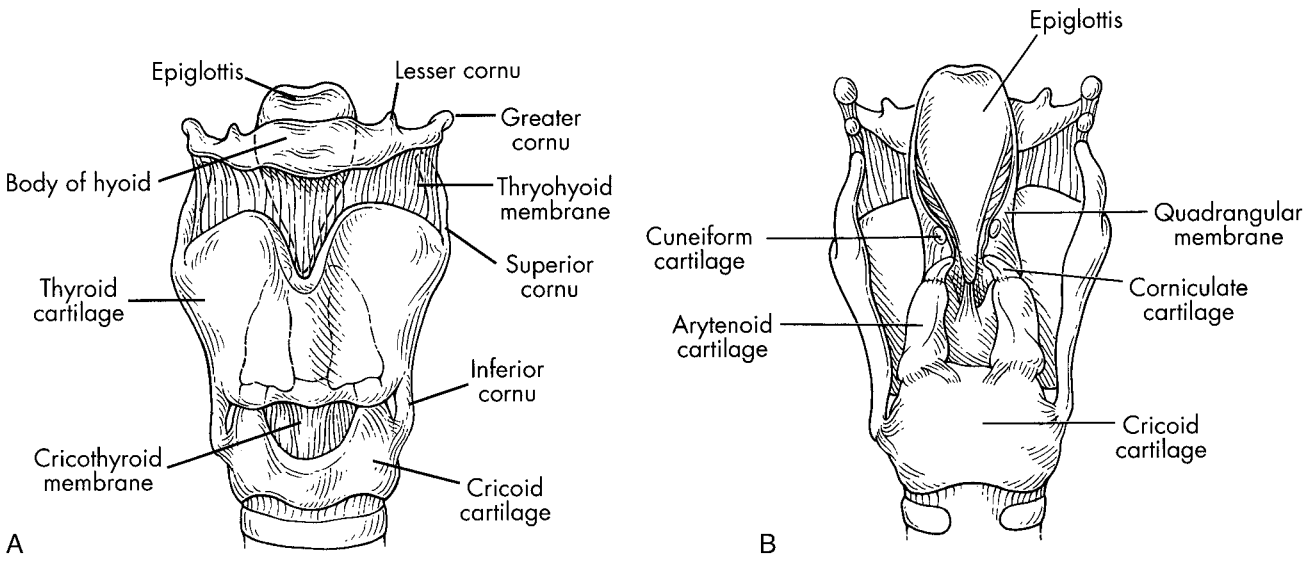

VIEW IMAGE

FIGURE 29-17 Normal larynx, cartilaginous and ligamentous components. The laryngeal cartilages are calcified or ossified in the adult, and each can be discretely seen on radiographs or CT. However, only the hyoid bone is calcified in the pediatric larynx, and the cartilaginous components cannot be visualized as separate structures on plain radiographs or CT. **A**, Anterior view. The hyoid bone, thyroid cartilage, and anterior ring of the cricoid cartilage are the anterior structures of the larynx. **B**, Posterior view. The laryngeal surface of the epiglottis, the arytenoids, and the posterior portion of the cricoid ring are the important cartilaginous portions of the larynx in this view.

dimension is slightly greater than the lateral dimension, except at the level of the innominate artery, where normal physiologic AP narrowing can occur. Absolute tracheal measurements on radiographs, fluoroscopic studies, CT, and MR imaging should be qualified with respect to phase of respiration because the trachea is a dynamic structure that changes shape and size during the respiratory cycle. The trachea is greatest in diameter during full inspiration and narrows slightly during expiration.[34] In normal infants the AP tracheal diameter may vary from 20% to 50% after breath-holding or crying.[34] In the newborn and infant, a tracheal diameter of 5 mm or more is considered normal. Normal tracheal measurements obtained on plain films or CT at maximal inspiration in children older than 10 years of age show coronal tracheal dimensions ranging from 0.9 to 1.8 cm and AP dimensions ranging from 1.1 to 1.8 cm.[35, 36] An abrupt change in tracheal diameter and configuration may be a more significant finding than any single measurement in the airway diameter.

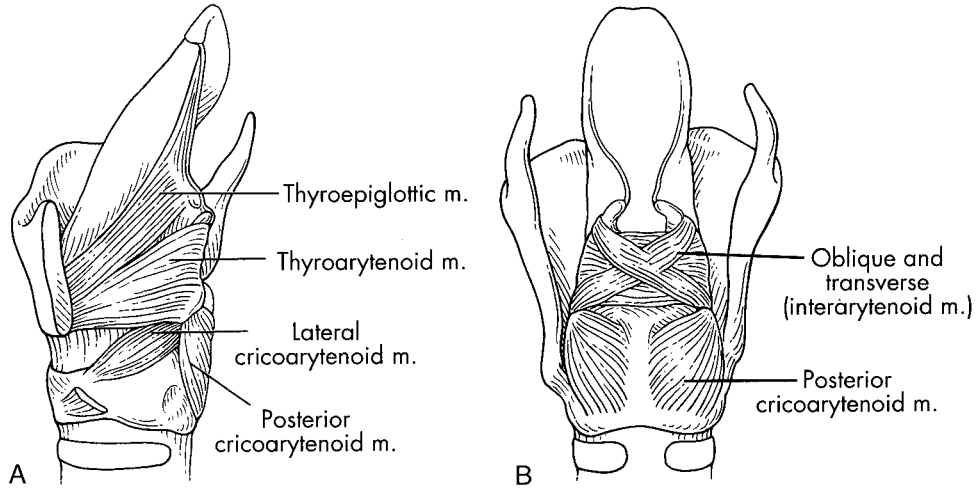

VIEW IMAGE

FIGURE 29-18 Intrinsic muscles of the larynx. **A**, Lateral view looking into the larynx, with half of the thyroid cartilage removed. **B**, Posterior view. Despite the complexity of the intrinsic laryngeal muscles, they cannot be routinely visualized individually on even high-resolution CT or MR imaging, but they appear as confluent soft tissue surrounding the airway.

Copyright © 2003, Mosby, Inc. All rights reserved.

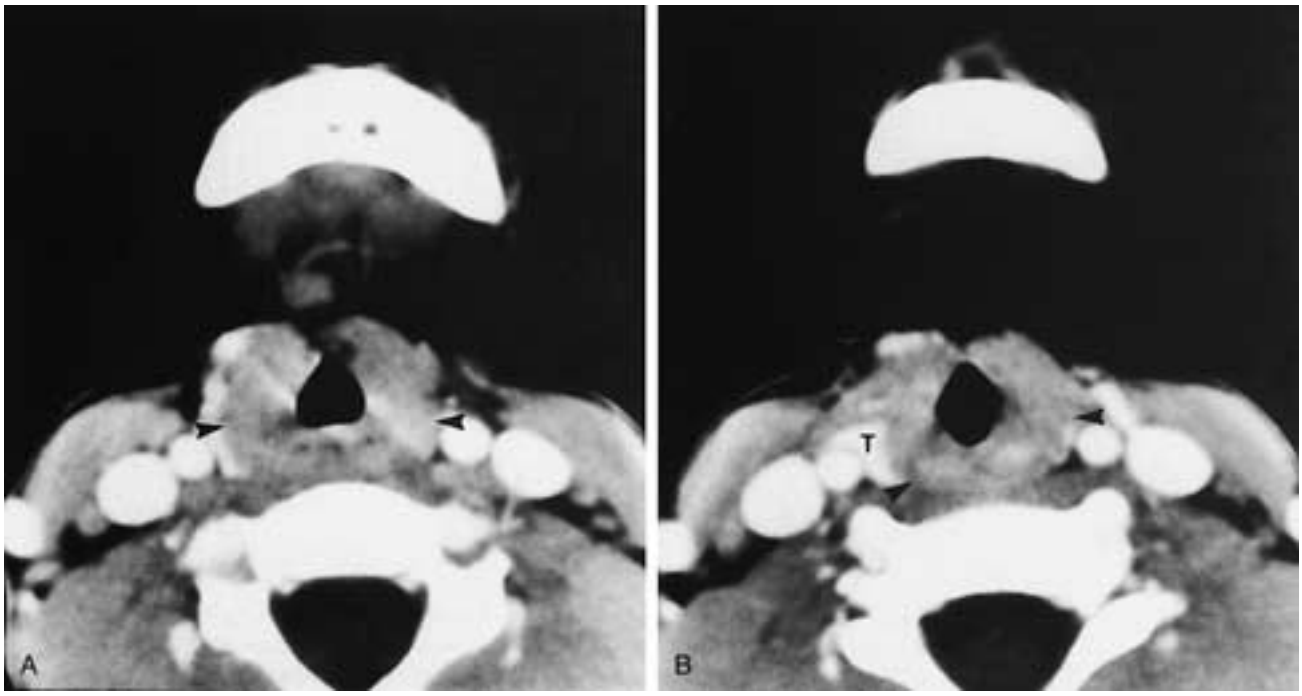

VIEW IMAGE

FIGURE 29-19 Normal larynx in a 5-year-old child without airway disease. **A**, Supraglottic larynx. Prominent circumferential soft tissue (*arrowheads*) surrounds the airway, but lack of calcification in the laryngeal cartilages makes more precise identification of the level difficult. **B**, Glottic level. The airway contour is oval. The thyroid gland (*T*) is separated from the airway by noncalcified laryngeal cartilages (*arrowheads*).

VIEW IMAGE

FIGURE 29-20 Normal larynx, gross specimen from a 9-month-old child who died from complications of complex congenital heart disease; no airway disease was found. The normal laryngeal anatomy contrasts dramatically with the featureless pediatric larynx on CT. **A**, True vocal cords. Note the thyroid and arytenoid cartilage, vocal cords, and cervical esophagus. **B**, View 3 mm caudal to **A** reveals thyroid and cricoid cartilage and the undersurface of the true vocal cords. Notice the oval contour to the airway. **C**, Trachea, 9 mm caudal to **B**. The trachea is round anteriorly and flat at the posterior membranous portion. The tissue surrounding the trachea is the thyroid gland.

Copyright © 2003, Mosby, Inc. All rights reserved.

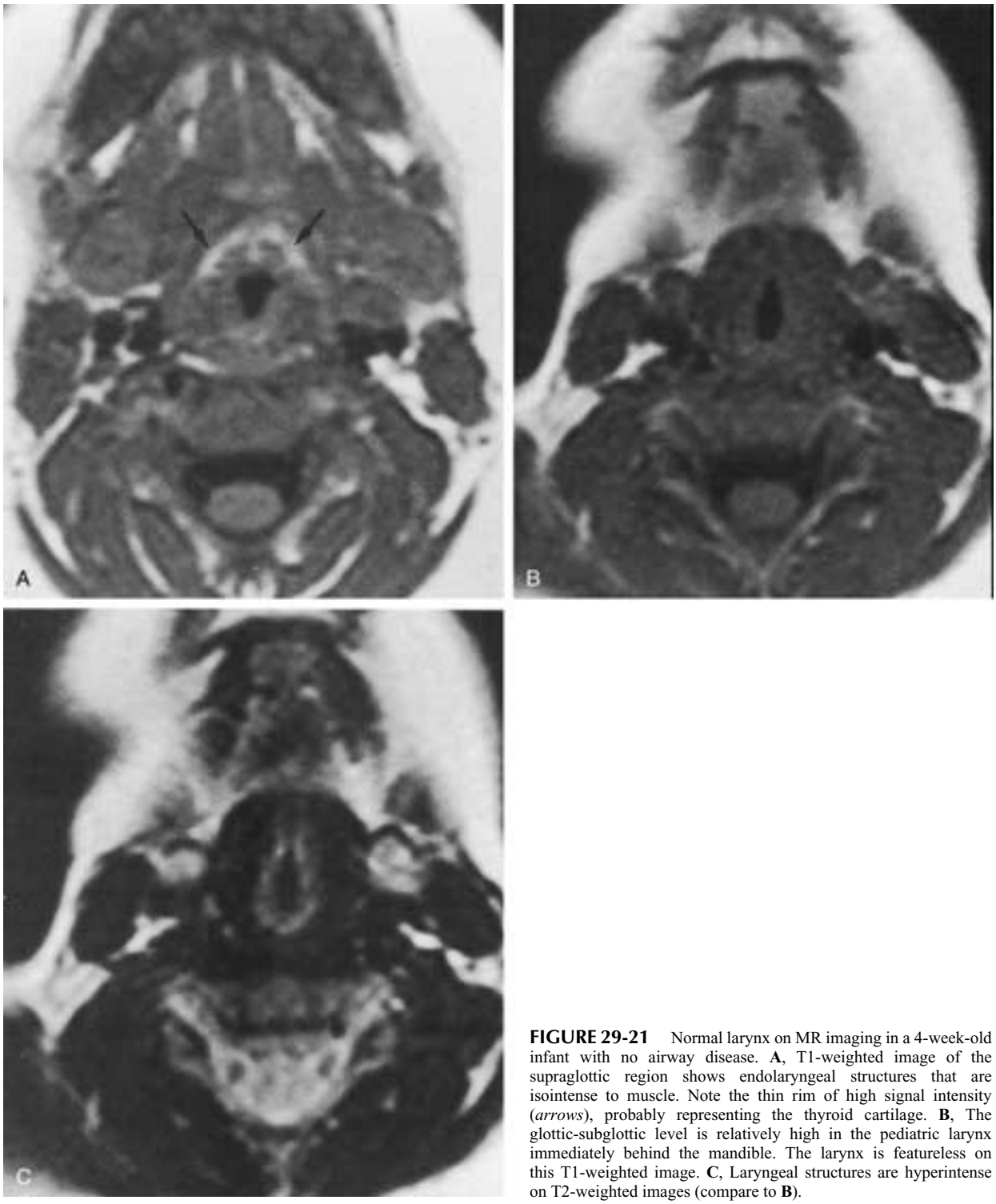

FIGURE 29-21 Normal larynx on MR imaging in a 4-week-old infant with no airway disease. **A**, T1-weighted image of the supraglottic region shows endolaryngeal structures that are isointense to muscle. Note the thin rim of high signal intensity (*arrows*), probably representing the thyroid cartilage. **B**, The glottic-subglottic level is relatively high in the pediatric larynx immediately behind the mandible. The larynx is featureless on this T1-weighted image. **C**, Laryngeal structures are hyperintense on T2-weighted images (compare to **B**).

VIEW IMAGE

Copyright © 2003, Mosby, Inc. All rights reserved.

SECTION FIVE

CONGENITAL AIRWAY DISEASES

NASAL OBSTRUCTION

Because the infant is an obligate nose breather, bilateral nasal airway disease often results in severe airway obstruction. Grunting, snorting, low-pitched stridor, and rhinorrhea are common presenting signs of nasal airway obstruction in the neonate or infant.[37] Although the most common cause of neonatal nasal airway obstruction is mucosal edema secondary to rhinitis, choanal atresia is the most common form of congenital nasal obstruction.[38, 39] Nasal airway obstruction may also result from turbinate hypertrophy, congenital syphilis (''snuffles''), pyriform aperture stenosis, and nasal cavity stenosis in association with craniofacial anomalies.[37, 38]

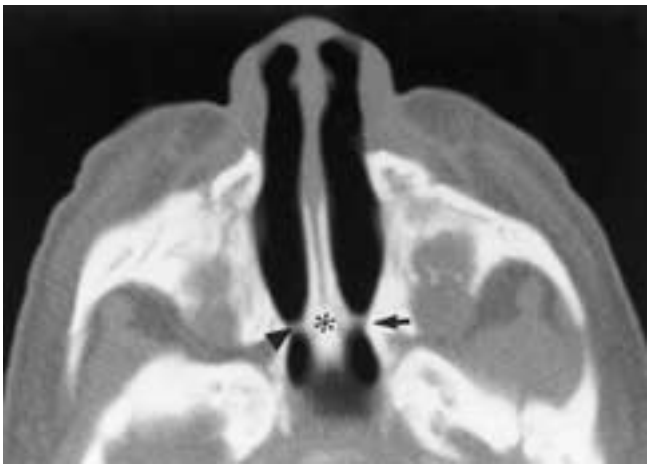

FIGURE 29-22 Bilateral membranous and bony choanal atresia in a 1-day-old girl. Axial CT scan obtained after suctioning the nasal cavity. There is thickening of the posterior vomer (*asterisk*). The posteromedial maxilla is bowed medially (*arrow*) and approximates the lateral margin of the vomer. There is a small membrane completing the atresia (*arrowhead*). Note the normal dimensions of the pyriform apertures anteriorly.

VIEW IMAGE

Choanal Atresia

Atresia of the posterior nasal cavity (choanae) is a developmental defect characterized by lack of communication between the nasal cavity and nasopharynx. This is the most common congenital abnormality of the nasal cavity, occurring in 1 of every 5000 to 10,000 live births.[38, 40] The anatomic classification of choanal atresia has been revised.[41] It was previously thought that choanal atresia was bony in 90% of cases and membranous in 10%.[42] However, with more accurate radiologic evaluation, it has been recognized that most if not all patients with choanal atresia have bony abnormalities. There is narrowing of the posterior nasal cavity with medial bowing and thickening of the lateral wall of the nasal cavity, with impingement at the level of the anterior aspect of the pterygoid plates and enlargement of the posterior portion of the vomer, with or without a central membranous connection (Fig. 29-22).[43] A combined bony and membranous malformation is found in approximately 70% of cases, and purely bony atresia occurs in about 30% of cases.[41] The existence of pure membranous atresia without a bony abnormality has been disputed.[41]

A number of theories have been proposed to explain choanal atresia: persistence of the buccopharyngeal membrane or of the bucconasal membrane, abnormal persistence or location of mesoderm-forming adhesions in the nasal choanal region, and misdirection of mesodermal flow.[40] The last mechanism links the development of choanal atresia to a mesodermal defect caused by faulty neural crest cell migration.[40, 44] Abnormal development, migration, or interaction of neural crest cells is thought to produce maldevelopment in the region of the nasal and palatal processes surrounding the nasobuccal membrane. The neural crest cell theory might help to explain the association of other craniofacial and distant malformations with choanal atresia.[44]

The clinical diagnosis of choanal atresia requires a high index of suspicion. Bilateral choanal atresia is a potentially life-threatening disorder that presents in the neonatal period. Symptoms range from intermittent mild to severe respiratory distress with cyanosis that is aggravated by feeding and alleviated by crying.[40, 45, 46] The diagnosis is suggested by an inability to pass nasal catheters or by absence of nasal mirror misting.[47] Bilateral choanal atresia should be promptly diagnosed and management initiated with insertion of an oral airway to alleviate symptoms.[45]

Approximately 75% of children with bilateral choanal atresia have other congenital abnormalities, as exemplified by the CHARGE association.[48, 49] The acronym CHARGE refers to a clustering of malformations that occurs more frequently together than expected on the basis of chance.[50, 51] These malformations include coloboma of the eye or microphthalmia (C), cardiovascular malformations (H), choanal atresia (A), developmental and growth delay (R), genital hypoplasia (G), typical external ear anomaly and/or hearing defects (E), and cranial nerve dysfunction.[52] The criteria for the diagnosis of CHARGE association have been recently revised.[52] Major criteria occur commonly in CHARGE association but are relatively rare in other conditions. These are coloboma, choanal atresia, characteristic ear abnormalities, and brainstem and cranial nerve dysfunction. Minor characteristics occur less commonly or are less specific for CHARGE. Heart defects, genital hypoplasia, orofacial clefting, tracheoesophageal fistula, short stature, and developmental delay are now considered minor criteria.[52, 53] The prevalence at birth of the CHARGE association is estimated at 1:100,000.[52] The diagnosis is firmly established when all four major criteria or three major and three minor criteria are present. The diagnosis also needs to be considered in any infant with one or two major and several minor characteristics.[52] The CHARGE complex is generally considered to be a sporadic condition. However, occasional familial cases, chromosomal abnormalities, and a significantly higher mean paternal age at conception have led some to consider an underlying genetic abnormality and to propose a subset of patients within the association who have a true syndrome.[54] Possible etiologies include defects of neural crest cells and the neural tube segment from which

Copyright © 2003, Mosby, Inc. All rights reserved.

these cells are derived, chromosomal deletion, and teratogenic exposure.[54, 55]

Although exact figures vary in the literature, about 50% to 60% of cases of choanal atresia are unilateral (Fig. 29-23).[41] Patients with unilateral choanal atresia usually present later in infancy or childhood with persistent unilateral nasal discharge or feeding problems. Although the presentation of unilateral choanal atresia is not as dramatic as bilateral choanal atresia, significant airway and/or feeding symptomatology may be present in a substantial number of children under 1 year of age.[56]

Radiologic evaluation of choanal atresia should be obtained after stabilization of the patient. CT is performed to identify the nature and severity of the anatomic deformity and to estimate the size of the nasopharynx. When the diagnosis is questionable, CT will differentiate other causes of bilateral nasal obstruction such as pyriform aperture stenosis or bilateral nasolacrimal duct cysts from choanal atresia (Fig. 29-24). Unilateral causes of nasal obstruction such as nasal foreign body, turbinate hypertrophy, septal deviation, antrochoanal polyp, or nasal tumor can also be differentiated from choanal atresia by CT.

The CT examinations are obtained with the patient supine. Agents can be suctioned and topical nasal vasoconstriction administered prior to commencing the scan to minimize accumulated nasal secretions in an effort to optimize assessment of any membranous component of atresia[24] (Fig. 29-22). Contiguous 1 to 1.5 mm scans of the nasopharynx should be obtained with the imaging plane parallel to the hard palate. Prospective high-resolution (edge enhancement) bone filters may be helpful because the skull base is only partially ossified at birth and conventional bone window settings may not permit adequate visualization of bone margins. Intravenous contrast is not required for the imaging of choanal atresia.

On CT scans the width of both posterior choanae at maximum stenosis and the maximum width of the inferoposterior vomer can be measured.[24] The major bony component of the atresia is an abnormal widening of the vomer (Fig. 29-22). Typically, the posteromedial maxilla is bowed medially and approximates or is fused with the lateral margin of the vomer. The mean width of the posterior choanal airspace in the newborn (measured from the lateral wall of the nasal cavity to the vomer) is 0.67 cm, increasing to 0.86 cm at 6 years and to 1.13 cm by 16 years of age.[24] In patients less than 8 years of age, the vomer generally measures less than 0.23 cm in width and should not exceed 0.34 cm; in children over 8 years, the mean vomer width is 0.28 cm and should not exceed 0.55 cm.[24] The thickness of the bony atretic plate should be reported because this may influence the surgical approach. In general, the thicker the plate, the more difficult the surgical repair.

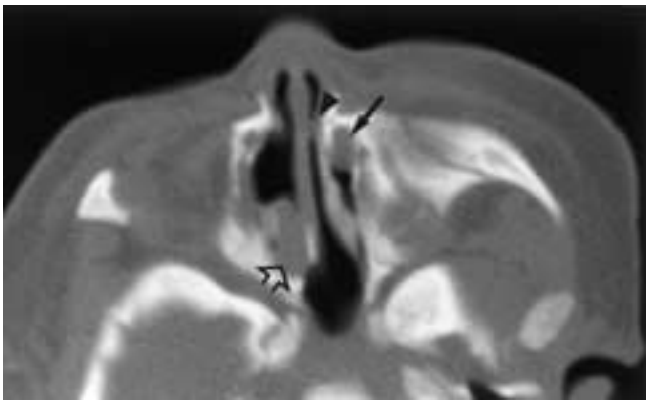

FIGURE 29-24 Nasal obstruction in a 2-day-old girl. Axial CT demonstrates unilateral choanal atresia (*open arrow*), pyriform aperture stenosis (*arrowhead*), and a nasolacrimal duct cyst (*black arrow*). Contrast these findings with those seen in Figure 29-22.

VIEW IMAGE

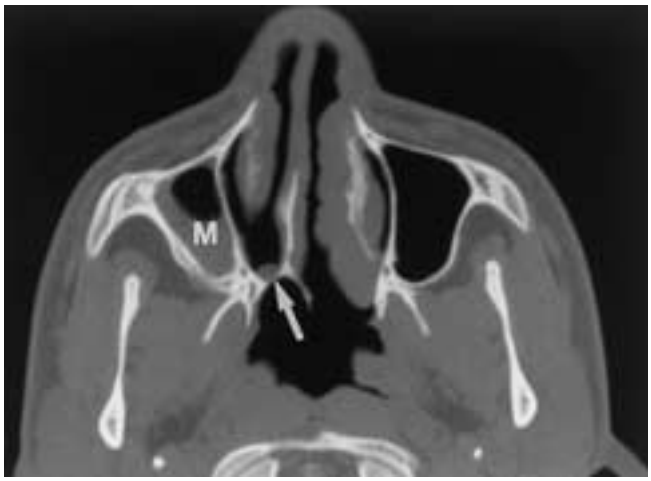

FIGURE 29-23 Unilateral choanal atresia in a 15-year-old boy. Axial CT demonstrates bony atresia of the right posterior choana. A thin wafer of bone (*arrow*) closes the space between the vomer and the posteromedial maxilla and pterygoid plates. There is hypoplasia of the right maxillary antrum (*M*), which contains mucoperiosteal thickening and secretions.

VIEW IMAGE

The membranous components of atresia are characterized by soft tissue filling the posterior choanae, associated with narrowing of the posterior choanae just anterior to the pterygoid plates (Fig. 29-22). The obstructing choanal membranes may be thin and strand-like or thick and plug-like. In patients with choanal abnormalities the nasal cavities may contain air, soft tissue, fluid secretions, or hypertrophied inferior turbinates. Topical vasoconstriction helps differentiate associated reversible changes from fixed obstructing lesions.

Surgical correction of bilateral choanal atresia is performed as soon as possible after the diagnosis has been made. The type of atresia and the thickness of the bony atresia plate, as determined by CT, determine the surgical approach. There has been little consensus regarding the optimal surgical approach to choanal atresia.[57] Transpalatal, transnasal, transseptal, and sublabial approaches have all been utilized, with varying results.[45, 57] Recently, the transnasal endoscopic drill-out procedure has emerged and been advocated as a safe and efficacious method with the best possibility of long-term nasal patency.[45, 57] This procedure usually entails the use of power instruments to perform mucosal incisions and bony resection of the atretic plate and vomer.[57] Puncture and curettage techniques without adequate resection of the vomer may lead to postoperative stenosis.[41] Multiple revisions are more likely to be required for small neonates and those with associated anomalies.[45] Postoperative nasal stenting is also frequently utilized.

Copyright © 2003, Mosby, Inc. All rights reserved.

Postsurgical persistent or recurrent choanal stenosis, usually caused by postoperative scar or an incompletely resected bony atretic plate, is also best evaluated with CT.[46] Laser resection can be considered for soft-tissue cicatrix.[41]

Nasolacrimal Duct Cysts

Most cases of nasolacrimal duct (NLD) cysts are thought to result from failure of canalization and partial or complete obstruction of the NLD. These cysts, which may be unilateral or bilateral, usually present in early neonatal life. The level of obstruction is usually at Hasner's valve, the most inferior point of the NLD, which is located beneath the inferior turbinate within the inferior meatus.[58] Retained secretions accumulate in the dilated NLD, with resultant cystic protrusion of the duct into the inferior meatus at the nasolacrimal ostium. In some cases, endoscopic contrast studies have demonstrated patency of the NLD in the presence of an NLD cyst. It has been suggested that these cases may be due to a diverticulum or duplication of the NLD.[58] Other etiologies of NLD obstruction typically present in older children and include tumors, granulomatous diseases such as sarcoid, tuberculosis, foreign body, and ectopic teeth. An increased incidence of NLD stenosis has also been noted in children with syndromic disorders such as trisomy 21 and branchio-oto-renal and branchi-oculo-facial syndromes.[59, 60]

Presenting signs of NLD cyst include a medial canthal mass due to dacryocystocele (dilatation of the lacrimal sac), epiphora, nasal obstruction, and respiratory distress. In the absence of a dacryocystocele, NLD cysts may be clinically indistinguishable from bilateral choanal atresia. Chronic inflammatory changes may be found in the walls of NLD cysts, suggesting the possibility of an intrauterine inflammation.[61] Bilateral NLD cysts present in early life with nasal obstruction. Unilateral mucoceles are uncommon.

CT evaluation should be performed using a technique similar to that described for choanal atresia. CT shows rounded, bilateral or unilateral, homogeneous soft-tissue density structures in the anterior and inferior nasal cavities (Figs. 29-24 to 29-26).[61] The inferior turbinates may be thinned and medially displaced. Unilateral cysts sometimes result in deviation of the nasal septum. NLD cysts may also occur in association with other abnormalities such as choanal atresia (Fig. 29-24).

Most cases of congenital NLD cysts resolve spontaneously within 12 months. For persistent NLD cysts, nasal endoscopy in conjunction with lacrimal probing is used to identify the precise site of opening of the NLD and the nature of obstruction. This technique minimizes the risk of creating a false passage, as may occur with blind lacrimal probing.[62]

Pyriform Aperture Stenosis

Congenital nasal pyriform aperture stenosis (PAS) is a rare anomaly characterized by narrowing of the anterior bony nasal apertures. The clinical presentation depends on the severity of the stenosis. Symptoms include respiratory distress immediately after birth, cyclical cyanosis relieved by crying, or difficulty breathing during feeding. It may be difficult or impossible to insert a nasogastric tube into the nose. Congenital PAS must be differentiated from other causes of nasal obstruction such as bilateral choanal atresia.

PAS may occur as an isolated anomaly or in association with dysmorphic features such as holoprosencephaly, hypopituitarism, a single central megaincisor, hypotelorism, cleft palate, and clinodactyly.[63, 64] Holoprosencephaly is a genetically and phenotypically heterogeneous disorder involving development of the forebrain and midface, with an incidence of 1:16,000 live born and 1:250 induced abortions.[65] Alobar holoprosencephaly, the most severe form, is associated with complete failure of division of the forebrain, as well as facial anomalies such as anophtalmia or cyclopia and a primitive nasal structure (proboscis) and/or midfacial clefting.[66] In milder forms, hypotelorism, single maxillary central incisor, and defects of the upper lip and/or nose characterize facial dysmorphism. Congenital PAS without a central megaincisor is generally an isolated anomaly with no intracranial defects.[63]

The etiology of PAS is unclear, but it may be related to bony overgrowth of nasal processes of the maxilla as part of

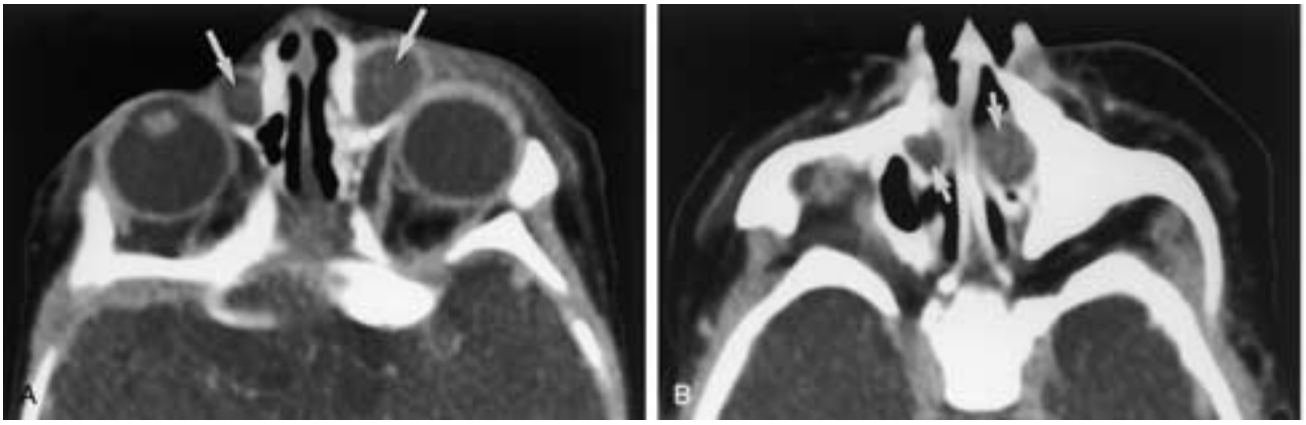

FIGURE 29-25 Bilateral nasolacrimal duct (NLD) cysts in a 4-day-old girl. Contrast-enhanced axial CT (soft-tissue windows) shows (**A**) dilated low attenuation and mildly ring-enhancing nasolacrimal sacs (*arrows*) and (**B**) NLD cysts (*arrows*).

VIEW IMAGE

Copyright © 2003, Mosby, Inc. All rights reserved.

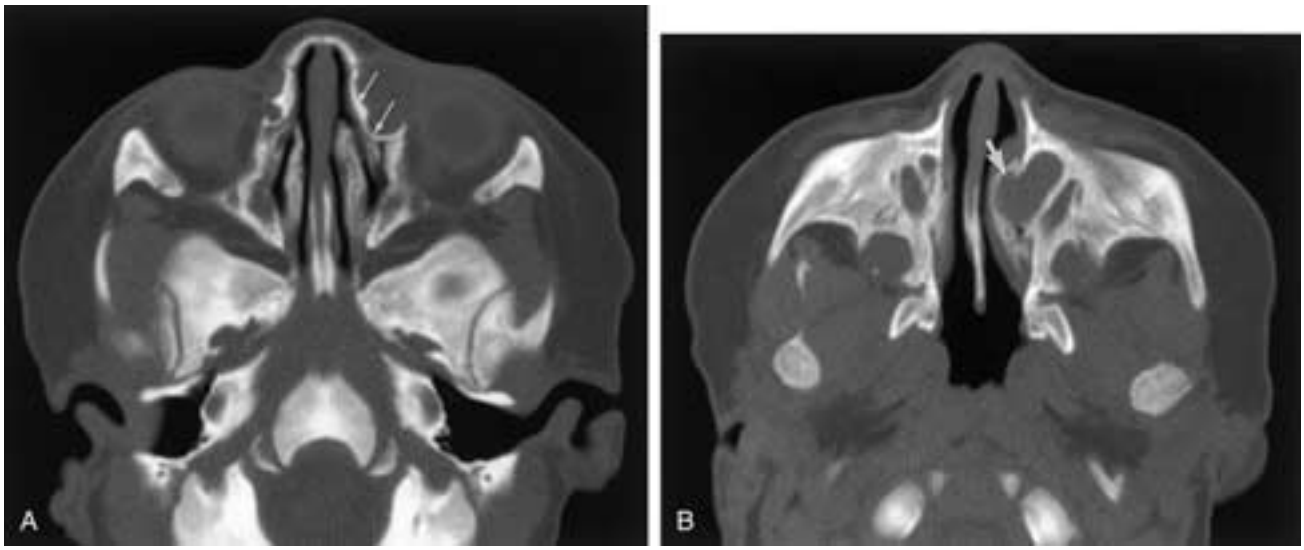

VIEW IMAGE

FIGURE 29-26 NLD cyst in a 4-week-old girl. Axial CT images (bone windows) demonstrate dilatation of (**A**) the left nasolacrimal sac and (**B**) the NLD. Note the smoothly marginated remodeling of the bony margins of the NLD (*arrows*). The NLD cyst protrudes beneath the inferior turbinate (*arrow*).

a developmental field defect or may be due to abnormal growth of the primary palate.[63, 67–69] Cytogenetic examination has revealed anomalies of chromosome 7, 13, or 18 in some cases.[64, 70] Defects in the cell signaling pathway involving the Sonic hedgehog gene, genes from other signaling pathways, defects in cholesterol biosynthesis, and teratogens have all been shown to cause holoprosencephaly in humans.[66, 71–73] Sonic hedgehog appears to have a role in coordinating the proliferation and survival of cells of the neural tube and cranial neural crest and is essential for morphogenesis of the frontonasal and maxillary processes, which give rise to the midface and upper face.[72, 73] Transient loss of sonic hedgehog signaling in the embryonic face inhibits growth of the primordia and results in defects analogous to hypotelorism and cleft lip/palate, characteristics of the mild forms of holoprosencephaly.[72]

CT of PAS should be performed as described for choanal atresia, but the scans should be extended through the maxillary alveolar ridge to evaluate for possible dental abnormalities. CT shows thickening of the nasal process of the maxilla, which results in narrowing of the anterior aperture, the narrowest portion of the nasal airway (Fig. 29-27). The adjacent anterior nasal septum may also be thinned. In addition to the pronounced narrowing of the anterior and inferior nasal apertures, the width of the nasal passage as a whole is generally also narrower than that of age-matched controls.[68] CT may also show a hypoplastic triangular hard palate with a marked midpalatal vomerine ridge and a median maxillary single central incisor tooth (megaincisor) (Fig. 29-27).[68, 69] Patients with a central megaincisor have an increased incidence of pituitary insufficiency and holoprosencephaly.[63] Therefore, MR imaging of the brain and pituitary is recommended in these patients. In addition to holoprosencephaly, MR imaging

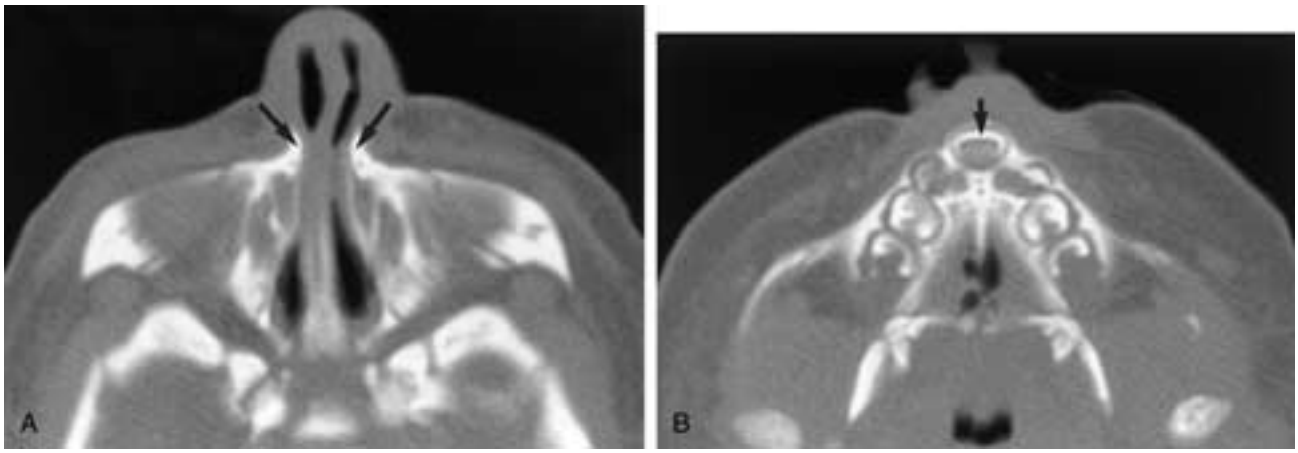

VIEW IMAGE

FIGURE 29-27 Bilateral pyriform aperture stenosis in a 2-day-old boy. Axial CT demonstrates (**A**) medial approximation of the nasal processes of the maxilla at the pyriform apertures (*arrows*). Contrast this appearance with the normal anatomy of the pyriform apertures in Figure 29-22. **B**, There is a single central megaincisor (*arrow*).

Copyright © 2003, Mosby, Inc. All rights reserved.

may demonstrate absence of the anterior pituitary gland and infundibulum.

Initial management of PAS is aimed at establishing an airway. Subsequent treatment is determined by the overall prognosis of the infant and the symptomatic severity of the stenosis.

Other Forms of Nasal Stenosis and Nasal Agenesis

Stenosis within the nasal cavity can be the result of maxillary hypoplasia or turbinate hypertrophy. In children with syndromic craniosynostosis, midfacial retrusion is generally associated with narrowing of the entire nasal and nasopharyngeal passages as well as some reduction in choanal dimensions.[74] Although there have been reports of ''choanal atresia'' in Apert syndrome, it is generally the anterior third to midportion of the nasal cavity that is maximally narrowed in these children, and a diagnosis of choanal stenosis is not usually supported by CT.[69] Nasal stenosis has also been reported to be a feature of the Antley-Bixler syndrome. This uncommon syndrome was first named in 1975 and is characterized by multiple malformations of cartilage and bone including multisynostotic osteodysgenesis, midface hypoplasia, choanal atresia or stenosis, femoral bowing, neonatal fractures and multiple joint contractures and, occasionally, urogenital, gastrointestinal, or cardiac defects.[75–77]

Congenital absence of the nose with failure of formation of the nose, nares, and nasal cavities is rare. Associated anomalies include maxillary hypoplasia, a high-arched or cleft palate, low-set ears, and ocular anomalies (e.g. hypertelorism, micropthalmia, coloboma, and occluded or absent nasolacrimal ducts) (Fig. 29-28).[78, 79] Associated intracranial anomalies may include frontal encephalocele, absence of the olfactory bulbs and tracts, minor frontal gyral abnormalities, and agenesis of the corpus callosum. Theories of pathogenesis include failure of invagination of the nasal placodes, premature fusion of the medial nasal processes, lack of resorption of the nasal epithelial plugs, and faulty neural crest cell migration.[80]

Congenital absence of the nose has been detected with antenatal sonography.[79] Postnatal evaluation of these infants involves the use of both CT and MR imaging. CT with 1 to 3 mm increment helical images in the axial plane is used to provide bony anatomic detail for surgical planning (Fig. 29-28). Thin-section high-resolution multiplanar MR images are obtained to assess for the presence of associated malformations such as frontal cephalocele, and to document the dimensions of the space between the anterior cranial fossa and the hard palate.[79]

Nasopharyngeal Atresia

Nasopharyngeal atresia (NA) is an extremely rare malformation that results in complete isolation of the nasal cavity from the oropharynx.[81] Patients present early in life with severe respiratory obstruction. The diagnosis is made when a nasogastric tube cannot be passed more than 3 to 4 cm. The most important differential diagnosis is choanal atresia. CT of NA demonstrates absence of air in the posterior nasal cavity or nasopharynx. The posterior choanal passages end blindly, the posterior vomer is wide, and both the vomer and the hard palate are fused to the central skull base (Fig. 29-29). The soft palate is absent. Soft-tissue density material occupies the nasal cavities. Imaging on conventional CT may not clearly delineate the abnormality, and therefore sagittal reformatted images or sagittal T1-weighted MR imaging should be performed. This study shows absence of the uvula and nasopharynx, confirming the

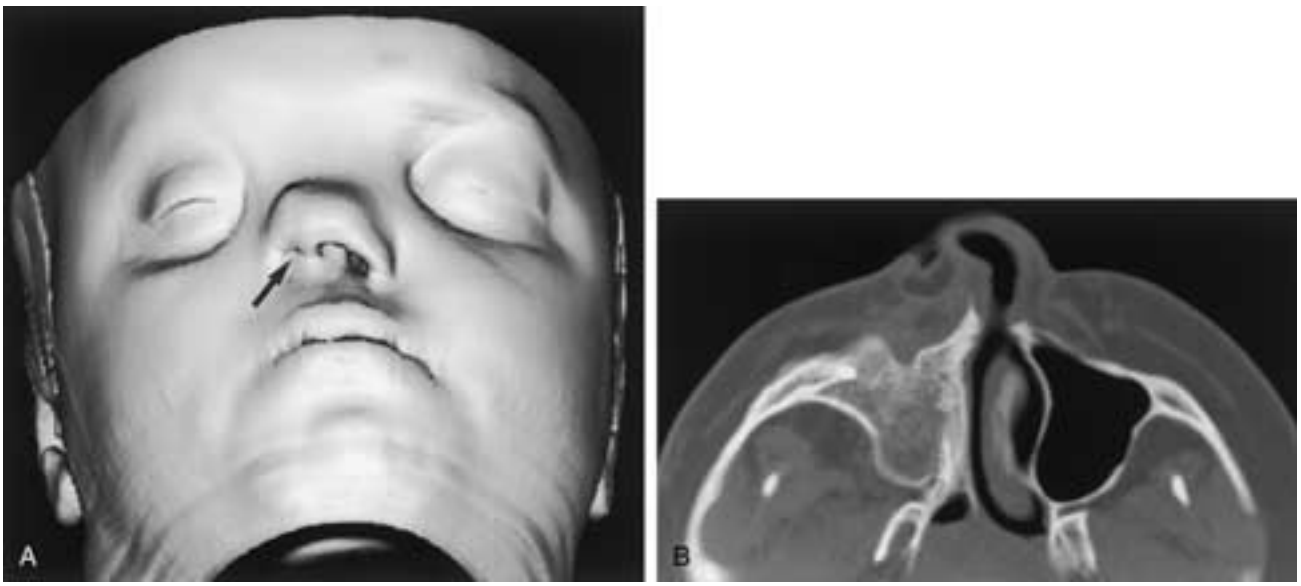

FIGURE 29-28 Frontoorbital and nasomaxillary dysplasia in a 16-year-old girl. **A**, Three-dimensional CT of the face reveals facial asymmetry and right nasal hypoplasia with a small depression at the location of the right nostril (*arrow*). There is hypertelorism and right micropthalmos. **B**, Axial CT shows absence of the right nasal cavity and right maxillary antrum.

VIEW IMAGE

Copyright © 2003, Mosby, Inc. All rights reserved.

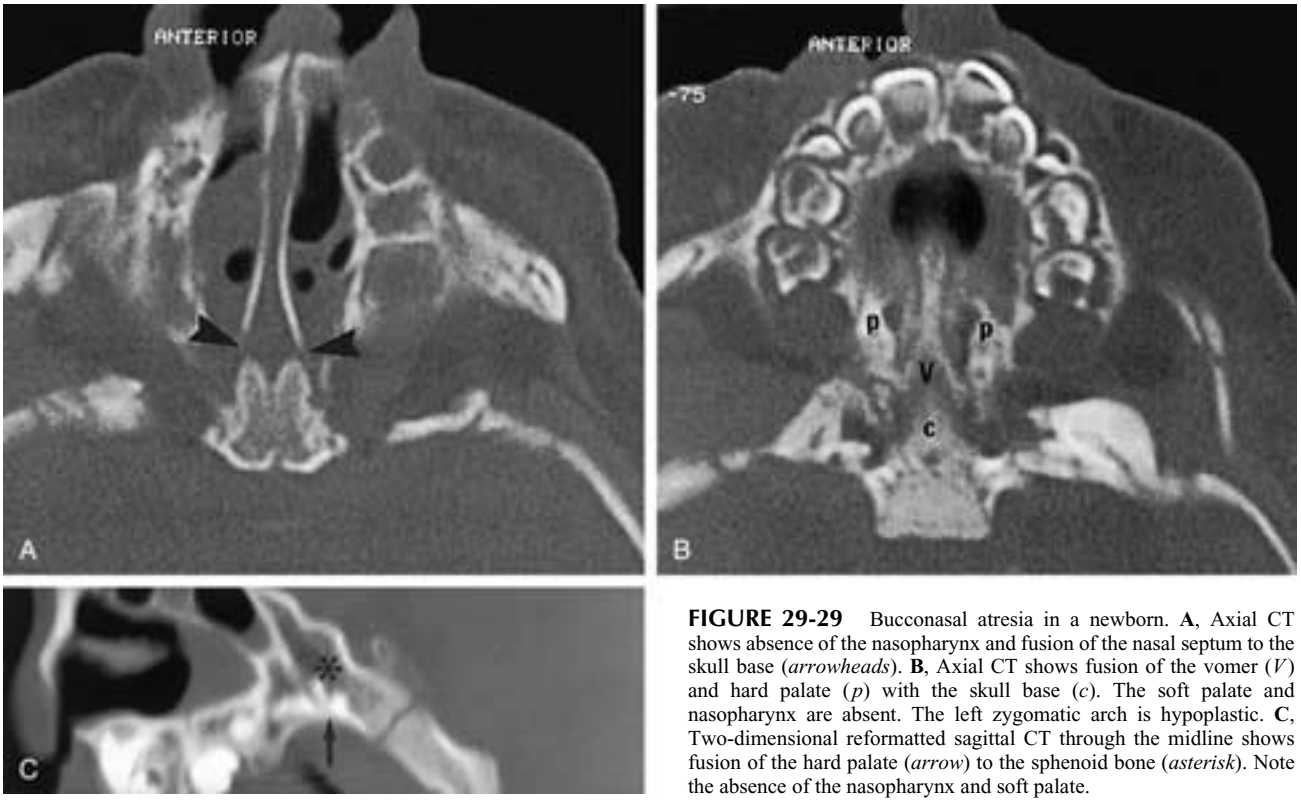

FIGURE 29-29 Bucconasal atresia in a newborn. **A**, Axial CT shows absence of the nasopharynx and fusion of the nasal septum to the skull base (*arrowheads*). **B**, Axial CT shows fusion of the vomer (*V*) and hard palate (*p*) with the skull base (*c*). The soft palate and nasopharynx are absent. The left zygomatic arch is hypoplastic. **C**, Two-dimensional reformatted sagittal CT through the midline shows fusion of the hard palate (*arrow*) to the sphenoid bone (*asterisk*). Note the absence of the nasopharynx and soft palate.

VIEW IMAGE

diagnosis. This complex anomaly is managed by tracheotomy and subsequent reconstruction. Cleft lip has been associated with NA.[81]

Meningocele, Encephalocele, Nasal Dermoid, and Neuroglial Heterotopia

Nasal obstruction resulting from meningoceles, encephaloceles, nasal dermoid, or nasal neuroglial heterotopia is uncommon and results from errors in nasofrontal development.[82–86] The embryologic basis and general description of these anomalies are discussed in detail in Chapter 1.

CRANIOFACIAL MALFORMATIONS

Upper airway obstruction is frequently a feature of craniofacial syndromes and is often due to compromise of the airway at more than one anatomic location. Excluding isolated cleft palate anomaly, approximately 20% of children with major craniofacial bony anomalies require tracheotomy to alleviate airway compromise.[74] Early severe airway obstruction in these children is most often associated with an inadequate nasal airway, usually in the setting of additional oropharyngeal anomalies. Severe midface retrusion with nasal and nasopharyngeal stenosis may be mistaken for choanal atresia or stenosis. This has important therapeutic implications, as operative procedures to enlarge the posterior choanae are not helpful with these midface deformities.[74] Upper airway compromise may manifest clinically as nasal obstruction, laborious breathing, and obstructive sleep apnea, sometimes with cor pulmonale. Severe airway obstruction for which tracheotomy is required is most commonly associated with syndromic forms of craniosynostosis (e.g., Crouzon, Pfeiffer, or Apert syndrome), mandibulofacial dysostosis (Treacher Collins or Nager syndrome), and hemifacial microsomia.[74] Severe variants of Apert and Pfeiffer syndromes sometimes also have tracheal sleeve abnormalities that produce distal tracheal stenosis and/or lack of tracheal distensibility with sometimes fatal lower airway compromise from respiratory inefficiency, inability to clear secretions, and/or increased vulnerability to surface injury from tracheal suctioning.[74, 87] Interestingly, the presence of a cleft palate seems to provide additional nasal airway in patients with midface retrusion who may require long-term tracheotomy following cleft palate repair.[74]

Procedures used to alleviate airway obstruction include midface advancement, mandibular expansion, tonsillectomy and adenoidectomy, uvulopalatopharyngoplasty, anterior tongue reduction, and endoscopic tracheal granuloma excision. The choice of treatment depends on the nature and severity of airway obstruction. Infant tracheotomy, when indicated, can normalize body growth and development until such time as sufficient facial growth has occurred or definitive surgery such as midfacial advancement can safely be performed.[74] In some patients, obstructive sleep apnea may become evident only when the size of the lymphoid tissues of Waldeyer's ring is maximal. In these children, adenotonsillectomy alone may produce symptomatic improvement.

Of all the cleft syndromes, unilateral cleft lip and palate has the most severe reduction in nasal airway area.[88] Nasal septal deformities, septal spurs, turbinate hypertrophy, and

Copyright © 2003, Mosby, Inc. All rights reserved.

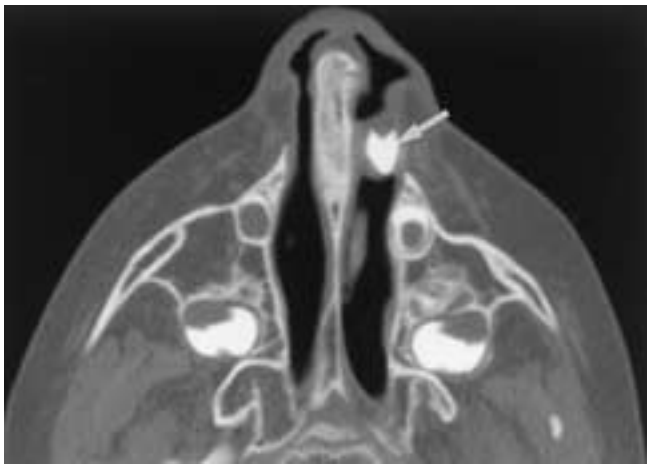

VIEW IMAGE

FIGURE 29-30 Supernumerary tooth in a 5-year-old boy with chromosomal abnormalities, multiple congenital anomalies, sleep apnea, and left facial pain. Axial CT shows the supernumerary tooth (*arrow*) obstructing the left pyriform aperture.

malpositioned teeth associated with cleft syndromes also result in nasal airway encroachment (Fig. 29-30). Although the nasal airways are accessible to direct clinical inspection, CT should be obtained before craniofacial surgery because size, asymmetry between sides, septal abnormalities such as lateral deviation or spurs, and turbinate anomalies or hypertrophy are details that should be conveyed to the surgeon.

Facial duplications are extremely rare and range from localized anomalies to complete doubling of all facial elements.[89] This anomaly is also known as *diprosopus*, referring to varying degrees of facial duplication with a single trunk and normal limbs.[90] Cleft lip and palate, macrostomia, multiple uvulae, hypertelorism, and intraoral or intranasal hamartomatous masses may accompany duplication of the maxilla, mandible, or both (Fig. 29-31).[89] Anomalies involving the brain, heart, kidneys, and spine have been described in children with facial duplications.[91, 92] It has been hypothesized that diprosopus results from duplicated neural crest cell derivatives following an initial duplication of the notochord.[92] The anomaly has also been linked to excessive Sonic hedgehog signaling.[72]

Helical CT with 3 mm increments in the axial plane with multiplanar 2D reformatted images and a three-dimensional (3D) model of the anomaly can be obtained to delineate the bony anatomy prior to reconstructive surgery (Fig. 29-31A). The skull base should be assessed for cephaloceles or defects, and the soft tissues of the nose, nasopharynx, and oropharynx should be assessed for hamartomatous masses (Fig. 29-31C). MR imaging provides useful ancillary evaluation for hamartomas, cephaloceles, and anomalies of the brain (Fig. 29-31D,E)

OROPHARYNGEAL OBSTRUCTION

Thyroglossal Duct Cyst and Ectopic Thyroid

The embryology of the thryoglossal duct is reviewed in Chapter 33. Of all the locations for thyroglossal duct cysts, those located at the base of tongue (foramen cecum) or vallecula are more likely to present with airway obstruction. CT or MR imaging is performed to characterize the mass, to define the extent of the cyst and its relationship to the larynx, and to exclude other lesions such as dermoid cyst, cervical adenopathy, hemangioma, lipoma, or lymphatic malformation. On CT, suprahyoid thyroglossal duct cysts are typically midline, rarely occurring more than 2 cm laterally (Fig. 29-32).[93] Simple thyroglossal duct cysts are low in density, with a thin rim that does not enhance significantly. If infected or if there is a history of infection, the cyst may have a higher density, with internal septations and rim enhancement.[94] On MR imaging, the cysts have either low or high signal on T1-weighted images and high signal on T2-weighted images. Rim enhancement is typical.

If a solid mass is seen in association with a presumed thyroglossal duct cyst, two entities should be considered: (1) ectopic thyroid tissue, which may occasionally be seen within the cyst wall or tract, or, rarely, (2) carcinoma, either papillary thyroid or squamous cell.[93, 95] If ectopic thyroid tissue coexists within a thyroglossal duct cyst and if this tissue is the patient's only functioning thyroid tissue, resection of the ectopic thyroid with the cyst will render the patient permanently hypothyroid.[96]

Malignancy, usually papillary adenocarcinoma, is a rare occurrence in a thyroglossal duct cyst. Most patients with thyroglossal duct cysts and associated malignancy are adults, but there are reports of carcinomas occurring in children as young as 6 years old.[97] Thyroid carcinoma arising in a thyroglossal duct cyst may be clinically indistinguishable from a benign thyroglossal duct cyst. However, carcinoma should be considered in thyroglossal duct cysts that have a mural nodule, calcification, or both (Fig. 29-33).[98]

The treatment of thyroglossal duct cysts is surgical excision using the Sistrunk procedure, in which the entire cyst, tract, and central body of the hyoid bone are resected en bloc.[99] Sistrunk's operative approach has been advocated to reduce the incidence of postoperative recurrence.[100]

Ectopic thyroid tissue at the base of the tongue, known as lingual thyroid, is the most common location for ectopic thyroid to occur, yet it is a rare cause of stridor in the infant.[101, 102] Of these patients, 70% have no other functioning thyroid tissue, and complete surgical resection may result in permanent hypothyroidism.[103] Congenital hypothyroidism and stridor suggest the diagnosis of lingual thyroid.[101] An ^{123}I scan, the diagnostic test of choice, shows uptake in the tongue base mass and can identify the presence of other thyroid tissue, usually in its normal location (Fig. 29-34). In most cases this is the only imaging test needed. If other imaging is required, ultrasound shows a solid mass, differentiating the ectopic thyroid from a thyroglossal duct cyst. CT without contrast shows a high-density mass at the tongue base. Iodinated contrast should not be used in this setting if it is anticipated that radionuclide imaging will be needed to confirm the diagnosis. On MR imaging, the lingual thyroid is hyperintense or isointense with respect to the intrinsic tongue muscles on both T1-weighted and T2-weighted images (Fig. 29-35). Regardless of the test performed, imaging should include the thyroid bed in an

Copyright © 2003, Mosby, Inc. All rights reserved.

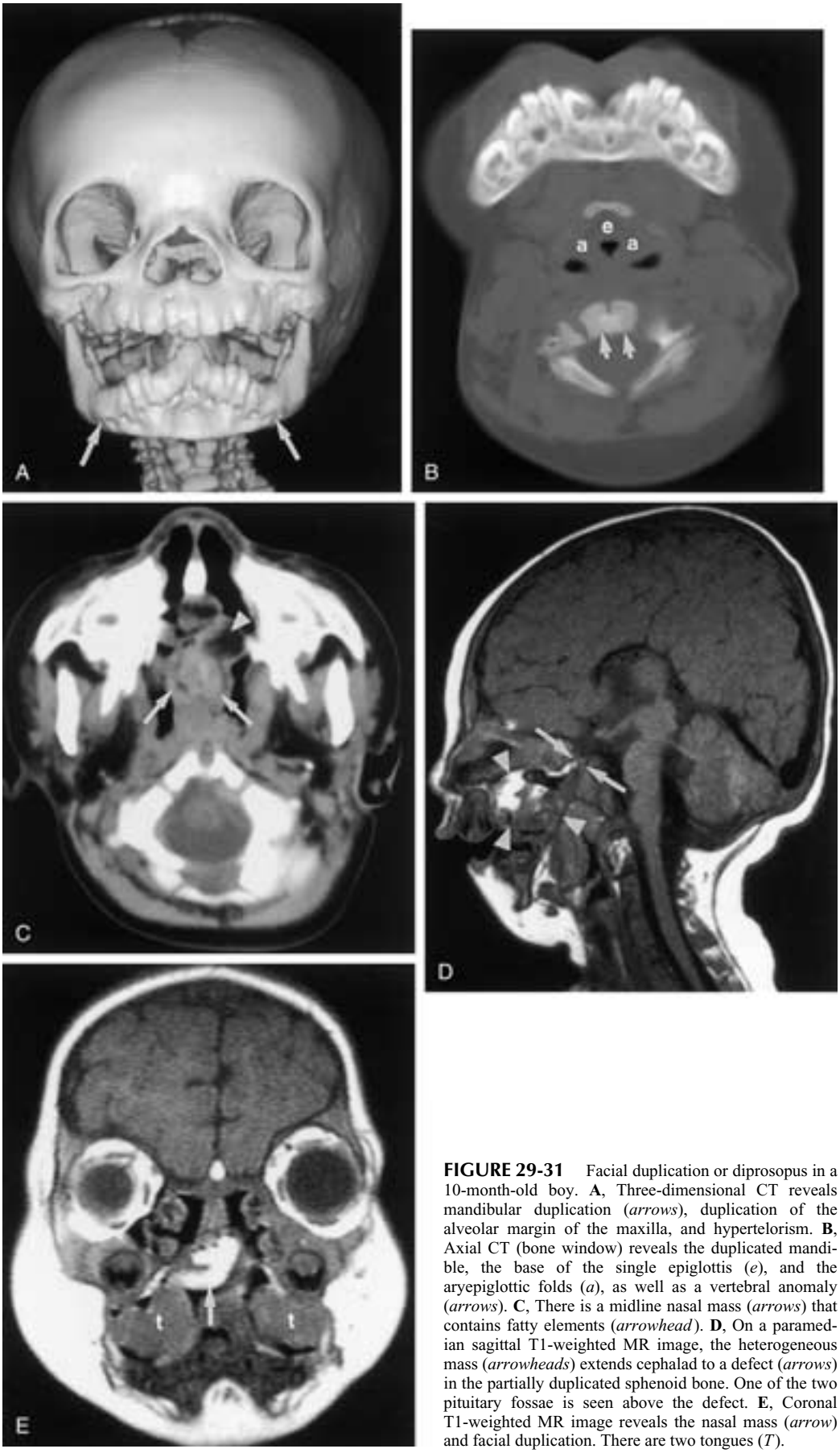

FIGURE 29-31 Facial duplication or diprosopus in a 10-month-old boy. **A**, Three-dimensional CT reveals mandibular duplication (*arrows*), duplication of the alveolar margin of the maxilla, and hypertelorism. **B**, Axial CT (bone window) reveals the duplicated mandible, the base of the single epiglottis (*e*), and the aryepiglottic folds (*a*), as well as a vertebral anomaly (*arrows*). **C**, There is a midline nasal mass (*arrows*) that contains fatty elements (*arrowhead*). **D**, On a paramedian sagittal T1-weighted MR image, the heterogeneous mass (*arrowheads*) extends cephalad to a defect (*arrows*) in the partially duplicated sphenoid bone. One of the two pituitary fossae is seen above the defect. **E**, Coronal T1-weighted MR image reveals the nasal mass (*arrow*) and facial duplication. There are two tongues (*T*).

VIEW IMAGE

Copyright © 2003, Mosby, Inc. All rights reserved.

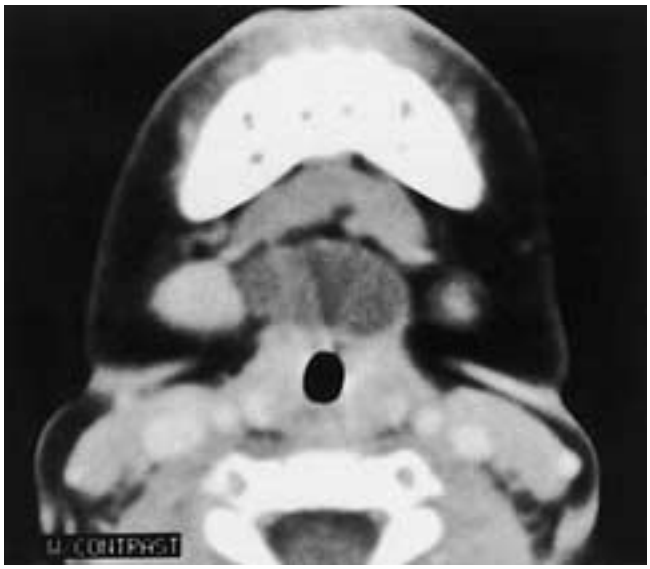

VIEW IMAGE

FIGURE 29-32 Thyroglossal duct cyst in a 1-year-old infant with a soft midline neck mass. Contrast-enhanced CT shows a low-density, nonenhancing unilocular midline mass in the midline floor of the mouth.

attempt to identify thyroid tissue in its normal location. Airway obstruction mandates surgical excision. Otherwise, hormonal suppression with thyroid hormone is the treatment of choice.

VIEW IMAGE

FIGURE 29-33 Papillary thyroid carcinoma arising within a thyroglossal duct cyst in a boy with a neck mass. Axial CT reveals a heterogeneous partially calcified nodule (*arrows*) within the thyroglossal duct cyst, which has an atypical multiloculated appearance.

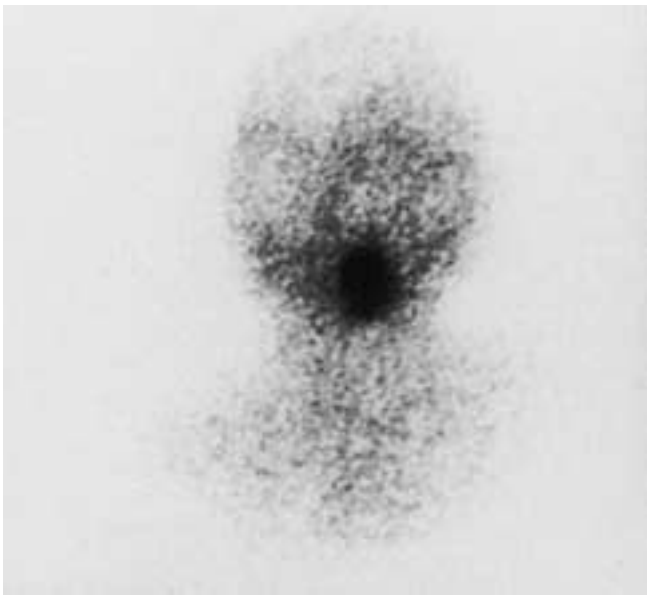

VIEW IMAGE

FIGURE 29-34 Lingual thyroid, with no functioning thyroid gland in the thyroid bed. ^{123}I nuclear medicine scan in a 1-year-old child with dysphagia. Note the uptake in the floor of the mouth, slightly eccentric to the left, with no radionuclide in the expected location of the thyroid gland. (Courtesy of Dr. John Alarcon, Scottish Rite Children's Medical Center, Atlanta, Georgia.)

Lingual Cysts

Various other cysts may occur in the lingual region, including mucous retention cysts, vallecular cysts, salivary retention cysts, dermoid cysts, and lingual cysts of developmental origin with either respiratory or gastric epithelium. Lingual cysts in infancy may be large enough to cause stridor and dyspnea, and occasionally result in sudden infant death.[104] A vallecular cyst, also known as a mucous retention cyst, often has to be differentiated from ectopic thyroid or a thyroglossal duct cyst on imaging studies (Fig. 29-36). The vallecular cyst may be similar in appearance to a thyroglossal duct cyst or dermoid cyst, but it is easily distinguished from a solid mass such as ectopic thyroid.

Dermoid cysts are uncommon benign developmental lesions that result from embryologic entrapment of ectodermal cells at lines of fusion in the embryo.[105] Oral cavity dermoids account for less than a quarter of head and neck dermoids and are usually located within the anterior floor of the mouth (Fig. 29-37). Most dermoids are seen in young adults; however, congenital sublingual dermoids occurring in infancy have been described.[106] Massive cysts may encroach upon the airway. Like thyroglossal duct cysts, dermoid cysts usually are midline, but they are not usually adherent to the hyoid bone. Like dermoid cysts elsewhere in the body, the lesion is usually sharply circumscribed and hypodense on CT (Fig. 29-38). On MR imaging, signal intensity ranges from intermediate to low on T1-weighted images and high on T2-weighted images (Fig. 29-37). Some signal heterogeneity may be observed. If focal regions of fat density (CT) or fat signal intensity (MR imaging) are seen within the cyst, the lesion is a dermoid.[107] Faint marginal enhancement may be seen. Dermoid cysts are treated by complete surgical resection of the cyst and any associated sinus tract or stalk. At surgery, the dermoid cyst may be

Copyright © 2003, Mosby, Inc. All rights reserved.

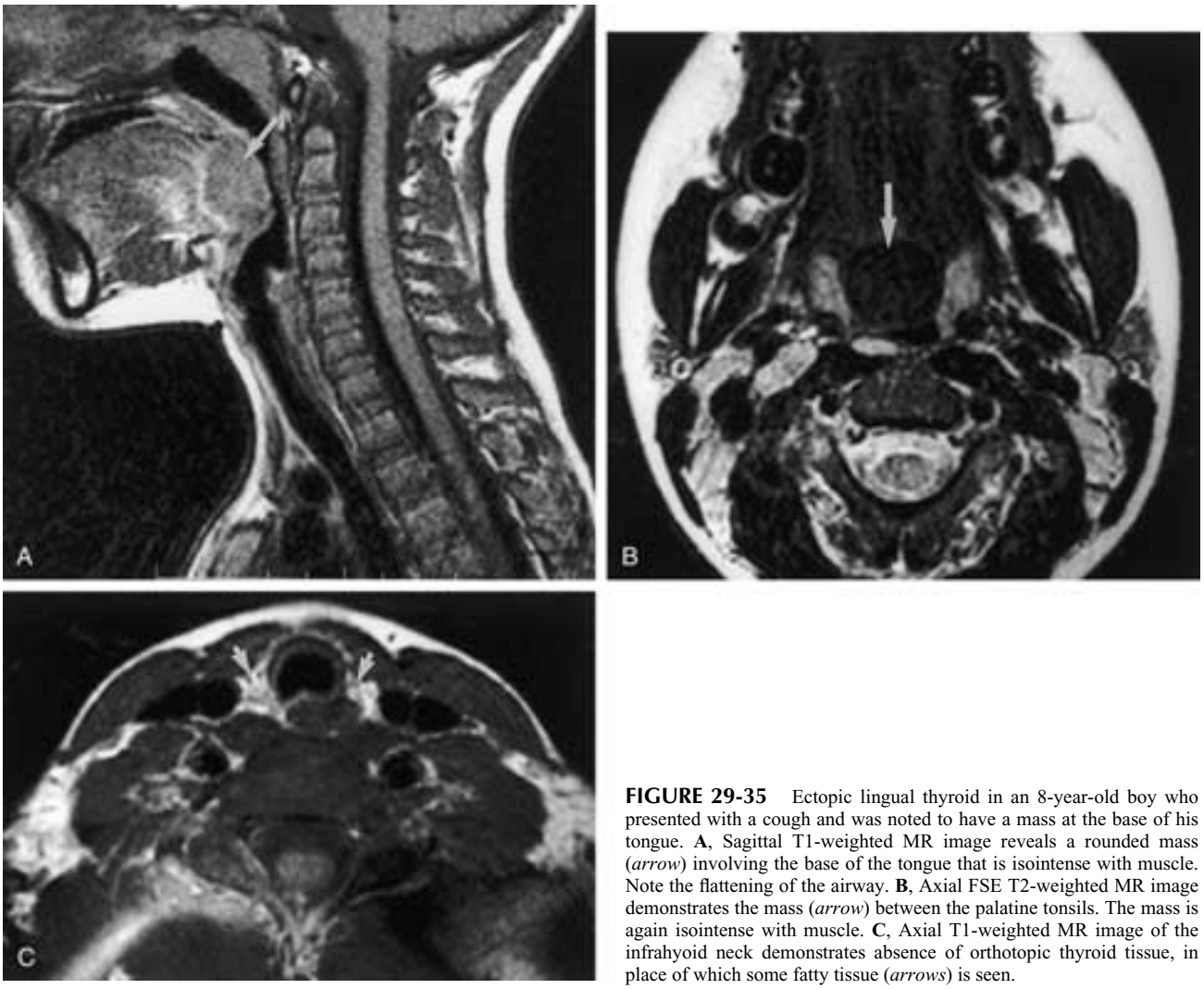

FIGURE 29-35 Ectopic lingual thyroid in an 8-year-old boy who presented with a cough and was noted to have a mass at the base of his tongue. **A**, Sagittal T1-weighted MR image reveals a rounded mass (*arrow*) involving the base of the tongue that is isointense with muscle. Note the flattening of the airway. **B**, Axial FSE T2-weighted MR image demonstrates the mass (*arrow*) between the palatine tonsils. The mass is again isointense with muscle. **C**, Axial T1-weighted MR image of the infrahyoid neck demonstrates absence of orthotopic thyroid tissue, in place of which some fatty tissue (*arrows*) is seen.

VIEW IMAGE

FIGURE 29-36 Vallecular cyst in a toddler with dysphagia. Lateral plain film reveals a smooth mass (*arrows*) anterior to the epiglottis cleft. (Courtesy of Dr. Carlo Buonomo, Children's Hospital, Boston, Massachusetts.)

VIEW IMAGE

filled with a cheesy white material containing skin, skin appendages, hair, or desquamated epithelium.

Obstruction of a sublingual gland duct may lead to an enlarging floor of the mouth or tongue mass known as a ranula. Although ranulas are common, airway obstruction from these lesions is unusual. Imaging shows a cystic mass in the floor of the mouth or tongue.

Primitive foregut cysts of either respiratory or alimentary origin are uncommon congenital defects of the developing airway and gastrointestinal tract.[108] When the oral cavity is involved, the cyst is usually located in the tongue or floor of the mouth (Figs. 29-39 and 29-40).[109] These cysts are usually discovered during infancy but may not appear until well into adulthood. The cyst may present as a mass or with symptoms such as difficulties with feeding, swallowing, and respiration.[108, 109] Heterotopic gastrointestinal cysts of the oral cavity have an enteric lining and are thought to originate from entrapment of undifferentiated endoderm within the oral cavity during the third to fourth week of fetal life.[108, 109] The cyst may range in size from less than 1 cm to 9 cm, with most lesions being 1 to 3 cm in size. Cysts containing respiratory epithelium have also been reported (Figs. 29-39 and 29-40).[110, 111] This developmental anomaly is believed to originate from abnormal detachments of accessory lung buds from the ventral foregut.[111] The histologic and clinical

Copyright © 2003, Mosby, Inc. All rights reserved.

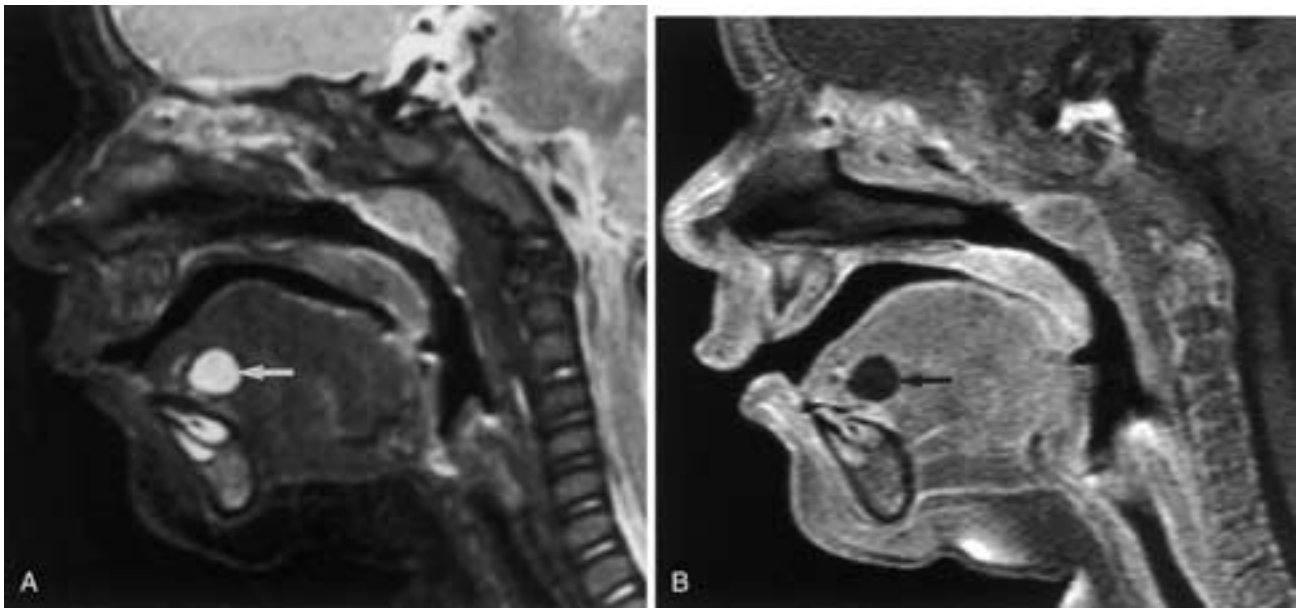

VIEW IMAGE

FIGURE 29-37 Dermoid cyst in a young child. **A**, Midline sagittal FSEIR image reveals that the sharply circumscribed cyst (*arrow*) is isointense with CSF. **B**, Contrast-enhanced, sagittal T1-weighted MR image reveals the hypointense, nonenhancing dermoid cyst (*arrow*) in the anterior floor of the mouth.

features and embryogenesis of both types of cysts overlap, and both respiratory and gastric epithelium may be present.[110] CT or MR imaging generally reveals a unilocular cyst with variable signal intensity, depending on the contents of the cyst (Fig. 29-39). Although usually hypointense on T1-weighted images, proteinaceous contents or blood products will produce T1 shortening (hyperintensity) (Fig. 29-40). The cyst contents are usually hyperintense on T2-weighted images. There is little if any marginal enhancement following the administration of gadolinium. The treatment of choice is complete surgical excision of the cyst.[111] However, aspiration of the cyst can be performed to improve access to the oropharynx for intubation prior to surgical resection.[112]

Macroglossia and Glossoptosis

Enlargement of the tongue with protrusion beyond the teeth or alveolar ridge in the resting position is termed *macroglossia*. Congenital macroglossia is associated with a variety of syndromes and conditions such as trisomy 21, Beckwith-Wiedemann syndrome, hypothyroidism, and the mucopolysaccharidoses. Macroglossia may result in respiratory compromise, dysphagia, and poor cosmesis.[113] Macroglossia is also a feature of lingual vascular anomalies (Fig. 29-41). The enlargement of the tongue that accompanies these lesions is sometimes also associated with ulceration and hemorrhage. Imaging is not usually required for evaluation of macroglossia per se unless an underlying primary lesion (e.g., vascular anomaly) is suspected. However, dynamic imaging of macroglossia as part of the assessment of obstructive sleep apnea is sometimes required.

Glossoptosis is a term used to describe posterior displacement of the tongue. This phenomenon has been

FIGURE 29-38 Dermoid cyst in the floor of the mouth in a young child with a palpable neck mass. The midline neck mass is low density, nonenhancing, and indistinguishable from the more common thyroglossal duct cyst. If fat globules are seen within such a mass, the diagnosis of dermoid cyst can be made preoperatively.

VIEW IMAGE

Copyright © 2003, Mosby, Inc. All rights reserved.

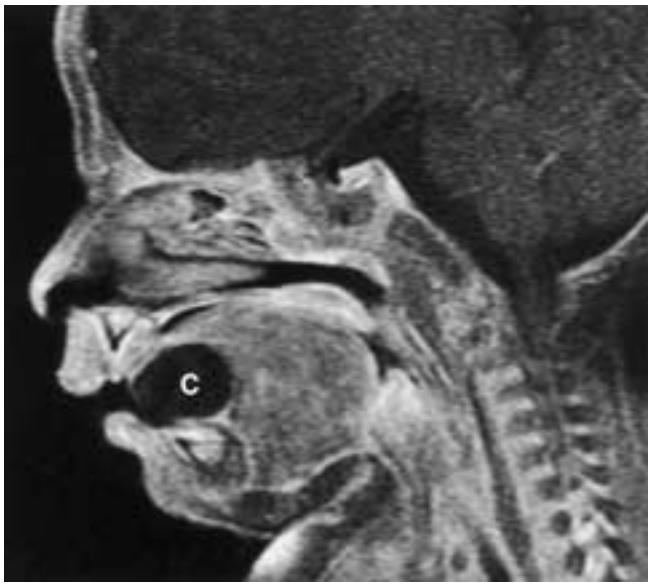

VIEW IMAGE

FIGURE 29-39 Primitive foregut cyst in a baby with a congenital tongue mass. Midline contrast-enhanced, fat-suppressed sagittal T1-weighted image shows a rounded, unilocular, sharply circumscribed cyst (c) located within the anterior third of the tongue. Note that the lesion is indistinguishable from the dermoid cyst shown in Figure 29-37.

observed in patients with macroglossia, micro- or retrognathia, and neuromuscular disorders and, in a minority of cases, in otherwise healthy patients.[14]

Micrognathia and Retrognathia

An abnormally small mandible is termed micrognathia. Abnormal posterior placement of the mandible is called retrognathia. There is often a combination of micro- and retrognathia (Figs. 29-42 and 29-43). Abnormal growth or position of the mandible can be caused by malformation, deformation, or connective tissue dysplasia.[114] The Robin sequence or complex (previously termed *Pierre Robin syndrome*) is characterized by micrognathia and/or retrognathia, glossoptosis, a wide U- or V-shaped cleft palate, and upper airway obstruction (Fig. 29-42). Factors that contribute to airway obstruction in the Robin sequence include micrognathia/retrognathia, glossoptosis, abnormal movement of the lateral pharyngeal wall, and sphincteric pharyngeal constriction.[115] The Robin sequence/complex is etiologically, phenotypically, and pathologically heterogeneous and occurs in syndromic and nonsyndromic forms.[114] Numerous monogenic, chromosomal, teratogenic, deformational (amniotic band disruption), and idiopathic syndromes are associated with Robin sequence. The most frequently encountered of these are the Stickler syndrome (hereditary arthro-opthalmopathy), deletion 22q11.2 syndrome (velocardiofacial syndrome), and Treacher Collins syndrome.[114, 116] In deletion 22q11.2 syndrome, the mandible is essentially normal in size but retrognathic as a result of an abnormally obtuse cranial base angle.[117] Also known as velocardiofacial syndrome, this autosomal dominant disorder is characterized by cleft palate, cardiac defects, learning disabilities and a typical facial appearance.[118] Less frequently, patients have manifestations of the DiGeorge complex including hypocalcemia, hypoplastic or absent lymphoid tissue, and T-cell deficiency.[119] This syndrome is also associated with medially positioned, tortuous, or kinked internal carotid arteries, low common carotid bifurcations,

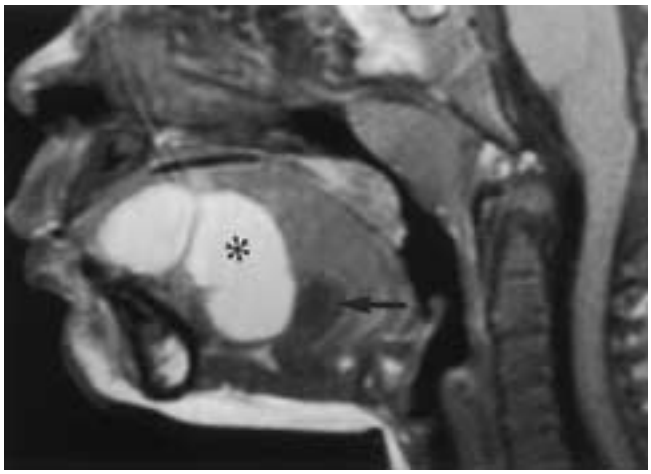

VIEW IMAGE

FIGURE 29-40 Primitive foregut cyst in a 2-year-old boy with a congenital tongue mass. Midline sagittal T1-weighted image shows a mixed-intensity bilobed cyst (*asterisk*) involving the anterior third of the tongue and the floor of the mouth. The ventral hyperintense component contained hemorrhage. The dorsal hypointense component contained clear fluid. Histologic examination revealed a cyst lined by respiratory and squamous epithelium, with seromucous glands and smooth muscle present in the cyst wall.

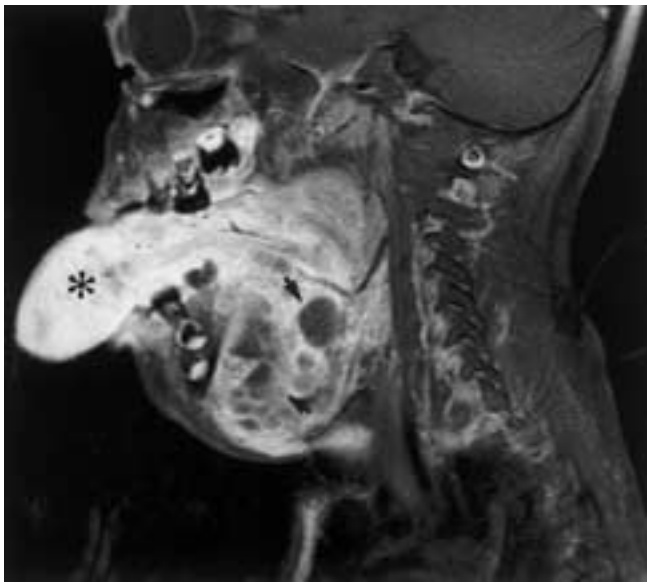

VIEW IMAGE

FIGURE 29-41 Macroglossia and complex mixed vascular malformation of the tongue, floor of the mouth, and neck. The patient presented with a mass and respiratory obstruction, for which tracheostomy was required. The malformation was complicated by multiple episodes of hemorrhage and ulceration. Contrast-enhanced, fat-suppressed sagittal T1-weighted image shows macroglossia with intense enhancement of the tongue (*asterisk*) and a macrocystic lymphatic malformation in the floor of the mouth (*arrows*). The patient was treated with a combination of embolization of the tongue and ethanol sclerotherapy to the tongue and floor of the mouth. There was subsequent resolution of hemorrhage and significant reduction in the size of the tongue.

Copyright © 2003, Mosby, Inc. All rights reserved.

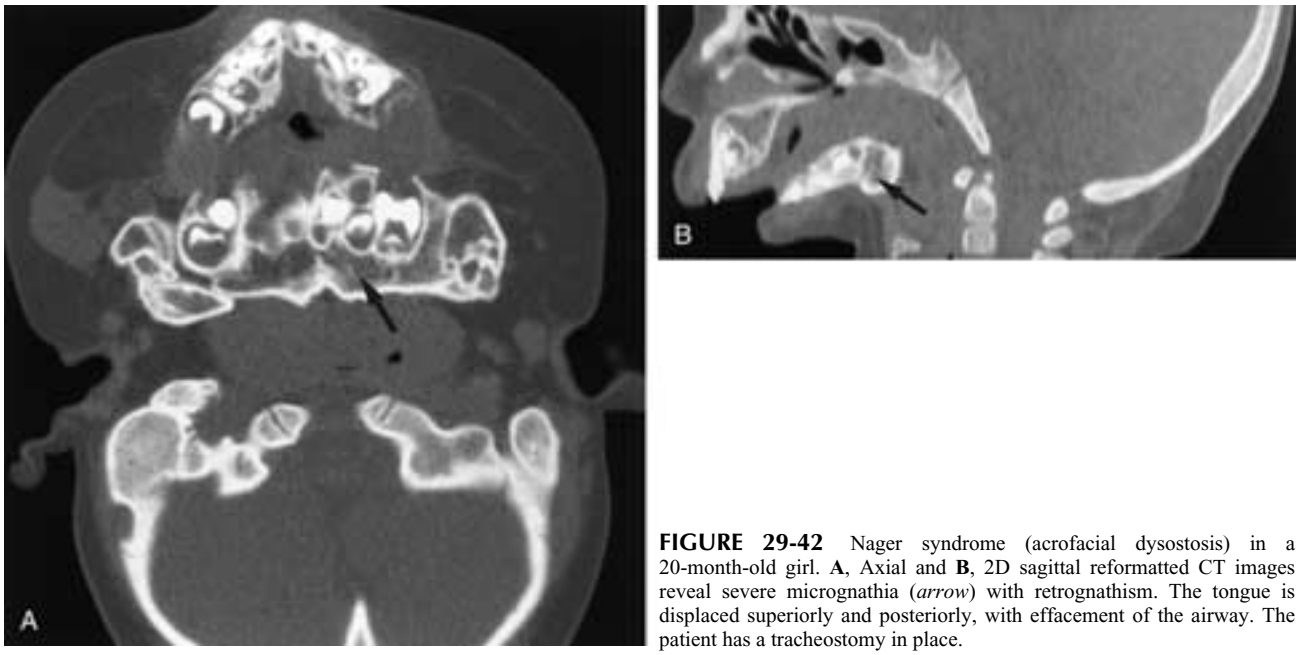

FIGURE 29-42 Nager syndrome (acrofacial dysostosis) in a 20-month-old girl. **A**, Axial and **B**, 2D sagittal reformatted CT images reveal severe micrognathia (*arrow*) with retrognathism. The tongue is displaced superiorly and posteriorly, with effacement of the airway. The patient has a tracheostomy in place.

VIEW IMAGE

and hypoplastic vertebral arteries.[120, 121] It is important to recognize this potentially dangerous implication, as pharyngoplasty for velopharyngeal incompetence and hypernasal speech may potentially damage the anomalous internal carotid arteries.[122]

Oculo-auriculo-vertebral spectrum encompasses a heterogeneous group of disorders ranging from minor unilateral ear anomalies or preauricular tags to severe manifestations with anotia, micrognathia, orbital dystopia, cervical spine anomalies, and ocular dermoids.[123] Terminology used to describe entities within this spectrum includes the first and second branchial arch syndrome, hemifacial microsomia, Goldenhar syndrome, and craniofacial dysplasia. In contrast to the Robin sequence, manifestations are typically asymmetric and usually unilateral. Airway abnormalities are produced by a combination of asymmetric micrognathia or hemimicrognathia, maxillary hypoplasia, and velopharyngeal insufficiency.[123] Asymmetric palatal and lateral pharyngeal wall motion have been attributed to unilateral hypoplasia of the pharyngeal constrictors and other pharyngeal muscles.[124] The structural abnormalities involving the pharynx and larynx predispose to obstructive sleep apnea and difficulties with intubation.[123]

Imaging modalities for airway assessment in children with micro- or retrognathia include cephalometrics, videofluoroscopy, CT, and MR imaging. If the patient is unable to tolerate the examination without sedation, a general anesthetic may be required. Cephalometrics are plain radiographs that are used to analyze the facial proportions based on specific osseous landmarks. Thin-section high-resolution helical CT with 2D (Fig. 29-42) and 3D reformatting provides multiplanar information including the size and proportions of the maxilla, nose, and mandible and the dimensions of the airway (Fig. 29-44). Two-dimensional sagittal reformatted images are useful for assessment of the vertical height of the pharynx, which may be reduced in children with coexistent spinal anomalies (oculo-auriculovertebral spectrum). The images should also be assessed for cranial base, temporal bone, and cervical spine anomalies as indicated by the clinical diagnosis. Patients with 22q11.2 syndrome who require pharyngeal flap surgery should undergo preoperative vascular imaging (CT angiography or 2D time-of-flight MR angiography) precisely to document the presence and location of anomalous internal carotid arteries in relation to the flap donor site.[121, 122]

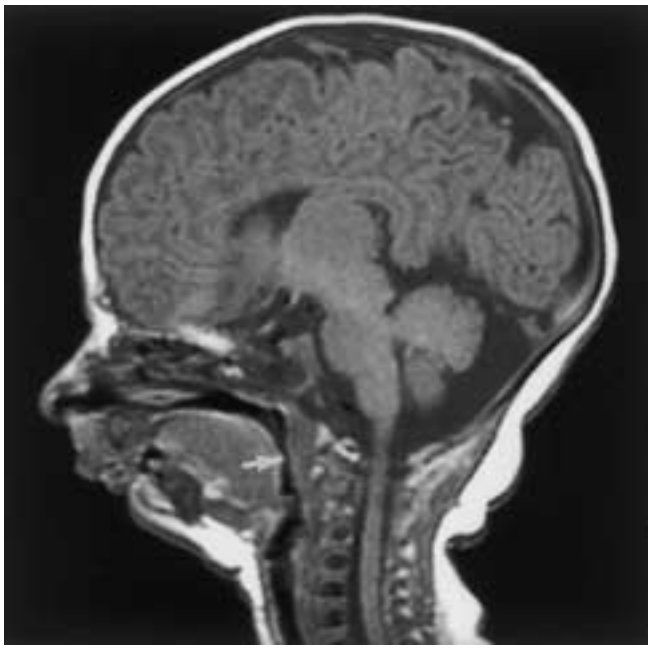

FIGURE 29-43 Prader-Willi syndrome in a young child with obstructive sleep apnea. Sagittal T1-weighted MR image shows micro- and retrognathia. The posterior displacement of the tongue and narrowed AP diameter of the airway (*arrow*) are well seen on MR imaging.

VIEW IMAGE

Copyright © 2003, Mosby, Inc. All rights reserved.

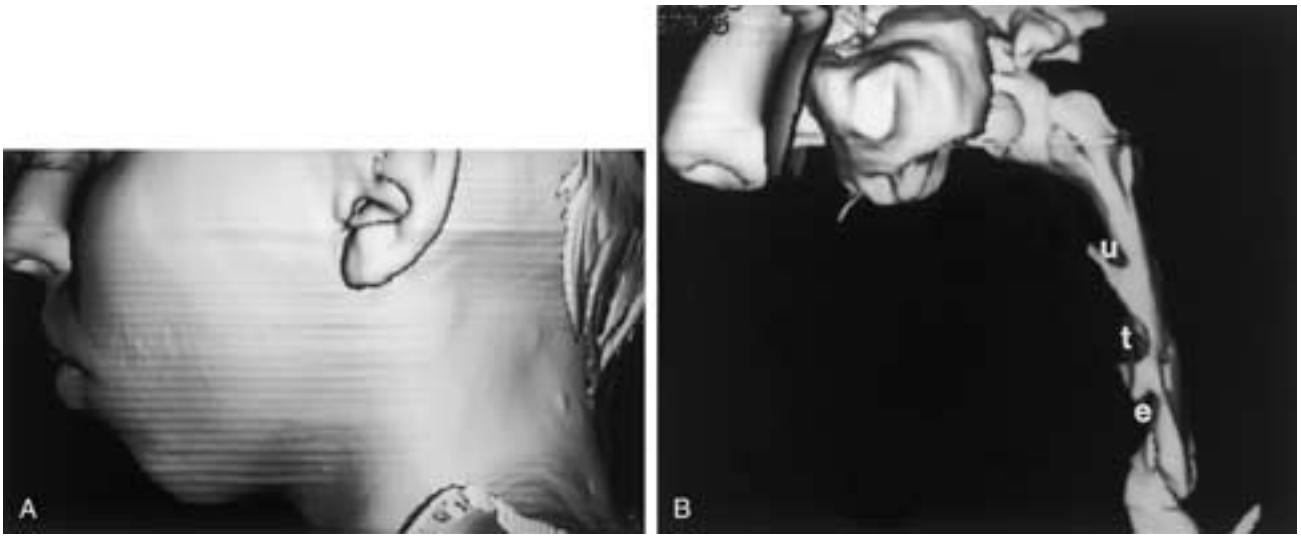

VIEW IMAGE

FIGURE 29-44 Obstructive sleep apnea in a 14-year-old girl with retrognathia. **A**, The 3D model of the face reveals retrognathia. **B**, The 3D model of the airway demonstrates ventral impressions on the airway from the soft palate and uvula, tongue, and epiglottis. Narrowing of the AP dimension of the airway is maximal at the level of the tongue base.

LARYNGEAL OBSTRUCTION

Laryngomalacia

Laryngomalacia is a disorder characterized by an abnormal redundancy of supraglottic tissue.[125] Laryngomalacia is the most common cause of stridor in the newborn and infant. The stridor is characteristically high-pitched and inspiratory and is most severe in the supine position.[30] The etiology is thought to be related to delayed development of neuromuscular control of the airway.[126] Laryngomalacia is usually a benign self-limited condition that typically presents within the first 2 weeks of life, often resolves by 2 years of age, and seldom requires surgical intervention.[125] It has been associated with other causes of airway obstruction, cardiovascular anomalies, gastroesophageal reflux, and neurologic deficits.[127]

In assessing children with laryngomalacia, pertinent clinical and anatomic information should be obtained. Clinical features include the severity of stridor, presence of synchronous airway lesions, failure to thrive, prematurity, age at presentation, and associated cardiovascular, neurologic, chromosomal, or syndromic abnormalities.[127] Fluoroscopy or plain radiographs obtained during inspiration show inferior and medial bowing of the arytenoids, aryepiglottic folds, and epiglottis, with ballooning of the laryngeal ventricle and hypopharynx. Definitive anatomic information is provided by fiberoptic examination. Flexible laryngoscopy may be used to confirm the diagnosis and assess the anatomy. Rigid endoscopy is reserved for selected cases in which the cause of stridor is cryptic, additional airway lesions are suspected, or operative management is planned. On direct laryngoscopic examination, laryngomalacia has been classified using anatomic factors as posterolateral, posterior, or anterior.[125] Posterolateral collapse is due primarily to redundant aryepiglottic folds, posterior collapse to excess arytenoid mucosal or cartilaginous bulk, and anterior collapse to excess pliability of the epiglottis.

Vocal Cord Paralysis

Vocal cord paralysis (VCP) is the second most common cause of stridor in infancy.[128] Bilateral VCP is usually central in origin, and unilateral paralysis typically has a peripheral cause. VCP can be congenital or acquired. Bilateral VCP is rarely seen in an otherwise normal child.[30] Brainstem malformations, particularly the Chiari II malformation, are the most common cause of VCP in children.[129] These children present with nonprogressive, high-pitched inspiratory stridor and usually have bilateral paralysis. Although the paralysis is probably multifactorial in etiology, possible mechanisms are mechanical traction on the vagus nerves from caudal displacement of the cerebellum and/or hindbrain herniation, congenital dysplasia of the brainstem, and lack of afferent information from the carotid bodies.[128] Other associated conditions include perinatal hypoxic ischemic injury, as well as multiple other disorders of the central and peripheral nervous systems. VCP can also be seen in conjunction with other congenital anomalies such as cardiac or pulmonary malformations, as well as other associated laryngeal malformations such as clefts or stenosis.[128, 130]

Unilateral VCP is most commonly left-sided and is seen in children with congenital cardiac anomalies, following tracheoesophageal fistula repair or corrective surgery for congenital heart disease, and following trauma, particularly traumatic delivery.[126]

VCP can affect any or all of the normal laryngeal functions, resulting in voice changes, stridor, feeding difficulties, ineffective cough, aspiration, and recurrent pneumonia.[131]

The investigation of choice for the evaluation of vocal

Copyright © 2003, Mosby, Inc. All rights reserved.

cord paralysis is flexible laryngoscopy.[128] Adjunctive techniques include airway fluoroscopy, CT, and MR imaging. Airway fluoroscopy shows limited abduction of the paralyzed vocal fold with respiration or crying. With unilateral paralysis, the AP film reveals thinning of the paralyzed cord, which may appear lower than the normal cord, the laryngeal ventricle is usually capacious, and the ipsilateral pyriform sinus may be larger than that on the normal side. If the lateral plain film is obtained during phonation, two separate air-filled laryngeal ventricles may be seen, the ventricle on the paralyzed side being lower and usually larger than the ventricle on the normal side.[132] MR imaging of the brain, posterior fossa, and skull base is important in the evaluation of bilateral paralysis to delineate posterior fossa malformations, hydrocephalus, posterior fossa tumors with cerebellar tonsillar herniation, and craniocervical malformation. Chest radiographs and a barium swallow may show anomalies of the heart, mediastinum, or great vessels as an explanation for unilateral VCP. CT or MR imaging of the neck may be required to trace the entire course of the vagus nerve from the skull base to the mediastinum in order to exclude a neoplasm as a source of vagal or recurrent laryngeal nerve dysfunction.

Laryngoceles and Laryngeal Cysts

A laryngocele is an air- or fluid-filled dilation of the laryngeal saccule that communicates with the laryngeal ventricle and is a rare cause of airway obstruction in infants.[133, 134] An internal laryngocele remains within the boundaries of the supraglottic laryngeal superstructure, and an external laryngocele, or combined laryngocele, the most common type, extends through the thyrohyoid membrane and has both an internal and an external component. Plain films are often nonspecific, showing a supraglottic airway mass. However, an air collection in the lateral neck, projected over the supraglottic larynx, is a highly suggestive finding. The external or combined laryngocele may present as a fluctuating soft lateral neck mass, and cross-sectional imaging shows the internal component submucosally filling the paraglottic space and obliterating the fat, and the external component extending through the thyrohyoid membrane into the lateral neck (Fig. 29-45). The CT density or the MR signal intensity of the laryngocele is variable, depending on whether the cyst is filled with air, fluid, or proteinaceous debris. Definitive therapy for laryngocele is excision.[133]

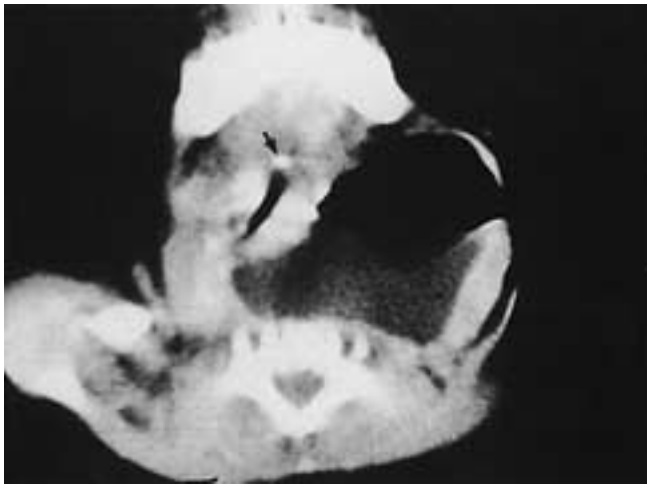

VIEW IMAGE

FIGURE 29-45 External laryngocele. This full-term infant developed a neck mass and respiratory distress within the first week of life. Axial CT scan shows a large left neck mass with an air-fluid level and compression of the airway at the level of the hyoid bone (*arrow*).

FIGURE 29-46 Cyst of the aryepiglottic fold in an infant with respiratory distress. A smooth, well-circumscribed mass (*arrows*) is seen projecting into the supraglottic airway.

VIEW IMAGE

In general, laryngeal cysts include a variety of lesions with different histogenetic origins and diverse symptoms related to their site and size. A recent classification system has been proposed that incorporates the genesis and development of laryngeal cysts and subdivides cysts into congenital cysts, retention cysts, and inclusion cysts.[135] Although encountered anywhere in the larynx, laryngeal cysts are fluid-filled and are most frequently found in the vallecula and true vocal cords.[136] Plain films show a smooth mass projecting into the airway (Fig. 29-46). Typically on CT, laryngeal cysts are well-circumscribed, submucosal, low-density, nonenhancing masses. On MR imaging the signal intensities vary. The T1-weighted signal intensity is usually low (water) but may be high (infection or hemorrhage), and the T2-weighted signal intensity is high. Treatment for laryngeal cysts is endolaryngeal microsurgery with marsupialization of the cyst.[135]

Copyright © 2003, Mosby, Inc. All rights reserved.

Anomalies of the Epiglottis

Anomalies of the epiglottis are extremely rare and include congenital absence of the epiglottis and bifid epiglottis. Clinical symptoms include aspiration and/or airway obstruction.[137] Bifid epiglottis has been reported in association with other laryngeal anomalies and in a syndromic form with other congenital anomalies, most often with polydactyly.[138] Pallister-Hall syndrome consists of polydactyly, hypothalamic hamartoma, imperforate anus, and absent or hypoplastic epiglottis with a laryngeal cleft.[139, 140] The diagnosis of epiglottic anomalies is made endoscopically. Radiologic investigation is indicated for assessment of other organ systems in children who have syndromic features.

Laryngeal Webs, Clefts, and Atresia

A laryngeal web is a membrane that partially occludes the airway lumen and results from failure of recannulation during embryogenesis.[141] Although laryngeal webs may occur anywhere in the larynx, most are at the glottic level, usually involving the anterior commissure. Presenting signs depend on the location and the degree of airway obstruction and may include stridor, hoarseness, weak voice, or feeding difficulties.[142] Endoscopy is the mainstay of diagnosis, but plain films may occasionally show a web of tissue within the airway.

Laryngeal clefts are rare anomalies that present with stridor and aspiration.[143] Although the diagnosis is usually made endoscopically, an esophagogram may show tracking of contrast from the upper esophagus into the trachea (Fig. 29-47). A Type I cleft is confined to the level of the interarytenoid space above the level of the vocal folds. A partial cricoid cleft is classified as Type II. Type III and IV lesions traverse the cricoid completely.[144]

Laryngeal atresia may occur at the supraglottic or glottic level and is extremely rare. Imaging plays little role in the postnatal management of this condition, as survival is unlikely unless the lesion is immediately recognized and emergent tracheotomy performed. However, laryngeal atresia has been diagnosed with antenatal sonography obtained during the second trimester with coronal images of the upper neck.[145] Images obtained during fetal breathing demonstrate the stenotic larynx in a closed position, and color Doppler fails to show movement of fluid across the atretic larynx. Additional sonographic features in the fetus with complete or near-complete upper airway obstruction include large echogenic lungs, flattened or inverted diaphragms, dilated airways distal to the obstruction, and fetal ascites and/or hydrops.[4] The fetus with laryngeal atresia should be carefully screened for coexistent anomalies of the central nervous system, renal anomalies, and esophageal atresia or fistula.[145] For isolated laryngeal atresia without significant hydrops, survival depends upon therapeutic maneuvers to bypass the site of airway obstruction while the fetus remains connected to the placenta. Antenatal diagnosis of laryngeal atresia may permit the implementation of the planned ex utero intrapartum treatment (EXIT) procedure, with immediate laryngoscopy and placement of a tracheostomy.[146]

FIGURE 29-47 Laryngoesophageal cleft in a baby girl. Contrast esophagogram reveals contrast within the esophagus (*asterisk*) and within the trachea (*arrows*). The patient was found to have a laryngoesophageal cleft. (Courtesy of Dr. Carlo Buonomo, Children's Hospital, Boston, Massachusetts.)

VIEW IMAGE

SUBGLOTTIC OBSTRUCTION

Congenital Subglottic Stenosis

Congenital subglottic stenosis is the third most common congenital laryngeal abnormality and is the most common lesion requiring tracheotomy in infants under 1 year of age.[142] Symptoms include biphasic or inspiratory stridor and a barking cough in the absence of a history of prior intubation or other cause of acquired subglottic stenosis. Congenital subglottic stenosis may be isolated or may be associated with congenital syndromes, especially trisomy 21, in which case the entire larynx is small.[141] Among infants with congenital subglottic stenosis, 7% to 10% have other laryngotracheal anomalies such as tracheoesophageal fistula, vocal cord paralysis, or tracheal stenosis.[147] The stenosis is usually associated with a small or malformed cricoid cartilage, with or without thickening of the underlying submucosal layer.[148]

The diagnosis of congenital subglottic stenosis is suggested on plain films and confirmed by endoscopy. Plain films show symmetric circumferential subglottic narrowing, the typical hourglass appearance. This narrowing extends for 1 to 1.5 cm and is fixed, not changing with the phase of respiration.[149] The diagnosis is considered when a 4 mm

Copyright © 2003, Mosby, Inc. All rights reserved.

scope or an age-appropriate-sized endotracheal tube cannot pass through the subglottic larynx in an infant who has not been intubated previously.[150] The lesion is generally self-limited, resolving with laryngeal growth.[151] However, if symptoms are severe, anterior laryngotracheal decompression (anterior cricoid split), laryngotracheal reconstruction, or tracheostomy may be required.[148]

TRACHEAL OBSTRUCTION

Tracheal anomalies associated with obstruction of the airway include agenesis or atresia of the trachea, fibrous strictures, stenoses and webs, and absence or deformity of the tracheal cartilages.[152] Stenotic lesions of the trachea can also be classified as causing intrinsic compression, extrinsic compression, or both. Intrinsic tracheal narrowing due to absence or deformity of tracheal cartilages incorporates tracheomalacia, tracheal deformity due to vascular compression, and tracheal cartilage anomalies. Conditions that produce both extrinsic and intrinsic narrowing include aberrant vessels and tracheoesophageal anomalies.

Tracheomalacia

Primary tracheomalacia is a rare entity due either to a deficiency of cartilage with increased width of the posterior membranous tracheal wall or to mechanical weakness that results in partial or total collapse of the airway and respiratory embarrassment.[153] Patients may experience stridor, wheezing, chronic cough, anoxic spells, and failure to thrive.

Endoscopic evaluation is used to provide a diagnosis, assess the severity of tracheomalacia, and exclude other lesions.[153] Airway fluoroscopy can also be used to confirm tracheomalacia in a symptomatic child when the tracheal diameter decreases more than 50% during expiration compared with the diameter during inspiration.[154] The change in diameter during a respiratory cycle helps differentiate tracheomalacia from a fixed stenotic lesion (Fig. 29-48).

Tracheomalacia usually resolves spontaneously by the second year of life.[152] However, severely symptomatic children may require treatment with continuous positive airway pressure, placement of an endotracheal stent, surgical resection, or the ''pexy'' procedure.[153, 155]

Intrinsic Tracheal Stenosis

Intrinsic tracheal stenosis can be congenital or acquired. Congenital tracheal stenosis results from one or more complete cartilaginous tracheal rings, with absence of the posterior membranous portion of the trachea that produces a circular cross section of the trachea.[156] Tracheal rings generally produce one of three types of tracheal stenosis: segmental stenosis with an hourglass configuration of the trachea, a funnel-shaped trachea with progressive tracheal narrowing from the cricoid to the carina, and narrowing of

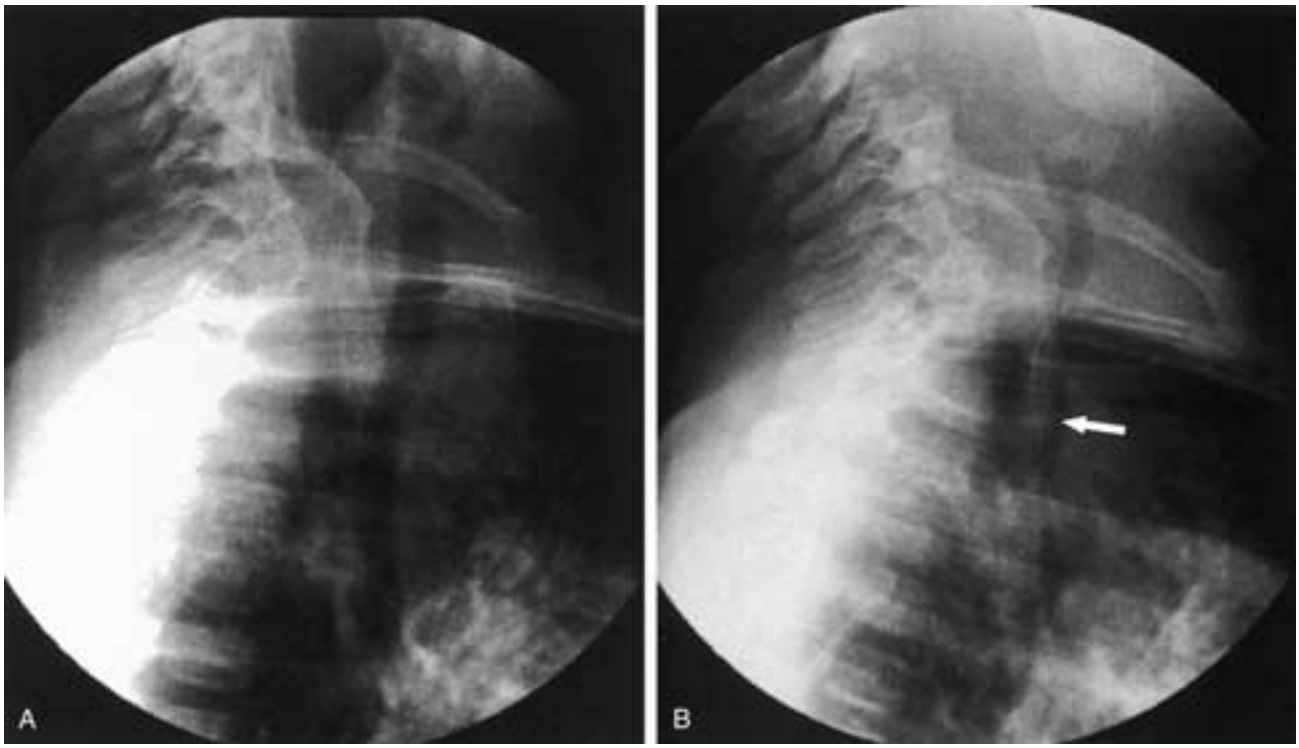

VIEW IMAGE

FIGURE 29-48 Tracheobronchomalacia with the innominate artery compressing the trachea, in a 5-month-old infant with stridor. **A**, Inspiratory oblique fluoroscopic film shows normal tracheal diameter. **B**, Same projection obtained during end expiration. Note the marked collapse of the entire trachea (*arrow*), which is most severe at the expected location of the innominate artery.

Copyright © 2003, Mosby, Inc. All rights reserved.

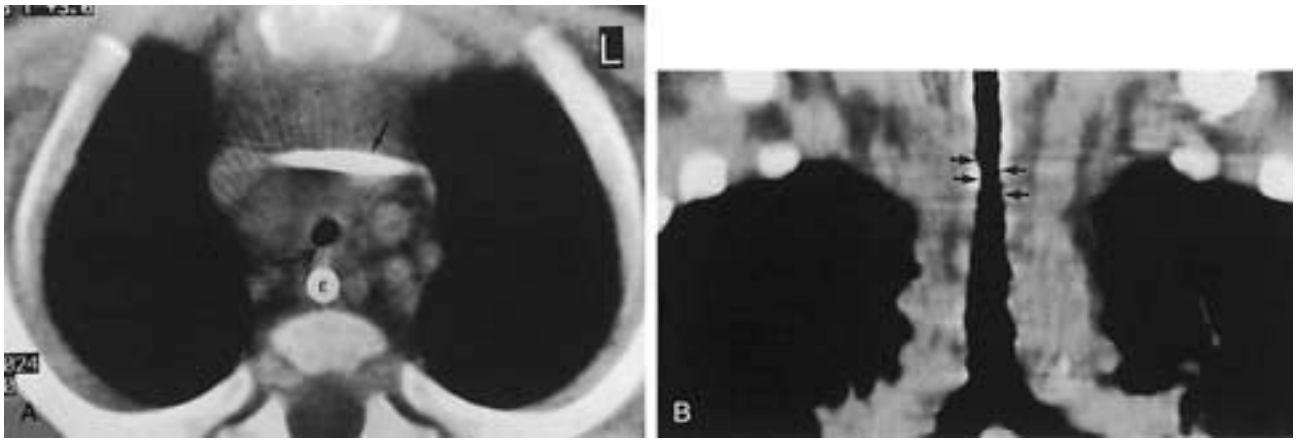

VIEW IMAGE

FIGURE 29-49 Congenital tracheal stenosis in a 2½-year-old boy with stridor. **A**, Axial spiral CT scan obtained immediately below the endotracheal tube shows a central venous line (*arrow*) and a nasogastric tube in the esophagus (*E*). The posterior membranous portion of the trachea is not flat but has a rounded contour (curved arrow). **B**, Two-dimensional coronal reformatted image shows the extent of the tracheal narrowing.

the entire trachea.[157, 158] Extensive malformation with a solid cartilaginous cylinder in place of the normal trachea has been termed *tracheal cartilaginous sleeve*.[159] This rare anomaly is often associated with other abnormalities, usually the syndromic forms of craniosynostosis such as Apert, Crouzon, and Pfeiffer syndromes.[87, 158, 160] Complete tracheal rings are also associated with other bronchial, vascular, cardiac, or intestinal abnormalities, tracheoesophageal fistula, eophageal atresia, and the VATER syndrome or complex (vertebral defects, anal atresia, tracheoesophageal fistula, esophageal atresia, renal anomalies, and aplasia of the radius).[156]

Clinical presentation of tracheal stenosis ranges from largely asymptomatic to symptoms such as stridor, increased mucus production, croup, sporadic cyanosis, and increased numbers of respiratory infections. Endoscopic evaluation reveals a smooth tracheal surface. Plain films may be normal and may underestimate the narrowing or show a narrowed tracheal air column. Cross-sectional imaging shows a rounded appearance of the trachea instead of the normal posterior membranous flattening (Fig. 29-49). CT is superior to high-kilovoltage plain films and chest radiography in evaluating the presence and extent of stenosis, and is sometimes superior to endoscopy for depicting the distal extent of disease.[161] Helical CT with 3D reconstruction provides excellent anatomic delineation of tracheobronchial anatomy and is safer and less invasive than conventional tracheobronchography (Fig. 29-50).[162]

Prognosis and treatment depend on the degree and extent of stenosis, with more severely affected infants requiring early surgical intervention. Surgical options include balloon dilatation, tracheostomy, tracheal resection and primary anastomosis, tracheoplasty, or tracheal stenting.[156]

Vascular Compression of the Airway

Vascular causes of tracheal stenosis include innominate artery compression, aortic arch anomalies, aberrant left pulmonary artery, and anomalous right subclavian artery.

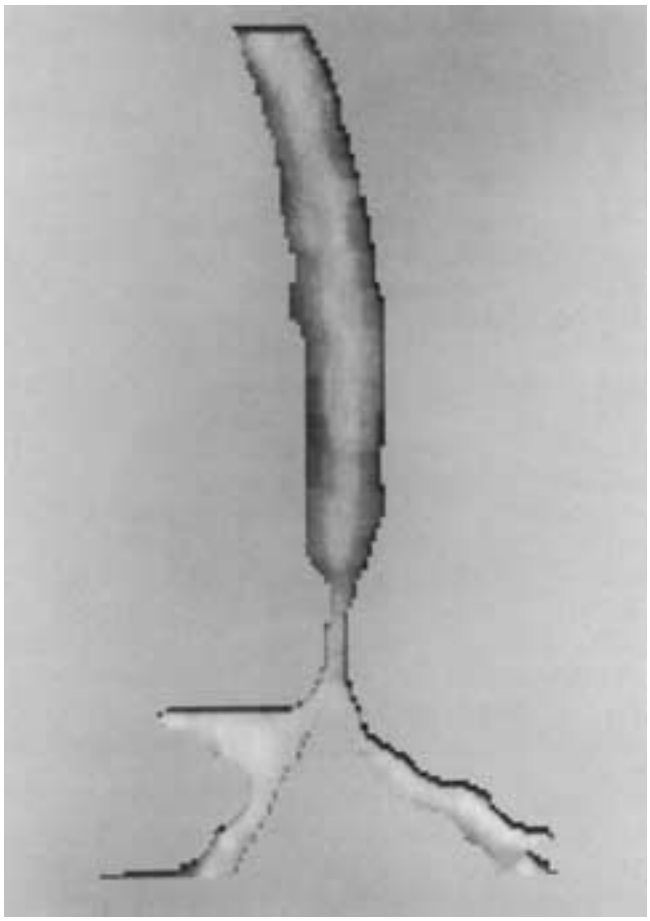

FIGURE 29-50 Tracheal stenosis in a newborn with stridor. Three-dimensional reconstructed images of the trachea and carina were obtained using a segmentation technique. T1-weighted axial images were obtained of the airway, and then coronal reformations confirmed the tracheal narrowing and best showed the cranial-caudal extent of the luminal compromise. The length of the narrowing was not appreciated at endoscopy because the endoscope could not pass through the narrowed segment.

VIEW IMAGE

Copyright © 2003, Mosby, Inc. All rights reserved.

Variations of normal vascular anatomy that can cause airway compression have an incidence of approximately 3%.[9] The most frequent presenting complaint is stridor, which is sometimes aggravated by agitation, feeding, or exertion. Other symptoms include episodic apnea, reflex apnea, croupy cough, recurrent respiratory tract infections, and dysphagia.[9] Mildly symptomatic cases can be managed conservatively. Surgical management is required for a variety of absolute and relative indications.

Historically, many aortic arch and great vessel anomalies were diagnosed by a characteristic combination of great vessel location on plain films, lateral deviations of the trachea and esophagus, indentation of the trachea, and rounded or oblique defects in the contour of the esophagus on barium swallow.[163] Based on plain films and esophagograms, four imaging patterns and their implications have been described: (1) anterior tracheal and posterior esophageal indentation: vascular ring; (2) normal trachea with posterior esophageal indentation: aberrant subclavian artery; (3) posterior tracheal and anterior esophageal indentation: pulmonary sling; and (4) anterior tracheal indentation, normal esophagus: innominate artery compression.[164] It is important to note that any vascular anomaly causing tracheal stenosis can be associated with tracheoesophageal fistulas or other forms of tracheal stenosis such as complete tracheal rings that should be diagnosed prior to any definitive surgical procedure.[153] More recently, MR imaging has become the imaging modality of choice to depict vascular anatomy and to exclude other forms of extrinsic tracheal compression such as mediastinal masses.[9] MR images are acquired using respiratory compensation techniques and cardiac gating, with data acquisition primarily during expiration.[154] Both 2D and 3D reconstructed images are useful for illustrating the degree of compression and the relationship of the extrinsic structures to the trachea (Figs. 29-51B,C, 29-52, and 29-53). Helical CT angiography has also been utilized and rapidly provides diagnostic images. For patients who are unable to suspend respiration, adequate images can generally be obtained during quiet breathing. Limitations of this technique include, in addition to exposure to ionizing radiation, inability to define nonenhancing ligamentous structures and appropriate timing of contrast injection.[165] Multidetector CT imaging may offer potential in terms of improved image quality and decreased exam time, but with an increased dose of radiation relative to older single-slice scanners.[166]

Vascular compression of the trachea is most frequently caused by the innominate artery.[153, 163] The anterior tracheal wall is compressed by the vessel as it crosses from left to right.[167] Possible etiologic factors implicated in symptomatic tracheal compression by the innominate artery include a more distal take-off from the aortic arch, increased tautness of the innominate artery, more compliant tracheal cartilages, and mediastinal crowding from enlargement of other neighboring structures.[9, 153] The diagnosis is controversial because normal children without clinical evidence of airway compromise may have, on fluoroscopy or plain films, prominent anterior tracheal impression at the level of the innominate artery.[168]

The most common symptomatic true vascular ring is the double aortic arch (Figs. 29-51 and 29-52).[169] A right-sided aortic arch associated with a left ductus or aberrant left subclavian also forms a complete vascular ring that produces less constriction than a double aortic arch (Fig. 29-53).[170]

The aberrant right subclavian artery occurs in approximately 1 in 200 persons.[9] The vessel originates from the aorta caudal to the origin of the left subclavian artery and courses posterior to the esophagus, producing dysphagia but seldom symptomatic airway compromise.

Pulmonary artery sling is an uncommon but typically symptomatic noncircumferential vascular variant in which the left pulmonary artery originates from the posterior aspect of the right pulmonary artery, compresses the right mainstem bronchus, and passes between the trachea and esophagus to reach the hilum of the left lung.[170] The combination of complete tracheal rings with a pulmonary artery sling is known as the *ring-sling complex*.[171]

VASCULAR ANOMALIES

The Mulliken and Glowacki classification is a biological classification of vascular anomalies that separates the vascular anomalies into two major categories: true vascular tumors (e.g., hemangioma and kaposiform hemangioendothelioma) and vascular malformations.[172] This distinction is clinically useful and guides the choice of appropriate therapy. Rapid growth, endothelial proliferation, and hyperplasia characterize vascular tumors such as hemangioma. Vascular malformations are nonproliferating lesions that consist of dysplastic vascular channels and are classified according to their dominant component and hemodynamic features. Slow-flow lesions include capillary malformations (CMs), venous malformations (VMs), and lymphatic malformations (LMs). High-flow malformations are arterial lesions (e.g., arteriovenous fistulae [AVFs], arteriovenous malformations [AVMs]). There are also complex malformations that contain a combination of elements. Malformations grow commensurate with the patient or expand secondary to hemodynamic alteration.

Hemangioma

Hemangiomas typically arise postnatally during the first few months of life, although true congenital tumors do occasionally occur.[173] Females are affected twice as often as males.[174] Hemangiomas proliferate during the first year of life and then involute during the ensuing several years. Subglottic hemangiomas produce hoarseness and biphasic stridor with potentially life-threatening respiratory compromise (Figs. 29-54 and 29-55).[175] The acronym PHACES has been proposed to emphasize an occasionally encountered association of the following characteristic features: *p*osterior fossa malformations, *h*emangiomas, *a*rterial anomalies, *c*oarctation of the aorta and cardiac defects, *e*ye abnormalities, and *s*ternal malformations.[176, 177]

In subglottic hemangioma, radiologic examination with AP plain films shows subglottic narrowing, classically asymmetric, unlike the concentric symmetric narrowing of congenital subglottic stenosis (Fig. 29-54A).[141, 178] However, 50% of the time the subglottic narrowing may be symmetric.[179] The lateral film shows a subglottic mass. On CT, hemangiomas appear as lobulated solid tumors that are

Copyright © 2003, Mosby, Inc. All rights reserved.

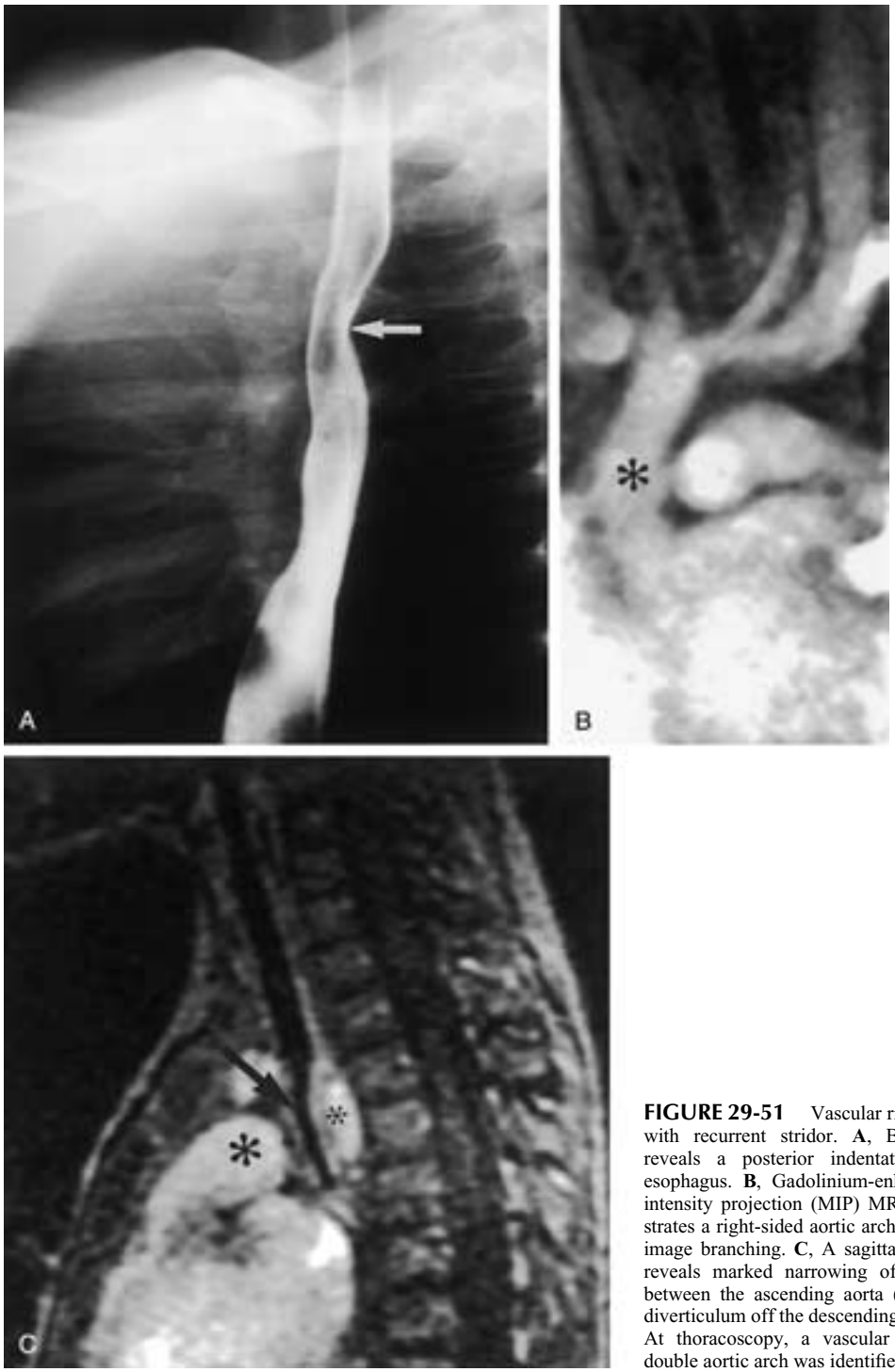

FIGURE 29-51 Vascular ring in a 4-year-old boy with recurrent stridor. **A**, Barium esophagogram reveals a posterior indentation (*arrow*) on the esophagus. **B**, Gadolinium-enhanced 3D maximum intensity projection (MIP) MR angiography demonstrates a right-sided aortic arch (*asterisk*) with mirror image branching. **C**, A sagittal gradient-echo image reveals marked narrowing of the trachea (*arrow*) between the ascending aorta (*large asterisk*) and a diverticulum off the descending aorta (*small asterisk*). At thoracoscopy, a vascular ring with an atretic double aortic arch was identified.

VIEW IMAGE

isodense with muscle and enhance rapidly and intensely following the administration of contrast (Fig. 29-54B). During the proliferative phase, MR imaging reveals a lobulated, moderately hyperintense mass on T2-weighted images (Fig. 29-55), with intense enhancement on contrast-enhanced, T1-weighted sequences (Fig. 29-56). Prominent vascularity within the tumor appears as flow voids on spin-echo pulse sequences (Fig. 29-55) and flow-related enhancement on short echo-time gradient-echo images. The presence of a parenchymal mass differentiates hemangioma from the other high-flow vascular anomalies such as AVM, which may exhibit reactive soft-tissue changes but no discrete mass. The enhancement pattern and vascularity differentiate the high-flow, enhancing hemangioma from the low-flow, nonenhancing lymphatic malformation. The vascularity and early enhancement may help to differentiate hemangioma from venous malformation. However, characteristic imaging features may not be as easily observed with small hemangiomas. Involuting hemangiomas enhance less intensely, have diminishing vascularity

Copyright © 2003, Mosby, Inc. All rights reserved.

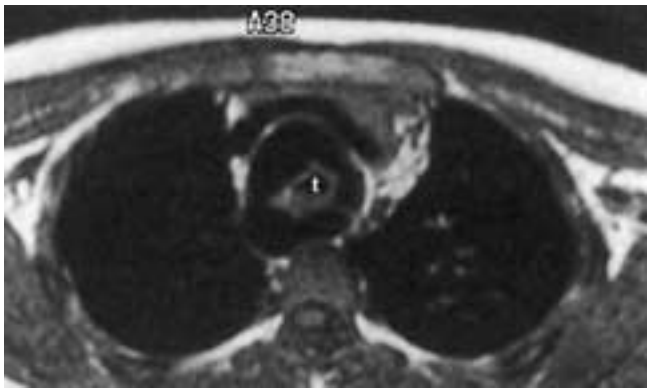

VIEW IMAGE

FIGURE 29-52 Double aortic arch causing tracheal compression in a 10-year-old child with chronic airway obstruction. T1-weighted axial image obtained with respiratory compensation shows a double aortic arch encircling the trachea (*t*).

over time, and have an increasing proportion of fibrofatty matrix.

Hemangiomas that do not interfere with vital functions can be managed expectantly, anticipating involution. However, medical treatment with antiangiogenic drugs such as steroids or alpha interferon, embolization, surgical resection, and sometimes tracheostomy may be required to treat or support patients with hemangiomas that interfere with vital functions such as breathing. Subglottic hemangiomas are also amenable to endoscopic ablation with laser therapy.[180, 181]

Lymphatic Malformation

Lymphatic malformations (LMs) are cystic masses composed of dysplastic endothelium-lined lymphatic channels filled with protein-rich fluid. LMs may be detected antenatally but usually present at birth or within the first few years of life. The usual mode of presentation is the presence of a mass and/or alteration of function from mass effect. However, these anomalies may remain clinically silent until sudden enlargement occurs as a result of hemorrhage or infection. LMs may obstruct the airway, and tracheostomy may be required. Skeletal distortion and overgrowth is a typical feature of LMs.[182] Most LMs are sporadic, but the malformation can occur as part of generalized disorders such as Turner syndrome (45XO), Noonan syndrome, trisomy 21, trisomy 13, and trisomy 18.[183, 184]

LMs can be characterized based on the size of the cysts as microcystic, macrocystic, or mixed. On clinical examination, a localized cystic mass or a solid or spongy mass is palpated or there may be diffuse infiltration and enlargement of the affected region. Macroglossia and overgrowth of the mandible with dental malocclusion can also occur. The most frequent complications of LMs are infection and hemorrhage.

The choice of imaging modality for LMs depends on the information required. MR imaging produces superior soft-tissue contrast and tissue characterization and is generally considered the imaging modality of choice in diagnosing and demonstrating the extent of LMs. However, where the clinical diagnosis of macrocystic LM is known, ultrasound or CT will adequately delineate the extent of the lesion in most cases (Fig. 29-57A). The appearance of LM on imaging depends on the size of the lymphatic spaces and on the presence of hemorrhage or infection (Fig. 29-57). LM has a tendency to involve multiple fascial compartments. The lesions generally appear cystic and septated. A very characteristic feature of LMs is the presence of fluid-fluid levels (Fig. 29-58). Large and/or anomalous adjacent venous channels are often seen, and communication between the LM and adjacent veins is frequently present.[185]

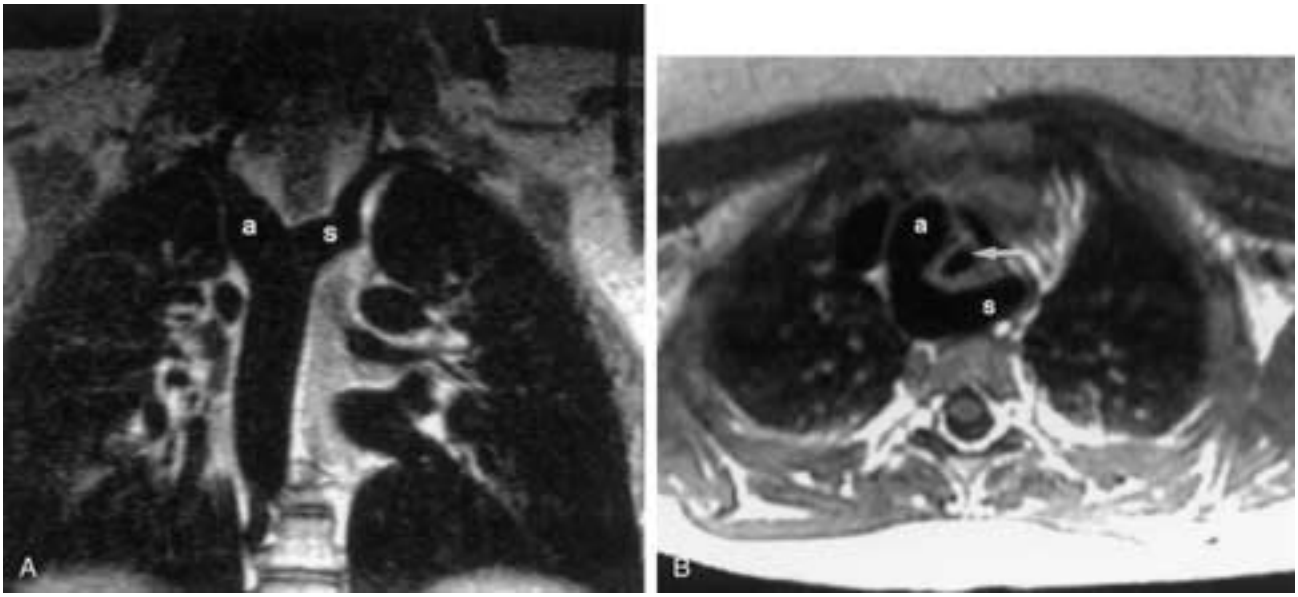

VIEW IMAGE

FIGURE 29-53 Right aortic arch with an aberrant left subclavian artery in a 6-year-old girl with a chronic cough and chest pain on deep inspiration. ECG-gated (**A**) oblique coronal and (**B**) axial T1-weighted images reveal the right aortic arch (*a*) and aberrant left subclavian artery (*s*). The trachea (*arrow*) is narrowed and partially encircled.

Copyright © 2003, Mosby, Inc. All rights reserved.

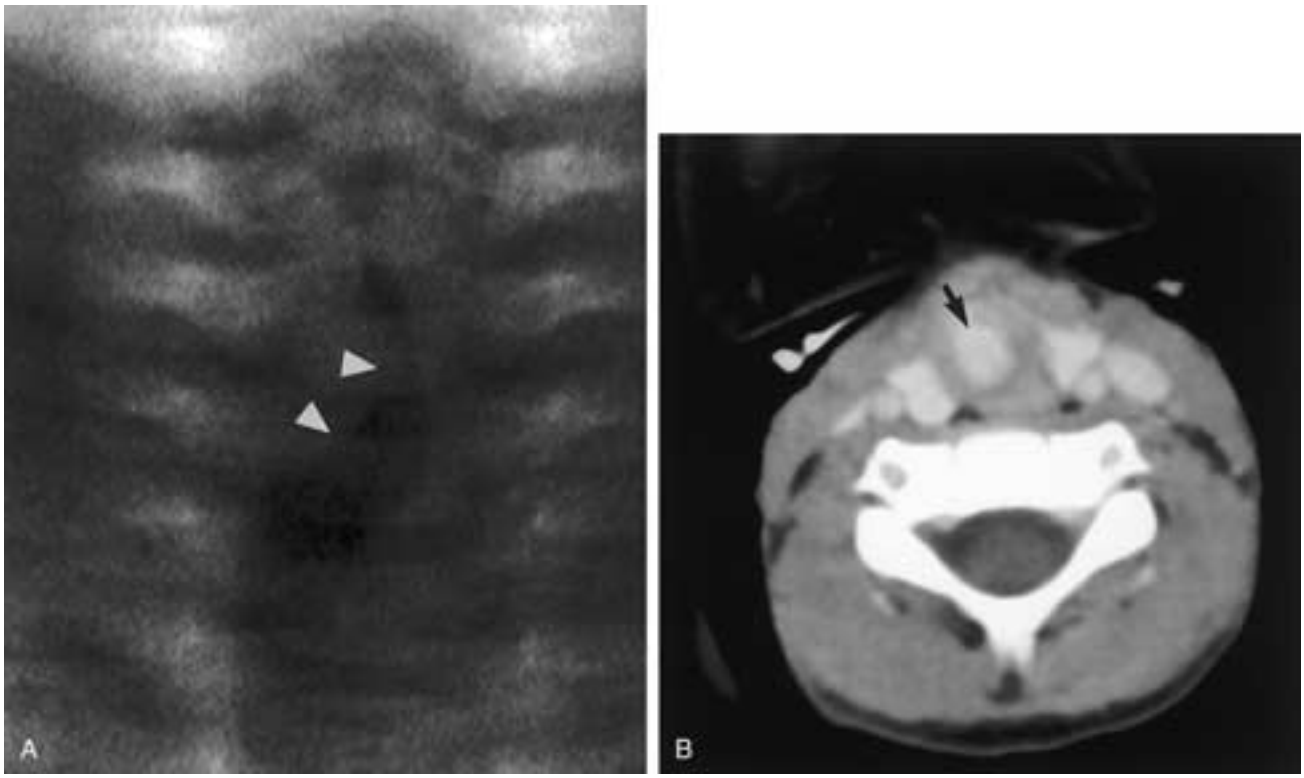

VIEW IMAGE

FIGURE 29-54 Subglottic hemangioma in a 6-week-old boy with stridor. **A**, Frontal plain film shows indentation of the trachea (*arrowheads*) by a right subglottic mass. An axial contrast-enhanced CT scan was obtained several weeks later. **B**, An image at the level of the thyroid gland shows interval enlargement due to proliferation of the intensely enhancing right subglottic hemangioma, which now fills the trachea (*arrow*). The patient had a tracheostomy tube in place.

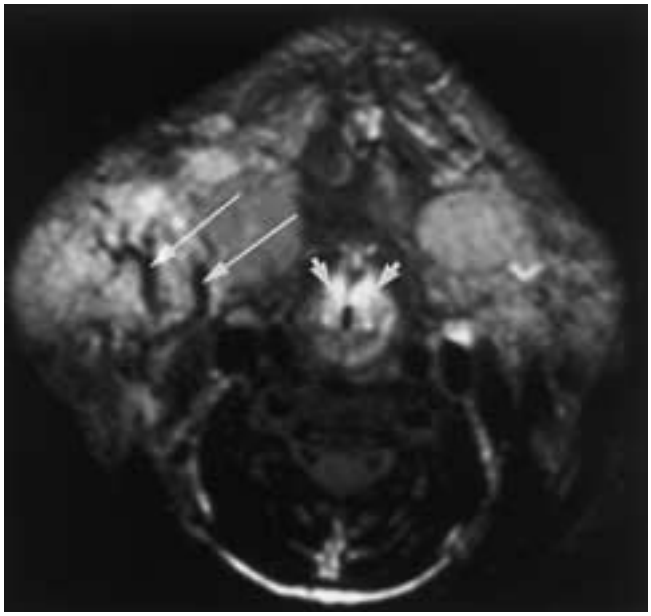

VIEW IMAGE

FIGURE 29-55 Subglottic and facial hemangioma in a 6-month-old girl. Axial FSE T2-weighted MR image with fat suppression reveals high signal intensity due to hemangioma (*short arrows*) surrounding and narrowing the airway. There is a large, lobulated right submandibular and facial hemangioma. Note the conspicuous flow voids (*long arrows*). The patient had a tracheostomy tube in place and received treatment with alpha interferon.

FIGURE 29-56 Congenital hemangioma of the tongue in a 4-week-old boy. Sagittal contrast-enhanced T1-weighted MR image reveals intense enhancement of the tumor (*asterisk*). The clinical course was complicated by massive hemorrhage. The patient underwent transarterial particle embolization of the lingual branches supplying the hemangioma, and steroid therapy was commenced. The hemangioma subsequently involuted.

VIEW IMAGE

Copyright © 2003, Mosby, Inc. All rights reserved.

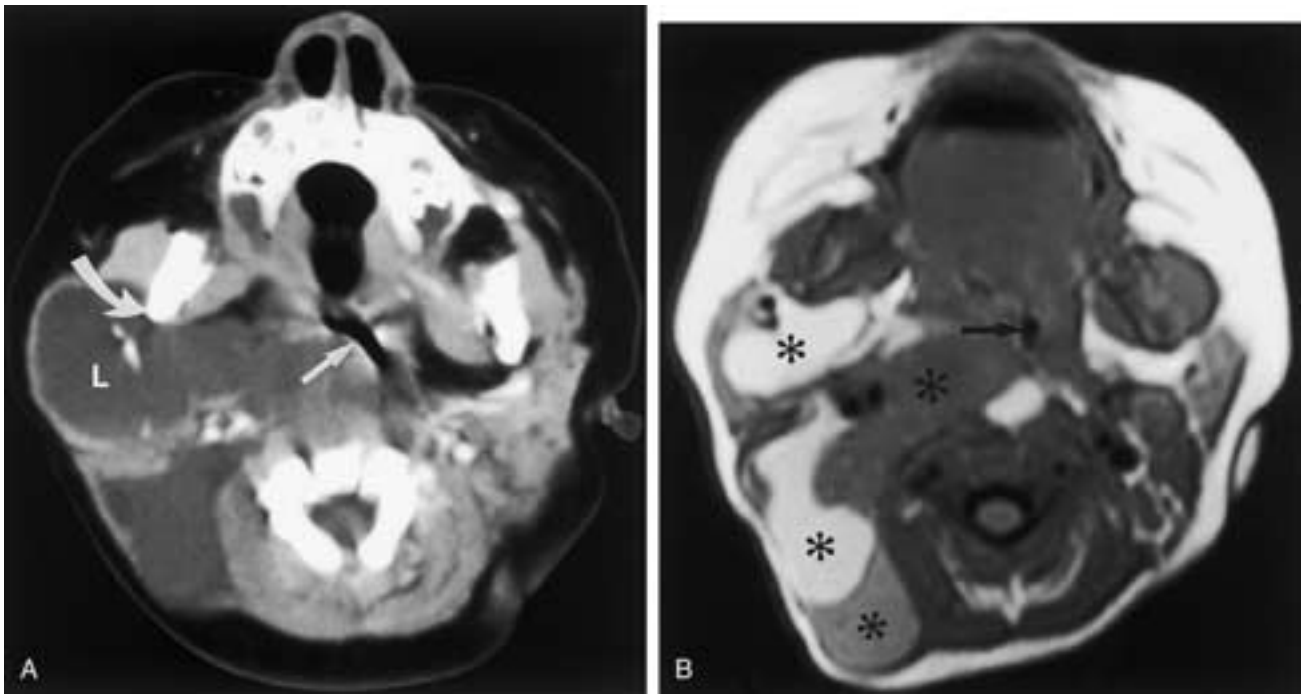

VIEW IMAGE

FIGURE 29-57 LM complicated by infection and subsequent hemorrhage in a 3-year-old boy. **A**, Axial contrast-enhanced CT reveals a low-attenuation macrocystic LM (*L*) encroaching on the airway (*straight arrow*). There is enhancement only of the margins and septations of the LM. Note the deformity and remodeling of the right mandibular ramus (*curved arrow*). This is a relatively common feature of LMs. **B**, Axial T1-weighted MR image reveals variegated high and intermediate signal intensity representing hemorrhage within the macrocystic LM (*asterisks*). The LM distorts and compresses the oropharynx (*arrow*).

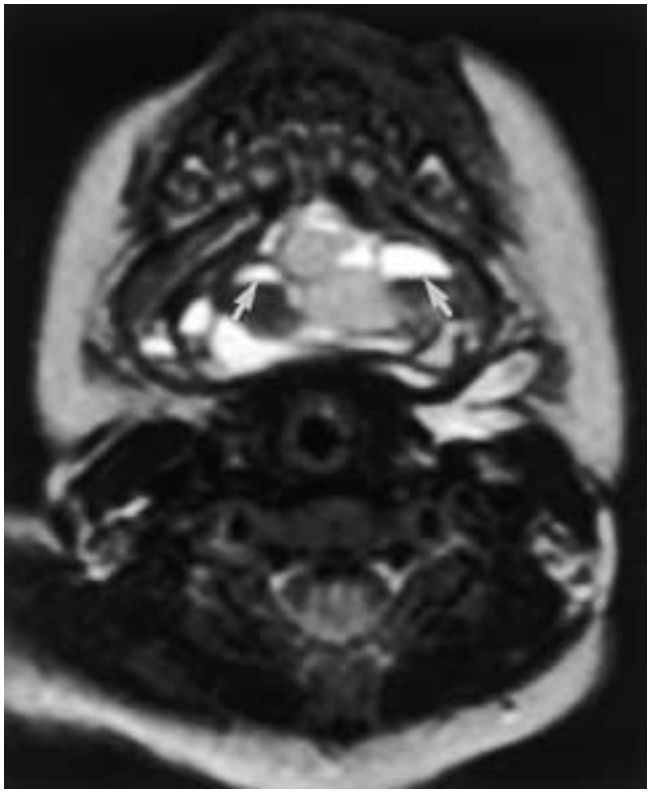

VIEW IMAGE

FIGURE 29-58 LM in a young boy. Axial FSE T2-weighted MR image demonstrates fluid-fluid levels (*arrows*) that are characteristic of LM.

Sonography of a macrocystic LM reveals a uni- or multilocular cystic mass sometimes containing echogenic debris. Microcystic LMs appear hyperechoic because of numerous interfaces.

Uncomplicated LMs usually appear hypodense on CT (Fig. 29-57) and markedly hyperintense on T2-weighted MR images. However, the density on CT, the signal intensity on MR imaging, and the presence of fluid-fluid levels vary, depending on the protein content and the presence of blood products. Depending on the time interval since hemorrhage, blood breakdown products produce T1 and T2 shortening or T2 prolongation on MR imaging (Figs. 29-57B and 29-58). Following the administration of contrast, the cyst walls/septations enhance but the fluid contained within the cystic space does not enhance (Fig. 29-57).

If a multicystic neck mass is diagnosed by antenatal ultrasound, fetal MR images can be obtained for diagnostic purposes and to provide further anatomic information including airway assessment. The half-fourier single shot turbo spin-echo (Haste) or the single-shot fast spin-echo (SSFSE) pulse sequence has been favored for delineation of masses and decreased motion artifacts.[186] The main differential diagnosis for multiseptated macrocystic lesions is teratoma in the fetus or newborn and venous malformation. The presence of fluid-fluid levels, lack of fluid enhancement, and absence of phleboliths differentiate LM from venous malformation. The absence of fat or calcification within the lesion differentiates LM from teratoma. Microcystic LMs produce more of a diagnostic dilemma, as

Copyright © 2003, Mosby, Inc. All rights reserved.

the cystic spaces may be so small that the lesion appears more diffusely enhancing.

The treatment of LMs includes the administration of antibiotics for infection and surgical resection. Postoperative complications and residual or recurrent disease are common. Intralesional injection with sclerosants such as ethanol or OK 432 may provide local control of the lesion in inoperable cases.[175, 187]

Venous Malformation

Venous malformations (VMs) are vascular malformations that consist of dysplastic venous channels. VMs are present at birth, but the age of presentation depends on size, location and interference with normal function. VMs grow proportionately to the child and frequently enlarge during puberty.[175] Clinical manifestations include pain and swelling, especially after recumbency. Clinical examination typically reveals blue or purplish discoloration of the skin and a soft or spongy, compressible mass that expands with the Valsalva maneuver or with dependent positioning.[185] VM can be single or multifocal and localized or extensive. Phlebothrombosis produces pain and a mass that is firm to palpation. Familial forms of VM include *Blue-rubber bleb nevus syndrome* (cutaneous and gastrointestinal VMs), *familial multiple glomangioma* (glomus cells line VM channels), and *cerebral cavernous malformations* (with or without cutaneous lesions).[175] Mafucci syndrome is characterized by multiple enchondromas associated with venous anomalies.

The characteristic imaging feature of VMs is the development of phleboliths associated with phlebothrombosis. Phleboliths appear as rounded, lamellated, calcific densities on CT. The fluid within VMs is venous blood that enhances, unlike the lymph contained within LMs. Early CT or MR images acquired during or immediately after bolus administration of IV contrast demonstrate enhancement of the VM that is initially heterogeneous. Delayed images show a more homogeneous pattern of enhancement (Fig. 29-59). MR imaging demonstrates some imaging similarities with LMs in that VMs are cystic and septated, and the fluid within the cystic spaces is markedly hyperintense on long TR images. Phleboliths appear as circumscribed signal voids (Fig. 29-59B) that should not be confused with flow voids. Unlike proliferating hemangiomas, arterial or rapid flow on flow-sensitive pulse sequences is not a feature of VMs. However, MR venography may reveal dilated or anomalous veins in the vicinity of VMs.

It is important, from a therapeutic standpoint, to differentiate VM from hemangioma or LM. The term *cavernous hemangioma* should be avoided when referring to VMs, as it is erroneous and frequently leads to the institution of inappropriate antiangiogenic drug therapy and subsequent therapeutic failure.[185] The treatment of VMs includes the use of elastic compressive garments, aspirin, percutaneous sclerotherapy, and surgical resection.[175, 185] Direct percutaneous cannulation with contrast injection of the VM typically shows interconnecting sinusoidal spaces and adjacent normal or dilated venous channels (Fig. 29-60).[185] For extensive VM of the airway, staged therapy with a combination of sclerotherapy and photocoagulation has been advocated.[188]

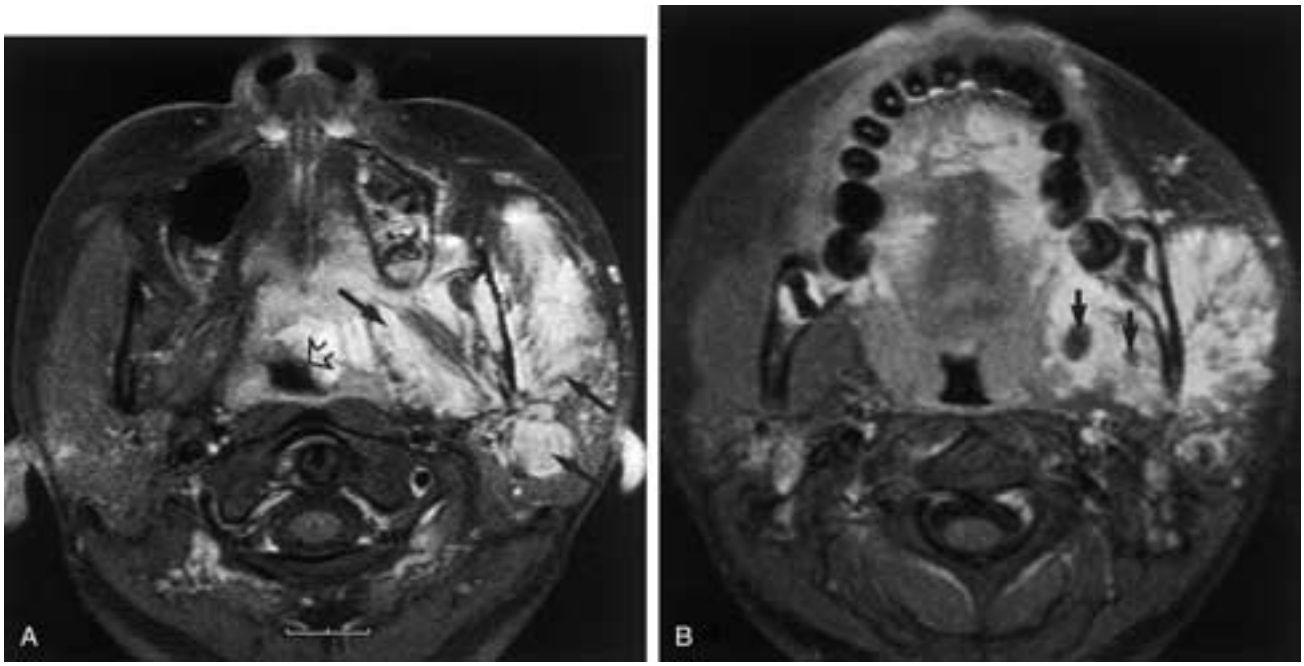

FIGURE 29-59 VM in a 13-year-old girl. Axial fat-suppressed, contrast-enhanced T1-weighted MR image (**A**) reveals a multiseptated enhancing mass (*arrows*) within the left muscles of mastication, the mandible, parotid space, parapharyngeal space, soft palate, and pharynx. There is distortion of the airway (*open arrow*). **B**, Phleboliths (*arrows*) are present.

VIEW IMAGE

Copyright © 2003, Mosby, Inc. All rights reserved.

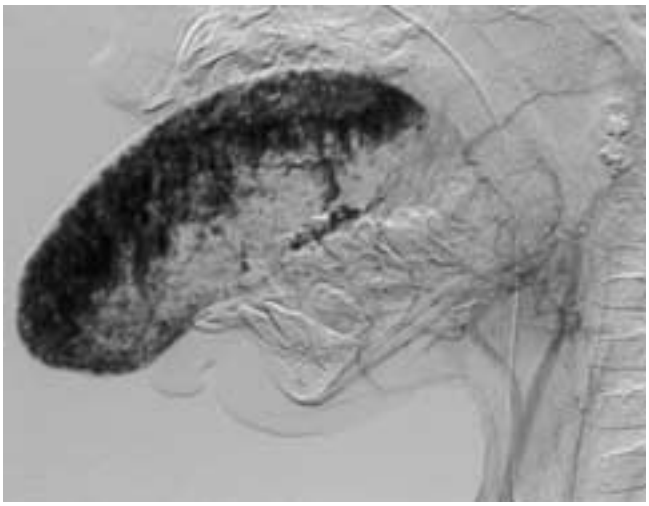

VIEW IMAGE

FIGURE 29-60 VM of the tongue in a 5-year-old girl. Lateral view with digital subtraction following direct percutaneous injection of contrast into the VM demonstrates the multiple small cysts that constitute the lesion. The cysts also communicate with normal lingual veins.

SECTION SIX

INFECTIOUS AND INFLAMMATORY DISORDERS

VIRAL ADENOTOSILLITIS AND LYMPHADENOPATHY

Nonspecific Viral Infection

Infections of the head and neck generally produce reactive enlargement of lymphoid tissue (adenoids, tonsils, and lymph nodes). Inflammatory adenotonsillitis with lymphadenopathy may be viral or bacterial in origin. Viral illnesses, with the exception of the acquired immunodeficiency syndrome (AIDS), are generally self-limited and do not usually require imaging. Mucocutaneous candidiasis, parotid enlargement, and cervical adenopathy have been reported in pediatric patients with AIDS, but imaging of the airway is not usually necessary.[189]

Infectious Mononucleosis (Epstein-Barr Virus)

Massive adenopathy with adenotonsillitis, fever, weakness and malaise, typically presenting in a teenager, is characteristic of infectious mononucleoisis, caused by the Epstein-Barr virus (EBV). Unlike other viral illnesses, EBV infection may produce massive, protracted enlargement of lymphoid tissues, sometimes with life-threatening compromise of the airway. In this situation, imaging is sometimes required to exclude secondary bacterial infection with abscess formation. CT with contrast demonstrates massive enlargement and enhancement of lymphoid tissues. The enlarged adenoids sometimes display streaky heterogeneous enhancement with interspersed low attenuation, indicative of adenoidal edema (phlegmonous change) (Fig. 29-61). This appearance should not be mistaken for abscess formation. An indistinguishable appearance can be seen in severe streptococcal pharyngitis with adenotonsillitis.

BACTERIAL ADENOTONSILLITIS, LYMPHADENOPATHY, CELLULITIS, AND ABSCESS

Acute Bacterial Infection

Acute adenotonsillitis and lymphadenopathy due to bacterial causes are most often due to infection with group A streptococci. Bacterial infections of the head and neck may progress to cellulitis, nodal suppuration, or abscess formation. Cellulitis can be seen with adenotonsillitis and lymphadenopathy with or without abscess formation. The most common site of abscess or cellulitis/adenopathy is the peritonsillar space, followed by the retropharyngeal and submandibular spaces.[190] The most frequently cultured organisms in neck infections are *Streptococcus pyogenes, Staphylococcus aureus,* and *Bacteroides melanogenicus*.[190] Peritonsillar infections are associated with suppurative tonsillitis, with extension of infection and pus between the tonsillar capsule and the anterior and posterior tonsillar pillars. Retropharyngeal and parapharyngeal infections result from suppurative lymphadenitis associated with tonsillitis, pharyngitis, sinonasal infection, otitis media, dental infection, or trauma to the neck and oropharynx. Causes of submandibular infection include dental infection, salivary calculi, and skin infection. Bilateral cellulitis of the submandibular space is known as Ludwig's angina. Necrotizing cellulitis is a fulminant and extensive form of cellulitis that involves multiple fascial compartments. Necrotizing cellulitis is uncommon and may occur in children with a primary dermatologic process, such as chicken pox or infantile eczema, who then develop secondary infection with hemolytic streptococci.

The primary symptoms of infection include fever, sore throat, and a focal neck mass or diffuse swelling. Stridor or other symptoms of respiratory distress, odynophagia, dysphagia, and trismus indicate compromise of the upper aerodigestive tract. Local complications of neck infections include airway compromise, torticollis due to muscle spasm, and involvement of the vessels within the carotid sheath. The most common vascular complication is septic thrombophlebitis of the internal jugular vein.[191] Distant complications include infection of the mediastinum, lungs, and pleural and pericardial spaces.

The clinical presentation of peritonsillar abscess differs from that of retropharyngeal and submandibular space infections. There is typically unilateral enlargement and medial displacement of the tonsil with contralateral deviation of the uvula. A peritonsillar abscess may spread around or through the superior constrictor muscle and into the parapharyngeal space, leading to a parapharyngeal space abscess. By contrast, the clinical presentation of a retropharyngeal abscess (RPA) includes neck stiffness, torticollis, and posterior pharyngeal wall swelling that is often asymmetric.

Imaging helps differentiate between cellulitis, lymphade-

Copyright © 2003, Mosby, Inc. All rights reserved.

nitis, and abscess formation. Cross-sectional imaging is also used to assess the location and extent of abscess formation and to diagnose complications. It follows that imaging is seldom obtained for uncomplicated adenotonsillitis and may not be required for peritonsillar abscess, as the clinical presentation is often diagnostic. For those patients in whom imaging is indicated, contrast-enhanced CT is currently the examination of choice (Figs. 29-62 to 29-67). However, initial lateral plain neck films are sometimes obtained prior to cross-sectional imaging (Figs. 29-65A and 29-66A). Retropharyngeal space infection is accompanied by widening of the retropharyngeal soft tissues on films taken during inspiration, loss of cervical lordosis, and, occasionally, air in the retropharyngeal soft tissues (Fig. 29-66A).

CT is performed with 3 mm axial images obtained during the administration of an intravenous bolus of iodinated contrast medium. Images should be acquired from the skull base to the mediastinum. After immediate image review, it

FIGURE 29-61 Infectious mononucleosis in an 11-year-old boy. The patient complained of fever, severe sore throat, neck swelling, and dysphagia for several days. Contrast-enhanced CT reveals (**A, B**) massive enlargement of the adenoids (*arrows*) with heterogeneous enhancement and interspersed edematous change. Enlarged retropharyngeal nodes (*n*) are present. The nasopharyngeal airway is completely effaced. **C**, There is enlargement of the tonsils (*t*) and retropharyngeal nodes (*n*).

VIEW IMAGE

Copyright © 2003, Mosby, Inc. All rights reserved.

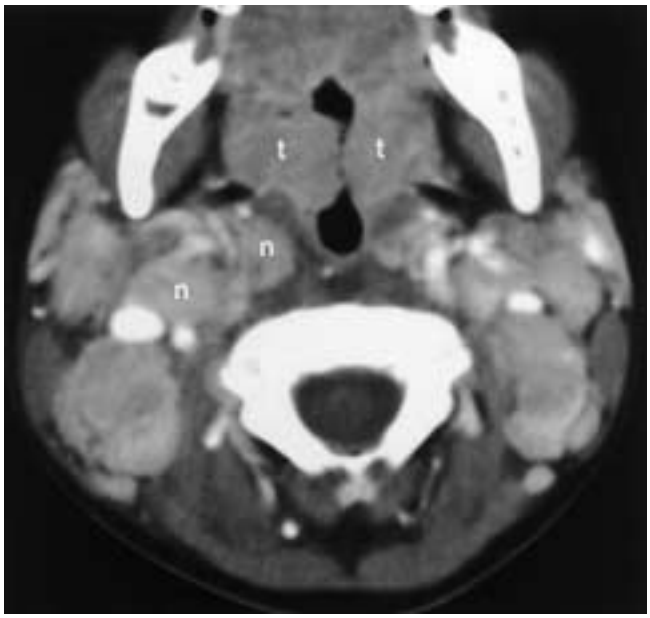

VIEW IMAGE

FIGURE 29-62 Streptococcal tonsillitis and lymphadenitis in a 4-year-old girl. Contrast-enhanced CT reveals marked enlargement and enhancement of the palatine tonsils (*t*) and lymph nodes (*n*) with narrowing of the airway. There is posterolateral displacement of the carotid sheath.

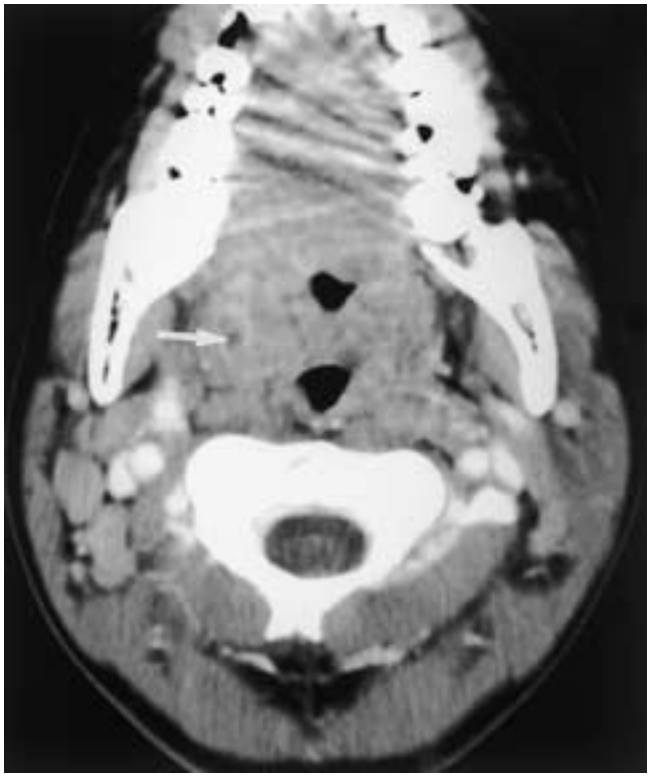

VIEW IMAGE

FIGURE 29-63 Streptococcal tonsillitis and lymphadenitis in an 11-year-old boy. Contrast-enhanced CT reveals heterogeneous streaky enhancement of the enlarged palatine tonsils with a focus of low attenuation (*arrow*).

FIGURE 29-64 Streptococcal pharyngitis and lymphadenitis in a 10-year-old boy with dysphagia. There are markedly enlarged, low-attenuation, edematous retropharyngeal lymph nodes (*short arrows*). This appearance is difficult to distinguish from early retropharyngeal abscess formation. There is also an enlarged, enhancing right lateral retropharyngeal lymph node (*arrowhead*). The airway is distorted and narrowed. There is compression or partial thrombosis of the left internal jugular vein (*long arrow*).

VIEW IMAGE

may be useful to obtain limited delayed images through any area that is equivocal for abscess versus edematous lymphadenitis. Inflamed lymphoid tissue may enhance homogeneously or heterogeneously or may appear edematous, with decreased attenuation and mild delayed peripheral enhancement, nodal edema, or suppuration (Figs. 29-62 to 29-64). Abscess formation is also characterized by low attenuation and ring enhancement, particularly if the margins of the lesion no longer conform to the morphology of the node in which the inflammatory process originated (Figs. 29-65 to 29-67). Since a similar appearance can be seen with edematous lymph nodes, the demonstration of a focal area of low attenuation with rim enhancement is predictive but not entirely diagnostic of abscess formation.[192] Therefore, CT provides invaluable information in determining the need for surgical intervention, but it is not entirely accurate in the diagnosis of abscess formation. Ultrasound has been proposed as an effective modality for differentiating adenitis from abscess and for providing guidance for intraoperative aspiration and drainage.[193] Effacement of the left pyriform sinus and recurrent perithyroidal suppurative infections should suggest the diagnosis of an underlying pyrifiorm sinus fistula (Fig. 29-68). A CT diagnosis of cellulitis is made when there is

Copyright © 2003, Mosby, Inc. All rights reserved.

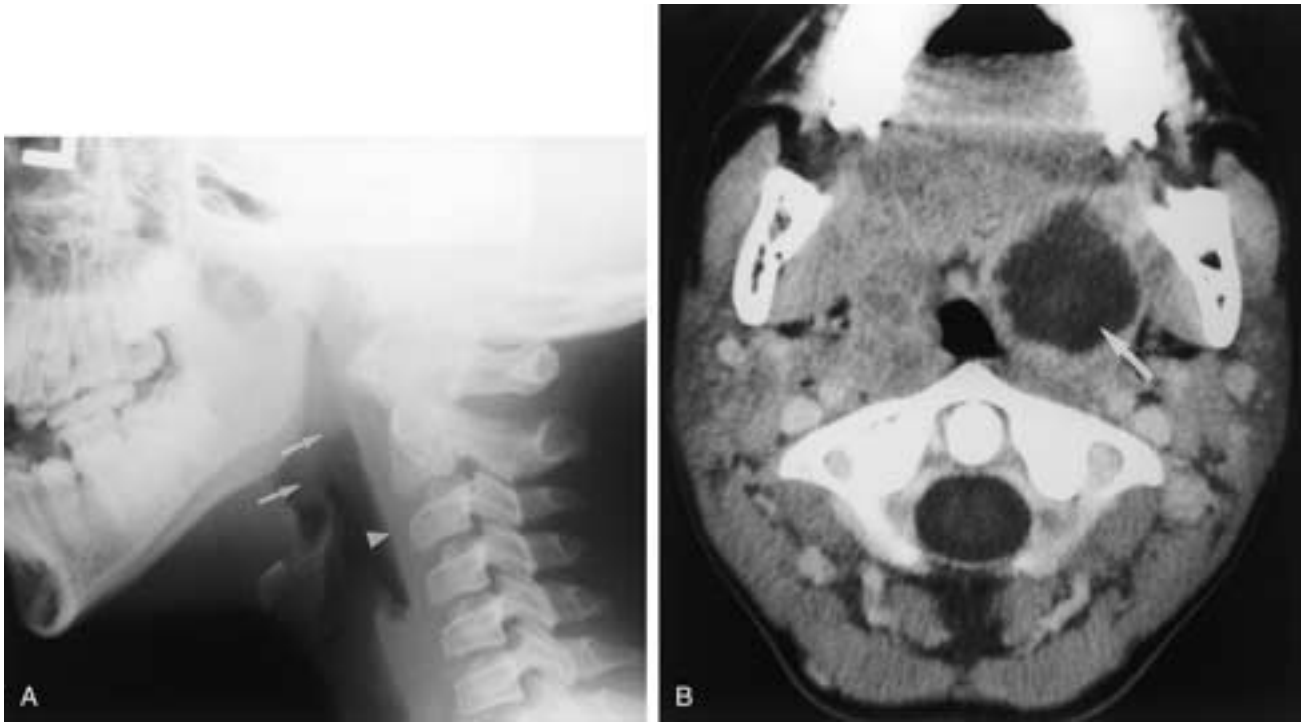

VIEW IMAGE

FIGURE 29-65 Peritonsillar abscess in a 13-year-old boy. **A**, Lateral plain film reveals some enlargement of the tonsils (*arrows*). Note the normal width of the retropharyngeal soft tissues (*arrowhead*). **B**, Contrast-enhanced CT reveals a large low-attenuation, ring-enhancing left peritonsillar abscess (*arrow*) that is distorting the airway.

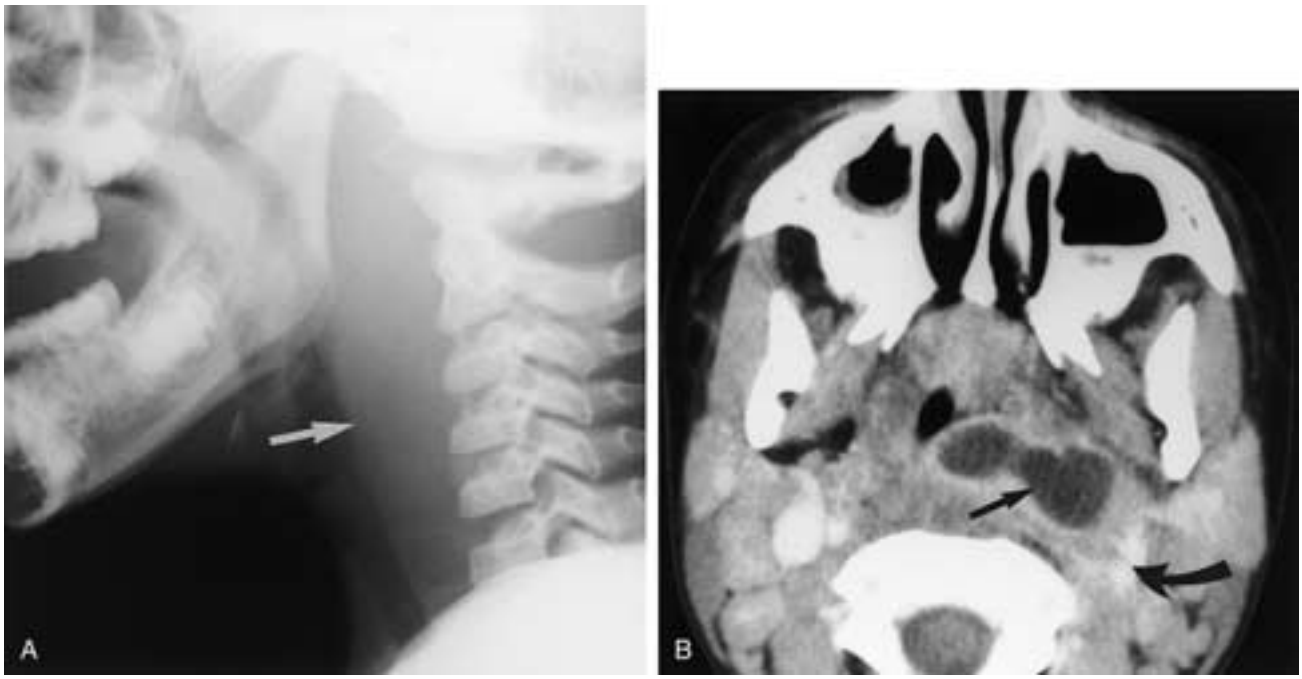

VIEW IMAGE

FIGURE 29-66 Retropharyngeal abscess in a 4-year-old boy. **A**, Lateral plain film reveals marked widening of the retropharyngeal soft tissues (*arrow*). Compare this appearance with that in Figure 29-65A. **B**, Contrast-enhanced CT reveals a large low-attenuation, ring-enhancing left retropharyngeal abscess (*arrow*) with distortion and narrowing of the airway. There is lateral displacement and attenuation of the left carotid artery and internal jugular vein (*curved arrow*).

Copyright © 2003, Mosby, Inc. All rights reserved.

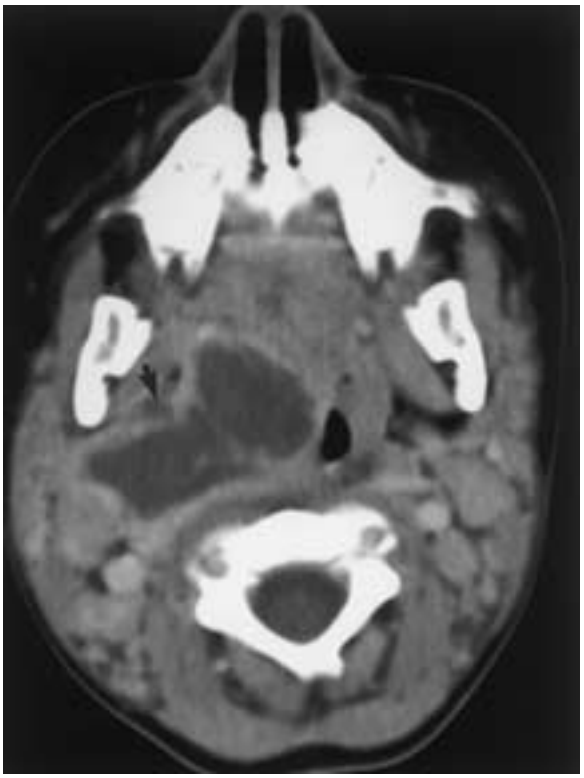

VIEW IMAGE

FIGURE 29-67 Large ruptured peritonsillar abscess in a 2-year-old girl with neck stiffness, fever, and poor oral intake. Contrast-enhanced CT shows a large right peritonsillar abscess that extends laterally and involves the parapharyngeal space (*arrow*).

edema of the soft tissues and obliteration of fat planes without rim enhancement (Fig. 29-69). Necrotizing cellulitis is characterized by extensive stranding of the subcutaneous fat, low-attenuation phlegmonous change, and involvement of multiple fascial compartments (Fig. 29-70).

Airway encroachment by the inflammatory process should be noted and reported to the patient's physician and to any medical attendant accompanying the patient as soon as possible. Quite frequently there is displacement and a relative decrease in the caliber of the ipsilateral internal carotid artery in association with retropharyngeal infections. This phenomenon may be due to spasm and is generally asymptomatic.[194] Similarly, the ipsilateral internal jugular vein is often compressed by the inflammatory process (Fig. 29-64). Thrombophlebitis is a less common but potentially serious complication, as thrombus may propagate proximally, with potential hemorrhagic venous infarction of the brain.

Surgical incision and drainage is indicated in a child with imaging findings of a deep neck abscess.

Granulomatous Infection

Chronically enlarged lymph nodes can be a manifestation of granulomatous infections associated with organisms such as *Mycobacterium tuberculosis* (MTB), nontuberculous mycobacteria (NTM), and *Rochalimaea henselae* (cat scratch disease). These disorders differ in terms of clinical presentation, physical examination, and, to a lesser extent,

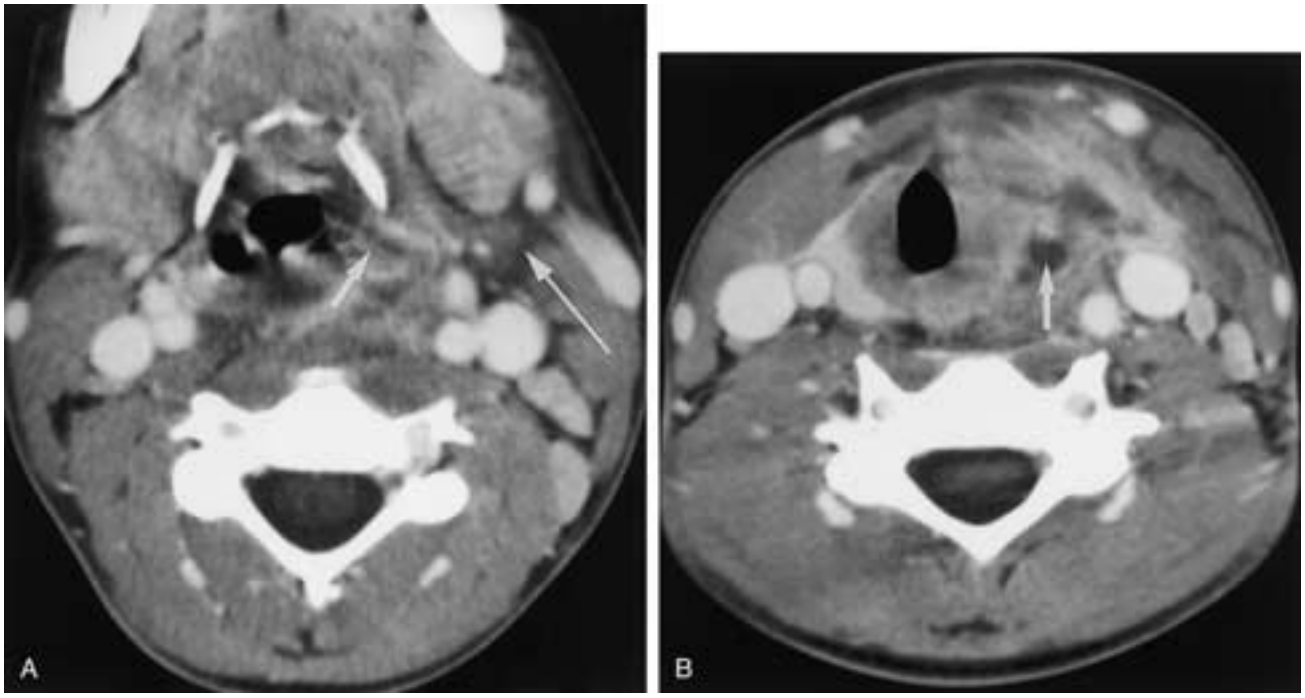

VIEW IMAGE

FIGURE 29-68 Pyriform sinus fistula in a 12-year-old girl with recurrent left perithyroidal suppurative infections. **A**, Contrast-enhanced CT shows effacement of the left pyriform sinus, with thickening of the mucosa (*short arrow*) and low-attenuation cellulitis of the left neck (*long arrow*). **B**, The left neck is swollen, the trachea is displaced to the right, and there is a small abscess (*arrow*) abutting the superior pole of the left lobe of the thyroid gland, with extensive surrounding inflammatory change. Several weeks after treatment and following resolution of inflammation, a pyriform sinus fistula was identified on an esophagogram.

Copyright © 2003, Mosby, Inc. All rights reserved.

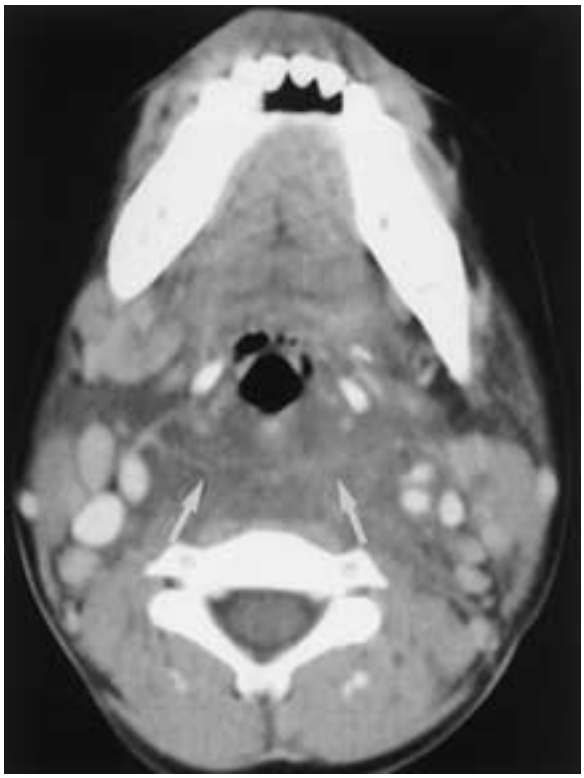

VIEW IMAGE

FIGURE 29-69 Retropharyngeal cellulitis in a 10-year-old boy. There is extensive thickening and diffuse low-attenuation change in the retropharyngeal and adjacent soft tissues (*arrows*) on this contrast-enhanced CT image.

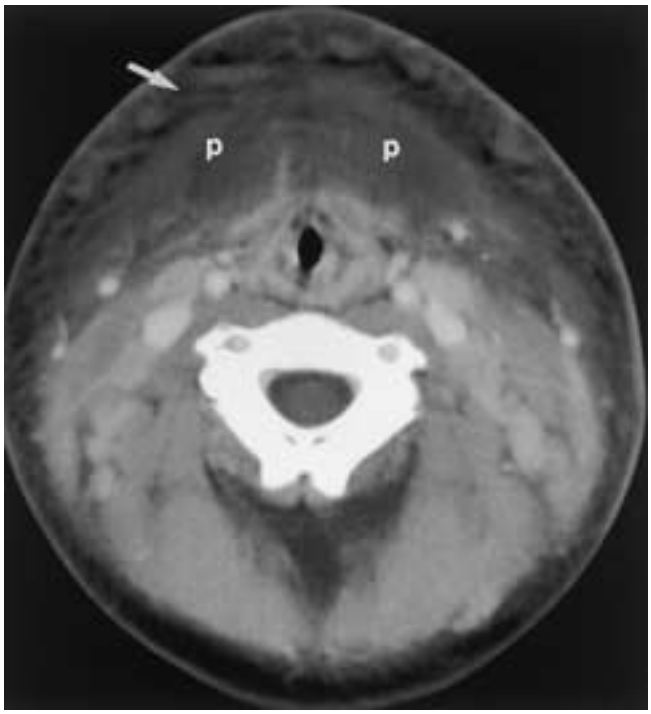

VIEW IMAGE

FIGURE 29-70 Streptococcal necrotizing cellulitis in a 2-year-old girl with a 6-day history of chicken pox and a 2-day history of rapidly progressive facial swelling. Contrast-enhanced CT shows massive swelling of the neck, diffuse stranding of the subcutaneous fat (*arrow*), low-attenuation phlegmonous change (*p*), and blurred muscle margins. The airway is narrowed.

imaging features.[195] Children with tuberculosis are usually systemically unwell. Children with NTM infection are usually aged between 2 and 5 years, are systemically well, and typically present with a unilateral nontender or minimally tender mass with overlying violaceous skin discoloration. Children with cat scratch disease usually have a history of a preexisting scratch from a cat.

Granulomatous adenopathy is occasionally massive enough to produce extrinsic airway compression. Involvement of retropharyngeal nodes can occasionally simulate a conventional bacterial abscess (Fig. 29-71).[196] On CT, involved lymph nodes typically have heterogeneous enhancement with foci of low attenuation and sometimes calcification. NTM infection is characterized by necrotic material extruding out of affected lymph nodes to involve the subcutaneous tissues and skin (Fig. 29-71).[196] Physical examination reveals associated violaceous skin discoloration. Inflammatory stranding of the soft tissues is not generally a feature of NTM infection but is usually seen with cat scratch disease.[196] It is important to differentiate granulomatous disorders from acute bacterial infection preoperatively, as surgical intervention, when indicated, should consist of excisional biopsy or curettage, as incision and drainage can lead to the formation of draining sinus tracts. Other causes of enlarged lymph nodes are described in Chapter 36.[197, 198]

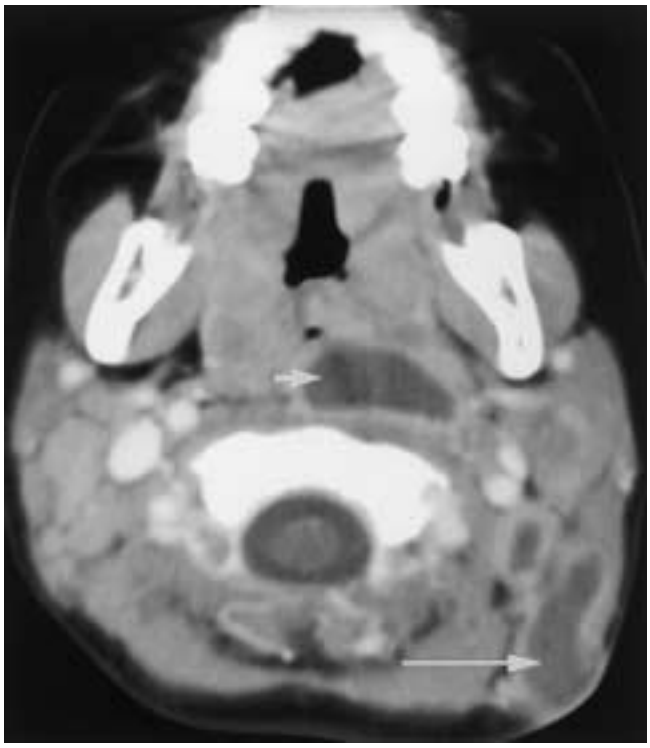

FIGURE 29-71 Nontuberculous mycobacterial infection in a 2½-year-old girl with a 4-week history of an enlarging left posterior triangle neck mass and deviation of the oropharynx to the right. Contrast-enhanced CT shows low-density, ring-enhancing spinal accessory adenopathy (*long arrow*), with extrusion of necrotic material involving the subcutaneous tissues and skin. Enlarged low-density, ring-enhancing left retropharyngeal adenopathy (*short arrow*) causes distortion and narrowing of the oropharynx (From Robson C.D. et al. Nontuberculous mycobacterial infection of the head and neck in immunocompetent children: CT and MR findings. AJNR 1999;20(10):1829–1835.)

VIEW IMAGE

Copyright © 2003, Mosby, Inc. All rights reserved.

SUPRAGLOTTITIS (EPIGLOTTITIS)

Supraglottitis, also known as *epiglottitis*, is an acute, potentially fulminating infection that occurs most commonly, though not exclusively, in children between 2 and 6 years of age. The infection is usually caused by *Haemophilus influenzae* type B. However, since the implementation of effective immunization against this organism, the incidence of epiglottitis has declined.[199] Previously immunized children with supraglottitis tend to be older and may have infection with other bacteria such as group A beta-hemolytic streptococci.[199] Invasive group A beta-hemolytic streptococcal infection with epiglottitis and necrotizing cellulitis has also been described as an unusual complication of varicella infection in children.[200]

Supraglottitis is characterized by an abrupt onset and a rapidly progressive course. Affected children present with drooling, fever, sore throat, dysphagia, restlessness, and inspiratory stridor with respiratory distress that may progress to complete airway obstruction. Bacterial supraglottitis must be clinically differentiated from other inflammatory causes of stridor such as viral laryngotracheobronchitis (croup) and bacterial tracheitis. As epiglottitis is considered to be a life-threatening condition, diagnosis and institution of appropriate therapy should be prompt. Every effort should be made to minimize patient manipulation, as this may exacerbate airway symptoms and provoke complete respiratory obstruction.

The diagnosis of supraglottitis can be based on clinical findings and endoscopic examination in the operating room. Physical examination reveals swelling and erythema of the epiglottis, aryepiglottic folds, false vocal cords, and arytenoids. However, if the diagnosis is uncertain and the patient's condition permits, a plain lateral radiograph of the neck can be obtained to help confirm the diagnosis and to exclude other causes of airway compromise. A physician should accompany the patient to the department, with equipment readily available for additional airway support. Ideally, radiographs should be obtained with the patient sitting comfortably in the erect position. The child should not be restrained or forced into a supine position, as this may exacerbate the respiratory obstruction. The typical plain film findings of supraglottitis include thickening of the free edge of the epiglottis, increased width of the aryepiglottic folds and arytenoids, and overdistention or ballooning of the hypopharynx (Figs. 29-72 and 29-73).[201]

FIGURE 29-73 Streptococcal supraglottitis in a 3-year-old boy with throat pain and drooling. The lateral plain film reveals thickening of the epiglottis and aryepiglottic folds (*arrowheads*). There is some overdistention of the hypopharynx.

VIEW IMAGE

FIGURE 29-72 Supraglottitis in a 17-year-old boy who complained of sore throat, dysphagia, and drooling. The lateral plain film reveals diffuse thickening of the supraglottic soft tissues (*arrow*) including the epiglottis (*e*). The diagnosis was confirmed endoscopically.

VIEW IMAGE

Other less common causes of epiglottic enlargement in the pediatric population include angioneurotic edema, epiglottic trauma, caustic laryngeal burns, abscess (Fig. 29-74), or hemorrhage within the epiglottis, radiation therapy, benign epiglottic lesions such as cysts or vascular malformations, or chronic epiglottitis, a rare persistent inflammatory process.[202, 203] The clinical presentation should aid in differentiating other lesions from acute bacterial supraglottitis. Treatment in children involves intravenous antibiotics and often nasotracheal intubation or tracheostomy.

LARYNGOTRACHEOBRONCHITIS (CROUP)

Laryngotracheobronchitis (LTB), or croup, is the most common inflammatory cause of stridor in young children. LTB may be spasmodic or follow an upper respiratory infection. Most infectious cases are viral in etiology and are usually attributable to the human parainfluenza viruses or, less commonly, to the influenza and respiratory syncytial viruses.[204] LTB is also a frequent and often severe complication of measles.[205]

Copyright © 2003, Mosby, Inc. All rights reserved.

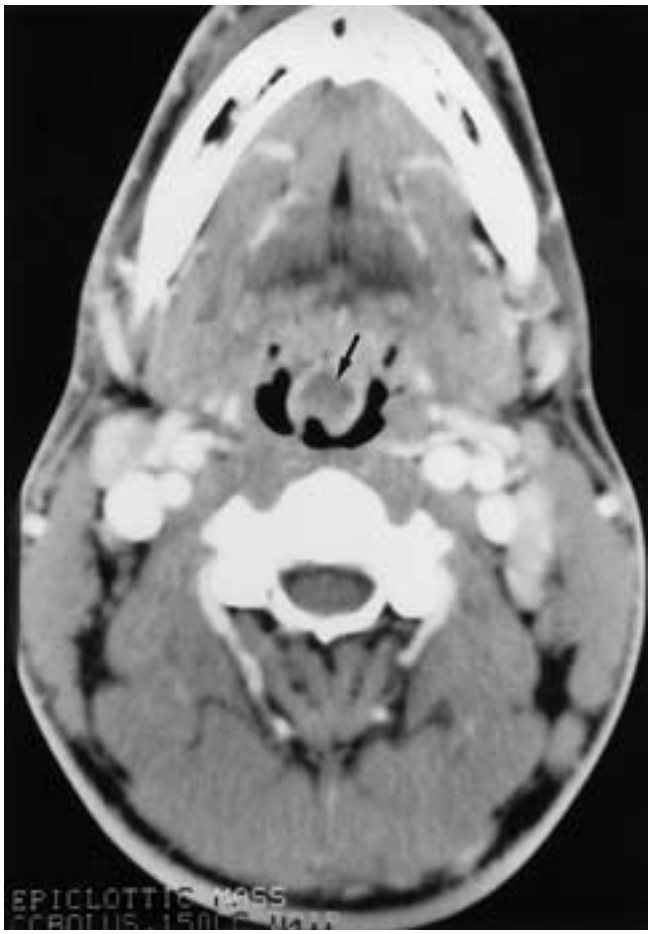

VIEW IMAGE

FIGURE 29-74 Epiglottic abscess in an adolescent with severe sore throat. Axial contrast-enhanced CT shows a mass in the epiglottis (*arrow*), with partial airway obstruction. At surgery this was found to be an epiglottic abscess.

Mucosal edema has a significant effect in the subglottic larynx. The loosely attached mucosa at this level helps make this portion of the airway especially vulnerable to compromise. However, unlike epiglottitis, infectious LTB is generally a benign process that occurs primarily in younger children 1 to 3 years of age.[206] There is gradual onset of upper or lower respiratory tract symptoms, followed by the development of a classic barking, brassy cough and intermittent inspiratory stridor. Drooling and odynophagia are uncommon.

The radiographic appearance of LTB is variable, depending on the amount of edema and the phase of respiration during which the film is acquired. Plain films should be interpreted within the context of the clinical setting. The sensitivity and specificity of radiographs in croup have been reported to be low and may be more valuable in excluding other causes of airway obstruction such as a foreign body or bacterial epiglottitis.[207] Inspiratory plain films show ballooning and overdistention of the hypopharynx, with narrowing of the subglottic region and collapse of the cervical trachea.[208] During expiration, overdistention of the cervical trachea, probably secondary to laryngeal obstruction, may be seen.[209] The vocal cords and larynx appear poorly defined. On the AP examination the subglottic region is narrowed for 1 to 2 cm (the *steeple sign*), a finding that does not vary significantly between inspiration and expiration (Fig. 29-75).[209] The epiglottis and aryepiglottic folds are normal, which excludes epiglottitis.

LTB is managed with humidification, hydration, and, in some cases, corticosteroids and nebulized racemic epinephrine.[210] Intubation may be required for severe cases.

BACTERIAL TRACHEITIS

Bacterial tracheitis is an acute lower airway infection characterized by subglottic edema and purulent tracheal secretions and is usually due to infection with *S. aureus* or *H. influenzae*.[211] Widespread vaccination has nearly eradicated diphtheria, a common organism responsible for supraglottitis and laryngotracheitis in the early 1900s. Bacterial tracheitis is thought to arise as a secondary bacterial infection following viral LTB. The clinical course consists of a prodromal upper respiratory tract illness with stridor, fever, and variable respiratory distress.[211] Thick, purulent tracheal secretions, pseudomembranes, and ulcerated mucosa are characteristic endoscopic findings. Lateral plain films, although nonspecific, show narrowing and

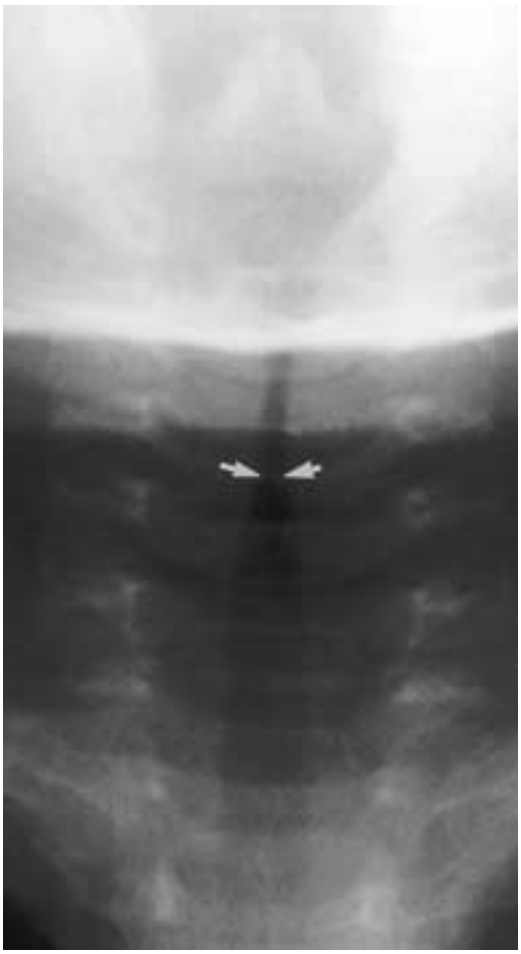

FIGURE 29-75 Laryngotracheal bronchitis in an 11-month-old boy. The AP plain film shows narrowing of the subglottic region, also called the *steeple sign* (*arrows*).

VIEW IMAGE

Copyright © 2003, Mosby, Inc. All rights reserved.

irregularity of the subglottic airway (Fig. 29-76), usually with a normal epiglottis and aryepiglottic folds. Treatment consists of establishment of an airway, frequent tracheal suctioning, and appropriate antimicrobial therapy.

MISCELLANEOUS CONDITIONS

Hereditary angioneurotic edema, a rare autosomal dominant disease, is due to a deficiency of C1 esterase inhibitor. Lack of this inhibitor leads to vascular damage, and the child presents with recurrent urticaria, subcutaneous soft-tissue swelling, and airway obstruction secondary to edema of the epiglottis and aryepiglottic folds.[202] The clinical setting helps differentiate this cause of airway obstruction from acute epiglottitis.

Thickening of the epiglottis and aryepiglottic folds may occur following radiation therapy for head and neck neoplasms. The laryngeal structures are symmetrically thickened, with stranding of the paraglottic fat. Chronic stenosis of the airway may also occur (Fig. 29-77).

Wegener's granulomatosis is a necrotizing vasculitis that is characterized by inflammatory lesions, usually granulomas or areas of necrosis, in the respiratory tract and kidneys.

VIEW IMAGE

FIGURE 29-76 Staphylococcal laryngotracheitis in a 6-month-old boy who presented with fever and respiratory distress. The lateral plain film of the neck reveals thickening of the retropharyngeal soft tissues, epiglottis, and aryepiglottic folds (*arrow*) and diffuse narrowing of the trachea (*open arrow*).

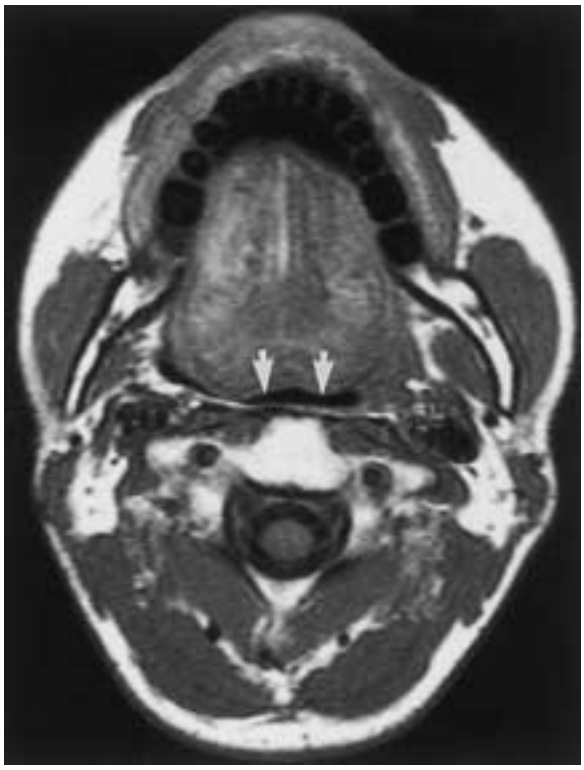

FIGURE 29-77 Radiation-induced oropharyngeal stenosis in a teenager who was irradiated as a child for rhabdomyosarcoma. Axial T1-weighted MR image reveals severe narrowing and asymmetry of the oropharynx (*arrows*).

VIEW IMAGE

Subglottic stenosis is a well-known manifestation of Wegener's granulomatosis in the pediatric population.[212] Tracheal stenosis causing stridor may also occur.[213] The differential diagnosis includes sarcoidosis, amyloidosis, and relapsing polychondritis, all uncommon pediatric lesions.[214]

SECTION SEVEN

TRAUMA

FACIAL TRAUMA

Direct trauma to the head and neck can affect the airway because of mass effect or distortion from hematoma, displaced bone fragments, and soft-tissue swelling. Clinical examination is the method of choice for establishing a diagnosis of nasal fracture or septal hematoma, although occasionally a nondisplaced fracture that is not palpable will be demonstrated radiographically. Fractures of the nose in younger children are poorly demonstrated due to the predominantly cartilaginous nasal framework and the presence of unfused nasal sutures.[215] Imaging, especially CT, may be useful for evaluating the complications of nasal trauma including nasal deformity and obstruction, secondary infection, septal hematoma (Fig. 29-78), and subsequent avascular necrosis of the nasal septal cartilage. In contrast to nasal fractures, imaging is helpful in the evaluation of acute

Copyright © 2003, Mosby, Inc. All rights reserved.

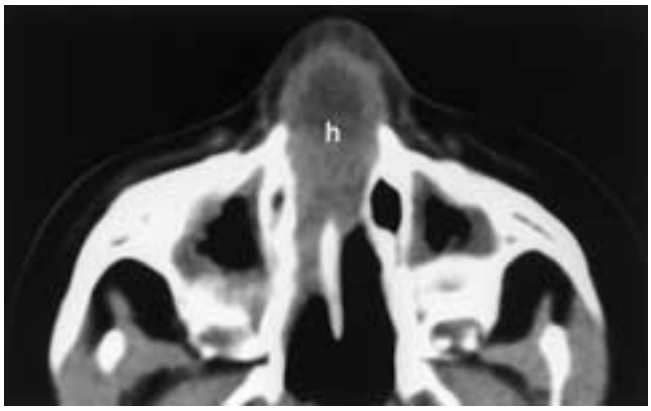

VIEW IMAGE

FIGURE 29-78 Nasal septal hematoma in a 2-year-old boy with facial trauma. Axial CT reveals the mixed-attenuation subacute nasal septal hematoma (*h*) obstructing the nasal airway.

nasoethmoidal and facial fractures. Axial 3 mm CT images should be obtained initially. Direct coronal images are obtained once the patient's cervical spine has been evaluated and spinal fracture or ligamentous instability has been excluded. Injuries to the nasoethmoidal, sphenoid, and frontal regions carry the additional risk of cerebrospinal fluid leak and posttraumatic meningoencephalocele. Mandibular fractures are often best assessed with panoramic radiographs and plain films.[216]

OROPHARYNGEAL TRAUMA

Penetrating oropharyngeal injury in children is common and is usually the result of impalement by a foreign object that was in the mouth at the time of a fall (e.g., lollipop or popsicle stick, toothbrush or pencil). The oropharyngeal injury ranges from a puncture wound with palatal or pharyngeal hematoma to a severe laceration. Complications of penetrating injuries include infection, subcutaneous emphysema, and vascular injuries with potential neurologic sequelae. The types of vascular injury include intimal dissection, transection, laceration, arteriovenous fistula formation, and pseudoaneurysm. Due to the proximity of the carotid artery to the lateral oropharynx, even apparently innocuous injuries can injure the vessel. Intimal dissection can lead to dissecting aneurysm or the formation of mural thrombus, with subsequent embolic cerebral infarction. Neither the mechanism of injury nor the degree of injury correlates with the potential for neurovascular sequelae, although there should be an increased index of suspicion with lateral oropharyngeal injuries.[217] In addition, neurovascular involvement may not become clinically apparent until days or weeks after the incident.

The radiographic evaluation and clinical management of penetrating oropharyngeal injury are controversial. Conventional angiography has been considered to be the examination of choice for the accurate diagnosis of arterial injuries if an abnormality is suspected clinically and immediate surgical intervention is not required.[218] An added benefit of the examination is the potential for endovascular intervention in selected cases. However, there are potential complications of conventional angiography, including stroke.

Cross-sectional imaging is useful for delineating the trajectory of the penetrating injury (Figs. 29-79 and 29-80) and provides objective evidence of proximity and actual injury to neck vessels (Fig. 29-81).[219] Penetrating injuries are often accompanied by extensive extraluminal air (Fig. 29-82). The sensitivity and specificity of helical CT are high for the detection of arterial occlusion, pseudoaneurysm, and arteriovenous fistula in teenagers and adults.[218] Helical CT images are rapidly obtained, and the modality is less invasive and less expensive than conventional angiography. However, the disadvantages compared with conventional angiography include the requirement of a higher volume of contrast agent, lower spatial resolution, potential degradation of image quality from imaging artifacts, and lack of immediate potential for endovascular intervention.[218]

MR angiography has been used to detect arterial injuries but not specifically penetrating or blunt trauma of the neck in children. The disadvantages of MR angiography include the need for patient monitoring and transport for the acutely ill patient, artifact caused by retained foreign body, and the presence of subcutaneous emphysema or air surrounding the great vessels.

LARYNGEAL AND TRACHEAL TRAUMA

The high position of the pediatric larynx, its mobility, and its flexibility make it less vulnerable or susceptible to blunt

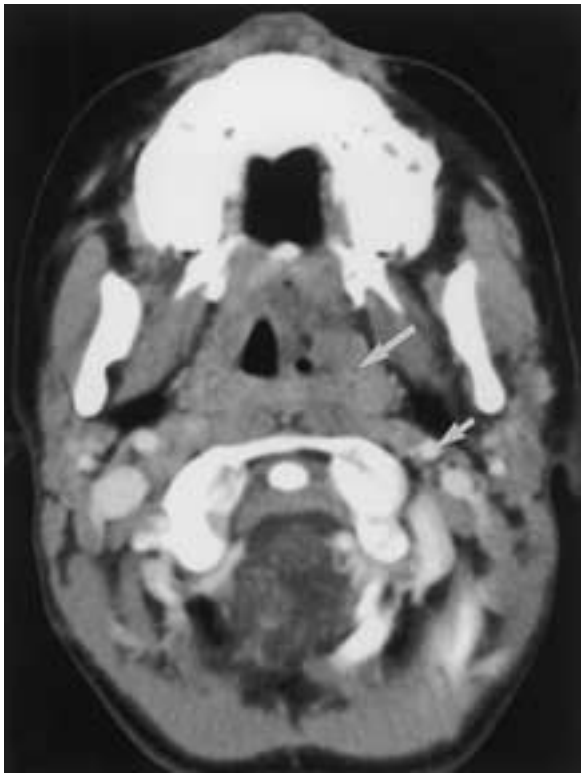

FIGURE 29-79 Oropharyngeal trauma in a toddler who fell with a toothbrush in his mouth. Contrast-enhanced CT reveals asymmetric thickening of the left pharyngeal mucosa and distortion of the airway but no extravasation of air (*long arrow*). The left internal carotid artery appears slightly smaller than the right (*short arrow*).

VIEW IMAGE

Copyright © 2003, Mosby, Inc. All rights reserved.

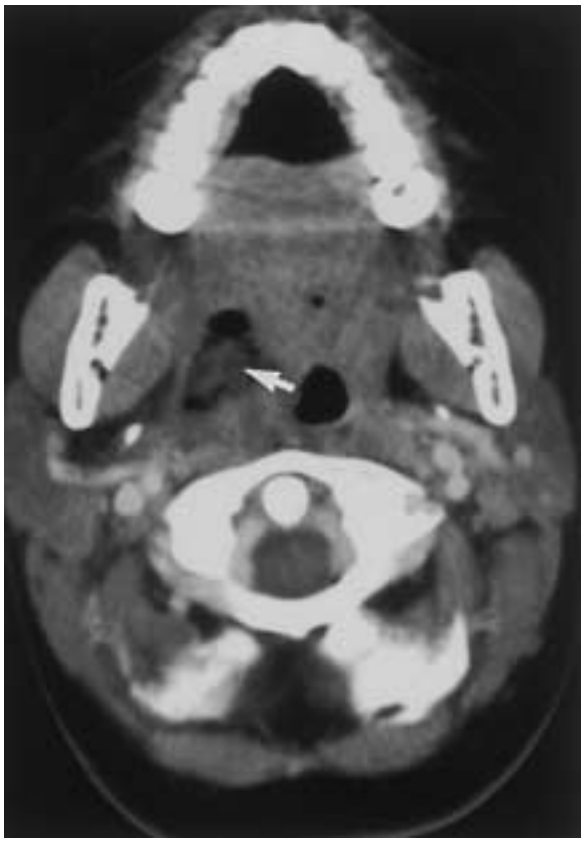

VIEW IMAGE

FIGURE 29-80 Penetrating injury to the tonsil in a 10-year-old child. On contrast-enhanced CT there is gas and low-attenuation change within the right tonsil indicating the trajectory of the injury (*arrow*).

nonpenetrating trauma than the adult larynx.[220] However, the submucosal tissues of the pediatric larynx are loosely attached to the underlying perichondrium, and there is a relative lack of fibrous tissue. These features predispose the pediatric larynx to massive soft-tissue swelling with edema or hemorrhage and significant functional consequences.[221] The mechanism of injury is often a direct blow to the child's extended neck, for example, against the dashboard of the car or against the handlebars of a bicycle. The laryngeal injury may not be recognized initially. Delayed recognition and treatment may result in chronic stenosis.

Acutely, the injury may result in contusion, hematoma, edema, or airway laceration. Additional injuries include arytenoid dislocation, recurrent laryngeal nerve injury (Fig. 29-83), true or false vocal cord avulsion, disruption of the thyroepiglottic ligament with posterior displacement of the epiglottis, and laryngotracheal separation.[221] Endoscopy and emergent tracheotomy are performed if complete or severe airway obstruction results. Endoscopic findings of laryngeal trauma include mucosal tears, hematomas, edema, immobile vocal cords, or cartilaginous fractures or dislocation, including cricoarytenoid disarticulation.[222] The endoscopic evaluation of partial airway obstruction, odynophagia, or hoarseness is limited when there is severe edema or blood in the endolaryngeal structures, and plain radiographs or CT may be requested. The advantage of CT in this setting is its ability to display the soft-tissue structures, and it is considered the definitive radiographic method for evaluating

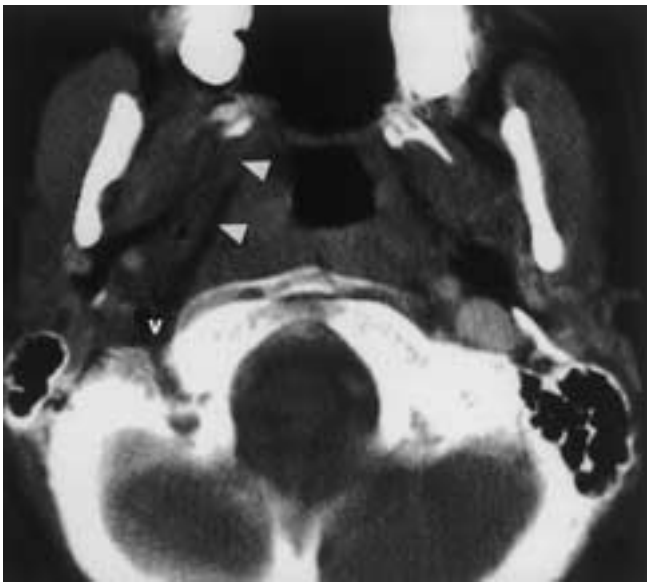

FIGURE 29-81 Popsicle-stick injury in a 7-year-old girl. Axial contrast-enhanced CT reveals the low-attenuation retained popsicle stick (*arrowheads*) within the soft tissues lateral to the pharynx, terminating in the expected location of the right internal jugular vein (*v*), which was thrombosed.

VIEW IMAGE

the injured larynx.[223] To best evaluate the noncalcified laryngeal cartilages in a child, delayed contrast-enhanced 1 to 3 mm helical axial images of the larynx should be obtained.

Edema, contusion, or laryngeal hematoma appears radiographically as swelling of the involved portion of the airway. Cervical or mediastinal emphysema suggests an

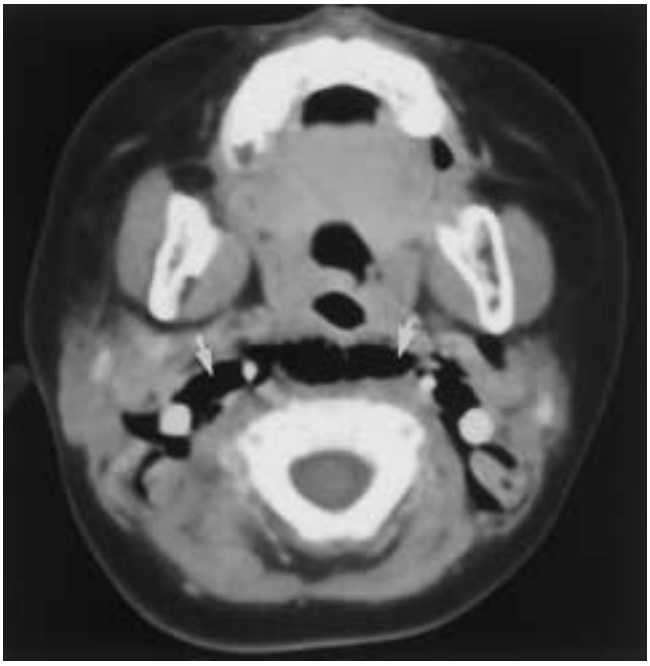

FIGURE 29-82 Penetrating injury in a 4-year-old boy who fell with a sharp stick in his mouth, puncturing his pharynx. Axial contrast-enhanced CT demonstrates extensive extraluminal air (*arrows*).

VIEW IMAGE

Copyright © 2003, Mosby, Inc. All rights reserved.

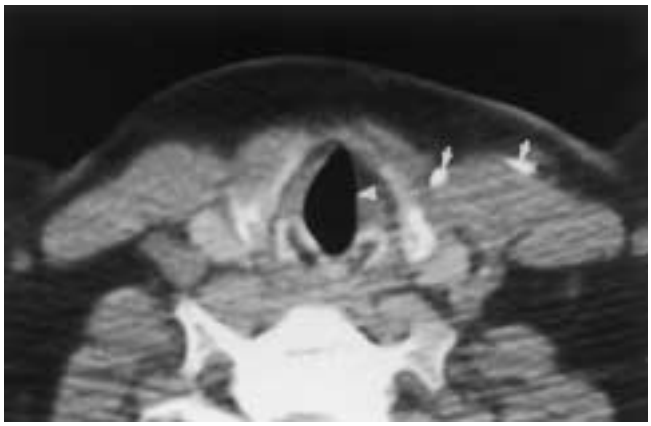

VIEW IMAGE

FIGURE 29-83 Vocal cord paralysis following insertion of a vagal nerve stimulator for refractory seizures. Axial CT reveals the radiopaque vagal nerve stimulator (*arrows*). The left vocal cord is paralyzed and does not abduct (*arrowhead*).

esophageal or laryngeal laceration or a laryngeal fracture (Fig 29-84). In the unusual instance that MR imaging is performed, edema of the injured laryngeal structure has a high T2-weighted signal intensity (Fig. 29-85). The degree and level of airway obstruction should be noted. Hyoid bone fracture can be detected on plain films and on CT. The epiglottis may be displaced posteriorly by edema or hematoma. Other cartilaginous fractures are difficult to detect in the noncalcified pediatric larynx, but they may be clinically suspected because of an abnormal thyroid eminence or an abnormal endoscopic airway contour.

Tracheal or laryngotracheal transection is a life-threatening injury and carries a high mortality. If the transection occurs at the thyrohyoid ligament, the supraglottic muscles pull the hyoid bone superiorly, and this can be seen on plain films.[224] Transection or avulsion of the recurrent laryngeal nerves is a complication of laryngotracheal transection, and vocal cord paralysis may be a chronic problem if the patient survives the initial injury.[225] Plain films or 2D coronal reformatted CT images show an increase in the craniocaudal extent of the larynx, as well as disruption of the tracheal air column.

Tracheal injuries or rupture from blunt trauma is not common but should be suspected with severe injury to the neck or chest.[226] Persistent pneumomediastinum or pneumothorax that is not relieved by a thoracotomy tube may be the only sign. Rupture of the anterior portion of the cervical trachea after severe coughing with the neck in extension has

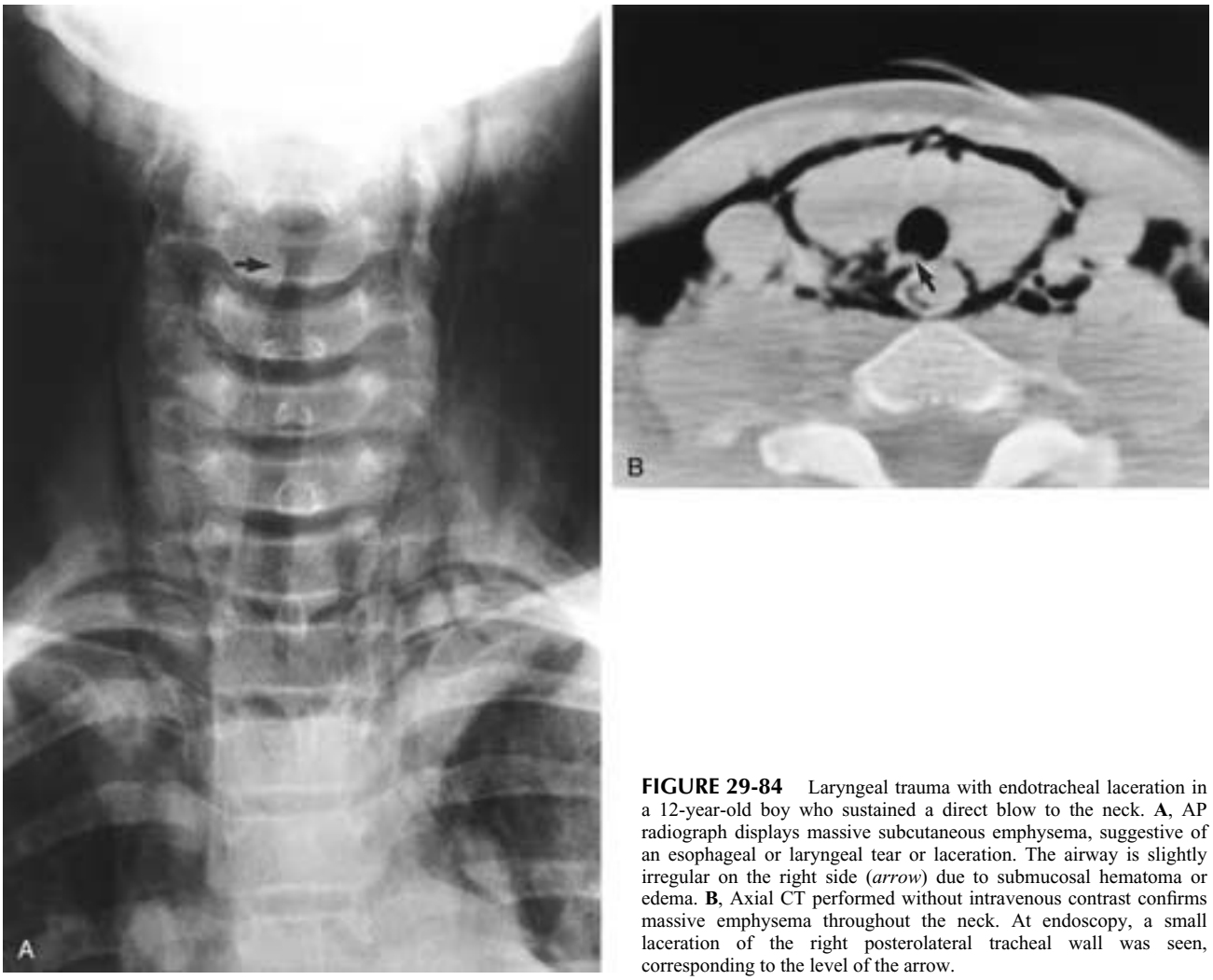

FIGURE 29-84 Laryngeal trauma with endotracheal laceration in a 12-year-old boy who sustained a direct blow to the neck. **A**, AP radiograph displays massive subcutaneous emphysema, suggestive of an esophageal or laryngeal tear or laceration. The airway is slightly irregular on the right side (*arrow*) due to submucosal hematoma or edema. **B**, Axial CT performed without intravenous contrast confirms massive emphysema throughout the neck. At endoscopy, a small laceration of the right posterolateral tracheal wall was seen, corresponding to the level of the arrow.

VIEW IMAGE

Copyright © 2003, Mosby, Inc. All rights reserved.

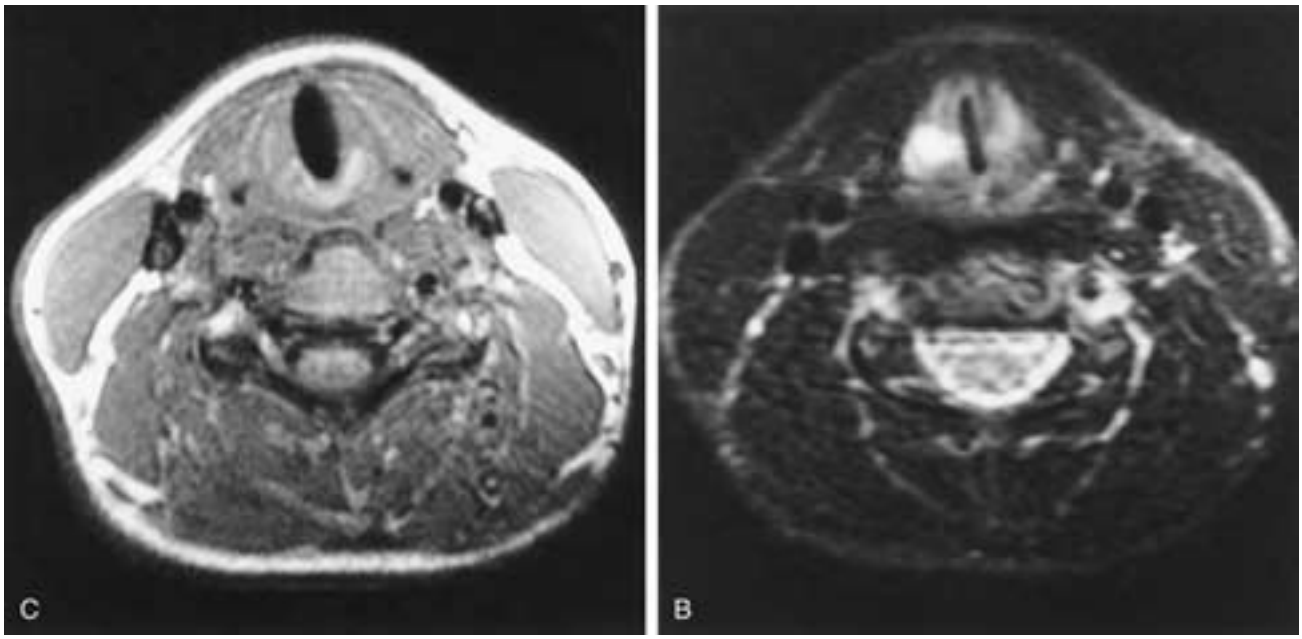

VIEW IMAGE

FIGURE 29-85 Contusion of the right true vocal cord in a 17-year-old girl who sustained a direct blow to the larynx in an automobile accident and complained of hoarseness. **A**, T1-weighted axial image shows mild fullness in the right true vocal cord. Note the normal high-signal intensity in the thyroid and cricoid cartilages and the oval contour of the airway. **B**, T2-weighted image obtained at the same level shows high-signal edema in the true vocal cord.

been described as ''subcutaneous rupture'' and results in extensive cervical emphysema (Fig. 29-86).[226]

THERMAL TRAUMA AND CAUSTIC INGESTION

Laryngeal edema and obstruction can result from accidental inhalation of steam, hot particles such as ash, or scalding liquids.[226, 227] The supraglottis receives the brunt of exposure to thermal or caustic substances and is thus the most commonly injured region of the pediatric airway. Mild supraglottic edema resolves with conservative therapy and does not require imaging. Severe cases share similar clinical features with acute infectious epiglottitis and are best served by immediate endotracheal intubation or direct laryngoscopy, depending on the presence and severity of respiratory distress.[228] Caustic ingestion of acidic or basic substances may cause significant injury to the airway. The most severe injuries result from ingestion of large quantities of industrial-strength alkali or direct aspiration of caustic substances. Usually the degree of oral mucosal injury does not reflect the severity of the laryngeal burn.

Plain films in children with thermal trauma or caustic ingestion are nonspecific and may show thickening of the laryngeal structures simulating epiglottitis or croup (Fig. 29-87). In more severe cases, pharyngeal stenosis may occur because of scarring. If aspiration occurs, significant glottic, subglottic, and tracheal injury may result, with the potential for permanent subglottic or tracheal stenosis.

INTUBATION TRAUMA

Complications of intubation most commonly occur at the glottic or subglottic level. Acute injuries from intubation occur at predictable locations, including the medial surface of the arytenoids, the cricoarytenoid articulation, the posterior commissure, and the anterior surface of the cricoid lamina.[229] Acute changes, which may be visualized endoscopically, include edema and hyperemia, mucosal erosion, and ulceration. Granulation tissue, intubation granulomas, glottic webs, submucosal cysts, and vocal cord immobility may eventually develop. Traumatic intubation may also dislocate one of the arytenoids or may fracture the cricoid. Endotracheal intubation is the most common cause of acquired subglottic stenosis.[230] However, there are other important etiologic risk factors, including gastroesophageal reflux, sepsis, low birth weight, and frequent self-extubations; the exact role of each of these risk factors is unknown.[231]

Stridor or hoarseness after extubation suggests a complication of intubation. Although imaging may be used to help localize the problem, endoscopy is the mainstay of diagnosis.

An intubation granulation may be focal or nodular, and it occurs most commonly at the vocal process of the arytenoid.[229] Airway fluoroscopy shows a focal mass projecting into the airway at the glottic level. Ischemic pressure necrosis from an endotracheal tube may result in posterior wall granulation tissue, which may lead to glottic stenosis. On imaging this will appear as airway narrowing at the glottic level.

Subglottic cysts are rare acquired retention cysts that usu-

Copyright © 2003, Mosby, Inc. All rights reserved.

VIEW IMAGE

FIGURE 29-86 Spontaneous subcutaneous emphysema following paroxysmal coughing in a 19-year-old girl. Lateral radiograph shows massive air in the retropharyngeal space and soft tissues of the neck. The patient noted crepitus in the neck following a paroxysm of coughing during an upper respiratory tract infection. The air gradually resolved.

ally follow long-term intubation in neonates (Fig. 29-88). The mechanism of formation is fibrosis and obstruction of the mucous glands with subsequent cyst formation.[232] Asymmetric subglottic narrowing may be seen on AP plain films and can mimic a subglottic hemangioma.[232]

The severity or extent of acquired subglottic stenosis may be determined on plain films or fluoroscopy of the airway. CT and MR imaging are usually not performed to evaluate intubation-related complications. Imaging is important, however, when there is complete or severe laryngeal stenosis and it is difficult to determine endoscopically the length of the stenosis. Helical CT with 2D coronal reformatted images and direct coronal MR imaging are helpful in evaluating severe grades of laryngotracheal stenosis and demonstrate the length of stenosis. The cross-sectional area of the airway can also be determined using either CT or MR imaging (Fig. 29-89). In this clinical setting, intravenous contrast is not required.

A tracheotomy often results in similar acquired lesions in the airway, including stomal and distal tracheal granulomas, subglottic stenosis, and collapse of the anterior tracheal wall.[233] The radiographic appearance of these lesions is similar to that of postintubation lesions (Fig. 29-90).

INGESTED OR ASPIRATED FOREIGN BODY

The majority of foreign bodies that are ingested pass undetected into the stool. Occasionally foreign bodies become impacted within the aerodigestive tract. The clinical presentation of foreign bodies lodged in the pharynx depends on the age of the patient and the site and morphology of the object. Older patients generally volunteer a history and complain of symptoms such as a pricking pain sensation, odynophagia, and a lump in the throat. Younger patients may simply refuse to eat, and blood-stained saliva may be observed.[234] Fish bones and radiolucent foreign bodies are associated with an increased risk of complications in patients under the age of 10 years.[235] Ingested sharp bones, which tend to lodge in the oropharynx or tonsils, can penetrate the mucosa and provoke local inflammatory complications such as retropharyngeal abscess. Foreign objects that are lodged in the oropharynx are amenable to direct inspection and removal with the aid of a tongue depressor or laryngoscope.[234] Other objects can be removed via transnasal flexible endoscopy. Plain films should be

FIGURE 29-87 Thermal inhalation injury in a 3-year-old boy who aspirated hot ashes through a straw. Severe perioral burns and respiratory distress were noted on presentation. Lateral radiograph in hyperextension shows marked thickening of the epiglottis and aryepiglottic folds (*arrows*).

VIEW IMAGE

Copyright © 2003, Mosby, Inc. All rights reserved.

VIEW IMAGE

FIGURE 29-88 Acquired subglottic cyst caused by long-term intubation in a 7-month-old boy who was born prematurely and required intubation for several months. The patient now has intermittent respiratory distress. Oblique film obtained during airway fluoroscopy shows a mass (*arrow*) projecting from the posterior wall at the subglottic level. Endoscopy showed a benign subglottic cyst.

reserved for patients in whom pain indicates obstruction below the level of the cricoid and for children with persistent symptoms despite a negative physical examination.[234] Contrast-enhanced CT should be performed if local complications such as abscess formation are suspected at the time of presentation or following removal of the foreign body.

Laryngotracheal inhaled foreign bodies are less common than bronchial foreign bodies, accounting for fewer than 20% of all aspirations.[236] However, because of the potential for complete airway obstruction, laryngotracheal foreign bodies are more hazardous than those lodged in a bronchus. The clinical presentation is generally obvious with severe airway obstruction and stridor.

Plain films of the neck detect foreign bodies that are radiopaque and help exclude croup, although subglottic edema and swelling may be seen with laryngotracheal foreign bodies.[237] Coins, pen caps, screws, pins including open safety pins, and small toy objects are common radiopaque foreign bodies that may lodge in the larynx,

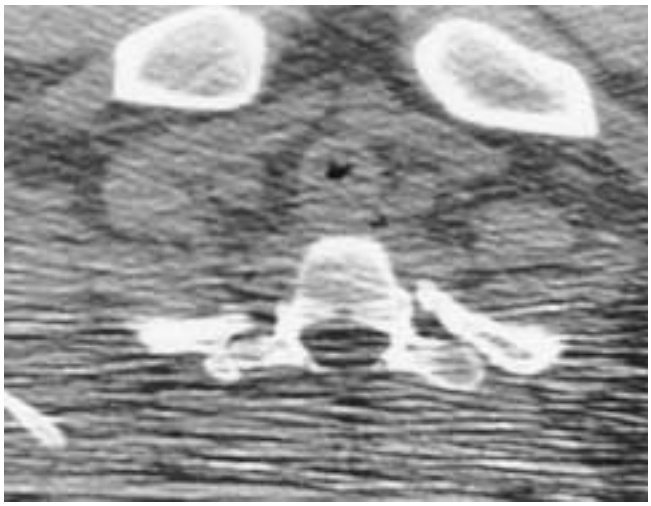

FIGURE 29-89 Circumferential granulation tissue causing tracheal stenosis in an 18-year-old boy with Down's syndrome and a history of long-term intubation following cardiac surgery. The patient now has intermittent respiratory distress. Spiral 1 mm thick axial CT scan shows circumferential endotracheal soft tissue causing marked airway compromise. The scan was performed during quiet respiration.

VIEW IMAGE

FIGURE 29-90 Tracheal granuloma after a tracheostomy tube in a 20-month-old boy with respiratory distress following decannulation. Lateral plain film shows a smooth mass in the cervical trachea (*arrow*).

VIEW IMAGE

Copyright © 2003, Mosby, Inc. All rights reserved.

trachea, or bronchi (Fig. 29-91). However, a significant proportion of foreign bodies, especially food particles such as peanuts or small vegetable matter, may not be seen, even with magnification views.[237] In this situation, indirect signs of aspiration such as subglottic swelling or airway narrowing should be reported.[238] Both AP and lateral neck films should be obtained to localize the object to the larynx or the esophagus and to determine the contour of the foreign body.

Unlike foreign bodies lodged within the upper airway, bronchial foreign bodies may present more insidiously. Smaller objects and particulate matter usually lodge in the distal bronchi. If the symptoms are mild, diagnosis may be delayed by weeks to months. As the aspiration is often not witnessed and physical findings are subtle, radiographs are an important part of the patient's evaluation.

In most cases, radiographic diagnosis is based upon changes secondary to unilateral obstruction of the airway. Partial occlusion of the bronchus produces a ball-valve effect with distal air trapping. This results in unilateral emphysema, mediastinal shift, and a decrease in pulmonary blood flow to the affected side. In the uncooperative child, lateral decubitus views usually suffice. Bronchial foreign bodies that have been present for longer periods may cause chronic inflammation in the bronchial lumen and complete bronchial obstruction, resulting in atelectasis, infiltrates, or effusions. However, in this situation it is also possible to have minimal radiographic findings. For instance, bilateral bronchial foreign bodies may not result in mediastinal shift or signs of air trapping. Endoscopy should be performed whenever clinical suspicion is high.

VIEW IMAGE

FIGURE 29-91 Aspirated foreign body in a young child with respiratory distress and dysphagia. The straight pin lodged obliquely in the vallecula is well seen on this lateral radiograph. AP examination should always follow the lateral film to lateralize and determine the width of the foreign body.

VIEW IMAGE

FIGURE 29-92 Esophageal foreign body, with perforation and abscess formation, in a young child who presented with respiratory distress. Lateral film from a barium swallow examination shows marked prevertebral soft-tissue swelling. A collection of barium is seen extending five vertebral bodies in length, which was caused by posterior esophageal wall perforation by a foreign body. The edema and the collection caused a mass effect on the airway, resulting in the presenting symptoms of airway compromise.

An esophageal foreign body may also present with airway obstruction secondary to direct pressure on the posterior larynx or trachea.[239] Impaction most commonly occurs at or just below the level of the cricopharyngeus muscle.[240] If the foreign body ulcerates and perforates the esophagus, the edema and inflammatory response may compromise the airway. Plain films are important for evaluating esophageal foreign bodies because most are coins. A barium swallow usually is performed to show the site of perforation and extravasation, and if perforation is likely, this study should be performed with water-soluble nonionic contrast (Fig. 29-92).[207] An esophageal stricture following a surgical repair for a congenital lesion such as esophageal atresia predisposes to obstruction by an esophageal foreign body.[201] A barium swallow helps delineate the location and extent of the stricture.

MISCELLANEOUS CONDITIONS

Nasopharyngeal stenosis, a rare cause of airway compromise, usually results from scarring after tonsillectomy and adenoidectomy, especially when surgery involved aggres-

Copyright © 2003, Mosby, Inc. All rights reserved.

sive circumferential cauterization of the nasopharyngeal tissues. Before the widespread availability of antibiotics, nasopharyngeal stenosis was a complication of syphilis or tuberculosis of the pharynx. Fusion of the soft palate and tonsillar pillar to the posterior pharyngeal wall causes complete or partial obstruction. Patients present with respiratory distress and nasal obstruction weeks to months after surgery. The diagnosis is usually made by the clinical history and endoscopy. Plain films may demonstrate narrowing or complete nasopharyngeal obstruction. Treatment involves pharyngoplasty with laterally based pharyngeal flaps.[201]

SECTION EIGHT

BENIGN TUMORS AND TUMOR-LIKE CONDITIONS

ADENOIDAL AND TONSILLAR HYPERTROPHY

Hypertrophy of the adenoids and palatine tonsils is common in the pediatric population. Adenoidal enlargement produces chronic nasal and nasopharyngeal obstruction and sometimes impairment of the ability to smell.[241] Clinical symptoms include a ''mouth-open'' posture, mouth breathing, hyponasal speech, and nocturnal snoring. Airway compromise or dysphagia caused by palatine tonsillar hypertrophy in the child is also common.[242] Less commonly, lingual tonsillar hypertrophy may be associated with airway obstruction.[243] Symptoms of airway obstruction from enlarged tonsils include obstructive sleep apnea and/or snoring, restless sleep, irritability, or decreased alertness.[244]

Although various measurements and ratios have been described to determine the normal adenoidal size, correlation of preoperative radiographic adenoidal size with surgical observations and specimens varies from excellent to poor.[245, 246] A lateral radiograph should be obtained during inspiration through the nose, with the mouth closed. The adenoid to nasopharyngeal (AN) ratio may aid in diagnosing prominent, clinically significant adenoids (Fig. 29-93).[247] Using this method, adenoidal hypertrophy can be reliably diagnosed in a symptomatic patient when the AN ratio is 0.8 or greater (Fig. 29-94).[247] Obstructive symptoms are not generally seen in patients with an AN ratio less than 0.5.[15] Because tremendous variation in adenoidal size exists in the normal pediatric patient, any measurement should be used with caution and clinical symptoms must always be considered. In assessing for obstruction, the airway anterior (between the anterior border of the adenoids and the posterior border of the maxillary antra) and inferior to the adenoids (from the inferior border of the adenoids to the superior border of the soft palate) should be assessed.[241] In certain craniofacial syndromes such as trisomy 21, because of the smaller nasopharyngeal size, a lower AN ratio may be clinically significant.[242] The presence of small mucous retention cysts within the adenoids is not uncommon and should not be mistaken for tumor (Fig. 29-95).

Palatine tonsillar hypertrophy appears as smooth, rounded, or oval soft-tissue masses on either side of the oropharynx, bulging into the pharyngeal column (Fig. 29-12). Sagittal MR images, obtained just off the midline, show similar findings, with the fullness in the tonsillar fossa being isointense to pharyngeal musculature on T1-weighted images and hyperintense to muscle on T2-weighted images (Fig. 29-14). On CT, palatine tonsillar tissue is isodense to the surrounding musculature. On MR imaging and CT, hypertrophic lingual tonsils are similar in appearance to palatine tonsils, but they occur at the tongue base, often filling the vallecula (Fig. 29-13).

The main indications for adenoidectomy, tonsillectomy, or adenotonsillectomy in childhood are recurrent infection and obstructive tonsillar and/or adenoidal enlargement.[244, 248] Infections include febrile tonsillitis (more than three episodes per year), peritonsillar abscess, and persistent or recurrent otitis media.

RECURRENT RESPIRATORY PAPILLOMATOSIS

Recurrent respiratory papillomatosis (RRP) is the most common benign neoplasm of the larynx in children and the second most frequent cause of childhood hoarseness.[249] The disease is caused by the human papilloma virus (HPV).[250, 251] RRP in children has been linked to maternal genital HPV infections, and vertical transmission of the virus has been observed.[252] However, few children exposed to genital warts at birth develop clinical symptoms.[253] RRP is generally diagnosed between 2 and 4 years of age.[251] Although the course of the disease is variable, there is a tendency for recurrence and for dissemination of lesions throughout the respiratory tract. Although spontaneous

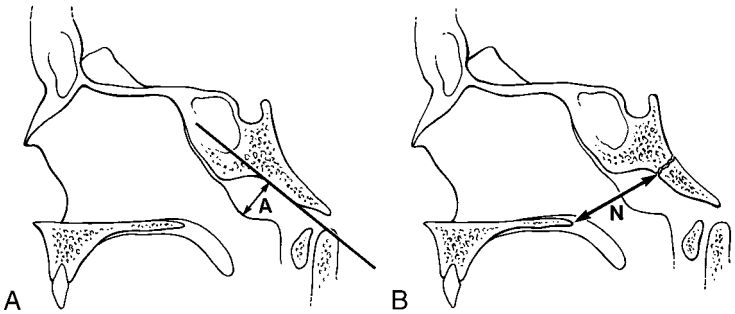

FIGURE 29-93 The AN ratio may be helpful in determining adenoidal size on the lateral radiograph. In the symptomatic child (with obstructive sleep apnea or recurrent otitis media), a ratio greater than 0.8 is considered abnormal. **A**, Adenoidal measurement. The distance (*A*) between the maximum convexity of the adenoids and a line drawn along the basiocciput is measured. **B**, Nasopharyngeal measurement. The distance (*N*) between the posterior hard palate and the sphenooccipital synchondrosis is determined. (From Fujioka M et al. Radiographic evaluation of adenoidal size in children: adenoidal-nasopharyngeal ratio. AJR 1979;133:401–404.)

VIEW IMAGE

Copyright © 2003, Mosby, Inc. All rights reserved.

VIEW IMAGE

FIGURE 29-94 Adenoidal hypertrophy in a 5-year-old boy with obstructive sleep apnea. Lateral plain film shows prominent adenoidal tissue (*arrows*) filling the posterior nasopharynx and narrowing the airway.

remission has been documented, childhood-onset RRP is more aggressive than its adult counterpart.[254] The papilloma lesions may be pedunculated or sessile and often occur in irregular exophytic clusters. Squamous cell carcinoma occasionally arises in RRP in the absence of known risk factors such as radiation therapy and smoking.[255, 256]

The classic symptoms of RRP are progressive hoarseness, stridor, and respiratory distress.[254] Because growth of the papillomas is gradual, acute airway obstruction is rare. Papillomas are often multiple and most commonly occur at the glottic level, but they can be found virtually anywhere in the aerodigestive tract.[257] Recurrent disease is often subglottic.[258] The preoperative diagnosis of RRP is best made with flexible fiberoptic endoscopy. Plain films show small, pedunculated nodular masses within the airway (Fig. 29-96). CT and MR imaging may show small nodules adherent to the airway wall and projecting into the lumen. Larger recurrent lesions may have transbronchial spread, with formation of lung masses and cavities.

No single treatment appears to be consistently effective in the eradication of RRP. The goal of therapy is complete surgical removal of papillomas with preservation of normal structures. The CO_2 laser has been the instrument most commonly used for surgical treatment. Recently, endoscopic microdebriders have also been used to debulk larger lesions and may cause less laryngeal scarring than CO_2 lasers.[254] Many adjuvant therapies have been evaluated, including antiviral and chemotherapeutic agents. The most commonly recommended adjuvant therapy is interferon.[259]

JUVENILE NASOPHARYNGEAL ANGIOFIBROMA

Juvenile nasopharyngeal angiofibroma (JNA) is a benign but aggressive vascular tumor found almost exclusively in adolescent males. Unilateral nasal obstruction and recurrent spontaneous epistaxis are the most common presenting symptoms.[260] JNA usually arises at the sphenopalatine foramen on the lateral nasopharyngeal wall. The tumor is locally destructive and spreads over time to involve contiguous structures: laterally the pterygopalatine and pterygomaxillary fissures and the infratemporal fossa; anteriorly the nasal fossa and maxillary antrum; and superiorly the ethmoid air cells, sphenoid sinus, orbit, cavernous sinus, and middle cranial fossa. Intracranial extension usually occurs via the superior orbital fissure. Although JNA is benign, it is extremely vascular, being primarily supplied by the ipsilateral internal maxillary artery, the ascending pharyngeal artery, and the palatine arteries. It also may recruit a vascular supply from the

FIGURE 29-95 Incidental adenoidal mucous retention cysts in a young boy. Coronal T2-weighted MR image obtained as part of a brain examination reveals rounded foci (*arrows*) within the adenoids that are isointense with CSF. The child also has adenotonsillar enlargement.

VIEW IMAGE

Copyright © 2003, Mosby, Inc. All rights reserved.

VIEW IMAGE

FIGURE 29-96 Laryngeal papillomatosis in a 2½-year-old child with stridor. Lateral plain film shows a glottic and supraglottic lobulated mass (*arrow*).

sphenoidal and ophthalmic branches of the internal carotid artery.[260]

The classic plain film findings include an ipsilateral nasal cavity and nasopharyngeal mass, widening of the pterygopalatine fossa, anterior displacement of the posterior wall of the maxillary sinus, erosion of the medial pterygoid plate, and extension of tumor to the sphenoid sinus. Axial and coronal CT images (3 mm slice thickness) are used to delineate bony erosion. Central skull base foramina and fissures that may be enlarged and/or eroded by pressure effects from the tumor include the sphenopalatine foramen, the foramen rotundum, the vidian canal, and the inferior and superior orbital fissures. On contrast-enhanced images there is immediate and intense tumor enhancement. On MR imaging the mass is generally heterogeneous, with prominent vascular flow voids (Fig. 29-97). One advantage of MR imaging over CT is the increased ability to differentiate obstructed secretions from intrasinus tumor. Conventional angiography shows the prominent vascular supply, usually from the ipsilateral external carotid artery branches but often involving the contralateral vessels as well. An internal carotid artery supply may be seen when the lesion has extended intracranially. A dense homogeneous blush persisting into the venous phase is typical.[261] Early draining veins are not common.

Treatment consists of surgical resection, often with preoperative embolization.[261] For patients with tumor involving the nasopharynx, nasal cavity, paranasal sinuses, and pterygopalatine fossa, the transnasal endoscopic technique offers minimally invasive resection of the entire tumor mass with minimal morphologic disturbance.[262] Radiation is not the primary treatment, but it may be considered in some cases.[263]

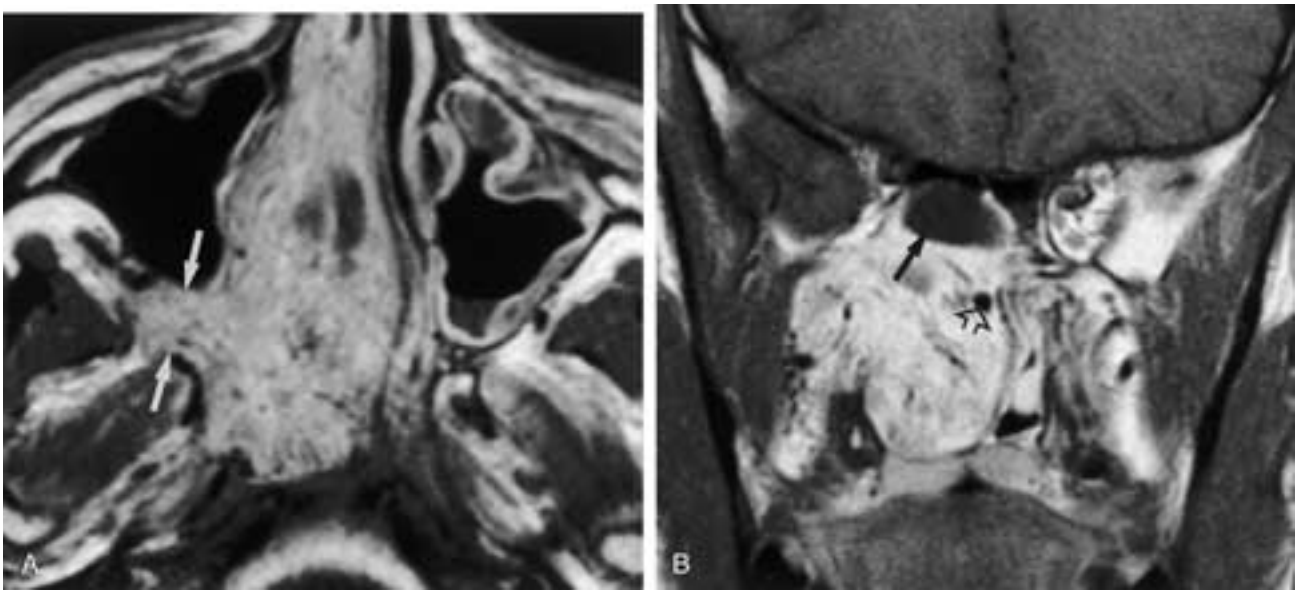

VIEW IMAGE

FIGURE 29-97 JNA in a 14-year-old boy with chronic nasal obstruction and epistaxis. **A**, Axial contrast-enhanced T1-weighted MR image shows an intensely enhancing tumor filling the right nasal cavity and deviating the nasal septum. The pterygopalatine fossa and pterygomaxillary fissure are widened and filled with tumor (*arrows*). There is anterior displacement of the posterior wall of the right maxillary antrum. **B**, The coronal contrast-enhanced T1-weighted image reveals flow voids within the tumor (*open arrow*). The cephalad extent of the tumor is well seen on the coronal images. There are retained secretions within the sphenoid sinus (*arrow*).

Copyright © 2003, Mosby, Inc. All rights reserved.

VIEW IMAGE

FIGURE 29-98 Antrochoanal polyp in a 14-year-old girl with troublesome snoring. **A**, Lateral plain film reveals a large opacity within the oropharynx and hypopharynx (*arrows*). **B,** Axial CT reveals the antrochoanal polyp filling the left maxillary antrum, left nasal cavity, and pharynx.

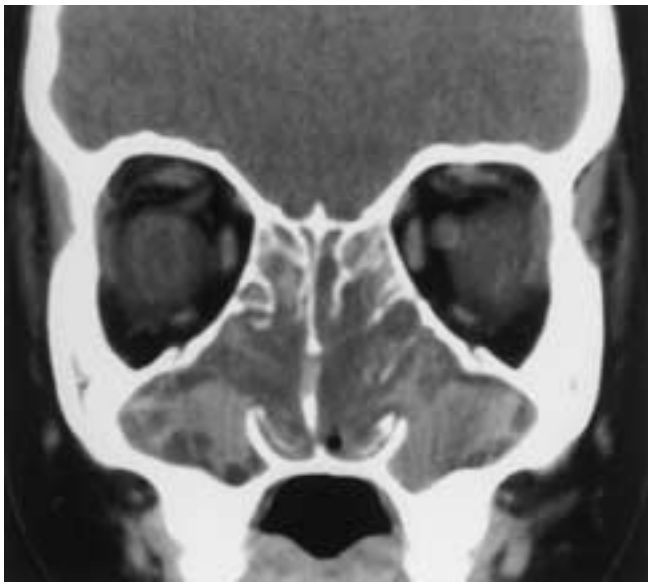

VIEW IMAGE

FIGURE 29-99 Cystic fibrosis in a teenager with nasal obstruction and a chronic cough. Coronal CT reveals foci of high density due to inspissated secretions with polypoid mucoperiosteal thickening within the paranasal sinuses protruding into and obstructing the nasal cavity.

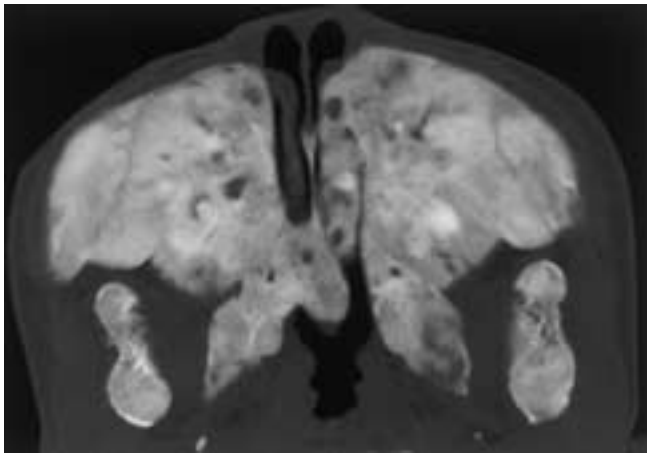

FIGURE 29-100 McCune-Albright syndrome in a 12-year-old boy with café au lait spots, polyostotic fibrous dysplasia, and precocious puberty. Axial CT reveals expansion with diffuse ground-glass opacification of the maxilla, pterygoid plates, mandible, and nasal turbinates. There is narrowing of the nasal cavity.

VIEW IMAGE

Copyright © 2003, Mosby, Inc. All rights reserved.

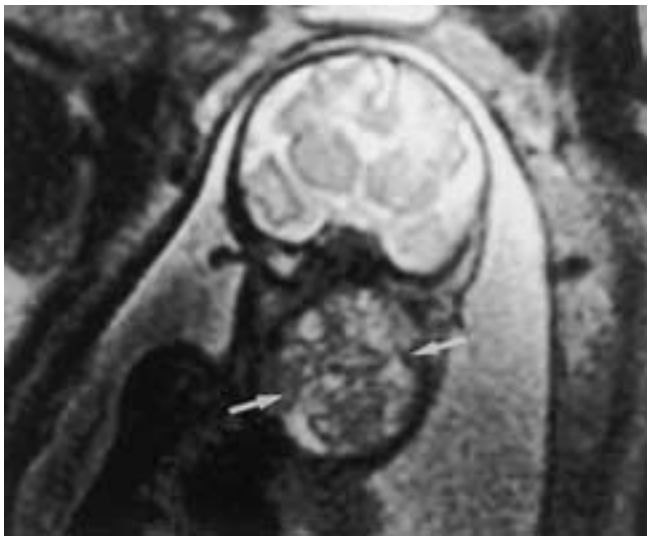

VIEW IMAGE

FIGURE 29-101 Fetal teratoma. Coronal single-shot FSE T2-weighted MR image reveals a heterogeneous neck mass (*arrows*) that is obstructing the trachea. Elective cesarean section was subsequently performed, the baby's airway was secured, and the teratoma was successfully resected.

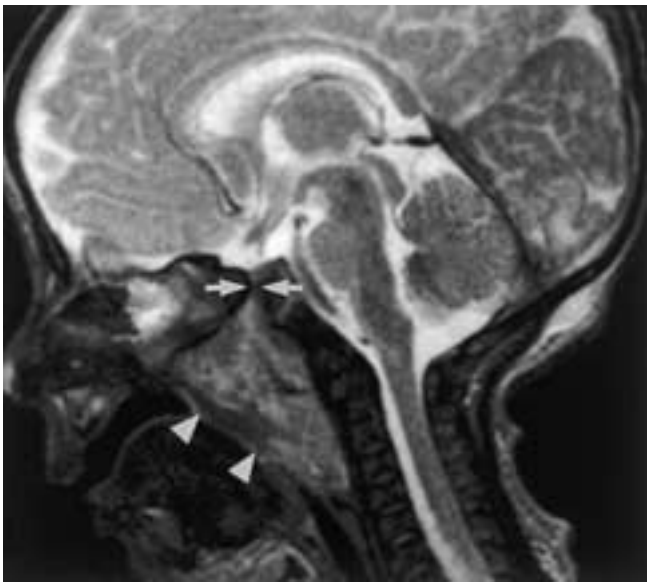

VIEW IMAGE

FIGURE 29-103 Neuroglial hamartoma in a 7-day-old boy with upper airway obstruction. Sagittal FSE T2-weighted MR image with fat suppression reveals a nasopharyngeal mass (*arrowheads*) that extends through a defect (*arrows*) in the sphenoid bone at the base of the pituitary fossa into the naso- and oropharynx. The mass is isointense with gray matter. The diagnosis was confirmed by biopsy.

MISCELLANEOUS CONDITIONS

Antrochoanal polyps and inflammatory sinonasal polyps, especially in children with cystic fibrosis, may cause nasal airway obstruction. Imaging findings are similar to those described in adults (Figs. 29-98 and 29-99).

Fibroosseous lesions such as fibrous dysplasia can also obstruct the airway due to involvement of facial bones and nasal turbinates (Fig. 29-100).

Teratomas are the most common congenital tumors. The head and neck region is the second most common location for teratomas in early infancy. Approximately 75% of childhood head and neck teratomas are diagnosed during the first year of life, and those involving the neck are usually noted at birth.[264] Antenatal diagnosis of teratoma can be made with sonography or MR imaging (Fig. 29-101). The postnatal clinical presentation of teratoma involving the neck is a large mass that causes respiratory difficulty and/or feeding problems. On CT teratomas appear heterogeneous but sharply circumscribed, with solid and cystic areas and variegated enhancement of the solid component. Hypodense areas indicating fat and/or hyperdense calcific foci are helpful in suggesting the preoperative diagnosis of teratoma and in differentiating the tumor from lymphatic malformation (Fig. 29-102).

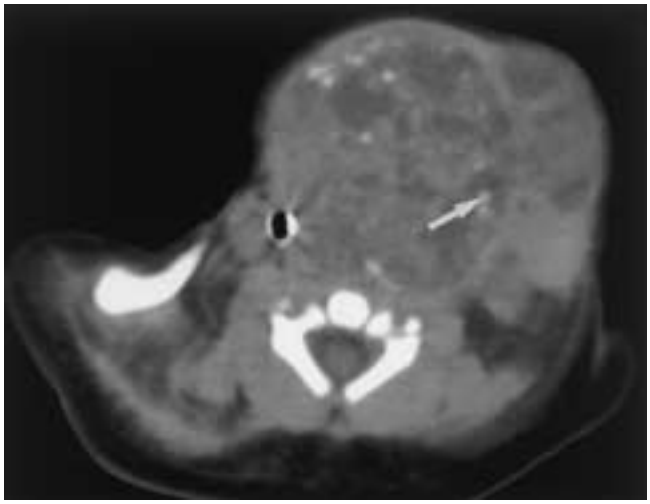

VIEW IMAGE

FIGURE 29-102 Teratoma in a 1-day-old boy, one of triplets, born with a large neck mass. The baby was intubated at birth. Axial nonenhanced CT demonstrates a heterogeneous solid and cystic tumor containing punctate calcifications (*arrow*). The endotracheal tube indicates the position of the displaced trachea.

Hamartomas are uncommon developmental masses that can produce airway obstruction. A neuroglial or hypothalamic hamartoma can occasionally extend through a skull base defect to present as a nasopharyngeal mass (Fig. 29-103).

Large neurofibromas and plexiform neurofibromas sometimes cause airway obstruction (Fig. 29-104). Neurofibroma is typically well circumscribed, with bone remodeling rather than frank bone destruction. Plexiform neurofibroma appears as a lobulated or poorly defined heterogeneous mass involving multiple fascial compartments. A characteristic cross-sectional imaging appearance is the *target sign*.[265] This refers to punctate central high attenuation and peripheral low attenuation within multiple tumor nodules on CT.

The larynx is the most common site for isolated amyloid, a rare benign condition in children.[266] On CT the solid laryngeal mass is similar in attenuation to muscle, and on MR imaging the signal intensities of the amyloid disease are isointense with muscle. The process enhances with gadolinium.[266]

Copyright © 2003, Mosby, Inc. All rights reserved.

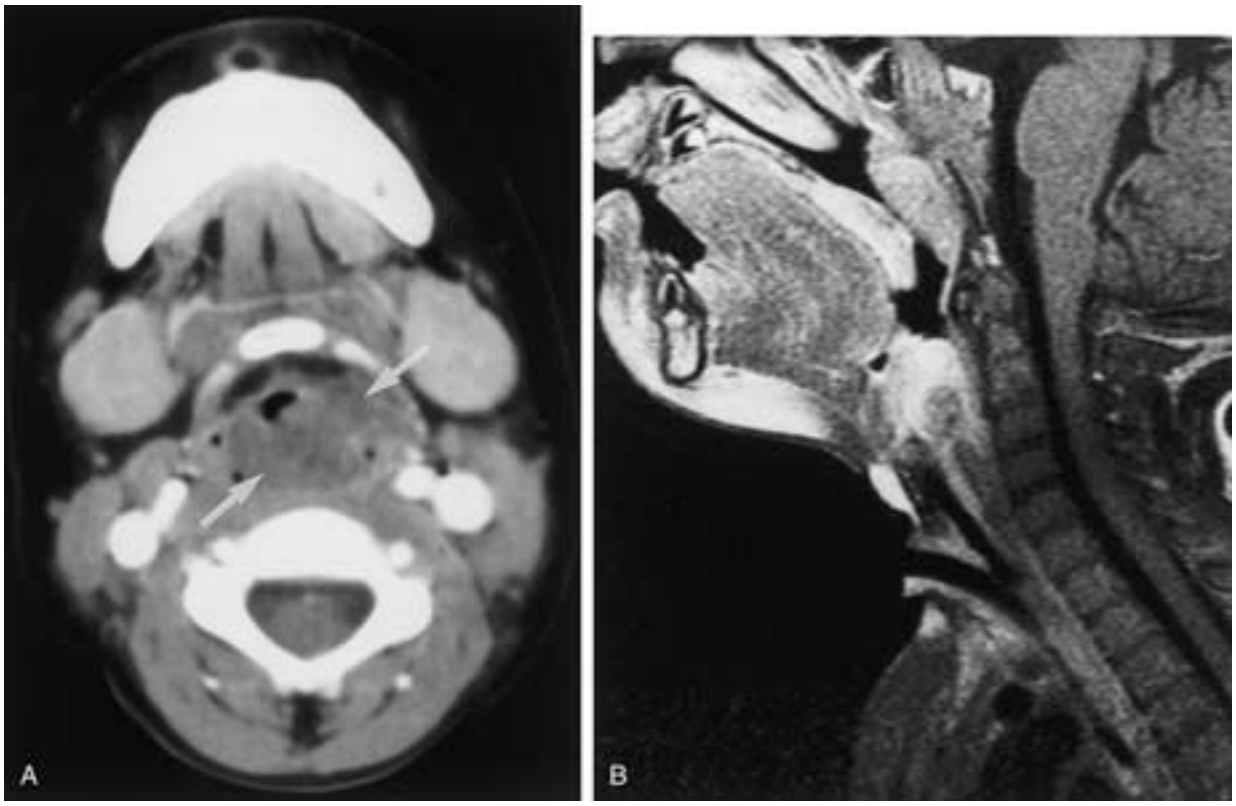

VIEW IMAGE

FIGURE 29-104 Supraglottic neurofibroma in a 2-year-old girl with neurofibromatosis type 1. **A**, Axial contrast-enhanced CT reveals an obstructing supraglottic mass (*arrows*). Since the image was acquired during the administration of contrast, enhancement of the tumor has not yet occurred. **B**, Sagittal contrast-enhanced T1-weighted MR image demonstrates the enhancing tumor extending between the epiglottis and the glottis. The patient has a tracheostomy tube in place.

Congenital hypothyroidism may be caused by dyshormonogenesis, resulting in a large thyroid gland that is in the normal thyroid bed.[267] The mass may be extensive and may result in airway compromise (Fig. 29-105).[268]

VIEW IMAGE

FIGURE 29-105 One-year-old child with congenital hypothyroidism and stridor. Axial contrast-enhanced CT shows symmetric enlargement of the thyroid gland. Note that the gland does not enhance normally. The common carotid arteries (*A*) and internal jugular veins (*V*) are deviated posterolaterally, and the trachea is compressed.

SECTION NINE

MALIGNANT TUMORS

Lymphoma is the most common malignant tumor of the head and neck. Sarcomas, specifically rhabdomyosarcomas, are the next most common tumors. Thyroid carcinoma and salivary gland malignancies are the most common tumors of glandular origin. The most common epithelial malignancy is nasopharyngeal carcinoma.[269, 270]

LYMPHOMA

Lymphoma is classified as Hodgkin's disease or non-Hodgkin's lymphoma. Both types of lymphoma display a male predilection. Hodgkin's disease (HD) is the most common type of lymphoma to involve the head and neck and is most common in adolescence. In children HD is primarily nodal, and at initial presentation, extranodal disease is rare.[269] During childhood, airway obstruction is not a common presenting symptom of HD. The presence of the Reed-Sternberg cell, a multinucleate giant cell, differentiates HD from other types of lymphoma.

Non-Hodgkin's lymphoma (NHL) primarily affects children between 2 and 12 years of age. It is classified as

Copyright © 2003, Mosby, Inc. All rights reserved.

U-cell (or undefined cell proliferations without specific markers), B-cell, T-cell, histiocytic, and unclassifiable types (technically insufficient for specific cytologic classification).[271] In children, although cervical adenopathy may be the presenting sign of disease, extranodal involvement is common, especially the lymphoid tissues of Waldeyer's ring.[269] When disease involves the airway, symptoms of airway obstruction occur. NHL occurs more frequently in patients with acquired or congenital immune disorders such as Wiskott-Aldrich syndrome and acquired immune deficiency syndrome (AIDS).[272–274] High grade B-cell lymphomas that arise in immunosuppressed transplant patients and those with AIDS occur in association with EBV infection.[273, 275] The posttransplantation lymphoproliferative disorders (PTLD) are typically associated with EBV infection and encompass a variety of disorders ranging from reversible polyclonal lymphoid hyperplasia to frankly malignant high-grade monoclonal lymphoma.

Burkitt lymphoma is a B-cell NHL with unique epidemiology. The disease occurs both as an endemic African form and as a nonendemic American form.[270] Antibody titers to EBV are high in the African type, but only 15% to 20% of American children have elevated viral titers.[276, 277] The African type commonly involves the oral cavity and jaw, and the American type more commonly presents as an abdominal mass. Involvement of the cervical lymph nodes, nasopharynx, and oropharynx is less common than in the other lymphomas.[278] However, Burkitt's lymphoma has an extremely short doubling time and is the fastest-growing human tumor. As a result, it may present with rapidly progressive airway obstruction.[276, 277]

CT and MR imaging cannot differentiate nodal disease caused by HL from that of NHL. Lymphadenopathy, sometimes only 1 cm in diameter, is seen in multiple locations, usually with a dominant larger node or group of nodes. However, because prominent hyperplastic nonneoplastic lymphadenopathy is common in the pediatric population, it may be impossible to differentiate lymphomatous from reactive nodes. Lymphomatous adenopathy is not commonly necrotic or calcified, although focal calcifications may be seen in treated nodes. Nodal biopsy is required to establish the diagnosis and the disease subtype.

NHL involving Waldeyer's ring is usually bilateral and fills or obliterates the airway. On CT the tumor is isodense to the pharyngeal musculature, and on MR imaging the tumor is isointense to muscle on T1-weighted images and generally hyperintense to muscle on T2-weighted images (Fig. 29-106). In children, extranodal lymphoma is nonspecific in appearance, but because lymphoma is one of the most common lesions in the head and neck, it should be included in the differential diagnosis of any large neck mass with malignant characteristics on CT or MR imaging (Fig. 29-107). Enlargement of lymphoid tissue in transplant recipients should raise the possibility of PTLD (Fig. 29-108).

Because of improved detection and staging and multimodality treatment regimens, the 5-year survival rate for lymphoma has improved over the past two decades. On follow-up CT or MR imaging after successful treatment, extranodal disease should appear smaller, or it should completely resolve. Lymphomatous nodes should decrease in size and number, although small nodes may remain. A new nodal or nonnodal mass following treatment for childhood lymphoma may represent recurrent disease or a new primary tumor because these patients are at risk for secondary malignant disease.[279]

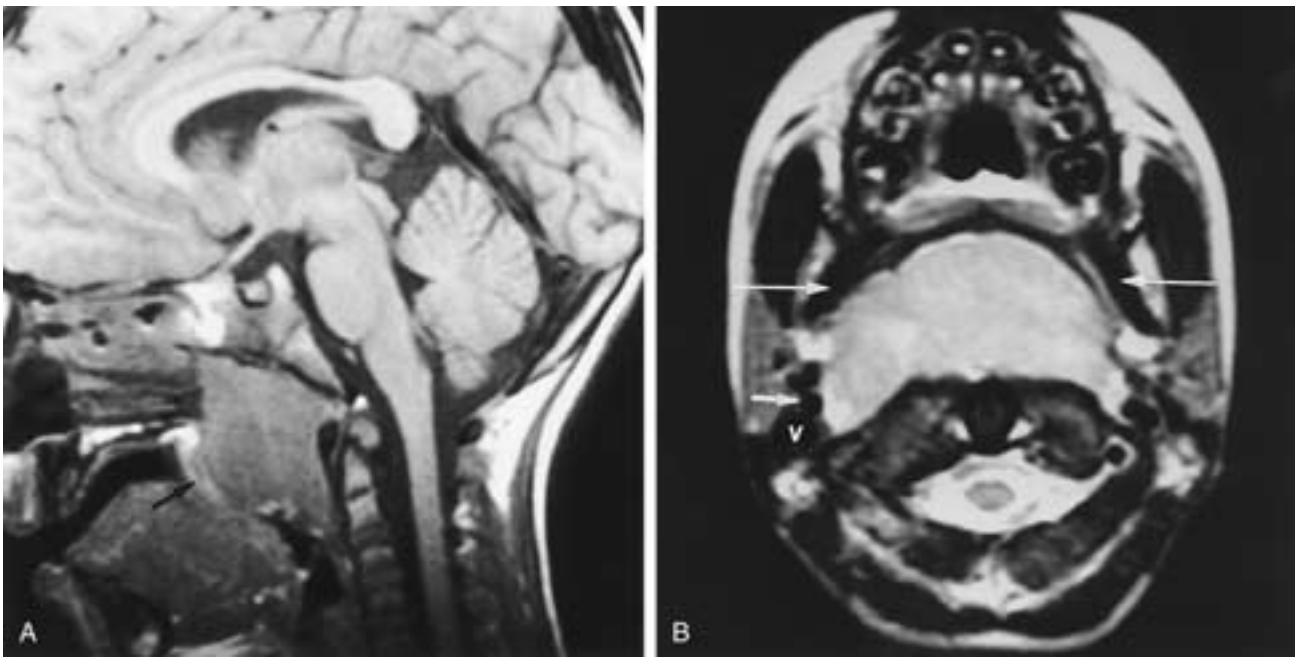

FIGURE 29-106 NHL in a 6-year-old boy with severe airway obstruction. **A**, T1-weighted sagittal image shows a large nasooropharyngeal mass obliterating the airway. The soft palate (*arrow*) is pushed anteroinferiorly by the mass. **B**, On this FSE T2-weighted axial image, the mass has pushed the vessels (*arrow*, internal carotid artery; *v*, internal jugular vein) and the pterygoid muscles (*long arrow*) laterally. Despite the large size, there is no skull base destruction and no cervical adenopathy.

VIEW IMAGE

Copyright © 2003, Mosby, Inc. All rights reserved.

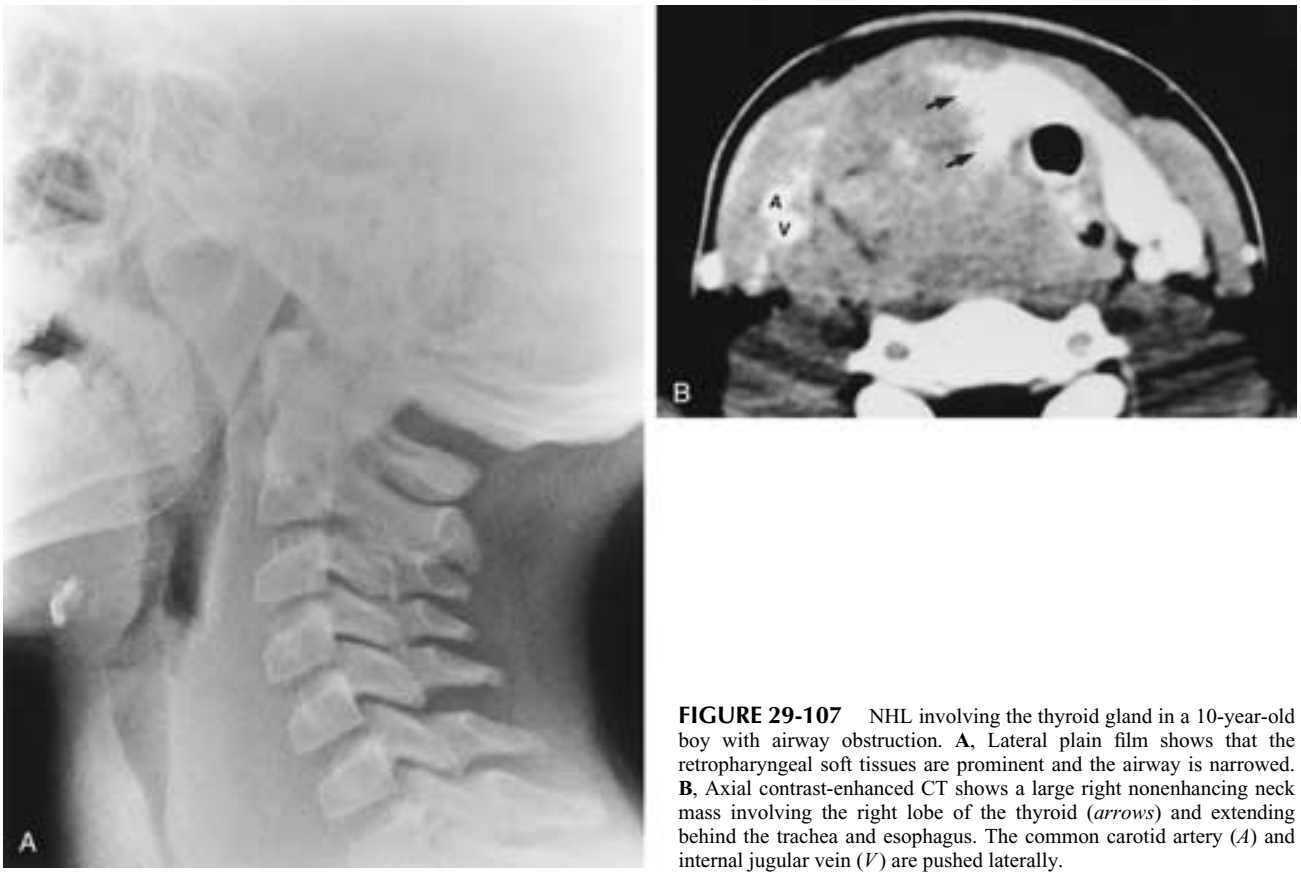

FIGURE 29-107 NHL involving the thyroid gland in a 10-year-old boy with airway obstruction. **A**, Lateral plain film shows that the retropharyngeal soft tissues are prominent and the airway is narrowed. **B**, Axial contrast-enhanced CT shows a large right nonenhancing neck mass involving the right lobe of the thyroid (*arrows*) and extending behind the trachea and esophagus. The common carotid artery (*A*) and internal jugular vein (*V*) are pushed laterally.

VIEW IMAGE

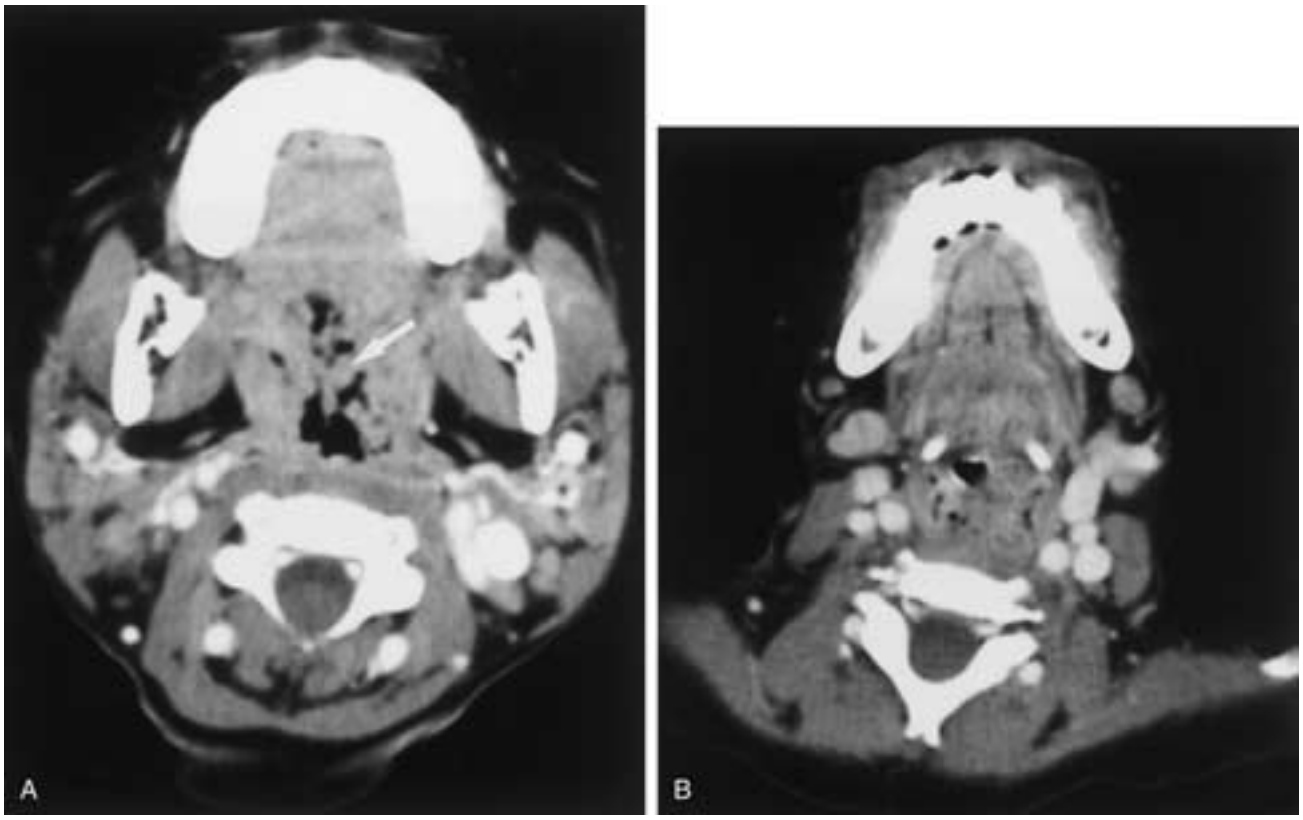

FIGURE 29-108 Posttransplant lymphoproliferative disorder in an immunosuppressed transplant recipient. **A**, Axial contrast-enhanced CT reveals frond-like enlargement of the lingual tonsils (*arrow*). **B**, The abnormal tissue extends into the hypopharynx and encroaches on the airway.

VIEW IMAGE

Copyright © 2003, Mosby, Inc. All rights reserved.

RHABDOMYOSARCOMA

Rhabomyosarcoma (RMS) is a malignant tumor of mesenchymal origin thought to arise from cells committed to a skeletal muscle lineage.[280] In the pediatric population, RMS is the most common soft-tissue sarcoma and the second most frequent head and neck malignancy.[281] The disease has a peak age presentation at 2 to 5 years and again at 15 to 19 years, and there is a slight male predominance.[282] Although most cases of RMS appear to be sporadic, some young children (aged < 3 years) have identifiable constitutional mutations of the *p53* tumor suppressor gene and a possible hereditary predisposition to cancer.[283] RMS has been associated with familial syndromes such as neurofibromatosis type 1.[284] There is also an association between bilateral or hereditary retinoblastoma of the orbit and RMS.[285]

Three main histopathologic types of rhabdomyosarcoma have been described: (1) embryonal, which accounts for 75% of tumors and is most common in younger children; (2) alveolar (20%), which has the worst prognosis and is seen in older children; and (3) pleomorphic, which accounts for 5% of the cases. The embryonal and alveolar subtypes of RMS have been found to have distinct genetic alterations that may play a role in the pathogenesis of these tumors.[280] Head and neck disease is further divided into three categories based on the site of occurrence: (1) orbital, which carries the best prognosis; (2) parameningeal, which has the poorest prognosis; and (3) other sites. Parameningeal disease arises from tumors in locations such as the middle ear space, posterior nasopharynx, nasal cavity, paranasal sinuses, and masticator space. Tumors erode directly through bone or extend through skull base foramina via perineural spread to produce an epidural mass and sometimes meningeal involvement. The incidence of metastatic cervical adenopathy at the time of presentation ranges from 3% to 25%.[282, 286] As with other head and neck malignancies in children, presenting signs and symptoms may initially be innocuous, resulting in a delay in diagnosis. Large nasopharyngeal, oropharyngeal, or laryngeal lesions may present with airway obstruction (Figs. 29-109 and 29-110). The prognosis, as reported by the Intergroup Rhabdomyosarcoma Study (IRS), is best with complete surgical resection.

Imaging shows a soft-tissue mass, often with bony tive, but bony remodeling can also be seen. The tumor is usually heterogeneous, may be hemorrhagic or necrotic, and has relatively well-circumscribed borders. The tumors enhance following the administration of contrast for CT or MR imaging. For baseline imaging, both CT and MR imaging should be performed. Axial and coronal CT images are used for assessment of bony destruction (Fig. 29-109A). The coronal images should be 3 mm thick, and the skull base should be carefully evaluated for erosion or widening of cranial nerve foramina. Multiplanar MR images should include T2-weighted or fast spin-echo inversion recovery pulse sequences and gadolinium-enhanced, fat-suppressed, T1-weighted images (Figs. 29-109B and 29-110). The signal intensity of tumors on the T2-weighted images is variable. Coronal contrast-enhanced, T1-weighted images are very useful for the detection of epidural masses and meningeal enhancement that indicate the presence of parameningeal disease (Fig. 29-109B). It is important to detect this preoperatively because combined craniofacial surgery may then be required.[281] A survey of the cervical lymph node

VIEW IMAGE

FIGURE 29-109 RMS in a 2-year-old girl with a 2-week history of unilateral nosebleeds, periorbital swelling, and proptosis. **A**, Axial CT demonstrates a large tumor with destruction of the sphenoid bone, right maxilla, and orbital floor. Tumor involves the right nasal cavity. **B**, Coronal fat-suppressed, gadolinium-enhanced, T1-weighted image demonstrates enhancing tumor involving the sphenoid sinus, posterior ethmoid air cells, right nasal cavity, and maxillary antrum. There are low signal intensity trapped secretions within the right maxillary antrum (*arrow*). Parameningeal extension is seen within the anterior cranial fossa (*arrowheads*).

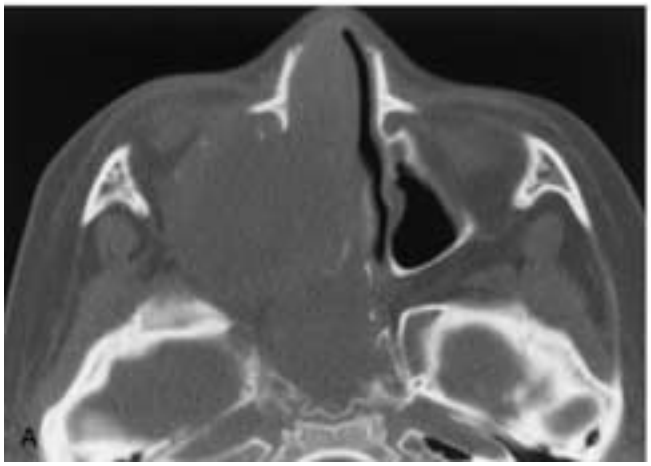

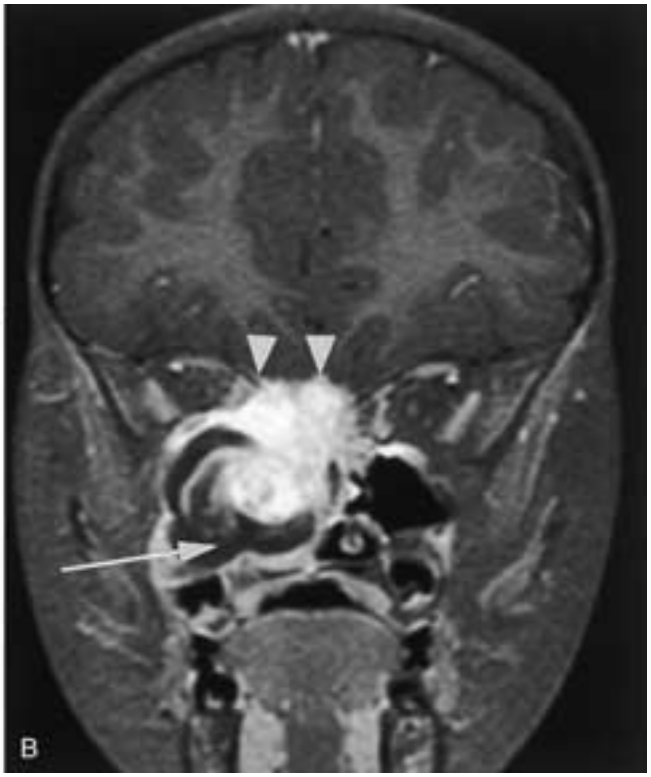

Copyright © 2003, Mosby, Inc. All rights reserved.

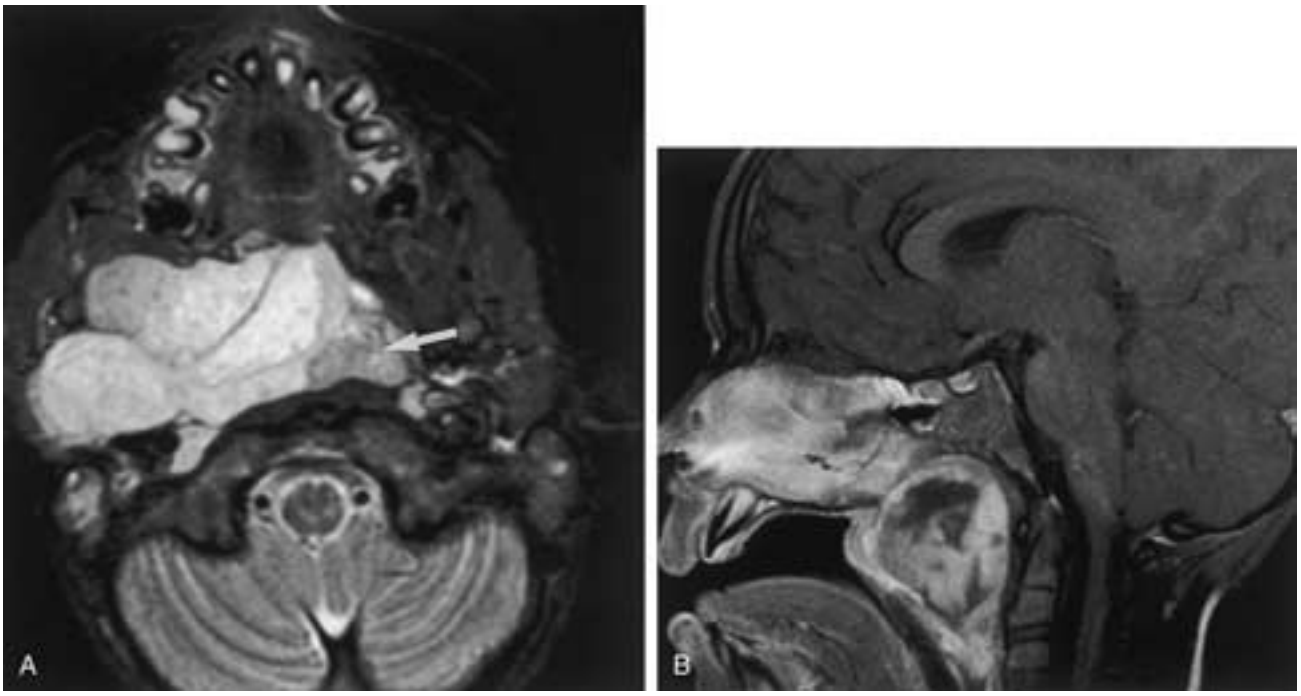

VIEW IMAGE

FIGURE 29-110 RMS of the pharynx in a 6-year-old boy with a 1-month history of nasal congestion, nasal voice, and noisy snoring. **A**, Axial FSEIR image reveals a large tumor involving the adenoids, extending anteriorly into the airway and laterally toward the muscles of mastication (*arrow*). **B**, Sagittal T1-weighted image reveals the heterogeneously enhancing tumor partially obstructing the nasopharynx.

chain also should be performed to detect metastatic adenopathy. The diagnosis is confirmed by biopsy.

Treatment involves surgery, radiation therapy, and chemotherapy. Posttreatment resolution of the tumor is a good indicator of the prognosis, but disease may recur at a later date, and serial scans are usually obtained to detect early disease recurrence.

NASOPHARYNGEAL CARCINOMA

Nasopharyngeal carcinoma, previously called lymphoepithelioma, is an uncommon malignancy in children. However, this tumor is the most common pediatric epithelial carcinoma and has the highest incidence in parts of Asia and Africa.[287] Nasopharyngeal carcinoma may be similar in presentation, imaging appearance, and even histology to the more common tumors, lymphoma and rhabdomyosarcoma.[270] As in the adult population with this disease, children commonly have elevated titers of EBV, suggesting an infectious etiology.[270] Unilateral nasal obstruction and otitis media, epistaxis, and rhinorrhea are common presenting findings.[269] Headache and cranial neuropathy imply skull base and intracranial extension. Most children have metastatic cervical adenopathy at the time of presentation.[270]

CT and MR imaging of nasopharyngeal carcinoma show a large, inhomogeneous mass filling the nasopharyngeal airway, often with skull base erosion and intracranial extension. Necrotic cervical adenopathy, particularly involving the retropharyngeal and high jugular chain nodes, is common.

A combination of radiotherapy and systemic chemotherapy is used for optimal disease-free survival.[287]

MISCELLANEOUS CONDITIONS

There are a variety of miscellaneous rare malignancies in the head and neck, which may have airway involvement. Neuroblastoma of the head and neck is most commonly metastatic from neural crest sympathetic precursor cells in the adrenal gland. There usually is disease in the cervical lymph nodes, the orbit, or the skull.[270] CT or MR imaging of the tumor is nonspecific, showing either a large cervical node or a mass in the orbit or skull, sometimes with dystrophic calcification and often with extensive bone destruction. Imaging of the primary lesion, especially the adrenal gland, should be performed.[270]

Malignant rhabdoid tumor is a rare aggressive pediatric neoplasm that originates either from the kidney or from extrarenal sites, including the head and neck.[288] The radiographic appearance is nonspecific (Fig. 29-111).

Thyroid carcinoma is rare in children and is strongly associated with a prior history of irradiation.[270] This tumor also may be increased in incidence in long-term survivors of acute lymphoblastic leukemia.[289] Patients present with a palpable neck mass, hoarseness, or dysphagia.[289] Ultrasound or an ^{123}I thyroid scan is often used to image the lesion and determine if the mass is ''cold.'' Cold nodules in children have a higher incidence of malignancy, up to 29% in some series, than in adults.[290] The definitive diagnosis is made by fine needle aspiration or surgical biopsy.

Laryngeal carcinoma, also a rare pediatric neoplasm, is

Copyright © 2003, Mosby, Inc. All rights reserved.

VIEW IMAGE

FIGURE 29-111 Malignant rhabdoid tumor in an infant. Sagittal postgadolinium T1-weighted sequence shows an inhomogeneously enhancing mass in the retropharyngeal and precervical soft tissues. (Courtesy of Dr. Suresh Mukerji.)

usually associated with RRP and is similar in CT and MR appearance to adult laryngeal carcinoma.[255, 291]

Synovial sarcomas may occasionally occur in proximity to the airway and produce airway symptoms (Fig. 29-112). Chondrosarcomas, other sarcomas, malignant teratomas, and other carcinomas have been reported in the head and neck in children, but they rarely cause airway compromise. Skull base lesions, when large, may affect the airway.

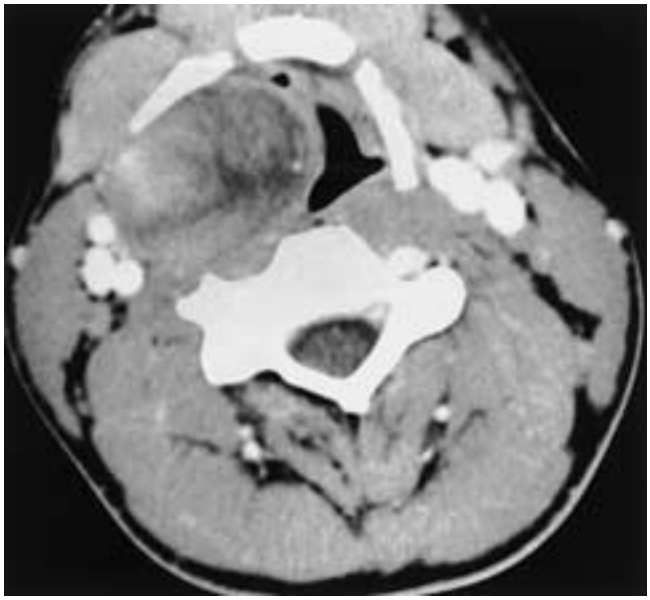

VIEW IMAGE

FIGURE 29-112 Biphasic synovial cell sarcoma in a 16-year-old boy with a right-sided neck mass. Biphasic synovial cell sarcoma. Axial contrast-enhanced CT demonstrates a large heterogeneously enhancing pharyngeal tumor narrowing the airway and distorting the hyoid bone.

Airway neoplasms in children with AIDS include NHL, bronchial leiomyomas, a benign smooth muscle tumor, and bronchial leiomyosarcomas.[270] However, inflammatory diseases such as chronic sinusitis and otitis media are more common in pediatric AIDs patients.

REFERENCES

1. Moore KL, Persaud TVN. Before We Are Born. Essentials of Embryology and Birth Defects, 5th ed. Philadelphia: WB Saunders, 1998.
2. Sadler TW. Langman's Medical Embryology, 7th ed. Baltimore: Williams & Wilkins; 1995.
3. Sanudo JR, Domenech-Mateu JM. The laryngeal primordium and epithelial lamina. A new interpretation. J Anat 1990;171:207–222.
4. Hedrick MH, Ferro MM, Filly RA, et al. Congenital high airway obstruction syndrome (CHAOS): a potential for perinatal intervention. J Pediatr Surg 1994;29(2):271–274.
5. Cotton RT, Reilly JS. Stridor and airway obstruction. In: Bluestone CD, Stool SE, Kenna MA, eds. Pediatric Otolaryngology, 3rd ed, Vol. 2, Philadelphia: WB Saunders, 1996;1275–1287.
6. Holinger LD. Etiology of stridor in the neonate, infant and child. Ann Otol Rhinol Laryngol 1980;89(5 Pt 1):397–400.
7. Soriano SG, Kim C, Jones DT. Surgical airway, rigid bronchoscopy, and transtracheal jet ventilation in the pediatric patient. Anesth Clin North Am 1998;16(4):827–838.
8. Jani P, Koltai P, Ochi JW, et al. Surgical treatment of laryngomalacia. J Laryngol Otol 1991;105(12):1040–1045.
9. Erwin EA, Gerber ME, Cotton RT. Vascular compression of the airway: indications for and results of surgical management. Int J Pediatr Otorhinolaryngol 1997;40(2-3):155–162.
10. Handler SD. Direct laryngoscopy in children: rigid and flexible fiberoptic. Ear Nose Throat J 1995;74(2):100–104, 106.
11. Gyepes MT, Nussbaum E. Radiographic–endoscopic correlations in the examination of airway disease in children. Pediatr Radiol 1985;15(5):291–296.
12. Bower CM, Gungor A. Pediatric obstructive sleep apnea syndrome. Otolaryngol Clin North Am 2000;33(1):49–75.
13. Potsic WP, Wetmore RF. Sleep disorders and airway obstruction in children. Otolaryngol Clin North Am 1990;23(4):651–663.
14. Donnelly LF, Strife JL, Myer CM 3rd. Glossoptosis (posterior displacement of the tongue) during sleep: a frequent cause of sleep apnea in pediatric patients referred for dynamic sleep fluoroscopy. AJR 2000;175(6):1557–1560.
15. Fernbach SK, Brouillette RT, Riggs TW, et al. Radiologic evaluation of adenoids and tonsils in children with obstructive sleep apnea: plain films and fluoroscopy. Pediatr Radiol 1983;13(5):258–265.
16. Gibson SE, Myer CM 3rd, Strife JL, et al. Sleep fluoroscopy for localization of upper airway obstruction in children. Ann Otol Rhinol Laryngol 1996;105(9):678–683.
17. Gilkeson RC, Ciancibello LM, Hejal RB, et al. Tracheobronchomalacia: dynamic airway evaluation with multidetector CT. AJR 2001;176(1):205–210.
18. Ardran GM, Kemp FH. The mechanism of changes in form of the cervical airway in infancy. Med Radiogr Photogr 1968;44(2):26–38.
19. Griscom NT. Diseases of the trachea, bronchi, and smaller airways. Radiol Clin North Am 1993;31(3):605–615.
20. Shorten GD, Opie NJ, Graziotti P, et al. Assessment of upper airway anatomy in awake, sedated and anaesthetised patients using magnetic resonance imaging [see comments]. Anaesth Intensive Care 1994; 22(2):165–169.
21. Ell SR, Jolles H, Keyes WD, et al. Cine CT technique for dynamic airway studies. AJR 1985;145(1):35–36.
22. Frey EE, Smith WL, Grandgeorge S, et al. Chronic airway obstruction in children: evaluation with cine-CT. AJR 1987;148(2): 347–352.
23. Brasch RC, Gould RG, Gooding CA, et al. Upper airway obstruction in infants and children: evaluation with ultrafast CT. Radiology 1987;165(2):459–466.

Copyright © 2003, Mosby, Inc. All rights reserved.

24. Slovis TL, Renfro B, Watts FB, et al. Choanal atresia: precise CT evaluation. Radiology 1985;155(2):345–348.
25. Scheerer WD, Lammert F. [Morphology and growth of the nasopharynx from three years to maturity (author's transl)]. Arch Otorhinolaryngol 1980;229(3–4):221–229.
26. Ardran GM, Kemp FH. A function for adenoids and tonsils. Am J Roentgenol Rad Ther Nucl Med 1972;114(2):268–281.
27. Tomaski SM. Embryology and anatomy of the mouth, pharynx and esophagus. In: Bluestone CD, Stool SE, Kenna MA, eds. Pediatric Otolaryngology, 3rd ed, Vol 2. Philadelphia: WB Saunders, 1996;918–938.
28. Isaacson G. Developmental anatomy and physiology of the larynx, trachea and esophagus. In: Bluestone CD, Stool SE, Kenna MA, eds. Pediatric Otolaryngology, 3rd ed, Vol 2. Philadelphia: WB Saunders, 1996;1202–1244.
29. Kahane JC. Growth of the human prepubertal and pubertal larynx. J Speech Hear Res 1982;25(3):446–455.
30. Holinger PH, Brown WT. Congenital webs, cysts, laryngoceles and other anomalies of the larynx. Ann Otol Rhinol Laryngol 1967;76(4):744–752.
31. Griscom NT. Cross-sectional shape of the child's trachea by computed tomography. AJR 1983;140(6):1103–1106.
32. Reed MH. Ossification of the hyoid bone during childhood. Can Assoc Radiol J 1993;44(4):273–276.
33. Goldbloom RB, Dunbar JS. Calcification of cartilage in the trachea and larynx in infancy associated with congenital stridor. Pediatrics 1960;26:669–673.
34. Wittenborg MH, Gyepes MT, Crocker D. Tracheal dynamics in infants with respiratory distress, stridor, and collapsing trachea. Radiology 1967;88(4):653–662.
35. Griscom NT. Computed tomographic determination of tracheal dimensions in children and adolescents. Radiology 1982;145(2): 361–364.
36. Breatnach E, Abbott GC, Fraser RG. Dimensions of the normal human trachea. AJR 1984;142(5):903–906.
37. Derkay CS, Grundfast KM. Airway compromise from nasal obstruction in neonates and infants [see comments]. Int J Pediatr Otorhinolaryngol 1990;19(3):241–249.
38. Chinwuba C, Wallman J, Strand R. Nasal airway obstruction: CT assessment. Radiology 1986;159(2):503–506.
39. Johnson PJ, Rydlund K, Hollins RR. Congenital nasal pyriform aperture stenosis. Plast Reconstr Surg 1999;103(6):1696–1699.
40. Hengerer AS, Strome M. Choanal atresia: a new embryologic theory and its influence on surgical management. Laryngoscope 1982;92(8 Pt 1):913–921.
41. Brown OE, Pownell P, Manning SC. Choanal atresia: a new anatomic classification and clinical management applications. Laryngoscope 1996;106(1 Pt 1):97–101.
42. Fraser JS. Congenital atresia of the choanae. Br J Med 1910;2:1698–1701.
43. Brown OE, Burns DK, Smith TH, et al. Bilateral posterior choanal atresia: a morphologic and histologic study and computed tomographic correlation. Int J Pediatr Otorhinolaryngol 1987;13(2): 125–142.
44. Cozzi F, Myers NA, Piacenti S, et al. Maturational dysautonomia and facial anomalies associated with esophageal atresia: support for neural crest involvement. J Pediatr Surg 1993;28(6):798–801.
45. Friedman NR, Mitchell RB, Bailey CM, et al. Management and outcome of choanal atresia correction. Int J Pediatr Otorhinolaryngol 2000;52(1):45–51.
46. Crockett DM, Healy GB, McGill TJ, et al. Computed tomography in the evaluation of choanal atresia in infants and children. Laryngoscope 1987;97(2):174–183.
47. Benjamin B. Evaluation of choanal atresia. Ann Otol Rhinol Laryngol 1985;94(5 Pt 1):429–432.
48. Castillo M. Congenital abnormalities of the nose: CT and MR findings. AJR 1994;162(5):1211–1217.
49. Wetmore RF, Mahboubi S. Computed tomography in the evaluation of choanal atresia. Int J Pediatr Otorhinolaryngol 1986;11(3): 265–274.
50. Pagon RA, Graham JM, Jr, Zonana J, et al. Coloboma, congenital heart disease, and choanal atresia with multiple anomalies: CHARGE association. J Pediatr 1981;99(2):223–227.
51. Hall BD. Choanal atresia and associated multiple anomalies. J Pediatr 1979;95(3):395–398.
52. Blake KD, Davenport SL, Hall BD, et al. CHARGE association: an update and review for the primary pediatrician. Clin Pediatr (Phila) 1998;37(3):159–173.
53. Kallen K, Robert E, Mastroiacovo P, et al. CHARGE association in newborns: a registry-based study [see comments]. Teratology 1999;60(6):334–343.
54. Tellier AL, Cormier-Daire V, Abadie V, et al. CHARGE syndrome: report of 47 cases and review. Am J Med Genet 1998;76(5):402–409.
55. Wyse RK, al-Mahdawi S, Burn J, et al. Congenital heart disease in CHARGE association. Pediatr Cardiol 1993;14(2):75–81.
56. Wiatrak BJ. Unilateral choanal atresia: initial presentation and endoscopic repair. Int J Pediatr Otorhinolaryngol 1998;46(1-2): 27–35.
57. Park AH, Brockenbrough J, Stankiewicz J. Endoscopic versus traditional approaches to choanal atresia. Otolaryngol Clin North Am 2000;33(1):77–90.
58. Calcaterra VE, Annino DJ, Carter BL, et al. Congenital nasolacrimal duct cysts with nasal obstruction. Otolaryngol Head Neck Surg 1995;113(4):481–484.
59. Lueder GT. Treatment of nasolacrimal duct obstruction in children with trisomy 21. J Aapos 2000;4(4):230–232.
60. Lin AE, Semina EV, Daack-Hirsch S, et al. Exclusion of the branchio-oto-renal syndrome locus (EYA1) from patients with branchio-oculo-facial syndrome [published erratum appears in Am J Med Genet 2000 Jul 17;93(2):169]. Am J Med Genet 2000;91(5): 387–390.
61. Castillo M, Merten DF, Weissler MC. Bilateral nasolacrimal duct mucocele, a rare cause of respiratory distress: CT findings in two newborns. AJNR 1993;14(4):1011–1013.
62. Ram B, Barras CW, White PS, et al. The technique of nasendoscopy in the evaluation of nasolacrimal duct obstruction in children [in process citation]. Rhinology 2000;38(2):83–86.
63. Arlis H, Ward RF. Congenital nasal pyriform aperture stenosis. Isolated abnormality vs developmental field defect. Arch Otolaryngol Head Neck Surg 1992;118(9):989–991.
64. Tavin E, Stecker E, Marion R. Nasal pyriform aperture stenosis and the holoprosencephaly spectrum. Int J Pediatr Otorhinolaryngol 1994;28(2-3):199–204.
65. Cohen MM Jr. Perspectives on holoprosencephaly: part I. Epidemiology, genetics, and syndromology. Teratology 1989;40(3):211–235.
66. Roessler E, Belloni E, Gaudenz K, et al. Mutations in the human sonic hedgehog gene cause holoprosencephaly. Nat Genet 1996; 14(3):357–360.
67. Brown OE, Myer CMD, Manning SC. Congenital nasal pyriform aperture stenosis. Laryngoscope 1989;99(1):86–91.
68. Belden CJ, Mancuso AA, Schmalfuss IM. CT features of congenital nasal piriform aperture stenosis: initial experience. Radiology 1999;213(2):495–501.
69. Ey EH, Han BK, Towbin RB, et al. Bony inlet stenosis as a cause of nasal airway obstruction. Radiology 1988;168(2):477–479.
70. Hui Y, Friedberg J, Crysdale WS. Congenital nasal pyriform aperture stenosis as a presenting feature of holoprosencephaly. Int J Pediatr Otorhinolaryngol 1995;31(2-3):263–274.
71. Muenke M, Cohen MM Jr. Genetic approaches to understanding brain development: holoprosencephaly as a model. Ment Retard Dev Disabil Res Rev 2000;6(1):15–21.
72. Hu D, Helms JA. The role of sonic hedgehog in normal and abnormal craniofacial morphogenesis. Development 1999;126(21):4873–4884.
73. Ahlgren SC, Bronner-Fraser M. Inhibition of sonic hedgehog signaling in vivo results in craniofacial neural crest cell death. Curr Biol 1999;9(22):1304–1314.
74. Sculerati N, Gottlieb MD, Zimbler MS, et al. Airway management in children with major craniofacial anomalies. Laryngoscope 1998; 108(12):1806–1812.
75. Antley R, Bixler D. Trapezoidocephaly, midfacial hypoplasia and cartilage abnormalities with multiple synostoses and skeletal fractures. Birth Defects Orig Artic Ser 1975;11(2):397–401.
76. Reardon W, Smith A, Honour JW, et al. Evidence for digenic inheritance in some cases of Antley-Bixler syndrome? J Med Genet 2000;37(1):26–32.
77. Lee HJ, Cho DY, Tsai FJ et al. Antley-Bixler syndrome, description of two new cases and review of the literature. Pediatr Neurosurg 2001;34(1):33–39.
78. Cohen D, Goitein KJ. Arhinia revisited. Rhinology 1987;25(4): 237–244.

Copyright © 2003, Mosby, Inc. All rights reserved.

79. Olsen OE, Gjelland K, Reigstad H, et al. Congenital absence of the nose: a case report and literature review. Pediatr Radiol 2001;31(4): 225–232.
80. Albernaz VS, Castillo M, Mukherji SK, et al. Congenital arhinia. AJNR 1996;17(7):1312–1314.
81. Smith JK, Castillo M, Mukherji S, et al. Imaging of nasopharyngeal atresia. AJNR 1995;16(9):1936–1938.
82. Handley GH, Reilly JS. Nasal obstruction in children. Otolaryngol Clin North Am 1989;22(2):383–396.
83. Wardinsky TD, Pagon RA, Kropp RJ, et al. Nasal dermoid sinus cysts: association with intracranial extension and multiple malformations. Cleft Palate Craniofac J 1991;28(1):87–95.
84. Choudhury AR, Taylor JC. Primary intranasal encephalocele. Report of four cases. J Neurosurg 1982;57(4):552–555.
85. Weiss DD, Robson CD, Mulliken JB. Transnasal endoscopic excision of midline nasal dermoid from the anterior cranial base. Plast Reconstr Surg 1998;102(6):2119–2123.
86. Barkovich AJ, Vandermarck P, Edwards MS, et al. Congenital nasal masses: CT and MR imaging features in 16 cases. AJNR 1991;12(1):105–116.
87. Cohen MM Jr, Kreiborg S. Upper and lower airway compromise in the Apert syndrome. Am J Med Genet 1992;44(1):90–93.
88. Warren DW, Hairfield WM, Dalston ET, et al. Effects of cleft lip and palate on the nasal airway in children [see comments]. Arch Otolaryngol Head Neck Surg 1988;114(9):987–992.
89. Fearon JA, Mulliken JB. Midfacial duplication: a rare malformation sequence. Plast Reconstr Surg 1987;79(2):260–264.
90. Turpin IM, Furnas DW, Amlie RN. Craniofacial duplication (diprosopus). Plast Reconstr Surg 1981;67(2):139–142.
91. al Muti Zaitoun A, Chang J, Booker M. Diprosopus (partially duplicated head) associated with anencephaly: a case report. Pathol Res Pract 1999;195(1):45–50.
92. Carles D, Weichhold W, Alberti EM, et al. Diprosopia revisited in light of the recognized role of neural crest cells in facial development. J Craniofac Genet Dev Biol 1995;15(2):90–97.
93. Telander RL, Deane SA. Thyroglossal and branchial cleft cysts and sinuses. Surg Clin North Am 1977;57(4):779–791.
94. Reede DL, Bergeron RT, Som PM. CT of thyroglossal duct cysts. Radiology 1985;157(1):121–125.
95. Solomon JR, Rangecroft L. Thyroglossal-duct lesions in childhood. J Pediatr Surg 1984;19(5):555–561.
96. Todd NW. Common congenital anomalies of the neck. Embryology and surgical anatomy. Surg Clin North Am 1993;73(4):599–610.
97. Butler EC, Dickey JR, Shill OS Jr, et al. Carcinoma of the thyroglossal duct remnant. Laryngoscope 1969;79(2):264–271.
98. Branstetter BF, Weissman JL, Kennedy TL, et al. The CT appearance of thyroglossal duct carcinoma. AJNR 2000;21(8):1547–1550.
99. Sistrunk WE. The surgical treatment of cysts of the thyroglossal tract. Ann Surg 1920;71:121.
100. Josephson GD, Spencer WR, Josephson JS. Thyroglossal duct cyst: the New York Eye and Ear Infirmary experience and a literature review. Ear Nose Throat J 1998;77(8):642–644, 646–647, 651.
101. Chan FL, Low LC, Yeung HW, et al. Case report: lingual thyroid, a cause of neonatal stridor. Br J Radiol 1993;66(785):462–464.
102. Mahboubi S, Tenore A, Kirkpatrick JA. Diagnosis of ectopic thyroid: value of pretracheal soft-tissue measurements. AJR 1981;137(4): 717–719.
103. Radkowski D, Arnold J, Healy GB, et al. Thyroglossal duct remnants. Preoperative evaluation and management [see comments]. Arch Otolaryngol Head Neck Surg 1991;117(12):1378–1381.
104. Kaneko K, Takahashi K, Unno A, et al. Lingual cyst in infancy: importance of palpation for diagnosis. Acta Paediatr Jpn 1997;39(4): 475–477.
105. al-Khayat M, Kenyon GS. Midline sublingual dermoid cyst. J Laryngol Otol 1990;104(7):578–580.
106. Gibson WS Jr, Fenton NA. Congenital sublingual dermoid cyst. Arch Otolaryngol 1982;108(11):745–748.
107. Hunter TB, Paplanus SH, Chernin MM, et al. Dermoid cyst of the floor of the mouth: CT appearance. AJR 1983;141(6):1239–1240.
108. Citardi MJ, Traquina DN, Eisen R. Primitive foregut cysts: a cause of airway obstruction in the newborn. Otolaryngol Head Neck Surg 1994;111(4):533–537.
109. Morgan WE, Jones JK, Flaitz CM, et al. Congenital heterotopic gastrointestinal cyst of the oral cavity in a neonate: case report and review of literature. Int J Pediatr Otorhinolaryngol 1996;36(1):69–77.
110. Manor Y, Buchner A, Peleg M, et al. Lingual cyst with respiratory epithelium: an entity of debatable histogenesis. J Oral Maxillofac Surg 1999;57(2):124–127; discussion 128–129.
111. Boue DR, Smith GA, Krous HF. Lingual bronchogenic cyst in a child: an unusual site of presentation. Pediatr Pathol 1994;14(2): 201–205.
112. Chen MK, Gross E, Lobe TE. Perinatal management of enteric duplication cysts of the tongue. Am J Perinatol 1997;14(3): 161–163.
113. Morgan WE, Friedman EM, Duncan NO, et al. Surgical management of macroglossia in children. Arch Otolaryngol Head Neck Surg 1996;122(3):326–329.
114. Cohen MM Jr. Robin sequences and complexes: causal heterogeneity and pathogenetic/phenotypic variability. Am J Med Genet 1999; 84(4):311–315.
115. Shprintzen RJ, Singer L. Upper airway obstruction and the Robin sequence. Int Anesthesiol Clin 1992;30(4):109–114.
116. van den Elzen AP, Semmekrot BA, Bongers EM, et al. Diagnosis and treatment of the Pierre Robin sequence: results of a retrospective clinical study and review of the literature. Eur J Pediatr 2001;160(1):47–53.
117. Arvystas M, Shprintzen RJ. Craniofacial morphology in the velo-cardio-facial syndrome. J Craniofac Genet Dev Biol 1984;4(1): 39–45.
118. Shprintzen RJ, Goldberg RB, Lewin ML, et al. A new syndrome involving cleft palate, cardiac anomalies, typical facies, and learning disabilities: velo-cardio-facial syndrome. Cleft Palate J 1978;15(1): 56–62.
119. Driscoll DA, Spinner NB, Budarf ML, et al. Deletions and microdeletions of 22q11.2 in velo-cardio-facial syndrome. Am J Med Genet 1992;44(2):261–268.
120. MacKenzie-Stepner K, Witzel MA, Stringer DA, et al. Abnormal carotid arteries in the velocardiofacial syndrome: a report of three cases. Plast Reconstr Surg 1987;80(3):347–351.
121. Mitnick RJ, Bello JA, Golding-Kushner KJ, et al. The use of magnetic resonance angiography prior to pharyngeal flap surgery in patients with velocardiofacial syndrome. Plast Reconstr Surg 1996;97(5):908–919.
122. Ross DA, Witzel MA, Armstrong DC, et al. Is pharyngoplasty a risk in velocardiofacial syndrome? An assessment of medially displaced carotid arteries. Plast Reconstr Surg 1996;98(7):1182–1190.
123. D'Antonio LL, Rice RD Jr, Fink SC. Evaluation of pharyngeal and laryngeal structure and function in patients with oculo-auriculo-vertebral spectrum. Cleft Palate Craniofac J 1998;35(4): 333–341.
124. Shprintzen RJ, Croft CB, Berkman MD, et al. Velopharyngeal insufficiency in the facio-auriculo-vertebral malformation complex. Cleft Palate J 1980;17(2):132–137.
125. Shah UK, Wetmore RF. Laryngomalacia: a proposed classification form. Int J Pediatr Otorhinolaryngol 1998;46(1-2):21–26.
126. Belmont JR, Grundfast K. Congenital laryngeal stridor (laryngomalacia): etiologic factors and associated disorders. Ann Otol Rhinol Laryngol 1984;93(5 Pt 1):430–437.
127. Altman KW, Wetmore RF, Marsh RR. Congenital airway abnormalities requiring tracheotomy: a profile of 56 patients and their diagnoses over a 9 year period [see comments]. Int J Pediatr Otorhinolaryngol 1997;41(2):199–206.
128. Grundfast KM, Harley E. Vocal cord paralysis. Otolaryngol Clin North Am 1989;22(3):569–597.
129. Kirsch WM, Duncan BR, Black FO, et al. Laryngeal palsy in association with myelomeningocele, hydrocephalus, and the Arnold-Chiari malformation. J Neurosurg 1968;28(3):207–214.
130. Daya H, Hosni A, Bejar-Solar I, et al. Pediatric vocal fold paralysis: a long-term retrospective study. Arch Otolaryngol Head Neck Surg 2000;126(1):21–25.
131. de Jong AL, Kuppersmith RB, Sulek M, et al. Vocal cord paralysis in infants and children. Otolaryngol Clin North Am 2000;33(1): 131–149.
132. Bachman AL. Benign, non-neoplastic conditions of the larynx and pharynx. Radiol Clin North Am 1978;16(2):273–290.
133. Chu L, Gussack GS, Orr JB, et al. Neonatal laryngoceles. A cause for airway obstruction. Arch Otolaryngol Head Neck Surg 1994;120(4): 454–458.
134. Holinger LD, Barnes DR, Smid LJ, et al. Laryngocele and saccular cysts. Ann Otol Rhinol Laryngol 1978;87(5 Pt 1):675–685.

Copyright © 2003, Mosby, Inc. All rights reserved.

135. Arens C, Glanz H, Kleinsasser O. Clinical and morphological aspects of laryngeal cysts. Eur Arch Otorhinolaryngol 1997;254(9-10):430–436.
136. Hsieh WS, Yang PH, Wong KS, et al. Vallecular cyst: an uncommon cause of stridor in newborn infants. Eur J Pediatr 2000;159(1-2): 79–81.
137. Killoran CE, Abbott M, McKusick VA, et al. Overlap of PIV syndrome, VACTERL and Pallister-Hall syndrome: clinical and molecular analysis. Clin Genet 2000;58(1):28–30.
138. Sturgis EM, Howell LL. Bifid epiglottis syndrome. Int J Pediatr Otorhinolaryngol 1995;33(2):149–157.
139. Squires LA, Constantini S, Miller DC, et al. Hypothalamic hamartoma and the Pallister-Hall syndrome. Pediatr Neurosurg 1995;22(6):303–308.
140. Hall JG, Pallister PD, Clarren SK, et al. Congenital hypothalamic hamartoblastoma, hypopituitarism, imperforate anus and postaxial polydactyly—a new syndrome? Part I: clinical, causal, and pathogenetic considerations. Am J Med Genet 1980;7(1):47–74.
141. Cotton RT, Richardson MA. Congenital laryngeal anomalies. Otolaryngol Clin North Am 1981;14(1):203–218.
142. Smith RJ, Catlin FI. Congenital anomalies of the larynx. Am J Dis Child 1984;138(1):35–39.
143. Benjamin B, Inglis A. Minor congenital laryngeal clefts: diagnosis and classification. Ann Otol Rhinol Laryngol 1989;98(6):417–420.
144. Moungthong G, Holinger LD. Laryngotracheoesophageal clefts. Ann Otol Rhinol Laryngol 1997;106(12):1002–1011.
145. Kalache KD, Chaoui R, Tennstedt C, et al. Prenatal diagnosis of laryngeal atresia in two cases of congenital high airway obstruction syndrome (CHAOS). Prenat Diagn 1997;17(6):577–581.
146. DeCou JM, Jones DC, Jacobs HD, et al. Successful ex utero intrapartum treatment (EXIT) procedure for congenital high airway obstruction syndrome (CHAOS) owing to laryngeal atresia. J Pediatr Surg 1998;33(10):1563–1565.
147. Marshak G, Grundfast KM. Subglottic stenosis. Pediatr Clin North Am 1981;28(4):941–948.
148. Hughes CA, Dunham ME. Congenital anomalies of the larynx and trachea. In: Wetmore RF, Muntz HR, McGill TJ, eds. Pediatric Otolaryngology: Principles and Practice Pathways, Vol. 1. New York: Thieme, 2000;775–786.
149. John SD, Swischuk LE. Stridor and upper airway obstruction in infants and children. Radiographics 1992;12(4):625–643; discussion 644.
150. Healy GB. Subglottic stenosis. Otolaryngol Clin North Am 1989;22(3):599–606.
151. Holinger LD, Oppenheimer RW. Congenital subglottic stenosis: the elliptical cricoid cartilage. Ann Otol Rhinol Laryngol 1989;98(9): 702–706.
152. Schild JA. Congenital malformations of the trachea and bronchi. In: Bluestone CD, Stool SE, Kenna MA, eds. Pediatric Otolaryngology, 3rd ed, Vol 2. Philadelphia: WB Saunders, 1996;1307–1328.
153. Rimell FL, Stool SE. Diagnosis and management of pediatric tracheal stenosis. Otolaryngol Clin North Am 1995;28(4):809–827.
154. Simoneaux SF, Bank ER, Webber JB, et al. MR imaging of the pediatric airway. Radiographics 1995;15(2):287–298; discussion 298–299.
155. Nicolai T, Huber RM, Reiter K, et al. Metal airway stent implantation in children: follow-up of seven children. Pediatr Pulmonol 2001;31(4):289–296.
156. Loeff DS, Filler RM, Vinograd I, et al. Congenital tracheal stenosis: a review of 22 patients from 1965 to 1987. J Pediatr Surg 1988;23(8):744–748.
157. Cantrell JR, Guild HG. Congenital stenosis of the trachea. Am J Surg 1964;108:297–305.
158. Lin SY, Chen JC, Hotaling AJ, et al. Congenital tracheal cartilaginous sleeve. Laryngoscope 1995;105(11):1213–1219.
159. Davis S, Bove KE, Wells TR, et al. Tracheal cartilaginous sleeve. Pediatr Pathol 1992;12(3):349–364.
160. Schmid H. [Synchrondrosis of the laryngotracheal skeleton and tracheostenosis in the Apert-Crouzon syndrome]. Zentralbl Allg Pathol 1971;114(3):326–337.
161. Hernandez RJ, Tucker GF. Congenital tracheal stenosis: role of CT and high kV films. Pediatr Radiol 1987;17(3):192–196.
162. Toki A, Todani T, Watanabe Y, et al. Spiral computed tomography with 3-dimensional reconstruction for the diagnosis of tracheobronchial stenosis. Pediatr Surg Int 1997;12(5/6):334–336.
163. Neuhauser EB. The roentgen diagnosis of double aortic arch and other anomalies of the great vessels. Am J Roentgenol Rad Ther 1946;56(1):1–12.
164. Berdon WE. Rings, slings, and other things: vascular compression of the infant trachea updated from the midcentury to the millennium—the legacy of Robert E. Gross, MD, and Edward B. D. Neuhauser, MD. Radiology 2000;216(3):624–632.
165. Hopkins KL, Patrick LE, Simoneaux SF, et al. Pediatric great vessel anomalies: initial clinical experience with spiral CT angiography. Radiology 1996;200(3):811–815.
166. McCollough CH, Zink FE. Performance evaluation of a multi-slice CT system. Med Phys 1999;26(11):2223–2230.
167. Chen JC, Holinger LD. Congenital tracheal anomalies: pathology study using serial macrosections and review of the literature [see comments]. Pediatr Pathol 1994;14(3):513–537.
168. Swischuk LE. Anterior tracheal indentation in infancy and early childhood: normal or abnormal? Am J Roentgenol Rad Ther Nucl Med 1971;112(1):12–17.
169. Backer CL, Ilbawi MN, Idriss FS, et al. Vascular anomalies causing tracheoesophageal compression. Review of experience in children. J Thorac Cardiovasc Surg 1989;97(5):725–731.
170. Wiatrak BJ, Myer CMD, Cotton RT. Atypical tracheobronchial vascular compression. Am J Otolaryngol 1991;12(6):347–356.
171. Cohen SR, Landing BH. Tracheostenosis and bronchial abnormalities associated with pulmonary artery sling. Ann Otol Rhinol Laryngol 1976;85(5 Pt 1):582–590.
172. Mulliken JB, Glowacki J. Hemangiomas and vascular malformations in infants and children: a classification based on endothelial characteristics. Plast Reconstr Surg 1982;69(3):412–422.
173. Boon LM, Enjolras O, Mulliken JB. Congenital hemangioma: evidence of accelerated involution. J Pediatr 1996;128(3):329–335.
174. Leikensohn JR, Benton C, Cotton R. Subglottic hemangioma. J Otolaryngol 1976;5(6):487–492.
175. Mulliken JB, Fishman SJ, Burrows PE. Vascular anomalies. Curr Probl Surg 2000;37(8):517–584.
176. Frieden IJ, Reese V, Cohen D. PHACE syndrome. The association of posterior fossa brain malformations, hemangiomas, arterial anomalies, coarctation of the aorta and cardiac defects, and eye abnormalities. Arch Dermatol 1996;132(3):307–311.
177. Boulinguez S, Teillac-Hamel D, Bedane C, et al. Cervicofacial hemangioma and a minor sternal malformation: inclusion in PHACES syndrome? Pediatr Dermatol 1998;15(2):119–121.
178. Sutton TJ, Nogrady MB. Radiologic diagnosis of subglottic hemangioma in infants. Pediatr Radiol 1973;1(4):211–216.
179. Cooper M, Slovis TL, Madgy DN, et al. Congenital subglottic hemangioma: frequency of symmetric subglottic narrowing on frontal radiographs of the neck. AJR 1992;159(6):1269–1271.
180. Healy G, McGill T, Friedman EM. Carbon dioxide laser in subglottic hemangioma. An update. Ann Otol Rhinol Laryngol 1984;93(4 Pt 1):370–373.
181. Kacker A, April M, Ward RF. Use of potassium titanyl phosphate (KTP) laser in management of subglottic hemangiomas. Int J Pediatr Otorhinolaryngol 2001;59(1):15–21.
182. Boyd JB, Mulliken JB, Kaban LB, et al. Skeletal changes associated with vascular malformations. Plast Reconstr Surg 1984;74(6): 789–797.
183. Azar GB, Snijders RJ, Gosden C, et al. Fetal nuchal cystic hygromata: associated malformations and chromosomal defects. Fetal Diagn Ther 1991;6(1-2):46–57.
184. Chervenak FA, Isaacson G, Blakemore KJ, et al. Fetal cystic hygroma. Cause and natural history. N Engl J Med 1983;309(14): 822–825.
185. Burrows PE, Laor T, Paltiel H, et al. Diagnostic imaging in the evaluation of vascular birthmarks. Dermatol Clin 1998;16(3): 455–488.
186. Hubbard AM, Crombleholme TM, Adzick NS. Prenatal MRI evaluation of giant neck masses in preparation for the fetal exit procedure. Am J Perinatol 1998;15(4):253–257.
187. Ogita S, Tsuto T, Deguchi E, et al. OK-432 therapy for unresectable lymphangiomas in children. J Pediatr Surg 1991;26(3):263–268; discussion 268–270.
188. Ohlms LA, Forsen J, Burrows PE. Venous malformation of the pediatric airway. Int J Pediatr Otorhinolaryngol 1996;37(2):99–114.
189. Williams MA. Head and neck findings in pediatric acquired immune deficiency syndrome. Laryngoscope 1987;97(6):713–716.

Copyright © 2003, Mosby, Inc. All rights reserved.

190. Ungkanont K, Yellon RF, Weissman JL, et al. Head and neck space infections in infants and children. Otolaryngol Head Neck Surg 1995;112(3):375–382.
191. Gidley PW, Ghorayeb BY, Stiernberg CM. Contemporary management of deep neck space infections. Otolaryngol Head Neck Surg 1997;116(1):16–22.
192. Stone ME, Walner DL, Koch BL, et al. Correlation between computed tomography and surgical findings in retropharyngeal inflammatory processes in children. Int J Pediatr Otorhinolaryngol 1999;49(2):121–125.
193. Glasier CM, Stark JE, Jacobs RF, et al. CT and ultrasound imaging of retropharyngeal abscesses in children. AJNR 1992;13(4):1191–1195.
194. Hudgins PA, Dorey JH, Jacobs IN. Internal carotid artery narrowing in children with retropharyngeal lymphadenitis and abscess. AJNR 1998;19(10):1841–1843.
195. Robson CD. Imaging of granulomatous lesions of the neck in children. Radiol Clin North Am 2000;38(5):969–977.
196. Robson CD, Hazra R, Barnes PD, et al. Nontuberculous mycobacterial infection of the head and neck in immunocompetent children: CT and MR findings. AJNR 1999;20(10):1829–1835.
197. Gersony WM. Diagnosis and management of Kawasaki disease. JAMA 1991;265(20):2699–2703.
198. Levine PH, Jahan N, Murari P, et al. Detection of human herpesvirus 6 in tissues involved by sinus histiocytosis with massive lymphadenopathy (Rosai-Dorfman disease). J Infect Dis 1992;166(2):291–295.
199. Midwinter KI, Hodgson D, Yardley M. Paediatric epiglottitis: the influence of the *Haemophilus influenzae* b vaccine, a ten-year review in the Sheffield region. Clin Otolaryngol 1999;24(5):447–448.
200. Slack CL, Allen GC, Morrison JE, et al. Post-varicella epiglottitis and necrotizing fasciitis. Pediatrics 2000;105(1):e13.
201. Macpherson RI, Leithiser RE. Upper airway obstruction in children: an update. Radiographics 1985;5(3):339–376.
202. McCook TA, Kirks DR. Epiglottic enlargement in infants and children: another radiologic look. Pediatr Radiol 1982;12(5):227–234.
203. Watts FB Jr, Slovis TL. The enlarged epiglottis. Pediatr Radiol 1977;5(3):133–136.
204. Marx A, Torok TJ, Holman RC, et al. Pediatric hospitalizations for croup (laryngotracheobronchitis): biennial increases associated with human parainfluenza virus 1 epidemics. J Infect Dis 1997;176(6):1423–1427.
205. Ross LA, Mason WH, Lanson J, et al. Laryngotracheobronchitis as a complication of measles during an urban epidemic. J Pediatr 1992;121(4):511–515.
206. Damm M, Eckel HE, Jungehulsing M, et al. Management of acute inflammatory childhood stridor. Otolaryngol Head Neck Surg 1999;121(5):633–638.
207. Kushner DC, Harris GB. Obstructing lesions of the larynx and trachea in infants and children. Radiol Clin North Am 1978;16(2):181–194.
208. Swischuk LE, Smith PC, Fagan CJ. Abnormalities of the pharynx and larynx in childhood. Semin Roentgenol 1974;9(4):283–300.
209. Currarino G, Williams B. Lateral inspiration and expiration radiographs of the neck in children with laryngotracheitis (croup). Radiology 1982;145(2):365–366.
210. Hughes PA, Lepow ML. Infections of the lower respiratory tract. In: Bluestone CD, Stool SE, Kenna MA, eds. Pediatric Otolaryngology, 3rd ed, Vol 2. Philadelphia: WB Saunders, 1996;1329–1340.
211. Donnelly BW, McMillan JA, Weiner LB. Bacterial tracheitis: report of eight new cases and review. Rev Infect Dis 1990;12(5):729–735.
212. Lebovics RS, Hoffman GS, Leavitt RY, et al. The management of subglottic stenosis in patients with Wegener's granulomatosis. Laryngoscope 1992;102(12 Pt 1):1341–1345.
213. Bohlman ME, Ensor RE, Goldman SM. Primary Wegener's granulomatosis of the trachea: radiologic manifestations. South Med J 1984;77(10):1318–1319.
214. Prasad S, Grundfast KW, Lipnick R. Airway obstruction in an adolescent with relapsing polychondritis. Otolaryngol Head Neck Surg 1990;103(1):113–116.
215. Alcaraz N, Lawson W. Trauma of the nose and nasoethmoid complex in children and adolescents. Facial Plast Surg Clin North Am 1999;7(2):175–183.
216. Marshall MD, Buchbinder D. Pediatric mandibular injury. Facial Plast Surg Clin North Am 1999;7(2):195–203.
217. Schoem SR, Choi SS, Zalzal GH, et al. Management of oropharyngeal trauma in children. Arch Otolaryngol Head Neck Surg 1997;123(12):1267–1270.
218. Munera F, Soto JA, Palacio D, et al. Diagnosis of arterial injuries caused by penetrating trauma to the neck: comparison of helical CT angiography and conventional angiography. Radiology 2000;216(2):356–362.
219. LeBlang SD, Nunez DB Jr. Noninvasive imaging of cervical vascular injuries. AJR 2000;174(5):1269–1278.
220. Fitz-Hugh GS, Powell JB 2nd. Acute traumatic injuries of the oropharynx, laryngopharynx, and cervical trachea in children. Otolaryngol Clin North Am 1970;3(2):375–393.
221. Link DT, Cotton RT. The laryngotracheal complex in pediatric head and neck trauma. Facial Plast Surg Clin North Am 1999;7(2):133–144.
222. Stanley RB Jr. Value of computed tomography in management of acute laryngeal injury. J Trauma 1984;24(4):359–362.
223. Schild JA, Denneny EC. Evaluation and treatment of acute laryngeal fractures. Head Neck 1989;11(6):491–496.
224. Polansky A, Resnick D, Sofferman RA, et al. Hyoid bone elevation: a sign of tracheal transection. Radiology 1984;150(1):117–120.
225. Snow JB Jr. Diagnosis and therapy for acute laryngeal and tracheal trauma. Otolaryngol Clin North Am 1984;17(1):101–106.
226. Greene R, Stark P. Trauma of the larynx and trachea. Radiol Clin North Am 1978;16(2):309–320.
227. Kulick RM, Selbst SM, Baker MD, et al. Thermal epiglottitis after swallowing hot beverages. Pediatrics 1988;81(3):441–444.
228. Sheridan RL. Recognition and management of hot liquid aspiration in children. Ann Emerg Med 1996;27(1):89–91.
229. Benjamin BNP. Special laryngoscopy techniques. In: Benjamin BNP, ed. Diagnostic Laryngology. Philadelphia: WB Saunders, 1990;59–63.
230. Holinger PH, Kutnick SL, Schild JA, et al. Subglottic stenosis in infants and children. Ann Otol Rhinol Laryngol 1976;85(5 Pt 1):591–599.
231. Grundfast KM, Morris MS, Bernsley C. Subglottic stenosis: retrospective analysis and proposal for standard reporting system. Ann Otol Rhinol Laryngol 1987;96(1 Pt 1):101–105.
232. Holinger LD, Toriumi DM, Anandappa EC. Subglottic cysts and asymmetrical subglottic narrowing on neck radiograph. Pediatr Radiol 1988;18(4):306–308.
233. Tom LW, Miller L, Wetmore RF, et al. Endoscopic assessment in children with tracheotomies. Arch Otolaryngol Head Neck Surg 1993;119(3):321–324.
234. Wai Pak M, Chung Lee W, Kwok Fung H, et al. A prospective study of foreign-body ingestion in 311 children. Int J Pediatr Otorhinolaryngol 2001;58(1):37–45.
235. Singh B, Kantu M, Har-El G, et al. Complications associated with 327 foreign bodies of the pharynx, larynx, and esophagus. Ann Otol Rhinol Laryngol 1997;106(4):301–304.
236. Daniilidis J, Symeonidis B, Triaridis K, et al. Foreign body in the airways: a review of 90 cases. Arch Otolaryngol 1977;103(10):570–573.
237. Esclamado RM, Richardson MA. Laryngotracheal foreign bodies in children. A comparison with bronchial foreign bodies. Am J Dis Child 1987;141(3):259–262.
238. Morioka WT, Maisel RH, Smith TW, et al. Unexpected radiographic findings related to foreign bodies. Ann Otol Rhinol Laryngol 1975;84(5 Pt 1):627–630.
239. Newman DE. The radiolucent esophageal foreign body: an often-forgotten cause of respiratory symptoms. J Pediatr 1978;92(1):60–63.
240. Smith PC, Swischuk LE, Fagan CJ. An elusive and often unsuspected cause of stridor or pneumonia (the esophageal foreign body). Am J Roentgenol Rad Ther Nucl Med 1974;122(1):80–89.
241. Paradise JL, Bernard BS, Colborn DK, et al. Assessment of adenoidal obstruction in children: clinical signs versus roentgenographic findings. Pediatrics 1998;101(6):979–986.
242. Potsic WP. Assessment and treatment of adenotonsillar hypertrophy in children. Am J Otolaryngol 1992;13(5):259–264.
243. Fitzgerald P, O'Connell D. Massive hypertrophy of the lingual tonsils: an unusual cause of dysphagia. Br J Radiol 1987;60(713):505–506.

Copyright © 2003, Mosby, Inc. All rights reserved.

244. Wolfensberger M, Haury JA, Linder T. Parent satisfaction 1 year after adenotonsillectomy of their children. Int J Pediatr Otorhinolaryngol 2000;56(3):199–205.
245. Cohen LM, Koltai PJ, Scott JR. Lateral cervical radiographs and adenoid size: do they correlate? Ear Nose Throat J 1992;71(12):638–642.
246. Hibbert J, Whitehouse GH. The assessment of adenoidal size by radiological means. Clin Otolaryngol 1978;3(1):43–47.
247. Fujioka M, Young LW, Girdany BR. Radiographic evaluation of adenoidal size in children: adenoidal-nasopharyngeal ratio. AJR 1979;133(3):401–404.
248. Paradise JL. Tonsillectomy and adenoidectomy. In: Bluestone CD, Stool SE, Kenna MA, eds. Pediatric Otolaryngology, 3rd ed, Vol 2. Philadelphia: WB Saunders, 1996;1054–1065.
249. Morgan AH, Zitsch RP. Recurrent respiratory papillomatosis in children: a retrospective study of management and complications. Ear Nose Throat J 1986;65(9):19–28.
250. Abramson AL, Steinberg BM, Winkler B. Laryngeal papillomatosis: clinical, histopathologic and molecular studies. Laryngoscope 1987;97(6):678–685.
251. Mounts P, Kashima H. Association of human papillomavirus subtype and clinical course in respiratory papillomatosis. Laryngoscope 1984;94(1):28–33.
252. Smith EM, Johnson SR, Cripe TP, et al. Perinatal vertical transmission of human papillomavirus and subsequent development of respiratory tract papillomatosis. Ann Otol Rhinol Laryngol 1991;100(6):479–483.
253. Tenti P, Zappatore R, Migliora P, et al. Perinatal transmission of human papillomavirus from gravidas with latent infections. Obstet Gynecol 1999;93(4):475–479.
254. Derkay CS. Recurrent respiratory papillomatosis. Laryngoscope 2001;111(1):57–69.
255. Solomon D, Smith RR, Kashima HK, et al. Malignant transformation in nonirradiated recurrent respiratory papillomatosis. Laryngoscope 1985;95(8):900–904.
256. Rady PL, Schnadig VJ, Weiss RL, et al. Malignant transformation of recurrent respiratory papillomatosis associated with integrated human papillomavirus type 11 DNA and mutation of *p53*. Laryngoscope 1998;108(5):735–740.
257. Benjamin B, Parsons DS. Recurrent respiratory papillomatosis: a 10 year study. J Laryngol Otol 1988;102(11):1022–1028.
258. Doyle DJ, Gianoli GJ, Espinola T, et al. Recurrent respiratory papillomatosis: juvenile versus adult forms. Laryngoscope 1994; 104(5 Pt 1):523–527.
259. Derkay CS. Task force on recurrent respiratory papillomas. A preliminary report. Arch Otolaryngol Head Neck Surg 1995;121(12): 1386–1391.
260. Gullane PJ, Davidson J, O'Dwyer T, et al. Juvenile angiofibroma: a review of the literature and a case series report. Laryngoscope 1992;102(8):928–933.
261. Davis KR. Embolization of epistaxis and juvenile nasopharyngeal angiofibromas. AJR 1987;148(1):209–218.
262. Scholtz AW, Appenroth E, Kammen-Jolly K, et al. Juvenile nasopharyngeal angiofibroma: management and therapy. Laryngoscope 2001;111(4 Pt 1):681–687.
263. Robinson AC, Khoury GG, Ash DV, et al. Evaluation of response following irradiation of juvenile angiofibromas. Br J Radiol 1989;62(735):245–247.
264. Tapper D, Lack EE. Teratomas in infancy and childhood. A 54-year experience at the Children's Hospital Medical Center. Ann Surg 1983;198(3):398–410.
265. Suh JS, Abenoza P, Galloway HR, et al. Peripheral (extracranial) nerve tumors: correlation of MR imaging and histologic findings. Radiology 1992;183(2):341–346.
266. O'Halloran LR, Lusk RP. Amyloidosis of the larynx in a child. Ann Otol Rhinol Laryngol 1994;103(8 Pt 1):590–594.
267. Wells RG, Sty JR, Duck SC. Technetium 99m pertechnetate thyroid scintigraphy: congenital hypothyroid screening. Pediatr Radiol 1986;16(5):368–373.
268. Optican RJ, White KS, Effmann EL. Goitrous cretinism manifesting as newborn stridor: CT evaluation. AJR 1991;157(3):557–558.
269. Cunningham MJ, Myers EN, Bluestone CD. Malignant tumors of the head and neck in children: a twenty-year review. Int J Pediatr Otorhinolaryngol 1987;13(3):279–292.
270. Cunningham MJ, Mcguirt WF, Myers EN. Malignant tumors of the head and neck. In: Bluestone CD, Stool SE, Kenna MA, eds. Pediatric Otolaryngology, 3rd ed, Vol 2. Philadelphia: WB Saunders, 1996;1557–1583.
271. Lukes RJ, Collins RD. Immunologic characterization of human malignant lymphomas. Cancer 1974;34(Suppl 4):1488–1503.
272. Raphael MM, Audouin J, Lamine M, et al. Immunophenotypic and genotypic analysis of acquired immunodeficiency syndrome-related non-Hodgkin's lymphomas. Correlation with histologic features in 36 cases. French Study Group of Pathology for HIV-Associated Tumors. Am J Clin Pathol 1994;101(6):773–782.
273. McGrath MS, Shiramizu B, Meeker TC, et al. AIDS-associated polyclonal lymphoma: identification of a new HIV-associated disease process. J Acquir Immune Defic Syndr 1991;4(4):408–415.
274. Thompson P, Standen GR. Wiskott-Aldrich syndrome: no evidence of chromosome instability. Cancer Genet Cytogenet 1993;69(1): 22–24.
275. Goldenberg D, Golz A, Netzer A, et al. Epstein-Barr virus and cancers of the head and neck. Am J Otolaryngol 2001;22(3): 197–205.
276. Ziegler JL. Burkitt's lymphoma. N Engl J Med 1981;305(13): 735–745.
277. Kearns DB, Smith RJ, Pitcock JK. Burkitt's lymphoma. Int J Pediatr Otorhinolaryngol 1986;12(1):73–84.
278. Levine PH, Kamaraju LS, Connelly RR, et al. The American Burkitt's Lymphoma Registry: eight years' experience. Cancer 1982;49(5):1016–1022.
279. Sullivan MP. Hodgkin's disease in children. Hematol Oncol Clin North Am 1987;1(4):603–620.
280. Dagher R, Helman L. Rhabdomyosarcoma: an overview. Oncologist 1999;4(1):34–44.
281. MacArthur CJ, McGill TJ, Healy GB. Pediatric head and neck rhabdomyosarcoma. Clin Pediatr (Phila) 1992;31(2):66–70.
282. Anderson GJ, Tom LW, Womer RB, et al. Rhabdomyosarcoma of the head and neck in children. Arch Otolaryngol Head Neck Surg 1990;116(4):428–431.
283. Diller L, Sexsmith E, Gottlieb A, et al. Germline *p53* mutations are frequently detected in young children with rhabdomyosarcoma. J Clin Invest 1995;95(4):1606–1611.
284. Yang P, Grufferman S, Khoury MJ, et al. Association of childhood rhabdomyosarcoma with neurofibromatosis type I and birth defects. Genet Epidemiol 1995;12(5):467–474.
285. Brookes CN, van Velzen D. Rhabdomyosarcoma presenting as a facial swelling in a child. A case report and review of the literature. Br J Oral Maxillofac Surg 1990;28(2):117–121.
286. Coene IJ, Schouwenburg PF, Voute PA, et al. Rhabdomyosarcoma of the head and neck in children. Clin Otolaryngol 1992;17(4): 291–296.
287. Zubizarreta PA, D'Antonio G, Raslawski E, et al. Nasopharyngeal carcinoma in childhood and adolescence: a single-institution experience with combined therapy. Cancer 2000;89(3):690–695.
288. Schmidt D, Leuschner I, Harms D, et al. Malignant rhabdoid tumor. A morphological and flow cytometric study. Pathol Res Pract 1989;184(2):202–210.
289. De Keyser LF, Van Herle AJ. Differentiated thyroid cancer in children. Head Neck Surg 1985;8(2):100–114.
290. White AK, Smith RJ. Thyroid nodules in children. Otolaryngol Head Neck Surg 1986;95(1):70–75.
291. Schwartz DA, Katin L, Lesser RD, et al. Juvenile laryngeal carcinoma: correlation of computed tomography and magnetic resonance imaging with pathology. Ann Clin Lab Sci 1990;20(3): 225–230.

Copyright © 2003, Mosby, Inc. All rights reserved.

Copyright © 2003, Mosby, Inc. All rights reserved.

30

The Larynx

Hugh D. Curtin

INTRODUCTION
SECTION ONE: ANATOMY
- Spaces
- Innervation and Blood Supply
- Lymphatic Drainage
- Regions

SECTION TWO: IMAGING
- Respiratory Maneuvers
- Plain Film Radiography
- Tomography
- Fluoroscopy
- Contrast Examinations
- Barium Swallow
- Computed Tomography Scanning
- Magnetic Resonance Imaging
- Ultrasonography, Nuclear Medicine, and Angiography

SECTION THREE: PATHOLOGIC CONDITIONS
SQUAMOUS CELL CARCINOMA
- General Considerations
- Voice Conservation Therapy
- Cartilage Involvement
- Nodal Metastasis
- Further Workup of the Patient with Squamous Cell Carcinoma

SITE-SPECIFIC EVALUATION
- Supraglottic Larynx
- Glottic and Infraglottic Regions
- Ventricular Tumors
- Pharynx

OTHER MALIGNANT TUMORS
BENIGN TUMORS
CYSTS AND LARYNGOCELES
INFECTION AND INFLAMMATION
- Croup
- Epiglottitis or Supraglottitis
- Tuberculosis and Other Granulomatous Lesions
- Neck Infection
- Rheumatoid and Collagen Vascular Disease
- Gastroesophageal Reflux

TRAUMA
CONGENITAL LESIONS
- Laryngomalacia
- Subglottic Stenosis
- Webs and Atresia
- Clefts
- Subglottic Hemangiomas
- Other Anomalies

STENOSIS
VOCAL CORD PARALYSIS
- Superior Nerve
- Recurrent Nerve
- Adductor Paralysis

MISCELLANEOUS CONDITIONS
- Benign Cartilage Changes
- Osteophytes of the Spine
- Carotid Position
- Postsurgical Changes
- Radiation Changes
- Stents, Tubes, and Teflon

INTRODUCTION

Although entirely within the soft tissues of the neck, the mucosal surfaces of the larynx are readily accessible to either indirect visualization using a mirror or direct visualization by employing an office endoscope. After the scope is passed through the nose and directed toward the larynx, almost all of the endolarynx can be seen and most tumors are diagnosed at the initial office visit. If voice problems are suspected, videotaping of the direct examina-

Copyright © 2003, Mosby, Inc. All rights reserved.

tion allows assessment of subtle movement disorders. Only if the initial clinical evaluation is inconclusive is a direct examination under anesthesia performed. This inspection allows better direct observation of the laryngeal mucosa, as well as the best direct examination of the laryngeal ventricle and the subglottic region. Biopsies can be performed to confirm a suspected diagnosis and to document subtle mucosal extension not appreciated on the office endoscopic examination. What cannot be visualized is deep soft-tissue extension or cartilaginous involvement. That evaluation falls into the domain of imaging, done as an adjunct to direct evaluation.

The larynx presents one of the true challenges of head and neck imaging. The organ is small and in almost constant motion. Breathing and swallowing create significant artifacts that can be controlled only briefly. The quality of laryngeal images has always been related to acquisition speed, and today, with multidetector spiral CT scanning and fast MRI techniques, excellent images can be achieved. Multidetector CT scanners can now cover the entire larynx in the time that, just a few years ago, could produce only a single axial image. The information obtained by modern imaging, when combined with the surface visualization of modern laryngoscopy, provides excellent understanding of pathology of the larynx.

This chapter first discusses the normal anatomy as seen using various imaging modalities. A discussion of the alterations of this anatomy, as a result of various types of pathology, follows. For completeness, some processes in which imaging is seldom helpful are also included. A discussion of the laryngopharynx (hypopharynx) is included because of its intimate relationship to posterior aspects of the larynx.

SECTION ONE

ANATOMY

There are three main functions of the larynx. The first, and most critical, is maintenance of the airway. The second is to help protect against aspiration, and the third is phonation. The anatomy[1] of the larynx is complex. It is a relatively tubular or cylindrical system of mucosal folds separated from an outer cartilaginous skeleton by intervening spaces filled with fat and muscle. Direct visualization of the endolarynx shows obvious landmarks including the epiglottis, aryepiglottic folds, false cords (folds), and true vocal cords (folds).

The region of the true cords, false cords, and intervening ventricle is particularly important in organizing the anatomy of the larynx. The true and false cords (vocal folds and vestibular folds) are axially oriented parallel structures situated at approximately the midlarynx along the craniocaudal axis. They extend from anterior to posterior, lying along the lateral aspect of the airway. The true cords converge anteriorly to attach to the midregion of the fused portion of thyroid cartilage. The vocal ligament is a thin fibrous band within the free margin of the true cord that extends the full length of the true cord from the vocal process of the arytenoid cartilage to the anterior commissure. The term *anterior commissure* refers to the region of the attachment of the vocal ligaments to the cartilage. This region includes the anterior cord, the thyroid cartilage, and Broyles' ligament, a fibrous structure connecting the vocal ligaments to the cartilage. Notably there is no perichondrium at that point, so the fibers extend directly from the vocal ligament into the structure of the cartilage.[2, 3]

The tubular airway extending from the cranial margin of the larynx to the level of the true vocal cords is referred to as the laryngeal vestibule. It has a circular or oval cross-sectional shape, and it is bounded by the epiglottis and the aryepiglottic (AE) folds. The AE folds sweep downward and posteriorly from the lateral margins of the midline anterior epiglottis to the arytenoid cartilages, just lateral to the midline in the posterior larynx. In the free posterior edge of the AE fold on either side, there are two small bumps or prominences. The more cranial one is the cuneiform cartilage, and the more caudal one is the corniculate cartilage. The corniculate cartilage is perched upon the superior aspect of the arytenoid cartilage. The interarytenoid area forms the posterior margin of the entrance to the larynx. Along the lateral surface of each AE fold is the pyriform sinus, which is actually an anterior recess of the hypopharynx (see also Chapter 28) (Figs. 30-1 and 30-2).

The skeleton of the larynx is made up of cartilage, fibrous sheets, and bands (Figs. 30-3 to 30-5). The cricoid cartilage is the only complete ring in the respiratory system and represents the foundation of the larynx. The shape of the cricoid cartilage resembles a signet ring with the quadrate lamina, or larger ''signet'' part, facing posteriorly. There is a vertically oriented midline ridge on the posterior surface of the quadrate lamina. The lateral aspect of the cricoid tapers gradually downward toward the much thinner anterior arch.

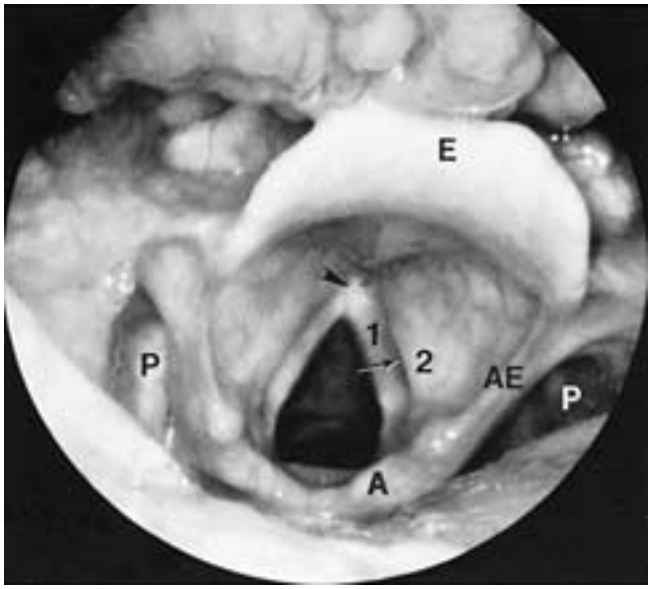

FIGURE 30-1 Endoscopic view of the larynx. *1*, True vocal cord; *2*, false vocal cord; *E*, epiglottis; *AE*, AE fold; *A*, arytenoid prominence; *P* pyriform; *arrowhead*, anterior commissure. Arrow points to the entrance of the ventricle. (From Hanafee W. Hypopharynx and larynx. In: Valvassori GE et al., eds. Head and Neck Imaging. New York: Thieme, 1988.)

VIEW IMAGE

Copyright © 2003, Mosby, Inc. All rights reserved.

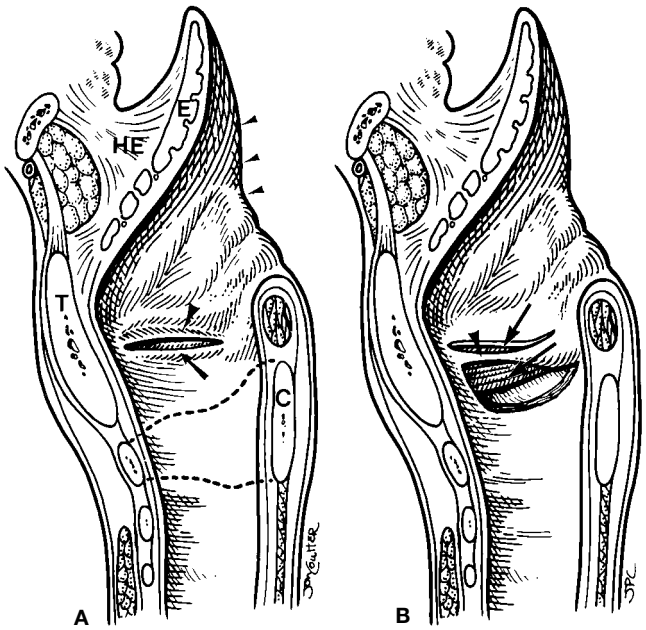

VIEW IMAGE

FIGURE 30-2 **A**, Lateral wall of the airway. The larynx has been sectioned sagittally in the midline. The true cord (*arrow*) and the false cord (*large arrowhead*) are separated by the slit-like ventricle. *Small arrowheads*, AE fold; *T*, thyroid cartilage; *C*, lamina of the cricoid cartilage (the projection of the arch of the cricoid is seen as a dashed line); *HE*, hyoepiglottic ligament; *E*, epiglottis. **B**, The mucosa of the true cord has been excised, showing the thyroarytenoid muscle (*arrows*) paralleling the margin of the true cord (*arrowhead*).

The lower edge of the entire cricoid is at the same horizontal level and defines the caudal aspect of the larynx. On either side, at the junction of the lateral arch and the quadrate lamina, there is a small facet for the articulation of the inferior horn of the thyroid cartilage. On the upper surface of the cricoid lamina are two paired articular facets, the cricoid portions of the cricoarytenoid joints (Figs. 30-4 and 30-6).

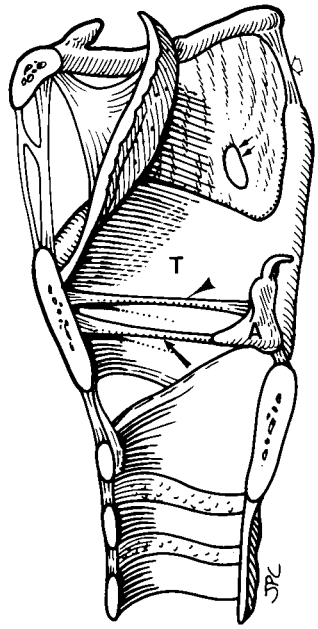

VIEW IMAGE

FIGURE 30-4 Lateral diagram of the larynx with the mucosa, laryngeal muscles, and paraglottic fat removed to show the skeleton of the larynx. The vocal ligament (*arrow*) stretches from the vocal process of the arytenoid (*A*) to the anterior thyroid cartilage. The ventricular ligament (*arrowhead*) stretches from the upper arytenoid to the thyroid cartilage. The small structure at the upper tip of the arytenoid is the corniculate cartilage. The lamina of the thyroid cartilage is represented by the letter T. The small hole (*double small arrows*) in the thyrohyoid membrane transmits the internal branch of the superior laryngeal nerve and the accompanying vessels. The posterior thyrohyoid ligament (*open arrow*) represents the posterior margin of the thyrohyoid membrane.

These facets are approximately 5 to 8 mm lateral to the midline.

The largest cartilage is the double-winged thyroid cartilage, with prominent superior and inferior cornua projecting from the posterior margin of either side of the

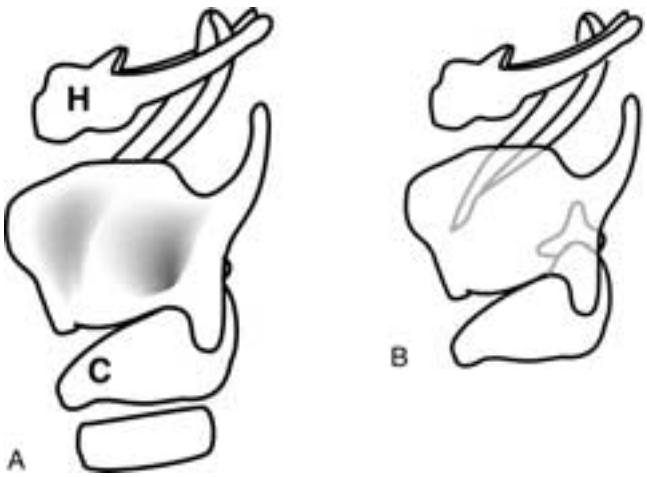

VIEW IMAGE

FIGURE 30-3 **A**, Lateral view of the cartilaginous skeleton shows the thyroid cartilage perched upon the cricoid cartilage (*C*). The epiglottis is partially shielded by the thyroid cartilage. Hyoid bone (*H*). **B**, Partial transparency of the thyroid cartilage shows the remaining outline of the lower epiglottis and demonstrates the arytenoid cartilage perched on the upper edge of the cricoid cartilage.

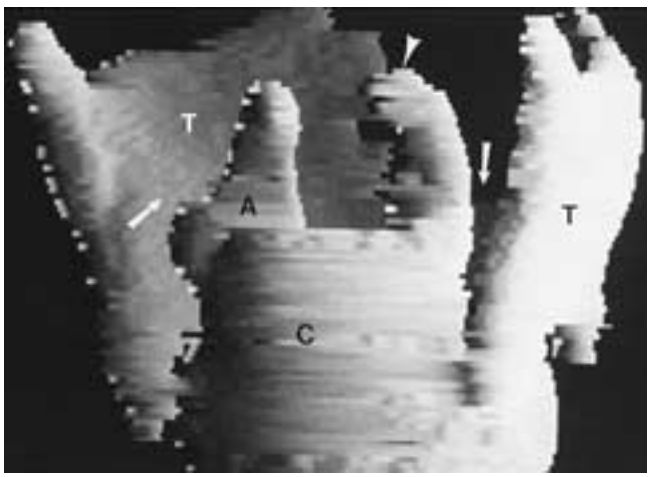

VIEW IMAGE

FIGURE 30-5 Computer reconstruction of the larynx, from axial CT scans, is viewed from posteriorly and slightly to the right. The arytenoid (*A*) is perched on the lamina of the cricoid cartilage (*C*). Thyroid cartilage is represented by the letter T. Arrows show the thyroarytenoid gap representing the position of the apex of the pyriform sinus. The arrowhead shows the corniculate cartilage.

Copyright © 2003, Mosby, Inc. All rights reserved.

thyroid ala (wings). The lower cornu articulates with the lateral facets of the cricoid cartilage, forming the cricothyroid joint. The superior thyoid cornu is connected to the dorsal tip of the greater cornu of the hyoid bone by the thyrohyoid ligament. The remaining gap between the upper surface of the thyroid cartilage and the hyoid bone is filled by the tough thyrohyoid membrane. There is a deep thyroid notch in the midline of the superior margin of the thyroid cartilage. Where the thyroid alae join at the bottom of this notch, there is a prominence that forms the Adam's apple. Thus, the fused portion of the thyroid cartilage extends from the bottom of the superior thyroid notch to the caudal margin of the anterior thyroid cartilage and, as mentioned, the anterior commissure is situated on the inner surface of the cartilage near the midpoint of this fused region. The thyroid and cricoid cartilages act as the external protective shield for the inner larynx.

On the outer lateral surface of the thyroid cartilage is the oblique line extending downward and anteriorly from the root of the superior thyroid cornu toward the lower border of the thyroid ala. The sternothyroid muscle, thyrohyoid muscle, and inferior pharyngeal constrictor muscles attach to this line.

Perched on the superior edge of the cricoid cartilage are the paired arytenoid cartilages. Each arytenoid cartilage is roughly pyramid-shaped. At the level of the arytenoid cartilage base (inferior aspect) are two projections: the muscular process, situated on the posterolateral margin, and the vocal process located anteriorly. The vocal ligament attaches to the vocal process of the arytenoid cartilage (Figs. 30-4 and 30-6). The superior process represents the apex of the pyramid, and the corniculate cartilage rests on this margin. The vertical height of the arytenoid cartilage spans the laryngeal ventricle. The vocal and muscular processes are at the level of the true cord, while the superior process is above the level of the ventricle at the level of the false cord.

The cricothyroid, cricoarytenoid, and corniculate-arytenoid joints are all true synovial joints and subject to all of the diseases that may afflict such joints.

The cricoid, thyroid, and arytenoid cartilages are all hyaline cartilages and ossify to varying degrees. Ossification occurs via an endochondral process, as found in the long bones of the extremities. Normally, the perichondrium of these cartilages is quite resistant to penetration of blood vessels. However, along the lines of attachment of the muscular ligamentous attachments to these cartilages, fibers violate the perichondrium and allow blood vessels to enter the cartilage. It is from these points that enchondral ossification proceeds. Thus, the first regions of the laryngeal cartilages to ossifiy are along the lines of attachment of the muscles to these cartilages. Unfortunately, ossification proceeds in a quite variable manner, and asymmetry between the left and right sides is common. In the ossified portions of the laryngeal cartilages, fatty marrow develops. As will be discussed later, these areas of ossification, intermixed with regions of nonossified cartilage, may confuse the imaging evaluation of cartilage invasion. In addition, cartilage is normally quite resistant to tumor invasion, while bone is not. Thus, the areas of ossified cartilage are more prone to direct tumor invasion from carcinomas arising within or adjacent to the larynx.

By comparison, the epiglottis consists of yellow elastic fibrocartilage and, unlike the hyaline cartilages, seldom calcifies unless damaged, usually by a granulomatous process. The epiglottis is extremely flexible and has a ''memory'' allowing it to return to its normal shape after being bent nearly to a right angle. The epiglottis has a flattened teardrop shape that tapers to an inferior point called the petiole. Although the major portion of the epiglottis extends down behind the protective shield of the thyroid cartilage, a small portion, often referred to as the suprahyoid epiglottis, extends above the level of hyoid bone. Although the suprahyoid portion of the epiglottis is a continuous sheet of cartilage, the laryngeal portion of the epiglottis is perforated with numerous holes. As a result, whenever a process is on the laryngeal mucosal surface of this cartilage, it is pathologically considered to have extended through the cartilage. The epiglottic cartilage is stabilized by the hyoepiglottic and thyroepiglottic ligaments. The thryroepiglottic ligament attaches to the inner cortex of the thyroid cartilage just above the anterior commissure. The hyoepiglottic ligament extends from the hyoid bone to the anterior surface of the epiglottis, and the mobile or flexible portion of the epiglottis lies cranial to this attachment. The laryngeal portion of the epiglottis lies caudal to this level, between the hyoepiglottic and thyroepiglottic ligaments. Along with the free edge of the epiglottis and the AE folds, the hyoepiglottic ligament defines the cranial margin of the larynx.

As mentioned, there are three smaller paired cartilages in the upper larynx. They are usually not radiologically significant, but are occasionally visualized. The corniculate cartilages are small and sit immediately superior to the arytenoid cartilages (Fig. 30-4). They may not be distinguished from the larger arytenoid cartilages or they may be seen as a small bump in the lowermost AE fold. Slightly lateral and cranial to the corniculate cartilages, buried in the

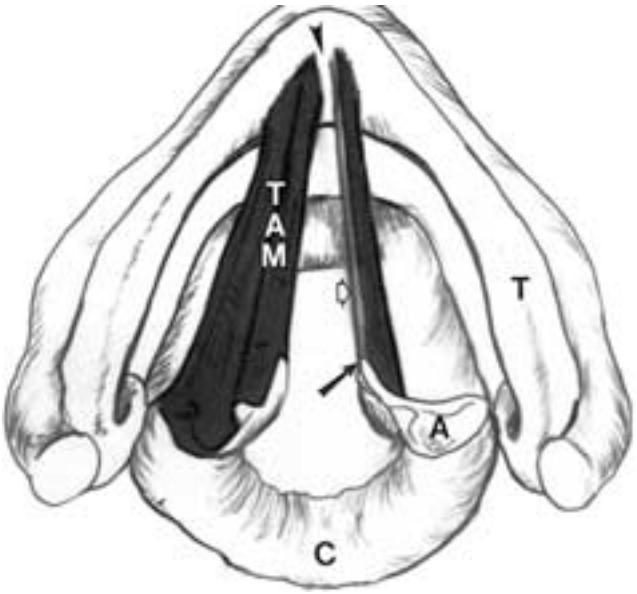

VIEW IMAGE

FIGURE 30-6 Larynx viewed from above; the mucosa and most of the soft tissues of the larynx have been removed to show the relationship of the arytenoid (*A*), cricoid ring (*C*), and thyroid cartilage (*T*). The vocal ligament (*open arrow*) stretches from the vocal process (*arrow*) of the arytenoid to the anterior commissure (*arrowhead*). *TAM*, thyroarytenoid muscle. Only the medial muscle bundle (vocalis) is seen on the right.

Copyright © 2003, Mosby, Inc. All rights reserved.

free edge of the AE folds, are the thin cuneiform cartilages, which are almost never visualized on sectional imaging. The triticeal (tritiate or triticeous) cartilage (cartilago triticea) is located in the thyrohyoid ligament in the posterior edge of the thyrohyoid membrane. This cartilage frequently calcifies and on plain films may mimic a foreign body.

The hyoid bone is the ''rafter'' from which the larynx is suspended. Muscles acting on the hyoid bone elevate the larynx and move it ventrally, providing the primary protection from aspiration. The hyoid bone is U-shaped, having an anterior body and two large (greater) cornua that project posteriorly. Two small (lesser) cornua project superiorly from the hyoid body. The stylohyoid ligaments attach to these lesser cornua. A sagittal section through the hyoid body has the shape of an inverted L open posteriorly and inferiorly.

Two parallel ligaments extend anteriorly from each arytenoid cartilage to attach to the inner lamina of the thyroid cartilage (Fig. 30-4). The more inferior vocal ligaments stretch from the vocal process of each arytenoid cartilage anteriorly to reach the anterior commissure, which, as mentioned, is in the middle third of the posterior surface of the midline thyroid cartilage. This vocal ligament forms the medial support of the true vocal cord.

The more superior ventricular ligament attaches to the anterior superior surface of the arytenoid cartilage and stretches across the larynx (parallel to the vocal ligament) to attach to the inner lamina of the thyroid cartilage just above the anterior commissure. This ligament is actually the lower free margin of the quadrangular membrane and supports the free edge of the false cord.

On either side, the quadrangular membrane is a fibrous sheet-like structure that extends from posteriorly, where it attaches to the upper arytenoid and corniculate cartilages, to anteriorly, where it attaches to the lateral margin of the epiglottis (Fig. 30-7). The anterior border of the quadrangular membrane is broader than the posterior edge. The lower margin is free, representing the ventricular ligament. The upper margin forms the support of the aryepiglottic fold. This membrane is just beneath the mucosa of the upper larynx and forms the medial boundary of the paraglottic space (see below).

A second membrane or fibrous layer, the conus elasticus, stretches downward from the vocal ligament of the true cord to attach to the upper inner margin of the cricoid cartilage (Fig. 30-7). Although some fibers of the conus may reflect along the inner margin of the cricoid to its lower inner surface, for purposes of this discussion it will be considered that the conus attaches primarily to the superior cricoid margin. The conus elasticus is a thicker, more clearly defined membrane than the quadrangular membrane. The conus spans part of the gap between the thyroid and cricoid cartilages and can be considered to consist of two parts. The lateral part extending from the vocal ligament to the cricoid cartilage is called the lateral cricothyroid ligament (cricovocal membrane). The anterior part of the conus is the anterior (or median) cricothyroid ligament, which extends in the midline from the lower margin of the thyroid cartilage to the upper margin of the arch of the cricoid. Fibers from these two parts merge together, and the entire complex taken together is called the conus elasticus. There are small gaps just lateral to the median cricothyroid ligament where the

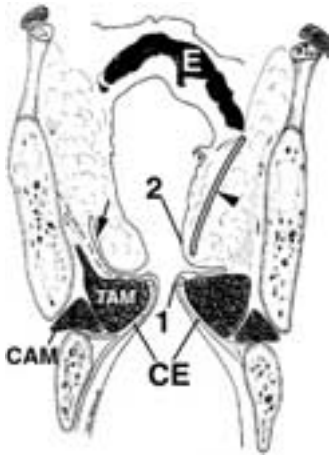

FIGURE 30-7 Diagram of a coronal section through the larynx. The thyroarytenoid muscle (*TAM*) forms the mass of the true cord. The lateral cricoarytenoid muscle (*CAM*) is seen slightly laterally and inferiorly. The conus elasticus (*CE*) extends from the vocal ligament at the cord level to the upper margin of the cricoid. On the left side of the diagram, the conus terminates at the upper margin of the cricoid cartilage. On the right side of the diagram, some fibers of the conus continue along the medial surface of the cricoid, as described by some authors. The paraglottic space is the soft tissue separating the quadrangular membrane and conus elasticus from the cartilage framework. *E*, Epiglottis; *1*, true cord; *2*, false cord; *arrowhead*, quadrangular membrane; *arrow*, ventricular appendix extending superiorly into the paraglottic space. The dashed line on the right describes the location of the thyroglottic ligament. (Modified from the original by Eric Jablonski.)

VIEW IMAGE

lowermost portion of the paraglottic space of the inner larynx is continuous with the extralaryngeal tissues.

As was previously mentioned, the primary supports of the epiglottis are the hyoepiglottic and thyroepiglottic ligaments. The hyoepiglottic ligament is a tough fibrous structure that extends from the ventral midline of the epiglottis to the dorsal margin of the body of the hyoid bone (Fig. 30-2). This fan-like ligament not only marks the line of separation between the suprahyoid and infrahyoid (laryngeal) portions of the larynx but is also considered the anterior upper margin of the larynx.[4] Immediately cranial to this ligament is the mucosa of the pharyngeal recesses referred to as the valleculae. They are formed by the three mucosal folds, the midline (median) glossoepiglottic fold and two more lateral pharyngoepiglottic folds. The valleculae are situated just caudal to the base of the tongue. Lingual tonsillar tissue may extend down along the anterior surface of the valleculae, but will not normally extend either into the floor or along the posterior mucosal surface of the valleculae.

Inferiorly the thyroepiglottic ligament extends from the petiole of the epiglottis to the midline inner surface of the thyroid cartilage just above the attachment of the anterior commissure. The epiglottis is also partially supported on either side by the quadrangular membranes.

One final membrane or fascial sheet should be mentioned. The thyroglottic ligament is described by Sato et al. as passing through the supraglottic fat (see Fig. 30-7).[5] This fascia is reported to sweep downward from its attachment to the inner lamina of the thyroid cartilage and is considered in descriptions of the paraglottic space. The layer passes around the lateral aspect of the ventricle to merge

Copyright © 2003, Mosby, Inc. All rights reserved.

with the vocal ligament and thyroarytenoid muscle. This ligament or fascial layer may be variable, but it is distinct from the quadrangular membrane.

The laryngeal muscles are described in terms of their origins and insertions. To the radiologist, the most important muscle is the thyroarytenoid muscle (TAM) because of its role as a landmark defining the level of the true vocal cord (Figs. 30-2, 30-6, 30-7 and 30-8).

Each TAM stretches from the anterior lower surface of the arytenoid cartilage to the inner aspect of the thyroid cartilage, paralleling the vocal ligament. Some fibers attach to the conus elasticus. The TAM is responsible for most of the bulk of the true cord, and has a medial belly and a lateral belly that run roughly parallel to each other. The medial portion, also called the vocalis muscle, consists of more parallel muscle fibers that form the medial part of the cord. The lateral belly forms the main bulk of the TAM and thus the true cord. Although most muscle fibers remain at the level of the true cord, a few fibers can extend superiorly to insert high on the thyroid cartilage above the level of the ventricle. The posterior space between the vocal cords at the level of the vocal processes of the arytenoid cartilages is referred to as the posterior commissure.

FIGURE 30-8 Coronal section of the larynx. The bulk of the true cord consists of the thyroarytenoid muscle (*TA*). The ventricle (*v*) is seen between the true and false cords. The paraglottic space (*arrowhead*) at the level of the false cord contains small slips of muscle but is filled predominantly with fat. *T*, Thyroid cartilage; *C*, cricoid cartilage; *E*, epiglottic cartilage.

VIEW IMAGE

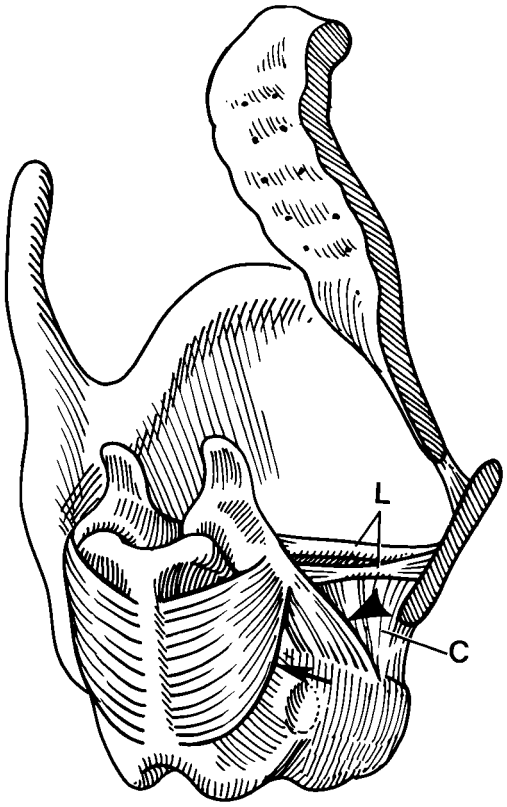

FIGURE 30-9 Diagram of a postero-right lateral view of the laryngeal skeleton (the right thyroid lamina has been removed) showing the posterior (*arrow*) and lateral (*arrowhead*) cricoarytenoid muscles. The posterior cricoarytenoid muscle is totally responsible for abduction of the true cord as the muscle pulls posteriorly on the lateral muscular process of the arytenoid. *C*, Conus elasticus; *L*, vocal ligaments.

VIEW IMAGE

Of equal importance to the function of the larynx, but not as crucial to the radiologist, are the cricoarytenoid muscles (Fig. 30-9). The lateral cricoarytenoid muscle stretches from the muscular process of the arytenoid to the upper lateral surface of the cricoid cartilage. The posterior cricoarytenoid muscle stretches from the posterior surface of the cricoid to the muscular process of the arytenoid. These small antagonistic muscles frequently can be identified on CT and MR imaging. The posterior cricoarytenoid muscle is the only muscle that directly swings the vocal cord laterally (abduction). The interarytenoid (transverse and oblique arytenoid) muscles stretch from one arytenoid to the other, completing the midline posterior wall of the larynx above the cricoid. The lateral cricoarytenoid and the interarytenoid muscle both adduct the true cords. The interarytenoid muscles are the only laryngeal muscles to have bilateral innervation from the recurrent laryngeal nerves; all of the other intrinsic muscles are innervated either by the left or the right recurrent laryngeal nerves (X). The cricothyroid muscle extends from the lower thyroid cartilage to the upper cricoid cartilage and is the only extrinsic laryngeal muscle. It is also the only laryngeal muscle supplied by the external branch of the superior laryngeal nerve (X). Small muscular slips are also present in the upper larynx. These include the thyroepiglotticus and the aryepiglotticus.

Copyright © 2003, Mosby, Inc. All rights reserved.

The pharyngeal constrictors attach posteriorly to a midline raphe and then sweep obliquely around the lumen of the pharynx to attach to the hyoid bone above and to the sides of the cricoid and thyroid cartilages more inferiorly. Notably the fibers attach to the lateral ala of the thyroid cartilage, not along the posterior margin of the cartilage, but along the oblique line on the lateral surface of this cartilage. This becomes important when evaluating pharyngeal tumors, as described in a later section. The pharyngeal constrictors are innervated by the pharyngeal plexus, with a major contribution from the vagus nerve (X) and a lesser contribution from the glossopharyngeal nerve (IX).

The muscle fibers of the three pharyngeal constrictors are attached in the posterior midline to a raphe. The fibers then extend obliquely downward to their attachment on the laryngeal cartilages. However, the lowermost fibers of the inferior pharyngeal constrictor are not attached to the midline raphe. These parallel fibers are continuous around the pharynx and are referred to as the cricopharyngeus. Between the lower edge of the oblique fibers of the inferior pharyngeal constrictor and the upper surface of the cricopharyngeus is a triangular space not supported by muscle, referred to as Killian's dehiscence. It is through this area that a Zenker's diverticulum extends. The cricopharyngeus is a sphincter between the pharynx and the esophagus that prevents esophagopharyngeal reflux. It also must open the gullet during swallowing (see Chapter 32). Anterior midline longitudinal fibers of the esophagus extend above the level of the cricopharyngeus to attach to the midline vertical crest on the posterior cricoid cartilage.

Spaces

The outer boundary of the larynx is formed by the lower hyoid bone, the thyrohyoid membrane and ligaments, the thyroid cartilage, the cricothyroid membrane, and the cricoid cartilage. Between this outer boundary and the mucosal surfaces of the larynx are spaces.

The preepiglottic space is an anterior space between the ventral surface of the epiglottis (posterior margin) and the anterior boundary of the larynx extending from the lowermost hyoid bone to the midthyroid cartilage (anterior margin). The cranial limit of this space is the thyrohyoid ligament, and the caudal limit is the thyroepiglottic ligament. The preepiglottic space is filled with fat and has a rich lymphatic and microvascular network.

The paraglottic space represents the deeper soft tissue of the lateral wall of the larynx. As described by Tucker and Smith, this area is bounded medially by the quadrangular membrane in the upper larynx and the conus elasticus in the lower larynx.[6, 7] The lateral boundary is the cartilaginous skeleton of the larynx represented predominantly by the thyroid cartilage (Figs. 30-7 and 30-8). The paraglottic space is the region deep to the mucosal surfaces of the true and false cords. At the false cord level, the paraglottic space is almost entirely composed of the fat lying between the quadrangular membrane and the thyroid cartilage. Although small slips of TAM may cross the space, no bulky muscle is present.

The laryngeal ventricle extends laterally into each space; however, the ventricle does not reach the inner surface of the thyroid cartilage. A narrow band of paraglottic fat is present lateral to each ventricle, and the paraglottic space is continuous from the level of the false cord to the level of the true cord, passing along the lateral aspect of the ventricle. At the level of the true cord, the TAM fills almost all of the paraglottic space (Fig. 30-8). The conus elasticus forms the lower boundary of the paraglottic space. However, the paraglottic space is not completely closed because, laterally and anteriorly, there is no major fascial barrier closing the space between the cricoid and thyroid cartilages. Thus, through this region the paraglottic space is continuous with the extralaryngeal soft tissues.

The terminology referring to this space is not universally accepted, and some authors describe the paraglottic space as being lateral to a thin membrane referred to as the thyroglottic ligament.[5, 8, 9] This ligament is described as arising from the inner surface of the thyroid cartilage above the ventricle and then sweeping downward and medially to reach the vocal ligament. Using this definition, there would be fat between the quadrangular membrane and the paraglottic space. This fat is considered a posterior extension of the preepiglottic fat. Tucker and Smith also described this thyroglottic ligament, but showed it to partially segment the paraglottic space rather than forming a complete boundary.[6] This chapter will use the terminology as originally presented by Tucker and Smith, and the paraglottic space will refer to all tissue between the quadrangular membrane and the outer cartilaginous laryngeal skeleton. The thyroglottic ligament lies within this space rather than forming a boundary of the space.

At the level of the false cord, a small recess projects superiorly from the anterior laryngeal ventricle into the paraglottic fat. This recess, called the laryngeal saccule or appendix, lies between the quadrangular membrane and the thyroid cartilage. Dilatation of the saccule causes a supraglottic cyst called a laryngocele.

The pyriform sinus is an anterior mucosa-lined recess of the hypopharynx situated between the medial aspect of the posterior one third of the thyroid cartilage and the lateral surface of the AE fold (Fig. 30-10). The anterior wall of much of the pyriform sinus is the posterior wall of the paraglottic space. The lowest aspect of the pyriform sinus, the apex, reaches the level of the true vocal cord, between the arytenoid cartilage and the thyroid cartilage. At imaging, this area, with a small amount of fat just deep to the mucosa, has been referred to as the thyroarytenoid gap.

Innervation and Blood Supply

The larynx is innervated by branches of the vagus nerve. The recurrent laryngeal nerve loops around the aortic arch on the left side and the subclavian artery on the right. Each nerve then travels in the tracheoesophageal groove at the anterolateral margin of the esophagus. Each nerve passes medial to the lower margin of the cricopharyngeus muscle and enters the larynx in the sulcus between the thyroid cartilage and the cricoid cartilage just above the cricothyroid joint. The recurrent laryngeal nerve innervates all of the intrinsic muscles of the larynx.

As mentioned, the only extrinsic laryngeal muscle, the cricothyroid muscle, is innervated by the external branch of the superior laryngeal nerve. This external branch never

Copyright © 2003, Mosby, Inc. All rights reserved.

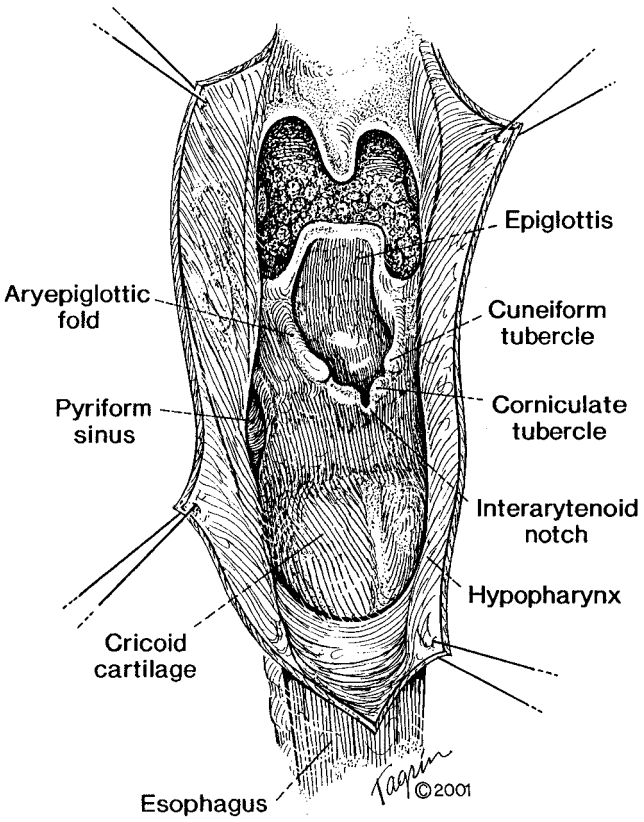

VIEW IMAGE

FIGURE 30-10 A view from posterior and to the left with the pharynx open. (Modified from Berman JM. Surgical anatomy of the larynx. In: Bailey BJ, Biller HF. Surgery of the Larynx. Philadelphia: WB Saunders, 1985; 20.)

enters the larynx. The internal branch of the superior laryngeal nerve does perforate the posterior lateral portion of the thyrohyoid membrane, providing sensation to the laryngeal mucosa.

The blood supply to the larynx accompanies the nerves. The superior laryngeal artery is a branch of the superior thyroid artery and follows the internal branch of the superior laryngeal nerve. The inferior laryngeal artery is a branch of the inferior thyroid artery, which in turn is a branch of the thyrocervical trunk. The inferior laryngeal artery accompanies the recurrent laryngeal nerve into the larynx.

Lymphatic Drainage

The lymphatic drainage of the deep larynx passes almost completely cephalad, as the supraglottic larynx is considered a derivative of the pharynx. The thyroid cartilages form from two centers, one on either side of the midline, and injection studies have shown that the submucosal lymphatics follow this bilateral developmental scheme and do not cross the midline.[10–12] However, the mucosa of the supraglottic larynx forms as a single structure, after development of the cartilage, and the mucosal lymphatics do cross the midline. The lymphatics of the supraglottic larynx drain superiorly through the thyrohyoid membrane to the upper jugular nodes (levels II and III).

The lymphatics of the subglottic larynx also drain in a cephalad direction. The low subglottic lymphatics drain slightly upward to and then through the cricothyroid membrane to the paratracheal and pretracheal nodes (level VI). The studies of Pressman et al. showed again that dye injections deep to the mucosa did not cross the midline, but that once the dye passed through the cricothyroid membrane, the subsequent drainage was bilateral. Mucosal dye injections ended abruptly at the lower margin of the cricoid cartilage and did not extend to the trachea. The lymphatic flow of the upper part of the subglottic larynx is also primarily cephalad, extending beyond the ventricle to the paraglottic network of the supraglottic larynx. The submucosa of the true cord has almost no lymphatic drainage.

The preepiglottic and paraglottic spaces are particularly rich in lymphatics, and the greater the tumor infiltration into these areas, the more likely it is that there will be cervical metastatic nodal disease. The Delphian node is anterior to the cricothyroid membrane. Tumor can reach this region either by direct extension or by lymphatic drainage from a tumor in the region of the anterior commissure and the subglottic larynx. Enlargement of this node has been suggested as an early clinical manifestation of the presence of subglottic tumor. Most commonly, the region in which this node is located is affected secondary to direct tumor extension, without involvement of a separate definable node.

The concept that the lymphatics of the deep portion of the larynx flow almost exclusively in the cephalad direction is important when planning a partial laryngectomy.

Regions

Certain anatomic terms are important when describing the larynx, particularly when discussing tumors. The larynx is subdivided by two theoretical horizontal (axial) planes; one extends through the apex of the two laryngeal ventricles, and the other parallel plane is 1 cm caudal to the first. The supraglottic larynx is that portion of the larynx cranial to the first plane or superior to the plane of the ventricle. This includes the epiglottis, AE folds, false cords, and so on. The upper margin of the supraglottic larynx, as described previously, is the free edge of the epiglottis and the AE folds and, more anteriorly, the hyoepiglottic ligament. The upper arytenoid cartilages are included in the supraglottic larynx. The glottis is the region between the two planes and includes the anterior and posterior commissures. The subglottis is the region between the lower plane and the inferior (caudal) margin of the cricoid cartilage.

The supraglottic larynx can be subdivided into infra- and suprahyoid regions separated by the hyoepiglottic ligament. The suprahyoid portion of the epiglottis is often called the free segment. The anterior surface of the free segment of the epiglottis, as well as the valleculae, are often included in discussions of the base of the tongue and the pharynx.

The postcricoid region is the mucosal covering of the posterior surface of the cricoid cartilage, representing the anterior wall of the hypopharynx at this level. Because of its relationship to both the pharynx and the larynx, the free edge of the AE fold is at times referred to as the junctional or marginal zone.

Copyright © 2003, Mosby, Inc. All rights reserved.

SECTION TWO

IMAGING

In this section, the various imaging modalities are discussed and the normal laryngeal anatomy visible on each examination is shown.[13–18] Several radiographic procedures are included for historical perspective, but are currently seldom if ever performed. A review of certain respiratory maneuvers is included because they can be used to accentuate different areas in the larynx during imaging. Although these respiratory maneuvers were used extensively with laryngography and multidirectional tomography, they were not as useful with earlier CT and MR imaging due to the longer imaging times they required. However, with today's faster imaging, examinations in different respiratory phases are again possible. The coronal plane is ideal for appreciating these movements, so some tomographic images are used for illustration.

Respiratory Maneuvers

In quiet respiration, the vocal cords are slightly separated from the midline but are not completely effaced against the lateral laryngeal wall. In the coronal plane, the cord is seen to have a flat upper surface and a lower downward-sloping surface that extends to the lateral wall of the subglottic laryngeal airway. This slope has been referred to as the subglottic arch. Although this slope is seen in quiet respiration, it is more pronounced in phonation. With slow inspiration the true cords and false cords further abduct, disappearing on imaging as they flatten against the now smooth lateral wall of the larynx. When the patient holds his or her breath and bears down (Valsalva maneuver), the cords go to the midline (adduct), squaring off the subglottic arch and forming the subglottic angle (between the inferior surface of the cord and the lateral wall of the airway). No airway is seen at the true cord level, and the false cords also approximate in the midline. The modified Valsalva maneuver is performed with the cheeks puffed and the patient allowing air to escape slowly from the mouth. This maneuver not only puffs the cheeks, but also dilates the pyriform sinuses and all the airway structures above the true cords. With phonation (the patient makes a high-pitched ''eeee'' sound), the cords tense and approach the midline, leaving a narrow airway. The ventricle may be expanded or collapsed in any maneuver. The reverse, or inspiratory ''e'' maneuver, usually dilates the ventricle. Although this maneuver may be difficult for many patients, usually any noise made while breathing in will suffice.

Although these maneuvers are expected to produce the described effects, many times the particular structure the radiologist is trying to visualize shows up on the ''wrong'' maneuver. A tomographic examination typically includes all of these maneuvers (Figs. 30-11 and 30-12).

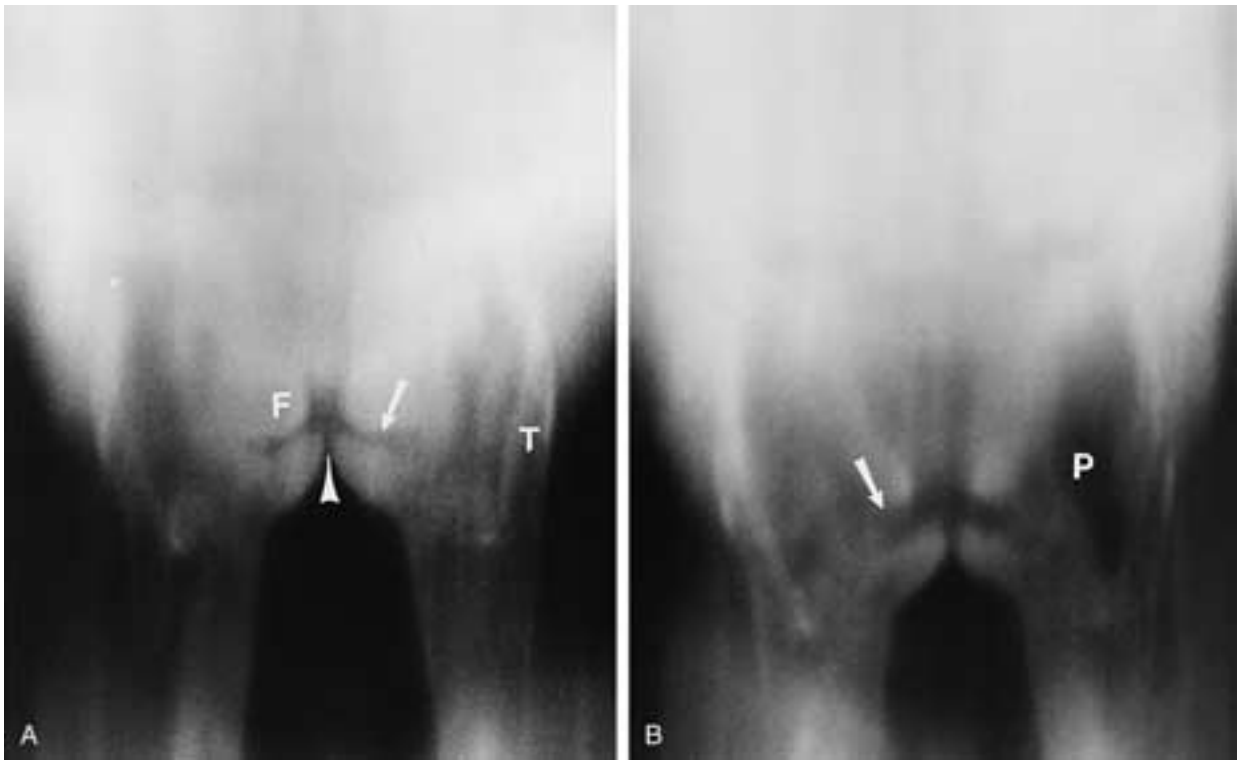

FIGURE 30-11 **A**, Coronal tomograms during phonation. The true cords approximate with only a small residual airway (*arrowhead*). The ventricle (*arrow*) is partially filled with air. *T*, Thyroid cartilage; *F*, false cord. **B**, Reverse phonation shows more dilatation of the ventricles (*arrow*). *P*, Pyriform sinus.

VIEW IMAGE

Copyright © 2003, Mosby, Inc. All rights reserved.

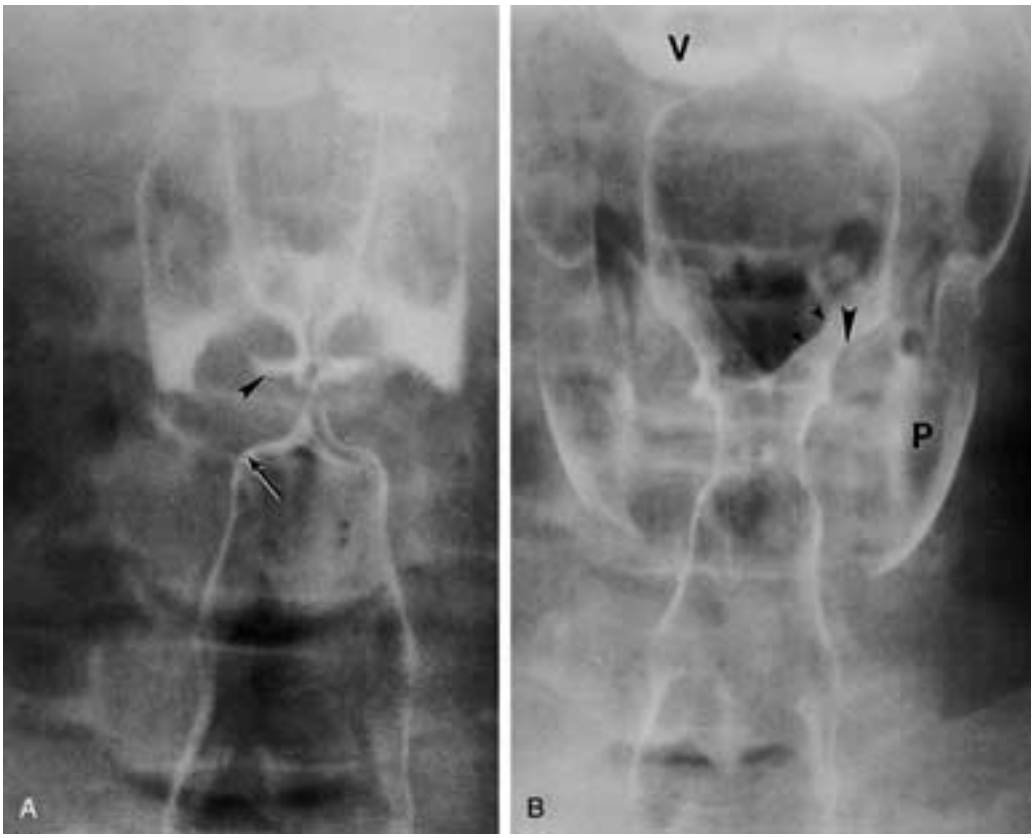

VIEW IMAGE

FIGURE 30-12 **A**, Laryngogram, frontal views, Valsalva maneuver. Note the squaring of the subglottic arch (*arrow*) and collapse of the ventricle (*arrowhead*). **B**, Laryngogram, puffed cheek, modified Valsalva maneuver. The pyriform sinuses (*P*) are distended. The AE fold (*small arrowheads*) and the inner wall of the larynx (*large arrowhead*) are well demonstrated. *V*, Valleculae.

Plain Film Radiography

The plain film soft-tissue technique uses less kilovoltage than that used for cervical spine films. These soft-tissue films of the neck use the normal air present in the upper airway to contrast the adjacent soft tissues of both the larynx and trachea (Fig. 30-13). The retropharyngeal soft-tissue thickness also can be appreciated on lateral films. The epiglottis and the AE folds usually are well visualized, and air in the ventricle often marks the position of the upper margin of the true cord. Portions of the cartilages can be visualized, depending on the degree of ossification.

The variability of ossification of the laryngeal cartilage makes any prediction of pathology affecting these cartilages hazardous on the plain films. Frequently the partly calcified cartilages create a diagnostic problem for the radiologist examining for foreign bodies. Because of this, the radiologist should be familiar with the most common pitfalls or false foreign bodies.

The superior margin of the cricoid lamina often calcifies early, before the remainder of the signet portion of the cricoid (Figs. 30-13 and 30-14). This linear calcification is easily mistaken for a foreign body. The triticeal cartilage in the posterior thyrohyoid ligament is another foreign body mimic (Fig. 30-14). Less commonly a calcified arytenoid or the cornua of the thyroid cartilage may be mistaken for a foreign body.

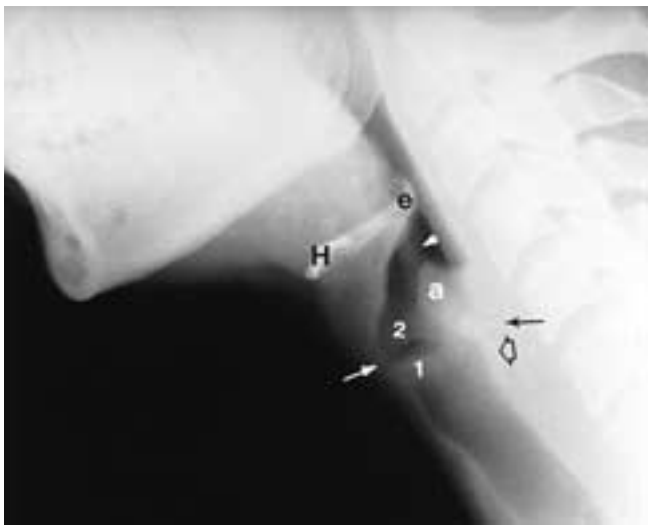

FIGURE 30-13 Lateral plain film of the neck shows the true cord (*1*) and the false cord (*2*) separated by the black air-filled linear ventricle. The white arrow points to the anterior ventricle. The anterior commissure (junction of the true cords) is just inferior to this point. The black arrow shows the calcified superior margin of the cricoid lamina, which is often mistaken for a foreign body. The open black arrow shows the calcified lower horn of the thyroid cartilage. *H*, Hyoid; *a*, arytenoid prominence; *e*, epiglottis; *arrowhead*, AE fold.

VIEW IMAGE

Copyright © 2003, Mosby, Inc. All rights reserved.

FIGURE 30-14 Lateral radiograph of the larynx and soft tissues. The triticeal cartilage (*upper black arrow*) is visualized between the thyroid cartilage and the hyoid. This cartilage is located in the posterior thyrohyoid membrane. The upper edge of the cricoid (*lower black arrow*) is mineralized. Ventricle (*white arrow*).

VIEW IMAGE

High-kilovolt (140 kV) films are used to ''soften'' the spine, allowing visualization of the airway in the frontal projection. A 1 mm copper filter can be placed between the tube and the patient to give a lowered film contrast.[19, 20]

Xeroradiography used edge enhancement technology to clearly show the anatomy of the airway, cartilages, and even muscle and fat planes (Fig. 30-15).[21] This technique was considered ideal for visualizing foreign bodies and for evaluating the trachea (e.g., for subglottic stenosis, granuloma). However, xeroradiography has an exposure three to five times that of the standard soft-tissue film. Its use in imaging soft tissues and cartilage has been superseded by CT and MR imaging.

Tomography

Today, conventional linear or multidirectional tomography seldom is used for the evaluation of the larynx, though occasionally it is utilized to assess the trachea. Tomography allows visualization of the airway anatomy in the frontal view without the problems of superimposition of the density of the spine (Fig. 30-11). The exposure can be made in several seconds, rapidly enough that the various maneuvers (e.g., phonation, Valsalva) can be used to show specific anatomic landmarks in the coronal plane. Only the surface deformity is visualized by this technique, and the deep extent of a tumor is estimated by the degree of distortion of the false and true cords. As the pyriform sinus protrudes between the thyroid cartilage and the inner wall of the larynx, the width of the wall can be estimated in an attempt to show tumor extending through the paraglottic space toward the true cord. Subglottic extension is well seen by the flattening of the subglottic arch.

Because tomography requires multiple slices and multiple maneuvers, the examination has a fairly high radiation exposure. Every attempt is made to place the airway in the plane of section parallel to the tabletop. Placing a bolster under the buttocks, with additional support of the knees, allows positioning without forcing the patient to straighten the natural angle between the thoracic and cervical spines.

Fluoroscopy

Because some patients will not tolerate direct clinical visualization of the larynx without anesthesia and because some patients may have a tumor blocking the clinician's view, fluoroscopy can be helpful in assessing vocal cord mobility. This procedure requires that the patient be awake and able to follow verbal commands. The examination is recorded on videotape to allow review without additional patient exposure.

Contrast Examinations

Contrast laryngography was developed to better define mucosal irregularities.[22–24] The information derived from the laryngogram is now routinely obtainable by endoscopy, and the submucosal regions can be better visualized with CT and MR imaging. Contrast laryngography was difficult for many patients to tolerate, and this procedure was contraindicated in those patients who had partial airway obstruction secondary to tumor, thus limiting direct clinical examina-

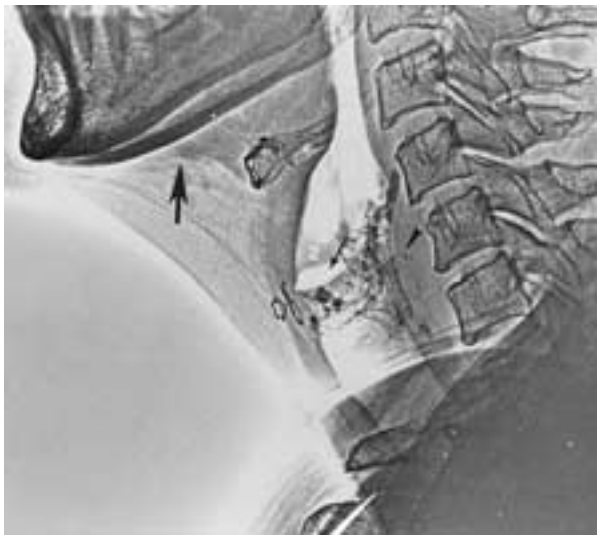

FIGURE 30-15 Xeroradiogram (lateral view) shows the true cord, false cord, and ventricle, with better definition of the fat planes. Note that the calcified upper margin of the cricoid lamina (*arrowhead*) is seen more obviously here than in Figure 30-13. Note how the muscles in the floor of the mouth (*large arrow*) can be seen against the fat. *2*, False cord; *small arrow*, ventricle; *open arrow*, partially calcified anterior thyroid cartilage.

VIEW IMAGE

Copyright © 2003, Mosby, Inc. All rights reserved.

tion. Unfortunately, these were the very patients who most needed such an examination. The examination is contraindicated in these patients because there is always some element of mucosal edema in response to the topical anesthetic and the contrast material, further narrowing an already compromised airway.

If there was no contraindication, the patient was given atropine (0.4 mg) and codeine (60 mg). The atropine decreased secretions, drying the mucosa, enabling better contrast coating, while the codeine limited coughing.

The anesthesia of the larynx was the most important part of the contrast laryngogram. After initial anesthesia with topical agents, a curved cannula was placed over the back of the tongue, and 2% xylocaine was dripped into the pyriform sinus and larynx as the patient breathed slowly in and out. Alternatively, a soft rubber tube was passed through the nose and directed over the larynx.

Some radiologists used 4% xylocaine, but with extreme caution. Xylocaine is rapidly absorbed through the mucosa and can precipitate cardiac arrhythmias, hypotension, or central nervous system aberrations.

Initially, the patient coughed as the xylocaine dripped into the laryngeal lumen, but as anesthesia occurred, the coughing stopped. The procedure continued with administration of the contrast medium. In the United States, oily propyliodone (Dionosil) was the most common contrast agent used. The contrast was warmed and mixed well, then dripped into the larynx using a syringe and a laryngeal cannula or nasal tube. The patient breathed in slowly as the contrast was administered, and the patient was asked to cough lightly to help distribute the contrast. Administration could be monitored in the lateral projection with intermittent fluoroscopy. The patient was placed in the frontal, lateral, and oblique positions and asked to perform the various previously described maneuvers (Fig. 30-12).

Historically, the laryngogram was considered especially helpful in imaging certain important areas of the larynx. The clinician's view of the ventricle and anterior commissure can be blocked by overhanging tumor. Phonation or inspiratory ''e'' may distend the ventricle. Because the two ventricles are superimposed on the lateral projection, frontal films were obtained to determine whether the ventricle filled on both sides. With modern endoscopy, these areas usually can be routinely visualized. The subglottic angle can be clearly defined with laryngography, but it is more easily assessed by CT or MR imaging.

Barium Swallow

The barium swallow is used to evaluate the pharyngeal wall. The barium column is followed through the pharynx into the esophagus. The motility and pliability of the pharyngeal wall and the mucosal surfaces are assessed. Demonstration of normal pliability of the pharyngeal wall suggests normal tissue. Tumor infiltration causes lack of pliability or distensibility, as well as mucosal irregularity (Fig. 30-16).

In the frontal view, the pyriform sinuses fill as the epiglottis deflects the barium column to either side, around rather than over the vestibule of the larynx (Fig. 30-17). As the larynx elevates, the pyriform sinuses lose their sharply curved lower borders, becoming continuous with the remaining hypopharynx. The barium is propelled through the cricopharyngeus into the esophagus. As the barium column splits to pass through the pyriform sinuses, the larynx becomes a ''filling defect'' in the barium column and should not be mistaken for a mass.

On the lateral view, the cricopharyngeus opens as the pharynx propels the bolus toward the pharyngoesophageal junction. The cricopharyngeus is inspected for late or incomplete relaxation and for the formation of an outpouching such as a Zenker's diverticulum. On the lateral film, irregularity is often seen on the anterior wall of the lower pharynx in the postcricoid area. This has been described as being due to a venous plexus or to normal mucosal redundancy, and at times differentiation from a tumor may be impossible. The relationship of the posterior pharyngeal wall to the cervical spine and possible anterior vertebral osteophytes is well seen in the lateral view.

Computed Tomography Scanning

CT scanning allows evaluation of the laryngeal structures deep to the mucosa.[24–26] A lateral scout view is obtained and the slice orientation is selected parallel to the laryngeal ventricle, seen as a dark air line in the laryngeal airway. If the ventricle is not seen well or if the airway is obscured by the shoulders in a patient with a short or thick neck, the slice orientation is estimated to be perpendicular to the axis of the spine at the level of the larynx. The axial images are made with a field of view corresponding to the size of the neck. The patient can pull on a strap passed around the feet to lower the position of the shoulders and diminish artifacts.

The use of sequential rapid (1 to 2 seconds) scanning can decrease respiratory and swallowing artifacts. The choice of slice thickness is arbitrary; however, most radiologists use either a 2 or 3 mm slice thickness. If the relationship of the lesion to the ventricle is still in question, once the area of the ventricle is identified, 1mm slices can be taken through the true cord–ventricle–false cord complex.

Spiral scanning rapidly acquires a complete data set through the larynx. The images then can be reconstructed to give overlapping slices at any level, and this is particularly helpful at the level of the ventricle. Coronal, sagittal, and even three-dimensional (3D) images can be generated from the same data set. The real advantage of spiral scanning is that the entire larynx can be examined in 10 to 20 seconds, and this minimizes motion artifact. In addition, with spiral CT scanning, examination of the larynx during respiratory maneuvers may be possible. This may be done to optimize visualization of a particular region of the larynx or the margin of a tumor. More clinical experience is necessary before the usefulness of these techniques is accepted. With new multidetector CT scanners, the collimation can be 1 mm and the larynx can be covered in a few seconds by varying the pitch of the scan.[27] Overlapping reconstructions can be made, giving excellent coronal reformatted images (Fig. 30-18). This technique makes correct patient positioning less important, as the recon-

Copyright © 2003, Mosby, Inc. All rights reserved.

VIEW IMAGE

FIGURE 30-16 Polypoid mass arising from the lateral wall of the pharynx. Pharyngogram using thicker barium. **A**, Anterior posterior view. The polypoid mass (*small arrow*) protrudes from the lateral wall of the pyriform sinus. Note the distention of the pyriform sinus (*small arrowheads*) as the patient puffs the cheek. There is distention of the pyriform apex (*large arrowhead*) on the opposite side. A small amount of contrast extends into the airway, coating the true cord (*large arrow*). *V*, Valleculae. **B**, Lateral view. The tumor (*T*) is seen contrasted against the distended pharynx. Note the coating of the laryngeal surface of the epiglottis (*arrowheads*) and the barium seen in the ventricle (*arrow*) along the upper margin of the true cord.

structed images can be adjusted to give images directly in the plane of the ventricle.

The region covered should extend below the level of the cricoid cartilage. The starting point can be the tip of the epiglottis or the hyoid bone, depending on the origin of the lesion (see the following discussions on squamous cell carcinoma, other malignancies, and benign tumors). If nodal regions are to be studied, the scan should start at the external auditory meatus. The examination can be done with the patient breathing quietly or breath-holding now that imaging speed is acceptable. Before the actual scan is started, the patient should practice any breathing maneuver, and the technologist should be confident that motion can be minimized during the scan. If the scan is done during quiet breathing, the patient should attempt as much as possible to breathe with the abdominal muscles, keeping the chest wall still. Intravenous contrast helps distinguish lymph nodes from blood vessels and thus is used in tumor cases, but it is not necessary in laryngeal trauma evaluation.

In the upper (cranial) axial slices, the epiglottis and connecting ligaments and folds (median glossoepiglottic and pharyngoepiglottic folds and the hyoepiglottic ligament) are seen (Fig. 30-19). More inferiorly, the lateral edges of the epiglottis merge with the AE folds, which in turn converge toward the midline and unite posteriorly at a more caudal level.

In the supraglottic larynx, the preepiglottic space is filled with fat, and portions of the hyoepiglottic ligament can be seen in the midline crossing the upper portion of this fat. The laryngeal vestibule has an ovoid shape, and the epiglottis may at times be partially folded upon itself. At the level of the false cords, the paraglottic region lateral to the airway is also predominantly fat density. As the axial slices pass the ventricle, the paraglottic space changes from predominantly fat density to muscle density (the thyroarytenoid muscle). The shape of the airway narrows at the cord level, becoming more slit-like, but then widening to a more oval or rounder appearance at the level of the subglottis. The paraglottic space, limited by the conus elasticus, stops at the upper margin of the cricoid. Thus there should be no soft tissue within the ring of the cricoid cartilage.

The appearance of the cartilage can vary considerably, depending on the degree of ossification and the amount of fatty marrow in the ossified medullary region. Both thyroid and cricoid cartilages are easily identified. The thyroid cartilage spans the level of the true and false cords. The axial slices are ideal for evaluating these cartilages, displaying them in perfect cross section. In general, the angle made by

Copyright © 2003, Mosby, Inc. All rights reserved.

the two thyroid alae is wider in women than in men. The arytenoid cartilages are important landmarks that can help identify the true cord, ventricle, and false cord relationships. Approached from cranially, the upper arytenoid is seen first at the level of the false cord as a square or triangular density. At more caudal levels, the anteriorly pointed vocal process can be identified projecting from the arytenoid base. The vocal process identifies the level of the true cord. Because the level of the vocal process is also at the level of the cricoarytenoid joint, the true cord level and the posterior commissure can be identified when the arytenoid cartilages are seen on the same axial scan as the top of the cricoid lamina. Unfortunately, there is no definite landmark on any of the cartilages that defines the exact level of the laryngeal ventricle.

The appearance of the vocal cords varies with the phase of respiration. In quiet breathing, the airway is open and the cords are slightly abducted. If the patient is breath-holding for each scan, the cords usually are adducted (Fig. 30-20). This maneuver may actually give a slightly clearer visualization of paraglottic fat along the outer lateral margin of the cords.

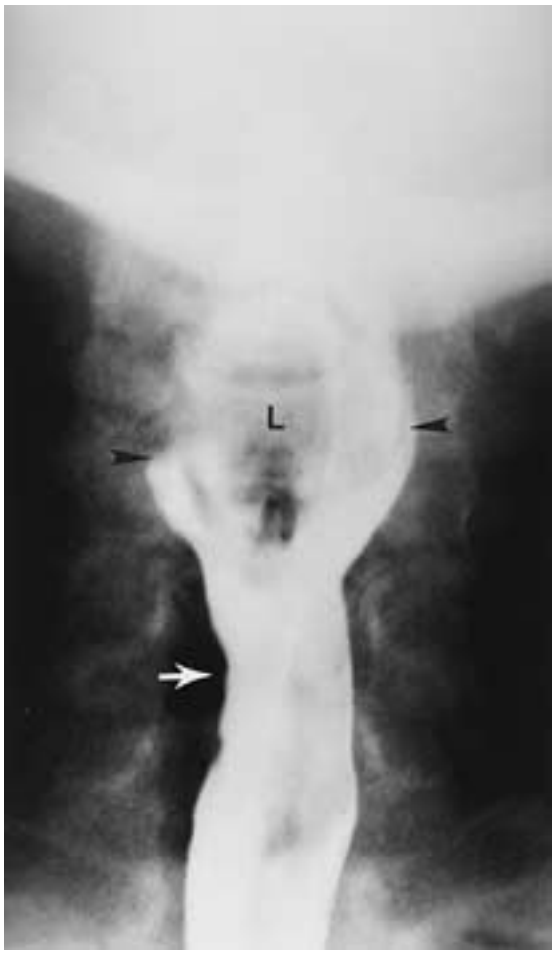

VIEW IMAGE

FIGURE 30-17 Frontal view of a barium swallow, normal. The barium (*arrowheads*) is deflected around the larynx, with an apparent filling defect caused by the larynx (*L*). The impression on the upper esophagus (*white arrow*) is caused by osteophytes.

The anterior commissure should have air closely approximating the cartilage. If this appearance is seen, the radiologist can be relatively confident that no disease is present at this site. On CT, obliteration of the anterior commissure can be seen secondary to tumor, but it may also be an artifact resulting from minor cord position changes or cord edema.

At the caudal margin of the cricoid cartilage, the appearance of the hypopharyngeal musculature changes from a flat, elongated semilunar appearance to a rounder ovoid configuration (Fig. 30-21). This signifies the change from the hypopharynx to the cervical esophagus, and the semilunar-shaped muscle is the cricopharyngeus. Its flatter shape is the result of its attachment to the lateral aspect of the thyroid and cricoid cartilages.

Magnetic Resonance Imaging

Because of motion artifact, the larynx has been difficult to image well with MR imaging. This modality does have the capability of multiplanar high-resolution imaging, and compared with CT, MR imaging has an increased ability to separate various soft tissues such as tumor and muscle.[13, 15–18, 26, 28, 29] However, the multiplanar capabilities of multidetector CT may challenge the abilities of MR imaging to better define lesions.

The actual pulse sequences used by different radiologists vary considerably and certainly will change with the continued evolution of this technology. As with CT, for MR imaging the patient is positioned with the airway as parallel to the tabletop as possible, but the plane of imaging can be angled when the patient is not in a perfect position. Currently, a sagittal T1-weighted localizer series is obtained to identify the axis of the larynx. This sequence ranges from one sternocleidomastoid muscle to the other to include the major lymph node groups.

A coronal T1-weighted series is performed with thin sections (3 to 5 mm), extending from the anterior vocal cords to the posterior larynx, in a plane perpendicular to the cords. An axial thin-section, T1-weighted sequence is then done, covering the larynx from the upper epiglottis to the lower cricoid. The anatomic level is chosen to cover the area of maximum interest (usually the true cord, ventricle, and false cord). Finally, an axial T2-weighted sequence is performed. The long TR allows multiple slices to be obtained, and thus the primary node-bearing areas can be covered. If there is a supraglottic lesion, the region from the midmandible to below the cricoid is imaged. With lower cord or subglottic lesions, the lower neck is evaluated.

Fast spin-echo (FSE) imaging gives excellent images with valuable T2 information. Fat suppression may be used, as the fat signal can be high on FSE images. This allows better appreciation of the higher signal intensity coming from abnormal soft tissues that may be bordered by fat. FSE T1-weighted images are also available (Fig. 30-22).

The use of gadolinium in laryngeal imaging is still controversial. Some feel that by using gadolinium, important information can be obtained regarding the interface of

Copyright © 2003, Mosby, Inc. All rights reserved.

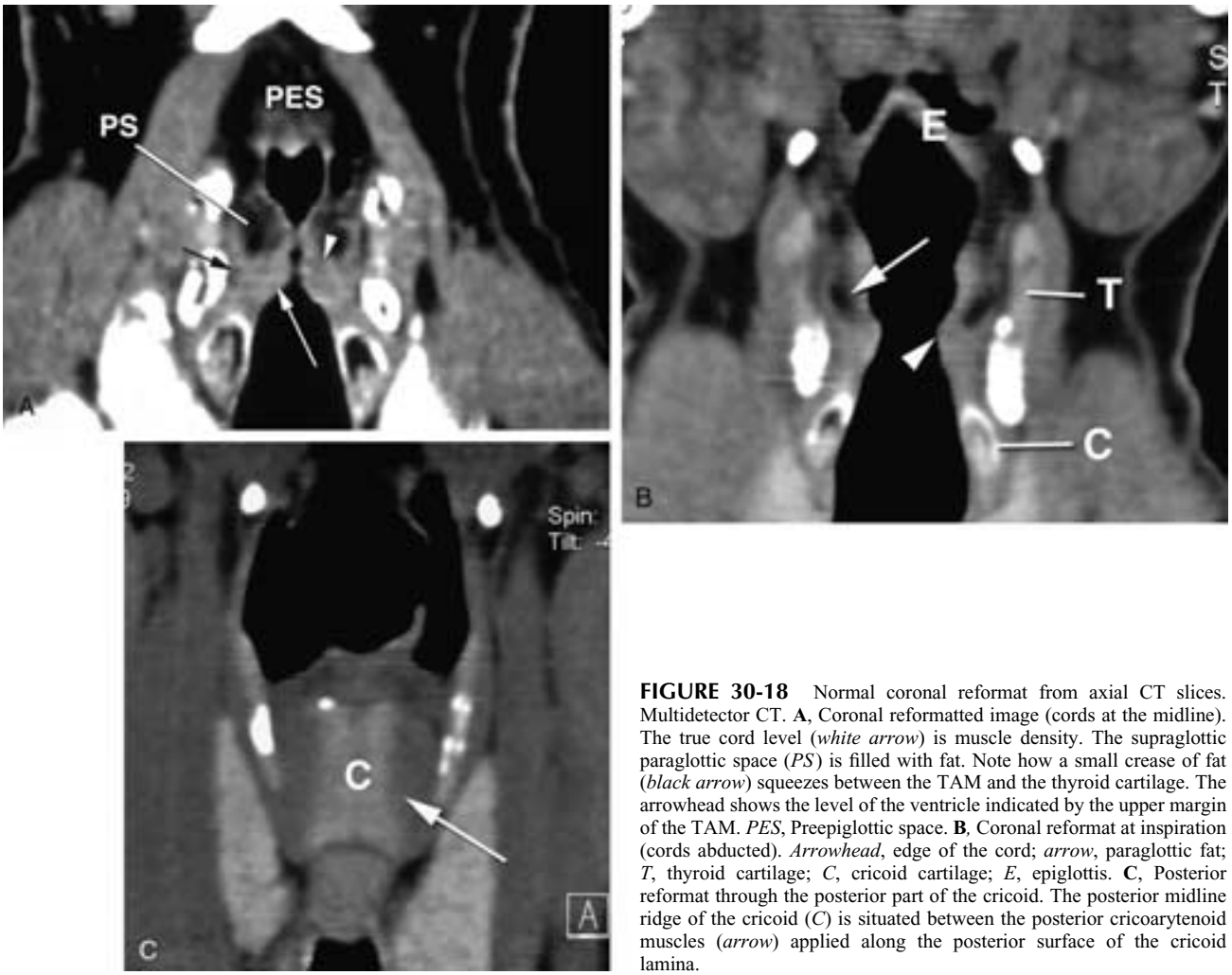

FIGURE 30-18 Normal coronal reformat from axial CT slices. Multidetector CT. **A**, Coronal reformatted image (cords at the midline). The true cord level (*white arrow*) is muscle density. The supraglottic paraglottic space (*PS*) is filled with fat. Note how a small crease of fat (*black arrow*) squeezes between the TAM and the thyroid cartilage. The arrowhead shows the level of the ventricle indicated by the upper margin of the TAM. *PES*, Preepiglottic space. **B**, Coronal reformat at inspiration (cords abducted). *Arrowhead*, edge of the cord; *arrow*, paraglottic fat; *T*, thyroid cartilage; *C*, cricoid cartilage; *E*, epiglottis. **C**, Posterior reformat through the posterior part of the cricoid. The posterior midline ridge of the cricoid (*C*) is situated between the posterior cricoarytenoid muscles (*arrow*) applied along the posterior surface of the cricoid lamina.

VIEW IMAGE

tumor with muscle. Often axial contrast-enhanced images are the most useful. However, FSE T2-weighted images may generate very similar information, obviating the need for gadolinium.

Motion artifacts from breathing, swallowing, and even pulsatile flow in the carotid arteries are major problems with MR imaging. In an attempt to eliminate or minimize these artifacts, a number of flow compensation techniques, respiratory and cardiac gating, and presaturation pulses have been tried, with varying results. Phase-encoding gradients are placed in the anteroposterior direction to move flow artifact away from the larynx in the axial images. Patient education is even more important with MR imaging than with CT. The patient is instructed to breathe quietly and to practice doing so without moving the neck. Shallow abdominal rather than chest breathing is encouraged, and the patient is instructed not to swallow or at least to swallow as seldom as possible during the sequence. However, if the patient must swallow, it should be done quickly rather than struggling to suppress the swallow, as struggling itself may cause even more motion artifact. The neck should not be hyperextended because this makes swallowing more difficult. The neck is kept in a more relaxed neutral position.

A surface coil is used as a receiver. Because the coil should move as little as possible, the technologist should take care to separate the coil from the chest wall while maintaining close approximation to the neck.

Sagittal images show the epiglottis, valleculae, and base of the tongue well (Fig. 30-23). The laryngeal surface of the epiglottis can be followed down to the petiole and the anterior commissure. The postcricoid area is seen well, and the arytenoid cartilage often can be visualized perched atop the cricoid cartilage. The preepiglottic fat is clearly seen on T1-weighted images.

The coronal view represents the ideal orientation for evaluation of the upper margin of the true cord (Figs. 30-24 and 30-25). The ventricle may not be seen, because the patient cannot maintain any particular breathing maneuver during the entire time required for the imaging sequence. The TAM represents the bulk of the true cord, and on T1-weighted images it can be seen contrasted against the high signal intensity fat of the false cord immediately above. Although slips of the TAM invariably extend up into

Copyright © 2003, Mosby, Inc. All rights reserved.

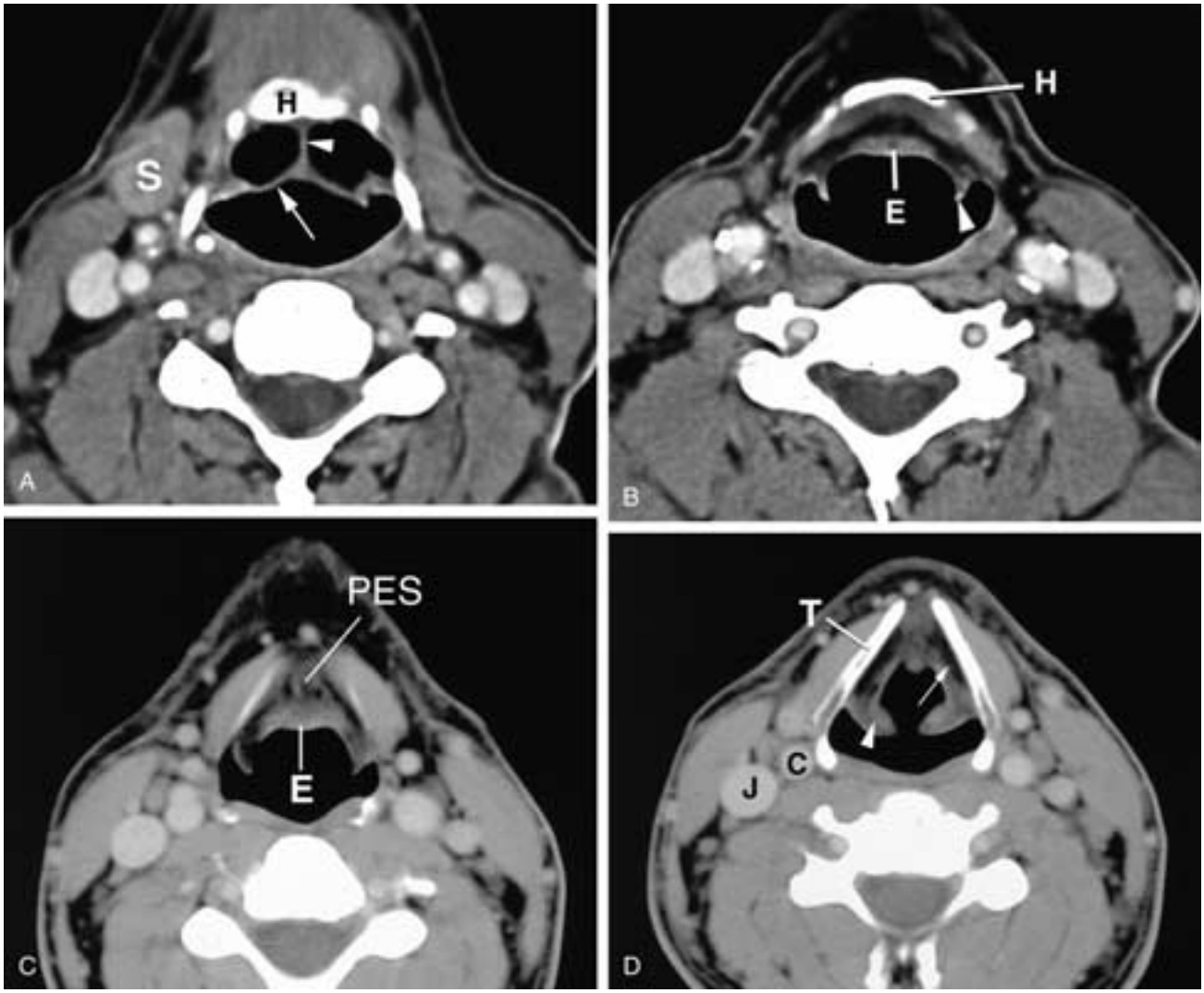

VIEW IMAGE

FIGURE 30-19 Axial CT scan through the larynx from superior to inferior. **A**, Hyoid (*H*) level, glossoepiglottic fold (*arrowhead*), edge of the epiglottis (*arrow*), submandibular gland (*S*). **B**, Hyoid (*H*), epiglottis (*E*), AE fold (*arrowhead*). **C**, Epiglottis (*E*), preepiglottic space (*PES*). **D**, Supraglottic level. Thyroid cartilage (*T*), paraglottic fat (*arrow*), AE fold (*arrowhead*), carotid artery (*C*), jugular vein (*J*).

Copyright © 2003, Mosby, Inc. All rights reserved.

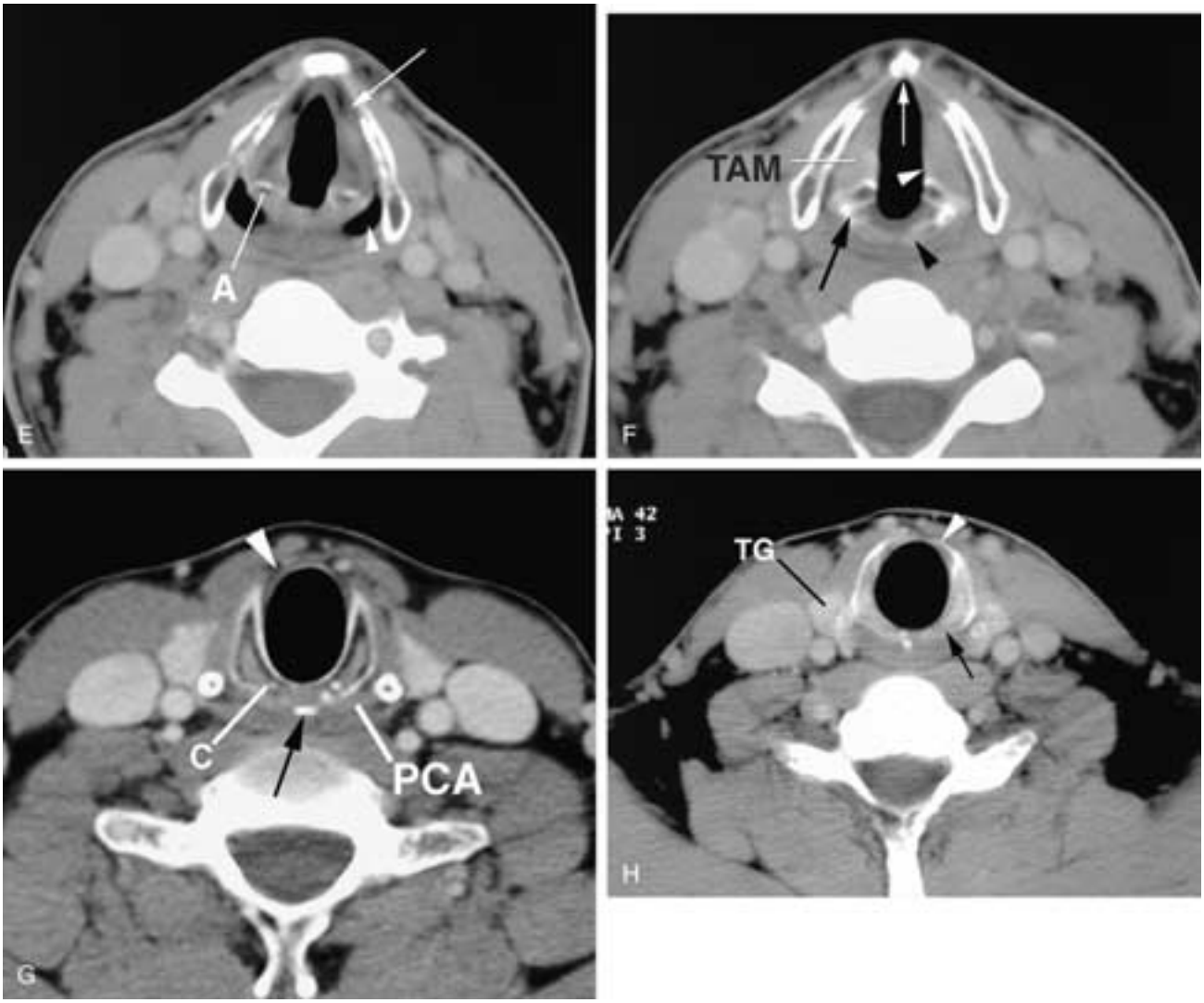

FIGURE 30-19 *Continued.* **E**, Axial slice just superior to the ventricle. Paraglottic fat (*arrow*), apex of the pyriform sinus (*arrowhead*), arytenoid cartilage (*A*). **F**, True cord level. The thyroarytenoid muscle (*TAM*) forms the bulk of the true cord. Anterior commissure (*white arrow*), vocal process of the arytenoid (*white arrowhead*), upper edge of the cricoid (*black arrowhead*), cricoarytenoid joint (*black arrow*). **G**, Cricothyroid membrane level. Note the slight fat pad just anterior to the airway (*white arrowhead*) is at the level of the cricothyroid membrane. Posterior cricoarytenoid muscle (*PCA*). Note the small amount of fat within the ossified lamina of the cricoid cartilage (*C*). The lamina (posteriorly) extends more superiorly than the anterior arch, which will be seen at a lower level. Midline posterior ridge of the cricoid (*black arrow*). **H**, Arch of the cricoid. In a more caudad slice than **G**, the lamina (*black arrow*) is still visualized, but now the anterior arch (*arrowhead*) is visible. Thyroid gland (*TG*).

VIEW IMAGE

Copyright © 2003, Mosby, Inc. All rights reserved.

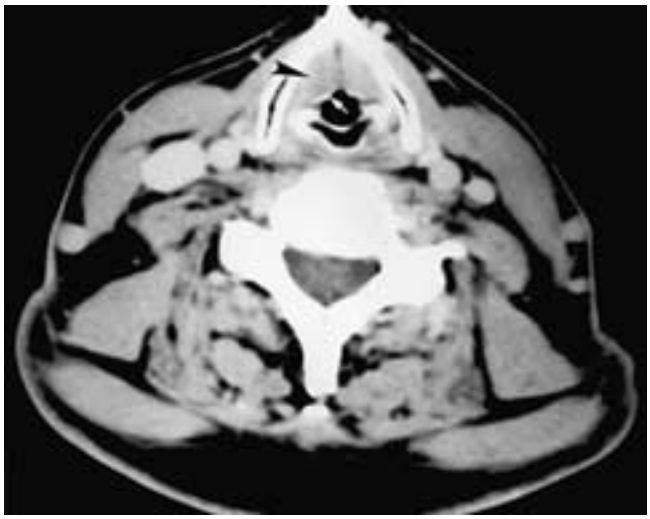

VIEW IMAGE

FIGURE 30-20 Axial CT with breath-holding. The true cords are apposed. *Arrowhead*, TAM; *arrow*, vocal process.

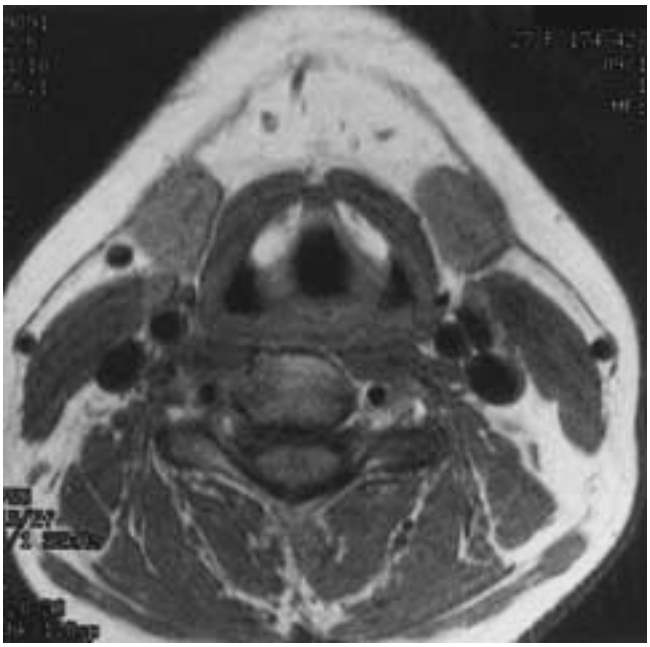

FIGURE 30-22 FSE T1-weighted image through the larynx. Axial 512 × 256 matrix shows excellent detail in the paraglottic space and pyriform sinuses.

VIEW IMAGE

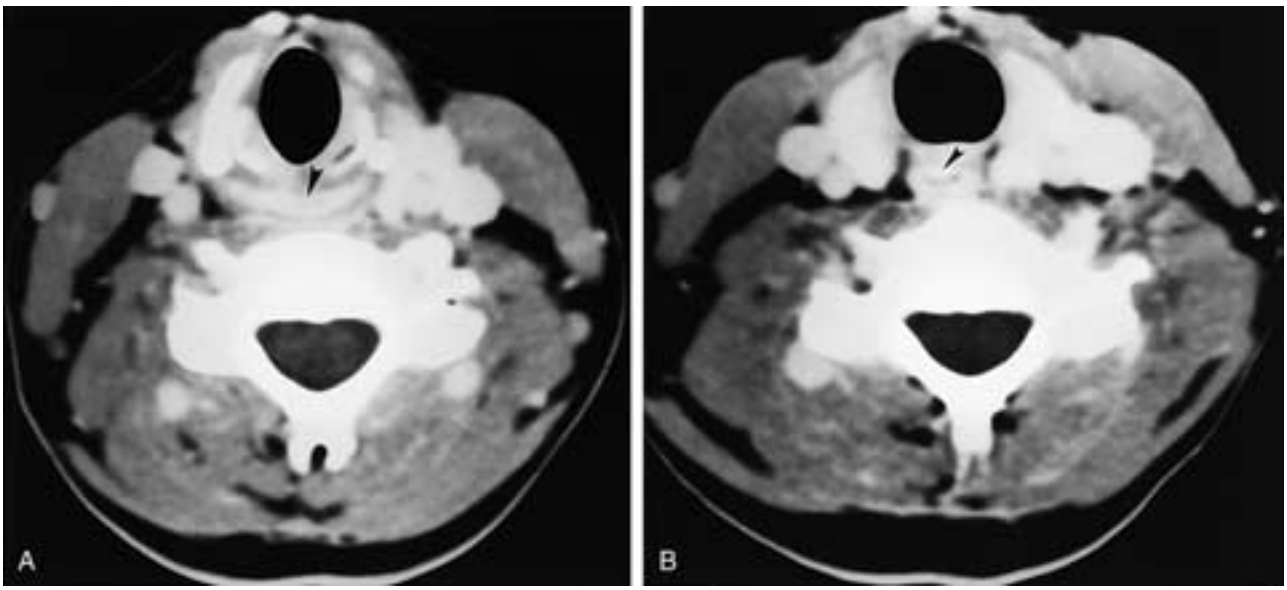

VIEW IMAGE

FIGURE 30-21 **A**, Axial scan with bolus contrast showing enhancement of the mucosa of the pharynx at the level of the lower pharynx. Note its flattened configuration (*arrowhead*) caused by the attachment of the pharyngeal musculature at the lateral aspect of the cricoid and thyroid. **B**, Lower scan showing the esophageal wall (*arrowhead*), with a rounder and narrower appearance than the wall of the pharynx.

Copyright © 2003, Mosby, Inc. All rights reserved.

the false cord level of the paraglottic space, these are very thin, and for practical purposes the upper margin of the true vocal cord is considered to be the upper margin of the muscle. Anteriorly, the petiole and the fat of the preepiglottic space are also visible just above the anterior commissure, whereas posteriorly, the arytenoids again are seen on the cricoid. The subglottic region is seen on the same images as the true cord.

The axial images represent slices perpendicular to the inner surface of the thyroid and cricoid cartilage, allowing assessment of cartilaginous erosion. Again, the appearance of the cartilage is quite variable, depending on the degree of ossification. Ossified cartilage with fat in the medullary space has a high signal intensity on T1-weighted sequences. By comparison, the nonossified cartilage tends to be dark on both T1-weighted and T2-weighted sequences. The ossified cartilage cortex is black on MR images.

The cord level can be identified on axial MR imaging in much the same way as it is with CT; the airway is narrow, and there is the low T1-weighted signal intensity of muscle in the cord. By comparison, a T1-weighted image through the false cord level shows the high T1-weighted signal intensity of fat in the paraglottic area.

Ultrasonography, Nuclear Medicine, and Angiography

Ultrasonography has significant limitations in the larynx. The proximity of the larynx to the skin surface allows the use of very high-resolution, high-frequency 5 to 10 mHz probes.[30] However, when ossified, the cartilage reflects most of the sound, thus limiting ultrasonic access to the larynx. The cystic nature of a laryngocele can be determined, and vocal cord mobility can be assessed.[31, 32] Perichondritis or tumor extension through the thyroid cartilage has been evaluated with ultrasound, but most centers use CT or MR imaging in this evaluation.[33]

Some work has been done using endolaryngeal ultrasound to visualize the deeper areas of the larynx during endoscopy.[34, 35] This method allows assessment of deep tissue infiltration as well as cartilage involvement, and more experience with this ultrasound technique may increase its future applicability.

Because the cartilage is not ossified in the pediatric patient, ultrasound can access the inner larynx.[36] Still, acoustic shadowing of the airway limits the ability to evaluate the posterior larynx, especially the cricoid. Mobility of the cords can be assessed, and invasion into the larynx by lesions such as lymphangiomas can be appreciated. Prenatal ultrasound is not compromised by air because the larynx, trachea, and bronchi are filled with fluid.[37] Thus, prenatal ultrasound has been used to predict laryngeal and tracheal atresia.

Nuclear medicine is seldom used specifically for pathologic conditions of the larynx. Increased uptake in inflammatory arthropathies or relapsing polychondritis occasionally has been mentioned in the literature.[38] Metabolic imaging such as positron emission tomography and single photon emission computed tomography are discussed in Chapter 45.

Arteriography can demonstrate the blood supply to the larynx. Although a primary glomus (paraganglioma) tumor or other vascular lesions can be evaluated by arteriography, this is seldom necessary.[39]

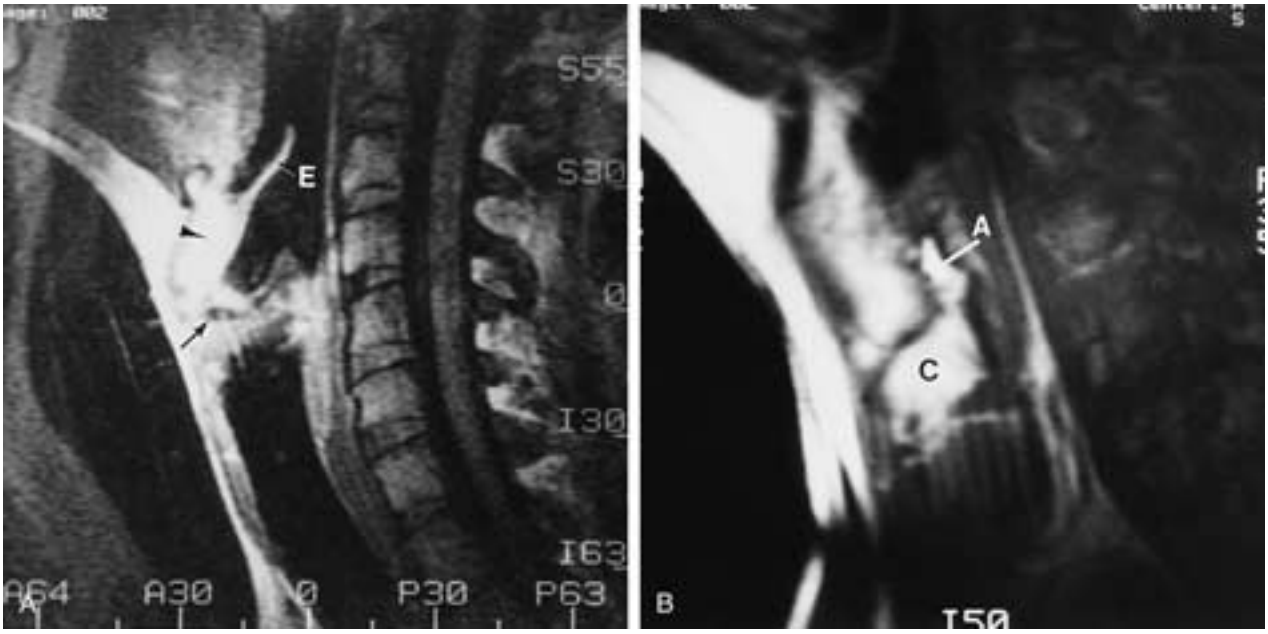

FIGURE 30-23 **A**, MR image, 1.5 Tesla, T1-weighted sagittal image, just off the midline, shows the true cord and false cord separated by the dark air-filled ventricle (*arrow*). *Arrowhead*, Preepiglottic fat; *E*, epiglottis. **B**, More lateral scan shows the cricoid (*C*) and arytenoid (*A*).

VIEW IMAGE

Copyright © 2003, Mosby, Inc. All rights reserved.

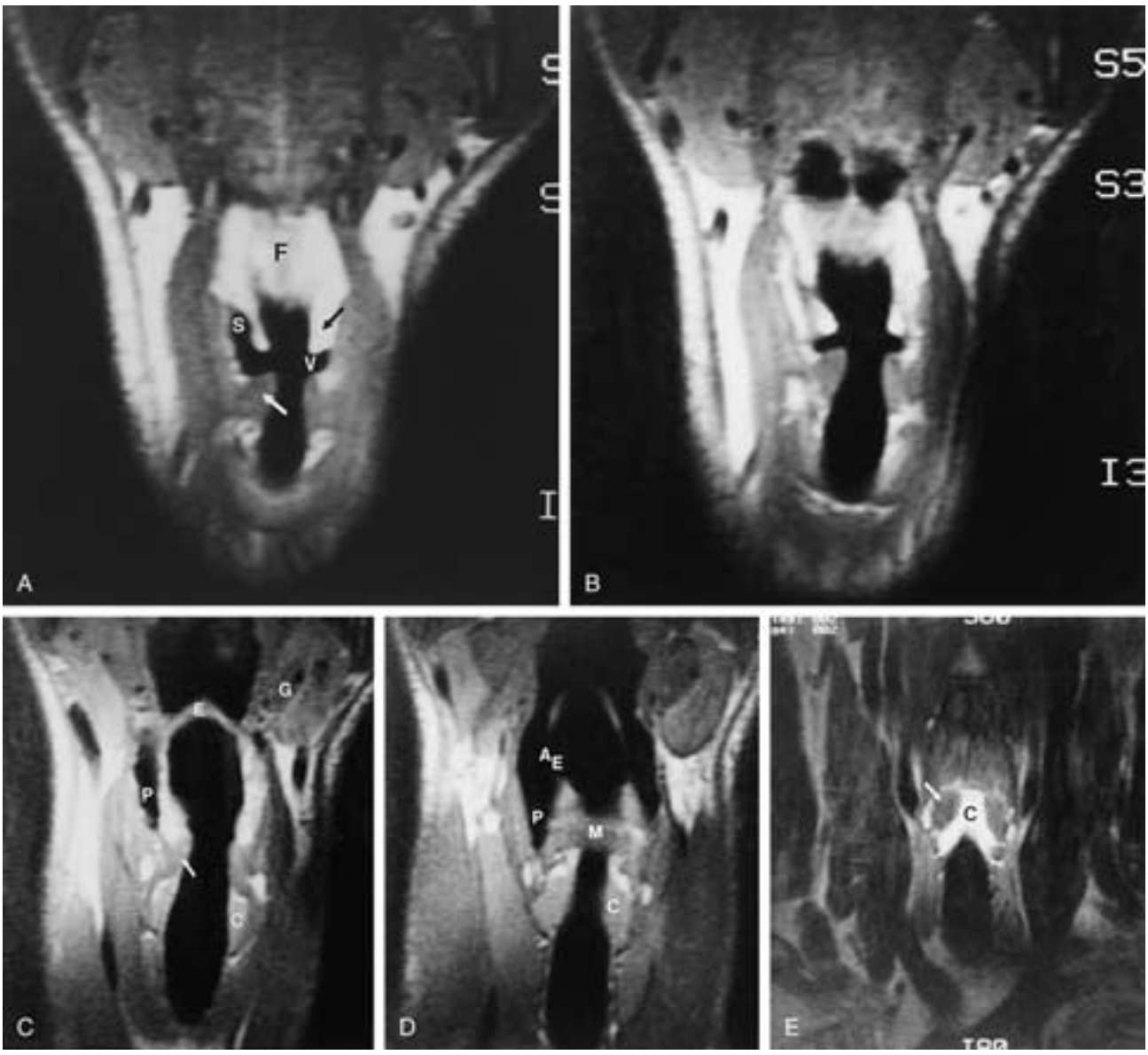

VIEW IMAGE

FIGURE 30-24 Coronal MR image, 1.5 Tesla, T1-weighted image seen from front to back. **A**, Anterior scan shows the muscle intensity (*white arrow*) of the TAM at the level of the cord. The paraglottic space at the level of the false cord shows bright fat intensity (*black arrow*). *V*, Ventricle; *S*, saccule of the ventricle; *F*, preepiglottic fat. **B**, Slightly more posterior scan. **C**, More posterior to **B**. *Arrow*, Posterior TAM; *P*, pyriform sinus; *E*, epiglottis; *C*, cricoid; *G*, submandibular gland. **D**, Posterior to **C**. *C*, Cricoid lamina; *M*, interarytenoid muscle; *AE*, AE fold; *P*, pyriform sinus. **E**, Posterior larynx shows the posterior cricoid (*C*). The muscle intensity to either side (*arrow*) represents the posterior cricoarytenoid muscle. (From Curtin HD. Imaging of the larynx: current concepts. Radiology 1989;713:1–11.)

Copyright © 2003, Mosby, Inc. All rights reserved.

VIEW IMAGE

FIGURE 30-25 Normal coronal MR image. Coronal image through the larynx shows the triangular TAM (*arrow*) forming the bulk of the true cord. The ventricle (*arrowhead*), preepiglottic space (*PS*).

SECTION THREE

PATHOLOGIC CONDITIONS

Congenital, inflammatory, neoplastic, and traumatic abnormalities all affect the larynx.[40, 41] Typically, the clinician has a good idea of the basic clinical problem and seeks the radiologist's help to determine the extent of the particular pathology. Because most modern imaging has been directed toward evaluation of neoplasms, this section begins with and emphasizes tumors. The evaluation of congenital, traumatic, and inflammatory lesions then follows. Although some pathologic conditions are not often evaluated by radiology, they are included here for completeness.

SQUAMOUS CELL CARCINOMA

General Considerations

Cancers of the larynx represent about 1% of all cancers diagnosed, and most laryngeal malignancies are squamous cell carcinomas.[42] Though there is no proven cause of laryngeal carcinoma, there are many strong etiologic associations. The most common risk factors for cancer of the larynx are considered to be smoking and alcohol. More than 95% of patients with laryngeal cancer have been found to have been smokers. About 2% of patients with laryngeal papillomas will develop laryngeal cancer, and the percentage of cancers is higher if the onset of the laryngeal papillomas is in the adult. These lesions are associated with human papilloma virus, and this virus has been found in large numbers of laryngeal cancers, with or without papillomas, again indicating an etiologic association. Other potential associations include mouthwash and gastroesophageal reflux, and many of the associated factors may be related or additive. For instance, smoking or drinking may increase reflux, while various other factors may influence the immune system and affect the body's ability to react to a developing cancer.

Because these cancers usually cause the early symptom of hoarsness, and because these are mucosal tumors and the larynx is accessible to direct visualization, the diagnosis is usually known prior to imaging. Very rarely, a squamous cell carcinoma can arise deep enough in the ventricle to avoid detection on indirect mirror examination. However, such lesions are almost always found if formal endoscopy is performed.

The laryngoscopist may be able to obtain all the information needed for treatment planning without imaging. However, the endoscopist is limited in the ability to define the deep extent of a lesion relative to precise landmarks utilized to determine whether the patient is a candidate for a speech conservation operation or radiotherapy. Because a tumor can cross the acceptable limits of a voice conservation operation by growing deeply through the paraglottic space, such tumor spread can go completely undetected by the laryngoscopist. A good approach to imaging of the larynx in the cancer patient is to concentrate on the specific anatomic landmarks that determine surgical planning. These landmarks are stressed in this chapter.

Clinically, tumors are staged by the TNM classification developed by the American Joint Committee on Cancer (AJCC). The AJCC system is now identical to that of the Union Internationale Contre le Cancer (UICC).[43] Although staging is done primarily by visual inspection, cross-sectional imaging is advised for analysis of areas of deeper tumor involvement. The AJCC system is presented in Box 30-1.

Certain points regarding the relationship of radiology and endoscopy must be emphasized. First, whenever possible, CT or MR imaging should be done prior to biopsy. This avoids confusion in differentiating the findings related to the local trauma of the biopsy procedure and the findings reflecting the tumor itself. Usually the diagnosis is strongly suspected by the clinician after mirror examination, and the clinician can help the radiologist best by initially localizating the lesion.

A second important point is that the mucosal surfaces are in the realm of the endoscopist, and the radiologist should not perform CT or MR imaging as a substitute for direct clinical visualization, as small but clinically obvious mucosal lesions may go undetected on these studies. It is impossible to exclude cancer of the larynx based only on imaging.

Voice Conservation Therapy

Voice conservation therapies include partial laryngectomies, radiation therapy, and organ preservation therapies that combine chemotherapy and radiation therapy. All of these treatments allow some preservation of the ability to have unassisted speech.[44–46] The alternative treatment is a total laryngectomy, which only allows assisted speech using either an esophageal voice valve or an external amplifier.

Although voice conservation surgery allows the patient to maintain the capability of speech using the remaining portion of the larynx, the ability of the remaining larynx to maintain a patent airway and protect the airway from

Copyright © 2003, Mosby, Inc. All rights reserved.

BOX 30-1
*DEFINITION OF TNM**

Primary Tumor (T)

TX Primary tumor cannot be assessed
T0 No evidence of primary tumor
Tis Carcinoma *in situ*

Supraglottis

T1 Tumor limited to one subsite of supraglottis with normal vocal cord mobility
T2 Tumor invades mucosa of more than one adjacent subsite of supraglottis or glottis or region outside the supraglottis (e.g., mucosa of base of tongue, vallecula, medial wall of pyriform sinus) without fixation of the larynx
T3 Tumor limited to larynx with vocal cord fixation and/or invades any of the following: postcricoid area, pre-epiglottic tissues, para
glottic space, and/or minor thyroid cartilage erosion (e.g., inner cortex)
T4a Tumor invades through the thyroid cartilage and/or invades tissues beyond the larynx (e.g., trachea, soft tissues of neck including deep extrinsic muscle of the tongue, strap muscles, thyroid, or esophagus)
T4b Tumor invades prevertebral space, encases carotid artery, or invades mediastinal structures

Glottis

T1 Tumor limited to vocal cord(s) (may involve anterior or posterior commissure) with normal mobility
T1a Tumor limited to one vocal cord
T1b Tumor involves both vocal cords
T2 Tumor extends to supraglottis and/or subglottis, and/or with impaired vocal cord mobility
T3 Tumor limited to the larynx with vocal cord fixation and/or invades paraglottic space,
and/or minor thyroid cartilage erosion (e.g., inner cortex)
T4a Tumor invades through the thyroid cartilage and/or invades tissues beyond the larynx (e.g., trachea, soft tissues of neck including deep extrinsic muscle of the tongue, strap muscles, thyroid, or esophagus)
T4b Tumor invades prevertebral space, encases carotid artery, or invades mediastinal structures

Subglottis

T1 Tumor limited to the subglottis
T2 Tumor extends to vocal cord(s) with normal or impaired mobility
T3 Tumor limited to larynx with vocal cord fixation
T4a Tumor invades cricoid or thyroid cartilage and/or invades tissues beyond the larynx (e.g., trachea, soft tissues of neck including deep extrinsic muscles of the tongue, strap muscles, thyroid, or esophagus)
T4b Tumor invades prevertebral space, encases carotid artery, or invades mediastinal structures

Regional Lymph Nodes (N)

NX Regional lymph nodes cannot be assessed
N0 No regional lymph node metastasis
N1 Metastasis in a single ipsilateral lymph node, 3 cm or less in greatest dimension
N2 Metastasis in a single ipsilateral lymph node, more than 3 cm but not more than 6 cm in greatest dimension, or in multiple ipsilateral lymph nodes, none more than 6 cm in greatest dimension, or in bilateral or contralateral lymph nodes, none more than 6 cm in greatest dimension
N2a Metastasis in a single ipsilateral lymph node, more than 3 cm but not more than 6 cm in greatest dimension
N2b Metastasis in multiple ipsilateral lymph nodes, none more than 6 cm in greatest dimension
N2c Metastasis in bilateral or contralateral lymph nodes, none more than 6 cm in greatest dimension
N3 Metastasis in a lymph node, more than 6 cm in greatest dimension

Distant Metastasis (M)

MX Distant metastasis cannot be assessed
M0 No distant metastasis
M1 Distant metastasis

**T*, Primary tumor; *N*, regional lymph nodes; *M*, metastasis.

From Green FL, et al. eds. American Joint Committee on Cancer: Cancer Staging Manual. 6th ed. New York: Springer-Verlag, 2002.

Copyright © 2003, Mosby, Inc. All rights reserved.

aspiration may be compromised. Immediately following most voice conservation surgery, the patient will aspirate. However, if the patient has the desire to go through a retraining period, if the hyoid bone is not fixed by scar tissue, and if there is an adequate pulmonary reserve, most often normal swallowing can be achieved. Some patients will not regain a normal swallow. Also, some voice conservation surgery patients will not be able to be decannulated, as a sufficient airway cannot be reestablished in the postoperative larynx.

The classic voice conservation operations are the (horizontal) supraglottic laryngectomy and the vertical hemilaryngectomy. The supraglottic laryngectomy is done for supraglottic carcinoma, whereas the vertical hemilaryngectomy is done for a lesion isolated to the true vocal cord. These procedures are described in the appropriate sections that follow. The anatomic landmarks used to determine the feasibility of each of these standard partial laryngectomies are also emphasized in the sections dealing with tumors of specific areas within the larynx.

Radiation therapy (RT) also has the ability to preserve voice function. The imaging approach for planning RT is similar to that for planning a partial laryngeal resection. In particular, the overall size of the tumor must be noted, as this is an important factor for the radiation therapist because both tumor volume and depth of penetration help predict the treatment outcome.[47, 48] In general, RT is more successful for superficial lesions than it is for deeply invasive tumors. However, because of patient treatment preferences or medical contraindications to surgery, RT is still used in some extensive lesions.

Only recently have studies appeared in the literature correlating imaging findings with RT outcome. Initial results have found higher recurrence rates with larger supraglottic lesions. In one study, volume was not as important in stage T2 true cord lesions, but the patient numbers were small.[49] Castelijns et al. compared recurrence rates with the involvement of cartilage as shown by MR imaging.[50] Higher recurrence rates were seen in patients with cartilage abnormality than in those with normal signal intensity within cartilage. This is an important concept because the outcome was compared directly with an imaging finding without exact histologic verification. The patient numbers in all of these studies are small, making definite conclusions somewhat premature. However, if absolute determinations are to be made, these preliminary studies do provide a rationale for further investigations.

If a tumor does recur after RT, a salvage total laryngectomy can be performed. This treatment sequence does, however, give a slightly lower overall survival than if a total laryngectomy is done at initial diagnosis.

Cartilage Involvement

The laryngeal cartilages should be assessed during the imaging evaluation of any tumor of the larynx. This evaluation is therefore discussed before the specific regions of the larynx are considered. In actual practice, a tumor confined to the supraglottic larynx very rarely invades the cartilage.[51] Cartilage invasion is much more of a problem in tumors of the true cord, subglottis, and hypopharynx.

Tumor invasion of the cricoid or thyroid cartilage is considered a negative predictor for the prognosis of patients treated with RT, and is considered a contraindication to the standard partial laryngeal operations. Thus, for any patient who is being considered for either RT or a conservation-type laryngectomy, cartilage involvement is an important consideration.

The epiglottis is not a crucial factor in planning treatment, as it is a poor barrier to tumor extension and it is routinely removed in a supraglottic laryngectomy without consequence to the patient. Similarly, minimum involvement of the vocal process of the arytenoid does not exclude a partial resection. Some of the more advanced types of partial laryngectomy may include a resection of one of the arytenoid cartilages if it is deemed necessary.

Mineralization of the cartilages is not uniform and is frequently asymmetric. By the age at which most patients develop laryngeal carcinoma, much of both the cricoid cartilage and the thyroid cartilage is ossified. As mentioned, ossification follows the line of attachment of the muscles to these cartilages, and thus the thyroid cartilage usually ossifies from the inferior margin superiorly and from the posterior margin anteriorly. Small islands of both ossified and nonossified cartilage are frequently seen in the broad, flat alar regions of the thyroid cartilage. The cricoid cartilage usually ossifies along the superior edge, the back of the lamina, and then along the upper margin of the cricoid arch. As a result of this partial ossification, the thyroid, the cricoid, and even the arytenoid cartilages may contain cortical bone, fatty marrow, and nonossified cartilage.

On CT, a tumor usually has an attenuation approximating that of nonossified cartilage or muscle (soft-tissue density), and minimal cartilage involvement is almost impossible to identify (Fig. 30-26). Gross cartilage destruction can be seen. The most reliable CT sign of cartilage invasion is the demonstration of through-and-through tumor spread, that is, the visualization of tumor on the opposite side of the cartilage from the primary lesion.[52] Obliteration of the marrow fat as tumor involves the medullary space of ossified cartilage may also be identified on CT.

Cartilage sclerosis seen on CT is a reactive phenomenon and thus does not necessarily mean that actual tumor invasion of the cartilage has occurred (Fig. 30-27). A tumor close to the perichondrium is thought to be able to cause cartilage sclerosis because of the adjacent inflammatory response that is frequently identified at the margin of a squamous cell carcinoma. Although more experience is needed to clarify this relationship, at present cartilage sclerosis is believed to indicate that tumor is either in or at least against the cartilage.

On MR, the most reliable imaging sign is still the demonstration of tumor spread through the cartilage, with tumor on the opposite side of the cartilage from the primary lesion. However, there is evidence that suggests that lesser degrees of tumor involvement may also be detectable with MR imaging, as variations in the signal patterns of normal and abnormal cartilage are seen on different pulse sequences.[29, 53–55]

MR imaging shows the cortex of ossified cartilage as a signal void, while fatty marrow is bright on T1-weighted sequences. Nonossified cartilage has a relatively low T1-weighted signal intensity and also has low signal on T2-weighted images. Although nonossified cartilage does not have as low a signal intensity as cortical bone, it

Copyright © 2003, Mosby, Inc. All rights reserved.

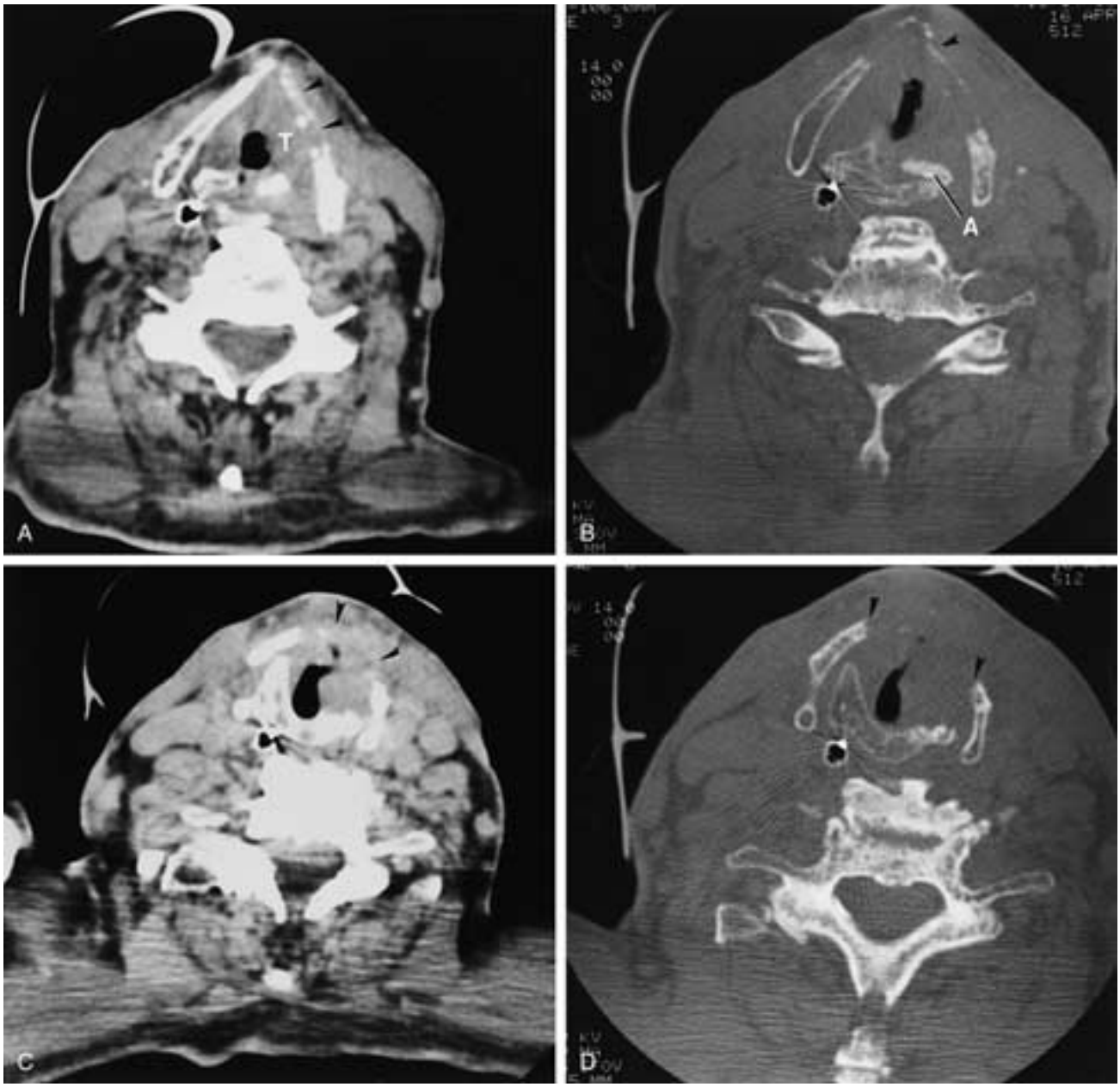

VIEW IMAGE

FIGURE 30-26 Axial CT scans of a transglottic tumor with cartilage destruction. **A**, The level close to the ventricle shows the tumor (*T*). There is definite demineralization of the thyroid ala (*arrowheads*) but no significant thickening of the strap muscles on the outer surface of the thyroid. **B**, Bone algorithm shows the demineralization of the cartilage, which is strongly indicative of tumor invasion. There has been slight buckling (*arrowhead*) of the thyroid ala because of the weakening of the cartilage. The arytenoid (*A*) is sclerotic. **C**, Scan through the cricoid shows tumor within the ring of the cricoid and, at this level, tumor extending outside of the larynx (*arrowheads*). **D**, Bone algorithm showing destruction of the thyroid cartilage (*arrowheads*).

has a much lower signal intensity than the either fat or tumor.

Since tumor has an intermediate signal intensity on T1-weighted sequences, any area that has a high (bright) T1-weighted szignal intensity typical of fat, represents ossified cartilage and can be reliably considered normal. A relatively dark segment of cartilage on T1-weighted images may represent either tumor or nonossified cartilage, and the T2-weighted image is used to help distinguish between these two possibilities (Figs. 30-28 to 30-30).

Tumors such as squamous cell carcinoma tend to have an intermediate or relatively high signal intensity on T2-weighted images, while nonossified cartilage has a lower T2-weighted signal intensity.[29, 53, 54] Thus, differentiation of tumor and nonossified cartilage is possible on T2-weighted images. Occasionally on T2-weighted images, tumor-infiltrated cartilage and uninvolved cartilage may actually

Copyright © 2003, Mosby, Inc. All rights reserved.

look the same, as tumor may have a relatively bright appearance and a fatty medullary area may retain a significant amount of signal because of its proximity to the surface coil. The important imaging finding is the change in appearance that occurs when short and long TR sequences are compared. Intermediate to low signal intensity on T1-weighted images and intermediate to high signal intensity on T2-weighted images suggest the presence of tumor. The use of FSE imaging with fat suppression has not only allowed highly detailed T2-weighted images, but with fat suppression the difference between tumor and the fat-containing medullary space may be accentuated.

Although Castelijns et al. used a midfield strength unit and an earlier echo (because of the diminishing signal on the later echo images), they demonstrated that tumor invasion of cartilage showed relative brightening on T2-weighted images compared with its appearance on T1-weighted images. Again, nonossified cartilage remained dark. Early experience using high field units and later echo times is encouraging, and although more experience is needed for verification, if proven reliable this finding will be diagnostically helpful.

Gadolinium also increases the signal intensity of the tumor. Limited experience using T1-weighted, contrast-enhanced, fat-suppressed images has indicated that one may be able to define early cartilage invasion (Fig. 30-29). However, high-quality T2-weighted FSE images may give the same information as gadolinium-enhanced, fat-suppressed images and therefore obviate the need for the contrast study.

The specificity of the high T2-weighted signal intensity has been questioned because the inflammatory changes that frequently accompany squamous cell carcinoma also give a relatively high T2-weighted signal. High T2-weighted signal intensity also can be present with ''red'' marrow, which may occasionally be found in the thyroid cartilage.[55] Currently, if the cartilage has normal signal (bright on T1), one can feel confident that the cartilage has not been invaded. If the signal is low to intermediate on T1-weighted and high on T2-weighted sequences or if the cartilage enhances, the cartilage is very likely abnormal. If the tumor abuts the questionable area, suspicion increases that the cartilage has been invaded by tumor. At times, one can see variations of signal intensity in the cartilage, suggesting either bulk tumor

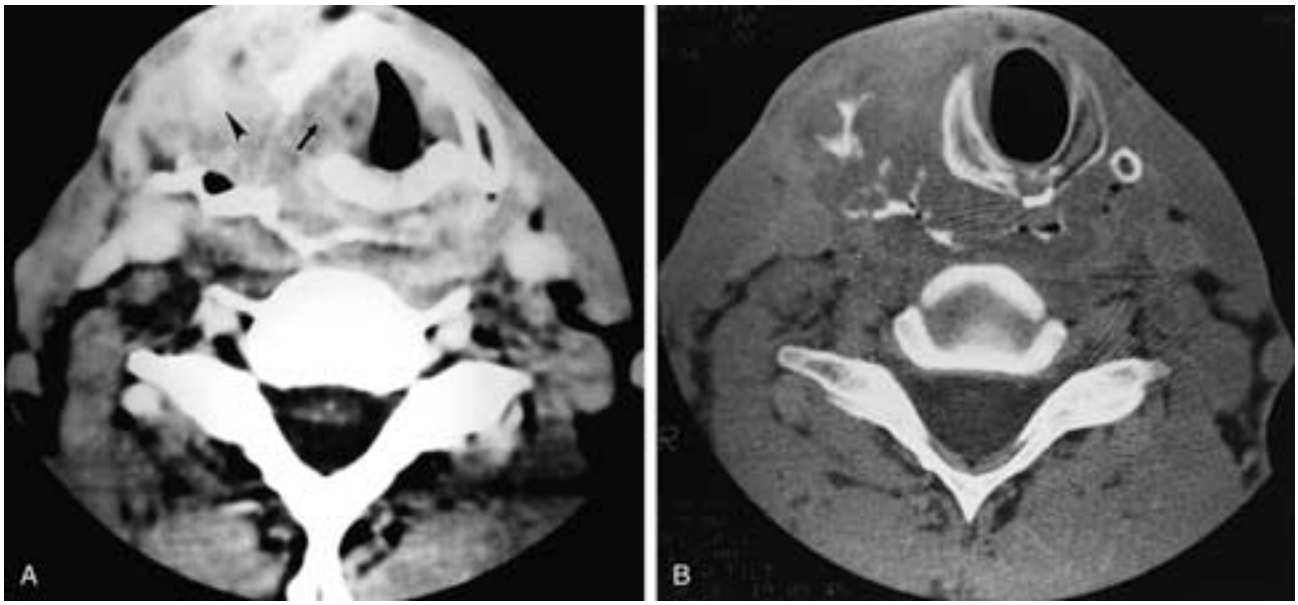

FIGURE 30-27 Axial CT scans show extensive pharyngeal tumor invading the larynx. **A**, Tumor of the pyriform sinus extending into the true cord level (*arrow*) and laterally (*arrowhead*). **B**, Lower level shows marked sclerosis of the cricoid cartilage on the involved side. The uninvolved side is normal. Tumor did not extend into the cartilage. The sclerotic reaction was definitely free of tumor histologically.

VIEW IMAGE

Copyright © 2003, Mosby, Inc. All rights reserved.

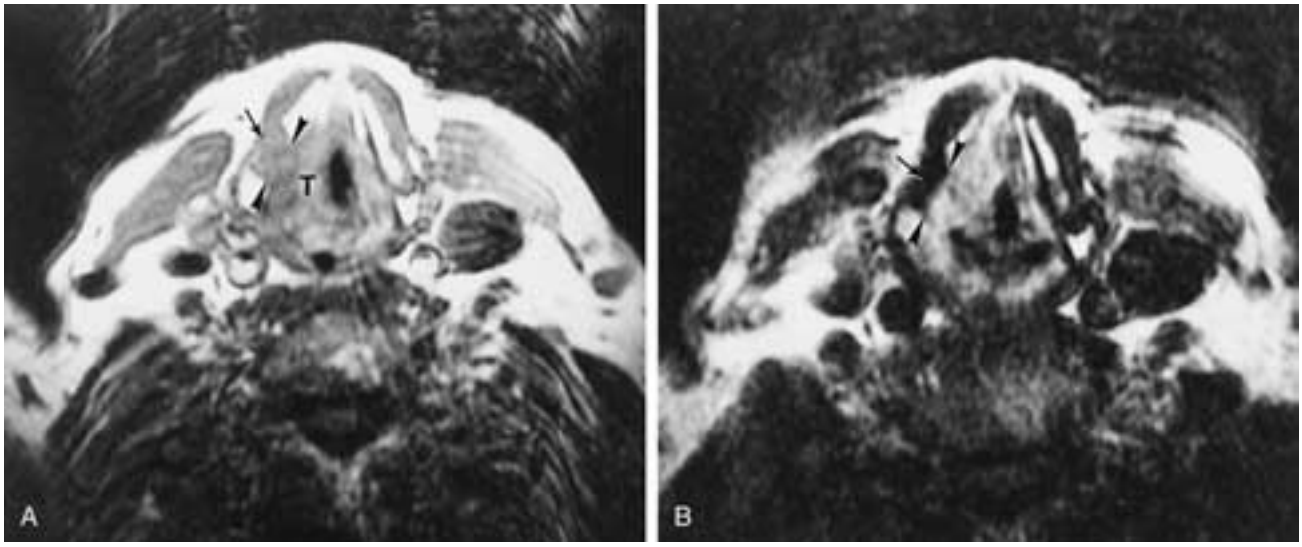

VIEW IMAGE

FIGURE 30-28 Axial MR image shows tumor against nonossified cartilage. **A**, T1-weighted image shows that tumor (*T*) and nonossified cartilage (*arrow*) both have intermediate signal intensity, and the tumor-cartilage junction between the arrowheads cannot be defined. **B**, T2-weighted image shows brightening of the tumor. The nonossified cartilage does not brighten (*arrow*). The margin between tumor and cartilage is now clearly defined (*between arrowheads*).

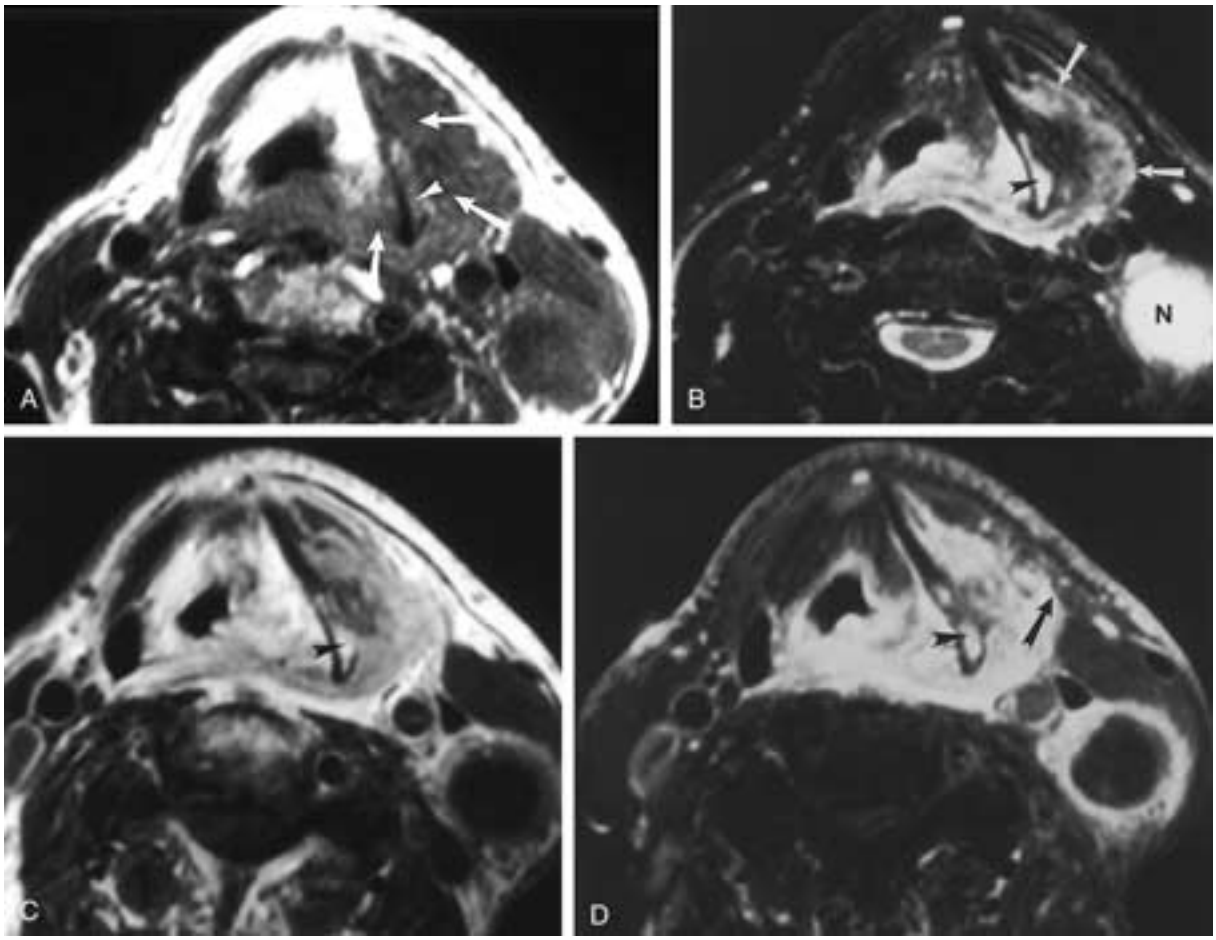

VIEW IMAGE

FIGURE 30-29 Carcinoma of the pyriform sinus invading the posterior thyroid cartilage and extending along the outer surface. **A**, Axial T1-weighted image without contrast. The tumor (*arrows*) is poorly seen relative to the strap muscles. Note the intermediate signal intensity (*arrowhead*) of the posterior thyroid cartilage. **B**, T2-weighted FSE image with fat suppression. The margins of the tumor (*arrows*) can be seen more distinctly. Note the high signal (*arrowhead*) within the posterior thyroid cartilage, indicating that it is abnormal. Note the abnormal node (*N*). **C**, Postcontrast without fat suppression T1-weighted image shows enhancement within the cartilage (compare with the T1-weighted image) and enhancement of the tumor. Enhancing thyroid cartilage (*arrowhead*). **D**, Postcontrast T1-weighted image with fat suppression. The margin of the tumor relative to the muscle (*arrow*) is clearly defined. Because fat suppression is used, the high signal within the thyroid cartilage (*arrowhead*) is not fat and is thus presumed to be abnormal. Again, note the metastatic node.

Copyright © 2003, Mosby, Inc. All rights reserved.

or edema (Figs. 30-31 and 30-32). The edema may be brighter on T2 sequences than actual bulk tumor. Again, further evaluation of this differentiation and its significance is warranted.

The significance of the inflammatory response is not known. It is possible that inflammatory edema may carry viable tumor cells. If this is the case, the inflammatory tissue would have to be treated as tumor and included in the resection or in the port of RT. Usually with cases that are questionable, there has been some other factor that tips the decision toward more radical treatment.

At times the tumor may have a relatively low signal intensity on T2-weighted images (Fig. 30-32). In this case, the involved cartilage will be relatively dark on both T1-weighted and T2-weighted images. However, the tumor within the cartilage should not be darker than the non-ossified cartilage and should follow the signal pattern of the tumor in the soft tissues of the larynx. This concept is relatively new, and further work is necessary before a definitive statement can be made regarding the importance of these findings.

Nodal Metastasis

Nodal metastasis is common with supraglottic tumors and rare with glottic tumors, but it should be considered during the assessment of any tumor arising at any site within the larynx.

The clinical presence or pathologic detection of metastatic adenopathy is accompanied by a lowered rate of survival.[56] More ominous is the presence of tumor extension through the capsule of a node (extracapsular spread). Although detection of large nodes by palpation is reliable, palpation fails to identify smaller or deeply situated nodes. Even on imaging, there can be false-positive and false-negative assessments.[57] This topic is discussed in Chapter 36.

Further Workup of the Patient with Squamous Cell Carcinoma

A patient with squamous cell cancer of the larynx, especially of the supraglottic larynx, has a relatively high risk (10% to 20%) of having or developing a second primary malignancy.[58] This may be the result of the common exposure of certain areas to carcinogens such as cigarette smoke or ethanol. The regions most likely to be involved are the oral cavity, larynx, pharynx, lung, esophagus, and, less often, the stomach (Fig. 30-33).

A barium swallow examination can be performed to search for second primary lesions in a patient diagnosed with a squamous cell carcinoma of the larynx. A truly negative barium swallow study is a very reliable test. Any area of mucosal irregularity, diminished pliability, or lack of distention should be evaluated by endoscopy and biopsy.

A chest radiograph is a good survey examination to evaluate for a second primary in the lung or the rare pulmonary metastasis. Some clinicians prefer the higher sensitivity of the chest CT study for the preoperative assessment of patients with head and neck carcinoma.

SITE-SPECIFIC EVALUATION

As stated in the section titled Anatomy, the larynx is subdivided into supraglottic, glottic, and subglottic areas. This classification is based on embryologic derivation, lymphatic drainage of the mucosa, and the clinical behavior of laryngeal tumors. The division is important for surgical statistics, but for the purposes of this chapter, the glottic and subglottic lesions are discussed together. Because of the proximity of the hypopharynx and the pyriform sinuses to the larynx, the discussion of carcinoma in one of these regions necessitates the discussion of carcinoma in the other; therefore, hypopharyngeal carcinoma is covered as well.

Supraglottic Larynx

Because the false cords are not directly used in vocalization, supraglottic tumors do not cause early hoarseness and are discovered somewhat later than are tumors arising in the true vocal cords. Therefore, at the time of diagnosis, supraglottic tumors are usually larger than tumors involving the true cord. Patients with a supraglottic tumor may have a ''hot potato'' voice, but they are not usually hoarse unless there is significant tumor extension onto the arytenoid cartilage or down into the true cord.

The standard voice conservation surgery related to the supraglottic larynx is the supraglottic laryngectomy (see Box 30-2).[59–62] Almost all of the larynx above the ventricle is removed, sparing the arytenoid cartilages if possible (Fig. 30-34). A horizontal cut is made through the upper thyroid cartilage, and the soft-tissue incision line is along the ventricle and just above the anterior commissure. More posteriorly, the incision moves upward over the AE fold just anterior to the arytenoid before passing along the medial wall of the pyriform sinus to complete the resection. The hyoid bone may or may not be removed.

The limits of the tumor are of obvious importance. Imaging is responsible for identifying some pathways of tumor spread more than others, as some tumor extension is

BOX 30-2 CONTRAINDICATIONS TO SUPRAGLOTTIC LARYNGECTOMY

1. Tumor extension onto the cricoid cartilage
2. Bilateral arytenoid involvement
3. Arytenoid fixation
4. Extension onto the glottis or impaired vocal cord mobility
5. Thyroid cartilage invasion
6. Involvement of the apex of the pyriform sinus or postcricoid region
7. Involvement of the base of the tongue more than 1 cm posteriorly to the circumvallate papillae

From Lawson W, Biller HF, Suen JY. Cancer of the larynx. In: Suen JY, Myers E, eds. Cancer of the Head and Neck. New York: Churchill Livingstone, 1989;533–591.

Copyright © 2003, Mosby, Inc. All rights reserved.

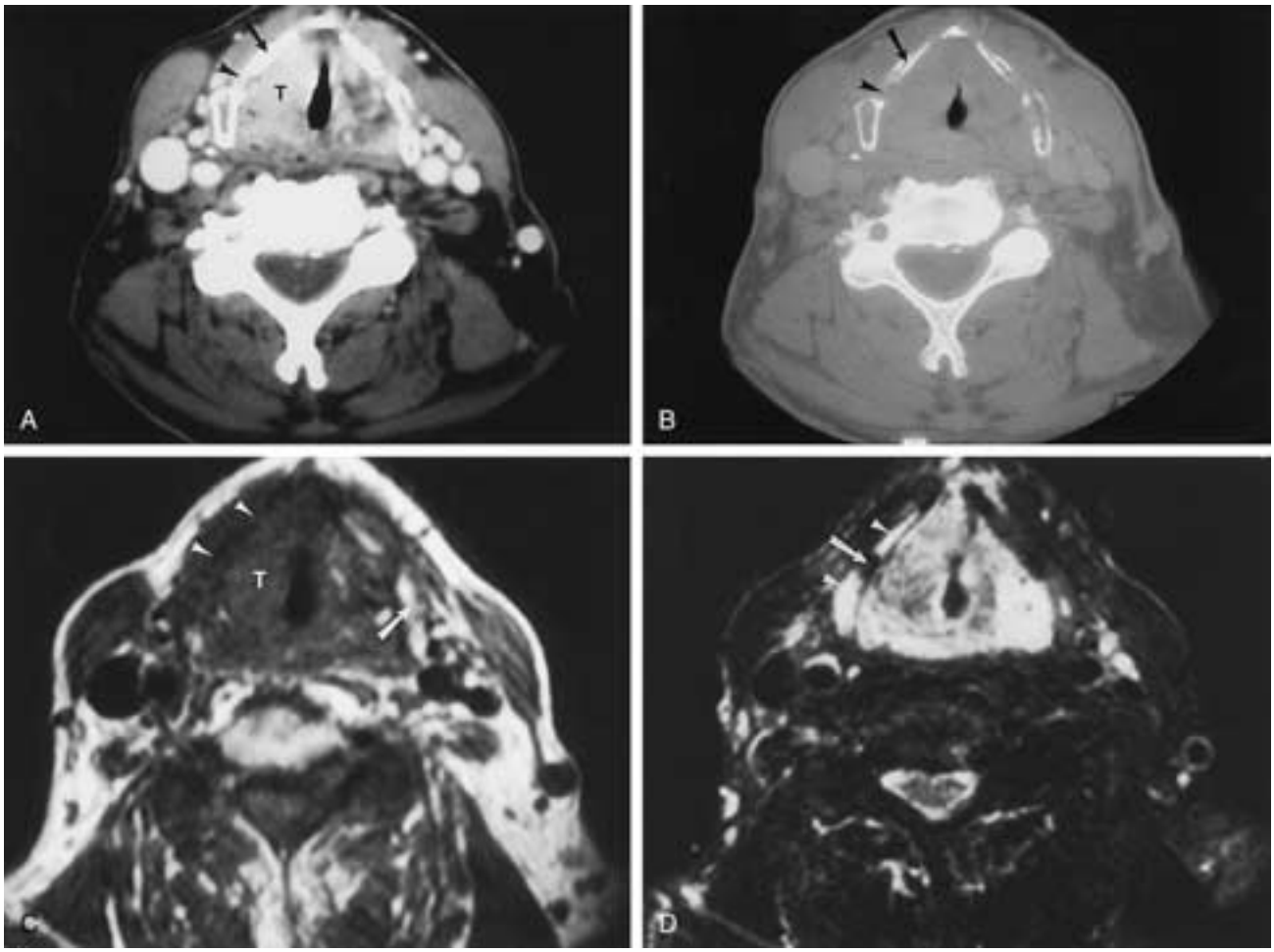

VIEW IMAGE

FIGURE 30-30 Carcinoma of the larynx invading the thyroid cartilage. **A**, Axial CT of the larynx shows a tumor (*T*). On the soft-tissue window the cartilage is unremarkable. Note the nonossified cartilage (*arrowhead*) and the ossified cartilage (*arrow*). **B**, Bone algorithm shows no definite abnormality. Again, both nonossified (*arrowhead*) and ossified (*arrow*) cartilage can be identified. **C**, MR T1-weighted image shows tumor (*T*). The thyroid cartilage (*arrowheads*) on the side of the tumor has intermediate signal, suggesting tumor involvement. On the opposite side there is fat in the medullary cavity of the cartilage (*arrow*). **D**, Axial T2-weighted image with fat suppression shows a definite increase in signal (*arrowheads*) in the involved thyroid cartilage. Note that there is relative sparing of the nonossified portion (*arrow*) of the cartilage.

easily seen endoscopically. By far the most important margin to assess is the inferior border of the tumor. In addition, the degree of spread into the preepiglottic and paraglottic regions relates to the likelihood of nodal metastasis. The supraglottic larynx may be subdivided into the suprahyoid and infrahyoid regions. Many tumors involve both regions, but some are small enough to be localized to only one area.

Suprahyoid lesions include tumors of the free margin of the epiglottis. Small tumors in this area can be resected without removing the entire supraglottic larynx. The hyoepiglottic ligament acts as a barrier to spread of suprahyoid or low tongue base lesions into the preepiglottic space (Fig. 30-35).[4] The management of the base of the tongue is often a clinical problem with suprahyoid cancers, because these lesions tend to extend anteriorly into the tongue (Fig. 30-36). Today many surgeons have expanded the classic criteria for a supraglottic laryngectomy to include lesions that extend less than 2 cm into the tongue base. Unless the lesion is very small, the true size of these lesions is difficult for the endoscopist to appreciate, as the lesion may indeed be the tip of an ''iceberg,'' with tumor extending deeply into the tongue base or the infrahyoid larynx. However, if the lesion extends into the infrahyoid larynx, the laryngeal surface of the epiglottis is usually involved and the extent of an infrahyoid tumor can often be appreciated at endoscopy.

The suprahyoid supraglottic larynx is well seen on axial CT and MR imaging. The lesion can extend laterally along the pharyngoepiglottic folds to reach the pharyngeal wall or along the glossoepiglottic fold in the midline of the floor of the valleculae to reach the tongue base. The extension into the tongue base is best seen on MR imaging, especially on sagittal views (Fig. 30-36).[28] The normal lingual tonsil is situated in the region of the valleculae and, as mentioned, can normally extend down to the anterior vallecular wall. It

Copyright © 2003, Mosby, Inc. All rights reserved.

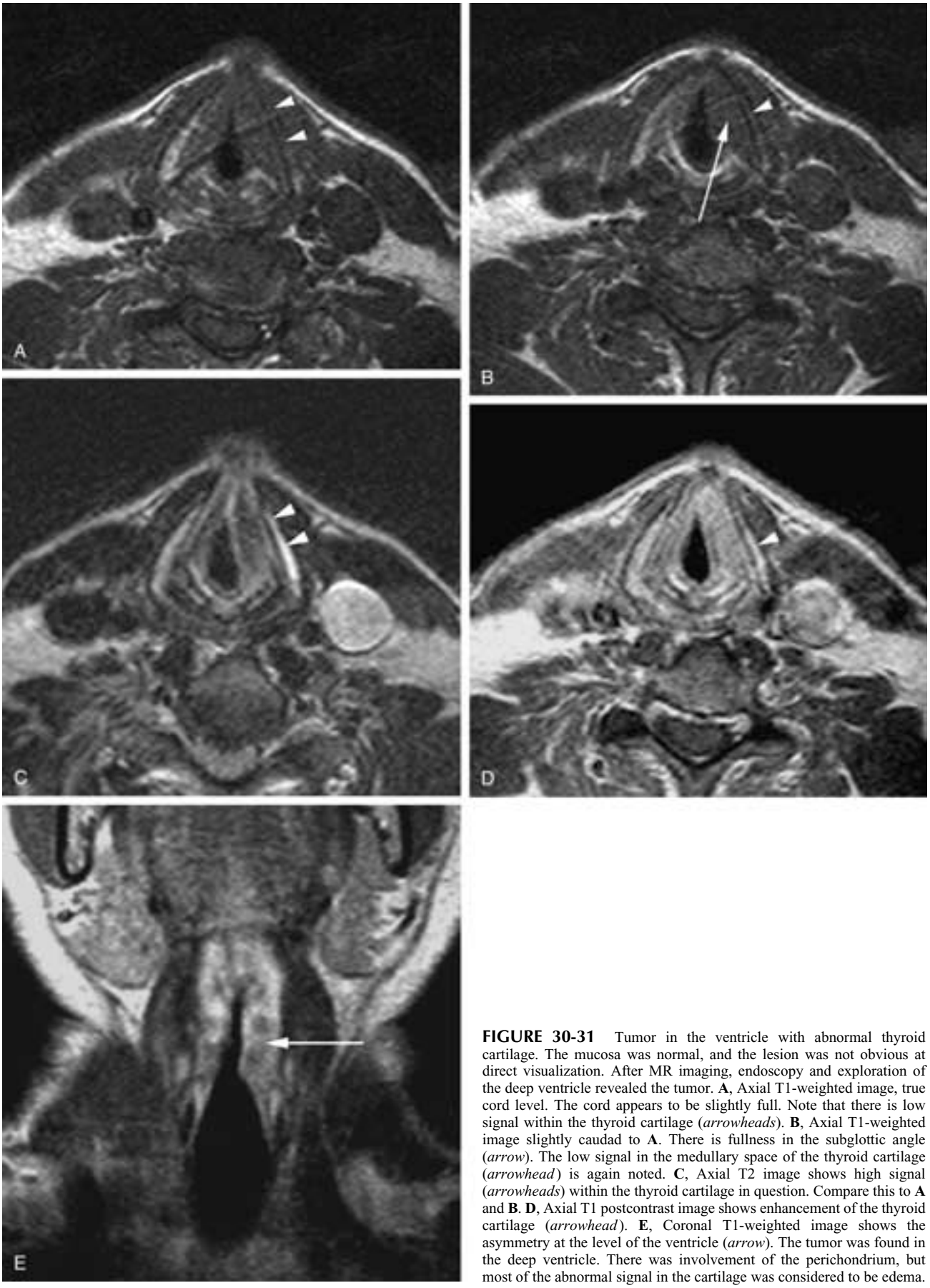

FIGURE 30-31 Tumor in the ventricle with abnormal thyroid cartilage. The mucosa was normal, and the lesion was not obvious at direct visualization. After MR imaging, endoscopy and exploration of the deep ventricle revealed the tumor. **A**, Axial T1-weighted image, true cord level. The cord appears to be slightly full. Note that there is low signal within the thyroid cartilage (*arrowheads*). **B**, Axial T1-weighted image slightly caudad to **A**. There is fullness in the subglottic angle (*arrow*). The low signal in the medullary space of the thyroid cartilage (*arrowhead*) is again noted. **C**, Axial T2 image shows high signal (*arrowheads*) within the thyroid cartilage in question. Compare this to **A** and **B**. **D**, Axial T1 postcontrast image shows enhancement of the thyroid cartilage (*arrowhead*). **E**, Coronal T1-weighted image shows the asymmetry at the level of the ventricle (*arrow*). The tumor was found in the deep ventricle. There was involvement of the perichondrium, but most of the abnormal signal in the cartilage was considered to be edema.

VIEW IMAGE

Copyright © 2003, Mosby, Inc. All rights reserved.

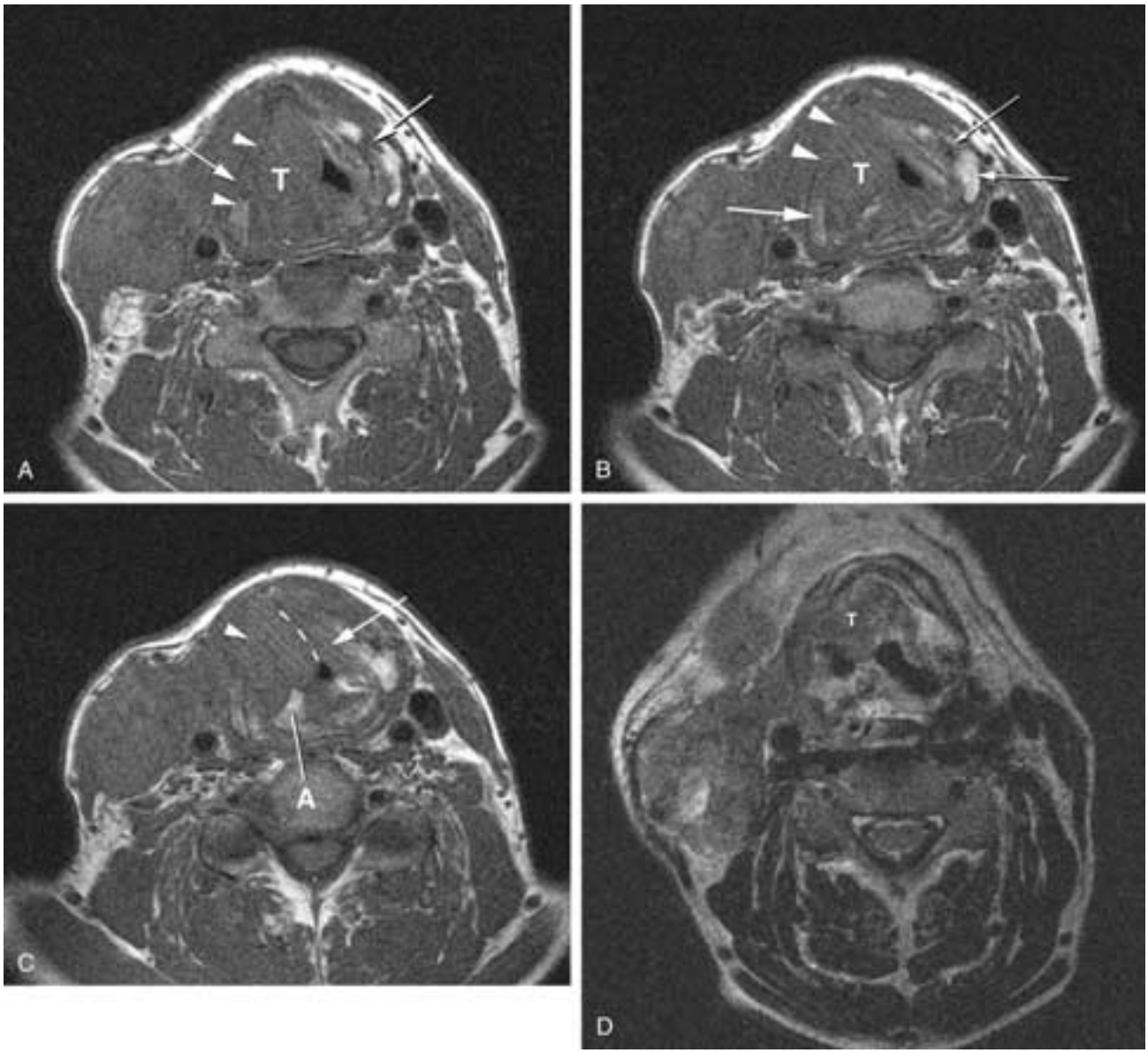

VIEW IMAGE

FIGURE 30-32 Transglottic tumor. Supraglottic primary tumor with paraglottic spread to the level of the true cord and beyond (same case as Fig. 30-39). **A**, T1-weighted axial image, level of the supraglottis. The tumor (*T*) infiltrates the paraglottic space. There is abnormal signal in the right ala of the thyroid cartilage (*arrowhead*). The abnormal signal in the ossified portion (*arrowheads*) is difficult to distinguish from the nonossified cartilage (*arrows*) on the T1-weighted sequence. Compare this with the appearance on the left side, where there is bright signal from the fat adjacent to the lower signal of nonossified cartilage (*arrow*). Compare with the T2-weighted image (**E**). **B**, Slightly caudad level shows the ventricle/glottic level. The tumor (*T*) fills the paraglottic region. There is abnormal signal in the anterior cartilage representing actual tumor invasion. More posteriorly (*large white arrow*) there is only partial obliteration of the fat signal. This area represents edema. Compare it with the normal nonossified portion of the cartilage (*small arrows*) on the opposite side. **C**, Axial T1-weighted image, cord level. The tumor infiltrates the thyroid cartilage (*arrowhead*). Normal TAM on the left side (*arrow*). Arytenoid (*A*). The dashed line approximates the position of the airway. **D**, T2-weighted image. The axial image at the level of the hyoid shows the tumor, with relatively low signal extending into the preepiglottic space.

Copyright © 2003, Mosby, Inc. All rights reserved.

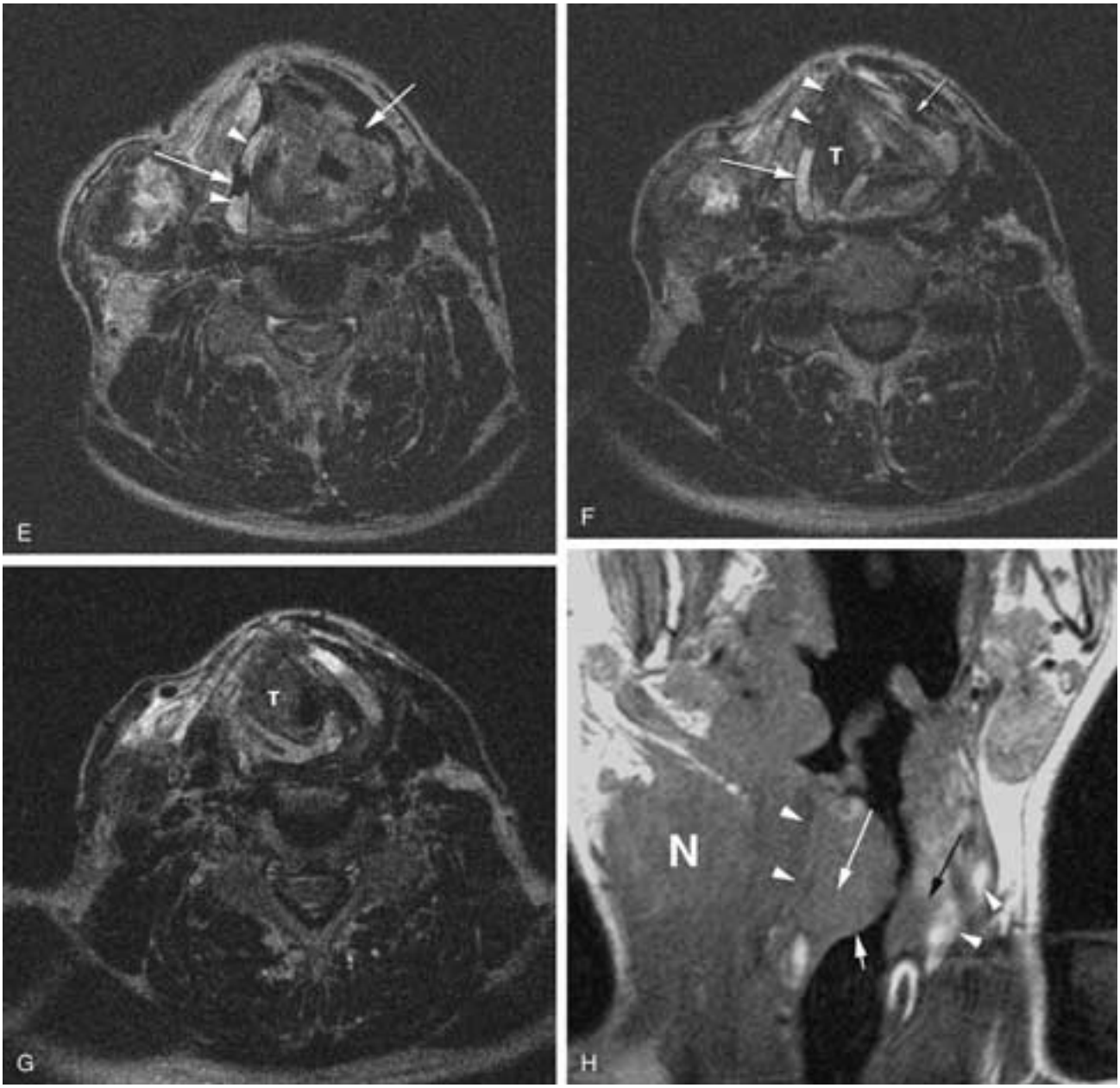

VIEW IMAGE

FIGURE 30-32 *Continued.* **E**, Axial T2-weighted image, same level as **A**, level of the false cord. Note the bright signal in the abnormal portions of the cartilage (*arrowheads*) compared to the dark signal of nonossified cartilage (*arrows*). **F**, Same level as **B**. Tumor (*T*) fills the paraglottic region, producing fullness in the cord. The anterior part of the right ala of the cartilage (*arrowheads*) has low signal. The signal approximates that of the tumor and thus separation of tumor and nonossified cartilage is difficult. (Compare with the opposite side [*arrow*].) Posteriorly (*large arrow*) the signal is higher, reflecting edema within the cartilage. **G**, Axial T2-weighted image at the subglottic level shows the tumor (*T*) within the cricoid ring. **H**, Coronal T1-weighted image shows the tumor following the paraglottic pathway (*large white arrow*). Note the smooth margin of the true cord (*small white arrow*). The tumor is forced laterally toward the cricothyroid interval. Compare the low signal in the abnormal right cartilage to the bright signal of fat in the normal left thyroid cartilage (*arrowheads*). On the normal side, the black arrow indicates the upper edge of the thyroarytenoid muscle, thus indicating the level of the ventricle. *N*, Metastatic node.

Copyright © 2003, Mosby, Inc. All rights reserved.

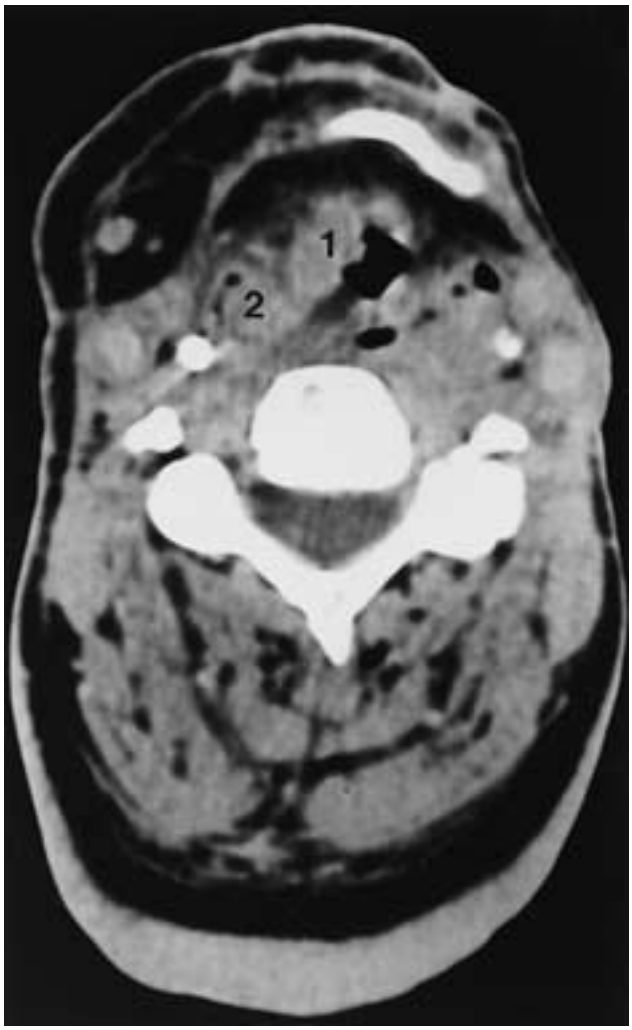

VIEW IMAGE

FIGURE 30-33 Axial CT shows multiple primary tumors. A patient with previous cancer in the floor of the mouth and radical neck dissection now has three separate primaries in the pharynx-larynx. Scan through the supraglottic level shows an endolaryngeal lesion (*1*) and a lesion of the pyriform sinus (*2*). These lesions were not directly connected. The patient also had a lesion of the opposite subglottic region.

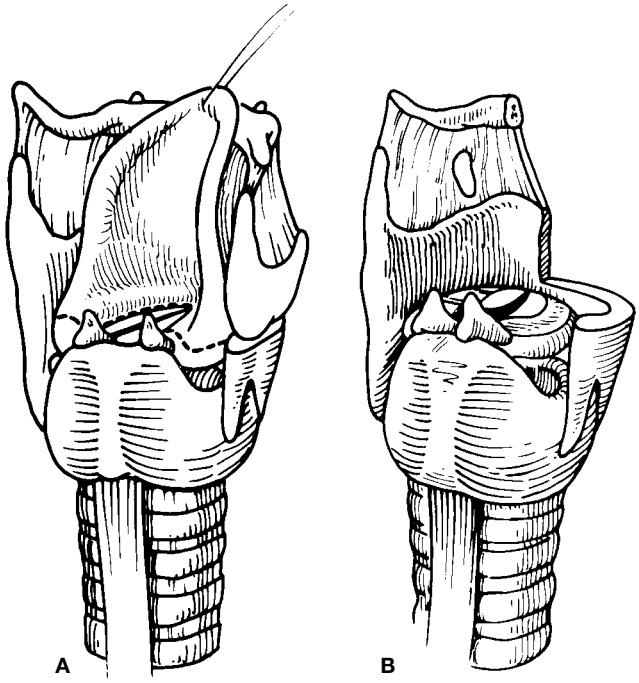

FIGURE 30-34 Diagram from the right posterior side of a supraglottic laryngectomy. **A**, Diagram shows the incision through the ventricle (the mucosa over the arytenoid has been removed for illustration). **B**, Diagram shows the postsurgical state. (From Curtin HD. Imaging of the larynx: current concepts. Radiology 1989;173:1–11.)

VIEW IMAGE

will not extend into the floor or posterior wall of the valleculae, and any such soft tissue must be considered tumor until proven otherwise. Even so, at times it may be impossible to differentiate normal tonsillar tissue from a tumor. Imaging can identify the unusually deep and caudad tumor extension of these suprahyoid epiglottic tumors into the infrahyoid larynx and the preepiglottic fat. These areas are well seen on either CT or MR imaging.

The infrahyoid supraglottic larynx is bordered by the easily visualized AE folds. Lesions at the posterior margin of the AE folds can spill over onto the pharyngeal wall. Lesions arising on the epiglottis usually have anterior extension through the epiglottis into the preepiglottic fat (Fig. 30-37). As mentioned, on gross inspection the cartilage itself is sieve-like, and the epiglottis is a poor barrier to tumor spread into the preepiglottic fat. The fact that the lesion has entered the preepiglottic fat does not preclude a supraglottic laryngectomy, but it does modify the surgical approach because neck metastases are more likely. On imaging, tumor is easily seen infiltrating into the fat density of the preepiglottic space on CT or into the high signal of the fat on T1-weighted MR imaging.

Because the resection line of a supraglottic laryngectomy is through the ventricles, the key to the feasibility of a supraglottic laryngectomy is the inferior tumor extension. Tumor cannot involve the ventricles, arytenoids, or anterior commissure. For the radiologist, the most important of these structures is the ventricle.

Because the slit-like ventricle is in the axial plane, it is poorly seen on axial scans. The ventricle is best visualized in the coronal plane, where it is seen in cross section. Thus, the coronal plane is the best plane to determine the relationship of the lower edge of the tumor to the ventricle.

Since the ventricle itself cannot be well visualized, as previously mentioned there are other anatomic landmarks that can be used to localize the level of the ventricle.

The arytenoid actually spans the ventricle. The upper arytenoid is at the level of the false cord, and the vocal process is at the level of the true cord. Also, the false cord is composed predominantly of fat, whereas the cord level is marked by the TAM. Thus, the soft tissue change from fat to muscle density marks the transition across the ventricle.

If the supraglottic laryngectomy is feasible, the radiologist should be able to show an axial image without tumor between the caudal margin of the tumor and the upper margin of the normal true cord (Fig. 30-38). On the other hand, if the lesion is seen both above and below the ventricle, it is trans-

Copyright © 2003, Mosby, Inc. All rights reserved.

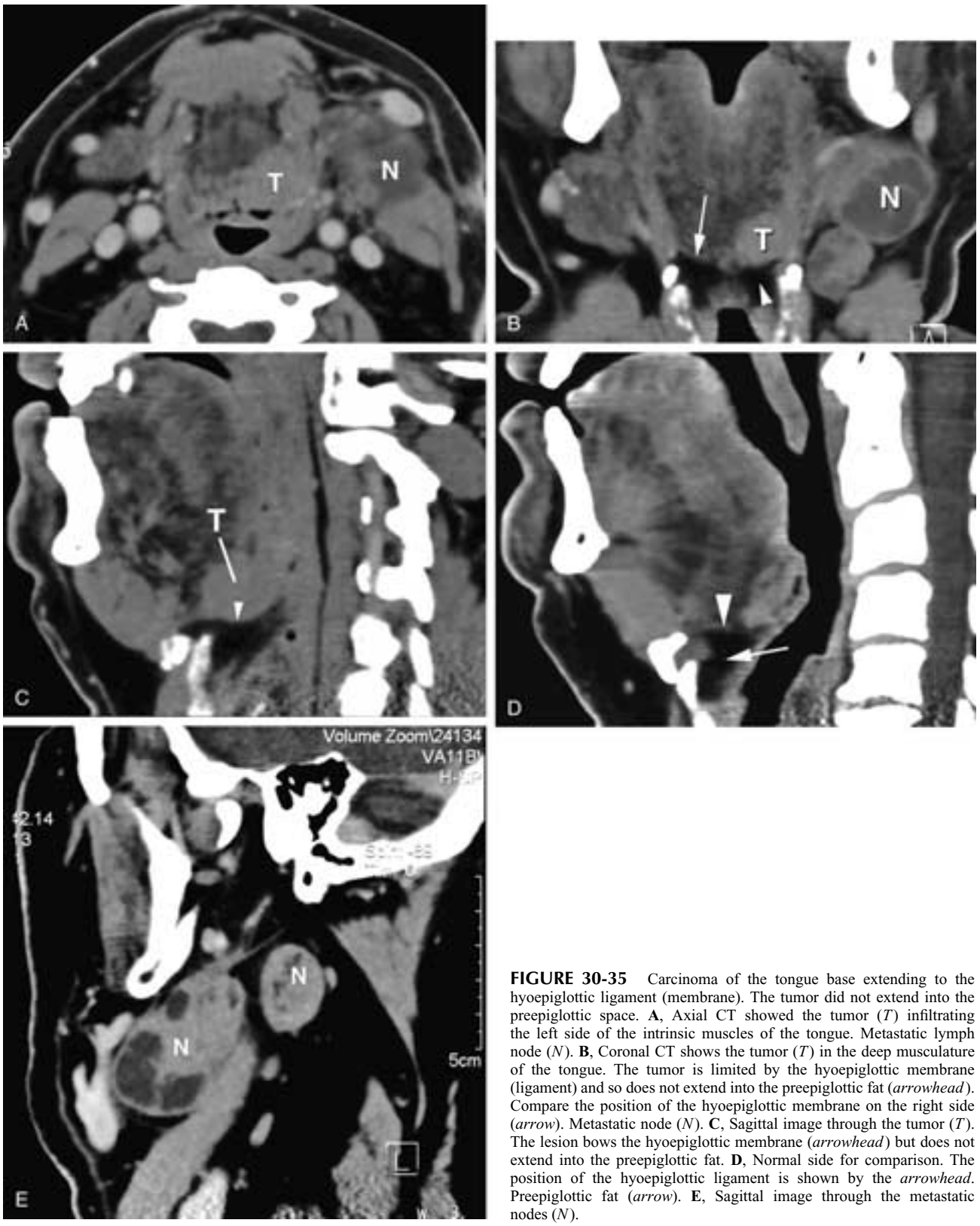

FIGURE 30-35 Carcinoma of the tongue base extending to the hyoepiglottic ligament (membrane). The tumor did not extend into the preepiglottic space. **A**, Axial CT showed the tumor (*T*) infiltrating the left side of the intrinsic muscles of the tongue. Metastatic lymph node (*N*). **B**, Coronal CT shows the tumor (*T*) in the deep musculature of the tongue. The tumor is limited by the hyoepiglottic membrane (ligament) and so does not extend into the preepiglottic fat (*arrowhead*). Compare the position of the hyoepiglottic membrane on the right side (*arrow*). Metastatic node (*N*). **C**, Sagittal image through the tumor (*T*). The lesion bows the hyoepiglottic membrane (*arrowhead*) but does not extend into the preepiglottic fat. **D**, Normal side for comparison. The position of the hyoepiglottic ligament is shown by the *arrowhead*. Preepiglottic fat (*arrow*). **E**, Sagittal image through the metastatic nodes (*N*).

VIEW IMAGE

Copyright © 2003, Mosby, Inc. All rights reserved.

FIGURE 30-36 Carcinoma of the free margin of the epiglottis, valleculae, and base of the tongue. Sagittal scan shows the margins of the lesion within the tongue (*arrowhead*) and the fat-filled high signal intensity of the preepiglottic space (*arrow*).

VIEW IMAGE

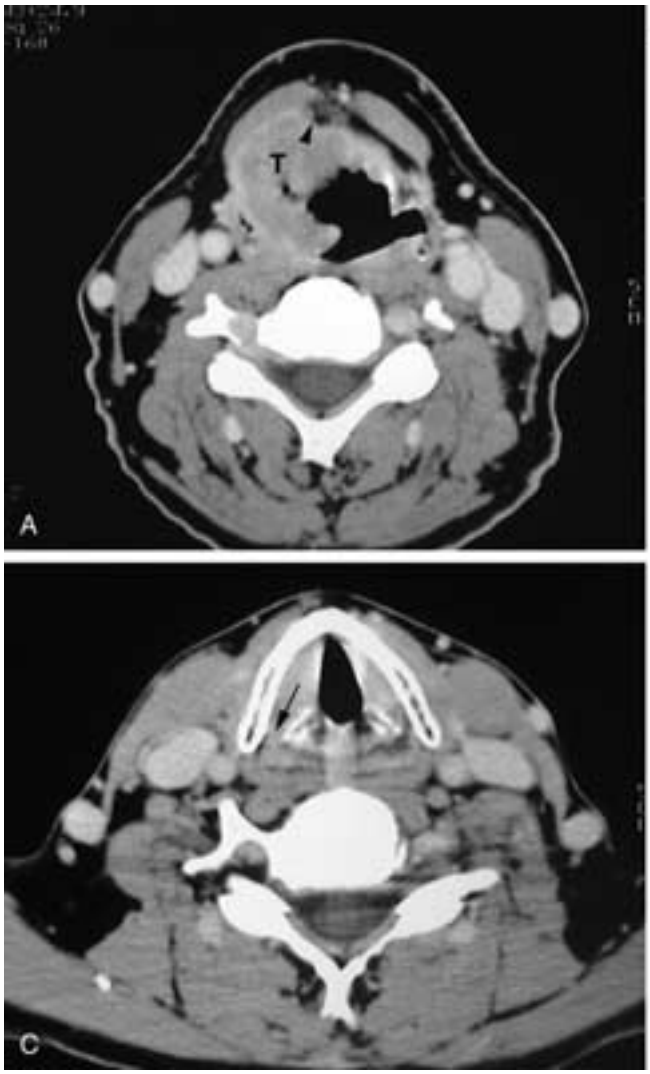

FIGURE 30-37 Supraglottic tumor reaching the outer edge of the true cord. Axial CT after contrast administration. **A**, The large bulk of the supraglottic tumor (*T*) impinges on the preepiglottic fat (*arrowhead*) and extends across the midline. **B**, The tumor (*T*) fills the paraglottic level of the false cord. **C**, The true cord level is relatively normal. A small amount of tumor (*arrow*) extends posterolaterally between the thyroid cartilage and the arytenoid. On this CT scan, it is difficult to clearly define the position of the tumor relative to the ventricle.

VIEW IMAGE

Copyright © 2003, Mosby, Inc. All rights reserved.

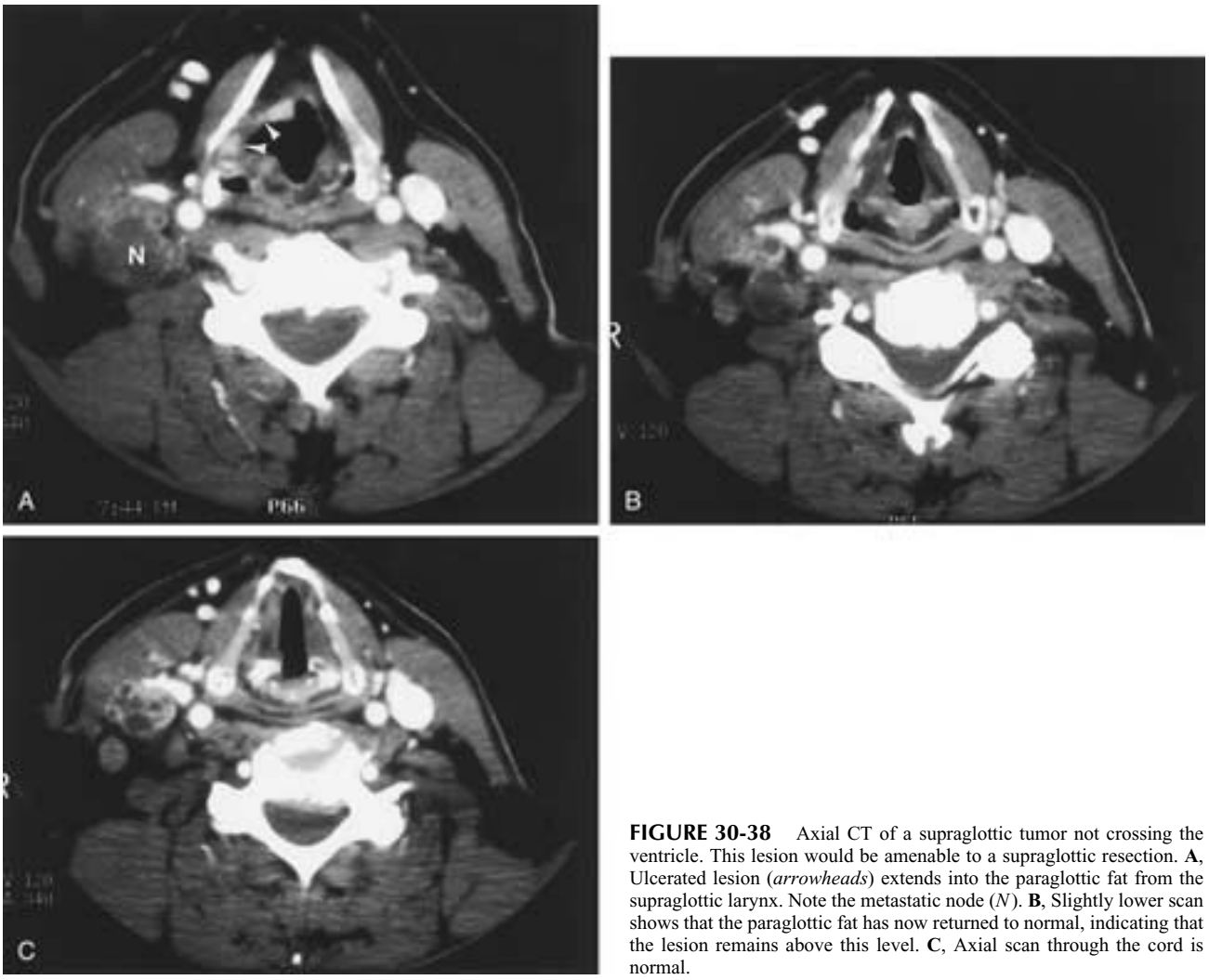

FIGURE 30-38 Axial CT of a supraglottic tumor not crossing the ventricle. This lesion would be amenable to a supraglottic resection. **A**, Ulcerated lesion (*arrowheads*) extends into the paraglottic fat from the supraglottic larynx. Note the metastatic node (*N*). **B**, Slightly lower scan shows that the paraglottic fat has now returned to normal, indicating that the lesion remains above this level. **C**, Axial scan through the cord is normal.

VIEW IMAGE

glottic (crosses the ventricle), and a supraglottic resection is not possible (Figs. 30-32, 30-39 and 30-40).

The greatest diagnostic challenge relates to those cases in which the tumor is very close to the ventricle. Definition of the inferior tumor boundary in these cases can be very difficult (Fig. 30-37). Tumor can cross the ventricle by growing along the mucosa either anterior to or posterior to the ventricle. Invasive supraglottic lesions can grow through the quadrangular membrane into the paraglottic space and then around the lateral margin of the ventricle to invade the outer margin of the true cord[63] (Fig. 30-41). This pathway is controversial, as some authors doubt that isolated paraglottic spread occurs without coexistent mucosal transglottic spread.[51, 64, 65]

As previously mentioned, some authors believe that the paraglottic space is at least partially compartmented and that the fascial layers that define the compartments could represent potential barriers to paraglottic tumor spread.[7] The thyroglottic ligament curves from the thyroid cartilage inward to the vocal ligament (see Fig. 30-7) and is considered by some authors as the boundary of the paraglottic space.[5] However, most authors consider the paraglottic space as bounded medially by the quadrangular membrane and the relatively thin thyroglottic ligament as a structure predominantly within the paraglottic space.

If there is enough tumor growth to actually invade the TAM, cord motion becomes limited. With more tumor invasion, the cord becomes fixed and the invasion can be clinically identified. However, more limited invasion can theoretically cross the ventricle without causing cord fixation, and such disease is best detected at imaging. In order to assess such tumor spread, the superolateral margin of the TAM becomes a key imaging landmark.

The coronal plane shows a perfect cross section of the ventricle and the thyroarytenoid muscle. Normally, there is a small amount of fat that can be seen ''tucking'' into the upper outer margin of the TAM (Fig. 30-42). The invading tumor will obliterate this fat and eventually will appear to ''pry'' the muscle away from the thyroid cartilage (Fig. 30-42). If this fat is seen intact, it is good evidence that the tumor has not crossed into the cord.

As previously noted, in the axial plane the ventricle is localized by the transition from the fat of the supraglottic larynx to the muscle of the glottic level. If thin scans are used, the small ''crease'' of fat at the upper outer margin of the TAM may be identified. Tumor infiltration is seen as it pries its way into this level (Figs. 30-42 to 30-44). This is best appreciated on MR imaging because the difference between the appearance of muscle and tumor is more definitive than on CT (Fig. 30-45). On CT, tumor has approximately the same attenuation as muscle. On T1-weighted MR imaging, tumor and muscle may also have similar signal intensity. However, on T2-weighted images, tumor usually has a relatively higher signal intensity than

Copyright © 2003, Mosby, Inc. All rights reserved.

does normal muscle. Tumor also tends to enhance more than muscle after the administration of gadolinium, and these factors are useful in evaluating tumor invasion of the upper margin of the TAM. Thus, relative brightening of the muscle may indicate tumor invasion, but caution must be exercised, as inflammation will also cause such brightening (Figs. 30-41 and 30-46).

As stated previously, squamous cell carcinoma can be associated with an inflammatory response along the margin of the tumor, and this gives a high signal intensity on T2-weighted images. Thus, abnormal signal may extend beyond the actual limit of the tumor. The significance of the inflammatory response is unknown. Some believe that it may be a protective effect, signaling a better therapeutic response. However, it is currently not known whether the inflamed area should be treated as tumor. In general, it is very likely that a muscle of normal signal intensity is uninvolved, and one that is bright on T2-weighted images and/or enhances must be considered abnormal.

Since the thin fat line along the lateral aspect of the TAM is not obvious in all patients, its lack of visualization does not necessarily mean that tumor is present. It may be due either to the phase of respiration or simply to a relative lack of fat at that level.

An epiglottic tumor in the midline tends to extend down along the laryngeal surface of the epiglottis toward the

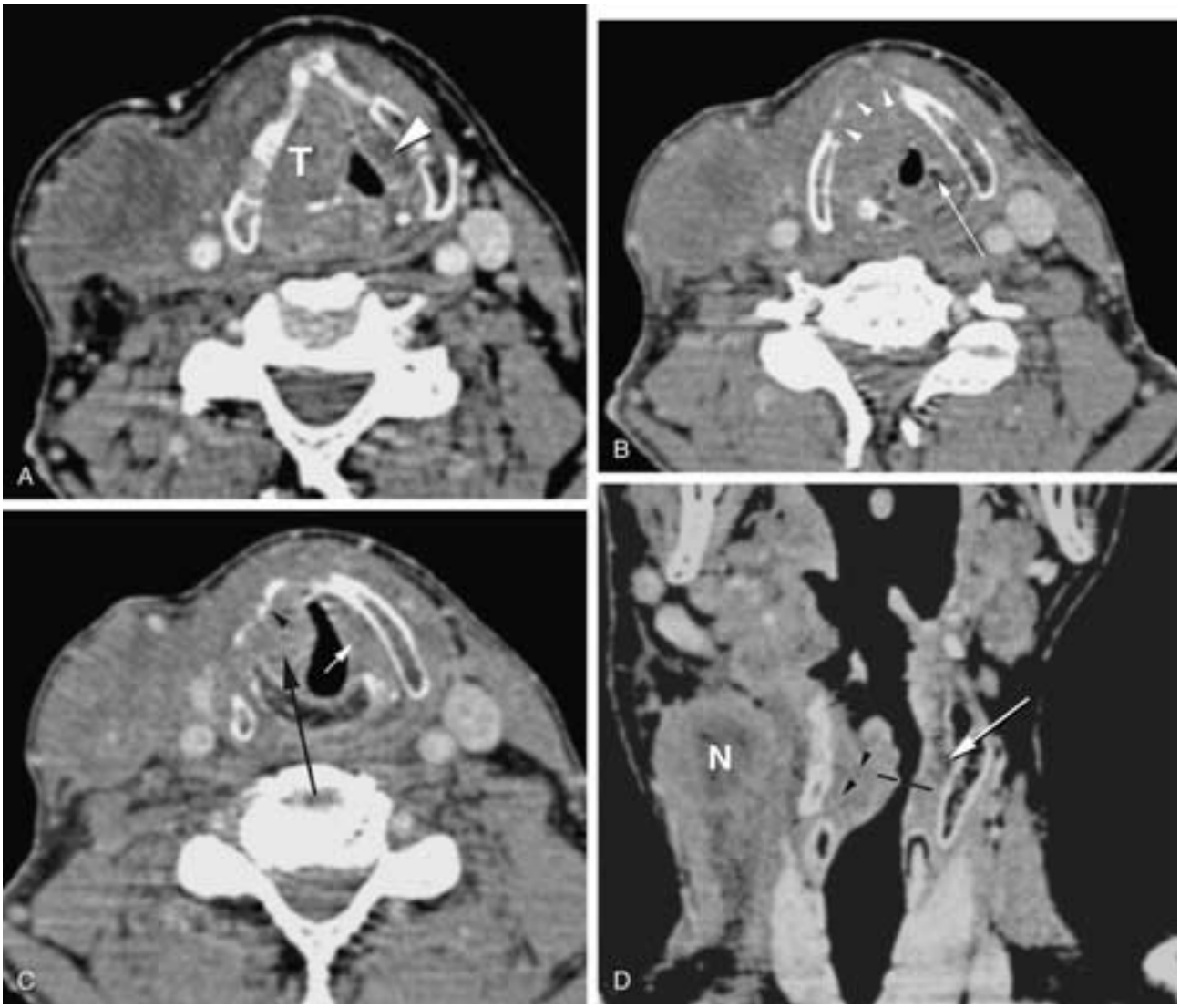

VIEW IMAGE

FIGURE 30-39 Carcinoma of the supraglottic larynx with transglottic spread via the paraglottic pathway. The mucosa of the true cord was normal. **A**, Axial CT image at the false cord level shows the tumor (*T*) filling the paraglottic space. Note the intact paraglottic fat (*arrowhead*) on the opposite side. The tumor extends posteriorly, obliterating the fat between the thyroid cartilage and the arytenoid (thyroarytenoid gap). **B**, Image at the level of the ventricle/true cord. The tumor extends into the thyroid cartilage (*arrowheads*), demineralizing the cartilage. Note the sclerosis of the cartilage contiguous to the erosion. Arytenoid (*arrow*). **C**, Axial slice through the glottic/subglottic level. The tumor (*arrow*) bulges into the subglottic level to the level of the cricoid. The scan angle is slightly oblique, showing the TAM (*white arrow*) on the opposite side. Residual cartilage (*arrowhead*). **D**, Coronal reformatted image shows the tumor (*arrowheads*) following the paraglottic pathway from the supraglottic to the glottic level. The conus elasticus restricts growth and forces the tumor laterally between the thyroid and cricoid cartilages. Note the normal paraglottic fat on the opposite side (*arrow*). The dashed line represents the level of the ventricle. Node (*N*). The fat in the thyroid cartilage is obliterated (compare with the opposite side).

Copyright © 2003, Mosby, Inc. All rights reserved.

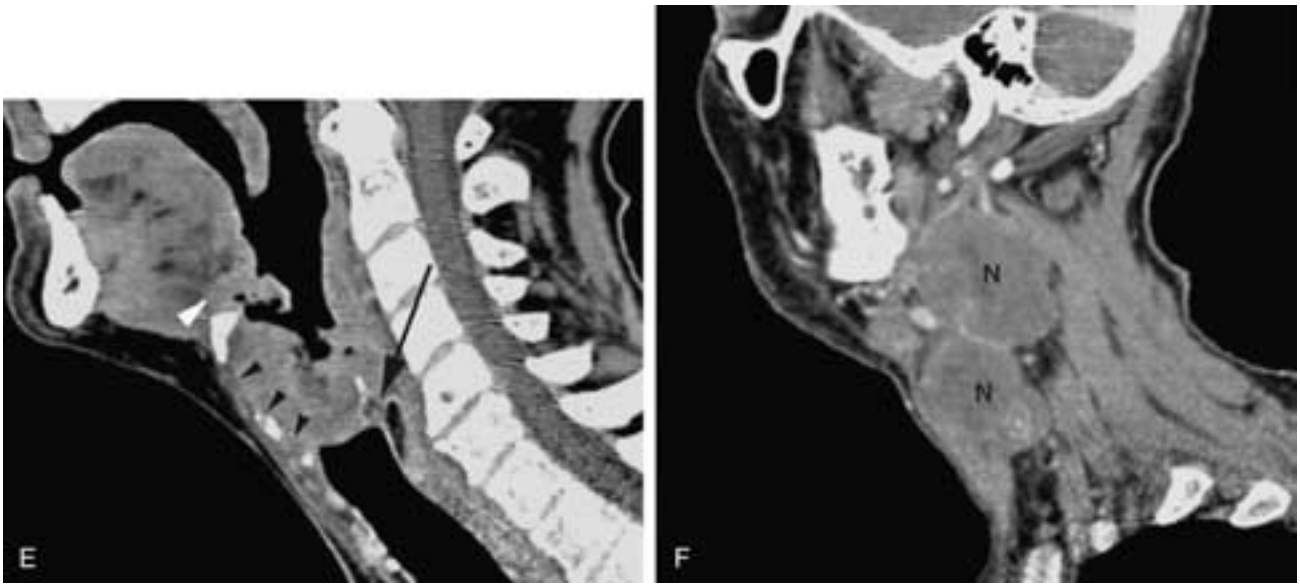

VIEW IMAGE

FIGURE 30-39 *Continued.* **E**, Sagittal reformat shows the tumor (*black arrowheads*) pushing forward, limited by the thyrohyoid membrane. This image is just off the midline at the level of the cricoarytenoid joint (*arrow*). There is destruction of the epiglottis, with tumor (*white arrowhead*) extending into the tongue base. The hyoepiglottic membrane (ligament) is destroyed. **F**, Sagittal image of the lateral neck shows several metastatic nodes.

anterior commissure rather than the ventricle (Figs. 30-47 and 30-48). If a standard supraglottic laryngectomy is to be performed for a midline lesion, there should be a 2 to 3 mm separation between the caudal margin of the tumor and the anterior commissure. When assessing this region on axial scans, the radiologist must be very careful to make the scan parallel to the ventricle. If this is not accomplished, the lower supraglottic larynx is usually seen anteriorly at the same level as the posterior commissure, giving the false impression that tumor may be present in the anterior commisssure. This altered oblique scan plane occurs most often because the patient's head is propped up slightly for comfort, bringing the plane of the larynx out of the plane of the tabletop.

On MR imaging, the fat on either side of the petiole can be seen, and on a sagittal image the integrity of the fat anteriorly, and the presence of air against the lower epiglottis, are relatively reliable signs that tumor has not extended to the anterior commissure. If the anterior true or false cords press against each other, a partial volume artifact can result and can give the false-positive impression that tumor has reached the anterior commissure. Because of this, the presence of air in this region is a more reliable negative sign than is the presence of soft tissue a positive sign of tumor presence.

In the posterior supraglottic larynx, the arytenoids are almost always assessed by direct visualization. If the upper level of one arytenoid is minimally involved by tumor, this arytenoid can be removed surgically. However, involvement of the interarytenoid area is considered a contraindication to supraglottic resection because the surgeon would have to remove both arytenoids to attain a clear margin, and the patient would have no true cords with which to generate a voice. Thus primary lesions of the interarytenoid area, even though small, are almost always treated by total laryngectomy if surgery is the treatment of choice (Figs. 30-49 and 30-50). The interarytenoid region is not usually a diagnostic concern for the radiologist because this area is very clearly seen at endoscopy.

Involvement of the thyroid cartilage is also a contraindication to supraglottic resection. This topic is discussed earlier in this chapter. However, it is extremely unusual for a supraglottic tumor to involve the cartilage unless the tumor has crossed the ventricle.

Lymph node involvement is common in supraglottic carcinoma. Nodal involvement is most common in lesions involving the AE fold and epiglottis that also involve the contiguous tongue and pharynx.[56] The incidence of nodal disease gradually diminishes with tumors that involve the margins of the larynx without contiguous spread and is lowest with small tumors that are isolated to the more central supraglottic larynx. Deeper tumor extension into the preepiglottic and paraglottic spaces is also generally associated with a higher incidence of lymph node metastasis.

The lymphatic drainage of the supraglottic larynx is to the upper jugular chain (levels II and III), and bilateral nodal involvement is common, especially if the lesion crosses the midline.[66] If the entire neck is not routinely scanned on CT, at least these upper nodes must be imaged. With MR imaging, coronal or sagittal imaging also visualizes these nodes.

Other procedures have been devised for supraglottic tumors that are considered as alternatives to, or extensions of, the classical supraglottic laryngectomy.

The near-total laryngectomy described by Pearson et al. resects one hemilarynx and continues down to resect the cricoid on the ipsilateral side.[67, 68] The pyriform sinus is taken on the same side. This operation is performed for supraglottic tumors extending to the true cord on one side or for an AE fold tumor extending into the pyriform sinus. One innervated cord remains, and a flap from the pharynx is used to reconstruct an air passage. If the cricoid is taken, the

Copyright © 2003, Mosby, Inc. All rights reserved.

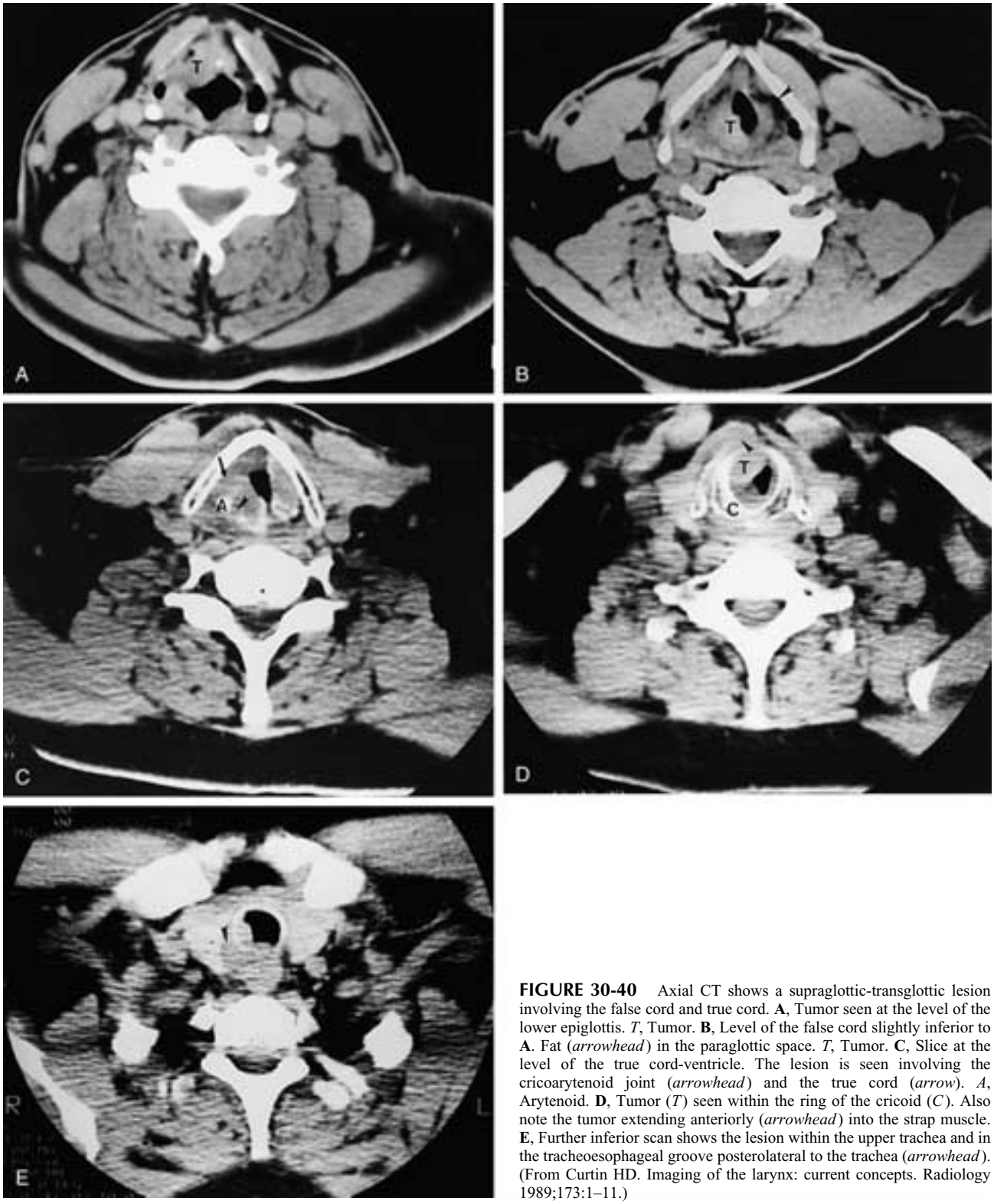

FIGURE 30-40 Axial CT shows a supraglottic-transglottic lesion involving the false cord and true cord. **A**, Tumor seen at the level of the lower epiglottis. *T*, Tumor. **B**, Level of the false cord slightly inferior to **A**. Fat (*arrowhead*) in the paraglottic space. *T*, Tumor. **C**, Slice at the level of the true cord-ventricle. The lesion is seen involving the cricoarytenoid joint (*arrowhead*) and the true cord (*arrow*). *A*, Arytenoid. **D**, Tumor (*T*) seen within the ring of the cricoid (*C*). Also note the tumor extending anteriorly (*arrowhead*) into the strap muscle. **E**, Further inferior scan shows the lesion within the upper trachea and in the tracheoesophageal groove posterolateral to the trachea (*arrowhead*). (From Curtin HD. Imaging of the larynx: current concepts. Radiology 1989;173:1–11.)

VIEW IMAGE

Copyright © 2003, Mosby, Inc. All rights reserved.

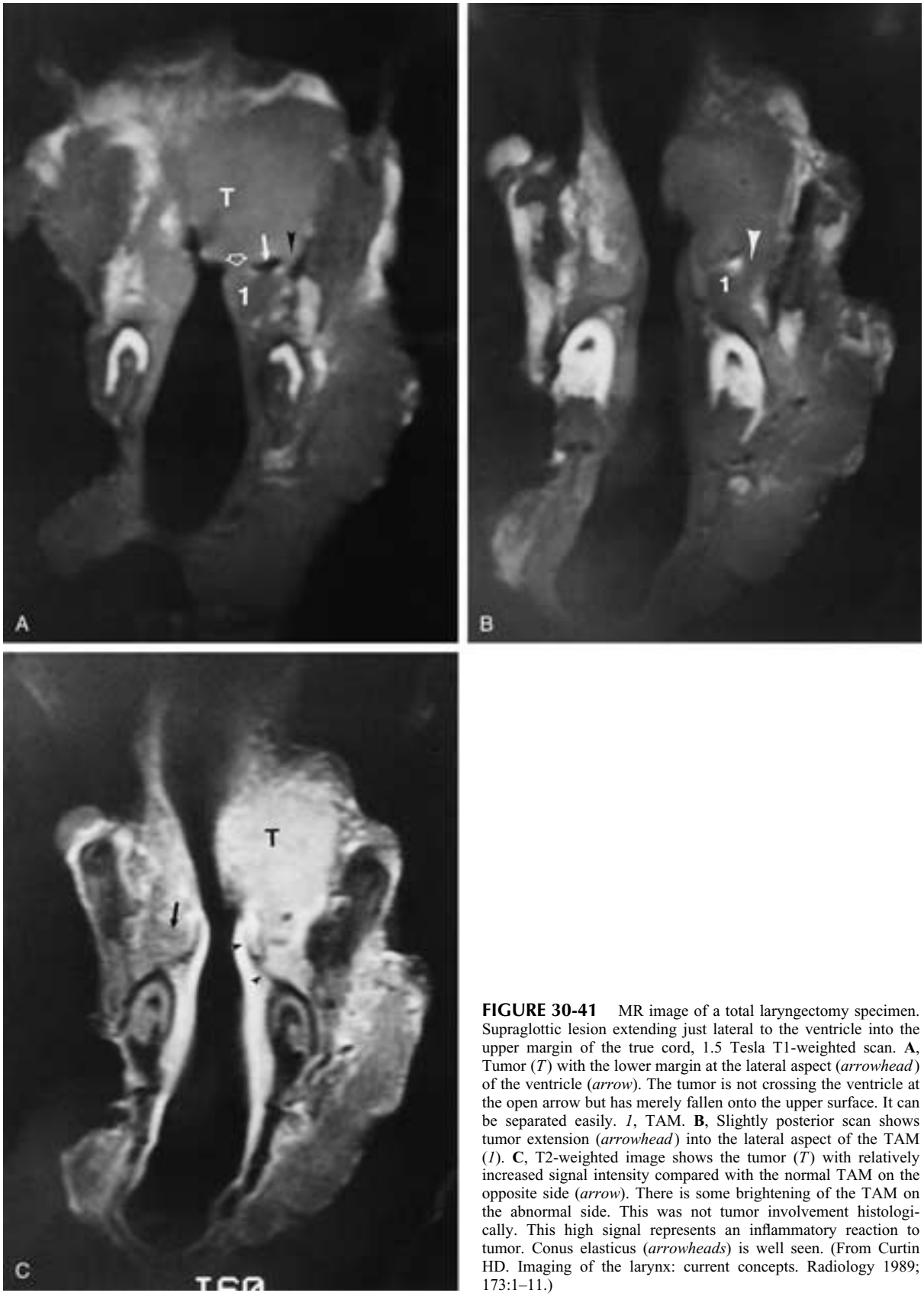

FIGURE 30-41 MR image of a total laryngectomy specimen. Supraglottic lesion extending just lateral to the ventricle into the upper margin of the true cord, 1.5 Tesla T1-weighted scan. **A**, Tumor (*T*) with the lower margin at the lateral aspect (*arrowhead*) of the ventricle (*arrow*). The tumor is not crossing the ventricle at the open arrow but has merely fallen onto the upper surface. It can be separated easily. *1*, TAM. **B**, Slightly posterior scan shows tumor extension (*arrowhead*) into the lateral aspect of the TAM (*1*). **C**, T2-weighted image shows the tumor (*T*) with relatively increased signal intensity compared with the normal TAM on the opposite side (*arrow*). There is some brightening of the TAM on the abnormal side. This was not tumor involvement histologically. This high signal represents an inflammatory reaction to tumor. Conus elasticus (*arrowheads*) is well seen. (From Curtin HD. Imaging of the larynx: current concepts. Radiology 1989; 173:1–11.)

VIEW IMAGE

Copyright © 2003, Mosby, Inc. All rights reserved.

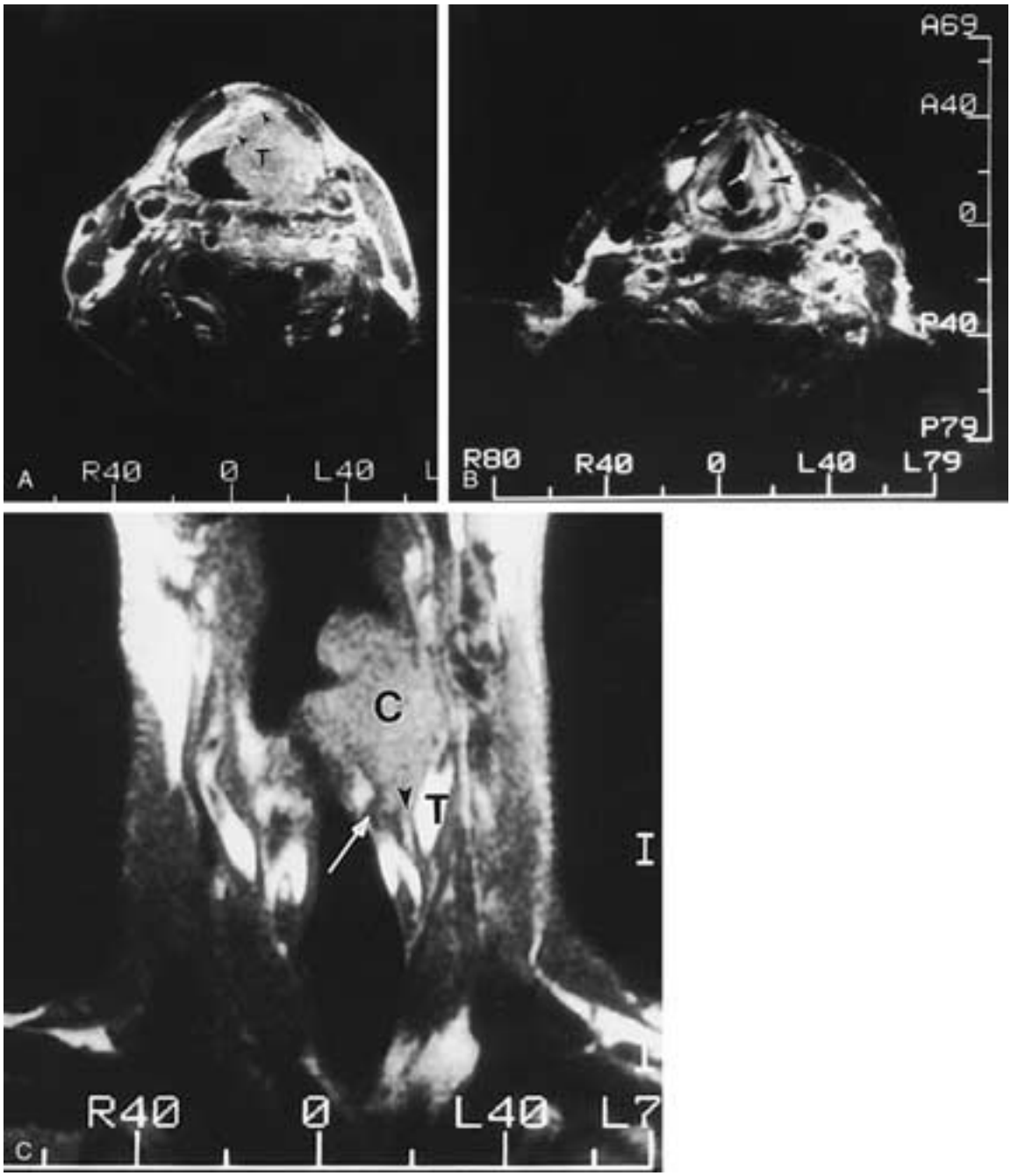

FIGURE 30-42 Supraglottic carcinoma crossing the ventricle via the paraglottic space. **A**, Axial T1-weighted image postcontrast. The tumor (*T*) is seen in the supraglottic larynx. Even with contrast, the margin (*arrowheads*) relative to the preepiglottic fat is clearly defined. **B**, Lower scan through the level of the cord. The tumor (*arrowhead*) is extending into the lateral portion of the TAM (*arrow*). This indicates that the lesion has crossed the ventricle into the true cord. **C**, Coronal image shows the carcinoma (*C*) following the paraglottic space around the ventricle. A very small amount of tumor (*arrowhead*) is squeezing between the thyroid cartilage (*T*) and the TAM (*arrow*). The upper edge of the muscle would indicate the level of the ventricle.

VIEW IMAGE

airway is unsupported and a tracheostomy must remain to ensure an adequate airway. However, the patient can speak through the reconstructed larynx.

The supracricoid partial laryngectomy with cricohyoidopexy removes not only the supraglottic larynx, but significant parts of the anterior true cords as well (see Fig. 30-141).[69] Ideally, both arytenoid cartilages remain; however, one may be resected if the tumor reaches the vocal process. The cricoid cartilage is left intact, and is pulled up and attached to the hyoid. This procedure is done for supraglottic lesions with extension to the cords. It can be done even with early cartilage invasion. As with true cord lesions, tumor reaching the cricoid cartilage is considered a contraindication, as is extensive cartilage invasion with tumor reaching the outer perichondrium of the thyroid cartilage. Hyoid invasion is a contraindication as well.

Copyright © 2003, Mosby, Inc. All rights reserved.

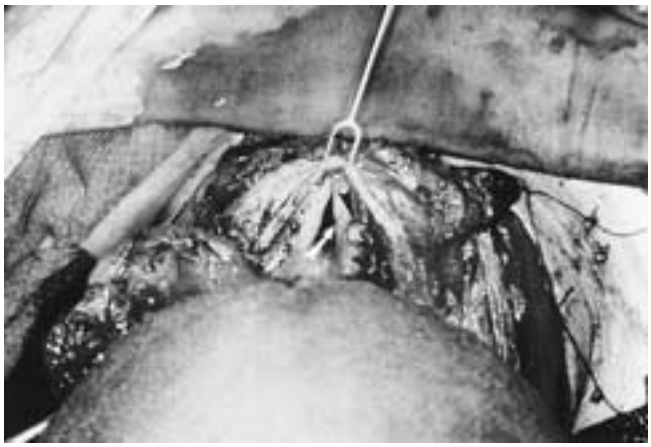

VIEW IMAGE

FIGURE 30-43 Supraglottic laryngectomy leaving tumor that was unsuspected passing along the paraglottic space. The mucosa of the true cords (*arrow*) is normal. A small amount of tumor (*arrowhead*) has been left because the incision was taken through the ventricle. Compare with Figure 30-40B. Note the characteristic cut through the thyroid cartilage performed as part of the supraglottic resection. (Courtesy of Dr. James Boyd.)

Endoscopic laser resection obviates the external incision.[70] The laser is used to excise rather than vaporize the lesion. Laser resection is easiest to perform for lesions that are readily visualized by the endoscope. The most amenable lesions arise at the false cord level, on the epiglottis, or on the AE fold. Tumors higher on the endolaryngeal surface of the epiglottis and the upper false cord are more difficult to see and therefore to excise by this technique.

Glottic and Infraglottic Regions

The region of the larynx inferior to the ventricle is divided into the glottic and subglottic or infraglottic levels. The boundary between the two regions is a plane parallel to, but 1 cm caudal to, an axial plane passing through the apex of each ventricle. Almost all tumors that occur in this region are squamous cell carcinomas. Unlike supraglottic lesions, tumors of the true cord usually present at a fairly early stage because they interfere with normal vocalization. Even very small lesions of the true cord will cause hoarseness. If the subglottic larynx is involved by tumor and the free margin of the true cord is uninvolved, the patient may not have hoarseness. Fortunately, these lesions are rare.

Many small true cord lesions are treated by RT, cord stripping, or laser resection.[71] The standard speech conservation partial laryngectomy applicable to this region is the vertical hemilaryngectomy.[60, 72, 73] The resection removes one false cord, one true cord, and the intervening ventricle, as well as most of the ipsilateral thyroid ala (Fig. 30-51). The outer perichondrium of the thyroid ala is retained. If the tumor is close to or minimally involves the vocal process of the arytenoid, this process can be resected, leaving most of the arytenoid. However, slightly greater involvement necessitates removal of the arytenoid. If there is deep tumor extension, especially involving the cricoarytenoid joint, the procedure is not performed. Similarly, if the lesion is deeply invasive, with total fixation of a cord, a vertical hemilaryngectomy is not done. Significant cartilage invasion is also considered a contraindication to this procedure.

With a glottic tumor, the key points for assessment are the inferior tumor extension, the anterior commissure, the arytenoid, the thyroid cartilage, and the paraglottic space at the level of the ventricle (Box 30-3). Although nodes are less of a problem than they are with supraglottic carcinoma, they should be sought, especially in the paratracheal and lower jugular areas (levels IV and VI). True cord tumors invading the paraglottic space can metastasize to the upper jugular nodes as well.

The most important consideration is the inferior extent of tumor. If the lesion reaches the upper margin of the cricoid, a routine vertical hemilaryngectomy cannot be done (Fig. 30-52). Some surgeons have resected the upper margin of the cartilage, and work is being done on near-total

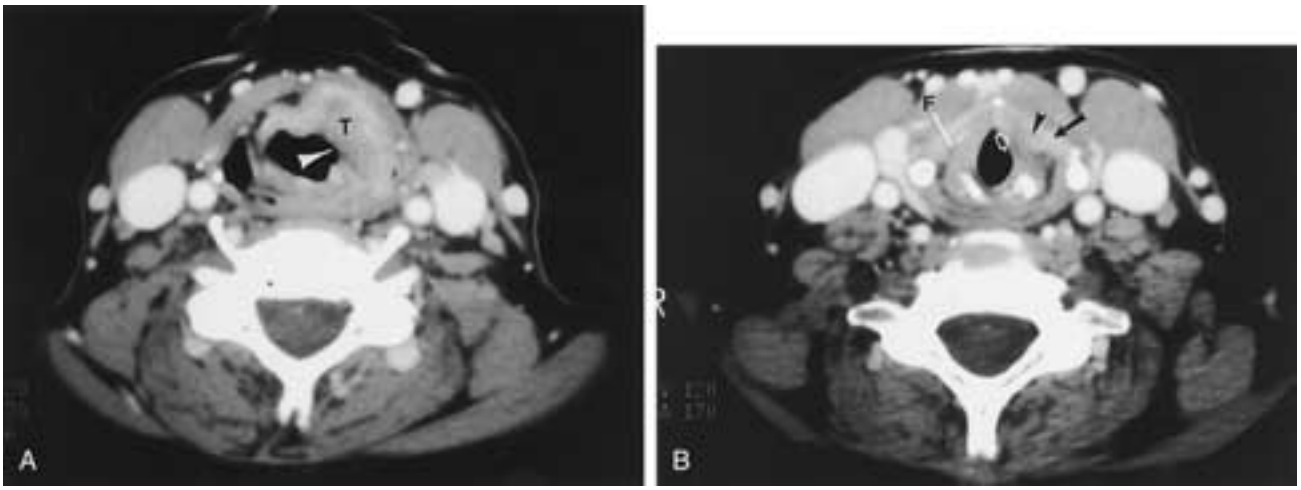

VIEW IMAGE

FIGURE 30-44 Supraglottic tumor extending beyond the ventricle via paraglottic pathways. **A**, Axial scan through a supraglottic lesion invading anteriorly and laterally. *T*, Tumor; *arrowhead*, ulceration. **B**, Scan through the level of the cord shows a small amount of tumor (*arrowhead*) obliterating the fat between the thyroid cartilage (*arrow*) and the TAM (*open arrow*). This scan would be just below the level of the ventricle. Compare with the fat (*F*) at the outer edge of the muscle on the opposite side.

Copyright © 2003, Mosby, Inc. All rights reserved.

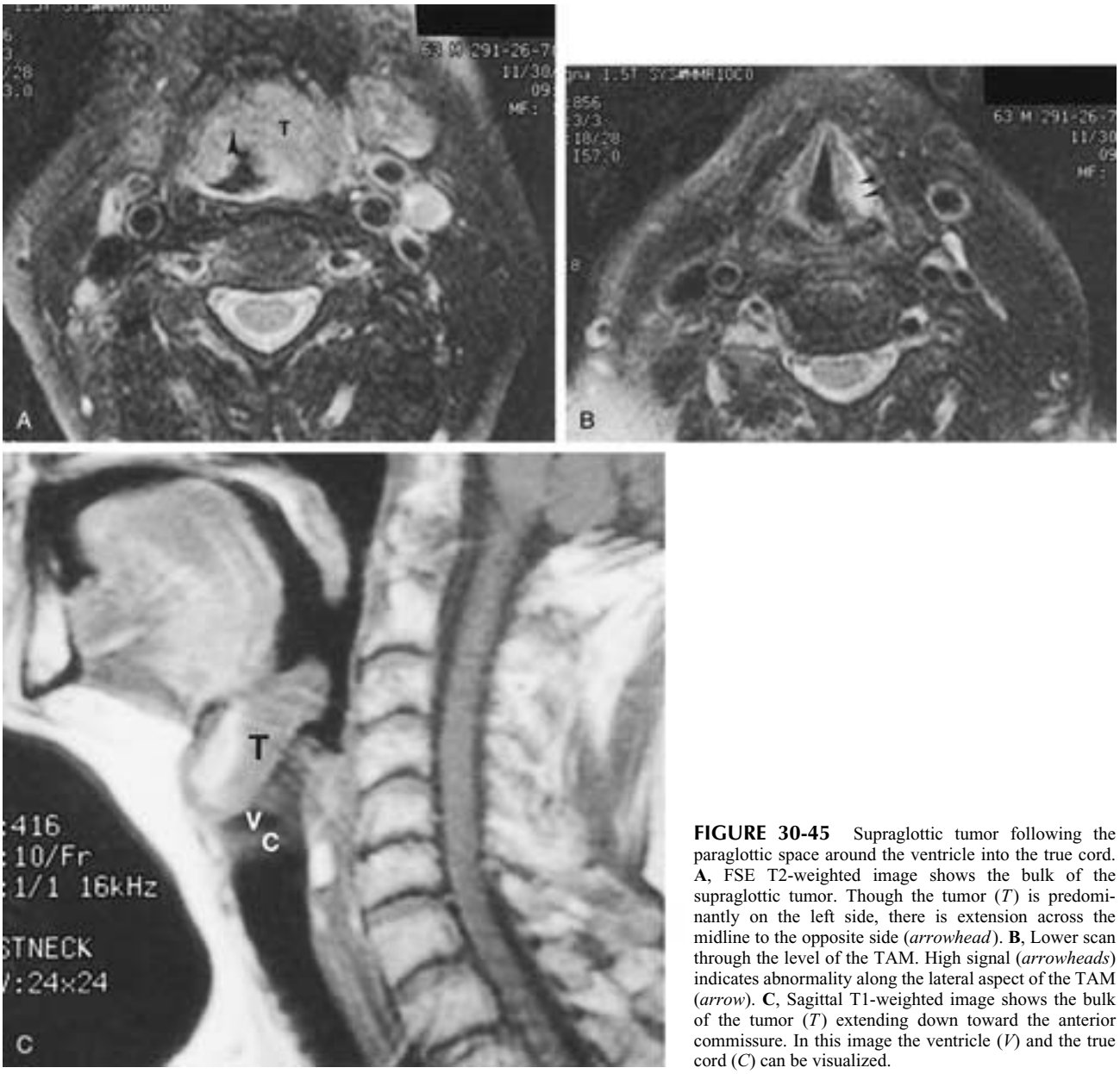

FIGURE 30-45 Supraglottic tumor following the paraglottic space around the ventricle into the true cord. **A**, FSE T2-weighted image shows the bulk of the supraglottic tumor. Though the tumor (*T*) is predominantly on the left side, there is extension across the midline to the opposite side (*arrowhead*). **B**, Lower scan through the level of the TAM. High signal (*arrowheads*) indicates abnormality along the lateral aspect of the TAM (*arrow*). **C**, Sagittal T1-weighted image shows the bulk of the tumor (*T*) extending down toward the anterior commissure. In this image the ventricle (*V*) and the true cord (*C*) can be visualized.

VIEW IMAGE

laryngectomies. However, the cricoid is the structural foundation of the larynx, and reconstruction of a usable larynx after partial removal of the cricoid is difficult. If the cricoid is involved with tumor, a total laryngectomy is usually performed.

The conus elasticus is thought to play an important role relating to the inferior growth of a true cord tumor (Fig. 30-7). This membrane represents the lower boundary of the paraglottic space and extends from the free edge of the true vocal cord to the upper margin of the cricoid cartilage. The membrane affects tumor extension in two situations. A mucosal true cord tumor that has grown caudally is separated from the deeper soft tissues and cartilage by the thick, ligamentous conus. However, caudal to the conus, a tumor invading the mucosa can immediately invade the cricoid cartilage. Alternatively, if a tumor has extended deep to the mucosa into the true cord and then grows caudally, the conus elasticus becomes a barrier to inferior growth and directs the tumor laterally. Although there may be no detectable subglottic mucosal tumor, the tumor may grow between the cricoid and thyroid cartilages into the extralaryngeal soft tissues.

The key imaging concept is the demonstration of whether or not the tumor has reached the upper margin of the cricoid cartilage. Such inferior extension is easily assessed on axial or coronal scans (Figs. 30-53 to 30-55).

Because of the cricoid's shape, the extent of tolerable inferior growth varies from anterior to posterior. Anteriorly, 1 cm of inferior extension is acceptable. More posteriorly, only 0.5 cm is allowed before the cartilage margin is reached. The cartilage is easily recognizable on axial scans, and if the lesion extends ''into the ring,'' a total laryngectomy is usually necessary if surgery is the chosen treatment. The cricoid also is easily identified on coronal

Copyright © 2003, Mosby, Inc. All rights reserved.

imaging, and tumor extending along its inner cortex is an ominous sign.

Although inferior tumor extension is the most important information sought by the radiologist, other findings also can alter surgical planning. The true vocal cords converge anteriorly, reaching the thyroid cartilage at the anterior commissure. At this midline point, the mucosa separating the airway and the thyroid cartilage is very thin, and a lesion can easily involve the cartilage early in the course of the disease. As mentioned previously, if air is seen against the inner lamina of the thyroid cartilage, tumor is unlikely. The finding of ''tissue'' against the cartilage is a less reliable finding because the cords may come together either physiologically or as a result of edema, obliterating the airway.

Even if the lesion crosses the anterior commissure, an extended vertical hemilaryngectomy may be done as long as the posterior half of one true cord is free of tumor and the cartilage is not eroded. The surgeon alters the cut through the thyroid cartilage, depending on the segment of the opposite cord that must be resected.

Superficial tumor extension along the cord or across the anterior commissure is best evaluated by direct clinical visualization. Some estimate of this disease can be made on imaging. However, if this tumor mapping is crucial in deciding the feasibility of voice-sparing surgery, confirmation by direct inspection is necessary even though the anterior commissure may at times be difficult to visualize directly.

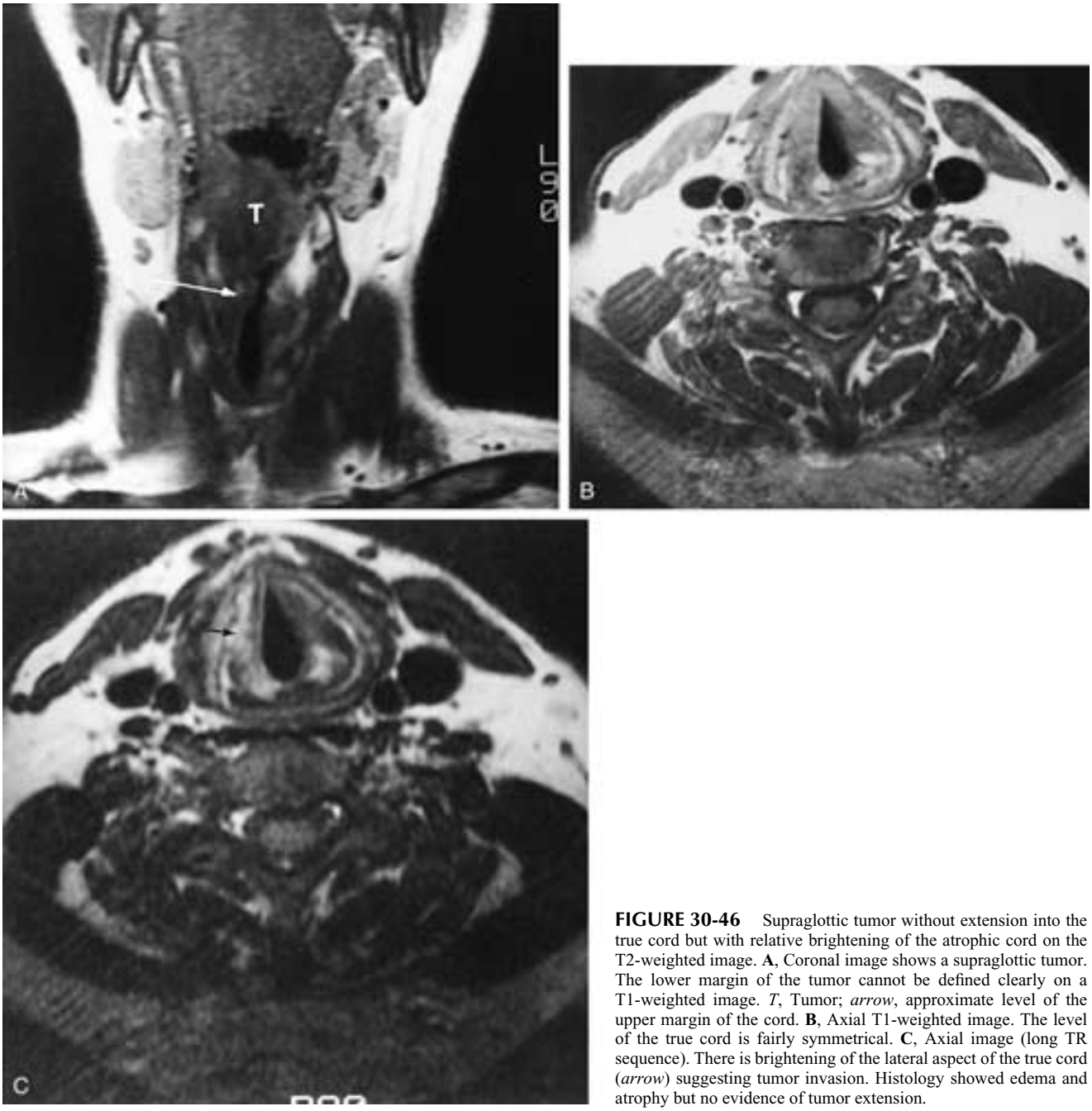

FIGURE 30-46 Supraglottic tumor without extension into the true cord but with relative brightening of the atrophic cord on the T2-weighted image. **A**, Coronal image shows a supraglottic tumor. The lower margin of the tumor cannot be defined clearly on a T1-weighted image. *T*, Tumor; *arrow*, approximate level of the upper margin of the cord. **B**, Axial T1-weighted image. The level of the true cord is fairly symmetrical. **C**, Axial image (long TR sequence). There is brightening of the lateral aspect of the true cord (*arrow*) suggesting tumor invasion. Histology showed edema and atrophy but no evidence of tumor extension.

VIEW IMAGE

Copyright © 2003, Mosby, Inc. All rights reserved.

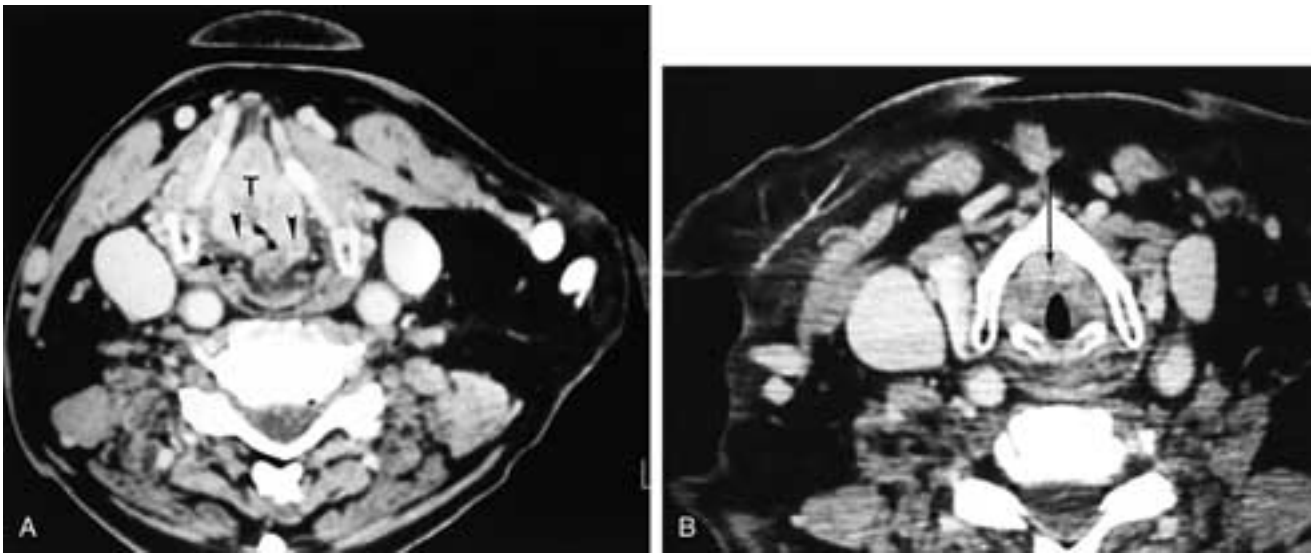

VIEW IMAGE

FIGURE 30-47 Axial CT scans. **A**, Supraglottic tumor extending to the anterior commissure. Supraglottic tumor (*T*) crosses the midline and involves both AE folds (*arrowheads*). **B**, More inferior scan at the level of the true cord shows involvement of the anterior commissure (*arrow*).

Particularly in the region of the anterior commissure, the radiologist's attention should be directed toward a search for deep tumor extension. Cartilage invasion may be assessed by CT or MR imaging, as previously discussed, and the demonstration of tumor anterior to the cartilage at this point is reliable evidence of cartilage invasion. Anterior tumor often grows through the cricothyroid membrane, just below the inferior margin of the thyroid cartilage (Fig. 30-56). In some cases, both the thyroid cartilage and the cricothyroid membrane are involved. This anterior extension can be undetectable on clinical examination.

The area just anterior to the cricothyroid membrane contains the so-called Delphian node. Lymphatic extension from the anterior commissure region and the subglottis to this node has been described.[74] However, a mass presenting in this position is usually the result of direct tumor extension through the cricothyroid membrane from a primary lesion in the anterior commissure and subglottis (Fig. 30-57).

If a vertical hemilaryngectomy is to be performed, the tumor cannot involve an entire arytenoid cartilage. However, as previously discussed, involvement of the vocal

VIEW IMAGE

FIGURE 30-48 Supraglottic tumor (*T*) with extension to the anterior commissure (*arrow*). Submucosal extension through the cricothyroid membrane involves the region of the Delphian node (*arrowhead*). Sagittal T1-weighted image, 1.5 Tesla.

FIGURE 30-49 Axial CT shows tumor at the interarytenoid area (*arrow*).

VIEW IMAGE

Copyright © 2003, Mosby, Inc. All rights reserved.

process is not a contraindication. If a large portion of the arytenoid is involved, the lesion will touch or be in close proximity to the cricoid cartilage, and a standard resection cannot be performed.

The degree of arytenoid involvement is usually assessed by endoscopy. However, deep extension to the region of the cricoarytenoid joint may be submucosal and thus is best established by CT or MR imaging.

Superior extension of a glottic tumor brings the tumor into the false cord (Fig. 30-58). Currently, significant extension to the false cord prohibits a vertical hemilaryngectomy. Tumors arising from the superior surface of the cord are in the ventricle and can spread directly into the paraglottic space. Unlike the regions above or below the ventricle, there is no fibrous barrier to limit lateral growth, and these tumors can grow upward into the paraglottic fat or downward into the TAM, eventually reaching the conus elasticus. From there the lesion may be directed anterolaterally through the defect or hiatus in the cricothyroid membrane.

More extended partial laryngectomies have been devised to treat tumors that have transgressed some of the boundaries allowed for the standard vertical laryngectomy.

The supracricoid partial laryngectomy with cricoidhy-

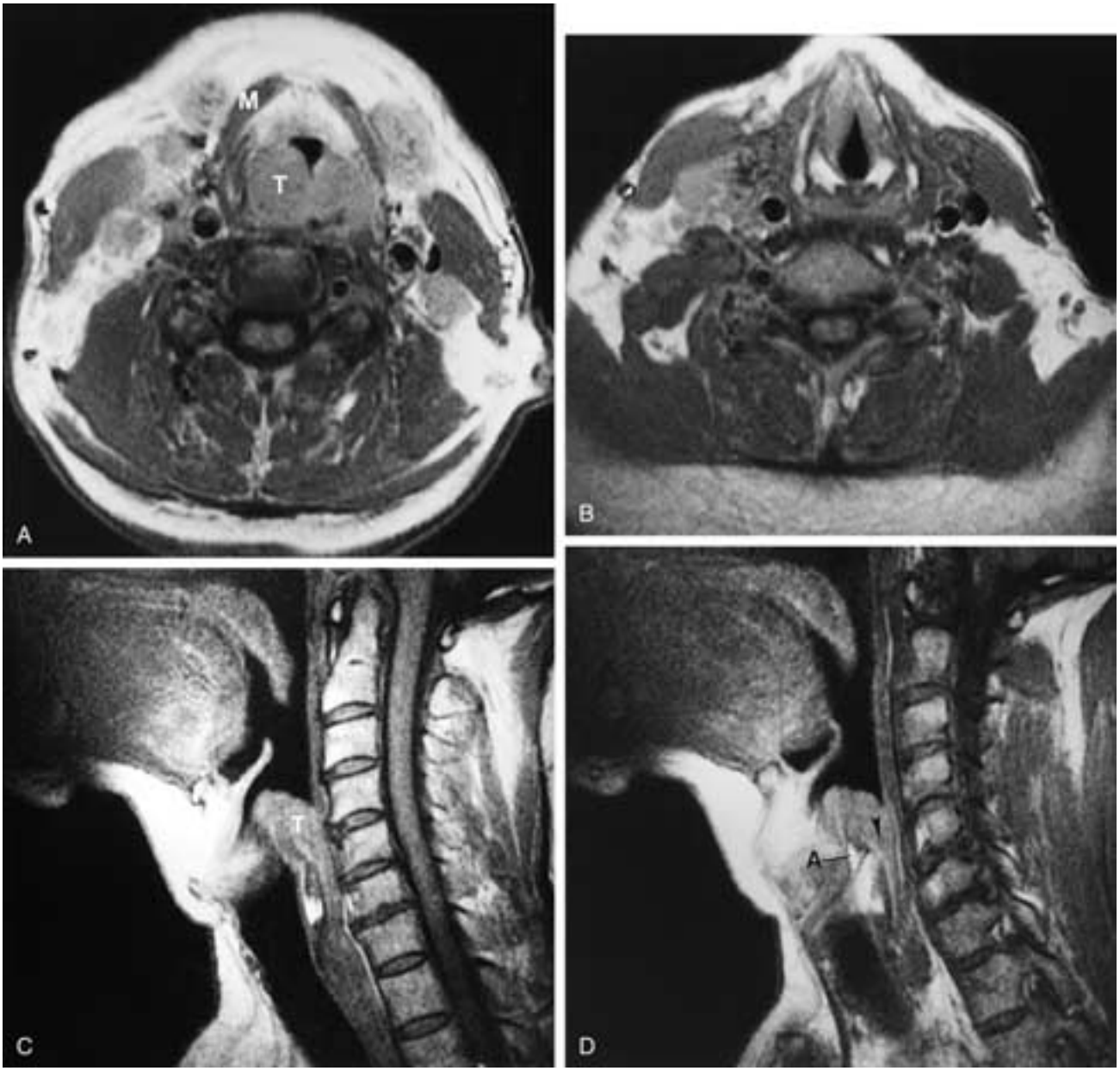

FIGURE 30-50 Interarytenoid tumor, .35 Telsa. **A**, Scan through the supraglottic larynx shows the tumor (*T*). *M*, Strap muscle. **B**, Level of the cricoid; tumor is no longer seen. **C**, Sagittal (near midline) T1-weighted image shows the tumor (*T*) just superior to the cricoid. **D**, Slightly lateral scan shows the tumor extending behind (*arrowhead*) the arytenoid (*A*). The lower margin of the tumor is at the level of the upper margin of the cricoid lamina. (Courtesy of Dr. Robert Lufkin.)

VIEW IMAGE

Copyright © 2003, Mosby, Inc. All rights reserved.

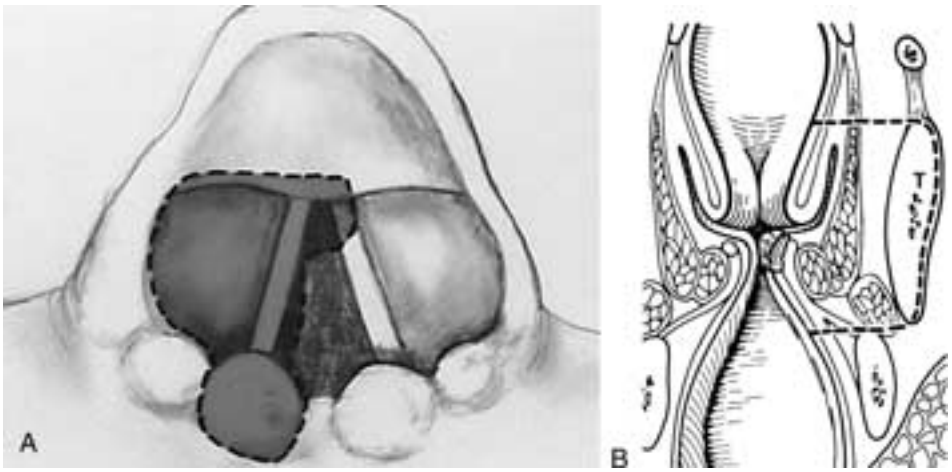

FIGURE 30-51 Vertical hemilaryngectomy. **A**, View from above. Diagram of tissue removed in a vertical hemilaryngectomy. One arytenoid can be resected. **B**, Coronal diagram showing the tissue resected in a vertical hemilaryngectomy. Note that the outer perichondrium of the thyroid cartilage (*T*) is retained. (**A** from Curtin HD. Imaging of the larynx: current concepts. Radiology 1989;173:1–11.)

VIEW IMAGE

oidoepiglottopexy is done for true cord lesions with limited extension above the ventricle to the lower supraglottic larynx. This is similar to the supracricoid partial laryngectomy with cricodhyoidopexy described in the section titled Supraglottic Larynx. A portion of the epiglottis is maintained and sutured to the cricoid.

Ventricular Tumors

Squamous cell carcinoma can arise in the ventricle itself. These lesions may arise from the inferior surface of the false cord or from the superior surface of the true cord. Thus, technically they can be either supraglottic or glottic in origin. These lesions may be deep enough in the ventricle that they cannot be directly visualized. Clinically, extension to the true cord can cause hoarseness, while superior tumor extension into the supraglottic paraglottic fat (Fig. 30-59) appears to follow the ventricular appendix and may cause a bulge in the supraglottic larynx suggesting a submucosal lesion.

BOX 30-3 CONTRAINDICATIONS TO VERTICAL FRONTOLATERAL HEMILARYNGECTOMY

1. Tumor extension from the ipsilateral vocal cord across the anterior commissure to involve more than one third of the contralateral vocal cord.
2. Extension subglottically more than 10 mm anteriorly and more than 5 mm posterolaterally.
3. This technique can still be used if the vocal process and anterior surface of the arytenoid are involved, but involvement of the cricoarytenoid joint, interarytenoid area, opposite arytenoid, or rostrum of the cricoid is a contraindication.
4. Extension across the ventricle to the false cord.
5. Thyroid cartilage invasion.
6. Impaired vocal cord mobility is a relative contraindication.

From Lawson W, Biller HF, Suen JY. Cancer of the larynx. In: Suen JY, Myers E, eds. Cancer of the Head and Neck. New York: Churchill Livingstone, 1989;533-591.

Pharynx

The lower pharynx (hypopharynx, laryngopharynx) has roughly the shape of a rectangular solid into whose anterior wall projects the supraglottic larynx. As a result, the lateral and posterior hypopharyngeal walls are rather simple in form, while the anterior wall is more complex. The postcricoid larynx bulges into the lower hypopharynx, the pyriform sinuses project forward on either side of the larynx, and the posterior aspect of the supraglottic larynx projects up into the midportion of the pharynx. The superior limit of the hypopharynx is the hyoid bone or valleculae, and the inferior margin is the lower edge of the cricopharyngeus, where the pharynx meets the esophagus.

The pyriform sinus invaginates between the thyroid cartilage and the AE fold. As such, the paraglottic space of the larynx is just anterior to the pyriform sinus mucosa. A lesion of the anterior wall of the pyriform sinus extending through the mucosa involves the paraglottic space at the level of the false cord (Fig. 30-60). On CT or MR imaging the lesion can be seen extending between the thyroid and arytenoid cartilages through the ‘‘thyroarytenoid gap.’’ The tumor may then extend further inferiorly into the vocal cord via the paraglottic pathway. Primary tumors of the lower false cord and ventricle can extend through the thyroarytenoid gap toward the pharyngeal mucosa, but they usually do not ulcerate this mucosa.

The apex of the pyriform sinus extends deeply into the thyroarytenoid gap and thus is very close to the cricoid cartilage. As a result, lesions of the pyriform apex usually require a total laryngectomy for complete resection. If a lesion is confined to the upper lateral aspect of the AE fold or the upper pyriform sinus, a partial pharyngectomy can be done in combination with a supraglottic laryngectomy (Fig. 30-61). Pearson et al.’s near-total laryngectomy (see above)

Copyright © 2003, Mosby, Inc. All rights reserved.

has also been applied to tumors of the AE fold extending into the pyriform apex.

Tumor extending into the pyriform apex can be visualized on axial CT or MR imaging as obliteration of the fat within or as widening of the thyroarytenoid gap (Figs. 30-60, 30-62). Today, most radiologists prefer to use either CT or MR imaging to determine the inferior tumor margin, and with the high-resolution scans now available, the extent of mucosal tumor can be defined at the same time that the deeper tumor extension is mapped. Alternatively, a pharyngogram can be done with thicker barium that will coat the mucosal surfaces of the hypopharynx and help define the margins of a pyriform sinus lesion. During this procedure, the patient performs a modified Valsalva maneuver to distend the pyriform sinus apex.

The postcricoid region is the lower anterior portion of the hypopharynx at the level of the posterior cricoid lamina. A pharyngeal lesion in this location usually necessitates a total laryngectomy because the resection must include the cricoid cartilage. Once a tumor is established in this area, the primary surgical concern becomes the lower extent of the lesion relative to the cricopharyngeus. Definition of this lower tumor margin helps the clinician decide whether the surgical resection involves only the pharynx or whether the resection must include the cervical esophagus with a reconstruction such as a jejunal interposition.

As previously mentioned, on axial CT or MR imaging, the level of the cricopharyngeus muscle is approximated by the lower margin of the cricoid cartilage (Fig. 30-21). Alternatively, the cricopharyngeus muscle can be identified as a semilunar-shaped muscle along the lower aspect of the cricoid cartilage lamina. Immediately caudal, the cervical esophagus is seen, with an ovoid or circular cross-sectional shape. The transition between these two shapes defines the esophagopharyngeal junction. Thus, this important transition zone usually can be identified at imaging. Lack of esophageal involvement by a tumor is suggested on axial images if the thickness of the pharyngeal wall at the lower margin of the cricoid cartilage returns to normal. However, minimum submucosal tumor spread into the esophagus will go undetected on these images, and often biopsy is the only way to accurately determine the caudal tumor extent. Sagittal MR images may also occasionally be helpful, with visualization of the lower tumor margin (Fig. 30-63).

The lower tumor margin also can be defined on a barium swallow. The cricopharyngeus muscle is almost always identified as a smooth posterior indentation into the barium column, so its relationship to the advancing edge of the tumor can be assessed.

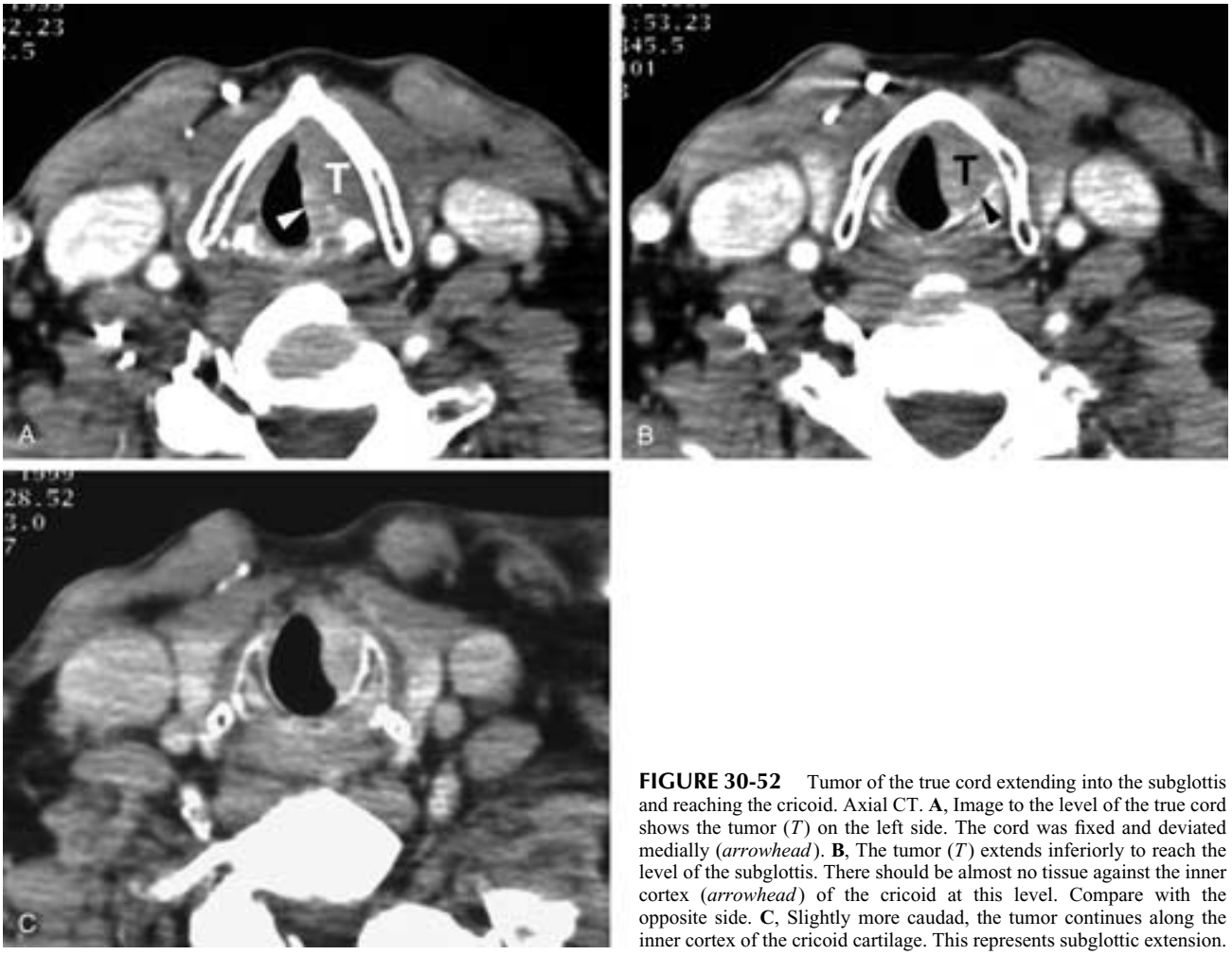

FIGURE 30-52 Tumor of the true cord extending into the subglottis and reaching the cricoid. Axial CT. **A**, Image to the level of the true cord shows the tumor (*T*) on the left side. The cord was fixed and deviated medially (*arrowhead*). **B**, The tumor (*T*) extends inferiorly to reach the level of the subglottis. There should be almost no tissue against the inner cortex (*arrowhead*) of the cricoid at this level. Compare with the opposite side. **C**, Slightly more caudad, the tumor continues along the inner cortex of the cricoid cartilage. This represents subglottic extension.

VIEW IMAGE

Copyright © 2003, Mosby, Inc. All rights reserved.

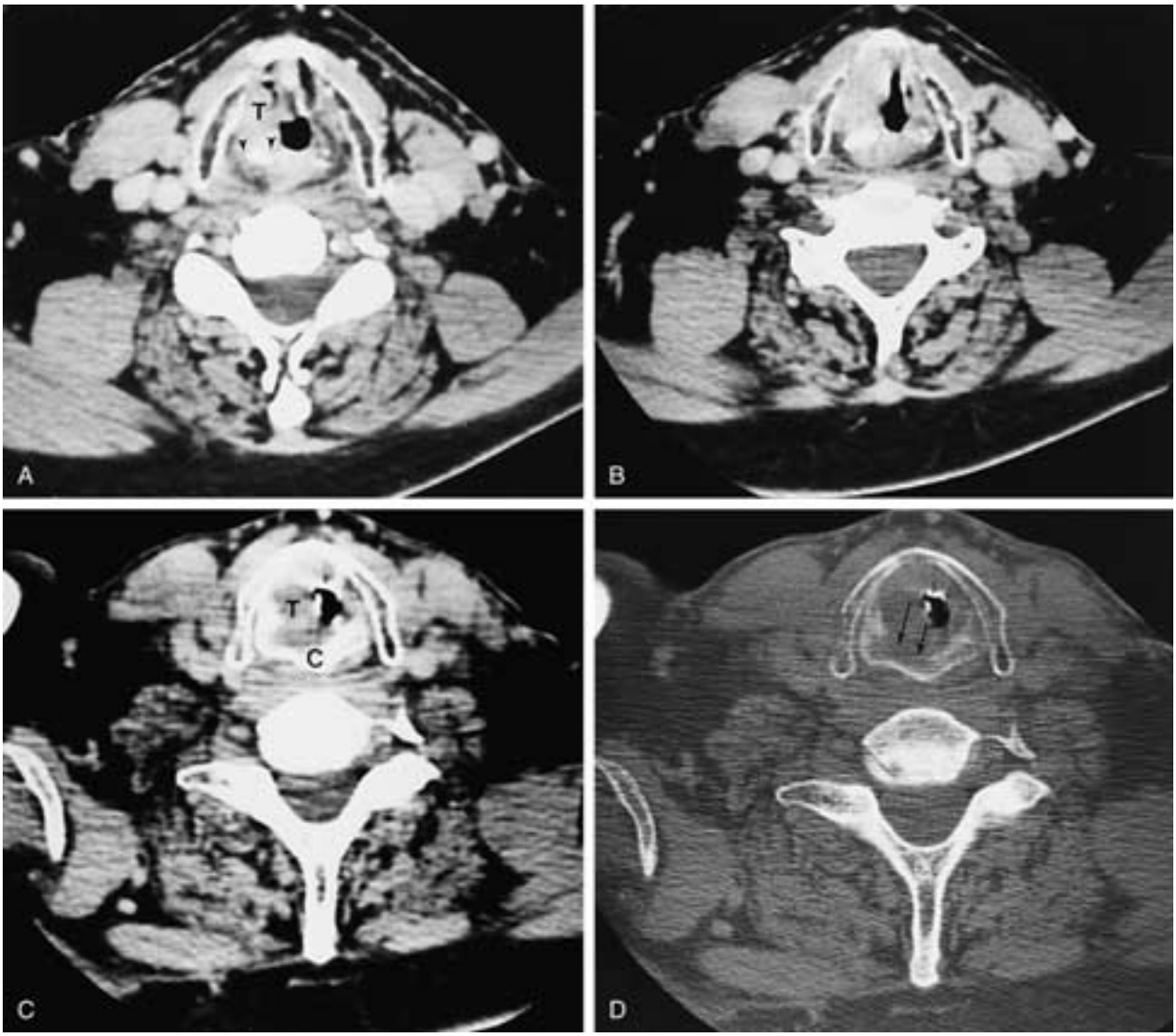

VIEW IMAGE

FIGURE 30-53 Axial CT scans show a predominantly glottic tumor, with extension into the false cord and subglottic extension. **A**, Supraglottic level shows tumor (*T*) with involvement of the anterior surface of the upper arytenoid (*arrowheads*). **B**, Lower scan shows the tumor at approximately the level of the ventricle. **C**, Inferior scan through the level of the cricoid shows tumor (*T*) within the ring. *C*, Cricoid. **D**, Bone algorithm shows loss of the cortical margin of the inner surface of the cricoid (*arrows*).

The actual mucosal surface in the postcricoid region can be difficult to evaluate on barium swallow because of the normal irregularity of the anterior wall that occurs secondary to mucosal redundancy or perhaps a prominent submucosal venous plexus. The pliability of the anterior wall of the postcricoid area is more difficult to assess than the pliability of the lateral or posterior pharyngeal walls because of the rigid support of the cricoid lamina. In addition, this area is relatively ''blind'' to the endoscopist, as the endoscope ''pops'' through the muscular ring into the cervical esophagus and so does not afford the clinician a good view of this important area. Thus, this region should be closely scrutinized by both radiologist and clinician, as failure to identify tumor spread into the esophagus can be disastrous for the patient.

The inferior pharyngeal constrictor muscles act as a relative barrier to lateral and posterior tumor spread. These muscles attach to the lateral aspect of the thyroid cartilage rather than the posterior edge of the thyroid ala. This configuration allows a tumor to ''wrap around'' the posterior margin of the thyroid cartilage along the outer surface of the cartilage, and this extension may occur before there is actual erosion of the cartilage (Fig. 30-60).

Direct lateral tumor extension from the lateral wall of the hypopharynx brings the tumor to the carotid artery, and any involvement of this artery is an important and ominous finding.[75] Neither CT nor MR imaging nor ultrasound has proven reliable in identifying tumor fixation to the arterial adventitia, and the best the radiologist can do is to report the degree to which the tumor encircles the artery.

Copyright © 2003, Mosby, Inc. All rights reserved.

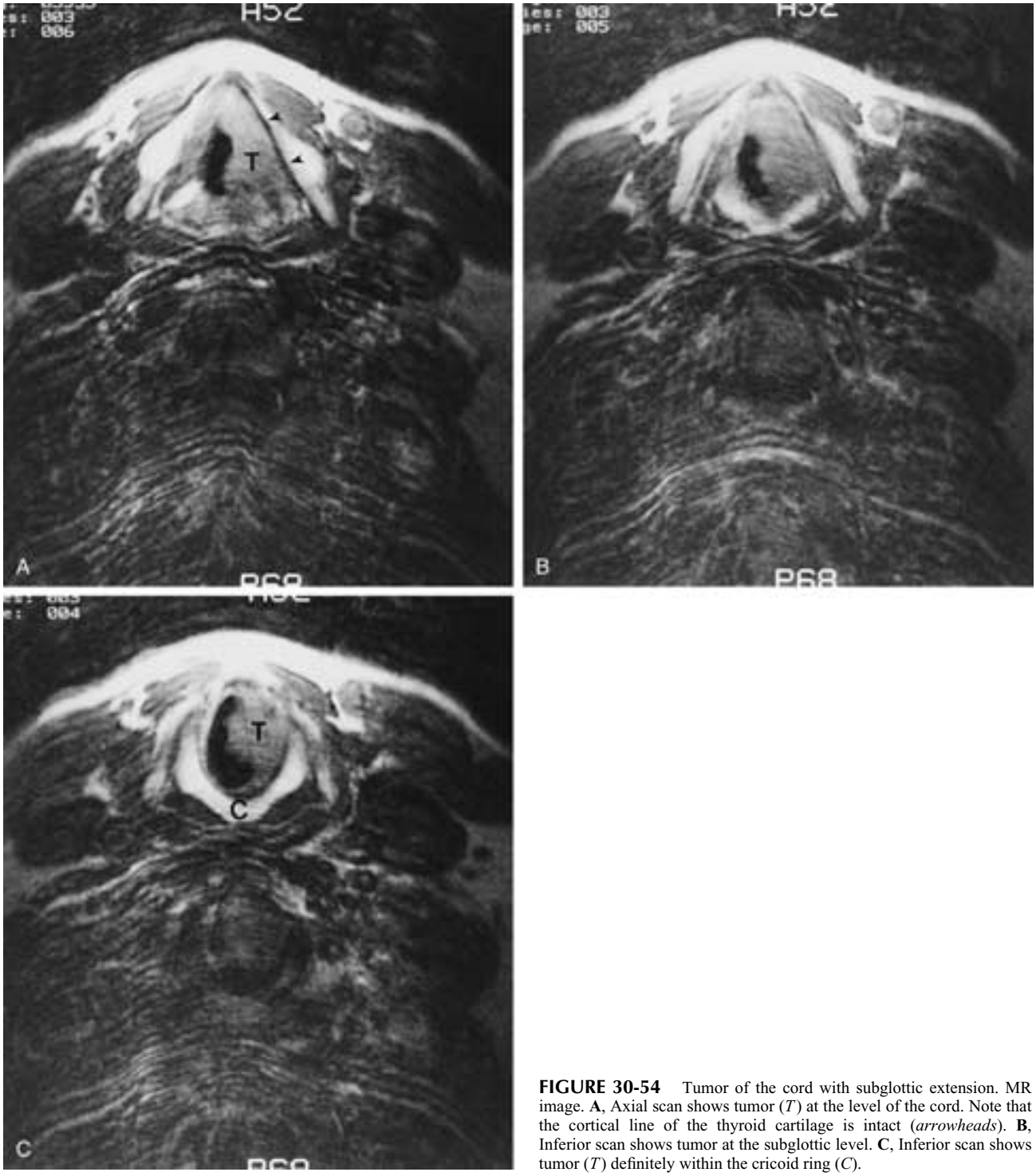

FIGURE 30-54 Tumor of the cord with subglottic extension. MR image. **A**, Axial scan shows tumor (*T*) at the level of the cord. Note that the cortical line of the thyroid cartilage is intact (*arrowheads*). **B**, Inferior scan shows tumor at the subglottic level. **C**, Inferior scan shows tumor (*T*) definitely within the cricoid ring (*C*).

VIEW IMAGE

Copyright © 2003, Mosby, Inc. All rights reserved.

Direct posterior tumor extension involves the posterior pharyngeal wall and brings the tumor to the prevertebral fascia and muscles. Fixation of this fascia or invasion of the prevertebral muscles worsens the prognosis and limits surgical resectability. If the lesion is ulcerative, fascial invasion is more likely; however, if the tumor is predominantly exophytic, the fascia may not be involved. This can be assessed on lateral fluoroscopy during a barium swallow, because a lesion not fixed to the fascia can slide up and down, relative to the spine, as the barium passes (Fig. 30-64). On MR imaging, a high T2-weighted signal intensity or enhancement after gadolinium administration in the longus colli muscles must be considered abnormal.[76] However, inflammation in these muscles also can have these MR findings. Thus, both false-positive and false-negative results have been reported.

Lymphatic spread from pharyngeal lesions initially reaches the high jugular nodes (levels II and III). Occasionally, a lesion arising in the lower pharynx can also spread superiorly to the high lateral retropharyngeal nodes (nodes of Rouviere) immediately beneath the skull base.

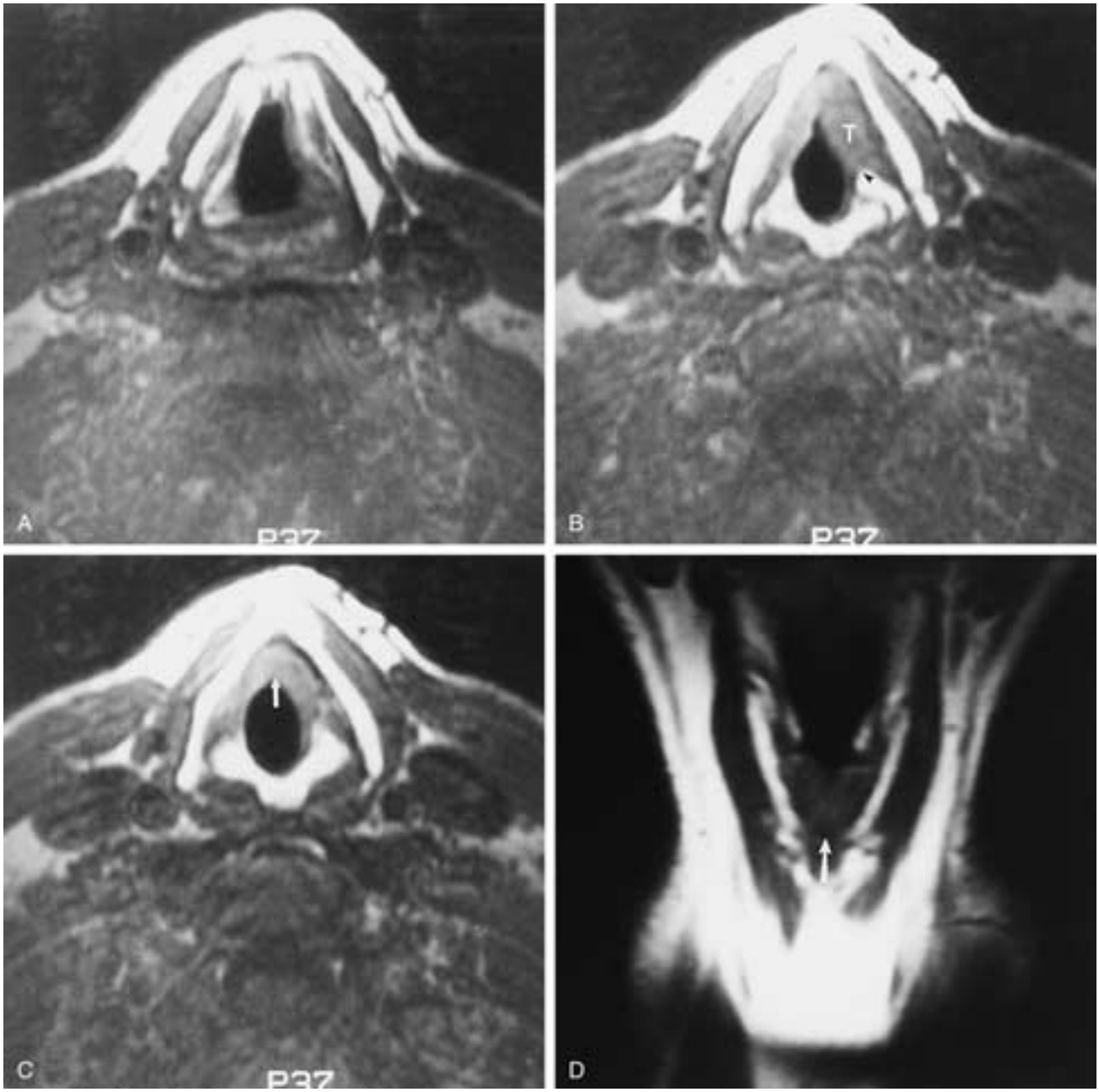

FIGURE 30-55 True cord lesion, 1.5 Tesla, MR image. **A**, Level of the false cord is relatively normal. Axial T1-weighted image. **B**, Tumor (*T*) at the level of the true cord. *Arrowhead*, vocal process. **C**, Level of the lower true cord. The tumor crosses the midline (*arrow*). **D**, Coronal image shows increased tissue (*arrow*) beneath the anterior commissure.

VIEW IMAGE

Copyright © 2003, Mosby, Inc. All rights reserved.

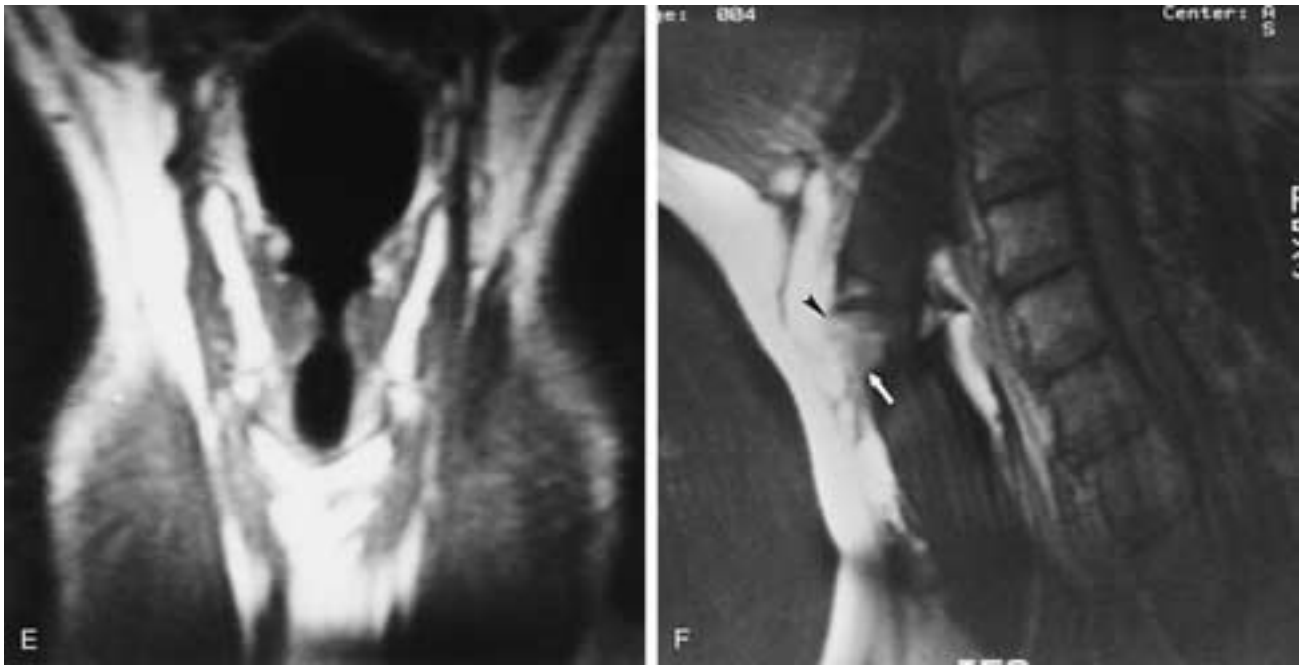

VIEW IMAGE

FIGURE 30-55 *Continued.* **E**, Slightly posterior scan shows only slight thickening of the right true cord. **F**, Sagittal T1-weighted image shows a small amount of tumor (*arrow*) immediately inferior to the anterior commissure (*arrowhead*). Evaluation of tumor in this anterior part of the cord can be unreliable because of partial volume artifact.

OTHER MALIGNANT TUMORS

Squamous cell carcinoma accounts for 95% of the malignancies of the larynx; however, other benign and malignant lesions do occur.[40, 41] Although the pathologic diagnosis is still made by endoscopy and biopsy, the radiologist may be able to direct the clinician toward a diagnosis other than typical squamous cell carcinoma.[77, 78] This is especially true when the lesion is completely submucosal.

Other carcinomas arising in the larynx include adenocarcinoma (1%), arising in the minor salivary glands, verrucous carcinoma, anaplastic carcinoma, and spindle cell carcinoma.[41]

Adenocarcinoma has the same subtypes as salivary gland neoplasms elsewhere in the body. Adenoid cystic carcinoma is slightly more common in the subglottic larynx, and mucoepidermoid and adenocarcinoma (not otherwise specified) are more common in the supraglottic larynx. Other subtypes of adenocarcinomas are rare.

Verrucous carcinoma is a primarily exophytic tumor. The lesion is wart-like and not very invasive. This tumor almost never metastasizes. Its appearance at endoscopy is very characteristic.

Anaplastic carcinoma, similar to oat cell carcinoma in the lung, is another rare carcinoma of the larynx. The prognosis is poor.

Spindle cell carcinoma is a rare lesion containing elements of a squamous cell carcinoma combined with a spindle cell stroma. There is a difference of opinion as to whether this is a peculiar kind of squamous cell carcinoma or a combination of squamous cell carcinoma and sarcoma.[79] Either or both components can metastasize. Other names for this lesion occasionally found in the literature include pseudosarcoma, carcinosarcoma, pleomorphic carcinoma, polypoid sarcoma, and pseudosarcomatous squamous cell carcinoma. The basic controversy depends on definition of the cell of derivation and the potential of the spindle cell stroma. Does the spindle cell develop directly from the squamous cell as a dedifferentiation toward the mesenchymal form? Is the spindle cell truly of a separate mesenchymal origin? One theory holds that the spindle cell stroma is a reactive phenomenon rather than a true sarcoma.

Any type of sarcoma can be found in the larynx.[80] As a group, sarcomas make up only 0.3% to 1% of all laryngeal malignancies. Although in rare cases they can be large or fungating, they are primarily submucosal. Other than chondrosarcoma, the masses are somewhat nonspecific at imaging, but a smooth mucosal covering should direct the radiologist away from a diagnosis of squamous cell carcinoma.

Special mention should be made of chondrosarcoma because the calcifications (often ring-like) can indicate a specific radiographic diagnosis. These calcifications may be suggested on MR imaging but are more obvious on CT (Figs. 30-65 and 30-66). Usually the origin of the lesion in the cartilage is easily identified by an obvious expansile defect in either the cricoid or the thyroid cartilage (Fig. 30-67). This pattern of cartilage abnormality usually is easily differentiated from the destruction associated with squamous cell carcinoma.

Separation of benign from malignant chondroid lesions is usually impossible based on imaging characteristics. However, most of these tumors behave in a low-grade manner. Even after histologic examination of the entire specimen, differentiation of benign and malignant tumors can be

Copyright © 2003, Mosby, Inc. All rights reserved.

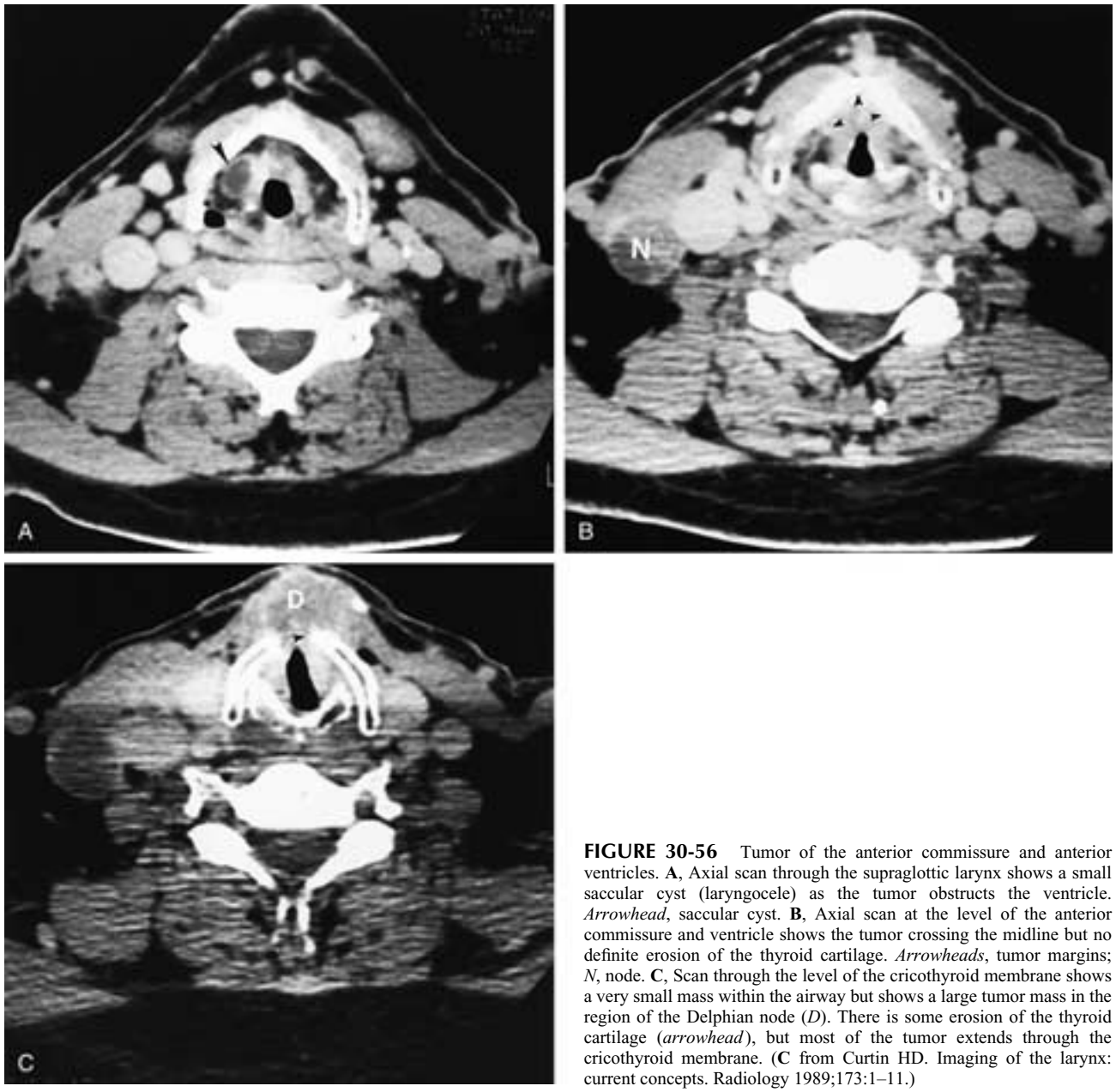

FIGURE 30-56 Tumor of the anterior commissure and anterior ventricles. **A**, Axial scan through the supraglottic larynx shows a small saccular cyst (laryngocele) as the tumor obstructs the ventricle. *Arrowhead*, saccular cyst. **B**, Axial scan at the level of the anterior commissure and ventricle shows the tumor crossing the midline but no definite erosion of the thyroid cartilage. *Arrowheads*, tumor margins; *N*, node. **C**, Scan through the level of the cricothyroid membrane shows a very small mass within the airway but shows a large tumor mass in the region of the Delphian node (*D*). There is some erosion of the thyroid cartilage (*arrowhead*), but most of the tumor extends through the cricothyroid membrane. (**C** from Curtin HD. Imaging of the larynx: current concepts. Radiology 1989;173:1–11.)

VIEW IMAGE

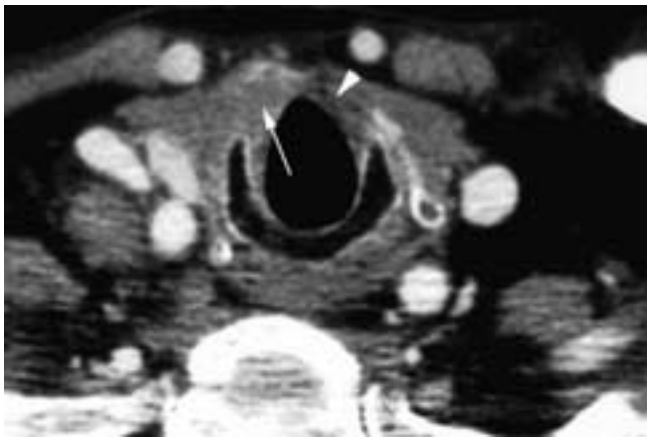

FIGURE 30-57 Tumor extension through the cricothyroid gap. Axial CT. The tumor originated at the true cord. Tumor extends anteriorly (*arrow*) between the cricoid and thyroid cartilages. Note the intact fat (*arrowhead*) on the opposite side related to the cricothyroid membrane.

VIEW IMAGE

Copyright © 2003, Mosby, Inc. All rights reserved.

FIGURE 30-58 Tumor of the ventricle involving the upper margin of the true cord and the lower margin of the false cord, 1.5 Tesla. **A**, Coronal image. Tumor extends around the ventricle involving the false cord (*arrowhead*) and the upper margin of the true cord (*open arrow*). T1-weighted image. **B**, Axial T1-weighted image with tumor at the level of the false cord (*arrow*). Normal fat indicates the false cord level (*arrowhead*). **C**, T2-weighted image shows brightening of the involved cord (*arrow*). Note the normal intermediate signal intensity of the TAM on the normal side (*arrowhead*).

VIEW IMAGE

difficult. Despite its fairly good prognosis, if a low-grade tumor has extensive cricoid involvement, a total laryngectomy may be considered. Rarely, chondroid lesions can arise from the cricoarytenoid joint (Fig. 30-68).

Chondrosarcoma tends to grow slowly; however, rarely, a secondary more malignant component can develop. This phenomenon is called a dedifferentiated chondrosarcoma (Fig. 30-69). A soft-tissue component appears to arise from the original chondroid lesion and grows rapidly. The soft-tissue component is usually a fibrosarcoma or a malignant fibrous histiocytoma.[81] Osteosarcoma and rhabdosarcoma elements, though less common, have also been described. The prognosis is extremely poor.

Rare primary and metastatic melanomas have been found in the supraglottic larynx and the true cord.[41] Other rare primary tumors involving the larynx include lymphoma, plasmacytoma, fibrous histiocytoma, and Kaposi's sarcoma (Fig. 30-70).[82]

Secondary involvement of the larynx by other than direct tumor extension is rare.[41, 83] Rare metastases from melanomas, renal cell, breast, and lung cancers as well as other rare primaries have been reported, as has involvement by leukemia and lymphoma.[84] No characteristic imaging appearances have been described. Metastasis can be to the soft tissues or can result in an expansile lesion of the cartilage.

BENIGN TUMORS

Benign lesions of the larynx include vocal cord nodules, juvenile papillomatosis, and a variety of nonepithelial tumors.

Copyright © 2003, Mosby, Inc. All rights reserved.

Vocal cord nodules (nonneoplastic, polyps) represent a stromal reaction that occurs in patients with a history of vocal abuse. Clinically, there may be a small fibrotic area on the cord or a more nodular, slightly vascular irregularity. The nodules may be an incidental imaging finding, but they usually are clinically diagnosed, with imaging considered unnecessary (Fig. 30-71). Vocal cord nodules occur on the free margin of the true vocal cord.

Papillomas, although benign and noninvasive, tend to recur after therapy. The wart-like lesions are frequently multiple and occur most often in children. Any part of the larynx can be affected, and involvement of the trachea and bronchial tree can occur in severe cases, especially if there is a history of a tracheostomy. Currently, the laser is used to excise papillomas in children; however, regrowth can be so rapid that many children require repeat procedures every few weeks. Most cases eventually go into remission, but some persist into adulthood, and although these lesions are benign, deaths have occurred secondary to pneumonia or airway compromise. The high correlation between children with juvenile papillomatosis and mothers with genital warts suggests a viral etiology. Papillomas do occur in adults, usually men; however, in these cases, the papillomas are less often multiple. Malignancy occurs in a small number of patients with papilloma (see above).

The lesions are exophytic, and CT or MR imaging is not usually done. On plain films, the multiple nodules may be seen impinging on the airway (Fig. 30-72). Chest films are used to evaluate possible pulmonary involvement, which is usually seen as small cavitating nodules.

Benign nonepithelial or mesenchymal tumors include hemangiomas, neural tumors, paragangliomas, lipomas, leiomyomas, rhabdomyomas, chondromas, and a few other rare lesions.[40, 41] Of these, lipomas have a characteristic appearance on both CT and MR imaging because of their high fat content (Fig. 30-73).[85] Chondromas often can be identified by their mineralized matrix and their relationship to the laryngeal cartilage. On imaging, the lesion cannot be reliably diagnosed as benign or malignant unless it has a very aggressive appearance.

Hemangiomas deserve special mention. They are more common in adults than in children, but the pediatric type is more likely to cause airway obstruction and so has received more attention.[86] In adults, hemangiomas (or vascular malformations) are usually localized (Fig. 30-74), tend to be glottic or supraglottic, enhance on CT and MR imaging, and have a fairly high T2-weighted signal intensity.

Hemangiomas of the young can occur anywhere in the larynx but have a predilection for the subglottic area (Figs. 30-75 to 30-77). Hemangiomas arising in the subglottic area are a major clinical problem because, even though they are

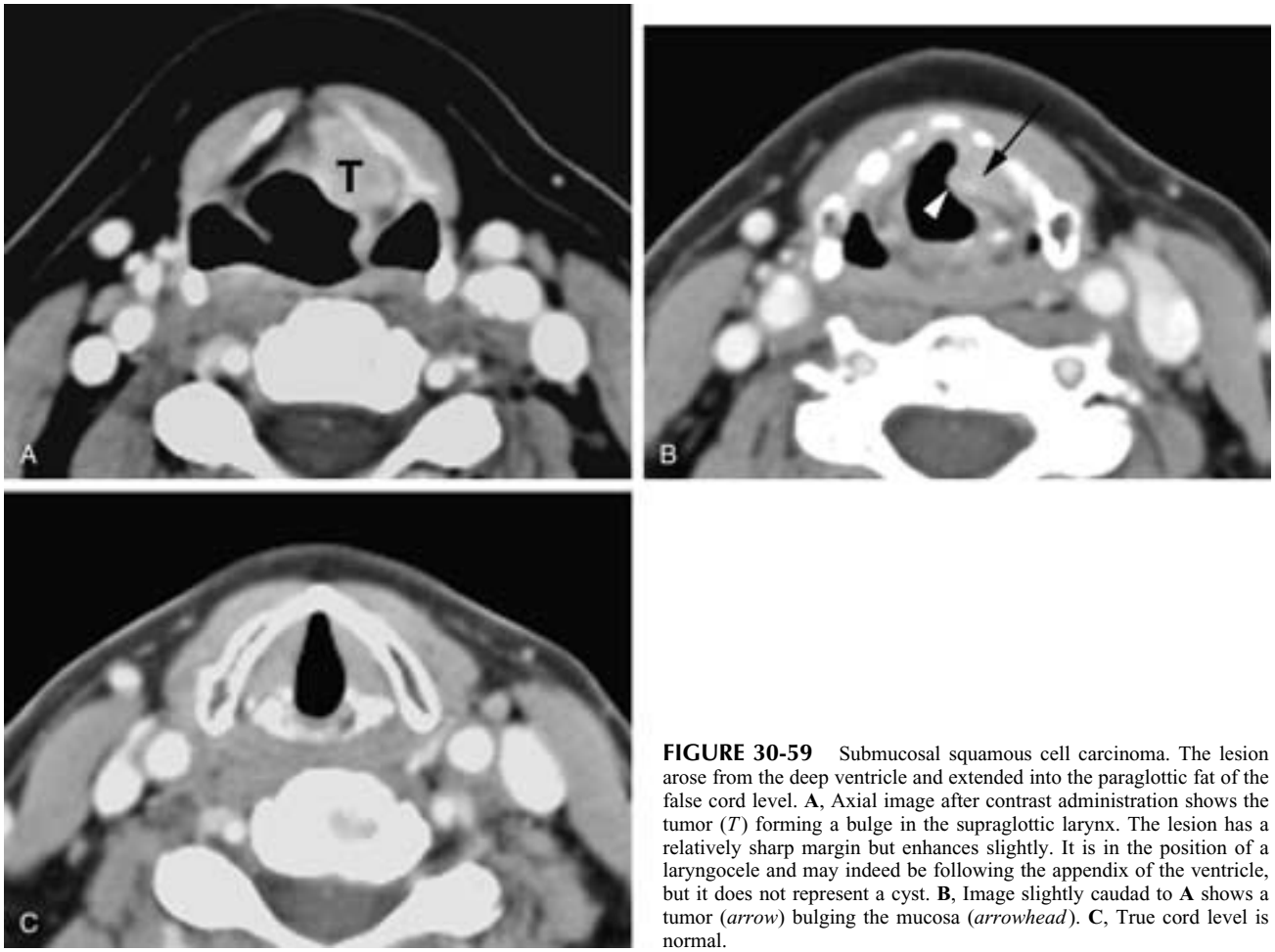

FIGURE 30-59 Submucosal squamous cell carcinoma. The lesion arose from the deep ventricle and extended into the paraglottic fat of the false cord level. **A**, Axial image after contrast administration shows the tumor (*T*) forming a bulge in the supraglottic larynx. The lesion has a relatively sharp margin but enhances slightly. It is in the position of a laryngocele and may indeed be following the appendix of the ventricle, but it does not represent a cyst. **B**, Image slightly caudad to **A** shows a tumor (*arrow*) bulging the mucosa (*arrowhead*). **C**, True cord level is normal.

VIEW IMAGE

Copyright © 2003, Mosby, Inc. All rights reserved.

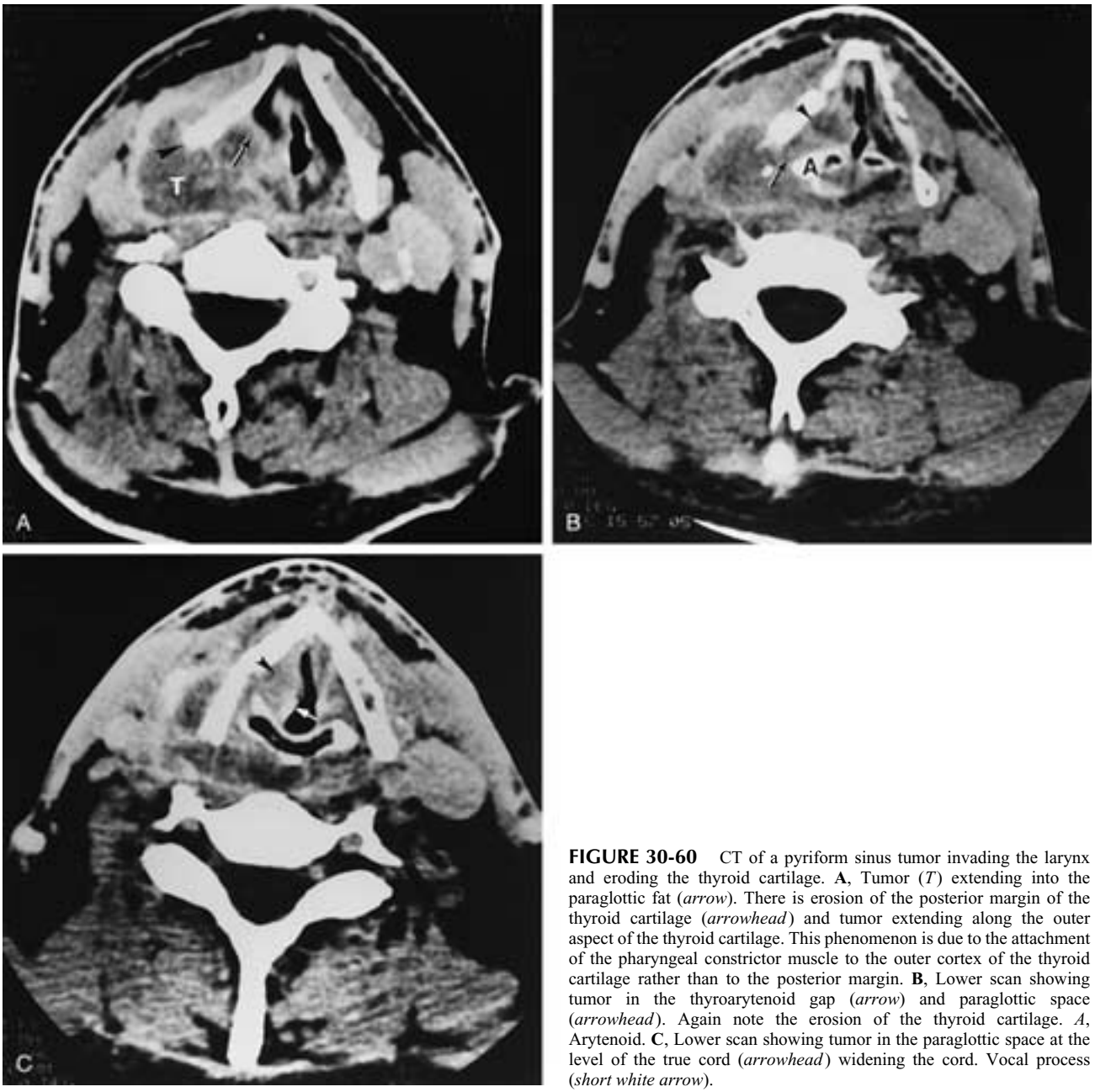

FIGURE 30-60 CT of a pyriform sinus tumor invading the larynx and eroding the thyroid cartilage. **A**, Tumor (*T*) extending into the paraglottic fat (*arrow*). There is erosion of the posterior margin of the thyroid cartilage (*arrowhead*) and tumor extending along the outer aspect of the thyroid cartilage. This phenomenon is due to the attachment of the pharyngeal constrictor muscle to the outer cortex of the thyroid cartilage rather than to the posterior margin. **B**, Lower scan showing tumor in the thyroarytenoid gap (*arrow*) and paraglottic space (*arrowhead*). Again note the erosion of the thyroid cartilage. *A*, Arytenoid. **C**, Lower scan showing tumor in the paraglottic space at the level of the true cord (*arrowhead*) widening the cord. Vocal process (*short white arrow*).

VIEW IMAGE

expected to regress, airway compromise can force intervention. In a typical pediatric hemangioma, the infant has partial airway obstruction within the first 6 to 12 months of life. Because any inflammation further compromises an already narrowed subglottic area, these patients may present with recurrent croup. Because of venous engorgement, crying also exacerbates the problem. The diagnosis may be suggested by radiography but is usually made by endoscopy when a compressible red or blue mass is seen. Topical epinephrine may cause the lesion to diminish in size; tracheostomy may be necessary while waiting for this to occur. Steroid therapy and surgery have been tried; however, currently, laser excision or reduction is used because of the lower associated operative bleeding. Eventual tracheal stenosis is not uncommon, especially after surgery. The laryngeal lesion is often associated with cutaneous or soft-tissue hemangiomas.

The most common radiographic appearance of a pediatric hemangioma is a localized bulge or concentric narrowing of the subglottic airway. This can be appreciated on CT or MR imaging in the axial, coronal, or sagittal planes. On MR imaging the lesion has a high T2-weighted signal intensity (Fig. 30-77), and on both CT or MR imaging the lesion enhances with contrast. The airway configuration can be easily appreciated on plain films done in several projections. Occasionally, phleboliths may be seen in a larger hemangioma, either with CT or with plain film (usually in somewhat older patients). Hemangiomas of the extralaryngeal neck rarely extend into the larynx.

Paragangliomas (glomus tumors) have been reported in

Copyright © 2003, Mosby, Inc. All rights reserved.

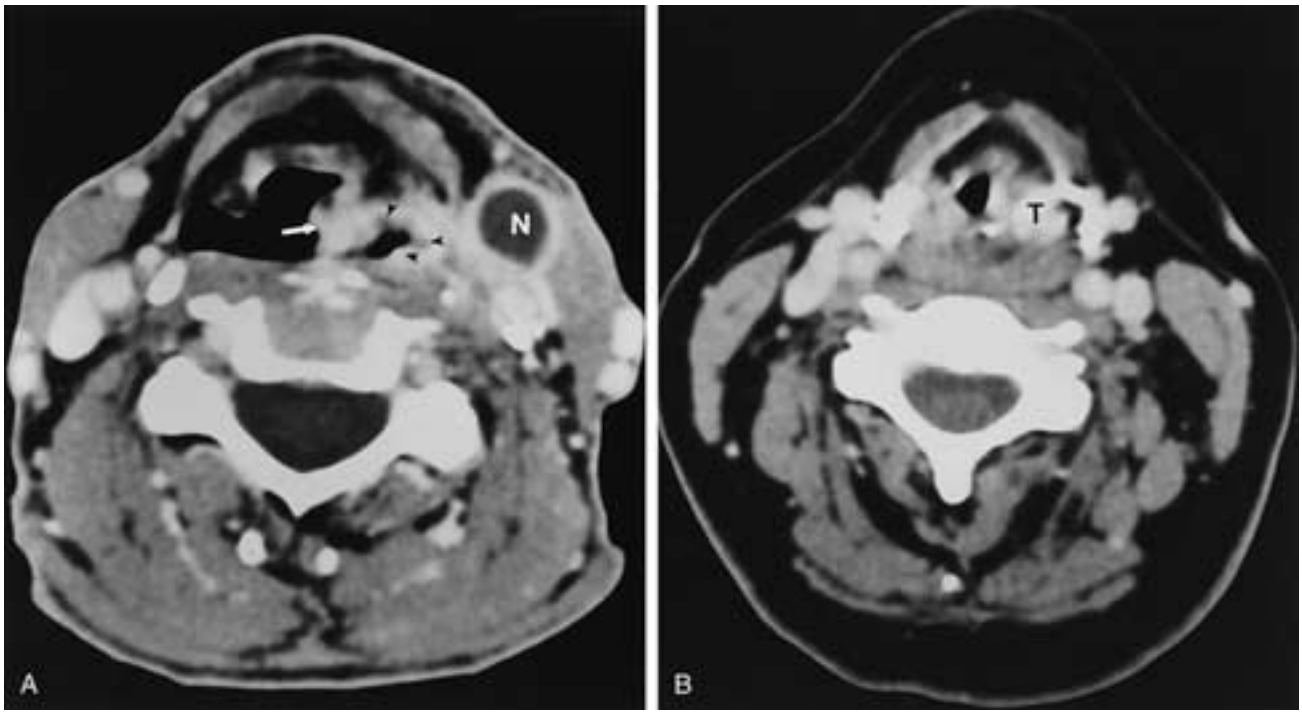

VIEW IMAGE

FIGURE 30-61 CT of a pharyngeal tumor limited to the level of the supraglottic larynx. **A**, The lesion (*arrowheads*) extends around the lateral wall of the pharynx onto the posterior wall. The AE fold (*arrow*) is involved. Typical appearance of a metastatic node (*N*). **B**, Lower margin of the tumor (*T*) is seen on the axial scan at the level of the supraglottic fat. The scan immediately inferior to this was normal.

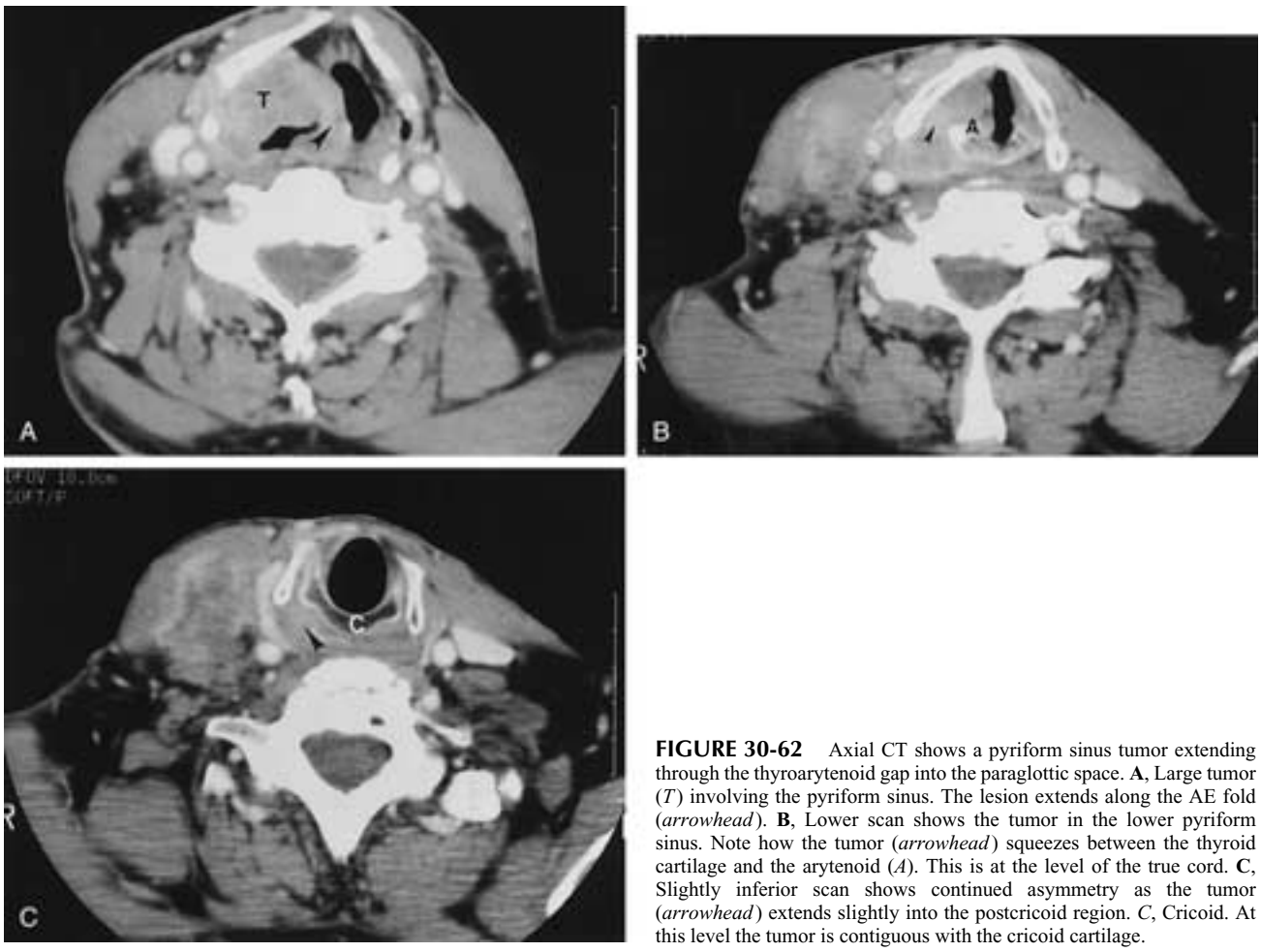

FIGURE 30-62 Axial CT shows a pyriform sinus tumor extending through the thyroarytenoid gap into the paraglottic space. **A**, Large tumor (*T*) involving the pyriform sinus. The lesion extends along the AE fold (*arrowhead*). **B**, Lower scan shows the tumor in the lower pyriform sinus. Note how the tumor (*arrowhead*) squeezes between the thyroid cartilage and the arytenoid (*A*). This is at the level of the true cord. **C**, Slightly inferior scan shows continued asymmetry as the tumor (*arrowhead*) extends slightly into the postcricoid region. *C*, Cricoid. At this level the tumor is contiguous with the cricoid cartilage.

VIEW IMAGE

Copyright © 2003, Mosby, Inc. All rights reserved.

VIEW IMAGE

FIGURE 30-63 MR image of a postcricoid tumor. Sagittal view shows the tumor (*T*). The inferior margin (*arrowhead*) is best defined in this view. Bright signal is fat in the medullary cavity of the cricoid lamina (*arrow*).

the larynx, usually in a supraglottic location (Fig. 30-78).[39] These lesions enhance on CT and, as might be expected from their vascular nature, tend to bleed if biopsied. Like hemangiomas, they have intermediate signal intensity on T1-weighted images and high signal intensity on T2-weighted images.

Schwannomas can occur as isolated submucosal tumors, usually in the supraglottic larynx. In neurofibromatosis, an isolated neurofibroma can occur; however, a plexiform, more infiltrative lesion also can diffusely involve the paraglottic structures (Fig. 30-79).[87, 88]

Granular cell tumor is a benign lesion of unknown origin that involves the mucosal membranes of the head and neck.[41] Most theories implicate either a Schwann cell or a more primitive mesenchymal cell origin. The larynx can be involved, and the most common site is the true cord. The epithelium over the granular cell tumor may be hyperplastic and thus may mimic squamous cell carcinoma at direct inspection. Biopsy establishes the diagnosis. The age of occurrence is usually 35 to 45 years, which is younger than the usual age of squamous cell carcinoma.

CYSTS AND LARYNGOCELES

Cysts of the larynx include submucosal cysts and laryngoceles or saccular cysts. Thyroglossal duct cysts may protrude into the supraglottic larynx.

Mucosal cysts can arise anyplace in the larynx that contains submucosal glands.[41, 89] Thus, only the free margin

VIEW IMAGE

FIGURE 30-64 Exophytic lesion of the posterior wall of the pharynx. The lesion is not fixed to the prevertebral fascia. Compare the positions of the upper and lower margins of the lesion (*arrows*) with the cervical spine interspace, C4 to C5. **A**, At rest. **B**, During swallowing.

Copyright © 2003, Mosby, Inc. All rights reserved.

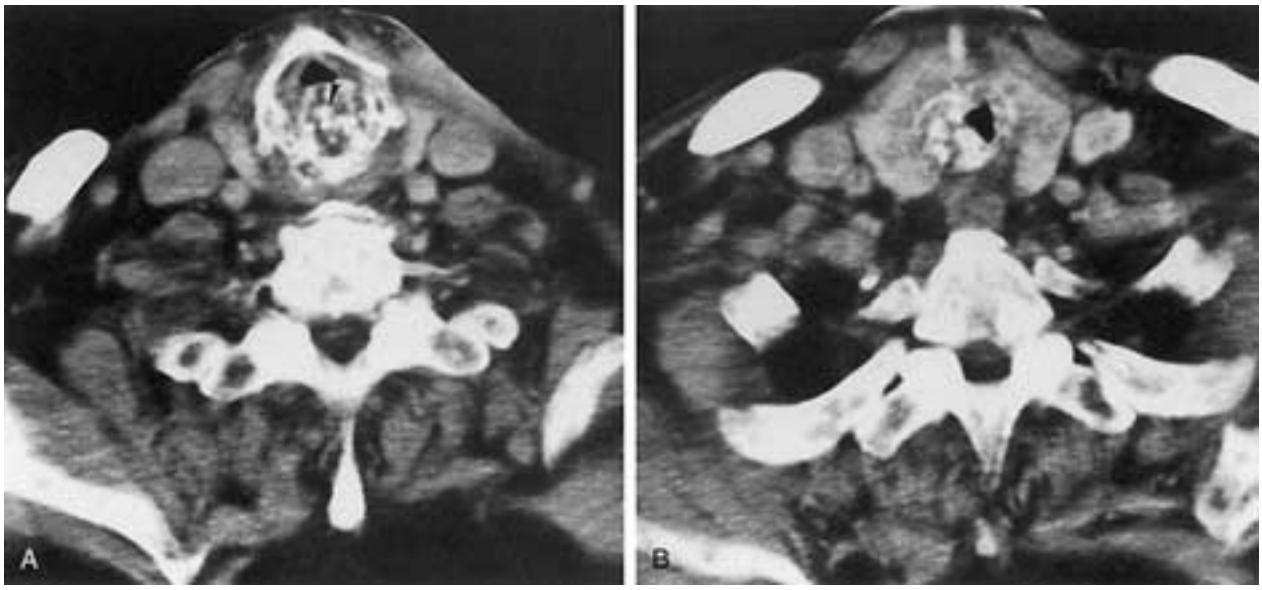

FIGURE 30-65 Chondrosarcoma of the larynx. **A**, CT shows definite ring-like calcifications (*arrowhead*) within the tumor mass. **B**, Inferior extension shows similar calcifications.

VIEW IMAGE

of the true cord is spared, and virtually any other location within the larynx is a possible site of cyst development. These cysts are superficial and submucosal, and they protrude into the airway. Symptoms depend on the size and location of the cyst and include dysphagia and respiratory distress. Deep extension is not seen. Vallecular cysts, which often occur in children, are seen anterior to the epiglottis (Fig. 30-80).

The saccule, or appendix, of the laryngeal ventricle is a tubular structure that normally extends cranially into the paraglottic region of the supraglottic larynx (Fig. 30-81). The saccular lumen communicates with the anterior ventricle. If the saccule enlarges, the resultant submucosal mass is called a laryngocele or saccular cyst.[90, 91] If the saccule remains air-filled, many authors refer to the abnormality as a laryngocele. However, if the saccular lumen fills with secretions, the terms *saccular cyst* and *laryngeal mucocele* are often preferred, although some authors simply use the terms *air-filled* and *fluid-filled laryngocele* to describe the lesions. Although a saccular cyst can result from inflammatory mucosal swelling, an obstructing lesion in the ventricle always must be sought.

A laryngocele is referred to as being internal, mixed or combined, or external in type. An internal laryngocele remains totally within the larynx, producing a submucosal supraglottic mass. A combined or mixed laryngocele protrudes through the thyrohyoid membrane, producing both an intralaryngeal and an extralaryngeal mass. The term *external laryngocele* refers to a combined laryngocele that produces little if any supraglottic mass. However, most lesions with an external component also have an internal component, even though it may be small.

A laryngocele can be diagnosed on CT, MR imaging, or even plain films (Figs. 30-82 to 30-87). The internal consistency of the fluid-filled cysts may vary somewhat, depending on their protein content; however, this is apparent only on MR or CT. On CT or MR imaging, the supraglottic ''mass'' can be followed down through the paraglottic area of the false cord to the level of the ventricle. The margin is usually smooth, and the supraglottic fat is not completely obliterated. Thus, the laryngocele is at least partially surrounded by the supraglottic fat. It should be noted that a normal air-filled ventricular appendix can often be seen on axial imaging. This should not be called a laryngocele unless it causes a submucosal deformity of the ipsilateral supraglottic margin.

As mentioned, a laryngocele, although always benign, can be associated with a malignancy in the region of the ventricle (Figs. 30-86, 30-88 and 30-89). The tumor obstructs the outflow of the saccule, causing either trapping of air or, more commonly, retention of mucous secretions. Thus, the ventricular area should be closely examined in patients with a laryngocele or a saccular cyst. In this regard, imaging cannot completely exclude a carcinoma and endoscopy should always be performed. Rarely, a laryngocele can develop after laryngeal surgery, presumably due to local scarring or from positioning of a prosthesis (Fig. 30-90).

The term *laryngopyocele* refers to an infected laryngocele (Figs. 30-91 and 30-92). Due to its size and the associated inflammation, a laryngopyocele can cause airway compromise. Cellulitis can also spread to the lateral neck.

The treatment of a symptomatic laryngocele is surgical. A tracheostomy is often performed because of concern that even minor postoperative swelling or bleeding can compromise the airway.

Although thyroglossal duct cysts (TGDC) are discussed in Chapter 35, they are also briefly mentioned here (Fig. 30-93). At the level of the larynx, a TGDC has a characteristic location just off the midline, insinuated between or deep to the strap muscles positioned against the anterior thyroid ala. These cysts are usually easily distinguished from a laryngocele, because the TGDC has a more anterior location and remains outside the larynx. Occasion-

Copyright © 2003, Mosby, Inc. All rights reserved.

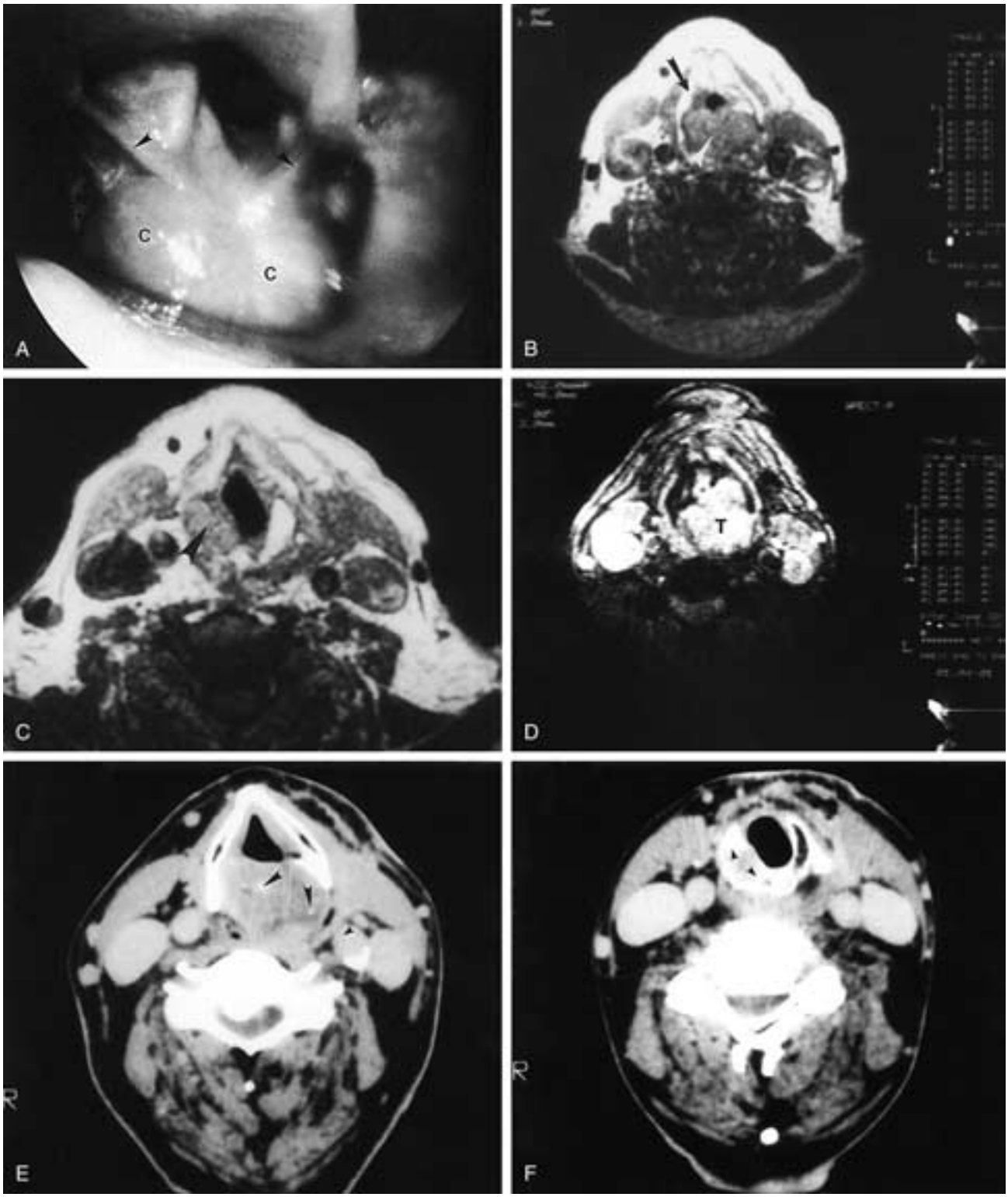

VIEW IMAGE

FIGURE 30-66 Chondrosarcoma of the larynx. **A**, Endoscopic view shows a large bulge in the region of the cricoid (*C*). Note that the mucosa is intact and is not ulcerated. *Arrowheads*, AE folds. **B**, T1-weighted image shows the large submucosal mass (*arrowhead*). Note its position in the posterior larynx. There is no abnormality in the paraglottic fat (*arrow*). **C**, Slightly lower than **B**. Axial image through the cricoid cartilage shows a well-defined defect (*arrowhead*). The sharp margin would be unusual in invasion by squamous carcinoma. This indicates the origin within the cricoid cartilage. **D**, T2-weighted axial image shows the tumor (*T*) to have the high signal characteristic of chondrosarcoma. **E**, Axial CT shows a large mass with small punctate calcifications (*arrowheads*). This suggests the chondroid nature of the lesion. **F**, Axial scan through the cricoid shows the sharp margin of the lesion (*arrowheads*) as it abuts the normal cartilage.

Copyright © 2003, Mosby, Inc. All rights reserved.

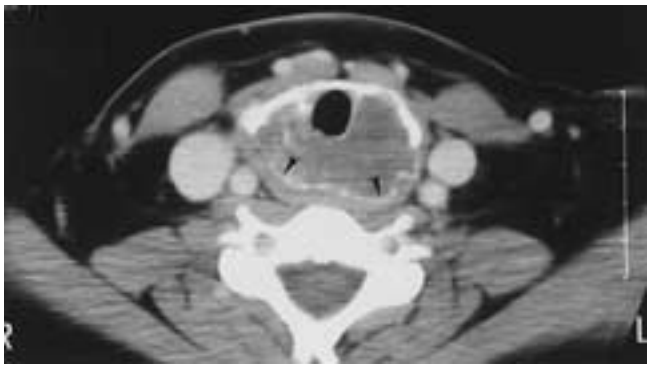

VIEW IMAGE

FIGURE 30-67 Low-grade chondrosarcoma of the cricoid that expands the cricoid cartilage. The cortex has been remodeled outward (*arrowheads*), leaving the general shape of the original cartilage.

ally, at imaging, a TGDC appears to protrude into the larynx through the superior thyroid notch. There have also been a few reports of long-standing large TGDCs that have caused deossification of the thyroid cartilage and bulged into the larynx, presenting clinically as a submucosal mass. The treatment was excision without resection of any of the larynx.

INFECTION AND INFLAMMATION

Infections that may come to the attention of the radiologist are usually those of childhood, including epiglottitis or croup. Tuberculosis or other granulomatous diseases are rare, as is perichondritis or infection of the laryngeal cartilages, usually associated with prior RT.[92] Previously, perichondritis and abscesses were caused by typhoid fever, measles, scarlet fever, erysipelas, anthrax, and mycoses.[93] Occasionally, infections of the soft tissues of the neck can involve the larynx secondarily, as can other inflammatory processes such as arthritis and collagen vascular disease.

Croup

Croup is an inflammation of the subglottic larynx with greater or lesser involvement of the trachea and bronchi.

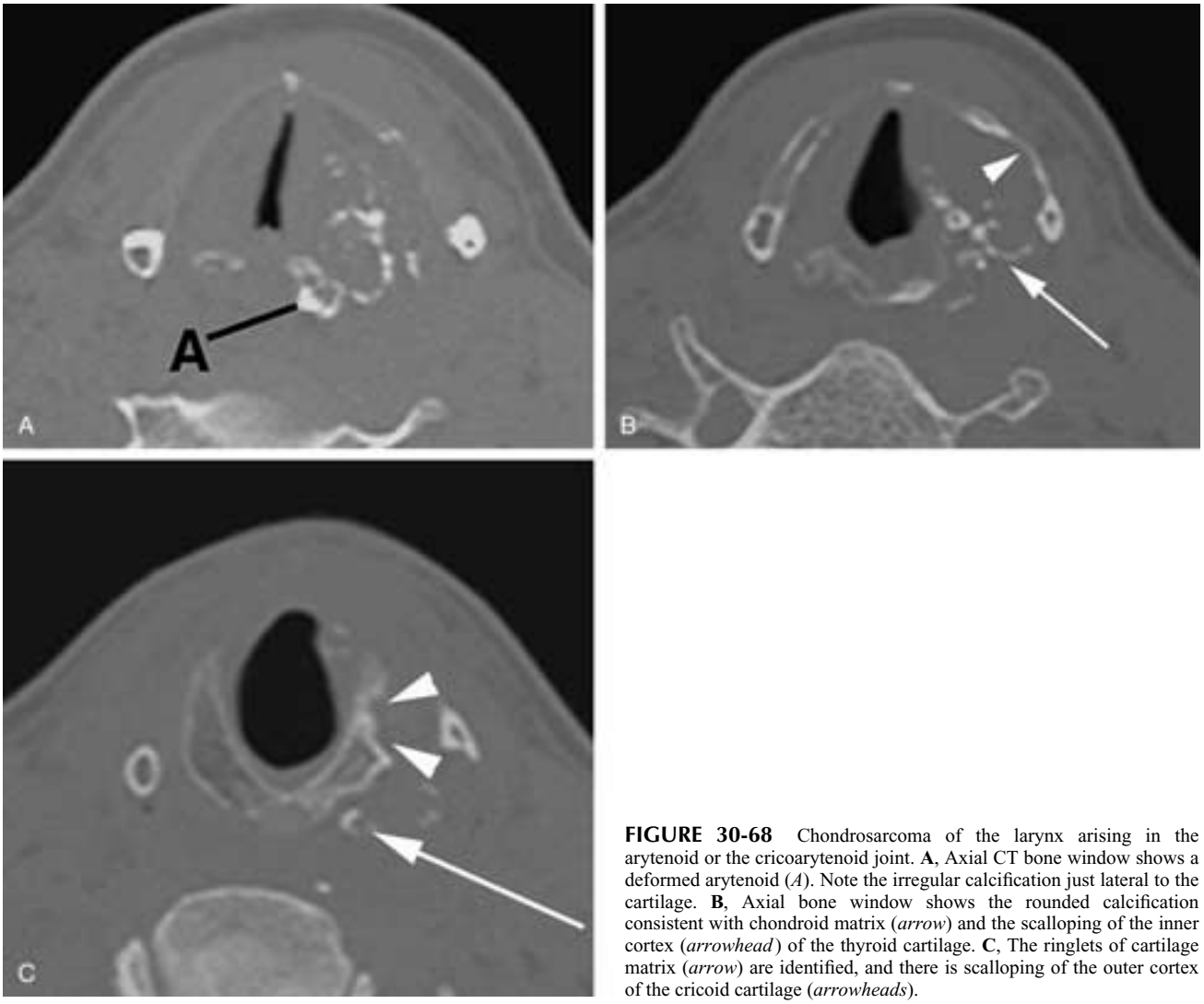

FIGURE 30-68 Chondrosarcoma of the larynx arising in the arytenoid or the cricoarytenoid joint. **A**, Axial CT bone window shows a deformed arytenoid (*A*). Note the irregular calcification just lateral to the cartilage. **B**, Axial bone window shows the rounded calcification consistent with chondroid matrix (*arrow*) and the scalloping of the inner cortex (*arrowhead*) of the thyroid cartilage. **C**, The ringlets of cartilage matrix (*arrow*) are identified, and there is scalloping of the outer cortex of the cricoid cartilage (*arrowheads*).

VIEW IMAGE

Copyright © 2003, Mosby, Inc. All rights reserved.

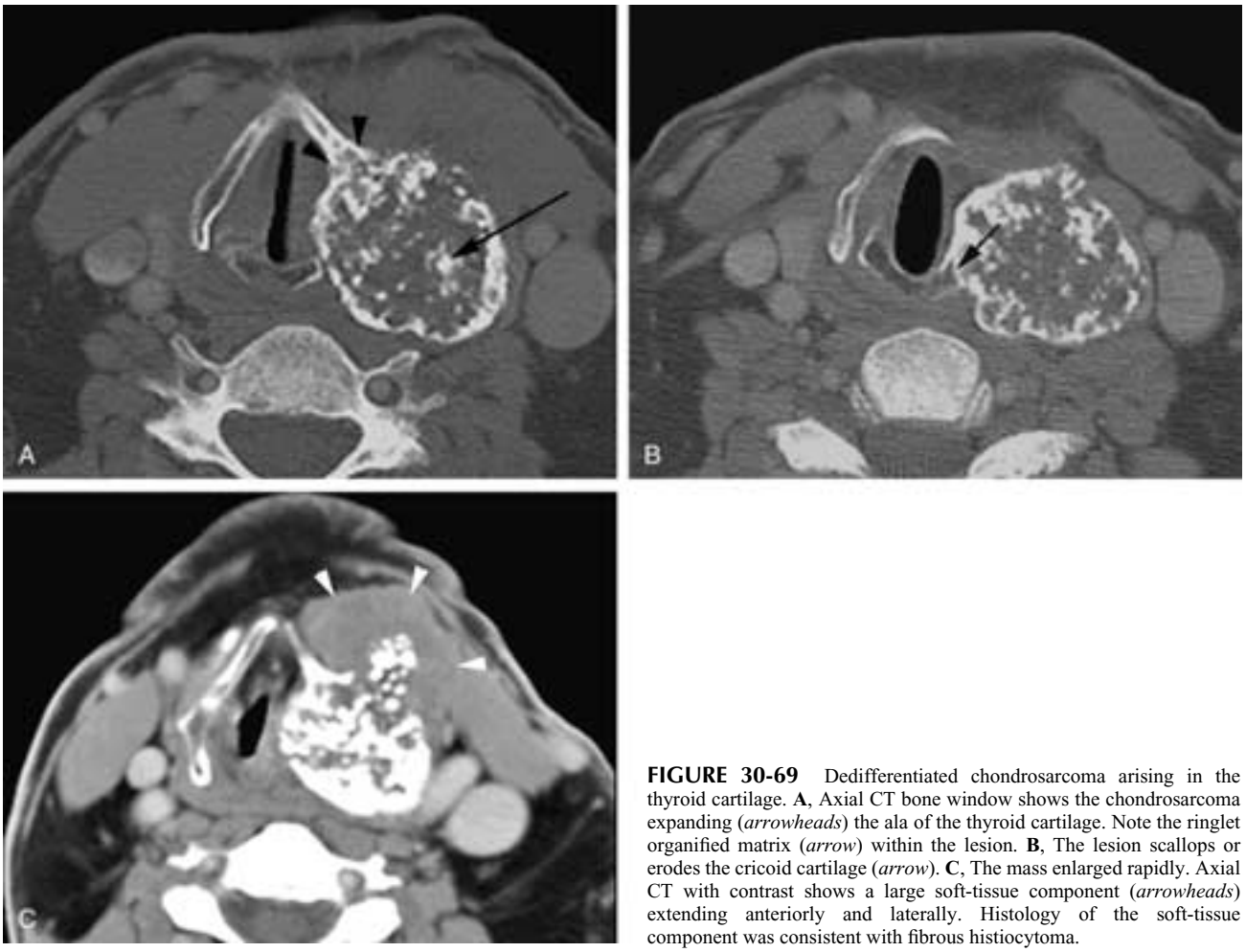

FIGURE 30-69 Dedifferentiated chondrosarcoma arising in the thyroid cartilage. **A**, Axial CT bone window shows the chondrosarcoma expanding (*arrowheads*) the ala of the thyroid cartilage. Note the ringlet organified matrix (*arrow*) within the lesion. **B**, The lesion scallops or erodes the cricoid cartilage (*arrow*). **C**, The mass enlarged rapidly. Axial CT with contrast shows a large soft-tissue component (*arrowheads*) extending anteriorly and laterally. Histology of the soft-tissue component was consistent with fibrous histiocytoma.

VIEW IMAGE

Occurring in young children (6 months to 3 years of age), croup is usually caused by type 1 parainfluenza virus, but many other organisms occasionally have been implicated. Croup produces a barking cough and stridor. The edema involves the mucosa of the subglottic larynx, and because this tissue is looser in children than in adults, the swollen mucosa can impinge upon the airway. This is usually appreciated best on a frontal film as the ''wine bottle'' or ''steeple-shaped'' airway, with loss of the subglottic arch (Fig. 30-94). If the film is taken during inspiration, there may be ballooning of the pharynx, including the pyriform sinuses. This paradoxical dilatation of the hypopharynx

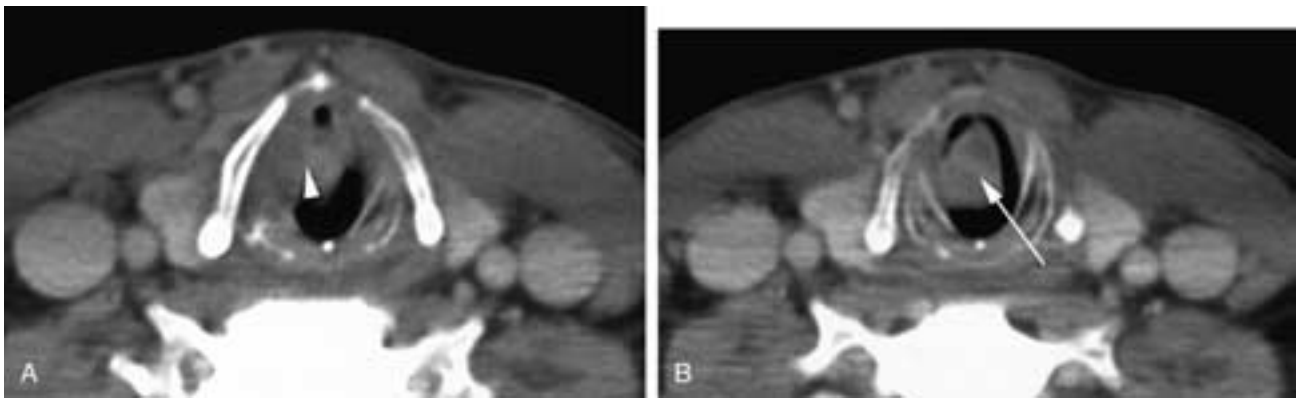

FIGURE 30-70 Kaposi's sarcoma. **A**, Axial CT to the level of the true cord (*arrowhead*). There is an exophytic lesion arising from the true cord and extending into the airway. **B**, The polypoid exophytic lesion (*arrow*) extended to the level of the cricoid. However, the tumor extension was exophytic into the lumen rather than extending along the mucosa.

VIEW IMAGE

Copyright © 2003, Mosby, Inc. All rights reserved.

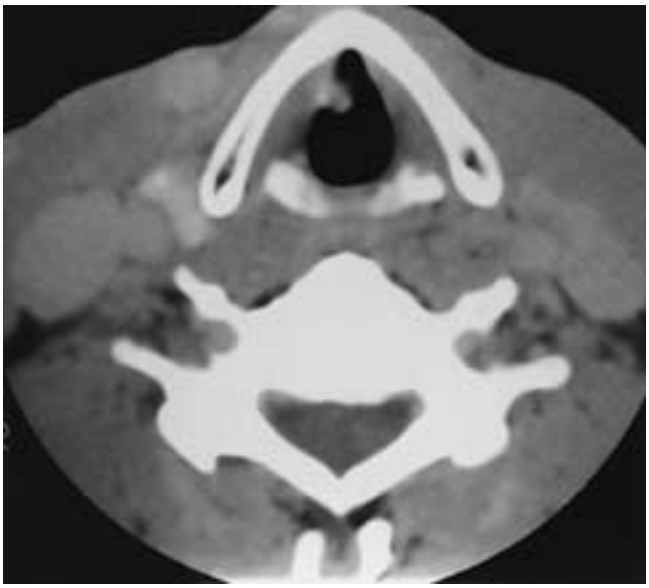

VIEW IMAGE

FIGURE 30-71 Axial CT shows a polyp of the right true cord. Incidental finding.

should alert the clinician to the diagnosis in these patients. On expiration the trachea and subglottis may be distended. Usually, however, the diagnosis is made clinically, and the factors that determine more extensive treatment, such as intubation or even tracheostomy, are clinical rather than radiographic. Plain films are used to confirm the diagnosis and to exclude a foreign body.

Epiglottitis or Supraglottitis

Epiglottitis or supraglottitis occurs in a slightly older age group than croup and is caused by *Haemophilus influenzae*. The child is usually 2 to 4 years old. A sore throat and the inability to swallow are the key clinical features, along with airway compromise. The epiglottis is swollen and has a typical ''cherry red'' appearance.

The lateral radiograph is characteristic and reflects the extent of the abnormality. The epiglottis is thickened, losing its normal sharp, thin or gracile, curvilinear shape (Fig. 30-95). The epiglottis blends into the enlarged AE folds. In severe cases the arytenoid prominence may be swollen. The radiograph is taken to document the disease and to exclude foreign bodies. Because epiglottitis can advance quickly to severe airway compromise, manipulation is minimized, including attempts at direct visualization of the enlarged epiglottis. The patient must never be out of an environment where an emergency tracheostomy can be performed; therefore, radiographs are usually done in the emergency room or even in the operating room. In most institutions, the child is not submitted to the risk of transportion to the radiology department. Therapy includes intubation or even tracheostomy, as well as administration of antibiotics. Decannulization is usually possible within 24 to 36 hours.

Adult epiglottitis or supraglottitis does occur, but it usually is not as life-threatening as it is in the pediatric patient. The findings may mimic radiation change, with enlargement of the AE folds and reticulated streaky density of the supraglottic fat. Rarely, emphysematous epiglottitis has been reported (Fig. 30-96).[94]

Tuberculosis and Other Granulomatous Lesions

Today tuberculosis of the larynx is rare. In the past, it was associated with pulmonary tuberculosis. Clinically, edema is present early, and with more severe involvement, ulceration and necrosis occur, producing a multinodular, irregularly enlarged epiglottis that can be seen on plain films (Fig. 30-97). There are reports of partial auto-epiglottectomies, in which the patient, in a fit of coughing, coughed up the necrotic epiglottic tip. The cricoarytenoid joint can also be involved, causing fixation; perichondritis can also occur.

Rhinoscleroma (Fig. 30-98), Wegener's granulomatosis, T-cell lymphoma (malignant midline granuloma, polymorphic reticulosis), pemphigus, leprosy, syphilis, and numerous mycotic infections all have been noted to rarely involve the larynx.[95] Involvement can be localized to the larynx or can occur in association with pharyngeal involvement (Fig. 30-99). The recent increase in immunocompromised patients has made these rare infections more of a diagnostic consideration.

Immunohistochemical studies have resulted in a reclassification of some midline destructive diseases. Although Wegener's granulomatosis remains an entity with histologic demonstration of noncaseating multinucleated giant cell granulomas and necrotizing vasculitis, midline granulomatosis has now been reclassified as a non-Hodgkin's T-cell lymphoma.[96]

Sarcoid can cause diffuse laryngeal thickening, small nodular lesions, or localized infiltrative lesions, almost all of which are submucosal. No radiographic finding is specific, and the patient usually has other systemic manifestations of this disease.

Neck Infection

Soft-tissue infection arising in the neck can rarely extend into the larynx (Fig. 30-100). Usually there is a diffuse supraglottic edema, although glottic and subglottic disease can occur. On CT, the diffuse soft-tissue thickening typically has an attenuation less than that of muscle, indicating its edematous nature. Although the clinical settings are quite different, the imaging findings of these cases of laryngitis are often similar to those seen in a recently irradiated larynx.

Rheumatoid and Collagen Vascular Disease

The cricoarytenoid and cricothyroid joints are true synovial joints and can be affected by any type of arthritis, including rheumatoid arthritis, that can affect the other synovial joints in the body.[97] Swelling of the cricoarytenoid joint may cause hoarseness, and late sequelae include joint fixation. On CT, this can be identified by irregular sclerosis

Copyright © 2003, Mosby, Inc. All rights reserved.

or erosions in the region of the cricoarytenoid joint, while the soft tissues close to the arytenoid may be swollen.

Relapsing polychondritis is a rare idiopathic, nonsuppurative inflammatory condition affecting various cartilages.[98–101] The cartilages in the ear, nose, larynx, trachea, and joints can be involved. Ocular findings and sensorineural hearing loss have also been described. Airway involvement is present in about half of the afflicted patients, often with significant airway compromise. When the laryngeal cartilages are involved, generalized laryngeal edema can occur.[102] Inflammation can present as high T2-weighted signal intensity along the margins of the cartilage. Sclerosis and enlargement of the cartilage can be present, presumably reflecting a reaction to the inflammation. There can also be demineralization of parts of the cartilage, and diffuse calcification of the involved areas may be present. One report showed considerable calcification in the region of the arytenoid cartilages. Radionuclide bone scans can be positive over the involved region of the larynx and over other affected areas of the body.[24] The tracheal rings may also be affected, with apparent thickening and sclerosis of the cartilage and contiguous soft-tissue changes. Once the carti-

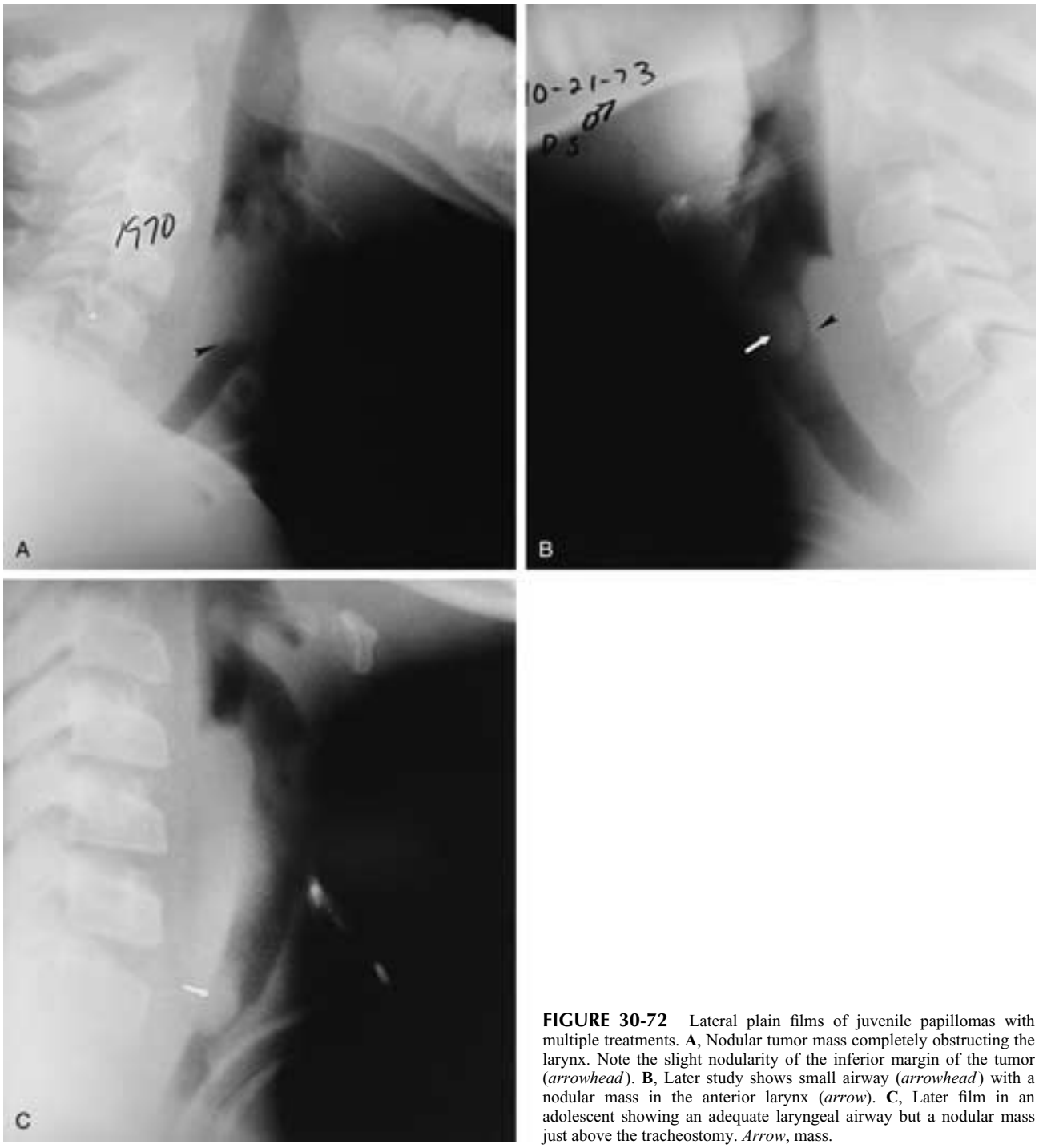

FIGURE 30-72 Lateral plain films of juvenile papillomas with multiple treatments. **A**, Nodular tumor mass completely obstructing the larynx. Note the slight nodularity of the inferior margin of the tumor (*arrowhead*). **B**, Later study shows small airway (*arrowhead*) with a nodular mass in the anterior larynx (*arrow*). **C**, Later film in an adolescent showing an adequate laryngeal airway but a nodular mass just above the tracheostomy. *Arrow*, mass.

VIEW IMAGE

Copyright © 2003, Mosby, Inc. All rights reserved.

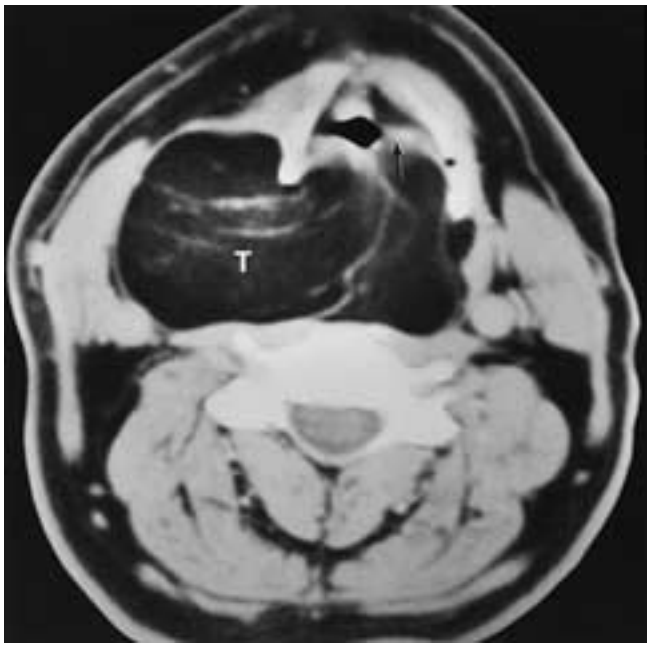

FIGURE 30-73 Axial CT shows a lipoma in the soft tissues of the neck and retropharyngeal space. Large tumor extending posterior to the larynx and displacing the larynx anteriorly. Note how the fat appears to bulge into the supraglottic-paraglottic space (*arrow*). The lesion at this level is actually retropharyngeal, with the pharyngeal lumen located between the tumor and the larynx. The anterior wall of the pyriform sinus is being pushed anteriorly, compressing the paraglottic fat but not invading. *T*, Tumor.

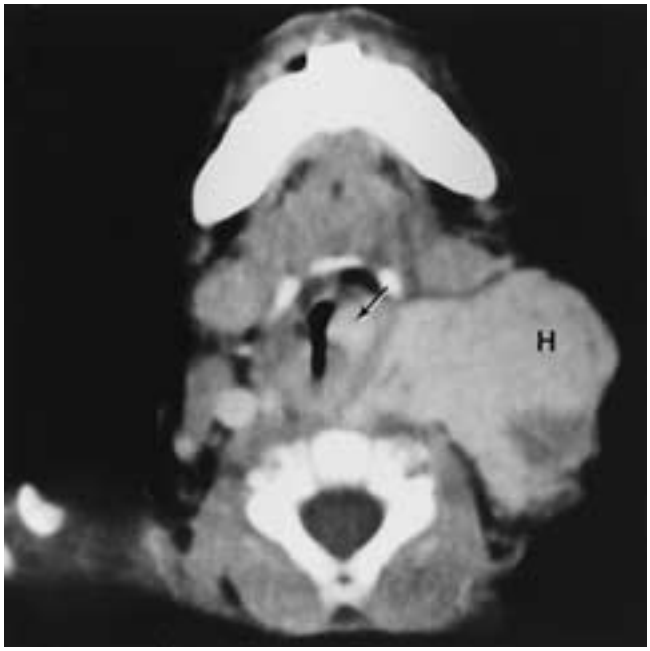

FIGURE 30-75 Axial CT of a child with large hemangioma (*H*) involving the soft tissues of the neck, with involvement of the AE fold and supraglottic paraglottic space (*arrow*).

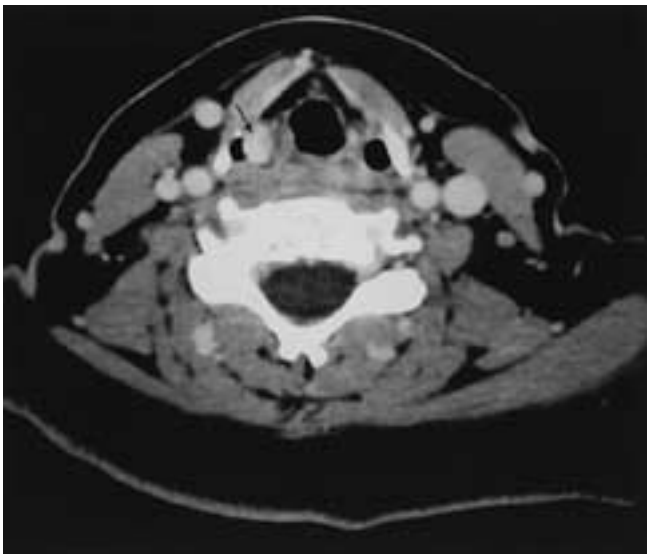

FIGURE 30-74 Axial CT of a hemangioma of the pyriform sinus shows enhancement of the small lesion attached to the medial wall of the pyriform sinus just below the aryepiglottic fold. *Arrow*, Tumor.

FIGURE 30-76 Lateral plain film of a large subglottic hemangioma protruding from the posterior wall, with significant narrowing of the airway (*arrowheads*). *Arrow*, Hemangioma. This patient is older than those who typically develop the infantile type of hemangioma.

Copyright © 2003, Mosby, Inc. All rights reserved.

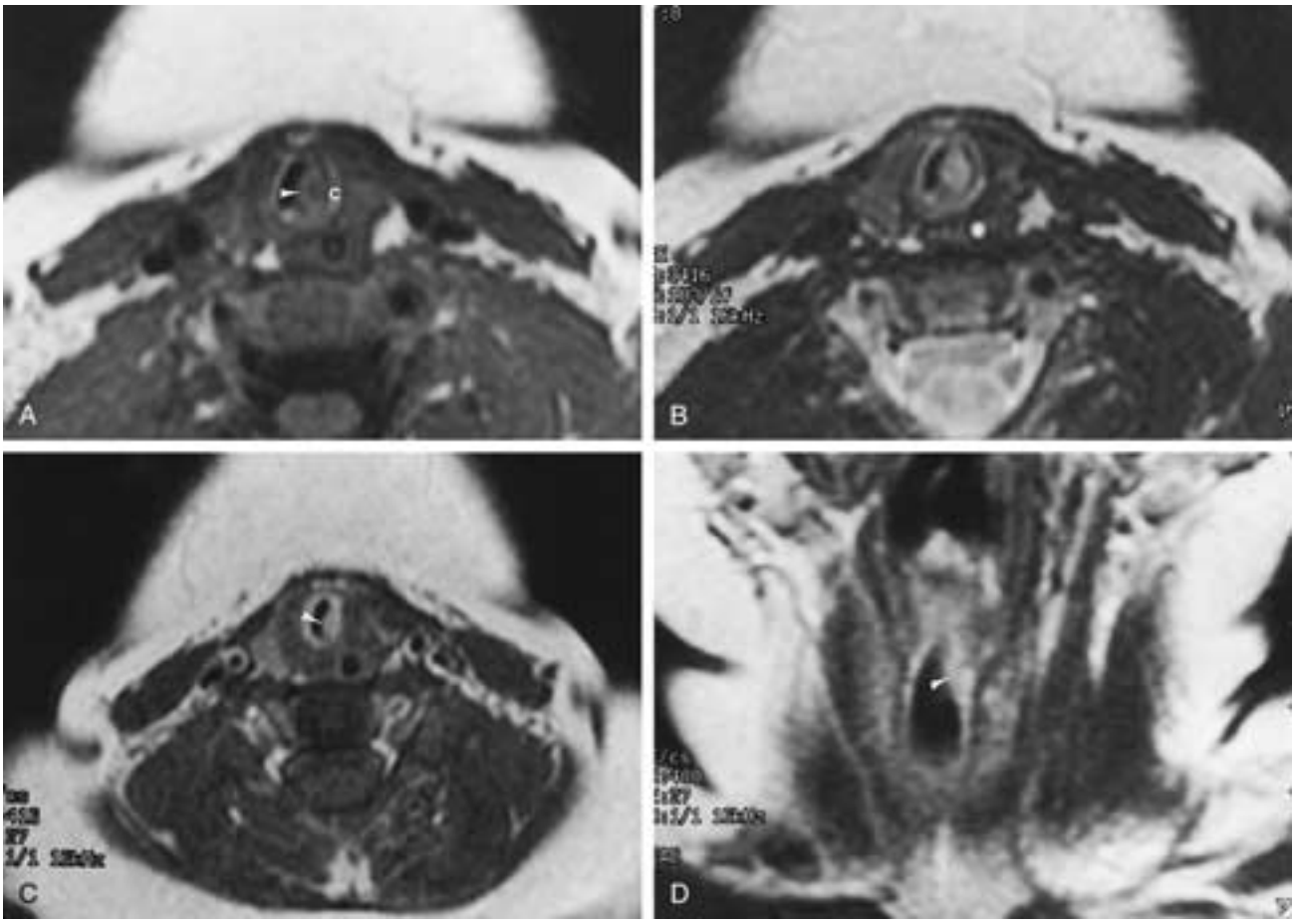

VIEW IMAGE

FIGURE 30-77 Subglottic hemangioma, MR image. **A**, Axial T1-weighted image shows a small bulge (*arrowhead*) at the level of the cricoid cartilage. *C*, Cricoid ring. **B**, T2-weighted image shows high signal in the abnormality characteristic of the hemangioma. **C**, Postcontrast T1-weighted image shows enhancement of the hemangioma (*arrowhead*) and the mucosa. **D**, Coronal image shows the enhancing lesion (*arrowhead*) in the subglottic angle. The lesion is limited to the mucosal area.

lage structure is destroyed, the affected tracheal rings collapse and airway compromise can result.

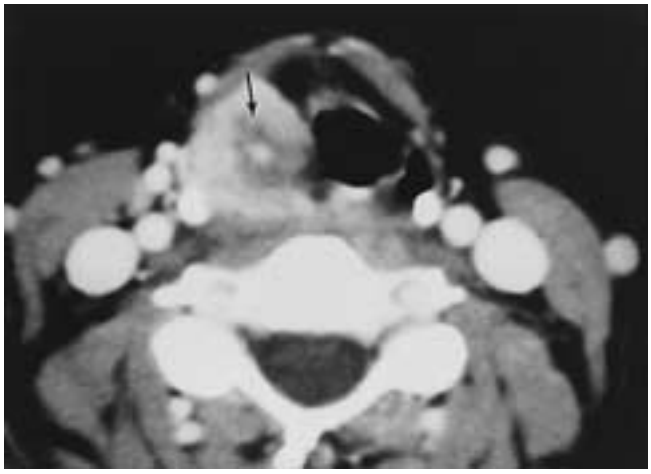

VIEW IMAGE

FIGURE 30-78 Axial CT of paraganglioma of the supraglottic larynx and pyriform sinus shows an enhancing mass in the AE fold and pyriform sinus (*arrow*). (Courtesy of Dr. Peter Som.)

Gastroesophageal Reflux

The presence of gastric acid in the larynx can cause a variety of problems related to the resulting inflammation.[103–105] So-called extraesophageal (esophagopharyngeal) reflux allows gastric secretions to extend above the cricopharyngeus muscle and cause inflammation in the posterior larynx, especially in the interarytenoid region, AE folds, and posterior cord area. As the arytenoid cartilages and true vocal cords become edematous, hoarseness can occur. Often these patients present with recurrent episodes of low-grade hoarseness, the onset of which is first noticed in the mornings. If laryngoscopy is performed shortly after the onset of symptoms, a characteristic redness can be seen localized to the arytenoids and posterior true cords. Gastric acid reflux has also been implicated in the formation of vocal cord nodules or granulomas, pharyngeal edema, and even inflammatory changes in the trachea. Some have suggested that the findings may mimic supraglottitis or other inflam-

Copyright © 2003, Mosby, Inc. All rights reserved.

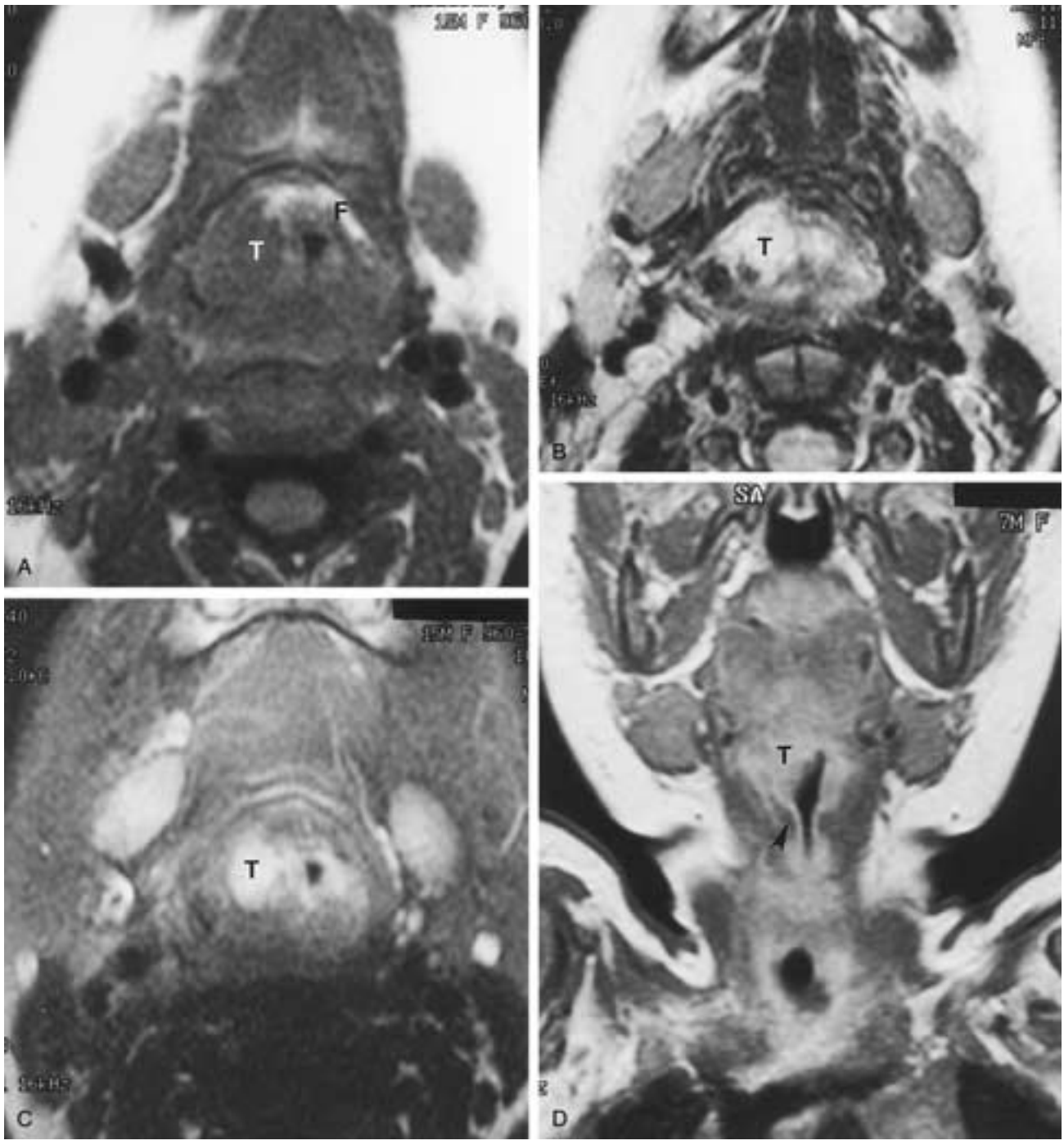

FIGURE 30-79 Neurofibromatosis with invasion of the larynx. Plexiform neurofibroma patient with neurofibromatosis. **A**, T1-weighted image through the supraglottic larynx. The tumor (*T*) extends anteriorly in the paraglottic fat. Note the normal paraglottic fat (*F*) on the opposite side. **B**, T2-weighted image (FSE) shows the high signal of the tumor (*T*). **C**, Postconstrast T1-weighted image with fat suppression. The tumor (*T*) enhances significantly. Compare with the enhancing mucosa. **D**, Coronal T1-weighted image with contrast, no fat suppression. The tumor (*T*) is seen in the paraglottic space. Note the normal TAM (*arrowhead*) at the cord level.

VIEW IMAGE

Copyright © 2003, Mosby, Inc. All rights reserved.

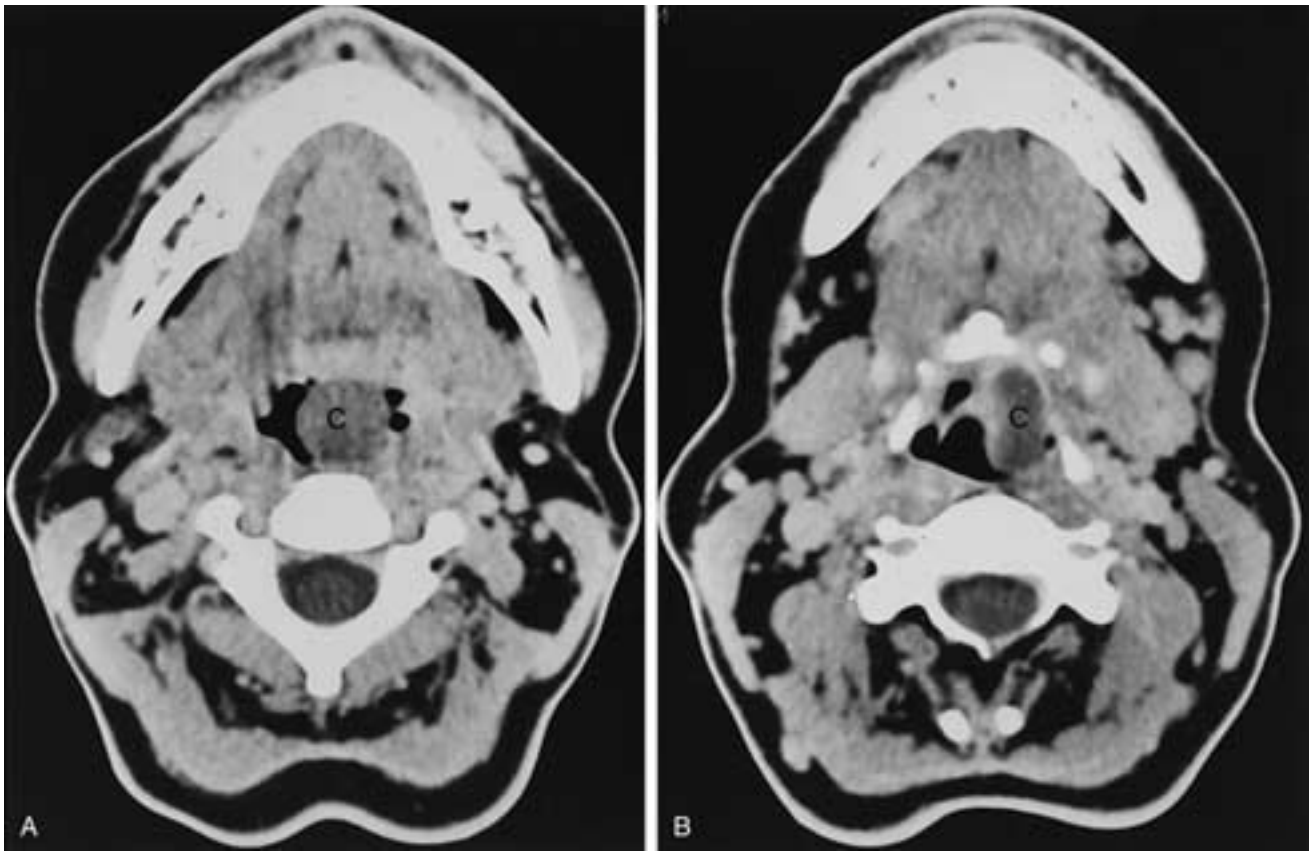

FIGURE 30-80 **A**, Vallecular cyst on CT. Midline cyst (*C*) seen at the level of the base of the tongue. **B**, Slightly lower level shows the origin of the cyst in the left valleculae deforming the epiglottis. *C*, Cyst.

VIEW IMAGE

matory disease in the larynx. The treatment is directed to the reflux, which, once controlled, allows the laryngeal lesions to resolve.

TRAUMA

A variety of direct blows and penetrating trauma to the neck can injure the larynx.[106] Vehicular accidents account for most of the significant trauma to the larynx and upper trachea, with the larynx being crushed between the dashboard or steering wheel and the cervical spine. In children, the larynx is higher in position relative to the mandible and is thus relatively protected. However, in the adult, the lower position of the larynx relative to the mandible makes it more vulnerable to trauma.

In many circumstances, the radiologic examination cannot be performed acutely because of airway compromise. However, as early definitive surgical intervention is associated with better results, the diagnostic evaluation should not be substantially delayed.

If the cartilage is well calcified, fractures can be seen on plain radiographs; however, CT usually gives better visualization.[107] Of particular interest should be the presence of any cartilage fragments that either impinge on the airway or appear to perforate the mucosa. These fractures and perforations predispose the region to infection of the

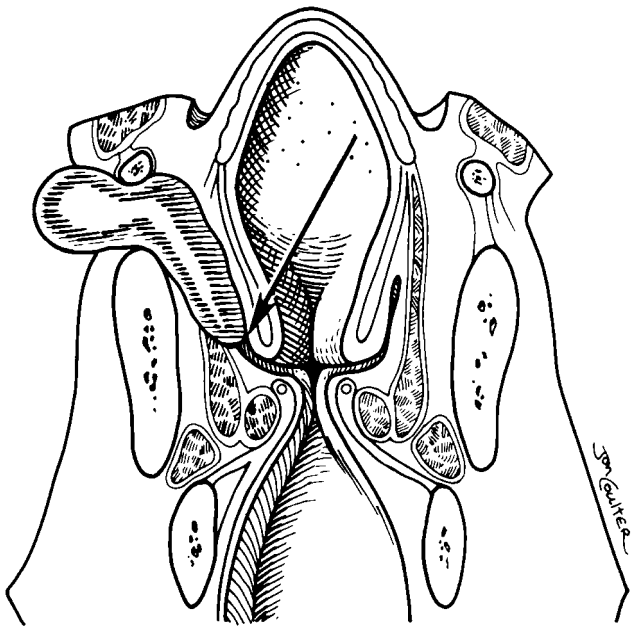

FIGURE 30-81 Diagram showing a laryngocele protruding between the hyoid and the thyroid cartilage. The laryngocele is caused by a relative obstruction (*arrow*) at the level of the ventricle.

VIEW IMAGE

Copyright © 2003, Mosby, Inc. All rights reserved.

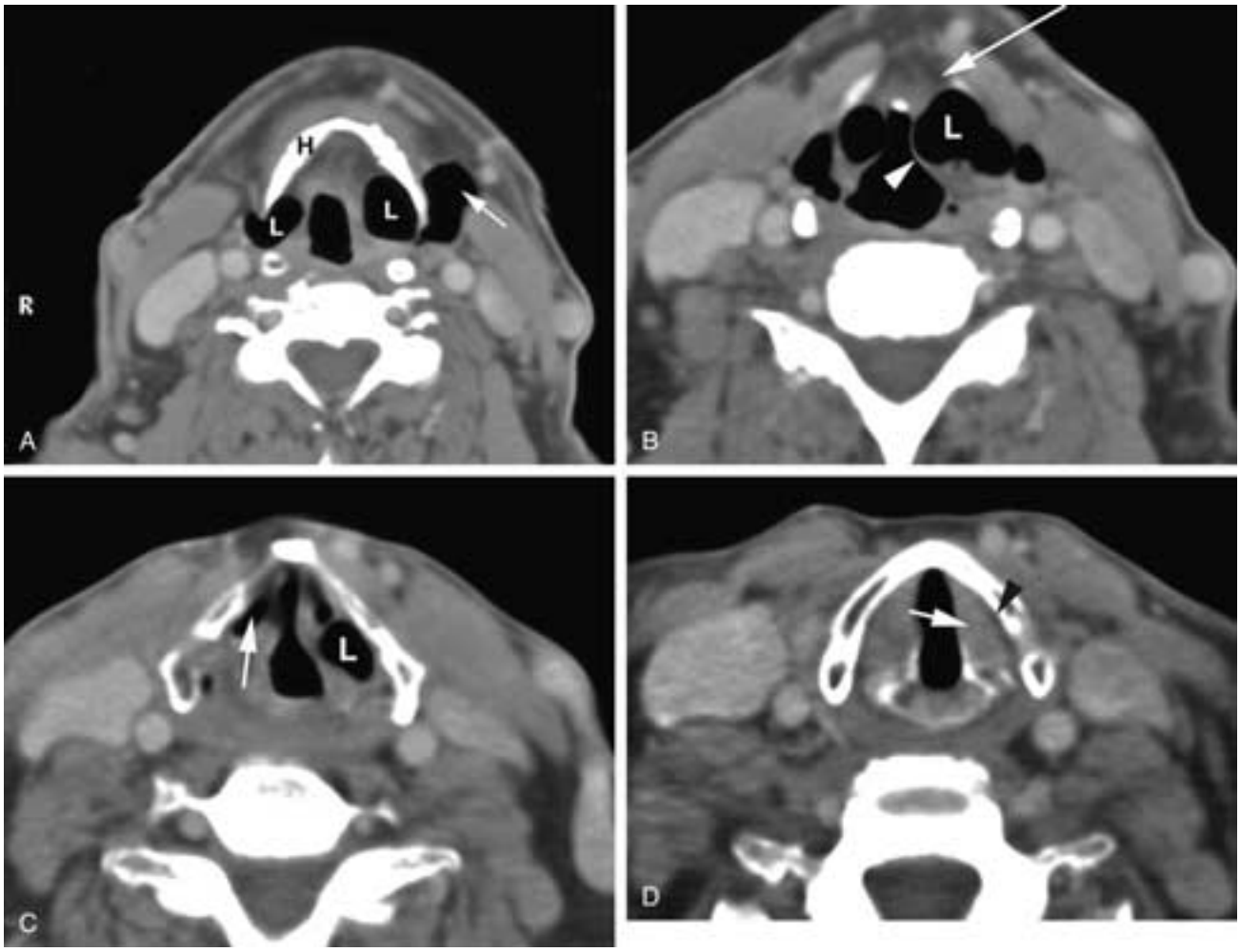

FIGURE 30-82 Bilateral air-filled laryngoceles. Axial CT. **A**, The laryngoceles (*L*) are bilateral. On the left, there is extension between the hyoid bone and the thyroid cartilage into the lateral soft tissues (*arrow*). This is a combined internal/external laryngocele. Hyoid bone (*H*). **B**, Slightly caudad slice shows the bulge of the mucosa (*arrowhead*) at the supraglottic level. Laryngocele (*L*); intact contiguous paraglottic and preepiglottic fat (*arrow*). **C**, Caudad to **B**. The laryngocele (*L*) can be followed anteriorly (*arrow*) as the dilated appendix approaches the ventricle. **D**, The true cord level of the TAM (*arrow*) is identified. Note the crease of fat (*arrowhead*) along the lateral aspect of the muscle representing the inferior extent of the paraglottic fat. The fat is normal.

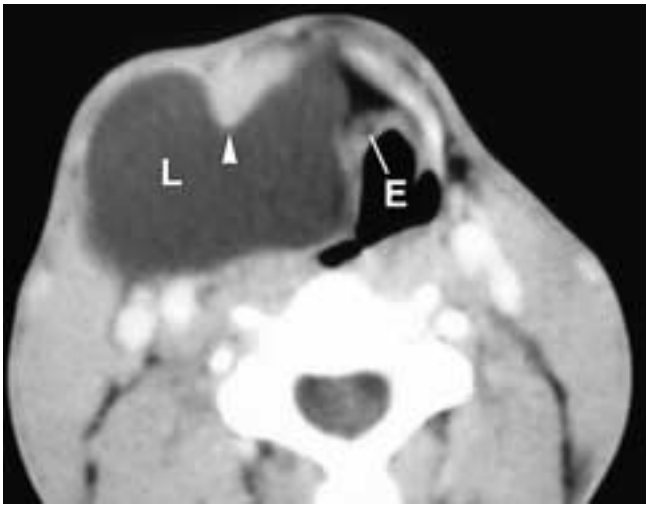

FIGURE 30-83 Large laryngocele. The patient presented with a mass in the right neck. The large fluid-filled saccular cyst (*L*) fills the supraglottic paraglottic space and extends laterally into the neck. The position of the thyrohyoid membrane is indicated by the arrowhead. Epiglottis (*E*).

Copyright © 2003, Mosby, Inc. All rights reserved.

VIEW IMAGE

FIGURE 30-84 Laryngocele. Tomography modified Valsalva maneuver with distention of the laryngocele (*L*) and widening of the communication with the ventricle (*arrowheads*).

cartilage and further airway compromise, so endoscopy is performed to assess for any mucosal tears. If the mucosa is torn, air can often be seen in the adjacent soft tissues and is visible on plain films and CT. A hematoma may develop and appear either as a mass or as an obliteration of the normal fat density in the upper larynx (Fig. 30-101).

Fractures of the larynx can involve the thyroid cartilage, cricoid cartilage, or both cartilages.[108] Thyroid cartilage fractures are either primarily vertical or horizontal (Figs. 30-102 and 30-103). Vertical fractures result from the splaying of the thyroid cartilage as it is pushed against the spine. A horizontal fracture usually crosses both thyroid alae, and there is often coexistent supraglottic soft-tissue injury (Fig. 30-104). The superior fragments of the thyroid cartilage can be displaced posteriorly, and the thyroepiglottic ligament or petiole of the epiglottis may be torn, resulting in a dislocated or avulsed epiglottis (Fig. 30-105).[109] The hyoid bone also may be fractured. Vertical fractures of the thyroid cartilage are best appreciated on CT. However, horizontal fractures are in the plane of the axial CT scan and therefore may be difficult to demonstrate on these images. As multidetector CT allows multiplanar visualization of these fractures, this technique may help in the diagnosis of horizontal fractures.

Occasionally on axial CT, a patient has an asymmetrical curvature to the thyroid cartilage, with one side bowing inward, often creating a submucosal fullness on that side. Although there is no immediate history of trauma, careful questioning may reveal a history of previous insult to the larynx. Although most authors believe that such an appearance represents the late sequelae of old trauma, a developmental variation is also a possibility.

Cricoid fractures cause a collapse of the normal cricoid ring (Figs. 30-106 and 30-107). Almost always there is more than one fracture, usually with both sides of the cricoid ring being broken to create anterior and posterior fragments. The anterior fragment is pushed posteriorly and impinges on the airway, and the free end of a fragment may perforate the mucosa. The fractures may be difficult to appreciate in younger patients because the arch of the cricoid cartilage is not as well calcified; however, usually the cartilage is dense enough that it can be seen on CT (Figs. 30-107 and 30-108).

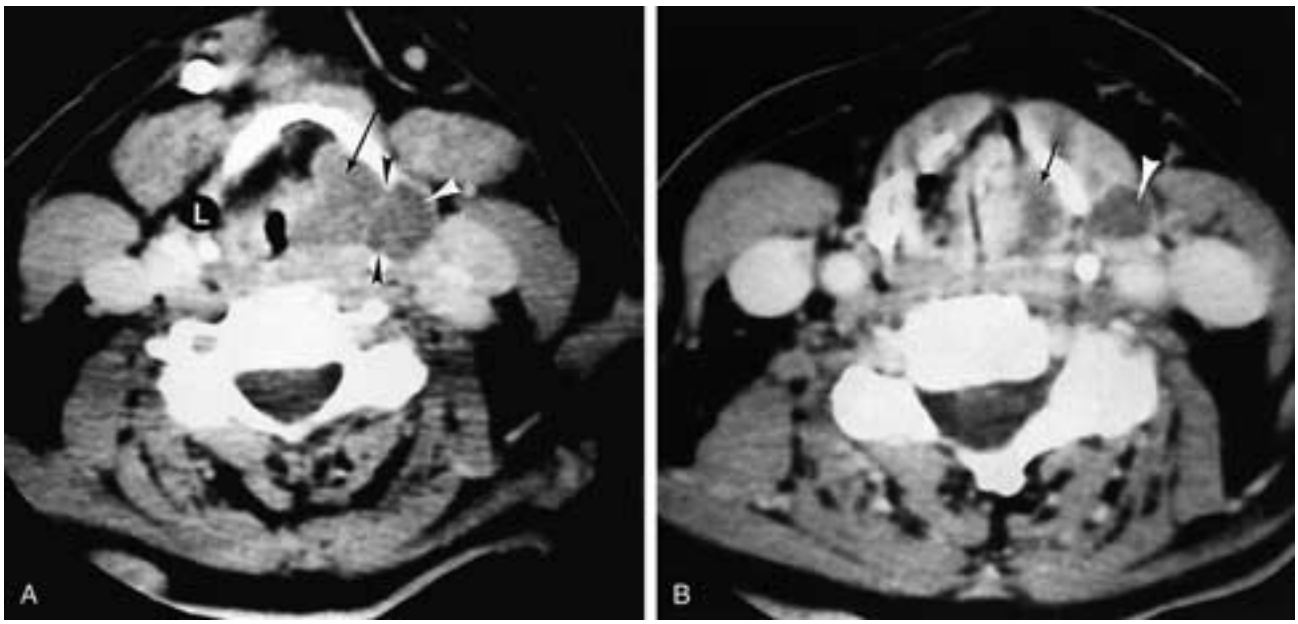

VIEW IMAGE

FIGURE 30-85 Axial CT of a laryngocele (saccular cyst). **A**, There is both an internal (*arrow*) and an external (*white arrowhead*) component. The position of the thyrohyoid membrane is signified by black arrowheads. A small air-filled external laryngocele (*L*) is seen on the opposite side. **B**, Lower scan through the supraglottic larynx shows the abnormality in the paraglottic space (*arrow*) and the external component (*arrowhead*).

Copyright © 2003, Mosby, Inc. All rights reserved.

FIGURE 30-86 Bilateral laryngocele with large supraglottic tumor on one side. **A**, Scout view shows the dilated air-filled sac (*arrow*). **B**, Axial scan through the upper larynx shows the air-filled laryngocele (*L*) on the left protruding through the thyrohyoid membrane. The lateral aspect of the laryngocele (*arrowhead*) caused a significant bulge in the neck. Tumor fills the opposite supraglottis (*T*). The smaller laryngocele (*arrow*) is seen on the side of the tumor with an air-fluid level. **C**, Lower scan shows the tumor (*T*), the intralaryngeal segment (paraglottic space) of the laryngocele (*arrow*) and the external component (*arrowhead*).

VIEW IMAGE

Key findings are the shape of the airway and the presence of subglottic swelling. At the level of the cricoid, the normal subglottic airway is slightly oval. A subtle fracture with minimal displacement gives the airway a rounder appearance, and edema causes increased soft tissue between the cartilage and the air column. If these important fractures are to be detected, familiarity with the normal appearance of the subglottic area is crucial. Fractures of the cricoid usually require surgical intervention, with repositioning of the fragments and stabilization with either sutures or a plate.

Laryngotracheal separation is a complete tear of the trachea, and because of loss of the airway, it is usually fatal (Fig. 30-109). Plain radiographs may show the malalignment of an incomplete separation. Few of these patients survive to be imaged. Those who do usually already have had a tracheostomy.

Arytenoid dislocation results in an abnormal position of the arytenoid relative to the cricoid cartilage (Fig. 30-110). Often there is an associated fracture of one of the larger laryngeal cartilages, but some dislocations have been reported with fairly minimal trauma to the side of the neck.

Copyright © 2003, Mosby, Inc. All rights reserved.

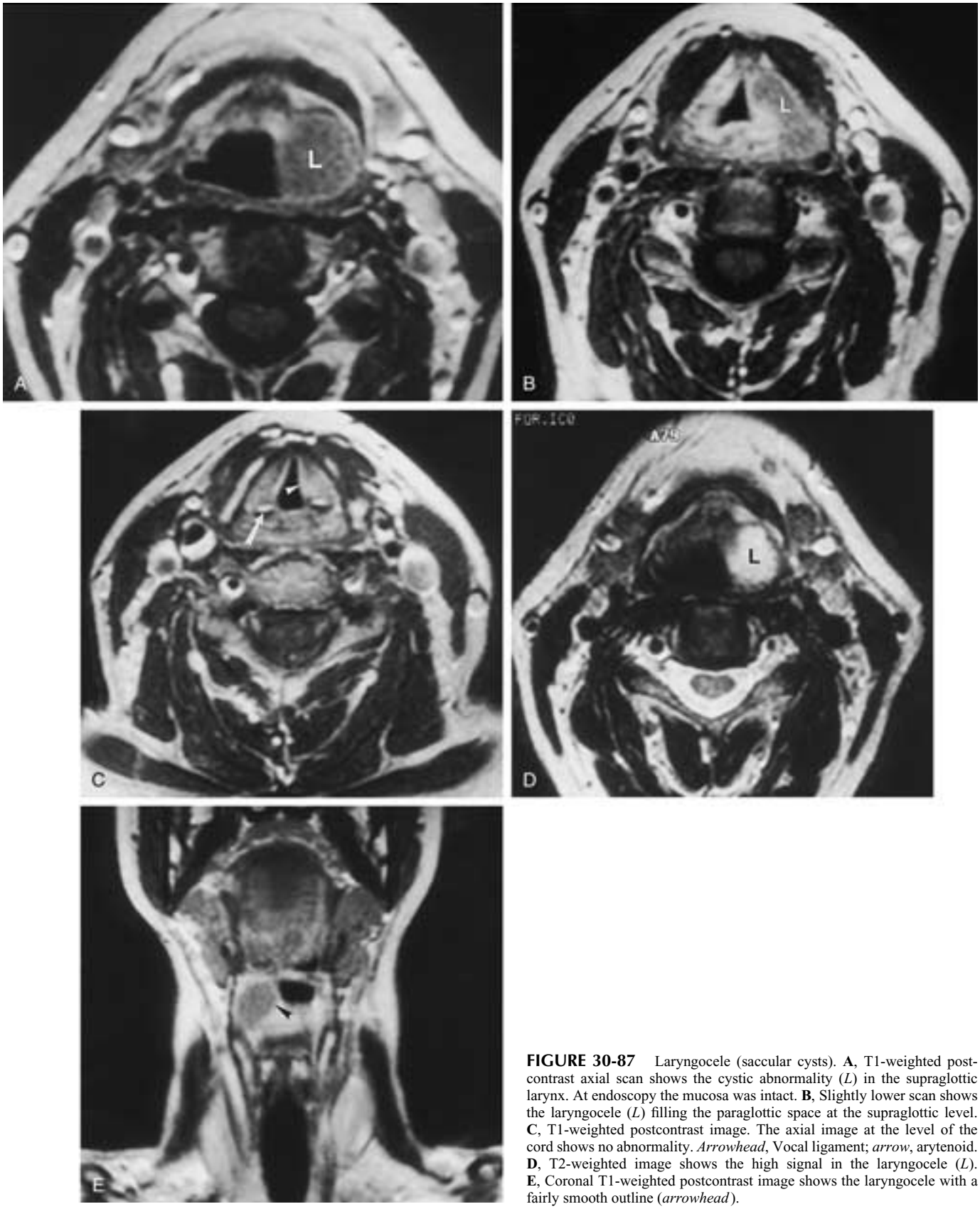

FIGURE 30-87 Laryngocele (saccular cysts). **A**, T1-weighted postcontrast axial scan shows the cystic abnormality (*L*) in the supraglottic larynx. At endoscopy the mucosa was intact. **B**, Slightly lower scan shows the laryngocele (*L*) filling the paraglottic space at the supraglottic level. **C**, T1-weighted postcontrast image. The axial image at the level of the cord shows no abnormality. *Arrowhead*, Vocal ligament; *arrow*, arytenoid. **D**, T2-weighted image shows the high signal in the laryngocele (*L*). **E**, Coronal T1-weighted postcontrast image shows the laryngocele with a fairly smooth outline (*arrowhead*).

VIEW IMAGE

Copyright © 2003, Mosby, Inc. All rights reserved.

Minimal dislocations probably can be missed at imaging, but the radiologist should comment on the position of the arytenoid cartilage relative to the articular tubercle on the upper margin of the cricoid.

A dislocation of the cricothyroid joint is seen as a malalignment of the thyroid and cricoid cartilages (Fig. 30-111). A true dislocation of this joint is considered to be very rare. Usually the inferior horn of the thyroid cartilage is fractured, allowing the apparent separation of the cartilages. The thyroid cartilage may be rotated to one side, while the cricoid retains a normal orientation. These ''dislocations'' usually result from more severe trauma, and usually other cartilage fractures are present. Before diagnosing a dislocation of the cricothyroid joint, it is important to follow the inferior horn of the thyroid cartilage to its articulation with the cricoid. Even slight obliquity of the scan can cause an apparent widening of the space between these two cartilages, and this effect should not be mistaken for a fracture.

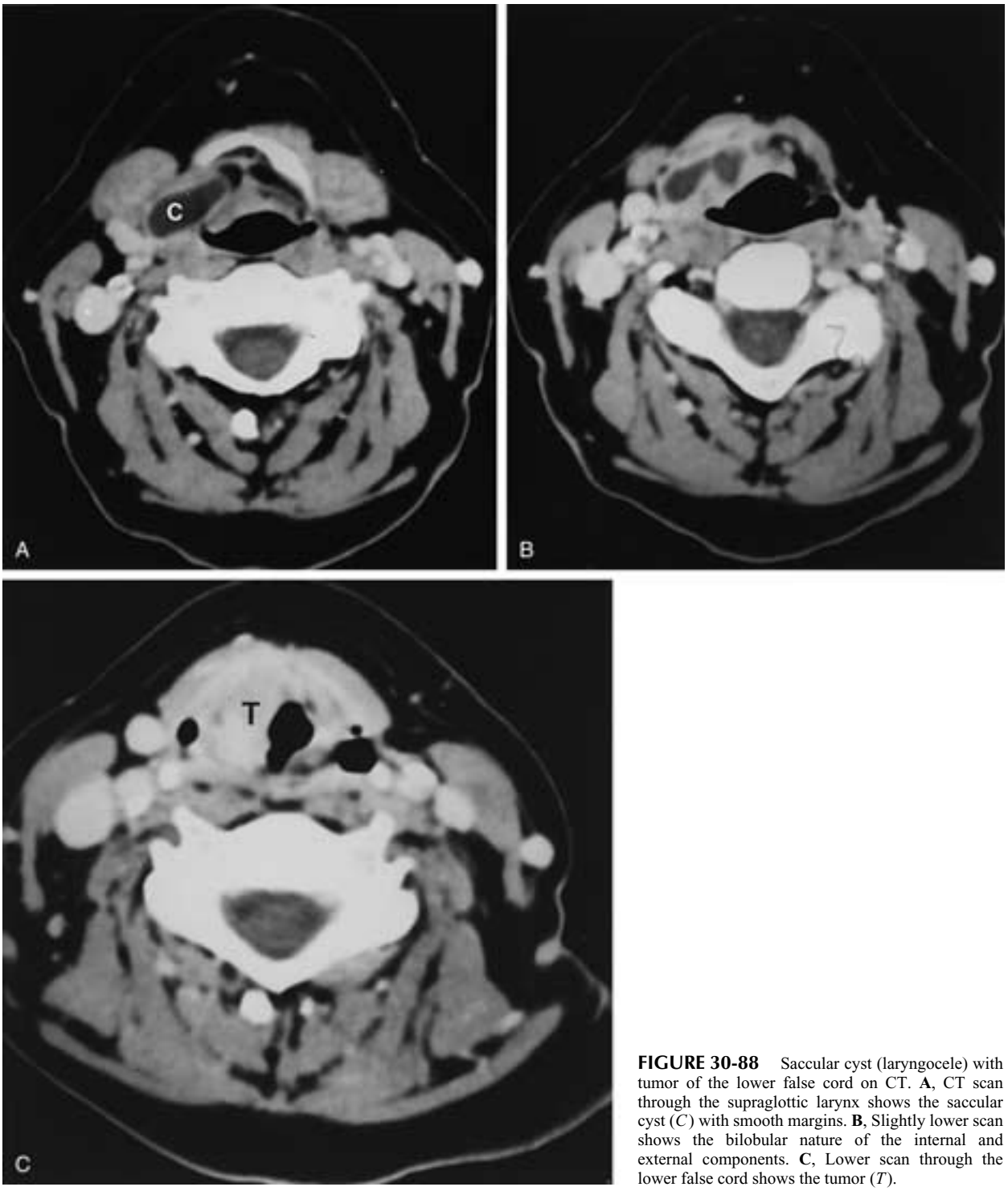

FIGURE 30-88 Saccular cyst (laryngocele) with tumor of the lower false cord on CT. **A**, CT scan through the supraglottic larynx shows the saccular cyst (*C*) with smooth margins. **B**, Slightly lower scan shows the bilobular nature of the internal and external components. **C**, Lower scan through the lower false cord shows the tumor (*T*).

VIEW IMAGE

Copyright © 2003, Mosby, Inc. All rights reserved.

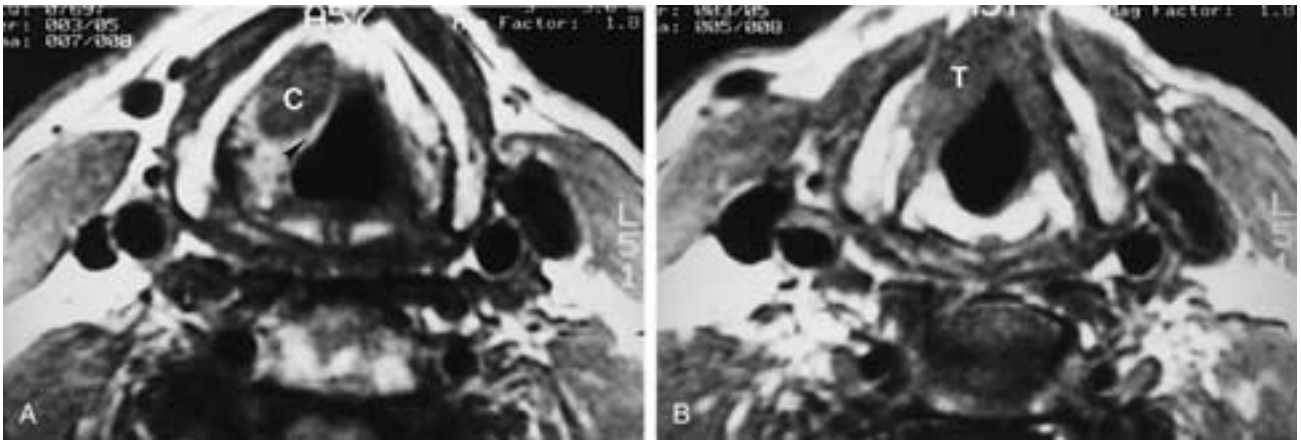

VIEW IMAGE

FIGURE 30-89 **A**, Saccular cyst (laryngocele). Well-defined cyst (*C*) fills the supraglottic larynx. Note the definite separation (*arrowhead*) from the mucosa. **B**, Scan inferior to **A** shows a tumor at the level of the ventricle and the true cord. *T*, Tumor.

Foreign bodies may be the result of penetrating trauma but more commonly are the result of either ingestion or aspiration. The pyriform sinus is a common location for a foreign body to lodge in, and from this point the foreign body can either enter the laryngeal airway and continue into the trachea or bronchi or penetrate anteriorly into the paraglottic space of the larynx.

Burn injury of the larynx can result from the inhalation or ingestion of hot material or gases.[110] The supraglottic larynx is most likely to be involved, and generalized edema can occur. Several cases of ingestion of hot foreign substances have been related to ''melting'' crack cocaine. Small bits of steel wool heated to melt the cocaine can cause a more localized burn in the pyriform sinus or AE fold (Fig. 30-112). The imaging findings can mimic tumor, creating diagnostic problems if the pertinent history is not available.

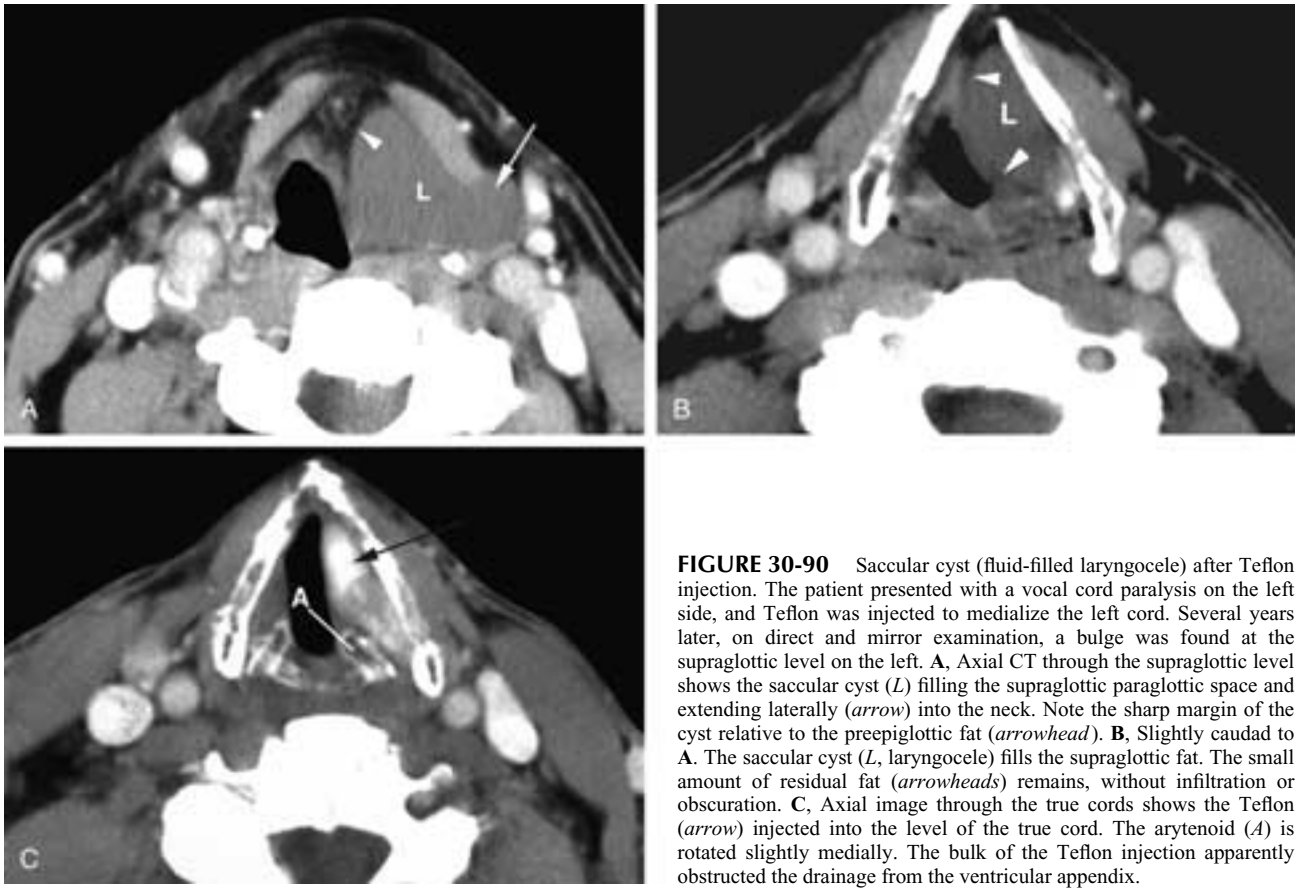

VIEW IMAGE

FIGURE 30-90 Saccular cyst (fluid-filled laryngocele) after Teflon injection. The patient presented with a vocal cord paralysis on the left side, and Teflon was injected to medialize the left cord. Several years later, on direct and mirror examination, a bulge was found at the supraglottic level on the left. **A**, Axial CT through the supraglottic level shows the saccular cyst (*L*) filling the supraglottic paraglottic space and extending laterally (*arrow*) into the neck. Note the sharp margin of the cyst relative to the preepiglottic fat (*arrowhead*). **B**, Slightly caudad to **A**. The saccular cyst (*L*, laryngocele) fills the supraglottic fat. The small amount of residual fat (*arrowheads*) remains, without infiltration or obscuration. **C**, Axial image through the true cords shows the Teflon (*arrow*) injected into the level of the true cord. The arytenoid (*A*) is rotated slightly medially. The bulk of the Teflon injection apparently obstructed the drainage from the ventricular appendix.

Copyright © 2003, Mosby, Inc. All rights reserved.

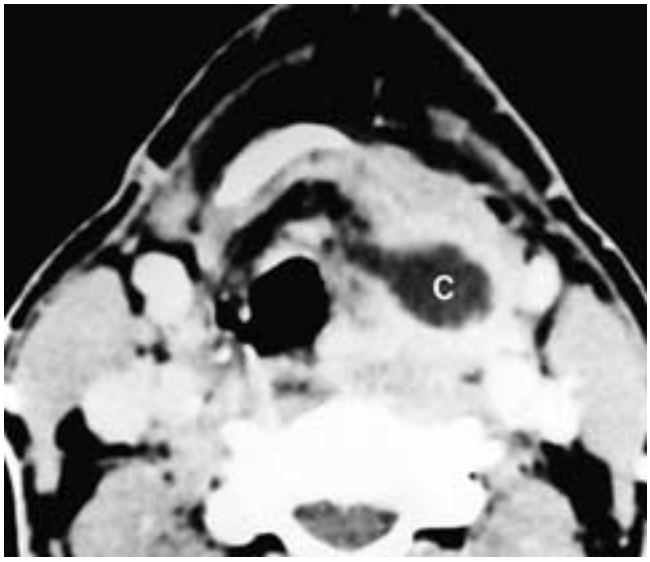

FIGURE 30-91 Laryngopyocele with contrast-enhanced CT shows the saccular cyst (*C*). There is irregular enhancement of the inflamed wall.

VIEW IMAGE

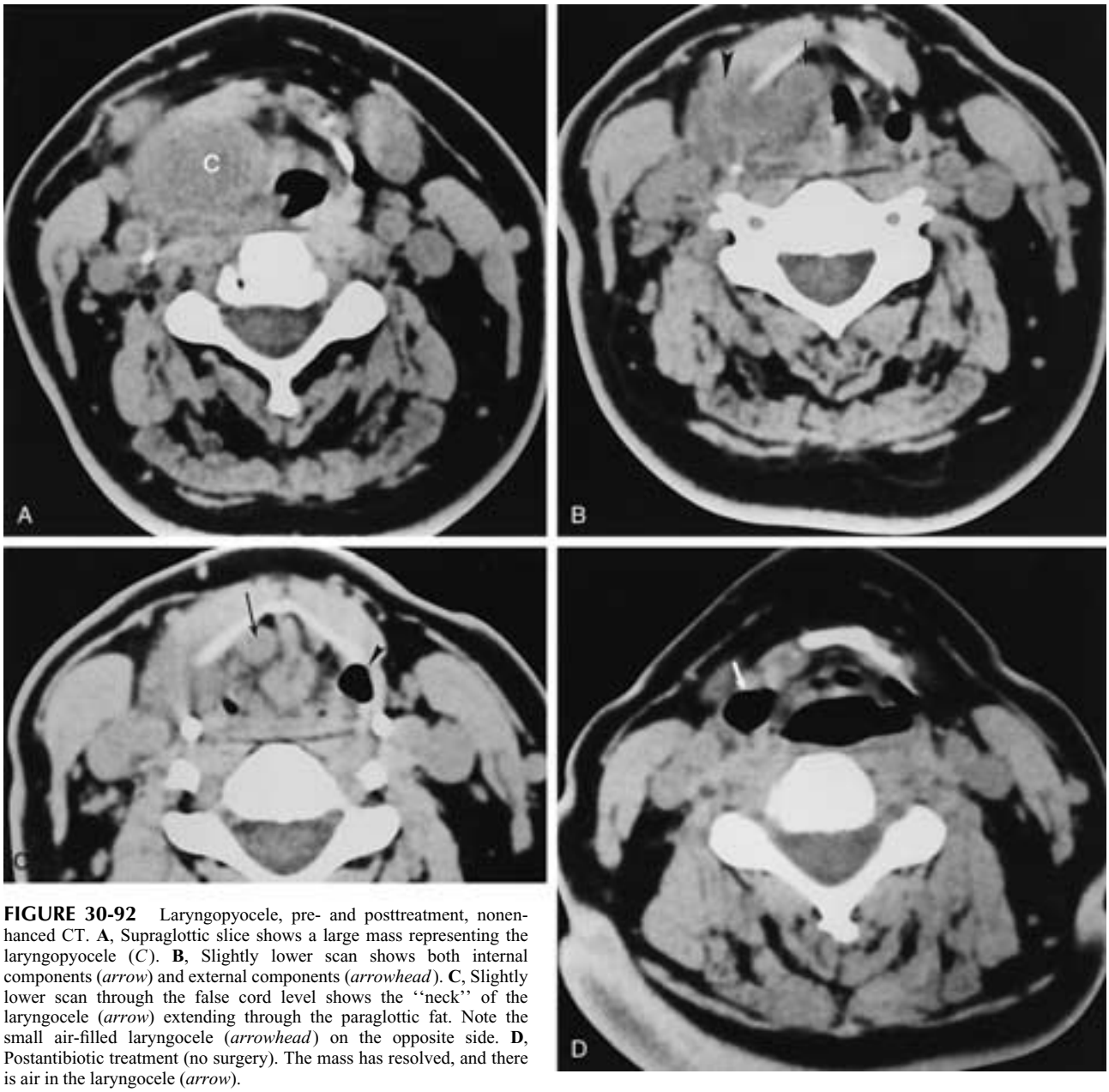

VIEW IMAGE

FIGURE 30-92 Laryngopyocele, pre- and posttreatment, nonenhanced CT. **A**, Supraglottic slice shows a large mass representing the laryngopyocele (*C*). **B**, Slightly lower scan shows both internal components (*arrow*) and external components (*arrowhead*). **C**, Slightly lower scan through the false cord level shows the ''neck'' of the laryngocele (*arrow*) extending through the paraglottic fat. Note the small air-filled laryngocele (*arrowhead*) on the opposite side. **D**, Postantibiotic treatment (no surgery). The mass has resolved, and there is air in the laryngocele (*arrow*).

Copyright © 2003, Mosby, Inc. All rights reserved.

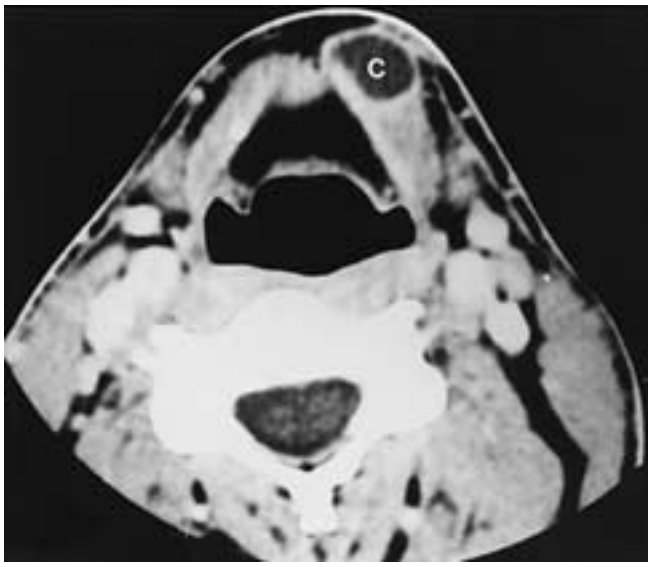

FIGURE 30-93 Thyroglossal duct cyst (*C*) on axial CT. Note that the fat within the larynx is normal. The paraglottic level would be normal as well.

VIEW IMAGE

CONGENITAL LESIONS

Radiology can be helpful in assessing congenital laryngeal anomalies. Plain radiographs can assess the size of the airway or the length of a stenosis. CT in the axial plane provides a good cross-sectional view of the airway, allows an estimate of the length of a stenosis, and characterizes the tissues deep to the mucosal surface. Spiral CT can acquire an entire set of images quickly and allows multiplanar reformations to better characterize the length of the abnormality.

FIGURE 30-95 Lateral plain film of the epiglottitis showing thickening of the epiglottis (*arrow*) and prominence of the arytenoid (*arrowhead*).

VIEW IMAGE

A very brief review of the embryology of the larynx is appropriate in this section. An outpouching, or bud, initially extends from the primitive pharynx to form the respiratory system. The cells on either side of the entrance to this respiratory diverticulum pinch together to form the tracheo-

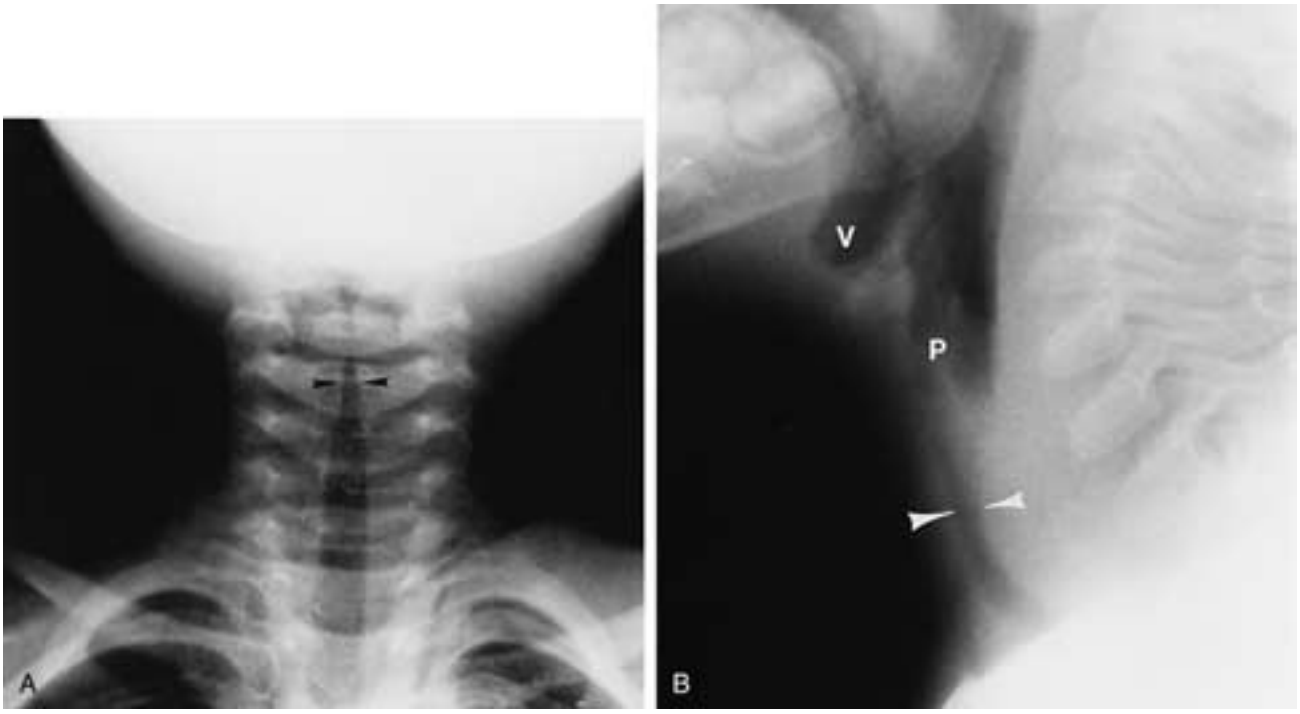

FIGURE 30-94 Croup. **A**, Frontal film shows narrowing of the airway between the arrowheads just beneath the cord. This is the so-called steeple-shaped or wine bottle sign. **B**, Lateral film shows dilatation of the pyriform sinuses (*P*) and the valleculae (*V*), with narrowing between the arrowheads of the subglottic larynx.

VIEW IMAGE

Copyright © 2003, Mosby, Inc. All rights reserved.

VIEW IMAGE

FIGURE 30-96 Lateral plain film of an emphysematous epiglottitis. There is enlargement of the epiglottis, but air is seen within the soft tissues (*arrow*). (Courtesy of Dr. William Nemzek.)

esophageal septum, isolating the trachea from the developing foregut. At one point, the laryngeal lumen is temporarily occluded but reopens or recanalizes. The cartilages form from the mesenchyme on either side of the primitive respiratory passage, and the components from either side fuse to form the cricoid and thyroid cartilages. Congenital abnormalities are related to problems of the developmental process or simply are the result of delays in normal maturation (see also Chapter 29).[111–113]

Laryngomalacia

Laryngomalacia represents delayed development of the laryngeal support system.[114] The structures are present but are not firm enough to keep the larynx continually open. The supraglottic larynx is primarily affected, and the epiglottis alone may be floppy or the entire supraglottic larynx may collapse on inspiration. The infant outgrows the abnormality as the cartilages mature; however, a tracheostomy may be needed to maintain an airway until this laryngeal maturation is completed.

Subglottic Stenosis

Subglottic stenosis is a narrowing of the subglottic larynx from the true cord down to the lower cricoid.[114–116] The patient normally outgrows this soft-tissue stenosis, but a tracheostomy may be needed before this maturation is completed. Plain radiographs can demonstrate the narrowing.

Less commonly, a rare cricoid abnormality can occur in which the cricoid shape is a narrow ellipse rather than round (Fig. 30-113). This elongated shape narrows the airway.[115] As the cricoid is not calcified at this age, imaging is unlikely to be helpful. However, because of the hard consistency of the subglottic wall, the diagnosis is suggested by endoscopy.

Webs and Atresia

Small webs can be seen at any level of the larynx, but they are usually at the level of the true cords. Subglottic webs may be associated with cricoid abnormalities. Webs are seldom evaluated radiographically, but radiographs may be done to exclude other abnormalities.

Atresia of the larynx is a failure of complete recanalization, and no airway exists through the larynx (Fig. 30-114). The trachea, however, is present, and a tracheostomy at birth is life-saving.

There have been reports of laryngeal or tracheal atresia diagnosed prenatally using ultrasound.[117, 118] Fluids are secreted into the lungs and cannot pass out of the bronchial tree unless there is a coexisting tracheoesophageal communication. Without such a communication, the bronchial tree

FIGURE 30-97 Laryngeal tuberculosis. Lateral view of the laryngogram shows a nodular, thickened epiglottis (*upper arrow*). The arytenoid mucosa is edematous (*lower arrow*). (Courtesy of Dr. Peter Som.)

VIEW IMAGE

Copyright © 2003, Mosby, Inc. All rights reserved.

VIEW IMAGE

FIGURE 30-98 Lateral laryngogram shows rhinoscleroma (caused by *Klebsiella rhinoscleromatis*). There is polypoid thickening of the epiglottis (*arrow*). (Courtesy of Dr. Peter Som.)

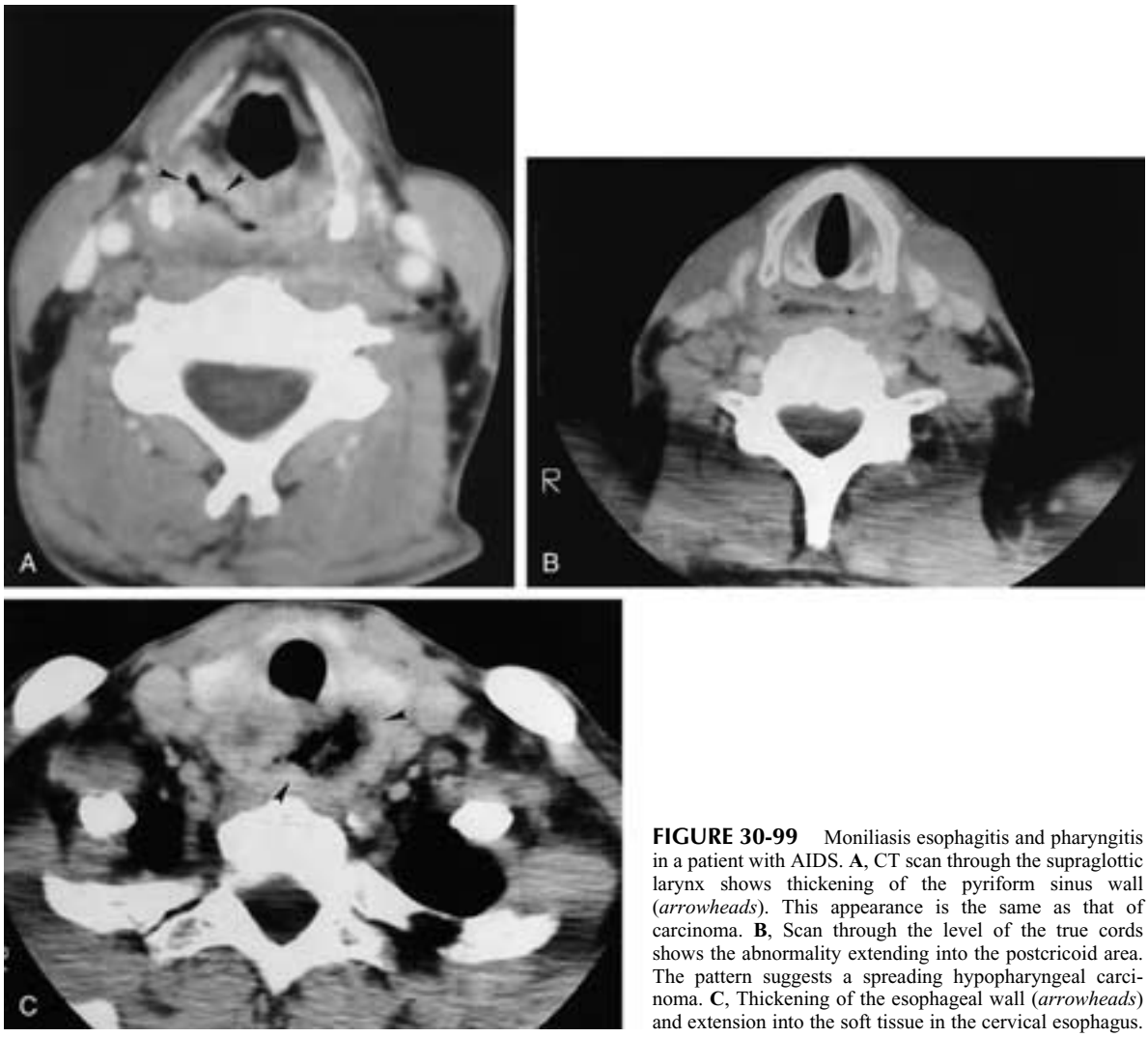

FIGURE 30-99 Moniliasis esophagitis and pharyngitis in a patient with AIDS. **A**, CT scan through the supraglottic larynx shows thickening of the pyriform sinus wall (*arrowheads*). This appearance is the same as that of carcinoma. **B**, Scan through the level of the true cords shows the abnormality extending into the postcricoid area. The pattern suggests a spreading hypopharyngeal carcinoma. **C**, Thickening of the esophageal wall (*arrowheads*) and extension into the soft tissue in the cervical esophagus.

VIEW IMAGE

Copyright © 2003, Mosby, Inc. All rights reserved.

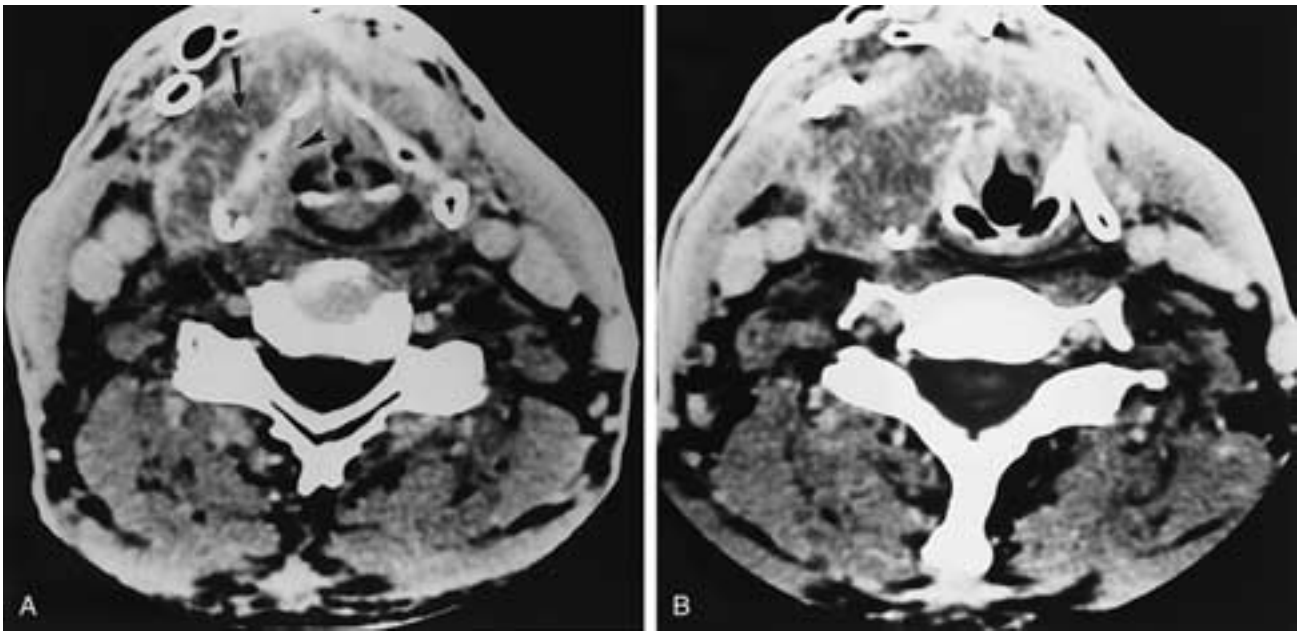

VIEW IMAGE

FIGURE 30-100 Axial CT scans. **A**, Infection of the soft tissues of the neck showing obscuration of the fat planes (*arrow*) and extension into the paraglottic fat of the larynx (*arrowhead*). The drains in the neck are from decompression of an abscess. **B**, Level of the cricoid showing considerable soft-tissue thickening impinging on the airway.

enlarges and the lungs become distended with fluid. The enlarged lungs are echogenic because of the small fluid-filled spaces present. A tracheostomy done at birth is crucial if there is to be any hope of survival; however, in most instances the anomaly is fatal.

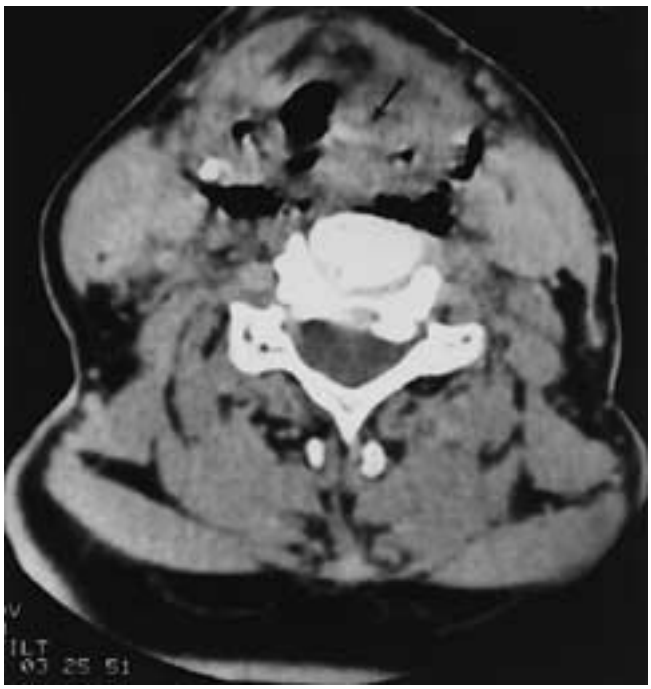

VIEW IMAGE

FIGURE 30-101 Vehicular injury. Axial CT of a hematoma of the larynx and laceration of the pharynx. There is a hematoma (*arrow*) of the AE fold. The gas in the soft tissues is from laceration of the pharyngeal wall.

Clefts

Laryngotracheal clefts are exceedingly rare and are presumed to be the result of failure of complete fusion of the tracheoesophageal septum as it grows to separate the trachea from the esophagus.[36, 114, 119] The cricoid cartilage, which results from a fusion of cells from the mesenchyme on either side of the airway, may also be affected. Although an isolated cleft of the larynx does occasionally occur, frequently a laryngeal cleft is associated with a tracheal cleft. The child aspirates and may have multiple pneumonias.[120]

Subglottic Hemangiomas

Subglottic hemangiomas were mentioned in the preceding section titled Benign Tumors, but they are included here because they are as much vascular malformations as they are tumors. The lesion usually can be seen as a subglottic narrowing on a lateral neck radiograph. Therapy is conservative, but tracheostomy may be necessary.

Other Anomalies

Other rare anomalies such as a bifid epiglottis or duplication anomalies have been reported.

STENOSIS

Stenosis of the larynx or upper trachea can be either a congenital anomaly, a sequela of trauma, or the result of therapy. The most common stenosis results from prolonged

Copyright © 2003, Mosby, Inc. All rights reserved.

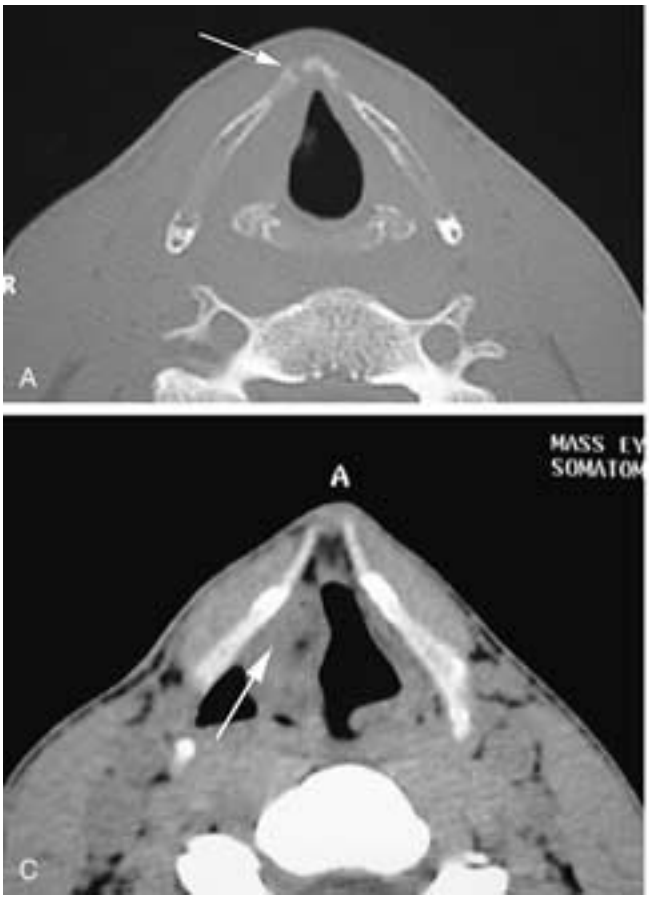

FIGURE 30-102 Vertical fracture with minimally displaced thyroid cartilage. **A**, Axial image through the level of the true cord shows the small lucent defect representing the fracture (*arrow*). **B**, Slightly caudad image shows the fracture (*arrow*) through the lower thyroid cartilage. **C**, In spite of the minimal displacement, there is a hematoma (*arrow*) in the paraglottic fat.

VIEW IMAGE

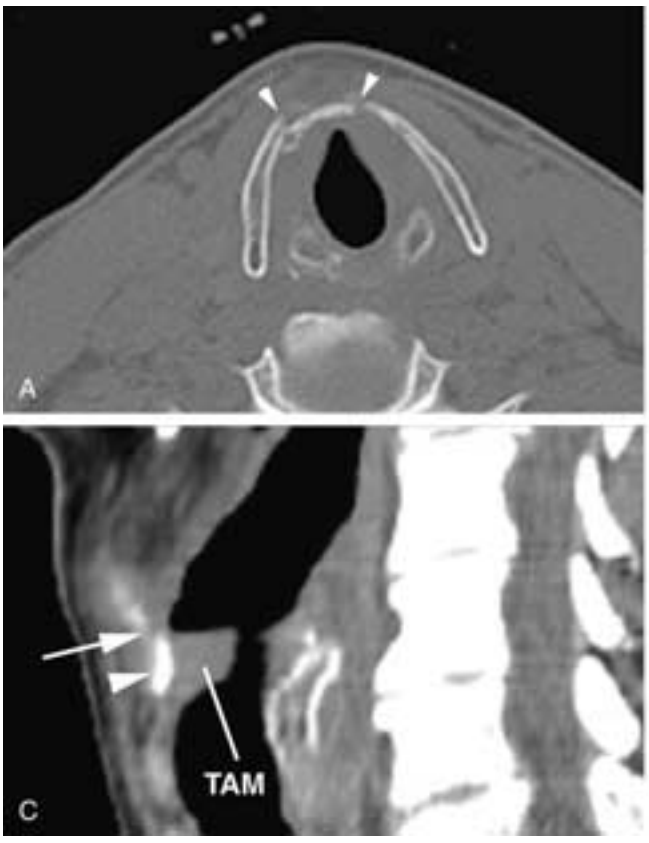

FIGURE 30-103 Vertical fractures through the lower thyroid cartilage. A fragment containing the attachment of the right cord is displaced posteriorly, decreasing tension on the true cord. **A**, Axial bone algorithm shows vertical fractures (*arrowheads*). The fragment (between the *arrowheads*) is posteriorly displaced. The patient cannot maintain tension on the cord and has an abnormal voice. **B**, Soft-tissue algorithm shows the fracture (*arrowhead*) and the TAM (*arrow*). **C**, Sagittal reformat shows the posteriorly displaced fragment (*arrowhead*). There is a horizontal fracture (*arrow*) through the thyroid cartilage as well. Thyroarytenoid muscle (*TAM*).

VIEW IMAGE

Copyright © 2003, Mosby, Inc. All rights reserved.

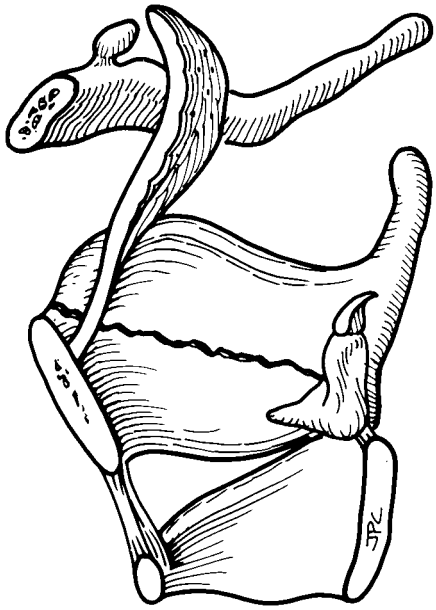

FIGURE 30-104 Diagram of a horizontal fracture crossing the thyroid cartilage. These fractures often can involve the petiole and lower epiglottis, causing dislocation of the upper epiglottis.

cuffed tube intubation (Figs. 30-115 and 30-116). The position of the stenosis secondary to such prolonged intubation or a tracheostomy is characteristic, starting first along unforgiving anterior and lateral walls. Eventually, circumferential stenosis occurs, with involvement of the posterior membranous wall. Stenosis secondary to trauma is more variable, while ingestion of corrosive materials usually causes strictures of the posterior supraglottic larynx. Plain films or conventional tomograms are still good methods for assessing the length of the stenosis or the extent of a ''granuloma'' (Fig. 30-117). Two projections are used, usually frontal and lateral. Alternatively, spiral CT can be used.

FIGURE 30-105 Avulsion of the epiglottis, sagittal MR image. In this midline scan the area of low signal, representing the epiglottis (*arrowheads*), is not straight, but rather bends abruptly in this patient with a fracture avulsion of the epiglottic cartilage. The point of angulation (*arrow*) is thought to represent a site of fracture. *T*, Tracheostomy. (From Duda JJ Jr, Lewin JS, Eliachar I. MR evaluation of epiglottic avulsion. AJNR 1996;17(3):563–566.)

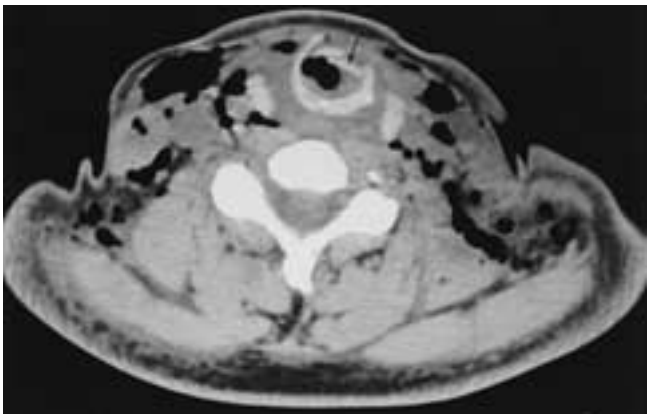

FIGURE 30-106 Axial CT shows fracture of the cricoid, with posterior positioning of the fragments (*arrow*) into the airway.

CT in the axial plane visualizes a cross section of the airway, and this allows characterization of the stenosis. Soft-tissue scars and granulomas can significantly compromise the airway, without any change in the cartilage, or the cartilage can collapse and be displaced into the airway, creating a ''hard'' stenosis (Fig. 30-118). This has obvious implications in planning therapy because if the cartilage is not involved, simple lysing of the soft tissues may be adequate therapy. However, if the cartilage itself is impinging on the airway, a more extensive reconstruction will be necessary. A limited segment of the trachea may be resected and the lower trachea may be surgically released and pulled up, to be anastomosed with the remaining normal trachea.

Although these problems primarily relate to the trachea rather than the larynx, a traumatically displaced fragment of the anterior cricoid can cause significant narrowing of the subglottic area, and scarring can further narrow the airway. Anterior and posterior commissure webs or scars are usually visible endoscopically. However if there is stenosis or scarring at the level of the cords, the lack of full abduction may limit distal visualization, and imaging may be performed to assess possible extension into the subglottis. Such scarring will be seen on imaging as soft-tissue fullness along the inner cortex of the cricoid, where normally no significant soft tissue is present separating airway and the cartilage.

Conventional CT has been limited to the axial plane. However, spiral CT, particularly with multidetector technology, provides excellent-quality reformatted images. Thus, the vertical exent of a stenosis can be defined at the same time that the character of the wall is examined. MR imaging can also provide good multiplanar images, but it does not show the calcified cartilages as well as CT. However, MR imaging has proven useful in the examination of lower tracheal narrowing and in the evaluation of various vascular rings.

When describing a tracheal stenosis, the radiologist should note how far the upper margin of the stenosis is from the bottom of the cricoid cartilage. Note should be made of the distance of the bottom of the stenosis from the carina. These landmarks are readily used anatomic reference points for the endoscopist. Secondly, the length of the stenosis

Copyright © 2003, Mosby, Inc. All rights reserved.

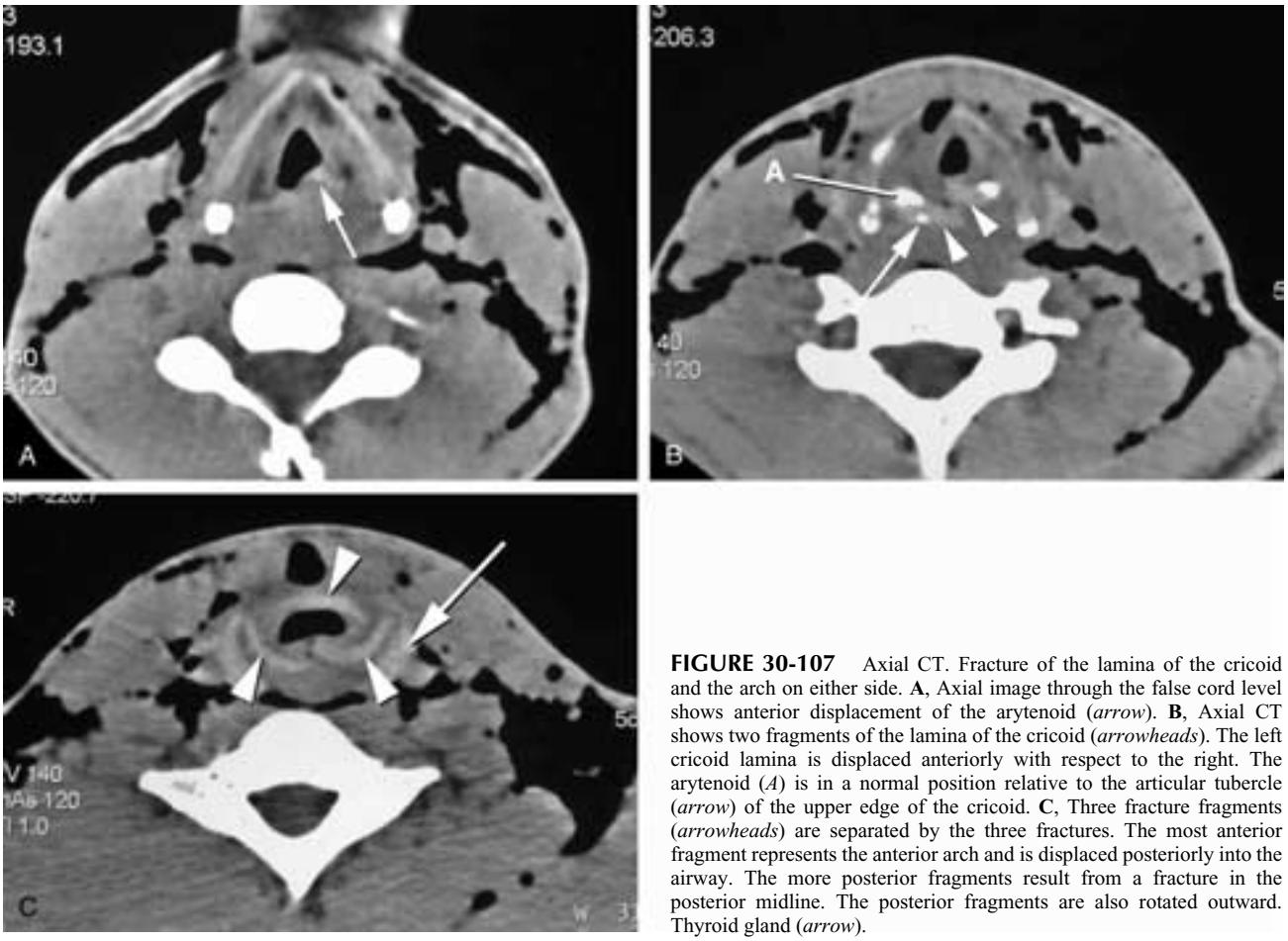

FIGURE 30-107 Axial CT. Fracture of the lamina of the cricoid and the arch on either side. **A**, Axial image through the false cord level shows anterior displacement of the arytenoid (*arrow*). **B**, Axial CT shows two fragments of the lamina of the cricoid (*arrowheads*). The left cricoid lamina is displaced anteriorly with respect to the right. The arytenoid (*A*) is in a normal position relative to the articular tubercle (*arrow*) of the upper edge of the cricoid. **C**, Three fracture fragments (*arrowheads*) are separated by the three fractures. The most anterior fragment represents the anterior arch and is displaced posteriorly into the airway. The more posterior fragments result from a fracture in the posterior midline. The posterior fragments are also rotated outward. Thyroid gland (*arrow*).

VIEW IMAGE

FIGURE 30-108 Axial CT shows fracture of the cricoid. The anterior arch of the cricoid has been fractured and pushed posteriorly. Several fragments (*arrowheads*) are noted as the ring collapses inward. The airway is narrowed, but no piece of the cartilage appears to project through the mucosa. The position of the fractures is shown in the lateral portion of the arch (*arrows*).

VIEW IMAGE

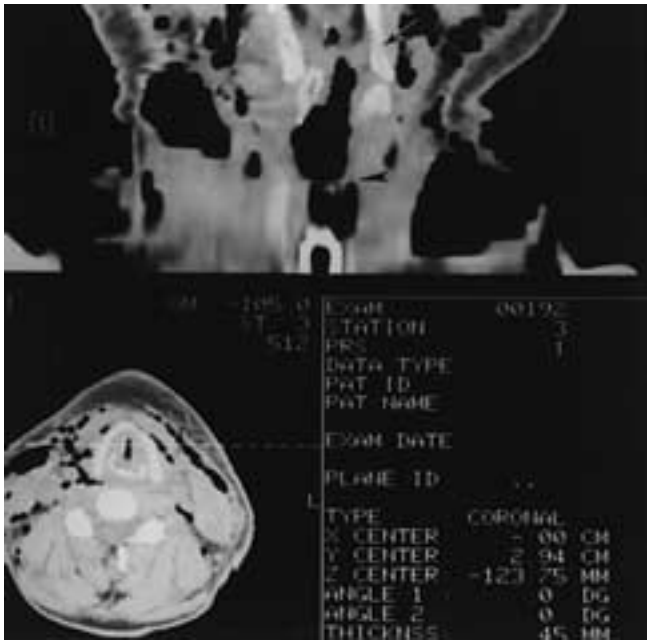

FIGURE 30-109 Coronal reformat of a horizontal fracture of the thyroid cartilage (*arrow*) and laryngotracheal partial separation. Note the lack of alignment of the trachea (*arrowhead*). This finding can be mimicked on reformatted CT slices by movement of the patient during the exam.

VIEW IMAGE

Copyright © 2003, Mosby, Inc. All rights reserved.

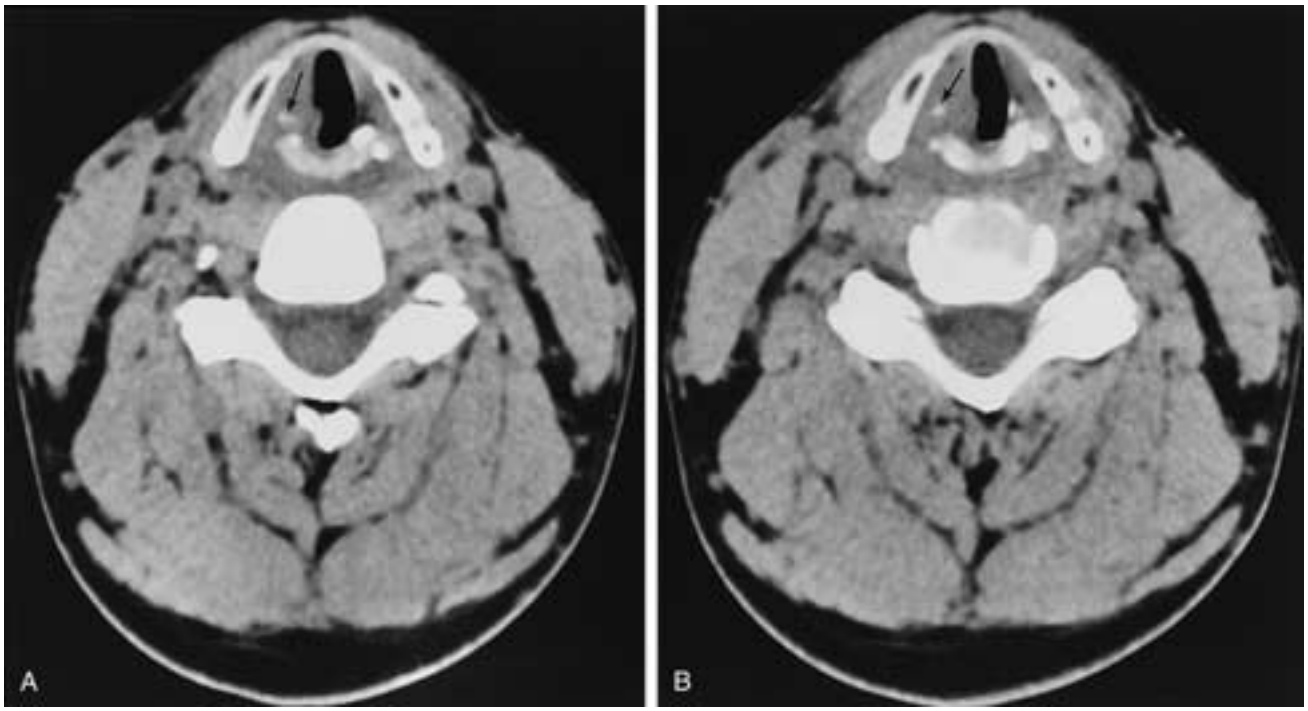

FIGURE 30-110 Axial CT. **A**, The arytenoid is anteriorly displaced (*arrow*). **B**, Slightly lower scan again shows the abnormal position of the arytenoid (*arrow*).

VIEW IMAGE

should be noted. Last, the maximal amount of reduction of the cross-sectional tracheal airway relative to the normal trachea either above or below the stenosis should be mentioned. As a general guide, if a patient has normal pulmonary function, a 50% cross-sectional airway narrowing is associated with dyspnea on exertion. With compromised pulmonary function, lesser degrees of stenosis will cause dyspnea on exertion. Greater degrees of stenosis are associated with dyspnea at rest.

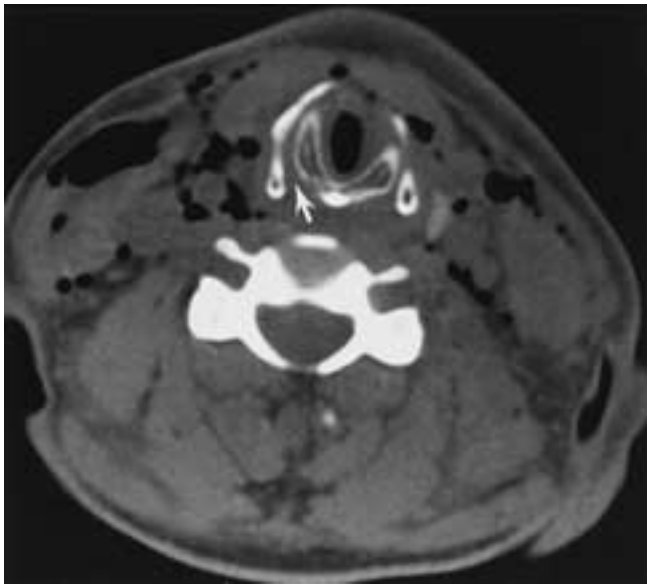

FIGURE 30-111 Axial CT shows cricothyroid separation. The cricoid is rotated relative to the thyroid, with widening of the space (*arrow*) between the lower thyroid and the cricoid. Compare with the opposite side.

VIEW IMAGE

VOCAL CORD PARALYSIS

Vocal cord paralysis can be categorized as a superior laryngeal nerve deficit, a recurrent laryngeal nerve deficit, or a total vagal nerve deficit.

Superior Nerve

The only muscle innervated by the superior laryngeal nerve is the only extrinsic muscle of the larynx, the cricothyroid muscle, which extends between the cricoid and thyroid cartilages. Contraction of the cricothyroid muscle normally pulls the anterior cricoid ring up toward the lower margin of the thyroid cartilage. This rotates the upper cricoid lamina and the attached arytenoids posteriorly, putting tension on the true vocal cords. If the cricothyroid muscle is paralyzed, unopposed contraction of the innervated contralateral muscle rotates the posterior cricoid to the paralyzed side. At laryngoscopy, the posterior larynx (arytenoid) is deviated toward the side of the nerve abnormality.

With this history, the radiologist should examine the neck for a lesion along the course of the vagus nerve (X), which passes through the pars nervosa of the jugular foramen and follows the carotid sheath to the level of the larynx. Usually in these cases, imaging fails to identify a lesion.

Copyright © 2003, Mosby, Inc. All rights reserved.

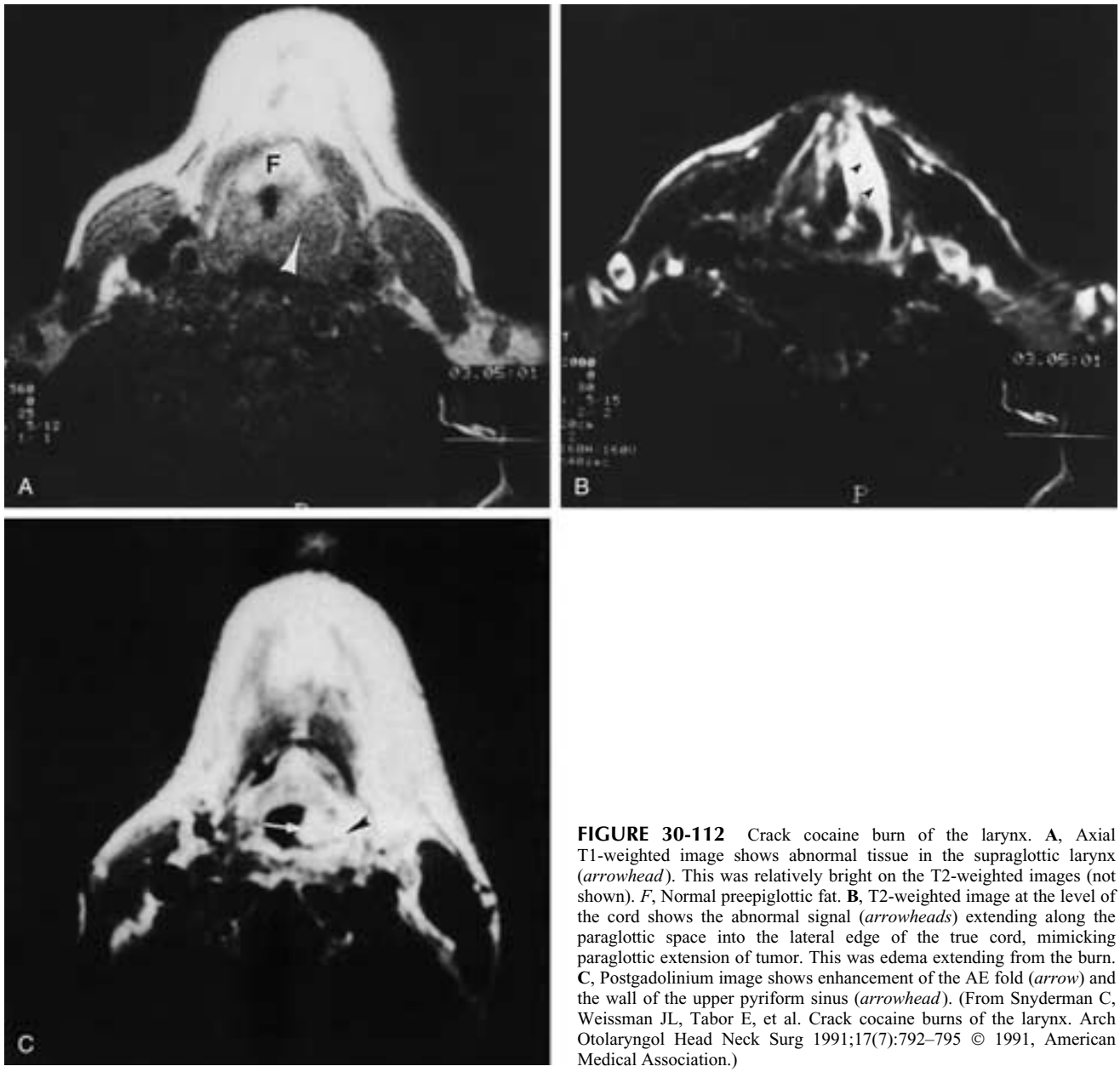

FIGURE 30-112 Crack cocaine burn of the larynx. **A**, Axial T1-weighted image shows abnormal tissue in the supraglottic larynx (*arrowhead*). This was relatively bright on the T2-weighted images (not shown). *F*, Normal preepiglottic fat. **B**, T2-weighted image at the level of the cord shows the abnormal signal (*arrowheads*) extending along the paraglottic space into the lateral edge of the true cord, mimicking paraglottic extension of tumor. This was edema extending from the burn. **C**, Postgadolinium image shows enhancement of the AE fold (*arrow*) and the wall of the upper pyriform sinus (*arrowhead*). (From Snyderman C, Weissman JL, Tabor E, et al. Crack cocaine burns of the larynx. Arch Otolaryngol Head Neck Surg 1991;17(7):792–795 © 1991, American Medical Association.)

VIEW IMAGE

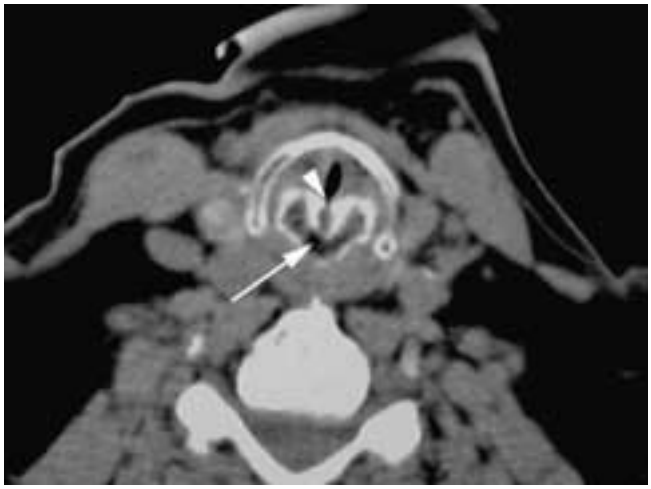

FIGURE 30-113 Elliptical cricoid cartilage; congenital malformation. The cricoid cartilage (*arrow*) pinches medially (*arrowhead*), causing significant narrowing of the lumen.

VIEW IMAGE

Copyright © 2003, Mosby, Inc. All rights reserved.

Recurrent Nerve

More commonly, one encounters a paralysis of the recurrent laryngeal nerve.[121] All of the intrinsic laryngeal muscles are innervated by this nerve. The classic findings of recurrent laryngeal palsy can be identified on plain films, tomography, CT, and MR imaging (Figs. 30-119 to 30-122).

Most of the findings are secondary to atrophy of the TAM. As the muscle atrophies, the cord becomes thinner and more pointed in the coronal plane, with loss of the subglottic arch. As the muscle diminishes in size, the ventricle enlarges and can be prominently seen on axial images, at times extending almost to the inner surface of the thyroid cartilage. The ipsilateral arytenoid is anteromedially placed, and the ipsilateral pyriform sinus enlarges as the AE fold falls medially and appears slightly thickened. The ispilateral vallecula may also be enlarged. On fluoroscopy, different maneuvers show the lack of motion of the paralyzed cord and normal motion of the contralateral side.

The posterior cricoarytenoid muscle is closely applied to the posterior surface of the cricoid, an area well seen on axial images. In cases of recurrent nerve paralysis, the muscle atrophies and fat infiltration may be appreciated.[122]

When studying an abnormality of the recurrent laryngeal nerve, the radiologist must examine the pathway of the vagus and recurrent laryngeal nerves. The vagus nerve exits the skull base in the jugular foramen and then runs in the posterior portion of the carotid sheath. Lower in the neck, the nerves move more anteriorly. On the left side, the recurrent nerve leaves the sheath and passes anterior to and then under the aortic arch before ascending in the tracheoesophageal groove to enter the larynx near the cricothyroid junction. On the right side, the recurrent nerve curves under and around the right subclavian artery to ascend in the tracheoesophageal groove to the larynx.

FIGURE 30-114 Congenital atresia of the larynx. The patient was born with complete atresia of the larynx. Emergency tracheostomy was done at birth. **A**, Proton density image suggests that the cricoid (*arrowheads*) is intact. **B**, Coronal T1-weighted image shows that the airway (*arrowhead*) extends up to the subglottic area. Some air (*arrow*) is seen in the vestibule of the larynx. It is impossible to determine the precise length of the stenosis without distention of the vestibule of the larynx. **C**, Coronal T1-weighted image shows the epiglottis (*arrowhead*).

VIEW IMAGE

Copyright © 2003, Mosby, Inc. All rights reserved.

FIGURE 30-115 Lateral plain film of tracheal stenosis characteristic of a tracheostomy site (*arrows*).

VIEW IMAGE

FIGURE 30-116 Coronal tomogram showing narrowing of the tracheal lumen (*arrowhead*) just below the cricoid. *VC*, Vocal cord. A narrowing resulting from prolonged intubation would be lower in position.

VIEW IMAGE

FIGURE 30-117 Lateral plain film shows granuloma of the posterior wall of the upper trachea (*arrow*).

VIEW IMAGE

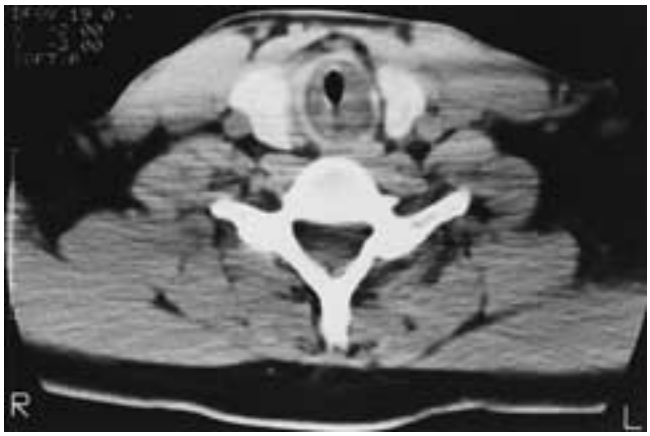

FIGURE 30-118 Axial CT of severe narrowing of the trachea by granulation tissue at the level of the thyroid shows an intact ring, with soft tissue filling the space between the ring and the airway. No portion of the tracheal ring has been pushed into the lumen.

VIEW IMAGE

Copyright © 2003, Mosby, Inc. All rights reserved.

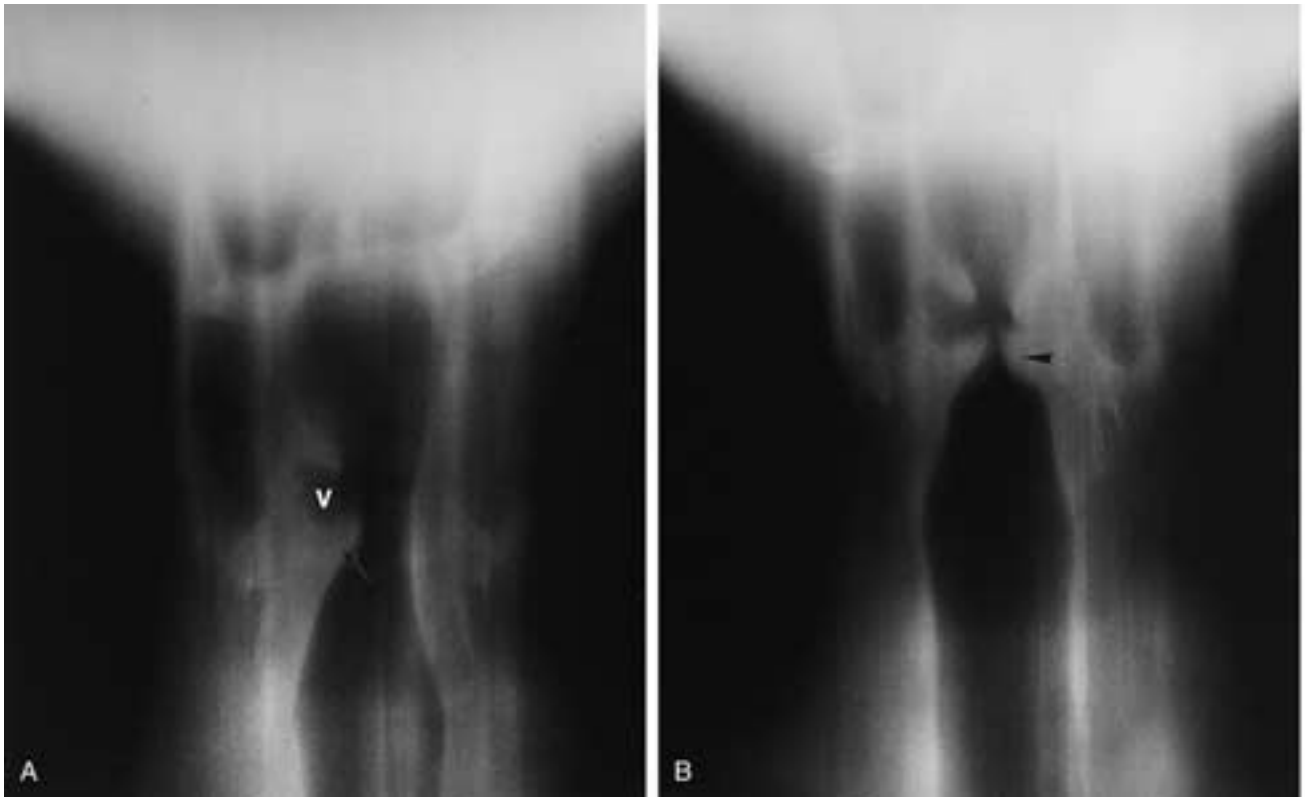

VIEW IMAGE

FIGURE 30-119 **A**, Coronal tomogram. Right cord paralysis, inspiration. The true cord on the affected side remains in the paramedian position and is more pointed than usual (*arrow*). The ventricle (*V*) is enlarged. **B**, Phonation. There is no change in the affected cord or ventricle. The normal cord now moves to the midline (*arrowhead*). Compare the size of the ventricle on the paralyzed side with that on the opposite side.

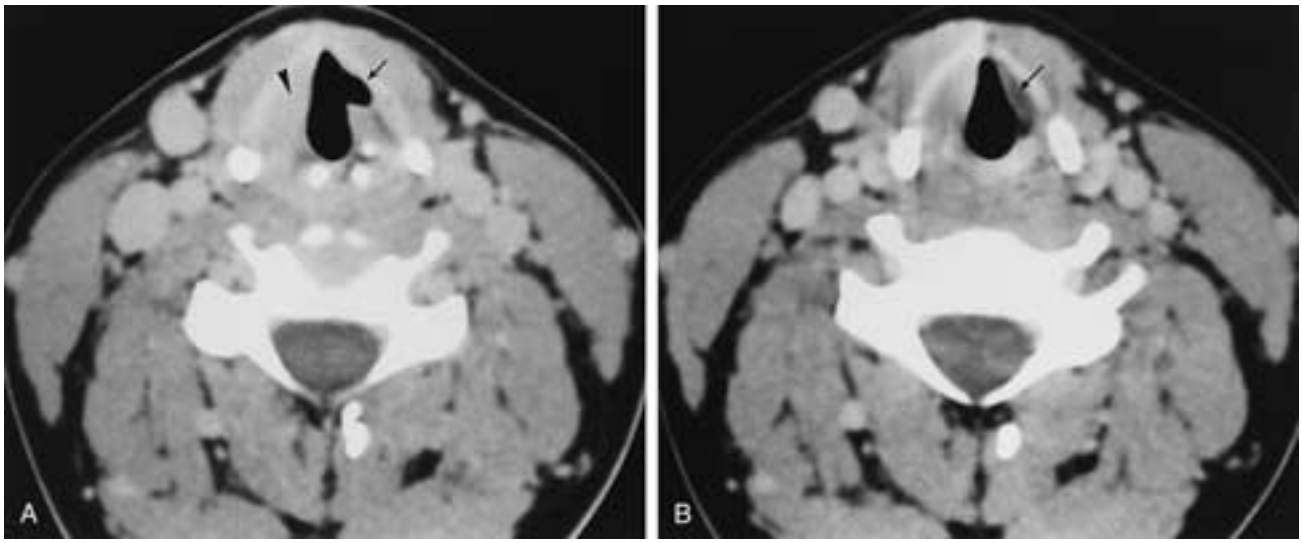

VIEW IMAGE

FIGURE 30-120 Vocal cord paralysis. **A**, Level of the cord shows a dilated ventricle (*arrow*). The TAM on the opposite side (*arrowhead*) is normal in size. **B**, Inferior scan again shows the decreased size of the TAM with decreased density (*arrow*) compared with the opposite side.

Copyright © 2003, Mosby, Inc. All rights reserved.

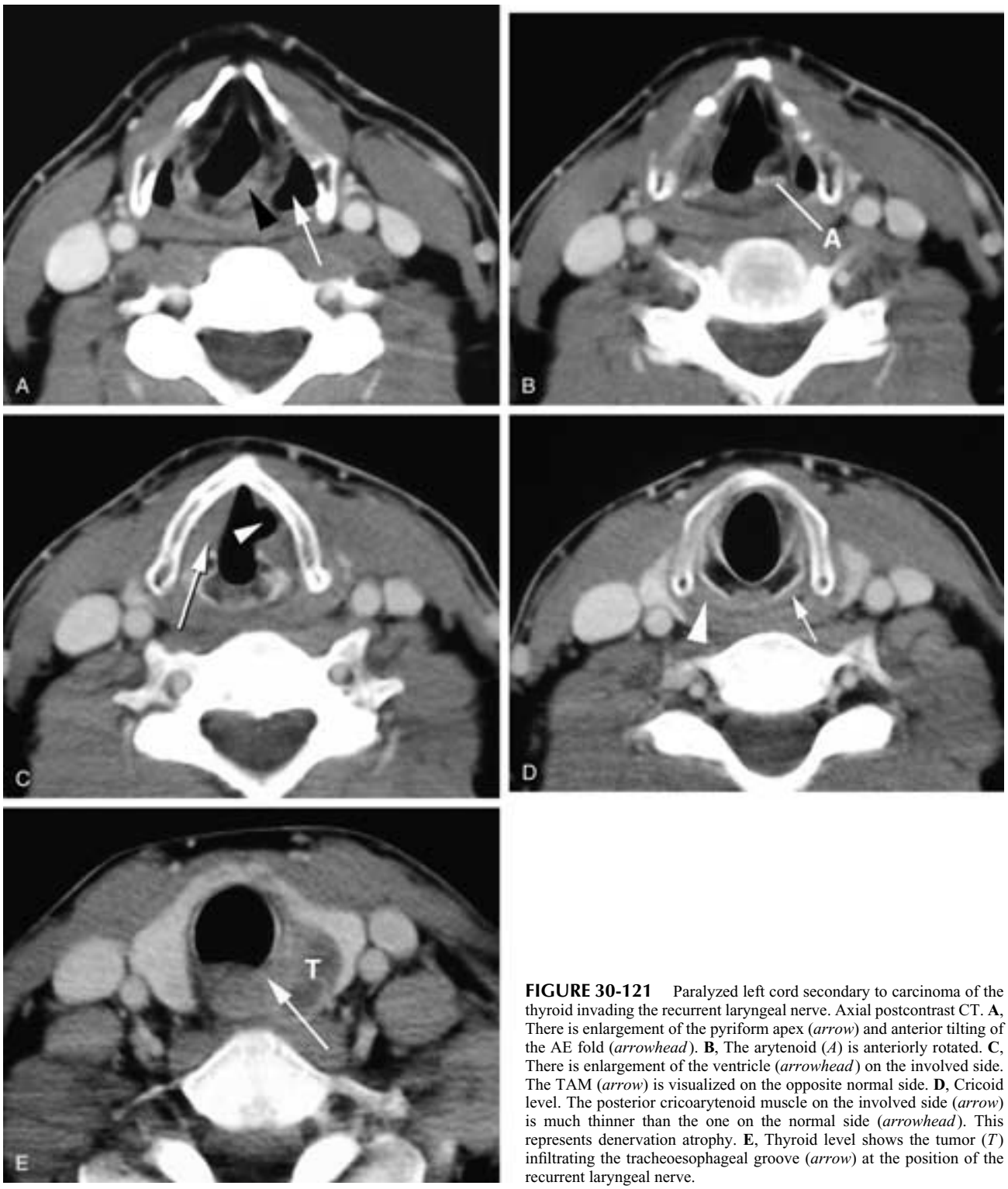

FIGURE 30-121 Paralyzed left cord secondary to carcinoma of the thyroid invading the recurrent laryngeal nerve. Axial postcontrast CT. **A**, There is enlargement of the pyriform apex (*arrow*) and anterior tilting of the AE fold (*arrowhead*). **B**, The arytenoid (*A*) is anteriorly rotated. **C**, There is enlargement of the ventricle (*arrowhead*) on the involved side. The TAM (*arrow*) is visualized on the opposite normal side. **D**, Cricoid level. The posterior cricoarytenoid muscle on the involved side (*arrow*) is much thinner than the one on the normal side (*arrowhead*). This represents denervation atrophy. **E**, Thyroid level shows the tumor (*T*) infiltrating the tracheoesophageal groove (*arrow*) at the position of the recurrent laryngeal nerve.

VIEW IMAGE

Copyright © 2003, Mosby, Inc. All rights reserved.

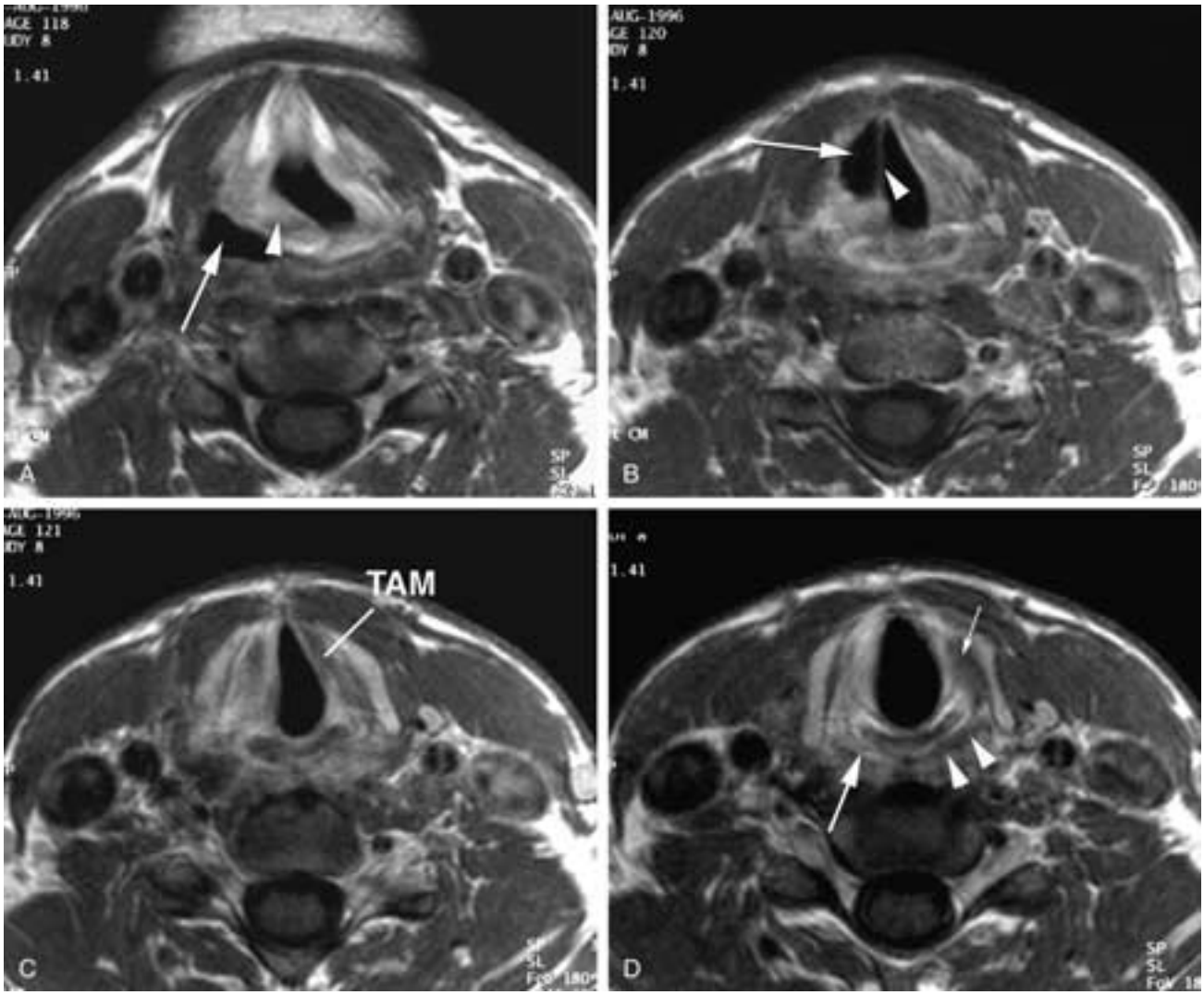

VIEW IMAGE

FIGURE 30-122 Vocal cord paralysis on the right side. MR image. **A**, Supraglottic level shows enlargement of the pyriform sinus (*arrow*) and anterior tilting of the AE fold (*arrowhead*). **B**, Level of the true cord. There is enlargement of the ventricle (*arrow*) as the TAM on the involved side atrophies. The vocal ligament (*arrowhead*) remains in place. **C**, The true cord on the left side shows a normal signal intensity. Thyroarytenoid muscle (*TAM*). **D**, Image slightly caudad to **C** shows the abnormal signal and decreased size of the posterior cricoarytenoid (*large arrow*) on the involved side. Compare with the bulk of the posterior cricoarytenoid muscle on the normal side (*arrowheads*). Anterior cricoarytenoid muscle on the normal side (*small arrow*).

Adductor Paralysis

Rare cases of adductor paralysis have been described. This paralysis affects the muscles that bring the cords together but spares the posterior cricoarytenoid muscle. This muscle stretches from the posterior surface of the cricoid to the lateral aspect of the muscular process of the arytenoid. It is the only muscle that rotates the cord outward, and because the posterior cricoarytenoid muscle is unopposed, the cord remains in a lateral position (Fig. 30-123). The lesion affects certain fibers of the recurrent laryngeal nerve while sparing others. The cause of this abnormality is poorly understood, although an intracranial etiology has been postulated.[123]

MISCELLANEOUS CONDITIONS

Amyloid can affect the larynx either as an isolated lesion (primary) or as part of a more generalized disease (secondary). The deposits produce nodules or thickened zones deep to the mucosal surface.[124] The findings on CT may be mistaken for a submucosal tumor (Fig. 30-124). Amyloid deposits may calcify (Fig. 30-125).

Diverticula of the pharynx are herniations of mucosa through dehiscences in the muscular constrictors. Pseudodiverticula are outpouchings of the pharynx due to focal weakness of the pharyngeal wall. These pharyngoceles have been noted in patients who play wind instruments, and most are located at the level of the thyrohyoid membrane (Figs.

Copyright © 2003, Mosby, Inc. All rights reserved.

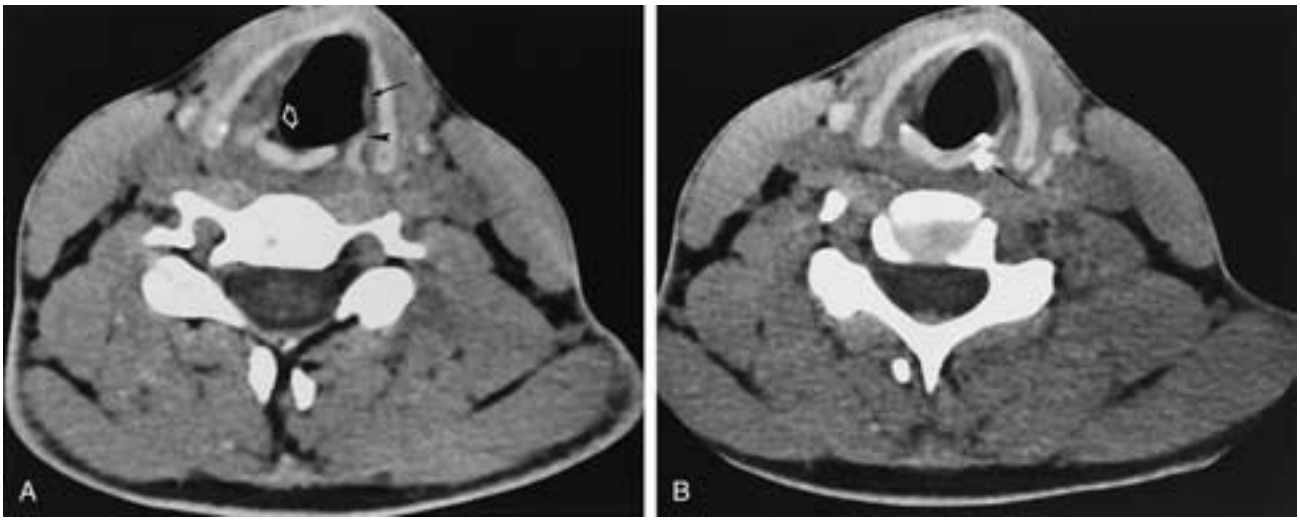

VIEW IMAGE

FIGURE 30-123 Axial CT. **A**, Adductor paralysis. Left side shows almost no TAM (*arrow*). The vocal process (*arrowhead*) is pulled laterally as the posterior cricoarytenoid muscle rotates the arytenoid laterally and posteriorly. Compare the position of the vocal process on the normal side (*open arrow*). **B**, Slightly lower scan shows a portion of the arytenoid pulled posteriorly and downward (*arrow*), overlapping the posterior surface of the cricoid.

30-126 and 30-127). The diverticula are usually incidental findings on barium swallow examinations and have been referred to as ''dog ears'' on a frontal barium swallow film.

A Zenker's diverticulum is an outpouching of pharyngeal mucosa through the inferior constrictor muscles. Most diverticula herniate through Killian's dehiscence, the weak area in the pharyngeal wall located in the gap between the uppermost cricopharyngeus and the inferior most oblique fibers of the inferior pharyngeal constrictors. Although the actual dehiscence or entrance to the diverticulum is in the midline, the diverticulum usually protrudes to the left side. The neck or the anterior wall of the diverticulum is well appreciated on a barium swallow, using oblique, frontal, and lateral projections (Fig. 30-128). Although a Zenker's diverticulum can occasionally be seen on CT (Fig. 30-129), it is easier to diagnose on a barium swallow.

A second weak point in the wall occurs laterally between the cricopharyngeus and esophageal musculature, at the so-called Killian-Jamieson area. Herniations through this area have been reported but are rare.

When there is a Zenker's diverticulum, the cricopharyngeus is usually prominent; however, the cricopharyngeus may also be prominent without a diverticulum (Fig. 30-130). Failure of the muscle to relax completely during swallowing can cause dysphagia, and occasionally a small collection of barium can be seen just above this muscle after the barium column has passed. This residual contrast is thought by

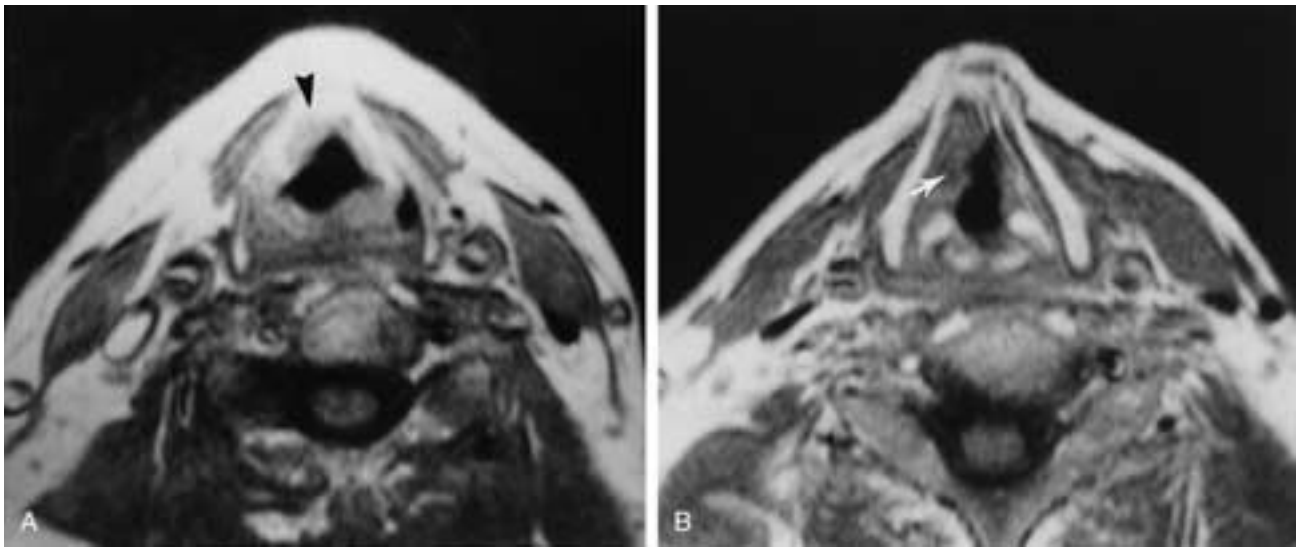

VIEW IMAGE

FIGURE 30-124 **A**, Submucosal amyloid. Axial scan through the supraglottis shows thickening of the lateral epiglottis, with soft tissue extending minimally (*arrowhead*) into the preepiglottic fat (.35 Tesla). **B**, Minor thickening of the true cord (*arrow*). (**A** courtesy of Dr. William Hanafee.)

Copyright © 2003, Mosby, Inc. All rights reserved.

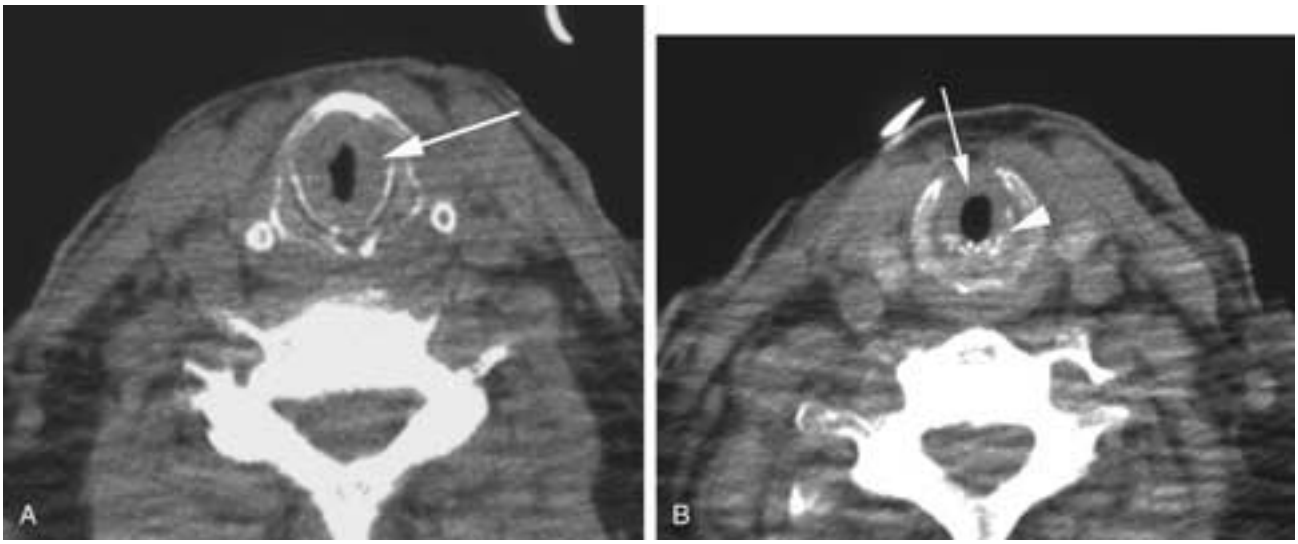

VIEW IMAGE

FIGURE 30-125 Submucosal amyloid infiltration. Axial noncontrast CT. **A**, In the subglottic position there is concentric narrowing (*arrow*) of the airway. At this level there should be no soft tissue within the cricoid ring. **B**, Slightly caudad to **A**. Note again the soft tissue (*arrow*) concentrically narrowing the airway. Note the calcifications (*arrowhead*) more posteriorly.

some to represent a ''primordial Zenker's diverticulum,'' although few of these cases are thought to develop into the classic Zenker's diverticulum. If there is cricopharyngeal achalasia, some authors have suggested that this condition can be related to the development of a Zenker's diverticulum. Failure of relaxation of the cricopharyngeus has also been associated with gastric reflux and other abnormal motility problems in the esophagus, as well as with neurologic conditions affecting the medulla.

VIEW IMAGE

FIGURE 30-126 Barium swallow, pharyngeal diverticula. There is a small outpouching extending through the pharyngeal wall (*arrows*).

Benign Cartilage Changes

Cartilage is a malleable tissue and can be remodeled by pressure or eroded by malignancy. Pressure capable of causing such remodeling can be the result of prominent osteophytes of the spine, benign tumors, or, rarely, an enlarged thyroid gland (Figs. 30-131 and 30-132).[125]

Occasionally, an ala of the thyroid cartilage can bow medially. As described earlier, this may be the result of old trauma, although most often there is no history of trauma. The abnormal cartilage shape may cause a medial bulge in the wall of the larynx that endoscopically mimics a submucosal mass. On CT or MR imaging, the lack of obliteration of the paraglottic fat makes tumor very unlikely (Fig. 30-133).

Osteophytes of the Spine

Large osteophytes arising from the anterior cervical spine can occasionally cause dysphagia.[126] These osteophytes can cause a significant mass effect on the posterior pharyngeal wall or even rarely interfere with the normal movement of the larynx during swallowing. Most often, such osteophytes are seen and the patient has no symptoms related to the area. However, if there is any cause of limitation of laryngeal movement (prior surgery, irradiation, tumor infiltration, neurologic deficit), these osteophytes can cause symptoms, presumably reflecting the combined effects of the limited laryngeal movement and the posterior retropharyngeal mass.

Copyright © 2003, Mosby, Inc. All rights reserved.

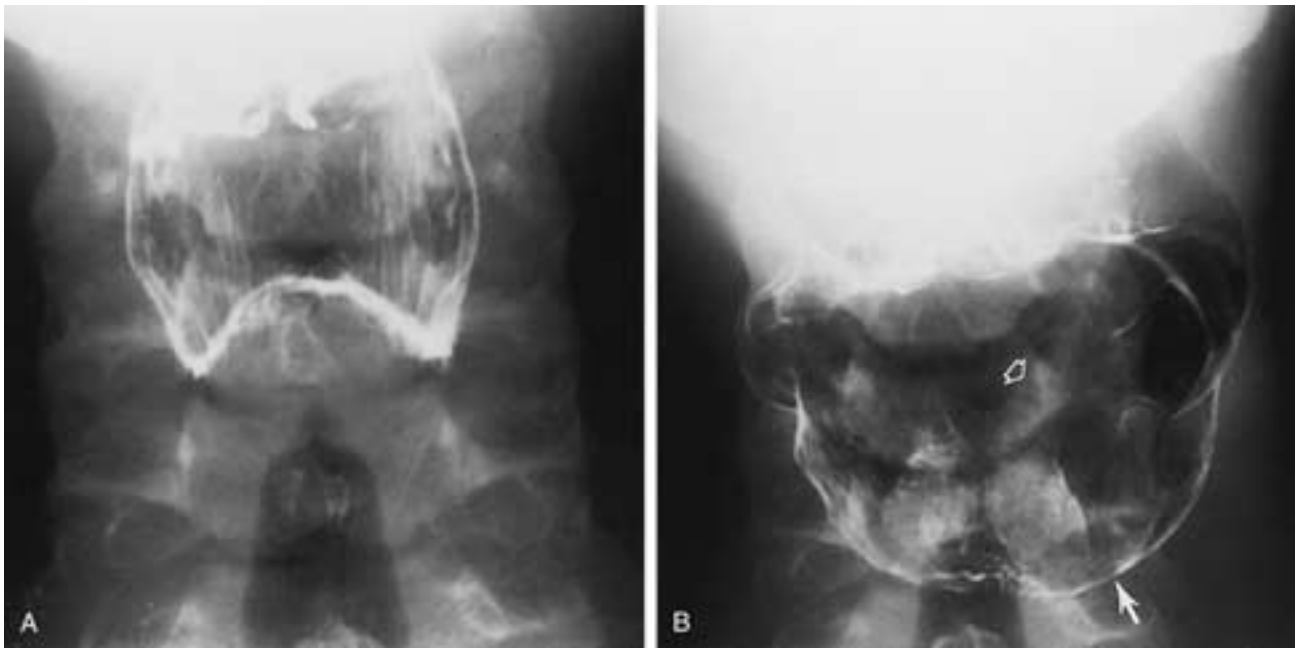

VIEW IMAGE

FIGURE 30-127 Barium swallow, ballooning of the pharynx in a trumpet player. **A**, At rest, the striated appearance of the pharynx is due to redundancy of the mucosa. **B**, On Valsalva maneuver, there is gross distention of the pharynx with bilateral ballooning. Lower margin of the pyriform (*arrow*). *Open arrow*, AE fold.

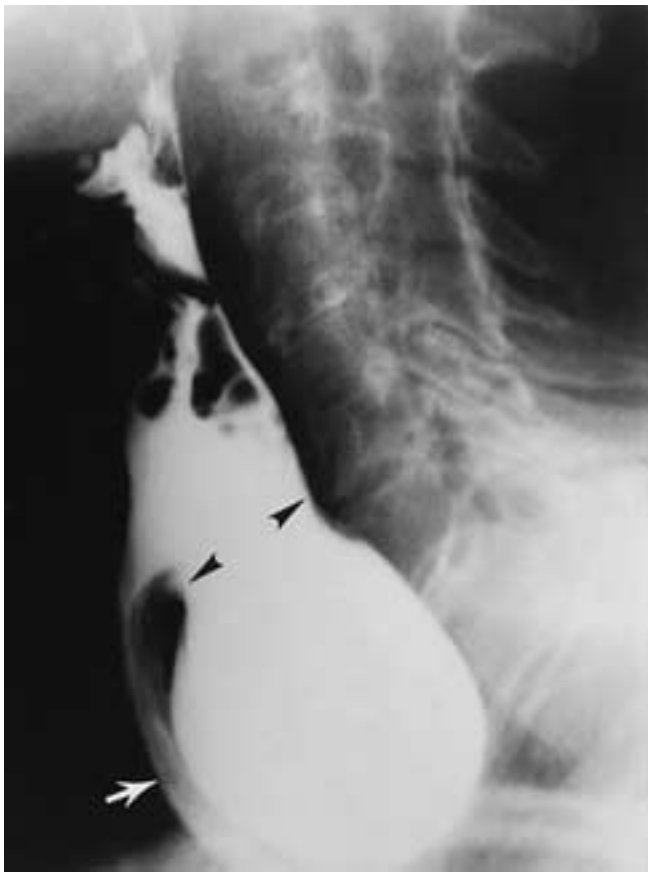

VIEW IMAGE

FIGURE 30-128 Zenker's diverticulum. Lateral film shows a large diverticulum with a wide entrance (*arrowheads*) and the barium column of the true esophagus continuing anterior to the diverticulum (*arrow*). The level of the persistent cricopharyngeus is at the level of the anterior arrowhead. This diverticulum was somewhat unusual because of its midline rather than its usual left-sided position.

Carotid Position

Frequently the carotid artery deviates medially between the pharynx and spine (Fig. 30-134). Although not likely to cause symptoms, this unusual position should be mentioned, especially in patients for whom surgery is contemplated.

Postsurgical Changes

The appearance of the neck after surgery varies, depending on the procedure performed. However, there are certain general postoperative and postradiation appearances in the larynx and neck that are fairly characteristic.

After a total laryngectomy, the normal laryngeal landmarks are no longer present. But as the fascial layers are disrupted during the surgery, the gullet or pharyngoesophageal remnant may migrate anteriorly and should not be mistaken for an airway. The esophagus may actually protrude between the lobes of the thyroid gland, mimicking the trachea (Fig. 30-135). The tracheostomy is usually seen just above the sternal notch, thus identifying the actual airway.

A radical neck dissection removes the sternocleidomastoid muscle and jugular vein, as well as the surrounding nodes.[127] The thyroid gland may assume a rounder shape than normal because of the disruption of the bordering fascial layers. This appearance may mimic a tumor recurrence.[128] The gland may also mimic a blood vessel because of the intrinsically high iodine content of the normally functioning thyroid gland and the highly vascular nature of the gland. The various modifications of neck dissections are described in Chapter 43.

The normal laryngeal structures are obviously missing on a barium swallow done after total laryngectomy.[129] At

Copyright © 2003, Mosby, Inc. All rights reserved.

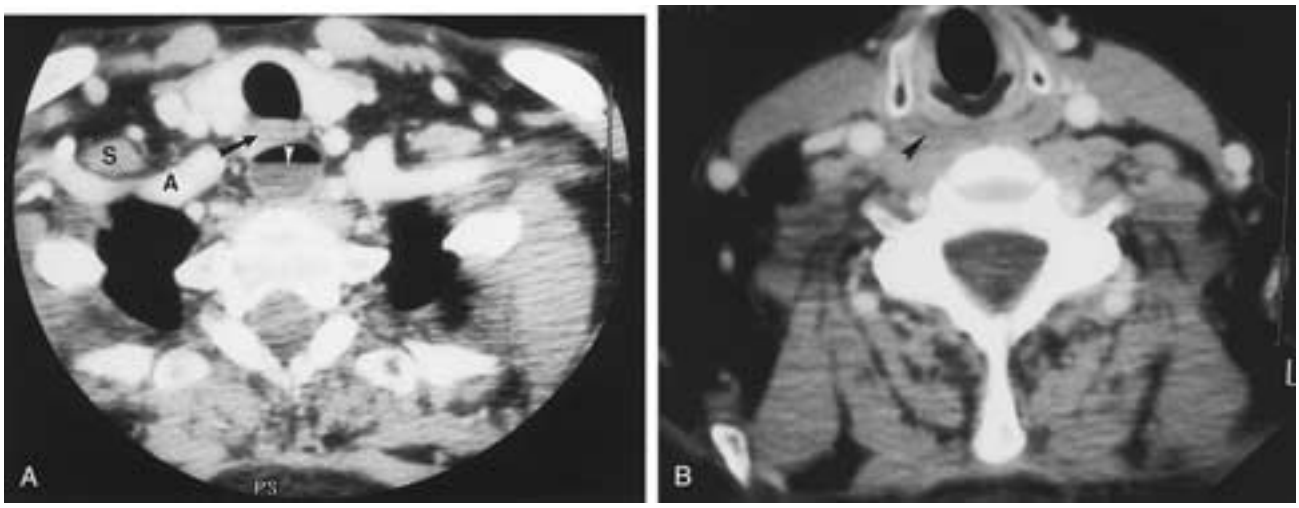

FIGURE 30-129 Zenker's diverticulum. Axial CT. **A**, An air-fluid level (*arrowhead*) is seen within the diverticulum. The actual esophagus (*arrow*) is seen just anteriorly. *A*, Subclavian artery; *S*, anterior scalene. **B**, More superior scan shows the intact pharyngeal wall (*arrowhead*) at the level close to the cricopharyngeus muscle. The abnormality (not shown) actually extends through the various fibers of the muscle.

surgical closure the mucosa is pulled together, often causing a ridge to form just posterior to the tongue base. This ridge can mimic an epiglottis (Fig. 30-136) and has been called the pseudoepiglottis. This is also the area where most postoperative fistulas occur.

Often, a contrast swallow is performed 7 to 10 days after laryngectomy, before the patient is allowed to eat. Barium can be used, but if a fistula into the soft tissues is present, the residual barium can interfere with follow-up studies. If there is no clinical concern that a fistula passes directly into the trachea, meglumine diatrizoate (Gastrografin) can be used as the contrast agent, with careful fluoroscopic control to exclude any communication with the airway. If significant aspiration occurs, the hypertonic Gastrografin can cause pulmonary edema. Care must be taken even if there is a sinus tract to the skin, because Gastrografin can track along the surgical dressing and then go into the tracheal stoma. Before choosing a contrast material, the radiologist should determine whether the surgeon has purposely created a fistula or placed a valve between the trachea and the esophagus. If a valve has been placed, a small amount of contrast material may pass into the trachea, and Gastrografin should not be used. The role of nonionic contrast in this situation has not been fully assessed.

In a supraglottic laryngectomy, all of the normal laryngeal structures above the true vocal cords are removed.

FIGURE 30-130 Lateral barium swallow, slightly prominent, persistent cricopharyngeus (*arrowhead*). There is a small collection of barium (*arrow*) just above the muscle band. This is sometimes referred to as a *primordial Zenker's diverticulum*.

FIGURE 30-131 Axial CT. Osteophyte (*arrow*) causing erosion (*arrowhead*) of the cricoid.

Copyright © 2003, Mosby, Inc. All rights reserved.

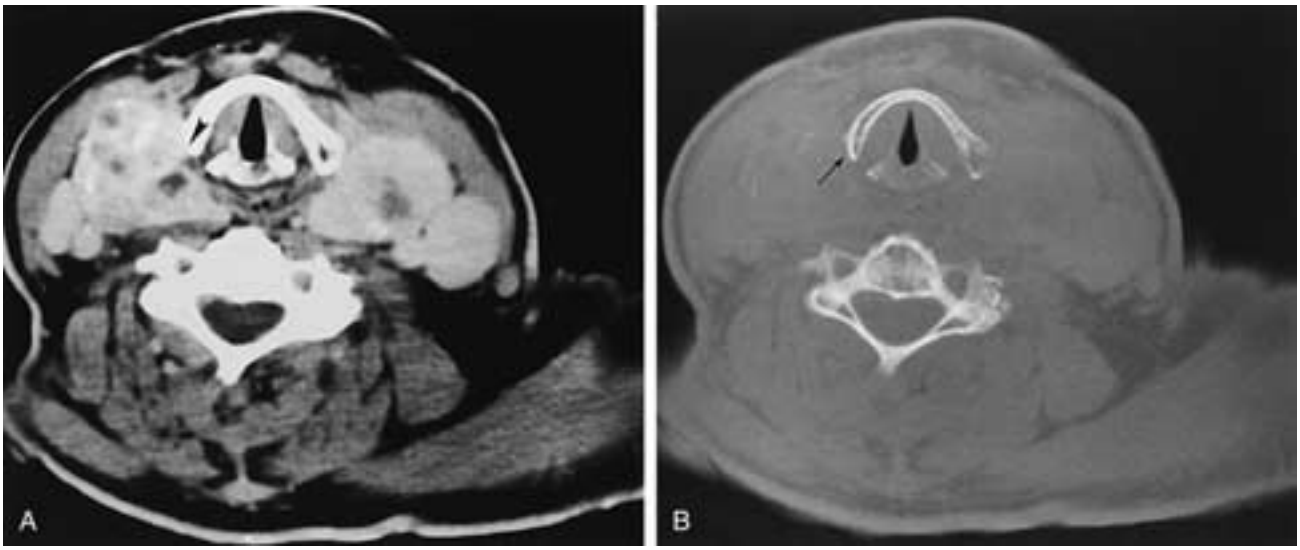

VIEW IMAGE

FIGURE 30-132 Axial CT. **A**, Large multinodular goiter causing shortening and remodeling of the lateral aspect of the thyroid ala (*arrowhead*). **B**, Bone algorithm showing the intact cortical line of the remodeled cartilage (*arrow*).

The hyoid may or may not be included in the resection. A CT scan through the true cords usually appears relatively normal, and the arytenoids usually remain, although one arytenoid may be removed (Figs. 30-137 and 30-138). Although a large portion of the thyroid cartilage has been removed, at the level of the true cords the cartilage should have a normal appearance.

After a supraglottic laryngectomy, in the early postoperative period, some aspiration is almost always present. Because of this, if a contrast swallow is done, Gastrografin should not be used. A barium swallow shows absence of the epiglottis and supraglottic structures, and usually some aspirated barium coats the vocal cords. A follow-up examination should be done after the patient has been trained in the various maneuvers used to help prevent aspiration.

Vertical hemilaryngectomy removes the true and false cords on one side of the larynx. The vertical hemilaryngectomy may also be extended to take the anterior portion of the opposite cord. The soft tissue on the resected side of the larynx may be flat, or a soft-tissue fullness may be present near the level of the true cord, representing either an

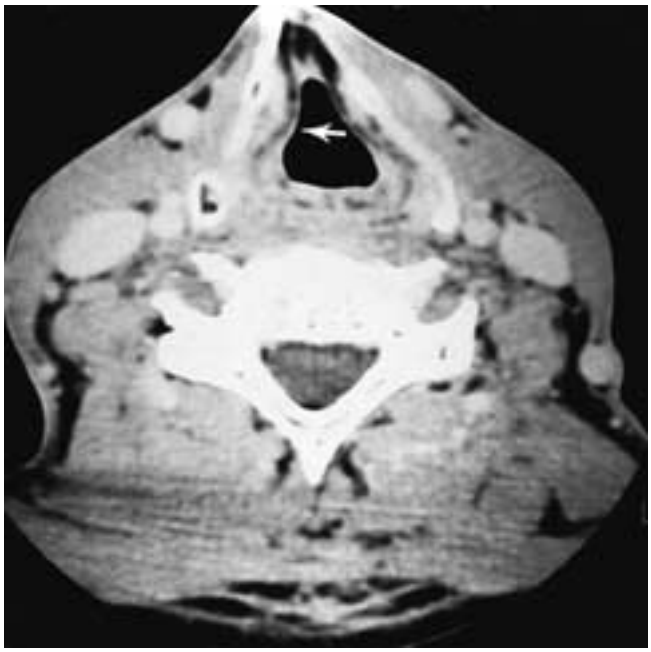

VIEW IMAGE

FIGURE 30-133 Axial CT. Asymmetrical shape of the thyroid cartilage causing a slight bulge in the supraglottic larynx (*arrow*), which could be confused with a submucosal tumor.

FIGURE 30-134 Axial T1-weighted MR image shows a tortuous carotid artery (*arrow*) causing a submucosal mass in the pharyngeal wall at the level of the epiglottis.

VIEW IMAGE

Copyright © 2003, Mosby, Inc. All rights reserved.

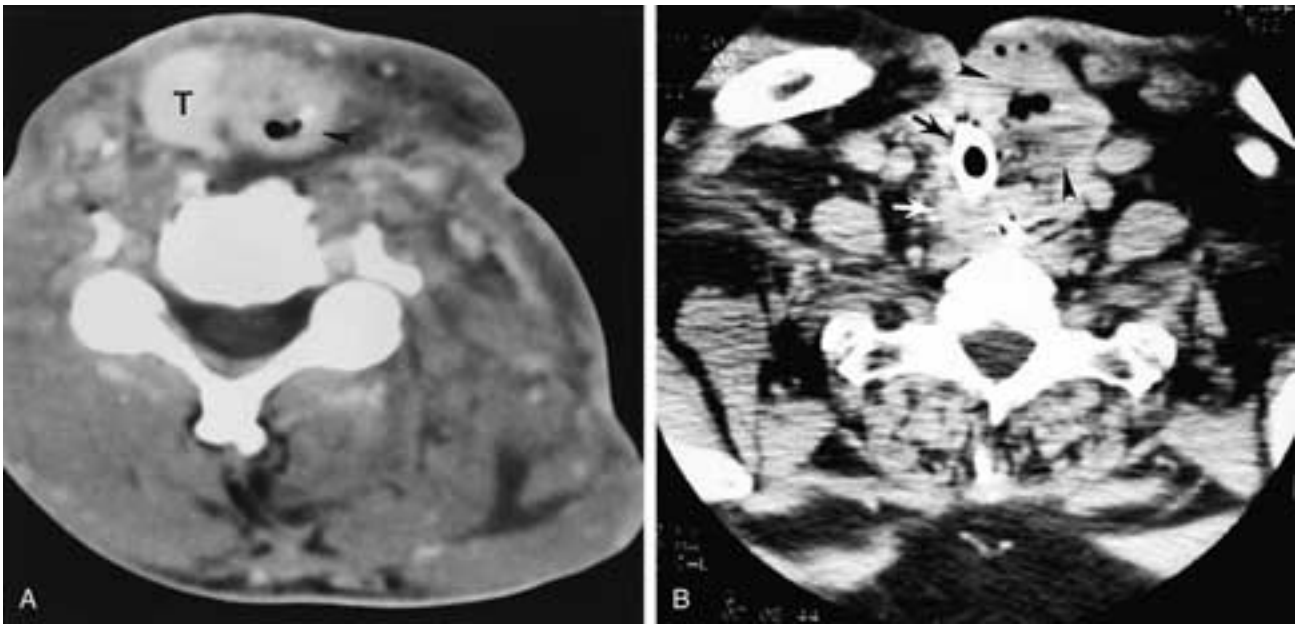

VIEW IMAGE

FIGURE 30-135 Axial CT. **A**, Postoperative laryngectomy and bilateral radical neck dissection. The esophagus has migrated anteriorly (*arrowhead*) to lie in the usual position of the trachea next to the thyroid gland (*T*). The sternocleidomastoid and jugular veins have been removed. **B**, Lower scan. The tracheostomy tube is seen documenting the position of the airway (*black arrow*). The esophagus is seen immediately posteriorly (*white arrow*). Note the large stomal recurrence (*arrowheads*).

VIEW IMAGE

FIGURE 30-136 Lateral barium swallow after laryngectomy with a fistula (*arrowhead*) extending to a collection in the soft tissues anteriorly. Note the pseudoepiglottis (*arrow*) caused by the drawing up of mucosal folds at the closure.

attempted reconstruction of the cord (Figs. 30-139 and 30-140) or a reaction of the mucosa to the trauma (pseudocord) resulting from the functioning contralateral cord hitting against it. In some cases, a strap muscle (sternohyoid) may be passed across the larynx and attached to the arytenoid, thus providing bulk against which the opposite cord can appose. In this instance, the corresponding muscle area outside the larynx is diminished, and there is excess tissue present within the larynx at the level of the cord on the resected side.

The amount of thyroid cartilage resected depends on the extent of the lesion. The resection always extends to the midline and often extends a variable distance along the opposite side. The outer perichondrium of the thyroid cartilage is left intact, and some regeneration of the thyroid ala often occurs. One arytenoid may be removed if the tumor reaches the vocal process. The cricoid usually remains intact, although some surgeons remove the upper portion of this cartilage if the tumor margin warrants such a resection.

The variability of the postoperative appearance is greater with the vertical hemilaryngectomy than it is with the supraglottic partial laryngectomy. Still, on imaging, some comments can be made regarding the possibility of deep recurrence, especially if a baseline scan is available.

The supracricoid partial laryngectomy (SCPL) with cricohyoidepiglottopexy (CHEP) or cricohyoidopexy (CHP) removes parts of the true cords. The cricoid is pulled up to the hyoid bone, and parts of the epiglottis remain in the CHEP (Fig. 30-141).

The near-total laryngectomy of Pearson et al. resembles a vertical laryngectomy but continues downward to include part of the upper cricoid.[67, 68] The contiguous soft tissue

Copyright © 2003, Mosby, Inc. All rights reserved.

is variable, depending on the pharyngeal flap used to reconstitute the airway.

Reconstruction of a pharyngeal defect can be done by a primary closure of the remaining soft tissues, a jejunal interposition, or various flaps (e.g., the deltopectoral flap). On imaging, the jejunal interposition can have a tortuous appearance through the neck, but usually it is in the midline.[130] A flap reconstruction alters the imaging appearance on the side of the neck; this topic is discussed in Chapter 43.[127]

Radiation Changes

Radiation is used to treat many laryngeal lesions, either as the primary therapy or in conjunction with surgery. If laryngeal irradiation has been performed, the resulting mucosal changes can confuse the postoperative imaging assessment of possible tumor recurrence.[131, 132]

Relatively low doses of radiation can cause mucositis and throat pain. Higher doses result in deeper edema and fibrosis and can be associated with perichondritis and chondronecrosis. Almost all patients receiving 60 to 65 Gy will have definable changes in the soft tissues of the larynx. Clinically, the epiglottis thickens and the arytenoids swell, often before the course of radiation is complete. Although gradual improvement is probable, some degree of change persists because of fibrosis and damage to the microvasculature.[133]

CT shows a diffuse thickening of the epiglottis and prominence of the soft tissues in the aryepiglottic folds, in the false cords, and around the arytenoids (Figs. 30-142 and 30-143). There is streaky increased attenuation in the

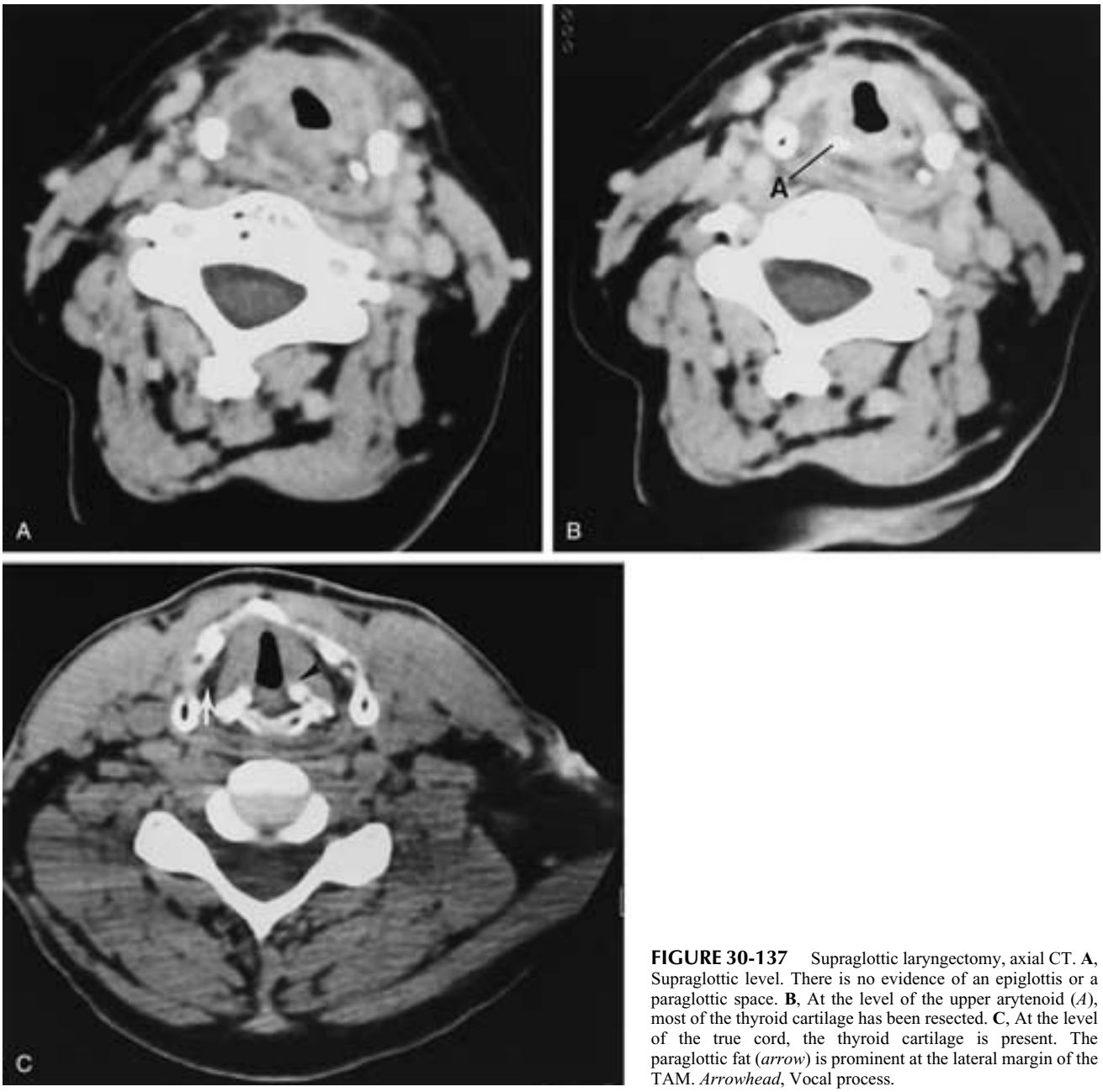

FIGURE 30-137 Supraglottic laryngectomy, axial CT. **A**, Supraglottic level. There is no evidence of an epiglottis or a paraglottic space. **B**, At the level of the upper arytenoid (*A*), most of the thyroid cartilage has been resected. **C**, At the level of the true cord, the thyroid cartilage is present. The paraglottic fat (*arrow*) is prominent at the lateral margin of the TAM. *Arrowhead*, Vocal process.

VIEW IMAGE

Copyright © 2003, Mosby, Inc. All rights reserved.

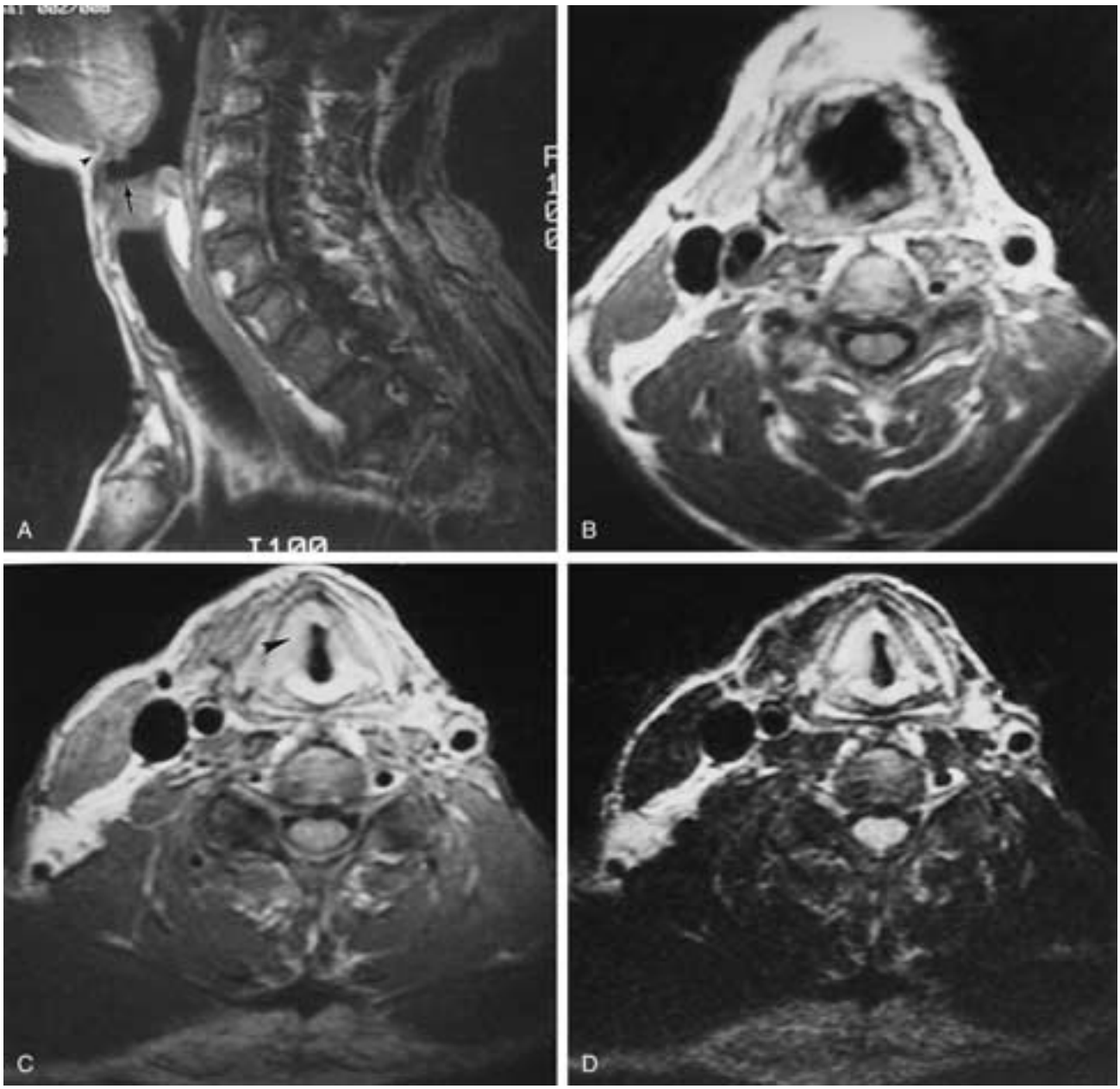

FIGURE 30-138 MR image of a supraglottic laryngectomy with recurrence at the cord level. **A**, Sagittal T1-weighted image shows the absence of supraglottic structures including the epiglottis. The upper margin of the larynx has taken on a rather square appearance (*arrow*). The larynx has been sutured to the base of the tongue and the mylohyoid (*arrowhead*). **B**, Axial T1-weighted image at the supraglottic level shows the irregular appearance of the supraglottic defect above the cord. **C**, Image shows thickening of the involved cord (*arrowhead*). **D**, T2-weighted image shows brightening of the involved cord. This could be from tumor or from edema. In this case it represented recurrence.

VIEW IMAGE

Copyright © 2003, Mosby, Inc. All rights reserved.

VIEW IMAGE

FIGURE 30-139 Vertical hemilaryngectomy on the right side. **A**, The right side of the thyroid cartilage has been removed, as has part of the paraglottic fat. Note the normal paraglottic fat (*arrow*) on the left side. The arytenoid (*A*) also remains on the left side. **B**, True cord level. The true cord including the thyroarytenoid muscle (*TAM*) has been removed, leaving little tissue (*arrow*) on the right side. The TAM remains on the left side, as does the thyroid cartilage.

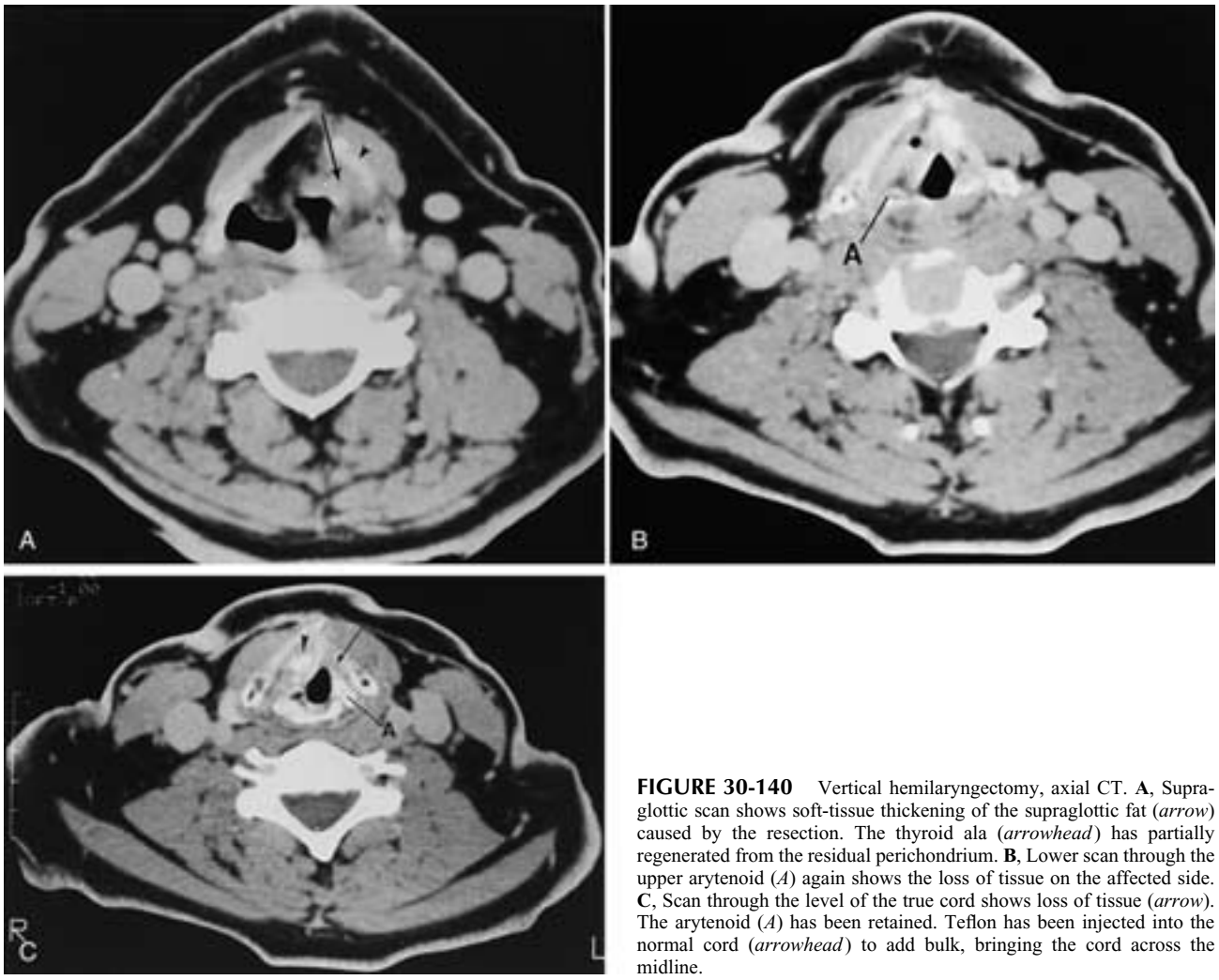

FIGURE 30-140 Vertical hemilaryngectomy, axial CT. **A**, Supraglottic scan shows soft-tissue thickening of the supraglottic fat (*arrow*) caused by the resection. The thyroid ala (*arrowhead*) has partially regenerated from the residual perichondrium. **B**, Lower scan through the upper arytenoid (*A*) again shows the loss of tissue on the affected side. **C**, Scan through the level of the true cord shows loss of tissue (*arrow*). The arytenoid (*A*) has been retained. Teflon has been injected into the normal cord (*arrowhead*) to add bulk, bringing the cord across the midline.

VIEW IMAGE

Copyright © 2003, Mosby, Inc. All rights reserved.

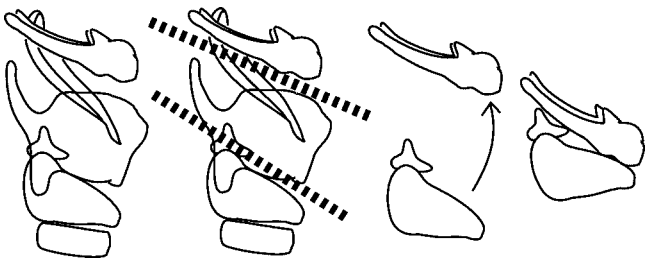

FIGURE 30-141 Supracricoid partial laryngectomy with cricohyoidopexy. Most of the thyroid cartilage and epiglottis (*dashed lines*) are resected. The cricoid is then elevated and attached to the hyoid bone.

VIEW IMAGE

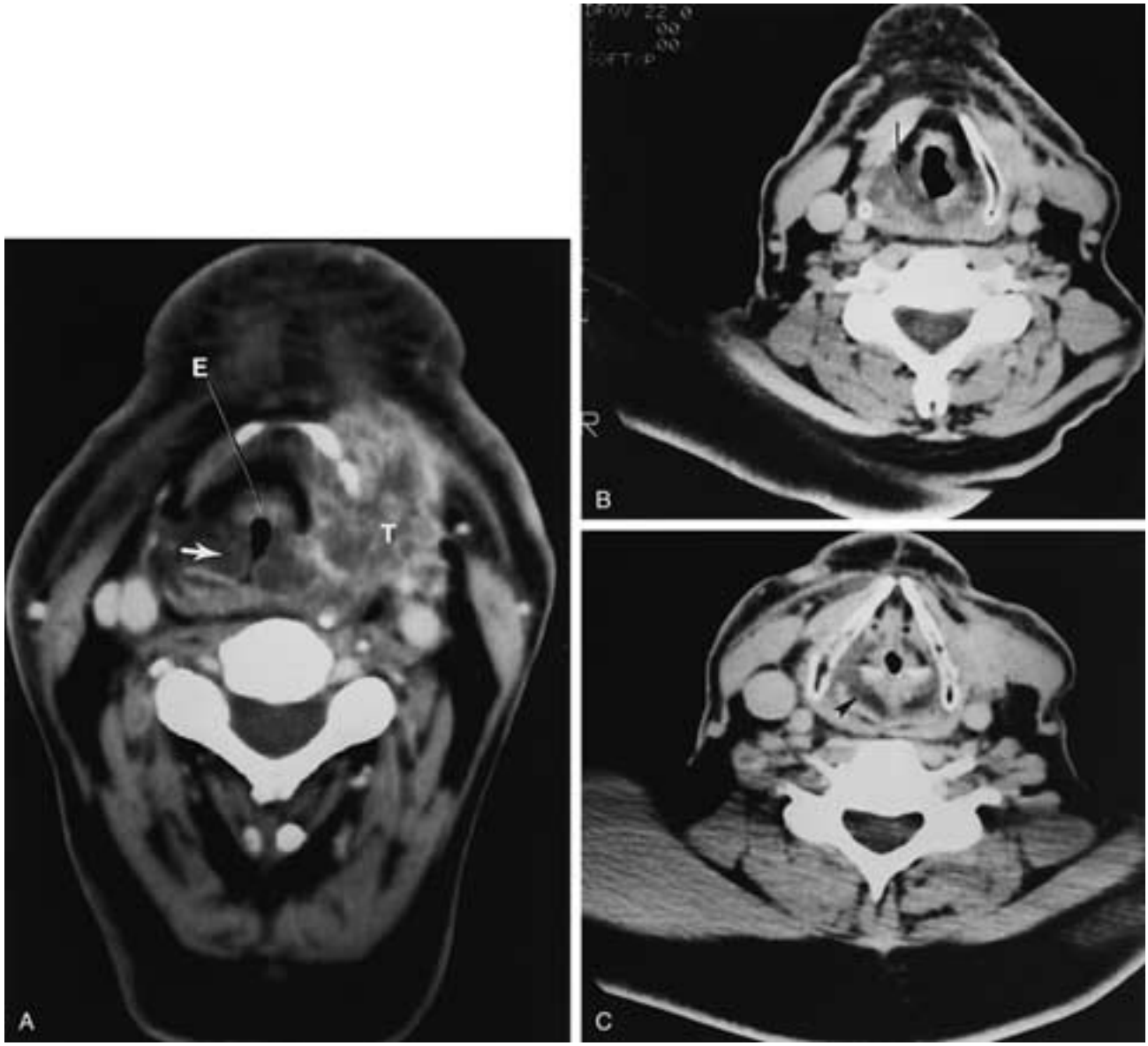

FIGURE 30-142 **A**, CT of postradiation tumor recurrence (*T*). Note the swelling of the AE fold (*arrow*) and apparent thickening of the epiglottic cartilage (*E*). **B**, Lower scan shows increased streaky density and thickening of the wall of the pyriform (*arrow*). Note also the streaky lymphedema (''dirty fat'') in the fat anterior to the larynx. **C**, Scan through the upper arytenoid shows continued swelling in the soft tissues (*arrowhead*) posterior to the arytenoid.

VIEW IMAGE

Copyright © 2003, Mosby, Inc. All rights reserved.

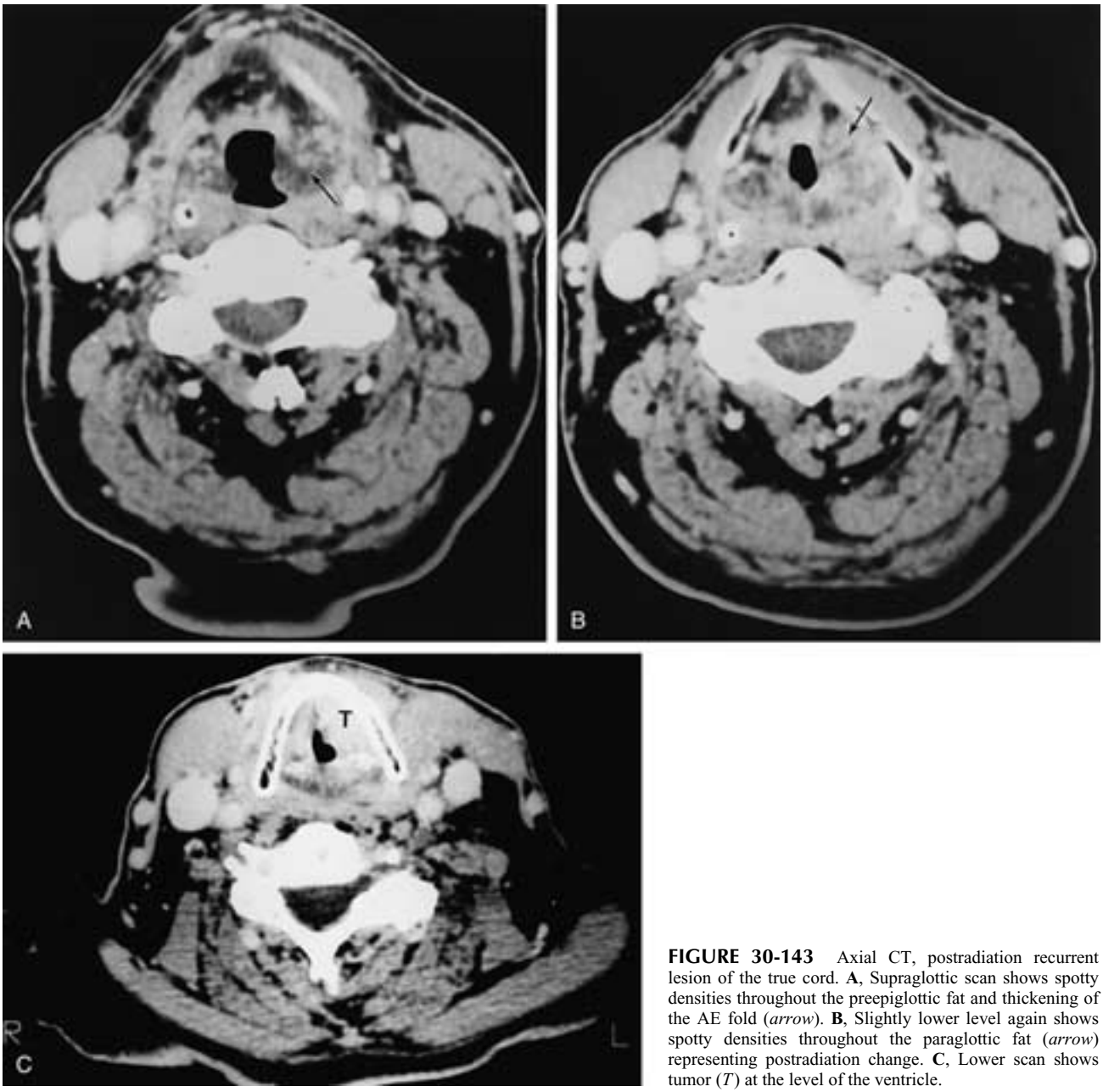

FIGURE 30-143 Axial CT, postradiation recurrent lesion of the true cord. **A**, Supraglottic scan shows spotty densities throughout the preepiglottic fat and thickening of the AE fold (*arrow*). **B**, Slightly lower level again shows spotty densities throughout the paraglottic fat (*arrow*) representing postradiation change. **C**, Lower scan shows tumor (*T*) at the level of the ventricle.

VIEW IMAGE

preepiglottic and paraglottic spaces (dirty fat or reticulation). The true vocal cords and subglottic larynx are usually fairly normal in appearance. However, in patients who have an excessive reaction to irradiation or who are heavily irradiated, edema of the true cords and subglottis can occur.

Perichondritis is an inflammation or infection of the cartilage. High doses of radiation can cause necrosis and collapse of the cartilages, and irradiated tissue is less resistant to infection than normal cartilage. A deep biopsy of an irradiated larynx (looking for a recurrent tumor) may result in perichondritis, and this may lead to chondritis and chondronecrosis. The CT findings are usually superimposed on the changes previously mentioned. Perichondritis causes edema around the cartilage, and at times gas bubbles can be seen. The cartilage may collapse and fragment, assuming unusual angles on the axial scans (Fig. 30-144). Both perichondritis and chondronecrosis are much more significant clinical problems than those encountered in an uncomplicated irradiated larynx.

Radiation may also lead to a collapse of cartilage invaded by a tumor. This is not necessarily due to a perichondritis or radiochondronecrosis. Rather, in these cases, tumor has replaced the cartilage and has actually become part of its support structure. As the tumor regresses in response to the irradiation, this support structure is lost, and the eroded cartilage collapses.

Stents, Tubes, and Teflon

Stents or bone grafts may be used to rebuild the anterior arch of the cricoid cartilage (Fig. 30-145). They are placed in

Copyright © 2003, Mosby, Inc. All rights reserved.

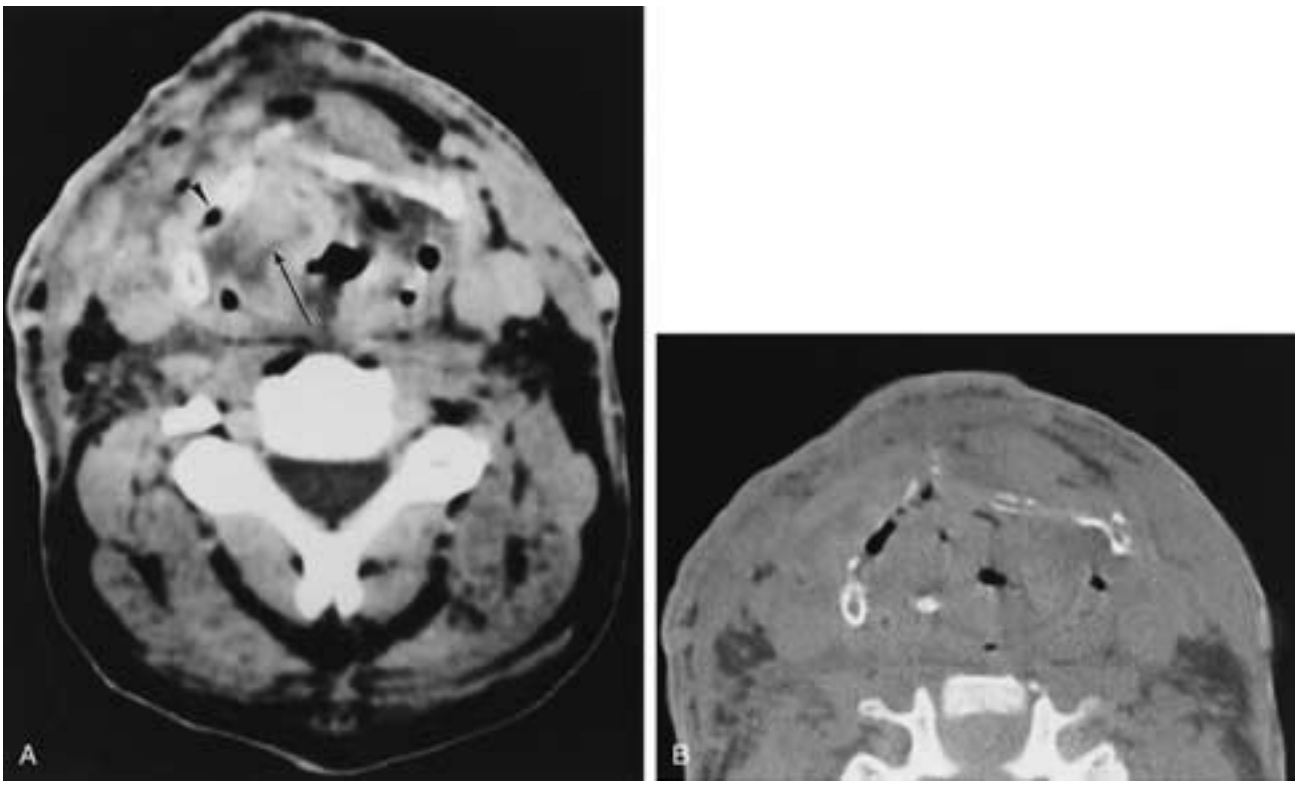

VIEW IMAGE

FIGURE 30-144 Axial CT, perichondritis and chondronecrosis of the thyroid cartilage after radiation therapy. **A**, Significant soft-tissue swelling of the wall of the larynx (*arrow*). There are gas bubbles within the thyroid cartilage (*arrowhead*). **B**, Bone algorithm shows partial collapse of the thyroid cartilage because of demineralization and chondronecrosis.

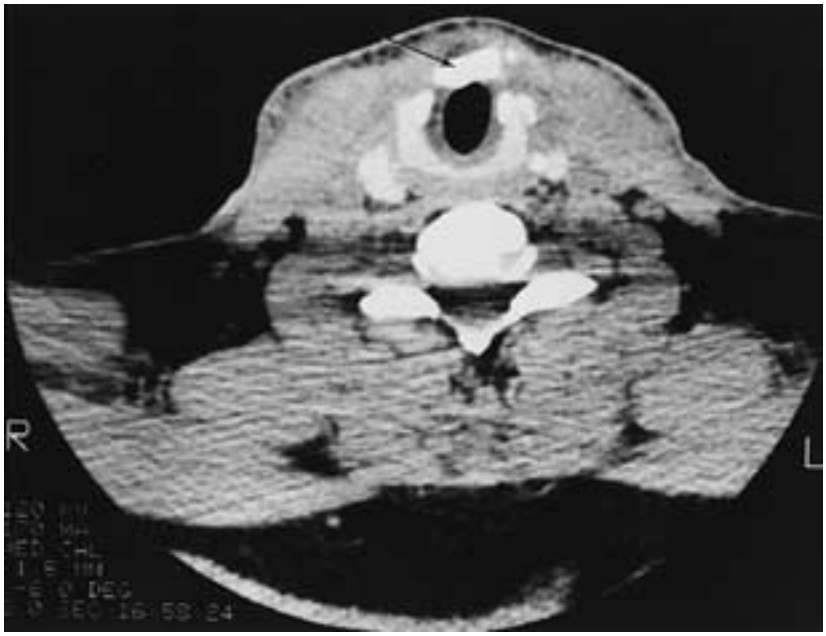

FIGURE 30-145 Axial CT, cartilaginous graft (*arrow*) placed in the anterior arch of the cricoid to support and maintain the lumen of the airway.

VIEW IMAGE

Copyright © 2003, Mosby, Inc. All rights reserved.

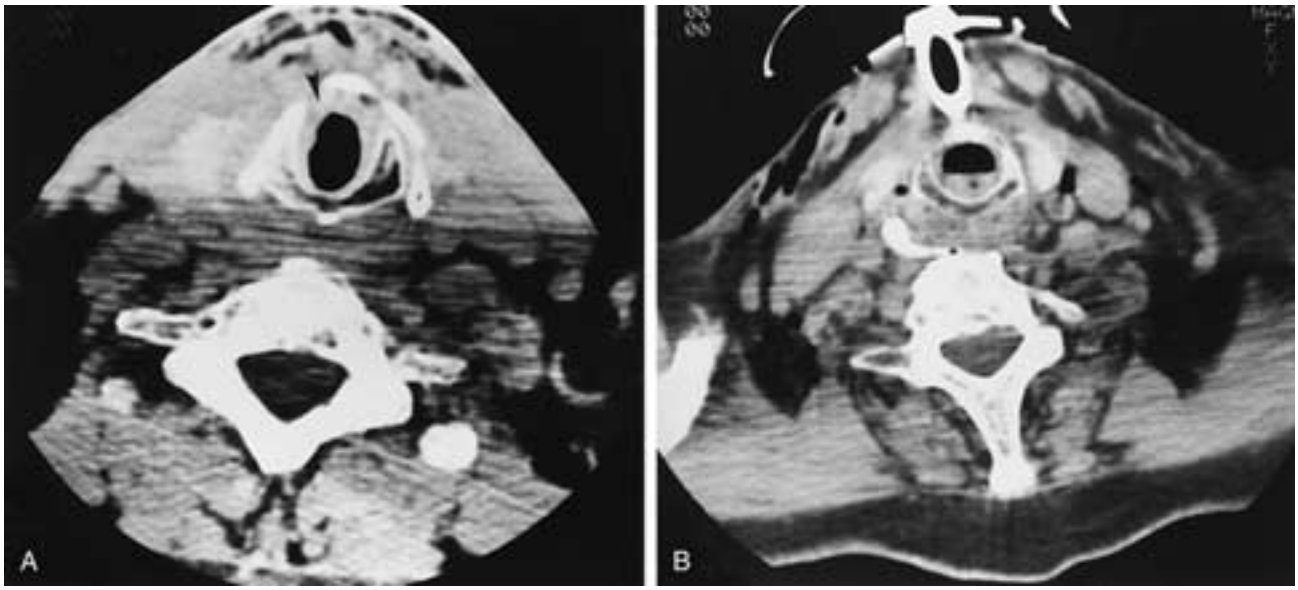

VIEW IMAGE

FIGURE 30-146 **A**, Tracheostomy tube. Axial CT scan through the cricoid shows swelling in the subglottic region (*arrowhead*) caused by recent tracheostomy placement. This can mimic tumor. **B**, Scan through the cricoid shows the extratracheal portion of the tracheostomy tube and an air-fluid level in the trachea.

an effort to maintain or improve the cricoid lumen as part of the treatment of laryngeal stenosis or as part of a reconstruction after trauma or surgery. Metal plates are usually used to stabilize the bone grafts and fragments.

Tracheostomy tubes and speaking (voice) tubes can be seen in the lower neck (Fig. 30-146). A tracheostomy tube is usually placed at the level of the midcervical trachea, but if the tracheostomy was done as an emergency procedure, it may extend through the cricothyroid membrane. Secretions can accumulate above the tracheostomy, and there is usually mucosal swelling extending up to include the subglottic larynx. This may mimic tumor, especially in the immediate subglottic region (Fig. 30-146). The secretions usually have a lower CT attenuation than does a recurrent tumor, particularly if contrast is given, and the mucosal edema tends to be very uniform in thickness, with no localized nodularity to suggest tumor.

The various voice valves used to force air from the trachea to the esophagus for use in esophageal speech are seen in the lower neck of patients who have had a total laryngectomy. These valves are most often noted on CT or barium swallow examinations. They are much smaller than a tracheostomy tube and rarely can be aspirated into the lung (Fig. 30-147).

Teflon can be injected into the paraglottic space just lateral to the true cord (Fig. 30-148). This is done to add bulk to a paralyzed cord so that the cords can better appose and thereby improve voice quality (Fig. 30-149). The procedure has also been performed to build up the resected side of a vertical hemilaryngectomy. Teflon is radiopaque and can easily be seen on CT. More recently, some otolaryngologists have used plastic preformed prostheses and other materials to add bulk to the cord and rotate the arytenoid slightly toward the midline (Fig. 30-150).[134, 135]

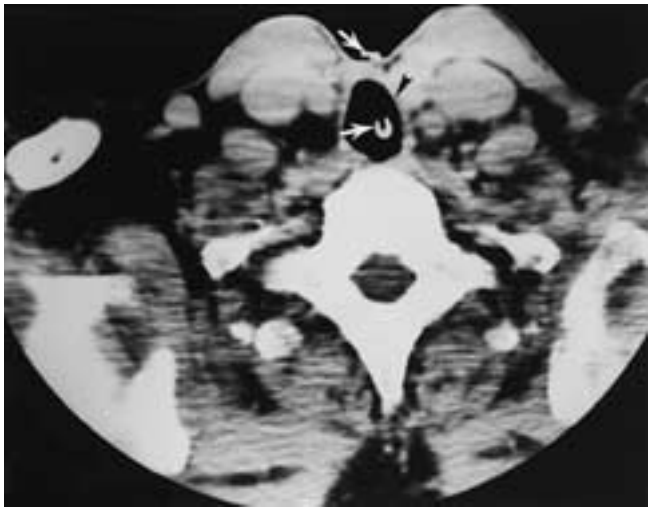

VIEW IMAGE

FIGURE 30-147 Axial CT, Blom-Singer valve used to pass air from the tracheostomy site into the esophagus. The tube (*arrows*) is too small to be a tracheostomy tube. The apparent airway (*arrowhead*) is actually a gas-filled esophagus. The airway would be seen on a lower scan. If the air-filled structure were the airway, one would expect to see the esophagus just posteriorly.

Copyright © 2003, Mosby, Inc. All rights reserved.

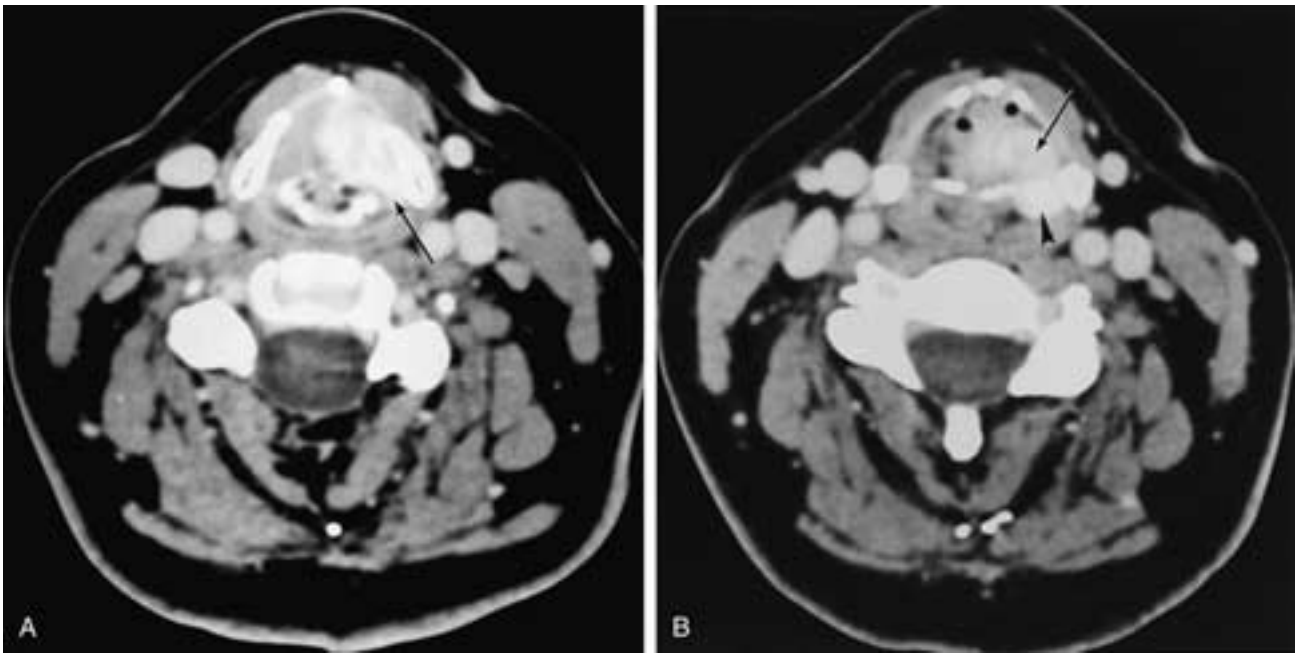

VIEW IMAGE

FIGURE 30-148 Axial CT. **A**, Radiopaque Teflon injected into the cord. Note the small amount of Teflon (*arrow*) squeezing between the thyroid cartilage and the arytenoid. **B**, Supraglottic scan. The radiopaque Teflon (*arrow*) again squeezes between the thyroid cartilage and the upper arytenoid (*arrowhead*). This amount of Teflon is more than is usually seen in a routine injection.

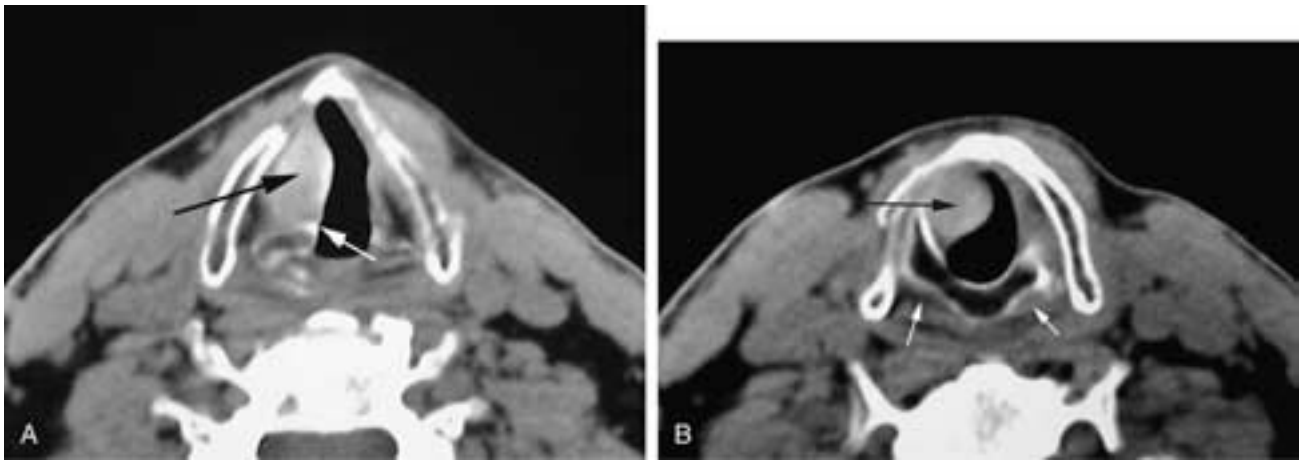

VIEW IMAGE

FIGURE 30-149 Teflon injection for vocal cord paralysis, right side. **A**, The Teflon (*black arrow*) is injected to add bulk to the right true cord and to medialize the cord. Note that the vocal process (*white arrow*) of the arytenoid is also rotated medially. **B**, More Teflon (*black arrow*) was injected than is necessary, causing a bulge into the subglottis. Note the atrophy of the posterior cricoarytenoid on the right compared to the left (*white arrows*).

Copyright © 2003, Mosby, Inc. All rights reserved.

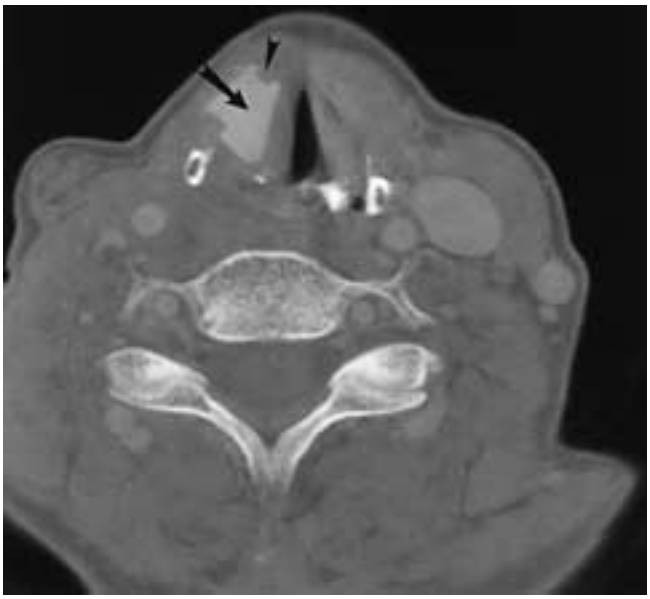

VIEW IMAGE

FIGURE 30-150 Axial CT, silastic stent for vocal cord paralysis. The preshaped silastic stent (*arrow*) is used to add bulk to the paralyzed cord. The notches seen in the anterior (*arrowhead*) and posterior edges stabilize the stent in the surgical opening in the thyroid cartilage.

REFERENCES

1. Gray H, Williams PL, Bannister LH. Gray's Anatomy: The Anatomical Basis of Medicine and Surgery, 38th ed. New York: Churchill Livingstone, 1995.
2. Tillmann B, Paulsen F. Functional and clinical anatomy of the anterior commissure. Adv Otorhinolaryngol 1995;49:201–206.
3. Broyles EN. The anterior commissure tendon. Ann Otol Rhinol Laryngol 1943;52:342–345.
4. Zeitels SM, Kirchner JA. Hyoepiglottic ligament in supraglottic cancer. Ann Otol Rhinol Laryngol 1995;104(10 Pt 1):770–755.
5. Sato K, Kurita S, Hirano M. Location of the preepiglottic space and its relationship to the paraglottic space. Ann Otol Rhinol Laryngol 1993;102(12):930–934.
6. Tucker GF, Smith HR. A histological demonstration of the development of laryngeal connective tissue compartments. Trans Am Acad Ophthalmol Otolaryngol 1962;66:303–318.
7. Tucker GF. Human Larynx: Coronal Section Atlas. Washington, DC: Armed Forces Institute of Pathology, 1971.
8. Reidenbach MM. The paraglottic space and transglottic cancer: anatomical considerations. Clin Anat 1996;9(4):244–251.
9. Reidenbach MM. Borders and topographic relationships of the paraglottic space. Eur Arch Otorhinolaryngol 1997;254(4):193–195.
10. Pressman JJ, Dowdy A, Libby R, Fields M. Further studies upon the submucosal compartments and lymphatics of the larynx by the injection of dyes and radioisotopes. Ann Otol Rhinol Laryngol 1956;65:963–980.
11. Pressman JJ. Submucosal compartmentation of the larynx. Ann Otol Rhinol Laryngol 1956;65:766–771.
12. Pressman JJ, Simon MB, Monell C. Anatomic studies related to the dissemination of cancer of the larynx. Trans Am Acad Ophthalmol Otolaryngol 1960;64:628–644.
13. Curtin H. Current concepts of imaging of the larynx. Radiology 1989;173:1–11.
14. Giron J, Joffre P, Serres-Cousine O, et al. [Magnetic resonance imaging of the larynx: its contribution compared to x-ray computed tomography in the pre-therapeutic evaluation of cancers of the larynx. Apropos of 90 surgical cases.] [French.] Original Title: L'imagerie par resonance magnetique du larynx. Apport comare a celui de la tomodensitometrie dans le bilan pre-therapeutique des cancers du larynx. A propos de quatre-vingt dix cas operes. Ann Radiol (Paris) 1990;33(3):170–184.
15. Lufkin R, Hanafee W. Application of surface coil to MR anatomy of the larynx. AJR 1985;145:483–492.
16. Lufkin R, Hanafee W, Wortham D, et al. Larynx and hypopharynx: MR imaging in surface coils. Radiology 1986;158:747–754.
17. McArdle C, Bailey B, Amparo E. Surface coil magnetic resonance imaging of the normal larynx. Arch Otolaryngol Head Neck Surg 1986;112:616–622.
18. Stark D, Moss A, Gamsu G, et al. Magnetic resonance imaging of the neck. I. Normal anatomy. Radiology 1984;150:447–452.
19. Maguire GH. The larynx: simplified radiological examination using heavy filtration and high voltage. Radiology 1966;87(1): 102–110.
20. Maguire G, Beigue R. Selective filtration: a practical approach to high kilovoltage radiography. Radiology 1965;85:345–351.
21. Doust BD, Ting YM. Xeroradiography of the larynx. Radiology 1974;110(3):727–730.
22. Powers WE, McGee HH, Seaman WB. The contrast examination of larynx and pharynx. Radiology 1957;68:169–172.
23. Momose KJ, Macmillan AS Jr. Roentgenologic investigations of the larynx and trachea. Radiol Clin North Am 1978;16(2):321–341.
24. Noyek A, Shulman H, Steinhardt M, Zizmor J, Som P. The larynx. In: Bergeron R, Osborne A, Som P, eds. Head and Neck Imaging: Excluding the Brain. St Louis: CV Mosby, 1983;402–490.
25. Mafee M, Schild J, GE V, et al. Computed tomography of the larynx: correlation with anatomic and pathologic studies in cases of laryngeal carcinomas. Radiology 1983;147:123–127.
26. Mancuso A, Hanafee W. Computed Tomography and Magnetic Resonance of the Head and Neck. Baltimore: Williams & Wilkins, 1985.
27. Bruning R, Sturm C, Hong C, et al. [The diagnosis of stages T1 and T2 in laryngeal carcinoma with multislice spiral CT.] Radiologe 1999;39(11):939–942.
28. Lufkin R, Larsson S, Hanafee W. Work in progress: NMR anatomy of the larynx and tongue base. Radiology 1983;148:173–177.
29. Castelijns J, Gerritsen G, Kaiser M, et al. MRI of normal or cancerous laryngeal cartilage: histopathologic correlation. Laryngoscope 1987;97:1085–1093.
30. Raghavendra B, Horii S, Reede D, et al. Sonographic anatomy of the larynx, with particular reference to the vocal cords. J Ultrasound Med 1987;6:225–230.
31. Chu L, Gussack GS, Orr JB, Hood D. Neonatal laryngoceles. A cause for airway obstruction. Arch Otolaryngol Head Neck Surg 1994;120(4):454–458.
32. Friedman EM. Role of ultrasound in the assessment of vocal cord function in infants and children. Ann Otol Rhinol Laryngol 1997;106(3):199–209.
33. Rothberg R, Noyek A, Freeman J, et al. Thyroid cartilage imaging with diagnostic ultrasound: correlative studies. Arch Otolaryngol Head Neck Surg 1986;112:503–515.
34. Arens C, Eistert B, Glanz H, Waas W. Endolaryngeal high-frequency ultrasound. Eur Arch Otorhinolaryngol 1998;255(5):250–255.
35. Arens C, Glanz H. Endoscopic high-frequency ultrasound of the larynx. Eur Arch Otorhinolaryngol 1999;256(6):316–322.
36. Garel C, Hassan M, Hertz-Pannier L, et al. Contribution of MR in the diagnosis of ''occult'' posterior laryngeal cleft. Int J Pediatr Otorhinolaryngol 1992;24:177–181.
37. Isaacson G, Birnholz J. Human fetal upper respiratory tract function as revealed by ultrasonography. Ann Otol Rhinol Laryngol 1991;100:743–747.
38. Noyek AM. Bone scanning in otolaryngology. Laryngoscope 1979;89(9 Pt 2 Suppl 18):1–87.
39. Konowitz P, Lawson W, Som P, et al. Laryngeal paraganglioma: update on diagnosis and treatment. Laryngoscope 1988;98:40–49.
40. Batsakis J. Tumors of the Head and Neck: Clinical Pathological Consideration, 2nd ed. Baltimore: Williams & Wilkins, 1979.
41. Barnes L, Gnepp D. Disease of the larynx, hypopharynx, and esophagus. In: Barnes L, ed. Surgical Pathology of the Head and Neck. New York: Marcel Dekker, 1985;141–226.
42. Koufman JA, Burke AJ. The etiology and pathogenesis of laryngeal carcinoma. Otolaryngol Clin North Am 1997;30(1):1–19.
43. Fleming ID, American Joint Committee on Cancer, American Cancer Society, American College of Surgeons. AJCC Cancer Staging Manual, 5th ed. Philadelphia: Lippincott-Raven, 1997.
44. Mendenhall WM, Parsons JT, Stringer SP, et al. Radiotherapy for carcinoma of the supraglottis. Otolaryngol Clin North Am 1997;30: 145–161.

Copyright © 2003, Mosby, Inc. All rights reserved.

45. Moose BD, Greven KM. Definitive radiation management for carcinoma of the glottic larynx. Otolaryngol Clin North Am 1997;30(1):131–143.
46. Hoffman HT, McCulloch T, Gustin D, Karnell LH. Organ preservation therapy for advanced-stage laryngeal carcinoma. Otolaryngol Clin North Am 1997;30(1):113–130.
47. Freeman D, Mancuso A, Parsons J, et al. Irradiation alone for supraglottic carcinoma: can CT findings predict treatment results? Int J Radiat Oncol Biol Phys 1990;19:485–490.
48. Lee W, Mancuso A, Saleh E, et al. Can pretreatment computed tomography findings predict local control in T3 squamous cell carcinoma of the glottic larynx treated with radiotherapy alone? Int J Radiat Oncol Biol Phys 1993;25:683–687.
49. Mukherji SK, Mancuso AA, Mendenhall W, Kotzur IM, Kubilis P. Can pretreatment CT predict local control of T2 glottic carcinomas treated with radiation therapy alone? AJNR 1995;16(4):655–662.
50. Castelijns JA, van den Brekel MW, Smit EM, et al. Predictive value of MR imaging-dependent and non-MR imaging-dependent parameters for recurrence of laryngeal cancer after radiation therapy. Radiology 1995;196(3):735–739.
51. Kirchner JA. Glottic-supraglottic barrier: fact or fantasy? Ann Otol Rhinol Laryngol 1997;106(8):700–704.
52. Becker M, Zbaren P, Delavelle J, et al. Neoplastic invasion of the laryngeal cartilage: reassessment of criteria for diagnosis at CT [see comments]. Radiology 1997;203(2):521–532.
53. Castelijns J, Gerritsen G, Kaiser M, et al. Invasion of laryngeal cartilage by cancer: comparison of CT and MR imaging. Radiology 1987;166:199–206.
54. Castelijns J, Kaiser M, Valk K, et al. MR imaging of laryngeal cancer. J Comput Assist Tomogr 1987;11(1):134–140.
55. Becker M, Zbaren P, Laeng H, Stoupis C, Porcellini B, Vock P. Neoplastic invasion of the laryngeal cartilage: comparison of MR imaging and CT with histopathologic correlation [see comments]. Radiology 1995;194(3):661–669.
56. Johnson J. A surgeon looks at cervical lymph nodes. Radiology 1990;175:607–610.
57. Curtin HD, Ishwaran H, Mancuso AA, Dalley RW, Caudry DJ, McNeil BJ. Comparison of CT and MR imaging in staging of neck metastases. Radiology 1998;207(1):123–130.
58. Wagenfeld D, Harwood A, Bryce D, et al. Second primary respiratory tract malignant neoplasms in supraglottic carcinoma. Arch Otolaryngol 1981;107:135–138.
59. Lawson W, Biller H. Supraglottic cancer. In: Bailey B, Biller H, eds. Surgery of the Larynx. Philadelphia: WB Saunders, 1985;243–256.
60. Lawson W, Biller H, Suen J. Cancer of the larynx. In: Suen J, Myers E, eds. Cancer of the Head and Neck. New York: Churchill Livingstone, 1989;533–591.
61. Thawley S, Sessions D. Surgical therapy of supraglottic tumors. In: Thawley S, Panje W, eds. Comprehensive Management of Head and Neck Tumors. Philadelphia: WB Saunders, 1987;959–990.
62. DeSanto LW. Cancer of the supraglottic larynx: a review of 260 patients. Otolaryngol Head Neck Surg 1985;93(6):705–711.
63. Weinstein GS, Laccourreye O, Brasnu D, Tucker J, Montone K. Reconsidering a paradigm: the spread of supraglottic carcinoma to the glottis. Laryngoscope 1995;105(10):1129–1133.
64. Kirchner JA. One hundred laryngeal cancers studies by serial section. Ann Otol Rhinol Laryngol 1969;78(4):689–709.
65. Bocca E, Pignataro O, Mosciaro O. Supraglottic surgery of the larynx. Ann Otol Rhinol Laryngol 1968;77(6):1005–1026.
66. Lutz CK, Johnson JT, Wagner RL, Myers EN. Supraglottic carcinoma: patterns of recurrence. Ann Otol Rhinol Laryngol 1990;99(1):12–17.
67. Pearson BW, Woods RDD, Hartman DE. Extended hemilaryngectomy for T3 glottic carcinoma with preservation of speech and swallowing. Laryngoscope 1980;90(12):1950–1961.
68. Pearson BW, DeSanto LW, Olsen KD, Salassa JR. Results of near-total laryngectomy. Ann Otol Rhinol Laryngol 1998;107(10 Pt 1):820–825.
69. Levine PA, Brasnu DF, Ruparelia A, Laccourreye O. Management of advanced-stage laryngeal cancer. Otolaryngol Clin North Am 1997;30(1):101–112.
70. Zeitels SM. Surgical management of early supraglottic cancer. Otolaryngol Clin North Am 1997;30(1):59–78.
71. Davis RK. Endoscopic surgical management of glottic laryngeal cancer. Otolaryngol Clin North Am 1997;30:79–86.
72. Lawson W, Biller H. Glottic and subglottic tumors. In: Thawley S, Panje W, eds. Comprehensive Management of Head and Neck Tumors. Philadelphia: WB Saunders, 1987;991–1015.
73. Bailey B. Glottic carcinoma. In: Bailey B, Biller H, eds. Surgery of the Larynx. Philadelphia: WB Saunders, 1985;257–278.
74. Olsen KD, DeSanto LW, Pearson BW. Positive Delphian lymph node: clinical significance in laryngeal cancer. Laryngoscope 1987;97(9):1033–1037.
75. Yousem DM, Hatabu H, Hurst RW, et al. Carotid artery invasion by head and neck masses: prediction with MR imaging. Radiology 1995;195(3):715–720.
76. Loevner LA, Ott IL, Yousem DM, et al. Neoplastic fixation to the prevertebral compartment by squamous cell carcinoma of the head and neck. AJR 1998;170(5):1389–1394.
77. Becker M, Moulin G, Kurt AM, et al. Non-squamous cell neoplasms of the larynx: radiologic-pathologic correlation. Radiographics 1998;18(5):1189–1209.
78. Becker M, Moulin G, Kurt AM, et al. Atypical squamous cell carcinoma of the larynx and hypopharynx: radiologic features and pathologic correlation. Eur Radiol 1998;8(9):1541–1551.
79. Olsen KD, Lewis JE, Suman VJ. Spindle cell carcinoma of the larynx and hypopharynx. Otolaryngol Head Neck Surg 1997;116(1):47–52.
80. McKiernan DC, Watters GW. Smooth muscle tumours of the larynx. J Laryngol Otol 1995;109(1):77–79.
81. Sakai O, Curtin HD, Faquin WC, Fabian RL. Dedifferentiated chondrosarcoma of the larynx. AJNR 2000;21(3):584–586.
82. Schiff NF, Annino DJ, Woo P, Shapshay SM. Kaposi's sarcoma of the larynx. Ann Otol Rhinol Laryngol 1997;106(7 Pt 1):563–567.
83. Batsakis JG Luna MA, Byers RM. Metastases to the larynx. Head Neck Surg 1985;7:458–462.
84. Fischbein NJ, Lim CC, Sloan SH. Metastatic chordoma to the larynx in a patient presenting with hoarseness. J Comput Assist Tomogr 2000;24(2):339–341.
85. Johnson J, Curtin H. Deep neck lipoma. Ann Otol Rhinol Laryngol 1987;96:472–473.
86. Jones S, Myers E, Barnes E. Benign neoplasms of the larynx. In: Fried M, ed. The Larynx: A Multidisciplinary Approach. Boston: Little, Brown, 1988;401–420.
87. Supance J, Queneue D, Crissman J. Endolaryngeal neurofibroma. Otolaryngol Head Neck Surg 1980;88:74–79.
88. Stines J, Rodde A, Carolus J, et al. CT findings of laryngeal involvement in von Recklinghausen disease. J Comput Assist Tomogr 1987;11(1):141–143.
89. Henderson L, Denneny JI, Teichgraeber J. Airway obstructing epiglottic cyst. Ann Otol Rhinol Laryngol 1985;94:473–475.
90. Glazer H, Mauro M, Aronberg D, et al. Computed tomography of laryngoceles. AJR 1983;140:549–552.
91. Hubbard C. Laryngocele. a study of five cases with reference to radiologic features. Clin Radiol 1987;38:639–643.
92. Michel J, Weinstein L. Laryngeal infections. In: Fried M, ed. The Larynx: A Multidisciplinary Approach. Boston: Little, Brown, 1988;237–247.
93. Souliere C, Kirchner J. Laryngeal perichondritis and abscess. Arch Otolaryngol 1985;111:481–484.
94. Nemzek W, Katzberg R, Van Slyke M, et al. A reappraisal of the radiologic findings of acute inflammation involving the epiglottis and supraglottic structures in adults. AJNR 1995;16:495–502.
95. Michaels L. Pathology of the Larynx. Berlin, New York: Springer-Verlag, 1984.
96. Borges A, Fink J, Villablanca P, Eversole R, Lufkin R. Midline destructive lesions of the sinonasal tract: simplified terminology based on histopathologic criteria. AJNR 2000;21(2):331–336.
97. Brageau-Lamontagne L, et al. Cricoarytenoiditis: CT assessment in rheumatoid arthritis. Radiology 1986;158:463–466.
98. Oddone M, Toma P, Taccone A, Hanau G, Delogu A, Gemme G. Relapsing polychondritis in childhood: a rare observation studied by CT and MRI. Pediatr Radiol 1992;22(7):537–538.
99. Mendelson DS, Som PM, Crane R, Cohen BA, Spiera H. Relapsing polychondritis studied by computed tomography. Radiology 1985; 157(2):489–490.
100. Casselman JW, Lemahieu SF, Peene P, Stoffels G. Polychondritis affecting the laryngeal cartilages: CT findings. AJR 1988;150(2): 355–356.
101. Hyams V, Heffner D. Laryngeal pathology. In: Tucker H, ed. The Larynx, 2nd ed. New York: Thieme, 1993;35–80.

Copyright © 2003, Mosby, Inc. All rights reserved.

102. Heman-Ackah YD, Remley KB, Goding GS Jr. A new role for magnetic resonance imaging in the diagnosis of laryngeal relapsing polychondritis. Head Neck 1999;21(5):484–489.
103. Wilson JA, White A, von Haacke NP, et al. Gastroesophageal reflux and posterior laryngitis. Ann Otol Rhinol Laryngol 1989;98(6): 405–410.
104. Carr MM, Nguyen A, Poje C, Pizzuto M, Nagy M, Brodsky L. Correlation of findings on direct laryngoscopy and bronchoscopy with presence of extraesophageal reflux disease [in process citation]. Laryngoscope 2000;110(9):1560–1562.
105. Benjamin B, Roche J. Vocal granuloma, including sclerosis of the arytenoid cartilage: radiographic findings. Ann Otol Rhinol Laryngol 1993;102(10):756–760.
106. Lahoz Zamarro MT, Valero Ruiz J, Royo Lopez J, Camara Jimenez F. [Open wound of the larynx caused by the horn of a bull.] Ann Otorrinolaringol Ibero Am 1990;17(1):77–84.
107. Schaefer S. Use of CT scanning in the management of the acutely injured larynx. Otolaryngol Clin North Am 1991;24(1):31–36.
108. Biller H, Lawson W. Management of acute laryngeal trauma. In: Bailey B, Biller H, eds. Surgery of the Larynx. Philadelphia: WB Saunders, 1985;149–154.
109. Duda JJ Jr, Lewin JS, Eliachar I. MR evaluation of epiglottic disruption. AJNR 1996;17(3):563–566.
110. Snyderman C, Weissman J, Tabor E, et al. Crack cocaine burns of the larynx. Arch Otolaryngol Head Neck Surg 1991;17(7):792–795.
111. Love J. Embryology and anatomy. In: Bluestone C, Stool S, eds. Pediatric Otolaryngology. Philadelphia: WB Saunders, 1983;1135–1140.
112. Tucker J. Developmental anatomy of the larynx. In: Bailey B, Biller H, eds. Surgery of the Larynx. Philadelphia: WB Saunders, 1985;3–14.
113. Sanudo J, Domenech-Mateu J. The laryngeal primordium and epithelial lamina. A new interpretation. J Anat 1990;171:207–222.
114. Cotton R, Reilly J. Congenital malformations of the larynx. In: Bluestone C, Stool S, eds. Pediatric Otolaryngology. Philadelphia: WB Saunders, 1983;1215–1224.
115. Schlesinger A, Tucker G. Elliptical cricoid cartilage: a unique type of congenital subglottic stenosis. AJR 1986;146:1133–1136.
116. McMillan W, Duvall A. Congenital subglottic stenosis. Arch Otolaryngol 1968;87:272–274.
117. Weston M, Porter H, Berry P, et al. Ultrasonographic prenatal diagnosis of upper respiratory tract atresia. J Ultrasound Med 1992;11:673–675.
118. Dolkart L, Reimers F, Wertheimer I, et al. Prenatal diagnosis of laryngeal atresia. J Ultrasound Med 1992;11:496–498.
119. Wilkinson A, Mackenzie S, Hendry G. Complete laryngotracheo-esophageal cleft: CT diagnosis and associated abnormalities. Clin Radiol 1990;41(6):437–438.
120. Ravich W, Donner M, Kashima H. The swallowing center: concepts and procedures. Gastrointest Radiol 1985;10(3):255–261.
121. Farooq P. Recurrent laryngeal nerve paralysis: laryngographic and computed tomography study. Radiology 1983;148:149–151.
122. Romo LV, Curtin HD. Atrophy of the posterior cricoarytenoid muscle as an indicator of recurrent laryngeal nerve palsy. AJNR 1999;20(3):467–471.
123. Levine H, Tucker H. Surgical management of the paralyzed larynx. In: Bailey B, Biller H, eds. Surgery of the Larynx. Philadelphia: WB Saunders, 1985;117–134.
124. McAlpine J, Fuller A. Localized laryngeal amyloidosis: a report of a case with a review of the literature. J Laryngol 1964;78:296–303.
125. Weissman JL, Curtin HD. Benign erosion of laryngeal cartilage: report of two cases. AJNR 1990;11(6):1215–1216.
126. Deutsch EC, Schild JA, Mafee MF. Dysphagia and Forrestier's disease. Arch Otolaryngol 1985;111:400–402.
127. Som P, Biller H. Computed tomography of the neck in the postoperative patient: radical neck dissection and the myocutaneous flap. Radiology 1983;148:157–161.
128. Weissman JL, Curtin HD, Johnson JT. Thyroid gland after total laryngectomy: CT appearance. Radiology 1998;207(2):405–409.
129. Niemeyer J, Balfe D, Hayden R. Neck evaluation with barium-enhanced radiographs and CT scans after supraglottic subtotal laryngectomy. Radiology 1987;162:493–498.
130. Williford M, Rice R, Kelvin F, et al. Revascularized jejunal graft replacing the cervical esophagus: radiographic evaluation. AJR 1985;145:533–536.
131. Mukherji S, Mancuso A, Kotzur I, et al. Radiologic appearance of the irradiated larynx. Part I. Expected changes. Radiology 1994;193: 141–148.
132. Mukherji S, Mancuso A, Kotzur I, et al. Radiologic appearance of the irradiated larynx. Part II. Primary site response. Radiology 1994;193:149–154.
133. Perez C, Marks J. Radiation therapy for carcinoma of the larynx. In: Bailey B, Biller H, eds. Surgery of the Larynx. Philadelphia: WB Saunders, 1985;417–434.
134. Orlandi R, Sercarz J, Calcaterra T. Custom silastic keel for anterior laryngeal reconstruction. Laryngoscope 1994;104(9):1167–1169.
135. Cummings C, Purcell L, Flint P. Hydroxylapatite laryngeal implants for medication. Preliminary report. Ann Otol Rhinol Laryngol 1993;102(11):843–851.

Copyright © 2003, Mosby, Inc. All rights reserved.

31

Trachea: Anatomy and Pathology

J. Pierre Sasson, Nadir G. Abdelrahman, Suzanne Aquino, and Michael H. Lev

INTRODUCTION
ANATOMY AND PHYSIOLOGY
- Gross Anatomy/Histology
- Innervation and Blood Supply
- Lymphatic Drainage
- Surrounding Anatomic Structures

RADIOGRAPHIC EVALUATION OF THE TRACHEA
- Plain Radiographs
- CT Scanning
- MR Imaging
- Virtual Bronchoscopy

PATHOLOGIC CONDITIONS
- Congenital Abnormalities
  - Tracheomalacia
  - Congenital Stenosis (Subglottic/Tracheal)
  - Tracheal Bronchus
  - Tracheal Diverticula (Tracheocele)
  - Tracheoesophageal Fistula
  - Vascular Rings and Slings
- Diffuse Disorders of the Trachea (Nonneoplastic)
  - Conditions Causing Narrowing of the Trachea
    - *Infection*
    - *Tuberculosis*
    - *Histoplasmosis*
    - *Relapsing Polychondritis*
    - *Granulomatous Disease of the Trachea*
    - *Sarcoidosis*
    - *Amyloidosis*
    - *Tracheopathia Osteochondroplastica*
    - *Saber-Sheath Trachea*
  - Diffuse Conditions Causing Widening of the Trachea
    - *Tracheobronchomegaly (Mounier-Kuhn Syndrome)*
    - *Secondary Tracheomegaly*
- Trauma
  - Posttracheostomy/Postintubation Complications
- Tracheal Tumors
  - General Considerations
  - Malignant Tumors
    - *Squamous Cell Carcinoma*
    - *Adenoid Cystic Carcinoma*
    - *Mucoepidermoid Carcinoma*
    - *Chondrosarcoma*
  - Benign Tumors
    - *Benign Vascular Tumor*
    - *Squamous Cell Papilloma*
    - *Cartilaginous Tumors and Hamartomas*
    - *Carcinoid Tumor*
    - *Benign Mixed Cell Tumors*
- Tumor-Like Conditions

INTRODUCTION

The trachea is a flexible cylindrical tube composed of cartilaginous rings, connected by a fibromuscular membrane and lined internally by mucosa. The trachea facilitates the passage of air between the larynx and the lungs. It is positioned midline in the neck and courses slightly to the right in the upper thorax. It extends from the cricoid cartilage superiorly (at about the level of the sixth cervical vertebra) to the carina inferiorly.[1] The location of the lower end of the trachea varies with body posture, and with inspiration and expiration, and in deep inspiration the carina may descend to the level of the sixth thoracic vertebra.[2] The length of the trachea ranges from 10 to 13 cm, averaging approximately 11 cm.[2] Viewed laterally, the trachea assumes an oblique course, running from superoanterior to in-

Copyright © 2003, Mosby, Inc. All rights reserved.

feroposterior. In severely kyphotic patients, the trachea may have a horizontal orientation.

The degree to which the laryngeal glottis (true vocal folds) is open significantly affects airflow patterns in the trachea. The glottis has the smallest, yet the most variable, cross-sectional area of the upper respiratory tract. Air currents in the upper trachea are typically turbulent during inspiration, with a transition to more laminar flow in the middle and distal trachea. The velocity of the air stream in the distal trachea during quiet respiration is approximately 1 mm/sec.[2] During forced expiration or coughing, intrathoracic pressure becomes positive, transmural pressure differences increase, and narrowing of the intrathoracic trachea occurs. This narrowing accelerates airflow and facilitates expectoration. The airflow in the central trachea during coughing has been estimated to be approximately 250 km/hr.[3] Airflow patterns in the trachea are significantly more complicated in cases with tracheal stenosis or tracheomalacia.

Gross Anatomy/Histology

The skeleton of the trachea is composed of 16 to 20 incomplete hyaline cartilaginous rings that are bound in a tight elastic connective tissue oriented longitudinally.[1] These cartilage rings may calcify with age and two or more cartilages may unite, either partially or fully. Rarely, they may bifurcate posteriorly. The cartilage forms about two thirds of the circumference of the trachea. Because the posterior border of the trachea is formed by fibromuscular membrane, the cross-sectional shape of the trachea is that of the letter D, with the flat side posterior. The first and last cartilaginous rings differ from the rest of the tracheal rings. The first ring, located approximately 1.5 to 2 cm below the true vocal cords, is partly recessed into the broader ring of the cricoid cartilage and is the broadest of all the cartilage rings. The first ring is sometimes merged to the cricoid cartilage or to the second tracheal ring. The second, third, and fourth rings are surrounded anteriorly and laterally by the thyroid gland.[2] The last tracheal ring is thicker and broad, and on its lower border there is a triangular process that curves downward and backward between the origins of the bronchi.[4] The mucosal portions of the posterior trachea are separated from the esophagus by a thin layer of connective tissue. This region is often referred to as the common party wall, as it separates the trachea in front from the esophagus behind.

The cartilaginous rings allow the tracheal lumen to retain its patency, even in the extreme circumstances of coughing and forced expiration. The diameter of the tracheal lumen, like its length, depends on the height, age, and gender of the individual. In men, tracheal diameter ranges from 13 to 25 mm in the coronal plane and 13 to 27 mm in the sagittal plane. Tracheal diameter is slightly less in women, ranging from 10 to 21 mm in the coronal plane and 10 to 23 mm in the sagittal plane.[1] Cross-sectional area correlates most closely with height in children. With increasing age, the transverse section of the tracheal lumen successively assumes the following shapes: round, lunate, flattened, and roughly elliptical. Respiratory cycle, certain maneuvers, and body position also contribute significantly to the variation in lumen shape. During rapid deep inspiration, the thoracic portion of the trachea widens and the cervical portion narrows. The opposite pattern occurs during expiration; the extrathoracic tracheal lumen increases in size during coughing, Valsalva maneuver, or forced expirations, whereas the intrathoracic portion decreases.[2]

The trachea is lined by pseudostratified columnar epithelium that sits on an elastic lamina propria. Goblet mucous cells and small subepithelial glands that secrete onto the luminal surface are interspersed among the ciliated columnar cells.[3] There has been recent interest in studying the small intercellular bridges (tight junctions) situated between the ciliated cells.[5] These junctions may explain the observation that cilia in the respiratory tract move in a synchronous and coordinated manner. The cilia beat about 1000 times per minute, propelling the mucous lining upward toward the pharynx, from which it can be coughed up several times a day. Normally, the amount of bronchotracheal secretions expelled is quite small, averaging 10 cc over a 24 hour period.[3] Mechanical irritation by endotracheal tubes or suction devices, however, can increase this volume 10-fold. During disease states, the amount and quality of the periciliary fluid and mucous can change, interfering with the drainage and protective functions of the mucosa.

Each tracheal cartilage has a perichondrium, continuous with a dense fibrous membrane that is between adjacent cartilages and within the posterior membranous wall. The perichondrium and membrane are composed primarily of collagen with some elastin fibers. Smooth muscle fibers (trachealis muscle) are in the membrane posteriorly. Most of these muscle fibers are transverse, attaching to the free ends of the tracheal cartilages and providing alteration in the tracheal cross-sectional area. There are also longitudinal fibers. The trachealis muscle can diminish the caliber of the tracheal lumen or prevent overdistention of the trachea when there is abdominal straining prior to coughing.

Innervation and Blood Supply

The trachea is innervated by parasympathetic tracheal branches of the vagus nerve, by the recurrent laryngeal nerve, and by sympathetic nerves. The *parasympathetic pre*ganglionic nerve fibers send their axons to local ganglia in the tracheal wall. The *sympathetic post*ganglionic supply comes from both the cervical ganglia and the second through fourth thoracic ganglia. The parasympathetic *post*ganglionic as well as the sympathetic fibers innervate seromucous glands, smooth muscles, and blood vessels.[6] Tracheal smooth muscle, controlled by these autonomic nerves, contracts to narrow and stabilize the tracheal lumen, preventing excessive invagination of the dorsal membrane.

Branches of the recurrent laryngeal nerve perforate the lateral tracheal wall, providing a rich supply of sensory afferents to the inner tracheal mucosa. The trachea has a segmental blood supply, shared largely with the esophagus and derived from multiple branches of the inferior thyroidal and bronchial arteries. The inferior thyroidal arteries, as well as the extreme right intercostal artery, supply the superior portion of the trachea; branches from both the bronchial arteries and the third intercostal artery supply the inferior

Copyright © 2003, Mosby, Inc. All rights reserved.

portion of the trachea. Tracheal venous drainage is to the inferior thyroid venous plexus.

Lymphatic Drainage

Numerous lymph nodes surround the trachea, most notably in the carinal region. The major lymph node groups are the inferior tracheobronchial nodes and the right and left superior bronchial nodes. The lymphatic drainage from the proximal two thirds of the trachea passes through to the pre- and paratracheal lymph nodes (level VI), eventually draining into the lower jugular nodes (level IV).

The pattern of tracheal lymph node drainage is important for the radiologist to be aware of for the purpose of lung cancer staging. For example, left apical lung cancers tend to drain to aortopulmonary window nodes rather than to hilar and paratracheal nodes. Lower-lobe cancers are more likely to drain to hilar nodes, followed in frequency by subcarinal and paratracheal region nodes. Staging of lung cancer, according to the American Thoracic Association, is based largely on knowledge of the nodal stations of the mediastinum—particularly the paratracheal nodes.[7]

Surrounding Anatomic Structures

The trachea is surrounded by the esophagus, thyroid gland, lungs, aorta, vagus nerves, recurrent laryngeal nerves, and azygos veins. It moves vertically with neck extension or flexion relative to these structures. The esophagus is positioned directly posterior to the cervical portion of the trachea and typically extends slightly to the left of the intrathoracic portion. Foreign bodies or tumors of the esophagus may therefore manifest with airway symptoms due to compression of the posterior membranous trachea (common party wall). On plain film radiography, the thin tracheal wall (1 to 2 mm) is well defined by air in the tracheal lumen, as well as by the adjacent mediastinal fat. As mentioned, cartilaginous calcification is increasingly common with age, especially in women.[1]

The vagus nerve exits the skull base at the jugular foramen and courses inferiorly along the posterolateral aspect of the carotid artery. On the left, the recurrent laryngeal nerve loops from anterior to posterior under the aortic arch, at the ductus arteriosus, where it begins its ascent. On the right, it similarly loops under the subclavian artery. The recurrent laryngeal nerves ascend bilaterally in the tracheoesophageal groove.[8] The course of the left recurrent laryngeal nerve is of clinical interest for several reasons. An aneurysm of the aorta, or another mass lesion, can apply traction to the nerve, resulting in recurrent laryngeal nerve palsy. A very rare mechanism of recurrent laryngeal nerve palsy relates to severe coughing spasms, during which the heart and great vessels can create traction on the left recurrent laryngeal nerve sufficient to cause neuropraxia.

Under normal conditions, the aortic arch courses anterior to the intrathoracic trachea, along the left and dorsally. The most fixed point of the trachea is in this region. The descending aorta may cause a slight impression at the lower left trachea. The innominate (brachiocephalic) artery crosses anterior to the trachea and can cause an indentation, particularly in infants. The azygos vein crosses the distal dorsal trachea toward the right tracheobronchial angle, and rarely produces an indentation. In infancy, the innominate vein lies anterior to the lower cervical trachea; in adulthood, this vein is intrathoracic.[9, 10]

RADIOGRAPHIC EVALUATION OF THE TRACHEA

The radiologic evaluation of the trachea includes plain films (both lateral neck and anteroposterior high-kilovoltage views), tomograms, computed tomography (CT), and magnetic resonance (MR) imaging.[11] CT is of great value in assessing the spectrum of disease that affects the trachea and has largely become the imaging modality of choice, especially now that two-dimensional and three-dimensional reformatted views can be routinely obtained through image postprocessing. Airway fluoroscopy, barium studies of the esophagus, angiography of vascular lesions, and conventional tomography all may play a part in the evaluation of tracheal pathology.

Plain Radiographs

Plain chest radiography in the posteroanterior (PA) and lateral projections is the most frequently used imaging tool for patient screening (Fig. 31-1). A high-kilovoltage (140 kVp) technique is preferred because it reduces the visibility of the bony thorax and improves imaging of the various mediastinal structures. There is considerable overlap of the trachea with the mediastinum and bony thorax, making many tracheal lesions difficult to visualize. The lateral neck film, obtained with the head slightly hyperextended, is useful for studying the cervical trachea. Flexion of the neck, especially in children, may cause buckling of the trachea, resulting in the appearance of a prevertebral ''pseudomass.'' The majority of patients with tracheal pathology require further imaging evaluation with CT scanning.

CT Scanning

CT has largely become the imaging modality of choice for most tracheal lesions. It allows direct visualization of the cross-sectional tracheal airway, and can be used to determine the size, extent, and attenuation value of a lesion. Helical (spiral) CT, with 1 to 1.5 mm thin sections, allows high-quality multiplanar reconstruction, facilitating detailed evaluation of disorders such as tracheal stenosis and tumors. CT is helpful in the evaluation of tracheal neoplasms that invade the mediastinum, as well as in the evaluation of other lesions such as goiters or vascular rings that may compress the trachea. CT can also be used to determine accurately the length of a tracheal lesion relative to the endoscopic reference points of either the larynx or the carina. CT can identify enlarged lymph nodes along the tracheal wall and in the mediastinum. It can also identify calcific or fatty

Copyright © 2003, Mosby, Inc. All rights reserved.

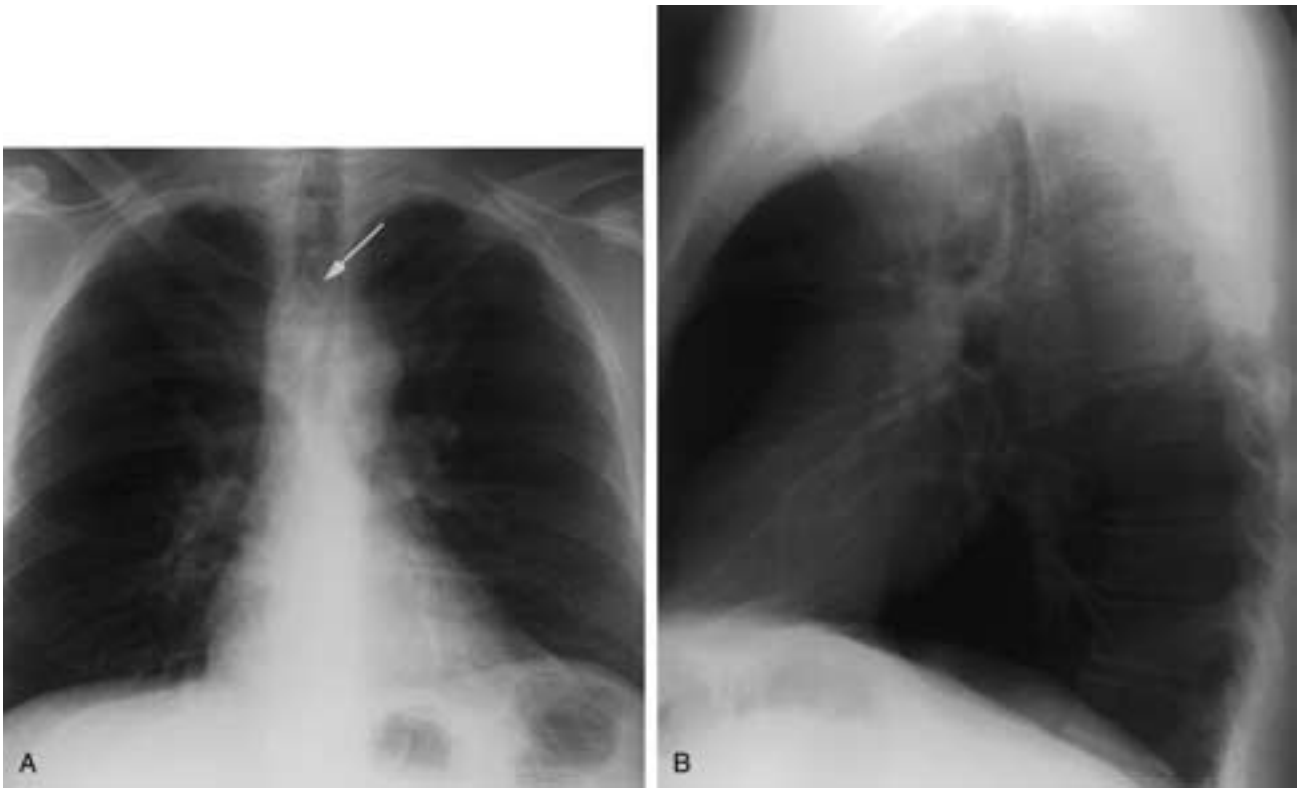

VIEW IMAGE

FIGURE 31-1 Large cell carcinoma. Posteroanterior (**A**) and lateral (**B**) views of the chest demonstrate a large, broad-based endoluminal mass arising from the right lateral tracheal wall (*arrow* in **A**).

densities, as well as vascular enhancement of tumors or aneurysms. Abnormal collapsibility of the trachea (i.e., tracheomalacia) can be identified by paired inspiratory/expiratory CT scans. CT is also useful in directing surgical or fine needle aspiration (FNA) biopsy of more aggressive lesions. Finally, spiral CT angiography with 3D reconstruction methods (Fig. 31-2) may reveal vascular anomalies affecting the tracheal lumen.

Congenital lesions affecting the trachea typically require a chest X-ray as a screening examination, followed by MR imaging or spiral CT to identify vascular anomalies or mediastinal masses. Inspiratory and expiratory CT can be used to investigate tracheal stenosis. CT is also the imaging modality of choice to investigate tracheal stenosis due to intubation or tracheotomy tubes. Finally, spiral CT is considered a valuable tool in the investigation and treatment planning of all lesions that will undergo endoscopic therapy.[12]

MR Imaging

MR imaging can be utilized in the assessment of tracheal stenosis and tumors. However, the current role of MR imaging is quite limited, as its spatial resolution does not permit adequate evaluation of the segmental bronchi and the longer scan times allow for respiratory motion image degradation. MR imaging, however, can depict a moderate degree of anatomic detail *without* employing ionizing radiation or iodinated intravenous contrast medium.[13] T1-weighted sequences demonstrate the anatomy of the trachea and surrounding structures in detail, whereas T2-weighted sequences add to the characterization of lesion signal differences, such as differentiation of cystic from solid masses. MR imaging is particularly useful in cases of tracheal compression by vascular rings and slings or by other mediastinal masses.

Virtual Bronchoscopy

Three-dimensional reconstruction of helical CT data permits navigation through the tracheobronchial tree via real-time simulated bronchoscopy. Recent advances in computer technology allow faster imaging times with a decrease in radiation dose and motion artifact. Unlike conventional fiberoptic bronchoscopy, virtual broncoscopy (VB) permits visualization of the relationship between an airway lesion and the surrounding mediastinal structures as well as airway patency beyond a stenosis. In addition, the viewer can repeatedly navigate through the airway without adverse consequences to the patient. The level of obstruction and the width and length of an airway stenosis can easily be measured. This information can be used in preoperative planning for resection of tracheal tumors or for palliative stent placement. VB also appears to be useful in imaging pediatric disorders such as vascular rings, tracheomalacia, and congenital tracheoesophageal fistula.

Despite initial enthusiasm, however, the practical application of volume rendering techniques remains in question.

Copyright © 2003, Mosby, Inc. All rights reserved.

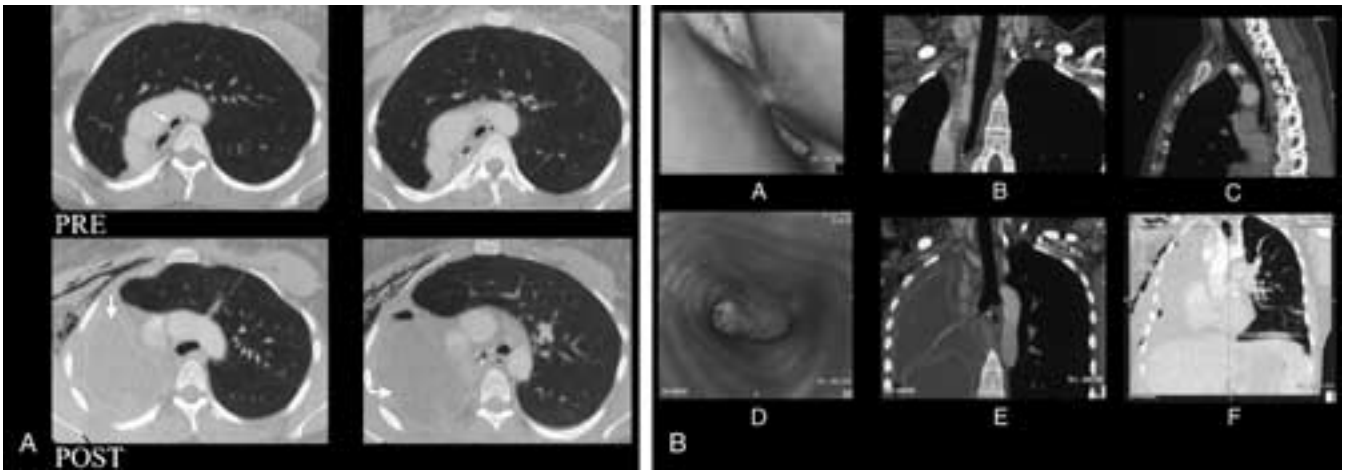

VIEW IMAGE

FIGURE 31-2 Postpneumonectomy syndrome. A 28-year-old female with congenital hypoplasia of the right lung who underwent right pneumonectomy following recurrent pulmonary infections. Several months after surgery, the patient developed severe shortness of breath. **A**, Contrast-enhanced axial CT scan of the chest shows right mediastinal shift, with herniation of the left lung into the right hemithorax (*upper row*). Note the compression of the proximal left mainstem bronchus between the transverse aorta and the vertebral body (*arrow, left upper row*). The mediastinal shift was corrected by insertion of saline breast implants (*short arrows, lower rows*) into the right pneumonectomy space. Following this, the trachea was midline and the compression of the left mainstem bronchus was resolved. **B**, Three-dimensional reconstructions from the dataset in **A** before and after placement of saline implants.

Conventional axial CT and virtual images are equally accurate in estimating the maximal luminal diameter and cross-sectional area of the central airways. Sufficient clinical data are not yet available to judge whether VB offers a true benefit to patients over that of the already high predictive values of conventional CT. Although VB may not offer improved diagnostic accuracy, it is a promising technique that tends to enhance the overall understanding of a disease process, and it will likely prove useful in surgical planning and communication of imaging results to referring clinicians (Figs. 31-2B, 31-3, and 31-4).[14, 15]

PATHOLOGIC CONDITIONS

Clinical detection of tracheal disease is notoriously difficult. With healthy lungs, occlusion of more than 75% of the tracheal lumen is necessary to cause symptoms of airway obstruction at rest.[1] Occlusion of about 50% of the cross-sectional tracheal airway is needed to produce symptoms of dyspnea on exertion. As a result, early identification of tracheal pathology is unusual. Symptoms such as hemoptysis, wheezing, or coughing may not manifest until disease is advanced. Radiographically, the trachea is often a blind spot on conventional X-rays, with lesions not identified until they are quite large. CT is the standard method for imaging a patient who has clinical symptoms suggesting tracheal obstruction.

Congenital Abnormalities

The trachea can be affected by an intrinsic anomaly isolated to the trachea or by an anomaly of the contiguous soft tissues that causes external pressure on the airway. Some abnormalities, such as stenosis or tracheomalacia, can occur as an isolated phenomenon or in conjunction with a second abnormality.

Tracheomalacia

Tracheomalacia is defined as collapse of the trachea on expiration, resulting in more than 10% to 20% obstruction of the airway. It is characterized by abnormal flaccidity of the trachea during the respiratory cycle, leading to abnormal collapse of the thoracic tracheal segment on expiration. Weakness of the tracheal wall results from softening of the supporting cartilage, with abnormal widening of the posterior membranous (noncartilaginous) wall. Frequently,

FIGURE 31-3 Squamous cell carcinoma. Three-dimensional virtual bronchoscopic images demonstrate intraluminal extension of tumor above the carina.

VIEW IMAGE

Copyright © 2003, Mosby, Inc. All rights reserved.

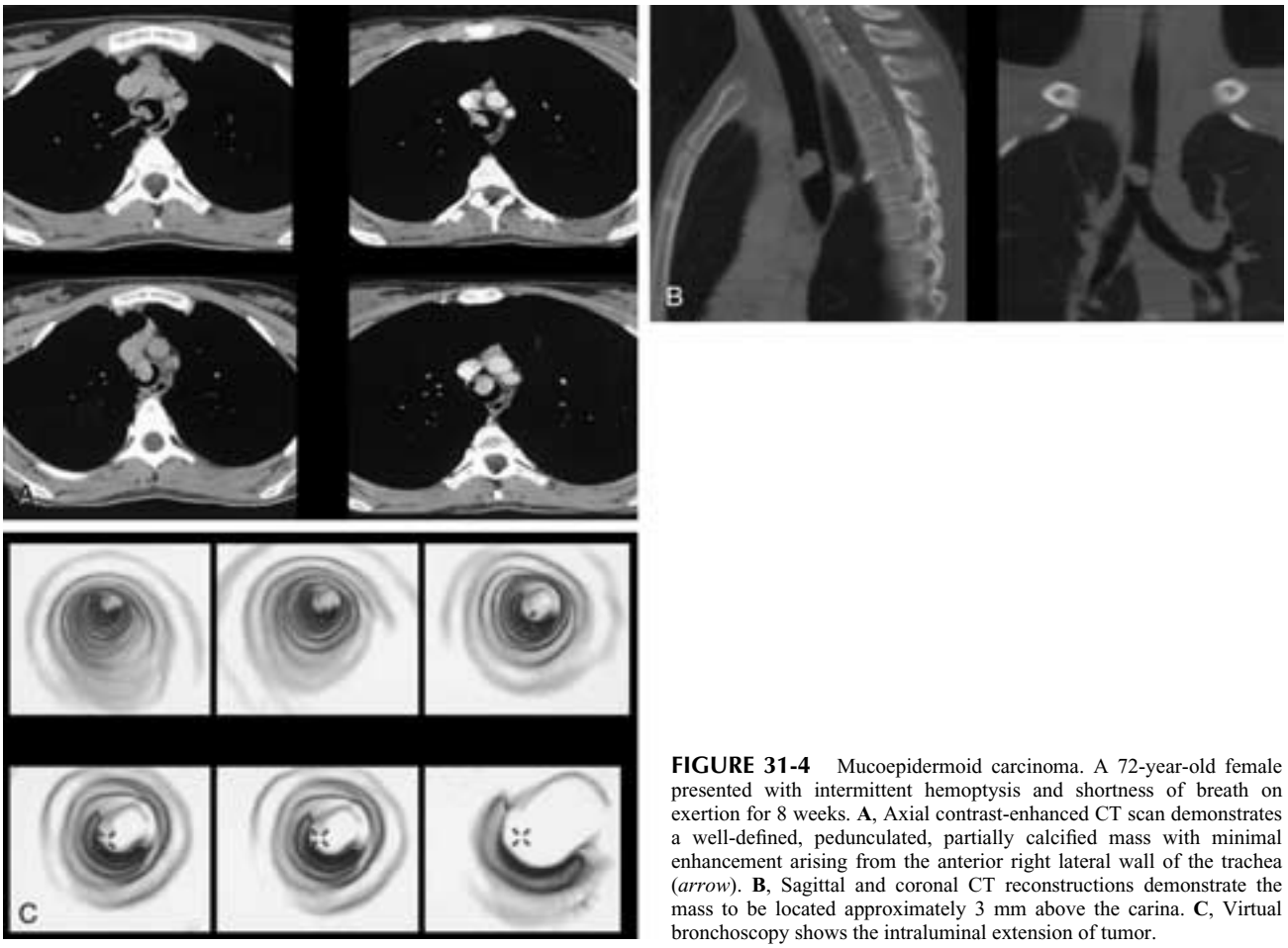

FIGURE 31-4 Mucoepidermoid carcinoma. A 72-year-old female presented with intermittent hemoptysis and shortness of breath on exertion for 8 weeks. **A**, Axial contrast-enhanced CT scan demonstrates a well-defined, pedunculated, partially calcified mass with minimal enhancement arising from the anterior right lateral wall of the trachea (*arrow*). **B**, Sagittal and coronal CT reconstructions demonstrate the mass to be located approximately 3 mm above the carina. **C**, Virtual bronchoscopy shows the intraluminal extension of tumor.

VIEW IMAGE

the anterior and posterior tracheal walls move closer together during respiration and coughing, reducing the intraluminal diameter (Figs. 31-5 and 31-6). The unsupported posterior wall may balloon anteriorly into the airway. Patients complain of inspiratory and/or expiratory stridor, wheezing, barking cough, or recurrent respiratory infections. The triad of an anterior bulging posterior tracheal wall, narrowed anteroposterior tracheal luminal diameter, and widened posterior membranous tracheal wall is typical. Tracheomalacia is the major cause of respiratory difficulty following repair of a tracheoesophageal fistula.

Patients with tracheomalacia may present with minimal symptoms or with severe, life-threatening airway obstruction. In children, the tracheobronchial tree is more collapsible than in adults. Hence, the classic expiratory stridor of tracheomalacia may be present at birth. Tracheomalacia can be categorized into either primary intrinsic or secondary extrinsic forms. Primary tracheomalacia is caused by an inherent defect of the tracheal cartilaginous rings. In secondary tracheomalacia, airway collapse on expiration may be due to extrinsic tracheal compression by a mass or vascular structure, as well as by conditions causing intrinsic weakness of the tracheobronchial structures. Secondary tracheomalacia may be associated with conditions such as tracheoesophageal fistula, laryngotracheal esophageal cleft, cardiac abnormalities, or vascular compression. Localized tracheomalacia is associated with tracheotomy.

Airway fluoroscopy, combined with a barium swallow, can demonstrate evidence of vascular compression. Rigid bronchoscopy is helpful for evaluating the degree of tracheobronchial tree collapse, as well as for documenting the presence of associated congenital airway anomalies. Cine CT imaging and 3D imaging of the trachea during inspiration and expiration are newer modalities that are likely to prove useful.[16] In cases of suspected vascular compression or cardiac anomalies contributing to tracheomalacia, MR imaging and echocardiography can also be performed.

Mild cases of primary tracheomalacia often do not require treatment, because they often resolve within the first 1 to 2 years of life. In cases of severe airway obstruction with tracheal collapse, tracheostomy with long-term positive airway pressure ventilation may be indicated. Surgical decompression of the trachea may lead to significant improvement in cases of vascular compression. Different surgical procedures have been developed for the treatment of tracheomalacia, with various degrees of success. These procedures include placement of internal and external stents, segmental resection, and cartilage grafting to the trachea.

Congenital Stenosis (Subglottic/Tracheal)

Congenital stenosis is an uncommon abnormality that usually is associated with other major or minor anomalies of the respiratory tract skeleton or other organ systems.

Copyright © 2003, Mosby, Inc. All rights reserved.

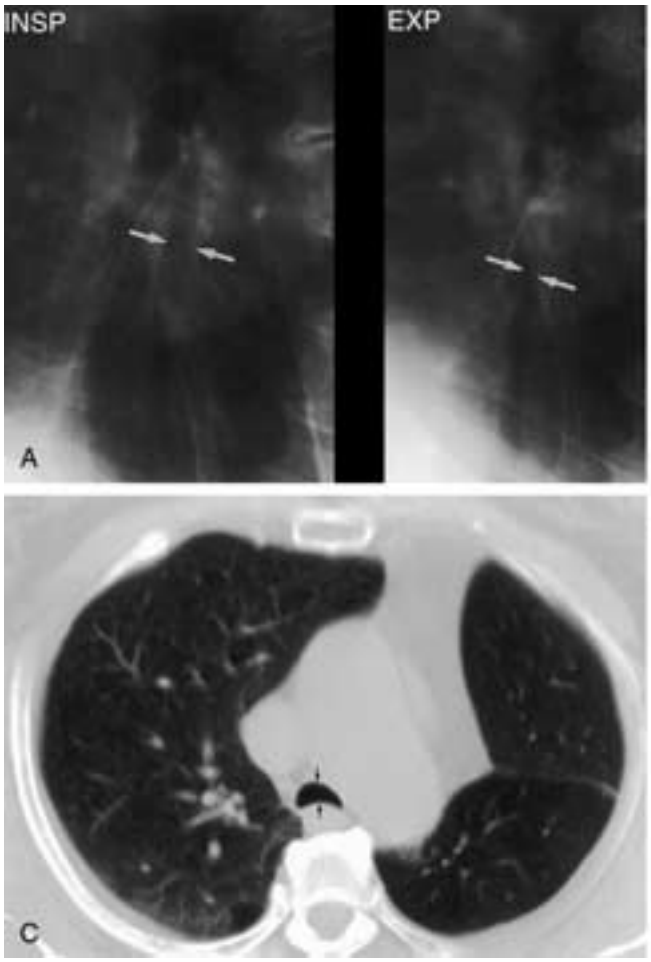

FIGURE 31-5 Tracheomalacia. **A**, Fluoroscopic evaluation of this 71- year-old man with a 5-year history of progressive stridor demonstrates diffuse narrowing of the trachea with expiration. The luminal diameter of the trachea was reduced by approximately 50% (*arrows*). Nonenhanced axial CT scan, filmed in lung windows, again demonstrates tracheal narrowing on expiration (**C**, *arrows*) compared with inspiration (**B**, *arrows*).

VIEW IMAGE

Commonly, there is an association with the H-type tracheoesophageal fistula, pulmonary hypoplasia, and a vascular sling. The affected segment of trachea has rigid walls with a narrowed lumen. The stenotic segment can be focal or affect the entire trachea, extending into the mainstem bronchi. Cartilages can be complete rigid rings.

Clinically, presentation occurs within the first weeks or months of life. Although segmental resection has been reported, it is rarely feasible due to the length of the stenotic segment. Most cases are treated conservatively and the patient may live with the stenosis, the tracheal lumen growing larger as the patient ages. However, approximately one half of these patients die either of the stenosis and associated pulmonary infections or of the major congenital anomalies associated with it.

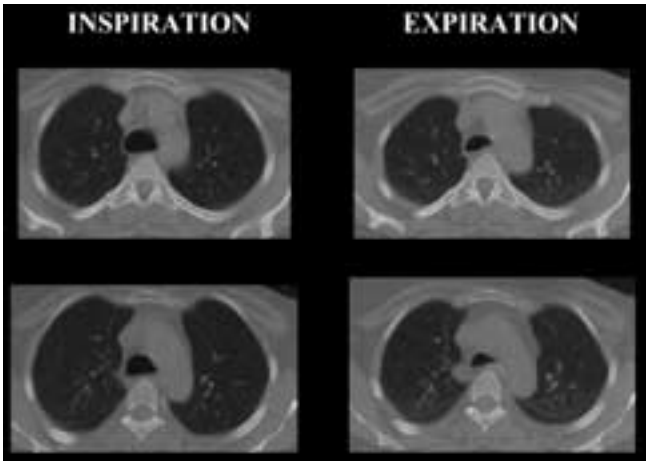

FIGURE 31-6 Tracheomalacia. A 62-year-old female with an increasingly loud, uncontrollable cough. Inspiratory and expiratory axial CT images of the upper thorax demonstrate a 44% reduction in the anteroposterior tracheal diameter on expiration. Both flexible and rigid bronchoscopy revealed a flattened, lax trachea with a redundant membranous wall.

VIEW IMAGE

Tracheal Bronchus

The term *tracheal bronchus* refers to any well-defined airway that arises from the trachea above the level of the carina. Although this anatomic configuration is normal for many mammals, it represents an anomaly in humans and is found in only 0.25% to 1% of the population.[17] Although the anomalous bronchus typically arises from the tracheal wall less than 2 cm above the tracheal bifurcation, it may arise as high as 6 cm above the carina. The tracheal bronchus originates more frequently from the right, rather than from the left, in which case it supplies a variable portion of the medial or apical right upper lobe (Fig. 31-7). The incidence of this anomaly is greatest in patients with other coexisting congenital malformations such as congenital tracheobronchial stenosis, aberrant pulmonary artery, Down's syn-

Copyright © 2003, Mosby, Inc. All rights reserved.

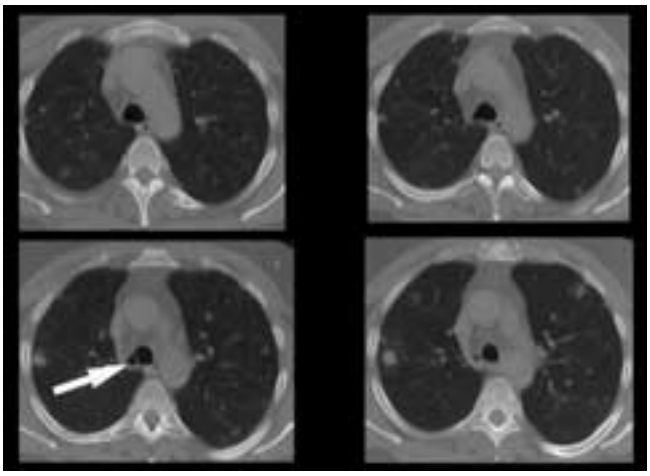

VIEW IMAGE

FIGURE 31-7 Right tracheal bronchus. Contiguous axial CT images through the upper thorax demonstrate an anomalous right upper lobe bronchus (*arrow*) arising directly from the trachea in this patient with metastatic bladder carcinoma.

drome, right aortic arch, or lung hypoplasia.[18] Although frequently asymptomatic, patients with tracheal bronchus may develop recurrent infections or bronchiectasis due to stenosis at the origin of the bronchus. Pooling of secretions, and/or obstruction of the orifice of the tracheal bronchus by an endotracheal tube, may cause atelectasis. Thus, it is important to keep this airway anomaly in mind when caring for patients with unusual sensitivity to endotracheal tube (ETT) position or with chronic right upper lobe atelectasis.

Tracheal Diverticula (Tracheocele)

A tracheocele is an outpouching or diverticulum of the posterolateral wall of the trachea.[19] Tracheocele is a rare condition that results from muscular weakness of the tracheal muscle. Wide-mouthed tracheoceles are likely acquired, whereas narrow-mouthed tracheoceles are likely congenital in origin (Fig. 31-8). Tracheoceles may be transient, seen only during periods of increased intratracheal pressure. Occasionally, on chest radiographs, they may present as thin-walled paratracheal air-filled cavities, with or without air-fluid levels. CT best displays these lesions and can provide 3D imaging of their size and extent, along with volumetric reconstruction. Although tracheoceles tend to be asymptomatic, they may become quite capacious and accumulate debris. This debris may spill into the lungs and cause pneumonia.

Tracheoesophageal Fistula

Tracheoesophageal fistula (TEF) is a common congenital anomaly, with an average frequency of 1 in 3000 to 4000 births, and is often associated with esophageal atresia.[20] TEF can exist in a number of forms (Fig. 31-9), the most common configuration being that of a proximal esophageal atresia with a distal TEF (Figs. 31-10 and 31-11). This anomaly may be associated with severe neonatal respiratory distress, often necessitating immediate tracheostomy. Approximately 85% of neonates with this TEF present within the first 24 hours of life with excessive mucus production, cough, choking, and cyanosis associated with feeding.[21] In approximately half of the patients with TEF and esophageal atresia, more than one fistula may be present. Associated

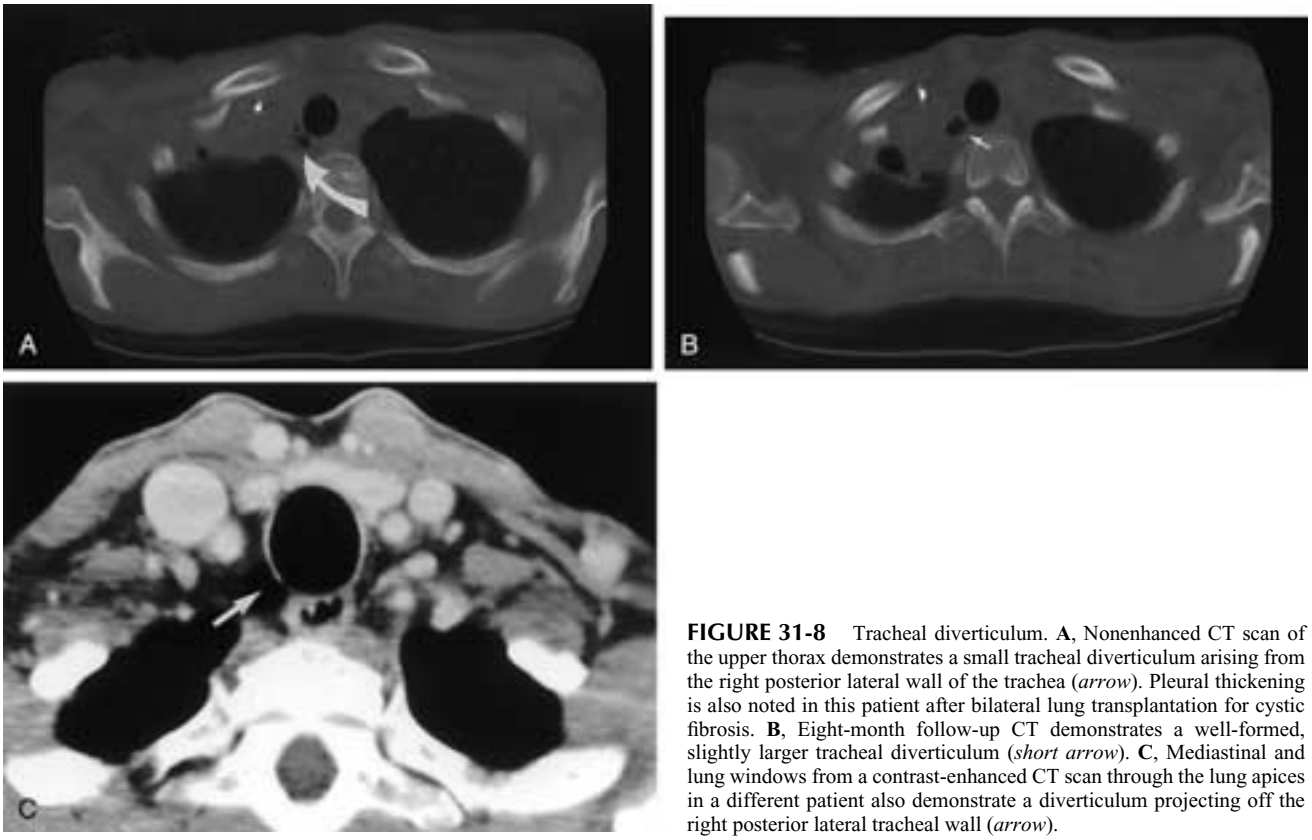

VIEW IMAGE

FIGURE 31-8 Tracheal diverticulum. **A**, Nonenhanced CT scan of the upper thorax demonstrates a small tracheal diverticulum arising from the right posterior lateral wall of the trachea (*arrow*). Pleural thickening is also noted in this patient after bilateral lung transplantation for cystic fibrosis. **B**, Eight-month follow-up CT demonstrates a well-formed, slightly larger tracheal diverticulum (*short arrow*). **C**, Mediastinal and lung windows from a contrast-enhanced CT scan through the lung apices in a different patient also demonstrate a diverticulum projecting off the right posterior lateral tracheal wall (*arrow*).

Copyright © 2003, Mosby, Inc. All rights reserved.

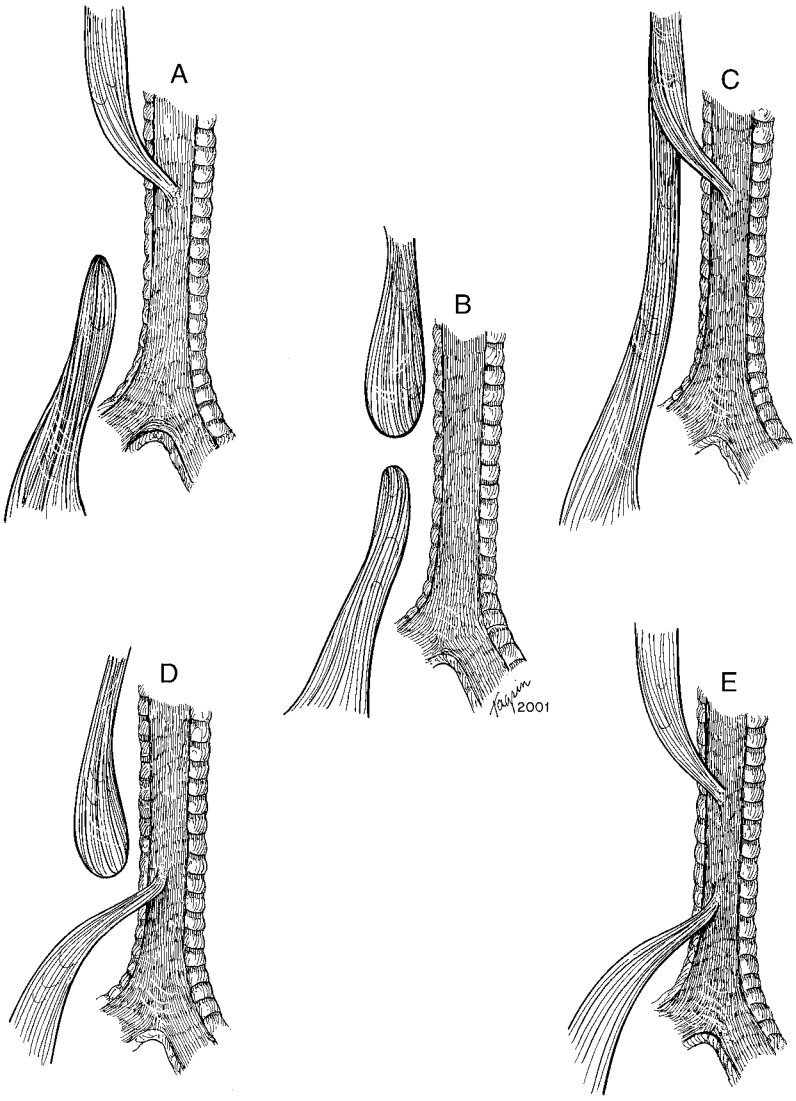

FIGURE 31-9 Classification of tracheoesophageal fistula. **A**, Atresia with upper fistula. **B**, Atresia with no fistula. **C**, No atresia, upper fistula (H type). **D**, Atresia with lower fistula. **E**, Atresia with upper and lower fistulas.

VIEW IMAGE

anomalies involving the cardiovascular, gastrointestinal, renal, or central nervous system may also be present.[22] Patients with normal birth weight and no other congenital malformations have the highest rates of survival. The overall survival rate is approximately 80%.[2]

H-type TEF, without esophageal atresia, is a less common type of TEF that has more subtle clinical manifestations and is characteristically associated with gastroesophageal reflux. Symptoms may include excessive oral secretions, respiratory distress, or immediate regurgitation of feedings; intermittent dysphagia and choking may also be present. The diagnosis of this type of TEF may be delayed until adulthood. Patients with H-type TEF usually have no associated congenital anomalies or can have congenital tracheal stenosis.

TEF *with* esophageal atresia is easily diagnosed by the failure to pass a radiopaque nasogastric tube into the stomach. The tube coils in the proximal esophageal pouch and can be seen on routine chest radiography or after the instillation of a small amount of water-soluble contrast material (Fig. 31-10B). Associated aspiration pneumonia may be present. Tracheomalacia may develop at the fistula site, usually resolves by the age of 2 years, and is best diagnosed by collapse of the airway structures on direct fluoroscopy. Patients with esophageal atresia and *both* proximal and distal TEFs (rare) may have gaseous distention of the gastrointestinal tract with aspiration pneumonia. This diagnosis can be confirmed by contrast studies. Barium swallow with fluoroscopy is typically employed to diagnose H-type fistulas. Cine-esophagography (cinefluorography or fluoroscopy with videotaping) can assist in differentiating TEF from simple laryngeal aspiration. Combined bronchoscopy and esophagoscopy have also been useful in increasing the ability to diagnose TEF. Surgery is the treatment of choice.[23]

Vascular Rings and Slings

Vascular anomalies of the great vessels include ''rings'' and ''slings''[11, 24, 25] (see also Chapter 29). Airway compression by vascular anomalies may be congenital or acquired. In children, vascular impressions on the trachea are generally congenital and may cause a spectrum of symptoms, from minimal to severe airway compression requiring intervention. Vascular compression syndromes in

Copyright © 2003, Mosby, Inc. All rights reserved.

adults are usually secondary to acquired aneurysmal dilatation of the great vessels. The radiologic evaluation of children with respiratory symptoms possibly due to vascular compression should include barium study of the esophagus, which is often affected along with the trachea by vascular rings. Contrast-enhanced CT angiography with 3D reconstructions and multiplanar reformatting is an excellent method of evaluating patients with complex great vessel anomalies. Alternatively, MR imaging can provide images of the vessels and the surrounding soft tissues.

Vascular *rings* are anomalies that completely encircle the trachea and esophagus, causing airway compression. The most common vascular ring is a double aortic arch (Fig. 31-12).[26] Patients with double aortic arch typically present early in life with airway obstruction and often require early surgical intervention. Another, less constricting, vascular ring is a right aortic arch with descending right aorta associated with an aberrant left subclavian artery and persistent ligamentum arteriosum. In both types of vascular ring, there is circumferential tracheal and esophageal indentation. Other findings include left-sided and anterior displacement of the distal trachea. Barium studies show a characteristic dorsal and left-sided impression on the esophagus.

Vascular *slings* are noncircumferential vascular anomalies that may also cause airway compromise. These anomalies may lead to significant morbidity and occasional mortality.[26] However, vascular rings often cause more severe airway symptoms than slings.[23] In the pulmonary artery sling, the left pulmonary artery originates from the right pulmonary artery and then passes between the trachea and esophagus to reach the left lung. The trachea is compressed from posteriorly, and there is an impression on the anterior esophagus seen at barium swallow.

Anterior impression on the trachea by the innominate artery in infants and children is much more common than compression by an aberrant left subclavian artery.[27] Although most patients develop symptoms during the first year of life, some reported cases have presented as late as 15 years of age. Symptoms include expiratory stridor, recurrent cough, apnea, and recurrent infection. Rigid bronchoscopy may establish the definitive diagnosis. In severe cases of airway obstruction, surgical intervention is warranted.

Diffuse Disorders of the Trachea (Nonneoplastic)

Various infections and inflammations involve the tracheal wall. They may cause infiltration with narrowing or, less commonly, widening of the trachea.

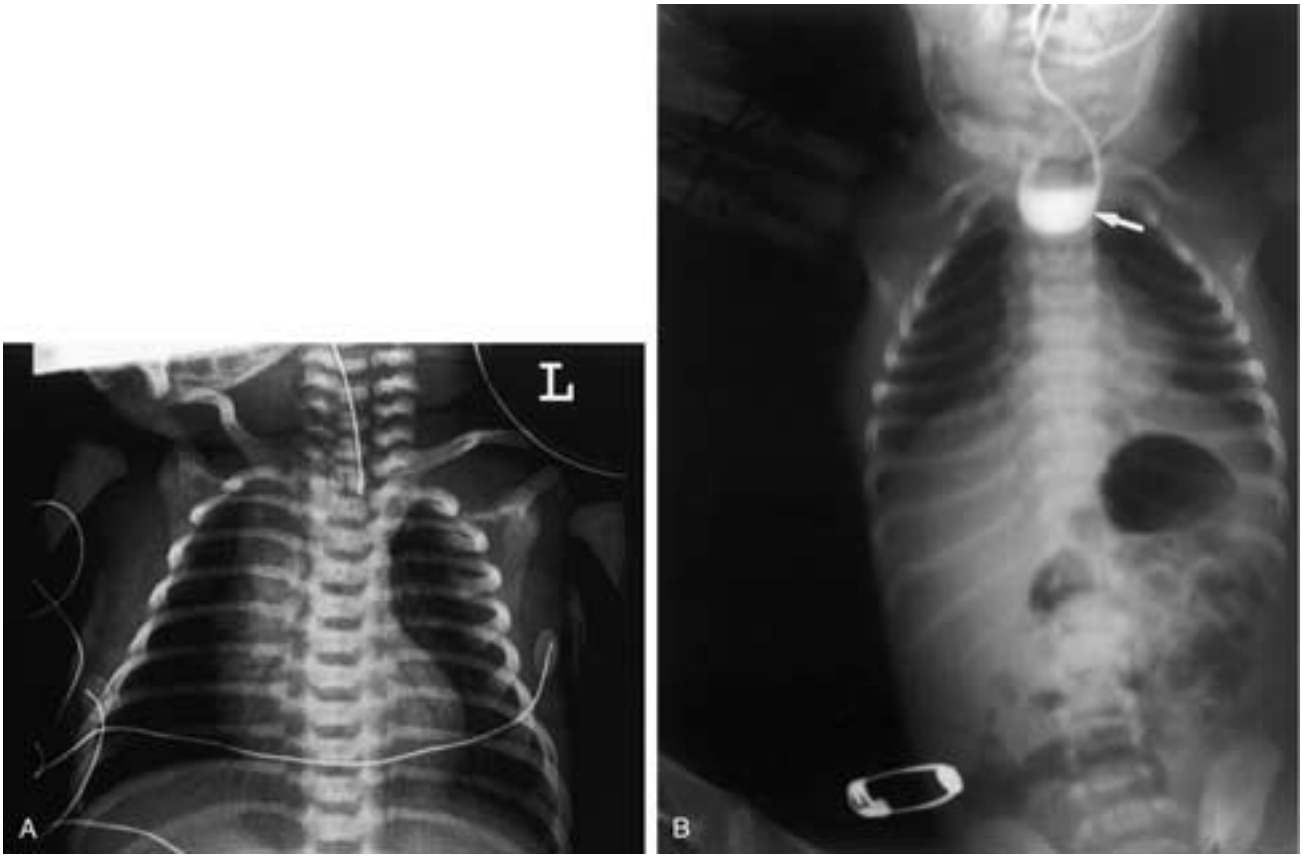

VIEW IMAGE

FIGURE 31-10 Tracheoesopheagal atresia. **A**, Multiple attempts to pass a nasogastric tube were unsuccessful in this full-term infant with esophageal atresia. The level of the nasogastric tube tip marks the level of the atresia. **B**, Chest X-ray from a different infant demonstrates a coiled nasogastric tube in the cervical esophagus, with contrast filling the proximal esophageal pouch (*arrow*). This premature infant presented with copious oral secretions and noisy respiration. Gas within the bowel indicates a distal communication between the tracheal bronchial tree and the gastrointestinal tract.

Copyright © 2003, Mosby, Inc. All rights reserved.

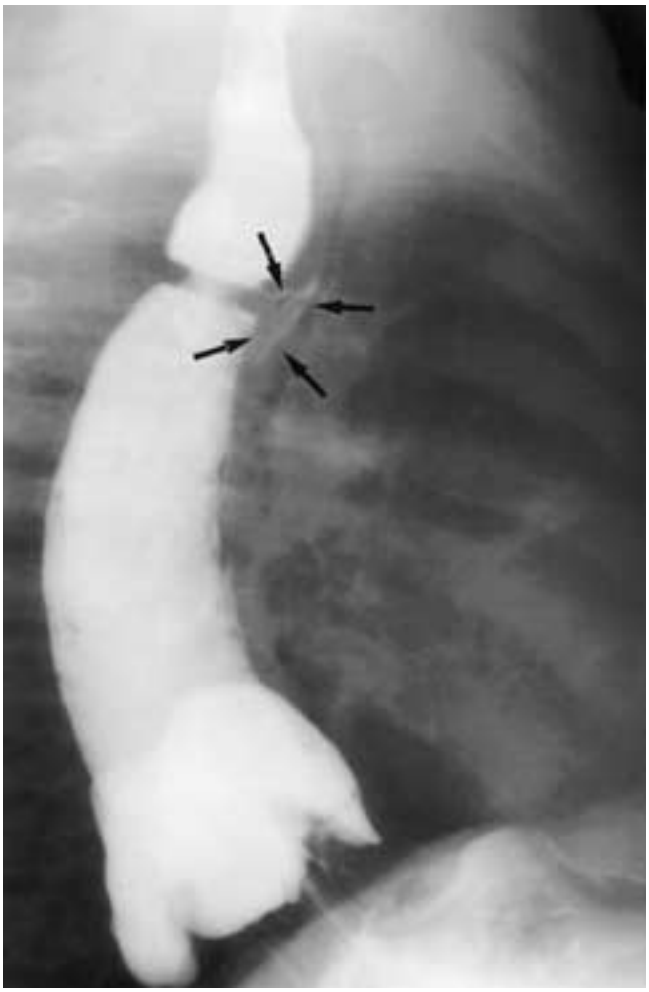

VIEW IMAGE

FIGURE 31-11 Recurrent tracheoesophageal fistula. A 1-year-old infant after repair of esophageal atresia and a distal tracheal esophageal fistula. The patient had also undergone Nissen fundoplication. Barium swallow demonstrates recurrent tracheal esophageal fistula at the level of the surgical anastomosis (*arrows*).

Conditions Causing Narrowing of the Trachea

Infection

Laryngotracheobronchitis (croup) is the most common infection of the trachea. Croup is a disease of infants and young children, with a peak incidence between the ages of 6 months and 3 years.[28] Parainfluenza and respiratory syncytial virus are the most common agents. Clinical symptoms include a ''barking'' cough and intermittent inspiratory stridor. Although typically infection involves the entire airway, critical narrowing usually occurs at the proximal 2 cm of the trachea. At this level, the tracheal mucosa is relatively loose, and therefore susceptible to edema and luminal narrowing. Anteroposterior radiographs demonstrate loss of the lateral convexities of the subglottic trachea, with luminal narrowing. This narrowing produces an inverted V configuration, with the point of the V at the level of the inferior margin of the true vocal cords. This subglottic narrowing is accentuated during expiration. It should be kept in mind that radiologic evaluation is not performed to *diagnose* croup, but to *exclude* other causes of stridor such as epiglottitis.

Bacterial tracheitis is an atypical form of croup, with a clinical picture more closely resembling that of epiglottitis.[29–31] The organisms most commonly involved are *Staphylococcus aureus*, group A beta-hemolytic streptococci, and *Haemophilus influenzae* type b.[29–31] Although early symptoms may mimic viral croup, they do not resolve with conventional medical therapies. The subsequent course is typically severe, with high fever, stridor, and dyspnea with production of purulent sputum. Intubation or tracheotomy may be required to prevent obstruction by purulent exudate. The primary focus of inflammation/obstruction is subglottic, with sparing of the epiglottis and supraglottic structures. The definitive diagnosis of *bacterial* tracheitis can be made by direct inspection of the purulent exudate, which is not present in viral croup. Laryngoscopy and bronchoscopy can be therapeutic; microbiologic tests are important in confirming the etiologic agent and in selecting or modifying antibiotic therapy.

Tuberculosis

Tuberculous tracheitis is rare and is usually associated with active pulmonary tuberculosis.[32, 33] The infection typically involves the distal trachea, where inflammation results in irregular circumferential tracheal wall thickening, leading to narrowing or even obstruction. Areas of necrosis and ulcerations may develop. Mediastinal and hilar lymphadenopathy are usually present. Fibrosis from chronic inflammation can lead to segmental stenosis of the trachea and bronchi. Erosion into adjacent mediastinal structures can lead to the development of a tracheoesophageal fistula or to severe hemorrhage from vascular invasion. Erosion of calcified lymph nodes into the airway can lead to expectoration of broncholiths.[34]

Histoplasmosis

Like tuberculosis, histoplasmosis can result in lymph node calcification. Granulomatous lesions arise outside the airways and tend to erode into the lumen. As with

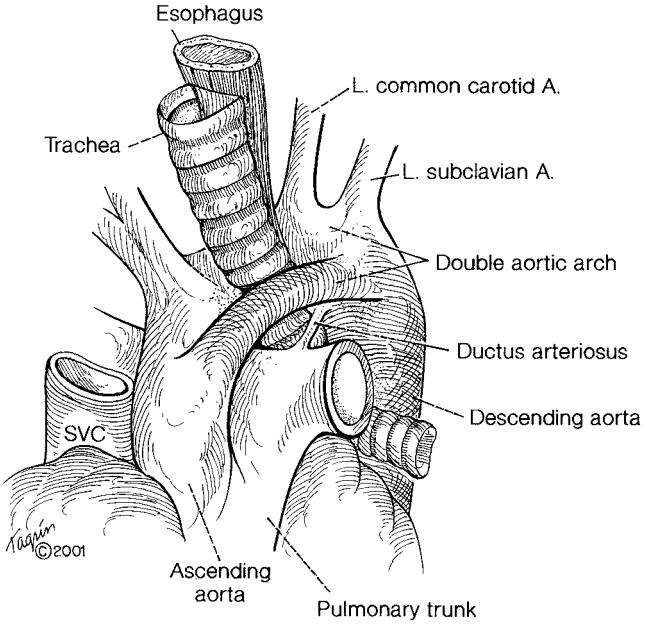

FIGURE 31-12 Double aortic arch.

VIEW IMAGE

Copyright © 2003, Mosby, Inc. All rights reserved.

tuberculosis, intraluminal extension is associated with hemoptysis and expectoration of broncholiths.

Fibrosing mediastinitis is a fibroinflammatory infiltrative process most commonly attributed to histoplasmosis.[25, 35–38] Large masses of fibrous tissue can form in the mediastinum. The accumulated fibrous tissue can squeeze the trachea or bronchi, resulting in long areas of airway narrowing. The patient can present with cough, hemoptysis, or difficulty breathing. The pulmonary arteries and veins can also be narrowed, resulting in significant vascular compromise. The lesions usually calcify and can have low signal intensity on T2-weighted images. These features may help differentiate the lesion from an invasive malignancy. Fibrosing mediastinitis has also been associated with tuberculosis, lymphatic obstruction, and methylsergide.

CT is the best single technique for diagnosing and assessing the severity of mediastinal fibrosis, as well as for evaluating tracheal luminal narrowing. CT studies performed both prior to and following the administration of intravenous contrast may be helpful in differentiating calcified lymph nodes from enhancing vessels.

Mediastinal granuloma is closely related to fibrosing mediastinitis. This term describes a well-demarcated mass of lymph nodes located in the mediastinum. It is commonly discovered as a mass lesion on routine chest radiography, typically in the right paratracheal or hilar regions. Mediastinal granuloma is often encapsulated and asymptomatic. If symptoms are present, they relate to compression of various mediastinal structures, including the major veins, tracheobronchial tree, esophagus, recurrent laryngeal nerves, pulmonary arteries, and heart. Narrowing of the tracheobronchial tree typically involves the major bronchi, with less frequent involvement of the distal trachea. Surgery is often indicated for diagnostic reasons (e.g., to exclude lymphoma) or for relief of specific symptoms.[39]

Relapsing Polychondritis

Relapsing polychondritis is a rare systemic disease characterized by recurrent episodes of inflammation, fragmentation, and fibrosis of cartilage tissue including the ears, nose, joints, and airways. Its incidence peaks in the fifth decade of life, and there is no sex predilection.[39] The upper airways (larynx and trachea) are affected in more than half of the patients. Tracheal involvement occurs late in the course of the disease. Diffuse tracheal inflammation is limited to the cartilage and perichondrium, with sparing of the mucosa and submucosa.[40] Respiratory manifestations are often severe and may be life-threatening.[41] Cardiovascular manifestations are present in one third of patients.

CT usually shows tracheal narrowing with diffuse wall thickening limited to the anterior and lateral tracheal walls, sparing of the posterior membrane, and narrowing of the lumen.[1] When calcification is seen within the tracheobronchial wall, the cartilage may appear thicker than normal. Both the inner and outer borders of the thickened tracheal wall are smooth, and areas of tracheomalacia may coexist. Fiberoptic bronchoscopy can be useful for both direct visualization and biopsy.

Granulomatous Disease of the Trachea

Wegener's granulomatosis is a hypersensitivity necrotizing granulomatous vasculitis that can involve the upper and lower respiratory tracts and may result in tracheal stenosis. It typically occurs in adults, with a peak incidence in the fourth and fifth decades of life.[42] Two or more organ systems may be affected simultaneously. Pulmonary and renal involvement together occurs in more than two thirds of cases.[43] The kidneys are frequently affected, as are other organs such as the skin, nervous system, eyes, ears, and heart. Tracheal involvement typically manifests as diffuse or focal tracheobronchial narrowing.[44] Although destruction of cartilage may result, malacia is not typical. Dyspnea and progressive airway obstruction develop over months or years following the initial diagnosis of the disease.

CT features include circumferential wall thickening with narrowing of the tracheal lumen. Enlarged, abnormally calcified tracheal cartilage may also be present.[44] Mediastinal and hilar lymphadenopathy are rare thoracic manifestations of Wegener's granulomatosis.[45]

Sarcoidosis

Sarcoidosis is a systemic granulomatous disease of unknown etiology. Involvement of the lungs, mediastinal lymph nodes, eyes, and skin is common. On rare occasion, the trachea can be involved.[46] Sarcoidosis can lead to diffuse narrowing of the trachea and main bronchi and can cause upper-airway obstruction (Fig. 31-13). Dyspnea and cough usually result from extensive fibrosis, which causes distortion and narrowing of the airway. Bronchial compression by mediastinal lymph nodes and airway hyperreactivity, presumably due to inflammation, contribute to the symptoms. While obstruction of the lower airway by granulomatous infiltration and chronic pulmonary fibrosis is common, tracheal stenosis is rare.

Amyloidosis

Amyloid infiltration of the airways may occur as an isolated phenomenon or as part of a diffuse systemic disease. The focal form of amyloidosis, in which amyloid deposits in a tumor-like fashion, is usually limited to one organ or organ system. This form can be found in approximately 10% of cases.[47] Primary solitary amyloidosis of the trachea is very rare and has no features to differentiate it from other tumors.[48] Deposition of amyloid in the submucosal and muscular layers of the trachea and bronchi can lead to tracheal narrowing and ulceration.

Tracheobronchial amyloidosis can involve the bronchial tree either as a single pseudotumorous mass or in a diffuse form.[49] The diffuse form is more frequent and is characterized by extensive subepithelial amyloid deposits. The elevated mucosa, which forms ridges and nodules (approximately 0.5 to 5 cm in diameter) that may calcify, can narrow the tracheal lumen.[2] Plain film radiographs and CT scanning demonstrate focal or diffuse narrowing of the trachea and bronchi (Fig. 31-14). The nodular form of tracheobronchial amyloid may appear on CT as a focal mass, partially or completely occluding the airway. There is often infiltration of adjacent peritracheal or bronchial tissue, frequently with calcified foci. In this form, it may mimic the appearance of both benign and malignant tracheal tumors. Depending on the size and calcification of the deposition, hemoptysis or airway obstruction may occur, ultimately resulting in atelectasis or recurrent pulmonary infection. Resection with a carbon dioxide laser and repeated bronchoscopic resection are successful methods of treatment.[39]

Copyright © 2003, Mosby, Inc. All rights reserved.

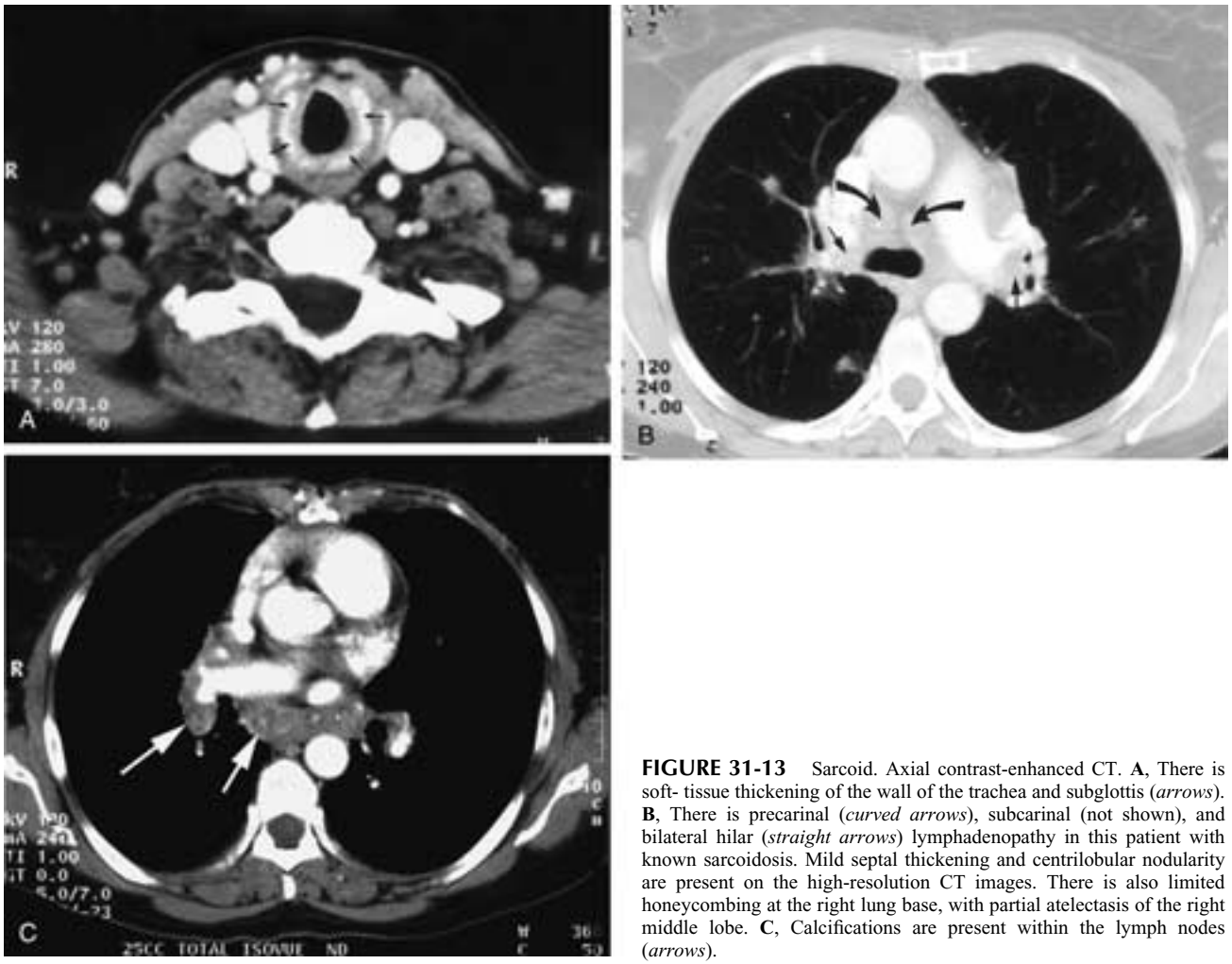

FIGURE 31-13 Sarcoid. Axial contrast-enhanced CT. **A**, There is soft- tissue thickening of the wall of the trachea and subglottis (*arrows*). **B**, There is precarinal (*curved arrows*), subcarinal (not shown), and bilateral hilar (*straight arrows*) lymphadenopathy in this patient with known sarcoidosis. Mild septal thickening and centrilobular nodularity are present on the high-resolution CT images. There is also limited honeycombing at the right lung base, with partial atelectasis of the right middle lobe. **C**, Calcifications are present within the lymph nodes (*arrows*).

VIEW IMAGE

Tracheopathia Osteochondroplastica

Submucosal cartilaginous and/or osseous nodules characterize this rare benign disease of the trachea. These nodules project into the lumen, causing considerable deformity. The lesions vary in size and are located mainly in the anterolateral tracheal wall, sparing the posterior membranous portion of the wall.[2] Most often, these lesions involve the inferior two thirds of the trachea, and frequently extend into the proximal portions of the major bronchi.[2]

The disease tends to occur in patients over 50 years of age, with equal frequency in males and females.[32] Patients may be asymptomatic but often present with cough, dyspnea, hemoptysis, and recurrent pneumonia. The etiology is unknown, although it has been suggested that tracheopathia osteochondroplastica develops secondary to metaplasia of the submucosal connective tissue.[32]

Chest radiographs may show tracheal scalloping, calcified nodules, or diffuse narrowing of the trachea. The tracheal wall may be calcified. CT scan can reveal nodular thickening and irregularity of the anterior and lateral walls of the trachea, with punctate calcification from the level of the thoracic inlet to the carina.[50, 51] Small calcified nodules along the inner aspect of the tracheal cartilage protrude into the tracheal lumen (Fig. 31-15). The differential diagnosis includes physiologic calcification of the tracheobronchial tree (in the elderly), tracheal amyloidosis, inflammatory conditions, and diffuse tumorous processes. Pulmonary function studies may indicate some degree of tracheal obstruction. Many patients with tracheopathia osteochondroplastica have a ''saber sheath'' tracheal deformity in the absence of obstructive lung disease.

Saber-Sheath Trachea

Saber sheath is a common variation of tracheal morphology that typically affects male smokers with chronic obstructive pulmonary disease.[44] Some patients with tracheopathia osteochondroplastica may present with this deformity.

The saber-sheath trachea is characterized by a marked decrease in the transverse diameter of the intrathoracic trachea associated with an increase in its sagittal diameter. The extrathoracic trachea is normal in these cases. In its earliest stages, narrowing is visible only at the thoracic inlet.[44] In more advanced cases, the stenosis involves all or part of the intrathoracic trachea. Saber-sheath trachea is clearly demonstrated on a CT scan obtained during forced expiration or a Valsalva maneuver. Inward bowing or displacement of the lateral tracheal walls is present and is due to weakness of the tracheal cartilages.[52]

Copyright © 2003, Mosby, Inc. All rights reserved.

Diffuse Conditions Causing Widening of the Trachea

Tracheobronchomegaly (Mounier-Kuhn Syndrome)

This rare condition, characterized by marked dilatation of the trachea and mainstem bronchi, is associated with atrophy of the cartilaginous, muscular, and elastic components of the tracheal wall. Patients commonly have associated bronchiectasis, with a history of recurrent pneumonia. The disease is most commonly diagnosed in males in their third to fourth decades of life. Patients typically have a long-standing, unusually loud, productive cough, with hoarseness and dyspnea. There is an association with other primary connective tissue disorders, such as Ehlers-Danlos syndrome and acquired cutis laxa.

The diagnosis of tracheobronchomegaly is made primarily by radiologic evaluation. On plain chest radiographs the trachea appears enlarged, and bronchiectasis is present. CT findings include tracheomegaly, with thinning of the tracheal wall, and a diameter of more than 3 cm below the level of the aortic arch or more than 2 cm above the level of the arch (Fig. 31-16). Tracheal scalloping or frank diverticulosis can also be present, although difficult to appreciate on cross-sectional imaging. Three-dimensional reconstructions

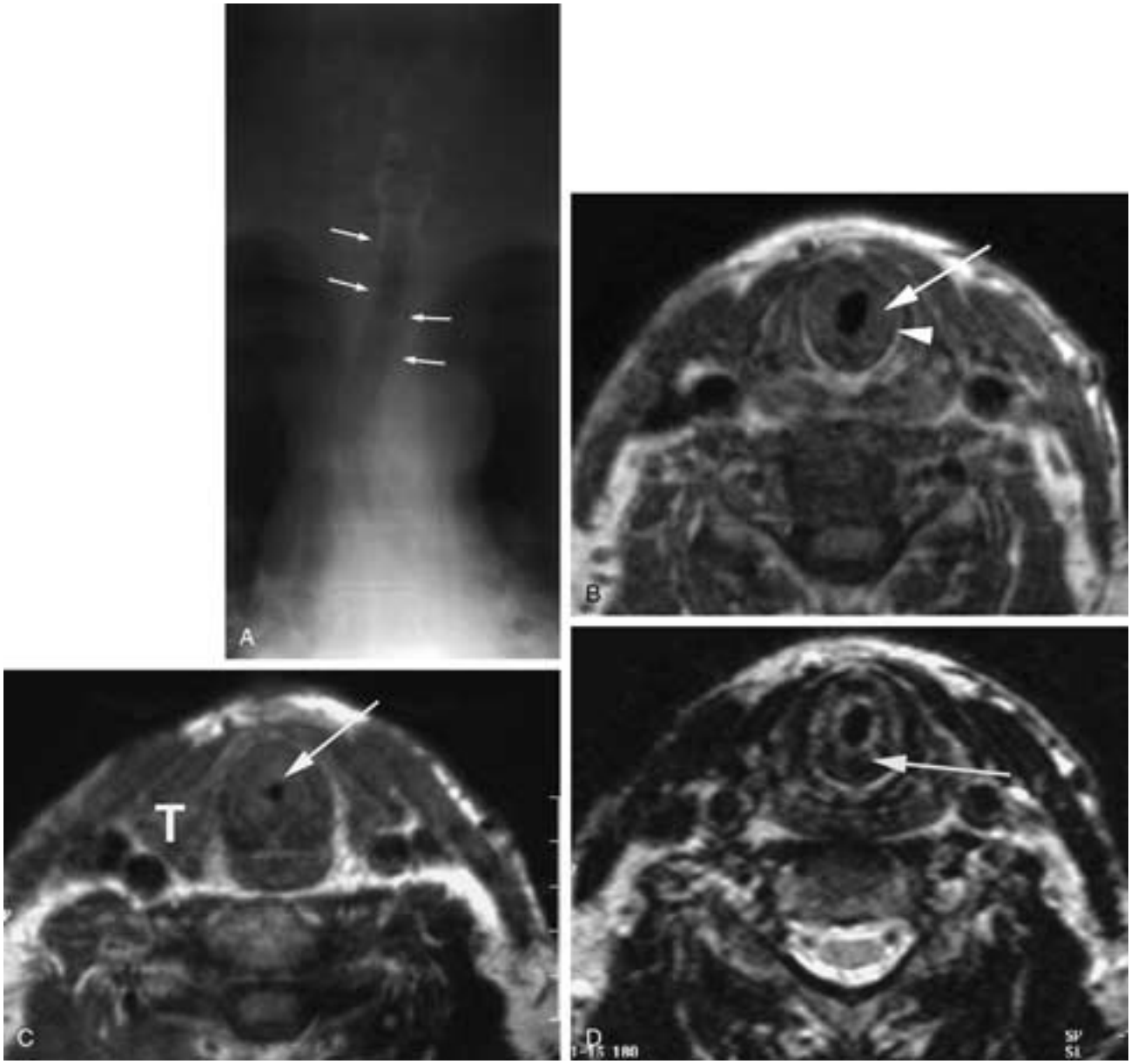

FIGURE 31-14 Amyloid. **A**, Chest radiograph of a 65-year-old man demonstrates a diffusely thickened tracheal wall on the posteroanterior view (*arrows*). **B**, T1-weighted MR image through the lower cricoid shows diffuse concentric soft tissue (*arrow*) narrowing the subglottic airway. The arrowhead indicates the position of the inner cortex of the cricoid cartilage. **C**, Axial T1-weighted image through the upper trachea shows the narrowing leaving a very narrowed airway (*arrow*). *T*, thyroid gland. **D**, T2-weighted axial image at the level of the lower cricoid shows that the abnormality has very low signal (*arrow*).

Illustration continued on following page

VIEW IMAGE

Copyright © 2003, Mosby, Inc. All rights reserved.

may be used to display this deformity. Another common association is marked tracheomalacia. There can be a significant decrease in the diameter of the trachea on expiration, even to the point of airway closure.

Secondary Tracheomegaly

Chronic coughing coupled with ongoing chronic inflammation has been blamed for diffuse acquired enlargement of the tracheal lumen. This has been described in cigarette smokers and in patients with cystic fibrosis.

Trauma

Tracheal trauma may result from either internal or external injury. Internal tracheal injuries are the result of inhalation of noxious fumes, gas, or steam or of aspiration. Edema, followed by rapid laryngotracheal airway obstruction, may result from chemical or thermal injury to the tracheal mucosa. Mechanical internal injuries are invariably due to iatrogenic causes, such as laryngotracheal intubation.

External traumatic tracheal injuries are more commonly due to blunt rather than penetrating trauma. The spectrum of injury includes small lacerations, tears of the posterior membranous wall, fracture of the cartilaginous rings, and complete separation. Penetrating trauma is most often the result of stab wounds or projectile injuries. Tracheal injuries most often occur in association with other severe injuries. Motor vehicle collisions are the most common cause of blunt tracheal injuries. Although rupture of the trachea in itself is a life-threatening injury, mortality is typically caused by damage to other surrounding vital organs.

Radiologic clues to tracheobronchial traumatic injury include pneumomediastinum, subcutaneous emphysema, and pneumothorax. Other signs of tracheal injury include elevation of the hyoid bone and distortion of the normal laryngotracheal air column.[53] Anteroposterior and lateral plain films of the neck are useful in identifying free air and

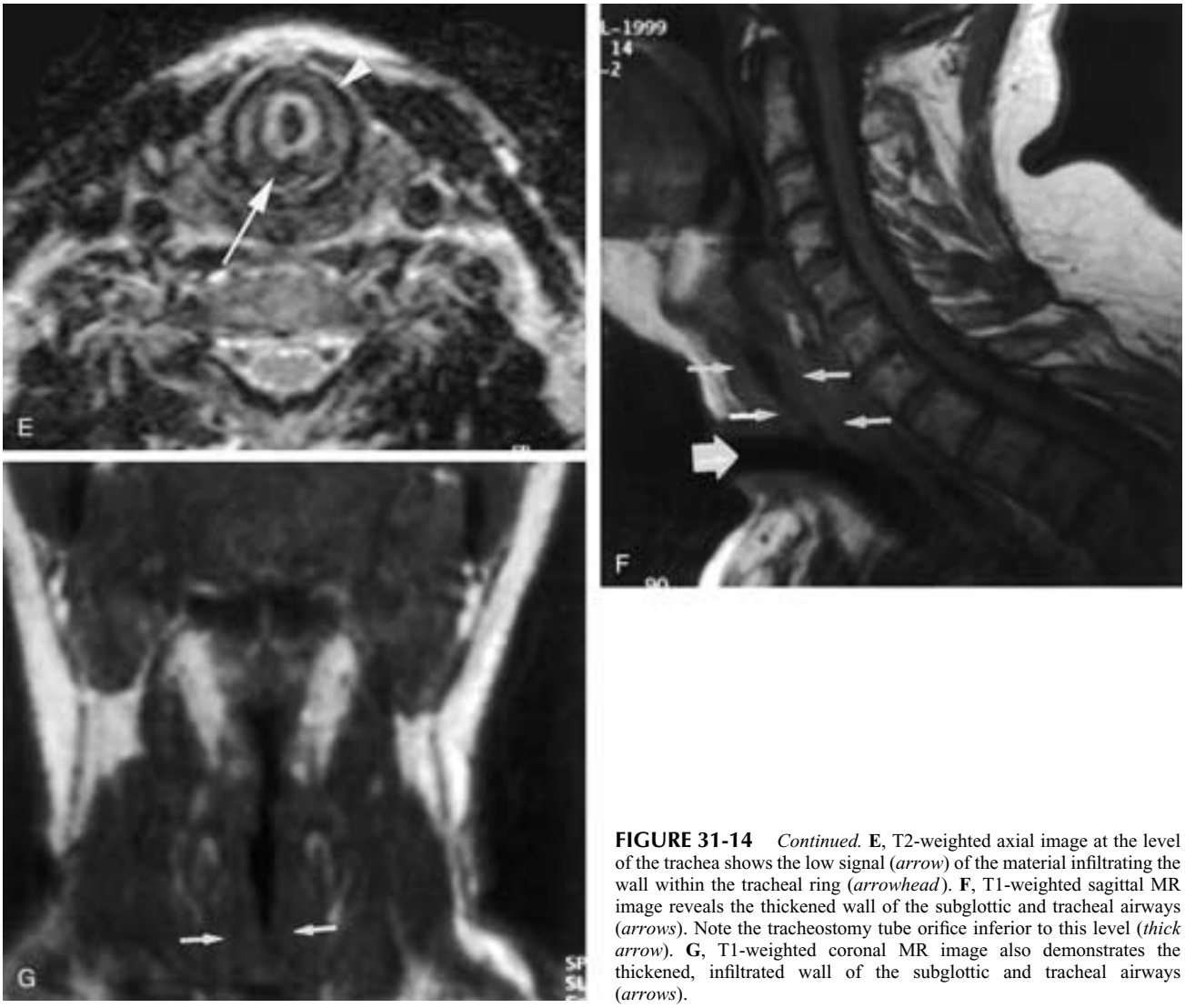

FIGURE 31-14 *Continued.* **E**, T2-weighted axial image at the level of the trachea shows the low signal (*arrow*) of the material infiltrating the wall within the tracheal ring (*arrowhead*). **F**, T1-weighted sagittal MR image reveals the thickened wall of the subglottic and tracheal airways (*arrows*). Note the tracheostomy tube orifice inferior to this level (*thick arrow*). **G**, T1-weighted coronal MR image also demonstrates the thickened, infiltrated wall of the subglottic and tracheal airways (*arrows*).

VIEW IMAGE

Copyright © 2003, Mosby, Inc. All rights reserved.

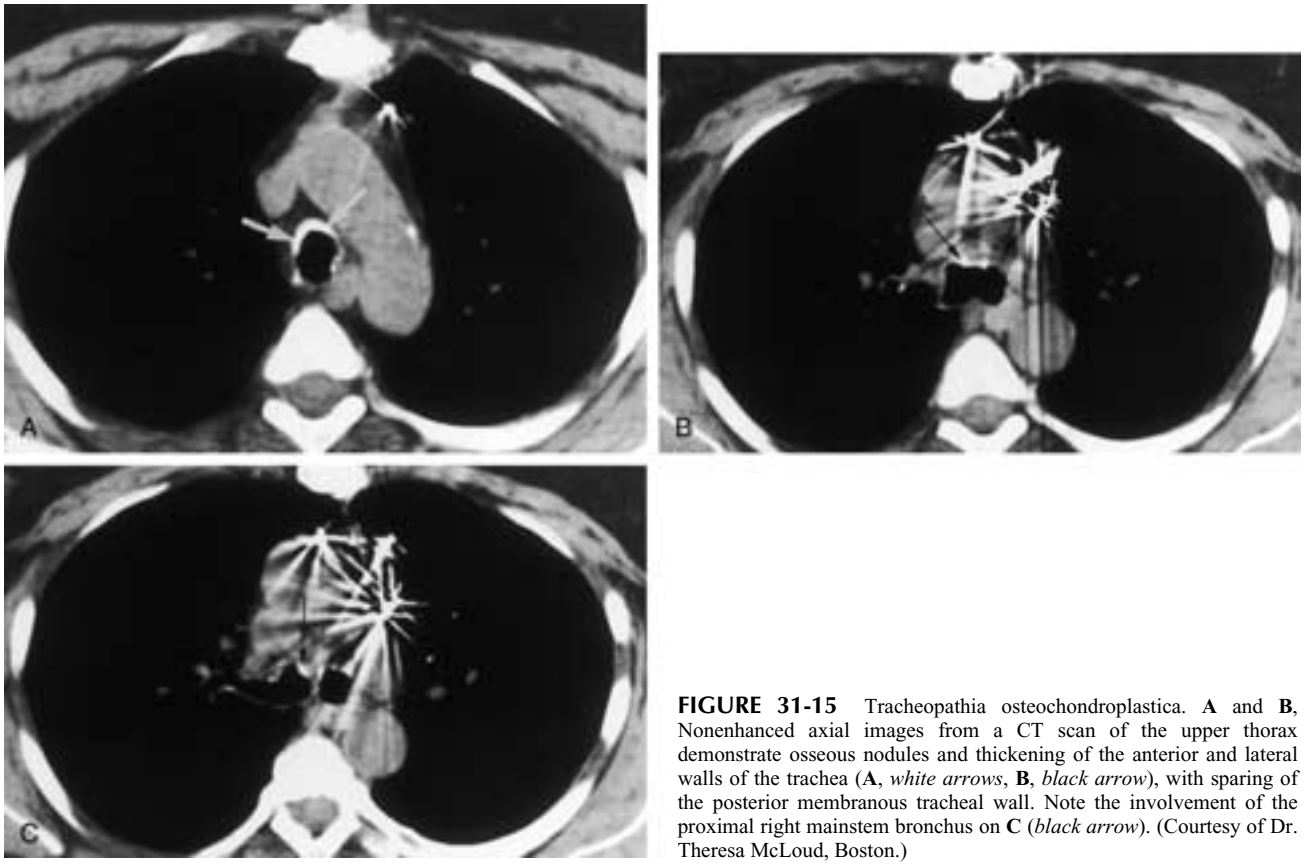

FIGURE 31-15 Tracheopathia osteochondroplastica. **A** and **B**, Nonenhanced axial images from a CT scan of the upper thorax demonstrate osseous nodules and thickening of the anterior and lateral walls of the trachea (**A**, *white arrows*, **B**, *black arrow*), with sparing of the posterior membranous tracheal wall. Note the involvement of the proximal right mainstem bronchus on **C** (*black arrow*). (Courtesy of Dr. Theresa McLoud, Boston.)

VIEW IMAGE

in evaluating for the presence of associated cervical spine trauma. Plain chest radiographs are essential in the evaluation of tension pneumothorax or hemothorax. Clinical findings include new onset of stridor, endobronchial bleeding, and respiratory failure. Direct bronchoscopy is often required for definitive diagnosis.[47]

Posttracheostomy/Postintubation Complications

The increasing use of cuffed endotracheal tubes and tracheostomy for long-term ventilation has led to characteristic injuries of the trachea. Complications from translaryngeal intubation may lead to acute airway obstruction due to postextubation glottic edema or laryngospasm. Alternatively, symptoms may develop months or even years after injury due to glottic or tracheal stenosis.[54]

A portable chest radiograph should be obtained following laryngotracheal intubation to ensure proper positioning of the endotracheal tube. Ideally, the tip of the endotracheal tube should be placed well above the carina, with the head and neck in a neutral position. It is important to recognize that flexion and extension of the neck will cause movement of the endotracheal tube of approximately 2 cm in either direction. In addition, rotation of the head can cause a 1 to 2 cm ascent of the tube. Unlike endotracheal tubes, tracheostomy tubes do not change position with head or neck movement, because tracheostomy tubes are not anchored to the nose or mouth.

Ideally, endotracheal tube lumens should be two thirds the diameter of the tracheal lumen to minimize airway resistance. Inflated tube cuffs are relatively easy to recognize on chest X-ray; their position should be checked whenever a chest X-ray is obtained. The inflated cuff should fill, but not bulge, the tracheal lumen. Rigid low-volume

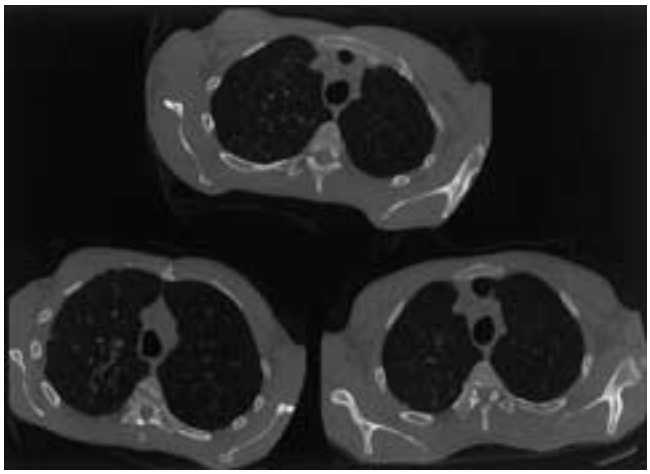

FIGURE 31-16 Tracheomegaly. Nonenhanced axial CT scan, obtained at three levels in the upper thorax, demonstrates marked dilatation of the trachea in this patient with recurrent pneumonia. Note that above the level of the aortic arch, the tracheal diameter is greater than 2 cm.

VIEW IMAGE

Copyright © 2003, Mosby, Inc. All rights reserved.

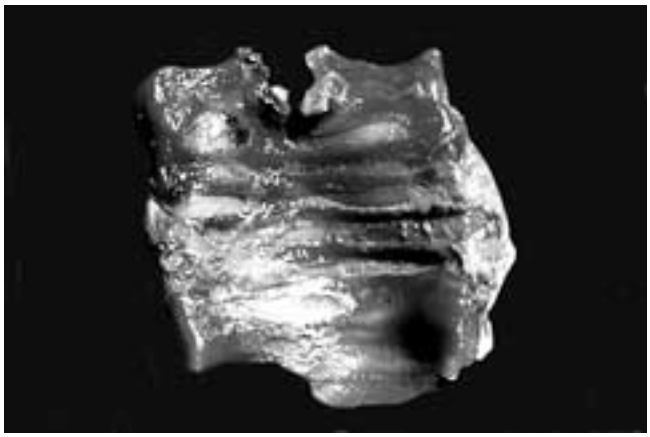

FIGURE 31-17 Resected specimen of a trachea (seen from behind) from a patient with cuffed tube injury. Hyperemic mucosa remains between the paler denuded tracheal cartilages. The mucosa overlying these cartilages is the first area damaged by the inflated cuff.

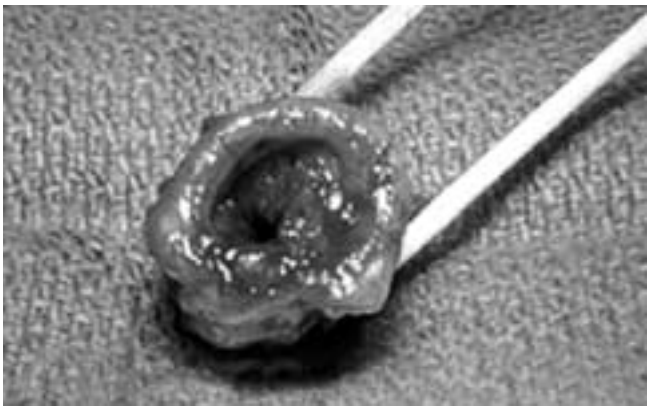

FIGURE 31-19 Resected specimen from a patient with cuffed tube tracheal injury. There is circumferential involvement of the trachea in this more advanced type of injury. The membranous posterior wall and the mucosa overlying the tracheal rings are involved.

cuffs have been replaced by high-volume, low-pressure cuffs, which are significantly more compliant and therefore adapt better to the variable cross-sectional shape of the tracheal lumen.[2] Most importantly, these newer cuffs provide sufficient sealing at approximately one tenth of the pressure required for rigid cuffs (about 20 to 30 mm Hg). Tracheal narrowing at the cuff site has dramatically decreased in frequency since the introduction of these high-volume, low-pressure cuffs. Immediate complications following laryngotracheal intubation can result from insertion of the tube into the right mainstem bronchus or positioning of the tube tip too close to the carina. The risk of aspiration is significantly increased if the cuff is malpositioned in the vocal cords or within the pharynx. In addition, overdistention of a malpositioned cuff may lead to vocal cord necrosis. Early complications of tracheostomy are usually associated with abnormal anterior, posterior, or lateral angulation of the tube. This can result in increased airway resistance, difficulty in clearing of secretions, or, if persistent, erosion or perforation of the tracheal wall. Anterior perforation may result in trachea-innominate artery fistula, whereas posterior perforation may lead to tracheoesophageal fistula.[55]

Late tracheostomy and postintubation stenosis can occur at the tracheostomy opening (stoma), at the balloon cuff site, or, rarely, where the tip of the tube abuts the tracheal mucosa. Most long-term complications are due to pressure necrosis at the cuff site.[44] When cuff pressure exceeds capillary pressure, the blood supply to the tracheal mucosa is compromised and ischemic necrosis results.[44] At first, the mucosa overlying the tracheal cartilages undergoes pressure necrosis. If the cuff is removed at this point, cicatricial healing usually results in an anterior tracheal web/scar. The flexible posterior wall is uninvolved. However, with greater cuff pressure, the posterior wall is also affected and a circumferential scar is produced. Usually this type of tracheal damage is limited to one or two tracheal rings at the level of the cuff-related injury (Figs. 31-17 to 31-22). Radiographically, the stenosis has a smooth edge. Typically, symptoms of stenosis develop 2 to 6 weeks postextubation and, in some patients, months or even years later.[44] Stenosis at the tracheostomy stoma may be prevented by improved

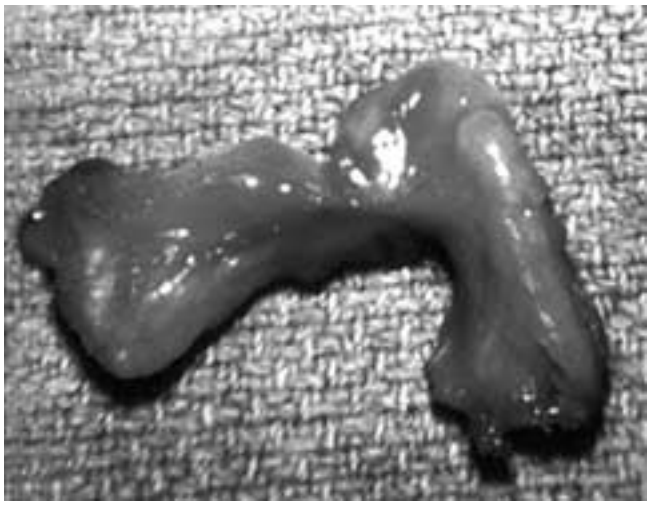

FIGURE 31-18 Resected specimen from a patient with cuffed tube tracheal injury. The scarred segment involved only the area overlying the rigid tracheal cartilages. This earlier type of stenotic injury has a semilunar configuration. The membranous posterior tracheal wall is not involved.

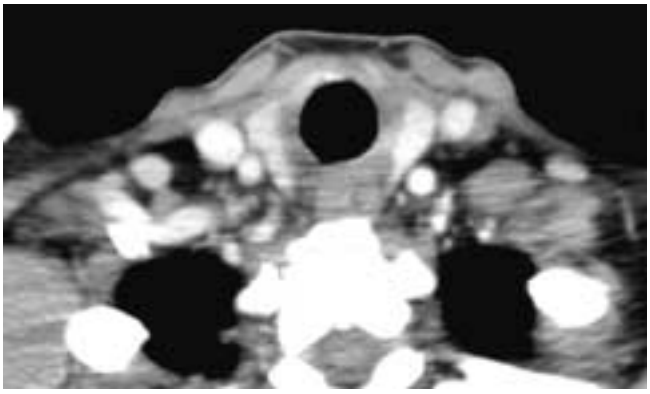

FIGURE 31-20 Axial contrast-enhanced CT scan shows a normal tracheal lumen at the level of the uppermost trachea.

Copyright © 2003, Mosby, Inc. All rights reserved.

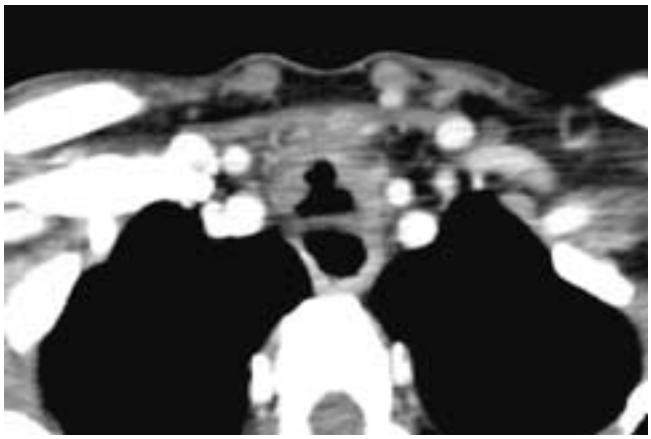

VIEW IMAGE

FIGURE 31-21 Axial contrast-enhanced CT scan shows a semilunar tracheal stenosis corresponding to the type of injury shown in Figure 31-18. The tracheal cartilages in this patient were poorly calcified.

surgical technique, control of local infection, and avoidance of heavy connecting equipment.[56]

Granuloma formation at the tracheostomy site is also common. Often on CT, such a granuloma is seen as a small incidental soft-tissue mass on the anterior tracheal wall. The differential diagnosis is with dessicated secretions at the tracheostomy site.

The configuration of the trachea is often altered after tracheostomy. Interruption of the integrity of the involved tracheal cartilages often identifies the site of a prior tracheostomy (Fig. 31-23). Side-to-side collapse of the anterior tracheal configuration can also result from loss of support from the violated tracheal rings (Fig. 31-24).

Resection of the stenotic segments with anastomosis is traditionally the treatment of choice for tracheal stenosis following extubation, provided that the stenotic segment does not exceed two or three tracheal rings. Polyurethane-covered, retrievable, expandable Nitinol stents are currently under investigation as a relatively new method for the treatment of tracheal strictures (Fig. 31-25). In cases of inoperable tracheal strictures with resultant dyspnea, these

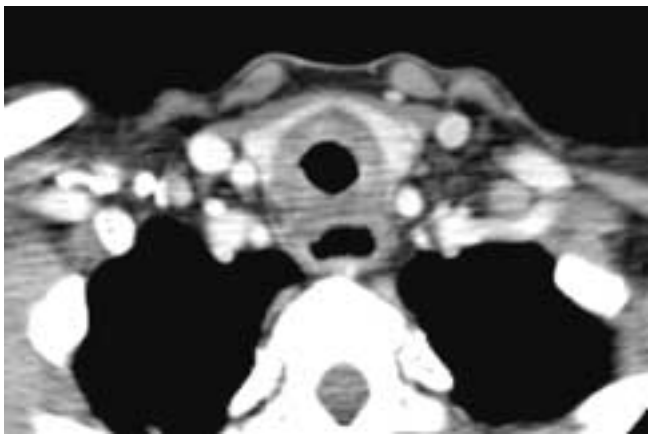

VIEW IMAGE

FIGURE 31-22 Axial contrast-enhanced CT scan shows a circumferential tracheal stenosis corresponding to the type of injury shown in Figure 31-19. The thyroid gland surrounds the anterior and lateral aspects of the trachea.

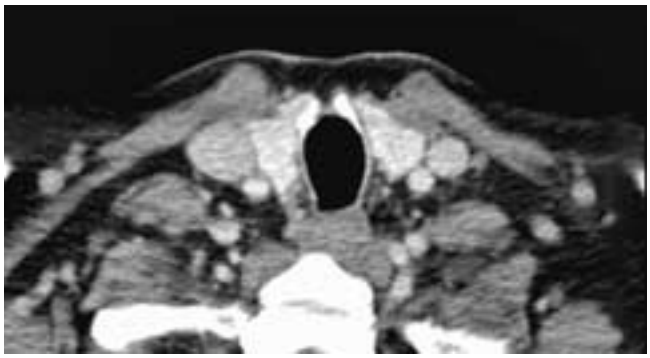

VIEW IMAGE

FIGURE 31-23 Axial contrast-enhanced CT scan shows separation of the anterior tracheal cartilage at the site of a prior tracheostomy.

stents are suggested to be a safe and convenient nonsurgical alternative.[57]

Other less common long-term complications of intubation include tracheomalacia and ulcerative tracheoesophageal fistula. When an indwelling esophageal tube is used along with intubation, particularly in neurologically impaired patients who are ventilated for long periods of time, tracheoesophageal fistula may result. The mechanism of injury is pressure necrosis resulting from the pressure exerted by the cuff on the tracheal wall abutting a foreign body within the esophagus. This type of fistula often results in recurrent pneumonia.

Tracheal Tumors

General Considerations

Primary tumors of the trachea are rare, with malignant neoplasms representing only 2% of all upper airway tumors.[58] These tumors include primary epithelial and mesenchymal neoplasms, as well as secondary neoplasia due to either metastases or, more commonly, direct tracheal invasion from adjacent mediastinal neoplasms. In adults, primary tumors are most commonly malignant, whereas in children, benign tumors are more likely.[59]

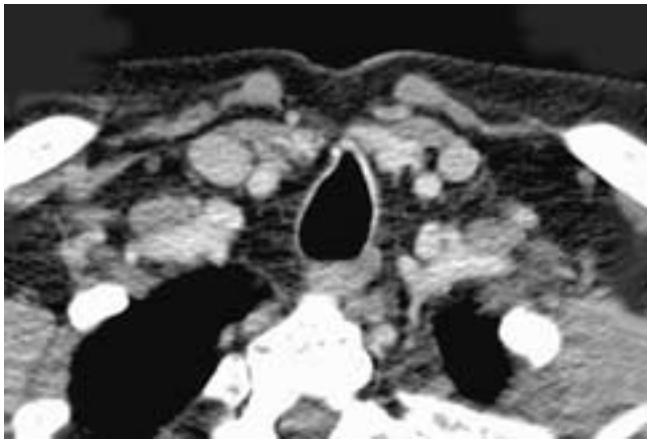

VIEW IMAGE

FIGURE 31-24 Axial contrast-enhanced CT scan shows a side-to-side collapse of the tracheal cross-sectional airway configuration due to injury of the tracheal cartilage from a prior tracheostomy.

Copyright © 2003, Mosby, Inc. All rights reserved.

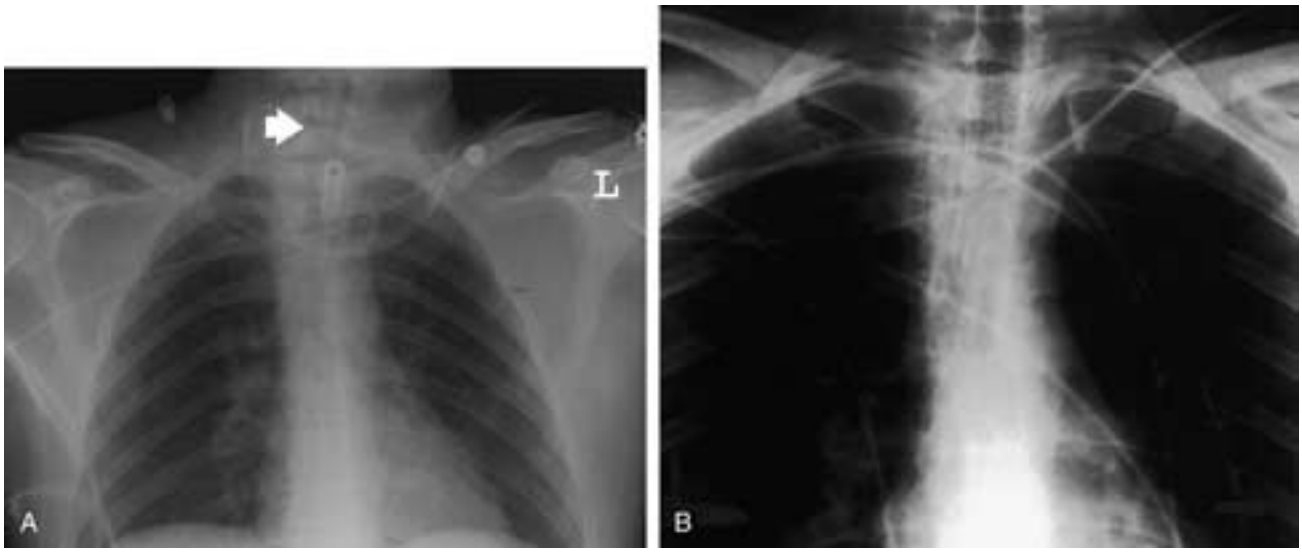

VIEW IMAGE

FIGURE 31-25 Tracheal stent. A 30-year-old male who suffered from an accidental pistol discharge was intubated for 20 days. Approximately 1 week following extubation, he developed difficulty breathing and was found to have granulation tissue causing tracheal stenosis. A covered tracheal stent was placed, providing relief of symptoms. **A**, Pre-stent AP chest X-ray shows narrowing of the subglottic airway above the level of the tracheostomy (*arrow*). **B**, Anteroposterior view of the chest following stent placement demonstrates the covered tracheal stent extending from the subglottic trachea to approximately 3 mm above the carina.

Adult tracheal tumors occur between the third and fifth decades of life, with no sex predominance. Most occur at the distal third of the trachea.[58] Symptoms associated with tracheal tumors include dyspnea, cough, hemoptysis, new-onset asthma or wheezing, dysphagia, stridor, change in voice and/or hoarseness, recurrent pneumonia, and emphysema. Approximately one third of patients with tracheal tumors are initially mistakenly treated for asthmatic bronchitis.[44]

Malignant Tumors

The most common malignant tracheal tumor in adults is squamous cell carcinoma, followed by adenoid cystic carcinoma. Together, these two neoplasms account for up to 86% of all malignant adult tracheal tumors.[1] Secondary malignant tumors are due to either metastases or direct tracheal invasion by adjacent mediastinal neoplasms. The most common primary carcinomas that spread directly to the trachea are from the lung, thyroid, or esophagus (Fig. 31-26).[1] The most common carcinomas to metastasize hematogenously to the trachea are breast, gastrointestinal, melanoma, lymphoma, renal cell carcinoma, or squamous cell carcinomas of the head and neck.[60, 61]

Squamous Cell Carcinoma

Squamous cell carcinoma (SCC) is the most common primary malignancy of the trachea. It typically affects middle-aged male smokers (mean age, 50 to 60 years).[2] SCC is associated with other malignant neoplasms of the respiratory and digestive tracts in one third of patients. The relatively high incidence of synchronous or metachronous tumors, found most frequently in the larynx, lung, or esophagus, makes comprehensive evaluation and follow-up imaging of the entire respiratory tract essential. Although SCC may arise at any level in the trachea, the lower trachea and the carina are the most common locations (Fig. 31-27).[58] At the time of presentation, the tumor is frequently locally advanced, with extension into the major bronchi and mediastinum.[58, 62] Malignant tracheoesophageal fistula can result from such extension. Lymph node metastases are generally seen in later disease stages, with distant metastases uncommon (Fig. 31-28). Patients may present with cough, dyspnea, hemoptysis, wheezing, stridor, and recurrent pneumonia.[2] The development of hoarseness usually indicates infiltration of the recurrent laryngeal nerve. The prognosis of patients with SCC is poor, with 5-year survival reported to be between 10% and 30%.[2]

Radiologic findings include focal and/or circumferential irregular thickening of the tracheal wall with luminal narrowing (Fig. 31-3). CT is useful in demonstrating the primary tumor, as well as extension of tumor into surrounding structures.[44]

Adenoid Cystic Carcinoma

Adenoid cystic carcinoma (ACC) is the second most common primary tracheal malignancy. Unlike SCC, there is no definite association with cigarette smoking, and the tumor occurs with equal frequency in males and females. The peak incidence of ACC is about 10 years earlier than in patients with SCC.[58] ACC arises from the tracheobronchial mucous glands and is usually located on the posterolateral wall of the trachea.[1] It is composed of small epithelial cells arranged in sheets, with fenestrations that produce a cribriform pattern. The tumor is a low-grade malignancy that tends to invade insidiously the submucosal plane of the trachea.[44] Occasionally, circumferential involvement of the trachea and bronchus without a distinct mass can be seen. ACC infiltrates through the fibrous membrane between adjacent cartilage plates and into surrounding tissues in the neck and mediastinum.[63] There may be perineural, intra-

Copyright © 2003, Mosby, Inc. All rights reserved.

neural, or pericardial great vessel involvement.[60] Indeed, perineural spread of tumor is a distinctive characteristic of ACC. ACC spreads to cervical and mediastinal lymph nodes in 10% of patients.[58] Involvement of the larynx or the recurrent laryngeal nerve may result in restriction of vocal cord motion. Hematogenous metastases spread most commonly to the lungs, with occasional spread to the brain or bony skeleton.[63]

ACC appears on radiographs as either a broad-based or pedunculated polypoid lesion. There may be smooth or nodular thickening of the tracheal wall, with associated luminal narrowing.[44] Barium swallow may demonstrate extrinsic esophageal compression or invasion. CT is useful in demonstrating the primary tumor and its extent (Fig. 31-29). However, because ACC may grow in the submucosal planes without producing a distinct mass, CT may underestimate the true extent of tumor.

The treatment of ACC involves surgical resection and anastomosis when possible. When surgical resection is performed, frozen section pathologic evaluation of the biopsy margins is recommended. Radiation therapy is used when surgery is not indicated. ACC has the best prognosis among the malignant tracheal neoplasms.[2] About 75% of patients are free of disease 5 years after therapy, but late recurrence, or survival with locally recurrent tumor for periods of 10 to 15 years, is common.[64, 65]

Mucoepidermoid Carcinoma

Mucoepidermoid carcinoma is a rare tumor that can occur as either a low-grade or a high-grade malignancy. The tumor arises from the minor salivary glands lining the tracheobronchial tree and consists of mucus-secreting cells, squamous cells, and intermediate cells that have no particular differentiating characteristics.

Mucoepidermoid carcinoma has been reported in patients ranging in age from 4 to 78 years, but nearly 50% of patients are under the age of 30.[66] The most common presenting symptoms relate to airway irritation (cough or hemoptysis) or obstruction (wheezing or pneumonia).[66] In its low-grade form, mucoepidermoid carcinoma grows slowly, is noninvasive, and therefore rarely metastasizes.[67] Completely resectable low-grade tumors have an excellent prognosis, and these patients rarely have tumor recurrence. Even in its high-grade form the tumor is slow-growing and has a better prognosis than do the more common bronchogenic carcinomas. In one study,[68] only 15% of high-grade mucoepider-

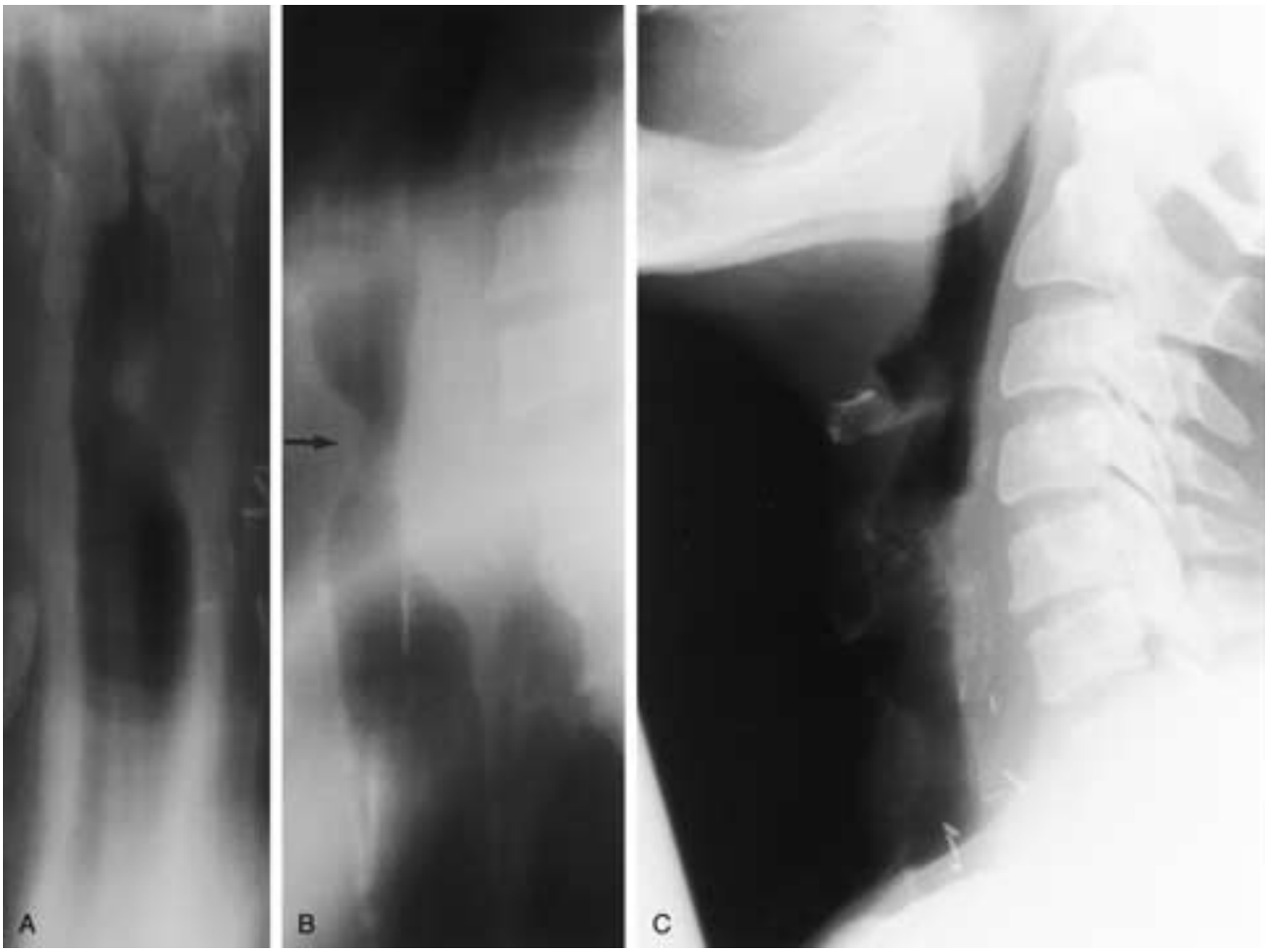

FIGURE 31-26 Carcinoma of the thyroid. Anterior (**A**) and lateral (**B**) conventional X-ray tomographic projections, as well as lateral plain film view of the neck (**C**), demonstrate a focal impression on the anterior left lateral wall of the trachea caused by an extrinsic thyroid carcinoma (**B**, *arrow*). The tracheal lumen is reduced to less than half of its normal width in the anteroposterior dimension.

VIEW IMAGE

Copyright © 2003, Mosby, Inc. All rights reserved.

moid carcinomas metastasized to regional lymph nodes. The tumor may manifest as a polypoid mass in the lumen of a main, lobar, or segmental bronchus. Radiographs may demonstrate a solitary pulmonary nodule or postobstructive ''pneumonic consolidation.''[68] CT scans may reveal punctate calcification within a smoothly oval or lobulated, mildly enhancing intraluminal mass (Fig. 31-4). The incidence of intratumoral calcification—up to 14%—is much higher than that of other pulmonary carcinomas.[12]

Chondrosarcoma

Tracheal chondrosarcoma is an extremely rare neoplasm with an excellent prognosis. The tumor is typically located in the middle to distal trachea. It grows slowly, expanding both into and away from the airway. Tracheal resection is the treatment of choice.

CT demonstrates a stereotypical soft-tissue mass with coarse or stippled calcifications. The hyaline tumor matrix is characterized by high signal intensity on T2-weighted images due to its high water content and low cellularity. The stippled calcifications are not as well seen on MR imaging studies as on CT, but they may appear as areas of low signal intensity on T1- and T2-weighted sequences. The distinction between benign chondroma, a nonmalignant form of chondroid tumor, and low-grade chondrosarcoma may be impossible on the basis of imaging studies alone.[13, 69]

Benign Tumors

Benign tumors of the trachea are rare and occur most frequently in children, in whom they account for 90% of primary tracheal neoplasms.[44] Squamous cell papilloma, fibroma, and hemangioma are the most common benign childhood tracheal neoplasms.[70] Other benign tracheal tumors include granular cell myoblastoma,[71] cartilaginous tumors,[61] neurilemmoma, lipoma, fibrous histiocytoma, intratracheal goiter, benign mixed tumor, and leiomyoma.[60]

Benign tracheal tumors tend to have a smooth contour and usually are less than 2 cm in size.[60] Presenting symptoms include cough, dyspnea, wheezing, recurrent pneumonia, and hemoptysis.[2] Chest X-ray can show tracheal luminal narrowing, postobstructive atelectasis, or tumor calcification. Because of their benign nature, benign tracheal tumors are usually well-circumscribed, sometimes lobulated intraluminal tumors, with limited spread into the tracheal wall (Fig. 31-30).[60] CT with 3D multiplanar reconstructions for surgical planning can delineate the precise location and extent of the mass. Calcification is typically present in cartilaginous-based lesions, including chondromas, low-grade chondrosarcomas, chondroblastomas, and hamartomas. Lipomas are hypodense on CT scanning, whereas they have increased signal intensity on T1-weighted and intermediate signal intensity on T2-weighted MR imaging exams.[60]

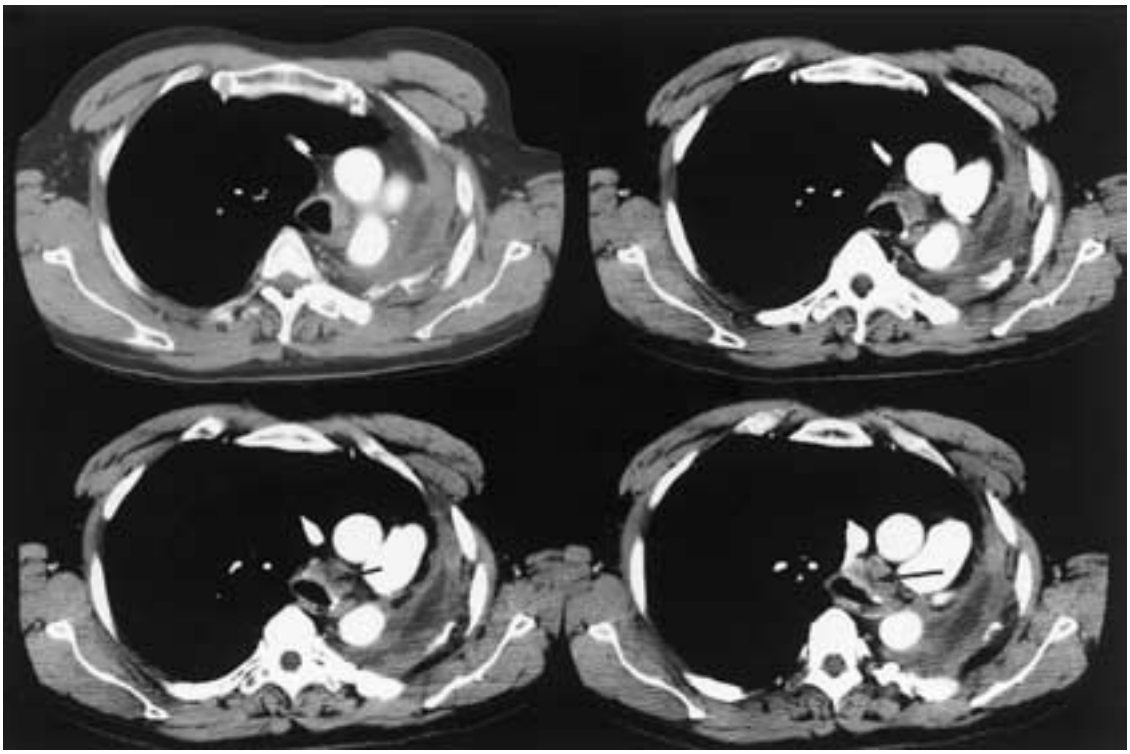

VIEW IMAGE

FIGURE 31-27 Recurrent squamous cell carcinoma at the carina. A 48-year-old male after pneumonectomy for SCC of the lung presented with cough and sputum production. Contiguous contrast-enhanced axial chest CT images demonstrate soft-tissue infiltration anterior to and to the left of the distal trachea extending to the carina (*arrows*). Irregularity of the anterior tracheal wall, carina, and left mainstem bronchus is indicative of neoplastic invasion. Postpneumonectomy changes are noted.

Copyright © 2003, Mosby, Inc. All rights reserved.

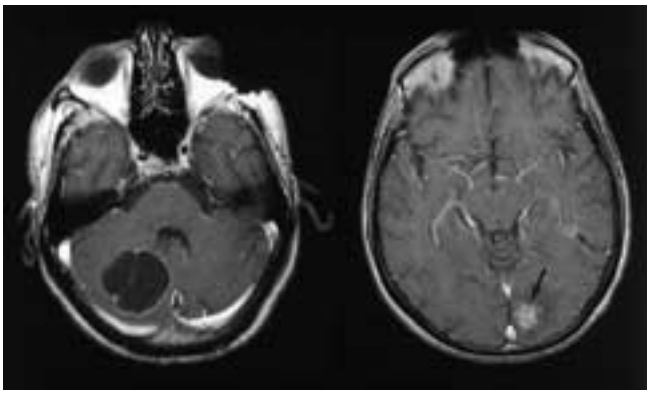

VIEW IMAGE

FIGURE 31-28 Hematogenous metastases. A 48-year-old male presented with a 3-month history of 40-pound weight loss, chronic cough, malaise, and drenching night sweats. A 5 cm diameter poorly differentiated SCC with necrosis was discovered in his distal trachea. T1-weighted postgadolinium MR image through the posterior fossa demonstrates a 3.5 cm diameter cystic mass with ring enhancement and internal septation. There is a slight mass effect on the fourth ventricle (left). Axial T1-weighted postgadolinium image at a more superior level (right) demonstrates an enhancing mass in the left occipital lobe (*large arrow*) with surrounding edema, as well as a small enhancing mass in the medial left temporal lobe (*small arrow*).

Benign Vascular Tumor

The most common benign pediatric large airway tumor is the hemangioma.[33] It is typically located in the subglottic portion of the larynx (i.e., subglottic hemangioma), not in the trachea. The cavernous form of hemangioma occurs more commonly than the capillary form. Neonates with airway hemangioma usually become symptomatic, with stridor and cough, within 3 months of birth.[33] Symptoms vary depending on the degree of vascular engorgement. These lesions rarely occur independently of other associated congenital vascular lesions such as hemangiomas of the skin, parotid gland, mediastinum, abdominal viscera, central nervous system, and retina. Because these lesions have a characteristic bronchoscopic appearance, biopsy is unnecessary and indeed may result in severe hemorrhage. Because many of these tumors regress spontaneously, the treatment of choice for both children and young adults is observation. For larger masses, temporary tracheostomy may be necessary for airway preservation. If the mass persists, tracheal resection may become necessary.

Hemangioendothelioma is an extremely rare lesion representing the benign counterpart of malignant hemangioendotheliosarcoma. This slow-growing tumor appears as a solid polypoid mass and contains endothelial cells surrounded by microscopic vascular channels.[72]

Squamous Cell Papilloma

The most common adult benign tracheal neoplasm is squamous cell papilloma. These tumors most often occur in middle-aged male smokers and typically involve the larynx or bronchi rather than the trachea. Squamous cell papilloma is characterized by single or multiple sessile or papillary nodular masses, with a central fibrovascular core and layers

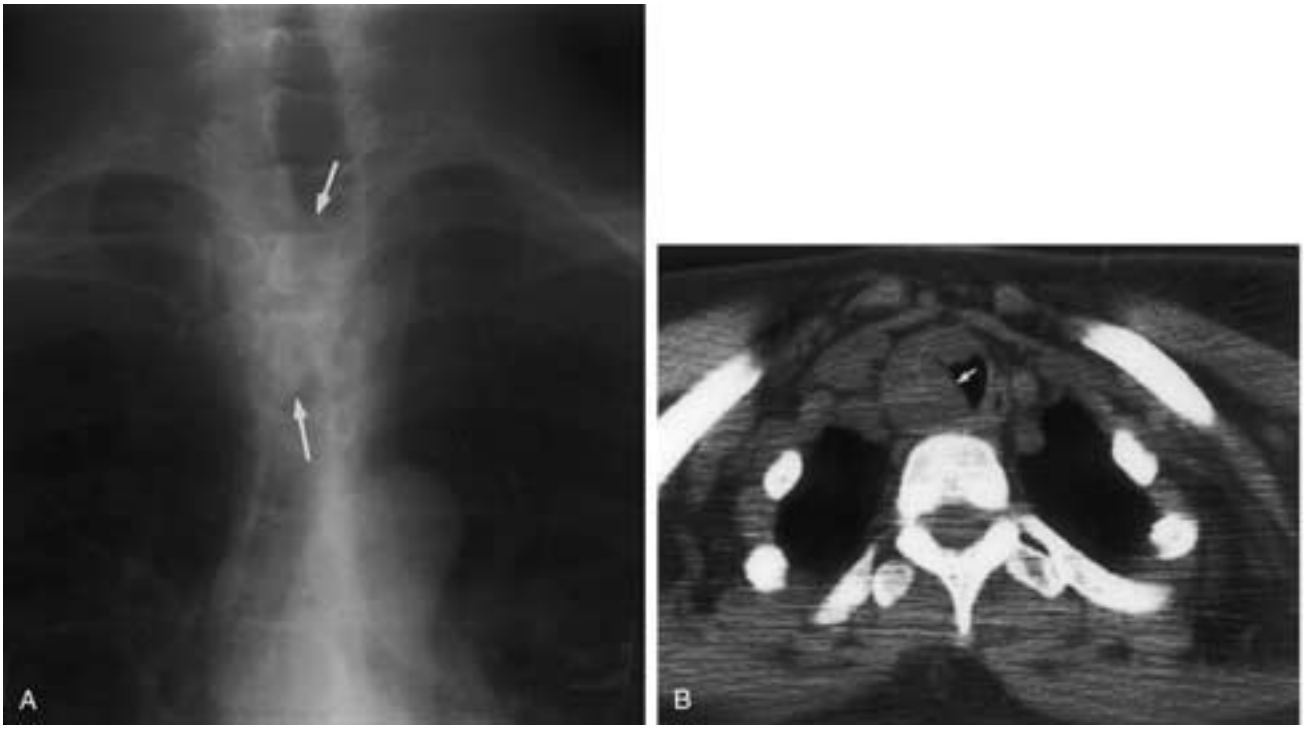

VIEW IMAGE

FIGURE 31-29 Adenoid cystic carcinoma. **A**, Chest radiograph demonstrates a large, broad-based endoluminal mass arising from the right tracheal wall (*arrows*) and partially obstructing the tracheal lumen. **B**, Axial nonenhanced CT scan demonstrates this large, lobulated, low-attenuation endoluminal mass arising from the right tracheal wall at the level of the thoracic inlet (*arrow*). Tumor is seen along the outer wall of the calcified cartilage as well, indicating infiltration either through or between the tracheal cartilages.

Copyright © 2003, Mosby, Inc. All rights reserved.

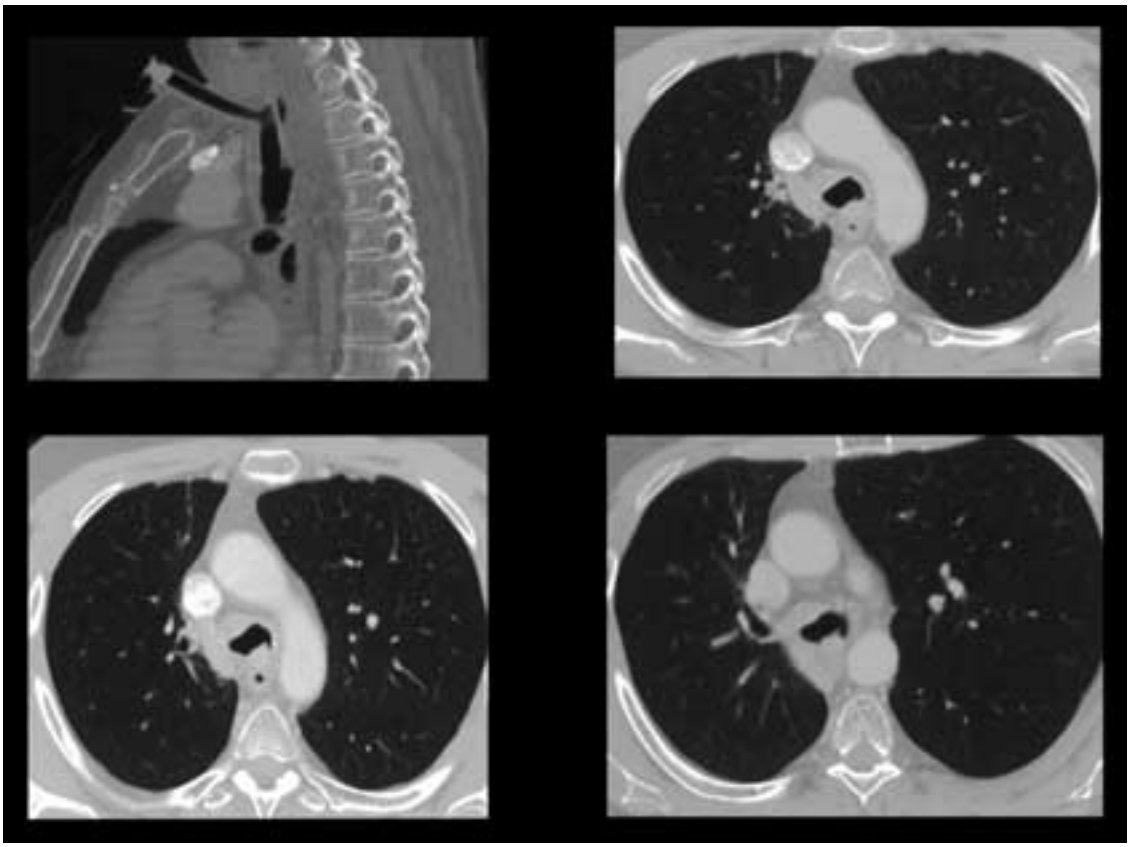

VIEW IMAGE

FIGURE 31-30 Glomus tumor. An 86-year-old male with episodic shortness of breath, cough, and hemoptysis. Rigid bronchoscopy and biopsy revealed multiple tracheal nodules and tracheal thickening. Biopsy demonstrated glomus tumor. Sagittal reconstruction of a contrast-enhanced CT scan demonstrates a tracheotomy tube that extends to the level of the transverse aorta (upper left corner). Diffusely thickened soft tissue with nodular components encases the trachea (remaining panels).

of well-differentiated squamous epithelium (Fig. 31-31). Papillomas tend to recur after resection and may undergo malignant degeneration.

Laryngotracheobronchial papillomatosis is a condition associated with multiple papillomas. Although histologically similar to solitary papillomas, the lesions associated with this condition more often occur in young children and tend to regress spontaneously after puberty.[58] Tracheobronchial papillomatosis results from a multicentric infection by the human papilloma virus. The disease is commonly acquired at birth as the infant passes through a birth canal infected with cervical condylomata. Papillomatosis has also been noted to occur in patients with the acquired immune deficiency syndrome (AIDS).[1] Although papillomatosis is usually restricted to the larynx, in a minority of patients one or more papillomas may develop in the trachea or bronchi, which can cause airway obstruction leading to atelectasis and bronchiectasis. Papillomas rarely spread to the lung, appearing on plain chest radiographs or CT scans as multiple small, widely scattered, round pulmonary nodules, which frequently develop thin-walled cavities with air-fluid levels (Fig. 31-32).[73] Clinically, laryngeal disease presents with hoarseness, whereas tracheobronchial disease presents with wheezing, atelectasis, or recurrent pneumonia. Asymmetric tracheal or bronchial wall thickening, causing eccentric tracheal luminal narrowing, may also be present.

Cartilaginous Tumors and Hamartomas

Cartilaginous tumors of the larynx and trachea are rare and include hamartoma, chondroma, and their malignant counterpart (already discussed), chondrosarcoma. Chondromas occur with equal frequency in males and females and are most common during the fourth to sixth decades.[61] These tumors present as sharply defined masses arising from the tracheal cartilage. They vary in size from very small, causing only a slight convexity of the endotracheal surface, to very large, forming an extensive mass.[61] They are usually located in the upper trachea.[58] The mucosa overlying these regions is usually intact, and calcification may be evident on chest radiographs and CT scanning. Distinction of chondroma from low-grade chondrosarcoma is controversial even at pathologic examination. The lesions in this area tend to grow slowly, and metastasis is rare.

A hamartoma is defined pathologically as a ‘‘tumor-like malformation composed of an abnormal combination of the normal constituents of the organ in which it is found.’’[61] Most endobronchial hamartomas therefore contain masses of cartilage, fat, or cystic fluid collections, with clefts lined by bronchial epithelium. They grow slowly and are usually solitary. The average age at presentation is 45 to 50 years. These tumors can be pedunculated; consequently, one lesion can obstruct different bronchi at different times. Clinical manifestations include bronchial obstruction or

Copyright © 2003, Mosby, Inc. All rights reserved.

occasionally hemoptysis. These tumors nearly always manifest stippled calcification, although clear-cut calcification is detected on plain films in 10% to 15% of patients in most series.[74] If calcification is of the typical ''popcorn'' configuration of cartilage calcification, the diagnosis of harmatoma is virtually certain. The contrast resolution of CT scanning improves the ability to identify calcium and fat within these lesions. Surgical excision is the treatment of choice.

Carcinoid Tumor

Carcinoid tumors of the trachea characteristically infiltrate the tracheal cartilage, growing slowly in a dumbbell configuration. The age range at presentation is variable, but the peak incidence is in the fifth to sixth decades. The atypical form of bronchial carcinoid has cellular and clinical features intermediate between those of typical carcinoid and SCC.[75] All types of carcinoid tumors are of neuroendocrine origin and are thought to form a spectrum of varying degrees of malignancy. Because these tumors are vascular, hemoptysis is a common presenting complaint. Other presenting symptoms include cough, pneumonia, atelectasis, and wheezing. The tumor may be predominantly intraluminal, assuming a polypoid configuration, or predominantly extraluminal (an ''iceberg'' lesion). Calcification and/or ossification within the tumor may occur.[76] Cushing's syndrome may develop due to secretion of corticotropins by tumor cells, and carcinoid *syndrome* uncommonly occurs as a complication of carcinoid tumor.[77] CT scanning provides superb anatomic localization of both the intraluminal and extraluminal components of the tumor. CT also may identify calcification and enhancement within the tumor.

Recurrence of carcinoid tumor is a significant problem, particularly after surgical resection of pedunculated tumors. Other methods of treatment, such as fulguration, cryotherapy, and laser ablation, seem to reduce recurrence rates more than local bronchoscopic resection.

Benign Mixed Cell Tumors

Benign mixed cell tumors (pleomorphic adenomas) of the trachea are histologically similar to benign mixed tumors of the major salivary glands. These contain a mixture of epithelial cells, cartilaginous elements, and mesenchymal cells. Although these lesions are less commonly found in tracheal or bronchial minor salivary glands than in major salivary glands, they constitute the fifth most common type of benign tracheal mass. Treatment consists of complete excision; recurrence is unusual.

Tumor-Like Conditions

Many nonneoplastic diseases can present as tracheal or bronchial masses. Infectious diseases such as tuberculosis, systemic histoplasmosis, or even coccidioidomycosis can form intraluminal granulomas that may simulate primary tumors. Traumatic injury of the trachea can also incite granuloma formation. Occasionally, aspirated foreign bodies may adhere to the tracheal wall and simulate tumor. Cysts and mucoceles in children must be differentiated from common tumors such as hemangiomas and fibromas.

Ectopic thyroid tissue in the trachea, although rare, can simulate neoplastic disease. Ectopic thyroid tissue is found in 1 of 7000 to 18,000 patients who undergo thyroid gland surgery (with a female predominance). It may come to clinical attention due to growth of normal thyroid tissue,

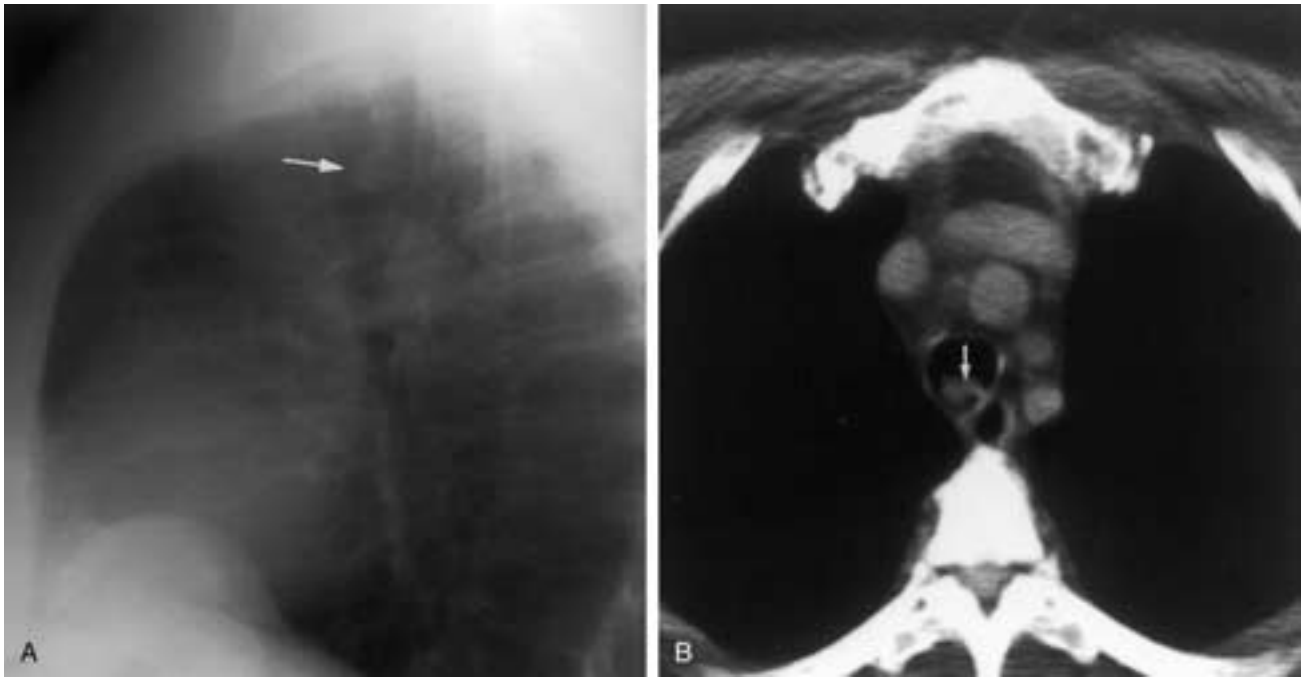

FIGURE 31-31 Squamous papilloma. Lateral chest radiograph (**A**) and noncontrast axial chest CT (**B**) demonstrate a polypoid endoluminal mass (**B**, *short arrow*, **A**, *long arrow*) protruding from the posterior left lateral wall of the midtrachea just above the level of the aortic arch.

VIEW IMAGE

Copyright © 2003, Mosby, Inc. All rights reserved.

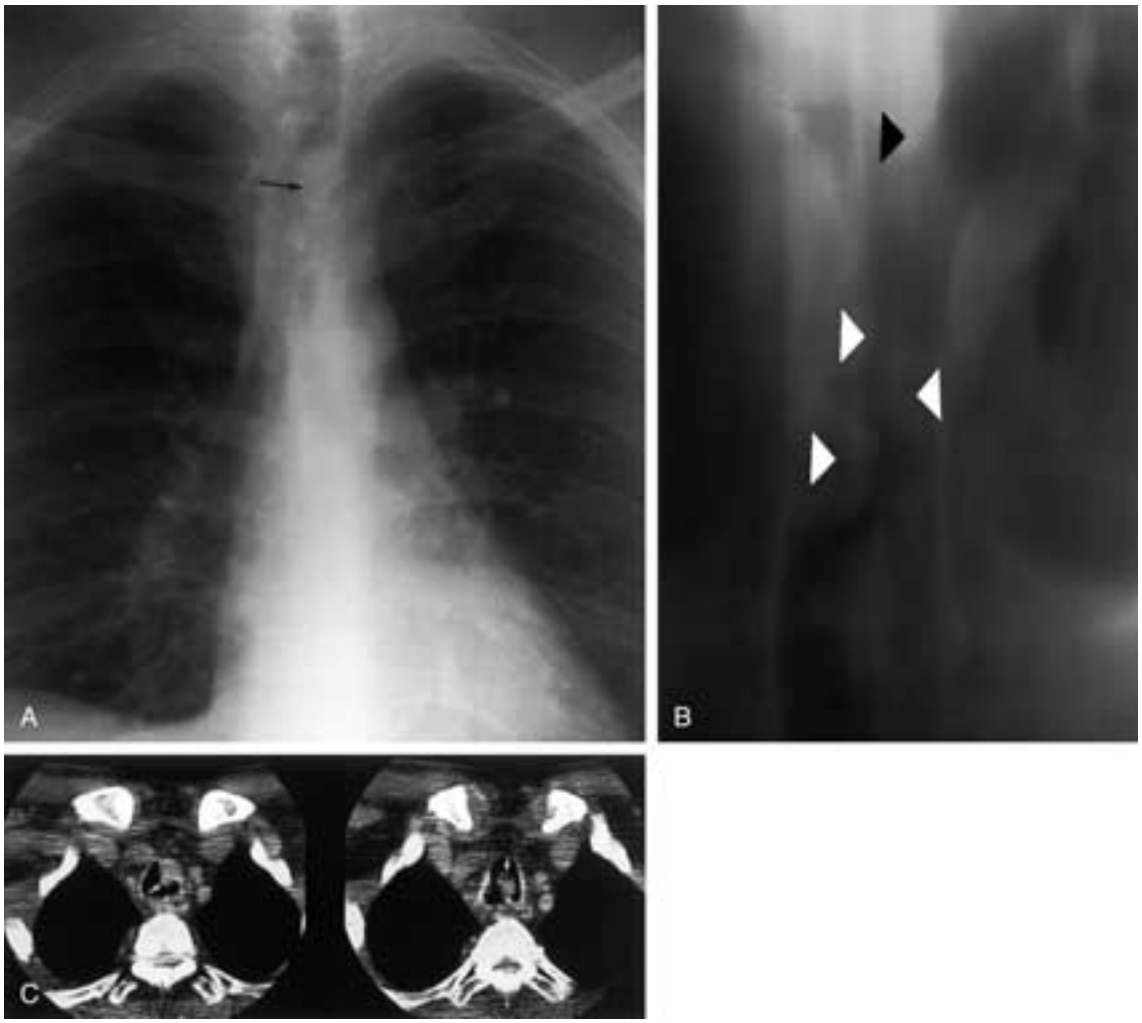

VIEW IMAGE

FIGURE 31-32 Tracheal papillomatosis. **A**, Anteroposterior chest radiograph demonstrates multiple exophytic masses projecting into the tracheal lumen (*arrow*). **B**, Coronal plain film tomography demonstrates multiple polypoid masses arising from the tracheal wall (*arrowheads*). **C**, Axial contrast-enhanced CT scan through the midtrachea demonstrates multiple pedunculated and broad-based exophytic polypoid masses arising from the tracheal wall (*arrows*).

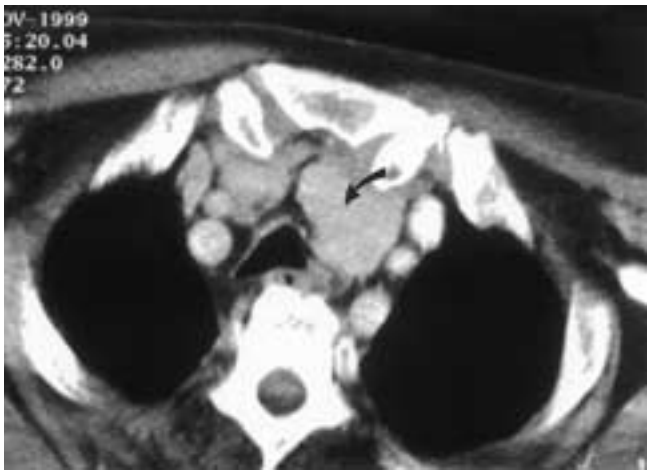

VIEW IMAGE

FIGURE 31-33 Substernal thyroid. Axial contrast-enhanced CT scan reveals an enlarged thyroid gland extending inferiorly to the level of, and posterior to, the sternum (*arrow*). There is mass effect on the trachea, which is compressed and displaced toward the right.

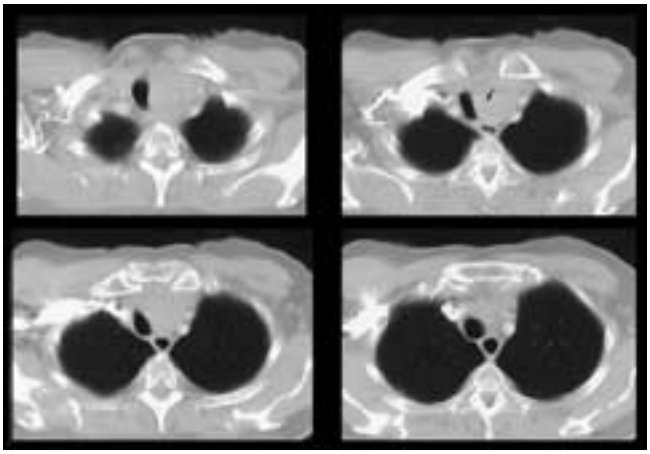

FIGURE 31-34 Goiter. A 75-year-old man with hyperthyroidism. Contiguous contrast-enhanced axial images from a CT scan demonstrate a 4 × 5 cm diameter left thyroid mass (*arrow*), which flattens and deviates the trachea toward the right. An adenomas goiter was discovered following partial thyroidectomy.

VIEW IMAGE

Copyright © 2003, Mosby, Inc. All rights reserved.

goitrous enlargement, or malignant degeneration (Fig. 31-33). A characteristic location is 2 to 3 cm below the vocal cords, although it may present more distally in the trachea. Frequently, intratracheal goiter is associated with goitrous enlargement of the normally positioned thyroid gland (Fig. 31-34). Intratracheal thyroid tissue may manifest years after thyroidectomy because of compensatory hyperplasia. Surgical resection is recommended, as malignant degeneration occurs in 10% of cases.

REFERENCES

1. Naidich DP, Webb R, Muller NL, Krinsky GA, Zerhouni EA, Siegelman SS, McGuiness G. Airways. In: Naidich DP et al., eds. Computed Tomography and Magnetic Resonance Imaging of the Thorax, 3rd ed. Philadelphia: Lippincott-Raven, 1999;161–291.
2. Lechner GL, Jantsch HS, Greene RE. Radiology of the trachea. In: Taveras JM, Ferrucci J, eds. Radiology Diagnosis Imaging Intervention, Philadelphia: Vol. 1. JB Lippincott, 1991;1–31.
3. Toremalm NG. Physiology. In: Cummings C, Frederickson J, Haker L, Krause C, Schuller D, eds. Otolaryngology Head and Neck Surgery, 2nd ed. St. Louis: Mosby-Year Book, 1993;2217–2222.
4. Graney DO, Marsh B. Anatomy. In: Cummings C, Frederickson J, Haker L, Krause C, Schuller D, eds. Otolaryngology Head and Neck Surgery, 2nd ed. St. Louis: Mosby-Year Book, 1993;2207–2216.
5. Lee A, Chow D, Haus B, Tseng W, Evans D, Fleiszig S, Chandy G, Machen T. Airway epithelial tight junctions and binding and cytotoxicity of *Pseudomonas aeruginosa*. Am J Physiol 1999;277(1 Pt 1): L204–L217.
6. Partanen M et al. Catecholamine and acetylcholinesterase-containing nerves in human lower respiratory tract. Histochemistry 1982;76:175.
7. Cymbalista M, Waysberg A, Zacharias C, Ajavon Y, Riquet M, Rebibo G, Grenier P. CT demonstration of the 1996 AJCC-UICC regional lymph node classification for lung cancer staging. RadioGraphics 1999;19(4):899–900 (poster).
8. Lev MH, Curtin HD. Larynx. In: Gentry LR, ed. Normal Anatomy of the Head and Neck: Neuroimaging Clinics of North America. Philadelphia: WB Saunders, 1998;235–256.
9. Gray's Anatomy: Anatomy, Descriptive and Surgical, 38th ed. Philadelphia: Running Press, 1995;1653–1657.
10. Moore KL. Clinically Oriented Anatomy, 3rd ed. Philadelphia: Lippincott, Williams & Wilkins, l996;114–115, 817.
11. Glazer HS, Siegel MJ. Diagnostic imaging of the trachea. In: Cummings CW, ed. Otolaryngology—Head and Neck Surgery, 3rd ed, Vol. 3. St. Louis: CV Mosby, 1998;2299–2342.
12. O'Keefe NE. Calcification in solitary nodules of the lung. AJR 1957;77:1023–1033.
13. Kiriyama M. Chondrosarcoma originating from the trachea. Ann Thorac Surg 1997;63(6):1772–1773.
14. Aquino SL, Vining DJ. Imaging: virtual bronchoscopy. Clin Chest Med 1999;20 (4):725–730.
15. Haponik EF, Aquino SL, Vining DJ. Flexible bronchoscopy in the 21st century, virtual bronchoscopy. Clin Chest Med 1999;20(1):201–217.
16. Aquino SL, Shepard JO, Ginns LC, et al. Acquired tracheomalacia: detection by expiratory CT scan. J Comput Assist Tomogr 2001;25:394–399.
17. Landing BH. Congenital malformations and genetic disorders of the respiratory tract (larynx, trachea, bronchi, and lungs). Am Rev Respir Dis 1979;120:151.
18. O'Sullivan BP, Frassica JJ, Raydner MM. Tracheal bronchus: a cause of prolonged atelectasis in intubated children. Chest 1998;113(2): 537–540.
19. Gronner AT. Tracheocoele. Br J Radiol 1971;44:979.
20. Kawahara H, Imura K, Yagi M, Kubota A. Clinical characteristics of congenital esophageal stenosis distal to associated esophageal atresia. Surgery 2001;129(1):29–38.
21. Swischuk LE, Hayden CK. Radiology of the Newborn and Young Infants. Baltimore: Williams & Wilkins, 1980.
22. Benjamin B. Congenital disorders of the trachea. In: Cummings C, Frederickson J, Haker L, Krause C, Schuller D, eds. Otolaryngology Head and Neck Surgery, 2nd ed. St. Louis: Mosby-Year Book, 1993;2288–2296.
23. Bone RC. Pulmonary and Critical Care Medicine. St. Louis: Mosby-Year Book, 1998.
24. Strife JL, Bisset GS. Cardiovascular system. In: Kirks DR, Ball WS, eds. Practical Pediatric Imaging: Diagnostic Radiology of Infants and Children, 2nd ed. Boston: Little, Brown, 1991;419–513.
25. Tarver RD, Conces DJ. Mediastinal disease. In: Haaga JR, ed. Computed Tomography and Magnetic Resonance Imaging of the Whole Body, 3rd ed. St. Louis: CV Mosby, 1994;737–771.
26. Sebening C, Jakob H, Tochtermann U, Lange R, et al. Vascular tracheobronchial compression syndromes—experience in surgical treatment and l literature review. Thorac Cardiovasc Surg 2000;48(3): 164–174.
27. Strife JL. Tracheal compression by the innominate artery in infancy and childhood. Radiology 1981;139:73.
28. Uba A. Infraglottic and bronchial infections. Prim Care 1996;23(4): 759–791.
29. Jones R, Santos JL, Overall JC. Bacterial tracheitis. JAMA 1979;242: 721–726.
30. Liston SL, Gehrz RC, Jarvis CW. Bacterial tracheitis. Arch Otolaryngol 1981;107:561–564.
31. Long SS. Bacterial tracheitis. Report Pediatr Infect Dis 1992;2:29–31.
32. Scully RE. Case Records of Massachusetts General Hospital, Case 32-1999. N Engl J Med 1999;341(17):1292–1299.
33. Dunbar JS. Upper respiratory tract obstruction in infants and children. AJR 1970;109:227.
34. Scully RE. Case Records of Massachusetts General Hospital, Case 1-1995. N Engl J Med 1995;332(2):110–115.
35. Rossi SE, McAdams HP, Rosado-de-Christenson ML, Franks TJ, Galvin JR. Fibrosing mediastinitis. RadioGraphics 2001;21(3): 737–757.
36. Rodriguez E, Soler R, Pombo F, Requejo I, Montero C. Fibrosing mediastinitis: CT and MR findings. Clin Radiol 1998;53(12):907–910.
37. Rholl KS, Levitt RG, Glazer HS. Magnetic resonance imaging of fibrosing mediastinitis. AJR 1985;145(2):255–259.
38. Atasoy C, Fitoz S, Erguvan B, Akyar S. Tuberculous fibrosing mediastinitis: CT and MRI findings. J Thorac Imaging 2001;16(3): 191–193.
39. Grum CM, Lynch JP. Tracheobronchial and esophageal manifestations of systemic disease. In: Cummings C, Frederickson J, Haker L, Krause C, Schuller D, eds. Otolaryngology Head and Neck Surgery, 2nd ed. St. Louis: Mosby-Year Book, 1993;2297–2319.
40. Webb EM, Elicker BM, Webb WR. Using CT to diagnose nonneoplastic tracheal abnormalities: appearance of the tracheal wall. AJR 2000;174:1315–1321.
41. Scully RE. Case Records of Massachusetts General Hospital, Case 46-1992. N Engl J Med 1992;327(21):1512–1518.
42. Carruthers DM, Watts RA, Symmons DP, Scott DG. Wegener's granulomatosis—increased incidence or increased recognition? Br J Rheumatol 1996;35(2):142–145.
43. Watts RA. Wegener's granulomatosis: unusual presentations. Hosp Med 2000;61(4):250–253.
44. Shepard JO. The trachea. In: McLoud TC, ed. Thoracic Radiology: The Requisites. St. Louis: CV Mosby, 1998;347–371.
45. George TM, Cash JM, Farver C, Sneller M, van Dyke CW, Derus CL, Hoffman S. Mediastinal mass and hilar adenopathy: rare thoracic manifestations of Wegener's granulomatosis. Arthritis Rheum 1997; 40(11):1992–1997.
46. Case Records of the Massachusetts General Hospital: weekly clinicopathological exercises. Case 31-1986. A 39-year-old woman with stenosis of the subglottic area and pulmonary artery. N Engl J Med 1986;7;315(6):378–387.
47. Himmelfarb R. The radiologic spectrum of cardiopulmonary amyloidosis. Chest 1977;72:327.
48. O'Regan A, Fenlon HM, Beamis JF, Steele MP, Skinner M, Berk JL. Tracheobronchial amyloidosis. The Boston University experience from 1984 to 1999. Medicine (Balt) 2000;79(2):69–79.
49. Rubinow A, Celli BR, Cohen AS, et al. Localized amyloidosis of the lower respiratory tract. Am Rev Respir Dis 1978;118:603.
50. Young RH, Sandstrom RE, Mark GJ. Tracheopathia osteochondroplastica: clinical, radiologic, and pathologic correlations. J Thorac Cardiovasc Surg 1980;79:537–541.
51. Meyer CA, White CS. Cartilaginous disorders of the chest. RadioGraphics 1998;18(5):1109–1123; quiz 1241–1242.
52. Shepard JO, McLoud TC. Imaging the airways: computed tomography and magnetic resonance imaging. Clin Chest Med 1991;12(1): 151–168.

Copyright © 2003, Mosby, Inc. All rights reserved.

53. Polansky A, Resnick D, Sofferman RA, et al. Hyoid bone elevation: a sign of tracheal transection. Radiology 1984;150:117.
54. Lewis RJ. Tracheostomies: indications, timing, and complications. Clin Chest Med 1992;13:137–149.
55. Staufer RL, Olson DE, Petty TL. Complications and consequences of endotracheal intubation and tracheotomy: a prospective study of 150 critically ill patients. Am J Med 1981;70:65.
56. Weber AL, Grillo HC. Tracheal stenosis: an analysis of 151 cases. Radiol Clin North Am 1978;2:291–308.
57. Song H, Shim TS, Kang SG, Jung GS, et al. Tracheobronchial strictures: treatment with a polyurethane-covered retrievable expandable Nitinol stent—initial experience. Radiology 1999;213(3):905–912.
58. Cardoso PF, Pearson FG. Diagnosis and management of tracheal neoplasms. In: Cummings C, Frederickson J, Haker L, Krause C, Schuller D, eds. Otolaryngology Head and Neck Surgery, 2nd ed. St. Louis: Mosby-Year Book, 1993;2339–2344.
59. Caldarola VT, Harrison EG Jr, Clagett OT, Schmidt HW. Benign tumors and tumorlike conditions of the trachea and bronchi. Ann Otol 1974;73:1042–1061.
60. Weber AL, Grillo HC. Tracheal tumors: radiological, clinical and pathological evaluation. Adv Otorhinolaryngol 1978;24:170–176.
61. Weber AL, Shortsleeve MJS, Goodman M, Montgomery W, Grillo HC. Cartilaginous tumors of the larynx and trachea. Radiol Clin North Am 1978;2:261–267.
62. Weber AL, Grillo HC. Tracheal lesions—assessment by conventional films, computed tomography and magnetic resonance imaging. Isr J Med Sci 1992;28:233–240.
63. Pearson FG, Thompson DW, Weillberg D, Simpson WJK, Kergin FG. Adenoid cystic carcinoma of the trachea. Ann Thorac Surg 1974;18:16–29.
64. Spizarny DL, Shepard JO, McLoud TC, Grillo HC, Dedreick CG. CT of adenoid cystic carcinoma of the trachea. AJR 1986;146:1129–1132.
65. Weber AL. Radiologic evaluation of the trachea. Chest Surg Clin North Am 1996;6(4):637–673.
66. Kim TS. Mucoepidermoid carcinoma of the tracheobronchial tree: radiographic and CT findings in 12 patients. Radiology 1999;212: 643–648.
67. Heitmiller RF, Mathisen DJ, Ferry JA, Mark EJ, Grillo HC. Mucoepidermoid lung tumors. Ann Thorac Surg 1989;47:394–399.
68. Yousem SA, Hochhlozer, L. Mucoepidermoid tumors of the lung. Cancer 1987;60:1346–1352.
69. Becker M. Larynx and hypopharynx. Radiol Clin North Am 1998;36(5):891–920.
70. Gilbert JG, Mazzarella LA, Feit LJ. Primary tracheal tumors in the infant and adult. Arch Otolaryngol 1953;58:1–9.
71. Canalis RF, Dodson TA, Turkell SB, et al. Granular cell myoblastoma of the cervical trachea. Arch Otolaryngol 1976;102:176–179.
72. Sabiston DC. Textbook of Surgery: The Biological Basis of Modern Surgical Practice, 15th ed. Philadelphia: WB Saunders, 1997.
73. Kramer SS. Pulmonary manifestations of juvenile laryngotracheal papillomatosis. AJR 1985;144:687–694.
74. Poirier TJ. Pulmonary chondromatous hamartoma: report of seventeen cases and review of the literature. Chest 1971;59:50–55.
75. Choplin RH, Rawamoto EH, Dryer RB, et al. Atypical carcinoid of the lung: radiographic features. AJR 1986;146:665–668.
76. Bateson EM, Whimster WF, Wwoo-Ming M. Ossified bronchial adenoma. Br J Radiol 1970;43:570–573.
77. Armstrong P. Neoplasms of the lungs, airways and pleura. In: Armstrong P, Wilson A, Dee P, Hansell D, eds. Imaging of Diseases of the Chest, 2nd ed. St. Louis: Mosby-Year Book, 1994;272–368.

Copyright © 2003, Mosby, Inc. All rights reserved.

32

Videofluoroscopic Evaluation of Oropharyngeal Swallowing

Tessa Goldsmith

INTRODUCTION
MULTIDISCIPLINARY NATURE OF THE VFSS
THE DIFFERENCE BETWEEN THE VFSS AND THE BARIUM SWALLOW
INDICATIONS FOR THE VFSS
CLINICAL EXAMINATION
PROCEDURE FOR THE VFSS
- Positioning
- Contrast Agents
- Recording
- Reporting the Findings

NORMAL SWALLOWING
- Oral Preparatory Stage
- Oral Transport Stage
- Pharyngeal Stage
- Esophageal Stage

EFFECTS OF AGING ON OROPHARYNGEAL SWALLOWING
INTERPRETATION OF FINDINGS
- Normal and Abnormal Anatomy
- Normal and Abnormal Biomechanical Movements
  - Lips and Cheeks
  - Tongue
  - Soft Palate or Velum
  - Epiglottis
  - Hyoid and Larynx
  - Pharyngeal Wall
  - Glottic Closure
  - Cricopharyngeus/Pharyngoesophageal Segment
  - Esophagus
- Temporal Coordination of Biomechanical Events in Relation to Bolus Flow
- Timeliness of Onset of Pharyngeal Swallow
- Duration of Oral and Pharyngeal Transit
- Laryngeal Penetration and Transglottic Aspiration
- Evaluation of Therapeutic Strategies

OVERVIEW OF A NORMAL VFSS
CONCLUSION

INTRODUCTION

The process of transferring food or liquids from the oral cavity to the esophagus consists of a series of intricately connected and exquisitely timed biomechanical events. When abnormalities of oropharyngeal swallowing occur, they can lead to potentially life-threatening health outcomes such as aspiration pneumonia, dehydration, and/or malnutrition, not to mention the devastating social consequences of the problem. While epidemiologic data are sparse, current estimates on the incidence and prevalence of dysphagia indicate that 16% to 22% of adults over 50 years of age experience swallowing difficulties; 12% to 13% of acute care hospitalized patients and about 60% of residents in long-term care facilities have dysphagia.[1]

Stroke is the leading cause of oropharyngeal dysphagia. Approximately 30% to 90% of patients with acute stroke have signs of dysphagia, and of those, 38% to 50% have aspiration on the videofluoroscopic swallowing study (VFSS).[2–4] Other progressive neurologic disorders such as amyotrophic lateral sclerosis, dementia, and Parkinson's disease also affect swallowing function. Moreover, oropharyngeal swallowing disorders can be manifestations of any of a multitude of systemic diseases such as those illustrated in Table 32-1.[1]

Oropharyngeal dysphagia is usually the result of a physiologic disorder of the swallowing process rather than a

Copyright © 2003, Mosby, Inc. All rights reserved.

Table 32-1
CAUSES OF OROPHARYNGEAL DYSPHAGIA

Iatrogenic
Medication side effects (neuroleptics, chemotherapy)
Postsurgical muscular or neurogenic
Radiation
Corrosive (pill injury, intentional)
Infectious
Botulism
Lyme disease
Syphilis
Mucositis (herpes virus, cytomegalovirus, *Candida*)
Metabolic
Amyloidosis
Thyrotoxicosis
Myopathic
Connective tissue disease
Dermatomyositis and polymyositis
Myasthenia gravis
Myotonic dystrophy
Oculopharyngeal muscular dystrophy
Paraneoplastic syndromes
Sarcopenia
Neurologic
Stroke (hemispheric, subcortical, brainstem)
Head trauma
Brain tumors
Cerebral palsy
Guillain-Barré syndrome
Huntington's disease
Parkinson's disease
Multiple sclerosis
Amyotrophic lateral sclerosis
Postpolio syndrome
Tardive dyskinesia
Metabolic encephalopathies
Dementia
Structural disorders
Cricopharyngeal prominence
Zenker's diverticulum
Cervical web
Pharyngoceles
Tumors of the oral cavity, oropharynx, hypopharynx, and larynx
Osteophytes and skeletal abnormalities
Congenital disorders (cleft palate)

mucosal or structural aberration. Therefore, diagnosis demands an understanding of the complexity of the multifaceted temporal, spatial, and pressure-related components of the swallowing process. While several instrumental diagnostic procedures are available for diagnosing oropharyngeal swallowing disorders, such as endoscopy, scintigraphy, and ultrasonography, each provides only limited information. The dynamic VFSS provides the most complete appreciation of the individual elements of the oral, pharyngeal, and laryngeal events that drive the bolus through the oral cavity into the cervical esophagus. Its comprehensiveness has earned it the status of the gold standard.[5, 6]

VFSS provides immediate information on bolus transit in relation to structural movements of the oral cavity and hypopharynx. The purpose of the examination is not simply to determine whether the patient is aspirating. The study is important because it helps define the underlying physiology of the swallowing disorder for rehabilitation planning. By careful analysis of the sequence of events during oropharyngeal swallowing, therapeutic strategies can be introduced systematically and their effectiveness evaluated. A critical objective is to determine a prescription for safe and effective feeding and swallowing.[7, 8]

Unlike the barium swallow, which has been the mainstay of fluoroscopic imaging of the upper aerodigestive tract for about 50 years, the VFSS is a relatively new examination in the armamentarium of speech language pathologists for examination of oropharyngeal swallowing. The VFSS is widely used in hospital and rehabilitation settings and has recently been adapted for mobile use with a C-arm fluoroscope in long-term care and school facilities. The study is alternatively known as a *cine-swallow study* after the cinefluorographic technology that preceded video recordings of dynamic radiographic events. It has also been called the *cookie swallow*, a term coined by Logemann[9] to emphasize the assessment of the oral stages of swallowing using cookies and barium as the contrast medium. The term most widely used today is *modified barium swallow*, which is frequently confused with *barium swallow*. Others have referred to the study as the *oropharyngeal motility swallowing study*,[10] *dynamic swallow study*,[11] and *videofluoroscopic oropharyngeal swallowing study*.[12, 13] For the purposes of this chapter, the term *videofluoroscopic swallowing study* (VFSS) will be used.

The VFSS has high clinical utility. In a recent study by Martin-Harris et al.,[7] 83% of their 608 consecutive heterogeneous subjects displayed abnormal swallowing on VFSS and 48.4% of those patients benefited from compensatory swallowing strategies that improved their swallowing safety and efficiency. However, the clinical utility of the examination depends on comprehensive evaluation of muscular movements in relation to bolus flow, not simply on evaluation of the bolus flow itself. Focus on the bolus flow alone, which is common among novice clinicians, provides information about symptomatology but not etiology. Successful therapeutic compensations or maneuvers are based on an understanding of the etiology of the disorder.

MULTIDISCIPLINARY NATURE OF THE VFSS

Optimally, the radiologist in collaboration with a speech pathologist trained in dysphagia evaluation and management perform the VFSS together, with each professional bringing his or her individual expertise. The radiologist is trained to identify structural abnormalities and disease processes, while the speech language pathologist possesses an in-depth understanding of the dynamics of oral and pharyngeal movements during normal and disordered swallowing and is familiar with the therapeutic strategies that can improve swallowing safety and efficiency. The speech language

Copyright © 2003, Mosby, Inc. All rights reserved.

pathologists should be acutely aware of his or her diagnostic range and should rely heavily on the radiologist for identification of disease. The radiologist provides input about radiation safety procedures and positions the fluoroscope to provide the clearest image of the area under consideration.[14] Together, both professionals estimate the risk of continuing to administer contrast to the patient and make recommendations for oral intake based on the results of the study.

THE DIFFERENCE BETWEEN THE VFSS AND THE BARIUM SWALLOW

The traditional barium swallow study differs from the VFSS in several ways. The routine procedure for the barium swallow includes a full-column, single-contrast or mucosal relief *double-contrast study* and a motility assessment of the esophagus.[15] The fluoroscopy unit is focused on the hypopharynx and follows the bolus as it traverses the esophagus into the stomach. The focus of this study is on the thoracic esophagus, and the oral manipulation of the bolus is not primarily evaluated. Aspiration is noted if it occurs, but the mechanism of aspiration cannot be determined unless the oral and pharyngeal stages of swallowing are carefully examined. Gas-producing granules and high-density barium may be administered for assessment of possible mucosal irregularities, and high-density liquid barium is used to assess esophageal motility. If a stricture or esophageal narrowing is suspected, a 13 mm barium tablet may be given. In the barium swallow, the patient is examined in upright and recumbent positions and in anterior-posterior (AP), lateral, and oblique projections. Usually single or sequential plane films taken during the swallow are generally adequate to capture the bolus as it moves through the esophagus.[15]

By comparison, the VFSS focuses on the oral cavity, oropharynx, nasopharynx, hypopharynx, larynx, and cervical esophagus. In an attempt to simulate the habitual swallowing function, patients are required to swallow controlled and uncontrolled volumes of barium contrast with a variety of consistencies while seated upright and imaged in the lateral and AP projections. Typically, esophageal function is not examined in detail during the VFSS. However, a survey scanning the esophagus to determine whether the contrast material has passed through the gastroesophageal junction provides some screening information about esophageal function and may suggest that further evaluation is needed. This is especially important since 35% of patients have combined pharyngeal and esophageal components to their dysphagia and the site of the lesion does not correspond accurately with the patient's complaint.[16]

INDICATIONS FOR THE VFSS

Patients who present with signs of pharyngeal dysphagia on xclinical examination are most appropriate for a VFSS study. Problems may include overt complaints of coughing and choking when eating or drinking as well as signs of food or liquid becoming ''caught in the throat.'' While aspiration may be obvious, it may also present silently in the form of a weak volitional cough or a wet or ''gurgly'' vocal quality after eating or drinking. Symptoms of silent aspiration are strongly related to transglottic aspiration on videofluoroscopic evaluation.[2] Splaingard et al.[17] observed that 40% of their subjects who aspirated on VFSS were not identified as having aspirated on the bedside examination.

Patients should be alert and be able to accept food by mouth in a reasonable length of time. If therapeutic strategies are to be evaluated, patient cooperation is necessary. Hemodynamically unstable patients or those with severe deconditioning who have not had practice sitting upright should be transported to the radiology suite only with extreme caution, as the effect of positioning the patient may overwhelm and fatigue the patient, affecting the outcome of the examination. In such cases, it may be prudent to defer the examination until the patient's health improves. Patients should be able to sit upright or close to upright comfortably for the procedure for several minutes.

CLINICAL EXAMINATION

In most instances, the patient is known to the speech language pathologist prior to the VFSS. Previous clinical encounters permit the clinician to obtain a comprehensive medical and swallowing history and to perform an assessment of oral motor and sensory function. In addition, it is likely that the speech language pathologist has observed the patient swallowing liquids and solids. The clinical swallowing evaluation allows the clinician to hypothesize about the nature of the underlying pathophysiology of the swallow and to attempt therapeutic strategies at the bedside. In addition, the patient may be taught compensatory swallowing strategies in preparation for the VFSS.

In certain settings, however, the VFSS may be the first encounter, and thus a detailed history is required to plan the study. Relevant history information details the onset and progression of the patient's dysphagia symptomatology as well as current diet, food consistency preferences and avoidances, duration of mealtimes, strategies the patient has found helpful to alleviate the problem, unintended weight loss, and medical consequences of the dysphagia. If the patient is fed nonorally via a gastrostomy or nasogastric tube, the circumstances surrounding its placement must be understood. The patient's medical and surgical history and current medications are examined for their etiologic contribution to the dysphagia, including recent hospitalizations for pneumonia, radiation therapy to the head and neck, and/or gradual changes in speech intelligibility.

Prior to the radiographic examination, an assessment of the motor and sensory function of the oral mechanism is performed. Note is made of asymmetries of labial, lingual, and palatal movements, reduction in range of motion, strength or coordination, and restricted sensation to light touch. An absent gag reflex is noted, as well as impairment of volitional coughing and laryngeal excursion during dry swallowing.

Copyright © 2003, Mosby, Inc. All rights reserved.

Table 32-2
PARAMETERS THAT GUIDE THE PROGRESS OF THE VFSS

From		To
Lateral projection	→	AP projection
Liquids	→	Semisolids, solids, and tablets
Small boluses	→	Large boluses
Clinician-delivered bolus delivery	→	Patient-controlled bolus delivery
Uncompensated swallows	→	Compensatory maneuvers

Adapted from Mills RH. Increasing the precision of the videofluoroscopic swallowing evaluation. In: Mills RH, ed. Evaluation of Dysphagia in Adults: Expanding the Diagnostic Options. Austin, TX: Pro-Ed, 2000;103-144.

PROCEDURE FOR THE VFSS

The VFSS aims to simulate habitual swallowing behavior as much as possible, taking into account that barium contrast does not closely resemble typical solid or liquid substances. Although several standard protocols have been described,[6, 18, 19] there is no real consensus about the most appropriate protocol, probably because no one protocol is suitable for all patients. The VFSS is tailored to the patient's complaints, medical profile, cognitive status, results of the clinical swallowing evaluation, and the patient's risk of aspiration. In all instances, efforts are made to limit aspiration of the contrast material. In some cases, the study is terminated when the patient aspirates. However, in most instances, controlled volumes of different barium consistencies coupled with swallowing maneuvers allow for evaluation of their effectiveness. The general sequence of the procedure is illustrated in Table 32-2 and is adapted from Mills.[20]

Positioning

The patient is seated upright in a comfortable posture in a chair. Chairs designed specifically for the VFSS are available. These chairs fit into the fluoroscopic unit and permit easy transfer of patients from stretchers or wheelchairs, as well as easy position changes from lateral to AP views. The VFSS always commences with the patient in the lateral view. The field of view includes the lips anteriorly, the posterior pharyngeal wall and cervical spine posteriorly, the nasopharynx superiorly, and the upper esophageal segment and C7 inferiorly (Fig. 32-1A). This wide view enables assessment of the various stages of swallowing at one time. After contrast with the various consistencies is administered and any necessary maneuvers are performed, the patient is turned to the AP projection for observation of the symmetry of muscular contraction. For the AP views, the fluoroscopic unit is focused on the oral cavity so that the palate forms the superior border of the image and the vocal folds and tracheal column form the inferior border. To improve the quality of the image, the field is collimated so that the lateral borders of the mandible are at the outer aspect of the field of view (Fig. 32-1B).

Contrast Agents

Patients are given small amounts of barium sulfate in various forms such as liquid, paste mixed with pudding or applesauce to create a semisolid consistency, and a portion of a cookie coated with barium paste. Since the study is not designed to identify mucosal pathology, it is not necessary to use a contrast agent with a very high weight/volume concentration. Some clinicians attempt to replicate the

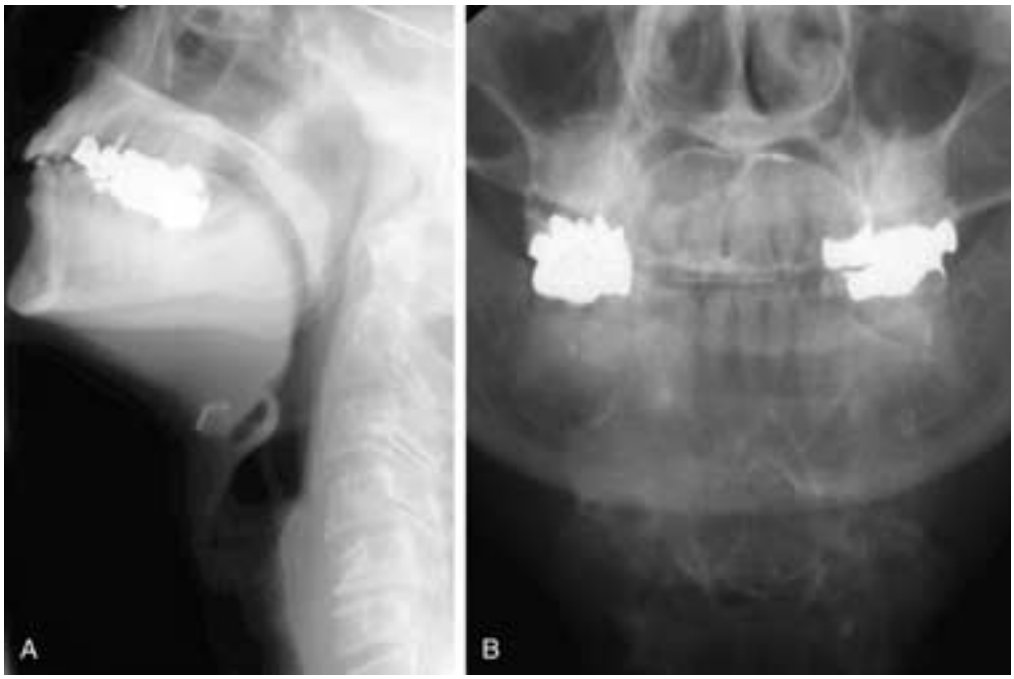

FIGURE 32-1 Ideal view for imaging oropharyngeal swallowing in the (**A**) lateral and (**B**) AP projections.

VIEW IMAGE

Copyright © 2003, Mosby, Inc. All rights reserved.

thinnest liquids, such as water or juice, by diluting the barium liquid. While this more closely resembles the viscosity of thin liquids, its reduced radiodensity reduces the reliability with which small amounts of aspiration can be accurately detected.

The boluses are measured and are given in increments to determine performance with a variety of volumes. Contrary to expectation, some patients have greater difficulty initiating a swallow with smaller liquid boluses than with larger ones. Sometimes it is necessary to evaluate the patient while swallowing thickened liquids or specially prepared foodstuffs such as bread and hard meats coated with barium. In some settings, patients are encouraged to bring foods with which they have difficulty, the goal being to simulate the scenario that causes the dysphagia. If the patient has difficulty taking pills, a 13 mm barium tablet may be given, although extreme caution should be exercised if the patient is seen to experience moderate to severe oropharyngeal dysphagia. Aspiration of a barium tablet can lead to significant complications, particularly in a compromised patient.

Recording

Fluoroscopic images are recorded in real time by high-definition video recording equipment for later analysis and review. Image data can be stored on videotape or, with new technology, in digital form on a hard drive or digital video disk. Because of the complexity of the events of the swallow occurring in a short period of time, video recorders should be capable of slow-motion review and frame-by-frame analysis. A microphone is needed to record the instructions to the patient and to record audible responses such as coughing and the patient's vocal quality. Static or spot films can be taken during the fluoroscopic procedure if suspected pathology is identified.

In an effort to reduce radiation exposure, some clinicians use pulse fluoroscopy, particularly during mastication of solid boluses. Since swallow onset after mastication is variable, it is possible to miss the important biomechanical events if the fluoroscope is turned off. Rapid-sequence digital radiography has become available in many hospitals. Among the advantages of this system are the excellent image resolution quality (1024 lines per inch), the relatively low-dose radiation, and the ability to enhance the image on a frame-by-frame basis.[20] However, one disadvantage is that its capture rate of six frames per second may be too slow to ensure visualization of the intricacies of the pharyngeal swallow, which in normal instances can be completed in less than 1 second.

While clinicians should be mindful of the cumulative recording time, the examination should be long enough to obtain the answers to the critical questions. Fluoroscopy time can be controlled by thorough preparation for the examination based on the history and the findings of the clinical swallowing assessment. Clinicians should take care to administer only that contrast necessary to answer particular questions reliably, expecting to extrapolate some information to slightly larger boluses or to consistencies that differ minimally in viscosity. For the beginning clinician, it may be necessary to review the video recording partway through the study before proceeding with the remainder of the examination.

Traditionally, the radiologist terminates the barium swallow examination when aspiration is detected. However, sometimes aspiration is observed early in the examination and terminating the study will not allow evaluation of the efficacy of therapeutic strategies that may indeed eliminate aspiration. Compensatory or rehabilitative maneuvers are introduced if the patient aspirates or demonstrates inefficient swallowing behaviors. Such maneuvers are assessed for their effectiveness in both the lateral and AP projections. Ideally, more than one trial per bolus is needed to improve the reliability of the findings.

Termination of the study will depend on patient-specific parameters such as the amount of aspiration, the patient's sensitivity to the aspiration, effectiveness of clearance from the trachea, and the underlying medical history. For example, an ambulatory patient, who has no history of aspiration pneumonia, is cognitively intact, and whose airway is effectively cleared with a cough is more likely to tolerate aspiration than a patient who is bed bound and has recently been mechanically ventilated, with a weak cough.

Reporting the Findings

In many facilities, the speech pathologist and radiologist generate separate reports on the results of the VFSS. Ideally, a report that details observations of the structural components of the oropharyngeal mechanism, as well as a description of the biomechanical events of the swallow and the results of therapeutic procedures, would reflect the collaborative nature of this radiographic procedure.

NORMAL SWALLOWING

Traditionally, the description of swallowing is divided into four stages: the oral preparatory stage, the stage of oral transit, the pharyngeal stage of swallowing, and the esophageal stage. This description is artificial in that it fails to capture the fluidity of the normal swallow and it ignores the impact one stage has on the progress of the next. In this section, an attempt is made to outline the features of the normal oropharyngeal swallow from a physiologic standpoint using the pressure generation model as the basis for the discussion. In the section on Interpretation of Findings, the radiologic manifestations of the normal and abnormal physiology of swallowing are discussed. However, in order to make clinical sense of radiographic findings, it is necessary to understand the complexity and fluidity of normal swallowing physiology.

The process of safe and efficient swallowing demands exquisite timing and coordination of more than 30 pairs of muscles and 6 cranial nerves that are under voluntary and involuntary nervous control. Boluses are prepared and propelled through the oral cavity, pharynx, and esophagus and enter the stomach in an extremely complex process that lasts for less than 20 seconds, with the longest phase occurring in the esophagus. A dynamic pressure gradient, generated by the opening and closing of a series of ''valves''

Copyright © 2003, Mosby, Inc. All rights reserved.

in the tube-like structure of the oral cavity and hypopharynx, is responsible for propagation of the bolus into the esophagus.

Oral Preparatory Stage

In the first preparatory stage, the food or liquid is manipulated until it is ready for swallowing. This stage involves mastication of solid boluses and positioning of semisolid or liquid boluses for transfer into the hypopharynx. Bolus preparation is under voluntary control and can be halted at any point. It is during this stage that pleasure is taken from the food by stimulation of the multiple chemoreceptors and sensory receptors located on the tongue dorsum and to a lesser degree in the pharynx. The length of this stage varies, depending on the consistency of the material being manipulated, the presence of saliva, the individual preference of bolus size for swallowing, and the style of chewing. Liquids, including saliva, and semisolid materials such as pudding require minimal manipulation. The bolus is formed by pressure generated by contraction of the buccinator and labial musculature, and elevation of the edges of the tongue aids in shaping the bolus and positioning it on the tongue dorsum in preparation for propulsion of the bolus to the pharynx. Simultaneously, the soft palate is depressed against the tongue base, creating a palatoglossal seal, which prevents leakage of liquids or semisolids into the pharynx before they are ready to be swallowed.

During mastication of solid foods, finely coordinated movements of intrinsic and extrinsic lingual muscles move the bolus to the dental arches. Opening of the jaw and lateral and rotary movements of the mandible against the maxilla grind food into smaller pieces. Cohesive bolus formation of solids and liquids depends on the presence of sufficient saliva that binds the material together, tongue movement that sweeps the crevices of the oral cavity, and lip closure that prevents spillage of food from the mouth. It is important to note that during mastication, unlike manipulation of liquids and semisolids, the bolus is not completely contained in the oral cavity. Here the rotary and lateral mandibular movements release the palatoglossal seal, and some material falls into the valleculae prior to the onset of the pharyngeal phase.

Oral Transport Stage

During the second stage of swallowing, the oral transit or oral transport phase, the prepared bolus is propelled into the pharynx by a series of anterior-to-posterior wave-like contractions of the tongue in contact with the incisors and the lateral borders of the palate. The soft palate elevates, permitting the bolus to enter the pharynx and preventing nasal regurgitation. Simultaneously, the floor of mouth muscle complex, including the suprahyoid muscles, contracts and the base of the tongue depresses and moves anteriorly, forming a chute down which the bolus can flow. This, in turn, causes pressure on the bolus and drives it cleanly into the pharynx. This stage of swallowing, illustrated in Figure 32-2, lasts for less than 1 second and is under voluntary neural control.

Pharyngeal Stage

The events of the pharyngeal stage of swallowing occur concomitantly with the oral transport stage and can be described as a single pressure-driven event in which the oral cavity, pharynx, and cervical esophagus form a single tube. The ‘‘valves’’ of the system (lip closure, contraction of the buccinators, closure of the velopharyngeal port, adduction of the vocal folds, and contraction of the pharyngeal musculature) act to close the cavity and, in conjunction with the ‘‘piston-like movement’’[21] of the tongue and contraction of the pharyngeal constrictor muscles, generate pressure within this continuous tube. A pressure differential occurs as the hyolaryngeal complex elevates superiorly and anteriorly, opening the upper esophageal segment and propelling the bolus into the cervical esophagus.[22]

The pharyngeal stage is the most complex stage of the swallow in terms of muscular coordination and timing. It is during this stage that airway protection must occur simultaneously with opening of the upper esophagus to prevent aspiration into the trachea and to facilitate transfer of the bolus into the esophagus.

Stimulation of the sensory impulses of cranial nerves IX, X, and XI (glossopharyngeal, vagus, and accessory, respectively) marks the onset of the pharyngeal stage of swallowing. The glossopharyngeal nerve transmits visceral sensation from the pharynx, taste sensation from the posterior one third of the tongue, and touch, pain, and thermal sensation from the mucous membranes of the oropharynx and posterior tongue.[23] The superior laryngeal branch of the vagus nerve supplies sensation to the mucosa covering the epiglottis and the posterior tongue and endolarynx, while the recurrent laryngeal nerve supplies sensation to the subglottis and the mucosa of the cervical esophagus.[24] These sensory impulses travel to the nucleus tractus solitarius (NTS) in the medullary reticular formation located within the brainstem, which integrates multiple functions related among others to respiration and swallowing[24] (p. 70). Neurons from the NTS project to other brainstem regions including the nucleus ambiguus (NA). The motor neurons of the NA innervate the palatal, pharyngeal, laryngeal, and esophageal muscles critical to the pharyngeal stage of swallowing. Together with input from higher cortical and subcortical structures, the coordinated and precisely timed actions occurring in the pharyngeal stages of swallowing are possible.

Airway protection, opening of the upper esophagus, and pharyngeal clearance transform the aerodigestive tract from its function as a respiratory system to a deglutitional system. Airway protection takes place in the horizontal and vertical planes, begins simultaneously with bolus entry into the pharynx, and can occur even when the bolus is first placed in the mouth.[25] Intrinsic laryngeal closure begins with adduction of the vocal folds (contraction of the thyroarytenoid, vocalis, interarytenoid, and lateral cricoarytenoid muscles) toward the midline.[26, 27] The vestibular vocal folds and the supraglottis also adduct to close the laryngeal airway. Vocal fold adduction is the first event to occur during the swallow and continues throughout the swallow sequence. Shaker et al.[27] noted that in one third of their normal subjects, true vocal fold approximation was incomplete prior to laryngeal elevation and during the pharyngeal swallow. This may

Copyright © 2003, Mosby, Inc. All rights reserved.

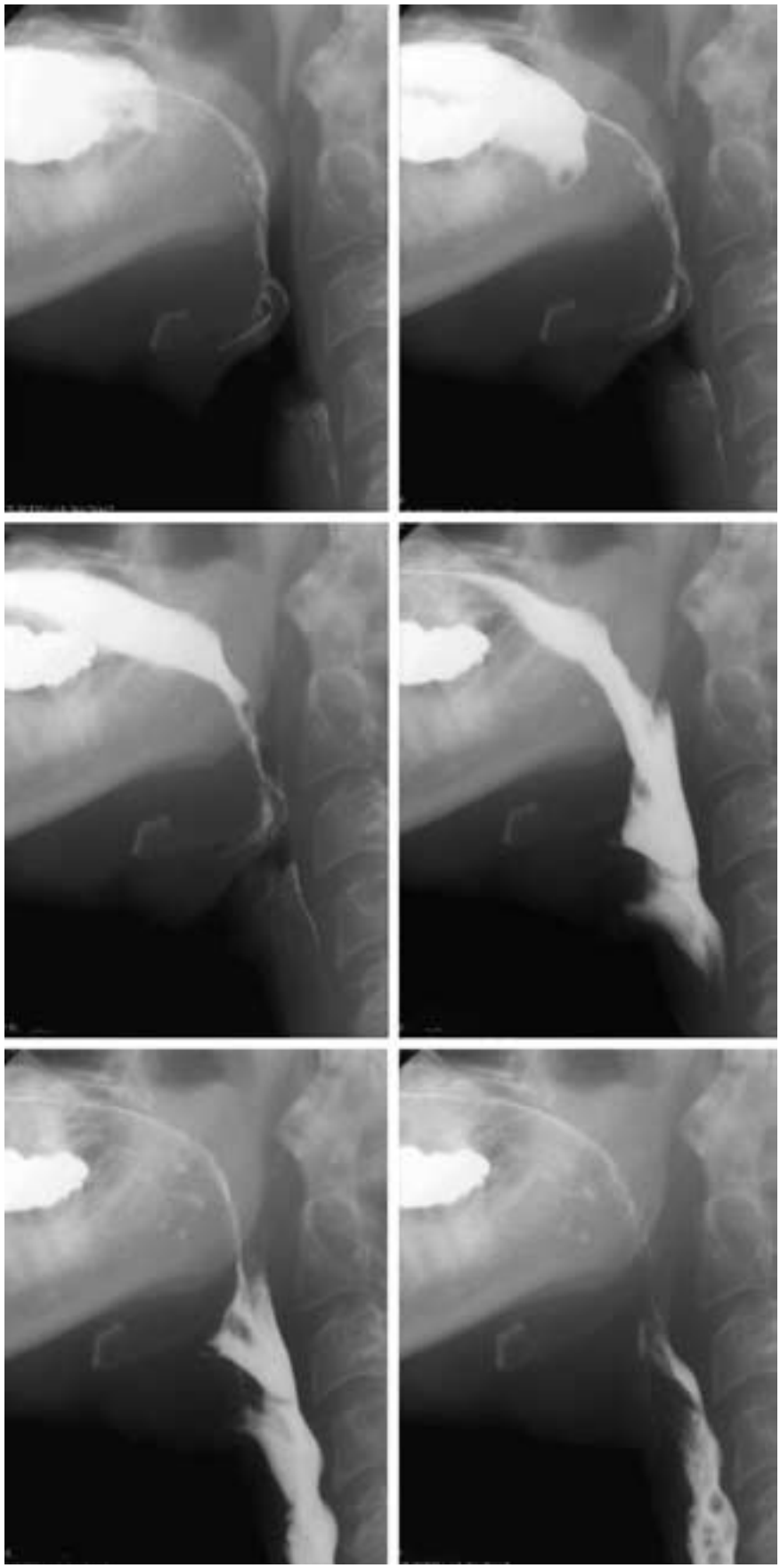

FIGURE 32-2 Phases of normal swallowing.

VIEW IMAGE

Copyright © 2003, Mosby, Inc. All rights reserved.

account for the frequently observed phenomenon in normal adults of trace and transient liquid penetration high in the laryngeal vestibule, which is extruded out as the swallow progresses.[28]

The upright suprahyoid portion of the epiglottis forms the posterior border of the vallecula at the base of the tongue, and acts to divide the advancing bolus and direct it down the lateral channels of the hypopharynx (pyriform sinuses) and into the cervical esophagus. As the pharyngeal stage of the swallow progresses the epiglottis inverts, contributing to the closure of the laryngeal inlet. The epiglottis moves passively, and its inversion is dependent on the contraction of its muscular attachments in a two-stage process. Contraction of the suprahyoid muscles pulls the hyolaryngeal complex anteriorly, and with it the epiglottis to the horizontal plane. Thereafter, contraction of the thyroepiglottic muscle inverts the epiglottis to a completely downfolded position assisted by pressure from the bolus above.[29–31] Of note, epiglottic downfolding may be inconsistent in occurrence. Ekberg and Nylander[32] noted that the epiglottis can remain upright in normal adults when a small bolus is swallowed. Appreciation of the passive nature of epiglottic movement per se is important in interpreting abnormal deflection on a radiographic examination because the function of the surrounding structures must be examined.

Respiration ceases for approximately 0.75 second during an obligatory apneic period. This period of apnea varies with bolus consistency and volume; the larger the bolus volume and/or the more viscous its consistency, the longer the duration of apnea.[25] Respiration resumes after the swallow on the expiratory phase of the respiratory cycle, which is thought to have a role in clearing material possibly penetrating the laryngeal vestibule.

Opening of the cervical esophagus occurs as the suprahyoid muscles contract, pulling the larynx upward, forward, and away from the posterior pharyngeal wall. Conventional wisdom suggests that opening of the upper esophagus is achieved through relaxation of the tonically contracted cricopharyngeus muscle. While intrinsic relaxation of the pharyngoesophageal segment must occur, research has shown that the movement of the entire larynx upward and forward approximately 2 to 2.5 cm under the tongue base affects the major opening force, assisted by intrinsic relaxation of the pharyngoesophageal segment and by the bolus pressure from above.[33, 34] Opening of the upper esophageal segment is modulated by bolus variables such that larger or more viscous boluses result in earlier onset, greater magnitude, and longer duration of opening than smaller, less viscous boluses.[25, 34]

Contraction of the obliquely arranged pharyngeal constrictor muscles generates additional pressures on the tail of the bolus, especially at the area between the valleculae and the arytenoid cartilages. These sequential contractions contact the tongue base, acting as a clearing force to remove boluses from the pharyngeal recesses and propel them into the cervical esophagus.[35] Pharyngeal bolus transit is very rapid, occurring in less than 1 second, and is consistent in duration regardless of the viscosity or volume of the bolus or the age of the patient.

Esophageal Stage

In contrast to the oral and pharyngeal stages of swallowing, the esophageal stage is the longest, lasting for 8 to 20 seconds in normal adults. The transfer of food from the mouth to the stomach via the esophagus results from the coordinated relaxation of the upper and lower esophageal sphincters and the peristaltic contraction waves that sweep the length of the conduit after the pharyngeal swallow. Primary and secondary peristaltic waves are the result of contraction of the striated and smooth esophageal regions, which shortens the esophagus in rostrocaudal sequences. The mass of the bolus entering the esophagus initiates primary and secondary esophageal contractions. If the cricopharyngeus does not close in an appropriately rapid manner, esophagopharyngeal reflux can occur. Thus, the timing of both the opening and closing of the cricopharyngeus is critical to a normal swallow. In addition, this region must remain open long enough to allow the entire bolus to enter the esophagus. These factors illustrate the delicate and precise timing of events during a normal swallow, and they are discussed later in the chapter.

EFFECTS OF AGING ON OROPHARYNGEAL SWALLOWING

The features of normal swallowing described above undergo changes with aging, even in the elderly normal. These changes must be recognized when evaluating the swallowing of older patients in order to avoid overdiagnosis and overtreatment of normally occurring phenomena. There is a natural progressive change in the sensory and motor components of oropharyngeal swallowing that may make older normal persons vulnerable to dysphagia. Physiologic features of swallowing in older individuals include slower manipulation of solids and a delay in initiating the pharyngeal stage of swallowing, which results in an unprotected airway for an increased length of time. The range of opening of the upper esophageal segment is reduced as a result of tissue fibrosis and degeneration, which in turn results in more pharyngeal retention than in a younger patient. High laryngeal penetration of the laryngeal vestibule may be observed in older individuals before completion of the swallow. However, persistent laryngeal penetration and aspiration is never normal, and the material is usually ejected from the laryngeal inlet as the swallow progresses. Aging can bring with it loss of skeletal muscle mass, as well as changes in muscle strength and muscle contraction, all of which may contribute to a weaker bolus drive and increased stasis in the oral cavity and pharynx. Furthermore, aging individuals are more susceptible to disease, which in turn restricts the functional reserve capacity in dealing with the normal structural and physiologic changes that accompany normal aging.

In elderly patients, dysphagia is frequently the result of combinations of several conditions such as diabetes, chronic obstructive pulmonary disease, congestive heart failure,

Copyright © 2003, Mosby, Inc. All rights reserved.

renal failure, immunocompromised status, and/or cachexia. Some conditions that are not sufficient to cause dysphagia in younger adults can challenge the naturally declining physiology of older adults. Such conditions include the presence of a nasogastric feeding tube, medication side effects, and chronic illness.[36–38]

INTERPRETATION OF FINDINGS

Interpretation of the dynamic images of the VFSS must accomplish two goals. The first is to identify the presence of an oropharyngeal swallowing disorder and to describe the physiologic underpinnings of its component parts. The second but equally important goal is to determine which therapeutic maneuvers are likely to facilitate improved swallowing safety and efficiency. A declaration of the presence or absence of aspiration or bolus obstruction or hesitation is insufficient. In order to exploit the therapeutic value of the VFSS, it is necessary to consider the reason for symptoms of aspiration or residue. Logemann,[12] a pioneer of the VFSS, takes a very strong position on this point: ''Aspiration and residue are symptoms of swallowing disorders, not swallowing disorders themselves . . . the anatomic and/or neurologic muscular dysfunctions are the actual disorders leading to the symptom for which the treatment is designed'' (p. 71). In contrast, an exhaustive interpretation of any of the many components of the swallow may not yield useful clinical information and may be too time-consuming. Clinicians should resist the urge to comment exclusively on bolus location in the oral cavity, pharynx, airway, or cervical esophagus and should consider the aberrant forces that caused the bolus to flow in the observed directions.

Therefore, the challenge is to develop a schema that permits identification of the salient abnormal events in order to arrive at an integrated understanding of the biomechanical basis of impairment. These data form a foundation for assessing therapeutic maneuvers. Assessment of the videofluoroscopic images involves description of abnormal anatomy, analysis of the timing and coordination of the biomechanical events of the swallow, and determination of laryngeal penetration. Finally, the effectiveness of swallowing strategies attempted during the VFSS is evaluated in order to make recommendations for oral nutrition. This schema, outlined in Table 32-3, follows the outline suggested by Murray.[39]

Dodds et al.[22] make the important point that the goal of interpretation is not to diagnose disease. There are very few typical presentations of diseases on the VFSS, and symptoms of a variety of diseases or conditions can appear similarly on the study. For example, a severely deconditioned patient with significant loss of muscle mass and pharyngeal weakness may closely resemble a patient with polymyositis with respect to solid bolus swallowing. Thus, it would not be possible to offer a differential diagnosis of polymyositis when viewing the results of a VFSS alone. The clinical history is very important and assists in generating hypotheses and recommendations for further diagnostic evaluation.

Table 32-3
SCHEMA FOR INTERPRETATION OF VFSS

Normal and abnormal anatomy
Normal and abnormal biomechanical movements of structures of the oral pharyngeal swallowing mechanism
Temporal coordination of biomechanical events in relation to bolus flow
Penetration/aspiration
Swallowing efficiency
Evaluation of therapeutic strategies
Changes in bolus volume, viscosity, rate of delivery
Changes in posture
Rehabilitative swallowing maneuvers

Adapted from Murray J. Manual of Dysphagia Assessment in Adults. San Diego, CA: Singular Publishing, 1999;113-151.

Normal and Abnormal Anatomy

Lateral and AP scout films taken prior to fluoroscopy can highlight variations in anatomy that may contribute to the swallowing problem and that may require closer scrutiny. If this is not possible, it is advisable to scan the oral cavity and pharynx fluoroscopically from the lips to the posterior pharyngeal wall, as well as the proximal trachea and esophagus, prior to the administration of contrast. The anatomic configuration of the mandible is observed for evidence of surgical resection and possible plated reconstruction (Fig. 32-3). In addition, gross deviations of mandibular–maxillary relationships are observed. The

FIGURE 32-3 Mandibular reconstruction.

VIEW IMAGE

Copyright © 2003, Mosby, Inc. All rights reserved.

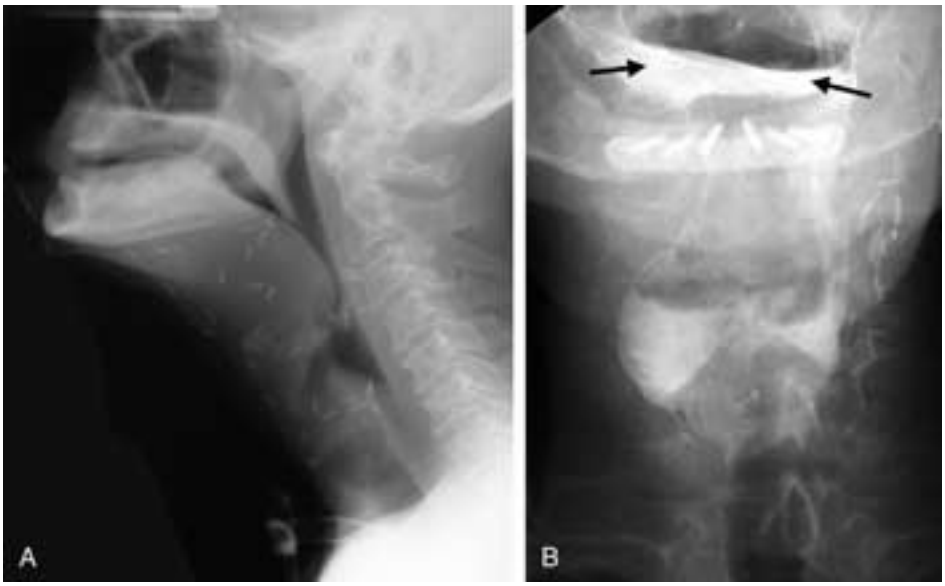

FIGURE 32-4 **A**, Patient with total glossectomy with free flap reconstruction. **B**, Patient with a glossectomy (*arrows*) where reconstruction of the tongue has failed.

VIEW IMAGE

tongue posture is observed at rest and in both lateral and AP projections. Observations can be made about tongue bulk, particularly in the area of the base of the tongue. Asymmetry of the tongue following surgical resection can be appreciated, although accurately differentiating the left from the right side is not possible in the lateral view. Sometimes surgical reconstruction of the tongue has the appearance of normal tongue bulk when in fact a myocutaneous flap is in place and anchors surrounding tissue (Fig. 32-4). In other situations, the tongue bulk may be atrophied, as in the patient with ALS or in a patient who is deconditioned. This may signal impaired bolus formation, control, and propulsion.

The structure of the soft palate at rest is observed for its completeness and bulk. The posture of the soft palate at rest and during speech tasks can provide information about bolus containment before the swallow as well as velopharyngeal sufficiency during swallowing. Palatal appliances should be examined for their purpose. For example, palatal obturators occlude fistulae of the hard palate or the nasopharynx; a palatal lift promotes improved velopharyngeal closure by elevating the soft palate during swallowing; and a palatal reshaping device may augment the contour of the hard and soft palates to form a surface against which the tongue can contact for bolus propulsion. Assessment of swallowing function with and without palatal appliances in position during swallowing may be indicated.

Nasogastric feeding tubes do not need to be removed during the fluoroscopic study, as they usually do not interfere directly with swallowing function. There are three exceptions: firstly, if the nasogastric tube is coiled in the pharynx, it may affect swallowing efficiency (Fig. 32-5); secondly, increased pharyngeal retention may be observed if the bore of the feeding tube is large and the tube itself is rigid in the context of a weakened swallow; and thirdly, if the feeding tube is located in the midline postcricoid region such that the arytenoid cartilages are stented open, and complete rotation of the cartilages and adduction of the vocal folds are restricted. This last scenario can best be appreciated in the AP view. In these cases, it may be wise to remove the nasogastric feeding tube and replace it if necessary after the study.

The epiglottis is observed for signs of surgical resection and evidence of edema or fibrosis as a result of radiation therapy (Fig. 32-6). The relationship of the tongue base to the posterior pharyngeal wall is noted with respect to the area that must be approximated to drive the bolus into the hypopharynx. However, it cannot automatically be assumed that reduced tongue base muscle mass or pharyngeal soft tissue at rest, that is, a vacuous pharyngeal lumen, will not adduct completely during swallowing. Sometimes compensatory pharyngeal wall adduction is observed with a reduced

FIGURE 32-5 Nasogastric tube coiled in the hypopharynx.

VIEW IMAGE

Copyright © 2003, Mosby, Inc. All rights reserved.

VIEW IMAGE

FIGURE 32-6 Radiation effects on structures of the hypopharynx, epiglottis, and arytenoid cartilages. The posterior pharyngeal wall is thickened (*arrow*).

tongue base mass, as occurs in patients with tongue base resections from carcinoma. In patients who have had pharyngeal resections with flap reconstructions, a soft-tissue fullness is seen, often simulating the pharyngeal constrictor muscles. However, the flap is bulkier than the normal pharyngeal muscles, and there is no observed contraction of the flap during swallowing.

The contour of the cervical spine is well appreciated in the lateral projection, and note is taken of the location and size of cervical osteophytes (Fig. 32-7A). Approximately 20% to 30% of the elderly population present with diffuse skeletal hyperostosis (DISH) manifesting as cervical osteophytes at C5-C6 and of these, 28% complain of symptoms of dysphagia.[40, 41] Osteophytes, if sufficiently large, may impinge directly on the cervical esophagus and hypopharynx, allowing only squirts of the bolus to pass. Periosteophytic edema or inflammation may increase the dysphagia. Osteophytes can coexist with reduced laryngeal closure and may additively cause more severe dysphagia than if either is present alone (Fig. 32-7B). It is important to resist the temptation to implicate the osteophyte solely as the predominant etiology of the swallowing difficulty, particularly in acute-onset dysphagia. Osteophytes develop over time, and most patients adapt unconsciously to their presence. In patients who have had surgery or radiation therapy that restricts the motion of the hyoid bone (and thus of the larynx), the coexistence of pronounced osteophytes can be a cause of dysphagia. Other causative biomechanical factors should be considered in these cases, such as weak laryngeal excursion or impaired tongue base retraction, particularly since surgical reduction of osteophytes is a risky and complex procedure. Valadka et al.[41] illustrate this point very clearly in a report on a patient who underwent resection of an anterior cervical osteophyte for relief of dysphagia after two separate diagnostic evaluations by two different otolaryngologists failed to detect base of tongue cancer.

Some patients have undergone cervical fusion procedures

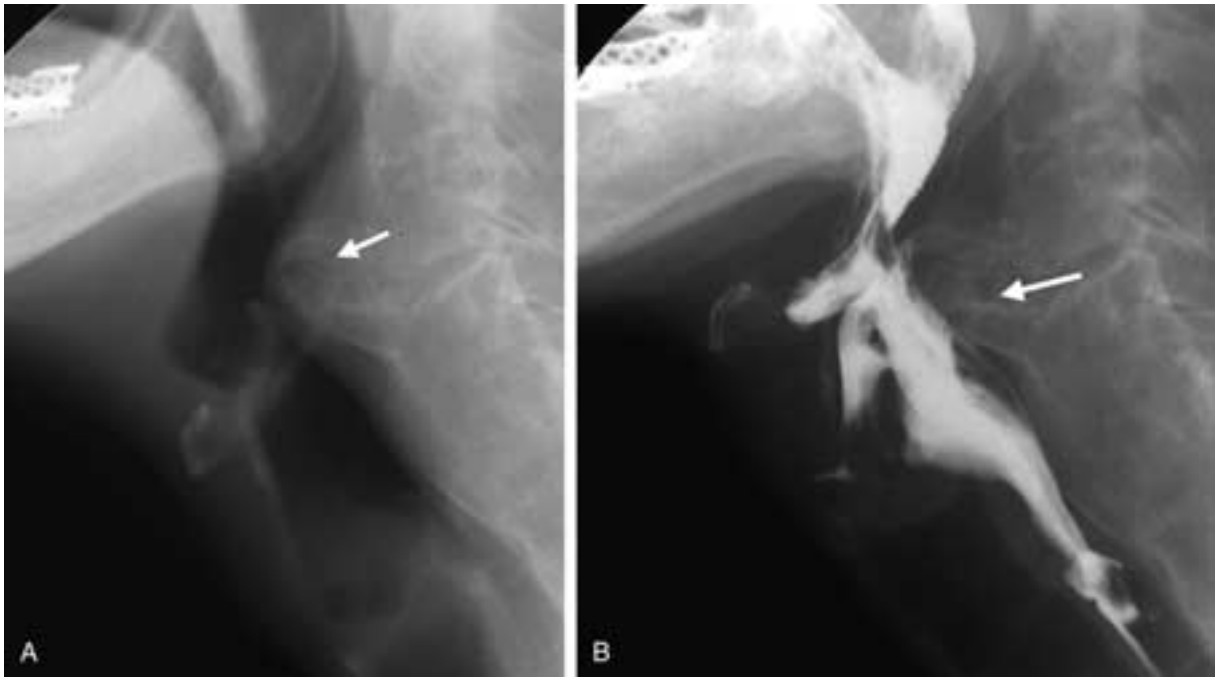

VIEW IMAGE

FIGURE 32-7 **A**, Cervical osteophyte (*arrow*) and its effect on swallowing, with inhibited epiglottic deflection and laryngeal closure resulting in aspiration. **B**, Osteophyte (*arrow)* aspiration is observed during the swallow as a result of restricted epiglottic deflection and hyolaryngeal excursion.

Copyright © 2003, Mosby, Inc. All rights reserved.

with autologous grafts or rod placements. These patients may present with hematoma formation, edema, infection, and denervation with injury to the recurrent laryngeal nerve as a result of the surgical necessity of shifting structures across the midline to reach the cervical spine. Usually the pharyngeal edema subsides within a few days of surgery; however, if severe, the pharyngeal contraction waves and bolus clearance, particularly during swallowing of solid foods, may be temporarily compromised. If fibrosis affects the pharyngeal constrictor muscles, poor pharyngeal contraction can be permanent. Increased prevertebral space soft tissue that is observed in patients treated with radiation therapy and/or chemotherapy for hypopharyngeal tumors subsides more slowly but has the same impact on the swallow. It is not uncommon to observe pharyngeal wall edema in these patients months after radiation therapy is completed, as seen in Figure 32-8.

The pharyngeal recesses form the conduit for bolus flow, and their capaciousness or lack thereof can assist in compensating for disordered pharyngeal contractions. For example, patients with recent pharyngeal wall resections may display edema such that the pyriform sinuses are unable to contain even a small amount of residue after the swallow, and this may lead to prompt aspiration. On the other hand, patients with generalized deconditioning and muscle wasting in the pharynx may present with generous pyriform sinuses that can contain considerable residue that does not empty into the laryngeal vestibule.

Calcifications of the laryngeal cartilages, carotid arteries, and various ligaments appear as areas of radiodensity at fluoroscopy and on x-ray films. Taking note of these areas prior to the administration of contrast will eliminate the misinterpretation of these sites of calcification as droplets of barium. This can decrease the overdiagnosis of laryngeal aspiration.

FIGURE 32-8 Severe edema of the posterior pharyngeal wall (*ppw*) and blunting of the epiglottis (*e*) in a patient 3 months after receiving radiation therapy for a pharyngeal tumor.

VIEW IMAGE

FIGURE 32-9 Stricture (*arrow*) of the cervical esophagus after laryngectomy.

VIEW IMAGE

The presence of a laryngectomy must be noted. These patients are generally not at risk for aspiration of contrast; however, they may present with bolus hesitation as a result of strictures at the surgical site, scarring or resection of the hyoid-related musculature, or as a result of radiation therapy (Fig. 32-9).

Vocal fold adduction is best observed in the AP projection. Glottic closure, as discussed previously, is critical for swallowing, and even cursory evaluation of vocal fold movements during phonation is helpful in determining the risk of aspiration and the presence of vocal fold asymmetry. However, the diagnosis of vocal fold paralysis should be made with caution, as image clarity can be obscured by the vocal folds superimposed on the dense bony structure of the cervical spine. Videofluoroscopy does not provide a detailed view of the laryngeal structure because of the poor resolution of the cartilaginous structures. Sometimes contrast present in the airway outlines the laryngeal structures more clearly and provides information about arytenoid cartilage edema, surgical resection, the contour of the aryepiglottic folds, and the amount of tracheal aspiration.

Patency of the airway should be appreciated and the presence of a tracheostomy tube noted. Tracheal or supraglottic stents may be present, and their location in the trachea should be noted, as at times the superior edge of the upper limb of a T-tube stents open the glottis, affecting airway protection. In most cases, however, sufficient superior and hyolaryngeal excursion prevents aspiration of contrast of certain consistencies. Unless the patient is mechanically ventilated, it is advisable to have the patient

Copyright © 2003, Mosby, Inc. All rights reserved.

swallow with the tracheostomy tube cuff deflated. Ideally, the tracheostomy tube should have a diameter that permits airflow around the tube in the trachea such that finger occlusion of the hub of the tube or capping is possible. A one-way speaking valve may also be used, allowing inhalation through the tracheostomy tube and exhalation through the oral cavity as the one-way valve closes. Closure of the vocal folds at the glottis permits a strong clearing cough if the patient aspirates. A cursory appreciation of the underlying anatomic variations allows the clinician to develop hypotheses about the potential swallowing problem and to speculate, at least in part, about the possible risks of performing the swallowing study.

Normal and Abnormal Biomechanical Movements

Lips and Cheeks

The lips must close around the spoon or cup in order to contain the bolus in the oral cavity. Lip protrusion is necessary for straw drinking. While lip seal functionality can readily be observed during the clinical swallowing evaluation, the ease with which the bolus is accepted can affect tongue posturing. Contraction of the buccinator muscles together with lip closure and tongue tip contact against the alveolar ridge facilitates cohesive bolus formation in the oral cavity. Weak lip closure may result in loss of the bolus anteriorly from the oral cavity, as in drooling. Absent lip and jaw closure occurs in patients with bulbar ALS and affects containment of saliva as well as food and contrast. Sometimes drooling occurs because of reduced sensation of the lips as well as reduced motor output. Resection of mandibular tumors or even lingual cancers necessitates mandibulotomy, severing the labial branch of the alveolar nerve and affecting awareness of lip closure, and resulting in lack of awareness of saliva or contrast on the lips or chin. In patients with facial droop, for example as a result of unilateral middle cerebral artery distribution cerebrovascular accident or acoustic neuroma resection affecting facial nerve function, the bolus may fall immediately into the lateral buccal sulcus of the affected side, where it pools.

Tongue

Movement of the tongue plays a central role in swallowing. Its function is to manipulate the bolus, position it carefully, and propel it from the oral cavity into the pharynx. There is a great deal of normal variability in bolus formation and propulsion. Dodds et al.[42] identified two types of oral swallowing events. In the first type, *tipper* swallows, the bolus is positioned on the dorsum of the tongue and the swallow is initiated with the tip of the tongue against the incisors (Fig. 32-10). In the second type, *dipper* swallows, the bolus is held under the tongue in the anterior sulcus of the floor of the mouth, and the tongue tip must scoop up the bolus and elevate it onto the tongue before swallowing. Dodds et al.[42] observed dipper swallows more commonly in older individuals. Furthermore, some normal individuals take large sips and bites and swallow large mouthfuls at once; others segment the bolus into distinct portions and swallow small amounts. In normal individuals, formed

FIGURE 32-10 Normal hold position of a liquid bolus in the lateral view.

VIEW IMAGE

liquid boluses are identified radiographically in the lateral projection as elliptically shaped entities contained on the tongue dorsum, prevented from spilling into the pharynx by depression of the soft palate against the back of the tongue (contraction of the palatoglossus muscle). In the AP projection, the bolus is seen enclosed in a central groove on the tongue dorsum, with the buccinators contracted against the dental ridges and the lateral borders of the tongue in contact with the alveolar ridge (Fig. 32-11).

During mastication, the material is placed on the tongue and the midline and lateral borders of the oral tongue move the bolus toward the dental arches. In the AP view, opening and closing of the jaw enables rotary tongue movements to the left and right. Frequently, some of the bolus spills into the lateral sulci but most normal individuals can sweep the sulci clean with the tongue tip and lateral borders and reassemble the bolus ready for swallowing. The palatoglossal seal observed in liquid and semisolid bolus manipulation is broken in mastication by the constant movements of the posterior tongue. Therefore, it is not unusual for the head of the bolus to be seen moving toward the vallecular space while mastication and bolus formation are in progress. If leakage of the bolus is observed during formation of semisolids or liquids, it is referred to as premature spillage and is an indication of muscle weakness either in the tongue or in the palatoglossus muscle. The risk is that the material will spill into the open airway and be aspirated prior to the onset of the pharyngeal swallow response. Once the bolus is formed, a series of wave-like movements of the tongue dorsum creates pressure on the bolus and propels it with a piston-like motion[21, 22] from anterior to posterior against the hard and soft palates toward the oropharynx. The tongue base depresses and moves anteriorly, forming a ramp or chute down which the bolus flows. The posterior tongue movement continues with the tongue base contacting the

Copyright © 2003, Mosby, Inc. All rights reserved.

posterior pharyngeal wall, helping to direct the bolus toward the vallecular space (Fig. 32-12). In the AP view, bolus propulsion is observed as cohesive midline bolus flow.

Abnormalities in swallowing resulting from impaired tongue function can affect the passage of the bolus to a minor or major degree. The most extreme impairment in tongue function is observed in patients with total reduction in tongue bulk and hence movement, as in total glossectomy, or marked lingual atrophy, as in advanced ALS. These patients present with difficulty positioning the bolus on the tongue, manipulating it, or controlling it for propulsion. In the case of semisolid boluses, videofluoroscopic images reveal stasis of material on the tongue or reconstructed tongue or in the valleculae. Less viscous consistencies fall into the lateral or anterior sulci or spill in an uncontrolled fashion into the pharynx. Mashing of the tongue against the palate or vertical movements of chewing lacking rotary actions are inefficient, as the tongue does not draw the bolus together in a cohesive manner. In compensation, the patient may extend the head to enlist the assistance of gravity for bolus propulsion. Sometimes opening and closing the jaw, especially in cases of total glossectomy, where the tongue has been reconstructed with a regional or free myocutaneous flap, helps to compress the bolus against the palate and slowly move it posteriorly to the pharynx. However, in these patients, it is not unusual to observe contrast adhering to the hard palate or coating the dorsum of the tongue. Improved efficiency in bolus propulsion may be observed by following bites of semisolid material with sips of liquids, provided that airway protection is intact. One of the compensatory strategies developed by patients with total glossectomy is what has been referred to as a *dump swallow maneuver*, in which the bolus is swallowed as a result of suprahyoid activity, laryngeal closure, and pharyngeal shortening. Mastication of solid boluses is unrealistic in these patients, as deforming the solid, mixing it with saliva, and reforming it are not possible. These patients are in danger of aspirating large, unmasticated boluses.

FIGURE 32-12 Contraction of the posterior pharyngeal wall seen as a bulge (*arrow*). The hyoid bone is elevated superiorly and anteriorly and the pharyngoesophageal segment is distended to receive the advancing bolus from above.

VIEW IMAGE

FIGURE 32-11 Right lateral floor of mouth resection and lateral hemiglossectomy resulting in stasis of contrast in the lateral buccal sulcus (*arrow*).

VIEW IMAGE

Partial glossectomy can have a profound effect on bolus control, manipulation, and deformation. The location of the resection and nature of reconstruction will dictate the nature and severity of the impairment and the location of the residue. The effects of structural changes can be variable and wide-ranging even among patients with similar operative procedures and radiation treatments. Patients with anterior oral tongue glossectomy crossing the midline or with floor of mouth resection have the greatest challenge in holding the bolus cohesively for propulsion. These patients display a marked amount of residue in the oral cavity and require head extension or careful placement of the bolus in the posterior pharynx. During VFSS it may be helpful to bypass assessment of the oral stage in order to determine pharyngeal swallow impairment by controlled injection of boluses into the pharynx via a catheter or syringe. Once the integrity of the pharyngeal swallow has been established, compensatory strategies increasing bolus volume may be attempted.

Tongue base resections affect tongue base retraction and bolus propulsion through the pharynx and hypopharynx. Disturbance of the suprahyoid musculature that sometimes accompanies these resections affects laryngeal excursion, and therefore epiglottic downfolding and airway protection. The outcome of bilateral tongue base resection may present radiographically as significant residue along the pharyngeal

Copyright © 2003, Mosby, Inc. All rights reserved.

wall and in the vallecular space, and aspiration may occur before the swallow because of uncontrolled spillage or after the swallow from the residue. Piecemeal swallowing may be observed in which the boluses are purposefully segmented and swallowed in small portions. Multiple swallows of the same bolus is a hallmark behavior of reduced tongue base function.

Patients with hemiglossectomy in which the tongue is resected only on one side may be able to compensate for their defects by containing the bolus on the unaffected side. Functionality, however, will depend on preservation of mobility of the tongue on the unaffected side. If the tongue is tethered in reconstruction by a regional or free flap, or is fibrosed as a consequence of radiation therapy, compensatory behaviors may be restricted. In these cases, residue will be observed along the oral cavity and pharynx in the area of the defect. AP views reveal asymmetric bolus flow very clearly.

The posterior tongue contributes to the glossopalatal seal, which is particularly important during liquid swallows. Compromise of this valve as a result of weakness or resection can result in loss of bolus control, and liquids may be presented prematurely to the pharynx prior to initiation of the pharyngeal swallow response, potentially resulting in aspiration.

Lingual tremors at rest may not result in oral stage swallowing disorders. However, patients with Parkinson's disease or Parkinson-like symptoms may have difficulty initiating bolus propulsion. Overall lingual weakness may co-occur and can manifest in searching movements of the tongue and repetitive small-amplitude AP movements slowly shuffling the bolus toward the pharynx in an action referred to as *tongue pumping*. This behavior mimics the festinating behaviors common in ambulation patterns of patients with Parkinson's disease. These patients may lack the range of motion for coordinated rotary lingual movements and uncontrolled boluses may spill prematurely into the pharynx, resulting in aspiration particularly with liquid contrast. Oral dyskinesia with lingual chorea may be observed in patients with Huntington's disease. In these cases, tongue movements are dyssynchronous, resulting in large bites, poor mastication, and rapid swallowing.[43, 44]

Bilateral tongue weakness can be observed in a variety of conditions, the most common of which is cerebrovascular accident, in which dysarthria and dysphagia are symptomatic. Thin liquids and textured solids present the greatest challenge to these patients, who are unable to cradle the boluses on the tongue or coordinate movements for mastication and run the risk of uncontrolled bolus loss. Limited tongue-driving force results in vallecular retention and weak bolus flow through the hypopharynx, and where sensation is preserved, multiple swallows represent the patient's attempt to clear the residue. Patients with unilateral tongue weakness, as in unilateral stroke or skull base tumors affecting the hypoglossal nerve, may be able to compensate for the weakness by chewing on the contralateral side, albeit in an awkward and protracted fashion. Retrieving boluses from the buccal sulci is complicated and may require digital removal.

Efficiency of swallowing can be affected by the habitual tongue posture. Normally, the tongue moves posteriorly along the palate, driving boluses into the pharynx. Tongue thrusting is a reverse swallow pattern, usually of neurologic origin such as in patients with cerebral palsy, in which the tongue thrusts forward between the incisors, pushing the food out of the mouth. Usually mastication as well as swallowing is affected in these patients.

Radiation therapy for oral cavity, pharyngeal, and laryngeal tumors carry the side effect of xerostomia, or dry mouth, and tongue function during swallowing can be disturbed as a result of radiation therapy alone. Reduced volume and consistency of saliva affect the ease of bolus formation, particularly with more solid textures, and can result in residue on the tongue or palate. In addition, the speed of tongue movement can be reduced in these patients as a result of tissue fibrosis, a condition that can occur immediately after radiation therapy or even a year after radiation treatments are completed.[9]

Soft Palate or Velum

The soft palate has two distinct purposes during the swallow. In the oral stage, contraction of the palatoglossus contains the bolus in the oral cavity. Once the pharyngeal swallow response is initiated, the soft palate elevates against the lateral and posterior pharyngeal walls, creating a seal of the velopharyngeal port.

Premature spillage into the pharynx and hypopharynx can occur due to weakness of the palatoglossal seal, increasing the risk of aspiration. As was mentioned earlier, premature spillage can only be considered such during liquid and semisolid bolus preparation, where mastication is not required. There is normal loss of the palatoglossal seal during mastication of solid boluses due to lingual and mandibular movements. Cranial nerve dysfunction or palatal resection can cause premature spillage. Careful inspection of soft palate elevation is required, as sometimes it appears that the soft palate is elevating when in fact the tongue is moving posteriorly, propping up the soft palate.

Nasal regurgitation of liquids or solids is the result of an incompetent velopharyngeal mechanism and can be observed in patients with palatal or tonsillar fossa resection, or cranial nerve or muscular dysfunction. Cranial nerve dysfunction can be the result of, for example, ALS, skull base tumor, or cerebral or brainstem stroke (Fig. 32-13). The increased pressure by the tongue to propel the bolus into the pharynx causes the bolus to take the path of least resistance, resulting in nasal regurgitation when there is reduced nasopharyngeal closure during swallowing. Nasal regurgitation is usually more pronounced with liquid boluses or when the patient's chin is tucked in. Patients may control their nasopharyngeal incompetence by adopting a head upright posture or by swallowing consistencies of higher viscosity than liquids.

Palatal obturators or palatal lifts are dental appliances constructed to reduce nasal regurgitation, increasing the integrity of the velopharyngeal port. In cases of severe incompetence when an appliance is not available, these patients can be instructed to hold the nose closed with their fingers in an attempt to improve the seal and increase pressure on the bolus without leakage into the nasopharynx.

Epiglottis

Downfolding of the epiglottis is frequently a focus in VFSS interpretation. It is important to bear in mind, though,

Copyright © 2003, Mosby, Inc. All rights reserved.

FIGURE 32-13 Nasopharyngeal regurgitation (*arrow*).

VIEW IMAGE

that the epiglottis is a cartilage with attachments to the hyoid bone, tongue base, and larynx. Since the epiglottis is a ''passive performer,''[24] its inversion depends on adequate function of these attached structures, which are most often implicated in impaired epiglottic movement. Biomechanical movements of structures attached to the epiglottis should receive attention when therapeutic maneuvers are selected for evaluation during the VFSS.

Prior to the onset of the pharyngeal swallow, the epiglottis deflects advancing secretions or boluses around the laryngeal inlet.[39] The laryngeal vestibule is shielded by the movement of the epiglottis from the upright to the horizontal position by thyrohyoid shortening and is clearly visualized on fluoroscopy, particularly in the lateral view.

FIGURE 32-15 Laryngeal penetration (*arrow*) during the swallow to the level of the true vocal folds in a patient with a supraglottic laryngectomy. In this procedure the hyoid bone, epiglottis, and supraglottis are resected. Aspiration is prevented by forceful adduction of the true vocal folds during the swallow.

VIEW IMAGE

Inversion of the epiglottis can also be visualized in the AP projection, appearing as a slit-like opacity within the column of barium (Fig. 32-14).

In the standard supraglottic laryngectomy procedure, the entire epiglottis is resected together with the carcinoma of the supraglottis, making the laryngeal vestibule vulnerable to penetration or aspiration of oral secretions, liquid materials, and solid materials (Fig. 32-15). Patients are

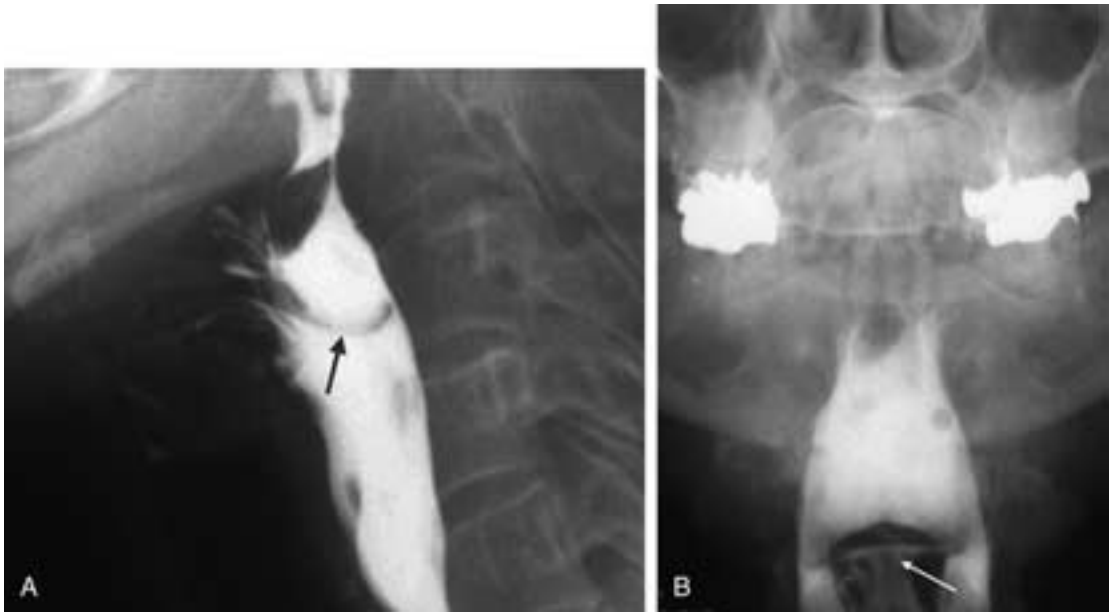

FIGURE 32-14 Normal epiglottic (*arrow*) deflection during swallowing in the lateral (**A**) and AP (**B**) views.

VIEW IMAGE

Copyright © 2003, Mosby, Inc. All rights reserved.

taught voluntary airway protection techniques, enabling them to swallow in most cases.

Thickening and fibrosis of the epiglottic mucosa and attached supporting structures occur after radiation therapy, affecting the extent of downfolding even if hyolaryngeal excursion is spared. An edematous epiglottis may attach to the tongue base and appear blunted in the lateral radiographic view, restricting the guarding function of the epiglottis and obliterating the valleculae.[39]

Impaired laryngeal excursion or tongue base retraction has the effect of maintaining vallecular continence, in contrast to the ''flattening out'' of the valleculae that occurs in normal epiglottic deflection, and stasis is observed in the valleculae after the swallow. Furthermore, transient penetration can occur along the laryngeal surface of the epiglottis during the pharyngeal swallow, which may or may not be extruded from the laryngeal vestibule, depending on the competence of hyolaryngeal excursion.

The danger of impaired epiglottic downfolding lies in the amount of residue remaining in the valleculae after the swallow. The greater the stasis, the greater the risk that material (liquid or solid) will spill over the tip of the epiglottis or over the aryepiglottic folds and penetrate the airway.[45]

Hyoid and Larynx

The radiodensity of the hyoid bone makes its movement trajectory quite easy to track during swallowing on VFSS. The hyoid bone is suspended by muscular attachments extending from the tongue and mandible to the larynx. Contractions of the geniohyoid, mylohyoid, and anterior belly of the digastric muscles are primarily responsible for superior and anterior movement of the hyoid bone.[15] The hyoid bone is attached along its inferior border to the thyroid cartilage by the thyrohyoid ligament, which is shortened during hyolaryngeal excursion. These movements are clearly viewed in the lateral radiographic projection. In the normal individual, the hyolaryngeal complex moves an average of 2 cm anteriorly and 2 to 2.5 cm superiorly from rest to maximal excursion (Fig. 32-12).[25, 34, 46] Increased bolus volume affects the duration and extent of maximal hyolaryngeal excursion.

The primary function of hyolaryngeal excursion is to pull the entire larynx away from the posterior pharyngeal wall, thus creating a continuous conduit for the advancing bolus from the hypopharynx through the cervical esophagus. This has the dual effect of opening the upper esophageal segment while simultaneously protecting the laryngeal vestibule as the epiglottis deflects. As the larynx elevates, the arytenoid cartilages rock and tilt anteriorly to contact the base of the epiglottis, closing the entrance to the airway.[12]

Impairment of hyolaryngeal excursion results therefore in stasis in the pyriform sinuses after the swallow or in penetration of the laryngeal vestibule during the swallow resulting from incomplete closure of the supraglottic entrance. While transglottic aspiration may not occur immediately, the presence of material in the larynx may make it more likely. Since pyriform sinus stasis can also result from impaired pharyngeal clearance or inadequate intrinsic relaxation of the cricopharyngeus muscles, all possibilities must be probed before reduced laryngeal excursion is held primarily responsible.

In most cases, anterior and superior movement coexist; however, it is possible to observe increased impact in one or the other movement plane. For example, it is possible for patients to present with reduced anterior excursion while superior movement is preserved. In reality, safe and efficient swallowing demands sufficient superior and anterior excursion.

Pharyngeal Wall

The pharyngeal constrictors move the pharyngeal wall anteriorly during the pharyngeal swallow to function as a surface that the tongue base can contact to drive the bolus into the hypopharynx. In addition, contraction of the constrictors and the longitudinal pharyngeal musculature (salpingopharyngeus, palatopharyngeus, and stylopharyngeus) shortens the pharynx, clearing the bolus from the pharyngeal recesses and propelling it into the cervical esophagus. In the lateral projection, pharyngeal contraction is seen as a progressive anterior bulge from superior to inferior along the posterior wall. Propagation in the pharynx is very rapid, 12 to 25 cm/sec, compared with 1 to 4 cm/sec in the esophageal phase.[26, 27] In the AP projection, medial excursion of the lateral pharyngeal walls is seen bilaterally in the normal individual, but in up to 20% of normal subjects, swallowing can occur down only one side.[47] The term *pharyngeal contraction wave* is preferable to *pharyngeal peristalsis*, as peristalsis applies to a circumferential muscular tube such as exists in the esophagus and does not pertain to the pharynx, as the anterior pharyngeal wall is composed of the tongue base, laryngeal vestibule, and larynx[12] (Fig. 32-12).

The effect of impaired pharyngeal wall motion is residue along its length or in the pharyngeal recesses. In unilateral impairment, the residue is located along the weak side and is best viewed in the AP projection. Usually the stronger side pushes the bolus over to the weaker side, which has increased flaccidity; hence the unilateral retention. However, in the AP plane, unilateral pharyngeal wall weakness is visualized as residue in one of the pyriform sinuses or in one side of the vallecula (Fig. 32-16). Double or multiple swallows per bolus may indicate pharyngeal weakness. The patient may also report the failure of bolus clearance.

Bilateral pharyngeal weakness can be seen in patients suffering from progressive neurologic disease, deconditioning, sarcopenia of the oropharyngeal musculature, and radiation fibrosis. Patients with pharyngectomy extending across the midline experience severe stasis even when tongue base retraction is relatively spared. Postural therapeutic maneuvers to be discussed later, which alter the dimensions of the pharynx, are sometimes helpful.

Weak pharyngeal contraction is difficult to separate from weak tongue base retraction. Each biomechanical movement must be inspected for its contribution in the event that pharyngeal residue is observed. Furthermore, impaired laryngeal elevation can affect epiglottic deflection and may erroneously implicate the pharyngeal constrictors.

Transient pharyngeal outpouchings may be observed during swallows of liquid boluses larger than 7 to 12 cc.[48] These outpouchings are the result of pharyngeal mucosa herniating through focal weakness in the thyrohyoid membrane anterior to the thyrohyoid ligament and are believed to occur due to dyssynchronous contraction of the

Copyright © 2003, Mosby, Inc. All rights reserved.

VIEW IMAGE

FIGURE 32-16 Unilateral weakness of the right pharyngeal wall resulting in stasis on that side. Contraction of the left lateral pharyngeal wall, indicated by the arrow, moves the bolus over to the weaker right side.

oblique and longitudinally oriented pharyngeal muscles[48] in the context of increased intrapharyngeal pressures (Fig. 32-17). While these outpouchings have been considered a normal variant, Curtis et al.[48] observed that they become symptomatic when the bolus arrival coincides with the appearance of the pharyngocele. When the bolus is in the esophagus once the outpouching occurs, the patient is asymptomatic.

Glottic Closure

Protection of the airway involves numerous biomechanical movements that change the aerodigestive tract from a respiratory to an alimentary system.[49] Epiglottic inversion and hyolaryngeal excursion close the airway in a vertical plane. Closure of the laryngeal vestibule in the horizontal plane is made possible by adduction of the true and vestibular vocal folds and can be first detected during the oral stage of swallowing. Respiration ceases at this point, increasing the subglottic pressure and helping to keep boluses from entering the airway. The airway remains closed for 0.6 to 0.7 second and opens again once the larynx descends and the epiglottis is in the resting position.[22, 50]

Glottic closure is not clearly observed with videofluoroscopy, and inferences about its integrity are based on the presence or absence of barium flow. In the lateral view, closure of the laryngeal vestibule is inferred when the air column disappears. Through frame-by-frame analysis of the video recording, it is possible to visualize rocking of the arytenoid cartilages anteriorly to appose the base of the epiglottis. In the AP projection, normal glottic closure is usually superimposed on the bony spine, compromising detection of midline vocal fold adduction. However, when aspiration occurs, an outline of the true and vestibular vocal folds and the laryngeal ventricle is clearly visible.

Laryngeal penetration and/or aspiration are the primary consequences of impaired closure of the glottis. Incoordinated timing of laryngeal closure is one of the major culprits and is discussed in a later section. Neuromuscular or structural defects can impair laryngeal closure, can occur unilaterally or bilaterally, and can involve small or large

VIEW IMAGE

FIGURE 32-17 Lateral (**A**) and AP (**B**) views of a patient with pharyngoceles (*arrows*).

Copyright © 2003, Mosby, Inc. All rights reserved.

sections of the larynx. Vocal fold paralysis can result from disease processes such as brainstem stroke, progressive motor neuron disease, skull base tumors, or infection. In addition, iatrogenic vocal fold paralysis is a well-documented risk in patients who have undergone thyroidectomy, cardiac surgery, carotid endarterectomy, or various thoracic surgical procedures. Some patients with injury to the recurrent laryngeal nerve resulting in unilateral vocal fold paralysis may, but do not always, demonstrate penetration of the airway during swallowing of liquids. Similarly, wide surgical resection of the larynx, as seen in supraglottic laryngectomy or hemilaryngectomy, affects closure of the airway in the horizontal or vertical plane. Since many of these patients also undergo pre- or postoperative radiation therapy, fibrosis of the laryngeal structures further compromises airway closure. Patients who have recently required endotracheal intubation may exhibit impaired laryngeal adduction as a result of trauma to the vocal folds. Patients who demonstrate aspiration during the swallow as a result of impaired airway closure are excellent candidates for using postural strategies such as rotation of the head to the affected side or compensatory maneuvers such as the supraglottic swallow technique described in a later section.

When glottic closure is impaired during the swallow, it is likely that the protective or reflexive cough in response to aspiration will also be involved. This increases the patient's risk of developing pulmonary compromise since they will be unable to clear material from the airway either reflexively or upon instruction.

Cricopharyngeus/Pharyngoesophageal Segment

The pharyngoesophageal region is located ''beneath the pharyngeal air column and posterior to the arytenoid cartilages'' (Murray,[39] p. 126) and is approximately 3 to 4 cm in length, with the cricopharyngeus muscle comprising 1 cm of this length.[51] It is difficult to identify precisely the high-pressure zone of the pharyngoesophageal segment because of the tight contact of the mucosal walls. Cook[52] suggested that its location corresponds to the middle and lower third of the cricoid cartilage.

Opening of the pharyngoesophageal segment occurs as a function of three factors: intrinsic relaxation of the cricopharyngeus muscle, intrabolus pressure, and, most importantly, anterosuperior distraction of the hyolaryngeal complex away from the posterior pharyngeal wall, as discussed above. Only the last can be reliably observed on VFSS, but all factors may be involved in failure of opening. In the normal condition, the cricopharyngeus muscle complex does not indent the barium column, and increased bolus volume increases the duration and diameter of opening of the pharyngoesophageal segment[25, 52] (Fig. 32-12).

Functional failure of opening of the pharyngoesophageal segment may be the result of failure of or incoordinated cricopharyngeal relaxation, as occurs in patients with oculopharyngeal muscular dystrophy, lateral medullary syndrome, and Parkinson's disease.[53] Impaired hyolaryngeal elevation may also affect opening of the pharyngoesophageal segment, as has been described, resulting in postswallow retention in the pyriform sinuses.

Structural pharyngoesophageal abnormalities are numerous. The most common, cricopharyngeal prominence (also

FIGURE 32-18 Lateral view of a cricopharyngeal prominence (*arrow*).

VIEW IMAGE

referred to as a cricopharyngeal bar, cricopharyngeal achalasia, or cricopharyngeal hypertrophy) is a controversial entity in terms of its role in dysphagia (see Fig. 32-20). It appears as a shelf in the posterior barium column at the level of the cricoid cartilage and can be reproducible or inconsistent. Its location can be variable in relation to the cervical vertebrae because of the superior excursion of the larynx during the swallow. The presence of a cricopharyngeal bar increases with age, with 6.3% to 22% of elderly normal persons displaying this phenomenon.[32, 54, 55]

Abnormal contraction (or lack of relaxation) of the cricopharyngeus muscle is visible only during swallowing. It may occur as a function of uncoordinated timing or may be the result of intrinsic muscle fibrosis, for example in postradiation stricture. In either case, the muscle contraction appears as an indentation in the barium column, which, if severe, can obstruct the lumen, and is particularly troublesome during swallows of solid food and pills. It is sometimes seen in primary muscle disease such as polymyositis, peripheral or central cranial nerve palsy, brainstem stroke, or pharyngeal paresis.[15] Radiographic imaging of the cricopharyngeal prominence is best visualized during swallowing of large mouthfuls of barium (Fig. 32-18). It is important to remember that fluoroscopic imaging only provides information about the degree of opening or obstruction of the bolus flow. It does not document the extent of spasm or pressure, which is measured by manometric recordings. If cricopharyngeal achalasia is suspected, manometric investigation may be necessary.

The functional significance of a cricopharyngeal prominence increases in the context of coexisting pharyngeal problems such as reduced pharyngeal contractions. In fact, there are instances when the pharyngoesophageal segment

Copyright © 2003, Mosby, Inc. All rights reserved.

only appears to be prominent in relation to absent or weak pharyngeal contraction forces. Careful evaluation of pharyngeal contractility independent of the cricopharyngeus muscle complex is necessary to determine the underlying etiology of reduced bolus flow through the pharyngoesophageal segment. Dynamic fluoroscopic imaging is necessary to make this distinction. Cricopharyngeal myotomy may be recommended as the treatment of impaired opening of the cricopharyngeal muscle complex. Recent studies have shown that this procedure has limited value in patients with abnormal laryngeal excursion. Without the mechanical traction of the larynx away from the posterior pharyngeal wall, bolus flow through the segment is markedly restricted even after myotomy.[56, 57] Ergun and Kahrilas[58] state that cricopharyngeal myotomy is indicated only when there is complete obstruction of bolus flow, with increased intrabolus pressure and a decreased transsphincteric flow rate, as seen on manometric study as well as fluoroscopic imaging.

Zenker's diverticulum represents an abnormality of the opening of the pharyngoesophageal segment and, if large, can affect swallowing of solids and liquids. A Zenker's diverticulum is defined as ''a mucosal outpouching of the hypopharyngeal wall located in Killian's triangle between the upper border of the cricopharyngeus and inferior pharyngeal constrictor muscles''[59] (p. 1229). Figure 32-19 presents images of a Zenker's diverticulum in the lateral and AP projections. The cricopharyngeus is described as fibrotic and stiff and reduces the opening of the lumen in the context of normal laryngeal excursion. During VFSS, contrast fills the pouch, and as the larynx descends and pressure is placed on the pouch, its contents are emptied and some of the regurgitated material may fall into the airway. Surgical correction is the appropriate treatment, with pexy or resection of the pouch and concurrent cricopharyngeal myotomy necessary to avoid formation of recurrent diverticula.[60]

Occasionally, a small irregularity is noted on the anterior wall of the hypopharynx that corresponds to the postcricoid region. This indentation has been attributed to a submucous venous plexus and/or redundant mucosa.[61] This irregularity is often pliable and not fixed, as in the case of a tumor, which can be confirmed if necessary with a CT scan or endoscopic evaluation. Table 32-4 provides a summary of impaired biomechanical movements in oropharyngeal swallowing and their related radiographic findings.

Esophagus

Propagation of boluses through the esophagus is the result of primary and secondary peristalsis lasting for approximately 8 seconds.[1] While a discussion of esophageal motility is beyond the scope of this chapter, it is important to emphasize the need to observe contrast moving through the entire lumen of the esophagus in patients who complain of solid food dysphagia and who present with normal oropharyngeal swallowing of semisolid and even textured boluses. Obstruction of the lower esophageal segment by a 13 mm barium tablet or failure to pass the tablet in these cases may support the need for further radiographic or endoscopic evaluation.

Temporal Coordination of Biomechanical Events in Relation to Bolus Flow

Up to this point, the focus of interpretation of VFSS has been on displacement of the bolus as a result of

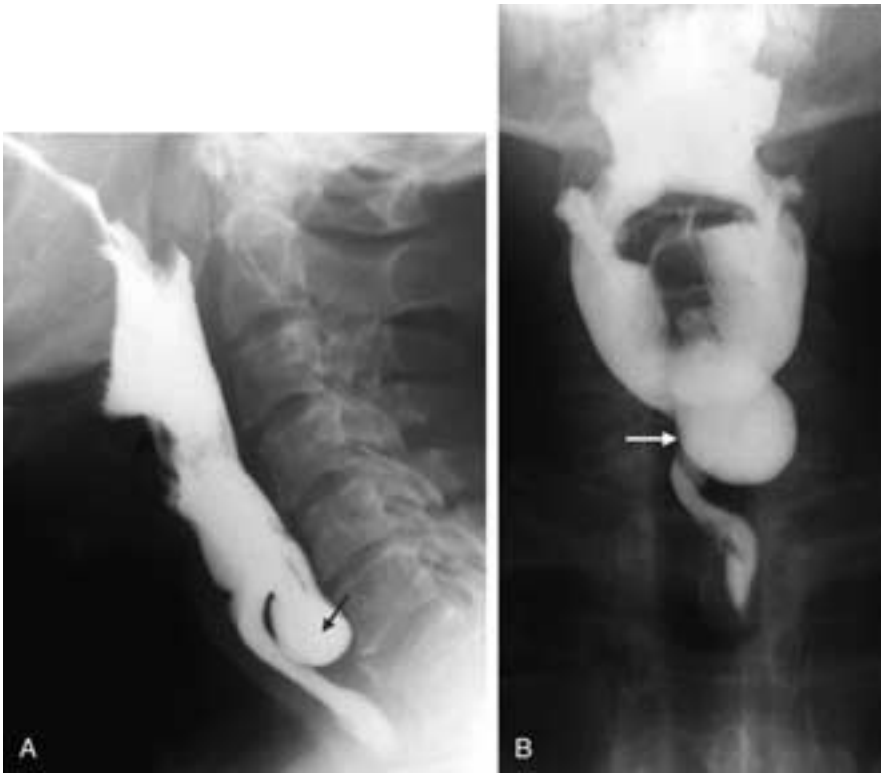

FIGURE 32-19 Lateral (**A**) and AP (**B**) views of a Zenker's diverticulum (*arrows*).

VIEW IMAGE

Copyright © 2003, Mosby, Inc. All rights reserved.

Table 32-4
COMMON OROPHARYNGEAL BIOMECHANICAL IMPAIRMENTS AND THEIR RELATED RADIOGRAPHIC FINDINGS

Biomechanical Impairment	Radiographic Findings
Reduced lip closure	Barium spills out from the lips
Reduced range of coordination of tongue movement	Bolus coats tongue diffusely
Reduced tongue lateralization	Bolus is not deformed promptly during chewing
Impaired cognitive function, neural function, or oral sensation	Hesitancy initiating swallowing
Reduced labial or buccal tension	Stasis in buccal sulci
Reduced tongue shaping	Stasis in floor of mouth
Impaired tongue motion	Abnormal AP lingual movements
Reduced tongue elevation	Poor tongue-to-palate contact
Parkinson's disease	Repetitive tongue rolling
Reduced tongue or palatal control	Premature spillage of bolus
	Penetration and/or aspiration before the swallow
Dry oral cavity	Diffuse coating of barium over tongue and pharynx
Impaired tongue movement	Slow oral transit time
Delayed onset of pharyngeal swallow	Bolus fills valleculae and/or pyriform sinuses before swallow is activated
Velopharyngeal insufficiency	Nasal regurgitation
Impaired tongue base retraction	Residue in valleculae and on pharyngeal wall
Reduced hyolaryngeal excursion	Residue in pyriform sinuses
	Incomplete epiglottic deflection
	Aspiration during and after the swallow
Hypertonic cricopharyngeus muscle	Reduced opening of the pharyngoesophageal segment
	Increased pyriform sinus residue
Large cervical osteophyte	Incomplete epiglottic deflection
Diminished pharyngeal wall contractions (unilateral or bilateral)	Stasis along pharyngeal wall
	Residue in valleculae and/or pyriform sinus
	Laryngeal penetration and/or aspiration after the swallow
Reduced hyolaryngeal excursion	Impaired epiglottic downfolding
	Impaired tongue base retraction
	Laryngeal penetration and/or aspiration
Incomplete laryngeal closure	Laryngeal penetration/aspiration during the swallow
Zenker's diverticulum	Regurgitation after swallow from pouch in cervical esophagus
Impaired vocal fold adduction	Laryngeal penetration and/or aspiration during the swallow

movements of the structures of the oral cavity, larynx, pharynx, and pharyngoesophageal segment as isolated events. It is the sequenced coordination of these events, many of which overlap temporally, that affects the direction or misdirection of the bolus through the upper aerodigestive tract.

Timeliness of Onset of Pharyngeal Swallow

Timing of onset of the pharyngeal swallow is important in determining the interaction between bolus flow in relation to airway protection. Delayed onset of the pharyngeal swallow response is also referred to as *pharyngeal delay*,[62] *duration of stage transition*,[63, 64] *stage transition duration*,[39] *delayed swallow* reflex,[65] or *delayed pharyngeal swallow*[12] (Fig. 32-20). It is affected by a number of conditions including stroke, Parkinson's disease, ALS, prior radiation therapy, postendotracheal intubation/tracheostomy, or oral cavity resection affecting laryngopharyngeal sensation. The longer the delay in initiating the pharyngeal swallow response after the bolus is in the pharynx, the greater the risk of latent material spilling into the airway.[45] Thin liquids travel rapidly through the oral cavity and pharynx, and an unprotected airway is vulnerable to an advancing bolus if the pharyngeal response is not elicited promptly. More viscous substances such as solids and semisolids travel more slowly and cohesively and allow the sensory system more time to respond with respect to initiating the motor responses for airway protection and opening of the pharyngoesophageal segment.

In the most extreme case, the pharyngeal response, with its sequence of events for driving the bolus through the oral pharynx and hypopharynx, can be absent. Fortunately, this is a relatively uncommon occurrence, but it can be seen in patients with lateral medullary syndrome where there is injury to the central swallowing pattern generator. In moderate brainstem dysfunction it may be possible to observe the onset of components of the pharyngeal swallow response, but these may be uncoordinated and may lack the correct sequence. For example, in the lateral projection, it may be possible to observe aspiration before the swallow

FIGURE 32-20 Pharyngeal delay with coating of the valleculae (*arrows*).

VIEW IMAGE

Copyright © 2003, Mosby, Inc. All rights reserved.

response is elicited, and/or mistimed tongue propulsion and pharyngeal clearance with failure of the bolus to enter the esophagus.[66, 67]

Bolus characteristics of volume and viscosity modulate the timing of the onset of the pharyngeal swallow with the beginning of vocal cord adduction and airway closure. Research in normal adults has shown that vocal cord adduction and the onset of hyolaryngeal elevation begins when large liquid boluses are placed in the oral cavity.[25, 26, 28] Radiographically, this is most easily observed in the lateral plane. The laryngeal vestibule narrows as the arytenoid cartilages rock and tilt toward the base of the epiglottis and the glottis closes. This results in a negative onset time in that the liquid bolus has not exited the oral cavity and yet the pharyngeal swallow response has begun. For example, Lazarus et al.[68] found that an average normal pharyngeal delay time for a 5 ml liquid bolus was -0.6 second in adults aged 18 to 80 years.

Different anatomic landmarks are used by different researchers in calculating pharyngeal delay in relation to bolus flow. In the most commonly used definition, the onset of the pharyngeal swallow occurs as the head of the bolus crosses the intersection of the ramus of the mandible and the tongue base.[13, 39] Pharyngeal delay time has been observed to increase with age,[28] in which a large portion of the bolus reaches the vallecular space before the onset of airway closure and hyolaryngeal elevation. This is thought to be the result of reduced sensory awareness of the bolus but is also considered a normal variant in older individuals (>70 years of age).

Purees and solid boluses have increased viscosity and therefore travel more slowly, presenting less of a threat to an open airway. During normal mastication, boluses move in small amounts over the tongue base and into the valleculae in the presence of an open airway, and the pharyngeal swallow response may not be triggered until the material reaches the pyriform sinuses or touches the aryepiglottic folds. This phenomenon is not considered abnormal in the case of solid bolus swallowing and does not necessarily increase the relative risk of laryngeal penetration or aspiration. Perlman et al.[69] suggested that only when the boluses remain in the pharynx longer than 1 second but less than 2 seconds before the beginning of laryngeal closure is the pharyngeal swallow onset considered mildly delayed. A delay of 5 seconds or more is considered severe.

Duration of Oral and Pharyngeal Transit

Swallowing efficiency is estimated by determining the duration of transit of the bolus through the oral cavity and pharynx. Counting the number of swallows required to clear a liquid or solid bolus provides a rough guide of swallow efficiency. Usually a 5 to 30 ml bolus is cleared in a single swallow and may be followed by a second clearing swallow. There is greater variability in solid boluses, particularly those that require longer mastication. Several swallows are required to clear boluses with hard textures.[70]

A more precise assessment of oropharyngeal swallow efficiency is described by Rademaker et al.[71] This measure depicts the interaction between the speed of bolus flow and the efficiency with which the material is cleared from the oropharynx, taking aspiration into account. The numerical value provided by this measure may be particularly helpful when determining change in function after treatment.

FIGURE 32-21 High laryngeal penetration (*arrow*) without aspiration.

VIEW IMAGE

Laryngeal Penetration and Transglottic Aspiration

Identification of material in the airway has traditionally been the key abnormal finding on a VFSS and is often the catalyst for terminating the study for fear of airway compromise. Aspiration or laryngeal penetration is not a binary event, and the physiologic circumstances surrounding its occurrence must be described to determine the full implications. The first challenge is definition. The literature is replete with ambiguous terminology to describe the entrance of barium contrast into the laryngeal vestibule, larynx or trachea. For purposes of this chapter the following definitions are used: Laryngeal penetration refers to the presence of barium contrast in the laryngeal vestibule that does not pass below the level of the true vocal folds into the trachea (Fig. 32-21). Aspiration refers to the presence of barium contrast below the level of the true vocal folds in the subglottis or trachea.

The most clinically useful way of resolving the confusion is to describe the amount and viscosity of barium in the airway, its lowest location, the timing of its occurrence in the airway, and the patient's response to its presence. Detection of silent aspiration, defined as aspiration in the absence of a reflexive patient response, is a distinct advantage provided by the VFSS and assists in prognostication. Rosenbek et al.[64] describe an 8-point penetration-aspiration scale based on videofluoroscopic data that fulfils this purpose (Table 32-5).

Copyright © 2003, Mosby, Inc. All rights reserved.

Table 32-5
EIGHT-POINT PENETRATION-ASPIRATION SCALE

Score	Description of Events
1	Material does not enter the airway
2	Material enters the airway, remains above the vocal folds, and is ejected from the airway
3	Material enters the airway, remains above the vocal folds, and is not ejected from the airway
4	Material enters the airway, contacts the vocal folds, and is ejected from the airway
5	Material enters the airway, contacts the vocal folds, and is not ejected from the airway
6	Material enters the airway, passes below the vocal folds, and is ejected from the airway
7	Material enters the airway, passes below the vocal folds, and is not ejected from the airway
8	Material enters the airway, passes below the vocal folds, and no effort is made to eject

From Rosenbek JC, Robbins J, Roecker EV, Coyle JL, Woods JL. A penetration-aspiration scale. Dysphagia 1996;11:93-98.

It is instructive to note that laryngeal penetration is not uncommon in normal healthy adults. Robbins et al.[28] found that 20% of their adult subjects showed high laryngeal penetration during the swallow and received a score of 2 on the penetration-aspiration scale, indicating that the material was ejected from the larynx before the swallow was completed. Given its occurrence in normal patients, it would be unnecessary to terminate the VFSS on the basis of laryngeal penetration alone, particularly if the patient senses the material in the airway.

In addition to defining the nature of the penetration or aspiration, it is necessary to understand the physiologic basis for its occurrence, particularly when therapeutic strategies are to be evaluated. Laryngeal penetration or aspiration can occur before, during, or after the pharyngeal swallow response is activated. Aspiration *before* the swallow usually is due to impaired tongue movement for bolus control, resulting in premature spillage into the pharynx and/or delayed onset of the pharyngeal swallow. Aspiration *during* the swallow implies that the swallow response has been initiated but laryngeal closure is incomplete, resulting in penetration or aspiration (Fig. 32-22). Any of the multiple airway protective forces such as true and vestibular vocal fold closure or hyolaryngeal elevation with epiglottic inversion may be impaired, resulting in an exposed laryngeal inlet. Aspiration *after* the swallow is usually the result of retention in the pharyngeal recesses from an impaired pharyngeal contraction clearing force, reduced hyolaryngeal elevation with a reduction in opening of the pharyngoesophageal segment, or hypertonicity of the cricopharyngeal region (Fig. 32-23). Residue may also appear in the pyriform sinuses after the swallow as a result of emptying of a Zenker's diverticulum or cervical esophageal dysmotility.

Commonly, if the penetration or aspiration occurs during the initial descent of the bolus during the swallow, it is referred to as primary penetration or aspiration. If the penetration or aspiration occurs after the initial descent of the bolus, from residual bolus in the valleculae or more commonly in the pyriform sinuses, it is referred to as secondary penetration or secondary aspiration.

FIGURE 32-22 Aspiration during the swallow.

VIEW IMAGE

Evaluation of Therapeutic Strategies

One of the major advantages of the VFSS is that it provides an opportunity to assess the value of therapeutic

FIGURE 32-23 Aspiration after the swallow in a patient who has undergone radiation therapy for a hypopharyngeal tumor. *ac*, Arytenoid cartilages; *e*, epiglottis; *h*, hyoid bone.

VIEW IMAGE

Copyright © 2003, Mosby, Inc. All rights reserved.

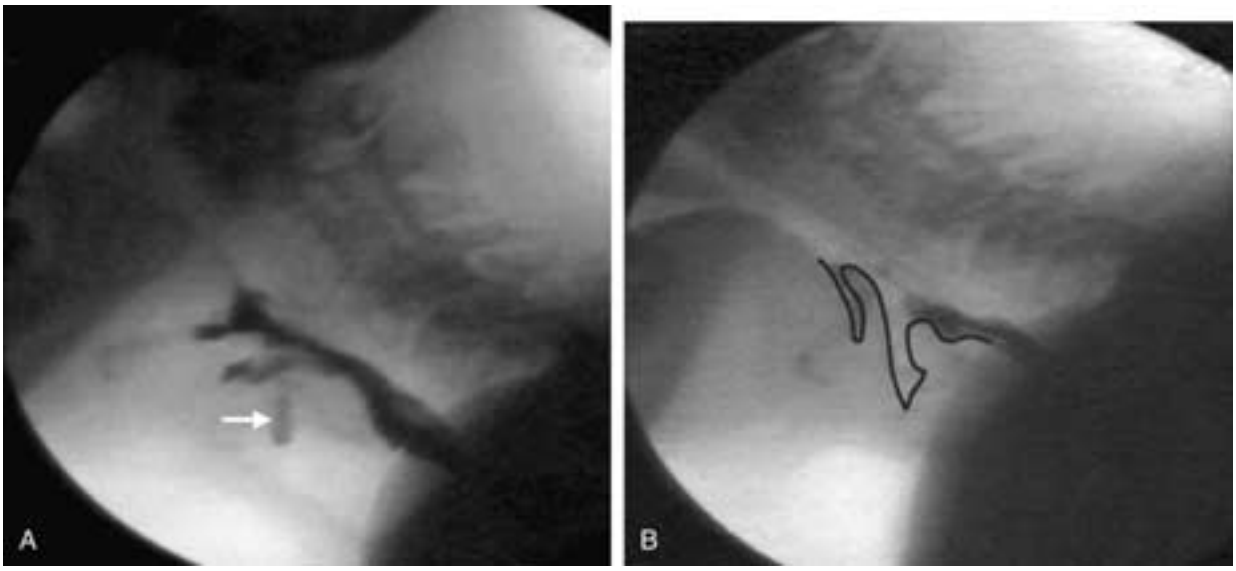

VIEW IMAGE

FIGURE 32-24 Aspiration (**A**) (*arrow*) eliminated by the chin-down posture (**B**), indicating increased narrowing of the laryngeal vestibule and greater tongue base retraction.

strategies. Appropriate selection of these strategies as isolated maneuvers or in combination depends on the precise characterization of the biomechanical and temporal events of the swallow resulting in impairment. Therapeutic procedures are either compensatory or rehabilitative in nature.[12] Compensatory strategies are designed to alter the bolus flow in an attempt to eliminate the patient's disordered symptoms. Postural changes involve changing the position of the head in order to alter the geometry of the oral, pharyngeal, and laryngeal systems. Individual techniques can reduce the angle of opening of the upper airway, as occurs in the chin-down (chin tuck) posture[72, 73] (Fig. 32-24), or can improve hyolaryngeal excursion and increase the propulsive force on the bolus by obstructing paretic pharyngeal musculature, as in head rotation[74, 75] (Fig. 32-25). Correct performance of these postural changes requires minimal cooperation from the patient since the instructions are single step and simple, for example, ''Put your chin on your chest.'' Matching the physiologic outcome of the postural change with the patient's swallowing problem increases the likelihood of the effectiveness of the technique. The frequently employed chin-down posture does not assist all patients. In fact, if contrast fills the pyriform sinus prior to the onset of the pharyngeal swallow, there is an increased risk of aspiration as the larynx elevates and the pyriform sinuses empty.

Other compensatory techniques involve manipulating bolus viscosity and volume and increasing sensory input. Changing bolus viscosity is a powerful tool in assisting patients with dysphagia, and a wide range of options is available, from thin liquids to textured solids.[13, 68] Increasing the bolus volume for liquids may be helpful in patients with incomplete oral or pharyngeal contraction, such as those with total glossectomy.[12, 25, 75] Smaller volumes of liquids may be indicated in patients with reduced laryngeal closure. The effectiveness of these trials can be evaluated by videofluoroscopy. Table 32-6 lists the most common compensations and their physiologic indications.

Rehabilitative therapy procedures place aspects of the patient's swallow under voluntary control and alter the physiology of the swallow[12]; they are listed in Table 32-7. These maneuvers require sophisticated cooperation by the patient, with the ability to understand, learn, and apply the treatment strategy. For example, the super-supraglottic swallow requires the patient to perform a Valsalva maneuver while swallowing a bolus and to cough after the swallow in an effort to invoke voluntary airway protection.[76] Since these therapeutic maneuvers take some time for the patient to learn, it is fitting for the speech pathologist to anticipate

FIGURE 32-25 Head rotation to the right in this patient with right-sided pharyngeal weakness obstructs bolus flow on the affected side, causing the bolus to flow down the left side of the pharynx.

VIEW IMAGE

Copyright © 2003, Mosby, Inc. All rights reserved.

Table 32-6
COMPENSATORY SWALLOWING STRATEGIES AND THEIR IMPACT ON SWALLOWING PHYSIOLOGY

	Functional Impairment	Physiologic Impact
Changes in Bolus Viscosity		
Increase bolus viscosity	Impaired tongue control	Reduces rate of liquid bolus flow
	Aspiration before the swallow	Allows improved lingual control
	Impaired laryngeal closure	Bolus remains cohesive
	No response to bolus placement	Increased sensory stimulation activates bolus manipulation (e.g., chewing of solids)
Decrease bolus viscosity	Impaired anterior posterior bolus propulsion	Reduced resistance to bolus flow
	Weak pharyngeal contraction	
Changes in Bolus Volume		
Increase bolus size	Delayed onset of pharyngeal swallow	Increases stimulation of sensory receptors to activate swallow response
Decrease bolus volume	Severe tongue weakness	Increased control
Postural Changes		
Chin down	Delayed onset of pharyngeal swallow	Widens vallecular space
	Reduced tongue drive on bolus	Displaces tongue posteriorly
	Aspiration before the swallow	Narrows angle of laryngeal vestibule
Head rotation to affected side	Unilateral pharyngeal weakness	Isolates damaged side from bolus flow
	Reduced laryngeal excursion and opening of pharyngoesophageal segment	Reduces pressure of pharyngoesophageal segment
	Unilateral vocal fold paralysis	Increases vocal fold adduction
Head tilt to unaffected side	Unilateral oral or pharyngeal weakness	Redirects bolus flow down unaffected side
Head extended	Reduced tongue propulsion	Gravitational forces assist bolus flow
	Velopharyngeal incompetence	Reduces nasal regurgitation

which therapeutic maneuvers may require assessment and to teach them to the patient before the study. The VFSS can be used to determine how accurately the patient has performed the maneuver and can be shown to the patient after completion of the study to assist with treatment recommendations.

Compensatory and rehabilitative procedures can be used in isolation or in combination. For example, a patient who presents with unilateral impaired pharyngeal weakness and weak tongue base retraction, resulting in pharyngeal retention and aspiration of residue after the swallow, may benefit from head rotation to the impaired side (to close off the weaker pharynx) together with a chin tuck (reducing the laryngeal opening size and increasing drive on the bolus) and an effortful swallow maneuver (to increase force on the bolus). Assessment of therapeutic maneuvers is conducted in the lateral and anterior projections, using several trials to ensure the reliability of the findings.

OVERVIEW OF A NORMAL VFSS

Although much detail regarding the normal swallow has been presented, it is useful to summarize the main points to observe on a normal VFSS. On the lateral view, there should be coordinated tongue movements and, in general, the bolus should remain on the upper surface of the tongue. The soft palate should be caudal, against the tongue base prior to initiation of the pharyngeal phase of the swallow. As the tongue thrusts dorsally, the soft palate should touch the

Table 32-7
REHABILITATIVE MANEUVERS THAT ALTER THE PHYSIOLOGY OF THE SWALLOW

	Indication	Physiologic Effect
Super supraglottic swallow instruction: ″Bear down, swallow, cough, and swallow again″	Aspiration before, during, and after the swallow	Improved airway protection with decreased amount of laryngeal penetration or aspiration
Effortful swallow instruction: ″Swallow as hard as you can″	Weak tongue base and pharyngeal wall contractions	Improved clearance of pharyngeal recesses
Mendelsohn maneuver instruction: ″Swallow and keep your larynx elevated until you have completed the swallow″	Poor coordination of tongue base movement to the posterior pharyngeal wall	Sustains laryngeal elevation during swallow
	Increased pharyngeal retention in the pyriform sinuses	Sustains opening of pharyngoesophageal segment

Copyright © 2003, Mosby, Inc. All rights reserved.

posterior pharyngeal wall, effectively closing off the nasopharynx. The posterior tongue may be seen to first descend slightly and then the tongue base should move dorsally, touching the posterior pharyngeal wall. The pharyngeal phase should normally initiate as the bolus reaches the upper posterior aspect of the tongue. The hyoid, and thus the larynx, should then move forward and upward, while the epiglottis should be seen to tilt passively downward, resting upon the arytenoid cartilages and muscles. Forward movement of the posterior pharyngeal wall should occur, signaling pharyngeal contraction, and as the bolus reaches the lower hypopharynx, the cricopharyngeus should open, with no posterior cricopharyngeal indentation being seen on the barium column. The cricopharyngeus should then close as cervical esophageal primary and secondary contractions are initiated. There should be no residual contrast in the vallecula or pyriform sinuses with liquids. Some residua may be seen with purees and solids; however, this should be cleared on subsequent swallows of saliva. Similarly, tongue or pharyngeal coating should be rapidly cleared on the next swallow of saliva.

In the AP or frontal projection, the lateral pharyngeal walls should be filled symmetrically by the bolus, bulging outward without any ''dog ears'' (pharyngoceles). The vocal folds may be seen to adduct fully, and the barium column should smoothly enter the cervical esophagus.

CONCLUSION

Diagnosis of oropharyngeal swallowing disorders demands an understanding of the complex normal and abnormal biomechanical events that drive boluses from the oral cavity through the hypopharynx and into the esophagus. The VFSS provides information about the physiologic substrates underlying the swallowing process that extends beyond the simple detection of aspiration. Thoughtfully executed studies that draw on the expertise of the radiologist and speech pathologist in understanding the problem permit evaluation of therapeutic strategies aimed at improving the chance that the patient can eat safely and efficiently by mouth.

ACKNOWLEDGMENTS

The author wishes to thank the following individuals:Cary Crehan, R.T., M.B.A., for his assistance in printing the images used in this chapter; Sandy Martin, M.S., C.C.C., Joanne Gutek, M.A., C.C.C., and Suzanne Danforth, M.S., C.C.C., for their invaluable editorial comments; and Hugh Curtin, M.D., for his generosity of spirit and knowledge.

REFERENCES

1. Cook IJ, Kahrilas PJ. AGA technical review on management of oropharyngeal dysphagia. Gastroenterology 1999 116:455–478.
2. Daniels SK, McAdam CP, Brailey K, Foundas AL. Clinical assessment of swallowing and prediction of dysphagia severity. Am J Speech-Language Pathol 1997;6:17–24.
3. Daniels SK, Brailey K, Priestly DH, Herrington LR, Wiesberg LA, Foundas AL. Aspiration in patients with acute stroke. Arch Phys Med Rehabil 1998;79:14–19.
4. Horner J, Massey EW, Brazer SR. Aspiration in bilateral stroke patients. Neurology 1990;40:1686–1688.
5. Wu CH, Hsiao TY, Chen JC, Chang YC, Lee SY. Evaluation of swallowing safety with fiberoptic endoscope: comparison with videofluoroscopic technique. Laryngoscope 1997;107:396–401.
6. O'Donoghue S, Bagnall A. Videofluoroscopic evaluation in the assessment of swallowing disorders in paediatric and adult populations. Folia Phoniatr Logop 1999;51:158.
7. Martin-Harris B, Logemann JA, McMahon S, Schleicher M, Sandidge J. Clinical utility of the modified barium swallow. Dysphagia 2000;15:136–141.
8. Palmer JB, DuChane AS, Donner MW. Role of radiology in rehabilitation of swallowing. In: Jones B, Donner MW, eds. Normal and Abnormal Swallowing: Imaging in Diagnosis and Therapy. Berlin: Springer-Verlag, 1991; 215–225.
9. Logemann JA. Evaluation and Treatment of Swallowing Disorders. San Diego, CA: College-Hill Press, 1983.
10. Stenson KM, MacCracken E, List M, Haraf DJ, Brockstein B, Weichselbaum R, Vokes EE. Swallowing function in patients with head and neck cancer prior to treatment. Arch Otolaryngol Head Neck Surg 2000;126:371–377.
11. Kendall K, McKenzie S, Leonard R. Dynamic swallow study: objective measures and normative data. In: Leonard R, Kendall K, eds. Dysphagia Assessment and Treatment Planning: A Team Approach. San Diego, CA: Singular Publishing, 1998;101–160.
12. Logemann JA. Evaluation and Treatment of Swallowing Disorders, 2nd ed. Austin, TX: Pro-Ed, 1998.
13. Logemann JA. Manual for the Videofluoroscopic Study of Swallowing. Austin, TX: Pro-Ed, 1993.
14. Beck TJ, Gayler BW. Image quality and radiation levels in videofluoroscopy for swallowing studies: a review. Dysphagia 1990;5:118–128.
15. Perlman AL, Lu C, Jones B. Radiographic contrast examination of the mouth, pharynx and esophagus. In: Perlman AL, Schulze-Delrieu K, eds. Deglutition and Its Disorders. San Diego, CA: Singular Publishing, 1997;153–199.
16. Jones B, Ravich WJ, Donner MW, Kramer SS. Pharyngoesophageal interrelationships: observations and working concepts. Gastrointest Radiol 1985;10:225–233.
17. Splaingard ML, Hutchins B, Sulton LD, Chaudhuri G. Aspiration in rehabilitation patients: videofluoroscopy vs. bedside clinical assessment. Arch Phys Med Rehabil 1988;69:637–640.
18. Robbins JA, Sufit R, Rosenbek J, Levine R, Hyland J. A modification of the modified barium swallow. Dysphagia 1987;2:83–96.
19. McKenzie S. Swallow evaluation with videofluoroscopy. In: Leonard R, Kendall K, eds. Dysphagia Assessment and Treatment Planning: A Team Approach. San Diego, CA: Singular Publishing, 1997;83–99.
20. Mills RH. Increasing the precision of the videofluoroscopic swallowing examination. In: Mills RH, ed. Evaluation of Dysphagia in Adults: Expanding the Diagnostic Options. Austin, TX: Pro-Ed, 2000;103–144.
21. McConnel FM, Cerenko D, Jackson RT, Guffin TN. Timing of major events of pharyngeal swallowing. Arch Otolaryngol Head Neck Surg 1988;114:1413–1418.
22. Dodds WJ, Logemann JA, Stewart ET. Radiologic assessment of abnormal oral and pharyngeal phases of swallowing. Am J Roentgenol 1990;154:965–974.
23. Miller AJ. The Neuroscientific Principles of Swallowing and Dysphagia. San Diego, CA: Singular Publishing, 1999;107–134.
24. Perlman AL, Christensen J: Topography and functional anatomy of the swallowing structures. In: Perlman AL, Schulze-Delrieu K, eds. Deglutition and Its Disorders. San Diego, CA: Singular Publishing, 1997;15–42.
25. Dantas RO, Kern MK, Massey BT, Dodds WJ, Kahrilas PJ, Brasseur JG, Cook IJ, Lang M. Effect of swallowed bolus variables on oral and pharyngeal phases of swallowing. Am J Physiol 1990;258:G675–G681.
26. Dua KS, Ren J, Bardan E, Xie P, Shaker R. Coordination of deglutitive glottal function and pharyngeal bolus transit during normal eating. Gastroenterology 1997;112:73–83.
27. Shaker R, Ren J, Zamir Z, Sarna A, Liu J, Sui Z. Effect of aging, position, and temperature on the threshold volume triggering pharyngeal swallows. Gastroenterology 1994;107:396–402.

Copyright © 2003, Mosby, Inc. All rights reserved.

28. Robbins J, Hamilton JW, Lof GL, Kempster GB. Oropharyngeal swallowing in normal adults of different ages. Gastroenterology 1992;103:823–829.
29. Ekberg O, Sigurjonsson V. Movement of the epiglottis during deglutition. Gastrointes Radiol 1982;7:101–107.
30. Logemann JA, Kahrilas PJ, Cheng J, Pauloski BR, Gibbons PJ, Rademaker AW, Lin S. Closure mechanisms of laryngeal vestibule during swallow. Am J Physiol 1992;262:G338–G344.
31. Van Daele DJ, Perlman AL, Cassell M. Intrinsic fiber architecture and attachments of the human epiglottis and their contribution to the mechanism of deglutition. J Anat 1995;186:1–15.
32. Ekberg O, Nylander G. Dysfunction of the cricopharyngeal muscle. A cineradiographic study of patients with dysphagia. Radiology 1982;143:481–486.
33. Cook IJ, Dodds WJ, Dantas RO, Massey BT, Kern MK, Lang JM, Brasseur JG, Hogan WJ. Opening mechanisms of the human upper esophageal sphincter. Am J Physiol 1989;257:G748–G759.
34. Jacob P, Kahrilas PJ, Logemann JA, Shah V, Ha T. Upper esophageal sphincter opening and modulation during swallowing. Gastroenterology 1989;97:1469–1478.
35. McConnel FM, Hood D, Jackson K, O'Connor A. Analysis of intrabolus forces in patients with Zenker's diverticulum. Laryngoscope 1994;104:571–581.
36. Barczi SR, Sullivan PA, Robbins JA. How should dysphagia care of older adults differ? Establishing optimal practice patterns. Semin Speech Lang 2000;21:347–361.
37. Price PA, Darvell BS. Force and mobility in the aging human tongue. Med J Aust 1981;1:75–78.
38. Nicosia M, Hind JA, Roecker EBM, Carnes M, Doyle J, Dengle GA, Robbins J. Age effects on the temporal evolution of isometric and swallowing pressure. J Gerontol A Biol Sci Med Sci 2000;55: 634–640.
39. Murray J. Manual of Dysphagia Assessment in Adults. San Diego, CA: Singular Publishing, 1999;113–151.
40. Di Vito J. Cervical osteophytic dysphagia: single and combined mechanisms. Dysphagia 1998;13:58–61.
41. Valadka AB, Kuhl WS, Smith MM. Updated management strategy for patients with cervical osteophytic dysphagia. Dysphagia 1995;10: 167–171.
42. Dodds WJ, Taylor AJ, Stewart ET, Kern MK, Logemann JA, Cook IJ. Tipper and dipper types of oral swallows. Am J Roentgenol 1989;153:1197–1199.
43. Leopold N. Kagel MC. Dysphagia in Huntington's disease. Arch Neurol 1985;42:57–60.
44. Leopold N, Kagel MC. Dysphagia in progressive supranuclear palsy: radiologic features. Dysphagia 1997;12:140–143.
45. Perlman AL, Grayhack JP, Booth BM. The relationship of vallecular residue to oral involvement, reduced hyoid elevation and epiglottic function. J Speech Hear Res 1992;35:734–741.
46. Sundgren P, Maly P, Gullberg B. Elevation of the larynx on normal and abnormal cineradiogram. Br J Radiol 1993;66:768–772.
47. Logemann JA, Kahrilas PJ, Kobara M, Vakil N. The benefit of head rotation on pharyngo-esophageal dysphagia. Arch Phys Med Rehabil 1989;70:767–771.
48. Curtis DJ, Cruess DF, Crain M, Sivit C, Winters C, Dachman AH. Lateral pharyngeal outpouchings: a comparison of dysphagic and asymptomatic patients. Dysphagia 1988;2:156–161.
49. Kahrilas PJ, Lin S, Rademaker AW, Logemann JA. Impaired deglutitive airway protection: a videofluoroscopic analysis of severity and mechanism. Gastroenterology 1997;113:1457–1464.
50. Shaker R, Dodds WJ, Dantas RO, Hogan WJ, Andorfer RC. Coordination of deglutitive glottic closure with oropharyngeal swallowing. Gastroenterology 1990;98:1478–1484.
51. Goyal R, Martin SB, Shapiro J, Spechler SJ. The role of cricopharyngeal muscle in pharyngoesophageal disorders. Dysphagia 1993;8:252–258.
52. Cook IJ. Opening mechanism of the human upper esophageal sphincter. Am J Physiol 1989;257:G748–G759.
53. Cook IJ. Cricopharyngeal function and dysfunction. Dysphagia 1993;8:244–251.
54. Baredes S, Shah CS, Kaufman R. The frequency of cricopharyngeal dysfunction on videofluoroscopic swallowing studies in patients with dysphagia. Am J Otolaryngol 1997;18:185–189.
55. Curtis DJ, Cruess D, Berg T. The cricopharyngeal muscle: a videorecording review. Am J Roentgenol 1984;142:497–500.
56. Buchholz DW. Cricopharyngeal myotomy may be effective treatment for selective patients with neurogenic oropharyngeal dysphagia. Dysphagia 1995;10:225–228.
57. Shin T, Tsuda K, Takagi S. Surgical treatment for dysphagia of neuromuscular origin. Folio Phoniatr Logop 1999;51:213–219.
58. Ergun GA, Kahrilas PJ. Medical and surgical treatment in interventions in deglutitive dysfunction. In: Perlman AL, Schulze-Delrieu K, eds. Deglutition and Its Disorders. San Diego, CA: Singular Publishing, 1997;463–490.
59. Cook IJ, Gabb M, Panagopoulos V, Jamieson GG, Dodds WJ, Dent J, Shearman DJ. Pharyngeal (Zenker's) diverticulum is a disorder of upper esophageal opening. Gastroenterology 1992;103:1229–1235.
60. Skinner KA, Zuckerbraun L. Recurrent Zenker's diverticulum: treatment with cricopharyngeal myotomy. Am Surg 1998;64:192–195.
61. Pitman RG. The post-cricoid impression on the esophagus (letter and reply). Am J Roentgenol 1992;158:690–691.
62. Langmore SE, Terpenning MS, Schork A, Chen Y, Murray JT, Lopatin D, Loesche WJ. Predictors of aspiration pneumonia: how important is a dysphagia? Dysphagia 1998;13:69–81.
63. Robbins J, Coyle J, Rosenbek J, Roecker E, Wood J. Differentiation of normal and abnormal airway protection during swallowing using the penetration-aspiration scale. Dysphagia 1999;14:228–232.
64. Rosenbek JC, Robbins J, Roecker EV, Coyle JL, Woods JL. A penetration-aspiration scale. Dysphagia 1996;11:93–98.
65. Lazarus C, Logemann JA. Swallowing disorders in closed head trauma patients. Arch Phys Med Rehabil 1987;68:79–84.
66. Aydogdu I, Ertekin C, Tarlaci S, Turman B, Kiylioglu N, Secil Y. Dysphagia in lateral medullary infarction (Wallenberg's syndrome): an acute disconnection syndrome in premotor neurons related to swallowing activity? Stroke 2001;32:2081–2087.
67. Martino R, Terrault N, Ezerzer F, Mikulis D, Diamant NE. Dysphagia in a patient with lateral medullary syndrome: insight into the central control of swallowing. Gastroenterology 2001;121:420–426.
68. Lazarus CL, Logemann JA, Rademaker AW, Kahrilas PJ, Pajak T, Lazar R, Halper A. Effects of bolus volume, viscosity, and repeated swallows in non-stroke patients. Arch Phys Med Rehabil 1993;74: 1066–1170.
69. Perlman AL, Booth PM, Grayhack JP. Videofluoroscopic predictors of aspiration in patients with oropharyngeal dysphagia. Dysphagia 1994;9:90–95.
70. Hiiemae K, Heath M, Heath G, Kazazoglu E, Murray J, Sapper D, Hamblett K. Natural bites, food consistency and feeding behaviour in man. Arch Oral Biol 1996;41:175–189.
71. Rademaker AW, Pauloski BR, Logemann JA, Shanahan TK. Oropharyngeal swallow efficiency as a representative measure of swallowing function. J Speech Hear Res 1994;37:314–325.
72. Shanahan TK, Logemann JA, Rademaker AW, Pauloski BR, Kahrilas PJ. Chin down posture effect on aspiration in dysphagic patients. Arch Phys Med Rehabil 1993;74:736–739.
73. Welch MV, Logemann JA, Rademaker AW, Kahrilas PJ. Changes in pharyngeal dimensions effected by chin tuck. Arch Phys Med Rehabil 1993;74:178–181.
74. Rasley A, Logemann JA, Kahrilas PJ, Rademaker AW, Pauloski BR, Dodds WJ. Prevention of barium aspiration during videofluoroscopic swallowing studies: value of change in posture. Am J Roentgenol 1993;160:1005–1009.
75. Lazarus C, Logemann JA, Gibbons P. Effects of maneuvers on swallowing function in a dysphagic oral cancer patient. Head Neck 1993;15:419.
76. Martin B, Logemann JA, Shaker R, Dodds W. Normal laryngeal valving patterns during three breath-holding maneuvers: a pilot investigation. Dysphagia 1993;8:11.

Copyright © 2003, Mosby, Inc. All rights reserved.

Copyright © 2003, Mosby, Inc. All rights reserved.

Section VII

Neck

Copyright © 2003, Mosby, Inc. All rights reserved.

Copyright © 2003, Mosby, Inc. All rights reserved.

33

Embryology and Anatomy of the Neck

Peter M. Som, Wendy R.K. Smoker, Armand Balboni, Joy S. Reidenberg, Patricia A. Hudgins, Jane L. Weissman, and Jeffrey Laitman

INTRODUCTION
BASIC TERMINOLOGY OF HEAD AND NECK DEVELOPMENT
- General Terminology
- Branchial Arches
- Basic Terminology of *Hox* Genes

EARLY EMBRYOLOGY OF THE HEAD AND NECK
- Mesodermal Layers, Somitomeres, and Somites

NORMAL EMBRYOLOGY OF THE BRANCHIAL APPARATUS
- General Embryology
- Pouch Derivatives
- The Thymus and Parathyroid Glands
- The Tongue and Thyroid Gland
- Pharynx, Larynx, and Trachea
- Branchial Arches

EMBRYOLOGY OF THE AORTIC ARCHES
EMBRYOLOGY OF THE VEINS
EMBRYOLOGY OF THE LYMPHATIC SYSTEM
- Tonsils

EMBRYOLOGY OF THE SALIVARY GLANDS
NORMAL POSTNATAL ANATOMY OF THE NECK
THE PERIPHERAL NERVOUS SYSTEM
- Cranial Nerves
- Spinal Nerves
- Sympathetic System
- Autonomic (Parasympathetic) Ganglia of the Face and Neck
  - The Ciliary Ganglion
  - The Pterygopalatine Ganglion
  - The Submandibular Ganglion
  - The Otic Ganglion

DIFFERENTIAL DIAGNOSIS

INTRODUCTION

Many of the structures in the head and neck are intimately related to the embryogenesis of the branchial apparatus (i.e., branchial arches, pharyngeal pouches, branchial grooves, and branchial membranes). These branchial structures are transient and undergo such substantial remodeling that their original embryonic form is unrecognizable in the adult. Nonetheless, knowledge of their development provides a basis for understanding how their derivatives acquire their adult forms, and it provides an understanding of the pathogenesis of the variety of congenital anomalies that may result from abnormal branchial apparatus development (Chapter 35). This chapter gives an overview of the early stages of head and neck embryology (the somatomere and somite phase of development) and reviews all of the branchial arches, with particular focus on the derivatives of the third through sixth arches.[1–7] A detailed discussion of the first and second arches and their contributions to the formation of the face, sinonasal cavities, and oral cavity appears in Chapter 1. The embryology of the eye and orbit is discussed in Chapters 8 and 9 and that of the skull base is described in Chapter 12, while the embryology of the temporal bone is discussed in Chapter 19. In addition, this chapter reviews the development of the aortic arches and arteries, the veins, and the lymphatics of the head and neck. The embryology of the larynx and the salivary glands is also discussed. Finally, the anatomy of the neck in the adult is described, and differential diagnosis based on anatomic location is reviewed.

Copyright © 2003, Mosby, Inc. All rights reserved.

BASIC TERMINOLOGY OF HEAD AND NECK DEVELOPMENT

General Terminology

As differing terms are often applied to the development of head and neck structures and the time frames within which this development occurs, it is important to establish briefly those terms that will be used in this chapter. First, the term *embryo* or *embryogenesis* is properly used to refer to the first 8 weeks of development in humans. This period largely corresponds to the appearance of organs and organ systems. The term *organogenesis* thus is largely equatable with the embryonic period.

Following the embryonic period is the *fetal* period. This is largely the time of growth and differentiation as opposed to the appearance of structures. Accordingly, one should not refer to an individual before the end of the eighth week as a fetus or after the ninth week as an embryo. It should be noted that these demarcations, terms, and time frames are based on humans. Other animals have different gestational periods from humans, and so the periods and terminology may not mirror those of humans. This is important to keep in mind in studies on comparative embryology in general, in which a number of mouse, rat, or avian species are used as experimental models.

Branchial Arches

The branchial arches are the main component of the branchial *apparatus*, which includes the branchial arches, pharyngeal pouches, branchial grooves, and branchial membranes. Branchial arches are transient embryonic structures from which will arise many of the adult structures of the head and neck. The word *branchial* derives from the Greek *branchia*, meaning ''gill.'' Early in development, the cranial region of an embryo has marked arch-like regions with intervening clefts. To early anatomists, this condition resembled the gills of a fish (they are, in fact, homologous to the precursors of gills in fish and immature amphibians), and hence the term *branchial* came into common use. As humans never develop gills, the term *pharyngeal arch* is frequently used. The term *branchial arch* will be used throughout this chapter, as it is the more commonly used term and is also used in discussing vertebrates.

Basic Terminology of *Hox* Genes

Over the last few years, a great deal has been learned about the establishment of the overall body plan, and much of this has come from our understanding of the genes involved. For example, the basic body plan—from *Drosophila* through humans—is highly conserved and follows the blueprints laid out by some basic genes. These basic genes, known collectively as homeotic genes, share a highly conserved 180 base pair sequence known as the homeobox.[8, 9] In vertebrates, specific homeotic genes are referred to as *Hox* genes. The positional commitment of head and neck structures may be the result of the specific overlapping expression of these *Hox* genes. Studies exploring these features of head and neck development will be referenced throughout this chapter.

EARLY EMBRYOLOGY OF THE HEAD AND NECK

Mesodermal Layers, Somitomeres, and Somites

Prior to the full appearance of the branchial arches, the somitomere and somite period of intrauterine development occurs. In fact, it is not until the late somite stage (fourth intrauterine week) that the branchial arches can be clearly seen. Starting at about the twenty-first gestational day, and lasting for approximately 10 days, the major event in embryonic development is the folding of the neural plate, from which the brain and spine will develop. Following this, the mesoderm differentiates into three aggregations: a lateral mesoderm, an intermediate mesoderm, and a paraxial mesoderm. The lateral mesoderm contributes to the development of the walls of the embryonic coelom, and from this will arise the pleural, pericardial, and peritoneal cavities.[10] In the head and neck, the lateral mesoderm has been described as forming considerable portions of the throat and larynx, such as the tracheal cartilages and connective tissues, as well as forming angiogenic precursors that may seed distant parts of the head.

The intermediate mesoderm is not present in the head and contributes to the formation of the gonads, kidney, and adrenal cortex. The paraxial mesoderm, which is alongside the notochord, gives rise to all striated voluntary muscles in the body. In the head and neck, the paraxial mesoderm develops seven rostral condensations of incompletely segmented *somitomeres* and a series of 42 to 44 paired more caudal segmented *somites*. Overall, there are 7 somitomeres and 4 occipital, 8 cervical, 12 thoracic, 5 lumbar, 5 sacral, and 8 to 10 coccygeal somites (Fig. 33-1).[10]

Each somite differentiates into three parts. The ventromedial part, or *sclerotome*, contributes to the development of the vertebral column and accounts for its segmental nature. As a result of notochordal secretion of procollagen and collagen, some of the sclerotomal cells are induced to convert into cartilage. The lateral part of the somite, or *dermatome,* gives rise to the development of the dermis and skin. With reference to muscular development, it is the intermediate part of the somite, or *myotome,* that eventually differentiates into the muscles of the trunk and limbs, as well as some of the orofacial muscles. The *somitomeres* are not as clearly delineated as the somites; nevertheless, their muscular derivatives arise from a somewhat comparable region known as the myomere.

It is the myomeres and the myotomes that form the primitive muscle cells, or *myoblasts*, which then divide and fuse to form *myotubes*. The myotubes, in turn, halt subsequent mitosis and become *myocytes*, or muscle fibers.[11] Although most muscle fibers develop prior to birth, they continue to increase in size during early infancy. It is motor innervation that stimulates muscle activity and further growth by hypertrophy. The craniofacial muscles develop

Copyright © 2003, Mosby, Inc. All rights reserved.

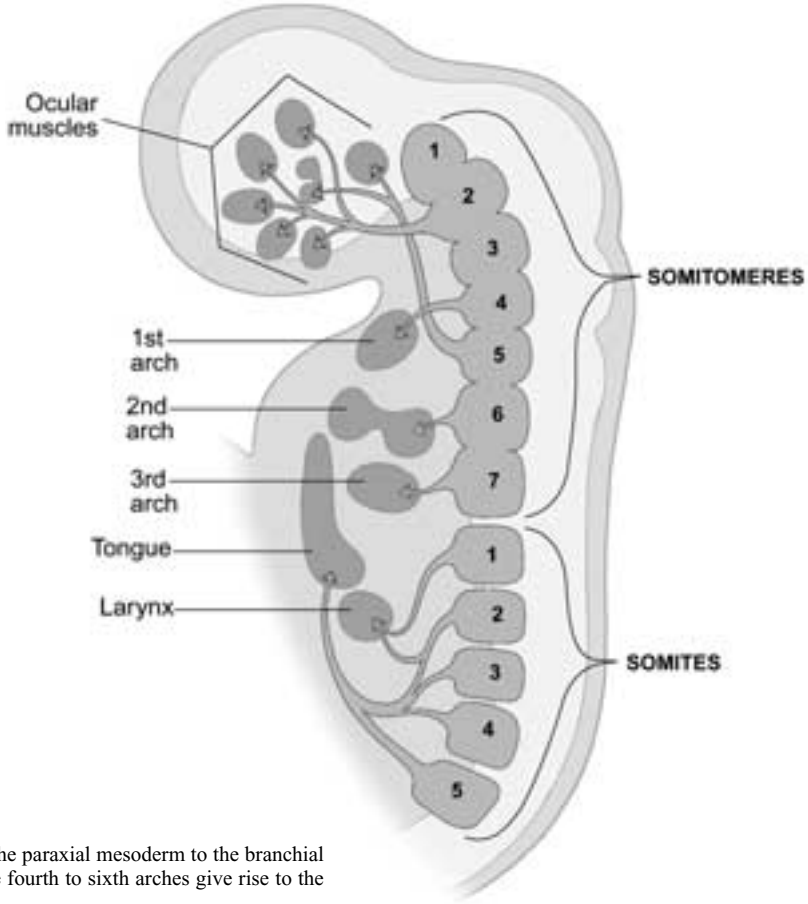

VIEW IMAGE

FIGURE 33-1 Schematic view of the contributions from the paraxial mesoderm to the branchial arches and muscles of the tongue and oculomotor system. The fourth to sixth arches give rise to the intrinsic laryngeal muscles.

initially from paraxial mesoderm that transiently resides in seven somitomeres and the five most rostral somites. The resultant muscles obtain their innervation, in a sequential manner, from the cranial nerves. Thus, four of the extraocular muscles (the superior rectus, medial rectus, inferior rectus, and inferior oblique) arise from the first two somitomeres and are supplied by the third cranial nerve (oculomotor, CN III) (note: the first two cranial nerves, the olfactory and optic, are not true nerves, but rather brain tracts historically called nerves). The superior oblique muscle develops from the third somitomere and is innervated by the fourth cranial nerve (trochlear, CN IV). The myomere of the fourth somitomere invades the first branchial arch and develops into the muscles of mastication (the masseter, medial pterygoid, lateral pterygoid, and temporalis) supplied by the fifth cranial nerve (trigeminal, CN V). The lateral rectus muscle comes from the fifth somitomere and is supplied by the sixth cranial nerve (abducent, CN VI). The myomere of the sixth somitomere invades the second branchial arch to form the facial muscles that are supplied by the seventh cranial nerve (facial, CN VII). The seventh somitomere forms the stylopharyngeus muscle of the third branchial arch, which is supplied by the ninth cranial nerve (glossopharyngeal, CN IX).[11, 12]

The development of the caudal arches (fourth to sixth) is much less clear than that of the rostral arches (9). Nevertheless, it appears that the myotomes of the first four (occipital) somites invade the fourth, (fifth?), and sixth branchial arches, bringing the tenth cranial nerve (vagus, CN X) and the eleventh cranial nerve (the cranial ''root'' portion of the spinal accessory, CN XI) to the extrinsic and intrinsic laryngeal muscles. The precursors of the tongue muscles are probably derived from occipital somites 2 to 4 and supplied by the twelfth cranial nerve (hypoglossal, CN XII), which migrates into the tongue to form the intrinsic and extrinsic tongue muscles. The derivatives of the third through seventh somites, innervated by the spinal root of CN XI (with initial cell bodies in the accessory, or spinal, nucleus in the spinal cord rather than in the nucleus ambiguus), form the sternocleidomastoid and trapezius muscles.[12] Overall, there is a cephalocaudal sequence of development so that the orofacial muscles are the first to develop. As the muscles form, their nerve and blood supplies also develop, and these are maintained as the muscles migrate from their sites of origin. As the muscle fibers differentiate, they gain their attachments to bone; this process is related to periosteal growth.[12]

NORMAL EMBRYOLOGY OF THE BRANCHIAL APPARATUS

General Embryology

The branchial apparatus is first identified at about the fourth week of development and is complete by the sixth to seventh week. Initially, ventrally migrating neural crest cells

Copyright © 2003, Mosby, Inc. All rights reserved.

interact with lateral extensions of the ventral pharyngeal endoderm that surrounds the six aortic arch arteries. This appears to initiate branchial arch development and results in the segmentation of the mesoderm lateral to the ventral foregut to form a series of five distinct bilateral mesenchymal swellings referred to as the branchial arches. The initial mesodermal core of each arch is then augmented by migrating neural crest cells that surround the mesodermal elements. This mesoderm will give rise to muscle myoblasts, while the neural crest cells will give rise to skeletal and connective tissues.

Externally, the ectodermally covered branchial arches are separated by branchial clefts or grooves, which correspond to five internal outpouchings of the endodermally lined foregut, referred to as the branchial pouches (Fig. 33-2A,B). The fifth arch does not appear on the surface but lies buried about the site of origin of the laryngotracheal outgrowth. Indeed, it is unclear whether or not the fifth arch ever develops in humans. For this reason, it is often placed together with the sixth arch and its derivatives, and is thus perhaps more conservatively described as originating from the *fifth-sixth* arches. This terminology will be used in this chapter. The branchial arches decrease in size from cranial to caudal, with each pair eventually merging midventrally.

Thus, there are five visible arches, which are numbered cranially to caudally as the first, second, third, fourth, and fifth-sixth branchial arches. These arches are prominent in a lateral profile of the embryo, and they are aligned transversely to the plane of the neck. Between each arch is a branchial cleft. The branchial cleft ectoderm forms a thin double-layered branchial or closing membrane where it transiently comes in contact with the endoderm of the primitive pharynx. However, mesoderm soon separates the ectodermal and endodermal layers of the membranes. The tympanic membrane, which is derived from the first branchial membrane, is the only branchial membrane structure to remain as such in the adult human. It should be noted that the clefts never communicate with the foregut lumen, as they do in the gill apparatus of the fish. The cleft and pouch (and thus the branchial membrane) of each arch are positioned caudally to the arch (mesoderm) of the same number. Each arch contains a central cartilaginous rod that is differentiated from neural crest tissue and forms the skeleton of the arch. This tissue is destined to become bone, cartilage, or ligamentous structures. There is also a muscular component, an aortic arch artery that runs around the developing pharynx from the ventral heart to the dorsal aorta, and a neural element that supplies the mucosa and muscles that will arise from that arch (Fig. 33-2C). These neural elements consist of sensory and specialized visceral motor fibers of one or more cranial nerves. It is the migrating cranial nerve fibers of each arch that initiate the development of that arch's muscles and, although some of these muscles may migrate from their sites of origin, these muscles retain their original arch nerve supply.[1, 4, 7, 13] It is also the migration of the muscles, which ''drag'' their neural supply with them, that accounts for the tortuous routes of many of the cranial nerves.

Shortly after the branchial arches appear, excessive mesodermal growth occurs in the first arch, the cranial portion of the second arch, obliterating the outer contour of the second through fourth grooves and forming the hyoid operculum. Overgrowth also occurs in the epipericardial ridge, which develops from the mesoderm lateral to the fifth-sixth arch. These accelerated growths result in a submerging of the intervening caudal portion of the second, third, and fourth arches into a shallow recessed ectodermal pit, the retrohyoid depression or the cervical sinus of His (Fig. 33-3).[14] Further growth about the cervical sinus results in narrowing of the external opening into a channel called the cervical duct. Soon the cervical duct is obliterated, as is the ectodermally lined cervical sinus, and eventually there is a smooth uniform contour to the external surface of the neck. In the adult, the site of the cervical sinus is located at the angle between the dorsal surface of the strap muscles and the anterior margin of the sternocleidomastoid muscle.[2]

The epipericardial ridge contains the rudiments of the sternocleidomastoid-trapezius muscle complex, the infrahyoid muscles, and the muscles of the floor of the mouth and tongue. Also contained within this mesodermal ridge are the spinal branches of the spinal accessory (XI) and hypoglossal (XII) cranial nerves. Based on this embryology, any communication persisting between the cervical sinus and the skin or the pharynx lies anterior to the derivatives of the epipericardial ridge and the hypoglossal nerve. Such developmental anomalies are discussed in Chapter 35.

The ganglia of cranial nerves V, VII, and IX and portions of the ganglia of cranial nerves VIII and X derive from neural crest cells. In addition, neuroblasts from superficial ectodermal thickenings, the epibranchial placodes, develop at the dorsal portions of the first through fourth branchial grooves and contribute to the ganglia of cranial nerves V, VII, IX, and X. Caudal to the region of the vagal ganglion, neural crest tissue in the occipital region contributes to the ganglia of cranial nerves XI and XII.[14]

Pouch Derivatives

There are four endothelially lined pouches that protrude laterally from the developing foregut. There is a rudimentary sixth pouch, but it is considered an appendage of the fourth pouch, as it has no independent communication with the pharyngeal lumen.[15] Later in development, as the pouches progressively extend away from the wall of the pharynx, their communication with the pharynx is maintained via an elongated pharyngobranchial duct.

The first and second pouches merge to form the tubotympanic recess, from which the middle ear and eustachian tube develop. Thus, the epithelial lining of the eustachian tube and the middle ear, including the inner lining of the tympanic membrane, is of endodermal origin. The ventral portion of the second pouch does not contribute to the tubotympanic recess, but rather eventually forms the palatine tonsillar fossa. The actual tonsillar tissue, however, comes from the underlying mesoderm of the second arch. The third, fourth, and sixth pouches give rise to glandular structures discussed below (Fig. 33-4).

The Thymus and Parathyroid Glands

The thymus develops from the outpouchings of the ventral portions of the third pharyngeal pouches during the

Copyright © 2003, Mosby, Inc. All rights reserved.

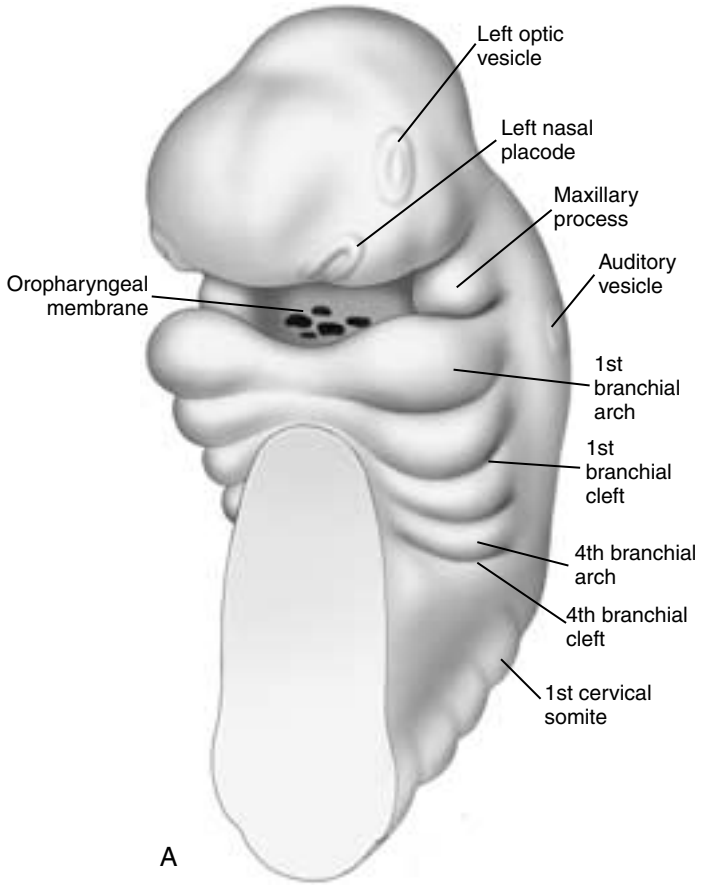

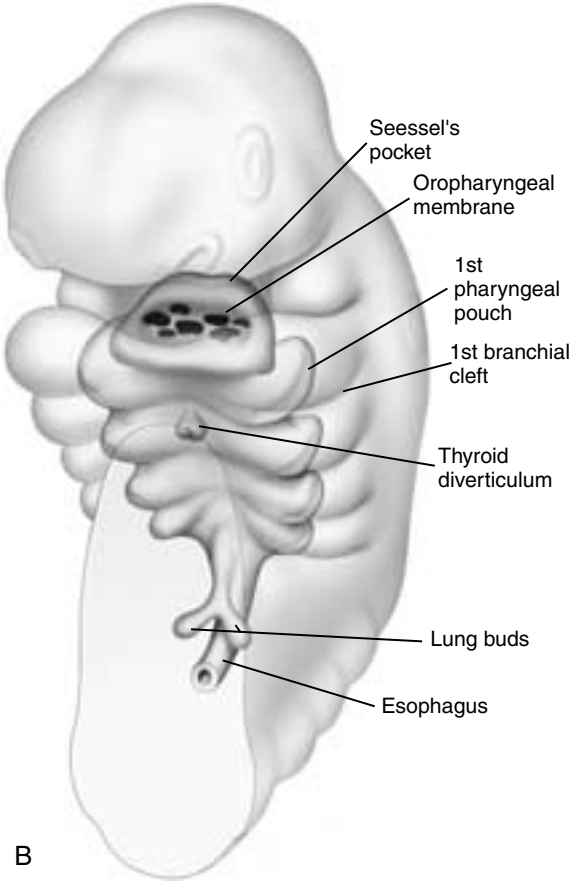

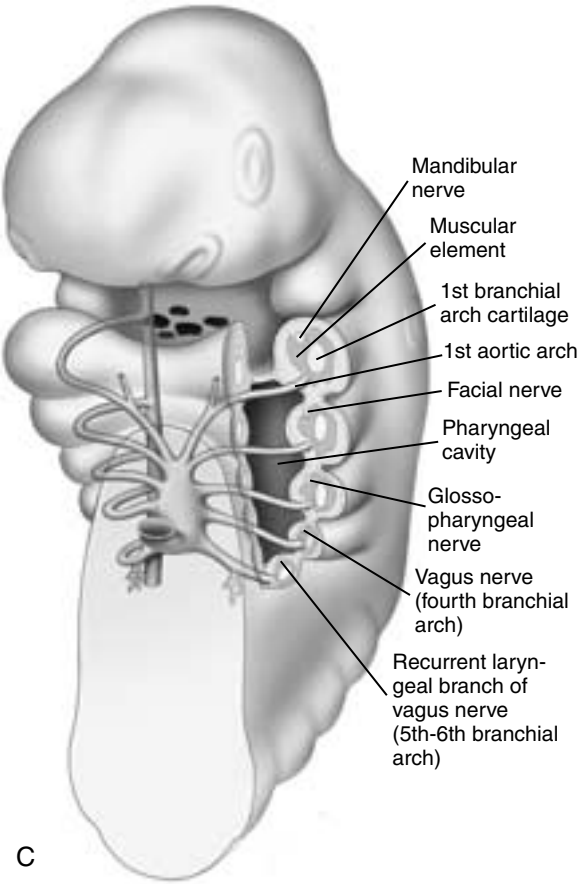

FIGURE 33-2 **A**, Oblique frontal view of a 27-day-old embryo shows the development of the branchial arches and clefts. The corresponding cleft is caudal to its arch. **B**, Oblique frontal view of a 27-day-old embryo shows the pharyngeal pouches within the embryo. The pouches correspond to the arches. Caudally, the lung buds and the connection of the pouches with the foregut are seen. **C**, Oblique frontal view of a 27-day-old embryo shows the aortic sac and the ventral aortic arches and their connection to the right dorsal aorta. On the left side, a wedge of tissue has been removed to expose the artery, nerve, cartilage, and muscular elements within each branchial arch.

Copyright © 2003, Mosby, Inc. All rights reserved.

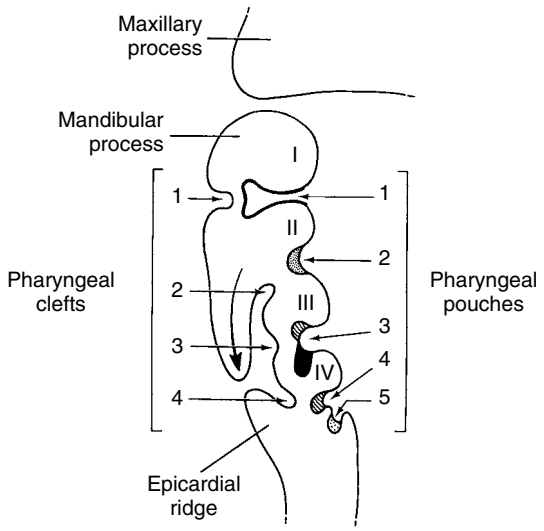

VIEW IMAGE

FIGURE 33-3 Coronal diagram of a 6-week-old fetus shows that the second arch overgrows the third and fourth arches and the epicardial ridge develops to oppose it. This creates the cavity referred to as the cervical sinus of His, which covers the second, third, and fourth arches and clefts. It is the failure of the sinus of His to obliterate that is believed to be the cause of the development of branchial cleft cysts, fistulas, or sinuses. (From Langman J. Medical Embryology, 4th ed. Baltimore: Williams & Wilkins, 1981:274.)

sixth week of gestation. These outpouchings are initially hollow. Rarely, the ventral portion of the fourth pouch gives rise to a rudimentary thymus that lies near the superior parathyroid glands. These outpouchings undergo caudal elongation, being connected to the pharynx by tubular structures referred to as thymopharyngeal ducts. By the end of the sixth week, these connections of the thymic primordia have continued to migrate caudally and medially, their lumina have become obliterated by epithelial proliferation, and the glands have increased in bulk. By the middle of the seventh week, obliteration of the thymopharyngeal ducts is complete, and the two solid masses of primitive thymus approach each other in the midline just below the thyroid gland. At the beginning of the eighth week, the bilateral thymic primordia join in the midline, attach to the pericardium, and begin to descend into the superior mediastinum. By the ninth week of gestation, the thymus is in its final position in the anterior mediastinum, and the elongated stalks through which their descent occurred undergo atrophy and disappear. This is followed by eventual invasion of the thymus by mesenchymal cells, with subsequent degeneration of the primitive endodermal cells into Hassall corpuscles.

The inferior and superior parathyroid glands develop from dorsal portions of the third and fourth pharyngeal pouches, respectively, and are thus sometimes called the parathyroid-3 and parathyroid-4 glands. The inferior parathyroids migrate in either side of the neck along the course of the thymopharyngeal duct, thus following the same caudal elongation pattern as the thymus. Their thymic connection, however, is lost at the level of the thyroid gland, where they reach their final destination near the inferior dorsal aspect of the gland. The dorsal aspect of each fourth pouch forms the superior parathyroid glands. Once these cells lose their connection to the fourth pouch, they attach to the caudally migrating thyroid gland and assume their position near the superior dorsal aspect of the gland. Thus, the craniocaudal relationship between the inferior and superior parathyroid glands is *reversed* due to differential migration, placing the cells derived from pouch three caudal to those derived from pouch four.

The sixth pouch and a portion of the fourth pouch give rise to the ultimobranchial body, which differentiates into glandular tissue that resembles fetal thyroid. Its ultimate fate in the adult is still unclear. However, as noted in the following section on The Tongue and Thyroid Gland, the calcitonin-secreting cells, which are derived from neural crest tissue, are eventually incorporated into both the thyroid gland and the ultimobranchial body.[13]

The Tongue and Thyroid Gland

Development of the thyroid gland begins early in embryonic life, starting between the second and third weeks and virtually finishing by the eleventh week. The thyroid arises simultaneously from three bodies, one median anlage and two lateral anlagen (Fig. 33-5).[16, 17] Although a few embryologists believe that only the median anlage forms the gland, this discussion will assume the majority opinion that the lateral anlagen exist, for without them, it is difficult to reconcile many of the nonmidline ectopic locations of thyroid anomalies.

The first branchial arch is responsible for the formation of the anterior two thirds of the tongue in the form of two anterior lingual swellings that fuse with the median tuberculum impar, which is a more posterior midline swelling. The two lateral lingual swellings overgrow the tuberculum impar and merge to form the anterior two thirds

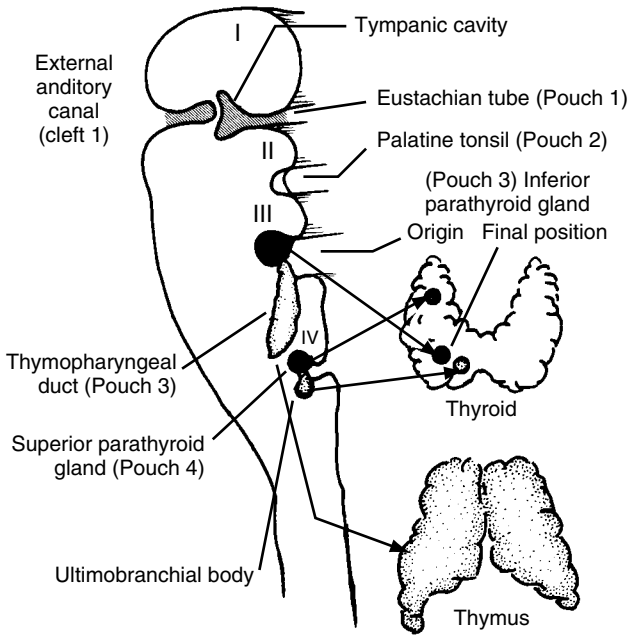

FIGURE 33-4 Coronal diagram showing the migration of the thymus, parathyroid glands, and ultimobranchial body. (Modified from Langman J. Medical Embryology, 3rd ed. Baltimore: Williams & Wilkins, 1975.)

VIEW IMAGE

Copyright © 2003, Mosby, Inc. All rights reserved.

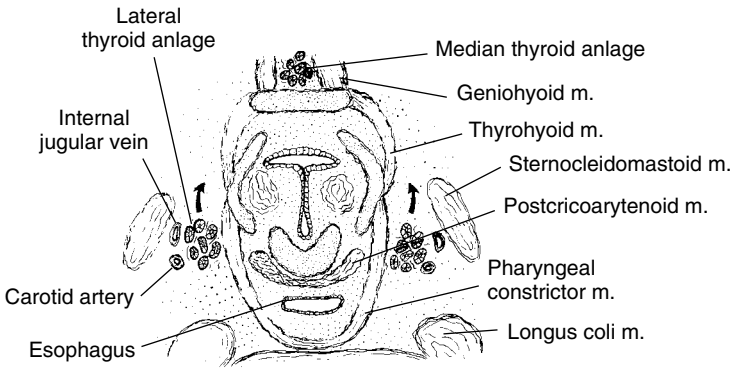

VIEW IMAGE

FIGURE 33-5 Axial diagram showing the position of the median and lateral thyroid primordia in relationship to the developing larynx.

of the tongue (Fig. 33-6). Since these are all first arch structures, the anterior portion of the tongue has its sensory innervation from the mandibular branch of the trigeminal nerve (V), the nerve of the first arch. The posterior third of the tongue is formed from the coalescence of the ventral aspects of the second and third branchial arches, as well as a lesser contribution from the fourth arch. The third arch is felt to be the major contributor to the posterior tongue since the glossopharyngeal nerve (IX), the nerve of the third arch, is responsible for sensory innervation of the posterior third of the tongue. The copula is a median elevation formed by the fusion of the ventromedial portion of the second branchial arch and the hypobranchial eminence, which develops from the mesoderm of the third and fourth branchial arches (Fig. 33-6). The large hypobranchial eminence overgrows the copula, which eventually disappears, and in the adult, the junction line between the ectoderm and endoderm is in front of the row of the vallate papillae. The anterior two thirds of the tongue is demarcated from the posterior one third of the tongue by a V-shaped groove, the terminal sulcus, which lies just behind the vallate papillae (Fig. 33-6).[15]

During the third week, the median thyroid anlage arises as an endodermal thickening, evaginating caudally from the ventral pharyngeal wall, in the midline between the first and second branchial arches, just caudal to the medial tongue swelling between the tuberculum impar and the copula. Thus, this evagination arises from the first pharyngeal pouch at the junction of the developing anterior and posterior portions of the tongue. In the adult, the site of this thickening is the foramen caecum. This thickening forms the thyroid diverticulum, which may start as a single diverticulum but divides very early into two lateral lobes.[16, 18] As the embryo grows, the thyroid diverticulum descends caudally in the neck, acquiring new cells from the surrounding endoderm. These existing cells then begin proliferating.[19] In the earliest stage of thyroid embryogenesis, the median thyroid diverticulum comes in contact with the aortic sac of the developing heart, located immediately below the pharynx. As the heart descends into the thorax, it pulls the median thyroid anlagen down, elongating its pharyngeal connection or stalk (Fig. 33-7). As the thyroid anlage descends, it interacts with the fourth and sixth pharyngeal arches, and by the end of the seventh week, the median thyroid anlage has reached its final position in front of the trachea, with a small median isthmus as well as two lateral lobes having been formed (Fig. 33-8). When the hyoid anlage rotates and fuses, the descending thyroid stalk can become adherent to its periosteum and a portion of the stalk can end up lying

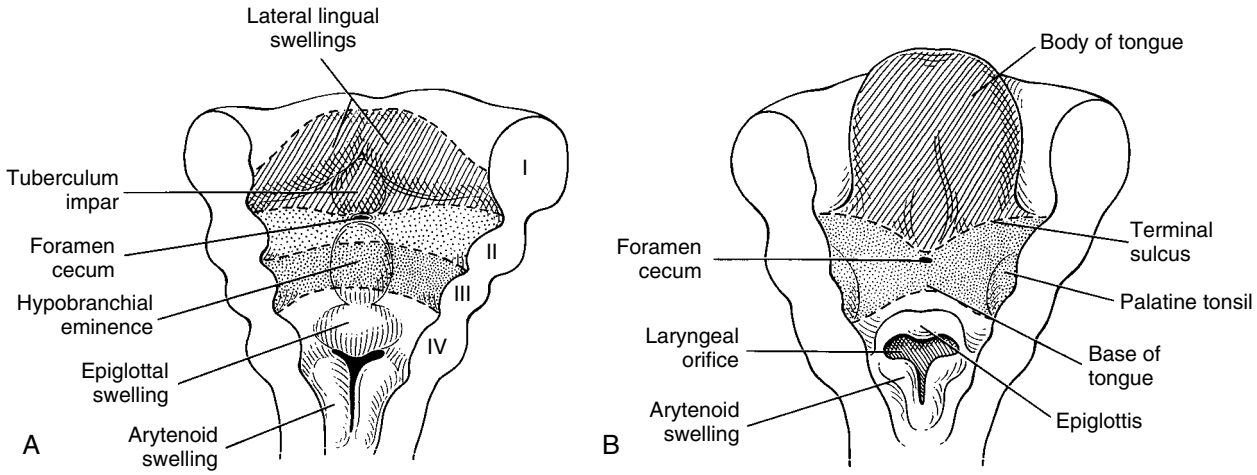

VIEW IMAGE

FIGURE 33-6 Development of the tongue. **A**, Drawing of a 5-week-old fetus shows that one medial (tuberculum impar) and two lateral lingual swellings have appeared, originating from the mesenchyme of the first pharyngeal arch. **B**, Drawing of a 5-month-old fetus shows that the terminal sulcus divides the anterior two thirds of the tongue from the posterior third. The foramen cecum is the site of origin of the thyroid gland. (**A** and **B**, From Langman J. Medical Embryology. 4th ed. Baltimore: Williams & Wilkins, 1981;277.)

Copyright © 2003, Mosby, Inc. All rights reserved.

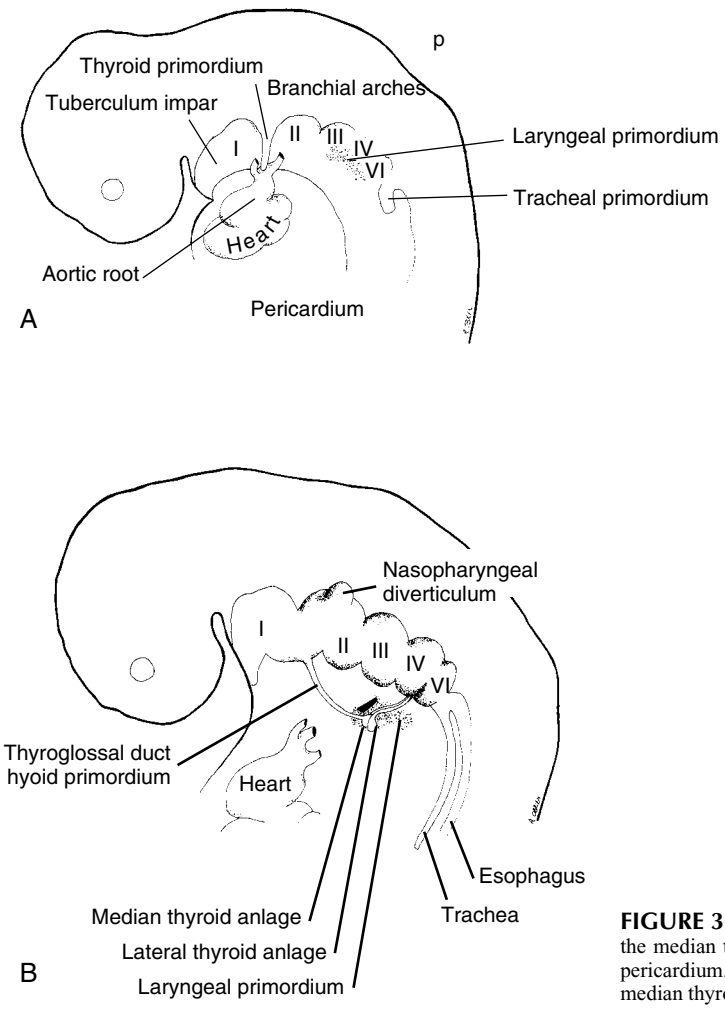

FIGURE 33-7 **A**, Drawing of a sagittal view of an embryo shows the origin of the median thyroid and its relationship to the branchial arch derivatives, aorta, and pericardium. **B**, Drawing of a sagittal view of an embryo shows the interaction of the median thyroid anlage with the branchial mesenchyme and the lateral thyroid anlage.

VIEW IMAGE

posterior to the hyoid bone, after first passing anterior to and then underneath the hyoid body.[20, 21]

Though the median thyroid stalk can be a solid tract of epithelial cells, it usually has a lumen and is referred to as the thyroglossal duct.[16] In fact, it has been shown that the process of pharyngeal evagination, or duct formation, and epithelial proliferation, or obliteration of the duct to form a solid tract, are separate processes. As it descends, the gland expands dorsally and laterally while losing its connection with the foramen cecum (Fig. 33-9). Norris, in 1918, postulated variations in the early development of the median thyroid anlage.[22] He described a pre-anlage stage, which represents the time prior to the appearance of the thyroid anlage. The early anlage stage demonstrates the earliest thyroid primordia with endodermal proliferation and a shallow evagination. Although the early growth stage deals largely with growth of the thyroid primordia, three distinct anatomic variations in form can develop. The connection with the pharynx can be solid, cystic, or bilobed. At the beginning of the separation stage, these three types of connecting stalks lengthen. During the complete separation stage, the thyroid severs its connection with the pharynx in a variety of ways. The separation can occur anywhere along the descent of the thyroid, and at this time, the gland itself can also have wide variation in form.

As previously mentioned, the existence of the lateral thyroid anlagen remains controversial; however, many nonmidline ectopic thyroid anomalies are best explained by the existence of such structures. The lateral lobes of the thyroid are thought to receive contributions from the ventral portion of the fourth and sixth branchial pouches, also called the caudal pharyngeal complex. In mammals, this lateral pharyngeal diverticulum is called the ultimobranchial body. As the median thyroid descends and interacts with this portion of the branchial apparatus, it loses its attachment to the aortic root. As the lateral anlagen migrate anteriorly, they fuse with the median thyroid anlage and simultaneously, during the sixth week of gestation, detach from the pharynx (Fig. 33-10). The contribution to the adult thyroid gland from these lateral thyroid primordia varies from 0% to 33% of the total gland volume.[16, 23]

The calcitonin-producing parafollicular cells originate from neural crest cells, which are of ectodermal origin, adjacent to the fourth and sixth pharyngeal pouches. These cells migrate and eventually become incorporated into the lateral thyroid primordia to form the ultimobranchial bodies (Fig. 33-11).

The morphogenesis of the thyroid gland is characterized by a proliferation of cells in the rudimentary thyroid that is followed by organization into double cellular plates. By the

Copyright © 2003, Mosby, Inc. All rights reserved.

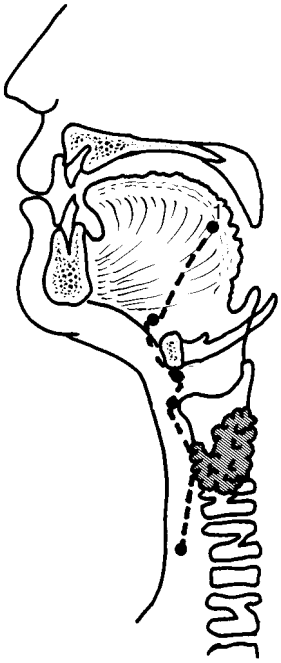

VIEW IMAGE

FIGURE 33-8 Lateral view drawing of the neck showing the path of descent of the median thyroid anlage. The path brings the tract against the anterior face of the developing hyoid bone. As the bone rotates to its adult position, the adherent tract is pulled up behind the lower body of the hyoid bone.

eighth week, these differentiate further into primary thyroid follicles, and secondary follicles result from further budding and subdivision.[24] Between the tenth and eleventh weeks of gestation, the fetal thyroid develops the ability to trap and organify iodine to form thyroxine.[25] The arterial blood supply for the developing thyroid anlage is acquired by the eighth week of gestation from the extensive fetal capillary network of the branchial arches supplied by the carotid and branchiocephalic systems.[16] The pathology of the thyroid gland is discussed in Chapters 37 and 40.

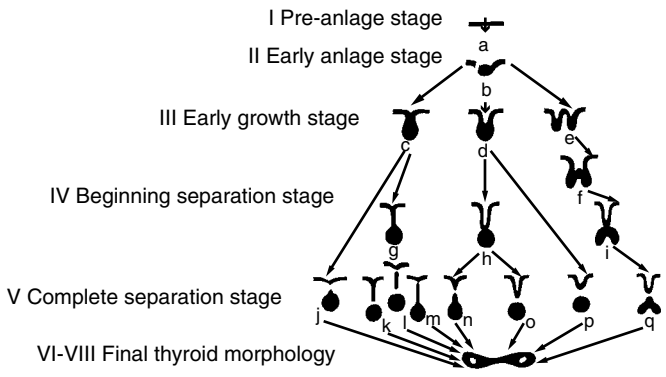

VIEW IMAGE

FIGURE 33-9 Schematic drawing of early developmental variations of the median thyroid anlage. The solid black areas represent epithelium arising from the pharyngeal floor, which eventually forms the thyroid gland over the depicted stages of thyroid morphogenesis. (Modified from Norris EH. The early morphogenesis of the human thyroid gland. Am J Anat 1918;24:443–466.)

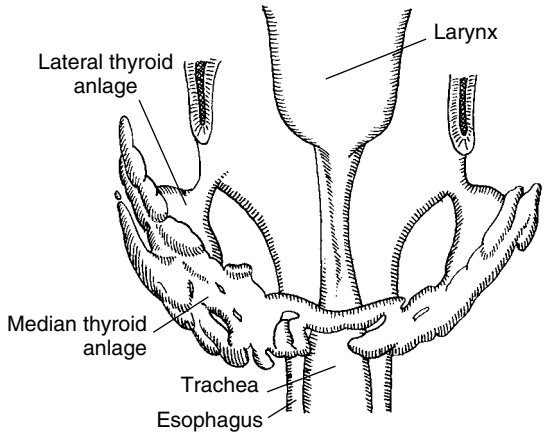

FIGURE 33-10 Drawing of the lateral thyroid anlage fusing with the median anlage before separation from the pharynx. (Modified from Weller GL. Development of the thyroid, parathyroid, and thymus glands in man. Contrib Embryol Carnegie Inst Wash 1933;24:93–142.)

VIEW IMAGE

Pharynx, Larynx, and Trachea

The respiratory primordium begins at about the fourth week of gestation with the formation of the laryngotracheal groove, which extends lengthwise in the floor of the gut just caudal to the pharyngeal pouches (Fig. 33-12). This groove deepens into the laryngotracheal diverticulum, whose ventral endoderm will become the larynx and trachea, while the more caudal endoderm will give rise to the bronchi and lungs. Lateral furrows develop on either side of the laryngotracheal groove or diverticulum, at the level of the junction between the groove and the future esophagus. These furrows gradually deepen and extend cephalad, elongating this structure to form the primitive laryngotracheal tube. The lateral furrows join, splitting off first the lung bud and then the trachea. The upper end of this tube advances slightly cephalad until it lies between the fourth branchial arches, and this region will form the primitive laryngeal aditus. A tracheoesophageal septum develops caudally to cranially and separates the respiratory system from the esophagus.[26]

It is at the end of the fourth week of gestation that the single lung bud appears at the caudal end of the laryngotracheal tube (Fig. 33-13). This bud soon divides into right and left bronchial buds, and these grow caudally and laterally into the pericardioperitoneal cavities. The primitive lung buds then subdivide into secondary and tertiary bronchi. Throughout fetal development, the surrounding pulmogenic mesoderm continues to develop into the lung parenchyma.[27]

The larynx develops on the proximal end of the laryngotracheal groove between the fifth and sixth gestational weeks, as three swellings appear at the laryngeal aditus. The anterior swelling, which is the future epiglottis, may be a derivative of the hypobranchial eminence from the fourth arch, although its actual origin and relationships to the branchial arches remain unclear. It should be noted that in contrast to the first, second, and third arches, little is clearly known about the precise development of the *caudal* arches, the fourth through sixth arches.[9] The two lateral masses give rise to the future arytenoids, from the fourth or fifth-sixth arches. These two lateral swellings migrate cranially and

Copyright © 2003, Mosby, Inc. All rights reserved.

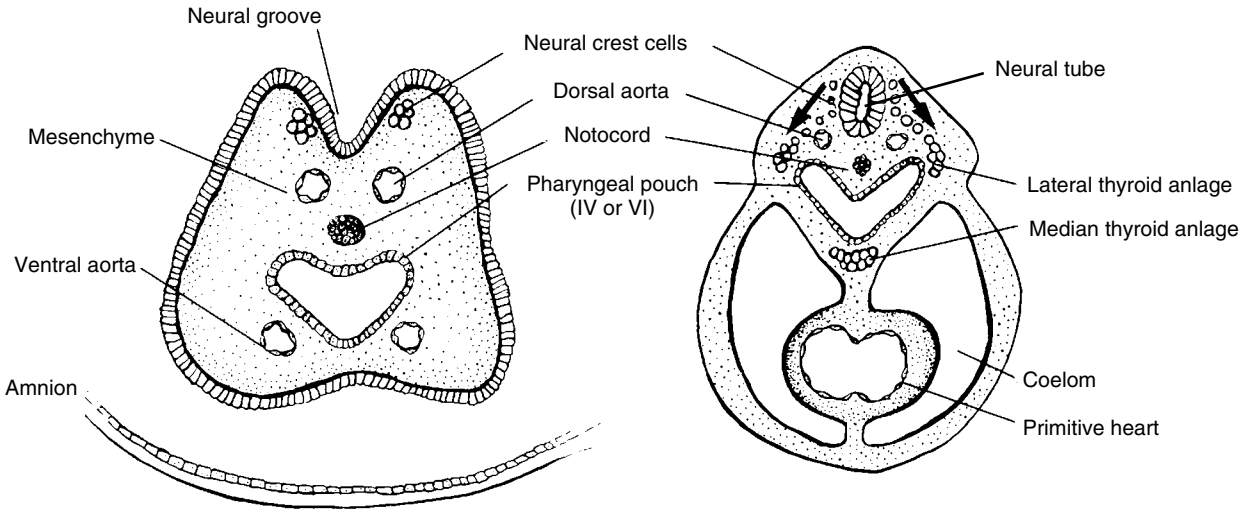

FIGURE 33-11 Drawings depicting the anatomic location of the neural crest cells as they migrate and incorporate into the lateral thyroid anlage (ultimobranchial body) during embryogenesis.

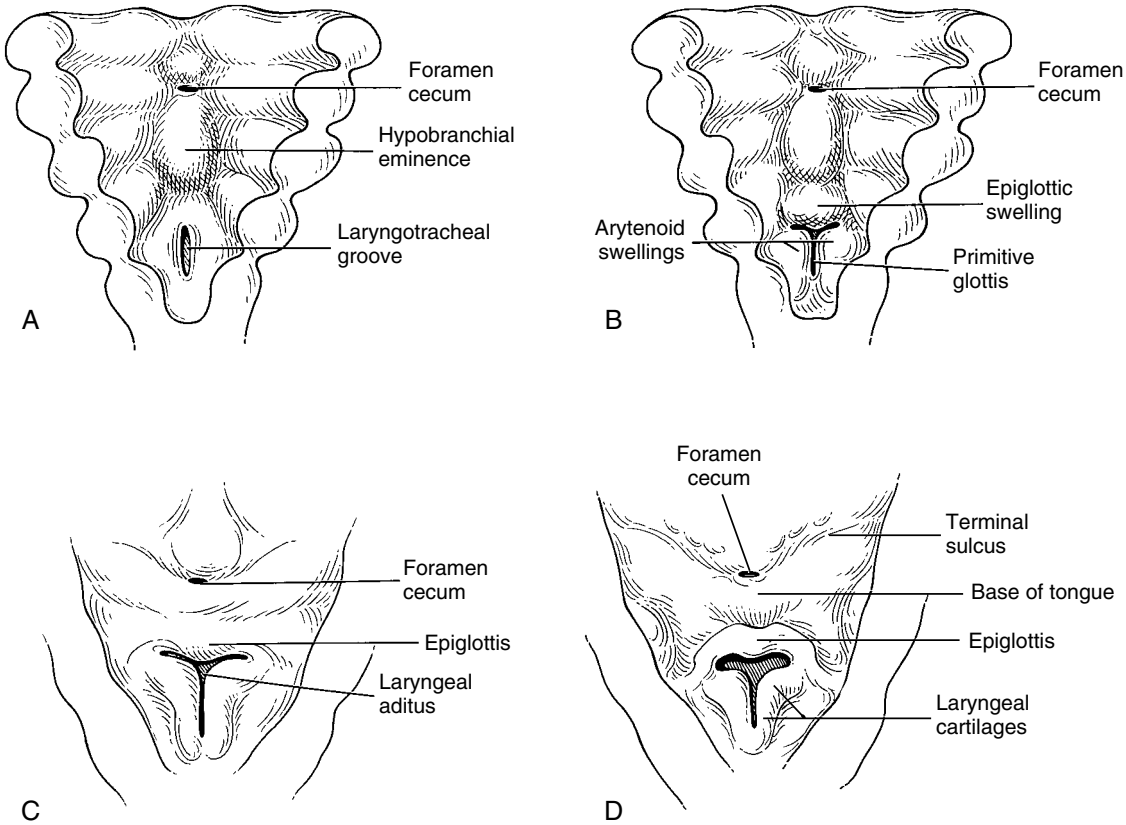

FIGURE 33-12 Development of the larynx. **A**, Drawing of 4- to 5-week-old fetus shows that the larynx develops on the proximal end of the laryngotracheal groove. **B**, Drawing of a 5-week-old fetus shows that the paired arytenoid swellings are found lateral to the laryngeal aditus. The anterior midline swelling, the future epiglottis, is a derivative of the hypobranchial eminence. **C**, Drawing of a 6-week-old fetus shows that the arytenoid swellings have migrated medially and toward the tongue, and the laryngeal aditus has become T-shaped. The laryngeal lumen is only a slit. **D**, Drawing of a 10-week-old fetus shows that the laryngeal cartilaginous and muscular structures have formed from the fourth and sixth branchial arches. (From Moore KL, Persaud TVN. The Developing Human. 5th ed. Philadelphia: WB Saunders, 1993;228.)

Copyright © 2003, Mosby, Inc. All rights reserved.

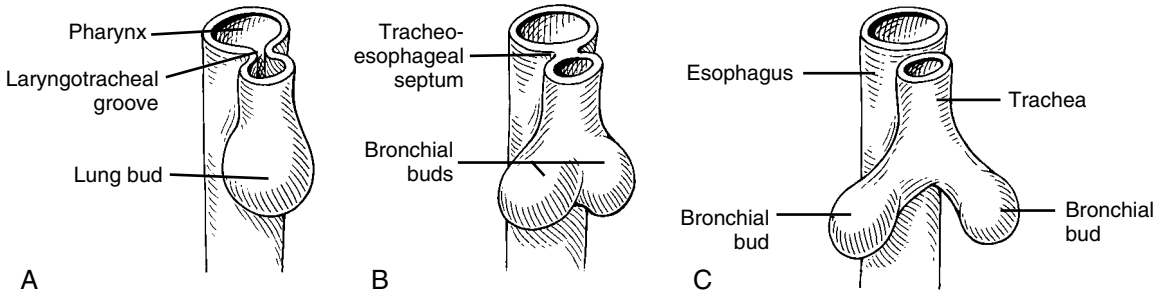

VIEW IMAGE

FIGURE 33-13 Development of the respiratory system. **A**, Drawing of a 4-week-old fetus shows the laryngotracheal groove developing from the ventral wall of the primitive pharynx. The proximal portion will be the future laryngeal aditus. **B**, Drawing of a 4- to 5-week-old fetus shows that the tracheoesophageal septum now separates the laryngotracheal tube from the primordium of the esophagus. The bronchial buds will become the bronchi. **C**, Drawing at a slightly later stage of development shows that the esophagus and the trachea are now completely separate. A tracheoesophageal fistula is an abnormal persistence of the original communication between the trachea and the esophagus (**A**). (From Moore KL, Persaud TVN. The Developing Human. 5th ed. Philadelphia: WB Saunders, 1993;227.)

medially to oppose each other and, together with the epiglottic swelling, surround a T-shaped laryngeal aditus.[28, 29] The laryngeal lumen becomes occluded at eight weeks of gestation due to epithelial proliferation. If normal recanalization does not occur during the tenth gestational week, a laryngeal web results. The formation of the vocal (true) and vestibular (false) folds (cords) is related to the condensation of mesenchyme and the outpouching of the laryngeal sinus or ventricle. The two vocal folds separate during the third gestational month, and failure of this recanalization process results in congenital atresia of the larynx.

The laryngeal cartilages develop from the branchial arches, with the more cranial cartilages possibly arising from the fourth arch and the more caudal ones from the sixth (with the caveat that the epiglottis may not be arch derived, as mentioned above) (Fig. 33-14). The thyroid cartilage develops from the fourth arch as two lateral plates that fuse in the midline. This process is almost completed by the ninth gestational week. The cricoid cartilage appears to begin as

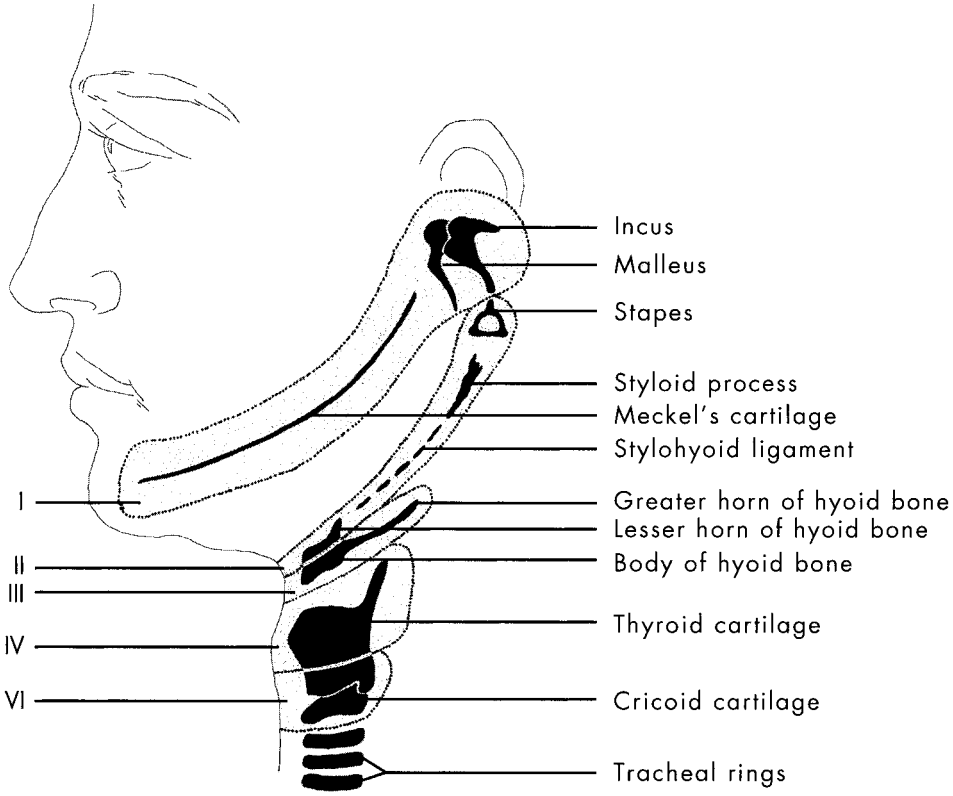

VIEW IMAGE

FIGURE 33-14 Diagram of the lateral face and neck showing the cartilaginous derivatives of the branchial arches. (Modified from Langman J. Medical Embryology, 3rd ed. Baltimore: Williams & Wilkins, 1975.)

Copyright © 2003, Mosby, Inc. All rights reserved.

two cartilaginous centers of the sixth arch. First, the centers grow and unite in the ventral midline; then, by the seventh gestational week, they fuse dorsally. The rostral advancement of the tracheoesophageal septum results in the fusion of the dorsal cricoid lamina. Failure of advancement of this septum results in a fistula. At first, the cricoid lumen is slit-like in shape, but eventually the ventral and lateral walls of the cricoid cartilage condense and there is progressive enlargement of the lumen. Failure of this condensation process results in congenital subglottic stenosis.

The arytenoid cartilages develop from the arytenoid swellings, most likely derivatives of the sixth arch but possibly arising from the fourth arch. They are initially fused to the cricoid cartilage, but they eventually separate from it and form the cricoarytenoid joints. The origins of the corniculate and cuneiform cartilages remain unclear. The intrinsic laryngeal muscles develop from the mesoderm of the fourth through sixth arches.[28, 29]

The tracheal tube elongates, and the future carina or point of bifurcation descends caudally eight somite segments. The right bronchus descends more directly than the left bronchus, a relationship that is maintained in the adult. The smooth muscle fibers and the cartilaginous tracheal rings differentiate from the surrounding mesenchyme at the end of the seventh week. The minor salivary glands develop as ingrowths from the epithelium after four months of gestation.[30]

Branchial Arches

As mentioned earlier, specific osseous, cartilaginous, and vascular structures arise from each branchial arch. However, the muscles of the different arches do not necessarily attach to the osseous or cartilaginous components of their own arches. In some cases, the muscles may migrate to the surrounding regions; however, the origins of these muscles can always be established through their nerve supply, which comes from their arch of origin.

The first or mandibular pair of branchial arches are the precursors of the jaws. On either side of the face, the first arch borders the lateral margin of the stomodeum. The maxilla is derived from the small maxillary prominence that extends ventrally from the much larger mandibular prominence (Fig. 33-15). The cartilage skeleton of the first arch is Meckel's cartilage, which can be identified between 41 and 45 days of gestation. Most of this cartilage disappears in the formed mandible. The smaller dorsal portion of this cartilage is related to the developing ear and eventually becomes ossified to form the upper portions of the malleus and incus. The intermediate portion of this cartilage regresses, and its perichondrium forms the anterior ligament of the malleus and the sphenomandibular ligament. The ventral portion of this cartilage largely disappears, and the mandible is formed around it by secondary intramembranous ossification (Fig. 33-14). The trigeminal or fifth cranial nerve (V) is the nerve of the first arch, and it innervates the muscles of the first arch, which include the muscles of mastication (the medial and lateral pterygoids, the masseter, and the temporalis), the mylohyoid, the anterior belly of the digastric, the tensor tympani, and the tensor veli palatini muscles. In addition to this motor supply, the trigeminal nerve provides sensory supply to the region of the first branchial arch, that is, the mandible, its covering mucosa and gingiva, the mandibular teeth, the mucosa of the anterior two thirds of the tongue, the floor of the mouth, and the skin of the lower one third of the face. The first arch artery contributes to portions of the maxillary artery and the common carotid artery.

Reichert's cartilage, the cartilage of the second branchial or hyoid arch, appears between 45 and 48 days of gestation. The dorsal margin of the second arch is also closely related to the middle ear and ossifies to form the manubrium of the malleus, the long process of the incus, the crura of the stapes, and the styloid process of the temporal bone. The footplate of the stapes is not a branchial arch derivative, as it is derived from the otic capsule.[1] The portion of the cartilage between the styloid process and the hyoid bone regresses, and its perichondrium forms the stylohyoid ligament. (It is interesting to note that many adult mammals exhibit a chain of bony elements spanning the styloid process and the hyoid bone [Fig. 33-14].[31])

The ventral end of Reichert's cartilage ossifies to form the lesser cornuae (horns) and the upper portion of the body of the hyoid bone. The muscles of the second arch include the posterior belly of the digastric, the stylohyoid, the stapedius, and muscles of facial expression, all of which are supplied by the nerve of the second branchial arch, the facial nerve (VII). Other than a small sensory branch of cranial nerve VII that may supply a portion of the external auditory canal, there is no sensory distribution from cranial nerve VII to the ectodermal derivatives.[1] The main sensory component of the facial nerve, the chorda tympani, invades the first arch as a pretrematic nerve (i.e., a nerve that joins the nerve of the arch above by traveling over the ''trema'' or inter-arch cleft). The chorda tympani is thus carried in a branch of the trigeminal nerve to supply (taste) to the mucosa of the anterior two thirds of the tongue. The artery of the second arch is the stapedial artery, which disappears during the fetal period. Its prior location is marked by the stapes' central foramen, the gap between the stapes crura. Portions of the stapedial artery persist as part of the internal carotid artery proximally and the external carotid artery distally.

The cartilage of the third branchial arch ossifies to form the greater cornu and lower portion of the body of the hyoid bone (Fig. 33-14). The musculature of this arch is limited to the stylopharyngeus muscle, which is innervated by the nerve of the third arch, the glossopharyngeal nerve (IX). Because the mucosa of the posterior one third of the tongue is also derived from the third branchial arch, its sensory innervation is supplied largely by the glossopharyngeal nerve. Neural crest tissue in the third arch forms the carotid bodies that appear as mesenchymal condensations about the third aortic arch artery. Thus, the glossopharyngeal nerve (IX) supplies innervation to the carotid body.[14] The artery of this arch contributes to the common carotid artery and part of the internal carotid artery.

The cartilages of the fourth and fifth-sixth branchial arches fuse to form the larynx, although the precise arch of origin for some of the laryngeal structures clearly remains uncertain. Overall, it is believed that the line of division between the fourth and sixth arches is the vocal folds (true vocal cords). It is generally thought that all laryngeal

Copyright © 2003, Mosby, Inc. All rights reserved.

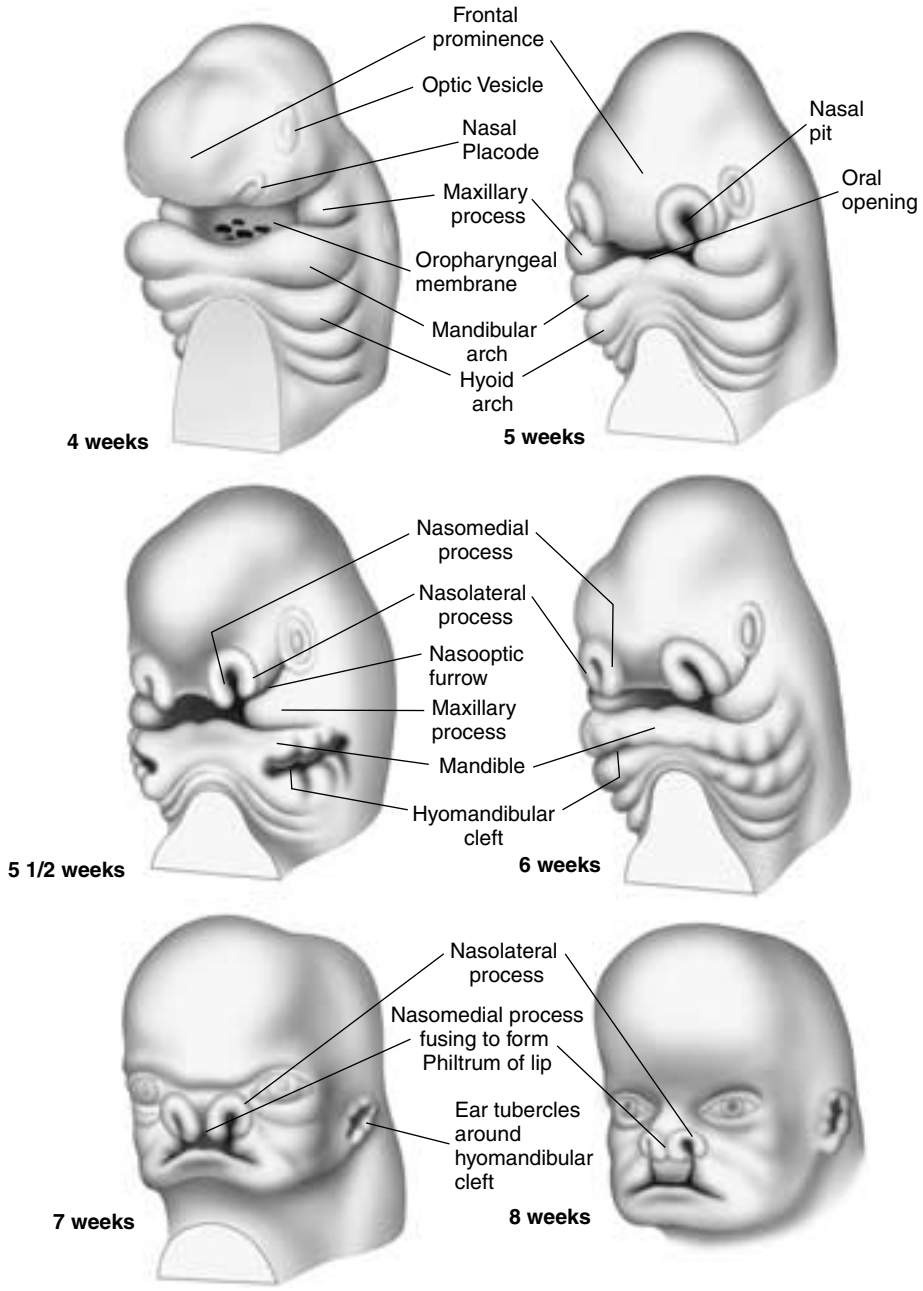

VIEW IMAGE

FIGURE 33-15 Drawings of the embryogenesis of the normal face at approximately 4, 5, 5½, 6, 7, and 8 weeks.

cartilages (with the possible exception of the epiglottis) are derived from the fourth through sixth arches (Fig. 33-14). It would appear logical that the cartilages are laid out in a craniocaudal arrangement corresponding to their arches of origin, but this remains to be shown (see the prior discussion on laryngeal embryology). The cricothyroid and constrictor muscles of the pharynx are derived from the fourth branchial arch. They are innervated by the nerve of this arch, the superior laryngeal branch of the vagus nerve (X), which also gives sensory innervation to the mucosa of the larynx above the vocal folds. The muscles of the fifth-sixth branchial arches are the intrinsic muscles of the larynx, innervated by the nerve of the sixth arch. This nerve is generally believed to be the cranial portion (i.e., *cranial root*) of the spinal accessory nerve (CN XI) whose fibers join the vagus (CN X) and are distributed within its recurrent laryngeal branch. The striated muscles of the upper half of the cervical esophagus are also derived from the sixth arch. The caudal portion of the esophagus is composed of smooth muscle and is derived from the splanchnic mesoderm of the primitive foregut.[1] In addition, the para-aortic bodies of chromaffin cells that secrete noradrenalin arise from the ectomesenchyme of the fourth and sixth arches.[14]

The left artery of the fourth arch forms the aortic arch. The right arch artery contributes to the right subclavian artery and the brachiocephalic arteries. The sixth arch arteries develop in part into the pulmonary arteries. The remainder of the artery disappears on the right side, while on the left side it forms the fetal ductus arteriosus that in the adult becomes the ligamentum arteriosum.

Copyright © 2003, Mosby, Inc. All rights reserved.

Of all the branchial clefts, only the first cleft contributes directly to an adult structure. It persists as the epithelium of the external auditory canal. The other branchial clefts, together with the cervical sinus of His, normally are obliterated as the neck develops.

In summary, the mesenchyme of the first branchial arch gives rise to the muscles of mastication (and some nonmasticatory muscles such as the tensor tympani and tensor veli palatini) and some of the swallowing muscles. The second arch mesenchyme gives rise to the muscles of facial expression (and some other muscles, such as the posterior belly of the digastric and stapedius). The mesenchyme of the third, fourth, and fifth-sixth arches merges into the palatofaucial, pharyngeal, and laryngeal muscles. The orofacial muscles are the first to develop in keeping with the craniocaudal sequence of fetal development.[12]

The specific adult derivatives of the branchial arches, their clefts and pouches, are summarized in Table 33-1.[32]

Table 33-1
DERIVATIVES OF THE BRANCHIAL ARCH ECTODERM, MESODERM, ENDODERM, ARTERIES, AND THE SPECIFIC ARCH NERVES

Arch	Ectodermal	Endodermal	Mesodermal	Arch Arteries	Nerve
First	External auditory canal and external layer of the tympanic membrane, contributes to anterior tongue mucosa	Eustachian tube, mucosa of middle ear, mastoid, and inner layer of tympanic membrane (from dorsal tubotympanic recess)	Malleus head and neck, incus body and short process, mandible and teeth, anterior ligament of malleus, sphenomandibular ligament, facial bones, middle layer of tympanic membrane, muscles of mastication, tensor tympani, tensor veli palatini, anterior belly of digastric, mylohyoid	External carotid and maxillary artery	Trigeminal (V); sensory V_1, V_2, V_3; motor V_3
Second	Skin of anterior triangle, contributes to anterior tongue mucosa	Tonsillar fossa and part of palatine tonsil	Manubrium of malleus, long process of incus, stapes crura, upper body and lesser cornua of hyoid, styloid process, stylohyoid ligament, muscles of facial expression, posterior belly of digastric, platysma, stapedius muscle, stylohyoid muscle, posterior belly of digastric muscle	Stapedial artery, ?part of facial artery	Facial (VII) motor to facial muscles, sensory to anterior two thirds of tongue
Third	Contributes to posterior tongue mucosa	Inferior parathyroid glands, thymus	Lower body and greater cornua of hyoid stylopharyngeus	Proximal one third of internal carotid artery, common carotid artery; cephalic portion fuses with dorsal aorta to form proximal internal carotid artery	Glossopharyngeal (IX) motor to pharyngeal plexus, sensory to posterior one third of tongue
Fourth	Skin of lower neck	Superior parathyroid glands, ultimobranchial body	Epiglottis, thyroid, and cuneiform cartilages, pharyngeal constrictors, some laryngeal muscles, ?palatoglossus	Arch of aorta (left), proximal right subclavian	Superior laryngeal nerve (X)
Fifth			Corniculate, arytenoid, and cricoid cartilages, some laryngeal muscles, striated muscles of cervical esophagus	Proximal part of both pulmonary arteries and ductus arteriosus	Recurrent laryngeal nerve (X)
Epipericardial Ridge			Sternocleidomastoid, trapezius muscles, infrahyoid muscles and muscles of the floor of the mouth, ?tracheal cartilages		Spinal accessory (XI), hypoglossal (XII)

Modified from Sperber GH, The branchial arches. In: Sperber G, ed. Craniofacial Embryology. London: Wright, 1989;64–65.

Copyright © 2003, Mosby, Inc. All rights reserved.

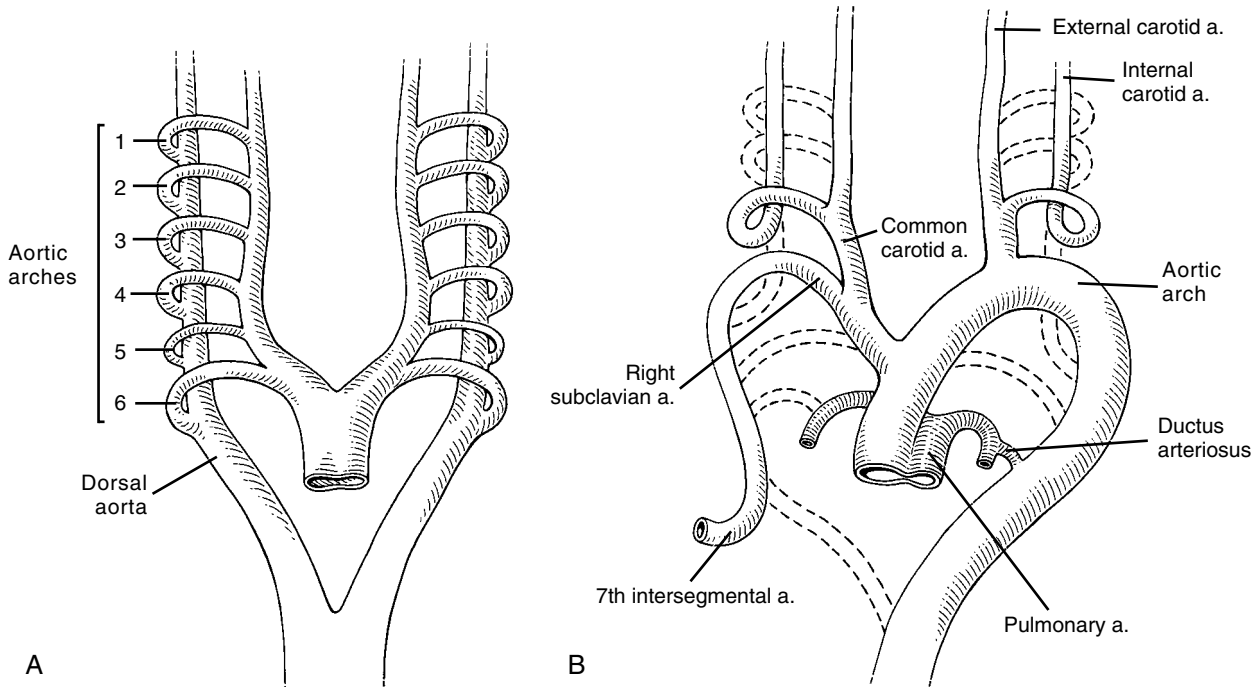

VIEW IMAGE

FIGURE 33-16 Development of the great vessels. **A**, Diagram of the paired dorsal and ventral aortas, which are connected by six pairs of aortic arches. Each of the six paired aortic arches is the arterial component of a branchial arch. **B**, Diagram at a later stage of development shows that the first, second, and fifth arches have disappeared (*broken lines*). Errors in the obliterative process result in vascular rings. (From Langman J. Medical Embryology. 4th ed. Baltimore: Williams & Wilkins, 1981;186.)

EMBRYOLOGY OF THE AORTIC ARCHES

A review of the vascular anatomy of the branchial apparatus aids in understanding the basis for classification of second, third, and fourth branchial anomalies. Each branchial arch contains an aortic arch that connects the paired dorsal and ventral aortas (Figs. 33-2C and 33-16). Although six pairs of aortic arches develop, they are not all present at the same time. The first two arches involute by the time the sixth pair is formed.[33] Parts of the maxillary artery and portions of the external carotid artery appear to be remnants of the transient first aortic arch.

The dorsal segment of the second arch artery transiently persists in fetal life as the *stapedial artery*, around which the stapes crura ossify. Rarely, this artery may persist in the adult. This is discussed in Chapter 26.

The third arch artery on either side persists, forming the common carotid artery and the proximal portion of the internal carotid artery. The origin of the external carotid artery is controversial.[33–35] It arises from either the persistence of the ventral aorta or the surrounding mesenchyme. In either case, it connects with the ventral aspect of the third aortic arch. The dorsal aspect of the third arch artery also fuses with the primitive cephalic portion of the dorsal aorta to form the remainder of the internal carotid artery.

The right fourth arch artery becomes the proximal portion of the right subclavian artery, while the left fourth arch artery forms part of the postnatal aortic arch. The fifth arch arteries appear to involute (which, if any, arteries are derived from it remains unclear), and the sixth pair form the pulmonary arteries and ductus arteriosus.

All of the branchial arch nerves lie cranial to the respective arch artery, except the nerve of the sixth arch, the recurrent laryngeal nerve, which lies caudal to its arch artery on the left side. Since the sixth artery persists as the ductus arteriosus into fetal life and sometimes beyond, the recurrent laryngeal nerve on the left side curves around this structure or its adult counterpart, the ligamentum arteriosum. On the right side, the dorsal portion of the sixth arch artery disappears, so that there is no ductus arteriosus on the right. This results in the right recurrent laryngeal nerve coursing under the next most cranial persisting arch vessel, the fourth, which is the subclavian artery.

In some patients, a retroesophageal right subclavian artery develops because of the persistence of the right dorsal aorta distal to the origin of the seventh dorsal intersegmental artery (the right subclavian artery). The sixth arch artery disappears distal to the point of origin of the pulmonary artery, and the right recurrent laryngeal nerve is shifted cranially, to course around the next most cranial persisting arch artery, the right internal carotid artery. Thus the right recurrent laryngeal nerve descends almost vertically near the internal carotid artery to then enter the larynx. This situation is called a nonrecurrence of the right recurrent laryngeal nerve. In these patients, the right subclavian artery arises from the dorsal aorta beyond the left subclavian artery, and then the right subclavian artery passes behind the esophagus.

Copyright © 2003, Mosby, Inc. All rights reserved.

EMBRYOLOGY OF THE VEINS

There are three systems of paired veins that can be identified in the 20 somite (about 3 mm long) embryo: the umbilical veins from the chorion, the vitelline veins from the yolk sac, and the cardinal veins from the embryo itself.[30] There are actually two sets of cardinal veins, the precardinals that drain blood from the region of the head and the postcardinals that drain blood from regions caudal to the heart. Both pairs of cardinal veins unite at the heart in the short common cardinal veins (ducts of Cuvier).

Each precardinal (or anterior cardinal) vein actually consists of two veins. One is the primary head vein, which courses ventrolateral to the meninges and calvaria, except at the most caudal end of the head, and eventually develops into the cerebral veins and the dural sinuses. The other is the precardinal vein (the *true* precardinal vein) itself, which is laterally situated in the segmented portion of the head and neck and empties into the common cardinal vein. These true precardinal veins start near the base of the head and run caudally into the heart (Fig. 33-17). During the eighth fetal week, an oblique cross-channel develops (the intercardinal vein), which shunts blood from the left precardinal vein to the right one. As a result of this diversion of blood, the caudal portion of the left precardinal vein loses its communication with the common cardinal vein on the left side and survives in the adult as the highest intercostal vein and most of the inconstant oblique vein of the left atrium.[30]

The right common cardinal vein and the right precardinal vein, up to the level of the intercardinal vein, become the superior vena cava. The intercardinal vein itself becomes the left brachiocephalic (innominate) vein. The portion of the right precardinal vein between the intercardinal vein and the subclavian vein becomes the right brachiocephalic vein. Even more cephalad, the precardinal veins continue as the internal jugular veins. The external jugular veins and the subclavian veins are both extraneous vessels that develop independently and attach secondarily.[15, 30]

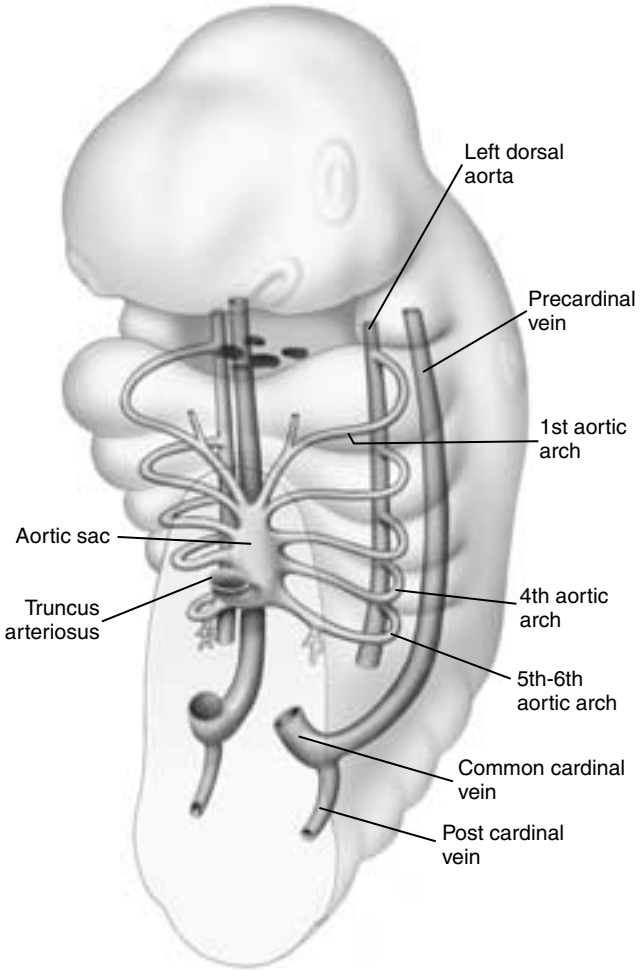

FIGURE 33-17 Oblique view of a 27-day-old embryo shows the developing arterial system and its relationship to the developing venous system.

VIEW IMAGE

EMBRYOLOGY OF THE LYMPHATIC SYSTEM

The development of the lymphatic system remains controversial. A number of different theories regarding their embryology have been proposed.[36]

Florence Sabin, in the early twentieth century, first proposed the theory that the lymphatics are formed from sprouts that arise from large central veins in certain locations. These sprouts then almost immediately demonstrate their own lymphatic character and form the primordial lymph sacs. Subsequently, the sacs enlarge, coalesce, and form new sprouts that grow in the periphery of the embryo (centrifugal spread).[37–39]

Huntington and McClure and then Kampmeier proposed that the lymphatic system develops independently of the mesenchyme. They believed that lymphatics are formed from the confluence of mesenchymal spaces in the periphery of the embryo. These lymphatic spaces spread centripetally by annexing other similar spaces, and anastomoses are eventually established with the venous system centrally.[40–43]

Van de Jagt and Kutsuna believed that the lymphatics originate from the confluence of small venules with spaces in the adjacent mesenchyme. These confluent spaces subsequently develop a lymphatic character.[44, 45]

S.C.J. van der Putte observed that the lymphatic system in humans arises from seven double and two single isolated primordia. He agreed with Sabin that the lymphatics are most likely of venous origin and that their subsequent development is due to centrifugal growth and sprouting.[46]

Today the most popular theory is closer to that proposed by Huntington, McClure, and Kampmeier in that it is believed that the lymphatic system originally develops in mesenchyme, independently of the venous system, and only later does any communication occur between the two systems. The lymphatics appear to develop as discrete mesenchymal lacunae with flattened mesenchymal cells, or endotheliocytes, bordering each space, and it is these cells that evolve into the endothelial cells of the lymphatics.[47–49]

The first spaces develop along the main primitive venous trunks near the anterior cardinal veins, at the site where eventually the primitive left and right internal jugular veins will meet the subclavian veins (Fig. 33-18). From these spaces sprouts develop, branch, and anastomose to form the jugular sacs at about six weeks of gestation. From these sacs,

Copyright © 2003, Mosby, Inc. All rights reserved.

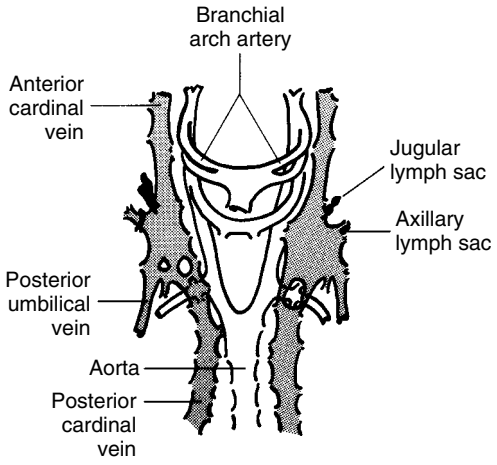

VIEW IMAGE

FIGURE 33-18 Eleven mm human embryo (about 7½ weeks' gestational age). Large prevertebral blood vessels and first lymphatic primordia are shown. The jugular and axillary lymph sacs are quite small. They communicate with the anterior cardinal veins as blind-ending vessels.

lymphatic capillary beds spread to the neck, head, arms, and thorax. The more direct channels of these capillary beds enlarge to form the lymphatic vessels, and the larger vessels acquire smooth muscle coats, nerve connections, and eventually contractility (Fig. 33-19).

The jugular sacs are the only primitive sacs to acquire permanent connections with the venous system. The jugular sacs unite with each other and meet upgrowths from the cysterna chyli to produce the longitudinally coursing thoracic duct, which links the several lymphatic sacs in the body into a common system.[47–50] The jugular sac at the cranial termination of the thoracic duct bends and extends caudally to form a connection with the left subclavian vein.

The most popularly held view is that in the mesenchyme surrounding the lymphatic plexuses, groups of mesenchymal cells differentiate independently into hemopoietic centers that eventually produce cells that subsequently organize into lymph node structures. The primary lymph nodes begin to develop during the third month of gestation in the capillary lymphatic plexuses that were formed out of the large lymph sacs as the sacs start to break down. That is, the primary lymph nodes arise from the transformation of the lymphatic sacs into plexuses, eventually giving rise to the lymph node chains. Secondary lymph nodes develop later, even after birth, in peripherally located capillary lymphatic plexes.[47–49] The structural and functional unit of a lymphatic vessel is the lymphangion, and it is the circular layer of smooth muscle of the lymphangion's wall that seems to play a basic role in the pumping function of the lymphangions.[51]

More specifically, this concept suggests that the lymph nodes develop from groups of mesenchymal cells that become surrounded by a network of lymphatic vessels. The mesenchymal cells develop into the lymphocytes, reticular cells, and fibroblasts of the lymph node, while the lymph node sinuses arise from the surrounding lymphatic network. Parallel with this multiplication of lymphocytes, the surrounding mesenchyme forms a connective tissue capsule and the hilum of the node. Some researchers believe that it is from the capsule that trabeculae carrying blood vessels grow into the lymphoid tissue. Others believe that it is from the hilar region that the trabeculae and vessels spread into the node. In the larger trabeculae, collagenous fibers are laid down and continue as reticular fibrils into smaller trabeculae. The mesenchymal cells of the larger trabeculae become fibroblasts, while those accompanying the reticular fibrils become reticular cells. The marginal sinuses of the node can be identified in the fifth fetal month, while a true nodal cortex with germinal centers is identified mostly after birth.[47–49]

It is also now known that the cell surface ligand (lymphotoxin LT) is involved in immune organ morphogenesis. That is, exposure to LT beta-R-IG during gestation can disrupt lymph development and splenic architecture.[52] It has also been shown in mice that during fetal and early neonatal life, when only mucosal addressin MadCAM-1 is expressed on high endothelial venules, an unusual subset of CD4+ CD3− cells, exclusively expressing alpha 4 beta 7 as homing receptors, enters the lymph nodes. Starting 24 hours after birth, a developmental switch occurs that causes the peripheral node addressins to be upregulated on the high endothelial venules in peripheral and mesenteric lymph nodes. This switch in addressin expression facilitates tissue-selective lymphocyte migration and mediates a sequential entry of different cell populations into the lymph nodes.[53] This genetically related research represents the beginning of our understanding of the mechanisms involved in the embryology of the lymphatic system.

Tonsils

As mentioned earlier, the endoderm of the ventral portion of the second pharyngeal pouch, in the region between the tongue and the palate, forms the tonsillar fossa and invades the mesenchyme as a group of solid buds. The central portions of these buds degenerate to form tonsillar crypts, and invading lymphoid cells from the surrounding mesenchyme eventually become grouped as lymphoid follicles. In fact, during the third to fifth fetal months, lymphoid tissue invades not only the palatine region, but also the mucosa in the region of the future pharyngeal (adenoids) tonsils and the mucosa of the root of the tongue in the region of the future lingual tonsils. Together, these lymphoid tissues encircle the oropharynx forming Waldeyer's ring.[14]

EMBRYOLOGY OF THE SALIVARY GLANDS

The salivary glands share an overall common embryogenesis in that they all develop from the ingrowth of local proliferations of surface epithelium into the underlying mesenchyme, and they all have a similar anatomic structure. The secretory or parenchymal tissues all arise from these proliferations of oral epithelium, which are of ectodermal origin for the major salivary glands and of either ectodermal or endodermal origin (depending upon the anatomic location) for the minor salivary glands. The stroma of the glands develop from mesodermal origins, although an additional component migrating from the neural crest has been postulated (Fig. 33-20).[14]

The parotid anlagen are the first to develop, and they appear between the fourth and sixth weeks of intrauterine

Copyright © 2003, Mosby, Inc. All rights reserved.

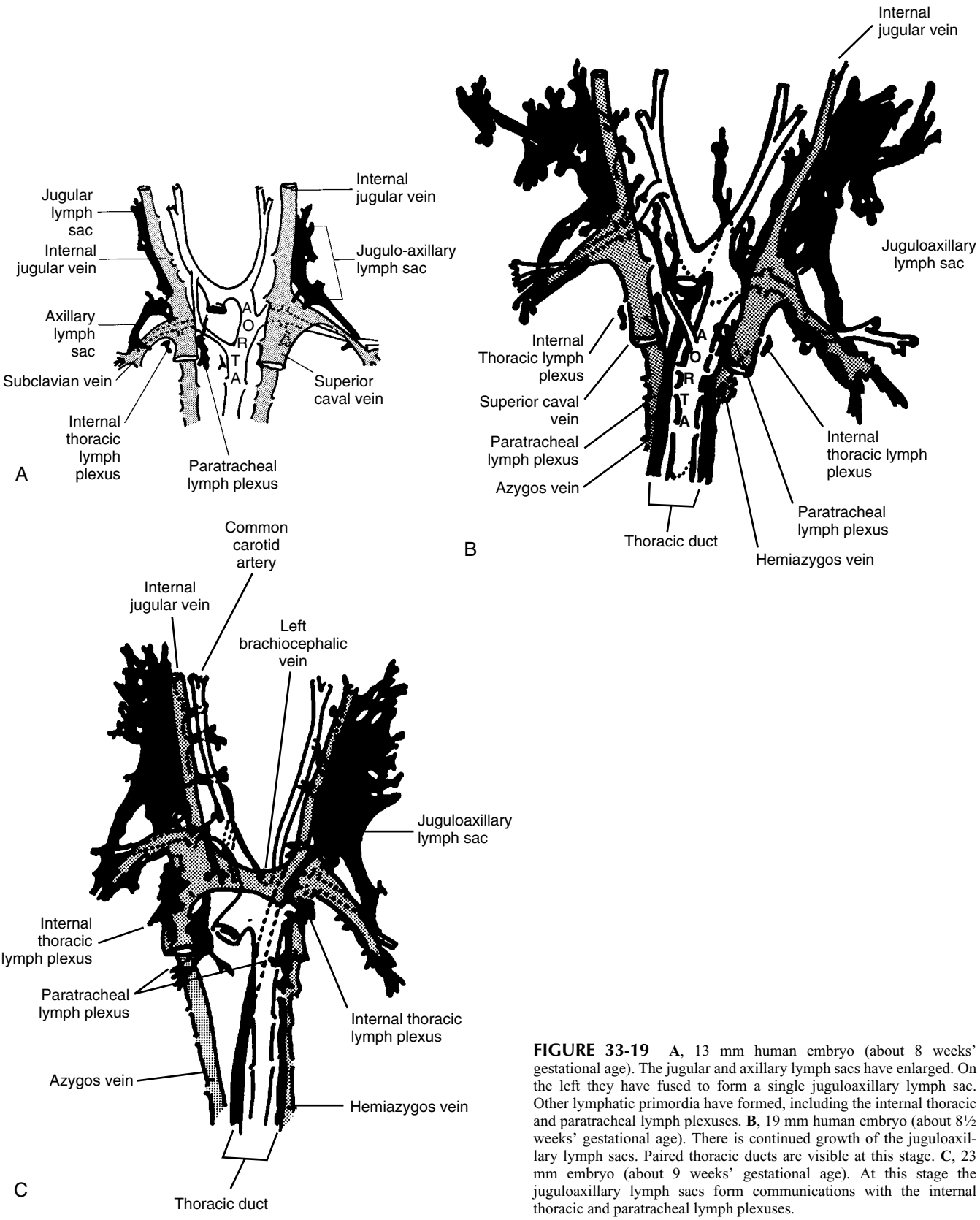

FIGURE 33-19 **A**, 13 mm human embryo (about 8 weeks' gestational age). The jugular and axillary lymph sacs have enlarged. On the left they have fused to form a single juguloaxillary lymph sac. Other lymphatic primordia have formed, including the internal thoracic and paratracheal lymph plexuses. **B**, 19 mm human embryo (about 8½ weeks' gestational age). There is continued growth of the juguloaxillary lymph sacs. Paired thoracic ducts are visible at this stage. **C**, 23 mm embryo (about 9 weeks' gestational age). At this stage the juguloaxillary lymph sacs form communications with the internal thoracic and paratracheal lymph plexuses.

VIEW IMAGE

Copyright © 2003, Mosby, Inc. All rights reserved.

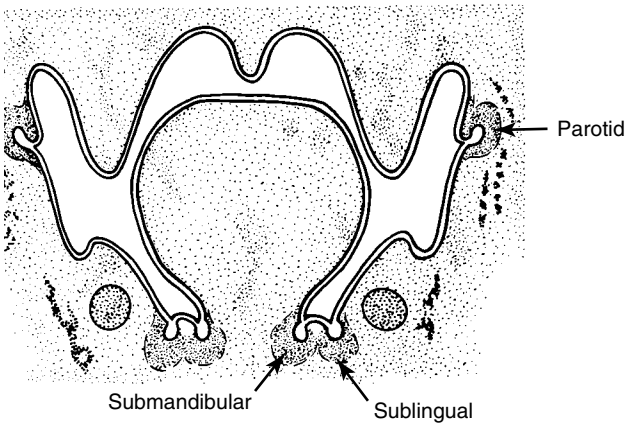

VIEW IMAGE

FIGURE 33-20 Diagram of coronal section of human embryo at about 7 weeks. Anlagen of major salivary glands can be seen extending into adjacent mesenchyme. (Modified from Mason DK, Chisholm DM. Salivary Glands in Health and Disease. Philadelphia: WB Saunders, 1975.)

life. The submandibular gland anlagen appear later in the sixth week, and the sublingual gland anlagen arise in the seventh to eight weeks, while the minor salivary glands do not start to develop until late in the twelfth week of intrauterine life.[14, 54–56]

The epithelial buds of each gland enlarge, elongate, and branch, the last process being induced by the mesenchyme surrounding the epithelium. Initially these buds are solid structures; however, they eventually canalize, creating lumina. The canalization process results from a differential in mitotic rate between the more rapidly dividing outer cell layers of the epithelial cords and the inner cells layers that divide more slowly. This canalization process is completed prior to the development of lumina in the terminal buds, which are the distal ends of the ductal epithelial buds and which eventually develop into the acini.[57]

The epithelial cells lining the ducts, tubules, and acini then proceed to differentiate both morphologically and functionally. Surrounding the acini are the contractile myoepithelial cells that reach their peak density by the twenty-fourth fetal week in the submandibular glands and the thirty-fifth fetal week in the parotid glands.[57]

Interaction of the salivary gland parenchymal and stromal elements with the autonomic nervous system is necessary for normal salivary development and function, as sympathetic nerve stimulation leads to acinar differentiation, while parasympathetic nerve stimulation is important for overall glandular growth.

In the parotid glands, the ducts are canalized by the tenth fetal week, the terminal buds are canalized by the sixteenth fetal week, and secretions commence in the eighteenth fetal week. In the submandibular glands, the acini start to differentiate by the twelfth fetal week. Serous secretory activity starts at the sixteenth fetal week, increases until the twenty-eighth fetal week, and then diminishes. These serous secretions contribute to the amniotic fluids, and contain amylase and possibly nerve and epidermal growth factors. The mucous acini develop postnatally. The mucosal minor salivary glands are not morphologically mature until the twenty-fifth fetal week.[57]

Although the parotid anlagen are the first to emerge, they become ''encapsulated'' or ensheathed in a loose condensation of fibroconnective tissue only after the submandibular and sublingual glands have become encapsulated. This delayed encapsulation is critical to the parotid gland's adult anatomy because although all of the glands are developing within a loose condensation of mesenchymal tissue, the emergence of the lymphatic system occurs after encapsulation of the submandibular and sublingual glands but before that of the parotid glands. Thus, at the completion of embryogenesis, the parotid glands have lymph nodes and lymphatic channels within the gland's capsule, while the submandibular and sublingual glands do not. In addition, salivary epithelial cells can be included within the intraparotid and periparotid lymph nodes during their process of encapsulation. This unusual situation of salivary epithelial inclusions within lymph nodes is unique to the parotid and periparotid nodes.[56] The intraparotid and periparotid lymph nodes are elements of the mucosal associated lymphoid tissue (MALT) system that is found throughout the gastrointestinal tract, and which may be important in supplying all of the major salivary glands with IgA-producing plasma cells that are important components of mucosa-based immunity. This special embryogenesis of the parotid glands and their lymph nodes is believed to play a role in the development of Warthin's tumors, as discussed in Chapter 39.

The parotid gland is also unique in that as its epithelial buds are growing and branching, they extend between the divisions of the facial nerve that have already started to develop in the region. As a result, when these structures have completed their embryologic development, the facial nerve and its branches extend through the substance of the parotid gland.[14, 54, 55, 58, 59] Clearly, any surgical approach to the parotid must be mindful of this anatomy lest the nerve be seriously damaged.

The organ of Chievitz, found near the oral cavity, arises in the embryo as an oral epithelial invasion of the corners of the mouth, developing earlier than the parotid analgen. It is a small 7 to 17 mm long strand that resembles a nerve, and it lies in the cheek region between the buccopharyngeal fascia and the site where the parotid (Stenson's) duct penetrates the buccinator muscle. The organ of Chievitz is situated close to the buccal branch of cranial nerve V, which innervates it. Eventually, it loses its connection with the buccal sulcus and becomes embedded in a dense connective tissue sheath. The function of the organ of Chievitz is not known, but it may be a sensory receptor.[57]

Table 33-2 shows the embryologic development of the various systems described in relation to gestational age.

NORMAL POSTNATAL ANATOMY OF THE NECK

Traditionally in physical diagnosis, the superficial neck is analyzed as being divided into several palpable triangles (Fig. 33-21). These triangles not only define anatomic location, but often allow an initial differential diagnosis to be generated. However, because these triangles are not defined by the layers of the deep cervical fascia, they do not function as barriers to the spread of disease. The fasciae and

Copyright © 2003, Mosby, Inc. All rights reserved.

Table 33-2
THE TEMPORAL RELATIONSHIP OF FETAL AGE AND THE EMBRYOLOGY OF VARIOUS SYSTEMS

Fetal Age (Weeks)	Embryology
2.5	The embryonic disc is flat, the primitive streak is prominent, and the neural groove is indicated. The gut is not yet distinct from the yolk sac. Blood islands appear in the chorion and yolk sac. The notochordal plate and groove are present.
3.5	The neural groove deepens and closes. The neural crest is a continuous band. The optic and otic placodes are present, and the acoustic ganglia appear. Branchial arches 1 and 2 are identified, the stomodeum is a definite pit, and the oral membrane ruptures. The pharynx is broad and flat, and the pouches are forming. The thyroid anlagen are identified. The respiratory primordium appears as a groove on the floor of the pharynx. The foregut and hindgut are present.
4	The branchial arches are complete, and all 40 somites are present. The maxillary and mandibular processes are prominant. Rathke's pouch is identified. Five pharyngeal pouches are present, with pouches 1–4 having closing plates. The primary tympanic cavity is present, and the thyroid is a stalked sac. The laryngeal opening is a simple slit, and the trachea and paired lung buds are prominent. The esophagus is short. The optic cup and lens pit are forming. The auditory pit closes, and the otocyst detaches. The olfactory placodes arise and differentiate into nerve cells. Nerves and ganglia are forming.
5	The nasal pits are present, and the jaws are outlined. Rathke's pouch is a stalked sac. The pharyngeal pouches attain dorsal and ventral diverticula. The thyroid is bilobed, and the thyroglossal duct atrophies. The arytenoid swellings and the epiglottis are identified. The bronchial buds presage future lung lobes. There are premuscular masses in the head and neck, and the epidermis has a second layer. The lens vesicle is free, and the vitrous anlage appears. The otocyst elongates and develops the endolymphatic duct. The olfactory pits deepen. The nerves and ganglia are better represented.
6	The upper jaw components are present but separate; the lower jaw halves fuse. The head becomes dominant in size, and cervical flexure is marked. The external ear appears. The lingual primordia fuse, and the foramen caecum is established. The parotid and submaxilliary buds appear, as do the labio-dental laminae. The thymic sacs, ultimobranchial sacs, and solid parathyroids are prominent and ready to detach. The thyroid becomes solid and converts internally to plates. Definitive pulmonary lobes are identified. The laryngeal cavity is temporarily obliterated. Myotomes fuse into a continuous column, and muscle segmentation is lost. Nerve plexes are present, and sympathetic ganglia are forming segmental masses. The optic cup has nervous and pigmented layers. The lens vesicle thickens, and the eyes are set at 160°. The nasolacrimal duct is formed. Modeling of the external, middle, and inner ears continues, and the vomer-nasal region is identified.
7	The branchial arches are lost. The cervical sinus of His is obliterated. The lingual primordia merge into a single tongue. Separate labial and dental laminae are distinguishable. The jaws are formed and start to ossify. The palate folds are present and separated by the tongue. The thymi elongate further and lose lumina. The parathyroids become trabeculated and associated with the thyroid. The ultimobranchial bodies fuse with the thyroid, and the thyroid becomes crescentic in shape. The larynx and epiglottis are well outlined, and the laryngeal orifice is T-shaped. The laryngeal and tracheal cartilages are identified. The posterior nasal conchae appear and the primary conchae ruptures, creating two internal nasal orifices. The cardinal veins are transforming. Chondrification is more generalized, and muscles are rapidly differentiating. The infundibulum and Rathke's pouch are in contact. The choroidal fissure closes in the eye, enclosing the central artery. Nerve fibers invade the optic stalk, and the lens cavity is lost by elongating lens fibers. The eyelids form, and the olfactory sacs open into the mouth.
8	The nose is flat, the eyes are far apart, and the head is elevating. The tongue muscle become well differentiated, and the taste buds are identified. Rathke's pouch detaches from the mouth. The sublingual gland appears. The eustachian tube, tympanic cavity, external ear, and inner ear are distinguishable. The sites of the palatine tonsil and fossa appear. The thymic halves unite, and the gland becomes solid. The thyroid follicles start to form. The nostrils are closed by epithelial plugs. The major blood vessels assume their final shape. The primitive lymph sacs develop. The first indications of ossification occur. Definitive muscles are present, and the fetus has movement. The olfactory lobes are visible, the dura, pia, and arachnoid are distinct, and the chromaffin bodies appear. The eyes are rapidly converging.
10	The head is erect. The fungiform and vallate papillae are differentiating. The lips are separate from the jaw, and the enamel organs and dental papillae form. The palatal folds fuse. The thymic epithelium is transforming into reticulum and thymic corpuscles. The ultimobranchial bodies disappear. The nasal passages are partitioned by fusion of the septum and palate. The nasal cartilages appear. The laryngeal cavity reopens, and the vocal cords appear. The earliest hair follicles develop on the face. The iris and ciliary body organize, the eyelids fuse and the lacrimal gland develops. The spiral organ of the ear begins to differentiate. Early lymph nodes appear.
12	The bridge of the nose is identified. The filiform and foliate papillae become more prominent. The tooth primordia form prominent cysts. The cheeks can be identified. The tonsillar crypts invaginate. The thymus forms medullary and lymphoid tissue. The thyroid gland attains a typical structure. The nasal conchae are prominent, and the nasal glands develop. Blood formation begins in the marrow. The notochord is rapidly degenerating. Ossification is more extensive, and some bones are clearly identified. The smooth muscle layers of the gut are identified. The eye attains its characteristic organization, and the retina becomes layered. Fusion of the nasal septum and palate is completed.
16	There is now a human facial appearance, and head hair appears. The muscles become spontaneously active, and the body outgrows the head size. The hard and soft palates are differentiating. The hypophysis is acquiring a definitive structure. Lymphocytes start to accumulate within the palatine tonsil, and the adenoids appear. The paranasal sinuses start to develop, and the tracheal glands appear. Most bones are distinct, and the joint cavities develop. Body hair appears, and the sweat glands and sebaceous glands start to differentiate. The eye, ear, and nose grossly approach their adult forms.
20–40	Lanugo hair appears (5 months), becomes prominent (7 months), and is shed (10 months). The subcutaneous fat collects, and skin wrinkles start to smooth (8–10 months). Enamel and dentin are deposited (5 months), and the permanent tooth primordia are identified (6–8 months). The lingual tonsil forms, and adult tonsilar structure is seen (5 months). The nasal bones begin to ossify (5 months), and the nostrils reopen (6 months). The frontal and sphenoid sinuses are still only rudimentary (10 months). Myelinization of the cord begins (5 months), and the cerebral fissures and convolutions rapidly appear (7 months). The vascular tunia of the lens attains its highest development (5 months). The retinal layers are completed, and light perception develops (7 months). The eyelids reopen (7–8 months). Taste sensation is present (8 months). The mastoid cells are still unformed (10 months).

Copyright © 2003, Mosby, Inc. All rights reserved.

fascial spaces are detailed in Chapter 34. For discussion of the anatomy of the neck during the fetal, perinatal, and infant periods, see references 60 to 63.

One of the dominant anatomic landmarks in the neck is the sternocleidomastoid muscle, which courses obliquely down the lateral neck, from the mastoid process to the clavicle and sternum. By definition, this muscle is used to divide the neck into anterior and posterior triangles.[1] Structures that are palpated ventral to the anterior edge of the sternocleidomastoid muscle are within the anterior triangle, while those structures that lie posterior to this muscle but anterior to the trapezius muscle are considered to be within the posterior triangle. The clinically inaccessible region deep to the sternocleidomastoid muscle is defined as being part of the anterior triangle of the neck.

Traditionally on either side of the neck, the boundaries of the anterior triangle are the anterior border of the sternocleidomastoid muscle, the undersurface of the body of the mandible, and the anterior midline of the neck. Each anterior triangle can be further subdivided into four smaller triangles. Thus, the anterior belly of the digastric muscle separates the anterior midline submental triangle from the submandibular triangle. The posterior belly of the digastric muscle separates the submandibular and carotid triangles, while the superior belly of the omohyoid muscle separates the carotid and muscular triangles. The borders of the

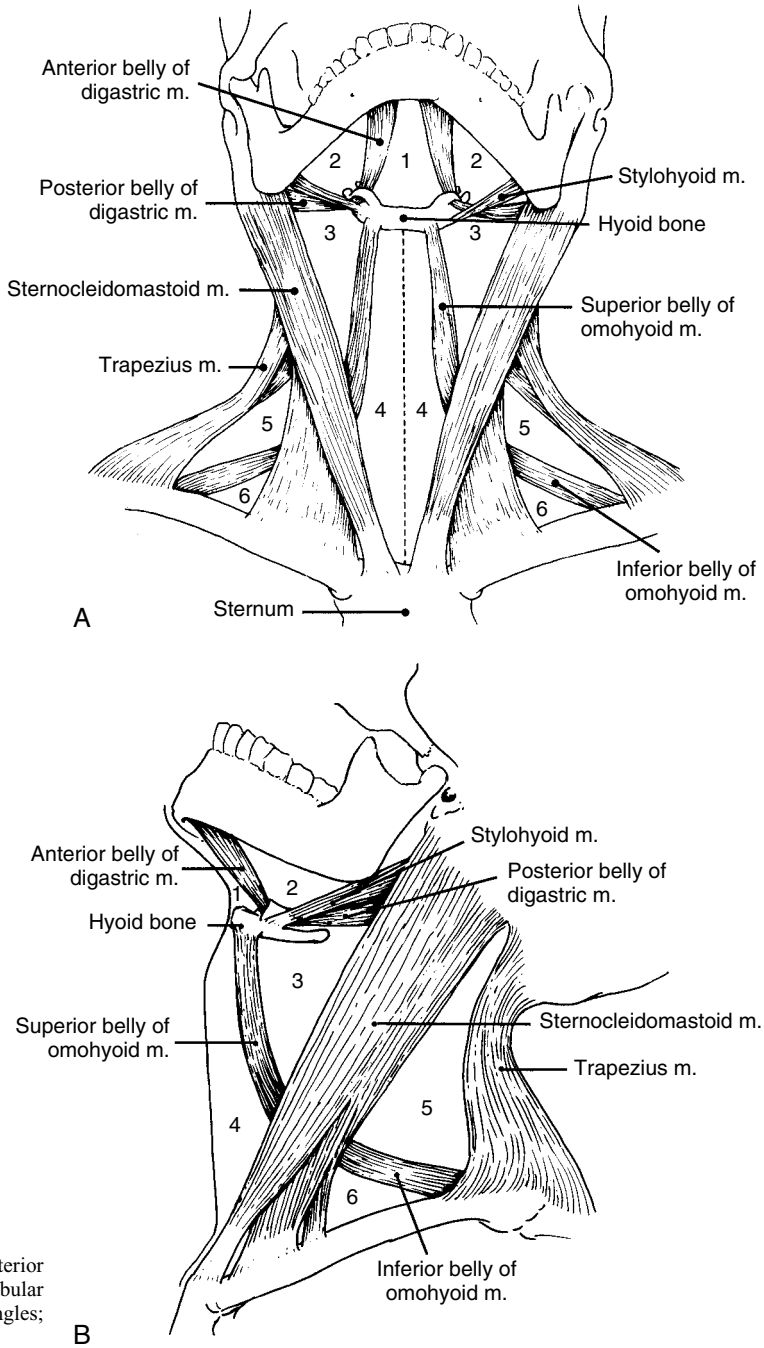

VIEW IMAGE

FIGURE 33-21 Triangles of the neck—line diagrams. **A**, Anterior view. **B**, Lateral view. *1*, midline submental triangle; *2*, submandibular triangles; *3*, carotid triangles, *4*, muscular triangles; *5*, occipital triangles; *6*, subclavian triangles.

Copyright © 2003, Mosby, Inc. All rights reserved.

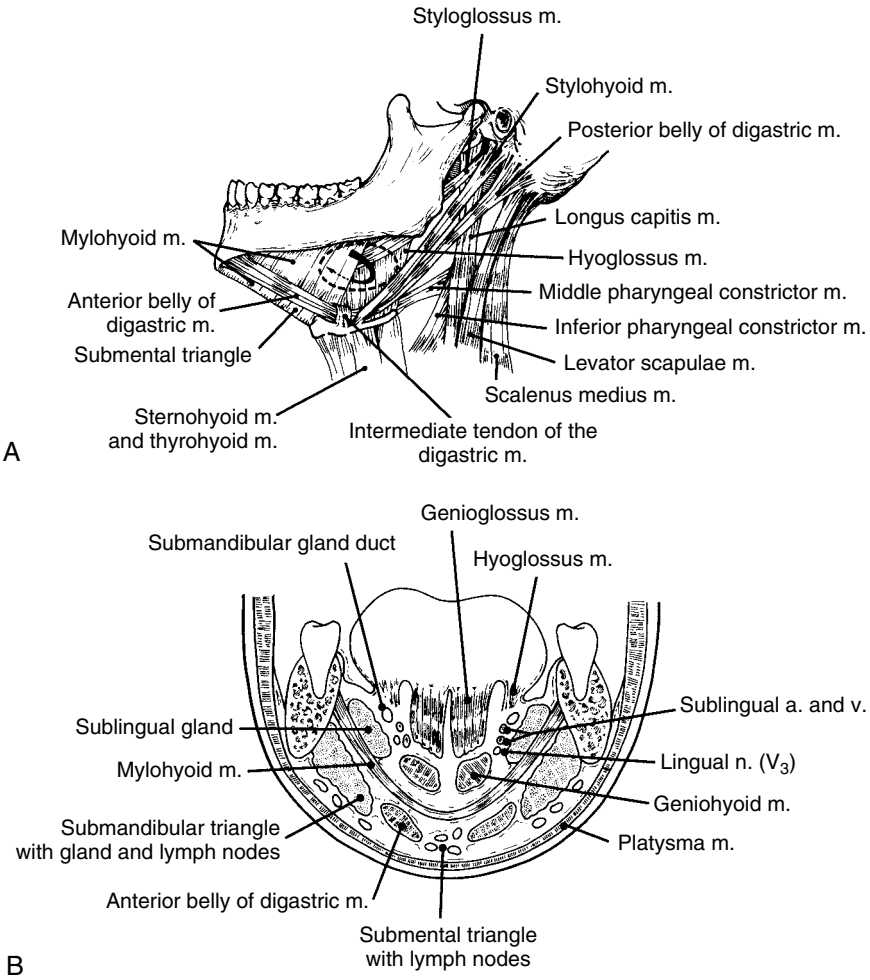

FIGURE 33-22 **A**, Suprahyoid region of neck—line diagram (lateral view). *Dotted circle* shows position of submandibular gland. Note gap between posterior margin of mylohyoid and hyoglossus muscles (*curved arrow*). **B**, Suprahyoid region of the neck—line diagram (coronal view). Note the muscular sling, primarily provided by the mylohyoid muscles, forming the floor of the mouth. The submandibular and submental triangles lie below this sling, and contents of the oral cavity lie above it.

VIEW IMAGE

posterior triangle are the dorsal edge of the sternocleidomastoid muscle, the anterior border of the trapezius muscle, and the middle third of the clavicle. The posterior triangle can be subdivided by the inferior belly of the omohyoid muscle into the occipital and subclavian (omoclavicular) triangles.[1, 64–67]

The hyoid bone can also be used to subdivide the anterior triangle into suprahyoid and infrahyoid compartments. In this classification, the suprahyoid compartment contains the solitary midline submental triangle and the paired (lateral) submandibular triangles. Functionally the suprahyoid compartment is related to the oral cavity, floor of the mouth, oropharynx, and hypopharynx. The infrahyoid compartment on either side contains the carotid and muscular triangles.

The submental triangle is a midline unpaired triangle bordered laterally by the anterior bellies of the digastric muscles, inferiorly by the hyoid bone, and superiorly by the lower border of the symphysis of the mandible. The mylohyoid muscles and their fibrous median raphe form the deep boundary (or floor) of the triangle, separating it from the oral cavity. The contents of the submental triangle include small submental lymph nodes (level IA) and branches of the facial artery and vein (Figs. 33-21 and 33-22).

Each of the submandibular triangles, or digastric triangles, is bordered superiorly by the lower border of the body of the mandible and inferiorly by the anterior and posterior bellies of the digastric muscle. The deep surface (or floor) of each submandibular triangle is formed by portions of the mylohyoid muscle anteriorly and the hyoglossus muscle posteriorly. The submandibular triangles communicate with the sublingual space at the posterior margins of the mylohyoid muscles. Each submandibular triangle is almost completely occupied by the superficial portion of the submandibular gland. Three to five submandibular lymph nodes (level IB, see Chapter 36) lie superficial to the gland, as do portions of the posterior (retromandibular) and anterior facial veins (Figs. 33-21 and 33-23). The anatomy of this region is discussed in more detail in Chapter 27.

Each carotid triangle is the region of the lateral neck in which the carotid sheath structures are relatively superficial in location. These triangles are bordered by the posterior belly of the digastric muscle, the superior belly of the omohyoid muscle, and the midportion of the sternocleidomastoid muscle. The contents include the carotid sheath structures: the common carotid and internal carotid arteries, a portion of the external carotid artery, portions of cranial nerves IX, X, XI, and XII, and the internal jugular vein. Also present are the cervical sympathetic trunk and the ansa cervicalis, a part of the cervical plexus (see the section on Spinal Nerves). In addition, there are a number of lymph nodes that are primarily related to the internal jugular vein and the carotid sheath (level III) (Figs. 33-21, 33-24, and 33-25).

Copyright © 2003, Mosby, Inc. All rights reserved.

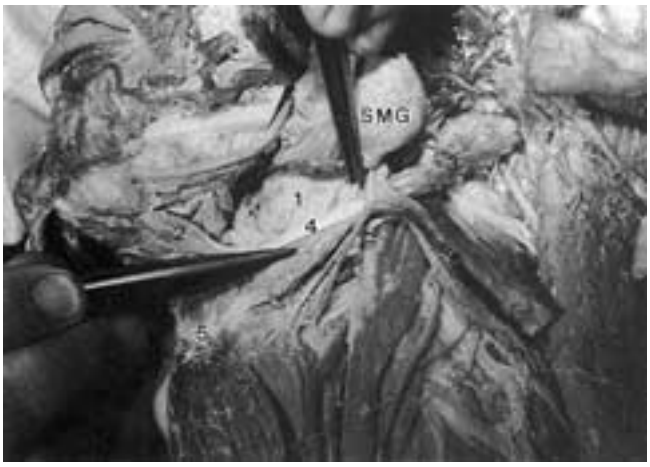

VIEW IMAGE

FIGURE 33-23 Submandibular triangle—gross dissection (lateral view). The submandibular gland (SMG) has been rotated cephalad to reveal the underlying fascia covering the hyoglossus and mylohyoid muscles (*1*), forming the roof of the triangle. The anterior (*2*) and posterior (*3*) bellies of the digastric muscle are united by a tendon (*4*) that has been released from the hyoid bone (*5*).

VIEW IMAGE

FIGURE 33-25 Carotid triangle—gross dissection (oblique view). Boundaries include the sternocleidomastoid muscle (which has been removed in this specimen) posterolaterally, the superior belly of the omohyoid muscle anteromedially (*1*) and the posterior belly of the digastric muscle superiorly (*2*). The forceps indicates the descending hypoglossal ramus of the ansa hypoglossi, coursing on the anterior border of the common carotid artery (*3*). The internal jugular vein (*4*) lies posterolateral to the artery within the triangle, and the vagus nerve (*arrowhead*) lies between them.

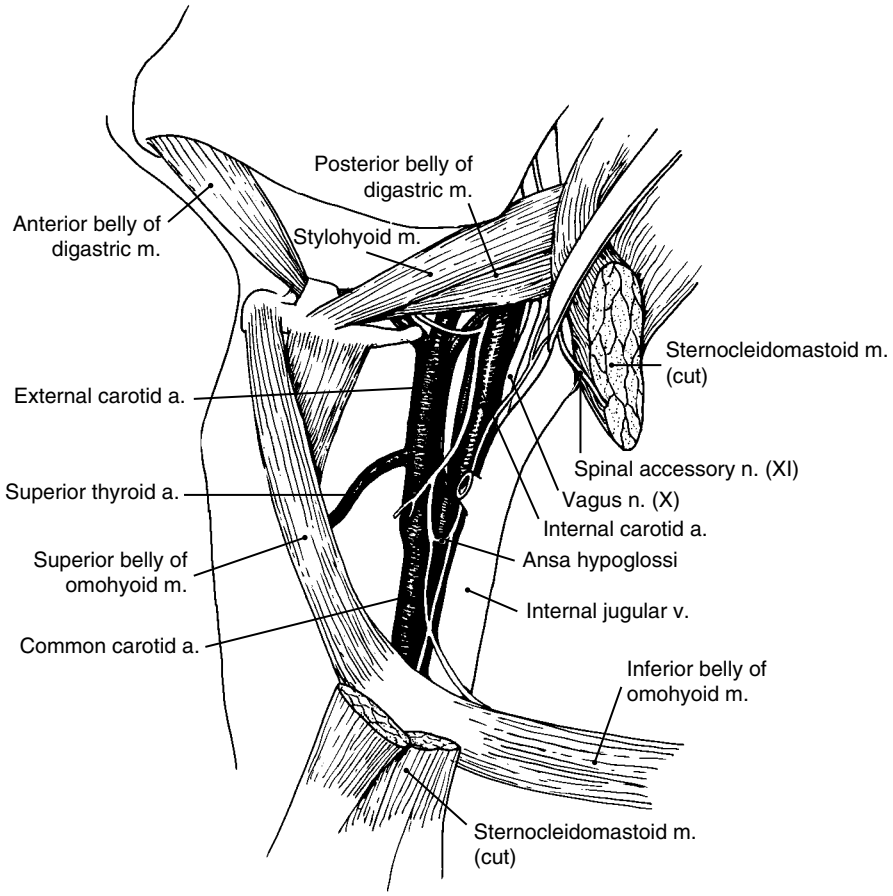

VIEW IMAGE

FIGURE 33-24 Carotid triangle—line diagram (lateral view). A midportion of the sternocleidomastoid muscle has been resected for visualization of carotid triangle structures. The vagus nerve lies posteriorly within the triangle. The ansa hypoglossi, formed by the descending hypoglossal and descending cervical rami, lies just inferior to the common carotid artery bifurcation.

Copyright © 2003, Mosby, Inc. All rights reserved.

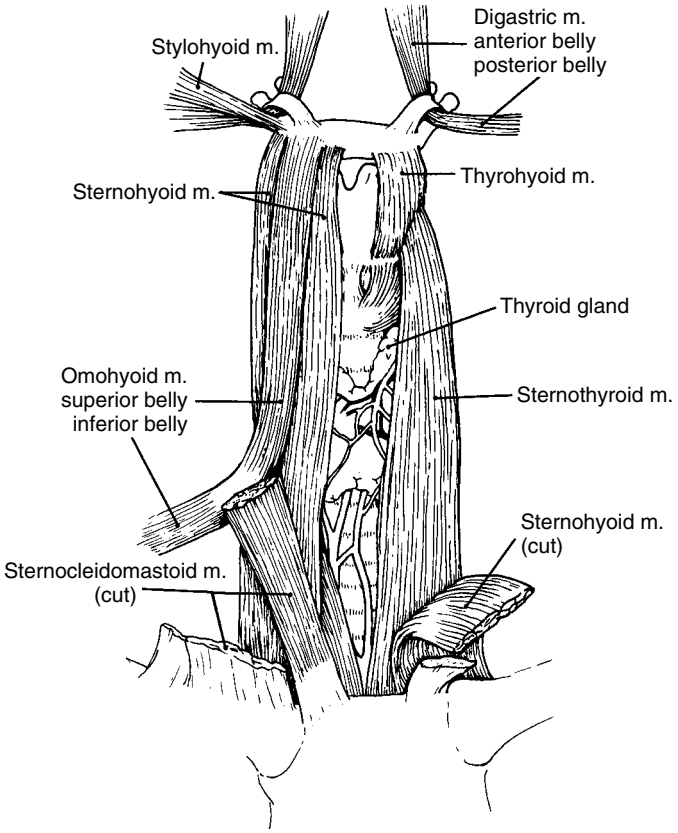

VIEW IMAGE

FIGURE 33-26 Muscular triangles—line diagram (AP view). Superficial strap muscles are identified on the left, and the deeper ones are labeled on the right.

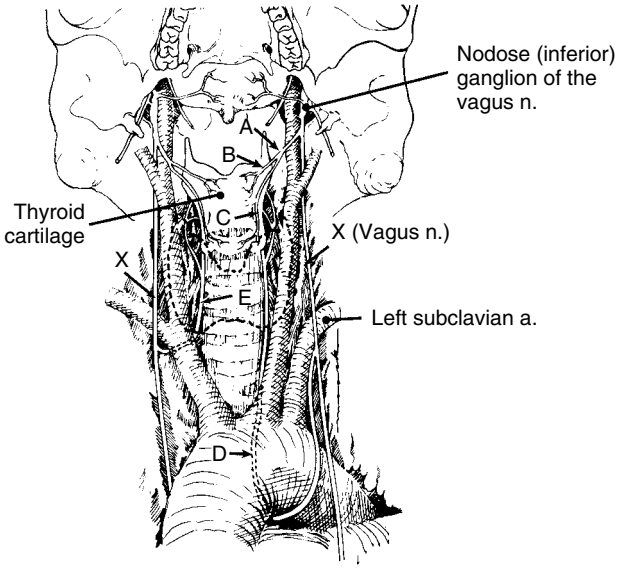

VIEW IMAGE

FIGURE 33-27 Anterior triangle of neck (strap muscles have been removed)—line diagram (AP view). Note the different levels of origin of the two recurrent laryngeal nerves; the left recurrent laryngeal nerve arises below the level of the aortic arch, under which it loops in the region of the aortopulmonary window. **A**, Superior laryngeal nerve. **B**, Internal branch of superior laryngeal nerve. **C**, External branch of superior laryngeal nerve. **D**, Left recurrent laryngeal nerve. **E**, Right recurrent laryngeal nerve.

Each muscular triangle is bordered posteriorly and superiorly by the superior belly of the omohyoid muscle, posteriorly and inferiorly by the sternocleidomastoid muscle, and anteriorly by the midline of the neck. Together, these paired triangles contain the infrahyoid ''strap'' muscles, larynx, hypopharynx, cervical portion of the trachea, esophagus, thyroid, and parathyroid glands, the vascular supply to these structures, and the recurrent laryngeal nerves coursing in the tracheoesophageal grooves. There are also the visceral (level VI) and some of the lower internal jugular (level IV) lymph nodes (Figs. 33-21, 33-26 to 33-28).

The infrahyoid ''strap'' muscles include the superior belly of the omohyoid muscle and the sternohyoid, sternothyroid, and thyrohyoid muscles. As a result of their muscular attachments, the sternothyroid and thyrohyoid muscles lie in a deeper plane than do the sternohyoid muscle and the superior belly of the omohyoid muscle (Fig. 33-29).

The thyroid gland (so named because it resembles a shield, *thyreos* in Greek) lies below and on both sides of the thyroid cartilage, covered by three of the four infrahyoid strap muscles. (The thyrohyoid muscle does not cover the thyroid gland.) The thyroid gland consists of two lateral lobes, one on either side of the upper trachea and lower

FIGURE 33-28 Muscular triangle—gross dissection (oblique view). The sternocleidomastoid muscle has been removed. The pointer indicates the sternohyoid muscle, one of the two superficial strap muscles. The other superficial strap muscle, the superior belly of the omohyoid muscle (*1*), has been slightly displaced posterolaterally to reveal underlying structures. The sternothyroid (*2*) and thyrohyoid (*3*) muscles can be identified on a deeper plane. *4*, Submandibular gland; *5*, internal jugular vein; *6*, common carotid artery; *7*, superior thyroid branch of the external carotid artery.

VIEW IMAGE

Copyright © 2003, Mosby, Inc. All rights reserved.

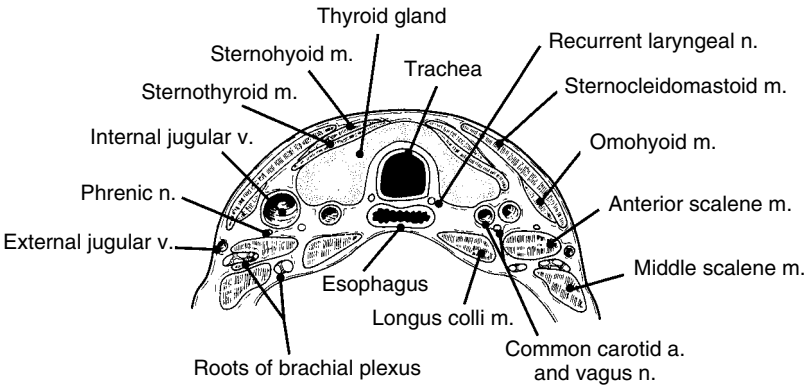

VIEW IMAGE

FIGURE 33-29 Infrahyoid region of neck (thyroid gland level)—line diagram (axial view). Superior belly of omohyoid muscle often can be seen as separate structure on deep surface of sternocleidomastoid muscle. Recurrent laryngeal nerves lie in tracheoesophageal grooves. Posterior aspect of thyroid gland is in intimate contact with common carotid artery. Note locations of vagus and phrenic nerves.

larynx, and an interconnecting isthmus that overlies the second to fourth tracheal rings, just below the cricoid cartilage. The gland varies greatly in size and is often larger in women and children than in men. In 40% of the population, a variably sized pyramidal lobe arises from the upper margin of the thyroid gland and projects superiorly, usually, but not always, in a midline location. It may be represented by a small stump of tissue or by a large, discrete lobe.[68] A remnant of the thyroglossal duct, the levator glandulae thyroideae, represented by a fibrous strand or a fibromuscular band, may attach the thyroid gland to the body of the hyoid bone. The parathyroid glands are usually embedded in the posterior surface of the thyroid gland, one pair in each lobe. The posterior aspect of each lobe of the thyroid gland is just medial to the common carotid artery. The anatomy of the thyroid gland is discussed in greater detail in Chapter 40.

The contents of the posterior triangle are the cutaneous branches of the cervical plexus (the lesser occipital, greater auricular, anterior cutaneous, and supraclavicular nerves), the spinal accessory nerve, the suprascapular and tranverse cervical arteries (branches of the thyrocervical trunk), the suprascapular, transverse cervical, and external jugular veins, and lymph nodes associated with the spinal accessory nerve (level V nodes). As mentioned, the inferior belly of the omohyoid muscle subdivides the posterior triangle into a larger occipital triangle and a smaller subclavian (omoclavicular) triangle (Figs. 33-21, 33-30, and 33-31).

Each occipital triangle is bordered anteriorly by the sternocleidomastoid muscle, posteriorly by the ventral edge of the trapezius muscle, and caudally by the inferior belly of the omohyoid muscle. Each triangle is primarily fat-filled and traversed by the spinal accessory and dorsal scapular nerves. Portions of the spinal accessory lymph node chain (level V) are contained in the midportion of this triangle, while portions of the transverse cervical artery and vein are contained in its inferior portion. From above downward (posteriorly to anteriorly), the floor of the posterior triangle is composed of the splenius capitus, levator scapulae, and posterior, middle, and anterior scalene muscles. The spinal accessory nerve enters the deep surface of the sternocleidomastoid muscle at Erb's point, which is just cranial to where the great auricular nerve surfaces from the deep neck (Fig. 33-32). Alternatively, the spinal accessory nerve can be located surgically where it disappears on the deep surface of the trapezius muscle, at a point roughly two finger-breadths

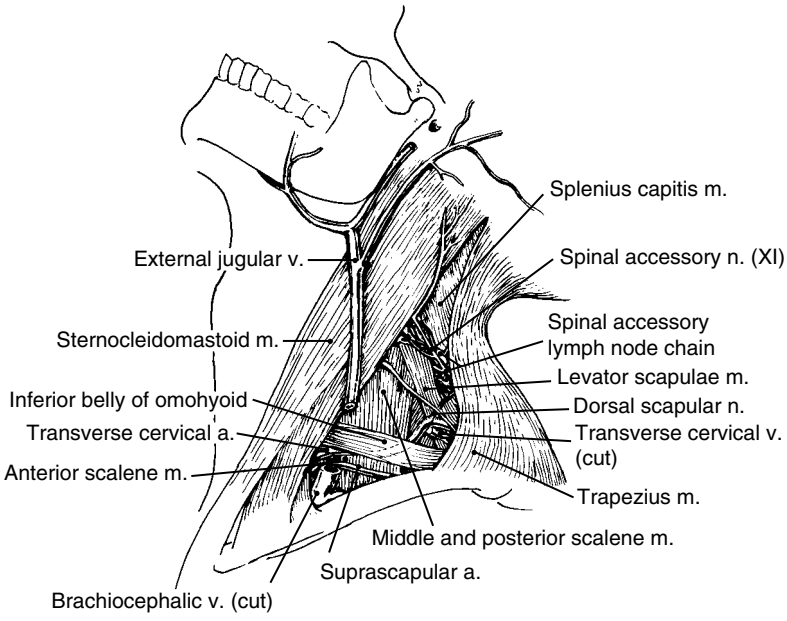

VIEW IMAGE

FIGURE 33-30 Posterior triangle of the neck—line diagram (lateral view). The inferior belly of the omohyoid muscle subdivides the posterior triangle into larger occipital and smaller subclavian triangles. The spinal accessory lymph node chain courses through the midportion of the posterior triangle, in association with the spinal accessory nerve.

Copyright © 2003, Mosby, Inc. All rights reserved.

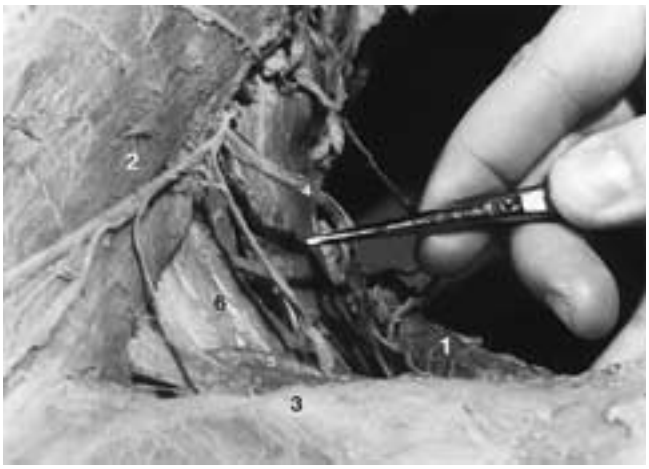

VIEW IMAGE

FIGURE 33-31 Posterior triangle of the neck—gross dissection (oblique view). The extensive amounts of fat have been removed during dissection. A portion of the trapezius muscle (*1*), forming the posterior border of the triangle, is visible as are the sternocleidomastoid muscle (*2*) and clavicle (*3*), forming the other two borders. The forceps is holding the spinal accessory nerve (cranial nerve XI) (*4*) as it traverses the posterior triangle. The suprascapular artery (*5*) is seen crossing the middle and posterior scalene muscles (*6*).

superior to the clavicle at the anterior border of the trapezius muscle. At the skull base, the spinal accessory nerve courses in front of the internal jugular vein at the level of the transverse process of the first cervical vertebra.[69]

The borders of each small subclavian triangle are anteriorly, the lower portion of the sternocleidomastoid muscle; superiorly, the inferior belly of the omohyoid muscle; and inferiorly, the middle third of the clavicle. Within each triangle is located the distal (third) portion of the subclavian artery, the trunks of the brachial plexus, and portions of the transverse cervical and suprascapular arteries and veins. Some of the supraclavicular lymph nodes are also located within this triangle (Figs. 33-21, 33-33, and 33-34).

The anterior scalene muscle is an important landmark for the anatomy of the lower neck, and it arises from the transverse processes of C3 to C6. The muscle then courses inferiorly, deep to the sternocleidomastoid muscle, to insert onto the first rib. The anterior scalene muscle separates the subclavian vein, which lies superficial (ventral) to the muscle, from the roots of the brachial plexus and the subclavian artery, which lie deep (dorsal) to it.[64, 66–68]

The anterior scalene muscle also can be used to subdivide the subclavian artery into three portions, all of which are within the subclavian triangle. The first portion lies medial to the anterior scalene muscle, the second portion lies deep to it, and the third portion extends from the lateral border of the muscle to the outer margin of the first rib. Beyond the first rib, the subclavian artery becomes the axillary artery.

THE PERIPHERAL NERVOUS SYSTEM

The peripheral nervous system (PNS) is composed of three components that communicate and interact to supply afferent and efferent fibers to the somatic and visceral portions of the head and neck. The three components of the PNS are the cranial nerves, the spinal nerves, and the autonomic nervous system. While a review of these systems in their entirety is beyond the scope of this book, a discussion of the anatomic location of the major components of the PNS will allow a better understanding of where to look for these structures within the neck. In addition, noting the communications between them may possibly explain how disease in one nerve may spread to another nerve or component of the system. Discussions of some of these cranial nerves also appear elsewhere in this book.

Cranial Nerves

Cranial nerves I, II, III, IV, VI, and VIII are confined to the intracranial compartment and orbit and, in general, do not have manifestations in the neck. These nerves are also discussed elsewhere in the book.

Cranial nerve V, the trigeminal nerve, has three divisions: ophthalmic (V_1), maxillary (V_2), and mandibular (V_3). The ophthalmic nerve courses within the cavernous sinus before it enters the orbit via the superior orbital fissure and eventually branches into the frontal, nasociliary, and lacrimal nerves. The maxillary nerve runs from the cavernous sinus through the foramen rotundum, crosses the pterygopalatine fossa directed laterally and downward, and enters the the orbit via the inferior orbital fissure. It continues in the floor of the orbit as the infraorbital nerve and exits on the face of the maxilla through the infraorbital foramen (Fig. 33-35). The zygomatic nerve arises in the pterygopalatine fossa, enters the orbit via the inferior orbital fissure, and has two branches: the zygomaticotemporal and zygomaticofacial. The former leaves the orbit through the zygomaticotemporal foramen or passes through the sphenozygomatic suture to reach the temporal fossa, where the *zygomaticotemporal nerve communicates with the facial nerve (VII) and the auriculotemporal branch of the mandibular nerve (V_3)*. While in the orbit, *V_2 sends a branch through the pterygopalatine ganglion that reaches the lacrimal gland. The zygomaticofacial nerve* leaves the anterior orbit via the zygomaticoorbital and zygomaticofacial formina to emerge on the face, where it *joins VII and the infraorbital branch of V_1*.

Within the pterygopalatine fossa, *V_2 gives off the pterygopalatine branches, which are important functional communications between the pterygopalatine ganglion and the maxillary nerve. The greater palatine nerve, a branch of the pterygopalatine nerves, communicates with the terminal branches of the nasopalatine nerve, while the terminal facial branches of V_2 communicate with filaments of VII.*

The mandibular nerve, V_3, is the largest division of the fifth cranial nerve and has two roots, a larger lateral sensory root and a smaller medial motor root. The two roots leave the middle cranial fossa via the foramen ovale and unite to form a main trunk just below the skull base. After only 2 to 3 mm, the trunk divides into a smaller anterior division and a larger posterior division (main trunk). The otic ganglion lies just medial to the main nerve trunk (Fig. 33-35). The *recurrent branch or nervus spinosus* of the main trunk reenters the skull base via the foramen spinosum to supply the dura. It *communicates with the meningeal branch of V_2*. Muscular branches then go to the medial pterygoid and the tensor veli

Copyright © 2003, Mosby, Inc. All rights reserved.

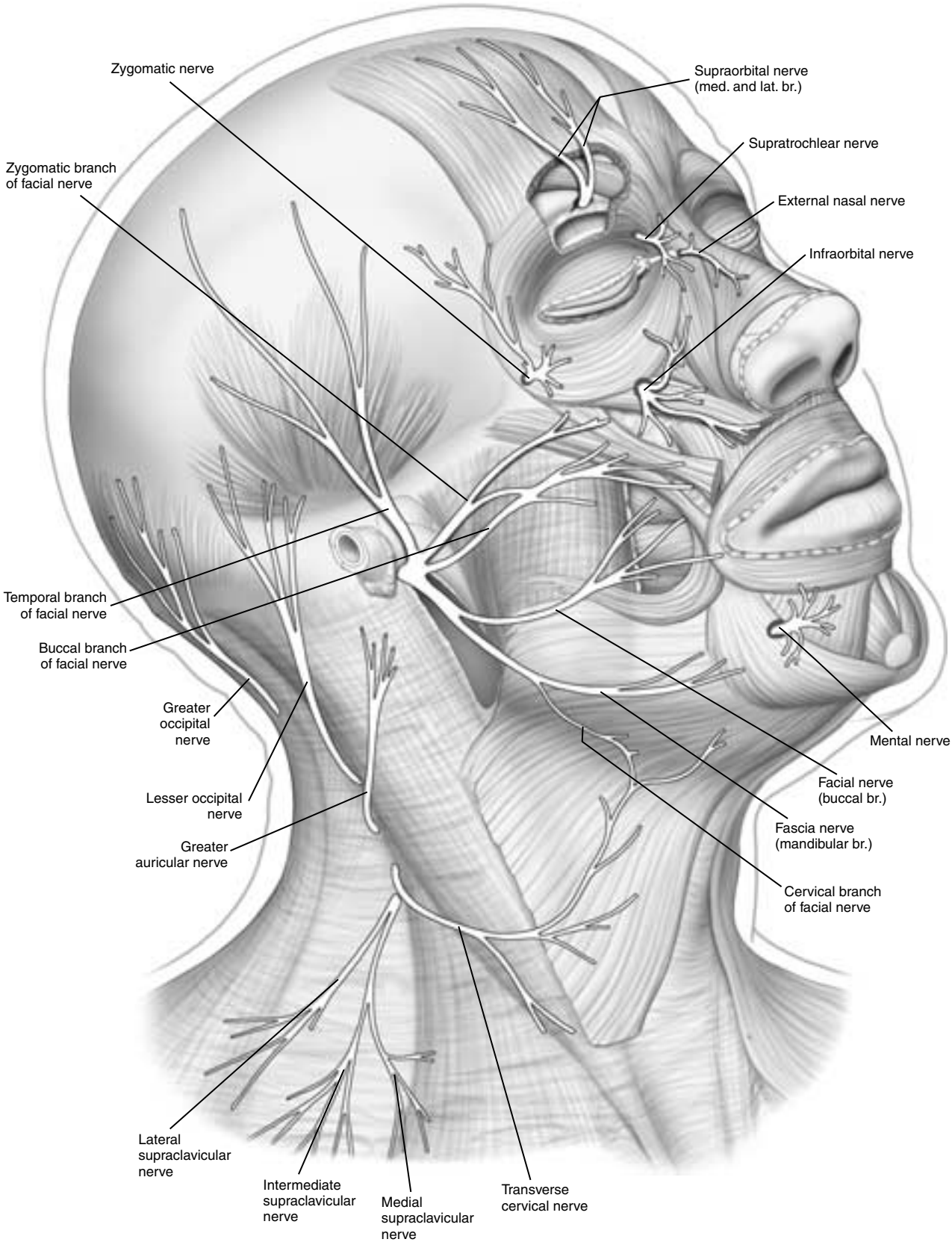

FIGURE 33-32 Drawing of the oblique frontal view of the face and neck showing the superficial innervation and the major facial nerve branches.

VIEW IMAGE

Copyright © 2003, Mosby, Inc. All rights reserved.

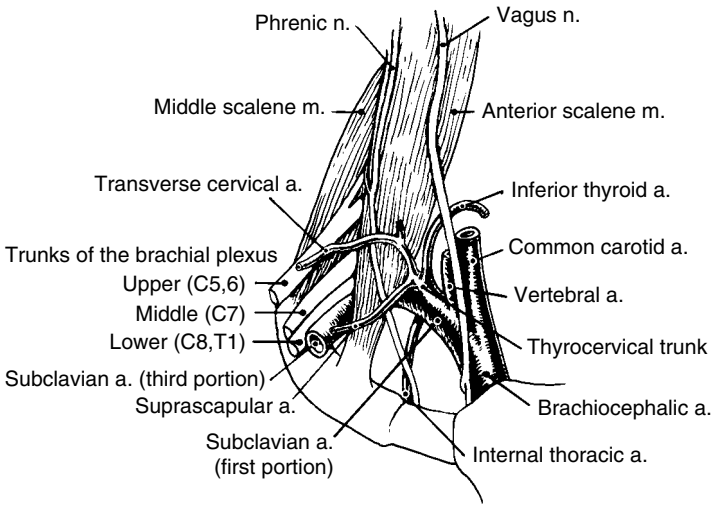

FIGURE 33-33 Right subclavian triangle—line diagram (AP view). Sternocleidomastoid muscle, brachiocephalic vein, and clavicle have been removed. Note relationship of subclavian artery and brachial plexus to scalene muscles. The phrenic nerve courses on the anterior surface of the anterior scalene muscle, as does the vagus nerve.

VIEW IMAGE

palatini muscles, entering these muscles near their cranial origins. Near its zygomatic arch origin, the anterior division of V_3 sends branches to the masseter muscle and then to the temporalis muscle. *The buccal nerve penetrates the lower temporalis muscle and ramifies over the surface of the buccinator muscle, communicating with buccal branches of VII.* The auriculotemporal nerve arises close to the foramen spinosum as two roots that encircle the middle meningeal artery and then join and run behind the neck of the mandible to pass upward with the superficial temporal artery (Fig. 33-35). The *auriculotemporal nerve communicates with the otic ganglion and with the facial nerve in the substance of the parotid gland. The lingual nerve of V_3 lies deep to the lateral pterygoid muscle, where it is joined by the chorda tympani nerve of VII.* The lingual nerve then runs between the medial pterygoid muscle and the mandible, crosses over the superior pharyngeal constrictor and styloglossus muscle, and reaches the side of the tongue. It then passes between the hyoglossus and the submandibular gland, crosses the lateral side of the submandibular (Wharton's) duct, and runs along the undersurface of the tongue to its tip, lying just deep to the mucosa (Fig. 33-35). *The lingual nerve has communications with the submandibular ganglion and the hypoglossal nerve (XII)* along the anterior margin of the hyoglossus muscle. The inferior alveolar nerve enters the ramus of the mandible through the mandibular foramen and runs within the mandibular canal. It has branches to the mylohyoid muscle and dental branches before it emerges from the mental foramen of the mandible as the mental nerve. *The terminal branches communicate freely with the mandibular branch of the facial nerve.*

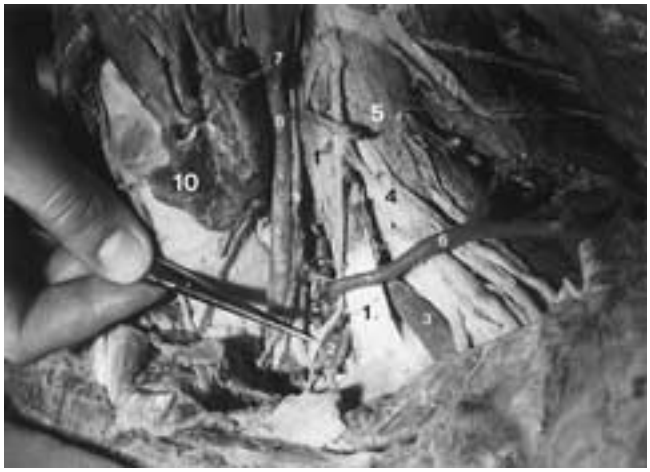

FIGURE 33-34 Left subclavian triangle—gross dissection (oblique view). Superficial musculature and veins have been removed. The forceps indicates the phrenic nerve as it crosses anterior to the first portion of the subclavian artery. Note the anterior scalene muscle (*1*) and its relationship to the subclavian artery, (*2*) first portion and (*3*) third portion (the second portion lies deep to the muscle tendon). The roots of the branchial plexus (*4*) course between the anterior scalene (*1*) and middle-posterior scalene (*5*) muscles. *6*, Transverse scapular artery (the suprascapular artery was absent in this specimen); *7*, internal jugular vein (cut); *8*, common carotid artery; *9*, vagus nerve; *10*, thyroid gland.

VIEW IMAGE

The facial nerve has two roots, a larger motor root and a smaller sensory and parasympathetic root called the nervus intermedius (see Chapter 19). Within the internal auditory canal, the *facial nerve communicates with the vestibulocochlear nerve (VIII). Via the geniculate ganglion it communicates with the pterygopalatine ganglion and sympathetic fibers.* Within the facial canal, just before it exits the stylomastoid foramen, *VII communicates with the auricular branch of the vagus nerve (X).* Below the skull base, *VII communicates with the glossopharyngeal nerve (IX), X, the great auricular nerve of the cervical plexus (C2,C3), and the auricular temporal nerve of V_3.* Within the parotid gland, the facial nerve then typically divides into five branches (Fig. 33-32). (The facial nerve is further discussed in Chapters 13 and 39).

The glossopharyngeal nerve exits the skull base through the jugular foramen, situated between the internal carotid artery and the internal jugular vein and posterior to the styloid process. Within the jugular fossa there is a smaller superior ganglion and a *larger inferior ganglion that communicate with X and the superior sympathetic ganglion.* Immediately below the skull base, *IX communicates with VII.* It then follows the posterior border of the stylopharyngeus muscle, which it supplies, for 2 to 3 cm and then curves

Copyright © 2003, Mosby, Inc. All rights reserved.

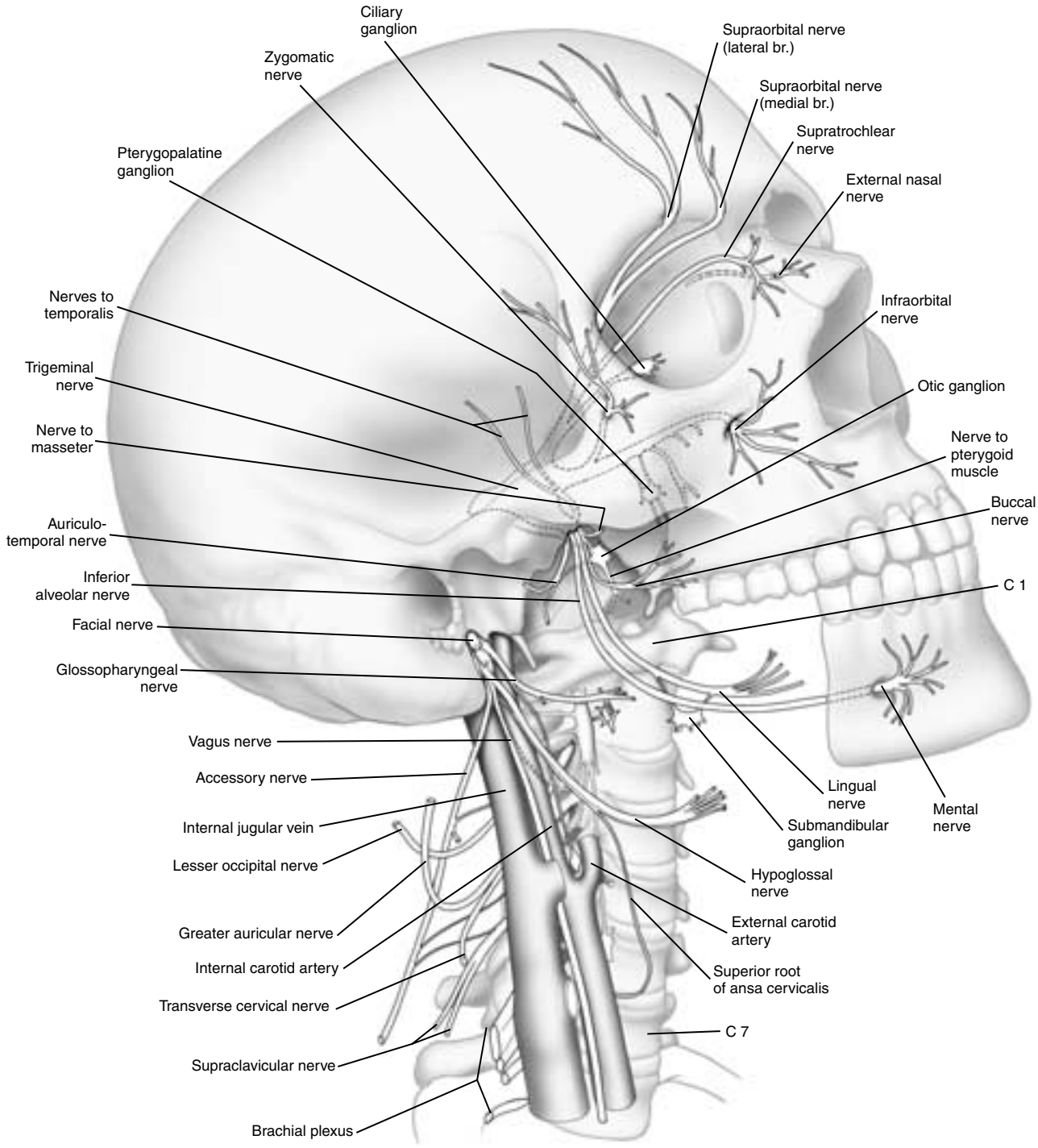

VIEW IMAGE

FIGURE 33-35 Drawing of the oblique frontal view of the skull and cervical spine showing the relationships of the cranial nerves, autonomic ganglia, and some of the connections with the cervical roots.

across the outer surface of the hyoglossus muscle. It then penetrates deeply, to be distributed to the palatine tonsil, the mucosa of the fauces and base of the tongue, and the minor salivary glands in the region (Fig. 33-35).

The vagus nerve is the longest of the cranial nerves, has the most extensive distribution of any of the cranial nerves, and leaves the skull base via the jugular foramen. Within the jugular foramen there is the 4 to 5 mm in diameter superior vagal (jugular) ganglion. About 1 cm below it and under the skull base is the 2.5 cm inferior (nodose) ganglion of X. The *jugular ganglion communicates with the spinal accessory nerve (XI), the inferior ganglion of IX, VII via the auricular branch, and the superior sympathetic cervical ganglion. The nodose ganglion communicates with XII, the superior sympathetic cervical ganglion, and the cervical plexus via the loop between the anterior rami of C1 and C2*. Within the neck, X lies within the carotid sheath, posterior to the internal carotid artery and anterior to the internal jugular

Copyright © 2003, Mosby, Inc. All rights reserved.

vein (Fig. 33-35). On the right side, the vagus nerve passes above and anterior to the subclavian artery, lying posterior to the brachiocephalic (innominate) vein (Fig. 33-27). As it passes under the subclavian artery, the right vagus contributes to the posterior pulmonary plexus, and below this it enters a plexus on the dorsal side of the esophagus. It then communicates with the left vagus and forms a single trunk, the posterior vagus nerve, which passes through the esophageal hiatus in the diaphragm. As the vagus nerve passes superficial to the first part of the subclavian artery, the right recurrent loops under this vessel and then ascends within the tracheoesophageal groove as the right recurrent nerve to enter the larynx near the posterior aspect of the cricothyroid joint.

The left vagus extends down around the left side of the aortic arch, passing above and anterior to it before going under it, lying between the aorta and the left pulmonary artery just distal to the ligamentum arteriosum (Fig. 33-27). Near the root of the lung, it contributes to the posterior pulmonary plexus and communicates with the right vagus to form the anterior vagus nerve, which then passes through the diaphragm. The left recurrent nerve arises near the posterior pulmonary plexus and ascends in the tracheoesophageal groove to enter the larynx near the posterior cricothyroid joint. Because of the nerves's low origin on the left, imaging of patients with paralysis of the left recurrent laryngeal nerve must be extended below the level of the aorticopulmonary window.

The vagus nerve has a meningeal branch to the dura and an auricular branch *(Arnold's nerve), which communicates with the inferior ganglion of IX* and then passes via the mastoid canaliculus into the temporal bone near the facial canal just above the stylomastoid foramen. *It communicates with VII* and then passes through the tympanomastoid fissure to be distributed on the skin of the posterior external auditory canal and the back of the pinna, joining *the posterior auricular nerve of VII*. There are *pharyngeal branches that arise just under the nodose ganglion and contain fibers from XI. The pharyngeal branches then communicate with IX, the sympathetics, and the external branch of X to form the pharyngeal plexus*, which is on the upper margin of the middle pharyngeal constrictor muscle. The *vagus also has branches to the carotid body, along with fibers from IX and the superior cervical sympathetic ganglion*. The superior laryngeal nerve arises near the lower border of the nodose ganglion and passes downward, near the internal carotid artery, to the thyrohyoid membrane of the larynx. The *superior laryngeal nerve communicates with the superior cervical sympathetic ganglion*.

The spinal accessory nerve has a cranial and a spinal portion. The *cranial portion (cranial root)* passes through the jugular foramen separately from the spinal portion (spinal root) and *joins X* proximal to the nodose ganglion. The spinal portion also passes through the jugular foramen, lying immediately adjacent to the cranial portion, and then passes below the skull base either anterior (two thirds) or posterior (one third) to the internal jugular vein. Then XI passes posterior to the stylohyoid muscle and the posterior belly of the digastric muscle to the upper portion of the sternocleidomastoid muscle, which it pierces. It then courses obliquely downward and backward across the posterior triangle of the neck to the anterior border of the trapezius muscle. Via the cervical plexus*, XI communicates with C1, C2, C3, and C4* (Figs. 33-35 and 33-36).

The hypoglossal nerve rootlets join to form two bundles that pass through the hypoglossal canal and then unite below the skull base. Nerve XII runs downward within the carotid sheath and becomes superficial to the internal carotid artery and internal vein near the angle of the mandible. Nerve XII then becomes anterior to the external carotid and lingual arteries below the tendon of the digastric muscle. It passes above the hyoid bone and goes deep to the stylohyoid and digastric muscles between the mylohyoid and hyoglossus muscles. It then continues forward near the genioglossus muscle to the tip of the tongue. *Nerve XII communicates with the nodose ganglion of X, the pharyngeal plexus, the superior cervical sympathetic ganglion, the lingual nerve of V, and the cervical plexus C1 and C2 loop* (Figs. 33-35 and 33-36).

Spinal Nerves

The spinal nerves have both ventral and dorsal rami. The dorsal rami supply the intrinsic muscles of the back (i.e., those muscles evolutionarily derived from the axial skeleton) and the skin of the midline areas of the occipital region of the skull and back. The suboccipital or C1 dorsal ramus emerges above the posterior arch of C1 and supplies the rectus capitis posterior (major and minor), oblique capitis (superior and inferior), and semispinalis capitis muscles. *The dorsal C1 ramus communicates with a filament of C2*. The dorsal division of C2 emerges between the posterior arch of C1 and the lamina of C2. It supplies the oblique capitis inferior muscle and then divides into the greater occipital nerve and the lateral branch. The *greater occipital nerve communicates with dorsal branches of C3 and supplies the scalp and vertex of the head, communicating with the lesser occipital nerve*. It also supplies the semispinalis captis. The *lateral branch* supplies the splenius capitis and semisplenius capitis and often *communicates with the lateral branch of C3*. The dorsal rami of C3 supply the skin of the lower back of the neck. The dorsal rami of C4 to C8 supply the semispinalis capitis and cervicis, the multifidus, interspinales, iliocostalis cervicis, and longissimus capitis and cervicis muscles and the skin of the back.

The cervical plexus is formed by the ventral primary rami of the upper four cervical nerves. The rami of C2 to C4 each divide into upper and lower branches, and these branches unite to form three loops. The *cervical plexus has communications with cranial nerves X, XI, and XII and the superior sympathetic ganglion* (Figs. 33-36 and 33-37). The ventral ramus of C1 leaves the spinal canal above the posterior arch of C1 and runs forward around the lateral aspect of the superior articular process while being medial to the vertebral artery. Most often it remains medial and anterior to the lateral rectus capitis muscle. The ventral rami of C2 to C4 extend out between the anterior and posterior intertransversarii muscles, lying on the grooved upper surfaces of the transverse processes of the vertebrae. The cervical plexus lies opposite the first four cervical vertebrae, anterior and lateral to the levator scapulae and middle scalene muscles and deep to the sternocleidomastoid muscle.

Copyright © 2003, Mosby, Inc. All rights reserved.

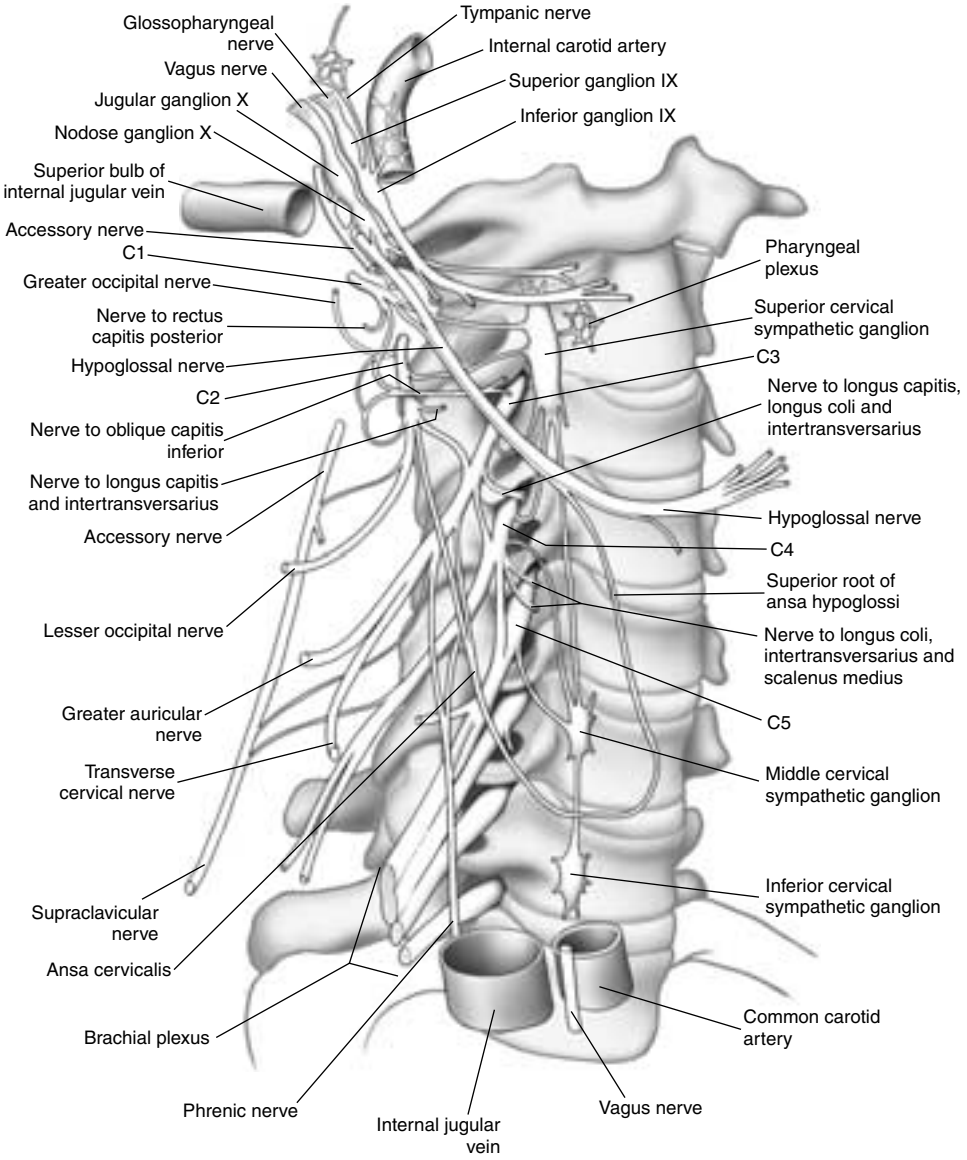

FIGURE 33-36 Drawing of the oblique frontal view of the cervical spine showing the relationship of the cervical nerves, the glossopharyngeal and vagus nerves, and the cervical sympathetic ganglia.

VIEW IMAGE

Following its exit from the skull base, the *hypoglossal nerve is joined by fibers from the loop between C1 and C2*, and these fibers course with the hypoglossal nerve until it crosses the internal carotid artery. At this point, most of the cervical nerve fibers separate from the main trunk and descend as the superior ramus of the ansa hypoglossi or the descending hypoglossal ramus. This ramus courses inferiorly on the internal carotid artery to unite with the inferior ramus of the ansa cervicalis (ansa hypoglossi) or the descending cervical ramus, formed by fibers from the C2 and C3 nerves. The ansa supplies motor innervation to the sternohyoid, omohyoid, and sternothyroid muscles. The thyrohyoid and geniohyoid muscles are supplied by the few C1 fibers that course with the hypoglossal nerve beyond the origin of the superior ramus.[1, 64–67] *The hypoglossal nerve sends a branch to communicate with the nodose ganglion of the vagus nerve, as do fibers from the loop between C1 and C2. Communication between the cervical plexus and the spinal accessory nerve occurs at several places; branches from the loop between C2 and C3 join XI to supply the sternocleidomastoid muscle; fibers from C3 join XI to supply the trapezius muscle; and proprioceptive fibers from C4 also join XI and go to the deep surface of the trapezius muscle* (Figs. 33-36 and 33-37).

Other deep or muscular branches of the cervical plexus include those from the loop between C1 and C2 to the anterior rectus capitis and lateral rectus capitis muscles; from C1 to C3 branches go to the longus capitis muscle and from C2 to C4 to the longus colli muscle; fibers from the C1/C2 loop run with XII and then leave it as the descending hypoglossi. Fibers from the descending hypoglossi supply the superior belly of the omohyoid muscle and the thyrohyoid and geniohyoid muscles prior to joining fibers from C2/C3 (the descending cervical nerve) to form the ansa cervicalis. The descendens hypoglossi supplies the inferior belly of the omohyoid muscle, and fibers from the ansa

Copyright © 2003, Mosby, Inc. All rights reserved.

(cervicalis) go to the sternohyoid and sternothyroid muscles (Fig. 33-37).

There are also superficial or cutaneous branches of the cervical plexus. *The lesser occipital nerve* usually arises from the C2/C3 loop and ascends along the sternocleidomastoid muscle to the retroauricular area, where it supplies the skin, *communicating with the greater occipital and great auricular nerves and the posterior auricular branch of VII. The great auricular nerve* arises from C2 and C3 and goes along the posterior border of the sternocleidomastoid muscle deep to the platysma muscle, where an anterior branch supplies the skin over the parotid gland and fibers *communicate with the substance of the gland*. The *posterior branch of the great auricular nerve* supplies the skin over the mastoid process and portions of the auricle. This branch *communicates with the lesser occipital nerve, the auricular branch of X, and the posterior auricular branch of VII. The cervical cutaneous nerve* arises from C2 and C3 and runs horizontally across the sternocleidomastoid muscle, deep to the external jugular vein and platysma, to form ascending and descending branches. The ascending branches go to the skin of the submaxillary region and the upper anterior lateral neck. A few fibers *communicate with the cervical branch of VII*. The descending branch supplies the lateral anterior neck down to the sternum. The *supraclavicular nerves* arise from C3 and C4 and extend posterior to the sternocleidomastoid muscle to form the following branches: the anterior supraclavicular nerves that supply the skin over the medial infraclavicular region to the midline; the middle supraclavicular nerves that supply the skin over the pectoralis major muscle and the deltoid muscle, *communicating with the cutaneous branches of the upper intercostal nerves*; and the posterior supraclavicular nerves that supply the skin over the upper and posterior shoulder (Figs. 33-32 and 33-35). The brachial plexus is formed by the ventral primary rami of the lower four cervical nerves and the first thoracic nerve, with occasional small contributions from the fourth cervical and second thoracic nerves (Fig. 33-36).[64, 66–68] These ventral rami course between the anterior and middle scalene muscles, superior to the second portion of the subclavian artery. The brachial plexus extends from the lateral border of the anterior scalene muscle to the lower border of the pectoralis minor muscle, at which point the cords divide into their terminal branches. The detailed anatomy and imaging of the brachial plexus are discussed in Chapter 42.

The phrenic nerve arises primarily from the fourth cervical nerve, with contributions from the third and fifth cervical nerves (Figs. 33-36 and 33-38). It courses inferiorly on the anterior scalene muscle, deep to the transverse cervical and suprascapular branches of the thyrocervical trunk and deep to the prevertebral fascia. It gains access to the medial surface of the pleura by crossing anterior to the first portion of the subclavian and internal thoracic (mammary) arteries.[64, 66–68]

Sympathetic System

The cervical portion of the sympathetic system consists of three ganglia (superior, middle, and inferior) connected by intervening cords (Figs. 33-36, 33-38). This system lies ventral to the transverse processes of the vertebrae, near the carotid artery, either embedded within the carotid sheath or between the sheath and the fascia over the longus capitis and longus colli muscles. Its preganglionic or white rami come from the upper five thoracic spinal nerves, primarily from T2 and T3, and travel up to the three cervical ganglia. The superior ganglion is the largest, being about 30 mm long by 8 mm wide. It is embedded in the connective tissues between the carotid sheath and the longus capitis muscle at the level

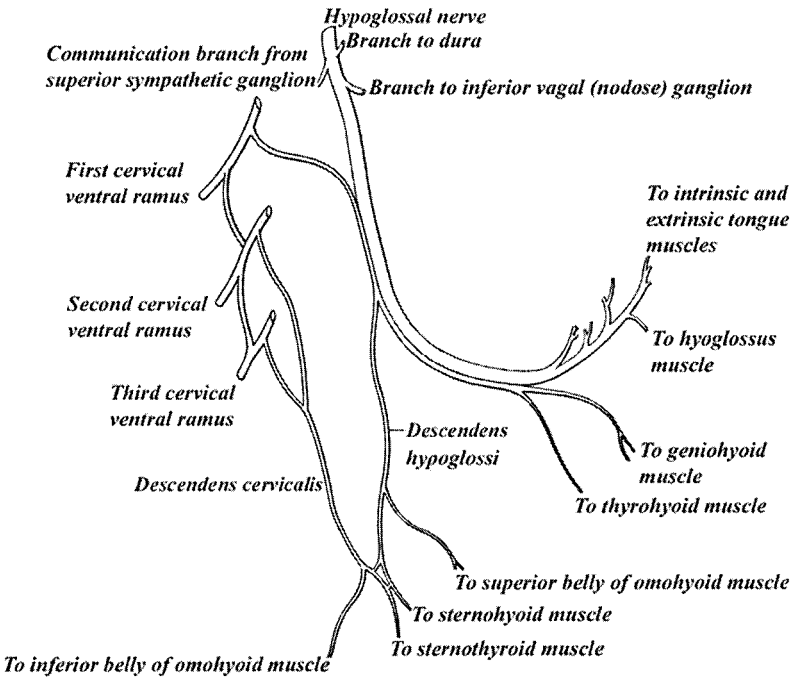

FIGURE 33-37 Diagram showing the ansa cervicalis and its relationship to the hypoglossal nerve and the first three cervical ventral roots.

VIEW IMAGE

Copyright © 2003, Mosby, Inc. All rights reserved.

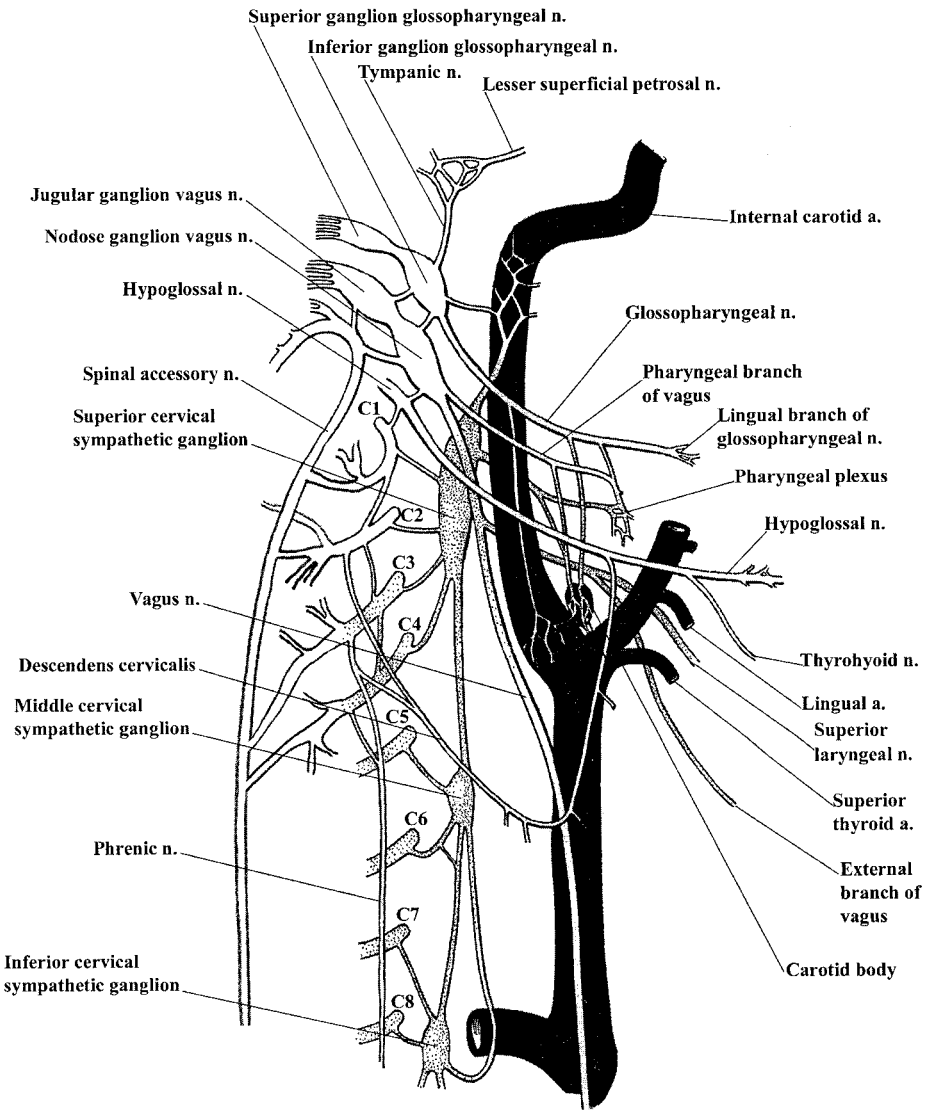

VIEW IMAGE

FIGURE 33-38 Diagram showing the relationship of the cervical sympathetic ganglia, the glossopharyngeal, vagus, and spinal accessory nerves, the cervical nerves, and the ansa cervicalis.

of the second cervical vertebra. The superior cervical ganglion gives off a collection of postganglionic fibers known as the *internal carotid nerve*, which extends into the head. *The superior ganglion communicates with the inferior ganglion of IX, the jugular and nodose ganglia of X, XII, branches (sympathetic roots or gray rami) to and ventral roots of C1, C2, and usually C3, and C4, a pharyngeal branch to the pharyngeal plexus, and branches to the external carotid artery, the intercarotid plexus, and the superior cardiac nerves*. These cardiac nerves have different courses on either side of the neck. On the right side, the nerves pass either anterior or posterior to the subclavian artery and then along the brachiocephalic artery to the deep cardiac plexus. On the left side, the cardiac nerve is anterior to the common carotid artery and then extends across the left side of the aortic arch to reach the superficial cardiac plexus.

The middle cervical ganglion is the smallest cervical ganglion and may be either double or missing. It is usually near the transverse process of the sixth cervical vertebra, on the longus colli muscle at the level of the bend of the inferior thyroid artery. It may also be at the level of the seventh cervical vertebra near the vertebral artery. *Sympathetic roots from the middle ganglion go to the C5 and C6 ventral roots*. There are also *middle cardiac nerves* that run down with the common carotid artery and *communicate with the superior cardiac nerve and the recurrent laryngeal nerve of X on either side*. Lastly, there is the *thyroid nerve*, which forms a plexus on the inferior thyroid artery and supplies the thyroid gland. It also *joins the plexus on the common carotid artery and may communicate with branches of the superior laryngeal nerve of X*.

The inferior cervical ganglion is situated near the transverse process of the seventh cervical vertebra and the neck of the first rib. It may be completely separate from the first thoracic ganglion or, more commonly, it may be fused with it and is then called the *stellate ganglion*. The *middle cervical ganglion has sympathetic roots to the ventral rami of C6, C7, and C8*. There are also the inferior cardiac nerve and the vertebral nerve, the latter accompanying the vertebral artery.

The *stellate ganglion* (when present) is usually formed by

Copyright © 2003, Mosby, Inc. All rights reserved.

a fusion of the inferior cervical and first thoracic ganglia, but may include the middle cervical and second thoracic ganglia. *Gray rami go to the spinal nerves C6, C7, C8, T1, and T2, and to the vertebral artery*.[64, 66–68]

Autonomic (Parasympathetic) Ganglia of the Face and Neck

Four parasympathetic ganglia are found in the head and upper neck: the ciliary, pterygopalatine, submandibular, and otic (Fig. 33-35). These ganglia are distinctive in that in contrast to the usual body plan of having secondary sympathetic cell bodies in discrete ganglia, these are the major instances in which secondary parasympathetic neurons occur in discrete ganglia rather than at or in the walls of the structures they innervate, as is usually found throughout the body. All four ganglia have a similar plan of composition. Traditionally, each ganglion is described as having four ''roots'': a motor root (preganglionic parasympathetic—the only site of any synapse), a sensory root, a sympathetic root, and a distribution root.

The Ciliary Ganglion

The ciliary ganglion is about 1 to 2 mm in diameter and lies on the lateral side of the optic nerve (II) just in front of the ophthalmic artery about 1 cm from the posterior globe. The motor root comes from the Edinger-Westphal nucleus of the third nerve and reaches the ganglion via the inferior division of this nerve within the orbit. The sympathetic root comes from the cavernous sinus plexus, whose postganglionic fibers come from the superior sympathetic cervical ganglion. The sensory fibers come from the nasociliary nerve, a branch of V_1. Via the short ciliary nerves, all three roots reach the eye. The parasympathetic fibers are distributed to the sphincter pupillae and ciliary muscles. The sympathetic fibers are vasoconstrictive fibers that go to the intraocular blood vessels. Some sympathetic fibers also go via the long ciliary nerves to the dilator pupillae muscle. The sensory fibers go to the entire globe, including the cornea.

The Pterygopalatine Ganglion

The pterygopalatine ganglion (sphenopalatine ganglion) is in the deep portion of the pterygopalatine fossa, just below the maxillary nerve as it crosses the fossa to the pterygopalatine canal. It is triangular in shape and about 5 mm in length. It is closely attached to the pterygopalatine branches of the maxillary nerve (V_2). The motor root comes from the superior salivary nucleus. The fibers leave the brainstem in the nervus intermedius that accompanies VII until the geniculate ganglion, where the motor fibers leave VII as the greater petrosal (greater superficial petrosal) nerve. The sympathetic root comes from the internal carotid plexus via the superior sympathetic cervical ganglion as the deep petrosal nerve. The sensory root comes from two short branches of the trigeminal ganglion that join the greater petrosal nerve. The joining of the greater petrosal and deep petrosal nerves forms the nerve of the pterygoid canal (the Vidian nerve). The parasympathetic fibers go to the lacrimal gland and the mucous glands of the nose, paranasal sinuses, nasopharynx, and palate. The sympathetic fibers are vasoconstrictive to the mucosa of the same region, and the sensory fibers provide sensation to the same mucosa.

The Submandibular Ganglion

The submandibular ganglion is 2 to 5 mm in diameter and is situated above the deep portion of the submandibular gland, on the hyoglossus muscle, near the posterior border of the mylohyoid muscle. The ganglion is suspended from the lower border of the lingual nerve by two 5 mm filaments. The motor root comes from the superior salivary nucleus, and the fibers leave the brainstem in the nervus intermedius that accompanies VII until the corda tympani nerve. The fibers then travel with the corda tympani nerve to join the lingual nerve of V_3. The sympathetic root comes from the superior sympathetic cervical plexus via the plexus around the facial artery. The sensory root comes from the trigeminal ganglion through the lingual nerve. The parasympathetic, sympathetic, and sensory fibers go to the sublingual and submandibular glands and the mucous glands in the floor of the mouth.

The Otic Ganglion

The otic ganglion is a flattened, oval, stellate ganglion 2 to 4 mm in diameter. It is closely approximated to the medial surface of V_3, just below the foramen ovale. It is lateral to the cartilaginous portion of the pharyngotympanic auditory, (eustachian) tube, anterior to the middle meningeal artery, and posterior to the origin of the tensor veli palatini muscle. The motor roots come from the inferior salivary nucleus and leave the brainstem with IX. They pass via the tympanic (Jacobson's) nerve to the tympanic plexus. Here they unite with fibers from the nervus intermedius part of the facial nerve, and the united fibers leave the tympanic plexus as the lesser petrosal (lesser superficial petrosal) nerve. The sympathetic root comes from the superior cervical sympathetic ganglion via the plexus on the middle meningeal artery. The sensory root enters the ganglion from the auriculotemporal nerve (V_3) from cells originating in the trigeminal ganglion. The branches are distributed to the parotid gland via the auriculotemporal nerve. They also go to the glands of the buccal mucosa and lower lip.

A detailed discussion of the lymphatics of the neck is presented in Chapter 36. The origins, insertions, motor innervations, and actions of the muscles discussed in this chapter, as well as other neck muscles discussed elsewhere in the book, are listed in Table 33-3. The normal anatomy of the neck, with emphasis on the muscles and major vessels, is shown in the atlas at the end of this chapter.

DIFFERENTIAL DIAGNOSIS

The formulation of a list of differential diagnoses of a neck lesion is based on several factors including the location of the mass, the patient's age, and physical findings such as tenderness, firmness, and fixation. A thorough discussion of the imaging for each area occurs in the respective chapters relating to these regions. This section presents an overview of differential diagnoses based on the location of the mass. The most likely causes of a mass are mentioned, as are the

Copyright © 2003, Mosby, Inc. All rights reserved.

Table 33-3
MUSCLES OF THE NECK, ORAL CAVITY, AND PHARYNX

Muscle	Origin	Insertion	Innervation	Action
Platysma	Fascia and skin over the upper part of the pectoralis and deltoid muscles	Lower border of the mandible and muscles of the lip	Cervical branch of the facial nerve (VII)	Produces a slight wrinkling of the skin surface of the neck, in an oblique direction, when the entire muscle is brought into action. Anterior portion depresses the lower jaw and draws the lower lip and angles of the mouth down on either side
Sternocleidomastoid	Sternum and medial third of the clavicle	Mastoid process of the temporal bone and the superior nuchal line	Spinal accessory nerve (XI) and C2	Acting alone, it bends the head to its own side and rotates so that the face is turned to the opposite side. The two muscles, acting together, flex the neck. If the neck is kept extended by the posterior vertebral muscles, the muscles act together to raise the sternum and assist in inspiration
Anteror Belly of the Digastric Muscle	Lower border of the mandible near the symphysis	Into an intermediate tendon, where it is united with the posterior belly	Mylohyoid nerve-branch of the inferior alveolar branch of the mandibular division of the trigeminal nerve (V_3)	
Posterior Belly of the Digastric Muscle	Digastric notch of the temporal bone	Into an intermediate tendon, where it is united with the anterior belly	Facial nerve (VII)	Chief action of both bellies, acting together, is to raise the hyoid bone during swallowing. Acting with the infrahyoid muscles, they fix the hyoid bone, forming a stable platform on which the tongue can move
Stylohyoid	Styloid process of the temporal bone	Distally it splits to surround the intermediate tendon of the digastric muscle before inserting on the hyoid bone	Facial nerve (VII)	Helps pull the hyoid up and backward during swallowing
Mylohyoid	Entire length of the mylohyoid line of the mandible	Into a midline fibrous raphe, extending from the mandibular symphysis to the hyoid bone	Mylohyoid nerve-branch of the inferior alveolar nerve branch of the mandibular division of the trigeminal nerve (V_3)	Raises the hyoid bone and tongue during swallowing and forms the muscular floor of the mouth
Hyoglossus	Body and greater cornu of the hyoid bone	Posterior half of the side of the tongue	Hypoglossal nerve (XII)	Depresses the side of the tongue and enlarges the cavity of the mouth
Geniohyoid	Inferior genial tubercle on the inner surface of the mandible	Anterior surface of the body of hyoid bone	Branch C1 through the hypoglossal nerve (XII)	Elevates the hyoid bone and tongue
Genioglossus	Upper genial tubercle on the inner surface of the mandible	Lowest fibers to the hyoid bone. Middle fibers to undersurface of the tongue, upper fibers to tip of the tongue	Muscular branches of the hypoglossal nerve (XII)	Posterior fibers protrude the tongue. Anterior fibers retract tongue, aided by styloglossus muscle. Tongue depressed by genioglossus and hyoglossus
Transverse and Verticalis Tongue Muscles	Transverse from median fibrous septum. Vertical from mucous membrane on dorsum and tip of tongue	Dorsum and sides of the tongue and from dorsum to undersurface of the tongue	Trigeminal (V_3) sensory anterior two thirds of the tongue. Corda tympani (VII) taste anterior two thirds of the tongue. Glossopharyngeal (XI) sensory and taste posterior one third of the tongue. Hypoglossal (XII) extrinsic and intrinsic muscles	Modifies shape of tongue. Transverse muscle narrows and elongates tongue. Verticalis muscle flattens and broadens tongue
Superior and Inferior Longitudinal Muscles of Tongue	Superior muscle fibers in back of tongue. Inferior muscle undersurface of tongue between genioglossus and hyoglossus	Tip of tongue	Trigeminal (V_3) sensory anterior two thirds of tongue. Corda tympani (VII) taste anterior two thirds of tongue. Glossopharyngeal (IX) sensory and taste posterior one third of tongue. Hypoglossal (XII) extrinsic and intrinsic muscles	Modifies shape of tongue. Superior: shortens tongue and turns tip and sides up. Inferior: turns tip and sides down

Table continues on following page

Table 33-3
MUSCLES OF THE NECK, ORAL CAVITY, AND PHARYNX *Continued*

Muscle	Origin	Insertion	Innervation	Action
Styloglossus	Anterior border of styloid process	Sides of tongue. Fibers mix with those of palatoglossus and hyoglossus	Hypoglossal nerve (XII)	Retracts tongue with aid of genioglossus. Elevates tongue with aid of palatoglossus
Palatoglossus	Anterior surface of soft palate	Dorsum and side of tongue, blending with styloglossus and transverse linguae	Pharyngeal plexus (sympathetic, IX, X), cranial portion XI	Narrows fauces and elevates back of tongue
Palatopharyngeus	Soft palate and mucous membranes	Posterior border of thyroid cartilage and aponeurosis of pharynx	Pharyngeal plexus (sympathetic, IX, X), cranial portion XI	Narrows oropharyangeal isthmus, elevates pharynx, shuts off nasopharynx
Superior Pharyngeal Constrictor	Lower third of posterior border of medial pterygoid plate, pterygomandibular raphe, and alveolar process of mandible	Median raphe of posterior pharynx and to pharyngeal tubercle	Cranial IX, X through pharyngeal plexus	Contracts pharynx in swallowing
Middle Pharyngeal Constrictor	Both cornua of hyoid bone, stylohyoid	Posterior pharyngeal raphe	Pharyngeal plexus (IX, X, sympathetic)	Contracts pharynx in swallowing
Inferior Pharyngeal Constrictor	Oblique line of thyroid cartilage, side of cricoid cartilage, posterior border of cricothyroid muscle	Posterior pharyngeal raphe	Pharyngeal plexus (IX, X, sympathetic), external and recurrent laryngeal branches of vagus X, and cranial XI	Contracts pharynx in swallowing
Stylopharyngeus	Medial root of styloid process. Passes between internal and external carotid arteries	Superior and posterior borders of thyroid cartilage and fibers of pharyngeal constrictors	Glossopharyngeal (IX)	Raises and dilates pharynx
Salpingopharyngeus	Pharyngeal end of eustachian tube near its orifice	Blends with palatopharyngeus	Pharyngeal plexus (IX, X, sympathetic), and cranial XI	Raises nasopharynx, helps open eustachian tube during swallowing with tensor veli palatini and levator veli palatini
Levator Veli Palatini	Lower surface of petrous temporal bone and medial side of eustachian tube	Fibers extend down to palate and blend with those of opposite side	Pharyngeal plexus (IX, X, sympathetic), and cranial XI	Raises soft palate in swallowing and helps open eustachian tube during swallowing with tensor veli palatini and salpingopharyngeus
Tensor Veli Palatini	Scaphoid fossa and spine of sphenoid and lateral side of eustachian tube	Tendon winds around hamulus into aponeurosis of soft palate and posterior palatal bone	Trigeminal (V_2)	Tenses soft palate and helps open eustachian tube during swallowing with levator veli palatini and salpingopharyngeus
Musculus Uvulae	Posterior nasal spine and palatal aponeurosis	Mucous membrane of uvula	Pharyngeal plexus (IX, X, sympathetic), and cranial XI	Raises uvula
Sternohyoid	Posterior manubrium and medial third of clavicles	Lower border of hyoid	Ansa hypoglossi	Depresses larynx and hyoid bone. Steadies hyoid bone
Sternothyroid	Posterior manubrium and first costal cartilage	Oblique line of thyroid cartilage lamina	Ansa hypoglossi	Depresses larynx and thyroid cartilage
Thyrohyoid	Oblique line of thyroid lamina	Lower border of body of hyoid bone	Thyrohyoid branch of C1 through descendens hypoglossi	Depresses larynx and hyoid bone and elevates thyroid cartilage
Superior Belly of Omohyoid	Body and greater cornu of hyoid bone	United with inferior belly by tendon deep to sternocleidomastoid muscle	Descendens hypoglossi (branches of C2 and C3)	Steadies hyoid bone and depresses and retracts hyoid and larynx
Inferior Belly of Omohyoid	Upper border of scapula	United with superior belly by tendon deep to sternocleidomastoid muscle	Descending cervical nerve of cervical plexus	Steadies hyoid bone and depresses and retracts hyoid and larynx
Longus Colli	Bodies of C3 to C7 and D1 to D3 vertebrae	Bodies of C2 to C4, atlas, and anterior tubercles of C2 to C6	Branches of anterior rami of C2 to C8	Flexes and assists in rotating cervical vertebrae and head. Acting singly, it flexes vertebral column laterally
Longus Capitis	Anterior tubercles of transverse processes of C3 to C6	Inferior basilar surface of occipital bone	Muscular branches of C1 to C4	Flexes and assists in rotating cervical vertebrae and head

Anterior Rectus Capitis	Lateral mass of atlas	Base of occipital bone in front of foramen magnum	Muscular branches of C1 and C2	Flexes and rotates head
Lateral Rectus Capitis	Upper transverse process of atlas	Inferior surface of jugular process of occipital bone	Branches of anterior rami of C1 and C2	Flexes head laterally
Anterior Scalene	Anterior tubercles of transverse processes of C3 to C6	Scalene tubercle and ridge of first rib	Anterior branches of C5 to C8	Acting from above, it elevates first rib. Acting from below, it flexes and rotates vertebral column
Middle Scalene	Posterior tubercles of transverse processes of C2 to C7	Upper surface of first rib behind subclavian groove	Posterior branches of anterior rami of C3 and C4, lateral muscular branches of C3 and C4	Flexes and assists in rotating cervical vertebrae and head. It flexes cervical column laterally. Acting from above, it elevates first rib on inspiration
Posterior Scalene	Posterior tubercles of transverse processes of C4 to C6	Outer surface of second rib behind attachment of serratus anterior	Posterior branches of anterior rami of C4 and C7 and lateral muscular branches of C3 and C4	Flexes and assists in rotating cervical verebrae and head. Acting alone, it flexes cervical column laterally. Acting from above, it elevates second rib on inspiration
Splenius Capitis	Lower half of ligamentum nuchae and spinous processes of C7, and D1 to D4	Mastoid process of temporal bone and lateral portion of superior nuchal line under sternocleidomastoid muscle	Lateral branches of posterior rami of C4 to C7	Bends the head and neck back and turns the face toward its own side
Trapezius	Medial portion of superior nuchal line, external occipital protuberance, nuchal ligament from spines of C7 and all dorsal vertebrae	Lateral third of clavicle, spine of scapula, acromion	Spinal accessory (XI) and C3 and C4	Adducts scapula, draws back acromion, rotates scapula, tilts chin
Levator Scapulae	Transverse processes of C1 to C4	Vertebral border of scapula between medial angle and root of spine	C3, C4, and possibly C5	
Temporalis	Floor of temporal fossa and temporal fascia	Anterior border of coronoid process and anterior border of mandibular ramus	Trigeminal (V)	Elevates jaw, retracts mandible, clenches teeth
Masseter	Lower border and deep surface of zygomatic arch	Lateral surface of coronoid process of mandible and outer surface of ramus and angle of the mandible	Trigeminal (V)	Elevates jaw and clenches teeth
Lateral (External) Pterygoid	Upper head from infratemporal surface of greater wing of sphenoid. Lower head from lateral surface of lateral pterygoid plate	Anterior neck of mandibular condyle and capsule of temporomandibular joint	Trigeminal (V)	Protrudes mandible, pulls articular disc forward, and assists in rotary motion while chewing
Medial (Internal) Pterygoid	Medial surface of lateral pterygoid plate, pyramidal process of palatine bone, and tuberosity of maxilla	Lower posterior medial surface of ramus and angle of mandible	Trigeminal (V)	Protracts and elevates mandible and assists in rotary motion while chewing
Buccinator	Alveolar process of mandible opposite molar teeth and anterior border of the pterygomandibular raphe	Fibers converge toward angle of mouth, where they blend with fibers of orbicularis oris muscle	Facial (VII)	Compresses cheeks, expels air from mouth, and aids in chewing

likely sites of primary tumors that commonly have nodal metastases to these regions. Abscesses may occur virtually anywhere in the neck, and their clinical presentation strongly suggests their diagnosis. Thus, although they can occur in every area, abscesses are not included in the various differential diagnoses.

In the submental triangle (level IA), a mass could be a dermoid, an epidermoid, a thyroglossal duct cyst, or lymphadenopathy. If it is lymphadenopathy, the probable source could be in the central lower lip, chin, anterior floor of the mouth, or tip of the tongue. The adenopathy may also be reactive or secondary to a lymphoma or another systemic disease such as sarcoidosis, mononucleosis, etc. (Table 33-4).

In the submandibular triangle (level IB), a mass could be due to enlargement of the submandibular gland (due to diffuse disease or a focal mass), a ranula, a solitary lymphangioma, or lymphadenopathy. If it is lymphadenopathy, the likely source could be in the submandibular or sublingual glands, the sides of the anterior two thirds of the tongue, the floor of the mouth or lower gums, the paranasal sinuses, the buccal cheek and lips, the anterior cheek, the sides of the nose, the upper lip and lateral lower lip, or the eyelids and conjunctiva. The adenopathy may also be reactive or secondary to a lymphoma or another systemic disease such as sarcoidosis, mononucleosis, etc. (Table 33-5).

In the carotid triangle, a mass could be a carotid body tumor, ectasia or an aneurysm of the carotid artery, phelbectasia of the internal jugular vein, a schwannoma or neurofibroma, a second or third branchial cleft cyst, a lateral thyroglossal duct cyst, a laryngocele, a lymphangioma, or lymphadenopathy. If it is lymphadenopathy, the likely source could be in the supraglottic larynx, the floor of the mouth, the sides or base of the tongue, the pharynx or palatine tonsil, the gums or palate, the posterior nasal cavity, the deep infratemporal or temporal fossa, the lower pinna of the ear, the occipital scalp, the parotid gland, the thyroid or parathyroid glands, or the upper cervical esophagus. Reactive nodes or lymphoma, metastasis from a distant site, or a systemic disease may also cause such lymphadenopathy (Table 33-6).

In the muscular triangle, a mass could represent diffuse enlargement of the thyroid gland or a localized thyroid mass, a parathyroid mass, a subglottic or cartilaginous laryngeal mass, a laryngocele, a third or fourth branchial cyst, a thyroglossal duct cyst, a cervical thymic cyst, an esophageal mass such as a Zenker's diverticulum, or lymphadenopathy. If it is lymphadenopathy, the likely source could be reactive nodes or a primary tumor in the thyroid or parathyroid

Table 33-4
DIFFERENTIAL DIAGNOSES BASED ON THE SUBMENTAL TRIANGLE OF THE NECK

- Submental triangle (level I)
  - Dermoid
  - Epidermoid
  - Thyroglossal duct cyst
  - Lymphadenopathy: likely source in:
    - Central lower lip
    - Chin
    - Anterior floor of mouth
    - Tip of the tongue
    - Reactive (hyperplastic)
    - Lymphoma
    - Systemic disease (sarcoidosis, etc.)

Table 33-5
DIFFERENTIAL DIAGNOSES BASED ON THE SUBMANDIBULAR TRIANGLE OF THE NECK

- Submandibular triangle (level II)
  - Submandibular gland
    - Diffuse disease (inflammatory)
    - Focal mass
    - Ranula
    - Solitary lymphangioma
    - Lymphadenopathy: likely source in:
      - Submandibular gland
      - Sublingual gland
      - Sides of the anterior two thirds of the tongue
      - Floor of the mouth or lower gums
      - Paranasal sinuses
      - Buccal cheek and lips
      - Anterior cheek
      - Sides of the nose
      - Upper lip and lateral lower lip
      - Eyelids and conjunctiva
      - Reactive (hyperplastic)
      - Lymphoma
      - Systemic disease (sarcoidosis, etc.)

Table 33-6
DIFFERENTIAL DIAGNOSES BASED ON THE CAROTID TRIANGLE OF THE NECK

- Carotid triangle
  - Carotid body tumor
  - Carotid ectasia
  - Carotid aneurysm
  - Phlebectasia of the internal jugular vein
  - Schwannoma
  - Neurofibroma
  - Second branchial cleft cyst
  - Third branchial cleft cyst
  - Lateral thyroglossal duct cyst
  - Laryngocele
  - Lymphangioma
  - Lymphadenopathy: likely source in:
    - Supraglottic larynx
    - Floor of mouth
    - Sides off tongue
    - Base of tongue
    - Pharynx
    - Palatine tonsil
    - Gums
    - Palate
    - Posterior nasal cavity
    - Deep infratemporal fossa
    - Deep temporal fossa
    - Lower pinna of the ear
    - Occipital scalp
    - Parotid gland
    - Thyroid gland
    - Parathyroid glands
    - Upper cervical esophagus
    - Reactive (hyperplastic)
    - Lymphoma
    - Metastasis (lung, breast, colon, kidney)
    - Systemic disease (sarcoidosis)

Copyright © 2003, Mosby, Inc. All rights reserved.

Table 33-7
DIFFERENTIAL DIAGNOSES BASED ON THE MUSCULAR TRIANGLE OF THE NECK

Muscular triangle
Thyroid gland
Diffuse enlargement (goiter, etc.)
Localized thyroid mass
Parathyroid mass
Larynx
Subglottic mass
Cartilaginous laryngeal mass
Laryngocele
Third branchial cleft cyst
Fourth branchial cleft cyst
Thyroglossal duct cyst
Cervical thymic cyst
Esophageal mass
Zenker's diverticulum
Lymphadenopathy: likely source in:
Reactive (hyperplastic) diseases
Thyroid tumor
Parathyroid tumor
Cervical esophagus
Postcricoid pharynx
Pharynx
Palatine tonsil
Lymphoma

glands, the cervical esophagus, the postcricoid pharynx, the pharynx, or the palatine tonsil. Lymphoma can also cause lymphadenopathy in this region (Table 33-7).

In the posterior triangle, the most likely cause of a mass could be a lymphangioma or hemangioma, a lipoma or rarely a liposarcoma, a neural tumor of either the spinal accessory nerve or part of the brachial plexus, an aneurysm of the subclavian artery, or lymphadenopathy. If it is lymphadenopathy, the most likely source would be lymphoma or a mass in the pharynx, the palatine tonsil, the base of the tongue, the parotid gland, or a metastasis from a distant primary below the clavicles. The adenopathy may also be reactive in etiology (Table 33-8).

Table 33-8
DIFFERENTIAL DIAGNOSES BASED ON THE POSTERIOR TRIANGLE OF THE NECK

Posterior triangle
Lymphangioma
Hemangioma
Lipoma
Liposarcoma
Neural tumor (schwannoma, neurofibroma)
Spinal accessory nerve
Brachial plexus
Subclavian artery aneurysm
Lymphadenopathy: likely source in:
Lymphoma
Pharynx
Palatine tonsil
Base of the tongue
Parotid gland
Reactive (hyperplastic) diseases
Metastasis (lung, breast, colon, kidney)

The following atlas reviews the neck anatomy as shown on computed tomographic (CT) scans and magnetic resonance (MR) images of normal necks.

Copyright © 2003, Mosby, Inc. All rights reserved.

CROSS-SECTIONAL ATLAS OF NORMAL NECK

FIGURE 1

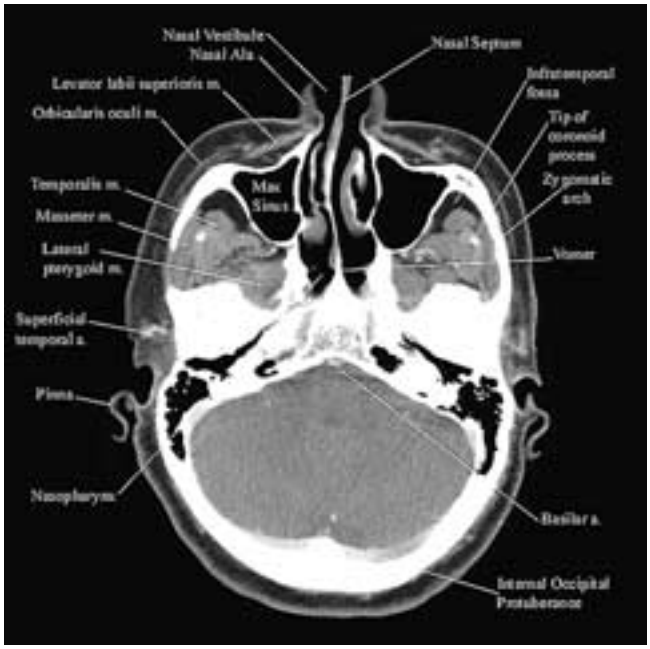

FIGURE 2

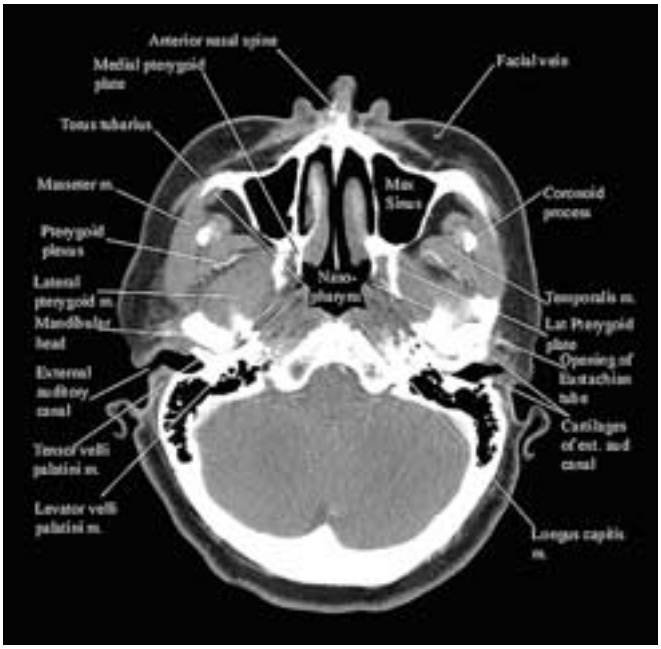

FIGURE 3

Copyright © 2003, Mosby, Inc. All rights reserved.

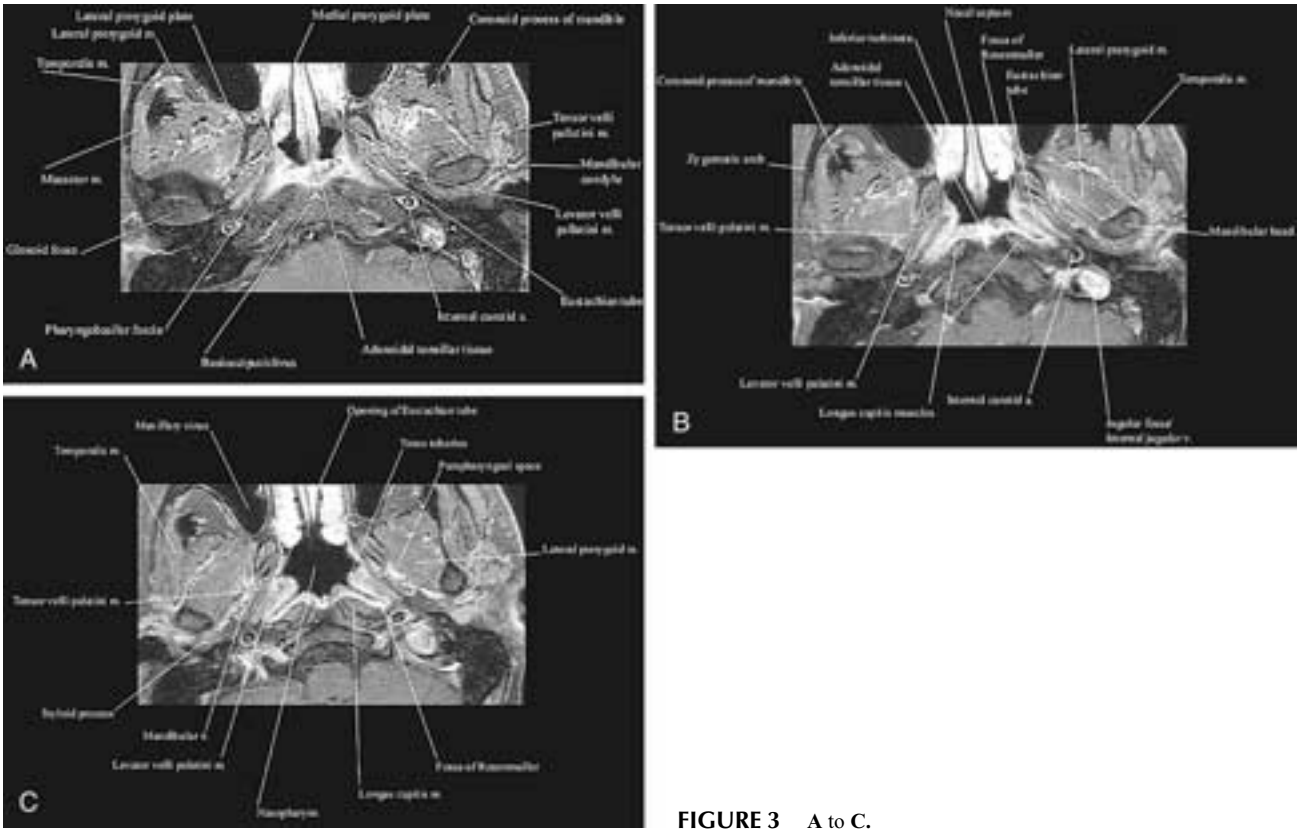

FIGURE 3 **A** to **C.**

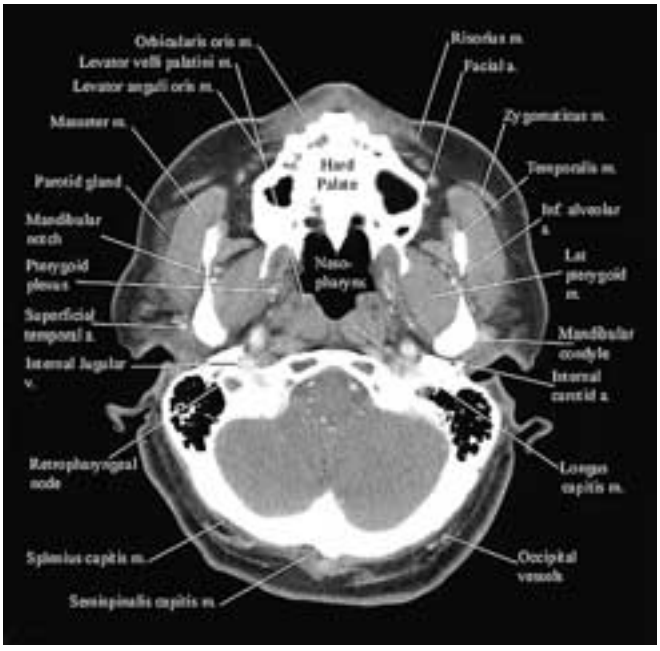

FIGURE 4

FIGURE 5

Copyright © 2003, Mosby, Inc. All rights reserved.

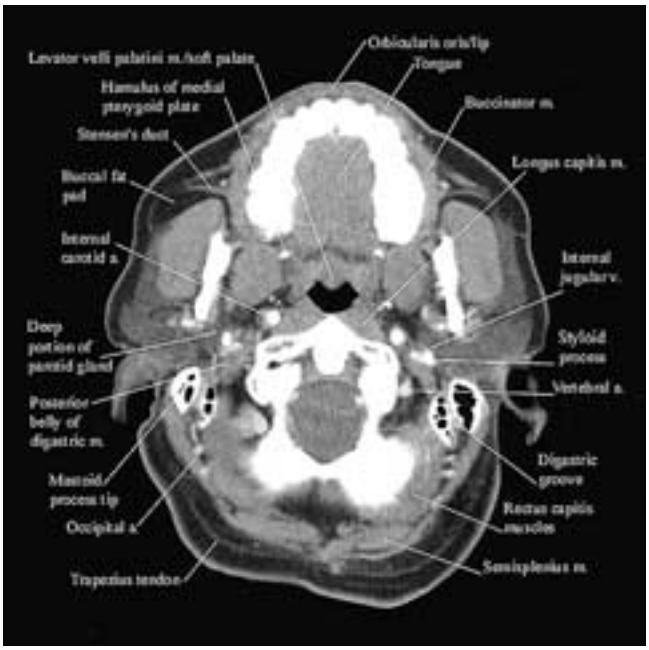

FIGURE 6

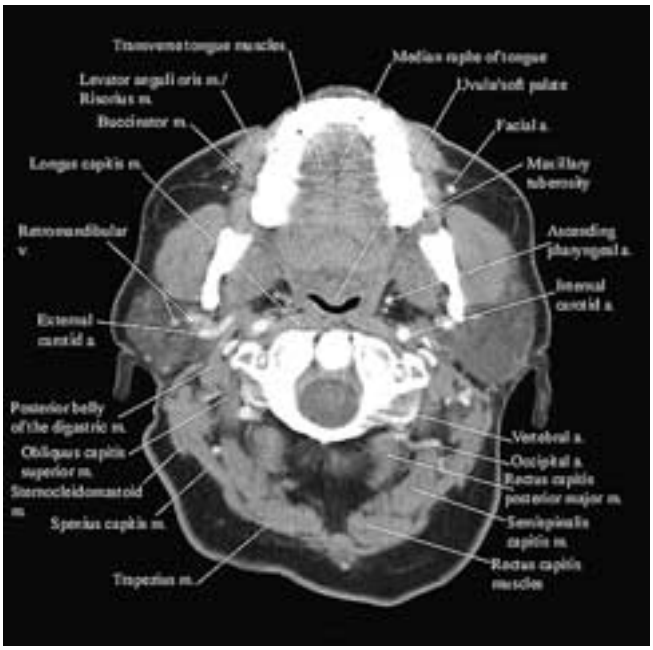

FIGURE 7

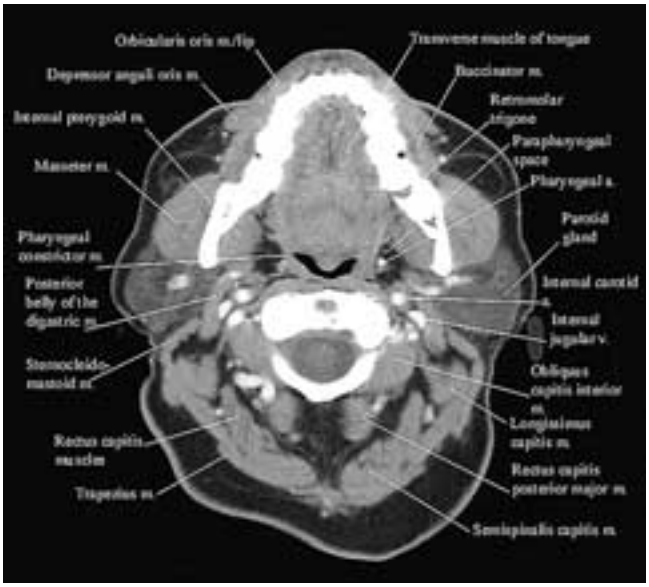

FIGURE 8

FIGURE 9

Copyright © 2003, Mosby, Inc. All rights reserved.

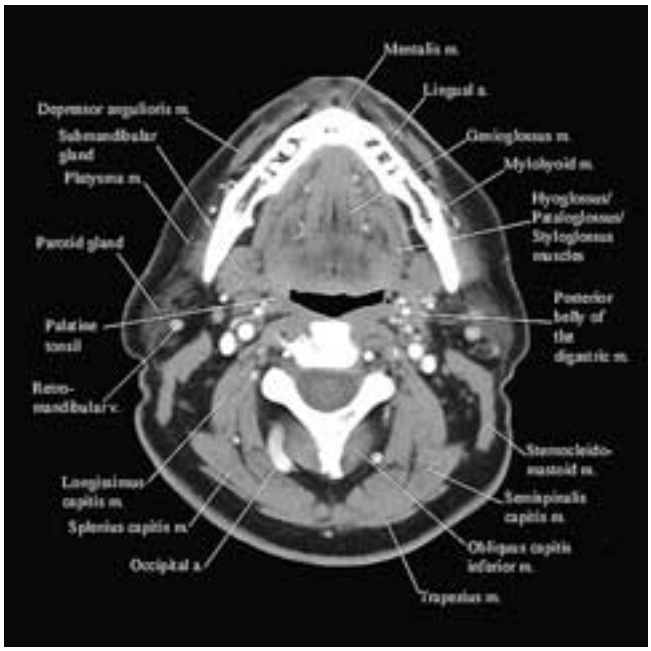

FIGURE 10

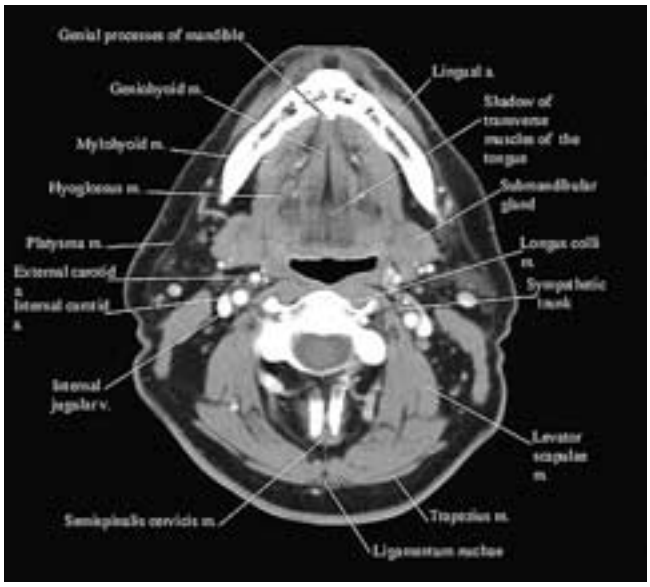

FIGURE 11

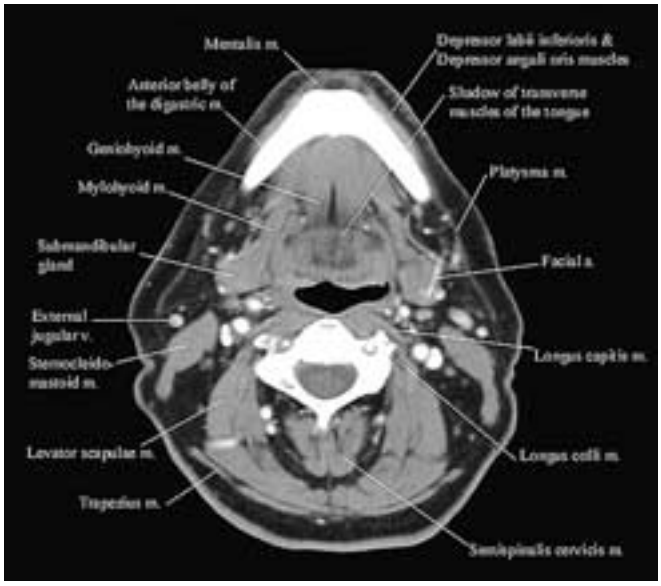

FIGURE 12

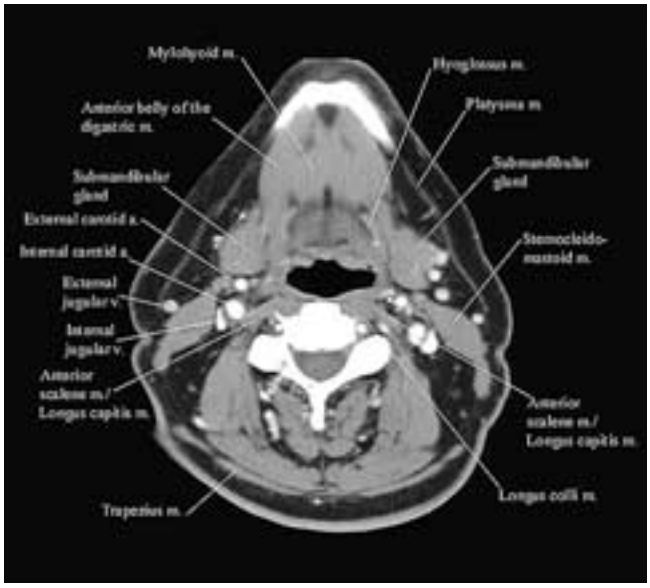

FIGURE 13

Copyright © 2003, Mosby, Inc. All rights reserved.

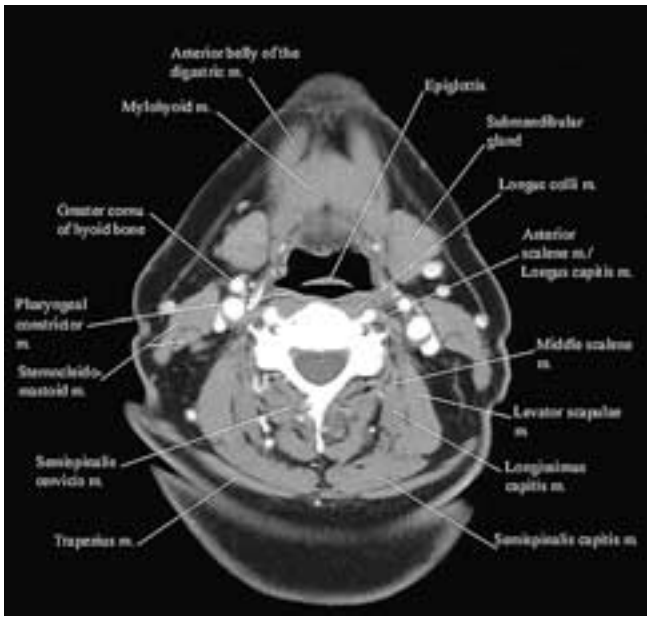

FIGURE 14

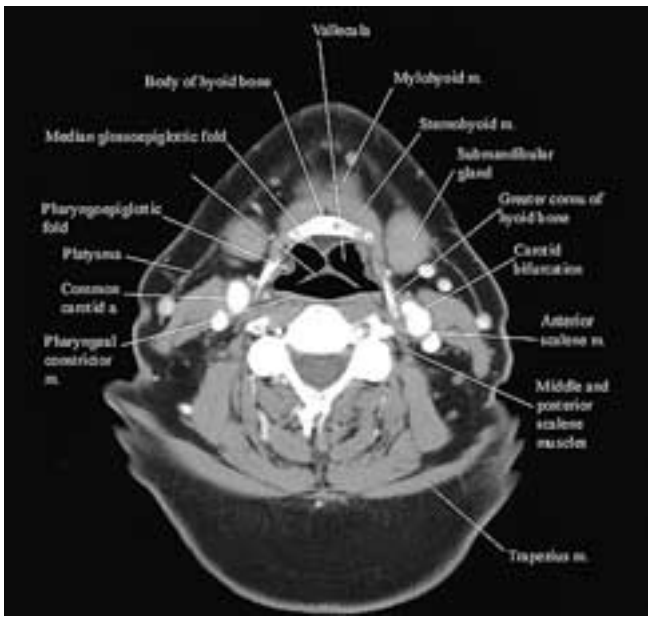

FIGURE 15

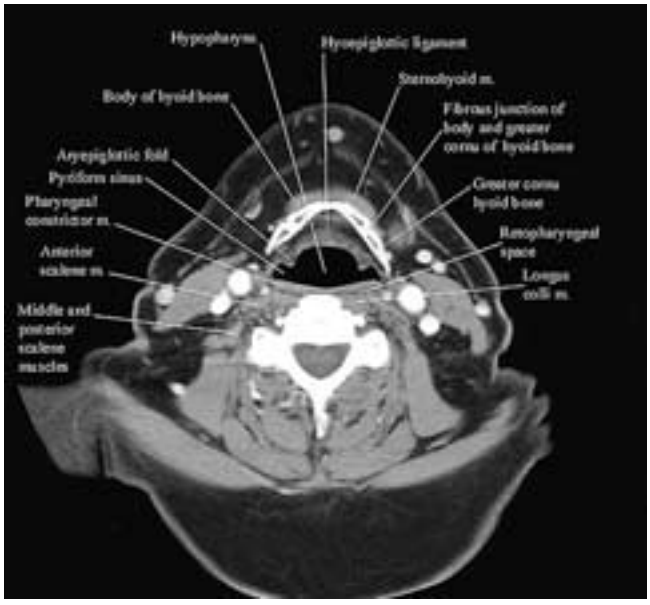

FIGURE 16

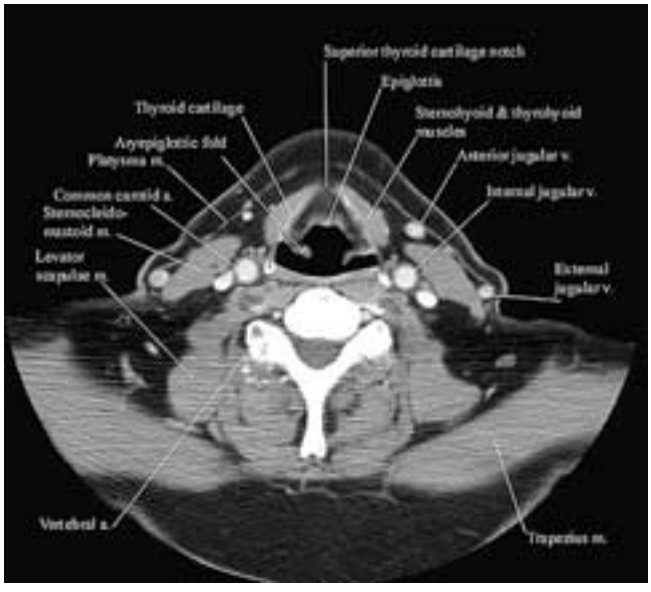

FIGURE 17

Copyright © 2003, Mosby, Inc. All rights reserved.

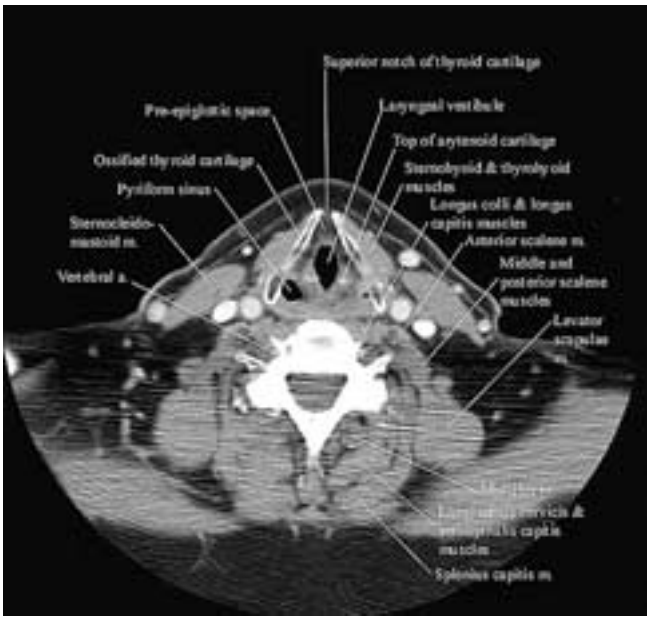

FIGURE 18

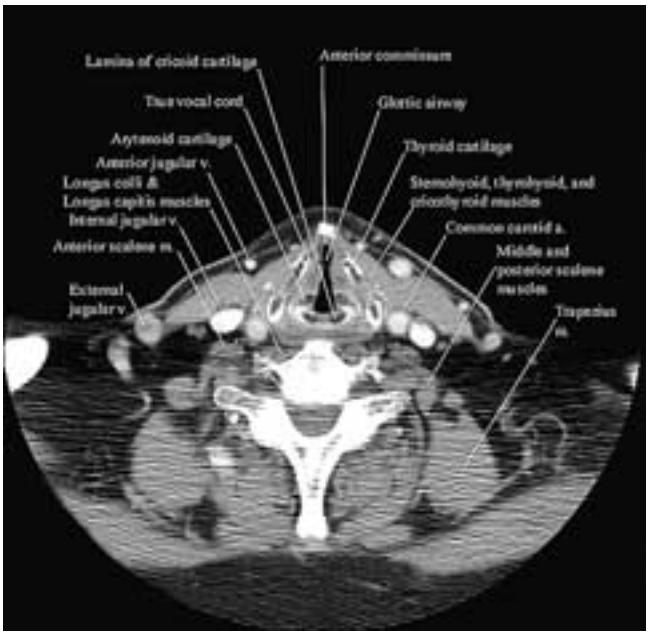

FIGURE 19

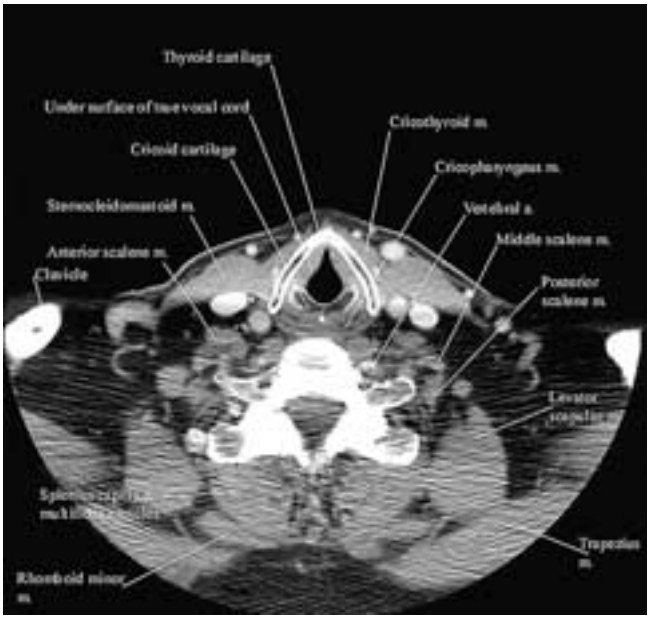

FIGURE 20

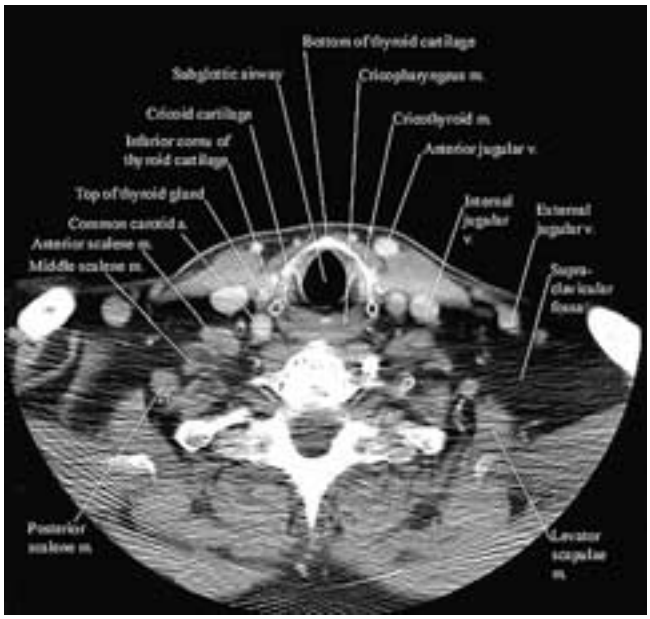

FIGURE 21

Copyright © 2003, Mosby, Inc. All rights reserved.

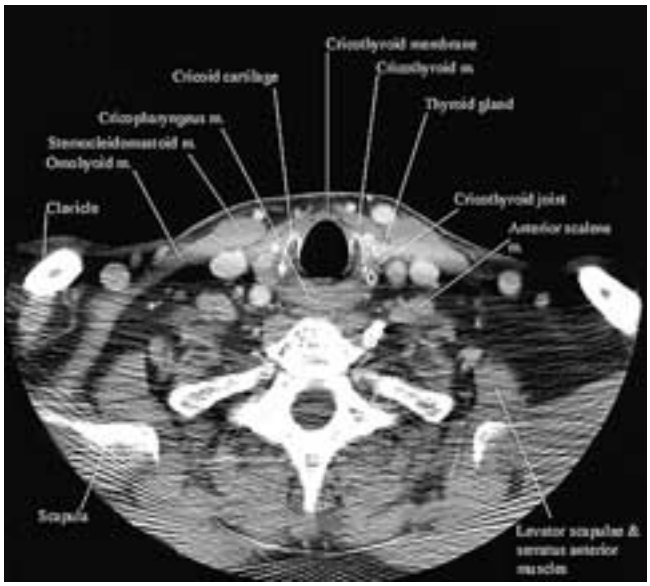

FIGURE 22

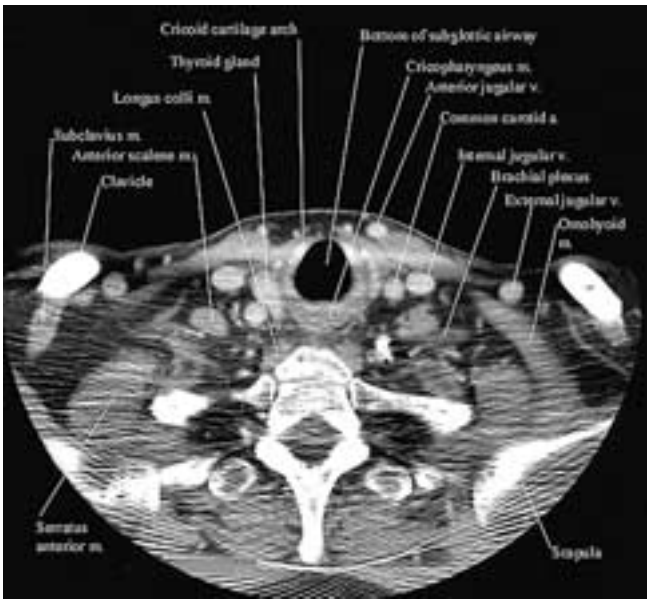

FIGURE 23

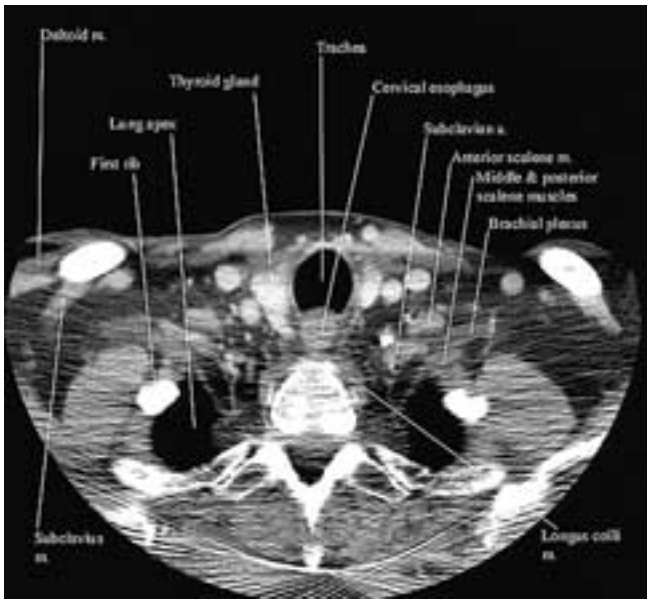

FIGURE 24

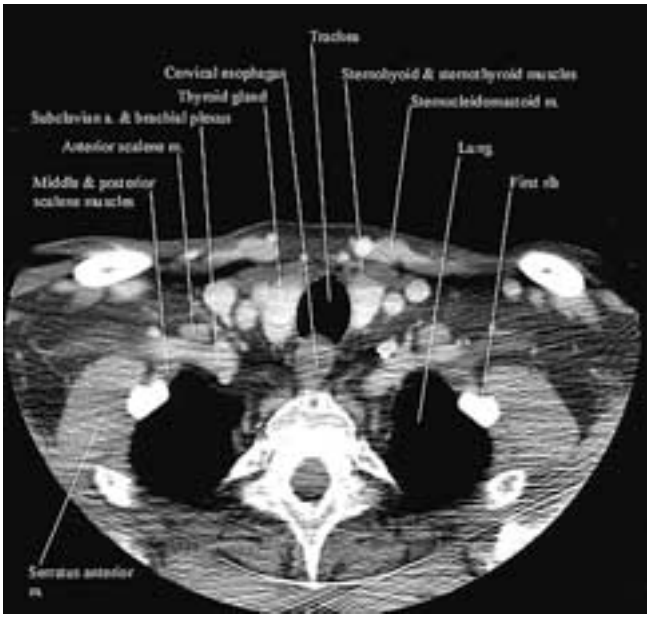

FIGURE 25

Copyright © 2003, Mosby, Inc. All rights reserved.

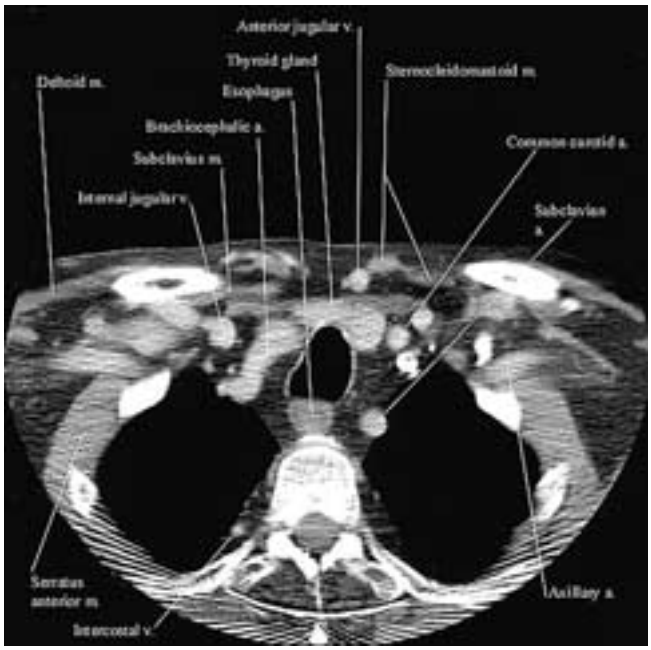

FIGURE 26

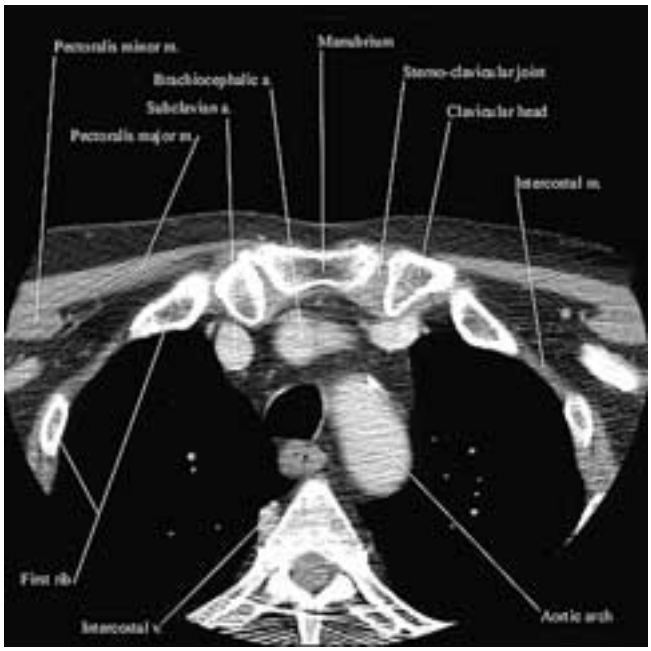

FIGURE 28

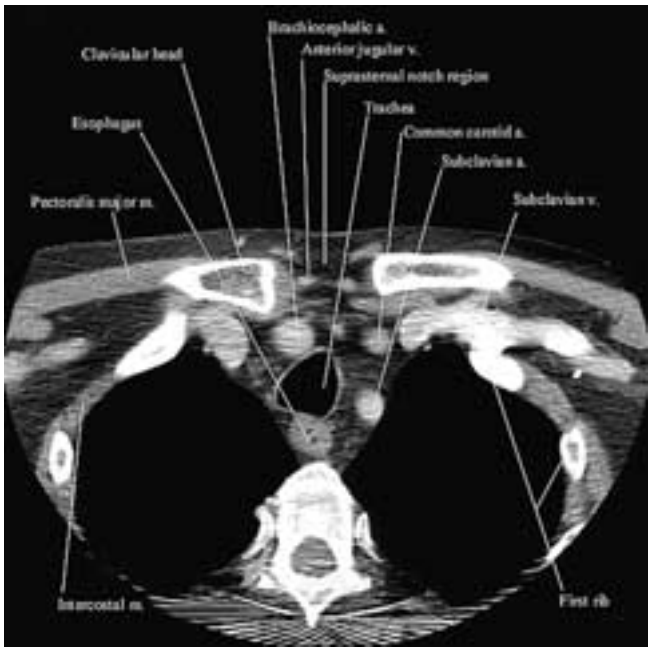

FIGURE 27

REFERENCES

1. Graney D. Developmental anatomy. In: Cummings C, Fredrickson J, Harker L, Krause C, Schuller D, eds. Otolaryngology: Head and Neck Surgery, 2nd ed., Vol. 2. St. Louis: Mosby-Year Book, 1993;1517–1529.
2. Donegan J. Congenital neck masses. In: Cummings C, Fredrickson J, Harker L, Krause C, Schuller D, eds. Otolaryngology: Head and Neck Surgery, 2nd ed., Vol. 2. St. Louis: Mosby-Year Book, 1993;1554–1565.
3. Chandler J, Mithchell B. Branchial cleft cysts, sinuses, and fistulae. Otolaryngol Clin North Am 1981;14:175–186.
4. Maran AGD, Buchanan DR. Branchial cysts, sinuses, and fistulae. Clin Otolaryngol 1978;3:77–92.
5. Pound L. Neck masses of congenital origin. Pediatr Clin North Am 1981;28:841–844.
6. Liston S, Siegel LG. Branchial cysts, sinuses, and fistulae. Ear Nose Throat J 1979;58:9–17.
7. Smith JF, Kielmovitch I. Branchial cysts anomaly in a newborn. Laryngoscope 1989;100:163–165.
8. Noden DM. The embryonic origins of avian cephalic and cervical muscles and associated connective and muscle tissue. Am J. Anat 1983;168:257–276.
9. Laitman JT, Noden DW, Van De Water TR. Formation of the larynx: from homeobox genes to critical periods. In: Rubin JS et al, eds. Diagnosis and Treatment of Voice Disorders. New York: Igaku-Shoin, 1995;9–24.
10. Dodd J, Jessell TM. Axon guidance and the patterning of neuronal projections in vertebrates. Science 1988;242:692–699.
11. Chen Z-F, Behrinber RR. Twist is required in head mesenchyme for cranial neural tube morphogenesis. Genes Dev 1995;7:686–699.
12. Sperber G. Muscle development. In: Sperber G, ed. Craniofacial Embryology. London: Wright, 1989;192–203.
13. Sperber G. The pharyngeal pouches and branchial grooves. In: Sperber G, ed. Craniofacial Embryology. London: Wright, 1989;69–75.
14. Sperber G. The branchial arches. In: Sperber G, ed. Craniofacial Embryology. London: Wright, 1989;188–191.
15. Collins P. Embryology and development. In: Bannister L, Berry M, Collins P, Dyson M, Dussek J, Ferguson M, eds. Gray's Anatomy, 38th ed. London: Churchill Livingstone, 1999;91–341.
16. Weller G. Development of the thyroid, parathyroid, and thymus glands in man. Contrib Embryol Carnegie Inst Wash 1933;24:93–142.
17. Hoyes A, Kershaw D. Anatomy and development of the thyroid gland. Ear Nose Throat J 1985;64:318–324.
18. Skandalakis J, Gray S, Todd N. The pharynx and its derivatives. In: Skandalakis J, Gray S, eds. Embryology for Surgeons. Baltimore: Williams & Wilkins, 1994.
19. Smuts M, Hyer S, Soarls R. Patterns of cellular proliferation during thyroid organogenesis. J Embryol Exp Morphol 1978;48:269–286.
20. Dalgaard J, Wetteland P. Thyroglossal anomalies: a follow-up study of 58 cases. Acta Chir Scand 1956;111:444–445.
21. Allard R. The thyroglossal cyst. Head Neck Surg 1982;5:134–146.
22. Norris E. The early morphogenesis of the human thyroid gland. Am J Anat 1918;24:443–466.

Copyright © 2003, Mosby, Inc. All rights reserved.

23. Kingsbury B. The question of a lateral thyroid in mammals with special references to man. Am J Anat 1939;65:333–359.
24. Norris E. The morphogenesis of the follicles in the human thyroid gland. Am J Anat 1916;20:411–448.
25. Shepard T, Andersen H, Andersen H. Histochemical studies of the human fetal thyroid during the first half of fetal life. Anat Rec 1964;149:363–380.
26. Moore K. The Developing Human—Clinically Oriented Embryology, 3rd ed. Philadelphia: WB Saunders, 1982.
27. Spooner B, Wessels N. Mammalian lung development: interactions in primordium formation and bronchial morphogenesis. J Exp Zool 1970;175:445–454.
28. Hast M. Developmental anatomy of the larynx. In: Hinchcliffe R, Harrison D, eds. Scientific Foundations of Otolaryngology. London: Heinemann Medical, 1976.
29. Spector G. Developmental anatomy of the larynx. In: Ballenger J, ed. Diseases of the Ear, Nose, and Throat. Philadelphia: Lea & Febiger, 1984.
30. Arey L, ed. Developmental Anatomy, 6th ed. Philadelphia: WB Saunders, 1954;377–383.
31. Reidenbrg J, Laitman J. Anatomy of the hyoid apparatus in Odontoceti (toothed whales): specializations of their skeleton and musculature compared with those of terrestrial mammals. Anat Rec 1994;240: 598–624.
32. Quiring D, Warfel J. The Head, Neck, and Trunk Muscles and Motor Points, 2nd ed. Philadelphia: Lea & Febiger, 1960.
33. Langman J, ed. Embryology, 3rd ed. Baltimore: Williams & Wilkins, 1975;234–236.
34. Barry A. The aortic arch derivatives in the human adult. Anat Rec 1951;111:221–238.
35. Himalstein M. Branchial cysts and fistulae. Ear Nose Throat 1980;59:47–54.
36. Langman J, ed. Medical Embryology, 7th ed. Baltimore: Williams & Wilkins, 1995;212–231.
37. Sabin F. The lymphatic system from the veins and the development of the lymph hearts and thoracic duct in the pig. Am J Anat 1902;1:367–391.
38. Sabin F. The lymphatic system in human embryos with a consideration of the morphology of the system as a whole. Am J Anat 1909;9:43–91.
39. Sabin F. On the origin of the abnormal lymphatics in mammals from the vena cava and renal veins. Anat Rec 1912;6:335–343.
40. Huntington G, McClure C. The anatomy and development of the jugular lymph sac in the domestic cat (*Felis domestica*). Anat Rec 1908;2:1–9.
41. McClure C. On the provisional arrangements of the embryonic lymphatic system. Anat Rec 1915;9:281–297.
42. Kampmeier O. The value of the injection method in the study of the lymphatic development. Anat Rec 1912;6:223–233.
43. Kampmeier O, ed. Evolution and Comparative Morphology of the Lymphatic System. Springfield, Ill: Thomas, 1969.
44. van der Jagt E. The origin and development of the anterior lymph sacs in the sea turtle (*Thalassochelys caretta*). Q J Micr Sci 1932;75:151–165.
45. Kutsuna M. Beitrage zur Kenntnis der Entwicklung des lymphgefaB-systems der Vogel. Acta Sch Med Kioto 1933;16:16–25.
46. van der Putte SCJ. The development of the lymphatic system in man. Adv Anat Ebryol Cell Biol 1975;51:3–60.
47. Kuisk H. Development, structure, and function of the lymphatic system. St. Louis: In: Kuisk H, ed. Technique of Lymphography and Principles of Interpretation. Green, 1971;5–14.
48. Battezzati M, Donini I. Embryology of the lymphatic system. In: Battezzati M, Donini I, eds. The Lymphatic System. Padua: Piccin Medical Books and Halsted Press Book, Wiley, 1972;27–34.
49. Hall J. The functional anatomy of lymph nodes. In: Stansfeld A, d'Ardenne A, eds. Lymph Node Biopsy Interpretation. Edinburgh and London: Churchill Livingstone, 1992;3–28.
50. Krutsiak VN, Polianskii I. Development of the thoracic duct in the prenatal period of human ontogeny. Arkh Anat Gistol Embriol 1983;85:79–84.
51. Borisov AV, Petrenko VM. The development of the thoracic duct lymphangions in the prenatal period of human ontogeny. Ontogenez 1992;23:254–259.
52. Rennert P, Browning J, Mebius R, Mackay F, Hochman P. Surface lymphotoxin alpha/beta complex is required for the development of peripheral lymphoid organs. J Exp Med 1996;184:1999–2006.
53. Mebius R, Steeter P, Michie S, Butcher E, Weissman I. A developmental switch in lymphocyte homing receptor and endothelial vascular addressin expression regulates lymphocyte homing and permits CD4-CD3 cells to colonize lymph nodes. Proc Natl Acad Sci USA 1996;93:11019–11024.
54. Dardick I, Burford-Mason A. Current status of histogenic and morphogenetic concepts of salivary gland tumorigenesis. Crit Rev Oral Biol Med 1993;4:639–677.
55. Dardick I, Dardick A, Mackay A, Pastolero G, Gullane P, Burford-Mason A. Pathobiology of salivary glands. IV. Histogenetic concepts and cycling cells in human parotid and submandibular gland cultures in floating collagen gels. Oral Surg Oral Med Oral Pathol 1993;76:307–318.
56. Batsakis J. Tumors of the major salivary glands. In: Batsakis J, ed. Tumors of the Head and Neck: Clinical and Pathological Considerations, 2nd ed. Baltimore: Williams & Wilkins, 1979;1–75.
57. Sperber G. The salivary glands. In: Sperber G, ed. Craniofacial Embryology. London: Wright, 1989;188–191.
58. Johns M. The salivary glands: anatomy and embryology. Otolaryngol Clin North Am 1977;10:261–271.
59. Moss-Salentijn L, Moss M. Development and functional anatomy. In: Rankow R, Polayes I, eds. Diseases of the Salivary Glands. Philadelphia: WB Saunders, 1976;17–31.
60. Magriples U, Laitman J. Developmental change in the position of the fetal human larynx. Am J Phys Anthropol 1987;72:463–472.
61. Wolfson V, Laitman J. Ultrasound investigation of fetal human upper respiratory anatomy. Anat Rec 1990;227:363–372.
62. Laitman J, Reidenberg J. Specializations of the human upper respiratory and upper digestive systems as seen through comparative and developmental anatomy. Dysphagia 1993;8:318–325.
63. Laitman J, Reidenberg J. The human aerodigestive tract and gastroesophageal reflux: an evolutionary perspective. Am J Med 1997;103:2–7.
64. Gray H. Anatomy of the Human Body, 27th ed. Goss C, ed. Philadelphia: Lea & Febiger, 1963.
65. Harnsberger H, ed. Handbook of Head and Neck Imaging, 2nd ed. St. Louis: CV Mosby, 1995.
66. Last R, ed. Anatomy: Regional and Applied, 6th ed. Edinburgh and London: Churchill Livingstone, 1978.
67. Paff G, ed. Anatomy of the Head and Neck. Philadelphia: WB Saunders, 1973.
68. Montgomery R, ed. Head and Neck Anatomy with Clinical Correlations. New York: McGraw-Hill, 1981.
69. Lingeman R. Surgical anatomy. In: Cummings C, Fredrickson J, Harker L, Krause C, Schuller D, eds. Otolaryngology: Head and Neck Surgery, 2nd ed., Vol. 2. St. Louis: Mosby-Year Book, 1993;1530–1542.

Copyright © 2003, Mosby, Inc. All rights reserved.

34

Fascia and Spaces of the Neck

Peter M. Som and Hugh D. Curtin

INTRODUCTION
THE FASCIAE
- The Superficial Fascia
- The Deep Cervical Fascia
- The Superficial Layer of the Deep Cervical Fascia
- The Deep Layer of the Deep Cervical Fascia
- Sibson's Fascia
- The Middle Layer of the Deep Cervical Fascia in the Infrahyoid Neck
- The Middle Layer of the Deep Cervical Fascia in the Suprahyoid Neck

THE CAROTID SHEATH
THE FASCIAL SPACES
- The Visceral Compartment and Its Spaces
- The Pretracheal Space
- The Retrovisceral Space
- The Danger Space
- The Prevertebral Space
- The Carotid Sheath
- The Space of the Body of the Mandible
- The Space of the Submandibular Gland
- The Space of the Parotid Gland
- The Submandibular Space
- The Masticator Space
- The Parapharyngeal Space
- The Peritonsillar Space
- The "Paravertebral Space"
- The "Posterior Triangle (Cervical) Space"

SUMMARY AND CONCLUSION

INTRODUCTION

The importance of the fasciae of the neck is their ability to define spaces that may limit to some degree the spread of most infections and some tumors. However, these fasciae vary in thickness and composition, and they have been described in numerous forms by a variety of authors. In fact, the literature is filled with such varying descriptions of the anatomy of the cervical fasciae and spaces that there is confusion due to unclear statements and contradictory reports. As a sign of this frustration, Malgaigne in 1838 was prompted to note that ''the cervical fasciae appear in a new form under the pen of each author who attempts to describe them.''[1–3]

Part of the problem is that there is no consistent definition of what constitutes fascia. Fascia has been variously described in the literature as a collection of fat and fibrous tissue that seems to equate with a ''fat layer''; a thin but firm, well-defined layer of fibrous tissue such as an aponeurosis; and a localized thickening or condensation of fibroadipose tissue within a larger, more diffuse area of such tissue. This problem prompted Hollinshead to write: ''If the reader will recall that there is no generally accepted definition as to how dense connective tissue must be before it can be regarded as forming a fascia, and that fascial spaces are simply areas of relatively loose connective tissues, the reasons for many of the discrepancies in various descriptions will be obvious.''[4]

Another part of the problem relates to the varied descriptions of the anatomic boundaries of the fasciae. However, when one considers that the fasciae may split to surround muscles, vessels, and nerves and then merge with other fascial layers, it becomes apparent that any description is somewhat arbitrary.[2, 4] In addition, many of the smaller muscles have their own surrounding fascia, or epimysium, which is not necessarily considered to arise from any of the classic fascial layers.

The interest in the fasciae and spaces of the neck stems from early anatomic investigations performed by surgeons who were seeking ways to predict the spread of infection.[5] They believed correctly that knowledge of such routes of spread would allow them to approach and drain abscesses more effectively. However, interest in this subject waned with the introduction of the antibiotic era and the advent of medical control of many of these infections. Hollinshead wrote in 1954, ''It should be noted that with the widespread use of antibiotics, the anatomy of these spaces is necessarily becoming less important.''[4] But with the emergence of the

Copyright © 2003, Mosby, Inc. All rights reserved.

HIV pandemic within the past decades, the incidence of infections not well controlled by medical therapy has risen and the need to understand the fascial and spatial anatomy of the neck has again gained importance. Lastly, with the utilization of CT and MR imaging, it has been noted that the growth of some tumors appears to be restricted by certain fasciae, and knowledge of the anatomy of these fasciae allows one to predict such growth patterns.

This chapter reviews the major anatomic descriptions of the fasciae and spaces of the neck, mentions the various synonyms used for the fascia and spaces, points out areas of confusion and divergent description, and presents what the authors believe is the present understanding of this topic.[1–15] Once the often complex anatomy of these fasciae is mastered, one can achieve a better understanding of the spread of both infections and some tumors in the neck.

THE FASCIAE

Traditionally, the fasciae of the neck are classified into two major divisions: superficial and deep. The superficial cervical fascia (SCF) is a fairly thick, well-defined, primarily fatty layer of relatively loose connective tissue that lies deep to the skin and superficial to the deep cervical fascia. The SCF covers the head, face, and neck and in its deeper portions contains the thin platysma muscles, the muscles of facial expression, and portions of the anterior and external jugular veins.

The deep cervical fascia (DCF) is more complex than the SCF and is made up of thinner but denser, better-defined discrete layers that are more deserving of the classic term *fascial sheet*. The DCF exists in the neck below the skull base and encloses the muscles of the neck, as well as the mandible and the muscles of mastication and deglutition.

The DCF is classically subdivided into three layers: (1) the superficial or investing layer of the deep cervical fascia (SLDCF), (2) the middle layer, which includes the pretracheal and visceral layers (MLDCF), and (3) the deep layer (DLDCF).[2, 4] This terminology itself may lead to some confusion, as there is both an SCF and an SLDCF. Although these two layers border one another, they are distinctly separate entities.

In the literature, there is reasonable agreement, except for some minor variations, regarding the descriptions of the SCF, the SLDCF, and the DLDCF. Thus, most of the variations in the fascial descriptions concern the MLDCF, which is found between the more uniformly described SLDCF and DLDCF layers.

The Superficial Fascia

Deep to the skin and superficial to the SLDCF, the subcutaneous tissues of the head and neck are referred to as the SCF. This superficial fascia is not a fascial sheet in the classic sense, but rather a fatty, loose connective tissue in which are embedded the voluntary muscles of facial expression and the platysma muscles. The subcutaneous nerves, venules, and lymphatics are also within the SCF, and in some descriptions portions of the anterior and external jugular veins are included in the SCF (Drawings 1–5) (Fig. 34-1).[2, 4]

In the neck, the fat of the SCF is fairly loose. However, in the facial area the fat is much denser, except in the region of the eyelids, where it is fairly loose on both the superficial and deep aspects of the orbicularis oculi. In the scalp, the subcutaneous fat is dense and contains the epicranius (frontalis) muscle in its deep portion. Beneath the epicranial aponeurosis, between it and the periosteum of the calvarium, there is loose areolar tissue that permits motion of this muscle and, like the tissue about the eyelids, can hold large accumulations of fluid.[2, 4]

The skin, the SCF, and the platysma muscle function as a complex morphologic unit, interconnected by a system of fine connective tissue fibers and less well defined muscular elements called the superficial musculo-aponeurotic system (SMAS). Although the muscles of facial expression are often considered to be a separate functional unit, the SMAS interlinks these facial muscles with the dermis and amplifies the effect on the skin caused by the contractions of the facial muscles. The SMAS extends from the temporalis and frontalis muscles superiorly to the platysma muscle inferiorly. Thus, the SMAS has come to be considered an important functional unit in plastic surgery of the face and upper neck. Many surgeons consider the SMAS to be the most important component of a rhytidectomy and the factor that most contributes to a longer-lasting result.[13]

The Deep Cervical Fascia

Deep to the SCF, the DCF surrounds and encloses the musculature of the neck. The DCF is traditionally subdivided into three layers: the SLDCF, the MLDCF, and the DLDCF.

As mentioned, the various descriptions in the literature of the SLDCF and the DLDCF are fairly uniform. However, the layers between the SLDCF and the DLDCF are more arbitrarily described—at times being assigned to the MLDCF, at other times referred to as derivations of the SLDCF or the DLDCF, and at still other times considered to be separate fasciae that are not ascribed to any of these layers. This discussion of the DCF will start by describing the less controversial SLDCF and DLDCF. Then the ''middle regions'' and layers will be discussed, exploring the labyrinth of fascial webs and partitions found in the perplexing zone that separates the SLDCF and DLDCF.

The Superficial Layer of the Deep Cervical Fascia

The SLDCF is a well-defined sheet of fibrous tissue that completely encircles the neck, incorporating the sternocleidomastoid and trapezius muscles and attaching posteriorly to the vertebral spines and ligamentum nuchae. This layer extends cranially into the face and caudally into the pectoral and axillary regions. The SLDCF may be thought of as arising from the cervical vertebral spines and the ligamentum nuchae. It extends to the left and right sides of the neck, splits to enclose each trapezius muscle, and then

Copyright © 2003, Mosby, Inc. All rights reserved.

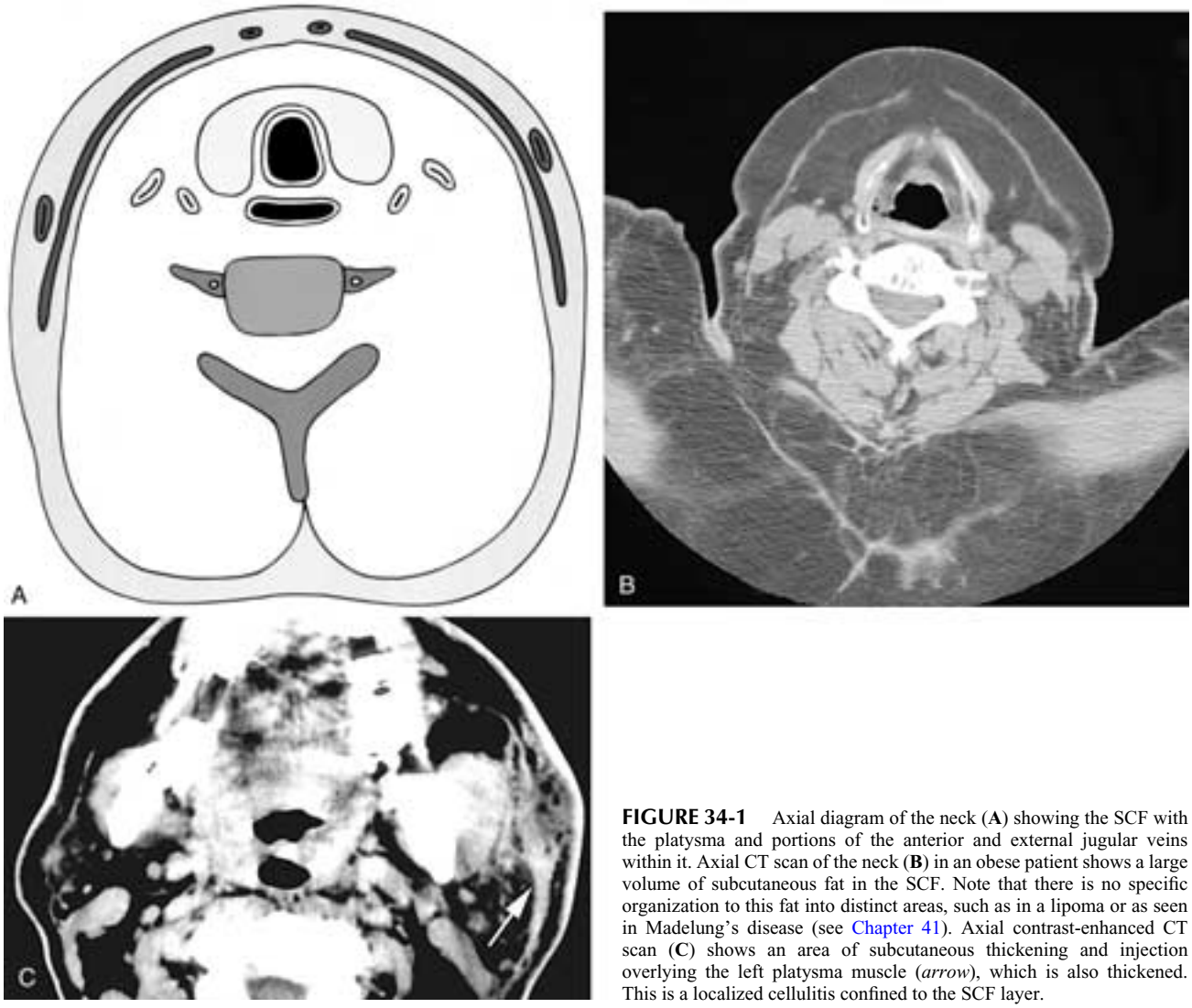

FIGURE 34-1 Axial diagram of the neck (**A**) showing the SCF with the platysma and portions of the anterior and external jugular veins within it. Axial CT scan of the neck (**B**) in an obese patient shows a large volume of subcutaneous fat in the SCF. Note that there is no specific organization to this fat into distinct areas, such as in a lipoma or as seen in Madelung's disease (see Chapter 41). Axial contrast-enhanced CT scan (**C**) shows an area of subcutaneous thickening and injection overlying the left platysma muscle (*arrow*), which is also thickened. This is a localized cellulitis confined to the SCF layer.

VIEW IMAGE

crosses the posterior triangle of the neck. The SLDCF then splits again to enclose each sternocleidomastoid muscle and finally crosses the anterior midline of the neck in front of the strap muscles as a single fascia connecting the anterior borders of the sternocleidomastoid muscles (Drawings 2–9) (Fig. 34-2).

Caudally in the midline, the SLDCF splits into two layers, one attaching to the anterior aspect and one to the posterior aspect of the manubrium. This creates the variably sized suprasternal space of Burns (or Gruber), which primarily contains fat and a communicating vein between the left and right anterior jugular veins (Drawings 8, 9). This space either can extend nearly halfway up the neck or can be localized to just above the manubrium. The clinical importance of this space lies in the fact that if it is entered during a tracheostomy, inadvertent transection of the communicating vein may result in considerable blood loss.[2, 14] Although of minor importance, even the small suprasternal space of Burns is somewhat controversial, as some authors describe the posterior layer of this space as being formed from the MLDCF.[2] Lateral to the sternum, the SLDCF attaches to the superior margin of each clavicle along the entire extent of this bone. Even more laterally, the fascia attaches to the acromion and spine of each scapula. Most portions of the anterior and external jugular veins are considered to be embedded in the superficial surface of the SLDCF, rather than lying between it and the deeper fascial layers. As mentioned, small portions of these veins also extend into the SCF.

The literature also contains ambiguity regarding the origin of the fascia around the strap muscles (sternothyroid, sternohyoid, and thyrohyoid muscles). Although some authors believe this fascia to be part of the SLDCF, most authors refer to it as being part of the MLDCF.[2, 4] However, the MLDCF has in turn been described as either encircling the strap muscles or as comprising only the most posterior layer of fascia, deep to the strap muscles.[4] There is also some controversy over the origin of the fascial sling between the superior and inferior bellies of the omohyoid muscle. This sling is attached below to the clavicle and first rib and maintains the angulated course of this muscle. Some authors believe the sling is formed by the SLDCF, while most other authors believe it is formed by the sternohyoid-omohyoid layer of the MLDCF.[2, 4] What is clearly apparent is that

Copyright © 2003, Mosby, Inc. All rights reserved.

these are only differences in nomenclature, and there is no controversy over the presence and location of these fascial planes and slings.

Above the hyoid bone, the SLDCF extends to the lower border of the mandible, and as this fascia passes over the muscles below the floor of the mouth, it fuses with the fascial covering of each digastric muscle. Grodinsky and Holyoke consider the fasciae about the anterior belly of each digastric muscle, the mylohyoid, the geniohyoid, the hyoglossus, and the genioglossus muscles to be separate fasciae related to each of these muscles and not actually part of the SLDCF.[2] However, more posteriorly these same authors considered the fascial sheaths of the posterior belly of the digastric muscles and the stylohyoid muscles to be direct derivatives of the SLDCF.

On either side of the neck in the submandibular triangle, a portion of the SLDCF splits to form a thin, often flimsy capsule about each submaxillary gland (Drawing 10). Then, as the SLDCF reaches the mandible, the fascia divides into superficial and deep leaflets. These leaflets extend superiorly, enclosing the muscles of mastication and forming the masticator spaces.[7, 12, 15, 16]

The superficial leaflet, or fascial sheet, overlies the masseter muscle and attaches to the zygomatic arch. The fascia here splits once again to enclose the zygomatic arch and creates a small space on the cranial surface of the arch that is filled with fat. The superficial fascial leaflet then continues cranially to overlie the temporalis muscle, attaching along the temporal ridge cranially and dorsally and along the lateral orbital margin ventrally (Drawings 10–13).

Anteriorly, the fascia covering the masseter muscle curves medially to attach to the mandible and to the fascia of

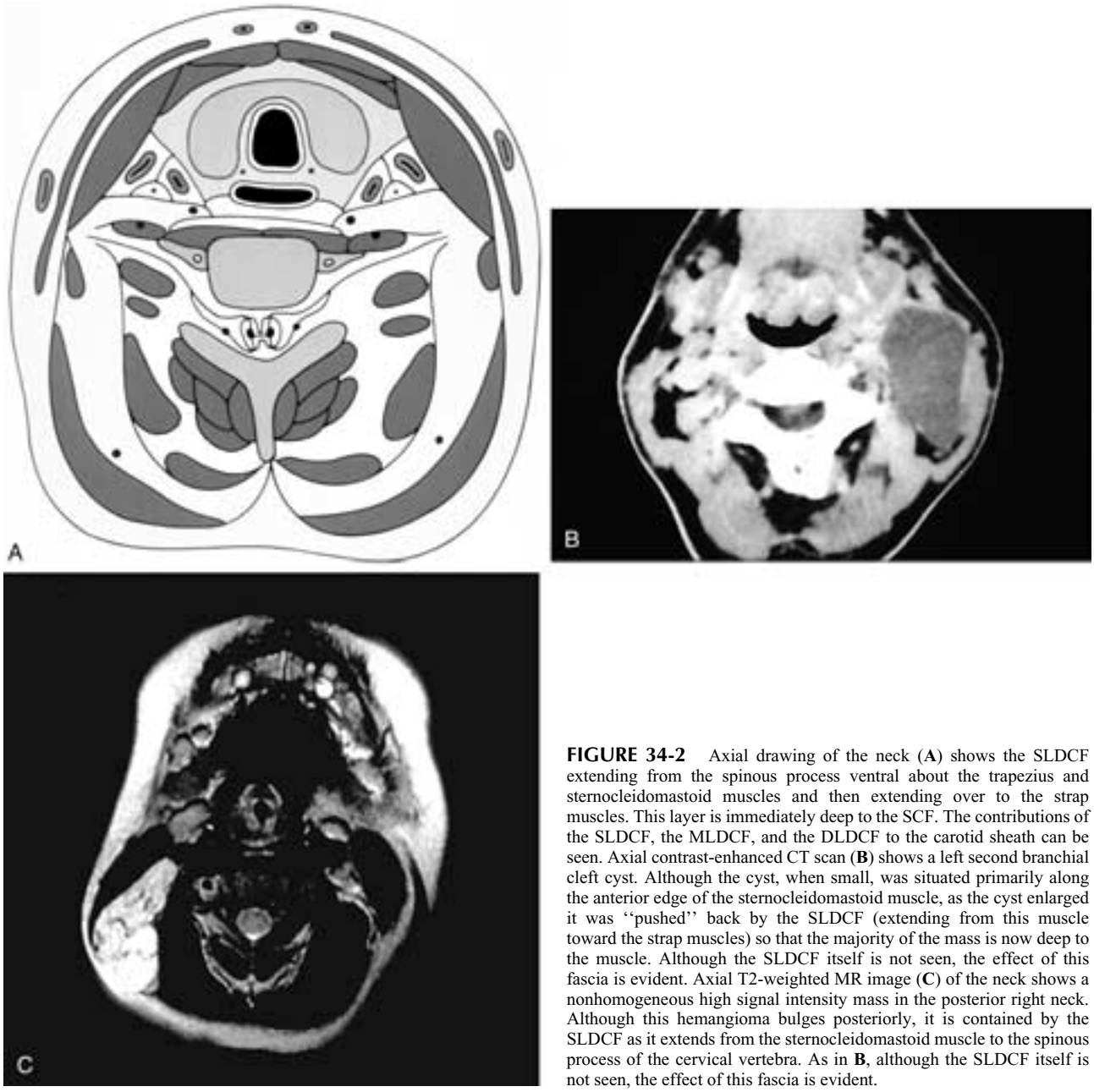

FIGURE 34-2 Axial drawing of the neck (**A**) shows the SLDCF extending from the spinous process ventral about the trapezius and sternocleidomastoid muscles and then extending over to the strap muscles. This layer is immediately deep to the SCF. The contributions of the SLDCF, the MLDCF, and the DLDCF to the carotid sheath can be seen. Axial contrast-enhanced CT scan (**B**) shows a left second branchial cleft cyst. Although the cyst, when small, was situated primarily along the anterior edge of the sternocleidomastoid muscle, as the cyst enlarged it was ''pushed'' back by the SLDCF (extending from this muscle toward the strap muscles) so that the majority of the mass is now deep to the muscle. Although the SLDCF itself is not seen, the effect of this fascia is evident. Axial T2-weighted MR image (**C**) of the neck shows a nonhomogeneous high signal intensity mass in the posterior right neck. Although this hemangioma bulges posteriorly, it is contained by the SLDCF as it extends from the sternocleidomastoid muscle to the spinous process of the cervical vertebra. As in **B**, although the SLDCF itself is not seen, the effect of this fascia is evident.

VIEW IMAGE

Copyright © 2003, Mosby, Inc. All rights reserved.

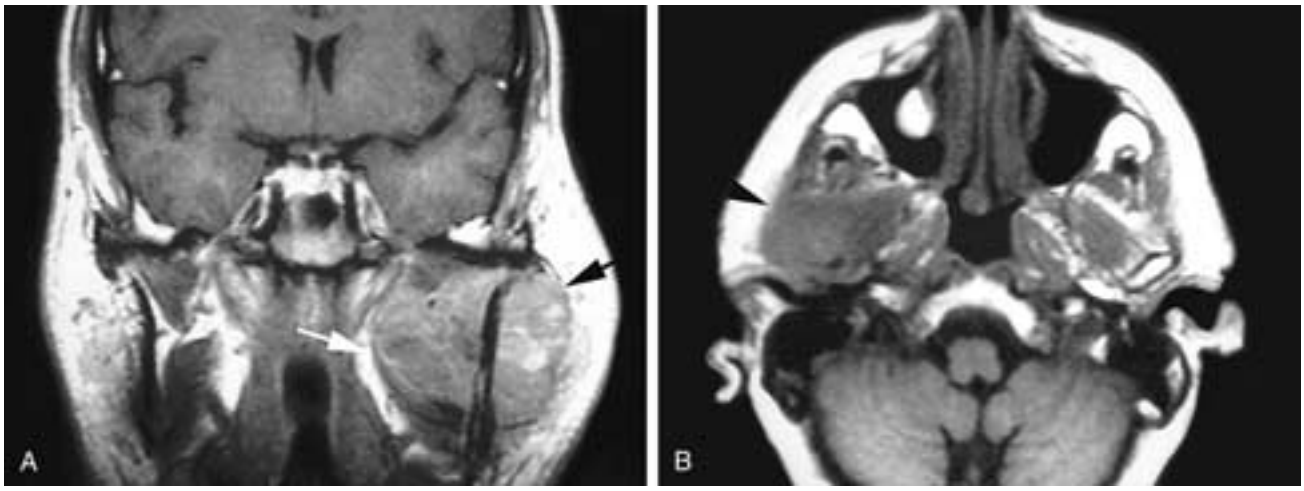

VIEW IMAGE

FIGURE 34-3 Coronal T1-weighted MR image (**A**) of a patient with a rhabdomyosarcoma in the left masticator space. Although this is an aggressive tumor, the deep (*white arrow*) and superficial (*black arrow*) leaflets of the SLDCF contain the tumor. In this instance, the integrity of the fascia belies the aggressive nature of the tumor. Axial T1-weighted MR image (**B**) shows an infiltrating mass in the right masticator space (*arrowhead*). Both the superficial and deep layers of the masticator space fascia have been violated, attesting to the invasive nature of this breast carcinoma metastasis.

the temporalis tendon and muscle as it attaches to the coronoid process of the mandible.[17] Fascia also extends from the temporalis muscle to the buccinator fascia near the pterygomandibular raphe. However, in some reports, a separate fascial leaflet is described as passing from the anterior margin of the masseter muscle directly to the buccinator fascia.[17, 18] In one or another of these ways, the fascia covering the masseter muscle attaches to the buccinator fascia and to the maxilla, and in so doing it encloses a small fat pad referred to as the masticator fat pad. This fat pad is intimately associated with the masticator space, often being included as part of the space, and the fat has small projections into the pterygopalatine fossa as well as along the lateral pterygoid muscle. Thus, these various fasciae, either with or without the masticator fat pad, attach to the maxilla and to the buccinator fascia and, in so doing, close the masticator space anteriorly (Drawings 2 and 12) (Fig. 34-3).

Just as the superficial leaflet of the SLDCF forms the outer boundary of the masticator space, the deep leaflet of the SLDCF extends cranially to form the medial or inner boundary of this space. The fascial covering of the medial pterygoid muscle is fairly thin, but does attach to the lower border of the mandible and thus can be considered a derivation of the SLDCF. A stronger fascia, the interpterygoid fascia (also probably derived from the SLSCF), attaches to the inner surface of the mandible, medial to the insertion of the medial pterygoid muscle. From here the interpterygoid fascia sweeps cranially to the superior edge of the medial pterygoid muscle, where the fascia covering the medial surface of the muscle fuses with the interpterygoid fascia. The resultant combined fascia continues up to the skull base and attaches along a line that extends from the root of the medial pterygoid plate to the sphenoid spine, just medial to the foramen ovale. The fascia then curves posterolaterally to reach the posterior glenoid fossa. The sphenomandibular ligament, which extends from the sphenoid spine to the ramus of the mandible, is a localized thickening of the interpterygoid fascia.

The superficial and deep leaflets of the SLDCF also fuse along the dorsal border of the mandibular ramus. The space thus enclosed by these leaflets contains the muscles of mastication (the temporalis, masseter, and pterygoid muscles). It was first described by Juvara in 1870 and was first called the masticator space by Coller and Yglesias in 1935 (Drawings 2 and 10–13) (Fig. 34-3).[2, 4, 7, 12]

On either side of the neck, between the angle of the dorsal edge of the mandibular ramus and the ventral border of the sternocleidomastoid muscle, the SLDCF splits again to form the capsule of the parotid gland. The deep layer, in particular, is quite thin and flimsy and in the opinion of many investigators is actually deficient. The external carotid artery, with adherent prolongations from the carotid sheath, and the posterior facial vein (retromandibular vein) each perforate the parotid gland capsule and pass through the substance of this gland (Drawings 2 and 12).[2] The SLDCF then attaches to the mastoid process of the skull and extends dorsally to attach to the external occipital protuberance.

The Deep Layer of the Deep Cervical Fascia

The DLDCF, like the superficial layer, can be considered to originate from the cervical vertebral spinous processes and the ligamentum nuchae. The fascia then extends to either side, covering and investing the muscles that form the floor of the posterior triangle of the neck. These muscles are, from dorsally to ventrally, the splenius capitis, the levator scapulae, and the posterior, middle, and anterior scalene muscles. The portion of the fascia that relates to the scalene muscles is often called the scalene fascia. On either side of the neck as the DLDCF extends between the middle and anterior scalene muscles, the fascia is reflected outward, forming a sleeve around

Copyright © 2003, Mosby, Inc. All rights reserved.

the brachial plexus and subclavian artery, which are all situated between these muscles. More laterally, this sleeve becomes the axillary sheath (Drawings 2–5, 7–9, and 14–16) (Fig. 34-4).

More specifically, the posterior scalene muscle arises from the posterior tubercles of the transverse processes of C4–C6 and the middle scalene muscle arises from the posterior tubercles of the transverse processes of the C2–C7 cervical vertebrae. By comparison, the anterior scalene muscle arises from the anterior tubercles of the transverse processes of C3–C6, and the respective anterior cervical nerve roots exit through the sulci or canals between the anterior and posterior tubercles. More caudally in the neck, the subclavian artery also passes between the anterior and middle scalene muscles. Thus, as the DLDCF extends ventrally over the middle and posterior scalene muscles, this fascia attaches to the origins of these muscles on the posterior tubercles of the transverse processes of the cervical vertebrae. The DLDCF then is reflected outward over the anterior cervical nerve roots and the subclavian artery (Fig. 34-5). Ventrally, the DLDCF then attaches again to the anterior tubercles about the origins of the anterior scalene muscle. The fascia then extends around the anterior scalene muscles, where it splits into two layers, both of which cross the anterior surface of the cervical vertebral bodies essentially extending between the anterior tubercles of the transverse processes on either side.

The dorsal layer, or the prevertebral fascia, lies closest to the vertebral bodies and covers the anterior surface of the longus capitis and colli muscles. This fascia extends from the skull base to the coccyx, and the proximal portion of each phrenic nerve lies deep to the prevertebral fascia on the anterior face of each anterior scalene muscle. The ventral layer, or alar fascia, lies anterior to the prevertebral fascia from which it is separated by loose connective tissue.[2] The alar fascia extends from the skull base caudally to a level between the sixth cervical and the fourth thoracic vertebrae, usually at the level of the seventh cervical vertebra, at which point it merges with the more anterior visceral fascia (see the discussion of the MLDCF) (Drawings 2–5, 8, 9, and 15) (Fig. 34-6).[4]

Charpy originally described a small, sagittally oriented fascial sheet that, on either side of the neck, extended from the fusion line of the DLDCF on the anterior tubercles of the cervical vertebrae ventrally toward the fascia over the posterolateral pharyngeal wall. He called this fascia the cloison sagittale, or sagittal partition, and it in effect separated the midline retropharyngeal and danger spaces from the more lateral parapharyngeal spaces.[1, 10]

However, 7 years later, Dean referred to this sagittal partition as the alar fascia and thus created confusion in terminology.[19] It was not until 19 years later that Grodinsky and Holyoke described the alar fascia as a coronally oriented fascial sheet that was parallel to and ventral to the prevertebral fascia.[2] Today, this coronally oriented fascia is generally accepted as the alar fascia, while the fascia

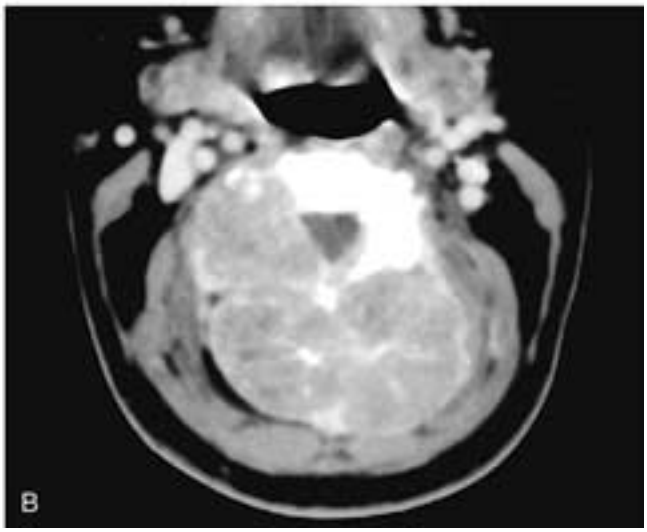

VIEW IMAGE

FIGURE 34-4 Axial drawing of the neck (**A**) shows the DLDCF extending from the spinous process over the muscles of the floor of the posterior triangle of the neck. After splitting to form the sheath about the brachial plexus and subclavian artery, the fascia attaches to the cervical vertebra. Ventrally, one layer of the DLDCF extends across the face of the flexor muscles of the cervical spine (prevertebral fascia). A second layer of fascia (alar fascia) also crosses the vertebral body and extends just ventral to the prevertebral fascia. These two layers form the boundaries of the danger space. Slips of fascia extend from the alar fascia (DLDCF) to contribute to the carotid sheath. Axial contrast-enhanced CT scan (**B**) of the neck shows a destructive lesion involving the right side of the cervical vertebra and all the muscles of the floor of the posterior triangles of the neck. Despite the aggressive nature of this metastatic breast cancer, the DLDCF contains the tumor.

Copyright © 2003, Mosby, Inc. All rights reserved.

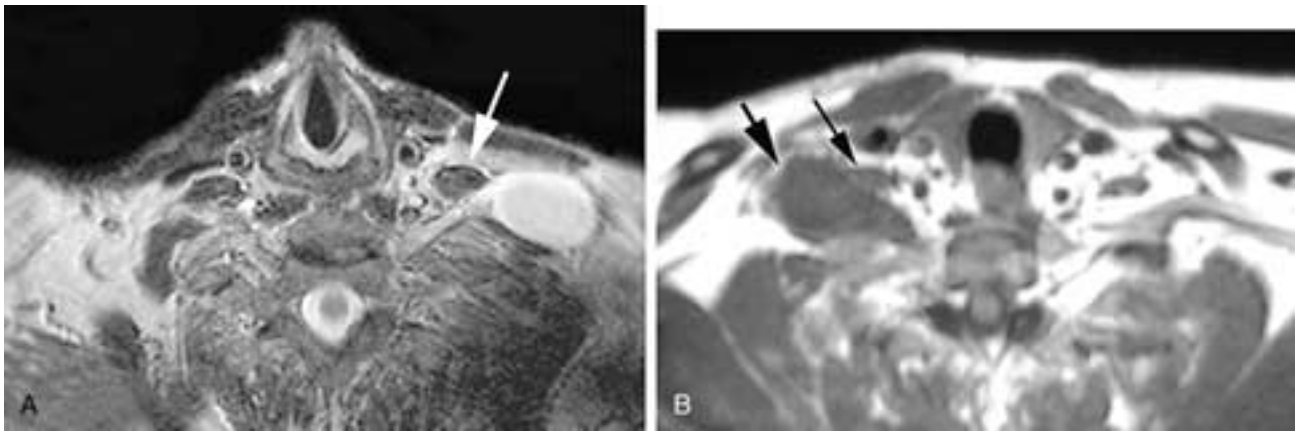

VIEW IMAGE

FIGURE 34-5 Axial T1-weighted, contrast-enhanced MR image (**A**) shows a schwannoma of the left brachial plexus. The thickened proximal nerve is seen extending toward the spinal cord, directly dorsal to the anterior scalene muscle (*arrow*). The DLDCF extends from the adjacent muscles of the floor of the posterior triangle of the neck out over the brachial plexus as a sheath, which more caudally also contains the subclavian artery. Axial T1-weighted MR image (**B**) shows a schwannoma of the right brachial plexus (*large arrow*) situated just dorsal to the anterior scalene muscle (*small thinner arrow*). This case illustrates how the anterior scalene muscle is a good marker for identifying the location of the brachial plexus in this region of the neck.

described by Dean is probably best referred to as the cloison sagittale, as described by Charpy.

Sibson's Fascia

On either side of the neck, the DLDCF extends laterally from the transverse process of the seventh cervical vertebra, covers the dome of the pleura, and then attaches to the medial surface of the first rib. This fascia, called Sibson's fascia, serves as a plane of separation between the lower neck and the thorax .[2, 4, 14]

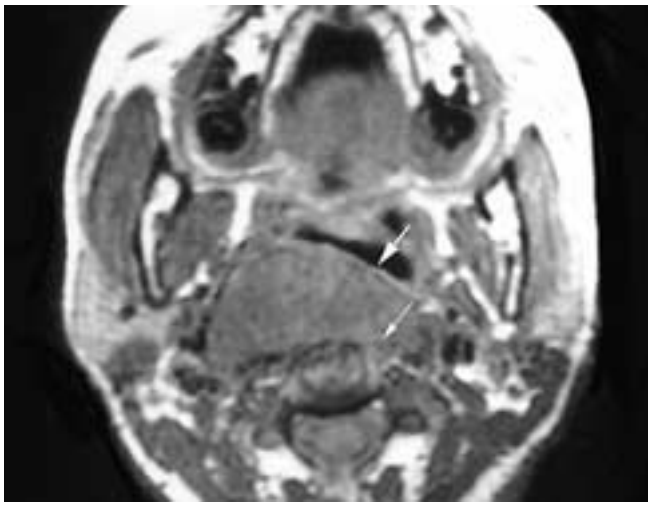

VIEW IMAGE

FIGURE 34-6 Axial T1-weighted MR image shows a mass involving the flexor muscles of the cervical spine (*small thinner arrow*) and pushing the pharyngeal constrictors forward (*large arrow*). This schwannoma was in the prevertebral space, pushing the danger and retropharyngeal spaces forward. Because the actual fascia (prevertebral, alar, and visceral) cannot be routinely seen on imaging, the involvement of the prevertebral muscles indicates the space of origin of the mass.

The Middle Layer of the Deep Cervical Fascia in the Infrahyoid Neck

As mentioned, the MLDCF is the most arbitrarily described of the fascial layers. Although originally described only as the fascia in the neck that takes its origin from the fascial covering of the omohyoid muscle, the term *middle layer of the deep cervical fascia* was subsequently used to describe the fascia associated with the strap muscles and the ''visceral'' fascia surrounding the esophageal and pharyngeal walls.

Hollinshead stated that the MLDCF most commonly is the fascia between the sternocleidomastoid muscles that passes behind the strap muscles, thus lying in front of the thyroid gland and trachea.[4] This description and relationship gave rise to the term *pretracheal fascia*. However, Grodinsky and Holyoke considered the MLDCF to be more complex and composed of three layers.[2] The first layer was called the sternohyoid-omohyoid layer, and it formed the sling of the omohyoid muscle and the fascia of the sternohyoid and omohyoid muscles. The second layer was called the sternothyroid-thyrohyoid layer, and it formed the fascia about these muscles. This layer was the one most analogous to the pretracheal fascia. The third layer was the deepest or most central of the three layers and was called the visceral or buccopharyngeal fascia (BPF). This last layer was closely adherent to the muscular walls of the esophagus and pharynx (Drawings 3–5, 7, 8, 15, and 16).

Whether one considers all of the fascia about the strap muscles to be formed by the MLDCF or the SLDCF, or instead believes that the MLDCF forms only the fascial layer deep to the strap muscles, is purely an academic issue. Regardless of the fascial derivation, the fascia about these muscles extends caudally behind the sternum to the origin of these muscles and then fuses with the fibrous pericardium as it is prolonged out along the great vessels and their adventitia in the superior mediastinum. This inferior fusion occurs at about the level of the fourth thoracic vertebra.

Copyright © 2003, Mosby, Inc. All rights reserved.

Cranially, this fascia fuses with the thyroid cartilage and the hyoid bone. Laterally, the fascia fuses with and contributes to the carotid sheath on either side of the neck.

The term *visceral fascia* refers to the layer of the MLDCF that is adherent to the outer surface of the esophagus and pharynx. This fascia is best defined at the level of the upper pharynx, and in this location it is often referred to as the buccopharyngeal fascia, which not only adheres to the outer surface of the pharyngeal constrictors but extends ventrally via the pterygomandibular raphe over the buccinator muscles.

Confusion was introduced when Grodinsky and Holyoke also stated that below the level of the thyroid cartilage, the ''visceral fascia'' surrounded not only the esophagus, but also the trachea and thyroid gland. They described a space (their space 3) that contained a small amount of loose adipose tissue and existed between the outer surface of this visceral fascia and the fasciae covering the inner surface of the strap muscles ventrally (SLDCF and/or MLDCF), the carotid sheaths laterally (all layers of the DCF contribute to this sheath), and the alar fascia (DLDCF) dorsally (Drawings 3–5, 7 and 8). However, Grodinsky and Holyoke referred to the structures within their visceral fascia (including the esophagus, trachea, and thyroid gland) as being in a visceral space (see discussion in the section on The Fascial Spaces).

Other authors, including Hollinshead, found it difficult to consider the loose, often incomplete connective tissue about the esophagus, trachea, and thyroid gland as a layer of fascia.[4] They considered the fascia immediately about the cervical esophagus and pharynx either to be the only true visceral fascia or to be analogous to the subperitoneal connective tissue of the serous coat of the thoracic esophagus and the bowel.[4] The trachea was considered to have its own fascia, and the thyroid gland capsule was considered to develop from the thyroid anlagen. These authors, in general, considered the visceral fascia of the esophagus and pharynx to be the deep division of the MLDCF and the fascia about the trachea, thyroid gland, and surrounding loose connective tissue not to be part of the MLDCF. Today, this is the view that is most commonly held.

Again, these are problems of nomenclature. There is no dispute that in the lower neck there is a thyroid gland capsule, a filmy loose connective tissue around the thyroid gland, trachea and cervical esophagus that is incomplete or absent in many people but that has a fairly consistent thickening on each side between the posterior margin of the thyroid gland and the esophagus. There also is a better-defined fascia about the cervical esophagus (which extends cranially to surround the pharynx) and a surrounding, less well defined connective tissue zone.

The Middle Layer of the Deep Cervical Fascia in the Suprahyoid Neck

Although the controversies concerning the fasciae in the infrahyoid neck are of limited clinical concern, the fasciae of the suprahyoid neck figure prominently in discussions of the clinically important retropharyngeal and parapharyngeal spaces. Critical to any discussion of this fasciae is an understanding of the anatomy of the cranial portion of the pharynx, the attachments of the tensor and levator veli palatini muscles to the skull base, and the relationship of these muscles to the eustachian tube as the visceral fascia attaches to and surrounds these structures.

The superior pharyngeal constrictor muscle attaches dorsally to the skull base at the midline pharyngeal tubercle via an aponeurosis. From this point, on either side, the muscle arches caudally to attach to the lower portion of the medial pterygoid plate. This arching shape results in a gap on either side of the midline between the skull base and the upper surface of the superior constrictor muscle. This gap is almost entirely filled by the thick pharyngobasilar fascia, which can be considered as the cranial continuation of this muscle and which helps define and restrict the shape of the nasopharynx.[2, 4] On either side, just under the skull base and dorsal to the posterior edge of the medial pterygoid plate, the pharyngobasilar fascia is deficient, creating a space known as the sinus of Morgagni, through which passes the cartilaginous portion of the eustachian tube and the levator veli palatini muscle (Drawings 2 and 13–16).

The levator veli palatini muscle arises from the undersurface of the petrous apex and the medial lamina of the cartilaginous eustachian tube. This muscle then passes through the sinus of Morgagni in the pharyngobasilar fascia, descending submucosally along the inner surface of the pharyngeal constrictor to finally reach the soft palate. Once through the sinus of Morgagni, the levator veli palatini muscle has been described as being enclosed in a fascial space ''la loge peristaphyline interne'' (box or space of the levator palatini) that is formed by small medial and lateral leaves of the BPF at the skull base, the skull base itself, the eustachian tube, and the pharyngobasilar fascia. The muscle moves freely within this fascial space, is partly responsible for maintaining the patency of the eustachian tube, and is an integral part of the pharyngeal wall. It is best considered as a part of the pharynx and is innervated by the pharyngeal plexus (Fig. 34-7).

The tensor veli palatini muscle arises from a scaphoid fossa and spine of the sphenoid bone near the base of the medial pterygoid plate and from the lateral lamina of the cartilaginous eustachian tube. It then descends lateral to the pharyngeal constrictor, between the medial pterygoid plate and the medial pterygoid muscle, which arises in the pterygoid fossa. Its tendon then wraps around the hamulus of the medial pterygoid plate, and the muscle inserts into the palatine aponeurosis. The tensor veli palatini muscle, which remains outside of the pharynx, is best considered to be part of the muscles of mastication and is supplied by the fifth cranial nerve. This muscle also helps maintain the patency of the eustachian tube and, as noted, is really part of the deglutitional group of muscles.

The visceral fascia or BPF extends from the skull base and follows the outer surface of the pharyngobasilar fascia and the pharyngeal constrictors. This fascia is firmly adherent to the muscular wall of the pharynx and the esophagus, and no real space exists between this fascia and the viscera. However, this potential space has caused some confusion in the literature because it has also been referred to as the visceral space. Today the visceral space is generally considered to be the space between the BPF and the alar fasciae (see the discussion in the section on The Fascial

Copyright © 2003, Mosby, Inc. All rights reserved.

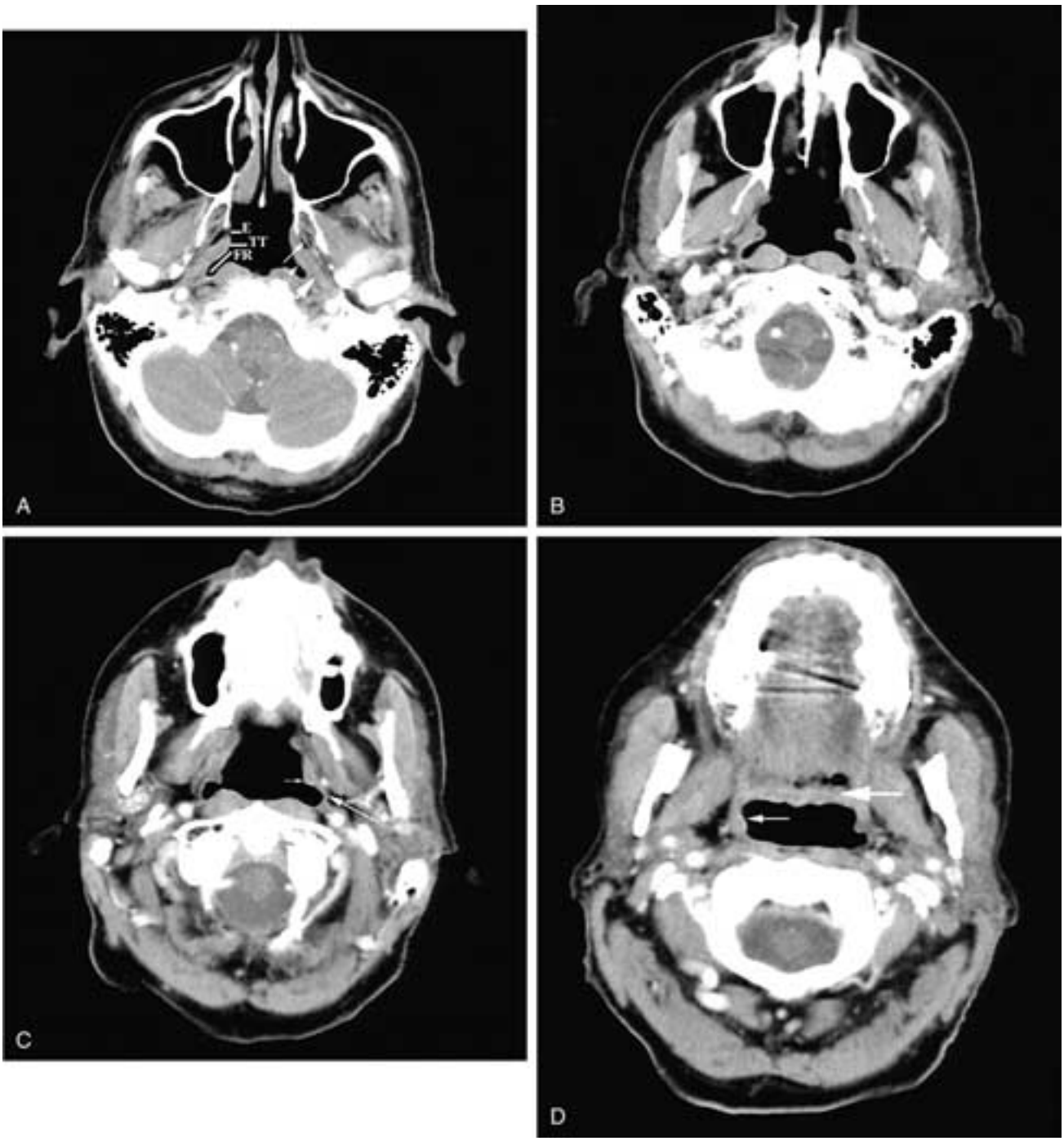

FIGURE 34-7 Axial sequential contrast-enhanced CT scans extending from cranially (**A**) to caudally (**D**). In **A**, the fossa of Rosenmueller (*FR*), the torus tubarius (*TT*), and the opening of the eustachian tube (*E*) are shown. The tensor velli palatini muscle (*small arrow*) is seen lateral to the pharyngeal constrictors (*arrowhead*). The tensor muscle remains outside the pharynx until its tendon extends around the hamulus of the medial pterygoid plate to reach the soft palate. The levator velli palatini muscle (*large arrow*) is seen extending from the skull base to lie within the pharyngeal constrictors. In **B**, the levator velli palatini muscle is seen extending caudally from the torus tubarius. In **C**, the tapering levator velli palatini muscle (*small arrow*) is seen within the pharyngeal constrictors (*large arrow*). In **D**, the caudal levator velli palatini muscle (*small arrow*) is seen heading toward the soft palate (*large arrow*), all within the pharyngeal constrictors.

VIEW IMAGE

Copyright © 2003, Mosby, Inc. All rights reserved.

Spaces) (Fig. 34-8). This current usage is virtually the opposite of that of Grodinsky and Holyoke.

Descriptions of the most superior visceral fascial attachments vary, with most authors indicating that the BPF has an intimate association with the eustachian tube and the levator veli palatini muscle. The BPF splits to enclose the more cranial portion of the levator muscle, and a lateral leaflet is sometimes described in association with the lateral margin of the tensor veli palatini muscle. According to most authors, a well-defined, fairly thick fascial sheet arises directly from the posteroinferior edge of the tensor veli palatini muscle and extends caudally and posterolaterally from this muscle to the styloid process and the styloid muscles, fusing inferiorly with the fascia covering the styloglossus muscle.[9, 16, 20] This fascial sheet thus closes the gap between the tensor veli palatini, the skull base (from the sphenoid spine along the medial side of the foramen ovale to the root of the medial pterygoid plate), and the styloid process with its associated musculature. Anteriorly this fascia reaches the pterygomandibular raphe and there fuses with the interpterygoid fascia as well as the BPF.

In the English literature this important fascia has been described by Gaughran, who referred to it as the vascular fascia because it contains the ascending palatine artery and vein.[9] Other names given to this fascia include the nerve-vessel sheath of Weintraub, the lame vasculaire, and the lateral aponeurosis of the pharynx.[9, 21, 22]

As to the origin of this fascia, it is clearly located between the SLDCF and the DLDCF and it is immediately contiguous with the BPF, which is derived from the MLDCF. However, the subclassification of the DCF into three different layers is not usually applied to the region above the hyoid bone and is rarely utilized in the area under the skull base. Some authors believe it to be part of the MLDCF; other authors describe it as an independent fascial layer. In either case, its derivation is less important than knowledge of its existence and its location. In this discussion, we will refer to this fascia by the anatomically descriptive name *tensor-vascular-styloid fascia*. This fascia plays a key role in the descriptions of the parapharyngeal space, as discussed in Chapter 38 (Drawings 2, 13–16).

THE CAROTID SHEATH

Most authors have described the primary fascial contributions to the middle and lower carotid sheath as coming from the SLDCF (from the fascia covering the sternocleidomastoid muscle) and from the DLDCF (from the alar fascia). There also may be contributions to the sheath from the MLDCF about the strap muscles (this fascia is variously thought to come from either the SLDCF or the MLDCF). Overlapping of these fascial contributions occurs in some areas, giving added strength to that portion of the carotid sheath, while in other areas there may be focal dehiscences, especially along the medial wall (Drawings 2–5, 8, 15 and 16).

The upper portion of the carotid sheath remains a composite compartment formed by the various regional fasciae. Typically, the upper carotid sheath is described as being formed by the SLDCF (represented by contributions from the adjacent muscular investing fasciae) that forms the lateral wall, the DLDCF (represented by the alar and/or prevertebral fasciae) that forms the posterior wall, the cloison sagittale (either part of the DLDCF or the MLDCF) that forms the medial wall, and the stylopharyngeal aponeurosis or the tensor-vascular-styloid fascia (MLDCF) that forms the anterior wall (see the discussion below).

There is general agreement among anatomists and surgeons that in the neck, caudal to the carotid artery bifurcation, the carotid sheath is a complete, well-defined structure. However, more cranially, many authors describe the internal carotid artery as being in an incomplete sheath with variable areas of dehiscence (Fig. 34-9).

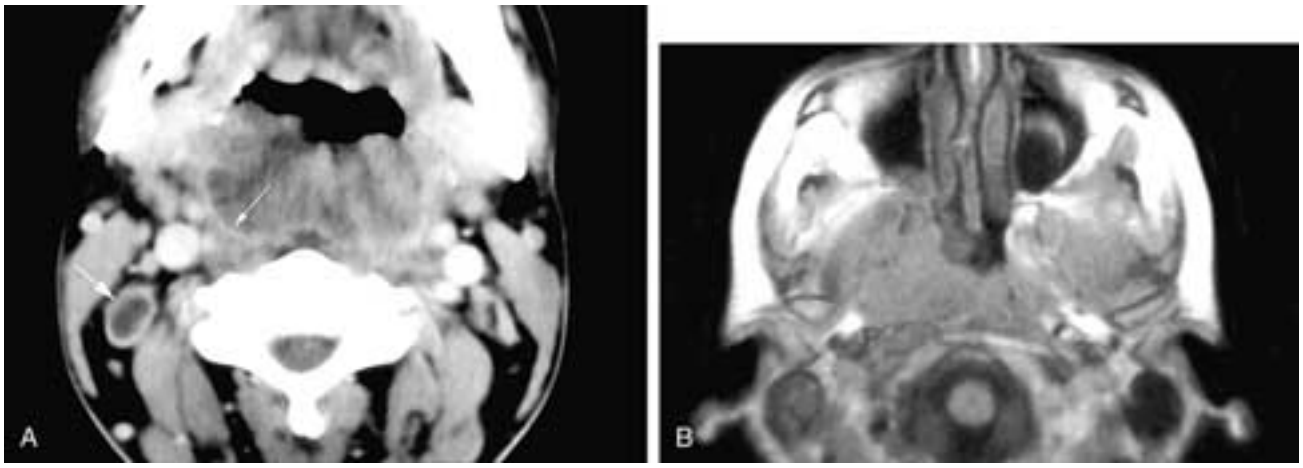

FIGURE 34-8 Axial contrast-enhanced CT scan (**A**) shows a large, bulky tumor in the pharynx. The visceral fascia around the pharyngeal constrictor muscles can be seen containing the tumor (*small arrow*). This imaging appearance is not uncommon with pharyngeal tumors and often belies the malignant nature of the tumor. However, a necrotic right level II node is present (*large arrow*), attesting to the aggressive nature of the cancer. Axial T1-weighted MR image (**B**) shows an infiltrative nasopharyngeal tumor that has violated the visceral fascia. The penetration of this fascia signifies the aggressive nature of the carcinoma.

VIEW IMAGE

Copyright © 2003, Mosby, Inc. All rights reserved.

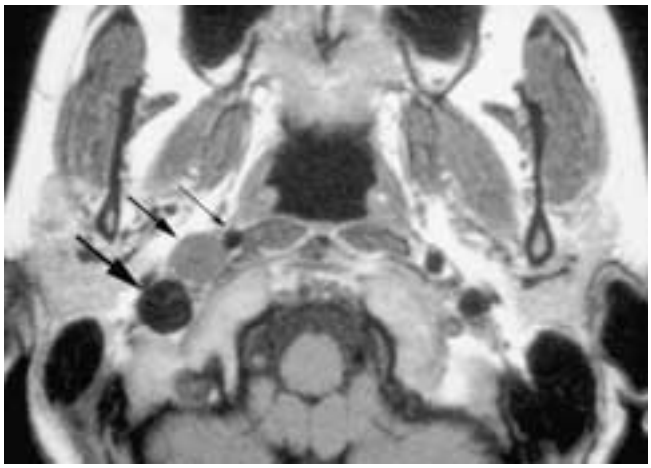

VIEW IMAGE

FIGURE 34-9 Axial T1-weighted MR image shows a mass (*medium arrow*) separating the internal carotid artery (*small arrow*) and the internal jugular vein (*large arrow*). Although the fascia forming the carotid sheath cannot be seen on imaging, its presence is noted by the fact that it restrains the vessels from simply sliding away from the schwannoma and thus allows the mass to separate them.

THE FASCIAL SPACES

The fascial spaces or compartments are regions of loose connective tissue that fill the areas between the fascial layers. In some cases these compartments are readily identifiable, while in others they represent more potential spaces. The descriptions of these fascial spaces vary almost as much as those of the fasciae themselves, and there is little agreement among surgeons and anatomists as to whether the spaces communicate freely with each other, allowing unobstructed spread of infections, or whether most of these spaces are closed and separate so that infections from one space must ''point'' and penetrate in order to spread to adjacent spaces. The explanation of these differing opinions may be the normal anatomic variations of the fasciae that occur among people.

Another difficulty when discussing the spaces of the neck is that there are no officially accepted names for many of these spaces. A number of the spaces do have names that have been so commonly utilized for years that they have become acceptable terms. However, throughout the literature, a variety of less common names have been employed for some spaces. These differences in nomenclature will be mentioned throughout the discussion of the spaces.

In the previous sections, a detailed description of the fasciae that form these spaces has been given. In this section a summary of the boundaries of these spaces will be given, and Drawings 17 to 22 show the overall relationship of each of the major spaces to one another.

The Visceral Compartment and Its Spaces

Probably the most controversial and confusing terminology is for the space that contains the pharynx, cervical esophagus, trachea, thyroid gland, parathyroid glands, larynx, recurrent laryngeal nerves, and portions of the sympathetic trunk. This space is referred to by various authors as either the visceral compartment or the visceral space. This region extends from the skull base down to the upper thorax. In its more cranial portion it is defined by the visceral fasciae or BPF ventrally, the alar fascia dorsally, the cloison sagittale fasciae on either side, and the skull base superiorly. In its caudal portion it has two sections. There is an anterior or ventral portion enclosed by the strap muscles ventrally, the carotid sheaths laterally, and the alar fascia dorsally. There is also a caudal or posterior continuation of the more cranial portion of this region around the cervical esophagus.

Most authors today refer to this region as the visceral space. It is considered to have two subdivisions: an anterior pretracheal space and a more posterior retrovisceral space.[2, 4] These spaces communicate freely between the levels of the thyroid cartilage and the inferior thyroid artery. However, caudal to this level, these spaces are separated by a fascia associated with the inferior thyroid artery. As a result, the pretracheal space extends down into the superior mediastinum, while the retrovisceral space extends into the middle mediastinum. As mentioned, the reader should be aware of the confusing terminology, as in the literature the entire visceral space is referred to by some authors as the visceral compartment, with two lower regions: the pretracheal space and the retrovisceral space.

The Pretracheal Space

The pretracheal space (itself a somewhat confusing term, as this space contains the trachea) extends from the hyoid bone and the attachments of the strap muscles and their fascia to the hyoid bone and thyroid cartilage down to the superior mediastinum about the upper border of the aortic arch and great vessels. This space contains the trachea, thyroid gland, parathyroid glands, larynx, cervical esophagus, recurrent laryngeal nerves, and portions of the sympathetic trunk. The pretracheal space communicates freely with the retrovisceral space around the sides of the larynx, the lowermost pharynx, and the upper cervical esophagus between the levels of the thyroid cartilage and the inferior thyroid artery. Caudal to this level, the pretracheal space is separated from the retrovisceral space by dense connective tissue that extends from each lateral wall of the visceral compartment to the lateral margins of the esophagus. This tissue accompanies the inferior thyroid artery on either side as it courses cranially from the thyrocervical trunk, extends ventral to the vertebral artery and the longus colli muscle, and then runs to the caudal and dorsal aspect of the thyroid gland (Drawings 3–5, 8, 9, and 17–22).[2, 4]

The Retrovisceral Space

The posterior portion of the visceral compartment, referred to as the retrovisceral space, is behind the pharynx and upper esophagus. It extends from the skull base down to the mediastinum, where its caudal limit is between the levels of the sixth cervical vertebra and the fourth thoracic vertebra, where the alar fascia fuses with the visceral fascia. Often the space actually stops at the more cranial of these levels, corresponding to the level of the tracheal bifurcation (Drawings 2–5, 8, 9, and 17–22).[2, 4] As the retrovisceral

Copyright © 2003, Mosby, Inc. All rights reserved.

space lies behind the pharynx and upper esophagus, in the upper neck it is often referred to as the retropharyngeal space.

More specifically, in its upper regions, this space lies between the BPF anteriorly (as this fascia surrounds the pharyngeal musculature) and the alar fascia posteriorly. On either side, the cloison sagittale separates the retropharyngeal space from the more laterally positioned parapharyngeal space. In the middle and lower neck, the continuation of this space surrounds the esophagus, and it is commonly referred to as the retroesophageal space. Thus the ''retropharyngeal'' and ''retroesophageal'' spaces are the upper and lower aspects of one space (the retrovisceral space or portion of the larger visceral space), which communicates freely with the pretracheal space between the levels of the thyroid cartilage and the inferior thyroid artery. This fascial anatomy explains why a retropharyngeal abscess can extend down into the pretracheal space and affect the thyroid gland and anterior mediastinum, or why a large thyroid goiter can extend behind the esophagus and grow either upward as a retropharyngeal mass or downward as a retroesophageal mass (Figs. 34-10 to 34-14).

To confuse the issue even further, a few authors have restricted the use of the term *visceral space* to the potential space between the visceral fascia and the enclosed viscera. However, this opinion is not held by most authors.

The Danger Space

Grodinsky and Holyoke described the danger space (their space 4) as lying between the alar fascia (ventrally) and the prevertebral fascia (dorsally).[2] The space extends from the skull base down into the posterior mediastinum to a level just above the diaphragm where the fused alar and visceral fascia, in turn, fuse with the prevertebral fascia. Grodinsky and Holyoke considered this space an important potential pathway for the spread of cranial and cervical infections into the middle and lower mediastinum. Since the space is closed superiorly, inferiorly, and laterally, infections must enter the space by penetrating its walls (Drawings 2–5, 8, 9, and 17–22).[2]

The Prevertebral Space

This space is a potential space that exists between the prevertebral fascia and the vertebrae, extending from the skull base to the coccyx.[2, 4] The prevertebral muscles are within this space (Drawings 2–5, 8, 9, and 17–22). The vast majority of the pathology that affects this space arises from the adjacent vertebral bodies, discs, and neural elements.

The Carotid Sheath

There is lack of agreement in the literature as to whether the potential cavity within the carotid sheath can act as a space that allows the spread of infections from the upper neck down into the lower neck and mediastinum. Coller and Yglesias, like Pearse, believed it to be a true pathway for the spread of infection.[7, 23] However, Grodinsky and Holyoke found this space to be of limited value as a pathway for infectious spread.[2] Their experimental injections into the sheath remained confined to the sheath around the common carotid artery between the carotid bifurcation and the root of the neck, levels where the sheath is closely adherent to the vessels. They suggested that it is probably most accurate to consider the carotid sheath as a true space only below the level of the carotid bifurcation and above the root of the neck.

There is some controversy in the literature as to whether the portion of the carotid sheath about the internal carotid artery (i.e., above the hyoid bone) should be considered as part of the parapharyngeal space or as a separate ''carotid space.'' Historically, the anatomic and surgical literature is of the opinion that this portion of the carotid sheath should be considered as part of the parapharyngeal space.[2, 4, 6, 9, 10, 15] The reasoning is based on three observations: (1) Grodinsky and Holyoke found that above the carotid bifurcation, the carotid sheath did not act as a space that allowed the spread of infection; (2) the anatomic literature traditionally has accepted that the posterior layers of the carotid sheath are the posterior boundary of the parapharyngeal space (Drawings 2–5, 8, 9, 15, 16, and 17–22); and (3) most importantly, during the surgical approach to the parapharyngeal space, the tensor-vascular-styloid fascia acts as a boundary between the more superficial prestyloid compartment (containing the retromandibular portion of the parotid gland) and the deeper retrostyloid compartment (containing the carotid sheath).

Harnsberger offered the concept that the carotid sheath and its contained structures should be considered as the carotid space.[24] Although this may not necessarily reflect the anatomic evidence regarding the true presence of a carotid space, the benefit of this concept lies in its ability to help generate a differential diagnosis of lesions that can be localized on imaging to the carotid sheath[25] (Fig. 34-9). The major limitation of this approach is that most surgeons use the prestyloid/retrostyloid terminology and are not as familiar with the carotid space concept.

The Space of the Body of the Mandible

As the SLDCF reaches the caudal border of the mandible, the fascia splits into two leaflets, with the outer leaflet firmly attaching along the lower buccal border of the mandible. The deep fascial leaflet attaches to the lingual surface of the mandible along the line of origin of the mylohyoid muscle that is 1 to 1.5 cm above the caudal edge of the mandible. This deep portion of the fascia can be elevated away from the bone, creating a potential space between the fascia and the lingual cortex of the bone. This potential space contains no loose connective tissue, is limited anteriorly by the attachment of the anterior belly of the digastric muscle, and is delineated posteriorly by the attachment of the internal pterygoid muscle.[2, 4]

The Space of the Submandibular Gland

This space is not a real space in the sense that the submaxillary gland can be easily shelled out of it, leaving the SLDCF behind as a capsule.[2, 4] Instead, the septa of the

Copyright © 2003, Mosby, Inc. All rights reserved.

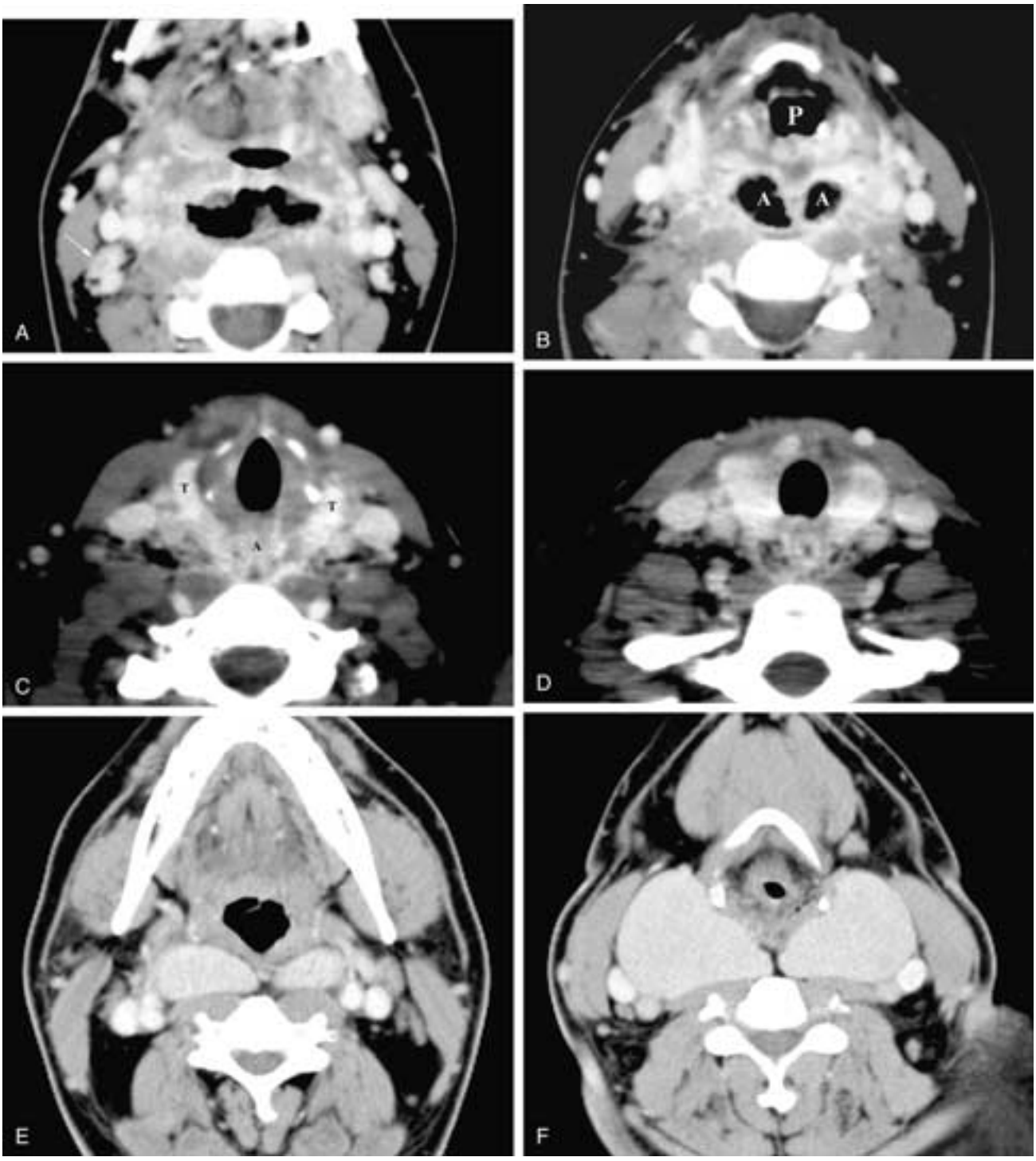

FIGURE 34-10 Serial contrast-enhanced CT scans from cranial (**A**) to caudal (**D**) show a retropharyngeal abscess with enhancing margins. In **A**, the abscess is behind the oropharynx and a necrotic inflammatory right level II node (*arrow*) is present. In **B**, the retropharyngeal abscess (*A*) is seen at the level of the upper hypopharynx (*P*). In **C**, the abscess (*A*) is seen involving the posterior aspects of each thyroid lobe (*T*), attesting to the common visceral space that includes the retropharyngeal portion and the visceral compartment containing the thyroid gland, trachea, and larynx. In **D**, the lowest portion of the abscess is still seen involving the thyroid lobes. Axial contrast-enhanced CT scans at the level of the oropharynx (**E**) and the thyroid bed (**F**) of a patient with a large goiter. The enlarged left and right thyroid lobes extend up behind the pharynx in the visceral (retropharyngeal) space.

Illustration continued on following page

VIEW IMAGE

Copyright © 2003, Mosby, Inc. All rights reserved.

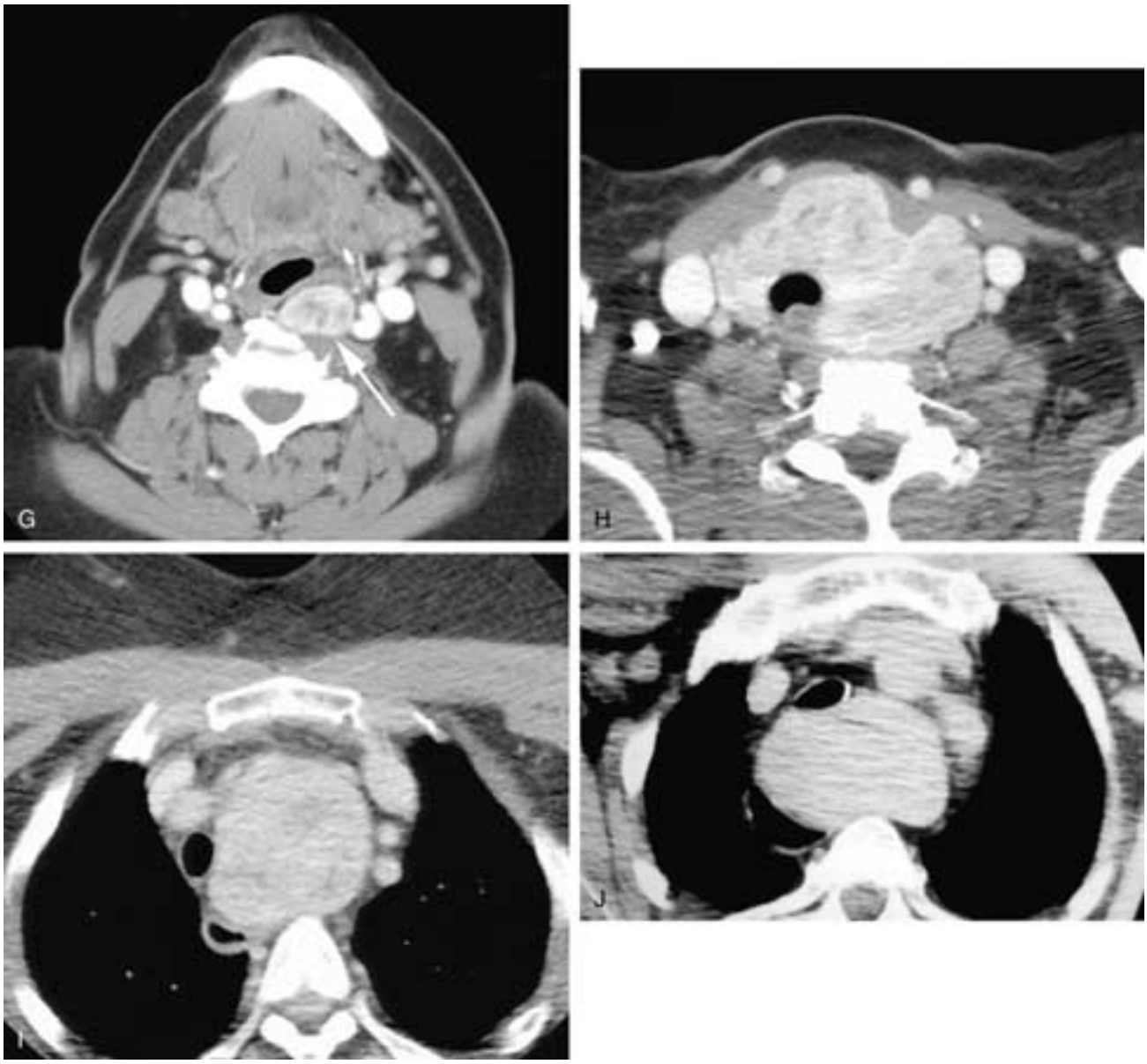

VIEW IMAGE

FIGURE 34-10 *Continued.* Axial contrast-enhanced CT scans at the level of the middle to upper oropharynx (**G**) and the thyroid bed (**H**) of another patient with a goiter. The larger left thyroid lobe (*arrow*) extends up via the retropharyngeal space. Axial contrast-enhanced CT scan (**I**) shows a thyroid goiter extending down into the pretracheal space portion of the visceral space behind the sternum. Axial CT scan (**J**) shows a thyroid goiter extending down into the retrovisceral portion of the visceral space behind the trachea.

gland are continuous with the capsule. However, the submandibular gland has its own volume and so can be thought of as occupying a space bounded by its own capsule or thin fascia (Drawing 13).

The Space of the Parotid Gland

The SLDCF also splits to enclose the parotid gland. Like the submaxillary gland space, the parotid gland cannot be shelled out, leaving behind a real compartment with strong fascial boundaries. In fact, the fascia about the parotid gland is attached by septae to the gland and is inseparable from the gland. The fascia along the medial or deep portions of the gland is also thin or deficient in most people. However, conceptually, this space encloses the parotid gland, the parotid lymph nodes, and portions of the external carotid artery and the posterior facial or retromandibular vein (Drawings 12, 21, and 22).[2, 4]

The Submandibular Space

Overall, this space is the volume described within the mandibular arch, limited above by the mucosa in the floor of the mouth and caudally by the SLDCF as it extends from the hyoid bone to the mandible. The space is divided into an upper and a lower portion by the mylohyoid muscle that

Copyright © 2003, Mosby, Inc. All rights reserved.

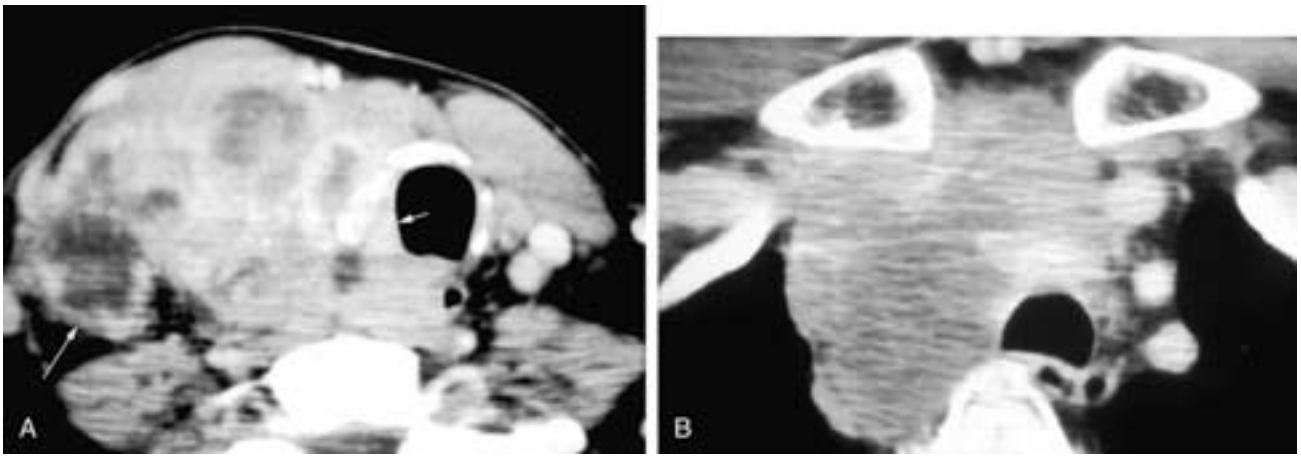

VIEW IMAGE

FIGURE 34-11 Axial contrast-enhanced CT scan (**A**) through the lower neck shows a nonhomogeneous thyroid mass replacing the right thyroid lobe. The mass has displaced the trachea to the left and has invaded the lower larynx (*short arrow*). The fat planes around the right thyroid lesion are infiltrated, obliterating the separation from the adjacent muscles and vessels. The right common carotid artery and internal jugular vein are obscured. All of these imaging findings are evidence of the aggressive nature of this anaplastic thyroid carcinoma as it violates the fascial planes. There also is a necrotic right metastatic level III node (*long arrow*). Axial contrast-enhanced CT scan (**B**) through the lower neck and anterior mediastinum shows an infiltrating thyroid mass that has violated the fascial boundaries, obscuring the adjacent structures. This imaging appearance attests to the aggressive nature of this anaplastic thyroid carcinoma.

attaches to the lingual surface of the mandible along the mylohyoid line. The submaxillary (submandibular) gland is folded around the back of this muscle so that the gland lies partially above and partially below its dorsal edge. In fact, the upper and lower portions of the submandibular space communicate freely with each other around this dorsal margin of the mylohyoid muscle. In general, there is also free communication between the left and right sides of this space (Drawings 10, 13, and 20–22) (Figs. 34-15 and 34-16). As the submandibular gland lies within the submandibular space, a distinction should be made between this larger space and the *space for the submandibular gland*, which essentially refers to the capsule of this gland (see above).

The upper or cranial portion of the submandibular space is often called the *sublingual space*. It is filled with loose connective tissue that surrounds both sublingual glands and their ducts, the lingual and hypoglossal nerves, the lingual arteries, and the smaller or deep portion of each submandibular gland along with its hilum and Wharton's duct. On either side, the lower or caudal portion of the submandibular space is usually referred to as the submaxillary space, and the larger superficial portion of the submandibular gland and its lymph nodes lie within its loose connective tissue. The facial artery and vein as well as the digastric muscle are also in each submandibular space. The submental triangle and the submandibular triangles of the neck are the superficial landmarks that correspond to the region of this space.[2, 4, 14]

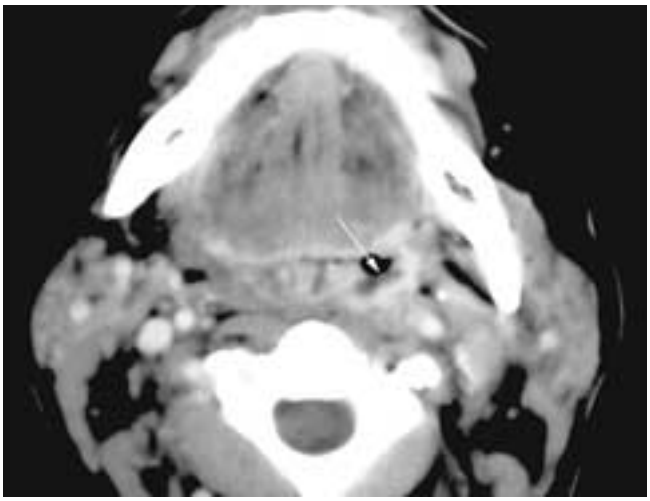

VIEW IMAGE

FIGURE 34-12 Axial contrast-enhanced CT scan through the oropharynx shows an enhancing, thickened mucosa on the left side. There is a mucosal ulceration (*arrow*); however, the visceral fascia appears to prevent the tumor from spreading further into the deep spaces of the neck. This is not an uncommon imaging appearance of pharyngeal carcinomas and illustrates the potential resistance of this fascia to tumor spread.

The Masticator Space

The SLDCF splits about the lower edge of the mandible, and the outer or superficial layer encloses the masseter muscle, extends over the zygomatic arch, and attaches to the calvarium about the dorsal and cranial margins of the temporalis muscle and the lateral orbital wall. The inner or deep layer of fascia covers the medial pterygoid muscle before fusing with the interpterygoid fascia and continuing to the skull base.[15, 16] The split layers of the SLDCF fuse again along the ventral and dorsal borders of the ramus of the mandible and, in so doing, close this space about the muscles of mastication. The lateral pterygoid muscle lies freely within this space, while the fasciae about the masseter, temporalis, and internal pterygoid muscles con-

Copyright © 2003, Mosby, Inc. All rights reserved.

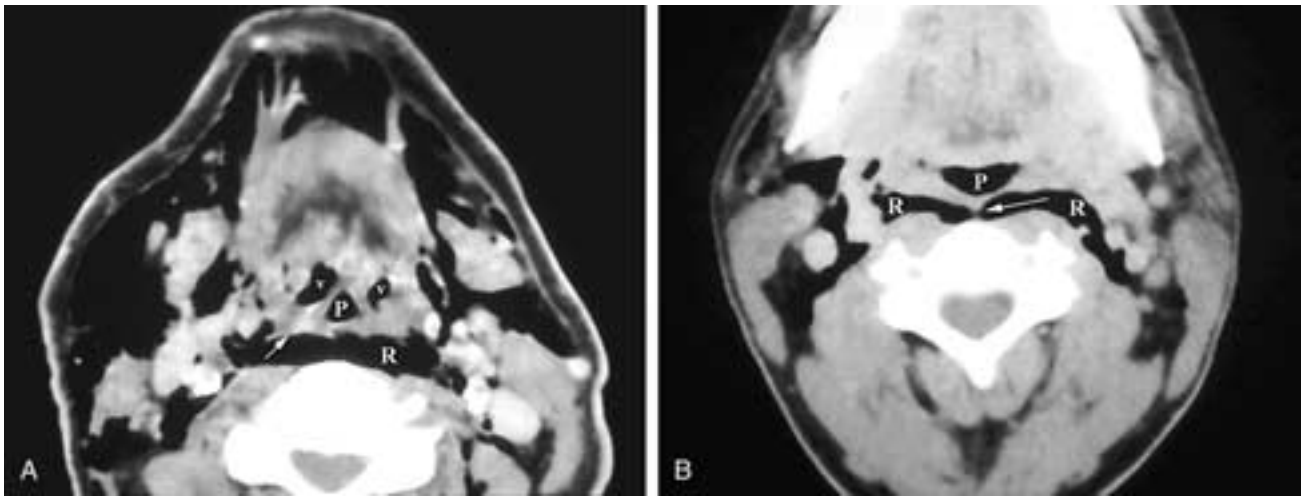

VIEW IMAGE

FIGURE 34-13 Axial contrast-enhanced CT scan (**A**) through the oropharynx shows air infiltrating throughout the neck in this patient who required an emergency tracheotomy. Air is seen in the retropharyngeal space (*R*) behind the pharyngeal airway (*P*) and the vallecullae (*v*). The posterior pharyngeal constrictor muscles are seen (*arrow*) between these air collections. Air is also dispersed throughout the soft tissues of the neck. Axial contrast-enhanced CT scan (**B**) through the oropharynx of another patient shows air in the retropharyngeal space in this patient who had a tracheotomy. Note that there is a midline attachment of the visceral fascia to the alar fascia (*arrow*), incompletely dividing the retropharyngeal space (*R*) into two compartments. This type of compartmentalization occurs in nearly half of the cases (compare to **A**, where there is no such division of the retropharyngeal space). The pharyngeal airway is indicated by *P*.

tribute to the boundaries of this space. The portion of the masticator space that extends cranially between the calvarium and the outer layer of the SLDCF is occasionally referred to as the temporal space, but it is probably better regarded as the cranial extension of the masticator space (Fig. 34-17). The internal maxillary artery and the third division of the trigeminal nerve run within the masticator space (Drawings 2, 10–13, 21, and 22) (Fig. 34-3); see Chapter 38.[2, 4, 7, 12, 15, 16]

The Parapharyngeal Space

What today is commonly referred to as the parapharyngeal space has also been referred to in the literature as the lateral pharyngeal, peripharyngeal, pharyngomaxillary, pterygopharyngeal, pterygomandibular, and pharyngomasticatory space, and it boundaries have been described with more variation than those of any other space of the neck (Drawing 2).[2, 4, 6, 8, 9, 15] The parapharyngeal space is a

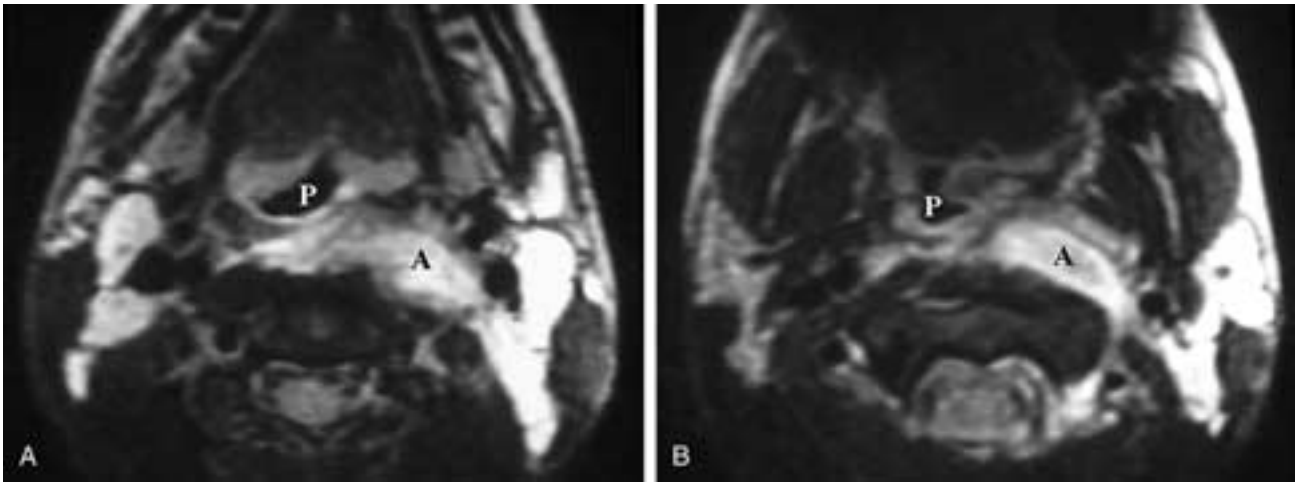

VIEW IMAGE

FIGURE 34-14 Axial T2-weighted MR image (**A**) shows an area of high signal intensity in the retropharyngeal space (*A*). Although the lesion is larger on the left side, the process extends across the midline to involve the right side. Thus, the entire retropharyngeal space is affected by this abscess. The pharyngeal airway is indicated by *P*. Axial T2-weighted MR image (**B**) shows an area of high signal intensity in the left retropharyngeal space (*A*). The remaining portions of the retropharyngeal space are uninvolved. This was an abscessed node, but in a different patient the same imaging appearance could represent a retropharyngeal metastatic node. It is the localized nature of this nodal disease that differentiates this case from the retropharyngeal space abscess shown in **A**. The pharyngeal airway is indicated by *P*.

Copyright © 2003, Mosby, Inc. All rights reserved.

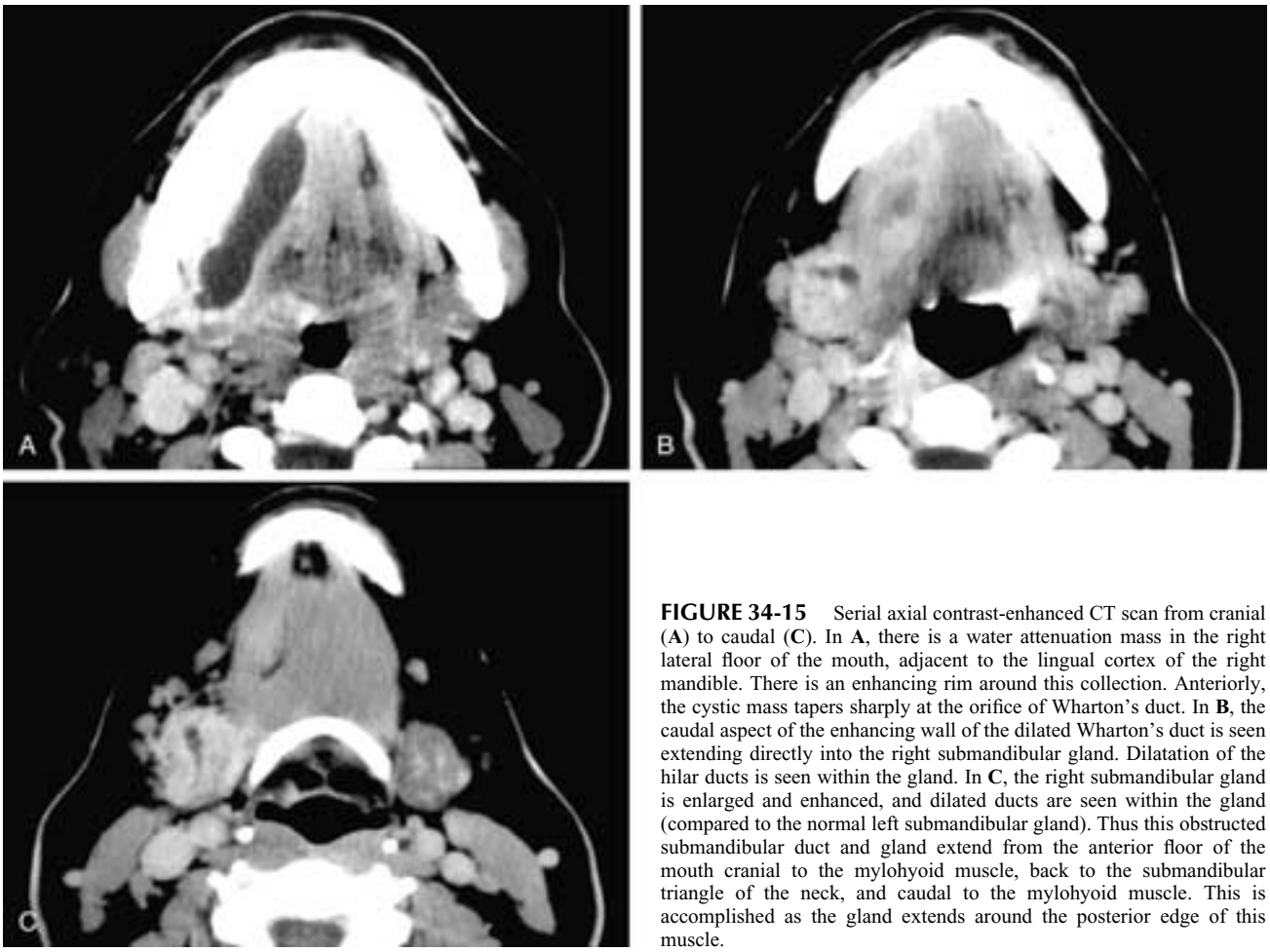

FIGURE 34-15 Serial axial contrast-enhanced CT scan from cranial (**A**) to caudal (**C**). In **A**, there is a water attenuation mass in the right lateral floor of the mouth, adjacent to the lingual cortex of the right mandible. There is an enhancing rim around this collection. Anteriorly, the cystic mass tapers sharply at the orifice of Wharton's duct. In **B**, the caudal aspect of the enhancing wall of the dilated Wharton's duct is seen extending directly into the right submandibular gland. Dilatation of the hilar ducts is seen within the gland. In **C**, the right submandibular gland is enlarged and enhanced, and dilated ducts are seen within the gland (compared to the normal left submandibular gland). Thus this obstructed submandibular duct and gland extend from the anterior floor of the mouth cranial to the mylohyoid muscle, back to the submandibular triangle of the neck, and caudal to the mylohyoid muscle. This is accomplished as the gland extends around the posterior edge of this muscle.

VIEW IMAGE

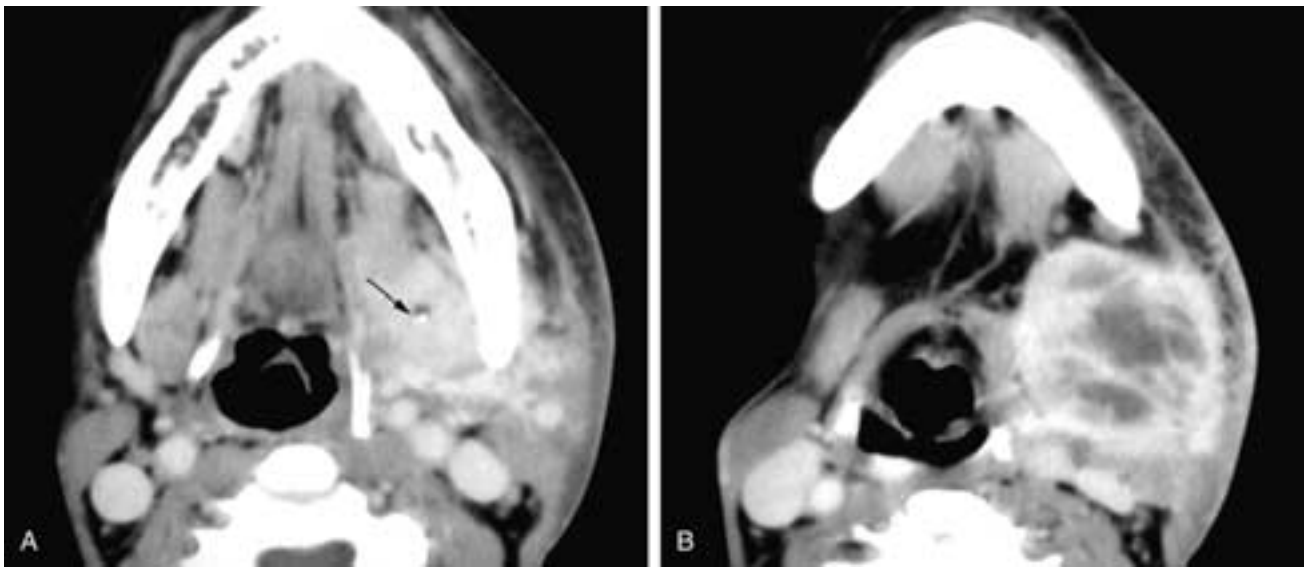

FIGURE 34-16 Axial contrast-enhanced CT scans through the floor of mouth (**A**) and the caudal suprahyoid neck (**B**). In **A**, there is an enhancing mass in the region of the left submandibular gland. A small calculus is present near the hilum of the gland (*arrow*), and the process extends beyond the gland into the adjacent floor of the mouth and the submandibular triangle. In **B**, an abscess is seen in the submandibular triangle, with adjacent thickening of the platysma muscle and thickening and injection of the overlying subcutaneous fat and skin. This abscess arose in the acutely obstructed submandibular gland and spread over the back of the mylohyoid muscle into the submandibular triangle of the neck. Such an abscess from an acutely obstructed gland is unusual. This patient turned out to be HIV positive, which accounted for the rapid spread of the infection.

VIEW IMAGE

Copyright © 2003, Mosby, Inc. All rights reserved.

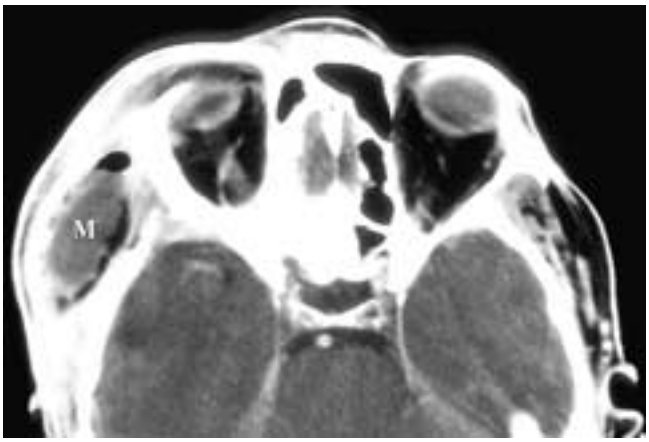

VIEW IMAGE

FIGURE 34-17 Axial contrast-enhanced CT scan through the upper facial area shows a mucoid collection (*M*) with air in the right temporal fossa adjacent to the skull. This was spread of a right masticator space abscess up into the cranial extension of the masticator space.

hatchet-shaped space on either side of the neck. Its ventral (prestyloid) compartment lies just lateral to the pharynx and deep to the masticator space and the ramus of the mandible. It is filled with fat and connective tissue, and the deep portion of the parotid gland protrudes into it. The dorsal (retrostyloid) compartment of the parapharyngeal space corresponds to the carotid sheath and its enclosed structures. The parapharyngeal space extends from the skull base down to the level of the angle of the mandible.

More specifically, the medial wall of the parapharyngeal space is formed by the BPF or visceral fascia as it extends from the skull base caudally, first covering the pharyngobasilar fascia and then the outer aspect of the pharyngeal constrictor muscles (Drawing 3).

On either side of the neck, the pterygomandibular raphe is a linear fascial condensation that extends from the hamulus of the medial pterygoid plate to the lingual surface of the mandible near the posterior margin of the mylohyoid line. This raphe serves as the point of attachment of the superior pharyngeal constrictor muscle, and it is also the origin of the buccinator muscle. In addition, the BPF (covering the pharyngeal constrictor and extending ventrally to cover the buccinator muscle) and the interpterygoid fascia (from the masticator space) both fuse with the pterygomandibular raphe. As the parapharyngeal space is between these fasciae, the pterygomandibular raphe is considered to be the anterior or ventral boundary of the parapharyngeal space.

Caudally, the parapharyngeal space has been described as extending down to the hyoid bone. However, in actuality, the fascia about the submaxillary gland, the sheaths of the styloid muscles, the fascia over the posterior belly of the digastric muscle, the fascia on the lingual aspect of the mandible, and the visceral fascia all fuse near the level of the angle of the mandible, functionally obliterating the parapharyngeal space. Running at the caudal aspect of this region is the styloglossus muscle, which is most often considered to be the inferior boundary of the parapharyngeal space.[2, 4, 6, 8, 9, 15]

The lateral boundary is the fascia on the medial aspect of the masticator space and the fascia over the deep surface of the parotid gland, both of which are formed by the superficial layer of the deep cervical fascia.

The posterior boundary of the parapharyngeal space is the most controversial. As already mentioned, most anatomists and surgeons have placed the carotid sheath in the retrostyloid compartment of the parapharyngeal space, while some radiologists have referred to the sheath as representing a separate carotid space.[2, 4, 6, 8–10, 15, 24, 26] In general, when communicating sectional imaging findings to surgeons, as well as for consistency with the clinical literature, the carotid sheath is considered to be the retrostyloid compartment of the parapharyngeal space. However, it should be remembered that in the literature there is no disagreement about the anatomy itself, only about the terminology used to describe this anatomy (Drawing 4).

Within the boundaries of each parapharyngeal space just described, the parapharyngeal space is usually subdivided into three compartments defined in various descriptions by the tensor-vascular-styloid fascia, the stylopharyngeal aponeurosis (aileron), and the sagittal partition (cloison sagittale) (Drawing 5).

As previously discussed, there is a well-defined, fairly thick fascial sheet, the tensor-vascular-styloid fascia, that closes the gap between the tensor veli palatini muscle and the medial pterygoid plate, the skull base, and the styloid process and its associated musculature (Drawings 3 and 5).[9, 10, 16, 20]

Gaughran mentioned a continuation of this fascia laterally from the styloid process to the posterior border of the mandibular ramus.[9] He referred to this fascial extension as the stylomandibular fascia; a thickening in the lower edge of this fascia is the stylomandibular ligament. This ligament, along with the posterior border of the mandibular ramus and the skull base, forms the stylomandibular tunnel, through which the deep or retromandibular portion of the parotid gland protrudes into the parapharyngeal space. This stylomandibular fascia may also be thought of as a fusing of the SLDCF, as it covers both the medial aspect of the parotid gland and the styloid musculature.

There are two more fascial layers that relate to the tensor-vascular-styloid fascia and further subdivide or partition the parapharyngeal space. The first layer is a roughly coronally oriented fascia that has been variously described as extending medially from either the tensor-vascular-styloid fascia or the styloid musculature to the BPF. It attaches to the BPF near the location of the lateral pharyngeal recess or fossa of Rosenmuller.[15] This fascia has been described by Testut, Zuckerkandl, and others and is most often referred to in the literature as the stylopharyngeal aponeurosis. Some French anatomists refer to it as the *aileron* (Drawings 3 and 5).[6, 8, 9]

The second fascial layer is positioned approximately in the sagittal plane and extends from the BPF, at or near the attachment of the stylopharyngeal aponeurosis, to the alar fascia and prevertebral fascia near their attachments to the transverse processes of the cervical vertebrae. This fascia is referred to by Charpy as the *cloison sagittale* (sagittal partition) (Drawings 3 and 5).[1, 2, 6, 8, 9, 15] Probably reflecting anatomic variation, Cazalas described this cloison sagittale fascia as extending directly from the tensor-vascular-styloid fascia (rather than from the BPF) to the alar fascia.[6] He also described the *aileron* as extending from the tensor-vascular-styloid fascia to the BPF. Cazalas used the term *sphenopharyngeal ligament* to identify the thickening in the tensor-vascular-styloid fascia from which, in his opinion, the cloison sagittale and the aileron had their origins.

Copyright © 2003, Mosby, Inc. All rights reserved.

Color plates 1 to 22 refer to Chapter 34.

VIEW IMAGE

DRAWING 1 Drawing of the head and neck shows the SCF as a loose fatty layer deep to the skin. The fat is more dense in the facial and scalp areas and less dense in the neck and about the eyelids.

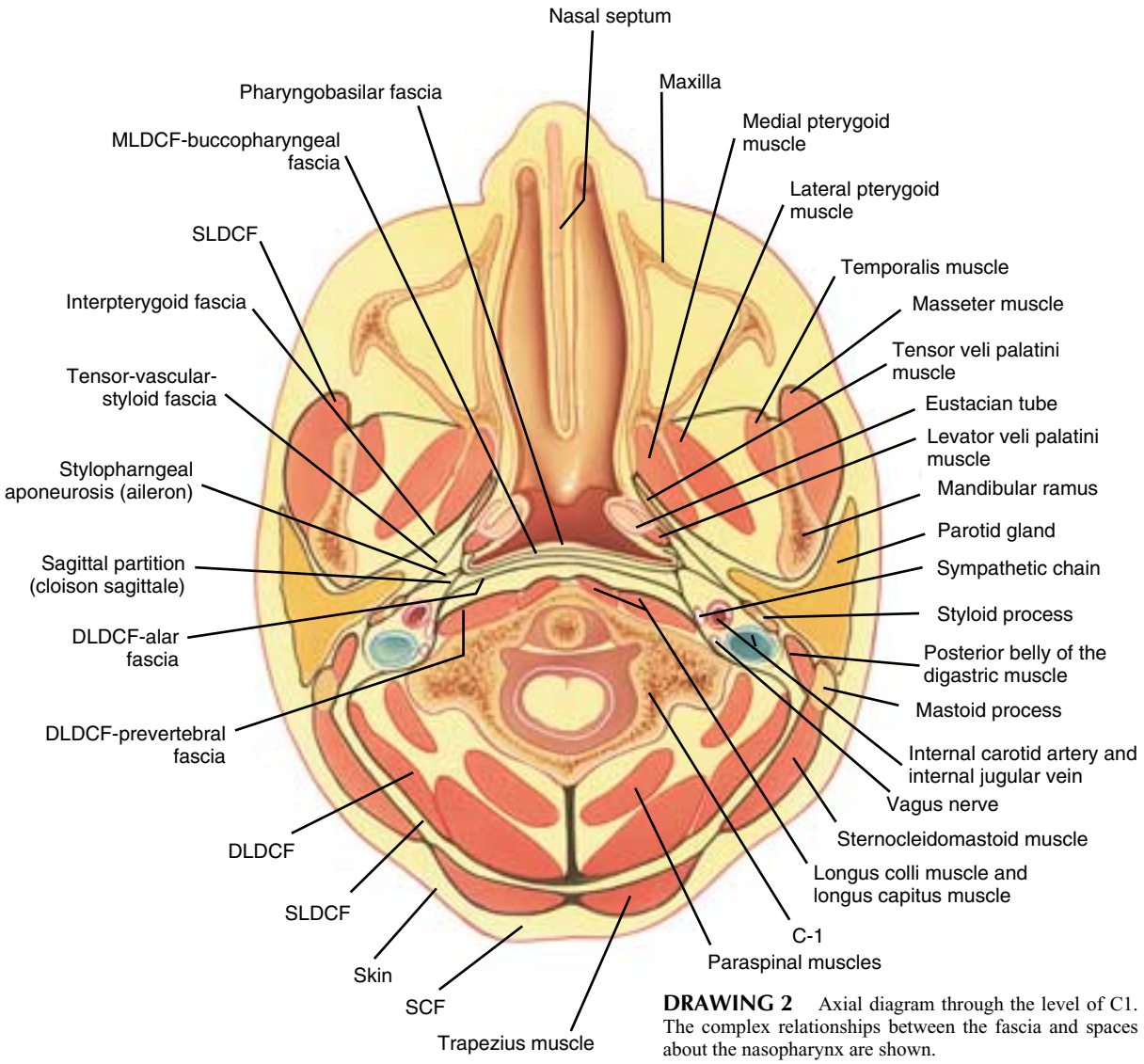

DRAWING 2 Axial diagram through the level of C1. The complex relationships between the fascia and spaces about the nasopharynx are shown.

VIEW IMAGE

Copyright © 2003, Mosby, Inc. All rights reserved.

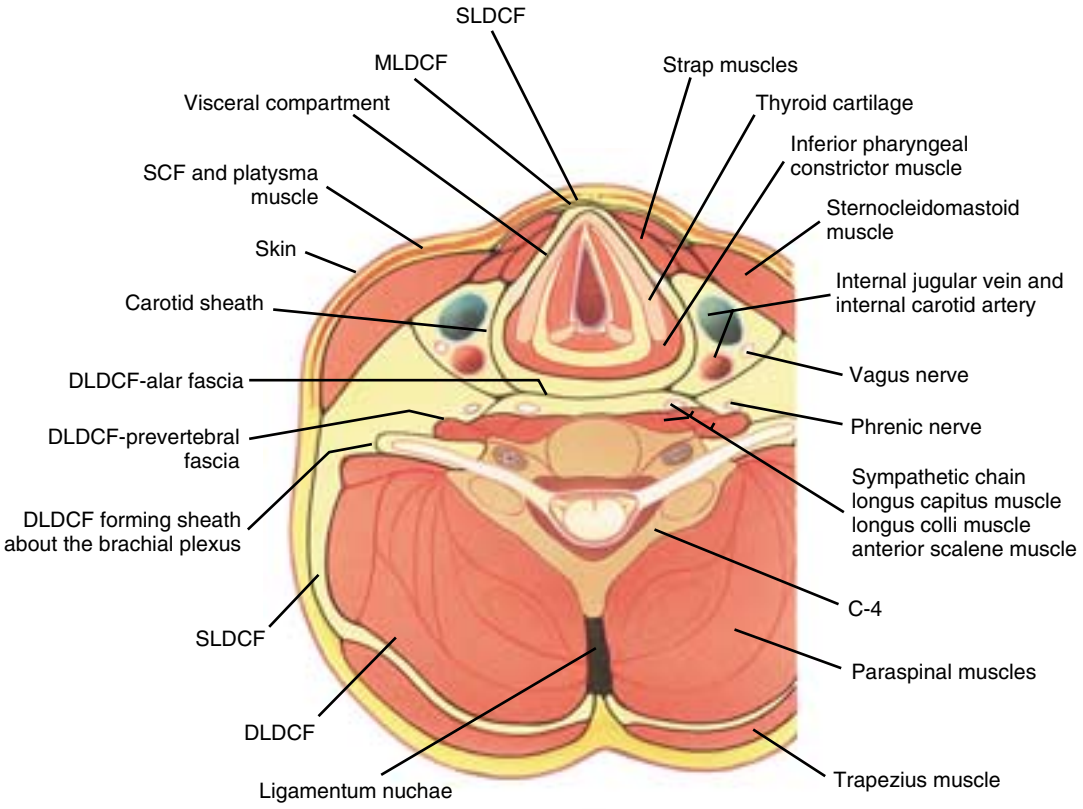

VIEW IMAGE

DRAWING 3 Axial diagram through the level of C4 shows the fascia near the level of the upper visceral compartment.

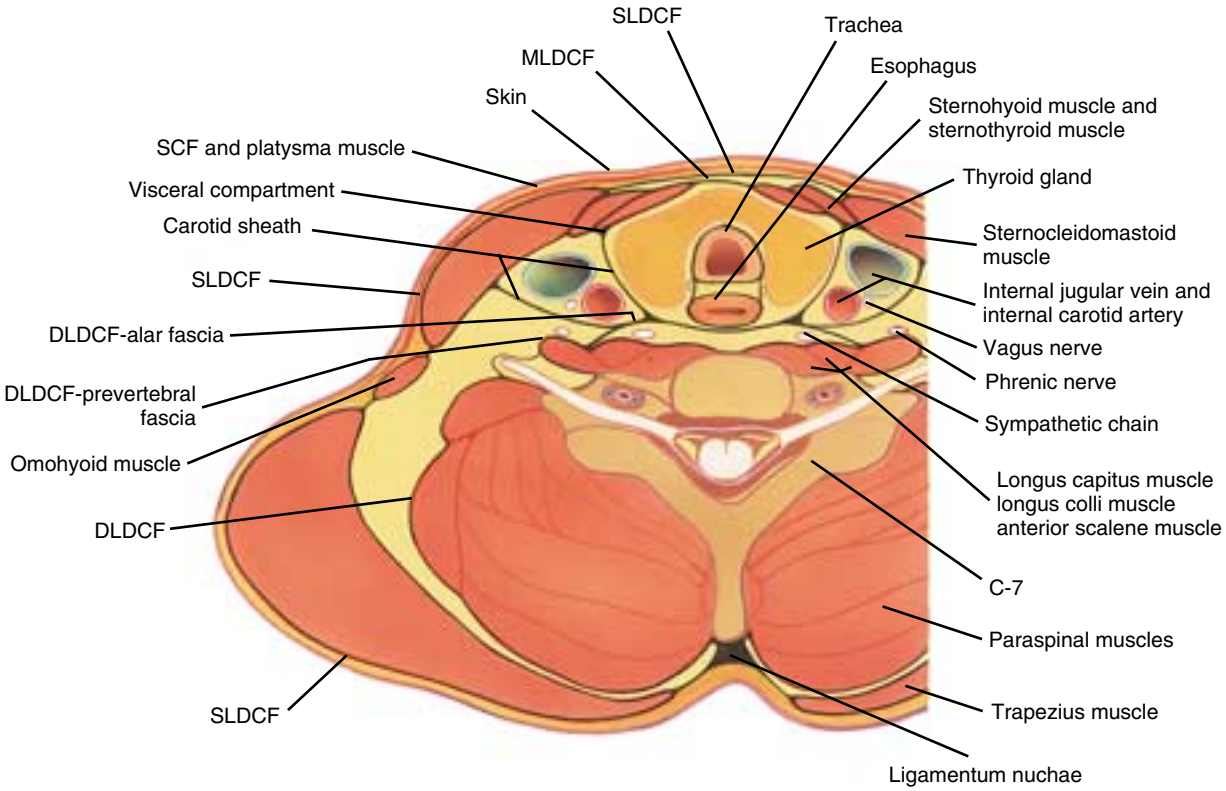

VIEW IMAGE

DRAWING 4 Axial diagram through the level of C7 shows the fascia through the level of the midvisceral compartment. Note that there is a common visceral space at this anatomic level.

Copyright © 2003, Mosby, Inc. All rights reserved.

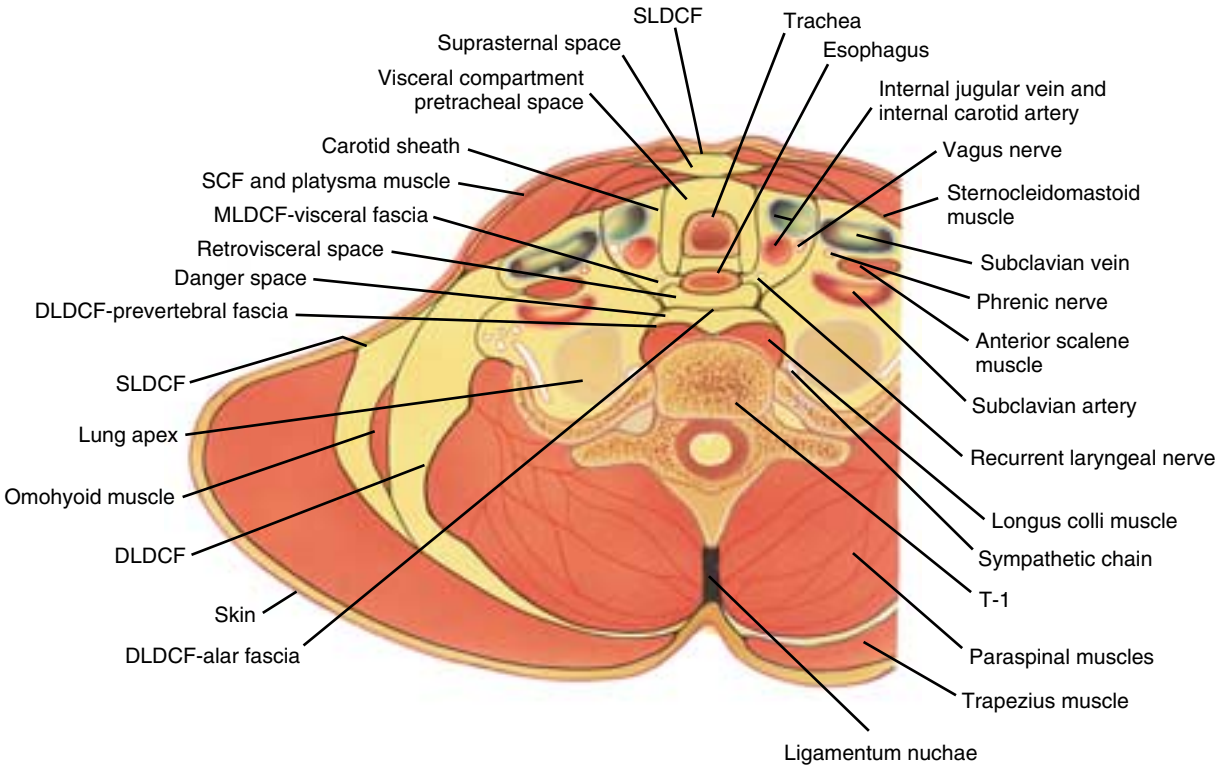

DRAWING 5 Axial diagram through the level of T1 shows the fascia at the level of the lower visceral compartment. Note that the visceral compartment is divided into pretracheal and retrovisceral spaces.

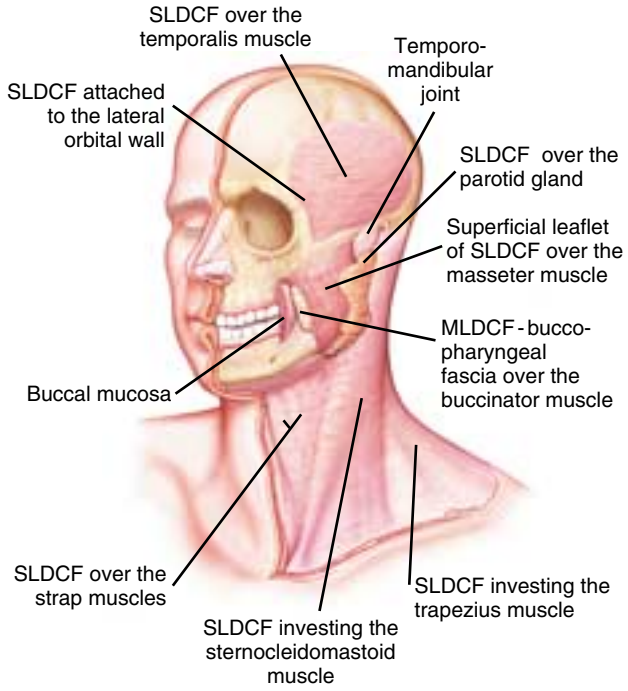

DRAWING 6 Drawing of the head and neck shows the SLDCF as a well-defined fibrous layer deep to the SCF. The SLDCF is seen investing the superficial muscles of the neck and the muscles of mastication.

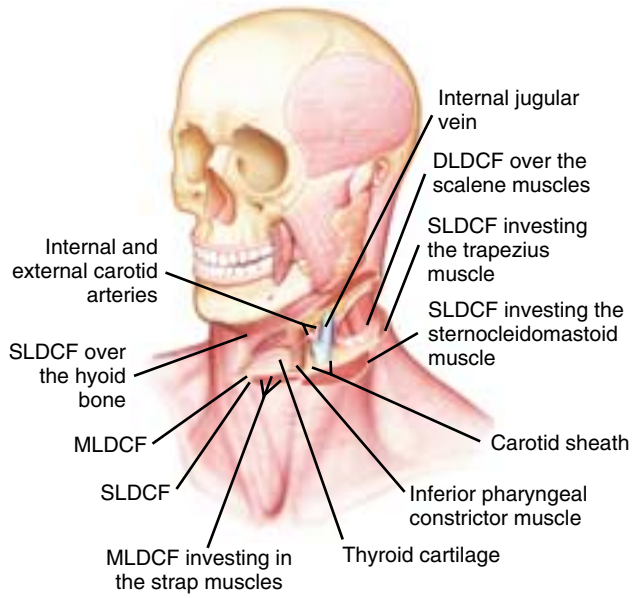

DRAWING 7 Drawing of the head and neck similar to Drawing 6, except that a wedge-shaped cutout has been made in the left neck to illustrate the SLDCF investing the muscles. Note the relationship to the more centrally positioned carotid sheath, the MLDCF, and the DLDCF.

Copyright © 2003, Mosby, Inc. All rights reserved.

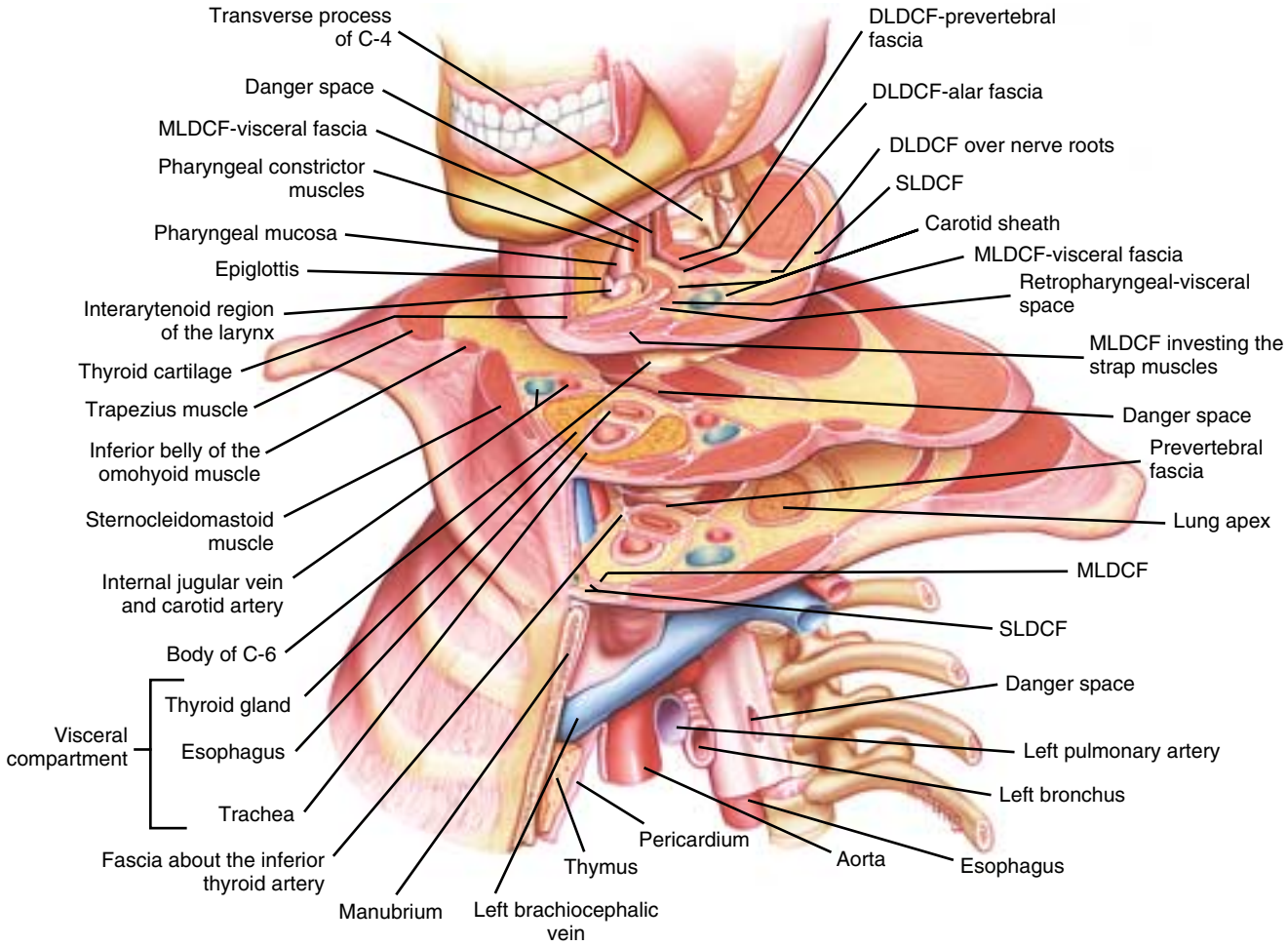

VIEW IMAGE

DRAWING 8 Drawing of the neck and upper chest with three axial cross-sectional slices. The most cranial cut is at the C4 to C5 level and shows the relationships of the upper neck spaces to one another. The middle cut is at the C6 to C7 level and shows the cranial portion of the common visceral compartment. The most caudal cut is at the C7 to T1 level and shows the division of the visceral compartment into the pretracheal and retrovisceral spaces. Also note the substernal extension of the pretracheal space.

Copyright © 2003, Mosby, Inc. All rights reserved.

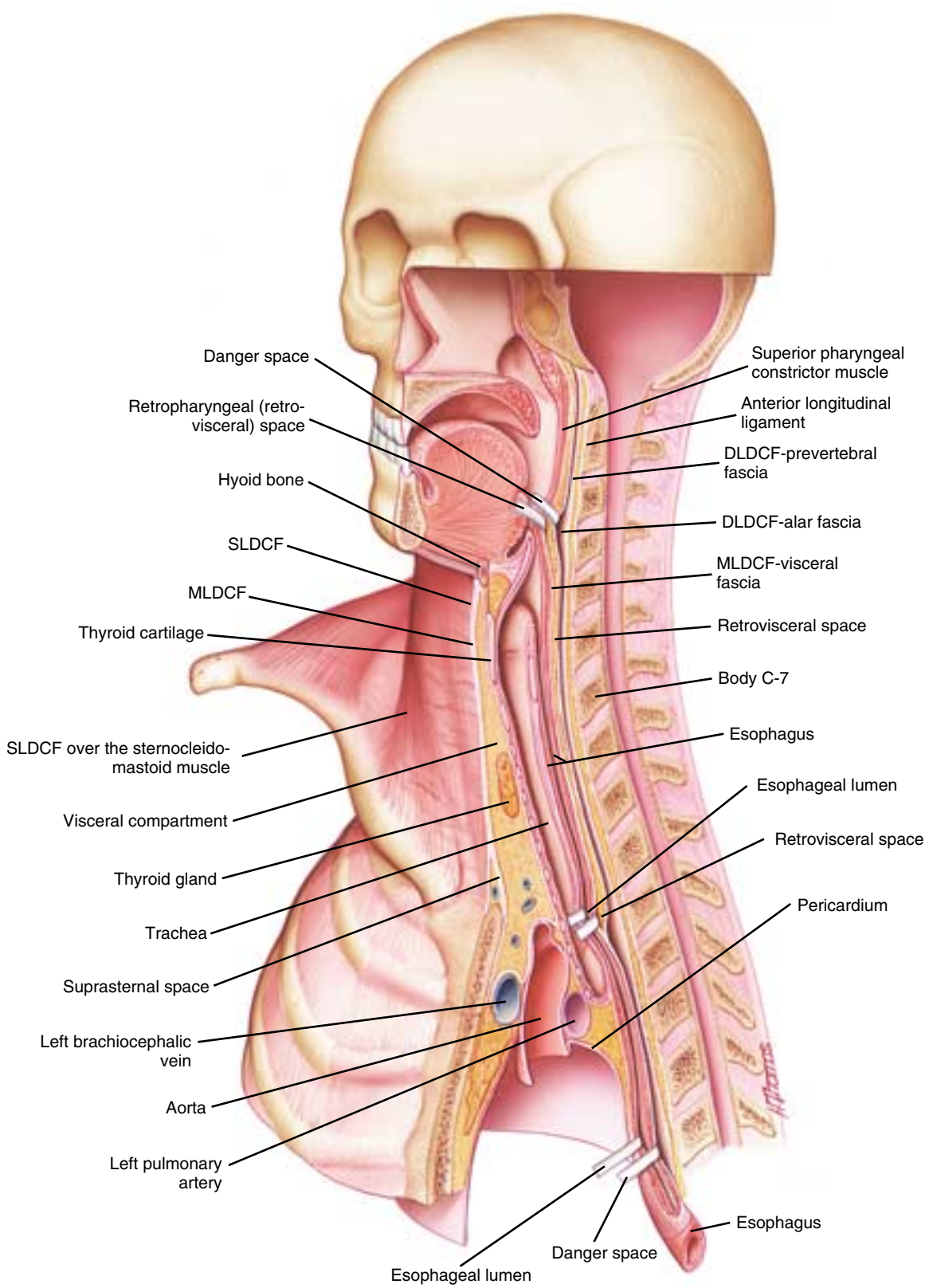

VIEW IMAGE

DRAWING 9 Drawing of a sagittal view of the skull base, neck, and upper chest shows the relationships of the fascia and spaces of the neck to one another and to the mediastinal structures.

Copyright © 2003, Mosby, Inc. All rights reserved.

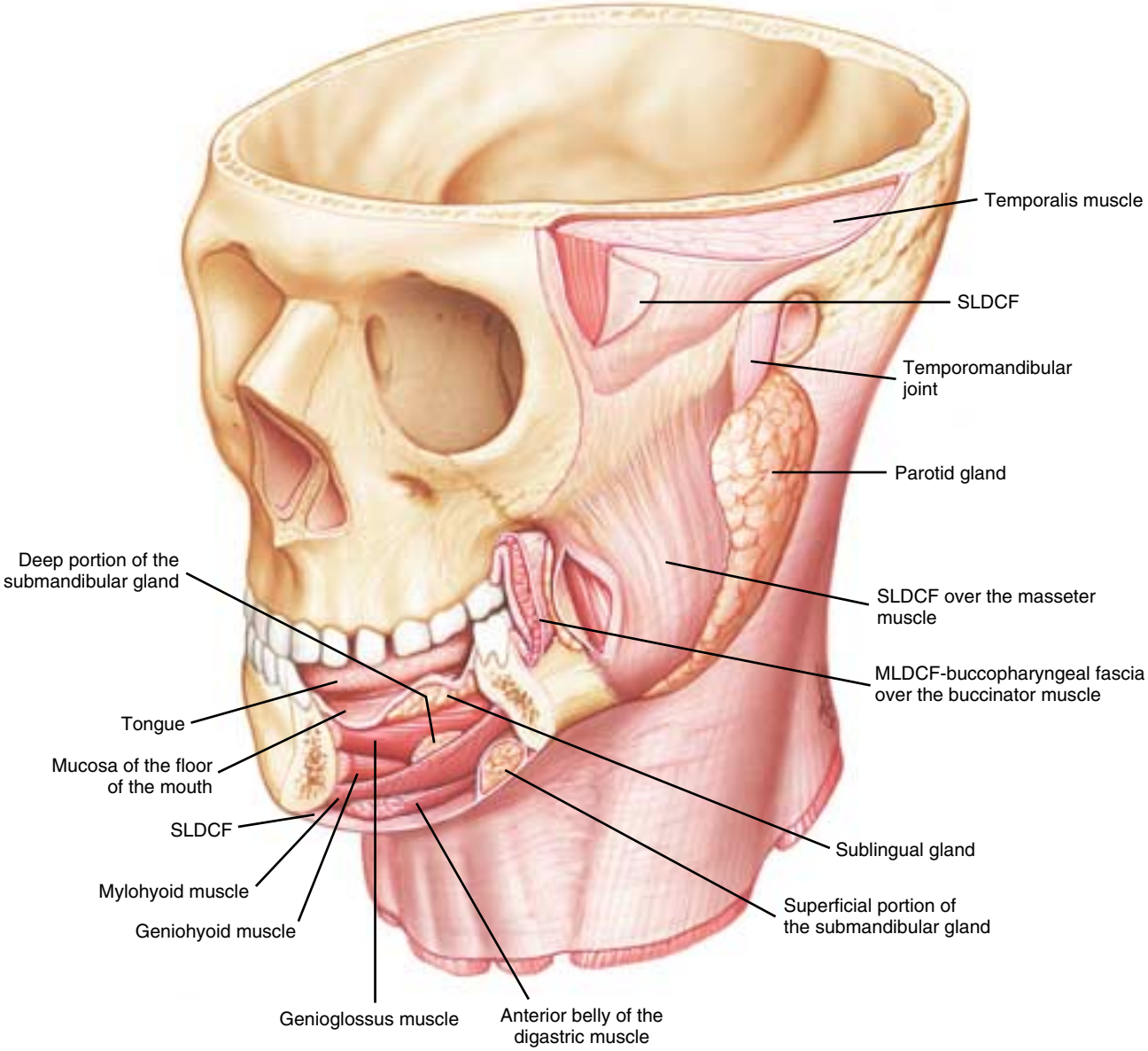

VIEW IMAGE

DRAWING 10 Drawing of the facial region and the upper neck shows the SLDCF with cuts in the fascia exposing the temporalis and masseter muscles. This fascia forms the lateral margin of the masticator space. A portion of the mandible has been removed to expose the structures of the floor of the mouth. Note how the mylohyoid muscle divides the overall submandibular space into an upper sublingual space and a lower submaxillary space.

Copyright © 2003, Mosby, Inc. All rights reserved.

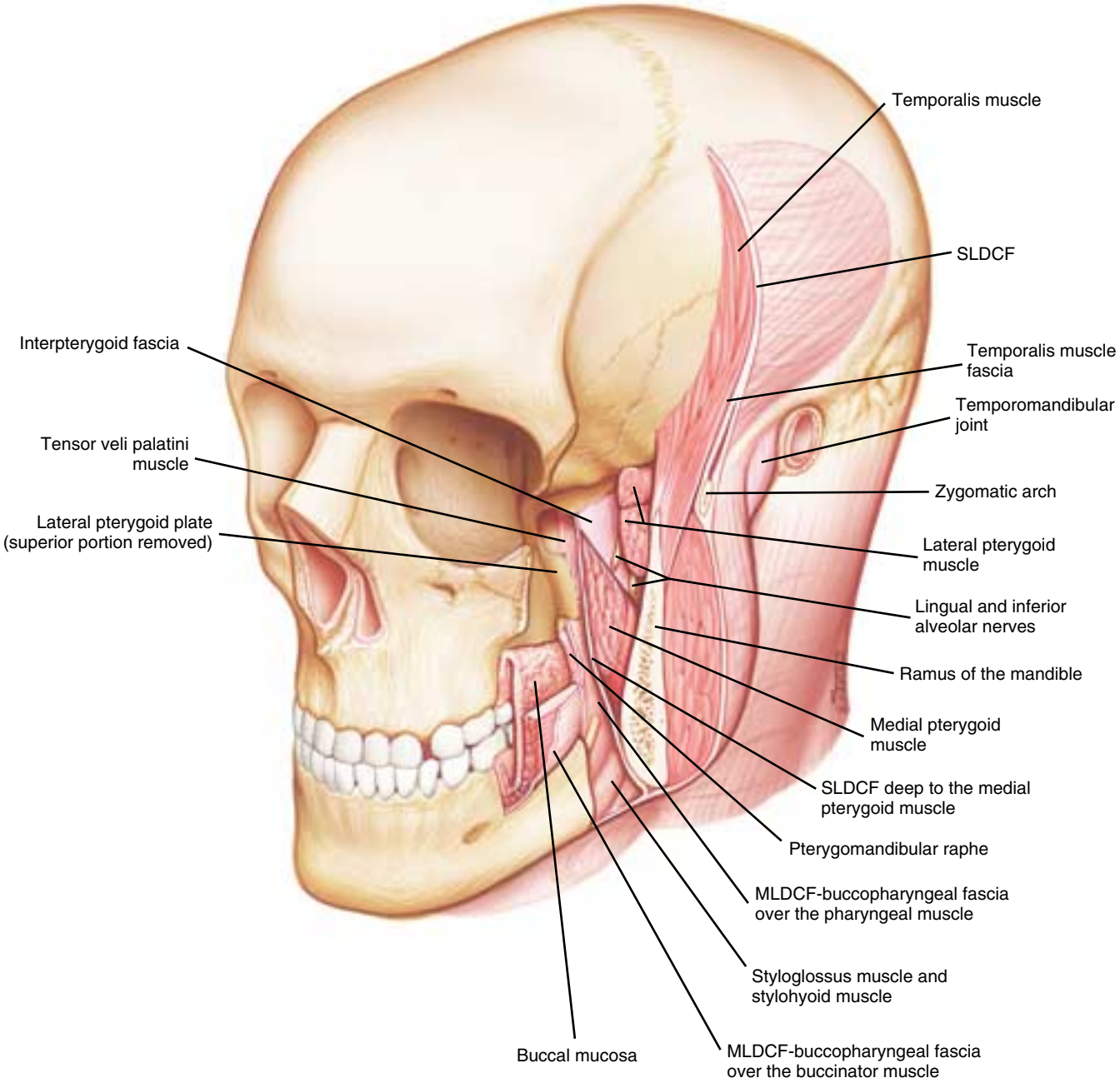

VIEW IMAGE

DRAWING 11 Drawing of the facial area and the skull with a coronal cut through the ramus of the mandible shows the relationships of the masticator space structures to each other and to the BPF. The left zygoma and most of the zygomatic arch have been removed to give better visualization of the deep structures. Note how the masticator space is continuous above and below the zygomatic arch.

Copyright © 2003, Mosby, Inc. All rights reserved.

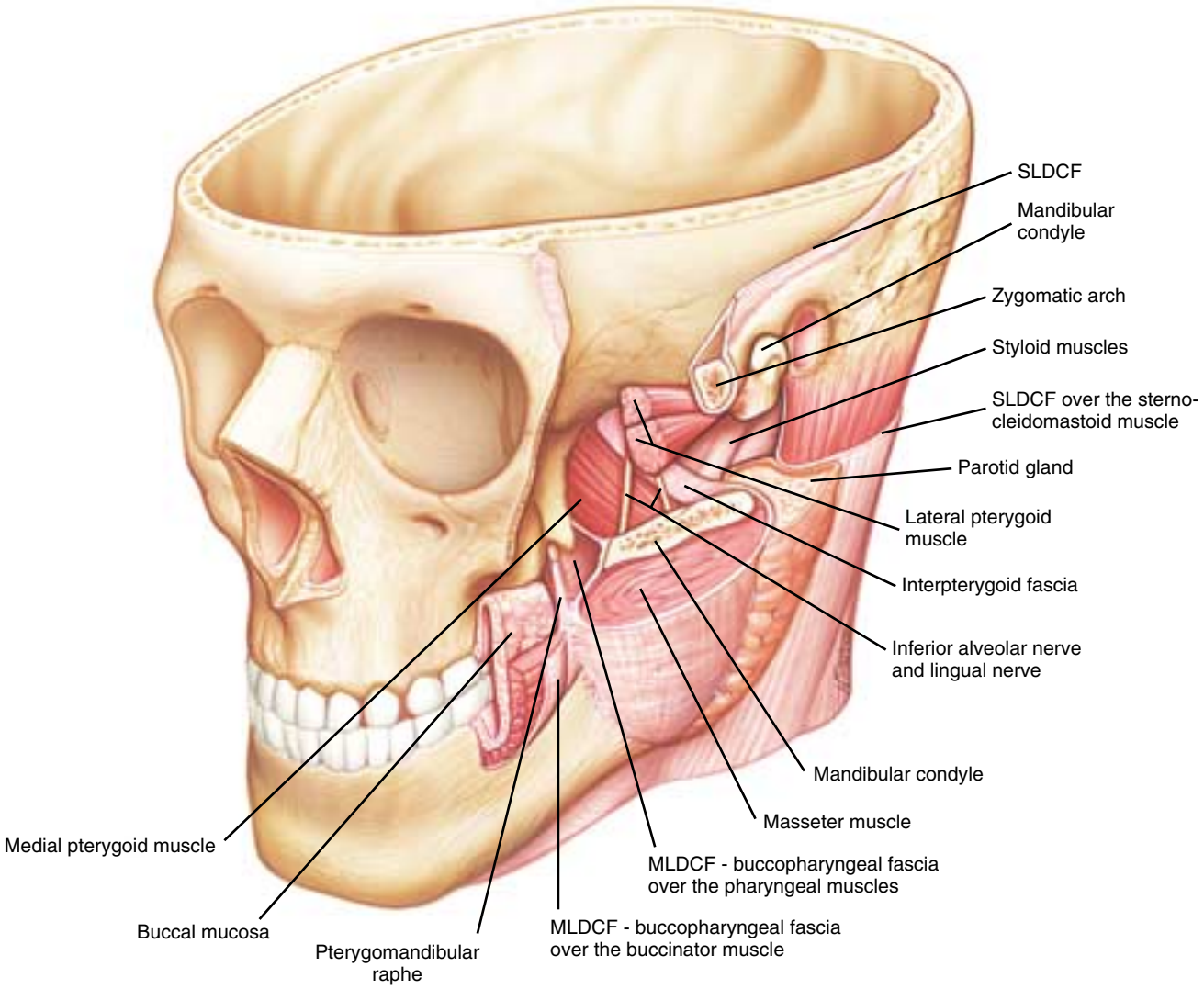

VIEW IMAGE

DRAWING 12 Drawing of the facial area with an axial cut through the level of the midmandibular ramus shows the relationships of the masticator space structures to each other and to the adjacent regional anatomy. The left zygoma and most of the zygomatic arch have been removed to provide better visualization of the deep structures. Note that the parotid gland borders the dorsal edge of the masticator space. The parapharyngeal space lies just deep to the masticator space and the parotid gland.

Copyright © 2003, Mosby, Inc. All rights reserved.

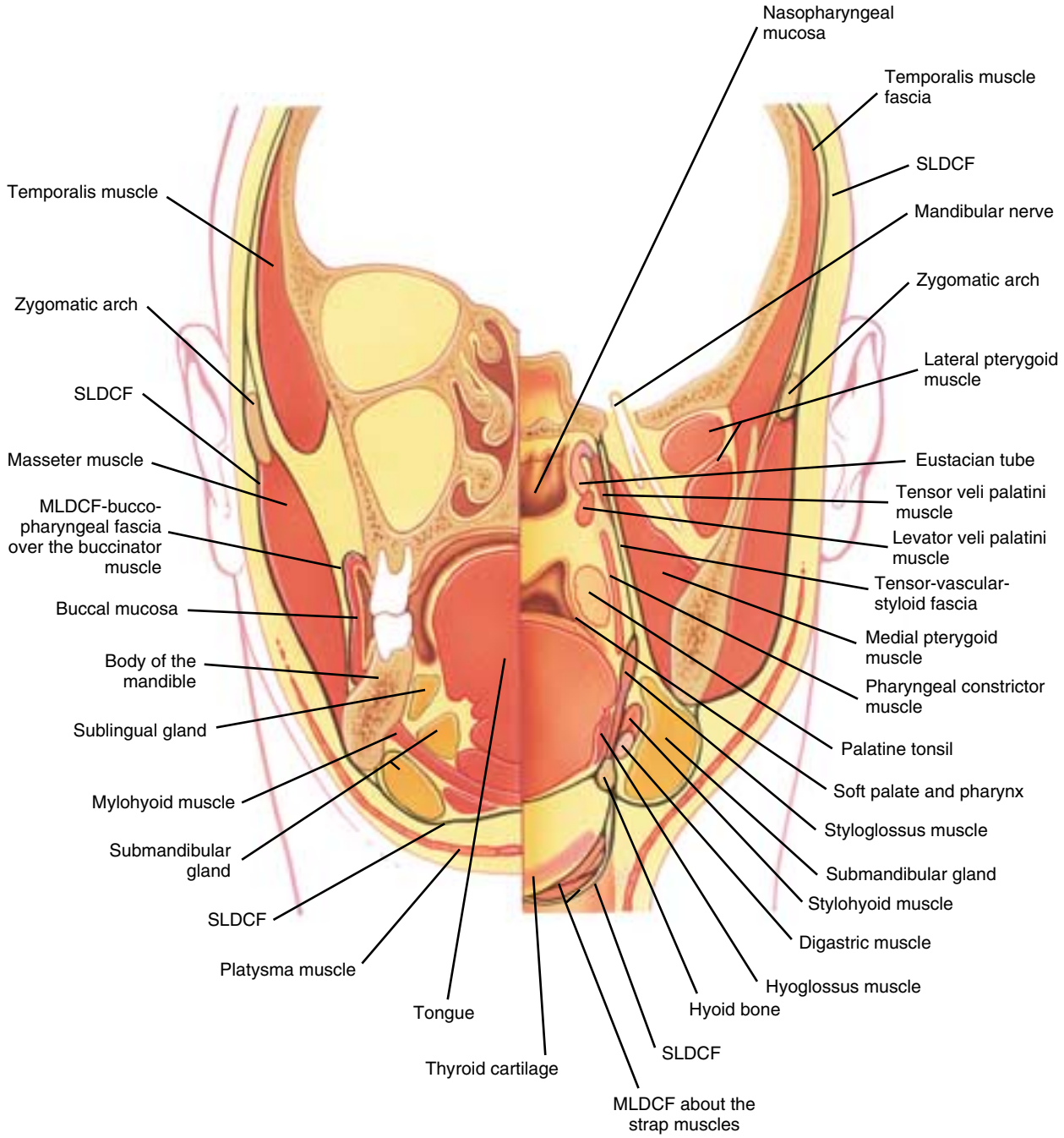

VIEW IMAGE

DRAWING 13 Coronal diagram of the facial area. On the left side, the level is through the foramen ovale and palatine tonsil. On the right side, the level is through the midfloor of the mouth. Note on the left side how the tensor-vascular-styloid fascia divides the parapharyngeal space that lies between the pharyngeal constrictor muscles and the medial side of the masticator space. The diagram also shows the styloglossus muscle as the effective floor of the parapharyngeal space.

Copyright © 2003, Mosby, Inc. All rights reserved.

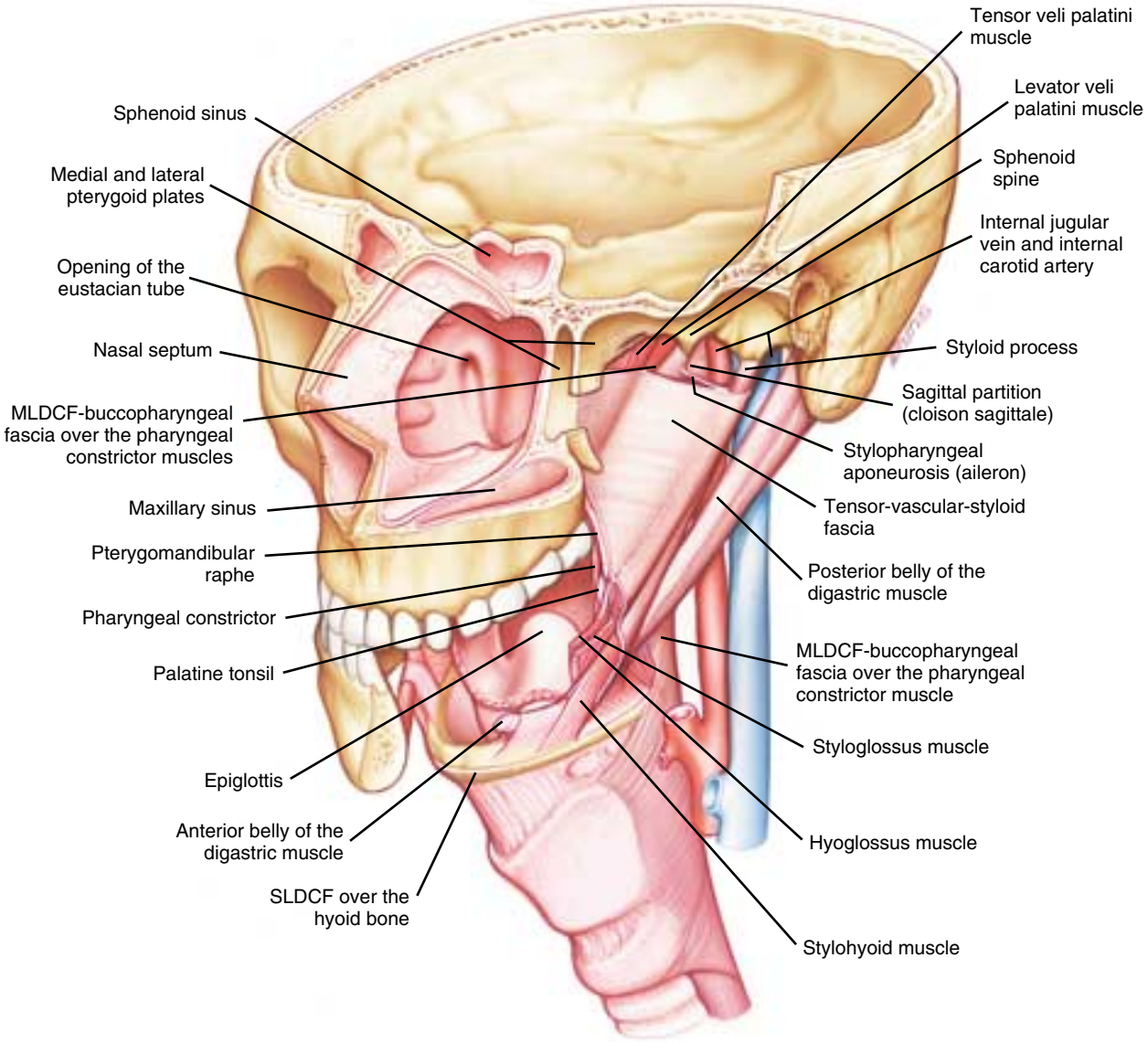

VIEW IMAGE

DRAWING 14 Drawing of the facial area and the upper neck with a coronal cut just ventral to the left external auditory canal, a sagittal cut just to the left of the nasal septum, and an axial cut through the level of the lower left maxillary sinus. The deep structures of the upper neck are visualized. The right nasopharyngeal mucosa can be viewed through the defect in the nasal septum. Note that the styloglossus muscle acts effectively as the caudal margin of the parapharyngeal space.

Copyright © 2003, Mosby, Inc. All rights reserved.

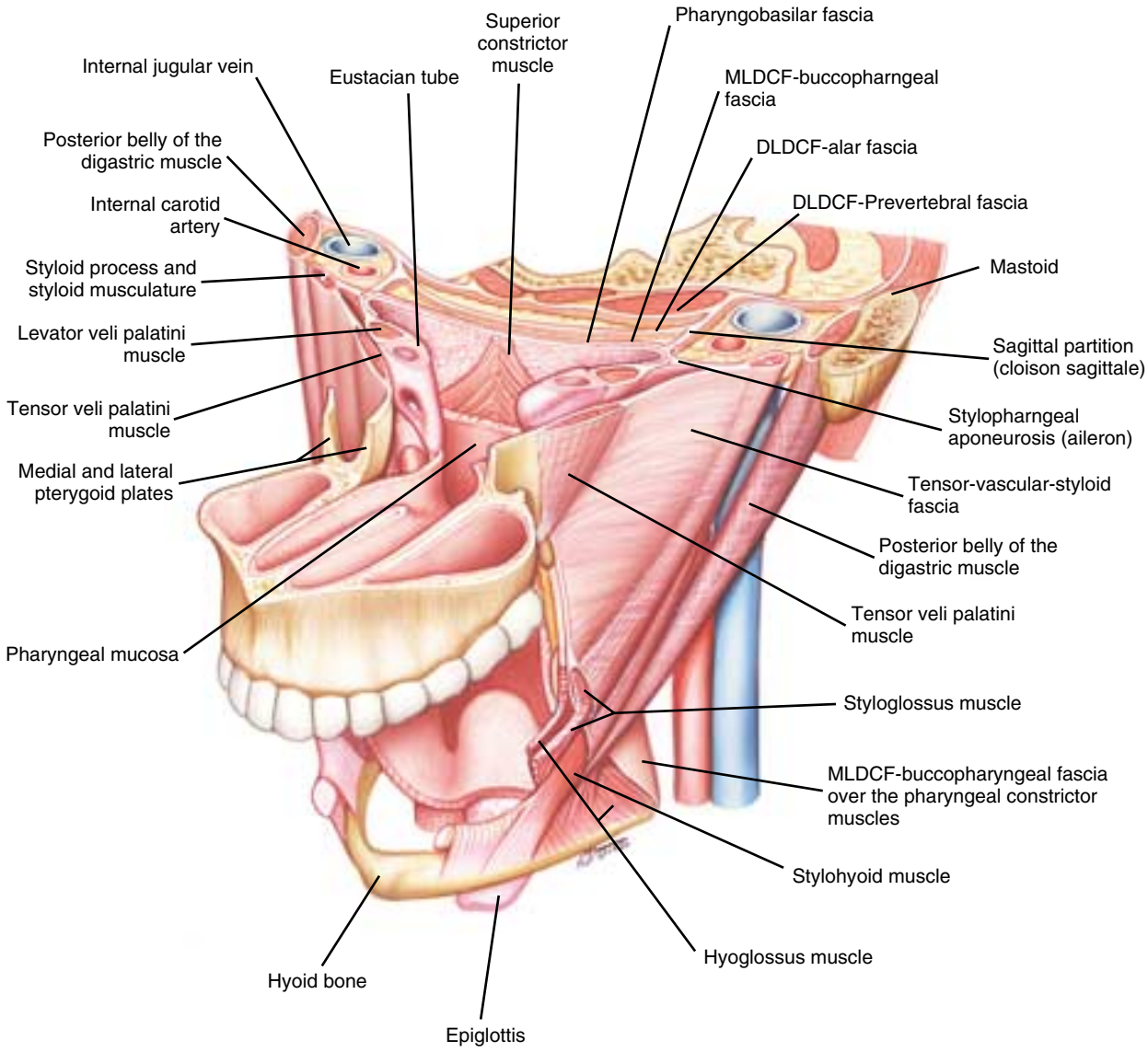

VIEW IMAGE

DRAWING 15 Drawing at the level of the face and upper neck. An axial cut has been made just caudal to the skull base, and additional axial and coronal cuts have removed the facial structures except for the caudal portions of the maxillary sinuses and the nasal fossae. The relationships of the parapharyngeal spaces are shown. Note that the area just lateral to the tensor-vascular-styloid fascia and deep to the masticator space (which is not shown on this drawing) is the prestyloid compartment of the parapharyngeal space.

Copyright © 2003, Mosby, Inc. All rights reserved.

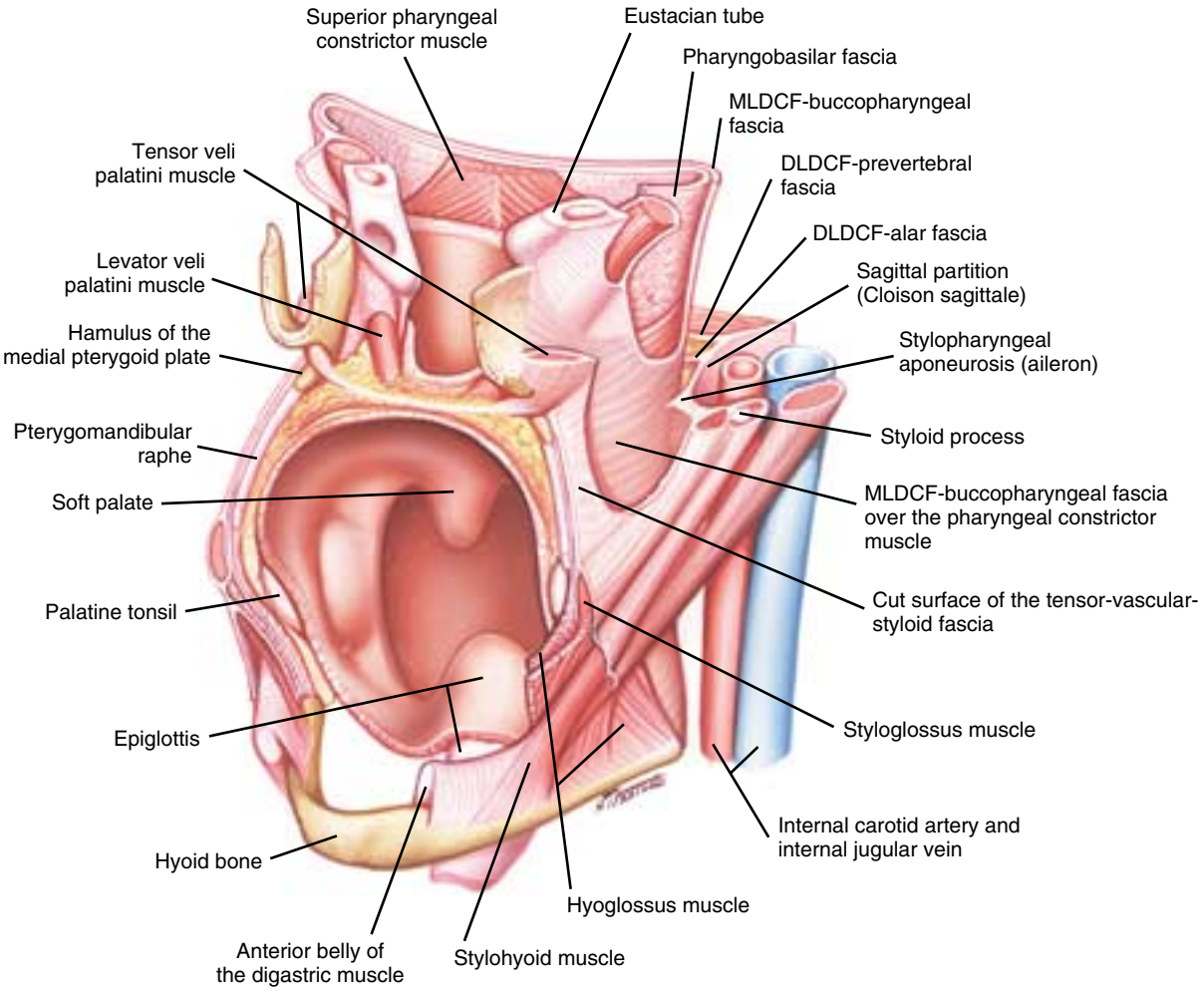

VIEW IMAGE

DRAWING 16 Drawing of a dissected view of the structures surrounding the nasopharynx and the oropharynx. A cut has been made in the left tensor-vascular-styloid fascia to show the relationship to the BPF.

Copyright © 2003, Mosby, Inc. All rights reserved.

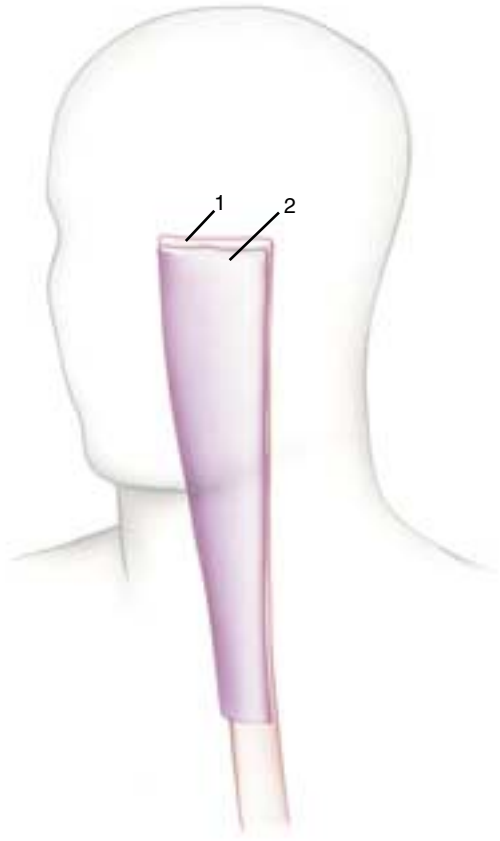

VIEW IMAGE

DRAWING 17 Block diagram of the prevertebral space (*1*) and the danger space (*2*). Note that the danger space actually extends down to the level of the diaphragm, while the prevertebral space extends to the coccyx.

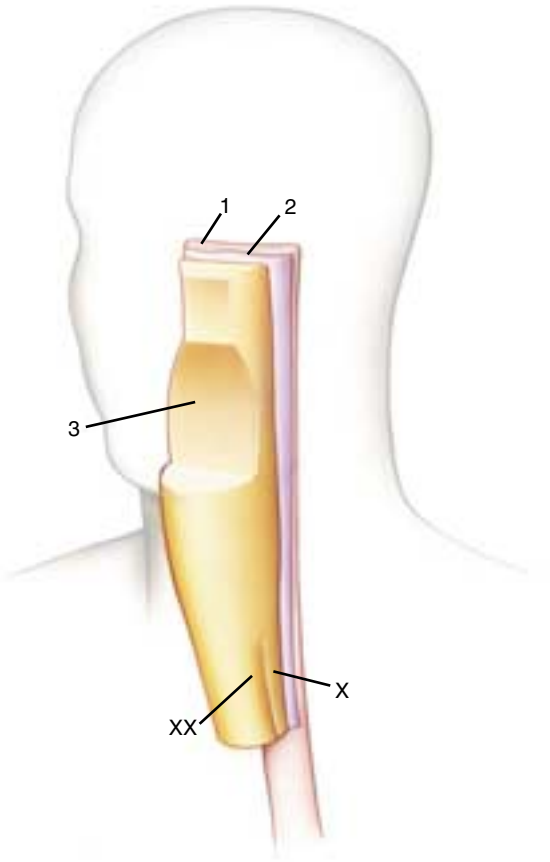

VIEW IMAGE

DRAWING 18 Block diagram of the prevertebral space (*1*), the danger space (*2*), and the visceral compartment (*3*). The division of the visceral compartment into the pretracheal space (*XX*) and the retrovisceral space (*X*) by the fascia that accompanies the inferior thyroid artery is shown as a cleft in the visceral compartment. Note that the retropharyngeal and retroesophageal spaces are actually parts of the common retrovisceral space. Also note that the pretracheal space extends substernally, while the retrovisceral space extends to about the level of the carina.

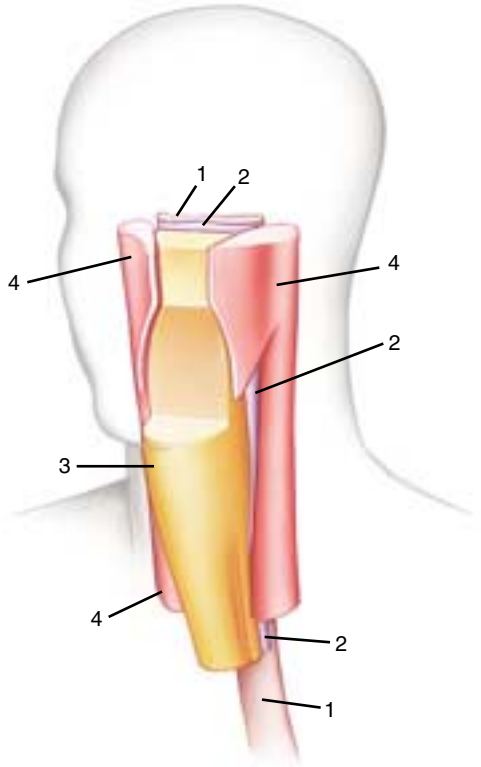

VIEW IMAGE

DRAWING 19 Block diagram showing the relationships of the prevertebral space (*1*), the danger space (*2*), the visceral compartment (*3*), and the parapharyngeal spaces with the carotid sheaths (*4*). Note that the parapharyngeal space includes the carotid sheath around the internal carotid artery and that this is continuous with the carotid sheath about the common carotid artery in the neck.

Copyright © 2003, Mosby, Inc. All rights reserved.

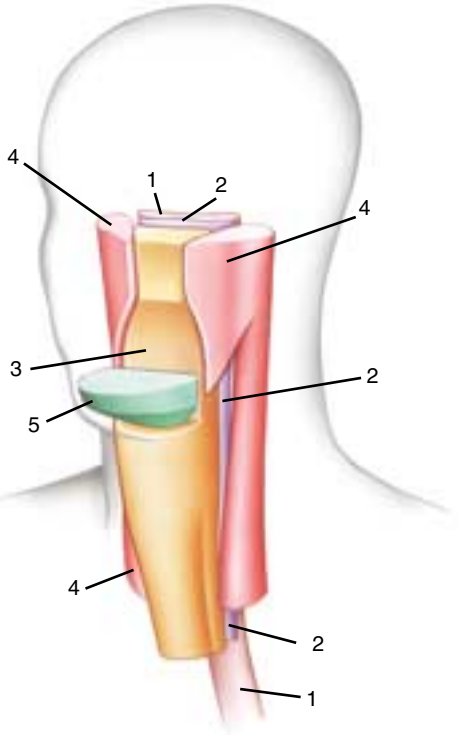

VIEW IMAGE

DRAWING 20 Block diagram showing the relationships of the prevertebral space (*1*), the danger space (*2*), the visceral compartment (*3*), the parapharyngeal spaces and the carotid sheaths (*4*), and the submandibular space (*5*).

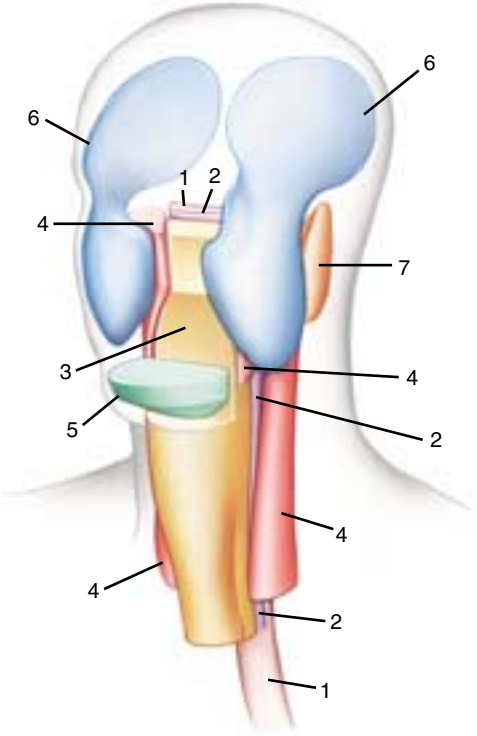

VIEW IMAGE

DRAWING 21 Block diagram showing the relationships of the prevertebral space (*1*), the danger space (*2*), the visceral compartment (*3*), the parapharyngeal spaces and the carotid sheaths (*4*), the submandibular space (*5*), the masticator spaces (*6*), and the parotid gland (*7*).

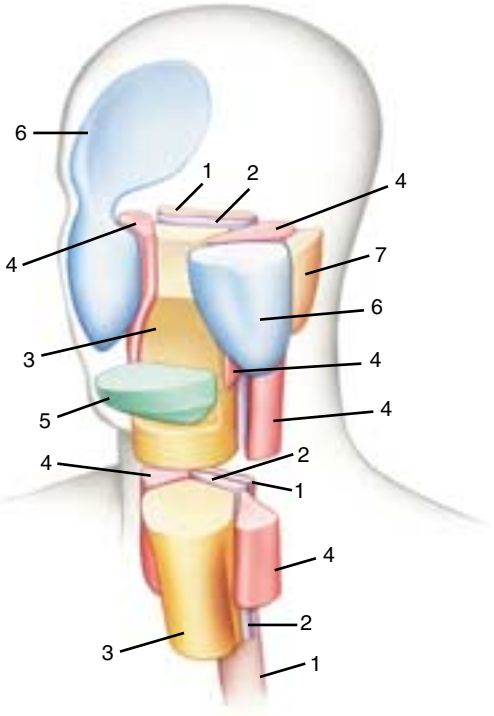

DRAWING 22 Block diagram showing the relationships of the prevertebral space (*1*), the danger space (*2*), the visceral compartment (*3*), the parapharyngeal spaces and the carotid sheaths (*4*), the submandibular space (*5*), the masticator spaces (*6*), and the parotid gland (*7*). This is the same diagram as Drawing 20 except that axial cuts have been made at a level just caudal to the skull base and at a level in the midneck to illustrate the cross-sectional relationships of these spaces. Compare the more cranial slice with Drawing 2, and the caudal slice with Drawings 3 and 4.

VIEW IMAGE

Copyright © 2003, Mosby, Inc. All rights reserved.

Color plates 1 to 6 refer to Chapter 44.

VIEW IMAGE

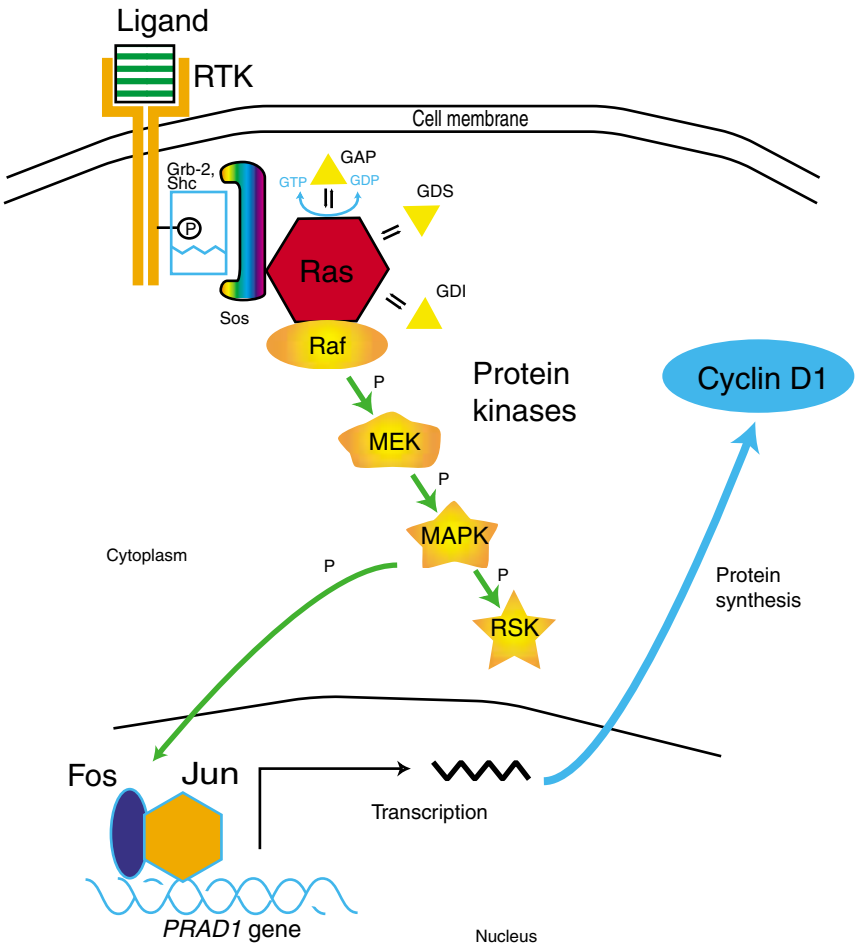

COLOR PLATE 1 The Ras-Map kinase pathway for intracellular growth factor signal transduction. The figure depicts signal transduction initiated by binding of a generalized growth factor to a dimerized receptor tyrosine kinase (RTK) at the cell plasma membrane. Ras is recruited to the inner surface of the membrane by the proteins shown in response to internal phosphorylation of tyrosine in the RTK. In its active GTP-bound form, Ras interacts with and activates the protein kinase Raf, initiating a cascade of protein phosphorylation events denoted by *P*. A GTPase-activating protein, GAP, interconverts active and inactive Ras forms. Mitogen-activated kinase (MAPK) can phosphorylate several transcription factors that enter the nucleus, as exemplified here by Fos and Jun, which together activate transcription of several genes, including the *PRAD1* gene, which encodes the protein cyclin D1. The protein kinase RSK is involved in translational aspects of protein synthesis. Mutation of genes encoding several proteins in this pathway can lead to self-sufficiency of growth signaling independence of the extracellular factor.

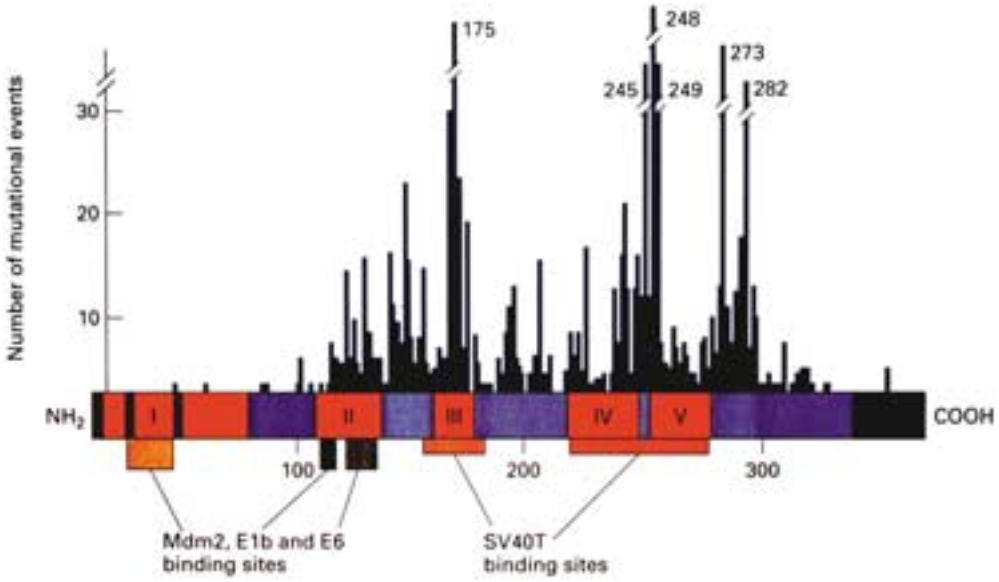

VIEW IMAGE

COLOR PLATE 2 Distribution of mutations in the *p53* tumor suppressor gene in various tumors. The p53 protein is schematized, and amino acids are enumerated on the x-axis.[19] On the y-axis, numbers of mutations at each amino acid position are presented as recorded in a variety of tumors. The majority of mutations occur in the central DNA-binding domains of p53. Note that regions in these domains are also targeted for binding by viral proteins that inactivate p53. E1b is an adenoviral protein, E6 is a papilloma viral protein, and the SV40 large T antigen is a simian virus 40 protein. The site specificity of the mutations is due in part to the environmental agents that caused them. For example, certain sites are preferentially mutated by aflatoxin B1 in hepatocellular carcinoma, and other sites are preferentially observed in lung adenocarcinoma, presumably mutated by benzo-a-pyrene or other agents in cigarette smoke. (From Denissenko MF, Pao A, Tang M, Pfeifer GE. Preferential formation of benzo [a]pyrene adducts at lung cancer mutational hotspots in P53. Science 1996;274:430. Copyright 1996 American Association for the Advancement of Science.)

Copyright © 2003, Mosby, Inc. All rights reserved.

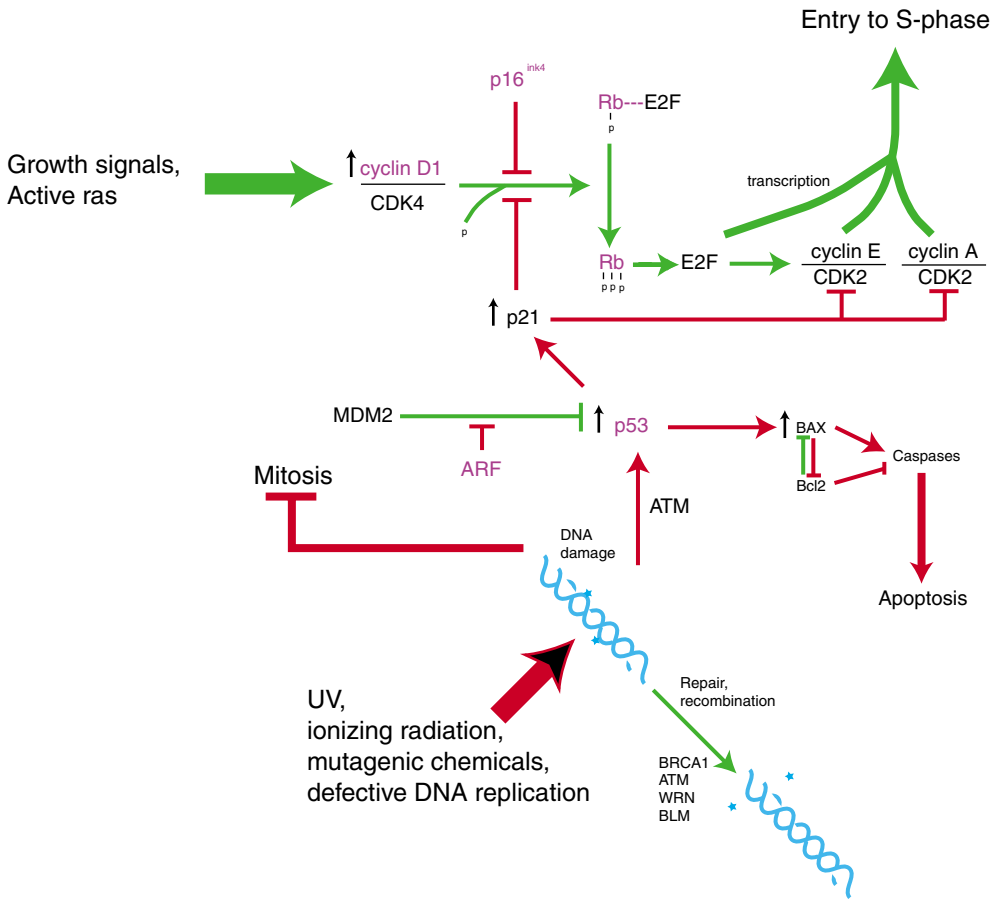

VIEW IMAGE

COLOR PLATE 3 Involvement of several tumor suppressor gene products in pathways leading to cessation of cell growth or to apoptosis in response to DNA damage. Processes leading to activated cell proliferation, that is, entry to S-phase of the cell cycle, are indicated in green. Processes inhibiting cell proliferation are indicated in red. In response to DNA damage, such as that caused by ionizing radiation, for example, the ATM protein kinase phosphorylates and activates p53. The p53 protein, in turn, through effects on gene transcription, activates pathways leading to either apoptosis or cessation of cell growth. Transcription of the *p21* gene is activated by p53. The p21 protein is an inhibitor of both CDK2, necessary for initiation of DNA replication, and CDK4, which catalyzes phosphorylation of Rb. Hyperphosphorylation of Rb is necessary to trigger events leading to the G1-S transition. Two different products of another tumor suppressor gene, *p16/ARF*, play important roles in inhibiting cell proliferation. ARF binds to MDM2 and prevents it from targeting p53 for proteolytic destruction. The p16 protein specifically inhibits CDK4 kinase activity, preventing phosphorylation of Rb. Several proteins are indicated in magenta. It is believed that at least one of the four genes encoding these proteins, *ARF/p16*, *cyclin D1*, *p53*, and *Rb*, is mutated in every neoplasia.

Copyright © 2003, Mosby, Inc. All rights reserved.

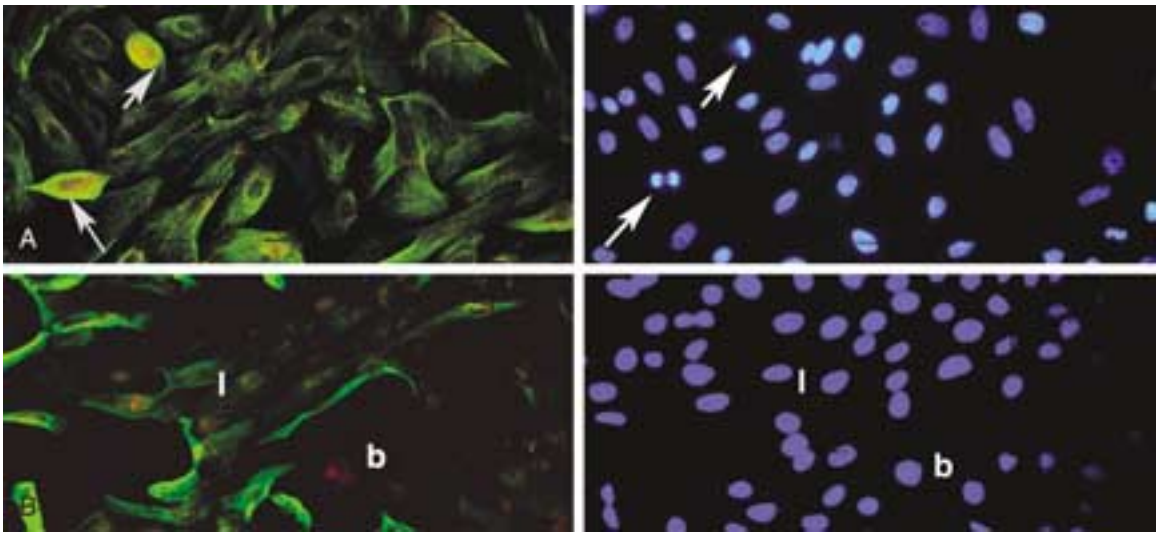

VIEW IMAGE

COLOR PLATE 4 Presence of the breast cancer tumor suppressor gene product BRCA1 in both basal and luminal epithelial cells of the breast. BRCA1 is detected in the nuclei of both basal and luminal cell types when using double immunofluorescence labeling. *Left panel*: **A**, Edge of the basal outgrowth costained with MAbs to BRCA1 (red) and vimentin (green). **B**, Edge of luminal outgrowth costained with MAbs to BRCA1 (red) and cytokeratin 19 (green). *Right panel*: **A** and **B**, DAPI counterstain of the same fields of cells. Note: photo mask was left in the light path to help orient fields and is visible in some of the photographs. *b*, Basal; *l*, luminal. Arrows are identified in text. (From Daniel DC. Cell Tissue Res 1999;298:481.)

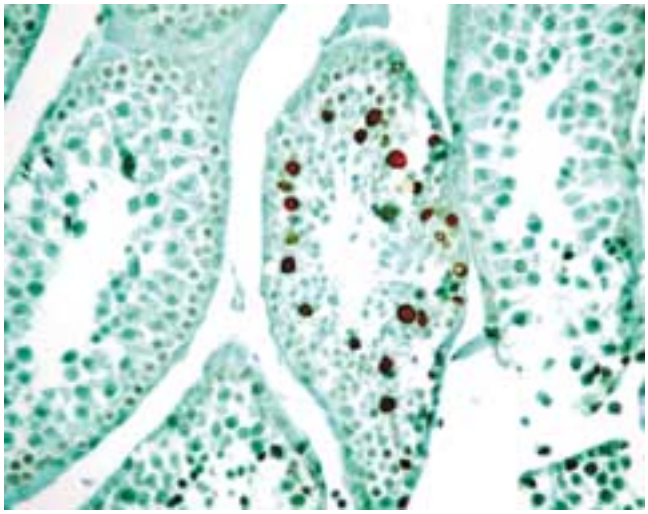

VIEW IMAGE

COLOR PLATE 5 Apoptosis is highly stage-specific in normal spermatogenesis in the mouse. Shown is a section from normal mouse testis approximately 20 days after birth. Staining for apoptosis, or programmed cell death, is done by the TUNEL assay, which detects DNA fragmentation. This is early in spermatogenesis, but cells develop toward the center of the seminiferous tubule. Note that darkly stained apoptotic cells are visualized in a specific layer in development. Note also how apoptosis, which affects specific cells in a defined region, differs from necrosis, a nonprogrammed form of cell death that usually affects multiple contiguous cells in a focus.

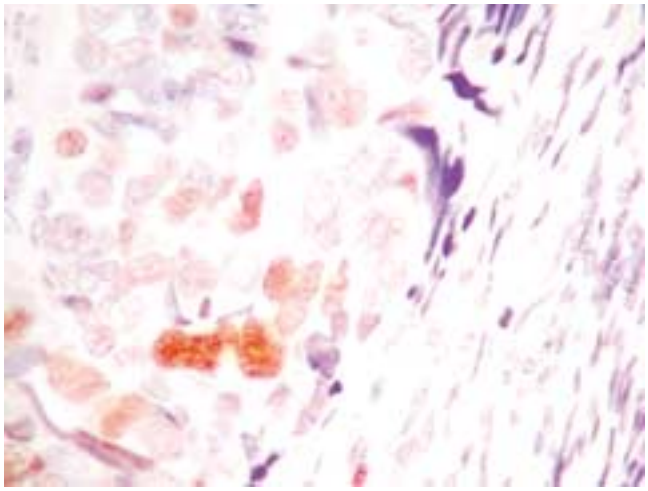

COLOR PLATE 6 DNA replication protein MCM7 as a marker for ovarian cancer. Many recently developed tumor cell markers are proteins involved in DNA replication. MCM7 is part of an MCM 4, 6, 7 DNA helicase complex essential for initiation of DNA replication. Its levels are cell-cycle regulated. Staining, visualized as red-brown, was with anti-MCM7 antibody and secondary antibody coupled to horseradish peroxidase. Note the high percentage of large tumor cells with mottled nuclear staining as opposed to the lack of staining of adjacent normal ovarian tissue on the right.

VIEW IMAGE

Copyright © 2003, Mosby, Inc. All rights reserved.

These three fascial planes subdivide the parapharyngeal space into three compartments. The first compartment (A) is lateral to the tensor-vascular-styloid fascia and deep to the medial boundary of the masticator space. This area contains a small amount of fat, and the deep or retromandibular portion of the parotid gland protrudes into its lateral margin. The second compartment (B) is a very thin, slit-like region between the BPF medially and the tensor-vascular-styloid fascia laterally. There is only a small amount of loose connective tissue in this second compartment, which is bounded posteriorly by the stylopharyngeal aponeurosis (aileron). The third compartment (C) of the parapharyngeal region is posterior to the stylopharyngeal aponeurosis and separated from the retropharyngeal space by the cloison sagittale. This third compartment contains the internal carotid artery, internal jugular vein, and, at various levels, cranial nerves IX to XII. Thus, this third compartment is primarily the carotid sheath and its contents. Almost all descriptions of the parapharyngeal space include some or all of these compartments, albeit under a variety of names and combinations.

Gaughran referred to the region between the BPF and the medial wall of the masticator space as the lateral pharyngeal cleft.[9] This cleft is analogous to the anterior part of the parapharyngeal space and includes the first two compartments (A+B) just described. Gaughran described the vascular fascia as extending from the tensor veli palatini and separating the lateral pharyngeal cleft into a very thin medial compartment and a larger, more lateral compartment called, respectively, the paratonsillar and paramasticator regions of the lateral pharyngeal cleft. This same fascial organization was described by Cazalas and Coulomb, who referred to the thin medial compartment as the meta-amygdalin space and the larger lateral compartment as the para-amygdalin space.[6, 8] Amygdalin refers to the tonsil, and in this nomenclature there is also a periamygdalin space between the tonsil and the constrictor muscles (referred to today as the peritonsillar space).

Hall used the terms *prestyloid* and *poststyloid parapharyngeal spaces*.[10] The poststyloid space was essentially the carotid sheath. The two spaces were separated by the stylopharyngeal aponeurosis, which indicates that the prestyloid compartment included the first two compartments described above (A+B). Hall did not describe any structure resembling the tensor-vascular-styloid fascia. Instead, he ascribed the entire region between the BPF overlying the constrictor muscles medially and the masticator space laterally to the prestyloid space. The paratonsillar and paramasticator spaces (meta- and para-amygdalin) were combined.

Hollinshead referred to the parapharyngeal space as the lateral pharyngeal space, stating that it was continuous with the retropharyngeal space.[4] He also stated that the area was subdivided by some authors into prestyloid and poststyloid compartments, referring to Hall, but not stating precisely which fascia, if any, divided the two compartments.

Som et al. referred to the prestyloid and retrostyloid compartments of the parapharyngeal space as being separated by the tensor-vascular-styloid fascia.[20] They mentioned a fascia extending from the tensor-vascular-styloid fascia to the prevertebral fascia, separating the retrostyloid compartment from the retropharyngeal space. This fascia is analogous to the cloison sagittale, as described by Charpy. Thus Som et al. combined the spaces on either side of the stylopharyngeal aponeurosis, the second and third compartment described above (B+C), into one compartment called the retrostyloid space. The prestyloid compartment referred to the first compartment (A) described above, which is lateral to the tensor-vascular-styloid fascia and into which protrudes the deep portion of the parotid gland (Fig. 34-18).

Support for the use of this prestyloid and retrostyloid compartment terminology comes from the surgeons, who note that in their operative approach to the parapharyngeal space, the plane of the tensor-vascular-styloid fascia acts as an important landmark, with the great vessels and cranial nerves lying deep to the plane. In this sense, this fascia and its boundaries act as a protective barrier to these vital structures. Today, this terminology for the parapharyngeal space is most often used by surgeons.[20]

In the radiology literature, the various compartments of the parapharyngeal space have been used to help generate a differential diagnosis for lesions arising in this region. As previously discussed, two conventions are used. The first uses the prestyloid and retrostyloid configuration emphasizing the tensor-vascular-styloid fascia.[16, 20] The second, discussed by Harnsberger, separates the region into the carotid space and the parapharyngeal space.[24, 26] In this second convention, the separation closely approximates the stylopharyngeal aponeurosis, as discussed by Hall.[10]

In the opinion of most authors, the parapharyngeal space is considered as a closed space that is surrounded by a number of other ‘‘spaces.’’[10] These include the pharynx, the submandibular space, the submaxillary gland space, the masticator space, the parotid gland space, the retropharyngeal space, the danger space, and the prevertebral space. However, when one considers the wide variety of descriptions of the fascial planes themselves, there is certainly a possibility that in some people, portions of these fasciae are weak or incomplete. This presumably explains why a few authors believe that the parapharyngeal space communicates freely with the submaxillary and retropharyngeal spaces.

One of the main reasons for interest in the parapharyngeal space is its critical location and anatomic relationships that allow it to act as a highway for the spread of infections and

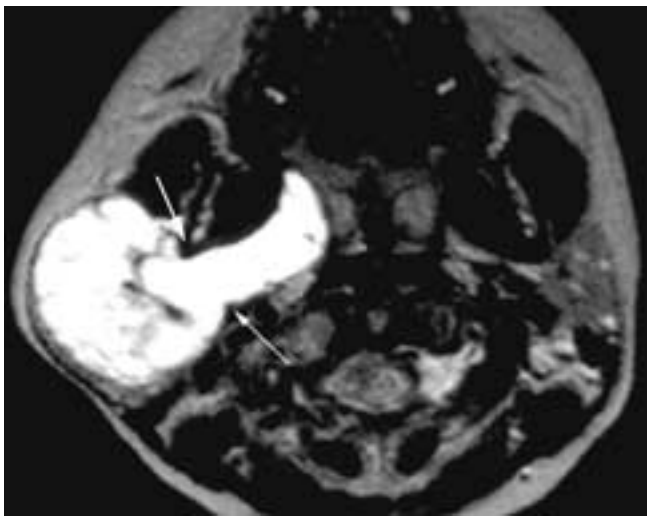

FIGURE 34-18 Axial T2-weighted MR image shows a high signal intensity lymphangioma filling the right parotid gland and extending through the stylomandibular tunnel into the prestyloid compartment of the parapharyngeal space. The thin arrow indicates the styloid process, and the thick arrow indicates the dorsal edge of the ramus of the mandible.

VIEW IMAGE

Copyright © 2003, Mosby, Inc. All rights reserved.

some tumors from any of the areas that surround it to any of the other bordering spaces (see Chapter 38).

The Peritonsillar Space

The palatine tonsil is surrounded by a capsule. Between this capsule and the laterally positioned superior pharyngeal constrictor muscle is a potential space that is limited anteriorly by the palatoglossus muscle and its fascia (the anterior tonsillar pillar) and posteriorly by the palatopharyngeus muscle and its fascia (the posterior tonsillar pillar). This space, called the peritonsillar or paratonsillar space, is filled with loose connective tissue. The space is inside (medial to) the constrictor muscles and the BPF and should not be confused with the paratonsillar division of the parapharyngeal space mentioned by Gaughran.[9]

A tonsillar infection can break through the tonsillar capsule into the peritonsillar space. Such an infection (quinsy) can produce bulging of the tissues about the tonsillar pillars, spreading cranially to the level of the hard palate and caudally to the pyriform sinus. However, these infections tend not to extend axially beyond the tonsillar pillars and their site of pointing.[4]

The "Paravertebral Space"

The DLDCF extends from the spinous processes of the cervical vertebrae and the ligamentum nuchae to the left and right transverse processes of the cervical vertebrae. In so doing, this fascia covers the muscles of the upper back and the muscles of the ''floor'' of the posterior triangle. This space deep to the DLDCF has no official name; however, the term *paravertebral space* has been suggested as being anatomically appropriate. The space is adjacent to but separate from the prevertebral space, the danger space, and the carotid sheath structures (Drawings 2–5 and 8). (Fig. 34-4).

However, using reasoning based on imaging studies and the observation that the DLDCF surrounds both spaces, Harnsberger has suggested that this space and the prevertebral space are actually one space, the perivertebral space, and he refers to the prevertebral and paraspinal portions of the perivertebral space to describe the spaces more commonly known to the surgical community as the prevertebral and paravertebral spaces.[27] It should be noted that the reluctance of most surgeons to utilize the Harnsberger classification stems from the observation that the DLDCF firmly attaches to the transverse processes of the cervical vertebrae, effectively separating the prevertebral and ''paravertebral'' spaces.

The "Posterior Triangle (Cervical) Space "

One final compartment or space deserves mention but lacks a common name. Grodinsky and Holyoke referred to this region as space 4A.[2] This compartment lies between the SLDCF and the DLDCF, dorsal to the carotid sheath and ventral to the cervical vertebral spinous processes and the ligamentum nuchae. Its deep boundary is the DLDCF over the so-called paravertebral space, and its superficial boundary is the SLDCF as it defines the posterior triangle of the neck.

This compartment contains mostly fat, hence the term *coussinet adipose*, or ''small cushion of fat,'' used in the French literature. The compartment also contains the spinal accessory nerve and its associated lymph node chain, and so has important surgical and radiologic significance. Potential descriptive terms include *spinal accessory nodal space*, *posterior cervical nodal space*, and *posterior triangle space* (Drawings 2–5 and 8) (Figs. 34-2, 34-19, and 34-20). Harnsberger has suggested the term *posterior cervical space*.[28]

SUMMARY AND CONCLUSION

The most often quoted descriptions of the fasciae, compartments, and spaces of the head and neck have been discussed, and we have given our opinion as to the anatomy and terminology that are most widely accepted. It should be noted that some controversy still remains in the literature regarding the actual anatomy and the descriptive terminology. Some of the variations in the descriptions may be explained by the observation that these fascial sheets may be incomplete or absent in some people; dissection techniques may also account for some reported differences. In the face of such variations in the descriptions of the anatomy itself, it is difficult to expect a uniform terminology. However, the use of a common nomenclature would be an advantage in comparing information and in reporting cases. Such a standard language should use terms acceptable and recognizable to all groups interested in the field including anatomists, surgeons, and radiologists. Drawings 17 to 22 summarize the various spaces in the neck. Table 34-1 summarizes the contents of the various spaces, and Table 34-2 provides an approach to differential diagnosis based on the spaces.

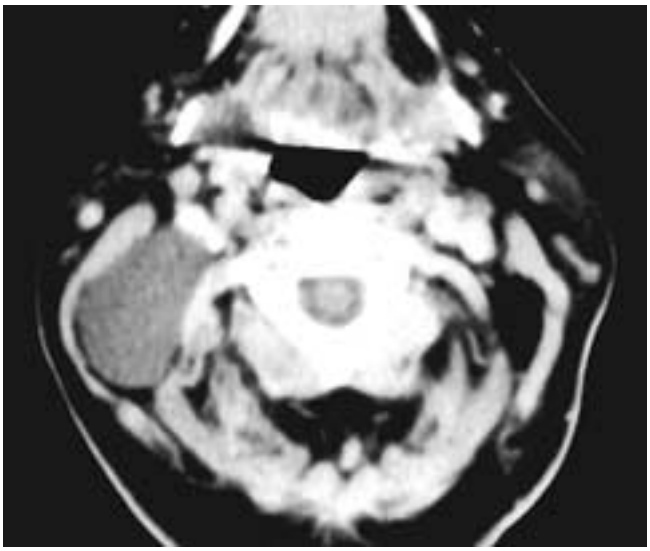

FIGURE 34-19 Axial contrast-enhanced CT scan shows a cystic mass in the right neck deep to the sternocleidomastoid muscle and superficial to the muscles that comprise the floor of the posterior triangle of the neck. The mass fills this space, which has been variously referred to as the spinal accessory nodal space, the posterior cervical nodal space, the posterior triangle space, and the posterior cervical space. This lesion was a solitary lymphangioma in an adult but could just as easily have been a node in a patient with lymphoma.

VIEW IMAGE

Copyright © 2003, Mosby, Inc. All rights reserved.

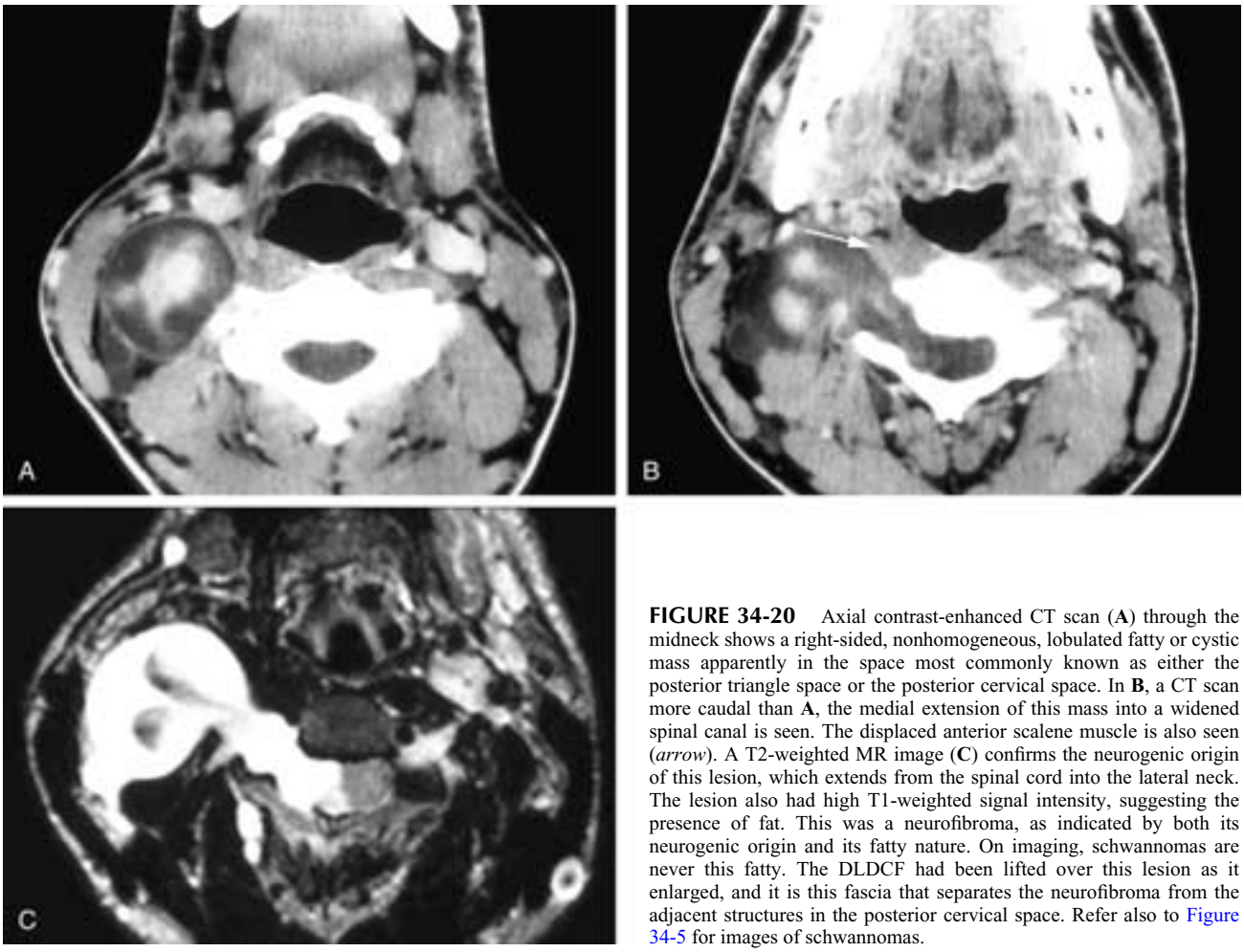

FIGURE 34-20 Axial contrast-enhanced CT scan (**A**) through the midneck shows a right-sided, nonhomogeneous, lobulated fatty or cystic mass apparently in the space most commonly known as either the posterior triangle space or the posterior cervical space. In **B**, a CT scan more caudal than **A**, the medial extension of this mass into a widened spinal canal is seen. The displaced anterior scalene muscle is also seen (*arrow*). A T2-weighted MR image (**C**) confirms the neurogenic origin of this lesion, which extends from the spinal cord into the lateral neck. The lesion also had high T1-weighted signal intensity, suggesting the presence of fat. This was a neurofibroma, as indicated by both its neurogenic origin and its fatty nature. On imaging, schwannomas are never this fatty. The DLDCF had been lifted over this lesion as it enlarged, and it is this fascia that separates the neurofibroma from the adjacent structures in the posterior cervical space. Refer also to Figure 34-5 for images of schwannomas.

VIEW IMAGE

Table 34-1
THE SPACES OF THE NECK AND THEIR CONTENTS

Space or Anatomic Region	Major Structures Either Within or Bordering Each Space
Superficial Fascia (subcutaneous tissues)	Subcutaneous fat, subcutaneous venules, lymphatics and nerves, platysma muscle, portions of anterior and external jugular veins
Visceral Compartment	
Retropharyngeal space	Pharynx, medial and lateral retropharyngeal lymph nodes, fat
Retrovisceral space (retroesophageal)	Esophagus, fat
Pretracheal space	Larynx, trachea, thyroid gland, parathyroid glands, recurrent laryngeal nerve, sympathetic trunk, level VI lymph nodes, thyroid arteries, fat
Danger Space	Fat, retropharyngeal and retroesophageal space in front, prevertebral space behind, parapharyngeal spaces on either side
Prevertebral Space	Anterior longitudinal ligament, cervical vertebrae and discs, longus coli and longus capitis muscles, phrenic nerve, fat
Carotid Sheath	Internal carotid artery, common carotid artery, internal jugular vein, cranial nerves IX, X, XI, XII, level II, III, and IV lymph nodes, fat
Space of the Body of the Mandible	Mandible, fat
Space of the Submandibular Gland	Submandibular gland, fat
Space of the Parotid Gland	Parotid gland, facial nerve, parotid lymph nodes, external carotid artery, retromandibular (posterior facial) vein, fat
Submandibular Space	
Sublingual space	Sublingual glands, deep portion (including hilum) of submandibular glands, Wharton's ducts, lingual artery, lingual vein, lingual nerve (sensory V3 and chorda tympani), cranial nerves XI and XII, fat
Submaxillary space	Superficial portion of the submandibular gland, anterior bellies of the digastric muscles, level I lymph nodes, facial artery, facial vein, fat

Table continued on following page

Copyright © 2003, Mosby, Inc. All rights reserved.

Table 34-1
THE SPACES OF THE NECK AND THEIR CONTENTS *Continued*

Space or Anatomic Region	Major Structures Either Within or Bordering Each Space
Masticator Space	Medial pterygoid muscle, lateral pterygoid muscle, masseter muscle, temporalis muscle, ramus of mandible, branches of V3, fat
Parapharyngeal Space	Fat, ascending pharyngeal artery, internal maxillary artery, pterygoid venous plexus, branches of V3, cervical sympathetic trunk, minor salivary glands. Deep portion of parotid gland
Peritonsillar Space	Fat, palatine tonsil medially, parapharyngeal space laterally
''Paravertebral'' Space	Anterior middle and posterior scalene muscles, levator scapulae muscle, splenius capitus and splenius cervicus muscles, brachial plexus (roots), vertebral artery, vertebral vein, fat
''Posterior Triangle'' Space	Fat, cranial nerve XI, brachial plexus (trunks, divisions, and chords), dorsal scapular and long thoracic nerves, cutaneous nerves of the cervical plexus, level V lymph nodes

Table 34-2
THE SPACES OF THE NECK AS A BASIS FOR DIFFERENTIAL DIAGNOSIS

Space or Anatomic Region	Differential Diagnosis
Superficial Fascia (subcutaneous tissues)	Keloids; scars; subcutaneous fat necrosis of the newborn; lipomas; obstructed lymphatics and venules from edema, cellulitis, radiation therapy, surgery; schwannomas; neurofibromas, plexiform neurofibromas, pilomatrixoma, Merkel cell tumor; lymphoma, squamous cell and basal cell carcinomas
Visceral Compartment	
Retropharyngeal space	Medial and lateral retropharyngeal lymph adenopathy, cellulitis, phlegm, abscess, extension of goiter, extension of pharyngeal tumor
Retrovisceral space	Cellulitis, phlegm, abscess, extension of goiter, extension of esophageal tumor, extension of thyroid tumor
Pretracheal space	Tracheal, thyroid, laryngeal, and parathyroid tumors, goiter, recurrent laryngeal nerve or sympathetic trunk schwannomas, level VI lymph adenopathy, cellulitis, phlegm, abscess
Danger Space	Phlegm, abscess
Prevertebral Space	Cervical vertebral and disc disease, longus coli and longus capitis muscle tumors, phrenic nerve schwannoma, minor salivary gland tumors, cellulitis, phlegm, abscess
Carotid Sheath	Carotid artery arteritis, aneurysm, or dissection, internal jugular vein thrombosis or phlebitis, cranial nerve IX, X, XI, and XII schwannomas, paragangliomas, level II, III, and IV lymph adenopathy, cellulitis, phlegm, abscess
Space of the Body of the Mandible	Mandibular and odontogenic disease, cellulitis, phlegm, abscess
Space of the Submandibular Gland	Submandibular gland disease, cellulitis, phlegm, abscess
Space of the Parotid Gland	Parotid gland disease, facial nerve schwannoma, parotid lymph adenopathy, external carotid artery aneurysm, retromandibular (posterior facial) vein thrombosis and disease
Submandibular Space (sublingual space)	Sublingual gland disease, especially ranula, dermoid, lingual artery aneurysm, lingual nerve schwannoma, cranial nerve XI and XII schwannomas, lymphangioma, level I lymph adenopathy, facial artery and facial vein disease
Masticator Space	Medial pterygoid, lateral pterygoid, masseter, and temporalis muscle inflammatory disease and tumors, mandibular disease, V3 retrograde tumor or schwannoma, cellulitis, phlegm, abscess
Parapharyngeal Space	Deep portion of parotid gland tumors, V3 schwannomas, cervical sympathetic trunk disease, minor salivary gland tumors, paragangliomas, cellulitis, phlegm, abscess
Peritonsillar Space	Phlegm, abscess, extension of tonsillar tumor
''Paravertebral'' Space	Anterior middle and posterior scalene muscles, levator scapulae muscle, splenius capitus and splenius cervicus muscle disease, brachial plexus (roots) schwannomas, vertebral artery aneurysm, vertebral vein thrombosis, metastasis
''Posterior Triangle'' Space	Cranial nerve XI or brachial plexus (trunks, divisions, and chords) schwannomas, lymphangioma, level V lymph adenopathy

Copyright © 2003, Mosby, Inc. All rights reserved.

REFERENCES

1. Charpy A. Aponeuroses de cou. In: Poirier P, Charpy A, eds. Traite de anatomic humaine, Vol 12. Paris: Masson, 1912;258–280.
2. Grodinsky M, Holyoke E. The fasciae and fascial spaces of the head, neck and adjacent regions. Am J Anat 1938;63:367–408.
3. Maligaigne J. Traite d'anatomie chirugicale. Quoted in Carpy, 1912;1838.
4. Hollinshead W. Fascia and fascial spaces of the head and neck. In: Hollinshead W, ed. Anatomy for Surgeons, Vol 1. New York: Hoeber-Harper, 1954;282–305.
5. Shapiro S. Deep cervical infection following tonsillectomy: report of thirty cases with a review of the literature. Arch Otolaryngol 1930;11:701–735.
6. Cazalas G. Les espaces intra et peri-pharyngiens etude anatomique et experimentale. Lyon: Considerations Medico-Chirugicales, 1938; 168:164.
7. Coller F, Yglesias L. Infections of the lip and face. Surg Gynecol Obstet 1935;60:277–290.
8. Coulouma P. La systematisation des espaces peri, meta et para-amygdaliens. Leur interet clinique. Echo Med Nord 1937;8:649–662.
9. Gaughran G. The lateral pharyngeal cleft. Ann Otol Rhinol Laryngol 1959;68:1082–1096.
10. Hall C. The parapharyngeal space: an anatomical and clinical study. Ann Otol Rhinol Laryngol 1934;43:793–812.
11. Heeneman H, Gilbert J, Rood S. The Parapharyngeal Space: Anatomy and Pathologic Conditions with Emphasis on Neurogenous Tumors, Vol. 79500. Rochester, Minn.: American Academy of Otolaryngology, 1980;1–61.
12. Juvara E. Anatomie de la region pterygo-maxillaire, Vol. Thesis No. 186. Paris: Battaille, 1895;1–65.
13. Lemmon M. Superficial fascia rhytidectomy. A restoration of the SMAS with control of the cervicomental angle. Clin Plast Surg 1983;10:449–478.
14. Paff G. Introduction to the anatomy of the neck. In: Paff G, ed. Anatomy of the Head and Neck. Philadelphia: W.B. Saunders, 1973;1–3.
15. Rouviere H. Lymphatic system of the head and neck. In: Anatomy of the Human Lymphatic System. Ann Arbor, Mich.: Edwards Brothers, 1938;5–28.
16. Curtin H. Separation of the masticator space from the parapharyngeal space. Radiology 1987;163:195–204.
17. Gaughran G. Fasciae of the masticator space. Anat Rec 1957;129: 383–400.
18. Salasche S, Bernstein G. Superficial musculoaponeurotic system. In: Salasche S, Bernstein G, eds. Surgical Anatomy of the Skin. Appleton and Lange, 1988;89–97.
19. Dean L. The proper procedure for external drainage of retropharyngeal abscesses secondary to caries of the vertebrae. Ann Otol Rhinol Laryngol 1919;28:566–572.
20. Som P, Biller H, Lawson W. Tumors of the parapharyngeal space: preoperative evaluation, diagnosis, and surgical approaches. Ann Otol Rhinol Laryngol 1981;90:3–15.
21. Weintraub J. A new anatomic and functional systematization of the connective tissues of the neck. Arch Otolaryngol 1941; 33:1–30.
22. Truffert P, Le Cou. Anatomie topographique. Les Aponeuroses-Les Loges. Paris: L. Arnette, 1922;1–142.
23. Pearse HJ. Mediastinitis following cervical suppuration. Ann Surg 1938;108:588–611.
24. Harnsberger H. CT and MRI of masses of the deep face. Curr Probl Diagn Radiol 1987;16:143–173.
25. Harnsberger H. The carotid space. In: Harnsberger H, ed. Handbook of Head and Neck Imaging. 2nd ed. St. Louis: C.V. Mosby, 1995;75–88.
26. Harnsberger H. The parapharyngeal space and the pharyngeal mucosal space. In: Harnsberger H, ed. Handbook of Head and Neck Imaging. 2nd ed. St. Louis: C.V. Mosby, 1995;29–45.
27. Harnsberger H. The perivertebral space. In: Harnsberger H, ed. Handbook of Head and Neck Imaging. 2nd ed. St. Louis: C.V. Mosby, 1995;105–119.
28. Harnsberger H. The infrahyoid neck: normal anatomy and pathology of the head and neck from the hyoid to the clavicles. In: Harnsberger H, ed. Handbook of Head and Neck Imaging. 2nd ed. St. Louis: C.V. Mosby, 1995;150–198.

Copyright © 2003, Mosby, Inc. All rights reserved.

35

Congenital Lesions

Peter M. Som, Wendy R.K. Smoker, Hugh D. Curtin, Joy S. Reidenberg, and Jeffrey Laitman

INTRODUCTION
THE BRANCHIAL ANOMALIES
FIRST BRANCHIAL ANOMALIES
GENERAL CONCEPTS REGARDING SECOND, THIRD, AND FOURTH ARCH ANOMALIES
SECOND BRANCHIAL ANOMALIES
THIRD BRANCHIAL ANOMALIES
Thymic Anomalies
FOURTH BRANCHIAL ANOMALIES
Parathyroid Anomalies
FOURTH TO SIXTH BRANCHIAL ANOMALIES
Laryngeal Anomalies
NONBRANCHIAL ANOMALIES
Thyroid Anomalies
Thyroglossal Duct Anomalies
Ectopic Thyroid Arising from the Median Anlage
Ectopic Thyroid Originating from the Lateral Anlage
Neoplasms Arising within Thyroglossal Duct Cysts
Neoplasms Arising within Ectopic Thyroid
Imaging the Postoperative Sistrunk Procedure
CONGENITAL MALFORMATIONS OF THE CERVICAL LYMPHATIC SYSTEM
Theories of Pathogenesis
Classification of Lymphangiomas
Cystic Hygroma
Cavernous Lymphangioma
Capillary Lymphangioma
Vasculolymphatic Malformations
VASCULAR LESIONS
Hemangiomas
Vascular Malformations
Capillary Malformations
Venous Malformations
Arterial Malformations
TERATOMAS, EPIDERMOID CYSTS, AND DERMOID CYSTS
RARE CYSTS AND LESIONS

INTRODUCTION

In the proper clinical setting, congenital lesions must be considered in the differential diagnosis of a neck mass. Because there is a wide age range over which these congenital lesions can be identified, varying from the newborn to the older adult, it is important for the physician to be familiar with the specific anatomic and clinical presentations of these lesions so that appropriate and, when necessary, early therapy can be instituted. This chapter will discuss anomalies, and in particular cysts, related to the branchial, thymic, thyroid, parathyroid, and lymphatic primordia. In addition, hemangiomas, vascular malformations, teratoma/epidermoid/dermoid cysts, and other rare lesions including abnormalities of the sternocleidomastoid muscle are discussed.

THE BRANCHIAL ANOMALIES

The most accepted theories to explain the development of branchial abnormalities propose that they are either vestigial remnants resulting from incomplete obliteration of the branchial apparatus or the result of buried epithelial cell rests.[1, 2] A cell rest is a collection of displaced fetal cells embedded within tissue of another character. The vestigial remnant theory suggests that if any portion of the cervical sinus (of His), a branchial pouch, or a branchial cleft fails to

Copyright © 2003, Mosby, Inc. All rights reserved.

obliterate during embryogenesis, it can result in a cyst, sinus, or fistula. The cell rest theory suggests that if cells become trapped anywhere in the branchial apparatus during embryogenesis, they can grow and canalize to form branchial cysts, sinuses, or fistulas later in life.

The branchial anomalies are classified as either first, second, third, or fourth according to their proposed pouch or cleft of origin. A fifth-sixth branchial anomaly has never been reported. In most cases, surgical confirmation of the branchial arch involved is achieved by identification of the course of an associated fistula or sinus tract. However, in some cases without such surgical confirmation, the cysts may be less accurately classified on the basis of their anatomic location. Subtypes of some cysts have been proposed based on even more detailed anatomic considerations.[3, 4]

The malformations of the branchial apparatus are best understood as representing a spectrum of developmental anomalies that includes fistulas, sinuses, and cysts. As discussed in Chapter 33, the cervical sinus of His is formed shortly after the branchial arches appear by accelerated mesodermal growth cranially of the first arch and a portion of the second arch and caudally by growth of the epipericardial ridge, which develops from the mesoderm lateral to the fifth-sixth arch. As a result of these growths, within the cervical sinus of His are the caudal portion of the second arch and the third and fourth arches with their associated closing membranes. Continued growth around the cervical sinus of His narrows the external opening to the sinus into the channel-like cervical duct. Normally, the cervical duct and the ectoderm-lined cervical sinus of His are obliterated at about the seventh fetal week, resulting in a smooth, uniform contour to the external surface of the neck. In the adult, the cervical sinus of His is located at the angle between the dorsal surface of the infrahyoid strap muscles and the anterior margin of the sternocleidomastoid muscle.[5, 6]

Of specific interest is the observation that the epipericardial ridge, which forms the caudal aspect of the cervical sinus of His, contains the rudiments of the sternocleidomastoid muscle and the hypoglossal nerve (XII). Thus, based on this embryology, any communication persisting between the cervical sinus of His and the skin or the pharynx must lie ventral to the derivatives of the epipericardial ridge, namely, the sternocleidomastoid muscle and the hypoglossal nerve. In addition, the rare congenital absence of the sternocleidomastoid muscle is related to maldevelopment of the epipericardial ridge.[7, 8]

Branchial fistulas result when there is persistence of both a branchial cleft and its corresponding pharyngeal pouch forming an epithelium-lined single communication.[9] Such a communication never occurs during the normal development of a human embryo. The branchial fistula is thus a malformation that connects the skin to the lumen of the foregut. Since a fistula is formed from the cleft and pouch of a particular arch, and since the arch is always cranial to its cleft and pouch, the fistula must lie caudal to the structures derived from that arch. A branchial fistula may or may not communicate with a branchial cyst.

A branchial sinus is, in effect, a partial fistula that may open either externally or internally. Most often the sinus communicates externally; only rarely does it open internally. It may or may not communicate with a branchial cyst.

Branchial cysts are believed to be remnants of the cervical sinus of His, and a pure cyst has no internal or external communication. Branchial cysts are lined by stratified squamous epithelium of ectodermal origin. Less commonly, cysts can arise from branchial pouch endoderm; in this case, they are lined by columnar epithelium. Virtually all cysts have mesodermally derived lymphoid tissue in their walls. Thus, branchial cysts, fistulas, and sinuses can be lined by either stratified squamous, ciliated, or columnar epithelium, and all usually have lymphoid tissue in their walls.[10]

Branchial cysts typically present as recurrent tender masses, enlarging within days after an upper respiratory tract infection. Often initially treated with antibiotics, the cyst may resolve both to physical palpation and on imaging, only to enlarge again after the next infection. Alternatively, the cyst may be aspirated and disappear clinically for months, enlarging again when an upper respiratory tract infection develops. The patient's history often includes multiple such episodes before the diagnosis is finally established.

FIRST BRANCHIAL ANOMALIES

Of the first branchial cleft anomalies, which account for up to 8% of all branchial anomalies, 68% are cysts, 16% are sinuses, and 16% are fistulas.[5, 11, 12] They may be the most difficult anomalies to conceptualize because of the complex role played by the first branchial apparatus in the embryology of facial development, as discussed in Chapter 1. Possibly because of this complicated embryologic role, the anatomic locations of the first arch anomalies are less predictable than those of the second, third, and fourth branchial arches. Arnot in 1971 suggested that there are two types of anomalies.[3] He defined a type I anomaly as a cyst or sinus in the parotid gland lined with squamous epithelium and clinically appearing in early adult life. His type II anomaly was a sinus or cyst in the anterior triangle of the neck that had a communicating tract to the external auditory canal. In 1972, Work reclassified the first arch anomalies into two types.[4] He defined a type I anomaly to be of ectodermal origin, and he considered it a duplication of the external auditory canal. His type II anomaly was a duplication anomaly of the membranous external auditory canal and pinna that contained both ectodermal (skin) and mesodermal (cartilage) derivatives. Both types of anomalies are related to the parotid gland.[5] Of these two classifications, Work's is more widely accepted today. However, in 1980, Olsen et al. reviewed 38 cases and concluded that it was difficult to subclassify all of the anomalies into one of these subtypes, and that it was probably better to consider the locations of first arch anomalies as a spectrum of malformations.[13, 14] Nonetheless, today most physicians consider a type I first branchial anomaly as a lesion in the preauricular region whose distal portion may be either anterior or posterior to the pinna. These lesions tend to be parallel to the external auditory canal, lateral to the facial nerve (VII), and they may be embedded in the parotid gland (Fig. 35-1A). There can be a cyst, sinus, or fistula, with a tract connecting to the external auditory canal. A type II first branchial cleft anomaly is usually situated immediately posterior or inferior

Copyright © 2003, Mosby, Inc. All rights reserved.

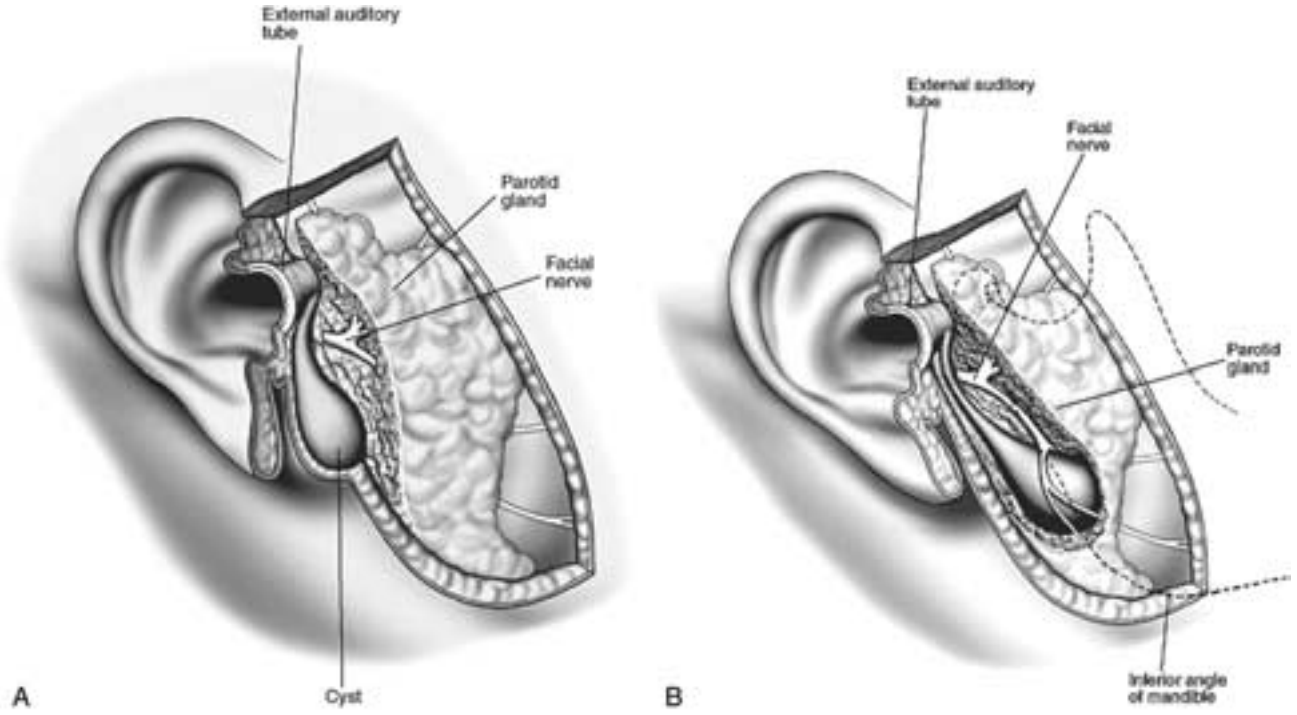

VIEW IMAGE

FIGURE 35-1 **A**, Oblique drawing of an embryo showing the location of a first branchial cyst located in the upper portion of the parotid gland. This is classified as a type I first branchial cyst. **B**, Oblique drawing of an embryo showing a first branchial cleft cyst located in the lower portion of the parotid gland. This is classified as a type II first branchial cyst.

to the angle of the mandible; it may lie lateral to, medial to, or between the branches of the facial nerve within the parotid gland (Fig. 35-1B). Its tract connects to the external auditory canal. Because of this relationship to the parotid gland, complete excision usually requires that a superficial parotidectomy be performed to expose the branches of the facial nerve.

The sinuses, fistulas, and cysts related to the first arch most often originate along the course of the external auditory canal, but have rarely been reported to originate in the middle ear cavity or nasopharynx. The anomalies that approach or involve the external auditory canal most commonly terminate at the junction of the cartilaginous and bony portions of this canal and can extend either anterior or posterior to the pinna.[2, 15] This variable position relative to the pinna is explained by the fact that the pinna itself has a multifocal origin, arising from the union of six mesenchymal proliferations or hillocks, three on either side of the first pharyngeal cleft. In addition, once formed, the pinna migrates from its initial location on the caudal and ventral side of the face to its final more cranial and dorsal adult location. Thus, the pinna has contributions from the first and second arches and the first branchial groove, which are the sites of origin of these anomalies. That is, the pinna lies in the center of this development and migration. Since conceptually a first branchial malformation may occur anywhere along the course of migration of the pinna, the rare occurrence of a first arch anomaly near the angle of the mandible is explained by its location near the initial site of pinna development.

As discussed in Chapter 33, between the sixth and eighth weeks of fetal development, the parotid gland forms from ectoderm within the mouth that branches dorsally and cranially toward the ear. At the same time, the facial nerve and associated second arch musculature are migrating ventrally and caudally. Because the facial nerve and parotid gland have a somewhat later embryologic development, a vestigial first branchial anomaly can insinuate itself in a variable relationship to the parotid gland and the facial nerve. Thus, these anomalies have been reported to be within, superficial to, or deep to the parotid gland.

Occasionally, isolated cysts may occur within the parotid gland. Such cysts may represent a first branchial cyst without a sinus or fistulous tract. However, as discussed in Chapter 39, such a cyst may also represent a lymphoepithelial cyst, presumably developed in response to chronic inflammation.[16]

On imaging, these first branchial cysts are usually related to the parotid gland and/or the lower margin of the pinna (Figs. 35-2). If a tract directed toward the external auditory canal can be identified, the diagnosis is established. However, if a tract is not seen and the cyst lies within the parotid gland, the final diagnosis could be either a first branchial cyst, a lymphoepithelial cyst, or a rare localized obstructive mucocele or sialocele. In all of these cases, the cyst contents usually are of mucoid attenuation on CT (10 to 25 HU), while on MR imaging there usually is low to intermediate T1-weighted and high T2-weighted signal intensity. If the cyst is infected and has a tract, coronal T2-weighted and postcontrast T1-weighted, fat-suppressed MR images may best demonstrate the tract. It is only on the contrast-enhanced images that the cyst wall can be clearly identified on MR imaging.

Copyright © 2003, Mosby, Inc. All rights reserved.

GENERAL CONCEPTS REGARDING SECOND, THIRD, AND FOURTH ARCH ANOMALIES

As Bailey had suggested in 1929, to best understand the second, third, and fourth branchial anomalies, they should be considered to represent a spectrum of manifestations that range from a fistula to an isolated cyst.[17] According to Fraser, the only way to truly determine the branchial level of origin of these vestigial structures is by careful anatomic examination, the most important considerations for each cyst, sinus, or fistula being (1) its connection with the foregut derivatives and (2) its relationship to both the main vascular (the carotid arteries and the aorta) and neural components (cranial nerves IX, X, XI, and XII).[18] Thus, if the arteries have a normal embryologic development, these relationships are absolutely fixed, and one can reliably predict the branchial level of origin of the malformation. Therefore, for each of the second, third, and fourth arch anomalies, the course of the entire fistula will be discussed, realizing that a branchial cyst can occur anywhere along each described course. These cysts are usually filled with turbid straw-colored fluid that contains cholesterol products.

SECOND BRANCHIAL ANOMALIES

Between 92% and 99% of branchial anomalies arise from the second branchial apparatus, and cysts are far more common than sinuses or fistulas.[9, 19] When a sinus or fistula is present, nearly 80% of the time the opening is to the skin. The external opening for a second branchial fistula is typically along the anterior border of the sternocleidomastoid muscle at the junction of its middle and lower thirds. The tract runs deep to the platysma muscle, ascends lateral to the carotid sheath, and courses lateral to and above the hypoglossal nerve (XII) and the glossopharyngeal nerve (IX). It then passes between the external and internal carotid arteries to end in the region of the palatine tonsillar fossa, a second pouch derivative (Fig. 35-3).[5] The fistula's relationship to the carotid arteries is explained embryologically by noting that when the first and second arch vessels disappear, the third arch vessel, which becomes the common carotid artery and proximal internal carotid artery, remains as the most cephalic vessel to persist.[15] The more distal internal carotid artery is formed by the dorsal aorta. Because the external carotid artery arises from a persistence of the ventral aorta or the surrounding mesenchyme, a second branchial fistula, which is formed above the third arch, must pass between the internal and external carotid arteries.

Bailey classified second branchial cleft cysts into four types.[17, 20] A type I cyst lies beneath the platysma and cervical fascia but anterior to the sternocleidomastoid muscle. It is believed to originate from a remnant of the tract connecting the cervical sinus of His to the skin. The type II cyst, which is the most common, originates from persistence of the cervical sinus of His and therefore technically could be considered a cyst of the combined second, third, and fourth branchial arches. It characteristically lies adjacent to the great vessels and may be adherent to them. The type III cyst courses between the internal and external carotid arteries and extends to the lateral wall of the pharynx. The type IV cyst, a columnar-lined cyst lying against the

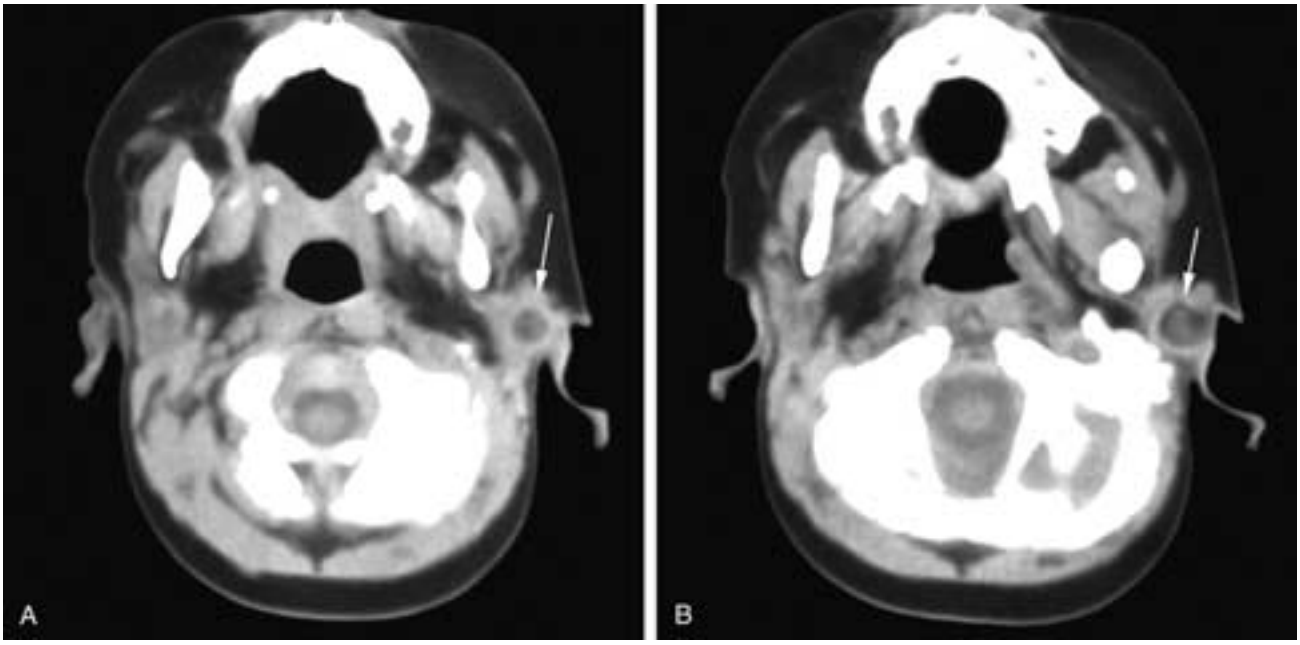

VIEW IMAGE

FIGURE 35-2 Axial CT scans just caudal to the skull base (**A**) and at the skull base (**B**). In **A**, there is a cyst (*arrow*) in the immediate infra-auricular region on the left side of this young child. In **B**, there is extension of the cyst into the left external auditory canal, which is widened by pressure from the cyst (*arrow*). This was a type I first branchial cleft cyst. Axial contrast enhanced CT scans cranial (**C**) to caudal (**D**). There is a cyst in (**C**) overlying the right parotid gland with enhancing inflammation surrounding it. This inflammation extends up to the right pinna (**D**). This patient had a type II first branchial cyst.

Copyright © 2003, Mosby, Inc. All rights reserved.

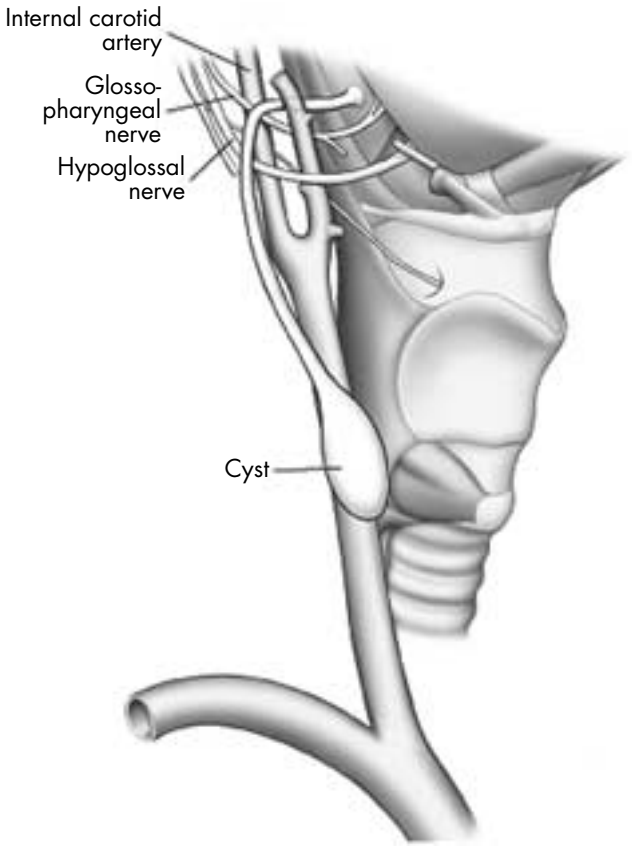

VIEW IMAGE

FIGURE 35-3 Lateral drawing of a second branchial cyst. Note that its tract enters in the region of the palatine tonsil.

pharyngeal wall, is believed to form from a remnant of the pharyngeal pouch. Type III and IV cysts can occasionally grow large, with elongations coursing cranially as far as the base of the skull.

Most second branchial cysts are first diagnosed when patients are between the ages of 20 and 40 years. Most often these cysts develop shortly after an upper respiratory tract infection, secondary to stimulation of the lymphoid tissue present in the cyst wall. Typically, the cyst is located in the lateral neck, superficial to the carotid sheath, dorsal to the submandibular gland, and ventral to the anterior edge of the sternocleidomastoid muscle. As these cysts enlarge, they may displace the submandibular gland anteriorly, while posteriorly the cysts extend deep to the sternocleidomastoid muscle (Fig. 35-4).

On CT, a noninfected cyst typically appears as a mucoid attenuation (10 to 25 HU) cyst with a uniformly thin, smooth wall. On MR imaging, the cyst typically has a low to intermediate T1-weighted and a high T2-weighted signal intensity. However, some cysts can have high T1-weighted signal intensity that may be related to chronic infection (Fig. 35-5). These variations in signal intensity reflect alterations in the protein content of the cyst.

If infected, the cyst wall becomes thickened and irregular, and it enhances with contrast (Fig. 35-6). Without clinical correlation, the imaging appearance is similar to that of a suppurative or metastatic lymph node (Fig. 35-7). Rarely, the inflamed walls of a sinus or fistulous tract can be seen, and there may be an associated thickening of the ipsilateral palatine tonsillar fossa (Fig. 35-6A).

Occasionally, septations can be seen on imaging within the cyst contents. Although septations usually occur after aspirations of the cyst, they can also be seen in nonmanipulated cysts. In addition, bleeding can occur into a cyst, usually correlating with a sudden enlargement of the cyst. The blood can increase the CT attenuation over that of muscle. On MR imaging, both the T1- and T2-weighted signal intensities are high.

THIRD BRANCHIAL ANOMALIES

The remaining branchial anomalies are rare. A complete third branchial fistula has a cutaneous opening along the anterior border of the sternocleidomastoid muscle, usually more caudal than the opening for a second branchial anomaly. The tract then courses cranially and dorsal to the common or internal carotid artery, cranial to the hypoglossal nerve (XII), and caudal to the glossopharyngeal nerve (IX), and then extends medially to pierce the posterolateral thyrohyoid membrane and open into the upper lateral piriform sinus. The tract opening into the thyrohyoid membrane is most often superior to the opening for the internal branch of the superior laryngeal nerve (Fig. 35-8).

The position of the tract dorsal to the proximal common carotid artery is a result of its cleft and pouch precursors arising dorsal to this vessel's origin from the ventral aorta. In addition, as noted earlier, the structures derived from a branchial arch lie cranial to the cleft and thus cranial to a fistula of the same arch. Involution of the dorsal aorta, a posterior structure between the third and fourth arches, enables a third branchial fistula to pass posterior to the distal common carotid and proximal internal carotid arteries. The tract passes anterior to the vagus nerve (X) and above the hypoglossal nerve (XII) but below the glossopharyngeal nerve (IX). This is to be expected since the glossopharyngeal nerve innervates the third arch derivatives and must therefore lie cranial to them. The tract ends in the thyrohyoid membrane, which extends between the third arch derivative hyoid bone (inferior portion of the body and greater cornua) and the fourth arch derivative thyroid cartilage, precisely at the level of the third pouch. The fistula then enters the piriform sinus and, as can be expected, lies above the internal branch of the superior laryngeal nerve—the nerve of the fourth branchial apparatus.

On imaging, the third branchial cyst is identified either in the same region as a second branchial cyst or slightly lower in the neck along the anterior edge of the sternocleidomastoid muscle and lateral to the carotid sheath. If the cyst is infected, there may be localized edema of the ipsilateral hypopharyngeal wall (Fig. 35-9). Its other imaging characteristics are similar to those of a second branchial cyst.

Thymic Anomalies

The normal development of the thymus, a third pouch derivative, is discussed in Chapter 33. Several anomalies of the thymus are attributed to abnormal embryologic descent of the thymic primordium into the mediastinum. These

Copyright © 2003, Mosby, Inc. All rights reserved.

anomalies can result from incomplete descent of the thymus into the chest, sequestration of thymic tissue being retained along the normal thymic pathway during descent, or failure of involution of the thymopharyngeal duct. Thymic tissue may be associated with an epithelial tract that communicates with the pharynx through the thyrohyoid membrane or it may maintain a connection with the thymus gland in the mediastinum. Thymic tissue may occur in the lateral neck, anterior or deep to the sternocleidomastoid muscle, and as such, it may be clinically similar to a branchial cyst. It also may occur as a mass in relationship to the piriform sinus. Thymic cysts are diagnosed by the presence of thymic tissue on histologic examination.[5, 21–26]

Two theories exist concerning the pathogenesis of aberrantly located thymic cysts. One theory suggests that the cysts result from acquired progressive cystic degeneration of epithelial remnants or Hassall corpuscles.[4] Histologically, there are Hassall corpuscles in a thymic cyst wall; however, the cause of such presumed degeneration is uncertain. The other, more popular theory states that the cysts represent persistence of portions of the thymopharyngeal duct and, uncommonly, a cyst may occur that extends from the upper neck caudally into the lower neck or even the anterior mediastinum. Such cysts are referred to as thymopharyngeal cysts, presumably following the course of a nonresorbed thymopharyngeal duct. It is interesting to note that the majority of these anomalies are found on the left side of the neck.

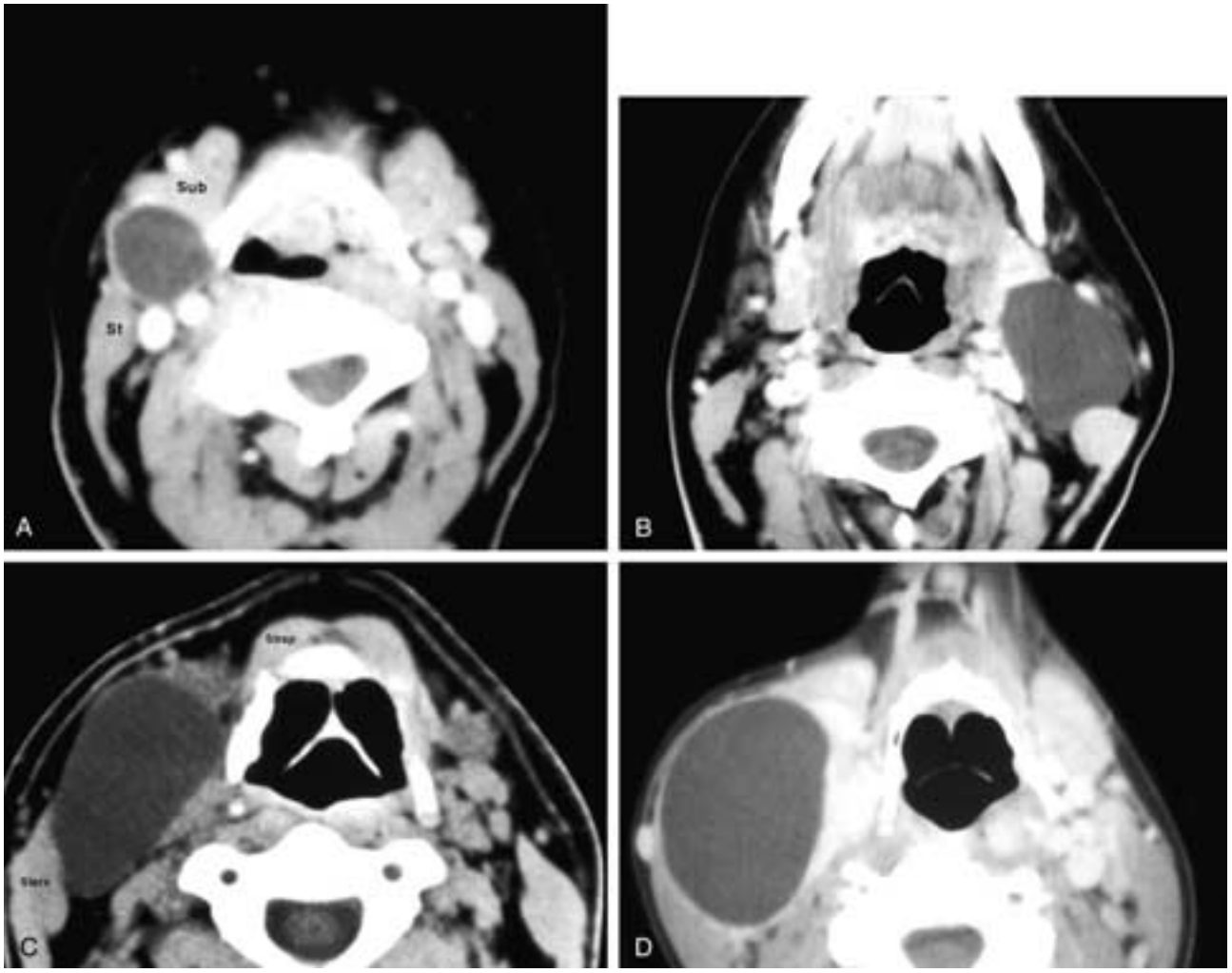

VIEW IMAGE

FIGURE 35-4 **A**, Axial contrast-enhanced CT scan shows a uniformly thin-walled right neck cyst positioned lateral to the carotid sheath structures, behind the right submandibular gland (*Sub*), and along the anterior border of the sternocleidomastoid muscle (*St*). This second branchial cleft cyst was located just caudal to the angle of the mandible. **B**, Axial contrast-enhanced CT scan shows a left neck cyst just behind the submandibular gland, lateral to the carotid sheath structures, along the anterior border of the sternocleidomastoid muscle, at or just caudal to the level of the angle of the mandible. This was a first branchial cleft cyst. **C**, Axial CT scan shows a large right neck cyst behind the submandibular gland, lateral to the carotid sheath structures, and just caudal to the level of the angle of the mandible. As this second branchial cleft cyst enlarges, the unseen superficial layer of the deep cervical fascia (extending from the sternocleidomastoid muscle (*Stern*) to the strap muscles (*Strap*) puts pressure on the cyst and pushes it dorsally deep to the Stern muscle. **D**, Axial contrast-enhanced CT scan shows a huge right second branchial cleft cyst lateral to the carotid sheath structures, behind the submandibular gland, just caudal to the level of the angle of the mandible, and partially deep to the sternocleidomastoid muscle (see **B**).

Copyright © 2003, Mosby, Inc. All rights reserved.

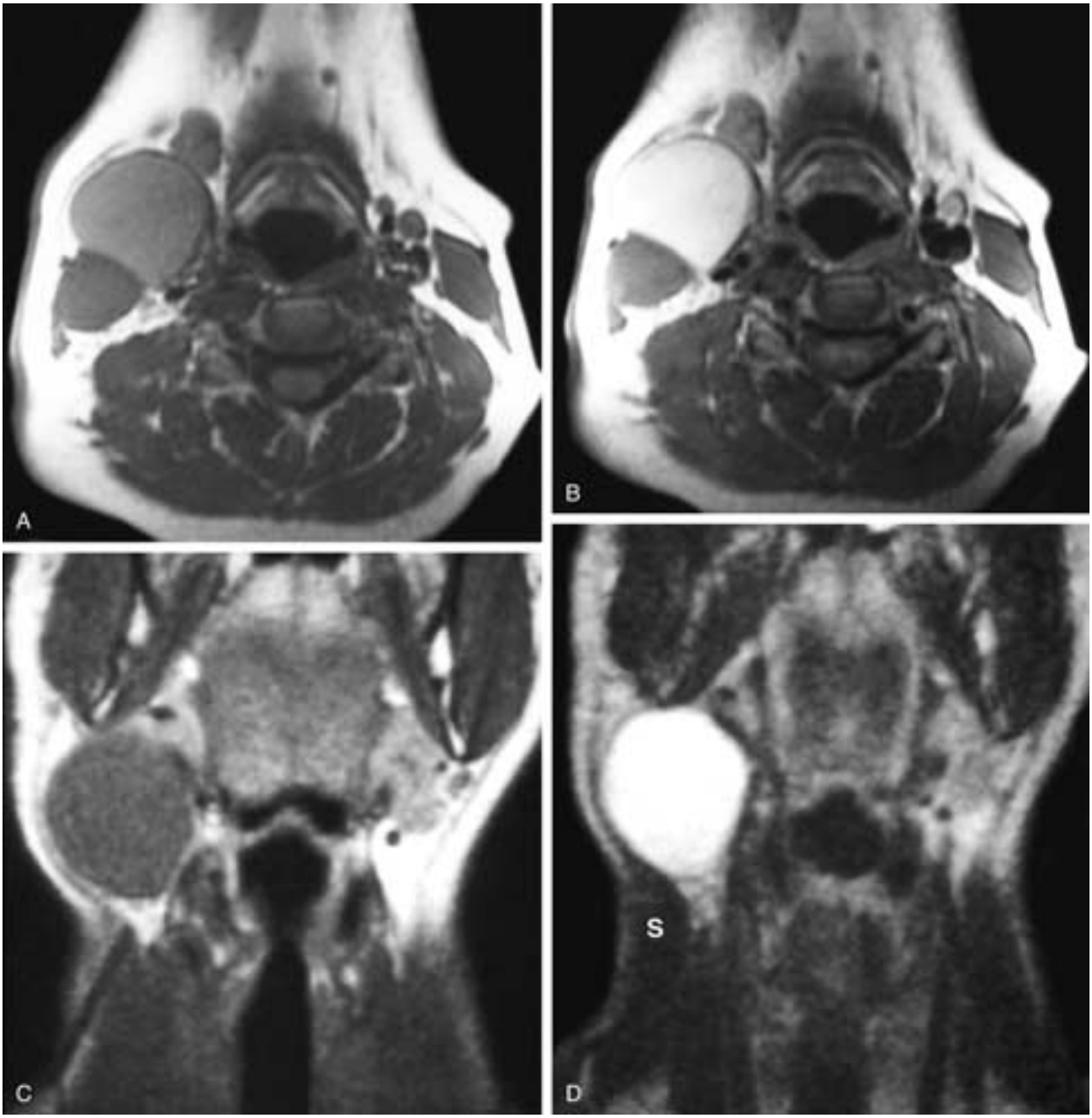

VIEW IMAGE

FIGURE 35-5 Axial T1-weighted (**A**) and T2-weighted (**B**) MR images show a spherical mass in the right neck that is lateral to the carotid sheath structures, behind the submandibular gland, and along the anterior margin of the sternocleidomastoid muscle. This second branchial cleft cyst has fairly low T1-weighted and high T2-weighted signal intensity. If contrast had been given, the cyst wall could have been differentiated from the cyst fluid. Coronal T1-weighted (**C**) and T2-weighted (**D**) MR images show a right-sided spherical mass with low T1-weighted and high T2-weighted signal intensity. This mass is just caudal to the mandible and just deep to the sternocleidomastoid muscle (*S*). Second branchial cleft cysts such as this one may have low to high T1-weighted signal intensity and almost always have high T2-weighted signal intensity. Without contrast, the cyst wall is rarely seen.

Copyright © 2003, Mosby, Inc. All rights reserved.

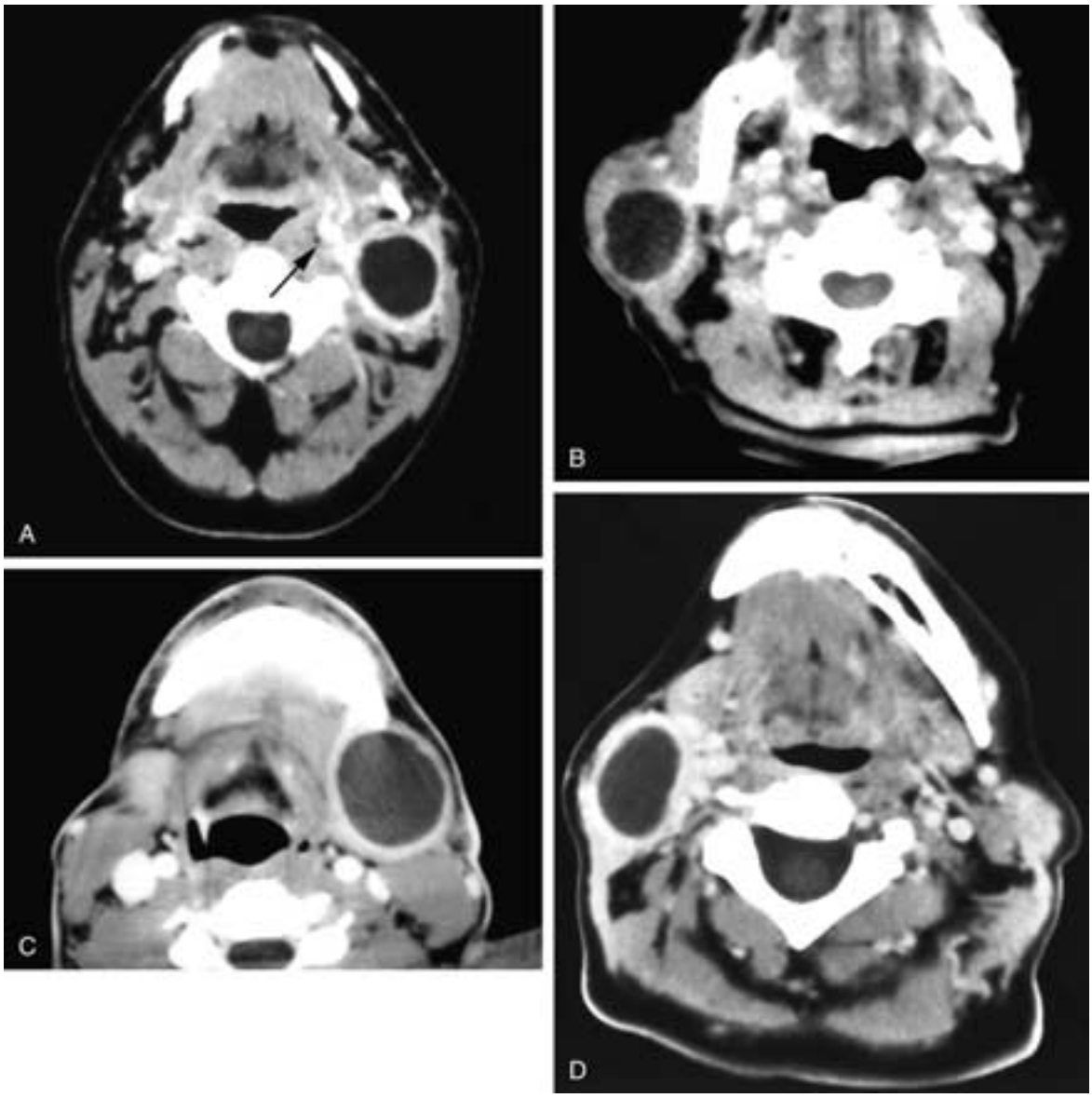

VIEW IMAGE

FIGURE 35-6 **A**, Axial contrast-enhanced CT scan shows a left-sided cyst with a thick, enhancing rim. This cyst is behind the submandibular gland, lateral to the carotid sheath structures, and deep to the anterior margin of the sternocleidomastoid muscle. There is an enhancing tract (*arrow*) extending from the cyst toward the left palatine tonsil. This was an infected second branchial cleft cyst with an internal tract. Such a tract typically passes between the internal and external carotid arteries and ends in the palatine tonsil. **B**, Axial contrast-enhanced CT scan shows a cyst in the right parotid gland with a thick but uniform cyst wall. This was a branchial cyst with no associated tract. Because of its fairly caudal location within the parotid gland, this most likely should be classified as a type II first branchial cyst. **C**, Axial contrast-enhanced CT scan shows a cyst in the left neck with a uniform, fairly thick, enhancing rim. The cyst is behind the submandibular gland, lateral to the carotid sheath structures, and along the anterior margin of the sternocleidomastoid muscle. This was an infected second branchial cleft cyst. **D**, Axial contrast-enhanced CT scan shows a cyst in the right neck with a fairly thick, enhancing rim. The cyst is behind the submandibular gland, lateral to the carotid sheath structures, and along the anterior margin of the sternocleidomastoid muscle. This was an infected second branchial cleft cyst.

Copyright © 2003, Mosby, Inc. All rights reserved.

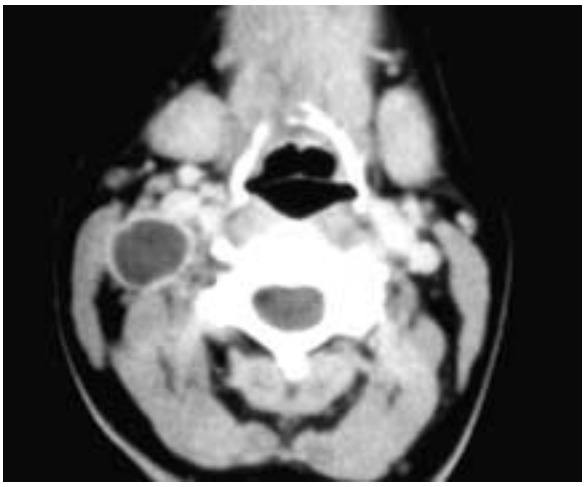

VIEW IMAGE

FIGURE 35-7 Axial contrast-enhanced CT scan shows a ''cyst'' in the right neck, completely deep to the sternocleidomastoid muscle, dorsal to the carotid sheath structures, and not touching the submandibular gland. Clinically, this was thought to be a second branchial cleft cyst, but the location of the lesion on the image is not that of a second branchial cleft cyst. This was a metastatic papillary thyroid carcinoma lymph node.

About two thirds of the cases of cervical thymic cyst occur in the first decade of life, and the remaining cases are distributed over the second and third decades. They can present anywhere in the neck from the angle of the mandible to the sternum, usually paralleling the sternocleidomastoid muscle. Most occur in the lower neck as a slowly enlarging mass, and sudden enlargement usually signifies hemorrhage into the cyst. The cysts may be isolated from the normal thymic tissue or attached to it by a fibrous band. Unlike mediastinal thymic cysts, cervical thymic cysts are not associated with myasthenia gravis.[27]

On imaging, a cervical thymic cyst usually appears as a solitary, off-midline, low anterior neck cyst, either adjacent to the lower piriform sinus or just caudal to the thyroid gland (Fig. 35-10). There usually is no demonstrable connection to the thymus in the anterior mediastinum. The cyst wall is thin and uniformly smooth, and the cyst contents are of mucoid attenuation (10 to 25 HU) on CT. On MR imaging, the cyst contents usually have low to intermediate T1-weighted and high T2-weighted signal intensity.

Although the inferior parathyroid glands develop from the third pharyngeal pouch endoderm, for the sake of brevity the abnormalities of the parathyroid glands will be discussed with the fourth arch anomalies, since the fourth arch contributes to the superior parathyroid glands.

FOURTH BRANCHIAL ANOMALIES

There are only a few documented complete fourth branchial fistulas. In 93% of the reported cases, the anomaly occurred on the left side and recurrent episodes of a low neck abscess or thyroiditis suggested the diagnosis.[28] The anomaly is most often diagnosed in a child, although it can present in an adult. The cutaneous opening is along the anterior border of the sternocleidomastoid muscle, usually along the lower third of the muscle and caudal to the openings of the second and third arch anomalies. On the left side, the tract courses superiorly to loop over the hypoglossal nerve (XII), extends between the internal and external carotid arteries, descends in the neck posteriorly to the common carotid artery, loops posteriorly around the aortic arch, and then ascends lateral to the trachea and the recurrent laryngeal nerve to end in the apex of the piriform sinus. On the right side, the fistula passes beneath the subclavian artery and then ascends to the apex of the piriform sinus (Fig. 35-11). These varied courses are explained by noting that a branchial fistula must pass inferior to its arch structures and the associated nerves and vessels of the same arch. Because the left fourth arch artery forms the aorta while the right fourth artery forms the subclavian artery, the fistulas descend respectively beneath the arch or subclavian artery anteriorly, then loop around the vessel posteriorly to extend cranially. Because the superior laryngeal nerve develops in association with the fourth arch and the recurrent laryngeal nerve with the sixth arch, a complete fourth branchial fistula passes inferior to the superior laryngeal nerve and superior to the recurrent laryngeal nerve.[29] It penetrates the thyrohyoid membrane behind the internal branch of the superior laryngeal nerve, unlike the more anterior third branchial fistula.[30] The tract then empties into the apex of the piriform sinus, more caudal than its third branchial counterpart.[31–35]

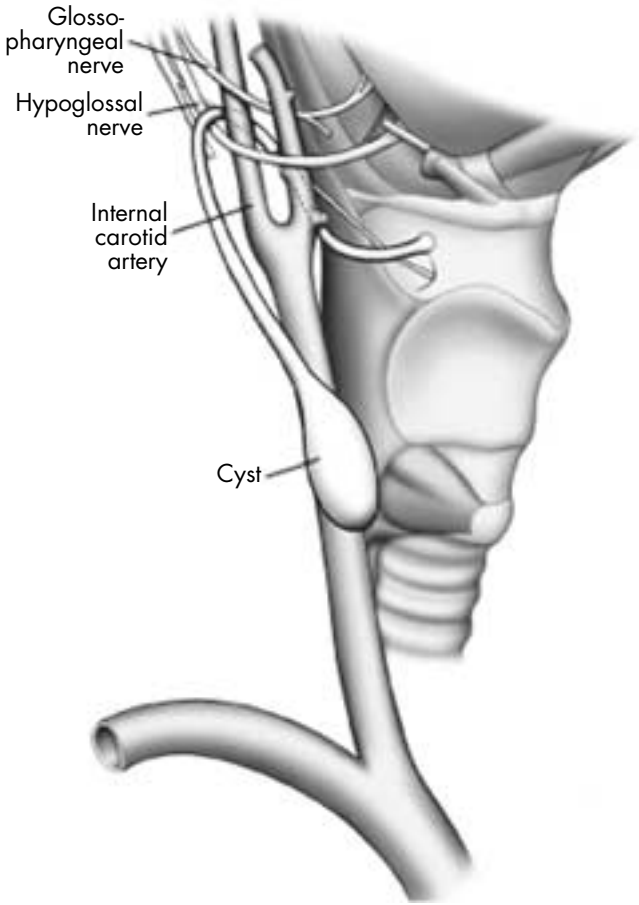

FIGURE 35-8 Lateral drawing of a third branchial cyst. Note that its tract enters in the region of the lateral wall of the upper pyriform sinus.

VIEW IMAGE

Copyright © 2003, Mosby, Inc. All rights reserved.

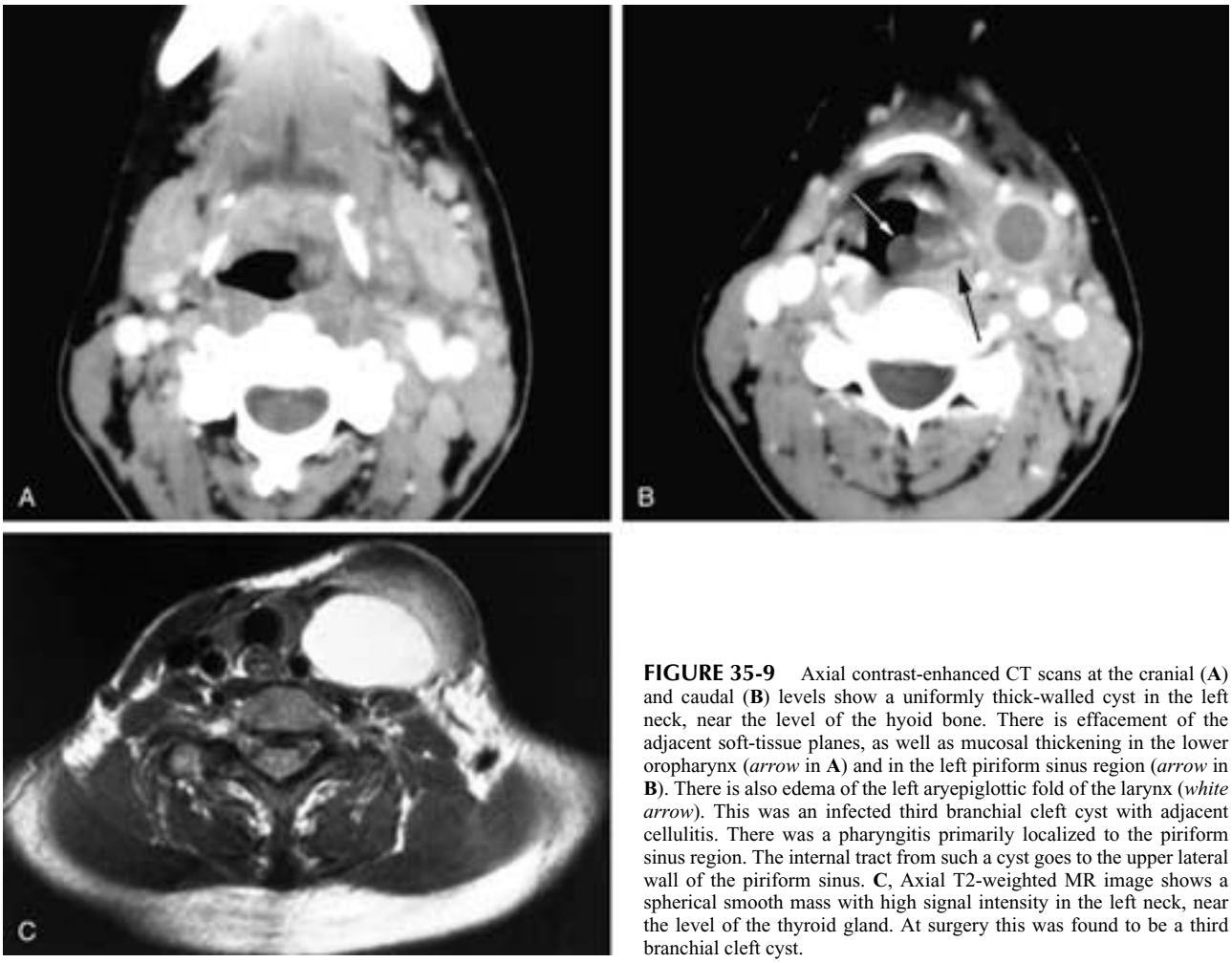

FIGURE 35-9 Axial contrast-enhanced CT scans at the cranial (**A**) and caudal (**B**) levels show a uniformly thick-walled cyst in the left neck, near the level of the hyoid bone. There is effacement of the adjacent soft-tissue planes, as well as mucosal thickening in the lower oropharynx (*arrow* in **A**) and in the left piriform sinus region (*arrow* in **B**). There is also edema of the left aryepiglottic fold of the larynx (*white arrow*). This was an infected third branchial cleft cyst with adjacent cellulitis. There was a pharyngitis primarily localized to the piriform sinus region. The internal tract from such a cyst goes to the upper lateral wall of the piriform sinus. **C**, Axial T2-weighted MR image shows a spherical smooth mass with high signal intensity in the left neck, near the level of the thyroid gland. At surgery this was found to be a third branchial cleft cyst.

VIEW IMAGE

A fourth branchial pouch cyst adjacent to the larynx, like a third branchial pouch cyst, must be clinically differentiated from a laryngocele. As mentioned, the literature supports the belief that a branchial cyst arising from the apex of the piriform sinus is more likely to be a fourth pouch remnant. Branchial cysts in the mediastinum without a connection to the larynx or the neck have also been described.[36] Such a cyst could represent either a fourth or fifth-sixth branchial remnant, depending on whether the remnant passes clearly beneath the aorta (fourth arch) or the pulmonary artery (fifth-sixth arch), respectively.

On imaging, a fourth branchial cyst usually appears as a solitary, often infected, cyst just anterior to the thyroid gland, usually on the left side. The adjacent thyroid lobe is involved, and on CT it has a lower attenuation, reflecting infection and the loss of iodine concentration (Fig. 35-12). On MR imaging, as a result of infection, there usually is high T2-weighted signal intensity within the involved thyroid. Rarely, there can be swelling of the ipsilateral hypopharynx reflecting a pharyngitis.

Parathyroid Anomalies

The normal development of the parathyroid glands was discussed in Chapter 33. As a result of that embryology, parathyroid cysts or aberrant glands can be located anywhere around the thyroid gland and are most commonly found inferior to the gland. Because of their proximity to the thymic primordia (particularly for the inferior parathyroid glands), these anomalies can be situated anywhere a thymic anomaly can be found, including the mediastinum.

Various theories have been proposed to explain the pathogenesis of parathyroid cysts, suggesting that these cysts arise from embryologic remnants of third and fourth pharyngeal pouches, cystic degeneration of parathyroid adenomas, gradual enlargement of microcysts as a result of accumulation of secretions, or fusion or coalescence of smaller microcysts. Although most parathyroid cysts are not associated with biochemical anomalies, nearly one third of them have been reported to be functioning and associated with hyperparathyroidism.[27, 37, 38]

Parathyroid cysts comprise only 0.6% of all thyroid and parathyroid masses. Although most patients present with an asymptomatic low neck mass, tracheal and esophageal compression can occur, as can hoarseness secondary to recurrent laryngeal nerve compression. Pain associated with hemorrhage into the cyst has also been reported.[39] Nearly 95% of parathyroid cysts occur below the level of the inferior thyroid border, and 65% are associated with the inferior parathyroid glands. However, these cysts can occur

Copyright © 2003, Mosby, Inc. All rights reserved.

anywhere from the angle of the mandible down to the mediastinum.[40, 41]

The cyst wall usually is composed of a solitary layer of cuboidal or low columnar epithelium, with scattered chief or oxyphil parathyroid cells. Some cysts have no parathyroid tissue in their wall, but analysis of the fluid content shows elevated parathyroid hormone levels.

The nonfunctioning cysts affect patients with a mean age of 43.3 years and are three times more likely to occur in women than in men. These cysts almost always involve the inferior parathyroid glands.[39] The functioning cysts, which represent about one third of these cysts, occur more commonly in men by a ratio of 1.6:1, affect patients with a mean age of 51.9 years, and tend to occur in the superior parathyroid glands or in ectopic locations.

On imaging, although both multiloculated and multiple cysts can occur, most often there is a solitary unilocular cyst just inferior to the thyroid gland in the anterior neck, varying in size from 1 to 10 cm (Fig. 35-13). A cleavage plane usually is seen between the cyst and the thyroid gland, making excision relatively easy. The cysts contain mucoid attenuation (10 to 25 HU) material and have a thin, uniform rim. On MR imaging, the signal intensities vary from low to high on T1-weighted images, and there is a high T2-weighted signal intensity. Rarely, an adenoma can be visualized within the cyst.[27]

FOURTH TO SIXTH BRANCHIAL ANOMALIES

Laryngeal Anomalies

The fourth branchial apparatus contributes to the embryology of the larynx, and the development of this structure is discussed in Chapter 33. The congenital abnormalities of the larynx are discussed in detail in Chapters 30 and 31.

NONBRANCHIAL ANOMALIES

Thyroid Anomalies

The embryology of the thyroid gland is discussed in detail in Chapter 33. The anomalies of the gland are varied and can present as complete or unilateral agenesis, an abnormality due to altered migration or incomplete degeneration, or an abnormality resulting from incomplete glandular descent that can lead to remnants of ectopic thyroid tissue anywhere along the course of the thyroglossal duct. During embryologic descent of the thyroid anlagen, the forming gland interacts with the developing branchial pouches, particularly the third and fourth pouches from which the parathyroid glands originate, as well as the ultimobranchial body, which is thought to contribute to the lateral thyroid

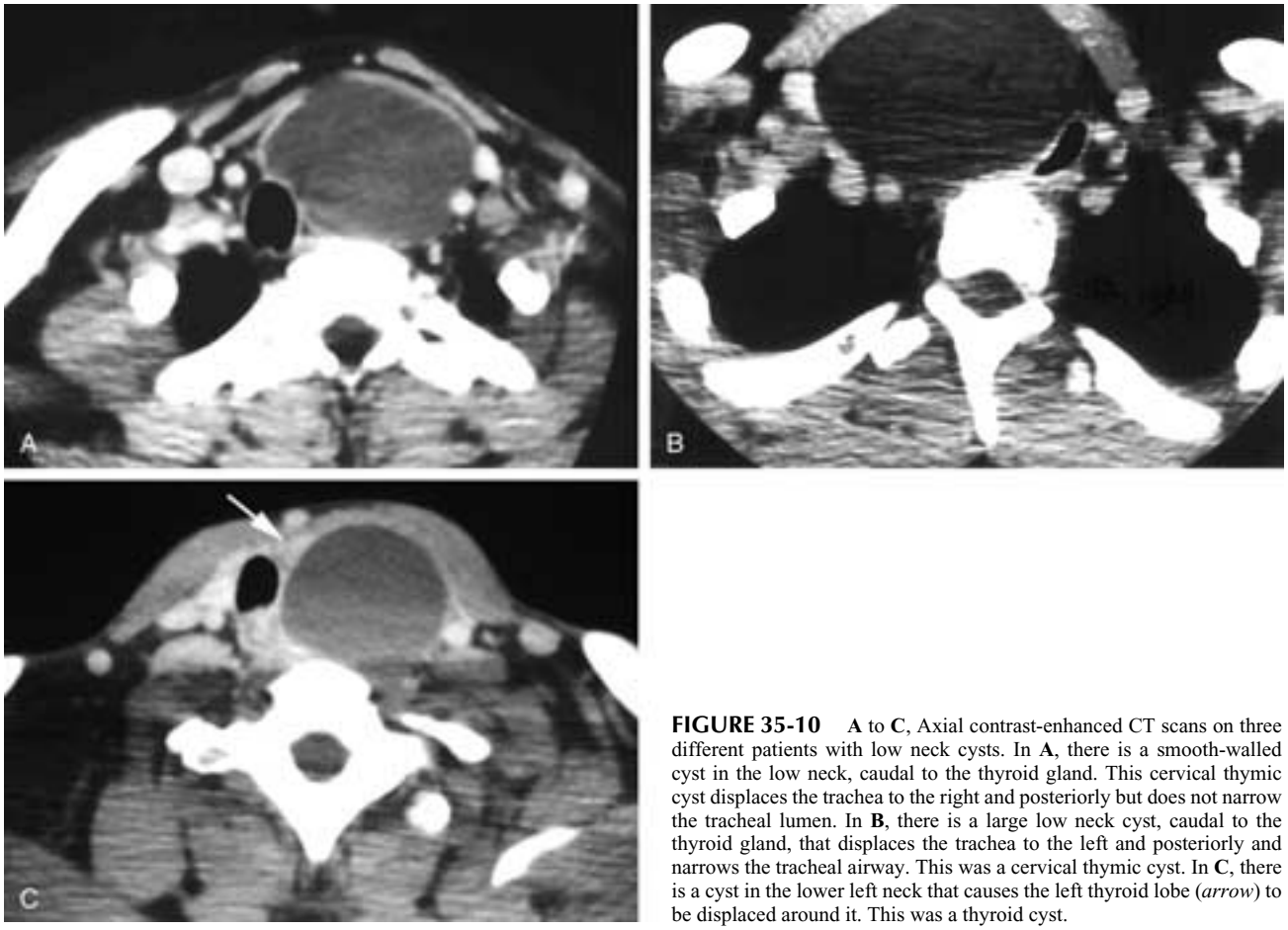

FIGURE 35-10 **A** to **C**, Axial contrast-enhanced CT scans on three different patients with low neck cysts. In **A**, there is a smooth-walled cyst in the low neck, caudal to the thyroid gland. This cervical thymic cyst displaces the trachea to the right and posteriorly but does not narrow the tracheal lumen. In **B**, there is a large low neck cyst, caudal to the thyroid gland, that displaces the trachea to the left and posteriorly and narrows the tracheal airway. This was a cervical thymic cyst. In **C**, there is a cyst in the lower left neck that causes the left thyroid lobe (*arrow*) to be displaced around it. This was a thyroid cyst.

VIEW IMAGE

Copyright © 2003, Mosby, Inc. All rights reserved.

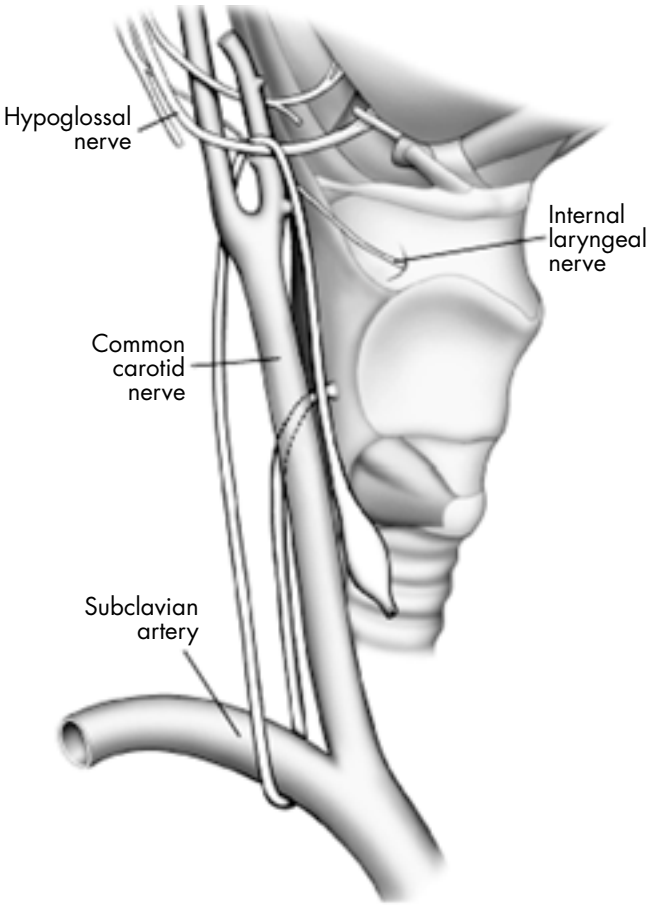

VIEW IMAGE

FIGURE 35-11 Lateral drawing of a fourth branchial cyst. Note that the tract enters the apex or floor of the pyriform sinus. Also note the relationship of the cyst and the distal tract to the location of the thyroid bed. Axial contrast-enhanced CT scans on three different patients.

FIGURE 35-13 Axial contrast-enhanced CT scan shows a cyst (*large arrow*) adjacent to the left thyroid lobe. There is an enhancing nodule (*small arrow*) within the cyst. This patient had a functioning parathyroid adenoma and the nodule was the adenoma.

VIEW IMAGE

anlage. Possibly as a result of the early embryologic position of the heart and great vessels relative to the developing branchial region, ectopic thyroid tissue may become located in the larynx, esophagus, lateral neck, mediastinum, pericardium, or heart.

Complete absence or agenesis of the thyroid gland is poorly understood because of the lack of any morphologic information. The complete lack of a thyroid gland at birth can be due either to congenital absence or possibly destruction in utero secondary to maternal antithyroid antibodies.[42, 43] When there is a congenitally absent thyroid, this anomaly appears to be quite specific, and there are no other associated anomalies of the branchial region.

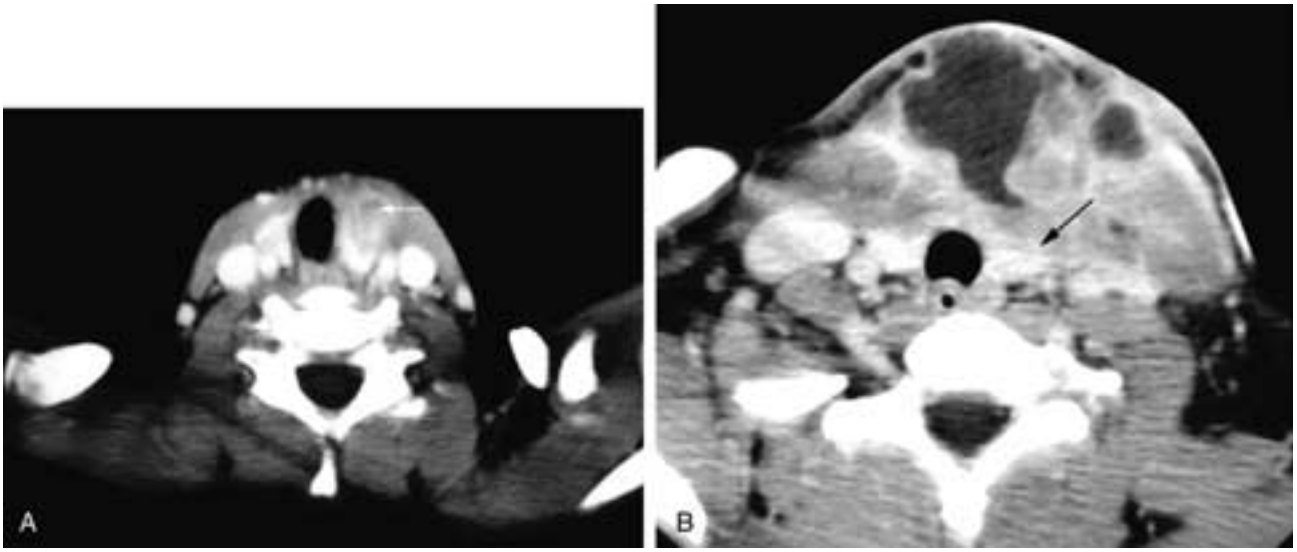

VIEW IMAGE

FIGURE 35-12 In **A**, there is a low-attenuation region (*arrow*) in the left neck. Associated with this process is effacement of the adjacent soft-tissue planes and extension of the process into the left thyroid lobe. The patient was a young child with a recurrent low neck abscess and clinical thyroiditis. At surgery, the lesion was found to be an infected fourth branchial cleft cyst with a tract extending to the apex of the left piriform sinus. In **B**, there is a low-attenuation region with an enhancing rim in the left side of the neck. There is associated cellulitis involving the anterior neck and the left thyroid lobe (*arrow*) is affected, having slightly lower attenuation than the normal right thyroid lobe. The patient was a young child with a recurrent low neck abscess and clinical thyroiditis. At surgery, the lesion was found to be an infected fourth branchial cleft cyst with a tract extending to the apex of the left piriform sinus.

Copyright © 2003, Mosby, Inc. All rights reserved.

The term *congenial hypothyroidism* refers to hypothyroidism present at birth. The etiologies are diverse and can be either congenital or acquired. One of the more common congenital etiologies is congenital dyshormonogenesis, which is caused by an enzyme defect in the synthesis of thyroglobulin, the matrix protein for thyroid hormone synthesis in the thyroid gland.[44] Other causes include thyroid agenesis or dysgenesis, congenital goiter due to maternal drug ingestion or the ingestion of iodide, genetic defects in thyroid hormone synthesis and metabolism, congenital endemic goiter, familial transient hypothyroidism secondary to transplacental thyrotropin-blocking antibodies, transient primary hypothyroidism in a sick premature newborn, and familial thyroid-stimulating hormone deficiency.[45, 46]

The adult thyroid gland can vary in both form and size.[47] Asymmetry in the size of the two lobes is very common, with the right lobe usually being longer than the left. True thyroid hemiagenesis is reported to be very uncommon and usually occurs on the left side.[48] More commonly, there are a variety of pathologic conditions that can render a lobe nonfunctioning, mimicking hemiagenesis on a radionuclide thyroid scan. Thyroid pathology is discussed in Chapter 40.

Thyroglossal Duct Anomalies

For a short time, the developing thyroid gland is connected to the tongue by a narrow tube, the thyroglossal duct. This duct courses from the region of the junction of the anterior two thirds and posterior one third of the tongue to the hyoid bone and then farther caudally to the region of the thyroid bed (Fig. 35-14). The thyroglossal duct begins to degenerate or atrophy between the fifth and sixth fetal weeks, and the foramen cecum of the tongue and the pyramidal lobe of the thyroid gland are the normal remnants of this duct, respectively occurring at its most proximal and most distal portions. The pyramidal lobe is a band of thyroid tissue that can be attached to the isthmus in the midline or project off either thyroid lobe, more often on the left side. It can extend up to the hyoid bone. Uncommonly, the pyramidal lobe can be detached from the main thyroid gland or it can be divided into two or more parts. The distal thyroglossal duct can also differentiate into fibrous tissue or even into a muscle referred to as the levator glandulae thyroidae, originating in the midline above at the body of the hyoid bone and extending either to the isthmus of the thyroid gland or to the pyramidal lobe.

VIEW IMAGE

FIGURE 35-14 Lateral diagram traces the course of the thyroglossal duct cyst from the foramen cecum (*F*) downward, at first ventral to the hyoid bone and then dorsal to the hyoid bone. The duct then descends in the neck to the level of the normal thyroid bed (*T*).

The most common congenital neck mass is the thyroglossal duct cyst, which accounts for nearly 90% of nonodontogenic congenital cysts.[10, 49] This usually midline or near-midline lesion can occur anywhere along the path of the duct and probably is due to a rest of secretory epithelial cells that fails to involute and, when stimulated by an inflammatory process, causes a cyst to develop. The distribution of these cysts in the neck is 20% to 25% in the suprahyoid neck, 15% to 50% at the level of the hyoid bone, and 25% to 65% in the infrahyoid neck.[10] Thus, these cysts most commonly occur near the hyoid bone, and they can be either superior, anterior, inferior, or posterior to this bone. This is explained by noting that during its maturation, the hyoid bone rotates (in a counterclockwise direction, as seen from the left side) before assuming its final adult position. During this rotation, the thyroglossal duct, which is adherent to the hyoid along its anterior inferior edge, may be drawn posteriorly and cranially to lie behind the body of the hyoid bone.[50] Rarely, the duct can be incorporated into the hyoid bone, presumably trapped between the second and third arch components of the hyoid's body.[51] Noting this close relationship between the thyroglossal duct and the body of the hyoid bone, Sistrunk proposed that the body of the hyoid bone should be removed during surgical resection of a thyroglossal duct cyst. When this was done, recurrences were reduced from nearly 50% to less than 4%.[52]

As mentioned, thyroglossal duct cysts are the most common midline neck mass, and 75% of them occur near the midline.[10] The lining of the cyst may be stratified squamous, pseudostratified ciliated, simple cuboidal, or columnar epithelium, and there may be residual thyroid tissue in the cyst wall.[53] The typical history is that of a gradually enlarging mass in the midline of the neck. The size of the mass may fluctuate with cyst infection, and fistulas are rare in patients who have not been operated on. Rarely, the cyst can rupture, and occasionally a residual portion of the duct can form a sinus or even a branched sinus tract.[54, 55] Although these are congenital lesions, with nearly 50% of patients being diagnosed before the age of 30 years, 15% are diagnosed in patients older than 50 years.

On imaging, those cysts that occur in the suprahyoid neck are almost always in the midline, and most lie immediately adjacent to the hyoid bone, often remodeling it (Fig. 35-15). Rarely, a lateral suprahyoid thyroglossal duct cyst can occur, clinically mimicking a second branchial cyst. However, these thyroglossal duct cysts have a medial tail-like component that ''dives'' into the hyoid bone, thus differentiating them from a branchial cyst (Fig. 35-16). If the cyst occurs just caudal to the hyoid bone, it lies at the level of the

Copyright © 2003, Mosby, Inc. All rights reserved.

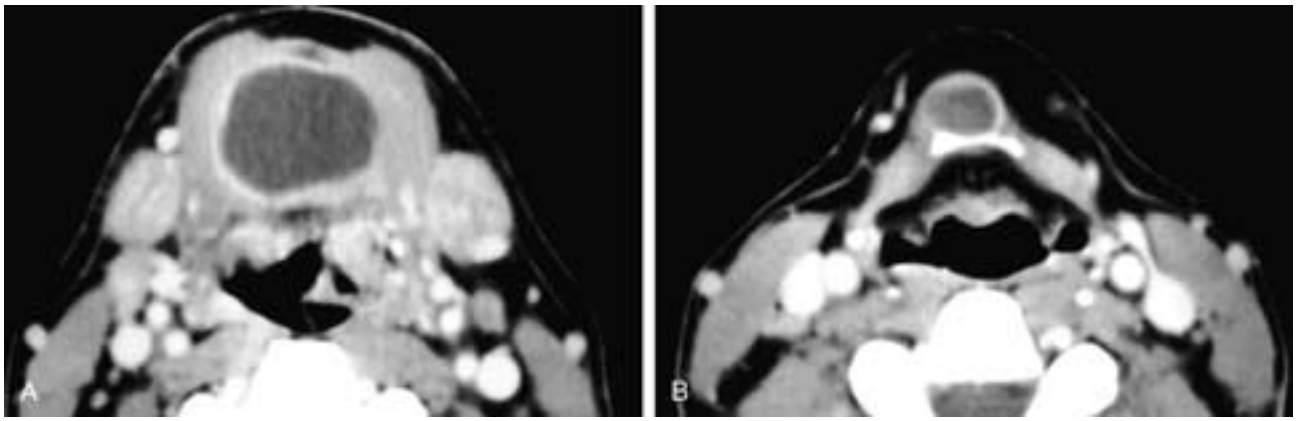

VIEW IMAGE

FIGURE 35-15 Axial contrast-enhanced CT scans at the cranial level (**A**) and a more caudal level (**B**). There is a midline thin-walled cyst in the region of the floor of the mouth. The caudal aspect of the cyst touches the hyoid bone and slightly remodels the anterior margin of this bone. This was a thyroglossal duct cyst.

thyrohyoid membrane of the larynx. These cysts can stretch this membrane, bowing it posteriorly, so that on imaging the cyst appears to lie in the preepiglottic space of the larynx (Fig. 35-17). In fact, the cyst remains outside the larynx, and at surgery, once a dissecting plane around the cyst can be identified, the cyst can be separated from the larynx without entering the larynx itself. In rare cases, such a cyst, occurring at the level of the larynx, can grow so large that it appears to destroy the laryngeal cartilages, and may initially appear both on imaging and clinically to be a submucosal supraglottic laryngeal tumor (Fig. 35-18). In actuality, the cyst has simply remodeled (and deossified) the laryngeal cartilages without destroying them. At surgery, once a dissection plane can be identified, the larynx again need not be entered. The imaging appearance of such a cyst, usually deforming the hyoid bone as well as the larynx, should lead to the correct diagnosis.[56]

In the infrahyoid neck, a thyroglossal duct cyst also has a classic imaging appearance. It is a cyst the lies just off of the midline, adjacent to the outer surface of the thyroid cartilage and deep to the infrahyoid strap muscles (Figs. 35-19 and 35-20). Once it is so identified on imaging, the diagnosis is established. Rarely, these cysts can occur in the lower neck, either in the midline or just off to one side (Fig. 35-21).

Regardless of their location in the neck, on imaging these cysts have a thin, smooth rim when not infected. If they are infected, the cyst wall thickens and enhances. On CT, the cyst contents usually have a mucoid attenuation (10 to 25 HU); however, if there has been previous infection or hemorrage, the attenuation of the cyst contents can approach

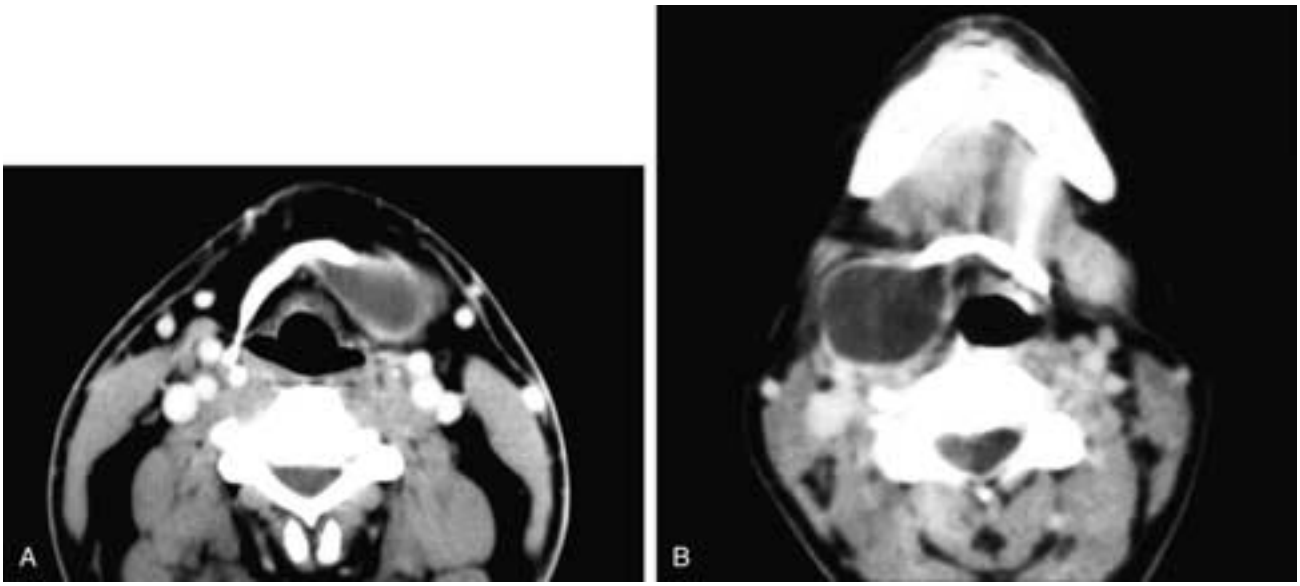

VIEW IMAGE

FIGURE 35-16 Axial contrast-enhanced CT scans on two different patients, each thought clinically to have a branchial cleft cyst. In **A**, a left-sided cyst ''dives'' into the hyoid bone. In **B**, a right-sided cyst ''dives'' into the hyoid bone. This finding establishes the diagnosis of thyroglossal duct cysts. Branchial cysts do not have such a relationship to the hyoid bone.

Copyright © 2003, Mosby, Inc. All rights reserved.

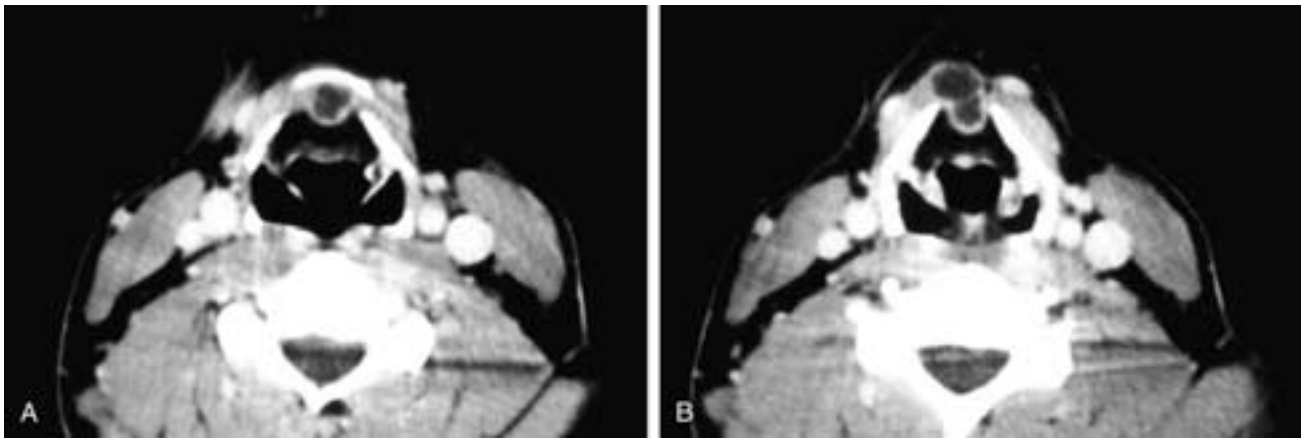

VIEW IMAGE

FIGURE 35-17 Axial contrast-enhanced CT scans at the cranial level (**A**) and a more caudal level (**B**). There is a slightly lobulated midline cyst that extends from the lower posterior margin of the hyoid bone (**A**), indents the thyrohyoid ligament, and projects into the superior thyroid notch of the thyroid cartilage of the larynx (**B**). Such a thyroglossal duct cyst was an incidental finding on this scan of the neck done for another reason. These cysts indent the thyrohyoid membrane but do not actually enter the preepiglottic space of the larynx.

that of muscle. On MR imaging, the T1-weighted signal intensity can vary from low to high, while the T2-weighted signal intensity remains high (Fig. 35-22). These variations in signal intensity reflect the variable protein content of the cyst.[57] As with branchial cysts, septations can occur within the cyst, with or without prior needle aspirations.

MR imaging also allows distinction from a vallecula cyst (Fig. 35-22C and D), which is a retention cyst on the mucosal margins, not along the thyroglossal duct tract.

Ectopic Thyroid Arising from the Median Anlage

Ectopic thyroid tissue occurs more commonly in females (7:1) and presents symptomatically during adolescence in approximately 78% of cases, often being attributed to hormonal disturbances that occur during puberty and pregnancy.[58] In autopsy studies, ectopic thyroid tissue measuring less than 3 mm in size was found in 10% of the normal population.[59] An understanding of the anatomic locations in which ectopic thyroid tissue can occur is based on knowledge of the embryologic course of the thyroglossal duct, as described in Chapter 33. If the gland fails to descend, it can actually ascend secondary to the growth of the developing tongue. For this reason, a thyroid in the tongue, the most common ectopic location (90% of cases), is by strict embryologic criteria an abnormally ascended gland. Partial failure of the gland to descend causes a prelaryngeal thyroid gland. Failure of the thyroglossal duct to degenerate completely can result in persistent thyroid tissue occurring anywhere along the course of this duct. However, when this happens, the thyroid tissue is usually normal and is most often in or near the location of a normal thyroid gland. To be

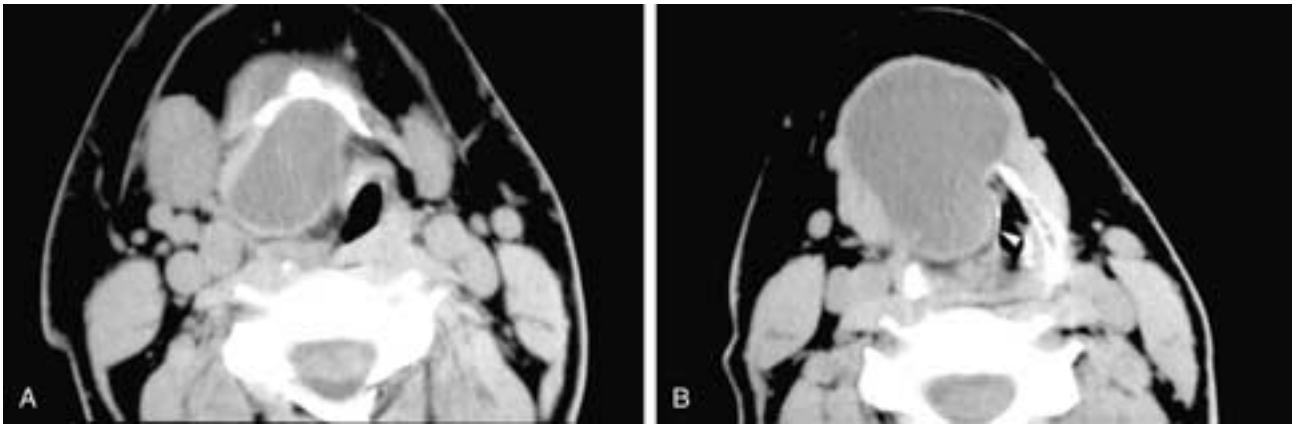

VIEW IMAGE

FIGURE 35-18 Axial contrast-enhanced CT scans at the cranial level (**A**) and a more caudal level (**B**). This patient presented with altered voice quality, and the clinical examination showed a large submucosal supraglottic mass that was thought to be a tumor. In **B**, the large cyst is seen apparently destroying the right side of the thyroid cartilage and bulging into the larynx deep to the mucosa (*arrowhead*). However, in **A**, the cranial aspect of the cyst not only touches the hyoid bone but remodels and widens the dorsal concavity of this bone. It is this latter finding that confirms the diagnosis of a huge thyroglossal duct cyst. This cyst was surgically elevated away from the larnyx without entering the larynx. The thyroid cartilage was only deossified from pressure exerted by the cyst.

Copyright © 2003, Mosby, Inc. All rights reserved.

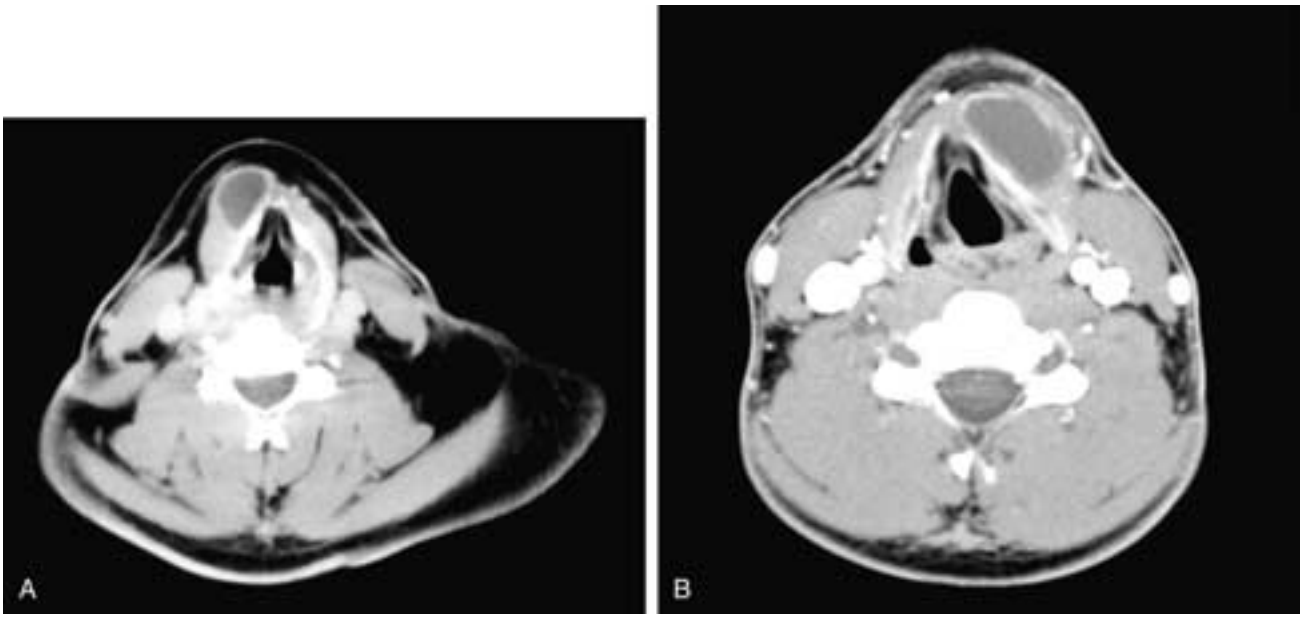

VIEW IMAGE

FIGURE 35-19 Axial contrast-enhanced CT scans on two different patients. In **A**, there is a smooth-walled cyst in the right neck, adjacent to the outer aspect of the thyroid cartilage and deep to the strap muscle. In **B**, a slightly larger but similar cyst is present on the left side. These were both thyroglossal duct cysts.

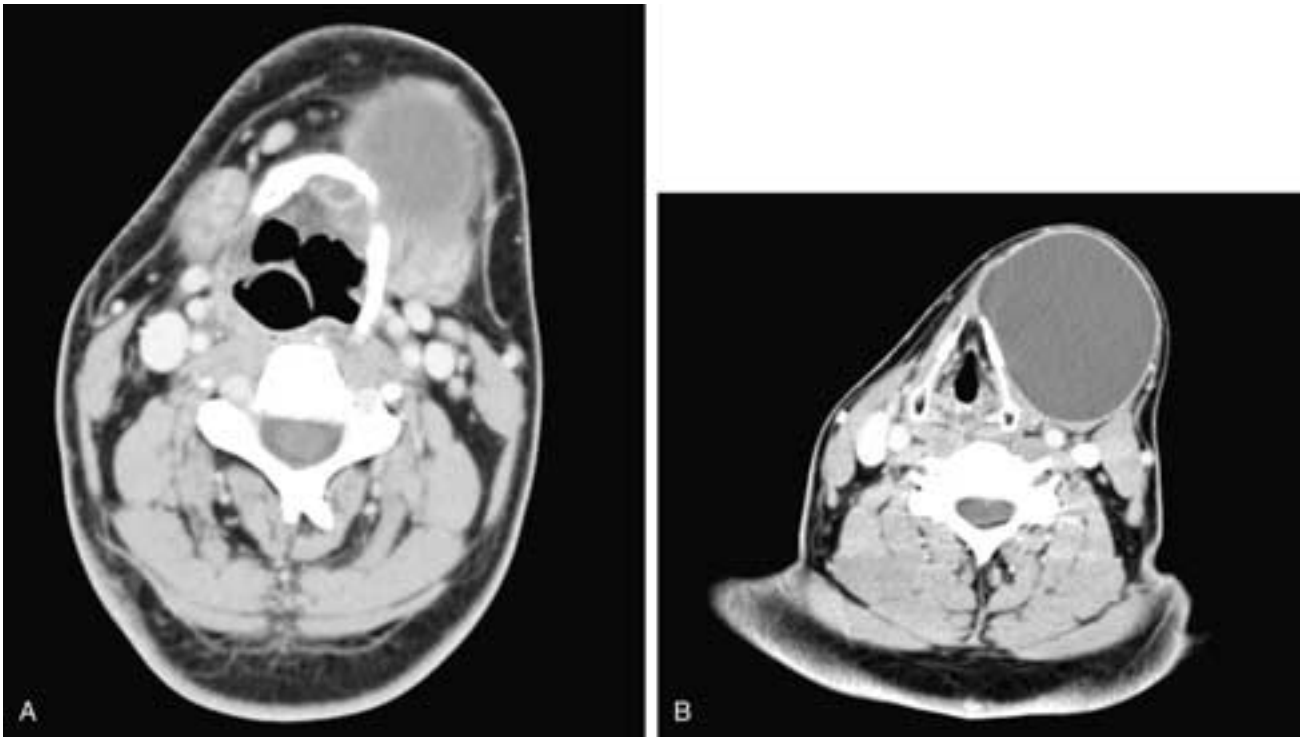

VIEW IMAGE

FIGURE 35-20 Axial CT scans at the cranial level (**A**) and a more caudal level (**B**). In **B**, there is a large cyst adjacent to the outer contour of the thyroid cartilage. However, the cyst is so large that the strap muscles cannot clearly be identified as draped over the cyst. In **A**, the upper aspect of the cyst touches the hyoid bone and a small lobulation extends dorsal to the body of the hyoid bone. This was a thyroglossal duct cyst.

Copyright © 2003, Mosby, Inc. All rights reserved.

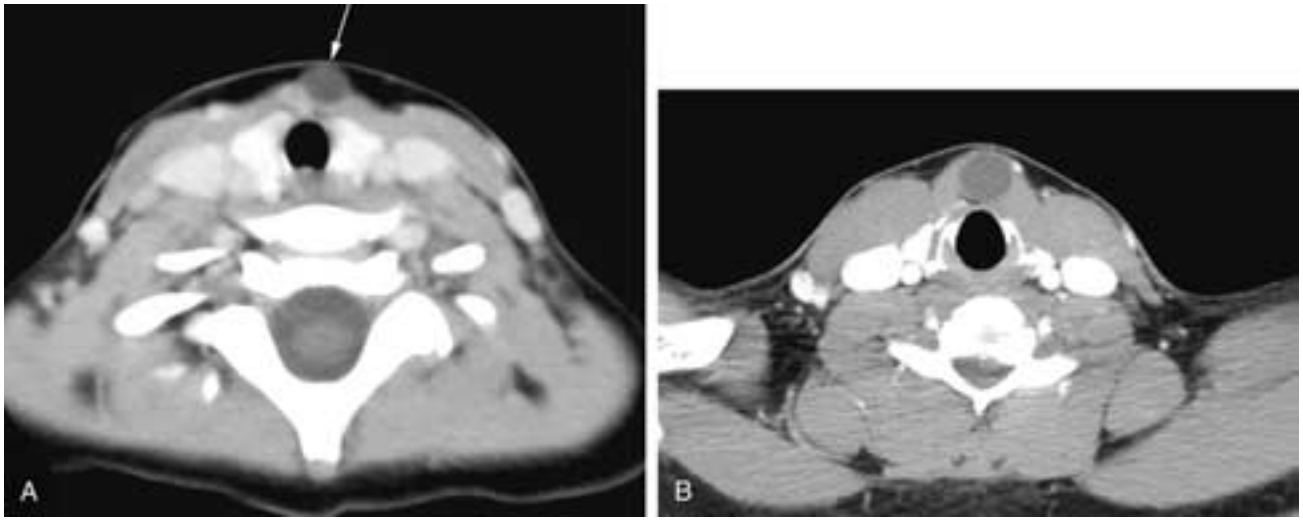

VIEW IMAGE

FIGURE 35-21 **A**, Axial contrast-enhanced CT scan shows a small midline cyst positioned superficial to the strap muscles (*arrow*). This is an unusual location for a thyroglossal duct cyst at this level of the neck. It illustrates that on occasion, such a variant will be encountered. The midline location should still suggest the diagnosis, despite the low neck location of the cyst. **B**, Axial contrast enhanced CT scan shows a midline cyst at the level of the upper trachea. As in Figure 35-21A, this is an unusual location for a thyroglossal duct cyst at this level of the neck.

VIEW IMAGE

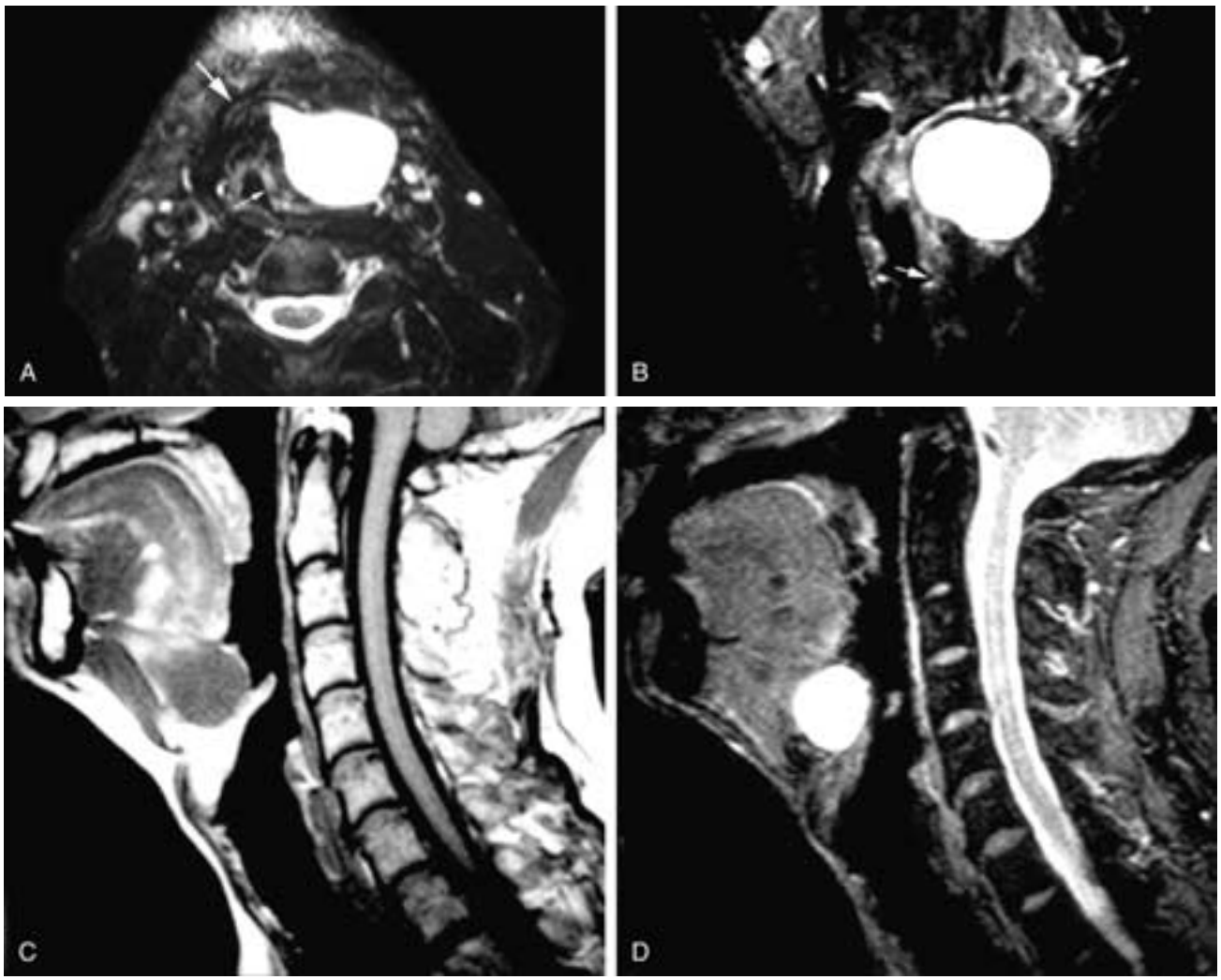

VIEW IMAGE

FIGURE 35-22 Axial (**A**) and coronal (**B**) T2-weighted MR images on a patient clinically thought to have a large submucosal laryngocele. In **A**, this high-attenuation cyst is seen to be in relationship to the dorsal aspect of the hyoid bone (*large arrow*) and to displace the supraglottic mucosa (*small arrow*) medially. In **B**, the cyst is seen to be cranial to the laryngeal ventricle (*arrow*), with no connection to the ventricle or any laryngeal appendix. This was a large thyroglossal duct cyst. Sagittal T1-weighted (**C**) and T2-weighted (**D**) MR images show a cyst in the vallecula with low T1-weighted and high T2-weighted signal intensity. This cyst is on the mucosal surface of the pharynx, and it is not within the tongue base. This is a vallecular or retention cyst, and its location is common for such cysts.

Copyright © 2003, Mosby, Inc. All rights reserved.

truly considered ectopic thyroid tissue, there must be no connection between the ectopic tissue and the normal thyroid bed.[60]

During normal embryogenesis, the thyroid anlage is adherent to the aortic root, which enables the thyroid tissue to descend until it interacts with the laryngeal primordia. These thyroid cells can become trapped within the developing laryngeal cartilages, the membranes, or the surrounding pharyngeal constrictor muscles.[61] Abnormal adherence of thyroid cells to the developing heart can lead to deposition of thyroid tissue anywhere along the descent of the heart into the thorax, including the low neck, mediastinum, pericardium, or even within the heart itself.[62, 63] Thyroid cells adhering to the developing tracheoesophageal bud can also contribute thyroid tissue adjacent to the diaphragm.

In a patient with a lingual thyroid, especially one in a stressful situation such as pregnancy, a goiter may develop and present clinically as dysphagia, dysphonia, stridor, dyspnea, hemorrhage, or hoarseness.[64–67] The actual development of a malignancy in lingual thyroid tissue is considered to be rare. The topic of thyroid disease is discussed in detail in Chapter 40.

On CT, ectopic thyroid tissue usually has high attenuation because normally functioning thyroid tissue has an active transport mechanism that concentrates iodine about 100 times over the serum concentration (Figs. 35-23 to 35-26). In addition, on contrast CT studies, the normally hypervascular thyroid tissue strongly enhances. The diagnosis is somewhat more difficult on MR imaging since the thyroid tissue is not as distinctly identified as on CT. On MR imaging, thyroid tissue is isointense to slightly hyperintense relative to muscle on both T1- and T2-weighted images and, as with CT, the thyroid does enhance strongly after contrast administration.

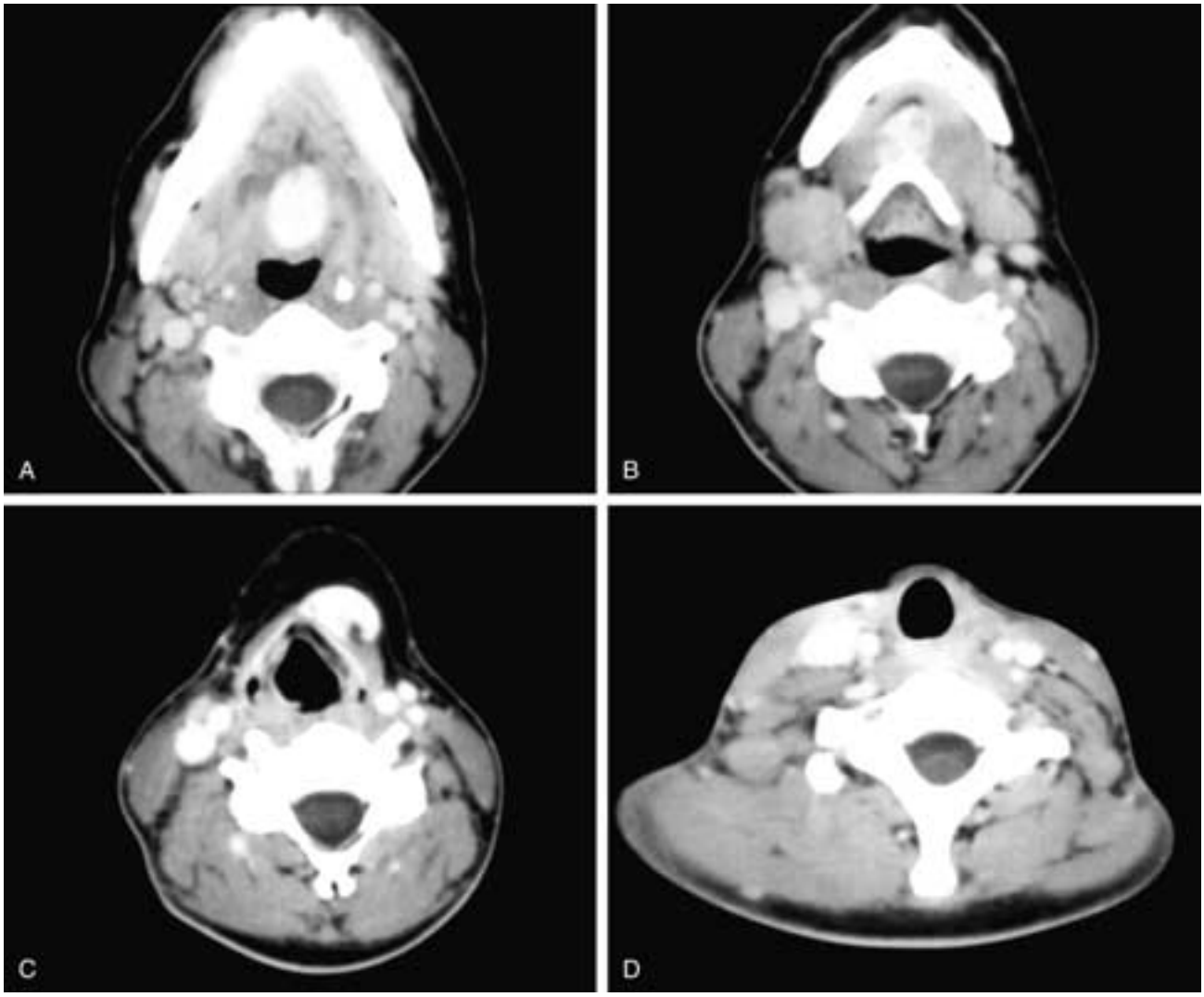

VIEW IMAGE

FIGURE 35-23 Serial axial contrast-enhanced CT scans from cranial (**A**) to caudal (**D**). In **A**, an enhancing mass is seen in the midline of the tongue. This was lingual thyroid tissue. In **B**, similar tissue is seen in the midline at the level of the hyoid bone. In **C**, similar tissue is seen adjacent to the outer contour of the thyroid cartilage and partially deep to the strap muscles. In all of these cases this was ectopic thyroid tissue, paralleling the location of the thyroglossal duct cysts in Figures 35-14 to 35-21. In **D**, there was no thyroid tissue in the normal location of the thyroid bed. This occurs in about 80% of patients with lingual thyroid tissue.

Copyright © 2003, Mosby, Inc. All rights reserved.

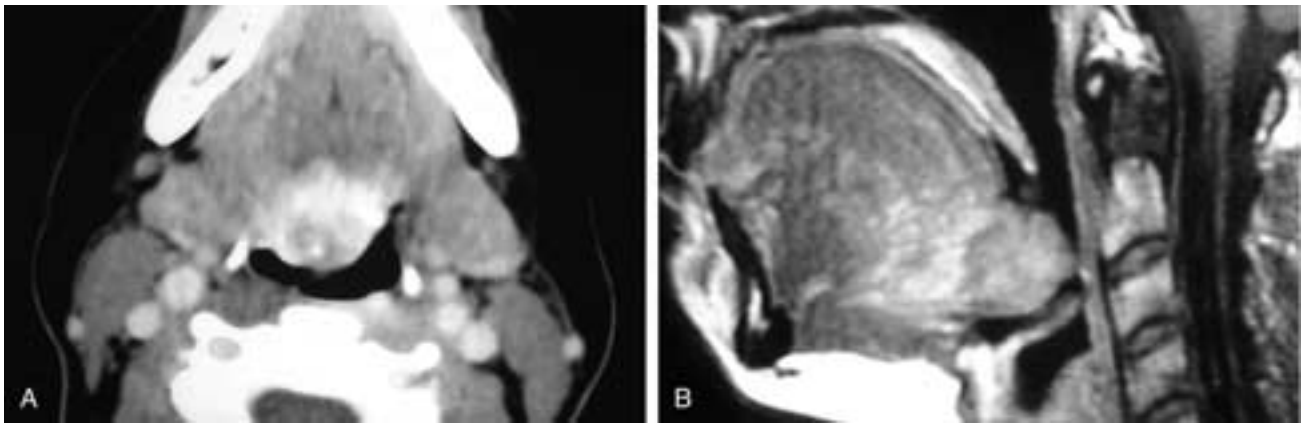

VIEW IMAGE

FIGURE 35-24 Axial contrast-enhanced CT scan (**A**) and a sagittal T1-weighted MR image (**B**) on a woman who developed dysphagia 1 week after delivering her first child. There is an enhancing mass in the midline base of the tongue. This was a goiter in a lingual thyroid, a fairly common occurrence in pregnant women. After surgery, pathologic examination revealed a focus of papillary thyroid carcinoma within the goiter.

Once a lingual thyroid is identified, one should always check the normal thyroid bed for the presence of any thyroid tissue. In 70% to 80% of these cases, the lingual thyroid is the only functioning thyroid tissue. Thus its complete removal, without any thyroid tissue reimplantation, will lead to permanent hypothyroidism and the need for thyroid replacement medication for the remainder of the patient's life. Nuclear thyroid scanning, usually with technetium 99m pertechnetate, can also identify the location of any ectopic thyroid tissue. Such imaging will visualize a small site of ectopic thyroid, provided that no dominant normal thyroid tissue is present in the neck. The presence of such normal thyroid tissue will trap virtually all of the radionuclide, making isotopic identification of ectopic thyroid tissue unlikely.

Ectopic Thyroid Originating from the Lateral Anlage

Ectopic thyroid tissue arising from the lateral anlage is extremely rare. As previously described, the lateral lobes of the thyroid receive contributions from the ventral aspect of the fourth through sixth branchial pouches. They migrate laterally around the developing laryngeal primordia to adhere to the median bilobed thyroid anlage. Although unproven, one theory postulates that endoderm originating from the caudal pharyngeal complex does not form thyroid tissue unless there is an interaction with the median anlage. The lateral thyroid anlage also has a less complicated embryology than the median thyroid anlage, including a

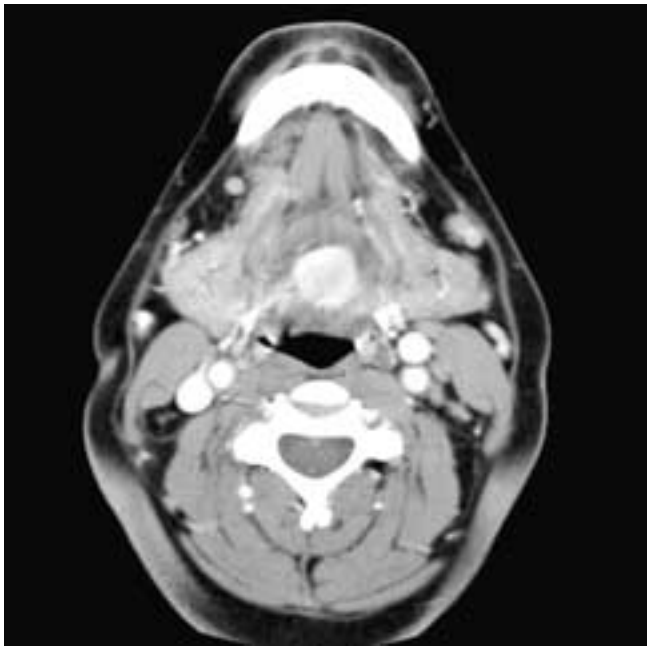

VIEW IMAGE

FIGURE 35-25 Axial contrast-enhanced CT scan shows an enhancing midline mass in the caudal posterior tongue. This was lingual thyroid tissue.

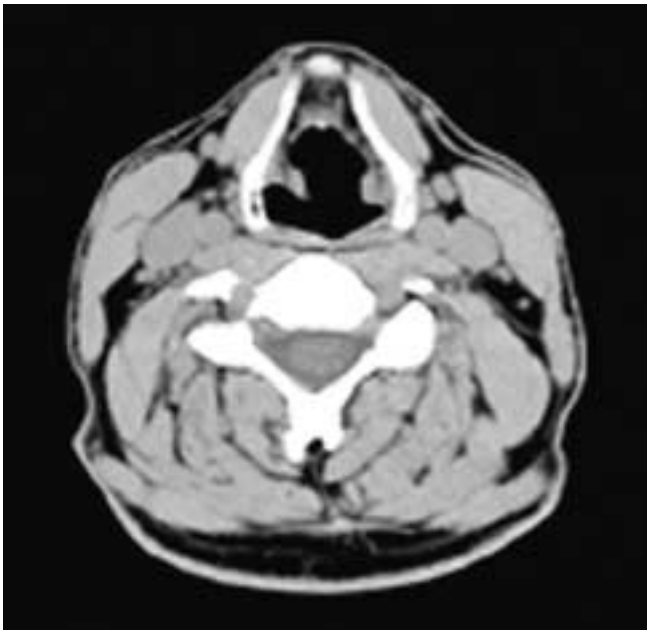

FIGURE 35-26 Axial CT scan shows a small, dense mass in the superior thyroid notch region of the larynx. This was ectopic thyroid tissue.

VIEW IMAGE

Copyright © 2003, Mosby, Inc. All rights reserved.

shorter distance to travel during development. These concepts could account for the rarity of ectopic tissue arising from the lateral thyroid anlage. Their pathogenesis is similar to that of the median anlage, and abnormal migration can lead to thyroid cells being left behind in the lateral neck or lateral floor of the mouth.[68] Lateral thyroid anlagen can also adhere to, or be trapped by, the developing neck musculature, vessels, lymph nodes, or laryngeal primordium. When trapped by the developing cartilages, membranes, and musculature of the laryngotracheal primordia, these ectopic clusters of thyroid tissue can migrate abnormally to the posterolateral wall of the trachea, the esophagus, or even the retroesophageal region.[61, 69, 70] Cells can also adhere to the developing nasopharyngeal diverticulum, which originates at the posterior aspect of the cervical foregut. This can lead to abnormal migration of ectopic thyroid to the nasopharynx.

Lateral ectopic thyroid tissue poses a unique problem in the setting of a known thyroid malignancy.[62] In some circumstances, exclusion of metastasis is straightforward. If an ectopic thyroid nodule is attached to the gland by a fibrous band, it can be considered a congenital group of cells pulled away from the thyroid during development. Similarly, thyroid tissue within the neck, not attached to the thyroid gland or lymph nodes, can be considered ectopic and due to abnormal migration of the lateral anlage. However, the presence of thyroid tissue within lymph nodes is a less clear-cut issue. It is well known that differentiated thyroid malignancy can frequently metastasize to lymph nodes. Although it is possible for ectopic thyroid tissue to be incorporated into a lymph node during normal embryogenesis, whenever such tissue is identified, it should be considered metastatic disease until proven otherwise.

Neoplasms Arising within Thyroglossal Duct Cysts

The literature on this subject was reviewed in 1988 by McNicoll et al.[71] Of the 133 reviewed cases, 89% were papillary or mixed papillary-follicular carcinoma, 7% squamous cell carcinoma, 2% adenocarcinoma, 1% follicular carcinoma, and 1% anaplastic carcinoma. Overall, carcinoma arising in a thyroglossal duct cyst occurs in less than 1% percent of the cases, and the diagnosis of malignancy is usually made postoperatively.[72, 73] If the malignancy is entirely within the resected cyst, simple cyst resection is considered adequate surgical treatment. Wider excision is considered necessary if the neoplasm extends beyond the cyst wall. Treatment remains controversial. Of the patients who underwent thyroidectomy for papillary or follicular carcinoma within a thyroglossal duct cyst, 11% had carcinoma in the native thyroid gland. The prognosis appears to be similar to that of the same malignancy when it occurs in normally located thyroid tissue.[72, 73]

On imaging, most of these cases appear to be normal cysts, with no evidence of a malignancy. However, a localized mass visualized in a portion of the cyst wall should suggest the possibility of a malignancy, while invasion of the adjacent soft tissues, without a history of infection, should strongly suggest that a neoplasm is present within the cyst (Fig. 35-27).

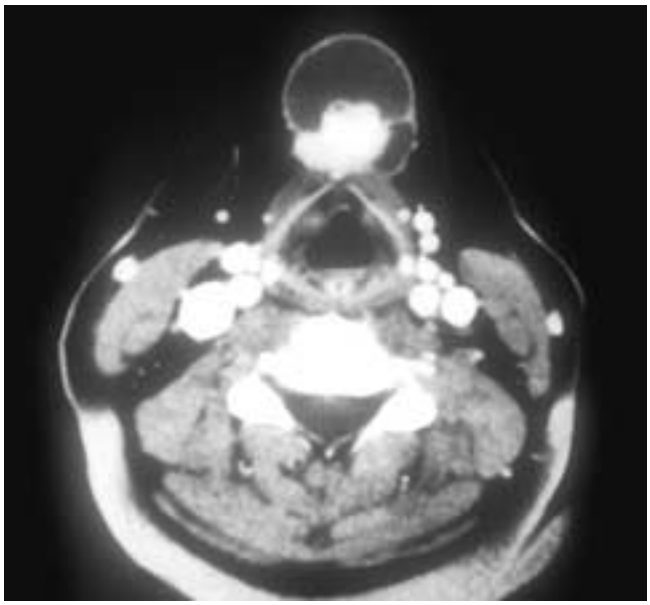

FIGURE 35-27 Axial contrast-enhanced CT scan shows a midline cyst just caudal to the level of the hyoid bone. Within the cyst is an enhancing nodule and there is some infiltration of the adjacent strap muscles. This was a papillary thyroid carcinoma within a thyroglossal duct cyst. At surgery, there was extension of the tumor into the strap muscles.

VIEW IMAGE

Neoplasms Arising within Ectopic Thyroid

Carcinoma arising in ectopic thyroid tissue is extremely rare.[74] Although the reported cases are few, they appear to involve the same cell types that affect the thyroid gland. Almost all reported cases are mixed papillary and follicular carcinoma.

The neural crest cells migrate to many areas in the body and are the origin for many polypeptide- or hormone-producing cells including those of the adrenal medulla.[75, 76] As described in Chapter 33, the parafollicular C cells of the lateral lobes of the thyroid gland are neural crest derivatives that secrete calcitonin, and medullary thyroid carcinoma arises from these cells. Most such tumors arise spontaneously, but they can also be part of the familial (autosomal dominant) multiple endocrine neoplasia syndromes (MEN types II and III). Medullary thyroid carcinoma is discussed in detail in Chapter 40.

Imaging the Postoperative Sistrunk Procedure

If a patient has had a Sistrunk procedure, on imaging a portion of the hyoid bone will have been resected and the space filled with fibrofatty tissue (Fig. 35-28). When seen, this classic imaging appearance indicates that the patient had surgery for a thyroglossal duct cyst.

CONGENITAL MALFORMATIONS OF THE CERVICAL LYMPHATIC SYSTEM

Lymphangiomas are congenital lymphatic malformations that comprise 5.6% of all benign lesions of infancy and childhood. They have no predilection for either sex or any

Copyright © 2003, Mosby, Inc. All rights reserved.

race.[77–79] From 50% to 60% of these lesions are present at birth, and nearly 80% to 90% are detected by the age of 2 years. Although the lesions that occur within the first 2 years of life may be unilocular, most are multilocular. In up to 10% of patients, lymphangiomas may not be discovered until adulthood, and only a few cases have been reported as late as the fifth decade of life. These latter lesions are most often unilocular, and there is some evidence that these adult lymphangiomas may not be congenital but rather posttraumatic in origin. They frequently present as a painless soft or semifirm mass.

Hemorrhage into the cystic spaces may cause rapid enlargement, and the mass effect of the lesion may cause compression of adjacent structures and lead to symptoms such as dysphagia, dyspnea, stridor, or pain.[5] Although the lesion tends to surround and sometimes invade normal anatomic structures, it has no malignant potential. Surgical excision is the treatment of choice, with a recurrence rate of up to 15%. More recently, new attempts to sclerose these lesions with agents such as OK-432 have met with more success than in the past.[80]

Typical lymphatic malformations cause little serious threat to life. However, due to aberrant peripheral lymphatics, nuchal cystic hygromas discovered in utero may have a poor prognosis when associated with Turner's syndrome and fetal hydrops. It has also been suggested that involution of a cervical lymphangioma in utero may be the origin of the ''wed neck'' associated with Turner's syndrome.[19]

The embryology of the lymphatic system is discussed in detail in Chapter 33. Familiarity with it allows an understanding of the pathogenesis and imaging appearance of congenital lymphatic malformations (lymphangiomas).

Theories of Pathogenesis

Three major theories have been proposed to explain the pathogenesis of lymphangiomas, and each of these theories helps us better understand the imaging appearance of these lesions.[81] These theories are as follows:

1. Failure of the primordial lymphatic sacs to drain into the veins: According to this theory, failure of the lymphatic sacs to drain into the veins results in dilation of the isolated lymphatic channels, which may eventually form lymphangiomas, particularly the larger, more central cystic hygromas.[81]
2. Abnormal sequestration of lymphatic tissue: According to this theory, abnormal sequestration of lymphatic tissue occurs early in embryogenesis.[82] This tissue subsequently fails to join the normal, more central lymphatic channels, and consequently lymphangiomas are formed. This theory helps explain the morphology of the more peripheral lesions such as capillary and cavernous lymphangiomas. The smaller lymphatic channels and the smaller overall size of these lesions are likely related to their primordium, which is a fine meshwork of lymphatic channels, the terminal branches of the lymphatic system.
3. Abnormal budding of the lymphatics: According to this theory, these aberrant buds lose their connections with the lymphatic primordia and eventually canalize to form lymph-filled cysts.[83] These cysts maintain their ability to branch and grow, and do so in an uncontrolled, disorderly manner. They have a strong tendency to penetrate and destroy normal anatomic structures. This theory helps explain the branching and permeative growth pattern of many lymphatic malformations, particularly the cavernous lymphangiomas. An aberrant primary bud arising directly from a primordial lymphatic sac is the likely explanation for the formation of a cystic hygroma near, but not in, the exact location of a primordial lymphatic sac.

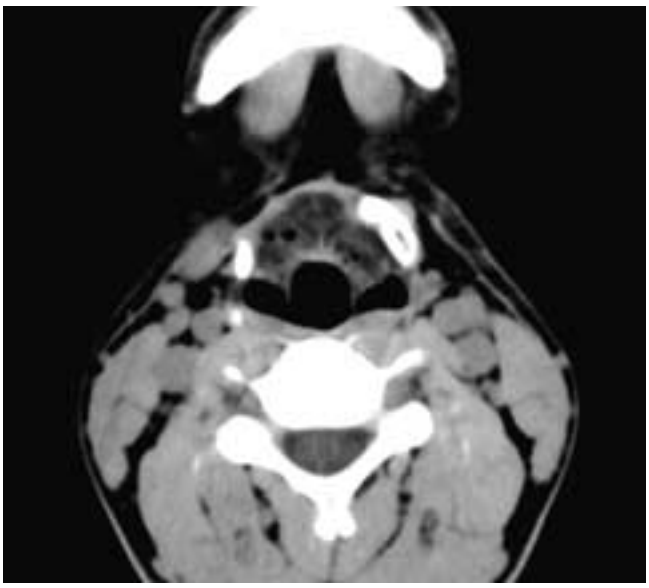

FIGURE 35-28 Axial CT scan on a patient who has had a Sistrunk procedure for a thyroglossal duct cyst. The body and a portion of the right greater cornu were resected.

VIEW IMAGE

Classification of Lymphangiomas

There are four histologic types of lymphangioma: cystic hygroma or lymphangioma, cavernous lymphangioma, capillary or simple lymphangioma, and vasculolymphatic malformation or lymphangiohemangioma. For at least two reasons, it is best to consider these four types of lymphangioma under a unified concept, as representing a spectrum of manifestations of the same pathologic process. First, combinations of these four types can often be seen in a single lesion. Second, these four types are differentiated from one another merely on the basis of the size of their lymphatic spaces. In all other respects, they are virtually pathologically identical, as all four types are composed of endothelium-lined lymphatic channels that are separated by connective tissue stroma.

The anatomic location of the lymphatic abnormality may also be very important in determining the histologic characteristic. Bill and Summer suggested that the loose fatty tissue in the axilla, neck, and chest may allow relatively unlimited growth of the lymphatic anomaly, leading to the formation of a cystic hygroma.[84] The subcutaneous portions of the lips, cheek, and tongue, however, permit only a more limited expansion, possibly resulting in a cavernous lymphangioma. Finally, in the tougher dermal and epidermal elements, expansion is further limited, possibly result-

Copyright © 2003, Mosby, Inc. All rights reserved.

ing in the formation of a capillary lymphangioma (e.g., lymphangioma circumscription congenitale).

Cystic Hygroma

Cystic hygroma, or cystic lymphangioma, is the most common form of lymphangioma. It consists of hugely dilated cystic lymphatic spaces. As mentioned, 75% of these malformations occur in the neck, particularly within the posterior triangle of the neck, and up to 10% of these nuchal hygromas may extend into the mediastinum. An additional 20% of these lesions are found in the axilla, and 5% arise in the mediastinum. Rarer locations include the retroperitoneum, abdominal viscera, and groin, although they can arise in any portion of the lymphatic system. These malformations tend to occur in or near the location of the primordial lymphatic sacs from which they presumably arise (jugular, axillary, internal thoracic, etc).

Cystic hygromas are often isolated malformations in which the remainder of the lymphatic system is normal. They may, however, be associated with a more generalized process, including an abnormally developed peripheral lymphatic system.

Fetal cystic hygromas occur most commonly in the posterior triangle of the neck. They are associated with abnormal peripheral lymphatics and varying degrees of lymphedema, and the prognosis worsens in the presence of fetal hydrops. They are frequently seen in aborted fetuses with Turner's syndrome. Smith believed that fetal cystic hygromas form when the juguloaxillary lymphatic sac fails to drain into the internal jugular vein.[85] He suggested that the accumulation of lymphatic fluid within a progressively dilating juguloaxillary lymph sac leads to the formation of the cystic hygroma. Secondary dilatation of the lymphatic channels draining the chest and extremities occurs, and peripheral edema and hydrops result. This series of events has been termed the *jugular lymphatic obstruction sequence*.[85] As previously noted, if lymphatic drainage is established prior to fetal death, the cystic hygroma may regress and the neck webbing characteristic of Turner's syndrome can result.[86]

Van der Putte studied aborted fetuses with cervical cystic hygroma and Turner's syndrome and confirmed that no lymphaticovenous communications were present near the jugulosubclavian junctions on either side.[87] He also found no communication between the juguloaxillary sac and the internal thoracic sac, paratracheal sac, or thoracic duct. Shaub and Wilson also helped prove this cause-and-effect relationship between failed lymphaticovenous communication and generalized lymphatic defects.[88] They described a fetus with a unilateral left cystic hygroma and edema of all body parts except the right arm. This pattern suggested that the left juguloaxillary lymph sac and the thoracic duct that emptied into it failed to communicate with the venous system, whereas the corresponding sac on the right and its tributaries formed normally due to adequate drainage into the venous system.

Van der Putte also noted that the peripheral lymphatics have a variable appearance in fetuses with nuchal cystic hygroma and Turner's syndrome. Increased numbers of very wide, valveless lymph vessels were seen in some fetuses, while in others, the extremities were devoid of lymphatic structures. Van der Putte concluded that the time in embryonic life at which the maldevelopment of the lymphaticovenous communication occurs is important in ultimately determining which portions of the lymphatic system will be hypoplastic. If the maldevelopment occurs early, a more hypoplastic system may be seen, since the wide, valveless lymphatic sprouts have not had time to reach the periphery. If the maldevelopment occurs late enough to allow these sprouts to reach the periphery but before further arborization occurs, the wide, valveless channels persist.[87]

Van der Putte also theorized that the disorder of lymphatic outgrowth is related to a chromosomal anomaly and mechanical factors. High pressures in the peripheral tissues have been shown to inhibit lymphatic growth, which sets up a vicious cycle of impaired lymph flow, lymphedema, and inhibition of lymphatic growth with a further diminution in lymph flow. Mechanical factors, however, are negligible in malformations of the juguloaxillary lymph sac, since the lower pressures within the loose, fatty connective tissue of the neck allow significant lymphatic sprouting and extension.

The differential diagnosis of a large neck mass identified in utero includes lymphangioma, teratoma, and possibly epidermoid.[89] Such imaging can be accomplished with either ultrasound or MR imaging and allows any compromise of the fetal airway to be assessed so that appropriate precautions for immediate intubation can be taken at the time of birth.

An isolated cystic hygroma may develop when one of several potential lymphaticovenous anastomoses fails to form. The resultant malformation is in or near the location of the primordial sac from which it arose. However, as long as the remainder of the lymphatic system is connected and the other lymphaticovenous anastomoses form, the remainder of the lymphatic system should drain well. Yet, an isolated cystic hygroma could develop even if the failed anastomosis involves the left juguloaxillary lymph sac, which is often responsible for the lymphatic drainage of most of the body. This is not unexpected, since the thoracic duct has more than one venous communication in 75% of all cases.[90] Connections with the venous system may also persist in other lymph vessels. These additional connections allow adequate lymphatic drainage for the rest of the body, thus preventing the jugular lymphatic obstruction sequence and fetal death.

An isolated cystic hygroma can also form if an aberrant bud loses its connection with the primordial lymph sac from which it arose. In conjunction with a normal lymphaticovenous communication, this situation also leads to the development of an isolated cystic hygroma in a patient with an otherwise normal lymphatic system.

In adults, solitary cystic hygromas can occur in the posterior triangle of the neck and in the submandibular triangle. These isolated lesions are cured by surgery and may be posttraumatic in origin.

On imaging, cystic hygromas typically are multiloculated cystic masses in the posterior triangle of the neck in a child or young adult. Rarely in uncomplicated cases is a cyst wall actually seen. However, if there has been infection within the lesion, the cyst wall thickens and enhances, and there is inflammatory infiltration of the adjacent fat planes (Figs. 35-29 through 35-31). On CT, the cyst content is typically of mucoid attenuation (10 to 25 HU) (Fig. 35-29). Fluid-fluid

Copyright © 2003, Mosby, Inc. All rights reserved.

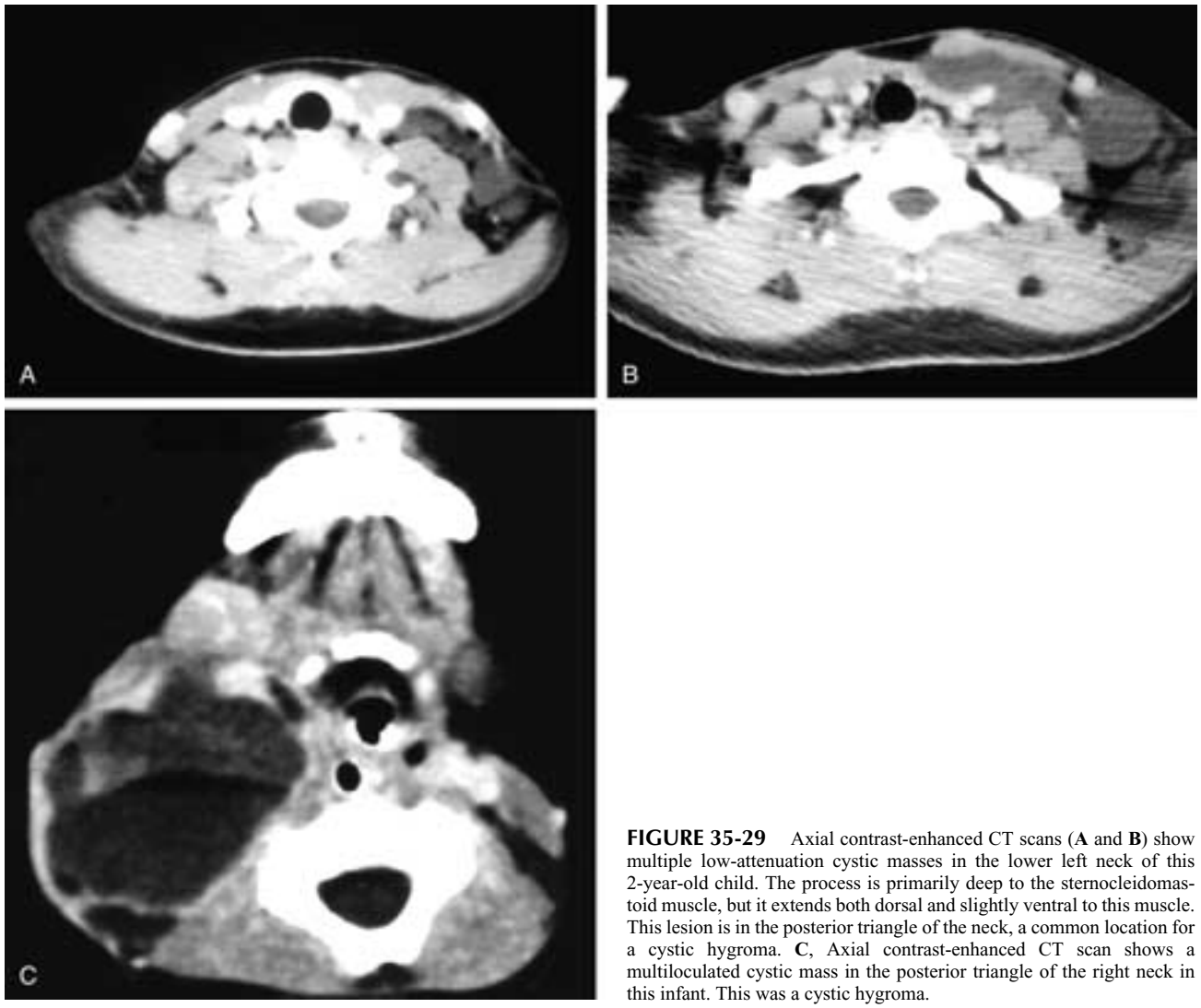

FIGURE 35-29 Axial contrast-enhanced CT scans (**A** and **B**) show multiple low-attenuation cystic masses in the lower left neck of this 2-year-old child. The process is primarily deep to the sternocleidomastoid muscle, but it extends both dorsal and slightly ventral to this muscle. This lesion is in the posterior triangle of the neck, a common location for a cystic hygroma. **C**, Axial contrast-enhanced CT scan shows a multiloculated cystic mass in the posterior triangle of the right neck in this infant. This was a cystic hygroma.

VIEW IMAGE

levels may be seen after hemorrhage into the lesion. On MR imaging, typically there is low T1-weighted signal intensity, but this may vary between low and high signal intensity. There almost always is high T2-weighted signal intensity. If hemorrhage has occurred, fluid-fluid levels are best seen on MR imaging; in fact, the appearance of a multicystic mass with fluid-fluid levels is characteristic of this lesion (Fig. 35-32).[77, 78, 91] Since blood entering these cysts does not clot, the fluid-fluid levels actually represent separation of fluids based on specific gravity. If a parotid lymphangioma hemorrhages, the lesion can become sufficiently rigid to cause facial nerve paresis and simulate an aggressive tumor (Fig. 35-33).[92] This subject is discussed in more detail in Chapter 39.

Cavernous Lymphangioma

Cavernous lymphangioma is a subcutaneous lesion composed of mildly dilated cavernous lymphatic spaces that are smaller than those of a cystic hygroma but larger than those of a capillary lymphangioma. These lesions also tend to be larger than capillary lymphangiomas. Cavernous lymphangioma commonly occurs in the tongue, floor of the mouth, or salivary glands. The margins of the lesion are not discrete, and the lesion tends to penetrate but not destroy contiguous structures such as muscles, glands, vessels, and nerves (Fig. 35-34).

These lymphatic malformations form during the last phase of lymphatic development, which occurs between the ninth and tenth weeks of gestation, when sprouts are sent in all directions to permeate all tissues. The lesion forms from an abnormally sequestered mesenchymal bud that loses its connection with the more central lymphatic channels but maintains its ability to branch and grow. It is believed that the prevalence of these lesions in the tongue and parotid gland, and the relative absence of cystic hygromas in these regions, are secondary to the cavernous lymphangioma's being a lesion that arises from the more peripheral, finely branched portions of the lymphatic primordium, and the fact that the tongue musculature and glandular tissues offer more resistance to growth than do the loose fatty connective tissues of the neck in which cystic hygromas tend to form.

Copyright © 2003, Mosby, Inc. All rights reserved.

Capillary Lymphangioma

The capillary or simple lymphangioma (lymphangioma simplex) is the least common form of lymphangioma and has the most diminutive lymphatic channels. This lesion is composed of a network of small lymph vessels that can be differentiated from capillaries by the absence of red blood cells, pericytes, and a basement membrane. The lymphatic endothelial cell cytoplasm is also extremely thin. The lesion occurs predominantly within the epidermis and/or dermis as a wart or a group of small vesicles. Most of the vesicles are white or pink, but a few can have a more dark red or purplish color. These cutaneous lesions may be further subdivided into two main groups, classic and localized.[93]

Although the classic form can occur anywhere on the body, it tends to develop over the proximal portions of a limb and the adjacent trunk. Involvement of the upper arm, axilla, and adjacent chest is especially common. The superficial vesicles described above are connected via lymphatic channels to larger dilated lymphatic spaces called cisterns. These cisterns are often surrounded by a muscular coat, the contractions of which may cause further dilation of the superficial vesicles with which the cisterns communicate. The relatively smaller component on the skin surface can mask an underlying lesion that may reach considerable size.

The localized form has no predilection for any definite area. It also differs from the other lymphangiomas by presenting at any age. Twenty-five percent of the cases are first seen in patients older than 45 years of age. This superficial epidermal lesion typically involves a discrete area of approximately 1 cm^2. The term *lymphangioma circumscriptum* was formerly used to describe all cutaneous lymphangiomas, but now it is used to describe any localized capillary lymphangioma that measures less than 5 cm in diameter.[94] Some authors have also described a ''spongy'' form of lymphangioma that is now believed to be merely a localized capillary lymphangioma that occurs in mucous membranes, lips, eyelids, and the external auditory canal.[93, 95]

Capillary lymphangioma forms during the last part of embryonic development. As lymphatic sprouts follow the vasculature into the periphery, an abnormal bud encounters the relatively tougher connective tissue of the skin. This tends to inhibit subsequent growth of these lymphangiomas more so than do the musculature or glandular elements throughout which cavernous lymphangiomas grow. In addition, capillary lymphangiomas arise from the terminal branches of the lymphatic primordium, which constitute a fine meshwork of capillary-sized vessels.

After penetrating trauma, the heat of the penetrating object usually seals the lymphatic capillaries. However, if such a sealing does not occur, lymph can accumulate in the wound site and a posttraumatic lymphocyst can develop. Such cysts often become infected and on imaging thus have a thickened, enhancing rim (Fig. 35-35).

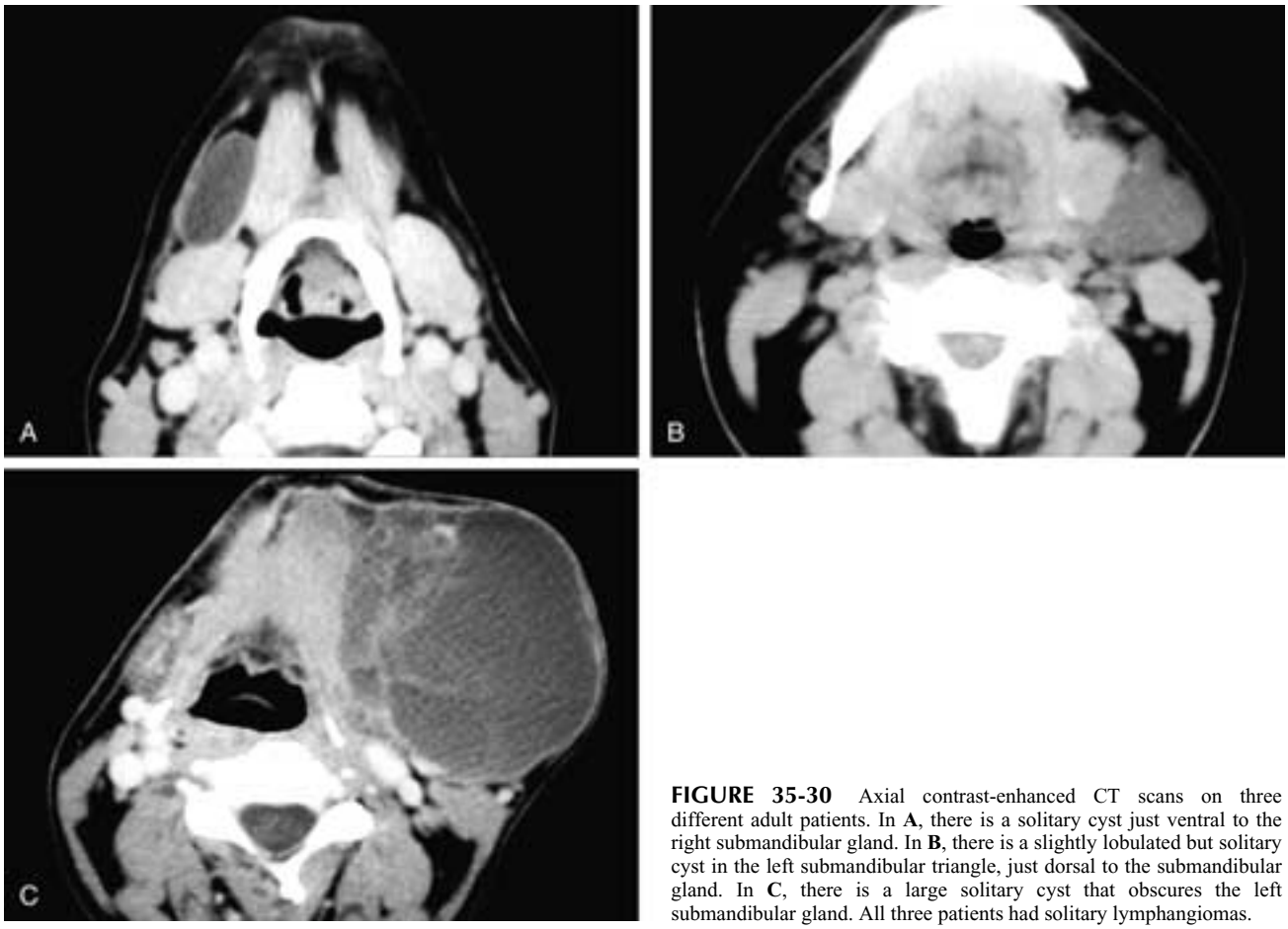

FIGURE 35-30 Axial contrast-enhanced CT scans on three different adult patients. In **A**, there is a solitary cyst just ventral to the right submandibular gland. In **B**, there is a slightly lobulated but solitary cyst in the left submandibular triangle, just dorsal to the submandibular gland. In **C**, there is a large solitary cyst that obscures the left submandibular gland. All three patients had solitary lymphangiomas.

VIEW IMAGE

Copyright © 2003, Mosby, Inc. All rights reserved.

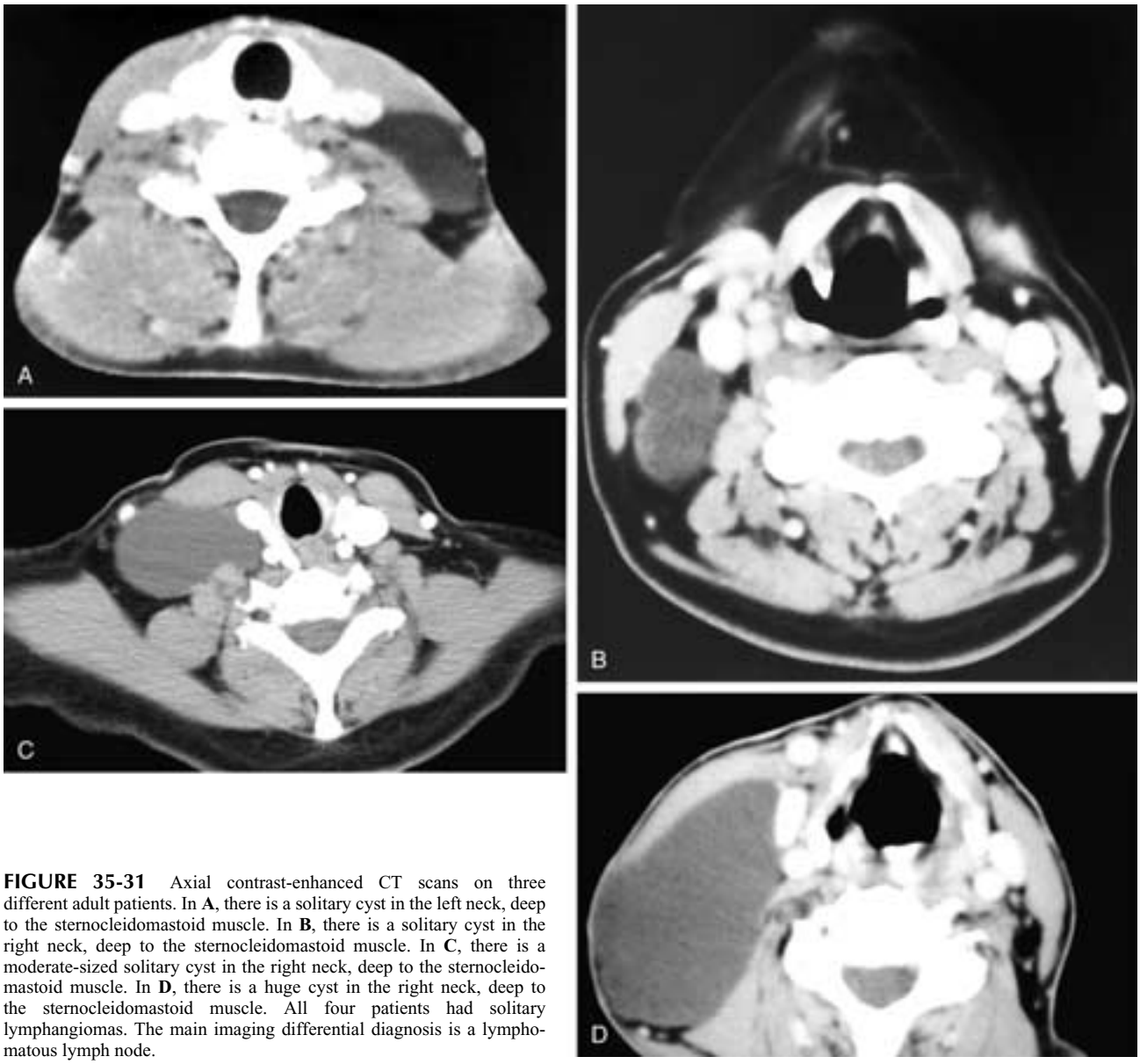

VIEW IMAGE

FIGURE 35-31 Axial contrast-enhanced CT scans on three different adult patients. In **A**, there is a solitary cyst in the left neck, deep to the sternocleidomastoid muscle. In **B**, there is a solitary cyst in the right neck, deep to the sternocleidomastoid muscle. In **C**, there is a moderate-sized solitary cyst in the right neck, deep to the sternocleidomastoid muscle. In **D**, there is a huge cyst in the right neck, deep to the sternocleidomastoid muscle. All four patients had solitary lymphangiomas. The main imaging differential diagnosis is a lymphomatous lymph node.

Vasculolymphatic Malformations

Vasculolymphatic malformations are composed of both lymphatic and vascular elements, and lymphangiohemangioma is a prime example. These lesions likely form from an abnormal bud that retains its original venous communication. For this reason, the mesenchyme of the venous structure and some vascular characteristics are maintained.

VASCULAR LESIONS

The classification of vascular lesions of the head and neck has been somewhat confusing in that overlapping terminology has made it difficult to compare certain lesions, follow their natural history, and plan appropriate treatment. In 1982, Mulliken and Glowacki proposed a classification for these vascular lesions that was based on their natural history as well as their cellular structure. This nomenclature provides insight into the natural history and management of these vascular lesions.[96] The authors identified two main categories of lesions: hemangioma and vascular malformations. The vascular malformations were, in turn, further subdivided into capillary, venous, arteriovenous, and lymphatic types.

Hemangiomas

Hemangiomas are neoplastic and exhibit increased proliferation and turnover of endothelial cells, mast cells, fibroblasts, and macrophages.[97] They are the most common tumors of the head and neck in infancy and childhood, accounting for approximately 7% of all benign soft-tissue tumors.[5, 98] Utilizing the classification proposed by Mulliken and Glowacki, the term *hemangioma* should be reserved

Copyright © 2003, Mosby, Inc. All rights reserved.

for those lesions that present in early infancy, rapidly enlarge, and ultimately involute by adolescence.[96]

Although they are rarely present at birth, hemangiomas typically become apparent during the first month of life.[98] Ninety-six percent of hemangiomas are clinically evident by the age of 6 months and about 80% occur as single lesions, with females being more commonly affected (4:1). One half of all hemangiomas resolve completely by 5 years of age, and 70% resolve by 7 years of age.[99]

Previously termed *strawberry hemangiomas*, these primarily superficial cutaneous hemangiomas are usually diagnosed clinically with ease. However, they may also occur as subcutaneous hemangiomas that extend deeply through the skin to infiltrate the underlying muscles, usually presenting as nonspecific soft-tissue masses. Osseous deformity or skeletal hypertrophy may be associated with these lesions, but intraosseous invasion is extremely uncommon.[100, 101] Clinically, these lesions present as either a diffuse skin lesion or a soft ''cystic'' mass in the oral cavity, pharynx, parotid gland, or neck. The deeper lesions usually exhibit characteristics such as compressibility, bluish discoloration of the overlying skin, bruits, and a change in size during crying or straining, and there may be other associated hemangiomas elsewhere on the body.[5]

The association of hemangiomas with a variety of intracranial arterial vascular anomalies has been reported as

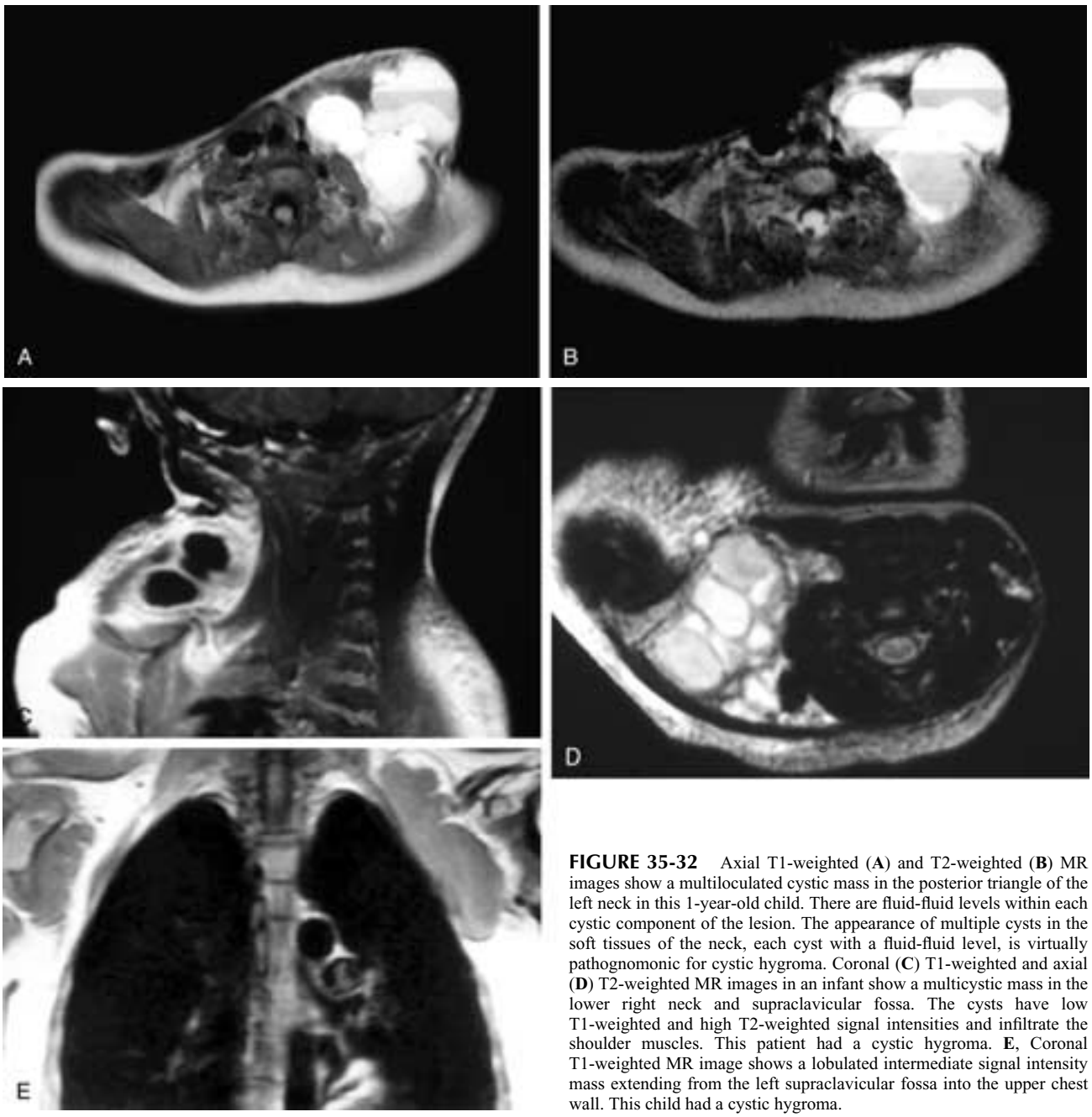

VIEW IMAGE

VIEW IMAGE

FIGURE 35-32 Axial T1-weighted (**A**) and T2-weighted (**B**) MR images show a multiloculated cystic mass in the posterior triangle of the left neck in this 1-year-old child. There are fluid-fluid levels within each cystic component of the lesion. The appearance of multiple cysts in the soft tissues of the neck, each cyst with a fluid-fluid level, is virtually pathognomonic for cystic hygroma. Coronal (**C**) T1-weighted and axial (**D**) T2-weighted MR images in an infant show a multicystic mass in the lower right neck and supraclavicular fossa. The cysts have low T1-weighted and high T2-weighted signal intensities and infiltrate the shoulder muscles. This patient had a cystic hygroma. **E**, Coronal T1-weighted MR image shows a lobulated intermediate signal intensity mass extending from the left supraclavicular fossa into the upper chest wall. This child had a cystic hygroma.

Copyright © 2003, Mosby, Inc. All rights reserved.

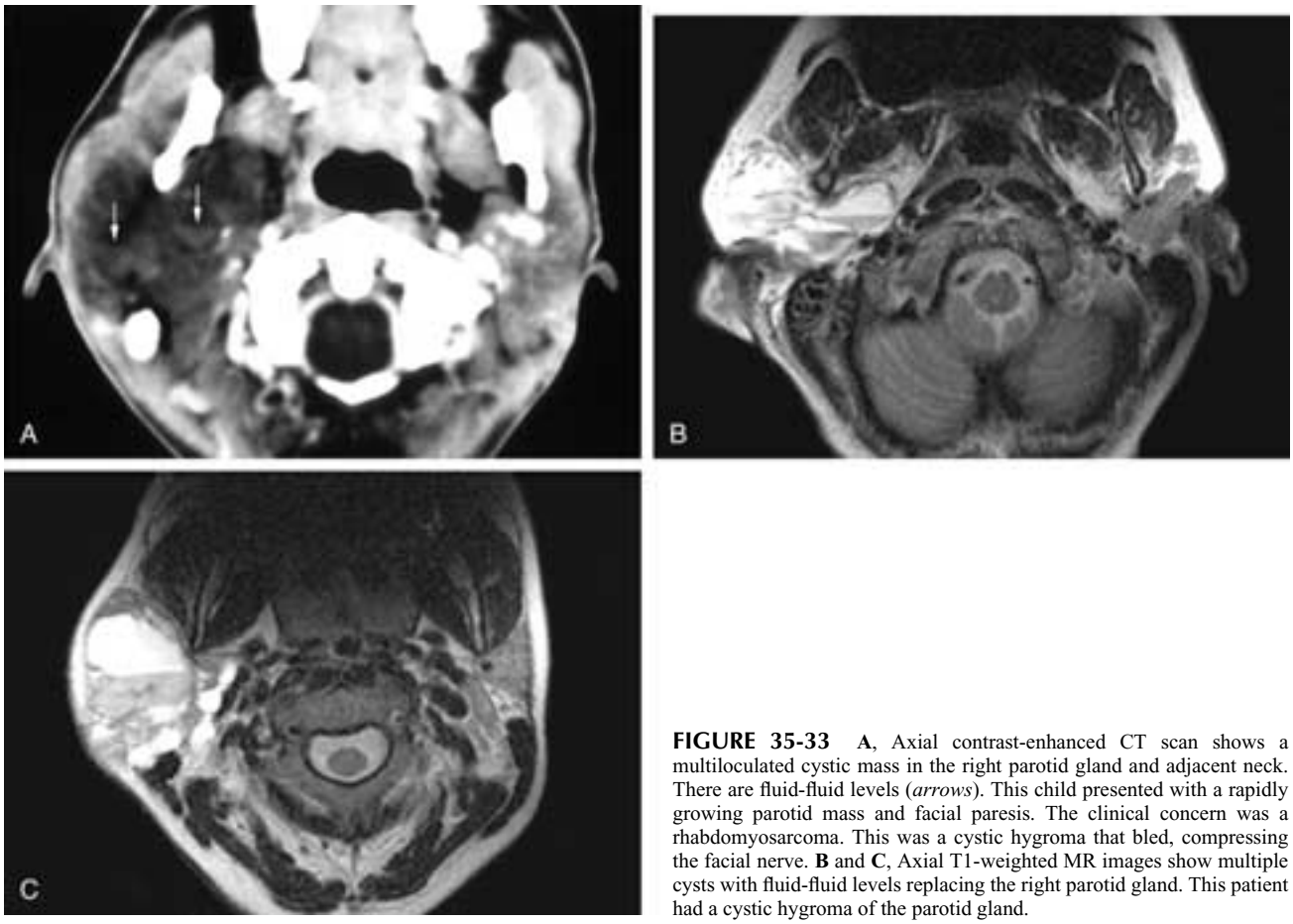

FIGURE 35-33 **A**, Axial contrast-enhanced CT scan shows a multiloculated cystic mass in the right parotid gland and adjacent neck. There are fluid-fluid levels (*arrows*). This child presented with a rapidly growing parotid mass and facial paresis. The clinical concern was a rhabdomyosarcoma. This was a cystic hygroma that bled, compressing the facial nerve. **B** and **C**, Axial T1-weighted MR images show multiple cysts with fluid-fluid levels replacing the right parotid gland. This patient had a cystic hygroma of the parotid gland.

VIEW IMAGE

the *cutaneous hemangioma–vascular complex syndrome*. There is an association between extensive craniofacial hemangiomas, these intracranial arterial vascular anomalies, and the presence of progressive occlusive cerebrovascular disease, with resultant cerebral infarction. One defined cluster of abnormalities associated with hemangiomas is referred to as the PHACE syndrome, consisting of posterior fossa abnormalities, facial hemangioma, arterial abnormalities, cardiovascular defects, and eye abnormalities, associated with a supraumbilical midline raphe.

Most hemangiomas require no treatment unless life-threatening complications occur. They usually present during the rapid proliferation phase and may be associated with a mortality rate as high as 20% to 30%. Complications may include Kasabach-Merritt syndrome (consumptive coagulopathy), compression of vital structures (i.e., airway), bleeding, and ulceration.

Hemangiomas are classified as high-flow lesions that are well circumscribed and angiographically exhibit a lobular pattern of intense, persistent tissue staining. The frequent arteriovenous shunting and high flow in these lesions may not permit their distinction from vascular malformations. On MR imaging, the solid component of the hemangioma demonstrates signal intensity isointense or slightly hyperintense to muscle on T1-weighted images, higher signal intensity on progressively more heavily T2-weighted scans, and enhancement following contrast administration (Fig. 35-36).[102, 103]

Vascular Malformations

Unlike hemangiomas, vascular malformations are not tumors. Rather, they are true congenital vascular anomalies that may not be clinically manifest until late infancy or early childhood. Their endothelial cell proliferation and turnover characteristics are normal, and they demonstrate slow, steady growth commensurate with the growth of the child. They also neither regress nor involute, and skeletal changes are more commonly associated with these vascular malformations (35%) than they are with hemangiomas. Rapid enlargement of these lesions is reported to occur in association with trauma, infection, or endocrine changes such as those occurring during puberty and pregnancy.[104, 105]

The vascular malformations are classified on the basis of their predominant type of anomalous vessels. Thus, there are the capillary, venous, arterial, and lymphatic malformations.[97, 101] A variety of therapies have been employed for the treatment of vascular malformations and rapidly enlarging hemangiomas, with varying degrees of success. These include steroid administration, laser photocoagulation, sclerotherapy, embolization, and surgical resection.[106–116]

Capillary Malformations

These lesions have been variably referred to as *port-wine stains, capillary hemangiomas*, and *nevus flammeus*.[117]

Copyright © 2003, Mosby, Inc. All rights reserved.

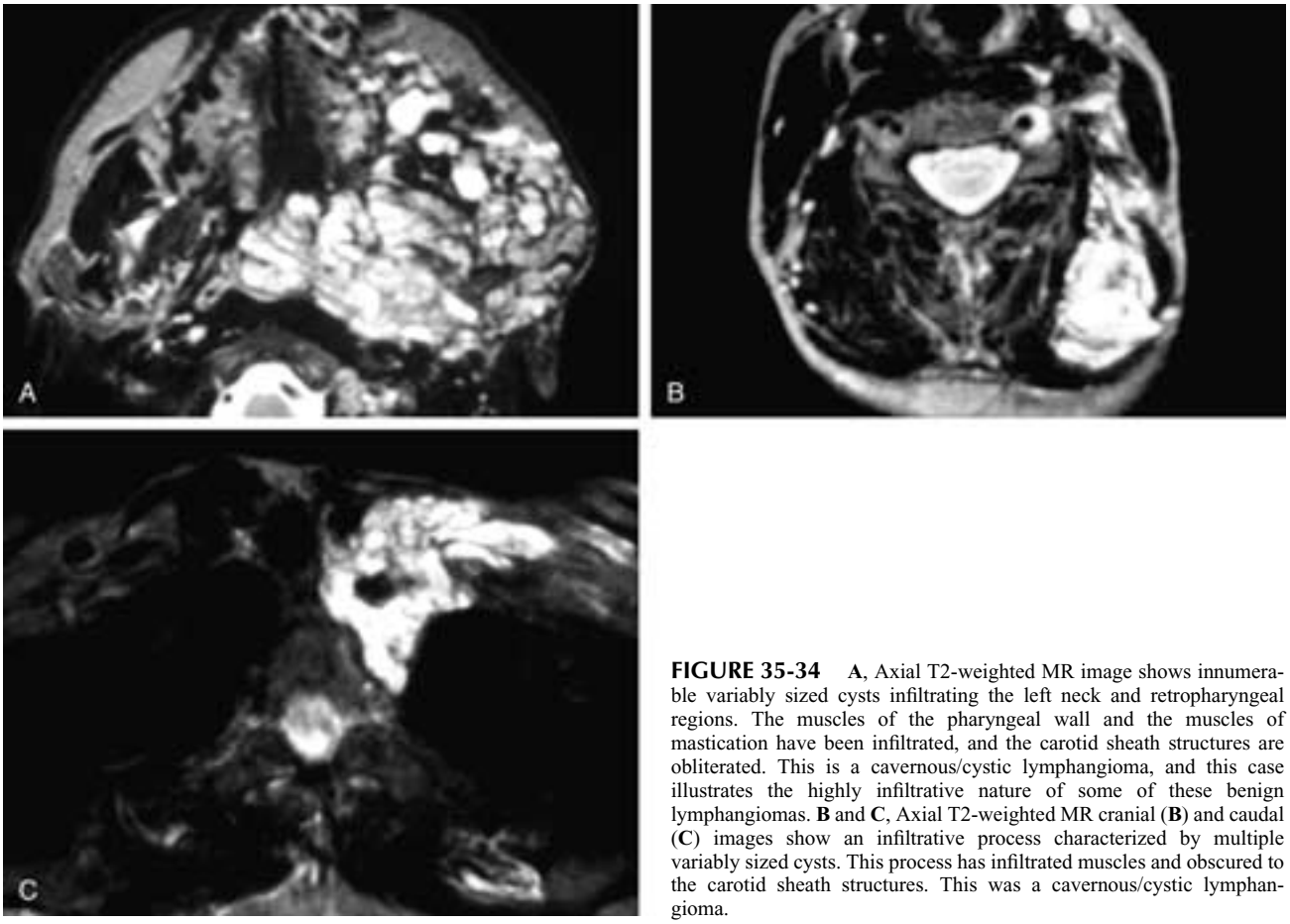

FIGURE 35-34 **A**, Axial T2-weighted MR image shows innumerable variably sized cysts infiltrating the left neck and retropharyngeal regions. The muscles of the pharyngeal wall and the muscles of mastication have been infiltrated, and the carotid sheath structures are obliterated. This is a cavernous/cystic lymphangioma, and this case illustrates the highly infiltrative nature of some of these benign lymphangiomas. **B** and **C**, Axial T2-weighted MR cranial (**B**) and caudal (**C**) images show an infiltrative process characterized by multiple variably sized cysts. This process has infiltrated muscles and obscured to the carotid sheath structures. This was a cavernous/cystic lymphangioma.

VIEW IMAGE

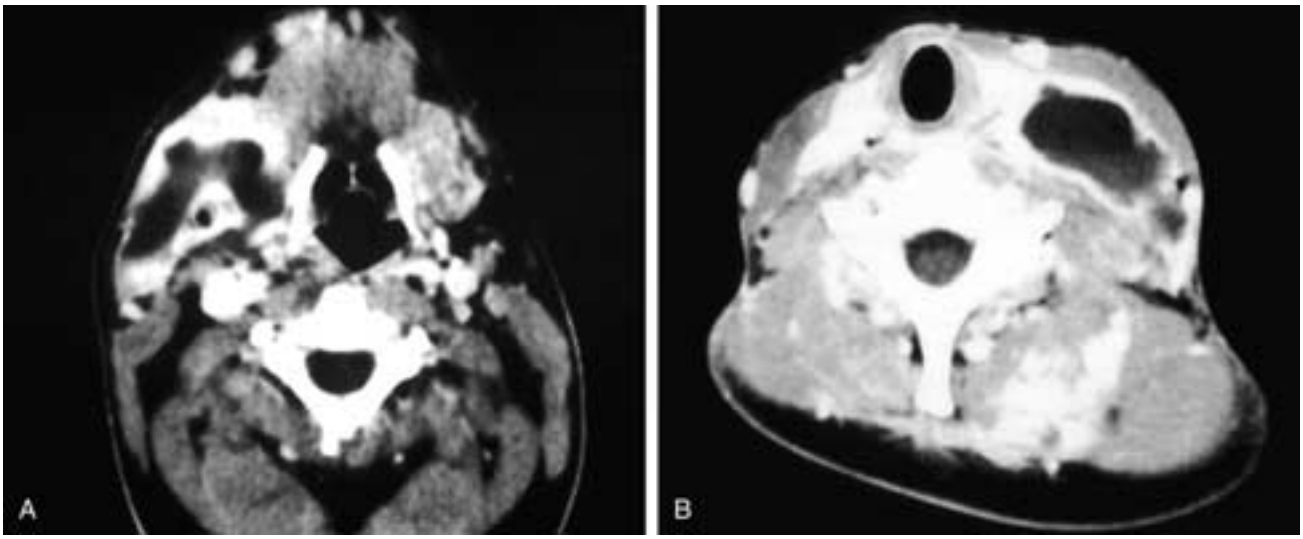

FIGURE 35-35 Axial contrast-enhanced CT scans on two different patients. In **A**, in the right neck, there is a slightly lobulated low-attenuation region surrounded by a thick zone of enhancement. This adult had been shot in the neck, and this mass developed 2 weeks later. At surgery, it was found to be an infected posttraumatic lymphangioma. In **B**, there is a cystic region in the left neck surrounded by a zone of enhancement deep to the sternocleidomastoid muscle. This adult had been stabbed in the neck, and this infected posttraumatic lymphangioma developed several weeks later.

VIEW IMAGE

Copyright © 2003, Mosby, Inc. All rights reserved.

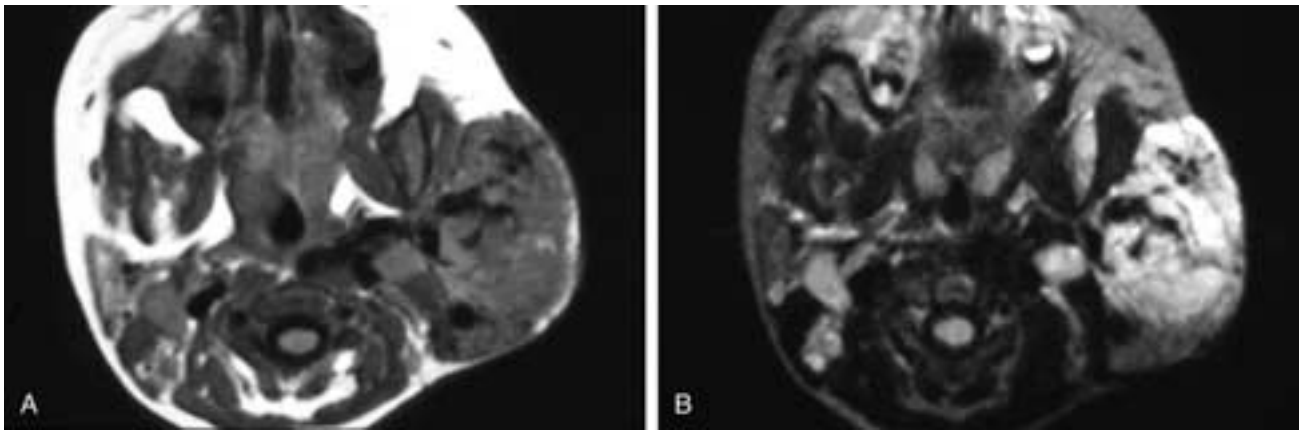

VIEW IMAGE

FIGURE 35-36 Axial T1-weighted (**A**) and T2-weighted (**B**) MR images show a large soft tissue mass replacing the ventral portion of the left parotid gland. Within the mass there are serpiginous vascular flow voids. This child had an hemangioma.

They are low-flow lesions that may be associated with the distribution of the trigeminal nerve as part of the Sturge-Weber syndrome. In this syndrome, these lesions also may involve, as an underlying vascular anomaly, the choroid plexus and leptomeninges. Other syndromes associated with capillary malformations include ataxia-telangiectasia (Louis-Barr) and Osler-Weber-Rendu (hereditary hemorrhagic telangiectasia), Wyburn-Mason (facial capillary malformation overlying retinal or optic pathway arteriovenous malformations), and Cobb (posterior thoracic capillary malformation overlying spinal cord arteriovenous malformations) syndromes.[97]

Venous Malformations

These lesions are occasionally erroneously termed *cavernous hemangiomas*, and unlike true hemangiomas, they may involve bone and they do not involute.[117] These lesions are the most common ones to affect the oral cavity and share many imaging features with subcutaneous hemangiomas. When located in the extracranial head and neck, these venous malformations may attain enormous size and cause airway compromise. Although they are predominantly soft-tissue masses, they may infiltrate deeply along fascial planes and, rarely, may be entirely intramuscular.[118, 119] Of all the skeletal muscle hemangiomas or venous malformations, approximately 14% occur in the head and neck region and in descending order involve the masseter, trapezius, and sternocleidomastoid muscles.[120, 121] On CT, these lesions typically show muscle attenuation on noncontrast images and variable patterns of enhancement on contrast studies.[122] Like their capillary counterparts, venous malformations are low-flow lesions that are supplied by small arteries. As a consequence of their slow blood flow, they may not demonstrate sufficient enhancement on CT to enable separation of their margins from the surrounding muscle, while angiographically, their arterial supply may not be identified.[123] On MR imaging, these lesions may appear very similar to deep hemangiomas in that they are either isointense or hyperintense to muscle on T1-weighted images, hyperintense to muscle on T2-weighted images, and typically enhance. The identification of discrete areas of homogeneous high signal intensity, representing venous lakes, or the presence of phleboliths may be extremely helpful in suggesting the diagnosis of a venous malformation (Figs. 35-37 and 35-38).[99, 123, 124]

Arterial Malformations

These lesions are high-flow malformations that result from abnormal blood vessel morphogenesis and arteriovenous malformations; fistulas are included in this category. The head and neck region is considered to be one of the more common sites for these congenital arterial malformations. Angiographically, arterial malformations are characterized by rapid flow and enlarged, tortuous arteries and draining veins. Parenchymal staining is unusual. On MR imaging, the enlarged arterial components appear as flow voids on T1- and T2-weighted images.

One subgroup of patients has combined vascular malformations with features of both high- and low-flow lesions.[100] These lesions may be highly invasive, become enormous in size with a tendency to involve the deep musculature and subcutaneous tissues, and be resistant to all forms of therapy. On MR imaging, these lesions demonstrate serpiginous flow voids, characteristic of arterial malformations, as well as a soft-tissue infiltrating component, typical of venous malformations (Figs. 35-39 and 35-40).[101]

There are other congenital vascular abnormalities that can occur in addition to the vascular malformations. Internal jugular vein phlebectasia is a rare entity that mostly involves the right side.[125, 126] It is usually discovered in childhood and is believed to be of congenital origin. Although it can occur at any age and can affect both genders, no case has been reported in a young adult male. The diagnosis is made clinically by noting a soft fullness in the lower neck that is most prominent when the patient is supine, or phonates in the erect position, and then disappears when the patient is erect and breathes normally. The diagnosis can be confirmed by Doppler ultrasonography, CT with contrast, and MR imaging.[125, 127] Even though most of these lesions have been excised surgically, the

Copyright © 2003, Mosby, Inc. All rights reserved.

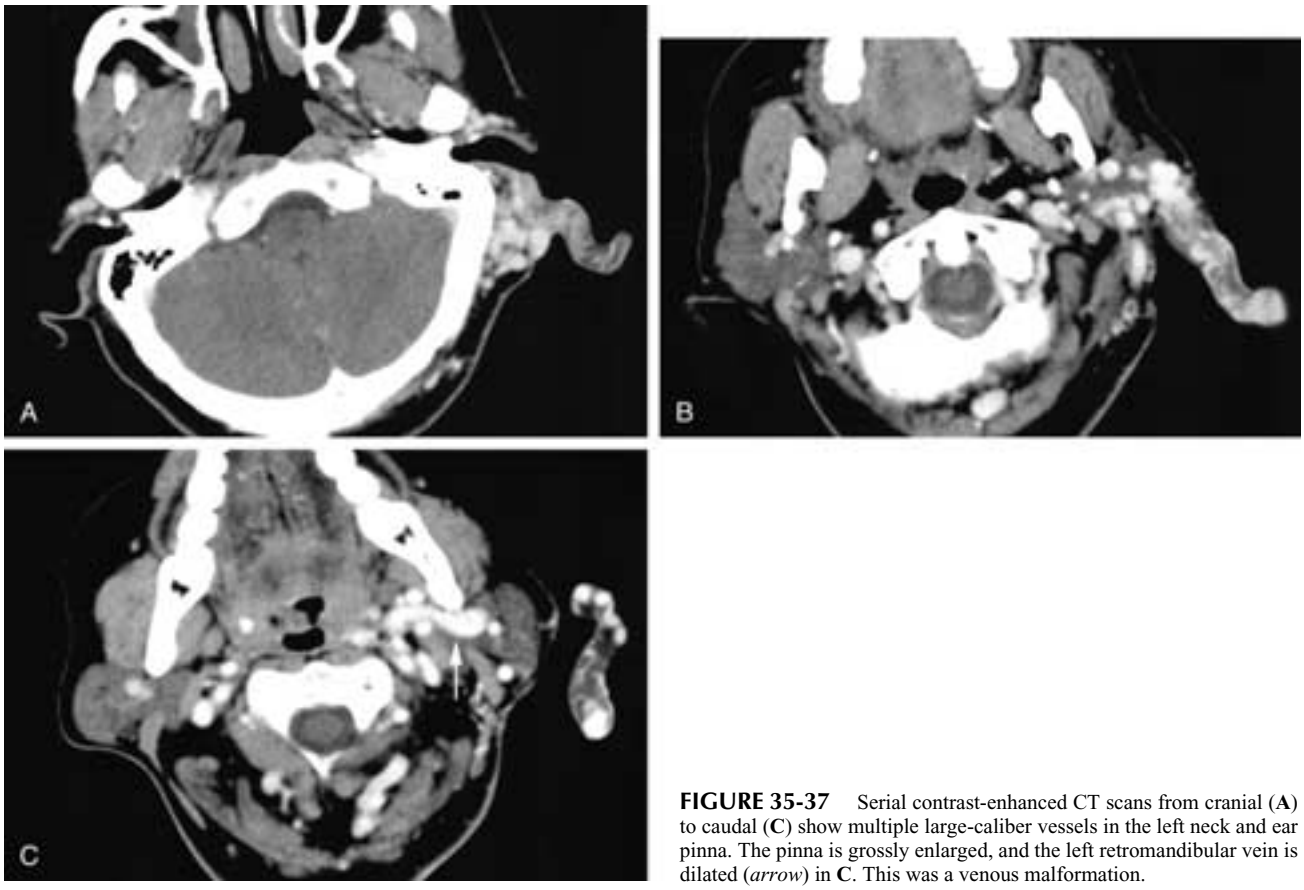

FIGURE 35-37 Serial contrast-enhanced CT scans from cranial (**A**) to caudal (**C**) show multiple large-caliber vessels in the left neck and ear pinna. The pinna is grossly enlarged, and the left retromandibular vein is dilated (*arrow*) in **C**. This was a venous malformation.

VIEW IMAGE

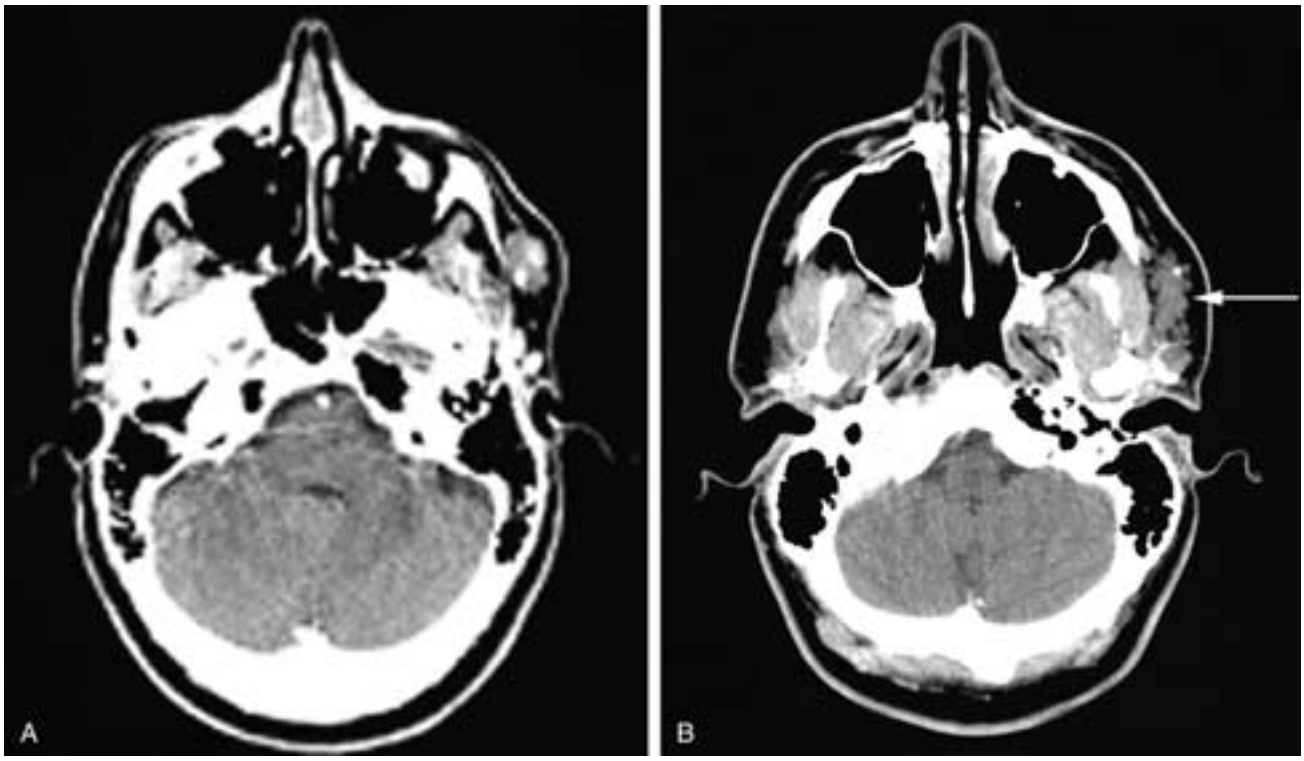

FIGURE 35-38 Coronal (**A**) and sagittal (**B**) T1-weighted MR images show large vascular flow voids in the right side of the tongue and floor of mouth. This patient had a venous malformation.

VIEW IMAGE

Copyright © 2003, Mosby, Inc. All rights reserved.

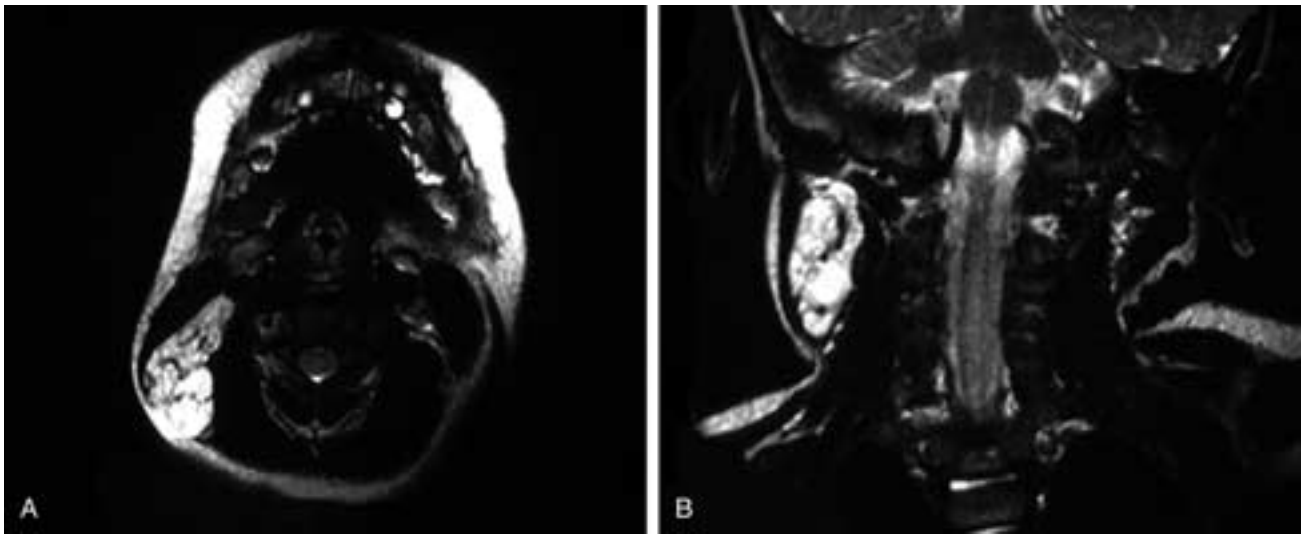

VIEW IMAGE

FIGURE 35-39 Axial (**A**) and coronal (**B**) T2-weighted MR images show a noninfiltrating mass with overall high signal intensity in the fat of the posterior right neck, deep to the sternocleidomastoid muscle. There are vascular flow voids within this arteriovenous vascular malformation.

treatment of choice should be conservative as long as the patient is asymptomatic.

TERATOMAS, EPIDERMOID CYSTS, AND DERMOID CYSTS

The nomenclature of these lesions is confusing, and overlapping definitions exist. There are two main categorical systems that use either the teratoma or the dermoid as the basic lesion and then define the other lesions as variants.

A teratoma is a neoplasm composed of multiple tissues that are foreign to the part of the body in which the lesion arises. The term *teratoma* is often used in the generic sense to include both teratoid and dermoid lesions. As such, teratomas occur in 1 in 4000 births, and less than 10% involve the head and neck structures. Most often affected are the sacrococcygeal, mediastinal, retroperitoneal, and gonadal regions.[5] The teratomas have been classified into four groups, differentiated by the germ layers involved and the degree of tissue organization. The most common form of teratoma is the demoid cyst, which contains ectodermally

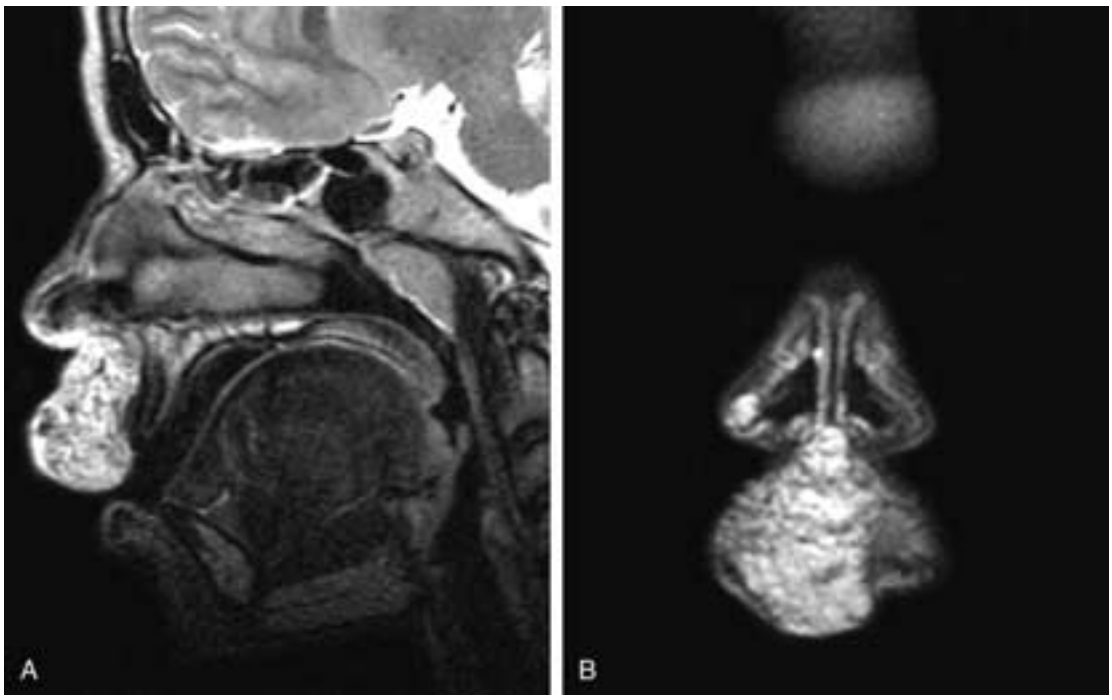

VIEW IMAGE

FIGURE 35-40 Sagittal (**A**) and coronal (**B**) T2-weighted MR images shows a mass with vascular flow voids within the columella and upper lip. The lesion also extended back into the right cheek. This was a vascular malformation in a 12-year-old girl.

Copyright © 2003, Mosby, Inc. All rights reserved.

and mesodermally derived tissues. The teratoid cyst is composed of tissues derived from ectoderm, mesoderm, and endoderm. The teratoma differs from the teratoid cyst in that the teratoma has cellular differentiation into recognizable organs. Congenital teratoid cysts have been reported to occur primarily in the floor of the mouth, with or without a median fistula, and two cases have been reported in the nasopharynx.[79, 128–137] The epignathi represents the highest form of differentiation, containing fetal organs and limbs. This rare anomaly is virtually incompatible with life.[5]

The term *dermoid cyst* has also been applied to a variety of dysontogenic cystic lesions that can occur in the body. Despite Meyer's detailed classification of these lesions into epidermoid, dermoid, and teratoid forms, the term *dermoid cyst* continues to be commonly used in reference to all three types of lesions, without regard to their differing histologies.[138] Being so loosely defined, as mentioned above, dermoid cysts of the head and neck account for 7% to 10% of all dermoid cysts.[139] Pathologically, epidermoid cysts consist of simple squamous cell epithelium with a fibrous wall. Dermoid cysts have, in addition, a variable number of skin appendages such as hair follicles and sebaceous glands. Teratoid cysts contain any number of diverse tissues derived from all three germ cell layers.[140] All three varieties may be filled with a cheesy keratinaceous material.

The most popular theory regarding the etiology of these lesions suggests that they are derived from epithelial rests that become enclaved during midline closure of the first and second branchial arches.[141] This theory may help to explain the simultaneous occurrence of multiple such cysts.[142] The other popular theory suggests that isolation of pluripotential cells occurs during embryogenesis and that subsequently disorganized growth of these cells occurs.[5]

Approximately 80% of the dermoid cysts that occur in the head and neck develop in the orbit (~50%), the oral cavity region (~24%), and the nasal region (~13%). The remainder of these lesions occur in the neck, frontal or occipital midline scalp, lower lip, or palate. There is apparent sparing of the upper lip.[139]

Median dermoid cysts of the nose represent 3% of all dermoids and about 7.6% of head and neck dermoids. Although they usually are clinically evident shortly after birth, the average age of diagnosis and treatment is 12 to 13 years. There is a 2:1 male predominance. This topic is discussed further in Chapter 1. Rarely, a tumor such as a hemangiopericytoma can present at birth and mimic such a congenital midline nasal mass.[143]

When they occur in the oral cavity, dermoid cysts most commonly involve the floor of the mouth (sublingual, submental, or submandibular regions), although other sites have been reported including the lips, tongue, and buccal mucosa.[141, 144–149] Extracapsular excision of cysts in the floor of the mouth is performed by either an intraoral or an external approach, depending on the relationship of the cyst to the mylohyoid muscle.[150] For those cysts that lie above the mylohyoid muscle (sublingual), an intraoral approach is preferable because it avoids a conspicuous scar, it preserves the mylohyoid muscle, and it is associated with a shorter recovery time. Those lesions that lie inferior to the mylohyoid muscle (submental and submandibular cysts) must usually be removed via an external approach. Therefore, the imaging identification of the cyst in relationship to the mylohyoid muscle is extremely helpful in surgical planning. Axial and especially coronal imaging are useful in this regard.[150]

Clinically, these lesions are rubbery or doughy and exhibit pitting after palpation due to their ''cheesy'' content. They are also usually nontender, nonpainful, slow-growing masses. Rapid growth may occur during pregnancy.

On CT, dermoid cysts typically appear as low-density, well-circumscribed, unilocular masses, less dense than muscle, that may or may not contain fat (Figs. 35-41 and 35-42). The wall of the cyst usually enhances following contrast administration. In the absence of fat globules, epidermoid and dermoid cysts are indistinguishable. On MR imaging, epidermoid cysts are of low signal intensity on T1-weighted images and high signal intensity on T2-weighted images, reflecting their fluid content. Dermoid lesions present a more variable appearance, depending upon their fat content, being either hypointense or hyperintense to muscle on T1-weighted images and typically hyperintense on T2-weighted sequences. The use of contrast permits determination of the thickness of the cyst wall (2 to 6 mm) (Fig. 35-43).[150]

Most of the dermoids that occur in the nasopharynx are present at birth and develop in the nasopharyngeal midline or the lateral wall. The patient is usually first diagnosed early in the third decade of life, and females are affected six times more often than males.[139]

The teratomatous lesions that occur in the nasopharynx and paranasal sinuses are usually composed of well-differentiated tissues, and neuroectodermal and neural tissues predominate. The rare malignant teratoma has a low level of differentiation and may be a teratosarcoma or present with metastases.[151] Cervical teratomas are rare, and are found in newborn full-term infants and in premature or stillborn infants. The infant usually has severe respiratory distress and dysphagia. There is no increased incidence of coexistent congenital anomalies, and maternal hydramnios is present in 19.6% of the cases.[139] The thyroid gland is involved in most of these cases and the lesions are large, usually between 5 and 12 cm.[152]

RARE CYSTS AND LESIONS

The term *choristoma* refers to a nidus of tissue that is histologically normal but is not normally present in the organ or structure in which it is located. Only a few cases have been described in the head and neck. In one case, there was a mediastinal choristoma that contained thymic, parathyroid, and salivary tissue. Another case was a mediastinal parathyroid adenoma that contained thymic tissue. In both of these instances the lesions were cystic, which may have led to their being confused with other low neck parenchymal cysts such as a large thyroid cyst, a parathyroid cyst, or a cervical thymic cyst.[27, 153] There have been reports of brain tissue in the back, the parapharyngeal space, the pterygopalatine fossa, and the lateral face.[154] There have also been reports of salivary tissue in the middle ear, a branchial cleft fistula in the neck, and respiratory epithelium in the tongue.[155–161] In addition, there has been a report of an adenocarcinoma developing in salivary tissue in the neck.[162]

Enterocystomas are rare lesions that are choristomas composed of gastric and/or intestinal mucosa. They usually occur in the floor of the mouth and tongue, and most have been reported in infants.[163–166]

Copyright © 2003, Mosby, Inc. All rights reserved.

A tracheoesophageal cyst has been reported in the neck of an infant. The mass was 12 cm in diameter and contained elements of both respiratory and upper esophageal wall origin. It was believed to have developed from a spurious sequestrum of the foregut that became separated before the development of the tracheoesophageal partition.[167]

Cervical bronchogenic cysts are derived from small buds that separate from the foregut during the formation of the tracheobronchial tree. As such, they occur primarily in the lung or mediastinum, but they have also been reported in the neck, presumably after erratic migration of primordial cells. They are more common in males (3:1) and range in size from 1 to 6 cm.[27, 168]

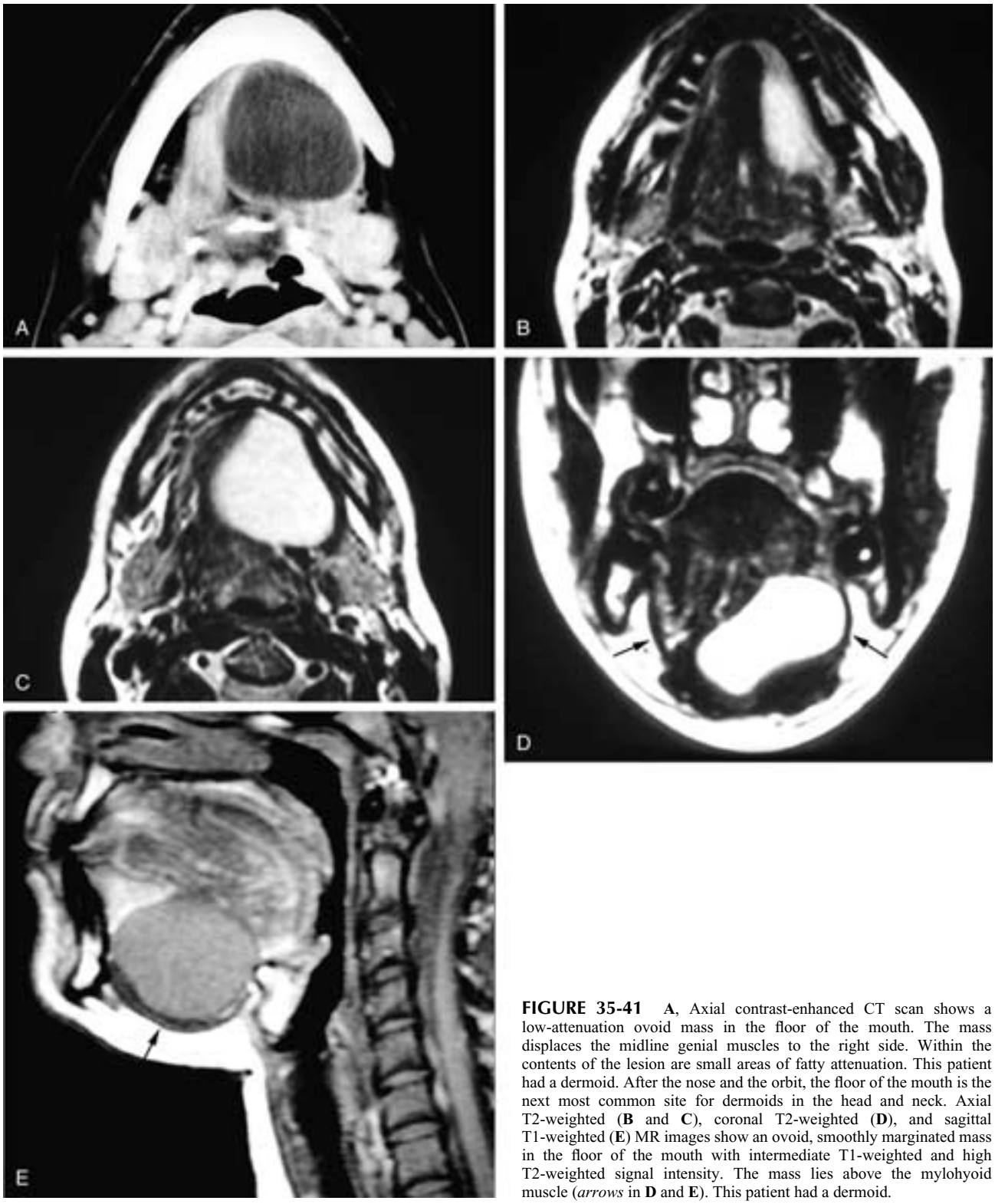

FIGURE 35-41 **A**, Axial contrast-enhanced CT scan shows a low-attenuation ovoid mass in the floor of the mouth. The mass displaces the midline genial muscles to the right side. Within the contents of the lesion are small areas of fatty attenuation. This patient had a dermoid. After the nose and the orbit, the floor of the mouth is the next most common site for dermoids in the head and neck. Axial T2-weighted (**B** and **C**), coronal T2-weighted (**D**), and sagittal T1-weighted (**E**) MR images show an ovoid, smoothly marginated mass in the floor of the mouth with intermediate T1-weighted and high T2-weighted signal intensity. The mass lies above the mylohyoid muscle (*arrows* in **D** and **E**). This patient had a dermoid.

VIEW IMAGE

Copyright © 2003, Mosby, Inc. All rights reserved.

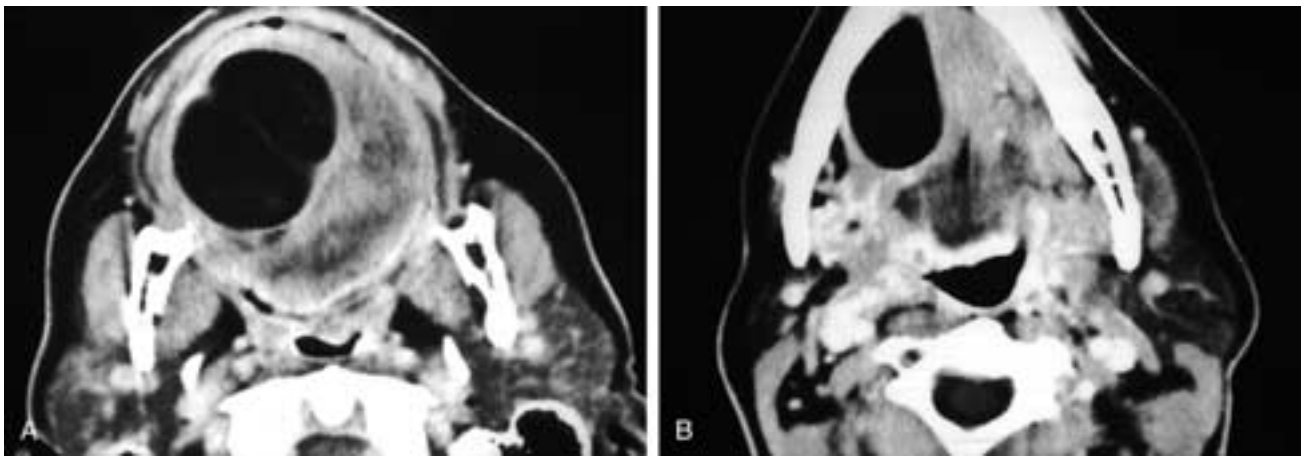

VIEW IMAGE

FIGURE 35-42 Axial contrast-enhanced CT scans through the tongue (**A**) and the floor of the mouth (**B**) show a well-delineated fat attenuation mass. This patient had a lipoma. Although dermoids may contain fat, they never consist predominantly of fat (compare this to Fig. 35-41).

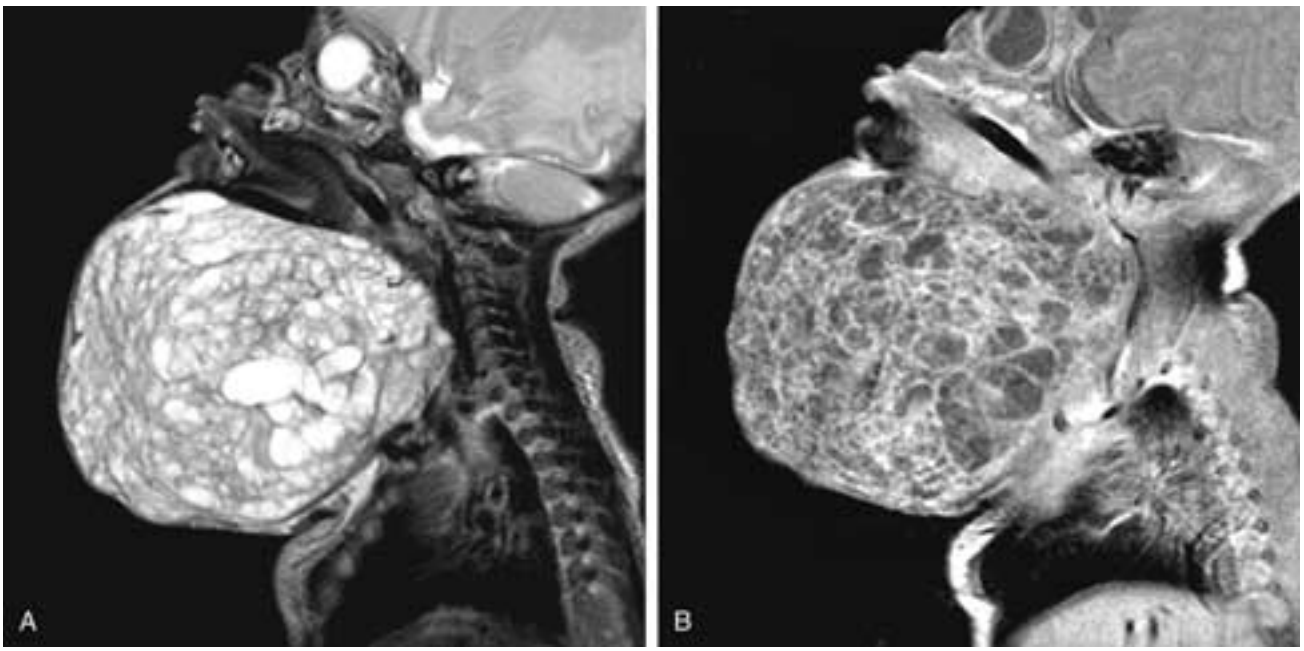

VIEW IMAGE

FIGURE 35-43 Sagittal T2-weighted (**A**) and T1-weighted, contrast-enhanced, fat-suppressed (**B**) MR images show a huge nonhomogeneous mass in the anterior neck of this newborn. The mandible is deformed and elevated, and the lesion extends down into the superior mediastinum. This was an epidermoid.

Copyright © 2003, Mosby, Inc. All rights reserved.

REFERENCES

1. Maran AGD, Buchanan DR. Branchial cysts, sinuses, and fistulae. Clin Otolaryngol 1978;3:77–92.
2. Chandler J, Mithchell B. Branchial cleft cysts, sinuses, and fistulae. Otolaryngol Clin North Am 1981;14:175–186.
3. Arnot R. Defects of the first branchial cleft. S Afr Surg 1971;9: 93–98.
4. Work W. Newer concepts of first branchial cleft defects. Laryngoscope 1972;82:1581–1593.
5. Donegan J. Congenital neck masses. In: Cummings C, Frederick J, Harker L, Krause C, Schuller D, eds. Otolaryngology Head and Neck Surgery. St. Louis: Mosby-Year Book, 1993;1554–1565.
6. Benson MT, Dalen K, Mancuso AA, Kerr HH, Cacciarelli AA, Mafee MF. Congenital anomalies of the branchial apparatus: embryology and pathologic anatomy. Radiographics 1992;12: 943–960.
7. Bayne SR, Lehman JA, Crow JP. Lung herniation into the neck associated with congenital absence of the sternocleidomastoid muscle. J Pediatr Surg 1997;32:1754–1756.
8. Penchaszadeh V. Facioscapulohumeral muscular dystrophy with congenital absence of sternocleidomastoid muscles. Birth Defects Orig Artic Ser 1971;7:116–117.
9. Liston S, Siegel LG. Branchial cysts, sinuses, and fistulae. Ear Nose Throat J 1979;58:9–17.
10. Pound L. Neck masses of congenital origin. Pediatr Clin North Am 1981;28:841–844.
11. Finn D, Buchalter I, Sarti E, Romo T, Chodosh P. First branchial cleft cysts: clinical update. Laryngoscope 1987;97:136–140.
12. Mukherji S, Tart R, Slattery W, Stringer S, Benson M, Mancuso A. Evaluation of first branchial anomalies by CT and MR. J Comput Assist Tomgr 1993;17:576–581.
13. Gainsford J, Anderson U. First branchial cleft cysts and sinuses. Plast Reconstr Surg 1975;55:299–304.
14. Olsen K, Maragos N, Weiland L. First branchial cleft anomalies. Laryngoscope 1980;90:423–436.
15. Himalstein M. Branchial cysts and fistulae. Ear Nose Throat 1980;59:47–54.
16. Som P, Brandwein M, Silvers A. Nodal inclusion cysts of the parotid gland and parapharyngeal space: a discussion of lymphoepithelial cysts, AIDS-related parotid cysts, branchial cysts, cystic Warthin's tumors, and cyst in Sjogren's syndrome (benign lymphoepithelial lesions). Laryngoscope 1995;105:1122–1128.
17. Bailey H. Branchial Cysts and Other Essays on Surgical Subjects in the Facio-Cervical Region. London: Lewis, 1929.
18. Frazer J. The nomenclature of diseased states caused by certain vestigial structures in the neck. Br J Surg 1923;11:131–136.
19. Cunningham M. The management of congenital neck masses. Am J Otolaryngol 1992;13:78–92.
20. Lingeman R. In: Surgical Anatomy. In: Cummings C, Fredrickson J, Harker L, Krause C, Schuller D, eds. Otolaryngology-Head and Neck Surgery; St. Louis: Mosby-Year Book, 1993. vol 2: 1530–1542.
21. Mouri N, Muraji T, Nishijima E, Tsugawa C. Reappraisal of lateral cervical cysts in neonates: pyriform sinus cysts as an anatomy-based nomenclature. J Pediatr Surg 1998;33:1141–1144.
22. Khochtali H, Guessous M, Mokni M, Tlili K, Mansouri N, Bakir A. [Thymic cyst in the neck. Apropos of a case]. Rev Stomatol Chir Maxillofac 1997;98:316–320.
23. Kelley DJ, Gerber ME, Willging JP. Cervicomediastinal thymic cysts. Int J Pediatr Otorhinolaryngol 1997;39:139–146.
24. Jones JE, Hession B. Cervical thymic cysts. Ear Nose Throat J 1996;75:678–680.
25. Nguyen Q, deTar M, Wells W, Crockett D. Cervical thymic cyst: case reports and review of the literature. Laryngoscope 1996;106: 247–252.
26. Cure JK, Tagge EP, Richardson MS, Mulvihill DM. MR of cystic aberrant cervical thymus. AJNR 1995;16:1124–1127.
27. Som P, Sacher M, Lanzieri C, et al. Parenchymal cysts of the lower neck. Radiology 1985;157:399–406.
28. Miller M, Cohn A. Case report: fourth branchial pouch sinus. Ear Nose Throat J 1993;72:356–358.
29. Tucker H, Skolnick M. Fourth branchial cleft (pharyngeal pouch) remnant. Trans Am Acad Ophthalmol Otolaryngol 1973;77:1368–1371.
30. Proctor B. Lateral vestigial cysts and fistulae of the neck. Laryngoscope 1955;65:355–400.
31. al-Ghamdi S, Freedman A, Just N, Rochon L, Frenkiel S. Fourth branchial cleft cyst. J Otolaryngol 1992;21:447–449.
32. Burstin PP, Briggs RJ. Fourth branchial sinus causing recurrent cervical abscess. Aust N Z J Surg 1997;67:119–122.
33. Chatzimanolis E, Dokianakis G, Gavalas G. [Congenital fistula of the 4th pharyngeal pouch and cleft]. Hno 1990;38:217–219.
34. Contencin P, Augui O, de Gaudemar I, Helardot P. [Recurrent thyroid abscess in children and malformations of the pyriform sinus]. Ann Chir 1997;51:76–81.
35. Cote DN, Gianoli GJ. Fourth branchial cleft cysts. Otolaryngol Head Neck Surg 1996;114:95–97.
36. Downey W. Branchial cleft cysts in the mediastinum. Arch Otolaryngol 1969;89:104–107.
37. Clark O. Parathyroid cysts. Am J Surg 1978;135:395–402.
38. Clark O. Hyperparathyroidism due to primary cystic parathyroid hyperplasia. Arch Surg 1978;113:748–750.
39. Som P. Cystic lesions of the neck. Postgrad Radiol 1987;7:211–236.
40. Shimizu M, Akamatsu H, Yoshizaki T, Tanaka H, Sakamoto T, Sunamori M. [Thoracoscopic resection of mediastinal parathyroid adenoma with cyst and hyperparathyroidism—a case report]. Nippon Kyobu Geka Gakkai Zasshi 1997;45:1972–1975.
41. Kuriyama K, Ikezoe J, Morimoto S, et al. Functioning parathyroid cyst extending from neck to anterior mediastinum. Diagnosis by sonography and computed tomography. Diagn Imag Clin Med 1986;55:301–305.
42. Blizzard R, Chandler R, Landing B, Pettit M, West C. Maternal autoimmunization to thyroid as a probable cause of athyrotic cretinism. N Engl J Med 1960;263:327–336.
43. Chandler R, Blizzard R, Hung W, Kyle M. Incidence of thyrocytotoxic factor and other antithyroid antibodies in the mother of cretins. New Engl J Med 1962;267:376–380.
44. Wells R, Sty J, Duck S. Technetium 99m pertechnetate thyroid scintigraphy: congenital hypothyroid screening. Pediatr Radiol 1986;16:368–373.
45. Taybi H. Metabolic disorders. In: Taybi H, Lachman R, eds. Radiology of Syndromes, Metabolic Disorders, and Skeletal Dysplasias, 4th ed. St. Louis: CV Mosby, 1996:635–637.
46. Iancu T, Boyanower Y, Laurian N. Congenital goiter due to maternal ingestion of iodide. Am J Dis Child 1974;128:528–530.
47. Anson B. An Atlas of Human Anatomy, 2nd ed. Philadelphia: WB Saunders, 1963.
48. Hamburger J, Hamburger S. Thyroidal hemiagenesis: report of a case and comments on clinical ramifications. Arch Surg 1970;100: 319–320.
49. Ward G, Hendrick J, Chamber R. Thyroglossal tract abnormalities, cysts, and fistula. Surg Gynecol Obstet 1949;89:727–734.
50. Allard R. The thyroglossal cyst. Head Neck Surg 1982;5:134–146.
51. Ellis P, Van Nostranel A. The applied anatomy of the thyroglossal tract. Laryngoscope 1977;87:765–770.
52. Sistrunk W. The surgical treatment of cysts of the thyroglossal tract. Ann Surg 1920;71:121–122.
53. Dische S, Berg P. An investigation of the thyroglossal tract using the radio-isotope scan. Clin Radiol 1963;14:298–303.
54. Hoyes A, Kershaw D. Anatomy and development of the thyroid gland. Ear Nose Throat J 1985;64:318–324.
55. Tovi F, Eyal A. Branched and polycystic thyroglossal duct anomaly. J Laryngol Otol 1985;99:1179–1182.
56. Loevner LA. Imaging of the thyroid gland. Semin Ultrasound CT MR 1996;17:539–562.
57. Blandino A, Salvi L, Scribano E, Chirico G, Longo M, Pandolfo I. MR findings in thyroglossal duct cysts: report of two cases. Eur J Radiol 1990;11:207–211.
58. Montgomery M. Lingual thyroid: a comprehensive review. West J Surg 1935;43:661–669.
59. Batsakis J. Parenchymal cysts of the neck. In: Batsakis J, ed. Tumors of the Head and Neck Clinical and Pathological Considerations, 2nd ed. Baltimore: Williams & Wilkins, 1979;233–239.
60. Waggoner L. Intralaryngeal intratracheal thyroid. Ann Otol Rhinol Laryngol 1958;67:61–71.
61. Meyers E, Pantangeo I. Intratracheal thyroid. Laryngoscope 1958;85:1833–1839.
62. Gray S, Skandalakis J. Embryology for Surgeons: The Embryological Basis for the Treatment of Congenital Defects. Philadelphia: WB Saunders, 1972.
63. Rogers W, Kesten H. Embryological basis for thyroid tissue in the heart. Anat Rec 1962;142:323.

Copyright © 2003, Mosby, Inc. All rights reserved.

64. Chan F, Low L, Yeung H, Saing H. Case report: lingual thyroid, a cause of neonatal stridor. Br J Radiol 1993;66:462–464.
65. Johnson J, Coleman L. Magnetic resonance imaging of a lingual thyroid gland. Pediatr Radiol 1989;19:461–462.
66. Shah H, Boyd C, Williamson M, Angtuaco T, Suen J, Eudy S. Lingual thyroid: unusual appearance on computed tomography. Comput Med Imag Graphics 1988;12:263–266.
67. Willinsky R, Kassell E, Cooper P, Chin-Sang H, Haight J. Computed tomography of lingual thyroid. J Comput Assist Tomogr 1987;11: 182–183.
68. Knoblich R. Accessory thyroid in the lateral floor of mouth. Oral Surg 1965;19:234–238.
69. Postlethwait R, Detmer D. Ectopic thyroid nodule in the esophagus. Ann Thorac Surg 1975;19:98–100.
70. Arriga M, Myers E. Ectopic thyroid nodule in the retroesophageal superior mediastinum. Otolaryngol Head Neck Surg 1988;99: 338–340.
71. McNicoll M, Hawkins D, England K, Penny R, Maceri D. Papillary carcinoma arising in a thyroglossal duct cyst. Otolaryngol Head Neck Surg 1988;99:50–54.
72. Renard T, Choucair R, Stevenson W, Brook W, Poulos E. Carcinoma of the thyroglossal duct. Surg Gynecol Obstet 1990;171: 305–308.
73. Fernandez J, Ordonez N, Schultz P, Samaan N, Hickey R. Thyroglossal duct carcinoma. Surgery 1991;110:928–934.
74. Fish J, Moore R. Ectopic thyroid tissue and ectopic thyroid carcinoma. Ann Surg 1963;157:212–222.
75. Weichert R. The neural ectoderm origin of the peptide-secreting endocrine glands. Am J Med 1970;49:232–241.
76. Janson K, Roberts J, Varela M. Multiple endocrine adenomatosis: in support of the common origin theories. J Urol 1978;119:161–165.
77. Siegel M, Glazer H, St Amour T. Lymphangiomas in children: MR imaging. Radiology 1989;170:467–470.
78. Yuh W, Buehner L, Kao S. Magnetic resonance imaging of pediatric head and neck cystic hygromas. Ann Otol Rhinol Laryngol 1991;100:737–742.
79. Faerber TH, Hiatt WR, Dunlap C. Congenital teratoid cyst of the floor of the mouth. J Oral Maxillofac Surg 1988;46:487–490.
80. Okubo T, Shimada T, Narita Y, et al. [A successful case report on intralesional OK-432 therapy for cystic mediastinal lymphangiomas]. Kyobu Geka 1998;51:1017–1021.
81. Weingasat G. Congenital lymphangiectasia with fetal cystic hygroma: report of two cases with coexistent Down's syndrome. J Clin Ultrasound 1988;16:663–668.
82. Phillips H, McGahan J. Intrauterine fetal cystic hygromata: sonographic detection. Am J Roentgenol 1981;136:799–802.
83. Lee K. Surgery of cysts and tumors of the neck. In Paparella M, Shunrick D, eds. Otolaryngology. Philadelphia: WB Saunders, 1980; 29–87.
84. Bill A, Summer D. A unified concept of lymphangioma and cystic hygroma. Surg Gynec Obstet 1965:79–86.
85. Smith D. Recognizable Patterns of Human Malformation: Genetic, Embryologic and Clinical Aspects, 3rd ed. Philadelphia: WB Saunders, 1982;472–473.
86. Chervenak F, Isaacson G. Fetal cystic hygroma, cause and natural history. N Engl J Med 1983;309:822–825.
87. van der Putte S. Lymphatic malformation in human fetuses. Virchows Arch A Path Anat Histol 1977;376:233–246.
88. Shaub M, Wilson R. Fetal cystic lymphoma (cystic hygroma): prepartum ultrasonic findings. Radiology 1976;121:449–450.
89. Hubbard AM, Crombleholme TM, Adzick NS. Prenatal MRI evaluation of giant neck masses in preparation for the fetal exit procedure. Am J Perinatol 1998;15:253–257.
90. Gray S, Skandalakis J. Embryology for Surgeons: The Lymphatic System. Philadelphia: WB Saunders, 1972;695–714.
91. Faerber E, Swartz J. Imaging of neck masses in infants and children. Crit Rev Diagn Imag 1991;31:283–314.
92. Som P, Zimmerman R, Biller H. Cystic hygroma and facial nerve paralysis—A rare association. J Comput Assist Tomogr 1984;8: 110–113.
93. Bauer B, Kernahan D. Lymphangioma circumscriptum: a clinicopathological review. Ann Plast Surg 1981;7:318–326.
94. Kinmonth J. The Lymphatics, 2nd ed. London: Arnold, 1982; 307–319.
95. Ajal M, Roche J, Turner J, Fagan P. Unusual lesions of the internal auditory canal. J Laryngol Otol 1998;112:650–653.
96. Mulliken J, Glowacki J. Hemangiomas and vascular malformations in infants and children: a classification based on endothelial characteristics. Plast Reconstr Surg 1982;69:412–420.
97. Chen J, Spetzler R, Reiff J, Beals S. Hemangiomas and vascular malformations. BNI Q 1994;10:19–25.
98. Watson W, McCarthy W. Blood and lymphatic vessel tumors: report of 1056 cases. Surg Gynecol Obstet 1940;71:569–588.
99. Bowers R, Graham E. The natural history of the strawberry nevus. Arch Dermatol 1960;82:667–673.
100. Kaban L, Mulliken J. Vascular anomalies of the maxillofacial region. J Oral Maxillofac Surg 1986;44:210–213.
101. Baker L, Dillon W, Hieshima G, Dowd C, Frieden I. Hemangiomas and vascular malformations of the head and neck: MR characterization. Am J Neuroradiol 1993;14:307–314.
102. Burrows P, Mulliken J, Fellows K, Strand R. Childhood hemangiomas and vascular anomalies: angiographic differentiation. Am J Roentgenol 1983;141:483–488.
103. Meyer J, Hoffer F, Barnes P, Mulliken J. Biological classification of soft-tissue vascular anomalies: MR correlation. Am J Roentgenol 1991;157:559–564.
104. Boyd JB, Mulliken JB, Kaban LB, Upton J 3rd, Murray JE. Skeletal changes associated with vascular malformations. Plast Reconstr Surg 1984;74:789–795.
105. Mulliken J. Vascular malformations of the head and neck. In Mulliken J, ed. Vascular Birthmarks, Hemangiomas and Malformations. Philadelphia: WB Saunders, 1988;301–342.
106. Bartlett J, Riding K, Salkeld L. Management of hemangiomas of the head and neck in children. J Otolaryngol 1988;17:111–120.
107. Edgerton M. The treatment of hemangiomas. Ann Surg 1976;183; 517–530.
108. Sasaki G, Pang C, Wittliff L. Pathogenesis and treatment of infant skin strawberry hemangiomas: clinical and in vitro studies of hormonal effects. Plast Reconstr Surg 1984;73:359–368.
109. Apfelberg D, Maser M, White D, Lash H. A preliminary study of the combined effect of Neodymium: YAG laser photocoagulation and direct steroid instillation in the treatment of capillary/cavernous hemangiomas of infancy. Ann Plast Surg 1989;22:94–104.
110. Waner M, Suen J, Dinehart S. Treatment of hemangiomas of the head and neck. Laryngoscope 1992;102:1123–1132.
111. Berthelsen B, Fogdestam I, Svendsen P. Venous malformations in the face and neck: radiologic diagnosis and treatment with absolute ethanol. Acta Radiol 1986;27:149–155.
112. Yakes W, Haas D, Parker S, et al. Symptomatic vascular malformations: ethanol embolotherapy. Radiology 1989;170:1059–1066.
113. Forbes G, Earnest F, Jackson I, Marsh W, Jack C, Cross S. Therapeutic embolization angiography for extra-axial lesions of the head. Mayo Clin Proc 1986;61:427–441.
114. Leikensohn J, Epstein L, Vasconez L. Superselective embolization and surgery of noninvoluting hemangiomas and A-V malformations. Plast Reconstr Surg 1981;68:143–152.
115. Biller H, Krespi Y, Som P. Combined therapy of vascular lesions of the head and neck with intra-arterial embolization and surgical excision. Otolaryngol Head Neck Surg 1982;90:37–47.
116. Persky M. Congenital vascular lesions of the head and neck. Laryngoscope 1986;96:1002–1015.
117. Mulliken J. Classification of vascular birthmarks. In: Mulliken J, ed. Vascular Birthmarks, Hemangiomas and Malformations. Philadelphia: WB Saunders, 1988;24–37.
118. Ott J. Hemangiomata in skeletal muscle. Br J Surg 1957;44:496–501.
119. Elahi M, Parnes L, Fox A. Hemangioma of the masseter muscle. J Otolaryngol 1992;21:177–179.
120. Wolf G, Daniel F, Krause C, Kaufman R. Intramuscular hemangioma of the head and neck. Laryngoscope 1985;95:210–213.
121. Ingalls G, Bonnington G, Sisk A. Intramuscular hemangioma of the mentalis muscle. Oral Surg Oral Med Oral Pathol 1986;60:476–481.
122. Braun I, Hoffman JJ, Reede D, Grist W. Computed tomography of the buccomasseteric region. II. Pathology. Am J Neuroradiol 1984;5:611–616.
123. Itoh K, Nishimura K, Togashi K, et al. MR imaging of cavernous hemangiomas of the face and neck. J Comput Assist Tomogr 1986;10:831–835.
124. Gelbert F, Riche M, Reizine D, et al. MR imaging of head and neck vascular malformations. J MRI 1991;1:579–584.
125. al-Dousary S. Internal jugular phlebectasia. Int J Pediatr Otorhinolaryngol 1997;38:273–280.

Copyright © 2003, Mosby, Inc. All rights reserved.

126. Bosshardt TL, Honig MP. Congenital internal jugular venous aneurysm: diagnosis and treatment. Milit Med 1996;161:246–247.
127. Shimizu M, Takagi Y, Yoshio H, Takeda R, Matsui O. Usefulness of ultrasonography and Doppler color flow imaging in the diagnosis of internal jugular phlebectasia. Heart Vessels 1992;7:95–98.
128. Bonilla JA, Szeremeta W, Yellon RF, Nazif MM. Teratoid cyst of the floor of the mouth. Int J Pediatr Otorhinolaryngol 1996;38:71–75.
129. Harada H, Kusukawa J, Kameyama T. Congenital teratoid cyst of the floor of the mouth—a case report. Int J Oral Maxillofac Surg 1995;24:361–362.
130. Nagar H, Baratz M. Congenital sublingual teratoid cyst. Case report. Int J Oral Maxillofac Surg 1993;22:44–45.
131. Sciubba JJ, Younai F. Epipalatus: a rare intraoral teratoma. Oral Surg Oral Med Oral Pathol 1991;71:476–481.
132. Jones AS. Two cases of nasopharyngeal teratoid tumours. J R Coll Surg Edinb 1986;31:187–188.
133. Ohishi M, Ishii T, Shinohara M, Horinouchi Y. Dermoid cyst of the floor of the mouth: lateral teratoid cyst with sinus tract in an infant. Oral Surg Oral Med Oral Pathol 1985;60:191–194.
134. Heffner DK. Problems in pediatric otorhinolaryngic pathology, III. Teratoid and neural tumors of the nose, sinonasal tract, and nasopharynx. Int J Pediatr Otorhinolaryngol 1983;6:1–21.
135. Mirsky I, Doyle JL. Sublingual teratoid cyst with unusual giant-cell reaction. Report of a case. Oral Surg Oral Med Oral Pathol 1967;23:428–432.
136. Cardesa A, Blesa G. [Teratoid tumor of possible branchiogenic origin]. Acta Oncol (Madr) 1964;3:238–243.
137. Kitagawa Y, Hashimoto K, Tanaka N, Ishii Y. Congenital teratoid cyst with a median fistula in the submental region: case report and ultrastructural findings. J Oral Maxillofac Surg 1998;56:254–262.
138. Meyer I. Dermoid cysts (dermoids) of the floor of the mouth. Oral Surg Oral Med Oral Pathol 1955;8:1149–1164.
139. Batsakis J. Teratomas of the head and neck. In: Batsakis J, ed. Tumors of the Head and Neck: Clinical and Pathological Considerations, 2nd ed. Baltimore: Williams & Wilkins, 1979;226–232.
140. Hunter T, Paplanus S, Chernin M, Coulthard S. Dermoid cyst of the floor of the mouth. AJR 1983;141:1239–1240.
141. Worley C, Laskin D. Coincidental sublingual and submental epidermoid cysts. J Oral Maxillofac Surg 1993;51:787–790.
142. Arcand P, Granger J, Brochu P. Congenital dermoid cyst of the oral cavity with gastric choristoma. J Otolaryngol 1988;15:219–222.
143. Sabini P, Josephson GD, Yung RT, Dolitsky JN. Hemangiopericytoma presenting as a congenital midline nasal mass. Arch Otolaryngol Head Neck Surg 1998;124:202–204.
144. Black E, Leathers R, Youngblood D. Dermoid cyst of the floor of the mouth. Oral Surg Oral Med Oral Pathol 1992;75:556–558.
145. Mathur S, Menon P. Dermoid cyst of the tongue: report of a case. Oral Surg Oral Med Oral Pathol 1980;50:217–219.
146. Quinn J. Congenital epidermoid cyst of anterior half of tongue. Oral Surg Oral Med Oral Surg 1960;13:1283–1285.
147. Rajayogeswaran V, Eveson J. Epidermoid cyst of the buccal mucosa. Oral Surg Oral Med Oral Pathol 1989;67:181–183.
148. Ruggieri M, Tine A, Rizzo R, Micali G, Fiumara A. Lateral dermoid cyst of the tongue: case report. Int J Pediatr Otorhinolaryngol 1994;30:79–84.
149. Rule D. Dermoid cyst of the lower lip: a case report. Br J Oral Surg 1976;131:543–545.
150. Vogl T, Steger W, Ihrer S, Ferrera P, Grevers G. Cystic masses in the floor of the mouth: value of MR imaging in planning surgery. AJR 1993;161:183–186.
151. Touran T, Applebaum H, Frost DB, Richardson R, Taber P, Rowland J. Congenital metastatic cervical teratoma: diagnostic and management considerations. J Pediatr Surg 1989;24:21–23.
152. Rothschild M, Catalano P, Urken M, et al. Evaluation and management of congenital cervical teratoma: case report and review. Arch Otolaryngol Head Neck Surg 1994;120:444–448.
153. Breckler I, Johnston D. Choristoma of the thymus. J Dis Child 1956;92:175–178.
154. Madjidi A, Couly G. Heterotopic neuroglial tissue of the face. Report of six cases and review of the literature. Oral Surg Oral Med Oral Pathol 1993;76:284–288.
155. Downing MT, Hamoudi AB, Besner GE. Brain heterotopia: choristoma of the back. Pediatr Surg Int 1997;12:183–185.
156. Forte V, Friedberg J, Thorner P, Park A. Heterotopic brain in the parapharyngeal space. Int J Pediatr Otorhinolaryngol 1996;37:253–260.
157. Heffner DK, Thompson LD, Schall DG, Anderson V. Pharyngeal dermoids (''hairy polyps'') as accessory auricles. Ann Otol Rhinol Laryngol 1996;105:819–824.
158. Hinni ML, Beatty CW. Salivary gland choristoma of the middle ear: report of a case and review of the literature. Ear Nose Throat J 1996;75:422–424.
159. Hwang SM, Ahn SK, Lee SH, Lee WS. Heterotopic salivary glands simulating bronchial cleft fistular in the lower neck. J Dermatol 1996;23:287–289.
160. Kallman JE, Loevner LA, Yousem DM, et al. Heterotopic brain in the pterygopalatine fossa. AJNR 1997;18:176–179.
161. Mahler V, Wurm J, Von den Driesch P. Ectopic respiratory epithelium associated with multiple malformations. Br J Dermatol 1997;136:933–934.
162. Hata T, Iga H, Imai S, Hirokawa M. Heterotopic salivary gland adenocarcinoma in the cervical region. Int J Oral Maxillofac Surg 1997;26:290–292.
163. Crawley DE, Miller RH. Enterocystoma of the head and neck. Otolaryngol Head Neck Surg 1983;91:492–496.
164. Grime PD. Giant enterocystoma within an infant's tongue. J Laryngol Otol 1990;104:814–818.
165. Huang SF, Chuang SM, Chen WJ. Heterotopic oral gastrointestinal cyst: report of a case. Taiwan I Hsueh Hui Tsa Chih 1989;88:621–623.
166. Katz A, Aimi K, Skolnik EM. Enterocystoma of the head and neck. Laryngoscope 1980;90:1441–1444.
167. Tenery J, Abul-Haj S, Burt G. A tracheoesophageal cyst of the neck. Plast Reconstr Surg 1960;25:517–524.
168. Landa Aranzabal M, Navarro Sanpedro JJ, Rivas Salas A, Rodriguez Garcia L, Cabeza Sanchez R, Algaba Guimera J. [A bronchogenic cervical cyst. A case report]. An Otorrinolaringol Ibero Am 1997;24:343–351.

Copyright © 2003, Mosby, Inc. All rights reserved.

36
Lymph Nodes

Peter M. Som and Margaret S. Brandwein

INTRODUCTION
THE LYMPHATIC SYSTEM
LYMPH AND LYMPHATIC FLOW
LYMPH NODES: STRUCTURE AND FUNCTION
PATHWAYS OF LYMPH NODE METASTASIS
CLINICAL SIGNIFICANCE OF METASTATIC NODAL CARCINOMA
THE CLINICAL IMPACT OF IMAGING METASTATIC LYMPH NODES
NODAL CLASSIFICATION
- The Rouvière System
- The Level Systems
- The Imaging-Based System
  - How to Scan the Neck
  - How to Use the Imaging-Based Classification
  - The Imaging-Based Classification

NODAL STAGING
- Nasopharyngeal Carcinoma Nodal Staging
- Thyroid Carcinoma Nodal Staging

PATHOLOGY
THE NONDIAGNOSTIC NODAL BIOPSY
CONSIDERATION OF THE PRIMARY TUMOR SITE
LIMITATIONS IN IMAGING CERVICAL LYMPH NODES
THE NECESSITY OF CLINICOPATHOLOGIC CORRELATION
SPECIFIC NODAL PATHOLOGIES
- Viral Lymphadenitides
  - Infectious Mononucleosis
  - Cytomegalovirus
  - Herpes Simplex Virus
  - Varicella
  - Vaccinia
  - Measles
  - Rubella (German Measles)
  - Human Immunodeficiency Virus
- Bacterial Lymphadenitides
  - Routine Bacterial Lymphadenitis
  - Lemierre's Syndrome
  - Cat-Scratch Lymphadenitis
  - Bacillary Angiomatosis
  - Syphilitic Lymphadenitis
  - Lyme Lymphadenitis
  - Mycobacterial Lymphadenitides
  - Mycobacterium Tuberculosis
  - Atypical Mycobacteria
  - Mycobacterium leprae
- Fungal Lymphadenitides
  - Cryptococcosis
  - Histoplasmosis
  - Coccidioidomycosis
  - Pneumocystosis
- Protozoal Lymphadenitis
  - Toxoplasmosis
- Reactive Lymphadenopathies
  - Atypical Lymphoid Hyperplasia
- Lymphadenopathies Associated with Clinical Syndromes
  - Kimura's Disease
  - Sinus Histiocytosis with Massive Lymphadenopathy
  - Kikuchi-Fujimoto Disease
  - Sarcoidosis
  - Dermatopathic Lymphadenopathy
  - Angiofollicular Lymph Node Hyperplasia
  - Angioimmunoblastic Lymphadenopathy
  - Kawasaki's Syndrome
  - Posttransplantation Lymphoproliferative Disorders
- Tumor-Reactive Lymphadenopathy
- Vascular Lymphadenopathies
- Foreign Body Lymphadenopathies
- Lymph Node Inclusions
- Lymphoproliferative Disorders
- Proliferative Histiocytic Disorders
- Spindle Cell Neoplasms of Lymph Nodes
- Vascular Neoplasms of Lymph Nodes
- Metastatic Lymph Nodes

Copyright © 2003, Mosby, Inc. All rights reserved.

IMAGING CRITERIA OF PATHOLOGIC ADENOPATHY
"Normal" Reactive Nodes
Criteria for Assessing Metastatic Nodes
Size Criteria
Central Necrosis
Subcapsular Nodal Tumor
Extranodal Tumor Extension
Arterial Invasion
Metastatic Thyroid Carcinoma
Enhancing Nodes
Nodal Calcifications
The Retropharyngeal Abscessed Node
NEWER IMAGING APPROACHES

INTRODUCTION

Most often, imaging of the cervical lymph nodes is performed incidental to mapping a potential primary tumor or a source of infection. When lymph nodes are assessed by imaging, the examination can confirm the clinical suspicion of an inflamed or metastatic node, further characterize a suspicious palpable lesion as being an enlarged lymph node, or identify occult lymphadenopathy. In addition, the therapeutic response can be monitored accurately with imaging. Regardless of the reason, imaging usually contributes new information to the overall evaluation of these patients, and it should be considered a basic adjunctive study to clinical evaluation.[1–15]

THE LYMPHATIC SYSTEM

The lymphatic system consists of a number of lymph nodes, mucosa-associated lymphoid tissue (Waldeyer's ring in the head and neck), the spleen, and the thymus. The lymph navigates via an extensive lymphatic capillary network that begins as blind channels that collect the lymph from the intercellular fluid. These channels then develop into afferent lymphatic vessels that carry lymph to the lymph nodes. Efferent lymphatic vessels carry lymph from peripheral lymph nodes to other lymph nodes and eventually, via the thoracic duct on the left side and the right lymphatic duct, to the blood through the great veins in the root of the neck. The embryology of the lymphatic system is discussed in Chapter 33.

LYMPH AND LYMPHATIC FLOW

The direction of the flow of fluid within the vascular and lymphatic capillary beds differs on the arterial and venous sides of these beds. On the arterial side, the blood pressure exceeds the osmotic pressure of the adjacent tissue spaces driving fluid from the capillaries into the interstitial spaces. On the venous side of the capillary bed, the blood pressure drops and the interstitial osmotic pressure rises sufficiently to drive fluid into the postcapillary venules. About 90% of the interstitial fluid is returned to the blood, while the remaining nearly 10% enters the lymph. Virtually any liquid or mobile solid material, including tumor cells, can also enter the lymph.

Lymph is a transparent, colorless, or slightly yellow, watery fluid with a specific gravity of 1.015. It closely resembles blood plasma but is more dilute. The term *peripheral lymph* refers to lymph that is formed in the peripheral tissues and that has not passed through a lymph node. This peripheral lymph is paucicellular. Lymph nodes are referred to as either peripheral or intermediate. Peripheral lymph nodes receive only peripheral lymph. After passing through a peripheral lymph node, the lymph becomes enriched with lymphocytes and is referred to as intermediate lymph.

The efferent lymphatic vessels of these peripheral lymph nodes function as the afferent vessels of the next lymph nodes in a nodal chain. These nodes are referred to as intermediate lymph nodes, and they have two types of afferent lymph supply: (1) the peripheral lymph from the immediate regions and (2) the intermediate lymph from the efferent lymphatics of other peripheral lymph nodes. In turn, the lymph passes to deeper lymph nodes and ultimately to the main lymph trunks and thoracic duct. The lymph within these central trunks and ducts is referred to as central lymph, as it does not pass through additional lymph nodes before reaching the blood.[16]

The peripheral lymph contains between 200 to 1000 cells/mm^3, of which about 15% are cells of the macrophage-monocyte series and the remaining cells are recirculating lymphocytes extravasated from the blood. Most of these lymphocytes are T cells; only about 10% are B cells. The cellularity of intermediate and central lymph varies greatly, ranging from 5000 to 50,000 white cells/mm^3. Most of these cells are small lymphocytes that have migrated from the lymph node paracortices. About 25% are B cells, and the remainder are subsets of T cells. Few macrophage-like cells are present, having apparently been retained by the first lymph nodes they encountered.[16] The population of cells in the lymph alters with stimulation. Large numbers of lymphoid blast cells (immunoblasts) can be seen after antigenic stimulation, comprising nearly half of the cells of efferent lymph from stimulated nodes. This change indicates the vigor of the immune response.[16]

The lymphatic capillaries have no valves; however, the lymphatic vessels have valves that are more closely spaced together than those in comparably sized veins. Expanded pouch-like sinuses are present immediately above the point of attachment of each lymphatic valve, imparting a distended beaded appearance to the lymph vessel when it is fully filled. The lymph is propelled by contractions of the larger vessel walls.

Copyright © 2003, Mosby, Inc. All rights reserved.

LYMPH NODES: STRUCTURE AND FUNCTION

The lymph nodes are the raison d'être of the lymphatic system. They are situated in either groups or chains so that the afferent lymphatic vessels leading to these lymph nodes drain discrete anatomic regions. In addition to mechanical filtration of the lymph, the lymph nodes are involved with recognition and processing of antigens and lymphopoiesis. Lymph emerging from efferent channels is always enriched with more lymphocytes than the corresponding afferent lymph. Most lymph nodes have an oval or bean shape with a slight depression on the hilar side. The hilum contains arterioles, venules, and efferent lymphatic vessels. There are usually only 2 or 3 efferent vessels at the hilum, but between 6 and 25 afferent lymphatic vessels that enter the nodal periphery away from the hilum (Fig. 36-1).[16–19]

Lymph nodes have a complex architecture that arranges a variety of specific cell populations so that they interact in a favorable environment that allows the various cellular components to process antigens, interact, and generate the immune response. This nodal architecture varies with the anatomic region and with the response to antigen stimulation. Thus, the lymph nodes that drain areas of active antigen stimulation, such as the neck, have larger and more numerous germinal centers, or areas of active lymphoid cell production, than do mesenteric lymph nodes.[19]

The circulating lymph travels to each node through the afferent lymphatic vessels. The lymph then circulates within a system of sinuses, first entering the marginal or subcortical sinuses, then the cortical or intermedullary sinuses, and lastly the medullary sinuses. Finally, the lymph exits the lymph node via the efferent lymph vessels in the nodal hilum. As the lymph flows through the lymph node, it first contacts the cortex, then the paracortex, and then the medulla. Each of these areas has a distinct morphology and function. The lymph brings antigens to the node and carries out antibodies, T cells and macrophage components of cellular immunity, and activated B lymphocytes of humoral immunity. In addition, the phagocytic apparatus of the sinuses filters the lymph, retaining foreign antigens and substances. The passage of the lymph and cells from one chain of lymph nodes to the next is a means by which the immune response is conveyed from the peripheral to the more central lymph nodes.[16–19]

The majority of lymphocytes are brought to the lymph node by the blood supply rather than by the afferent lymphatic vessels. The blood enters the lymph node at the nodal hilum via one or more arterioles. The vessels then divide into branches in the medulla, ramify further into capillary networks in the cortex and paracortex, and then exit the node via a parallel venous system. The blood vessels within the lymph node are morphologically identical to those in other organs, except for the postcapillary venules of the paracortex. These vessels are lined by high endothelial venules (HEV) that are tightly bound together by close interdigitations. The HEV have specialized lymphocyte-homing receptors that are recognized by the circulating lymphocytes and that facilitate lymphocyte migration from the circulating blood into the lymphoid tissue. HEV are also

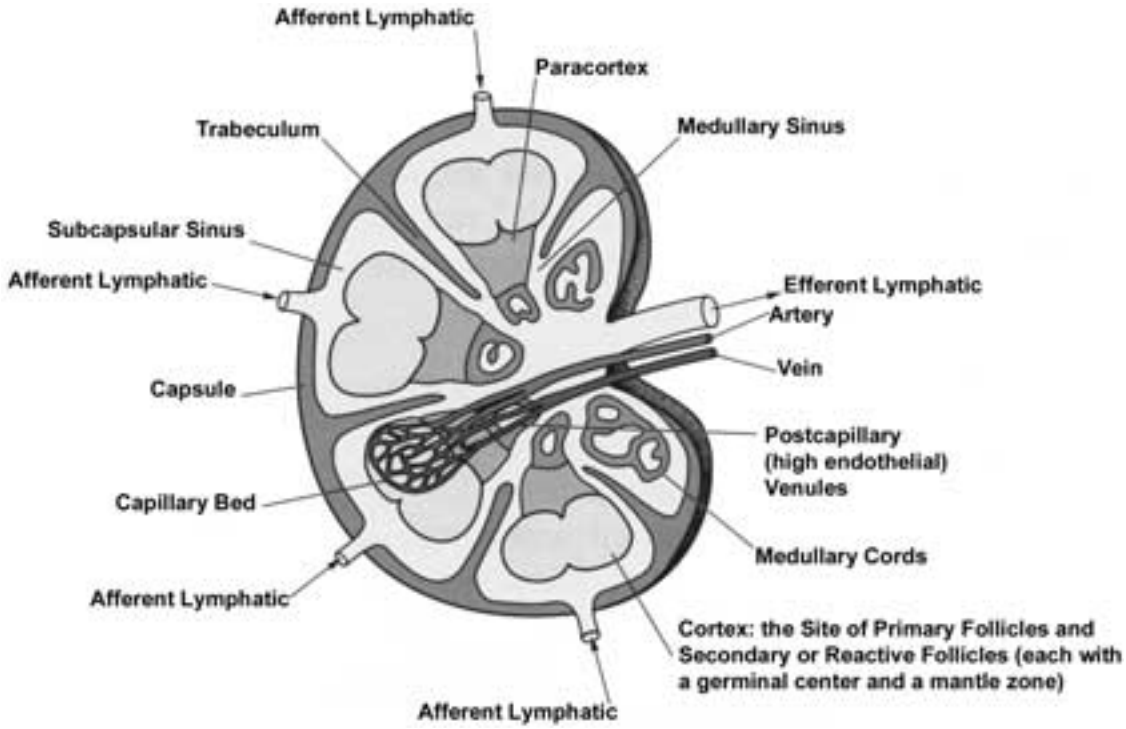

FIGURE 36-1 Diagram of a lymph node. The arrows indicate the direction of the flow of lymph. Afferent lymphatics bring the lymph to the node, and the lymph exits the node via the efferent vessels in the hilum. In the cortex of the node are the primary follicles and the secondary or reactive follicles, each with a germinal center and mantle. It is through the HEV in the paracortex that 10% to 20% of circulating lymphocytes enter the node. (Modified from Iochim H. Lymph Node Pathology. 2nd ed. Philadelphia: JB Lippincott, 1994;1.)

VIEW IMAGE

Copyright © 2003, Mosby, Inc. All rights reserved.

present in extranodal mucosa-associated lymphoid tissue (MALT) such as tonsillar tissue and the gastrointestinal tract. The blood vessels of the cortex and the medulla are not specialized and thus do not allow exit of lymphocytes.[16, 19]

More specifically, it is known that CD44, an 80- to 90-kDa hyaluronate-binding glycoprotein, is involved in binding cells to the HEV of the postcapillary venules, and LECAM-1, a 75- to 85-kDa glycoprotein with lectin activity, is also known to interact with human peripheral lymph node vascular addressin (PNAd) on the HEV. Both CD44 and LECAM-1 are expressed on B lymphocytes. L-Selectin is a cell adhesion molecule that mediates homing of lymphocytes to peripheral lymph nodes and is speculated to bind with the carbohydrate determinant specifically expressed by HEV in the peripheral lymph nodes. It is also probable that sialyl leX determinants, having complex carbohydrate structures, also serve as the ligand for L-selectin on HEV cells.[20–29]

The stroma or supporting framework of the node is formed by the lymph node capsule, trabeculae, and a network of reticular cells and fibers that form the main extracellular matrix of the lymph node and maintain the structure of the node by connections to the trabeculae. These fibers are reinforced by fine collagen fibers, and together this framework supports the lymphoid cells within the lymph node. The main components of the capsule and trabeculae are fibroblasts; however, there are also smooth muscle cells, nerves with Schwann cells, and blood vessels with pericytes.

The cortex, or superficial cortex, is the seat of humoral immunity, mediated by B-cell lymphocytes. Thus, the cortex consists mostly of B cells. The cortex contains lymphoid follicles (primary follicles) that, when stimulated, develop reactive germinal centers (secondary follicles). Reactive follicles are surrounded by a peripheral mantle zone composed of small, mature, circulating, nonactivated B-cell lymphocytes.[19] These lymphocytes enter the node via the postcapillary venules and, failing activation, return to the general circulation within a few hours through the efferent lymphatics. If the small B-cell lymphocytes in the peripheral mantle zone become stimulated by antigens, they undergo blastic transformation and migrate into the germinal zone as small cleaved cells (nondividing centocytes). These cells acquire a narrow rim of pyroninophilic cytoplasm as they reach the large cleave cell stage. The nuclear cleavage then disappears as the nuclei become round or oval, and mitosis of these cells results in small noncleaved (dividing centroblasts) cells that further mature into large noncleaved cells (immunoblasts) that typify germinal follicles. Stimulated immunoblasts then give rise to plasma cells. In the cortex, there are also dendritic reticulum cells that aid in antigen presentation to the lymphocytes. In addition, there are a few T-cell lymphocytes.[16, 19] Thus, when naive B cells are activated by antigen, they mature and produce an expanded population of identical dedicated cells that recognize the same antigen. Histologically, this is seen as an increase in the number and size of germinal centers, with the above-mentioned mantle zone and pale centers containing abundant immunoblasts, and ''tingible body'' macrophages with cytoplasmic nuclear debris.

The paracortical area, or deep cortex, is a densely cellular subcortical area extending between the lymphoid follicles and interdigitating to the corticomedullary junction. It contains postcapillary venules and lymphoid cells. The paracortex is the main site of cellular immunity.[19]

The T cells also enter the lymph node via the postcapillary HEV and, unless activated, leave the node within a few hours through efferent lymphatics. If activated, the T cells enlarge, proliferate, and produce a clone of cells that disseminate peripherally, where they are most active. The T cells are composed of two major subpopulations: T4 (helper cells, CD4 cells) and T8 (suppressor cells, CD8 cells).[19]

The medulla contains lymphocytes, plasmatoid lymphocytes, and mature plasma cells and is the main site of plasma cell proliferation and antibody production. Under intense antigenic stimulation, the medullary cords may extend deep into the cortex. The cords of plasma cells and precursors are separated by wide medullary sinuses containing lymphocytes, monocytes, plasma cells, and macrophages. The plasma cells are primarily responsible for the memory-recall type of antibody stimulation.[19] Additional accessory immunologic cells involved in antigen presentation and processing (monocytic/histiocytic cells) migrate from the peripheral tissues and the bone marrow to the lymph node.

Normally, the lymph node is estimated to recirculate its entire population of lymphocytes within about 12 days. This flow can double or treble when the node is antigenically challenged. In part, this reflects the normal rich lymph node blood flow of about 1 ml/minute/gram and the normal lymph flow of about 10 ml/minute/gram. These flows also increase with antigenic challenge. As the blood flows through the node, between 10% and 20% of the blood lymphocytes extravasate out. Within 5 hours, these lymphocytes migrate through the node and emerge in the efferent lymph.[16]

PATHWAYS OF LYMPH NODE METASTASIS

The ability of tumor to invade basement membrane and underlying connective tissue and gain access to vascular/lymphatic channels is dependent upon the elaboration of extracellular proteases such as matrix metalloproteinases (MMP) and plasminogen activators (see Chapter 44).[30, 31] Lymphatico-lymphatic spread is the dominant pathway by which invasive tumor cells enter the lymph capillaries and metastasize to the lymph nodes. That is, tumor cells enter the lymph and pass into a node via the afferent lymphatic vessels. However, there is also evidence for a hematogenous route, or veno-lymphatic pathway, that allows tumor cells to enter the lymph node via the blood circulation at the nodal hilum and then enter the central region of the lymph node via the HEV cells of the postcapillary paracortical venules following the pathway taken by lymphocytes.[32] This mechanism accounts for the occasional observation of isolated tumor metastasis in the paracortical zone, away from afferent lymphatics.

It has been established that tumor cells may recognize nodal homing sites on the HEV cells of the postcapillary venules.[33–38] There is also evidence that squamous cell carcinoma cells have specific surface markers that may influence their propensity to metastasize to lymph nodes.[20, 21, 23–29, 33–44]

CD44 is a membrane protein involved in cell adhesion, lymphocyte activation, and cellular homing. Numerous splice variants have been described, one of which (CD44v6)

Copyright © 2003, Mosby, Inc. All rights reserved.

has been found upregulated in metastatic adenocarcinoma.[45, 46] However, conflicting data exist regarding the relationship of CD44v6 and metastatic potential. Downregulation of CD44 has also been associated with metastatic potential, and it has been hypothesized that the lack of ''anchorage'' may enable a tumor to metastasize.[47]

CLINICAL SIGNIFICANCE OF METASTATIC NODAL CARCINOMA

The presence of cervical metastatic nodal disease is a major prognostic determinant for patients with head and neck cancer, significantly reducing patient survival.[48] Historically, surgeons believed that a cure could only be achieved if the primary tumor site was controlled. It is now known that patient mortality may result from recurrent cervical nodal disease and distant metastasis despite control of the primary tumor. In fact, the presence of positive lymph nodes at initial presentation is the strongest prognosticator for the recurrence of cervical nodal metastases and the eventual development of distant metastases.[1–15, 49–52] The presence of a solitary ipsilateral or contralateral positive lymph node, or extracapsular tumor spread, each reduces the expected survival by nearly 50% for all head and neck sites. Presumably due to a reseeding effect, it has also been observed that the persistence or recurrence of tumor at the primary site is associated with an increased incidence of both nodal and distant metastases.

As a result of better local and regional control, patients with head and neck cancers are surviving longer, allowing for the development of distant metastases. Usually the lungs, bones, and liver are involved as a reflection of the natural history of this disease.[8, 53] The potential for distant metastases provides the rationale for neoadjuvant chemotherapy, although this is not presently a universally accepted part of standard initial therapy.

An important issue for upper aerodigestive tract carcinoma is the treatment of the clinically and radiographically negative (N0) neck. When all upper aerodigestive tract sites are considered, about 15% of such N0 necks will eventually develop metastatic disease.[49] The resultant dilemma is how to predict which patients will fall into this 15% group and require treatment, thus avoiding overtreating 85% of these patients. Alternatively, there are the conflicting survival data regarding the approach of awaiting the clinical development of metastatic cervical nodal disease versus treating the neck prophylactically at initial presentation.[54]

One approach to identifying those N0 cases that may require treatment is to examine the risk factors at the primary tumor site. It has been advocated that either a selective neck dissection or radiotherapy should be offered to patients with N0 necks when the risk of occult metastasis exceeds 20%.[55, 56] In multivariate analysis of risk factors, the following are significant independent predictors of occult metastases: tumor site, T stage, tumor thickness, histologic grade, vascular embolization, and perineural infiltration.[55, 57] The number of microvessels in the primary tumor may also be closely associated with the tumor's potential to metastasize to regional lymph nodes.[58] Additionally, metastases with a desmoplastic pattern are associated with a sevenfold increase in the risk of subsequent recurrent neck disease.[59]

There is a wide range of metastatic rates (1% to 85%) for all upper aerodigestive tract sites. For T3/T4 carcinomas of the oral cavity, oropharynx, hypopharynx, and supraglottic larynx, the ipsilateral metastatic rate is greater than 50%.[55] The rate for bilateral metastases or isolated contralateral metastases ranges from 2% to 35%. Tables 36-1 to 36-3 summarize different experiences regarding the incidence of nodal metastasis associated with various head and neck primary tumors. These factors may be helpful in predicting which primary tumors within N0 necks require treatment.

THE CLINICAL IMPACT OF IMAGING METASTATIC LYMPH NODES

Once metastatic adenopathy is identified within the neck, the information derived about the number of nodes, the unilaterality or bilaterality of the disease, the location of the nodes, and the size of the nodes can be used in two different formats to aid prognostication and patient treatment. First, nodal classification incorporates the location of involved lymph nodes to allow selection of the proper type of neck dissection. Second, N status as part of the overall TNM staging system is a critical predictor of survival and dictates treatment philosophy. The ability of imaging to identify clinically silent adenopathy does not necessarily correlate

Table 36-1
INCIDENCE OF IPSILATERAL AND CONTRALATERAL METASTASIS ACCORDING TO STAGE

Tumor Site	% of Cases with Ipsilateral Metastasis				% of Cases with Contralateral Metastasis
	T1	T2	T3	T4	
Inferior lip	4	42	77	87	1
Oral tongue	6	37	63	74	17
Floor of mouth	31	44	67	81	17
Retromolar trigone	100	46	50	56	2
Soft palate	31	28	53	74	18
Base of tongue	0	86	91	76	39
Tonsil	38	48	61	77	10
Supraglottis	78	73	69	76	18
Glottis/transglottic	5	5	31	60	5
Pyriform sinus	100	77	80	84	22

Source: Modified from Kowalski L, Medina J. Nodal metastases: predictive factors. Otolaryngol Clin North Am 1998; 31:621–631.

Copyright © 2003, Mosby, Inc. All rights reserved.

Table 36-2
HEAD AND NECK PRIMARY TUMOR SITES AND THEIR CORRELATION WITH CERVICAL NODAL METASTASIS

Primary Site	Common Nodal Levels	% Presenting with Nodes	% with Bilateral Nodes
Oral tongue	I, II, III	34–65	11.8
Floor of mouth	I, II	30–59	7.8
Retromolar trigone			
Anterior tonsillar pillar	I, II, III	39–56	8.8
Soft palate	II	37–56	25
Nasopharynx	II, III, IV, V (22.3%)	86–90	32.8
Oropharynx	II, III, V (10.9%)	50–71	20.2
Tonsillar fossa	I, II, III, IV, V (9.0%)	58–76	13
Hypopharynx	II, III, IV, V (8.4%)	52–72	9
Base of tongue	II, III, IV, V (6.7%)	50–83	21.3
Supraglottic larynx	II, III, IV	31–54	22.5

with ''upstaging'' for all patients, as, among other reasons, enlarged nodes may be hyperplastic rather than metastatic.

Various literature reports reveal that imaging can identify 7.5% to 19% of clinically silent metastatic nodes.[1, 3, 4, 6, 7, 60] However, the actual impact of these nodes on staging is not obvious, and several series reflect a wide variation in imaging upstaging. Mancuso et al. reported that 6% of necks were upstaged from N0 to N1.[2] Stevens et al. reported that 2.5% of 40 cases were upstaged from N0 to N1, 10% of cases were upstaged from N0 to N2, and 10% of cases were upstaged from N1 to N2 necks.[4] However, at the other extreme, Close et al. reported imaging upstaging in 67% of N0 necks, while van den Brekel et al. reported imaging upstaging in 71% of N0 necks.[6, 7] These latter two studies probably reflect a smaller number of patients. We believe that larger series would no doubt reflect a lower rate of N0 to N1 upstaging, probably closer to 5% of the time.

Pretreatment imaging may also identify lymph nodes outside of the typical treatment areas (e.g., retropharyngeal or high level II nodes, low level IV or V nodes, or nodes in levels VI and VII), thus expanding the typical treatment fields and potentially improving patient survival.

Postsurgical and/or postradiation surveillance imaging is a mainstay of patient follow-up. Such surveillance probably has very little impact on facilitating cures after local recurrence, but imaging surveillance certainly improves palliation and prolonged disease-free survival (see Chapter 43). Untreated local recurrences usually result in a rapid, uncomfortable death. The treatment of local recurrence thus can result in good palliation, often lasting for several years, which is of incalculable value to these patients and their families.

Table 36-3
PATTERNS OF NODAL METASTASES

	% of Nodal Metastases Based on Palpation					
Primary Tumor	IA	IB	II	III	IV	V
Palatine tonsil	0.6	9.2	59.5	14.4	8.1	8.1
Base of tongue	0.8	4.4	56.4	25.3	5.8	7.1
Pharyngeal wall	1.5	3.6	56.9	22.6	5.1	10.2
Hypopharynx	0.3	0.6	44.2	33.4	12.8	8.6
Nasopharynx	1.1	2.6	44.8	16.8	8.6	26.1

Source: Based on Medina J. A rational classification of neck dissections. Otolaryngol Head Neck Surg 1989; 100:169–176.

NODAL CLASSIFICATION

Initially, the aim of developing a classification for identifying the cervical lymph nodes was to achieve anatomic precision. Prior to the early 1900s, there was little established nodal classification, and there was a relative lack of understanding of the cervical lymphatic pathways and their respective drainage regions. The scope of the problem of developing an acceptable nodal nomenclature for the head and neck is exemplified by noting that of the estimated 800 lymph nodes in the body, about 300 are located in the head and neck.[61] Thus, approximately 40% of the lymph nodes in the body are located in about 20% of the body's volume. Further complicating nodal identification is the fact that all of these lymph nodes are situated in fat and, if not reactively or pathologically enlarged, they are almost impossible to identify at surgery or autopsy.

For nearly four decades, the most commonly used classification for the cervical lymph nodes was that developed by Rouviere in 1938.[61] His work followed an earlier classification by Trotter in 1930, which was based on earlier work by Poirer and Charpy in 1909.[62, 63] Many of the landmarks used in these classifications were based on the superficial triangles of the neck, areas that were easily accessible to palpation and referred to by familiar names (Fig. 36-2).

In 1981, Shah et al. suggested that the anatomically based terminology be replaced with a simpler level-based system. Since then, a number of clinically and radiologically based classifications have been proposed that employ such nonanatomic terminology.[2, 50, 64–72] The aim of these more recent classifications was more functional than anatomic. That is, their purpose was to aid the surgeon in selecting the most appropriate type of nodal dissection based on the nodal groups involved. This was accomplished by grouping the cervical nodes into *levels* that were based on pathophysiologic observation of cancer spread. Thus, the distinction between the upper internal jugular and spinal accessory nodes described by Rouviere was replaced by one group of level II nodes.

The landmarks used to separate the nodal levels in these various clinically based classifications vary from those determined by physical palpation to those identified at surgery. This has led to some confusion regarding nodal level boundaries. One of the most recent and most widely utilized classifications is the 1997 version of the American Joint Committee on Cancer (AJCC) (Table 36-4) (Fig. 36-3).[70] Although this work is the product of many years of modification, dis-

Copyright © 2003, Mosby, Inc. All rights reserved.

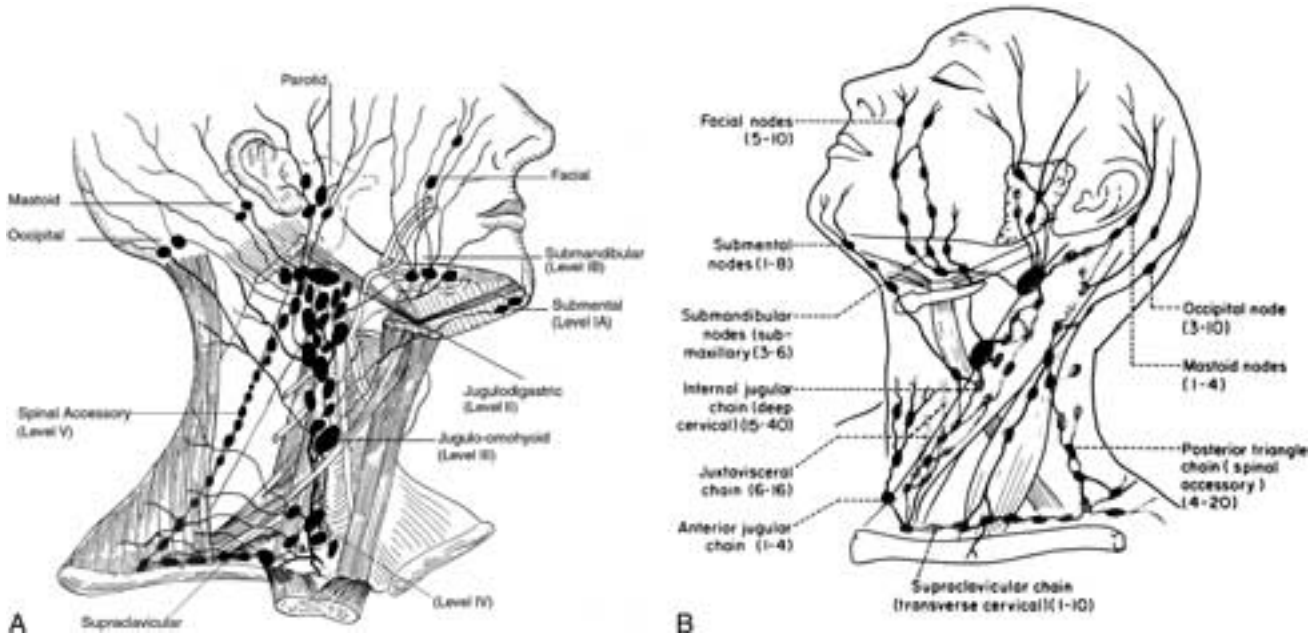

FIGURE 36-2 **A**, Drawing of the head and neck region as seen from the right side. The major nodal chains, as described by Rouviere, are identified, and their corresponding nodal levels are noted. Several of the important superficial nodal groups are also shown. **B**, Drawing of the head and neck region as seen from the left side also shows the important nodal groups described by Rouviere, and the approximate number of nodes usually seen within each nodal group is noted. The retropharyngeal nodes and other deep nodes are not shown.

Table 36-4
1997 AJCC NODAL CLASSIFICATION

Level I	Contains the submental and submandibular triangles bounded by the posterior belly of the digastric muscle, the hyoid bone inferiorly, and the body of the mandible superiorly.
Level II	Contains the upper jugular lymph nodes and extends from the level of the skull base superiorly to the hyoid bone inferiorly.
Level III	Contains the middle jugular lymph nodes from the hyoid bone superiorly to the cricothyroid membrane inferiorly.
Level IV	Contains the lower jugular lymph nodes from the cricothyroid membrane superiorly to the clavicle inferiorly.
Level V	Contains the lymph nodes in the posterior triangle bounded by the anterior border of the sternocleidomastoid muscle anteriorly and the clavicle inferiorly. For descriptive purposes, level V may be further subdivided into upper, middle, and lower levels corresponding to the superior and inferior planes that define levels II, III, and IV.
Level VI	Contains the lymph nodes of the anterior compartment from the hyoid bone superiorly to the suprasternal notch inferiorly. They lie between the medial borders of the carotid sheaths.
Level VII	Contains the lymph nodes inferior to the suprasternal notch in the upper mediastinum.

Note: Retropharyngeal, parotid, facial, occipital, and other nodes are referred to by these names.

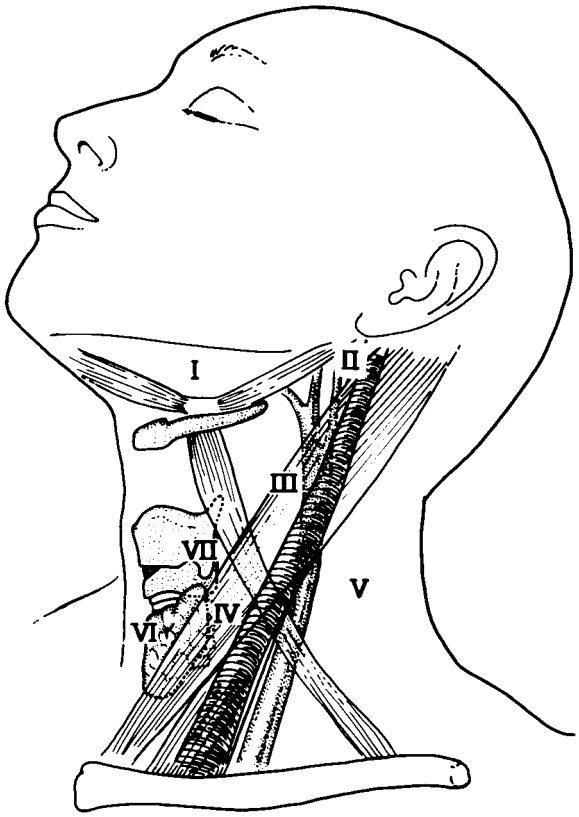

FIGURE 36-3 Drawing of the head and neck region as seen from the left side showing the AJCC nodal levels. Note that the internal jugular vein parallels the oblique orientation of the sternocleidomastoid muscle, and the vein is lateral to the internal carotid artery, which runs more vertically in the neck. Thus, the vein is dorsal to the artery at the skull base but ventral to the artery at the root of the neck. The digastric and omohyoid muscles are indicated for reference. Nodal levels I to VII of the AJCC classification are indicated.

Copyright © 2003, Mosby, Inc. All rights reserved.

cussion, and pathologic correlation, there are several areas that are somewhat broadly defined and may lack reproducibility. The American Academy of Otolaryngology-Head and Neck Surgery (AAO-HNS) classification was modified by Robbins in 1998.[73] Differences between these two classifications include the separation of level II nodes into the internal jugular chain (IIA) and the spinal accessory chain (IIB), the separation of level IV nodes into those deep to the sternal head of the sternocleidomastoid muscle (IVA) and those that lie deep to the clavicular head (IVB) of this muscle, and the division of the level V nodes into upper (VA) and lower (VB) divisions rather than into the three divisions suggested in the AJCC classification. These alterations were suggested because (1) involvement of level IIB nodes most often is associated with tumors in the oropharynx and nasopharynx, (2) involvement of level IVA nodes has a high risk of nodal disease in level VI, (3) disease in level IVB is associated with nodal metastasis in level V, and (4) the observation that the upper level V nodes of the AJCC system actually contain few, if any, nodes. It was thus considered more reasonable to divide level V simply into an upper and a lower group based on the position of the inferior belly of the omohyoid muscle. Having noted these differences, it should be mentioned that there is no present consensus as to the need to split some of the nodal levels into separate subcategories.

To address specific issues raised in both the AJCC and the AAO-HNS classifications, and to bring the anatomic detail and reproducibility of imaging to nodal classification, an imaging classification was suggested in 1999.[74] This classification can be applied to either the clinical examination or imaging studies using landmarks readily identified with either. The system is not meant to replace the clinical assessment, but rather to allow clinicians and radiologists to use the same system. Imaging was chosen to be the basis of the modification for three reasons: (1) most patients with head and neck cancer today have an initial computed tomography (CT) or magnetic resonance (MR) imaging study to assess both the primary tumor and the extent of nodal disease; this is especially true for deeply situated tumors. It is estimated that over 80% of cancer patients obtain such imaging. (2) Imaging can identify clinically silent nodes (usually in areas inaccessible to palpation such as retropharyngeal nodes, nodes deep to the sternocleidomastoid muscle, and deep low visceral nodes).[1–8, 60] (3) Imaging has the potential to best reveal precise anatomic landmarks that lend themselves to a consistent definition of nodal groups or levels. This classification is presented in Table 36-5 and is summarized in Figures 36-4 and 36-5, and a comparison between the three clas-

Table 36-5
SUMMARY OF THE IMAGING-BASED LEVEL NODAL CLASSIFICATION

Level I	The submental and submandibular nodes. They lie above the hyoid bone, below the mylohyoid muscle and anterior to the back of the submandibular gland.
Level IA	The submental nodes. They lie between the medial margins of the anterior bellies of the digastric muscles.
Level IB	The submandibular nodes. On each side, they lie lateral to the level IA nodes and anterior to the back of each submandibular gland.
Level II	The upper internal jugular nodes. They extend from the skull base to the level of the bottom of the body of the hyoid bone. They are posterior to the back of the submandibular gland and anterior to the back of the sternocleidomastoid muscle.
Level IIA	A level II node that lies either anterior, medial, lateral, or posterior to the internal jugular vein. If posterior to the vein, the node is inseparable from the vein.
Level IIB	A level II node that lies posterior to the internal jugular vein and has a fat plane separating it from the vein.
Level III	The midjugular nodes. They extend from the level of the bottom of the body of the hyoid bone to the level of the bottom of the cricoid arch. They lie anterior to the back of the sternocleidomastoid muscle.
Level IV	The low jugular nodes. They extend from the level of the bottom of the cricoid arch to the level of the clavicle. They lie anterior to a line connecting the back of the sternocleidomastoid muscle and the posterior-lateral margin of the anterior scalene muscle. They are also lateral to the carotid arteries.
Level V	The nodes in the posterior triangle. They lie posterior to the back of the sternocleidomastoid muscle from the skull base to the level of the bottom of the cricoid arch and posterior to a line connecting the back of the sternocleidomastoid muscle and the posterior-lateral margin of the anterior scalene muscle from the level of the bottom of the cricoid arch to the level of the clavicle. They also lie anterior to the anterior edge of the trapezius muscle.
Level VA	Upper level V nodes. They extend from the skull base to the level of the bottom of the cricoid arch.
Level VB	Lower level V nodes. They extend from the level of the bottom of the cricoid arch to the level of the clavicle as seen on each axial scan.
Level VI	The upper visceral nodes. They lie between the carotid arteries from the level of the bottom of the body of the hyoid bone to the level of the top of the manubrium.
Level VII	The superior mediastinal nodes. They lie between the carotid arteries below the level of the top of the manubrium and above the level of the innominate vein.
Supraclavicular Nodes	They lie at or caudal to the level of the clavicle and lateral to the carotid artery on each side of the neck as seen on each axial scan.
Retropharyngeal Nodes	Within 2 cm of the skull base they lie medial to the internal carotid arteries.

Note: The parotid nodes and other superficial nodes are referred to by their anatomic names.

Copyright © 2003, Mosby, Inc. All rights reserved.

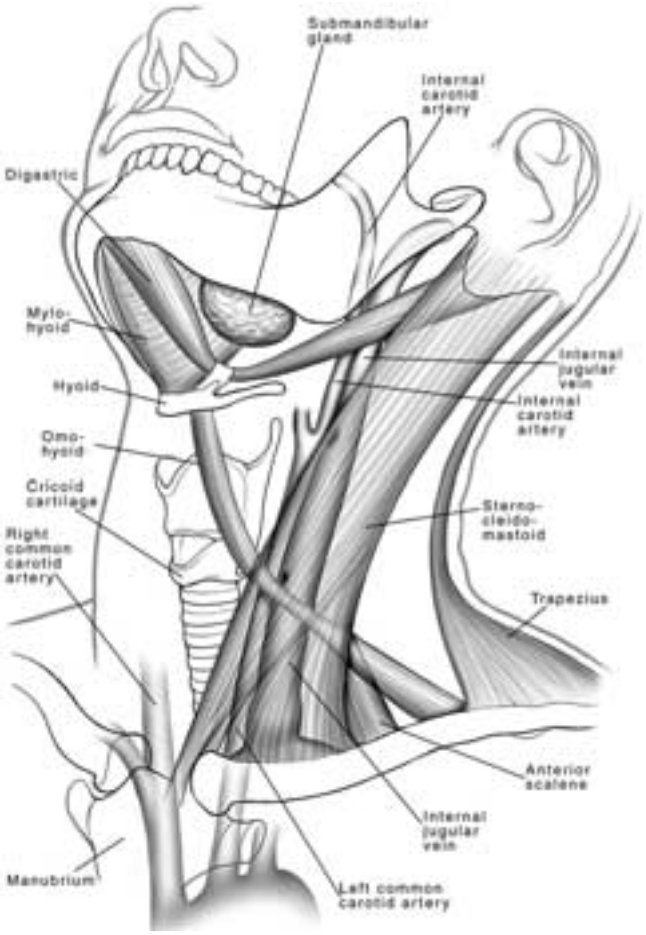

VIEW IMAGE

FIGURE 36-4 Diagram of the head and neck viewed from the left anterior oblique projection. The anatomic landmarks used in the imaging-based nodal classification are shown.

sifications is shown in Table 36-6. Nodal classifications are continuously evolving, with modifications constantly being proposed to better allow surgeons to plan the most appropriate surgery. Thus, these classifications are presented with the understanding that modifications can be anticipated. The enthusiastic clinical acceptance of the imaging-based classification hopefully has ushered in an era in which classification and staging of head and neck malignancies will require CT or MR imaging studies.

The Rouvière System

The predominant nodal classification used for nearly 40 years was that of the French anatomist Rouvière (Fig. 36-2).[61] He described a lymphoid ''collar'' of nodes encircling the top of the neck composed of the occipital, mastoid, parotid, facial, retropharyngeal, submaxillary, submental, and sublingual lymph nodes. Anterior and lateral cervical groups of lymph nodes, respectively, descended from the collar along the front and sides of the neck. Rouviere described the deep lateral cervical group as being composed of an internal jugular chain, a spinal accessory (posterior triangle) chain, and a transverse cervical (supraclavicular) chain. These three chains, joined at their edges, formed a lateral triangle of nodes in the neck. The deep cervical or internal jugular lymph node chain is the primary drainage pathway of the head and neck and ultimately receives lymph from all of the other nodal chains. Two nodes in this chain are of special importance. The first is the jugulodigastric (JD), or sentinel, node, which lies near the angle of the mandible and receives lymph from the tonsils, pharynx, mouth, and facial region. As a result of numerous infections in its drainage area, this node tends to be hyperplastic and larger than most other lymph nodes. The second node is the juguloomohyoid (JO) node, which lies near the point at which the omohyoid muscle crosses the internal jugular chain. The JO node receives all of the lymph from the tongue, and if enlarged, it may be the first physical finding to suggest an otherwise clinically silent tongue tumor.[61]

As summarized by Last, the lymphatics of the head and neck, with the exception of the tongue, are organized into two circles or cylinders: an outer one that contains the superficial nodes extending from the chin to the occiput (the submental, submandibular, buccal, mandibular, preauricular, and occipital nodes) and an inner one that lies within the outer one and surrounds the upper aerodigestive tract. Specifically, the nodal groups included in the inner circle are the retropharyngeal, pretracheal, and paratracheal nodes. Lying vertically between these two circles and accompanying the internal jugular veins are the deep cervical

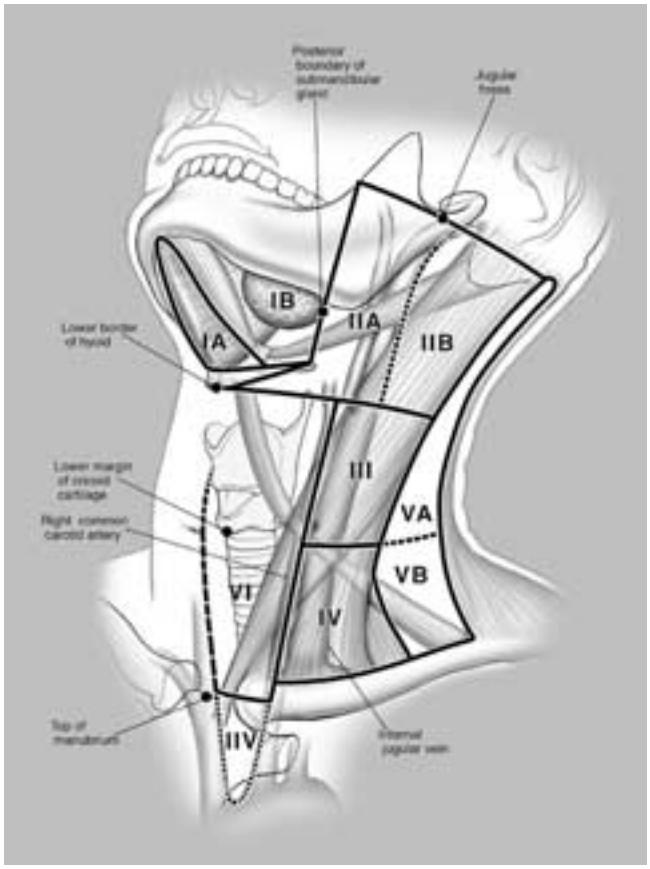

FIGURE 36-5 Diagram of the head and neck viewed from the left anterior oblique projection. The broad lines outline the boundaries of the nodal levels, and I to VII identify the specific nodal levels of the imagery-based nodal classification.

VIEW IMAGE

Copyright © 2003, Mosby, Inc. All rights reserved.

Table 36-6
COMPARISON OF AJCC, AAO-HNS, AND IMAGING NODAL CLASSIFICATIONS

	1997 AJCC	1998 Modification of the 1991 AAO-HNS	1999 Imaging
Level I	Contains the submental and submandibular triangles bounded by the posterior belly of the digastric muscle, the hyoid bone inferiorly and the body of the mandible superiorly.	Submental and submandibular nodes from the mandible to the hyoid and anterior to the posterior bellies of the digastric muscle.	The submental and submandibular nodes. They lie above the hyoid bone, below the mylohyoid muscle and anterior to the back of the submandibular gland.
Level IA		Submental nodes between the anterior bellies of the digastric muscles, above the hyoid bone and below the mandible.	The submental nodes. They lie between the medial margins of the anterior bellies of the digastric muscles.
Level IB		Submandibular nodes between the anterior and posterior bellies of the digastric muscle below the body of the mandible.	The submandibular nodes. On each side, they lie lateral to the level IA nodes and anterior to the back of each submandibular gland.
Level II	Contains the upper jugular lymph nodes and extends from the level of the skull base superiorly to the hyoid bone inferiorly.	Upper jugular nodes from the skull base to either the carotid bifurcation or the hyoid bone. Anterior to the posterior border of the sternocleidomastoid muscle and posterior to the lateral border of the stylohyoid muscle.	The upper internal jugular nodes. They extend from the skull base to the level of the bottom of the body of the hyoid bone. They are posterior to the back of the submandibular gland and anterior to the back of the sternocleidomastoid muscle.
Level IIA		Level II nodes anterior to the spinal accessory nerve.	A level II node that lies either anterior, medial, lateral, or posterior to the internal jugular vein. If posterior to the vein, the node is inseparable from the vein.
Level IIB		Level Il nodes posterior to the spinal accessory nerve.	A level II node that lies posterior to the internal jugular vein and has a fat plane separating it and the vein.
Level III	Contains the middle jugular lymph nodes from the hyoid bone superiorly to the cricothyroid membrane inferiorly.	Middle jugular nodes from the hyoid bone or carotid bifurcation to the cricothyroid membrane or where the omohyoid muscle crosses the internal jugular vein bone. They are anterior to the posterior border of the sternocleidomastoid muscle and posterior to the lateral border of the stylohyoid muscle.	The midjugular nodes. They extend from the level of the bottom of the body of the hyoid bone to the level of the bottom of the cricoid arch. They lie anterior to the back of the sternocleidomastoid muscle.
Level IV	Contains the lower jugular lymph nodes from the cricothyroid membrane superiorly to the clavicle inferiorly.	Lower jugular nodes from the level where the omohyoid muscle crosses the internal jugular vein to the level of the clavicle. Anterior to the posterior border of the sternocleidomastoid muscle and posterior to the lateral border of the sternohyoid muscle.	The low jugular nodes. They extend from the level of the bottom of the cricoid arch to the level of the clavicle. They lie anterior to a line connecting the back of the sternocleidomastoid muscle and the posterior-lateral margin of the anterior scalene muscle. They are also lateral to the carotid arteries.
Level IVA		Level IV nodes deep to the sternal head of the sternocleidomastoid muscle.	
Level IVB		Level IV nodes deep to the clavicular head of the sternocleidomastoid muscle.	
Level V	Contains the lymph nodes in the posterior triangle bounded by the anterior border of the sternocleidomastoid muscle anteriorly and the clavicle inferiorly. For descriptive purposes, level V may be further subdivided into upper, middle, and lower levels corresponding to the superior and inferior planes that define levels II, III, and IV.	Posterior triangle nodes lying between the posterior border of the sternocleidomastoid muscle, the anterior border of the trapezius muscle, and above the clavicle.	The nodes in the posterior triangle. They lie posterior to the back of the sternocleidomastoid muscle from the skull base to the level of the bottom of the cricoid arch and posterior to a line connecting the back of the sternocleidomastoid muscle and the posterior-lateral margin of the anterior scalene muscle from the level of the bottom of the cricoid arch to the level of the clavicle. The also lie anterior to the anterior edge of the trapezius muscle.
Level VA		Level V nodes lying above the level of the posterior belly of the omohyoid muscle.	Upper level V nodes extend from the skull base to the level of the bottom of the cricoid arch.

Copyright © 2003, Mosby, Inc. All rights reserved.

Table 36-6
COMPARISON OF AJCC, AAO-HNS, AND IMAGING NODAL CLASSIFICATIONS *Continued*

	1997 AJCC	1998 Modification of the 1991 AAO-HNS	1999 Imaging
Level VB		Level V nodes lying below the level of the posterior belly of the omohyoid muscle.	Lower level V nodes extend from the level of the bottom of the cricoid arch to the level of the clavicle as seen on each axial scan.
Level VI	Contains the lymph nodes of the anterior compartment from the hyoid bone superiorly to the suprasternal notch inferiorly. On each side, the lateral border is formed by the medial border of the carotid sheath.	Central compartment nodes extending from the hyoid bone to the suprasternal notch and lying between the medial border of each carotid sheath.	The upper visceral nodes. They lie between the carotid arteries from the level of the bottom of the body of the hyoid bone to the level of the top of the manubrium.
Level VII	Contains the lymph nodes inferior to the suprasternal notch in the upper mediastinum.		The superior mediastinal nodes. They lie between the carotid arteries below the level of the top of the manubrium and above the level of the innominate vein.
Supraclavicular Nodes	They lie below the level of Ho's triangle.		They lie at or caudal to the level of the clavicle and lateral to the carotid artery on each side of the neck, as seen on each axial scan.
Retropharyngeal Nodes			Within 2 cm of the skull base, they lie medial to the internal carotid arteries.

Note: Retropharyngeal, parotid, facial, occipital, and other nodes are referred to by these names for all classifications.

(jugular chain) nodes, into which virtually all of the lymph from both the inner and outer circles of nodes drains. Table 36-7 compares the Rouviere nomenclature with the level systems.[75]

The Level Systems

Since the introduction of the initial level nodal classification, there have been a number of classifications that define the nodal groups slightly differently.[2, 50, 64–72] Of these various proposals, the 1997 AJCC classification, the 1991 AAO-HNS classification and its 1998 modification, and the 1999 imaging modification[70, 73, 74] are the most widely used. They are summarized in Tables 36-4 to 36-7.

The Imaging-Based System

How to Scan the Neck

It is imperative that any nodal classification based on CT and MR imaging be reproducible no matter what scanner is utilized or where the imaging study is performed. In order to accomplish this, a consistent technique must be used. This is especially true for CT, where patient positioning and gantry angulation are variables. There is no one universal technique that is utilized to perform CT scans of the neck. However, the following technique is used by many head and neck radiologists, and slight variations from it do not effectively influence the nodal levels.

The axial plane referred to in this classification is obtained with the patient's head in a comfortable neutral position, with the hard palate perpendicular to the table top and the shoulders down as far as possible. The scanner gantry is aligned along the inferior orbital meatal (IOM) plane and, if possible, the examination should be performed with the administration of intravenous contrast to allow the best possible differentiation of nodes from vessels. The recommended field of view is 16 to 18 mm. With CT, the examination is performed as contiguous 3-mm scans from the skull base to the manubrium or as a spiral study reconstructed as contiguous 2-mm or 3-mm slices. With MR imaging, the scans should be no thicker than 5 mm (preferably 3 to 4 mm), with either no interslice gap or a 1-mm interslice gap. If there is a history of thyroid or cervical esophageal cancer, the caudal margin of the studies should be extended down to the level of the carina to ensure inclusion of the superior mediastinum.

When imaging a neck, the entire neck should be studied to evaluate both a potential primary tumor or infection site as well as any lymphadenopathy. Thus, the routine neck imaging examination should include the skull base and extend down to the manubrium. Using this imaging approach, the most likely potential primary sites along Waldeyer's ring, as well as all of the nodal chains, are visualized. This approach is especially pertinent when imaging the 3% to 9% of patients who present with metastatic adenopathy and no known primary tumor site. A discussion of ultrasound imaging of the neck appears in Chapter 37.

How to Use the Imaging-Based Classification

The classification was designed to be easily and readily usable. Each side of the neck should be evaluated separately. That is, the ''lines'' that are used to define the boundaries of the levels should be ''drawn'' separately for each side of the neck. The lines need not actually be drawn, as when one becomes familiar with the classification, they can be easily approximated visually or a straight-line guide or ruler can be placed on the film or monitor. Whenever a lymph node is transected by one of the lines that define the levels, the side

Copyright © 2003, Mosby, Inc. All rights reserved.

of the line on which the majority of the nodal cross-sectional area lies is the level in which the lymph node should be classified. The supraclavicular fossa is defined on each axial scan whenever any portion of the clavicle is identified on one side of the neck. That is, if the scan level is cranial to any portion of the clavicle, the nodes in the lower lateral neck should be classified as being in either level IV or level VB. Once any portion of the clavicle is seen on the scan, the level VB nodes are classified as supraclavicular nodes. If nodes are seen below the level of the clavicle and lateral to the ribs, they are axillary nodes. The clinically important internal jugular nodes described by Rouviere are now classified as level II, III, or IV nodes, depending on their location with reference to the axial scan levels of the bottom of the body of the hyoid bone and the bottom of the arch (anterior rim) of the cricoid cartilage (Figs. 36-4 and 36-5).

The Imaging-Based Classification

Level I includes all of the nodes above the bottom of the body of the hyoid bone, below the mylohyoid muscles, and anterior to a transverse line drawn on each axial image through the posterior edge of the submandibular gland (Figs. 36-6 to 36-8). Thus, level I nodes include the previously classified submental and submandibular nodes. Level I nodes can be subclassified into levels IA and IB.

Level IA represents the nodes that lie between the medial margins of the anterior bellies of the digastric muscles, above the bottom of the body of the hyoid bone and below the mylohyoid muscle (previously classified as submental nodes) (Figs. 36-7 and 36-9).

Level IB represents the nodes that lie below the mylohyoid muscle, above the bottom of the body of the hyoid bone, posterior and lateral to the medial edge of the anterior belly of the digastric muscle, and anterior to a transverse line drawn on each axial image tangent to the posterior surface of the submandibular gland on each side of the neck (previously classified as submandibular nodes) (Figs. 36-6 to 36-8).

Level II extends from the skull base, at the lower level of the bony margin of the jugular fossa, to the level of the lower body of the hyoid bone (Figs. 36-6 to 36-10). Level II nodes lie anterior to a transverse line drawn on each axial image through the posterior edge of the sternocleidomastoid muscle and lie posterior to a transverse line drawn on each axial scan through the posterior edge of the submandibular gland. If a node situated within 2 cm of the skull base lies anterior, lateral, or posterior to the carotid sheath, it is classified as a level II node. If the node lies medial to the internal carotid artery, it is classified as a *retropharyngeal node* (Figs. 36-9 and 36-11). Caudal to 2 cm below the skull base, level II nodes can lie anterior, lateral, medial, and posterior to the internal jugular vein. Level II nodes can be subclassified into levels IIA and IIB.

Level IIA nodes are level II nodes that lie posterior to the internal jugular vein and are inseparable from the vein, or they are nodes that lie anterior, lateral, or medial to the vein (previously classified as upper internal jugular nodes) (Figs. 36-6 to 36-10).

Level IIB nodes are level II nodes that lie posterior to the internal jugular vein and have a fat plane

Table 36-7
COMPARISON OF THE ROUVIERE AND LEVEL SYSTEMS OF NODAL CLASSIFICATION

Rouviere System	AJCC Level System	Imaging-Based Level System
Submental nodes	I	I (IA) (medial to the medial edge of the anterior belly of each digastric muscle)
Submandibular nodes	I	I (IB) (lateral to IA nodes and anterior to the back edge of the submandibular gland)
Internal jugular nodes	II (skull base to hyoid bone, anterior to back edge of sternocleidomastoid muscle)	II (skull base to bottom of body of hyoid bone, anterior to back edge of sternocleidomastoid muscle)
Retropharyngeal nodes		Retropharyngeal node medial to internal carotid artery within 2 cm of skull base
	III (hyoid to cricothyroid membrane, anterior to back edge of sternocleidomastoid muscle)	III (bottom of body of hyoid bone to bottom of cricoid arch, anterior to back edge of sternocleidomastoid muscle)
	IV (cricothyroid membrane to clavicle, anterior to back edge of sternocleidomastoid muscle)	IV (bottom of cricoid arch to top of manubrium, anterior to back edge of sternocleidomastoid muscle)
Spinal accessory nodes	V (posterior to sternocleidomastoid muscle, anterior to trapezius, above clavicle)	V (posterior to sternocleidomastoid muscle, anterior to trapezius, above clavicle) VA (level V nodes from skull base to the level of the bottom of the cricoid arch) VB (level V nodes from level of bottom of cricoid arch to level of clavicle)
Anterior compartment nodes	VI (below hyoid bone, above suprasternal notch, between carotid sheaths)	VI (below bottom of body of hyoid bone, above top of manubrium, medial to carotid arteries)
Upper mediastinal nodes	VII (below suprasternal notch)	VI (below top of manubrium and above innominate vein)

Note: Facial, parotid, retropharyngeal, occipital, and other nodes are referred to by these names for all classifications.

Copyright © 2003, Mosby, Inc. All rights reserved.

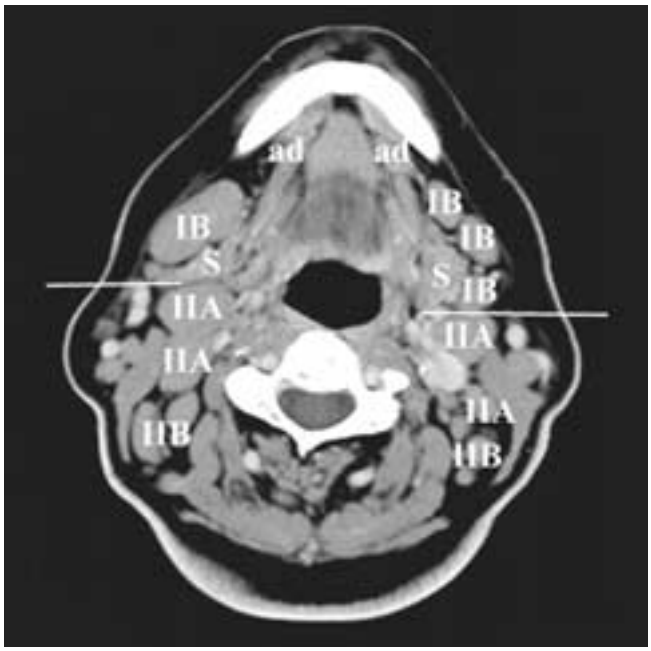

VIEW IMAGE

FIGURES 36-6 TO 36-19 Representative axial contrast-enhanced CT scans of the neck illustrating the use of the imaging-based nodal classification. In Figures 36-6 to 36-9, note that the dorsal edge of the submandibular gland (*S*) separates levels I and II. The medial edge of the anterior belly of the digastric muscle (*ad*) separates levels IA and IB. Also, note that level IIA nodes can be medial, anterior, or lateral to the internal jugular vein (*v*). They can also be posterior to the vein and touching it. Level IIB nodes are posterior to the vein and are not touching the vein. The back edge of the sternocleidomastoid muscle separates levels II, III, and IV from level V.

In Figures 36-10 and 36-11, note that the medial border of the internal carotid artery separates level II nodes from retropharyngeal nodes. Figures 36-12 and 36-13 are between the levels of the bottom of the body of the hyoid bone and the bottom of the cricoid cartilage. They define the level III nodes. In Figures 36-14 to 36-18, a line drawn from the back of the sternocleidomastoid muscle and the lateral edge of the anterior scalene muscle separates level IV from level V. Whenever a portion of the clavicle is seen on the image (Figs. 36-16 to 36-18), the level V nodes are referred to as *supraclavicular nodes.*

Below the bottom of the hyoid, the medial borders of the carotid arteries separate level IV nodes from level VI nodes. The upper border of the manubrium separates levels VI and VII (Fig. 36-19).

separating the nodes and the vein (previously classified as upper spinal accessary nodes) (Figs. 36-6 to 36-8).

Level III nodes lie between the level of the lower body of the hyoid bone and the level of the lower margin of the cricoid cartilage arch (Figs. 36-12 and 36-13). These nodes lie anterior to a transverse line drawn on each axial image through the posterior edge of the sternocleidomastoid muscle. Level III nodes also lie lateral to the medial margin of either the common carotid artery or the internal carotid artery. On each side of the neck, the medial margin of these arteries separates level III nodes (which are lateral) from level VI nodes (which are medial). Level III nodes were previously known as the midjugular nodes.

Level IV nodes lie between the level of the lower margin of the cricoid cartilage arch and the level of the clavicle on each side, as seen on each axial scan. These nodes lie anterior and medial to an oblique line

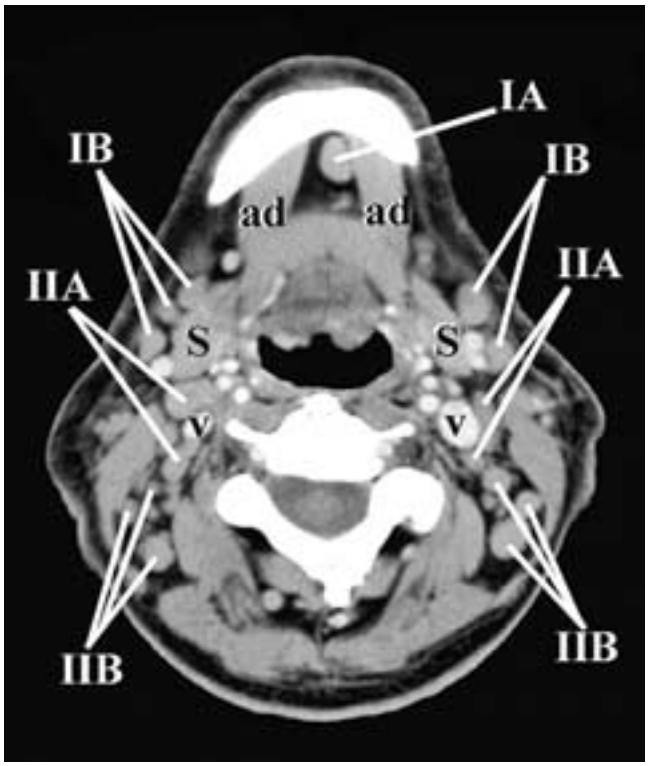

VIEW IMAGE

FIGURE 36-7 *Continued*

drawn through the posterior edge of the sternocleidomastoid muscle and the lateral posterior edge of the anterior scalene muscle (Figs. 36-14 to 36-18). The medial aspect of the common carotid artery is the landmark that separates level IV nodes (which are lateral) from level VI nodes (which are medial) to this artery (Figs. 36-14 and 36-18). Level IV nodes were previously known as the low jugular nodes (including the prescalene nodes).

Level V nodes extend from the skull base, at the posterior border of the attachment of the sternocleidomastoid muscle, to the level of the clavicle, as seen on each axial scan (Figs. 36-8, 36-10, and 36-12 to 36-16).

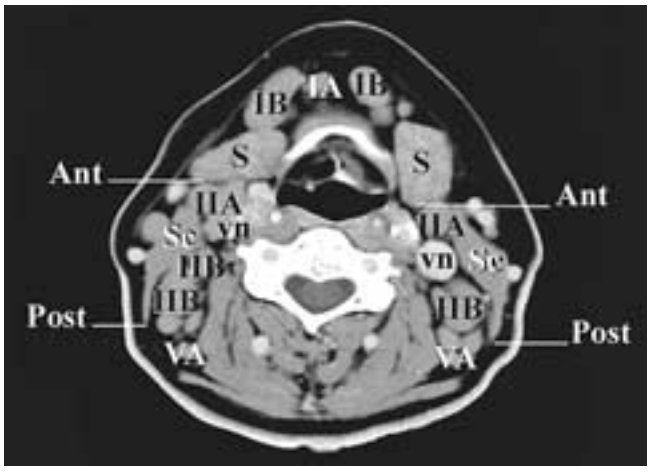

VIEW IMAGE

FIGURE 36-8 *Continued*

Copyright © 2003, Mosby, Inc. All rights reserved.

VIEW IMAGE

FIGURE 36-9 *Continued*

VIEW IMAGE

FIGURE 36-10 *Continued*

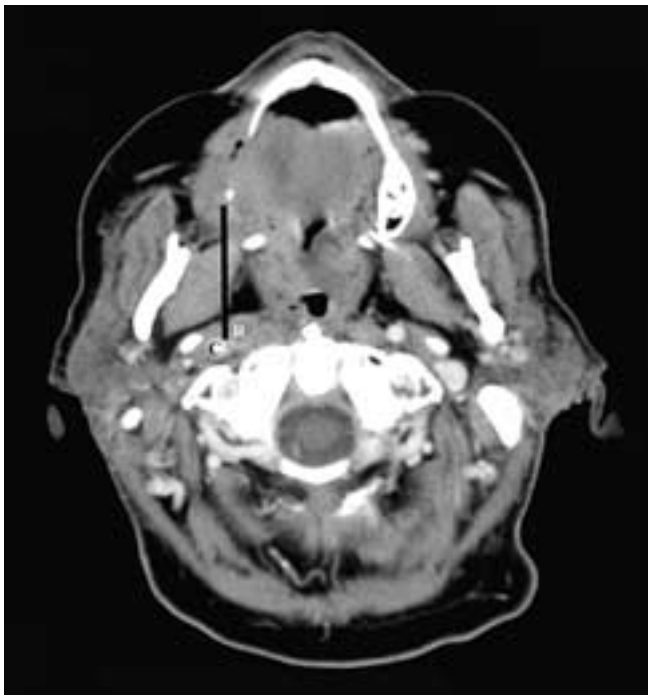

VIEW IMAGE

FIGURE 36-11 *Continued*

Level V nodes all lie anterior to a transverse line drawn on each axial scan through the anterior edge of the trapezius muscle. Between the levels of the skull base and the bottom of the cricoid arch, these nodes are situated posterior to a transverse line drawn on each axial scan through the posterior edge of the sternocleidomastoid muscle (Figs. 36-8, 36-10, 36-12, and 36-13). Between the axial level of the bottom of the cricoid arch and the level of the clavicle, level V nodes lie posterior and lateral to an oblique line through the posterior edge of the sternocleidomastoid muscle and the lateral posterior edge of the anterior scalene muscle (Figs. 36-14 to 36-16). The level V nodes can be subdivided into VA and VB nodes.

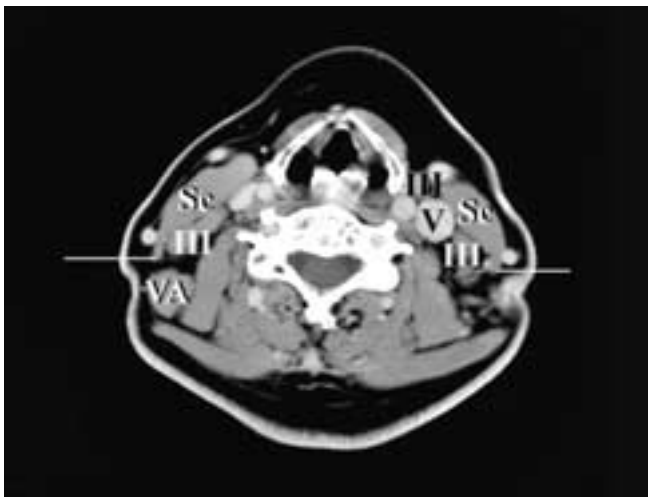

VIEW IMAGE

FIGURE 36-12 *Continued*

Copyright © 2003, Mosby, Inc. All rights reserved.

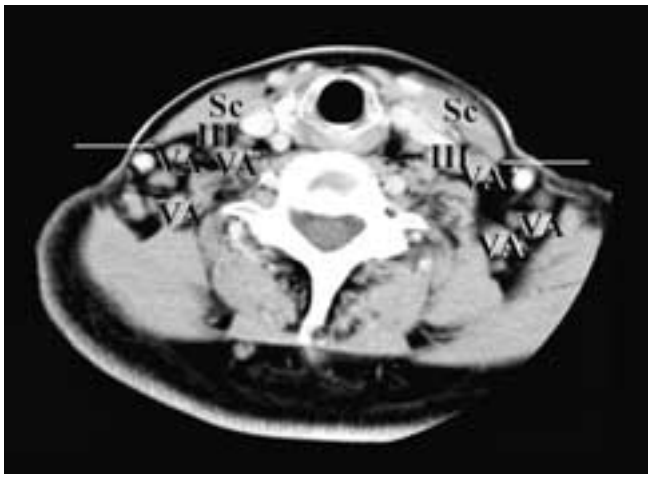

VIEW IMAGE

FIGURE 36-13 *Continued*

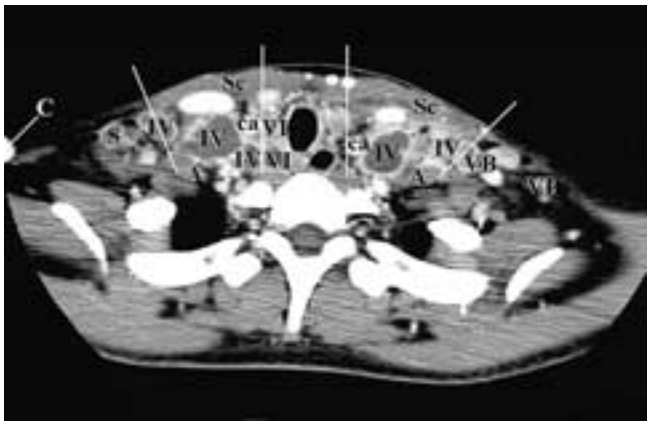

VIEW IMAGE

FIGURE 36-14 *Continued*

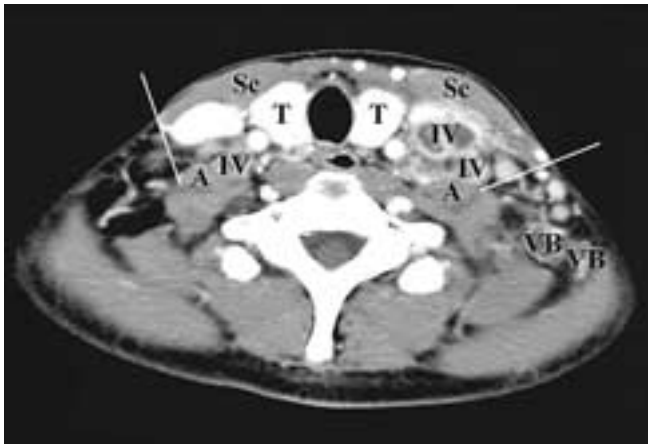

VIEW IMAGE

FIGURE 36-15 *Continued*

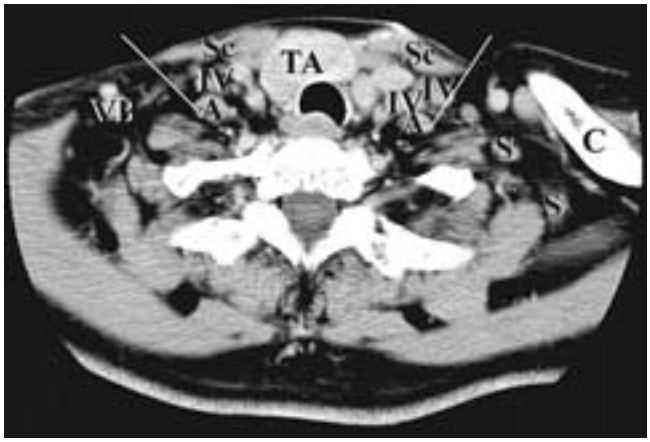

VIEW IMAGE

FIGURE 36-16 *Continued*

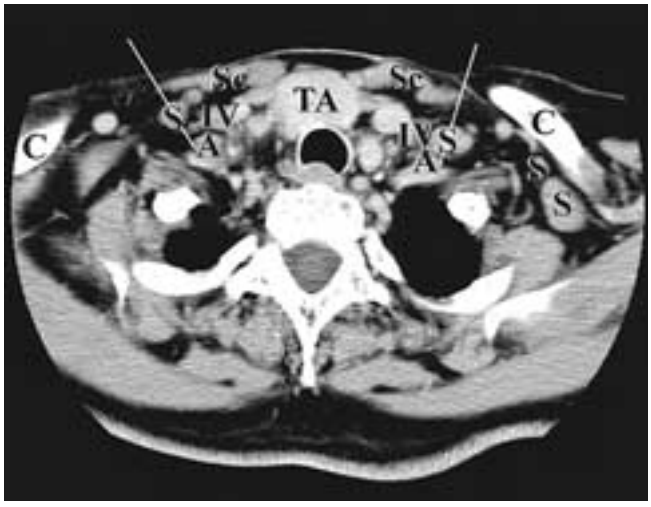

VIEW IMAGE

FIGURE 36-17 *Continued*

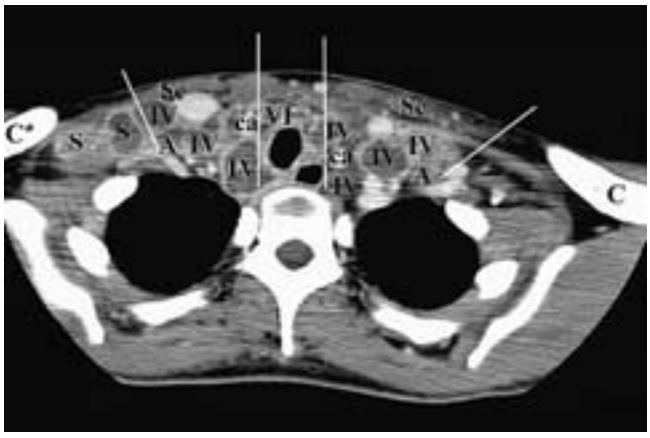

VIEW IMAGE

FIGURE 36-18 *Continued*

Copyright © 2003, Mosby, Inc. All rights reserved.

VIEW IMAGE

FIGURE 36-19 *Continued*

Level VA (*upper level V*) nodes lie between the skull base and the level of the lower margin of the cricoid cartilage arch. They are behind the posterior edge of the sternocleidomastoid muscle (Figs. 36-8, 36-10, 36-12, and 36-13).

Level VB (*lower level V*) nodes on each side lie between the level of the lower margin of the cricoid cartilage arch and the level of the clavicle, as seen on each axial scan. They are behind an oblique line through the posterior edge of the sternocleidomastoid muscle and the lateral posterior edge of the anterior scalene muscle (Figs. 36-14 to 36-16).

Level VI nodes lie inferior to the lower body of the hyoid bone, superior to the top of the manubrium, and between the medial margins of the left and right common carotid arteries or the internal carotid arteries. They are the visceral nodes (Figs. 36-14 and 36-18).

Level VII nodes lie caudal to the top of the manubrium in the superior mediastinum, between the medial margins of the left and right common carotid arteries (Fig. 36-19). These superior mediastinal nodes extend caudally to the level of the innominate vein.

To maintain consistency with the prior classifications, the following nodal groups continue to be referred by their anatomic names: supraclavicular, retropharyngeal, parotid, facial, occipital, postauricular, and the other superficial nodes.

It is also important to recognize that from both a clinical and an imaging perspective, once a metastatic lymph node is identified, knowledge of the lymphatic anatomy of the neck often allows the likely location of a primary tumor to be suggested. This is summarized in Tables 36-2, 36-3, 36-8, and 36-9).[70, 76]

As mentioned earlier, in the ever-changing world of nodal classification, there has been some clinical discussion about subdividing level IV nodes into IVA and IVB nodes. However, the imaging identification of the IVA nodes deep to the sternal head of the sternocleidomastoid muscle is inconsistent. It may be that these nodes, if they are added to the clinical nodal classification, along with the supraclavicular nodes, may be better and more consistently classified clinically.

NODAL STAGING

Nodal staging differs from nodal classification. Whereas nodal classification identifies the nodal groups involved and, hopefully, is useful in assisting the clinician in determining the type of surgery that is best for that specific nodal disease, nodal staging relates the overall number, size, and location of the affected nodes to the prognosis. That is, rather than being concerned with the precise location of any nodal disease, as with a classification, staging is concerned with the presence or absence of nodal disease, nodal size, and a limited assessment of nodal number. Initially, the assessment of cervical lymphadenopathy was based on clinical evaluation, and the criteria included nodal size, nodal mobility or fixation, the unilateral or bilateral location of the nodes, and whether the disease represented single or multiple nodal involvement.[48] The primary limitations to this clinical approach were the variations in the subjective evaluation of some of these criteria.

In 1987, the AJCC and the International Union Against Cancer (IUCC) developed a common staging system that eliminated the subjective criterion of nodal fixation, which varied with nodal location and with the skill of the clinician.[68] Table 36-10 shows the refinements in this system as of 1997.[70] It is a TNM-based system that assesses the size of the primary tumor (T), regional lymph node involvement (N), and distant metastasis (M). Although this single reporting system is now used worldwide, this categorization still does not address a number of pathophysiologic issues such as the significance of a node's location in relation to the primary tumor site, the specific nodal chain involved, the reactive lymphoid response, tumor histology, and the effect of the primary site on the prognosis.

The initial clinical pretreatment classification is referred to as the cTNM classification. Once the pathologic assessment of a resected specimen is made, pathologic staging (pTNM) can be performed. If a cancer recurs after therapy, it is restaged using the same criteria utilized in the initial staging; however, this restaging is referred to as rTNM staging. A final classification after autopsy, if available, is referred to as the aTNM classification. If imaging becomes recognized by the AJCC as a staging modality, its classification might be referred to as iTNM. Other descriptors can be used to assess multiple primary tumors (m), the effect of neoadjuvant therapy (y), histopathologic grade (G), lymphatic vessel invasion (L), venous invasion (V), and residual tumor after treatment (R). Unfortunately, as with all such staging systems, interobserver inconsistencies and errors in measurements and assessments remain potentially confounding factors.[70]

By definition, direct extension of the primary tumor into a lymph node is considered lymph node metastasis. Metastasis to any lymph node other than a regional node is considered distant metastasis. If a microscopic tumor nodule measuring up to 3 mm in greatest dimension is found, it is considered discontinuous tumor extension and it is classified in a T category. If the tumor nodule is greater than 3 mm and even if there is no evidence of residual lymph node tissue, it is

Copyright © 2003, Mosby, Inc. All rights reserved.

Table 36-8
PRIMARY TUMOR LOCATIONS AND THEIR LYMPH NODE DRAINAGE AREAS

Anatomic Area	Anatomic Subdivision(s)	Primary Nodal Drainage Group(s)
Scalp	Frontal region	Preauricular, parotid
	Temporoparietal region	Parotid, retroauricular
	Occipital region	Occipital, III, IV
Pinna and external auditory canal	Anterior portion	Preauricular, parotid
	Posterior portion	Retroauricular, II, III
	Inferior portion	Superficial, II, III
Face	Eyelids and conjunctiva	IB (submandibular), parotid
	Posterior cheek	Parotid
	Anterior cheek, side of nose, upper lip, and lateral lower lip	IB (submandibular)
	Deep portion of temporal and infratemporal fossae	Deep facial, II, III
	Buccal cheek and lips	IB (submandibular)
	Central lower lip and chin	IA (submental)
Nasal cavities	Anterior nose	IB (submandibular)
	Posterior two-thirds of nasal cavities and paranasal sinuses	Retropharyngeal, II, III
		IB (submandibular)
Mouth	Lower gums	IB (submandibular)
	Upper gums and hard palate	II, III
	Soft palate	Retropharyngeal, parotid, II, III
	Anterior floor of mouth	IA (submental), II, III
	Rest of floor of mouth	II, III, IB (submandibular)
Pharynx	Nasopharynx, oropharynx	Retropharyngeal, II, III, V
	Hypopharynx	II, III, V, retropharyngeal
	Postcricoid	II, IV, VI
Palatine tonsil	Palatine tonsil	II, III, IV, V
Tongue	Tip	IA (submental)
	Sides of anterior two-thirds and floor of mouth	IB (submandibular), II, III
	Posterior third	Bilateral II, III, (jugulo-omohyoid), IV, V
Larynx	Supraglottic	II, III
	Glottic	
	Subglottic	VI, IV, III
Esophagus	Cervical esophagus	VI, VII, IV, III
Thyroid and parathyroid	Thyroid, parathyroid	VI, III, IV, I, V, VII
Salivary glands	Parotid	II, III, V, superficial
	Submandibular	IB (submandibular)
	Sublingual	IA, IB (submental and submandibular)
Orbit	Eye	Preauricular, parotid, II
	Lacrimal gland	

Table 36-9
NAMED LYMPH NODE GROUPS: THEIR PRIMARY DRAINAGE AREAS AND WHERE THEY DRAIN

Nodes	Drainage Regions	Drain To
Occipital	Occipital region of scalp	II (superior deep cervical nodes)
Retroauricular (mastoid)	Posterior temporoparietal region Upper pinna, dorsal external auditory meatus	II
Preauricular	Lateral pinna, skin of frontal and temporal regions	II
Parotid	Root of the nose, eyelids, frontotemporal region, external acoustic meatus, tympanic cavity posterior palate	II, III
Subparotid	Posterior nasal cavity, nasopharynx	II, III
Facial (infraorbital or maxillary, buccinator, supramandibular)	Eyelids, conjunctiva, skin and mucous membrane of nose and cheek	IB (submandibular)
Deep facial	Temporal and infratemporal fossae, nasopharynx	II, III
Retropharyngeal	Nasal cavities, nasopharynx, eustachian tubes, oropharynx, palate, hypopharynx	II, III
Submandibular	Medial palpebral commissure, cheek, side of nose, upper lip, lateral lower lip, gums, anterior lateral tongue	II, III
Submental	Central lower lip and floor of mouth, tip of tongue	IB (submandibular), II, III
Superficial cervical	Superficial to sternocleidomastoid muscle, lower pinna, parotid	II, III
Anterior cervical	Superficial, prelaryngeal, pretracheal larynx, thyroid, upper trachea	IV
Spinal accessory	Pharynx, tonsil, base of tongue	IV, supraclavicular (transverse cervical)

Copyright © 2003, Mosby, Inc. All rights reserved.

Table 36-10
1997 AJCC NODAL (N) STAGING SYSTEM FOR CERVICAL LYMPH NODES

NX	The regional lymph nodes cannot be assessed (clinically)
N0	There are no regional metastatic lymph nodes present
N1	There is metastasis to a single ipsilateral lymph node that is 3 cm or less in greatest dimension
N2	There is metastasis in a single ipsilateral lymph node that is between 3 and 6 cm in greatest dimension; there are multiple ipsilateral lymph nodes, none of which are greater than 6 cm in greatest dimension; or there are bilateral or contralateral lymph nodes, none of which are greater than 6 cm in greatest dimension
N2a	There is metastasis in a single ipsilateral lymph node that is between 3 and 6 cm in greatest dimension
N2b	There are multiple ipsilateral lymph nodes, none of which are greater than 6 cm in greatest dimension
N2c	There are bilateral or contralateral lymph nodes, none of which are greater than 6 cm in greatest dimension
N3	There is metastasis in lymph nodes that are more than 6 cm in greatest dimension

classified as a regional lymph node metastasis. A final comment on nodal assessment relates to the observation that generally most nodal masses greater than 3 cm in diameter are not single nodes, but are either confluent nodes or tumor in the soft tissues of the neck.[70]

There are two primary head and neck tumors whose distribution of nodal metastases and the prognosis associated with such regional metastases are sufficiently different from those of the other head and neck cancers that they have been recognized by the AJCC as requiring separate nodal (N) classifications. These tumors are nasopharyngeal carcinoma and thyroid carcinoma.

Nasopharyngeal Carcinoma Nodal Staging

The AJCC staging utilizes Ho's triangle, which is a surface triangle formed by the upper medial and lateral ends of the clavicle and the point dorsally where the neck meets the shoulder. This triangle defines the supraclavicular fossa, and the AJCC classification is given in Table 36-11.[70]

Thyroid Carcinoma Nodal Staging

Regional lymph node spread for thyroid cancer is common, but is of less prognostic significance in the generally well-differentiated tumors (papillary, follicular) than in the medullary cancers. The first echelon of nodal metastasis is the paralaryngeal, paratracheal, and prelaryngeal (Delphian) nodes adjacent to the thyroid (level VI), but involvement of these nodal stations has no prognostic value and therefore is not part of the staging system. Metastases secondarily involve the middle and lower jugular (level III and IV) nodes, supraclavicular nodes, and, much less commonly, the submental (level IA), submandibular (level IB), and spinal accessory nodes (level V). Upper mediastinal nodal spread

Table 36-11
NODAL CLASSIFICATION FOR NASOPHARYNGEAL CARCINOMAS

NX	Regional lymph nodes cannot be assessed (clinically)
N0	No regional metastatic lymph nodes are present
N1	Unilateral metastasis in lymph node(s), 6 cm or less in greatest dimension, above the supraclavicular fossa
N2	Bilateral metastasis in lymph node(s), 6 cm or less in greatest dimension, above the supraclavicular fossa
N3	Metastasis in lymph node(s)
N3a	More than 6 cm in greatest dimension
N3b	Extension to the supraclavicular fossa

Note: The supraclavicular fossa is defined by Ho's triangle, a plane defined by the upper sternal and lateral ends of the clavicle and the point posteriorly where the neck meets the shoulder.

occurs frequently, both anteriorly (level VII) and posteriorly. Retropharyngeal nodal metastases may be seen, usually in the presence of extensive cervical metastases. Bilateral metastases are common. Metastases from medullary thyroid carcinoma follow a similar pattern of spread but are associated with a poorer prognosis. The AJCC classification schema for thyroid neoplasia is given in Table 36-12.[70]

PATHOLOGY

The detection of metastatic disease can be a multidisciplinary diagnostic problem. That is, the surgeon identifies palpable disease, the radiologist detects nonpalpable disease, and the pathologist may discover microscopic disease. When one considers that an estimated 1 billion malignant cells are required to create a mass of only 1 mm^3, the limitations of even pathologic detection become clear. Only careful pathologic analysis of the nodes can be considered the ''gold standard,'' and as mentioned, even histologic examination of the lymph nodes is not free of potential error. It has been found that up to 30% of lymph node metastases may be missed if the lymph node is simply bisected sagitally. In addition, micrometastases in supraomohyoid neck dissection specimens were not initially diagnosed in 7.6% of cases.[55] These types of sampling errors may explain why 4% to 8% of patients with pathologically N0 necks develop recurrences in the neck.[48] Between 20% and 40% of clinically N0 necks are pathologically staged as N1 (reported range, 4% to

Table 36-12
NODAL CLASSIFICATION FOR THYROID CARCINOMAS

NX	Regional lymph nodes cannot be assessed (clinically)
N0	No regional metastatic lymph nodes are present
N1	There is regional lymph node metastasis
N1a	Metastasis in ipsilateral cervical lymph node(s)
N2b	Metastasis in bilateral, midline, or contralateral cervical or mediastinal lymph node(s)

Note: Regional lymph nodes are the cervical and upper mediastinal lymph nodes.

Copyright © 2003, Mosby, Inc. All rights reserved.

60% of cases). Interestingly, a clinically N0 neck is just as likely to contain multiple positive nodes (13%) as it is to have a solitary positive node (16%).[48, 77, 78] Van den Brekel and colleagues examined the value of additional pathologic sectioning (step sectioning or ''leveling'' the paraffin tissue block) and of adding cytokeratin immunohistochemistry in detecting micrometastases. They performed step sections on 600 lymph nodes from 64 patients originally classified histopathologically as negative. Five further patients (7.8%) were found to have positive lymph nodes. Antikeratin staining revealed four micrometastases in 739 originally histopathologically negative lymph nodes. However, as no adjuvant therapy was offered to these ''new N1'' patients, and as the prognostic significance of this group is still unknown, these authors concluded that the massive additional work of immunostaining and deeper sectioning was not yet warranted for routine use in clinical practice.[79] Thus, the ultimate use of pathology as the gold standard may some day require the caveat that multiple slices of the nodes and immunostaining be obtained. Table 6-1 describes the immunohistochemical testing of tumors.

THE NONDIAGNOSTIC NODAL BIOPSY

A definitive diagnosis can be made in more than half of the enlarged lymph nodes that are biopsied.[19] Of the remainder, most are diagnosed as nonspecific reactive lymphoid hyperplasia. Longitudinal follow-up on 100 children with nondiagnostic biopsies revealed that 37 were finally diagnosed with reactive hyperplasia, and 74% of these children were alive and well at 20 years. In adults, there is a greater likelihood of eventually establishing a diagnosis of malignancy. Half of the adults followed remained without a specific diagnosis, and 25% to 53% of these patients eventually received a specific diagnosis 8 months to 1 year after initial biopsy. Twenty percent of the adults were ultimately diagnosed with malignant lymphoma. When only cases of atypical lymph node hyperplasia were considered for the adults, 37% of patients ultimately were diagnosed with lymphoma.[80] Thus, only between 25% and 47% of patients with either Hodgkin's lymphoma or large cell lymphoma received a specific diagnosis on submission of the initial specimen.[19] Diagnostic problems were due either to sampling errors (surgeons should biopsy the largest lymph node in a group, not just the most surgically accessible node) or to improper specimen processing (poor fixation, inadequate sectioning, or poor staining).

CONSIDERATION OF THE PRIMARY TUMOR SITE

When evaluating a patient with cervical nodal metastasis, the mapping of the primary upper aerodigestive tract (UADT) tumor site is critical to the imaging study. In fact, the relationship between various primary sites and the location and frequency of cervical metastasis has been well studied (Tables 36-1 to 36-3).[7, 48, 81] In general, for carcinomas of the oral cavity, soft palate, true vocal cord, paranasal sinuses, and nasal cavity, there is a direct relationship between the size of the primary tumor and the risk of metastatic neck disease. However, this relationship is not direct for other UADT carcinomas such as nasopharyngeal carcinomas. Nonetheless, of special note is the observation that tumors arising in Waldeyer's ring are the ones most likely to present with metastatic adenopathy. They are also the tumors most likely to present with bilateral neck disease and posterior triangle (level V) adenopathy. In patients who present with nodal disease and no known primary tumor site, knowledge of the nodal drainage areas may help direct attention to the most likely primary areas (Tables 36-8 and 36-9).

LIMITATIONS IN IMAGING CERVICAL LYMPH NODES

Despite the normal imaging appearance of a hyperplastic or reactive cervical node, a variety of diseases may still have affected the node. In most of these cases, the precise pathology may not be predicted on imaging and, in the final analysis, it is the pathologist who determines the diagnosis. Although elective fine needle aspiration (FNA) biopsies have their limitations, FNA cytology is a reasonable next diagnostic step.[54] A definite positive diagnosis can triage the patient and set the therapeutic wheels in motion, and a negative FNA diagnosis should not be taken as the absence of pathology.

Newer approaches such as MR spectroscopy (MRS), PET, and Thallium-201 SPECT may become alternative, noninvasive techniques to quickly identify the presence of nodal metastasis. These topics are discussed in Chapter 45. Even if microscopic tumor cannot be identified, it is possible that in the near future the current capabilities of both clinical and imaging evaluations can be advanced to a new, more refined level.

Most of the research addressing the assessment of size criteria and nodal architecture has been done to evaluate squamous cell carcinoma metastasis. In summary, classically such a metastatic node will be enlarged, have central tumor and necrosis, and have extracapsular tumor spread (Fig. 36-20). However, even when all of these imaging criteria are present, the histology may still reveal some form of lymphoma or infectious process. As already mentioned, it must always be remembered that in a patient with a head and neck tumor, hyperplastic-appearing lymph nodes may still harbor microscopic metastases, highlighting a persistent limitation of clinical and radiographic evaluation.

THE NECESSITY OF CLINICOPATHOLOGIC CORRELATION

Imaging analysis is limited by the lack of specificity in the CT and MR imaging appearances of many different diseases. Correlation with the clinical history, physical findings, and laboratory test results allows the radiologist and clinician to hone the differential diagnosis to a pertinent few possibilities rather than suggesting a long list of potential diagnoses. Thus, a tender, painful, firm node usually signifies an acute inflammation. Conversely, a hard,

Copyright © 2003, Mosby, Inc. All rights reserved.

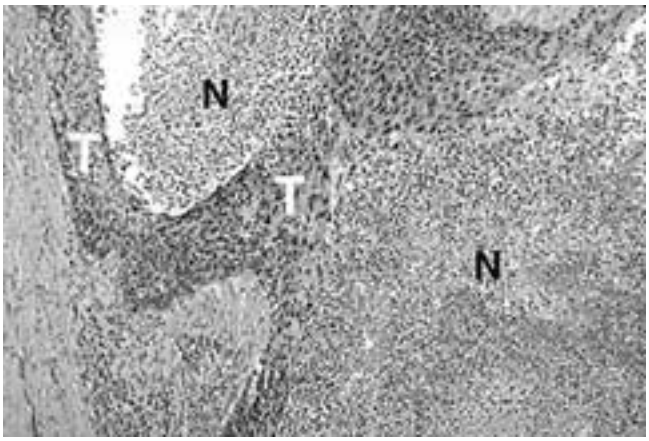

VIEW IMAGE

FIGURE 36-20 There are ribbons of viable tumor (*T*) within this metastatic lymph node, with shedding of necrotic cells (*N*). This is seen as central necrosis on CT and MR imaging.

fixed, nontender, painless node is the classic nodal metastasis. However, even clinical findings can be misleading in rare cases, and uncommonly, metastatic nodes, if acutely enlarged, may be painful and tender. A soft, nontender, painless node could be either hyperplastic, lymphoma, or even an infection. Nonetheless, correlation with clinical information usually limits the vast majority of the imaging differential diagnoses and makes the imaging contribution to the case more pertinent.

The number and the specific chains of lymph nodes involved may also suggest a diagnosis. Diffuse nodal disease (especially if suboccipital nodes are involved) suggests a systemic process such as infectious mononucleosis, acquired immune deficiency syndrome, sarcoidosis, or lymphoma. Unilateral involvement of lymph nodes is less specific and can be found in many diseases including metastatic carcinoma, lymphoma, tuberculosis, and a variety of local infections. Nodes in the infraomohyoid neck (levels IV and VB, including Virchow's node), without supraomohyoid nodes (levels II and III) suggest that the source of the nodes lies in the thyroid, in the cervical esophagus, or in a primary tumor caudal to the clavicles, most often in the lung or breast (Fig. 36-21).

Obviously, a history of a previous primary tumor or a recent infection may strongly suggest the etiology of cervical adenopathy. However, occasionally even such a history may be misleading, as new or multiple pathologic processes can occur.

Whenever possible, imaging should be performed prior to any biopsy procedures so that the images reflect the disease process and not obfuscating iatrogenic effects. Whatever the limitations of establishing an imaging-based diagnosis, clearly in most cases the contribution of imaging is more focused if the history and clinical information is available at the time of the examination.

SPECIFIC NODAL PATHOLOGIES

With regard to the clinical and imaging evaluation of the cervical lymph nodes, although the primary concern is usually with metastatic squamous cell carcinoma, there are a number of other diseases that require consideration. In most of these instances, the imaging characteristics are nonspecific and the diagnosis is based on a combination of the history, clinical findings, imaging, and laboratory data. The role of imaging in these cases is to map the disease, namely, to identify the number and location of lymph nodes, potentially

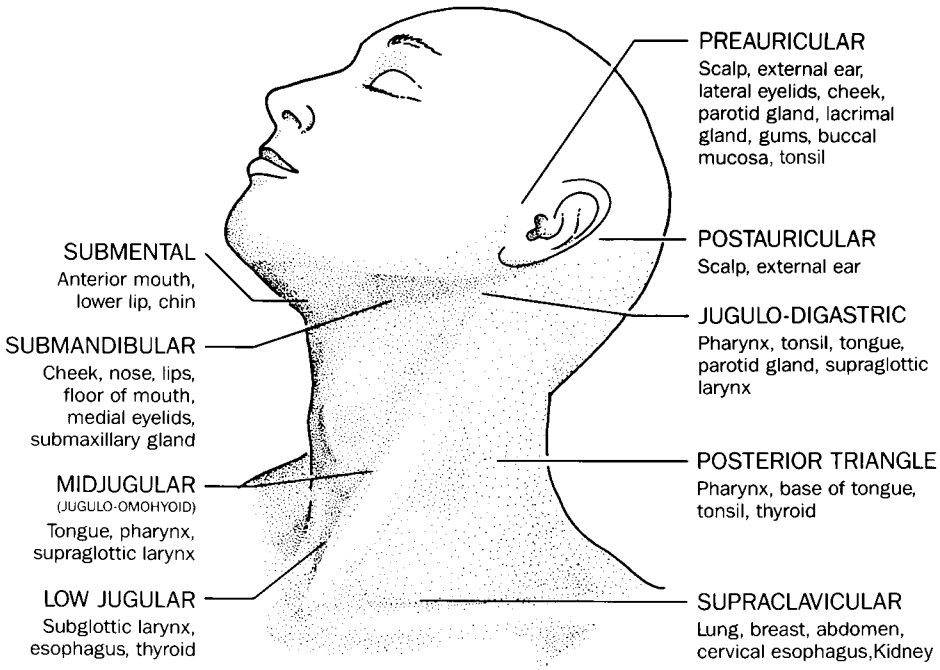

VIEW IMAGE

FIGURE 36-21 Diagram of the head and neck viewed from the left anterior oblique projection shows the most likely locations of primary tumor sites when metastatic lymph nodes are identified in the neck or facial region.

Copyright © 2003, Mosby, Inc. All rights reserved.

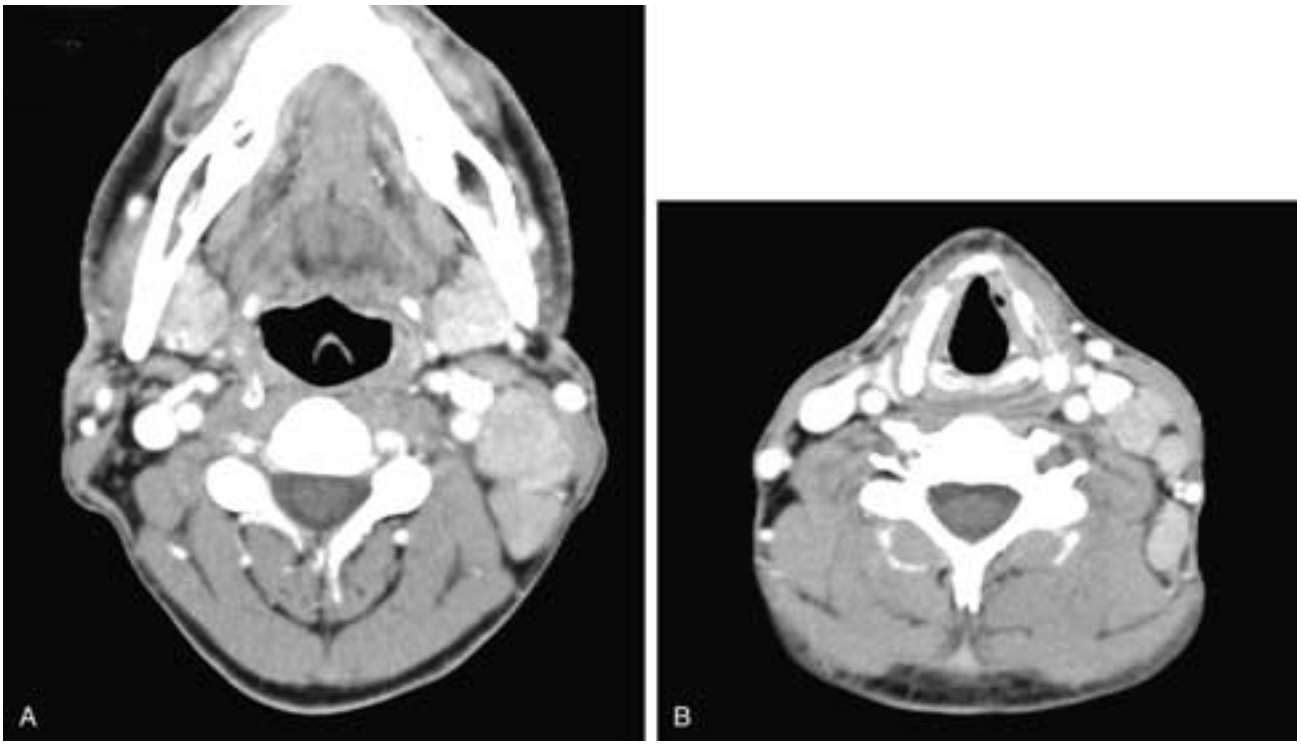

VIEW IMAGE

FIGURE 36-22 Cranial (**A**) and caudal (**B**) axial contrast-enhanced CT scans show multiple enlarged, enhancing, fairly homogeneous, well-delineated nodes in the left neck. Nodes are seen in levels II, III, and V. This patient had EBV infection.

determine the site of primary pathology, and evaluate any associated findings such as soft-tissue infiltration, necrosis and/or abscess formation, bone involvement, and so on. The following are capsule reviews of the diseases, other than squamous cell carcinoma, that can affect the cervical nodes. For each of the pathologic sections described, a brief summary of the imaging findings for affected lymph nodes in that group of diseases is included.

Viral Lymphadenitides

There are a number of viruses that may cause acute or chronic lymphadenitis. In some cases, the viruses can be demonstrated within the lymph node; in other cases, the presence of virus can only be suspected. Some of the nonspecific reactive lymphadenitides may be in this latter group.[19]

On imaging, these lymphadenitides can have a variable appearance. There usually is diffuse nodal involvement, with most nodes being either normal in size or mildly enlarged. As a rule, there is little, if any, adjacent inflammation. The nodes are usually homogeneous, often with an attenuation slightly less than that of muscle, with mild enhancement on CT and MR imaging (Figs. 36-22 to 36-24). They most often have low to intermediate T1-weighted and high T2-weighted signal intensities.[82] It is in this group of diseases that the occipital nodes are most often affected.

Infectious Mononucleosis

The Epstein-Barr virus (EBV) is a Herpesvirus with 173-kb double-stranded linear DNA, which is strongly trophic for B lymphocytes, epithelium, and T lymphocytes by binding complement receptor type 2 (CR2) via a viral envelope glycoprotein (gp350/220). Infection with EBV usually occurs in early life with worldwide ubiquity. Nearly 100% of children have positive serology by the age of 3 years, and in the Western world, only about 50% of those exposed to EBV actually become infected. Acute EBV infection is infectious mononucleosis (IM), which is a self-limited disease that primarily affects adolescents and young adults. In the United States the incidence is 50 per 100,000, or about 100,000 cases per year. Patients with acute IM present with cervical adenopathy, pharyngitis, abdominal pain, and fever after a nonspecific prodromal period of 3 to 5 days. The pharyngitis and tonsillitis may be ulcerative and exudative. In extreme cases, the tonsillitis may cause upper airway obstruction. There is generalized adenopathy (including the posterior cervical chain) and hepatosplenomegaly. Multiple cranial nerve palsies may rarely occur, possibly secondary to brainstem encephalitis.[83]

The diagnostic feature of IM is the peripheral lymphocytosis with significantly elevated (10% to 20%) atypical lymphocytes (Downey cells) of T-cell origin (Fig. 36-25). IgM antibodies to viral capsid antigen (VCA) rise at first and disappear within a week, replaced by rising IgG titers to VCA, which persist for life. Elevated VCA titers indicate reactivation of latent infection. Early antigen-diffuse type and Epstein Barr nuclear antigen (EBNA) antibodies also rise early in the course of the acute illness. Antibodies to EBNA-1 rise after the first month and remain elevated throughout life. Antibodies to EBNA-2 peak during the acute phase of IM and then drop off. Failure to generate

Copyright © 2003, Mosby, Inc. All rights reserved.

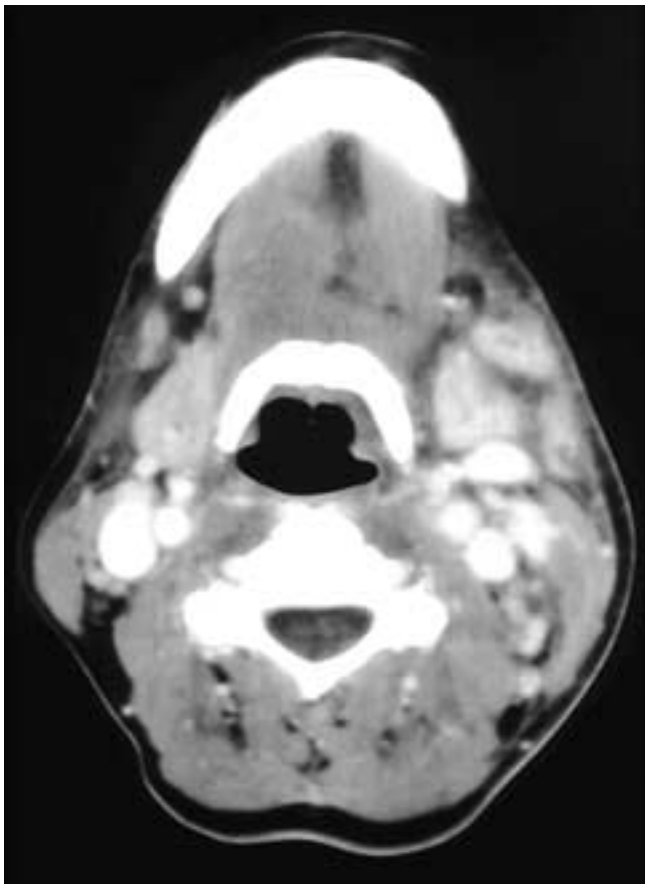

VIEW IMAGE

FIGURE 36-23 Axial contrast-enhanced CT scans show enhancing left level I and II adenopathy in this patient with herpes zoster affecting the lower left face. There are also findings of local inflammation in the overlying skin and subcutaneous soft tissues.

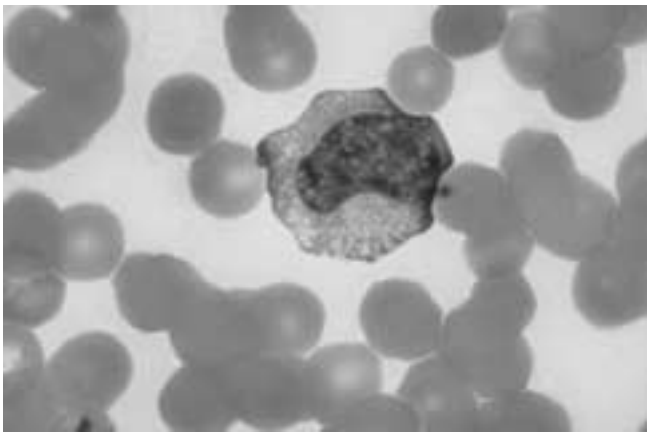

FIGURE 36-25 Downy cell: Atypical, enlarged, circulating lymphocyte in the setting of acute infectious mononucleosis (EBV).

VIEW IMAGE

EBNA antibodies indicates a failure in immune surveillance. Low titers to EBNA in the face of recent EBV infection have been seen in chronic EBV infections and in X-linked lymphoproliferative disorder.[84]

Uncomplicated IM can resolve within 3 to 4 weeks, but occasional patients remain symptomatic for months. Progressive fatal cases may occur in patients with inherited immunodeficiences (see below) or in rare patients with ''normal'' immunity. The T cells of these latter patients develop exuberant graft-versus-host responses that may result in myocarditis, hepatitis, nephritis, and encephalitis. Rather than being immunosuppressed, Purillo et al. point out, they are ''immune dysregulated'' in the vigorous self-directed immune reaction in response to EBV infection.[85]

Children with IM tend to be less symptomatic and have

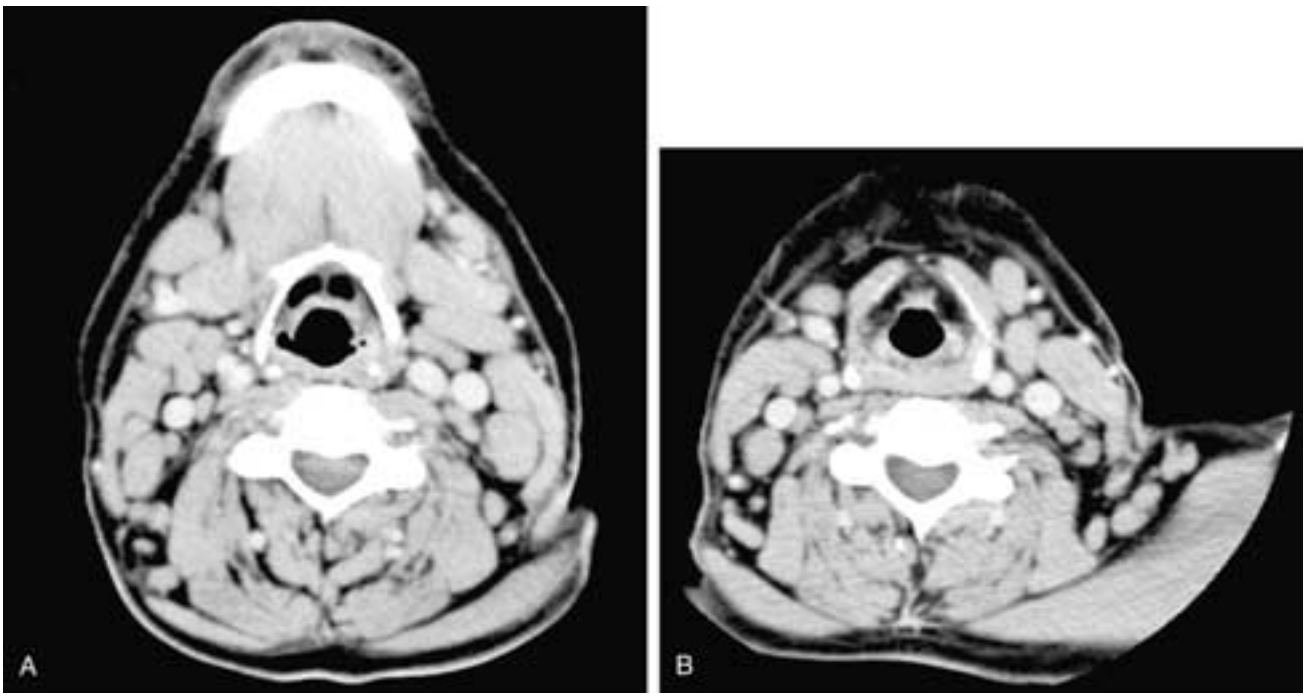

VIEW IMAGE

FIGURE 36-24 Cranial (**A**) and caudal (**B**) axial contrast-enhanced CT scans show multiple enlarged, homogeneous lymph nodes in virtually every nodal level. The nodes are sharply defined in this HIV-positive patient. These are nonspecific findings and could also be seen in any reactive adenopathy or even in lymphoma.

Copyright © 2003, Mosby, Inc. All rights reserved.

shorter illnesses than young adults or, as mentioned, have subclinical illnesses. The infecting viral dose and the maturity of the host's immune system are thought to explain the differences between the pediatric and adolescent disease courses. Resolution of acute IM occurs as killer T lymphocytes eliminate the infected B lymphocytes. A small residual pool of infected lymphoblastoid cells always remain, kept in check by sensitized cytotoxic T cells. Reactivation of latent infection will not occur unless this balance is disturbed by various possible mechanisms.[85–87]

Cytomegalovirus

Cytomegalovirus (CMV) is a double-stranded DNA Herpesvirus (180 nm in diameter) trophic for endothelial cells, B and T lymphocytes, mononuclear cells, and salivary gland epithelium. CMV has a high prevalence worldwide. It is ubiquitous in AIDS patients, nearly all of whom have serum antibodies to primary or reactivated CMV infection. CMV reactivation is caused potentially by viral/viral interactions with HIV. CMV directly impairs cell-mediated immunity through a variety of mechanisms: infected monocytes have inhibited antigen-presenting functions and downregulation of interleukin-1 production.[88] The marked decrease in interleukin-1 may contribute to the depressed lymphocyte responses. Fresh clinical isolates from various strains of CMV can also directly suppress null killer cell function and inhibit mitogen-induced T-cell proliferation.[89]

In general, viral/viral interactions play a crucial role in the clinical downward spiral of immune function. CMV interacts with HIV and EBV to potentiate immunosuppression. A general mechanism of viral/viral interaction is the cross-reactivity of viral activating factors. CMV (as well as EBV and HIV) produce transactivating proteins that activate the flanking long terminal repeat (LTR) regions of HIV, thereby upregulating viral transcription and promoting active HIV replication. Specifically, CMV protein transcripts of the immediate-early region-2 can transactivate HIV LTR.[90] In turn, HIV infection potentiates CMV and is responsible for reactivation of latent CMV infection. H9 lymphoblastoid cell lines coinfected with HIV-1 and CMV demonstrate enhanced transcription CMV late region antigens, as well as enhanced HIV replication.[91]

The clinical course of most CMV infections is basically asymptomatic, subclinical, or may cause mononucleosis-like illnesses in immunocompetant individuals. After primary infection, CMV may be shed in saliva, urine, semen, and cervical secretion for extended periods of time.[92] The virus then remains latent in the host, to be potentially reactivated at any time, producing chronic persistent infection.

Serious disseminated CMV infections are seen as a result of some congenital infections and immunosuppression (e.g., posttransplant and AIDS). An autopsy study of 164 AIDS patients revealed that almost half had evidence of active CMV infection; adrenalitis, pneumonia, gastrointestinal ulceration, central nervous system infection, and retinitis were the most common findings.[93]

Involvement of the upper respiratory tract was seen in only 4% of these cases. CMV infection may result in large oropharyngeal and nasopharyngeal ulcerations in patients with active AIDS, causing odynaphagia and dysphagia.[94, 95] The ulcers have a ''well-punched-out'' appearance without induration of the periphery or the base.[96] These lesions are self-limiting, and most resolve with gancyclovir (Fig. 36-26). CMV parotitis has been reported; FNA revealed the characteristic and diagnostic cytomegalic cells.[97]

The larynx and trachea may be sites for ulcerative CMV infections in the absence of CMV pneumonitis.[98, 99] Vocal cord paralysis (without mucosal ulceration) due to laryngeal neuritis has been seen: CMV inclusions have been demonstrated at autopsy within the recurrent laryngeal nerve.[100] Concomitant supraglottic diffuse large cell lymphoma and CMV epiglottitis have been reported. Although CMV is not firmly established as having oncogenic potential, it may reactivate latent EBV infection, which, of course, is associated with B-lymphocyte neoplasia.[101]

Herpes Simplex Virus

Herpes simplex virus (HSV) is a double-stranded DNA (150 kb pairs) Herpesvirus that is trophic for epithelium and nerve ganglia. HSV causes oropharyngeal and genital infections, recurrent episodic infections, and a serious disseminated infection in neonates and immunosuppressed individuals.

The pathobiology of HSV infection is similar to that of other Herpesviruses. HSV may produce either an active replicating lytic infection or a latent quiescent infection that can be reactivated under certain conditions. HSV binds to target cells by attaching to heparin sulfate proteoglycan molecular receptors.[102] HSV enters by envelope fusion with cell membranes rather than by phagocytosis. HSV DNA is then extruded from the capsid via nuclear pores into the host nucleus, where it becomes circularized. The ability of HSV to effect productive infection depends on several viral talents. HSV subterfuges host RNA polymerase II for viral transcription.[103] HSV also causes a decline in most cellular synthetic processes.[104] This is efficiently accomplished early on by integument proteins present between the viral envelope and capsid.[102] It is also postulated that functional redundancy in the estimated 70 HSV encoded proteins allows successful viral adaptation to various cellular environments.[102]

After primary infection, HSV travels retrograde via axons to nerve ganglia, where it remains in a latent state; thus, reactivated infection will occur along neural dermatomes.[105] Ex-

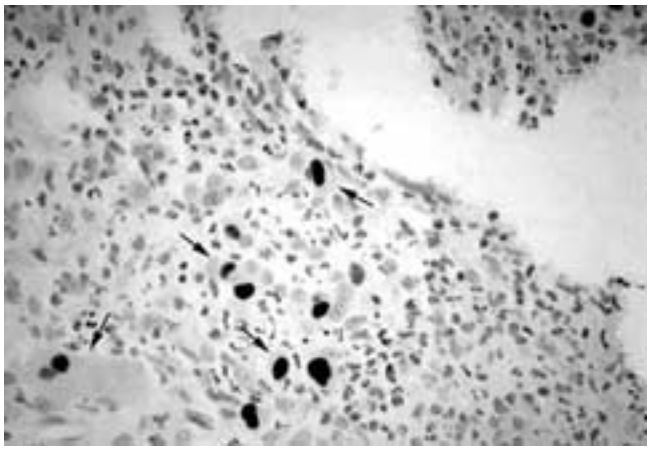

FIGURE 36-26 Enlarged cells (*arrows*) with nuclear inclusions stain for CMV immediate early antigen by immunohistochemistry.

VIEW IMAGE

Copyright © 2003, Mosby, Inc. All rights reserved.

perimental explantation of ganglia months after primary experimental infection results in viral reactivation.

Cell-mediated and humoral immunity play crucial roles in protecting against primary infection and controlling against reactivation of latent infection. The topic of cell-mediated immunity and HSV infection has been extensively reviewed.[106] Natural killer (NK) effector lymphocytes normally lyse HSV-infected cells, even in the absence of anti-HSV antibodies. This may be seen in patients with antibody deficiencies who retain NK activity against HSV-infected cells.[107] The very stress of prolonged physical restraint in animals has been shown to result in decreased NK activity, with attendant reactivation of HSV infection.[108] A longitudinal study revealed that interleukin-2, alpha-interferon, and cell-mediated cytotoxicity decreased 3 to 7 days prior to the development of recurrent herpes labialis.[109]

Clinically, HSV I is a ubiquitous virus contracted through routine household contact. HSV I may commonly infect normal hosts ''above the waist'' and is responsible for oral and labial disease (cold sores), cutaneous disease (''herpetic whitlow''), and herpetic conjunctivitis. HSV II is less common than HSV I and usually hits ''below the belt,'' is transmitted through sexual contact, and causes genital infections.

Primary HSV I infection occurs during childhood in the majority of cases and may be subclinical. Adult-onset herpetic gingivostomatitis is much more severe than the pediatric form. Acute primary herpetic gingivostomatitis presents after a nonspecific prodrome of fever, headache, and myalgias. The gums are red, swollen, and friable. Painful vesicles erupt on the labial, anterior gingival, and intraoral mucosa. Tiny vesicles may also appear around the nose. The lesions heal within 2 weeks. Both acute gingivostomatitis and subclinical infection result in latent infection of sensory ganglion nuclei. An infrequent sequela of primary gingivostomatitis is herpetic encephalitis, which is commonly fatal; survivors are left with severe morbidities.

Reactivation of latent infection may occur in up to half of infected individuals. It can be stimulated by emotional factors, hormonal changes, excessive sunlight, and fever. Reactivation, heralded by tingling and pain, results in clusters of coalescing vesicles. It has been noted that immunocompetent individuals tend to have labial lesions (herpes labialis), not intraoral lesions, while AIDS patients tend to have recurrences widely distributed throughout the oral cavity, which persist longer.[110–112] In fact, mucocutaneous HSV lasting for more than 1 month was one of the original criteria for defining AIDS prior to the advent of serologic testing, and it remains a diagnostic criterion.

Herpetic whitlow, consisting of painful digital pustules and vesicles, occurs after autoinoculation through skin abrasions from oral or genital lesions. It is an occupational hazard of hospital personnel and dentists. Herpetic paronychia is the result of deep vesicles under the nail bed.

HSV II is the cause of genital herpes. Primary infection is associated with fever, malaise, and lymphadenopathy. Men develop painful penile vesicles and ulcerations with dysuria and a penile discharge. Women develop vulvar and cervical lesions with vulvar pain and burning dysuria. Recurrent episodes are not uncommon and are associated with milder symptoms. Intrauterine transmission of HSV II occurs uncommonly and results in ''TORCH'' infection sequelae: mental retardation, microencephaly, microphthalmia, and blindness. Active genital herpes at the time of delivery results in neonatal infection with serious sequelae such as encephalitis, keratoconjunctivitis, and hepatitis, with high morbidity and mortality.

Disseminated HSV infection with visceral involvement occurs in immunosuppressed and cancer patients. Localized HSV lymphadenitis, and also tonsillitis, in the absence of disseminated disease has been rarely reported.[112–115] Some (but not all) of these patients had underlying hematopoietic diseases. In immunosuppressed patients, herpetic esophagitis and infection of the lower respiratory tract may lead to a chronic and severe disease. It is in this latter group of patients that herpes simplex lymphadenitis primarily occurs, and it is the regional lymph nodes that tend to be affected.[116, 117]

Varicella

Varicella zoster virus (VZV) is a Herpesvirus that causes varicella (chicken pox) and herpes zoster (shingles). Primary exposure to the highly contagious VZV results in malaise, anorexia, and mild fever, followed by vesicles and maculopapular eruptions within 24 to 48 hours. The dermal eruptions begin centrally on the trunk and progress distally to the limbs and head. Childhood infections are self-limiting, but primary VZV in adults may lead to more serious manifestations such as pneumonia. Herpes zoster infection represents an adult reactivation of VZV, which may occur in the setting of chronic illness, neoplasm, and so on. The cutaneous lesions of herpes zoster resemble those of varicella but usually are limited to one or several sensory dermatomes. Generalized lymphadenitis can occur in the setting of both VZV and herpes zoster.[118]

Vaccinia

Vaccinia is a DNA poxvirus that causes vesicular skin eruptions less serious than those of smallpox. Vaccinia is antigenically similar to the smallpox virus and has been employed as a vaccination against smallpox. Parenthetically, it has been theorized that the spread of HIV in Central Africa is in no way coincidental with the massive vaccination campaign against smallpox in Africa in the late 1960s and 1970s.[119] Cervical or axillary lymphadenopathy may develop 1 to 3 weeks after vaccination. The morphologic changes are similar to those of other virus infections such as Herpesvirus, measles, and other unidentified viral agents.

Measles

Measles, or rubeola, is a highly contagious acute exanthematous childhood illness caused by an RNA paramyxovirus. Measles is uncommon in the United States due to use of the live measles virus (MV) vaccine, but it may still occur among nonimmunized children. In Third World countries where nutrition and immunity are poor, measles may be a routinely fatal disease. Measles is transmitted by oral/respiratory secretions. The incubation period averages 10 to 12 days, after which the child develops a prodrome of high fever, conjunctivitis, photophobia, lymphadenopathy, and intraoral small, erythematous vesicles and ulcers (Koplick's spots), usually on the lower buccal mucosa. A generalized skin rash develops, beginning on the face and spreading downward to involve the trunk and extremities; this pattern of spread distinguishes measles from chicken pox. The rash

Copyright © 2003, Mosby, Inc. All rights reserved.

usually resolves within 10 days. Pneumonia (interstitial giant cell pneumonia) and acute encephalitis are serious immediate complications of measles; they occur, albeit rarely, in normal patients.[120, 121] Subacute sclerosing panencephalitis (SSPE) is a rare, progressive, fatal, late sequela of measles characterized by mental deterioration and motor abnormalities. SSPE is detectable 5 to 10 years after primary measles and is the result of defective, nonreplicative MV persistence in the brain. Patients with AIDS, malignancies, or immunosuppression due to other causes are quite likely to develop serious sequelae. They may also fail to develop the characteristic rash, or develop an atypical rash that takes longer to resolve, thus obscuring the clinical diagnosis. Fatal disseminated cases may also rarely occur after vaccination with attenuated virus in immunosuppressed children.[122] Vaccines are prepared from live, attenuated strains of measles virus, and regional lymphadenitis, most often cervical, axillary, and inguinal, may develop within a few days to 2 weeks after vaccination.

Histologically, Warthin-Finkeldey (WF) cells were first observed in tonsillectomy specimens from children who subsequently developed measles; they are characteristic of this infection. Immunohistochemical studies reveal them to be of T-cell origin. The nuclei of these syncytial giant cells are numerous and crowded; up to 100 nuclei may be present, with a ''bunch of grapes'' appearance. Eosinophilic inclusions are present in both the nuclei and the cytoplasm. WF cells can be seen in the stratum corneum and tonsils, as well as in other organs, most notably the lungs, in disseminated cases.

Rubella (German Measles)

Rubella, or German measles, is a childhood disease characterized by mild constitutional symptoms, a rash similar to that of mild rubeola or scarlet fever, and enlarged, tender, postoccipital, retroauricular, and posterior cervical lymphadenopathy. The lymphadenopathy precedes the rash by at least 24 hours; the latter may last for about 1 week. In older patients rubella can be more severe, with arthralgias and purpura. Prior to the development of the vaccine, rubella was quite common; now it is rarely encountered. Maternal rubella in early pregnancy will cause severe congenital anomalies in the newborn infant, first noted in 1941.[118]

Human Immunodeficiency Virus

Human immunodeficiency virus type 1 (HIV-1) is a member of the lentiviruses, a subfamily of retroviruses, with a strong tropism for components of the mononuclear phagocyte system (MPS), namely, CD4+ T lymphocytes, monocytes, macrophages, and dendritic cells.[123] The HIV viremia follows infection, peaking at about 6 weeks and becoming undetectable after about 8 weeks. Antibody seroconversion is detectable after 6 weeks and peaks at approximately 8 to 10 weeks. After seroconversion, proviral host integration is established and a latency/quiescent period of variable duration follows, with normal T4 counts and immune function. HIV may not be detectable at all in circulating lymphocytes. A vigorous cytotoxic T-lymphocyte response immediately follows HIV infection, specifically targeted against envelope proteins and internal proteins such as Gag and Nef. This cytotoxic immune response selects against active viral replication early in the disease, and the selection pressure is toward early viral integration. The pressure toward integration and latency allows HIV to effectively elude the host immune system while it is still intact. Specific cytotoxic immunity is also apparently eluded and exhausted as AIDS becomes manifest. The switch from a quiescent/latent state to actively productive infection is not completely understood, but may represent a progressive move from imperceptible infection to immune deterioration, exhaustion, and a fatal downward spiral. This course may play out over a decade or longer. Although little or no HIV may be detected in circulating T cells during latency, HIV is actively replicating in tissue lymphocytes.[124]

Primary HIV infection may be entirely asymptomatic, with seroconversion as the only clue to infection. More than half of patients infected with HIV may present with a range of symptoms: fever, malaise, myalgias, diarrhea, pharyngitis, macular erythematous rash, lymphadenopathy, splenomegaly, and weight loss, akin to the presenting symptoms of infectious mononucleosis. The acute illness occurs 3 to 6 weeks after exposure and may last for up to 2 weeks, though milder symptoms may persist for months. Mucosal ulcerations accompanying acute HIV seroconversion, thought to be a direct result of HIV infection (the ''chancre of HIV''), has been reported. Multiple, painful, small (0.3 to 1.5 cm) discrete ulcers have been reported on the palate, esophagus, anus, and penis of patients during acute seroconversion that relate to sexual activity.

A large percentage of AIDS cases initially come to medical attention because of complaints related to the head and neck, especially oral complaints. The three most common general complaints are skin lesions such as Kaposi's sarcoma (KS), oropharyngeal symptoms such as candida oropharyngitis or HSV infections, and cervical lymphadenopathy. Among 375 homosexual males (AIDS and non-AIDS patients) presenting to an oral medicine clinic, candidiasis was diagnosed in 66%, KS in 53%, and hairy leukoplakia in 28%.[125] Persistent generalized adenopathy (PGA) is a common presenting symptom of AIDS. Early in the course of HIV, lymph node infection reveals reactive follicular hyperplasia and follicular lysis: an influx of mantle cells and polymorphonuclear cells into germinal centers, with their architectural disruption.[126] Multinucleated giant cells and monocytoid B cells can be seen in sinusoids. As the reactive hyperplasia regresses, follicles become fewer, with a ''washed-out'' paucicellularity. Terminal lymph nodes may have virtually no lymphocytes; one sees only macrophages, fibroblasts, and granulocytes. On imaging, when there is a diffuse lymphadenitis (lymphadenopathy) and multiple benign-appearing parotid cysts (lymphoepithelial cysts; see Chapter 39), the diagnosis of AIDS can be established. In approximately one third of these patients, there also is considerable enlargement of the adenoids.[116]

Bacterial Lymphadenitides

Bacteria cause localized direct cell injury by secretion of exotoxins or release of endotoxins with bacteriolysis. Lymph nodes draining infected tissues may reveal acute suppuration with abscess formation and necrosis, reactive germinal centers, and scar formation. On imaging, bacterial lymphadenitides may appear similar to viral lymphadeni-

Copyright © 2003, Mosby, Inc. All rights reserved.

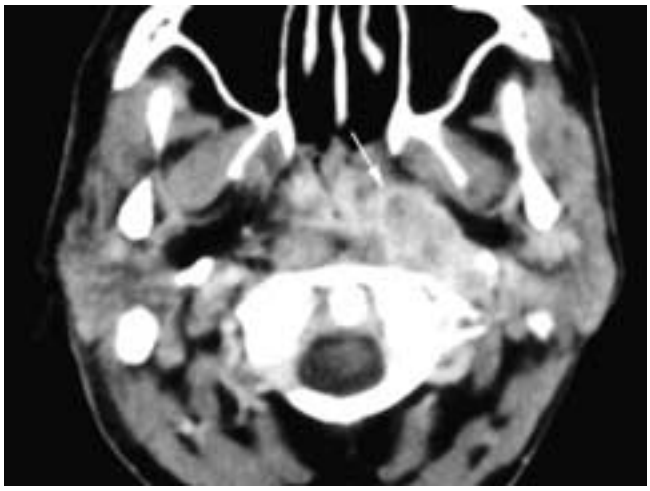

FIGURE 36-27 Axial contrast-enhanced CT scan shows an abscessed left retropharyngeal node (*arrow*) with an enhancing nodal capsule in a patient with an acute bacterial pharyngitis. Note that only the node and not the entire retropharyngeal space is enhancing, a differentiating point from a retropharyngeal abscess.

tides in that there are nonnecrotic enhancing nodes. However, often the nodes are more enlarged. There is a tendency toward central nodal necrosis with a thick, irregular, enhancing nodal wall and adjacent cellulitis. If one does not consider the clinical presentation, the imaging appearance may mimic that of metastatic carcinoma (Figs. 36-27 to 36-32).

FIGURE 36-28 Axial contrast-enhanced CT scan shows multiple variably enhancing left level II and level V lymph nodes with some effacement of the immediate nodal fat planes in this patient with tuberculosis.

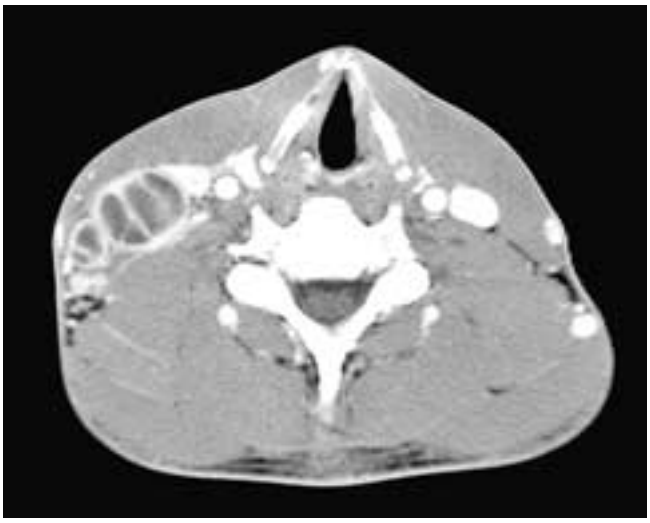

FIGURE 36-29 Axial contrast-enhanced CT scan shows several right partially necrotic, partially enhancing level III nodes. There is little effacement of adjacent fat planes in this patient with tuberculosis.

Routine Bacterial Lymphadenitis

Acute, suppurative lymphadenitis is most often caused by staphylococci. Abscess and or sinus formation may completely obliterate lymph node architecture. Acute lymphadenitis may also be caused by yersiniosis, listeriosis, fungal infections, and cat-scratch disease. Rarely, gonorrhea may cause acute suppurative lymphadenitis. Because of the widespread availability of antibiotics, suppurative lymphadenitis

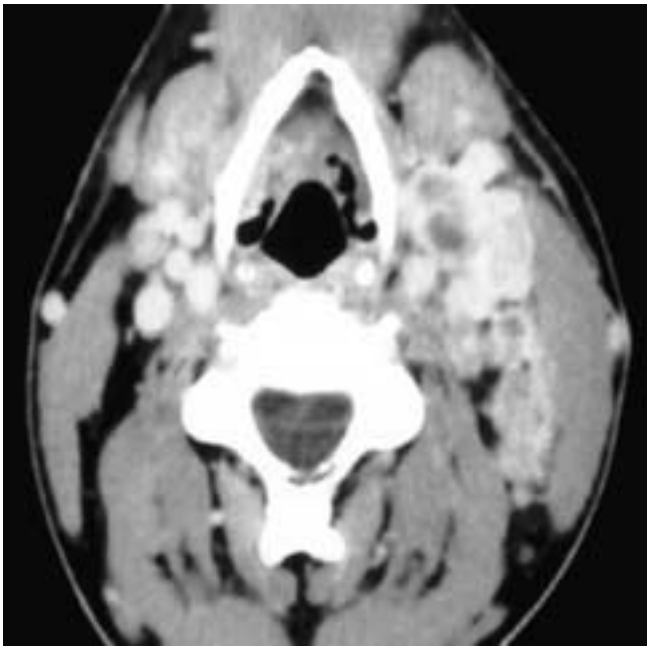

FIGURE 36-30 Axial contrast-enhanced CT scan shows multiple left level II nodes and one right level II node. These nodes have a variable imaging appearance with some nodes enhancing, some with an attenuation close to that of muscle, and some that are necrotic. Despite the number of affected nodes, there is virtually no infiltration of the adjacent fat planes. Although this imaging appearance could be that of lymphoma, this patient had tuberculosis.

Copyright © 2003, Mosby, Inc. All rights reserved.

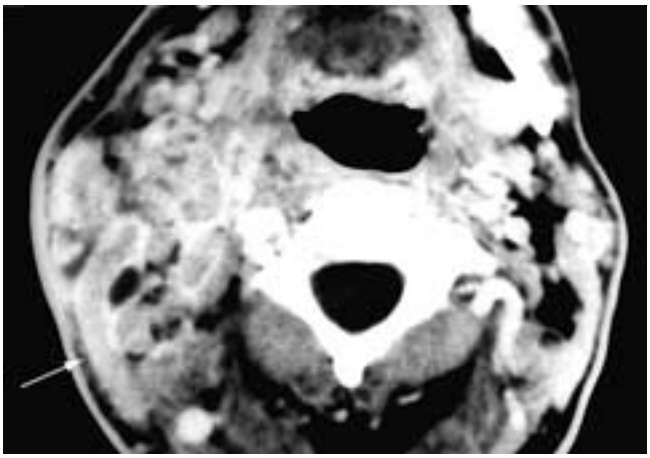

VIEW IMAGE

FIGURE 36-31 Axial contrast-enhanced CT scan shows multiple enhancing right level II nodes with some effacement of adjacent fat planes, involvement of the right sternocleidomastoid muscle (*arrow*), and overlying skin and subcutaneous fat planes. This patient was HIV positive and had tuberculosis. Possibly his HIV status accounted for the more aggressive imaging appearance of his tuberculosis.

is rarely encountered. The involved nodes are enlarged, tender, and soft, and there are secondary changes of inflammation in the adjacent soft tissues.[127, 128]

Lemierre's Syndrome

Lemierre's syndrome represents an uncommon complication of an acute pharyngotonsillitis in which an anaerobic oropharyngitis results in septic thrombophlebitis of the ispsilateral internal jugular vein, with subsequent septicemia and septic emboli, most often to the lungs and large joints.[129] There usually is an associated regional reactive lymphadenitis (see Chapter 41).

Cat-Scratch Lymphadenitis

Cat-scratch disease (CSD) has an associated necrotizing granulomatous regional lymphadenitis that is caused by *Rochalimaea henselae*, a member of the Rickettsiaceae. Most often, the bacteria are introduced at a skin site by either a scratch, splinter, or thorn. Children and young adults are most often affected.[128] An erythematous lesion develops at the site, and the lesion resolves spontaneously within 1 to 3 weeks. CSD then comes to medical attention when regional lymph nodes become painfully enlarged within weeks of the

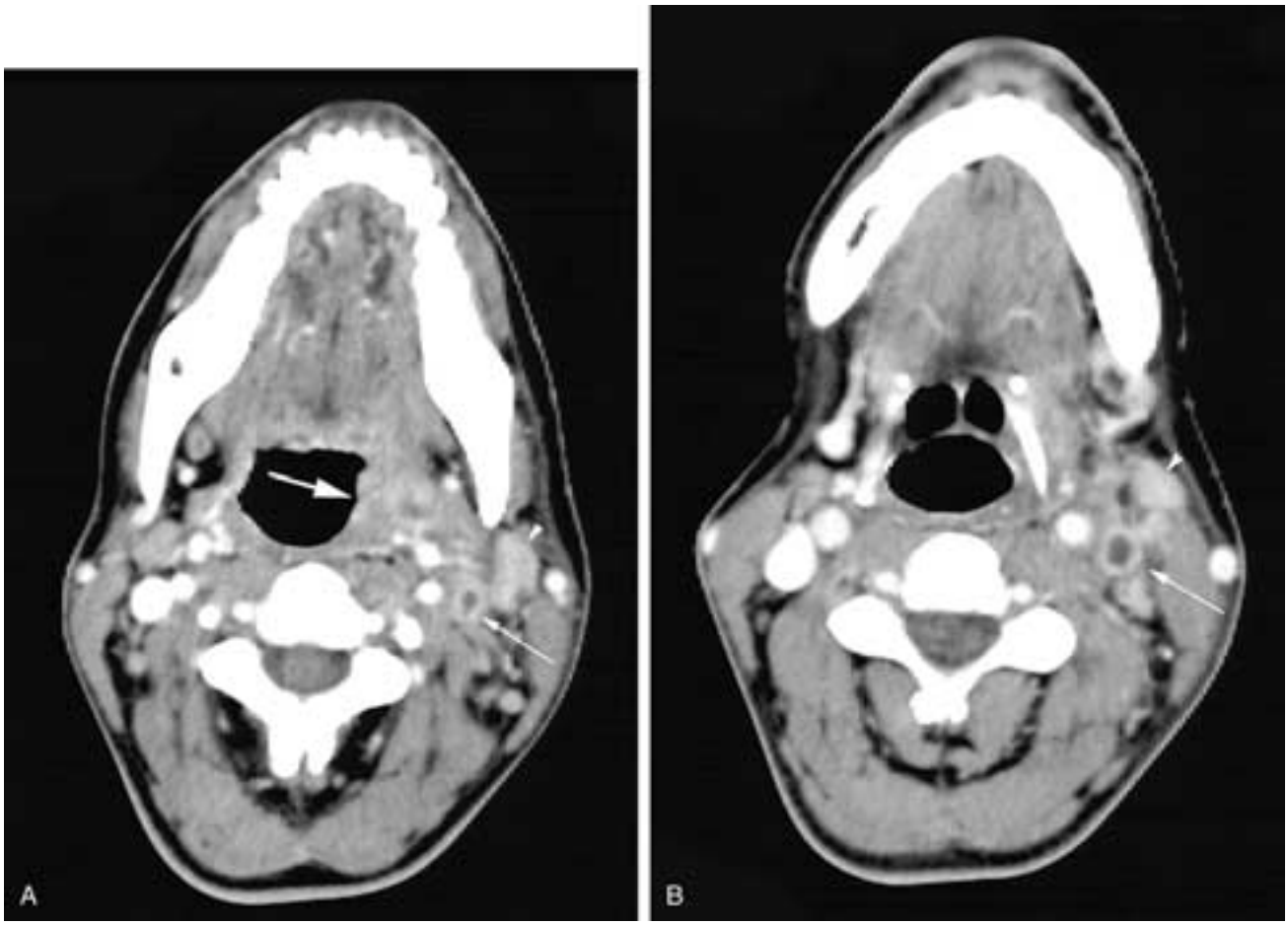

VIEW IMAGE

FIGURE 36-32 Axial contrast-enhanced CT scans from cranial (**A**) to caudal (**B**) show thickening of the left oropharyngeal wall (*large arrow*) due to a clinically evident acute pharyngitis. There is infiltration of the adjacent fat planes extending toward the lateral neck, and there is thrombosis of the left internal jugular vein (*small arrows*). There are also enhancing reactive left level II nodes (*arrowheads*). This patient had Lemierre's syndrome.

Copyright © 2003, Mosby, Inc. All rights reserved.

primary lesion. Lymphadenopathy may be accompanied by fever, headache, and myalgias. An erythema nodosum–type rash may follow but may also be manifest as erythema annulare, erythema multiforme, or thrombocytopenic purpura. This illness runs a self-limiting course within 2 to 4 months.

Occasionally, though, 1% to 2% of patients with CSD may progress to severe systemic infections such as encephalitis, osteomyelitis, hepatitis, and pleuritis. Histologically, early CSD lymphadenitis may reveal only nonspecific reactive changes. The finding of coalescent epithelioid granulomata forming stellate necrotizing microabscesses suggests the diagnosis of CSD, but bacilli are rarely present within the granulomata. The bacilli stain with Warthin-Starry silver stain, stain weakly with Brown and Hopp stain, and have been noted in capillaries and within macrophages. In practice, histologically they may be very difficult to distinguish from background.

Bacillary Angiomatosis

Bacillary angiomatosis (BA) is a *Rochalimaea* infection occurring in patients with AIDS that is related to CSD.[130] Patients with BA as well as those with CSD share a history of exposure to cats. BA presents clinically as solitary or multiple tender (or nontender) red or violaceous, friable, cutaneous papules or nodules 0.5 to 4.0 cm in size, which may crust over. These papules occur on the face, extremities, and scrotum. Deeper subcutaneous nodules, resembling cellulitis, may also develop and erode underlying bone. Lesions involving regional lymph nodes and internal organs such as bone, spleen, liver, and brain may also develop in AIDS victims. Clinically, the cutaneous lesions of BA may resemble KS, and have also been noted to bear a resemblance to verruga peruana, the chronic cutaneous manifestation of infection with *Bartonella bacilliformis* (the agent of Carrion's disease, or Oroyo fever). BA is responsive to antibiotics; erythromycin-type drugs are the drugs of choice.[127]

Histologically, BA reveals nodular proliferations of small vessels lined by enlarged cuboidal endothelial cells, which may be markedly atypical, mimicking malignancy. On the other hand, there is a resemblance to pyogenic granulomata, as these lesions are polypoid, with a collarette of epidermis. An acute inflammatory infiltrate and debris are seen. Clusters of slender rods may be observed on Warthin-Starry stain, and variably observed on Steiner treponeme silver stain and Brown and Brenn stain, similar to the bacilli seen in CSD.

Syphilitic Lymphadenitis

Syphilitic lymphadenitis is caused by the sexually transmitted bacterium *Treponema pallidum* (*treponema*—Greek: ''turning thread''; *palidum*—Latin: ''pale''), a long, slender spirochete that rotates along its long axis in fluid and may creep and crawl along solid surfaces. Syphilis may be divided clinically into three distinct phases: primary, secondary, and tertiary. Primary acquired syphilis develops 1 week to 3 months following initial exposure and is characterized by chancre formation at the site of infection. Only the regional lymph nodes are involved at this stage. Typically, cutaneous chancres are painless, hard, raised lesions that develop shallow ulcerations with sharp, raised borders. On mucosal surfaces, primary chancres may appear as silvery gray erosions, granulation tissue, or nonspecific ulcers or may even mimic carcinoma. Chancres are self-healing, with minimal scarring (''cigarette paper thin'' and semitranslucent), so individuals may not be prodded into seeking medical attention. Secondary syphilis occurs weeks to months after the primary chancre and is the result of systemic generalization of the infection. Individuals develop fever, pharyngitis, and a generalized macular/papular rash. The rash can affect the hair follicles of the scalp, eyebrows, and beard, causing a patchy, ''moth-eaten'' alopecia (alopecia syphilitica). These macular/papular lesions coalesce in warm, moist areas such as the anogenital and intertriginous areas to form hyperplastic lesions: condyloma lata or flat condylomata. As condyloma lata arise from the systemic spread of *T. pallidum*, they are not dependent on the initial site of inoculation. Like chancres, they are also infectious. Rarely, ulcerative lesions also occur in secondary syphilis: lues malignum. Generalized lymphadenopathy occurs during the secondary stage, with a predisposition for periarticular lymph nodes, such as those in the epitrochlear and inguinal areas. Secondary syphilis will lapse into a latent state, but patients may experience recurrent mucocutaneous symptoms of secondary syphilis.

Symptomatic tertiary syphilis is a late manifestation seen years to decades after primary infection; a minority of untreated patients (as shown by the infamous Tuskeegee study) progress to the tertiary form.[131] Tertiary syphilis most commonly affects the cardiovascular system and the central nervous system. Cardiovascular syphilis results in a coronary artery vasculitis and aortitis that may progress to aneurysmal dilatation. The aortic intima becomes contracted and scarred, resulting in a characteristic ''pebbled'' or ''tree bark'' appearance. Neurosyphilis results in a chronic syphilitic meningitis with a lymphoplasmacytic endarteritis. The brain and nerves may be directly infiltrated by *Treponema*, causing neural loss and resulting in psychiatric disorders, progressive dementia, cranial nerve deficits (e.g., eighth nerve deafness, vestibular symptoms), and sensory/motor losses (tabes dorsalis, taboparesis). Large necrotic lesions or gummas can occur. They are seen most commonly in the liver but may occur anywhere. Lymphadenopathy may also be associated with latent or early tertiary syphilis.

Lyme Lymphadenitis

Lyme disease is caused by the spirochete *Borrelia burgdorferi* and is at present the most common arthropod-borne infectious disease in Europe and the United States. It is transmitted primarily by *Ixodes dammini* ticks, or deer ticks, in the Northeast and Upper Midwest, by *Ixodes pacificus* in Western states, and by *Ixodes ricinus* in Europe. The disease is transmitted to humans primarily in the spring, summer, and early fall. Lyme disease can affect the skin, nervous system, heart, eyes, and joints and is diagnosed in patients with these characteristic clinical features: exposure to an endemic area and usually a positive serologic test for *B. burgdorferi* 6 or more weeks after infection. Lymphadenopathy usually occurs in regional draining nodes. Full recovery is possible with early diagnosis and treatment.[132] However, if Lyme disease is not treated with antibiotics in the early stages, neurologic complications can occur.[133]

Copyright © 2003, Mosby, Inc. All rights reserved.

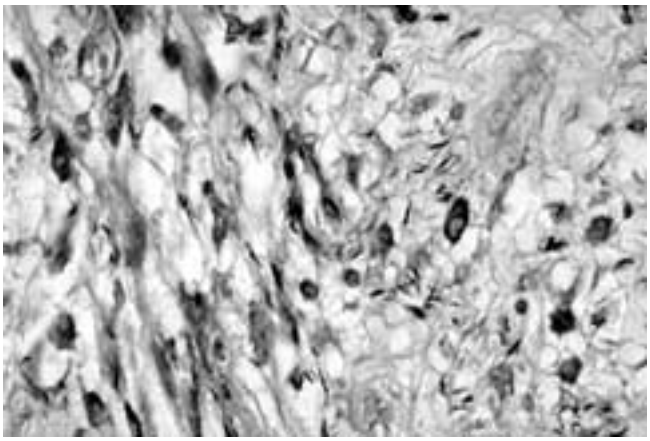

VIEW IMAGE

FIGURE 36-33 Numerous magenta mycobacterial bacilli seen on Ziehl Neelson stain.

Mycobacterial Lymphadenitides

Mycobacteria are aerobic, non-spore-forming, nonmotile bacteria with a thick, multilayered cell of complex lipids and waxes, which accounts for their staining and immunogenic properties. Once stained, they are resistant to decolorization by acid alcohol and hence are acid-fast (Fig. 36-33). Generally, the imaging findings of the mycobacterial lymphadenitides, particularly those of tuberculosis, are variable and include multiple hyperplastic nodes, a localized abscessed node (cold abscess), and on CT multiple nodes, some of which enhance, some of which are necrotic, and some of which have an attenuation similar to that of muscle. There usually is little infiltration of the adjacent fat planes, and there may be nodal calcification. Level V nodes tend to be involved, usually unilaterally, although diffuse adenopathy can occur. Overall, the imaging findings may be indistinguishable from those of lymphoma or even squamous cell carcinoma, and the clinical presentations may be identical. However, unlike these tumors, with tuberculosis there is often imaging evidence of prior pulmonary disease.[134, 135]

Mycobacterium Tuberculosis

A definite resurgence of tuberculosis has been reported in the United States, as a result of (1) immigration from endemic countries, (2) reactivation of disease in the elderly population, and (3) the AIDS pandemic. Primary *Mycobacterium tuberculosis* (MTB) infection is usually subclinical, occurring in the upper lobes, where the oxygen tension is highest (Simon's focus). The pulmonary infection and draining lymph nodes (Ghon complex) heal as calcified granulomata, which are usually negative for acid-fast bacilli. Latent bacilli are still present in these foci and are capable of reactivation. Primary infections become inactivated, but patients are at lifelong risk for developing active disease. Less commonly, primary infections progress to symptomatic pulmonary disease (progressive primary infection); children and young adults are most susceptible.

The more common scenario is that reactivation occurs years after latent primary infection, referred to as progressive secondary infection or endogenous reinfection tuberculosis. Patients present with fever, weight loss, and pulmonary symptoms such as bloody sputum. Cavitary tuberculosis develops, which can seed systemically (miliary spread), favoring the kidneys, adrenals, bone marrow, spleen, ovaries, testes, meninges, and bones. However, extrapulmonary tuberculosis is actually an uncommon event following secondary infection. Head and neck involvement in tuberculosis is rare, thought to be the result of direct infection from expectorated sputum and also hematogenous/lymphatic spread. A total of 136 cases of extrapulmonary tuberculosis were collected: 16 (12%) patients had head and neck involvement; 13 patients had tuberculosis lymphadenitis of cervical, supraclavicular, or submental nodes (scrofula); and there was 1 case each of gingivitis, otitis, and laryngitis.[136] Nasopharyngeal/sinonasal tuberculosis can occur more commonly secondary to pulmonary tuberculosis or uncommonly as a primary upper airway infection of Waldeyer's ring.[137] Primary nasopharyngeal infection presumably is the direct result of inhalation, and clinically and histologically it may mimic Wegener's granulomatosis. Nasopharyngeal tuberculosis can also be accompanied by lymphadenopathy. Clinically, this may mimic nasopharyngeal carcinoma, especially in the Asian population at risk for this neoplasm.

Lupus vulgaris (LV) consists of ragged, ulcerated mucocutaneous lesions, usually facial, that occur in secondary tuberculosis usually as a result of hematogenous or lymphatic spread. There is a significant association between LV (40% of cases) with cervical lymphadenitis or upper airway mucosal lesions.[138] Mucosal LV may occur in the nasal cavity, causing cartilaginous destruction of the palate, pharynx, or gingiva. LV is usually seen in patients with strong immune responses (strong reactors to purified protein derivative), so hypersensitivity to acid-fast bacilli is thought to be responsible for the destructiveness of these lesions. These lesions heal with dense scarring that may deform the underlying tissues. This may be a point of distinction between LV and syphilitic chancres. Laryngeal tuberculosis (''laryngeal phthisis''; *phthisis*: ''to dry up'') was one of the most common laryngeal diseases in the preantibiotic era.[134, 135]

Atypical Mycobacteria

Atypical mycobacteria (also referred to as *mycobacteria other than tuberculosis* [MOTT]) represents a large group of acid-fast bacilli other than *Mycobacterium tuberculosis*, only some of which are human pathogens. MOTT are present in water, milk (especially unpasteurized milk), dust, soil, and birds (*M. avium*). Human-to-human transmission of MOTT is not thought to occur. There are four common presentations of disease caused by MOTT: (1) pulmonary infection in those with underlying pulmonary diseases such as emphysema (e.g., *M. kansasii*), (2) ulcerative skin disease (*M. ulcerans, M. marinium*), (3) serious pneumonias and generalized infections in AIDS patients (e.g., *M. avium-intracellulare*), and (4) cervical lymphadenitis (e.g., *M. scrofulaeum, M. kansasii*). Cervical lymphadenitis (scrofula, scrofulous gumma, scrofuloderma gummosa, tuberculosis colliquativa) is a common presentation of MOTT in nonimmunocompromised patients. Patients are generally afebrile, with enlarged, erythematous lymph nodes mostly in the upper cervical region. Involvement of submental, preauricular, middle, or lower cervical nodes is much less common than upper cervical involvement.[139] Lymph nodes may spontaneously fisualize to the skin of the neck or upward to

Copyright © 2003, Mosby, Inc. All rights reserved.

the face. Primary cervical atypical MTB lymphadenitis is thought to gain entrance to the lymphatics possibly through a mucosal break on the tonsils. The most common MOTT cultured from these lesions are *M. scrofulaceum, M. kansasii*, and *M. avium-intracellulare*. The treatment of choice for MOTT cervical lymphadenitis is surgical excision, not incision and drainage.[140] MOTT are not susceptible to standard anti-MTB therapeutic agents (isoniazid, streptomycin, rifampin), so antibiotic therapy is not indicated. However, scrofula may also be caused by *M. tuberculosis* and *M. bovis*. The distinction between MOTT and MTB relies on cultures or special hybridization techniques, which has important epidemiologic and treatment repercussions. One third to one half of patients with mycobacterial lymphadenitis have radiographic evidence of pulmonary disease, indicating that mycobacterial cervical lymphadenitis can be the presenting symptom of pulmonary MTB disease. These patients then require the recommended full anti-MTB therapy (isoniazide and rifampin for 9 months) to eradicate the pulmonary focus. In the latter instance, it has been postulated that the primary pulmonary infection gives rise to cervical infection via drainage to mediastinal lymph nodes, and subsequently inferior deep cervical lymph nodes, or from the pleura to axillary lymph nodes to inferior deep cervical lymph nodes.

Mycobacterium leprae

Mycobacterium leprae, the causative agent of leprosy, is seen mostly in tropical climates. Leprosy affects more than 11 million people worldwide, mostly in rural areas of Latin America, South and Southeast Asia, Saharan Africa, the Mediterranean basin, and Northern Europe.[141] Endemic U.S. states include Florida, Louisiana, Texas, California, and Hawaii. The number of indigenous U.S. cases of leprosy has remained stable (10 to 29 per year) over the last two decades. On the other hand, the number of imported cases reported in the United States (which fluctuated between 100 and 150 reported cases per year) dramatically increased (up to 300 cases per year) starting in the late 1970s. Forty-five percent of these excess cases involved Vietnamese, Cambodian, and Laotian refugees; 21% were from the Philippines. Leprosy is a disease of low infectivity transmitted through prolonged exposure through either nasal secretions or injured skin. Nasal secretions contain concentrated amounts of infectious bacilli, while the amount of bacilli in skin lesions is variable. Other modes of transmission may include breast milk, mosquitos, and bed bugs. The rate of infection is higher for those with known household contacts than for those without known contacts; the risk of contact with lepromatous leprosy (LL) patients is much higher than that of contact with tuberculoid leprosy (TL) patients, indicating the importance of the exposure dose. The exact interval from exposure to clinical onset of disease is difficult to determine, as one is never certain of the time of initial exposure in endemic areas. However, the median incubation period for war veterans serving in endemic areas has been estimated to be 2 to 5 years for the development of TL and 8 to 12 years for the development of LL.[142]

Immunologically, leprosy can be graded by the host's histopathologic response as TL, BL (borderline leprosy), or LL. BL can be further subdivided into borderline tuberculoid (BT), borderline (BB), and borderline lepromatous (BL).[143] A clinically significant feature of this grading system is that the polar groups (TL and LL) are relatively stable and their immunologic responses do not shift, whereas in patients with BL, the immunologic response may be either upgraded or downgraded. TL is characterized by a robust immunologic response with few bacilli, with the possibility for spontaneous cures. LL is characterized by anergy to the lepromin test (purified suspension of killed *M. leprae*) and abundant bacilli.

Leprosy has a predisposition to affect cooler peripheral areas such as the digits, ears, and nose. It presents as cutaneous hypopigmented or hyperpigmented, hypesthetic, isolated macular lesions. Early lesions may also be tender, erythematous, and indurated (erythema nodosum leprosum) and can ulcerate. Neural involvement is common to all types of leprosy and results in severe pain and muscular atrophy. Sensory loss ultimately leads to repeated mechanical trauma and secondary infections. The classic signs of leprous nerve involvement include claw hand, foot drop, lagophthalmos (failure of the upper eyelid to move down), and anesthesias.[142] Clinically, LL presents with a widespread symmetric facial distribution of lesions leading to coarsening of features (leonine facies). The earlobes and nose are especially enlarged and infiltrated. Intranasal and paranasal sinus involvement is common and occurs after cutaneous nasal involvement. Sinus involvement may present with mucopurulent rhinitis, producing mucus with copious mycobacteria. Early mucosal lesions are plaque-like. Late sinonasal lesions are nodular and ulcerative and may ultimately lead to nasal collapse. LL is also associated with mycobacillemia and involvement of the liver, spleen, and bone marrow. Retrograde laryngeal involvement usually follows nasal disease. In a study of 973 untreated leprous patients, laryngeal involvement was common in LL (65%), with the strongest association seen in the most advanced cases. The epiglottis was most often involved, appearing thickened and irregular. This mirrors *M. leprae's* predisposition for cooler sites.[144, 145]

Fungal Lymphadenitides

Generally, mycotic infections tend to be superficial, limited to the mucocutaneous tissues; however, fungi can cause pulmonary infection, and also disseminated infections in the immunocompromised patient. Only those fungi that may have an associated lymphadenitis are discussed below. In general, the nonspecific imaging findings are similar to those of the bacterial lymphadenitides; often the nodes are enlarged and hyperplastic.[146]

Cryptococcosis

Cryptococcus neoformans is a ubiquitous yeast of worldwide distribution. Cryptococcosis (torulosis) is the result of inhalation of aerosolized bird droppings. It may cause asymptomatic, localized pulmonary granulomas; cryptococcal pneumonia or disseminated disease can develop in the immunosuppressed. It is reported to occur in about 7% of AIDS patients, and the lymph nodes involved may be in association with either an occult focus or part of the disseminated form of the disease. The meningeal infection seen in the AIDS population is thought to follow respiratory infection.

Gomori methenamine silver will stain the organism,

Copyright © 2003, Mosby, Inc. All rights reserved.

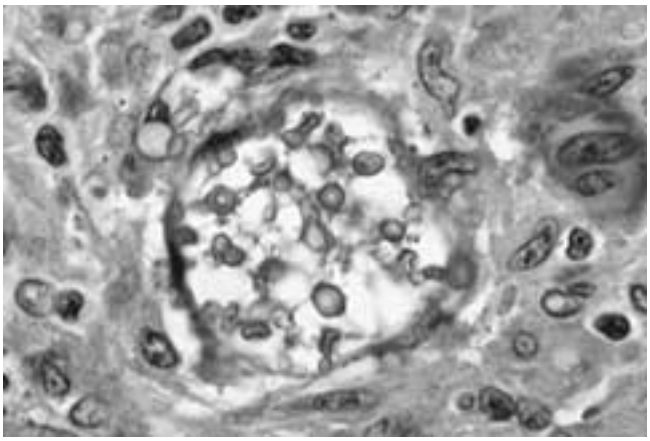

FIGURE 36-34 Cryptococcal organisms can be seen (center), their capsules staining with mucocarmine.

VIEW IMAGE

while mucicarmine and digested periodic acid–Schiff stain will accentuate the polysaccharide capsule. Uncollapsed round yeasts are the size of erythrocytes (6–7 μm), but may be as large as 20 μm (Fig. 36-34). Collapsed, deformed yeasts take on a "boat-like" or sickle-type shape similar to that of *Pneumocystis*. Single budding yeasts with narrow necks may be seen.

Histoplasmosis

Histoplasmosis (Darling's disease) was described early in the twentieth century by Samuel Darling.[147] The organisms he found were intracellular, within histiocytes; therefore, he coined the term *Histoplasma*. *Capsulatum* was further derived from the ''refractile rim'' observed around the organisms.

The introduction of a major vector of histoplasmosis, the European starling (*Sturnus vulgaris linnaeus*), lies in New York City and is an example of life imitating art. One of the features of Central Park, which was designed in the late nineteenth century, was the importation of pairs of all the birds mentioned in the writings of Shakespeare, including the starling. A murmuration of 60 starlings were released in Central Park in 1890. In 1895, Frank M. Chapman, an ornithologist, noted: ''They seemed to have left the park and have established themselves in various favorable places in the upper part of the city. They have bred for three successive years in the roof of the Museum of Natural History and at other points in the vicinity as they have already endured our most severe winters, we may doubtless regard the species as thoroughly naturalized.''[148, 149] Since this initial introduction, the starlings multiplied successfully and rapidly, to become one of the most numerous birds in North America. This tremendous ecological success has been attributed to the adaptation of a south-west migratory pattern and to the ability of starlings to oust other birds from their roosts—thus the lines ''I'll have a starling shall be taught to speak, Nothing but 'Mortimer,' and give it to him.''[150] Starlings were indirectly responsible for countless cases of histoplasmosis, as well as ruined crops and downed airplanes in the United States.

In the United States, histoplasmosis is endemic in the Midwest and Central states and in the Southeast. A dimorphic fungus, its hyphal form, *Emmonsiella capsulatum*, can be isolated from starling roosts, bat caves, pigeons' excrement, and chicken coops. Exposure occurs via aerosolized bird or bat droppings and contaminated soil and fertilizers. Starling congregations are especially risky, as these gregarious birds amass by the thousands in a ''Hitchcock-like'' fashion, and their accumulated droppings are especially dense, necessitating public health measures to decontaminate heavily infected soil.[151] Point source epidemics have been associated with construction and renovation sites, either through turning contaminated soil or by working on sites where birds had been roosting.[152]

As with most inhaled mycotic pathogens, the most common manifestation of histoplasmosis is a subclinical pulmonary infection, usually because of a small exposure source and normal patient immunity. Patients may develop acute pneumonia after massive inhalation. Chronic cavitating and fibrosing pulmonary infection, sclerosing mediastinitis, and disseminated infection with involvement of bone marrow and adrenals (resulting in Addison's disease) are more serious sequelae of histoplasmosis. Prior to the AIDS epidemic, disseminated histoplasmosis was seen very rarely, usually in elderly patients or in those immunosuppressed by chemotherapy or hematologic malignancy. Disseminated and extrapulmonary histoplasmosis in the face of HIV seropositivity has been included in the criteria for AIDS. Disseminated histoplasmosis presents with fever, septicemia, pneumonia, hepatic or renal failure, central nervous system infection, or skin lesions. It is thought to be due to reinfection or, less frequently, to reactivation of latent disease.[153] Cervical adenopathy, pharyngitis, tonsillitis, and ulcerating oral lesions may occur in AIDS patients.[154, 155]

Histologically, *Histoplasma* is seen as tiny intracellular and extracellular hematoxylinophilic bodies, each surrounded by a small halo (Fig. 36-35). A granulomatous reaction may be present. The overlying mucosa can be hyperplastic. The aforementioned ''halo'' or ''capsule'' does not stain and in actuality is an artifact of tissue embedding. Solitary and multiple thin-necked budding may be seen.

Coccidioidomycosis

Coccidioides immitis is endemic in the southern United States (southern Texas, New Mexico, Arizona, and Califor-

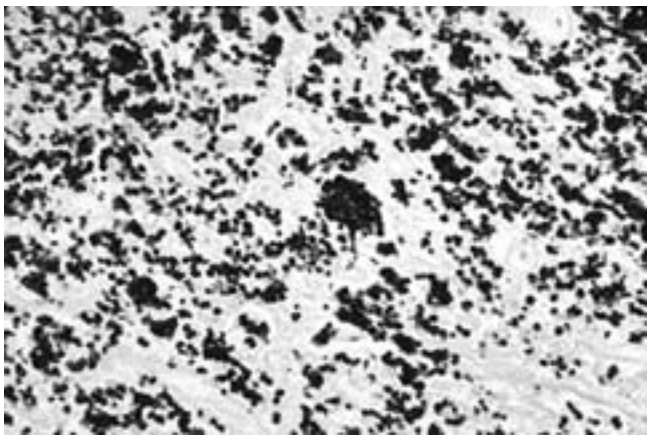

FIGURE 36-35 These small intracellular *Histoplasma* organisms stain with Gomori methamine.

VIEW IMAGE

Copyright © 2003, Mosby, Inc. All rights reserved.

nia) and in northern Mexico, as well as in Central America and South America. Coccidioidomycosis (San Joaquin Valley fever, desert rheumatism, the bumps) affects immunocompetent patients. It has also been estimated that 20% of the cases reported yearly are diagnosed outside the endemic areas, thus widening the relevance of the causative organism.[156] The endospores of *Coccidioides* are released and germinate to form hyphae and highly infectious arthrospores. There is seasonal variation in the rate of skin-test conversion: the higher rate of infection is seen at the end of summer during dry, dusty periods. Any profession that involves the movement of soil (e.g., construction, archaeology) places individuals in endemic areas at risk of infection. Point source epidemics have been related to archaeological digs, such as those at Indian sites, with an especially high rate of symptomatic pulmonary infection and an erythema multiforme hypersensitivity rash among individuals visiting from nonendemic areas.[157] *Coccidioides* is extraordinarily infectious; just 10 arthroconidia will cause infection in animals.[158] Handling petri dishes of laboratory cultures has caused disease, as has handling and washing infected glassware. Direct human-to-human transmission does not occur, as the tissue endospores are not infectious; they must first go through germination to yield the infectious arthrospores. Several hospital staff developed infections after removing a plaster cast from a patient with an osteomyelitis caused by *Coccidioides*.[159] It was postulated that the dressing under the cast had supported the growth of the mycelial phase, which gave rise to the infectious arthrospores.

Illnesses range from subclinical infections to disseminated and often lethal infections, depending on the patient's immune status, infectious dose, nationality, and other factors such as pregnancy. Pulmonary infection occurs through inhalation of arthrospores, and commonly causes self-limiting pulmonary and mediastinal disease. In an outbreak involving military personnel, third-trimester pregnant women are more likely to develop disseminated and fatal infections than are first-trimester pregnant women.[160]

Laryngotracheal coccidiomycoses may be seen, with or without concurrent pulmonary disease.[161] Patients with upper airway involvement present with hoarseness and stridor, which may progress to complete upper airway obstruction. The larynx and trachea have edematous, erythematous, polypoid-type tissue. Other sites of involvement of the head and neck include skin and scalp nodules, cervical soft tissue and lymph nodes, and peritonsillar and retropharyngeal tissues.[162]

AIDS patients living in or visiting regions endemic for *Coccidioidomyces* may present clinically with pulmonary infiltrates or erythematous skin lesions indistinguishable from the infections manifested in the nonimmunocompromised population. On the other hand, AIDS patients with disseminated coccidioidomycosis may have atypical presentations such as lymph node, hepatic, or cerebral involvement or pustular skin lesions.[163] Histologically, *Coccidioidomyces* evokes a granulomatous reactions with foreign body–type giant cells. The fungal spherules are large, measuring 30 to 80 μm, with thick spherule capsules that have a "double-walled" appearance (Fig. 36-36). Serum acute antibodies and a newly converted skin reaction to coccidioidin antigen may be helpful clinical diagnostic adjuncts; these tests may be falsely negative early in the course of infection. Additionally, patients with disseminated disease are likely to become anergic.

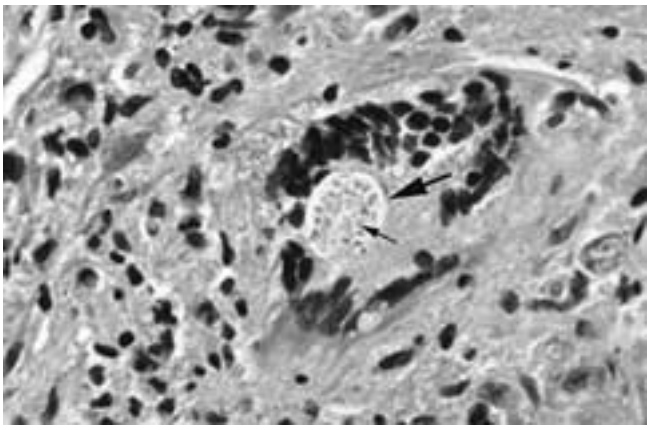

FIGURE 36-36 A multinucleated giant cell (center) containing a spherule (*large arrow*) filled with coccidioidomycosis organisms (*small arrow*).

VIEW IMAGE

Pneumocystosis

Pneumocystis carinii, the agent of pneumocystosis, is ubiquitous in nature, and exposure occurs in early childhood. The nature of *Pneumocystis* was generally unknown but had been assumed to be protozoal. Studies comparing the 16S-like ribosomal RNA of *Pneumocystis* with that of fungi and protozoa revealed that it is more closely related to fungi.[164] *P. carinii* is the most common opportunistic infection associated with AIDS and occurs in more than 60% of these patients, often leading to death. Lymph nodes may be involved in cases of bilateral pneumonia or in the rare disseminated form. Extrapulmonary pneumocystosis may be seen in AIDS patients, often in the absence of *Pneumocystis* pneumonia. These infections have occurred in patients maintained on aerosolized pentamidine, since it offers only pulmonary prophylaxis and is not systemically absorbed.

Extrapulmonary pneumocystosis of the head and neck appears to have a predisposition for the ear. Otitis externa forming external canal polyps and subcutaneous nodules and/or middle ear infections have been reported.[165–168] A suggested explanation is that *Pneumocystis* may colonize the nasopharynx and ascend the eustachian tube. Pneumocystosis appears as a foamy, frothy, granular exudate without much inflammatory response. Only the faint basophilic nuclei may be seen on hematoxylin and eosin stain. The Gomori methenamine silver stain can reveal the cystic formation of organisms that are partially collapsed, ''cup-shaped'' or ''boat-shaped,'' generally the size of erythrocytes.

Protozoal Lymphadenitis

Only *Toxoplasma* will be discussed, as this is the only protozoan that causes lymphadenopathy.

Toxoplasmosis

Toxoplasma was first isolated at the turn of the twentieth century in gondis, which are rodents in Tunis.[169] Domestic

Copyright © 2003, Mosby, Inc. All rights reserved.

cats and small rodents are major natural reservoirs for these protozoa. Feline coinfections with *T. gondii* and *Toxocara cati* had led to the initial conclusion that *T. gondii* was transmitted within *T. cati* larvae. This issue was resolved when it was shown that *Toxocara*-free cats could transmit infectious *T. gondii* oocysts.[170] The oocysts, 10 to 12 μm in size, are formed in the cat intestinal epithelium. Stray and household cats involved in catching mice or birds can pass tremendous numbers of infectious oocysts in their feces. For instance, 45% of stray cats in Kansas City have been exposed to *Toxoplasma*.[171] Cats usually develop immunity after primary infection. The excreted oocystes are unsporulated when first passed and thus are noninfectious. They require oxygen for sporulation, which can occur up to 5 days later. By contrast, feces remain infectious for up to 1 year.[172] Oocysts are resistant to drying, freezing, and disinfectants but not to boiling water. They may also become aerosolized or dispersed by houseflies or roaches.

Toxoplasmosis may be transmitted by direct inhalation of oocytes, or by ingestion of meat from secondary hosts. It may also be present in soil or sand. Oocytes in the soil also infect grazing herbivore hosts, such as cows, lambs, and pigs, and cause toxoplasmosis via ingestion of raw or rarely cooked meat. France has a higher rate of infection by *Toxoplasma* than other European countries, which is directly related to its culinary habits. For example, barely seared meat was customarily served at a tuberculosis sanitarium in France in the 1960s. The rate of *Toxoplasma* seropositivity in children increased from 0% to 18% after entrance to the sanitarium and increased further when the ration of undercooked meat was raised.[173]

Inhaled sporulated oocytes result in the release of tachyzoites (trophozoites) that invade and infect cells. The tachyzoites divide to form cysts (10 to 100 μm) filled with thousands of organisms, which can then remain latent in host tissue and serve as potential reservoirs for reactivation or chronic infection. Normal hosts commonly have asymptomatic infection. Cervical lymphadenopathy as well as fever, myalgias, anorexia, headache, sore throat, and rash are uncommon symptoms. Rarely, patients may develop necrotizing systemic infections such as retinitis, encephalitis, myocarditis, hepatitis, and pneumonitis. Chronic or recurrent infection is the result of persistence of tissue cysts.

Transplacental *T. gondii* infection may be entirely asymptomatic or result in fetal loss. The risk of fetal loss is greatest in first-trimester infections, while the risk of delivering a baby with evidence of severe congenital infection is greatest with third-trimester infections. The overall risk of fetal infection was 7.4% in a cohort of 339 pregnant women from France who contracted toxoplasmosis during pregnancy.[174] Transplacental transmission may result in severe intracranial infections causing microcephaly, hydrocephaly, cerebral calcifications, chorioretinitis, mental retardation, blindness, and seizure disorders. Immunosuppressed patients or those with AIDS are much more likely to develop severe and fatal infections such as encephalitis, myocarditis, pneumonitis, and hepatitis. *Toxoplasma* encephalitis is the most frequent cause of intracerebral mass lesions in AIDS.

Histologically, the tachyzoites, especially in an extracellular location, are hardly perceptible on hematoxylin and eosin stain but might be observed with a tissue Giemsa stain. They are banana-shaped or crescent-shaped, with a nucleus. The encysted forms of *T. gondii* are more easily visualized: they can be seen on hematoxylin and eosin stain but are rarely present in lymph nodes. Disseminated infections reveal areas of necrosis, intracellular and extracellular tachyzoites, and encysted tachyzoites adjacent to necrosis.

Reactive Lymphadenopathies

Reactive lymphoid hyperplasia may have many causes: bacterial or viral infection, exposure to chemicals, environmental pollutants, drugs, or foreign antigens. The reaction may be an acute inflammatory one or a chronic immune response. Histologically, the response may be focused within the germinal centers, there may be a sinusoidal pattern with antigen-processing cells filling the sinuses, or the pattern may be mixed. The imaging findings are nonspecific and usually consist of homogeneous, normal or slightly enlarged, variably enhancing, well-delineated nodes, similar to the findings of the viral lymphadenitides (see 'Normal' Reactive Nodes in the section on Imaging Criteria of Pathologic Adenopathy).

Atypical Lymphoid Hyperplasia

Atypical lymphoid hyperplasia is seen as activated germinal centers with peculiar dumbbell or serpentine shapes. The germinal centers may be distorted by an influx of small lymphocytes (follicular lysis). The crowded appearance of the follicles may bring to mind follicular lymphoma. Most commonly, atypical lymphoid hyperplasia may be seen in the early phase of AIDS.

Lymphadenopathies Associated with Clinical Syndromes

The following entities involve lymphadenopathies that may be localized to cervical lymph nodes or may have additional generalized manifestations. Two different imaging patterns can be seen. With Kimura's disease and Kikuchi-Fujimoto disease, usually only regional lymph nodes are involved. The nodes are enlarged and necrotic and enhance on imaging, and there is soft-tissue infiltration, often involving the parotid and/or submandibular glands. With other entities such as sinus histiocytosis with massive lymphadenopathy, sarcoidosis, dermatopathic lymphadenopathy, angiofollicular lymph node hyperplasia, angioimmunoblastic lymphadenopathy, and tumor-reactive lymphadenopathy, the lymph nodes are either hyperplastic or considerably enlarged, homogeneous, and often similar in imaging appearance to lymphomatous nodes (Figs. 36-37 to 36-42).[175–178]

Kimura's Disease

This disease, described by Kimura et al. in 1948, is endemic to Asia. The disease involves lymph nodes and deep subcutaneous tissues. By comparison, angiolymphoid hyperplasia with eosinophilia, once considered synonymous with Kimura's disease, is primarily restricted to the dermis. Kimura's disease occurs mainly in young adults age 27 to 40

Copyright © 2003, Mosby, Inc. All rights reserved.

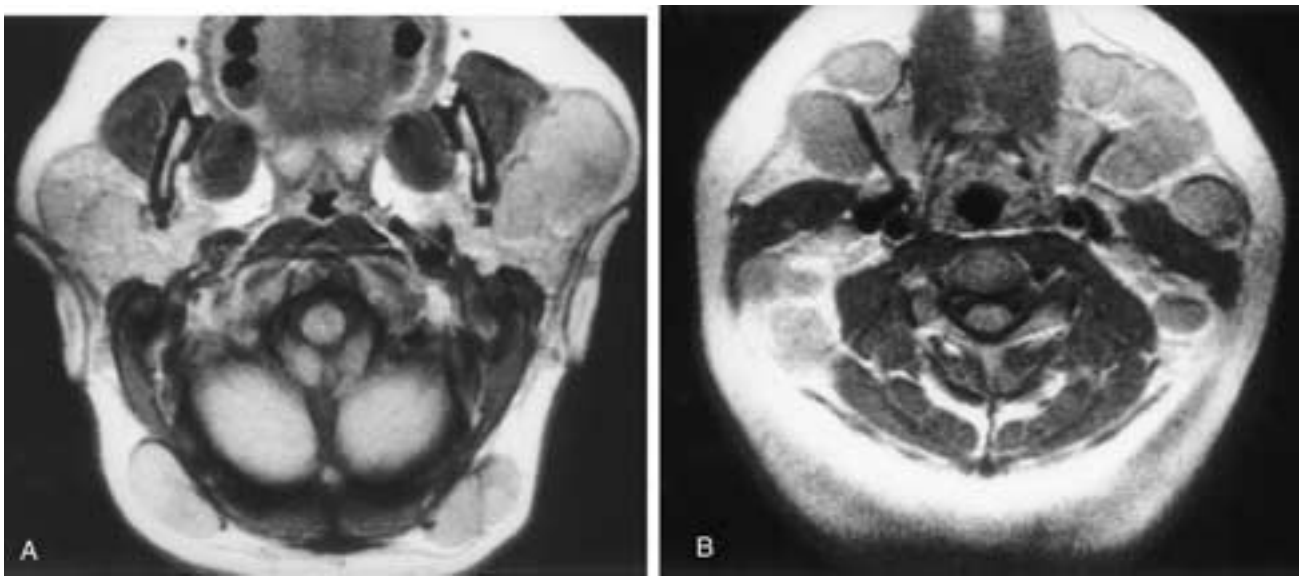

VIEW IMAGE

FIGURE 36-37 Axial T1-weighted MR images from cranial (**A**) to caudal (**B**) on a patient with sarcoidosis. There are multiple homogeneously enlarged lymph nodes in the parotid gland and in the occipital region. There are also nodes in levels I, II, and V. There was no infiltration of the adjacent fat planes. Although this imaging appearance can be seen in lymphoma, the presence of the suboccipital nodes makes a viral adenopathy or sarcoidosis more likely.

years, and there is a male-female ratio of 3:1. The onset is insidious, with nodular masses enlarging mainly in the head and neck. Often the parotid and periauricular regions are involved, although the oral cavity, axilla, groin, and limbs can also be affected. Peripheral blood eosinophilia of 10% to 15% and elevated serum immunoglobulin E (IgE) levels are common. Histologically, Kimura's disease is characterized by intense infiltrates of eosinophils and vascular proliferation with plump reactive endothelium (Fig. 36-43). While the disease process is usually localized, systemic symptoms (allergic asthma, myocarditis, and focal segmental glomerulosclerosis) may occur as a result of the peripheral eosinophilia.[179, 180]

Surgery is the treatment of choice, and the disease usually has a benign course.[175]

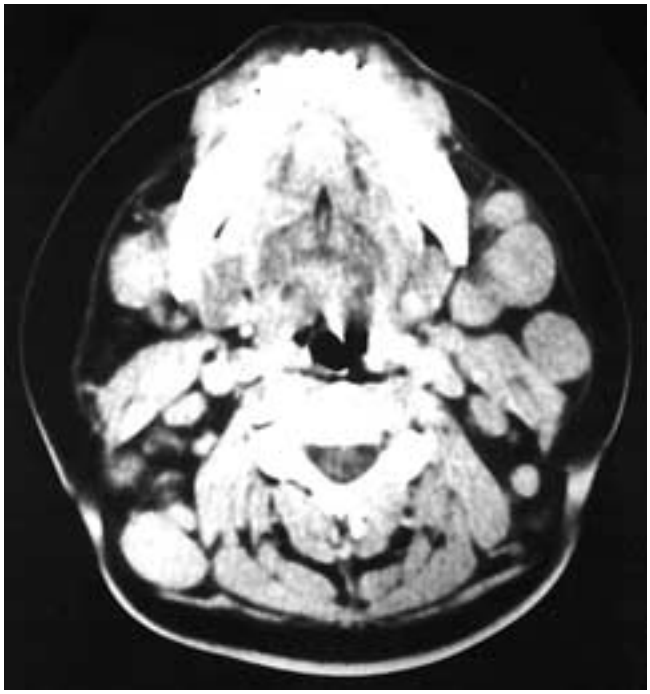

VIEW IMAGE

FIGURE 36-38 Axial contrast-enhanced CT scan shows multiple enlarged, homogeneous nodes with no infiltration of the adjacent fat planes. This patient had sarcoidosis.

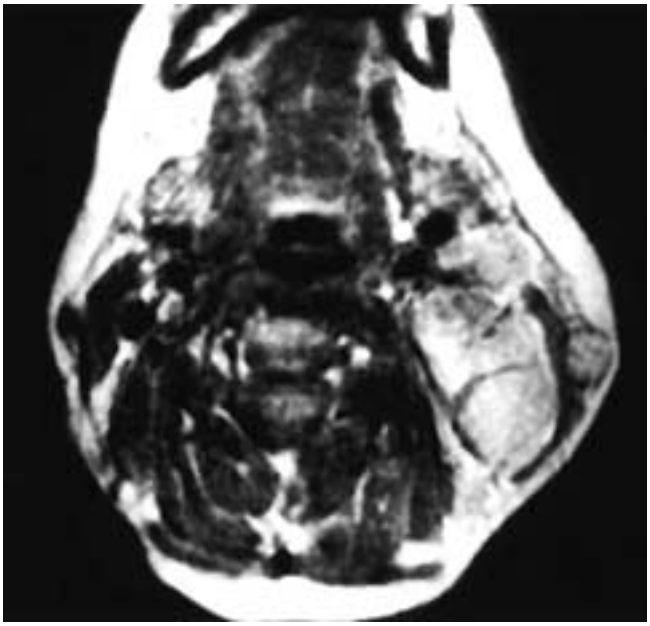

FIGURE 36-39 Axial T1-weighted MR image shows multiple enlarged, homogeneous left level II nodes. Although this imaging appearance is most suggestive of lymphoma, this patient had sarcoidosis.

VIEW IMAGE

Copyright © 2003, Mosby, Inc. All rights reserved.

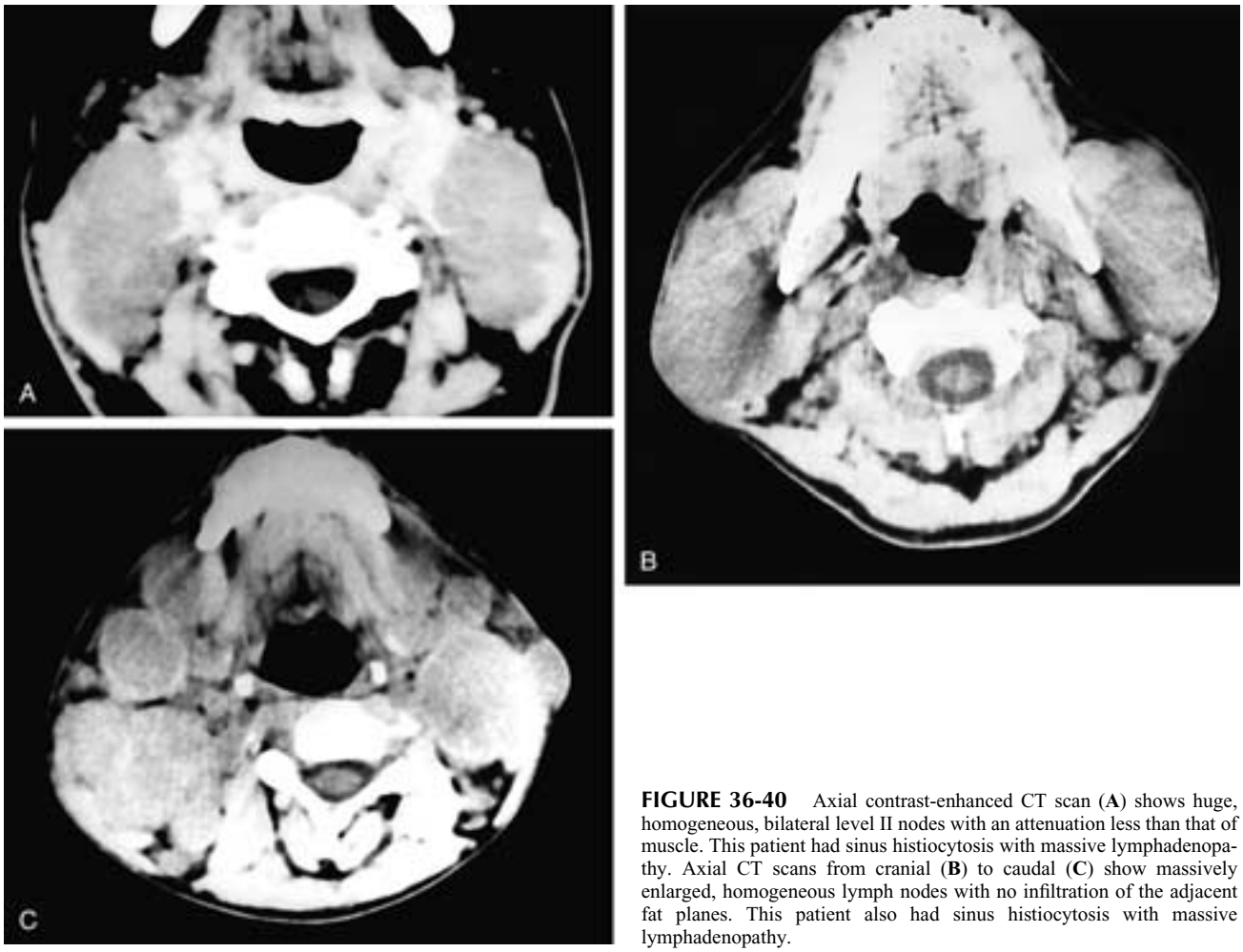

FIGURE 36-40 Axial contrast-enhanced CT scan (**A**) shows huge, homogeneous, bilateral level II nodes with an attenuation less than that of muscle. This patient had sinus histiocytosis with massive lymphadenopathy. Axial CT scans from cranial (**B**) to caudal (**C**) show massively enlarged, homogeneous lymph nodes with no infiltration of the adjacent fat planes. This patient also had sinus histiocytosis with massive lymphadenopathy.

VIEW IMAGE

Sinus Histiocytosis with Massive Lymphadenopathy

Sinus histiocytosis with massive lymphadenopathy (SHML) has also been referred to as Rosai-Dorfman disease, lymphadenitis with massive hemophagocytic sinus histiocytosis of Lennert, and histiocytose lipdique ganglionnaire pseudotumorale of Destombes.[181] There is a wide age range (newborn to age 74 years), although most cases involve children and teenagers. The male-female ratio is 6:4, and there is a worldwide distribution with no racial predisposition. SHML can affect lymph nodes and cause soft-tissue infiltrates of the ear, upper respiratory and gastrointestinal tracts, meninges, and other extranodal sites. Painless, enlarged lymph nodes may persist for several years, but the disease is self-limited. Lymph nodes reveal a proliferation of histiocytes within distended sinuses. These histiocytes contain ingested lymphocytes (emperipolesis). Soft-tissue infiltrates of SHML likewise reveal a lympho/histiocytic infiltrate with emperipolesis. Rarely, there is more aggressive involvement of underlying bone or vital organs, with resultant morbidity and mortality. There is no effective treatment.[176]

Kikuchi-Fujimoto Disease

Kikuchi-Fujimoto lymphadenopathy (KFL) has also been referred to as Kikuchi's disease, necrotizing lymphadenitis of Kikuchi and Fujimoto, and histiocytic necrotizing lymphadenitis without granulocytic infiltration. KFL commonly affects Japanese and is sporadic in Western countries. The majority of patients are female (80%), with a mean age younger than 30 years. The cervical nodes are involved, commonly unilaterally but occasionally bilaterally, and may be tender. There are occasional systemic symptoms such as fever, chills, myalgia, sore throat, skin rash, localized pain, leukopenia, or leukocytosis. Less often, patients complain of weight loss, nausea, vomiting, night sweats, arthralgias, and hepatosplenomegaly. Rarely, skin and bone marrow have also been involved.

KFL follows a self-limiting course, usually resolving spontaneously within a few weeks to months. The lymph nodes show a necrotizing process, with patchy or confluent areas of necrosis associated with karyorrhexis and absence or paucity of granulocytes. A proliferating component of large blastic cells, T lymphocytes, and histiocytes, mimicking lymphoma can be seen.[178, 182] The etiology of KFL is unknown, but an autoimmune process has been suggested based on the histologic resemblance to systemic lupus erythematosus.

Sarcoidosis

Sarcoidosis is a self-limiting systemic granulomatous disease that affects lymph nodes, upper aerodigestive tract mucosa, parotid gland, lungs, liver, skin, and spleen and is presumably the result of infection by a mycobacterial agent.

Copyright © 2003, Mosby, Inc. All rights reserved.

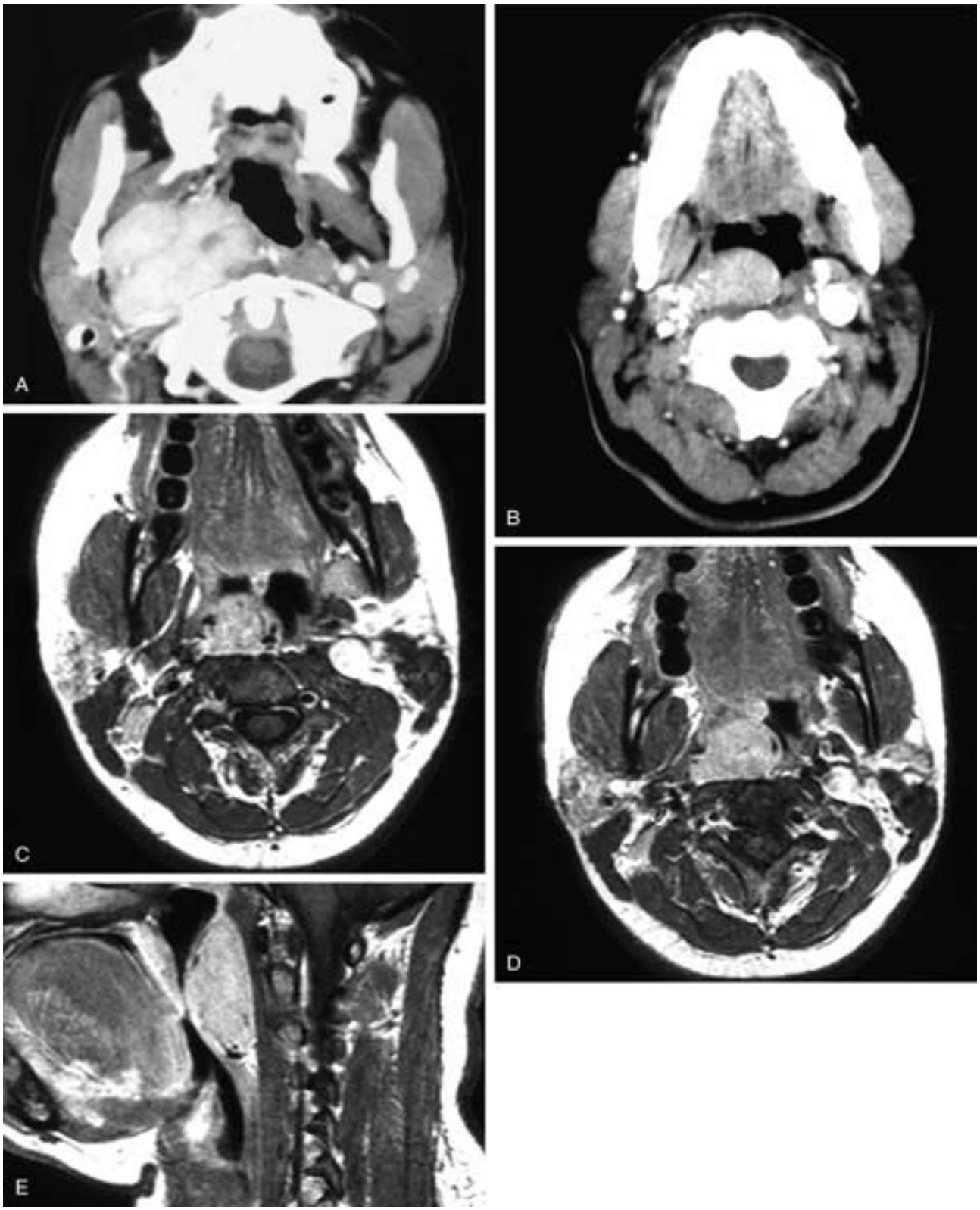

FIGURE 36-41 Axial contrast-enhanced CT scan (**A**) shows a large, enhancing mass in the right parapharyngeal space/carotid sheath region obliterating the silhouette of the internal carotid and internal jugular vein. The mass pushes the right pharyngeal wall forward and medially. At surgery, this was found to be Castleman's disease in a retropharyngeal node. Axial contrast-enhanced CT scan (**B**) on another patient shows findings similar to those in **A**; however, the enhancing mass is seen to be along the medial border of the carotid sheath, in the region of a retropharyngeal node. Axial T1-weighted images (**C**, **D**) show the mass to have an intermediate signal intensity with vascular flow voids. Sagittal T1-weighted, contrast-enhanced image (**E**) shows enhancement of the mass with vascular flow voids at its margins. At surgery, this was found to be Castleman's disease in a retropharyngeal node.

VIEW IMAGE

Copyright © 2003, Mosby, Inc. All rights reserved.

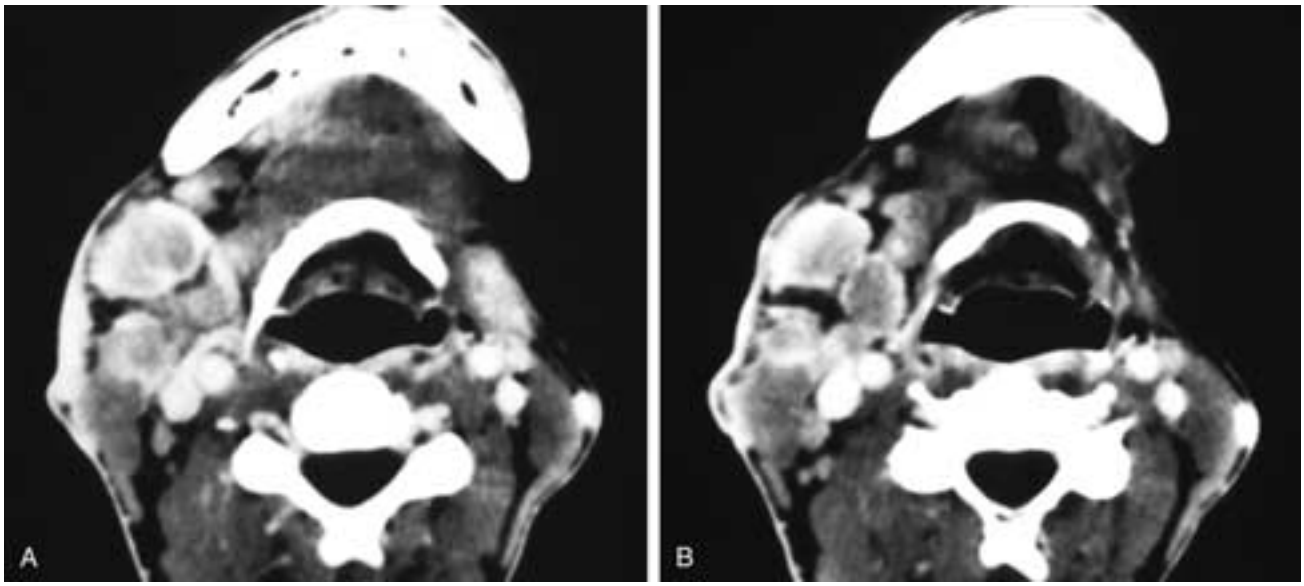

VIEW IMAGE

FIGURE 36-42 Axial CT scans from cranial (**A**) to caudal (**B**) show enlarged, enhancing, fairly homogeneous right level I and II nodes and a smaller left level II node. There is also thickening and enhancement of the adjacent skin in the right neck, and there is involvement of the right parotid gland in this Asian patient with Kimura's disease.

Sarcoidosis is most often diagnosed between the second and fourth decades of life. Worldwide, the highest incidence of sarcoidosis has been seen in Sweden, Norway, the Netherlands, and England. In the United States, it is 10 times more common among African Americans than among Caucasians. Sarcoid is most prevalent in the southeastern United States, and there is also an increased incidence in persons who have migrated from the South. Generally, there is an inverse relationship between susceptibility to MTB and sarcoid. Sarcoid is virtually nonexistent among ethnic populations with a high susceptibility to MTB, such as the Inuit, Native Americans, and Chinese.

Patients may present with nonspecific symptoms such as fever, malaise, weight loss, and erythema nodosum, or they may present with lymphadenopathy, and hepatosplenomegaly, as well as pulmonary, arthritic, and ocular symptoms.

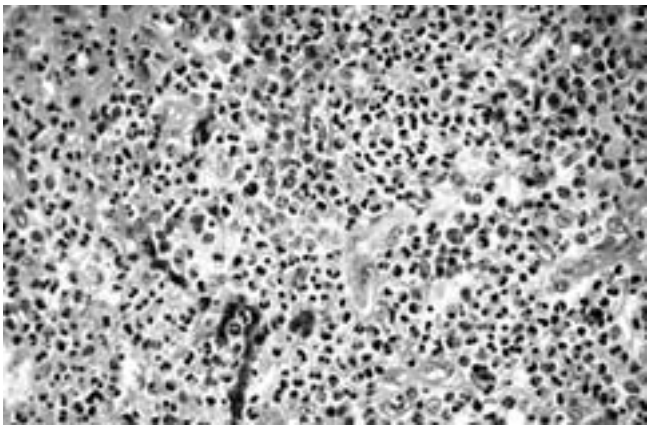

VIEW IMAGE

FIGURE 36-43 Plump vessels and a lymphocytic infiltrate with prominent eosinophilia (note the binucleated cells) are seen within the periparotid soft tissue. The eosinophilia was also present in adjacent lymph nodes in this patient with Kimura'a disease.

Other individuals are totally asymptomatic; an incidental chest x-ray will reveal enlarged hilar lymph nodes and a diffuse pulmonary reticular pattern. A pulmonary screening program for sarcoid in Denmark in the early 1960s estimated that asymptomatic sarcoid was four times more prevalent than symptomatic cases. A Swedish autopsy study revealed the incidence of subclinical sarcoidosis to be even greater.[183] The majority of clinically symptomatic individuals follow a self-limiting course in which the disease ''burns out,'' usually within 2 years. Fewer individuals progress to severe pulmonary fibrosis and renal involvement. Death is only uncommonly attributed to sarcoidosis.[184]

In the head and neck, sarcoid may involve the anterior or posterior cervical lymph node chains. Extranodal head and neck manifestations can be seen in 38% of sarcoid patients. In one report, 20% of patients had ophthalmic involvement, 7% had parotid gland involvement, 6% had lacrimal gland involvement, and 3% had upper respiratory tract submucosal involvement.[184] Heerfordt's syndrome (uveoparotid fever) is an acute, febrile, self-limiting involvement of the parotid and lacrimal glands and the retina. Involvement of the temporal bone and of nerves VII and VIII results in neurosensory hearing loss, vertigo, and facial paralysis.

The relationship between sarcoidosis and a specific infectious agent has not yet been firmly established. Tissue homogenates from sarcoid patients injected into mice result in sarcoid-like granulomas with a distribution similar to that seen in humans (lungs, lymph nodes, liver, spleen).[185] However, direct inoculation of sarcoid tissue into athymic mice failed to lead to isolation of an infectious agent.[186]

Mycobacteria other than *M. tuberculosis* (MOTT) have been implicated in the etiology of sarcoid. Acid-fast bacilli are observed on rare occasion within granulomata of tuberculin-negative sarcoid patients after considerable inspection.[187] Moscovic studied cases in great detail by histochemistry and electron microscopy and described pleomorphic spindled, almond-shaped and round bodies

Copyright © 2003, Mosby, Inc. All rights reserved.

with electron-dense cores (nucleoids) and without cell walls. He concluded that they were consistent with L-forms of mycobacteria, the result of viral bacteriophage infection.[188] Bacteriophages cause mutated bacterial forms with loss of cell walls (L-forms, Much's granules, lysogenic forms). Bacteriophages have been isolated from the stools of 36% of tuberculosis patients and 6% of control patients. Interestingly, 94% of patients with pathologically proven sarcoidosis have been shown to harbor bacteriophages. On the other hand, serum antibodies to bacteriophages were present in tuberculosis patients but were absent in sarcoid patients. These antibodies could, in vitro, prevent the formation of L-forms.[189, 190] The presence of bacteriophages and the absence of neutralizing antibodies in sarcoid patients is consistent with the interpretation that sarcoidosis is the result of infection with mutated or lysogenic mycobacterial strains. Possibly, certain populations are genetically predisposed to a lack of immunity to certain bacteriophages (as well as the ''sarcoid mycobacterium''). This would explain the elevated incidence of sarcoid in particular populations. The majority of patients with sarcoid have been found to contain antibodies against an unclassified mycobacterium.[191] Sera from 23 sarcoid patients had elevated antibodies to *M. paratuberculosis* compared to a control group.[192] These antibodies, though, are not species specific and may cross-react with other MOTT. Application of more specific and highly sensitive techniques, such as in situ polymerase chain reaction, will probably illuminate the issue of mycobacterial and bacteriophage interaction in the development of sarcoid.

The granulomas seen in sarcoid are sufficiently characteristic to allow immediate recognition (Fig. 36-44). They are usually small, nonconfluent, nonnecrotic, and densely hyalinized. On rare occasions, patients with clinically confirmed sarcoidosis may have necrotizing granulomas. The pathologist must then make certain that these granulomas are not the result of MTB or fungal infection. Pathognomonic features of sarcoid include asteroid bodies (star-like crystalline inclusions within multinucleated giant cells), Schaumann bodies (calcified, laminated concretions within multinucleated giant cells), and Hamasaki-Wesenberg inclusions (coccoid, oval, or rod-shaped golden brown inclusions measuring 3 to 15 μm).

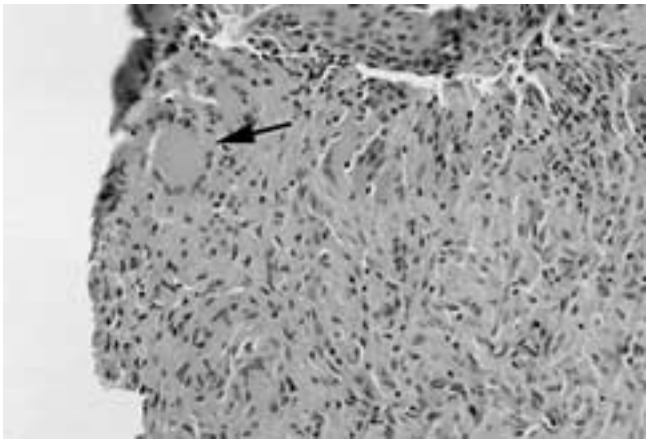

VIEW IMAGE

FIGURE 36-44 Sarcoid granulomas are characterized by epithelioid histiocytes and multinucleated giant cells (*arrow*). Necrosis is usually not present.

The Kveim test relies on the specific hypersensitivity that sarcoid patients have to the ''sarcoid antigen.'' It involves subcutaneous injection of heat-sterilized tissue homogenates from tissue (spleen or liver) involved by sarcoid. The injection site is biopsied 4 to 6 weeks later. A positive Kveim test reveals sarcoid granulomas at the injection site. The sensitivity of this test varies with disease activity: up to almost 90% of patients recently diagnosed with subacute cases may have a positive Kviem test, while patients with chronic or inactive sarcoid may have low or nonexistent rates of reactivity to this test. On the other hand, false positivity with the Kviem test is rare.[184]

Angiotensin converting enzyme (ACE) is responsible for the conversion of angiotensin I to angiotensin II. Its main tissue sources are foamy histiocytes and epithelioid histiocytes. Elevated serum ACE can be seen in sarcoidosis, especially in patients with active pulmonary disease, and may be helpful in clinically establishing the diagnosis. ACE is not elevated in inactive sarcoidosis, pulmonary tuberculosis, or berylliosis. Other conditions in which serum ACE may be elevated include liver disease, leprosy, silicosis, and asbestosis.[193]

On imaging, sarcoidosis usually has multiple reactive-appearing lymph nodes or enlarged ''foamy-type'' nodes similar to those of lymphoma. There is rarely any imaging evidence of extracapsular disease. When there is cervical adenopathy and multiple parotid lymph nodes, the most likely diagnosis is either sarcoidosis or lymphoma.

Dermatopathic Lymphadenopathy

Dermatopathic lymphadenopathy (DPL) is a reactive lymph node hyperplasia associated with chronic inflammatory skin disease. Axillary, inguinal, and regional nodes are most commonly involved, and there is an associated peripheral eosinophilia in 35% of patients.[194] Cervical or facial lymph nodes may be involved with facial dermal conditions.[195] Pruritis is a common finding. In 22.5% of cases, there is associated mycosis fungoides. Histologically, DPL is characterized by a paracortical proliferation of histiocytes and melanin deposition. Interdigitating reticulum cells (IDCs), which are antigen-presenting cells with broad cytoplasm, innumerable cytoplasmic interdigitation, and bizarre-shaped nuclei, are the most striking cell type in DPL.

Angiofollicular Lymph Node Hyperplasia

Angiofollicular lymph node hyperplasia (AFLNH) is also referrred to as Castleman's disease, giant lymph node hyperplasia, and angiomatous lymphoid hamartoma. This disease may be either unicentric, presenting as a solitary mass, or multicentric and systemic, presenting with widespread lymphadenopathy. There are two histologic subtypes: hyaline vascular and plasma cell types. The hyaline vascular type, which constitutes 91% of the cases of AFLNH, affects patients with a wide age range, without gender predominance. Most patients are young and present with single, asymptomatic masses of either cervical or mediastinal lymph nodes. Periparotid/intraparotid lymph nodes may be involved, as well as extranodal soft tissue.[196] Histologically, one sees lymphoid follicles with central hyalinized blood vessels surrounded by an ''onion skin'' arrangement of lymphocytes. Surgery is curative.

Copyright © 2003, Mosby, Inc. All rights reserved.

The plasma cell type is not restricted to the mediastinum and often has systemic manifestations including the POEMS syndrome (polyneuropathy, organomegaly, endocrinopathy, monoclonal gammopathy, and skin abnormalities). These patients tend to be older. There can also be associated anemia, hypoferremia, antierythropoietin factor, and polyclonal hypergammaglobulinemia. Histologically, one sees germinal center hyperplasia with interfollicular sheets of plasma cells. The plasma cell type of AFLNH may pursue a different course from the hyaline vascular type in that it may persist, relapse, or progress to malignant lymphoma.[197]

Angioimmunoblastic Lymphadenopathy

Synonyms include *angioimmunoblastic lymphadenopathy with dysproteinemia* and *immunoblastic lymphadenopathy with dysproteinemia*. Patients are usually middle-aged and present with generalized lympadenopathy, skin rash, fever, and hyperglobulinemia. Immunologic and molecular studies have demonstrated that the majority of cases are T-cell clonal disorders; most cases show rearrangements of the T-receptor genes. Histologically, one sees effaced lymph nodes with a polymorphous cellular infiltrate including immunoblasts. Prominent proliferating postcapillary venules can be seen, along with proteinaceous deposition. Eighty percent of the cases follow an aggressive course with short median survival, especially if a complete response with chemotherapy is not achieved. There may be progression to immunoblastic lymphoma of either the T-cell or B-cell type, and the 5-year survival is only 20%.[177, 198]

Kawasaki's Syndrome

Kawasaki's syndrome, also known as mucocutaneous lymph node syndrome, is a systemic disorder of unknown etiology that manifests during infancy or early childhood. Children present with fever, skin rash, aseptic meningitis, conjunctivitis, uveitis, hyperemic tympanic membranes, fissured lips, injected pharynx, strawberry tongue, and diffuse lymphadenopathy. Neurologic complications are reported in 1% of patients and include facial nerve palsy, seizures, ataxia, encephalopathy, hemiplegia, and cerebral infarction.[199] An acute necrotizing coronary arteritis is common, leading to aneurysm, which may be fatal. When gamma globulin is administered in combination with oral aspirin within the first 10 days of the illness, there may be a reduced incidence of coronary artery abnormalities.[200–202]

Posttransplantation Lymphoproliferative Disorders

The posttransplantation lymphoproliferative disorders (PTLD) are a group of disorders ranging from lymphoid hyperplasia to lymphoma that occur in patients who have had chronic immunosuppression after solid organ transplantation.[203] PTLD occurs with a reported frequency of 1% to 10%, depending on the organ transplanted and the type and duration of immunosuppression. PTLD is an uncontrolled B-cell proliferation that can range from a polymorphic cellular process of large and small lymphocytes to large cell non-Hodgkin's lymphoma. Epstein-Barr virus has been shown to play a role in the pathogenesis of PTLD. In one study, the interval between transplantation and the onset of symptoms varied from 3½ to 108 months.[203] On imaging, reported abnormalities include enlargement of the adenoids and/or palatine tonsils and/or lingual tonsils, as well as adenopathy that can vary from a grossly enlarged lymph node to multiple reactive-appearing nodes. It is suggested that when these findings are seen in a transplanted patient, PTLD should be suspected.

Tumor-Reactive Lymphadenopathy

Frequently, lymph nodes adjacent to a neoplasm may be enlarged yet may not contain metastatic disease. Histologically, one sees typical reactive hyperplasia. On occasion, sarcoid-type granulomas may also be seen in lymph nodes draining from tumors.

Vascular Lymphadenopathies

These vascular-related lymphadenopathies can be the result of obstruction of nodal blood flow secondary to compression by tumor, vascular embolization and thrombosis, surgery, or, rarely, needle biopsy. Such changes can also be found with the nonneoplastic angiomatoses like angioimmunoblastic lymphadenopathy, AFLNH, Kimura's disease, HIV lymphadenitis type C, and vascular transformation of sinuses. The importance of these vascular lymphadenopathies lies in their potential confusion with vascular neoplasms in lymph nodes. In most recorded cases, the nonspecific imaging findings are those of reactive lymph nodes.[134, 200, 204–206] Lymph node infarction is rare due to abundant normal lymph node vascularity. The most common cause of massive lymph node infarction is nodal involvement by either lymphoma or metastatic carcinoma. Vascular transformation of sinuses is a benign vascular proliferation of lymph nodes with a characteristic sinus distribution. It is rare and in most cases is an incidental finding in lymph nodes excised at tumor surgery. It has also been associated with a distal lymphatic or venous obstruction.

Foreign Body Lymphadenopathies

Regional lymph nodes may drain endogenous or exogenous material which can cause reactive adenopathy. These substances may be endogenous, such as lipids (seen in elderly and obese patients or in those with diabetes mellitus or hyperlipidemia) and proteins (such as amyloid). Exogenous substances causing lymphadenopathy include agents used for lymphangiography, silicone (used for reconstructive or orthopedic surgery), Teflon (injected into a paralyzed vocal cord to improve vocal quality), and gold (previously used for the treatment of rheumatoid arthritis). Radiodense foreign material may be visualized as focal lymph node densities on CT; nonradiodense material manifests as nonspecifically enlarged lymph nodes.

Lymph Node Inclusions

Benign cellular inclusions within lymph nodes are important to recognize, as they may be confused with metastatic processes. These inclusions are usually microscopic, although on imaging they may be the cause of enlarged lymph

Copyright © 2003, Mosby, Inc. All rights reserved.

nodes. For instance, it is common to find salivary duct and acinar inclusions within parotid and periparotid lymph nodes. Nevus cell inclusions may be seen within peripheral lymph nodes, probably as a result of embryonal migration of neural crest cells. In the lower cervical lymph nodes, thyroid follicles may be found within the nodes (Fig. 36-45). This raises the obvious question of metastasis from an occult thyroid primary. Usually, metastatic papillary thyroid carcinoma contains some of the histologic hallmarks (papillae formation, overlapping oval nuclei), allowing for the correct diagnosis. Even if these findings are absent, it behooves the clinician, under these circumstances, to make sure that the thyroid gland is properly imaged. We have had occasion to examine thyroidectomies performed after the discovery of cervical lymph node thyroid ''inclusions.'' On one occasion, an exhaustive search failed to uncover any primary malignancy, confirming the possible existence of benign lymph node thyroid inclusions.

Lymphoproliferative Disorders

On imaging, lymphomas can appear as normal-sized to enlarged lymph nodes with variable enhancement. On CT, these nodes may be hyperdense, isodense, or hypodense relative to muscle. Central necrosis can be seen, although it is not as frequently observed as in comparably sized nodes containing metastatic squamous carcinoma. The fat planes adjacent to the nodes can be effaced, but there is usually little infiltration into the surrounding neck. Although there is no typical CT appearance for a lymphomatous node, the most common appearances are (1) slightly enlarged, homogeneous, reactive-appearing nodes; (2) enlarged, ''foamy''-appearing nodes; (3) an enlarged lymph node with a thin nodal capsule and a central homogeneous attenuation similar to that of water; or (4) a cluster of nodes with variable enhancement, some of which may have central necrosis. There usually is relatively little ''extracapsular'' infiltration of the adjacent fat planes compared to that of comparably sized nodes containing squamous carcinoma. Either a single lymph node or diffuse disease may be present. The adenopathy is usually nontender. The imaging appearance of lymph nodes in leukemia is similar to that of lymphoma. In addition, the imaging appearance of tuberculosis may be similar to that of lymphoma. If there is cervical adenopathy and multiple parotid lymph nodes, the most likely causes are lymphoma and sarcoidosis (Figs. 36-37 to 36-39 and 36-46 to 36-55).

Leukemia is a neoplastic proliferation of either myelocytic or lymphocytic precursor cells manifested within the circulating blood compartment; a tissue infiltrate may or may not be discernible. By comparison, lymphoma, by nature, usually arises within lymph nodes but may extend to the bone marrow compartment; it may also disseminate and produce a leukemic phase. Cytologically, leukemias and lymphomas can appear similar, as the same cell type gives

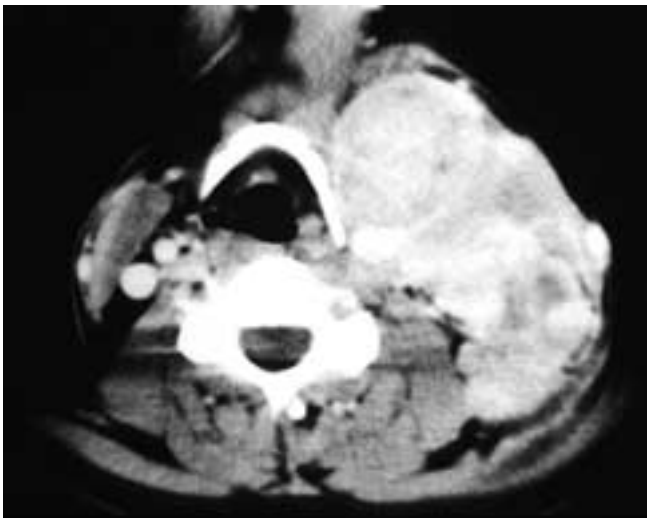

FIGURE 36-46 Axial contrast-enhanced CT scan shows multiple grossly enlarged, enhancing left level I, II, and III nodes. There is minimal involvement of the adjacent fat planes in this patient with large cell lymphoma.

VIEW IMAGE

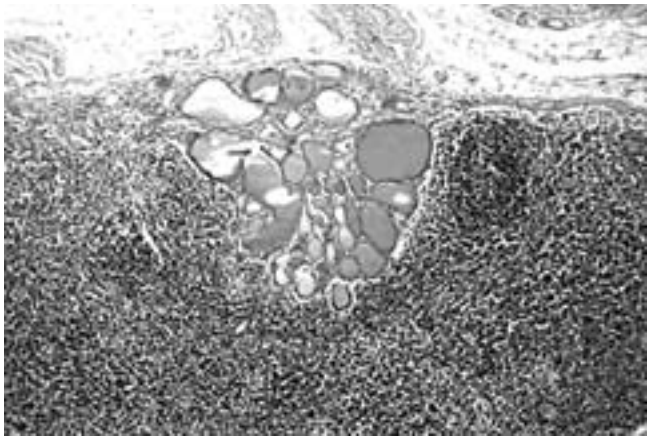

FIGURE 36-45 A collection of thyroid follicles is seen beneath the capsule of this lymph node. In some cases (though not this one), there may be histologic features suggesting metastatic papillary thyroid carcinoma. Regardless, the thyroid gland should be evaluated for a primary tumor.

VIEW IMAGE

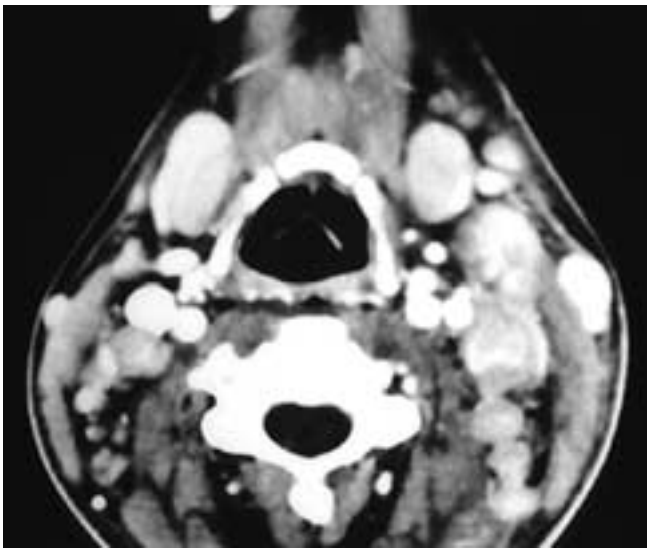

FIGURE 36-47 Axial contrast-enhanced CT scan shows multiple bilateral enlarged, enhancing lymph nodes with little involvement of the adjacent fat planes. Nodes at multiple levels were involved bilaterally in this patient with large cell lymphoma.

VIEW IMAGE

Copyright © 2003, Mosby, Inc. All rights reserved.

FIGURE 36-48 Sagittal T1-weighted MR image shows multiple homogeneous, grossly enlarged lymph nodes with no involvement of the adjacent fat planes. This patient had large cell lymphoma.

VIEW IMAGE

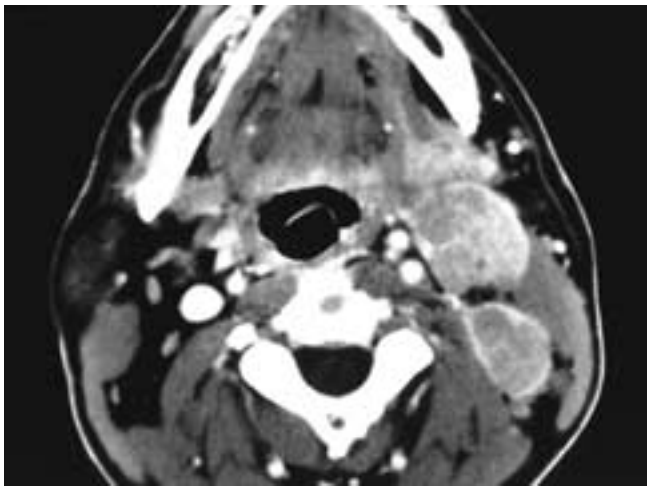

FIGURE 36-49 Axial contrast-enhanced CT scan shows several left level II nodes that are enlarged, with scattered enhancement within the nodes and with capsular enhancement. There is little involvement of the adjacent fat planes. This patient had chronic lymphocytic leukemia. More commonly, large cell lymphoma has this imaging appearance. Rarely, metastatic squamous cell carcinoma can have a similar imaging appearance.

VIEW IMAGE

rise to both localized and systemic neoplastic proliferations.

The two most popular lymphoma classifications are the European Keil classification, by Lenner, and the Working Formulation, proposed by an international panel of American experts. A recently proposed Revised European-American Lymphoma (REAL) classification has been drafted by the International Lymphoma Study Group.[207, 208] This is a much broader, more complex schema than the Working Formulation, which includes Hodgkin's disease, non-Hodgkin's lymphomas, lymphoid leukemias, plasma cell neoplasms, extranodal lymphomas, and ''maltomas'' (mucosa-associated lymphoid tumors). It is based on both the morphologic and functional properties of the neoplastic cells (Fig. 36-56). The newly proposed REAL classification and the Working Formulation are compared in Table 36-13.

Proliferative Histiocytic Disorders

The advent of immunohistochemical cell typing has allowed characterization of disorders of true monocyte-macrophage cells. Prior to this, all large hematopoietic cells, including neoplastic T and B lymphocytes, were referred to as histiocytic proliferations. This group of disorders is still

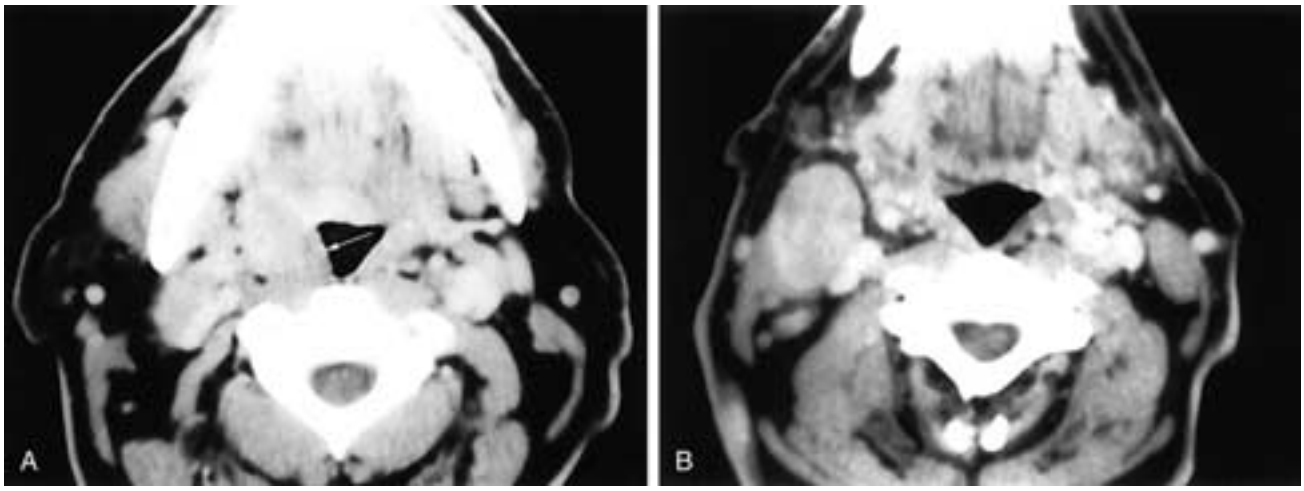

FIGURE 36-50 Axial CT scans from cranial (**A**) to caudal (**B**) show thickening of the right pharyngeal tonsil and oropharyngeal wall (*arrow* in **A**) and an enlarged right level II node. The lymph node is fairly homogeneous, and there is no involvement of the adjacent fat planes. This patient had large cell lymphoma.

VIEW IMAGE

Copyright © 2003, Mosby, Inc. All rights reserved.

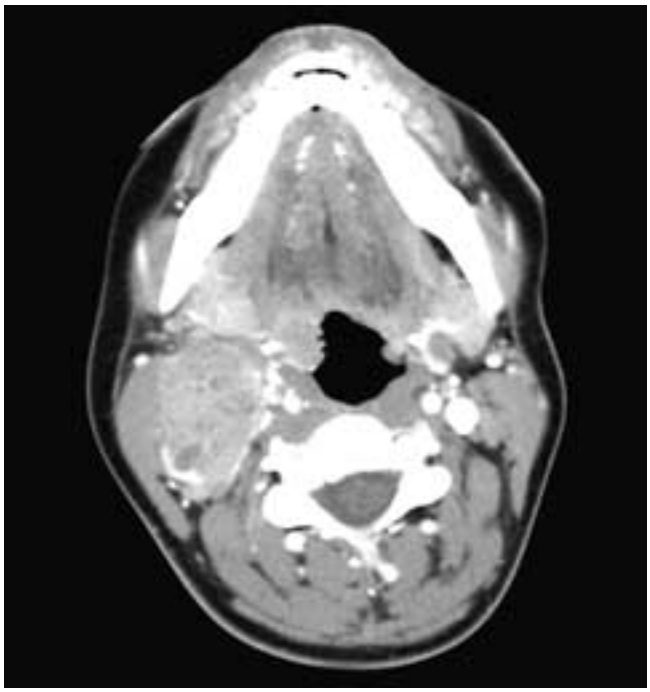

FIGURE 36-51 Axial contrast-enhanced CT scan shows prominence of the right palatine tonsil and an enlarged, slightly nonhomogeneous right level II node. There is no involvement of the adjacent fat planes in this patient with large cell lymphoma.

broad, albeit better classified, and includes entities such as true histiocytic lymphoma, hemophagocytic syndromes (viral-associated hemophagocytic syndrome, familial erythrophagic lymphohistiocytosis, Rosai-Dorfman disease [covered above] and Langerhan's cell histiocytosis [granulomatosis] [LCG or histiocytosis X]). *LCG* is the term applied to a group of childhood disorders, including eosinophilic granuloma (EG), Hand-Schuller Christian (HSC) disease, and Letterer-Siwe (L-S) disease. EG is a localized form of LCG,

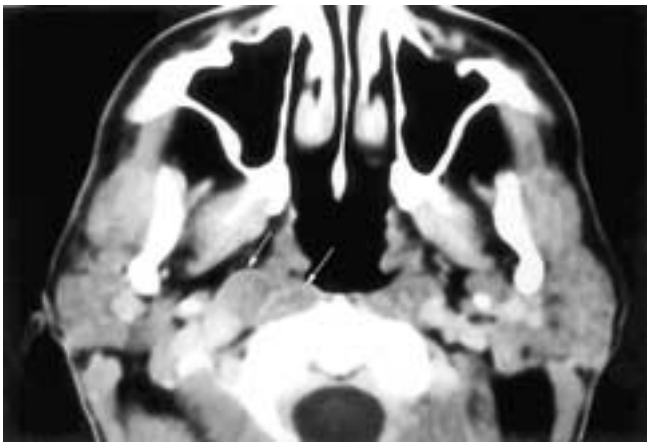

FIGURE 36-53 Axial contrast-enhanced CT scan shows enlarged medial and lateral right retropharyngeal lymph nodes with an attenuation slightly less than that of muscle (*arrows*). This patient had large cell lymphoma.

often manifesting as a solitary bone lesion, whereas the latter two syndromes have multifocal or disseminated disease, with involvement of lymph nodes, skin, liver, spleen, lung, head and neck, or the gastrointestinal tract. The etiology is unknown, however, a recent report suggests that all forms of LCG are clonal. Others, however, believe LCG to be a benign, possibly reactive process.

The head and neck are frequently involved in LCG. In a recent study, 82% of patients with LCG had head and neck disease, causing the presenting symptom in 40% of patients. Facial rash and cervical adenopathy are common. The skull is the most frequently involved flat bone; the mandible and temporal bone are also common sites. Otitis media and/or destructive lesions of the temporal bone may be the initial presentation in up to 60% of cases. Histologically, LCG is characterized by a polymorphous cellular infiltrate of mononuclear or multinucleated histiocytes (Langerhans

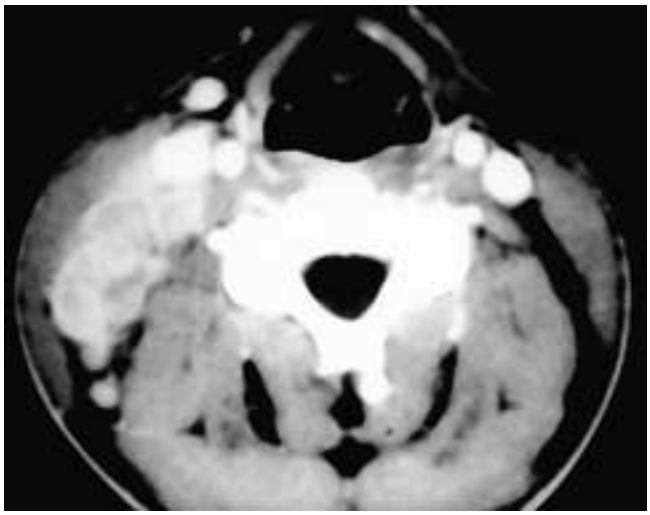

FIGURE 36-52 Axial contrast-enhanced CT scan shows multiple nonhomogeneously enlarged right level II nodes. Anteriorly, there is some involvement of the adjacent fat planes. The enhancing nodal capsules give an appearance suggesting numerous ''rings'' within the nodal mass, a sign highly suggestive of nodal disease. This patient had Hodgkin's disease.

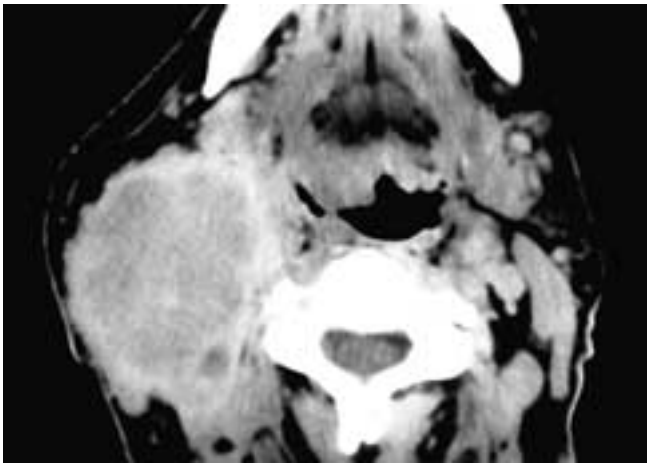

FIGURE 36-54 Axial contrast-enhanced CT scan shows a grossly enlarged right level II node with an enhancing rim and some involvement of the adjacent fat planes. The node is fairly homogeneous and has an attenuation less than that of muscle. Although metastatic squamous cell carcinoma nodes can have similar-appearing capsular enhancement with extracapsular disease, it would be unusual to find a node this large without central necrosis. This patient had large cell lymphoma.

Copyright © 2003, Mosby, Inc. All rights reserved.

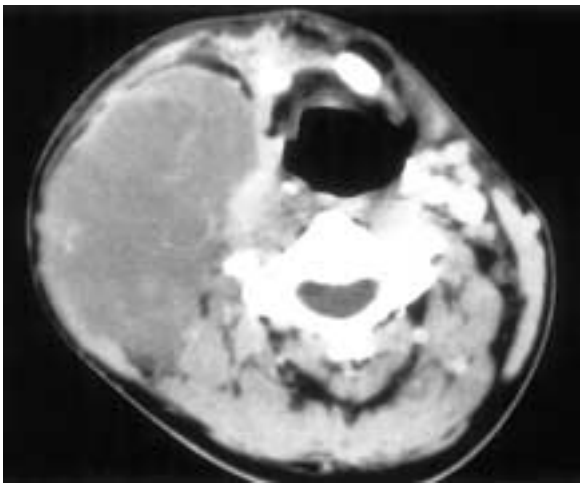

VIEW IMAGE

FIGURE 36-55 Axial contrast-enhanced CT scan shows a huge conglomerate nodal mass in the right level II region. The nodes are fairly homogeneous and have an attenuation less than that of muscle. This imaging appearance is highly suggestive of lymphoma. This patient had large cell lymphoma.

cells), having oval, lobated or grooved (clefted) nuclei, mixed with varying numbers of eosinophils, granulocytes, and lymphocytes (Fig. 36-57). These cells are typically positive for S-100 protein and, more specifically, for CD1a.

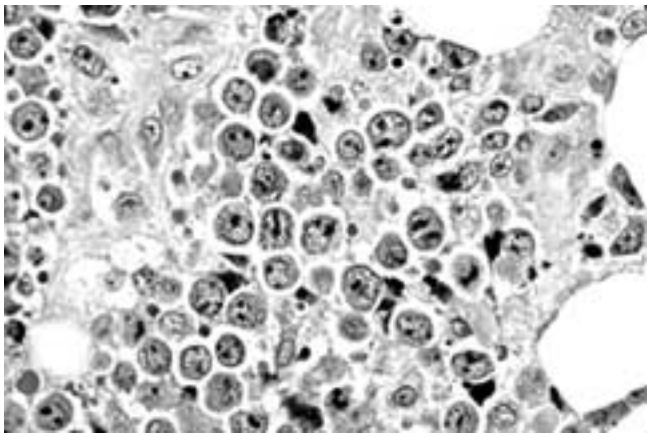

FIGURE 36-56 Malignant lymphoma, diffuse, large cell type.

VIEW IMAGE

Intracytoplasmic ''Birbeck'' granules are diagnostic of LCG cells on ultrastructural analysis.

Malignant histiocytosis (MH) and true histiocytic lymphoma (THL) are hematopoietic malignancies of the mononuclear phagocytic system distinguished from each other by their clinical presentation and presumed cell of origin. THL presents as a localized mass derived from the tissue histiocytes; it may or may not disseminate. MH originates from the circulating monocyte or tissue macro-

Table 36-13
COMPARISON OF THE WORKING FORMULATION AND THE REVISED EUROPEAN-AMERICAN LYMPHOMA (REAL) CLASSIFICATION

Working Formulation	REAL Classification
	B-Cell Neoplasms
Lymphoblastic lymphoma	Precursor B-lymphoblastic leukemia/lymphoma
Small lymphocytic/CLL	B-CLL/prolymphocytic leukemia/small lymphocytic lymphoma
Plasmacytoid	Lymphoplasmacytoid
	Mantle cell lymphoma
Follicular, small cleaved cell	Follicle center lymphoma, follicular, grade I
Follicular, mixed small and large cell	Follicle center lymphoma, follicular, grade II
Follicular, large cell	Follicle center lymphoma, follicular, grade III
Diffuse, small cleaved cell	Follicle center lymphoma, diffuse, small cell
	Extranodal marginal zone B-cell lymphoma (MALT)
	Nodal marginal zone B-cell lymphoma (monocytoid)
	Splenic marginal zone B-cell lymphoma
	Hairy cell leukemia
	Plasmacytoma/plasma cell myeloma
Diffuse, mixed small and large cell	Diffuse large B-cell lymphoma
Diffuse, large cell	Diffuse large B-cell lymphoma
Immunoblastic	Diffuse large B-cell lymphoma
	Primary mediastinal large B-cell lymphoma
Small non-cleaved cell (Burkitt's)	Burkitt's lymphoma
Small non-cleaved cell (Non-Burkitt's)	High-grade B-cell lymphoma, Burkitt-like
	T-Cell Neoplasms
Lymphoblastic lymphoma	Precursor T-lymphoblastic leukemia/lymphoma
Small lymphocytic/CLL	T-CLL/prolymphocytic leukemia
	Large granular lymphocytic leukemia
	T-cell type
	NK-cell type
Miscellaneous	Mycosis fungoides/Sezary syndrome
	Peripheral T-cell lymphoma, unspecified
	Peripheral T-cell lymphoma, specified
	Angioimmunoblastic T-cell lymphoma
	Angiocentric lymphoma
	Intestinal T-cell lymphoma
	Adult T-cell lymphoma/leukemia
	Anaplastic large cell lymphoma

Copyright © 2003, Mosby, Inc. All rights reserved.

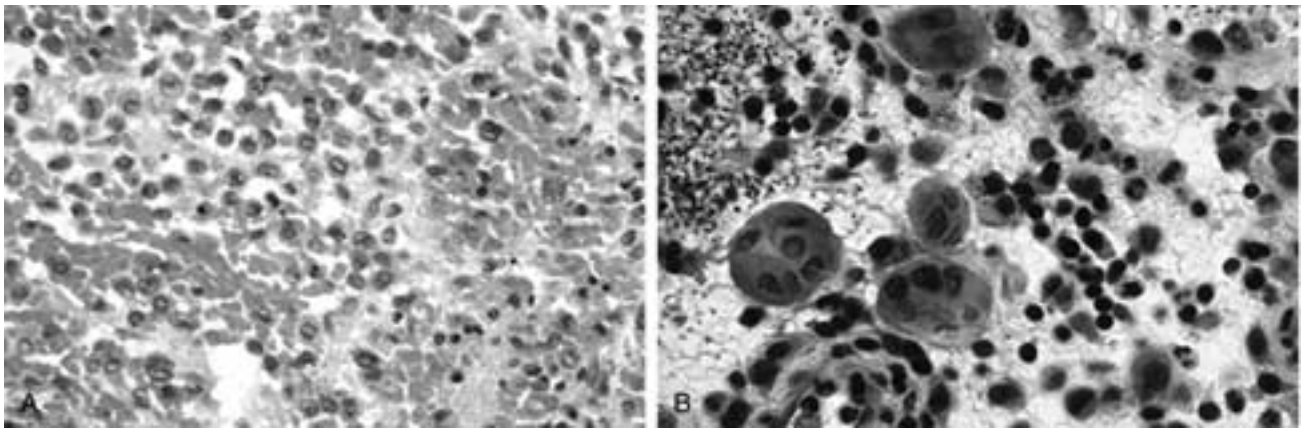

VIEW IMAGE

FIGURE 36-57 Histiocytosis. Cellular infiltrate of mononuclear or multinucleated histiocytes (**A**), or Langerhan's cells, having oval, lobated, or grooved (clefted) nuclei (**B**).

phage and is characterized by a syndrome of systemic symptoms, pancytopenia, adenopathy, hepatosplenomegaly, and wasting. The distinction between MH and THL is at times arbitrary, and overlap exists between these syndromes (Fig. 36-58).[209–217]

Spindle Cell Neoplasms of Lymph Nodes

A list of the various entities that can appear as spindle cell lesions within lymph nodes is given in Table 36-14. Intranodal myofibroblastoma is a rare primary spindle cell tumor that usually arises within inguinal lymph nodes. It is often a solitary mass but occasionally may be multicentric. The tumors consist of a fascicular proliferation of spindle cells with focal nuclear pallisading and acellular stellate-shaped, collagen-rich areas (so-called amianthoid fibers).[217] Intranodal myofibroblastoma is thought to arise from intranodal myofibroblasts. This lineage can be demonstrated by the immunohistochemical expression of muscle actin and the ultrastructural findings of intracytoplasmic microfilaments and rough endoplasmic reticulum. These tumors are generally cured by resection, although occasional recurrences have been documented.

Inflammatory pseudotumor of lymph nodes (IPT) can be considered to be vaguely related to intranodal myofibroblastoma in that myofibroblastic differentiation is also seen here; hence, *inflammatory myofibroblastic tumor* (IMFT) is the currently preferred term. IMFT is most likely a number of different entities with overlapping histologic features, the true nature of which is only beginning to be elucidated. The lung, liver, and gastrointestinal tract (omentum and mesentery) are the most common sites for IMFT. Lymph nodes at various sites (cervical, supraclavicular, inguinal, mesenteric, mediastinal, paraaortic) can be involved. In the head and neck, IMFT has been reported in the epiglottis, endolarynx, parapharyngeal space, maxillary sinus, submandibular region, and oral cavity. There is no pronounced gender predominance, and the tumor tends to occur in the first two decades of life. Occasionally, systemic symptoms such as fatigue, abdominal pain, weight loss, fever of unknown origin, pelvic inflammatory disease, nausea, or night sweats may occur.

Histologically, one sees a characteristic fibrosing/

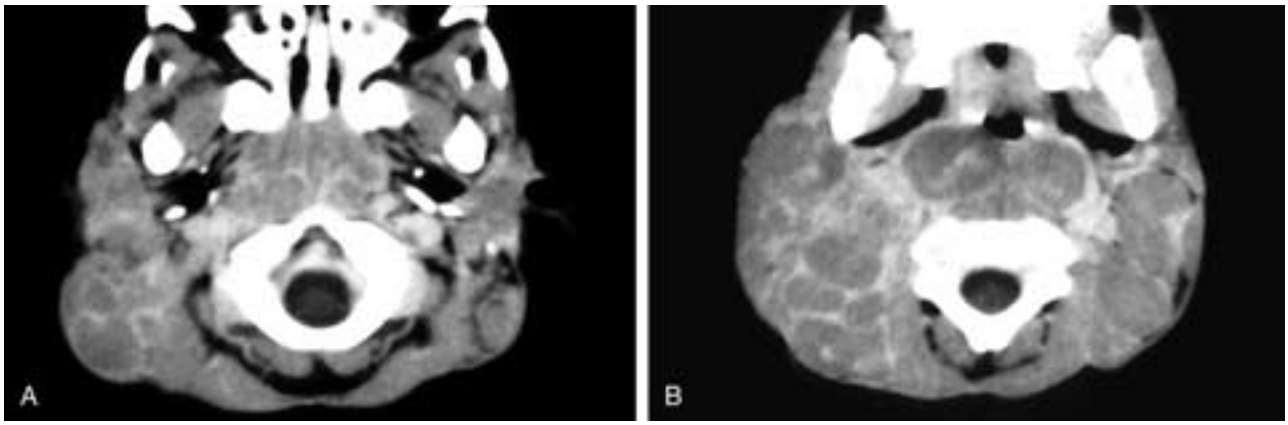

VIEW IMAGE

FIGURE 36-58 Axial CT scans from cranial (**A**) to caudal (**B**) show considerable enlargement of virtually every node in this 1-month-old infant. Note that the retropharyngeal nodes are also involved, and all of the nodes have a fairly low attenuation. In an older patient, this imaging appearance would suggest a lymphoma. However, in a patient this young, histiocytosis must be considered. This patient had histiocytosis.

Copyright © 2003, Mosby, Inc. All rights reserved.

Table 36-14
THE DIFFERENTIAL DIAGNOSIS OF SPINDLE CELL LESIONS WITHIN LYMPH NODES

Metastatic
Sarcoma (smooth muscle, skeletal muscle, fibroblastic, etc.)
Carcinomas (spindle cell carcinoma [carcinosarcoma, pseudosarcoma], nasopharyngeal carcinoma)
Melanoma
Vascular (Kaposi's sarcoma, angiosarcoma, etc.)
Hematopoietic
Dendritic reticulum cell sarcoma
Interdigitating reticulum cell sarcoma
Nodular sclerosis variant of Hodgkin's disease
Benign
Intranodal palisaded myofibroblastoma (inflammatory/infectious)
Inflammatory pseudotumor (inflammatory myofibroblastic tumor) of lymph nodes
Spindled atypical mycobacterial infection

inflammatory process with a prominent inflammatory background. The myofibroblastic proliferation is variable. The polymorphous appearance of IMFT may reflect its variable etiology or its shifting histology during the disease course. Lymphocytes, plasma cells, histiocytes, fibroblasts, and myofibroblasts are the basic components of IMFT, with mutable proportions. Four basic histologic patterns have emerged: (1) a dominant lymphoplasmacytic infiltrate, (2) a dominant lymphohistiocytic infiltrate, (3) a predominantly ''young and active'' myofibroblastic process, and (4) a predominantly collagenized process with a lymphoplasmacytic infiltrate.

Many IMFT may resolve or regress with conservative excisional biopsy and/or steroid therapy. However, some cases may persist and worsen. Single or multiple recurrences developed in 25% of patients with IMFT at all body sites after excision. Histologic evidence of sarcomatous transformation can occur. Recurrence or transformation was more likely to occur with mesenteric or retroperitoneal multinodular tumors. These cases tend to remain localized.

Spindled atypical mycobacteriosis (SAM), or mycobacterial pseudotumors, is a mycobacterial infection, usually caused by an atypical mycobacterium, that produces an unusual myofibroblastic reaction. This lesion occurs in immunosuppressed patients, usually those with AIDS, hence the inability to mount a granulomatous or epithelioid histiocytic reaction. SAM may occur within lymph nodes, subcutaneous tissue, brain, bone marrow, spleen, lungs, and retroperitoneum. The spindled cells are actual myofibroblasts that act as facultative histiocytes, ingesting the mycobacteria.[219–224]

Vascular Neoplasms of Lymph Nodes

The primary disease in this category is Kaposi's sarcoma (KS). Imaging of lymph nodes affected by this disease usually shows nodes that are enhanced, enlarged, and often nonhomogeneous in appearance.

Prior to the AIDS epidemic, KS was rarely encountered in the head and neck. The classic form of KS is an indolent tumor seen most commonly as soft red nodules on the lower limbs and, less commonly, on the upper limbs. Lesions may be multicentric and coalescent but rarely exceed 2 cm. Patients with classic KS usually have long survivals and died ''with but not of KS.''

Gnepp et al. compiled a total of 83 cases of classic KS from the literature and from the files of the Armed Forces Institute of Pathology (AFIP) that affected the head and neck. Eight percent of all classic KS cases affected cutaneous sites on the head and neck, and only 2% affected the mucosal surfaces. Mucosal sites included conjunctiva, palate, tongue, gingiva, and tonsil; skin sites included eyelids, nose, ears, and face. By comparison, AIDS KS cases commonly affected skin of the head and neck (32%) and upper airway mucosal surfaces (19%). Common sites for AIDS KS cases in the head and neck include palate, gingiva, buccal mucosa, tongue, larynx, trachea, and sinuses. Patients with classic KS are usually over the age of 50 years at the time of tumor diagnosis, although 3% to 4% of cases with the classic form are diagnosed in those less than 15 years old. Patients with AIDS diagnosed with head and neck KS tend to be decades younger than those with classic KS (mean age, 38 years), although there is overlap in both age groups.

Histologically, KS appears as long, plump, spindle-shaped nuclei forming slit-like spaces. The description ''slit-like'' is emphasized to differentiate KS from high-grade angiosarcomas, which form incomplete, anastomosing channels, with protrusion of the malignant nuclei into the lumina. Mitotic figures are easily recognized. Erythrocytes are usually abundant within the slit-like spaces. Intracellular eosinophilic globules, or red bodies, are seen. They are usually smaller than erythrocytes, which have been mistaken for Russell bodies and even fungal conidia. These eosinophilic bodies have high sensitivity and specificity for KS. KS may frequently metastasize to lymph nodes, and early metastases may be confined to subcapsular sinusoids.

Original observations were derived from KS cell lines that revealed Herpesvirus type virions by ultrastructural examination.[225] Cytomegalovirus had long been suspected as a possible viral promoter. More recently, Human Herpes virus 8 has been implicated as promoting the KS lesion and precursor lesions.[226–229]

Metastatic Lymph Nodes

As mentioned in the section on Clinical Significance of Metastatic Nodal Carcinoma, metastases to lymph nodes carry a poor prognosis. Metastases can be found with high frequency in certain histologically well defined tumors (Fig. 36-59) (head and neck squamous cell carcinomas, breast carcinoma, and melanoma); with tumors that have poor cellular differentiation and a resemblance to lymphomas (neuroblastoma, Ewing's sarcoma, alveolar rhabdomyosarcoma, and small cell carcinoma of lung); with tumors that have characteristic histologic patterns such as clear cell tumors (renal cell carcinomas and seminoma) and mucinous carcinomas (adenocarcinomas primarily in the gastrointestinal tract, breast, ovary, and prostate); or with occult tumors (nasopharyngeal carcinomas, thyroid carcinomas, and melanomas). There are also hypervascular primaries that metastasize (hypernephroma and thyroid), as well as a variety of uncommon

Copyright © 2003, Mosby, Inc. All rights reserved.

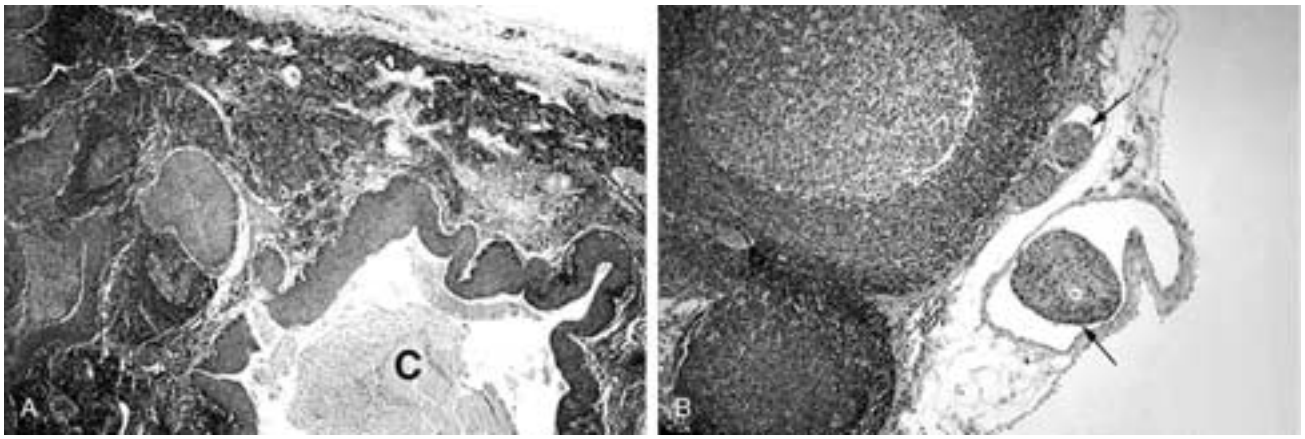

VIEW IMAGE

FIGURE 36-59 **A**, Cystic degeneration (*C*) of metastatic carcinoma in a lymph node. **B**, Emboli (*arrow*) of squamous cell carcinoma within lymphatic channels.

primary tumors. For a discussion on the imaging of metastastic lymph nodes, see the section on Criteria for Assessing Metastatic Nodes.[19] Table 36-15 summarizes the diseases that are associated with specific tumor locations presenting with lymph nodes.

IMAGING CRITERIA OF PATHOLOGIC ADENOPATHY

"Normal" Reactive Nodes

Normal nonchallenged lymph nodes are small, on the order of a few millimeters in greatest diameter, and both on imaging and at surgery are very difficult to identify and separate from the normal fat of the neck in which they are situated. Once a lymph node is challenged by infection, it enlarges, reflecting the increase in the number and size of the germinal centers. Pathologically, this is referred to as reactive follicular hyperplasia. Lymph nodes that are so challenged over many years enlarge more than nodes that drain areas of less frequent infection. Thus, the jugulodigastric (level II) and submandibular (level I) nodes tend to be larger than other cervical nodes because they are the primary drainage nodes for, among other things, the inflammations associated with teething, tonsillitis, pharyngitis, sinusitis, and skin infections of the facial region.[1–8]

On imaging, these nodes are homogeneous, with smooth, noninfiltrating margins, and they enhance slightly (Fig. 36-60). On MR imaging, the nodes typically have homogeneously low to intermediate T1-weighted and fairly high T2-weighted signal intensities. On CT, such nodes usually have an attenuation similar to or slightly less than that of muscle.

Criteria for Assessing Metastatic Nodes

A number of CT criteria have been proposed to assess the presence of cervical nodal metastasis and to distinguish such nodes from reactive nodes.[2–7] More recently, there have been a variety of studies utilizing MR imaging and helical CT.[9–15, 78, 230–239] The two major imaging criteria used are nodal size and the presence of central nodal necrosis or nodal nonhomogeneity. If imaging shows a cervical lymph node to be highly suspicious for metastasis, clinicians will modify their treatment plan to include such a node.

Size Criteria

Surgeons have long recognized the ''normal'' size variation in hyperplastic lymph nodes, and over several decades they have developed clinical criteria for assessing cervical lymphadenopathy based on nodal size. In a patient suspected of having a head and neck carcinoma, when a lymph node was greater than 1.5 cm in maximum diameter, either in the jugulodigastric region (level II) or in the submandibular triangles (level I), or when a node was greater than 1 cm in maximum diameter elsewhere in the neck, it was considered likely to contain metastatic carcinoma. These size criteria alone are inaccurate in 20% to 28% of cases, either underestimating or overestimating the presence of tumor (Figs. 36-60 and 36-61). Subsequently, a

Table 36-15
AN APPROACH TO DIFFERENTIAL DIAGNOSIS WHEN THERE ARE CERVICAL LYMPH NODES AND AN IDENTIFIABLE MASS

Location of Mass with Nodes	Main Differential Diagnosis
Waldeyer's ring and nodes	Lymphoma, mononucleosis, HIV infection, squamous cell carcinoma
Skin lesion and lymph nodes	Basal cell carcinoma, squamous cell carcinoma, melanoma, lymphoma, Kaposi's sarcoma, Kikuchi-Fujimoto disease, actinomycosis, mycobacterial infection, cat-scratch fever
Parotid gland masses and/or cysts and lymph nodes	HIV infection, sarcoid, lymphoma, Kimura's disease, cat-scratch fever, and, rarely, Sjogren's syndrome

Copyright © 2003, Mosby, Inc. All rights reserved.

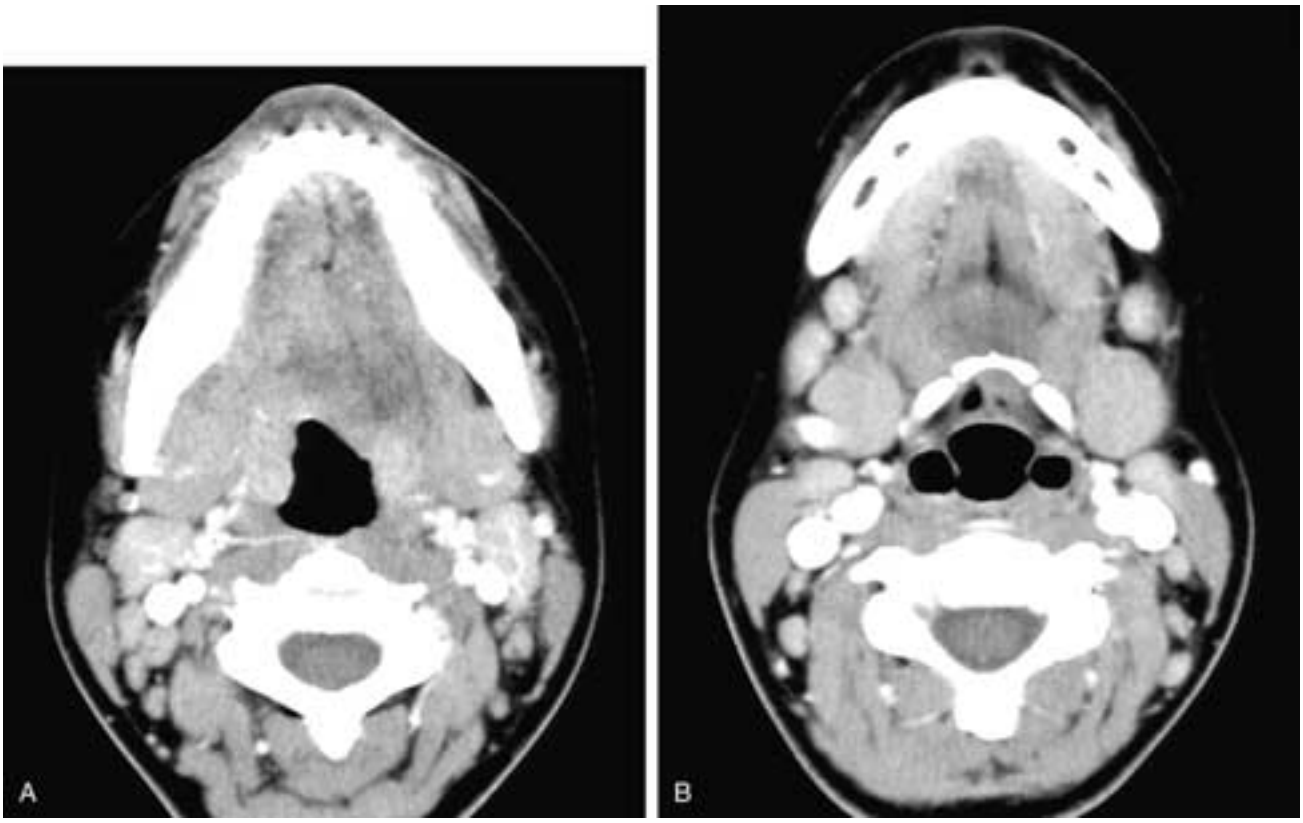

VIEW IMAGE

FIGURE 36-60 Axial CT scans from cranial (**A**) to caudal (**B**) show bilateral level I and level II lymph nodes that do not exceed the size criterion to suspect pathologic adenopathy. The nodes are sharply delineated, and there is some enhancement. These were reactive lymph nodes in this 22-year-old female who had a pharyngitis. Note the slight prominence of the right palatine tonsil.

number of imaging studies have reaffirmed these measurements and, in addition, have suggested using the minimum axial diameter of the node, with normal nodes not exceeding 11 mm in the jugulodigastric region and 10 mm elsewhere in the head and neck.[2–7] It has also been proposed that retropharyngeal nodes should not exceed 8 mm in maximum diameter or 5 mm in minimal transverse (short-axis) diameter.[2, 239] More recently, it has been suggested that the ratio of the maximum longitudinal nodal length to the maximum axial nodal length (L/T) should be greater than 2 for normal hyperplastic nodes, while a value of less than 2 strongly suggests that the node contains metastatic carcinoma.[1–8] This last approach is based on the concept that a normal lymph node tends to be oblong or lima bean–shaped, while a metastatic node often is spherical in shape. However, to some degree, the shape can vary with the location of the lymph node in the neck.

It has also been observed that a group of three or more lymph nodes with maximal diameters of 8 to 15 mm or minimum axial diameters of 9 to 10 mm in the jugulodigastric region and 8 to 9 mm in the remaining neck are suggestive of metastatic lymphadenopathy, provided that they are in the drainage area of the primary tumor site. All of these imaging criteria describe homogeneous, sharply outlined lymph nodes. Interestingly, regardless of which of these criteria are used, the overall error rates for both false-positive and false-negative diagnoses are between 15% and 20%, reflecting the limitations of imaging and the use of size criteria. Many im-

FIGURE 36-61 Axial contrast-enhanced CT scan shows two homogeneous left level I nodes. The more anterior node exceeds the normal size criterion; the posterior node does not. This appearance could be seen in a patient with lymphoma. However, these were reactive nodes that became smaller after a course of antibiotics in a patient who had an oral cavity infection.

VIEW IMAGE

Copyright © 2003, Mosby, Inc. All rights reserved.

Table 36-16
SIZE CRITERIA FOR HOMOGENEOUS CERVICAL LYMPH NODES ON CT AND MR IMAGING

Lymph nodes are considered pathologic if they exceed these measurements:
Maximal Longitudinal Diameter
Jugulodigastric and submandibular nodes >15 mm are abnormal
All other nodes except retropharyngeal nodes >10 mm are abnormal
Retropharyngeal nodes >8 mm are abnormal
Minimum Axial Diameter
Jugulodigastric nodes >11 mm are abnormal
All other nodes >10 mm are abnormal
L/T Ratio (Longitudinal Length/Transaxial Width)
<2 is suggestive of metastasis (round node vs. lima bean–shaped node)
For a group of three or more nodes in the drainage area of the tumor, suspect metastases if:
The maximal longitudinal diameter is greater than 8 to 15 mm
The minimum axial diameters are greater than 9 to 10 mm in level II or greater than 8 to 9 mm in the remaining neck

agers continue to use the greatest nodal diameter because it is that dimension that is used by the clinicians. However, at this time, there is no documented statistical advantage to any of these systems, so that radiologists can choose whichever one they are most comfortable with, provided that it is familiar to their clinicians. Stated differently, all of these methods are equally inadequate. Table 36-16 summarizes these size criteria.

In 1998, the Radiological Diagnostic Oncology Group compared CT and MR imaging in the staging of neck metastases and found that CT performed better for all interpretive criteria, especially if both nodal size and internal abnormalities were considered. However, a high negative predicative value (NPV = true negatives/true negatives + false negatives) was achieved only when small nodal size was considered, and this was associated with a low positive predicative value (PPV = true positive/true positives + false positives). Thus, in this study, if 10 mm was used as the upper size limit of a normal node, then the NPV was 84% and the PPV was 50%. That is, 16% of the patients with negative imaging would actually have metastases, while 50% of the patients with positive imaging would not have metastases.[72] In order to achieve a 90% NPV, this study found that it was necessary to go to a 5-mm or 6-mm node as the indicator of positivity, with a concomitantly unacceptably low PPV. The reason for seeking a 90% NPV was that a number of clinicians stated that if a population of patients could be defined by imaging in which a negative node had only a 10% chance of eventually harboring tumor, the clinicians would consider a ''wait and watch'' strategy.

Using sonography, van den Brekel et al. in 1998 found that smaller size criteria should be used for the evaluation of nodal metastases.[240] Their conclusion was that size criteria alone were in general not very accurate, especially in the clinically negative neck. They noted that although lymph nodes with minimum axial diameters of 10 mm in level I, 12 mm in level II, and 9 mm in level III were almost always metastatic, such large nodes without clinical evidence of metastasis (N0 neck) were rare. They suggested that a compromise between sensitivity and specificity could be achieved using a minimal axial diameter of 7 mm for level II and 6 mm for the rest of the neck in necks without palpable metastases. When considering all necks (with and without clinical disease), the minimal axial diameters should be 8 to 9 mm for level II and 7 to 8 mm for the rest of the neck. The authors also suggested the use of early sonographically guided aspiration cytology.[54]

Central Necrosis

Regardless of the route of metastatic spread to the nodal center, within this region there are tumor cells, residual lymph node tissues, and areas of necrosis. Despite this resulting complex cellular mixture, it has become common practice to simply refer to such lymph nodes as being *necrotic* or *having central necrosis*. In part, this may reflect the observation that on CT, such a node has a central region of ''water'' attenuation that represents all of these components. However, on MR, the necrosis (by its high T2-weighted signal intensity) can be distinguished from the other cellular components, more realistically representing the pathologic findings in these nodes.

When greater than 3 mm in size, nodes with central nodal necrosis have been observed by imaging in approximately one third of metastatic nodes.[71] On contrast-enhanced CT, such nodes have a central region of low ''water''attenuation (10 to 25 HU) and a variably thick and variably enhancing nodal rim (Figs. 36-62 to 36-67). On T2-weighted MR images, such nodes have areas of both high and intermediate

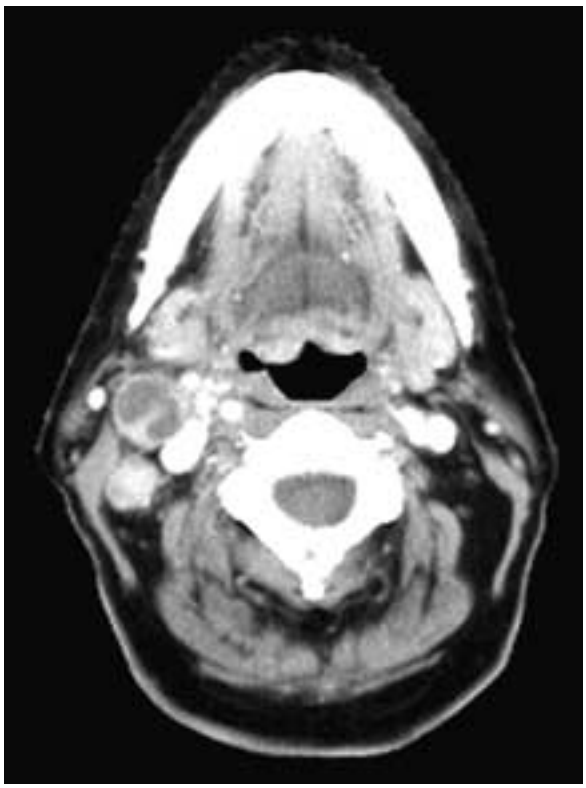

FIGURE 36-62 Axial contrast-enhanced CT scan shows two right level II lymph nodes. The more anterior node is enlarged and necrotic, with an irregular, enhancing rim. There is no gross extranodal tumor spread. The second node is enhancing, but normal by the size criterion. This patient had a right oropharyngeal carcinoma, and both of these nodes were metastatic.

VIEW IMAGE

Copyright © 2003, Mosby, Inc. All rights reserved.

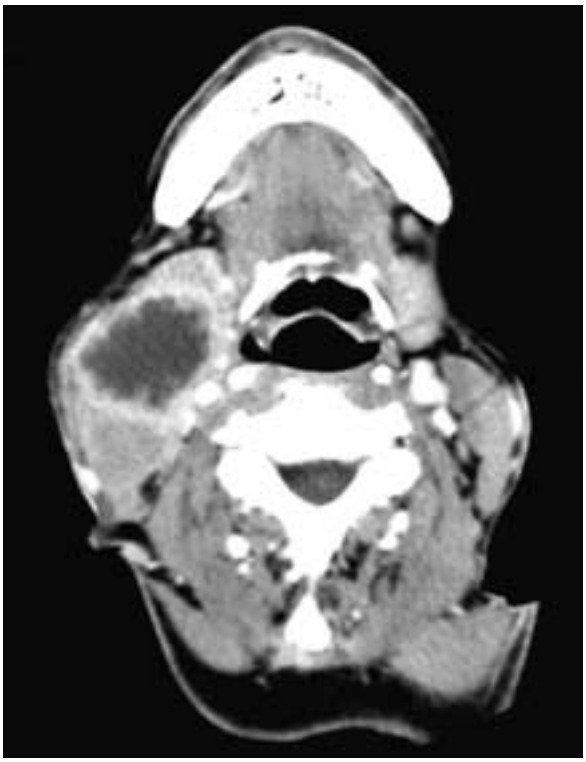

VIEW IMAGE

FIGURE 36-63 Axial contrast-enhanced CT scan shows a large right level II node with a highly nodular enhancing rim and slight infiltration of the adjacent tissues. The nodularity of the wall differentiates this metastatic squamous cell carcinoma node from a cyst.

VIEW IMAGE

FIGURE 36-64 Axial contrast-enhanced CT scan shows two necrotic right level II nodes. Each enhancing nodal capsule is of uneven thickness, and there is extracapsular tumor spread, as noted by infiltration of the adjacent fat planes. Also note that the carotid artery is surrounded by tumor, making it likely that the arterial wall has been invaded by tumor.

VIEW IMAGE

FIGURE 36-65 Axial contrast-enhanced CT scan shows an enlarged, partially necrotic left level II node with some extracapsular tumor spread, as noted by minimal infiltration of the adjacent fat planes. In particular, the fat planes are obliterated along the lateral 180° of the left carotid artery. This suggests invasion of the arterial wall. The primary tumor is seen at the base of the tongue and in the hypopharynx.

signal intensity. The high signal intensity corresponds to the areas of necrosis, while the intermediate signal intensity corresponds to tumor cells and residual normal lymph node tissues. As such, the areas of high T2-weighted signal intensity are always smaller than the central region of low attenuation seen on CT (Figs. 36-68 to 36-70). Because fast spin-echo (FSE) T2-weighted images are comparable to conventional spin-echo (SE) T2-weighted images, either technique can be routinely used. However, since the FSE

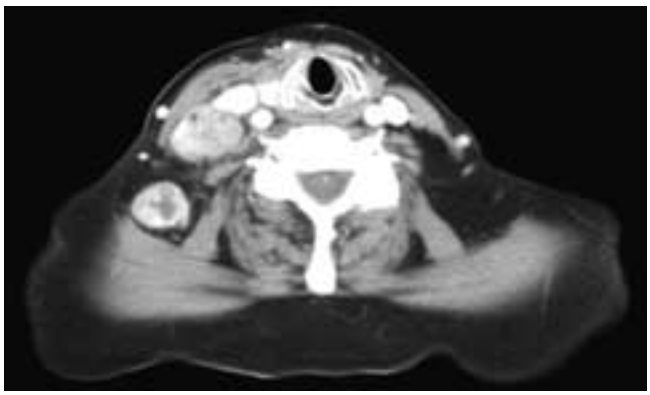

VIEW IMAGE

FIGURE 36-66 Axial contrast-enhanced CT scan shows a right level III enlarged, nonhomogeneously enhancing metastatic node. There also is an enlarged, enhancing, partially necrotic right level V node in this patient with metastatic squamous cell carcinoma.

Copyright © 2003, Mosby, Inc. All rights reserved.

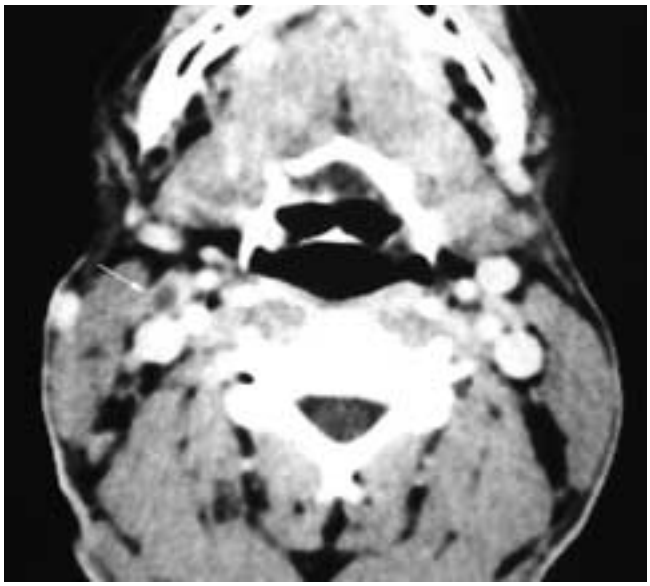

FIGURE 36-67 Axial contrast-enhanced CT scan shows a right level II node (*arrow*) that is normal in size and sharply delineated from the adjacent fat planes. However, the node has central necrosis and an unevenly thick, enhancing nodal rim. This was a metastatic squamous cell carcinoma node.

VIEW IMAGE

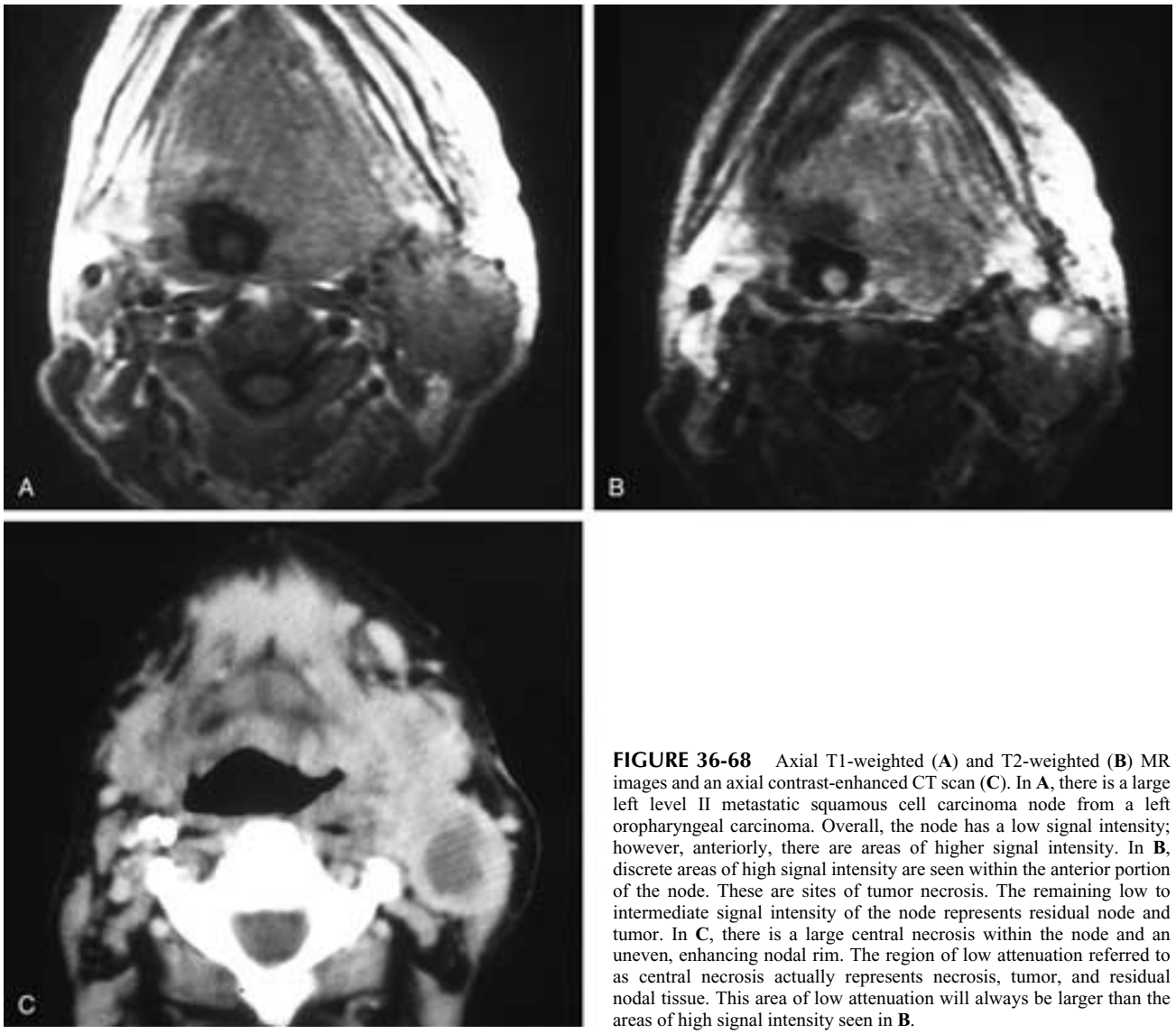

FIGURE 36-68 Axial T1-weighted (**A**) and T2-weighted (**B**) MR images and an axial contrast-enhanced CT scan (**C**). In **A**, there is a large left level II metastatic squamous cell carcinoma node from a left oropharyngeal carcinoma. Overall, the node has a low signal intensity; however, anteriorly, there are areas of higher signal intensity. In **B**, discrete areas of high signal intensity are seen within the anterior portion of the node. These are sites of tumor necrosis. The remaining low to intermediate signal intensity of the node represents residual node and tumor. In **C**, there is a large central necrosis within the node and an uneven, enhancing nodal rim. The region of low attenuation referred to as central necrosis actually represents necrosis, tumor, and residual nodal tissue. This area of low attenuation will always be larger than the areas of high signal intensity seen in **B**.

VIEW IMAGE

Copyright © 2003, Mosby, Inc. All rights reserved.

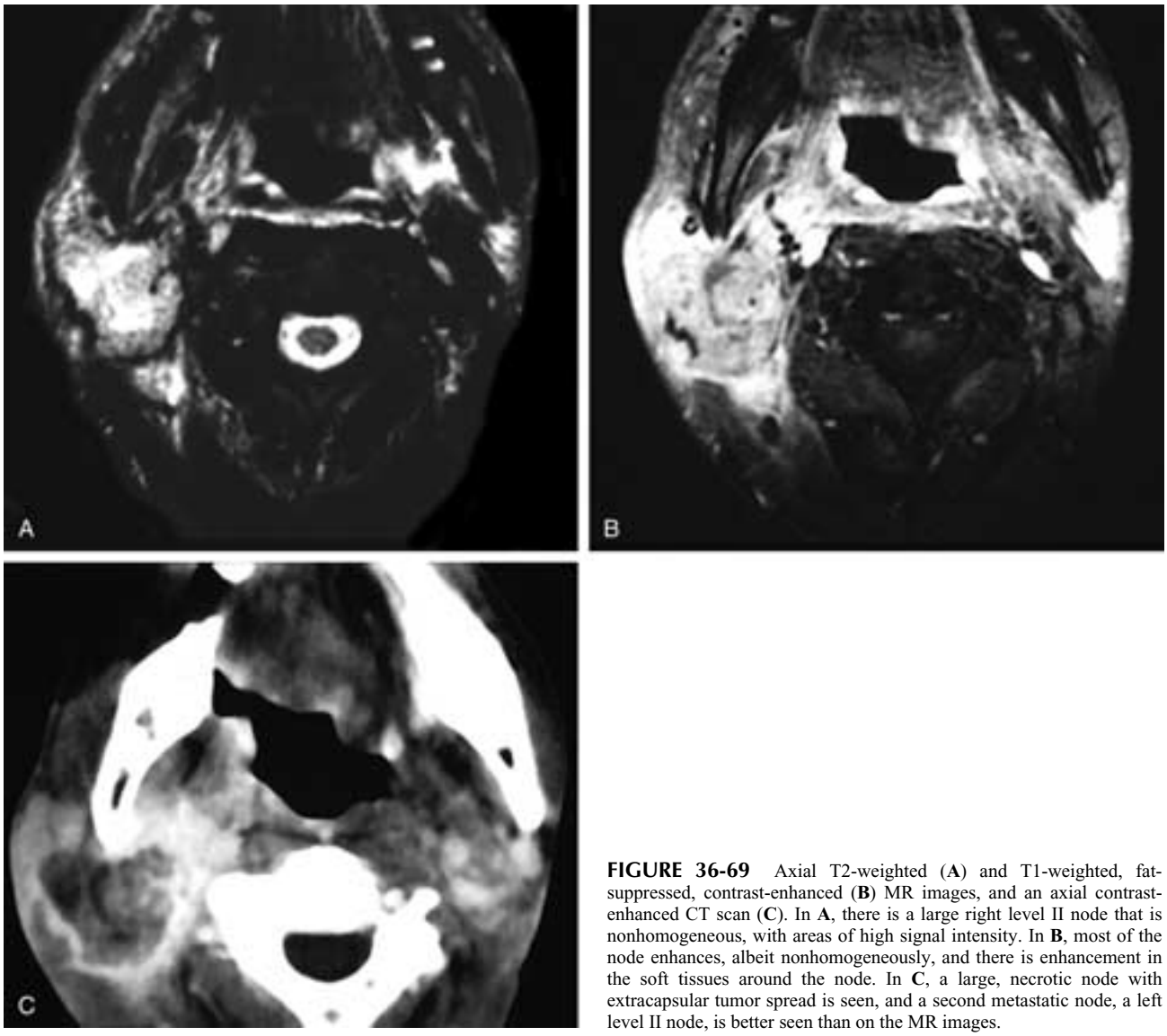

FIGURE 36-69 Axial T2-weighted (**A**) and T1-weighted, fat-suppressed, contrast-enhanced (**B**) MR images, and an axial contrast-enhanced CT scan (**C**). In **A**, there is a large right level II node that is nonhomogeneous, with areas of high signal intensity. In **B**, most of the node enhances, albeit nonhomogeneously, and there is enhancement in the soft tissues around the node. In **C**, a large, necrotic node with extracapsular tumor spread is seen, and a second metastatic node, a left level II node, is better seen than on the MR images.

VIEW IMAGE

images can be obtained with less scan time, this technique has become increasingly popular.[235]

Regardless of lymph node size, the most reliable imaging finding of metastatic disease is the presence of central nodal necrosis on contrast-enhanced CT and, as mentioned, when such areas are larger than 3 mm, they are routinely identified on CT.[7] On noncontrast MR, as described, the most reliable finding is variable T2-weighted signal intensity. A less reliable criterion is the presence on T1-weighted MR images of low signal intensity areas that do not enhance.[72] Although nodes with central nodal necrosis may be easily identified on contrast-enhanced CT scans, on routine SE noncontrast MR, such nodes may have homogeneously low to intermediate T1-weighted and high T2-weighted signal intensity. Unfortunately, this appearance is the same as that of a hyperplastic node, and it is only on a T1-weighted, contrast-enhanced, fat-suppressed MR image that a central nonenhancing region (akin to the central nodal necrosis appearance on CT) can be seen in these nodes (Fig. 36-71). Thus, a thorough MR examination should include noncontrast T1-weighted and T2-weighted (FSE) scans and a contrast-enhanced, T1-weighted, fat-suppressed sequence. Equivalent imaging sequences are also acceptable.

The primary imaging differential diagnosis of central tumor necrosis is fatty hilar metaplasia, which occurs almost exclusively at the periphery of the node, usually giving the node a pronounced lima bean configuration. Specifically, the central region of low attenuation can be seen to extend to the peripheral outer surface of the node. Such metaplasia is usually in response to chronic nodal infection and, if large enough, can be measured to have the attenuation of fat (Fig. 36-72). Rarely, metaplasia may occur centrally within a node. When this happens, the imaging distinction from a metastatic lymph node may be impossible.[7]

Subcapsular Nodal Tumor

Because the majority of the tumor load enters a lymph node via the afferent lymphatics, the tumor cells first start to proliferate within the node in the subcapsular regions. Occasionally on CT scans, low-attenuation focal areas can

Copyright © 2003, Mosby, Inc. All rights reserved.

be seen in these subcapsular nodal regions (Fig. 36-73). When present, they may be considered a suggestive imaging finding of nodal metastasis.

Extranodal Tumor Extension

Once tumor penetrates the nodal capsule, it extends into the adjacent soft tissues. This tumor growth has been variously referred to as extranodal, extracapsular, or transcapsular tumor spread, and it is associated with a decrease in survival. The presence of such macroscopic extranodal tumor extension is identified on contrast-enhanced CT as an enhancing, often thickened nodal rim, usually with infiltration of the adjacent fat planes (Figs. 36-74 to 36-76). These imaging changes reflect the presence of such macroscopic extranodal tumor spread, and their absence on imaging indicates the lack of this type of macroscopic disease. Histologically, such disease was found in 40% of lymph nodes less than 2 cm in diameter and in 23% of lymph nodes 1 cm in greatest length.[1–8, 48] This means that in approximately one quarter of lymph nodes considered normal by size criteria, extracapsular tumor spread can be present. As the node enlarges, the incidence of extracapsular tumor spread rises, so that it is reported to be present in 53% of lymph nodes 2 to 3 cm in size and in 74% of lymph nodes larger than 3 cm. Overall, such tumor spread occurs in 60% of nodes less than 3 cm in diameter.[52, 53, 241] It is also known that when macroscopic transcapsular tumor spread is present, the patient has a nearly 10 times greater risk of recurrence compared with patients with either microscopic tumor spread or no transcapsular spread.[48] Table 36-17 summarizes these findings.

Several other circumstances can result in imaging findings similar to those of extranodal capsular spread. All of these situations cause an inflammation of the nodal capsule, including recent nodal infection, irradiation, and surgical manipulation (Table 36-18).[242] However, if these clinical possibilities can be eliminated by the history, the contrast CT findings described previously are diagnostic of such extranodal tumor extension. For reasons that remain unclear, such extranodal spread overall is less reliably identified on MR than on CT, especially when present to only a minimal degree. It may simply be that the low attenuation of fat on CT is the best ''background'' in which to identify such early nodal changes. On imaging, it is important to identify if the extracapsular nodal tumor has invaded adjacent structures such as the internal carotid artery, common carotid artery, retropharyngeal soft tissues, or bone.

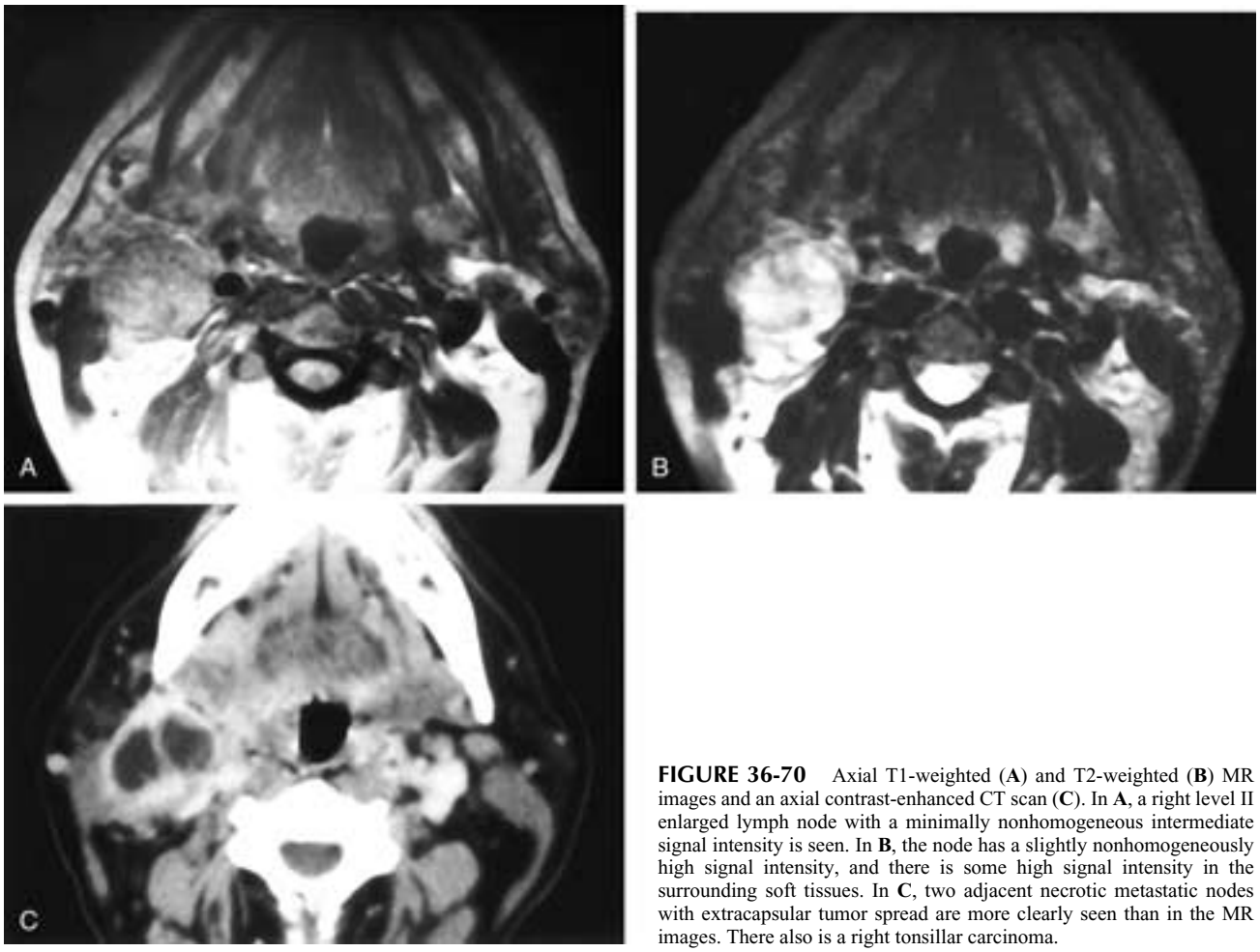

FIGURE 36-70 Axial T1-weighted (**A**) and T2-weighted (**B**) MR images and an axial contrast-enhanced CT scan (**C**). In **A**, a right level II enlarged lymph node with a minimally nonhomogeneous intermediate signal intensity is seen. In **B**, the node has a slightly nonhomogeneously high signal intensity, and there is some high signal intensity in the surrounding soft tissues. In **C**, two adjacent necrotic metastatic nodes with extracapsular tumor spread are more clearly seen than in the MR images. There also is a right tonsillar carcinoma.

VIEW IMAGE

Copyright © 2003, Mosby, Inc. All rights reserved.

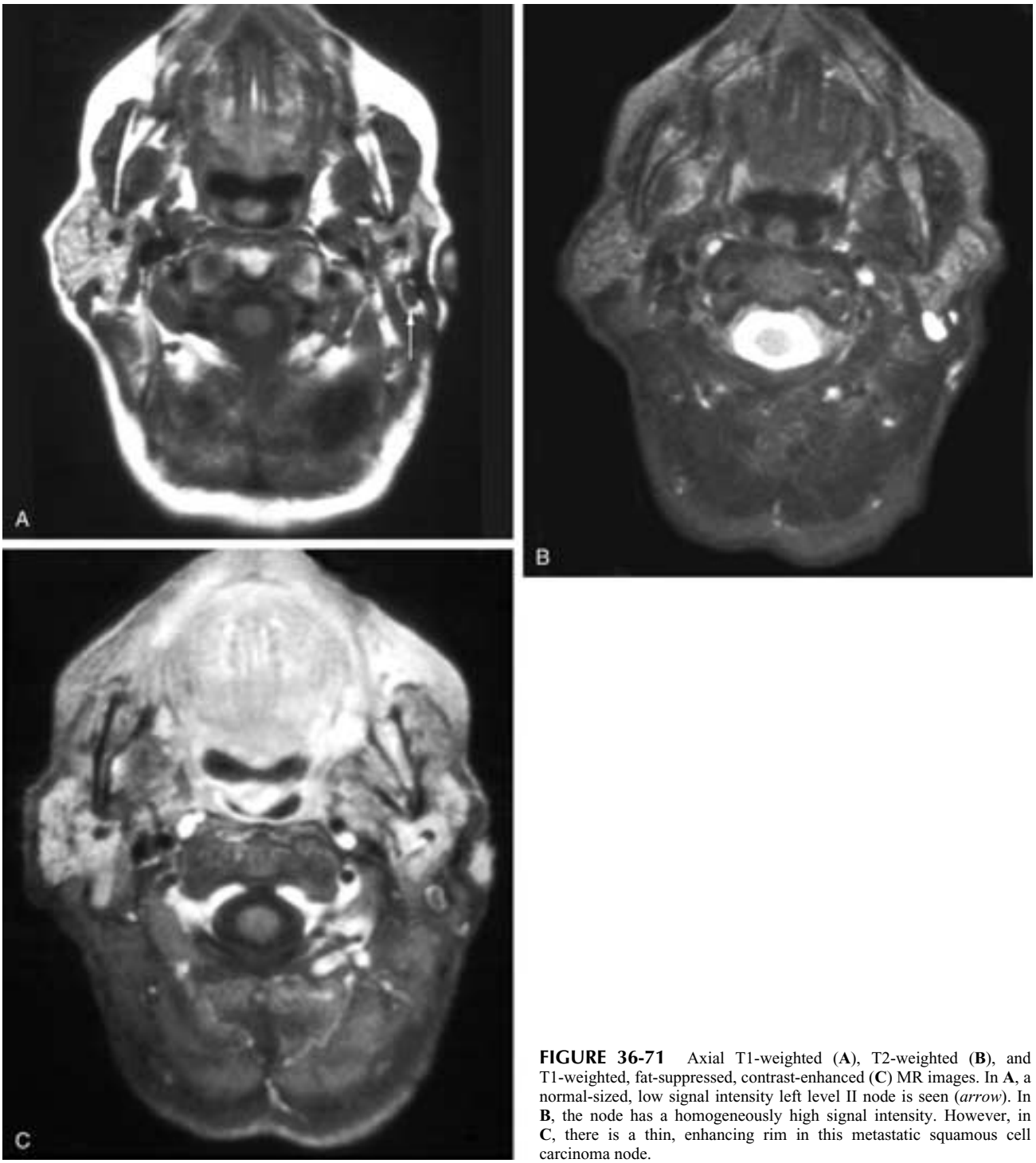

FIGURE 36-71 Axial T1-weighted (**A**), T2-weighted (**B**), and T1-weighted, fat-suppressed, contrast-enhanced (**C**) MR images. In **A**, a normal-sized, low signal intensity left level II node is seen (*arrow*). In **B**, the node has a homogeneously high signal intensity. However, in **C**, there is a thin, enhancing rim in this metastatic squamous cell carcinoma node.

VIEW IMAGE

Arterial Invasion

The extension of nodal tumor to the adjacent internal carotid artery is a grave prognostic finding. Although the salvage of patients with arterial tumor invasion is small, there is evidence to suggest that if the involved artery is resected and, if possible, replaced with a graft at the time of surgery, the patient does better than if the tumor is dissected off of the artery and the patient is irradiated after surgery.[243, 244] However, in either case, this situation is associated with a poor prognosis.

The degree of arterial wall invasion can be variable, but from an oncologic consideration, tumor invasion of the arterial adventitia is as important as greater degrees of arterial invasion into the muscularis and intima that may be seen on imaging as narrowing of the arterial lumen. Because microscopic adventitial tumor infiltration is beyond the scope of current imaging detection, the best one can do is to

Copyright © 2003, Mosby, Inc. All rights reserved.

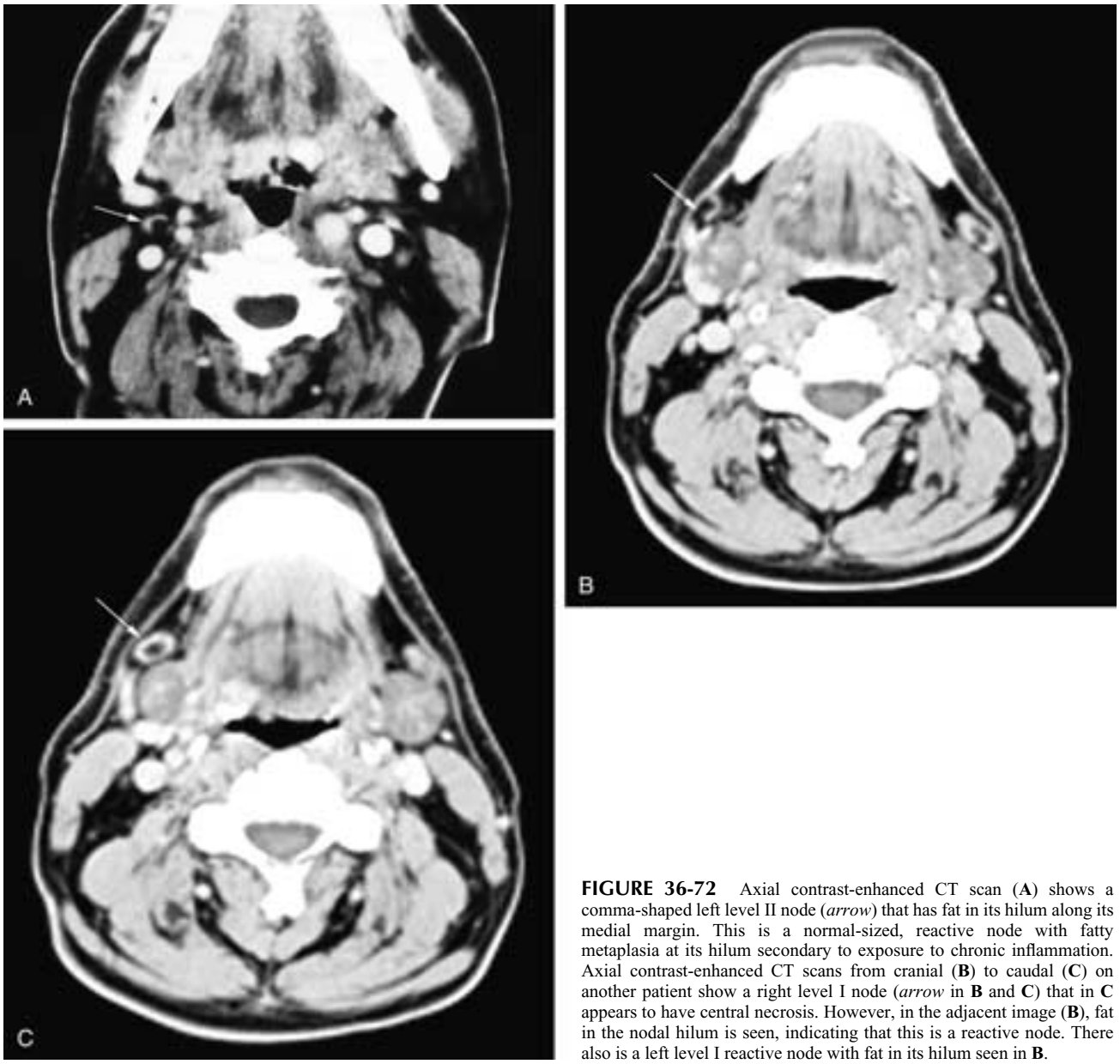

FIGURE 36-72 Axial contrast-enhanced CT scan (**A**) shows a comma-shaped left level II node (*arrow*) that has fat in its hilum along its medial margin. This is a normal-sized, reactive node with fatty metaplasia at its hilum secondary to exposure to chronic inflammation. Axial contrast-enhanced CT scans from cranial (**B**) to caudal (**C**) on another patient show a right level I node (*arrow* in **B** and **C**) that in **C** appears to have central necrosis. However, in the adjacent image (**B**), fat in the nodal hilum is seen, indicating that this is a reactive node. There also is a left level I reactive node with fat in its hilum seen in **B**.

VIEW IMAGE

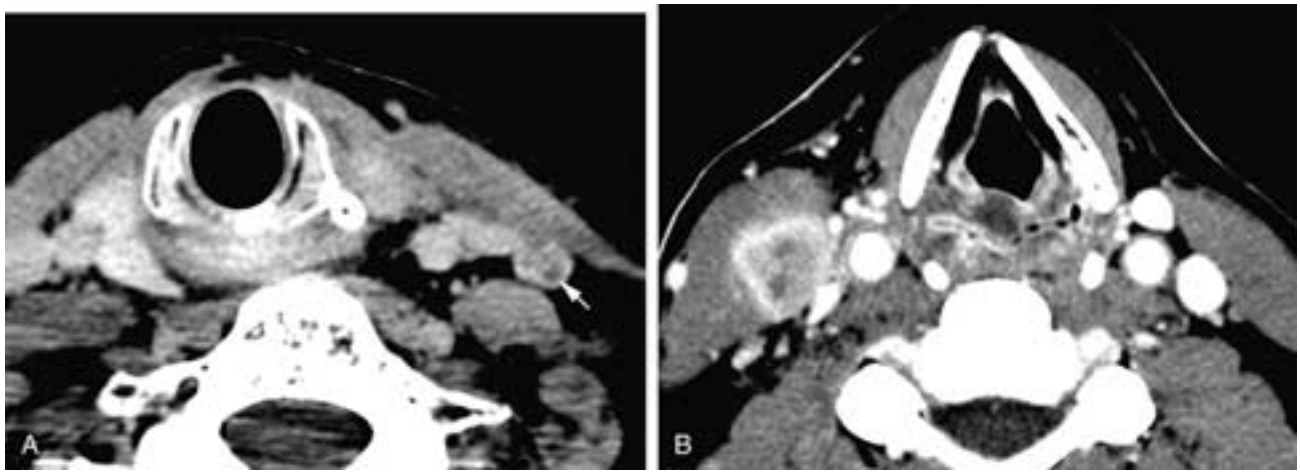

FIGURE 36-73 Axial contrast-enhanced CT scan (**A**) shows a 1-cm left level III node with focal areas of low attenuation (*arrow*) in the subcapsular region. Axial contrast-enhanced CT scan (**B**) on another patient shows an enlarged, enhancing right level III node with focal areas of subcapsular low attenuation. There is also enhancement of a hazy-appearing nodal rim indicating extracapsular tumor spread. Both of these nodes contained metastatic squamous cell carcinoma. (Courtesy of Dr. Anthony Mancuso.)

VIEW IMAGE

Copyright © 2003, Mosby, Inc. All rights reserved.

FIGURE 36-74 Axial contrast-enhanced CT scan shows a necrotic left level II node with a thick, nodular, enhancing rim. The enhancement extends into the adjacent soft tissues, indicating extracapsular tumor spread. This extranodal disease is adjacent to the carotid artery, suggesting invasion of the arterial wall.

note the degree of the artery's circumference that is potentially involved by tumor. This is noted not only by observing the gross tumor, but also by identifying the degree of obliteration of the normal fat plane that surrounds the artery. If the artery is entirely surrounded by tumor, it is most likely that the artery is invaded, yet there are some cases that at surgery have no adventitial involvement. Conversely, if just a tip of tumor touches the artery, it is unlikely that the arterial wall has been invaded, yet at surgery such cases may have adventitial tumor spread. In general, the greater the tumor extension around the artery,

FIGURE 36-75 Axial contrast-enhanced CT scan shows multiple right level II necrotic metastatic squamous cell carcinoma nodes with extracapsular tumor spread. The right carotid artery is almost surrounded by this disease, making it highly probable that the arterial wall has been invaded. There is also a nonenlarged necrotic right level V node.

the more likely it is that the artery is involved. Thus, when more than 270° of the arterial circumference is surrounded by tumor, it is likely that the arterial wall has been invaded.[244]

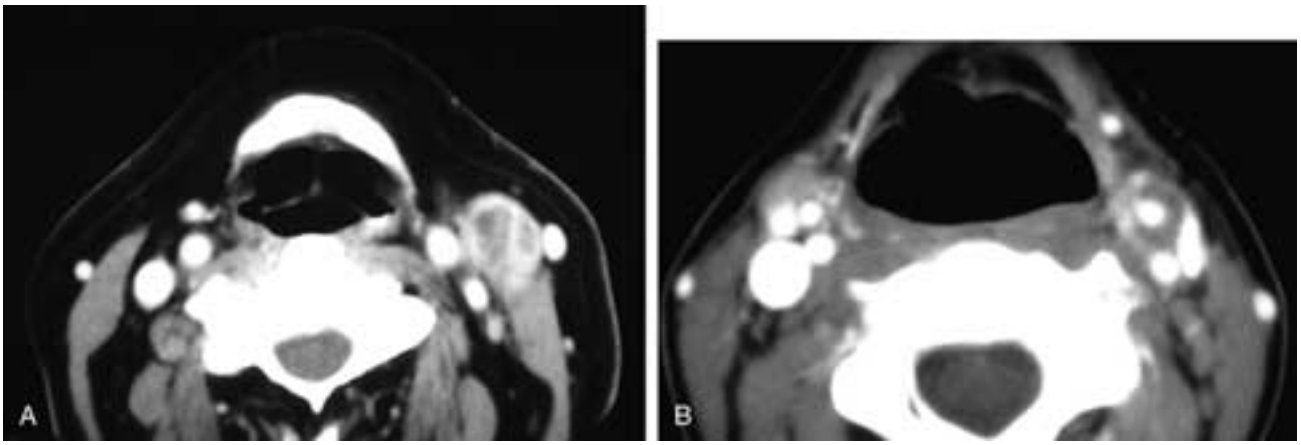

FIGURE 36-76 Axial contrast-enhanced CT scans on two different patients, both of whom had a slightly tender, pulsatile mass in the left neck. In **A**, there is a necrotic metastatic node adjacent to the carotid artery. The arterial pulsations were transmitted by the node to the skin surface. In **B**, there is a nonenhancing zone around the left carotid artery, and the lumen of the artery is slightly reduced compared to the right carotid artery. This patient had an arteritis.

Copyright © 2003, Mosby, Inc. All rights reserved.

Table 36-17
EXTRANODAL TUMOR SPREAD

Occurs in:
- 23% of lymph nodes <10 mm
- 53% of lymph nodes 20 to 30 mm
- 74% of lymph nodes >30 mm
- Overall occurs in 60% of lymph nodes <30 mm

All measurements are maximal longitudinal diameter

A patient with macroscopic transcapsular (extranodal) tumor spread has nearly a 10 times greater risk of neck recurrence than does a patient with either microscopic extranodal tumor spread or no transcapsular spread.

Metastatic Thyroid Carcinoma

Because of its variable imaging appearance, metastatic thyroid carcinoma deserves special comment. The most common thyroid cancers to metastasize to the cervical lymph nodes are the papillary and follicular types. Less often, medullary carcinoma involves the cervical nodes; this tumor has a predilection for osseous metastasis. Although anaplastic carcinoma may spread to nodes, its locally aggressive nature often causes the demise of the patient prior to imaging evidence of nodal metastases is noted.

The involved lymph nodes from thyroid carcinomas may appear as hyperplastic nodes; or they may have a variety of imaging presentations, including enhancement and small, dystrophic, scattered calcifications (true psammomatous calcifications are identified only microscopically); or they may be completely cavitated, often mimicking the imaging appearance of a benign cyst (Figs. 36-77 to 36-79). Rarely, areas of hemorrhage (also fairly commonly seen in metastatic hypernephroma) may occur (Fig. 36-80). On MR imaging, most metastatic thyroid carcinomatous nodes have a fairly low to intermediate T1-weighted and a high T2-weighted signal intensity. They also usually enhance fairly significantly. However, some of the nodes, especially those from papillary thyroid carcinoma, may have high T1-weighted and T2-weighted signal intensities (Figs. 36-81 and 36-82). This is ostensibly due to high intranodal concentrations of the macromolecular protein thyroglobulin. As previously mentioned, rare intranodal hemorrhage may occur. This also causes high T1-weighted and T2-weighted signal intensities.[245, 246]

Enhancing Nodes

It was once thought that contrast enhancement of a lymph node suggested only a limited differential diagnosis. However, there are a great number of diseases that can be associated with enhancing lymphadenopathy. In general, nodal enhancement seems to imply increased nodal vascularity, and the most common causes are acute infections. Often such nodes are slightly enlarged, are homogeneous, and enhance to a variable degree. If an acute virulent infection such as staphylococcus is present, nodal necrosis may occur and the imaging may simulate a necrotic metastatic lymph node. Lymphomas, tuberculosis, HIV infection, metastatic papillary and medullary thyroid carcinomas, metastatic hypernephroma, KS, and rare diseases such as angioimmunoblastic lymphadenopathy with dysproteinemia, angiolymphoid hyperplasia with eosinophilia (ALHE and Kirmura's disease), ALNH, and Kikuchi's disease all can have enhanced lymph nodes.[66, 175–178, 200, 204–206, 245–247] Although not typically observed, metastatic squamous carcinoma containing nodes may also enhance (Figs. 36-83 and 36-84). These diseases are summarized in Table 36-19.

It has also been suggested that nodal vascularity may be related to the response of nodes to chemotherapy, and there may be evidence to suggest that color flow Doppler may aid in predicting the response of metastatic nodes to chemotherapy.[14] Color flow Doppler imaging is also helpful in diagnosing pulsatile neck masses (separating a node adjacent to the carotid artery from vascular lesions) and in fine-needle aspiration biopsies of nonpulsatile masses.[248]

Nodal Calcifications

Overall, nodal calcifications in the neck are uncommon, occurring in about 1% of cases.[249] Most frequently, such calcifications are still seen in patients with tuberculosis. Nodal calcifications may also be seen with healed necrotic, abscessed nodes and in benign diseases such as amyloidosis and, rarely, sarcoidosis. Of the primary head and neck tumors, the most common ones associated with nodal calcifications are metastatic papillary thyroid carcinomas. Nodal calcifications also occur with both non-Hodgkin's and Hodgkin's lymphomas, particularly after irradiation and chemotherapy. Calcifications may also be seen in metastatic mucinous adenocarcinomatous nodes, primarily from breast, lung, and colon primary tumors. A patient with sinus histiocytosis with massive lymphadenopathy developed nodal calcifications after interferon treatment. If there is extensive pulmonary disease, rarely calcification can also be seen in supraclavicular nodes in patients with silicosis. These diseases are summarized in Table 36-20 (Fig. 36-85). Calcifications have also been reported with metastatic prostate, seminoma, carcinoid, olfactory neuroblastoma, and angiofollicular lymph node hyperplasia. Egg shell–type calcifications (peripheral nodal calcifications) have been reported in silicosis, sarcoidosis, scleroderma, tuberculosis, and amyloidosis. Nodal radiodensities can also be seen on CT in areas of nodal hyalinization and keratinization.[245, 250–276]

Table 36-18
IMAGING EXTRANODAL TUMOR SPREAD

On imaging, there is:
1. Enhancement, thickening, and usually irregularity of the nodal rim
2. Infiltration of the adjacent fat planes

Look for tumor extension to:
1. Internal carotid artery and common carotid artery
2. Retropharyngeal soft tissues
3. Bone

Imaging caution: Recent surgery, irradiation, or infection can cause similar imaging findings.

Copyright © 2003, Mosby, Inc. All rights reserved.

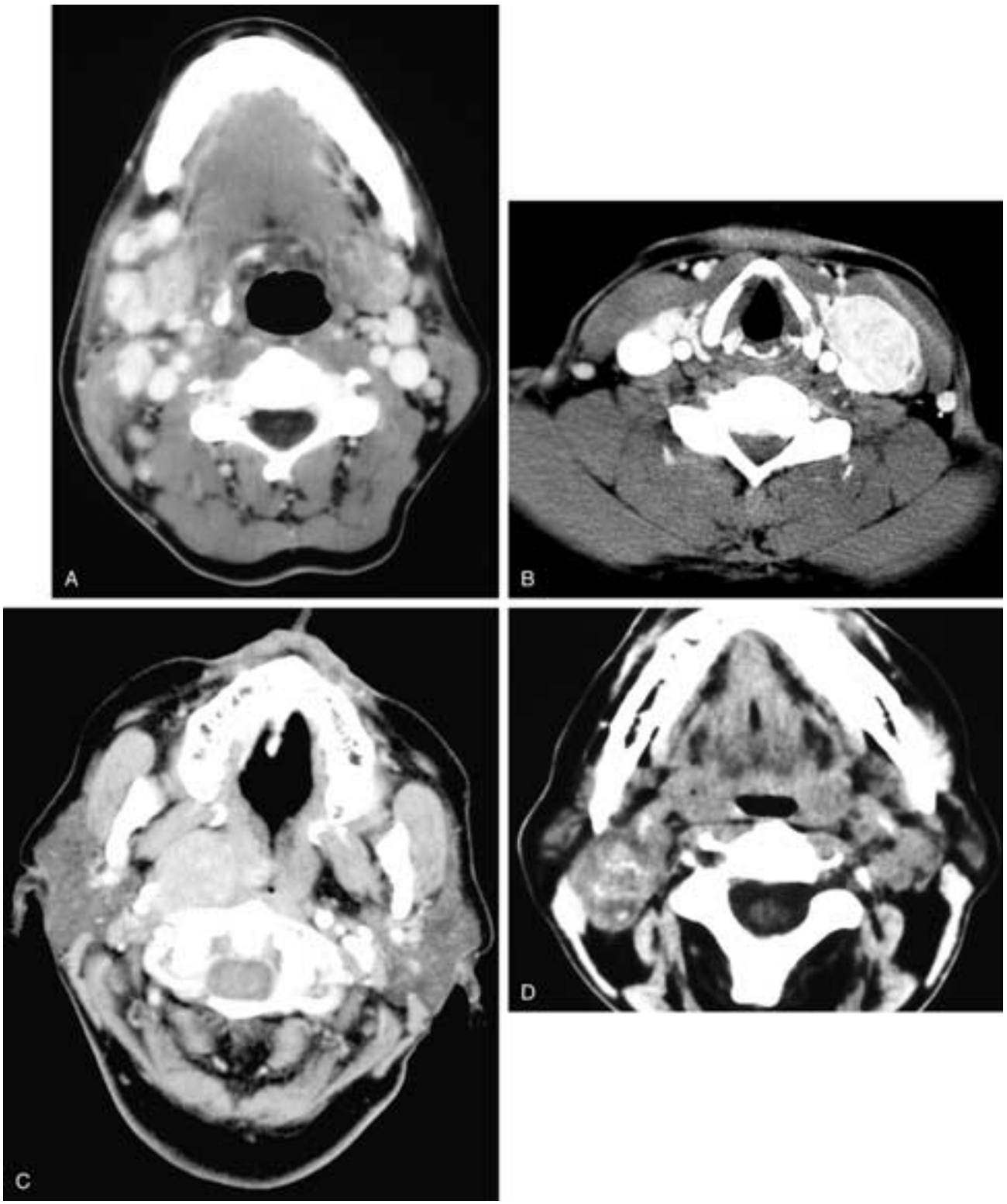

VIEW IMAGE

FIGURE 36-77 Contrast-enhanced CT scans on four different patients. In **A**, there are multiple right, densely enhancing level I and II nodes. There are also bilateral smaller, posterior level II nodes that enhance to a lesser degree. The larger right-sided nodes were metastatic papillary thyroid carcinoma. The smaller posterior nodes were reactive. In **B**, there is an enlarged, densely enhancing left level III node that was a metastatic papillary thyroid carcinoma node. In **C**, there is an enlarged, enhancing right retropharyngeal node that was a metastatic papillary thyroid carcinoma node. In **D**, there is a right, enlarged, and enhancing level II node with calcifications in this patient with metastatic papillary thyroid carcinoma.

Copyright © 2003, Mosby, Inc. All rights reserved.

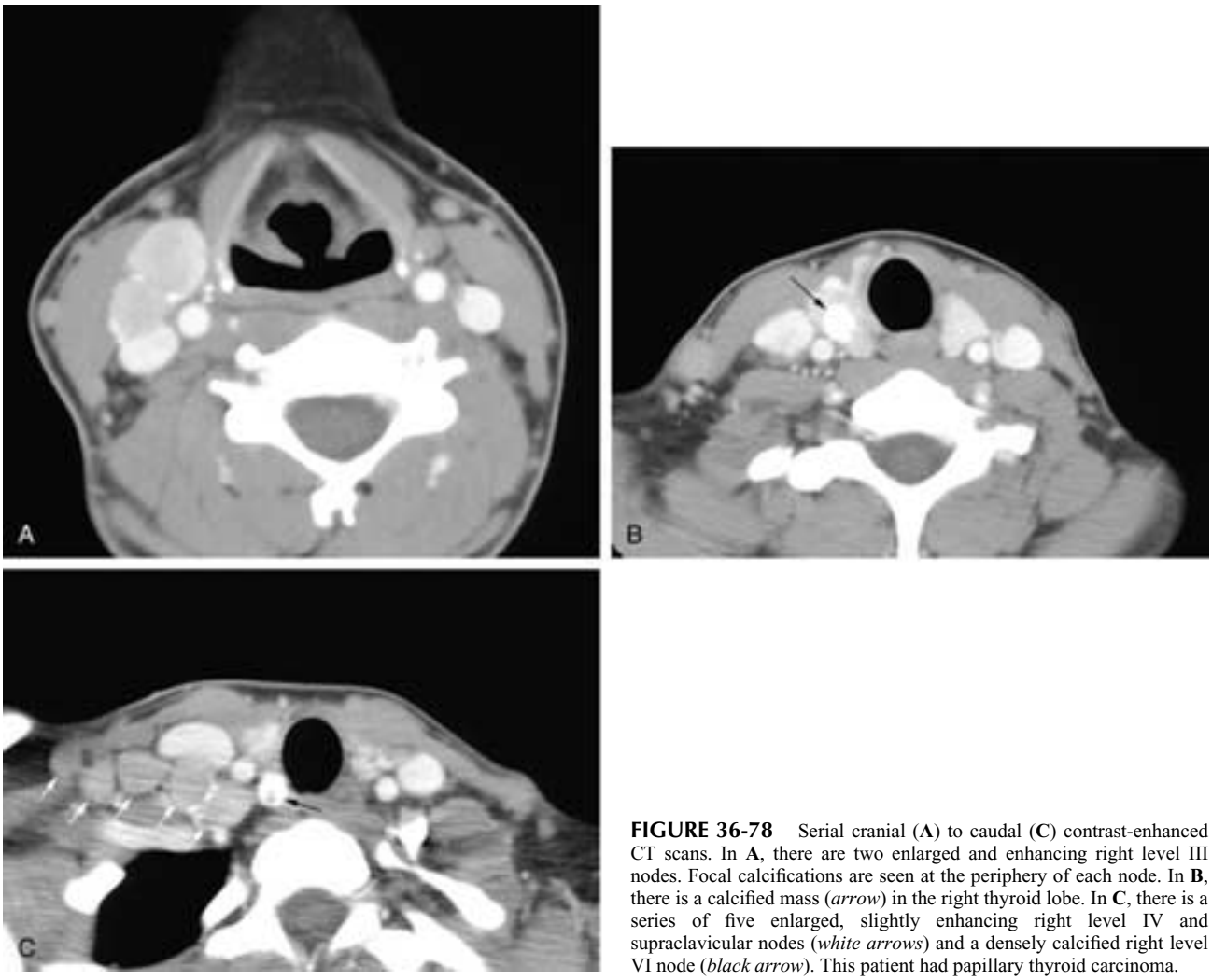

FIGURE 36-78 Serial cranial (**A**) to caudal (**C**) contrast-enhanced CT scans. In **A**, there are two enlarged and enhancing right level III nodes. Focal calcifications are seen at the periphery of each node. In **B**, there is a calcified mass (*arrow*) in the right thyroid lobe. In **C**, there is a series of five enlarged, slightly enhancing right level IV and supraclavicular nodes (*white arrows*) and a densely calcified right level VI node (*black arrow*). This patient had papillary thyroid carcinoma.

VIEW IMAGE

The Retropharyngeal Abscessed Node

Retropharyngeal lymph nodes, especially in children, have a tendency to become necrotic when infected. On imaging, this may at first suggest the presence of a retropharyngeal abscess; however, the findings of these two entities are different. With the necrotic node, there is an enhancing irregular rim about a necrotic nodal center. The remaining margins of the retropharyngeal space are not involved. When a retropharyngeal abscess is present, there is enhancement of the walls of this space, and mucoid attenuation material fills the space (Fig. 36-86). The distinction between these two forms of infection has clinical implications. Today, a necrotic retropharyngeal node is usually initially treated with intensive intravenous antibiotic therapy without surgery. Most patients have an excellent clinical response within 48 hours, and surgery can be avoided. With a retropharyngeal abscess, the initial treatment remains surgical drainage.

NEWER IMAGING APPROACHES

Different imaging approaches beyond conventional CT and MR imaging have been tried in an attempt to further refine the early detection of metastatic lymphadenopathy (also see Chapters 43 and 45). One such technique is to apply magnetization transfer analysis to differentiate benign from malignant disease.[235] This approach presently remains unproven. It cannot be routinely applied on all MR scanners, and necrotic areas within a metastatic node may lead to unreliable results.

A second technique employs a type of functional MR imaging. The patient has a pre-drug MR imaging scan, then is injected intravenously with Dextran-coated superparamagnetic iron oxide particles, and finally gets a 24-hour post-drug MR imaging scan. Normally, hyperplastic lymph nodes filter the superparamagnetic iron oxide, and this gives them very low signal intensity on the MR study. The concept is that the absence of such filtration indicates tumor replacement of nodal tissue (Fig. 36-87). However, the problem of interpreting these studies arises when there is partial ''blackening'' of a node after the superparamagnetic iron oxide is given. Because repeated infections cause nodal scarring and this, like tumor, may cause a lack of nodal filtering of the drug, the ultimate usefulness of this technique remains in question. If one uses the criterion that more than 50% blackening of a node indicates that it is probably metastatic, early reports suggest

Copyright © 2003, Mosby, Inc. All rights reserved.

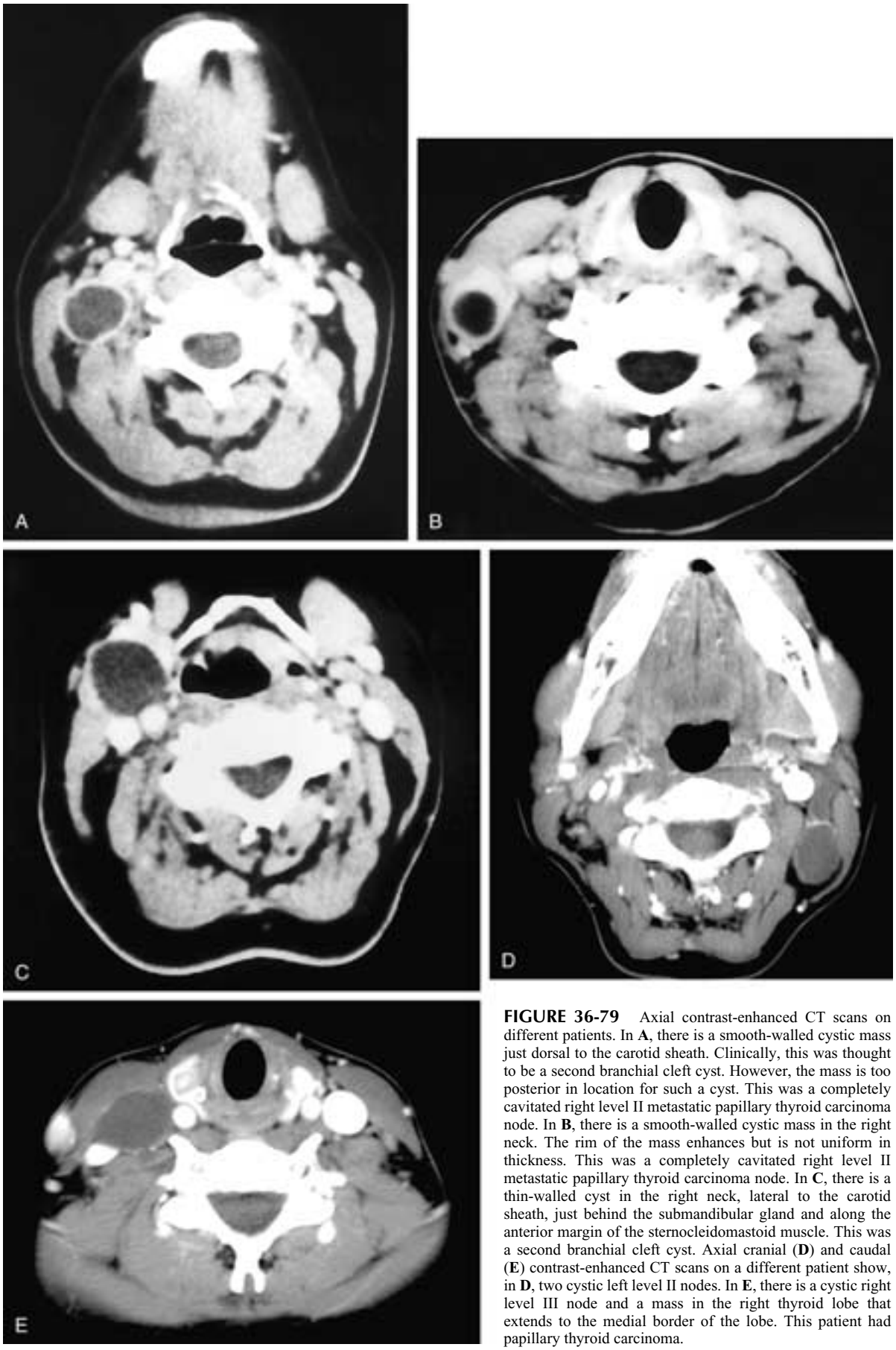

FIGURE 36-79 Axial contrast-enhanced CT scans on different patients. In **A**, there is a smooth-walled cystic mass just dorsal to the carotid sheath. Clinically, this was thought to be a second branchial cleft cyst. However, the mass is too posterior in location for such a cyst. This was a completely cavitated right level II metastatic papillary thyroid carcinoma node. In **B**, there is a smooth-walled cystic mass in the right neck. The rim of the mass enhances but is not uniform in thickness. This was a completely cavitated right level II metastatic papillary thyroid carcinoma node. In **C**, there is a thin-walled cyst in the right neck, lateral to the carotid sheath, just behind the submandibular gland and along the anterior margin of the sternocleidomastoid muscle. This was a second branchial cleft cyst. Axial cranial (**D**) and caudal (**E**) contrast-enhanced CT scans on a different patient show, in **D**, two cystic left level II nodes. In **E**, there is a cystic right level III node and a mass in the right thyroid lobe that extends to the medial border of the lobe. This patient had papillary thyroid carcinoma.

VIEW IMAGE

Copyright © 2003, Mosby, Inc. All rights reserved.

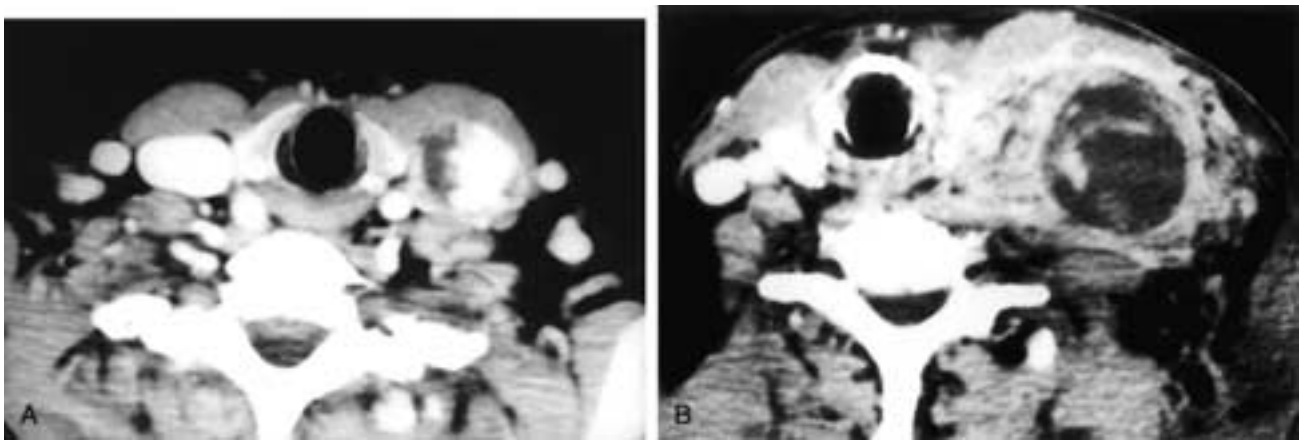

VIEW IMAGE

FIGURE 36-80 Axial contrast-enhanced CT scans. In **A**, there is a partially enhancing, partially cystic left level IV node. This was a metastatic papillary thyroid carcinoma node with hemorrhage. In **B**, there is a large, necrotic left level IV node with extracapsular tumor spread. Within the node are areas of higher attenuation that represent hemorrhage in this patient with metastatic hypernephroma.

that this approach increases the sensitivity of this technique compared to CT and more conventional MR imaging for detecting early nodal metastasis.[237, 238] The downside of this approach is that the patient must make at least two visits to the radiology department, one to be injected and one to be imaged.

The use of metabolic imaging has also made strides in the diagnosis of head and neck cancer and in following treatment changes in these patients. Studies have shown that the kinetic characteristics and tracer uptake intensity are similar in both primary tumors and their lymph node metastases. These topics are also dealt with in Chapter 45. In these studies, all tumors were demonstrated by PET, although there was a tendency to overestimate tumor size, and the authors concluded that FDG-PET could be useful in detecting occult primary tumors and nodal metastases.[277, 278] In following metastatic lymph nodes after irradiation, FDG-PET showed an initial increase in nodal metabolic activity. After 30 Gy was given, the deeper nodes returned to their initial levels of activity. The metabolic activity of superficial nodes remained high even after administration of 60 Gy, and anti-granulocyte scans showed intense inflammation in these latter nodes.[279] FDG-PET may thus be useful in predicting a good nodal response to irradiation by identifying such an inflammatory response to treatment. Another study reported results of static, nonattenuation-corrected PET starting 40 minutes after the intravenous injection of 370 MBq of fluorodeoxyglucose F 18. The authors noted that the diagnostic accuracy of PET for detecting ''neck sides'' with malignant involvement was

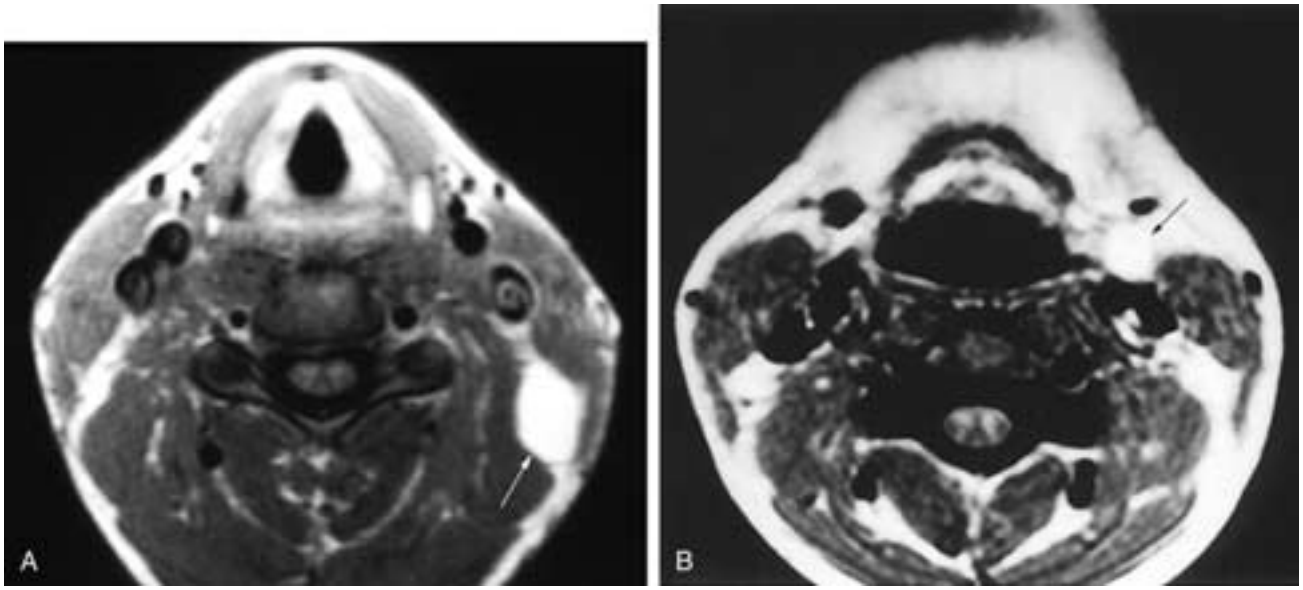

VIEW IMAGE

FIGURE 36-81 Axial T1-weighted MR images on two different patients. In **A**, there is a left level II node with high signal intensity (*arrow*) deep to the sternocleidomastoid muscle. In **B**, there is a left level II node with high signal intensity (*arrow*) adjacent to the carotid artery. Both of these nodes contained metastatic papillary thyroid carcinoma.

Copyright © 2003, Mosby, Inc. All rights reserved.

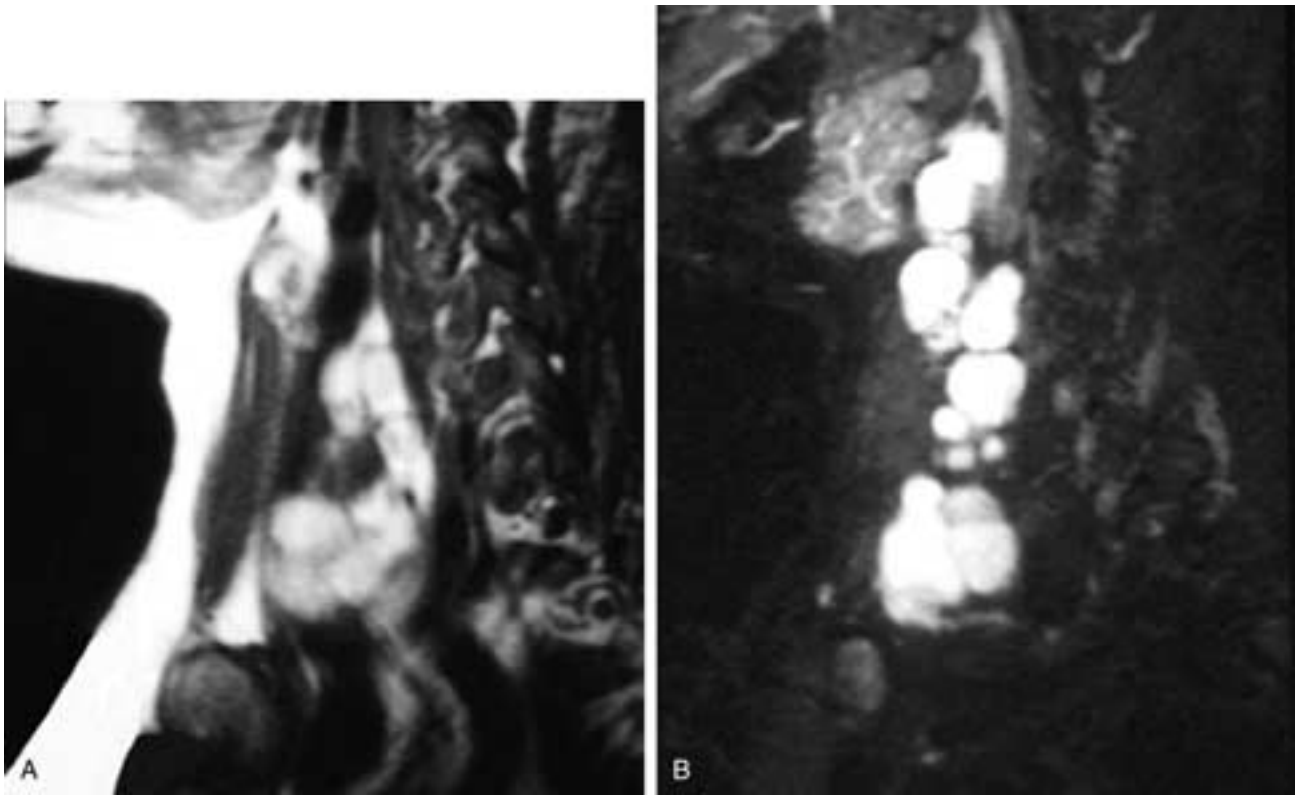

VIEW IMAGE

FIGURE 36-82 Sagittal T1-weighted (**A**) and T2-weighted (**B**) MR images show multiple high signal intensity nodes in levels II to IV. These were all metastatic papillary thyroid carcinoma nodes.

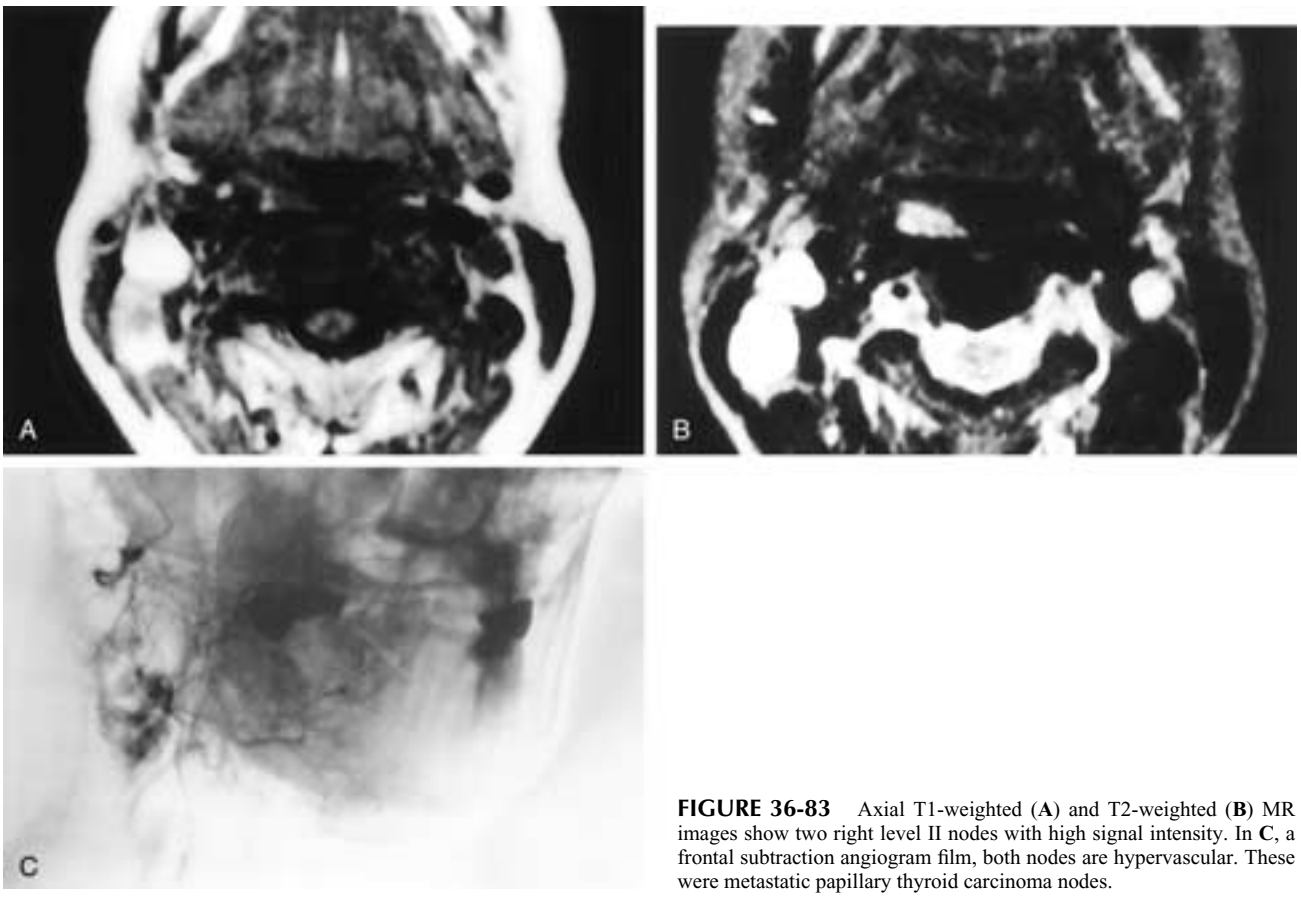

FIGURE 36-83 Axial T1-weighted (**A**) and T2-weighted (**B**) MR images show two right level II nodes with high signal intensity. In **C**, a frontal subtraction angiogram film, both nodes are hypervascular. These were metastatic papillary thyroid carcinoma nodes.

VIEW IMAGE

Copyright © 2003, Mosby, Inc. All rights reserved.

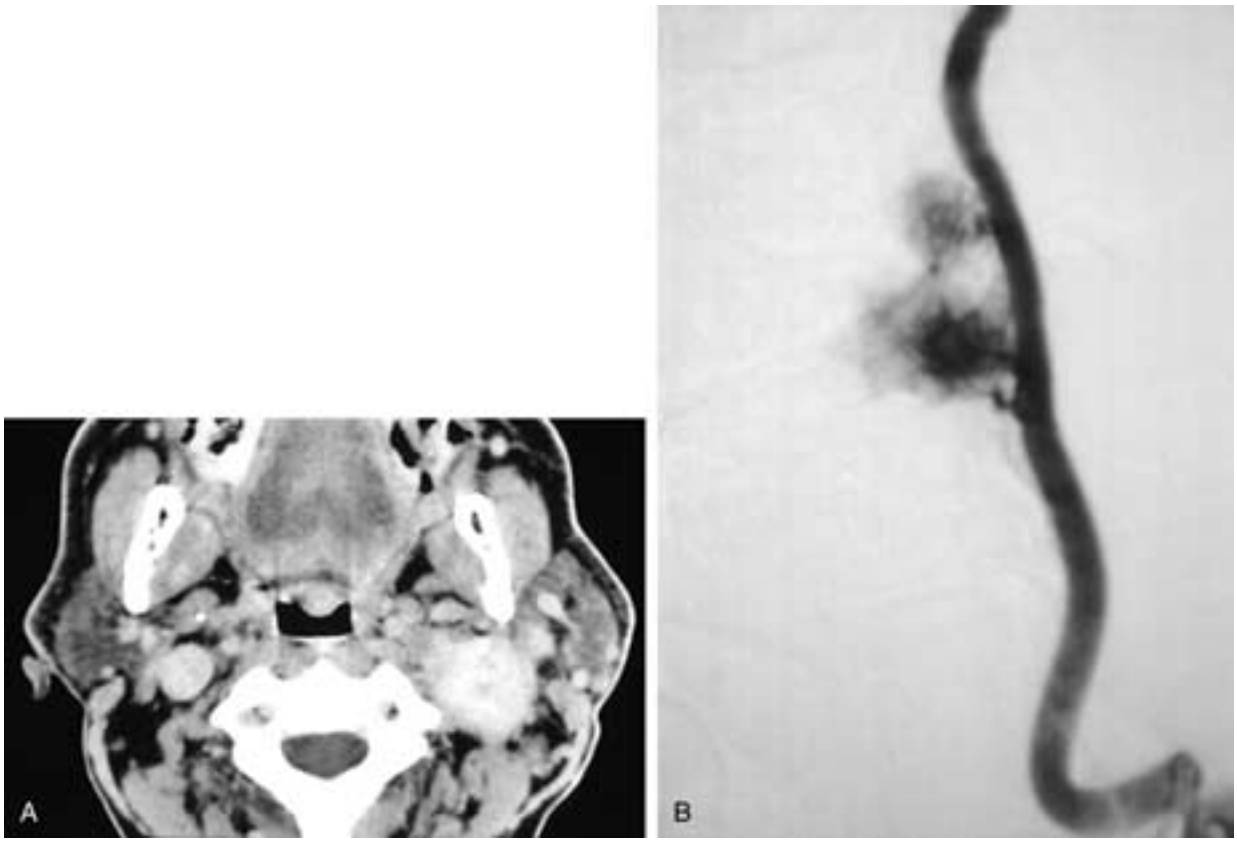

VIEW IMAGE

FIGURE 36-84 Axial contrast-enhanced CT scan (**A**) shows an enlarged, enhancing left level II node. In **B**, a lateral subtraction angiogram film, this mass is seen to actually be two adjacent hypervascular nodes. These were squamous cell carcinoma nodes.

superior to that of morphologic procedures, with a sensitivity and specificity of 87% and 94%, respectively.[280]

Thallium-201 SPECT may also be useful in head and neck cancer patients, especially for detecting occult tumors and for assessing recurrences.[281] Similarly, thallium-201 SPECT has been shown to be useful in predicting the response of lymph nodes and primary tumors to irradiation.[282] However, when such a scan is utilized, there are other lesions, such as Kimura's disease, that show increased thallium-201 uptake.[283]

SPECT using 99m-technetium-MIBI also demonstrated uptake in both tumors and metastatic lymph nodes. This approach may be a good adjunctive technique to CT and MR imaging.[284] Another approach, with limited testing to date, that may correctly identify both the primary tumor site and nodal metastases involves the use of SPECT immunoscintigraphy with 111In-(Fab′)2-anti-carcinoembryonic-antigen monoclonal antibody, SQ174 monoclonal antibody, and

Table 36-19
DISEASES THAT CAUSE ENHANCED CERVICAL LYMPH NODES ON IMAGING

Nodal angiomatoses
Acute bacterial infections (including tuberculosis, etc.)
Viral infections (mononucleosis, HIV, etc.)
Other infections (Lyme disease, toxoplasmosis, cat-scratch fever, etc.)
Non-Hodgkin's lymphoma and Hodgkin's lymphoma
Squamous cell carcinoma
Vascular metastases (thyroid, renal, melanoma, etc.)
Sarcomas (Kaposi's and angiosarcoma)
Nonneoplastic angiomatoses
Angioimmunoblastic lymphadenopathy
Angiofollicular lymph node hyperplasia (Castleman's disease)
Kimura's lymphadenopathy
Kikuchi-Fujimoto's lymphadenopathy
HIV lymphadenitis, type C
Benign vascular proliferation (distal venous or lymphatic obstruction)
Inflammatory pseudotumor of lymph nodes

Table 36-20
DISEASES ASSOCIATED WITH NODAL CALCIFICATIONS

Infections
Tuberculosis
Healed bacterial nodal necrosis (usually staphylococcal infections in children)
Silicosis (rare)
Unknown etiology
Amyloidosis
Sarcoidosis
Malignancies
Thyroid carcinoma (usually papillary)
Metastatic adenocarcinoma (usually from breast, lung, or colon primaries)
Squamous cell carcinoma (rare)

Copyright © 2003, Mosby, Inc. All rights reserved.

E48IgG or (Fab′)2 mononclonal antibodies.[285–287] These newer approaches illustrate how adjunctive testing may complement more conventional CT and MR imaging to increase the accuracy of imaging in identifying occult primary tumors, recurrent tumors, and nodal metastases.

Last, but by far not least, ultrasound has been used to detect cervical nodal metastasis.[288] However, the major limitations of this modality remain its great dependence on user technique and skill and its difficulty in precisely imaging the deeper spaces of the neck, especially those adjacent to the airway. Its main current use appears to be in imaging superficial masses in children or in imaging and biopsy of some superficial masses in adults. It is not the mainstay modality for survey studies of the neck to detect nodal disease and to evaluate primary tumor extension.

Recently, the application of power Doppler sonography to detect cervical nodal metastasis has shown some promise.[289] These authors showed that when there was no hilar flow, peripheral nodal flow, and a transverse-longitudinal ratio of more than 0.65, the node was likely to

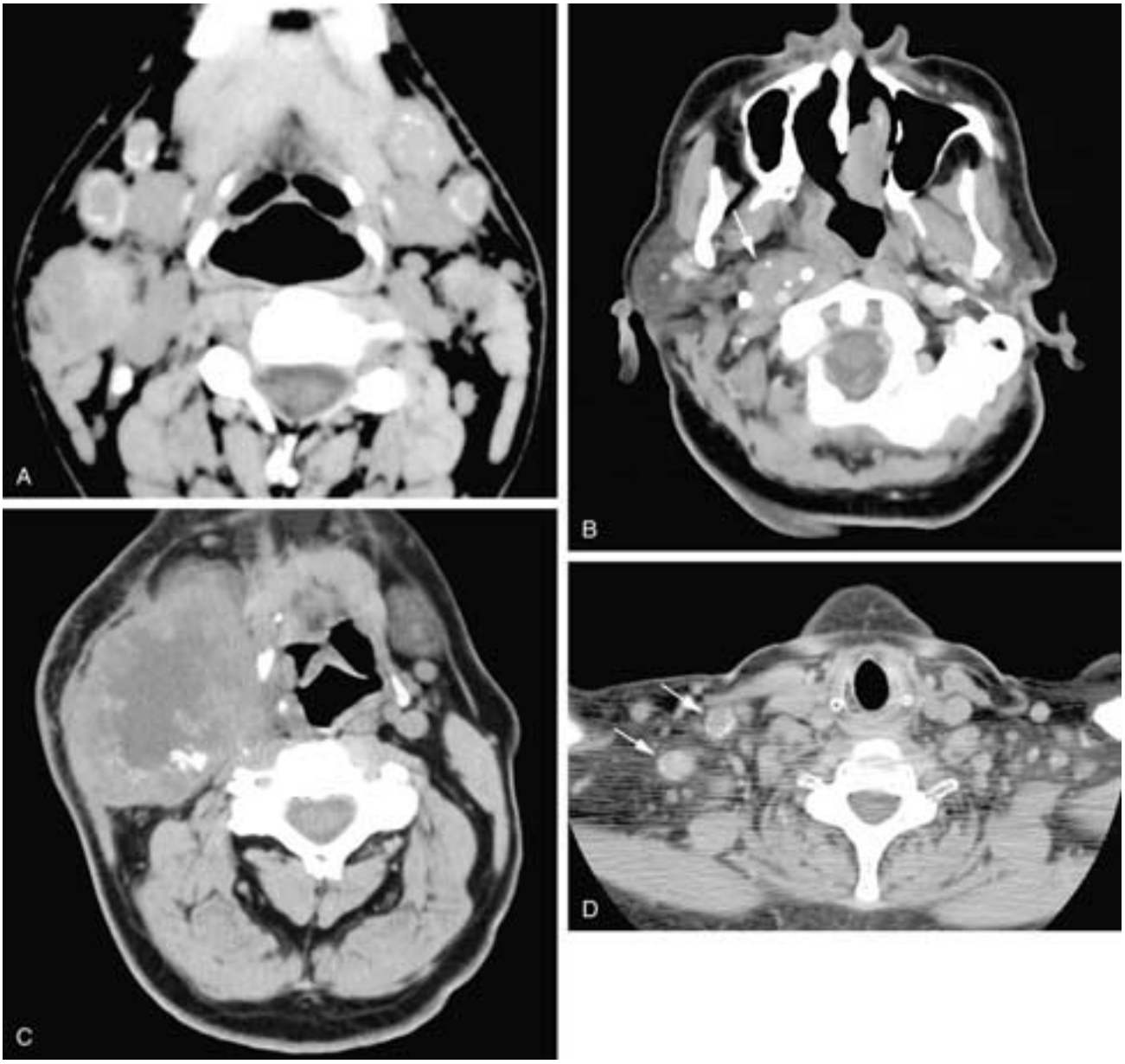

VIEW IMAGE

FIGURE 36-85 Axial contrast-enhanced CT scans. In **A**, there are multiple bilateral level I nodes with punctate calcifications around their peripheries. There is a small, dense calcification in the right level V area that was also a lymph node. This patient had amyloidosis. In **B**, there is a large right retropharyngeal lymph node (*arrow*) with calcifications both within it and at its periphery. This patient had squamous cell carcinoma. In **C**, there is a huge right level I node that is necrotic, with extracapsular tumor spread. In addition, there are calcifications within the periphery of the necrotic region. This patient had squamous cell carcinoma. In **D**, there are two right supraclavicular nodes with calcifications both within the nodal substance and at the nodal periphery (*arrows*). This patient had metastatic adenocarcinoma.

Illustration continued on following

Copyright © 2003, Mosby, Inc. All rights reserved.

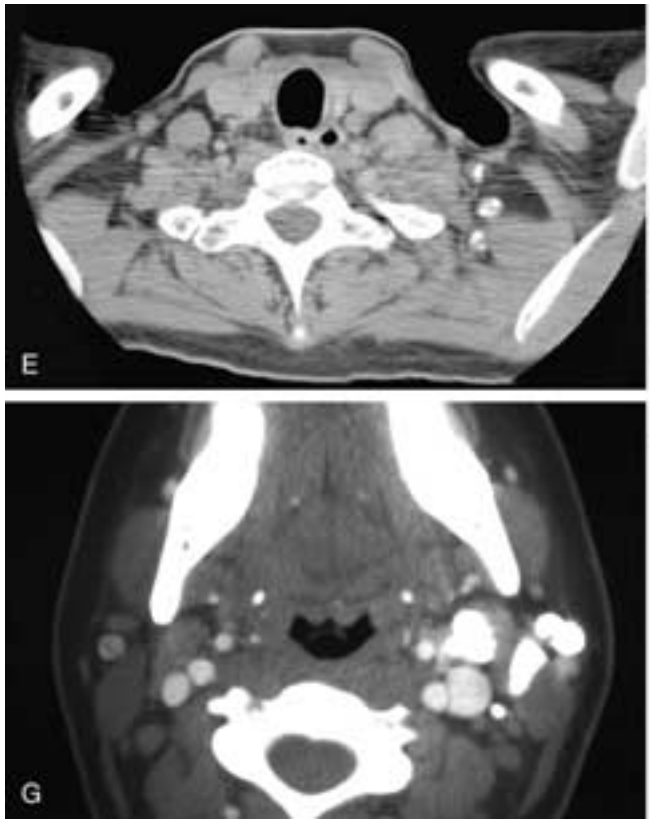

FIGURE 36-85 *Continued.* In **E**, there are three left supraclavicular nodes with calcifications in this patient with metastatic adenocarcinoma. In **F**, there are right level IV, VI, and supraclavicular nodes, and there are left level IV and supraclavicular nodes in this patient with extensive silicosis. In **G**, there are multiple very dense masses (denser than the vessels) in the left level II region. These were calcified/ossified tuberculous lymph nodes.

VIEW IMAGE

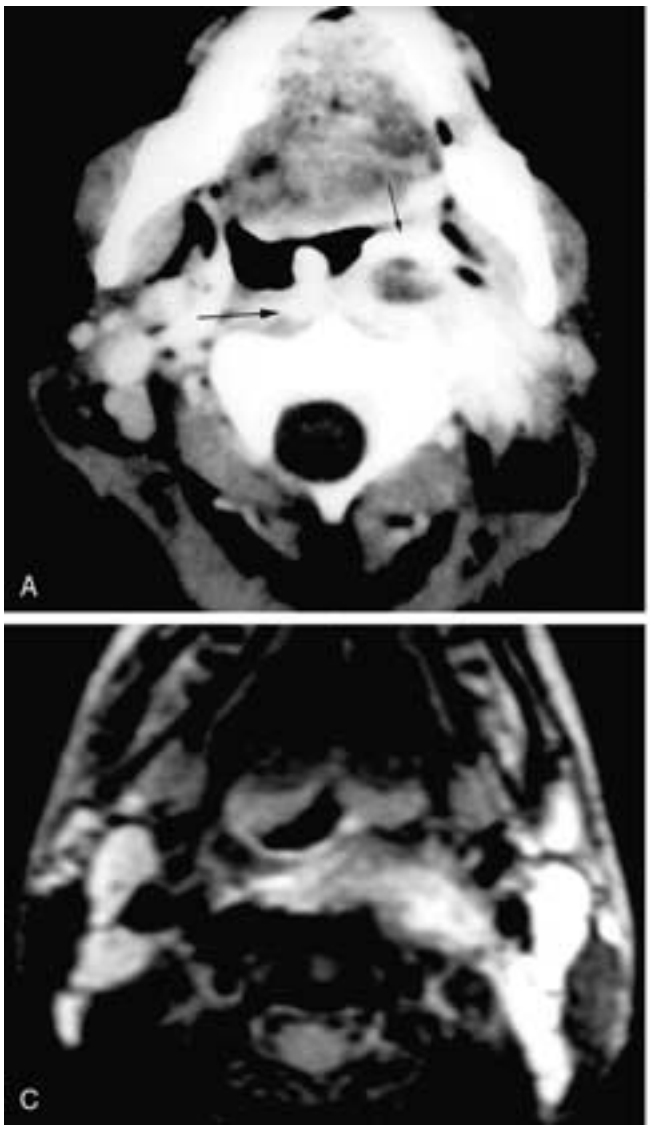

FIGURE 36-86 Axial contrast-enhanced CT scan (**A**) shows a necrotic left retropharyngeal node (*small arrow*) with a thick, enhancing rim. The enhancement extends to fill almost the entire retropharyngeal space (*large arrow*) and extends beyond the space into the left posterior neck. This was an abscessed node with a retropharyngeal abscess. Axial T1-weighted MR images (**B**) of another patient. There is a localized area of high signal intensity that is an abscessed left retropharyngeal node (*arrow*). Note that the remainder of the retropharyngeal space is not involved. In a third patient (**C**), there is a left abscessed retropharyngeal node; however, the remainder of the retropharyngeal space is also affected by an abscess. It is this latter extension that differentiates a retropharyngeal abscess with an abscessed node (**C**) from an abscessed retropharyngeal node alone (**B**).

VIEW IMAGE

Copyright © 2003, Mosby, Inc. All rights reserved.

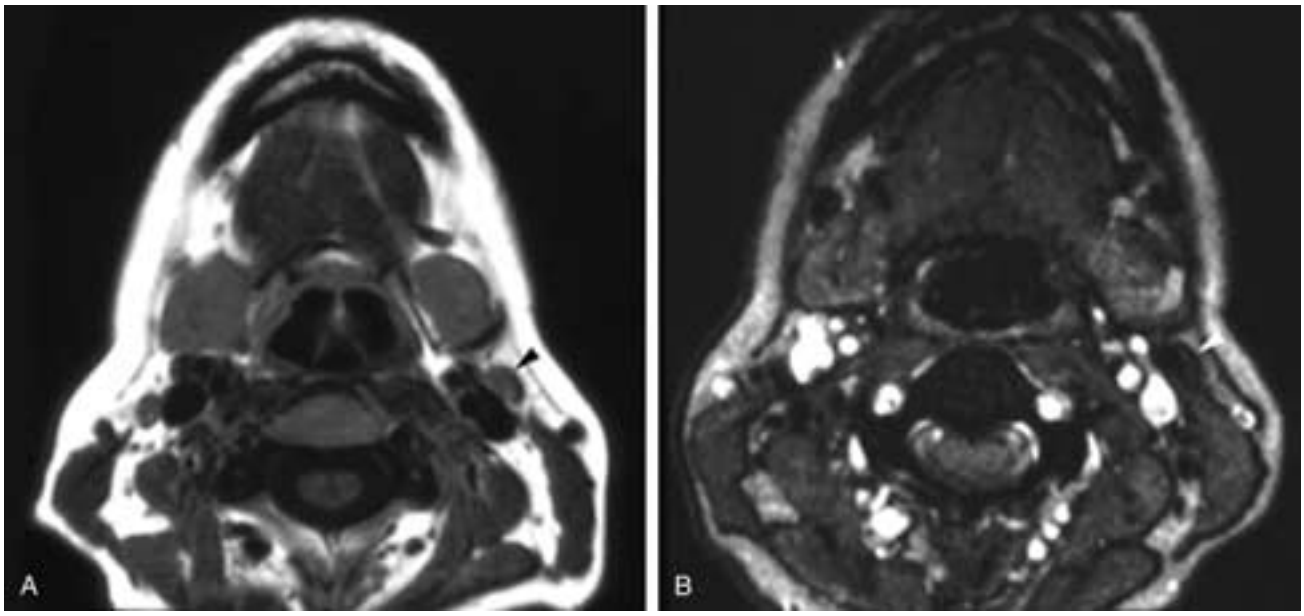

VIEW IMAGE

FIGURE 36-87 Axial T1-weighted MR image (**A**) shows a small left level II homogeneous node (*arrowhead*). Axial gradient echo MR image (**B**) taken 24 hours after **A** and the injection of 2.6 mg/kg Combidex, a superparamagnetic iron oxide chelated dextran. The level II node in **A** now has a very low signal intensity (*arrowhead*) due to the uptake of Combidex. This was a reactive node. (Courtesy of Dr. C. Douglas Phillips.)

be metastatic. This preliminary study suggested that power Doppler may be an important tool in diagnosing superficial cervical nodal metastasis.

REFERENCES

1. Mancuso A, Maceri D, Rice D, Hanafee W. CT of cervical lymph node cancer. AJR 1981;136:381–385.
2. Mancuso A, Harnsberger H, Muraki A, Stevens M. Computed tomography of cervical and retropharyngeal lymph nodes: normal anatomy, variants of normal, and application in staging head and neck cancer. Part II. Radiology 1983;148:715–723.
3. Friedman M, Shelton V, Mafee M, et al. Metastatic neck disease: evaluation by computed tomography. Arch Otolaryngol Head Neck Surg 1984;110:443–447.
4. Stevens M, Harnsberger R, Mancuso A, et al. Computed tomography of cervical lymph nodes: staging and management of head and neck cancer. Arch Otolaryngol Head Neck Surg 1985;111:735–739.
5. Feinmesser R, Freeman J, Nojek A, Birt B. Metastatic neck disease: a clinical/radiographic/pathologic correlative study. Arch Otolaryngol Head Neck Surg 1987;113:1307–1310.
6. Close L, Merkel M, Vuitch M, et al. Computed tomographic evaluation of regional lymph node involvement in cancer of the oral cavity and oropharynx. Head Neck 1989;11:309-317.
7. van den Brekel M, Stel H, Castelijns J, et al. Cervical lymph node metastasis: assessment of radiologic criteria. Radiology 1990;177:379–384.
8. Som P. Detection of metastasis in cervical lymph nodes: CT and MR criteria and differential diagnosis. AJR 1992;158:961–969.
9. Shah J, Medina J, Shaha A, et al. Cervical lymph node metastasis. Curr Probl Surg 1993;30:1–335.
10. Jones A, Roland N, Field J, Phillips D. The level of cervical lymph node metastases: their prognostic relevance and relationship with head and neck squamous carcinoma primary sites. Clin Otolaryngol 1994;19:63–69.
11. Don D, Anzai Y, Lufkin R, et al. Evaluation of cervical lymph node metastases in squamous cell carcinoma of the head and neck. Laryngoscope 1995;105:669–674.
12. Kaji A, Mohuchy T, Swartz J. Imaging of cervical lymphadenopathy. Semin Ultrsound CT MR 1997;18:220–249.
13. Atula T, Varpula M, Kurki T, et al. Assessment of cervical lymph node status in head and neck cancer patients: palpation, computed tomography and low field magnetic resonance imaging compared with ultrasound-guided fine needle aspiration cytology. Eur J Radiol 1997;25:152–161.
14. Maremonti P, Califano L, Longo F, et al. Detection of laterocervical metastases from oral cancer. J Craniomaxillofac Surg 1997;25: 149–152.
15. Atula T, Silvoniemi P, Kurki T, et al. The evaluation and treatment of the neck in carcinoma of the oral cavity. Acta Otolaryngol Suppl (Stockh) 1997;529:223–225.
16. Hall J. The functional anatomy of lymph nodes. In: Stansfeld A, d'Ardenne A, eds. Lymph Node Biopsy Interpretation. Edinburgh and London: Churchill-Livingstone, 1992;3–28.
17. Kuisk H. Development, structure, and function of the lymphatic system. In: Kuisk H, ed. Technique of Lymphography and Principles of Interpretation. St. Louis: Green, 1971;5–14.
18. Battezzati M, Donini I. Embryology of the lymphatic system. In: Battezzati M, Donini I, eds. The Lymphatic System. Padua: Piccin Medical Books and Halsted Press Book, Wiley, 1972;27–34.
19. Ioachim H. Lymph Node Pathology. 2nd ed. Philadelphia: JB Lippincott, 1994.
20. Duijvestijn A, Kerkhove M, Bargatze R, Butcher E. Lymphoid tissue and inflammation specific endothelial cell differentiation defined by monoclonal antibodies. J Immunol 1987;138:713–719.
21. Ager A, Humphries M. Use of synthetic peptides to probe lymphocyte high endothelial cell interactions. Lymphocytes recognize a ligand on the endothelial surface which contains the CS1 adhesion motif. Int Immunol 1990;2:921–928.
22. Berg E, Robinson M, Warnock R, Butcher E. The human peripheral lymph node vascular addressin is a ligand for LECAM-1, the peripheral lymph node homing receptor. J Cell Biol 1991;114: 343–349.
23. Weston S, Parish C. Calcein: a novel marker for lymphocytes which enter lymph nodes. Cytometry 1992;13:739–749.
24. Anderson A, Shaw S. T cell adhesion to endothelium: the FRC conduit system and other anatomic and molecular features which facilitate the adhesion cascade in lymph node. Semin Immunol 1993;5:271–282.
25. Michie S, Streeter P, Bolt P, et al. The human peripheral lymph node vascular addressin. An inducible endothelial antigen involved in lymphocyte homing. Am J Pathol 1993;143:1688–1698.

Copyright © 2003, Mosby, Inc. All rights reserved.

26. Sawada M, Takada A, Ohwaki I, et al. Specific expression of a complex sialy Lewis X antigen on high endothelial venules of human lymph nodes: possible candidate for L-selectin ligand. Biochem Biophys Res Commun 1993;193:337–347.
27. Hemmerich S, Butcher E, Rosen S. Sulfation-dependent recognition of high endothelial venules (HEV)—ligands by L-selectin and MECA79, an adhesion blocking monoclonal antibody. J Exp Med 1994;180:2219–2226.
28. Hemmerich S, Bertozzi C, Leffler H, Rosen S. Identification of the sulfated monosaccharides of GlyCAM-1, an endothelial derived ligand for L-selectin. Biochemistry 1994;33:4820–4829.
29. Crommie D, Rosen S. Biosynthesis of GlyCAM-1, a mucin-like ligand for L-selectin. J Biol Chem 1995;270:22614–22624.
30. Porte H, Triboulet J, Kotelevets L, et al. Overexpression of stromelysin-3, BM-40/SPARC, and MET genes in human esophageal carcinoma: implications for prognosis. Clin Cancer Res 1998;4: 1375–1382.
31. Johansson N, Vaalamo M, Grenman S, et al. M collagenase-3 (MMP-13) is expressed by tumor cells in invasive vulvar SCCs. Am J Pathol 1999;154:469–480.
32. Ivanov K, Som P, Zhang D, et al. The Back Door: venous metastasis into cervical lymph nodes as an alternative metastatic pathway for squamous carcinoma. Mod Pathol 1999;12:683–688.
33. Moller P, Eichelmann A, Leithauser F, et al. Venular endothelial binding molecules CD44 and LECAM-1 in normal and malignant B-cell populations. A comparative study. Virchows Arch A Pathol Anat Histopathol 1992;421:305–313.
34. Dall P, Heider K, Hekele A, et al. Surface protein expression and messenger RNA-splicing analysis of CD44 in uterine cervical cancer and normal cervical epithelium. Cancer Res 1994;54:3337–3341.
35. Sakumoto M, Tsukuda M, Mochimatsu I, et al. Secretion of a fibronectin-like substance from head and neck carcinomas. J Otorhinolaryngol Relat Spec 1994;56:213–216.
36. Harada T, Shinohara M, Nakamura S, Oka M. An immunochemical study of the extracellular matrix in oral squamous cell carcinoma and its association with invasive and metastatic potential. Virchows Arch 1994;424:257–266.
37. Wenzel C, Scher R, Richtsmeier W. Adhesion of head and neck squamous cell carcinoma to endothelial cells. The missing links. Arch Otolaryngol Head Neck Surg 1995;121:1279–1286.
38. Tozeren A, Kleinman H, Grant D, et al. E-selectin mediated dynamic interactions of breast and colon cancer cells with endothelial cell monolayers. Int J Cancer 1995;60:426–431.
39. Prieto V, Reed J, McNutt N, et al. Differential expression of CD44 in malignant cutaneous epithelial neoplasms. Am J Dermatopathol 1995;17:447–451.
40. Kainz C, Kohlberger P, Sliutz G, et al. Splice variants of CD44 in human cervical cancer stage IB to IIB. Gynecol Oncol 1995;57: 383–387.
41. Tempfer C, Gitsch G, Hanzal E, et al. Expression of the adhesion molecule CD44v3 is a prognostic factor in vulvar carcinoma. Anticancer Res 1996;16:2029–2031.
42. Mende CH, Seiter S, Born A, et al. Expression of CD44 splice variants in squamous epithelia and squamous cell carcinomas of the head and neck. Pathology 1996;179:66–73.
43. Kunishi M, Kayada Y, Tsumura M, et al. Expression of CD44 variant 6 and its metastatic potential in squamous cell carcinoma of the oral cavity. Gan To Kagaku Ryoho 1996;23:1045–1048.
44. Tempfer C, Gitsch G, Haeusler G, et al. Prognostic value of immunohistochemically detected CD44 expression in patients with carcinoma of the vulva. Cancer 1996;78:273–277.
45. Penno M, August J, Baylin S, et al. Expression of CD44 in human lung tumors. Cancer Res 1994;54:1381–1387.
46. Fox S, Fawcett J, Jackson D, et al. Normal human tissues, in addition to some tumors express multiple different CD44 isoforms. Cancer Res 1994;54:4539–4546.
47. Spafford M, Koeppe J, Pan Z, et al. Correlation of tumor markers p53, bcl-2, CD34, CD44H, CD44v6, and Ki-67 with survival and metastasis in laryngeal SCC. Arch Otolaryngol Head Neck Surg 1996;122:627–632.
48. Cummings B. Radiation therapy and the treatment of the cervical lymph nodes. In: Cummings C, Fredrickson J, Harker L, et al, eds. Otolaryngology Head and Neck Surgery. Vol 2. 2nd ed. St. Louis: Mosby Year Book, 1993;1626–1648.
49. Johnson J. A surgeon looks at cervical lymph nodes. Radiology 1990;175:607–610.
50. Spiro R. The management of neck nodes in head and neck cancer: a surgeon's view. Bull NY Acad Med 1985;61:629–637.
51. Batsakis J, ed. Tumor of the Head and Neck: Clinical and Pathological Considerations. 2nd ed. Baltimore: Williams & Wilkins, 1979;144–176.
52. Batsakis J, ed. Tumor of the Head and Neck: Clinical and Pathological Considerations. 2nd ed. Baltimore: Williams & Wilkins, 1979; 240–250.
53. Collins S. Controversies in management of cancer of the neck. In: Thawley S, Panje W, eds. Comprehensive Management of Head and Neck Tumors. Philadelphia: WB Saunders, 1987;1386–1443.
54. van den Brekel M, Castelijns J, Snow G. Diagnostic evaluation of the neck. Otolaryngol Clin North Am 1998;31:601–620.
55. Kowalski L, Medina J. Nodal metastases: predictive factors. Otolaryngol Clin North Am 1998;31:621–637.
56. Weiss M, Harrison L, Isaacs R. Use of decision analysis in planning a management strategy for the stage N0 neck. Arch Otolaryngol Head Neck Surg 1994;120:699–702.
57. Woolgar J, Scott J. Prediction of cervical lymph node metastasis in squamous cell carcinoma of the tongue/floor of mouth. Head Neck 1995;17:463–472.
58. Mikami Y, Tsukuda M, Ito K, et al. Peritumoral angiogenesis in carcinomas of the head and neck. Auris Nasus Larynx 1996;23: 57–62.
59. Olsen K, Caruso M, Foote R, et al. Primary head and neck cancer. Histopathologic predictors of recurrence after neck dissection in patients with lymph node involvement. Arch Otolaryngol Head Neck Surg 1994;120:1370–1374.
60. Som P. Lymph nodes of the neck. Radiology 1987;165:593–600.
61. Rouviere H. Lymphatic System of the Head and Neck. Ann Arbor, Mich: Edwards Brothers, 1938;5–28.
62. Poirer P, Charpy A. Traite d'anatomie humaine. 2nd ed. Paris: 1909. Vol 2me tome, 4me fascicule:
63. Trotter H. The surgical anatomy of the lymphatics of the head and neck. Ann Otol Rhinol Laryngol 1930;39:384–397.
64. Shah J, Strong E, Spiro R, Vikram B. Surgical Grand Rounds: neck dissection: current status and future possibilities. Clin Bull 1981;11:25–33.
65. Som P. An approach to tumors of the head and neck: the role of computed tomography in the staging and follow-up of patients. Margulis A, Gooding C, eds. Diagnostic Radiology. San Francisco: University of California Press, 1985;347–352.
66. Som P, Norton K, Shugar J, et al. Metastatic hypernephroma to the head and neck. AJNR 1987;8:1103–1106.
67. Medina J. A rational classification of neck dissections. Otolaryngol Head Neck Surg 1989;100:169–176.
68. Beahrs O, Henson D, Hutter R, Meyers M. Manual for Staging Cancer. 3rd ed. Philadelphia: JB Lippincott, 1988.
69. Robbins K, ed. Pocket Guide to Neck Dissection and TNM Staging of Head and Neck Cancer. Alexandria, Va: American Academy of Otolaryngology-Head and Neck Surgery Foundation, 1991.
70. Fleming I, Cooper J, Henson D, et al. American Joint Committee on Cancer Staging Manual. 5th ed. Philadelphia: Lippincott-Raven, 1997.
71. van den Brekel M. Assessment of Lymph Node Metastases in the Neck: A Radiological and Histopathological Study. Utrecht: University of Amsterdam, 1992; 1–152.
72. Curtin H, Ishwaran H, Mancuso A, et al. Comparison of CT and MR imaging in staging of neck metastases. Radiology 1998;207:123–130.
73. Robbins K. Classification of neck dissection: current concepts and future considerations. Otolaryngol Clin North Am 1998;31:639–655.
74. Som P, Curtin H, Mancuso A. An imaging-based classification for the cervical nodes designed as an adjunct to recent clinically based nodal classifications. Arch Otolaryngol Head Neck Surg 1999;125: 388–396.
75. Last R. Lymph drainage of the head and neck. In: Last R, ed. Anatomy: Regional and Applied. 6th ed. Edinburgh and London: Churchill-Livingstone, 1978;443–444.
76. Surgical grand rounds: Neck dissection: Current status and future possibilites. Clin Bull 1981;11:25–33.
77. Gallo O, Boddi V, Bottai G, et al. Prognostic significance of clinically false positive cervical lymph nodes in patients with laryngeal carcinoma. Cancer 1995;75:1077–1083.
78. Lee A, Weissleder R, Brady T, Wittenberg L. Lymph nodes: microstructural anatomy at MR imaging. Radiology 1991;178: 519–522.

Copyright © 2003, Mosby, Inc. All rights reserved.

79. van den Brekel M, Stel H, van der Valk P, et al. Micrometastases from squamous cell carcinoma in neck dissection specimens. Eur Arch Otorhinolaryngol 1992;249:349–353.
80. Schroer K, Franssila K. Atypical hyperplasia of lymph nodes. A follow-up study. Cancer 1979;44:1155–1163.
81. Lindberg R. Distribution of cervical lymph node metastases from squamous cell carcinoma of the upper respiratory and digestive tracts. Cancer 1972;29:1446–1449.
82. Garten A, Mendelson D, Halton K. CT manifestations of mononucleosis. Clin Imaging 1992;16:114–116.
83. Madden B, Werhaven J, Wessel H, et al. Infectious mononucleosis with airway obstruction and multiple cranial nerve palsies. Otolaryngol Head Neck Surg 1991;104:529–532.
84. Jones J, Shurin S, Abramowsky C, et al. T-cell lymphomas containing EBV DNA in patients with chronic EBV infection. N Engl J Med 1988;318:733–741.
85. Purtillo D, Sakamoto K, Saemundsen A, et al. Documentation of EBV infection in immunodeficient patients with life-threatening lymphoproliferative diseases by clinical, virological, and immunopathological studies. Cancer Res 1981;41:4226–4236.
86. Purtillo D. Immunodeficiency predisposing to EBV-induced lymphoproliferative disease: The X-linked lymphoproliferative syndrome as a model. Adv Cancer Res 1981;34:279–312.
87. Epstein M, Achong B. Pathogenesis of infectious mononucleosis. Lancet 1977;2:1270–1273.
88. Smith P, Miyake Y, Rook A, et al. CMV infection depresses monocyte production of interleukin-1. In: The physiologic, metabolic, and immunologic actions of interleukin-1; Alan R Liss, 1985;319–326.
89. Schrier R, Oldstone MBA, Rice GPA. Suppression of natural killer cell activity and T cell proliferation by fresh isolates of human cytomegalovirus. J Infect Dis 1986;153:1084–1091.
90. Davis M, Kenney S, Kamine J, et al. Immediate-early gene region of human CMV transactivates the promoter of HIV. Proc Natl Acad Sci USA 1987;84:8642–8646.
91. Skolnick P, Kosloff B, Hirsch M. Bidirectional interactions between HIV type 1 and CMV. J Infect Dis 1988;157:508–513.
92. Jeffries D. The spectrum of CMV infection in AIDS. J Antimicrob Chemother 1989;23:1–10.
93. Klatt E, Shibata D. CMV infection in AIDS. Arch Pathol Lab Med 1988;112:540–544.
94. Lalwani A, Snyderman N. Pharyngeal ulceration in AIDS patients secondary to CMV infections. Ann Otol Rhinol Laryngol 1991;100:484–487.
95. Kanas R, Jensen J, Abrams A, et al. Oral mucosal CMV as a manifestation of AIDS. Oral Surg Oral Med Oral Pathol 1987;64:183–189.
96. Langford A, Kunze R, Timm H, et al. CMV associated oral ulcerations in HIV-infected patients. L Oral Pathol Med 1989;19:71–76.
97. Redleaf M, Bauer C, Robinson R. Fine-needle detection of CMV parotitis in a patient with AIDS. Arch Otolaryngol Head Neck Surg 1994;120:414–416.
98. Imoto E, Stein R, Shellito J, et al. Central airway obstruction due to CMV-induced necrotizing tracheitis in a patient with AIDS. Am Rev Respir Dis 1990;142:884–886.
99. Marelli R, Biddinger P, Gluckman J. Cytomegalovirus infection of the larynx in the acquired immunodeficiency syndrome. Otolaryngol Head Neck Surg 1992;106:296–301.
100. Small P, McPhaul L, Sooy C, et al. CMV infection of the laryngeal nerve presenting as hoarseness in AIDS patients. Am J Med 1989;86:108–110.
101. Siegal R, Browning D, Schwartz D, Hudgins P. CMV laryngitis and probable malignant lymphoma of the larynx in a patient with AIDS. Arch Pathol Lab Med 1992;116:539–541.
102. Roizman B, Sear A. Herpes simplex virus and their replication. In: Fields B, Knipe D, et al, eds. Virology. 2nd ed. New York: Raven Press, 1990; Chapter 65.
103. Rice S, Long M, Lam V. RNA polymerase II is aberrantly phosphorylated and localized to viral replication compartments following Herpes Simplex virus infection. J Virol 1994;68:988–1001.
104. Kemp L, Latchman D. Induction and repression of cellular gene transcription during Herpes Simplex virus infection are mediated by different viral IE gene products. Eur J Biochem 1988;174:443–449.
105. Galloway D, Fenoglio C, Shevchuk M, et al. Detection of Herpes Simplex virus RNA in human sensory ganglia. Virology 1979;95:265–268.
106. Rinaldo C, Torpey D. Cell-mediated immunity and immunosuppression in Herpes Simplex virus infection. Immunodeficiency 1993;5:33–90.
107. Lopez C, Fitzgerald-Bocarsly P. Natural killing of Herpes Simplex virus–infected fibroblasts. J Infect Dis 1986;154:1043–1044.
108. Bonneau R, Sheridan J, Feng N, et al. Stress-induced suppression of Herpes Simplex virus–specific cytotoxic T lymphocyte and natural killer cell activity and enhancement of acute pathogenesis following local Herpes Simplex virus infection. Brain Behav Immun 1991;5:170–192.
109. Kuo Y, Lin C. Recurrent Herpes Simplex virus type I infection precipitated by the impaired production of interleukin-2, alpha interferon and cell-mediated cytotoxicity. J Med Virol 1990;31:183–189.
110. Eversole L. Viral infections of the head and neck among HIV-seropositive patients. Oral Surg Oral Med Oral Pathol 1992;73:155–163.
111. Higgins C, Schofield J, Tatnall F, et al. Natural history, management and complications of herpes labialis. J Med Virol Suppl 1993;1:22–26.
112. Epstein J, Ambinder R, Kuhajda F, et al. Localized Herpes Simplex lymphadenitis. Am J Clin Pathol 1986;86:444–448.
113. Gaffey M, Ben Ezra J, Weiss L. Herpes Simplex lymphadenitis. Am J Clin Pathol 1991;95:709–714.
114. Howat A, Campbell A, Stewart D. Generalized lymphadenopathy due to Herpes Simplex virus-I. Histopathology 1991;19:563–564.
115. Wat P, Strickler J, Myers J, et al. Herpes Simplex virus infection causing acute necrotizing tonsillitis. Mayo Clin Proc 1994;69:269–271.
116. Shugar J, Som P, Jacobson A, et al. Multicentric parotid cysts and cervical adenopathy in AIDS patients. A newly recognized entity: CT and MR manifestations. Laryngoscope 1988;98:772–775.
117. Cose S, Jones C, Wallace M, et al. Antigen-specific CD8+ T cell subset distribution in lymph nodes draining the site of herpes simplex virus infection. Eur J Immunol 1997;27:2310–2316.
118. Blattner R. Viral infections and those presumed to be caused by viruses. In: Vaughan I, McKay R, Nelson W, eds. Nelson Textbook of Pediatrics. 10th ed. Philadelphia: WB Saunders, 1975;653–662.
119. Siebert C. Smallpox is dead. Long live smallpox. New York Times 1994;section 6:31–55.
120. The Measles Emergency. An Epidemic Alert. New York: New York City Department of Health, 1991;10:1.
121. Akang E, Ekweozor C, Pindiga H, et al. Childhood infections in Nigeria: an autopsy study. J Trop Med Hyg 1993;96:231–236.
122. Monafo W, Haslam D, Roberts R, et al. Disseminated measles infection after vaccination in a child with congenital immunodeficiency. J Pediatr 1994;124:273–276.
123. Dalgleisheish A, Beverly P, Clapham P, et al. The CD4 (T4) antigen is an essential component of the receptor for the AIDS retrovirus. Nature 1984;312:763–767.
124. Pantaleo G, Graziosi C, Butini L, et al. Lymphoid organs function as major reservoirs for HIV. Proc Natl Acad Sci USA 1991;88:9838–9842.
125. Silverman S, Migliorati C, Lozarda-Nur F, et al. Oral findings in people with or at high risk for AIDS: a study of 375 homosexual males. Journal of the American Dental Association 1986;112:187–192.
126. Burns B, Wood G, Dorfman R. The varied histopathology of lymphadenopathy in the homosexual male. Am J Surg Pathol 1985;9:287–297.
127. Haught W, Steinbach J, Zander D, Wingo C. Case report: bacillary angiomatosis with massive visceral lymphadenopathy. Am J Med Sci 1993;306:236–240.
128. Wong T, Kruskal J, Kane R, Trey G. Cat-scratch disease simulating lymphoma. J Comput Assist Tomogr 1996;20:165–166.
129. Sceaton N, Ravenel J, Lehner P, et al. Lemierre syndrome: forgotten but not extinct—report of four cases. Radiology 1999;213:369–374.
130. Koehler J, Quinn F, Berger T, et al. Isolation of *Rochalimaea* species from cutaneous and osseous lesions of bacillary angiomatosis. N Engl J Med 1992;327:1625–1631.

Copyright © 2003, Mosby, Inc. All rights reserved.

131. Deibert A, Bruyer M. Untreated syphilis in the male Negro. III. Evidence of cardiovascular abnormalities and other forms of morbidity. Vener Dis Inform 1946;27:301–317.
132. Duffy J. Lyme disease: a clinical review. Minn Med 1991; 74:21–26.
133. Gerber MA, Shapiro ED. Diagnosis of Lyme disease in children. J Neurosci Nurs 1991;23:211–217.
134. Reede D, Bergeron R. Cervical tuberculous adenitis: CT manifestations. Radiology 1985;154:701–704.
135. Moon W, Han M, Chang K, et al. CT and MR imaging of head and neck tuberculosis. RadioGraphics 1997;17:391–402.
136. Alvarez S, McCabe W. Extrapulmonary tuberculosis revisited: a review of experience at Boston City and other hospitals. Medicine 1984;63:25–55.
137. Chopra R, Kerner M, Calcaterra T. Primary nasopharyngeal tuberculosis: a case report and review of this rare entity. Otolaryngol Head Neck Surg 1994;111:820–823.
138. Sehgal V, Wagh S. Cutaneous tuberculosis. Current concepts. Int J Dermatol 1990;29:237–252.
139. Saitz E. Cervical lymphadenitis caused by atypical mycobacteria. Pediatr Clin North Am 1981;28:823–839.
140. Stewart M, Starke J, Coker N. Nontuberculous mycobacterial infections of the head and neck. Arch Otolaryngol Head Neck Surg 1994;120:873–876.
141. Mastro T, Redd S, Breiman R. Imported leprosy in the United States, 1978 through 1988: an epidemic without secondary transmission. Am J Pub Health 1992;82:1127–1130.
142. Fine P. Leprosy: the epidemiology of a slow bacterium. Epidemiol Rev 1982;4:162–188.
143. Ridley D, Jopling W. Classification of leprosy according to immunity—a five group system. Int J Leprosy 1965;34:255–273.
144. Yoshie Y. Clinical and histopathological studies on leprosy of the larynx. Int J Leprosy 1955;24:352–353.
145. Soni N. Leprosy of the larynx. J Laryngol Otol 1992;106: 518–520.
146. Rivron R, Evans E. Enlarged cervical lymph node due to African histoplasmosis. J Laryngol Otol 1988;102:945–946.
147. Darling S. A protozoon general infection producing pseudotubercles in the lungs and focal necrosis in the liver, spleen and lymph nodes. JAMA 1906;46:1283–1285.
148. Feare C, ed. The Starling. Oxford: Oxford University Press, 1984.
149. Chapman F. Handbook of Birds in Eastern North America. New York: Appleton, 1895.
150. Shakespeare W. The First Part of Henry IV; act I, Scene 3: line 224.
151. Furcolow M, Tosh F, Larsh H, et al. The emerging pattern of urban histoplasmosis. Studies on an epidemic in Mexico, Missouri. N Engl J Med 1961;264:1226–1230.
152. Parrott T, Taylor G, Poston M, et al. An epidemic of histoplasmosis in Warrenton, North Carolina. South Med J 1955;48:1147–1150.
153. Wheat L, Conolly-Stringfield P, Baker R, et al. Disseminated histoplasmosis in AIDS: clinical findings, diagnosis and treatment, and review of the literature. Medicine 1990;69:361–374.
154. Mello KA, Wheat LJ, Lis R, et al. Ketoconazole-responsive tonsillar infection due to *Histoplasma capsulatum* in an HIV-1-seropositive individual (letter). AIDS 1991;5:908–910.
155. Oda D, McDougal L, Fitsche T, et al. Oral histoplasmosis as a presenting disease in AIDS. Oral Surg Oral Med Oral Pathol 1990;70:631–636.
156. Drutz D, Catanzaro A. State of the art: coccidioidomycosis. Part I. Am Rev Respir Dis 1978;117:559–585.
157. Werner S, Pappagianis D, Heindl I, et al. An epidemic of coccidioidomycosis among archeology students in northern California. N Engl J Med 1972;286:507–512.
158. Pappagianis D. Epidemiology of coccidioidomycosis. Curr Top Med Mycol 1988;2:199–238.
159. Eckmann B, Schaeffer G, Huppert M. Bedside interhuman transmission of coccidioidomycosis via growth on fomites. An epidemic involving six persons. Am Rev Respir Dis 1964;89: 175–185.
160. Van Bergen W, Fleury F, Cheatle E. Fatal maternal disseminated coccidioidomycosis in a nonendemic area. Am J Obstet Gynecol 1976;124:661–663.
161. Boyle J, Coulthard S, Mandel R. Laryngeal involvement in disseminated coccidioidomycosis. Arch Otolaryngol Head Neck Surg 1991;117:433–438.
162. Fish D, Ampel N, Galgiani J, et al. Coccidioidomycosis during HIV infection. A review of 77 patients. Medicine 1990;69:384–390.
163. Prichard J, Sorotzkin R, James R. Cutaneous manifestations of disseminated coccidioidomycosis in AIDS. Cutis 1987;39:203–205.
164. Edman J, Kovacs J, Masur H, et al. Ribosomal RNA sequence shows *Pneumocystis carinii* to be a member of the Fungi. Nature 1988;334:519–522.
165. Henneberry J, Smith R, Hruban R. *Pneumocystis carinii* infection of the external auditory canal. Arch Otolaryngol Head Neck Surg 1993;119:466–469.
166. Sandler E, Sandler J, Le Boit P, et al. *Pneumocystis carinii* otitis media in AIDS: a case report and review of the literature regarding extrapulmonary pneumocystosis. Otolaryngol Head Neck Surg 1990;103:817–821.
167. Wasserman L, Haghighi P. Otic and ophthalmic pneumocystosis in AIDS. Arch Pathol Lab Med 1992;116:500–503.
168. Biavanti M, Khan A, Kessler C. Disseminated *Pneumocystis carinii* infection involving the neck and nasopharynx. Otolaryngol Head Neck Surg 1993;109:773–776.
169. Frenkel J. Pursuing toxoplasma. J Infect Dis 1970;122:553–559.
170. Hutchinson W, Dunachie J. The life cycle of the coccidian parasite, *Toxoplasma gondii*, in the domestic cat. Trans R Soc Trop Med Hyg 1971;65:380–399.
171. Dubey J, Miller N, Frenkel J. Characterization of the new fecal form of *Toxoplasma gondii.* J Parasitol 1970;56:447–456.
172. Frenkel J, Dubey J. Toxoplasmosis and its prevention in cats and man. J Infect Dis 1972;126:664–673.
173. Desmonts G, Couvrier J, Alison F, et al. Etude epidemiologique sur la Toxoplasmose: de l'influence de la cuisson des viandes de boucherie sur la frequence de l'infection humaine. Rev Franc Etudes Clin et Biol 1965;10:952–958.
174. Hohlfeld P, Daffos F, Costa J, et al. Prenatal diagnosis of congenital toxoplasmosis with a PCR test on amniotic fluid. N Engl J Med 1994;331:695–699.
175. Smith J, Hadgis C, Hasselt Av, Metreweli C. CT of Kimura disease. AJNR 1989;10 (Suppl):34–36.
176. Naidu R, Urken M, Som P, et al. Extranodal head and neck sinus histiocytosis with massive lymphadenopathy. Otolaryngol Head Neck Surg 1990;102:764–767.
177. Locksmith J, Brannon M. Diffuse CT contrast enhancement of cervical lymph nodes in angioimmunoblastic lymphadenopathy. J Comput Assist Tomogr 1991;15:703–704.
178. Na D, Chung T, Byun H, et al. Kikuchi disease: CT and MR findings. AJNR 1997;18:1729–1732.
179. Nakagawa C, Sakaguchi Y, Nakajima T, et al. A case of eosinophilic myocarditis complicated by Kimura's disease (eosinophilic hyperplastic lymphogranuloma) and erythroderma. Jpn Circ J 1999;63: 141–144.
180. Romao J, Saldanha L, Ianez L, Sabbaga E. Recurrence of focal segmental glomerulosclerosis associated with Kimura's disease after kidney transplantation. Intern Med 1998;37:1064–1067.
181. Rosai J, Dorfman R. Sinus histiocytosis with massive lymphadenopathy. A newly recognized benign clinicopathological entity. Arch Pathol 1969;87:63–70.
182. Menasce L, Banerjee S, Edmondson D, Harris M. Histiocytic necrotizing lymphadenitis (Kikuchi-Fujimoto disease): continuing diagnostic difficulties. Histopathology 1998;33:248–254.
183. Siltzbach L. Editorial: Current thoughts on the epidemiology and etiology of sarcoidosis. Am J Med 1965;39:361–368.
184. Siltzbach L. Sarcoidosis: clinical features and management. Med Clin North Am 1967;51:483–502.
185. Mitchell D, Rees R, Goswami K. Transmissible agents from human sarcoid and Crohn's disease tissues. Lancet 1976;2:761–765.
186. Grizzanti J, Rosenstreich D. Effect of inoculation of sarcoid tissue into thymic (nude) mice. Sarcoidosis 1988;5:136–141.
187. Schaumann J, Hallberg V. Koch's bacilli manifested in the tissue of lymphogranulomatosis benigna (Schaumann) by using Hallberg's staining method. Acta Med Scand 1941;152:499–501.
188. Moscovic E. Sarcoidosis and mycobacterial L-forms. A critical reappraisal of pleomorphic chromogenic bodes (Hamazaki corpuscles) in lymph nodes. Pathol Annu 1978;2:69–164.
189. Mankiewicz E. On the etiology of sarcoidosis. Can Med Assoc J 1963;88:593–595.
190. Mankiewicz E, van Walbeek M. Mycobacteriophages. Their role in tuberculosis and sarcoidosis. Arch Environ Health 1962;5: 122–128.

Copyright © 2003, Mosby, Inc. All rights reserved.

191. Chapman J, Baum J, Clark J, et al. Mycobacterial antibodies in immunoglobulins IgA and IgM of patients with sarcoidosis. Am Rev Respir Dis 1966;95:612–617.
192. Reid J, Chiodini R. Serologic reactivity against *Mycobacterium paratuberculosis* antigens in patients with sarcoidosis. Sarcoidosis 1993;10:32–35.
193. Rohrbach M, DeRemee R. Pulmonary sarcoidosis and serum angiotensin converting enzyme. Mayo Clin Proc 1982;51:64–66.
194. Murphy T, Mowad C, Feig S, et al. Breast imaging case of the day. Dermatopathic lymphadenopathy. RadioGraphics 1998;18:536–539.
195. Hochman M, Anonsen C. Dermatopathic lymphadenopathy presenting as a parotid mass. Otolaryngol Head Neck Surg 1990;102: 281–284.
196. Yi A, deTar M, Becker T, Rice D. Giant lymph node hyperplasia of the head and neck (Castleman's disease): a report of five cases. Mod Pathol 1998;11:93–98.
197. Schwarzenberg H, Wacker H, Elfeldt R, et al. Castleman's disease: evaluation of 338 cases. Rofo Fortschr Geb Rontgenstr Neuen Bildgeb Verfahr 1995;163:474–479.
198. Sallah S, Gagnon G. Angioimmunoblastic lymphadenopathy with dysproteinemia: emphasis on pathogenesis and treatment. Acta Haematol 1998;99:57–64.
199. Chung C, Stein L. Kawasaki disease: a review. Radiology 1998;208:25–33.
200. Park A, Batchra N, Rowley A, Hotaling A. Patterns of Kawasaki syndrome presentation. Int J Pediatr Otorhinolaryngol 1997;40: 41–50.
201. Fischer P, Uttenreuther-Fischer M, Naoe S, Gaedicke G. Kawasaki disease: update on diagnosis, treatment, and a still controversial etiology. Pediatr Hematol Oncol 1996;13:487–501.
202. Fanconi A, Lips U. Interesting cases in clinical practice concerning Kawasaki syndrome and child abuse. Schweiz Rundsch Med Prax 1996;85:1211–1216.
203. Loevner LA, Karpati RL, Kumar P, Yousem DM, et al. Posttransplantation lymphoproliferative disorder of the head and neck: Imaging features in seven adults. Radiology 2000;216:363–369.
204. Herts B, Megibow A, Birnbaum B, et al. High attenuation lymphadenopathy in AIDS patients: significance of findings at CT. Radiology 1992;185:777–781.
205. Davis R, Warnke R, Dorfman R. Inflammatory pseudotumor of lymph nodes: additional observations and evidence for an inflammatory etiology. Am J Surg Pathol 1991;15:744–756.
206. Lamer S, Sigal R, Lassau N, et al. Radiologic assessment of intranodal vascularity in head and neck squamous cell carcinoma. Correlation with histologic vascular density. Invest Radiol 1996;31: 673–679.
207. Harris N, Jaffe E, Stein H, et al. A revised European-American classification of lymphoid neoplasms: a proposal from the International Study Group. Blood 1994;87:1361.
208. Chan J, Banks P, Cleary M, et al. A revised European-American classification of lymphoid neoplasms proposed by the International Study Group: a summary version. Am J Clin Pathol 1995; 103:543.
209. Egeler R, Schmitz L, Sonneveld P, et al. Malignant histiocytosis: a reassessment of cases formerly classified as histiocytic neoplasms and review of the literature. Med Pediatr Oncol 1995;25:1–7.
210. Jaffe H, Lichtenstein L. Eosinophilic granuloma of bone; condition affecting one, several or many bones, but apparently limited to skeleton, and representing mildest clinical expression of peculiar inflammatory histiocytosis also underlying Siwe disease and Schuller-Christian disease. Arch Pathol 1944;37:99–118.
211. Lichtenstein L. Histiocytosis X: integration of eosinophilic granuloma of bone; Letterer Siwe's disease and Schuller-Christian disease as related manifestations of a single nosologic entity. Arch Pathol 1953;55:84–102.
212. Lieberman P, Jones C, Steinman R, et al. Langerhans cell (eosinophilic) granulomatosis: A clinicopathologic study encompassing 50 years. Am J Surg Pathol 1996;20:519–552.
213. Willman C, Busque L, Griffith B, et al. Langerhans'-cell histiocytosis (histiocytosis X): a clonal proliferative disease. N Engl J Med 1994;331:154–160.
214. DiNardo L, Wetmore R. Head and neck manifestations of histiocytosis-X in children. Laryngoscope 1989;99:721–724.
215. Alessi D, Maceri D. Histiocytosis X in the head and neck in a pediatric population. Arch Otolaryngol Head Neck Surg 1992;118: 945–948.
216. Jones R, Pillsbury H. Histiocytosis X of the head and neck. Laryngoscope 1984;94:1031–1035.
217. De Schepper A, Ramon F, Van Marck E. MR imaging of eosinophilic granuloma: report of 11 cases. Skeletal Radiol 1993;22: 163–166.
218. Brandwein M, Choi H, Strauchen J, et al. Spindled nontuberculous mycobacteriosis in AIDS mimicking neoplasia. Evidence of dual histiocytic and fibroblast-like characteristics of spindle cells. Virchows Arch 1990;416:281–286.
219. Hisaoka M, Hashiomoto H, Daimaru Y. Intranodal palisaded myofibroblastoma with so-called amianthoid fibers: a report of two cases with a review of the literature. Pathol Int 1998;48:307–312.
220. Creager A, Garwacki C. Recurrent intranodal palisaded myofibroblastoma with metaplastic bone formation. Arch Pathol Lab Med 1999;123:433–436.
221. Lioe T, Allen D, Bell J. A case of multicentric intranodal palisaded myofibroblastoma. Histopathology 1994;24:173–175.
222. Moran C, Suster S, Abbondanzo S. Inflammatory pseudotumor of lymph nodes: a study of 25 cases with emphasis on morphological heterogeneity. Hum Pathol 1997;28:332–338.
223. De Vuysere S, Hermans R, Sciot R, et al. Extraorbital inflammatory pseudotumor of the head and neck: CT and MR findings in three patients. Am J Neuroradiol 1999;20:1133–1139.
224. Coffin C, Watterson J, Priest J, Dehner L. Extrapulmonary inflammatory myofibroblastic tumor (inflammatory pseudotumor): a clinicopathologic and immunohistochemical study of 84 cases. Am J Surg Pathol 1995;19:859–872.
225. Giraldo G, Beth E, Haguenau F. Herpes-type virus particles in tissue culture of Kaposi's sarcoma from different geographic regions. JNCI 1972;49:1509–1526.
226. Oettle A. Geographic and racial differences in the frequency of Kaposi's sarcoma as evidence of environmental or genetic causes. Acta Unio Internat Contra Cancrum 1962;18:330–363.
227. Gnepp D, Chandler W, Hyams V. Primary Kaposi's sarcoma of the head and neck. Ann Intern Med 1984;100:107–114.
228. Memar O, Rady P, Tyring S. Human herpesvirus-8: detection of novel herpesvirus-like DNA sequences in Kaposi's sarcoma and other lesions. J Mol Med 1995;73:603–609.
229. Boshoff C, Schulz T, Kennedy M, et al. Kaposi's sarcoma–associated herpesvirus infects endothelial and spindle cells. Nat Med 1995;1: 1274–1278.
230. Dooms G, Hricak H, Moseley M, et al. Characterization of lymphadenopathy by magnetic relaxation times: preliminary results. Radiology 1985;155:691–697.
231. Dooms G, Hricak H, Crooks L, Higgins C. Magnetic resonance imaging of the lymph nodes: comparison with CT. Radiology 1984;153:719–728.
232. Yousem D, Som P, Hackney D, et al. Central nodal necrosis and extracapsular neoplastic spread in cervical lymph nodes: MR imaging versus CT. Radiology 1992;182:753–759.
233. Lewin J, Curtin H, Ross J, et al. Fast spin-echo imaging of the neck: comparison with conventional spin-echo, utility of fat suppression, and evaluation of tissue contrast characteristics. AJNR 1994;15:1351–1357.
234. Steinkamp H, Hosten N, Richter C, et al. Enlarged cervical lymph nodes at helical CT. Radiology 1994;191:795–798.
235. Yousem D, Hurst R. MR of cervical lymph nodes: comparison of fast spin-echo and conventional spin-echo T2W scans. Clin Radiol 1994;49:670–675.
236. Yousem D, Montone K, Sheppard L, et al. Head and neck neoplasms: magnetization transfer analysis. Radiology 1994;192:703–707.
237. Anzai Y, Blackwell K, Hirschowitz S, et al. Initial clinical experience with dextran-coated superparamagnetic iron oxide for detection of lymph node metastases in patients with head and neck cancer. Radiology 1994;192:709–715.
238. Anzai Y, Prince M. Iron oxide-enhanced MR lymphography: the evaluation of cervical lymph node metastases in head and neck cancer. JMRI 1997;7:75–81.
239. Mizowaki T, Nishimura Y, Shimada Y, et al. Opitmal size criteria of malignant lymph nodes in the treatment planning of radiotherapy for esophageal cancer: evaluation by computed tomography and magnetic resonance imaging. Int J Radiat Oncol Biol Phys 1996;36:1091–1098.
240. van den Brekel M, Castelijns J, Snow G. The size of lymph nodes in the neck on sonograms as a radiologic criterion for metastasis: how reliable is it? Am J Neuroradiol 1998;19:695–700.

Copyright © 2003, Mosby, Inc. All rights reserved.

241. Snow G, Annyas A, Slooten Ev, et al. Prognostic factors of neck node metastasis. Clin Otolaryngol 1982;7:185–192.
242. Som P, Biller H. Computed tomography of the neck in the postoperative patient: radical neck dissection and myocutaneous flap. Radiology 1983;148:157–160.
243. Biller H, Urken M, Lawson W, Haimov M. Carotid artery resection and bypass for neck carcinoma. Laryngoscope 1988;98:181–183.
244. Yousem D, Hatabu H, Hurst R, et al. Carotid artery invasion by head and neck masses: prediction with MR imaging. Radiology 1995;95: 715–720.
245. Som P, Brandwein M, Lidov M, et al. The varied presentations of papillary thyroid carcinoma cervical nodal disease: CT and MR findings. AJNR 1994;15:1123–1128.
246. Pombo F, Rodriguez E, Cao J, Isla CM. Cervical lymph node metastases of medullary thyroid carcinoma: CT findings. Evr Radiol 1997;7:99–101.
247. DePena C, Tassel PV, Lee Y. Lymphoma of the head and neck. Radiol Clin North Am 1990;28:723–744.
248. Takeuchi Y, Numata T, Suzuki H, et al. Differential diagnosis of pulsatile neck masses by Doppler color flow imaging. Ann Otol Rhinol Laryngol 1995;104:633–638.
249. Eisenkraft B, Som P. The spectrum of benign and malignant etiologies of cervical nodal calcification. AJR 1999;172:1433–1437.
250. McLoud T, Putnam C, Pascual R. Eggshell calcification with system sarcoidosis. Chest 1974;66:515–517.
251. Schacherl M, Holzman H. Eggshell-like calcification of enlarged hilus lymph nodes in progressive scleroderma. Zschr Haut Geschl Krkh 1968;43:273–276.
252. Stark P. Egg shell calcification of lymph nodes: a rare feature of Boeck's sarcoid. Prax Klin Pneumol 1981;35:440–442.
253. Sun M. A study of clinical radiology of egg shell calcification of the hilar lymph nodes in silicosis. Chin J Prevent Med 1981;15:167–168.
254. Yang Z. The analysis of 42 cases of egg shell calcification hilum lymph node in coal worker's pneumoconiosis. Chin J Tuberculosis Respir Dis 1980;3:49–51.
255. Ibeas R, Carles J, Miguel A, et al. Calcification of lymph node metastases from prostate carcinoma after hormonal treatment: a case report (letter). Prostate 1997;33:147.
256. Pantongrag-Brown L, Buetow PC, Carr NJ, et al. Calcification and fibrosis in mesenteric carcinoid tumor: CT findings and pathologic correlation. AJR 1995;164:387–391.
257. Burdeny DA, Reed MH, Ferguson CA. Calcification of axillary lymph nodes following BCG vaccination. Can Assoc Radiol J 1989; 40:92–93.
258. Williams MP, Cherryman GR. Lymph-node calcification in Lennert's lymphoma. Br J Radiol 1987;60:1131–1132.
259. Kumar V, Shetty NC, Kumar KB, Murthy VS. Calcification of lymph node in Hodgkin's lymphoma. Indian J Cancer 1986;23:163–172.
260. Wiersma ES. De novo calcification in lymph node metastasis. Diagn Imaging Clin Med 1986;55:282–284.
261. Strijk SP. Lymph node calcification in malignant lymphoma. Presentation of nine cases and a review of the literature. Acta Radiol [Diagn] (Stockh) 1985;26:427–431.
262. Thornton A, Pancharatnam MD. Testicular tumor presenting with lymph node calcification on computed tomography: a case report. J Comput Tomogr 1984;8:245–248.
263. Yang ZL. [The analysis of 42 cases of egg-shell calcification hilum lymph node in coal worker's pneumoconiosis (author's trans.)]. Chung Hua Chieh Ho Ho Hu Hsi Hsi Chi Ping Tsa Chih 1980;3:49–51.
264. Shibuya H, Horiuchi J, Matsubara S, et al. [Lymph node calcification in Hodgkin's disease following irradiation (author's trans.)]. Nippon Igaku Hoshasen Gakkai Zasshi 1978;38:936–939.
265. Bertrand M, Chen JT, Libshitz HI. Lymph node calcification in Hodgkin's disease after chemotherapy. AJR 1977;129:1108–1110.
266. De Giuli E. Lymph node calcification after radiotherapy in 2 cases of seminoma testis. Tumori 1977;63:543–548.
267. Nakayama E, Ariji E, Shinohara M, et al. Computed tomography appearance of marked keratinization of metastatic cervical lymph nodes: a case report. Oral Surg Oral Med Oral Pathol Oral Radiol Endod 1997;84:321–326.
268. Gawne-Cain ML, Hansell DM. The pattern and distribution of calcified mediastinal lymph nodes in sarcoidosis and tuberculosis: a CT study. Clin Radiol 1996;51:263–267.
269. Kim JH, Jun TG, Sung SW, et al. Giant lymph node hyperplasia (Castleman's disease) in the chest. Ann Thorac Surg 1995;59:1162–1165.
270. Hasegawa T, Matsumoto H, Tomioka H, et al. [A case of sarcoidosis with systemic lymph node involvement presenting as multiple high-density masses on chest and abdominal CT]. Nippon Kyobu Shikkan Gakkai Zasshi 1994;32:1125–1130.
271. Sweeney DJ, Low VH, Robbins PD, Yu SF. Calcified lymph node metastases in adenocarcinoma of the colon. Australas Radiol 1994;38:233–234.
272. McCluggage WG, Bharucha H. Lymph node hyalinisation in rheumatoid arthritis and systemic sclerosis. J Clin Pathol 1994;47: 138–142.
273. da Silva AL, Giacomin RT, Deoti e Silva B. [Calcified abdominal lymph node paracoccidioidomycosis]. Rev Soc Bras Med Trop 1991;24:253–255.
274. Evans HL, Batsakis JG. Polymorphous low-grade adenocarcinoma of minor salivary glands. A study of 14 cases of a distinctive neoplasm. Cancer 1984;53:935–942.
275. Chiesura P, Terribile P, Bardellini G. Egg shell calcifications in silicosis: findings observed in 52 cases. Minerva Med 1968;59:5960–5968.
276. Strada L, Storto AL. On the origin of egg shell calcifications of the hilar lymph nodes in silicosis. Med Lavoro 1970;61:677–682.
277. Rege S, Maass A, Chaiken L, et al. Use of positron emission tomography with fluorodeoxyglucode in patients with extracranial head and neck cancers. Cancer 1994;73:3047–3058.
278. Laubenbacker C, Saumweber D, Wagner-Manslau C, et al. Comparison of fluorine-18-fluorodeoxyglucose PET, MRI and endoscopy for staging head and neck squamous carcinomas. J Nucl Med 1995;36:1747–1757.
279. Hautzel H, Muller-Gartner H. Early exchange in fluorine-18 FDG uptake during radiotherapy. J Nucl Med 1997;38:1384–1386.
280. Kau RJ, Alexiou C, Laubenbacher C, et al. Lymph node detection of head and neck squamous cell carcinomas by positron emission tomography with fluorodeoxyglucose F 18 in a routine clinical. Arch Otolaryngol Head Neck Surg 1999;125:1322–1328.
281. Nagamachi S, Jinnouchi S, Flores, LG. 2nd, et al. The use of 201Tl SPECT to predict the response to radiotherapy in patients with head and neck cancer. Nucl Med Commun 1996;17:935–942.
282. Olmos RV, Balm A, Hilgers F, et al. Thallium-201 SPECT in the diagnosis of head and neck cancer. J Nucl Med 1997;38:873–879.
283. Nagamachi S, Hoshi H, Ohnishi T, et al. Tl-201 SPECT in Kimura's disease involving the parotid and cervical nodes. Clin Nucl Med 1996;21:125–128.
284. Tomura N, Hirano H, Watanabe O, et al. Evaluation of single photon emission computed tomography of tumors in the head and neck with technetium-99m MIBI. Kaku Igaku 1997;34:471–479.
285. Rossi GD, Maurizi M, Almadori G, et al. The contribution of immunoscintigraphy to the diagnosis of head and neck tumours. Nucl Med Commun 1997;18:10–16.
286. Heissler E, Grunert B, Fritsche L, et al. Radioimmunoscintigraphy of squamous cell carcinoma in the head and neck region. Int J Oral Maxillofac Surg 1994;23:149–152.
287. Bree RD, Roos J, Quak J, et al. Clinical imaging of head and neck cancer with technetium-99m labeled monoclonal antibody E48 IgG or (Fab′)2. J Nucl Med 1994;35:775–783.
288. van den Brekel M, Castelijns J, Stel H, et al. Modern imaging techniques and ultrasound guided aspiration cytology for the assessment of neck node metastases: a prospective comparative study. Eur Arch Oto Rhinol Laryngol 1993;250:11–17.
289. Ariji Y, Kimura Y, Hayashi N, et al. Power Doppler sonography of cervical lymph nodes in patients with head and neck cancer. Am J Neuroradiol 1998;19:303–307.

Copyright © 2003, Mosby, Inc. All rights reserved.

37

Ultrasound of the Neck

J.A. Castelijns, Michiel W.M. van den Brekel, Suresh K. Mukherji, and J.S. Lameris

EXAMINATION TECHNIQUE OF THE NECK
ULTRASOUND-GUIDED FINE-NEEDLE ASPIRATION CYTOLOGY
SONOGRAPHIC ANATOMY OF THE NORMAL NECK
- Thyroid Gland
- Parathyroid Gland
- Salivary Glands
- The Neck (Cervical Lymph Nodes)

ULTRASONOGRAPHY OF NECK PATHOLOGY
- Thyroid Gland
  - Diffuse Thyroid Disease
  - Focal Thyroid Disease
  - Percutaneous Aspiration Under Ultrasound Guidance
  - Tumor Recurrence After Thyroidectomy
  - Ultrasound-Guided Sclerotherapy of Thyroid Cysts
- Parathyroid Gland
  - Primary Hyperparathyroidism
  - Imaging Indications

SALIVARY GLAND
- Sialolithiasis
- Tumors and Tumor-Like Conditions
  - Pleomorphic Adenoma
  - Warthin's Tumor
  - Malignant Tumors

NODAL NECK DISEASE
- Nonneoplastic Lymphadenitis
- Malignant Lymphomas
- Metastatic Lymphadenopathy

OTHER CERVICAL SITES: CONGENITAL CYSTIC LESIONS AND NONNODAL MASSES OF THE NECK
- Cystic Lesions
- Infectious Disease
- Lipomas
- Neurogenic Tumors

THE ROLE OF ULTRASOUND FOR EVALUATION OF INFANTS AND YOUNG CHILDREN

Although CT and MR imaging can be used for the evaluation of a variety of head and neck disorders, ultrasound may be the initial modality for evaluating superficial structures. Ultrasound may also be preferred for guiding needle aspirations (punctures) of all types of lesions in the neck. Ultrasound, and if necessary ultrasound-guided fine-needle aspiration cytology, is also useful for evaluating thyroid and parathyroid gland lesions, for evaluating cervical nodes, and for the diagnostic evaluation of salivary gland tumors. The noninvasiveness of ultrasound makes this an ideal modality for evaluating neck masses in infants and children. This chapter will review the potential of ultrasound and ultrasound-guided fine-needle aspiration cytology for evaluating a variety of disorders involving the extracranial head and neck.

EXAMINATION TECHNIQUE OF THE NECK

The patient is examined in a supine position with the neck mildly hyperextended. The neck should be examined with a high-frequency linear array transducer ranging from 7.5 to 10 MHz. Blood flow can be studied using Duplex sonography, in which gray scale 2D sonography is combined with pulsed Doppler. With color Doppler imaging (CDI), the pulsed Doppler information is encoded for flow direction and (mean) flow velocity and displayed in the 2D image. The relative direction of flow (toward or away from the transducer) is shown by the use of a suitable color (e.g., red or blue). Power Doppler shows the intensity of flow, which is proportional to the square of the amplitude of the Doppler signal. It is usually presented in a unidirectional

Copyright © 2003, Mosby, Inc. All rights reserved.

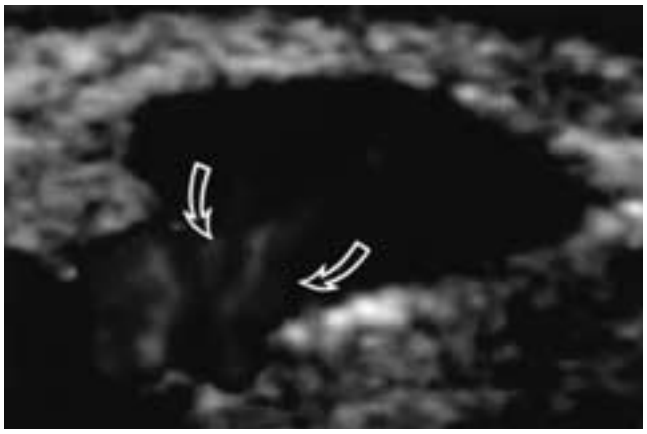

FIGURE 37-1 Power Doppler ultrasound shows hilar flow (*arrows*) inside a small normal lymph node, which is seen with low signal intensity.

VIEW IMAGE

form (Fig. 37-1). CDI is generally used to examine intravascular flow, while the more sensitive power Doppler is used to detect parenchymal flow. Flow patterns (velocity in time) during the cardiac cycle are studied with duplex scanning. Many indices of waveform analysis have been described, but only the *resistance index* (RI = (maximum velocity – minimum velocity) / maximum velocity) is used to characterize parenchymal flow. The RI is particularly sensitive to changes in downstream flow resistance. Neovascularization, as seen in many tumors, causes a decrease in the RI compared to normal tissue. Depending on the indication (swelling of the neck, suspicion of a thyroid or parathyroid lesion, etc.), particular attention should be given to certain regions of the neck. Level I should be evaluated in the coronal plane. Generally, levels II to V should be evaluated longitudinally (craniocaudally) and in the axial plane. The thyroid gland should be imaged entirely in both the transverse and longitudinal planes. Potential enlargement of the parathyroid gland should be evaluated, particularly if there are indications of adenoma, hyperplasia, and so on. The parotid gland should be examined in the axial plane. Sometimes it may be difficult to assess the origin of a lesion (intra- or extraparotid), and imaging in other directions should be performed. Levels I to V of both sides of the neck should be examined for the presence of enlarged nodes, particularly in patients known to have head and neck cancer or parotid lesions or when a suspicious thyroid nodule is encountered. All nodes that are visible on ultrasound are measured in the axial plane. We prefer to measure the minimal axial diameter, since we consider this to be the most accurate size criterion in differentiating between benign and malignant disease.

ULTRASOUND-GUIDED FINE-NEEDLE ASPIRATION CYTOLOGY

Fine-needle aspiration cytology (FNAC) has a major role in the diagnosis of palpable or nonpalpable thyroid lesions because of the absence of reliable clinical or ultrasonographic criteria for differentiation between benign and malignant disease. The procedure is safe and easily performed in an outpatient setting (Fig. 37-2). Ultrasound-guided FNAC can provide a cytologic diagnosis in a large percentage of lesions. We prefer ''freehand'' FNAC using a syringe holder (Cameco, Tayby, Sweden). A 22-gauge (25-mm) noncutting needle equipped with 10- or 20-ml aspiration syringes should be used. A longer needle should be used for deeper lesions. After antiseptic preparation, the needle should be advanced 0.5 to 1 cm from the middle of the long axis of the transducer. After visualization of the needle tip in the lesion, syringe suction should be applied and the needle moved gently but rapidly through the mass. An ideal specimen for cytologic analysis consists of 1 or 2 drops of orange-red fluid. Cutting needles generally yield very cellular specimens but are more difficult to insert than the sharper noncutting needle.[1] The smears are fixed using 70% ethanol, stained with Papanicolaou stain, and air-dried and stained with May-Grunwald-Giemsa solution. The needle and syringe are washed with Carbowax to obtain additional smears. Repeated ultrasound-guided FNAC, possibly with the use of on-site cytopathology review, may reduce the number of nondiagnostic aspirates. Spring-activated automated biopsy guns may also allow more accurate histologic diagnosis without a significant increase in the complication rate.[2]

If the aspirate obtained by ultrasound-guided FNAC contains blood, a nonaspiration technique may be used in which the 22-gauge needle is inserted without suction. Capillary action causes cells to move into the needle as it is moved in a back-and-forth excursion within the mass.[1] This technique may be especially useful when aspirating thyroid nodules.

SONOGRAPHIC ANATOMY OF THE NORMAL NECK

This section describes the normal ultrasonographic anatomy of the thyroid gland, the parathyroid glands, the salivary glands, and the cervical nodes. The axial anatomy

FIGURE 37-2 Ultrasound-guided aspirations are performed by using a syringe holder and preferentially a 0.6 × 25 mm needle. The needle should be introduced 0.5 to 1.0 cm from the middle of the long axis of the 7.5- to 10-MHz linear array transducer.

VIEW IMAGE

Copyright © 2003, Mosby, Inc. All rights reserved.

VIEW IMAGE

FIGURE 37-3 Thyroid gland. The thyroid gland consists of two lateral lobes (*arrows*) connected by a median structure, the isthmus. This axial image shows thyroid tissue as highly uniform tissue with medium-level echogeneity, with little identifiable internal architecture. Small, dilated veins may be visualized as small, rounded structures or as small, linear structures. The concave posterior surface of the thyroid is located adjacent to the first tracheal rings.

of the neck has been extensively discussed in Chapter 33. In this chapter, selected topics will be discussed; in particular, potential applications and limitations of ultrasound will be indicated, along with anatomic features of each structure.

Thyroid Gland

The thyroid gland consists of two lateral lobes connected by a median structure, the isthmus, at the junction of the lower and middle thirds of each lobe (Fig. 37-3). The concave posterior surface of the thyroid is applied against the anterolateral surfaces of the larynx and the first tracheal rings. Average lobe dimensions are: height, 4 to 6 cm; width and thickness, 1 to 2 cm. Ultrasound allows volumetric analysis of the thyroid lobes. Each lobe can be considered as a separate sphere whose volume is given by $v = (\pi/6 \times \text{height} \times \text{width} \times \text{depth})$. The average volume has been estimated at between 12 and 40 cm^3. The average distance between the inferior lobe and the sternum may be 1 to 2 cm, but this position varies from one individual to another. If the caudal extreme is much lower, the neck should be extended considerably for accurate examination. The thyroid lobes are often slightly asymmetric, with the right lobe tending to be larger than the left. The isthmus may vary from 1 to 2 cm in height. The pyramidal lobe is an inconstant conical structure projecting upward from the isthmus, either along the midline or off to one side. Normal thyroid parenchyma has a characteristic sonographic appearance of homogeneous medium-level echoes, with little identifiable internal architecture. The use of color Doppler imaging identifies multiple small vessels within and adjacent to the thyroid gland. Parts of the paired superior and inferior thyroid arteries, which provide the blood supply to the thyroid, can usually be visualized as they enter the gland.

The esophagus often projects to the left of the trachea and may be seen at the posteromedial border of the left thyroid lobe. The esophagus is visualized sonographically as a semicircular bull's eye with a hyperechogenic center (esophageal lumen) and less echogenic contours (esophageal wall). However, this image may vary. An esophageal deviation to the left side of the neck should not be mistaken for a cervical mass. The mobility of this structure can be examined by having the patient swallow.

As the internal jugular vein is not always spontaneously visible, a Valsalva maneuver can be performed to dilate the jugular vein. The vagus nerve lies in the posterior angle of the common carotid artery and the internal jugular vein (Fig. 37-4). The posteromedial border of each thyroid lobe is intimately related to the corresponding recurrent laryngeal nerve. Enlargement of the thyroid gland, especially if secondary to malignancy, may cause paralysis of the vocal cord.

FIGURE 37-4 The major neurovascular bundle comprises the common carotid artery, the internal jugular vein (lateral to the artery and more or less spontaneously visible), and the vagus nerve. This axial image low in the neck shows both vascular structures, lateral to the thyroid lobe and deep to the sternocleidomastoid muscle.

VIEW IMAGE

Copyright © 2003, Mosby, Inc. All rights reserved.

Parathyroid Gland

In most people there are four parathyroid glands (two superior and two inferior ones) dorsal to the thyroid gland and its capsule. In approximately 5% of people there are more than four glands. Normal glands are oval or bean-shaped. The normal parathyroid gland averages 3 to 6 mm in length, 2 to 4 mm in width, and 1 to 3 mm in thickness. However, normal parathyroid glands cannot be visualized because they have an echogenicity similar to that of the thyroid gland. Normally positioned parathyroid glands are characteristically located around the terminal branches of the inferior thyroid artery. Superior glands are located behind the upper pole or midportion of each thyroid lobe. The inferior glands are usually located just inferior to the posterior aspect of the lower thyroid poles. If they fail to dissociate from the adjacent thymus during development, they may migrate more inferiorly into the superior mediastinum. Most frequent sites of ectopic glands are mediastinal, retropharyngeal, or retroesophageal.

Salivary Glands

The parotid gland is the largest salivary gland and is bounded anteriorly by the ascending ramus of the mandible and posteriorly by the mastoid process (Fig. 37-5). This gland has a homogeneous, hyperechoic appearance. Ultrasound cannot visualize the portion of the gland that extends deep to the mandible. The facial nerve emerges from the skull through the stylomastoid foramen. It enters the superior deep portion of the parotid gland anterior to the posterior belly of the digastric muscle. As the nerve courses inferiorly, it is located lateral to the retromandibular vein. After crossing the vein, the facial nerve divides into its branches. The facial nerve is encased in a fibrous sheath that is easily recognized by the surgeon but is indistinguishable sonographically from surrounding parotid gland tissue.[3] The external carotid artery may be visible sonographically, terminating 4 cm above the angle of the mandible, where it divides into the maxillary and superficial temporal arteries. Lymph nodes are also located in the parotid gland. Normal intraparotid lymph nodes cannot be visualized by ultrasonography.

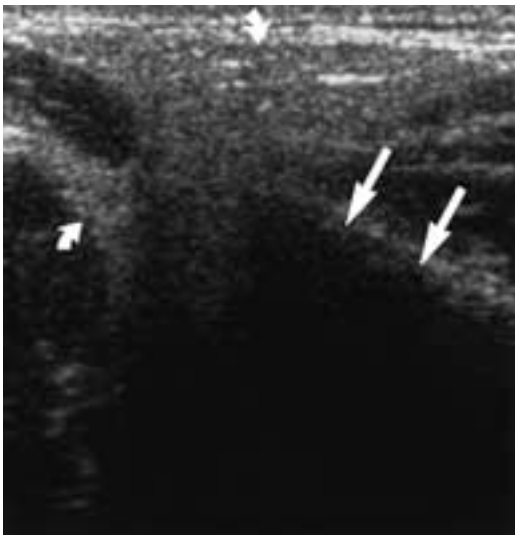

VIEW IMAGE

FIGURE 37-5 This axial image shows the parotid gland (*curved arrows*) with a homogeneous, hyperechoic appearance. Ultrasound cannot visualize the part of the deep portion of the gland that extends deep to the mandible (*straight arrows*), which is the anechogenic area on this image.

FIGURE 37-6 This frontal image shows the submandibular gland adjacent to the anechoic mandible (*curved arrow*), with a homogeneous appearance similar to that of the parotid gland. The entire gland can be seen by ultrasound. Submandibular ducts (*small arrows*) may be visualized inside the gland.

VIEW IMAGE

The submandibular gland (Fig. 37-6) is located in the submandibular region. The submandibular duct (Wharton's duct) emerges from the gland's superior surface and terminates at the side of the frenulum of the tongue. The entire submandibular gland can be seen by ultrasound, with an appearance similar to that of the parotid gland.

The Neck (Cervical Lymph Nodes)

Familiarity with the normal anatomy and features of the cervical nodes is essential for complete evaluation of patients with head and neck malignancies. Of the estimated 800 lymph nodes in the human body, 300 are situated in the neck. Until recently, the regional categorization of lymph nodes, as described by Rouvière, was the most widely used for lymphadenopathy.[4] Today, most centers use the classification into levels proposed by the Memorial Sloan-Kettering Cancer Center and described by Som[5] (Fig. 37-7). Also see Chapter 36 for updated classifications.

In this classification system, level I corresponds to the submandibular and submental regions. Levels II, III, and IV correspond to the jugular chain nodes around the internal jugular vein (high, mid-, and low jugular). Level II is situated above the level of the hyoid bone. Level III lies between the bottom of the body of the hyoid bone and the

Copyright © 2003, Mosby, Inc. All rights reserved.

crossing with the omohyoid muscle and the jugular vein (or the bottom of the cricoid cartilage arch). Level IV lies underneath this crossing and above the clavicle. Level V represents the lymph nodes posterior to the posterior border of the sternocleidomastoid muscle (posterior triangle) and above the clavicle (supraclavicular). The trapezius muscle forms the posterior border of this level. Level VI corresponds to the juxtavisceral, such as the paratracheal lymph nodes. The superficial, facial, parotid, nuchal, and retropharyngeal lymph nodes that were recognized by Rouvière are not outlined in this scheme, as these are not commonly removed in neck dissections.

Although many different pathways and anastomoses of the lymphatics in the neck exist, most primary tumors metastasize via predictable routes following local and deep lymphatic pathways.[6] The primary echelon lymph nodes, that is, the sentinel lymph nodes, are at highest risk of harboring occult metastases in an N0 neck. For anterior oral and nasal cavity as well as lip carcinomas, level I is at highest risk. In posterior oral cavity and oropharyngeal tumors, level II lymph nodes are at highest risk, whereas in laryngeal and hypopharyngeal tumors, levels II and III can both harbor the sentinel lymph node. Hypopharyngeal and proximal esophageal as well as subglottic tumors can also spread to the paratracheal nodes in an early stage. Tumors from the skin of the face and scalp often spread to parotid, facial, or nuchal lymph nodes. For the radiologist, it is important to look for lymph nodes especially in the first echelon, and if ultrasound-guided FNAC is used, preferably to aspirate from lymph nodes in these regions.

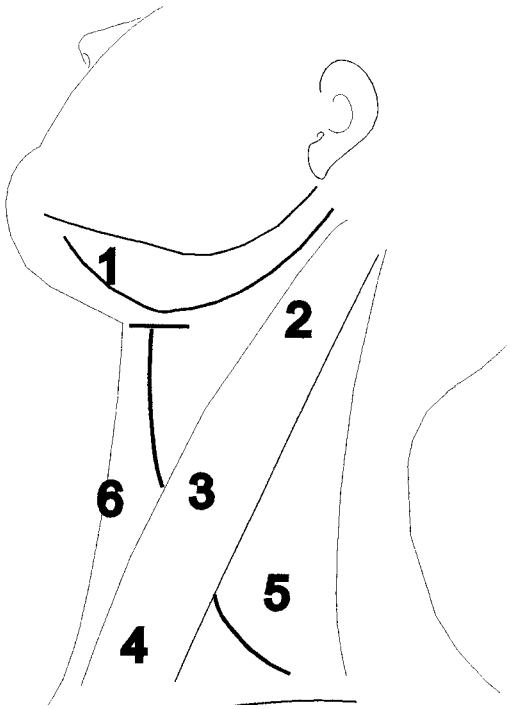

FIGURE 37-7 Anatomic classification of cervical nodes according to the American Academy of Otolaryngology. Level 1: submandibular and submental region; level 2: high jugular or subdigastric; level 3: midjugular; level 4: low jugular; level 5: posterior triangle; level 6: juxtavisceral.

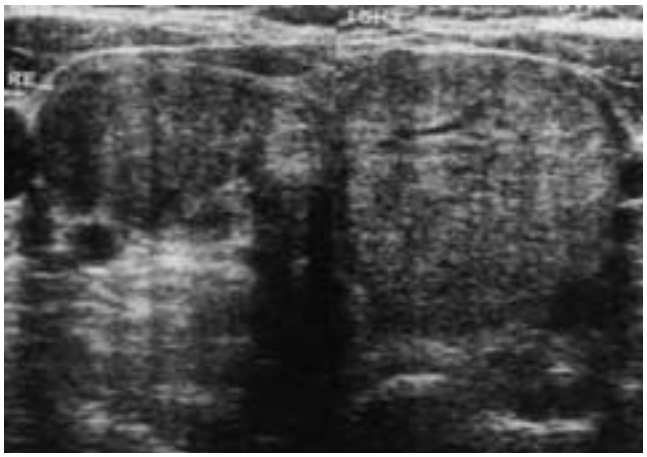

FIGURE 37-8 Multinodular goiter. Both lobes of the thyroid gland are enlarged, and are seen with moderate heterogeneity (mainly solid).

ULTRASONOGRAPHY OF NECK PATHOLOGY

Thyroid Gland

The thyroid gland is ideally situated for high-frequency sonography due to its superficial location. High-resolution ultrasound permits excellent visualization of the thyroid parenchyma. Ultrasound is generally the first choice for evaluation of thyroid morphology because of its sensitivity in detecting both small nodules and subtle variations like nodularity, calcifications, septations, and cyst formations. Many thyroid nodules discovered incidentally at sonography may not be clinically significant.[7] Sonography is an excellent tool for evaluating the thyroid gland to assess the volume of thyroid tissue, to provide image guidance for punctures and follow-up during and after therapy (thyroidectomy or prior neck irradiation). Ultrasound is less expensive than scintigraphy, allows easier comparison during follow-up, and has no accompanying radiation exposure or intravenous injections.

Diffuse Thyroid Disease

Generalized thyroid enlargement, or goiter, may be caused by a number of distinct entities, including multinodular goiter, Graves' disease, Hashimoto's thyroiditis, and infectious thyroiditis.[8, 9] A goiter is simply an enlarged thyroid gland, which may be seen with hyperthyroidism or hypothyroidism. Multiple hyperplastic nodules exhibiting varying degrees of colloid, necrosis, or hemorrhage characterize pathologically multinodular goiter (Figs. 37-8 and 37-9). Generally, laboratory values, the clinical history, and the physical examination differ in these entities. However, ultrasound findings may demonstrate mixed solid and cystic zones within an enlarged nodular thyroid gland. Calcifications may occasionally be present.[10] Sonography provides information regarding the size of the thyroid gland, disease extent, and surrounding lymphadenopathy. The incidence of carcinoma in a multinodular goiter is very low (less than 3%), and on scintigraphy the characteristic appearance of multiple cold areas interspersed with hot areas in a large gland will usually obviate the need for aspiration. A large,

Copyright © 2003, Mosby, Inc. All rights reserved.

VIEW IMAGE

FIGURE 37-9 Multinodular goiter. The thyroid gland is minimally enlarged. A large cystic lesion is located in the right lobe of the thyroid.

dominant, hard, or growing mass amid a goiter should probably be sampled. Serial ultrasound examination can monitor the disease progression and the therapeutic response.[11, 12]

Graves' disease (diffuse toxic goiter) is characterized clinically by signs and symptoms of thyrotoxicosis and enlargement of the thyroid gland (Fig. 37-10). The most common cause of hyperthyroidism, Graves' disease is an autoimmune disorder mostly found in women. Carcinoma of the thyroid gland in a patient with Graves' disease is rare, reported in only 0.15% to 0.5% of patients. The gray-scale sonographic pattern ranges from normal echogenicity to diffusely hypoechogenic. The thyroid tends to be more heterogeneous in patients with multinodular goiter than in patients with Graves' disease. The diagnosis is made clinically. Color Doppler imaging of the thyroid gland affected by Graves' disease may show a striking pattern of increased vascularity, both in systole and in diastole.[13] Some studies suggest that thyroid vascularity and thyroid artery blood flow are significantly higher in the active stage of Graves' disease. These findings suggest that color Doppler could be a useful marker for inflammatory activity, independent of hormone production.[14]

Another cause of thyroid enlargement is Hashimoto's thyroiditis, the most common form of thyroiditis (Fig. 37-11). It is mostly found in middle-aged women as a painful, diffusely enlarged gland. Gland size may also be normal. About 50% of patients are hypothyroid. The disease shows no greater risk of thyroid carcinoma, but patients appear to be at greater risk of developing non-Hodgkin's lymphoma. On ultrasound, the thyroid gland is enlarged and hypoechoic. Multiple ill-defined hypoechoic areas separated by thickened fibrous strands may be seen. A diffuse micronodular pattern is suggestive of Hashimoto's disease. However, the diagnostic accuracy of this finding has not been reported.[15] The final diagnosis still requires serologic tests. An enlarged thyroid gland may also be seen with acute infectious thyroiditis. Ultrasound may be useful for patients with a painful thyroid gland, particularly those with focal tenderness, to evaluate for the presence of a thyroid abscess.

Focal Thyroid Disease

Nodular disease in the thyroid gland is characterized by the presence of one or more palpable or nonpalpable nodules (Fig. 37-12). In the general population, thyroid nodules are exceedingly common. Noncystic nodules were detected on sonography in about 20% in a large prospective study of patients who had a normal thyroid gland on palpation. Clinical assessment is generally considered to be unreliable in attempting to differentiate a benign from a malignant nodule. The primary role of scintigraphy in the evaluation of focal thyroid masses is to determine whether a lesion is ''hot'' (a relatively low incidence of malignancy: less than 5%) or ''cold'' (a relatively high incidence of malignancy: 20% to 30%).[16] The low accuracy of radionuclide scanning has led to an effort to define reliable sonographic criteria to differentiate between malignant and benign thyroid nodules.

High-resolution ultrasonography can detect very small nodules. However, no single sonographic criterion enables reliable differentiation between benign and malignant thyroid nodules.[9, 11, 14, 17, 18] Nevertheless, there are certain findings that can help to make this important differentiation. The presence of microcalcifications is highly suggestive of malignancy.[18] An irregular, thick margin, especially in the presence of a halo or microcalcification, suggests malignancy.[14] Ultrasonography is accurate in distinguishing solid from cystic thyroid nodules. Malignant thyroid cysts are rare. Most cystic masses arise from preexisting solid nodules and are therefore complex.[19] The presence of colloid material within the cyst can cause a series of closely spaced, discrete echoes (a particular form of reverberation), the so-called comet tail artifact. Conversely, the presence of coarse calcifications, a regular margin, and a thin-rimmed anechoic cyst with a well-defined halo suggests benignity.[19–22] Multiplicity of nodules has not been shown to affect the likelihood of malignancy.[23] There may be considerable overlap in the sonographic appearance of

FIGURE 37-10 Graves' disease. Diffuse enlargement of both lobes (*curved arrows*) of the thyroid gland is present. The thyroid gland has low echogeneity.

VIEW IMAGE

Copyright © 2003, Mosby, Inc. All rights reserved.

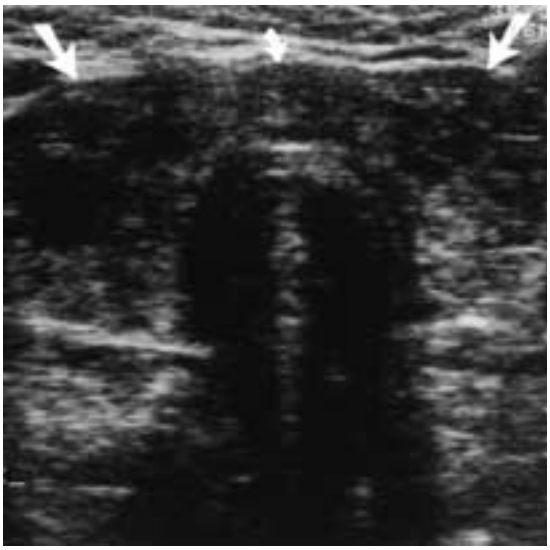

VIEW IMAGE

FIGURE 37-11 Hashimoto's thyroiditis. The thyroid gland is symmetrically enlarged (*straight arrows*), as noted especially at the isthmus (*curved arrow*). The gland has an overall homogeneous, hypoechoic appearance. Multiple ill-defined hypoechoic areas are separated by thickened fibrous strands.

benign and malignant nodules. Therefore, caution should be used in relying on sonographic features alone to characterize thyroid nodules. There are also many similarities in the appearances of benign and malignant nodules on color Doppler imaging.[24] Often an ultrasound-guided puncture is required to obtain cytologic evidence.

During routine ultrasound examination of the neck, nonpalpable (incidental) thyroid nodules that are less than 1 cm in diameter may often be detected.[14] The question arises as to what should be done with the many unsuspected, mostly benign thyroid nodules. Radiologists should be familiar with the above-mentioned morphologic features that increase the probability of malignancy. Based on the work of several authors,[25, 26] an algorithm for dealing with incidental nodules was developed. Patients with nodules at least 1.5 cm in size, or with nodules with suspicious ultrasound features or a history of thyroid cancer, should undergo ultrasound-guided FNAC. Patients with nodules smaller than 1.5 cm, or with nodules with benign-appearing features and without a history of thyroid cancer, can be followed by physical examination. If during follow-up the nodule is found to be increasing in size, patients should undergo ultrasound-guided FNAC. Most papillary carcinomas, which account for 55% to 75% of thyroid cancer, grow slowly and remain definitely curable if and when they become clinically apparent at approximately 1.0 to 1.5 cm in size.

Percutaneous Aspiration Under Ultrasound Guidance

FNAC has a major role in the management of palpable thyroid nodules because of the absence of reliable clinical or ultrasonographic criteria for differentiation of benign from malignant thyroid nodules.[14] Aspiration findings can be classified as benign (no evidence of malignancy), suspicious (features suggestive of but not diagnostic for malignancy, including Hurthle cell neoplasms and follicular neoplasms), malignant (definite evidence of papillary, anaplastic, or metastatic cancer), or nondiagnostic. Regarding the majority of palpable thyroid nodules, FNAC can be performed under palpation guidance with a high degree of accuracy (up to 85%). Ultrasound-guided FNAC has been reported to have higher accuracy than conventional FNAC.[27] Ultrasound-guided FNAC is useful for patients in whom conventional FNAC was not successful; for patients with suspicious, nonpalpable nodules; and for patients with a worrisome clinical history, such as significant neck irradiation. Approximately 60% of the nondiagnostic, palpation-guided nodule biopsies are reported to be diagnostic when repeated using ultrasound guidance.[9]

Tumor Recurrence After Thyroidectomy

Whole body scanning using radioiodine has traditionally been the mainstay in diagnosing recurrent tumor following surgery. However, Antonelli et al. have reported that ultrasound is capable of detecting recurrent tumor in the thyroid bed as well as cervical lymph node metastasis[28] (Fig. 37-13). Some studies suggest that ultrasound may have higher diagnostic accuracy than scintigraphy.[29] Routine ultrasonography may be used for follow-up of patients with thyroid cancer.[14] Because of the considerable overlap in the size and appearance of benign and malignant lymph nodes, we recommend percutaneous ultrasound-guided FNAC of all suspicious lymph nodes.

Ultrasound-Guided Sclerotherapy of Thyroid Cysts

True thyroid cysts can be punctured and aspirated. However, these cysts will very often regain their original size within a few days. An alternative approach is to sclerose the cyst wall by injecting absolute ethanol or tetracycline hydrochloride. After aspiration of the cystic fluid with a 22-gauge needle, approximately one-half to two-thirds of the original volume is replaced by a sclerosing agent. A small amount of saline is injected before the needle is

FIGURE 37-12 Euthyroid patient. The right lobe of the thyroid is almost entirely replaced by a large cystic nodule, which proved to be hemorrhagic.

VIEW IMAGE

Copyright © 2003, Mosby, Inc. All rights reserved.

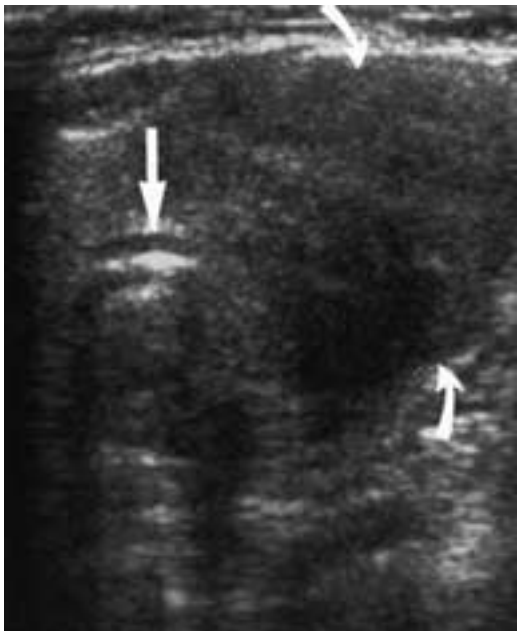

VIEW IMAGE

FIGURE 37-13 Tumor recurrence after thyroidectomy. A large, inhomogeneous mass (*curved arrows*) is found in the left lobe of the thyroid adjacent to the trachea (*straight arrow*).

retracted. In this manner, pain due to spilling of the sclerosing agent in the surrounding tissue is avoided. In approximately 80% to 90% of cases, the cyst will be reduced in size or disappear. Large cysts respond better than small cysts.[30]

Parathyroid Gland

Primary Hyperparathyroidism

The main indication for ultrasonography of the parathyroid glands is the evaluation of patients with hypercalcemia. Hypercalcemia is a fairly common disorder that may occur in the absence of clinical symptoms in 1 out of 1000 cases. About 80% of cases are related to hyperparathyroidism. Females are affected twice as often as males, and although the condition can occur at any age, most patients are over 40 years of age.[31] Primary hyperparathyroidism is caused by an excess of parathyroid hormone secretion by a parathyroid adenoma (nearly 80% of cases and almost always limited to one gland), hyperplasia (less than 20% of cases and affecting all four glands), or carcinoma (only 1% and affecting one gland).

The typical parathyroid adenoma may be seen in a patient with biochemical evidence of hyperparathyroidism as an oval, solid mass of homogeneously low echogenicity. The size of the adenoma usually ranges between 0.8 and 1.5 cm in length; however, larger lesions may occasionally be encountered.[32] They may occasionally be multilobular and heterogeneous and may contain internal calcification or cysts.[33] An echogenic line separating thyroid and parathyroid tissue may allow the distinction between adenoma and adjacent thyroid.

The sensitivity of sonography for localizing parathyroid adenomas in patients with primary hyperthyroidism has been reported to range between 70% and 80%.[34, 35] Sonographic examination of a patient with hyperparathyroidism may give a false-negative result in three situations: minimally enlarged adenomas, adenomas displaced and obscured by an enlarged thyroid goiter, and adenomas in ectopic parathyroid glands located in regions difficult to evaluate by ultrasonography. Such areas include locations behind air-containing viscera (pharynx, esophagus) or bone (sternum, clavicle).

Posterior exophytic thyroid nodules and cervical lymph nodes may cause false-positive sonographic results. Thyroid nodules have mixed echogenicity, including cystic and calcified components, and are usually intrathyroid. Lymph nodes may contain a characteristic hilum and are generally more lateral in the neck. Ultrasound-guided FNAC may be performed to differentiate suspected parathyroid adenomas from lymph nodes and thyroid nodules.

Imaging Indications

Routine preoperative imaging is not performed because morbidity is rare when an experienced surgeon performs parathyroidectomy. Ultrasound may occasionally be used in preoperative evaluation of patients with primary hyperparathyroidism. Unilateral parathyroid exploration with adenoma removal and identification of a normal parathyroid gland is an accepted surgical approach for the treatment of patients with primary hyperparathyroidism. In experienced hands, high-resolution sonography can be a cost-effective means of localizing parathyroid adenomas when unilateral exploration is considered an accepted surgical approach.[36] In contrast, preoperative imaging may be beneficial in patients undergoing a second surgical procedure for persistent or recurrent hyperparathyroidism (Fig. 37-14). In this patient group, ultrasound has demonstrated higher sensitivity (60% to 82%) than MR imaging or CT.[37] Ultrasound may also be used to guide the fine-needle aspiration of suspicious lesions.

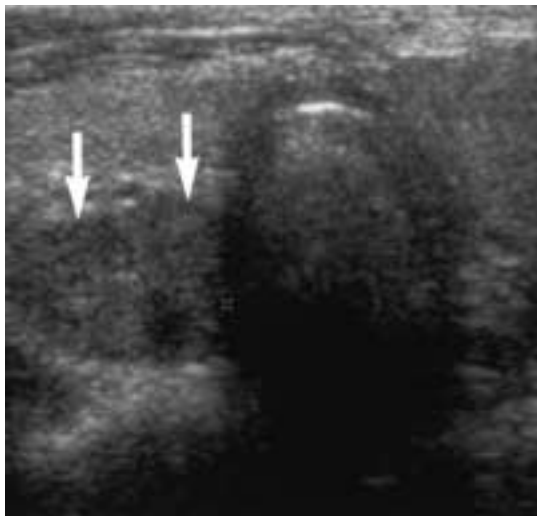

FIGURE 37-14 Recurrent hyperplasia of the parathyroid gland. Dorsally to the right lobe of the thyroid gland, an enlarged parathyroid gland (*arrows*) is demonstrated, with low and somewhat inhomogeneous echogenicity.

VIEW IMAGE

Copyright © 2003, Mosby, Inc. All rights reserved.

SALIVARY GLAND

Sialolithiasis

Inflammatory disease can be best investigated by other modalities, such as CT or sialography, and is not an indication for ultrasound. However, ultrasound may be beneficial for evaluating patients with sialolithiasis. Plain films or CT are usually performed first. If they are negative, sialography remains a reliable method for detecting sialolithiasis.[38] Ultrasound is a noninvasive method for detecting calculi and assessing the surrounding parenchyma. A dilated duct can be identified, as can nonradiopaque calculi. Ultrasound may detect calculi in up to 91% of cases.[39] It may also be helpful when ductal cannulation is impossible.

Tumors and Tumor-Like Conditions

Tumors are 10 to 15 times more common in the parotid gland than in the submandibular glands. Benign lesions account for about 80% of all parotid tumors. In contrast, the frequency of malignant tumors in the submandibular gland is much higher (approximately 33% to 50%). Pleomorphic adenoma is the most frequent tumor (60% to 70%) of the salivary glands. Warthin's tumor, also called adenolymphoma, accounts for 6% to 10% of all parotid tumors. Only 5% of cases are bilateral. Benign nonepithelial tumors may arise within glandular spaces and include lipomas, schwannomas, and vascular tumors. Like benign tumors, epithelial lesions are the most frequent forms of malignancy. Metastases and lymphomas of the salivary glands are rare. Pleomorphic adenomas have a tendency to recur if the capsules are damaged at surgery. For that reason, partial or total parotidectomy should be performed. Warthin's tumor has an excellent prognosis and almost never recurs; malignant degeneration is extremely rare. Therefore, enucleation or continuous follow-up without removal may be sufficient.

High-resolution ultrasound is considered by some authors to be the modality of first choice for detection of neoplasms in the salivary glands. However, ultrasound is unable to evaluate that portion of the parotid gland situated deep to the mandible. If the lesion needs to be identified before surgery, ultrasound-guided FNAC may be performed. MR imaging is an important adjunct for evaluating the full extent of tumor and evaluating for perineural spread. In cases of malignancy, the neck should also be examined for enlarged lymph nodes.

Pleomorphic Adenoma

Approximately 90% of pleomorphic adenomas are located in the superficial lobe (Fig. 37-15). Consequently, ultrasonography may detect the large majority of these lesions. The possibility of malignant transformation of pleomorphic adenomas remains controversial. Small (<3 cm) pleomorphic adenomas are usually visualized as a homogeneous, well-delineated, lobular nodule of decreased signal intensity compared to surrounding parotid gland tissue.[40, 41] The absence of either sharp margins or homogeneity may suggest malignancy. Reports from the literature regarding the potential of color Doppler sonography to differentiate malignant and benign tumors are contradictory.[42, 43] Large tumors (>3 cm) are prone to cystic and hemorrhagic degeneration, which modifies their internal architecture. In cases of recurrent tumor, ultrasound examination may be hindered by echogenic scar. MR imaging is indicated in these cases.

FIGURE 37-15 Pleomorphic adenoma. Axial image shows a pleomorphic adenoma as a somewhat lobulated, homogeneous area (*curved arrow*) in the parotid gland and adjacent to the mandible (*straight arrow*).

VIEW IMAGE

Warthin's Tumor

Ultrasound shows a well-defined, anechoic mass or a mass with multiple anechoic areas, often at the lower pole of the parotid[40, 41] (Fig. 37-16). However, the pattern may vary. In certain cases, multiple septa and the thickness of

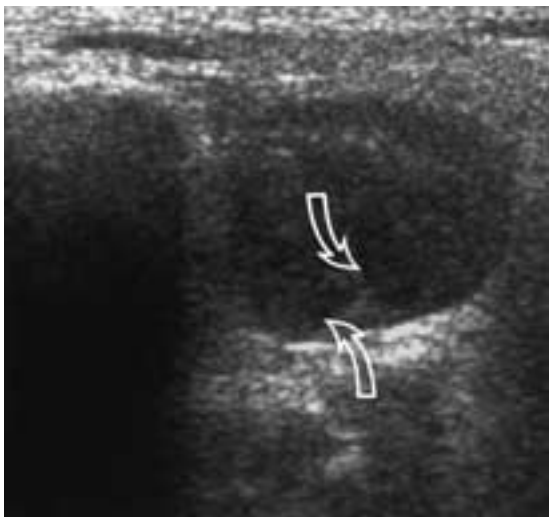

FIGURE 37-16 Warthin's tumor. Axial image shows a large, well-defined mass with multiple anechoic areas (*arrows*) and septa in the parotid gland adjacent to the mandible.

VIEW IMAGE

Copyright © 2003, Mosby, Inc. All rights reserved.

VIEW IMAGE

FIGURE 37-17 Warthin's tumor. Axial image shows a small, well-defined mass (*curved arrow*) in the superficial lobe of the parotid gland and adjacent to the masseter muscle (*straight arrows*).

intratumoral fluid give an inhomogeneous echogenic pattern (Fig. 37-17). Because Warthin's tumor may be bilateral, the contralateral gland should always be examined carefully.

Malignant Tumors

There are many types of malignant epithelial tumors. The most frequent are mucoepidermoid cancer (5% to 10% of all salivary gland tumors), adenoid cystic carcinoma, acinic cell tumors (Fig. 37-18), undifferentiated carcinoma, and epidermoid carcinoma. Malignant tumors may often show attenuated posterior echoes, heterogeneous internal echoes, or a polygonal shape. There are no consistent criteria to differentiate between malignant and benign lesions. MR imaging is necessary to show the extent of disease, particularly to demonstrate perineural spread of tumor tissue.

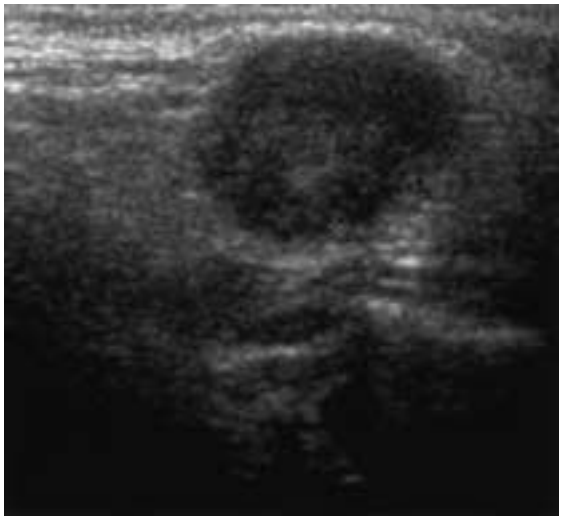

VIEW IMAGE

FIGURE 37-18 Acinic cell carcinoma. Axial image shows a mass with heterogeneous, low echogeneity in the parotid gland.

NODAL NECK DISEASE

Nonneoplastic Lymphadenitis

As the neck lymphatics play a key role in upper aerodigestive tract infections, reactively enlarged lymph nodes are very common (Fig. 37-19). Most often these are caused by viral or bacterial infections. The history, serology, and cultures of the primary infection, together with intracutaneous testing (e.g., Mantoux testing for mycobacteria), and, if needed, cytology can in general establish the diagnosis. However, ultrasound can sometimes help in the diagnostic workup of cervical lymphadenopathy. In suppurative lymphadenitis, the assessment of abscess formation and eventually ultrasound-guided drainage can be of great importance.[44] In this respect, the hypervascularity shown using Doppler sonography is a reliable diagnostic criterion. In a study of 50 lesions, a peripheral blood flow pattern was observed only in abscesses. Other patterns, such as a mixed pattern (flow within and around the lesion) and a central pattern (flow in the central region of the mass), were seen most frequently in lymphadenitis but were not specific for that diagnosis.[45] Ultrasound-guided drainage is especially useful if the abscess is located deep and is difficult to reach surgically.[46, 47] For this indication, CT-guided drainage can be used as well. A single mass with central heterogeneous reflection patterns is most often caused by a suppurative lymph node, an (atypical) mycobacterial infection, or cat-scratch disease caused by *Bartonella henselae*. Multiple enlarged, conglomerate lymph nodes that are hypoechoic or have inhomogeneous echotexture with enhanced through-transmission may be indicative of tuberculous lymphadenopathy (Fig. 37-20). In these cases, nonspecific abscess-forming lymphadenitis, lymph node metastases, and malignant lymphoma still should be excluded.[48, 49] Bilateral diffuse lymph node enlargement without necrosis is most frequently caused by viral infections, such as mononucleosis, herpes, cytomegalovirus, rubella, or HIV. HIV infections can also present with cystic lesions in the parotid

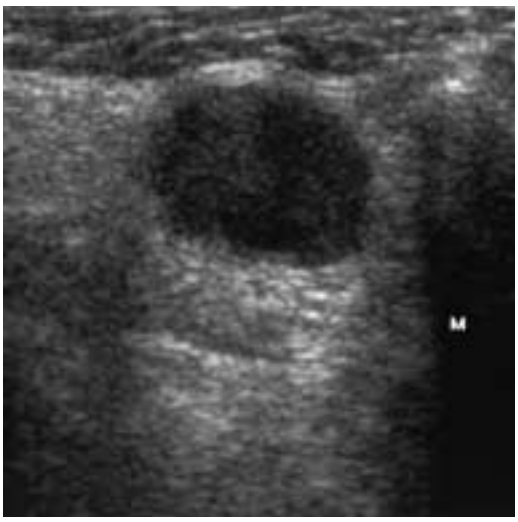

FIGURE 37-19 Reactive lymph node. A reactive enlarged node with a homogeneous pattern is identified in the submandibular region close to the mandible (*M*).

VIEW IMAGE

Copyright © 2003, Mosby, Inc. All rights reserved.

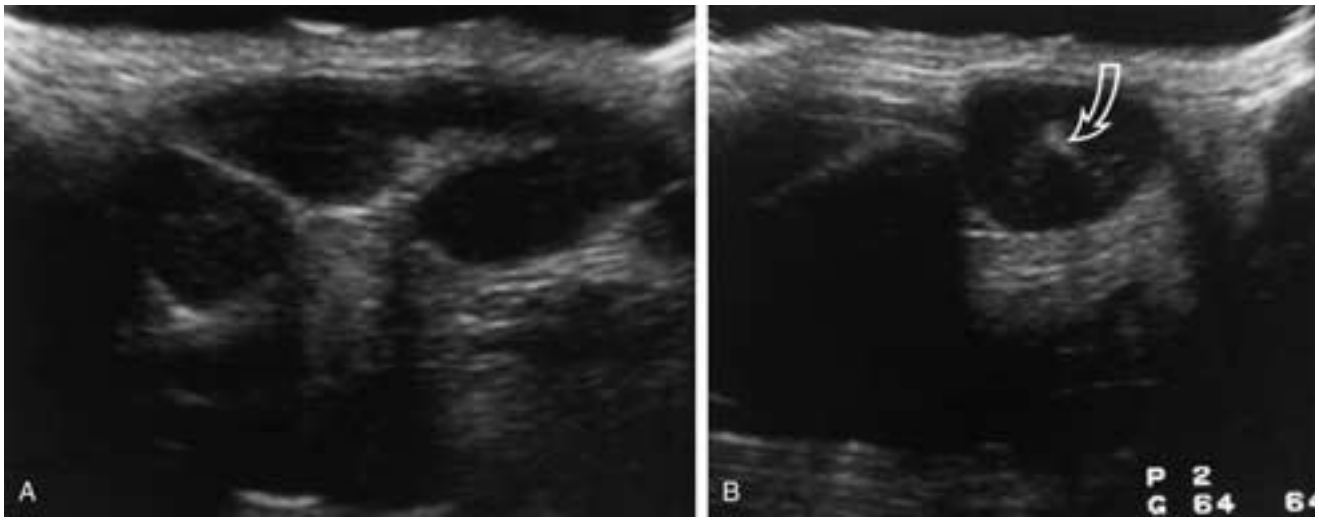

VIEW IMAGE

FIGURE 37-20 **A** and **B**, Tuberculous lymphadenopathy. Multiple enlarged, conglomerating lymph nodes that are hypoechoic, with enlarged through-transmission, are seen. This large submandibular node appears to be partly calcified (*arrow*). (Courtesy of Dr. F.B.L.M. Joosten.)

glands or with associated malignancies. Toxoplasmosis and sarcoidosis are rare causes of multiple cervical nodal enlargement. In sarcoidosis the salivary glands can be swollen, and a chest x-ray may reveal mediastinal lymph node enlargement. The diagnosis is made by serologic tests (angiotensin converting enzyme, muramidase), bronchial lavage, and histopathology. In cases of single or multiple nodal enlargements with homogenous reflection patterns, Castleman's disease should be in the differential diagnosis.[50]

Malignant Lymphomas

Hodgkin's and non-Hodgkin lymphomas can present with multiple or single abnormal nodes in the neck, either as the initial presenting symptom or as part of a more generalized disease. Ultrasound shows clearly delineated lymph nodes with a homogeneous, weak internal echo pattern, although spotty or dendritic hyperechoic areas can sometimes be seen. Power Doppler sonography shows highly perfused nodes with color signals in the center as well as in the nodal periphery in most lymphomas. However, this flow pattern with a reduced resistance index is not specific. It is reported that contrast-enhanced Doppler sonography can be useful in differentiating lymphoma from reactive nodes.[52]

Metastatic Lymphadenopathy

Metastases to the cervical lymph nodes most frequently originate from squamous cell carcinomas of the mucosal lining of the upper aerodigestive tract. Other primary sites of metastases are salivary gland, thyroid, and skin neoplasms. Metastatic patterns from skin melanomas differ from and are more variable than metastases from mucosal carcinomas.[53] Metastases from skin tumors are more often located in the superficial lymph nodes, such as those in the parotid gland, the nuchal area, or the posterior triangle. Their appearance on ultrasound, CT, and MR imaging is identical to that of squamous metastases, although melanoma metastases are more often hypervascular. Well-differentiated thyroid carcinomas have a very high rate of neck metastases, although these are often clinically occult. On ultrasound, every slightly enlarged node should be regarded as suspicious. Discrete calcifications or internal cysts may occasionally be seen. Imaging has relatively little utility in the management of papillary carcinoma in patients with N0 necks since the treatment is radioactive iodine.

Head and neck squamous cell carcinomas metastasize primarily to the cervical lymphatic system. The number and extent of metastases are important for the prognosis. Whereas only 7% of patients without lymph node metastases develop distant metastases, almost 50% of patients with more than three tumor-positive lymph nodes do so.[53] Palpation is the most widely used staging technique for the neck, but its sensitivity and specificity are both between 60% and 70%. As a consequence, there is a substantial risk of clinically occult metastases.[54, 55] For T1 to T3 oral, oropharyngeal, and supraglottic tumors, the risk of occult metastases is between 20% and 50%. In many head and neck primaries, both the ipsilateral and contralateral sides are at substantial risk of developing nodal metastases. The risk increases further if the primary has grown close to or extends across the midline.

Imaging can play a significant role in the staging and management of cervical nodal metastases. An accurate imaging method can help to detect occult metastases in the clinically N0 neck or to lower the risk of occult metastasis. In the latter case, one should realize that imaging can only decrease the risk of occult metastases; it can never reduce the risk to zero. In general, ultrasound is reported to be superior to palpation in detecting lymph node metastases.[56, 57] Whereas some authors report ultrasound to be superior to contrast-enhanced CT and MR imaging,[57, 58] others have found similar accuracy rates.[56, 59] Ultrasound examination of level I is assumed to be more difficult because of the presence of the submandibular gland and artifact caused by the adjacent mandible (Fig. 37-21).

Copyright © 2003, Mosby, Inc. All rights reserved.

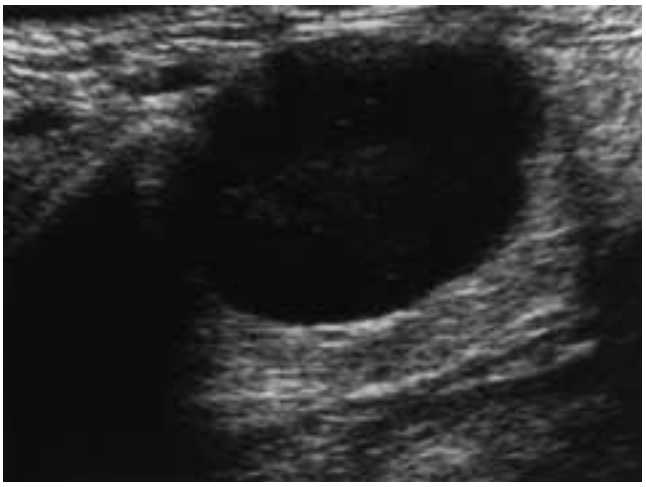

VIEW IMAGE

FIGURE 37-21 B-cell lymphoma. Adjacent to the mandible, a clearly delineated lymph node with homogeneous low echogeneity is seen. No hilar pattern can be seen. (Courtesy of Dr. F.B.L.M. Joosten.)

In patients with palpable suspicious lymph nodes, the role of imaging is quite limited, although it can help determine the tumor extent. If lymph nodes are fixed to the deep structures, most authors cite preference for CT or MR imaging to assess the extent of the tumor. However, it has been reported that ultrasound, in combination with palpation (i.e., sonopalpation),[60] can identify carotid wall invasion. The accuracy of ultrasound and other imaging techniques for the neck is dependent on the diagnostic criteria used in assessing for lymph node metastases.[61, 62] Although the resolution has improved in recent years, it is still not possible to detect small tumor deposits within lymph nodes.

Table 37-1
CRITERIA CONCERNING THE SIZE, SHAPE, AND GROUPING OF LYMPH NODES, AS REPORTED BY DIFFERENT AUTHORS

Author	Criteria
Van den Brekel[59]	Ax-min 11 mm at level II or 10 mm elsewhere or a grouping of three or more measuring 8 to 10 mm
Vassallo[63]	No size criterion; long/ax-min <2 or absence of a hilus or focal cortical widening
Bruneton[67]	8 mm ax-max and long/ax-max <1.5
Stern[97]	15 mm at all levels
Som[98]	15 mm at levels I and II or 10 mm elsewhere
Mancuso[99]	8 mm retropharyngeal or 15 mm at all other levels
Hillsamer[100]	Grouping of three or more measuring 8 to 15 mm
Friedman[101]	10 mm at all levels
Close[102]	30 mm ovoid shape or 10 mm round shape or a grouping of two or more measuring 10 to 30 mm
Steinkamp[103]	8 mm ax-min or 8 mm ax-max and long/ax-min <2
Tachimori[104]	5 mm minimal diameter and long/ax-min <2

Abbreviations: long, longitudinal diameter; ax-max, maximal axial diameter; ax-min, minimal axial diameter.

Diagnostic criteria include an increased size, a rounder shape, and the presence of irregular ultrasound reflection patterns caused by the tumor or by tumor necrosis or keratinization (Table 37-1). An echogenic hilus can be seen in 60% of nonmetastatic nodes and is not present in lymph nodes totally replaced by tumor. However, the hilus can remain when small tumor deposits are present. Focal cortical widening by tumor is reported to be a reliable criterion, as is a cystic pattern.[63, 64] In general, a round shape is considered more suspicious than an oval or flat shape.[65, 66] In reactive nodes, a transverse to longitudinal ratio of less than 0.5 is present in more than 80% of the cases.[67] However, most of the characteristic ultrasound features cannot be appreciated in lymph nodes smaller than 1 cm. As a consequence, for the clinically N0 neck, the size of lymph nodes remains an important criterion as well.[66] In this respect, the minimal diameter is the preferred axis to measure. However, any size criterion is a compromise, as a small cutoff point has high sensitivity and low specificity and vice versa. In a recent study on the ultrasound size criteria in the N0 neck,[69] it was shown that the often used 1-cm criterion provides a low sensitivity for this patient category. For level II nodes, a size criterion of 7 mm was optimal, whereas for the rest of the neck, lymph nodes with a minimal diameter of 6 mm were considered suspicious. In spite of these refinements, it is clear that size, shape, and irregular echo patterns are not very accurate for the clinically N0 neck.

In recent reports on power Doppler sonography, a parenchymal blood flow signal throughout the entire lymph node was present in over 80% of the larger metastatic lymph nodes, whereas reactively enlarged lymph nodes showed characteristic hilar perfusion.[70] Other characteristics that have been reported in metastatic lymph nodes include avascular areas, displacement of intranodal vessels, aberrant course of central vessels, and accessory peripheral vessels.[71] However, again with the use of Doppler sonography, it is not possible to make a histopathologic diagnosis, and some authors found skepticism about the applicability of this modality.[72, 73] Administration of galactose-based ultrasound contrast may improve the assessment of hilar and other adjacent vascularity. However, measured Doppler indices do not add to the criteria for a differential diagnosis. A combination of peripheral parenchymal nodal flow, internal architecture, and size will probably be the most accurate. However, application of these criteria to small lymph nodes may be impossible.

To enhance the accuracy of ultrasound, ultrasound-guided aspiration of lymph nodes has been used. To use this technique, considerable training is required.[74, 75] It is, of course, mandatory to be aware of the patterns of lymphatic spread from different tumors in order to select the lymph nodes at highest risk. It has been shown that ultrasound-guided FNAC has a very high specificity, approaching 100%. To obtain a high enough sensitivity, lymph nodes as small as 4 to 5 mm in the first two echelons should be aspirated. If ultrasound is used during follow-up, not only the size of the node is important, but also its evolution over time. In a previous report, we found that the diagnostic accuracy of ultrasound-guided FNAC had a sensitivity of 73% and a specificity of 100% in N0 necks.[59, 74] This was significantly better than the results obtained with CT or MR imaging. Only one other study compared ultrasound-guided

Copyright © 2003, Mosby, Inc. All rights reserved.

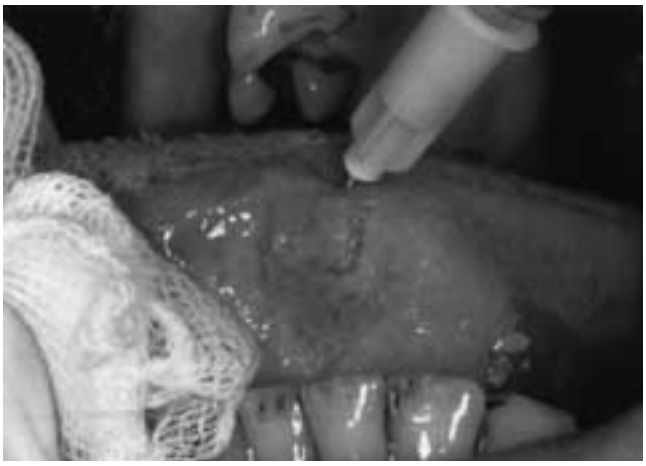

VIEW IMAGE

FIGURE 37-22 The sentinel node procedure. Initially, technetium-99-labeled colloidal albumin should be injected around the tumor in three or four locations.

FNAC to CT and MR imaging and found it to be superior as well.[76] Recently, however, in a multi-institutional study using ultrasound-guided aspiration, Takes et al. reported a sensitivity of only 42% in the N0 neck.[77, 78] However, in this series, only a few elective neck dissections were included in most centers, and some patients were irradiated before surgery. Righi et al. found a sensitivity of 50%, which was worse than the 60% for CT in their relatively small study.[79] However, in their study, most false negatives were found at the beginning of the study, and some of these involved irradiated patients or non–squamous cell carcinoma patients.

As these different sensitivities at least shed doubt on the accuracy of the technique, we recently started a study to define the causes of false-negative results. Using very sensitive molecular markers for the detection of tumor cells in the aspirate, preliminary results show that only a few positive aspirates are missed by the pathologist.[80] Recently, the most likely nodal drainage of a particular tumor has been identified by injecting a radiotracer into the region of the primary tumor and measuring the activity over various nodal regions. With the use of scintigraphic detection of this sentinel lymph node (Figs. 37-22 and 37-23) and subsequent

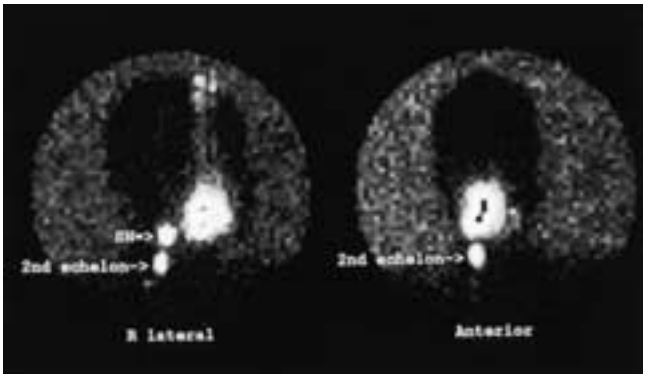

VIEW IMAGE

FIGURE 37-23 Several minutes after injection of technetium-99, the first-echelon node may be located with a gamma camera on lateral and posteroanterior (PA) images. It is essential to obtain both PA and lateral images; otherwise, the sentinel node may be missed by overprojection of the injection site.

Table 37-2
REPORTS OF DIFFERENT AUTHORS WHO ADOPTED A WAIT-AND-SEE POLICY FOR T1 AND T2 ORAL CARCINOMAS

Author	Patients Observed	Neck Recurrences	Patients Salvaged
Kligerman[105]	33	11 (33%)	3 (27%)
Ho[106]	28	10 (36%)	3 (30%)
Fakih[107]	40	23 (57%)	7 (30%)
Cunningham[108]	43	18 (42%)	9 (50%)
McGuirt[109]	103	37 (36%)	22 (59%)
Khafif[110]	396	90–95 (24%)*	53 (59%)
Vandenbrouck[111]	36	17 (47%)	14 (82%)
Van den Brekel[112]	77	14 (18%)	10 (71%)

Note: Only Van den Brekel et al. used ultrasound-guided FNAC in the initial assessment and follow-up.

ultrasound-guided aspiration of the node, we found that it is possible to aspirate from the sentinel node reliably and to confirm its identity by scintillation counting of the aspirate.[81] The aspirate is then examined for tumor cells. The use of sentinel node scintigraphy and the use of different aspiration techniques or needles might thus further improve the ultrasound-guided aspiration technique.

We have found ultrasound-guided FNAC to be highly specific and quite sensitive in detecting palpably occult metastases. In selected patients who can be treated with transoral excision for T1 and T2 oral, oropharyngeal, and supraglottic carcinomas, we rely on the ultrasound-guided FNAC findings and do not routinely treat the neck electively. These patients are followed very meticulously, using ultrasound-guided FNAC at regular intervals during the first year. So far, our preliminary experiences with this ''wait and see'' policy have been encouraging. Of the 77 patients who underwent a transoral excision without neck treatment in the last 4 years, and who have been followed for at least 1 year, 14 have failed in the neck (18%). Ten of these 14 were salvaged and are alive without tumor (a 71% salvage rate). This high salvage rate is certainly related to the short delay of the diagnosis of these 14 neck failures. These figures compare favorably to those quoted in the literature (Table 37-2).

The role of ultrasound in evaluating the posttreatment neck is controversial. The use of ultrasound or duplex Doppler for the follow-up of the treated neck has been investigated by several authors.[82–86] Westhofen showed that ultrasound-guided FNAC was superior to CT in detecting neck recurrences after previous treatment.[82]

OTHER CERVICAL SITES: CONGENITAL CYSTIC LESIONS AND NONNODAL MASSES OF THE NECK

In neck masses of unknown etiology, ultrasound provides a noninvasive method that can help differentiate between solid and cystic masses and may help in identifying the origin of a mass. Depiction of anatomic structures often allows differentiation of lymphadenopathy from tumors of the salivary glands or other soft tissues of the neck. Exact

Copyright © 2003, Mosby, Inc. All rights reserved.

localization of a mass, as well as typical ultrasound or Doppler sonography characteristics, can help differentiate between a primary mass such as a carotid body tumor and an enlarged lymph node.[87, 88] Congenital cystic masses such as branchial cleft cysts, thyroglossal duct cysts, and plunging ranulas have a characteristic sonographic appearance. Extralaryngeal laryngoceles can be followed through the thyrohyoid membrane and can be filled with air as well as fluid. Ultrasound can also be used to guide aspiration cytology of small masses or masses in proximity to the large vessels.

Cystic Lesions

This section describes the cysts in the neck apart from those in solid organs: the thyroglossal duct cyst, ranula, branchial cyst, cystic lymphangioma, and dermoid cyst.

The thyroglossal duct cyst (Fig. 37-24) accounts for the majority of cystic neck lesions. The cysts may occur at almost any age. They may be complicated by fistulas. Carcinomatous change occurs in 1% of cases. The anatomic location along the course of the thyroglossal duct usually suggests the diagnosis. The cysts may occur anywhere along the course of the duct remnant, from the base of the tongue to the suprasternal region, but most are located in the region of the hyoid bone. Most commonly, they are located in the midline, but approximately 33% may be located slightly off midline. The majority of off-midline cysts are located adjacent to the outer surface of the thyroid cartilage, deep to the strap muscles. High-resolution ultrasonography remains the ideal imaging modality. The sonographic appearance may vary from truly anechoic, to predominantly anechoic but containing internal debris (due to proteinaceous content), to a complex heterogeneous pattern and a uniformly heterogeneous appearance.[89] Posterior enhancement, a characteristic feature of an uncomplicated cyst, is reported to be present in approximately 90% of cases.[89, 90] Often it is difficult to identify this enhancement, particularly if the lesions occur in proximity to the airway. The cysts are well defined. The walls may be thin, thick (probably due to infection or cellular debris), or, rarely, imperceptible. The presence of a solid component is suspicious for carcinoma. Ultrasound-guided FNAC may not be necessary in patients undergoing surgery.

Ranulas are of two types. The simple ranula occurs in the floor of the mouth above the mylohoyoid muscle in the region of the sublingual gland and is truly an epithelium-lined cyst. A ''diving'' or ''plunging'' ranula results after the rupture of the simple ranula's wall. These are pseudocysts lined by dense connective tissue or granulation tissue. On ultrasound, ranulas are usually well-defined, cystic-appearing lesions. When simple they are confined to the sublingual region. When diving, the bulk of the lesion is typically identified in the submandibular region (Fig. 37-25).

Branchial cysts can be classified on the basis of their location (see Chapter 35). Superficial cysts may be seen in the region of the parotid or anterior to the sternocleidomastoid muscle. Deeper cysts are seen anterior to the great vessels (type 2 is the most frequent type) (Fig. 37-26). Extensions between the carotid arteries and toward the pharyngeal wall can be followed on ultrasound. Branchial cysts are most commonly discovered in young adults between 15 and 40 years of age. Clinically, branchial cysts appear rapidly over a period of several days as a mostly painless swelling in the upper region of the neck. Less often, the diagnosis is suggested by a history of a recurrent inflammatory neck mass, always at the same location. Ultrasound can usually confirm the diagnosis of a branchial cyst. Branchial cleft cysts may be difficult to distinguish from thyroglossal duct cysts (Fig. 37-27). However, the characteristic location and FNAC are helpful in differentiating the two cystic lesions.

A dermoid cyst is usually located at or near the midline around the hyoid bone. These cysts have an echogenic,

FIGURE 37-24 **A**, Thyroglossal duct cyst. Ultrasonography shows a large midline bilobular cystic lesion immediately caudal to the hyoid bone. The sonographic appearance is anechoic. **B**, CT confirms the ultrasonographic findings. (Courtesy of Dr. F.B.L.M. Joosten.)

VIEW IMAGE

Copyright © 2003, Mosby, Inc. All rights reserved.

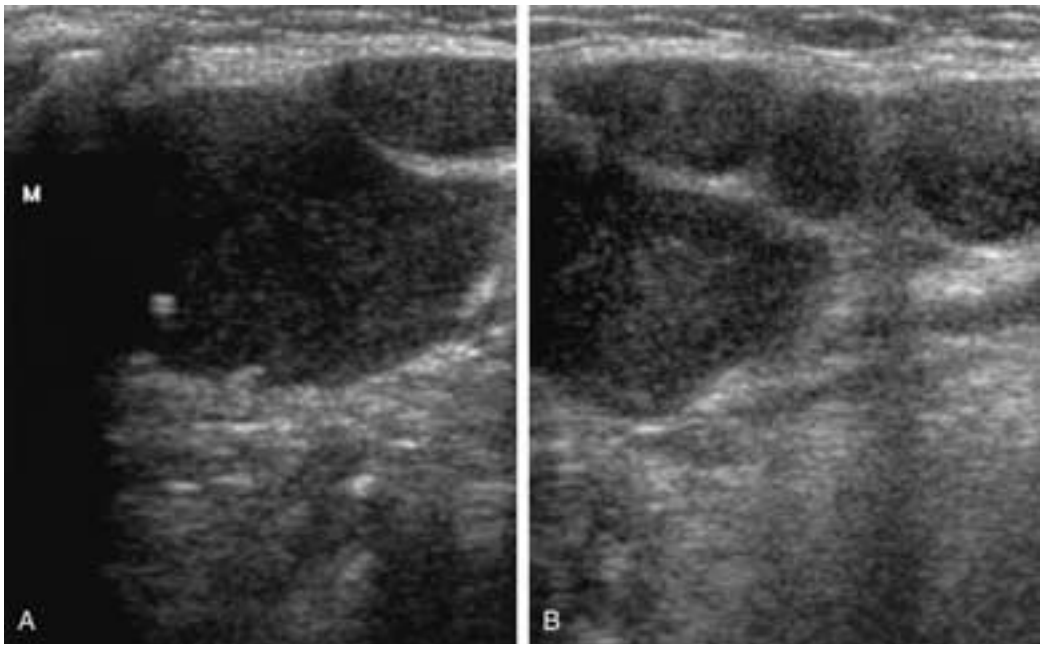

FIGURE 37-25 **A** and **B**, Plunging ranula. Coronal ultrasound demonstrates a multilobular cystic lesion in the submandibular space adjacent to the mandible (**M**) but extending beyond the mylohyoid muscle. The cysts are well defined and are not truly anechoic due to their high protein content.

VIEW IMAGE

pseudosolid appearance similar to that of a thyroglossal duct cyst. Preoperative differentiation between the two is not necessary, as this can be done at surgery.

Cystic hygroma and lymphangioma are discussed in the last section of this chapter.

Infectious Disease

In our experience, ultrasonography should not be the modality of first choice when there is a suspicion of inflammatory disease or abscesses in the neck. The appearance of abscesses may be misleading on ultrasonography, and they may be underdiagnosed. We recommend CT for confirming the diagnosis of a neck abscess or suppurative adenitis and for delineating the extent of disease. In selected cases, ultrasound may be used to guide aspiration or drain placement.

Lipomas

Lipomas are the most common benign mesenchymal tumor. They can arise in any location where fat is located.

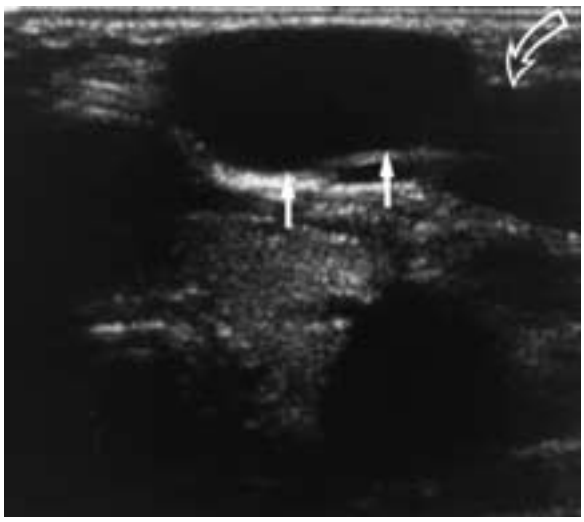

FIGURE 37-26 Brachial cleft cyst. This lateral cyst (*straight arrows*) lies beneath the platysma anterior to the sternocleidomastoid muscle (*curved arrow*). (Courtesy of Dr. F.J.A. Beek.)

VIEW IMAGE

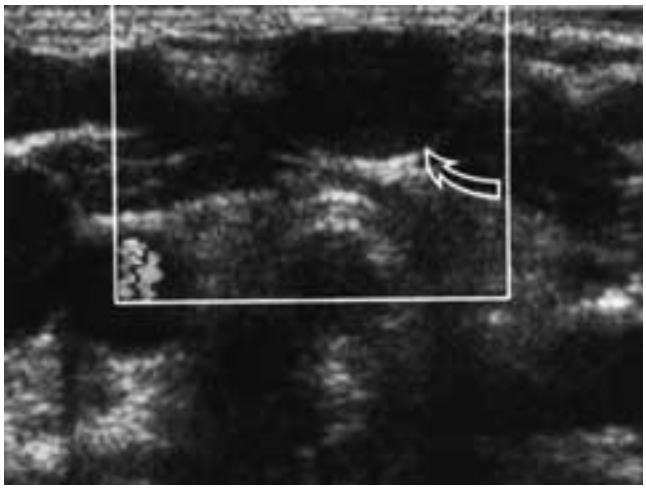

FIGURE 37-27 Thyroglossal duct cyst. Located near the midline, this homogeneous lesion (*arrow*) has low echogeneity. (Courtesy of Dr. F.J.A. Beek.)

VIEW IMAGE

Copyright © 2003, Mosby, Inc. All rights reserved.

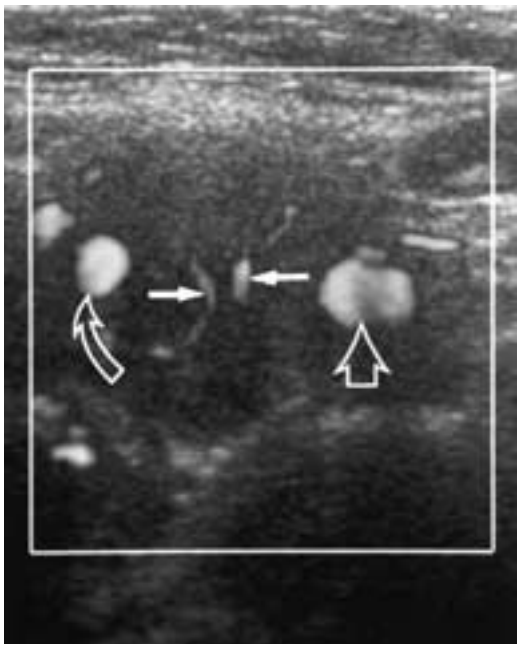

VIEW IMAGE

FIGURE 37-28 Carotid body paraganglioma. A large mass with vascular channels (*small arrows*) fills the crotch of the carotid artery, splaying the external carotid artery (*large curved arrow*) and the internal carotid artery (*large straight arrow*).

Fifteen percent of all lipomas occur in the head and neck. They are uncommon in children and most commonly present in the fifth and sixth decades. They are multiple in 5% of cases.

Clinical examination is often insufficient to identify the nature and exact origin of the mass, in which case imaging is necessary. The sonographic appearance of head and neck lipomas appears to be characteristic.[91, 92] Ahuja and coworkers found that head and neck lipomas are compressible. In most cases they are well-defined, elliptical masses parallel to the skin surface and hyperechoic relative to adjacent muscle. They typically have linear echoes at right angles to the ultrasound beam and display no distal enhancement or attenuation.[89] FNAC may be indicated if the diagnosis is not compatible with clinical symptoms. CT or MR imaging may be indicated to show the extent of the mass.

The differential diagnosis of lipoma includes epidermoid cysts, branchial cleft cysts, thyroglossal duct cysts, hemangiomas, and lymph nodes. In epidermoid, branchial cleft, and thyroglossal cysts, the linear echogenic lines so characteristic of a lipoma are not seen.[91] Hemangiomas may have a similar shape and similar echogenic lines but are hypoechoic, with a heterogeneous echo pattern, and contain cystic and sinusoidal spaces as well as the occasional phlebolith.[93] Normal nodes in the neck are hypoechoic and may have an anechoic hilum. Nodes from papillary carcinoma are hyperechoic relative to adjacent muscle. However, they do not have echogenic lines parallel to the skin surface.[94]

Neurogenic Tumors

Neurogenic lesions are relatively rare. The most commonly encountered neurogenic tumors in the neck are schwannomas, neurofibromas, and paragangliomas. Small neurofibromas and schwannomas appear as solid nodules. However, the diagnosis can be obtained with high certainty by performing MR imaging.

Color Doppler ultrasound may suggest the diagnosis of paraganglioma by showing flow in the vascular channels and the characteristic relationship of the mass to the carotid arteries (Fig. 37-28). Sonographic findings alone are insufficient for a conclusive diagnosis of these tumors. In practice, the value of ultrasound appears limited compared to MR imaging and angiography for the diagnosis of paraganglioma.

THE ROLE OF ULTRASOUND FOR EVALUATION OF INFANTS AND YOUNG CHILDREN

Ultrasound examination of neck masses in infants and children is very useful and is often the initial imaging modality.[95, 96] It provides immediate information regarding the location of a mass and determines whether the mass is cystic or solid. An indication of blood flow to the lesion can be assessed by color Doppler. Ultrasound is especially useful for soft, fluctuant masses (i.e., lymphangiomas, hemangiomas, and lipomas), because the ultrasonographic pattern of each of these lesions is quite distinct.

The characteristic appearance of many cystic lesions, including branchial cleft and thyroglossal duct cysts, has been discussed. Cystic hygromas or lymphangiomas are predominantly cystic, with multiple septations and loculations that can be variable in size.[96] Hemangiomas are solid lesions and are the most variable of all of these lesions sonographically; the appearance depends mainly on the size of vascular lesions. Cavernous hemangiomas consist of feeding vessels and larger sinuses that are seen as round or linear hypoechogenic areas within the otherwise echogenic mass (Fig. 37-29). Color Doppler imaging readily detects flow within this type of hemangioma. Capillary hemangiomas usually consist of small vessels that are not clearly resolved with ultrasound, giving the lesion a coarse, echogenic aspect.[96] Hemorrhage may occur often in lym-

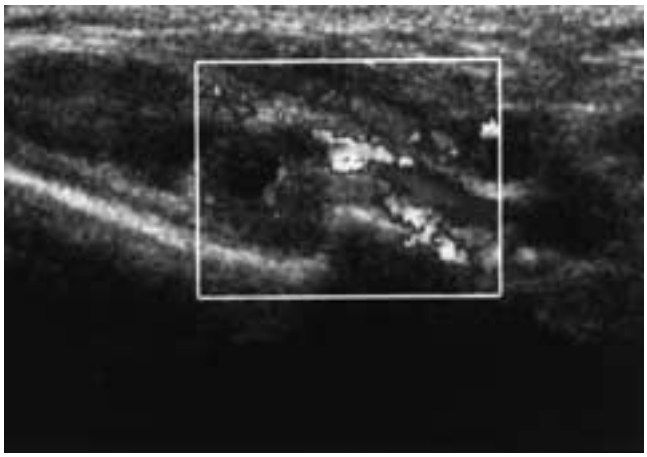

FIGURE 37-29 Cavernous hemangioma. Duplex Doppler ultrasonography shows a large, inhomogeneous lesion consisting of feeding vessels and larger sinuses that are seen as round or linear vascular areas. (Courtesy of Dr. F.J.A. Beek.)

VIEW IMAGE

Copyright © 2003, Mosby, Inc. All rights reserved.

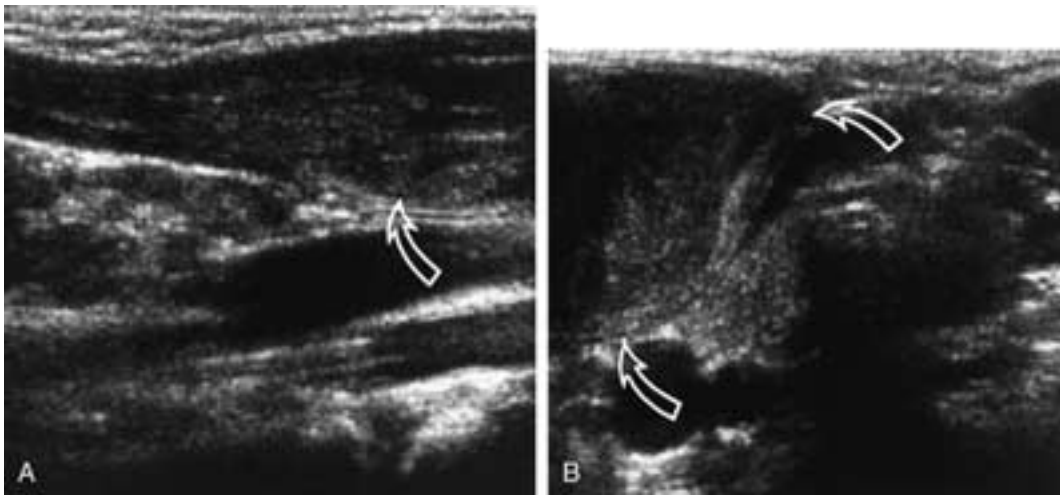

VIEW IMAGE

FIGURE 37-30 Fibromatosis colli. Oblique coronal ultrasound-image (**A**) shows that part of the caudal area (*curved arrow*) of the sternocleidomastoid muscle is enlarged. The axial image (**B**) shows the abnormality in the sternocleidomastoid muscle (*curved arrows*), which is slightly inhomogeneous and isoechoic. (Courtesy of Dr. F.J.A. Beek.)

phangiomas. If it is present, the normal anechoic fluid may become echogenic. Generally, CT or MR imaging is indicated in fluctuant lesions to demonstrate the extent of disease, particularly infiltration of surrounding structures.[96]

Fibromatosis colli or fibroma is a common benign tumor in a young infant (Fig. 37-30). Ultrasonography often shows an oval echogenic mass located in the sternocleidomastoid muscle. The clinical picture of torticollis combined with this ultrasound appearance secures the diagnosis.

In infants, carotid body tumors, malignant tumors of the neck such as sarcomas and neuroblastoma, may occur but are relatively uncommon. On ultrasonography, malignant tumors generally are echogenic, but if necrosis occurs, hypoechoic foci may be scattered throughout the tumor. CT and particularly MR imaging are usually required for delineation of the tumor extent.

REFERENCES

1. Santos JEC, Leiman G. Nonaspiration fine needle cytology: application of a new technique to nodular thyroid diseases. Acta Cytol 1988;32:353–356.
2. Taki S, Kakuda K, Kakuma K, et al. Thyroid nodules: evaluation with U.S.-guided core biopsy with an automated biopsy gun. Radiology 1997;202:874–877.
3. Sonography, CT, CT sialography, MRI and MRI sialography in investigation of the facial nerve and the differentiation between deep and superficial parotid lesions. Neuroradiology 1997;39(7):506–511.
4. Rouvière H: Anatomie des lymphatiques de l'homme. Paris: Masson, 1932.
5. Som PM. Lymph nodes of the neck. Radiology 1987;165:593–600.
6. Shah JP. Patterns of cervical lymph node metastasis from squamous carcinomas of the upper aerodigestive tract. Am J Surg 1990;160: 405–409.
7. Ezzat S, Sarti DA, Cain DR, et al. Thyroid incidentalomas: prevalence by palpation and ultrasonography. Arch Intern Med 1994:154:1838–1840.
8. Mulder JE. Thyroid disease in women. Med Clin North Am 1998;31:103–125.
9. Hopkins CR, et al. Thyroid and parathyroid imaging. Semin Ultrasound CT MR 1995;16(4):279–295.
10. Katz JF, Kane RA, Reyes J, et al. Thyroid nodules: sonographic-pathologic correlation. Radiology 1984;151:741–745.
11. De Marco D, Burgi U. Monitoring of treatment in thyroid diseases. Ther Umsch 1999;56(7):400–402.
12. Reading CC. Thyroid, parathyroid and cervical lymph nodes. In: Rifkin MD, ed. Syllabus: Special Course—Ultrasound. Oakbrook, Ill: RSNA, 1991;363–377.
13. Ralls PW, Mayekawa DS, Lee KP, et al. Color-flow Doppler sonography in Graves' disease: ''thyroid inferno.'' AJR 1988;150: 781–784.
14. Tessler FN. Thyroid sonography: current applications and future directions. AJR 1999;173(2):473–434.
15. Yarman S, Mudun A, Alagol F, Azizilerli H, Ogunz H, Cantez S. Scintigraphic varieties in Hashimoto's thyroiditis and comparison with ultrasonography. Nucl Med Comm 1997;18:951–956.
16. Sabel MS, Staren ED, Gianakakis LM, et al. Effectiveness of the thyroid scan in evaluation of the solitary thyroid nodule. Am Surg 1997;63:660.
17. Aluja A, Chick W, King W, et al. Clinical significance of the comet-tail artifact in thyroid ultrasound. J Clin Ultrasound 1996;24: 129–133.
18. Cotran RS, Kumar V, Robbins SL. Robbins Pathologic Basis of Disease. 5th ed. Philadelphia: WB Saunders, 1994;1121–1171.
19. Hatabu H, Kasagi K, Yamamoto K, et al. Cystic papillary carcinoma of the thyroid gland: a new sonographic sign. Clin Radiol 1991;43:121–124.
20. Solbiati L, et al. Ultrasonography of the neck. Radiol Clin North Am 1992;30(5):941–945.
21. Burch HB. Evaluation and management of the solid thyroid nodule. Endocrinol Metab Clin North Am 1995;24:663–710.
22. Rago T, Vitti P, Chiovato L, et al. Role of conventional ultrasonography in predicting malignancy in ''cold'' thyroid nodules. Eur J Endocrinol 1998;138:41–46.
23. Belfiore A, La Rosa GL, La Porta GA, et al. Cancer risk in patients with cold thyroid nodules: intake, sex, age, and multinodularity. Am J Med 1992;93:363–369.
24. Shimamoto K, Endo TM, Ishigaki T, et al. Thyroid nodules: Evaluation with color Doppler ultrasonography. J Ultrasound Med 1993;12:673–678.
25. Ezzat S, Sart DA, Cain DR, et al. Thyroid incidentalomas: prevalence by palpation and ultrasonography. Arch Intern Med 1994;154:1838–1840.
26. Tan GH, Gharib H. Thyroid incidentalomas: management approaches to nonpalpable nodules discovered incidentally on thyroid imaging. Ann Intern Med 1997;126:226–231.
27. Danese D, Sciacchitano S, Farsetti A, et al. Diagnostic accuracy of conventional versus sonography-guided fine-needle aspiration biopsy of the thyroid nodules. Thyroid 1998;8:15–21.
28. Antonelli A, Miccoli P, Ferdeghini M, et al. Role of neck ultrasonography in the follow-up of patients operated on for thyroid cancer. Thyroid 1995;5:25–28.

Copyright © 2003, Mosby, Inc. All rights reserved.

29. Sutton RT, Reading CC, Charboneau JW, et al. Ultrasound-guided biopsy of neck masses in postoperative management of patients with thyroid cancer. Radiology 1988;168:769–772.
30. Giammarile F, Bielle E, Fattapposta A, et al. Sclerotherapy of thyroid cysts with tetracycline hydrochloride. Minerva Endocrinol 1994; 19(3):143–147.
31. Boonstra CE, Jackson CE. Hyperparathyroidism detected by routine serum calcium analysis. Prevalence in the clinical population. Ann Intern Med 1965;63:468–479.
32. McIvor NP, Freeman JL, Salem S. Ultrasonography of the thyroid and parathyroid glands. ORL 1993;55:303–308.
33. Randel SB, Gooding GA, Clark OH, et al. Parathyoid variants: U.S. evaluation. Radiology 1987;165:191–194.
34. Clark OH, Duh QY. Primary hyperparathyroidism, a surgical perspective. Endocrinol Metab Clin North Am 1989;18:701–704.
35. Gooding GA. Sonography of the thyroid and parathyroid. Radiol Clin North Am 1993;967–989.
36. Koslin DB, Adams J, Andersen P, et al. Preoperative evaluation of patients with primary hyperparathyroidism: role of high-resolution ultrasound. Laryngoscope 1997;107(9):1249–1253.
37. Higgins CB. Role of MR imaging in hyperparathyroidism. Radiol Clin North Am 1993;31:1017–1028.
38. Rice DH. Advances in diagnosis and management of salivary gland diseases. West J Med 1984;140:238–249.
39. Yoshimura Y, Inoue Y, Odagawa T. Sonographic examination of sialolithiasis. J Oral Maxillofac Surg 1989;47(9):907–912.
40. Bruneton JN, Fenart D, Vallicioni J, et al. Semeiologie echographique des tumeurs de la parotide. A propos de 40 observations. J Radiol 1980;61:151–154.
41. Shimizu M, Ussmuller J, Hartwein J, et al. Statistical study for sonographical differential diagnosis of tumorous lesions in the parotid gland. Oral Surg Oral Med Oral Pathol Oral Radiol Endod 1999;88:226–233.
42. Schick S, Steiner E, Gahleiter A, et al. Differentiation of benign and malignant tumors of the parotid gland: value of pulsed Doppler and color Doppler sonography. Eur Radiol 1998;8(8):1462–1467.
43. Cerovac SS, Vowles RH, Bleach NR. Sudden parotid swelling due to spontaneous haemorrhage. J Laryngol Otol 1998;112(5):497–498.
44. Lazor JB, Cunningham MJ, Eavey RD, et al. Comparison of computed tomography and surgical findings in deep neck infections. Otolaryngol Head Neck Surg 1994;111:746–750.
45. Latifi HR, Siegel MJ. Color Doppler flow imaging of pediatric soft tissue masses. J Ultrasound Med 1994;13:165–169.
46. Ochi K, Ogino S, Fukamizu K, et al. US-guided drainage of deep neck space abscess. Acta Otolaryngol 1994;1:120–123.
47. Yeow KM, Hao SP, Liao CT. US-guided percutaneous catheter drainage of a deep retropharyngeal abscess. J Vasc Intervent Radiol 1999;10:1365–1369.
48. Ying M, Ahuja AT, Evans R, et al. Cervical lymphadenopathy—sonographic differentiation between tuberculous nodes and nodal metastases from non-head and neck carcinomas. J Clin Ultrasound 1998;26:383–389.
49. Winkelbauer F, Denk DM, Ammann M, et al. Sonographic diagnosis of cervical lymph-node tuberculosis. Ultraschall Med 1993;14:28–31.
50. Kooper DP, Tiwari RM, van der Valk P. Castleman's disease as an uncommon cause of a neck mass. Eur Arch Otorhinolaryngol 1994;251:370–372.
51. Tesoro-Tess JD, Balzarini L, Ceglia E, et al. Magnetic resonance imaging in the initial staging of Hodgkin's disease and non-Hodgkin lymphoma. Eur J Radiol 1991;12:81–90.
52. van den Brekel MW, Pameijer FA, Koops W, et al. Computed tomography for the detection of neck node metastases in melanoma patients. Eur J Surg Oncol 1998;24:51–54.
53. Leemans CR, Tiwari RM, Nauta JJP, et al. Regional lymph node involvement and its significance in the development of distant metastases in head and neck carcinoma. Cancer 1993;71:452–456.
54. Martinez Gimeno C, Rodriguez EM, Vila CN, et al. Squamous cell carcinoma of the oral cavity: a clinicopathologic scoring system for evaluating risk of cervical lymph node metastasis. Laryngoscope 1995;105:728–733.
55. Prayer L, Winkelbauer H, Gritzmann N, et al. Sonography versus palpation in the detection of regional lymph-node metastases in patients with malignant melanoma. Eur J Cancer 1990;26:827–830.
56. Ishii J, Amagasa T, Tachibana T, et al. US and CT evaluation of cervical lymph node metastasis from oral cancer. J Craniomaxillofac Surg 1991;3:123–127.
57. Furukawa M, Kaneko M, Mochimatsu I, et al. Comparative studies of diagnosis with US or CT of the cervical lymph node metastases in head and neck cancer. [In Japanese.] Nippon Jibiinkoka Gakkai Kaiho 1991;4:577–586.
58. Quetz JU, Rohr S, Hoffmann P, et al. B-image sonography in lymph node staging of the head and neck area. A comparison with palpation, computerized and magnetic resonance tomography. [In German.] HNO 1991;39:61–63.
59. van den Brekel MW, Castelijns JA, Stel HV, et al. Modern imaging techniques and ultrasound-guided aspiration cytology for the assessment of neck node metastases: a prospective comparative study. Eur Arch Otorhinolaryngol 1993;250:11–17.
60. Mann WJ, Beck A, Schreiber J, et al. Ultrasonography for evaluation of the carotid artery in head and neck cancer. Laryngoscope 1994;104:885–888.
61. van den Brekel MW, Castelijns JA, Snow GB. Detection of lymph node metastases in the neck: radiologic criteria [editorial; comment]. Radiology 1994;192:617–618.
62. Don DM, Anzai Y, Lufkin RB, et al. Evaluation of cervical lymph node metastases in squamous cell carcinoma of the head and neck [abstract]. Laryngoscope 1995;105:669–674.
63. Vassallo P, Wernecke K, Roos N, et al. Differentiation of benign from malignant superficial lymphadenopathy: the role of high-resolution US. Radiology 1992;183:215–220.
64. Ahuja A, Ying M, King W, et al. A practical approach to ultrasound of cervical lymph nodes. J Laryngol Otol 1997;111:245–256.
65. Steinkamp HJ, Heim T, Zwicker C, et al. Feasibility of the differential diagnostic imaging of neck lymphomas. [In German.] Aktuelle Radiol 1993;3:226–237.
66. Steinkamp HJ, Cornehl M, Hosten N, et al. Cervical lymphadenopathy: ratio of long- to short-axis diameter as a predictor of malignancy. Br J Radiol 1995;68:266–270.
67. Bruneton JN, Balu-Maestro C, Marcy PY, et al. Very high frequency (13 MHZ) ultrasonographic examination of the normal neck: detection of normal lymph nodes and thyroid nodules. J Ultrasound Med 1994;13:87–90.
68. Van den Brekel MWM, Stel HV, Castelijns JA, et al. Cervical lymph node metastasis: assessment of radiologic criteria. Radiology 1990;177:379–384.
69. Van den Brekel MWM, Castelijns JA, Snow GB. The size of lymph nodes in the neck on sonograms as a radiologic criterion for metastasis: How reliable is it? AJNR 1998;19:695–700.
70. Steinkamp HJ, Teichgraber UK, Mueffelmann M, et al. Differential diagnosis of lymph node lesions. A semiquantitative approach with power Doppler sonography. Invest Radiol 1999;34:509–515.
71. Tschammler A, Wirkner H, Ott G, et al. Vascular patterns in reactive and malignant lymphadenopathy. Anal Biochem 1996;6: 473–480.
72. Giovagnorio F, Rusticali A, Araneo AL. Color and pulsed Doppler evaluation of benign and malignant adenopathy. Clin Imaging 1997;21:163–169.
73. Chang DB, Yuan A, Yu CJ, et al. Differentiation of benign and malignant cervical lymph nodes with color Doppler sonography. AJR 1994;162:965–968.
74. van den Brekel MWM, Castelijns JA, Stel HV, et al. Occult metastatic neck disease: detection with US and US-guided fine-needle aspiration cytology. Radiology 1991;180:457–461.
75. McIvor NP, Freeman JL, Salem S, et al. Ultrasonography and ultrasound-guided fine-needle aspiration biopsy of head and neck lesions: a surgical perspective. Laryngoscope 1994;104:669–674.
76. Atula TS, Varpula MJ, Kurki TJI, et al. Assessment of cervical lymph node status in head and neck cancer patients—palpation, computed tomography and low field magnetic resonance imaging compared with ultrasound-guided fine-needle aspiration cytology. Eur J Radiol 1997;25:152–161.
77. Takes RP, Knegt P, Manni JJ, et al. Regional metastases in head and neck squamous cell carcinoma: revised value of US with US-guided FNAB. Radiology 1996;198:819–823.
78. van den Brekel MWM. US-guided fine-needle aspiration cytology of neck nodes in patients with N0 disease [letter; comment]. Radiology 1996;201:580–581.
79. Righi PD, Kopecky KK, Caldemeyer KS, et al. Comparison of ultrasound fine needle aspiration and computed tomography in patients undergoing elective neck dissection. Head Neck Surg 1997;19:604–610.
80. Brakenhoff RH, Stroomer JGW, ten Brink C, et al. Sensitive detection of squamous cells in bone marrow and blood of head and

Copyright © 2003, Mosby, Inc. All rights reserved.

neck cancer patients by e48 reverse transcriptase polymerase chain reaction. Clin Cancer Res 1999;5:725–732.
81. Nieuwenhuis EJC, Colnot DR, Pijpers HJ, et al. Lymphoscintigraphy and ultrasound guided aspiration cytology of sentinel nodes in head and neck cancer patients. Recent Results Cancer Res 2000;157:206–217.
82. Westhofen M. Ultrasound b-scans in the follow-up of head and neck tumors. Head Neck Surg 1987;9:272–278.
83. Ahuja A, Ying M, Leung SF, et al. The sonographic appearance and significance of cervical metastatic nodes following radiotherapy for nasopharyngeal carcinoma. Clin Radiol 1996;51:698–701.
84. Szmeja Z, Wierzbicka M, Kaczmarek J, et al. The value of ultrasound examination in early detection of nodal disease in the neck in follow-up patients operated for head and neck cancer. Br J Cancer 1998;77(Suppl 1):15.
85. Steinkamp HJ, Maurer J, Cornehl M, et al. Recurrent cervical lymphadenopathy: differential diagnosis with color-duplex sonography. Eur Arch Oto-Rhino-Laryngol 1994;251:404–409.
86. Hessling KH, Schmelzeisen R, Reimer P, et al. Use of sonography in the follow-up of preoperatively irradiated efferent lymphatics of the neck in oropharyngeal tumours. J Cranio-Maxillo-Fac Surg 1991;19: 128–130.
87. Schroder RJ, Maurer J, Hidajat N, et al. Signal-enhanced colour-coded duplex sonography of reactively and metastatically enlarged lymph nodes. [In German.] Rofo 1998;168:57–63.
88. Toriyabe Y, Nishimura T, Kita S, et al. Differentiation between benign and metastatic cervical lymph nodes with ultrasound. Clin Radiol 1997;52:927–932.
89. Ahuja AT, King AD, King W, et al. Thyroglossal duct cysts: sonographic appearances in adults. AJNR 1999(20):579–582.
90. Wadsworth DT, Siegel M. Thyroglossal duct cyst: variability of sonographic findings. AJR 1994;163:1475–1477.
91. Ahuja AT, King AD, Kew J, et al. Head and neck lipomas: sonographic appearance. AJNR 1998;19:505–508.
92. Gritzman N, Schratter M, Traxler M, et al. Sonography and computed tomography in deep cervical lipomas and lipomatosis of the neck. J Ultrasound Med 1988;7:451–456.
93. Yang WT, Ahuja A, Metreweli C. Sonographic features of head and neck hemangiomas and vascular malformations: review of 23 patients. J Ultrasound Med 1996;16:39–44.
94. Ahuja A, Chow L, Mok CO, et al. Metastatic cervical lymph nodes in papillary carcinoma of the thyroid: ultrasound and histological correlation. Clin Radiol 1995;50:229–231.
95. Kraus R, Han BK, Babcock DS, et al. Sonography of neck masses in children. AJR 1986;146:609–614.
96. Swischuk LE, John SD. Neck masses in infants and children. Pediatr Oncol Imaging Radiol Clin North Am 1997;35(6):1329–1340.
97. Stern WBR, Silver CE, Zeifer BA, et al. Computed tomography of the clinically negative neck. Head Neck 1990;12:109–113.
98. Som PM. Detection of metastasis in cervical lymph nodes: CT and MR criteria and differential diagnosis. [review]. AJR 1992;158: 961–969.
99. Mancuso AA, Harnsberger HR, Muraki AS, et al. Computed tomography of cervical and retropharyngeal lymph nodes: normal anatomy, variants of normal, and applications in staging head and neck cancer. Part II: pathology. Radiology 1983;148:715–723.
100. Hillsamer PJ, Schuller DE, McGhee RB, et al. Improving diagnostic accuracy of cervical metastases with computed tomography and magnetic resonance imaging. Arch Otolaryngol Head Neck Surg 1990;116:1297–1301.
101. Friedman M, Roberts N, Kirshenbaum GL, et al. Nodal size of metastatic squamous cell carcinoma of the neck. Laryngoscope 1993;103:854–856.
102. Close LG, Merkel M, Vuitch MF, et al. Computed tomographic evaluation of regional lymph node involvement in cancer of the oral cavity and oropharynx. Head Neck 1989;11:309–317.
103. Steinkamp HJ, Hosten N, Richter C, et al. Enlarged cervical lymph nodes at helical CT. Radiology 1994;191:795–798.
104. Tachimori Y, Kato H, Watanabe H, et al. Neck ultrasonography for thoracic esophageal carcinoma. Ann Thoracic Surg 1994;57:1180–1183.
105. Kligerman J, Lima RA, Soares JR, et al. Supraomohyoid neck dissection in the treatment of T1/T2 squamous cell carcinoma of oral cavity. Am J Surg 1994;168:391–394.
106. Ho CM, Lam KH, Wei WI, et al. Treatment of neck nodes in oral cancer. Surg Oncol 1992;1:73–78.
107. Fakih AR, Rao RS, Patel AR. Prophylactic neck dissection in squamous cell carcinoma of oral tongue: a prospective randomized study. Semin Surg Oncol 1989;5:327–330.
108. Cunningham MJ, Johnson JT, Myers EN, et al. Cervical lymph node metastasis after local excision of early squamous cell carcinoma of the oral cavity. Am J Surg 1986;152:361–366.
109. McGuirt WF Jr, Johnson JT, Myers EN, et al. Floor of mouth carcinoma. The management of the clinically negative neck. Arch Otolaryngol Head Neck Surg 1995;121:278–282.
110. Khafif RA, Gelbfish GA, Tepper P, et al. Elective radical neck dissection in epidermoid cancer of the head and neck. A retrospective analysis of 853 cases of mouth, pharynx, and larynx cancer. Cancer 1991;67:67–71.
111. VandenBrouck C, Sancho-Garnier H, Chassagne D, et al. Elective versus therapeutic radical neck dissection in epidermoid carcinoma of the oral cavity: results of a randomized clinical trial. Cancer 1980;46:386–390.
112. Van den Brekel MWM, Reitsma LC, Quak JJ, et al. Sonographically guided aspiration cytology of neck nodes for selection of treatment and follow-up in patients with N0 head and neck cancer. AJR 1999;20:1727–1731.

Copyright © 2003, Mosby, Inc. All rights reserved.

38

Parapharyngeal and Masticator Space Lesions

Peter M. Som and Hugh D. Curtin

INTRODUCTION
CLINICAL AND IMAGING ASSESSMENT OF THE PARAPHARYNGEAL SPACE
PARAPHARYNGEAL SPACE ANATOMY
CLINICAL PRESENTATIONS OF PARAPHARYNGEAL SPACE MASSES
IMAGING PATHOLOGY AFFECTING THE PARAPHARYNGEAL SPACE
Diseases and Tumors Arising in the Parapharyngeal Space
Infections
Tumors
Salivary Gland Tumors
Neurogenic Tumors
Paragangliomas
Other Tumors
Lymph Nodes
Benign Soft-Tissue Masses and Cysts
Vascular and Neurologically Related Abnormalities
Trauma
Diseases and Tumors Arising in the Skull Base
Diseases and Tumors Arising Intracranially
MASTICATOR SPACE ANATOMY
The Masticator Muscles and Mastication
CLINICAL PRESENTATION OF MASTICATOR SPACE MASSES
THE BUCCAL FAT
IMAGING PATHOLOGY AFFECTING THE MASTICATOR SPACE
Inflammatory Diseases
Denervation Atrophy
Masticator Muscle Hypertrophy
Tumors and Nonneoplastic Masses

INTRODUCTION

By the 1930s, the parapharyngeal and masticator spaces had been described; their anatomy is presented in Chapter 34.[1–5] In the past few decades, further refinement of knowledge regarding their anatomy has helped explain either the containment or spread of diseases affecting these spaces.[6–9] As pathology, either inflammatory or neoplastic, involving one of these spaces often affects the other, it is appropriate to discuss these two important spaces together.

CLINICAL AND IMAGING ASSESSMENT OF THE PARAPHARYNGEAL SPACE

Of the two spaces, the parapharyngeal space is the more difficult to examine clinically, as it lies buried deep in the upper neck. It is immediately lateral to the pharynx and deep to the mandibular ramus, the pterygoid muscles, and the parotid gland (Figs. 38-1 and 38-2). Thus protected, it is often only by bimanual palpation that one can detect clinically even a moderate-sized mass (1 to 1.5 cm). When a mass becomes sufficiently large, usually 1.5 to 4 cm, it initially displaces the lateral pharyngeal wall and tonsil medially and then pushes the parotid gland laterally. It is only when a very large parapharyngeal space mass (5 to 6 cm) fills the entire space that a fullness near the angle of the mandible can be detected clinically. Thus, clinical evaluation of this space is quite limited, and over the past three decades the clinician has turned to the radiologist for help in assessing pathology in this region.

Prior to the CT era, very limited radiologic information could be gleaned from plain films and multidirectional tomograms. The degree of lesion vascularity could be identified on a conventional angiogram; however, only a lesion such as a paraganglioma, with its characteristic

Copyright © 2003, Mosby, Inc. All rights reserved.

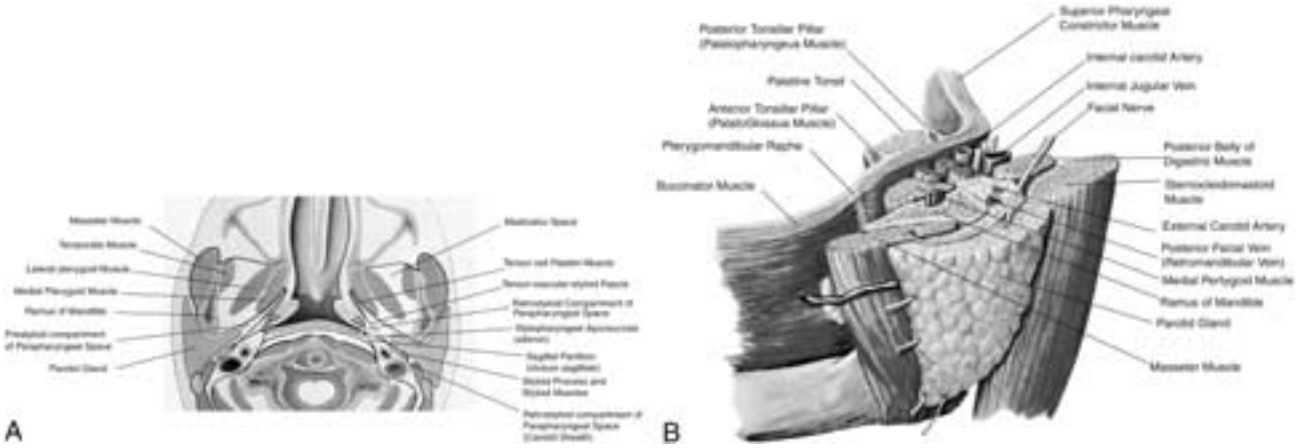

VIEW IMAGE

FIGURE 38-1 Axial diagram (**A**) through the level of C1. Note the complex relationships between the fascia and spaces about the nasopharynx. In particular, note the fascia surrounding the mandibular ramus, as well as the masseter, medial pterygoid, and lateral pterygoid muscles. This fascia defines the masticator space. Immediately deep to the masticator space is the prestyloid compartment of the parapharyngeal space. Medial and posterior to the prestyloid compartment is the retrostyloid compartment of the parapharyngeal space. Diagram (**B**) of the normal anatomic relationships of the left parapharyngeal space, as seen obliquely and from above. Note how the deep portion of the parotid gland extends into the parapharyngeal space.

VIEW IMAGE

hypervascular appearance, or an aneurysm could be confidently diagnosed. A lesion could also be identified as being hypovascular, but a salivary gland tumor could not be differentiated from a schwannoma or other such pathology. If there was parotid gland fullness, a conventional sialogram could, in most cases, distinguish an intraparotid from an extraparotid mass. This was accomplished by noting if the parotid ducts encircled the mass completely or only partially. A completely encircled mass arose within the parotid gland, while a partially encircled mass could be of either intraparotid or extraparotid origin. Using this diagnostic approach, it is estimated that a preoperative diagnosis was possible in only 20% to 40% of cases and necessitated performing angiograms and sialograms on virtually all patients.[10–15]

In the late 1970s, the clinical application of CT scanning to head and neck lesions allowed the radiologist for the first time to visualize directly a soft-tissue mass in the parapharyngeal space. However, the relatively low resolution of these early CT scanners made the use of CT sialography necessary to clearly identify the parotid gland parenchyma and to distinguish it from the fat in the parapharyngeal space.[16–18] When high-resolution CT scanners were developed, CT sialography was no longer required to accomplish this localization.[7, 19]

Concurrent with the development of CT scanning, surgery also experienced new advances. Prior to the late 1970s, all parapharyngeal space lesions were approached via a parotid incision, regardless of whether or not the tumor was truly of parotid origin. This approach reflected the surgeon's belief that a confident preoperative distinction between an intraparotid and an extraparotid mass could not be made. As most of these tumors were parotid in origin, a transparotid approach was deemed necessary to protect the facial nerve. However, even in the best hands, manipulation of this nerve was accompanied by a small but significant morbidity. If this could be avoided, it would be better for patient and physician alike.

In the late 1970s and early 1980s the surgical philosophy changed, in part, because of the new developments in sectional imaging. If the surgeon could know preoperatively that a mass was extraparotid in origin, then a transcervical approach could be used without manipulation of the facial nerve (Fig. 38-3). The result was that only those patients with true intraparotid tumors would require a transparotid approach.[7, 20] Because of this new surgical concept, the surgeon relied even more on the imaging diagnosis, and this in turn prompted the radiologist to develop sectional imaging criteria that distinguished intraparotid from extraparotid masses.

The most reliable CT criterion used to make this distinction was the observation of the effect of a mass on the fat within the prestyloid compartment of the parapharyngeal space. If this fat was seen separating the deep portion of the parotid gland and a mass on all axial scans through the lesion, the mass was of extraparotid origin. If this fat was not visualized on all scans, the lesion was probably of parotid origin. However, a very large extraparotid mass could so compress this fat that the fat was not seen on CT. Assessing these circumstances, most surgeons concluded that if the fat plane was not seen on all scans, a transparotid approach should be used to protect the facial nerve during surgery.

CT also provided information about the internal architecture of the lesion, so that a solid mass could be differentiated from a cystic one, and the size of the mass could be accurately evaluated for proper surgical planning. In addition, clinically silent lymph nodes or other pathology could be identified.

Dynamic CT also gave information on the rate of contrast enhancement within a lesion. This enhancement may result either from the progressive extravascular accumulation of contrast material in a hypovascular mass (a schwannoma or salivary gland tumor) or from the rapid intravascular accumulation of contrast in a hypervascular mass (a paraganglioma).[8, 21, 22] To differentiate between a vascular and a hypovascular mass, dynamic scans

Copyright © 2003, Mosby, Inc. All rights reserved.

VIEW IMAGE

FIGURE 38-2 Block diagram showing the relationships of the prevertebral space (*1*), the danger space (*2*), the visceral compartment (*3*), the parapharyngeal spaces and the carotid sheaths (*4*), the submandibular space (*5*), the masticator spaces (*6*), and the parotid gland (*7*). Axial cuts have been made at a level just caudal to the skull base and at a level in the midneck to illustrate the cross-sectional relationships of these spaces. In particular, note the relationship of the masticator space to the parapharyngeal space and the temporal extension of the masticator space.

must be obtained during the vascular filling phase, which occurs within the first seconds after contrast administration. After this time, the contrast is in an equilibration phase in both vascular and hypovascular lesions, and any distinction between the mode of contrast accumulation is impossible (Fig. 38-4).

Hypervascular lesions have a very rapid filling phase and, because of their rich venous drainage, a rapid washout phase. By contrast, hypovascular lesions have a slow ''shoulder'' of contrast filling and, because of a paucity of veins, a prolonged washout phase. Thus, on scans taken after the contrast filling phase, the hypovascular mass often has more retained contrast than the hypervascular lesion and on CT appears more enhanced. For this reason, routine contrast-enhanced CT scans should not be used to critically assess lesion vascularity.

As a result of these advances, radiologists were now able to improve the rate of preoperative diagnosis of parapharyngeal space masses to 80% to 90%. In most cases, parotid tumors could now be distinguished from extraparotid lesions and paragangliomas could be distinguished from hypovascular tumors. However, the confident differentiation of a schwannoma from an extraparotid salivary gland tumor remained impossible.

MR imaging provided an even more reliable distinction between intraparotid and extraparotid lesions, and it allowed differentiation between most schwannomas and extraparotid salivary gland tumors. This was possible because compared to CT, MR imaging more consistently visualized the parapharyngeal space fat, and the internal carotid artery (ICA) was more reliably identified by its MR signal flow void than by its enhancement on CT.[9, 23–26] The more consistent visualization of the ICA was key to the imaging differential diagnosis, as both parotid and extraparotid salivary gland tumors displaced the ICA posteriorly. By comparison, the paragangliomas and most schwannomas displaced the ICA anteriorly.[8, 27–35] An additional advantage of MR imaging over CT was the observation that the contour of a mass was usually better identified on MR imaging, and

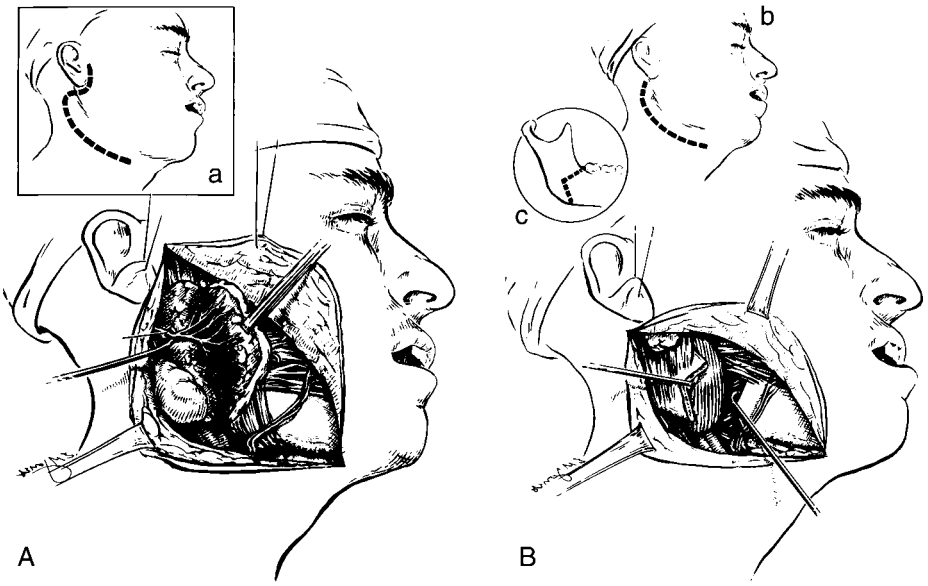

FIGURE 38-3 Diagrams of the right neck illustrating the typical parotid incision (a) and the typical parotid exposure of the facial nerve (**A**). The typical transcervical incision is shown in (b) and the typical transcervical exposure is illustrated in **B**. Note that in the transcervical exposure, the facial nerve is not within the surgical field. A variety of mandibular surgical maneuvers allow delivery of the intact tumor. An angle mandibulotomy is illustrated in (c).

VIEW IMAGE

Copyright © 2003, Mosby, Inc. All rights reserved.

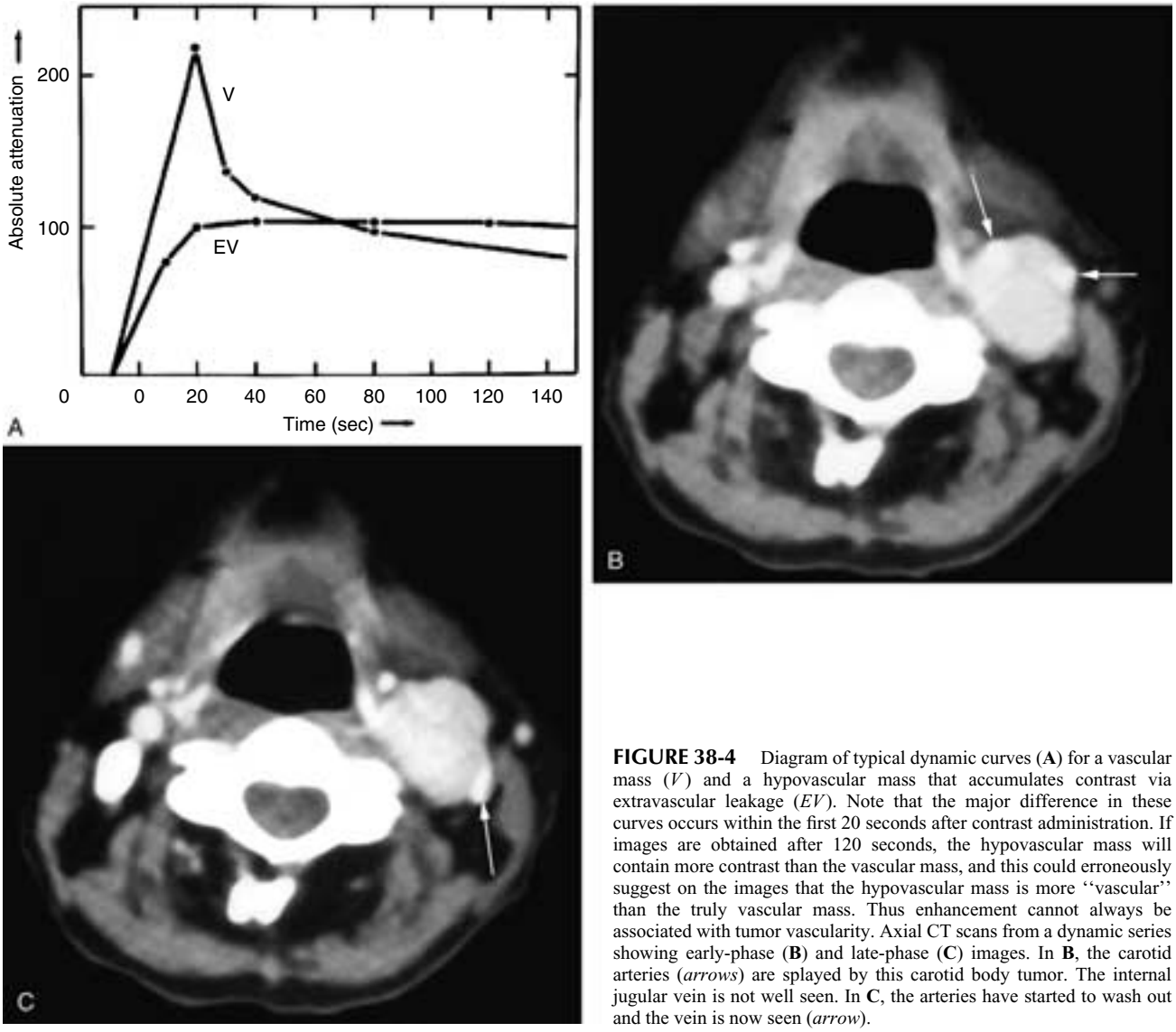

FIGURE 38-4 Diagram of typical dynamic curves (**A**) for a vascular mass (*V*) and a hypovascular mass that accumulates contrast via extravascular leakage (*EV*). Note that the major difference in these curves occurs within the first 20 seconds after contrast administration. If images are obtained after 120 seconds, the hypovascular mass will contain more contrast than the vascular mass, and this could erroneously suggest on the images that the hypovascular mass is more ''vascular'' than the truly vascular mass. Thus enhancement cannot always be associated with tumor vascularity. Axial CT scans from a dynamic series showing early-phase (**B**) and late-phase (**C**) images. In **B**, the carotid arteries (*arrows*) are splayed by this carotid body tumor. The internal jugular vein is not well seen. In **C**, the arteries have started to wash out and the vein is now seen (*arrow*).

VIEW IMAGE

the smooth contours of a paraganglioma could be differentiated from the invasive margins of a vascular metastasis.[9] Lastly, with MR imaging, moderate- to large-caliber, rapid-flow vessels could be identified by their flow voids, using flow-sensitive sequences, or by MR angiography. Only small-caliber, slow-flow vessels could not be visualized on MR imaging; their identification required conventional angiography.

At present, if the radiologist utilizes both clinical and imaging information, a correct preoperative diagnosis can be made in 90% to 95% of patients with a parapharyngeal space mass. These figures reflect the dramatic influence that CT and MR imaging have had on the diagnosis and surgical planning of these cases.

Inherent in the imaging localization of a parapharyngeal space mass is a precise assessment of the size of the lesion, as this helps determine the surgical approach.[36] This information applies primarily to the deep parotid masses; this topic is discussed in Chapter 39.

PARAPHARYNGEAL SPACE ANATOMY

The anatomy of the parapharyngeal space is discussed in detail in Chapter 34. In summary, the parapharyngeal space extends on either side of the neck from the skull base to the styloglossus muscle at the level of the angle of the mandible. The space extends along the sides of the nasopharynx up to the pterygomandibular raphe anteriorly. The parapharyngeal space is separated from the retropharyngeal space by the sagittally oriented cloison sagittale fascia. It is also separated from the danger space by the deep layer of the deep cervical fascia (Figs. 38-1, 38-2, and 38-5).

Each fat-filled parapharyngeal space is subdivided by the tensor-vascular-styloid fascia into a prestyloid and a retrostyloid compartment. For the purposes of this discussion, the carotid sheath will be considered to be in the retrostyloid compartment, as described in Chapter 34. The deep portion of the parotid gland bulges into the lateral aspect of the prestyloid compartment, extending through the

Copyright © 2003, Mosby, Inc. All rights reserved.

stylomandibular tunnel anterior to the styloid process, the styloid muscles, and the retrostyloid compartment.

CLINICAL PRESENTATIONS OF PARAPHARYNGEAL SPACE MASSES

The most pliable border of the parapharyngeal space is its medial wall. The pharyngeal constrictor muscles are immediately adjacent to the medial aspect of the prestyloid compartment of the parapharyngeal space. Most masses greater than 1.5 cm in diameter cause some medial displacement of the nasopharyngeal and oropharyngeal walls, often depressing the ipsilateral soft palate.

Most of the lateral wall of the parapharyngeal space is rigid, supported by the ramus of the mandible and the pterygoid muscles. However, long-standing lesions can remodel the mandible, displacing it laterally and anteriorly. The only truly pliable portion of the lateral wall is where the retromandibular portion of the parotid gland protrudes into the prestyloid compartment, and almost any parapharyngeal space mass can displace this gland laterally. In such cases, a clinician may mistake an extraparotid mass, and its resulting parotid fullness, for a parotid lesion. Only a very large parapharyngeal space mass can distend the most caudal aspect of this space, producing a fullness near the angle of the mandible.[15, 18, 37–41] If the lesion is large enough, the temporomandibular joint may also be dislocated.

Parapharyngeal space masses produce relatively few symptoms, which may explain why such lesions often grow

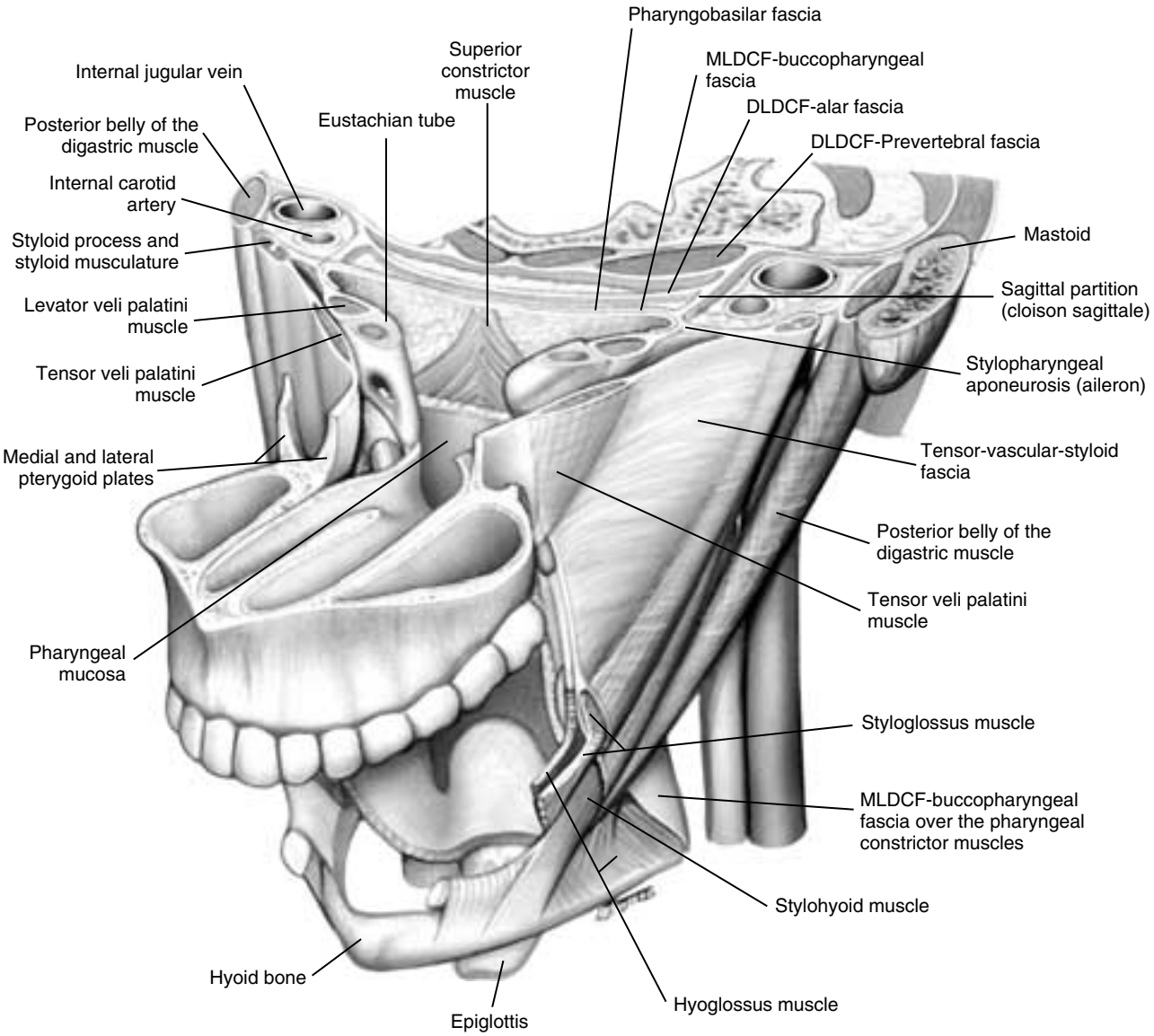

FIGURE 38-5 Drawing of the face and upper neck as seen from the left oblique view and from above. The parotid glands and the masticator space structures have been removed, as has the fat in the prestyloid compartment of the parapharyngeal space. This fat would have been just lateral to the tensor-vascular fascia. A horizontal cut has been made just below the level of the skull base, and an additional horizontal cut has been made through the lower maxillary sinuses, removing the facial structures.

VIEW IMAGE

Copyright © 2003, Mosby, Inc. All rights reserved.

to 4 to 6 cm in diameter before diagnosis. The displacement of the pharyngeal wall and the parotid gland rarely produces pain, and these masses are usually discovered incidentally either by the patient or by a clinician during a routine examination. However, patients with parapharyngeal space masses may have specific complaints such as sore throat, a change in voice quality, dysphagia, trismus, nasal obstruction, or a sensation of aural fullness. With schwannomas, paragangliomas, and malignant lesions, deficits of any or all of the last four cranial nerves may occur, and if the skull base is involved by a malignancy or an infection, headache or local pain may be present.[13, 41, 42]

In terms of imaging, the most important landmarks to note when evaluating a parapharyngeal space mass are (1) the deep portion of the parotid gland and the stylomandibular tunnel region; (2) the ICA, its size, shape, and the direction of any displacement; (3) the direction of any displacement of the fat of the prestyloid compartment; and (4) the effect of a mass on the surrounding structures, including the pharynx, masticator space, mandible, and skull base.

A discussion of the differential diagnoses of diseases that affect the prestyloid and retrostyloid compartments of the parapharyngeal space follows. A summary of these differential diagnoses is given in Tables 38-1 and 38-2.

Table 38-1
PARAPHARYNGEAL SPACE MASSES: PRESTYLOID COMPARTMENT

Tumors of Salivary Gland Origin	
Deep portion of parotid gland	
Common benign:	pleomorphic adenoma
Rare malignant:	mucoepidermoid carcinoma
	adenoid cystic carcinoma
	acinic cell carcinoma
Salivary rest:	pleomorphic adenoma
Lipoma	
Prominence of Pterygoid Venous Plexus	
Common:	normal variant
Uncommon:	reflecting venous hypertension in the neck
Branchial Cyst	
Abscess Of:	
Pharyngeal origin (primarily tonsillitis)	
Parotid origin (acute sialadenitis)	
Masticator space origin (primarily odontogenic in origin)	
Extension of abscess in lower neck	
Spread From:	
Pharyngeal tumor:	squamous cell carcinoma
	minor salivary gland carcinoma
	lymphoma
	common: non-Hodgkin's lymphoma
	uncommon: Hodgkin's lymphoma
Metastatic nodes:	level II nodes
	retropharyngeal nodes
Parotid tumor:	mucoepidermoid carcinoma
	squamous cell carcinoma
	adenocarcinoma not otherwise specified
Masticator space tumor:	metastatic squamous cell carcinoma
	sarcoma
Intracranial origin:	meningioma
	rare glioma
Skull base:	osteochondroma
	osteoma
	chondrosarcoma
	chordoma
Neurogenic Tumor	
Uncommon: schwannoma, usually of the sympathetic plexus	
Rare: neurofibroma	

IMAGING PATHOLOGY AFFECTING THE PARAPHARYNGEAL SPACE

Diseases and Tumors Arising in the Parapharyngeal Space

Infections

Most infections that involve the parapharyngeal space arise in adjacent spaces and spread via the parapharyngeal space pathway to other areas. In one series, 50% of the patients with abscesses in the parapharyngeal space had received antibiotics for an infection of the ear, nose, or throat prior to the development of the abscess.[43] In another study, most patients had a history of a recent upper aerodigestive tract infection, especially tonsillitis, with or without treatment, prior to the spread of disease to the parapharyngeal space. The most common isolates were *Streptococcus*, *Staphylococcus*, *Bacteroides*, *Micrococcus*, *Neisseria*, *Candida*, *Enterobacter*, *Enterococcus*, *Peptostreptococcus*, *Proteus*, *Proprionobacter*, and *Pseudomonas*. There were patients with no growth on culture but with organisms found on Gram's stain. The main complications of parapharyngeal space infections were jugular vein thrombosis, carotid artery aneurysm and rupture, mediastinitis, and, rarely, meningitis from a large retropharyngeal-parapharyngeal space abscess.[43]

In another study of adult patients, the distribution of abscesses in the major deep spaces of the neck was five sublingual, four parapharyngeal, three retropharyngeal, three submaxillary, three visceral, and one in the deep posterior triangle. The source of infection was odontogenic in six patients, pharyngeal in three, otogenic in one, and not identified in six. Most patients presented with pain and neck swelling; a positive culture was obtained in only 56.2%, with no predominant organism identified. Antibiotic therapy and surgical drainage were the mainstay of treatment, and two cases were complicated by internal jugular vein thrombophlebitis.[44]

In one review, intraoperative findings confirmed the CT diagnosis of parapharyngeal space abscess in 76.3% of the patients. The false-positive rate was 13.2%, and the false-negative rate was 10.5%. The sensitivity of CT for detection of parapharyngeal space or retropharyngeal space abscess was 87.9%. This study's documentation emphasizes the importance of correlating the imaging interpretation with the clinical examination findings before surgical intervention, a belief shared by most clinicians.[45, 46]

In still another study, the spaces involved by abscesses were the peritonsillar space (72 patients), the parapharyngeal space (8 patients), the submandibular space (7 patients), the retropharyngeal space (1 patient), the subcutaneous region (1 patient), the anterior visceral compartment (1 patient), and the carotid sheath (1 patient). Of the 19 patients who did not have a peritonsillar space infection, the origin of the infection was found in 8, and 4 of these were

Copyright © 2003, Mosby, Inc. All rights reserved.

odontogenic. Thirty-eight patients required surgical drainage of the abscess, and five patients underwent a tracheotomy for dyspnea. The combination of early imaging diagnosis, effective antimicrobial therapy, and intensive surgical management contributed to the good prognosis.[47]

Finally, in a study involving the incidence of deep space abscesses in children, peritonsillar abscesses were the most common (49%), followed by retropharyngeal (22%), submandibular (14%), buccal (11%), parapharyngeal (2%), and mandibular (2%) space infections. The most common pathogens isolated were the aerobes beta-hemolytic streptococcus (18%) and *Staphylococcus aureus* (18%), the anaerobes *Bacteroides melaninogenicus* (17%) and *Veillonella* (14%), and the gram-negative organism *Haemophilus parainfluenzae* (14%). Beta-lactamase production by aerobic pathogens was detected in 22% of cultures. In this study, the sensitivity of CT in detecting the presence of an abscess versus cellulitis was high (91%); however, the specificity was low (60%). It was concluded that the treatment of head and neck space infections in children should consist of accurate physical diagnosis aided by imaging studies, empiric antibiotic therapy that covers gram-negative and beta-lactamase-producing organisms as well as gram-positive organisms and anaerobes, and timely surgical intervention when indicated.[48]

Thus, most infections that result in a parapharyngeal space abscess arise either in the palatine tonsil or pharynx or are odontogenic in origin. The CT findings of cellulitis involving the parapharyngeal space are those of ''dirty'' fat and often some swelling of the fat in the prestyloid compartment (Fig. 38-6). On MR imaging, there usually is a decrease in the normal high T1-weighted signal intensity of fat and an increase in the T2-weighted signal intensity due to fluid accumulation.

Identification of an abscess is the critical contribution that imaging adds to these cases. The abscess cavity, as elsewhere in the body, has a low-attenuation necrotic, pus-filled center with a thick, irregular, enhancing rim on CT. On MR imaging, the central pus or necrotic region has a low or intermediate T1-weighted and a high T2-weighted signal intensity, and there is enhancement of a thick, irregular abscess rim. The presence of the abscess rim differentiates phlegmon from an abscess, and this is best identified on a contrast-enhanced study, either CT or MR imaging. In fact, many authors believe that the imaging diagnosis of an abscess should be made only when an enhancing rim is identified about the central region of pus. If no such rim is seen, the imaging diagnosis should be that of phlegmon and cellulitis.

The differentiation of a parapharyngeal space abscess from cellulitis is clinically important because an abscess should be drained expeditiously, as a mycotic aneurysm of the internal carotid artery has been reported to occur in as few as 10 days after the development of such an abscess. On the other hand, surgical exploration of cellulitis in the vain pursuit of a nonexistent abscess is inadvisable.[49, 50]

Tumors

Almost all of the tumors that occur in the parapharyngeal space arise either from the deep portion of the parotid gland

Table 38-2
PARAPHARYNGEAL SPACE MASSES: RETROSTYLOID COMPARTMENT

Neurogenic Origin:	common:	schwannoma of cranial nerves IX, X, XI, XII
	uncommon:	neurofibroma of cranial nerves IX, X, XI, XII
	rare:	neurosarcoma
neurogenic tumor spread:		nasopharyngeal carcinoma lymphoma: non-Hodgkin's meningioma
Vascular Origin:	internal carotid artery:	aneurysm/pseudoaneurysm dissection thrombosis ectasia medial deviation congenital arteriosclerotic
	internal jugular vein:	thrombosis/thrombophlebitis tumor invasion ectasia
Paraganglioma:	glomus jugulare glomus vagale carotid body tumor	
Abscess/Cellulitis		
Spread From:		
Pharyngeal tumor:	squamous cell carcinoma minor salivary gland carcinoma lymphoma common: non-Hodgkin's lymphoma uncommon: Hodgkin's lymphoma	
Metastatic nodes:	level II nodes retropharyngeal nodes	
Parotid tumor:	mucoepidermoid carcinoma squamous cell carcinoma adenocarcinoma not otherwise specified	

Copyright © 2003, Mosby, Inc. All rights reserved.

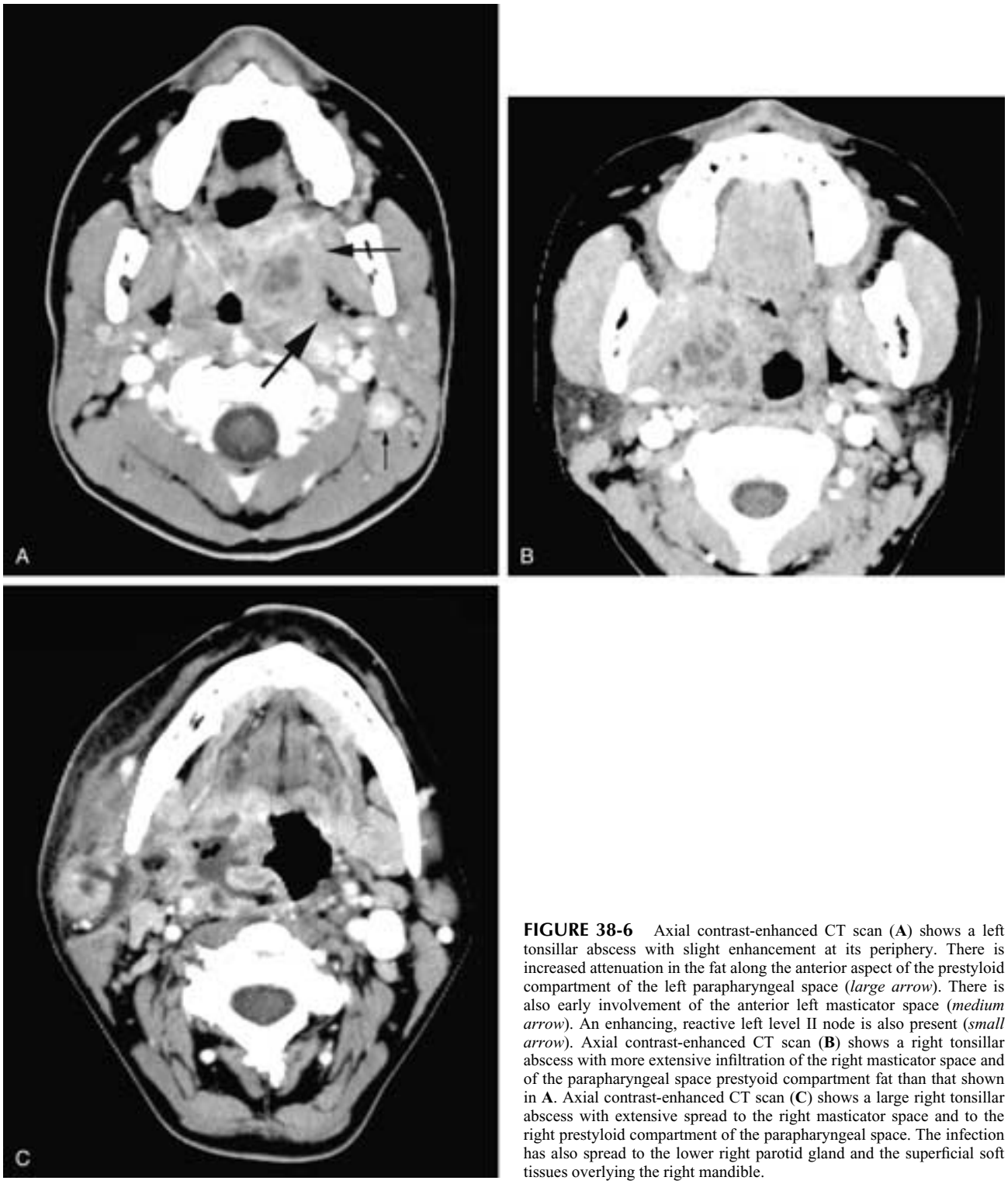

FIGURE 38-6 Axial contrast-enhanced CT scan (**A**) shows a left tonsillar abscess with slight enhancement at its periphery. There is increased attenuation in the fat along the anterior aspect of the prestyloid compartment of the left parapharyngeal space (*large arrow*). There is also early involvement of the anterior left masticator space (*medium arrow*). An enhancing, reactive left level II node is also present (*small arrow*). Axial contrast-enhanced CT scan (**B**) shows a right tonsillar abscess with more extensive infiltration of the right masticator space and of the parapharyngeal space prestyoid compartment fat than that shown in **A**. Axial contrast-enhanced CT scan (**C**) shows a large right tonsillar abscess with extensive spread to the right masticator space and to the right prestyloid compartment of the parapharyngeal space. The infection has also spread to the lower right parotid gland and the superficial soft tissues overlying the right mandible.

VIEW IMAGE

in the prestyloid compartment or from neural–related elements in the retrostyloid compartment. Although statistically the most common masses in the parapharyngeal space are hyperplastic or metastatic level II lymph nodes, they are not included in most clinical series of parapharyngeal space masses, as they are not considered to be primary lesions of this space. The imaging of such lymph nodes is discussed in Chapter 36. They are mentioned in this chapter only as they pertain to the differential diagnosis of other parapharyngeal space masses. There are also a number of reviews of imaging of the parapharyngeal space. They all agree that MR imaging should be the initial study of choice and that CT is better for detecting the presence of early bone changes and calcifications.[9, 27, 51–55]

Copyright © 2003, Mosby, Inc. All rights reserved.

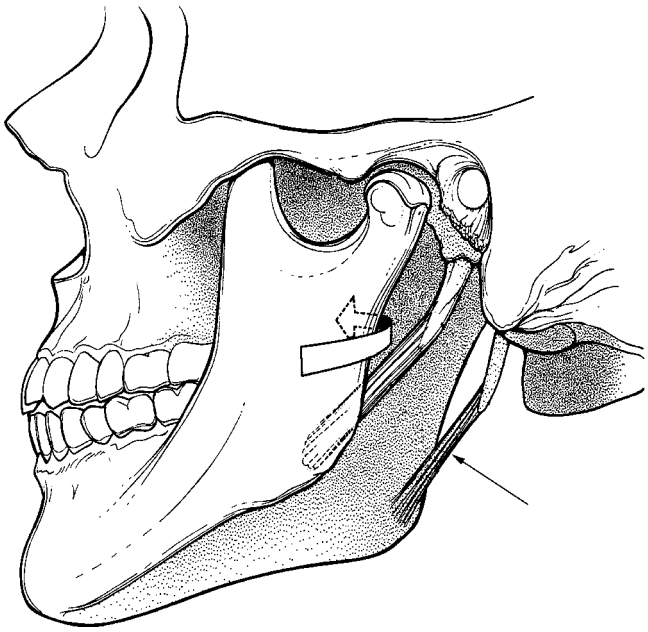

VIEW IMAGE

FIGURE 38-7 Drawing of a lateral view of the left side of the mandible and skull base. The stylomandibular ligament (*arrow*) is shown extending from the styloid process to the inner aspect of the ramus of the mandible. The curved arrow extends through the stylomandibular tunnel. It is through this tunnel that the deep portion of the parotid gland extends. This always places this portion of the parotid gland ventral to the styloid process and its muscles. Since the carotid sheath (or retrostyloid compartment of the parapharyngeal space) is dorsal to the styloid process, the ICA is always dorsal to the deep portion of the parotid gland.

Salivary Gland Tumors

The most common primary neoplasms to arise in the parapharyngeal space are of salivary gland origin. These include tumors arising in the parotid gland, in salivary rests within the prestyloid compartment fat of the parapharyngeal space, and in the minor salivary glands of the pharyngeal mucosa. As a group, they account for 40% to 50% of all parapharyngeal space masses, and 80% to 90% of these tumors are benign pleomorphic adenomas. The most common malignancies are mucoepidermoid carcinomas, adenoid cystic carcinomas, and acinic cell carcinomas. Hughes et al. found that 40% of their series were benign salivary gland tumors and 13% were malignant salivary gland lesions.[56] Those salivary gland tumors that arise in the pharyngeal mucosa and then spread into the parapharyngeal space are not usually considered in the analysis of parapharyngeal space lesions. Those tumors are discussed in Chapter 28.

The vast majority of primary tumors affecting the parapharyngeal space arise from the deep portion of the parotid gland, and almost all of them are pleomorphic adenomas. The next most common benign lesions arise in extraparotid salivary rests in the prestyloid compartment fat, and they are also predominantly pleomorphic adenomas. The tumors that arise from the pharyngeal mucosal minor salivary glands are primarily malignant, and they, along with nasopharyngeal carcinoma, account for most of the malignancies that affect the parapharygneal space.

The deep or retromandibular portion of the parotid gland (deep to the facial nerve) lies behind and just medial to the mandibular ramus (Fig. 38-1). The parotid gland actually passes through the rigid stylomandibular tunnel, whose margins are the posterior edge of the ramus of the mandible, the undersurface of the middle cranial fossa, and the styloid process and stylomandibular ligament (Fig. 38-7). Thus, the deep portion of the parotid gland lies in the lateral aspect of the prestyloid compartment of the parapharyngeal space and anterior to the retrostyloid compartment and the internal carotid artery.[8, 27] Most of the tumors arising in the deep portion of the parotid gland are roughly ovoid in shape; however, occasionally they have a dumbbell shape, with the waist of the tumor lying in the plane of the rigid stylomandibular tunnel (Figs. 38-8 and 38-9). In such dumbbell tumors, the deep portion of the mass is often clinically unappreciated, and imaging studies are necessary to fully identify the extent of the lesion. Most surgeons believe that any large or relatively immobile parotid mass requires an imaging study so that the palpable portion of the mass is not clinically misinterpreted as representing the entire tumor.

An unusual case of a Warthin's tumor of the deep portion of the parotid gland was reported, with extensive protrusion into the parapharyngeal space. The tumor was partially cystic and had the MR imaging characteristics suggestive of a Warthin's tumor, as discussed in Chapter 39. This is an atypical location for this tumor, and rarely does it grow large enough to present as a parapharyngeal space mass.[57]

On imaging, pleomorphic adenomas have noninfiltrating margins. When small, they are spherical in shape and primarily homogeneous (Figs. 38-8 and 38-9). When larger than 1.5 to 2 cm in diameter, they tend to develop lobulated contours; are nonhomogeneous, with sites of cystic degeneration and necrosis; and may contain areas of hemorrhage (Fig. 38-10). Occasionally calcification within the tumor

FIGURE 38-8 Drawing of a large pleomorphic adenoma of the deep portion of the left parotid gland as viewed from obliquely and above. The mass displaces the pharyngeal wall toward the midline and lies anterior to the internal carotid artery. See Figure 38-1B.

VIEW IMAGE

Copyright © 2003, Mosby, Inc. All rights reserved.

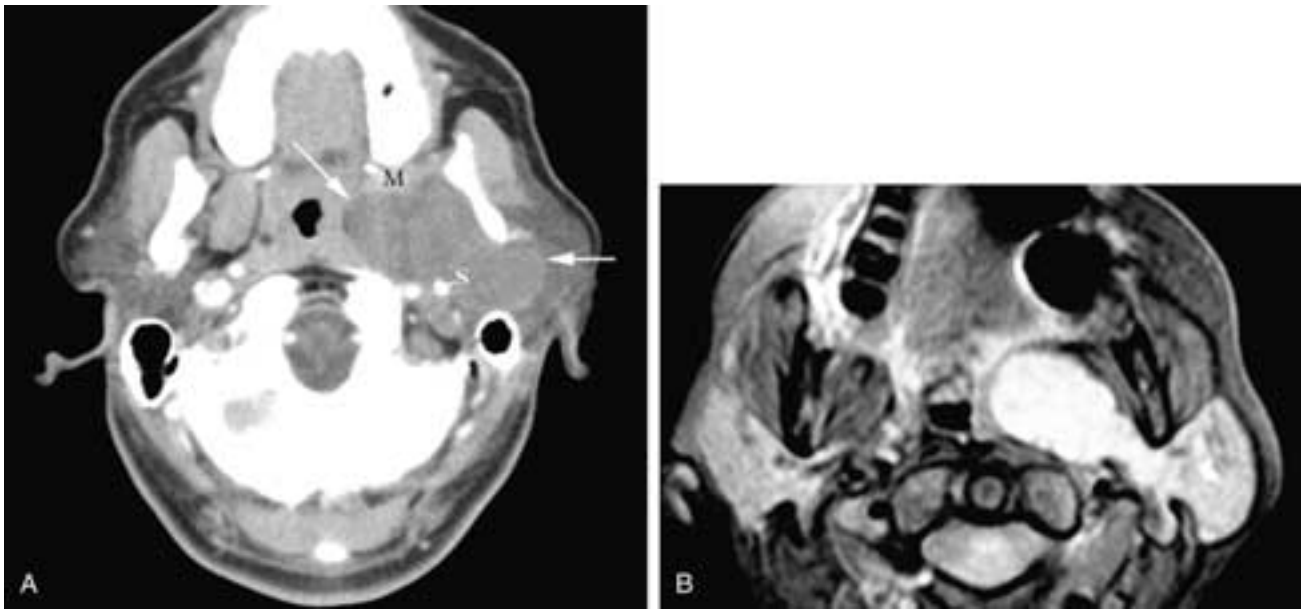

VIEW IMAGE

FIGURE 38-9 Axial contrast-enhanced CT scan (**A**) shows a pleomorphic adenoma (*arrows*) with near-water attenuation in the deep portion of the left parotid gland extending into the prestyloid compartment of the parapharyngeal space. The mass has displaced the internal pterygoid muscle (*M*) ventrally and had widened the stylomandibular tunnel. *S* represents the styloid process. The left pharyngeal wall has been displaced medially. Axial T1-weighted, fat-suppressed, contrast-enhanced MR image (**B**) shows a slightly dumbbell-shaped pleomorphic adenoma extending from the deep portion of the left parotid gland into the prestyloid compartment of the parapharyngeal space. The waist of the tumor is at the level of the rigid stylomandibular tunnel.

matrix—not around the periphery, as seen in aneurysms—is present; rarely, areas of ossification can occur (Fig. 38-11). Typically, the cystic areas are small and multiple rather than large and solitary. If the mass has a solitary large cystic region with a thin, fairly uniform wall and a localized tumor nodule, a Warthin's tumor is a more likely diagnosis. If the mass has a large central cystic region with thick, irregular walls, a high-grade malignancy is a more likely diagnosis.

On CT, pleomorphic adenomas are of a soft-tissue attenuation. The cystic and necrotic areas are of a lower attenuation, while calcifications, or the rare ossification, are clearly seen as high-attenuation regions. However, the contours of the tumor are better identified on MR imaging than on CT and, regardless of homogeneity, overall these tumors have low to intermediate T1-weighted and high T2-weighted signal intensities. If the tumor suddenly increases in size, hemorrhage has probably occurred. Because it is unusual for patients to come to scanning with fresh intratumoral hemorrhage, most such hemorrhagic sites are usually more than a day old and have high T1-weighted and high T2-weighted signal intensities (Fig. 38-10D). If fresh blood is imaged, the appearance is similar to that of necrosis and cystic change, with low T1-weighted and high T2-weighted signal intensities.

If a tumor is seen on imaging to lie in the prestyloid compartment of the parapharyngeal space and there is no intervening fat between the tumor and the parotid gland, the tumor must be considered to arise from the parotid gland. Actually, one of four possibilities may account for the nonvisualization of the fat: (1) the tumor is truly of parotid origin (about 80% of cases); (2) the tumor is extraparotid but is so large that it compresses the fat, preventing its identification on the images; (3) the tumor is adherent to the gland's capsule but not truly arising from the parotid gland (about 20% of cases); or (4) the tumor is extraparotid but has invaded the parotid gland. The last is considered a rare occurrence. In all of these cases, most surgeons employ a transparotid approach to protect the facial nerve from inadvertent damage during surgery.

In some patients, only a thin isthmus of tissue can be seen connecting the parotid gland to the pedunculated parapharyngeal space portion of the tumor (Fig. 38-9B). If this isthmus is not identified on the images, an erroneous diagnosis of an extraparotid tumor could be made, and this could lead the surgeon to approach the tumor from the neck. However, once the tumor is exposed, attempted extirpation through the neck could pull on the attached parotid gland, which in turn would put tension on the facial nerve and lead to avulsion of the nerve. To avoid this problem, thin-section 3-mm contiguous axial scans should be used through the tumor; this soft-tissue detail is much better seen on MR images than it is on CT scans.[9, 27] In almost all of these cases, the fat of the parapharyngeal space will also be seen separating the medial contour of the lesion from the pharyngeal musculature. This indicates that the mass is not arising from the pharyngeal wall. Lastly, if fat is clearly seen surrounding a prestyloid mass, the lesion is not arising either from the parotid gland or from the pharyngeal wall.

Only a relatively few extraparotid, prestyloid compartment, parapharyngeal space salivary gland tumors have been reported, and traditionally they were regarded as developing directly from the minor salivary glands of the pharyngeal wall.[58–60] However, this belief now seems to require a qualifying statement. These tumors are believed to arise

Copyright © 2003, Mosby, Inc. All rights reserved.

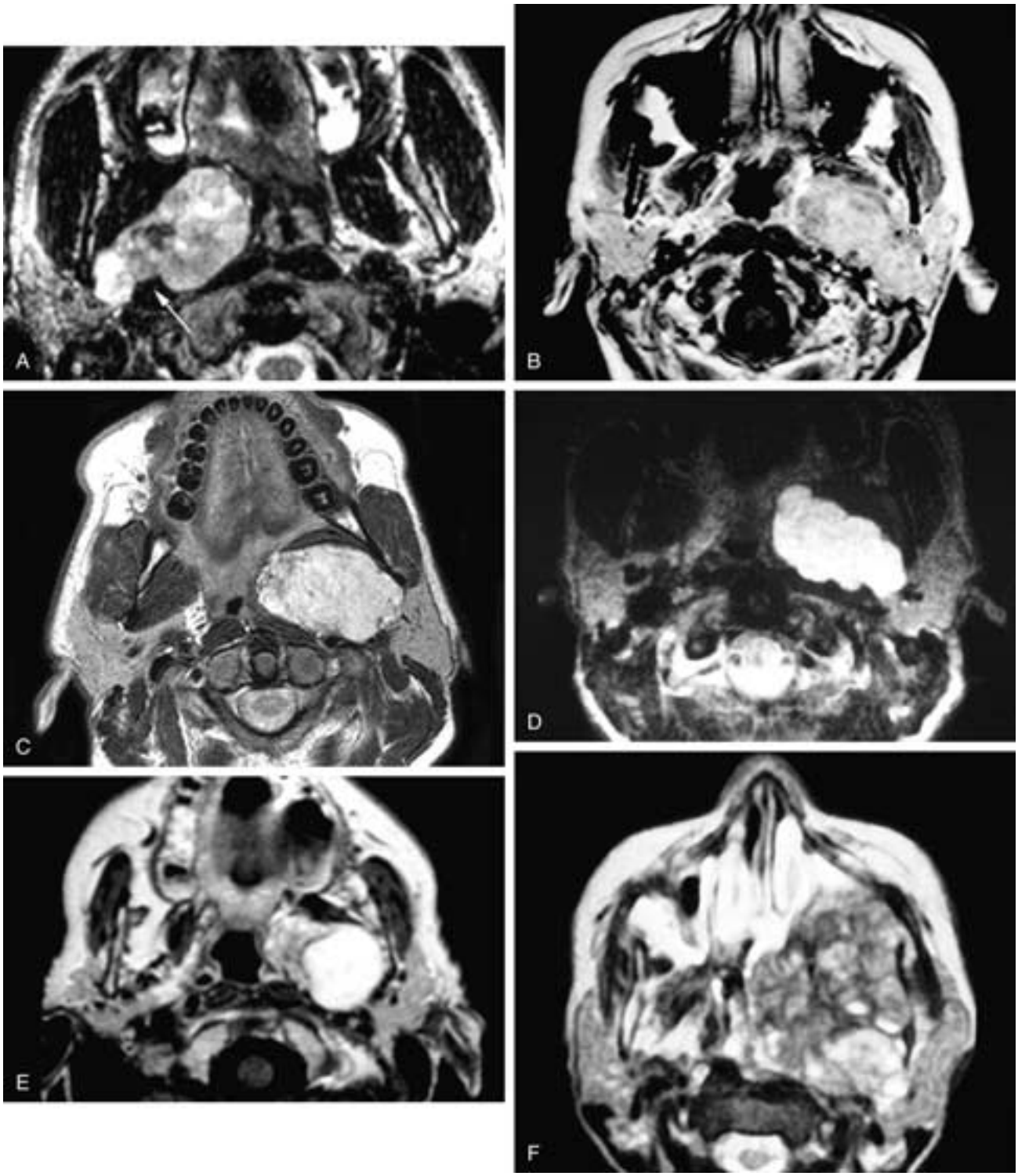

VIEW IMAGE

FIGURE 38-10 Axial T2-weighted MR image (**A**) shows a pleomorphic adenoma of the right parotid gland extending into the parapharyngeal space and displacing the right pharyngeal wall across the midline to the left side. The tumor has cystic areas of high signal intensity, and the mass is ventral to the ICA (*arrow*). Axial T1-weighted, contrast-enhanced MR image (**B**) shows a mass in the left parotid gland and parapharyngeal space. Although the fat planes around the tumor are displaced but otherwise normal, the interface of the lesion with the parotid parenchyma is indistinct. This was an adenoid cystic carcinoma. Axial T1-weighted, contrast-enhanced MR image (**C**) shows a large left parapharyngeal space mass that lies anterior to the ICA artery and is inseparable from the deep portion of the left parotid gland. The left pharyngeal wall is displaced far to the right. Parotid pleomorphic adenoma. Axial T2-weighted MR image (**D**) shows the lobulated contour of a left pleomorphic adenoma extending from the deep portion of the parotid gland into the prestyloid compartment of the parapharyngeal space. This silhouette is highly suggestive of a pleomorphic adenoma. Axial T1-weighted MR image (**E**) shows a left parotid pleomorphic adenoma extending into the prestyloid compartment of the parapharyngeal space. Clinically there was a sudden enlargement of this mass. There is an area of high signal intensity in the lateral portion of the tumor, which at surgery was found to be hemorrhage. Axial T1-weighted MR image (**F**) shows a huge mass arising in the left parotid gland and extending into all of the deep spaces of the upper neck. Despite the aggressive appearance of the tumor, at surgery it was diagnosed as a pleomorphic adenoma. This case illustrates that when such tumors become very large, the extreme distortion of the adjacent imaging landmarks may falsely suggest a malignancy.

Copyright © 2003, Mosby, Inc. All rights reserved.

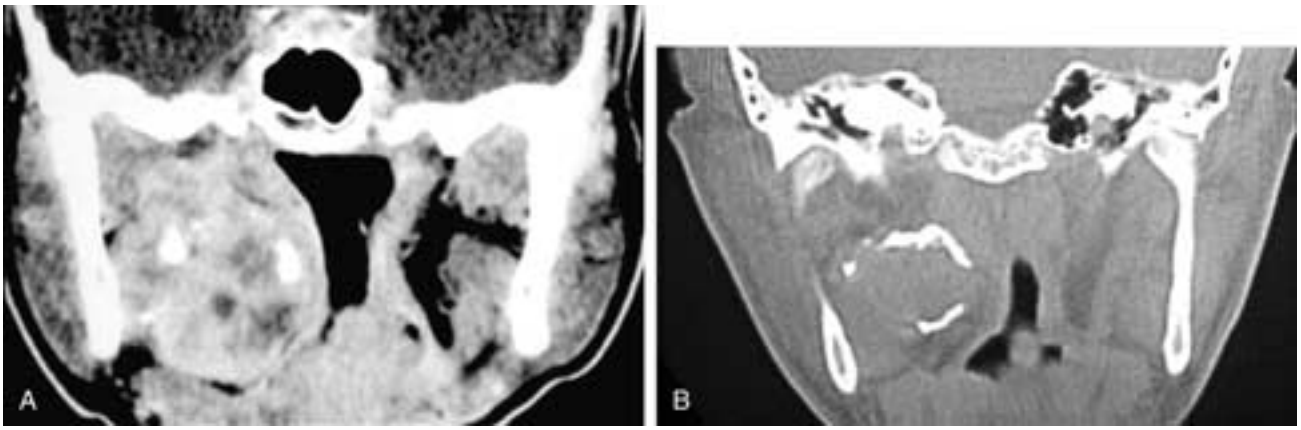

VIEW IMAGE

FIGURE 38-11 Coronal contrast-enhanced CT scan (**A**) shows a right pleomorphic adenoma that arose within the deep portion of the parotid gland and extended into the parapharyngeal space. Areas of dystrophic calcification are seen within the tumor matrix, as are areas of cystic degeneration. This appearance is highly suggestive of a pleomorphic adenoma, but occasionally it can be seen in a schwannoma. Coronal CT scan (**B**) viewed at wide window settings shows a circular area of calcification around the periphery of a right parapharyngeal space mass. Note the difference in the pattern of calcification compared to **A**. This was an aneurysm of the ICA. Whenever calcifications are seen at the periphery of a mass, an aneurysm must be ruled out by other studies.

from salivary epithelial rests within the prestyloid compartment fat. Although it was thought that these rests were derivatives of the parotid anlagen migration, it now appears that they may be derived from the minor salivary glands of the pharyngeal mucosa. Since these tumors arise within the prestyloid fat, they have fat on both their medial and lateral margins (Fig. 38-12). These extraparotid tumors are almost always benign pleomorphic adenomas, and their imaging characteristics are those of the parotid pleomorphic adenomas, except that they are located in the prestyloid compartment fat. If the margins of the tumor are not clearly defined, the possibility of an uncommon malignancy must be considered; such tumors are likely to be mucoepidermoid, adenoid cystic, or adenocarcinomas. The rare tumor that arises directly from the pharyngeal wall has fat only on its lateral contour (Fig. 38-13). Most of these tumors are malignancies of the minor salivary glands, and they usually have infiltrative margins into the prestyloid fat.

All of these salivary gland tumors, regardless of whether they arise from the parotid gland, from salivary rests in the prestyloid fat, or from the pharyngeal minor salivary glands, are anterior to the ICA and, if large enough, will displace the ICA posteriorly.[27]

Neurogenic Tumors

Neurogenic lesions comprise 17% to 25% of the lesions. In Hughes et al.'s series, they represented 14% of the cases.[56] Most are schwannomas of the vagus nerve, less

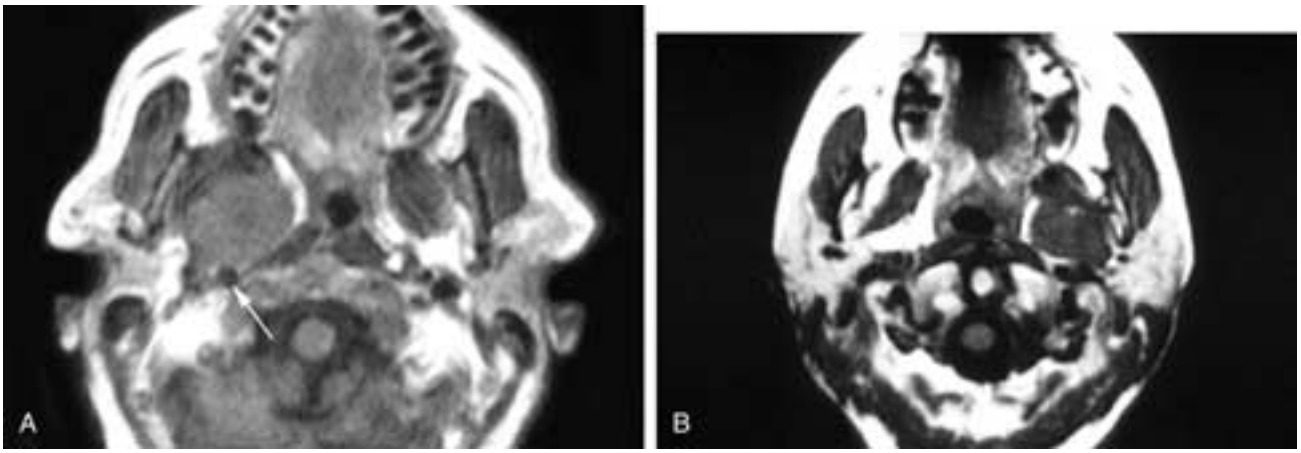

VIEW IMAGE

FIGURE 38-12 Axial T1-weighted MR image (**A**) shows an ovoid mass in the right prestyloid parapharyngeal space fat. A fat plane is present along its medial side, separating it from the pharyngeal constrictor muscles. A fat plane also separates the mass from the parotid gland. This was an extraparotid pleomorphic adenoma arising from minor salivary gland rest cells. The ICA is dorsal to the mass (*arrow*). A rare schwannoma, usually of the sympathetic chain, can also have this imaging appearance. Axial T1-weighted MR image (**B**) shows an ovoid mass in the left prestyloid parapharyngeal space fat. Fat planes are present along both its medial and lateral sides, separating it from the pharyngeal constrictor muscles and the parotid gland. The mass is ventral to the ICA. This was an extraparotid pleomorphic adenoma.

Copyright © 2003, Mosby, Inc. All rights reserved.

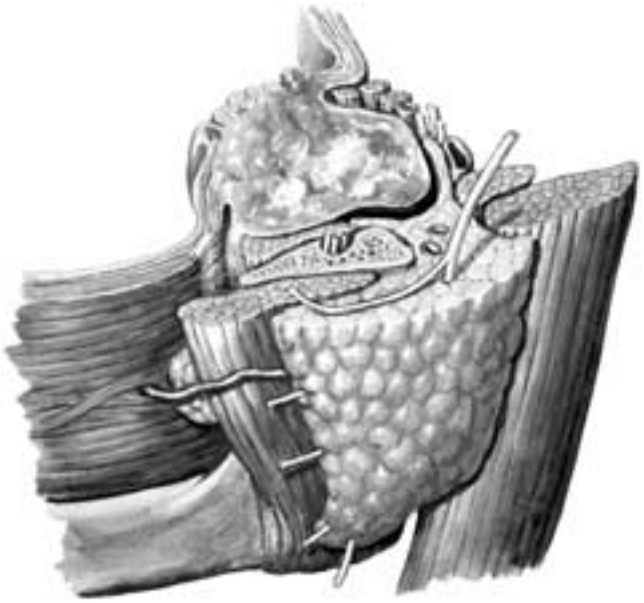

VIEW IMAGE

FIGURE 38-13 Drawing viewed obliquely and from above shows a large minor salivary gland tumor arising from the pharyngeal submucosal glands. The mass displaces the prestyloid parapharyngeal space fat and the parotid gland laterally. Since the tumor arises from the mucosal margin of the pharynx, no fat plane is present between the mass and the pharyngeal constrictors.

commonly of the glossopharyngeal nerve, and uncommonly of the superior sympathetic chain. By comparison to schwannomas, neurofibromas are rare, and although they can occur as solitary lesions, they usually are associated with neurofibromatosis (Fig. 38-14). A solitary parapharyngeal space neurofibroma is reported to be one of the rare complications of neurofibromatosis. Such tumors represent less than 5% of all parapharyngeal space neoplasms.[61]

The vagus nerve is situated behind the ICA within the carotid sheath. As a result, tumors of this nerve tend to displace the ICA ventrally and usually medially. The superior sympathetic chain lies along the medial and posterior border of the carotid sheath, and although these tumors may displace the ICA anteriorly, they can also displace it posteriorly.[27] In the latter instance, a sympathetic schwannoma may be indistinguishable on imaging from an extraparotid salivary gland tumor arising in the prestyloid compartment of the parapharyngeal space. Both of these lesions are ovoid, well-defined masses with fat planes on their medial and lateral sides that displace the ICA posteriorly. Thus, the displacement of the ICA is an important imaging finding differentiating tumors of salivary gland origin from the most common schwannomas arising within the parapharyngeal space (Fig. 38-15).

When a schwannoma arises within the jugular fossa, there can be both caudal and cranial growth creating a dumbbell-shaped mass whose waist is at the rigid skull base. Multiple benign schwannomas also rarely occur within the parapharyngeal space.[62–67]

Most schwannomas are fairly homogeneous soft-tissue masses. However, areas of necrosis and hemorrhage can occur, just as in pleomorphic adenomas. Thus, on imaging, with the possible exception of the displacement of the ICA, these two lesions may have the same appearance. By comparison, some neurofibromas undergo significant fatty degeneration and, on imaging, may appear as predominantly lipid-containing lesions (Fig. 38-14A).

As previously discussed, despite the fact that schwannomas are hypovascular, they can enhance significantly on both CT and MR images and mimic the appearance of a vascular lesion such as a paraganglioma (Fig. 38-15). The enhancement of these schwannomas is seen on images taken at least 2 minutes after the administration of contrast. The reason appears to be related to the hypovascular nature of these lesions and their associated poor venous drainage of the contrast. Once contrast enters the schwannoma's tumor bed, it remains in the equilibrium phase for several minutes. This phase occurs well after a vascular tumor, with its rich venous component, has lost most of its contrast enhancement due to a rapid washout phase. Thus, on images taken after the vascular filling phase, paradoxically the hypovascular schwannoma will appear to be more enhanced than the vascular lesion.[8, 68] The only way to identify the true nature of the lesion's vascularity is to examine the mode of contrast accumulation within the first 30 to 60 seconds after contrast administration. This can be accomplished by using either a dynamic scan technique, helical CT, or a conventional angiogram.

If a schwannoma extends through a skull base foramen, the foramen is smoothly enlarged. This differentiates it from a paraganglioma, which, when it extends through a skull base foramen, causes irregular, shaggy-appearing bony margins, not unlike those caused by a malignancy.

Ganglioneuromas have also rarely been reported in the parapharyngeal space. On imaging, they are indistinguishable from schwannomas.[69, 70]

Malignant peripheral nerve sheath tumors are rare, and although they can occur as sporadic tumors, 25% to 50% are associated with von Recklinghausen's disease.[71] Between 9% and 14% of these malignant tumors occur in the head and neck, with the cranial nerves, large cervical nerves, the sympathetic chain, and the inferior alveolar nerve being most commonly affected.[72] These tumors usually have the same imaging findings as schwannomas, and it is only at pathologic examination that their malignant nature is identified. Rarely, they have infiltrative margins suggesting their invasive nature.[73, 74] Although continuity with a major nerve cannot often be confidently seen on imaging, if such continuity can be established the neurogenic origin of the lesion is identified (Fig. 38-15H).

The presence of neurologic symptoms relating to the last four cranial nerves or the superior sympathetic chain can be a useful aid in distinguishing salivary gland tumors from neurogenic tumors. This statement reflects the observation that most salivary gland tumors are benign and thus rarely cause neurogenic complaints. When small, schwannomas rarely cause symptoms. However, when they are large, as is commonly found in the parapharyngeal space, neurogenic symptoms may be present. Neurologic symptoms are not a useful differentiating point when a malignancy is present, as both salivary gland tumors and schwannomas tend to invade nerves.

Paragangliomas

Paragangliomas represent 10% to 15% of all the lesions in this region, although Hughes et al. found them to

Copyright © 2003, Mosby, Inc. All rights reserved.

represent 20% of their series.[56] They occur in three different varieties, depending on their site of origin. The most common form is the glomus vagale tumor, which arises from the paraganglionic cells about the nodose ganglion (Fig. 38-16). This ganglion is the more caudal of the two vagal ganglia and is located just below the skull base. These tumors usually lie entirely within the parapharyngeal space, although, when large, they may have a relatively small extension through the jugular foramen into the posterior fossa. Lateral bone destruction in the skull base, extending toward the middle ear cleft, is uncommon with these tumors but is common with the glomus jugulare paraganglioma (Fig. 38-17).

Some large vagale tumors may extend caudally toward the carotid bifurcation, splaying the internal and external carotid arteries. However, the vagale tumors, unlike the carotid body tumors, rarely fill the crotch of the carotid bifurcation.[75] Rarely, these vagale tumors may become very large, extending down into the lateral neck as far caudally as the larynx. In these cases, the internal and external carotid arteries, the carotid bifurcation, and the common carotid artery all may be displaced around the tumor (Fig. 38-18).

The second most common paraganglioma of this region is the carotid body tumor, which originates from the carotid body cells near the carotid bifurcation (Fig. 38-19). Classically, this tumor completely fills the splayed carotid bifurcation, which distinguishes it from almost all glomus vagale tumors. Only 8% of carotid body tumors are large enough to present clinically as a parapharyngeal space mass. The carotid body cells are variably located about the carotid bifurcation, usually being situated in the crotch between the internal and external carotid arteries. However, in some patients, the carotid bodies may entirely surround the external carotid artery or, rarely, the ICA.

Glomus jugulare tumors are the third most common paraganglioma of this region, and they arise from the paraganglionic cells around the jugular ganglion. This ganglion is the more cranial of the two vagal ganglia and is located in the jugular fossa. Both intracranial and extracranial tumor growth occurs, even in relatively small lesions, and spread above and below the skull base is usually nearly of equal bulk, distinguishing these neoplasms from glomus vagale tumors. In addition, glomus jugulare lesions tend to erode the skull base laterally, extending into the middle ear cleft (Fig. 38-17).

Apparently, the chronic, minimally invasive nature of these tumors can cause developmental anomalies if the tumor arises early enough in life. There is a report of a

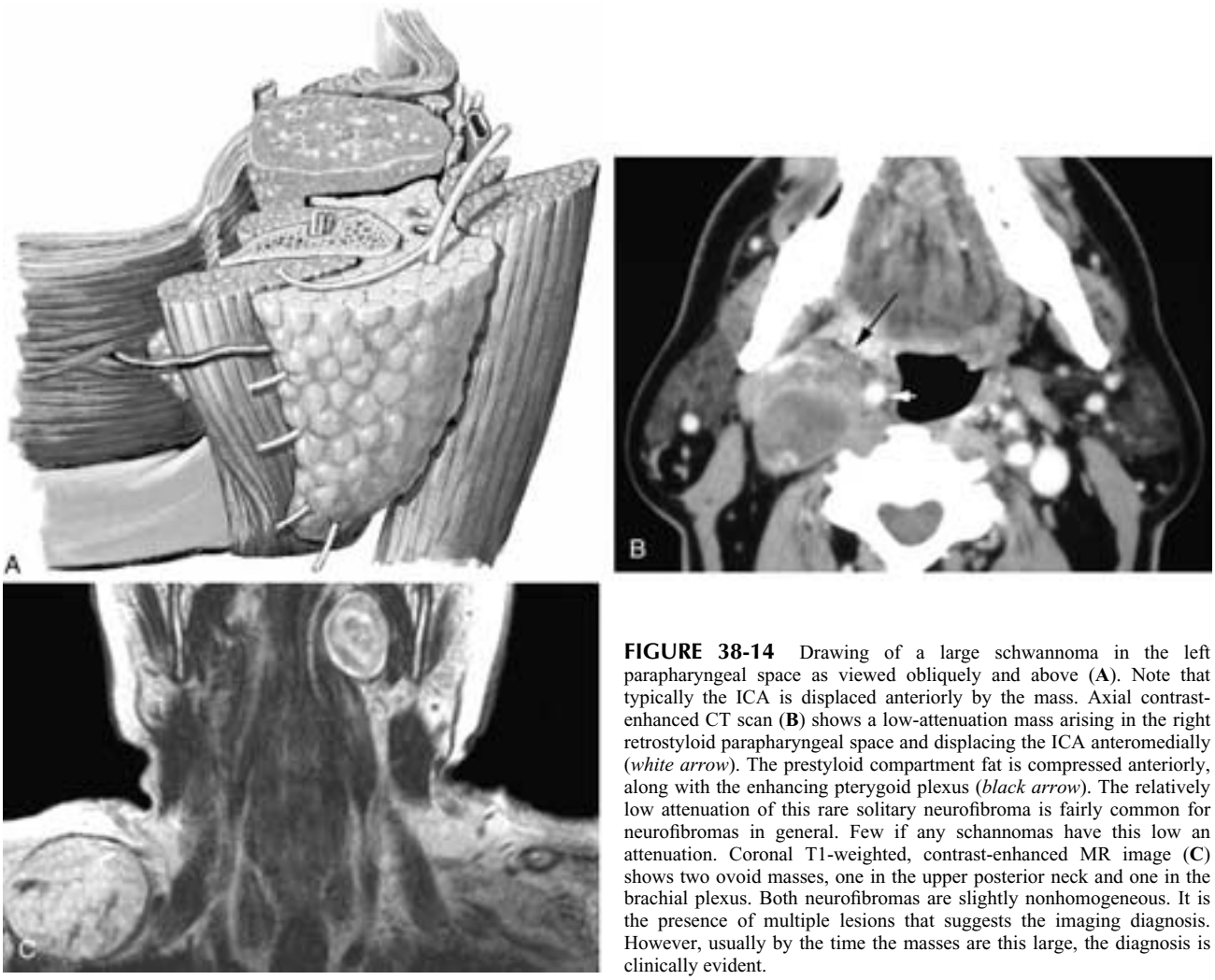

FIGURE 38-14 Drawing of a large schwannoma in the left parapharyngeal space as viewed obliquely and above (**A**). Note that typically the ICA is displaced anteriorly by the mass. Axial contrast-enhanced CT scan (**B**) shows a low-attenuation mass arising in the right retrostyloid parapharyngeal space and displacing the ICA anteromedially (*white arrow*). The prestyloid compartment fat is compressed anteriorly, along with the enhancing pterygoid plexus (*black arrow*). The relatively low attenuation of this rare solitary neurofibroma is fairly common for neurofibromas in general. Few if any schannomas have this low an attenuation. Coronal T1-weighted, contrast-enhanced MR image (**C**) shows two ovoid masses, one in the upper posterior neck and one in the brachial plexus. Both neurofibromas are slightly nonhomogeneous. It is the presence of multiple lesions that suggests the imaging diagnosis. However, usually by the time the masses are this large, the diagnosis is clinically evident.

VIEW IMAGE

Copyright © 2003, Mosby, Inc. All rights reserved.

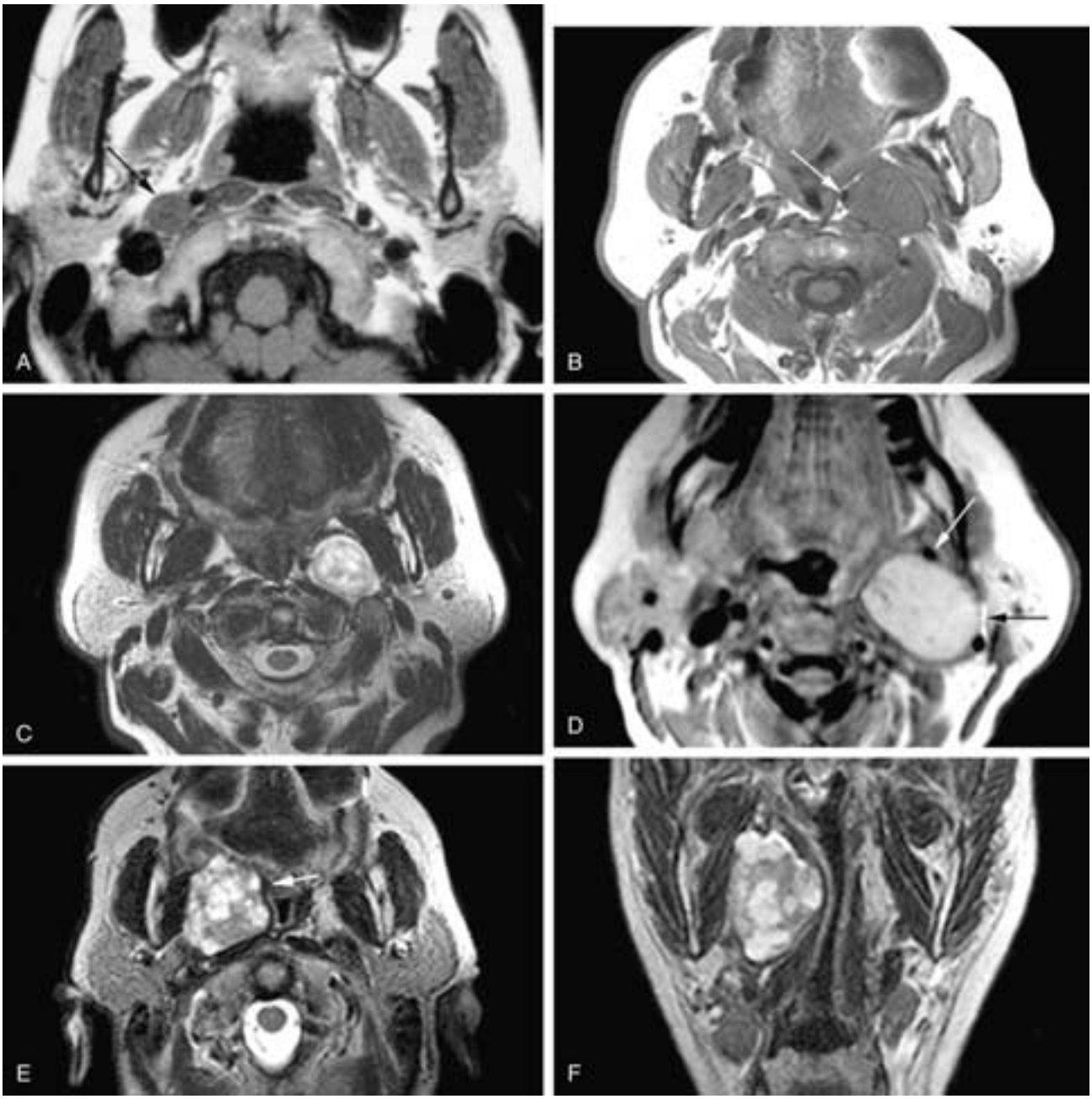

VIEW IMAGE

FIGURE 38-15 Axial T1-weighted MR image (**A**) shows a small ovoid mass (*arrow*) in the right carotid sheath (retrostyloid compartment of the parapharyngeal space) that pushes the ICA anteromedially and the internal jugular vein posterolaterally. This was a schwannoma of the vagus nerve. Axial T1-weighted (**B**) and T2-weighted (**C**) MR images show an ovoid mass in the left parapharyngeal space displacing the ICA anteromedially (*arrow* in **B**). This vagal schwannoma has a fairly homogeneous low T1-weighted signal intensity and a nonhomogeneous T2-weighted signal intensity. Axial T1-weighted MR image (**D**) shows a left parapharyngeal space mass that displaces the ICA anterolaterally (*white arrow*). This vagal schwannoma is separated from the parotid gland by a thin fat plane (*black arrow*). Axial (**E**) and coronal (**F**) T2-weighted MR images show an ovoid, nonhomogeneous right parapharyngeal space vagal schwannoma that displaces the ICA (*arrow* in **E**) anteromedially.

Copyright © 2003, Mosby, Inc. All rights reserved.

FIGURE 38-15 *Continued.* Sagittal T1-weighted MR image (**G**) shows a parapharyngeal space mass that bows the ICA (*arrow*) anteriorly. This vagal schwannoma has a fairly homogeneous signal intensity. This appearance of arterial bowing on sagittal images is fairly typical of schwannomas and glomus vagale tumors. Sagittal T1-weighted, fat-suppressed, contrast-enhanced MR image (**H**) shows a vagal schwannoma. The tail of this tumor extends cranially up the nerve into the jugular fossa. When such a relationship to the nerve can be identified, the diagnosis of a schwannoma is virtually assured. Axial T1-weighted MR image (**I**) shows an ovoid right parapharyngeal space mass that displaces the ICA anterolaterally (*arrow*). This was a schwannoma of the sympathetic chain.

VIEW IMAGE

24-year-old female with a right carotid body tumor that had been present since she was 9 years old. Presumably the chronic pressure of the tumor caused a disturbance of the osseous development of her occipito-atlantoaxial complex, resulting in anterior basilar invagination, hypoplasia of the clivus, kyphoscoliosis, and aplasia of the posterior arch of the atlas.[76]

Paragangliomas can occur sporadically or as autosomal dominant familial tumors, and the incidence of multicentric tumors is higher in the familial cases. Bilateral carotid body tumors can occur in 5% to 14% of sporadic tumors (Fig. 38-20). Multiple tumors may develop within a period ranging from several months to a few years of each other or up to 20 years later. Bilateral carotid body tumors may occur in 26% to 33% of patients with familial cases, and the combination of a carotid body tumor, a glomus vagale tumor, or a glomus jugulare tumor is less common than bilateral carotid body tumors. For this reason, both the left and right carotid arteries should be routinely examined in patients with a suspected paraganglioma to rule out multiple tumors.[75] The imaging study should extend from the temporal bones down to the lower neck.

The specific function of most of the extraadrenal paraganglia remains unknown. Unlike the adrenal medulla, they are sparsely innervated and are believed to be directly responsive to chemical signals such as changes in pH (hence the term *chemodectoma* suggested by Mulligan in 1950).[77] Compensatory hypertrophy of the paraganglia is known to occur only in the parasympathetic carotid body in patients with prolonged hypoxia and hypercapnia.[78] In fact, populations living at high altitudes and chronically exposed to hypoxic conditions also have a 10-fold increased prevalence of carotid body paragangliomas but no increase of such tumors at other sites.[79] Carotid body tumors occurring at altitudes higher than 2000 m above sea level in Mexico City were found to differ significantly from those in inhabitants of cities in the United States or Europe less than 1500 m above sea level. Those tumors occurring at high altitudes have an evident female predominance (8.3∶1), a low rate of bilaterality (5%), and a family history of 1% versus a discrete female predominance (2∶1), bilaterality ranging from 10% to 20%, and a family history ranging from 7% to 25% in tumors occurring at low altitudes.[80]

As previously discussed, these hypervascular tumors have significant enhancement on routine contrast CT and MR scans. However, if there is a delay of more than several minutes in imaging after contrast administration, the rich tumor blood flow may wash out the contrast, and these lesions may not appear to be highly enhanced. Dynamic scanning will reveal a hypervascular curve, with a sharp filling peak and a rapid washout phase.[8, 20, 21] Such a curve differentiates this vascular tumor from a hypovascular lesion such as a schwannoma, which enhances because of the slow extravascular accumulation of contrast in the tumor bed.

Copyright © 2003, Mosby, Inc. All rights reserved.

When small, these tumors enhance homogeneously. However, when large, they are usually nonhomogeneous, with areas of both necrosis and hemorrhage. They tend to be ovoid or pear-shaped, and they are smoothly contoured. If the tumor extends through the skull base, it usually has an hourglass shape, with the waist at the level of the skull base. The margins of the skull base involvement have irregular, infiltrative contours, differentiating these tumors from schwannomas. On MR imaging, they have an overall intermediate signal intensity background matrix on all imaging sequences, usually with some ''brightening'' on T2-weighted images. Scattered sites of high T2-weighted signal intensity can be seen, which help give the tumor a ''salt and pepper'' appearance. These high-signal regions primarily appear to be areas of slow flow within the tumor. In larger tumors, a characteristic MR finding is serpentine, channel-like areas of signal void within the tumor matrix, which are present on all imaging sequences. These vascular flow voids represent the larger-caliber, rapid-flow dominant vessels of the tumor (Figs. 38-16 to 38-18).[9, 27, 81] These flow voids often are not seen in lesions smaller than 2 cm in diameter, and occasionally they may not be seen in large tumors. Such tumors have a predominance of small-caliber, slower-flow vessels that can only be identified on a

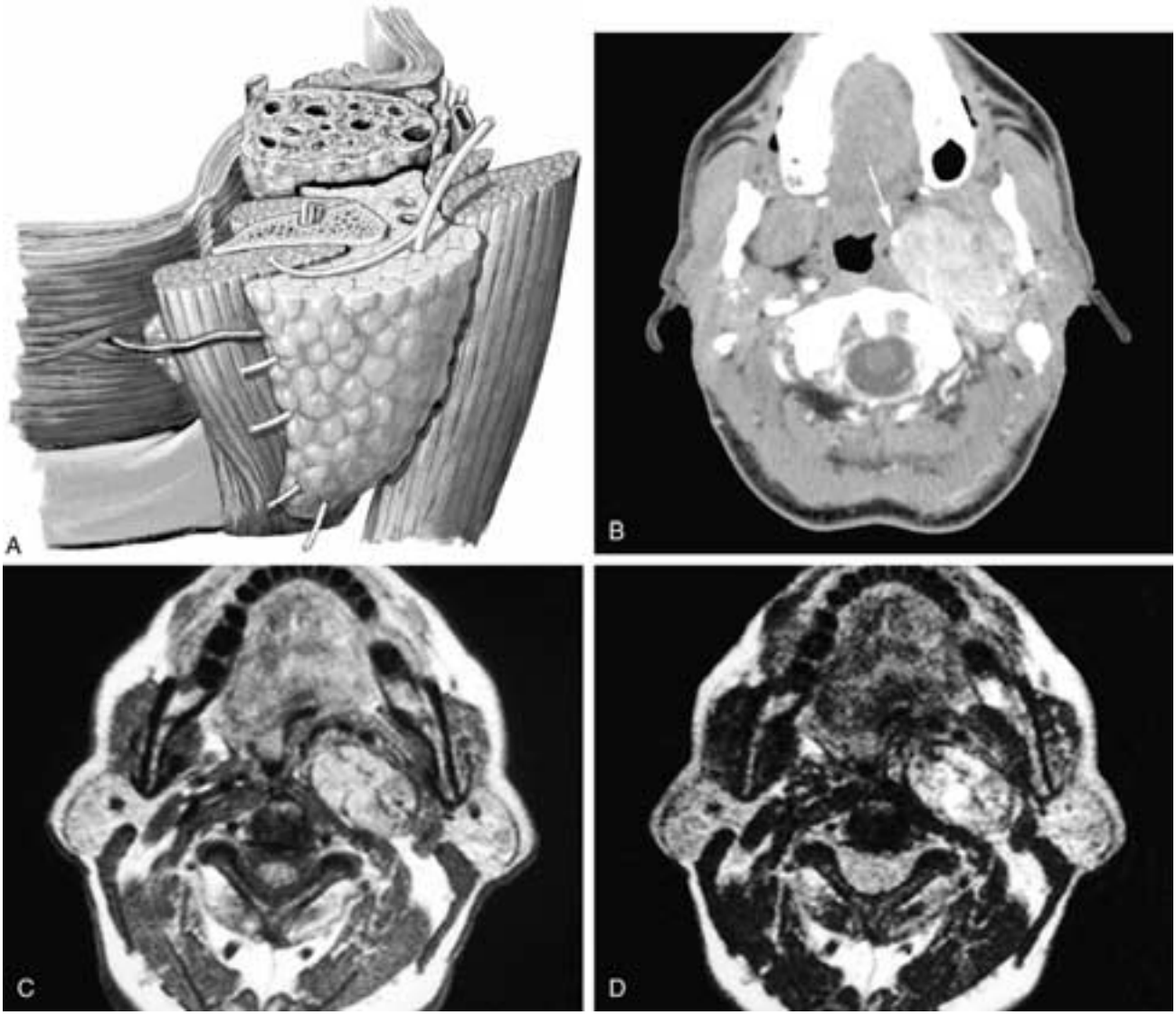

VIEW IMAGE

FIGURE 38-16 Drawing of a large glomus vagale tumor in the left parapharyngeal space as viewed from obliquely and above (**A**). Note that the mass is separate from and displaces the pharyngeal wall medially while also being separate from and displacing the parotid gland laterally. Thus, fat planes will separate such a mass from both the pharyngeal wall and the deep portion of the parotid gland. Typically, the ICA is anteriorly displaced. This tumor configuration also applies to a schwannoma within the parapharyngeal space. Axial contrast-enhanced CT scan (**B**) shows an enhancing mass in the left parapharyngeal space that has displaced the ICA (*arrow*) anteromedially. This glomus vagale tumor extended from the skull base to near the carotid bifurcation. Axial T1-weighted (**C**) and T2-weighted (**D**) MR images show an ovoid glomus vagale tumor in the left parapharyngeal space. The carotid arteries have been displaced anteriorly, and within the mass are serpiginous areas of signal void. In **D**, intermixed with the areas of signal void are areas of high signal intensity. This gives the ''salt and pepper'' appearance associated with these glomus tumors.

Copyright © 2003, Mosby, Inc. All rights reserved.

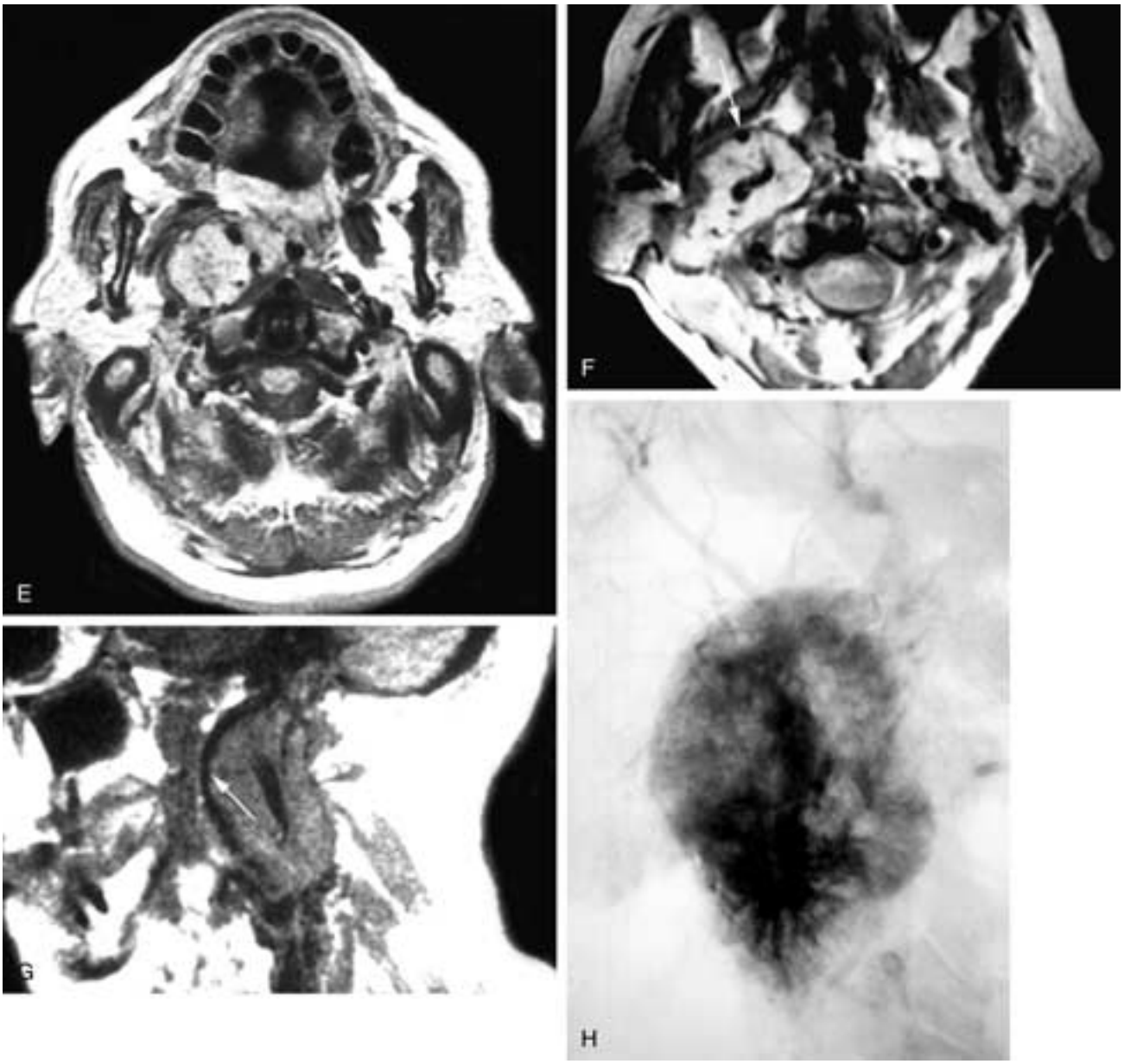

VIEW IMAGE

FIGURE 38-16 *Continued* Axial T1-weighted MR image (**E**) shows a spherical mass in the right parapharyngeal space. There are signal voids within the mass, and the carotid arteries have been displaced anteromedially. This was a glomus vagale tumor. Axial T1-weighted (**F**) and sagittal T1-weighted (**G**) MR images show an oblong mass with a large central region of signal void. In **F**, there are also smaller scattered signal voids. The ICA is displaced anteriorly (*arrow* in **F** and **G**). In **H**, a lateral subtraction angiogram film, the hypervascular nature of this glomus vagale tumor is seen. There is also considerable internal atrioventricular shunting into a large internal draining vein.

conventional angiogram, which is still considered the gold standard for evaluating tumor vascularity. It has been suggested that MR contrast is unnecessary in studying paragangliomas and that the diagnosis is most reliably made on T2-weighted images. This study also confirmed that flow voids are more likely to be found in tumors greater than 2 cm in diameter and on T2-weighted images.[82]

Both glomus vagale and glomus jugulare tumors arise around the vagus nerve that is dorsal to the ICA. Thus, these tumors tend to displace the ICA anteriorly. The carotid body tumors also usually displace the internal carotid artery anteriorly; however, splaying of the internal and external carotid arteries is a more constant feature.[27] This splaying causes a lyre-shaped widening of the carotid bifurcation, a distinctive imaging feature well seen on MR imaging, CT scanning, and on CT, MR, and conventional angiography. When there is gross asymmetry in the splaying of the internal and external carotid arteries, the possibility of a vascular-type nodal metastasis should be considered. In these cases, the metastatic node is usually lateral to the carotid vessels.

The classic imaging diagnosis of a paraganglioma is

Copyright © 2003, Mosby, Inc. All rights reserved.

based on the presence of a smoothly contoured, ovoid parapharyngeal space mass, with vascular flow voids, anterior displacement of the ICA, and possibly a ''salt and pepper'' T2-weighted appearance. This imaging appearance usually obviates the need for an invasive angiogram, which remains necessary for a definitive diagnosis in those cases without vascular flow voids on MR imaging or MR angiography (MRA). A further indication for a conventional angiogram is preoperative tumor embolization, which reduces blood loss at surgery, especially for the larger tumors. The tumors most often embolized preoperatively are the glomus jugulare and vagale lesions. Because of concern that the embolization material may reflux into the ICA, the carotid body tumors are less frequently embolized.

Compared to the conventional digital subtraction angiograms, multislice 3D time-of-flight (TOF) MRA was superior to 3D phase-contrast and 2D TOF MRA for identifying the first- and second-order vessels in the neck. However, the sensitivity of MRA was too low to replace conventional angiography, especially for carotid body tumors.[83] Today, CT angiography (CTA) is also being utilized to demonstrate the blood vessels associated with these tumors, and this technique appears to be comparable to MRA.

Paragangliomas may cause disabling symptoms and even death by slow, progressive enlargement, with encroachment on vital organs and contiguous structures, or by the development of regional and distant metastases.[84] Carotid body tumors are malignant in 10% to 15% of cases. Most metastases are to regional lymph nodes. Distant metastases have been reported in the lungs, liver, pleura, heart, kidney, skin, thyroid, spinal dura, pancreas, trachea, and brain. Glomus vagale tumors also have an approximately 10% incidence of malignancy, with regional lymph node metastases and distant metastases to lung and bone. Glomus jugulare tumors have a metastatic frequency of only about 3%, with regional cervical metastases and distant metastases to lung, liver, bone, brain, parotid, nasopharynx, and the posterior neck.[75]

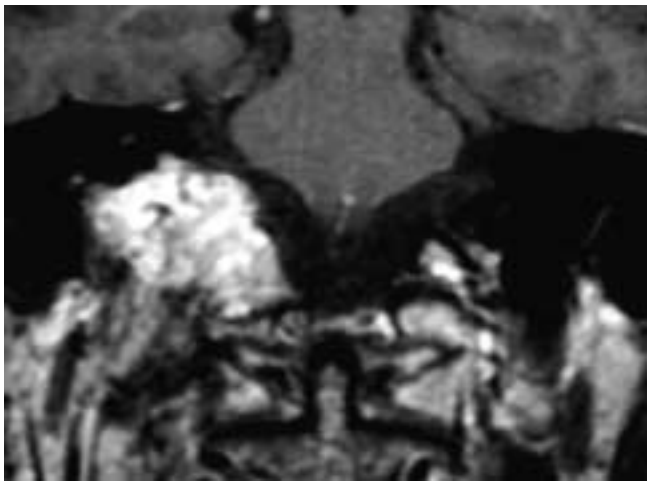

VIEW IMAGE

FIGURE 38-17 Coronal T2-weighted MR image shows a mass centered in the right jugular fossa. This glomus jugulare tumor has high signal intensity and serpiginous areas of signal void. Laterally, the tumor extends into the middle ear, and the lesion extends about as much into the posterior fossa as it does below the skull base.

The presence of a hypervascular tumor on CT and MR imaging is not specific for a paraganglioma. If the lesion has invasive margins, a vascular metastasis from a renal cell or thyroid carcinoma should be considered (Fig. 38-21). Some venous hemangiomas may also have a similar hypervascular imaging appearance, although the flow voids on MR imaging may not be as dominant a feature as in the other tumors.[9]

Other Tumors

A large number of cellular lesions have been reported to involve the parapharyngeal space, usually infiltrating and obliterating the tissue planes. Among these, nasopharyngeal and oropharyngeal carcinomas are the most common in adults, while in children, the most common tumors are either rhabdomyosarcomas or lymphomas.[85, 86] Rare tumors such as hemangiopercytoma and synovial sarcoma have also been reported.[87, 88] In the case of synovial sarcoma in a 21-year-old man, CT was found to be very useful for identifying the presence of tumoral calcifications, which may portend a favorable prognosis. CT was also useful in excluding involvement of cortical bone. The CT and MR imaging findings were nonspecific, but MR imaging was superior to CT for assessing the topographic relationships of the tumor (Fig. 38-22).[87] Extramedullary plasmacytoma has also been reported in the parapharyngeal space and showed significant enhancement, a finding possibly suggestive of this rare diagnosis.[89] Rarely, liposarcomas can occur in the parapharyngeal space. They are identified on imaging by their fatty content, which often may comprise only about half of the tumor mass (Fig. 38-23). Aggressive fibromatosis can also involve the parapharyngeal space, and parotid malignancies can invade this space.[90–92] Solitary fibrous tumors arise in the pleura and, less commonly, in extrapleural sites that in the head and neck regions have included the nose and paranasal sinuses, soft palate, epiglottis, thyroid, parotid gland, and submandibular gland, as well as the infratemporal fossa and the parapharyngeal space. A solitary fibrous tumor arising in the parotid gland and extending to the parapharyngeal space was documented on CT and MR imaging.[93] A rare aggressive juvenile laryngeal papillomatosis was reported in a patient who had had laryngeal papillomas since the age of 3 years. The papillomas gradually spread to the entire respiratory system, and over 30 years the patient was operated on more than 80 times. MR imaging documented an invasive tumor spreading from the tongue into the parapharyngeal space and extending to the cranial base.[94] A very rare osteolipoma has also been reported in the lower parapharyngeal space.[95] Metastases from distant primary tumors to the parapharyngeal space come most commonly from primary tumors in the kidney and the thyroid gland.

Benign tumors such as rhabdomyomas and processes other than tumors, such as the granulomatous reaction from a malignant external otitis, can also occur in the parapharyngeal space.[96, 97] Pseudotumors have rarely been reported in the parapharyngeal space. They appear on imaging as infiltrating lesions that are indistinguishable from carcinomas.[98]

Unfortunately, for the most part, the CT and MR imaging findings of these entities are nonspecific. On CT, almost all of these lesions are fairly homogeneous, with an attenuation

Copyright © 2003, Mosby, Inc. All rights reserved.

FIGURE 38-18 Axial T1-weighted (**A**) and T2-weighted (**B**) MR images show a huge left glomus vagale tumor in the left parapharyngeal space. The ICA is displaced anteromedially, and there are vascular signal voids within the tumor. In **C**, a coronal T2-weighted MR image, the massive extent of the tumor can be appreciated as it extends down almost to the level of the supraclavicular fossa. In **D**, a left oblique view of an MRA, the lateral bowing of the common carotid artery (*large arrow*) is seen. There is also slight splaying of the carotid bifurcation as a portion of the tumor bulges laterally between the internal and external carotid arteries (*small arrows*). Coronal T1-weighted MR image (**E**) on a different patient than in **A** to **D** shows another huge glomus vagale tumor in the right neck. A few vascular flow voids are present within the tumor.

VIEW IMAGE

Copyright © 2003, Mosby, Inc. All rights reserved.

similar to that of muscle, show minimal enhancement, and diffusely infiltrate the region. When they are large, areas of necrosis may develop. On MR imaging, these processes also tend to be homogeneous, and most have a low to intermediate T1-weighted and a slightly higher T2-weighted signal intensity. Although the degree of enhancement is variable, most of these tumors enhance.

As a general rule, lymphomas tend to be less infiltrative and cause relatively little bone erosion compared to carcinomas and most sarcomas. Often their MR imaging signal intensities are the same as those of normal adenoidal tissue, thereby suggesting the possible diagnosis.[8, 9] There is no consistent difference between the signal intensities of lymphomas and carcinomas to use these MR findings as a differentiating point.

Tumors of the nasopharynx are discussed in depth in Chapter 28. These carcinomas are mucosal tumors that may have extensive submucosal and parapharyngeal space extension, often with skull base erosion and intracranial spread.[24]

Lymph Nodes

Lymph nodes within the parapharyngeal space are part of either the upper spinal accessory or upper internal jugular chains and are now all classified as level II nodes. The retropharyngeal nodes, as the name implies, are not within the parapharyngeal space. Most lymph nodes in the parapharyngeal space do not occur in isolation; they are usually part of a more extensive lymphadenopathy in the neck, and the source of a causative infection or the primary tumor is often also identified in the pharynx.[99] As mentioned earlier in this chapter, a necrotic lymph node and an abscess

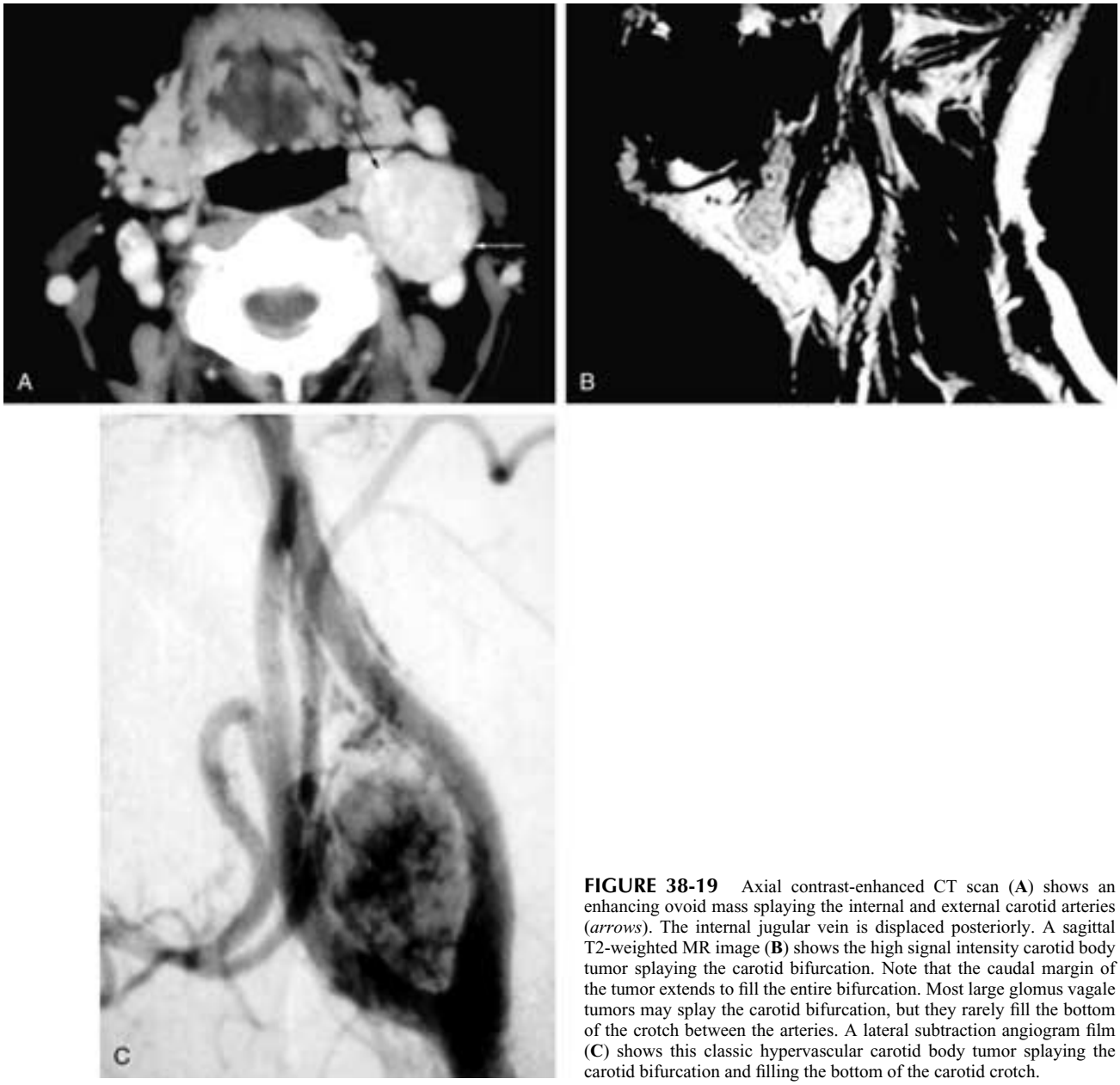

FIGURE 38-19 Axial contrast-enhanced CT scan (**A**) shows an enhancing ovoid mass splaying the internal and external carotid arteries (*arrows*). The internal jugular vein is displaced posteriorly. A sagittal T2-weighted MR image (**B**) shows the high signal intensity carotid body tumor splaying the carotid bifurcation. Note that the caudal margin of the tumor extends to fill the entire bifurcation. Most large glomus vagale tumors may splay the carotid bifurcation, but they rarely fill the bottom of the crotch between the arteries. A lateral subtraction angiogram film (**C**) shows this classic hypervascular carotid body tumor splaying the carotid bifurcation and filling the bottom of the carotid crotch.

VIEW IMAGE

Copyright © 2003, Mosby, Inc. All rights reserved.

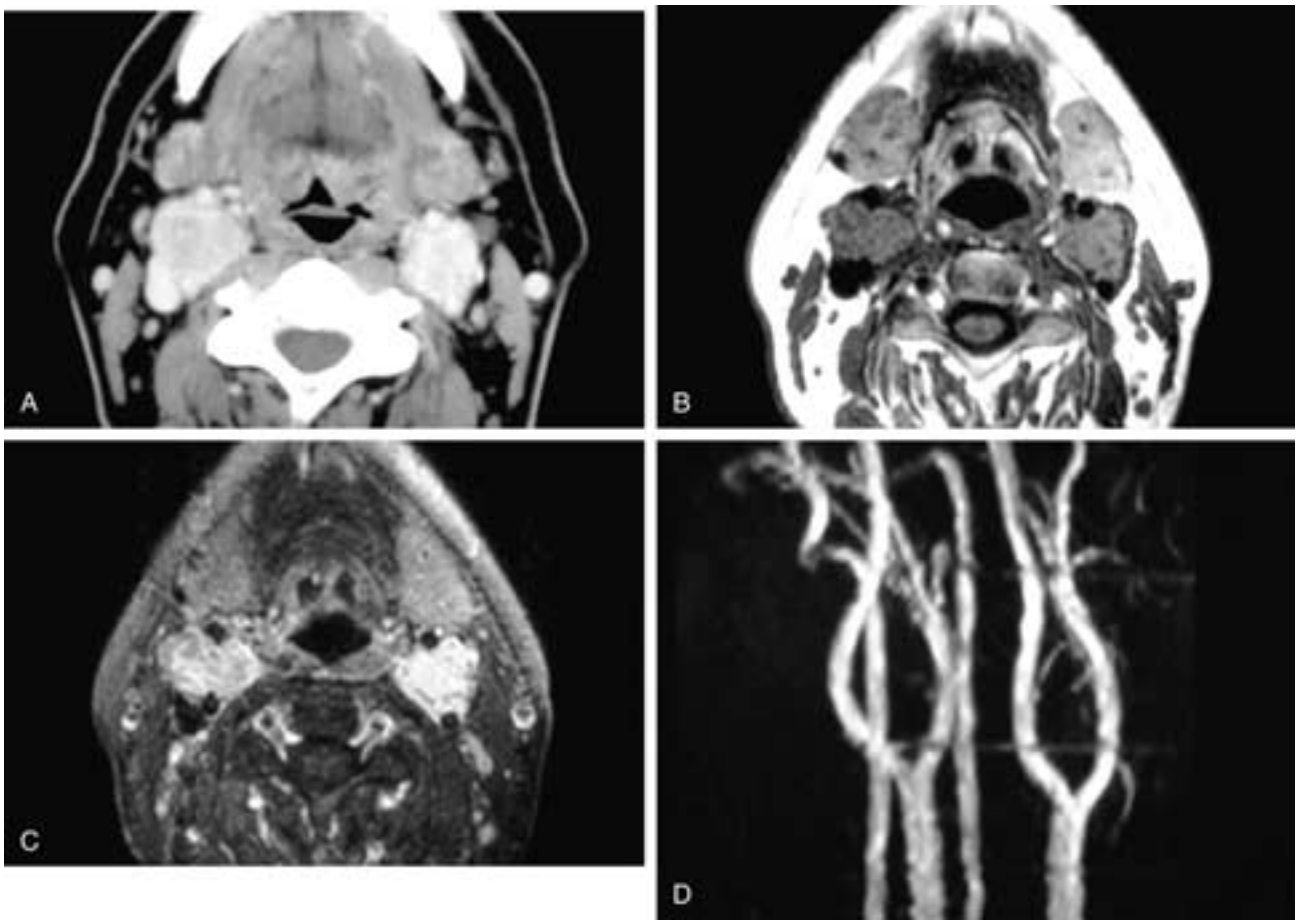

VIEW IMAGE

FIGURE 38-20 Axial contrast-enhanced CT scan (**A**) shows bilateral enhancing ovoid masses that splay the carotid arteries. Axial T1-weighted MR image (**B**) shows the bilateral carotid body tumors to have virtually no vascular flow voids. A T1-weighted, fat-suppressed, contrast-enhanced MR image (**C**) shows marked enhancement of the tumors. A left anterior oblique projection of an MRA (**D**) shows the splaying of both carotid bifurcations but virtually no tumor vascularity. On a conventional arteriogram, these tumors each had dense hypervascularity.

may have identical imaging findings. In these cases, it is the history that distinguishes the two diagnoses (Fig. 38-24). Patients with abscesses in the parapharyngeal space are acutely ill, often with severe malaise. By comparison, patients with metastatic nodes usually are asymptomatic or complain of localized discomfort or pain. The imaging appearance of lymph nodes is discussed in Chapter 36.

Benign Soft-Tissue Masses and Cysts

The remaining lesions that occur in the parapharyngeal space are statistically rare. As a group, they represent 10% to 33% of all the cases, with the latter number including lymph nodes.

Teratomas involving the parapharyngeal space are rare, and most have occurred in newborns or infants. The child often presents in acute respiratory distress. On CT these lesions may have calcifications, ossifications, cystic areas, and fatty regions. Usually the margins are infiltrative, and CT has been found to be most useful in their diagnosis. Components of all three germ layers are present, and histologic examination of one patient showed the presence of a large amount of mature brain tissue, a moderate amount of collagenous fibers and smooth muscle cells, and a minute amount of cartilage and epithelial structures.[100, 101]

There have been numerous reports of various types of heterotopic tissue in the head and neck, with heterotopic cartilage, gastric tissue, thyroid tissue, and salivary gland tissue having been found in such varied locations as the tongue, gingiva, palate, nasopharynx, parapharyngeal space, and neck. Heterotopic brain tissue in the parapharyngeal space causing airway obstruction in the neonate has been described, and three cases were reported that caused significant airway and feeding difficulties.[102]

Solitary fibrous tumors and desmoplastic fibromas are uncommon spindle cell neoplasms that most often affect serosal surfaces, especially the pleura. However, recently, these tumors have been documented in a number of extrapleural sites, including the head and neck, and there has been direct involvement of the parapharyngeal space (see Chapter 41). The rare location of these uncommon lesions gives rise to difficulty in diagnosis, and the final diagnosis is not made until the excised tumor is examined by histopathology and immunohistochemistry.[103–107] As with such fibrous tumors elsewhere in the body, the MR signal

Copyright © 2003, Mosby, Inc. All rights reserved.

intensities tend to be intermediate to low on T1-weighted and low on T2-weighted images.

Nodular fasciitis is a benign lesion composed of fibrous tissue. It most commonly affects the upper extremity, which accounts for half of all cases. From 10% to 20% of the lesions occur in the head and neck area, most of which are subcutaneous (see Chapter 41). One case of nodular fasciitis presented as an unusually large submucosal tumor of the pharynx. The tumor extended from the retropharyngeal to the parapharyngeal space and measured $8 \times 4 \times 3$ cm. Since nodular fasciitis is known for its tendency to spontaneous regression, this tumor was transorally debulked by the use of YAG laser.[108]

Branchial cysts can occur in the parapharyngeal space and are of either a first or second arch derivation. Currently, most authors refer to them as second branchial arch cysts; they are probably of branchial pouch origin.[109] This conclusion is related to the observation that although second branchial apparatus problems usually occur along the anterior border of the sternocleidomastoid muscle, the tract of this arch courses between the internal and external carotid arteries in the parapharyngeal space, heading toward the palatine tonsil. In addition, the second branchial pouch contributes to the tonsillar fossa, and these parapharyngeal space cysts are usually deep to this fossa.[110] These cysts most often are located in the medial aspect of the parapharyngeal space, adjacent to the retropharyngeal space, and anteromedial to the carotid sheath (Fig. 38-25). Less often, the cysts occur laterally, adjacent to or involving the deep portion of the parotid gland. All of these cysts usually are less than 2 cm, are well delineated, and are spherical or ovoid in shape. Rarely, a large cyst can fill the entire parapharyngeal space, extending down to the level of the submandibular gland. In one case, the mass effect of the cyst caused cranial nerve palsies.[111]

On CT, the cysts usually have a homogeneous low-attenuation (10 to 20 HU) central region with a thin, uniformly smooth wall. On MR imaging, they usually appear as homogeneous masses with a low or intermediate T1-weighted and a high T2-weighted signal intensity. The signal intensities of the cyst's contents reflect the protein content of the cyst fluid. Their cystic nature may not be evident on noncontrast images. After contrast injection the cyst wall enhances, verifying the cystic nature of the mass (Fig. 38-25).[109–113]

When a cyst becomes infected, its protein content increases, and this is seen on CT as an increase in attenuation. In addition, the cyst wall thickens and enhances, and the surrounding soft-tissue planes become effaced due to cellulitis. On MR imaging, the findings are probably best appreciated on T2-weighted images and on T1-weighted, fat-suppressed, contrast-enhanced images. Such an infected cyst is, in effect, an abscess, and its imaging appearance is similar to that of an abscess. Two points may aid in the distinction between an abscess and an infected parapharyngeal space cyst: (1) The abscess usually arises secondary to an infection of the soft tissues surrounding the parapharyngeal space, with the seeding source often being in the palatine tonsil or teeth. A tonsillar abscess or evidence of a pharyngitis is usually seen on the images. (2) With an

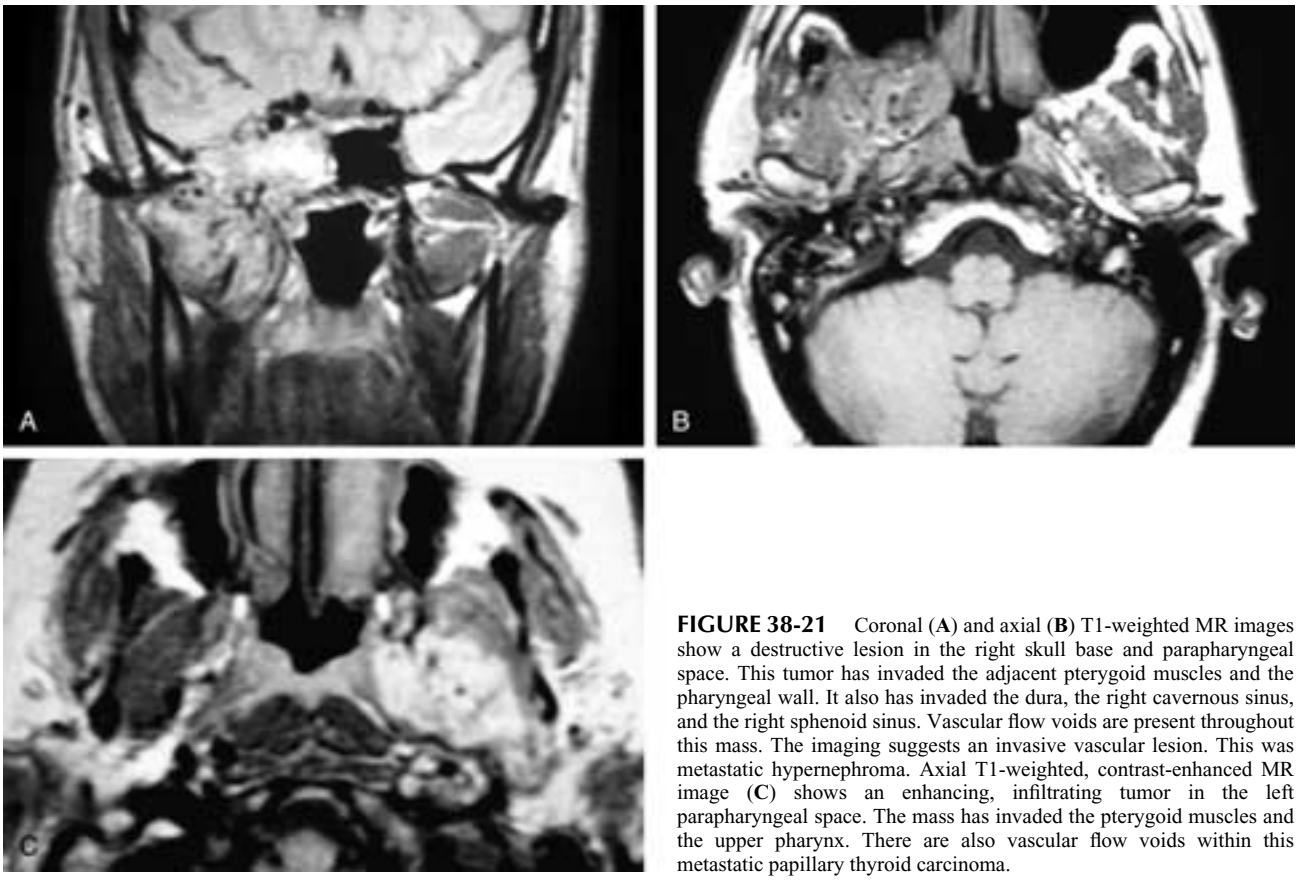

FIGURE 38-21 Coronal (**A**) and axial (**B**) T1-weighted MR images show a destructive lesion in the right skull base and parapharyngeal space. This tumor has invaded the adjacent pterygoid muscles and the pharyngeal wall. It also has invaded the dura, the right cavernous sinus, and the right sphenoid sinus. Vascular flow voids are present throughout this mass. The imaging suggests an invasive vascular lesion. This was metastatic hypernephroma. Axial T1-weighted, contrast-enhanced MR image (**C**) shows an enhancing, infiltrating tumor in the left parapharyngeal space. The mass has invaded the pterygoid muscles and the upper pharynx. There are also vascular flow voids within this metastatic papillary thyroid carcinoma.

VIEW IMAGE

Copyright © 2003, Mosby, Inc. All rights reserved.

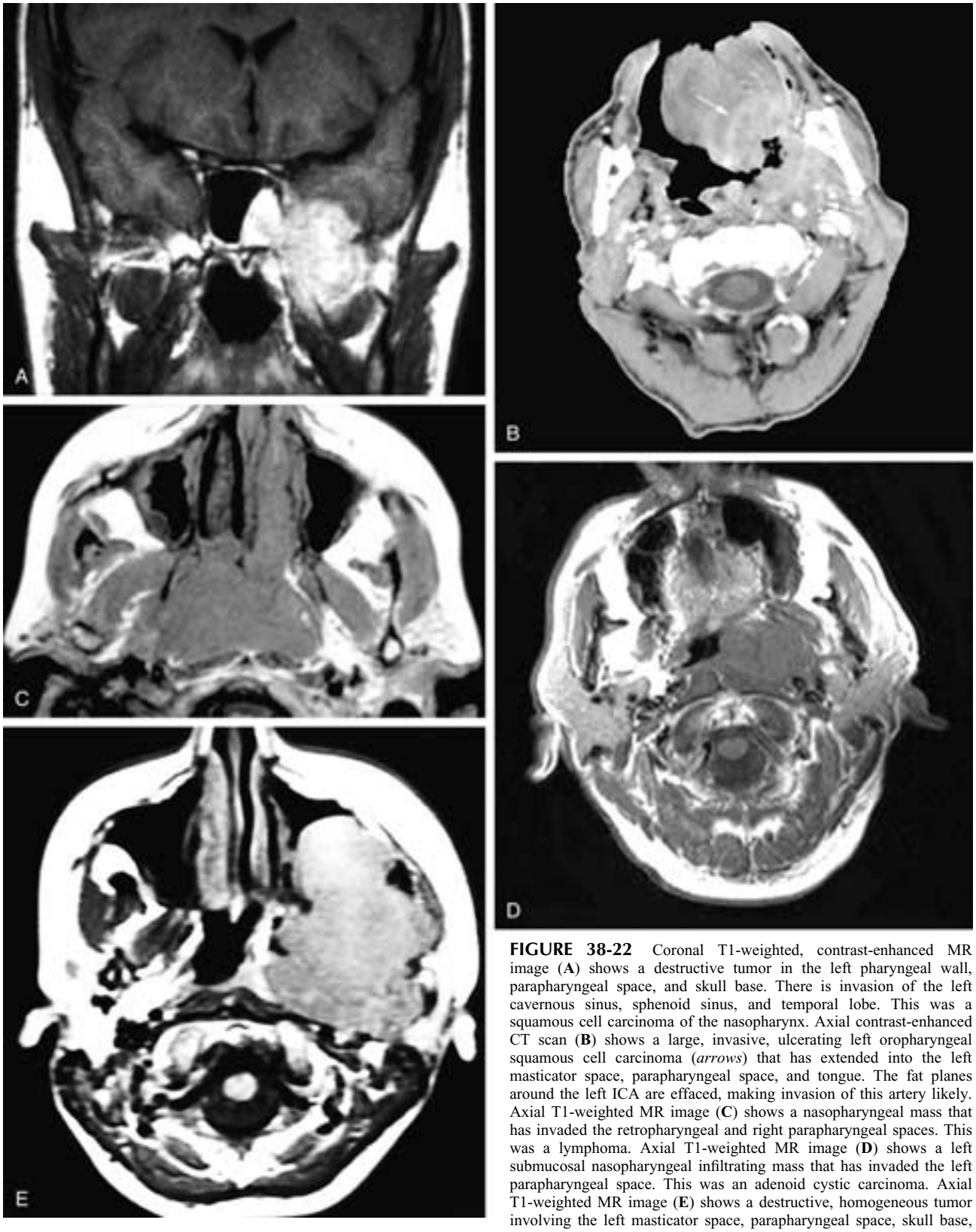

FIGURE 38-22 Coronal T1-weighted, contrast-enhanced MR image (**A**) shows a destructive tumor in the left pharyngeal wall, parapharyngeal space, and skull base. There is invasion of the left cavernous sinus, sphenoid sinus, and temporal lobe. This was a squamous cell carcinoma of the nasopharynx. Axial contrast-enhanced CT scan (**B**) shows a large, invasive, ulcerating left oropharyngeal squamous cell carcinoma (*arrows*) that has extended into the left masticator space, parapharyngeal space, and tongue. The fat planes around the left ICA are effaced, making invasion of this artery likely. Axial T1-weighted MR image (**C**) shows a nasopharyngeal mass that has invaded the retropharyngeal and right parapharyngeal spaces. This was a lymphoma. Axial T1-weighted MR image (**D**) shows a left submucosal nasopharyngeal infiltrating mass that has invaded the left parapharyngeal space. This was an adenoid cystic carcinoma. Axial T1-weighted MR image (**E**) shows a destructive, homogeneous tumor involving the left masticator space, parapharyngeal space, skull base, and posterior maxilla. This was a rhabdomyosarcoma.

VIEW IMAGE

Copyright © 2003, Mosby, Inc. All rights reserved.

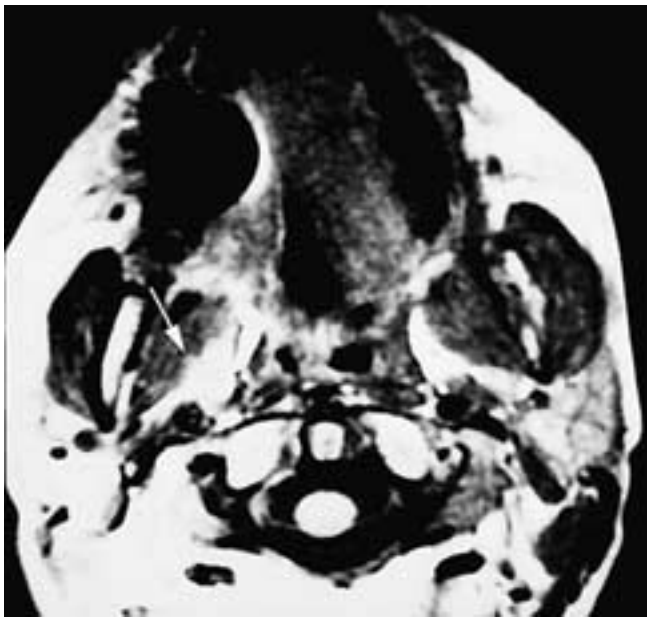

VIEW IMAGE

FIGURE 38-23 Axial T1-weighted MR image shows slightly increased fat in the right parapharyngeal space. The feature differentiating a benign lipoma (see Fig. 38-28) from this liposarcoma is the infiltration of the right medial pterygoid muscle (*arrow*).

abscess, multiple enlarged lymph nodes usually are present in the adjacent neck. By comparison, with an infected branchial cyst there rarely are adjacent lymph nodes. As mentioned earlier, the primary role of the radiologist in such cases is to differentiate between cellulitis and abscess.

Cystic lymphangiomas or cystic hygromas are rarely found in adults, with 90% of the cases being discovered by age 2 years. When the parapharyngeal space is involved, there usually are multicystic extensions of a posterior triangle mass. Less commonly, there may be an anterior triangle mass with extension into the parapharyngeal space; rarely, large cystic hygromas can involve the entire parapharyngeal space and floor of the mouth. The cyst walls are normally so thin that they are not clearly identified as a rim on sectional imaging. However, if infection has occurred, the cyst wall thickens and enhances, and the normally sharp contours of noninfected cysts become blurred and effaced. During surgery on large lymphangiomas, intraoperative neurologic monitoring has been suggested so that cranial nerves hidden or encased in the lesion are not damaged.[114]

On CT, cystic hygromas usually are composed of multiple conglomerate cysts with well-delineated borders (Fig. 38-26). Increased attenuation within the cyst's contents usually reflects either infection or hemorrhage, and a fluid-fluid level may be seen. The individual cysts are usually better seen on MR imaging, and the cyst's contents usually have a low to intermediate T1-weighted and a high T2-weighted signal intensity (Fig. 38-27).[115–118] If the cyst is infected, both the T1-weighted and T2-weighted signal intensities are usually high. If hemorrhage has occurred, intracystic fluid-fluid levels are seen. These actually represent the separation of fluids with different specific gravities, as the blood does not clot within the cysts. Such hemorrhage can occur with or without an antecedent history of trauma. The classic MR appearance is that of multiple cysts, each with a fluid-fluid level.

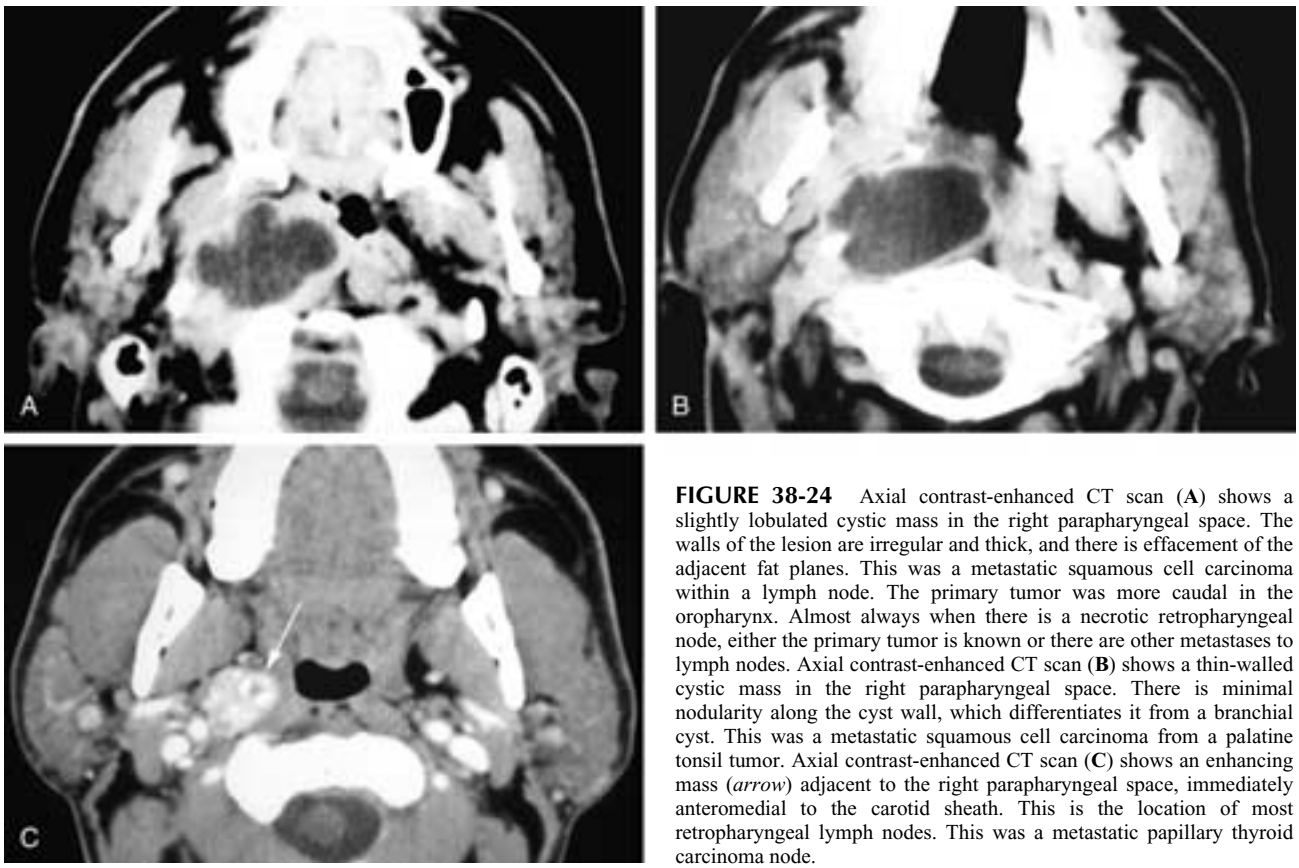

VIEW IMAGE

FIGURE 38-24 Axial contrast-enhanced CT scan (**A**) shows a slightly lobulated cystic mass in the right parapharyngeal space. The walls of the lesion are irregular and thick, and there is effacement of the adjacent fat planes. This was a metastatic squamous cell carcinoma within a lymph node. The primary tumor was more caudal in the oropharynx. Almost always when there is a necrotic retropharyngeal node, either the primary tumor is known or there are other metastases to lymph nodes. Axial contrast-enhanced CT scan (**B**) shows a thin-walled cystic mass in the right parapharyngeal space. There is minimal nodularity along the cyst wall, which differentiates it from a branchial cyst. This was a metastatic squamous cell carcinoma from a palatine tonsil tumor. Axial contrast-enhanced CT scan (**C**) shows an enhancing mass (*arrow*) adjacent to the right parapharyngeal space, immediately anteromedial to the carotid sheath. This is the location of most retropharyngeal lymph nodes. This was a metastatic papillary thyroid carcinoma node.

Copyright © 2003, Mosby, Inc. All rights reserved.

Lipomas and fatty neurofibromas involving the parapharyngeal space may have similar appearances on CT and MR imaging (Fig. 38-28). The MR findings of these fat-dominated lesions are those of high T1-weighted and intermediate T2-weighted signal intensities. However, occasionally a lipoma contains hemorrhage. This can cause the CT attenuation to approach that of muscle and can cause the MR T1-weighted and T2-weighted signal intensities to be high. In such cases, the imaging diagnosis can be quite difficult.[119–124]

Angiolymphoid hyperplasia with eosinophilia (ALHE) is an uncommon benign condition characterized by cutaneous nodules with a predilection for the head and neck region. Extracutaneous involvement is rare. A 44-year-old woman has been reported with a large submucosal ALHE tumor in the parapharyngeal space, diagnosed at pathology.[125]

Two cases of eumycotic mycetomas in the head and neck region were reported, one localized to the soft tissue of the neck. It was completely excised, and the patient needed no further treatment. In the second case, the lesion extensively

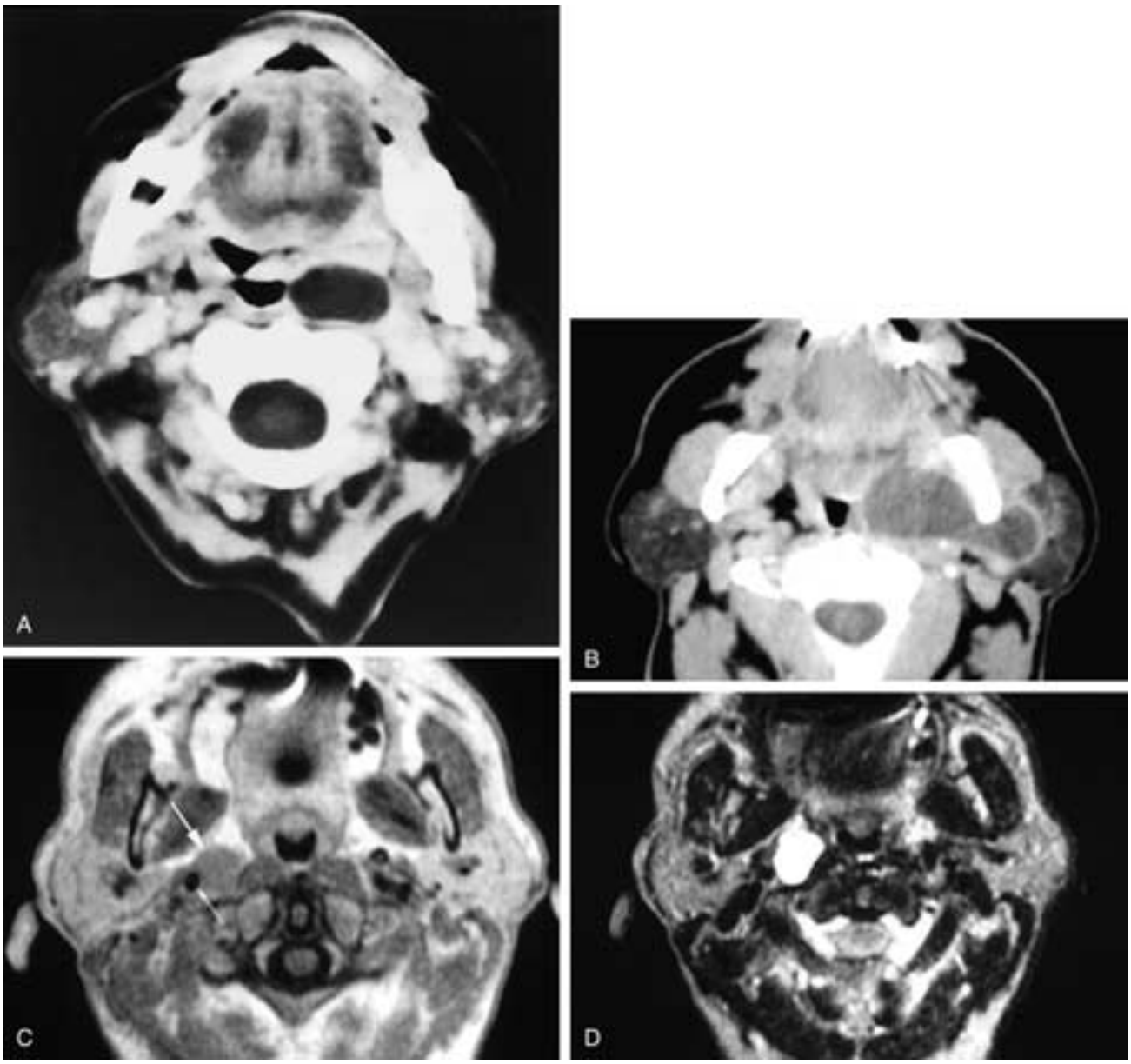

VIEW IMAGE

FIGURE 38-25 Axial contrast-enhanced CT scan (**A**) shows a smooth-walled cyst in the left parapharyngeal space. The cyst pushes the left pharyngeal wall toward the midline and is just anteromedial to the left carotid sheath. This was a branchial cyst. Axial CT scan (**B**) shows a dumbbell-shaped cyst in the deep portion of the left parotid gland and within the left parapharyngeal space. The narrowest portion of the cyst is at the level of the stylomandibular tunnel. This was a branchial cyst. Axial T1-weighted MR image (**C**) shows a small ovoid mass (*large arrow*) just anteromedial to the right carotid sheath and thus the ICA (*small arrow*). This branchial cyst had high T2-weighted signal intensity. Compare this image to Figure 38-15A, which shows a schwannoma within the carotid sheath. Axial T2-weighted MR image (**D**) shows a smooth-walled, high signal intensity ovoid lesion in the right parapharyngeal space lying immediately anteromedial to the carotid sheath. This is a slightly larger branchial cyst than that shown in **C**.

Illustration continued on following page

Copyright © 2003, Mosby, Inc. All rights reserved.

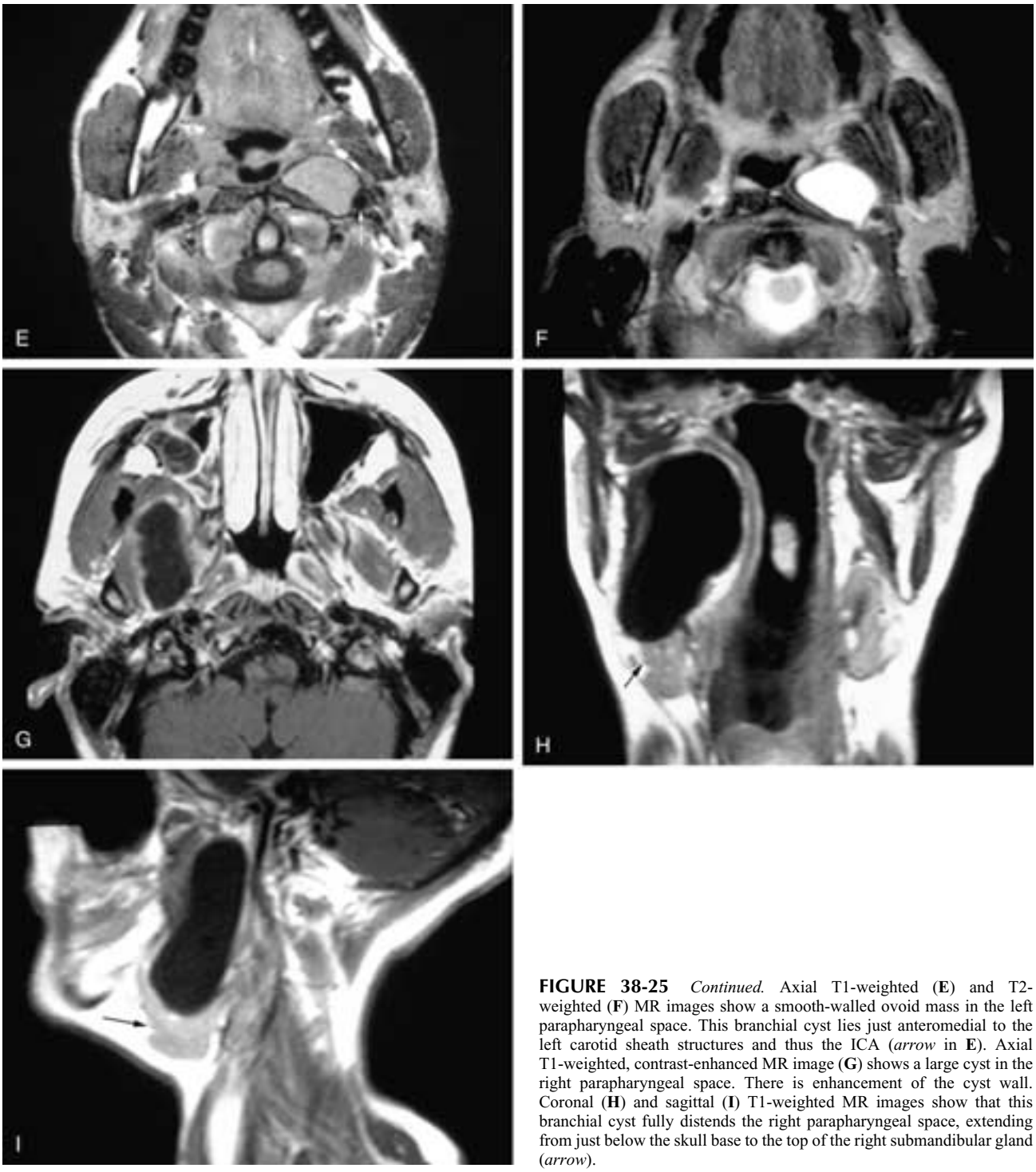

FIGURE 38-25 *Continued.* Axial T1-weighted (**E**) and T2-weighted (**F**) MR images show a smooth-walled ovoid mass in the left parapharyngeal space. This branchial cyst lies just anteromedial to the left carotid sheath structures and thus the ICA (*arrow* in **E**). Axial T1-weighted, contrast-enhanced MR image (**G**) shows a large cyst in the right parapharyngeal space. There is enhancement of the cyst wall. Coronal (**H**) and sagittal (**I**) T1-weighted MR images show that this branchial cyst fully distends the right parapharyngeal space, extending from just below the skull base to the top of the right submandibular gland (*arrow*).

VIEW IMAGE

involved the structures in the parapharyngeal space, submandibular space, and carotid sheath, extending to the skull base. The patient was treated by a combination of wide excision with a radial forearm flap and antifungal agents.[126]

Vascular and Neurologically Related Abnormalities

A partially or totally occluded vessel may occasionally present a diagnostic problem on sectional imaging. If internal jugular vein thrombosis is present, it is most often iatrogenic, either the result of a catheter, a needle, or prior surgery or irradiation. ICA occlusions usually are secondary to atherosclerotic disease or surgical trauma. Although on a single axial image a thrombosed internal jugular vein or an occluded carotid artery may simulate a cystic mass, the tubular configuration of the vessel is easily identified once all of the scans are examined serially (Fig. 38-29). On MR imaging, with the use of gradient-echo and short flip angle techniques, slow flow through a partially occluded vessel can be identified, and the high signal intensity of the clotted

Copyright © 2003, Mosby, Inc. All rights reserved.

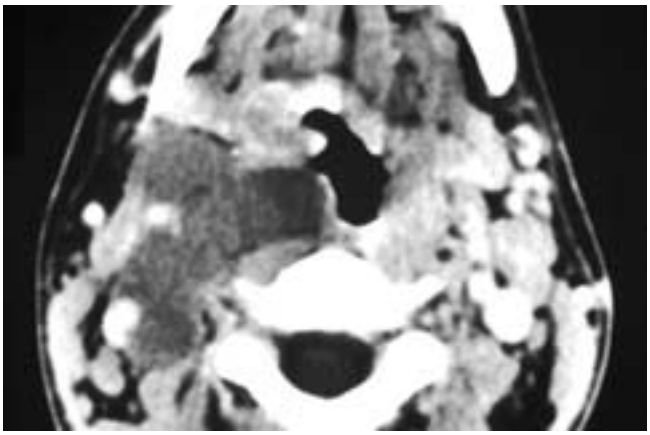

VIEW IMAGE

FIGURE 38-26 Axial contrast-enhanced CT scan shows a multiloculated cystic mass in the right parapharyngeal space. Although no cyst wall is clearly identified, this cystic lymphangioma (hygroma) remains clearly differentiated from the adjacent soft tissues.

or slowly flowing blood can be helpful in diagnosing these lesions.

Aneurysms tend to occur at the carotid bifurcation and often are the result of either atherosclerotic disease or trauma. When an aneurysm is present, there often is peripheral rim calcification, which distinguishes it from a pleomorphic adenoma, a schwannoma, or another rare tumor in which any dystrophic calcifications occur within the lesion's matrix. Calcifications may also be seen within the parapharyngeal space lymph nodes, most often secondary to metastatic papillary thyroid carcinoma. The topic of nodal disease is discussed in Chapter 36.

On imaging, an aneurysm also obliterates the silhouette of the involved artery. Thus, whenever a mass is seen, especially with peripheral calcification, and the ICA adjacent to the mass cannot be identified, the diagnosis of an aneurysm should be made. Further studies such as CTA, MRA, or conventional angiography should be performed to confirm this diagnosis (Fig. 38-30).[127–129]

Of all the masses that occur in the parapharyngeal space, the aneurysm is most immediately life-threatening. In addition, if surgery is performed on the parapharyngeal space and the surgeon is not preoperatively aware of the diagnosis of an aneurysm, catastrophic complications may result. Thus, the imager must always be prepared to ensure that the diagnosis of an aneurysm can either be established or excluded.

Dissection of the ICA is recognized as a common cause of ischemic stroke in young adults and occurs in approximately 10% to 20% of these patients.[130] Although the most common clinical presentation is headache, patients may also present with focal neurologic deficits. In the majority of patients, the dissection involves the extracranial portion of the ICA and only infrequently extends intracranially or involves the intracranial segment alone. The etiology of spontaneous dissection of the ICA is broad and includes minor trauma, fibromuscular dysplasia, Marfan's syndrome, cystic medial necrosis, idiopathic regressing arteriopathy, type IV Ehlers Danlos syndrome, hypertension, ICA redundancy, and alpha 1-antitrypsin deficiency.[130] The presumption that there is preexisting arterial disease that

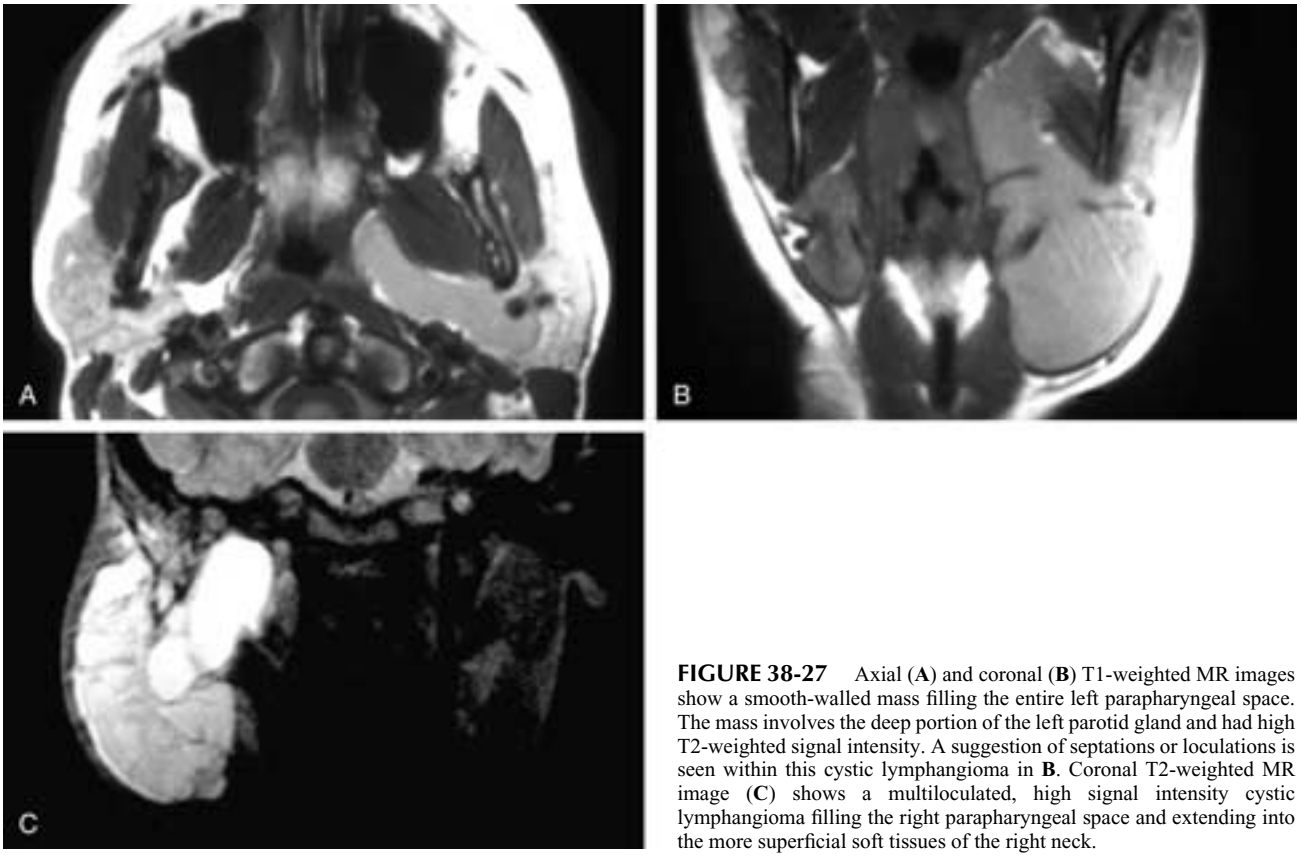

FIGURE 38-27 Axial (**A**) and coronal (**B**) T1-weighted MR images show a smooth-walled mass filling the entire left parapharyngeal space. The mass involves the deep portion of the left parotid gland and had high T2-weighted signal intensity. A suggestion of septations or loculations is seen within this cystic lymphangioma in **B**. Coronal T2-weighted MR image (**C**) shows a multiloculated, high signal intensity cystic lymphangioma filling the right parapharyngeal space and extending into the more superficial soft tissues of the right neck.

VIEW IMAGE

Copyright © 2003, Mosby, Inc. All rights reserved.

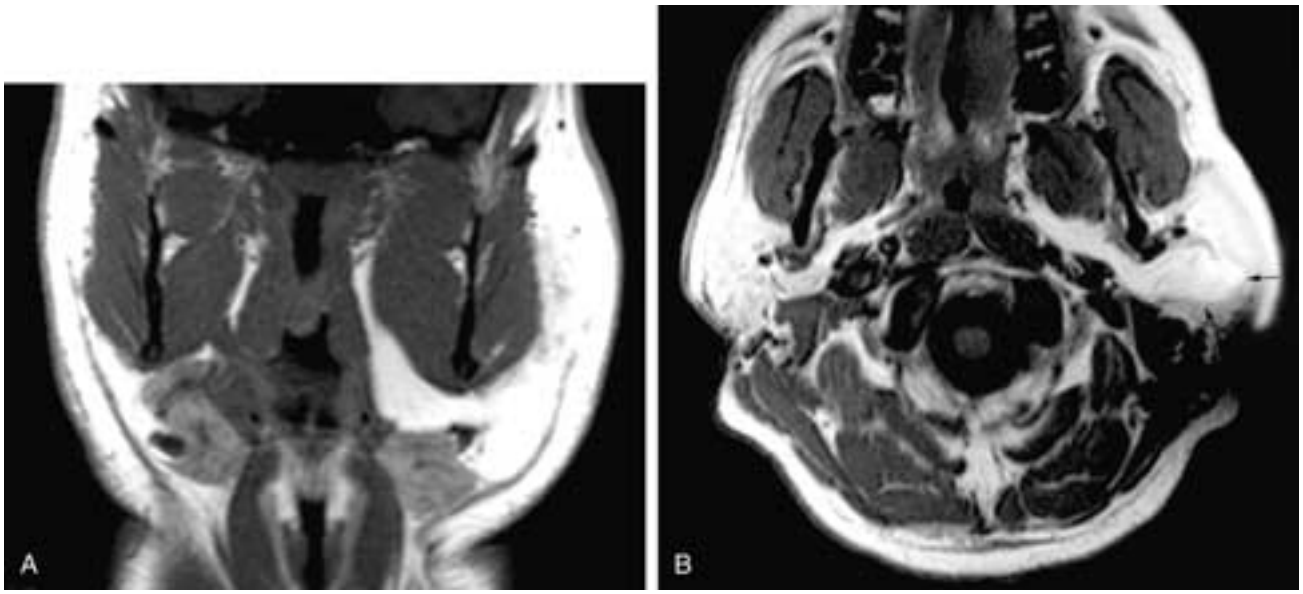

VIEW IMAGE

FIGURE 38-28 Coronal (**A**) and axial (**B**) MR images show a fat signal intensity mass filling and expanding the left parapharyngeal space and extending well into the left parotid gland (*arrows* in **B**). This was a benign lipoma.

predisposes cervical arteries to dissection is supported by reports of intracranial aneurysms associated with spontaneous cervical artery dissection, a familial association of intracranial aneurysms and cervical artery dissection, a familial occurrence of cervical artery dissections, and the occurrence of multivessel dissections.

Mokri et al. reported that cranial nerve palsy was present in 12% of 190 adults diagnosed with spontaneous dissection of the extracranial ICA.[131] Of these patients with cranial nerve findings, 65% presented with isolated cranial nerve palsy. The most common isolated cranial nerve to be involved in this series was cranial nerve V. There are also two distinct syndromes of cranial nerve palsies that are recognized in association with dissection of the ICA: a syndrome of ocular motor palsies (III, IV, VI) and a syndrome of lower cranial nerve palsies (IX, X, XI, XII). These lower cranial nerves can be affected in multiple combinations; however, cranial nerve XII is almost always involved, and frequently there is an associated ipsilateral headache. When the dissection involves the cavernous portion of the ICA, ocular motor palsy is seen.[131] Isolated vagal neuropathy has also been reported.[130]

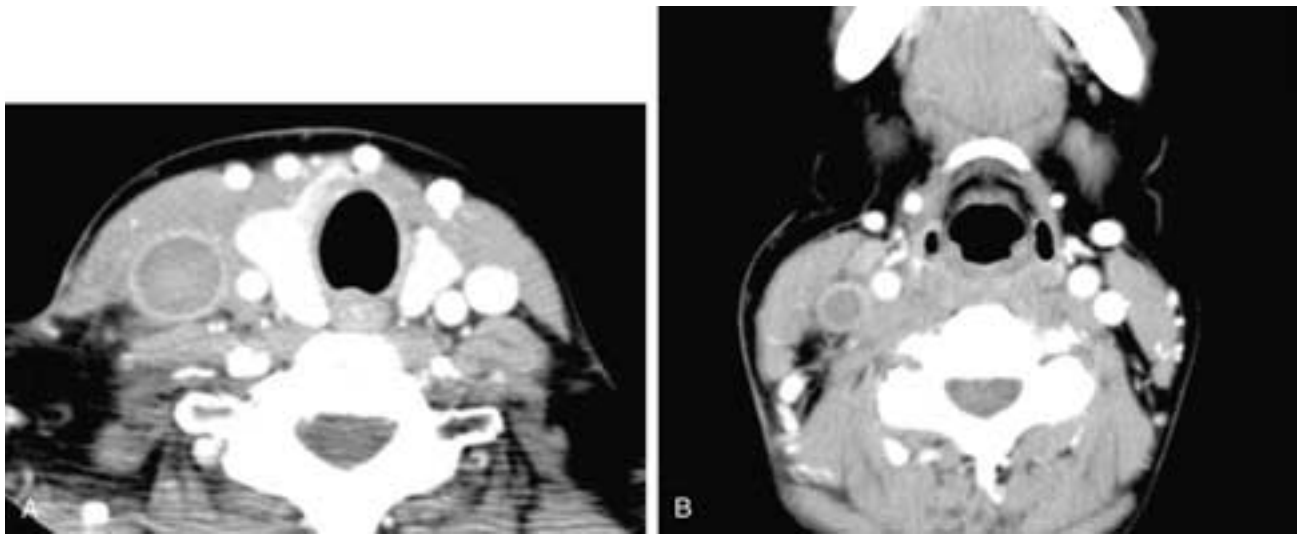

VIEW IMAGE

FIGURE 38-29 Axial contrast-enhanced CT scan (**A**) shows a ''cyst'' in the right neck. The internal jugular vein is not identified. More cranially in the neck (**B**), the thrombosed internal jugular vein is again seen. The tubular configuration and its replacement of the internal jugular vein establishes the diagnosis.

Copyright © 2003, Mosby, Inc. All rights reserved.

The traditional method of imaging cervical cephalic arterial dissection has been catheter angiography, in which findings may include smooth or slightly irregular luminal narrowing, pseudoaneurysm, an intimal flap, or distal branch occlusions secondary to embolization. CT and MR imaging provide a noninvasive means of diagnosing arterial dissection, and findings on each of these studies include an eccentric rim of mural thickening surrounding a narrowed lumen. On CT, the intramural hemorrhage usually is hypodense to muscle, and a thin rim of enhancement may be seen around the hematoma, presumably representing enhancement of the vasa vasorum. On MR imaging, typically the eccentric or circumferential periarterial rim of the intramural hematoma demonstrates hyperintense signal on T1-weighted and T2-weighted images (Fig. 38-30). The utility of MRA in the diagnosis of dissection is limited, and probably the most useful MR imaging sequence is fat-suppressed, axial T1-weighted images with inferior saturation pulses.[130] Other authors prefer a non-fat-suppressed, noncontrast sequence to best identify the bright signal of the dissection with a ring around it. Duplex sonography is less reliable than angiography and MR imaging, primarily because the dissection is usually distal to the region that can be well visualized on ultrasound. Findings on ultrasound may include an echogenic intimal flap or an echogenic thrombus, and Doppler waveforms may show a highly resistive, obstructive pattern.

Variations in the course of the ICA are reported to occur, with an incidence of 15% to 40%. They are mainly the result of degenerative atherosclerosis, with elongation, slight coiling, and kinking of the vessel. In addition, a sigmoid-shaped tortuosity represents an occasional congenital anomaly.[132] Commonly, the tortuous ICA causes an impression on the pharyngeal wall, and this may be an uncommon cause of a retropharyngeal or parapharyngeal ''mass.'' Such a fullness has also been related to minor globus syndromes. The ICA can also come into direct contact with the tonsillar fossa, creating a significant surgical risk during tonsil surgery.[132, 133] This abnormal positioning of the artery is well seen on contrast CT and MR images, and it is extremely important that the

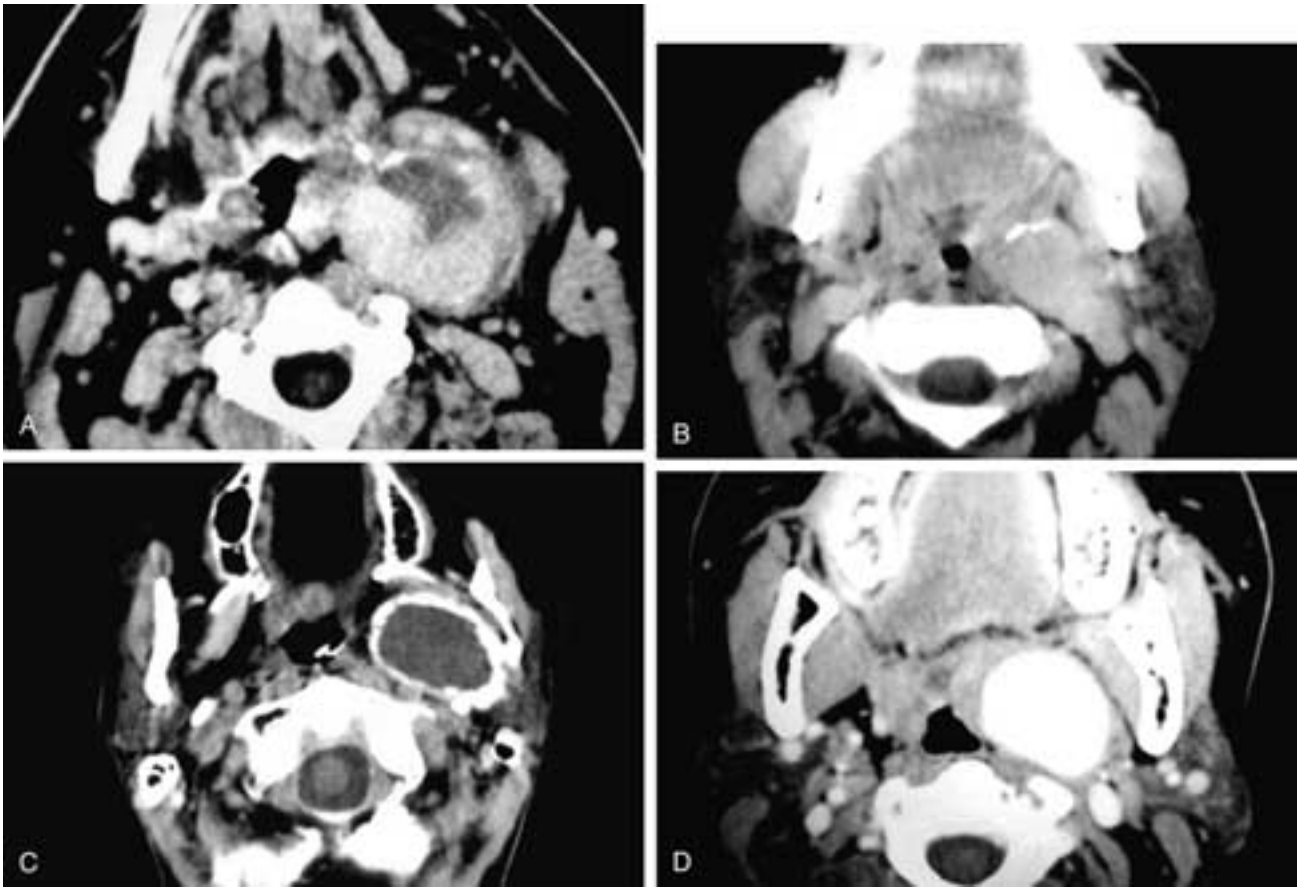

VIEW IMAGE

FIGURE 38-30 Axial contrast-enhanced CT scan (**A**) shows an ovoid, partially enhancing mass with peripheral calcifications in the left parapharyngeal space. The ICA could not be identified. This was an aneurysm of the ICA. Axial contrast-enhanced CT scan (**B**) shows an oblong enhancing mass with peripheral calcification in the left parapharyngeal space. The ICA could not be identified. This was an aneurysm of the ICA. Axial CT scan (**C**) shows an ovoid water attenuation mass in the left parapharyngeal space with peripheral calcification. Compare this aneurysm of the ICA with that in Figure 38-11B. Axial contrast-enhanced CT scan (**D**) shows a large, spherical, enhancing mass in the left parapharyngeal space replacing the left ICA.

Illustration continued on following page

Copyright © 2003, Mosby, Inc. All rights reserved.

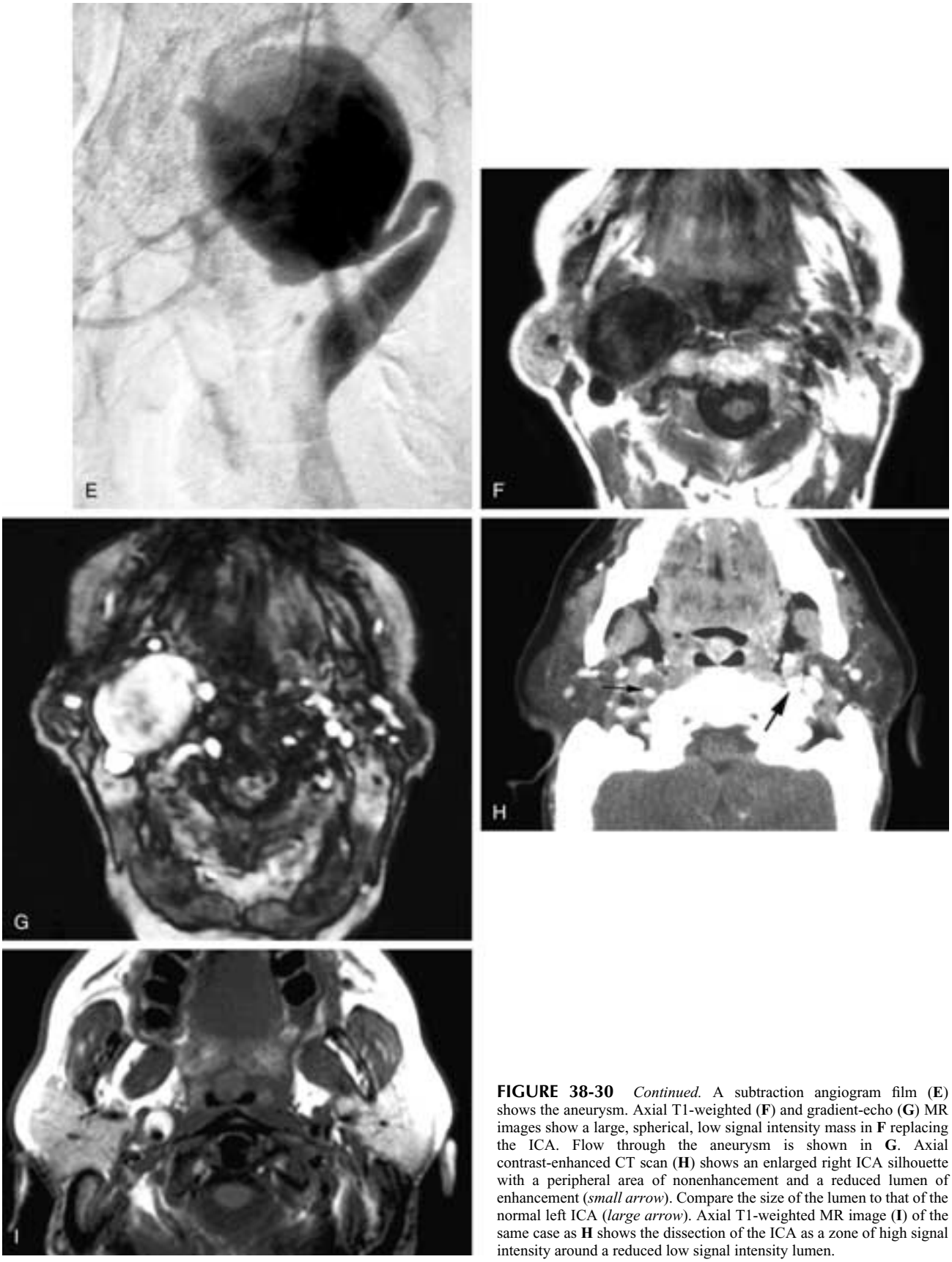

FIGURE 38-30 *Continued.* A subtraction angiogram film (**E**) shows the aneurysm. Axial T1-weighted (**F**) and gradient-echo (**G**) MR images show a large, spherical, low signal intensity mass in **F** replacing the ICA. Flow through the aneurysm is shown in **G**. Axial contrast-enhanced CT scan (**H**) shows an enlarged right ICA silhouette with a peripheral area of nonenhancement and a reduced lumen of enhancement (*small arrow*). Compare the size of the lumen to that of the normal left ICA (*large arrow*). Axial T1-weighted MR image (**I**) of the same case as **H** shows the dissection of the ICA as a zone of high signal intensity around a reduced low signal intensity lumen.

VIEW IMAGE

Copyright © 2003, Mosby, Inc. All rights reserved.

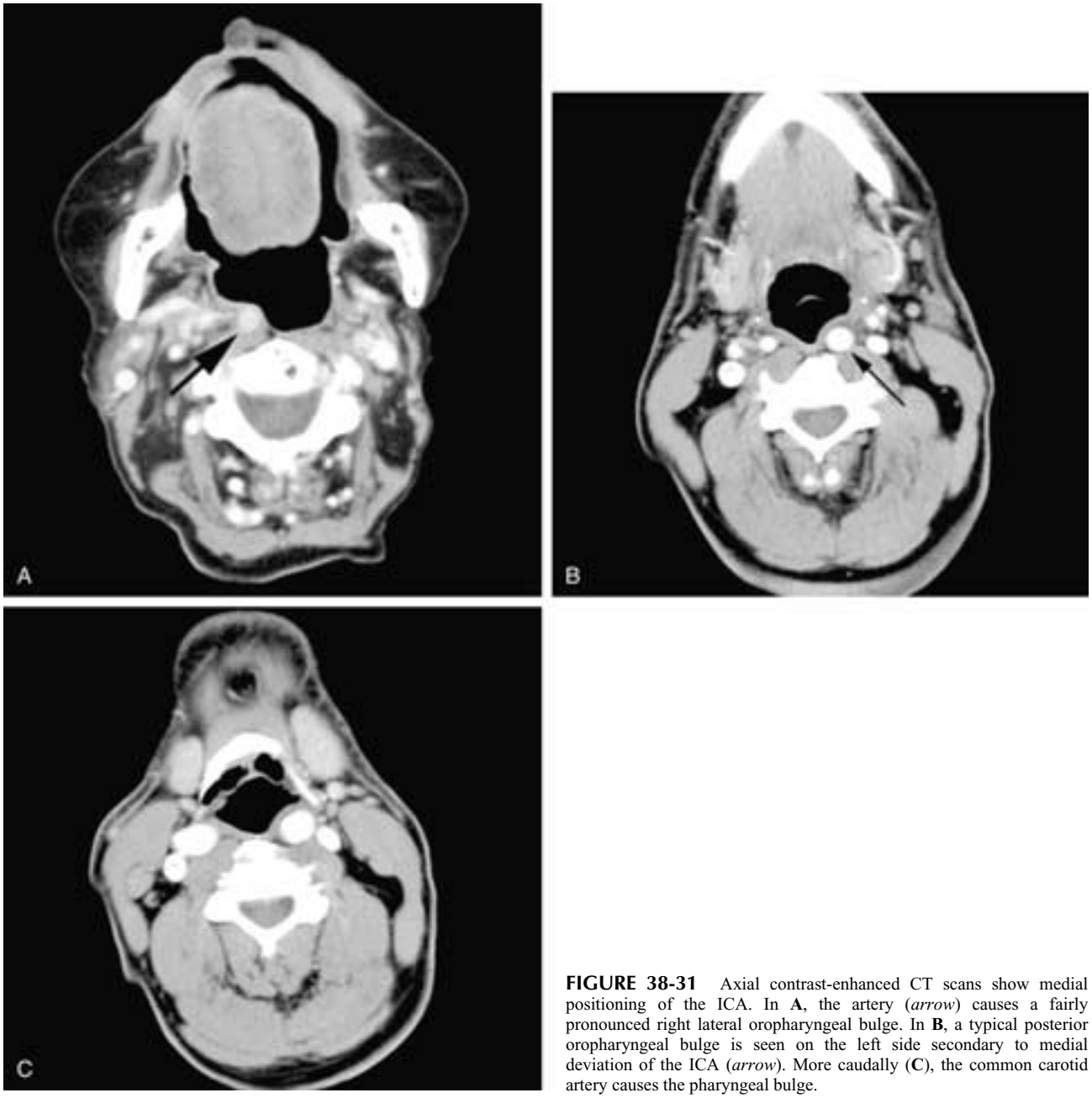

FIGURE 38-31 Axial contrast-enhanced CT scans show medial positioning of the ICA. In **A**, the artery (*arrow*) causes a fairly pronounced right lateral oropharyngeal bulge. In **B**, a typical posterior oropharyngeal bulge is seen on the left side secondary to medial deviation of the ICA (*arrow*). More caudally (**C**), the common carotid artery causes the pharyngeal bulge.

VIEW IMAGE

clinician be notified of this vascular aberration so that an ill-fated biopsy is not attempted (Fig. 38-31) (also see Chapters 28 and 41).

An intense vasovagal reaction characterizes those reflex cardiovascular syncopes in which the glossopharyngeal nerve constitutes the main afferent nerve pathway. In these syndromes, afferent fibers of the glossopharyngeal nerve project from the baroreceptor area to the medullary cardiac, and vasomotor centers and efferent fibers then descend to the vagus nerve. The most common reflex cardiovascular syndromes linked to cranial nerve IX are carotid sinus syndrome (CSS) and the glossopharyngeal neuralgia-asystole syndrome (GNS). Most patients are males, with a mean age of 65.4 years. The episodes are characterized by weakness, general malaise, pallor, sudation (sweating), very low (40 to 60 mmHg) systolic pressure, mental disorientation, and/or syncope. Often the admission diagnosis in these patients is CSS, but the clinical picture differs in that a triggering factor is not present, the vasovagal episodes are longer, syncope is more frequent and severe, and cranial nerve pacing is ineffective. In all of these patients, imaging shows either a malignant or a benign mass compressing the parapharyngeal space. The pathogenesis of syncope may be similar to that occurring in GNS, except for the absence of neuralgia. Surgical carotid sinus denervation or atrioventricular (A-V) sequential (DDD) pacing is ineffective in completely controlling symptoms, and intracranial sectioning of cranial nerve IX appears to be the most effective mechanism for controlling the syndrome.[134, 135]

Copyright © 2003, Mosby, Inc. All rights reserved.

Trauma

Many different types of trauma can involve the parapharyngeal space, either accidentally or intentionally. The trauma can vary from the unusual explosion of a bottle in a child's mouth, to pellets or bullets, to sharp foreign objects often accidentally placed in food, to knives. In particular, lateral oropharyngeal injuries raise increased concern regarding potential neurovascular impairment via extension into the parapharyngeal space. Unfortunately, neither the mechanism of injury nor the degree of injury correlates well with the potential for neurovascular sequelae, which may not become clinically apparent until days or weeks after the incident.[136–141]

Diseases and Tumors Arising in the Skull Base

Osseous and cartilaginous lesions of the skull base, cervical vertebrae, and mandible are uncommon. These tumors can extend, usually via a stalk-like extension, into the parapharyngeal space. Osteomas (exostoses), osteogenic sarcomas, chondromas, chondrosarcomas, osteochondromas, chordomas, and fibroosseous lesions have all been reported.[124, 142–144] These patients present with signs and symptoms related to the mass effect in the parapharyngeal region. Malignant degeneration of a benign osteocartilaginous exostosis into osteosarcoma and chondrosarcoma has also been reported, and it has been suggested that the differentiation of these benign and malignant osteocartilaginous tumors is best accomplished by examining the imaging features of the cartilage cap.[142] Because of either an osseous matrix or calcifications, these lesions are usually better diagnosed on CT. Often, the final diagnosis is made only by pathologic examination (Fig. 38-32).

Chordomas usually arise in the clivus. Those tumors that arise in the petrous apex are now referred to as chondrosarcomas. Rarely, they may extend caudally into the parapharyngeal space. About 35% of all chordomas occur in the bones of the skull, and the usual natural history is that of relentless local recurrences. However, recent skull base surgery has shown promise of improving this prognosis. About 7% of skull base chordomas can metastasize, usually to the lungs, other bones, skin, lymph nodes, and liver. On CT, most tumors have a nonhomogeneous enhancing appearance, with multiple scattered areas of ''calcification'' that presumably represent residual skull base fragments. On MR imaging, these tumors have a variable nonhomogeneous signal intensity on all imaging sequences, depending upon the histologic makeup of the tumor.[9] In general, because of their bony matrix and the presence of scattered calcifications, some authors believe that these tumors are more easily diagnosed on CT than on MR imaging studies.[124, 142, 143]

Diseases and Tumors Arising Intracranially

Intracranial masses rarely extend through the skull base to project into the parapharyngeal space, and only a few such cases have been reported. Meningiomas represent 13% to 18% of all primary intracranial tumors, and they are the most common of the intracranial neoplasms to extend into the parapharyngeal space. They exit the intracranial compartment either by extending through the jugular fossa or other neurovascular canals or by invading the skull base bone itself.[145] The involved bone can be permeated but otherwise intact, or there can be erosion or some remodeling. Hyperostotic thickening of the bone is a common finding.[7–9, 146] Once the meningioma extends below the skull base, it can grow rapidly, becoming a bulky mass that most often causes the patient to seek medical attention. Meningiomas are enhancing, homogeneous tumors that may have calcifications either in a localized portion of the lesion or scattered throughout the tumor (Fig. 38-33). On MR imaging, they usually have signal intensities similar to those

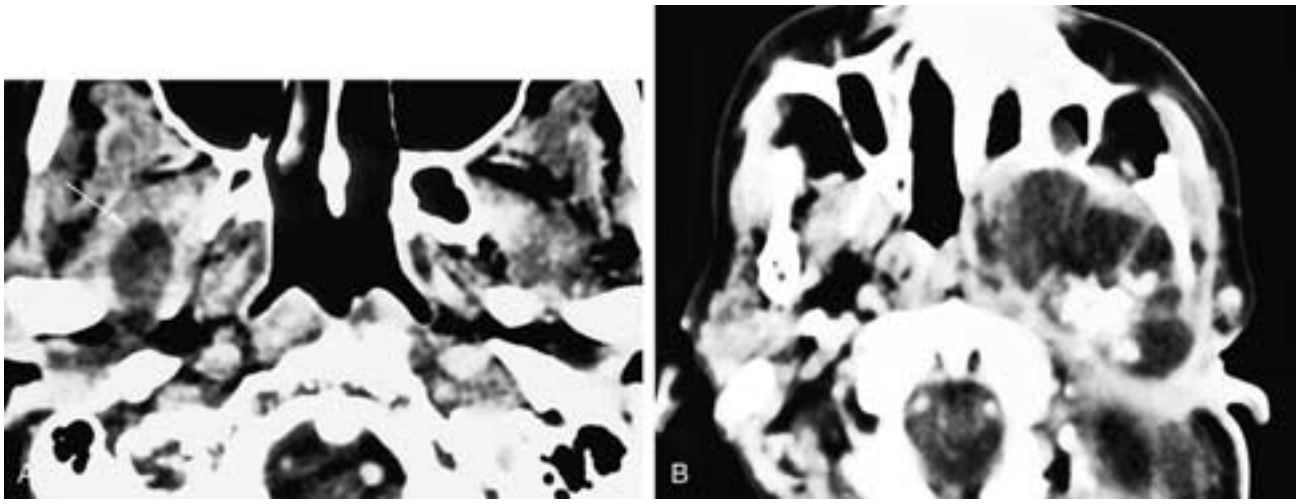

VIEW IMAGE

FIGURE 38-32 Axial contrast-enhanced CT scan (**A**) shows a fairly low-attenuation, sausage-shaped mass (*arrow*) extending from the skull base down into the parapharyngeal and masticator spaces. This was a chondroma. Axial contrast-enhanced CT scan (**B**) shows an overall low-attenuation mass in the left masticator and parapharyngeal spaces, with destruction of the posterior left maxilla. Within the mass are large tumoral calcifications. Note the difference in the appearance of the calcifications in this chondrosarcoma from those in aneurysms (see Figs. 38-14B and 38-27).

Copyright © 2003, Mosby, Inc. All rights reserved.

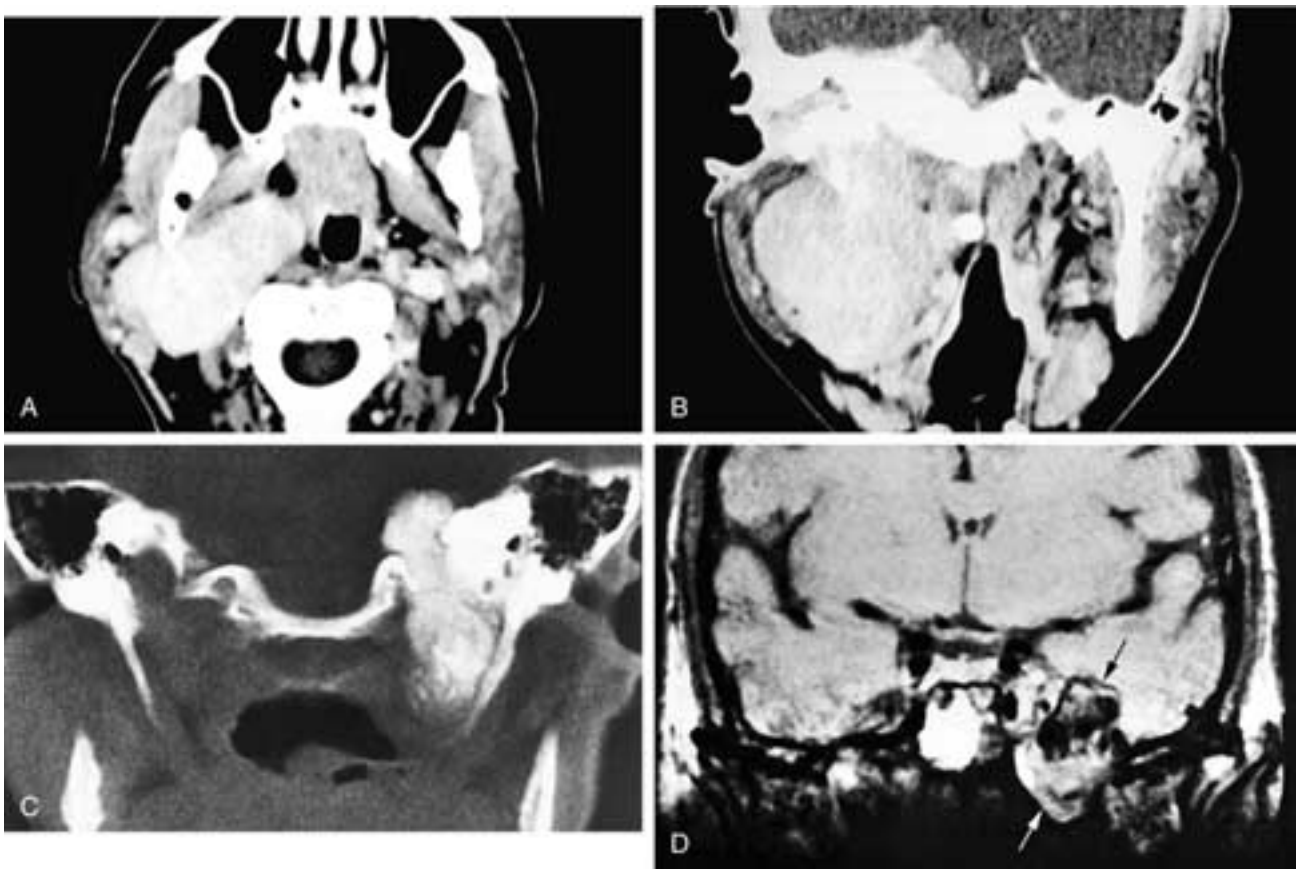

VIEW IMAGE

FIGURE 38-33 Axial (**A**) and coronal (**B**) contrast-enhanced CT scans show a homogeneously enhancing mass in the right parapharyngeal space, the right skull base (which is thickened and sclerotic), and the right posterior fossa. This is a fairly typical imaging appearance for a meningioma. Coronal CT scan (**C**) shows a heavily calcified meningioma extending from the left posterior fossa down into the left parapharyngeal space via the jugular fossa. Coronal T1-weighted MR image (**D**) shows a nonhomogeneous giant aneurysm in the left middle cranial fossa (*black arrow*) that extends down into the left parapharyngeal space (*white arrow*).

of brain. Most of these tumors are in the posterior fossa and extend down through the petrous apex, jugular fossa, and central skull base. Despite their vascularity on angiography, vascular flow voids are rarely seen on MR imaging.

Rarely, a giant aneurysm can erode through the skull base and present as a mass in the parapharyngeal space. These long-standing aneurysms usually have wall calcifications that are best seen on CT. On MR imaging, peripheral signal voids reflect hemosiderin, fibrosis, and/or calcification in the aneurysm (Fig. 38-33). There are also rare reports of glial tumors that extend below the skull base.[147]

There is a case report of a newborn with an extracerebral, intracranial mass that extended from the right middle cranial fossa through the base of the skull to the parapharyngeal space. The mass was composed predominantly of immature brain tissue, and it was enclosed by its own leptomeninges and dura. It was classified as a glioneural hamartoma.[148]

MASTICATOR SPACE ANATOMY

Throughout the literature, there has been relatively little ambiguity about the description of the fascial boundaries of the masticator space, which contains the muscles of mastication: the temporalis, masseter, lateral pterygoid, and medial pterygoid muscles. This space was first described by Juvara in 1870 and was first referred to as the masticator space by Coller and Yglesias in 1935.[3, 5, 6, 149–151]

The anatomy of the masticator space is discussed in detail in Chapter 34. In summary, the fascia that forms the borders of the masticator space is well-defined fibrous tissue that is more on the order of an aponeurosis (Fig. 38-34). The fascia surrounds the muscles of mastication, with the lateral pterygoid muscle lying freely within the space, while the other muscles contribute to the surrounding fascia.[3, 5, 6, 149–153] Most of the medial boundary is the strong interpterygoid fascia, which sweeps cranially from the mandible to the skull base, attaching along a line that extends from the root of the medial pterygoid plate to the sphenoid spine, just medial to the foramen ovale. When viewed in a coronal plane, this fascia runs obliquely downward and laterally from the skull base. Immediately deep (medial) to this fascia is the fat within the prestyloid compartment of the parapharyngeal space. This fat provides an excellent imaging boundary by which to determine whether pathology has grossly violated the medial fascial boundary of the masticator space.[7, 9, 20, 23, 25–27, 30, 32, 42, 151, 153–156] The lateral fascia extends from the bottom of the mandible upward to

Copyright © 2003, Mosby, Inc. All rights reserved.

encase the zygomatic arch. The fascia then continues cranially to the temporal ridge of the calvarium. The fascia also attaches to the lateral orbital margin of the temporal fossa, encasing the temporalis muscle. The medial and lateral fasciae join both anteriorly and posteriorly around the mandibular ramus, closing this space. The parotid gland lies immediately dorsal to the masticator space, and the buccal fat pad is either along the ventral border of this space or within the space.

The differential diagnosis of masses that occur within the masticator space is summarized in Table 38-3.

The Masticator Muscles and Mastication

With regard to the muscles of mastication, opening the mouth is accomplished on either side by the lateral pterygoid muscle (whose medial [upper] head attaches to the temporomandibular articular disc and whose lateral head [lower] attaches to the neck of the mandible) pulling the mandibular condyle forward in a gliding motion. Mouth opening is also assisted, to a small degree, by the superficial portions of the masseter muscle and the medial pterygoid muscle, while the chin is pulled downward and backward by the digastric muscles. If the hyoid bone is fixed in place by contraction of the infrahyoid muscles (strap muscles), and there is some contraction of the temporalis muscles, then contraction of both bellies of the digastric muscles also can open the mouth. Closing the mouth requires relaxation of the lateral pterygoid muscles and digastric muscles, while the temporalis (posterior or horizontal fibers), medial pterygoid, and masseter muscles pull the mandible upward.

Chewing, which is a slewing or grinding motion, is accomplished by both anteroposterior and lateral excursions of the mandible. The anteroposterior motion is produced on either side by alternating actions of the lateral pterygoid muscle and the posterior fibers of the temporalis muscle. The lateral excursion is caused by the medial pterygoid muscle, which on either side pulls the angle of the mandible upward, forward, and medially.[157]

In anatomic summary, the ramus of the mandible lies almost centrally within the masticator space. It is surrounded by the masticator muscles, which, in turn, are contained by firm fascial boundaries.

Table 38-3
MASTICATOR SPACE MASSES

Arising Within Muscle
Hemangioma: usually within masseter muscle
Lymphangioma
Benign masticator muscle hypertrophy
Denervation of masticator muscles (disease or surgery to V_3)
Rhabdomyosarcoma
Rhabdomyoma
Leiomyoma
Lymphoma (non-Hodgkin's)
Metastasis
Arising Within Mandible
Osteomyelitis (usually secondary to odontogenic infection)
Radiation necrosis
Osteoblastoma
Osteosarcoma
Chondrosarcoma
Odontogenic
Dentigerous cyst
Keratocyst
Ameloblastoma
Metastasis
Arising Within Nerve
Schwannoma
Neurofibroma
Neurosarcoma
Spread From:
Acute sialadenitis: either parotid gland or accessory parotid tissue
Salivary gland malignancy
Mucoepidermoid carcinoma
Squamous cell carcinoma
Adenocarcinoma not otherwise specified
Retromolar trigone squamous cell carcinoma
Oropharyngeal squamous cell carcinoma

VIEW IMAGE

FIGURE 38-34 Drawing of the facial region as seen from the left anterior oblique view. A coronal slice has been made through the left masticator space showing the masseter and temporalis muscles laterally and the medial pterygoid muscle medially. The lateral pterygoid muscle lies freely within the masticator space.

CLINICAL PRESENTATION OF MASTICATOR SPACE MASSES

Symptoms referable to the masticator space are pain and trismus. The third division of the trigeminal nerve, the mandibular nerve, exits the skull base at the foramen ovale, descends in the masticator space to the inner aspect of the ramus of the mandible, and then enters the mandible through

Copyright © 2003, Mosby, Inc. All rights reserved.

the mandibular canal as the inferior alveolar nerve, supplying sensation to the teeth. Thus the mandibular nerve contains both motor fibers (for the muscles of mastication) and sensory fibers. The sensory fibers supply the skin of the temporal region, auricle, external auditory meatus, mastoid air cells, cheek, lower face, lower lip, mucous membrane of the cheek, tongue, lower teeth and gums, mandible, temporomandibular joint, and some of the dura. However, through the first and second divisions of the trigeminal nerve, pain of masticator space origin can present as referred pain to the upper face and orbit. Thus, a patient may complain of numbness in the lower teeth, temporomandibular joint pain, ear pain, midfacial pain, pain over the temporal fossa region, temporal headache, or pain in the orbit or forehead. Tumors involving the masticator space often extend in a retrograde manner along the mandibular nerve, through the foramen ovale, into the lateral margin of the cavernous sinus, and occasionally back to the Gasserian ganglion. Tumor spread can also extend into the cavernous sinus proper.

An additional important branch of the mandibular nerve is the auricular temporal nerve, which arises near the middle meningeal artery at the foramen spinosum. This nerve runs laterally deep to the external (or lateral) pterygoid muscle, along the medial side of the mandible, and then turns upward with the superficial temporal artery, under the cover of the parotid gland. The peripheral branches then communicate with the facial nerve, in the substance of the parotid gland, and connect to the otic ganglion. It is this auricular temporal nerve that may act as a pathway for a parotid tumor to extend in a retrograde manner not only along the facial nerve, but along the mandibular nerve. The topic of neural tumor spread is discussed in Chapter 13.

Infections are more common in the masticator space than are tumors, and most of these infections are odontogenic in origin. Often, the offending source is related to a recent tooth extraction, especially a mandibular molar tooth. Less commonly, chronic caries with severe gingivitis and even osteomyelitis of the mandible are the offending sites. Rarely, a traumatic extraction of a maxillary molar tooth may lead to a masticator space infection. Other infectious sources include parotid (and less often submandibular) gland sialadenitis, extension of a severe retropharyngeal space infection or a pharyngitis, and extension of a palatine tonsillar abscess.[158–165]

Noninfectious pathology that affects the masticator space can arise from components within it, can be extensions of processes that arise in proximity to it, or can be metastases to it. Lesions that have been reported to arise within the space include schwannomas, fibrous dysplasia, ossifying fibroma, osteomas, dentigerous cysts, odontogenic keratocysts, ameloblastomas, pigmented vilonodular synovitis, synovial chondromatosis, hemangiomas, lymphangiomas, lipomas, masticator hypertrophy, and a variety of sarcomas including osteosarcoma, chondrosarcoma, fibrosarcoma, rhabdomyosarcoma, hemangiosarcoma, hemangiopericytoma, ameloblastic sarcoma, Ewing's sarcoma, juxtacortical osteosarcoma, myxosarcoma, malignant fibrous histiocytoma, and large cell lymphoma. Metastases to this space from a variety of primary tumors have been reported including adenocarcinoma of the breast, prostate, colon, and stomach; urinary bladder, renal cell, hepatocellular, and follicular thyroid carcinomas; squamous cell carcinoma of the lip; and metastases from chordomas and meningiomas. There can also be extension of carcinomas arising in the nasopharynx, retromolar trigone, buccal region, and parotid and submandibular glands. Cases of recurrent maxillary ameloblastomas have also been reported, with tumor extension from the maxilla into the infratemporal fossa, infraorbital fissure, masticator space, and left ethmoid sinus. A postbiopsy traumatic aneurysm of the buccal artery has also been reported.[166–190]

THE BUCCAL FAT

There is a well-encapsulated collection of fat that lies superficial to the posterior aspect of the buccinator muscle and along the anterior edge of the masseter muscle. This fat pad is clearly separated from the superficial layer of the deep cervical fascia as it covers the masseter muscle and from the buccopharyngeal fascia (middle layer of the deep cervical fascia) as it covers the buccinator muscle. This fat pad fills the groove between these muscles and in the adult is called the buccal fat pad. In the newborn, this same fat pad is referred to as the suctorial pad, as it is alleged to help prevent indrawing of the cheeks during sucking. Extensions from this fat pad are thought, by some, to reach between the masseter and temporalis muscles and to extend deeply into the infratemporal fossa, separating the external pterygoid and temporalis muscles from the maxilla. Stenson's duct from the parotid gland lies over the buccal fat pad before penetrating the buccinator muscle at the level of the second upper molar tooth.

Also in this buccal region are the facial artery and vein, which lie adjacent to the superior and middle pharyngeal constrictors and deep to the platysma, risorius, and zygomaticus muscles. The facial artery is especially tortuous and ends as the angular artery, rising along the side of the nose and ending near the medial orbital commissure. The buccal region is often affected by disease arising in the masticator space, the parotid gland, the buccal oral cavity margin, and the retromolar trigone.

IMAGING PATHOLOGY AFFECTING THE MASTICATOR SPACE

Inflammatory Diseases

The classic imaging manifestation of inflammation is cellulitis, which is seen as a swelling of the fat planes in the involved region, with a rete pattern of soft-tissue stands that represent dilated venules and lymphatics. This ''dirty'' fat appearance is a nonspecific finding that reflects any type of inflammation, whether from infection, trauma, or irradiation. On CT, the attenuation of the fat is greater than that of normal fat, while on MR imaging, the fat may have a lower than normal T1-weighted signal intensity and a high T2-weighted signal intensity, reflecting the increased fluid within it.

When the masticator muscles become inflamed they enlarge, and on CT they usually have a lower attenuation

Copyright © 2003, Mosby, Inc. All rights reserved.

than normal muscle. On MR imaging, the inflamed muscle has a higher T2-weighted signal intensity than normal muscle, and on both CT and MR imaging, the muscle enhances and is usually nonhomogeneously affected (Figs. 38-6 and 38-35).[158] Clinically, the patient has an acute history, with pain in the masticator region, swelling and redness of the overlying facial area, and often trismus.

The ramus, angle, and posterior body of the mandible are within the masticator space, and they are the least likely of the masticator space structures to be affected by routine infections. It is only the unusual case of osteomyelitis spreading from the alveolar region of the mandible or an infected radiation osteitis that affects the masticator space portions of the mandible. Early changes of osteomyelitis are not commonly seen on CT, while on MR imaging there is loss of the normal fatty marrow high T1-weighted signal intensity as inflammatory cells invade the bone. On CT, there may be focal areas of cortical deossification and some loss of the bony medullary septae. In more advanced osteomyelitis, sequestra, a periosteal reaction, and gross demineralization of the bone are present, again changes better seen on CT than on MR imaging (Fig. 38-36). Extension outside of bone can distort the soft tissues, and a ''cloaca'' may be seen as a defect in the cortex.

The most critical imaging steps in treatment planning of a masticator space infection are identifying the presence of an abscess, mapping the boundaries of the disease, and identifying a carious tooth as the potential source of the problem. An abscess, as elsewhere in the body, is seen as a localized area of low-attenuation, nonenhancing pus surrounded by an irregular, enhancing, often fairly thick capsule. Not only is the distinction between the central pus and the abscess rim best seen after contrast administration on both CT and MR imaging, identification of the abscess wall may be missed on noncontrast images. On MR imaging, the pus has a low to intermediate T1-weighted and

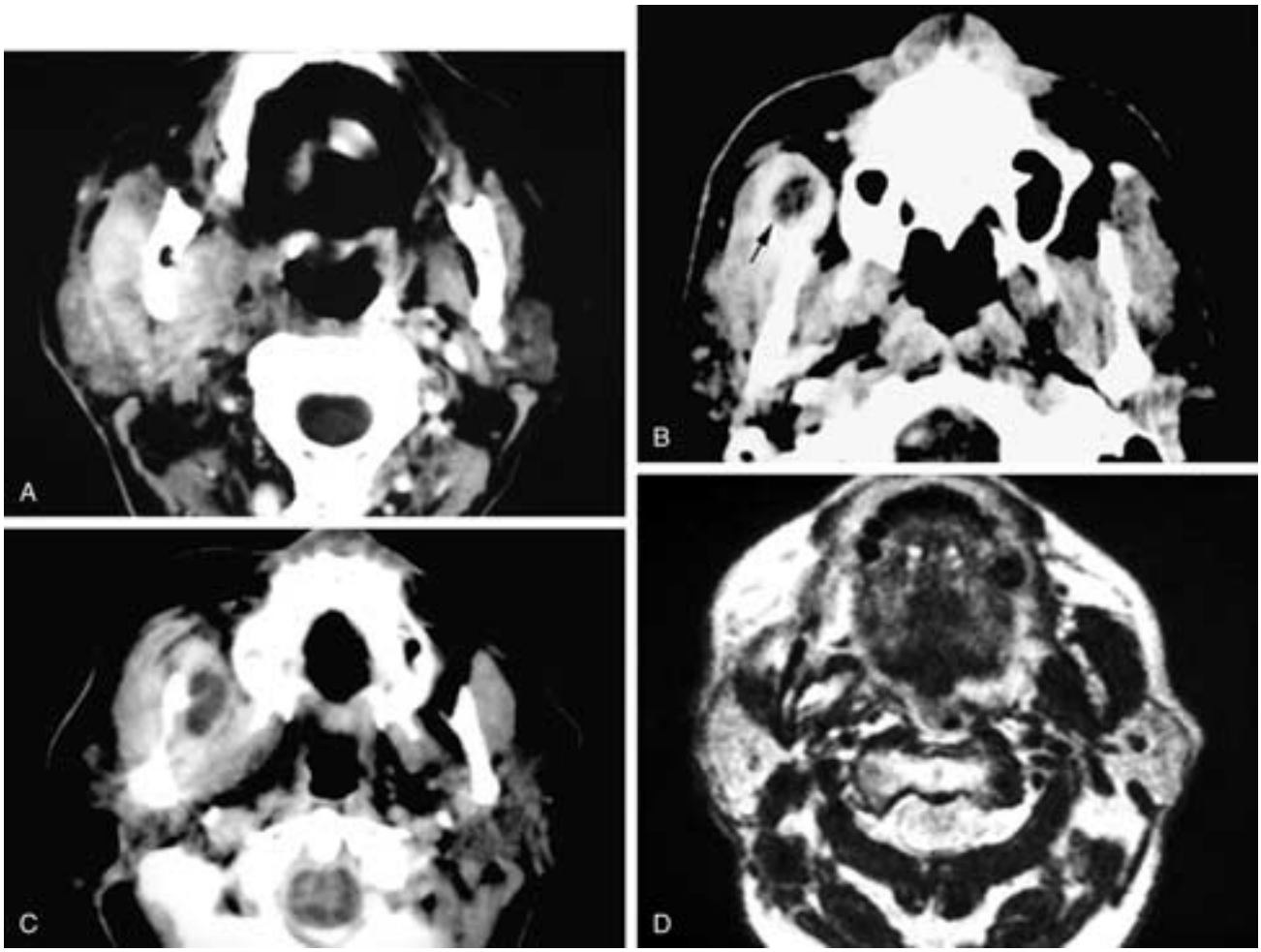

FIGURE 38-35 Axial contrast-enhanced CT scans show (**A**) enlargement and enhancement of the right masticator space muscles, with effacement of the adjacent fat planes including the fat in the right prestyloid compartment of the parapharyngeal space. There is also enhancement of the right parotid gland representing a secondary parotitis. This was an acute cellulitis of the masticator space. In **B**, there is swelling and enhancement of the right masseter muscle, with a low-attenuation abscess (*arrow*) anteriorly within the muscle. There is also enhancement of the medial pterygoid muscle in this patient with a masticator cellulitis and abscess. There is virtually no effacement of the adjacent fat planes. In **C**, there is a right masticator space cellulitis and abscess, with virtually no effacement of the adjacent fat planes. In **D**, an axial T2-weighted MR image shows the right masticator space muscle to have high signal intensity (compared to that of the normal left masticator muscles). This patient had a right masticator space cellulitis.

VIEW IMAGE

Copyright © 2003, Mosby, Inc. All rights reserved.

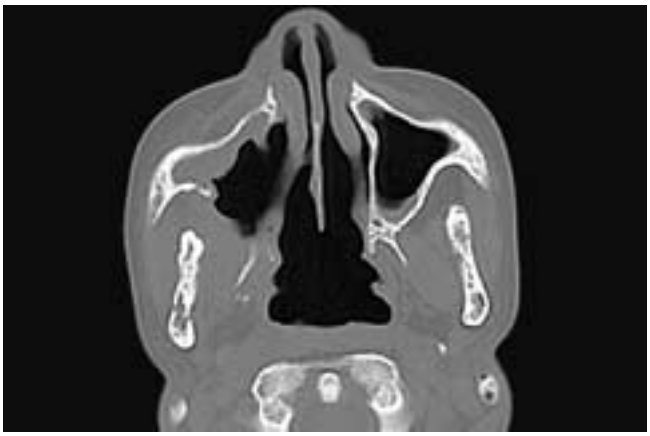

VIEW IMAGE

FIGURE 38-36 Axial CT scan viewed at wide window settings shows interruption of the cortices of both mandibular rami. There is loss of some of the medullary septations and there are areas of sclerosis. There is a non-displaced fracture of the anterior left ramus. Similar changes are also present in the zygomas. This patient had radiation osteitis after RT treatment and surgery for a right medial wall maxillary sinus carcinoma. The surgical defect is seen as is the partial resection of the right pterygoid plates.

a high T2-weighted signal intensity. Due to beam hardening artifact from the mandible and/or dental amalgams, a small abscess along the dorsal aspect of the ramus of the mandible may be difficult to identify in some patients. Angled CT scans or sagittal or oblique MR images may occasionally be necessary in these cases. It is important to identify an abscess, as this usually indicates the need for immediate surgical intervention in association with intravenous antibiotic therapy. Without an abscess, antibiotic therapy alone usually causes the infection to resolve within a few days.

Mapping the infection is also important in treatment planning, as the disease may have spread to the masticator space from adjacent areas such as the submandibular space, the parapharyngeal space, or the parotid gland.[191] Parotid gland involvement is identified by enlargement of the gland, increased attenuation on CT, and a higher T2-weighted signal intensity than normal (compared to the uninvolved side) (Fig. 38-35A). Spread of the infection into the parapharyngeal space is noted as a ''dirty'' appearance of the prestyloid compartment fat and a blurring of the normally sharp interface between the medial masticator space and the parapharyngeal space. Similarly, if the infection has spread to the submandibular space, the fat planes are blurred and the digastric muscles and muscles of the floor of the mouth may be enlarged, as occurs with the muscles in the masticator space. In virtually all cases, there is cellulitis of the overlying face, as noted by thickening of the subcutaneous fat, a ''dirty'' fat appearance, and possible thickening of the skin.

Denervation Atrophy

The imaging changes of inflammation should not be confused with denervation atrophy of the masticator muscles.[191–198] Patients with denervation of the masticator muscles usually have a prior history of trauma or surgery involving the mandibular nerve (also see Chapter 41). There may be bite weakness and flattening of the side of the face; pain is rarely present. Occasionally, clinically unexpected early denervation may be observed on imaging studies. When this is seen, attention should be directed to the foramen ovale and along the course of the mandibular nerve, as the denervation may signal the presence of an otherwise clinically silent tumor. Neural and perineural tumor spread is discussed in detail in Chapter 13.

If there is masticator muscle denervation, within the first 4 weeks there usually is mild muscle enlargement, and there may be some muscle enhancement and increased T2-weighted signal intensity. During the next 20 months after denervation, the muscle volume starts to decrease as muscle fibers progressively undergo fatty replacement, which is seen as progressive low attenuation on CT and as high T1-weighted signal intensity on MR imaging. There is also muscle enhancement and an increase in T2-weighted signal intensity. With long-standing denervation, there is progressive fatty replacement of the muscle, decrease in muscle size, loss of muscle enhancement, and loss of the high T2-weighted signal intensity (Fig. 38-37).[193]

Masticator Muscle Hypertrophy

Masticator muscle hypertrophy can affect all the muscles of mastication, several muscles, or just one muscle (also see Chapter 41). It can occur either bilaterally or unilaterally, and most commonly the masseter muscles alone are affected.[199–201] The involved muscles, which are variably enlarged and can be up to three times the normal size, are otherwise normal on all imaging studies. Flaring of the mandibular angle on the involved side can also occur.[202] The process usually starts in adolescence or early adulthood, and there is a history of slowly progressive muscle growth. The facial fullness is located anterior to the usual location of a parotid lesion, and the mass enlarges when the patient's teeth are clenched. The mass feels like muscle on palpation and is not tender or painful. The etiology is unclear but may be related to bruxism and gum chewing. Plain films may show an exostosis of the lateral aspect of the angle of the mandible at the line of attachment of the masseter muscle. A sialogram demonstrates lateral bowing of Stensen's duct around the enlarged masseter muscle, and CT and MR imaging show an enlarged, otherwise normal muscle (Fig. 38-38). Surgery is performed only for cosmesis, and microscopic examination of resected muscle demonstrates either normal muscle or muscle with true work hypertrophy.

Muscle hypertrophy can also occur as a compensatory mechanism; this has been reported in cases of hemifacial microsomia with unilateral condylar hypoplasia. CT has shown the ipsilateral medial pterygoid muscle to be larger. This was considered likely to be a compensatory adjustment to help keep the mandible centered.[203]

There is sparse quantitative information on the normal size range of the masticatory muscles, and such data may be needed for the successful treatment of facial asymmetry. In one study, the muscles were scanned from their origins to their insertions, and the maximum cross-sectional area (MCSA) and its location relative to the mandibular foramen were noted. The MCSA of the masseter muscle was centered 8 mm above the mandibular foramen, while that of the medial pterygoid muscle was centered at the level of the

Copyright © 2003, Mosby, Inc. All rights reserved.

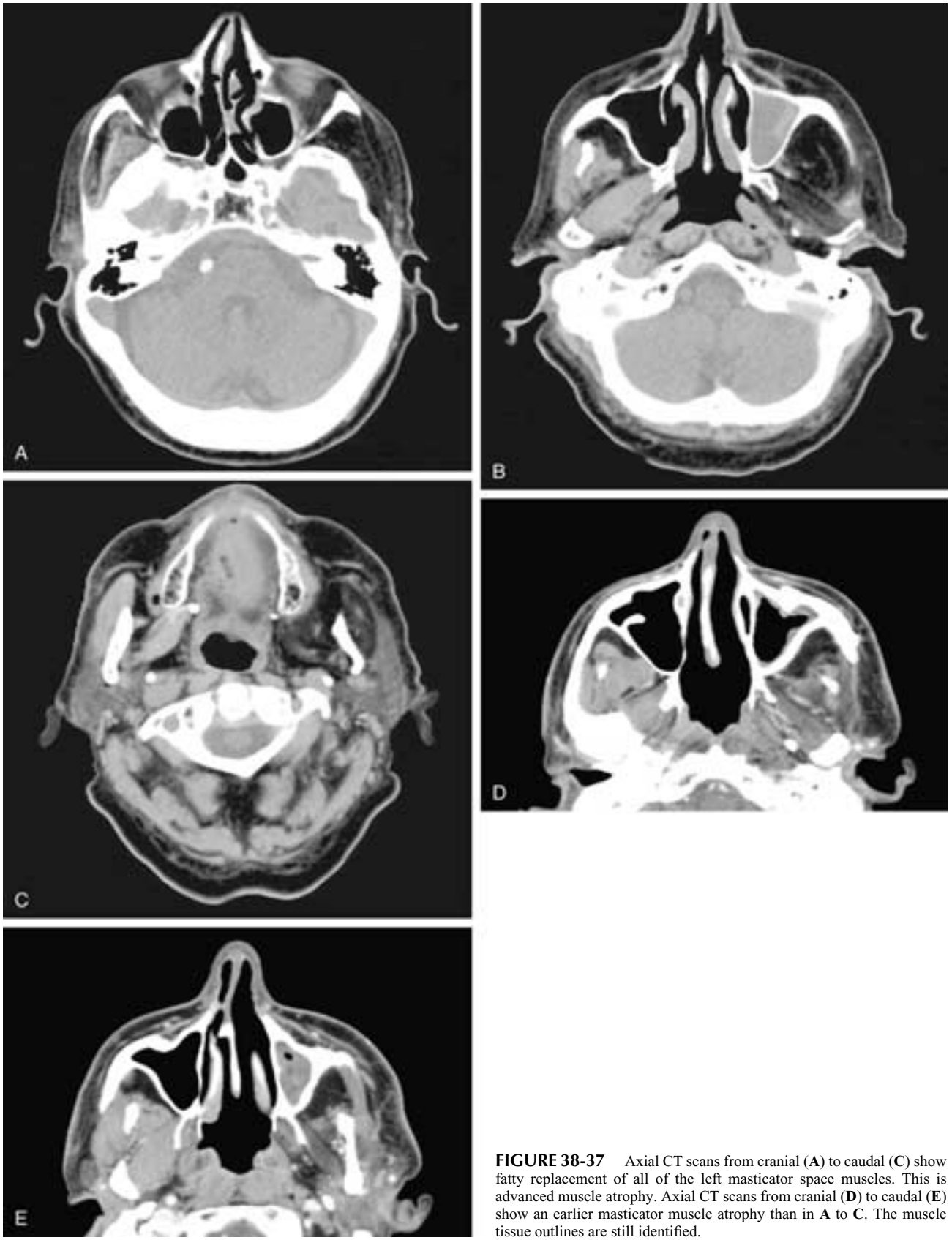

FIGURE 38-37 Axial CT scans from cranial (**A**) to caudal (**C**) show fatty replacement of all of the left masticator space muscles. This is advanced muscle atrophy. Axial CT scans from cranial (**D**) to caudal (**E**) show an earlier masticator muscle atrophy than in **A** to **C**. The muscle tissue outlines are still identified.

VIEW IMAGE

Copyright © 2003, Mosby, Inc. All rights reserved.

foramen. It was noted that the MCSA of both muscles was highly correlated with their volumes, suggesting that this parameter might serve as an indicator of their volume.[204] In this article, the mean MCSA of the masseter muscle in males was 535.9 mm^2 and in females it was 434.9 mm^2. The mean MCSA for the medial pterygoid muscle was 363.7 mm^2 in males and 310.6 mm^2 in females.

Tumors and Nonneoplastic Masses

Three helpful imaging criteria are used to determine the presence of an invasive malignancy in the masticator space: (1) erosion of the mandible, (2) invasion of the muscles, and (3) violation of the surrounding fascial planes.

Erosion of the mandible by a malignancy can occur as a tumor from outside the masticator space spreads into this space, first involving the masticator space fascia, then the muscles, and finally the mandible. This may be noted especially in tumors involving the retromolar trigone and the anterior tonsillar pillar regions. Alternatively, tumor may extend from the oral cavity, erode into the mandibular alveolus, and spread into the posterior body and ramus of the mandible. In this circumstance, initially the surrounding muscles and fascia may be uninvolved or only minimally affected.

Because most tumors, especially squamous cell carcinomas, arise adjacent to the masticator space and extend toward the bone, there often is erosion of the cortex only at the point of tumor entry. With more extensive disease, the bone is eroded and often fragmented, and there are infiltrative rather than sharp borders of the uninvolved bone. On MR imaging, the fatty marrow is replaced with tumor that has an intermediate T1-weighted and a slightly higher T2-weighted signal intensity. The tumor usually enhances to a moderate degree (Fig. 38-39).

Fragmentation of the bone may occur as a result of radiation osteitis. In these circumstances, the bone is sclerotic in areas, there are sequestra, and there are regions of demineralization. Often there are also mild inflammatory changes in the masticator muscles and the adjacent soft tissues (Fig. 38-40). Osteoradionecrosis is not a true necrosis of bone, but rather a particularly severe osteitis that evolves in bone and is related to compromise of the bone's vascularity. It may occur from 1 to 20 years after irradiation and is directly related to the total dose, the dosing rate, the presence of local infection or trauma, and the concurrent administration of chemotherapy.[205–207]

Bone production is also associated with tumors such as osteosarcomas, Ewing's sarcomas, plasmacytomas, metastatic meningioma, and keratocysts (Fig. 38-41). In addition, bone production or thickened bone can be seen with fibrous dysplasia, ossifying fibroma, and Paget's disease. These diseases are discussed in detail in Chapters 6 and 17. Multiple calcifications or ossifications about the ramus of the mandible can also be seen with osteosarcoma, chondrosarcoma, osteochondroma, hemangioma, and temporomandibular diseases such as synovial chondromatosis and chondrocalcinosis. These latter diseases are discussed in Chapter 18.

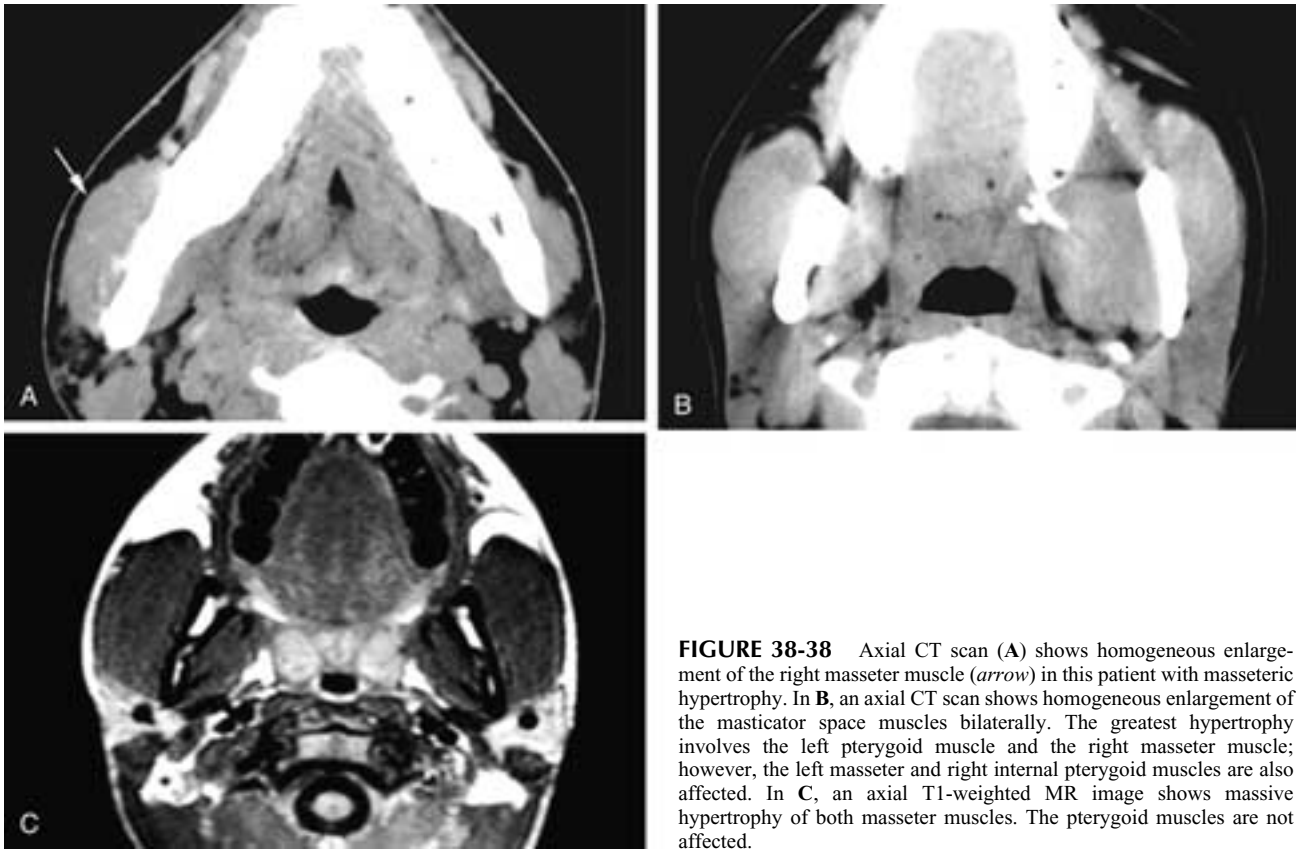

FIGURE 38-38 Axial CT scan (**A**) shows homogeneous enlargement of the right masseter muscle (*arrow*) in this patient with masseteric hypertrophy. In **B**, an axial CT scan shows homogeneous enlargement of the masticator space muscles bilaterally. The greatest hypertrophy involves the left pterygoid muscle and the right masseter muscle; however, the left masseter and right internal pterygoid muscles are also affected. In **C**, an axial T1-weighted MR image shows massive hypertrophy of both masseter muscles. The pterygoid muscles are not affected.

VIEW IMAGE

Copyright © 2003, Mosby, Inc. All rights reserved.

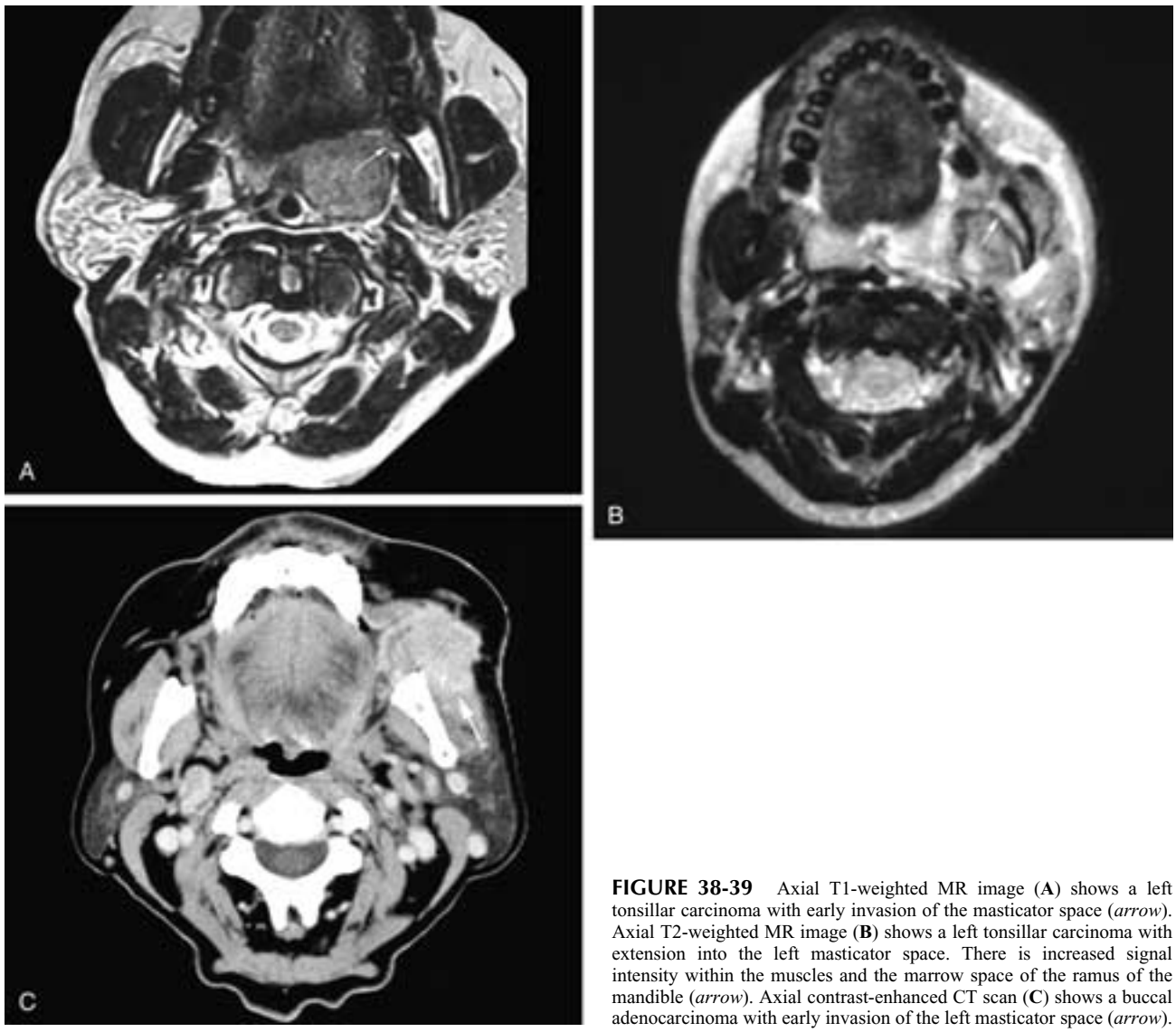

FIGURE 38-39 Axial T1-weighted MR image (**A**) shows a left tonsillar carcinoma with early invasion of the masticator space (*arrow*). Axial T2-weighted MR image (**B**) shows a left tonsillar carcinoma with extension into the left masticator space. There is increased signal intensity within the muscles and the marrow space of the ramus of the mandible (*arrow*). Axial contrast-enhanced CT scan (**C**) shows a buccal adenocarcinoma with early invasion of the left masticator space (*arrow*).

VIEW IMAGE

Copyright © 2003, Mosby, Inc. All rights reserved.

VIEW IMAGE

FIGURE 38-40 Coronal CT scan shows irregular areas of sclerosis, erosion, and fracture on both sides of the mandible in this patient with the typical imaging findings of radiation necrosis.

With regard to the de novo or postradiation mandibular osteosarcomas, nearly half of the cases are osteoblastic and occasionally a periosteal reaction is present. Tumor matrix mineralization occurs in more than 75% of the cases, and osteoid matrix calcification is frequent, even though most tumors are chondroblastic. Soft-tissue extension of tumor is present in all cases, and it contains calcifications in more than half of the cases. CT provides excellent detection of any tumor calcification, cortical involvement, and, in most instances, soft-tissue and intramedullary extension. However, MR imaging is even more effective in demonstrating the intramedullary and extraosseous tumor components on both T1-weighted and T2-weighted images. However, CT and plain films are superior to MR in detecting the matrix calcifications and bone destruction or reaction (Fig. 38-41). There can be dense sclerosis, an aggressive periosteal reaction, or multiple ossifications or calcifications.[142, 208–211]

Cystic expansion of the ramus may be seen with large dentigerous cysts, cherubism, aneurysmal bone cysts, keratocysts, and rare metastases (Fig. 38-42). The identifica-

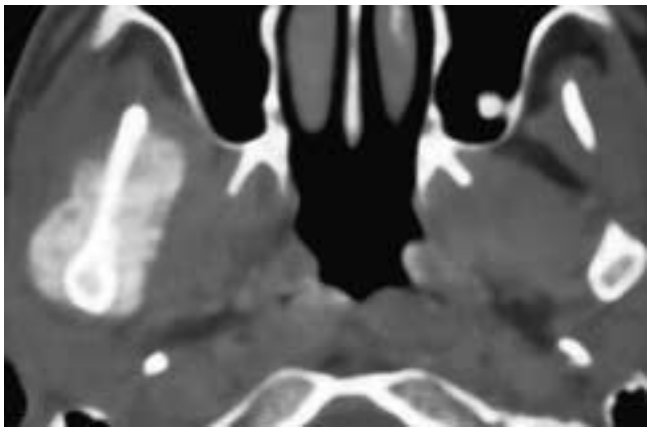

VIEW IMAGE

FIGURE 38-41 Axial CT scan shows thickening and sclerosis of the right mandibular ramus, with an exuberant periosteal bone reaction along both the buccal and lingual cortices. There was a minimal adjacent soft-tissue mass effect in this patient with an osteosarcoma of the mandible.

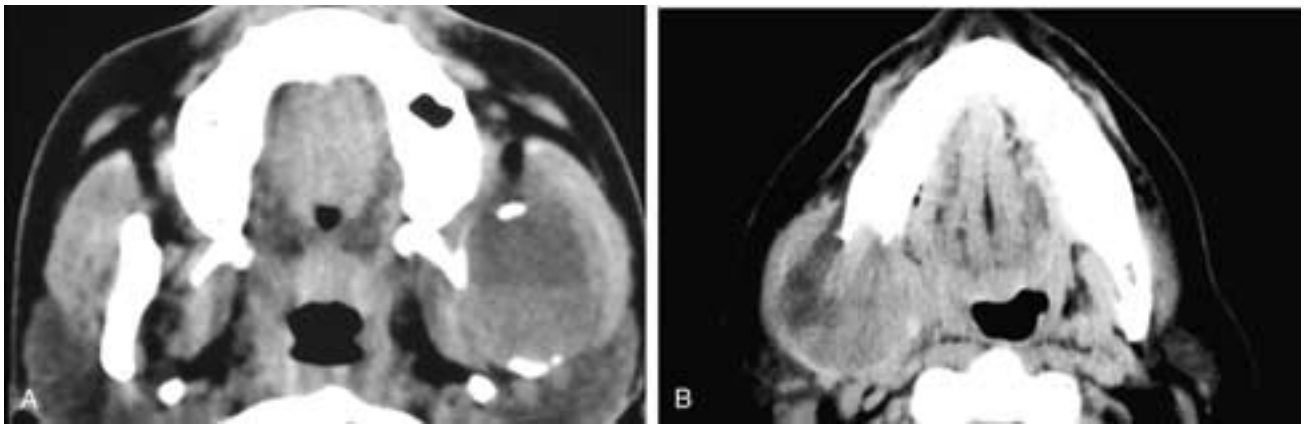

VIEW IMAGE

FIGURE 38-42 Axial CT scan (**A**) shows an expansile cyst arising in the left mandibular ramus. Only a small region of cortex remains along the anterior and posterior edges of the ramus. The masticator space muscles are displaced away from the ramus but are otherwise normal. There is a fluid-fluid level in this benign bone cyst with hemorrhage. Axial CT scan (**B**) shows an area of cystic expansion of the right posterior body of the mandible, with erosion of the cortex around the mass. The masticator muscles are poorly seen as they are stretched around the lesion. This was a rare metastatic meningioma.

Copyright © 2003, Mosby, Inc. All rights reserved.

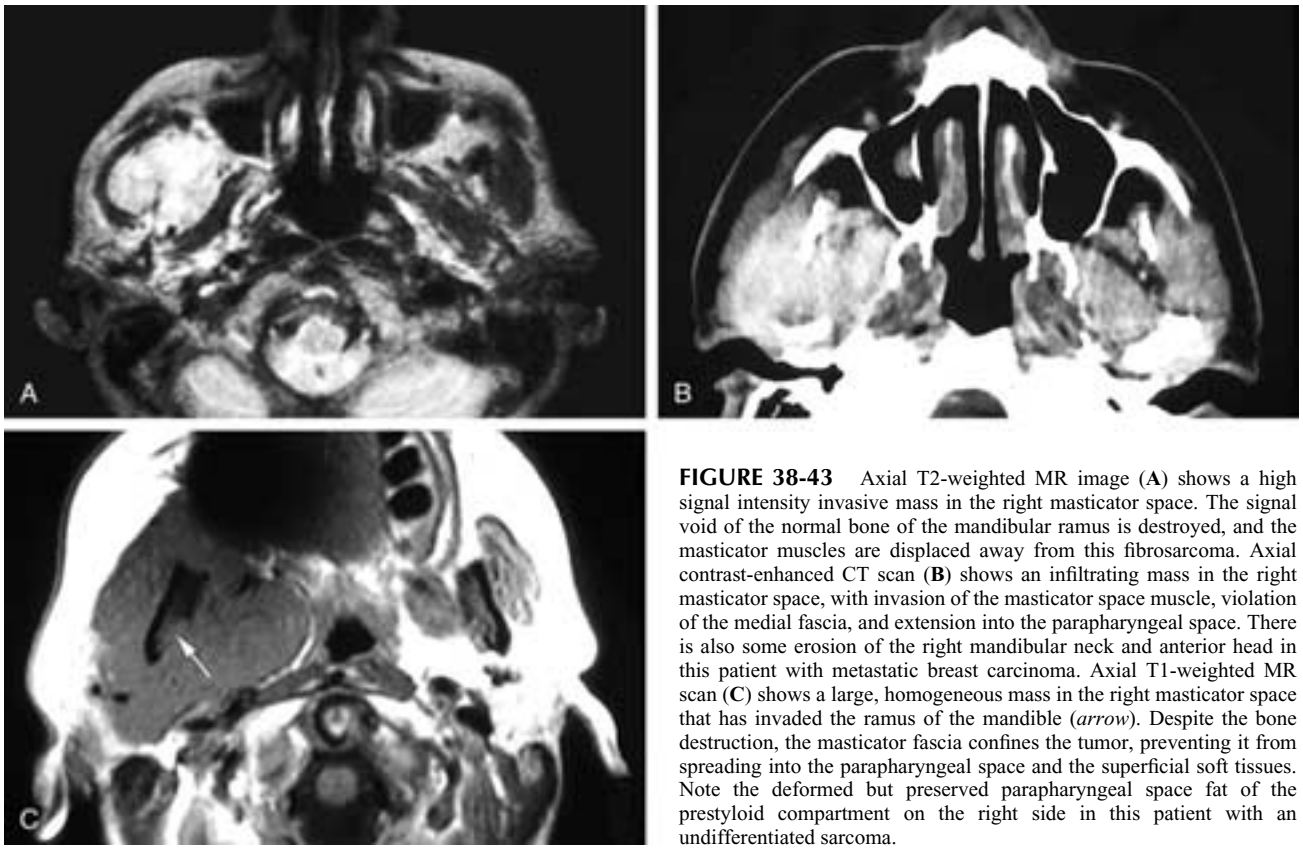

FIGURE 38-43 Axial T2-weighted MR image (**A**) shows a high signal intensity invasive mass in the right masticator space. The signal void of the normal bone of the mandibular ramus is destroyed, and the masticator muscles are displaced away from this fibrosarcoma. Axial contrast-enhanced CT scan (**B**) shows an infiltrating mass in the right masticator space, with invasion of the masticator space muscle, violation of the medial fascia, and extension into the parapharyngeal space. There is also some erosion of the right mandibular neck and anterior head in this patient with metastatic breast carcinoma. Axial T1-weighted MR scan (**C**) shows a large, homogeneous mass in the right masticator space that has invaded the ramus of the mandible (*arrow*). Despite the bone destruction, the masticator fascia confines the tumor, preventing it from spreading into the parapharyngeal space and the superficial soft tissues. Note the deformed but preserved parapharyngeal space fat of the prestyloid compartment on the right side in this patient with an undifferentiated sarcoma.

VIEW IMAGE

tion of a tooth within the cyst is diagnostic of the dentigerous cyst. These odonogenic lesions are discussed in Chapters 6 and 17.

Muscle invasion by tumor is better seen on MR imaging than on CT, as most cellular tumors have an attenuation similar to that of muscle. On MR imaging, the tumor has an intermediate T1-weighted and a slightly higher T2-weighted signal intensity, usually enhances to a moderate degree, and has infiltrative, unsharp margins. Thus, on MR imaging, the tumor is usually well seen silhouetted against the normal low T2-weighted signal intensity of muscle. The affected muscle is usually enlarged, and either a localized portion or the entire muscle may be infiltrated (Figs. 38-43 and 38-44).

Fascial invasion at first appears to be a very reliable sign of malignancy extending either into or out of the masticator space. This is, in fact, true when tumor extends into the masticator space, since the neoplasm must cross these strong fascial layers in order to gain entrance to this space. However, this is not always true when the tumor arises within the masticator space, and often, despite erosion of the mandible and involvement of the muscles, the outer masticator space fascia remains intact. In fact, high-grade malignancies can arise within the masticator space without evidence of either bone destruction or fascial invasion.[177] More commonly than tumor, infections cross the fascia, mimicking a tumor on CT and MR imaging. However, the history distinguishes inflammatory disease from neoplasm in almost all cases. Although both may present with trismus, tumors usually are painless, with a nontender or slightly tender mass. Infections produce pain, tenderness, and an associated elevated white blood cell count with a shift to the left.

Importantly with regard to tumors in the masticator space, it should be remembered that high-grade malignancies can be present without evidence of either bone erosion or fascial violation. When such a mass is seen within this space, especially in a patient less than 30 years of age, biopsy should be performed without delay (Fig. 38-44).[177]

Anatomically, after exiting the skull base via the foramen ovale, the third division of the trigeminal nerve lies along the medial margin of the lateral pterygoid muscle. Thus, schwannomas of this nerve may smoothly expand the foramen ovale and then present as a well-defined mass in the masticator space, with imaging characteristics similar to those of the neurogenic tumors described in the section on Diseases and Tumors Arising in the Parapharyngeal Space. (Fig. 38-45). Retrograde tumor extension along the third division of the trigeminal is discussed in detail in Chapter 13.

Copyright © 2003, Mosby, Inc. All rights reserved.

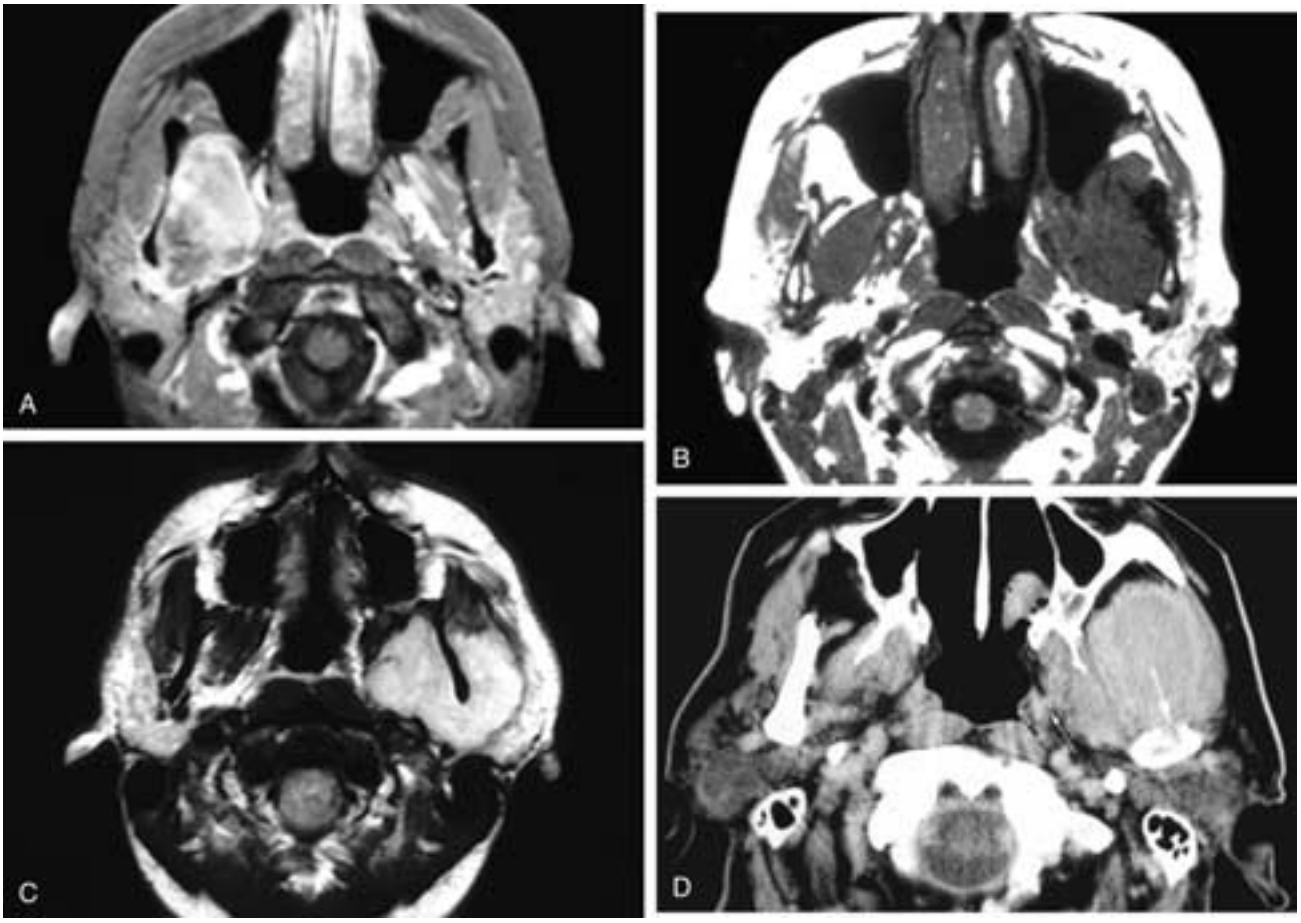

VIEW IMAGE

FIGURE 38-44 Axial T1-weighted MR image (**A**) shows an enhancing mass in the right masticator space. This periosteal osteosarcoma causes the medial masticator space fascia to bulge medially, but there is no invasion of the parapharyngeal space. Axial T1-weighted MR image (**B**) shows a left masticator space mass that has invaded the pterygoid muscles and is limited to the medial portion of the masticator space. This undifferentiated sarcoma is contained by the medial masticator fascia, and there is no extension into the parapharyngeal space. Axial T2-weighted MR image (**C**) shows a left masticator space sarcoma with high signal intensity that has invaded the masticator muscles but remains contained by the masticator space fascia. Axial contrast-enhanced CT scan (**D**) shows a destructive left masticator space mass that has eroded the anterior left mandibular head (*large arrow*). Despite its aggressive nature, the masticator fascia prevents this sarcoma from spreading outside the masticator space except in the most anterior medial margin of this space (*small arrow*).

Illustration continued on following page

Copyright © 2003, Mosby, Inc. All rights reserved.

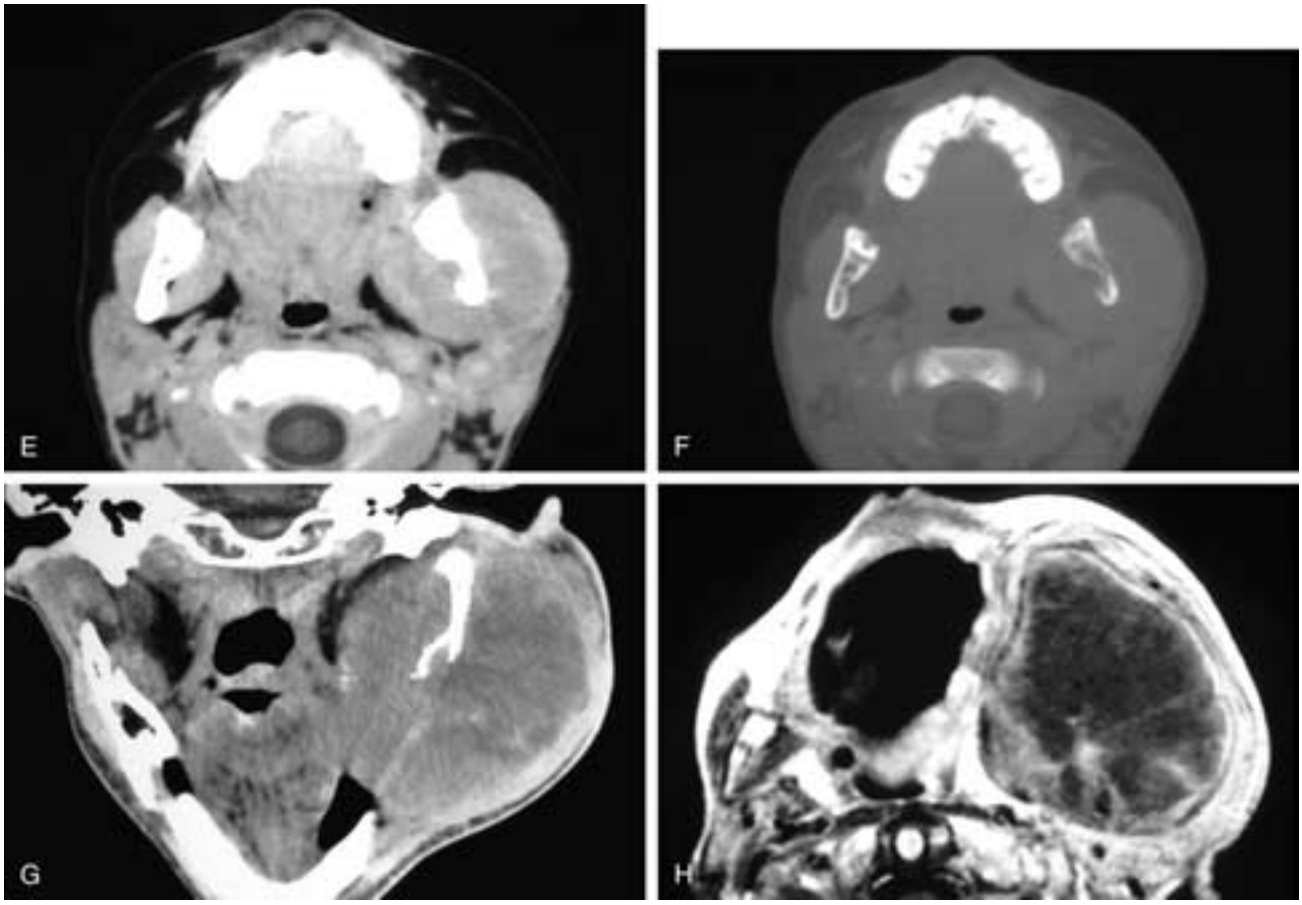

FIGURE 38-44 *Continued.* Axial CT scans viewed at narrow soft-tissue window settings (**E**) and wide bone window settings (**F**) show a rhabdomyosarcoma in the left masticator space that has permeated the mandibular ramus but is contained by the masticator space fascia. Coronal CT scan (**G**) and axial T1-weighted MR image (**H**) show a large, destructive left masticator space mass. Much of the left mandible has been destroyed by this metastatic melanoma. However, the masticator space fascia contains the tumor, and there is no extension into the parapharyngeal space or the superficial soft tissues.

VIEW IMAGE

Copyright © 2003, Mosby, Inc. All rights reserved.

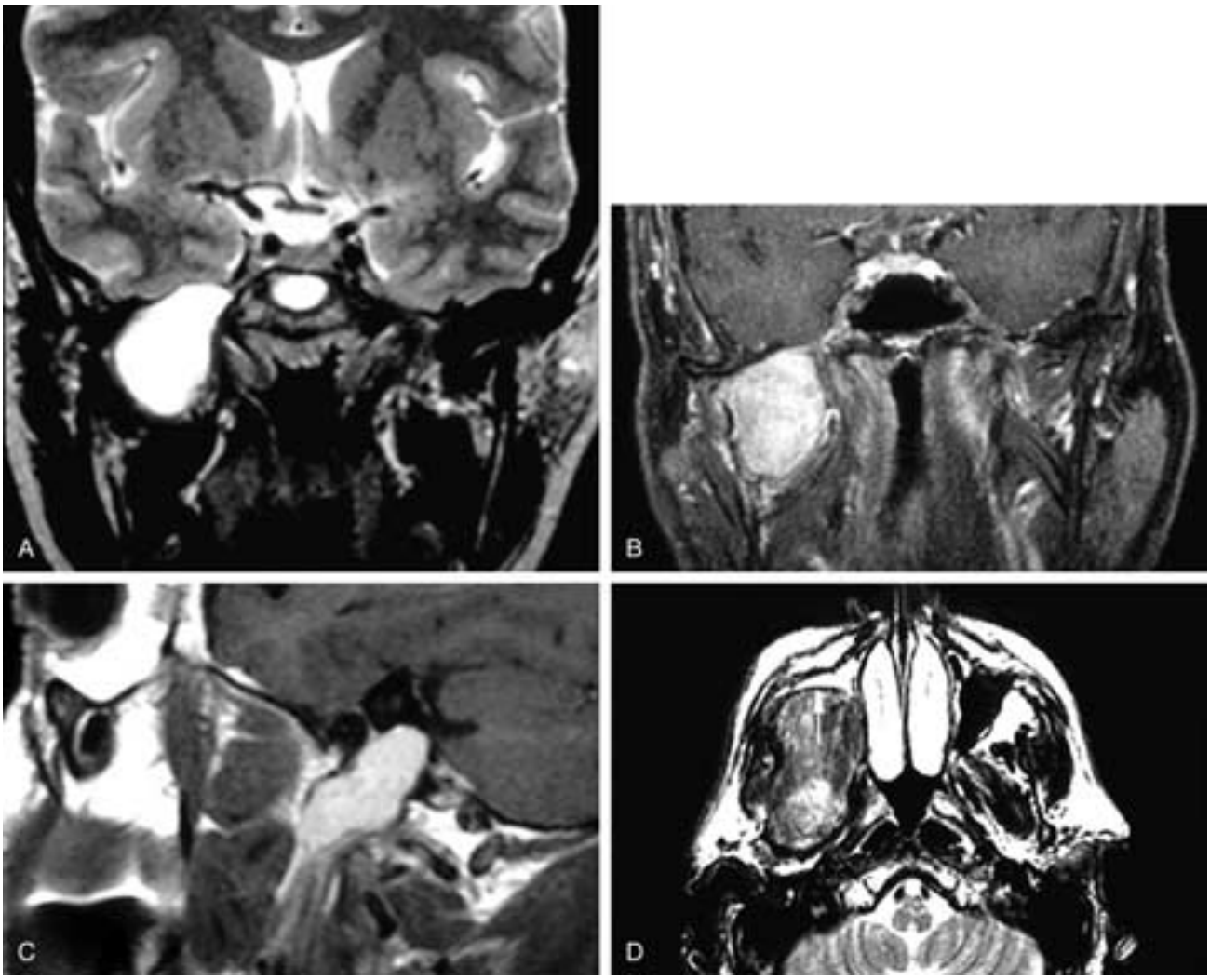

VIEW IMAGE

FIGURE 38-45 Coronal T2-weighted MR image (**A**) shows a high signal intensity mass within a smoothly widened right foramen ovale. This schwannoma extends both toward the cavernous sinus and down below the skull base into the masticator space. Although on coronal images such masses appear to lie directly above the parapharyngeal space, such schwannomas extend along the third division of the trigeminal nerve into the masticator space. Coronal T1-weighted, fat-suppressed, contrast-enhanced MR image (**B**) shows a schwannoma of V_3. The tumor extends from the smoothly widened foramen ovale down into the medial mandibular ramus, displacing the pterygoid muscles medially. Sagittal T1-weighted, fat-suppressed, contrast-enhanced MR image (**C**) shows a schwannoma of V_3 extending down into the masticator space. Axial T2-weighted MR image (**D**) shows a huge schwannoma of V_3 that extends through a smoothly widened foramen ovale down into the masticator space, where it has expanded the medial aspect of this space, filled the infratemporal fossa, and remodeled the posterior right antral wall forward (*arrow*).

REFERENCES

1. Hall C. The parapharyngeal space: an anatomical and clinical study. Ann Otol Rhinol Laryngol 1934;43:793–812.
2. Cazalas G. Les espaces intra et peri-pharyngiens etude anatomique et experimentale. Lyon: Considerations Medico-Chirugicales, 1938; 168:164.
3. Coller F, Yglesias L. Infections of the lip and face. Surg Gynecol Obstet 1935;60:277–290.
4. Coulouma P. La systematisation des espaces peri, meta et para-amygdaliens. Leur interet clinique. Echo Med Nord 1937;8: 649–662.
5. Grodinsky M, Holyoke E. The fasciae and fascial spaces of the head, neck and adjacent regions. Am J Anat 1938;63:367–408.
6. Curtin H. Separation of the masticator space from the parapharyngeal space. Radiology 1987;163:195–204.
7. Som P, Biller H, Lawson W. Tumors of the parapharyngeal space: preoperative evaluation, diagnosis, and surgical approaches. Ann Otol Rhinol Laryngol 1981;90:3–15.
8. Som P, Biller H, Lawson W. Parapharyngeal space masses: an updated protocol based upon 104 cases. Radiology 1984;153: 149–156.
9. Som P, Braun I, Shapiro M, et al. Tumors of the parapharyngeal space and upper neck: MR imaging characteristics. Radiology 1987;164:823–829.
10. Einstein R. Sialography in the differential diagnosis of parotid masses. Surg Gynecol Obstet 1966;122:1079–1083.
11. Potter G. Sialography and the salivary glands. Otolaryngol Clin North Am 1973;6:509–522.
12. Calcaterra T, Hemenway G, Hansen G, Hanafee W. The value of sialography in the diagnosis of parotid tumors. Arch Otolaryngol 1977;103:727–729.

Copyright © 2003, Mosby, Inc. All rights reserved.

13. Som P, Biller H. The combined CT-sialogram. Radiology 1980;135: 387–390.
14. Tsai F, Goldstein J, Parhad I. Angiographic features of lateral cervical masses. Trans Am Acad Ophthalmol Otolaryngol 1977;84: 840–850.
15. Work W. Tumors of the parapharyngeal space. Trans Am Acad Ophthalmol Otolaryngol 1969;73:389–394.
16. Carter B, Karmody C. Computed tomography of the face and neck. Semin Roentgenol 1978;13:257–266.
17. Mancuso A, Rice D, Hanafee W. Computed tomography of the parotid gland during contrast sialography. Radiology 1979;132: 2111–2113.
18. Som P, Biller H. The combined CT-sialogram: a technique to differentiate deep lobe parotid tumors from extraparotid pharyngo-maxillary space tumors. Ann Otol Rhinol Laryngol 1979;88: 590–595.
19. Bryan R, Miller R, Ferreyro R, Sessions R. Computed tomography of the major salivary glands. Am J Roentgenol 1982;139:547–554.
20. Lau W, Lam K, Wei W. Parapharyngeal space tumors. Aust NZ J Surg 1986;56:835–842.
21. Mafee M. Dynamic CT and its application to otolaryngology. Head Neck Surg J Otolaryngol 1982;11:307–318.
22. Shugar M, Mafee M. Diagnosis of carotid body tumors by dynamic computerized tomography. Head Neck Surg 1982;4:518–521.
23. Lloyd G, Phelps P. Demonstration of tumours of the parapharyngeal space by magnetic resonance imaging. Br J Radiol 1986;59:675–683.
24. Dillon W, Mills C, Kjos B, et al. Magnetic resonance imaging of the nasopharynx. Radiology 1984;152:731–738.
25. Dillon W. Applications of magnetic resonance imaging to the head and neck. Semin Ultrasound CT MR 1986;7:202–215.
26. Mancuso A, Hanafee W. Nasopharynx and parapharyngeal space. In: Mancuso A, Hanafee W, eds. Computed Tomography and Magnetic Resonance Imaging of the Head and Neck. 2nd ed. Baltimore: Williams & Wilkins, 1985;428–497.
27. Som P, Sacher M, Stollman A, et al. Common tumors of the parapharyngeal space: refined imaging diagnosis. Radiology 1988; 169:81–85.
28. Lufkin R, Hanafee W. Magnetic resonance imaging of the nasopharynx and skull base. Acta Radiol Suppl (Stockh) 1986;369: 325–326.
29. Tom B, Rao V, Guglielmo F. Imaging of the parapharyngeal space: anatomy and pathology. Crit Rev Diagn Imag 1991;31:315–356.
30. Carrau R, Myers E, Johnson J. Management of tumors arising in the parapharyngeal space. Laryngoscope 1990;100:583–589.
31. Noyek A, Kassel E, Chapnik J, et al. Parotid gland and parapharyngeal space imaging: the surgical significance. Isr J Med Sci 1992;28:193–197.
32. Castelijns J, van den Brekel M. Magnetic resonance imaging evaluation of extracranial head and neck tumors. Magn Reson Q 1993;9:113–128.
33. Kase Y, Yamane M, Ichimura K, Iinuma T. Comparison of CT and MRI in diagnosis of parapharyngeal tumors. Nippon Jibinkoka Gakkai Kaiho J Oto Rhino Laryngol Soc 1992;95:655–664.
34. Cross R, Shapiro M, Som P. MRI of the parapharyngeal space. Radiol Clin North Am 1989;27:353–378.
35. Modder U, Lenz M, Steinbrich W. MRI of facial skeleton and parapharyngeal space. Eur J Radiol 1987;7:6–10.
36. Olsen KD. Tumors and surgery of the parapharyngeal space. Laryngoscope 1994;104:1–28.
37. Work W, Hybels R. A study of tumors of the parapharyngeal space. Laryngoscope 1974;84:1748–1755.
38. Baker D, Conley J. Treatment of massive deep lobe parotid tumors. Am J Surg 1979;138:572–575.
39. McLean W. Differential diagnosis and management of deep lobe parotid tumors. Laryngoscope 1976;86:28–35.
40. Lawson V, LeLiever W, Makerewich L, et al. Unusual parapharyngeal lesions. J Otolaryngol 1979;8:241–249.
41. Heeneman H, Gilbert J, Rood S. The Parapharyngeal Space: Anatomy and Pathologic Conditions with Emphasis on Neurogenous Tumors. Vol 79500. Rochester, Minn.: American Academy of Otolaryngology, 1980;1–61.
42. Lederman M. Cancer of the Nasopharynx: Its Natural History and Treatment. Springfield, Ill: Charles C Thomas, 1961;3–52.
43. Gidley PW, Ghorayeb BY, Stiernberg CM. Contemporary management of deep neck space infections. Otolaryngol Head Neck Surg 1997;116:16–22.
44. el-Sayed Y, al Dousary S. Deep-neck space abscesses. J Otolaryngol 1996;25:227–233.
45. Lazor JB, Cunningham MJ, Eavey RD, Weber AL. Comparison of computed tomography and surgical findings in deep neck infections. Otolaryngol Head Neck Surg 1994;111:746–750.
46. Sichel JY, Gomori JM, Saah D, Elidan J. Parapharyngeal abscess in children: the role of CT for diagnosis and treatment. Int J Pediatr Otorhinolaryngol 1996;35:213–222.
47. Sakaguchi M, Sato S, Ishiyama T, et al. Characterization and management of deep neck infections. Int J Oral Maxillofac Surg 1997;26:131–134.
48. Ungkanont K, Yellon RF, Weissman JL, et al. Head and neck space infections in infants and children. Otolaryngol Head Neck Surg 1995;112:375–382.
49. de-Marie S, Tjon A, Tham R, et al. Clinical infections and nonsurgical treatment of parapharyngeal space infections complicating throat infection. Rev Infect Dis 1989;11:975–982.
50. Urquhart A, Leontsinis T, Bodenstein N. Acute parapharyngeal space infections. A report of 12 cases. S Afr J Surg 1991;29:161–163.
51. Castelijns JA, van den Brekel MW. Magnetic resonance imaging evaluation of extracranial head and neck tumors. Magn Reson Q 1993;9:113–128.
52. Leverstein H, Castelijns JA, Snow GB. The value of magnetic resonance imaging in the differential diagnosis of parapharyngeal space tumours. Clin Otolaryngol 1995;20:428–433.
53. Miller FR, Wanamaker JR, Lavertu P, Wood BG. Magnetic resonance imaging and the management of parapharyngeal space tumors. Head Neck 1996;18:67–77.
54. Som PM, Curtin HD. Lesions of the parapharyngeal space. Role of MR imaging. Otolaryngol Clin North Am 1995;28:515–542.
55. Vogl TJ, Balzer JO. Base of skull, nasopharynx, and parapharyngeal space. Neuroimaging Clin North Am 1996;6:357–378.
56. Hughes KV 3rd, Olsen KD, McCaffrey TV. Parapharyngeal space neoplasms. Head Neck 1995;17:124–130.
57. Takashima S, Sone S, Honjho Y, et al. Warthin's tumor of the parotid gland with extension into the parapharyngeal space. Eur J Radiol 1997;24:227–229.
58. McIlrath D, ReMine W, Devine K, Dockerty M. Tumors of the parapharyngeal region. Surg Gynecol Obstet 1963;116:88–94.
59. Batsakis J, ed. Tumor of the Head and Neck: Clinical and Pathological Considerations. 2nd ed. Baltimore: Williams & Wilkins, 1979;1–99.
60. Peel R, Gnepp D. Diseases of the salivary glands. In Barnes L, ed. Surgical Pathology of the Head and Neck. Vol 1. Baltimore: Williams & Wilkins, 1985;533–645.
61. Szmeja Z, Szyfter W, Szymiec E, et al. [Neurofibroma of the parapharyngeal space: a case report]. Otolaryngol Pol 1998;52: 215–217.
62. Hamza A, Fagan JJ, Weissman JL, Myers EN. Neurilemmomas of the parapharyngeal space. Arch Otolaryngol Head Neck Surg 1997;123:622–626.
63. Matsuyama T, Shimomura T, Kawata K, Ohnishi H. [Huge skull base neurofibroma: case report]. No Shinkei Geka 1996;24:563–566.
64. Michida A, Ryoke K, Ishikura S, Hamada T. Multiple schwannomas of the neck, mediastinum, and parapharyngeal space: report of case. J Oral Maxillofac Surg 1995;53:617–620.
65. Nibu K, Kamata S, Tayama N, et al. Dumbbell-shaped schwannoma of the jugular foramen. J Otorhinolaryngol Relat Spec 1993;55: 49–53.
66. Santoro R, De Meester W, Coscarelli S, Polli G. Multiple neurinomas of the parapharyngeal space. Eur Arch Otorhinolaryngol 1997;254: 301–303.
67. Yumoto E, Nakamura K, Mori T, Yanagihara N. Parapharyngeal vagal neurilemmoma extending to the jugular foramen. J Laryngol Otol 1996;110:485–489.
68. Kumar A, Kuhajda F, Martinez C, et al. Computed tomography of extracranial nerve sheath tumors with pathological correlation. J Comput Assist Tomogr 1983;7:857–865.
69. Ozdzinski W, Norozny W, Debniak E, Mikaszewski B. [Parapharyngeal space tumors]. Otolaryngol Pol 1995;49:36–39.
70. Andre P, Laccourreye H, Haguet JF. [Parapharyngeal nerve tumors (10 recent cases)]. Ann Otolaryngol Chir Cervicofac 1975;92: 345–356.
71. Elias MM, Balm AJ, Peterse JL, et al. Malignant schwannoma of the parapharyngeal space in von Recklinghausen's disease: a case report and review of the literature. J Laryngol Otol 1993;107:848–852.

Copyright © 2003, Mosby, Inc. All rights reserved.

72. Barnes L, Peel R, Verbin R. Tumors of the nervous system. In: Barnes L, ed. Surgical Pathology of the Head and Neck. New York: Marcel Dekker, 1985;659–724.
73. Cabay JE, Collignon J, Dondelinger RF, Lens V. Neurosarcoma of the face: MRI. Neuroradiology 1997;39:747–750.
74. al-Otieschan AA, Saleem M, Manohar MB, et al. Malignant schwannoma of the parapharyngeal space. J Laryngol Otol 1998;112:883–887.
75. Zak F, Lawson W. The Paraganglionic Chemoreceptor System: Physiology, Pathology, and Clinical Medicine. New York: Springer-Verlag, 1982;287–411.
76. Ishii N, Sawamura Y, Tada M, et al. Basilar invagination associated with an intercarotid paraganglioma—case report. Neurol Med Chir (Tokyo) 1997;37:279–283.
77. Mulligan R. Chemodectoma in the dog. Am J Pathol 1950;26: 680–681.
78. Arias J, Valcerel J. Chief cell hyperplasia in the human carotid body at high altitudes. Hum Pathol 1976;7:361–373.
79. Saldana M, Salem L, Travezan R. High altitude hypoxia and chemodectomas. Hum Pathol 1973;4:251–263.
80. Rodriguez-Cuevas S, Lopez-Garza J, Labastida-Almendaro S. Carotid body tumors in inhabitants of altitudes higher than 2000 meters above sea level. Head Neck 1998;20:374–378.
81. Olsen W, Dillon W, Kelly W, et al. MR imaging of paragangliomas. Am J Roentgenol 1987;148:201–204.
82. van Gils A, van den Berg R, Falke T, et al. MR diagnosis of paraganglioma of the head and neck: value of contrast enhancement. Am J Roentgenol 1994;162:147–153.
83. van den Berg R, Wasser MN, van Gils AP, et al. Vascularization of head and neck paragangliomas: comparison of three MR angiographic techniques with digital subtraction angiography. AJNR 2000;21:162–170.
84. Namyslowski G, Czecior E, Bluszcz A, Poloczek R. [A case of glomus caroticum malignum]. Otolaryngol Pol 1995;49:593–597.
85. Bauer GP, Volk MS, Siddiqui SY, et al. Burkitt's lymphoma of the parapharyngeal space. Arch Otolaryngol Head Neck Surg 1993;119: 117–120.
86. Hanazawa T, Kimura Y, Sakamaki H, et al. Burkitt's lymphoma involving the mandible: report of a case and review of Japanese cases. Oral Surg Oral Med Oral Pathol Oral Radiol Endod 1998;85:216–220.
87. Tillich M, Ranner G, Humer-Fuchs U, Lang-Loidolt D. Synovial sarcoma of the parapharyngeal space: CT and MRI [in process citation]. Neuroradiology 1998;40:261–263.
88. Rosignoli M, Cadoni G, Rabitti C, Galli J. [Hemangiopericytoma of parapharyngeal space]. Acta Otorhinolaryngol Ital 1993;13:455–465.
89. Vogl TJ, Steger W, Grevers G, et al. MR characteristics of primary extramedullary plasmacytoma in the head and neck. AJNR 1996;17:1349–1354.
90. Weber B, Kempf H, Lenz M, Gartner H. Diagnosis and therapy of aggressive fibromatosis (extra-abdominal desmoid) in the head and neck area. Laryngol Rhinol Otol 1991;70:367–374.
91. Carluccio F, Amendola S. [Parapharyngeal oncocytoma of the parotid gland]. Acta Otorhinolaryngol Ital 1996;16:57–61.
92. Yokoyama M, Nomura Y, Semba T. Acinic cell carcinoma of the parapharyngeal space: case report. Head Neck 1993;15:67–69.
93. Sato J, Asakura K, Yokoyama Y, Satoh M. Solitary fibrous tumor of the parotid gland extending to the parapharyngeal space. Eur Arch Otorhinolaryngol 1998;255:18–21.
94. Petersen BL, Buchwald C, Gerstoft J, et al. An aggressive and invasive growth of juvenile papillomas involving the total respiratory tract. J Laryngol Otol 1998;112:1101–1104.
95. Ohno Y, Muraoka M, Ohashi Y, et al. Osteolipoma in the parapharyngeal space. Eur Arch Otorhinolaryngol 1998;255: 315–317.
96. Bizakis J, Segas J, Tsardis M, et al. Pathologic quiz case 1. Adult rhabdomyoma of the parapharyngeal space. Arch Otolaryngol Head Neck Surg 1993;119:350–352.
97. Goldfarb D, Lowry LD, Keane WM. Recurrent rhabdomyoma of the parapharyngeal space. Am J Otolaryngol 1996;17:58–60.
98. Hytiroglou P, Brandwein MS, Strauchen JA, et al. Inflammatory pseudotumor of the parapharyngeal space: case report and review of the literature. Head Neck 1992;14:230–234.
99. Som P. Lymph nodes of the neck. Radiology 1987;165:593–600.
100. Saing H, Lau WF, Chan YF, Chan FL. Parapharyngeal teratoma in the newborn. J Pediatr Surg 1994;29:1524–1525.
101. Gullane PJ, Lampe HB, Slinger R. Erosive parapharyngeal space teratoma. J Otolaryngol 1986;15:317–321.
102. Forte V, Friedberg J, Thorner P, Park A. Heterotopic brain in the parapharyngeal space. Int J Pediatr Otorhinolaryngol 1996;37:253–260.
103. Gangopadhyay K, Taibah K, Manohar MB, Kfoury H. Solitary fibrous tumor of the parapharyngeal space: a case report and review of the literature. Ear Nose Throat J 1996;75:681–684.
104. Fucci MJ, Lowry LD, Eriksen C, Kelly MF. Desmoplastic fibroma of the parapharyngeal space. Otolaryngol Head Neck Surg 1994;110: 341–344.
105. Porter MJ, Suen WM, John DG, van Hasselt CA. Fibromatosis of the parapharyngeal space. J Laryngol Otol 1994;108:1102–1104.
106. Safneck JR, Alguacil-Garcia A, Dort JC, Phillips SM. Solitary fibrous tumour: report of two new locations in the upper respiratory tract. J Laryngol Otol 1993;107:252–256.
107. Sato J, Asakura K, Yokoyama Y, Satoh M. Solitary fibrous tumor of the parotid gland extending to the parapharyngeal space [in process citation]. Eur Arch Otorhinolaryngol 1998;255:18–21.
108. Nakagawa T, Sugimoto T, Komiyama S, et al. Giant tumor formed by nodular fasciitis of the pharynx: a case report. Auris Nasus Larynx 1994;21:196–199.
109. Som PM, Brandwein MS, Silvers A. Nodal inclusion cysts of the parotid gland and parapharyngeal space: a discussion of lymphoepithelial, AIDS-related parotid and branchial cysts, cystic Warthin's tumors, and cysts in Sjogren's syndrome. Laryngoscope 1995;105: 1122–1128.
110. Shidara K, Uruma T, Yasuoka Y, Kamei T. Two cases of nasopharyngeal branchial cyst. J Laryngol Otol 1993;107:453–455.
111. Durrant TJ, Sevick RJ, Lauryssen C, MacRae ME. Parapharyngeal branchial cleft cyst presenting with cranial nerve palsies. Can Assoc Radiol J 1994;45:134–136.
112. Guneri A, Gunbay MU, Guneri EA, et al. Management of parapharyngeal space cysts. J Laryngol Otol 1994;108:795–797.
113. Chabot M, Fradet G, Theriault R, Morrissette YP. The excision of branchial parapharyngeal cysts by transbuccal or lateral cervical approach. J Otolaryngol 1996;25:108–112.
114. Deitmer T. [Therapy of cystic lymphangioma in childhood. Report of 4 cases with manifestations in the area of the head-neck]. Laryngorhinootologie 1996;75:166–170.
115. Reede D, Whelan M, Bergeron R. Computed tomography of the infrahyoid neck. II, Pathology. Radiology 1982;145:397–402.
116. Reede D, Whelan M, Bergeron R. CT of the soft-tissue structures of the neck. Radiol Clin North Am 1984;22:239–250.
117. Harnsberger H, Mancuso A, Muraki A, et al. Branchial cleft anomalies and their mimicks: computed tomographic evaluation. Radiology 1984;152:739–748.
118. Som P. Cystic lesions of the neck. Postgrad Radiol 1987;7:211–236.
119. Wolfram-Gabel R, Kahn JL, Bourjat P. The parapharyngeal adipose corpus: morphologic study. Surg Radiol Anat 1997;19:249–255.
120. Hellin Meseguer D, Garcia Ortega F, Merino Galvez E. [Pharyngeal lipoma]. Otorrinolaringol Ibero Am 1994;21:247–254.
121. Elango S. Parapharyngeal space lipoma. Ear Nose Throat J 1995;74:52–53.
122. Barbiera F, Pappalardo S, Saraniti C, Incandela S. [A case of lipoma of the parapharyngeal space. Report of an unusual clinico-radiologic finding]. Radiol Med (Torino) 1996;92:317–320.
123. Abdullah BJ, Liam CK, Kaur H, Mathew KM. Parapharyngeal space lipoma causing sleep apnoea. Br J Radiol 1997;70:1063–1065.
124. Gomersall L, Needham G. Case report: mesenchymal chondrosarcoma occurring in the parapharyngeal space. Clin Radiol 1990;42: 359–361.
125. Backhouse SS, Shone GR, Douglas-Jones AG. Angiolymphoid hyperplasia with eosinophilia of the parapharyngeal space. J Laryngol Otol 1998;112:802–804.
126. Supanakorn S, Rungruxsirivorn S, Patradul A, et al. Head and neck mycetoma. J Med Assoc Thai 1998;81:1019–1022.
127. Sirotnak JJ, Loree TR, Penetrante R. Papillary carcinoma of the thyroid metastatic to the parapharyngeal space. Ear Nose Throat J 1997;76:342–344.
128. Ferrario F, Roselli R, Macchi A. Occult thyroid carcinoma presenting as a parapharyngeal mass. J Laryngol Otol 1995;109:1204–1206.
129. Carter LC, Uthman A, Drinnan AJ, Loree TR. Diagnostic dilemma involving calcification in the parapharyngeal space: metastatic thyroid carcinoma masquerading as a deep lobe parotid mass. Oral Surg Oral Med Oral Pathol Oral Radiol Endod 1997;84:697–702.

Copyright © 2003, Mosby, Inc. All rights reserved.

130. Nusbaum O, Som P, Dubois P, Silvers A. Isolated vagal nerve palsy secondary to a dissection of the extracranial internal carotid artery. Am J Neuroradiol 1998; 19:1845–1847.
131. Mokri B, Silbert P, Schievink W, Piepgras D. Cranial nerve palsy in spontaneous dissection of the extracranial internal carotid artery. Neurology 1996;46:356–359.
132. Jackel M. [Anatomic variants of the internal carotid artery as differential parapharyngeal space-occupying lesions diagnosis]. Hno 1997;45:1018–1021.
133. Tillmann B, Christofides C. [The ''dangerous loop'' of the internal carotid artery. An anatomic study]. Hno 1995;43:601–604.
134. Cicogna R, Bonomi FG, Curnis A, et al. Parapharyngeal space lesions syncope-syndrome. A newly proposed reflexogenic cardiovascular syndrome. Eur Heart J 1993;14:1476–1483.
135. Chiodi L, Cordopatri F, Rossi D, et al. [Reflex syncope as a preliminary symptom of a rhinopharyngeal lymphoma. A case report]. Minerva Cardioangiol 1995;43:501–503.
136. Tostevin PM, Hollis LJ, Bailey CM. Pharyngeal trauma in children—accidental and otherwise. J Laryngol Otol 1995;109:1168–1175.
137. Tselishchev VA. [A foreign body of the parapharyngeal space]. Vestn Otorinolaringol 1997;1:60.
138. Schoem SR, Choi SS, Zalzal GH, Grundfast KM. Management of oropharyngeal trauma in children. Arch Otolaryngol Head Neck Surg 1997;123:1267–1270.
139. Osinubi OA, Osiname AI, Pal A, et al. Foreign body in the throat migrating through the common carotid artery. J Laryngol Otol 1996;110:793–795.
140. Mitchell RB, Pereira KD, Younis RT, Lazar RH. The management of asymptomatic firearm injuries in children. J R Coll Surg Edinb 1997;42:418–419.
141. Efrati Y, Sarfaty S, Klin B, et al. Oral blast injury caused by an accident. Ann Otol Rhinol Laryngol 1993;102:528–530.
142. Russell EJ, Levy JM, Breit R, McMahan JT. Osteocartilaginous tumors in the parapharyngeal space arising from bone exostoses. AJNR 1990;11:993–997.
143. Ikeda K, Kikuta N, Sasaki Y, et al. Extracranial chondroma of the skull base. Arch Otolaryngol Rhinol Laryngol 1987;243:424–428.
144. Wang DH, Guan XL, Xiao LF, et al. Soft-tissue chondroma of the parapharyngeal space: a case report. J Laryngol Otol 1998;112:294–295.
145. Kawahara N, Sasaki T, Nibu K, et al. Dumbbell type jugular foramen meningioma extending both into the posterior cranial fossa and into the parapharyngeal space: report of 2 cases with vascular reconstruction. Acta Neurochir 1998;140:323–330.
146. Kado H, Ogawa T, Okudera T, et al. Parapharyngeal meningioma extending from the intracranial space evaluated by FDG PET. J Nucl Med 1998;39:302–304.
147. Fisher A, Som P, Mosesson R, et al. Giant intracranial aneurysms with skull base erosion and extracranial masses: CT and MR findings. J Comput Assist Tomogr 1994;18:939–942.
148. Moritz JD, Emons D, Wiestler OD, et al. Extracerebral intracranial glioneural hamartoma with extension into the parapharyngeal space. AJNR 1995;16:1279–1281.
149. Hollinshead W. Fascia and fascial spaces of the head and neck. In: Hollinshead W, ed. Anatomy for Surgeons. Vol 1. New York: Hoeber-Harper, 1954;282–305.
150. Juvara E. Anatomie de la region pterygo-maxillaire. Vol. Thesis No.186. Paris: Battaille, 1985;1–65.
151. Gaughran G. Fasciae of the masticator space. Anat Rec 1957;129:383–400.
152. Rouviere H. Lymphatic system of the head and neck. In: Anatomy of the Human Lymphatic System. Ann Arbor, Mich.: Edwards Brothers, 1938;5–28.
153. Dean L. The proper procedure for external drainage of retropharyngeal abscesses secondary to caries of the vertebrae. Ann Otol Rhinol Laryngol 1919;28:566–572.
154. Truffert P. Le Cou. Anatomie topographique. Les Aponeuroses-Les Loges. Paris: L. Arnette, 1922;1–142.
155. Harnsberger H. CT and MRI of masses of the deep face. Curr Probl Diagn Radiol 1987;16:143–173.
156. McIleath D, ReNine W, Devine K, Dockerty M. Tumors of the parapharyngeal region. Surg Gynecol Obstet 1963;116:88–94.
157. Last R. The temporo-mandibular joint. In: Last R, ed. Anatomy: Regional and Applied. 6th ed. Edinburgh and London: Churchill Livingstone, 1978;444–447.
158. Ariji E, Moriguchi S, Kuroki T, Kanda S. Computed tomography of maxillofacial infection. Dentomaxillofac Radiol 1991;20:147–151.
159. Bird JS, Smith RL. Auditory canal drainage from a masticator space cellulitis. J Oral Surg 1973;31:854–857.
160. Caruso VG. Masticator space abscess complicating removal of suspension wires: case report. Ann Otol Rhinol Laryngol 1978;87:266–269.
161. Fenton RS, Rotenberg D. Actinomycosis of the parotid. Is it usually a masticator space infection? J Otolaryngol 1977;6:233–238.
162. Hardin CW, Harnsberger HR, Osborn AG, et al. Infection and tumor of the masticator space: CT evaluation. Radiology 1985;157:413–417.
163. Kim HJ, Park ED, Kim JH, et al. Odontogenic versus nonodontogenic deep neck space infections: CT manifestations. J Comput Assist Tomogr 1997;21:202–208.
164. Newman MH Jr, Emley WE. Chronic masticator space infection. Arch Otolaryngol 1974;99:128–131.
165. Nishimura T, Okabe Y, Furukawa M. A chronic organized masseter abscess causing trismus resolved by hemi-masseter myotomy. Auris Nasus Larynx 1996;23:140–142.
166. Messina S, Notarantonio A, Pancotti G, Feyles E. Primary sarcomas of the maxillofacial area. Clinical assessment of a case of angiosarcoma with a rare location. Minerva Stomatol 1993;42:57–62.
167. Zhang G. Digital image processing of radiography of 32 cases with mandible sarcomas. Chung Hua Kou i Hsueh Tsa Chih Chinese J Stomatol 1992;27:323–325.
168. Fernandez Sanroman J, Alonso del Hoyo J, Diaz F, et al. Sarcomas of the head and neck. Bri J Oral Maxillofacial Surg 1992;30:115–118.
169. Batsakis J. Osteogenic and chondrogenic sarcomas of the jaws. Annal Otol Rhinol Laryngol 1987;96:474–475.
170. Abdul-Karim F, Ayala A, Chawla S, et al. Malignant fibrous histiocytoma of jaws. A clinicopathologic study of 11 cases. Cancer 1985;56:1590–1596.
171. Altini M, Thompson S, Lownie J, Berezowski B. Ameloblastic sarcoma of the mandible. J Oral Maxillofacial Surg 1985;43:789–794.
172. Bale P, Parsons R, Stevens M. Diagnosis and behavior of juvenile rhabdomyosarcoma. Hum Pathol 1983;14:596–611.
173. Lian S, Naga T, Kawasaki H, et al. Reticulum cell sarcoma of the jaws. Report of two cases and comparison of incidence in Japan and other countries. Oral Surg Oral Med Oral Pathol 1980;50:110–115.
174. Lam K, Wong J, Lim S, Ong G. Primary sarcomas of the jaws. Aust NZ J Surg 1979;49:668–675.
175. Doval D, Naresh K, Sabitha K, et al. Carcinoma of the urinary bladder metastatic to the oral cavity. Ind J Cancer 1994;31:8–11.
176. Peters E, Cohen M, Altini M, Murray J. Rhabdomyosarcoma of the oral cavity and parol region. Cancer 1989;63:963–966.
177. Som PM, Curtin HD, Silvers AR. A re-evaluation of imaging criteria to assess aggressive masticator space tumors. Head Neck 1997;19:335–341.
178. Aspestrand F, Boysen M. CT and MR imaging of primary tumors of the masticator space. Acta Radiol 1992;33:518–522.
179. Ceysens C, Horvath M, Termote JL, Lemahieu SF. Extranodal non-Hodgkin lymphoma of the head and neck presenting as a mandibular swelling: report of two cases. J Belge Radiol 1992;75:37–39.
180. Chong VF, Fan YF. Pictorial review: radiology of the masticator space. Clin Radiol 1996;51:457–465.
181. Chua DT, Sham JS, Kwong DL, et al. Prognostic value of paranasopharyngeal extension of nasopharyngeal carcinoma. A significant factor in local control and distant metastasis. Cancer 1996;78:202–210.
182. Daniels RL, Haller JR, Harnsberger HR. Hemangiopericytoma of the masticator space. Ann Otol Rhinol Laryngol 1996;105:162–165.
183. DelBalso AM, Herz P, Miller L, et al. Ki-1-positive anaplastic large cell lymphoma of the masticator space with intracranial extension. AJNR 1996;17:1388–1391.
184. Mizutani H, Ohba S, Mizutani M, et al. [MR studies of extension and spread pattern of nasopharyngeal carcinoma]. Nippon Igaku Hoshasen Gakkai Zasshi 1991;51:487–497.
185. Ohtsuka H, Katayama S, Shioya N. Unusual facial hemangioma. Plast Reconstr Surg 1979;64:13–16.
186. Work WP, Penner JA, Hybels RL. Lymphomas of the masticator space. Arch Otolaryngol 1976;102:532–534.

Copyright © 2003, Mosby, Inc. All rights reserved.

187. Walker AT, Chaloupka JC, Putman CM, et al. Sentinel transoral hemorrhage from a pseudoaneurysm of the internal maxillary artery: a complication of CT-guided biopsy of the masticator space. AJNR 1996;17:377–381.
188. Tryhus MR, Smoker WR, Harnsberger HR. The normal and diseased masticator space. Semin Ultrasound CT MR 1990;11:476–485.
189. Doxey GP, Harnsberger HR, Hardin CW, Davis RK. The masticator space: the influence of CT scanning on therapy. Laryngoscope 1985;95:1444–1447.
190. Danikas D, Theodorou SJ, Arvanitis ML, et al. Malar metastasis from rectal carcinoma: a case report. Am Surg 1999;65:1150–1152.
191. Yonetsu K, Izumi M, Nakamura T. Deep facial infections of odontogenic origin: CT assessment of pathways of space involvement. AJNR 1998;19:123–128.
192. Petersilge CA, Pathria MN, Gentili A, et al. Denervation hypertrophy of muscle: MR features. J Comput Assist Tomogr 1995;19:596–600.
193. Russo CP, Smoker WR, Weissman JL. MR appearance of trigeminal and hypoglossal motor denervation. AJNR 1997;18:1375–1383.
194. Kullmer K, Sievers KW, Reimers CD, et al. [Magnetic resonance tomography and histopathologic findings after muscle denervation. A comparative animal experiment study during a two month follow-up]. Nervenarzt 1996;67:133–139.
195. Schellhas KP. MR imaging of muscles of mastication [see comments]. AJR 1989;153:847–855.
196. Polak JF, Jolesz FA, Adams DF. Magnetic resonance imaging of skeletal muscle. Prolongation of T1 and T2 subsequent to denervation. Invest Radiol 1988;23:365–369.
197. Shabas D, Gerard G, Rossi D. Magnetic resonance imaging examination of denervated muscle. Comput Radiol 1987;11:9–13.
198. Murakami R, Baba Y, Nishimura R, et al. MR of denervated tongue: temporal changes after radical neck dissection. AJR 1998;19: 515–518.
199. Gniadecka M, Weismann K, Herning M. Swelling of the temporal region: a case of benign masticatory muscle hypertrophy. Br J Dermatol 1997;136:242–244.
200. Rosa RA, Kotkin HC. That acquired masseteric look. ASDC J Dent Child 1996;63:105–107.
201. Staffenberg DA, McCarthy JG, Hollier LH, et al. Hypertrophy and asymmetry of the facial muscles: a previously unrecognized association [in process citation]. Ann Plast Surg 1998;40:533–537.
202. Waldhart D, Lynch D. Benign hypertrophy of the masseter muscles and mandibular angles. Arch Surg 1971;102:115–118.
203. Nakata S, Mizuno M, Koyano K, et al. Functional masticatory evaluation in hemifacial microsomia. Eur J Orthod 1995;17:273–280.
204. Xu JA, Yuasa K, Yoshiura K, Kanda S. Quantitative analysis of masticatory muscles using computed tomography. Dentomaxillofac Radiol 1994;23:154–158.
205. Basso Ricci S, Guzzon A, Milani F, Ceglia E. [Somatic sequelae induced by radiotherapy in bone segments in adults]. Radiol Med (Torino) 1987;73:83–90.
206. Gola R, Lachard J, Zattara H, Nerini A. [Recent advances in the therapy of osteoradionecrosis of the maxillomandibular bones (author's trans.)]. Rev Stomatol Chir Maxillofac 1979;80:146–151.
207. Keus R, Noach P, de Boer R, Lebesque J. The effect of customized beam shaping on normal tissue complications in radiation therapy of parotid gland tumors. Radiother Oncol 1991;21:211–217.
208. Mendelsohn DB, Hertzanu Y, Glass RB. Computed tomographic findings in primary mandibular osteosarcoma. Clin Radiol 1983;34: 153–155.
209. De Batselier P, Reychler H, Yousefpour A, et al. [Osteosarcoma of the mandible]. J Radiol 1997;78:461–463.
210. Shibuya H, Kurabayashi T, Iwaki H, et al. CT findings in primary osteosarcoma of the jaw. Rofo Fortschr Geb Rontgenstr Neuen Bildgeb Verfahr 1991;154:139–142.
211. Lee YY, Van Tassel P, Nauert C, et al. Craniofacial osteosarcomas: plain film, CT, and MR findings in 46 cases. AJR 1988;150:1397–1402.

Copyright © 2003, Mosby, Inc. All rights reserved.

Copyright © 2003, Mosby, Inc. All rights reserved.

39

Salivary Glands: Anatomy and Pathology

Peter M. Som and Margaret S. Brandwein

INTRODUCTION
- Normal Anatomy
  - Parotid Gland
  - Submandibular Gland
  - Sublingual Gland
  - Minor Salivary Glands
- Developmental Anomalies
- Physiology

IMAGING
- An Overall Imaging Approach
- Plain Films
- Sialography
  - Parotid Gland Study
  - Submandibular Gland Study
- Computed Sectional Imaging
  - General Considerations
  - CT and MR Imaging
    - *Parotid Gland: CT*
    - *Normal Parotid Gland: MR Imaging*
    - *Normal Submandibular Glands: CT and MR Imaging*
    - *Normal Sublingual Glands: CT and MR Imaging*
  - MR Sialography
  - Other Approaches
    - *Three-Dimensional MR Imaging*
    - *MR Spectroscopy*
    - *CT Sialography*
- Noncomputed Tomographic Sialography
  - Ultrasound
  - Radionuclide Salivary Studies
  - Angiography
  - Catheter Dilatation and Endoscopy
  - Fine Needle Aspiration
  - Positron Emission Tomography Scanning

NONNEOPLASTIC DISORDERS
- Infections
  - Acute Infections
    - *Bacterial Infections*
    - *Viral Infections*
  - Chronic Inflammations
    - *Mycobacteria*
    - *Syphilis*
    - *Cat-Scratch Disease*
    - *Toxoplasmosis*
    - *Actinomycosis*
    - *Sarcoidosis*
  - Other Causes: "Iodine Mumps"
- Sialolithiasis
- Chronic Recurrent Sialoadenitis
- Sialodochitis Fibrinosa (Kussmaul's Disease)
- Ductal Foreign Bodies
- Trauma
- Autoimmune Diseases (Including Benign Lymphoepithelial Lesion)
- Hyperlipidemia
- Sialosis
- Postirradiation Sialoadenitis
- Necrotizing Sialometaplasia
- Adenomatoid Hyperplasia of Mucous Salivary Glands
- Cystic Processes
  - Congenital Cysts
    - *Lymphoepithelial Cyst*
    - *True Branchial Cleft Cyst*
    - *Epidermoid Inclusion Cyst*
    - *Polycystic (Dysgenetic) Disease*
    - *Congenital Sialectasis and Merkel's Cyst*
  - Acquired Cysts
    - *Ductal Cysts/Sialocysts*
    - *Pneumoceles*
    - *AIDS-Related Parotid Cysts*
    - *Ranula*

TUMORS AND TUMOR-LIKE CONDITIONS
- Epithelial Tumors
  - Pleomorphic Adenoma (Benign Mixed Tumor) and Carcinoma ex Pleomorphic Adenoma (Malignant Mixed Tumor)
  - Warthin's Tumor

Copyright © 2003, Mosby, Inc. All rights reserved.

- **Benign and Malignant Oncocytic Tumors**
  - ***Major Salivary Gland Oncocytic Tumors***
  - ***Oncocytic Tumors of Minor Salivary or Seromucinous Gland Sites***
    - *Larynx*
    - *Oral Cavity*
    - *Sinonasal Cavity*
- **Oncocytic Papillary Cystadenoma**
- **Basal Cell Adenoma and Basal Cell Adenocarcinoma**
- **Canalicular Adenoma**
- **Myoepithelioma and Myoepithelial Carcinoma**
- **Epithelial-Myoepithelial Carcinoma**
- **Clear Cell Carcinoma**
- **Mucoepidermoid Carcinoma**
- **Adenoid Cystic Carcinoma**
- **Acinic Cell Carcinoma**
- **Polymorphous Low-Grade Adenocarcinoma and Low-Grade Papillary Adenocarcinoma of Salivary Origin**
- **Salivary Duct Carcinoma (Plus Low-Grade Salivary Duct Carcinoma)**
- **Adenosquamous Carcinoma and Basaloid Squamous Carcinoma**
- **Sebaceous Neoplasms of Salivary Gland Origin**
- **Primary Squamous Cell Carcinoma**
- **Lymphoepithelial Carcinoma**
- **Undifferentiated Carcinoma**
  - ***Small Cell Undifferentiated Carcinoma***
  - ***Large Cell Undifferentiated Carcinoma***
- **Hybrid Carcinoma**
- **Sialoblastoma**
- **Sclerosing Adenosis**
- **Adenocarcinoma, Not Otherwise Specified**
- **Carcinoma Metastatic to the Salivary Glands**
- **Nonepithelial Tumors**
  - **Hemangioma**
  - **Lymphangioma**
  - **Lymphoma**
  - **Intraparotid Lymphadenopathy**
  - **Lipoma**
  - **Neurogenic Tumors**
  - **Fibrous Tissue Lesions**
- **Miscellaneous Lesions**
  - **Masseteric Hypertrophy**
  - **Temporomandibular Joint and Mandibular Lesions**
  - **Other Miscellaneous Conditions**
  - **Kimura's Disease**
- **SUMMARY OF DISEASE PATTERNS**

INTRODUCTION

The salivary tissues can be affected by a variety of pathologic processes: inflammatory, infectious, obstructive, systemic, and neoplastic. The diversity of benign and malignant salivary neoplasia is probably greater than that of any other organ system. On the other hand, the incidence of salivary neoplasia is extremely low. Salivary tumors comprise less than 3% of all head and neck tumors and cause less than 0.1% of all cancer deaths.[1] As to the relative incidence of salivary gland involvement, it is estimated that for every 100 parotid tumors, there are 10 submandibular tumors, 10 minor salivary tumors, and 1 sublingual tumor.[2]

Little data are available on the epidemiology of salivary neoplasia. Radiation is a known promoter of both benign and malignant salivary gland tumors.[3] Sun exposure may also be causally related to salivary tumorigenesis, as there is a greater than expected coincidence of skin malignancies with salivary tumors.[4] There are a few associations between viruses and salivary tumor neogenesis. Transgenic mice infected with mouse mammary tumor virus have developed acinic carcinoma-like tumors.[5] Epstein-Barr virus (EBV) has been demonstrated within the parotid counterpart of nasopharyngeal carcinoma, the undifferentiated lymphoepithelial carcinoma found in the Aleutian population, or the so-called Eskimo tumor.[6] A finding of EBV genomic clonality in these tumors is strong evidence for a causal relationship.

Concerning the mechanism of salivary tumor genesis, it was assumed for decades that there were but two potential stem cells from which the scores of different salivary tumors originated. It was generally accepted that the basal cells of the excretory duct and the intercalated duct cells acted as the reserve cells for the more differentiated cells of the salivary gland unit. It was also believed that all of the epithelial tumors arose from these reserve cells rather than from the acini.[7, 8] The basal cells of the excretory duct gave rise to the columnar and squamous cells, while the intercalated duct cells gave rise to the acinar cells, striated duct cells, and other intercalated duct cells. The myoepithelial cells function to contract ductules, moving secretions along the ductal system. It was believed that the origins of most salivary tumors could be traced back to their corresponding ductal elements. So, for instance, pleomorphic adenoma, the most common salivary tumor, arose from the intercalated cell/myoepithelial unit, while tumors such as mucoepidermoid carcinoma and squamous cell carcinoma arose from the excretory duct reserve cell. Implicit in the assumption that there were but two basic stem cells was the notion that *end-differentiated* specialized cells, (e.g., acinar and striated duct cells) were incapable of mitotic division and hence incapable of giving rise to tumors.[8] However, there is

Copyright © 2003, Mosby, Inc. All rights reserved.

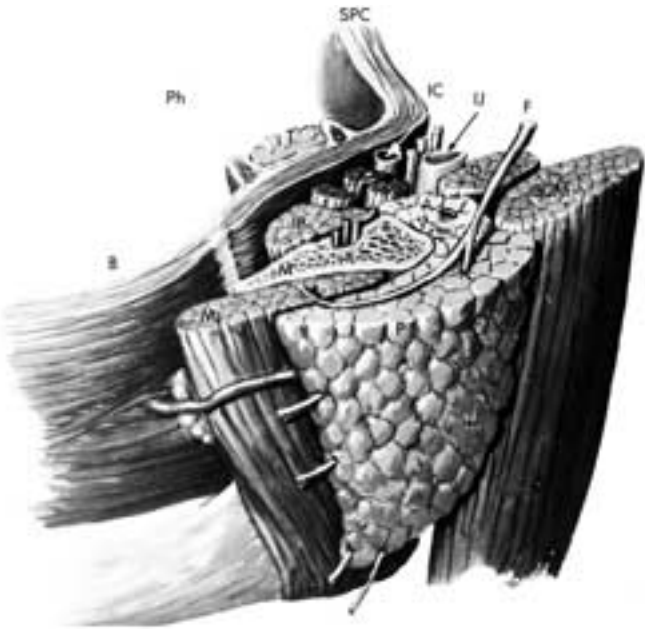

VIEW IMAGE

FIGURE 39-1 Normal anatomy of the left parotid gland and the parapharyngeal space viewed obliquely and from above. Note how the deep portion of the parotid gland extends behind the ramus of the mandible and in front of the sternocleidomastoid muscle and the posterior belly of the digastric muscle. Pharynx (*Ph*), superior pharyngeal constrictor muscle (*SPC*), tonsil (*T*), buccinator muscle (*B*), masseter muscle (*Ms*), sternocleidomastoid muscle (*SCM*), posterior belly of the digastric muscle (*D*), internal pterygoid muscle (*IP*), mandible (*M*), internal carotid artery (*IC*), internal jugular vein (*IJ*), parotid gland (*P*), facial nerve (*F*), external carotid artery (*A*), posterior facial vein (*V*). The combined CT-sialogram. (From Som PM, Biller H. Radiology 1980;135:387–390.)

evidence demonstrating the proliferative and regenerative ability of rat salivary tissue that is not confined to one cell type. Acinar cells, intercalated duct cells, striated duct cells, and excretory duct cells may all cycle.[9] Further, in cell cultures from human salivary glands, all differentiated cell types have now been shown to be capable of cycling.[10] Thus the pathogenesis of the salivary gland tumors appears to be far more diverse than was previously thought. The embryology of the salivary glands is discussed in Chapter 33.

Normal Anatomy

The paired parotid, submandibular, and sublingual glands are referred to as the major salivary glands; each is anatomically, histologically, and functionally unique. The minor salivary glands are submucosal clusters of salivary tissue present in the oral cavity, paranasal sinuses, pharynx, and upper respiratory tract. It has been estimated that more than 750 minor salivary gland clusters are present.

Parotid Gland

The parotid is the largest salivary gland, and the palpable superficial portion of the gland lies beneath the skin and over the mandibular ramus. The fascia that surrounds the parotid is derived from the superficial layer of the deep cervical fascia. Its thickness varies, being densest over the lateral and inferior aspects of the gland and filmy or incomplete over the medial surface of the gland. Fascial extensions into the parotid parenchyma subdivide the gland into lobules. The parotid weighs between 14 and 28 g in the adult male and measures, on average, 5.8 cm craniocaudally and 3.4 cm ventrodorsally.[8, 11] The female parotid gland tends to be slightly smaller.

Most of the gland (~80%) is superficial to the masseter muscle, ascending ramus, and angle of the mandible; it rarely extends cranially to the zygoma. The superficial parotid lies below and anterior to the external auditory canal and the mastoid tip, usually extending caudally to about the level of the angle of the mandible. The remaining deep aspect of the parotid gland (~20%) extends medially through the stylomandibular tunnel and is present between the posterior edge of the mandibular ramus and the anterior borders of the sternocleidomastoid muscle and the posterior belly of the digastric muscle (Fig. 39-1). The stylomandibular tunnel actually is formed by the skull base, the back of the mandibular ramus, and the stylomandibular ligament and styloid process (Fig. 39-2). The stylomandibular ligament also separates the parotid gland from the submandibular gland.

As a result of these anatomic relationships, the retromandibular or deep portion of the parotid gland is anterior to the styloid process (and its musculature) and the carotid sheath, which places the deep portion of the parotid gland within the prestyloid compartment of the parapharyngeal space (see Chapters 34 and 38) (Fig. 39-3).[8, 11] There are several lobulations (outward projections) or recesses (indentations) of the parotid gland related to (1) the external auditory meatus, (2) the mastoid process, (3) the anterior border of the sternocleidomastoid muscle, (4) the anterior border of the posterior belly of the digastric muscle, and (5) the styloid process and the styloid muscles. These lobulations or

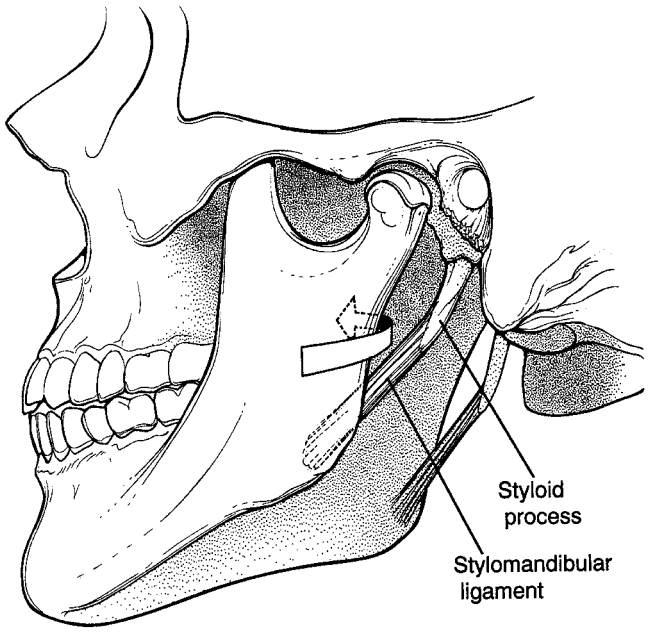

FIGURE 39-2 Left lateral drawing of the facial region shows the stylomandibular tunnel, through which passes the deep portion of the parotid gland (*arrow*).

VIEW IMAGE

Copyright © 2003, Mosby, Inc. All rights reserved.

recesses vary in size or may be nonexistent. Despite the commonly used terminology, there is actually no anatomic division into separate superficial and deep parotid lobes, a nomenclature based on the facial nerve as a reference plane within the gland. By convention, parotid tissue situated deep to this plane is referred to as the deep lobe, while parotid tissue superficial to this plane is considered to be the superficial lobe. This terminology persists despite its anatomic inaccuracy. However, anatomically correct terminology in which the mandible has become the reference point is gaining popularity. Parotid tissue external to the mandible is referred to as superficial, whereas the smaller amount of parotid tissue that resides behind and deep to the mandible is referred to as the retromandibular or deep portion of the parotid gland. Although anatomically these are different nomenclatures, either is appropriate to use. The main trunk of the facial nerve exits the skull base via the stylomastoid foramen, immediately producing three small branches: the posterior auricular, posterior digastric, and stylohyoid nerves. The facial nerve then courses laterally around the styloid process and is immediately superficial to the posterior belly of the digastric muscle. Distal to this, it pierces the posterior capsule of the parotid gland. The nerve continues within the gland lateral to the posterior facial vein (retromandibular vein) and the more medially situated external carotid artery. It then divides via variable anatomic patterns into the temporal, zygomatic, buccal, mandibular, and cervical branches (Fig. 39-4).[12]

The parotid ductal organization has an arborizing or tree-like branching pattern. As one traces proximally from the main parotid duct (Stensen's duct) toward the terminal acini, the ducts become progressively smaller, with more numerous branches (Fig. 39-5). Histologically, the main excretory ducts can be seen to lead into the striated ducts (columnar, oncocytic epithelium), the intercalated ducts (cuboidal epithelium surrounded by myoepithelial cells),

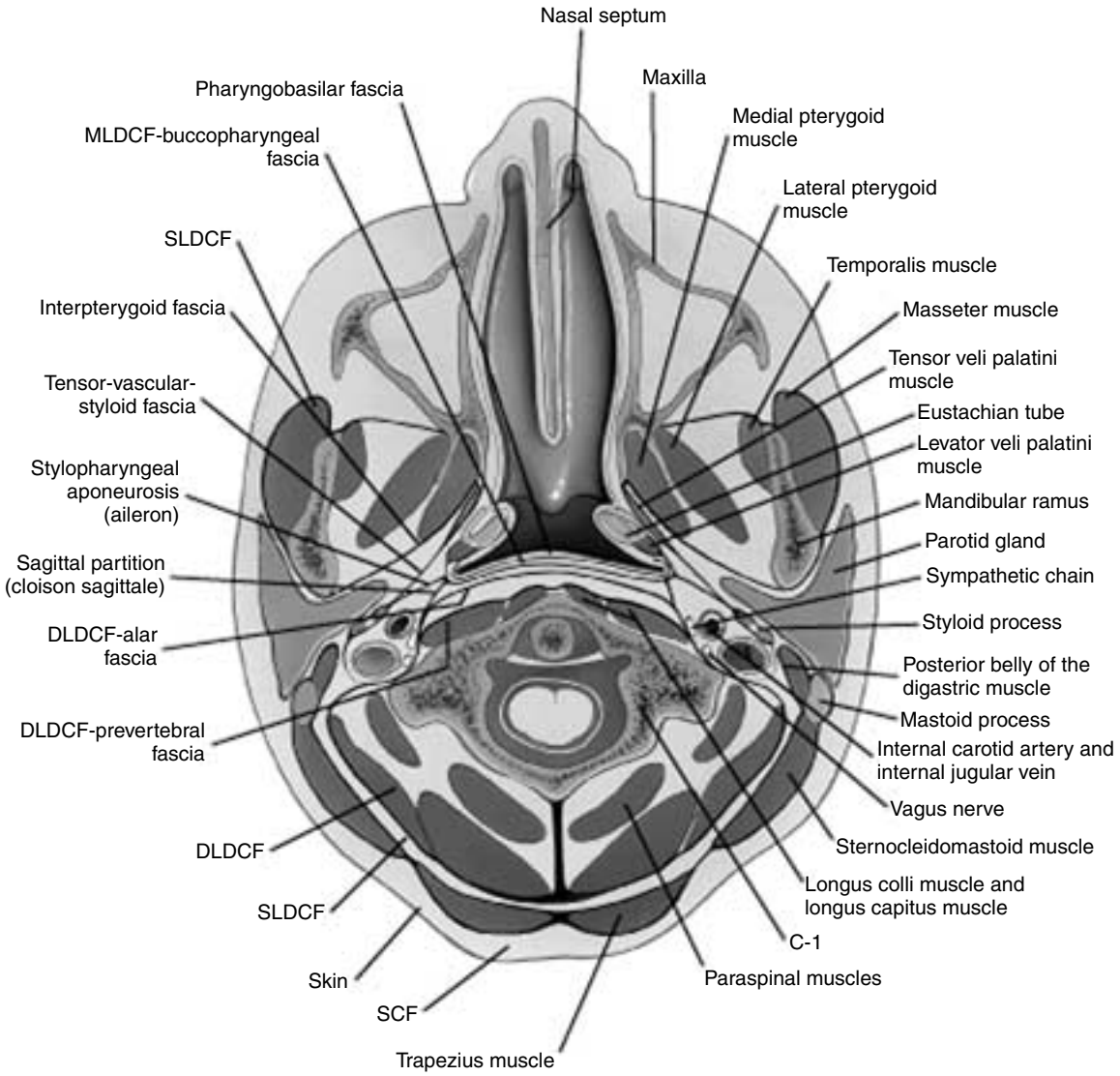

FIGURE 39-3 Diagram of the fascia at the level of C1. Note that the parotid gland is dorsal to the masticator space structures and that the deep portion of the parotid gland lies in the prestyloid compartment of the parapharyngeal space, anterior to the internal carotid artery.

VIEW IMAGE

Copyright © 2003, Mosby, Inc. All rights reserved.

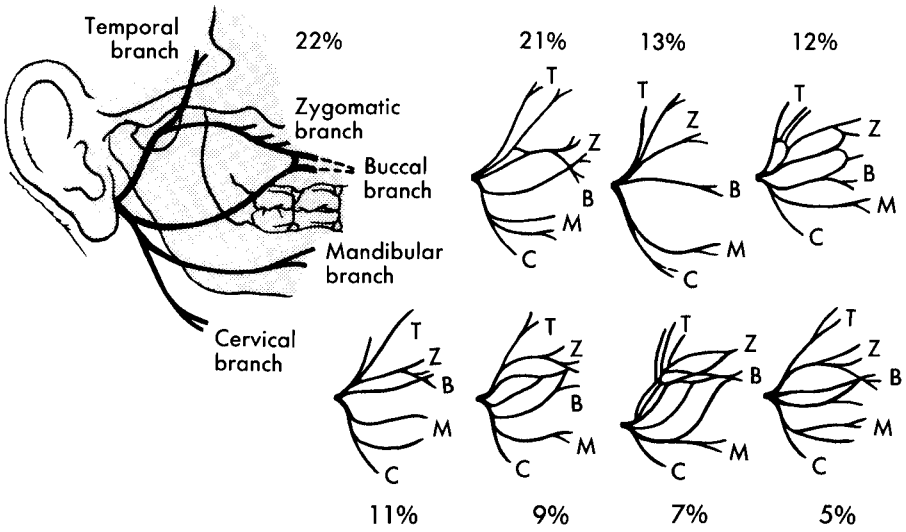

VIEW IMAGE

FIGURE 39-4 Variations of facial nerve branching in the parotid gland. (From Davis PA, Anson BJ, Budinger JM, et al. Surgical Anatomy of the Facial Nerve and Parotid Gland Based upon a Study of 350 Cervicofacial Halves. Surg Gynecol Obstet 1956;102: 385–412.)

and the terminal acini. In the adult, the parotid acini are purely serous; it is only in the neonatal period that some mucous cells are found.[8, 11] Sebaceous elements may be uncommonly found in the parotid gland and are thought to explain the sebaceous differentiation that may be seen in some salivary tumors. The parotid parenchyma has abundant adipose tissue, with a ratio of adipose to glandular tissue of 1:1. The parotid intercalated ducts are long and thin compared to the submandibular gland. The sublingual gland has the shortest and widest intercalated ducts. These variations in intercalated duct morphology may be related to the types of secretions in each of these glands.

Stensen's duct is about 7 cm long; after emerging from the anterior parotid gland, it courses over the masseter muscle and buccal fat pad, and then abruptly courses medially to pierce the buccinator muscle, forming a nearly 90° angle with this muscle. It then courses obliquely and inferiorly for a short distance between the buccinator muscle and the oral mucosa, terminating in a papilla of the buccal mucosa, opposite the second upper molar tooth (see Fig. 39-1). An accessory parotid duct may join Stensen's duct as the latter passes over the masseter muscle.[13]

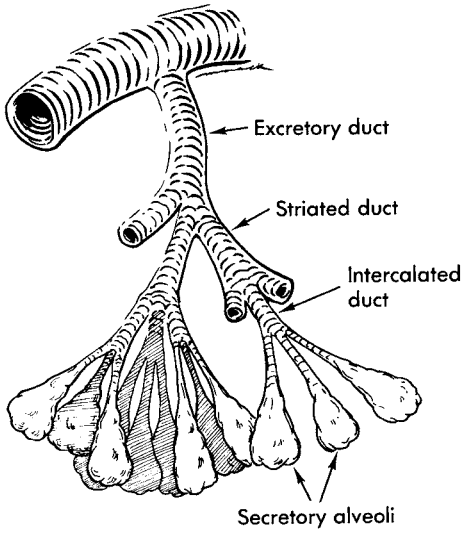

VIEW IMAGE

FIGURE 39-5 Diagram of the major salivary gland ductal system. (From Batsakis JG. Tumors of the Head and Neck: Clinical and Pathological Considerations. 2nd ed. Baltimore: Williams & Wilkins, 1979.)

Accessory parotid tissue is present in about 20% of the population, usually about 6 mm anterior to the main parotid gland, adjacent to Stensen's duct as it passes over the masseter muscle. This accessory tissue is usually cranial to Stensen's duct, with only one excretory duct entering Stensen's duct. There may be multiple accessory glands, each with its own primary drainage into Stensen's duct.

The parotid gland contains 3 to 32 (average, 20) intraglandular lymph nodes interconnected by a plexus of lymphatics that drain the ipsilateral upper and midfacial skin. The palatine tonsil also drains into the parotid lymph nodes. The parotid lymph nodes drain primarily into the internal jugular chain (level IIA) and also into the upper spinal accessory chain (level IIB).

The parotid is innervated from the sympathetic plexus on the carotid artery, while the parasympathetic parotid innervation is derived from the auriculotemporal nerve of the mandibular division of the trigeminal nerve via the glossopharyngeal nerve; parasympathetic fibers may also be contributed via the facial nerve through the otic ganglion. The sympathetic nerves regulate chiefly vasoconstriction, while the parasympathetic nerves regulate secretion.[13]

Proper surgical planning requires that the surgeon be informed as to whether a parotid mass is limited to the superficial gland or extends to the deep portion of the gland. If a parotid mass extends into the parapharyngeal space, its size is important, as such a mass will require one of several modifications of the standard surgical parotidectomy for successful extirpation without violation of the tumor capsule. The surgical modifications vary, depending on tumor size, from simple anterior dislocation of the temporomandibular joint (TMJ), to an angle mandibulotomy, to a midline mandibular split with dislocation of the TMJ. If the deep neck mass can be shown not to be of parotid gland origin, a lateral neck or submandibular approach is used.

Copyright © 2003, Mosby, Inc. All rights reserved.

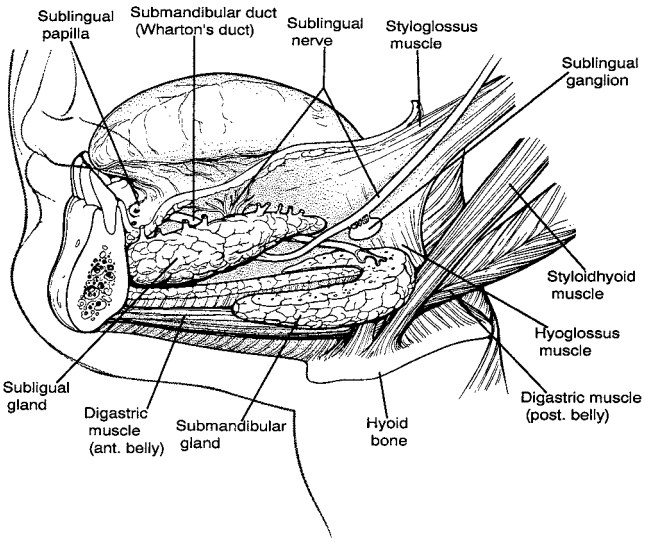

VIEW IMAGE

FIGURE 39-6 Drawing of a lateral view of the anatomy of the left submandibular and sublingual glands in the floor of the mouth. Note that the sublingual gland is lateral to Wharton's duct and that the submandibular gland wraps around the back edge of the mylohyoid muscle.

Thus it is important for the radiologist not only to map the lesion, but also to measure its size accurately.

Submandibular Gland

The submandibular gland is the second largest salivary gland, weighing between 10 and 15 g, or about one half the size of the parotid gland. It occupies most of the submandibular triangle of the neck; actually, the gland is folded around the dorsal free edge of the mylohyoid muscle. Despite the fact that there are no separate lobes to the gland, by convention it is also often referred to as being divided into superficial and deep lobes. The larger superficial lobe lies in the submandibular triangle superficial to the mylohyoid muscle. This portion of the gland is bounded anteriorly and inferiorly by the anterior belly of the digastric muscle, posteriorly by the posterior belly of the digastric and stylohyoid muscles, and laterally by the lower border of the mandible and the medial pterygoid muscle (Fig. 39-6). Posteriorly, it is separated from the parotid gland by the stylomandibular ligament. The floor or deep surface of the submandibular triangle is formed by the mylohyoid and hyoglossus muscles. The superficial portion of the submandibular gland is covered by the superficial layer of the deep cervical fascia, the platysma muscle, and the anterior facial vein, and the marginal mandibular nerve runs adjacent to the gland. The facial artery runs upward on the gland's posterior aspect, then turns downward and forward between the submandibular gland and the mandible. The anterior facial vein has been suggested as a useful imaging landmark to help determine if a mass arises within or adjacent to the submandibular gland. A lesion arising within the gland will never be separated from the gland by this vein. If the vein separates the mass and the gland, the lesion may have originated from submandibular lymph nodes (level IB) or the adjacent soft tissues.[14]

The deep portion of the submandibular gland lies deep (or cranial) to the mylohyoid muscle and contains the hilum of the gland. The lingual nerve and submandibular ganglion are superficial (lateral) to the submandibular gland, and the hypoglossal nerve with its accompanying vein lie deep to it. Wharton's duct is the main duct of the submandibular gland and is about 5 cm long, with thinner walls than Stensen's duct. The duct exits the gland anteriorly, occasionally making a sharp turn at the posterior edge of the mylohyoid muscle, and then extending anteriorly and superiorly, medial to the sublingual gland and lateral to the genioglossus muscle. Along this course, the duct is angled at approximately 45° to both the sagittal and axial planes. It terminates within the sublingual papilla in the anterior floor of the mouth. As the duct courses upward, the lingual nerve winds around it, first laterally, then inferiorly, and finally medially (Fig. 39-7).

Histologically, the submandibular gland is composed predominantly of serous acini (90%), with a mucinous acinar component (10%). Adipose tissue is not a significant component of the glandular parenchyma, as it is in the parotid. The arterial supply is derived from branches of the external maxillary and lingual arteries. Its sympathetic innervation comes from the carotid plexus, while its parasympathetic innervation is derived from the facial nerve and possibly the glossopharyngeal nerves via the chorda tympani nerve and the submandibular ganglion.[13] The glandular lymphatic drainage is into the submandibular nodes (level I).

Sublingual Gland

The sublingual gland is the smallest of the major salivary glands, about half the size of the submandibular gland, weighing only about 2 g, measuring about 2.5 cm, and shaped like a flattened almond (see Figs. 39-6 and 39-7). It

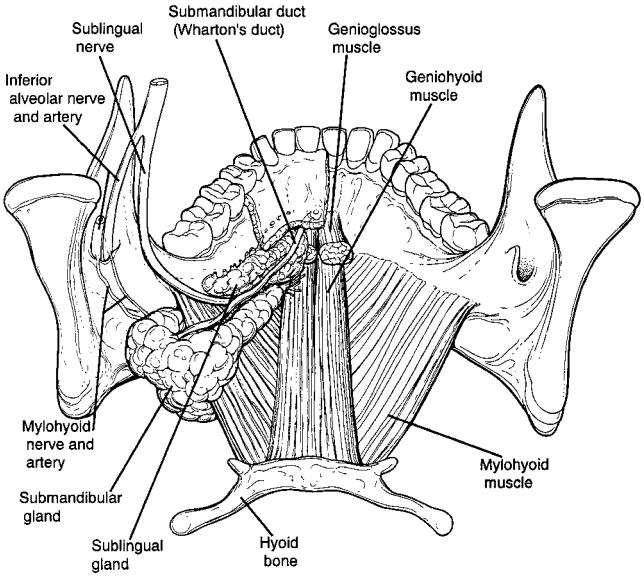

FIGURE 39-7 Drawing of a dissected view of the mandible seen from above and behind shows the muscles of the floor of the mouth, the sublingual and submandibular glands, and the branches of the lingual nerve. Note that in the floor of the mouth, the nerve and Wharton's duct lie medial to the sublingual gland and lateral to the genioglossus and geniohyoid muscles.

VIEW IMAGE

Copyright © 2003, Mosby, Inc. All rights reserved.

lies submucosally against the sublingual depression of the lingual mandibular surface, adjacent to the symphysis, and rests on the mylohyoid muscle. The lingual nerve and Wharton's duct separate the medial sublingual gland contour from the genioglossus muscle. There is no well-defined capsule, and histologically the gland is composed entirely of mucinous acini. There are about 20 individual small ducts (the ducts of Rivinus), most of which open independently into the floor of the mouth along the sublingual papilla and fold. Occasionally some of these ducts fuse to form Bartholin's duct, which in turn opens into Wharton's duct.[11, 13] The sublingual innervation is identical to that of the submandibular gland. The gland's lymph drains into the submental and submandibular lymph nodes (level I).

Minor Salivary Glands

The minor salivary glands (MSG) lie within the submucosa of the oral cavity, palate, paranasal sinuses, pharynx, larynx, trachea, and bronchi. They are particularly concentrated in the buccal, labial, palatal, and lingual regions. The gingivae, anterior hard palate, and true vocal cords have relatively sparse concentrations of MSG. The concentration of MSG within the nasal cavity has been estimated at 7 to 10 glands /mm^2, which is less than that of the palate but greater than that of the paranasal sinuses.[15] Histologically, the MSG acini are either entirely mucinous (e.g., hard palate) or mixed seromucous glands (e.g., sinonasal, oral). The acinar clusters lead to intercalated ducts, striated ducts, and excretory ducts that terminate as mucosal pores. The autonomic secretory function of the upper aerodigestive tract MSG is controlled by the following ganglia: the sphenopalatine (pterygopalatine) ganglia, located near the sphenopalatine foramina of the medial pterygopalatine fossae, innervate the paranasal sinuses, nasal cavity, portions of the palate, and the uppermost pharynx; the otic ganglia, located along the medial aspect of the mandibular nerves below the skull base, innervate the buccal mucosa; the submandibular ganglia, adjacent to the submandibular gland hili at the posterior border of the mylohyoid muscle and the lingual nerve, innervate the floor of the mouth and the anterior tongue; and finally, the pharyngeal plexus innervates the pharynx.[16, 17]

Developmental Anomalies

Developmental salivary gland aplasia, atresia, or agenesis are rare occurrences usually associated with other facial abnormalities (Fig. 39-8). They may be either unilateral or bilateral, and these anomalies of the salivary glands are associated with xerostomia, sialoadenitis, and dental caries. Parotid gland agenesis has been reported with hemifacial microstomia, mandibulofacial dysostosis, cleft palate, and anophthalmia. Agenesis of the parotid duct has been reported, and unilateral aplasia of the parotid gland can occur.[18] Atresia of one or more major salivary gland ducts is very rare. This condition usually occurs in the sublingual and submandibular ducts and may be associated with a cyst.[11, 19] Congenitally imperforate submandibular ducts and duplications of the submandibular gland and duct have also been reported.[20]

FIGURE 39-8 Axial contrast-enhanced CT scan shows a normal left parotid gland (*arrow*). In the right parotid bed, there is only fat and some interstitial stranding. This patient had a congenital absence of the right parotid gland. Incidentally noted is a retention cyst in the right maxillary sinus.

VIEW IMAGE

Hypoplasia of the parotid gland has been reported in the Melkersson-Rosenthal syndrome: an episodic condition of unknown etiology characterized by the triad of orofacial swelling, facial nerve palsy, and lingual plicata (furrowed tongue). Congenital fistulas of the parotid ductal system have been associated with branchial cleft abnormalities, accessory parotid ducts, and diverticula.[11]

A salivary choristoma is ectopic, histologically mature salivary tissue at abnormal sites. Such heterotopic salivary tissue has been reported in a large number of locations including the middle ear cleft associated with ossicular abnormalities, the external auditory canal, the lower neck near the sternoclavicular joints, the upper neck, the hypopharynx, the inner posterior mandible (Stafne cyst), the anterior mandible, the thyroglossal duct, the pituitary (pars nervosa), and the cerebellopontine angle.[7, 11, 21]

Congenital intraglandular cysts occur in a variety of forms and are discussed in the section on ''Congenital Cysts'' later in this chapter. Accessory salivary gland tissue is uncommon and usually occurs in relationship to the parotid gland. A congenital fistula to the cheek from an ectopic accessory parotid gland located lateral to the masseter muscle was demonstrated by CT sialography and CT fistulography.[22]

With regard to salivary abnormalities associated with syndromes or generalized diseases, in the familial form of amyloidosis (an autosomal dominant condition with high penetrance) there is an association with Sjogren's syndrome. Cystic fibrosis (an autosomal recessive disease mapped to chromosome 7, q21–31) is associated with pneumoparotitis

Copyright © 2003, Mosby, Inc. All rights reserved.

and sialolithiasis. The lacrimo-auriculo-dento-digital syndrome (autosomal dominant) is a rare malformation complex consisting of lacrimal, aural, digital, and dental anomalies and is also associated with salivary gland hypoplasia.[23, 24] The hypoglossia-hypodactylia syndrome (sporadic, no sex predilection) is a complex of variable tongue hypoplasia, micrognathia, and abnormalities of the upper extremities. It can be associated with sublingual and submandibular glandular hypertrophy. The spectrum of oculo-auriculo-vertebral abnormalities includes Goldenhar syndrome, Goldenhar-Gorlin syndrome, facio-auriculo-vertebral sequence, hemifacial microsomia, first and second arch syndrome, lateral facial dysplasia, and unilateral craniofacial microsomia. These syndromes are usually sporadic but occasionally are transmitted in an autosomal dominant fashion. They are associated with parotid aplasia and ectopic salivary gland tissue. The Treacher Collins (TCS) syndrome is an autosomal dominant disorder with an incidence of approximately 1 in 50,000 live births that is caused by mutations in the *TCOF1* gene mapped to chromosome 5q32–33.1. TCS is characterized by bilaterally symmetric midfacial hypoplasia, downward-slanting palpebral fissures, cleft palate, colobomata of the lower lids, microtia, and other ear deformities often leading to conductive hearing loss. Parotid aplasia can be associated with TCS.[25]

Physiology

Salivation is physiologically controlled almost entirely by the autonomic nervous system. Either parasympathetic or sympathetic stimulation will produce secretions; parotid or submandibular secretions probably never occur without autonomic input. Parasympathetic stimulation predominates, and parasympathetic denervation results in glandular atrophy. Conversely, sympathetic denervation causes little, if any, effect.[26]

Normal saliva is composed predominantly of water (99.5%) with a specific gravity of 1.002 to 1.012. Between 1 and 1.5 liters of saliva are produced daily, usually during meals. The parotids contribute about 45% (450 to 675 ml) of the total secretions, the submandibular glands about 45% (450 to 675 ml), the sublingual glands 5% (50 to 75 ml), and the minor salivary glands 5% (50 to 75 ml).[27] The basal secretory rate is low (parotid gland = 0.04/ml/minute/gland and submandibular gland = 0.05ml/minute/gland). During sleep, the flow rate is virtually nil.

Saliva is formed in the acini (Fig. 39-9). The secretion of electrolytes into saliva is under parasympathetic control via acinar cholinergic receptors. Their stimulation activates cytoplasmic guanylate cyclase and the conversion of GTP to GMP, necessary for the transport of sodium. Sodium enters along the basal cell membrane following an electrochemical gradient, which is the result of acetylcholine-induced enhanced permeability of the basal cell membrane to potassium and sodium. The result of this process is the formation of an isotonic, high-sodium, low-potassium fluid. The saliva becomes hypotonic as sodium is reabsorbed and potassium is excreted in the striated ducts, which are histologically, ultrastructurally, and functionally similar to the renal distal convoluted tubules. This sodium reabsorption is influenced by aldosterone.[11, 28]

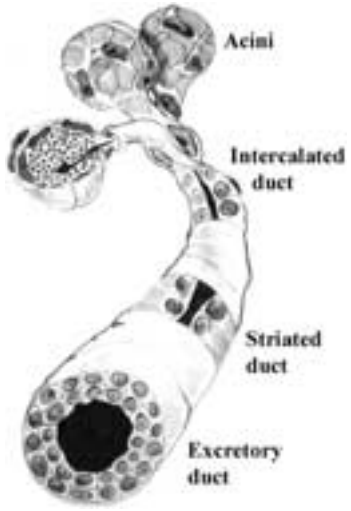

FIGURE 39-9 Schematic representation of the ducto-acinar salivary apparatus.

VIEW IMAGE

Saliva is multifunctional: it protects mucosa from the harmful effects of microbial toxins, noxious stimuli, and minor trauma. The salivary mucins are glycoproteins, which act as lubricants. Although the minor salivary and sublingual glands produce 10% of the total saliva volume, they secrete the majority the of mucinous components of saliva, and functional compromise of these glands (e.g., by autoimmune disease or irradiation) results in xerostomia.[11, 27] The antibacterial activity of saliva is accomplished by secretory IgA, plus enzymes such as lysozyme, peroxidase, alpha-amylase, and lactoferrin and ions such as thiocyanate and hydrogen. Normal salivary pH ranges from 5.6 to 7.0 (average, 6.7).[11, 27] The pH varies directly with the blood pH (CO_2 content).[25]

IMAGING

An Overall Imaging Approach

Salivary imaging has shifted from predominantly utilizing plain films and sialograms to nearly complete reliance upon computed tomography (CT), magnetic resonance (MR) imaging, and ultrasound. After two decades of debate, some consensus has been achieved regarding recommendations as to which imaging modality is indicated for a specific clinical situation. CT is the modality of choice for patients with a clinical history and findings suggestive of inflammatory disease, such as acute, painful, diffuse parotid or submandibular swelling. Similarly, recurrent, subacute episodes of mildly painful and tender parotid or submandibular swelling indicate an inflammatory related process, either infectious or noninfectious. As the imaging identification of calcifications (sialoliths) is important in the diagnosis of these inflammatory processes, either CT or ultrasound is the preferred modality.[29–35]

MR imaging is the primary modality of choice when a mass is palpated, whether or not it is tender, solitary or

Copyright © 2003, Mosby, Inc. All rights reserved.

multiple, or discrete or diffuse.[20, 36–50] Although MR imaging best delineates the morphology of the mass, CT can be an acceptable alternative; ultrasound is generally utilized as a complementary study. It should be noted that some clinicians and radiologists believe that children and adolescents with inflammatory and superficially located disease should be approached primarily by ultrasound, while MR imaging should be utilized for deeply positioned masses.[29]

When imaging minor salivary gland tumors, either CT with contrast or MR imaging (usually with contrast) is recommended as the initial examination. Imaging of these lesions is discussed in the chapters on the sinonasal cavities, oral cavity, pharynx, and larynx (respectively Chapters 6, 27, 28, and 30).

With CT, major salivary gland tumors require intravenous contrast agents, whenever possible, to enhance tumor conspicuity. However, the use of contrast agents with MR imaging below the skull base is less well established, as contrast may enhance tumor visualization for some cases and obfuscate lesion conspicuity in others. For the majority of such MR imaging studies, the addition of contrast yields little diagnostic information. In addition, most radiologists use fat suppression pulses to improve lesion conspicuity. However, this may also add artifact to the images. The additional required examination time, the added cost of the contrast agent, and the relatively low positive yield has led many radiologists not to employ contrast routinely. A notable exception to this is the detection of perineural tumor spread, as contrast-enhanced MR imaging is more sensitive than contrast-enhanced CT.[48] Sectional imaging with contrast-enhanced MR imaging is indicated, for instance, for patients with the diagnosis of adenoid cystic carcinoma of the parotid gland. The topic of perineural tumor spread is discussed in Chapter 13.

Plain Films

Plain films are rarely used today for the imaging evaluation of the major salivary glands. They are best for grossly detecting radiopaque sialolithiasis, dystrophic calcifications, or adjacent mandibular bone and dental disease. Although plain film studies can be obtained quickly and relatively inexpensively, they are of limited clinical value since they only identify moderately large, fairly dense calcifications (Figs. 39-10 and 39-11). Thus, a negative plain film may miss a clinically significant small sialolith or soft-tissue calcification that is easily identified by either ultrasound or CT. In fact, CT has about a 10-fold increased sensitivity compared to plain films for detecting soft-tissue calcifications, and one of the primary strengths of ultrasound is its ability to identify small, solid soft-tissue densities.

Even if calcifications are identified on plain films, further imaging is indicated to detect other possible and clinically important calcifications, findings that can potentially alter the treatment plan. For instance, a sialolith may be localized to a subsegment of the gland or a contralateral sialolith may be identified. Thus, either noncontrast CT or ultrasound is the current standard for investigation of soft-tissue calcifications. If plain films are to be obtained for the parotid region, the survey examination should consist of an extended-chin, open-mouth lateral film with both posteroanterior views (with or without the cheeks blown out for detection of Stensen's duct stones or other calcifications) and oblique views (Fig. 39-10).

For the submandibular gland, an extended-chin, open-mouth lateral view with the patient's finger depressing the tongue, an intraoral occlusal film, and oblique views are routinely obtained (Fig. 39-11). Fluoroscopy may also help the radiologist to detect a small calculus by allowing visualization of the stone's motion and/or by providing a means to optimize the patient's position in order to demonstrate the calculus.[51]

Sialography

Sialography is rarely employed today due to the continual improvements in CT and MR imaging, as well as changes in the clinical management of major salivary gland nonneoplastic disease. Sialography is an imaging examination that uses a positive contrast medium to demonstrate radiographically the ductal anatomy of either the parotid gland or the submandibular gland. This examination remains the only imaging study for examining the fine anatomy of the salivary ductal system. The sublingual and MSG are not studied by this technique, as MSG cannot be cannulated and the sublingual gland ducts can rarely be cannulated.

On routine CT and MR imaging, gross pathologic ductal dilatation or stenosis can be imaged, but small to moderate degrees of functional and anatomic alteration cannot be

FIGURE 39-10 Frontal plain film of the parotid gland shows multiple calculi in a patient with chronic sialadenitis.

VIEW IMAGE

Copyright © 2003, Mosby, Inc. All rights reserved.

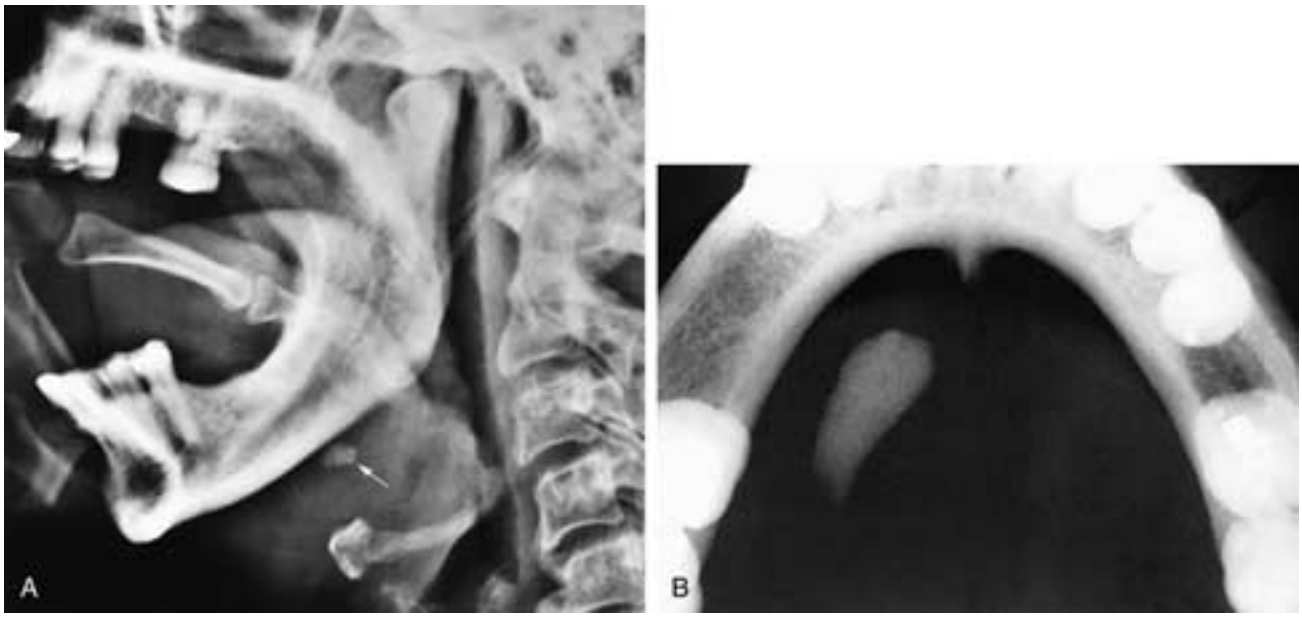

VIEW IMAGE

FIGURE 39-11 Lateral plain film (**A**) with the patient's index finger depressing the tongue demonstrates a submandibular gland calculus (*arrow*) that was hidden by the mandible on a routine lateral film. Intraoral occlusal film (**B**) shows a large calculus in Wharton's duct. Stones in this location may go unobserved on plain film studies if an intraoral occlusal film is not used.

seen. Because the quality of MR sialography continues to improve (see the section on MR Sialography), in the few remaining clinical situations that require analysis of ductal morphology, many of these patients can be sufficiently studied by MR sialography (which allows visualization of Stensen's or Wharton's ducts and the major and secondary intraglandular ducts). If even finer detail is needed, a situation rarely necessary for clinical decision making, sialography remains the examination of choice.

In the past, sialography was important in differentiating between certain cases of subacute and chronic sialoadenitis, autoimmune disease and sialosis, as neither the clinical presentation nor conventional sectional imaging can confidently distinguish among these entities.[52, 53] However, serology (general autoimmune antibodies, plus those specific for Sjogren's sydrome: SS-A and SS-B) now aids in the diagnosis of autoimmune sialoadenitis. In addition, improved understanding of the pathophysiology of these diseases and advances in surgical techniques have limited the need for conventional sialography despite its diagnostic specificity.

Sialography is an invasive procedure in which radiopaque contrast material is injected retrograde into the gland's ductal system via the intraoral opening of either Wharton's or Stensen's duct. The procedure is contraindicated for clinically active infection, as it will often spread the infection retrograde into the gland. Additionally, as acute sialoadenitis is already painful, the patient will not tolerate the additional discomfort of the retrograde pressure injection required for an adequate sialogram; thus a technically adequate study is usually not feasible.

In the event that a patient is recovering from a recent acute sialoadenitis, although the gland may have returned to an apparently normal clinical state, a sialogram can reactivate a clinically quiescent infection. Prophylactic administration of oral antibiotics after a sialogram is indicated in such cases to avoid reinfection. A sialogram is also contraindicated for patient with a history of allergic sensitivity to iodine compounds (contrast materials).

Indications to perform a sialogram include (1) the detection or confirmation of small parotid or submandibular gland sialoliths or foreign bodies (either calcified or noncalcified); (2) the evaluation of the extent of irreversible ductal damage present as a result of infection; (3) the differentiation of diseases such as chronic sialoadenitis, Sjogren's syndrome, and sialosis; (4) the evaluation of fistulas, strictures, diverticula, communicating cysts, and ductal trauma; and (5), rarely, as a dilating procedure for mild ductal stenosis.[54]

The original sialographic contrast agents, such as Lipiodol or Pantopaque, were lipid soluble and viscid, had high iodine concentrations, and produced sharp boundaries with the salivary secretions. These agents, however, were reported to cause foreign body reactions following ductal perforation during sialography. When water-soluble agents became available, they did not initially have as high an iodine content, they were too watery to remain within the ductal system long enough to produce a good study, and their boundary with saliva was unsharp. When Ethiodol was introduced, it became the agent of choice because it had all the benefits of the lipid-soluble media and a very low reported incidence of foreign body reactions. The few reported reactions secondary to Ethiodol were autopsy studies of subclinical reactions.[55]

Recently, the water-soluble agents have been further improved, but they remain generally less viscid and more miscible with saliva than the fat-soluble agents. Water-soluble Sinografin has an iodine content (38%) similar to that of Ethiodol (37%) and its viscosity facilitates injection, but it is not so watery as to empty rapidly from the main

Copyright © 2003, Mosby, Inc. All rights reserved.

ductal system. Additionally, there have been no reported foreign body reactions subsequent to perforation. If the sialographic radiographs are taken quickly, before Sinografin mixes with saliva, the study demonstrates clear, sharp ductal anatomy, equivalent to that seen on an Ethiodol study. Therefore, water-soluble agents such as Sinografin have replaced the fat-soluble agents as the sialographic contrast materials of choice.

The equipment used to perform a sialogram varies with the examiner's preferences. However, a general list includes the following:

1. Sialographic cannulas. The most commonly employed are the Rabinov-type cannulas with tips ranging from 0.012 to 0.033 inch (Fig. 39-12).[56] Variations such as the Manashil modification of the Rabinov cannula and cannulas designed by Lowman and Belleza are also commercially available. Modifications of butterfly needles also can be used for parotid cannulazations.[57] In general, the larger-diameter cannulas are used for the parotid gland and the smaller ones for the submandibular gland. Although cannulas without a polyethylene connecting tube can be used, if such a flexible connecting tube is employed, the examiner can work outside of the patient's mouth and therefore have greater mobility during the procedure.
2. A set of lacrimal dilators ranging from 0000 through 0 caliber.
3. A 5-ml or 10-ml syringe.
4. 4 × 4 inch gauze sponge pads.
5. Sinografin (or an equivalent contrast agent).
6. Secretogogue such as fresh lemon, lemon extract, or lemon concentrate.
7. Adequately focused lighting, usually a head-light unit.
8. High-powered magnifying glasses.

Once the salivary duct is cannulated, the injection is usually made with hand pressure.[55] The patient may complain of local pressure or mild pain during the injection; however, a slow, constant injection technique usually can accomplish complete ductal filling without much patient discomfort. This can be done when monitored by fluoroscopy. The patient's sensation of glandular fullness and pressure usually abates within minutes after the study. The patient should be alerted that there should be no residual discomfort by 24 hours after the examination. If local pain increases and becomes more intense 24 to 36 hours after the study, a postsialogram infection is probably present and antibiotic therapy should be started immediately.

FIGURE 39-12 Examples of some of the sialography catheters and needles commonly used. They are available with end holes, side holes, or both.

VIEW IMAGE

Parotid Gland Study

The intraoral opening of Stensen's duct is opposite the second upper molar tooth. In some patients this opening is easily seen; however, in others, it may be very difficult to identify, especially in individuals who have a dry, obstructed gland or a mucosal bite ridge across the region. After drying of the mucosa with gauze, milking of the gland and Stensen's duct may produce a drop of saliva that allows identification of the duct opening. In this regard, the use of a secretogogue (lemon) may also be helpful. Once the opening is identified, the dilators can be used to widen the opening for easier cannula placement. Slight abduction of the cheek with the thumb and index finger often provides better exposure and a better angle for cannula insertion. The cannula is then gently inserted and 0.5 to 1.5 ml of contrast material is slowly injected. The injection is often best made under fluoroscopic control so that optimal ductal filling without excessive acinar filling can be achieved. Optimal gland positioning can also be achieved, and spot filming is best used to document the examination.

Stensen's duct is approximately 6–7 cm long and has a small C-shaped curve anteriorly as it bends around the buccal fat pad and pierces the buccinator muscle to open opposite the second upper molar tooth. The duct's normal luminal caliber is only 1 to 2 mm, and on a direct conventional posteroanterior film, the duct should lie within 15 to 18 mm of the lateral mandibular cortex (Figs. 39-13 and 39-14). If the duct is more laterally placed, there is either hypertrophy of the masseter muscle or a mass in or near the masseter muscle (better seen on CT or MR imaging).

There is no specific parotid ductal branching pattern, and variation is noted from side to side within the same person as well as among different individuals.[58, 59] Usually there are main upper and lower hilar-intraglandular ducts, and it is from these that the glandular arborization pattern takes form. The overall appearance is that of a leafless tree, and no area of the gland should be devoid of peripheral ducts. As the ducts arch behind the ramus of the mandible, they may appear slightly stretched on frontal films. This appearance should not be confused with a mass lesion; on lateral films, no mass effect will be seen (Figs. 39-13 and 39-14). Normally, the ducts do not lie parallel to one another in any plane. If this appearance is seen, it usually indicates that a mass is present displacing some of the ducts away from their normal arborization configuration and causing them to appear parallel to one another.

Acinar filling can be accomplished in most patients and is a normal effect of slight overfilling of the ductal system.[59] It can be a useful technique to help identify small masses;

Copyright © 2003, Mosby, Inc. All rights reserved.

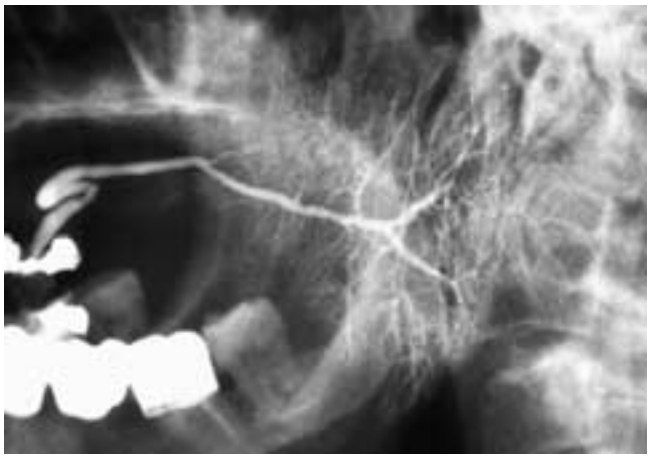

VIEW IMAGE

FIGURE 39-13 Lateral view of a normal parotid sialogram. Anteriorly, Stensen's duct enters the mouth by piercing the buccinator muscle near the second upper molar tooth; then the duct bends around the buccal fat pad and overlies the masseter muscle. Within the gland there is a ductal ''arborization'' pattern, with no area of the gland devoid of ducts.

however, the acinar filling should be carefully limited so that it does not obscure the ductal anatomy (Fig. 39-15).

The evacuation film should reveal complete, rapid ductal emptying. In some patients, more complete evacuation can be achieved if a secretogogue is given. Any delayed ductal emptying or trapping of the contrast material indicates the presence of a functional obstruction.[60] By comparison, if

VIEW IMAGE

FIGURE 39-14 Frontal view of a normal parotid sialogram. The hilum of the gland (*arrow*) is within 15 to18 mm of the lateral cortex of the mandible on a standard 40-inch TSD film. The posterior deep ducts often appear stretched or splayed as they arch behind the mandible. A lateral view, however, will show no splaying, confirming that no mass is present.

FIGURE 39-15 Lateral view of a normal parotid sialogram showing acinar filling throughout the gland, with many of the major ducts still being clearly identified. This technique made it easier to identify a mass by noting the abscence of acinarization at the site of the mass.

VIEW IMAGE

any acinar filling occurred during the sialogram, the water-soluble contrast will remain until its absorption occurs. Thus the presence of a persistent (usually less than 1 hour) acinar ''stain'' does not indicate the presence of an obstruction.

Multiple or solitary accessory parotid glands may be present and are usually situated above Stensen's duct, anterior to the main parotid gland.[60] These accessory glands are routinely filled in a retrograde manner as the contrast material courses through Stensen's duct. These accessory glands have a normal branching ductal pattern similar to that seen within the main parotid gland.

Submandibular Gland Study

The orifice of Wharton's duct lies in the floor of the mouth on or near the sublingual papilla. The opening is smaller than that of Stensen's duct, and thus it is usually more difficult to cannulate than is Stensen's duct. To best visualize the orifice of Wharton's duct, the area should be dried with gauze and the tongue pushed upward and backward to put some tension on the papilla. Milking the gland or using a secretogogue can aid in identifying the orifice by producing a drop of saliva.[37] Once the duct is cannulated, care must be taken to advance the cannula gently because painless perforation into the floor of the mouth can easily occur. Only 0.2 to 0.5 ml of contrast material should be injected. This volume reflects the facts that the submandibular gland is smaller than the parotid gland and that the ductal walls of the submandibular gland are more easily perforated than are those of the parotid gland. If

Copyright © 2003, Mosby, Inc. All rights reserved.

extensive perforation or acinarization occurs due to administration of too much contrast material, ductal detail can be completely obscured, rendering the examination virtually useless. Care must be taken not to obscure the ductal anatomy (Fig. 39-16).

Wharton's duct is seen to run downward and laterally at about a 45° angle to both the sagittal and horizontal planes.[60, 61] It is about 5 cm long and has a luminal caliber of 1 to 3 mm. Just before the duct enters the submandibular gland, it may curve caudally over the back edge of the mylohyoid muscle. The intraglandular ducts are shorter and taper more abruptly than those in the parotid gland (Fig. 39-16).

Occasionally, Bartholin's duct will be filled, extending from Wharton's duct (Fig. 39-16). In some cases the sublingual gland may be visualized, resembling an accessory gland with a normal branching ductal pattern. The most common causes of sialogram failure or of a poor sialogram are (1) failure to locate and cannulate the salivary duct, (2) perforation of the duct into either the cheek or the floor of the mouth, (3) suboptimal filling of the ductal system so that areas of the gland are not visualized, and (4) complete acinarization of the gland so that all ductal detail is obscured. The last problem is especially prone to occur in the submandibular gland and can best be avoided by fluoroscopically monitoring the injection volume.

If there has been previous surgery in the floor of the mouth, the scarring and altered anatomy probably account for more failures to cannulate Wharton's duct than any other single reason. A ''dry'' duct may be caused by prior surgery, scarring, irradiation, or obstruction by either a stone or a tumor, and the absence of saliva is the major cause of failure to identify the openings of either Stensen's or Wharton's duct.[60]

Computed Sectional Imaging

General Considerations

The inability of MR imaging to visualize small, potentially clinically significant calcifications detracts from its usefulness in imaging suspected inflammatory diseases. However, the final choice between CT and MR imaging may depend on the clinical presentation of the case and the expected differential diagnosis. Quite often the preferred examination is recognized only in retrospect.

In general, CT is the examination of choice for inflammatory related diseases. The study can identify the presence and number of sialoliths, differentiate between cellulitis and cellulitis with an abscess, map the extension of disease, and differentiate between clinically confused parotid and masticator space disease. CT can also distinguish between submandibular gland sialadenitis and adjacent reactive lymphadenitis.

If a mass is palpated, CT and MR imaging can confirm the presence of a clinically palpable mass or identify the presence of a clinically silent mass either in the same gland or in the opposite gland; map the location of a lesion within the gland and, in the case of the parotid gland, identify its position relative to the facial nerve; determine whether the mass has smooth or infiltrating margins; show if the mass is solid or cystic; and demonstrate if the mass is confined to the gland or if it has extended outside the gland capsule into the

FIGURE 39-16 Lateral view (**A**) and frontal view (**B**) of a normal submandibular sialogram demonstrates some acinar filling with shorter, more tapered ducts than those seen in the parotid gland. The bend in the course of Wharton's duct is at the point at which this duct arches around the dorsal free edge of the myohyoid muscle. There is also partial filling of a Bartholin's duct (*arrow*). In **B**, the usual 45° downward and outward angulation of Wharton's duct is seen.

VIEW IMAGE

Copyright © 2003, Mosby, Inc. All rights reserved.

upper neck and skull base. In general, a salivary mass is better seen on MR imaging than on CT, and in most cases MR imaging is the preferred modality when a mass is palpated or clinically suspected. Thus, each modality offers some benefits over the other.

CT has a reported overall sensitivity that approaches 100% in the detection of salivary tumors.[62] Since the literature also suggests that MR imaging is even more sensitive than CT in identifying such a mass, it is evident that either modality is excellent for localizing and mapping a clinically evident or occult lesion. When these nearly perfect figures are compared to the 85% sensitivity of sialography (even in the hands of an experienced sialographer) in detecting a salivary tumor, it is clear why CT and MR imaging have replaced sialography as the modalities of choice.[63–65]

The distinction between benign and malignant lesions frequently cannot be made on the basis of the morphology, as demonstrated by sectional imaging. However, by utilizing the radiologic and clinical findings, this distinction can be made in almost 90% of the cases.[40] The difficulties on sectional imaging arise because most benign salivary lesions (i.e., cysts, nodes, and tumors) have a capsule, and thus are smoothly contoured and sharply delineated from the adjacent salivary tissues. However, some of the most common low-grade malignancies (i.e., low-grade mucoepidermoid carcinomas, acinic cell carcinomas, and some adenoid cystic carcinomas) develop pseudocapsules that cause them to appear on sectional imaging as smoothly outlined, benign-appearing lesions.

By comparison, high-grade malignancies (i.e., high-grade mucoepidermoid carcinomas, adenocarcinomas, undifferentiated carcinomas, and squamous cell carcinomas) have irregular, infiltrating, indistinct margins with the adjacent salivary tissue. However, rarely, a benign mass is surrounded by inflammation and/or hemorrhage (possibly from vigorous palpation) that can present an aggressive appearance on sectional imaging.

Sectional imaging of a tumor's architecture also does not allow for a confident distinction between benign and malignant salivary tumors. However, on MR imaging, highly cellular tumors (usually high-grade malignancies) tend to have low to intermediate signal intensities on all imaging sequences, while the less cellular, better-differentiated masses (benign tumors and low-grade malignancies) tend to have low T1-weighted and high T2-weighted signal intensities. These signal intensities reflect the fact that the benign tumors and low-grade malignancies are sufficiently differentiated to produce secretory serous and mucous products, and these secretions have a high water content. In addition, there is a fairly high cytoplasmic/nuclear ratio so that there is a relatively high intracellular water content. As a result, these tumors have MR signal intensities that reflect this water.

On the other hand, the high-grade, aggressive tumors are poorly differentiated, are very cellular with a high nuclear/cytoplasmic ratio, and have little tendency to produce secretory products. These factors yield a net low water content, which is reflected in the lower T2-weighted signal intensities of these lesions.[66] However, such a relatively low T2-weighted signal intensity is not specific for an aggressive tumor, and other lesions including fibrosis, granulomas, and, rarely, some benign tumors can have similar signal intensities (Fig. 39-17). Thus, a lower T2-weighted signal intensity should only serve to alert the radiologist to the possibility that a high-grade malignancy may be present.

Clinically, benign tumors tend to be slow growing, painless, nontender, mobile, and firm but not rock hard. Facial nerve paralysis usually does not occur. Benign cysts usually develop rapidly over several days and are nontender unless infected, in which case they are tender and painful. These cysts are moderately firm to palpation, and patients often have a history of prior recurrent clinical episodes. By comparison, malignant tumors tend to enlarge fairly rapidly over several weeks or months, and they are either not painful (more insidious growth) or are slightly painful and minimally tender. In general, the faster these malignancies grow, the more symptomatic they are. When palpated, these malignancies are usually rock hard, and they may be fixed in position. There may be an associated facial nerve paralysis. In fact, the overall incidence of facial nerve paralysis with a parotid malignancy is 12% to 14%.[26] Often, such high-grade tumors are estimated to be larger on palpation than they are seen to be on CT and MR imaging. This discrepancy is the result of the presence of a zone of early microscopic infiltration extending from the mass into the adjacent tissues.

CT and MR Imaging

Parotid Gland: CT

In the adult, the parotid gland normally is a relatively fatty structure with numerous thin interstitial strands interlacing throughout it, as well as through the branches of the facial nerve and the ductal system. The gland produces serous secretions. The resulting usual CT attenuation of the gland (15 to 25 HU) is lower than that of muscle but greater than that of fat.[62] In children and some adults, a clinically normal parotid gland can have an attenuation similar to that of muscle. Presumably, such a CT appearance reflects a lower glandular fat content and is of no clinical significance. However, in such a ''dense'' gland it is more difficult to identify a small mass. Additionally, CT does not allow for the distinction between a dense normal gland and one that has been infiltrated with cells due to a variety of causes.

The fine anatomy of the intraglandular ducts is not normally visualized on CT, and Stensen's duct is seen only if abnormally dilated. The external carotid artery and the posterior facial (retromandibular) vein are seen situated posterior to the ramus of the mandible (Fig. 39-18). The vein extends caudally to drain into the external jugular vein, while the external carotid artery courses superiorly to become the superficial temporal artery. Some variable but normal glandular lobulations can also be seen primarily in relationship to the sternocleidomastoid muscle and the mastoid tip.

On axial CT scans, an area of high attenuation is routinely visualized near the caudal root or the attachment of the pinna of the ear. This musculotendinous region may mimic a small mass in the upper pole of the parotid gland; however, coronal images and clinical correlation almost always resolve any such imaging question.

The facial nerve normally cannot be seen on CT scans. However, the course of the nerve can be traced on the scans. The nerve exits the skull base via the stylomastoid foramen,

Copyright © 2003, Mosby, Inc. All rights reserved.

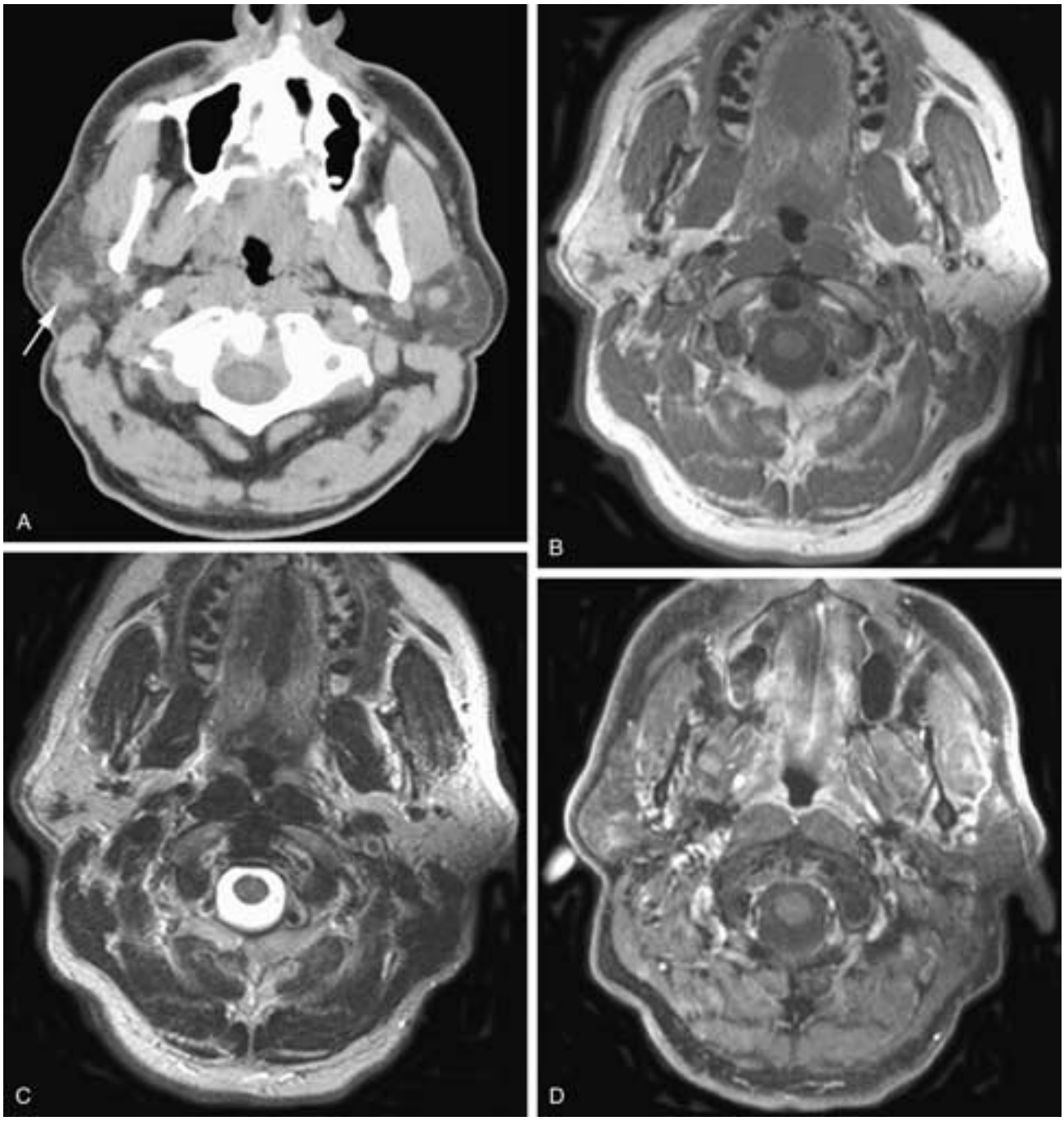

VIEW IMAGE

FIGURE 39-17 Axial CT scan (**A**) shows an irregular soft-tissue mass in the right parotid gland (*arrow*). Axial T1-weighted (**B**), T2-weighted (**C**), and T1-weighted, fat-suppressed, contrast-enhanced (**D**) MR images show the mass to have low signal intensity on the T1- and T2-weighted images and to enhance. This was a scar at the site of a biopsy performed many years prior to this study.

bends lateral to the styloid process, extends down along the lateral surface of the posterior belly of the digastric muscle, pierces the posterior gland capsule, and runs lateral to the posterior facial vein and external carotid artery. With these landmarks, an accurate estimate can be made in most cases as to whether a mass is medial or lateral to the facial nerve. More direct visualization of the nerve may be possible with the use of high-resolution, three-dimensional Fourier transform MR imaging.[67]

Artifacts from adjacent metallic dental restorations often badly degrade axial CT images through the parotid gland. In these cases, exaggerated inferior orbitomeatal (IOM) angled scans or modified coronal scans can be obtained. Although these images distort the axial anatomy, they are superior to the routine axial studies for avoiding these artifacts. In many such cases, less image distortion may be seen on MR imaging; however, even here, significant image degradation may occur.

Copyright © 2003, Mosby, Inc. All rights reserved.

Normal Parotid Gland: MR Imaging

On MR imaging, it is primarily the fat content of the parotid gland that accounts for its signal intensities, namely, an overall intermediate to high T1-weighted and a low to intermediate T2-weighted signal intensity.[37, 41, 68, 69] The T1-weighted signal intensity of the gland is nonhomogeneous, with multiple irregular areas of lower signal intensity that represent interstitial tissues, salivary ducts, and possibly branches of the facial nerve. The major vessels are identified by their flow voids.

The facial nerve and the intraparotid ducts can be identified on MR imaging.[70] One such technique employs high-resolution T1-weighted images of the parotid gland, acquired with a prototype three-dimensional Fourier transform gradient-echo sequence that permits a very short echo time (4.2 msec) coupled with a modified phase-encoded, time-reduced acquisition scheme. The sequences were obtained at 1.5 T with a head and neck coil. Postprocessed multiplanar, curved, and volumetric images were obtained. Using this technique, the most clinically useful images were acquired at parameters of 40/4.2 (TR/TEeff), a flip of 30°, a field of view of 18 to 20 cm, a matrix of 512×288 or 512×256, an axial plane, 60 images, no gaps, and a section thickness of 1.5 mm.[71] The resulting image contrast obtained was similar to that of a standard spin-echo, T1-weighted image. That is, the parotid gland showed intermediate signal intensity and the fat spaces showed high signal intensity. The vessels had variable signal intensity, depending on the saturation. The nerves, muscles, ducts, and saliva had lower signal intensity. In all patients, the facial nerve could be seen from the brain stem to the parotid gland. In addition, the parotid duct could be seen from the mouth to the hilum of the gland. The proximal intraparotid facial nerve to the level of the retromandibular vein was seen in 72% of the subjects, and the main intraparotid ducts were seen in 66%.[71]

The normal parotid gland has this appearance on conventional and fast spin-echo, T1-weighted images. On spin-echo, T2-weighted scans, the overall signal intensity of the gland is low to intermediate (Fig. 39-19). However, on fast spin-echo, T2-weighted images the gland maintains an intermediate to high signal intensity reflecting both its fat

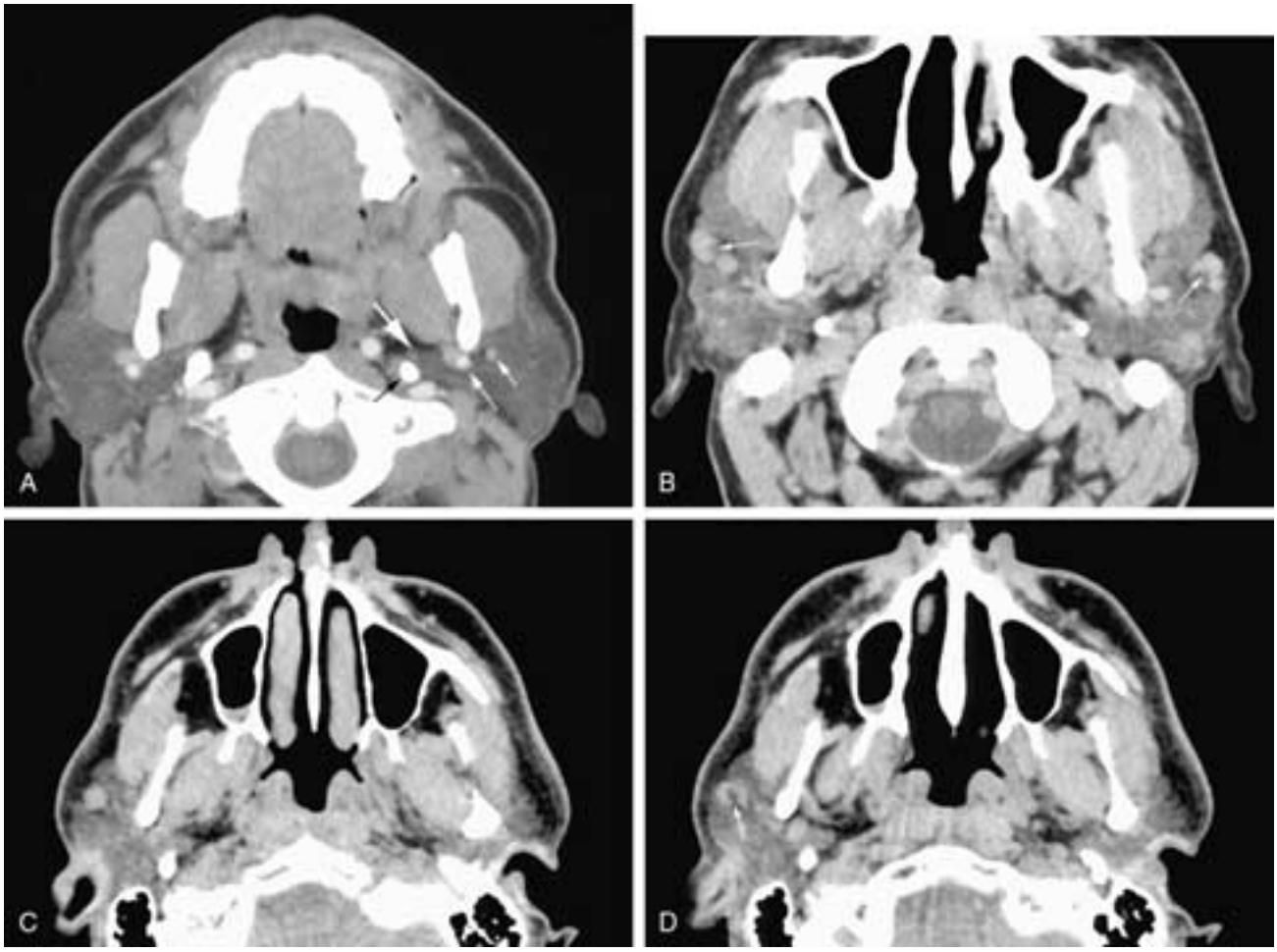

FIGURE 39-18 Axial contrast-enhanced CT scan (**A**) shows the parotid glands to be of lower attenuation than muscle but of higher attenuation than subcutaneous fat. The retromandibular vein (*long thin arrow*) and the external carotid artery (*short thin arrow*) are seen. At this level, the artery is lateral as it starts to ascend to become the superficial temporal artery. The styloid process (*black arrow*) is dorsal to the deep portion of the parotid gland (*large white arrow*) as it projects into the parapharyngeal space. Axial CT scans (**B** to **D**) show examples of parotid lymph nodes. Note the superficial location of the nodes and fat in the hilum (*arrow* in **B**).

VIEW IMAGE

Copyright © 2003, Mosby, Inc. All rights reserved.

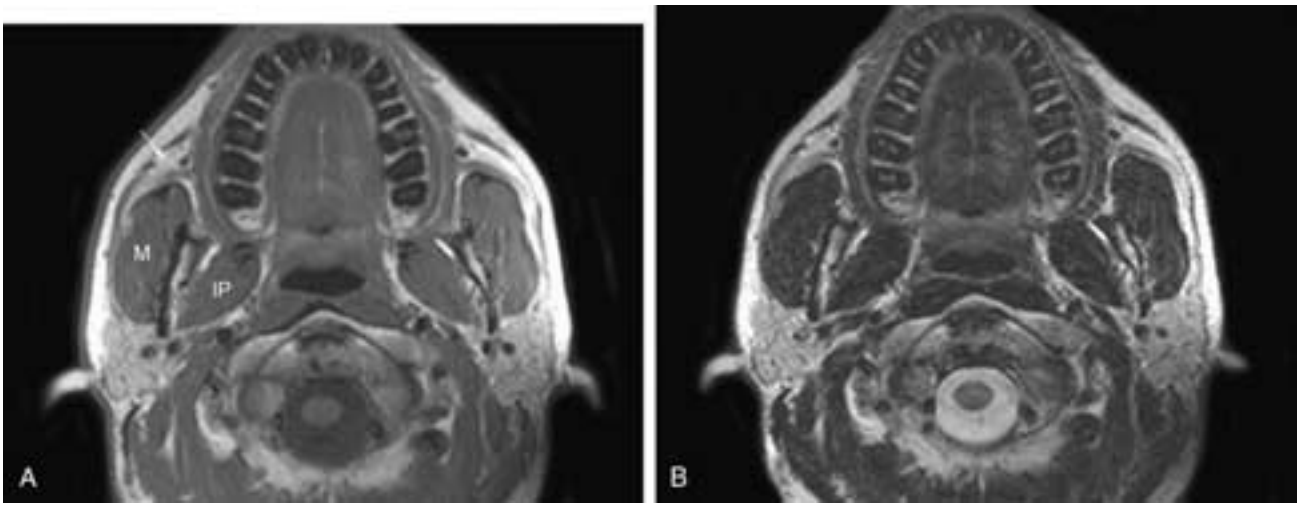

VIEW IMAGE

FIGURE 39-19 Axial T1-weighted (**A**), and T2-weighted (**B**), MR images through the parotid glands. Note the signal voids of the retromandibular vein and external carotid artery just dorsal to the ramus of the mandible. Also note the relationship of the masticator space (*M*, masseter muscle; *IP*, internal pterygoid muscle) and the buccal fat pad (*arrow* in **A**) to the parotid gland.

content and the gland's water content. Inversion recovery fast spin-echo imaging and inversion recovery (STIR) images have been reported to increase lesion conspicuity over routine spin-echo images by lowering the high T1-weighted signal intensity of fat.[37, 40, 72]

Although some authors have suggested that MR contrast is routinely needed to optimize the diagnostic results of MR imaging, as mentioned, most authors believe that MR contrast is not necessary in the majority of cases.[73] In fact, the use of such contrast can decrease the lesion's conspicuity against the fatty parotid gland unless fat suppression techniques are used. Furthermore, on inversion recovery sequences, not only is there a decreased signal intensity from fat, but any high signal intensity from contrast enhancement is not seen. In general, MR contrast may be beneficial only when a clinically palpable mass is not visualized on the noncontrast-enhanced MR image. It has also been noted that T1-weighted images may be the best overall sequence to localize a mass.[74] Although this may be true in some cases, the T2-weighted scans often best show the tumor margins, and in general, both T1-weighted and T2-weighted sequences are usually obtained in order to best assess the pathology.

Normal Submandibular Glands: CT and MR Imaging

The submandibular glands have a less fatty parenchyma than the parotid glands. As a result, compared to the parotid glands, the submandibular glands are more homogeneous and have a higher attenuation on CT, and slightly lower T1-weighted and higher T2-weighted signal intensities on MR imaging (Fig. 39-20). Occasionally mucoid secretions can normally be identified in the major collecting ducts and hilum of the submandibular gland. However, such ductal visualization may indicate some element of ductal obstruction, and careful scrutiny is required to rule out an obstructing lesion. After contrast administration, both submandibular glands should enhance to the same degree. If not, one gland is functioning abnormally, usually the gland that is more enhanced.

Normal Sublingual Glands: CT and MR Imaging

In general, the sublingual glands are the least well studied of the major salivary glands. This reflects the fact that inflammatory disease and tumors in these glands are rare. The most common abnormality is the ranula, an obstructed mucocele of the gland. Each sublingual gland is located just along the lingual aspect of the anterior third of the mandible. It lies in the floor of the mouth, above the mylohyoid muscle. The gland enhances with contrast and has either a linear or slightly medial concave configuration.

On MR imaging, the T1-weighted signal intensity of the sublingual gland is lower than that of the surrounding fat but higher than that of muscle. The T2-weighted signal intensity is high (Fig. 39-20). The sublingual glands show an age-related decrease in size, with approximately 25% of the gland's thickness present in the second decade of life being lost by the seventh decade. Although the T1-weighted signal intensity of the parotid gland increases with age, the T1-weighted signal intensity of the sublingual and submandibular glands does not.[75]

MR Sialography

MR sialography is a study that is performed without injection of any intraductal contrast material, intravenous contrast, or ductal catheterization. It is thus noninvasive and painless. Several different techniques have been proposed, including a heavily T2-weighted, fast spin-echo sequence (TR 3600 msec/TE 800 msec) with a slice thickness of 30–40 mm using an 8 cm surface coil,[76–78] a T2-weighted single-shot (TSE) sequence (TR/TE 2800/1100 msec, acquisition time 7 seconds) using a quadrature head or a surface coil,[79] a heavily T2-weighted sequence (TR = 3600 msec, TE = 80 msec),[80] and a heavily T2-weighted, two-dimensional, fast spin-echo technique with a 12-cm circular surface coil. Contiguous 3-mm axial images with frequency-selective fat suppression were then acquired through the symptomatic gland.[81] In another study, after being given lemon as a secretogogue, patients had MR

Copyright © 2003, Mosby, Inc. All rights reserved.

imaging using T2-weighted, 3D, constructive interference in steady-state (CISS) imaging. In this study, MR sialography was found to be superior to ultrasound and comparable to digital sialography of the submandibular glands.[82]

In all of these sequences there was depiction of the fluid-filled parotid ducts, with the main duct, primary branches, and secondary branches being clearly seen (Fig. 39-21). In addition, both intraparotid and extraglandular duct widening and ductal strictures were well seen, and sialolithiasis in the main duct was also visualized. By comparison, conventional sialography showed all of the parotid ducts up to the tertiary branches. However, in half of the submandibular gland studies, the ductal system was not seen due to difficulty in canalizing Wharton's duct. The

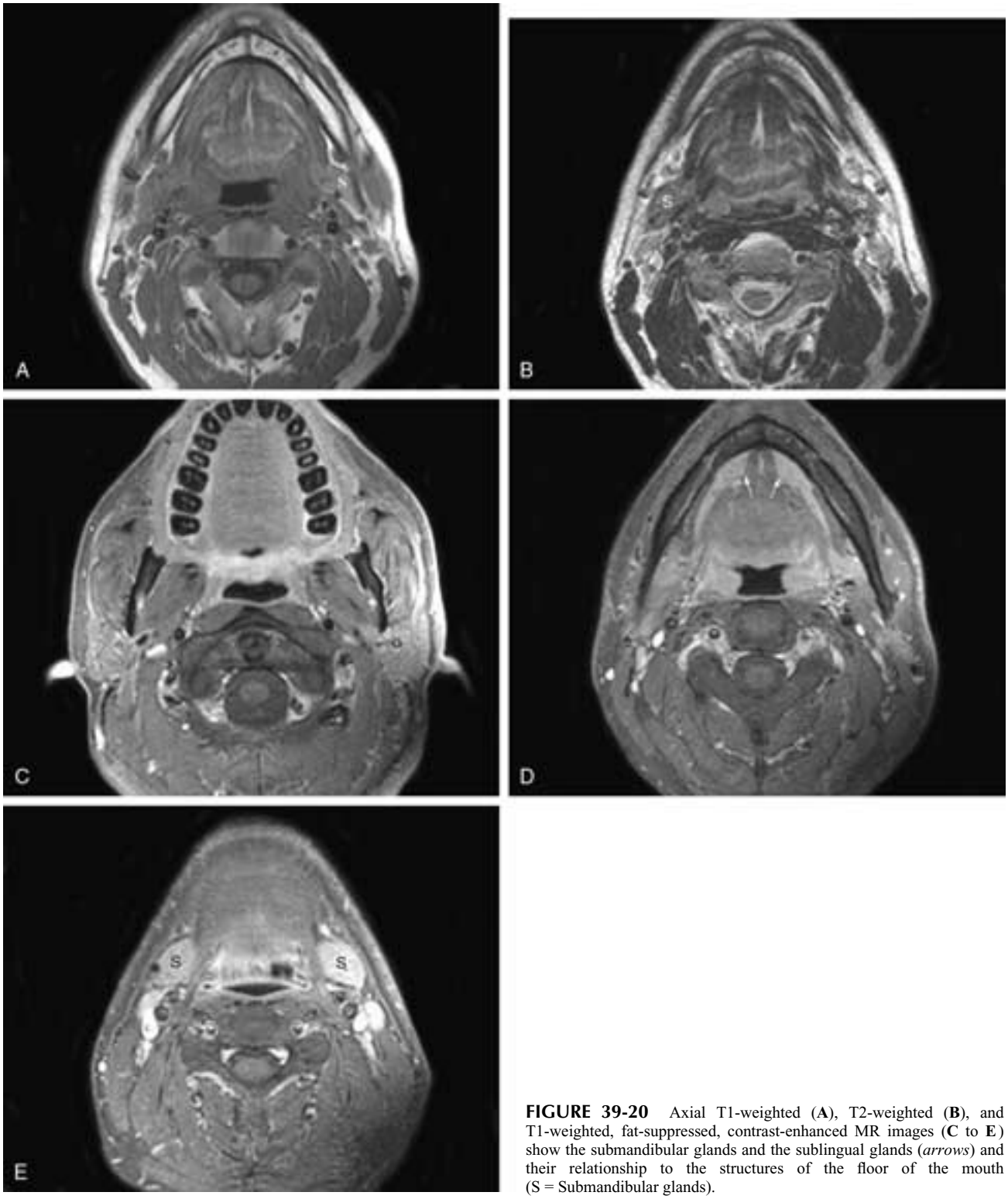

FIGURE 39-20 Axial T1-weighted (**A**), T2-weighted (**B**), and T1-weighted, fat-suppressed, contrast-enhanced MR images (**C** to **E**) show the submandibular glands and the sublingual glands (*arrows*) and their relationship to the structures of the floor of the mouth (S = Submandibular glands).

VIEW IMAGE

Copyright © 2003, Mosby, Inc. All rights reserved.

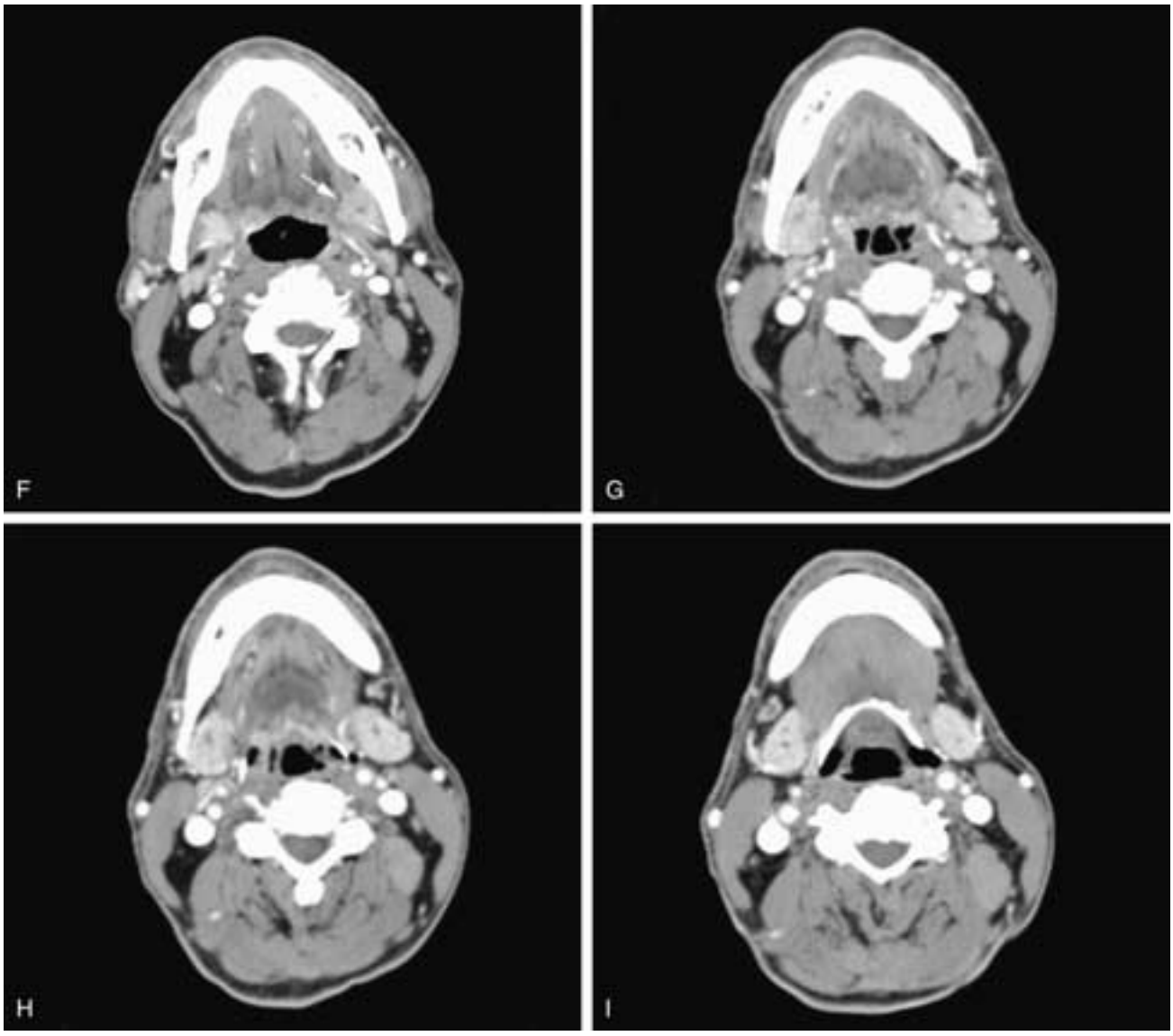

VIEW IMAGE

FIGURE 39-20 *Continued.* Serial contrast-enhanced CT scans from cranial (**F**) to caudal (**I**) show the normal symmetric enhancement of the submandibular glands. In **F**, the hilum of the gland is seen above the posterior edge of the mylohyoid muscle (*arrow*). In **G** to **I**, there is minimal symmetric visualization of the intraglandular ducts. This is a normal imaging appearance.

submandibular gland ducts were seen in all cases of MR sialography.

Unfortunately, the MR sialographic study may be time consuming to perform and clinically useful images may be difficult to obtain. As a result, it is presently not routinely performed as a part of the MR salivary gland study.

VIEW IMAGE

FIGURE 39-21 Sagittal MR sialography image shows some of the proximal Stensen's duct and the primary and secondary intraglandular ducts in this normal volunteer.

Other Approaches

Dynamic contrast examinations have been studied as a means of furthering sectional imaging diagnosis. With regard to CT, a two-phase helical CT study was performed to characterize salivary gland tumors. After the injection of 90 ml of contrast material at a rate of 3 ml/second, helical CT scans were obtained at early and delayed phases, with scanning delays of 30 and 120 seconds, respectively. The attenuation change and enhancement patterns in the tumors were then assessed. There was an increase in attenuation in 86% of pleomorphic adenomas and a decrease in 89% of Warthin's tumors. A multinodular enhancement pattern was found in only 34% of pleomorphic adenomas. With malignant tumors, there was an increase in 55% and no change in 40% of the cases at delayed phase scanning. This study concluded that the ratio of CT numbers was

Copyright © 2003, Mosby, Inc. All rights reserved.

significantly different between Warthin's tumors and pleomorphic adenomas and between Warthin's tumors and malignant tumors.[83] Although this technique does improve diagnosis, its clinical benefits are limited and it is not commonly performed.

With regard to MR imaging, the efficiency of dynamic contrast-enhanced MR imaging for the diagnosis of salivary gland masses was studied. Both T1-weighted and T2-weighted images were obtained, dynamic studies on each mass were performed, and the enhancement patterns were correlated with pathology. Four enhancement patterns of a mass were recognized: type 1 showed marked, homogeneous enhancement; type 2 had slight, homogeneous enhancement; type 3 had marginal enhancement; and type 4 had poor enhancement. Most pleomorphic adenomas had a type 1 enhancement pattern, but two had a type 2 pattern. Warthin's tumor generally showed the type 4 pattern. Primary malignant tumors of the salivary gland all showed the type 3 pattern. One inflammatory cyst and one Warthin's tumor also showed the type 3 pattern.[84] These studies show that although there is some improvement in imaging diagnosis, at present their clinical significance seems limited. Because of this and the additional time needed for these calculations, most people do not perform these dynamic studies.

Three-Dimensional MR Imaging

Three-dimensional MR imaging has been proposed as a good communication tool when describing pathology to clinicians who have difficulty assimilating serial images to display pathology. The use of MR contrast has been proposed to improve the identification of salivary masses on such 3D images.[85] At present, few radiologists routinely use 3D MR imaging because they find it adds little to their imaging information. However, as technology advances and CT and MR data can be rapidly combined to produce a 3D image, the use of this approach may become more popular.

MR Spectroscopy

MR spectroscopy is a relatively new field as applied to clinical imaging. One study has shown that ^{31}P spectroscopy of salivary malignancies demonstrated a significant increase in the concentration of phosphomonoesters, phosphodiesters, and inorganic phosphates compared to the concentrations in normal individuals, and there was a large reduction in creatine phosphate.[86] This early work may lead the way to attainment of more pathologic and prognostic information on the MR study. At present, because of the considerable time necessary to gather sufficient data and the limited clinical application of MR spectroscopy, it is primarily an investigative tool. MR spectroscopy has also been used to study various physiologic functions of the salivary glands. One review summarized the results of studies of energy metabolism and acid-base balance [using ^{31}P and ^{14}N nuclear magnetic resonance (NMR)], electrolytes transport (^{23}Na, ^{39}K, ^{35}Cl, and ^{87}Rb NMR), and water transport (^{1}H NMR). The study noted that the three-dimensional structure of salivary glands can be observed with ca. 60-µm resolution; it is also possible to observe circulation, flow, and volume changes during secretion. The study concluded that MR spectroscopy may open up new fields in the study of exocrine secretion.[87]

CT Sialography

The CT sialogram was developed to provide better definition of major salivary gland masses than was attainable with the early low-resolution CT scanners.[88–91] The study was a combination of a sialogram and a simultaneous CT scan of the gland. Acinarization of the gland provided a background density that silhouetted virtually any mass (Fig. 39-22). However, as a result of the development of high-resolution CT scanners and MR imaging, this cumbersome double examination is no longer performed.

Noncomputed Tomographic Sialography

In a manner similar to CT sialography, conventional multidirectional tomography of the parotid gland was performed immediately after a sialogram that intentionally had acinarization. If a mass was present, it was outlined by the contrast material and was more easily identified than on the routine sialographic study. In the present era of high-resolution CT and MR imaging, this technique is no longer employed.

Ultrasound

Ultrasound has traditionally been used to differentiate solid and cystic salivary gland masses and to identify salivary calculi. More recently, it has been used to make more specific diagnoses. Autoimmune disease (Sjogren's disease) can be diagnosed by ultrasound when the disease is in its more advanced stages. However, when the disease is in its early stages, it cannot be consistently diagnosed by ultrasound (or, for that matter, by MR imaging), and the improved reliability of labial minor salivary gland biopsies, sialochemical studies, and serum studies has made the current diagnosis of Sjogren's disease less dependent on imaging than it was in prior decades. Similarly, although in some cases lymphomatous and nonlymphomatous nodes can be distinguished by ultrasound, biopsy is still necessary. The diagnosis of multiple parotid cysts in HIV-positive patients can also be made by ultrasound. It is fair to say that overall in the last decade, ultrasound has become a more useful imaging technique, particularly for the parotid and submandibular glands. Although ultrasound can differentiate some intraglandular lesions from extraglandular masses, this technique is not used frequently in this regard because of the routinely superior visualization of the deep spaces of the upper neck, skull base, and floor of mouth attainable by CT and MR imaging.[29–31, 92, 93]

It has also been suggested that color Doppler ultrasound can be used to differentiate between a peripheral parotid mass that is near the caudal tip of the gland and a soft-tissue mass in this area that is adjacent to the gland. The technique is based on identifying the origin of the feeding vessels to the mass, with those masses deriving their vascular supply from the parotid gland being of parotid origin.[94]

Usually the ultrasound examination is performed with a linear probe, high-frequency (7- to 10-MHz) transducer. This gives higher-resolution images but does not penetrate as deeply as the lower-MHz transducers. This limitation is one of the reasons that ultrasound is not utilized as frequently as CT or MR imaging to examine patients with possible deep extensions of their salivary lesions. Sono-

Copyright © 2003, Mosby, Inc. All rights reserved.

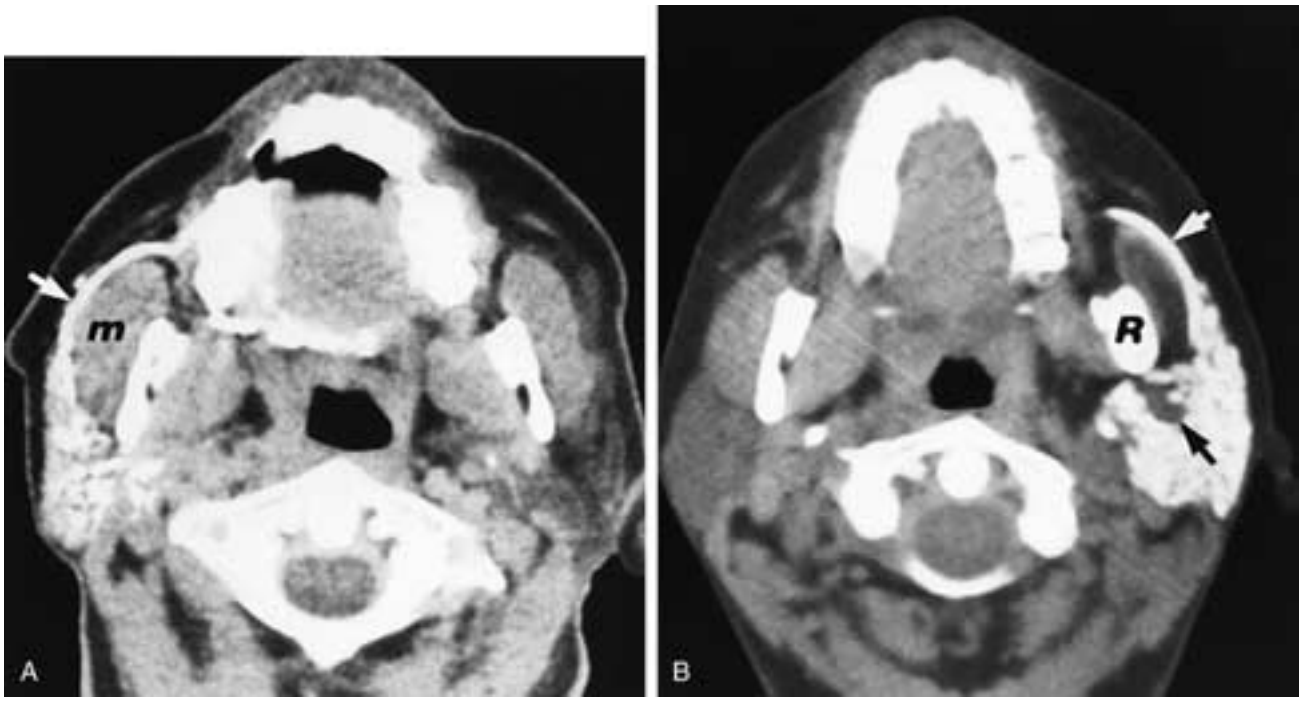

VIEW IMAGE

FIGURE 39-22 Axial CT scans (**A**, **B**) of a normal CT-sialogram of the parotid gland on two different patients. Contrast is seen in the gland and in Stensen's duct (*arrow*) as the duct bends around the masseter muscle (*m*). The location of the posterior facial vein and the external carotid artery can be identified (*black arrow*). Ramus of mandible (*R*).

graphically guided biopsy of masses and lymph nodes related to the salivary glands is now commonly performed. This approach adds a degree of pretreatment diagnosis in those cases where the surgeon needs this information.[95] Many surgeons are of the opinion that a mass in a major salivary gland must be resected; in such situations, a presurgical biopsy is usually not performed.

Radionuclide Salivary Studies

The major advantage of salivary gland scintigraphy, compared to other imaging modalities, is that both parenchymal function and the excretion fraction of both parotid and submandibular glands can be quantified simultaneously with a single well-tolerated intravenous injection.[96]

The salivary glands normally concentrate ^{99m}Tc pertechnetate, and there is a generalized decreased uptake of this radionuclide associated with aging. Although masses that excessively accumulate the radionuclide can be identified, they are not as accurately localized as on CT or MR imaging studies. In addition, masses that do not accumulate excessive radionuclide are poorly seen, if they are even identified. As a result, radionuclide sialograms are not routinely used to study parotid and submandibular gland masses.

The lesions that are most often examined by radionuclide sialograms are those that are suspected of highly concentrating ^{99m}Tc. These tumors are primarily Warthin's tumors and oncocytomas.[60, 97, 98] Salivary gland function can also be assessed, and hyperfunction can be demonstrated in acute sialoadenitis, granulomatous disease, lymphoma, and sialosis. A cold area within a gland that has overall increased activity may represent an abscess in a patient with an acute purulent sialoadenitis. Decreased glandular activity is seen in Sjogren's syndrome and in most primary and metastatic tumors. A viral sialoadenitis causes a generalized decreased uptake, and ductal obstruction can be estimated by the degree of prolongation of the secretory phase of the radionuclide study. Patchy decreased uptake may indicate chronic and atrophic salivary gland disease.[60, 99–101]

In one study, dual-isotope (^{99m}Tc and ^{201}Tl) Single Proton Emission Computed Tomography (SPECT) imaging was compared to CT and MR imaging in the differentiation of various lesions of the major salivary glands. The uptake ratio and retention index for ^{99m}Tc and ^{201}Tl were calculated by drawing regions of interest on the involved and normal glands. All malignant tumors were detected by all three modalities. Warthin's tumors were specifically identified by dual-isotope SPECT imaging; however, MR imaging failed to differentiate Warthin's tumor from pleomorphic adenoma. Of 16 tumors showing a cold defect on the ^{99m}Tc images, parametric analysis with ^{201}Tl had an accuracy of 94%, whereas CT had an accuracy of 70% to 90%. MR imaging was 73% to 91% accurate in differentiating between Warthin's and malignant tumors.[102] Although one may question the clinical significance of being able to specifically identify a Warthin's tumor, this approach clearly has merit in selected cases.

Angiography

Interventional vascular studies play little role in the diagnosis and treatment of most salivary gland diseases. With the rare exception of the embolization of an unusually large hemangioma or another rare vascular lesion, angiographic studies are not used in the salivary glands.

Copyright © 2003, Mosby, Inc. All rights reserved.

Catheter Dilatation and Endoscopy

In recent years, manufacturing techniques have progressed so that smaller-diameter catheters are now available. These catheters have started to be utilized both diagnostically and therapeutically in disease involving Stensen's duct.[101] The procedure, referred to as *sialendoscopy*, allows direct inspection of the salivary ductal system by means of a microendoscope. This technique is performed under local anesthesia on an outpatient basis.[103] It is presently considered a research technique and is rarely employed in the average clinical setting.

Fine Needle Aspiration

Fine needle aspiration of salivary masses is becoming increasingly popular. It is performed with a 22-gauge needle and can be done with or without CT or MR imaging guidance.[29, 31, 104–107] Diagnostic yields are highest when a cytopathologist or a cytotechnologist is present during the procedure and can check the specimen for adequacy. With greater experience, the concurrence between the cytologic and histologic findings can be expected to rise above the present 91%.[60]

Positron Emission Tomography Scanning

Early clinical work with positron emission tomography (PET) scanning has shown that when imaging using 2-(F-18) fluoro-2-deoxy-D-glucose (FDG), tumors with increased metabolic activity are seen as areas of increased PET activity.[108] However, initial results have also indicated that although PET can identify the higher-grade malignancies, there is confusion with the common benign Warthin's tumor, which also has high metabolic activity. Because of this limitation, the high cost of this examination, and the long procedure time, PET scanning appears to have a limited future in this area.

In fact, FDG is not a very tumor-specific substance, and its accumulation in benign lesions with increased glucose metabolism may give rise to false-positive results and hence cause FDG PET to display relatively low specificity, frequently below 85%. Correct interpretation of FDG PET studies is predicated upon both detailed knowledge of morphologic abnormalities and the correlation of functional and morphologic information derived from CT or MR imaging. False-positive findings may be obtained in patients with acute inflammatory lesions or benign salivary gland tumors. It has been suggested that these problems may be alleviated by means of multitracer studies, for example, using ^{11}C-labeled aminoisobutyric acid for quantification of A-type amino acid transport. Finally both radiotherapy and chemotherapy can cause increased FDG uptake, complicating diagnosis and evaluation.[109]

In another study using CT or MR imaging, FDG PET studies were performed in 28 patients with parotid lesions. All lesions except two showed higher accumulation of FDG than the normal parotid gland. High accumulation was found in all 5 carcinomas, all 6 Warthin's tumors, and 8 of 12 pleomorphic adenomas, with standardized uptake values (SUVs) of over 3.0. The mean SUVs of carcinomas, Warthin's tumors, and pleomorphic adenomas were 5.92 ± 2.05, 7.03 ± 2.49, and 4.07 ± 1.55, respectively. On the other hand, all five inflammatory lesions demonstrated low accumulation, with a mean SUV of 1.66 ± 0.89. The authors concluded that it is difficult to differentiate malignant from benign parotid lesions by SUV on FDG PET.[110]

NONNEOPLASTIC DISORDERS

Infections

Acute parotitis has only a few etiologies; most commonly it is caused by infections. By comparison, chronic salivary inflammation may be caused by numerous processes: infectious, autoimmune, systemic, and certain neoplasms. In this clinical setting, the radiologist may play an important role in resolving some diagnostic dilemmas.

Acute Infections

As a group, bacterial and viral infections are the most common causes of salivary abnormalities. Most of the bacterial infections ascend from the oral cavity and are related to a decrease in salivary flow. In fact, maintenance of normal salivary flow is the single best deterrent to infections. Many situations can decrease saliva flow: prior infections, dehydration, trauma, surgery, irradiation, some medications, and obstructing masses such as stones or tumors.[60] Ascending infections are more common in the parotid gland than in the submandibular gland. Reasons for this include the following: the orifice of Stensen's duct is larger than that of Wharton's duct, the parotid duct orifice is more easily injured by cheek biting and by the presence of dental prostheses and other mechanical trauma, and the overall smaller caliber of Stensen's duct itself may allow easier interruption of salivary flow by epithelial tears and thickened secretions.[7, 8] In addition, parotid secretions are primarily serous, while saliva from the submandibular and sublingual glands is more mucinous. Such mucoid secretions contain antibacterial elements such as lysosomes and IgA antibodies. Mucins also contain sialic acid, which agglutinates bacteria, preventing adherence to host tissues, and specific glycoproteins that bind epithelial cells, competitively inhibiting bacterial attachment to those cells.[111]

Dehydration classically occurs in the postoperative patient, especially after major abdominal surgery. Typically, such parotitis develops 2 to 7 weeks after surgery; however, cases can develop in the immediate postoperative period after spinal anesthesia, which causes peripheral vasodilatation, hypovolemia, and dehydration. In addition, patients with debilitating conditions and immunosuppression are at risk of developing acute sialadenitis. Such conditions include diabetes mellitus, malnutrition, HIV infection, Sjogren's syndrome, renal and hepatic failure, depression, anorexia, bulimia, cystic fibrosis, Cushing's disease, hyperuricemia, hyperlipoproteinemia, and lead intoxication.[111] There are also a number of medications that can contribute to dehydration and thus predispose the patient to acute sialadenitis. These medications include diuretics, barbiturates, antitricyclics, antihypertensives, antidepressants, antihistamines, and parasympathetic drugs.[111, 112]

Eosinophil-rich mucous plugs have been associated with acute bacterial parotitis in children, especially those with a history of allergies. In addition, foreign body materials such as food, seeds, and feathers have been reported to obstruct the salivary ducts.

Copyright © 2003, Mosby, Inc. All rights reserved.

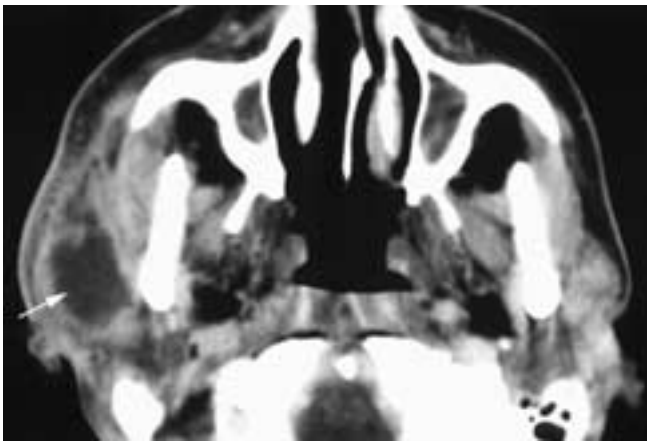

VIEW IMAGE

FIGURE 39-23 Axial contrast-enhanced CT scan shows a solitary low-attenuation area (*arrow*) in the right parotid gland. There is a thick, indistinct, enhancing rim, and the remaining gland is denser than normal. There is also thickening of the overlying skin and increased density in the subcutaneous fat. This patient had a parotid abscess with cellulitis.

There are two age groups particularly at risk of developing acute sialadenitis. Neonates can develop suppurative parotitis, usually within the first 2 weeks of life, and the elderly are prone to acute sialadenitis, usually due to debilitation.[111]

Bacterial Infections

Acute suppurative sialoadenitis is an acute, painful, diffuse disease primarily of the parotid gland. The gland is swollen and tender, and a purulent exudate can be seen in the buccal orifice of Stensen's duct. This disease usually occurs in debilitated, dehydrated patients, usually with poor oral hygiene.[112–114] The dry mouth may be caused by general debilitation, fluid restriction, irradiation, or medications that decrease salivary flow. The incidence of acute suppurative sialoadenitis varies between 0.004% and 0.74% of patients who have had a major surgical procedure.[60] Good oral hygiene and hydration have markedly reduced the incidence of this condition. The most common offending agents are *Staphylococcus aureus*, *Streptococcus viridans*, *S. pneumoniae*, *Haemophilus influenzae*, *Streptococcus pyogenes*, and *Escherichia coli*. Intraparotid and periparotid lymph nodes may be involved in the inflammatory reaction. The treatment of choice is antibiotic therapy.[60, 112]

Suppurative parotitis can also occur in neonates, usually affecting premature infants (35% to 40% of cases), and dehydration is the main predisposing factor.[113] The onset is usually between 7 and 14 days after delivery, and there is erythema of the skin overlying the parotid glands. The offending agents are *Staphylococcus*, *Pseudomonas Streptococcus*, *Pneumococcus*, and *Escherichia*.[60] Hydration and antibiotic therapy usually cure the infection. Patients with an undiagnosed or incompletely treated acute suppurative sialoadenitis can develop an intraglandular abscess (Figs. 39-23 and 39-24) regardless of their age. Uncommonly, the infection may progress to an abscess despite aggressive medical treatment. Small abscesses may form (Fig. 39-25) and coalesce to form a larger abscess, or a solitary abscess may develop. Patients with such abscesses have fever and malaise. The abscess may extend into the parapharyngeal space or the upper neck. Surgical drainage with adequate antibiotic therapy is the treatment of choice.

Acute suppurative sialoadenitis can also involve the submandibular gland, although the incidence is lower than that in the parotid gland. Such submandibular gland disease can occur in the absence of parotid disease. The lower incidence in the submandibular gland is related both to the protective anatomy of Wharton's duct and to the fact that the saliva of the submandibular gland is more bacteriostatic than that of the parotid gland. The submandibular glands also have a faster resting salivary flow rate, which helps prevent ascending infection from the oral cavity.[114] The presence of sialolithiasis is a major factor in the development of submandibular sialoadenitis, and a calculus is found either within the gland and/or within Wharton's duct in most cases of acute submandibular sialoadenitis.[60] The periglandular submandibular nodes are often enlarged, causing painful swelling of the gland. These enlarged nodes are a characteristic clinical presentation (Fig. 39-26).

Sialodochitis is inflammation of either Stensen's or Wharton's duct. Usually the duct is dilated secondary to a distal obstruction near the mouth. The enlarged duct can have a fusiform shape or appear as a ''string of sausages'' resulting from multiple areas of ductal stenosis (Figs. 39-27 and 39-28).

Because of the acute, painful nature of these inflammatory diseases and their usually short duration, sialography is rarely performed. In fact, it is contraindicated in these patients, as retrograde injection of contrast may drive the infection back into the gland and cause either exacerbation or recurrence of a clinically quiescent infection. If a sialogram is performed on a patient with acute sialoadenitis, the study shows peripheral tapering of the ducts, giving a

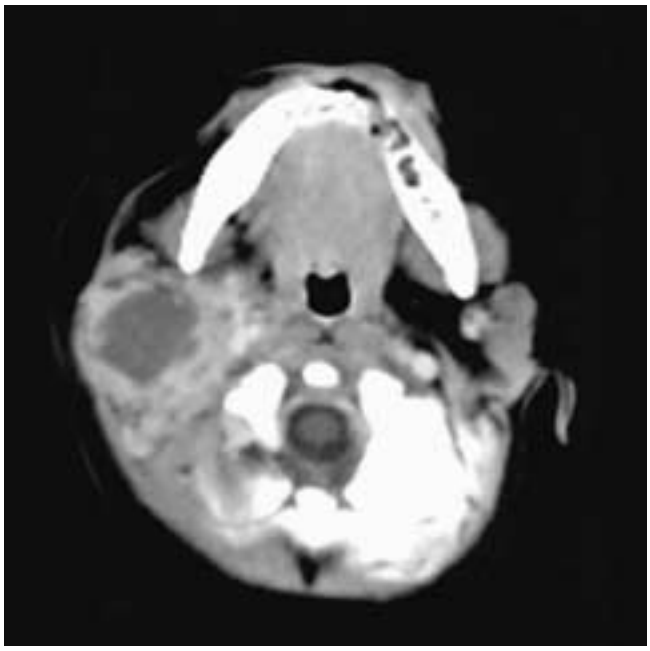

FIGURE 39-24 Axial contrast-enhanced CT scan on a child shows a large right parotid abscess. This child had been severely dehydrated prior to developing this abscess.

VIEW IMAGE

Copyright © 2003, Mosby, Inc. All rights reserved.

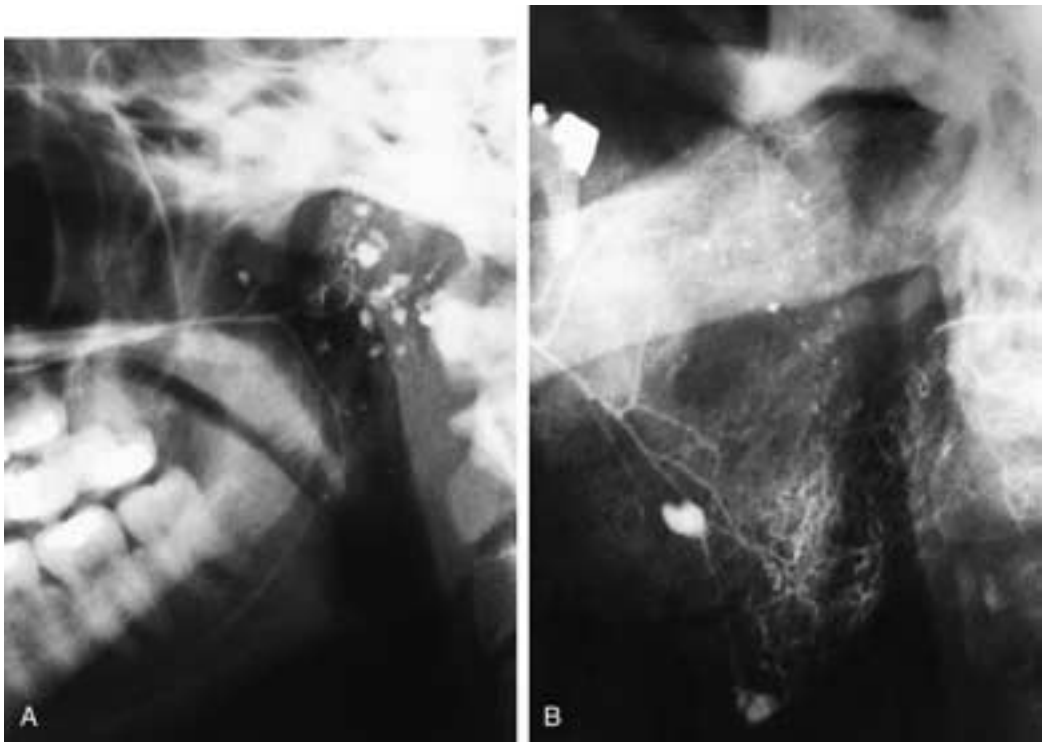

VIEW IMAGE

FIGURE 39-25 Left lateral views (**A**, **B**) of parotid sialograms on two different patients. In **A**, there are multiple collections of varying size of contrast material primarily located in the posterior portion of the gland. These were old abscesses in a clinically normal patient. In **B**, the patient had a vaguely palpable mass (superiorly, just below the mandible, where there is an absence of filled ducts). There are also scattered collections of contrast material in the upper and lower poles of the gland. This patient had tuberculous abscesses.

pruned appearance to the ductal system. This appearance results from periductal cellular infiltration of acute inflammatory cells, which is confined by the gland capsule and thus exerts pressure on the ductal system. Focal areas of major ductal dilatation can occur secondary to areas of ectasia, and narrowing at the ductal branch points due to functional spasm may also be seen.[113–115]

On CT scans obtained very early in an acute infection, the central ducts are dilated and the walls of the central ducts and of Stensen's duct may enhance (Figs. 39-29 and 39-30). The gland itself is variably enlarged and has an increased attenuation on noncontrast scans reflecting the cellular infiltration.[114] There may be diffuse enhancement of the gland on postcontrast studies, reflecting the associated increased vascularity (Fig. 39-30). Calcified sialolithiasis can be clearly identified on CT and may be located within the ductal system of the gland and/or within Stensen's duct (Figs. 39-31 to 39-35). Occasionally, even a noncalcified stone can be identified in Stensen's duct. It may appear as a low-attenuation area within a dilated, obstructed, saliva-filled duct (Fig. 39-36). If Stensen's duct is dilated and has thickened, enhancing walls (Figs. 39-28 to 39-30), sialodochitis is present.

On MR imaging, the parotid gland is variably enlarged, and the usual interstitial and ductal components are poorly seen compared to those of a normal gland. The gland can have either higher or lower than normal signal intensity on T2-weighted scans, depending on whether edema or cellular infiltration predominates.

In cases of acute sialoadenitis, the submandibular gland is enlarged and it enhances. Submandibular adenopathy is usually present. As in the parotid gland, calcified sialolithiasis may be present within the gland and/or in Wharton's duct (Figs. 39-26, 39-37 to 39-42).

Viral Infections

By far the most common cause of viral parotitis is mumps, which is caused by an RNA virus of the paramyxovirus group. Mumps is the most common of all salivary gland diseases.[12] It primarily involves the parotid glands but can occur in the submandibular and sublingual glands. The disease is most reliably diagnosed during epidemics, and the diagnosis can be confirmed by measuring serum antibody titers.[8] The incubation period is between 2 and 3 weeks, and parotid involvement is clinically unilateral in about 20% to 33.3% of the cases. The patient may experience a prodromal period of general malaise. During this period, there may be redness at the orifices of Stensen's or Wharton's ducts. The disease is then characterized by an acute, painful swelling of the involved gland that may persist for 1 or more weeks. Ingestion of sour liquids at this stage will result in an acute exacerbation of the discomfort. During the acute phase, the saliva is clear but contains virus. Mumps can be subclinical, and this type of infection may account for some misdiagnosed or apparently idiopathic cases of parotid gland enlargement. It may also account for adults who have no history of mumps but have a positive complement-fixation test for the virus (serum antibodies to mumps S and

Copyright © 2003, Mosby, Inc. All rights reserved.

V antigens). One episode of mumps provides immunity. Although about 75% of patients have an uncomplicated course, mumps can cause epididymo-orchitis, meningoencephalitis, pancreatitis, and thyroiditis. It may also be responsible for some cases of unilateral neurosensory hearing loss.

Other viral agents can cause parotitis, including coxsackie viruses, parainfluenza viruses (types I and III), influenza virus type A, herpes virus, echo virus, and choriomeningitis virus.[8, 60, 112, 116, 117] EBV may remain latent within the ductal epithelium and is a potential source (along with latently infected pharyngeal mucosa) of secreted virus in the saliva of patients. Cytomegalovirus (CMV) may also infect salivary tissue. HIV has not, to date, been shown to infect the salivary glands directly, although it does interact with and potentiate the effects of CMV and EBV.[118–120]

The imaging findings are nonspecific. The gland is usually enlarged and has a slightly greater CT attenuation than normal. On MR imaging, the gland tends to have a slightly higher T2-weighted signal intensity than normal.

Chronic Inflammations

The chronic inflammatory diseases of the major salivary glands may be due to recurrent bacterial infection or infection with other agents, as discussed below. Noninfectious conditions such as prior irradiation, autoimmune disease, or idiopathic causes may also lead to chronic inflammation.

Clinically, these chronic conditions have one of three general presentations. The first is that of repeated episodes of acute sialoadenitis with associated painful swelling of the involved gland. There are intervening intervals characterized by lack of symptoms and decreased gland size. The second presentation is that of a slowly progressive enlargement of the gland with periodic episodes of acute sialoadenitis. The third presentation is that of a slowly

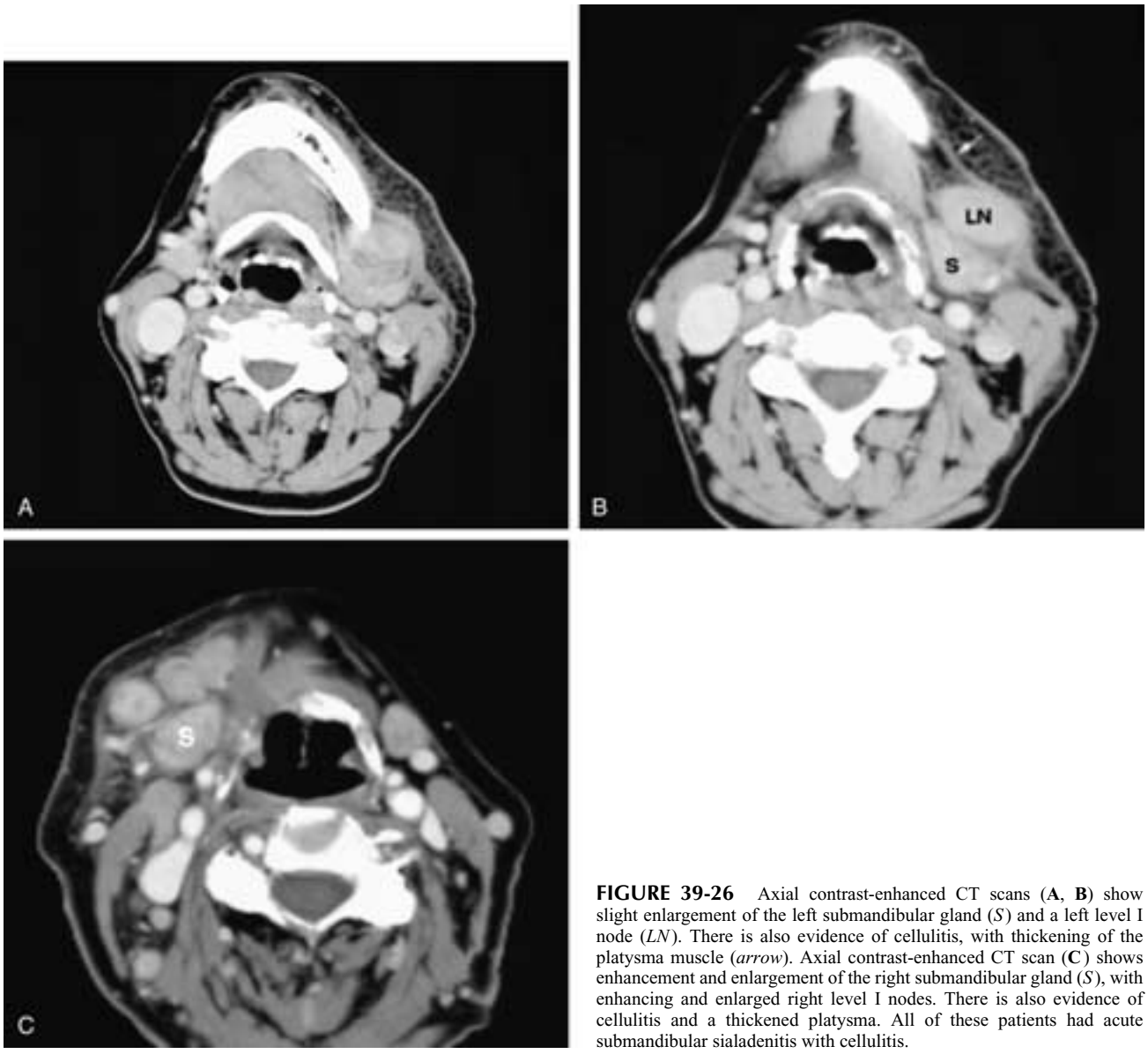

FIGURE 39-26 Axial contrast-enhanced CT scans (**A**, **B**) show slight enlargement of the left submandibular gland (*S*) and a left level I node (*LN*). There is also evidence of cellulitis, with thickening of the platysma muscle (*arrow*). Axial contrast-enhanced CT scan (**C**) shows enhancement and enlargement of the right submandibular gland (*S*), with enhancing and enlarged right level I nodes. There is also evidence of cellulitis and a thickened platysma. All of these patients had acute submandibular sialadenitis with cellulitis.

VIEW IMAGE

Copyright © 2003, Mosby, Inc. All rights reserved.

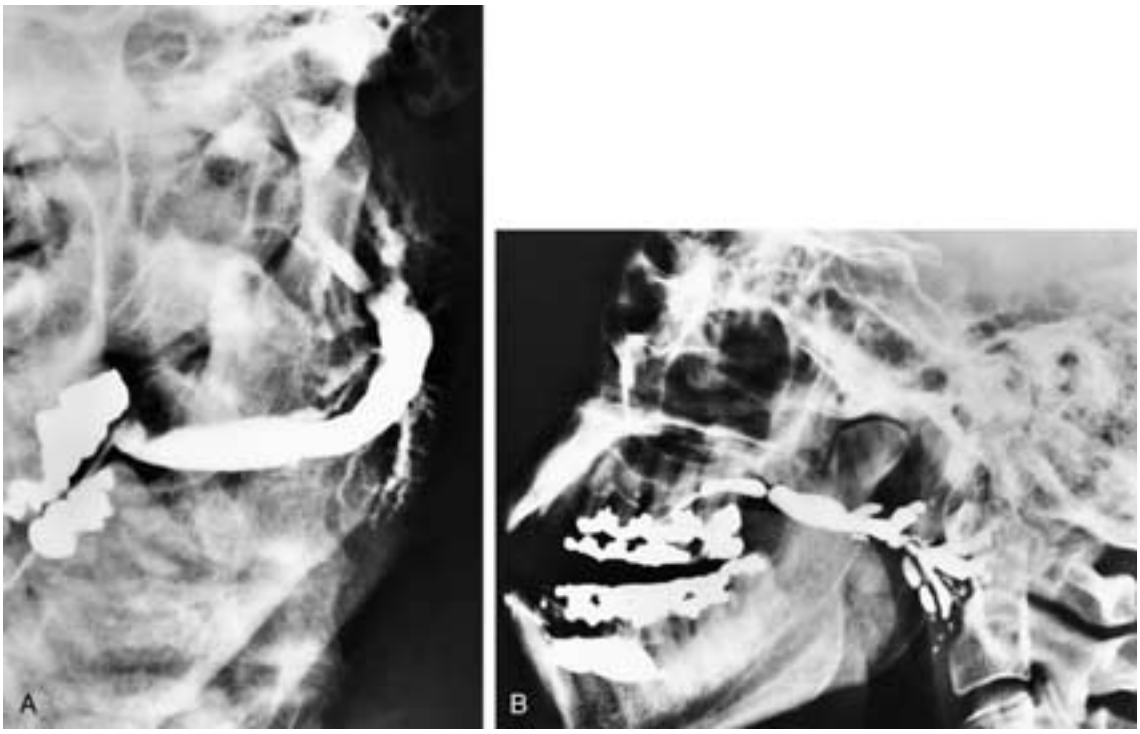

VIEW IMAGE

FIGURE 39-27 Frontal oblique view of a left parotid sialogram (**A**) shows dilatation of the entire Stensen's duct and some central dilatation of the glandular ducts. The peripheral ducts are not visualized. This patient had sialodochitis secondary to obstruction at the buccal orifice. Lateral view of a parotid sialogram (**B**) on a different patient shows dilatation of Stensen's duct and of the central parotid ducts. The peripheral ducts are not visualized. Strictures along Stensen's duct create a ''string of sausage'' appearance. This patient had sialodochitis and severe sialadenitis. A parotidectomy was necessary.

progressive, painless enlargement of the salivary glands. This last group of patients may be confused clinically with those who have neoplasms.

An attempt should be made to differentiate the obstructive and nonobstructive diseases, since their treatment and prognosis often vary considerably. The chronic nonobstructive diseases involve the parotid glands more frequently than they do the submandibular glands. Conversely, the obstructive disorders are more common in the submandibular glands.

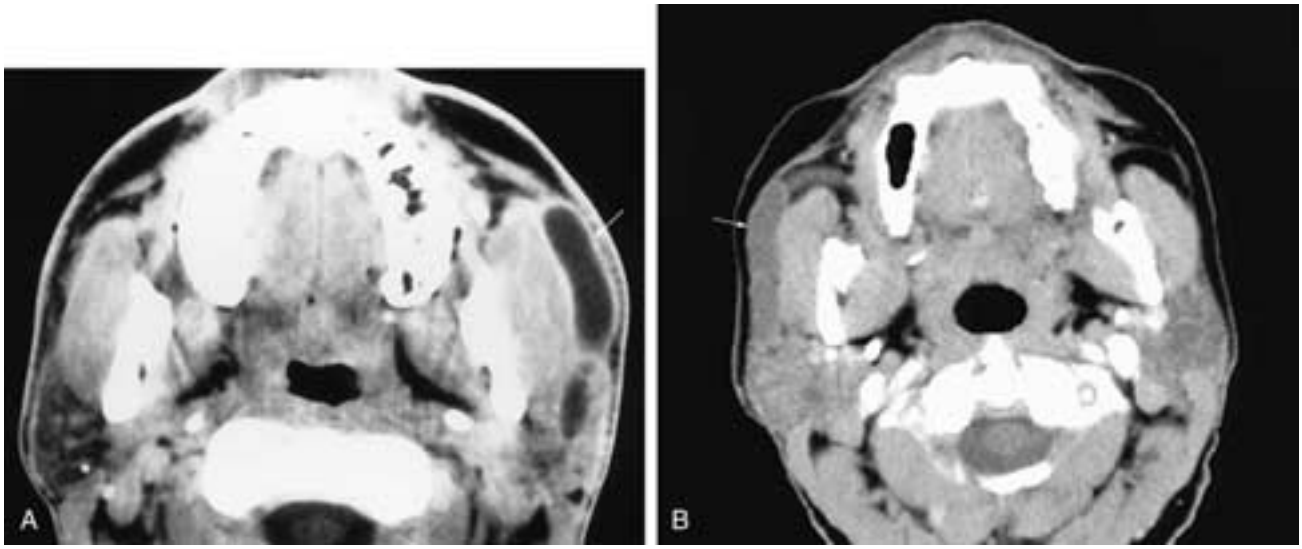

VIEW IMAGE

FIGURE 39-28 Axial contrast-enhanced CT scan (**A**) shows increased density in the left parotid gland, with enhancement and thickening of the walls of some intraglandular ducts and Stensen's duct (*arrow*). A small sialolith is present in the right parotid gland. Axial contrast-enhanced CT scan (**B**) in another patient shows mild generalized increased density in the right parotid gland and dilatation of Stensen's duct (*arrow*). Both of these patients had sialodochitis and sialadenitis.

Copyright © 2003, Mosby, Inc. All rights reserved.

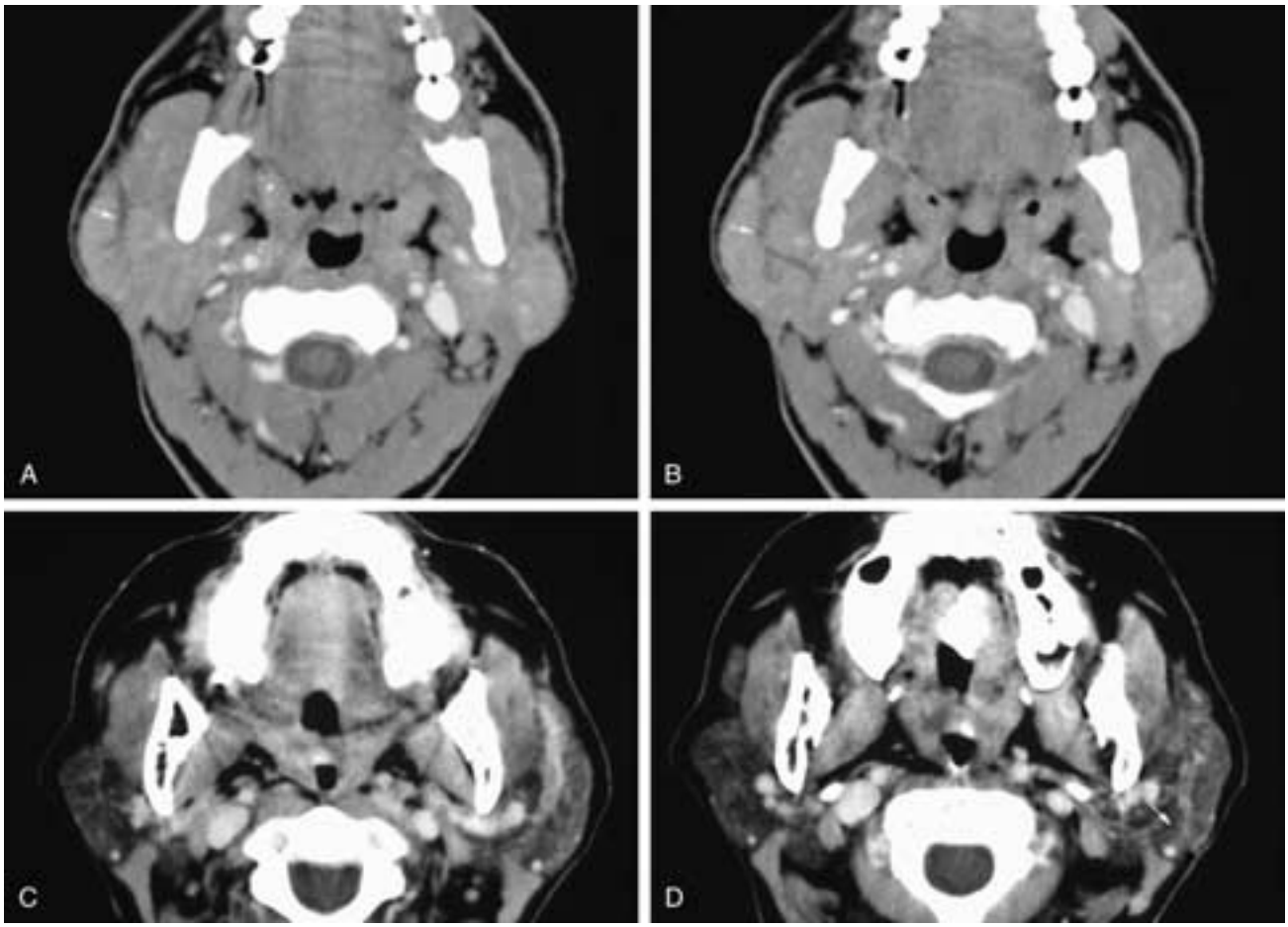

VIEW IMAGE

FIGURE 39-29 Axial contrast-enhanced CT scans (**A**, **B**) show minimal dilatation of the intraglandular ducts (*arrows*) within a slightly enlarged right parotid gland. This patient had very early right acute sialadenitis. Axial contrast-enhanced CT scans (**C**, **D**) show the early changes of a left sialadenitis. The left parotid gland parenchyma is denser than the normal right side secondary to edematous fluid and cellular infiltration. There is enhancement of the walls of the dilated intraglandular central parotid ducts.

The following discussion will focus on other infectious agents that can also affect the intraparotid or juxtaglandular lymph nodes, either as an ascending infection from the oral cavity or as part of a systemic process: tuberculosis, atypical mycobacterial infections, syphilis, cat-scratch fever, toxoplasmosis, actinomycosis, and sarcoidosis.[60, 121]

Mycobacteria

Primary tuberculous involvement of the salivary glands is rare. However, with the recent increase in the reported number of patients with tuberculosis (TB) in the United States, more of these cases are likely to be encountered in the next decade. Extrapulmonary TB is an uncommon event. In a review of patients with TB from Boston City Hospital during the years 1968 to 1977, it was estimated that 4.5% of all cases (over 1500 in total) had extrapulmonary TB.[122] Head and neck involvement in TB is an even rarer event. The authors had collected 136 cases of extrapulmonary TB; 16 (12%) patients had head and neck involvement: 13 patients had TB lymphadenitis of cervical, supraclavicular, or submental nodes; 1 patient had TB gingivitis; 1 had TB otitis; and 1 had TB laryngitis. For cases that do affect the salivary glands, 70% involve the parotid glands, 27% involve the submandibular glands, and only 3% involve the sublingual glands.[60] Most often the salivary disease arises from a focus in the tonsils or teeth and spreads to the gland via the regional lymph nodes. Sialadenitis occurs as the infection extends from the nodes into the gland proper. The clinical presentation may either be that of an acute tuberculous sialadenitis, which can mimic other acute infections, or a more indolent disease that may mimic a tumor.[112] In cases of chronic disease, the overlying skin may become inflamed and develop a fistulous tract. Secondary salivary TB occurs in cases of generalized TB and tends to affect the submandibular glands.[8]

The sialographic findings are primarily those of bacterial sialoadenitis, and focal abscesses tend to develop within the gland (Fig. 39-25). Adjacent tuberculous cervical adenitis may have an appearance similar to that of benign hyperplastic adenopathy or may have more extensive findings, which are described in Chapter 36.

Atypical mycobacterial infections of the salivary glands similarly tend to represent extensions from cervical adenopathy and are radiographically indistinguishable from tuberculous disease. This disease is most often found in immunosuppressed patients. Granulomatous reactions are

Copyright © 2003, Mosby, Inc. All rights reserved.

lacking in mycobacterial infections in the immunosuppressed population because of defects in cell-mediated immunity. Atypical mycobacterial infections are usually seen as diffuse infiltrates of foamy macrophages with abundant acid-fast bacilli.

The imaging findings are nonspecific and are generally those of a slightly enlarged, dense, congested gland, which may have microabscesses scattered irregularly throughout the gland.

Syphilis

Syphilis is a sexually transmitted bacterial infection caused by *Treponema pallidum* (*treponema*—Greek: turning thread, *pallidum*—Latin: pale), a long (5 to 20 μm), slender spirochete that rotates along its long axis in fluid and may ''creep'' and ''crawl'' along solid surfaces. Primary and secondary syphilis has a propensity to affect skin and mucosal surfaces. A chancre forms at the site of the primary infection. Cutaneous chancres are painless, hard, raised lesions with shallow ulcerations and sharp, raised borders. Mucosal primary chancres may appear as silvery gray erosions, granulation tissue, or nonspecific ulcers. Head and neck manifestations of secondary syphilis include condyloma lata, hyperplastic wart-like lesions that may occur in the larynx, ears, and nasolabial folds; ''mucous patches,'' oral raised and flattened, macerated lesions with a thin, grayish membranous covering; and a generalized maculopapular rash that may also occur intraorally. Tertiary syphilis tends to affect the central nervous system and the cardiovascular system. In the head and neck, tertiary syphilis is manifested as *gummas*, large necrotizing lesions with a proclivity for membranous bones. Gummas most commonly affect the palate; however, the nose, larynx, temporal bones, and ossicles may also be involved. Sinonasal gummas may present clinically with chronic sinusitis and drainage, as well as radiologic evidence of a destructive inflammatory mass that may easily mimic Wegener's granulomatosis or

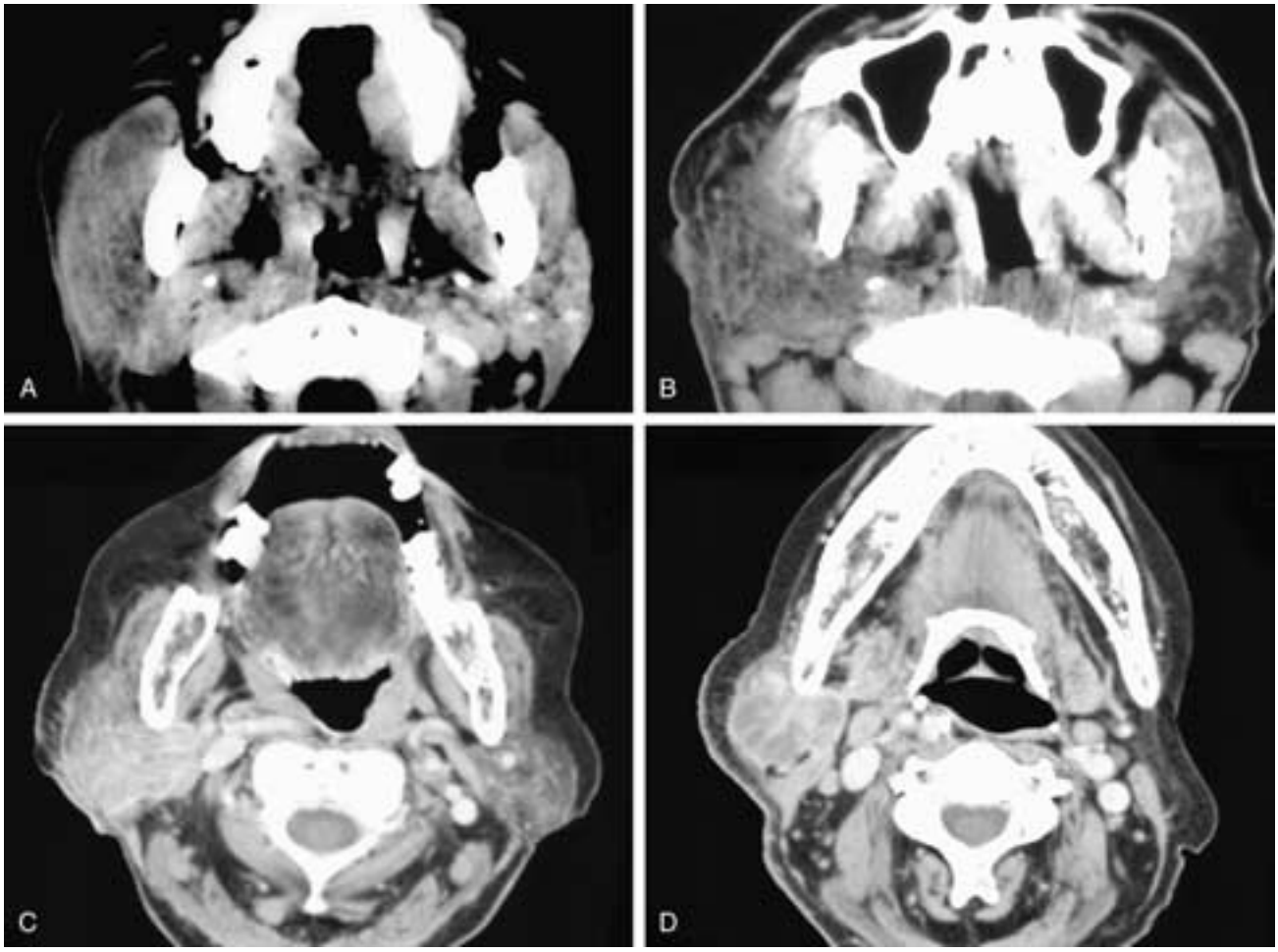

VIEW IMAGE

FIGURE 39-30 Axial contrast-enhanced CT scans on four different patients, all with acute sialadenitis. In **A**, there is enlargement of the right parotid gland, with blurring of the gland's margins. The adjacent masseter muscle is also enlarged, and there is involvement of the overlying subcutaneous tissues and skin. Thickening of the central parotid duct can be identified. The left parotid gland is dense, and there are small calcifications in the peripheral ducts. These are changes of chronic sialadenitis. In **B**, there is diffuse enlargement of the right parotid gland with a myositis of the right masseter and internal pterygoid muscles and an associated cellulitis. In **C**, there is enlargement and enhancement of the right parotid gland with adjacent cellulitis. There is minimal involvement of the right masseter muscle. In **D**, the right parotid gland is swollen, and the dilated glandular lobules can be identified. There is also evidence of cellulitis.

Copyright © 2003, Mosby, Inc. All rights reserved.

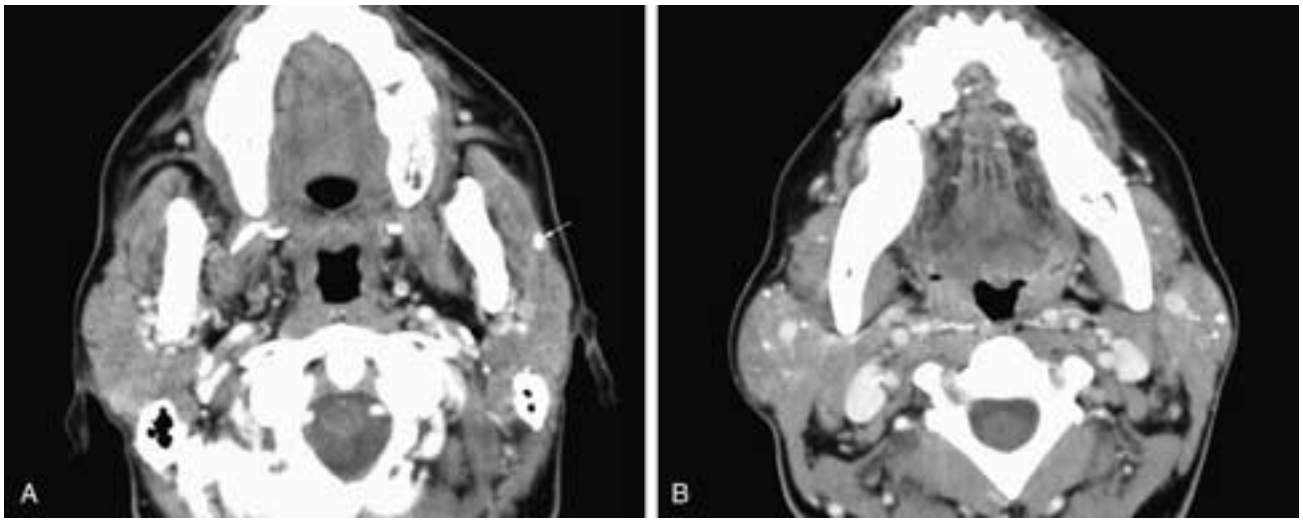

VIEW IMAGE

FIGURE 39-31 Axial contrast-enhanced CT scans (**A**, **B**) show multiple sialoliths in both parotid glands. Only the stone near the hilum of the left parotid gland (*arrow*) is causing symptoms of acute sialadenitis as it obstructs and dilates the main glandular duct immediately proximal to it.

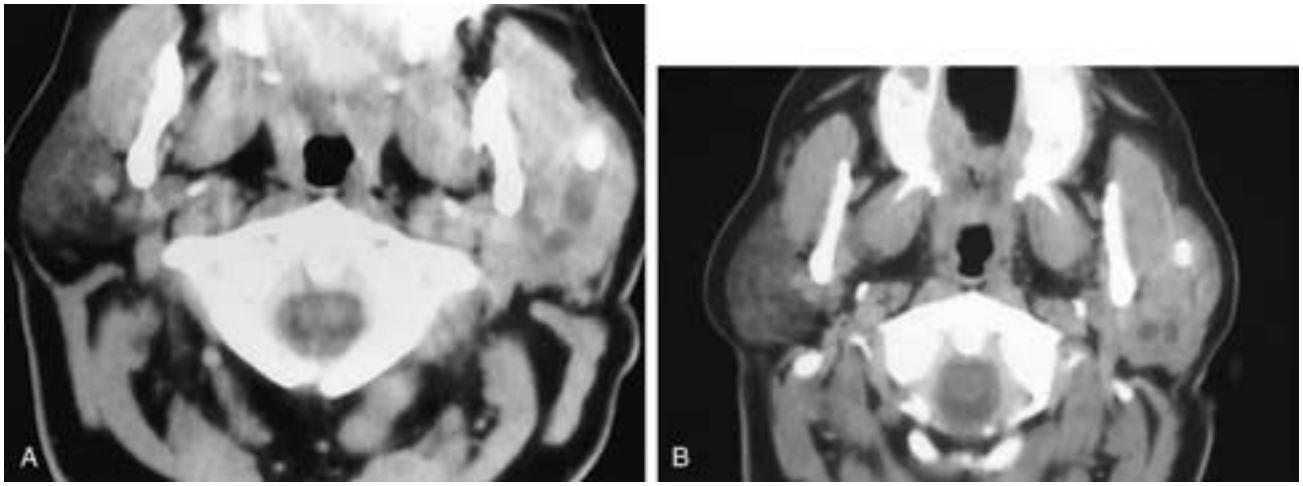

VIEW IMAGE

FIGURE 39-32 Axial CT scans (**A**, **B**) on two different patients. In **A**, there is a calculus in the hilum of the left parotid gland. Mucoid secretions are present in the dilated intraparotid central duct. The left parotid gland is diffusely denser than the normal right gland. In **B**, there is a calculus in the left parotid hilum, and dilated ducts are seen within the gland. The left parotid gland is also denser than the normal right parotid gland. Both of these patients had acute sialadenitis and sialolithiasis.

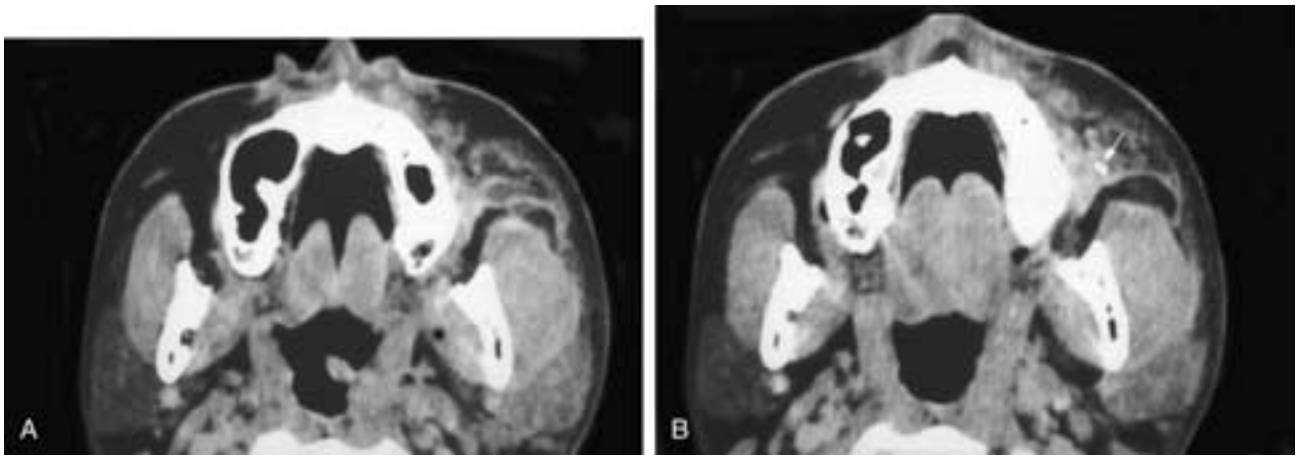

VIEW IMAGE

FIGURE 39-33 Axial CT scans (**A**, **B**) show increased density in the left parotid gland, thickening of the left masseter muscle, and increased density in the buccal fat pad region. There is also cellulitis in the overlying soft tissues in this patient with normal plane films of this region. In **B**, a more caudal scan shows a small calculus (*arrow*) in Stensen's duct. This patient had sialadenitis, sialodochitis, sialolithiasis, cellulitis, and myositis.

Copyright © 2003, Mosby, Inc. All rights reserved.

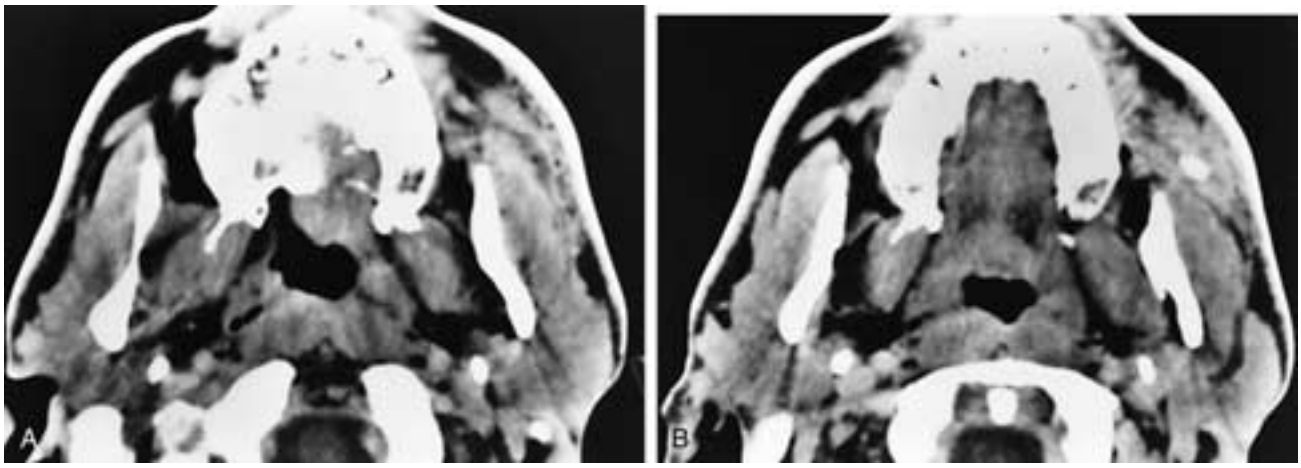

VIEW IMAGE

FIGURE 39-34 Axial contrast-enhanced CT scans (**A**, **B**) show increased attenuation in the left subcutaneous soft tissues overlying the region of the left part of Stensen's duct. There is also thickening of the left masseter muscle. In **B**, a more caudal scan, there is a small calculus in Stensen's duct with surrounding inflammatory changes. The routine plain films on this patient were normal. This patient had sialodochitis, sialolithiasis, and cellulitis.

sinonasal fungal disease. Another manifestation of tertiary syphilis is atropic glossitis resulting from obliterative vasculitis. Syphilis rarely affects the parotid glands. When this does occur, it is reported to have a distribution and an appearance similar to those of TB, and its imaging findings are similar to those of sarcoidosis.[8]

Cat-Scratch Disease

Cat-scratch disease (CSD), first described in France in 1950, is an infection caused by a rickettsia-like gram-negative bacterium introduced through a skin break and resulting in regional lymphadenitis. Children and young adults are most often affected. Patients present with lymphadenopathy following a cat scratch or bite. An erythematous lesion develops at the site of the scratch or bite, which resolves spontaneously within 1 to 3 weeks. CSD comes to medical attention when regional lymph nodes become painfully enlarged within weeks of development of the primary lesion. This nodal enlargement may be accompanied by fever, headache, myalgias, and rash. An atypical presentation is seen in up to 25% of cases, manifesting as ocular involvement, encephalopathy, granu-

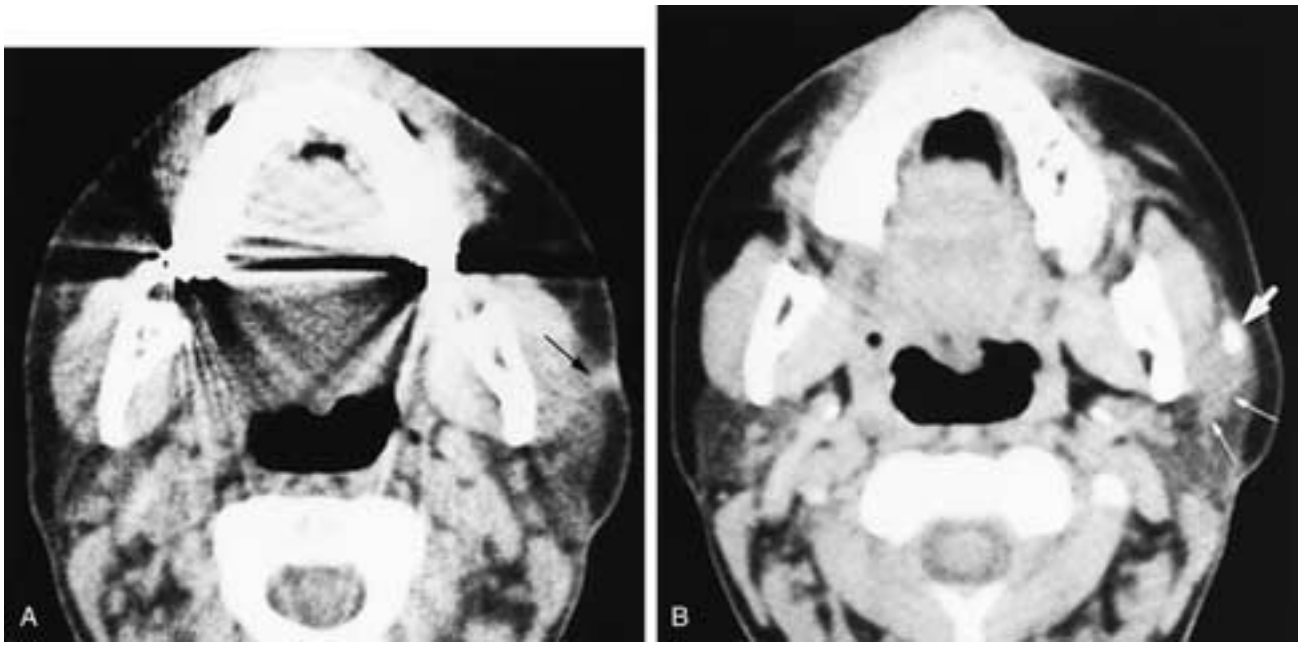

VIEW IMAGE

FIGURE 39-35 Axial CT scans (**A**, **B**) show a small sinus tract (*black arrow*) opening to the skin of the cheek. Clear fluid was draining from this site. In **B**, a more caudal scan, a small calculus (*short arrow*) is seen that caused obstruction of the saliva and that was not seen on routine plain films. There is increased attenuation in the obstructed parotid ducts just behind the calculus (*thin arrows*). This patient had sialodochitis, sialadenitis, sialolithiasis, and a sinus tract.

Copyright © 2003, Mosby, Inc. All rights reserved.

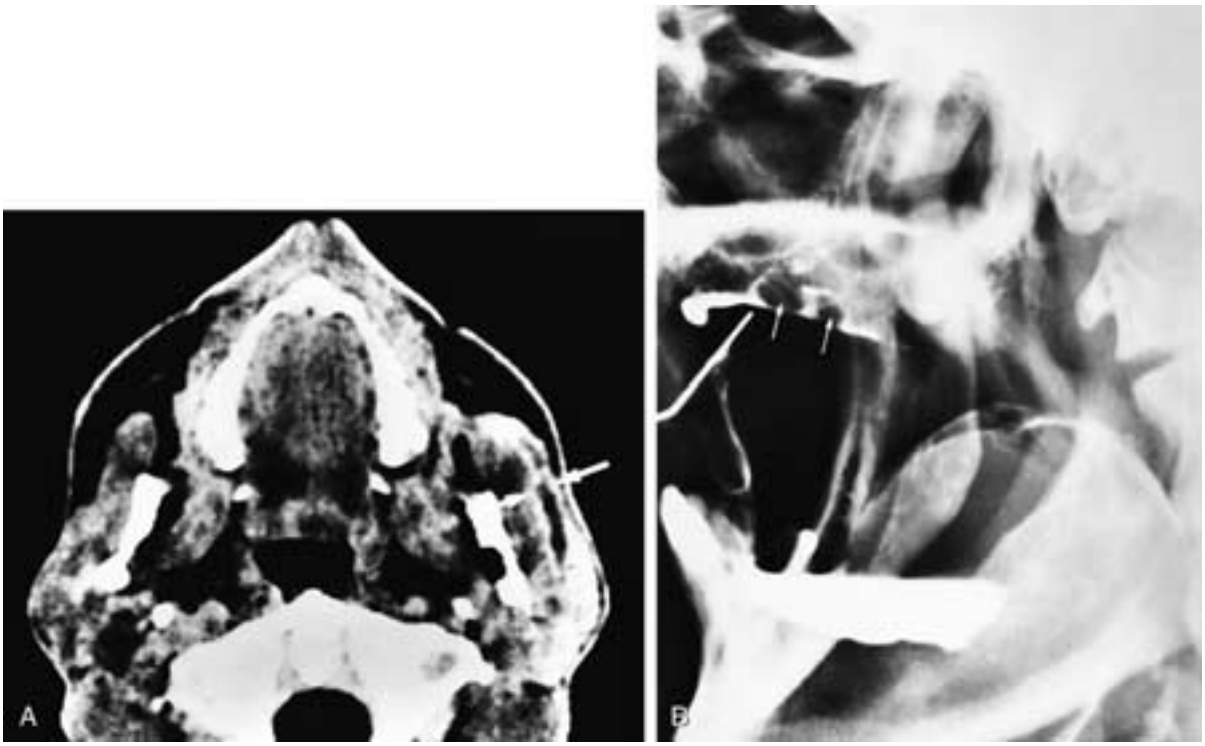

FIGURE 39-36 Axial contrast-enhanced CT scan (**A**) shows increased attenuation in the left parotid gland. There is also thickening and enhancement of the walls of Stensen's duct (*arrows*), and two lower-attenuation areas are present within the dilated duct. A lateral view of the left parotid sialogram (**B**) on the same patient shows two noncalcified stones in Stensen's duct (*arrows*). This patient had noncalcified sialolithiasis with sialodochitis and sialadenitis.

lomatous hepatitis, hepatosplenic infection, endocarditis, and osteomyelitis. The parotid lymph nodes may be involved with the lymphadenopathy, thus mimicking primary salivary gland disease.[8, 60] The imaging findings are nonspecific and are generally those of enlarged intraparotid lymph nodes. As such, the imaging findings can resemble either those of sarcoidosis or those of TB; therefore, CSD may be indistinguishable from these diseases.

The exact cause of CSD was uncertain until the 1990s. Initially, *Afipia felis* was thought to be the cause; however,

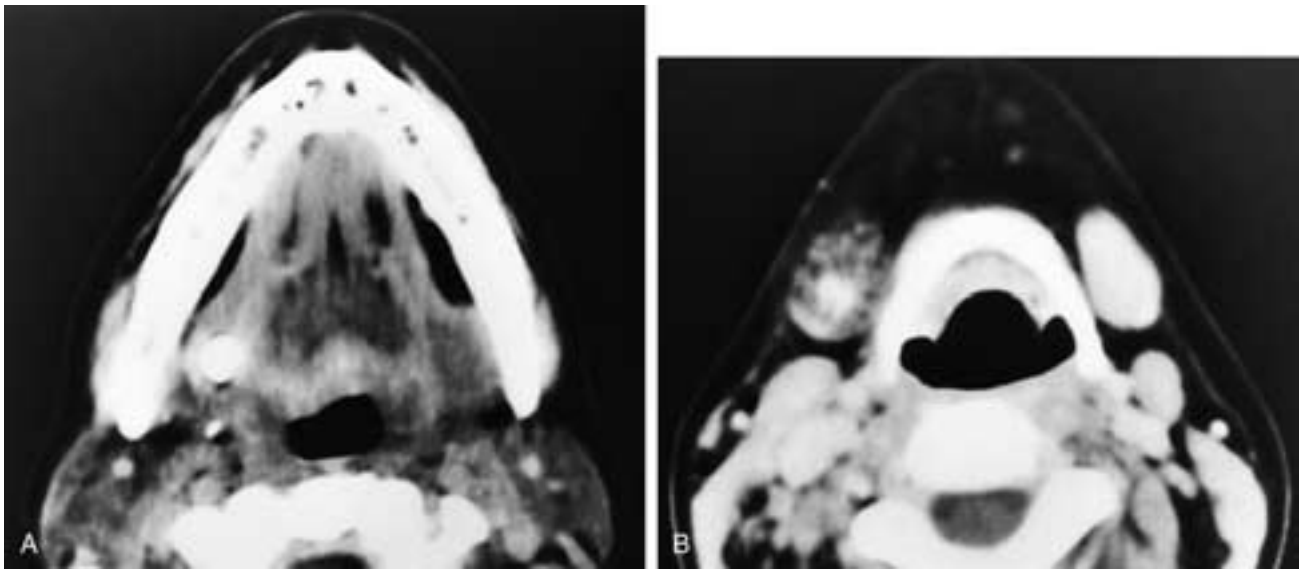

FIGURE 39-37 Axial contrast-enhanced CT scans (**A**, **B**) show a calculus near the hilum of the right submandibular gland. There is also some inflammatory thickening of the right mylohyoid muscle. In **B**, a more caudal scan, the lower portion of the calcification is seen in a somewhat diffusely fatty, atrophic gland. This patient had chronic submandibular sialolithiasis, sialadenitis, and early glandular atrophy.

Copyright © 2003, Mosby, Inc. All rights reserved.

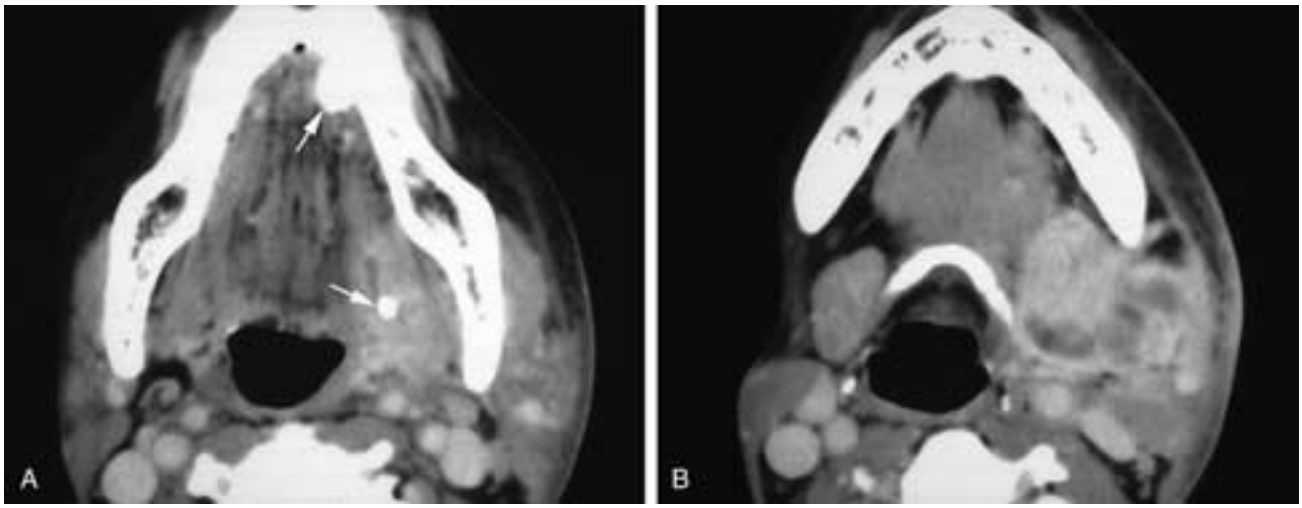

VIEW IMAGE

FIGURE 39-38 Axial contrast-enhanced CT scans (**A**, **B**) show two calculi in the left submandibular gland system (*arrows*). The stone at the hilum of the gland has caused an acute sialadenitis with a cellulitis. In **B**, an abscess is also seen around the gland. The formation of an abscess in acute submandibular sialadenitis is uncommon, and testing found this male to be HIV positive. This patient had submandibular sialolithiasis, sialadenitis, cellulitis, and an abscess.

subsequent study failed to confirm this. During the 1990s, it was demonstrated that *Rochalimaea henselae*, later reclassified as *Bartonella henselae*, was a causative agent. Multiple studies have subsequently shown that three *Bartonella* species may produce either CSD in humans, usually *B. henselae* or *B. clarridgeiae*, or bacteremia in healthy cats. Also, these two bacteria and *B. quintana* cause bacillary angiomatosis, bacillary peliosis, and relapsing bacteremia in humans.

Histologically, early cat-scratch lymphadenitis may reveal only nonspecific reactive changes and sinus histiocytosis. Epithelioid granulomas coalesce to form necrotizing microabscesses with polymorphonuclear cells and fibrin. Palisading epithelioid histiocytes rim ''stellate'' zones of necrosis. Bacilli are rarely present within the granulomas but have been noted within capillaries and macrophages.

CSD follows a self-limiting course of 2 to 4 months. Rarely, patients with CSD may progress to severe systemic infections such as encephalitis, osteomyeitis, hepatitis, or pleuritis. In complicated CSD, treatment with trimethoprim-sulfamethoxazole, ciprofloxacin, azithromycin, or gentamicin may be necessary.[123–125]

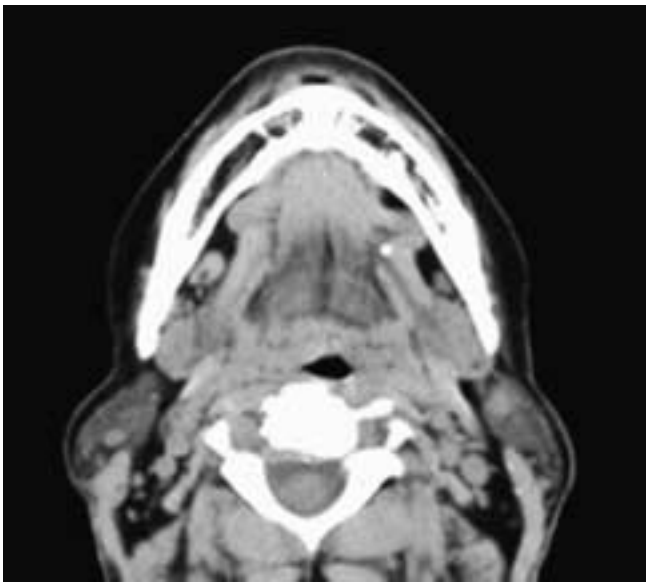

VIEW IMAGE

FIGURE 39-39 Axial CT scan shows a small calculus in the midportion of the left Wharton's duct. The duct is obstructed and dilated proximal to this stone. This patient had submandibular sialolithiasis and early sialadenitis.

Toxoplasmosis

Toxoplasmosis is a protozoan infection caused by *Toxoplasma gondii* transmitted by (1) inhalation of oocysts passed through cat feces, (2) ingestion of oocysts from poorly cooked or raw meats, (3) transplacental infection, or, rarely, (4) blood transfusions or organ transplantation. It is one of the most common infections affecting humans, infecting 5% to 95% of the population, depending on the geographic location. Normal hosts commonly have an asymptomatic infection. Cervical lymphadenopathy as well as fever, myalgias, anorexia, headache, sore throat, and rash are uncommon symptoms. In the parotid region, the disease may be clinically and radiographically indistinguishable from CSD, sarcoidosis, and TB.

Necrotizing systemic infections (retinitis, encephalitis, myocarditis, hepatitis, pneumonitis) rarely develop in the immune competent. But patients with AIDS or those who are immunosuppressed for other reasons are much more likely to develop severe and fatal infections. Toxoplasma encephalitis is the most frequent cause of intracerebral mass lesions in AIDS, and chronic or recurrent infection is the result of persistence of tissue cysts.

The histology of acute toxoplasmosis is characteristic. One sees epithelial granulomas with central ''stellate necrosis'' and an influx of monocytoid lymphocytes. Tachyzoites, especially in an extracellular location, may be observed with a tissue Giemsa stain. They are banana-

Copyright © 2003, Mosby, Inc. All rights reserved.

shaped or crescent-shaped, with a nucleus. The encysted forms of *T. gondii* are more easily visualized; they can be seen with hematoxylin and eosin stain, but are rarely present in lymph nodes.

Severe infection may be treated with pyrimethamine and sulfadiazine. Immune-competent patients require no specific therapy, as the lesion is self-limited due to the onset of cell-mediated immunity in the host.

Actinomycosis

Actinomycosis is caused by an anaerobic commensal gram-positive, filamentous, branching bacterium, *Actinomyces israelli*, and may result in oropharyngeal and locoregional draining infections. *Actinomyces israelii* is normally present in tonsillar crypts and around teeth, especially those with caries. Antecedent trauma or other precursors are necessary predisposing factors for invasive infection. The three common sites of *Actinomyces* infections are cervicofacial, thoracic, and abdominal. The most common form is cervicofacial infection. Soft-tissue abscesses and draining cervical fistulas develop as a result of secondary actinomyces infection of periapical abscesses. Actinomycosis can also present as a neck mass without the characteristic sinuses. Sinus tracts may occasionally become very extensive, creeping into the soft tissues of the back and chest. Parotid and submandibular lymph nodes may become secondarily infected via sinus tract extension of chronic mandibular infection.[60] The surrounding soft tissues have an inflammatory infiltrate; thus, a parotid infection may extend into the masticator space. Rarely, the disease can spread to the parotid in a retrograde manner from the oral cavity. Parotid disease can be acute, presenting with pain, swelling, abscess, and fistula formation. The presentation of chronic parotid infection is similar to that of TB, manifesting as a painless parotid mass.

The pale yellow ‘‘sulfur granules’’ or grains observed clinically represent microcolonies of bacilli. On hematoxylin and eosin stain, one sees only blue amorphous masses;

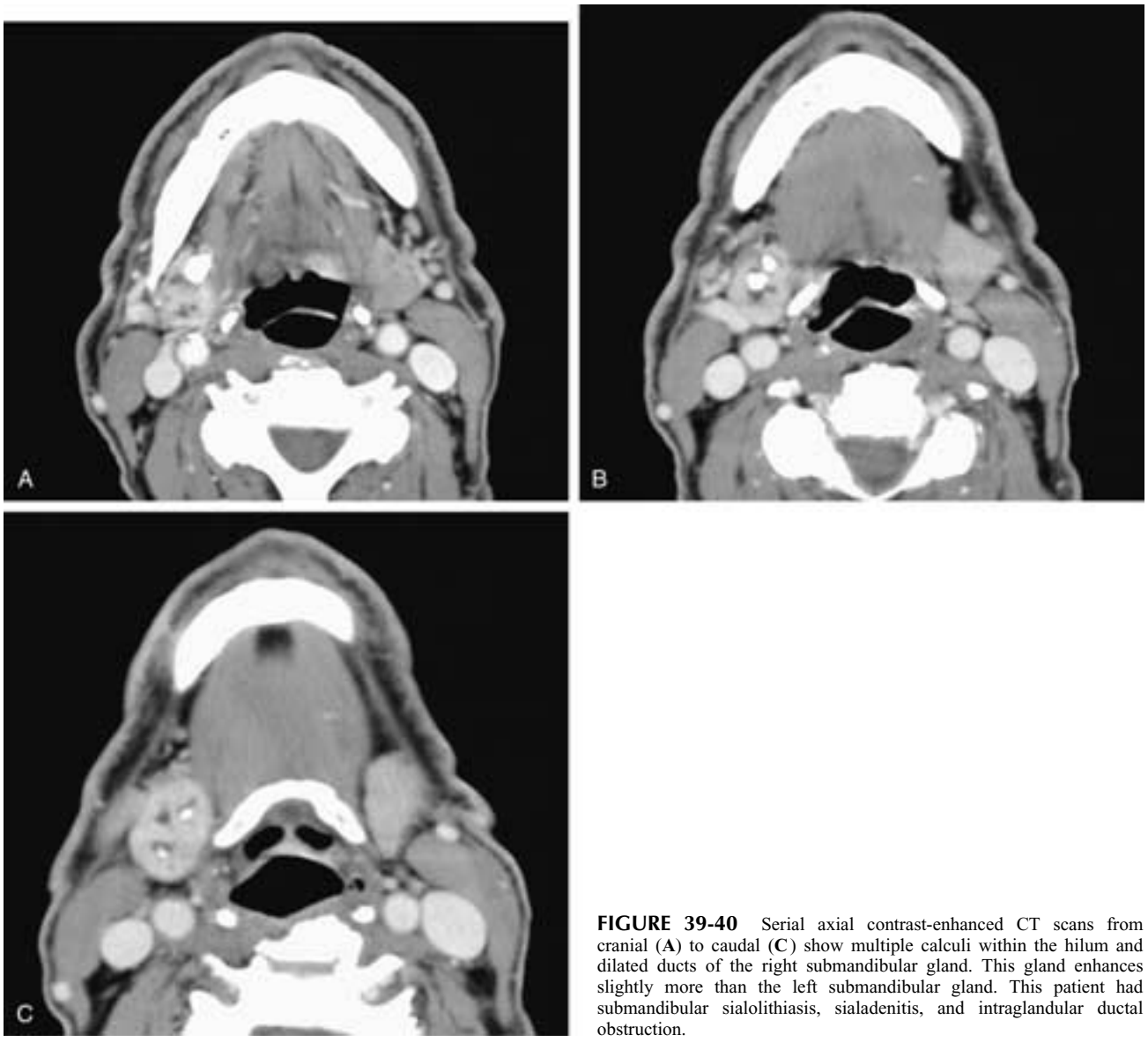

FIGURE 39-40 Serial axial contrast-enhanced CT scans from cranial (**A**) to caudal (**C**) show multiple calculi within the hilum and dilated ducts of the right submandibular gland. This gland enhances slightly more than the left submandibular gland. This patient had submandibular sialolithiasis, sialadenitis, and intraglandular ductal obstruction.

VIEW IMAGE

Copyright © 2003, Mosby, Inc. All rights reserved.

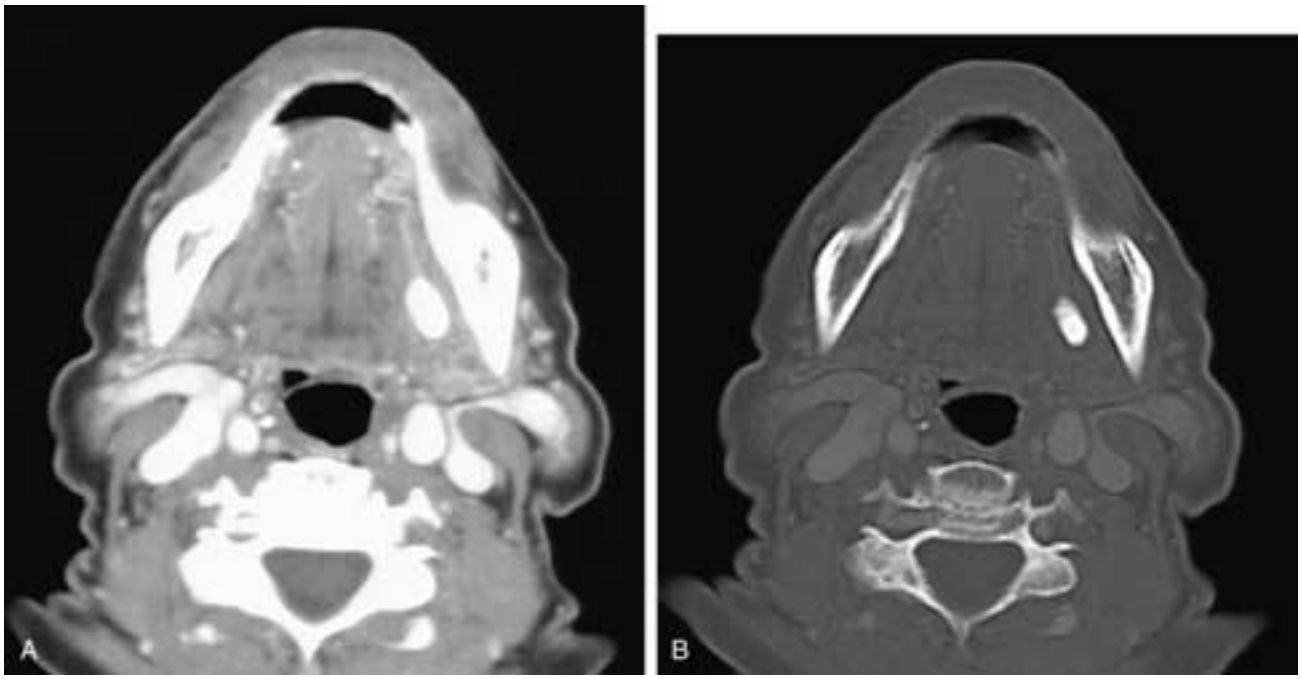

FIGURE 39-41 Axial CT scans viewed at narrow (**A**) and wide (**B**) windows show a calculus in the left hilum and the proximal portion of Wharton's duct. This patient had submandibular sialolithiasis and early sialadenitis.

VIEW IMAGE

the slender, filamentous nature of these bacilli is apparent on Brown and Brenn stain or Gomori methenamine silver stain. The filaments have a club-shaped or ''beaded'' end. The diagnosis of actinomycosis is confirmed by anaerobic culture.

Sarcoidosis

Sarcoidosis is a systemic disease of presumed infectious etiology characterized by noncaseating granulomas involving multiple organ systems. The exact agent of sarcoid is unknown, but existing data implicate an L-form of mycobacteria. The parotid glands are affected in 10% to 30% of patients, and in some cases the parotid disease may be the initial and only manifestation of the disease. Usually in such patients, a careful medical history will indicate that there was prior pulmonary disease, albeit presently quiescent. In 83% of these patients bilateral parotid gland enlargement is present, and there is decreased salivary flow. In some patients, involvement of the minor salivary glands can cause xerostomia.[60, 126] In most patients, a nontender, nonpainful, chronic enlargement of the gland occurs. The gland is often multinodular and clinically may mimic a malignancy.

The parotid glands can also be involved in patients with sarcoidosis who have uveitis and facial nerve paralysis. This triad of findings is called *Heerfordt's syndrome*.

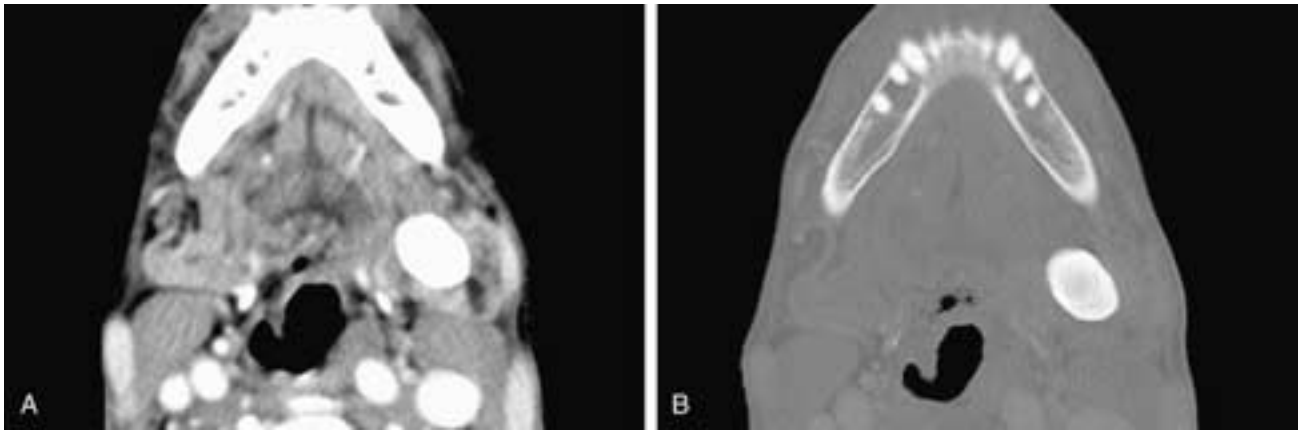

FIGURE 39-42 Axial CT scans viewed at narrow (**A**) and wide (**B**) windows show a large laminated calculus in the hilum of the left submandibular gland. There is some intraglandular ductal dilatation. This patient had submandibular sialolithiasis and early sialadenitis.

VIEW IMAGE

Copyright © 2003, Mosby, Inc. All rights reserved.

Importantly, one should not confuse parotid fullness or a mass and an ipsilateral facial nerve paralysis with a parotid gland malignancy. Most cases of such salivary gland sarcoidosis usually resolve as the underlying disease is treated.

On CT or MR imaging the parotid granulomas are usually multiple, benign-appearing, noncavitating masses. In fact, these nodes are frequently described radiographically as being ''foamy'' in appearance. This appearance most often is associated with adjacent cervical adenopathy (Figs. 39-43 and 39-44). In this circumstance, the diagnosis can be suggested on the basis of the radiologic findings. The main differential diagnosis is lymphoma. However, if the sarcoid granuloma is a solitary parotid mass, it cannot be differentiated from the other benign-appearing parotid lesions. Occasionally, small interstitial sarcoid granulomas may occur within the parotid gland. These are usually subclinical and are discovered incidentally if surgery is performed for other reasons. At present, they cannot be diagnosed reliably on either CT or MR imaging.

Other Causes: "Iodine Mumps"

A case of iodine mumps after a CT examination with 100 ml iopamidol was reported in a 70-year-old woman with a history of right nephrectomy due to right renal cancer. Three hours after the CT study, she complained of nausea, vomiting, facial flushing, bilateral jaw pain, and fever. The laboratory findings 12 hours after CT showed an increased white blood cell count and elevated serum amylase enzymes, 86% of which originated from the salivary glands. Her symptoms continued for 4 days, with decreasing severity.[127]

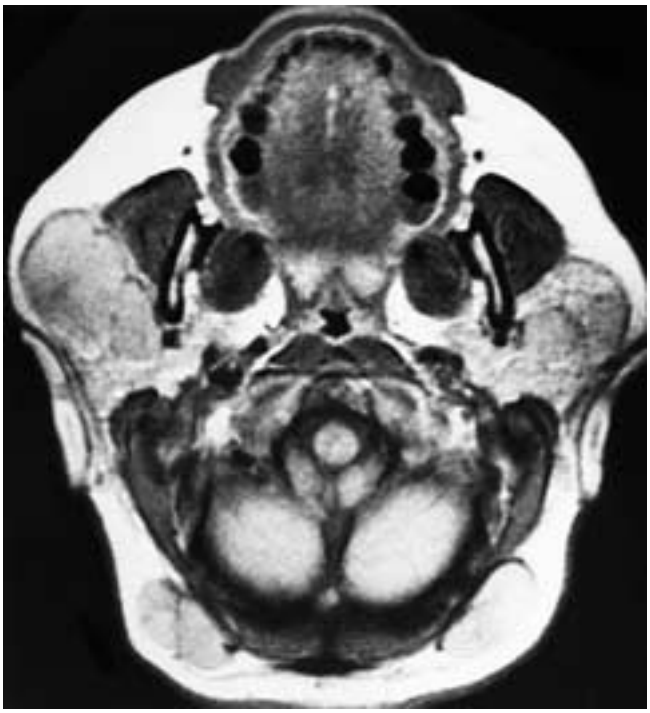

FIGURE 39-43 Axial proton density MR scan shows multiple masses within both parotid glands and enlarged occipital and posterior triangle lymph nodes. This patient had sarcoidosis.

VIEW IMAGE

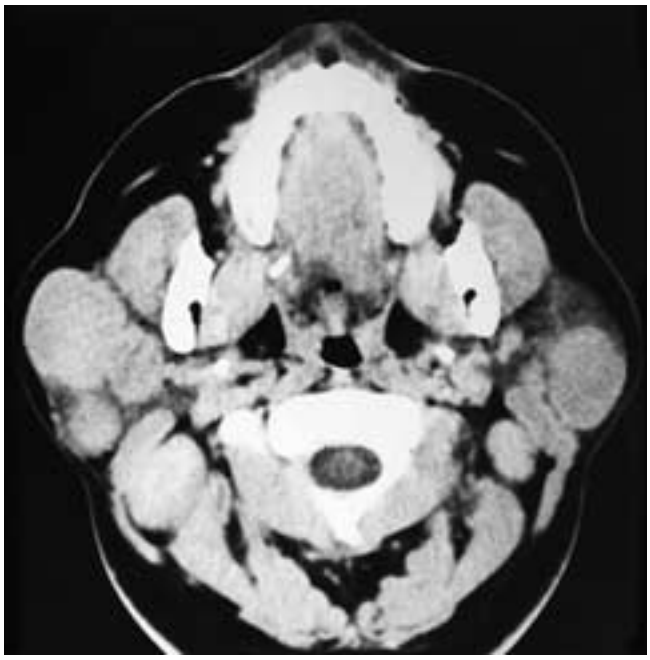

FIGURE 39-44 Axial CT scan shows multiple bilateral enlarged, homogeneous parotid lymph nodes. This patient had sarcoidosis.

VIEW IMAGE

Sialolithiasis

Between 80% and 90% of salivary gland stones occur in the submandibular gland, 10% to 20% occur in the parotid glands, and only 1% to 7% occur in the sublingual glands.[8, 60] Minor salivary gland calculi are rare, occurring most often in the upper lip and buccal mucosa.[21] About 75% of stones are solitary; however, about 25% of patients with one stone have multiple stones, with 32% of parotid calculi and 22% of submandibular stones being multiple. Bilateral salivary stones are rare (2.2%).[60, 62] In patients with chronic sialoadenitis, at least one calculus is present in two thirds of the cases, and 80% of submandibular stones and 60% of parotid stones are radiopaque on plain films.[12]

Some of the reasons given for the increased incidence of sialolithiasis in the submandibular gland compared to the parotid gland include the thicker, more mucous nature of submandibular gland secretions; their more alkaline pH, which helps precipitate salts; the higher concentration of hydroxyapatite and phosphatase; the narrower orifice of Wharton's duct compared to the caliber of the duct itself; and the uphill grade in the erect position of Wharton's duct.[8, 12, 60, 112]

About 85% of submandibular gland stones occur within Wharton's duct: 30% near the duct's ostium, 20% in the middle portion of the duct, 35% at the bend in the duct as it goes around the back of the mylohyoid muscle, and only 15% in the hilum and gland proper (see Figs. 39-11, 39-37 to 39-42).[60, 128] Symptomatic parotid gland stones occur primarily in Stensen's duct; however, incidental asymptomatic, small intraparotid ductal calculi are not uncommonly seen on CT scans (Figs. 39-31 to 39-36).

Sialoliths in Wharton's duct are diagnosed after longer symptomatic periods than those stones in Stensen's duct (up to 1 year versus up to 2 months, respectively). This is

Copyright © 2003, Mosby, Inc. All rights reserved.

because Wharton's duct can accommodate to the obstruction, and saliva will still flow due to the wide duct width and the presence of ductal pseudodiverticula. If the stone causes a ball-valve effect, the patient has intermittent obstruction and glandular swelling, usually at times of increased salivation. Larger stones may cause complete obstruction with an initial prolonged glandular swelling that, if left untreated, may eventually result in glandular atrophy. Stasis may result in a secondary bacterial infection. Rarely, a giant intraparotid calculus has been reported in a patient with recurrent parotitis.[129]

Gout is the only systemic disease known to cause salivary calculi, which are composed of uric acid. The majority of routine salivary calculi are composed primarily of calcium phosphate, with small amounts of magnesium, ammonium, and carbonate in a carbohydrate and amino acid organic matrix.

The initial radiographic investigation of sialolithiasis is the plain film examination. Larger, well-calcified stones are clearly seen with this technique (Figs. 39-10 and 39-11); however, small or partially calcified stones may elude detection. It is estimated that about 20% of submandibular gland stones and 40% of parotid gland stones are unseen on routine plain films.[112] Because CT has a 10-fold increased sensitivity compared to plain films in detecting focal calcium deposits, noncontrast CT scans can identify most of the stones that are unobserved on the plain film examination. Such small, faintly calcified stones may also be obscured on a sialogram and may be undiagnosed unless a plain scout film or a CT scan was obtained prior to the introduction of sialographic contrast medium. Noncalcified stones are best seen on a sialogram; however, some of the larger ones can also be identified on postcontrast CT scans (see Fig. 39-36A).

A stricture of a major salivary gland duct can occur secondary to a calculus, with or without associated recurrent infection. Less often, trauma or ill-fitting dentures can cause a stricture near the duct orifice or along the course of the duct. Whatever the cause, if there is significant obstruction to salivary flow, recurrent or chronic bacterial infection results. Treatment is either by periodic dilatation, surgical repair if the stricture is near the oral cavity, or a partial parotidectomy or submandibular gland resection if the stricture is closer to the hilum of the gland.[112] If salivary flow is completely obstructed, glandular atrophy eventually occurs. If incomplete obstruction occurs, the gland usually continues to produce saliva and a glandular mucocele may develop.

A Küttner tumor is a palpably enlarged, firm mass of the submandibular gland that results from chronic inflammation. One third of these cases are due to sialolithiasis; other cases may be autoimmune or idiopathic in origin.

A cavernous hemangioma in the submandibular gland was reported that clinically and radiologically (both on plain radiographs and on CT) resembled salivary calculous disease. Numerous phleboliths were present in the hemangioma.[130] In most cases, phleboliths are circular, laminated, and multiple.[21]

In general, stones within the distal parotid and submandibular salivary ducts are easily removed by transoral ductotomy, while more proximal stones are usually treated by excision of the salivary gland and its duct. Since the 1980s, extracorporeal shock wave lithotripsy has been used for the treatment of renal and gallbladder stones. In the early 1990s, this technique was used to treat sialolithiasis.[131] After this treatment, clinical symptoms such as pain and swelling disappeared, and gland excision was unnecessary. However, stones larger than 10 mm have a tendency to respond incompletely. Although CT findings correlated with success in breaking up gallstones, they did not predict success in destroying salivary stones. It was concluded that sialolithiasis can be treated successfully by extracorporeal shock wave lithotripsy without adverse effects in selected patients.[132] In the opinion of some investigators, the results of this procedure are uncertain, and it has not become a modality of choice in the treatment of salivary stones.

Chronic Recurrent Sialoadenitis

Chronic recurrent sialoadenitis is characterized by recurrent diffuse or localized, painful swelling of the salivary gland. It usually is associated with an incomplete obstruction of the ductal system; however, on occasion, a nonobstructive variant is present.[112, 116] A sialogram performed during a clinically quiescent period in a patient with the obstructive form of this disease usually shows a focal narrowing (stricture) of the main duct and central ductal dilatation (sialectasia); these dilated ducts often taper rather dramatically to normal peripheral ducts (and acini). In these patients, if the obstruction in the main salivary duct can be relieved, the gland may function normally and may not require resection (Figs. 39-45 and 39-46). This is because the

FIGURE 39-45 Lateral view of a parotid sialogram shows dilatation of Stensen's duct and the central parotid ducts behind a noncalcified stone (*arrow*). Most of the peripheral ducts are not visualized, and the patient eventually required a parotidectomy because of recurrent infections after initial surgery for removal of the stone. This patient had sialadenitis, sialolithiasis, and ductal stricture.

VIEW IMAGE

Copyright © 2003, Mosby, Inc. All rights reserved.

FIGURE 39-46 Frontal view of a parotid sialogram shows a stricture (*arrow*) in the anterior portion of Stensen's duct. There is marked dilatation of Stensen's duct and the central parotid ducts behind the stricture. The peripheral ducts are almost normal. The patient did well after dilatation of the stricture site. This patient had sialodochitis, sialadenitis, and a ductal stricture.

salivary acini were not entirely destroyed despite the often considerable dilatation of the main ductal system. Alternatively, the peripheral ducts and acini may not be visualized on a technically good sialogram. In these cases, the acini are not visualized because they are compressed and destroyed by the cellular infiltrate (Figs. 39-47 to 39-50). As a result, saliva production decreases, causing further sialoadenitis. Thus, if the peripheral ducts and acini are not visualized on a technically adequate sialogram, it is unlikely that this gland will function normally, and eventually a partial gland resection will probably have to be performed.

Areas of ductal branch point narrowing may in part represent focal inflammatory changes. In addition, scattered localized globular collections of contrast material may be encountered. These represent focal abscesses. When multiple, they usually are nonuniform in size and distribution throughout the gland, a factor that distinguishes most cases from the autoimmune diseases (Figs. 39-24, 39-25, 39-49, and 39-50).

On CT, the involved gland is usually enlarged, diffusely dense, and enhancing, and there may be a few scattered areas of calcification. Surrounding fasciitis and reactive adenopathy are usually not present. On MR imaging, the gland is usually enlarged, and there is a nonhomogeneously low T1-weighted and an intermediate to high T2-weighted signal intensity. The signal intensity apparently reflects the degree of a chronic inflammatory cellular infiltrate versus the presence of associated edema fluid.

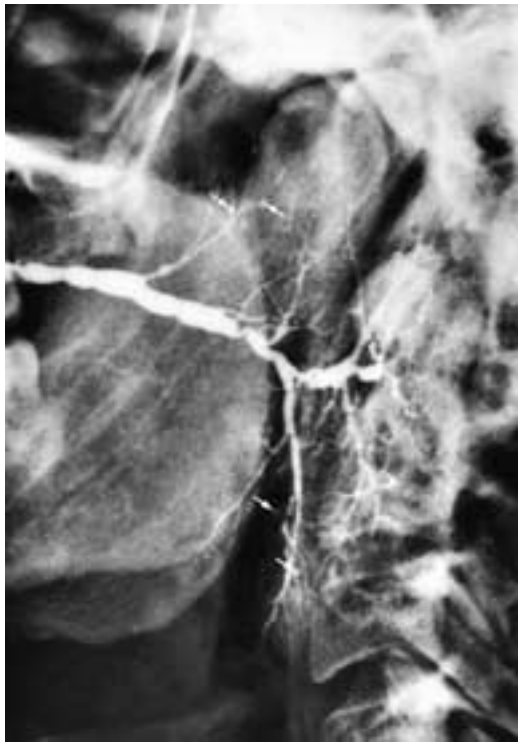

FIGURE 39-47 Lateral view of a parotid sialogram shows dilatation of Stensen's duct and the central intraparotid ducts. The peripheral ducts are not dilated. There are scattered small collections of contrast material (*arrows*), which represent small abscesses. Areas of stricture and functional spasm are also seen in the central ducts. This patient had sialadenitis.

FIGURE 39-48 Lateral view of a parotid sialogram shows mild dilatation of Stensen's duct and some of the central parotid ducts. There are areas of branch point narrowing and small abscesses (*arrows*). The majority of the peripheral ducts are visualized. This patient had chronic sialadenitis.

Copyright © 2003, Mosby, Inc. All rights reserved.

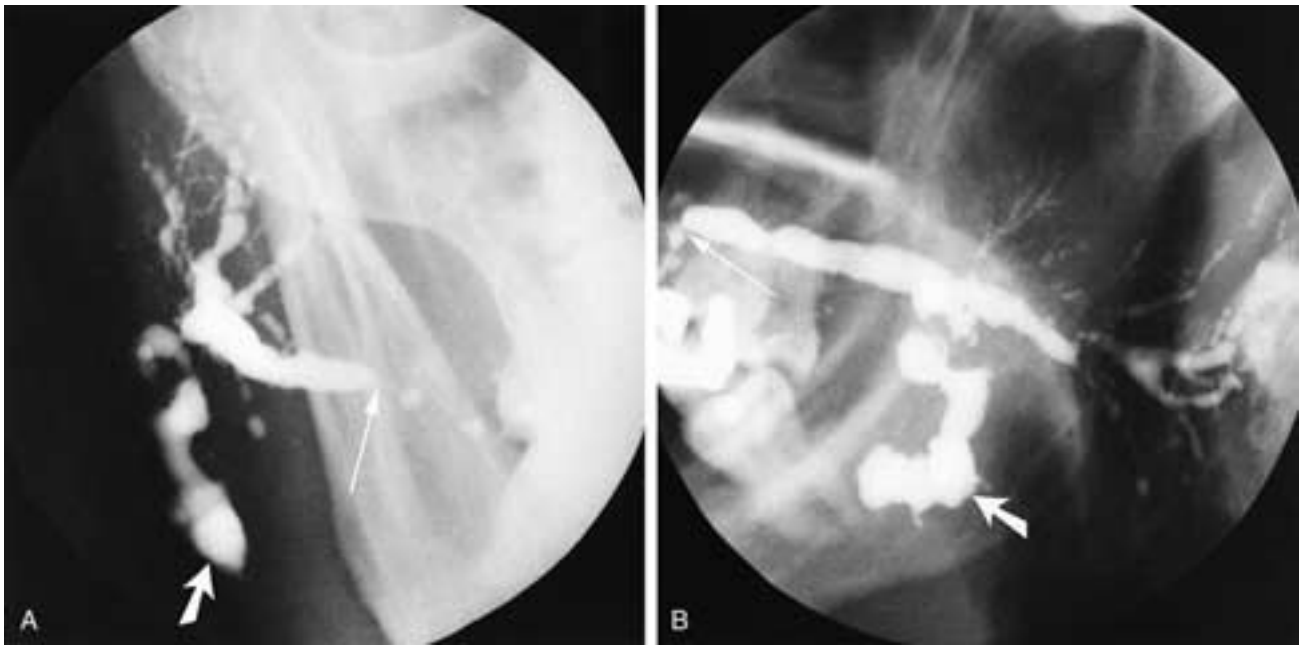

VIEW IMAGE

FIGURE 39-49 Frontal (**A**) and lateral (**B**) views of a right parotid sialogram show a stricture (*long arrow*) of the anterior portion of Stensen's duct. There is dilatation of Stensen's duct and the central and peripheral parotid ducts, and there is a fistulous tract (*short arrow*) to the skin. This patient had sialodochitis, sialadenitis, ductal stricture, and a fistula.

VIEW IMAGE

FIGURE 39-50 Frontal view of a left parotid sialogram shows a fairly normal Stensen's duct and parotid ducts, with the exception of multiple scattered collections of contrast material in small abscesses. These abscesses are not uniformly distributed throughout the gland. This patient had chronic sialadenitis with abscesses.

Sialodochitis Fibrinosa (Kussmaul's Disease)

Sialodochitis fibrinosa is an unusual disease characterized by recurrent, acute, painless or painful attacks of parotid or submandibular gland swelling secondary to a mucous or fibrinous ductal plug. The clinical appearance of this plug in either Stensen's or Wharton's duct orifice is diagnostic. This disease occurs primarily in dehydrated and debilitated patients. The treatment is glandular massage, the use of secretogogues to release the plug, ductal orifice dilatation to help prevent a recurrence, and, when clinically possible, rehydration.[112, 133]

Ductal Foreign Bodies

Ductal foreign bodies have been reported approximately 50 times in the literature. The cause in unknown, and spontaneous resolution has been reported in some cases. Most of the foreign bodies have been vegetable products such as grass seeds. The foreign body may cause chronic recurrent sialoadenitis, calculus formation about the foreign body, abscess formation, and sinus tract formation.[121]

Trauma

Blunt trauma injuries occur mainly in the parotid gland and result in edema, contusions, hemorrhage, and/or hematoma. Such injury is uncommon to the submandibular glands and sublingual glands, presumably due to the protection of the mandible.[21] Penetrating injuries may result

Copyright © 2003, Mosby, Inc. All rights reserved.

in laceration of Stensen's duct, the parotid parenchyma, and/or the facial nerve.

Stenosis of Stensen's duct orifice can occur as a result of repeated cheek biting or ill-fitting dentures, or secondary to epithelial injury from either stones or surgical manipulation. Injury to the gland parenchyma can also result in either a parenchymal laceration or an intracapsular hematoma. Calcification of such intraparenchymal hemorrhage can occur.[60]

Autoimmune Diseases (Including Benign Lymphoepithelial Lesion)

Sjogren's syndrome (SS) is a systemic autoimmune disorder of the exocrine glands that occurs either alone (referred to as *primary Sjogren's syndrome*) or with any of several connective tissue diseases (referred to as *secondary Sjogren's syndrome*). Traditionally, the diagnosis is established when two or more of the following clinical hallmarks are present: keratoconjunctivitis sicca, xerostomia, and/or a connective tissue disease, usually rheumatoid arthritis.[133] Patients complain of oral dryness, difficulty in swallowing food, oral soreness and intraoral ulcers, decreased ability to taste foods, severe dental problems, ''grittiness'' in the eyes, and inability to cry. The autoimmune diseases represent a diffuse exocrinopathy that primarily affects the lacrimal and salivary glands. However, other exocrine glands can also be involved. Thus, clinically, the exocrine involvement may cause not only dryness of the eyes and mouth, but also bronchial dryness (tracheobronchitis with a nonproductive cough), dry skin (itching), esophageal dryness (dysphagia), and genital dryness (atrophic vaginitis with burning and/or dyspareunia). Involvement of the glands of the gastrointestinal tract also occurs but is less frequent.[134, 135] Often the involvement of these other exocrine gland systems is histologically present but not clinically apparent.[128]

In the late nineteenth century, Mikulicz described the clinical findings in a Prussian farmer who presented with symmetric enlargement of all of his major salivary glands and his lacrimal glands, which was most likely of autoimmune etiology. Soon afterward, a similar clinical entity was observed in children and became known as recurrent parotitis in children. In the late 1930s, the term *Mikulicz's syndrome* was introduced to describe patients who presented with what clinically appeared to be Mikulicz's disease but who actually had another disease such as lymphoma, TB, or sarcoidosis. Unfortunately because of the overlapping terminology, confusion ensued between what comprised Mikulicz's disease and Mikulicz's syndrome, and this eventually lead to the complete elimination of the name Mikulicz. The term *sicca syndrome* temporarily replaced *Mikulicz's disease*. Currently, the term that refers to autoimmune disease limited to the salivary and/or lacrimal glands is primary Sjogren's syndrome.[134–136]

SS is the result of a lymphocyte-mediated destruction of exocrine glands that causes decreased secretions and dryness. SS is often associated with extrasalivary manifestations. In a study of 114 patients with SS, 42% had articular manifestations, 35% had neurologic manifestations, 21% had pulmonary involvement, and 13% had hepatic manifestations.[137] The pulmonary invasion leads to an intense lymphocytic infiltration, diffuse interstitial pneumonitis, fibrosis, or restrictive lung disease.[138] Eleven of these patients (9%) also developed vasculitis associated with hepatitis C infection, and three (2%) developed lymphoproliferative disorder. Involvement of the central nervous system is typified by polyneuropathy and/or mononeuritis multiplex.

Histologically, SS is characterized by periductal lymphocytic aggregates that extend into and destroy the salivary acinar parenchyma. The lymphocytes are mainly (CD45RO+) CD4-positive T lymphocytes. As the inflammation progresses, ectopic germinal centers are seen. When SS involves the major salivary glands, most often the parotid gland, the lymphoid infiltrate produces a localized parenchymal mass referred to as a benign lymphoepithelial lesion (BLEL) or Godwin's tumor[135] (Fig. 39-51). The BLEL is seen as a localized lymphoid infiltrate within the major salivary glands, usually the parotid. It is composed of small lymphocytes, germinal centers, and a periductal lymphoid infiltrate. Proliferation of ductal epithelium results in the obliteration of ductal lumina and the production of epithelial (epimyoepithelial) islands, which may undergo squamous metaplasia and hyalinization. Although these islands may be few in number, their identification is necessary for a pathologic diagnosis of BLEL to be made.[134, 135] BLEL is usually solid but occasionally may have a pronounced cystic component. BLEL may present clinically in the setting of a known autoimmune disease or independently of autoimmune symptomatology.

The mechanism of SS involves altered ductal cell antigenic statement. The ductal epithelial cells are activated in SS, expressing elevated levels of human leukocyte antigen-DR (HLA-DR) and secreting high levels of proinflammatory cytokines. This results in inappropriate activation and retention of B cells within the major and minor salivary glands. Once recruited, these lymphocytes survive due to their low rate of apoptosis, which is facilitated in part by alterations in cytokine production (interleukin-2, interleukin-10, tumor necrosis factor alpha).[139]

Although no specific virus has been identified as the cause of SS, retroviruses are now believed to be involved in the induction of autoimmunity. There have been eight case reports of the combination of human T-cell lymphocytic virus type 1 (HTLV-1)–associated myelopathy, SS, and lymphocytic pneumonitis, all occurring in areas endemic for HTLV-1.[140]

The actual incidence of SS is difficult to establish because the symptoms can be nonspecific and the specific autoimmune antibodies (SS-A and SS-B) may be elevated only during active disease or not elevated at all, as in the case of antibody-negative men with SS. An autopsy study in 1957 estimated the incidence to be 1 case per 225 people. Thus, of the autoimmune diseases, SS was considered second in frequency only to rheumatoid arthritis.[134] There is a marked female predominance for SS, and the mean age of diagnosis is within the sixth decade of life.[137] However, there is a subgroup of patients diagnosed within the first two decades of life (see below).[141]

A slight male predominance has been described in some series of juvenile SS but not in other series.[141, 142] The

Copyright © 2003, Mosby, Inc. All rights reserved.

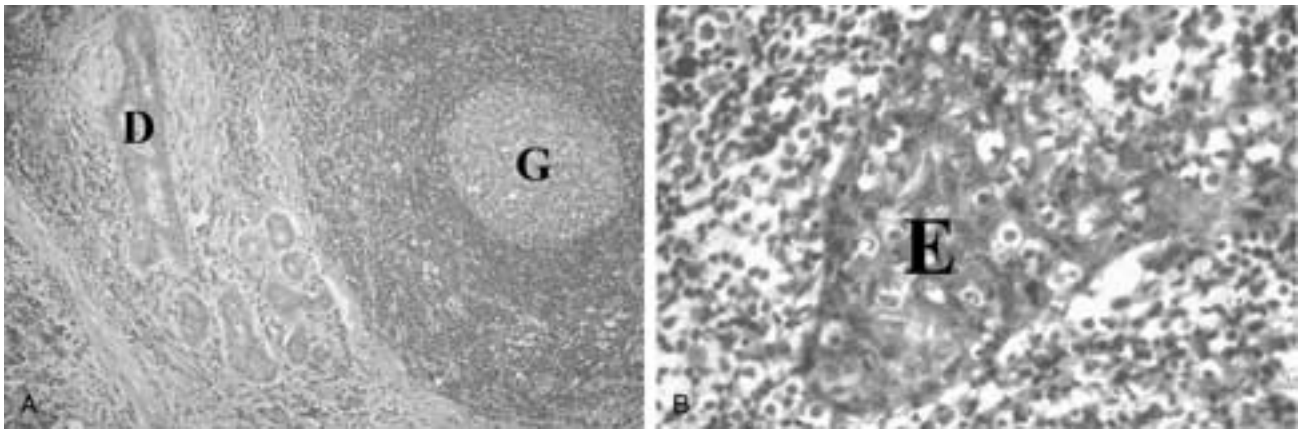

VIEW IMAGE

FIGURE 39-51 Benign lymphoepithelial lesion. **A**, Lymphoid infiltrate with a germinal center (*G*) adjacent to the parotid ducts (*D*). **B**, High-power view of one of these epithelial islands (*E*), which represent transformed ducts.

clinical picture of juvenile SS is similar to that of adults, but oral involvement is generally milder and there is an extremely high prevalence of recurrent parotitis. Most juvenile cases resolve spontaneously at puberty. Thus it is important to establish the diagnosis as early in the course of the disease as possible so that unnecessary surgery prior to puberty can be avoided. There are only a few cases of recurrent parotitis in children that have progressed to the adult form of the disease.[143]

The adult form of SS is most commonly diagnosed between the ages of 40 and 60 years. As mentioned, there is a striking female predominance (90% to 95%) and the parotid disease tends to be progressive, occasionally requiring a parotidectomy to relieve symptoms of recurrent infection.[60, 134]

Parotid gland enlargement is slightly more common in the primary form of SS than in the secondary form of the disease. The incidence of parotid enlargement has varied from 25% to 55% of cases, and either parotid or submandibular gland enlargement occurs in 80% of all patients with SS.[128]

Secondary SS occurs in 50% to 67% of all patients with SS. Most patients with the secondary form of the disease have rheumatoid arthritis. Conversely, the incidence of the sicca complex (dry eyes and mouth) in patients with rheumatoid arthritis is estimated to be 15% to 25%.[134] Other connective tissue diseases associated with secondary SS are systemic lupus erythematosus (SLE), progressive systemic sclerosis, polymyositis, polyarteritis nodosa, and mixed connective tissue disease.

Establishing the diagnosis of SS requires (1) clinical symptoms of dry eyes and dry mouth, (2) clinical confirmation of xerostomia and xerophthalmia, (3) serologic evidence of autoantibodies, and (4) histologic evidence of a minor salivary lymphocytic infiltrate. Confirmation of decreased saliva production can be assessed by unstimulated and stimulated whole saliva collection, salivary gland scintigraphy, and parotid sialography. Decreased lacrimation can be confirmed by the Schirmer's test, tear fluid lactoferrin level, and Rose Bengal score.[144] Serologic elevation of antinuclear antibodies can be seen in 50% to 70% of the patients—specifically, SS-A and SS-B antibodies in patients with either active SS or SLE. Up to 70% to 80% of SS patients have high titers of serum antibodies against the RO (60 kd and 52 kd) and LA (48 kd) ribonucleoproteins. Thus the absence of both of these antinuclear antibodies excludes the diagnosis of SS. A notable exception occurs in men with primary SS; they have a strong tendency to be seronegative for rheumatoid factor, SS-A, and SS-B (78%, 91%, and 94%, respectively).[145] Furthermore, patients who are SS-A positive are more likely to have parotid gland enlargement, vasculitis, and a serologic profile that suggests an exaggerated immune response. Patients with primary SS tend to have the haptotypes HLA-B8 and HLA-DRW3, while patients with secondary SS do not have an association with these antigens but are associated with HLA-DRW4, an antigen found in patients with rheumatoid disease.[128] Phenotypic characterization of the glandular infiltrative lymphocytes in SS shows a predominance of CD4-positive T cells. Biopsy of the labial minor salivary glands is also considered a useful diagnostic test of SS (positive in about 60% of cases), and this procedure is usually performed in consort with the antinuclear antibody studies. However, some reports suggest that incisional biopsies of the superficial lobe of the parotid gland are more diagnostic and have less morbidity than incisional labial biopsy.[126, 134–136, 142, 143, 145, 146]

The clinical presentations of patients with SS and parotid gland involvement vary from recurrent acute episodes of tender glandular swelling, to chronic glandular enlargement with superimposed acute attacks, to nontender, nonpainful glandular enlargement.[128] Although the gland is usually diffusely affected, in some patients a localized area may be more involved, clinically simulating a solitary mass. If accessory parotid glands are present, they can also be affected by SS, and they present as a mass in the cheek. If surgery is performed for the BLEL tumor, the surgeon should be aware of the possibility of a recurrent mass involving the ipsilateral, contralateral, or accessory glands. Submandibular gland enlargement is less common than parotid gland enlargement, with a clinical incidence

Copyright © 2003, Mosby, Inc. All rights reserved.

varying between 2.5% and 16% of cases with parotid gland disease.

The risk of developing non-Hodgkin's lymphoma in the setting of SS is estimated to be about 44 times greater in patients with SS than in control subjects. The tendency is to develop lymphoma in extraparotid as well as intraparotid sites.[128, 135, 143] Clinical findings associated with the development of lymphoma include parotid gland enlargement, lymphadenopathy, and splenomegaly. Local irradiation or immunosuppression (either secondary to therapy or a primary disease) further increases the risk of developing lymphoma. Lymphoma development is related to a malignant transformation in the autoreactive B-cell clonal expansion.[60, 128, 143] Loss of immunoregulation and prolonged B-cell clonal expansion promote this transformation. Gene rearrangement studies reveal that clonal rearrangements are common to the precursor benign lymphoepithelial lesions, indicating a prelymphomatous state.[60, 134, 147]

Lymphomas developing in SS are classified as MALT (mucosa-associated lymphoid tissue) lymphomas, which can be further subclassified as either low- or high-grade. The majority of these lymphomas are extranodal (78.8%), most often involving the salivary glands (54.6%). Associated lymphadenopathy (65.6%), skin vasculitis (33.3%), peripheral nerve involvement (24.2%), low-grade fever (25.0%), anemia (48.1%), and lymphopenia (78.6%) are more common in these patients than in the general SS patient population.[148–150]

Because SS initially involves the most peripheral intraglandular ducts and acini, in the initial stages of the disease the sialogram shows a normal central ductal system and numerous peripheral punctate (1 mm or less in diameter) collections of contrast material scattered uniformly throughout the gland. These punctate changes are the earliest sialographic findings that are diagnostic of SS (Figs. 39-52 to 39-55). On a sialogram, larger or globular collections of contrast material may also be seen scattered uniformly throughout the gland. This may represent a progression from the punctate appearance of the disease (Figs. 39-52 and 39-54). These sialographic appearances have been referred to as looking like a ''leafless fruit-laden tree'' or a ''mulberry tree.'' Once the disease has progressed to the point where there is sufficient acinar destruction, salivary production decreases and ascending infection develops. Sialographically, this is seen as dilatation of the central ducts, with the other associated changes of sialoadenitis superimposed on the punctate or globular findings of SS (Figs. 39-56 and 39-57). Thus the so-called cavitary and destructive forms of SS represent progressive inflammatory changes in the gland that eventually result in large peripheral collections of contrast material combined with the central changes of sialodochitis and sialoadenitis. This process finally leads to abscess formation that usually involves the entire gland (Fig. 39-58).[52]

If a secretogogue is given at the end of the sialogram, the contrast material drains from the main ducts but remains within the punctate and globular collections (Fig. 39-53B). The sialographic changes of SS described above are sufficiently specific that they allow the sialographer to differentiate cases of SS from those of sialosis and from most cases of chronic sialoadenitis. Occasionally, patients with a chronic bacterial or granulomatous infection can develop multiple abscesses within the parotid gland (Figs. 39-25, 39-49 and 39-50). These collections tend to vary in size and are not usually distributed uniformly throughout the gland. By comparison, the collections associated with SS tend to be uniform in size and uniformly distributed throughout the gland.[52, 151, 152]

On both CT and MR in the earliest stages of SS, the involved glands appear normal. This is a limitation of sectional imaging in these patients. As the disease progresses, glandular enlargement occurs, and on CT the gland is denser than normal. The appearance is similar to that seen in patients with either chronic sialoadenitis or sialosis (Fig. 39-59). If a prior sialogram was performed with fat-soluble contrast material, the retained droplets of contrast in the punctate and globular glandular collections will be seen on CT for many years after the initial sialogram was done (Fig. 39-60). As the parotid disease continues to progress, on CT a honeycomb glandular appearance develops. This CT appearance was once thought to be diagnostic of SS; however, other granulomatous diseases and even chronic sialoadenitis can also produce similar CT findings. On MR imaging, once globular changes are present within the parotid glands, these collections can be seen on T1-weighted scans as discrete collections of low signal intensity, reflecting the watery saliva contained within them (Fig. 39-61). This MR

FIGURE 39-52 Lateral view of a parotid sialogram shows a normal central ductal system with multiple uniformly sized punctate collections of contrast material evenly distributed throughout the gland. This patient had autoimmune disease. (From Som P, Shugar J, Train J, Biller H. Manifestations of parotid gland enlargement: radiologic, pathologic and clinical correlations, part I: the autoimmune pseudosialectasias. Radiology 1981;141:415–419.)

VIEW IMAGE

Copyright © 2003, Mosby, Inc. All rights reserved.

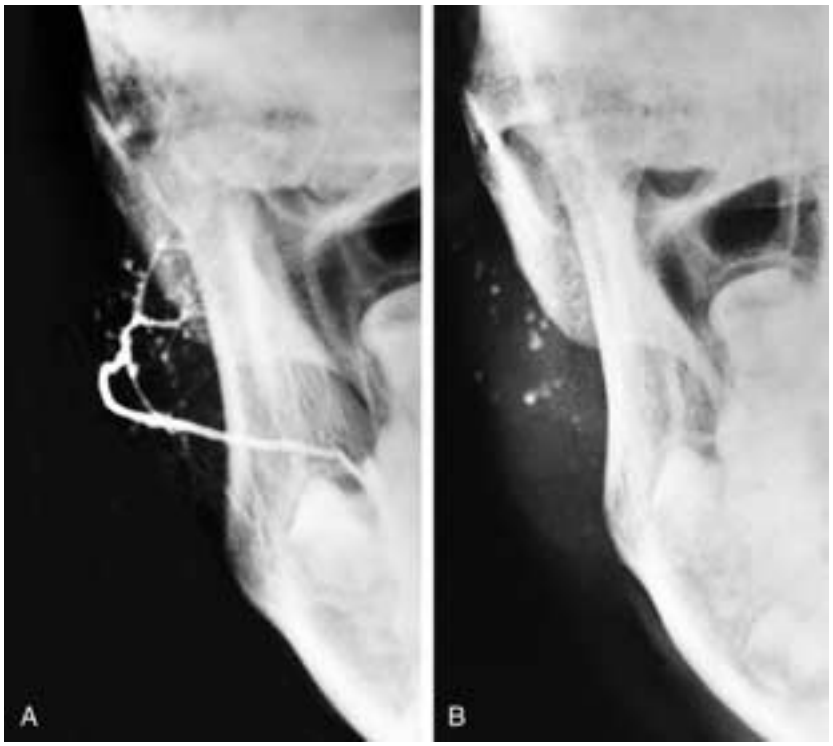

FIGURE 39-53 Frontal view of a right parotid sialogram (**A**) shows a normal Stensen's duct and central parotid ducts. Punctate collections of contrast material are uniformly scattered throughout the gland. In **B**, a frontal postevacuation film on the same patient, there is residual contrast within the punctate collections and good drainage of the main ducts. This patient had autoimmune disease.

VIEW IMAGE

appearance is diagnostic of SS. However, the development of lymphoma in BLEL has no characteristic imaging appearance.

A study analyzed the fat deposition in the parotid and submandibular glands of 33 patients with SS by using short inversion time inversion recovery (STIR) and fat-saturation MR sequences and CT. All three in vivo techniques substantially confirmed premature deposition of fat in the major salivary glands in association with SS. Furthermore, this change was characteristic of SS, and the severity of fat deposition correlated well with the impaired rates of salivary flow in these patients. It was concluded that monitoring of fat deposition might be useful in diagnosing SS and

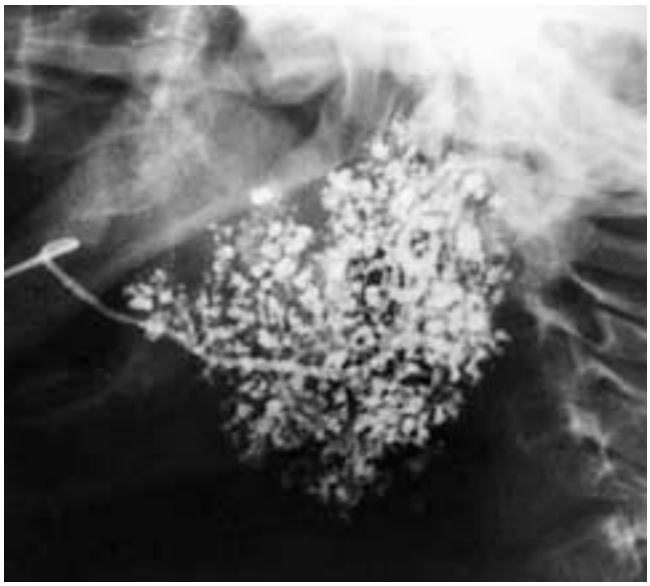

FIGURE 39-54 Lateral oblique view of a parotid sialogram shows larger globular collections of contrast material that are fairly uniform in size and distribution throughout the gland. The central ductal system is normal. This patient had autoimmune disease.

VIEW IMAGE

FIGURE 39-55 Lateral view of a parotid sialogram shows globular collections of contrast material uniformly distributed throughout the gland, with some dilatation of Stensen's duct. This patient had early sialodochitis, sialadenitis, and autoimmune disease. (From Som P, Shugar J, Train J, Biller H. Manifestations of parotid gland enlargement: radiologic, pathologic and clinical correlations, part I: the autoimmune pseudosialectasias. Radiology 1981;141:415–419.)

VIEW IMAGE

Copyright © 2003, Mosby, Inc. All rights reserved.

FIGURE 39-56 Lateral view of a parotid sialogram shows multiple punctate collections of contrast material uniformly scattered throughout the gland. Several collections in the inferior pole of the gland are larger, and there are changes of sialodochitis and central ductal sialadenitis. This patient had early cavitary autoimmune disease.

FIGURE 39-57 Lateral view of a parotid sialogram shows changes of sialodochitis and sialadenitis superimposed on those of autoimmune disease. Several focal areas appear to be coalescing to form larger collections or abscesses. Some contrast material is seen layering out in the floor of the mouth (*x*). This patient had early destructive autoimmune disease.

FIGURE 39-58 Frontal oblique view of a right parotid sialogram shows coalescent abscesses and changes of sialodochitis and sialadenitis superimposed on those of autoimmune disease. This patient had destructive autoimmune disease.

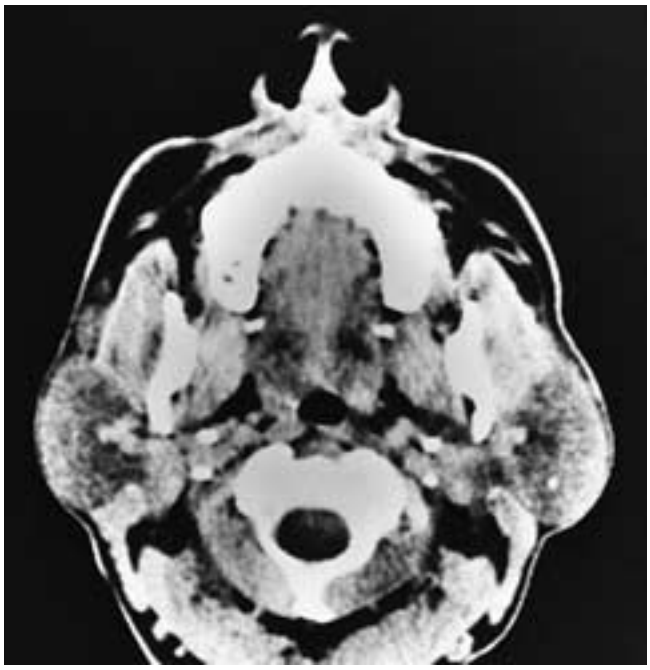

FIGURE 39-59 Axial contrast-enhanced CT scan shows larger and slightly denser parotid glands than normal. This is a nonspecific finding, and this patient had early autoimmune disease.

Copyright © 2003, Mosby, Inc. All rights reserved.

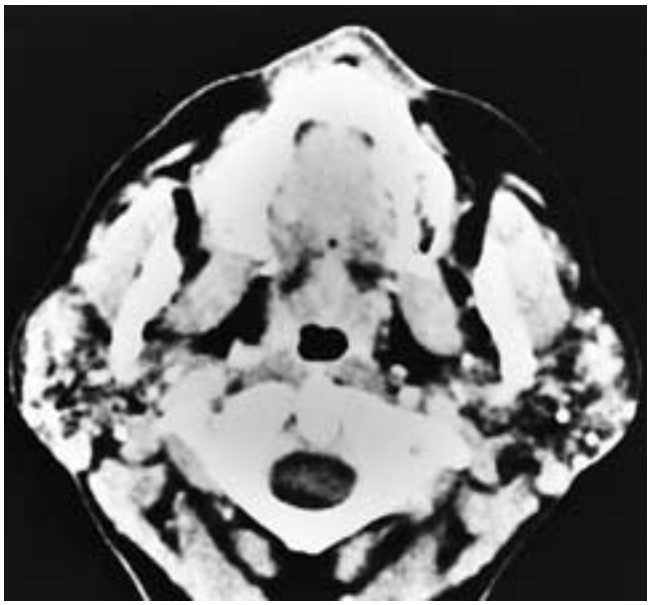

VIEW IMAGE

FIGURE 39-60 Axial contrast-enhanced CT scan on a patient who had had bilateral parotid sialograms 15 years earlier. The glands are enlarged, and residual globular collections of contrast material can be seen scattered throughout both salivary glands. This patient had autoimmune disease.

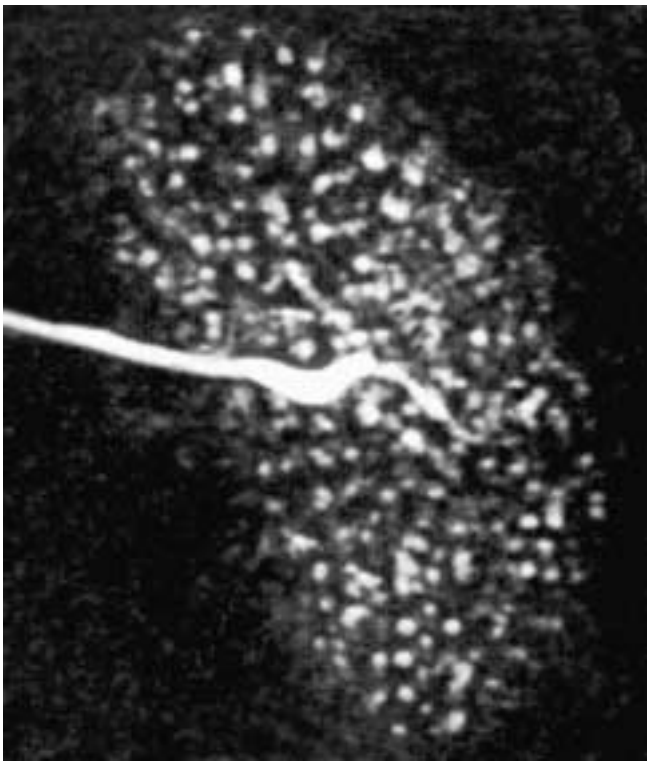

FIGURE 39-62 Frontal oblique MR sialogram shows multiple punctate collections throughout the left parotid gland in this patient with SS. Note that Stensen's duct is normal.

VIEW IMAGE

assessing its progress in patients whose clinical and serologic findings are suggestive of the disease.[153]

MR sialography was discussed earlier. This technique has specifically been applied to SS (Fig. 39-62). Gradient and spin-echo MR sialography was performed with a 1.5-T system, and the MR sialographic findings were compared with conventional sialographic findings. In 89% of the patients, the stage of salivary gland disease determined with MR sialography accurately correlated with that determined with conventional sialography. Both the sensitivity and the specificity of MR sialography in the diagnosis of SS were 100%.[154] In another study, MR sialography was performed on a 1.5-T unit with a neck phased-array coil. MR sialographic source images were obtained using a heavily T2-weighted, fast spin-echo sequence with spectral fat suppression. All images were analyzed on the basis of maximum intensity projection reconstruction. In patients with SS, a punctate, globular, cavitary, or destructive appearance was well seen within the parotid glands. Findings obtained at MR sialography correlated well with the results of labial gland biopsy.[155]

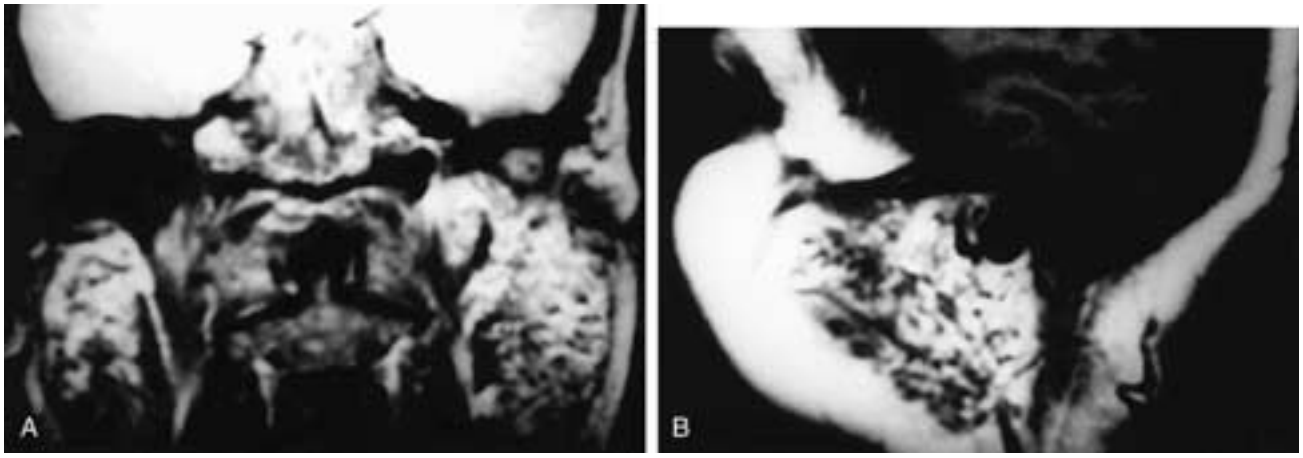

VIEW IMAGE

FIGURE 39-61 Coronal T2-weighted (**A**) and sagittal T1-weighted (**B**) MR images show multiple punctate low signal intensity areas in both parotid glands. These areas are evenly distributed throughout both glands. The patient had moderately advanced autoimmune disease.

Copyright © 2003, Mosby, Inc. All rights reserved.

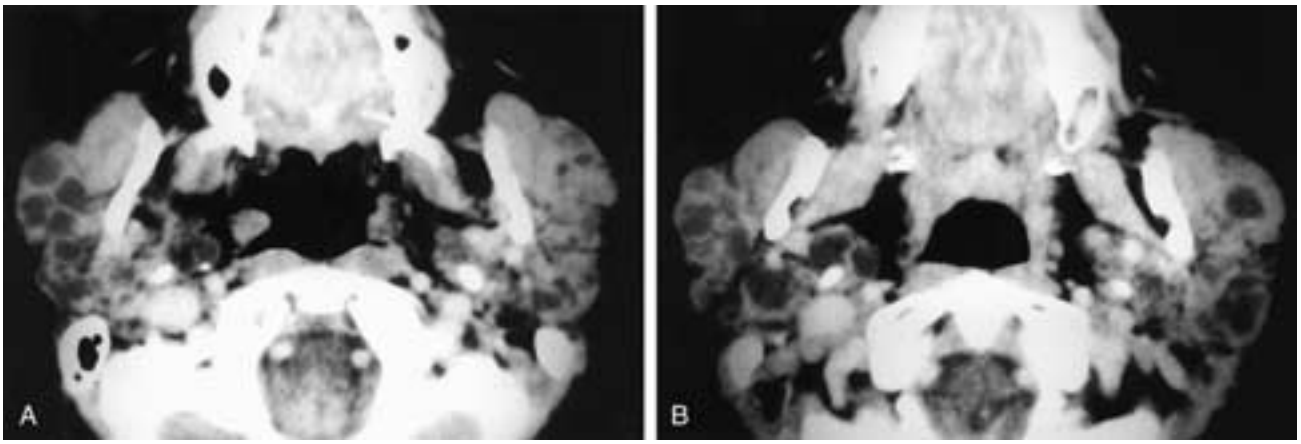

VIEW IMAGE

FIGURE 39-63 Axial contrast-enhanced CT scans (**A**, **B**) show multiple bilateral parotid cysts of varying size. The parotid parenchyma is denser than normal, and the parotid glands are slightly enlarged. This patient had end-stage cystic changes of autoimmune disease (SS).

Rarely, diffuse, bilateral macroscopic cystic change within the BLEL can develop. The cysts can vary from a few millimeters to several centimeters in diameter. When this occurs, the CT and MR appearances in the parotid gland are similar to that of the lymphoepithelial cysts associated with HIV infection (Figs. 39-63 and 39-64). The distinguishing feature is that in the autoimmune disease there is no diffuse cervical adenopathy, while such lymph node enlargement is part of the HIV disease process (especially in patients who have not yet received treatment).

Sicca syndrome can also occur in other conditions not necessarily associated with other clinical and serologic manifestations of SS. Symptomatic xerostomia and xerophthalmia can occur with viral infections [HIV and hepatitis C virus (HCV)], sialosis, sarcoidosis, amyloidosis, primary biliary cirrhosis, and graft-versus-host disease.[134, 156, 157] A recent report on 35 patients with chronic HCV infection and documented SS (SS-HCV) revealed some distinctions when compared with 60 patients with primary SS and negative HCV serology. Parotidomegaly was less common in the SS-HCV group; elevated anti-parietal cell gastric antibodies, antimitochondrial antibodies, and cryoglobulins, plus hypocomplementemia and a lower prevalence of anti-Ro/SS-A, were more common to the SS-HCV group.[158]

Diffuse infiltrative lymphocytosis syndrome (DILS) occurs in patients who are HIV positive. The patients have parotid gland enlargement, and only a few have xerostomia and keratoconjunctivitis sicca. As discussed, lymphoepithelial parotid cysts may be present. Minor salivary gland labial biopsies may show at least 50 lymphocytes per 4 mm^2 of tissue, a grade 4 positive biopsy for SS according to the Mason and Chisholm criteria.[143] Phenotypic characterization of the glandular infiltrative lymphocytes shows a predominance of CD8-positive T cells. Extraglandular manifestations of DILS include generalized lymphadenopathy, lymphocytic interstitial pneumonitis, and, less often, lymphocytic hepatitis, gastritis, nephritis, and neurologic involvement. HIV infection also produces a sicca syndrome and has a CD8 phenotype in the lymphocytic infiltration.

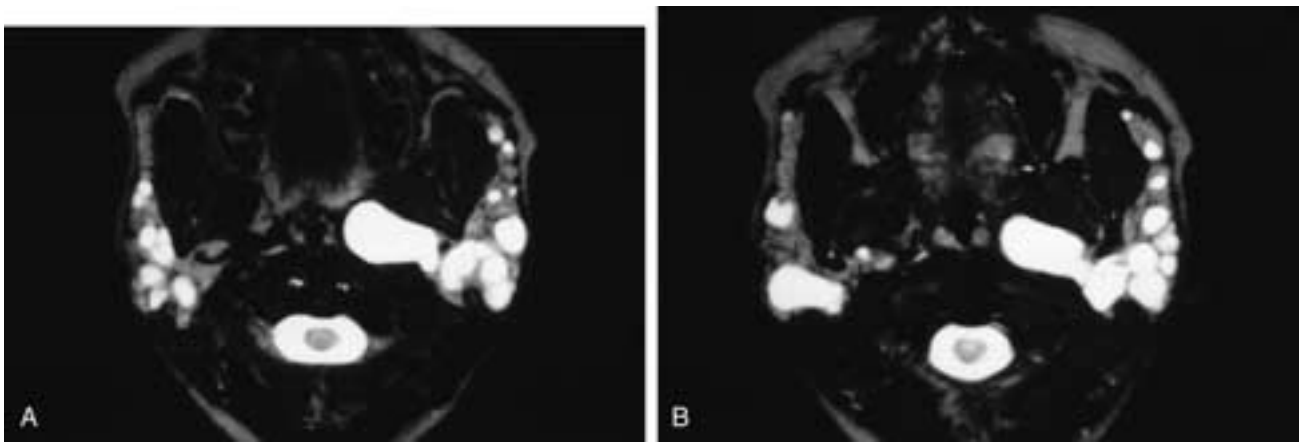

VIEW IMAGE

FIGURE 39-64 Axial T2-weighted MR images (**A**, **B**) show multiple bilateral parotid cysts of varying size. There was no cervical adenopathy. This patient had end-stage cystic changes of autoimmune disease.

Copyright © 2003, Mosby, Inc. All rights reserved.

Chronic graft-versus-host disease can produce a sicca syndrome and has associated extraglandular manifestations that are primarily cutaneous, gastrointestinal, and pulmonary. The phenotype of the infiltrative lymphocyte is CD8; however, there are no related autoantibodies or HLA associations.[159] These instances indicate that in atypical cases of apparent SS, further immune testing may lead to the proper diagnosis and thus to appropriate treatment.

SLE is a disease that may affect a number of organ systems, particularly the joints, skin, kidneys, heart, lungs, and immune system. Salivary gland involvement is usually associated with SS, in which lymphocytic acinar infiltrates predominate histologically. A case was presented of a 29-year-old woman with SLE who developed bilateral parotid gland enlargement with a unilateral focus of parotid necrosis that was consistent with a cystic mass on CT. A biopsy specimen from this lesion was histologically similar to a cervical lymph node biopsy specimen from the same patient, with both specimens showing loss of architecture and foci of necrosis consisting of nuclear dust, histiocytes, and scattered plasma cells without formation of granulomas or the presence of multinucleated giant cells; these findings are classic for SLE lymphadenopathy. This was believed to be the first reported case of focal necrosis in the parotid gland directly associated with SLE.[160]

Hyperlipidemia

Hyperlipidemia is characterized by elevated levels of plasma triglycerides and/or total cholesterol, especially low density lipoprotein cholesterol. Such elevations are considered risk factors for cardiovascular disease. Although some patients with hyperlipidemia can have symptoms of a sicca syndrome that clinically may mimic SS, these two diseases can be easily distinguished by other criteria. A few patients with hyperlipidemia have been reported to have parotid gland enlargement. In these patients, there is extensive uniform lipid infiltration of the parotid glands that can be well seen on MR imaging. Elevated plasma triglyceride levels correlate with parotid swelling, and elevated cholesterol levels adversely affect salivary flow. The submandibular glands may also be affected, albeit to a lesser degree.[161]

Sialosis

Sialosis is a nonneoplastic, noninflammatory, nontender, chronic or recurrent enlargement of the parotid glands.[143, 146] Far less commonly, the submandibular, sublingual, and minor salivary glands can be affected.[7]

The parotid disease is usually bilateral and symmetric but can be unilateral and/or asymmetric. The onset is usually insidious, with no symptoms of inflammation. The disease may worsen or improve, depending on whether the underlying condition is treated, and resolution of the sialosis can occur in only a few days if fatty replacement of the gland has not taken place. Decreased salivary flow and/or xerostomia may or may not occur; however, these findings usually reflect the underlying disease and are not specific findings of sialosis.[126]

Sialosis is associated with a variety of endocrine diseases, nutritional states, and certain medications. Sialosis is found especially in patients with diabetes, and the parotid gland enlargement may be the first clinical evidence of the underlying disease. Sialosis has also been reported with abnormalities of the ovaries, thyroid glands, and pancreas, and it has been associated with acromegaly.[126, 128] Sialosis is found in 26% to 86% of patients with chronic alcoholism and alcoholic cirrhosis, as well as with other states of malnutrition or abnormal nutrition such as prolonged starch ingestion (Argo laundry starch), causing zymogen depletion and compensatory acinar hypertrophy, pellagra, kwashiorkor, anorexia nervosa, and bulimia.[159, 162] The term *nutritional mumps* has been coined for these conditions. Other conditions associated with sialosis include hypertension, hyperlipidemia, obesity, pregnancy, brucellosis, bacillary dysentery, Chagas' disease, esophageal carcinoma, ankylostomiasis, and celiac disease.[21]

Sialosis has also been associated with a variety of medications, including phenylbutazone, oxyphenbutazone, sulfisoxazole, iodide, isoproterenol, atropine, imipramine, chloramphenicol, oxytetracycline, phenothiazides, benzodiazepines, monoamine oxidase (MAO) inhibitors, reserpine, guanethidine, heavy metals (lead, copper, mercury), methimazole, thiocyanates, and thiourea drugs such as thiouracil and propylthiouracil. With these pharmacologic sialoses both the submandibular and parotid glands may be involved, and the glandular swelling may be painful.[126, 134, 146] Sialosis may also lead to xerostomia.[163]

Pathologically, enlargement and degranulation of the parenchymal cells and/or fatty replacement of the parenchyma can occur. Usually acinar hypertrophy with increased zymogen granulation is the predominant early finding, while fibrosis and fatty atrophy dominate the later stages of the process. The fibrosis is confined to the interlobular septa, and there is no pathologic evidence of inflammatory changes. Experimental destruction of the sympathetic nervous system has resulted in tissue changes similar to those of sialosis, and it has been suggested that degeneration of the autonomic nervous system may be the common pathologic principle in all types of sialosis.[164]

In the end stages of sialosis, lipomatosis of the parotid gland can occur. Such deposition of lipid is distinguished from a lipoma of the parotid gland by the lack of a fibrous capsule in the former condition.[15]

On sialography, the parotid gland is enlarged, and the ducts are usually normal in appearance but splayed by the increased gland volume. There may be some compression of the smaller peripheral ductal branches by the increased interstitial fibrosis and/or fat. Because these sialographic changes are sufficiently different from those of chronic sialoadenitis or SS, sialosis can be distinguished sialographically from these entities (Fig. 39-65).

On both CT and MR imaging, the parotid glands are enlarged but may appear either dense or fatty, depending on the dominant pathologic change. As such, the CT and MR imaging appearances may be similar to those seen in SS and chronic sialoadenitis (Fig. 39-66).[165]

Copyright © 2003, Mosby, Inc. All rights reserved.

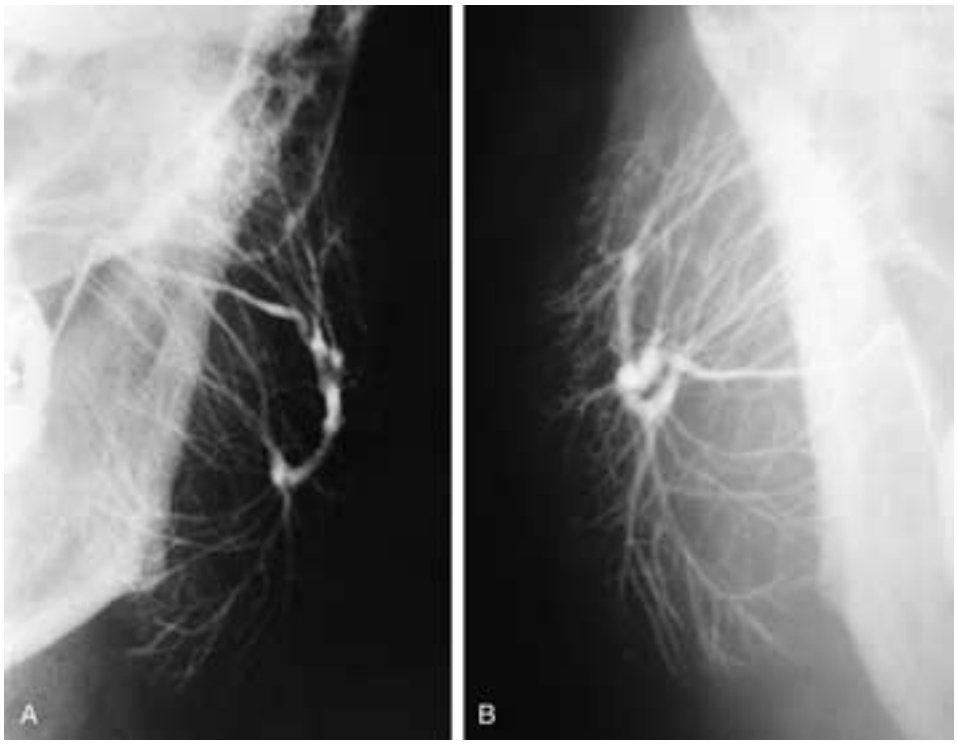

VIEW IMAGE

FIGURE 39-65 Frontal views of a left (**A**) and a right (**B**) parotid sialogram of two different patients. Both studies show a normal Stensen's duct. The intraparotid ducts are also normal, except for being widely separated as they are distributed within the enlarged gland. These patients had sialosis (From Som P, Shugar J, Train J, Biller H. Manifestations of parotid gland enlargement: radiologic, pathologic, and clinical correlations, part II. The diseases of Mikulicz's syndrome. Radiology 1981;141:421–426.)

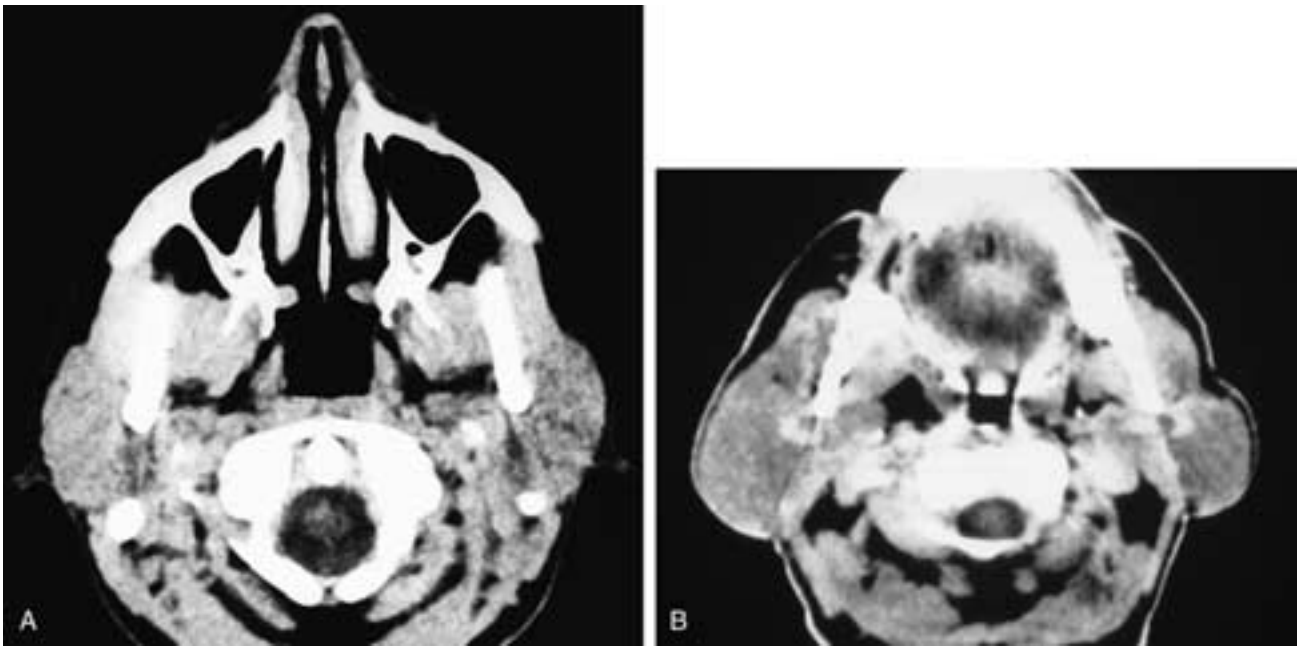

VIEW IMAGE

FIGURE 39-66 Axial CT scans (**A**, **B**) on two different patients. Both patients have enlarged and minimally dense parotid glands. This is a nonspecific finding. These patients had sialosis.

Copyright © 2003, Mosby, Inc. All rights reserved.

Postirradiation Sialoadenitis

Postirradiation sialoadenitis can occur in an acute or a chronic form. The acute type is rare today and is characterized by a tender, painful swelling of the gland within 24 hours after it has been irradiated, usually by a single dose of 1000 cGy or more. These manifestations usually subside within 3 to 4 days, and there may be an associated transient xerostomia. The chronic form occurs in glands irradiated as part of a curative treatment plan, usually for oral cavity or pharyngeal tumors. Animal studies and investigations of patients receiving radiotherapy reveal that the initial response to irradiation is a reduction in salivary flow rate. The observed increase in salivary viscosity is then a result of this reduced flow rate rather than of salivary compositional alterations.[166, 167] The parotid gland is more sensitive to the effects of irradiation than is the submandibular gland. Experimentally, parotid saliva reveals a decrease in total protein concentration and amylase activity, the severity of which increases with time in a radiation dose-dependent manner. Less effect is observed for the submandibular saliva. Saliva electrolyte concentrations are flow-rate dependent, decreasing with decreasing salivary flow rate.

If a portion of the gland is spared the full tumoricidal dose, there may be some hyperplasia of the residual acini. This corresponds to the clinical observation of decreasing xerostomia, usually after 6 to 12 months.[121] After a full dose of irradiation, the gland atrophies and xerostomia occurs because of direct effects on both the major and minor salivary glands. A sialogram shows patchy areas of lack of acinar filling and focal areas of ductal pruning. Sectional imaging shows a usually smaller than normal cellular and fibrotic gland that is dense on CT and that can enhance after contrast administration. On MR imaging, the glands usually have low to intermediate signal intensity on all imaging sequences. External irradiation is a tumor promoter, with an increased incidence of benign and malignant salivary tumors as a late sequela (10 to 25 years) in children who were irradiated for nonmalignant conditions.[134, 168]

It has been suggested that partial parotid gland sparing is feasible by using three-dimensional planning in patients undergoing bilateral head and neck irradiation. Approximately 50% of the saliva flow from the spared glands may be retained, and most of these patients have no or mild xerostomia in the early period after the completion of radiation treatment. Whether tumor control and late complications are comparable to those of standard irradiation will be assessed as more experience is gained.[169]

Necrotizing Sialometaplasia

Necrotizing sialometaplasia is a benign, self-limiting disorder that can be mistaken for a malignancy. This entity is found three times more commonly in males than in females, and most patients are over the age of 40 years. It usually involves the mucoserous glands of the hard palate, although it can arise in any salivary gland tissue including the major salivary glands. Most often there is a painless, round, deep ulcer in the palate. Less commonly, the ulcers can be linear and multiple. The process probably is reparative secondary to ischemic necrosis of the minor salivary gland tissue.[7] In the major salivary glands, the lesion appears as a consequence of focal lobular sialoadenitis. The lesion(s) heals slowly but spontaneously over a 6- to 10-week period. It can occur in two forms: (1) as a spontaneous mucosal ulcer, usually of the palate, or (2) as a reaction to injury to the minor salivary gland tissue of the oral cavity, nasal fossae, or larynx, or to a major salivary gland.[21] Necrotizing sialometaplasia is associated with squamous metaplasia as part of the regenerative process. Because it is an unfamiliar lesion to the general surgical pathologist, it may be misdiagnosed as either squamous cell carcinoma or mucoepidermoid carcinoma. On imaging, a nonspecific soft-tissue mass may be seen in the palate, without any associated bone erosion.

Adenomatoid Hyperplasia of Mucous Salivary Glands

Adenomatoid hyperplasia of mucous salivary glands is a rare entity that arises as a nonulcerated, asymptomatic, tumor-like sessile mass or swelling. The majority of cases occur on the palate, but other intraoral sites (e.g., the retromolar trigone) are occasionally affected. The condition is usually mistaken for a salivary gland neoplasm or fibroma. The overlying mucosa may appear normal or slightly blue. The etiology of this lesion has remained idiopathic, although it has been suggested that chronic local trauma may be an important factor in its development. Microscopically, adenomatoid hyperplasia appears as a predominance of lobules of normal mucinous acini coalescing with the lamina propia and submucosa. These lesions are well circumscibed but unencapsulated. Treatment is simple excision; recurrence has not been reported.[7, 170] Such masses are usually biopsied and excised without any imaging procedures.

Cystic Processes

Salivary gland cysts can be classified according to their site (major salivary versus minor salivary). Major salivary cysts can be subclassified as developmental (branchial cleft, lymphoepithelial, or dermoid) versus ductal (sialocyst, ranula). Minor salivary cysts are mucoceles. Additionally, various tumor-like entities, such as AIDS-related parotid cysts (benign lymphoepithelial cysts), can have a major cystic component and are discussed with acquired cysts. The clinical differential diagnosis of salivary cysts will be influenced by the patient's age. In children, an intraparotid cystic lesion may be a dermoid, an epidermoid, an inclusion cyst, a cystic hygroma (or another lymphangioma), an inflammatory cyst, a branchial cyst, or polycystic disease. In adults, most cystic masses are Warthin's tumors or AIDS-related parotid cysts (ARPC). Branchial cleft cysts, mucoceles, retention cysts, lymphangiomas, and some of the lesions of childhood may also occur in adults. Some salivary malignancies may also present as cysts. Low-grade mucoepidermoid carcinoma, the papillo-cystic variant of acinic cell carcinoma, and mucus-producing papillary adenocarcinoma are the three low-grade lesions that may also present as parotid cystic tumors.

Copyright © 2003, Mosby, Inc. All rights reserved.

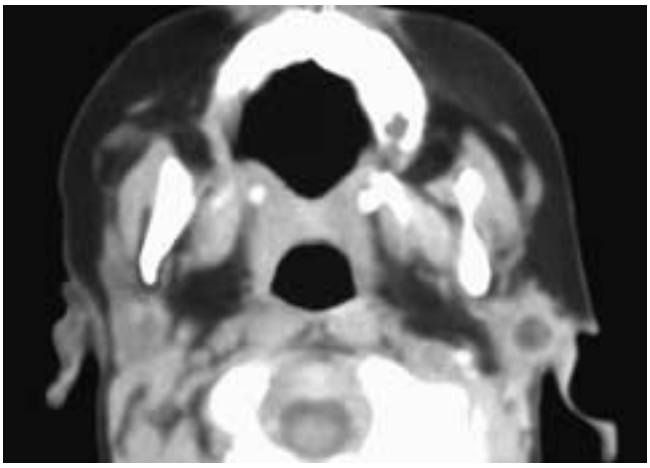

VIEW IMAGE

FIGURE 39-67 Axial CT scan shows a small cyst in the uppermost left parotid gland just caudal to the external auditory canal. This child had a type 1 first branchial cyst.

Congenital Cysts

Developmental cysts may be present at birth but often do not become clinically evident until adulthood. They present as painless unilateral parotid swellings. Pain may be present if the cyst becomes infected; sinus tracts and fistulas to the skin and external auditory canal may coexist (Figs. 39-67 to 39-72).[7]

Lymphoepithelial Cyst

Lymphoepithelial cysts are rare lesions that historically have been erroneously termed *branchial* cysts. This terminology is misleading, since the probable origin of these lesions is from intra–lymph nodal salivary gland inclusions. This reasoning is based on the observation that the branchial apparatus normally disappears by the 45th day of intrauterine (iu) life, while the lymphatic system does not start to develop until the second month (iu), and lymph nodes cannot be recognized until after the third month (iu). According to the proponents of this theory, the presence of lymphoid tissue makes it unlikely, on a temporal basis, that the inclusions are of branchial origin. In addition, the branchial cleft theory fails to explain (1) the rare occurrence of these cysts within the parotid gland, which is not at all of branchial origin; (2) the fact that these cysts are seldom present at birth, as are branchial cysts; and (3) the observation that these cysts are rarely connected to either the external auditory canal, the pharynx, or the skin. Therefore, the term *lymphoepithelial cyst* rather than *branchial cleft cyst* was proposed.

These lesions arise in adults, presenting as painless masses. They have a predilection for men (1.6 to 2.9∶1 ratio); however, they may also have a 5∶1 female-to-male ratio for intraparotid cysts and an equal sex incidence for periparotid cysts. The average age at presentation is in the mid-forties to early fifties, with a range in several series of 13 to 81 years. Rare cases have been associated with facial paralysis. The vast majority of lymphoepithelial cysts are unilateral; however, rare patients present with bilateral involvement. The cysts can measure up to 6 cm in diameter (average, 2.5 cm) and generally occur within and around the parotid gland.

Grossly, the cysts are well circumscribed and predominantly unilocular; a multilocular presentation is unusual. The cyst content is variable, ranging from fluid to mucoid to yellow-white and caseous in appearance. The luminal surface is frequently granular. Microscopically, the typical lesion is an encapsulated, smooth-walled cyst, free of internal papillae, lined by stratified squamous epithelium, although cuboidal, columnar, mucous, and sebaceous cells may be present. The cyst wall exhibits dense lymphoid tissue composed of small lymphocytes, plasma cells,

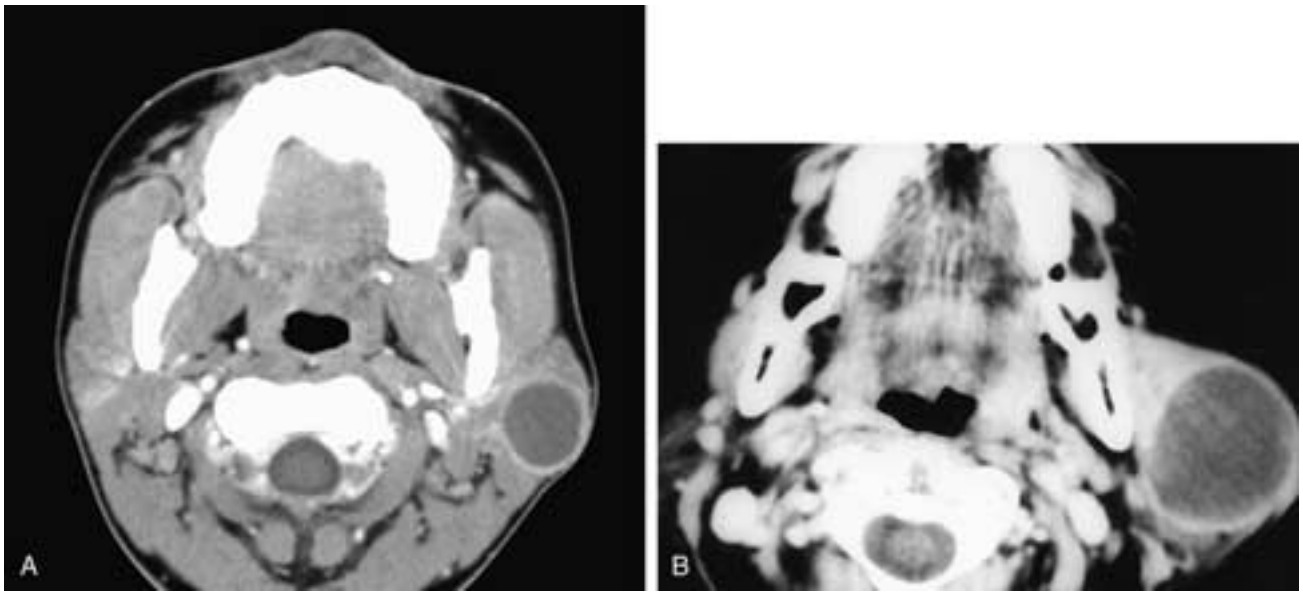

VIEW IMAGE

FIGURE 39-68 Axial CT scan (**A**) shows a smooth-walled cyst in the superficial portion of the right parotid gland. This patient had a type 1 first branchial cyst. Axial contrast-enhanced CT scan (**B**) on another patient shows a smooth-walled left parotid cyst. At surgery this was found to be a type 2 branchial cyst.

Copyright © 2003, Mosby, Inc. All rights reserved.

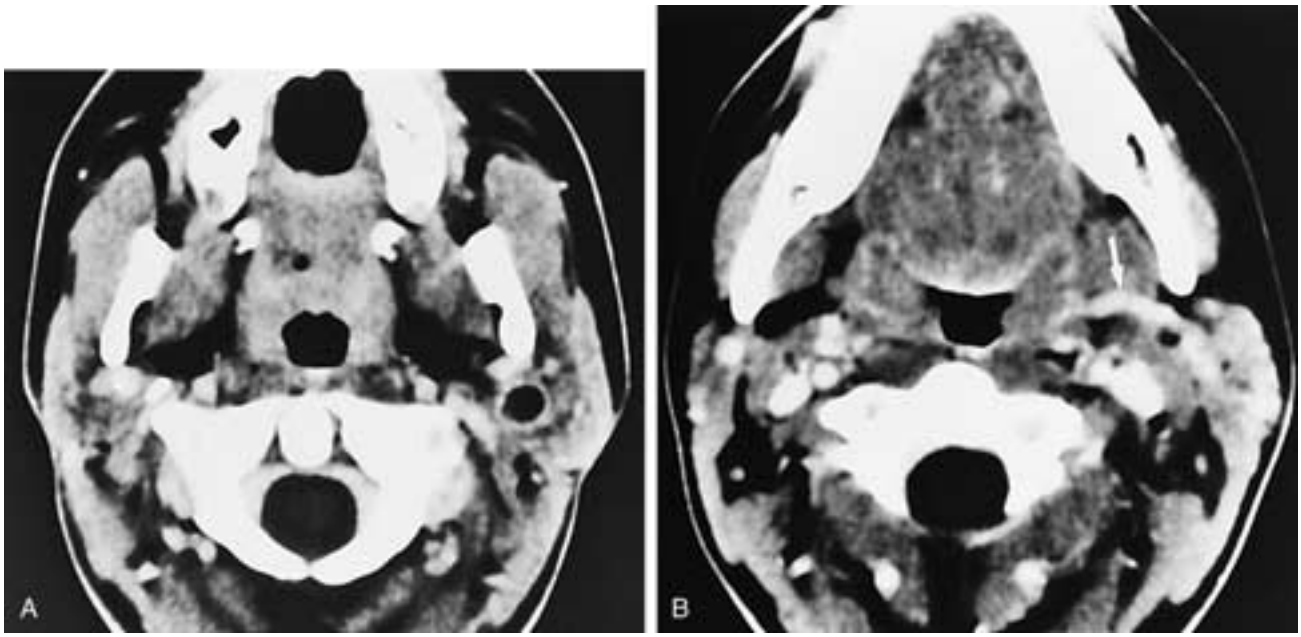

VIEW IMAGE

FIGURE 39-69 Axial contrast-enhanced CT scans through the parotid glands (**A**) and more caudally in the neck (**B**). There is a solitary smooth-walled cyst in the retromandibular portion of the left parotid gland. Extending from it is an enhancing sinus tract (*arrow*) that leads to the left palatine tonsil. This patient had an infected intraparotid second branchial cyst with an infected tract.

germinal centers, and a surrounding thick band of collagen. The nodal origin of the lesion can frequently be demonstrated by the persistence of subcapsular and/or medullary sinusoids (Figs. 39-73 to 39-77).

True Branchial Cleft Cyst

True branchial cleft cysts within the major glands are rare. Remnants of the first branchial groove, and presenting within and adjacent to the parotid gland, they comprise less than 5% of all branchial anomalies (see Chapter 35). Clinical correlation is necessary to make this diagnosis. When such a cyst has a fistulous connection in or around the external auditory canal, its origin from the first branchial cleft is clear. First branchial cleft cysts are classified as either type I or type II. Type I cysts are related only to the membranous external auditory canal, while type II cysts occur primarily near the angle of the mandible, and any tract extends through the parotid gland toward the membranous and cartilaginous external auditory canals. These cysts usually occur in the preauricular region of the parotid gland and can vary from 1 to 7 cm in diameter. Histologically, they are lined by squamous epithelium, ciliated columnar epithelium, or a mixture of both. Most of these cysts contain both skin appendages and cartilage, a feature not seen in lymphoepithelial cysts (Figs. 39-67 to 39-71).[7, 52]

Second branchial cleft anomalies usually occur along the anterior border of the sternocleidomastoid muscle, and any tract courses between the internal and external carotid

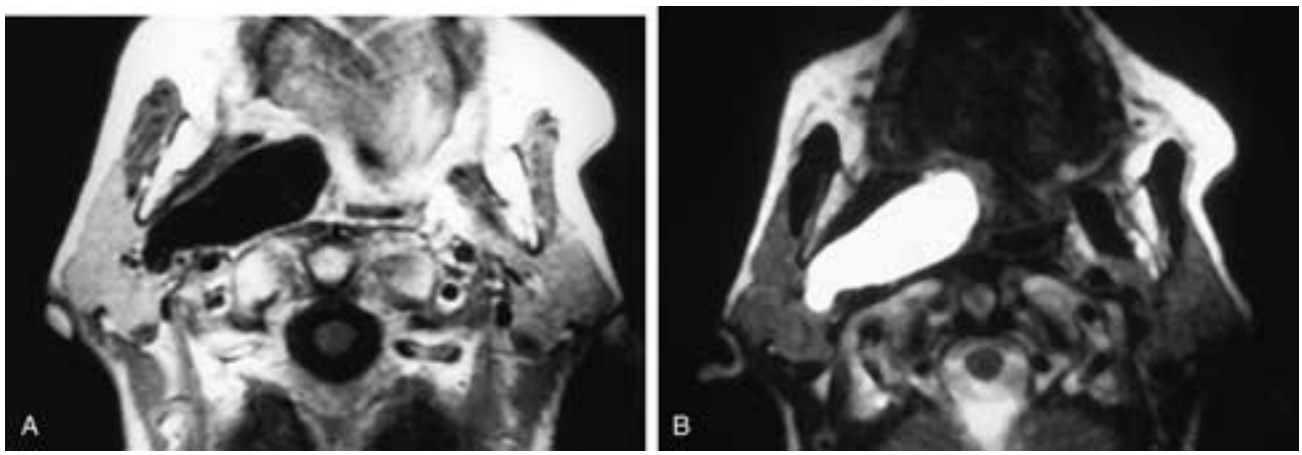

VIEW IMAGE

FIGURE 39-70 Axial T1-weighted (**A**) and T2-weighted (**B**) MR images show a large cyst extending from the right parotid gland into the right parapharyngeal space. The entire deep portion of the gland is occupied by the cyst. This patient had a second branchial (pouch) cyst.

Copyright © 2003, Mosby, Inc. All rights reserved.

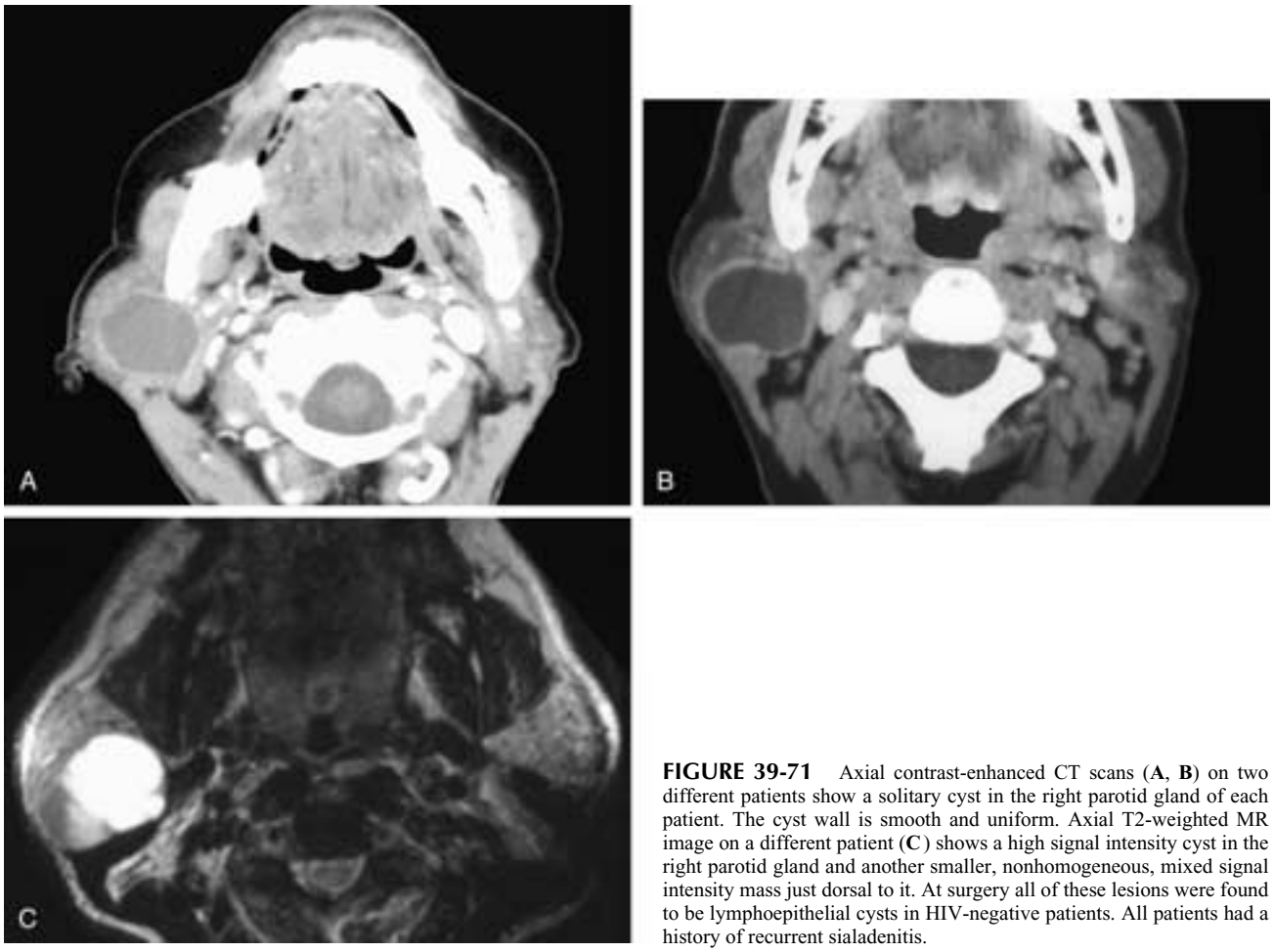

FIGURE 39-71 Axial contrast-enhanced CT scans (**A**, **B**) on two different patients show a solitary cyst in the right parotid gland of each patient. The cyst wall is smooth and uniform. Axial T2-weighted MR image on a different patient (**C**) shows a high signal intensity cyst in the right parotid gland and another smaller, nonhomogeneous, mixed signal intensity mass just dorsal to it. At surgery all of these lesions were found to be lymphoepithelial cysts in HIV-negative patients. All patients had a history of recurrent sialadenitis.

VIEW IMAGE

arteries heading toward the palatine tonsil. Occasionally, cysts occurring in the lower pole of the parotid gland are classified as being of second branchial origin, although without a demonstrable tract, this origin is of questionable validity.

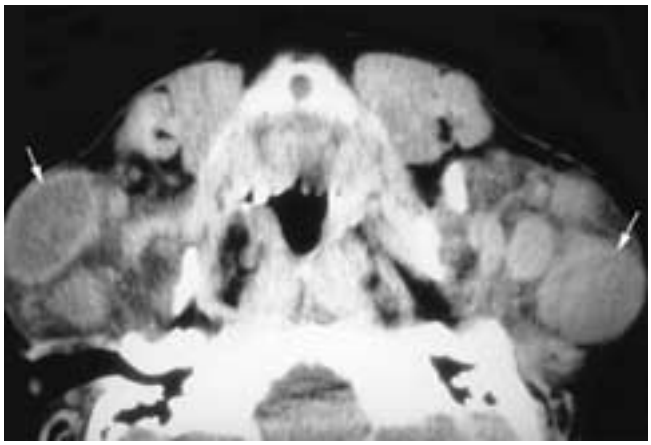

FIGURE 39-72 Axial CT scan shows multiple bilateral parotid masses and cervical lymphadenopathy in a patient with sarcoidosis. On either side, there is a solitary cyst (*arrows*) that developed several years after the appearance of the multiple sarcoid granulomas. At biopsy these were found to be lymphoepithelial cysts in a patient with long-standing sarcoidosis.

VIEW IMAGE

Epidermoid Inclusion Cyst

Rarely, epidermoid or dermoid cysts also occur within or adjacent to the major salivary glands. In the head and neck, dermoid cysts generally occur in the midline nose, the orbit, or the midline floor of the mouth. Distinction from an epidermoid cyst is based on the presence of skin adnexa in a dermoid cyst. The midline location and the lack of a lymphoid infiltrate, moreover, aid in distinguishing dermoid cysts from branchial cleft remnants.

Polycystic (Dysgenetic) Disease

Polycystic (dysgenetic) disease is a developmental abnormality of the salivary gland duct system that has histologic similarity to polycystic disease of the kidney. Extraordinarily rare, its incidence is 0.02% to 0.06% of large salivary series. Seventeen cases have been reported to date, 16 in the parotid gland and 1 in the submandibular gland. There is a pronounced female predominance, with an age range from 6 to 65 years. Most patients have bilateral involvement; however, occasionally a single gland is involved. Patients typically present with recurrent, painless swelling of the affected gland, with no abnormality of salivary flow. Sialography exhibits multicystic ductal changes.

Microscopically, the parotid parenchyma is replaced by varying degrees of honeycombed cystic change. The cysts are of variable size, but are usually no more than several

Copyright © 2003, Mosby, Inc. All rights reserved.

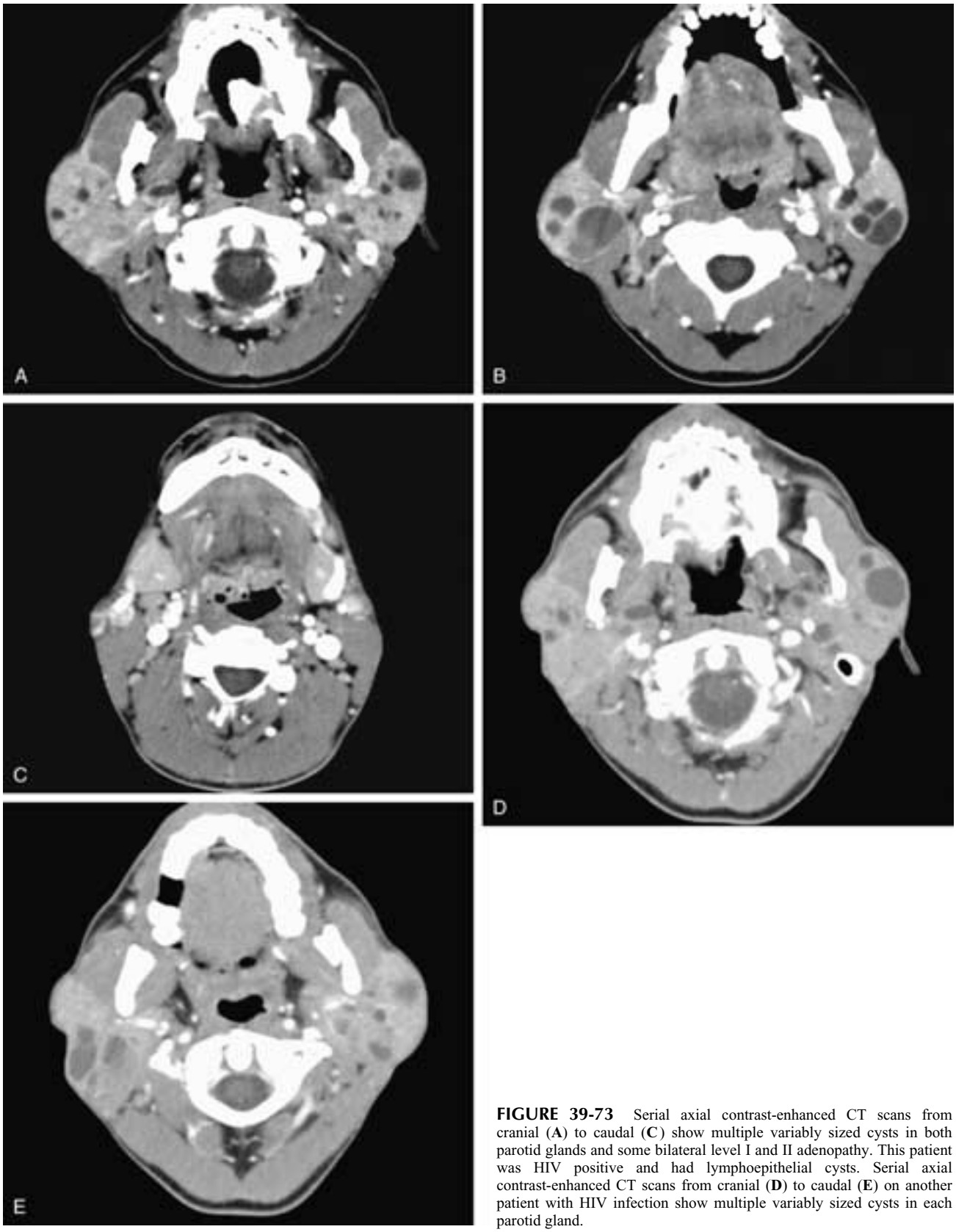

FIGURE 39-73 Serial axial contrast-enhanced CT scans from cranial (**A**) to caudal (**C**) show multiple variably sized cysts in both parotid glands and some bilateral level I and II adenopathy. This patient was HIV positive and had lymphoepithelial cysts. Serial axial contrast-enhanced CT scans from cranial (**D**) to caudal (**E**) on another patient with HIV infection show multiple variably sized cysts in each parotid gland.

VIEW IMAGE

Copyright © 2003, Mosby, Inc. All rights reserved.

millimeters in diameter, and are lined with a flat, cuboidal, and/or columnar epithelium. The cysts may be filled by inspissated proteinaceous secretions and eosinophilic bodies with concentric radial patterns similar to those of spheroliths and microliths. This cystic process may affect ectopic salivary gland tissue in cervical lymph nodes; therefore, involvement of cervical nodes should not be construed as evidence of a malignancy. Polycystic disease is a completely benign process. It may be necessary to remove the involved glands surgically for cosmetic reasons or to establish the diagnosis.[171, 172]

Congenital Sialectasis and Merkel's Cyst

Congenital sialectasis is a rare unilateral or bilateral cystic condition arising in children and adults. It accounts for 1.4% of nonneoplastic salivary gland cysts. Histologically, the salivary ducts are dilated with inspissated secretions. If there is no secondary sialadenitis, then the histology will support a congenital process. However, patients with congenital sialectasis eventually develop recurrent sialadenitis; thus, the histology will appear identical to that of acquired duct ectasia. Merkel's cysts are developmental simple cysts of the submandibular gland.

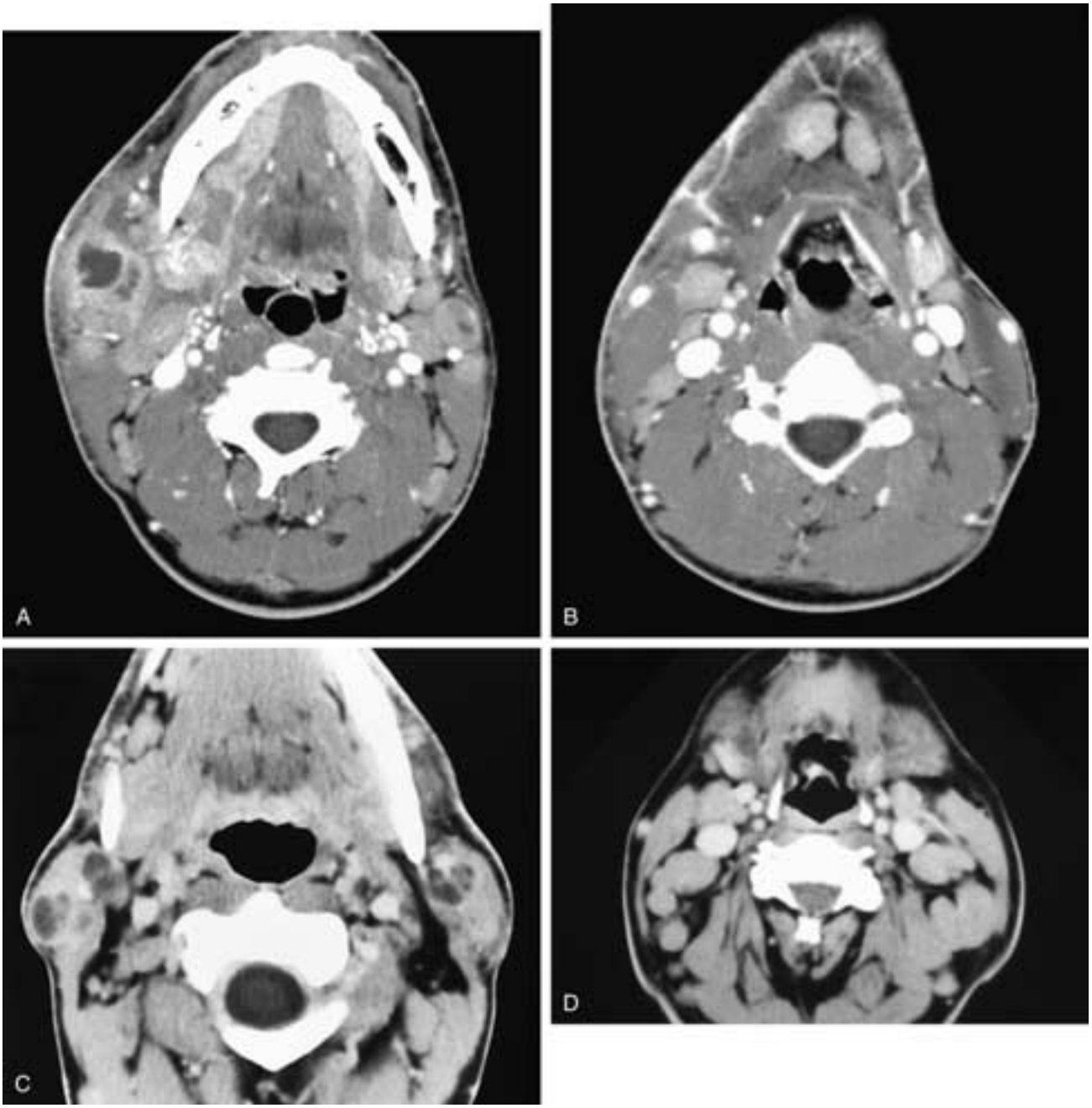

FIGURE 39-74 Axial CT scans (**A**, **B**) show cysts in both parotid glands with bilateral level I and II lymphadenopathy. This patient was HIV positive and had lymphoepithelial cysts. Axial contrast-enhanced CT scans on another patient show multiple cystic masses in both parotid glands (**C**) and diffuse cervical adenopathy (**D**). This patient was HIV positive and had lymphoepithelial cysts.

VIEW IMAGE

Copyright © 2003, Mosby, Inc. All rights reserved.

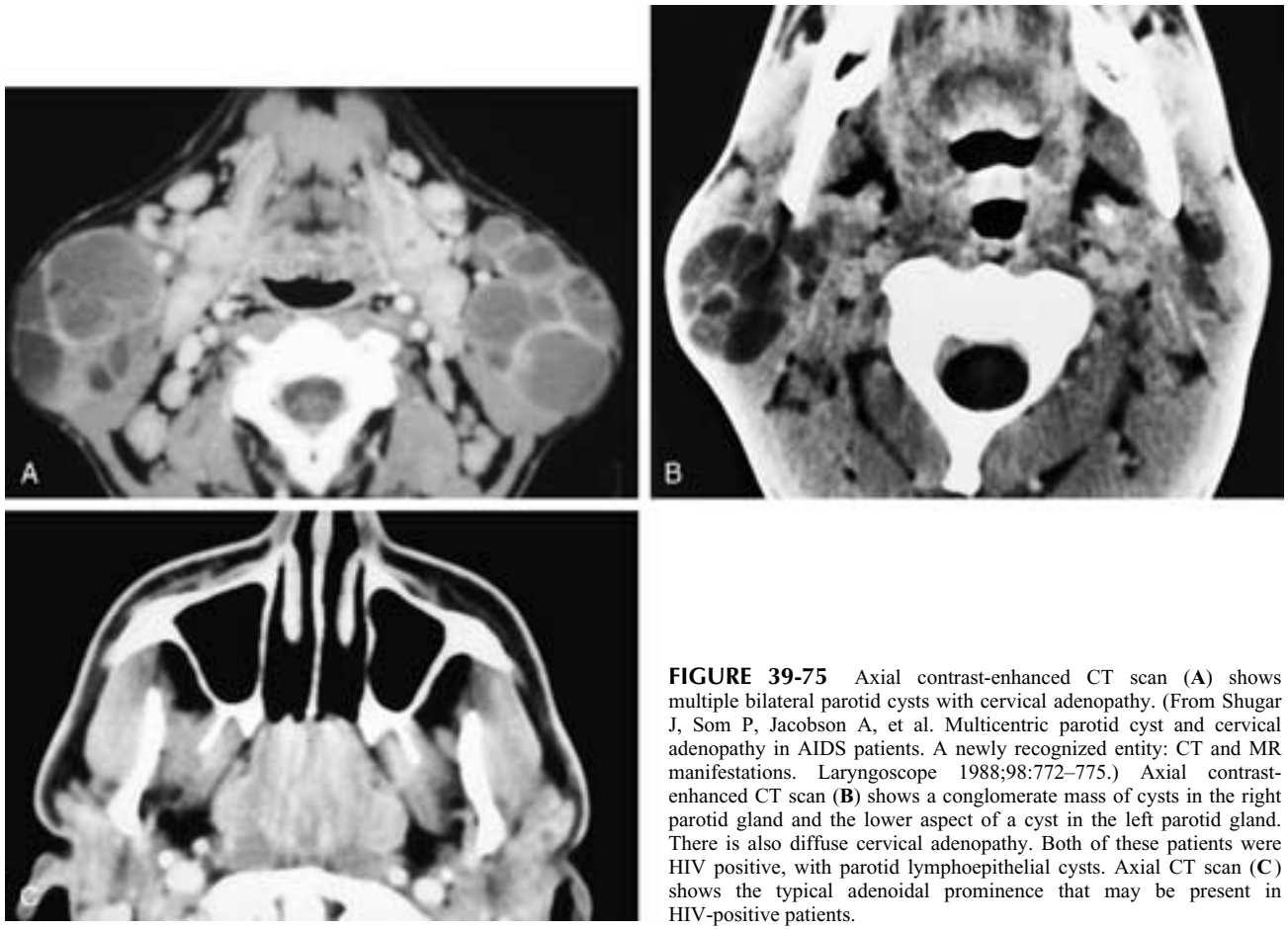

FIGURE 39-75 Axial contrast-enhanced CT scan (**A**) shows multiple bilateral parotid cysts with cervical adenopathy. (From Shugar J, Som P, Jacobson A, et al. Multicentric parotid cyst and cervical adenopathy in AIDS patients. A newly recognized entity: CT and MR manifestations. Laryngoscope 1988;98:772–775.) Axial contrast-enhanced CT scan (**B**) shows a conglomerate mass of cysts in the right parotid gland and the lower aspect of a cyst in the left parotid gland. There is also diffuse cervical adenopathy. Both of these patients were HIV positive, with parotid lymphoepithelial cysts. Axial CT scan (**C**) shows the typical adenoidal prominence that may be present in HIV-positive patients.

VIEW IMAGE

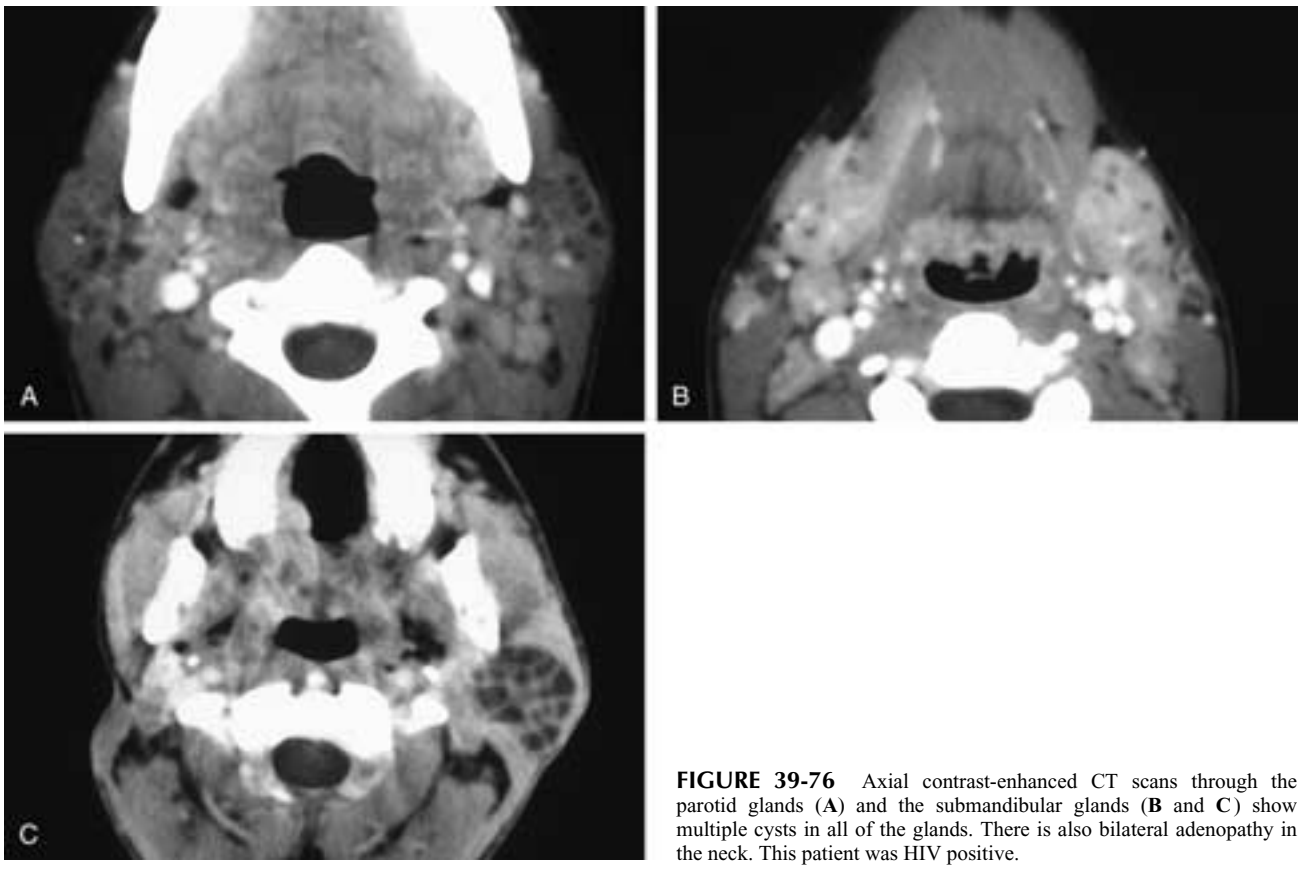

FIGURE 39-76 Axial contrast-enhanced CT scans through the parotid glands (**A**) and the submandibular glands (**B** and **C**) show multiple cysts in all of the glands. There is also bilateral adenopathy in the neck. This patient was HIV positive.

VIEW IMAGE

Copyright © 2003, Mosby, Inc. All rights reserved.

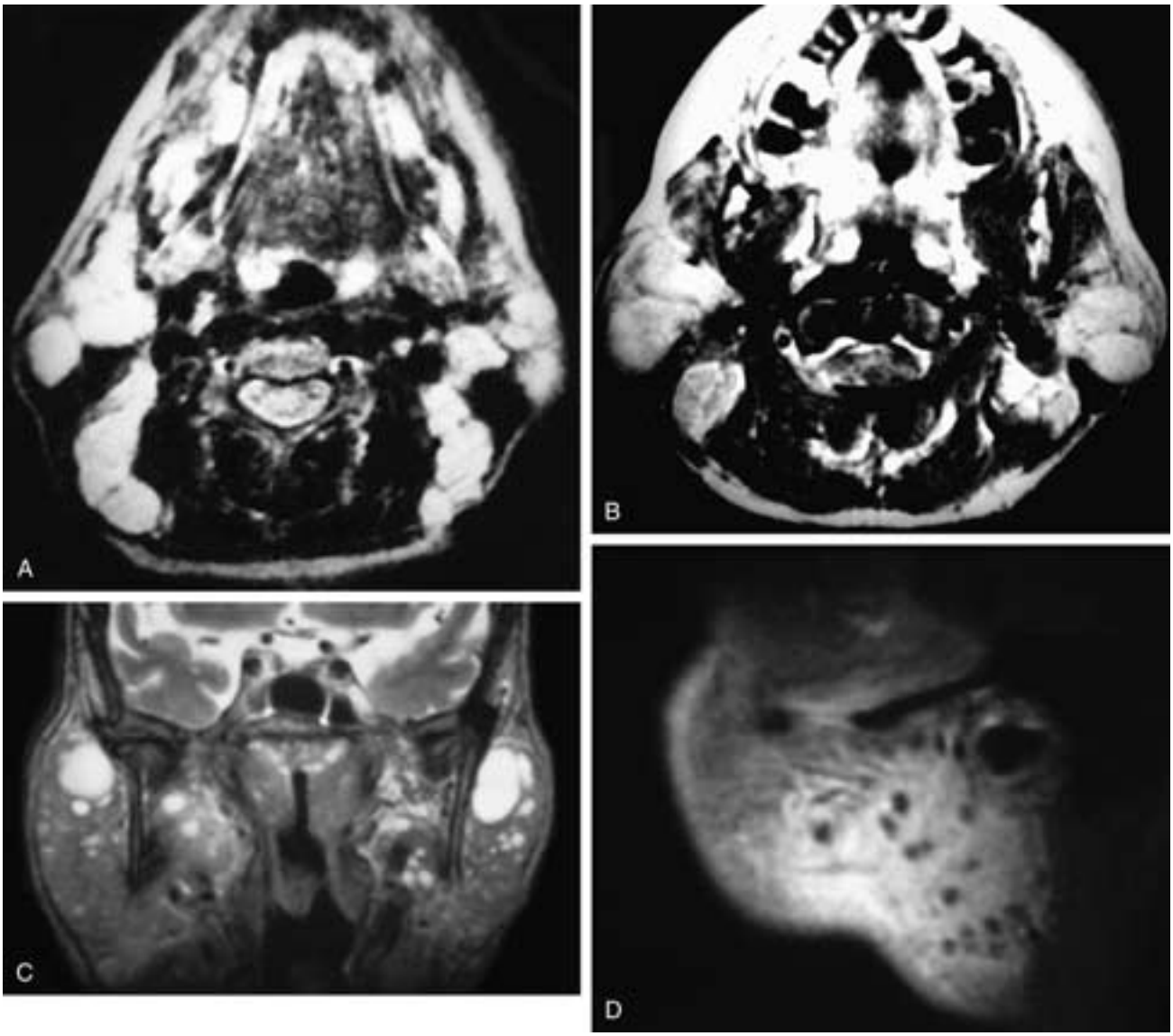

VIEW IMAGE

FIGURE 39-77 Axial T2-weighted MR images through the parotid glands (**A**) and more caudally in the neck (**B**) show multiple bilateral parotid masses and diffuse cervical adenopathy. This HIV-positive patient had lymphoepithelial cysts and cervical adenopathy. Coronal T2-weighted (**C**) and sagittal T1-weighted (**D**) MR images on another patient show multiple variably sized cysts in both parotid glands. In **D** note that the cysts are not uniformly distributed throughout the gland, as they are in SS (Fig. 39-61). This patient was HIV positive and had lymphoepithelial cysts.

Acquired Cysts

Ductal Cysts/Sialocysts

Many acquired cysts of the major salivary glands develop as a result of ductal obstruction that may be caused by a postinflammatory stricture, a calculus, trauma, a postsurgical complication (from stenosis or ligature of a duct), or a mass. Almost always the causative obstruction is incomplete or intermittent, since an initial complete obstruction of the glandular ducts results in acinar and glandular atrophy rather than cyst formation (Figs. 39-78 to 39-83).[7, 143] The resultant thin-walled cyst has been called a ductal cyst, sialocyst, retention cyst, major salivary gland mucocele, or extravasation cyst. It is believed that all of these cysts are different stages of the same pathogenetic process. Salivary duct cysts, or sialocysts, usually arise in the parotid gland and represent true cysts with epithelial linings. When seen in the sublingual gland, the cyst is called a ranula (see below).

Patients most commonly present in the fifth decade of life with a slowly enlarging, painless, mass-like lesion. The most common site for a sialocyst is the submandibular gland. Histologically, sialocysts may be multicystic or show ectasia of the adjacent ducts. The epithelial lining may be cuboidal/columnar, squamous, or mucous (goblet), and/or clear cells may be seen. These cysts are treated by complete but conservative surgical excision. They should not recur if completely excised.

A sialocele arises when saliva accumulates within a cystic area that develops secondary to a complete or incomplete traumatic interruption of the excretory ducts draining the region. If some communication with the main

Copyright © 2003, Mosby, Inc. All rights reserved.

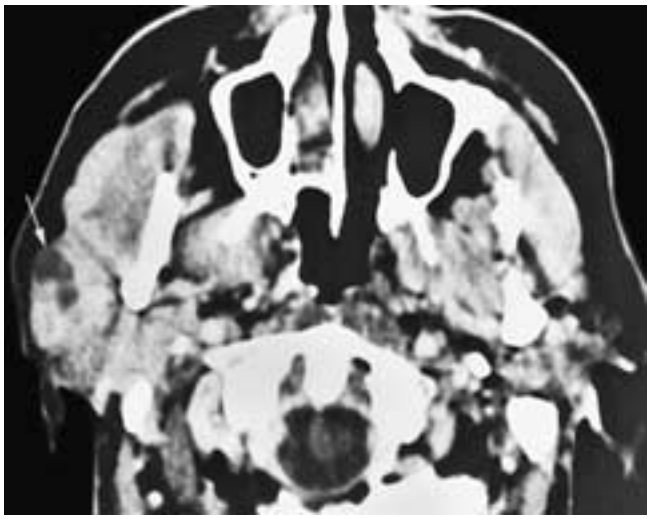

VIEW IMAGE

FIGURE 39-78 Axial contrast-enhanced CT scan shows several small cysts in the anterior superficial portion of the right parotid gland (*arrow*). The right parotid gland is denser than normal. These were posttraumatic acquired cysts.

ductal system persists, a sialogram will reveal a communicating cyst within the gland (Figs. 39-84 to 39-86). If no such communication exists, the sialogram will appear as a benign mass that displaces the adjacent ducts. These sialoceles develop rapidly after trauma, and needle aspiration of saliva from the cyst confirms the diagnosis.[152]

Pneumoceles

A pneumocele is a rare cause of a sialocyst. It is caused by the retention of air in a major salivary gland duct that may extend into the parenchyma. This occurs after an increase in intrabuccal pressure. Although it is associated with adult occupations such as glass blowing and trumpet playing, it commonly occurs in children who cause retrograde insufflation of air into the gland via Stensen's duct or, less commonly, Wharton's duct (Figs. 39-87 and 39-88). It has been suggested that in children, Stensen's duct has a more perpendicular insertion into the buccal mucosa than in adults, in whom the angle of insertion is more acute posteriorly. This allows a buccal mucosal fold to provide better protection in adults against the retrograde air traveling into Stensen's duct when intraoral pressure is increased. The clinical presentation of a recurrent painless soft-tissue glandular fullness usually establishes the diagnosis.[152]

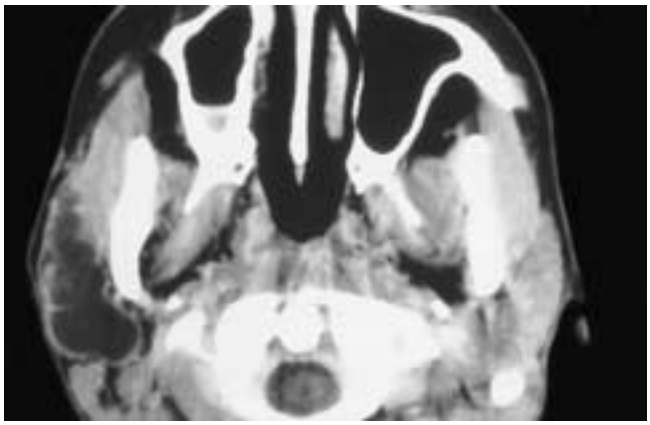

VIEW IMAGE

FIGURE 39-79 Axial postcontrast CT scan shows a large cyst occupying almost the entire right parotid gland. This cyst developed in a partially obstructed gland secondary to a stricture near the hilum of the gland. This patient had an obstructive cyst (mucocele, sialocele).

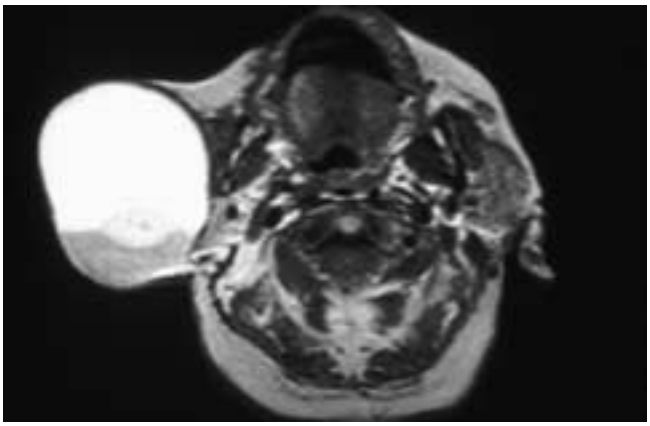

FIGURE 39-80 Axial T1-weighted MR image shows a large cyst in the right parotid gland. Hemorrhage is present in the upper portion of the cyst. This patient had an acquired hemorrhagic cyst. (Courtesy of Dr. Charles Schatz.)

VIEW IMAGE

AIDS-Related Parotid Cysts

HIV infection may manifest itself in the head and neck under myriad guises. Kaposi's sarcoma (KS), candidial or herpetic oropharyngitis, and cervical lymphadenopathy are the three most common presenting head and neck complaints for HIV infection. Less commonly, patients with AIDS develop cystic and solid intraparotid tumors that have been referred to as either cystic benign lymphoepithelial lesions, or BLEL in AIDS, or AIDS-related parotid cysts (ARPC). The last term is recommended, as the other terms may cloud the distinctions between BLEL and AIDS, two clinically and prognostically different entities. Patients typically present with unilateral or bilateral painless, enlarging masses; imaging studies reveal that bilaterality is the rule rather than the exception, even when the involvement clinically appears unilateral (Figs. 39-73 to 39-77). Cervical lymphadenopathy and nasopharyngeal lymphoid enlargement commonly accompany the parotid findings. In recent years, as better medical control of HIV-infected patients has developed, multiple ARPCs have been seen without associated cervical lymphadenopathy and/or adenoidal hypertrophy. In such cases, history as to medical therapy becomes important.

Histologically, ARPC appears as cystic spaces lined by squamous epithelium, accompanied by abundant reactive lymphoid stroma. Florid follicular hyperplasia, loss of mantle zone lymphocytes, and follicle lysis can be seen. The lesions may have an encapsulated, segmented appearance, or the inflammatory infiltrate can extend into the parotid parenchyma without encapsulation. Epimyoepithelial islands, identical to those seen in BLEL, can often be observed. Warthin-Finkeldey-type multinucleated giant cells may also be seen within involved lymph nodes.

What is the relationship between ARPC, BLEL, and SS?

Copyright © 2003, Mosby, Inc. All rights reserved.

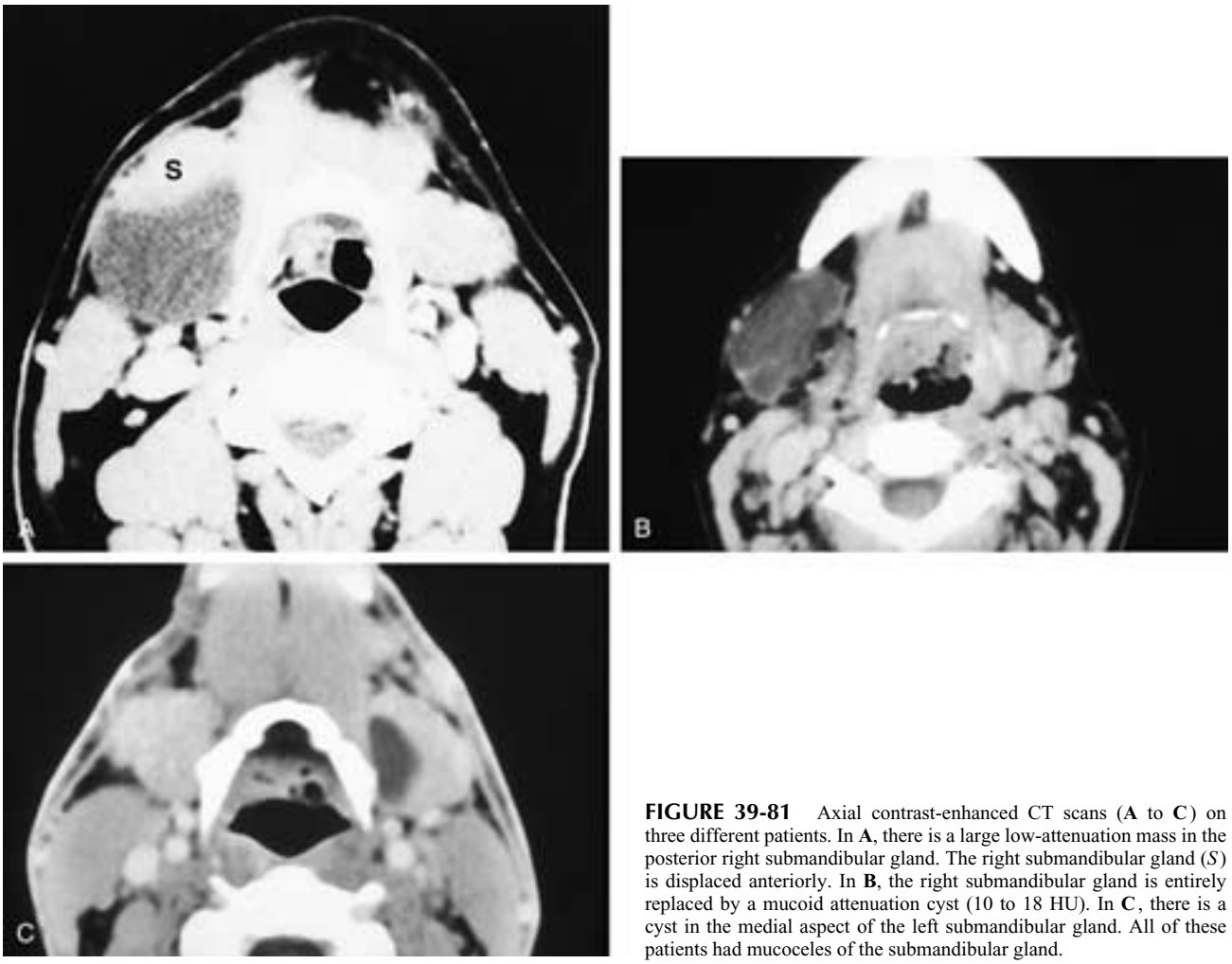

FIGURE 39-81 Axial contrast-enhanced CT scans (**A** to **C**) on three different patients. In **A**, there is a large low-attenuation mass in the posterior right submandibular gland. The right submandibular gland (*S*) is displaced anteriorly. In **B**, the right submandibular gland is entirely replaced by a mucoid attenuation cyst (10 to 18 HU). In **C**, there is a cyst in the medial aspect of the left submandibular gland. All of these patients had mucoceles of the submandibular gland.

VIEW IMAGE

The majority of patients with ARPC have no autoimmune symptomatology and lack serum autoimmune antibodies. The prevailing theory is that ARPC is the result of AIDS-related hyperplastic adenopathy [persistent generalized lymphadenopathy (PGL)] of periparotid/intraparotid lymph nodes causing obstruction, squamous metaplasia, and cystification of intranodal ducts. However, a recent study by Ihrler and colleagues did not support this theory. They found a continuous spectrum of lymphoepithelial salivary parenchymal lesions, developing initially from lymphoid infiltra-

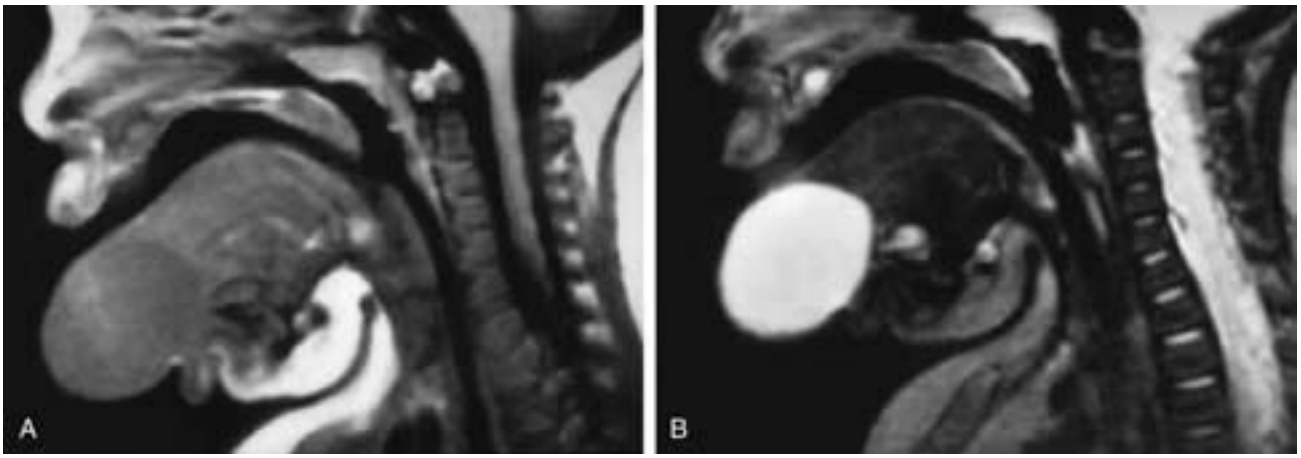

FIGURE 39-82 Sagittal T1-weighted (**A**) and T2-weighted (**B**) MR images show a large cyst in the anterior tongue of this child. This was a retention cyst.

VIEW IMAGE

Copyright © 2003, Mosby, Inc. All rights reserved.

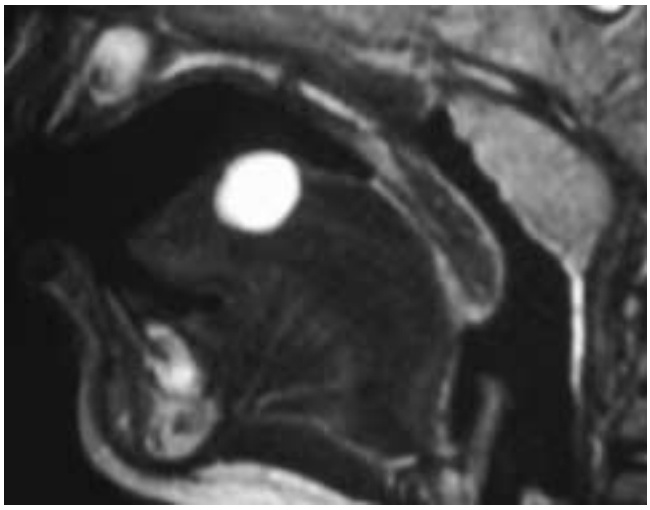

VIEW IMAGE

FIGURE 39-83 Sagittal T2-weighted MR image shows a cyst in the upper midline tongue of this child. This was a retention cyst.

tion of salivary lobules to lymphoepithelial duct lesions with cystic dilatation, up to large ductal cysts (up to 3.5 cm in diameter) with parenchymal atrophy. The ductal and cystic lesions demonstrate an intense basal cell hyperplasia without participation of myoepithelial cells. The MR imaging findings indicated involvement of the entire tissue of both parotid glands. The authors concluded that the enormous cystic dilatation of the duct lesions presumably is a consequence of ductal obstruction due to basal cell hyperplasia of striated ducts and intense intraglandular

VIEW IMAGE

FIGURE 39-84 Frontal view of a left parotid sialogram shows a cystic dilatation of Stensen's duct, with no evidence of communication with the remaining parotid ductal system. This patient had a posttraumatic stricture of Stensen's duct near the hilum of the gland.

FIGURE 39-85 Lateral view of a sialogram shows a normal-caliber Stensen's duct. From the proximal end of the duct, droplets of contrast material (*arrow*) fill a large cyst within the parotid gland. This patient had a posttraumatic communicating cyst (sialocele).

VIEW IMAGE

lymphofollicular hyperplasia. At present, it is believed that both pathophysiologies may coexist. Thus, cystification of lymph nodes and periductal obstruction may both be causes of the observed ARPC.

A small, distinct subgroup of AIDS patients also have Sjogren's-type symptoms of xerostomia, xerophthalmia, and arthritic pain; however, autoantibodies (antinuclear antibodies) have been identified in only one of all the reported patients.[173–175] Labial biopsies of minor salivary glands have revealed, for some patients, severe sialadenitis on a par with that seen in SS. Nonetheless, although ARPC and the BLEL of SS share similar histologic features, their

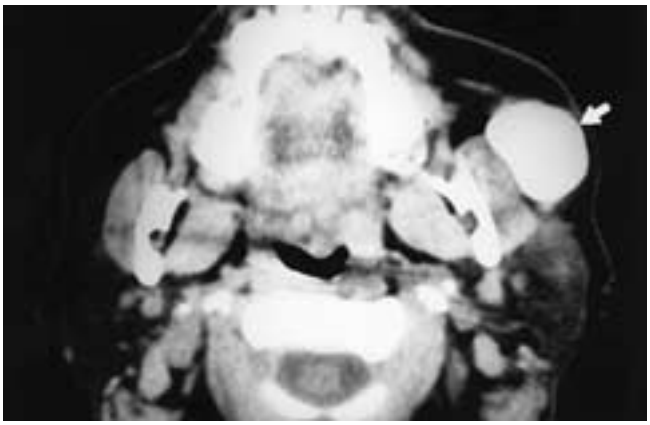

FIGURE 39-86 Axial CT scan taken after contrast injection into a cystic mass along the course of Stensen's duct (*arrow*). This patient had received trauma to this area of the cheek. The patient had a noncommunicating sialocele.

VIEW IMAGE

Copyright © 2003, Mosby, Inc. All rights reserved.

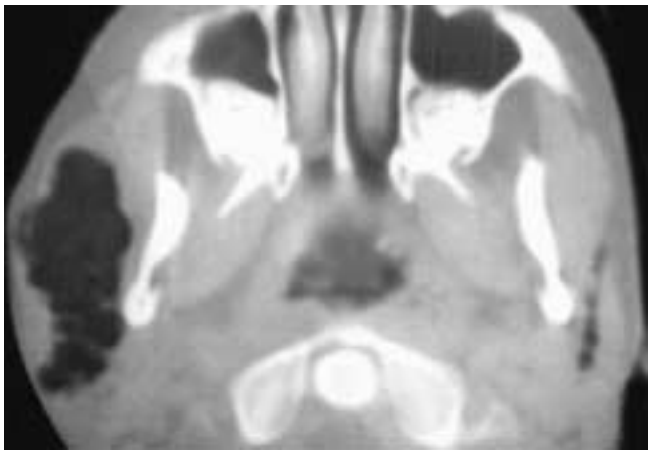

VIEW IMAGE

FIGURE 39-87 Axial CT scan shows a considerable amount of air in the right parotid gland and a small amount of air in the left parotid gland. This child had bilateral pneumoparotitis.

underlying pathophysiology is different, and therefore they warrant separate clinical and pathologic designations. There can be significant morphologic overlap between the individual features of ARPC and BLEL; obviously, this differential diagnosis has an enormous clinical impact, as ARPC may herald the diagnosis of HIV infection. Epimyoepithelial islands, a prominent feature of BLEL, may also be observed in ARPC. Warthin-Finkeldey-type multinucleated giant cells are more often seen in ARPC but are occasionally seen in BLEL. BLEL also tends to be less cystic and generally more solid, although cystic change has been observed in 3% of patients with BLEL.

An established radiologic/cytologic diagnosis of ARPC obviates the need for surgical excision. Patients treated by fine needle aspiration may develop repeated collections of cyst fluid and may require periodic fine needle aspiration.[174, 176–181]

Ranula

The term *ranula* refers to a mucous retention cyst that occurs primarily in the sublingual gland. Rarely, this term is also applied when a minor salivary gland in the oral cavity is involved. A ranula occurs in two forms. A simple ranula, which is the most common form, is a retention cyst (almost always of the sublingual gland) that remains in the floor of the mouth above the level of the mylohyoid muscle. The simple ranula is a true cyst because it has an epithelial lining. This lining is either the capsule of the sublingual gland or the epithelial wall or capsule of a minor salivary gland (Figs. 39-89 to 39-93). The second type of ranula is the deep or plunging ranula, which is a mucocele that develops from the rupture of the wall of a simple ranula. The irritating saliva is rapidly contained by an inflammatory response. Thus, the wall of the ranula is composed of both epithelium and inflammatory elements and, in reality, is a pseudocyst. It may or may not extend below the mylohyoid muscle; however, usually it does extends below this level (Figs. 39-91 and 39-93). Although a plunging ranula is also said to be present whenever the lesion simply extends below the mylohyoid muscle, this is not always true, and the pathologic definition remain the final means of establishing this diagnosis.

Plunging ranulas appear to occur more frequently in the Maori and Pacific Island Polynesian populations. The precise etiology of their predisposition is unknown, although local trauma or inherent mylohyoid dehiscences may play an important role. Removal of the sublingual gland via either a cervical or an intraoral approach is the treatment of choice.[182]

The simple ranula occurs as a mass in the floor of the mouth, off the midline in the area of the sublingual gland.

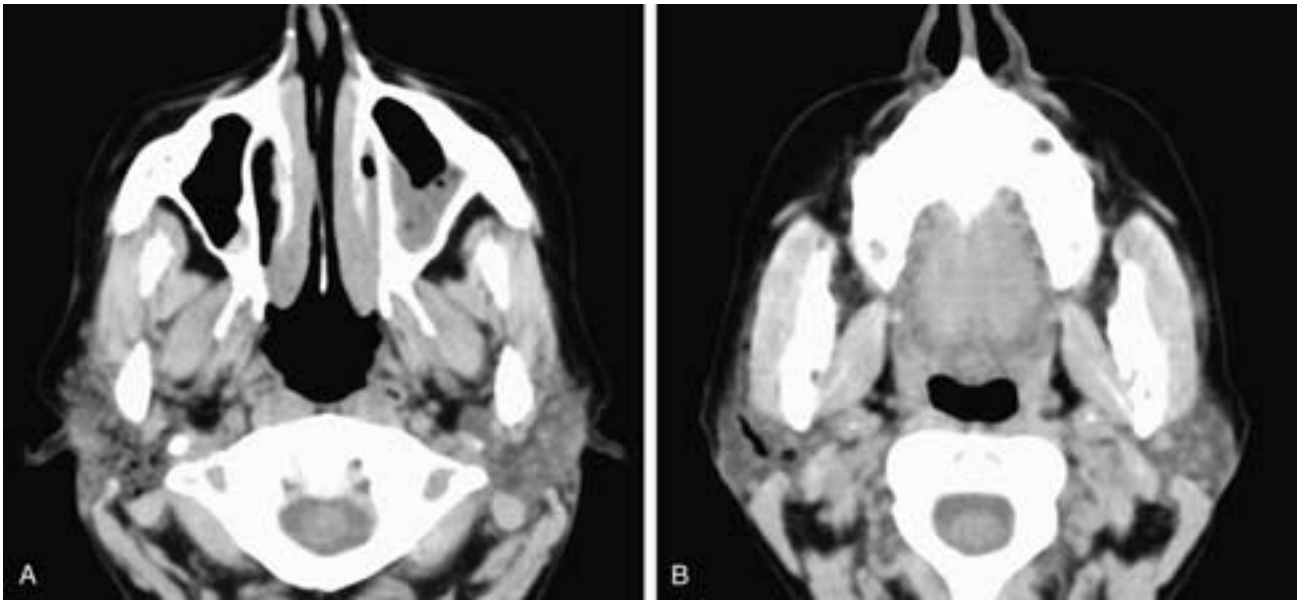

VIEW IMAGE

FIGURE 39-88 Axial CT scans through the upper (**A**) and lower (**B**) parotid glands. There is air within the right parotid ducts, and a small amount of air is seen in Stensen's duct. This patient had pneumoparotitis.

Copyright © 2003, Mosby, Inc. All rights reserved.

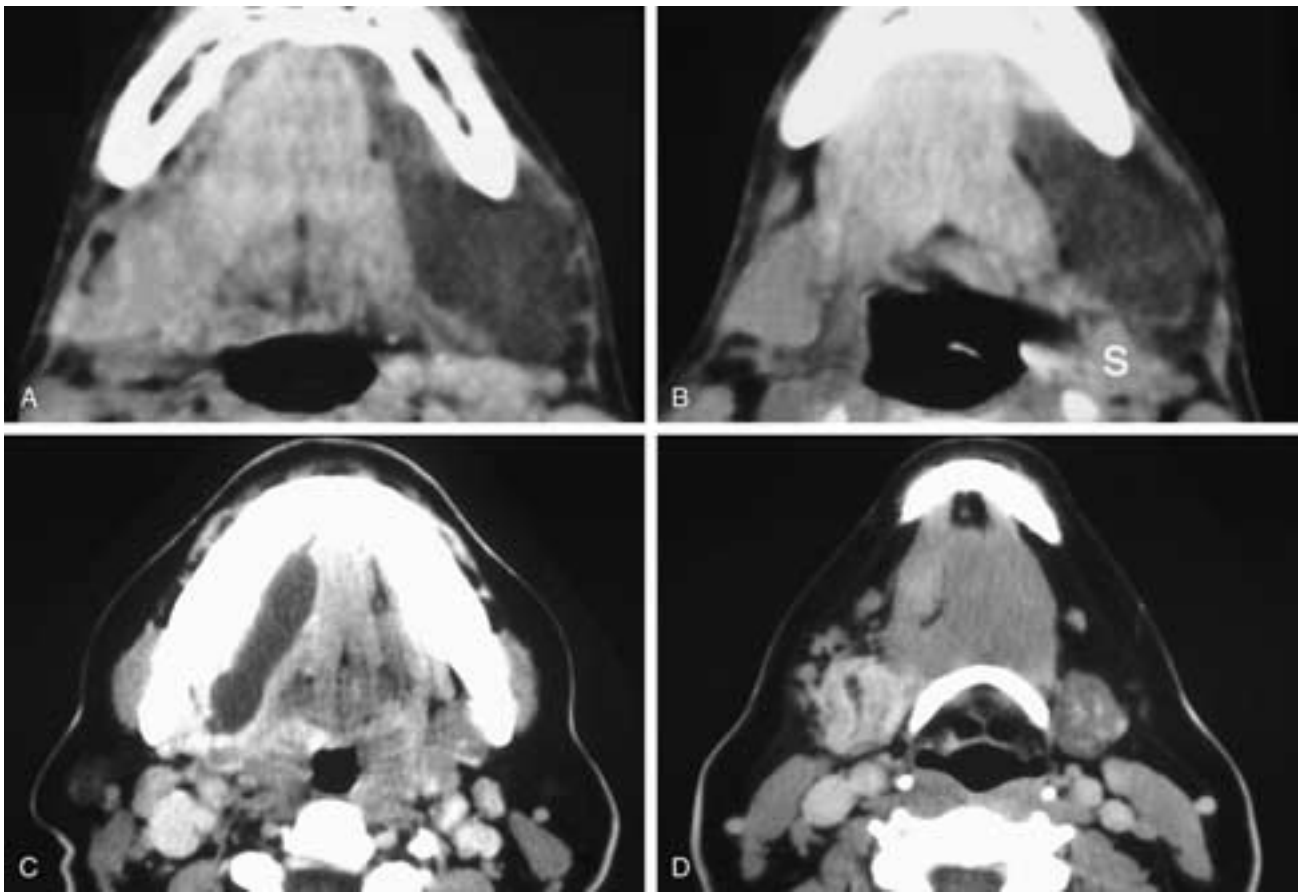

VIEW IMAGE

FIGURE 39-89 Axial CT scans through the floor of the mouth (**A**) and through the submandibular glands (**B**) show a cystic mass in the left lateral floor of the mouth that extends down into the left submandibular triangle. The left submandibular gland (*S*) is displaced backward by the cyst. This patient had a ranula. By comparison, axial contrast-enhanced CT scans through the floor of the mouth (**C**) and the submandibular glands (**D**) on another patient show a massively dilated right Wharton's duct and dilatation of the intraglandular ducts. The gland also enhances. This patient had a stricture of the opening of Wharton's duct, with dilatation of the ducts and sialadenitis.

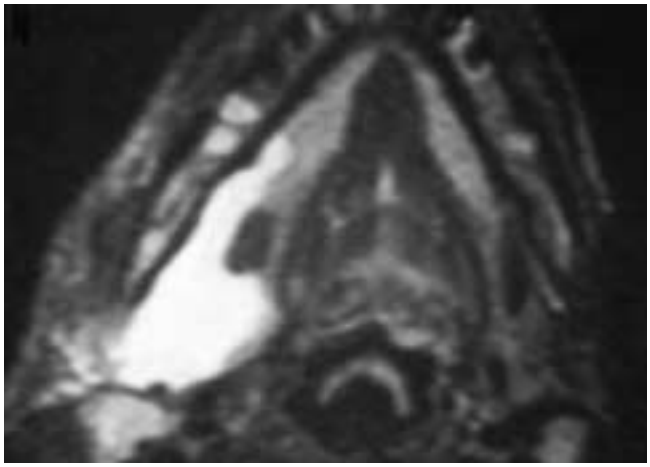

VIEW IMAGE

FIGURE 39-90 Axial T2-weighted MR image shows a high signal intensity mass in the right lateral floor of the mouth. The mass extends dorsal to the mylohyoid muscle and projects into the submandibular triangle. This patient had a ranula.

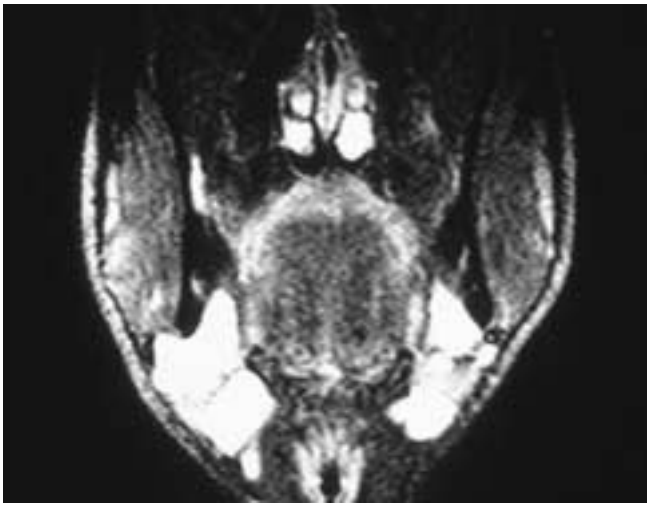

FIGURE 39-91 Coronal T2-weighted MR image shows bilateral cystic high signal intensity masses extending from the floor of the mouth into the submandibular triangles. This patient had bilateral ranulas.

VIEW IMAGE

Copyright © 2003, Mosby, Inc. All rights reserved.

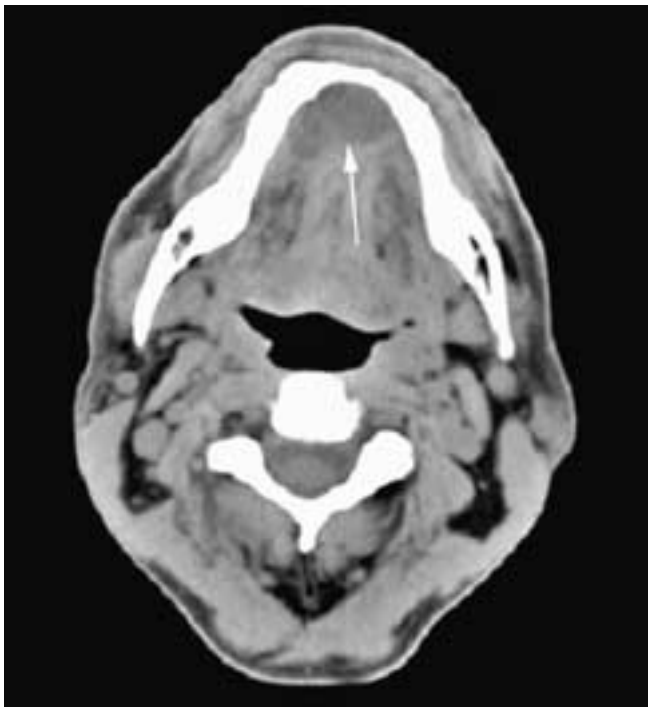

FIGURE 39-92 Axial CT scan shows a localized low-attenuation mass (*arrow*) in the midline extending from the anterior right sublingual gland across to the left side. This ranula remained above the mylohyoid muscle. This long-standing ranula has slightly remodeled the lingual cortex of the mandibular symphysis.

VIEW IMAGE

The elevated mucosa of the floor of the mouth often has a characteristic bluish color, and the appearance of this mucosa is reminiscent of the appearance of the gullet pouch of a frog (dim. French *rana*). Because of the simple ranula's location, the differential diagnosis includes lateral dermoid or epidermoid cyst, lipoma, and salivary gland tumor. The plunging ranula appears clinically as a painless mass in the submandibular or submental triangles of the neck, with or without evidence of a mass in the floor of the mouth. The differential diagnosis includes dermoid and epidermoid cysts, thyroglossal duct cysts, cystic hygroma, and lymphadenopathy.[151]

Although there is a diversity of proposed etiologies, ranulas most commonly result from trauma (including surgery) or obstruction to the sublingual salivary gland or its ductal elements. Ranulas are reported in approximately 5% to 12% of patients undergoing submandibular duct relocation for management of uncontrolled sialorrhea, presumably because, during this procedure, there is invariably surgical trauma to the sublingual gland components.[166, 168] Treatment of ranulas is directed primarily to transoral drainage of the cyst and excision of the ipsilateral sublingual gland.[169, 170] The more surgically difficult complete dissection of the ranula's lining or the exteriorization of the cyst have been shown to be unnecessary.[166, 167, 171, 172]

A sialogram performed on a patient with a cyst reveals smooth displacement of the glandular ducts around the mass. In general, no direct communication with the ductal system is demonstrated; however, the best method of demonstrating a communicating cyst is by sialography (Figs. 39-84 and 39-85). In patients with main ductal stenosis, the site and degree of this stenosis can be assessed accurately by a sialogram, provided that the stenosis is not at the main ductal orifice. Similarly, lacerations of the ducts can be identified by sialography, and in some cases any fistulas or sinus tracts can be visualized. In cases of parenchymal laceration or intracapsular hematoma, the sialogram reveals an area(s) of absent parenchymal filling, with splaying of the ducts around the region(s).

On CT, a cyst is identified as a smooth, well-delineated ovoid mass that usually has a homogeneous, low central attenuation of 10 to 20 HU. The cyst wall in these cases is easily identified, and is usually thin and uniform in

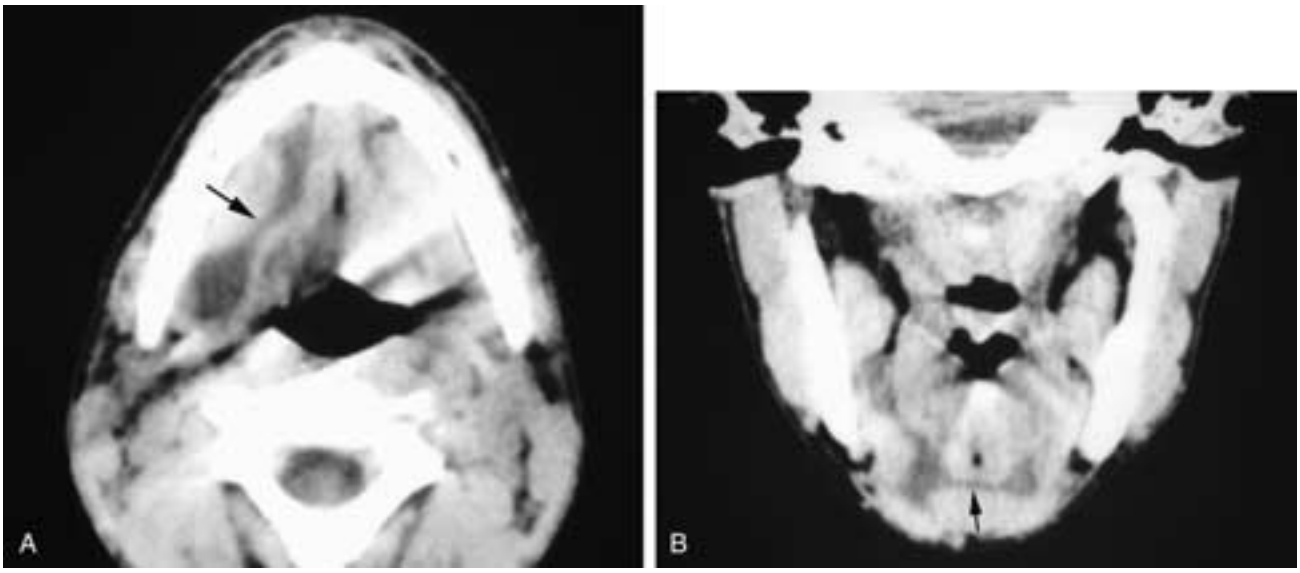

FIGURE 39-93 Axial (**A**) and coronal (**B**) CT scans show a low-attenuation (mucoid) collection (*arrows*) in the right floor of the mouth that has tracked down and across the midline floor of the mouth to the left side. This patient had a plunging ranula.

VIEW IMAGE

Copyright © 2003, Mosby, Inc. All rights reserved.

appearance. If the cyst contents are very proteinaceous (usually after repeated episodes of infection and/or hemorrhage), the attenuation of the cyst contents increases, approaching that of the cyst wall. In these uncommon cases, the cyst can appear on CT as a homogeneous, benign-appearing solid mass. If the cyst has become infected, the cyst wall enhances and becomes thicker and less well differentiated from the adjacent glandular parenchyma; the central portion of the cyst remains of lower attenuation. This CT appearance is indistinguishable from that of an abscess. The adjacent parenchyma in such cases usually has increased attenuation (compared to that of the normal gland), reflecting the cellular infiltration associated with the inflammation. In some cases, fistulas or sinus tracts can be demonstrated on CT scans; however, these are usually better identified by sialography. If contrast has been injected into a sialocele, the lesion will be well seen on CT (Fig. 39-86).

On CT, the simple ranula is usually a roughly ovoid-shaped cyst with a homogeneous central attenuation region of 10 to 20 HU. The cyst wall is either very thin or not seen, and the lesion is positioned lateral to the genioglossal muscles and above the mylohyoid muscle (Fig. 39-89). Uncommonly, the cyst can extend anteriorly, behind the symphysis of the mandible, above the genial muscles (Fig. 39-92). The plunging ranula often infiltrates the adjacent tissue planes, extending inferiorly and dorsally to the submandibular gland region, while ventrally it may cross the midline to the contralateral floor of the mouth (Fig. 39-93). The CT differential diagnosis includes dermoid, epidermoid, cystic lymphangioma, lipoma, lateral thyroglossal duct cyst, and cystic/necrotic lymph node.[152] A Wharton's duct that is obstructed anteriorly near the papilla may dilate and simulate a ranula in the lateral floor of the mouth on imaging. However, the changes in the obstructed duct extend back into the submandibular gland, and the gland has dilated ducts and usually enhances more than the contralateral normal submandibular gland. Although a plunging ranula may extend into the submandibular triangle and displace the submandibular gland, it does not intrinsically affect this gland.

On MR imaging, the ranula's characteristic appearance is usually dominated by its high water content. Thus, it has a low T1-weighted, an intermediate proton density, and a high T2-weighted signal intensity (Figs. 39-90 and 39-91). This appearance, especially in a plunging ranula, may be similar to that of a lymphangioma, a lateral thyroglossal duct cyst, and possibly an inflamed lymph node. However, if the protein concentration of the ranula's contents is high, the signal intensities can vary, often being high on all imaging sequences. In such cases, the MR differential diagnosis includes entities such as dermoids, epidermoids, and lipomas.

On MR imaging, the cyst wall's thickness, smoothness, or uniformity may occasionally be defined on T1-weighted images, but this is usually better accomplished on postcontrast fat-suppressed studies. One of the potential difficulties with noncontrast-enhanced MR images is that cysts and solid lesions that have a high water content can appear identical. The cyst wall may not be adequately visualized on any MR imaging sequence. This problem rarely exists with CT or ultrasound. The treatment of choice for ranulas and cysts is surgery.[165, 183–190]

TUMORS AND TUMOR-LIKE CONDITIONS

In the general population, salivary gland neoplasms represent less than 3% of all tumors.[191] It has been estimated that about 1% of all head and neck malignant tumors arise in the salivary glands, and these tumors result in about 750 deaths annually. However, a higher incidence of such salivary neoplasms has been reported in selected populations such as Eskimos, survivors of atomic bomb blasts, and persons exposed to previous radiation.[192, 193] From 70% to 80% of parotid gland tumors, 40% to 58% of submandibular gland tumors, 15% to 30% of sublingual gland tumors, and 20% to 51% of minor salivary gland tumors are benign. Generally, these figures indicate that the smaller the salivary gland involved, the greater the likelihood that a tumor is malignant.[192–194]

The TNM staging of salivary gland tumors according to the American Joint Committee on Cancer is weighted heavily on the size of the primary lesion and is presented in Table 39-1. Generally, tumor stage correlates inversely with overall survival for salivary malignancies. However, tumor grade is also an important prognosticator. In most circumstances, tumor stage and grade are more significant predictors than actual histologic subclassification. One exception to this rule concerns salivary duct carcinoma (see below). This high-grade neoplasm has a dismal prognosis despite its presentation as a T1 neoplasm.

Although overall cure rates traditionally are calculated on the basis of no evidence of disease (NED) for 5 years, several of the major salivary gland tumors (notably adenoid cystic carcinoma) may have late recurrences, some appearing 10 to 25 years after the initial treatment. For this reason, statistics citing 5 years of curability must be viewed with some circumspection.[192, 195]

Although salivary gland tumors are uncommon in children, there is a higher frequency of malignancies in children compared to adults. Thirty-five percent of all epithelial and nonepithelial salivary gland tumors in children are malignant.[196] The most common tumors in the pediatric age group are hemangiomas, followed in descending frequency by pleomorphic adenomas, mucoepidermoid carcinomas, lymphangiomatous tumors, acinic cell carcinomas, and undifferentiated carcinomas.[197]

For all parotid malignancies, the presence of metastatic regional lymph node disease indicates a poor prognosis. The frequencies of clinically palpable lymph node metastases per specific histologic diagnosis are: high-grade mucoepidermoid carcinoma, 44%; squamous cell carcinoma, 37%; adenocarcinoma, 25%; undifferentiated carcinoma, 23%; carcinoma ex pleomorphic adenoma, 21%; acinic cell carcinoma, 13%; and adenoid cystic carcinoma, 5%. The rates of occult nodal metastasis per diagnosis are: salivary duct carcinoma, 60%; squamous cell carcinoma, 40%; high-grade mucoepidermoid carcinoma, 16%; adenocarcinoma, 9%; and acinic cell carcinoma, 6%.[196] For malignancies of the submandibular, sublingual, and minor salivary glands, the rates of occult nodal metastasis per diagnosis are: carcinoma ex pleomorphic adenoma, 42%; mucoepidermoid carcinoma (all grades), 33%; squamous cell carcinoma, 33%; and adenoid cystic carcinoma, 13%. The difference between these two sets of data reflects the parotid predilection for salivary duct carcinoma and

Copyright © 2003, Mosby, Inc. All rights reserved.

Table 39-1
TNM SALIVARY GLAND STAGING SYSTEM

Primary Tumor (T)	
TX	Primary tumor cannot be assessed.
T0	No evidence of primary tumor.
T1	Tumor 2 cm or less in greatest dimension without extraparenchymal extension.
T2	Tumor more than 2 cm but not more than 4 cm in greatest dimension without extraparenchymal extension.
T3	Tumor more than 4 cm and/or tumor having extraparenchymal extension.
T4a	Tumor invades skin, mandible, ear canal, and/or facial nerve.
T4b	Tumor invades base of skull, and/or pterygoid plates and/or encases carotid artery.

Note: Extraparenchymal extension is clinical or macroscopic evidence of invasion of soft tissues. Microscopic evidence alone does not constitute extraparenchymal extension for classification purposes.

Regional Lymph Nodes (N)	
NX	Regional lymph nodes cannot be assessed.
N0	No regional lymph node metastasis.
N1	Metastasis in a single ipsilateral lymph node, 3 cm or less in greatest dimension.
N2	Metastasis in a single ipsilateral lymph node, more than 3 cm but not more than 6 cm in greatest dimension, or in multiple ipsilateral lymph nodes, none more than 6 cm in greatest dimension, or in bilateral or contralateral lymph nodes, none more than 6 cm in greatest dimension.
N2a	Metastasis in a single ipsilateral lymph node, more than 3 cm but not more than 6 cm in greatest dimension.
N2b	Metastasis in multiple ipsilateral lymph nodes, none more than 6 cm in greatest dimension.
N2c	Metastasis in bilateral or contralateral lymph nodes, none more than 6 cm in greatest dimension.
N3	Metastasis in a lymph node, more than 6 cm in greatest dimension.

Distant Metastasis (M)	
MX	Distant metastasis cannot be assessed.
M0	No distant metastasis.
M1	Distant metastasis.

Stage Grouping			
Stage I	T1	N0	M0
Stage II	T2	N0	M0
Stage III	T3	N0	M0
	T1	N1	M0
	T2	N1	M0
	T3	N1	M0
Stage IVA	T4a	N0	M0
	T4a	N1	M0
	T1	N2	M0
	T2	N2	M0
	T3	N2	M0
	T4a	N2	M0
Stage IVB	T4b	Any N	M0
	Any T	N3	M0
Stage IVC	Any T	Any N	M1

Source: AJCC Cancer Staging Manual 6th edition. Springer-Verlag, New York.

acinic cell carcinoma. Salivary malignancy that can be classified only as undifferentiated has a high rate of cervical metastasis.[198]

Facial nerve tumor invasion correlates directly with an increased rate of nodal metastasis (66% to 77%). Facial nerve paralysis is most commonly associated with parotid undifferentiated carcinoma (24%), squamous cell carcinoma (19%), adenoid cystic carcinoma (17%), adenocarcinoma (11%), mucoepidermoid carcinoma (9%), carcinoma ex pleomorphic adenoma (7%), and acinic cell carcinoma (1%). Overall, if the facial nerve is paralyzed at clinical presentation, the 5-year survival rate is only between 9% and 14%.[196]

The presence of pain is not necessarily a criterion of malignancy, since 5.1% of benign tumors and 6.5% of malignant tumors present with parotid pain. However, pain in a patient with a known malignancy is a very poor sign, as it is principally secondary to neural invasion.[196] Overall, the 5-year survival rate in patients with salivary malignancy and pain is 35% compared to 68% for those with no pain.

Distant metastasis also indicates a poor prognosis. Overall, about 20% of all parotid malignancies have distant metastases: salivary duct carcinoma, 57%; adenoid cystic carcinoma, 42%; undifferentiated carcinoma, 36%; adenocarcinoma, 27%; carcinoma ex pleomorphic adenoma, 21%; squamous cell carcinoma, 15%; acinic cell carcinoma, 14%; and mucoepidermoid carcinoma, 8%.[196]

In the past decade, the treatment philosophy for parotid gland malignancies has changed as the limitations of surgery for the more aggressive neoplasms have become known. Postoperative irradiation is now used frequently to improve local control, and chemotherapy is being utilized more often to control distant metastasis. Although specific chemotherapy regimens are constantly changing, the adenocarcinomas, adenoid cystic carcinomas, acinic cell carcinomas, and carcinoma ex pleomorphic adenomas seem to respond to a combination of adriamycin, cisplatinum, and 5-fluorouracil. The squamous cell carcinomas and the mucoepidermoid carcinomas have exhibited some response to a combination of methotrexate and cisplatinum.[196]

Many classifications of salivary gland tumors have been proposed.[8, 26, 199] Table 39-2 presents the most recent World Health Organization Classification of salivary tumors. Table 39-3 presents a refinement of that classification proposed in 1996.

Epithelial Tumors

Pleomorphic Adenoma (Benign Mixed Tumor) and Carcinoma ex Pleomorphic Adenoma (Malignant Mixed Tumor)

Pleomorphic adenoma, also referred to as *benign mixed tumor*, is the most common salivary gland tumor and represents 70% to 80% of all benign tumors of the major salivary glands. Table 39-4 shows the distribution of almost 700 pleomorphic adenomas seen at the Armed Forces Institute of Pathology.

Of all pleomorphic adenomas, 84% occur in the parotid gland, 8% in the submandibular gland, 6.5% in the minor salivary glands, and 0.5% in the sublingual glands. Of the parotid tumors, 90% arise lateral to the plane of the facial nerve.[7, 192] Although about 50% of all minor salivary gland tumors are malignant, pleomorphic adenoma is still the single most common tumor of these glands. Most of the minor salivary gland tumors occur in the palate and upper lip region; however, these tumors have also been reported in the lower lip, nasal septum, paranasal sinuses, base of the tongue, and larynx.[7]

Typically, these tumors occur as a slow-growing, painless mass that has an average interval between the onset of signs and symptoms and initial workup of 1 to 6 years. The tumors vary greatly in size from a few millimeters to

Copyright © 2003, Mosby, Inc. All rights reserved.

several centimeters. There is a female predominance, and most cases occur over the age of 40 years. The lesions are usually solitary, ovoid, well-demarcated masses despite having a capsule of variable thickness and completeness. The larger tumors may have pedunculated outgrowths from the main lesion that grossly simulate multiple masses.

The term *pleomorphic adenoma* summarizes the multifaceted (hence ''pleomorphic'') appearance of these tumors. They contain epithelial elements, which may be either glandular, ductal, or solid. The intercalated duct–myoepithelial cell unit is the proported origin of these tumors; certainly pleomorphic adenomas recapitulate these structures.[7] They also contain mesenchyma-like tissue, derived from the myoepithelial cells, which may contain chondroid and fibromyoid tissue (Fig. 39-94). Sites of necrosis, hemorrhage, hyalinization, calcification, and, rarely, ossification may be present.[7]

The recurrence rate varies between 1% and 50% and is directly related to the initial surgical procedure. The higher reported recurrence rates are in studies that included patients who were treated by enucleation rather than parotidectomy, as well as patients who had capsular rupture at surgery. For this reason, tumor enucleation is no longer considered an acceptable surgical technique. Conversely, some studies have very low reported recurrence rates because their follow-up period was of insufficient duration, since some recurrences take many years to develop. When recurrences occur, they are often multiple and clustered about the region

Table 39-2
WHO HISTOLOGIC CLASSIFICATION OF SALIVARY GLAND TUMORS (1991)

Adenomas
Pleomorphic adenoma
Myoepithelioma (myoepithelial adenoma)
Basal cell adenoma
Warthin's tumor (adenolymphoma)
Oncocytoma (oncocytic adenoma)
Canalicular adenoma
Sebaceous adenoma
Ductal papilloma
Inverted ductal papilloma
Intraductal papilloma
Sialadenoma papilliferum
Cystadenoma
Papillary cystadenoma
Mucinous cystadenoma
Carcinomas
Acinic cell carcinoma
Mucoepidermoid carcinoma
Adenoid cystic carcinoma
Polymorphous low-grade adenocarcinoma (terminal duct adenocarcinoma)
Epithelial-myoepithelial carcinoma
Basal cell adenocarcinoma
Sebaceous carcinoma
Papillary cystadenocarcinoma
Mucinous adenocarcinoma
Oncocytic carcinoma
Salivary duct carcinoma
Adenocarcinoma
Malignant myoepithelioma (myoepithelial carcinoma)
Carcinoma in pleomorphic adenoma (malignant mixed tumor)
Squamous cell carcinoma
Small cell carcinoma
Undifferentiated carcinoma
Other carcinomas
Nonepithelial Tumors
Malignant Lymphomas
Secondary Tumors
Unclassified Tumors
Tumor-Like Lesions
Sialadenosis
Oncocytosis
Necrotizing sialometaplasia (salivary gland infarction)
Benign lymphoepithelial lesion
Salivary gland cysts
Chronic sclerosing sialadenitis of submandibular gland (Küttner tumor)
Cystic lymphoid hyperplasia in AIDS

Table 39-3
CLASSIFICATION OF ELLIS AND AUCLAIR

Benign Epithelial Neoplasms
Mixed tumor (pleomorphic adenoma)
Myoepithelioma
Warthin's tumor
Basal cell adenoma
Canalicular adenoma
Oncocytoma
Cystadenoma
Ductal papillomas
Sialadenoma papilliferum
Inverted ductal papilloma
Intraductal papilloma
Lymphadenomas and sebaceous adenomas
Sialoblastoma
Malignant Epithelial Neoplasms
Mucoepidermoid carcinoma
Adenocarcinoma
Acinic cell adenocarcinoma
Adenoid cystic carcinoma
Polymorphous low-grade adenocarcinoma
Malignant mixed tumors
Carcinoma ex mixed tumor
Carcinosarcoma
Metastasizing mixed tumor
Squamous cell carcinoma
Basal cell adenocarcinoma
Epithelial-myoepithelial carcinoma
Clear cell adenocarcinoma
Cystadenocarcinoma
Undifferentiated carcinomas
Small cell undifferentiated carcinoma
Large cell undifferentiated carcinoma
Lymphoepithelial carcinoma
Oncocytic carcinoma
Salivary duct carcinoma
Sebaceous adenocarcinoma and lymphadenocarcinoma
Myoepithelial carcinoma
Adenosquamous carcinoma
Mucinous adenocarcinoma
Mesenchymal Neoplasms
Benign
Sarcomas
Malignant Lymphomas
Metastatic Tumors
Nonneoplastic Tumor-Like Conditions

Source: Ellis G, Auclair P. Benign epithelial neoplasms. In: Atlas of Tumor Pathology: Tumors of the Salivary Glands. Washington, D.C.: Armed Forces Institute of Pathology, 1996; Third series, Fascicle 17.

Copyright © 2003, Mosby, Inc. All rights reserved.

Table 39-4
ANATOMIC DISTRIBUTION OF 6880 CASES OF PLEOMORPHIC ADENOMA FROM THE ARMED FORCES INSTITUTE OF PATHOLOGY

Anatomic Site	Cases	%
Major Sites		
Parotid	4359	63.4
Submandibular	657	9.5
Sublingual	10	0.1
Neck nodes	89	1.3
Minor Sites		
Palate	711	10.3
Lip	297	4.3
Tongue	16	0.2
Cheek	126	1.8
Floor of mouth	7	0.1
Tonsil/oropharynx	38	0.6
Retromolar	3	—
Other	79	1.1
Not Stated	488	7.1

of the original tumor (cluster of grapes appearance). Recurrences result from transection of the finger or pod-like tumor projections, which characteristically cause a multinodular recurrence pattern. It has been noted that pleomorphic adenomas with a high stromal chondroid/myoid content have a greater recurrence rate than predominant cellular epithelial tumors.[200, 201] Myxoid-predominant pleomorphic adenomas have more numerous, obvious pseudopods and thinner capsules. Recurrences may be single but are more characteristically multiple. Myssiorrek et al. noted that the interval to recurrence was somewhat predictive. Patients with more than one recurrence tended to have their first recurrence earlier (mean, 47 months) than patients who were cured after reexcision of their only recurrence (mean, 105 months).[200] In a similar vein, MacGregor et al. noted that pleomorphic adenomas that ultimately recurred were more likely to have their initial onset prior to the age of 30 years.[201] Other series have indicated that younger patients tend to develop recurrences more often than older ones. Most investigators report a 10% to 18% incidence of further recurrence after surgery for the first recurrence (range, 5% to 60%).[202] Radiation has been used to treat recurrences; however, its utility is still uncertain.

True multiple pleomorphic adenomas are rare, with only isolated reports in the literature, and a primary multicentric origin is estimated to occur in 0.5% of parotid mixed tumors. The less common Warthin's tumors and oncocytomas are far more often multicentric than are pleomorphic adenomas.[7, 44, 98]

Three types of malignancies are associated with pleomor-

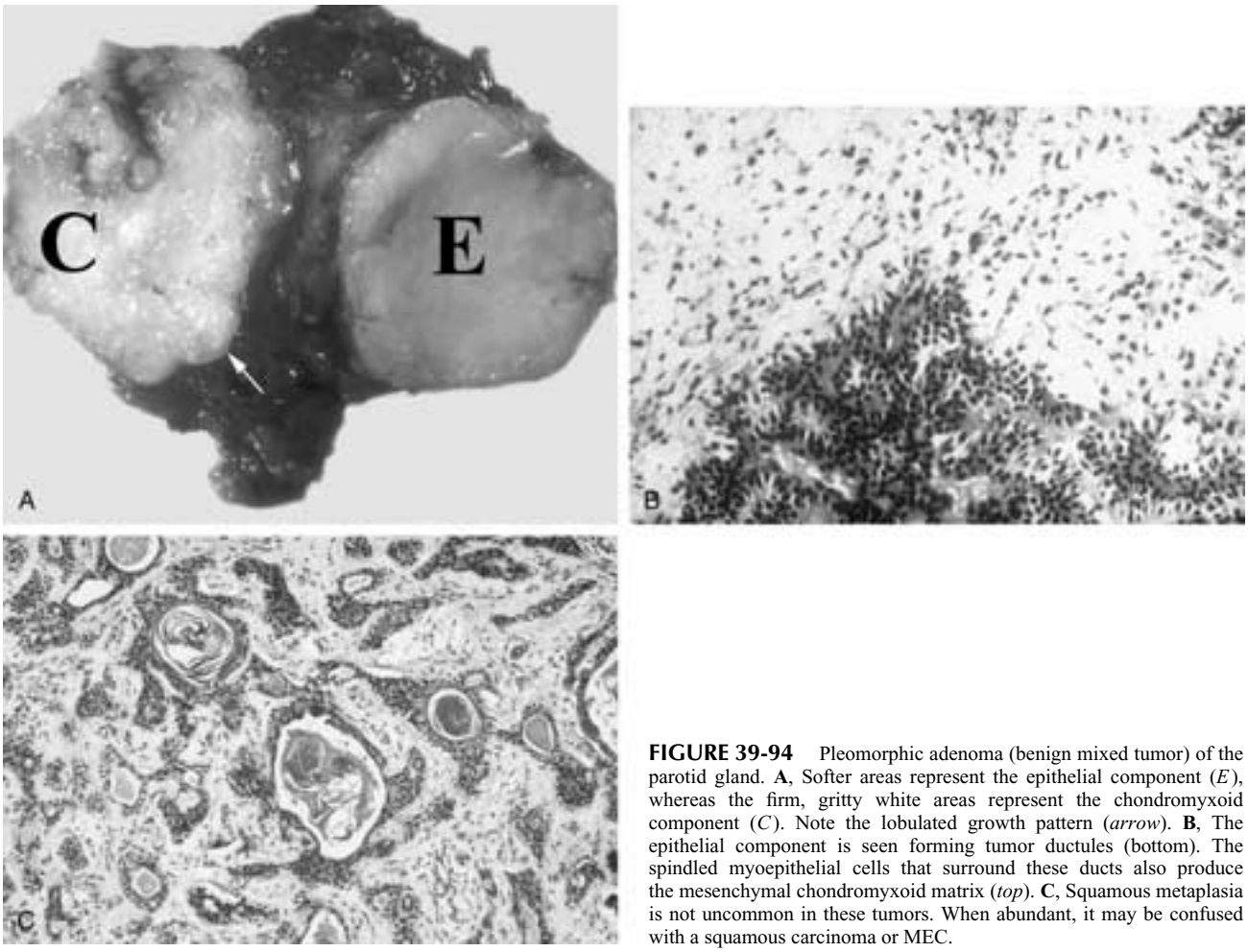

FIGURE 39-94 Pleomorphic adenoma (benign mixed tumor) of the parotid gland. **A**, Softer areas represent the epithelial component (*E*), whereas the firm, gritty white areas represent the chondromyxoid component (*C*). Note the lobulated growth pattern (*arrow*). **B**, The epithelial component is seen forming tumor ductules (bottom). The spindled myoepithelial cells that surround these ducts also produce the mesenchymal chondromyxoid matrix (*top*). **C**, Squamous metaplasia is not uncommon in these tumors. When abundant, it may be confused with a squamous carcinoma or MEC.

VIEW IMAGE

Copyright © 2003, Mosby, Inc. All rights reserved.

phic adenomas: carcinoma ex pleomorphic adenoma (also referred to as malignant mixed tumor) and rarer variants such as true malignant mixed tumor (also referred to as carcinosarcoma) and metastasizing benign mixed tumor.[203, 204] The carcinoma ex pleomorphic adenoma is either a malignant change in a benign mixed tumor in which elements of the benign lesion can still be identified or the development of a malignant tumor in a patient known to have a previously resected pleomorphic adenoma. Usually the malignancy is an adenocarcinoma, but any epithelial subtype can and does occur in approximately 2% to 5% of all mixed tumors.[7, 44, 203] The usual clinical presentation is in a patient with a long history (average, 10 to 15 years) of a benign mixed tumor that suddenly demonstrates a period of rapid growth (average, 3 to 6 months). Pain and facial nerve paralysis are often present; these patients most commonly are about 60 years of age. However, malignancies may be seen, usually a carcinoma ex pleomorphic adenoma, developing rapidly in a young person.[205, 206]

The malignant degeneration within a pleomorphic adenoma may be a function of time, and it has been estimated that, left untreated, nearly 25% of all pleomorphic adenomas may undergo malignant change.[7, 44] For this reason, surgeons no longer widely hold the concept of not operating readily on a benign mixed tumor because it is a ''benign'' lesion. In essence, the longer this tumor remains in the patient, the greater the chances that it will undergo malignant transformation. Carcinoma ex pleomorphic adenomas also have an accelerated recurrence rate and a high metastatic rate, which varies from 25% to 75%. Overall, the 5-year survival rate is approximately 50%; however, death usually occurs within 1 year of the discovery of metastases. The main sites of metastases are the regional lymph nodes, lungs, bones, and brain.[193] The degree of invasion of these tumors into the surrounding parotid parenchyma is an important prognosticator of survival.[207] A subgroup of noninvasive or minimally invasive malignant mixed tumor has recently been reported. This tumor has a better prognosis than the classic malignant mixed tumor.[205] No locoregional metastases or disease-related deaths have been reported in these minimally invasive (low-grade) malignant mixed tumors (Fig. 39-95).

The true malignant mixed tumor (*true* referring to truly mixed) is rare and contains both epithelial and stromal malignant elements. It is thus a true carcinosarcoma and usually has a grave prognosis. The metastasizing ''benign'' mixed tumor is the rarest form of malignancy associated with pleomorphic adenomas. Curiously, there are no tumor features (histology, flow cytology) that predict a malignant course. It has been postulated that multiple recurrences and surgical procedures allow some tumors to gain venous access and ''benignly'' metastasize. Karyotypic chromosomal analysis in one such tumor has revealed numerous translocations, including unbalanced rearrangements of chromosomes 1–13, 9–12, and monosomy 22, which differ from the typical balanced 8Q or 12Q translocations seen in pleomorphic adenomas. This suggests that more than happenstance allows a mixed tumor to gain venous access.[208–211]

Metastases may be multiple; involve lungs, bones, and soft tissues; and occur over many decades. Despite their indolent course, the pulmonary metastases may be massive, resulting in patient death. Therefore, it was recommended

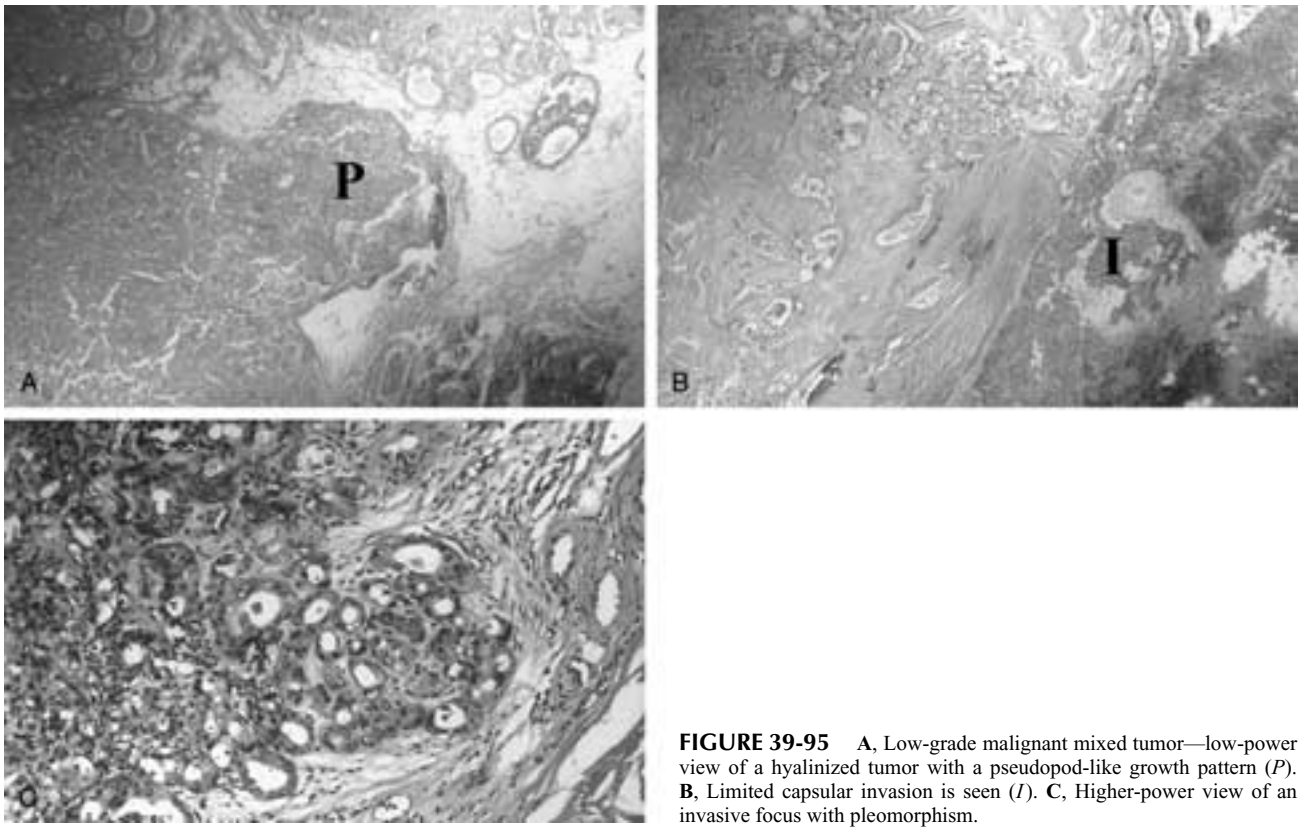

FIGURE 39-95 **A**, Low-grade malignant mixed tumor—low-power view of a hyalinized tumor with a pseudopod-like growth pattern (*P*). **B**, Limited capsular invasion is seen (*I*). **C**, Higher-power view of an invasive focus with pleomorphism.

VIEW IMAGE

Copyright © 2003, Mosby, Inc. All rights reserved.

that the adjective *benign* be deleted from the name of this tumor.[7, 44, 212]

The treatment of choice is surgical excision, with aggressive treatment of distant metastases. Half of the tumors metastasize to bone, 30% to the lung, and 30% to the lymph nodes; rarely, tumors metastasize to other body sites. Forty percent of patients died with disease, usually from distant metastases, 47% were alive and well, and 13% were alive with disease.

Carcinosarcoma (true malignant mixed tumor) is composed of a mixture of carcinomatous and sarcomatous elements. Unlike carcinoma ex pleomorphic adenoma, in which only the carcinomatous elements may metastasize, both the carcinomatous and sarcomatous elements of carcinosarcoma may metastasize. Carcinosarcoma is extremely rare, slightly over 40 cases having been reported to date.[213, 214] Two thirds of these tumors have arisen in the parotid glands, approximately 19% in the submandibular glands, and 14% in the palate; one case has been reported in the tongue. The mean age at presentation was 58 years, with a range of 14 to 87 years. A number of patients had a history of recurrent pleomorphic adenoma. Elements of chondrosarcoma and osteosarcoma are the most common sarcomatous elements, and moderate to poorly differentiated ductal carcinoma or undifferentiated carcinoma is the most common carcinomatous component. Local tissue infiltration and destruction are characteristic of this neoplasm.

Treatment is wide surgical excision combined with radiotherapy. Almost 60% of patients die of local recurrence and/or metastatic disease (lungs, bones, central nervous system), usually within 30 months.

The imaging of a pleomorphic adenoma shows the typical picture of a benign-appearing mass. On sialography, pleomorphic adenoma displaces the parotid ducts smoothly around the tumor mass (Fig. 39-96). On CT, most small benign mixed tumors are smoothly marginated, spherical tumors that have a higher attenuation than the surrounding parotid parenchyma. On occasion, these tumors can have a lower attenuation than the surrounding parotid parenchyma and mimic the appearance of a cyst. A good correlation between CT attenuation and tumor histology has not yet been established. All of these tumors enhance variably on contrast-enhanced studies (Figs. 39-97 to 39-102). The smaller lesions are usually fairly homogeneous in appearance. If delayed contrast-enhanced CT scanning is not performed in these cases, the mass may be overlooked. The larger masses most often have a nonhomogeneous appearance, with sites of lower attenuation representing areas of necrosis, old hemorrhage, and cystic change (Fig. 39-101). Localized areas of increased attenuation most often represent sites of recent hemorrhage and are associated clinically with a sudden increase in tumor size and localized pain. The larger tumors tend to develop a lobulated contour that, when present, is highly suggestive of the diagnosis (Figs. 39-99 and 39-100). Such a lobulated mass on CT may appear as multiple adjacent masses rather than a solitary lesion; however, on MR imaging they are clearly seen as a solitary mass (Fig. 39-99). On MR imaging, these tumors typically have a low T1-weighted and a high T2-weighted signal intensity (Fig. 39-102). A low signal intensity ''capsule'' is often seen on T2-weighted scans and on fat-suppressed, contrast-enhanced, T1-weighted images (Fig. 39-103). Dystrophic calcifications or ossifications can occasionally be seen scattered throughout the tumor, and such densities are highly suggestive of this diagnosis (Fig. 39-104) (also see the section on Clinical and Imaging Assessment of the Parapharyngeal Space in Chapter 38).

FIGURE 39-96 Lateral view of a parotid sialogram shows a mass (*arrows*) that smoothly displaces the adjacent parotid ducts around it. This patient had a pleomorphic adenoma (benign mixed tumor).

VIEW IMAGE

On CT, occasionally the outer contour of a pleomorphic adenoma may appear to be slightly indistinct. This is usually secondary to surrounding inflammation and/or hemorrhage. In these cases, the CT appearance can simulate that of a more aggressive tumor. However, on MR imaging, the lesion's contour is sharp and benign-appearing (Fig. 39-100).

Overall on MR imaging, these tumors, when small, have a fairly homogeneous low T1-weighted and a high T2-weighted signal intensity. However, when large, these tumors usually have a nonhomogeneous, low to intermediate T1-weighted and an intermediate to high T2-weighted signal intensity. Areas of hemorrhage appear as regions of high signal intensity on both T1-weighted and T2-weighted images. Regions of necrosis usually have low T1-weighted and high T2-weighted signal intensity. The nonhomogeneous MR appearance is not unique to this tumor and can be seen in other lesions, including malignancies. On MR imaging, the dystrophic calcifications seen on CT usually cannot be visualized or distinguished from focal areas of fibrosis.[45, 68, 69]

A carcinoma ex pleomorphic adenoma may have one of several CT appearances: (1) It may look like a large pleomorphic adenoma, with no CT evidence of malignancy. (2) It may look like a benign mixed tumor with a focally aggressive appearance. This aggressive area has a necrotic center, thick, irregular walls, and infiltrating margins. (3) Last, the tumor may be entirely aggressive in its CT

Copyright © 2003, Mosby, Inc. All rights reserved.

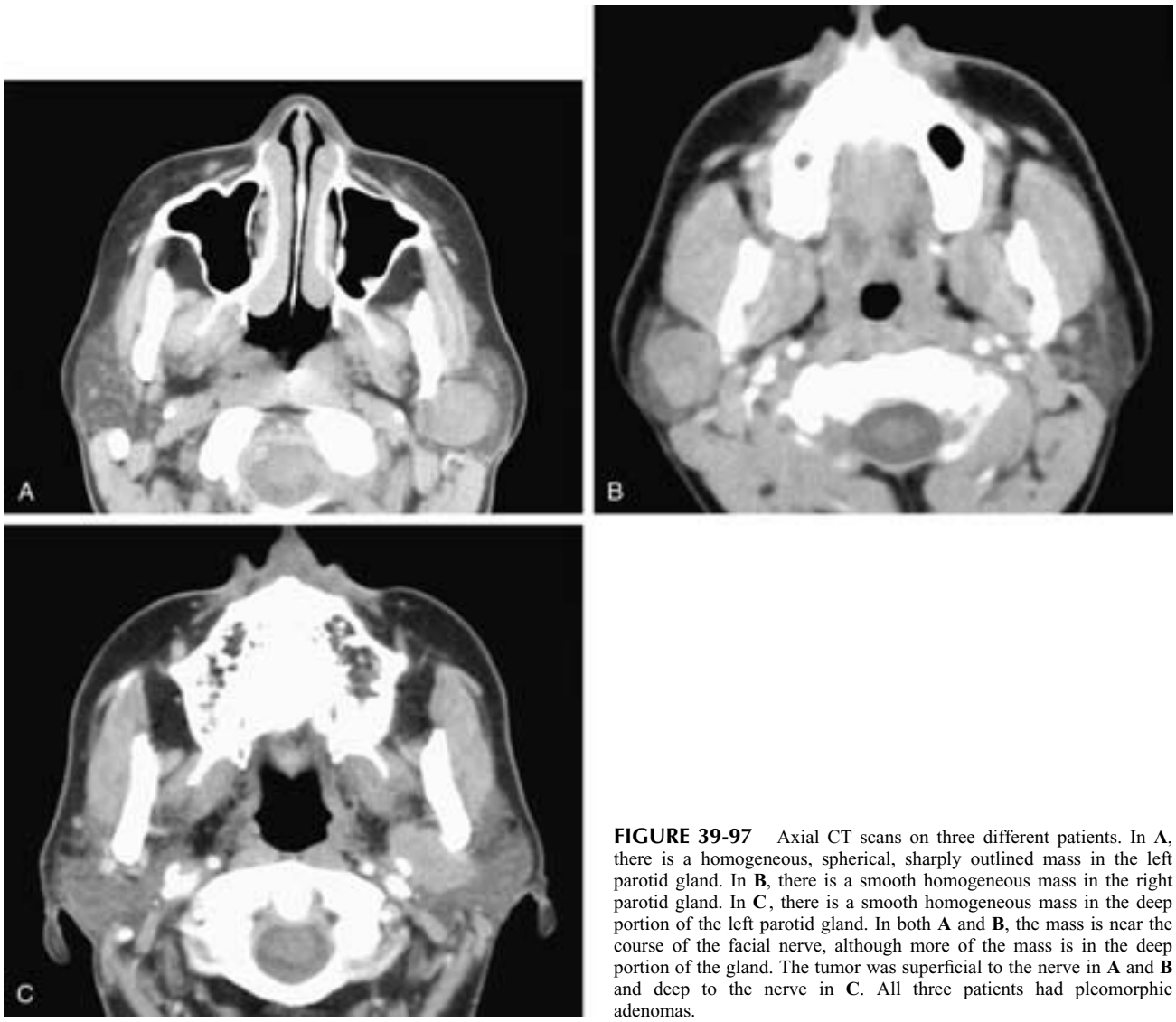

FIGURE 39-97 Axial CT scans on three different patients. In **A**, there is a homogeneous, spherical, sharply outlined mass in the left parotid gland. In **B**, there is a smooth homogeneous mass in the right parotid gland. In **C**, there is a smooth homogeneous mass in the deep portion of the left parotid gland. In both **A** and **B**, the mass is near the course of the facial nerve, although more of the mass is in the deep portion of the gland. The tumor was superficial to the nerve in **A** and **B** and deep to the nerve in **C**. All three patients had pleomorphic adenomas.

VIEW IMAGE

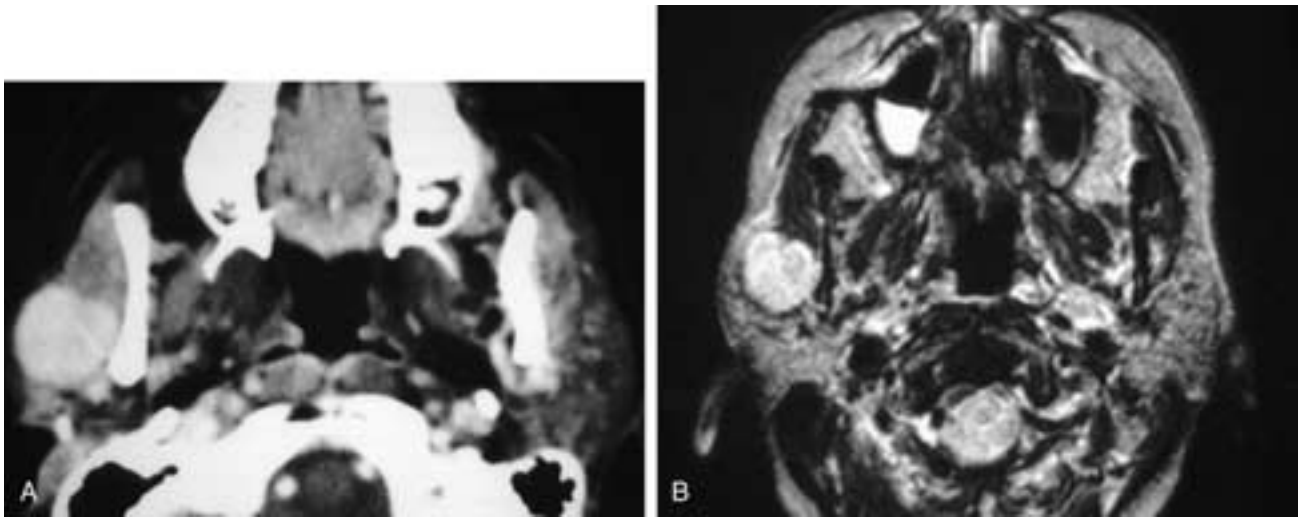

FIGURE 39-98 Axial contrast-enhanced CT scan (**A**) shows a well-delineated mass in the superficial portion of the right parotid gland. Axial T2-weighted MR image (**B**) shows this pleomorphic adenoma equally well. Although this may occur, the tumor margins usually are better seen on an MR study.

VIEW IMAGE

Copyright © 2003, Mosby, Inc. All rights reserved.

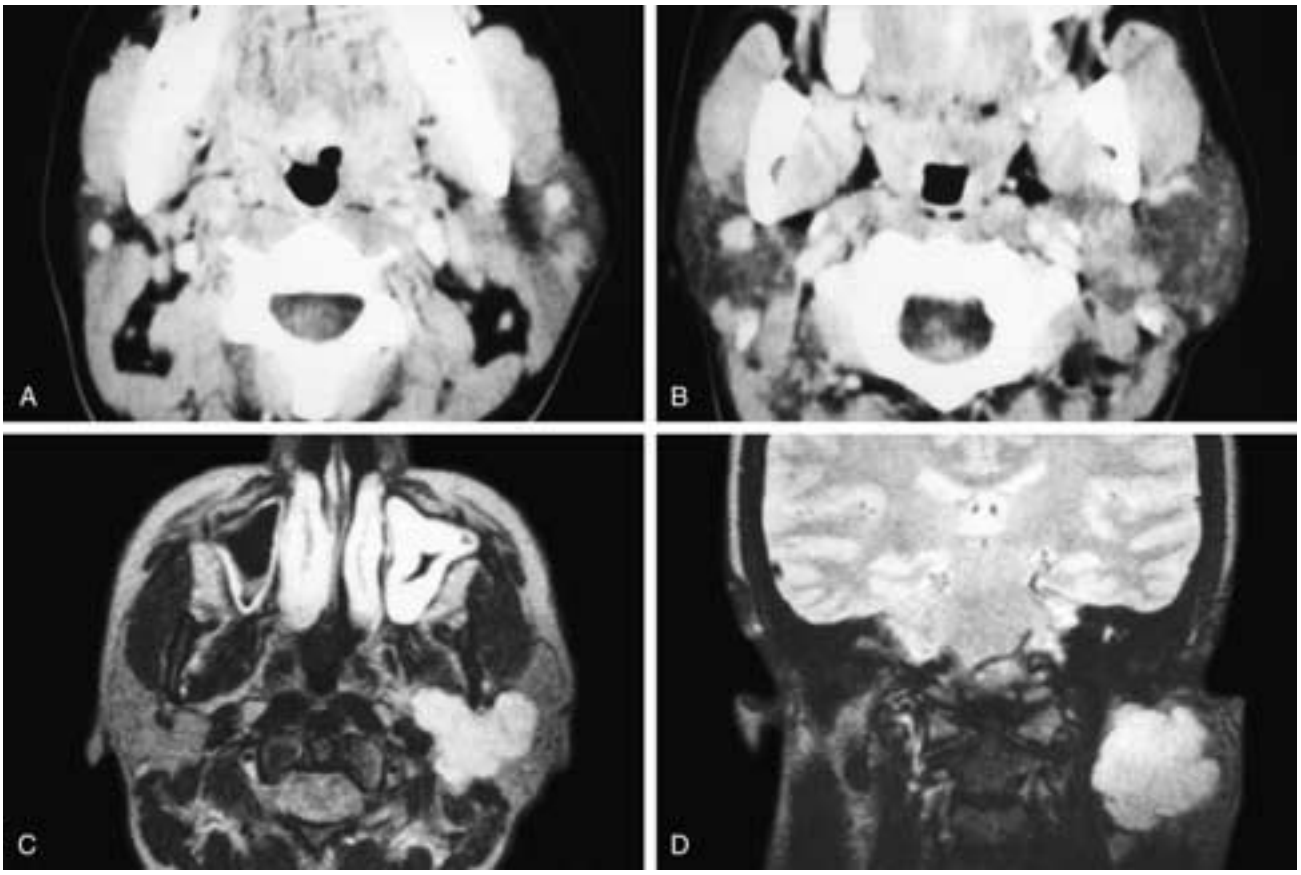

VIEW IMAGE

FIGURE 39-99 Axial contrast-enhanced CT scans (**A**, **B**) show a vaguely delineated mass in the deep portion of the left parotid gland. Axial (**C**) and coronal (**D**) T2-weighted MR images on the same patient show a lobulated solitary mass in the left parotid gland. The lesion is far better seen than on the CT scans. This patient had a pleomorphic adenoma.

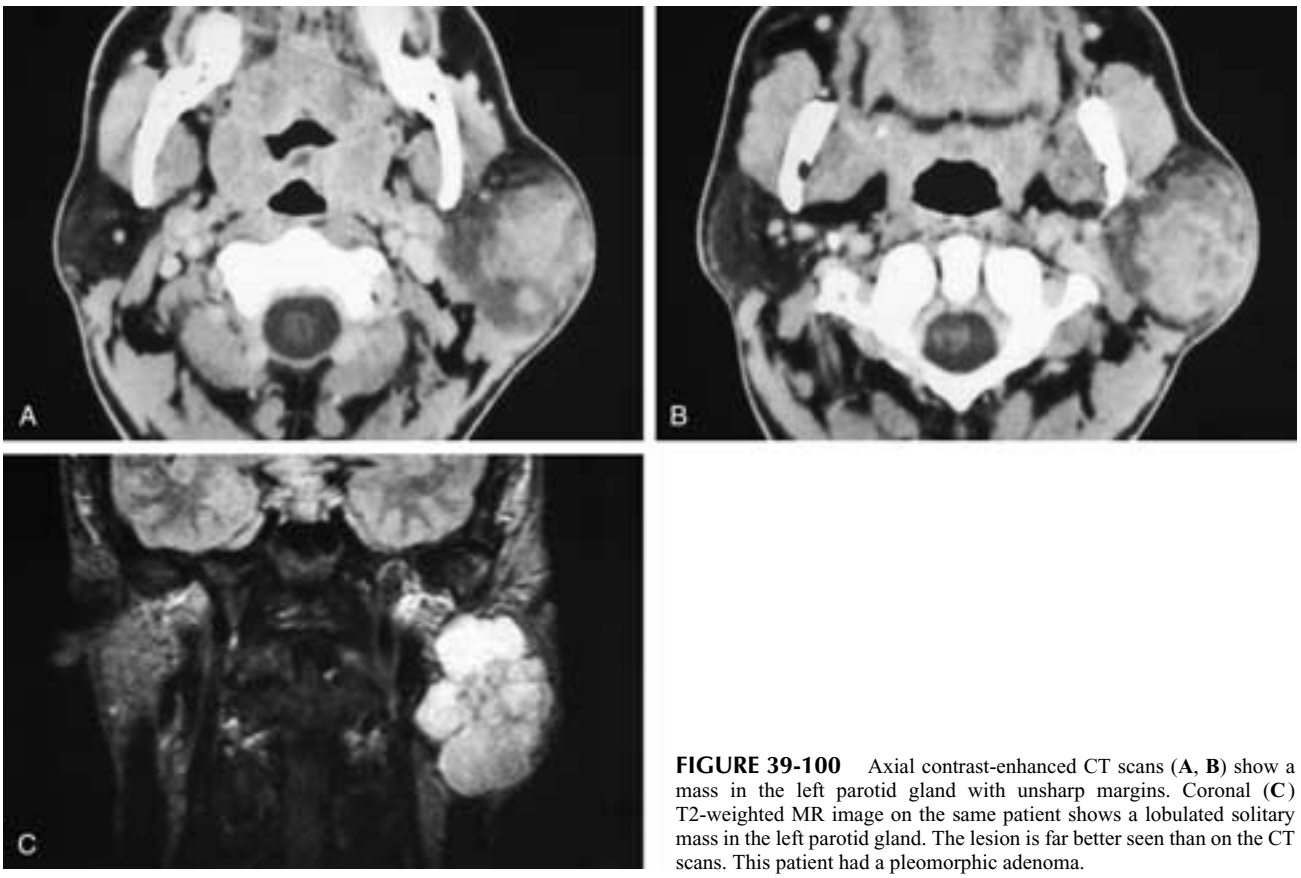

FIGURE 39-100 Axial contrast-enhanced CT scans (**A**, **B**) show a mass in the left parotid gland with unsharp margins. Coronal (**C**) T2-weighted MR image on the same patient shows a lobulated solitary mass in the left parotid gland. The lesion is far better seen than on the CT scans. This patient had a pleomorphic adenoma.

VIEW IMAGE

Copyright © 2003, Mosby, Inc. All rights reserved.

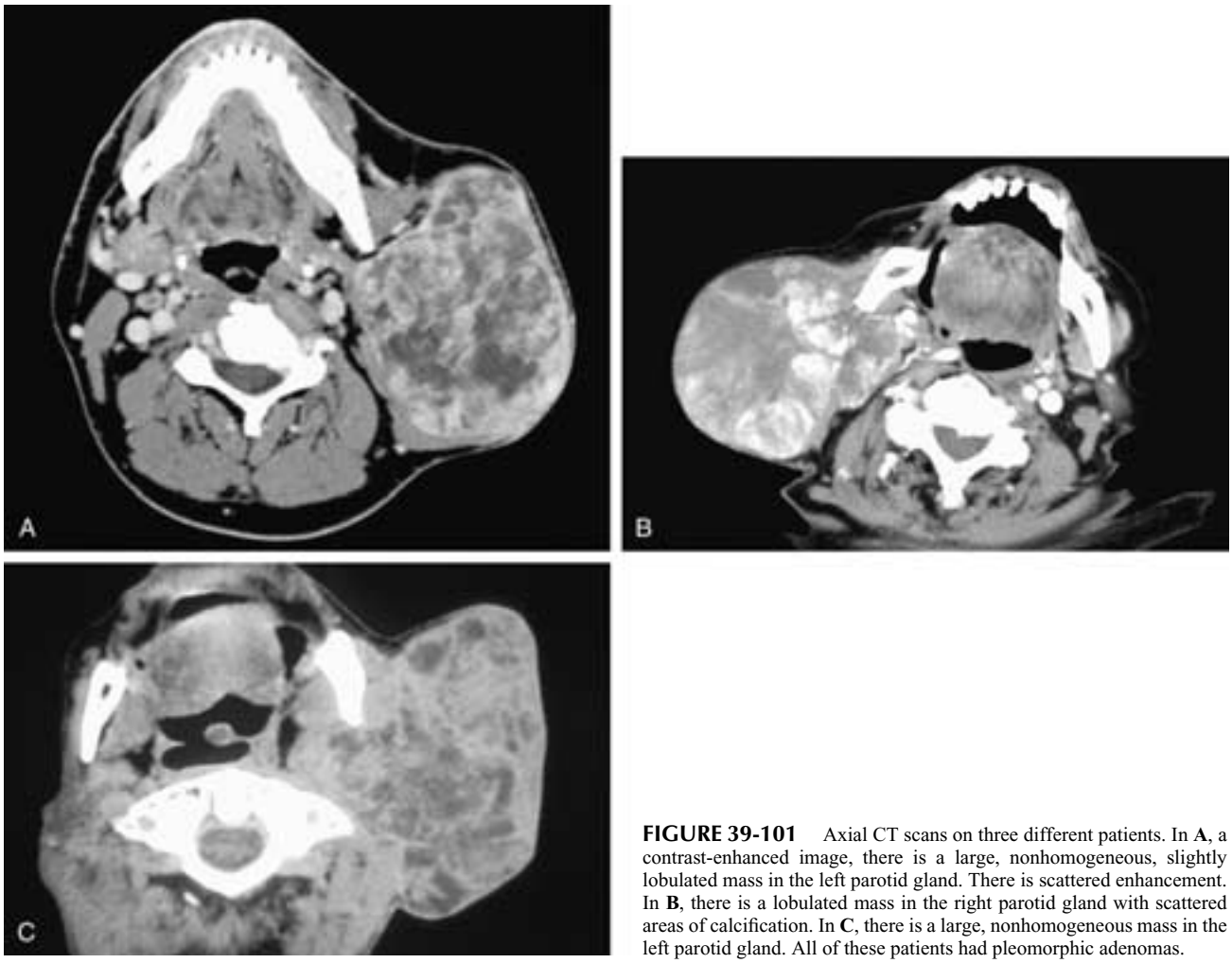

FIGURE 39-101 Axial CT scans on three different patients. In **A**, a contrast-enhanced image, there is a large, nonhomogeneous, slightly lobulated mass in the left parotid gland. There is scattered enhancement. In **B**, there is a lobulated mass in the right parotid gland with scattered areas of calcification. In **C**, there is a large, nonhomogeneous mass in the left parotid gland. All of these patients had pleomorphic adenomas.

VIEW IMAGE

appearance, with no remaining evidence of a benign pleomorphic adenoma. On MR imaging a similar variation can be encountered, with such a tumor having either a smooth margin or a focally or totally invasive margin (Fig. 39-105). Occasionally, like problems encountered with cervical lymph node metastasis, obviously necrotic, thick-walled areas of tumor seen on CT may be poorly identified on MR imaging. In such cases, contrast-enhanced, fat-suppressed, T1-weighted images usually show the necrotic region (Fig. 39-106).

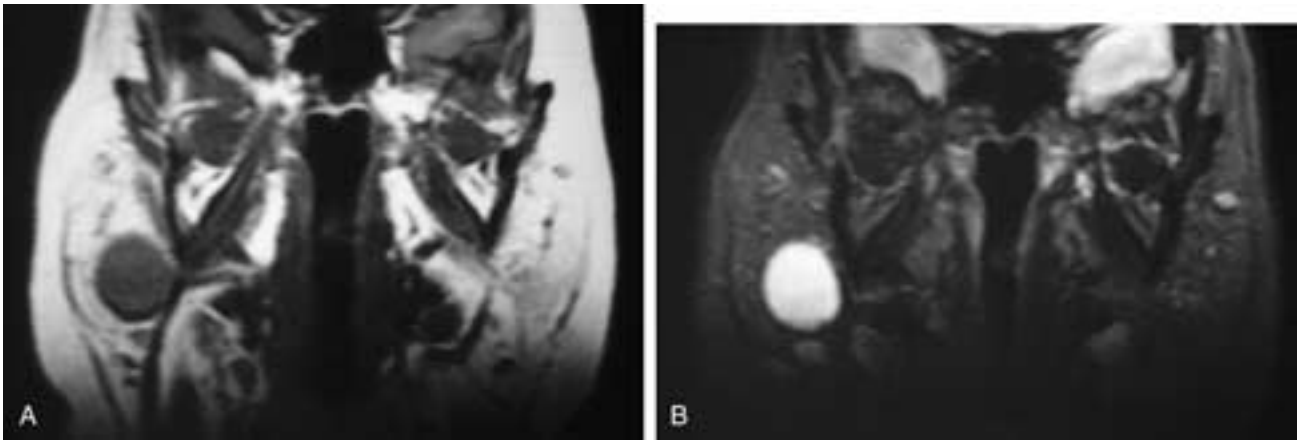

VIEW IMAGE

FIGURE 39-102 Coronal T1-weighted (**A**) and T2-weighted (**B**) MR images show a well-delineated right parotid mass that has a low signal intensity in **A** and a high signal intensity in **B**. These ''water'' signal intensities reflect the high serous and mucinous differentiation of this tumor. This is a nonspecific appearance. This patient had a pleomorphic adenoma.

Copyright © 2003, Mosby, Inc. All rights reserved.

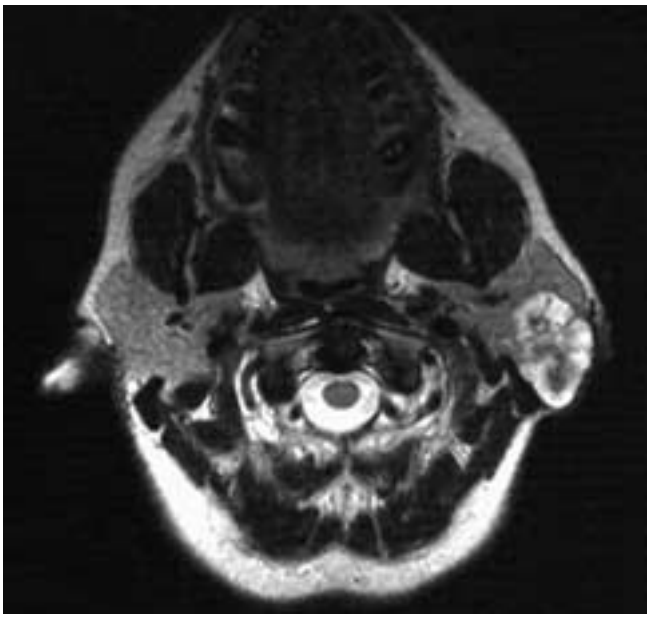

VIEW IMAGE

FIGURE 39-103 Axial T2-weighted MR image shows a nonhomogeneous but primarily high signal intensity, well-delineated mass in the left parotid gland. Although this is a nonspecific appearance, it is suggestive of a pleomorphic adenoma. The patient had a pleomorphic adenoma.

Most of the carcinomas that occur in pleomorphic adenomas are high-grade cellular masses, and they tend to have fairly low signal intensities on both T1-weighted and T2-weighted sequences. Thus, when a benign-appearing parotid mass is seen that has a low T2-weighted signal intensity, the diagnosis of a benign mixed tumor should be questioned and an explanation for the low signal intensity must be sought. Most often it is the result of a high-grade tumor; however, other lesions can cause similar signal intensities, including fibrosis, granulation tissue, and occasionally some benign or low-grade neoplasms. As previously mentioned, the presence of a low T2-weighted signal intensity only serves to alert the radiologist that a carcinoma ex pleomorphic adenoma may be present.

These imaging appearances hold true whether the pleomorphic adenoma is in the parotid gland proper, the deep portion of the parotid gland extending into the parapharyngeal space (Fig. 39-107), an accessory parotid gland (Fig. 39-108), or the submandibular gland (Figs. 39-109 and 39-110). There may be a tendency for the tumors within the submandibular gland to have a greater cystic component.

When postoperative recurrences occur, invariably there was violation of the original tumor capsule at surgery. This results in seeding of the operative bed, and tumor regrowth can occur anywhere from a few years to decades after sur-

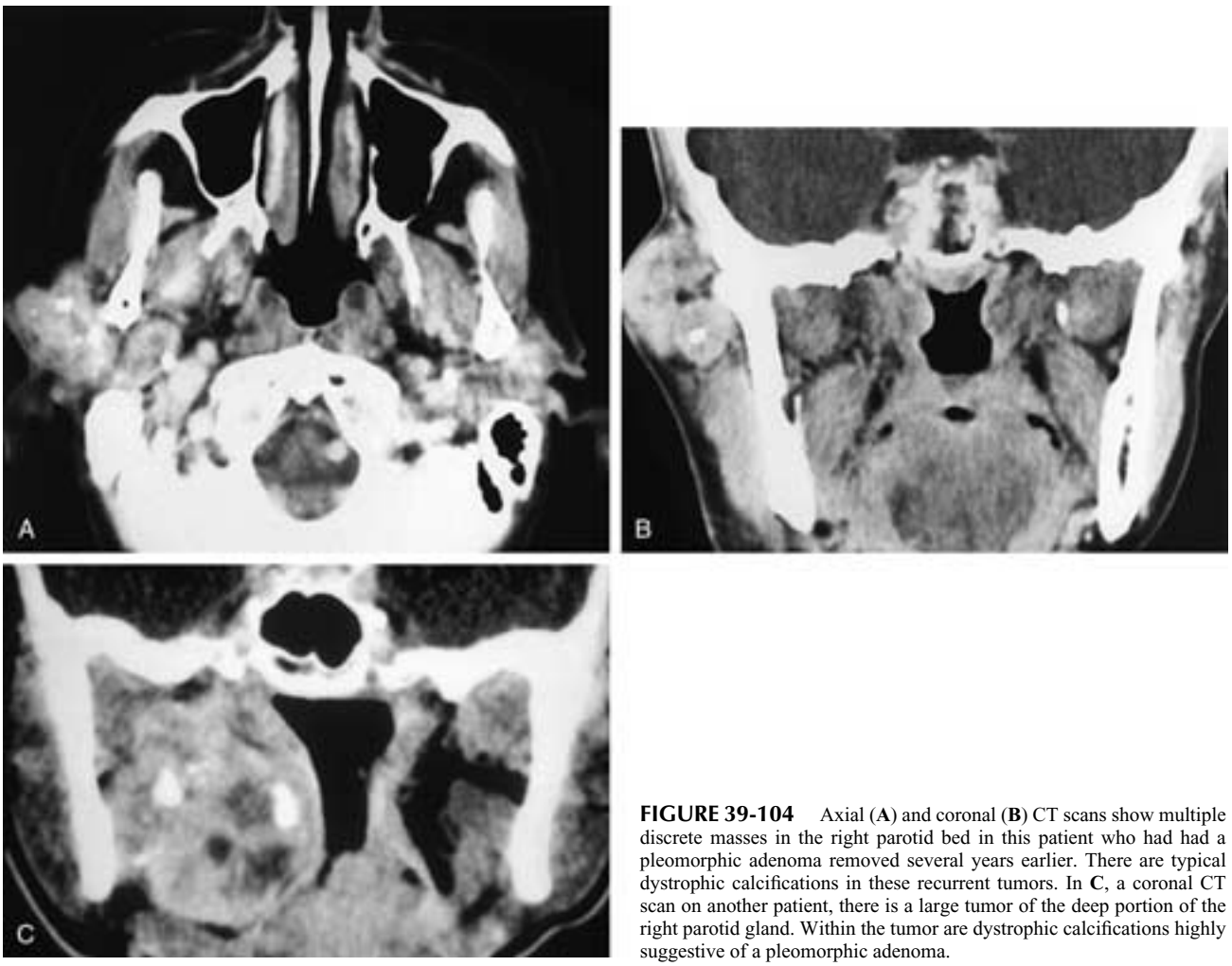

FIGURE 39-104 Axial (**A**) and coronal (**B**) CT scans show multiple discrete masses in the right parotid bed in this patient who had had a pleomorphic adenoma removed several years earlier. There are typical dystrophic calcifications in these recurrent tumors. In **C**, a coronal CT scan on another patient, there is a large tumor of the deep portion of the right parotid gland. Within the tumor are dystrophic calcifications highly suggestive of a pleomorphic adenoma.

VIEW IMAGE

Copyright © 2003, Mosby, Inc. All rights reserved.

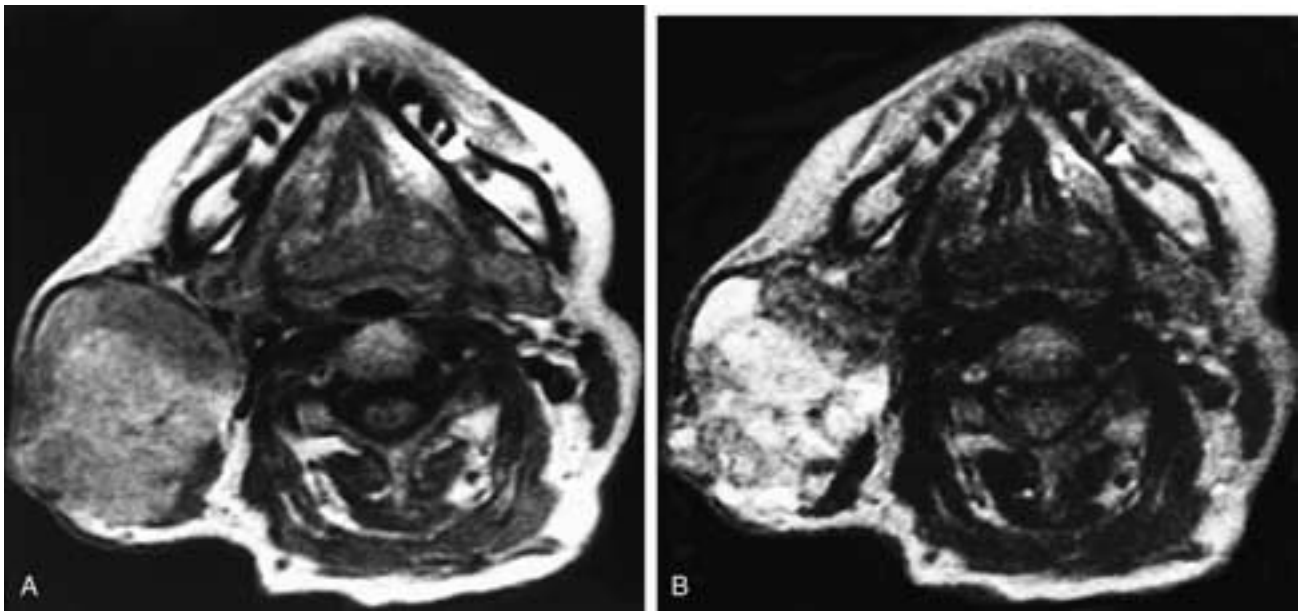

VIEW IMAGE

FIGURE 39-105 Axial T1-weighted (**A**) and T2-weighted (**B**) MR images show a large right nonhomogeneous parotid mass with well-defined margins except laterally, where the tumor has broken through to the skin. This patient had a carcinoma ex pleomorphic adenoma. With the exception of the focal tumor invasion of the skin, this imaging appearance suggests a pleomorphic adenoma.

gery. MR imaging is the best way to identify these recurrent tumors, as they have high T2-weighted signal intensity and are grouped like a cluster of grapes (Fig. 39-111).

Warthin's Tumor

Warthin's tumor, also referred to as papillary cystadenoma lymphomatosum, is the second most frequent benign tumor arising in the parotid gland after benign mixed tumor. Previously, it was referred to in the literature as adenolymphoma; this is a misnomer, as it may give the mistaken impression that one is dealing with a lymphoma. Warthin's tumor comprises 4% to 15% of all salivary gland epithelial tumors and 4% to 10% of all parotid tumors, with occasional series showing relative frequencies as high as 30%. It is a slow-growing, commonly cystic neoplasm that arises almost exclusively in the parotid gland, frequently in its lower portion over the angle of the mandible. Occasional tumors (2.7% to 12%) may arise in extraparotid locations, most frequently in periparotid lymph nodes in the area of the parotid tail or in the upper neck, where they can mimic a

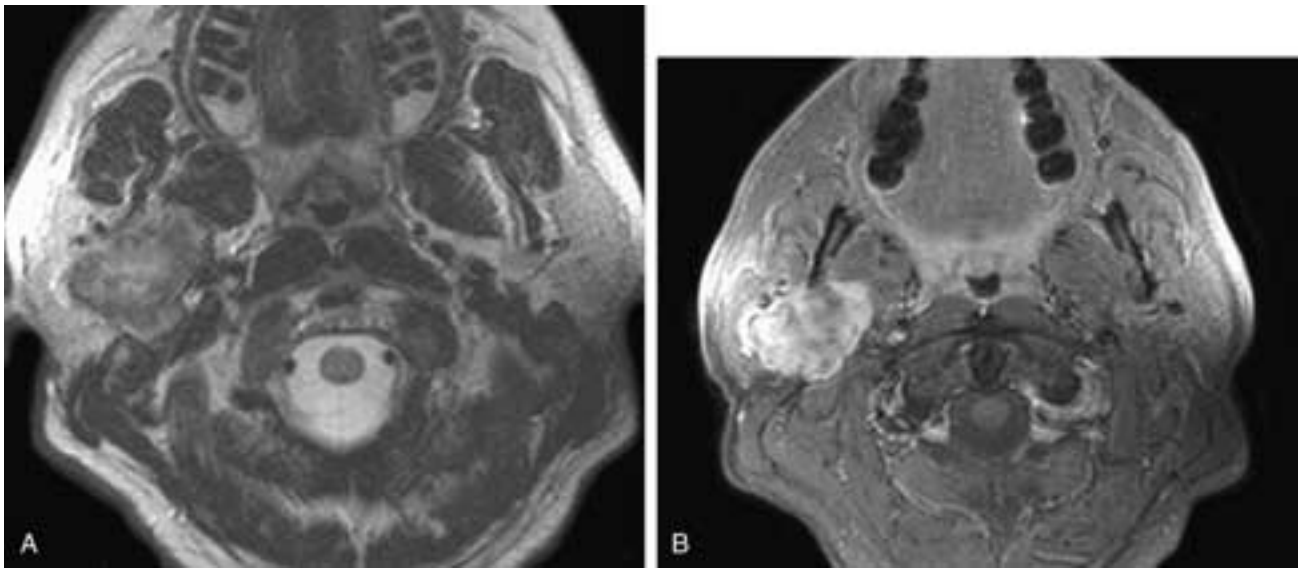

VIEW IMAGE

FIGURE 39-106 Axial T2-weighted MR image (**A**) shows a right deep parotid mass with slightly unsharp margins. The mass has a fairly low signal intensity. Axial T1-weighted, fat-suppressed, contrast-enhanced MR image (**B**) shows the mass to enhance nonhomogeneously. This was a carcinoma ex pleomorphic adenoma.

Copyright © 2003, Mosby, Inc. All rights reserved.

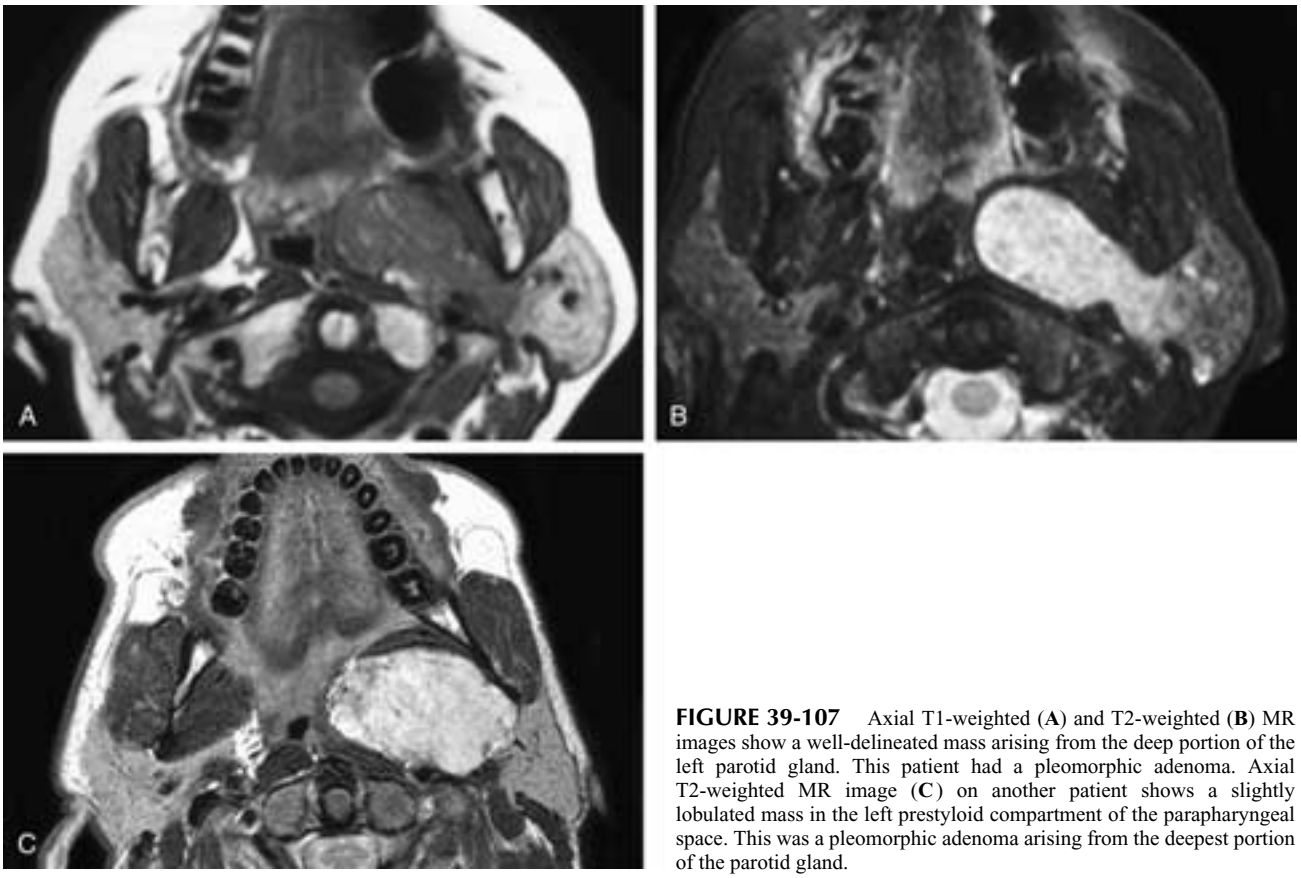

FIGURE 39-107 Axial T1-weighted (**A**) and T2-weighted (**B**) MR images show a well-delineated mass arising from the deep portion of the left parotid gland. This patient had a pleomorphic adenoma. Axial T2-weighted MR image (**C**) on another patient shows a slightly lobulated mass in the left prestyloid compartment of the parapharyngeal space. This was a pleomorphic adenoma arising from the deepest portion of the parotid gland.

VIEW IMAGE

lymph node metastasis. Rare Warthin's-like tumors have also been reported in the oral cavity, larynx, lacrimal gland, and nasopharynx, although these tumors may actually be oncocytomas.

Patients typically present with swelling, and only an occasional patient complains of pain. Warthin's tumor has a peak incidence in the fifth to seventh decades of life, with the youngest and oldest patients in one review being 2.5 and 92 years, respectively. It is considered to be more common in males than in females, with earlier studies demonstrating male:female ratios of up to 10:1; however, more recent reports have demonstrated a more equal incidence between the sexes. There appears to be a definite positive association between Warthin's tumor and cigarette smoking, and there is an increasing incidence of this tumor associated with increasing radiation exposure. It is the most common salivary gland tumor to present with multifocal or bilateral involvement, with 5% to 14% of patients presenting with bilateral masses, 25% of which present simultaneously and 75% metachronously.

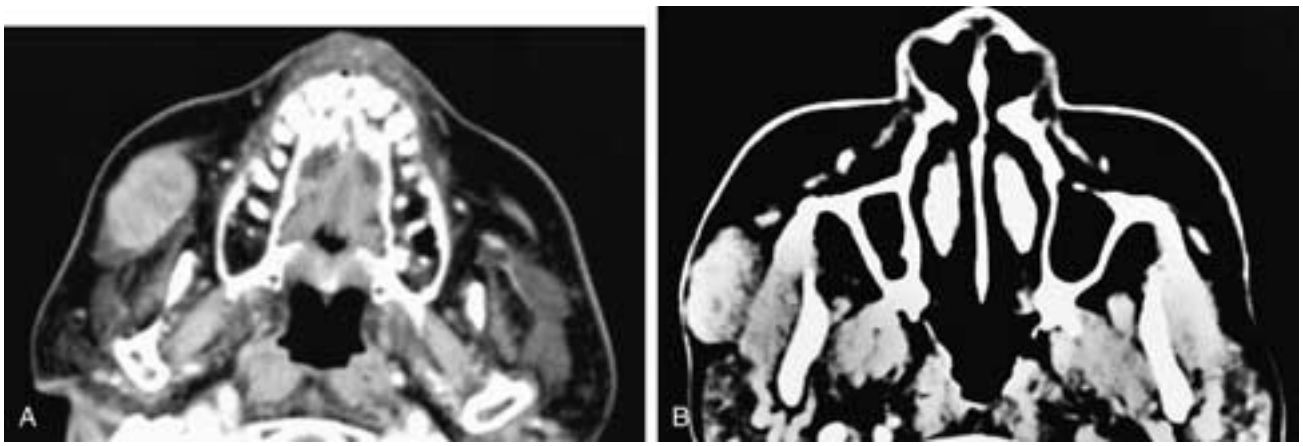

FIGURE 39-108 Axial CT scans (**A**, **B**) on two different patients, each with a slightly lobulated mass overlying the right masseter muscle. Both patients had pleomorphic adenomas of the accessory parotid glands.

VIEW IMAGE

Copyright © 2003, Mosby, Inc. All rights reserved.

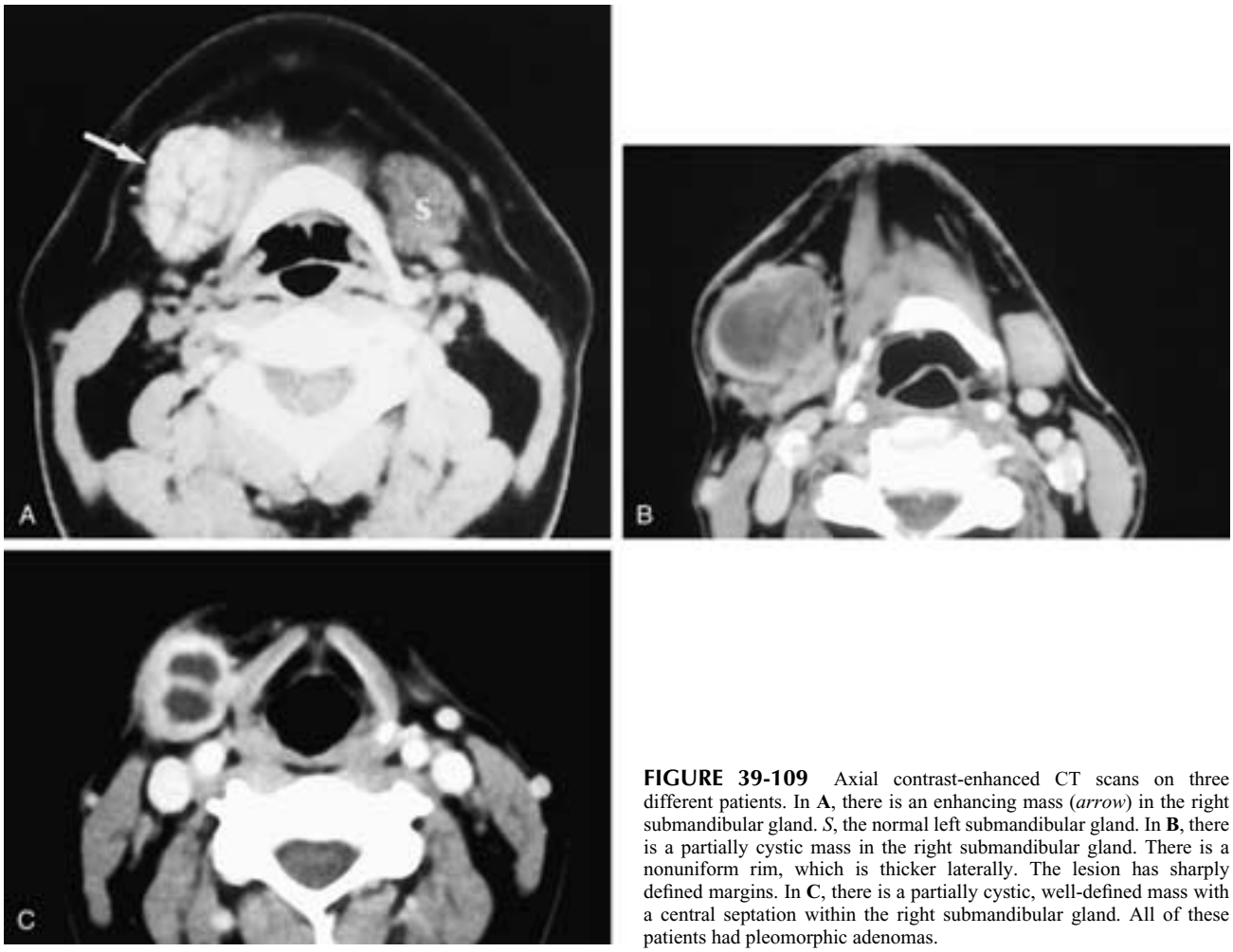

FIGURE 39-109 Axial contrast-enhanced CT scans on three different patients. In **A**, there is an enhancing mass (*arrow*) in the right submandibular gland. *S*, the normal left submandibular gland. In **B**, there is a partially cystic mass in the right submandibular gland. There is a nonuniform rim, which is thicker laterally. The lesion has sharply defined margins. In **C**, there is a partially cystic, well-defined mass with a central septation within the right submandibular gland. All of these patients had pleomorphic adenomas.

VIEW IMAGE

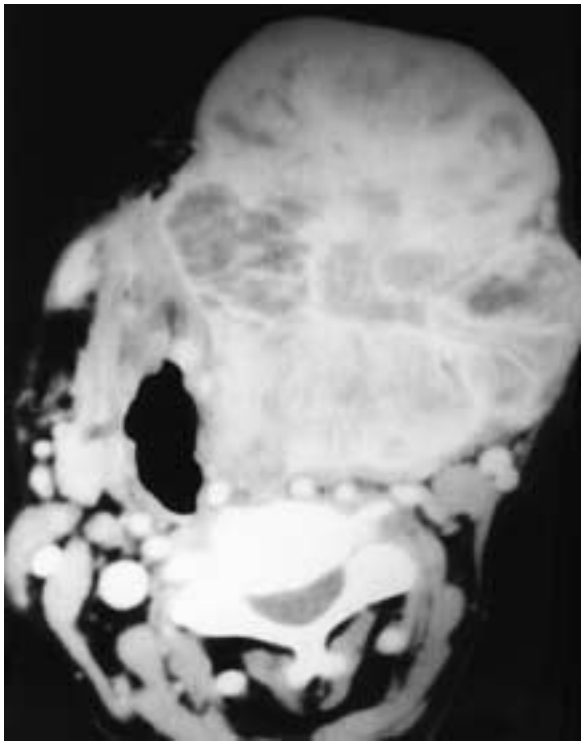

FIGURE 39-110 There is a large, nonhomogeneous mass in the left submandibular gland. Septations are present within the mass, and there is a lobulated contour. This was a carcinoma ex pleomorphic adenoma.

VIEW IMAGE

Copyright © 2003, Mosby, Inc. All rights reserved.

Warthin's tumors present grossly as round to oval, well-circumscribed masses that are typically encapsulated. Their cut surfaces range from a brown to a tan-white color, depending on the relative percentage of oncocytic epithelium to lymphoid stroma, and contain a variable number of cysts that exude yellowish, mucoid, brown to clear fluid and, rarely, semisolid caseous material. Most tumors measure 2 to 4 cm in diameter; however, occasional tumors may be over 12 cm in their greatest dimension. Histologically, the appearance of Warthin's tumor is distinctive and pathognomonic, composed of varying proportions of lymphoid stroma and epithelium. The epithelial component is characterized by epithelium-lined cystic spaces, often with numerous papillary projections and containing homogeneous eosinophilic, granular material. This lining and the papillae are composed of two layers of oncocytic cells, an inner row of tall columnar cells with central or luminally located nuclei and an outer layer of cuboidal and polygonal cells. The cytoplasm in both cells is usually granular and intensely eosinophilic due to abundant mitochondria, which is one of the classic characteristics of this neoplasm. Frequently, scattered mucin-secreting cells and foci with squamous metaplasia are seen. The lymphoid stroma is always benign and reactive, with germinal centers (Fig. 39-112).

Malignancy developing in Warthin's tumor is an extremely rare event, representing less than 1% of Warthin's tumors in several large series. Carcinomas and lymphomas occur with approximately equal frequency, with squamous cell carcinoma, mucoepidermoid carcinoma, undifferentiated carcinoma, adenocarcinoma (oncocytic and other types), and other carcinomas having been reported.

Several theories concerning the pathogenesis of Warthin's tumor have been advocated. The most popular of these contends that the tumor develops from heterotopic salivary gland epithelium present in preexisting intra- or periparotid lymph nodes. However, other authors have suggested that these tumors result from an adenomatous or metaplastic epithelial proliferation with secondary lymphocytic infiltration. Epstein-Barr virus (EBV) appears to have some role in the pathogenesis of Warthin's tumor. The virus has been found in tumor epithelium, especially in patients with multifocal and/or bilateral lesions, and there appears to be a higher frequency of autoimmune disorders in patients with

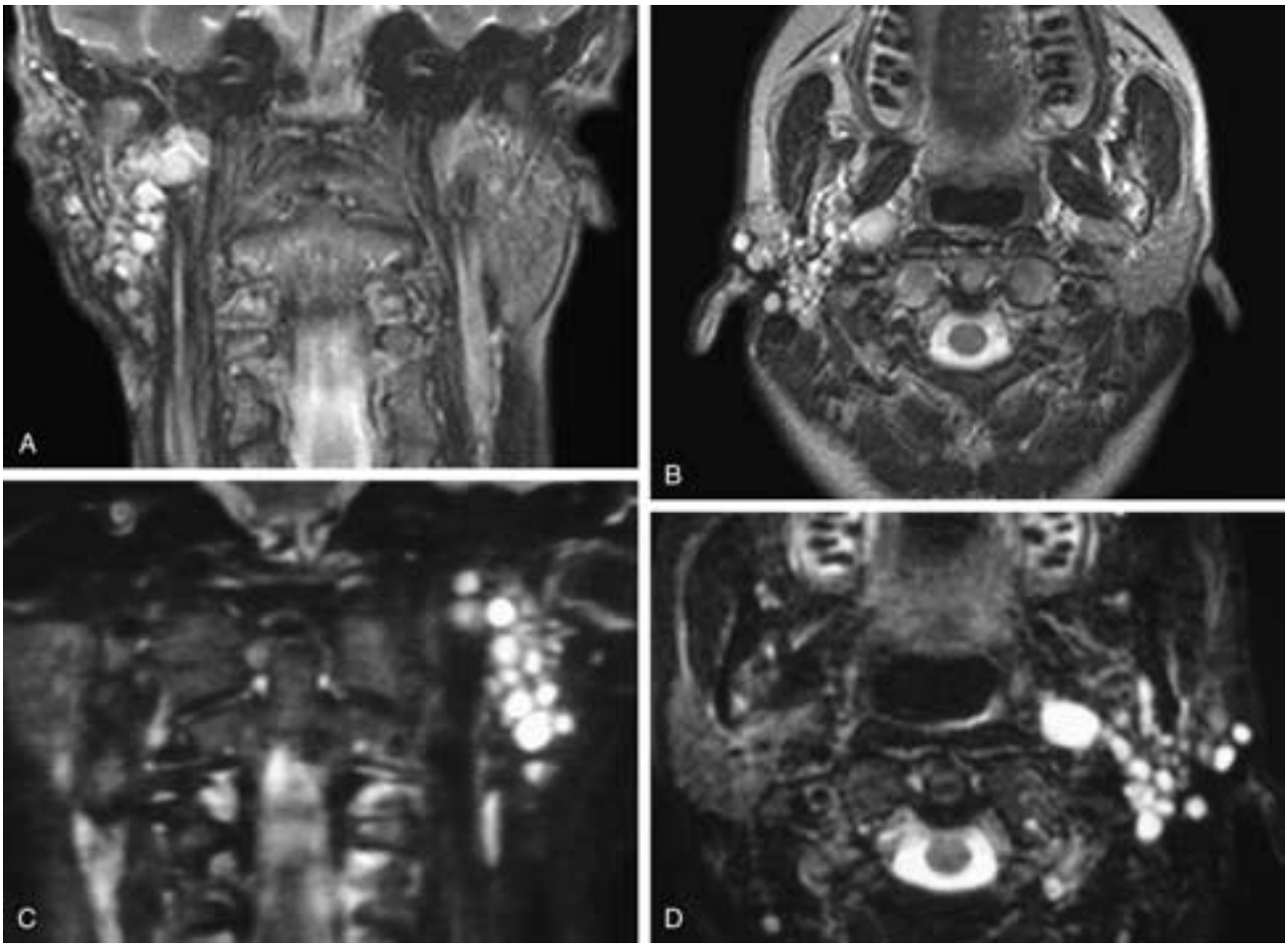

VIEW IMAGE

FIGURE 39-111 Coronal (**A**) and axial (**B**) T1-weighted, fat-suppressed, contrast-enhanced MR images show multiple discrete enhancing masses in the right parotid bed and parapharyngeal space. Coronal (**C**) and axial (**D**) T2-weighted images on another patient show multiple discrete high signal intensity masses within the left parotid bed and parapharyngeal space. Both of these patients had multiple recurrences of pleomorphic adenomas after parotidectomies.

Copyright © 2003, Mosby, Inc. All rights reserved.

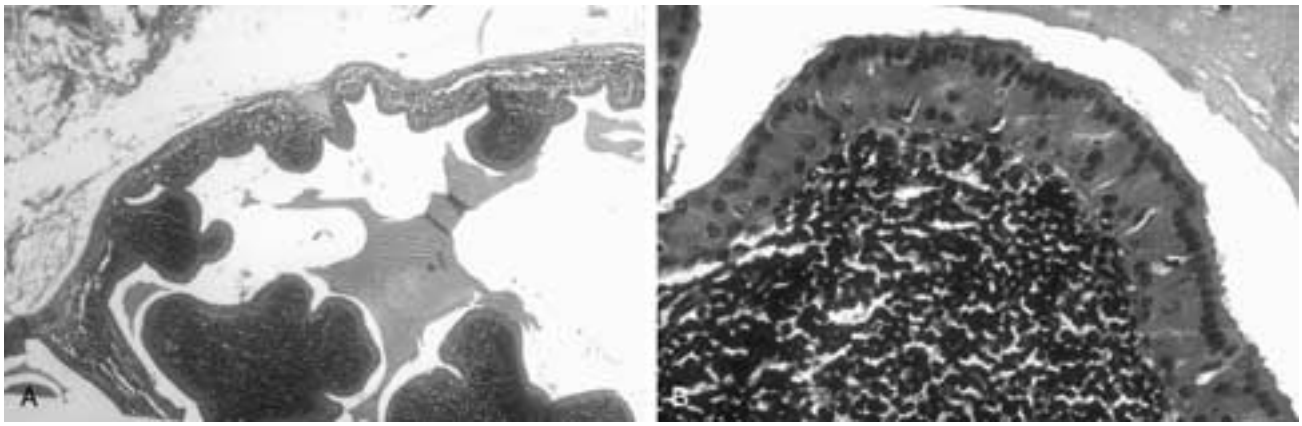

VIEW IMAGE

FIGURE 39-112 **A**, Warthin's tumor—low-power view showing a lymphoid tumor with cystic spaces. **B**, The papillary and cystic spaces are lined by a bilayer of tall and cuboidal oncocytes.

Warthin's tumor than in patients with mixed tumors or in healthy subjects.[215–221]

The recommended treatment is superficial parotidectomy, with preservation of the facial nerve plus good operative exposure to exclude multifocal disease, especially in periparotid lymph nodes. To reduce the risk of facial nerve damage, some observers recommend enucleation whenever feasible. Earlier studies demonstrated recurrence rates as high as 25%, most likely due to multifocal disease, but the majority of recent studies document rates of 2% or less. Similar results are achieved by investigators using enucleation.

VIEW IMAGE

FIGURE 39-113 Oblique frontal technetium sialograms show multiple masses with intense uptake in both parotid glands. This patient had bilateral Warthin's tumors.

The mitochondrium-rich oncocytes of Warthin's tumors are the cells that accumulate ^{99m}Tc pertechnetate on salivary radionuclide scans (Fig. 39-113). The only other tumor to accumulate ^{99m}Tc pertechnetate is an oncocytoma.[222] On CT, most Warthin's tumors appear as small, ovoid, smoothly marginated masses in the posterior aspect of the superficial lobe (tail) of the parotid gland. They are homogeneous soft-tissue density lesions with no dystrophic calcifications. However, cyst formation is common, and on CT the cyst contents usually consist of a homogeneous (10 to 20 HU) material. The cyst wall is usually thin and fairly smooth, but at some point there is a focal tumor nodule, which indicates that this lesion is a cystic tumor rather than a branchial cleft or lymphoepithelial cyst (Figs. 39-114 to 39-117). When a Warthin's tumor is large and arises either from the periphery of the parotid gland or from a juxtaparotid lymph node, most

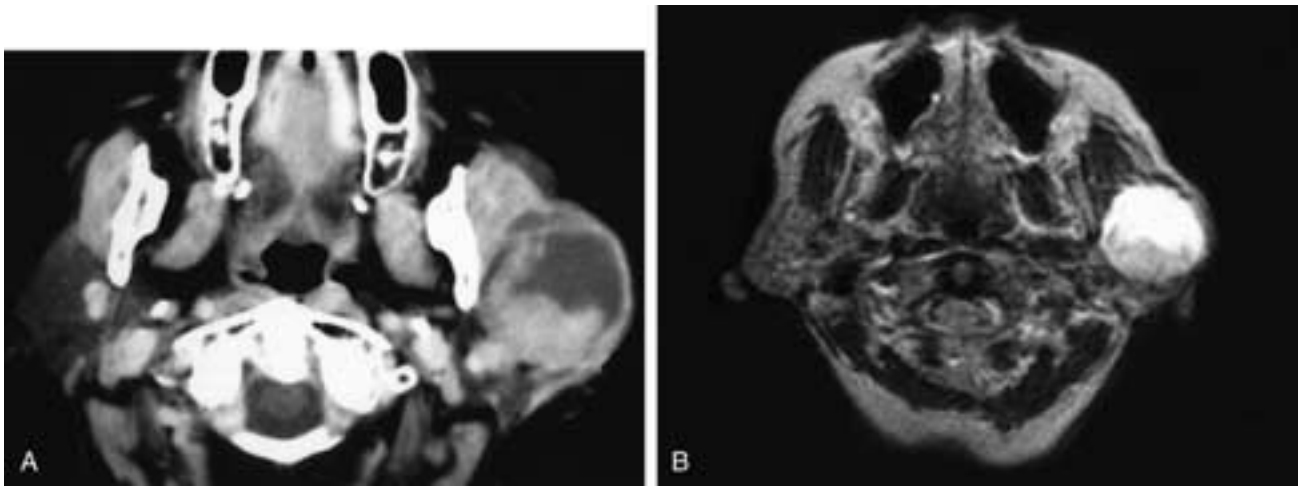

VIEW IMAGE

FIGURE 39-114 Axial contrast-enhanced CT scan (**A**) and T2-weighted MR image (**B**) show a partially cystic mass in the left parotid gland. The noncystic region is the residual tumor mass. This patient had a Warthin's tumor.

Copyright © 2003, Mosby, Inc. All rights reserved.

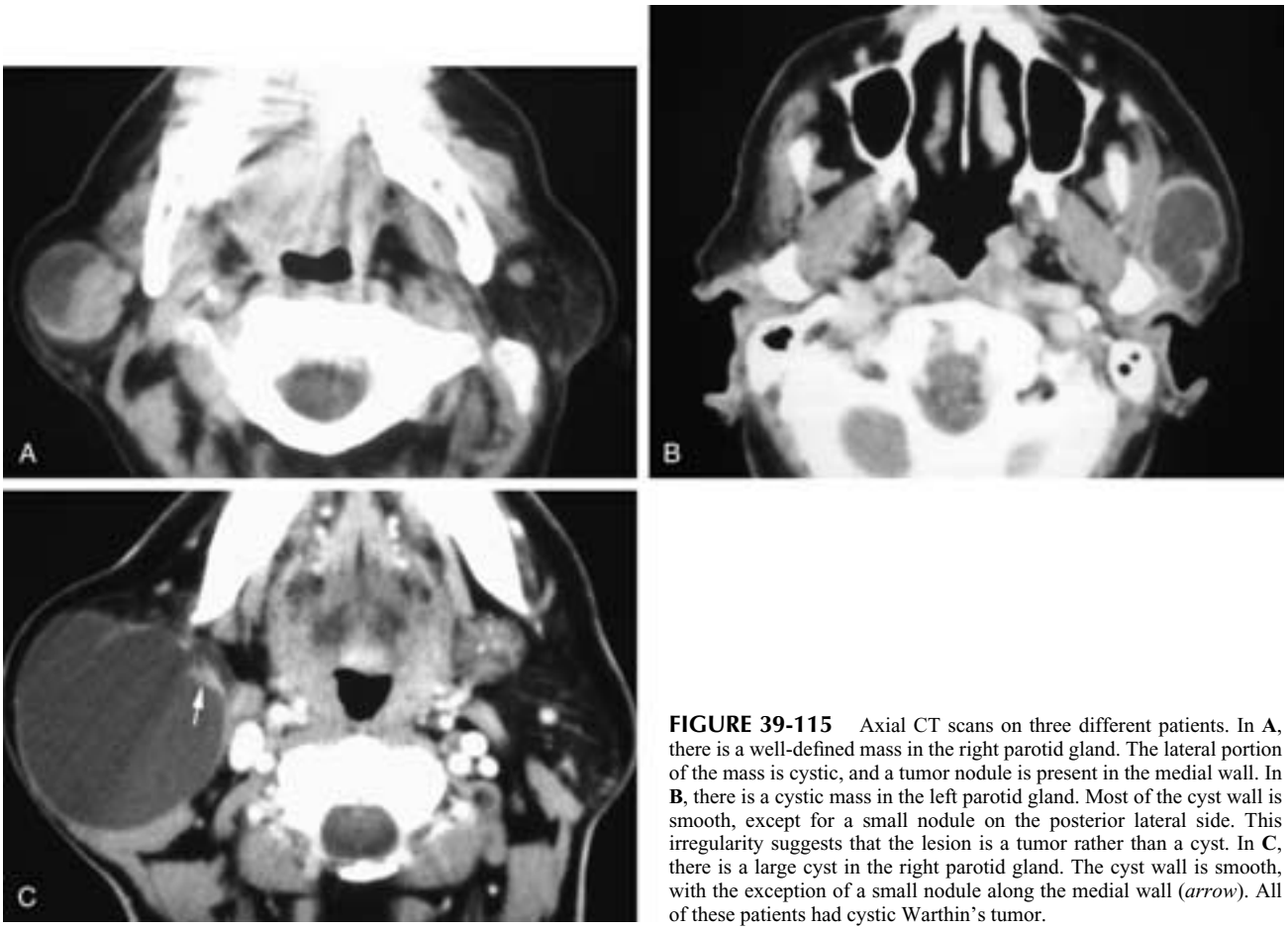

FIGURE 39-115 Axial CT scans on three different patients. In **A**, there is a well-defined mass in the right parotid gland. The lateral portion of the mass is cystic, and a tumor nodule is present in the medial wall. In **B**, there is a cystic mass in the left parotid gland. Most of the cyst wall is smooth, except for a small nodule on the posterior lateral side. This irregularity suggests that the lesion is a tumor rather than a cyst. In **C**, there is a large cyst in the right parotid gland. The cyst wall is smooth, with the exception of a small nodule along the medial wall (*arrow*). All of these patients had cystic Warthin's tumor.

VIEW IMAGE

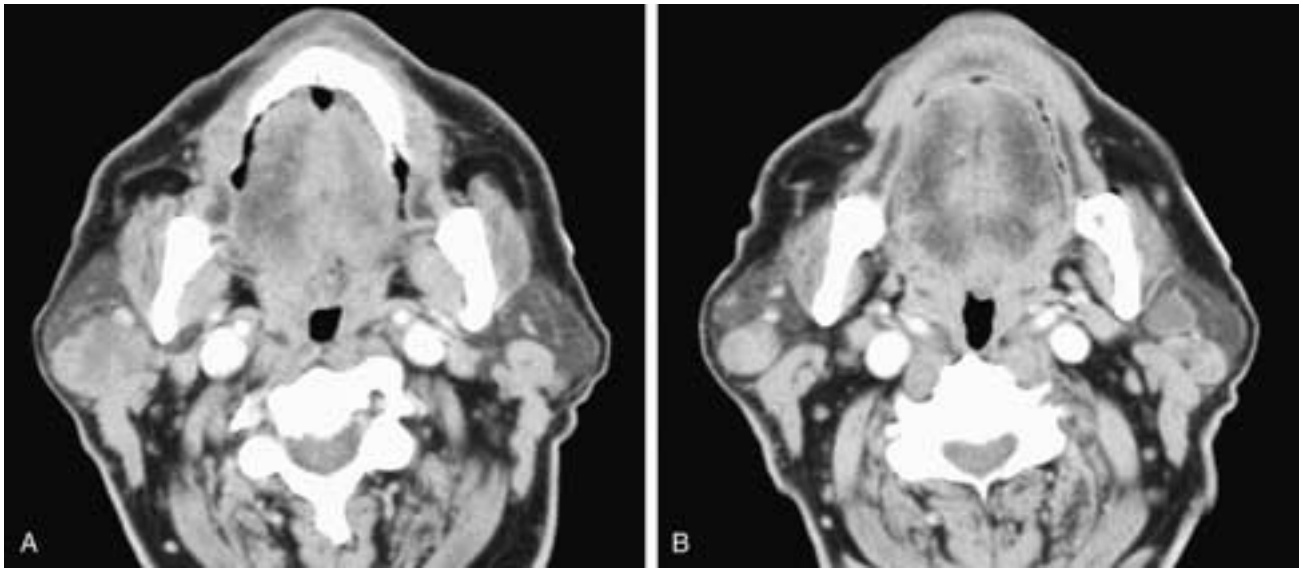

FIGURE 39-116 Axial contrast-enhanced CT scans (**A**, **B**) show multiple well-defined, partially cystic masses in both parotid glands. This patient had Warthin's tumors.

VIEW IMAGE

Copyright © 2003, Mosby, Inc. All rights reserved.

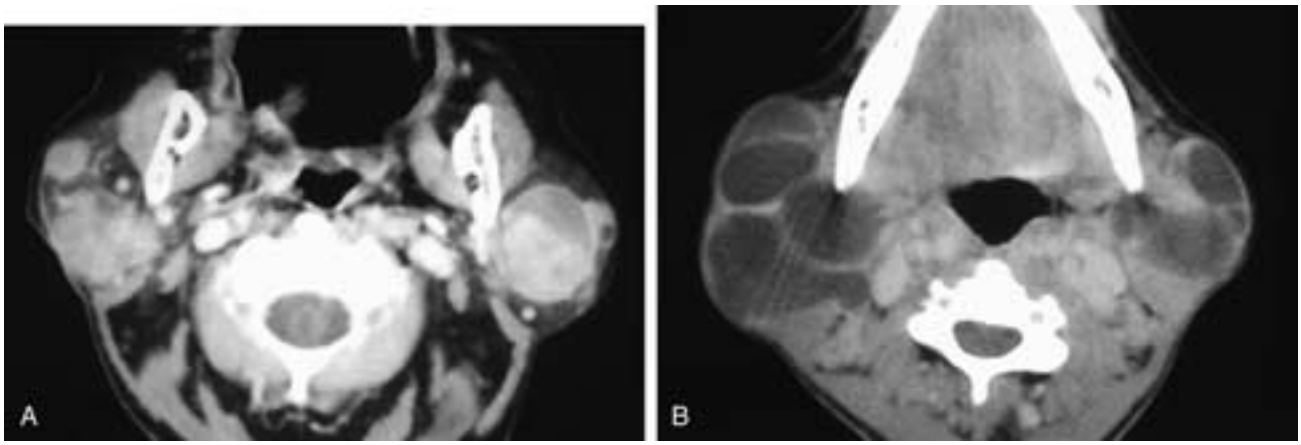

VIEW IMAGE

FIGURE 39-117 Axial contrast-enhanced CT scan (**A**) shows multiple bilateral parotid masses. The largest lesion on the left side is partially cystic. This patient had Warthin's tumors. In **B**, an axial contrast-enhanced CT scan shows multiple thinned-walled cysts in both parotid glands. No tumor nodules were seen in the cyst walls. This patient also had cervical adenopathy. These were lymphoepithelial cysts in an HIV-positive patient.

or all of the tumor is outside the normal gland contour. In such cases, imaging confusion with a second branchial cleft cyst or a necrotic node may occur.

When multiple lesions are seen either in one parotid gland or bilaterally, the most likely diagnosis is Warthin's tumor. If the neoplasms are cystic or partially cystic, the differential diagnosis includes lymphoepithelial cysts of HIV-positive patients, end-stage parotid Sjögren's syndrome, and possibly multiple cavitated metastatic nodes. If the multiple Warthin's tumors are not cavitated, the radiologic differential diagnosis includes lymphoma, granulomatous disease (primarily sarcoidosis), and benign adenopathy.

On MR imaging, when solid, these tumors appear similar to pleomorphic adenomas in that they have low T1-weighted, intermediate proton density, and high T2-weighted signal intensities. However, if the Warthin's tumor is cystic, the cyst fluid usually has a sufficiently different signal intensity from the solid tumor component that the cyst can be identified on some or all of the imaging sequences (Fig. 39-114). For this reason, when small or moderate in size, Warthin's tumors may be more nonhomogeneous than pleomorphic adenomas. When large, both of these tumors tend to be nonhomogeneous. Occasionally, the cystic nature of some of these tumors is not as apparent on MR imaging as it is on CT.

Benign and Malignant Oncocytic Tumors

Major Salivary Gland Oncocytic Tumors

Oncocytes derive their name from the Greek word *onkos*, meaning ''swelling.'' These cells are swollen with abundant pink granular cytoplasm as a result of a mitochondrial ''defect'' or proliferation. The mitochondria have abnormal rounded shapes or are stacked like erythrocytes in a rouleaux formation. Oncocytes are normally found within endocrine organs (thyroid, parathyroid, pituitary, etc.) And oncocytic metaplasia of minor salivary glands is especially common in older individuals.[7, 8]

Oncocytic tumors are relatively rare, representing 1.6% of 13,749 primary epithelial salivary gland tumors and 1.9% of over 8000 parotid gland tumors at the Armed Forces Institute of Pathology. The major salivary glands were the dominant site, comprising 86% of 226 cases (200 benign and 26 malignant). In general practice, oncocytomas represent 1% or less of all parotid tumors. In a series of 68 patients with oncocytic salivary tumors, 84% occurred in the parotid gland and 11% in the submandibular gland, and 5% were incidental findings within cervical lymph nodes. There is no gender predilection for these tumors, and most patients present with unilateral painless masses. A history of previous radiation exposure has been documented in 20% of patients with oncocytic tumors; these patients tend to present with oncocytomas two decades earlier than the mean. Oncocytomas may be multifocal or bilateral, and in up to 7% of cases they may consist of diffuse oncocytosis rather than single tumor nodules.

Most oncocytic carcinomas, also referred to as malignant oncocytomas, arise in the parotid gland; about 10% arise in the submandibular gland. To date, slightly over 50 cases have been reported. The average age of patients is about 60 years (range, 29 to 91 years), and there is a 2:1 male:female predominance.[2, 12] The most common clinical presentation is that of a slow-growing mass often associated with pain or facial paralysis.

On gross examination, parotid or submandibular oncocytomas appear as single, small, well-circumscribed brown tumors, which may have central star-like fibrosis and occasional cyst formation. Oncocytomas may also occur as part of a generalized process, oncocytosis, in which the entire gland undergoes multifocal oncocytic metaplasia and hyperplasia. In this case, the glandular architecture is entirely replaced by multiple brown or tan nodules, some of which may have central scarring, with one or more dominant tumor nodules that overgrow and distort the normal architecture (Fig. 39-118). Oncocytic carcinomas range from well circumscribed to widely invasive.

On imaging, solitary or multiple solid masses with sharp, well-delineated margins are seen. These lesions also accumulate ^{99m}Tc pertechnetate on salivary radionuclide scans (Fig. 39-119).

Copyright © 2003, Mosby, Inc. All rights reserved.

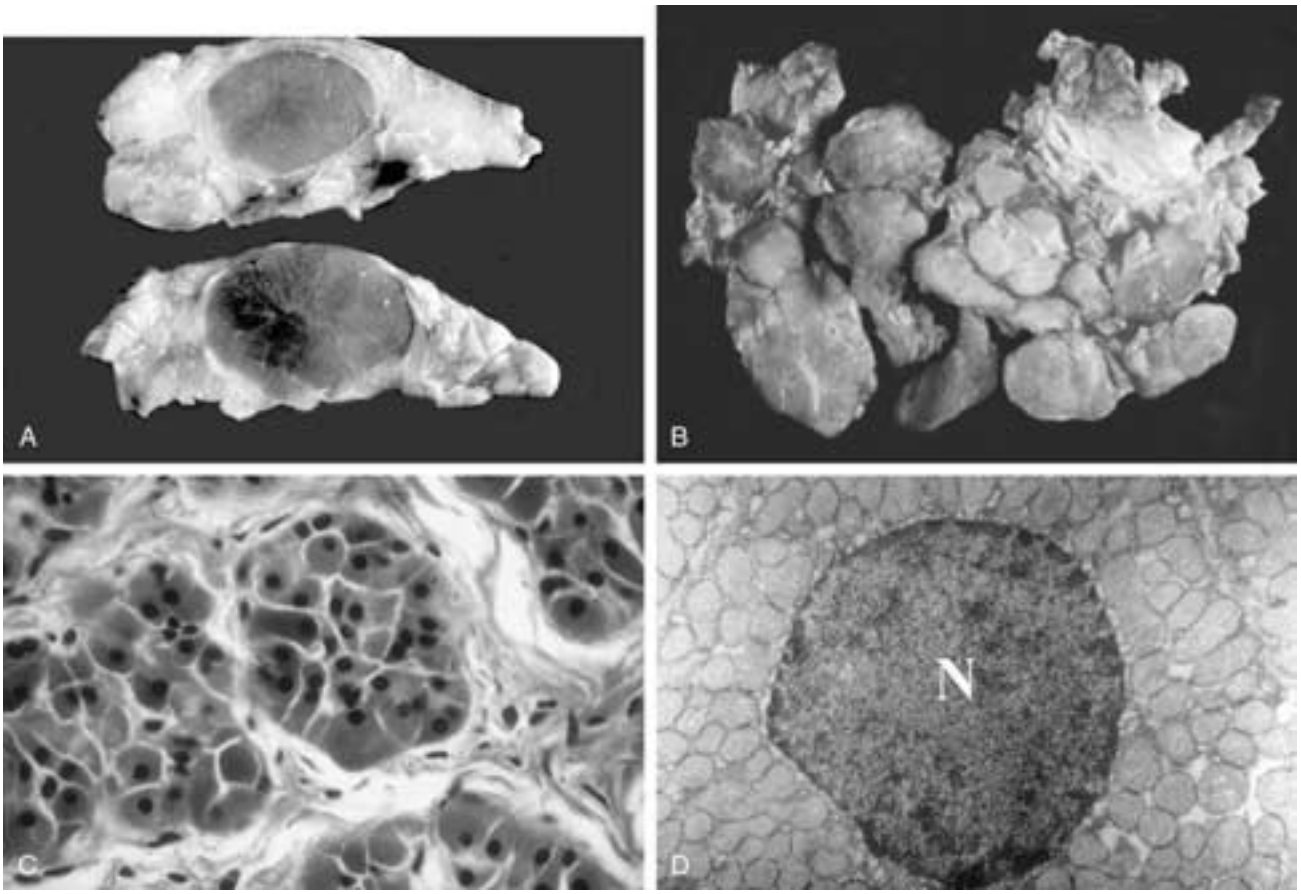

VIEW IMAGE

FIGURE 39-118 Oncocytoma. **A**, Single dark nodule within the parotid gland. **B**, Oncocytosis. This parotid is entirely replaced by dark nodules, some with central scars. **C**, High-power view. Oncocytomas are composed of nests of cuboidal oncocytes, with round nucleoli and abundant, dense, pink, granular cytoplasm. **D**, Electron microscopic image of an oncocyte. The nucleus (*N*) is surrounded by densely packed mitochondria.

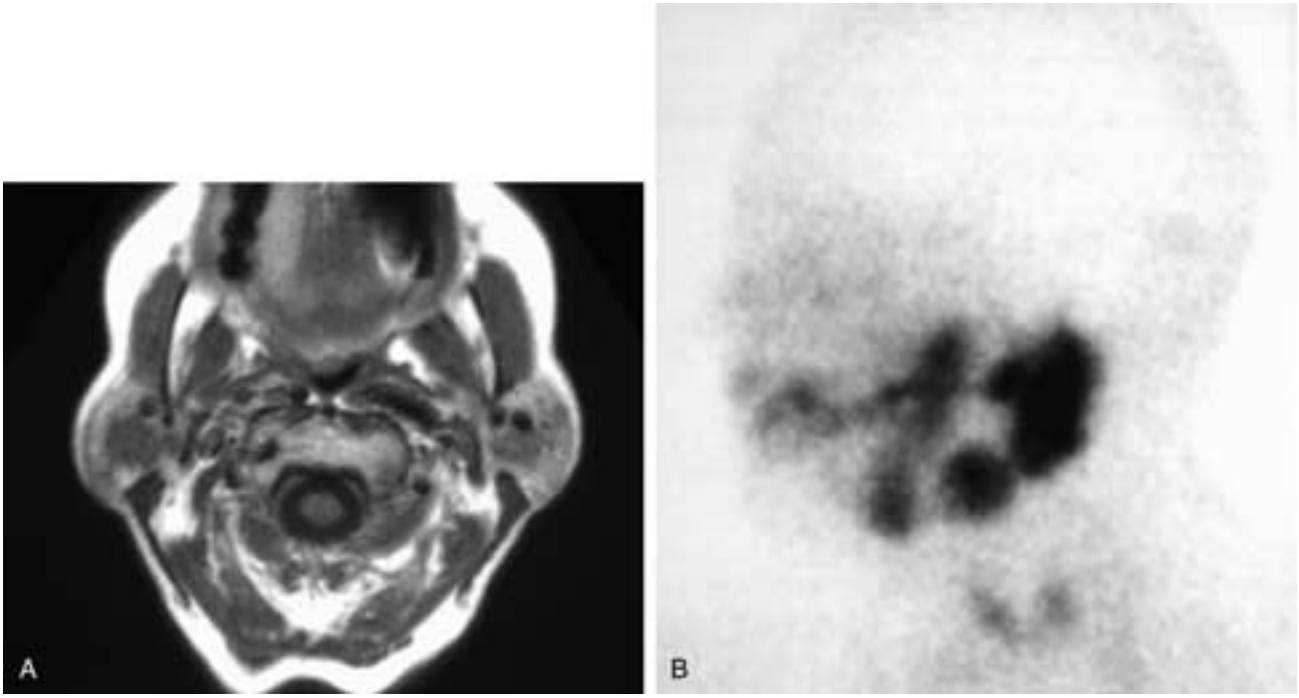

VIEW IMAGE

FIGURE 39-119 Axial T1-weighted MR image (**A**) shows multiple masses in each parotid gland. A left lateral ^{99m}Tc sialogram (**B**) shows multiple bilateral masses with intense accumulation of the nucleide. This patient had bilateral multiple oncocytomas.

Copyright © 2003, Mosby, Inc. All rights reserved.

Oncocytic Tumors of Minor Salivary or Seromucinous Gland Sites

Larynx The clinicopathologic features of minor salivary or seromucinous gland oncocytic tumors are sufficiently distinctive from those of major salivary tumors to warrant separate discussion. Laryngeal oncocytic lesions produce polypoid masses, most often involving the supraglottis. Rather than being true neoplastic processes, laryngeal oncocytic lesions, referred to as papillary oncocytic cystadenomas, are the result of oncocytic metaplasia and hyperplasia of minor salivary glands, with prominent cyst formation. They have been appropriately likened to extraparotid Warthin's tumors.

Oral Cavity A small fraction (5%) of all oncocytic lesions arise in the oral cavity; the palate and cheek are the most common sites. These lesions may span the spectrum from oncocytic papillary cystic tumors (oncocytic papillary cystadenomas) with a variable degree of lymphocytic infiltration to more solid oncocytomas. An association of parotid Warthin's tumors and oral oncocytic papillary cystadenomas has been reported. These lesions may occur on the lips, buccal mucosa, tonsillar fossa, or palate. They form submucosal circumscribed swellings; only one case has been documented as locally invasive.

Sinonasal Cavity Oncocytic processes at this anatomic site are classified as variations of oncocytic Schneiderian (cylindrical cell) papilloma (OSP), as discussed in Chapter 6, or as seromucinous gland neoplasia. Unlike major salivary gland oncocytomas, which are usually benign, sinonasal oncocytic tumors have a greater tendency toward local aggression. These tumors have a predilection for the lower septum or vestibule. Oncocytic tumors of the superior nasal cavity may also originate from the lacrimal apparatus.

A number of sinonasal oncocytic tumors have shown histologic evidence of local invasion from the onset. These tumors have a male preponderance (male:female ratio of 5:3), and most are diagnosed after the fifth decade of life. They are generally larger than benign tumors and more clinically aggressive, with a propensity to affect the maxillae or nasal cavity.

Histologically, oncocytic tumors of the salivary gland are classified as oncocytosis (nodular or diffuse) or oncocytoma (benign or malignant), as well as tumors with oncocytic metaplasia (oncocytic mixed tumor, oncocytic mucoepidermoid carcinoma, etc.). Oncocytosis is the replacement of normal portions of the salivary gland with oncocytes. These may diffusely replace normal parenchyma (diffuse oncocytosis) or, more typically, produce multiple nodules (oncocytic hyperplasia or nodular oncocytosis). The distinction between a large, hyperplastic nodule and oncocytoma is sometime difficult and often arbitrary. Usually an oncocytoma presents as a mass lesion, is larger than other adjacent hyperplastic nodules, and is well circumscribed, with at least a partially formed capsule. Most benign oncocytic tumors are solid, with a variable cystic component. The oncocytes form organoid nests and trabeculae with very occasional ducts. Cytologically, oncocytes are cuboidal or columnar, with abundant bright pink granular cytoplasm, and have decreased nuclear/cytoplasmic ratios compared to normal parotid ductal cells. Oncocytic nuclei are typically very round and centrally placed; the nucleoli may be single and prominent.

Patients with oncocytic carcinoma typically present with a single or multinodular unencapsulated gray-brown mass. The tumor cells are usually more pleomorphic than their benign counterparts. Their nuclei are often centrally located and contain large, irregular nucleoli, although occasional cases may lack significant atypia. Invasive growth into adjacent tissues is characteristic; scattered mitotic figures and perineural invasion are frequent, and foci of necrosis may be found.

The majority of parotid and submandibular oncocytomas behave in a benign fashion after complete surgical resection, even if rare aggressive features such as perineural invasion have been identified. Local recurrence of an oncocytoma is unusual and is often the result of persistent multifocal oncocytosis in the remaining deep parotid lobe. Most malignant parotid or submandibular oncocytomas are high-grade neoplasms with frequent recurrences and metastatic spread. They should be treated by wide local excision. Adjuvant radiation therapy should be strongly considered, and the appropriate neck should be treated either surgically or with radiation. These tumors are often locally aggressive and infiltrative and can metastasize, either to cervical lymph nodes or in a widespread fashion to the central nervous system, bone, liver, and lung. Although many of these reports have short follow-up periods, some of them have documented a protracted course with single or multiple local recurrences and distant metastases. In a recent review of 37 cases with follow-up, almost 85% of malignant oncocytomas developed regional or distant metastases and 32% developed local recurrences. Half of the patients died of disease with the average survival for patients with metastasizing tumors being 3.8 years. Distant metastasis is a poor prognostic sign, with all patients dying of disease. Tumor-related mortality may occur up to a decade after the original diagnosis. Malignant parotid and submandibular oncocytomas usually appear aggressive from the onset; rarely is there evidence of a preexisting benign oncocytoma or oncocytosis.

Locally invasive sinonasal oncocytic tumors appear to follow a low-grade malignant course with multiple recurrences. Three of eight patients developed recurrent disease 3 to 7 years after the initial diagnosis. Two of these patients had multiple recurrences—one at 3 and 10 years, the other at 5 and 7 years. Both of these patients were disease free 1 year after treatment of the second recurrence. It appears that recurrent tumors remain localized, with no attributable deaths due to disease.[98, 223–225]

Oncocytic Papillary Cystadenoma

Oncocytic papillary cystadenoma is a rare lesion that can occur in the parotid gland, although it most often occurs in the larynx. It may represent oncocytic metaplasia and hyperplasia of preexisting salivary gland ductal epithelial rather than a true neoplasm. This lesion is usually a benign rounded cyst. In the parotid gland, it is somewhat of a hybrid between an oncocytoma and a Warthin's tumor.[7]

Basal Cell Adenoma and Basal Cell Adenocarcinoma

Basal cell adenoma (BCA), as defined by the World Health Organization, is a distinctive benign neoplasm composed of basaloid cells organized with a prominent basal cell layer and distinct basement membrane–like material. It

Copyright © 2003, Mosby, Inc. All rights reserved.

lacks the myxochondroid stromal component of pleomorphic adenoma. Although it was first established as a specific entity in the late 1960s, there has been disagreement about the spectrum of tumors belonging to this group and about their proper designation. Many series in the 1970s and 1980s classified these tumors with other nonmixed tumors, including canalicular adenomas, into the category of monomorphic adenomas. In 1991 the World Health Organization separately classified BCA and its malignant counterpart, basal cell adenocarcinoma, as well as canalicular adenoma. BCA accounts for 1% to 2% of all salivary gland epithelial tumors, and over 80% of them arise in the major salivary glands, mostly the parotid gland. Less frequently, these tumors may be found in minor glands, with the upper lip being the most common site, followed by the buccal mucosa. BCAs arise almost exclusively in adults, with the average patient age being 57.7 years, more than a decade older than the average age of patients with pleomorphic adenoma. There is a 2:1 female predominance for most BCAs; however, the membranous variant has an equal male:female distribution. Clinically indistinguishable from pleomorphic adenoma, the typical BCA presents as a mobile superficial parotid tumor.

BCAs present as round to oval, well-encapsulated, soft to firm neoplasms; most measure 3 cm or less in diameter. On cut section, they are typically uniform and solid, without necrosis; however, they can occasionally be cystic. Membranous-type BCAs are noteworthy in that they can be multifocal, with a multinodular growth pattern.

Microscopically, BCAs are benign tumors composed of relatively basaloid cells, a conspicuous basal cell layer, and distinctive basement membrane–like material. Most tumors are well circumscribed and encapsulated, although any of the subtypes may have a multinodular microscopic pattern (Fig. 39-120). BSAs lack the characteristic myxochondroid matrix of pleomorphic adenoma. Based on their architecture, BSAs may be divided into four subtypes: solid, trabecular, tubular, and membranous. The solid variant is most common, and individual tumors commonly display several architectural growth patterns. BCAs are composed of two cell types. The first type, the basaloid cells, are found peripherally, frequently in a palisading arrangement within the cell nests and cords. They are cuboidal or columnar small cells with round, deeply staining nuclei and little discernible cytoplasm. The second cell type, the epithelioid cells, are larger, with modest cytoplasm, indistinct cell borders, and a pale-staining oval nucleus; the nuclei may exhibit small, eosinophilic nucleoli. Larger cells predominate centrally within the epithelial nests, sheets, and trabeculae. The membranous BCA, also known as the dermal anlage tumor, deserves special mention. A small percentage of patients with membranous BCAs may develop multiple dermal cylindromas (turban tumors), trichoepitheliomas, eccrine spiradenomas, trichilemmomas, and basal cell epitheliomas. In contrast to the other subtypes, membranous BCA tends to be multilobulated or multinodular and is often not encapsulated. This explains the high recurrence rate of 25% to 37%, similar to that of dermal cylindroma. Despite its multinodularity, no BCA should demonstrate soft-tissue invasion or perineural invasion. If these features are seen, diagnoses such as basal cell adenocarcinoma (see below) or adenoid cystic carcinoma should be considered.

BCAs are amenable to conservative resection (i.e., superficial parotidectomy). However, recurrence may develop in a significant percentage of patients (25%) with the membranous variant of BCA. Although exceedingly rare, malignant transformation of BCA has been reported.[226, 227]

Basal cell adenocarcinoma (BCAC) is a distinct type of low-grade carcinoma that is the malignant counterpart of BCA. BCAC may arise either de novo or from a preexisting BCA. These tumors account for 1.6% of all salivary gland tumors and 2.9% of malignant salivary gland neoplasms. Almost 90% of cases arise in the parotid gland, where they account for 0.6% of parotid tumors and up to 5% of primary parotid carcinomas. Less commonly, they occur within the submandibular gland, minor salivary glands, or sinonasal tract and, rarely, in the sublingual gland. No gender predominance has been noted. BCAC occurs over a wide age range (third to tenth decades), with a mean age at diagnosis of 60 years. The majority of BCACs arise de novo; however, slightly less than one quarter of cases have been

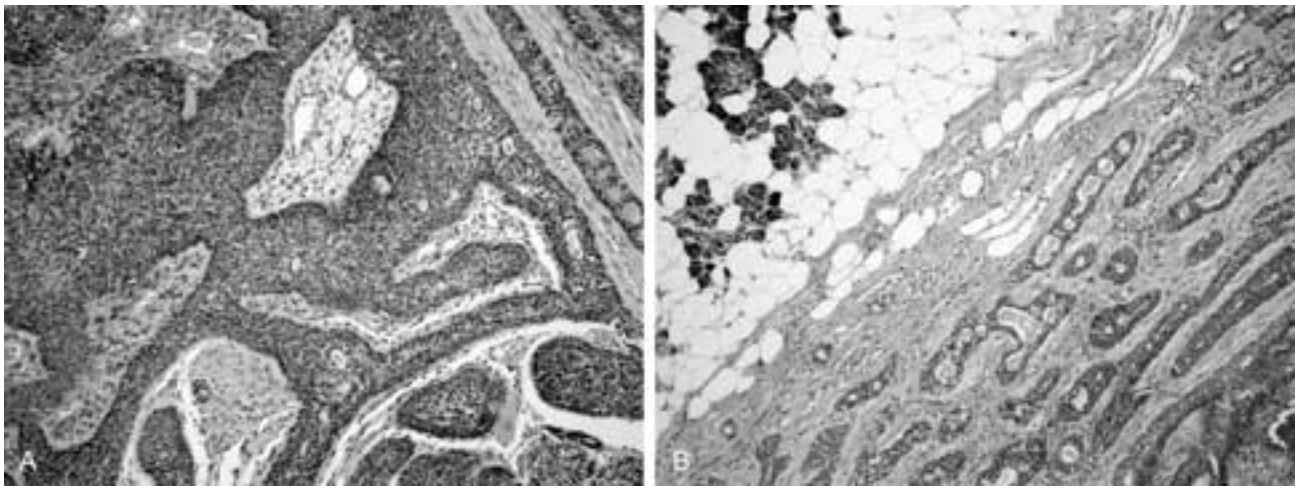

FIGURE 39-120 **A**, Low power reveals an encapsulated parotid mass. **B**, Interconnecting trabeculae of benign basaloid cells with oval nuclei and scanty cytoplasm, with characteristic pallisading. Basal cell adenoma (BCA).

VIEW IMAGE

Copyright © 2003, Mosby, Inc. All rights reserved.

documented to arise within their benign counterpart, the BCA. The presenting symptoms are nonspecific, including a parotid or submandibular mass and occasionally pain. Facial nerve involvement is uncommon. Association with concurrent skin adnexal tumors (especially eccrine cylindromas and trichoepitheliomas) has been noted in 14% of patients with BCAC, which is less frequent than the association of concurrent BCA and adnexal tumors (25% to 35%).

BCAC ranges in size from 0.7 to 7.0 cm. Histologically, BCAC mimics the architectural patterns of BCA: solid, membranous, trabecular, or tubular. The solid pattern, most commonly encountered, has predominantly confluent tumor islands with areas of palisading basaloid cells. Low-power scanning of BCAC reveals the standard features of aggressive neoplasia: infiltration into or destructive overgrowth of surrounding tissue, possible necrosis, and perineural or vascular invasion. Multicentricity is rarely seen in major salivary gland BCAC. Basement membrane hyaline can be quite prominent in the trabecular, membranous, and tubular patterns, with hyaline material deposition dissecting between tumor cells, resulting in a pseudocribriform pattern. Nuclear palisading is frequent at the periphery of the infiltrating nests and islands. Squamous differentiation with keratin pearls can be seen toward the center of islands. Cytologically, BCAC is composed of basaloid cells with oval to round nuclei and usually a high nuclear/cytoplasmic ratio. Mitotic figures and cellular pleomorphism may be marked, although tumors frequently have minimal atypia, with the diagnosis of carcinoma being based on invasive growth and/or perineural or vascular invasion. Perineural and/or intravascular invasion are common, and when they are present in an otherwise typical BCA, the diagnosis of BCAC should be given serious consideration.

BCAC is optimally treated by wide surgical resection with negative margins. With adequate resection, additional therapy is not warranted; however, adjuvant radiotherapy may be used for cases with close or positive resection margins. Elective neck dissection is not warranted. Reported cases of major salivary BCAC with clinical follow-up reveal a low-grade malignant biology. The general impression is that major salivary gland BCAC is less aggressive than adenoid cystic carcinoma. Muller and Barnes culled 45 cases of BCAC with clinical follow-up from the literature that demonstrated a local recurrence rate of 37%, a local metastatic rate of 8%, and a distant metastatic rate of 4%; disease-related mortality occurred in 2% of patients. In addition, Nagao et al. recently reported 11 cases, 10 with follow-up: 50% recurred, none metastasized, and there were no deaths from disease. Minor salivary or seromucinous gland BCACs have a more aggressive course due to the advanced tumor stage at presentation and the inherently poorer resectability of minor salivary gland tumors. Four of 12 patients reported by Fonseca and Soares with intraoral or sinonasal BCAC died of disease within 4 to 7 years.[228–233]

Canalicular Adenoma

Until the World Health Organization's classification in 1991, canalicular adenoma was classified as a variant of BCA or monomorphic adenoma. There are, however, sufficient clinicopathologic and histologic differences between BCA and canalicular adenoma to warrant separate classification.

Canalicular adenoma is a benign neoplasm that arises almost exclusively from the minor salivary glands of the oral cavity, where it accounts for 4% to 6% of minor salivary gland tumors. These tumors commonly affect older patients, with a peak incidence in the seventh decade. Females are more commonly affected than males; the female : male ratio ranges from 1.2 to 1.8 : 1. Clinically, canalicular adenoma presents as a slow-growing, asymptomatic, mobile nodule, most commonly arising in the upper lip (73% to 100% of cases in reported series). It is the second most common upper lip salivary gland tumor after benign mixed tumor. In decreasing frequency of occurrence, these tumors may occasionally arise in the buccal mucosa, lower lip, palate, and major salivary glands. Rarely, canalicular adenoma may present with multiple clinically palpable nodules; metachronous tumors may also be seen. The tumor is usually small at the time of diagnosis, with a mean diameter of 1.7 cm. The overlying mucosa is usually intact and normal; occasionally, it is slightly bluish, mimicking a mucocele.

Microscopically, canalicular adenoma is characterized by a circumscribed or encapsulated tumor composed of interconnecting strands or cords of uniform, single, cuboidal to columnar cells, usually with scanty eosinophilic cytoplasm, oval nuclei with diffuse granular nuclear chromatin, and indistinct borders. The tumor cells form characteristic parallel columns, producing long canaliculi with scattered duct-like or gland-like structures. Because of the absence of myoepithelial cells, the epithelial cells are sharply demarcated from the surrounding stroma. Cellular pleomorphism is minimal, and mitoses, if present, are rare. In addition, occasional tumors have papillary projections into the cystic spaces. The stroma separating parallel rows of cells is delicate, well vascularized, commonly mucoid, and sparsely cellular. Multifocal microscopic foci of canalicular adenoma are common (22% in one series of 49 patients); in these cases, the main tumor frequently is encapsulated, while the smaller foci often are not.

Treatment is complete surgical excision. Recurrence after surgical removal is rare and most likely is due to multifocality rather than true recurrence.[234–236]

Myoepithelioma and Myoepithelial Carcinoma

Myoepithelial cells are integral to the normal functioning of the salivary glands and are common components of benign and malignant salivary neoplasia. The contractions of normal myoepithelial intracytoplasmic myofibrils help express secretions from the salivary glands.[7] Myoepithelial cells are ectodermally derived but can function as mesodermal cells, producing mesenchyme-type products.

Myoepithelioma (benign myoepithelioma) is a rare salivary tumor composed entirely or predominantly of myoepithelial cells; it represents one extreme in the histologic spectrum of pleomorphic adenoma. Generally, if a tumor's composition contains more than 95% of myoepithelial elements, it is classified as a myoepithelioma, whereas if more than 5% of the tumor is composed of epithelial, ductal, or mesenchymal components, it is classified as a myoepithelium-rich pleomorphic adenoma. Myoepitheliomas are rare, accounting for less than 2% of salivary tumors, 2.2% of all major benign salivary tumors, and 5.7% of all benign minor salivary tumors. Approximately half of all cases arise in the parotid gland, 10% in the submandibular gland,

Copyright © 2003, Mosby, Inc. All rights reserved.

and 42% in minor salivary gland sites, most commonly the palate. There is no significant sex predilection. The reported age range is wide: from 6 to 85 years. The most common presentation is that of a slow-growing, asymptomatic mass.

Myoepithelioma is a well-circumscribed or encapsulated tumor. However, those arising on the palate or in other minor salivary gland sites are circumscribed but not usually encapsulated.

Histologically, the tumor is composed of various proportions of spindle-shaped, plasmacytoid, polygonal epithelioid, and, rarely, clear myoepithelial or modified myoepithelial cells commonly arranged in sheets, irregular collections, nests, interconnecting trabeculae, or ribbons. Nuclear pleomorphism is usually minimal; however, similar to mixed tumors, a mild to moderate degree of nuclear pleomorphism and/or atypia may be noted in occasional tumors. Stroma may be minimal or abundant and is usually acellular and mucoid, myxoid, or hyalinized.

Since benign myoepitheliomas are considered to represent one extreme of the histologic spectrum of mixed tumors, the treatment and prognosis are essentially the same as for benign mixed tumors. Patients with these tumors should be treated by complete excision that ensures a tumor-free margin; in minor gland sites this usually involves surgical excision with a rim of normal surrounding tissue.

Occasional myoepithelial tumors can behave in a locally aggressive or malignant fashion. These malignant myoepitheliomas are also referred to as *myoepithelial carcinomas.* Histologically, they appear cytologically and architecturally similar to benign myoepitheliomas. Additionally, however, they are characterized by cellular atypia and/or an infiltrative growth pattern, often with prominent necrosis and mitotic activity, and are capable of metastasis. Seventy cases of myoepithelial carcinoma culled from three series reveal that 64% (45 cases) arose in the parotid gland, 23% (16 cases) in the minor salivary glands sites, most frequently the palate, and 11% (8 cases) in the submandibular gland. Patients' age ranged from 14 to 86 years, with a mean in the sixth decade. A 4:1 male:female ratio was seen in one series, but others revealed a similar sex distribution. The tumors ranged in dimension from 2 to 20 cm and were usually unencapsulated.

These tumors should be considered intermediate to high-grade neoplasms. Treatment consists of wide surgical excision combined with radiation therapy. Tumor recurrence developed in 63% of 46 patients with follow-up, and multiple recurrences were frequent. The mortality rate was 28% (13 patients); 20% (9 patients) were alive with persistent disease, and 37% (17 patients) developed distant metastases, most frequently to the lung. Thirty-three percent (15 patients) were free of disease.[237, 238]

The CT findings show a fairly well defined heterogeneous lesion with smooth margins and slight enhancement. MR images show a mass with intermediate T1-weighted and relatively high T2-weighted signal intensities. The CT and MR studies are nonspecific.[239]

Epithelial-Myoepithelial Carcinoma

As experience with rare salivary tumors accrues, it is becoming increasingly evident that *primary clear cell tumors* (not variants of other known salivary tumors) represent a heterogeneous group of neoplasms. Historically, the entire group of primary salivary clear cell tumors had been referred to as clear cell carcinoma, clear cell adenoma, glycogen-rich adenoma, glycogen-rich adenocarcinoma, and so on. In 1979, Donath et al. described eight cases of a previously unrecognized clear cell tumor of salivary gland origin, which they termed *epithelial myoepithelial carcinoma* (EMEC).[7] However, it was not until 1982 that Corio and colleagues introduced this neoplasm into the English language literature and expounded upon it in their report on 16 cases from the Armed Forces Institute of Pathology series.[240] Prior to that publication, many cases of EMEC referred to in the literature as clear cell carcinoma, glycogen-rich adenoma, and so on. Thus EMEC became recognized as a distinct biphasic tumor forming ductules and glands surrounded by a variable clear cell component of myoepithelial origin and a variable hyaline background.

A literature meta-analysis of 96 patients with EMEC reveals a median age of 67 years and a female:male ratio of 2.4:1. Eighty-three percent of cases occurred in the parotid gland, 6% were intraoral, and 9% arose in the submandibular gland. Patients typically present with slowly enlarging masses, occasionally associated with facial nerve pain or weakness. Grossly, EMECs are well-delineated, firm, bulky tumors that may infiltrate adjacent soft tissue.

Histologically, they are often well circumscribed and may have a single or multinodular growth pattern; they are usually surrounded, at least partially, by a thick, fibrous capsule. They are biphasic tumors with islands, large nests, or sheets of tumor cells composed of scattered small ducts lined by cuboidal epithelium similar to normal intercalated ducts. The ducts are immediately surrounded by varying numbers of clear cells that often, in turn, are surrounded by dense hyalinized basement membrane material. Occasionally, columnar cells and small foci of early squamous metaplasia may be seen proliferating within ductal structures. The clear cell component may also be arranged in solid nests or sheets. The proportion and arrangement of nodular aggregates of the biphasic component and the sheets of clear cells are quite variable from tumor to tumor. In occasional tumors, the clear cell component may predominate and the more typical biphasic portions of the neoplasm may not be readily apparent. Mitotic figures, necrosis, perineural invasion, and, less frequently, intravascular growth may be found. Wide surgical excision is the treatment of choice for this neoplasm.

There is a significant likelihood (60%) of recurrence, which may be multiple and may happen up to two decades after the initial presentation (median 3 years). The rates of metastatic disease and tumor-related mortality are 9% and 9%, respectively, which may also happen after two decades. Metastases have involved regional lymph nodes, as well as hematogenous spread to the lung and kidney.[237, 240–242]

The imaging appearance is nonspecific, but in general these tumors are low-grade, benign-appearing masses, which may be cystic. As such, their imaging findings may be similar to those of a Warthin's tumor (Fig. 39-121).

Clear Cell Carcinoma

Milchgrub and colleagues first distinguished clear cell carcinoma [hyalinizing clear cell carcinoma (HCC)] as

Copyright © 2003, Mosby, Inc. All rights reserved.

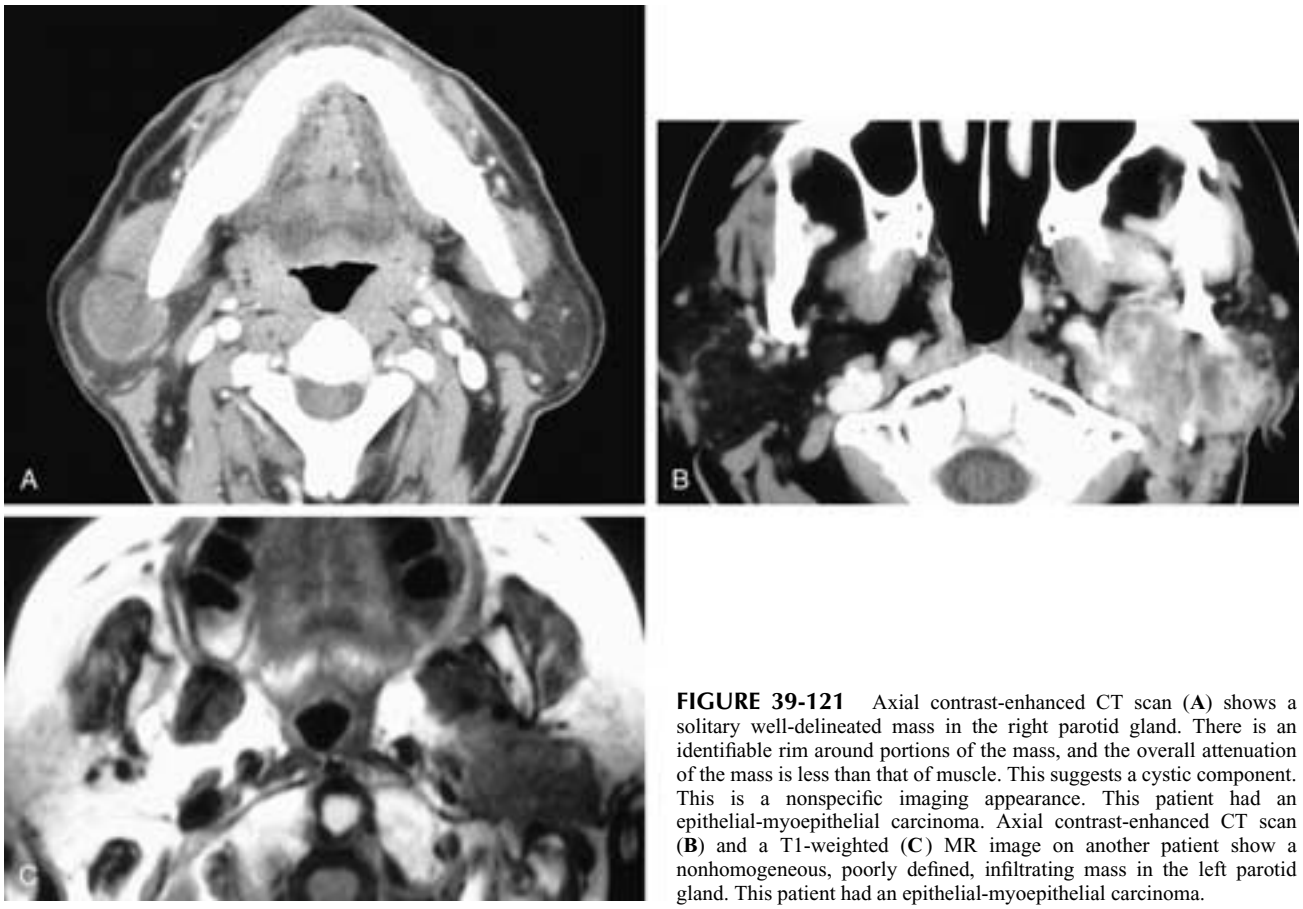

FIGURE 39-121 Axial contrast-enhanced CT scan (**A**) shows a solitary well-delineated mass in the right parotid gland. There is an identifiable rim around portions of the mass, and the overall attenuation of the mass is less than that of muscle. This suggests a cystic component. This is a nonspecific imaging appearance. This patient had an epithelial-myoepithelial carcinoma. Axial contrast-enhanced CT scan (**B**) and a T1-weighted (**C**) MR image on another patient show a nonhomogeneous, poorly defined, infiltrating mass in the left parotid gland. This patient had an epithelial-myoepithelial carcinoma.

VIEW IMAGE

an entity distinct from EMEC.[243] A literature meta-analysis of 103 cases reveals a wide age range (1 to 86 years; median, 52.5 years) and a slight female predominance (female:male ratio of 1.6:1). The majority of cases occur within the oral cavity (65%), usually on the palate, followed by the tongue; 21% of cases occur in the parotid gland. Patients typically present with a painless mass that had been present for months to several years.

Grossly, this tumor has been described as infiltrating and scar-like. Microscopically, clear cell carcinoma is a low-grade carcinoma characterized by nests of clear cells in a densely amyloid-like, fibrous, hyalinizing stroma surrounding cords, nests, sheets, and trabeculae of tumor cells. This hyalinization is not a constant feature, and some tumors may be relatively solid. The tumor cells are characterized as round to polygonal in shape, with clear, periodic acid-Schiff–positive cytoplasm and a high nuclear/cytoplasmic ratio. The nuclei are relatively peripheral, with mild pleomorphism, condensed chromatin, and inconspicuous nucleoli. Ductule formation is not seen.

Surgical resection with negative margins is the recommended treatment. The recurrence rate is 17%, and recurrence can occur up to two decades after initial therapy (median, 84 months). Multiple recurrences are possible. The metastatic rate is 21%, involving cervical lymph nodes, lungs, and soft tissue. Nevertheless, clear cell carcinoma is an indolent tumor, and no direct tumor-related deaths have been described, even after pulmonary metastases.[243–245]

Mucoepidermoid Carcinoma

Mucoepidermoid carcinoma (MEC) comprises 2.8% to 15.5% of all salivary gland tumors, 12% to 29% of malignant salivary gland tumors, and 6.5% to 41% of minor salivary gland tumors, representing the most common type of malignant minor salivary gland tumor in most series. About half of the cases occur in the major salivary glands; over 80% of these occur in the parotid gland, 8% to13% in the submandibular gland, and 2% to 4% involve the sublingual gland. In the minor salivary glands, MEC most commonly arises on the palate, but a significant number may also be found in the retromolar area, floor of the mouth, buccal mucosa, lip, and tongue. Rarely, MEC can arise as primary jaw or heterotopic intranodal tumors or as laryngeal, lacrimal, nasal, paranasal sinus, tracheal, or pulmonary tumors. MEC is most frequently seen in the 35- to 65-year age group but may be found at any age. It is the most common malignant salivary gland tumor to arise in children and adolescents under 20 years of age. MEC has a slight predilection for women. The most commonly implicated etiologic factor is radiation; as many as 44% of patients with a history of a radiation-associated salivary tumor developed MEC. Latency periods in this group ranged from 7 to 32 years.

On gross examination, MEC may appear circumscribed but it is seldom encapsulated. High-grade tumors have poorly defined margins and may grossly infiltrate adjacent skin and soft tissues. The cut surface ranges from gray to tan-yellow to pink, and cystic features are common and may

Copyright © 2003, Mosby, Inc. All rights reserved.

be prominent. The tumors usually range in size from 1 to 4 cm in their greatest dimension; however, occasional patients may present with larger tumors (over 12 cm).

Microscopically, MEC is composed of varying proportions of epidermoid cells, mucus-secreting cells, and cells intermediate between the other two cell types. Intermediate cells include the smaller basal cells, as well as larger cells that are differentiating toward squamous and mucin-secreting cells. Clear cells, many of which contain glycogen and/or mucin, are present in most MECs and often are a prominent feature. Tumors, especially low-grade neoplasms, frequently have distinct columnar cells containing intracellular mucin (goblet-like cells). Epidermoid cells have abundant eosinophilic cytoplasm and are occasionally associated with keratin production, including pearl formation. A given tumor may have a large variety of cell types. Cellular pleomorphism and atypia may be found and range from minimal to severe (Fig. 39-122).

Traditionally, MECs were classified histologically as low, intermediate, and high-grade based on the relative proportions of cell types. Other suggested grading criteria have included the degree of tumor invasiveness, anaplasia, the pattern of invasion, the degree of maturation of the various cellular components, mitotic rates, the presence or absence of necrosis, neural or vascular invasion, and the proportion of tumor composed of cystic spaces relative to solid growth. Grading of MEC is subjective, with different criteria used in various series. Auclair et al. established a set of more uniform histologic criteria that correlated with the clinical outcome.[246] Brandwein and colleagues have recently shown that this grading system, while enhancing reproducibility, tends to ''downgrade MEC,'' and they have proposed further refinements to this weighted grading criteria[247] (Table 39-5).

Treatment planning for MEC starts with a preoperative biopsy and diagnosis. However the issue of preoperative grading is often raised with respect to treatment planning. The major decision point here would be grade I MEC versus grade II/III MEC, as a grade I tumor would have no (or minimal) likelihood of requiring addition lymph node dissection. Lymph node dissections are included as standard therapy for grade III tumors, and grade II tumors are left to the surgeon's discretion. However, it is difficult to establish the tumor grade on a preoperative biopsy specimen due to the possibility of sampling error. Thus these biopsy specimens are often graded as MEC ''at least grade I'' or ''at least grade II,'' allowing for final grading after excision.

Prognosis is a function of the histologic grade, adequacy of excision, and clinical staging. Complete surgical excision is the treatment of choice for MEC. Adequate excision is important for all grades of tumor, with much higher recurrence rates reported for tumors with positive surgical margins (on the order of 50% for low- and intermediate-grade tumors and slightly over 80% for high-grade tumors). Adjuvant radiation therapy should be added for high-grade tumors and for patients with residual microscopic disease at the surgical margins.

Patients with low-grade tumors have a 5-year survival rate of 90% to 100%; with the exception of submandibular gland tumors, these tumors have been reported to recur or metastasize, albeit rarely. Metastatic, recurrence, and death rates from low-grade submandibular gland tumors have been reported as 13%, 9%, and 13%, respectively. Spiro et al. also found more frequent metastases from submandibular gland MEC than from other major gland sites; however, other series have not confirmed this association.[7] This may be a technical issue: when resecting the submandibular gland, surgeons may be more inclined to hug the capsule for

Table 39-5
GRADING OF MUCOEPIDERMOID CARCINOMA

	Characteristic Features	Defining Features
Grade I	Prominent goblet cell component Cyst formation Intermediate cells may be prominent Circumscribed growth pattern	Lack of grade III defining features Lack of aggressive invasion pattern
Grade II	Intermediate cells predominate in mucinous component Mostly solid Squamous cell may be seen	Aggressive invasion pattern Lack of grade III defining features
Grade III	Squamous cells predominate	Necrosis

Feature		Points
Tumor front invades in small nests and islands		2
Lymphatic invasion		2
Vascular invasion		3
Bony invasion		3
>4 mitoses/10 high-power fields		3
Perineural spread		3
Necrosis		3
Total points	Grade I	0
Total points	Grade II	2–3
Total points	Grade III	4 or more

Source: Brandwein M, Ivanov K, Wallace D, et al. Mucoepidermoid carcinoma: a clinicopathologic study of 80 patients with special reference to histological grading. Am J Surg Pathol 2001;25:835–845.

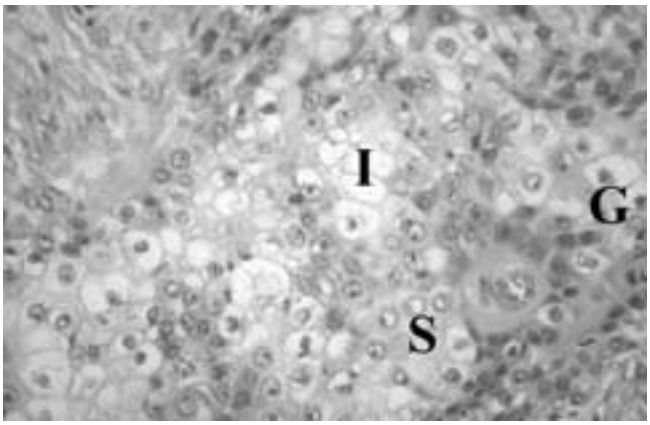

FIGURE 39-122 Mucoepidermoid carcinoma. The three cytologic components necessary for diagnosis are squamoid cells (*S*), larger, cleared intermediate cells (*I*), and mucinous goblet cells (*G*). The mucinous component is confirmed by mucicarmine stain.

VIEW IMAGE

Copyright © 2003, Mosby, Inc. All rights reserved.

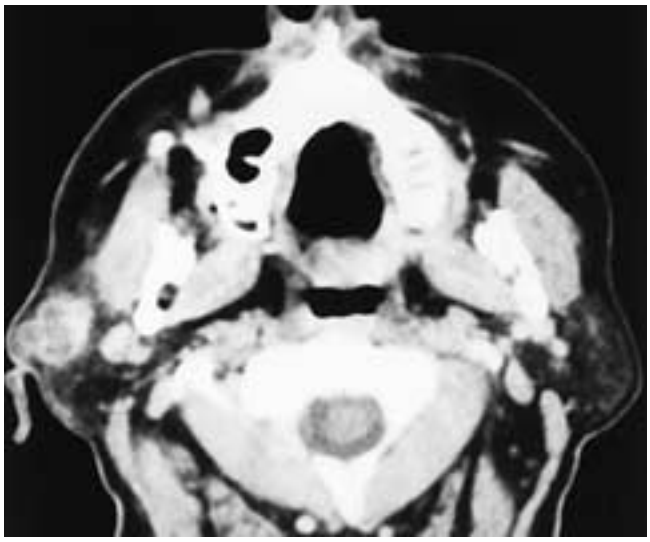

VIEW IMAGE

FIGURE 39-123 Axial CT scan shows a nodular mass in the right parotid gland. The mass has cystic areas within it, and the medial wall of the lesion is nodular and slightly unsharp as it merges with the adjacent parotid gland. This patient had a low-grade MEC.

fear of damaging the marginal mandibular nerve. Thus there is usually less of a cuff of surrounding normal tissue compared to the parotid gland. Therefore any tumor of the submandibular gland, irrespective of grade, should be treated aggressively.

Intermediate- and high-grade tumors have a greater tendency to infiltrate, recur, and metastasize. For intermediate-grade tumors, Healy reported a recurrence rate of 20%. Brandwein et al.[247] reported a recurrence rate of 30%, a rate of metastasis to cervical lymph nodes of 18%, and a disease-related mortality rate of 5%. For high-grade tumors, Brandwein et al.[247] reported a recurrence rate of 70%, a rate of metastasis to cervical lymph nodes of 63% and to distant sites of 6%, and a disease-related mortality rate of 63%. Survival is improved for tumors arising in younger patients and among females but is poorer in patients over 60 years of age. In a recent study, Plambeck et al. reported 5- and 10-year survival rates of 91.9% and 89.5%, respectively, regardless of tumor grade.[253] Stage appeared to be a better prognosticator: all patients who died had stage 3 or 4 disease with 5- and 10-year survivals for this group of 63.5% and 52%, respectively.[246–253]

The CT findings of mucoepidermoid lesions vary with the grade of the tumor (Figs. 39-123 to 39-129). Low-grade lesions are benign in appearance, with apparently well-delineated, smooth margins. Cystic areas may be present, with a low attenuation of 10 to 18 HU (Figs. 39-123, 39-124 and 39-126). Rarely, focal calcification may be seen. The appearance is similar to that of a benign mixed tumor. On MR imaging, these low-grade tumors also have signal intensities that are indistinguishable from those of pleomorphic adenomas. By comparison, the high-grade lesions have indistinct infiltrating margins and may destroy salivary ducts (Fig. 39-128). On CT they usually have few cystic areas, and they tend to be more homogeneous in appearance than the low-grade tumors. On MR imaging, these cellular tumors tend to have low to intermediate signal intensities on both T1-weighted and T2-weighted images (Fig. 39-129).

Adenoid Cystic Carcinoma

Adenoid cystic carcinoma (AdCC) accounts for 2% to 6% of parotid gland tumors, 12% of submandibular gland tumors, 15% of sublingual gland tumors, 30% of minor salivary gland tumors, and 50% of lacrimal gland tumors.[7, 194, 254–256] Overall, 4% to 8% of all salivary gland tumors are adenoid cystic carcinomas, and they occur most commonly in the parotid gland, the submandibular gland, and the palate. AdCC occurs over a very wide age range, from the first to the ninth decades of life, but with a preponderance in the fourth to seventh decades. The female:male ratio is approximately 3:2.

Typically, AdCC is a slow-growing, widely infiltrative tumor with a tendency toward perineural spread. Patients present with symptoms of pain and a mass that may have evolved over several years. Mucosal ulceration, especially of the palate, is common. Occasional tumors present with intracranial involvement, closely mimicking a meningioma clinically and radiographically; rarely, a tumor may have an occult presentation. Table 39-6 presents a compilation of tumor sites for AdCC derived from over 1600 cases. The parotid gland, palate, submandibular gland, and sinonasal tract are the most commonly affected upper aerodigestive tract sites; minor salivary sites are more frequently involved than all the major salivary glands combined. AdCC is the second most frequent malignant tumor of the trachea after squamous carcinoma; 45.5% of patients have tumors in the upper trachea. At this site, the male:female ratio is almost 1:1, and the average age at presentation is between 45 and 60 years (range, 15 to 80 years).

Grossly, these tumors are firm and gray-white, and can appear as subtle scar-like lesions. Smaller tumors may be circumscribed or, rarely, encapsulated. They have a tendency to extend along nerves, and ''skip lesions'' may be seen considerable distances away from the main tumor mass.

The World Health Organization's classification divides AdCC into the following microscopic patterns: tubular, cribriform (glandular), and solid. The cribriform type is the

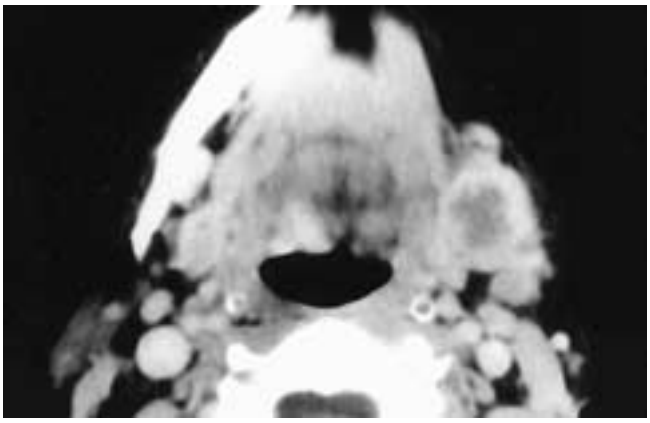

FIGURE 39-124 Axial CT scan shows a necrotic mass in the left submandibular gland. The tumor has a thick, irregular rim and an infiltrative outer contour. This patient had a high-grade MEC.

VIEW IMAGE

Copyright © 2003, Mosby, Inc. All rights reserved.

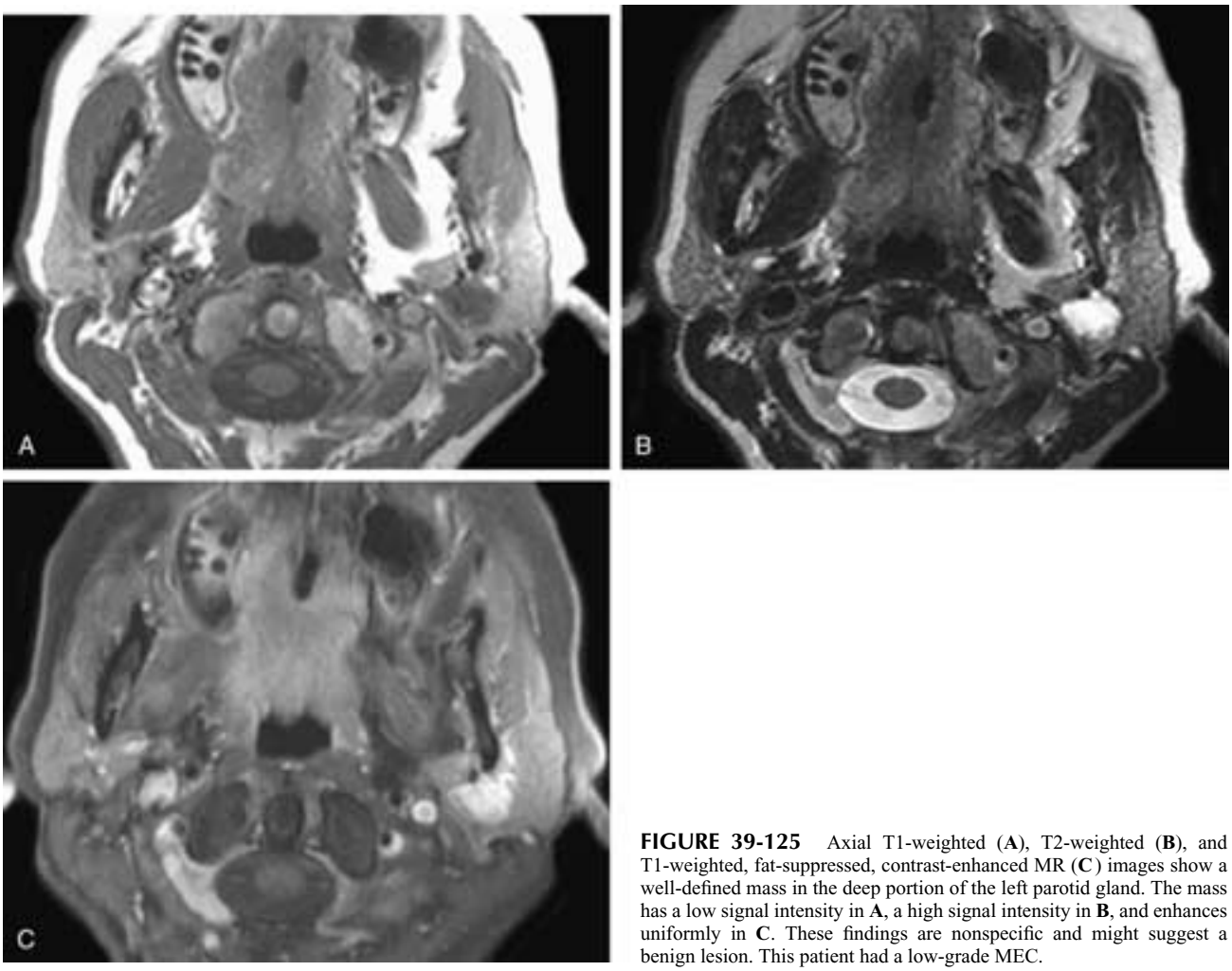

FIGURE 39-125 Axial T1-weighted (**A**), T2-weighted (**B**), and T1-weighted, fat-suppressed, contrast-enhanced MR (**C**) images show a well-defined mass in the deep portion of the left parotid gland. The mass has a low signal intensity in **A**, a high signal intensity in **B**, and enhances uniformly in **C**. These findings are nonspecific and might suggest a benign lesion. This patient had a low-grade MEC.

VIEW IMAGE

most frequent pattern observed; the solid pattern is least common. Adenoid cystic carcinomas are composed of two types of cells: ductal and abluminal myoepithelial. Cytologically, they are composed of a somewhat uniform, bland population of cells with oval basophilic nuclei with a homogeneous chromatin distribution, and usually with little cytoplasm, reminiscent of basal cell carcinoma of the skin. The nuclei are frequently angulated and rarely have coarse chromatin and prominent nucleoli (Fig. 39-130). While these latter two features are more likely to occur in the solid high-grade tumors, high-grade cytology may occasionally be seen with intermediate-grade tumors. A mixture of architechtural patterns is common, and grading depends on the predominant pattern. If a tumor has more than 30% of the solid pattern, it is classified as the solid variant. The tubular pattern (well differentiated or grade I) is characterized by slender tubules, solid cords, and glandular structures infiltrating a well-hyalinized background. These tumors are composed of myoepithelial cells often surrounding central lumina forming epithelial structures. The cribriform pattern (moderately differentiated or grade II) is characterized by invasive tumor islands with multiple ''holes'' (pseudocysts or pseudolumina) punched out in a ''Swiss cheese'' or sieve-like pattern. The solid pattern (poorly differentiated or grade III) consists of large islands of carcinoma composed predominantly of myoepithelial cells with infrequent true lumina lined by cuboidal epithelial cells, with only occasional punctuation by pseudocysts. Perineural spread is a feature common to all patterns. Mitotic figures and apoptotic cells are occasionally present in intermediate-grade tumors and are common to high-grade tumors. Necrosis is seen usually only in the solid pattern.

Pathologists are often reluctant to diagnose AdCC on the basis of a limited biopsy, especially in the absence of definite tumor infiltration. The cribriform pattern so typical of AdCC may also be seen rarely in BCA, in mixed tumors, and in polymorphous low-grade adenocarcinomas. The diagnosis of minor salivary gland tumors based on limited biopsy material is especially challenging, as benign minor salivary tumors are rarely encapsulated but are well circumscribed.

On imaging, these tumors may appear either as a benign or a malignant process (Figs. 39-131 to 39-135). The parotid lesions tend to appear as benign, well-delineated tumors, while the minor salivary gland neoplasms usually have malignant infiltrative margins. Retrograde tumor extension to the skull base often occurs via the facial nerve or the mandibular nerve. Although this neural invasion may be demonstrated by CT, it is more consistently and more reliably identified on MR imaging. On contrast CT, a grossly

Copyright © 2003, Mosby, Inc. All rights reserved.

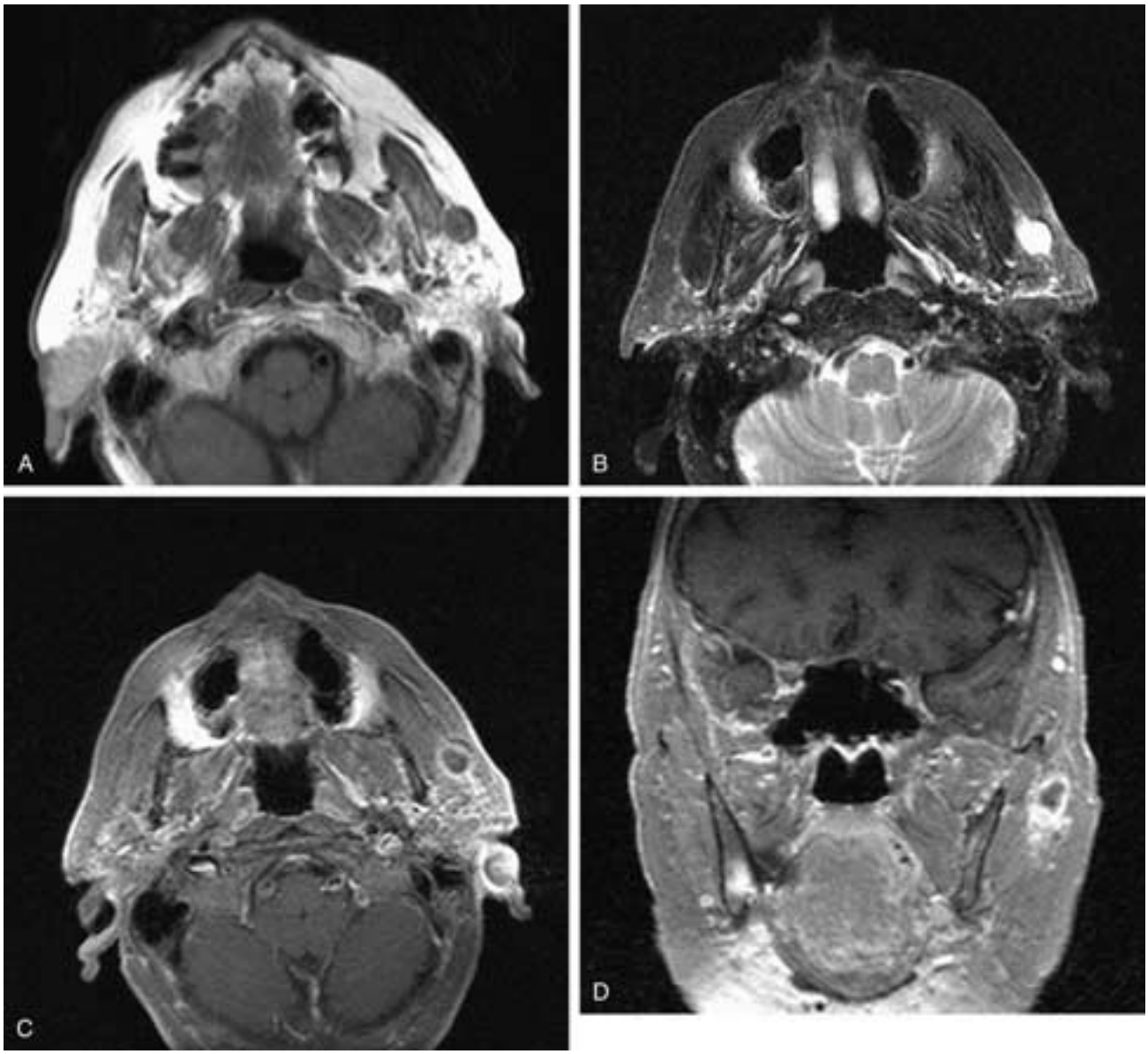

VIEW IMAGE

FIGURE 39-126 Axial T1-weighted (**A**), T2-weighted (**B**), and axial (**C**) and coronal (**D**) T1-weighted, fat-suppressed, contrast-enhanced MR images show a well-defined mass in the superficial left parotid gland. It has low T1-weighted and high T2-weighted signal intensity and is partially cystic, as seen after contrast administration. The finding might suggest a benign lesion such as a Warthin's tumor. This patient had a low-grade MEC.

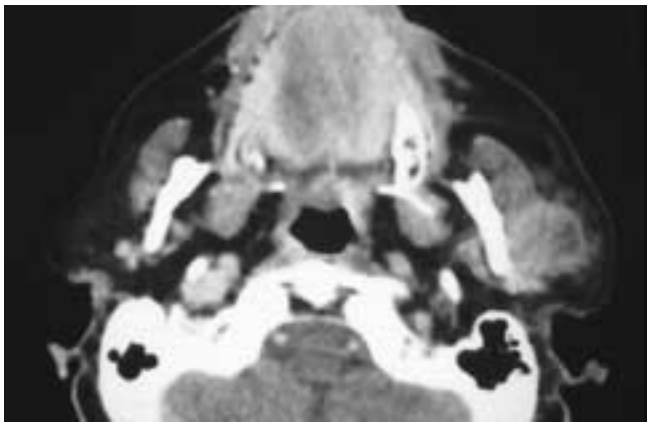

FIGURE 39-127 Axial contrast-enhanced CT scan shows a partially necrotic mass with irregular walls in the left parotid gland. The mass has an infiltrative margin with the adjacent parotid tissue. This patient had a high-grade MEC.

VIEW IMAGE

Copyright © 2003, Mosby, Inc. All rights reserved.

VIEW IMAGE

FIGURE 39-128 Lateral view of a parotid sialogram shows a mass that has caused ductal erosion and lack of parenchymal filling. These findings suggest a high-grade malignancy. This patient had a high-grade MEC.

widened nerve may be seen in a widened bony neural canal and obliterating the normal fat present at the extracranial opening of these canals (see Chapter 13). MR imaging is more sensitive than CT in detecting lesser degrees of neural tumor invasion, and on contrast MR imaging, nerve enhancement can be identified, often in a minimally enlarged nerve (Fig. 39-134). MR imaging has proven to be especially useful when evaluating postoperative recurrences (Fig. 39-135). Clinically, these patients most often have had

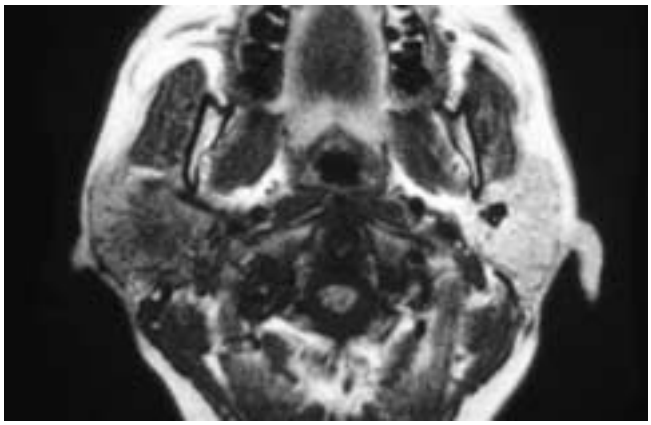

VIEW IMAGE

FIGURE 39-129 Axial T1-weighted MR image shows a poorly defined low signal intensity mass occupying the medial three quarters of the right parotid gland. The tumor also had a low signal intensity on a T2-weighted image. This patient had a high-grade MEC.

Table 39-6
DISTRIBUTION OF SITES FOR AdCC OF THE UPPER RESPIRATORY TRACT

Site (Total Number)	%
Parotid gland (336)	21.0
Palate (271)	17.0
Other site, not stated (242)	15.0
Submandibular gland (210)	13.0
Sinonasal, nasopharynx (184)	11.0
Tongue, floor of mouth (129)	8.0
Tonsil, pharynx (69)	4.3
Lip (53)	3.3
Buccal (44)	2.7
Sublingual gland (30)	1.8
Retromolar trigone (21)	1.3
Gingiva (10)	0.6
Larynx / trachea (10)	0.6
Lacrimal gland (5)	0.3
Total: 1614	

a prior total parotidectomy and return with pain either in the postoperative bed or in the skull base. The examination of choice should be a contrast MR imaging study that at least includes coronal scans of the base of the skull.

Wide surgical resection with negative margins is the standard primary therapy. Adjuvant radiotherapy is usually indicated for most tumors; however, some would argue that well-resected T1 AdCC may not require adjuvant radiotherapy. Primary conventional radiotherapy has never been shown to provide sufficient local disease control. However, there are emerging data suggesting that neutron therapy, which involves larger particles of greater energy, can achieve reasonable local control as a primary therapeutic modality. Also, adoptive immunotherapy in combination with chemoradiotherapy has recently shown promising results. Larger series with more patients are necessary to confirm these preliminary data.

AdCC has been noted to have a greater local recurrence rate compared to other malignant salivary tumors (p = 0.0059). This propensity for local recurrence (up to 62%) is highest within the first 5 years, but a significant number of patients develop local recurrence after 10, 15, and 20 years.

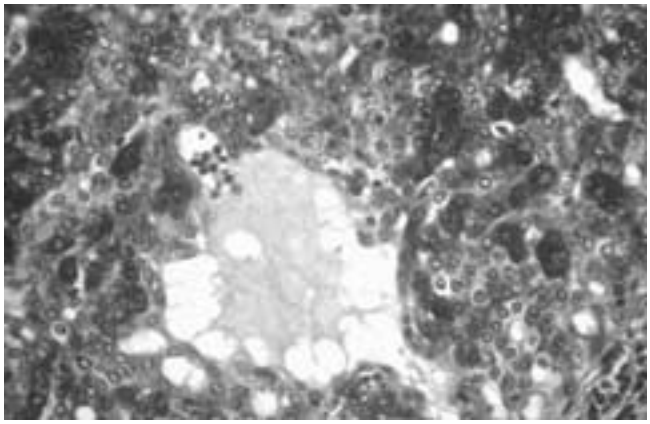

FIGURE 39-130 ACC. Higher power shows tumor cells with dense granular basophilic cytoplasm and small nuclei.

VIEW IMAGE

Copyright © 2003, Mosby, Inc. All rights reserved.

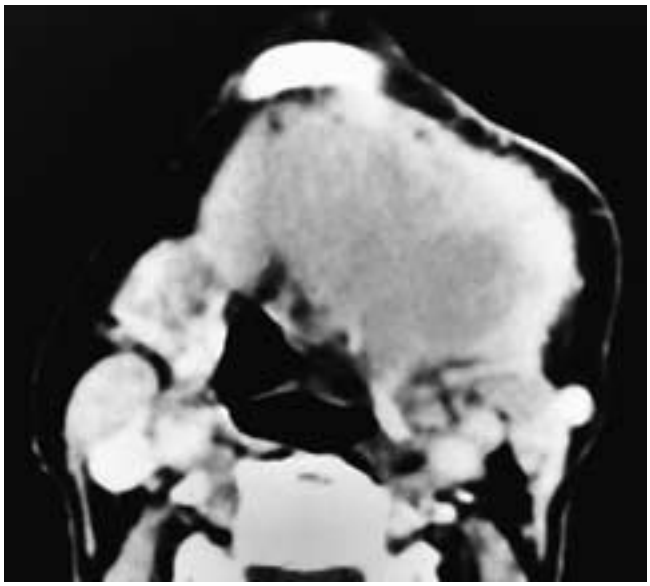

VIEW IMAGE

FIGURE 39-131 Axial contrast-enhanced CT scan shows a large, infiltrating mass of the left submandibular gland. The tumor has invaded the floor of the mouth. This patient had an AdCC.

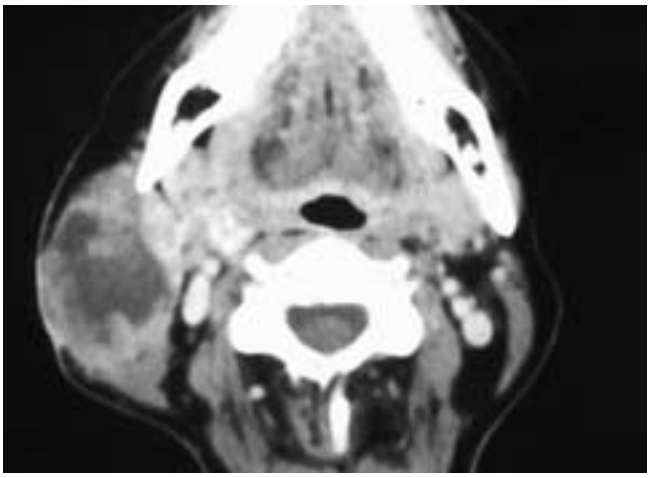

VIEW IMAGE

FIGURE 39-132 Axial contrast-enhanced CT scan shows a necrotic mass in the right parotid gland with poorly defined margins. Multiple tumor nodules are seen along the wall of the lesion. This appearance suggests a high-grade tumor. This patient had an AdCC. This is a more aggressive tumor than most of these parotid adenoid cystic carcinomas.

Actuarial local control rates at 5, 10, and 15 years of 95%, 86%, and 79%, respectively, have been reported. Distant metastases are much more frequent than local lymph node metastases. The rate of development of distant metastases is 40% to 50% for all adenoid cystic carcinomas, and these metastases may occur 10 to 108 months (median, 96) after initial diagnosis. Approximately 3% to 8% of patients have metastases at initial presentation. Tumors most frequently metastasize to lung and, less frequently, to bone and soft tissues. Distant metastasis usually occurs in conjunction with local recurrence but may develop in the absence of locoregional disease; it was the most common type of treatment failure in one recent series.

Spiro reported disease-free intervals after adequate primary therapy ranging from 1 month to 19 years (median, 36 months) and disease-free intervals of more than 10 years in 9 of 113 patients (8%).[262] Survival with distant metastases was less than 3 years in 54% but more than 10 years (with a maximum of 16 years) in 10% of patients. A recent series from the MD Anderson Cancer Center of 160 patients using consistent surgery and radiation therapy in 87.5% of patients yielded survivals at 5, 10, and 15 years of 89.0%, 67.4%, and 39.6%, respectively. Treatment failure was documented in 37% of patients ranging from 2 months to 19 years. Eight percent failed locoregionally, 22% failed distantly, and 7% had both locoregional and distant failures. Major (named) nerve invasion, positive margins, and solid histologic features predicted treatment failures, while nodal metastases, major nerve involvement, solid histologic features, and four or more symptoms present at diagnosis were associated with increased disease mortality.

Surgical prognosticators in other series include tumor

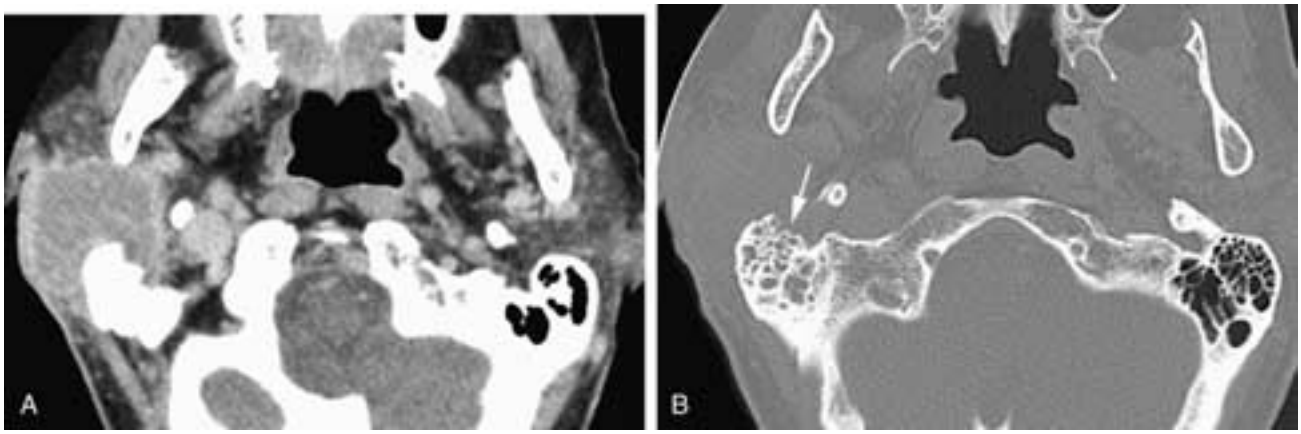

VIEW IMAGE

FIGURE 39-133 Axial CT scans at a narrow window setting (**A**) and a wide window setting (**B**) show a necrotic mass in the right parotid gland. Despite the fact that the lesion's contours in the gland are sharply defined, the upper edge of the tumor has invaded the mastoid tip, with erosion of the cortex (*arrow*). There was also tumor extension into the mastoid portion of the facial nerve. This patient had an AdCC with retrograde tumor spread and bone invasion.

Copyright © 2003, Mosby, Inc. All rights reserved.

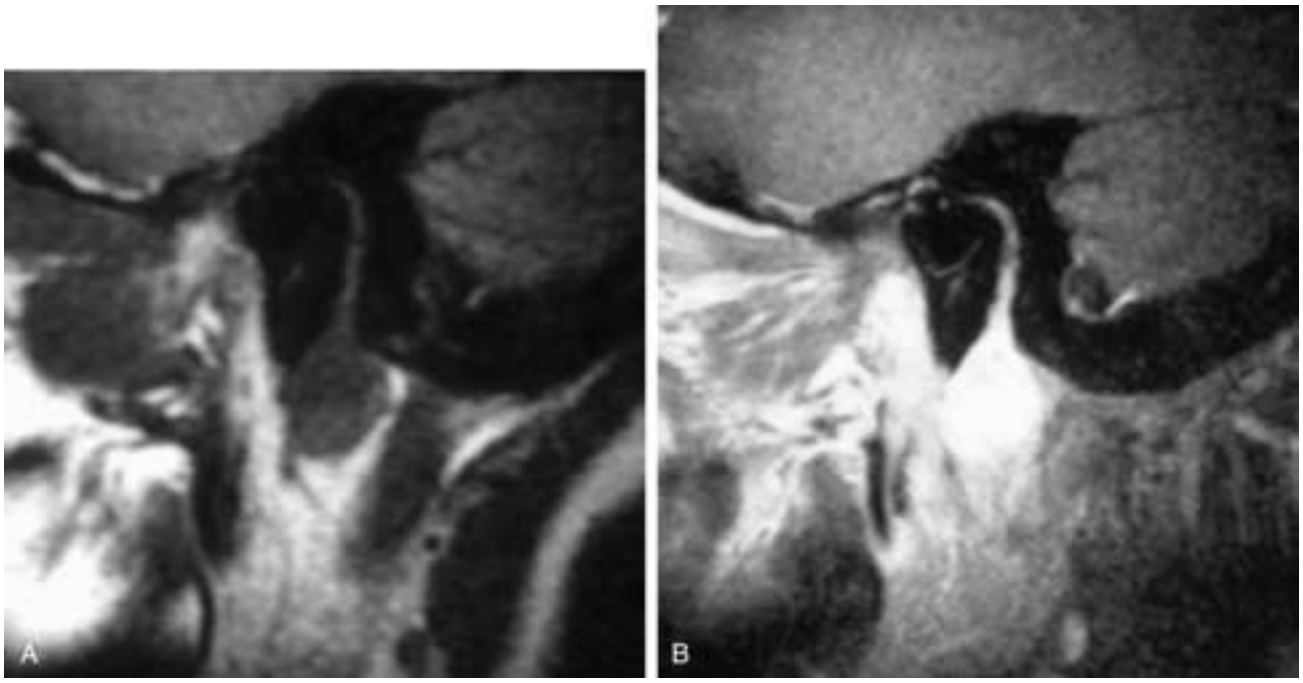

VIEW IMAGE

FIGURE 39-134 Sagittal T1-weighted (**A**) and T1-weighted, fat-suppressed, contrast-enhanced (**B**) MR images show a well-defined mass in the left parotid gland with widening and enhancement of the facial nerve up into the midmastoid portion of the nerve canal. This patient had an AdCC with retrograde tumor spread.

grade, stage, site, nerve involvement, and resection margins. A number of studies confirm that the grading system, based on the pattern of differentiation and tumor stage, correlates with survival for adenoid cystic carcinoma. When grade is considered as a prognosticator, the cumulative survival at 5, 10, and 15 years is 92%, 65%, and 14%, respectively, for grade I tumors; 76%, 26%, and 5% for grade II tumors; and 39%, 26%, and 5% for grade III tumors. Tumor site is another important prognosticator: generally, major salivary gland sites have a more favorable outcome than minor salivary gland sites. AdCCs of the trachea have a better prognosis than their counterparts in the upper respiratory tract, with 5-year survival ranging between 66% and 100% and 10-year survival ranging between 50% and 75%. These data are summarized in a recent review by Azar and colleagues. Sites such as the sinonasal tract are inherently less resectable and have the worst prognosis. Spiro and Huvos have shown that tumor stage is a better prognostic discriminator than tumor grade. This fact has been underappreciated, as AdCCs are not commonly encountered as stage I tumors. Patients with stage I tumors had a lower rate of local recurrence (23%) than those with stage II to IV tumors (60%). Their cumulative 10-year survival rates per stage were 75% (stage I), 43% (stage II), and 15% (stage III/IV). Histologic grade did have an impact on survival early in the disease course; one third of recurrences were evident within 1 year for intermediate- and high-grade tumors, whereas only 14% of low-grade tumors recurred within 1 year.

VIEW IMAGE

FIGURE 39-135 Coronal T1-weighted MR image of a patient who previously had had a right parotidectomy. The recurrent tumor has grown from the parotid bed up along the auriculotemporal nerve to the third division of the trigeminal nerve and then via the foramen ovale it invades the right cavernous sinus (*arrow*). This patient had recurrent AdCC. (From Som PM, Braun IF, Shapiro MD, et al. Tumors of the parapharyngeal space and upper neck: MR imaging characteristics. Radiology 1987;164: 823–829.)

Garden et al. reported on 83 patients (42%) with microscopic positive margins and 55 patients (28%) with close margins (defined as 5 mm or less) or uncertain margins. Perineural spread was seen in 69% of cases, and invasion of a major (named) nerve occurred in 28% of patients. Local recurrences developed in 18% of patients with positive margins compared to 9% of patients with close or uncertain margins and 5% of patients with negative margins ($p = 0.02$). Patients with a major (named) nerve involvement had a crude failure rate of 18% (10 out of 55) compared to 9% (13 out of 143) for patients without major nerve involvement ($p = 0.02$).

Copyright © 2003, Mosby, Inc. All rights reserved.

DNA ploidy has shown promise as a prognosticator and may be especially helpful in the preoperative planning phase. Franzen et al. studied 51 AdCCs and found that 39 tumors were diploid and 12 were aneuploid. Grade III tumors were more often associated with aneuploidy than grade I and II tumors ($p = 0.011$), and ploidy also correlated with clinical stage ($p = 0.011$). The authors found that the combination of an S phase greater than 6% and aneuploidy is a sensitive predictor of treatment failure. Recently, Franchi et al. found that E-cadherin statement was a prognostic marker of the disease-free interval and survival in AdCC, independent of clinical stage and other histopathologic parameters. Reduced statement correlated with shorter disease-free intervals and actual survival rates.[257–267]

Acinic Cell Carcinoma

Acinic cell carcinoma (ACC) comprises 7% to 17.5% of all salivary malignancies and 10% to 30% of primary parotid malignancies. The vast majority (90%) of ACCs arise in the parotid gland. The minor salivary glands are the second most common site, usually the upper lip, buccal mucosa, and palate. ACC rarely affects the submandibular and sublingual glands. Given that ACC of the submandibular gland is rare, the surgeon should be directed to investigate the deep parotid lobe, where the primary tumor may be identified. The reported age range for patients with ACC is 3 to 91 years; the female:male ratio is approximately 2:1. Interestingly, the average age at diagnosis, 38 to 46 years, is nearly a decade younger than that of patients with other parotid malignancies. After MEC, ACC is the second most common malignant salivary gland neoplasm of childhood. ACC is the third most common bilateral salivary gland tumor after Warthin's tumor and pleomorphic adenoma. It is the most frequent malignant tumor to present bilaterally. Nearly all patients present with a mass; up to 50% also complain of facial pain. However, facial nerve involvement with paresis or paralysis is less common at presentation, seen in up to 7.5% of patients.

Grossly, the typical ACC appears as a circumscribed, tan-gray, rubbery mass and may be cystic. Recurrent tumors can be multinodular. There are four principal histologic patterns: solid, microcystic, papillary-cystic, and follicular; however, a mixture of patterns is common. Microscopically, ACCs characteristically grow as solid sheets of basophilic serous cells. The tumor cells recapitulate the serous acinar cells of the normal parotid gland and contain cytoplasmic zymogen granules, the packaged secretory product of acinar cells. These granules are responsible for the tumor's prominent cytoplasmic basophilia.

Surgical excision with negative margins is the goal of primary treatment. Superficial lobectomy is adequate for the majority of parotid tumors. However, for those involving the deep lobe, total parotidectomy is necessary. Elective neck dissection is not indicated. Recurrences tend to be multiple and require rigorous surgical reexcision.[40, 41] Most studies suggest that radiation therapy is of little utility in the treatment of ACC.

ACC is capable of a notoriously protracted clinical course. Disease-free and determinate survival curves do not level off for a decade. Five-year survival ranges from 76% to 90% and drops to 44% to 67% beyond 15 years. The expected rates of recurrence, metastasis, and mortality after adequate resection are approximately 30%, 13%, and 13%, respectively. Patients may succumb to progressive locoregional or metastatic disease. The latter may occur by either lymphatic and/or hematogenous lymphatic spread. Lung and bone are the most common sites of hematogenous spread. Long-term survival is possible after documentation of metastatic disease.[268–277]

The clinical stage at presentation gives the most prognostic information. Accordingly, metastases, large tumor size, deep lobe parotid involvement, and tumor multinodularity are all associated with a poor clinical outcome.

The imaging characteristics of these tumors are nonspecific, with most lesions having a generally benign appearance, often occurring on CT and MR imaging as a pleomorphic adenoma.

Polymorphous Low-Grade Adenocarcinoma and Low-Grade Papillary Adenocarcinoma of Salivary Origin

Polymorphous low-grade adenocarcinoma (PLGA) was first described in the 1980s by Freedman and Lumerman as lobular carcinoma, and by Batsakis and coworkers as terminal duct carcinoma. Evans and Batsakis subsequently coined the term polymorphous low-grade adenocarcinoma to describe this low-grade salivary malignancy, which usually occurs at minor salivary gland sites. It is the second most common intraoral malignant salivary gland neoplasm after MEC, accounting for 26% of carcinomas. Approximately 60% of the cases involve the palate, and most of the other cases occur at other intraoral sites. PLGA can rarely arise in the major salivary glands. There is a 2:1 female:male ratio, and most affected patients are in their fifth to eighth decade of life. Patients usually present with firm, elevated, painless, nonulcerated masses that range from 0.6 to 6 cm in maximum dimension.

Histologically, PLGA is characterized by an infiltrative growth pattern, histologic blandness, cytologic uniformity, and cellular organizational diversity, hence the descriptor *polymorphous*. PLGA is unencapsulated but is characterized by an infiltrative growth pattern. The tumor cells are arranged in varied patterns ranging from sheets, interconnecting cords, small tubules, solid islands, ducts, and cystic and cribriform areas to other foci having a characteristic infiltrating ''Indian file'' pattern (Fig. 39-136). Tumors commonly invade adjacent soft-tissue and salivary gland lobules and may infiltrate adjacent bone; perineural growth is common and is as frequent in PLGA as in AdCC. The overlying surface epithelium is usually intact but may be ulcerated. Mitoses may be present but are usually sparse. Atypical mitotic figures are usually not found, and necrosis is usually not seen. The absence of these two features aids in distinguishing PLGA from AdCC. Two recent studies have also shown that the proliferative rates (^{67}Ki) for PLGA and AdCC are quite different, with little or no overlap in their ranges, which may also be useful in distinguishing these two tumors.

Some authors consider low-grade papillary adenocarcinomas arising in the palate to be a subtype of PLGA. These tumors are histologically different and distinctive from PLGA because they lack the pleomorphic growth patterns and contain almost exclusively papillary and cystic structures (PLGA may have papillary-cystic foci, but the

Copyright © 2003, Mosby, Inc. All rights reserved.

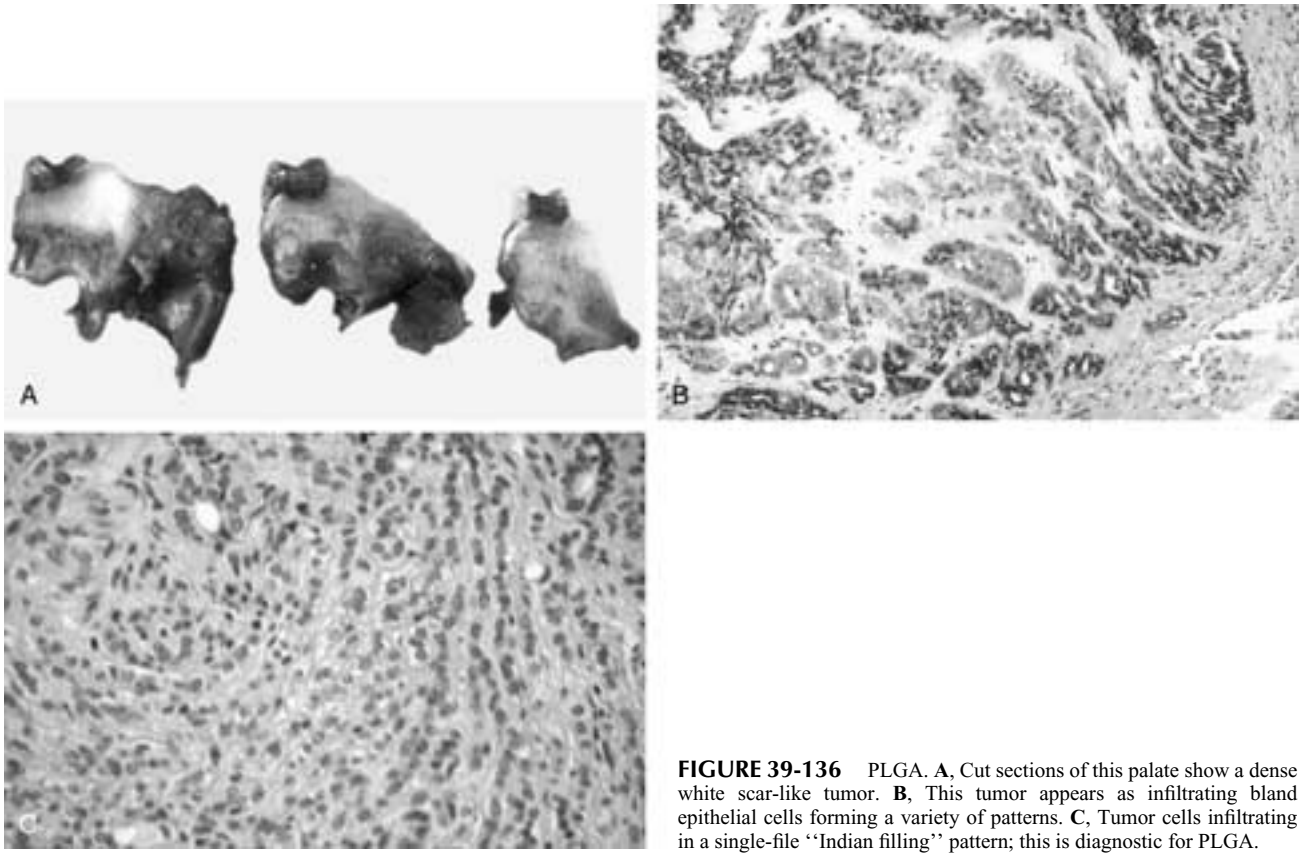

FIGURE 39-136 PLGA. **A**, Cut sections of this palate show a dense white scar-like tumor. **B**, This tumor appears as infiltrating bland epithelial cells forming a variety of patterns. **C**, Tumor cells infiltrating in a single-file ''Indian filling'' pattern; this is diagnostic for PLGA.

VIEW IMAGE

predominant growth pattern is not papillary.) They are also more aggressive biologically and therefore are more properly classified under the designation of papillary cystadenocarcinoma, which we prefer, or low-grade papillary adenocarcinoma.

Treatment consists of wide local surgical excision with possible adjuvant radiation therapy for insufficient margins or for recurrent tumors, although the literature indicates that the majority of recurrences are controlled by surgical reexcision alone. A lymph node dissection is indicated in the presence of cervical lymphadenopathy. Overall survival of patients with PLGA is excellent. The tumor behaves in an indolent fashion but may locally recur in 9% to 17% of patients. The rate of metastasis to cervical lymph nodes is low (varying from 0% to 9%). Two patients have been reported with pulmonary metastases, and to date, only three persons have died from PLGA.[278–287]

The imaging features are nonspecific and are similar to those of AdCC.

Salivary Duct Carcinoma (Plus Low-Grade Salivary Duct Carcinoma)

Salivary duct carcinoma (SDC) is a clinicopathologically distinct salivary tumor that gained wider recognition in the middle to late 1980s. Over 150 cases have been described, and some demographic features have emerged: there is a distinct male predominance (at least 4:1), most patients present after the age of 50 years, and the parotid gland is the most common site of origin. Occasionally SDC has been reported from the submandibular and sublingual glands and from minor salivary gland sites.

Grossly, tumors are usually firm, solid, tan, white, or gray, with a variable cystic component. Infiltration into the surrounding parenchyma is usually obvious, but occasional tumors may appear to be circumscribed. Microscopically, SDC can be subclassified as either high-grade or low-grade, infiltrative, or predominantly (>90%) intraductal.

The *high-grade* infiltrative tumor was the entity first recognized and reported, as it is the one most commonly encountered, representing more than 90% of cases. High-grade SDC resembles grade II and III intraductal and infiltrating breast ductal carcinoma both architecturally and cytologically. Comedonecrosis within ducts, a ''Roman bridge'' formation, and an intraductal cribriform pattern are typically seen. Perineural spread (60% of cases) and intravascular tumor emboli (31% of cases) are common. Cytologically, these cells have abundant light pink cytoplasm and large pleomorphic nuclei with prominent nucleoli and coarse chromatin. Mitotic figures are usually abundant (Fig. 39-137).

The cytologically *low-grade variant* was recognized and reported by Delgado and coauthors and by Tatemoto in 1996. Unlike the more frequent and familiar high-grade tumor, low-grade SDC has smaller cells with finely dispersed chromatin and small nucleoli, and may have apocrine-type cytoplasmic microvacuoles that may indent the nuclear contour. The cytoplasm may contain fine yellow to brown pigment, and the cytoplasmic membranes

Copyright © 2003, Mosby, Inc. All rights reserved.

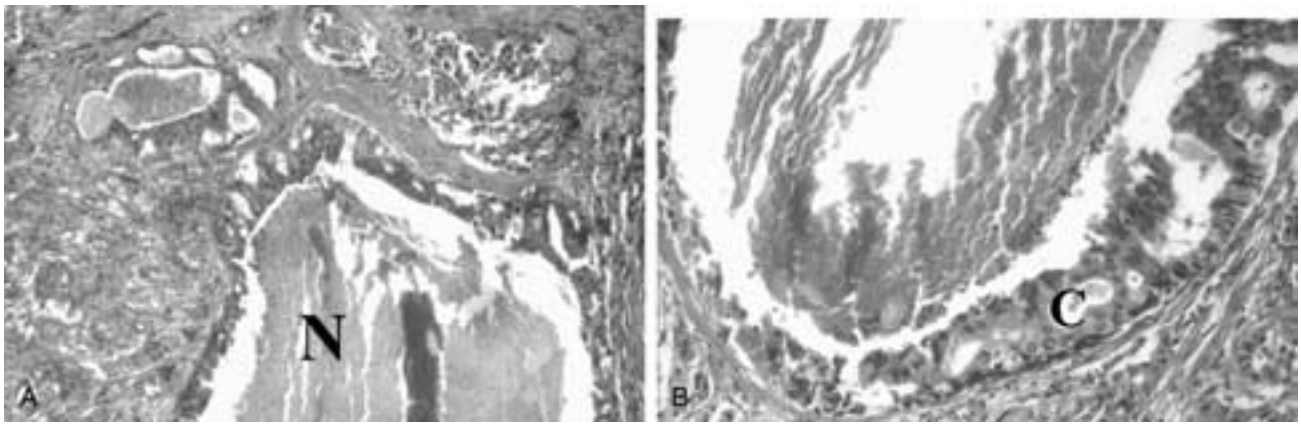

VIEW IMAGE

FIGURE 39-137 **A**, SDC. This tumor is reminiscent of breast carcinoma in its tendency to form ''comedonecrotic'' foci (*N*). **B**, High- power view of pleomorphic epithelial tumor cells forming a ''sieve-like'' cribriform pattern (**C**).

may be indistinct. The papillae can contain fibrovascular cores. Mitotic figures are negligible, and necrosis is minimal.

There have also been some reports suggesting that purely *intraductal* or *minimally invasive SDC* might be associated with an improved prognosis. The intraductal lesions may be seen in multiple, enlarged, adjacent ducts, resulting in a crowded appearance. In a purely intraductal tumor, the surrounding basement membrane and fibrous tissue of the large ducts are still intact and discernible.

High-grade SDC is one of the most aggressive salivary malignancies, and therefore should be treated with wide surgical excision combined with radiation therapy and possibly with chemotherapy. In addition, because of the high risk of cervical nodal metastases (59%), the neck should be treated with a lymph node dissection or by radiation. Barnes et al. compiled 104 cases of SDC from the literature, concluding that 33% of reported patients developed local recurrence and 46% developed distant metastasis. Sites for distant metastasis (in decreasing order of occurrence) include lungs, bones, liver, brain, and skin. Sixty-five percent of patients die of disease between 5 months and 10 years of diagnosis, usually within 4 years. The clinical course is characterized by distant metastases early in the course of the disease.

For *low-grade, in situ*, or *minimally invasive tumors*, wide resection with negative margins is recommended. Adjuvant therapy can be withheld, with watchful waiting. Estrogen receptor positivity is an infrequent finding, so antiestrogen adjuvant therapy is generally not an option.

Of the six patients reported by Delgado et al. with low-grade SDC, all were disease-free at 2 to 12 years of follow-up (mean, 7 years). Of the two patients in Brandwein et al.'s original report with long disease-free survival, one could be classified as having low-grade SDC and was disease free after 5 1/2 years of follow-up. To date, the low-grade variant appears to have a much better prognosis than the higher-grade variant. However, data on additional cases are necessary to confirm this trend.[288–294]

The imaging picture, although nonspecific, is that of a high-grade, infiltrating mass.

Adenosquamous Carcinoma and Basaloid Squamous Carcinoma

Adenosquamous carcinoma (ASC) and basaloid squamous carcinoma (BSC) are actually variants of mucosa-based squamous cell carcinoma (SCC), with a predilection, in the upper aerodigestive tract, for the base of the tongue and the hypopharynx.[295] However, clinically, radiologically, and even histologically they bear a resemblence to salivary tumors; therefore, they are included in this discussion.

Their clinical appearance is distinct from that of SCC. The typical white to red, firm, exophytic mucosal component seen in the usual SCC is lacking in BSC and ASC. Rather, these tumors appear to be entirely submucosal and possibly ulcerated, just like a typical salivary malignancy.

Histologically, BSC is made up of small cells with a high nuclear/cytoplasmic ratio forming glands, either with a cribriform and pallisading (hence the term *basaloid*) appearance reminiscent of either an AdCC or a small cell–type carcinoma. The strong tendency toward perineural infiltration seen in AdCC is lacking in BSC. The other tumor, ASC, produces typical glands of adenocarcinoma without the features of MEC, SDC, or other salivary malignancies. Carcinoma-in-situ of the overlying mucosa, which would be consistent with squamous origin, is focal. Carcinoma-in-situ is not seen in the mucosa overlying a salivary malignancy. Sometimes many histologic sections are necessary to reveal this; at other times, one may assume that any in-situ changes have been abolished by the mucosal ulceration. Keratin pearls are also focally seen in these tumors and again point to squamous differentiation.

The tumors reported to date generally have been aggressive, and survival has been dismal.[296–298] The question has been raised as to whether these tumors may represent more aggressive variants of SCC. It appears, though, that when stage, tumor site, and treatment are matched with those of typical SCC, the prognoses of both are similarly poor. One can conclude, however, that BSC and ASC rarely present as T1 or T2 tumors.[299, 300]

Sebaceous Neoplasms of Salivary Gland Origin

Salivary sebaceous neoplasia can be classified into five categories: sebaceous adenoma, sebaceous lymphadenoma,

Copyright © 2003, Mosby, Inc. All rights reserved.

sebaceous carcinoma, sebaceous lymphadenocarcinoma, and finally, sebaceous differentiation within other tumors. Although benign sebaceous differentiation of the parotid and submandibular glands is relatively common, primary sebaceous tumors are extremely rare here. Approximately 149 primary sebaceous salivary tumors have been reported: 24 sebaceous adenomas, 40 sebaceous lymphadenomas, 29 sebaceous carcinomas, 3 sebaceous lymphadenocarcinomas, and 53 other tumors with sebaceous differentiation.[301–303]

Sebaceous adenomas are rare benign tumors, comprising less than 0.1% of all salivary gland neoplasms and less than 0.5% of all salivary adenomas. The mean age at initial clinical presentation is 58 years (range, 22 to 90 years); the male:female ratio is approximately 1.6:1. Half of the tumors reported originated in the parotid, two were from the submandibular gland, and seven were at minor salivary intraoral sites. These tumors are commonly encapsulated or circumscribed. Microscopically, they are composed of sebaceous cell nests with minimal atypia, pleomorphism, and no invasive tendency. Sebaceous cells are characterized by their small nuclei and abundant clear cytoplasm. The cytoplasm has tiny bubbles that indent the nuclei, which aid in the distinction from other salivary clear cells. Sebaceous adenomas are cured by surgical excision.

Sebaceous lymphadenomas are rare benign tumors composed of well-differentiated nests of sebaceous glands within a lymphoid background. As with adenomas, there is minimal atypia and no invasion. These tumors appear to arise from sebaceous nests within lymph nodes, analogous to the pathogenesis of Warthin's tumors. Most tumors arise in older individuals, with no gender predominance. The vast majority of cases reported arose in the parotid gland. Sebaceous lymphadenomas are usually encapsulated and can be solid or cystic. Cheesy sebum is commonly found in many cystic tumors. Complete surgical excision is curative.

Sebaceous carcinoma is the malignant counterpart of sebaceous adenoma. These tumors have been reported with a biphasic age distribution with a peak incidence (the third decade and the seventh and eighth decades), with no gender predominance. The majority of cases arise in the parotid gland. Patients most frequently present with a painful mass, with varying degrees of facial nerve paralysis and occasional fixation to the skin. Tumors can be well circumscribed or locally infiltrating. Histologically, there is more pronounced pleomorphism and atypia than in the benign counterparts, and necrosis and perineural invasion can be seen. The treatment of choice is complete surgical excision with negative margins when feasible. Adjunctive radiation therapy is recommended for higher-stage and high-grade tumors. The overall 5-year survival rate is 62%.[304]

Sebaceous lymphadenocarcinoma is the malignant counterpart of sebaceous lymphadenoma and is the rarest salivary sebaceous tumor. Only three cases have been reported.[301, 302, 305] These carcinomas are locally invasive. Histologically, one sees foci of sebaceous lymphadenoma intermixed with pleomorphic carcinoma. These tumors should be treated with wide local excision, with possible adjuvant radiation therapy. Available follow-up information is minimal, but pulmonary metastasis did occur in one patient.

Primary Squamous Cell Carcinoma

Primary squamous cell carcinoma (SCC) of the parotid and submandibular glands is extremely rare. The reported incidence of primary parotid SCC ranges from 0.3% to 8.9% of all parotid tumors and from 2.1% to 11.4% of all submandibular gland tumors.[306, 307] The diagnosis of primary parotid SCC requires the exclusion of possible metastases from skin of the upper face and scalp or from the upper aerodigestive tract. Direct extension from the external auditory canal or overlying skin SCC must also be excluded, as well as other primary parotid tumors with squamous elements (high-grade MEC and SDC). The diagnosis of primary submandibular SCC requires the exclusion of direct extension from SCC of the floor of the mouth or extension from metastasis to level I lymph nodes. Rarely, SCC arises in an accessory parotid duct, sublingual gland, or minor salivary ducts. These latter tumors have not received any attention in the literature and are treated as routine upper aerodigestive tract SCCs. Primary parotid SCC is much more common than primary submandibular SCC.[308, 309] Male predominance is seen, and most cases occur after the fifth decade. An association with previous irradiation has been noted.

Histologically, salivary SCC is similar to other upper aerodigestive tract SCCs. However, in situ ductal dysplasia can be seen and is helpful in establishing the diagnosis of a primary neoplasm. On the other hand, its absence does not obviate the possibility of a primary tumor. The pathologic differential diagnosis includes MEC, SDC, carcinoma ex pleomorphic adenoma, and carcinoma ex benign lymphoepithelial lesion (the Eskimo tumor; see the next section). We have recently seen a case of primary parotid SCC with extensive perineural spread. This man presented with a dermal SCC and slight facial nerve palsy. The dermatologist erroneously concluded that the dermal SCC was unrelated to the facial nerve palsy and commenced Mohs surgery. The patient underwent this surgery for 3 days without achieving negative margins. He was transferred to our institution, where a parotidectomy and temporal bone resection were performed. A 1-cm SCC was present in the deep lobe of the parotid gland. Extensive perineural spread was found, which explained the dermal satellite as well as the failure to obtain clear resection margins. Of note, the surrounding skin did not reveal actinic damage, which speaks against the possibility of a dermal primary.

Patients have been treated either with primary surgery or with combined surgery and radiation therapy. Disease course and survival are dictated, as with almost all salivary tumors, by tumor stage and grade. Elective neck dissection appears to be warranted, as there is a significant rate of lymphatic spread. Gaughan et al. reported a 50% survival rate at 5 years, while the Memorial Sloan Kettering group reported survival at 5, 10, 15, and 20 years to be 21%, 15%, 13%, and 10%, respectively.[306, 307]

On imaging, these are infiltrating, often partially necrotic tumors (Figs. 39-138 to 39-142). Like other high-grade tumors, they tend to have low T2-weighted signal intensity on MR imaging.

Lymphoepithelial Carcinoma

The topic of BLEL was previously addressed in the section on ''Autoimmune Diseases.'' The tendency of

Copyright © 2003, Mosby, Inc. All rights reserved.

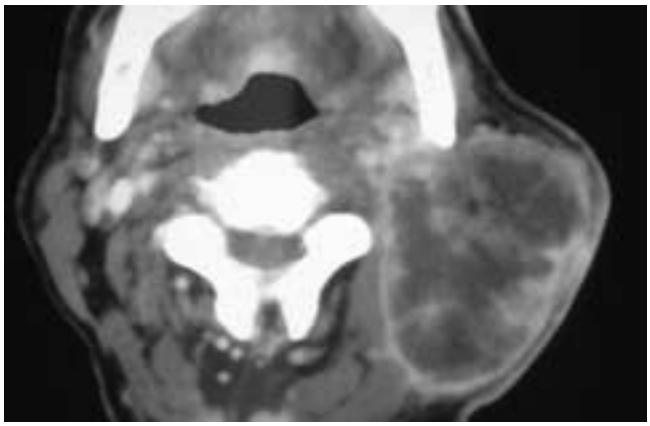

FIGURE 39-138 Axial contrast-enhanced CT scan shows a large necrotic mass in the left parotid gland. Some of the tumor borders are poorly defined. Clinically, this was a rapidly enlarging mass. This patient had an SCC of the parotid gland.

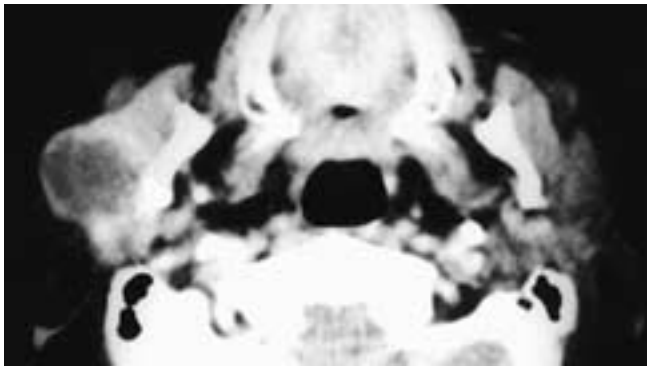

FIGURE 39-139 Axial contrast-enhanced CT scan shows a necrotic right parotid mass that has infiltrated the entire gland and the adjacent masseter muscle. This patient had an SCC of the parotid gland.

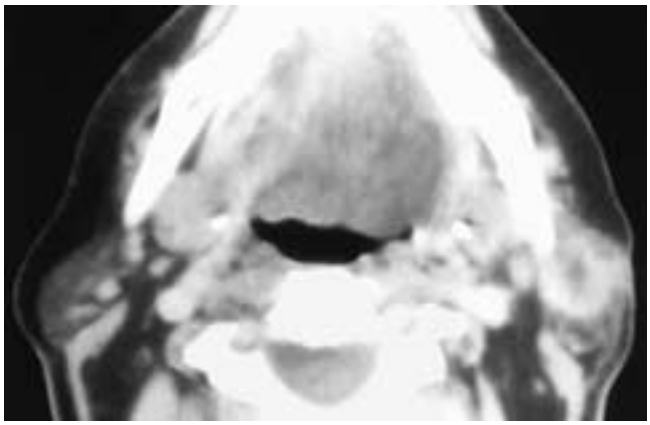

FIGURE 39-140 Axial contrast-enhanced CT scan shows a partially necrotic infiltrating mass in the left parotid gland in continuity with localized disease in the overlying skin. This patient had an SCC of the skin with extension to the parotid gland.

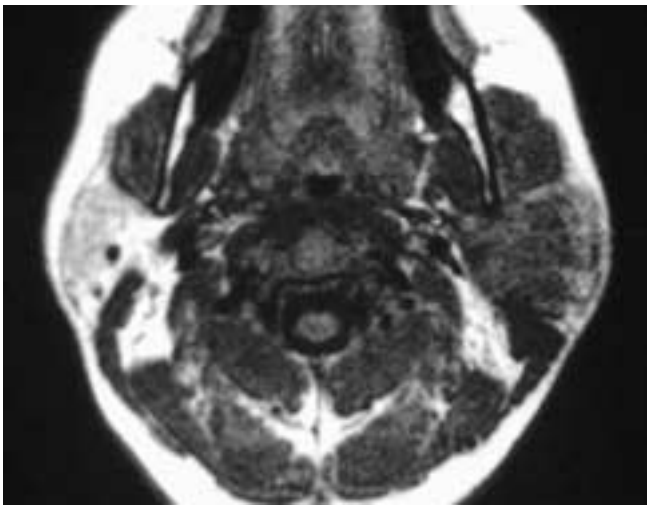

FIGURE 39-141 Axial T1-weighted MR image shows a poorly defined low signal intensity mass in the left parotid gland. The mass also had low T2-weighted signal intensity. The imaging appearance is that of a high-grade tumor. This patient had an SCC.

BLEL to undergo malignant transformation inspired the recommendation to change this diagnosis to myoepithelial sialoadenitis (MESA), a nosology that was never popularized. Most commonly, lymphoma will arise in BLEL in SS. The other possibility is that a carcinoma can develop; this is referred to as lymphoepithelial carcinoma (LEC), malignant lymphoepithelial lesion (MLEL), or undifferentiated carcinoma with lymphoid stroma (UCLS). Hilderman et al. initially described these tumors in 1962.[310]

The more colorful appellation ''Eskimo tumor'' is a reflection of the fact that this rarely encountered neoplasm has been described in patients from the Arctic region—Alaskan Eskimos, Aleuts, Greenland Inuits—as well as in oriental patients. LEC is very rare, accounting for 0.4% of

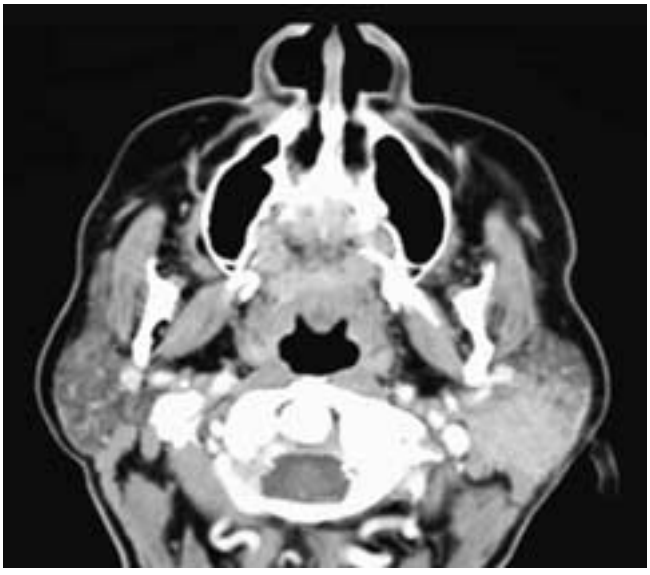

FIGURE 39-142 Axial CT scan shows an irregularly marginated, infiltrative mass in the left parotid gland. The tumor has started to extend beyond the parotid gland capsule. This patient had an SCC.

Copyright © 2003, Mosby, Inc. All rights reserved.

all salivary gland neoplasms in the Armed Forces Institute of Pathology Tumor Registry.[311] These tumors are histologically indistinguishable from the similarly named neoplasms of nasopharyngeal origin. Approximately 75% of reported cases have occurred in North American or Greenland Eskimos and southern Chinese individuals. A familial association has also been described, and the parotid gland is involved in over 90% of cases. The median age of affected persons is 39 years, and there is a 3:2 female predominance.[312–314]

These tumors may arise de novo, as well as within a BLEL. There is no association with SS or malignant lymphoma. As with LEC of nasopharyngeal origin, EBV has been strongly implicated in the oncogenesis of these tumors. In addition to elevated serum titers of anti-EBV antibodies in some patients, the EBV genome and mRNA have been demonstrated in tumor cells via in situ hybridization techniques. Most EBV-related tumors have been in patients of the Mongoloid race; however, occasional tumors in Caucasians may be associated with EBV. Conversely, epithelial cells in benign lymphoepithelial lesions appear negative for EBV infection.[315]

Patients present with an indurated mass of variable duration. Not uncommonly, the history is that of a long-standing mass with a recent rapid increase in size. Associated pain and discomfort are common, and facial nerve palsy is seen in up to 20% of cases. Cervical lymph node involvement is present in 41% of patients at presentation, although many of these nodal metastases are clinically occult.

Grossly, LEC may appear either encapsulated or infiltrative. Microscopically, these tumors are defined as undifferentiated carcinomas intimately intermingled with a dense lymphoid stroma. They are composed of sheets, strands, and/or irregular nests that may interconnect and are surrounded by a benign, dense lymphoid stroma. Tumor cells are large and polygonal or slightly spindled, with vesicular nuclei. Syncytial nests of tumor cells are typical, characterized by overlapping nuclei and indistinct cell borders. Perineural invasion is present in at half of LECs, and mitotic activity is variable. The differential diagnosis of LEC includes BLEL, metastatic tumors, and malignant lymphoma.

LEC is treated by complete surgical excision with negative surgical margins and adjuvant radiotherapy. Like LEC of nasopharyngeal origin, salivary LEC appears, at least in some cases, to be particularly radiosensitive. Given the high incidence of regional metastases, treatment of the cervical lymphatic chain with either surgery and/or radiotherapy is warranted in all cases. The prognosis correlates with the initial stage of disease. Advanced-stage disease has a poor prognosis. These tumors have been reported to have higher mitotic rates, necrosis, and greater anaplasia. Reported overall 5-year survival rates vary widely and are likely sullied by early reports of high mortality in patients who received suboptimal treatment. Five-year survival rates of 66% to 80% have been achieved with a combination of surgery and radiotherapy.[316–318] Nevertheless, up to 20% of patients develop local recurrence and/or distant metastases within 3 years of diagnosis.

Undifferentiated Carcinoma

Undifferentiated carcinomas of the salivary glands are rare tumors. Analogous to salivary adenocarcinoma, NOS, undifferentiated salivary carcinomas lack specific histologic features to allow for subclassification as other known salivary malignancies. Undifferentiated carcinomas are separated into two groups: small cell (undifferentiated) carcinoma and large cell undifferentiated carcinoma. LEC can be considered a subtype of undifferentiated large cell carcinoma, but it is unique in its resemblance to nasopharyngeal carcinoma, its association with EBV, and its marked predilection for southern Chinese and Eskimos. These features justify its distinct nosology.

Small Cell Undifferentiated Carcinoma

Small cell undifferentiated carcinoma has been reported to arise from major salivary glands (the majority within the parotid gland) and, less commonly, within the larynx, sinonasal cavity, oral cavity, pharynx, and upper esophagus. First reported by Koss et al. in 1972, it is remarkable for its resemblance to small cell carcinoma (oat cell carcinoma) of the lung.[319, 320] Importantly, the prognosis of salivary small cell carcinoma is better than the dismal one associated with pulmonary small cell carcinoma. Affected patients are usually in their fifth decade of life or older, and there is a slight male predominance.

Histologically, this tumor is composed of sheets, ribbons, and/or nests of tumor cells, which are as large as or slightly larger than lymphocytes. Appearing as small blue round cells, they have round to oval nuclei and scanty eosinophilic cytoplasm. Malignant features (infiltration, necrosis, pleomorphism, etc.) are seen. Vascular and perineural invasion are commonly found. Histologic, ultrastructural, and immunohistochemical studies have demonstrated the ductal and/or neuroendocrine characteristics of this tumor. The differential diagnosis includes tumors metastatic to the parotid gland such as pulmonary small cell carcinoma,[321] Merkel cell carcinoma from facial skin, metastatic BSC, malignant melanoma, and primary tumors such as solid-type AdCC and malignant lymphoma.

Wide local excision and lymph node dissection is indicated, and adjuvant chemotherapy and/or radiotherapy may be warranted. The 2- and 5-year survival rates for small cell carcinomas arising in the major salivary glands are 70% and 46%, respectively, while the rates for those arising in the larynx are only 16% and 5%, respectively.[320, 322]

Large Cell Undifferentiated Carcinoma

Large cell undifferentiated carcinoma (LCUC) represents a group of high-grade carcinomas that are too poorly differentiated to be classified as any other salivary carcinoma. As this tumor is extremely rare, little demographic data are available. The majority of patients with LCUC seen in consultation at the Armed Forces Institute of Pathology Tumor Registry presented in the seventh and eighth decades of life.[323] The majority of cases involve the parotid gland; up to 25% of cases arise in the submandibular gland. There is no gender predominance, and unlike LEC, there is no association with EBV and no racial predilection. Patients typically present with a rapidly growing, fixed parotid mass. Facial nerve palsy and palpable cervical adenopathy are common at presentation.

Microscopically, LCUC appears as a poorly differentiated carcinoma composed of large polygonal epithelioid tumor cells with brisk mitotic activity. There may be

Copyright © 2003, Mosby, Inc. All rights reserved.

ultrastructural evidence of squamous or glandular differentiation, but neuroendocrine differentiation is rare. The differential diagnosis includes metastatic tumors to the parotid gland (poorly differentiated adenocarcinoma, nasopharyngeal carcinoma, SCC, melanoma) and primary tumors such as poorly differentiated adenocarcinoma, MEC, and squamous carcinoma. LCUC can also occur as part of anaplastic progression of other tumors, either benign or malignant.

LCUC is best treated with wide local excision and aggressive radiotherapy. LCUC is aggressive: local recurrences, regional nodal metastases, and distant metastases develop in more than half of the patients, and over 60% of patients die of their disease.[324]

Hybrid Carcinoma

A salivary hybrid tumor is defined as a salivary tumor composed of two or more disparate patterns that are not included in each other's histologic realm. Tumors with features of both MEC and AdCC, or of ACC and cribriform SDC, are examples of hybrid tumors. There is presently no other nomenclature with which to adequately describe these types of tumors. The disparity inherent in hybrid tumors comes from the fact that either element differentiates toward distinctly different salivary elements: for example, excretory duct versus acini or excretory duct versus intercalated duct. Shared foci of phenotypic differentiation may be seen within salivary tumors; these cases would not be considered hybrid tumors. For instance, Grenko and colleagues have described AdCCs with foci of epithelial myoepithelial carcinoma–like differentiation, and vice versa. Both of these tumors are composed of ductal and myoepithelial elements, and presumably it is the degree of the local genetic statement that dictates the histologic phenotype. Therefore, these tumors would not be considered hybrid tumors, but rather variations in differentiation.[325, 326] By this definition, tumors with patterns of both canalicular adenoma and BCA, or AdCC and BCAC, would also not be considered hybrid tumors. Also, hybrid tumors would not show evidence of evolution from one entity to another. For instance, a tumor with features of MEC and pleomorphic adenoma is not a hybrid tumor and is better classified as MEC-ex-pleomorphic adenoma.

There are only a few acceptable examples of salivary hybrid tumors in the literature, and it has been estimated that they comprise less that 0.1% of all salivary tumors.[327–330] The reported combinations include parotid Warthin's tumor with sebaceous gland lymphadenoma; parotid cribriform SDC with ACC, sebaceous carcinoma with MEC, and palatal cribriform SDC with AdCC. More experience is necessary with salivary hybrid tumors before this group can be better characterized.

The treatment and prognosis should be based on the most poorly differentiated (highest-grade) component of the hybrid tumor.

Sialoblastoma

Salivary neoplasia is rare in children and adolescents. These patients comprise less than 3% of all patients with primary salivary tumors, and the majority of these tumors occur between the ages of 5 and 16 years. Tumors occurring in even younger patients are vanishingly rare. There is a 37% likelihood that a major salivary gland tumor in a child or adolescent will be malignant. By comparison, the rate of malignant tumors in the major salivary glands for all patients is generally between 15% and 20%. The most common tumors in the younger age group are pleomorphic adenoma, MEC, and ACC.

Sialoblastoma was first reported by Vawter and Tefft in 1966 as an *embryoma*.[331] Since that time, many terms have been used to describe this group of tumors, including congenital basal cell adenoma, basaloid adenoma, monomorphic adenoma, congenital hybrid basal cell adenoma–adenoid cystic carcinoma, low-grade basaloid carcinoma, adenoid cystic carcinoma, and sialoblastoma.[1, 4, 6] In his case report, Taylor drew an analogy between this tumor and others with a blastomatous appearance, suggesting the use of the term sialoblastoma.[332] To date, approximately 23 tumors have been reported that fit into the broad definition of sialoblastoma.[1–6]

Sialoblastomas arise almost exclusively in the major glands; over 80% involve the parotid gland and the remainder the submandibular gland. They are slightly more common in females than in males. Sialoblastomas arise almost exclusively in the perinatal period. Grossly, these tumors range up to 15 cm in greatest dimension[7] and are usually encapsulated or at least well circumscribed, but they may be locally infiltrative. Microscopically, these tumors try to recapitulate the embryonic development of the major salivary glands, with their histologic patterns reflecting the various stages of phenotypic expression and differentiation. Sialoblastomas frequently have variable histologic patterns within the same tumor and in different tumors. These patterns consist of solid multinodular nests and sheet-like collections of primitive-appearing epithelial cells with a basaloid morphology focally forming ducts and duct-like structures that may have peripheral palisading. The primitive nest-like pattern is frequently destructive and aids in separating this tumor from AdCC and BCA or BCAC. BCA does not exhibit destructive growth, while AdCC or BCAC grows in a less destructive pattern. Occasional acinar differentiation may also be seen. This latter feature helps to separate sialoblastoma from hamartoma, which usually has much more prominent acinar differentiation.

The nuclei in sialoblastoma are round to oval, usually with minimal to moderate amounts of cytoplasm. Nuclear pleomorphism is variable, as is the presence of nucleoli. Necrosis may be present and is more frequent in malignant tumors. Surrounding the nests and collections of epithelium is a loose mesenchyme that often has an embryonic appearance.[2] Mitoses are frequently found and may be plentiful; atypical mitoses are not usually seen. We have advocated the following grading subclassification scheme: well differentiated (grade 1) (including the basal cell subtype as well as tumors without cytologic atypia or invasive growth); moderately differentiated (grade 2) (including cases with invasive growth, greater cytologic atypia, and necrosis, but without definitive evidence of malignancy, i.e., no neural or vascular invasion or metastatic spread); and poorly differentiated tumors (grade 3) (which have definite evidence of malignancy).

Complete surgical excision with negative margins is the treatment of choice. Adjuvant chemotherapy and radiother-

Copyright © 2003, Mosby, Inc. All rights reserved.

apy have been tried; however, the limited number of cases hampers assessment of these modalities.[1, 4] The limited number of cases and short follow-up of reported cases also preclude drawing definitive conclusions about the tumor's biologic behavior; however, published data do indicate that sialoblastoma can be locally aggressive and malignant. Five of the 23 reported cases have recurred; several recurred multiple times or patients had local persistence of disease, and two patients developed regional lymph node metastases.[1, 4, 7, 10] Progression of tumor grade with recurrence and increasing mitotic rates has been seen.[4] One patient had four recurrences, with inoperative tumor extending into the skull at 43 months.[7] Low-grade tumors appear to be less aggressive than higher-grade tumors, with only one recurrence in eight tumors.[1]

MR imaging in one patient showed that the tumor was isointense with muscle on T1-weighted images, it had a high-intermediate signal intensity similar to that of fat on T2-weighted images, and it enhanced sparsely and nonhomogeneously (Fig. 39-143).[331–341]

Sclerosing Adenosis

Sclerosing polycystic adenosis is a recently described rare pseudoneoplastic reactive inflammatory process somewhat similar to sclerosing adenosis of the breast. It was first reported in 1996 by Smith and colleagues, who described a series of nine patients from the Armed Forces Institute of Pathology.[342] Since this initial report there have been only two other series, bringing the total number of cases in the literature to 18.[2, 3] Patients ranged in age from 12 to 63 years (mean, 29.4 years), with a male : female ratio of 2 : 7. Sixteen cases involved the parotid gland and two affected the submandibular gland. Presenting symptoms ranged from 10 days to 2 years. Patients typically presented with a slow-growing mass; three, in addition, had pain or a tingling sensation.

Grossly, most tumors were firm or rubbery, well circumscribed, and embedded in a normal salivary gland; five were multinodular. Tumors ranged in size from 1 to 7 cm in greatest dimension and had cut surfaces that were pale and glistening; a few had tiny visible cysts 1 to 2 mm in diameter. They were unencapsulated and consisted of multiple densely sclerotic, irregularly defined lobules composed of abundant hyalinized collagen surrounding areas of ductal cystic change. Hyperplasia of ductal and acinar elements with areas of apocrine-like metaplasia were typical. In addition, mucin-containing cells, squamous cells, and ballooned cells occasionally lined ducts and cystic spaces. The intraluminal epithelial proliferation infrequently formed a cribriform pattern, some of which was associated with nesting basement membrane–like material, similar to collagenous spherulosis of the breast. The differential diagnosis consists of polycystic (dysgenetic) disease, sclerosing sialadenitis, and carcinoma.

Until more cases with longer follow-up periods are available, treatment should consist of complete surgical excision with good surgical margins. Follow-up information is available in the Armed Forces Institute of Pathology series for six cases (mean, 43 months; range, 7 months to 9 years) and for two of the cases reported by Donath and Seifert.[3, 334]

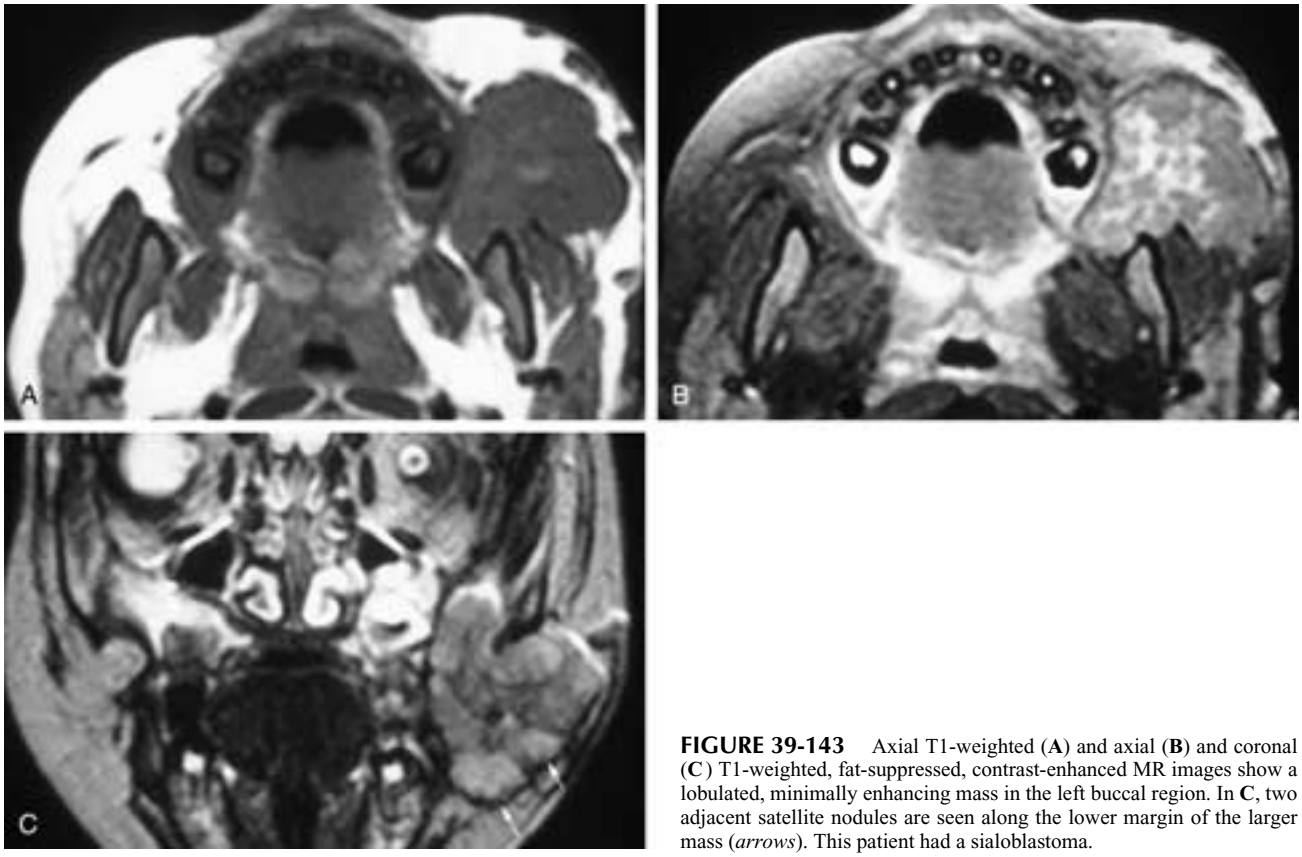

FIGURE 39-143 Axial T1-weighted (**A**) and axial (**B**) and coronal (**C**) T1-weighted, fat-suppressed, contrast-enhanced MR images show a lobulated, minimally enhancing mass in the left buccal region. In **C**, two adjacent satellite nodules are seen along the lower margin of the larger mass (*arrows*). This patient had a sialoblastoma.

VIEW IMAGE

Copyright © 2003, Mosby, Inc. All rights reserved.

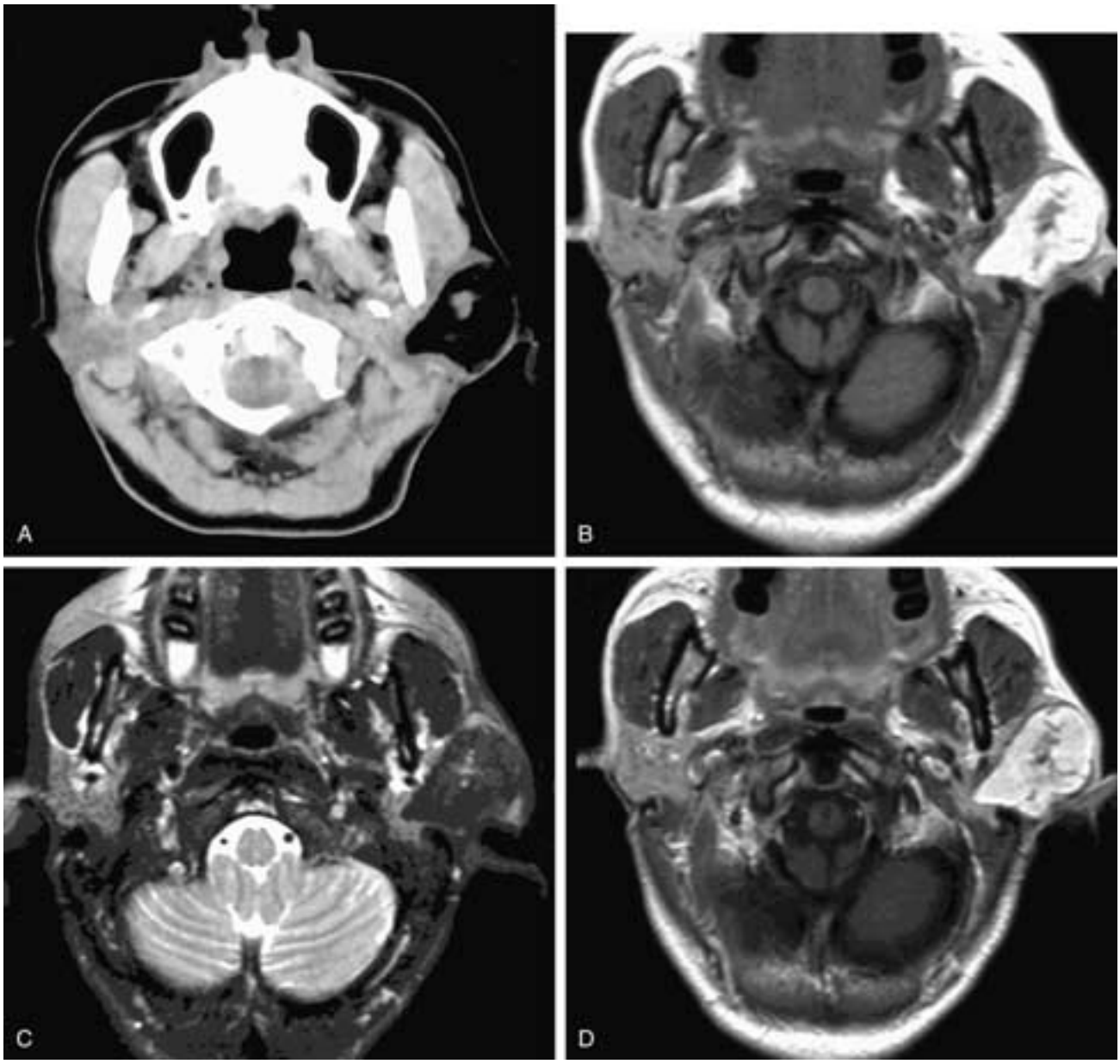

VIEW IMAGE

FIGURE 39-144 Axial CT scan (**A**) shows a fat attenuation mass in the left parotid gland and the adjacent soft tissues. Axial T1-weighted (**B**), T2-weighted (**C**), and T1-weighted, fat-suppressed, contrast-enhanced (**D**) MR images show a mass with a high T1-weighted and a low T2-weighted signal intensity. There is faint enhancement. Within the mass are structures of low T1-weighted and high T2-weighted signal intensity. These structures do not enhance. This patient had sclerosing adenosis.

To date, four cases have recurred; one patient had a single recurrence at 4 years 8 months, a second had multiple recurrences over a 9-year period,[1] and two patients had recurrences at 8 years.[3] The other two patients reported in Donath and Seifert's series were alive without evidence of disease at unknown lengths of time.[3] In addition, none of the cases reported by Batsakis have recurred.[2, 343]

Radiographically, these tumors can appear similar to other benign solid and cystic salivary tumors. However, we have recently seen a case with a prominent adipose component mimicking a parotid lipoma, albeit with an atypical radiographic cystic component (Fig. 39-144).[342–344]

Adenocarcinoma, Not Otherwise Specified

Despite the scores of well-recognized diagnostic categories of salivary tumors, some tumors persist in eluding current classsification schemes. As some type of gland formation is common to most of these tumors, the group is referred to as adenocarcinoma, not otherwise specified (NOS). These tumors usually are painful, rapidly enlarging masses, but occasionally they may be painless, slow-growing swellings. In 1982, Spiro et al. reported on 204 cases of unclassifiable salivary adenocarcinomas, that is, adenocarcinoma NOS, which represented about 9% of their total salivary cases. The majority of tumors occur at minor

Copyright © 2003, Mosby, Inc. All rights reserved.

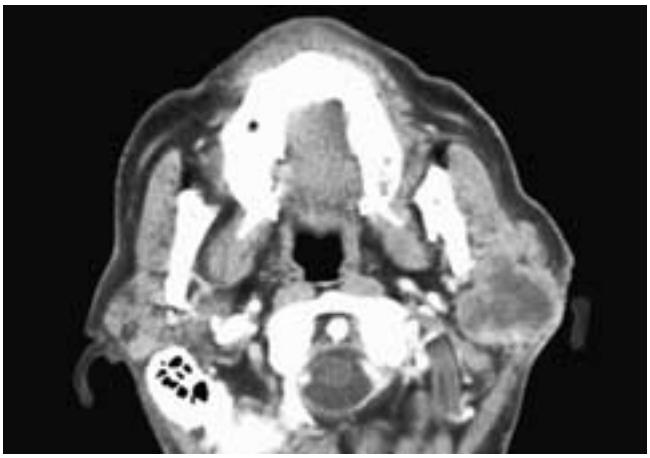

VIEW IMAGE

FIGURE 39-145 Axial contrast-enhanced CT scan shows a necrotic, ill-defined mass in the left parotid gland. This patient had an adenocarcinoma.

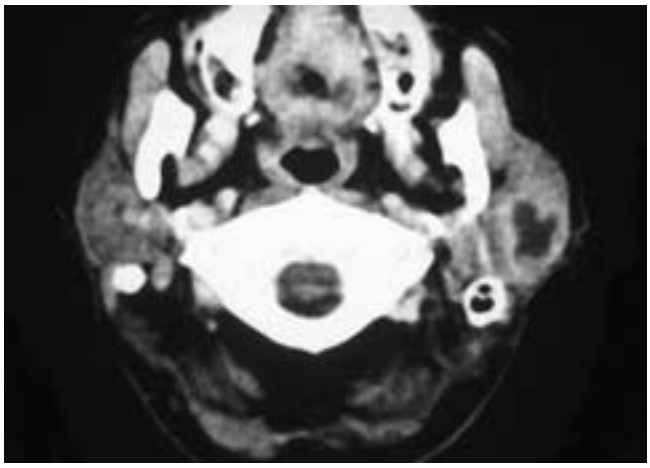

VIEW IMAGE

FIGURE 39-146 Axial contrast-enhanced CT scan shows a necrotic, irregularly walled, invasive tumor in the left parotid gland. This patient had an adenocarcinoma.

salivary gland sites (68%), followed by the parotid gland (28%), and the submandibular gland (4%). A review of 881 cases of adenocarcinoma NOS from the Armed Forces Institute of Pathology Tumor Registry revealed an almost opposite distribution of cases: 50% occurred in the parotid gland, 12% in the submandibular and sublingual glands, and 38% in minor salivary gland sites, most commonly the palate. The authors acknowledged that not all 881 cases were re-reviewed and that perhaps some could be reclassified currently as PLGA or BCAC. However, due to the relative rarity of these two tumors, they believed that the overall statistics would not have changed significantly.[345]

Adenocarcinoma can be subclassified according to cytologic and architectural grade: grade I tumors are circumscribed and minimally invasive, with mild features of pleomorphism; grade III tumors are more solid and pleomorphic, with a higher mitotic rate; and grade II tumors can be found between these two extremes. Tumor stage and site are important predictors of survival, as determined by the Memorial study.[345] The 5-, 10-, and 15-year survival rates for low-grade tumors were found to be 92%, 90%, and 82%, respectively. The 5-, 10-, and 15-year survival rates for high-grade tumors were predictably poorer: 49%, 42%, and 33%, respectively. Tumor site, as a reflection of tumor resectibility, was also an important prognosticator: patients with tumors of the paranasal sinuses had poorer survival. The 5-, 10-, and 15-year survival rates were 21%, 15%, and 10%, respectively. The Memorial data, albeit two decades old, represent the largest study correlating grade and stage with prognosis. However, because of improvements in surgical techniques, radiotherapeutic techniques, and chemotherapy protocols, one could hope for an improvement in survival even for patients with high-grade tumors. As more and more new salivary tumors are being recognized and categorized, the pool of NOS tumors may shrink, while the list of established salivary tumors will continue to grow. Radical surgery is the treatment of choice, and the imaging characteristics are those of a high-grade cellular infiltrating tumor (Figs. 39-145 to 39-150).[8, 345–349]

Carcinoma Metastatic to the Salivary Glands

Metastasis to the major salivary glands or adjacent lymph nodes is a frequent occurrence, accounting for one third of all metastases to the head and neck and comprising 4% of

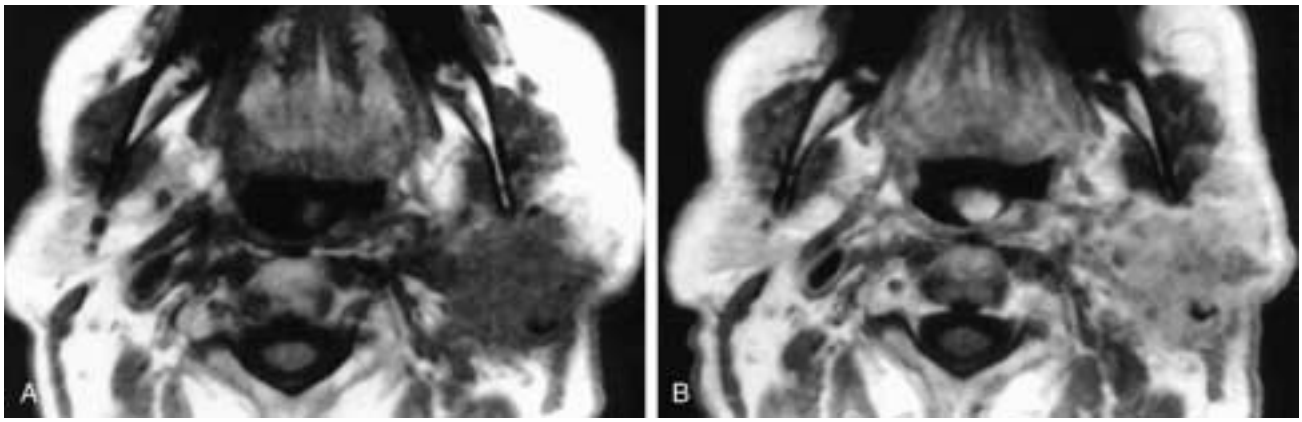

VIEW IMAGE

FIGURE 39-147 Axial T1-weighted (**A**) and T1-weighted, contrast-enhanced (**B**) MR images show a poorly defined infiltrating mass in the left parotid gland that has irregular enhancement. The tumor had low signal intensity on T2-weighted images. This patient had an adenocarcinoma.

Copyright © 2003, Mosby, Inc. All rights reserved.

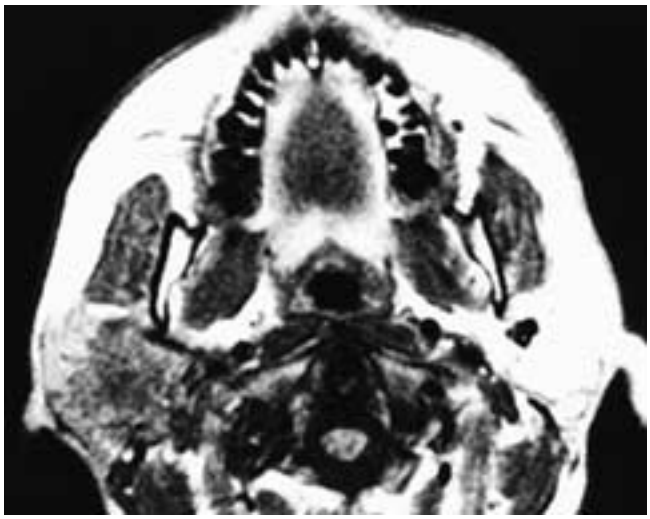

VIEW IMAGE

FIGURE 39-148 Axial T1-weighted MR image shows an infiltrating mass in the deep portion of the right parotid gland. The mass has low to intermediate T2-weighted signal intensity. This patient had a high-grade adenocarcinoma.

salivary gland neoplasms in various series.[350, 351] The parotid glands contain 3 to 32 (average, 20) intraglandular lymph nodes connected by a plexus of lymphatics that drain the ipsilateral facial skin of the upper face and midface. In contrast, the submandibular and sublingual glands proper do not contain any intraparenchymal lymph nodes. Approximately 90% of metastases involve the parotid region; the remainder involve the submandibular gland. Metastases to the sublingual gland have not been reported to date. SCC and malignant melanoma are the most common neoplasms metastasizing to the major salivary gland area, accounting for 60% and 14.5% of diagnoses, respectively. The vast majority (85% to 88%) of parotid metastases from known primaries originate in the head and neck, and the majority of them (84% to 89%) arise from the skin. Regarding parotid metastases from known nonhead and nonneck primary sites, tumors most commonly originate from the lung, kidney, and

FIGURE 39-150 Frontal view of a right parotid sialogram shows an amorphous pooling of contrast material within a necrotic high-grade parotid tumor. Parotid-lymphatic backflow occurs to the lower cervical lymphatic ducts. This patient had an adenocarcinoma. (From Som PM, Shugar JM. Parotolymphatic backflow: a new sign of malignancy. Ann Otol Rhinol Laryngol 1981;90:64–66.)

VIEW IMAGE

breast. Other primary sites include, in decreasing order of incidence, the colorectum, prostate, skin, stomach, uterus, and pancreas. The relationship between submandibular metastases and primary sites of malignancies is the opposite of that seen in the parotid gland. The majority (85%) of

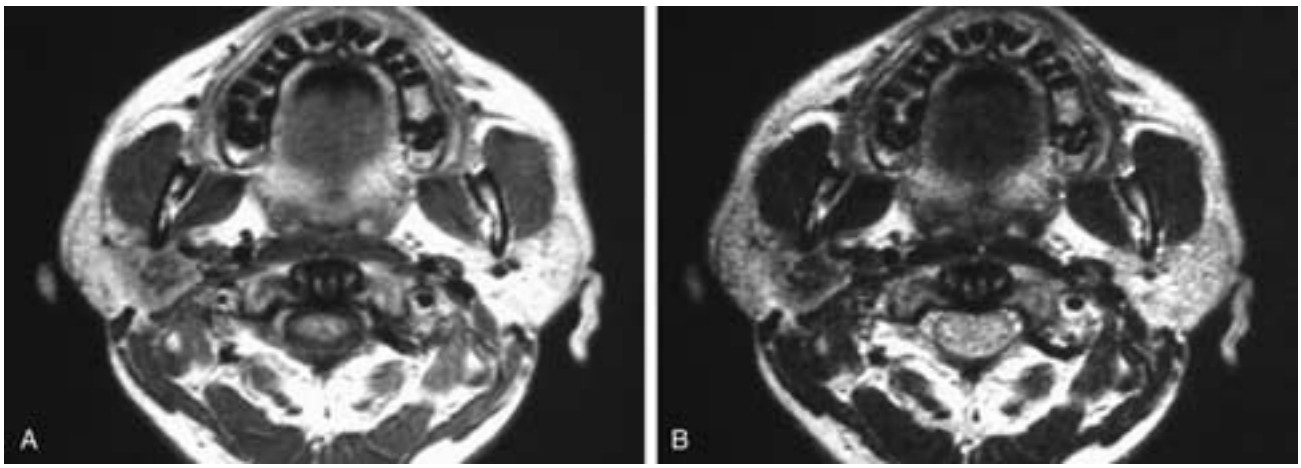

VIEW IMAGE

FIGURE 39-149 Axial proton density (**A**) and T2-weighted (**B**) MR images show a poorly defined mass in the deep portion of the right parotid gland. The mass had low signal intensity on all imaging sequences. This patient had an adenocarcinoma.

Copyright © 2003, Mosby, Inc. All rights reserved.

malignancies metastasizing to the submandibular gland originate in infraclavicular sites, most commonly the breast, kidney, and lung. The most frequent age at diagnosis for metastases to the major salivary glands is the seventh decade, and there is an approximately 2:1 male:female ratio. In most cases, the primary tumor is known; however, occasionally the metastasis is the initial presentation of disease and, rarely, bilateral involvement may be seen.[352, 353]

Appropriate treatment consists of complete surgical resection and cervical lymph node dissection if there is clinical or radiographic evidence of adenopathy. The addition of adjuvant radiotherapy is controversial, with varying recommendations. The primary location and tumor type will influence final therapeutic recommendations. Postoperative radiation therapy may also be warranted. It is difficult to generalize about the prognosis due to the different tumor types and variable primary locations encountered. For most tumors, metastatic disease implies a poorer prognosis for a given primary tumor. If the metastasis is from an infraclavicular primary and is only one of many metastatic deposits, the prognosis is usually poor. However, if the metastasis is only a single focus, local control of the primary and the metastasis is possible.

The prognosis for facial skin primaries that have metastasized to the parotid gland is better if the metastasis is confined to lymph nodes than if it infiltrates the parotid parenchyma (8% vs. 79% local recurrence rates).[354] The 5-year local disease control rate for facial squamous carcinoma metastatic to the parotid gland is 82%, and the overall 5-year survival is 54%.[355] Patients with head and neck mucosal primaries have a very poor prognosis, with only 1 of 10 patients alive and disease free at 5 years.[356] Ironically, patients with malignant melanoma of the parotid gland have a better prognosis if no primary site is found.[357] In a series of 19 patients, no primary tumor was found in 6 patients. Five of them were disease free (mean, 4.2 years; range, 14 months to 7.5 years), and one patient died of disease at 17 months. Extraparotid primary melanomas were found in the other 13 cases (10 cutaneous and 3 mucosal: sinonasal tract and occular). None of these patients were disease free at follow-up: nine died of melanoma (mean, 2.6 years; range, 10 months to 5 years), and three had metastatic disease (mean, 4.3 years, range, 3 to 6 years); only one patient was disease free at 2 years.

If a metastasis to the parotid gland is a solitary mass, it is indistinguishable from a primary high-grade salivary tumor. The typical imaging appearance of metastases to the parotid gland is that of multiple, invasive masses, often with some element of necrosis (Figs. 39-151 to 39-156).

Nonepithelial Tumors

Nonepithelial tumors of the salivary glands represent less than 5% of all salivary gland neoplasms. However, in children, they may comprise over 50% of the lesions.[7, 8] The only tumors of statistical consequence are hemangiomas, lymphangiomas, lymphomas, neurogenic lesions, lipomas, and sarcomas.

Hemangioma

Hemangiomas of the parotid gland represent 1% to 5% of all salivary gland tumors, but they are the most common salivary gland neoplasm in children.[7, 8, 358] Submandibular gland involvement is rare, and in these cases it has been difficult to distinguish between tumors that arose within the gland and those that arose in the soft tissues adjacent to the gland. Hemangiomas can be classified as capillary (composed of small capillary-sized vessels with plump endothelial cells) or cavernous (composed of large, thin-walled vessels with flattened endothelial cells). Congenital capillary hemangioma is the predominant tumor in the first year of life, representing 90% of parotid gland tumors in this age group. This lesion is usually discovered shortly after birth; it is unilateral, compressible, and soft. Rapid enlargement can occur and a bluish coloration can be seen in the overlying skin, especially when the infant is crying. There also may be an associated hemangioma in the overlying skin. These nonencapsulated and lobulated lesions are more common in girls than in boys. The differential diagnosis includes cystic lymphangioma and the rare malignant hemangioendothelioma, both of which can be distinguished histologically. If possible, surgery is to be avoided until adulthood since many of these tumors may regress spontaneously.[7] In addition, there are no known instances of malignant transformation of this lesion.[358] Cavernous hemangiomas occur in older children and adults, with most patients being older than 16 years of age. These tumors tend to be well circumscribed and involve the extralobular parotid tissues. Surgery is the treatment of choice since spontaneous regression is unlikely.[7]

Capillary hemangiomas (or vascular malformation: see Chapter 41 for a discussion of an alternate terminology) appear to be very rare in the parotid gland. For this reason, their characteristics have not been reported in sufficient numbers to allow any general conclusions.

On CT these tumors enhance, are often lobular in contour, may be seen to extend to the overlying skin, or have phleboliths within the tumor tissues (Figs. 39-157 to 39-159). Often, the mass effect of the tumor on the surrounding soft tissues is relatively small, reflecting the soft nature of these lesions. On MR imaging, the lesion can have sites of high signal intensity on both T1-weighted and T2-weighted images, which are caused by prior hemorrhage and slow flow. There also can be vascular flow voids, and the majority of the tumor has a low to intermediate, nonhomogeneous signal intensity on T1-weighted and proton density sequences. There usually is a high T2-weighted signal intensity (Figs. 39-160 and 39-161).

Lymphangioma

Lymphangiomas are benign tumors composed primarily of lymphatic vessels. These tumors are classified into three pathologic groups: lymphangioma simplex, cavernous lymphangioma, and cystic lymphangioma or cystic hygroma. Histologically, lymphangiomas consist of thin-walled spaces with flattened endothelium, without a significant erythrocyte component, as is seen in cavernous hemangiomas. All three pathologic types may coexist within the same tumor. Most of the lesions found in the head and neck are cystic hygromas. Lymphangiomas represent 5% to 6% of all benign tumors of infancy and childhood, with 50% to 60%

Copyright © 2003, Mosby, Inc. All rights reserved.

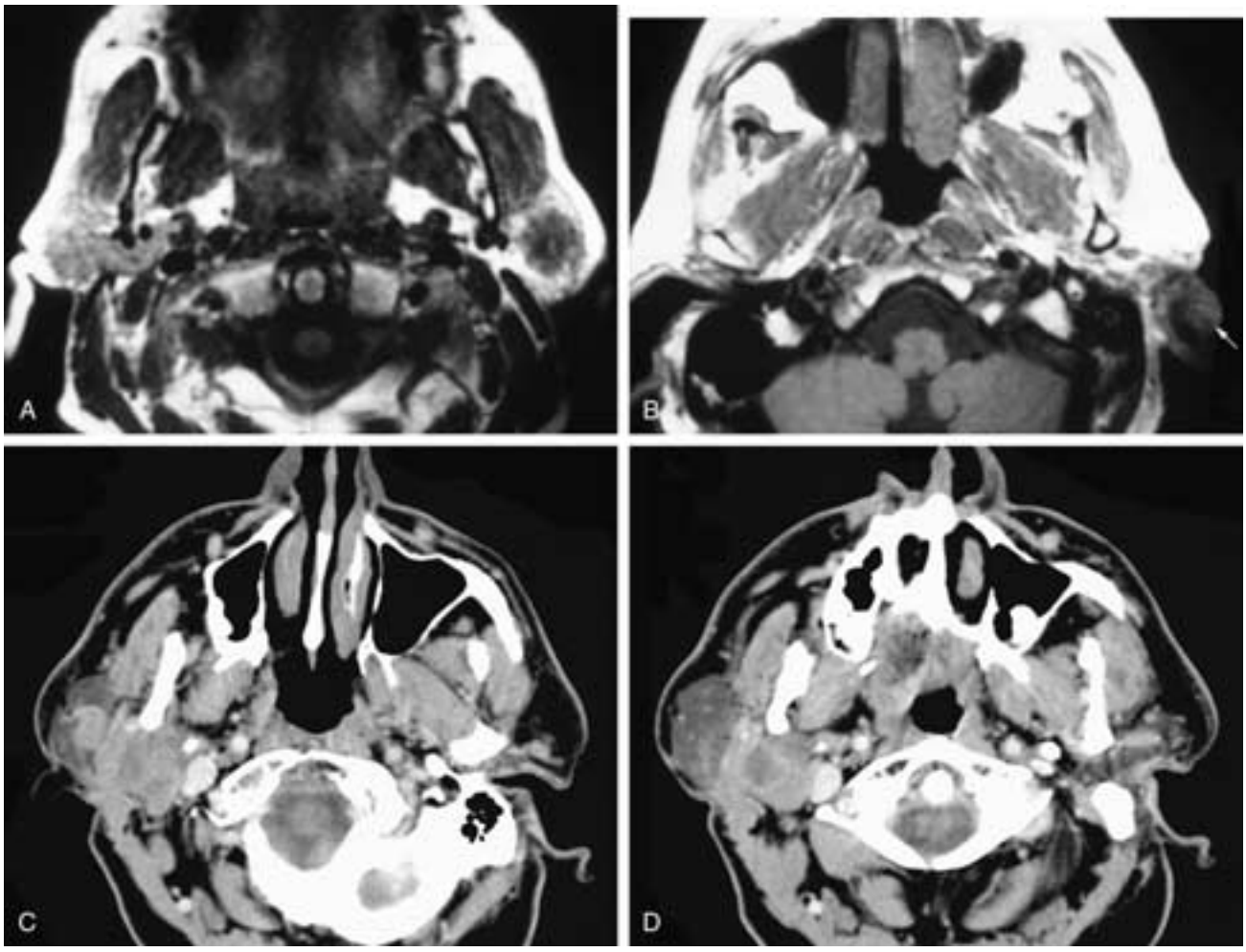

VIEW IMAGE

FIGURE 39-151 Axial T1-weighted MR images through the parotid gland (**A**) and the pinna of the left ear (**B**). There is a poorly defined low signal intensity mass in the left parotid gland. This mass also had low T2-weighted signal intensity. The imaging findings suggest a high-grade tumor. In **B**, there is a mass in the left ear pinna (*arrow*). This patient had metastatic disease to the parotid gland from a primary SCC of the ear. Axial contrast-enhanced CT scans (**C, D**) on another patient show multiple poorly defined masses in the right parotid gland. Some lesions are necrotic. This patient had metastatic SCC from a scalp primary.

VIEW IMAGE

FIGURE 39-152 Axial contrast-enhanced CT scan shows a necrotic mass with an enhancing rim within a swollen left ear pinna. The left parotid gland is dense and enlarged, and there are cellulitis-type changes overlying the gland. This patient had an abscess in the left pinna (secondary to an ear piercing) with cellulitis and parotitis. Compare this scan to Figure 39-151.

of the cases being present at birth. Between 80% and 90% of patients are diagnosed by the age of 2 years. This age range corresponds to the period of greatest lymphatic growth. It is uncommon for cystic hygromas to be reported in adults.[19, 187, 358–360]

Most commonly, these lesions arise in the posterior triangle of the neck. They can spread to invade the parotid and submandibular glands, muscles, and vessels. Most tumors are painless, soft or semifirm masses, and some fluctuation in size is common. Sudden enlargement is associated with infection or hemorrhage. Facial nerve paralysis can occur either secondary to nerve compression by a parotid lesion with hemorrhage or secondary to an acute otitis media caused by a lesion obstructing the eustachian tube.[360]

Cystic hygromas rarely occur in adults and usually develop as a solitary cyst either in the submandibular triangle or in the posterior triangle of the neck. Whether these lesions represent the congenital type of lymphangioma or a posttraumatic lesion is still unresolved.[187]

On CT, these lesions are usually cystic masses filled with homogeneous low-attenuation (10 to 20 HU) material. The

Copyright © 2003, Mosby, Inc. All rights reserved.

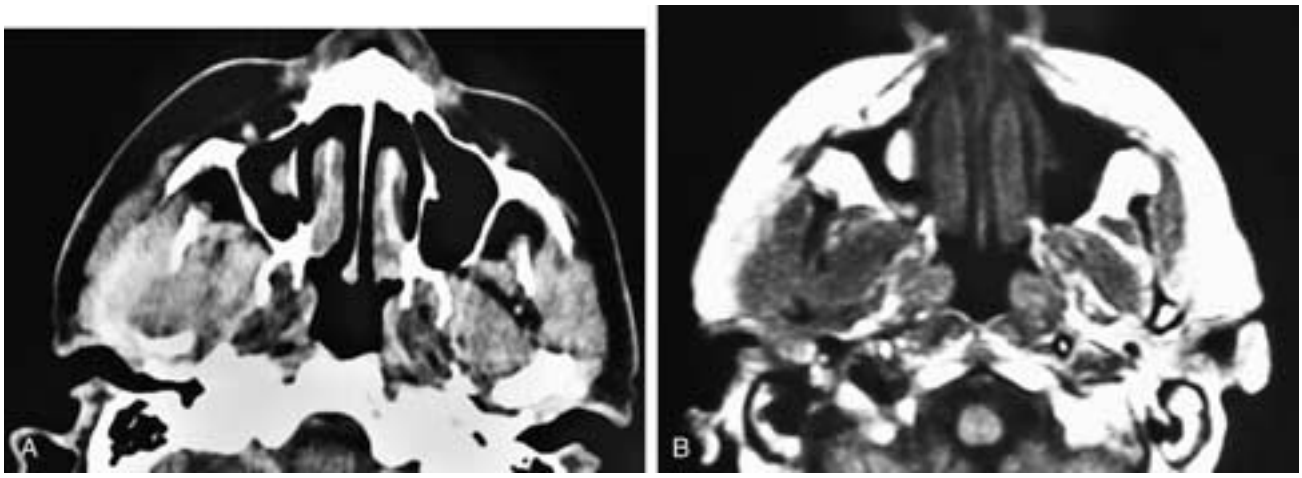

VIEW IMAGE

FIGURE 39-153 Axial contrast-enhanced CT scan (**A**) shows an infiltrating mass in the right infratemporal fossa, parotid gland, and parapharyngeal space. The mass has eroded the head of the mandible. In **B**, an axial proton density MR image, the mass has low to intermediate signal intensity. This patient had metastatic lung carcinoma.

cysts usually have thin walls that are often not clearly seen on the images. Most commonly there are multiple intercommunicating cystic components, although solitary cysts can occur, usually in adults in the submandibular triangle and deep to the sternocleidomastoid muscle (Figs. 39-162 and 39-163). Areas of higher attenuation within the cysts usually correspond to sites of hemorrhage.[360] Septation can occur within cysts even if they have not been previously aspirated. Infection is identified by an enhanced thickening of the cyst wall and infiltration of the adjacent soft tissues. In cases of multiple repeated infections, the attenuation of the cyst contents may approach that of muscle.

On MR imaging, the dominant water content of the cysts is revealed in their signal intensities, which are low on T1-weighted images and high on T2-weighted images. The multiple, intercommunicating nature of the cysts and any fluid-fluid levels are best seen on MR imaging, especially on T2-weighted scans (Figs. 39-163 and 39-164).

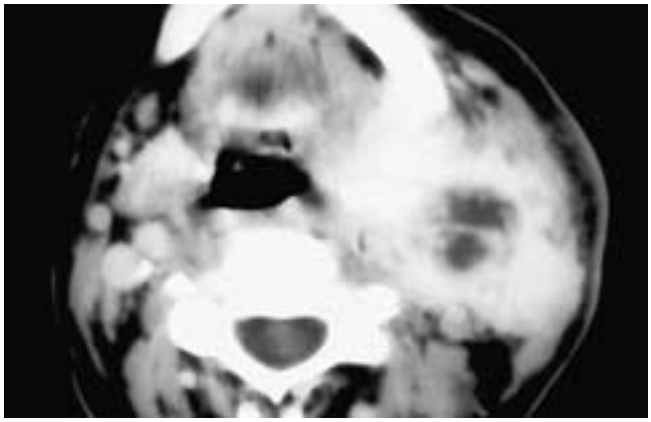

VIEW IMAGE

FIGURE 39-154 Axial contrast-enhanced CT scan shows a large, infiltrating, necrotic mass that invades the left parotid gland, adjacent neck soft tissues, and the submandibular gland. There are central areas of necrosis. This patient had metastatic breast carcinoma.

Lymphoma

Primary lymphoma of the salivary glands is a rare entity. The parotid gland is affected in 80% of the reported cases, and the submandibular gland is involved in nearly 20%. There are only isolated reports of primary lymphoma in the sublingual gland and the minor salivary glands. These lymphomas are classified as MALT (mucosa-associated lymphoid tissue) lymphomas in the classification schema (see Table 6-2). In the series of 33 patients with primary parotid lymphomas reported by Barnes et al., there were 15 men and 18 women aged 26 to 100 years (mean, 66 years). Patients invariably presented with enlarging painless masses. Autoimmune disease was associated with seven (21%) of these patients.[361]

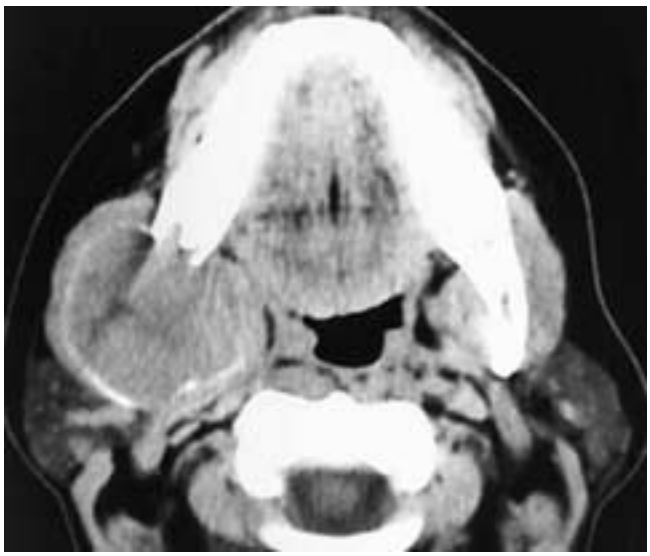

FIGURE 39-155 Axial CT scan shows an expansile and destructive mass of the right mandible, which clinically simulated a parotid tumor. This patient had metastatic meningioma. (From Som PM, Sacher M, Strenger SW, et al. ''Benign'' metastasizing meningiomas. AJNR 1987;8: 127–130.)

VIEW IMAGE

Copyright © 2003, Mosby, Inc. All rights reserved.

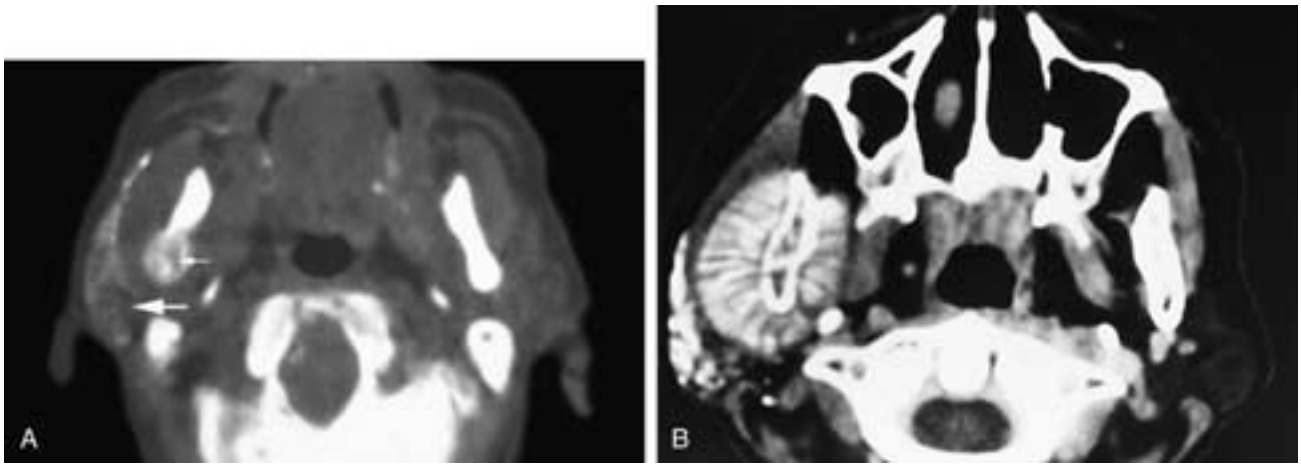

VIEW IMAGE

FIGURE 39-156 Axial CT-sialogram scan (**A**) shows an invasive tumor of the right parotid gland (*large arrow*) and a destructive lesion of the posterior right mandible (*small arrow*). This patient had metastatic lung carcinoma. Axial CT-sialogram scan (**B**) shows a normal contrast-filled right parotid gland. The right mandible is expanded by a lesion that causes an aggressive periosteal reaction. The resulting mass was clinically interpreted as a parotid tumor. This patient had a plasmacytoma.

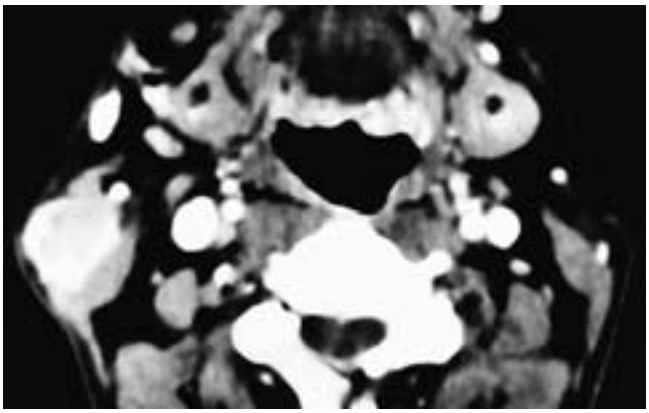

FIGURE 39-157 Axial contrast-enhanced CT scan shows an enhancing, benign-appearing mass in the right parotid gland. This patient had a hemangioma.

VIEW IMAGE

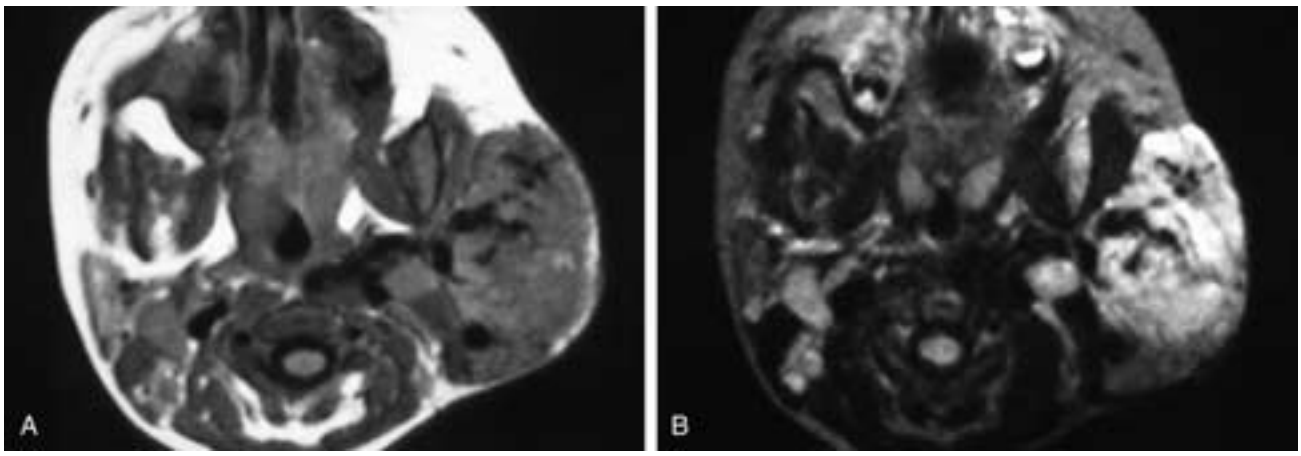

VIEW IMAGE

FIGURE 39-158 Axial T1-weighted (**A**) and T2-weighted (**B**) MR images show a soft-tissue mass in the left parotid gland. The lesion has a low T1-weighted and a high T2-weighted signal intensity, and there are large vascular flow voids within the lesion. This patient had a hemangioma.

Copyright © 2003, Mosby, Inc. All rights reserved.

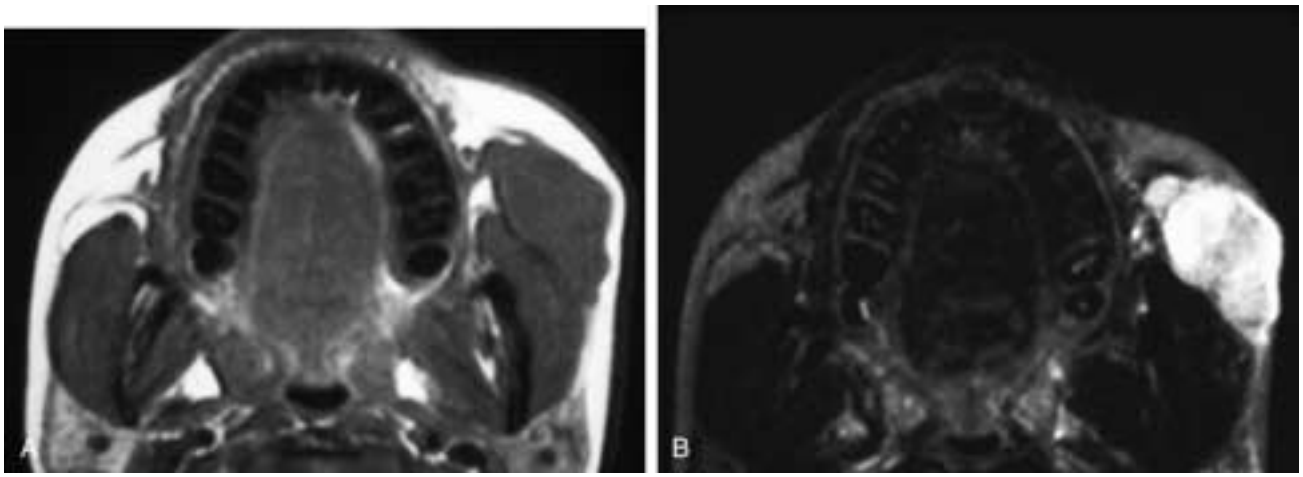

VIEW IMAGE

FIGURE 39-159 Axial T1-weighted (**A**) and T2-weighted (**B**) MR scans show a soft-tissue mass in the left cheek overlying the masseter muscle. There is slight nonhomogeneity on the T2-weighted image. Despite its size, there is relatively little mass effect, suggesting a soft lesion. Clinically, this mass was thought to arise in the parotid gland of this child. This patient had a hemangioma.

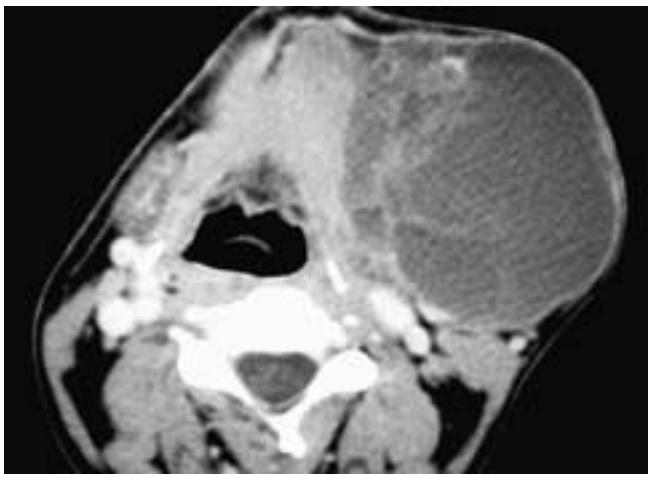

VIEW IMAGE

FIGURE 39-160 Axial CT scan shows a large cystic mass with slightly unsharp margins in the left submandibular gland. This patient had a cystic lymphangioma.

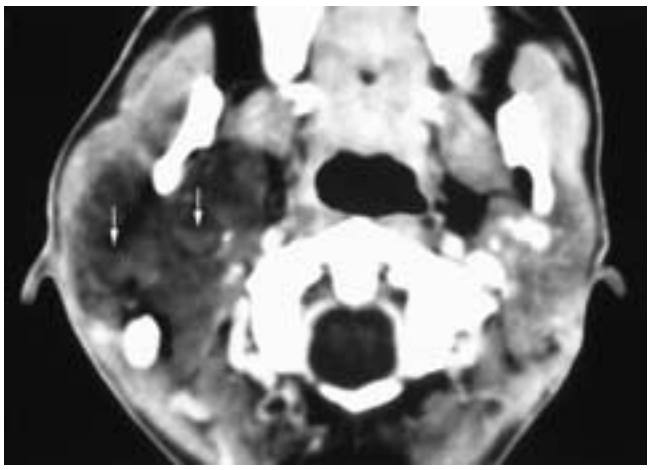

VIEW IMAGE

FIGURE 39-161 Axial contrast-enhanced CT scan through the parotid gland shows a low-attenuation, partially cystic mass in the right parotid gland. The lesion extends into the parapharyngeal space and caudally into the neck. Fluid-fluid levels are present within the mass (*arrows*). This child presented with a parotid mass and facial nerve paresis. The patient had a cystic lymphangioma of the parotid gland, with hemorrhage compressing the facial nerve.

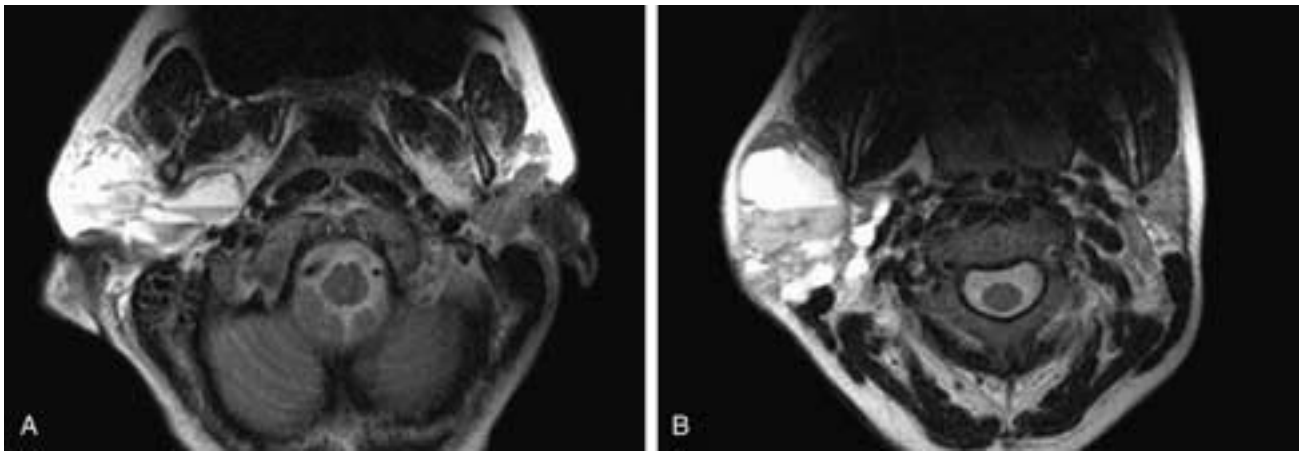

VIEW IMAGE

FIGURE 39-162 Axial T1-weighted, fat-suppressed, contrast-enhanced MR images (**A**, **B**) show a multicystic mass within the right parotid gland. Within the cysts there are fluid-fluid levels. This patient had a lymphangioma of the parotid gland.

Copyright © 2003, Mosby, Inc. All rights reserved.

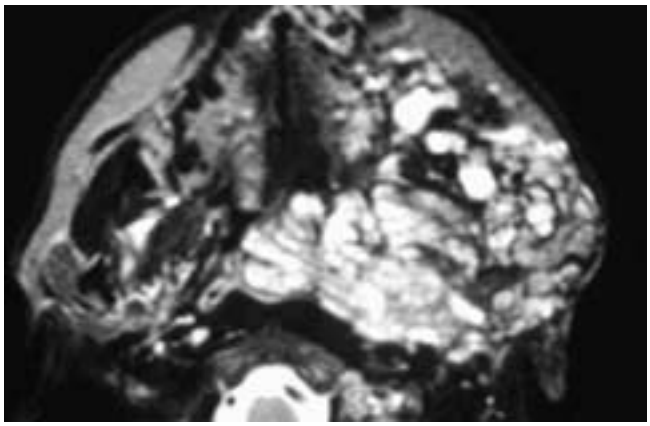

VIEW IMAGE

FIGURE 39-163 Axial T2-weighted MR scan shows multiple cystic components of varying size forming part of an overall bulky and infiltrating mass. The lesion involves the parotid gland, the adjacent superficial soft tissues in the face, and the deeper planes in the pharynx. This patient had a cystic lymphangioma.

The diagnosis of primary salivary gland MALT lymphoma is based on the demonstration of lymphocyte clonality (light chain restriction) and on morphology. Maltomas characteristically appear as infiltrates of small centrocytes and monocytoid B cells with variable plasma cell differentiation. These lymphocytes can invade parotid ductal and acinar tissue, which may be reflected in the radiographic imaging. The majority of MALT lymphomas type as B cells (L26, KiB3, LN2 positive) and are also low grade. However, some may be classified as intermediate- or high-grade lymphomas, which may also correlate with their imaging appearance, parotid infiltration, and tumor inhomogeneity. The differential diagnosis includes BLEL (or myoepithelial sialadenitis). Extensive sampling and immunohistochemistry may be required to make this distinction. Plasmacytoma and granulocytic sarcoma also enter into the differential diagnosis (see below).

If a diagnosis of parotid lymphoma is suspected, fine needle aspiration may be attempted, as this has the potential to establish the diagnosis. Systemic workup and bone marrow examination are necessary for staging. The majority of patients present with stage I_E disease (see Table 39-7).

Stage I and II MALT lymphomas are usually treated with either surgery or radiotherapy, with similar outcomes (see below). Parotidectomy may be initially performed for diagnostic purposes. If the MALT lymphoma is then found to be stage I or II, adjuvant therapy may not be necessary. The treatment choice between primary surgery and primary radiation therapy becomes important if the diagnosis is established preoperatively and the tumor is stage I or II. Surgery has an advantage since postirradiation xerostomia and mucositis are avoided. However, the cosmetic outcome is better with irradiation.

The overall prognosis of salivary MALT lymphomas is very good, as this is generally an indolent disease. Of 25 patients available for a minimal 2-year follow-up, 16 (64%) were alive with or without disease. Relapses are usually

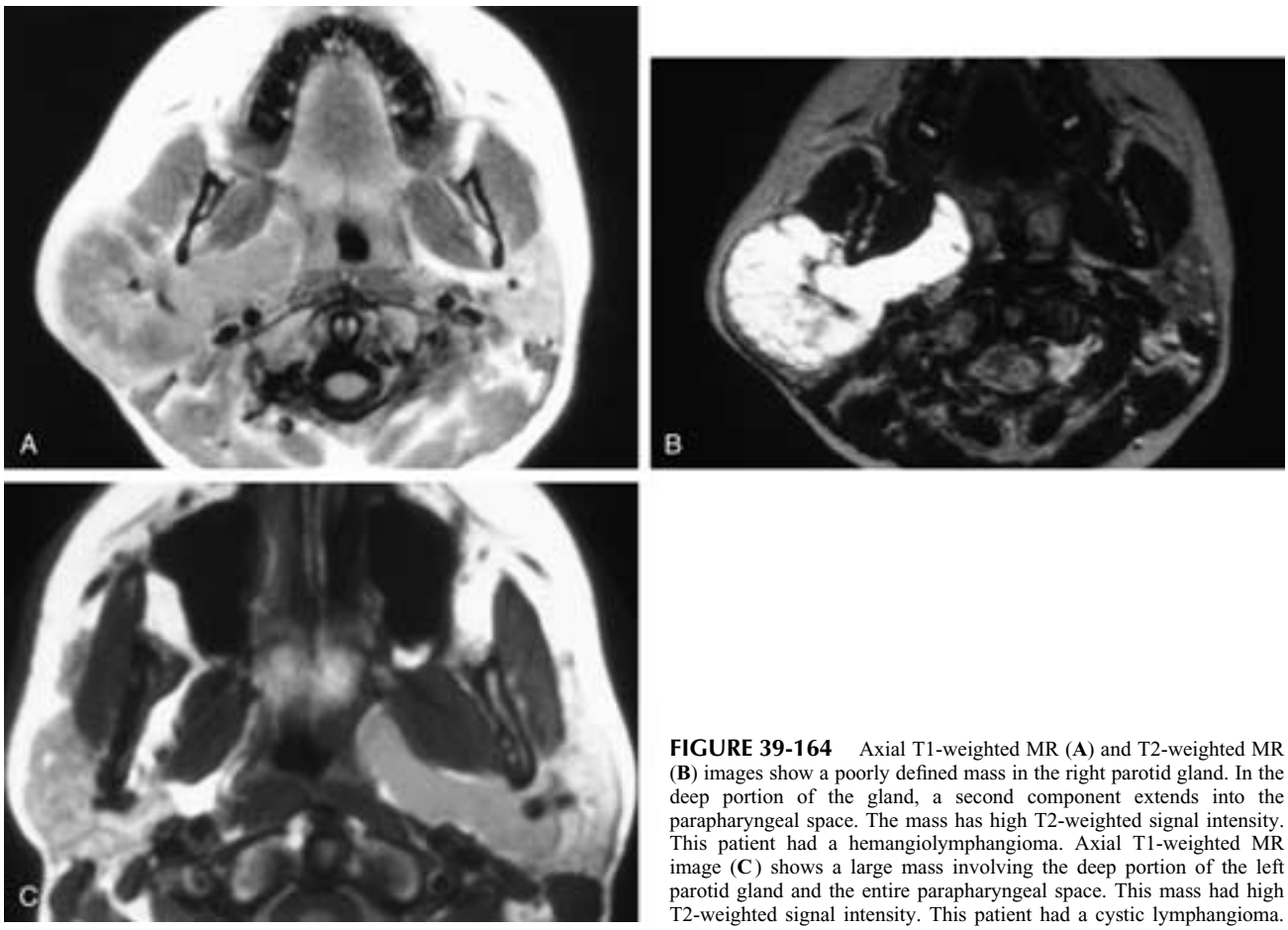

FIGURE 39-164 Axial T1-weighted MR (**A**) and T2-weighted MR (**B**) images show a poorly defined mass in the right parotid gland. In the deep portion of the gland, a second component extends into the parapharyngeal space. The mass has high T2-weighted signal intensity. This patient had a hemangiolymphangioma. Axial T1-weighted MR image (**C**) shows a large mass involving the deep portion of the left parotid gland and the entire parapharyngeal space. This mass had high T2-weighted signal intensity. This patient had a cystic lymphangioma.

VIEW IMAGE

Copyright © 2003, Mosby, Inc. All rights reserved.

Table 39-7
STAGE GROUPING OF THE AMERICAN JOINT COMMITTEE ON CANCER

Stage I	Involvement of a single lymph node region (I) or localized involvement of a single extralymphatic organ or site (I_E).
Stage II	Involvement of two or more lymph node regions on the same side of the diaphragm (II) or localized involvement of a single associated extralymphatic organ or site and its regional lymph node(s) with or without involvement of other lymph node regions on the same side of the diaphragm (II_E).
Note: The number of lymph node regions involved may be indicated by a subscript (e.g., II_3).	
Stage III	Involvement of lymph node regions on both sides of the diaphragm (III), which may also be accompanied by localized involvement of an associated extralymphatic organ or site (III_E), by involvement of the spleen (III_S), or both (III_{E+S}).
Stage IV	Disseminated (multifocal) involvement of one or more extralymphatic organs, with or without associated lymph node involvement, or isolated extralymphatic organ involvement with distant (nonregional) nodal involvement.

Source: AJCC Cancer Staging Manual 5th edition. Lippincott-Raven, Philadelphia 1997.

associated with a higher stage (stage II) or grade (intermediate or high grade) at initial presentation, and patients require additional radiotherapy combined with chemotherapy. Relapse may also be associated with progression in grade.

Lymphoma may also involve the salivary glands (usually parotid) secondary to diffuse disease. This secondary parotid involvement is not classified as MALT lymphoma. It occurs in 1% to 8% of lymphomas and is most commonly seen with high-grade, diffuse large cell lymphoma. Parotid lymphomas presenting in HIV patients usually can be classified as high-grade and secondary rather than MALT lymphoma. The prognosis is usually poor due to presentation with a high-stage and high-grade tumor.

The association of lymphoma and BLEL has been previously discussed (see the section on Autoimmune Diseases).

Solitary extramedullary plasmacytomas have a propensity for the upper respiratory tract but occur rarely in the parotid gland. This diagnosis requires a clinical workup to exclude multiple myeloma. The treatment of choice should be surgical excision followed by radiotherapy. The prognosis of solitary extramedullary plasmacytoma is generally good.

Granulocytic sarcoma represents the tissue manifestation of myeloid leukemia. It has been reported in the head and neck, and rarely may also be localized to the parotid gland. It is often misdiagnosed as a malignant lymphoma, which may delay proper treatment. The appearance of granulocytic sarcoma often precedes systemic relapse or progression from the chronic to the acute blastic form.[361–369]

The CT appearance of secondary lymphoma of the parotid gland varies with the pathologic distribution of the disease. Most commonly, the parotid disease is confined to the intraparotid lymph nodes, and one to six benign-appearing masses are identified within the gland. Usually, each node is homogeneous and may enhance slightly on postcontrast CT scans; however, nodal necrosis can occur (Figs. 39-165 to 39-167). If the parenchyma is involved, a diffuse infiltration will be seen either with poorly defined margins or involving the entire gland. The identification of extraparotid nodal disease can be helpful in suggesting the diagnosis. On MR imaging, the lymphoma tends to have a homogeneous intermediate signal intensity on all imaging sequences. There is also a tendency for the mass to ''fade'' into the signal intensity of the parotid gland on T2-weighted and contrast-enhanced, fat-suppressed, T1-weighted MR images (Figs. 39-168 to 39-171). In the uncommon patient with Hodgkin's disease involving the parotid gland, on both CT and MR imaging the nodes usually are nonhomogeneous.[358] Primary parotid lymphoma usually has a nodular, diffuse infiltrative pattern of the gland. As such, it is nonspecific and can mimic some cases of chronic sialadenitis. By definition, there are no affected parotid lymph nodes.

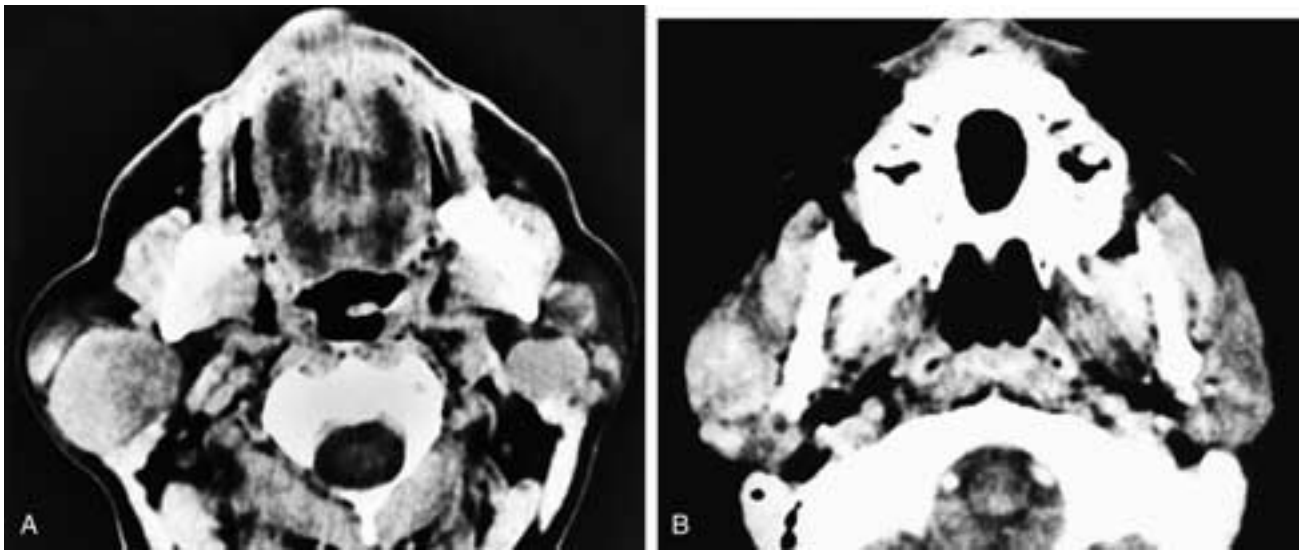

FIGURE 39-165 Axial CT scan (**A**) shows multiple benign-appearing masses in both parotid glands; the largest mass is in the right parotid gland. This patient had lymphoma. Axial contrast-enhanced CT scan (**B**) shows a slightly enhancing, benign-appearing mass in the right parotid gland. This was a hyperplastic lymph node. Note the similarity to **A**. These cases reinforce the fact that histology cannot be determined by imaging alone.

VIEW IMAGE

Copyright © 2003, Mosby, Inc. All rights reserved.

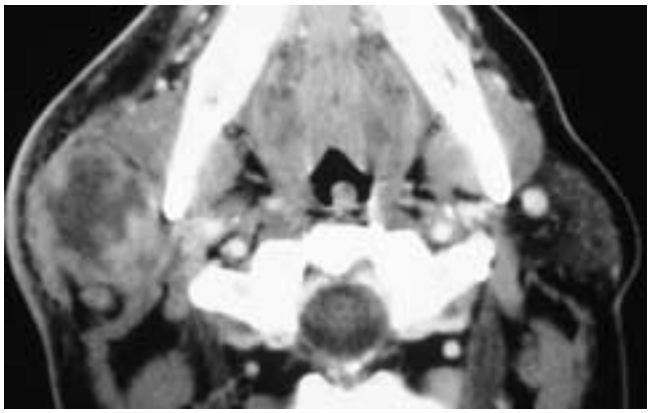

VIEW IMAGE

FIGURE 39-166 Axial contrast-enhanced CT scan shows a necrotic, irregularly walled, infiltrating mass in the right parotid gland. Edematous changes are also present in the overlying skin. This patient had systemic large cell lymphoma with involvement of the parotid gland.

Intraparotid Lymphadenopathy

Enlargement of intraparotid lymph nodes can occur from a variety of causes, most of which have already been discussed: acute viral or bacterial adenopathy, lymphoma, chronic infectious disease, and metastatic disease from the scalp, midface, or infraclavicular sites. Reactive hyperplastic lymphadenopathy can also involve periparotid lymph nodes and may be the result of an adjacent inflammatory process, the first stages of a systemic process (e.g., acute HIV infection), or of unknown etiology. Rapid, painful lymph node enlargement may simulate a parotid malignancy, especially in children. If facial nerve paralysis is present, this may further mimic malignancy. However, acute otitis media (AOM), a common pediatric event, can present with reactive lymphadenopathy of periparotid lymph nodes and facial nerve paralysis: about 5% of facial nerve paralysis is caused by AOM. Clinically, the child presents with a tender, rapidly growing parotid mass and accompanying facial nerve paralysis, bringing suspicions of rhabdomyosarcoma to mind. If MR imaging is performed, the lymph node usually has a fairly high T2-weighted signal intensity, whereas the high-grade malignancies tend to have low to intermediate T2-weighted signal intensities. This information can be helpful in distinguishing these entities, but in most cases needle aspiration or surgery will be necessary to establish the diagnosis. Such inflammatory nodes may enhance on postcontrast CT scans and have a slightly irregular margin due to the inflammatory reaction, further simulating a malignancy (Fig. 39-165B).

Heerfordt's syndrome consists of an enlarged parotid lymph node, facial nerve paralysis, and uveitis due to sarcoidosis. However, the clinical presentation of a parotid mass with a facial nerve paralysis has been misdiagnosed many times as a parotid gland malignancy.

Even when a parotid node is enlarged with metastatic disease, the mass may simulate a benign lesion on imaging. This is especially true in cases of metastatic melanoma from a facial or scalp primary. In such cases, the node usually has a well-delineated margin and is homogeneously enhanced.

Lipoma

Lipomas can arise either within the parotid gland or in the immediate periparotid region. At times, it may be clinically and radiographically impossible to distinguish the true site of origin. Series of parotid region lipomas reveal that 57% arose within the gland and 43% were of periparotid origin. Lipomas represent about 1% of parotid gland tumors, and approximately 90% of the cases are ordinary lipomas. The remaining lesions are either infiltrating lipomas or occurred as part of a lipomatosis syndrome.[19, 192, 370]

The ordinary lipomas are discrete lesions that usually have a homogeneously low attenuation (−65 to −125 HU). They have no definable capsule on imaging, yet they are easily delineated from the adjacent soft tissues (Fig. 39-172). The infiltrating lipoma is similar in appearance to the ordinary lipoma, except that it has poorly defined margins (Fig. 39-173). Actual infiltration of adjacent muscles may be demonstrated on imaging. Hemorrhage and

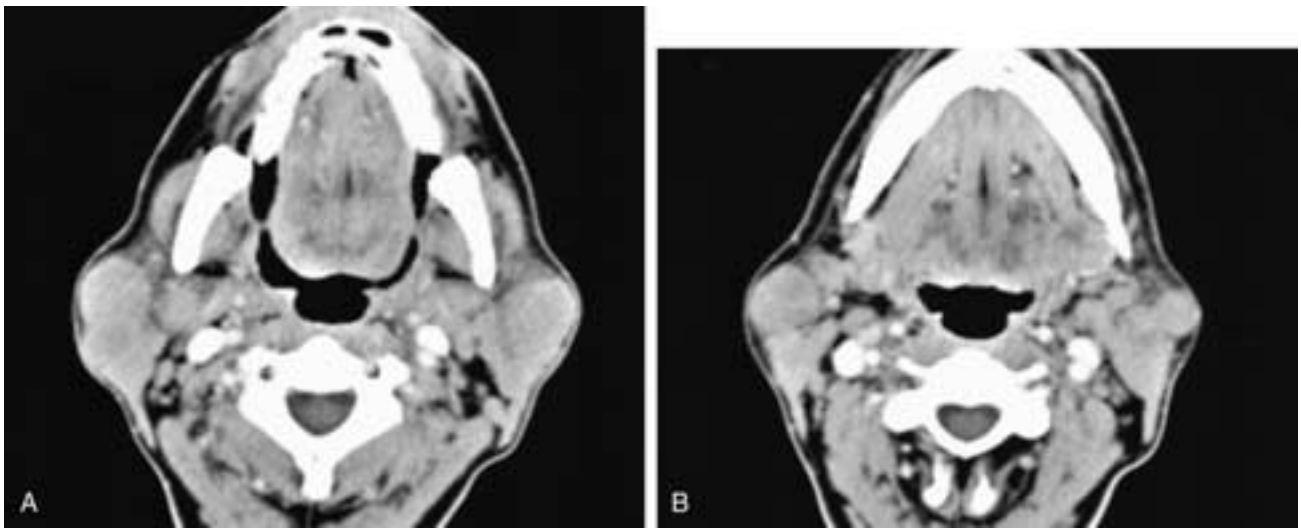

VIEW IMAGE

FIGURE 39-167 Axial contrast-enhanced CT scans (**A**, **B**) show multiple well-defined masses in both parotid glands. There is also lymphadenopathy in the neck bilaterally. This patient had large cell lymphoma.

Copyright © 2003, Mosby, Inc. All rights reserved.

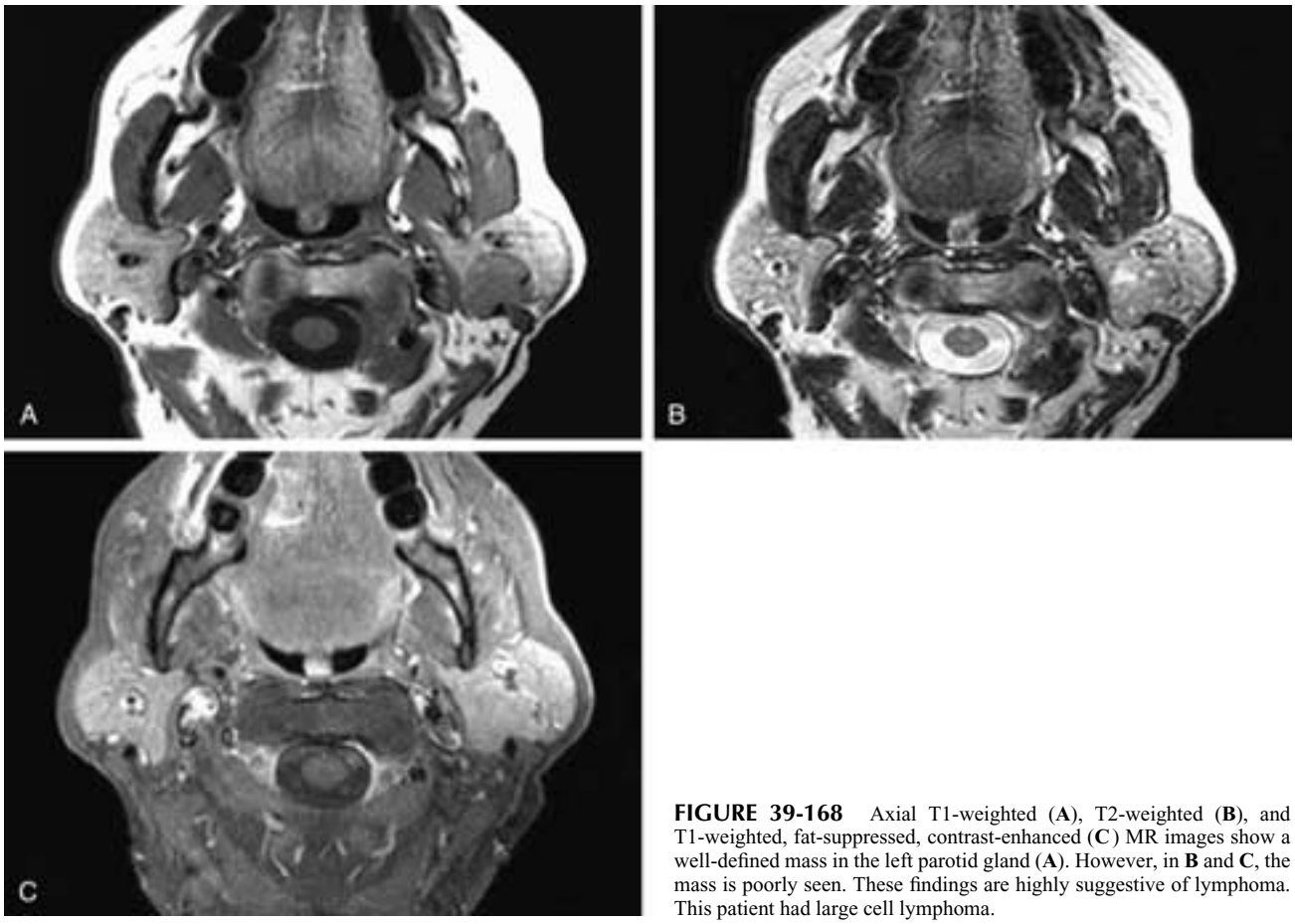

FIGURE 39-168 Axial T1-weighted (**A**), T2-weighted (**B**), and T1-weighted, fat-suppressed, contrast-enhanced (**C**) MR images show a well-defined mass in the left parotid gland (**A**). However, in **B** and **C**, the mass is poorly seen. These findings are highly suggestive of lymphoma. This patient had large cell lymphoma.

VIEW IMAGE

fibrotic changes can occur within lipomas, and on CT these changes may cause increased attenuation approaching that of muscle. Usually these changes are focal within the lipoma; however, the entire lesion may be hemorrhagic, rendering impossible the CT diagnosis of a lipoma. On MR imaging, lipomas have a high T1-weighted and an intermediate T2-weighted signal intensity, which may be minimally heterogeneous. An important diagnostic point to note is that whenever a lipomatous mass has an overall heterogeneously dense matrix, it may represent a liposarcoma.[19, 370]

Neurogenic Tumors

Neurogenic tumors of the parotid gland are the second most common benign mesenchymal neoplasm after vascular/lymphatic tumors. They may be either schwannomas or neurofibromas. Both lesions are usually ovoid, sharply delineated masses that arise primarily from the facial nerve trunk or its branches. Schwannomas are solitary, whereas neurofibromas often are multiple and associated with other manifestations of von Recklinghausen's disease. On CT these tumors can enhance, be cystic, or be isodense with muscle. The cystic changes usually are small and multiple. Neurofibromas may have a low, almost fatty attenuation that may simulate a lipoma. On MR imaging, these tumors in general have a low to intermediate T1-weighted and a high T2-weighted signal intensity. However, nonhomogeneous regions of higher and lower signal intensity can occur, making these lesions on MR imaging indistinguishable from a pleomorphic adenoma (Figs. 39-174 and 39-175).[371, 372]

The histologic distinction between these two benign peripheral nerve sheath tumors can be made as follows: a neurofibroma arises from actual neuronal and perineuronal tissue. A fairly uniform distribution of thin, wavy spindle cells is seen within a myoid-type stroma. To excise a neurofibroma is to sacrifice the nerve from which it arises. By contrast, a schwannoma arises from neural supporting elements, not from the actual neuronal elements. It arises eccentrically to the nerve and can theoretically be ''peeled'' off from the nerve. Histologically, one sees the classic yin/yang of the cellular (Antoni A) and paucicellular (Antoni B) areas. The wavy spindle cells have a tendency to palisade and form rows of palisading cells called Verocay bodies.

Solitary neurofibromas affecting the major salivary gland are uncommon. They are usually seen in the setting of von Recklinghausen's disease but may occur in the absence of manifestations of this disease.[373] Large and long-standing plexiform neurofibromas in patients with von Recklinghausen's disease are at risk for malignant transformation (malignant peripheral nerve sheath tumor). Histologically, malignant transformation is seen as an increase in tumor cellularity, mitotic figures, pleomorphism, and necrosis.

Primitive neuroectodermal tumor (PNET) is a rare tumor found in children and young adults, commonly in the gluteal

Copyright © 2003, Mosby, Inc. All rights reserved.

region, thighs, shoulder, and arms. Isolated cases of PNET have been reported in visceral sites such as the kidney, uterus, ovary, testis, urinary bladder, and pancreas. In the head and neck area, these tumors have been described in the maxilla, orbit, and soft tissues of the neck. PNET has rarely been reported to involve the parotid region.[374]

Histologically, tumor cells are small and round or oval, with minimal cytoplasm and clumped chromatin. Rosettes are frequently found, and mitoses vary from moderate to numerous. The differential diagnosis includes small cell carcinoma and BSA. Prominent rosette formation and MIC2 positivity support a diagnosis of PNET. PNETs are, in general, highly aggressive tumors requiring a combined approach consisting of surgery, radiation therapy, and chemotherapy.[375]

Fibrous Tissue Lesions

A number of benign lesions of fibroblastic origin may affect the periparotid region, including fibromatosis (or desmoid tumor), nodular fasciitis, myofibromatosis, fibrous histiocytoma, and plexiform fibrous histiocytoma. Fibromatosis, or desmoid tumor, is a histologically bland proliferation of fibroblasts in a collagenous background. The significance of this tumor lies in its insidiously infiltrative nature. For this reason, fibromatosis is considered a low-grade fibrosarcoma. The surgeon is never assurred that he or she is beyond the lesion, and resection margins have a tendency to be positive. A high rate of recurrence after surgery is not surprising. Surgical resection is the mainstay of therapy. Radiation therapy has been utilized in recurrent cases, but there have been cases of high-grade malignant transformation occurring after irradiation. Antiestrogen therapy (Tamoxifen) has resulted in some regression of unresectable recurrences.[376] The differential diagnosis includes nodular fasciitis, benign peripheral nerve sheath tumor (neurofibroma or schwannoma), fibrous histiocytoma, and myofibromatosis. Infantile myofibromatosis may be present as an isolated single tumor or, less commonly, as

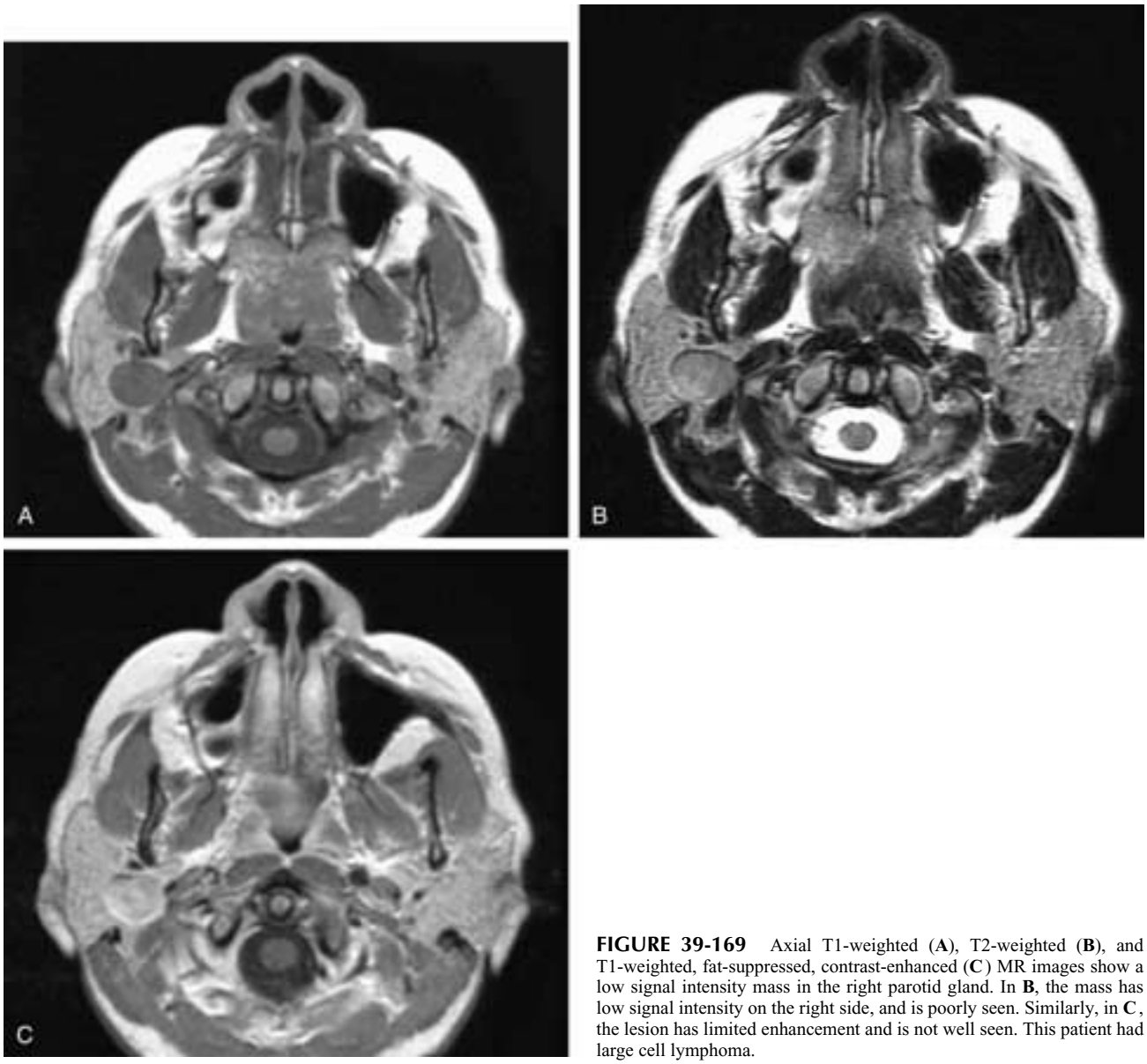

FIGURE 39-169 Axial T1-weighted (**A**), T2-weighted (**B**), and T1-weighted, fat-suppressed, contrast-enhanced (**C**) MR images show a low signal intensity mass in the right parotid gland. In **B**, the mass has low signal intensity on the right side, and is poorly seen. Similarly, in **C**, the lesion has limited enhancement and is not well seen. This patient had large cell lymphoma.

VIEW IMAGE

Copyright © 2003, Mosby, Inc. All rights reserved.

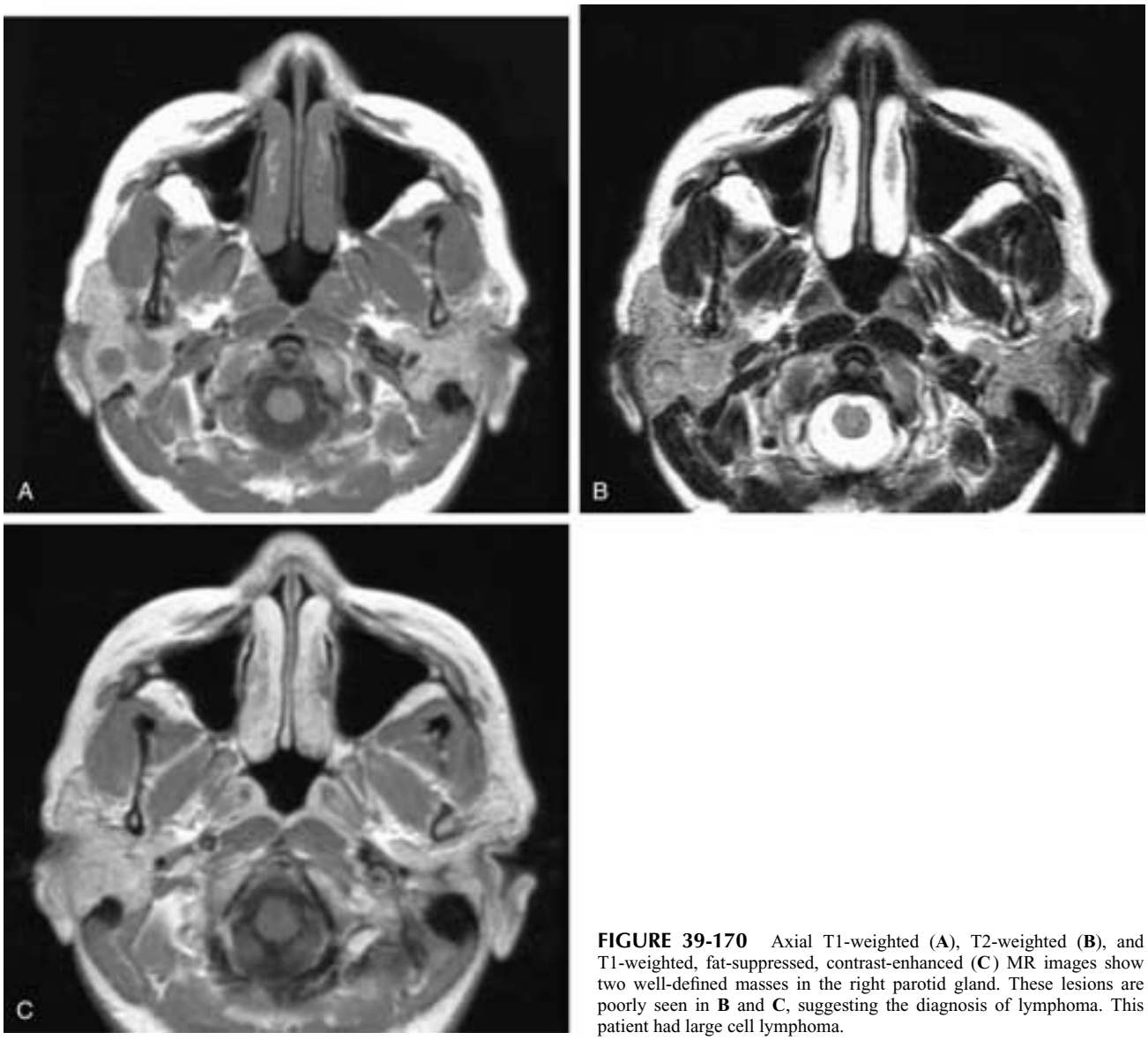

FIGURE 39-170 Axial T1-weighted (**A**), T2-weighted (**B**), and T1-weighted, fat-suppressed, contrast-enhanced (**C**) MR images show two well-defined masses in the right parotid gland. These lesions are poorly seen in **B** and **C**, suggesting the diagnosis of lymphoma. This patient had large cell lymphoma.

VIEW IMAGE

multiple tumor masses. The important clinical distinction between this entity and fibromatosis is that myofibromatosis is circumscribed, amenable to resection, and may occasionally regress spontaneously.

Nodular fasciitis is a benign reactive lesion of fibroblasts. Commonly, it presents as a rapidly growing, tender mass. Unlike fibromatosis, it is circumscribed, without an infiltrative growth pattern, and recurs uncommonly after excision, 7% in a series of 54 cases.[377] Histologically, one may see zones of necrosis and degeneration bordered by ''wild''-looking immature reactive fibroblasts. A tendency toward maturation with zones of whorled, bland fibroblasts may be seen.

Fibrous histiocytoma is a benign tumoral proliferation of fibroblasts and histiocytes. It is usually seen as a subcutaneous neoplasm but may occasionally arise in periparotid tissue (Fig. 39-176). Histologically, it enters the differential diagnosis with fibromatosis and nodular fasciitis.

Plexiform fibrohistiocytic tumor (PFT), a relatively newly described entity, is a soft-tissue neoplasm with low malignant potential that most commonly affects children and young adults and rarely occurs in the head and neck region. In the original description by Enzinger and Zhang, two thirds of patients were under 20 years of age, and there was a clear female predominance. The majority of PFTs occur in the superficial subcutaneous tissues of the upper extremities. Less frequently, they present in the lower extremities or trunk. PFTs affect the head and neck rarely: 10% of the cases reported by Enzinger and Zhang, 7% of the cases reported by Hollowood et al., and none of the cases reported by Remstein et al.[378–380]

Clinically, PFTs almost invariably present as slow-growing superficial masses, usually measuring less than 3 cm, which are painless and firm or rubbery. Generally, PFT can be asymptomatic, although one study reported a lower extremity lesion with an associated foot drop and contractures. The lesions may be raised and sometimes show a

Copyright © 2003, Mosby, Inc. All rights reserved.

central depression, but usually show little discoloration and no ulceration. Most often, the tumors are located in subcutaneous adipose tissue and may extend into dermis or skeletal muscle.

PFTs are characterized by a plexiform proliferation of mononuclear histiocyte-like cells, multinucleated osteoclast-like cells, epithelioid mononuclear cells, and spindle fibroblast-like cells in variable proportions. The stroma consists of a variable admixture of collagen or loose stroma. Cellular atypia and pleomorphism are usually minimal or absent. Mitoses are frequent, and atypical mitoses can also be seen.

PFT should be treated with complete resection and negative margins. Enzinger and Zhang originally emphasized the benign nature of these tumors, citing a low metastatic rate to regional lymph nodes and no distant metastasis. However, there is a significant local recurrence rate after surgical resection, indicating that PFTs are in fact locally aggressive and require complete excision. We have recently seen a 17-year-old boy with a cheek PFT that was initially treated only by shave biopsy. The tumor subsequently recurred, infiltrated the parotid gland, and metastasized to the cervical lymph nodes 3 years after initial biopsy. Distant pulmonary metastasis and a mortality reported by Remstein et al. indicate that PFT is capable of presenting with or progressing to systemic metastatic disease. However, the overall mortality rate for PFT is low (3 of 63 patients or 4.7%), and it appears more likely that patients will survive their disease.

Miscellaneous Lesions

Masseteric Hypertrophy

Masseteric hypertrophy is the most common form of an uncommon entity that is more accurately called masticator hypertrophy, since all of the muscles of mastication may be involved. Usually the condition occurs bilaterally, but it may be unilateral. Muscle enlargement may vary from minimal to up to three times the normal size.[372] Flaring of the mandibular angle(s) can occur. The process usually starts in adolescence or early adulthood, and there is a history of slowly progressive muscle growth. The facial fullness is located anterior to the usual location of a parotid mass and enlarges when the patient's teeth are clenched. The mass feels like muscle on palpation, and the muscle is nontender and not painful. Excessive gum chewing or bruxism has been suggested as playing an etiologic role, but many cases have no known cause. Plain films may show an exostosis of the lateral aspect of the angle of the mandible at the line of attachment of the masseter muscle. A sialogram demonstrates lateral bowing of Stensen's duct around the enlarged masseter muscle. Computed sectional imaging demonstrates the enlarged muscle mass(es), which otherwise appears as normal muscle tissue (Figs. 39-177 and 39-178). Surgery is performed only for cosmesis, and microscopic examination of resected muscle demonstrates either normal muscle or muscle with true work hypertrophy.[381]

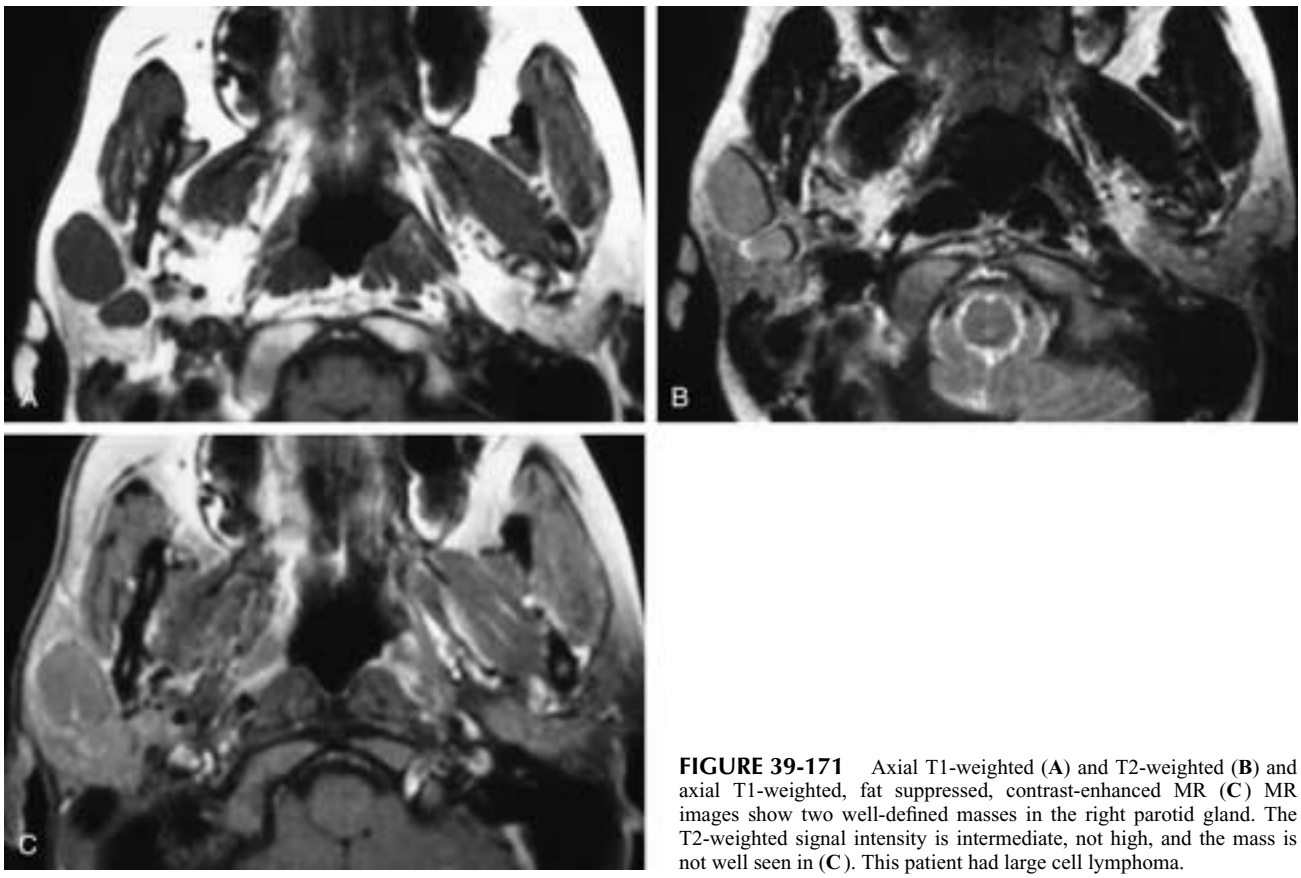

FIGURE 39-171 Axial T1-weighted (**A**) and T2-weighted (**B**) and axial T1-weighted, fat suppressed, contrast-enhanced MR (**C**) MR images show two well-defined masses in the right parotid gland. The T2-weighted signal intensity is intermediate, not high, and the mass is not well seen in (**C**). This patient had large cell lymphoma.

VIEW IMAGE

Copyright © 2003, Mosby, Inc. All rights reserved.

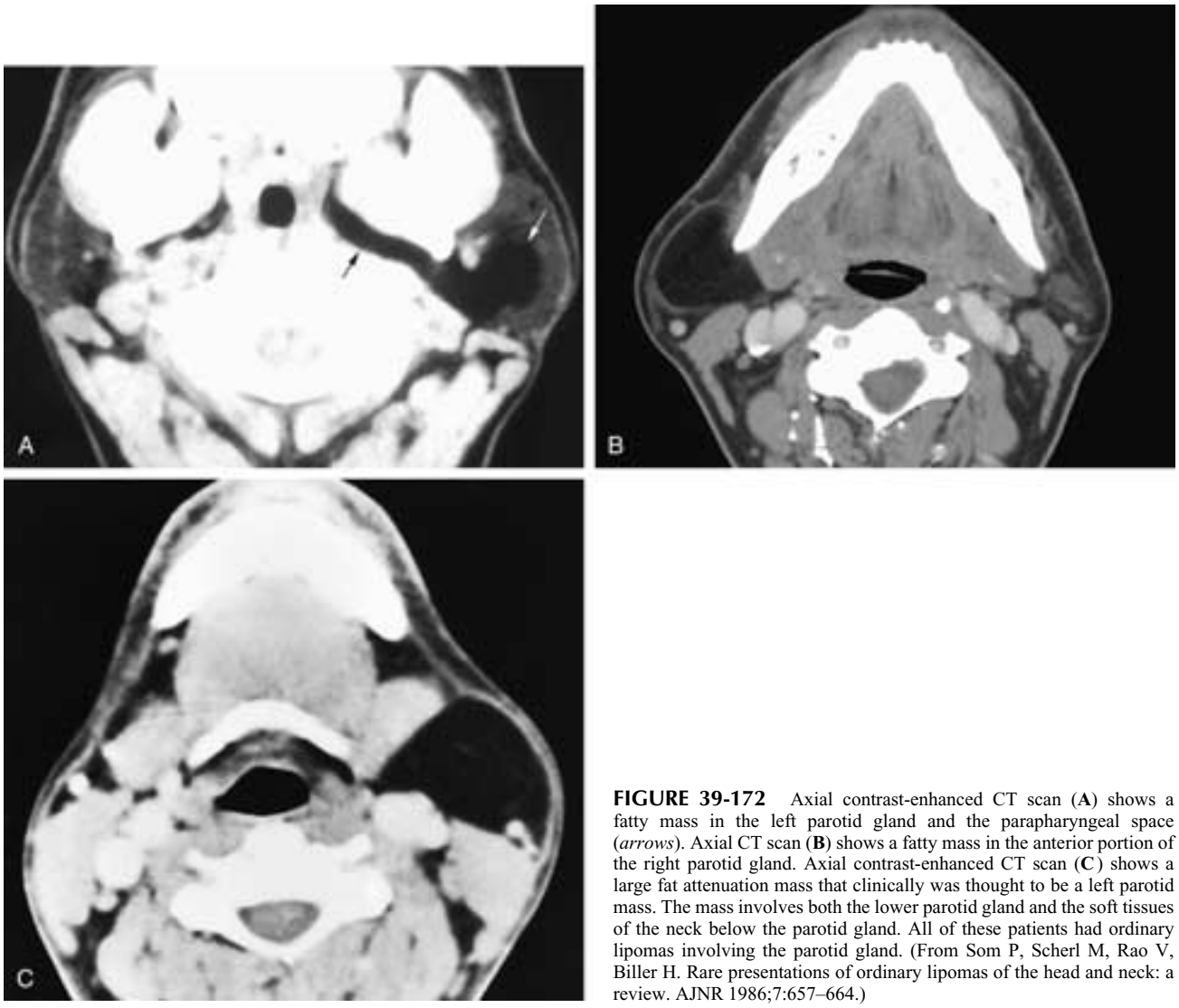

FIGURE 39-172 Axial contrast-enhanced CT scan (**A**) shows a fatty mass in the left parotid gland and the parapharyngeal space (*arrows*). Axial CT scan (**B**) shows a fatty mass in the anterior portion of the right parotid gland. Axial contrast-enhanced CT scan (**C**) shows a large fat attenuation mass that clinically was thought to be a left parotid mass. The mass involves both the lower parotid gland and the soft tissues of the neck below the parotid gland. All of these patients had ordinary lipomas involving the parotid gland. (From Som P, Scherl M, Rao V, Biller H. Rare presentations of ordinary lipomas of the head and neck: a review. AJNR 1986;7:657–664.)

VIEW IMAGE

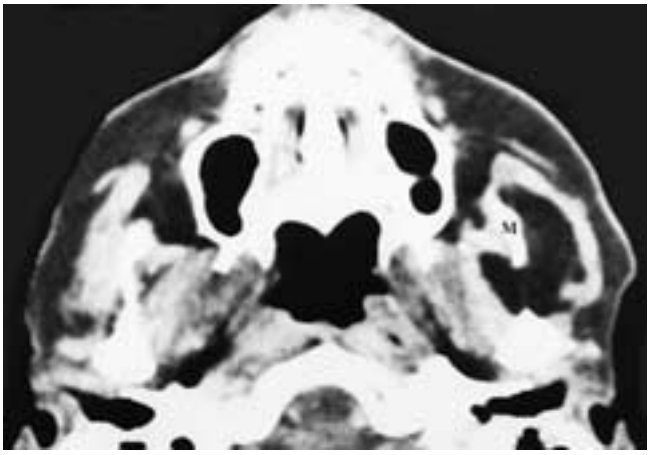

FIGURE 39-173 Axial CT scan shows a fat attenuation mass that has extended from the superficial portion of the left parotid gland back around the mandible (*M*) into the deep portion of the gland. The masseter muscle was also involved. This was an infiltrating lipoma. (From Som P, Scherl M, Rao V, Biller H. Rare presentations of ordinary lipomas of the head and neck: a review. AJNR 1986;7:657–664.)

VIEW IMAGE

Temporomandibular Joint and Mandibular Lesions

A variety of lesions can occur within the region of the temporomandibular joint (TMJ) that may clinically mimic parotid gland disease. Usually degenerative changes and internal joint derangements can be identified clinically as being of primary TMJ origin. However, fibroosseous lesions and exuberant degenerative productive changes involving the TMJ can occasionally present clinically as a mass in the parotid region, as can joint diseases such as synovial chondromatosis (Fig. 39-179). Similarly, in some circumstances, mandibular cysts and odontogenic masses in the mandibular ramus (i.e., dentigerous cysts and ameloblastomas) may be confused clinically with parotid lesions. Metastases to the mandibular ramus and TMJ region may also mimic salivary masses (Figs. 39-180 and 39-181). In these patients, computed sectional imaging provides the most accurate assessment of the true anatomic origin of the process. Metastases often have a cystic, destructive appearance, and the primary tumor usually arises in the lungs, breast, kidneys, or gastrointestinal tract.

Copyright © 2003, Mosby, Inc. All rights reserved.

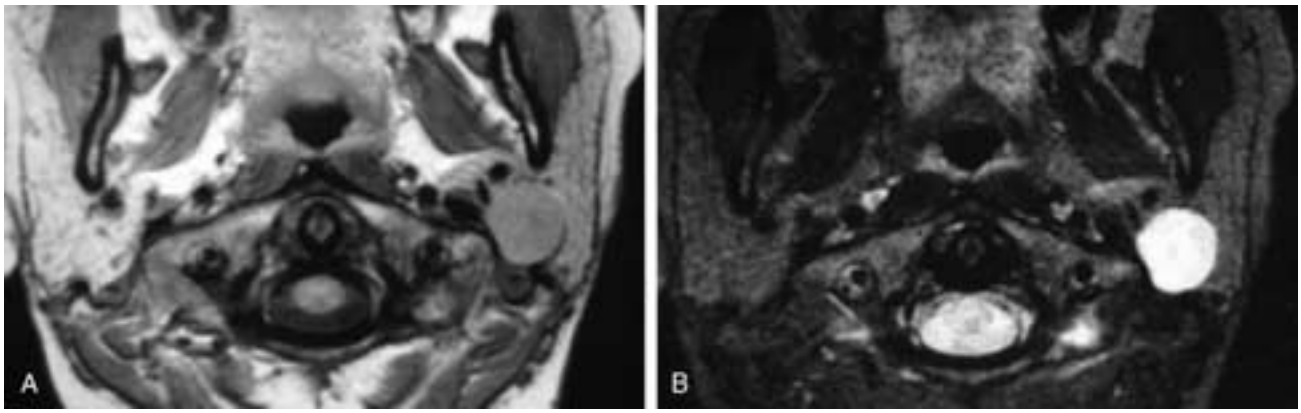

VIEW IMAGE

FIGURE 39-174 Axial T1-weighted (**A**) and T2-weighted (**B**) MR scans show a sharply defined mass in the posterior left parotid gland, along the course of the facial nerve. This is a nonspecific imaging appearance. This patient had a schwannoma of the facial nerve.

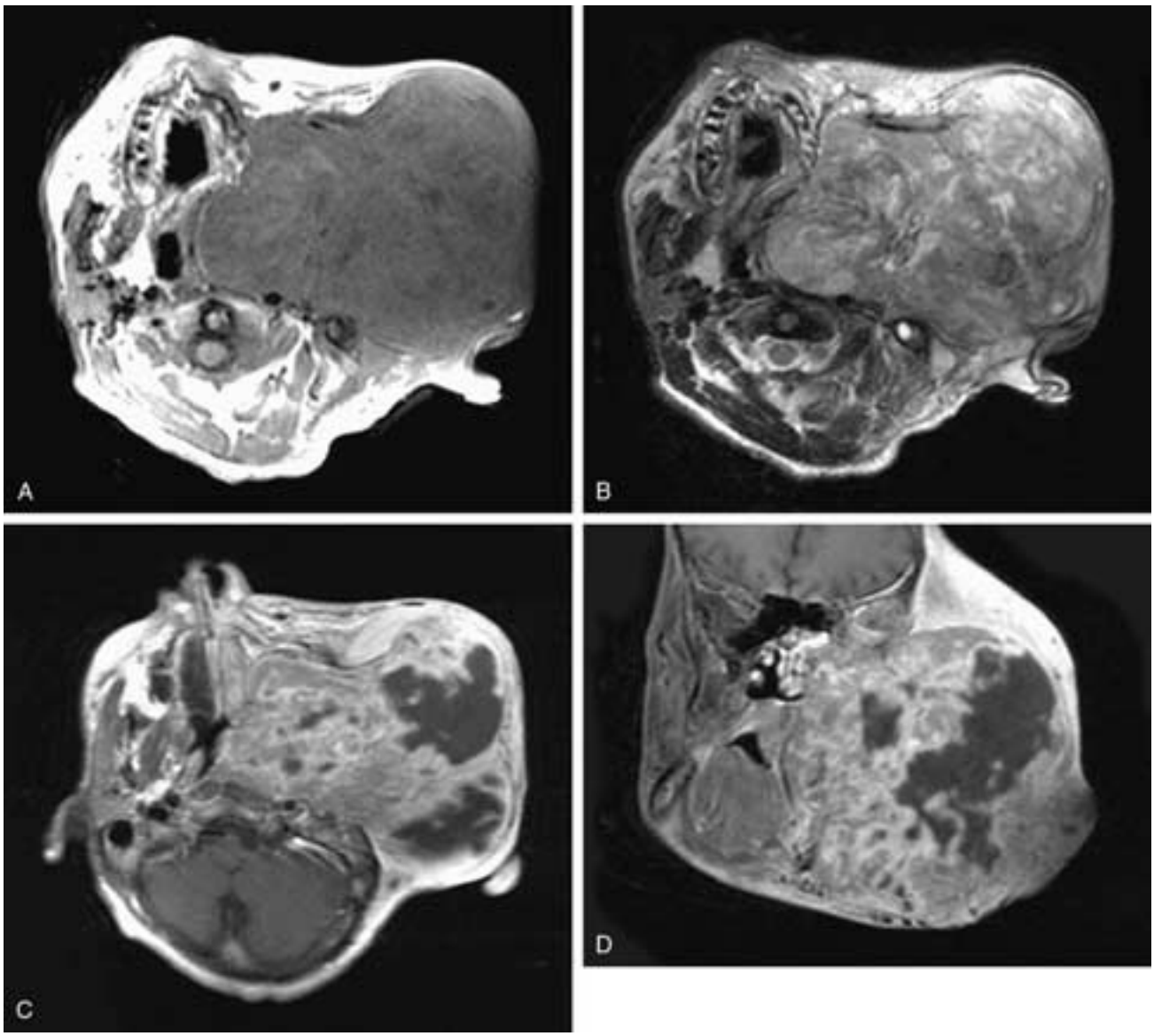

VIEW IMAGE

FIGURE 39-175 Axial T1-weighted (**A**), T2-weighted (**B**), and axial (**C**) and coronal (**D**) T1-weighted, fat-suppressed, contrast-enhanced MR images show a huge nonhomogeneous mass arising within the left parotid gland and extending into the adjacent soft tissues, maxillary sinus, and skull base. This was a neurofibroma, with malignant degeneration.

Copyright © 2003, Mosby, Inc. All rights reserved.

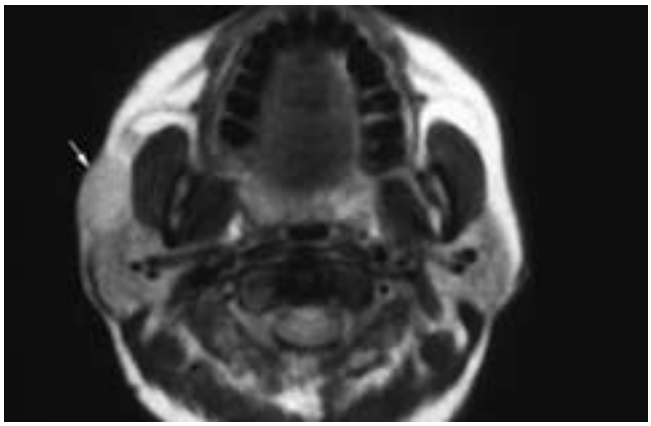

VIEW IMAGE

FIGURE 39-176 Axial proton density MR image shows an intermediate signal intensity well-delineated mass (*arrow*) arising in the anterior portion of the right parotid gland and overlying the masseter muscle. This patient had a fibrous histiocytoma.

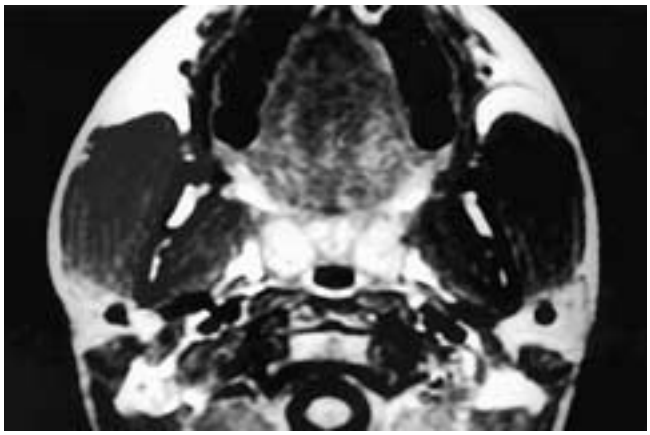

VIEW IMAGE

FIGURE 39-178 Axial T2-weighted MR image shows bilateral enlargement of the masseter muscles. The internal pterygoid muscles may also be slightly enlarged. This patient had bilateral masseteric (masticator) muscle hypertrophy.

Other Miscellaneous Conditions

Frey's syndrome, also known as auricular temporal syndrome or gustatory sweating, is an unusual entity that results from an injury to the auriculotemporal nerve. Clinically, sweating and flushing of the skin occur in the area of this nerve's distribution when the patient has a stimulus to salivate. Its true incidence is unknown, but it is estimated to occur in as many as 35% to 60% of postparotidectomy patients. It probably results from a communication between the postganglionic parasympathetic fibers from the otic ganglion and the sympathetic nerves from the superior cervical ganglion. Most patients are not bothered sufficiently to seek medical treatment. If the gland has not been removed, the sialogram and computed sectional imaging studies are normal.[26, 382]

Rarely, skin or subcutaneous lesions such as sebaceous cysts or dermoid cysts overlying the parotid gland may clinically mimic a parotid tumor. By comparison, a prominent transverse process of the second cervical vertebra may be clinically confused on palpation with a deep parotid mass. Tumors arising in the soft tissues around the parotid gland and masseter muscles rarely may also clinically simulate a parotid mass. These lesions include schwannomas, Merkel cell tumors, and rare carcinomas and sarcomas.[192] (See Chapter 41 for a discussion of these lesions (Figs. 39-184 and 39-185).)

Kimura's Disease

Kimura's disease occurs in Orientals, primarily of Chinese or Japanese extraction. The disease has a male predominance (87%), and most cases occur in patients in their second and third decades of life. Lesions can be solitary or multiple, localized or disseminated. Most lesions occur in the head and neck, with the majority of patients having disease in the major salivary glands and regional lymph nodes. The tumoral masses may range in size from 2 to 11 cm, and many reported patients have had these lesions for one to two decades.[383, 384] Histologically, one sees a

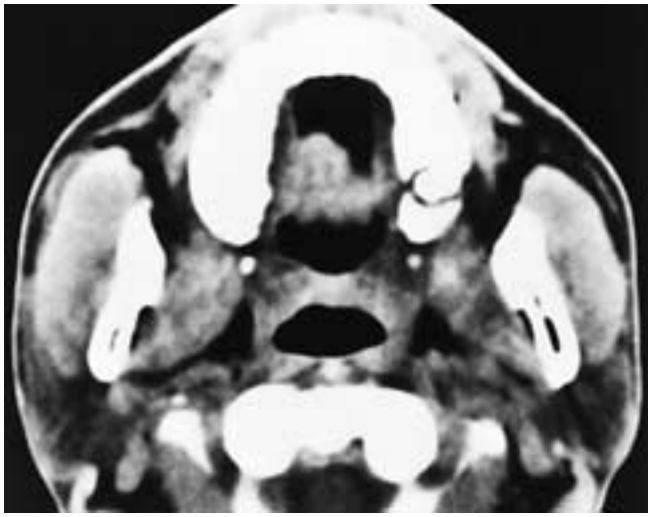

VIEW IMAGE

FIGURE 39-177 Axial CT scan shows moderate enlargement of the right masseter muscle and possibly the right internal pterygoid muscle. This patient had hypertrophy of the right masticator muscles.

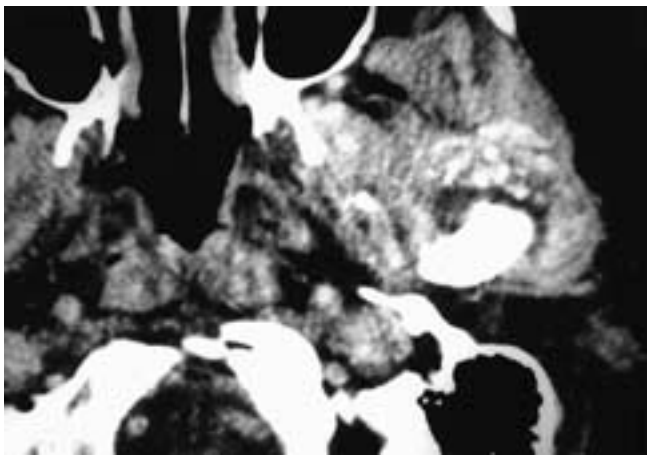

VIEW IMAGE

FIGURE 39-179 Axial CT scan shows a partially calcified mass involving the left TMJ. There is also fluid in the joint. This mass was clinically suspected of being a parotid tumor. This patient had a synovial chondromatosis.

Copyright © 2003, Mosby, Inc. All rights reserved.

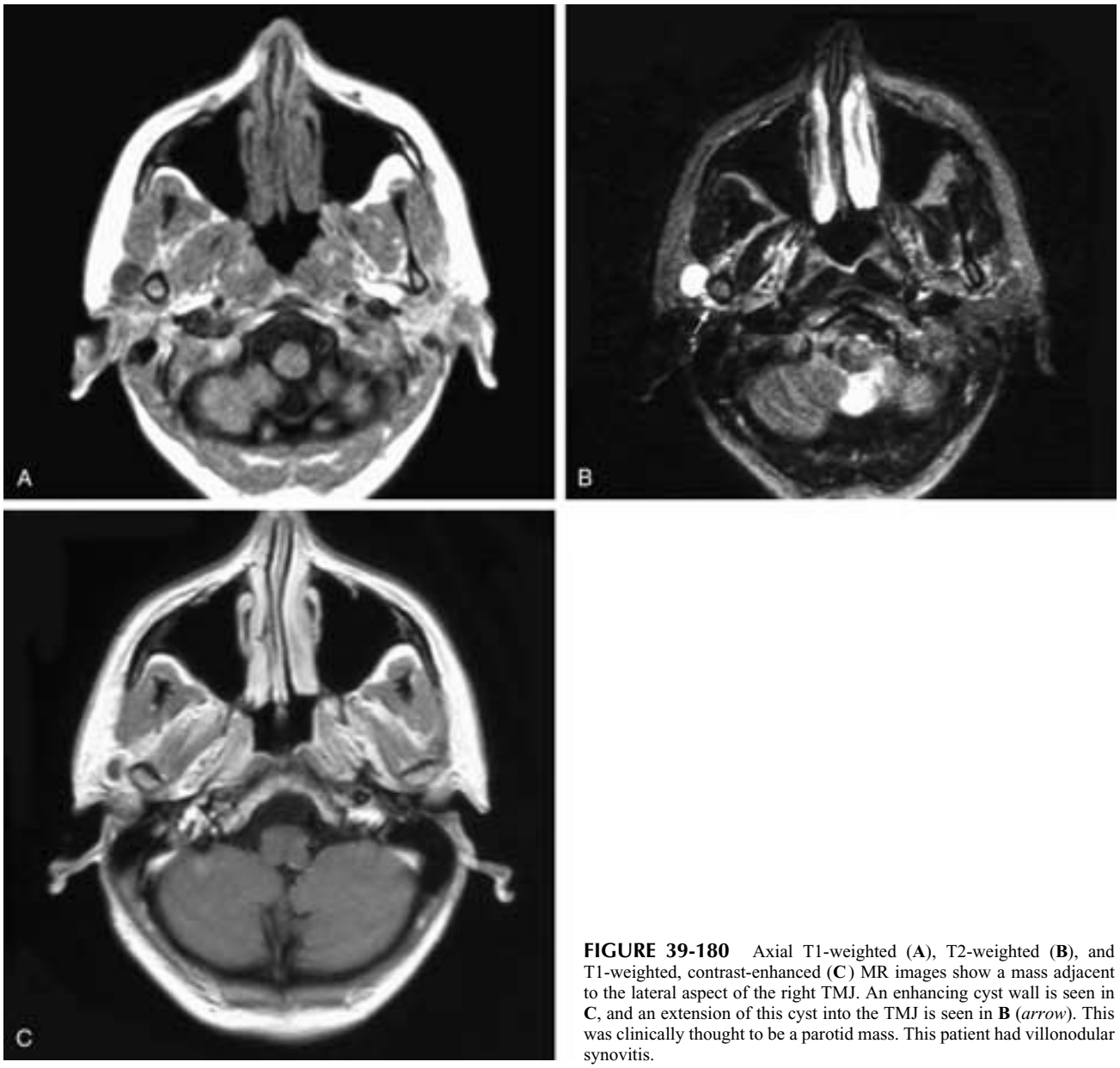

FIGURE 39-180 Axial T1-weighted (**A**), T2-weighted (**B**), and T1-weighted, contrast-enhanced (**C**) MR images show a mass adjacent to the lateral aspect of the right TMJ. An enhancing cyst wall is seen in **C**, and an extension of this cyst into the TMJ is seen in **B** (*arrow*). This was clinically thought to be a parotid mass. This patient had villonodular synovitis.

VIEW IMAGE

vascular and lymphoid proliferation with eosinophilia. The cause of this lesion is unknown. There often is associated blood eosinophilia (10% to 70%) and elevated serum IgE (800 to 35,000 U/ml). Treatment is usually surgical excision. Irradiation has been reported to produce a local control rate of 80%; however, many clinicians are reluctant to irradiate young patients. On CT, the lesions enhance intensely, while on MR imaging, the lesions may have variable T1-weighted signal intensity and usually high T2-weighted signal intensity. Occasionally, flow voids may be present (Figs. 39-182 and 39-183).[383, 384]

Two cases of Kimura's disease with parotid gland and postauricular lymph node involvement were reported. Elevated Tl-201 single photon emission computed tomography (SPECT) uptake was noted on both early and delayed images, and it was concluded that Kimura's disease should be included in the differential diagnosis when increased Tl-201 uptake in head and neck mass lesions is noted.[385]

The clinical differential diagnosis of bilateral parotid swelling includes sialadenosis, mumps, benign lymphoepithelial lesions, Warthin's tumors, clear cell oncocytosis, sarcoidosis, Wegener's granulomatosis, SS, amyloidosis, and polycystic (dysgenetic) disease. The last, an extremely rare condition, has rarely been reported in the literature. It has been reported exclusively in females, in almost all cases is bilateral, and may have its clinical onset either in childhood or in adulthood. Histologically, the parotid gland is entirely replaced by a honeycomb-type meshwork of cysts containing inspissated material with spheroliths. The cysts are the result of dilated ductoacinar units, and very few normal residual acini are seen. Despite its histologic similarity to cystic transformation of other organs such as polycystic kidney

Copyright © 2003, Mosby, Inc. All rights reserved.

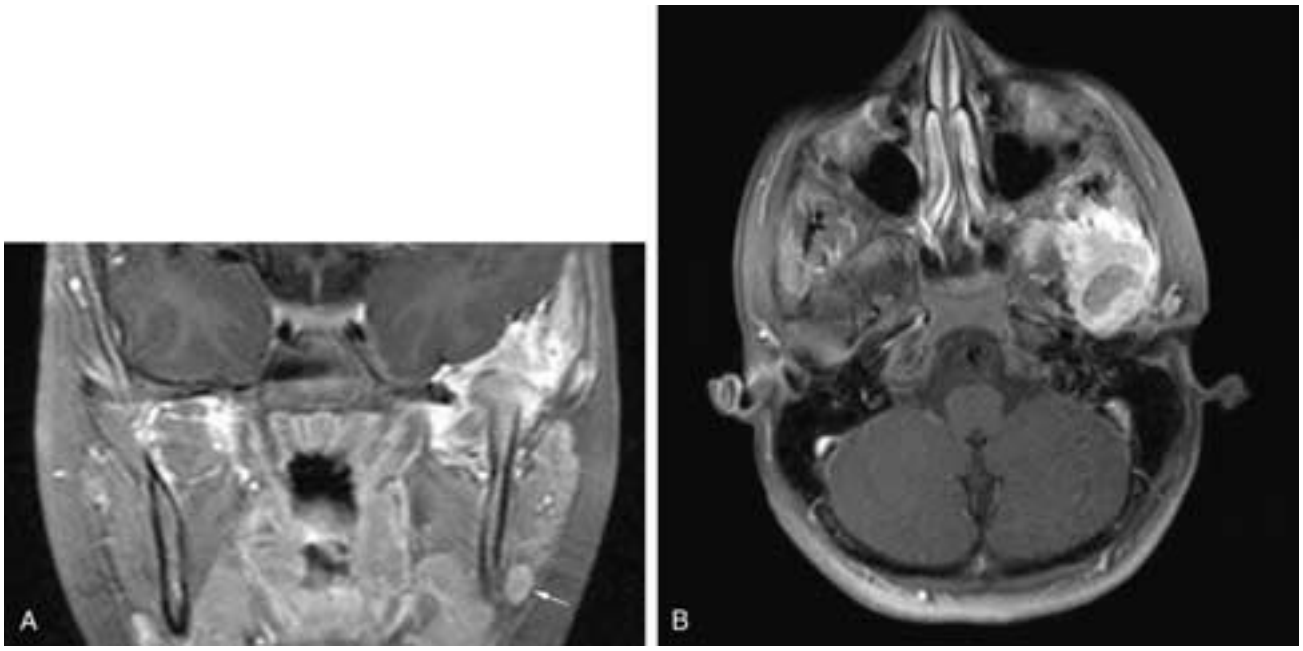

VIEW IMAGE

FIGURE 39-181 Coronal (**A**) and axial (**B**) T1-weighted, fat-suppressed, contrast-enhanced MR images show a destructive mass in the left TMJ and skull base. In **A**, there is a mass (*arrow*) in the lower left parotid gland that was a metastatic lymph node. This patient had a synovial sarcoma with metastasis to the parotid nodes.

disease, no other associated parenchymal involvement has been reported.[172, 386]

SUMMARY OF DISEASE PATTERNS

A history of recurrent parotid swelling, with or without associated pain, suggests an inflammatory process. A CT scan may identify a calcified sialolith, show the sialadenitis with or without adjacent inflammation, or suggest SS or sialosis. A sialogram can help determine the amount of damage that has occurred to either the parotid or submandibular gland by showing whether the acinar regions can be visualized. If the acini are not seen, it is unlikely that there will be normal saliva formation and surgery to remove the gland should be performed. On the sialogram, scattered collections of contrast material usually indicate abscesses. Multiple collections of contrast material that are uniform in size and distribution throughout the gland suggest SS. MR can also identify SS in its more advanced stages. An enlarged gland with an otherwise normal sialogram makes sialosis most likely.

Salivary tumors in children are uncommon and represent less than 5% of tumors in all age groups. Hemangioma is the

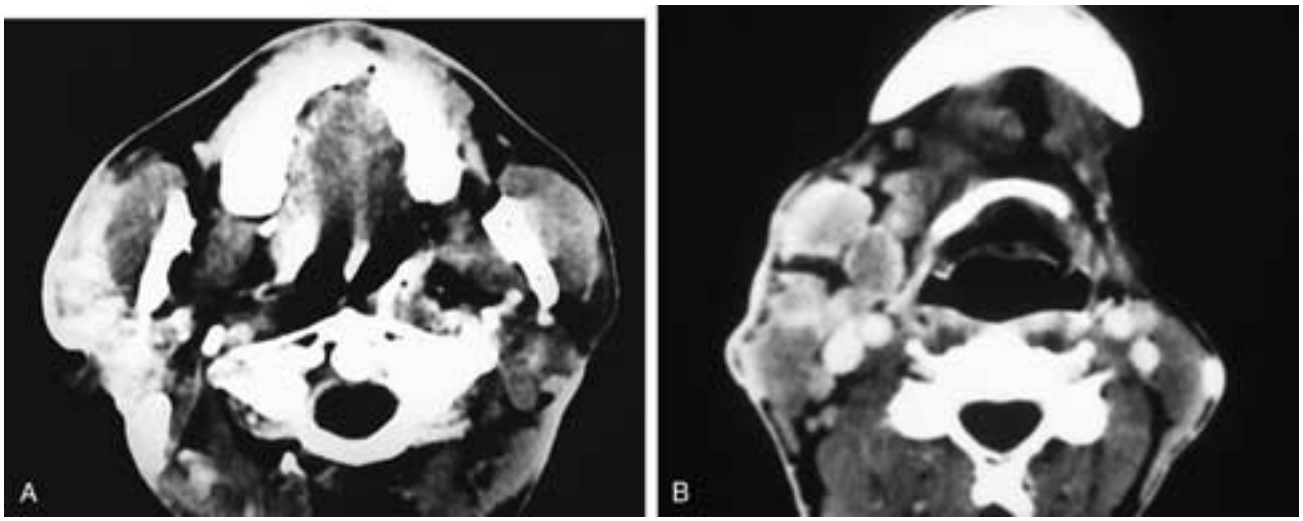

VIEW IMAGE

FIGURE 39-182 Axial contrast-enhanced CT scans through the level of the parotid glands (**A**) and more caudally in the neck (**B**) show an intensely enhancing infiltrative process involving the right parotid gland, the adjacent soft tissues, and the lymph nodes. This Asian male had Kimura's disease.

Copyright © 2003, Mosby, Inc. All rights reserved.

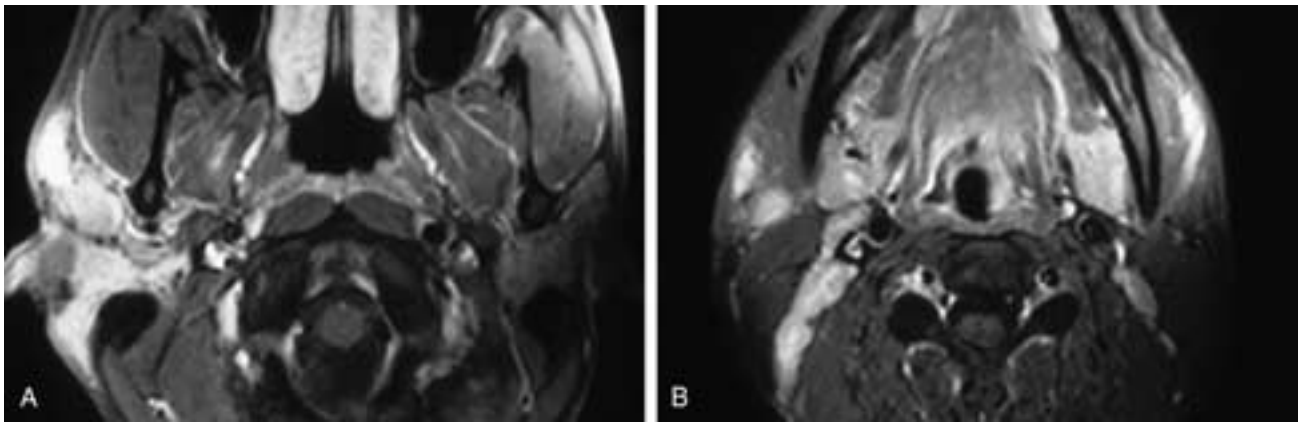

VIEW IMAGE

FIGURE 39-183 Axial T1-weighted, fat-suppressed, contrast-enhanced MR images through the parotid glands (**A**) and more caudally in the neck (**B**) show an enhancing mass in the right parotid gland and adjacent soft tissues. There are also involved right level II and V nodes. This patient had Kimura's disease.

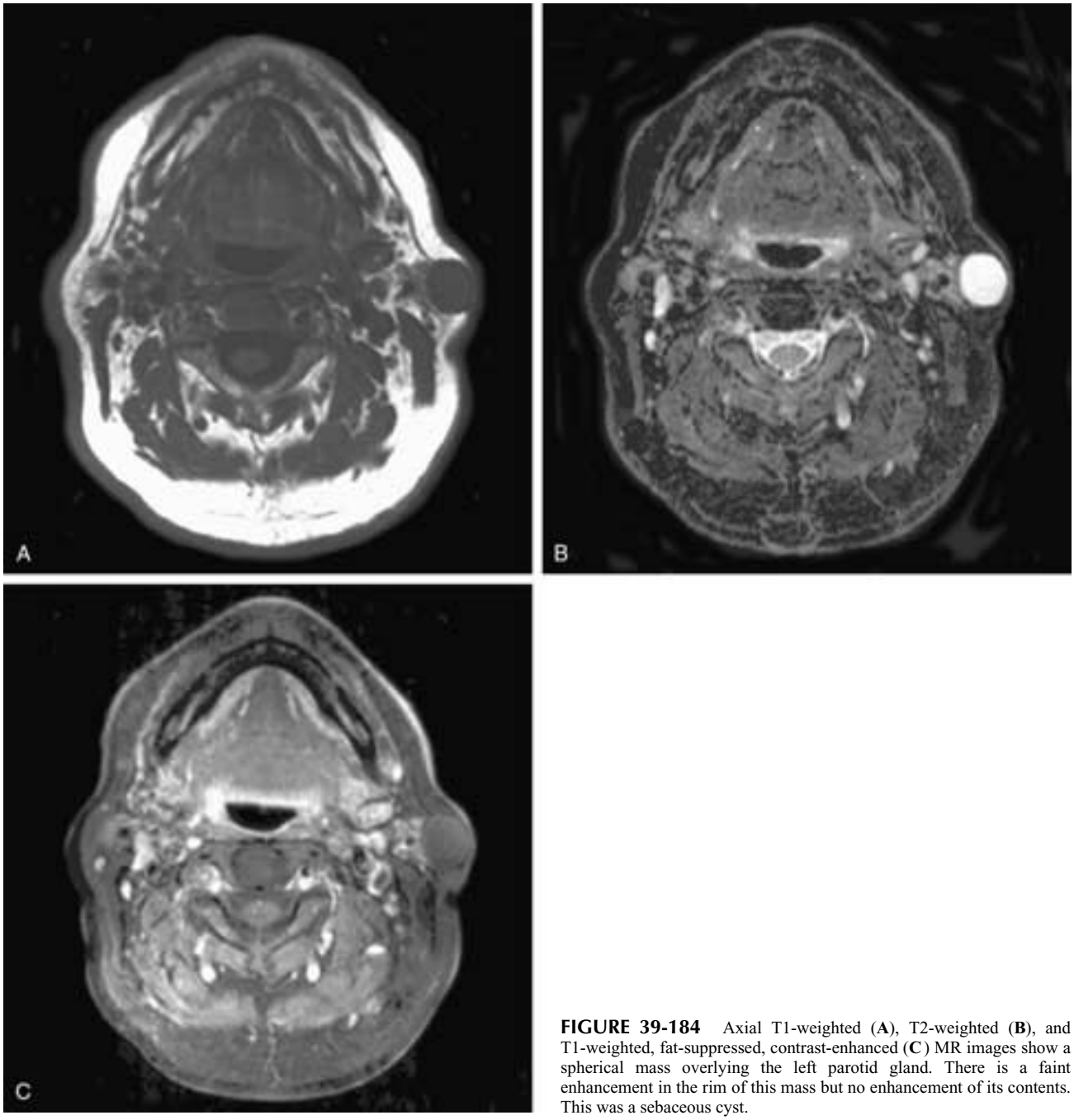

FIGURE 39-184 Axial T1-weighted (**A**), T2-weighted (**B**), and T1-weighted, fat-suppressed, contrast-enhanced (**C**) MR images show a spherical mass overlying the left parotid gland. There is a faint enhancement in the rim of this mass but no enhancement of its contents. This was a sebaceous cyst.

VIEW IMAGE

Copyright © 2003, Mosby, Inc. All rights reserved.

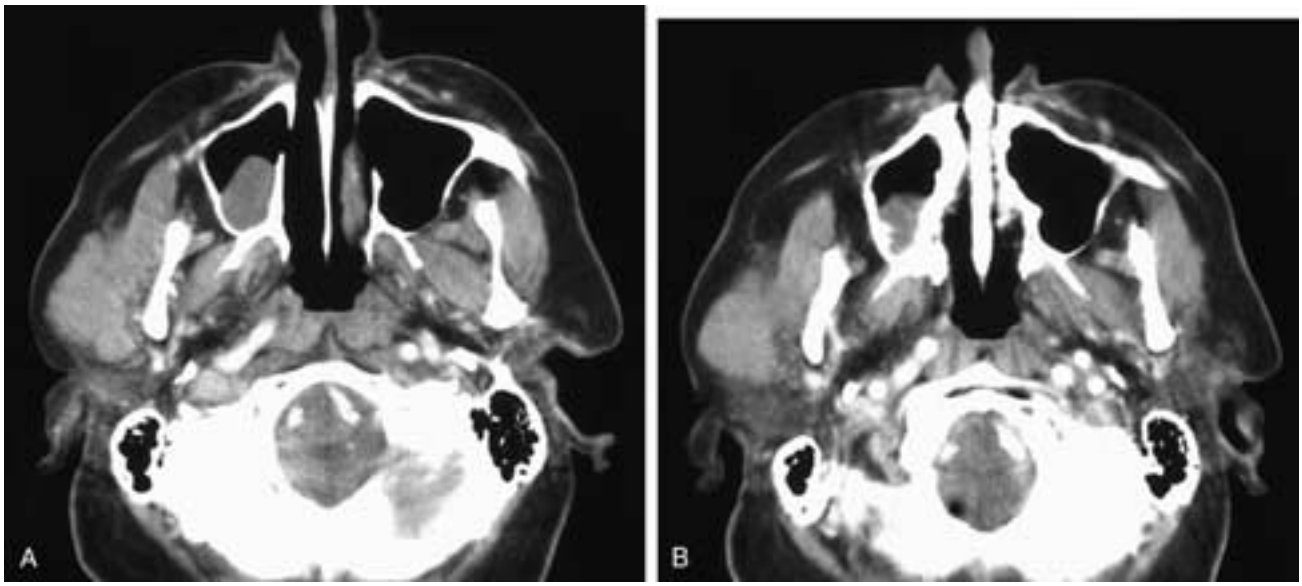

VIEW IMAGE

FIGURE 39-185 Axial contrast-enhanced CT scans (**A** and **B**) show a mass arising in the soft tissues overlying the right parotid gland. The tumor invades the parotid gland and the masseter muscle. Clinically, this was thought to be a parotid malignancy. This patient had a Merkel cell carcinoma.

most common tumor, representing over 50% of all lesions. Next in decreasing frequency are pleomorphic adenomas, MEC, lymphangiomas, and ACC. Rarely, undifferentiated carcinomas, adenocarcinomas, and AdCC can occur. About 30% to 35% of the cases are malignant, a higher percentage than found in adults.[8, 192, 197, 387] Masses that result from autoimmune disease and chronic sialadenitis may on occasion simulate a parotid tumor, and intraparotid lymphadenopathy may also mimic a parotid neoplasm.

A solitary benign-appearing mass in a pediatric patient is probably a lymph node, an hemangioma, a benign mixed tumor, a low-grade MEC, or a lymphangioma.

A solitary benign-appearing mass in an adult patient is probably a benign mixed tumor, a Warthin's tumor, a lymph node, an ACC, a low-grade MEC, a carcinoma ex pleomorphic adenoma, or an AdCC. A solitary malignant-appearing mass is most likely to be a high-grade MEC, an adenocarcinoma, or an undifferentiated carcinoma. Multiple masses suggest Warthin's tumors, acinic cell tumors, lymphoma, chronic inflammatory disease, oncocytic tumors, pleomorphic adenomas, or metastases. Multiple cystic masses, especially in association with benign cervical adenopathy, suggest that the patient is HIV positive.

If a cyst is present within a salivary gland, the limited differential diagnosis includes Warthin's tumor, lymphoepithelial cyst, branchial cleft cyst, sialocele, low-grade MEC, the papillocystic variant of ACC, and oncocystic cystadenoma. CT is the best modality for consistently evaluating the presence of a cyst and any cyst wall characteristics. On MR imaging, it is often difficult to distinguish a solid mass from a cyst unless there are contrast-enhanced images. This is because the watery cyst fluid gives the same signal intensities as the high water content of most benign and low-grade tumors. After contrast administration, the cyst wall enhances but the cyst contents do not. By comparison, the entire tumor usually enhances.

CT and MR imaging findings were reported on two patients with known HIV infection, bilateral parotid lymphoepithelial cysts, and bilateral multiple submandibular gland cysts with no evidence of obstructive glandular disease, autoimmune disease, or other organ system cysts. These cases of presumed submandibular gland lymphoepithelial cysts are rare in the literature.[388]

All salivary masses are probably better identified on MR imaging than on CT. However, calcifications are better seen on CT.

If the tumor accumulates ^{99m}Tc pertechnetate, a Warthin's tumor or oncocytoma is present.

If a tumor mass has low to intermediate signal intensity on all MR imaging sequences, a high-grade malignancy may be present. Although other entities can give these signal intensities, the high-grade lesion is the most important one to rule out of the differential diagnosis.

Calcifications may also be useful in generating a differential diagnosis. Solitary or multiple calcifications usually indicate the presence of chronic sialoadenitis. If calcification is seen within a salivary gland mass, most often the lesion is a pleomorphic adenoma. Less often, calcification can be seen within a schwannoma or an MEC. Parotid lymph node calcifications may occur in such conditions as posttreatment lymphoma and long-standing amyloidosis. Calcification may also occur within chronic hemorrhage. Ossification within a parotid mass is rare, the most common lesion being a pleomorphic adenoma. Phleboliths indicate a hemangioma. The inability of MR imaging to detect such small calcifications is one of the major limitations of this modality when imaging the major salivary glands.

When a solid salivary mass is present, MR imaging usually shows the margins more sharply than CT. What may appear on CT as a vague fullness in the parotid gland or a mass with unsharp margins will usually be seen as a discrete mass on MR. What may appear to be possibly several adjacent masses on CT can be seen either as a highly lobulated solitary mass or as several discrete adjacent

Copyright © 2003, Mosby, Inc. All rights reserved.

masses on MR imaging. Thus, in most cases, MR imaging better resolves the borders of such lesions. Evaluation of tumor extension outside the gland can be well achieved by either CT or MR imaging, as can gross erosion of the mandible or skull base. However, focal bone erosion or subtle bone sclerosis must be evaluated with CT.

With regard to the floor of the mouth and the sublingual glands, a study reported that the T1-weighted signal intensity of carcinomas in and near the sublingual space was lower than that of the sublingual glands, but the T2-weighted signal intensity of carcinomas may exceed that of the glands. Gadolinium enhancement occasionally diminished the contrast between invading carcinomas and the glands. T1-weighted MR imaging shows that sublingual glands affected by SS exhibit features analogous to those of the other major salivary glands; however, the sublingual glands seem to be less severely involved overall in this syndrome than the other major glands. Lastly, fat suppression and short time inversion recovery are useful for assessment of sialadenitis of the sublingual gland.[75]

REFERENCES

1. Boring C, Squires T, Tong T. Cancer statistics 1993. CA Cancer Journal for Clinicians 1993;43:18–19.
2. Thackray A, Lucas R. Tumors of major salivary glands. In: Atlas of Pathology. Washington, D.C.: Armed Forces Institute of Pathology 1974.
3. Spitz M, Tilley B, Batsakis J, et al. Risk factors for major salivary gland carcinoma: a case-comparison study. Cancer 1984;54:1854–1859.
4. Spitz M, Sider J, Newell G. Salivary gland cancer and risk of subsequent skin cancer. Head Neck 1990;12:254–256.
5. Dardick I, Burford-Mason A, Garlick D, et al. The pathology of salivary glands. II. Morphological evaluation of acinic cell carcinoma in the parotid gland of male transgenic (*MMTV/v-Ha-ras*) mice as a model for human tumors. Virchows Arch A Pathol Anat Histopathol 1992;421:105–113.
6. Krishnanmurthy S, Lanier A, Dohan P, et al. Salivary gland cancer in Alaskan natives. 1966–1980. Hum Pathol 1987;18:986–996.
7. Peel R, Gnepp D. Diseases of the salivary glands. In:, ed. Surgical Pathology of the Head and Neck. New York: Marcel Dekker, 1985;533–645.
8. Batsakis J, ed. Tumor of the Head and Neck: Clinical and Pathological Considerations. 2nd ed. Baltimore: Williams & Wilkins, 1979;1–120.
9. Dardick I, Burford-Mason A. Current status of histogenic and morphogenetic concepts of salivary gland tumorigenesis. Crit Rev Oral Biol Med 1993;4:639–677.
10. Dardick I, Dardick A, Mackay A, et al. Pathobiology of salivary glands. IV. Histogenetic concepts and cycling cells in human parotid and submandibular glands cultures in floating collagen gels. Oral Surg Oral Med Oral Pathol 1993;76:307–318.
11. Mason D, Chisholm D. Salivary Glands in Health and Disease. London: WB Saunders, 1975;3–18.
12. Moss-Salentijn L, Moss M. Development and functional anatomy. In: Rankow R, Polayes I, eds. Diseases of the Salivary Glands. Philadelphia: WB Saunders, 1976;17–31.
13. Gray H. Anatomy of the Human Body. Philadelphia: Lea & Febiger, 1959;1237–1241. Goss C, ed.
14. Weissman JL, Carrau RL. Anterior facial vein and submandibular gland together: predicting the histology of submandibular masses with CT or MR imaging [published erratum appears in Radiology 1999;210(2):585]. Radiology 1998;208:441–446.
15. Saleh HA, Ram B, Harmse JL, et al. Lipomatosis of the minor salivary glands. J Laryngol Otol 1998;112:895–897.
16. Gray H. Anatomy of the Human Body. Philadelphia: Lea & Febiger, 1959;951–1001. Goss C, ed.
17. Netter F. Nervous System. The CIBA Collection of Medical Illustrations. Vol. 1. Summit, N.J.: CIBA Pharmaceutical Products, 1953;80–87.
18. Almadori G, Ottaviani F, Del Ninno M, et al. Monolateral aplasia of the parotid gland. Ann Otol Rhinol Laryngol 1997;106:522–525.
19. Johns M. The salivary glands: anatomy and embryology. Otolaryngol Clin North Am 1977;10:261–271.
20. Pownell P, Brown O, Pransky S, Manning S. Congenital abnormalities of the submandibular duct. Int J Pediatr Otolaryngol 1992;24:161–169.
21. Rice DH. Noninflammatory, non-neoplastic disorders of the salivary glands. Otolaryngol Clin North Am 1999;32:835–843.
22. Moon WK, Han MH, Kim IO, et al. Congenital fistula from ectopic accessory parotid gland: diagnosis with CT sialography and CT fistulography. AJNR 1995;16:997–999.
23. Azar T, Scott J, Arnold J, Robin N. Epiglottic hypoplasia associated with lacrimo-auriculo-dental-digital syndrome. Ann Otol Rhinol Laryngol 2000;109:779–781.
24. Murdoch-Kinch C, Miles D. Clinical and radiographic features of the lacrimo-auriculo-dento-digital syndrome. Oral Surg Oral Med Oral Pathol Oral Radiol Endod 1996;81:727–735.
25. Taybi H, Lachman R, eds. Radiology of Syndromes, Metabolic Disorders, and Skeletal Dysplasias. St. Louis: CV Mosby, 1996.
26. Snyderman N, Suen J. Neoplasms. In: Cummings C, Fredrickson J, Harker L, et al, eds. Otolaryngology—Head and Neck Surgery. Vol. 2. St. Louis: CV Mosby, 1986;1027–1069.
27. Wotson S, Mandel I. The salivary secretions in health and disease. In: Rankow R, Polayes I, eds. Diseases of the Salivary Glands. Philadelphia: WB Saunders, 1976;32–53.
28. Sperber G. Craniofacial Embryology. 4th ed. London: Wright, 1989;144–146.
29. Diederich S, Roos N, Bick U, et al. Diagnostic imaging of the salivary glands in children and adolescents. Radiologe 1991;31:550–557.
30. Kawamura H, Taniguchi N, Itoh K, et al. Salivary gland echography in patients with Sjogren's syndrome. Arthritis Rheum 1990;33:505–510.
31. Mann W, Wachter W. Ultrasonic diagnosis of the salivary glands. Laryngol Rhinol Otol 1988;67:355–361.
32. March D, Rao V, Zwillenberg D. Computed tomography of salivary glands in Sjogren's syndrome. Arch Otolaryngol 1989;115:105–106.
33. Cholankeril J, Ravipati M, Khedekar S, et al. Unusually large sialocele: CT characteristics. J Comput Assist Tomogr 1989;13:367–368.
34. Coit W, Harnsberger H, Osborn A, et al. Ranulas and their mimics: CT evaluation. Radiology 1987;163:211–216.
35. Roebker J, Hall L, Lukin R. Fractured submandibular gland: CT findings. J Comput Assist Tomogr 1991;15:1068–1069.
36. Vogl T, Balzer J, Grevers G. Magnetic resonance tomography in questionable lesions of the ENT area. Examination technique and results of a prospective study of 1,493 patients. Laryngol Rhinol Otol 1992;71:439–452.
37. Chaudhuri R, Bingham J, Crossman J, Gleeson M. Magnetic resonance imaging of the parotid gland using the STIR sequence. Clin Otolaryngol 1992;17:211–217.
38. Marsot-Dupuch K, Brunereau L, Meyer B, et al. Parotid metastases: value of imaging. Review of the literature apropos of 4 cases. Ann Otolaryngol Chir 1991;108:338–342.
39. Sigal R, Monnet O, de Baere T, et al. Adenoid cystic carcinoma of the head and neck: evaluation with MR imaging and clinical-pathologic correlation in 27 patients. Radiology 1992;184:95–101.
40. Panush D, Fulbright R, Sze G, et al. Inversion-recovery fast spin-echo imaging: efficacy in the evaluation of head and neck lesions. Radiology 1993;187:421–426.
41. Tabor E, Curtin H. MR of the salivary glands. Radiol Clin North Am 1989;27:379–392.
42. Mees K, Vogl T, Kellermann O. Magnetic resonance tomography in tumors of the salivary glands—a diagnostic advantage? Laryngol Rhinol Otol 1988;67:355–361.
43. Smith F, Deans H, McLay K, Rayner C. Magnetic resonance imaging of the parotid glands using inversion-recovery sequences at 0.08T. Br J Radiol 1988;61:480–491.
44. Som P, Shugar J, Sacher M, et al. Benign and malignant parotid pleomorphic adenomas: CT and MR studies. J Comput Assist Tomogr 1988;12:65–69.

Copyright © 2003, Mosby, Inc. All rights reserved.

45. Mirich D, McArdle C, Kulkarni M. Benign pleomorphic adenomas of the salivary glands: surface coil MR imaging versus CT. J Comput Assist Tomogr 1987;11:620–623.
46. Rice D, Becker T. Magnetic resonance imaging of the salivary glands. A comparison with computed tomographic scanning. Arch Otolaryngol Head Neck Surg 1987;113:78–80.
47. Casselman J, Mancuso A. Major salivary gland masses: comparison of MR imaging and CT. Radiology 1987;165:183–189.
48. Parker G, Harnsberger H. Clinical-radiologic issues in perineural tumor spread of malignant diseases of the extracranial head and neck. Radiographics 1991;11:383–399.
49. Dalimonte P, Cerofolini E, Leoni A, et al. 1.5T MR in the diagnosis of parotid masses: comparison with ultrasonography. Eur J Radiol 1989;9:224–230.
50. Tien R, Hesselink J, Chu P, Szumowski J. Improved detection and delineation of head and neck lesions with fat suppression spin-echo MR imaging. AJNR 1991;12:19–24.
51. Kushner D, Weber A. Sialography of salivary gland tumors with fluoroscopy and tomography. AJR 1978;130:941–944.
52. Som P, Shugar J, Train J, Biller H. Manifestations of parotid gland enlargement: radiologic, pathologic and clinical correlations, part I: the autoimmune pseudosialectasias. Radiology 1981;141:415–419.
53. Som P, Shugar J, Train J, Biller H. Manifestations of parotid gland enlargement: radiologic, pathologic and clinical correlations, part II. The diseases of Mikulicz's syndrome. Radiology 1981;141:421–426.
54. Osier J, Peasants J. Distension sialography. Radiology 1966;87: 116–118.
55. Lowman R, Chang G. Diagnostic Radiology. In: Rankow R, Player I, eds. Diseases of the Salivary Glands. Philadelphia: WB Saunders, 1976;54–98.
56. Rabinov K, Jaffe N. A blunt-tip side injecting cannula for sialography. Radiology 1969;92:1438.
57. Som P, Khilnani M. Technical note: a modification of a butterfly infusion set for sialography. Radiology 1982;143:791.
58. Yoel J. Pathology and Surgery of the Salivary Glands. Springfield, Ill: Charles C Thomas, 1975;31–87.
59. Ollerenshaw R, Ross S. Radiological diagnosis of salivary gland disease. Br J Radiol 1951;24:538–548.
60. Rabinov K, Weber A. Radiology of the Salivary Glands. Boston: G Hall, 1985;1–221.
61. Manashil G. Clinical Sialography. Springfield, Ill: Charles C Thomas, 1978;19–28.
62. Bryan R, Miller R, Ferreyro R, Sessions R. Computed tomography of the major salivary glands. AJR 1982;139:547–554.
63. Calcaterra T, Hemenway W, Hansen G, Hanafee W. The value of sialography in the diagnosis of parotid tumors. Arch Otolaryngol 1977;103:727–729.
64. Potter G. Sialography and the salivary glands. Otolaryngol Clin North Am 1973;6:509–522.
65. Work W, Johns M. Symposium on salivary gland diseases. Otolaryngol Clin North Am 1977;10:261–328.
66. Som P, Biller H. The MR identification of high-grade parotid tumors. Radiology 1989;173:823–826.
67. McGhee RJ, Chakeres D, Schmalkbrock P, et al. The extracranial facial nerve: high resolution three-dimensional fourier transform MR imaging. AJNR 1993;14:465–472.
68. Mandelblatt S, Braun I, Davis P, et al. Parotid masses: MR imaging. Radiology 1987;163:411–414.
69. Teresi L, Lufkin R, Wortham D, et al. Parotid masses: MR imaging. Radiology 1987;163:405–409.
70. Thibault F, Halimi P, Bely N, et al. Internal architecture of the parotid gland at MR imaging: facial nerve or ductal system. Radiology 1993;188:701–704.
71. Dailiana T, Chakeres D, Schmalbrock P, et al. High-resolution MR of the intraparotid facial nerve and parotid duct. AJNR 1997;18: 165–172.
72. Zoarski G, Mackey J, Anzai Y, et al. Head and neck: initial clinical experience with fast spin-echo MR imaging. Radiology 1993;188: 323–327.
73. Chaudhuri R, Gleeson M, Graves P, et al. MR evaluation of the parotid gland using STIR and gadolinium-enhanced imaging. Eur Radiol 1992;2:357–364.
74. Schlakman B, Yousem D. MR of intraparotid masses. AJNR 1993;14:1173–1180.
75. Sumi M, Izumi M, Yonetsu K, Nakamura T. Sublingual gland: MR features of normal and diseased states. AJR 1999;172:717–722.
76. Fischbach R, Kugel H, Ernst S, et al. MR sialography: initial experience using a T2-weighted fast SE sequence. J Comput Assist Tomogr 1997;21:826–830.
77. Schroder U, Jungehulsing M, Fischbach R, Krug B. [Magnetic resonance sialography. A new diagnostic method for imaging salivary duct patency]. Hno 1998;46:38–43.
78. Alamdari A, Pierucci F, Leclerc JC, et al. [The value of sialo-MRI in the study of salivary gland duct pathology]. Rev Stomatol Chir Maxillofac 1999;100:184–186.
79. Heverhagen JT, Kalinowski M, Rehberg E, et al. Prospective comparison of magnetic resonance sialography and digital subtraction sialography. J Magn Reson Imag 2000;11:518–524.
80. Jungehulsing M, Fischbach R, Schroder U, et al. Magnetic resonance sialography. Otolaryngol Head Neck Surg 1999;121:488–494.
81. Varghese JC, Thornton F, Lucey BC, et al. A prospective comparative study of MR sialography and conventional sialography of salivary duct disease. AJR 1999;173:1497–1503.
82. Jager L, Menauer F, Holzknecht N, et al. Sialolithiasis: MR sialography of the submandibular duct—an alternative to conventional sialography and US? Radiology 2000;216:665–671.
83. Choi DS, Na DG, Byun HS, et al. Salivary gland tumors: evaluation with two-phase helical CT. Radiology 2000;214:231–236.
84. Park J, Inoue S, Ishizuka Y, et al. [Salivary gland masses: dynamic MR imaging and pathologic correlation]. Nippon Igaku Hoshasen Gakkai Zasshi 1997;57:581–585.
85. Vogl T, Wilimzig C, Assal J, et al. 3D MR imaging with Gd-DTPA in head and neck lesions. Eur Radiol 1991;1:151–157.
86. Vogl T, Dadashi A, Jassoy A, et al. The 31-phosphorus spectroscopy of space occupying lesions of the salivary glands. The clinical results and differential diagnosis. Rofo. Fortschritte Gebiete Rontgenstrahlen Neuen Bildgebenden Verfahren 1993;158:31–38.
87. Seo Y, Murakami M. NMR studies of salivary glands: from energy metabolism to morphology. Eur J Morphol 1998;36 Suppl:98–102.
88. Som P, Biller H. The combined CT-sialogram: a technique to differentiate deep lobe parotid tumors from extraparotid pharyngomaxillary space tumors. Ann Otolaryngol 1979;88:590–595.
89. Som P, Biller H. The combined CT-sialogram. Radiology 1980;135: 387–390.
90. Carter B, Karmody C. Computed tomography of the face and neck. Semin Roentgenol 1978;13:257–266.
91. Mancuso A, Rice D, Hanafee W. Computed tomography of the parotid gland during contrast sialography. Radiology 1979;132:211–213.
92. Neiman H, Phillips J, Jaques D, Brown T. Ultrasound of the parotid gland. J Clin Ultrasound 1976;4:11–13.
93. Gooding G. Gray scale ultrasound of the parotid gland. AJR 1980;134:469–472.
94. Martinoli C, Giovagnorio F, Pretolesi F, Derchi L. Identification of feeding arteries to establish the intra- or extraparotid location of jugulodigastric nodules: value of color doppler sonography. AJR 2000;175:1357–1360.
95. Feld R, Nazarian LN, Needleman L, et al. Clinical impact of sonographically guided biopsy of salivary gland masses and surrounding lymph nodes. Ear Nose Throat J 1999;78:905, 908–912.
96. Klutmann S, Bohuslavizki KH, Kroger S, et al. Quantitative salivary gland scintigraphy. J Nucl Med Technol 1999;27:20–26.
97. Cogan M, Gill P. Value of sialography and scintigraphy in diagnosis of salivary gland disorders. Int J Oral Surg 1981;10(Suppl 1):216–222.
98. Brandwein M, Huvos A. Oncocytic tumors of major salivary glands. A study of 68 cases with follow-up of 44 patients. Am J Surg Pathol 1991;15:514–528.
99. Schall G. The role of radionuclide scanning in the evaluation of neoplasms in the salivary glands: a review. J Surg Oncol 1971;3:699–714.
100. Schall G, Smith R, Barsocchini L. Radionuclide salivary imaging usefulness in a private otolaryngology practice. Arch Otolaryngol 1981;107:40–44.
101. Pretorius D, Taylor A. The role of nuclear scanning in head and neck surgery. Head Neck Surg 1982;4:427–432.
102. Arbab AS, Koizumi K, Toyama K, et al. Various imaging modalities for the detection of salivary gland lesions: the advantages of 201Tl SPET [in process citation]. Nucl Med Commun 2000;21:277–284.

Copyright © 2003, Mosby, Inc. All rights reserved.

103. Gundlach P, Hopf J, Linnarz M. Introduction of a new diagnostic procedure: salivary duct endoscopy (sialendoscopy) clinical evaluation of sialendoscopy, sialography, and X-ray imaging. Endosc Surg Allied Technol 1994;2:294–296.
104. Trappe M, Marsot-Dupuch K, Le Roux C. Study of the salivary glands in 1990. Ann Radiol 1991;34:114–117.
105. Gatenby R, Mulbern C, Strawitz J. CT-guided percutaneous biopsies of head and neck masses. Radiology 1983;146:717–719.
106. Lufkin R, Teresi L, Hanafee W. New needle for MR-guided aspiration cytology of the head and neck. AJR 1987;149:380–382.
107. Abemayor E, Ljung B, Ward P, et al. CT-directed aspiration biopsies of masses in the head and neck. Laryngoscope 1985;95: 1382–1386.
108. Jabour B, Choi Y, Hoh C, et al. Extracranial head and neck: PET imaging with 2-[F-18] fluoro-2-deoxy-D-glucose and MR imaging correlation. Radiology 1993;186:13–15.
109. Strauss LG. Fluorine-18 deoxyglucose and false-positive results: a major problem in the diagnostics of oncological patients. Eur J Nucl Med 1996;23:1409–1415.
110. Okamura T, Kawabe J, Koyama K, et al. Fluorine-18 fluorodeoxyglucose positron emission tomography imaging of parotid mass lesions. Acta Otolaryngol Suppl 1998;538:209–213.
111. McQuone SJ. Acute viral and bacterial infections of the salivary glands. Otolaryngol Clin North Am 1999;32:793–811.
112. Miglets A. Infections, part III, clinical entities. In: Cummings C, Fredrickson J, Harker L, et al, eds. Otolaryngology—Head and Neck Surgery. Vol 2. St. Louis: CV Mosby, 1986;999–1006.
113. Travis L, Hecht D. Acute and chronic inflammatory diseases of the salivary glands: diagnosis and management. Otolaryngol Clin North Am 1977;10:329–338.
114. Leake D, Leake R. Neonatal suppurative parotitis. Pediatrics 1970;46:203–207.
115. Spratt JJ. Etiology and therapy of acute pyogenic parotitis. Surg Gynecol Obstet 1961;112:391–405.
116. al-Deeb S. Herpes simplex encephalitis mimicking mumps. Clin Neurol Neurosurg 1993;95:49–53.
117. Chapnik J, Noyek A, Berris B, et al. Parotid gland enlargement in HIV infection: clinical/imaging findings. Otolaryngol Clin North Am 1990;19:189–194.
118. Scoidt M, Greenspan D, Levy J, et al. Does HIV cause salivary gland disease? AIDS 1989;3:819–822.
119. Tunkel D, Loury M, Fox C, et al. Bilateral parotid enlargement in HIV seropositive patients. Laryngoscope 1989;99:590–595.
120. Skolnick P, Kosloff B, Hirsch M. Bidirectional interactions between HIV type 1 and CMV. J Infect Dis 1988;157:508–513.
121. Bailey B. Trauma. In: Cummings C, Fredrickson J, Harker L, et al., eds. Otolaryngology—Head and Neck Surgery. Vol. 2. St. Louis: CV Mosby, 1986;1015–1026.
122. Alvarez S, McCabe W. Extrapulmonary tuberculosis revisited: a review of experience at Boston City and other hospitals. Medicine 1984;63:25–55.
123. Windsor J. Cat-scratch disease: epidemiology, aetiology and treatment. Br J Biomed Sci 2001;58:101–110.
124. Chomel B. Cat-scratch disease. Rev Sci Technol 2000;19: 136–150.
125. Margileth A. Recent advances in diagnosis and treatment of cat scratch disease. Curr Infect Dis Rep 2000;2:141–146.
126. Marx R, Hartman K, Rethman K. A prospective study comparing incisional labial to incisional parotid biopsies in the detection and confirmation of sarcoidosis, Sjogren's disease, sialosis and lymphoma. J Rheumatol 1988;15:621–629.
127. Kuwatsuru R, Katayama H, Minowa O, Tsukada K. Iodide mumps after contrast enhanced CT with iopamidol: a case report. Radiat Med 1995;13:147–148.
128. Levy D, ReMine W, Devine K. Salivary gland calculi. JAMA 1962;181:1115–1119.
129. Kesse WK, Shehab ZP, Courteney-Harris R. A megalith of the parotid salivary gland. J Laryngol Otol 1998;112:784–785.
130. McMenamin M, Quinn A, Barry H, et al. Cavernous hemangioma in the submandibular gland masquerading as sialadenitis: case report. Oral Surg Oral Med Oral Pathol Oral Radiol Endod 1997;84: 146–148.
131. Iro H, Waitz G, Nitsche N, et al. Extracorporeal piezoelectric shockwave lithotripsy of salivary gland stones. Laryngoscope 1992;102:492–494.
132. Yoshizaki T, Maruyama Y, Motoi I, et al. Clinical evaluation of extracorporeal shock wave lithotripsy for salivary stones. Ann Otol Rhinol Laryngol 1996;105:63–67.
133. Work W, Hecht D. Inflammatory diseases of the major salivary glands. In: Paparella M, Shumrick D, eds. Otolaryngology. Vol. 3. Philadelphia: WB Saunders, 1973;258–265.
134. Hudson N. Manifestations of systemic disease. In: Cummings C, Fredrickson J, Harker L, et al, eds. Otolaryngology—Head and Neck Surgery. Vol. 2. St. Louis: CV Mosby, 1986;1007–1013.
135. Godwin J. Benign lymphoepithelial lesion of the parotid gland (adenolymphoma, chronic inflammation, lymphoepithelioma, lymphocytic tumor, Mikulicz disease): report of eleven cases. Cancer 1952;5:1089–1103.
136. Rabinov K, Weber A. Radiology of the Salivary Glands. Boston: G. Hall, 1985;222–264.
137. Selva O'Callaghan A, Angel Bosch Gil J, Solans Laque R, et al. Primary Sjogren's syndrome: clinical and immunological characteristics of 114 patients. Med Clin (Barc) 2001;116:721–725.
138. Moutsopoulos H, Chused T, Mann D, et al. Sjogren's syndrome (sicca syndrome): current issues. Ann Intern Med 1980;92: 212–226.
139. Amft N, Bowman SJ. Chemokines and cell trafficking in Sjogren's syndrome. Scand J Immunol 2001;54:62–69.
140. Kompoliti A, Gage B, Sharma L, Daniels JC. Human T-cell lymphotropic virus type 1–associated myelopathy, Sjogren syndrome, and lymphocytic pneumonitis. Arch Neurol 1996;53: 940–942.
141. Ostuni PA, Ianniello A, Sfriso P, et al. Juvenile onset of primary Sjogren's syndrome: report of 10 cases. Clin Exp Rheumatol 1996;14:689–693.
142. Bloch K. Sjogren's syndrome. In: Stein J, ed. Internal Medicine. Boston: Little, Brown, 1983;1034–1036.
143. Mason D, Chisholm D. Salivary Glands in Health and Disease. London: WB Saunders, 1975;167–206.
144. Vitali C, Moutsopoulos HM, Bombardieri S. The European Community Study Group on diagnostic criteria for Sjogren's syndrome. Sensitivity and specificity of tests for ocular and oral involvement in Sjogren's syndrome. Ann Rheum Dis 1994;53: 637–647.
145. Molina R, Provost T, Arnett F, et al. Primary Sjogren's syndrome in men. Clinical, serologic, and immunogenetic features. Am J Med 1986;80:23–31.
146. Moutsopoulos H, Chused T, Mann D, et al. Sjogren's syndrome (sicca syndrome): current issues. Ann Intern Med 1980;92:212–226.
147. Muller-Hermelink H, Greiner A. Autoimmune disease and malignant lymphoma. Verhandlungen Deutsch Gesellschaft Pathol 1992;76: 96–109.
148. Biasi D, Caramaschi P, Ambrosetti A, et al. Mucosa-associated lymphoid tissue lymphoma of the salivary glands occurring in patients affected by Sjogren's syndrome: report of 6 cases. Acta Haematol 2001;105:83–88.
149. Ihrler S, Baretton GB, Menauer F, et al. Sjogren's syndrome and MALT lymphomas of salivary glands: a DNA-cytometric and interphase-cytogenetic study. Mod Pathol 2000;13:4–12.
150. Voulgarelis M, Dafni UG, Isenberg DA, Moutsopoulos HM. Malignant lymphoma in primary Sjogren's syndrome: a multicenter, retrospective, clinical study by the European Concerted Action on Sjogren's Syndrome. Arthritis Rheum 1999;42:1765–1772.
151. Rabinov K, Weber A. Radiology of the Salivary Glands. Boston: G. Hall, 1985;265–291.
152. Som P, Shugar J, Biller H. Parotid gland sarcoidosis and the CT-sialogram. J Comput Assist Tomogr 1981;5:674–677.
153. Izumi M, Eguchi K, Nakamura H, et al. Premature fat deposition in the salivary glands associated with Sjogren syndrome: MR and CT evidence. AJNR 1997;18:951–958.
154. Ohbayashi N, Yamada I, Yoshino N, Sasaki T. Sjogren syndrome: comparison of assessments with MR sialography and conventional sialography. Radiology 1998;209:683–688.
155. Tonami H, Ogawa Y, Matoba M, et al. MR sialography in patients with Sjogren syndrome [see comments]. AJNR 1998;19:1199–1203.
156. Itescu S. Diffuse infiltrative lymphocytosis syndrome in human immunodeficiency virus infection—a Sjogren's like disease. Rheum Dis Clin North Am 1991;17:99–115.
157. Schima W, Amann G, Steiner E, et al. Case report: sicca syndrome due to primary amyloidosis. Br J Radiol 1994;67:1023–1025.

Copyright © 2003, Mosby, Inc. All rights reserved.

158. Ramos-Casals M, Garcia-Carrasco M, Cervera R, et al. Hepatitis C virus infection mimicking primary Sjogren's syndrome. A clinical and immunologic description of 35 cases. Medicine 2001;80:1–8.
159. Levin P, Falko J, Dixon K, et al. Benign parotid enlargement in bulimia. Ann Intern Med 1980;93:827–829.
160. Carron JD, Karakla DW, Watkins DV. Focal parotid necrosis in systemic lupus erythematosus: case report and review of the literature. Oral Surg Oral Med Oral Pathol Oral Radiol Endod 1999;88:455–460.
161. Izumi M, Hida A, Kawabe Y, et al. MR imaging of the salivary glands in sicca syndrome: comparison of lipid profiles and imaging in patients with hyperlipidemia and patients with Sjogren's syndrome. AJNR 2000;175:829–834.
162. Hasler J. Parotid enlargement: a presenting sign in anorexia nervosa. Oral Surg Oral Med Oral Pathol 1982;53:567–572.
163. Gibson J, Lamey P, Lewis M, Frier B-. Oral manifestations of previously undiagnosed non-insulin-dependent diabetes mellitus. J Oral Pathol Med 1990;19:284–287.
164. Donath K. Swellings of the cheek from sialosis. HNO 1979;27: 113–118.
165. Whyte A, Bowyer F. Sialosis diagnosed by computed tomography. Br J Radiol 1987;60:400–401.
166. Leslie M, Dische S. The early changes in salivary gland function during and after radiotherapy given for head and neck cancer. Radiother Oncol 1994;30:26–32.
167. Valdes Olmos R, Keus R, Takes R, et al. Scintigraphic assessment of salivary function and excretion response in radiation-induced injury of the major salivary glands. Cancer 1994;73:2886–2893.
168. Land C, Saku T, Hayashi Y. Incidence of salivary gland tumors among atomic bomb survivors, 1950–1987. Evaluation of radiation risk. Radiat Res 1996;146:28–36.
169. Eisbruch A, Ship JA, Martel MK, et al. Parotid gland sparing in patients undergoing bilateral head and neck irradiation: techniques and early results. Int J Radiat Oncol Biol Phys 1996;36: 469–480.
170. Barrett A, Speight P. Adenomatoid hyperplasia of oral minor salivary glands. Oral Surg Oral Med Oral Pathol Oral Radiol Endod 1995;79:482–487.
171. Seifert G, Thomsen S, Donath K. Bilateral dysgenetic polycystic parotid glands: morphological analysis and differential diagnosis of a rare disease of salivary glands. Virchows Arch A Pathol Anat Histopathol 1981;390:273–288.
172. Batsakis J, Bruner J, Luna M. Polycystic (dysgenetic) disease of the parotid glands. Arch Otolaryngol Head Neck Surg 1988;114:1146–1148.
173. Couderc L, D'Agay M, Danon F, et al. Sicca complex and infection with HIV. Arch Intern Med 1987;147:898–901.
174. Schoidt M, Greenspan D, Levy J, et al. Does HIV cause salivary gland disease? AIDS 1989;3:819–822.
175. Ulirisch R, Jaffe E. Sjogren's syndrome–like illness associated with the AIDS-related complex. Hum Pathol 1987;18:1063–1068.
176. Smith F, Rajdeo H, Panesar N. Benign lymphoepithelial lesion of the parotid gland in intravenous drug users. Arch Pathol Lab Med 1988;112:742–745.
177. D'Agay M, de Roquancourt A, Peuchmaur M. Cystic benign lymphoepithelial lesion of the salivary glands in HIV positive patients. Report of two cases with immunohistochemical study. Virchows Arch A Pathol Anat Histopathol 1990;417:353–356.
178. Ferraro FJ, Rush BJ, Ruark D. Enucleation of parotid lymphoepithelial cyst in patients who are human immunodeficiency virus positive. J Surg Gynecol Obstet 1993;177:524–526.
179. Sperling N, Lin P, Lucente F. Cystic parotid masses in HIV infection. Head Neck 1990;12:337–341.
180. Som P, Brandwein M, Silvers A. Nodal inclusion cysts of the parotid gland and parapharyngeal space: a discussion of lymphoepithelial cysts, AIDS-related parotid cysts, branchial cysts, cystic Warthin's tumors, and cyst in Sjogren's syndrome (benign lymphoepithelial lesions). Laryngoscope 1995;105:1122–1128.
181. Ihrler S, Zietz C, Riederer A. HIV-related parotid lymphoepithelial cysts. Immunohistochemistry and 3-D reconstruction of surgical and autopsy material with special reference to formal pathogenesis. Virchows Arch A Pathol Anat Histopathol 1996;429:139–147.
182. Davidson J, Khan Y, Gilbert R, et al. Is selective neck dissection sufficient treatment for the N0/Np+ neck? [in process citation]. J Otolaryngol 1997;26:229–231.
183. Batsakis J, ed. Tumors of the Head and Neck: Clinical and Pathological Considerations. 2nd. Baltimore: Williams & Wilkins, 1979; 514–530.
184. Mihalyka E. Congenital bilateral polycystic parotid glands. JAMA 1982;181:634–635.
185. Work W. Cysts and congenital lesions of the parotid gland. Otolaryngol Clin North Am 1977;10:339–343.
186. Manashil G. Clinical Sialography. ed. Springfield, Ill: Charles C Thomas 1978;74–81.
187. Som P. Cystic lesions of the neck. Postgrad Radiol 1987;7:211–236.
188. Shugar J, Som P, Jacobson A, et al. Multicentric parotid cysts and cervical adenopathy in AIDS patients. A newly recognized entity: CT and MR manifestations. Laryngoscope 1988;98:772–775.
189. Morris M, Moore D, Shearer G. Bilateral multiple benign lymphoepithelial cysts of the parotid gland. Otolaryngol Head Neck Surg 1987;97:87–90.
190. Olsen W, Jeffrey RJ, Sooy C, et al. Lesions of the head and neck in patients with AIDS: CT and MR findings. AJR 1988;151:785–790.
191. Eneroth C. Salivary gland tumors in the parotid gland, submandibular gland and the palate region. Cancer 1971;27:1415–1418.
192. Rabinov K, Weber A. Radiology of the Salivary Glands. Boston: G Hall, 1985;292–367.
193. Rankow R, Polayes I, eds. Surgical treatment of salivary gland tumors. In: Rankow R, Polayes I, eds. Diseases of the Salivary Glands. Philadelphia: WB Saunders, 1976;239–283.
194. Audair P, Ellis G, Gnepp D, et al. Salivary gland neoplasms: general considerations. In: Ellis G, Audair P, Gnepp D, eds. Surgical Pathology of the Salivary Glands. Philadelphia: WB Saunders, 1991.
195. Johns M. Parotid cancer: a rational basis for treatment. Head Neck Surg 1980;3:132–141.
196. Thackray A, Sobin L. Histological typing of salivary gland tumors. In: International Histological Classification of Tumors. Geneva: World Health Organization, 1972.
197. Lack E, Upton M. Histopathologic review of salivary gland tumors in children. Arch Otolaryngol Head Neck Surg 1988;114:898–906.
198. Andersen L, Therkildsen M, Ockelmann H, et al. Malignant epithelial tumors in the minor salivary glands, the submandibular gland and the sublingual gland. Cancer 1991;68:2431–2437.
199. Cornug J, Gray S. Surgical and clinical pathology of salivary gland tumors. In: Rankow R, Polayes I, eds. Diseases of the Salivary Glands. Philadelphia: WB Saunders, 1976;99–142.
200. Myssiorek D, Ruah C, Hybels R. Recurrent pleomorphic adenomas of the parotid gland. Head Neck 1990;12:332–336.
201. McGregor A, Burgoyne M, Tan K. Recurrent pleomorphic salivary adenoma—the relevance of age at first presentation. Br J Plast Surg 1988;41:177–181.
202. Laskawi R, Schott T, Schröder M. Recurrent pleomorphic adenomas of the parotid gland: clinical evaluation and long-term follow-up. Br J Oral Maxillofac Surg 1998;36:48–51.
203. Batsakis J. The pathology of head and neck tumors: nasal cavity and paranasal sinuses. Part 5. Head Neck Surg 1980;2:410–419.
204. Gnepp D. Malignant mixed tumors of the salivary glands: a review. Pathol Annu 1993;28:279–328.
205. Brandwein M, Huvos AG, Dardick I, et al. Noninvasive and minimally invasive carcinoma ex mixed tumor: a clinicopathologic and ploidy study of 12 patients with major salivary tumors of low (or no?) malignant potential. Oral Surg Oral Med Oral Pathol Oral Radiol Endod 1996;81:655–664.
206. Gerughty R, Scofield H, Brown F, Hennigar G. Malignant mixed tumors of salivary gland origin. Cancer 1969;24:471–486.
207. Tortoledo M, Luna M, Batsakis J. Carcinoma ex pleomorphic adenoma and malignant mixed tumors. Histomorphologic indexes. Arch Otolaryngol Head Neck Surg 1984;110:172–176.
208. Wenig B, Hitchcock C, Ellis G, Gnepp D. Metastasizing mixed tumor of salivary glands. A clinicopathologic and flow cytometric analysis. Am J Surg Pathol 1992;16:845–858.
209. Jin Y, Jin C, Arheden K. Unbalanced chromosomal rearrangements in a metastasizing salivary gland tumor with benign histology. Cancer Genet Cytogenet 1998;102:59–64.
210. Hoorweg J, Hilgers F, Keus R. Metastasizing pleomorphic adenoma: a report of three cases. Eur J Surg Oncol 1998;24:452–455.
211. Goodisson D, Buff R, Creedon A. A case of metastasizing pleomorphic adenoma. Oral Med Oral Surg Oral Pathol Oral Radiol Endod 1999;87:341–345.

Copyright © 2003, Mosby, Inc. All rights reserved.

212. Wenig B, Hitchcock C, Ellis G, Gnepp D. Metastasizing mixed tumors of salivary glands. A clinicopathologic and flow cytometric analysis. Am J Surg Pathol 1992;16:845–857.
213. Takata T, Nikai H, Ogawa I, Ijuhin N. Ultrastructural and immunohistochemical observations of a true malignant mixed tumor (carcinosarcoma) of the tongue. J Oral Pathol Med 1990;19:261–265.
214. Julie C, Aidan D, Arkwright S. Carcinosarcome de la glande sous-maxillaire. Ann Pathol 1997;17:35–37.
215. Ellies M, Laskawi R, Argleba C. Extraglandular Warthin's tumours: clinical evaluation and long-term follow-up. Br J Oral Maxillofac Surg 1998;36:52–53.
216. Ellis G, Auclair P. Benign epithelial neoplasms. In: Atlas of Tumor Pathology: Tumors of the Salivary Glands. Washington, D.C.: Armed Forces Institute of Pathology, 1996; Third Series, Fascicle 17, 39–153.
217. Pinkston J, Cole P. Incidence rates of salivary gland tumors: results from a population-based study. Otolaryngol Head Neck Surg 1999;120:834–840.
218. Yoo G, Eisele D, Askin F. Warthin's tumor: a 40-year experience at the Johns Hopkins Hospital. Laryngoscope 1994;104:799–803.
219. Nagao T, Sugano I, Ishida Y. Mucoepidermoid carcinoma arising in Warthin's tumour of the parotid gland: report of two cases with histopathological, ultrastructural and immunohistochemical studies. Histopathology 1998;33:379–386.
220. Medeiros L, Rizzi R, Lardelli P, Jaffe E. Malignant lymphoma involving a Warthin's tumor: a case with immunophenotypic and gene rearrangement analysis. Hum Pathol 1990;21:974–977.
221. Aguirre J, Echebarria M, Martinez-Conde R. Warthin tumor: a new hypothesis concerning its development. Oral Surg Oral Med Oral Pathol Oral Radiol Endod 1998;85:60–63.
222. Shugar J, Som P, Biller H. Warthin's tumor, a multifocal disease. Ann Otol Rhinol Laryngol 1982;91:246–249.
223. Nakada M, Nishizaki K, Akagi H. Oncocytic carcinoma of the submandibular gland: a case report and literature review. J Oral Pathol Med 1998;27:225–228.
224. Ellis G, Auclair P. Atlas of Tumor Pathology: Tumors of the Salivary Glands. Washington, D.C.: Armed Forces Institute of Pathology, 1996: Third Series, Fascicle 17, 103–114, 318–324.
225. Thompson L, Wenig B, Ellis G. Oncocytomas of the submandibular gland. A series of 22 cases and a review of the literature. Cancer 1996;78:2281–2287.
226. Ellis G, Auclair P. Atlas of Tumor Pathology: Tumors of the Salivary Glands. Washington, D.C.: Armed Forces Institute of Pathology, 1996; Third Series, Fascicle 17:39–153.
227. Nagao K, Matsuzaki O, Saiga H. Histopathologic studies of basal cell adenoma of the parotid gland. Cancer 1982;50:736–745.
228. Ellis G, Wiscovitch J. Basal cell adenocarcinomas of major salivary glands. Oral Surg Oral Med Oral Pathol 1990;69:461–469.
229. Batsakis J, Luna M. Basaloid salivary carcinomas. Ann Otol Rhinol Laryngol 1991;100:785–787.
230. Ellis G, Auclair P. Atlas of Tumor Pathology: Tumors of the Salivary Glands. Washington, D.C.: Armed Forces Institute of Pathology, 1996; Third Series, Fascicle 17:257–267.
231. Nagao T, Sugano I, Ishida Y. Basal cell adenocarcinoma of the salivary glands: comparison with basal cell adenoma through assessment of cell proliferation, apoptosis, and expression of *p53* and *bcl-2*. Cancer 1998;82:439–447.
232. Fonseca I, Soares J. Basal cell adenocarcinoma of minor salivary and seromucous glands of the head and neck region. Semin Diagn Pathol 1996;13:128–137.
233. Muller S, Barnes L. Basal cell adenocarcinoma of the salivary glands. Report of seven cases and review of the literature. Cancer 1996;78:2471–2477.
234. Dardick I, ed. Salivary Gland Tumor Pathology. New York: Igaku-Shoin, 1996;61–67.
235. Ellis G, Auclair P. Atlas of Tumor Pathology: Tumors of the Salivary Glands. Washington, D.C.: Armed Forces Institute of Pathology, 1996;Third Series, Fascicle 17:95–103.
236. Rousseau A, Mock D, Dover D, Jordan R. Multiple canalicular adenomas: a case report and review of the literature. Oral Surg Oral Med Oral Pathol Oral Radiol Endod 1999;87:346–350.
237. Savera A, Sloman A, Huvos A, Klimstra D. Myoepithelial carcinoma of the salivary glands: a clinicopathologic study of 25 patients. Am J Surg Pathol 2000;24:761–774.
238. El-Mofty S, O'Leary T, Swanson P. Malignant myoepithelioma of salivary glands: clinicopathologic and immunophenotypic features: review of literature and report of 2 new cases. Int J Surg Pathol 1994;2:133–140.
239. Hsiao CH, Cheng CJ, Yeh KL. Immunohistochemical and ultrastructural study of malignant plasmacytoid myoepithelioma of the maxillary sinus. J Formos Med Assoc 1997;96:209–212.
240. Corio R, Sciubba J, Brannon R, Batsakis J. Epithelial-myoepithelial carcinoma of intercalated duct origin: a clinicopathologic and ultrastructural assessment of sixteen cases. Oral Surg Oral Med Oral Pathol 1982;53:280–287.
241. Corio R. Epithelial-myoepithelial carcinoma. In: Ellis G, Auclair P, Gnepp D, eds. Surgical Pathology of the Salivary Glands. Philadelphia: WB Saunders, 1991.
242. Hamper K, Brugmann M, Koppermann R. Epithelial-myoepithelial duct carcinoma of salivary glands: a follow-up and cytophotometric study of 21 cases. J Oral Pathol Med 1989;18:299–304.
243. Milchgrub S, Gnepp D, Vuitch F. Hyalinizing clear cell carcinoma of salivary gland. Am J Surg Pathol 1994;18:74–82.
244. Rinaldo A, McLaren K, Boccato P, Maran A. Hyalinizing clear cell carcinoma of the oral cavity and of the parotid gland. Orl J Otorhinolaryngol Relat Spec 1999;61:48–51.
245. Tang S, Wan S, Chan J. Hyalinizing clear cell carcinoma of salivary gland: report of a case with multiple recurrences over 12 years. Am J Surg Pathol 1995;19:240–241.
246. Auclair P, Goode R, Ellis G. Mucoepidermoid carcinoma of intraoral salivary glands. Evaluation and application of grading criteria in 143 cases. Cancer 1992;69:2021–2030.
247. Brandwein M, Ivanov K, Wallace D, et al. Mucoepidermoid carcinoma: a clinicopathologic study of 80 patients with special reference to histological grading. Am J Surg Pathol 2001;25:835–845.
248. Suzuki M, Ichimiya I, Matsushita F. Histologic features and prognosis of patients with mucoepidermoid carcinoma of the parotid gland. J Laryngol Otol 1998;112:944–947.
249. Batsakis J, Luna M. Pathologic consultation—histopathologic grading of salivary gland neoplasms: I. Mucoepidermoid carcinomas. Ann Otol Rhinol Laryngol 1990;99:835–838.
250. Goode R, Auclair P, Ellis A. Mucoepidermoid carcinoma of the major salivary glands: clinical and histologic analysis of 234 cases with evaluation of grading criteria. Cancer 1998;82:1217–1224.
251. Hicks J, El-Naggar A, Flaitz C. Histologic grading of mucoepidermoid carcinoma of major salivary glands in prognosis and survival: a clinicopathologic and flow cytometric investigation. Head Neck 1995;17:89–95.
252. Kaste S, Hedlund G, Pratt C. Malignant parotid tumors in patients previously treated for childhood cancer: clinical and imaging findings in eight cases. Am J Roentgenol 1994;162:655–659.
253. Plambeck K, Friedrich R, Heller D. Mucoepidermoid carcinoma of the salivary glands. Clinical data and follow-up of 52 cases. J Cancer Res Clin Oncol 1996;122:177–180.
254. Conley J, Casler J. Adenoid Cystic Cancer of the Head and Neck. New York: Theime, 1991.
255. Conley J, Dingman D. Adenoid cystic carcinoma in the head and neck (cylindroma). Arch Otolaryngol 1974;100:81–90.
256. McFall MR, Irvine GH, Eveson JW. Adenoid cystic carcinoma of the sublingual salivary gland in a 16-year-old female—report of a case and review of the literature. J Laryngol Otol 1997;111:485–488.
257. Spiro R, Huvos A. Stage means more than grade in adenoid cystic carcinoma. Am J Surg 1992;164:623–628.
258. Garden A, Weber R, Morrison W. The influence of positive margins and nerve invasion in adenoid cystic carcinoma of the head and neck treated with surgery and radiation. Int J Radiat Oncol Biol Phys 1995;32:619–626.
259. Brunori A, Scarano P, Iannetti G, Chiappetta F. Dumbbell tumor of the anterior skull base: meningioma? No, adenoid cystic carcinoma! Surg Neurol 1998;50:470–474.
260. Ueta E, Osaki T, Yamamoto T, Yoneda K. Induction of differentiation in maxillary adenoid cystic carcinomas by adoptive immunotherapy in combination with chemoradiotherapy. Oral Oncol 1998;34:105–111.
261. Beckhardt R, Weber R, Zane R. Minor salivary gland tumors of the palate: clinical and pathologic correlates of outcome. Laryngoscope 1995;105:1155–1160.
262. Spiro R. Distant metastasis in adenoid cystic carcinoma of salivary origin. Am J Surg 1997;174:495–498.

Copyright © 2003, Mosby, Inc. All rights reserved.

263. Fordice J, Kershaw C, El-Naggar A, Goepfert H. Adenoid cystic carcinoma of the head and neck: predictors of morbidity and mortality. Arch Otolaryngol Head Neck Surg 1999;125:149–152.
264. Huang M, Ma D, Sun K. Factors influencing survival rate in adenoid cystic carcinoma of the salivary glands. Int J Oral Maxillofac Surg 1997;26:435–439.
265. Franzen G, Nordgard S, Boysen M. DNA content in adenoid cystic carcinomas. Head Neck 1995;17:49–55.
266. Azar T, Abdul-Karim F, Tucker H. Adenoid cystic carcinoma of the trachea. Laryngoscope 1998;108:1297–1300.
267. Franchi A, Gallo O, Bocciolini C. Reduced E-cadherin expression correlates with unfavorable prognosis in adenoid cystic carcinoma of salivary glands of the oral cavity. Am J Clin Pathol 1999;111:43–50.
268. Batsakis J, Luna M, El-Naggar A. Histopathologic grading of salivary gland neoplasms: II. Acinic cell carcinomas. Ann Otol Rhinol Laryngol 1990;99:929–933.
269. Spiro R. Salivary neoplasms: overview of a 35-year experience with 2,807 patients. Head Neck Surg 1986;8:177–184.
270. Guimaraes D, Amaral A, Prado L. Acinic cell carcinoma of salivary glands: 16 cases with clinicopathologic correlation. J Oral Pathol Med 1989;18:396–399.
271. Hamper K, Mausch H, Caselitz J. Acinic cell carcinoma of the salivary glands: the prognostic relevance of DNA cytophotometry in a retrospective study of long duration (1965–1987). Oral Surg Oral Med Oral Pathol 1990;69:68–75.
272. Ellis G, Auclair P. Acinic cell adenocarcinoma. In: Ellis GL, Auclair P, Gnepp DR, eds. Surgical Pathology of the Salivary Glands. Philadelphia: WB Saunders, 1991;81–90.
273. Eveson J, Cawson R. Salivary gland tumours. A review of 2410 cases with particular reference to histological types, site, age and sex distribution. J Pathol 1985;146:51–58.
274. Spafford P, Mint D, Hay J. Acinic cell carcinoma of the parotid gland: review and management. J Otolaryngol 1991;20:262–266.
275. Castro E, Huvos A, Strong E, Feet J. Tumors of the major salivary glands in children. Cancer 1972;29:312–317.
276. Jones A, Lam A, Martin H. Acinic cell carcinoma of the parotid in children. Austral Radiol 1997;41:44–48.
277. Lewis J, Olsen K, Weiland L. Acinic cell carcinoma: clinicopathologic review. Cancer 1991;67:172–179.
278. Freedman P, Lumerman H. Lobular carcinoma of intraoral minor salivary gland origin: report of twelve cases. Oral Surg Oral Med Oral Pathol 1983;56:157–165.
279. Batsakis J, Pinkston G, Luna M. Adenocarcinomas of the oral cavity: a clinicopathologic study of terminal duct carcinomas. J Laryngol Otol 1983;97:825–835.
280. Evans H, Batsakis J. Polymorphous low-grade adenocarcinomas of minor salivary glands: a study of 14 cases of a distinctive neoplasm. Cancer 1984;53:935–942.
281. Gnepp D, Chen J, Warren C. Polymorphous low-grade adenocarcinoma of minor salivary gland: an immunohistochemical and clinicopathologic study. Am J Surg Pathol 1988;12:461–468.
282. Skalova A, Simpson R, Lehtonen H, Leivo I. Assessment of proliferative activity using the MIB1 antibody helps to distinguish polymorphous low-grade adenocarcinoma from adenoid cystic carcinoma of salivary glands. Pathol Res Pract 1997;193:695–703.
283. Perez-Ordonez B, Linkov I, Huvos A. Polymorphous low-grade adenocarcinoma of minor salivary glands: a study of 17 cases with emphasis on cell differentiation. Histopathology 1998;32:521–529.
284. Castle J, Thompson L, Frommelt R. Polymorphous low-grade adenocarcinoma (PLGA): a clinicopathologic study of 164 cases. Cancer 1999;86:207–219.
285. Mills S, Garland T, Allen M. Low-grade papillary adenocarcinoma of palatal salivary gland origin. Am J Surg Pathol 1984;8:367–374.
286. Tanaka F, Wada H, Inui K. Pulmonary metastasis of polymorphous low-grade adenocarcinoma of the minor salivary gland. Thorac Cardiovasc Surg 1995;43:178–180.
287. Thomas K, Cumberworth V, McEwan J. Orbital and skin metastases in a polymorphous low-grade adenocarcinoma of the salivary gland. J Laryngol Otol 1995;109:1222–1225.
288. Brandwein M, Jagirdar J, Patil J. Salivary duct carcinoma (cribriform salivary carcinoma of excretory ducts). A clinicopathologic and immunohistochemical study of 12 cases. Cancer 1990;65:2307–2314.
289. Lewis J, McKinney B, Weiland L. Salivary duct carcinoma: clinicopathologic and immunohistochemical review of 26 cases. Cancer 1996;77:223–230.
290. Barnes L, Rao U, Krause J, Contis L. Salivary duct carcinoma. Part I. A clinicopathologic evaluation and DNA image analysis of 13 cases with review of the literature. Oral Surg Oral Med Oral Pathol 1994;78:64–73.
291. Delgado R, Klimstra D, Albores-Saavedra J. Low grade salivary duct carcinoma. A distinctive variant with a low grade histology and a predominant intraductal growth pattern. Cancer 1996;78: 958–967.
292. Anderson C, Muller R, Piorkowski R. Intraductal carcinoma of major salivary gland. Cancer 1992;69:609–614.
293. Barnes L, Rao U, Contis L. Salivary duct carcinoma. Part II. Immunohistochemical evaluation of 13 cases for estrogen and progesterone receptors, cathepsin D, and c-erbB-2 protein. Oral Surg Oral Med Oral Pathol 1994;78:74–80.
294. Hellquest H, Karlsson M, Nilsson C. Salivary duct carcinoma—a highly aggressive salivary gland tumour with overexpression of c-erbB-2. J Pathol 1994;172:35–44.
295. Luna M, El-Naggar A, Parichatikanond P, et al. Basaloid squamous carcinoma of the upper aerodigestive tract. Clinicopathologic and DNA flow cytometric analysis. Cancer 1990;66:537–542.
296. Banks E, Frierson H, Mills S, et al. Basaloid squamous cell carcinoma of the head and neck. Am J Surg Pathol 1992;16:939–946.
297. Gerughty R, Hennigar G, Brown F. Adenosquamous carcinoma of the nasal oral and laryngeal cavities. A clinicopathologic survey of ten cases. Cancer 1968;22:1140–1155.
298. Klijanienko J, El-Naggar A, Ponzo-Rion A, et al. Basaloid squamous carcinoma of the head and neck. Arch Otolaryngol Head Neck Surg 1993;119:887–890.
299. Ferlito A, Devaney K, Rinaldo A, et al. Mucosal adenoid squamous cell carcinoma of the head and neck. Ann Otol Rhinol Laryngol 1996;105:409–413.
300. Barnes L, Ferlito A, Altavilla G, et al. Basaloid squamous cell carcinoma of the head and neck: clinicopathological features and differential diagnosis. Ann Otol Rhinol Laryngol 1996;105: 75–82.
301. Gnepp D, Brannon R. Sebaceous neoplasms of salivary gland origin, report of 21 cases. Cancer 1984;53:2155–2170.
302. Gnepp D. Sebaceous neoplasms of salivary gland origin: a review. Pathol Annu, Part 1 1983;18:71–102.
303. Auclair P, Ellis G, Gnepp D. Other benign epithelial neoplasms. In: Ellis GL, Auclair P, Gnepp DR, eds. Surgical Pathology of the Salivary Glands. Philadelphia: WB Saunders, 1991;252–267.
304. Boniuk M, Zimmerman L. Sebaceous carcinoma of the eyelid, eyebrow, caruncle, and orbit. Trans Am Acad Ophthalmol Otolaryngol 1968;72:619–642.
305. Linhartova A. Sebaceous glands in salivary gland tissue. Arch Pathol Lab Med 1974;98:320–324.
306. Shemen L, Huvos A, Spiro R. Squamous cell carcinoma of the salivary gland origin. Head Neck Surg 1987;9:235–240.
307. Gaughan R, Olsen K, Lewis J. Primary squamous cell carcinoma of the parotid gland. Arch Otolaryngol Head Neck Surg 1992;118: 798–801.
308. Sterman B, Kraus D, Sebek B. Primary squamous cell carcinoma of the parotid gland. Laryngoscope 1990;100:146–148.
309. Ellis G, Auclair P. Atlas of Tumor Pathology: Tumors of the Salivary Glands. Washington, D.C.: Armed Forces Institute of Pathology, 1996; Third Series, Fascicle 17:155–373.
310. Hilderman W, Gordon J, Large HJ. Malignant lymphoepithelial lesion with carcinomatous component apparently arising in parotid gland: a malignant counterpart of a benign lymphoepithelial lesion? Cancer 1962;15:606–610.
311. Ellis G, Auclair P. Malignant Epithelial Tumors. Tumors of the Salivary Glands. Washington, D.C.: Armed Forces Institute of Pathology, 1996; Third Series, Fascicle 17:311–318.
312. Krishnamurthy S, Lanier A, Dohan P. Salivary gland cancer in Alaskan natives 1966–1980. Hum Pathol 1987;18:986–996.
313. Saw D, Lau W, Ho J. Malignant lymphoepithelial lesion of the salivary gland. Hum Pathol 1986;17:914–923.
314. Borg M, Benjamin C, Morton R. Malignant lympho-epithelial lesion of the salivary gland: a case report and review of the literature. Australas Radiol 1993;37:288–291.
315. Nagao T, Ishida Y, Sugano I. Epstein-Barr virus–associated undifferentiated carcinoma with lymphoid stroma of the salivary gland in Japanese patients. Comparison with benign lymphoepithelial lesion. Cancer 1996;78:695–703.

Copyright © 2003, Mosby, Inc. All rights reserved.

316. Sheen T, Tsai C, Ko J. Undifferentiated carcinoma of the major salivary glands. Cancer 1997;80:357–363.
317. Bosch J, Kudryk W, Johnson G. The malignant lymphoepithelial lesion of the salivary glands. J Otolaryngol 1988;17:187–190.
318. Povah W, Beecroft W, Hodson I. Malignant lympho-epithelial lesion—the Manitoba experience. J Otolaryngol 1984;13:153–159.
319. Koss L, Spiro R, Hajdu S. Small cell (oat cell) carcinoma of minor salivary gland origin. Cancer 1972;30:737–741.
320. Gnepp D, Corio R, Brannon R. Small cell carcinoma of the major salivary glands. Cancer 1986;58:705–714.
321. Hisa Y, Tatemoto K. Bilateral parotid gland metastases as the initial manifestation of a small cell carcinoma of the lung. Am J Otolaryngol 1998;19:140–143.
322. Gnepp D, Ferlito A, Hyams V. Primary anaplastic small cell (oat cell) carcinoma of the larynx: review of the literature and report of 18 cases. Cancer 1983;51:1731–1745.
323. Eversole L, Gnepp D, Eversole G. Undifferentiated carcinoma. In: Ellis G, Auclair P, Gnepp D, eds. Surgical Pathology of the Salivary Glands. Philadelphia: WB Saunders, 1991;422–440.
324. Hui K, Luna M, Batsakis J. Undifferentiated carcinomas of the major salivary glands. Oral Surg Oral Med Oral Pathol 1990;69:76–83.
325. Grenko R, Abendroth C, Davis A. Hybrid tumors or salivary gland tumors sharing common differentiation pathways? Reexamining adenoid cystic and epithelial-myoepithelial carcinomas. Oral Surg Oral Med Oral Pathol Oral Radiol Endod 1998;86:188–195.
326. Hanada T, Hirase H, Ohyama M. Unusual case of myoepithelioma associated with adenoid cystic carcinoma of the parotid gland. Auris Nasus Larynx 1995;22:65–70.
327. Seifert G, Donath K. Hybrid tumours of salivary glands. Definition and classification of five rare cases. Eur J Cancer B Oral Oncol 1996;32B:251–259.
328. Dreyer T, Battmann A, Silberzahn J. Unusual differentiation of a combination tumor of the parotid gland. A case report. Pathol Res Pract 1993;189:577–581.
329. Evans R, Cruickshank A. Epithelial tumors of the salivary glands. In: Evans R, Cruickshank A, eds. Major Problems in Pathology. Philadelphia: WB Saunders, 1970;267.
330. Kamio N, Tanaka Y, Mukai M. A hybrid carcinoma: adenoid cystic carcinoma and salivary duct carcinoma of the salivary gland. An immunohistochemical study. Virchows Arch A Patholol Anat Histopathol 1997;430:495–500.
331. Vawter G, Tefft M. Congenital tumors of the parotid gland. Arch Pathol Lab Med 1966;82:242–245.
332. Taylor G, Case 6: congenital epithelial tumor of the parotid—sialoblastoma. Pediatr Pathol 1988;8:447–452.
333. Som PM, Brandwein M, Silvers AR, Rothschild MA. Sialoblastoma (embryoma): MR findings of a rare pediatric salivary gland tumor. AJNR 1997;18:847–850.
334. Seifert G, Donath K. The congenital basal cell adenoma of salivary glands. Contribution to the differential diagnosis of congenital salivary gland tumours. Virchows Arch A Path Anat Histopathol 1997;430:311–319.
335. Batsakis J, Frankenthaler R. Pathology consultation: embryoma (sialoblastoma) of salivary glands. Ann Otol Rhinol Laryngol 1992;101:958–960.
336. Batsakis J, Mackay B, Ryka A, Seifert R. Perinatal salivary gland tumours (embryomas). J Laryngol Otol 1988;102:1007–1011.
337. Brandwein M, Al-Naeif N, Manwani D, et al. Sialoblastoma: clinicopathological/immunohistochemical study. Am J Surg Pathol 1999;23:342–348.
338. Hsueh C, Gonzalez-Crussi F. Sialoblastoma: a case report and review of the literature on congenital epithelial tumors of salivary gland origin. Pediatr Pathol 1992;12:205–214, 631.
339. Adkins G. Low-grade basaloid adenocarcinoma of the salivary gland in childhood—the so-called hybrid basal cell adenoma–adenoid cystic carcinoma. Pathol 1990;22:187–190.
340. Daley T, Dardick I. An unusual parotid tumor with histogenetic implications for salivary gland neoplasms. Oral Surg Oral Med Oral Pathol 1983;55:374–381.
341. Simpson P, Rutledge J, Schaefer S, Anderson R. Congenital hybrid basal cell adenoma–adenoid cystic carcinoma of the salivary gland. Pediatr Pathol 1986;6:199–208.
342. Smith BC, Ellis GL, Slater LJ, Foss R. Sclerosing polycystic adenosis of major salivary glands: a clinicopathologic analysis of nine cases. Am J Surg Pathol 1996;20:161–170.
343. Batsakis J. Sclerosing polycystic adenosis: newly recognized salivary gland lesion—a form of chronic sialadenitis? Adv Anat Pathol 1996;3:298–304.
344. Donath K, Seifert G. Sklerosierende polyzystische sialadenopathie: Eine seltene nichttumorose erkrankung. Pathologie 1997;18: 368–373.
345. Spiro R, Huvos A, Strong E. Adenocarcinoma of salivary origin: clinicopathologic study of 204 patients. Am J Surg Pathol 1982;144:423–431.
346. Mills S, Garland T, Allen M. Low-grade papillary adenocarcinoma of palatal salivary gland origin. Am J Surg Pathol 1984; 8:367–374.
347. Auclair P, Ellis G. Adenocarcinoma not otherwise specified. In: Ellis G, Auclair P, Gnepp D, eds. Surgical Pathology of the Salivary Glands. Philadelphia: WB Saunders, 1991.
348. van der Wal J, Leverstein H, Snow G. Parotid gland tumors: histologic reevaluation and reclassification of 478 cases. Head Neck 1998;20:204–207.
349. Matsuba H, Mauney M, Simpson J. Adenocarcinoma of major and minor salivary gland origin: a histopathologic review of treatment failure patterns. Laryngoscope 1988;98:784–788.
350. Bouquot J, Weiland L, Kurland L. Metastases to and from the upper aerodigestive tract in the population of Rochester, Minnesota, 1935–1984. Head Neck 1989;11:212–218.
351. Gnepp D. Metastatic disease to the major salivary glands. In: Ellis G, Auclair P, Gnepp D, eds. Surgical Pathology of the Salivary Glands. Philadelphia: WB Saunders, 1991.
352. Hisa Y, Tatemoto K. Bilateral parotid gland metastases as the initial manifestation of a small cell carcinoma of the lung. Am J Otolaryngol 1998;19:140–143.
353. Saiz A, Sachdev U, Brodman M, Deligdisch L. Metastatic uterine leiomyosarcoma presenting as a primary sarcoma of the parotid gland. Obstet Gynecol 1998;92:667–668.
354. Lee K, McKean M, McGregor I. Metastatic patterns of squamous carcinoma in the parotid lymph nodes. Br J Plastic Surg 1985;38:6–10.
355. del Charco J, Mendenhall W, Parsons J. Carcinoma of the skin metastatic to the parotid area lymph nodes. Head Neck 1998;20: 369–373.
356. Pisani P, Krengli M, Ramponi A. Metastases to parotid gland from cancers of the upper airway and digestive tract. Br J Oral Maxillofac Surg 1998;36:54–57.
357. Wang B, Lawson W, Robinson R. Malignant melanoma of the parotid: comparison of survival for patients with metastases from known vs. unknown primary tumor sites. Arch Otolaryngol Head Neck Surg 1999;125:635–639.
358. Touloukian R. Salivary gland diseases in infancy and childhood. In: Rankow R, Polayes I, eds. Diseases of the Salivary Glands. Philadelphia: WB Saunders, 1976;284–303.
359. Barnes L, Verbin R, Gnepp D. Diseases of the nose, paranasal sinuses and nasopharynx. In: Barnes L, ed. Surgical Pathology of the Head and Neck. Vol. 1. New York: Marcel Dekker, 1985; 725–880.
360. Som P, Zimmerman R, Biller H. Cystic hygroma and facial nerve paralysis—a rare association. J Comput Assist Tomogr 1984;8: 110–113.
361. Barnes L, Myers E, Prokopakis E. Primary malignant lymphoma of the parotid gland. Arch Otolaryngol Head Neck Surg 1998;124: 573–577.
362. Hirokawa N, Hareyama M, Akiba H, et al. Diagnosis and treatment of malignant lymphoma of the parotid gland. Jpn J Clin Oncol 1998;28:245–249.
363. Biasi D, Caramaschi P, Ambrosetti A, et al. Mucosa-associated lymphoid tissue lymphoma of the salivary glands occurring in patients affected by Sjogren's syndrome: report of 6 cases. Acta Haematol 2001;105:83–88.
364. Wolvlus E, van der Valk P, van der Wal J, et al. Primary non-Hodgkin's lymphoma of the salivary glands. An analysis of 22 cases. J Oral Pathol Med 1996;25:177–181.
365. Takahashi H, Cheng J, Fujita S, et al. Primary malignant lymphoma of the salivary gland: a tumor of mucosa-associated lymphoid tissue. J Oral Pathol Med 1992;21:318–325.
366. Suchy B, Wolf S. Bilateral mucosa-associated lymphoid tissue lymphoma of the parotid gland. Arch Otolaryngol Head Neck Surg 2000;126:224–226.

Copyright © 2003, Mosby, Inc. All rights reserved.

367. Ustun M, Ekinci N, Payzin B. Extramedullary plasmacytoma of the parotid gland. Report of a case with extensive amyloid deposition masking the cytologic and histopathologic picture. Acta Cytol 2001;45:449–453.
368. Gonzalez-Garcia J, Ghufoor K, Sandhu G, et al. Primary xtramedullary plasmacytoma of the parotid gland: a case report and review of the literature. J Laryngol Otol 1998;112:179–181.
369. Cankaya H, Ugras S, Dilek I. Head and neck granulocytic sarcoma with acute myeloid leukemia: three rare cases. Ear Nose Throat J 2001;80:224–226.
370. Som P, Scherl M, Rao V, Biller H. Rare presentations of ordinary lipomas of the head and neck: a review. AJNR 1986;7:657–664.
371. Kumar A, Kuhajda F, Martinez C, et al. Computed tomography of extracranial nerve sheath tumors with pathological correlation. J Comput Assist Tomogr 1983;7:857–865.
372. Som P, Biller H, Lawson W. An approach to parapharyngeal space masses: an updated protocol based upon 104 cases. Radiology 1984;153:149–156.
373. Tsutsumi T, Oku T, Komatsuzaki A. Solitary plexiform neurofibroma of the submandibular salivary gland. J Laryngol Otol 1996;110: 1173–1175.
374. Helsel J, Mrak R, Hanna E, et al. Peripheral primitive neuroectodermal tumor of the parotid gland region: report of a case with fine-needle aspiration findings. Diagn Cytopathol 2000;22:161–166.
375. Deb RA, Desai SB, Amonkar PP, et al. Primary primitive neuroectodermal tumour of the parotid gland [see comments]. Histopathology 1998;33:375–378.
376. Wilcken N, Tattersall M. Endocrine therapy for desmoid tumors. Cancer 1991;67:1384–1388.
377. Montgomery E, Meis J. Nodular fasciitis: its morphologic spectrum and immunohistochemical profile. Am J Surg Pathol 1991;15: 942–948.
378. Enzinger F, Zhang R. Plexiform fibrohistiocytic tumor presenting in children and young adults. Am J Surg Pathol 1988;12:818–826.
379. Remstein E, Arndt C, Nascimento A. Plexiform fibrohistiocytic tumor: clinicopathologic analysis of 22 cases. Am J Surg Pathol 1999;23:662–670.
380. Hollowood K, Holley M, Fletcher C. Plexiform fibrohistiocytic tumor: clinicopathological, immunohistochemical and ultrastructural analysis in favour of a myofibroblastic lesion. Histopathology 1991;19:503–513.
381. Waldhart E, Lynch J. Benign hypertrophy of the masseter muscles and mandibular angles. Arch Surg 1971;102:115–118.
382. Mason D, Chisholm D. Salivary Glands in Health and Disease. London: WB Saunders, 1975;106–118.
383. Som P, Biller H. Kimura disease involving parotid gland and cervical nodes: CT and MR findings. J Comput Assist Tomogr 1992;16: 320–322.
384. Urabe A, Tsuneyoshi M, Enjoji M. Epithelioid hemangioma versus Kimura's disease. A comparative clinicopathologic study. Am J Surg Pathol 1987;11:758–766.
385. Nagamachi S, Hoshi H, Ohnishi T, et al. Tl-201 SPECT in Kimura's disease involving the parotid glands and cervical nodes. Clin Nucl Med 1996;21:125–128.
386. Brown E, August M, Pilch B, Weber A. Polycystic disease of the parotid glands. Am J Neuroradiol 1995;16:1128–1131.
387. Luna M, Batsakis J, El-Naggar A. Pathology consultation: salivary gland tumors in children. Ann Otol Rhinol Laryngol 1991;100: 869–871.
388. Gottesman RI, Som PM, Mester J, Silvers A. Observations on two cases of apparent submandibular gland cysts in HIV positive patients: MR and CT findings. J Comput Assist Tomogr 1996;20: 444–447.

Copyright © 2003, Mosby, Inc. All rights reserved.

40

Thyroid and Parathyroid Glands: Anatomy and Pathology

Laurie A. Loevner

SECTION ONE: THE THYROID GLAND
ANATOMY OF THE THYROID GLAND
ENDOCRINOLOGY OF THE THYROID GLAND
CLINICAL MANIFESTATIONS OF THYROID DISEASE
THYROID IMAGING
- Nuclear Scintigraphy
- Cross-Sectional Imaging
- Ultrasonography

PATHOLOGY OF THE THYROID GLAND
- Congenital Anomalies
- Autoimmune Disease and Thyroiditis
  - Graves' Disease
  - Hashimoto's Thyroiditis
  - Silent, Painless Thyroiditis and Postpartum Thyroiditis
  - De Quervain's Thyroiditis (Subacute Granulomatous Thyroiditis)
  - Acute Suppurative Thyroiditis
  - Riedel's Thyroiditis (Struma)
- Thyroid Goiter
- Nodular Thyroid Disease

NEOPLASMS OF THE THYROID GLAND
- Adenomas
- Malignant Neoplasms
  - Papillary Carcinoma
  - Follicular Carcinoma
  - Hurthle Cell Tumors
  - Medullary Carcinoma
  - Anaplastic Carcinoma
  - Primary Lymphoma
  - Rare Malignancies
  - Metastatic Disease

SECTION TWO: THE PARATHYROID GLANDS
ANATOMY OF THE PARATHYROID GLANDS
ENDOCRINOLOGY OF THE PARATHYROID GLANDS
CLINICAL MANIFESTATIONS OF PARATHYROID DISEASE
- Hyperparathyroidism
- Hypoparathyroidism

IMAGING OF PATHOLOGY OF THE PARATHYROID GLANDS
- Parathyroid Adenoma
  - Ultrasonography
  - Cross-Sectional Imaging
  - Nuclear Scintigraphy
- Reoperation for Hyperparathyroidism
- Parathyroid Hyperplasia
- Parathyroid Carcinoma
- Parathyroid Cyst

SECTION ONE

THE THYROID GLAND

The thyroid gland plays a critical role in the regulation of several metabolic functions including cardiac rate and output, lipid catabolism, and skeletal growth, as well as oxygen and heat production. As a result, patients with hormonally active thyroid abnormalities (hypothyroidism or hyperthyroidism) present with a wide range of symptoms. The evaluation of such patients requires an understanding of the hormonal functions carried out by the thyroid gland.

In addition to the pathophysiology resulting from abnormal thyroid function, cross-sectional imaging to assess the morphologic features of the thyroid gland may be necessary for comprehensive patient care. Nuclear scintigraphy reveals functional information about the thyroid gland,

Copyright © 2003, Mosby, Inc. All rights reserved.

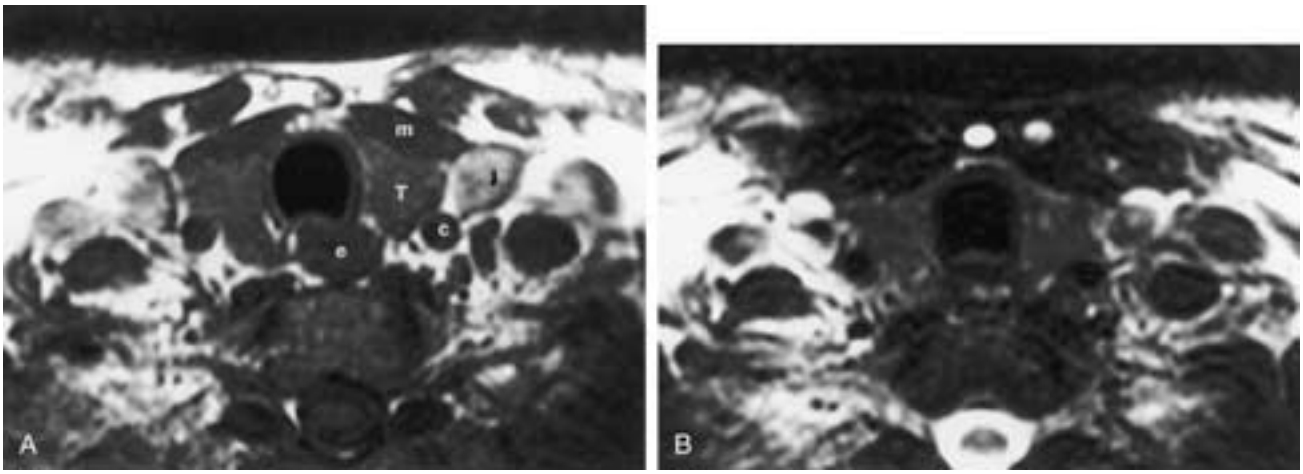

VIEW IMAGE

FIGURE 40-1 Normal thyroid gland on MR imaging. **A**, Unenhanced axial T1-weighted MR image shows the normal appearance of the thyroid gland (*T*), which is homogeneously hyperintense to the neck musculature (*m*). The normal anatomic relationship of the gland to the jugular vein (*J*), carotid artery (*c*), esophagus (*e*), and musculature (*m*) is shown. **B**, Axial T2-weighted image at the same level as **A** shows the normal gland to be hyperintense relative to the neck musculature.

while imaging including ultrasound, computed tomography (CT), and magnetic resonance (MR) imaging provide important adjunctive anatomic information. In addition to evaluating the intrinsic structure of the thyroid gland, these modalities provide important information about the related structures in the neck, including the presence of lymphadenopathy, and extension of disease into adjacent soft tissues of the neck such as the mediastinum, trachea, and carotid sheath.

The anatomy and physiology of the thyroid gland will be reviewed. Congenital, autoimmune, inflammatory, metabolic, and neoplastic diseases of the thyroid will then be discussed, and the diagnostic utility of radiologic imaging to evaluate each of these thyroid abnormalities will be addressed.

ANATOMY OF THE THYROID GLAND

The thyroid gland is shield-shaped in the majority of patients. It consists of right and left lobes that are usually joined by the isthmus, though occasionally the isthmus may be absent. The thyroid isthmus is anterior to the trachea, usually overlying the first through third tracheal rings. Uncommonly, it may be more cranial, positioned at or just caudal to the anterior cricoid cartilage arch. The right and left lobes of the thyroid gland are on either side of the trachea, and each lobe has a superior and an inferior pole. The normal thyroid gland is situated with its upper margin near the oblique line on the thyroid cartilage and its lower margin at the level of the fourth or fifth tracheal cartilage; a region referred to as the thyroid bed. The normal thyroid gland weighs between 15 and 35 grams and in males the average thyroid volume is 19.6 ml, while in females it is 18.6 ml. The gland size varies with patient weight, age, and gender and the thyroid gland is enlarged in females during menstruation and pregnancy. The average thyroid lobe measures 3 cm in greatest anteroposterior dimension and 2 cm in width. The thyroid is anterior to the prevertebral (longus colli) and paraspinal musculature and posterior (deep) to the sternothyroid and sternohyoid muscles (Fig. 40-1). Usually, the entire thyroid gland is in the neck above the level of the clavicles; however, substernal extension into the superior mediastinum may occur. An accessory lobe, referred to as the pyramidal lobe, may be present in 50% to 70% of people. It usually arises from the isthmus of the gland and extends superiorly along the course of the distal thyroglossal duct.[1] The pyramidal lobe may be attached to the hyoid bone or, uncommonly, it may arise from the medial aspect of the right or left thyroid lobe. A pyramidal lobe is most commonly recognized in patients with Graves' disease because it is enlarged and readily identified on nuclear scintigraphy (Fig. 40-2).

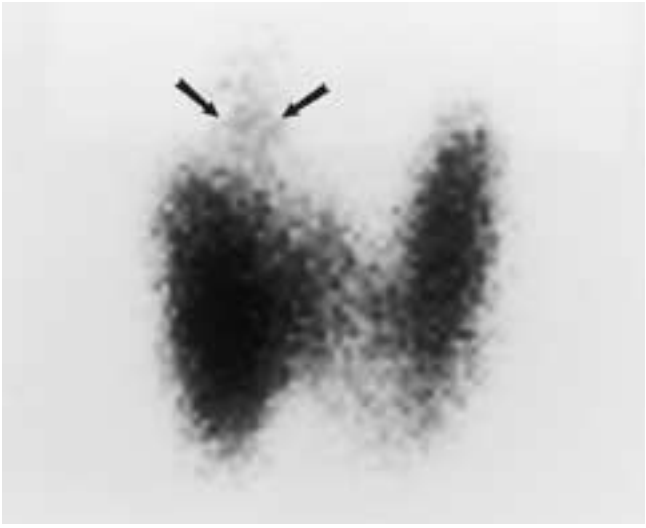

FIGURE 40-2 Iodine-131 scan in a patient with Graves' disease. There is diffuse enlargement and uptake of I-131 by the thyroid gland. A pyramidal lobe is noted (*arrows*). The 24-hour uptake was 48% (normal, 10% to 30%).

VIEW IMAGE

Copyright © 2003, Mosby, Inc. All rights reserved.

As discussed in Chapter 34, the pharynx and cervical esophagus are surrounded posteriorly and along their lateral margins by the retrovisceral space. At the level of the pharynx, this space is often referred to as the retropharyngeal space, while at the level of the cervical esophagus, this same space is usually referred to as the retroesophageal space. At the level of the thyroid cartilage and the attachment of the inferior pharyngeal constrictor muscles to this cartilage, the retrovisceral space has an anterior projection that extends around the sides of the cervical esophagus to encompass the larynx, trachea, thyroid gland, and parathyroid glands. This ventral extension is often referred to as the visceral compartment. This fascia thus attaches the thyroid gland to the larynx and trachea. As a result, the thyroid gland moves with the larynx during swallowing. The thyroid gland is encapsulated, and from this capsule septae extend into the substance of the gland.

Projecting up into the lower aspect of this visceral compartment is a fold of fascia containing the inferior thyroid artery. As a result, this fascial fold divides the lower visceral compartment into anterior and posterior sections. The anterior section, or pretracheal space, extends down behind the sternum to the level of the innominate vessels (sternoclavicular joint) in the anterior mediastinum. The posterior section of the visceral compartment is the retroesophageal space, which extends behind the esophagus down into the posterior mediastinum to approximately the level of the carina. Thus, the entire visceral space is a single, somewhat complex-shaped common space that contains in its anterior portion the larynx, trachea, thyroid gland, and parathyroid glands and surrounds the cervical esophagus and pharyngeal constrictor muscles.

The superior mediastinum is defined as being separated from inferior mediastinum by a plane connecting the joint between the manubrium and the body of the sternum (second costal cartilage) and the lower border of the fourth thoracic vertebra. The inferior mediastinum is further subdivided into anterior (in front of pericardium), middle (pericardium and heart and roots of the great vessels), and posterior (behind the pericardium) compartments. The anterior mediastinum is continuous with the pretracheal space while, as mentioned, the posterior mediastinum is continuous with the retropharyngeal space and the spaces lateral to the esophagus and trachea, between the carotid sheaths.[3]

If a thyroid gland enlarges sufficiently, it will extend outside the normal volume of the thyroid bed. Direct caudal growth is downward into the pretracheal space. As such, the thyroid extension lies in the retrosternal region, anterior to the common carotid arteries and the internal jugular veins. In this location, the thyroid enlargement is usually referred to as a retrosternal or substernal goiter. These goiters are usually resected via a cervical approach, without the need for a sternotomy. If the caudal thyroid gland enlargement is posteriorly directed, the goiter can grow along the sides of the esophagus and eventually extend behind the esophagus. Once behind the esophagus, the goiter can project either down into the posterior mediastinum or up behind the pharynx. If the thyroid growth is into the posterior mediastinum, the goiter is referred to as a mediastinal goiter and it lies dorsal to the great vessels. In this location, many surgeons prefer to resect the goiter via a sternectomy approach. Cranial extension behind the pharynx is resected via a cervical approach.

The thyroid gland has a rich vascular supply. There are paired superior and inferior thyroidal arteries. The right and left superior thyroidal arteries are the first branches off of the respective external carotid arteries, and travel inferiorly from their origin to the thyroid gland. The thyrocervical trunks, which originate from the subclavian arteries, each give rise to an inferior thyroidal artery. The thyroidea ima is an inconstant vessel that, when present, arises directly from the aortic arch and helps supply the inferior thyroid gland. The venous drainage of the thyroid gland is via the superior and middle thyroidal veins, which empty into the internal jugular vein, and an inferior vein, which drains into the innominate vein. The thyroid gland is innervated by the tenth cranial (vagus) nerve and the cervical sympathetic neural plexus. The sympathetic fibers descend from the ganglia of the sympathetic trunk, while the parasympathetic fibers course along with the vagus nerve. This autonomic innervation is believed to strongly influence thyroid gland perfusion.

The thyroid gland contains multiple lobules, each of which is composed of multiple follicles. Thyroglobulin is stored within colloid in these follicles, and the follicular cells secrete thyroid hormones. Parafollicular (C) cells are also dispersed throughout the stroma of the gland and secrete thyrocalcitonin.

ENDOCRINOLOGY OF THE THYROID GLAND

The primary function of the thyroid gland is to synthesize hormones that play a vital role in the regulation of a variety of metabolic functions. Two hormones, triiodothyronine (T3) and thyroxine (T4), are synthesized within the thyroid. They are released from the thyroid in response to a feedback mechanism with the pituitary-hypothalamic axis. Ultimately, the secretion of thyroid hormones is mediated by thyrotropin-stimulating hormone (TSH) secreted by the anterior lobe of the pituitary gland. Pituitary secretion of TSH is in turn regulated by thyrotropin-releasing hormone (TRH) secreted by the hypothalamus.

The synthesis of hormones within the thyroid is a regulated, systematic process. The first step involves trapping of iodide, in which iodide from the circulating plasma is actively transported into the thyroid gland and concentrated within follicular cells. This active transport mechanism traps iodine to a concentration of approximately 100 times more than that in the serum. Iodide is then oxidized by *thyroid peroxidase* into its chemically active form. Subsequently, organification, a process in which tyrosine residues on thyroglobulin molecules are iodinated to form monoiodotyrosine (MIT) and diiodotyrosine (DIT), occurs. The coupling of MIT and DIT forms T3, and the coupling of two molecules of DIT forms T4. Next, T3 and T4 are released from thyroglobulin and secreted into the circulation in free and bound forms.[2] Simultaneously, deiodination of free MIT and DIT occurs for iodide salvage and recycling within the thyroid gland. Aberrant organification usually results from enzymatic defects that interfere

Copyright © 2003, Mosby, Inc. All rights reserved.

with the oxidation of iodide or the iodination of tyrosine. Rarely, there may be failure of iodide trapping.

In the circulation, several carrier proteins transport thyroid hormones. Thyroxine-binding globulin carries approximately 70% of T3 and T4, thyroxine-binding preglobulin carries about 5% of T3 and 25% of T4, and albumin carries the remaining hormones. The active form of T3 and T4 is the free or unbound form, representing only 0.3% of T3 and 0.03% of T4. T3 is approximately three to four times more active physiologically than T4. T4 is synthesized entirely within the thyroid, while 80% to 95% of T3 is synthesized by peripheral conversion of T4.

Temporary interference with the organification of iodide may occur with several medications and with the iodinated contrast materials that are frequently used in CT studies (Table 40-1). The result is altered (decreased) radioactive iodine uptake measurements. Hence, these medications and contrast CT studies should be discontinued prior to nuclear scintigraphy (see below).

CLINICAL MANIFESTATIONS OF THYROID DISEASE

Thyrotoxicosis refers to a clinical syndrome that develops when circulating levels of T4 and T3 are increased (TSH is usually suppressed). Hyperthyroidism refers to sustained thyroid hyperfunction with increased thyroid hormone synthesis and release. Thyrotoxicosis is manifested by a variety of symptoms including warmth and flushing reflecting peripheral vasodilatation, increased heat loss, weight loss, myopathy, and increased appetite. Patients, especially children, may be hyperactive. Cardiac manifestations are more common in older patients and include tachycardia, palpitations, arrhythmias, and cardiomegaly.

Thyrotoxicosis associated with hyperthyroidism is most frequently seen with Graves' disease but may also be seen with toxic multinodular goiter or a hyperfunctioning adenoma. Toxic multinodular goiter associated with hyperthyroidism (Plummer's disease) commonly develops in patients over the age of 50 years and is related to a hyperfunctioning thyroid nodule.[3] Rarely, thyrotoxicosis may be associated with a TSH-secreting pituitary adenoma or thyroid neoplasms. Thyrotoxicosis not associated with hyperthyroidism (low radioactive iodine uptake) may be related to inflammatory thyroid disease or ectopic thyroid tissue (ovarian strumii), or it may be factitious (exogenous hormone use or Munchausen syndrome) (Table 40-2).

Table 40-1
COMMON MEDICATIONS THAT MAY DECREASE THYROID IODIDE UPTAKE

Iodine-containing contrast agents
Oral cholecystographic agents
Thyroxine (Synthroid)
Cytomel (T3)
Antithyroid medications (propylthiouracil)
Iodide preparations
Antibiotics
Antihistamines

Table 40-2
EVALUATION OF THE HYPERTHYROID PATIENT

	RAIU (Normal)	RAIU (Low)	RAIU (High)
TFTs elevated	Plummer's disease	Thyroiditis De Quervain's thyroiditis Subacute lymphocytic disease Struma ovarii Factitious disease	Graves' disease

RAIU, 24-hour radioactive iodine uptake (normal, 10% to 30%); *TFTs*, thyroid function tests.

Thyroid storm characterized by hypertension, tachycardia, and fever may present as a clinical emergency in patients with unrecognized or inadequately treated thyrotoxicosis. If unrecognized, it may result in death.

Thyroid ophthalmopathy, more common in women, is characterized by proptosis usually secondary to enlargement of the extraocular muscle bellies, with sparing of their tendinous insertions. Although most commonly seen in Graves'disease and hyperthyroidism, thyroid ophthalmopathy may occur in euthyroid and even hypothyroid patients. The most common patterns of extraocular muscle involvement are enlargement of the inferior rectus muscle, enlargement of both the inferior and medial rectus muscles, and enlargement of all of the muscles (Fig. 40-3).[4] There usually is relative sparing of the lateral rectus muscles, and isolated involvement of this muscle should raise the suspicion of a different disease process such as myositis or pseudotumor. Proptosis may also be related to an increase in orbital fat secondary to edema and lymphocytic infiltration, as well as due to an increase in the volume of the extraocular muscles. Although most commonly symmetric, exophthalmos (proptosis) may be asymmetric or even unilateral.[4] Clinical signs and symptoms include proptosis, lid retraction, decreased ocular range of motion, and corneal exposure caused by eyelid retraction. Extraocular muscle enlargement may result in compression of the optic nerve at the orbital

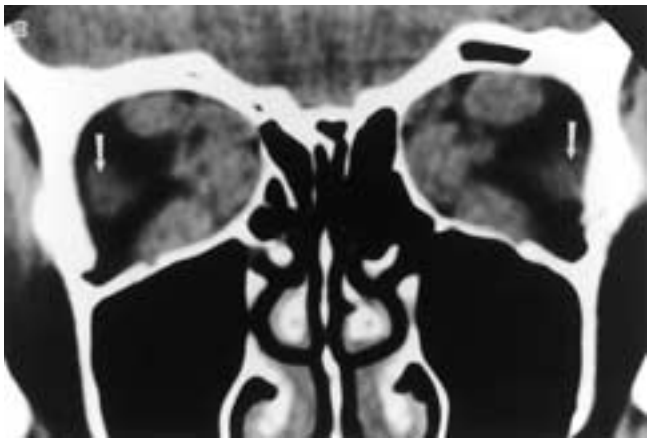

FIGURE 40-3 Thyroid ophthalmopathy in a 43-year-old woman with Graves' disease. Coronal CT scan shows bilaterally symmetric enlargement of the bellies of the extraocular muscles, with relative sparing of the lateral rectus muscles (*arrows*).

VIEW IMAGE

Copyright © 2003, Mosby, Inc. All rights reserved.

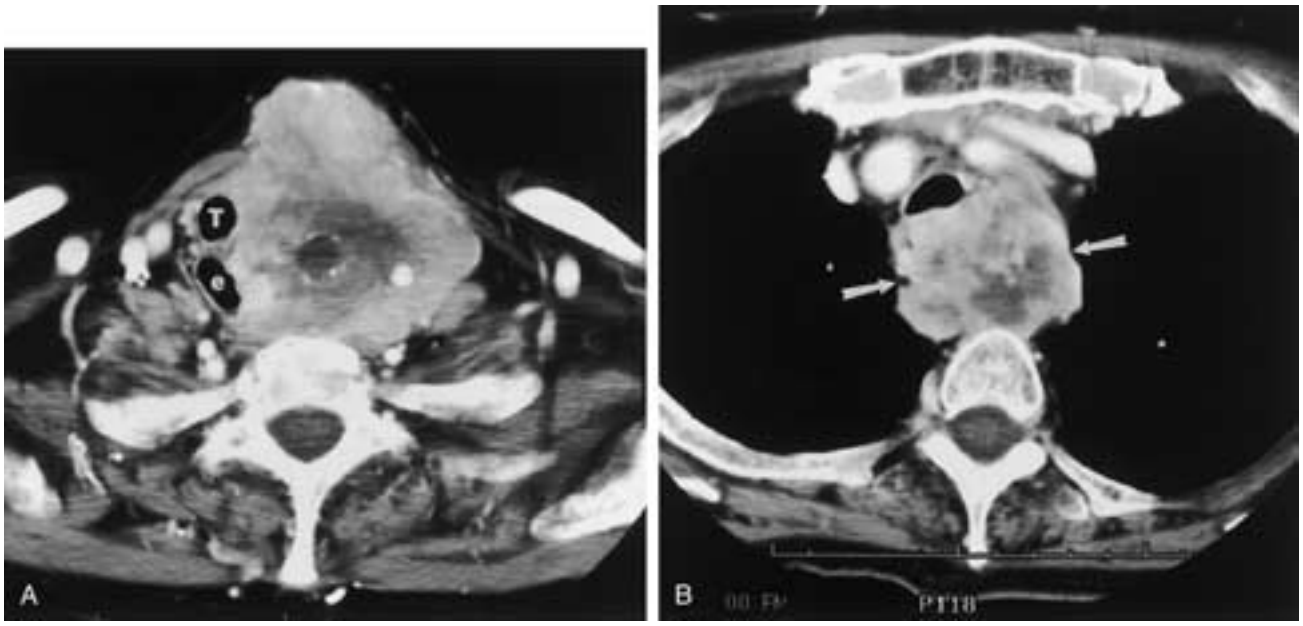

VIEW IMAGE

FIGURE 40-4 Enhanced CT scan of a multinodular goiter with substernal extension and compression of the trachea and esophagus. **A**, Axial CT scan at the level of the upper trachea shows diffuse nodular enlargement of the thyroid gland that is heterogeneous in density. There is marked displacement of the trachea (*T*) and esophagus (*e*) from left to right. **B**, There is extension of goiter (*arrows*) behind the trachea into the middle mediastinum.

apex, resulting in visual loss. Surgical decompression of the orbit is frequently necessary to preserve vision. Late in the disease, contractures and fibrosis of the extraocular muscles may lead to abnormal eye movements (see Chapter 9).

Hypothyroidism refers to decreased thyroid hormone synthesis (serum TSH is high, while T3 and T4 levels are low). Primary hypothyroidism may be secondary to structural or functional derangements of the thyroid gland, and in adults it most often results from processes that destroy thyroid tissue such as autoimmune disease or iodine-131 (^{131}I) treatment. In children it may be related to enzyme deficiencies, defects in organification, or congenital anomalies such as lingual thyroid or thyroid agenesis.[5] Central hypothyroidism refers to decreased thyroid stimulation by TSH related to pituitary disease (secondary hypothyroidism) or hypothalamic TRH deficiency (tertiary hypothyroidism). Unless readily identified and managed, hypothyroidism occurring prenatally or during infancy will result in cretinism. Hypothyroidism occurring in older children and adults is termed *myxedema*. Clinical manifestations are extremely variable, ranging from fatigue to coma.

Many of the secondary manifestations of thyroid disease are frequently responsible for the clinical presentation of such patients. Any condition that causes marked enlargement of the thyroid gland, most commonly multinodular goiters, but also neoplastic and inflammatory processes, may compress the adjacent esophagus and trachea, causing dysphagia and respiratory distress, respectively (Fig. 40-4). Similarly, there may be compression and displacement of the jugular vein and carotid artery. Because the recurrent laryngeal nerve travels in the tracheoesophageal groove, thyroid lesions that extend to this area may present with vocal cord paralysis. Cervical lymphadenopathy in the presence of a thyroid mass, violation of the thyroid gland capsule's integrity, or direct extension of a thyroid lesion into the trachea or carotid sheath structures are findings highly suggestive of a thyroid malignancy.

THYROID IMAGING

Nuclear scintigraphy and ultrasonography are frequently the first imaging modalities used to assess patients with suspected thyroid disorders. CT and MR imaging are frequently utilized to address specific issues regarding thyroid disease such as the extent of thyroid goiter or extension of neoplasm outside the thyroid capsule and into adjacent structures in the neck. They are used in assessing for regional nodal metastases in the setting of thyroid cancer and in the evaluation of recurrent disease following treatment for thyroid cancer.

Nuclear Scintigraphy

Nuclear scintigraphy provides excellent functional information about the thyroid because the radionuclides used to image the gland do so by utilizing some step of hormone synthesis within the thyroid. The primary role of scintigraphy in the evaluation of a focal thyroid mass is to determine whether a lesion is ''hot'' (low incidence of malignancy) or ''cold'' (higher incidence of malignancy).[6, 7] Nuclear imaging of the thyroid gland is performed with a gamma scintillation camera. The patient is usually placed in a hyperextended supine position. Images are typically obtained from the chin to the sternal notch in multiple views including anterior, posterior, and bilateral oblique projec-

Copyright © 2003, Mosby, Inc. All rights reserved.

tions. Findings on imaging are correlated with those on palpation of the gland.

Currently, morphologic detail of the thyroid gland is obtained using technetium (Tc-99m) pertechnetate, iodine 123 (I-123), and iodine 131 (I-131). Routes of administration, doses, and some physical properties of these agents are reviewed in Table 40-3. Imaging is performed approximately 20 minutes following administration of Tc-99m pertechnetate, 4 to 24 hours following oral ingestion of I-123, and 24 to 72 hours following administration of I-131. The normal thyroid gland shows homogeneous radionuclide uptake and distribution. The isthmus of the thyroid gland may demonstrate slightly less activity than the right and left thyroid lobes.

I-131 is used for determining 24-hour thyroid iodine uptake, measured with a dedicated probe centered 1 inch above the sternal notch. Thyroid uptake reflects the percentage of the dose given to the patient that is accumulated within the thyroid gland, corrected for radioactive decay. Normal 24-hour uptake ranges from 10% to 30%. Several medications such as propylthiouracil, methimazole, and iodine-containing contrast agents used for imaging may temporarily interfere with the organification of iodide, altering radioactive iodine uptake measurements for as long as 6 weeks (Table 40-1).[8–11] The uptake of I-131 may be reduced by as much as one half 1 week following injection of iodinated agents for CT examination.[8–10] Furthermore, in over one third of patients with underlying thyroid disease, temporary changes in thyroid function may occur following injection of iodinated contrast material.[8] Therefore, if CT imaging is believed to be necessary in a patient who will also be studied with nuclear scans using iodinated radionuclides, it should be performed without contrast administration. If contrast is desired, then CT should be performed after nuclear scintigraphy. Medications that interfere with thyroid function should be withdrawn for adequate periods of time prior to nuclear scanning. In general, if CT contrast is administered, one should wait at least 6 weeks before performing nuclear scintigraphy.

I-131 is used in both the evaluation and treatment of patients with thyroid cancers that concentrate iodine. It is particularly useful in the follow-up of patients after thyroidectomy to evaluate for residual thyroid tissue in the operative bed as well as to assess for distant metastatic disease (see Neoplasms of the Thyroid Gland).

More recently, fluorodeoxyglucose positron emission tomography (^{18}FDG-PET) has played an increasingly important role in the follow-up of patients with thyroid cancer due to increased glucose metabolism by malignant tumors. It may be particularly useful in assessing metastatic thyroid tumors that do not concentrate radioiodine [12, 13]. It is frequently used in evaluating patients with rising thyroglobulin levels following thyroidectomy.[14] Whole body scans are obtained to identify regions of FDG uptake (Fig. 40-5). Potential pitfalls include indolent or well-differentiated thyroid tumors that take up FDG poorly and FDG uptake in areas that are not related to metastatic thyroid cancer.

Cross-Sectional Imaging

While scintigraphy provides functional information about the thyroid, CT and MR imaging provide important adjunctive anatomic information that is superior to that of nuclear imaging. These modalities not only provide better delineation of lesions within the thyroid, but also play a critical role in the detection of lymph node metastases, as well as extension of thyroid disease to adjacent tissues in the neck. Specifically, invasion of the paraspinal musculature, esophagus, trachea, and carotid sheath structures may be assessed [15] (Fig. 40-6). The detailed anatomic information provided by CT and MR imaging is also valuable in guiding the surgical approach.

For CT and MR examinations, patients are typically scanned in the supine position with the neck mildly hyperextended so that the hard palate is roughly perpendicular to the tabletop. When possible, the patient is scanned with quiet breathing and swallowing suspended. Contiguous 3 mm thick axial sections are obtained from the level of the cavernous sinuses (upper level of the external auditory canal) to the superior mediastinum, including the aortic arch. In cases where small lesions are being evaluated, thinner sections (1 to 2 mm) may be obtained.

The normal thyroid gland (due to its iodide content) has a density of approximately 80 to 100 HU on CT. That is, since the thyroid gland normally concentrates iodine approximately100 times over the iodine concentration in the serum, and since iodine is the basis of the CT contrast agents, the radiodensity of the thyroid gland on noncontrast CT images correlates well with thyroid function. Thus, a well-seen thyroid gland usually indicates a normally functioning

Table 40-3
RADIONUCLIDES COMMONLY USED IN IMAGING THE THYROID GLAND

Radionuclide	Administration	Dose	Half-life	Energy
Tc-99m	Intravenous	2–10 mCi	6.02 hr	140 keV
I-123	Oral	200–400 µCi	13.6 hr	159 keV
I-131 (diagnostic)	Oral	30–100 µCi	8.05 days	364 keV
I-131 (whole body)*	Oral	2–5 mCi		
I-123 (whole body)*	Oral	1–2.5 mCi		
I-131 (treatment)†	Oral	100 mCi		
I-131 (treatment)‡	Oral	100–200 mCi		

*Diagnostic whole body scan following thyroidectomy to evaluate for residual thyroid tissue in the thyroid bed or to detect distant metastases; to detect ectopic thyroid tissue such as struma ovarii; in hyperthyroid patients with no demonstrable iodine uptake in the thyroid.
† Cancer treatment following thyroidectomy with the goal of ablating residual thyroid tissue (may require hospital admission, depending on the dose).
‡ Cancer treatment with the goal of ablating thyroid metastases (may require hospital admission, depending on the dose).

Copyright © 2003, Mosby, Inc. All rights reserved.

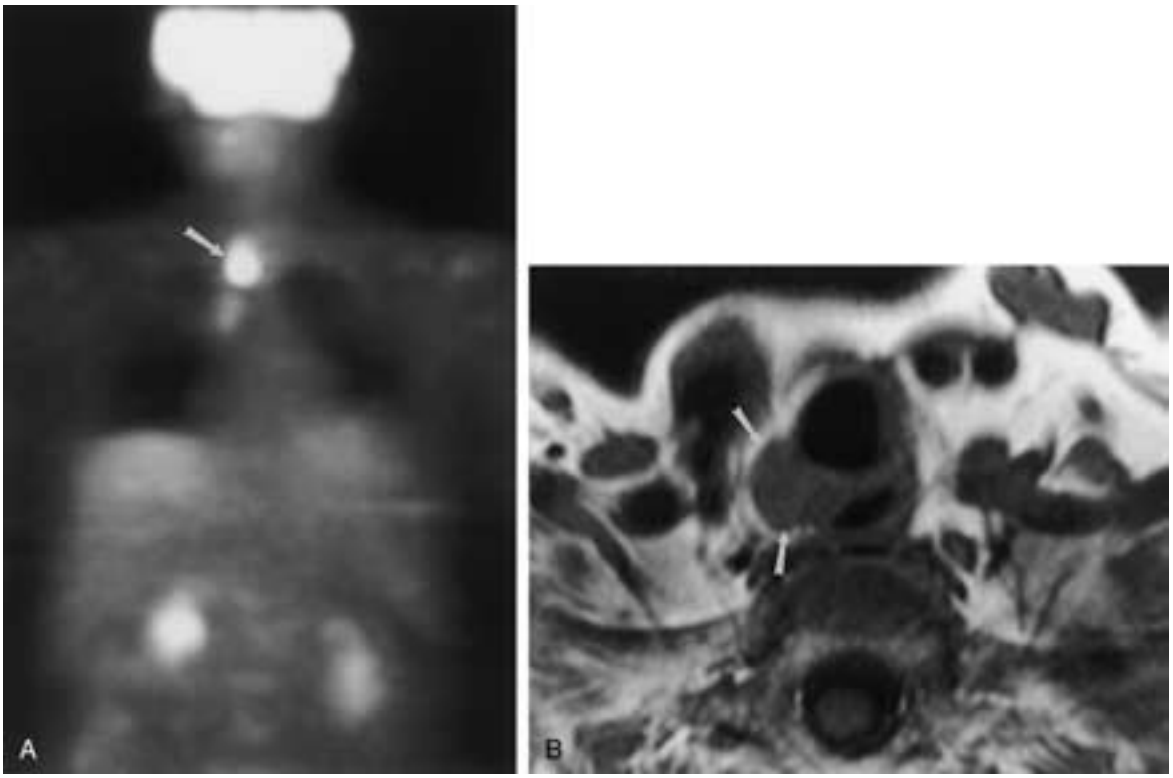

VIEW IMAGE

FIGURE 40-5 Recurrent thyroid cancer in a 64-year-old woman following thyroidectomy for papillary carcinoma, tall cell variant. **A**, ^{18}FDG-PET image shows a region of intense radiotracer uptake (*arrow*) in the base of the right neck. **B**, Unenhanced axial T1-weighted MR image shows a corresponding soft-tissue mass in the right tracheoesophageal groove (*arrows*), confirmed to be recurrent tumor at surgery.

thyroid. Conversely, a poorly seen gland, or portion of a gland, correlates with poor thyroid function. The injection of iodinated contrast material intravenously usually increases the density of the gland diffusely. While iodinated contrast material may provide additional information about lesions within the thyroid, as mentioned, such contrast will alter radioactive iodine uptake measurements for up to 6 weeks following the study. Therefore, in patients in whom nuclear scintigraphy will also be performed, either contrast should not be administered for the CT study or the nuclear imaging

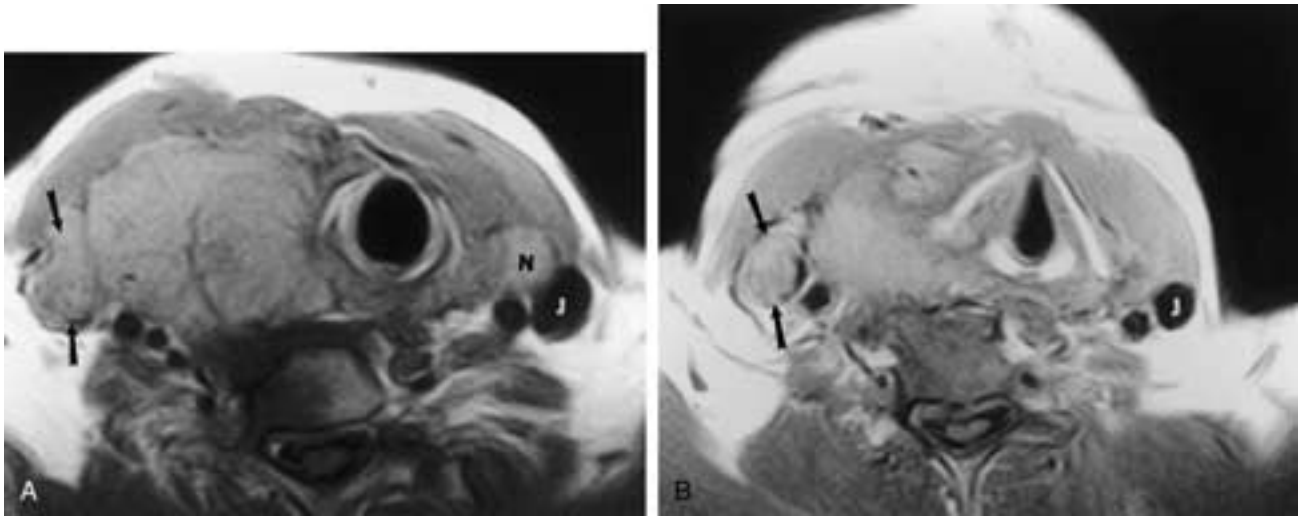

VIEW IMAGE

FIGURE 40-6 A 68-year-old man presented with a rapidly enlarging right neck mass and facial swelling. MR imaging revealed a right thyroid tumor with extension to the jugular vein. **A**, Unenhanced axial T1-weighted MR image shows a poorly defined mass originating in the right thyroid lobe with extracapsular extension and direct invasion of the jugular vein, which is filled with tumor (*arrows*). *J*, Left jugular vein with normal flow void; *N*, metastatic disease. **B**, Unenhanced axial T1-weighted MR image superior to **A** shows tumor in the right jugular vein.

Copyright © 2003, Mosby, Inc. All rights reserved.

should be performed prior to CT. Alternatively, MR with contrast material (gadolinium) may be used in conjunction with scintigraphy, as this contrast agent does not interfere with iodide uptake or organification by the thyroid. Another advantage of MR imaging is that it readily identifies blood vessels (signal voids) that on CT may be confused with lymph nodes.

MR imaging is performed with an anterior neck coil centered over the thyroid gland, which provides high-quality images with a high signal-to-noise ratio and the best soft-tissue resolution. Nodules as small as 4 mm may be detected.[16] Multiple pulse sequences should be obtained including noncontrast sagittal and axial T1-weighted images, as well as axial fast spin-echo T2-weighted images with the application of fat saturation. Following intravenous contrast administration, axial T1-weighted images with the application of fat saturation are usually acquired. On T1-weighted images, the normal thyroid gland shows homogeneous signal intensity slightly greater than that of the musculature in the neck. On T2-weighted images, the thyroid gland is hyperintense relative to the neck musculature (Fig. 40-1). Following contrast administration, the normal gland enhances diffusely and homogeneously.

Ultrasonography

Real-time ultrasound of the thyroid gland is usually performed with high-resolution linear array transducers ranging from 7.5 to 10 MHz.[17] The neck is mildly hyperextended, and the thyroid gland is imaged in its entirety in both the transverse and longitudinal planes. The carotid arteries and jugular veins are posterior and lateral to the thyroid lobes, respectively, and provide excellent anatomic markers during the examination. The thyroid gland is normally uniformly hyperechoic.[17] The more hypoechoic a focal lesion is relative to the normal thyroid gland, the higher the likelihood of malignancy.[18]

The advantages of ultrasound are three: it is accessible, inexpensive, and noninvasive. It is a quick and highly sensitive modality for distinguishing cystic from solid lesions. Focal lesions meeting all of the criteria for a simple cyst (thin wall with smooth margins, anechoic, distinct back wall, and enhanced through transmission) are usually benign. However, any complicated cyst may represent a carcinoma. When calcifications are present, they appear as foci of increase echogenicity with distal acoustic shadowing. Calcifications are nonspecific and may be seen in benign as well as malignant lesions.[18] Ultrasound may also be used to guide fine needle aspiration of nodular disease within the thyroid or to guide aspiration of suspicious cervical lymph nodes in the setting of thyroid cancer (Fig. 40-7).[19–21]

Drawbacks of ultrasound are that the quality of the images as well as their interpretation are dependent on the expertise of the examiner. Another limitation is that ultrasound is not as good as cross-sectional imaging techniques in identifying lymphadenopathy or in evaluating for extension of thyroid disease into the soft tissues of the neck, chest, or air-filled structures.

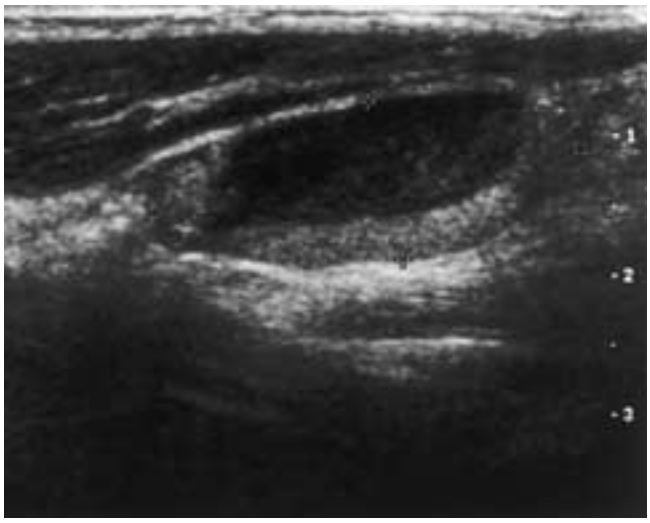

FIGURE 40-7 Ultrasonography in a patient previously treated for thyroid cancer shows a metastatic cervical lymph node (denoted by markers). (Courtesy of Dr. Jill Langer, Department of Radiology, Ultrasound Division, University of Pennsylvania Medical Center.)

VIEW IMAGE

PATHOLOGY OF THE THYROID GLAND

Congenital Anomalies

The thyroid gland develops in the first trimester of pregnancy, beginning around the fifth week of gestation, and its development is completed by the tenth week of gestation. It develops from median and paired lateral anlages. The median anlage arises in the midline oropharynx at the fourth to fifth gestational week and gives rise to follicular thyroid tissue, which will ultimately secrete hormones.[22] The lateral anlages are believed to arise from the ultimobranchial bodies, which in turn are derived from the fourth and fifth branchial pharyngeal pouches at around the fifth week of gestation. They give rise to the parafollicular C cells that are thought to derive from the neural crest.[22] The parafollicular cells ultimately secrete calcitonin. By the tenth week in utero, the right and left lateral anlages fuse with the median anlage, resulting in the bilobed thyroid gland (see also Chapter 33).[22, 23]

During fetal development, the thyroid gland must descend from its place of origin, the foramen cecum, located at the anterior, midline base of the tongue, to its final adult destination in the lower neck both anterior and lateral to the trachea. The thyroid is attached to the tongue base by the thyroglossal duct, which is lined by squamous epithelium. During the caudal descent of the gland, this duct elongates and subsequently degenerates and atrophies.

Abnormal development or aberrant caudal descent of the thyroid gland results in a variety of congenital anomalies. Arrest of descent can occur anywhere from the tongue down to the lower neck. Ectopic thyroid has rarely been reported in the submandibular and lateral neck regions.[24] In these cases, these ectopias may be misinterpreted as metastatic disease. Failure of descent of the median thyroid anlage, or complete failure of descent of the thyroid, results in a lingual thyroid gland at the base of the tongue, the most common type of functioning ectopic thyroid tissue (Fig. 40-8). In

Copyright © 2003, Mosby, Inc. All rights reserved.

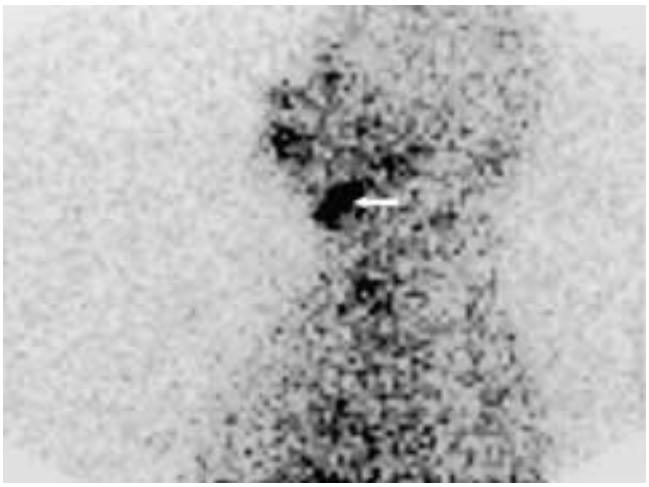

VIEW IMAGE

FIGURE 40-8 Lingual thyroid. Lateral I-123 scintigraphy showing increased radiotracer uptake at the base of the tongue region consistent with lingual thyroid (*arrow*). (Courtesy of Dr. Joseph Sam, Department of Radiology, Nuclear Medicine Division, University of Pennsylvania Medical Center.)

such cases, up to 75% of patients may have no functioning thyroid tissue in the neck.[25–27] As a result, if tissue at the base of the tongue is not recognized as thyroid and is resected, the patient may become acutely and severely hypothyroid.[28] Nuclear imaging plays the major role in establishing the diagnosis of a lingual thyroid gland as well as in determining whether there is normal functioning thyroid tissue in the neck. On noncontrast CT, lingual thyroid is hyperdense due to its iodine content, and on MR imaging it has high signal intensity on T1-weighted and T2-weighted images compared to the tongue musculature. Avid enhancement is seen following contrast administration.

Overdescent of the thyroid may result in ectopic normal thyroid in the lower neck or mediastinum. On rare occasions, thyroid tissue may be found in remote locations, such as within the heart and within ovarian teratomas (struma ovarii).[29, 30] In the handful of reported cases of intracardiac thyroid tissue, all arose from the right ventricular aspect of the interventricular septum, and none were associated with abnormalities of thyroid function.[30] Intratracheal thyroid ectopia may also occur, with aberrant thyroid tissue most often located at or just below the cricoid cartilage.[31] The overwhelming majority of patients with this condition are female, and most present with respiratory distress that may be acute or chronic. The intratracheal thyroid tissue may be contiguous with the thyroid lobe by a bridge of tissue or a thin fibrous strand.[31]

Any pathology that may arise within normally located thyroid may also arise in ectopic tissue. Though extremely rare, carcinoma has been described in ectopic tissue.[27, 32] Scintigraphy using Tc-99m pertechnetate or I-131 should be performed when ectopic thyroid is suspected.[33]

Other developmental anomalies of the thyroid gland include agenesis or hemiagenesis of one lobe, with normal formation of the contralateral lobe and isthmus.[6, 33, 34]

Incomplete degeneration of the thyroglossal duct may result in a persistent fistulous tract or in a thyroglossal duct cyst along the path of migration of the thyroid gland from the foramen cecum at the tongue base to the anterior lower neck. Thyroglossal duct cysts most often are anterior midline neck masses, although they may be located in a paramedian location especially when infrahyoid. Over half of these cysts have normal thyroid follicular tissue in their walls.[35] Approximately 65% of thyroglossal duct cysts are infrahyoid in location and are encased by the thyroid strap muscles (Fig. 40-9). Cysts may also occur in the suprahyoid region (20%) at the tongue base/floor of the mouth (Fig. 40-10) or in the hyoid region (15%) above the strap muscles.

On cross-sectional imaging, uncomplicated thyroglossal duct cysts are usually well demarcated. On CT, they most often are isodense to water; however, they may be hyperdense when there is high protein content. On MR imaging, they typically have low T1-weighted and high T2-weighted signal intensities. However, when the contents of the cyst are proteinaceous, the cysts may be hyperintense on T1-weighted images (Fig. 40-11) and usually remain intermediate to hyperintense on T2-weighted images. Thick peripheral enhancement is unusual unless a cyst is secondarily infected. On sonography, these lesions have typical features of a cyst. They may also demonstrate internal echoes when proteinaceous or infected, similar to other complicated cysts. Nuclear scintigraphy is usually not necessary in the evaluation of thyroglossal duct cysts. The one exception is a cyst in a child without a palpable thyroid gland; in this case, nuclear scintigraphy may be necessary to determine if the cyst contains the patient's only functional thyroid tissue.

When large, these cysts are clinically detected as palpable midline or near-midline neck masses. A highly suggestive clinical finding of a thyroid origin is vertical motion of the mass with swallowing or tongue protrusion. These larger

FIGURE 40-9 Infrahyoid thyroglossal duct cyst. Enhanced axial CT scan shows a thyroglossal duct cyst (*C*) in a right paramedian location. Note the small portion of the cyst extending into the superior thyroid notch and bowing the thyrohyoid membrane backward (*arrow*).

VIEW IMAGE

Copyright © 2003, Mosby, Inc. All rights reserved.

VIEW IMAGE

FIGURE 40-10 Suprahyoid thyroglossal duct cyst. T2-weighted MR image shows the cyst (*C*) in the region of the foramen cecum at the base of the tongue.

cysts may have multiple septations on imaging (Fig. 40-12). Small thyroglossal duct cysts are usually clinically occult and may be recognized only if they become secondarily infected or traumatized, or if they are incidentally noted on imaging studies of the neck being performed for unrelated reasons. Rarely, thyroglossal duct cysts may undergo malignant degeneration, usually into papillary carcinoma. This should be suspected when a soft-tissue component or nodule exists within or around the cyst or if the cyst has calcifications.[36]

Thyroglossal duct cysts may be excised for a variety of indications including secondary infection, a mass effect resulting in pain or dysphagia, or for cosmesis. Acutely infected cysts should be treated with a full course of antibiotics prior to surgical excision. In cases where a cyst is associated with a sinus tract, excision of the entire tract is necessary. The general operation for a thyroglossal duct cyst is the Sistrunk procedure. Sistrunk proposed that the body of the hyoid bone should be removed during surgical resection of a thyroglossal duct cyst. In so doing, recurrences were reduced from nearly 50% to less than 4%.

In cases of small thyroglossal duct cysts with carcinoma, surgical resection alone may be considered adequate therapy when there is no evidence of angio-invasion, the surgical margins are clear, the remainder of the thyroid gland is normal on ultrasound, and the patient is young and has no significant risk factors. Otherwise, in a patient of advanced age, or with unfavorable pathologic findings or nodularity in the thyroid gland, management may require surgical resection of the cyst accompanied by total thyroidectomy and/or radioiodide therapy.

Autoimmune Disease and Thyroiditis

Thyroiditis is infiltration of the thyroid gland with inflammatory cells. This may be seen in a diverse group of autoimmune, inflammatory, and infectious processes. Thyroiditis may be acute and self-limiting or chronic and progressive.

Several autoimmune disorders may affect the thyroid gland including Graves' disease, Hashimoto's thyroiditis, and silent/postpartum thyroiditis. Each differs in pathophysiology and clinical presentation. Graves' disease and silent thyroiditis are usually associated with thyroid hyperfunction, while Hashimoto's disease (chronic lymphocytic thyroiditis) is typically associated with hypofunction. As will be discussed later, the term *goiter* simply refers to a clinically evident enlargement of the thyroid gland.

Graves' Disease

Graves' disease is the most common of the autoimmune disorders, occurring in approximately 0.4% of the U.S. population.[2] The peak incidence is in the third to fourth decades of life, with a female predominance. There is a familial predisposition. In Graves' disease the thyrotropin receptor on the follicular cells is the target for thyroid autoantibodies, which bind to these receptors, stimulating them as though TSH triggered the receptor. This results in constant autonomous function of the thyroid resulting in hyperthyroidism. Serologic tests for specific autoimmune markers may be elevated, confirming the diagnosis. Marked enlargement of the thyroid gland without focal nodules referred to as diffuse toxic goiter results. There may be prominent enlargement of a pyramidal lobe (Fig. 40-2). Pathologically, in the thyroid gland there is diffuse hyperplasia of the follicular epithelial cells and depletion of

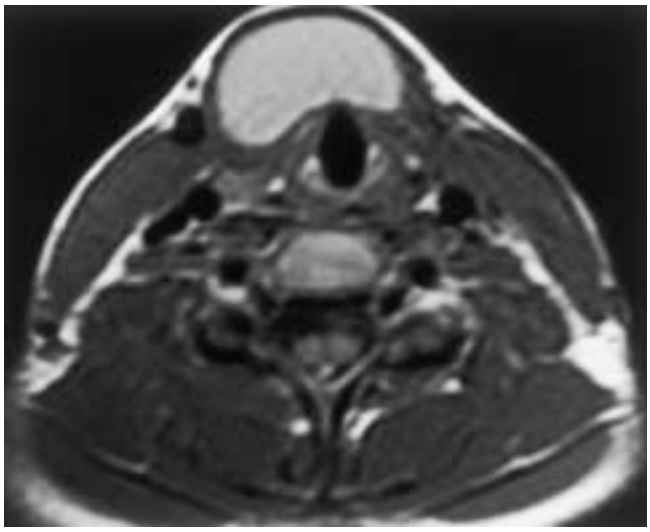

FIGURE 40-11 Thyroglossal duct cyst containing proteinaceous material. Unenhanced axial T1-weighted image shows a midline cyst that is hyperintense due to its proteinaceous contents.

VIEW IMAGE

Copyright © 2003, Mosby, Inc. All rights reserved.

colloid. Vascularity is increased. Graves' disease is associated with other autoimmune diseases of the thyroid including Hashimoto's thyroiditis.

Radionuclide scintigraphy may be useful in evaluating a patient with suspected Graves' disease as well as in differentiating it from acute thyroiditis. Typically in Graves' disease, the thyroid gland is diffusely enlarged with intense radiotracer uptake, often as high as 80% in 24 hours (Fig. 40-13).

The differential diagnosis includes thyroiditis, toxic multinodular goiter, and toxic adenoma. In contrast to Graves' disease, where there is concordance between the clinical presentation of thyrotoxicosis and the radionuclide uptake, in the acute phase of thyroiditis when the patient is clinically hyperthyroid, the gland may be so impaired that there is little observable radionuclide uptake (Fig. 40-14), which is usually less than 10% (normal, 10% to 30%). On scintigraphy, tracer uptake is often inhomogeneous and reduced. During the subacute phase of thyroiditis, the radiotracer uptake usually returns to normal if the gland recovers and the patient reverts to a euthyroid state. Differentiation between Graves' disease and subacute thyroiditis is important for appropriate patient management, as patients with Graves' disease often require medication to

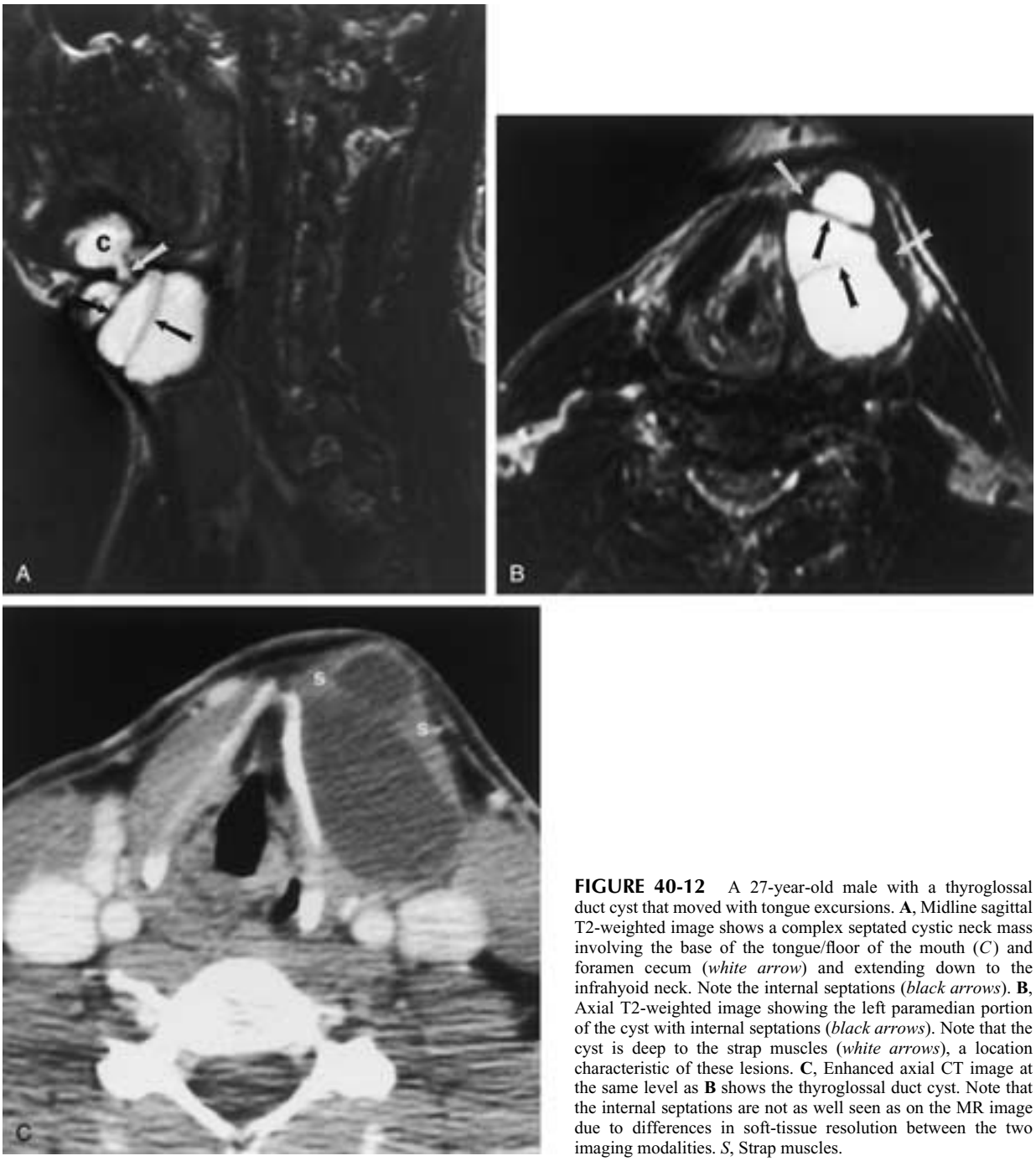

FIGURE 40-12 A 27-year-old male with a thyroglossal duct cyst that moved with tongue excursions. **A**, Midline sagittal T2-weighted image shows a complex septated cystic neck mass involving the base of the tongue/floor of the mouth (*C*) and foramen cecum (*white arrow*) and extending down to the infrahyoid neck. Note the internal septations (*black arrows*). **B**, Axial T2-weighted image showing the left paramedian portion of the cyst with internal septations (*black arrows*). Note that the cyst is deep to the strap muscles (*white arrows*), a location characteristic of these lesions. **C**, Enhanced axial CT image at the same level as **B** shows the thyroglossal duct cyst. Note that the internal septations are not as well seen as on the MR image due to differences in soft-tissue resolution between the two imaging modalities. *S*, Strap muscles.

VIEW IMAGE

Copyright © 2003, Mosby, Inc. All rights reserved.

FIGURE 40-13 Graves' disease. I-131 scintigraphy shows diffuse increased radiotracer uptake throughout the thyroid gland. The 2 hour uptake was 25.5% and the 24 hour uptake was 57%, with the upper limits of normal being 10% and 30%, respectively. (Courtesy of Dr. Joseph Sam, Department of Radiology, Nuclear Medicine Division, University of Pennsylvania Medical Center.)

VIEW IMAGE

FIGURE 40-14 Thyroiditis. I-123 scintigraphy in a 50-year-old woman who presented with hyperthyroidism. Note that the gland is so impaired that there is little observable radionuclide uptake, which was 7.3% at 24 hours (normal, 10% to 30%). Sternal notch (*arrow*). (Courtesy of Dr. Joseph Sam, Department of Radiology, Nuclear Medicine Division, University of Pennsylvania Medical Center.)

VIEW IMAGE

treat the secondary manifestations of hyperthyroidism (beta blockers for tachycardia) as well as thyroid medication, radioiodine ablation of the thyroid gland, or surgery when required. Subacute thyroiditis is treated conservatively.

In toxic multinodular goiter, there are areas of both increased and decreased uptake within an enlarged gland (Fig. 40-15) distinct from the homogeneous uptake seen in Graves' disease, and the overall uptake is not as avid as that in Graves' disease. In toxic adenoma, there is focal uptake in a single nodule. If the nodule is autonomous, suppression of the normal glandular tissue may be observed.

On cross-sectional imaging, the findings in Graves' disease are nonspecific. The thyroid is enlarged. On ultrasound, the gland is often diffusely hyperechoic, without discrete nodules. A characteristic increase in thyroid vascularity is observed on color Doppler studies in both systole and diastole, particularly in patients with active hyperthyroidism.[37, 38] On CT and MR imaging, the enlarged thyroid demonstrates avid enhancement. The noncontrast CT density is actually decreased, reflecting a decrease in iodine concentration even though there is an overall increase in the iodine content of the gland. Even after treatment, density values may not return to normal.[39]

Hashimoto's Thyroiditis

Hashimoto's thyroiditis (chronic lymphocytic thyroiditis) is the prototype autoimmune thyroiditis. Pathologically, the thyroid gland is enlarged and demonstrates lymphocytic and plasma cell infiltration, follicular cell atrophy, and interlobular fibrosis.[40] Additionally, the normal follicular epithelial cells may be altered, being replaced with pink oxyphilic epithelium (Hurthle or Askanazy cells).[41] It is usually associated with a goiter. The pathogenesis of Hashimoto's thyroiditis involves both cellular and humoral mechanisms. Autoantibodies have been identified against thyroglobulin, thyroperoxidase, and TSH receptors. In reported cases, when TSH receptor-blocking antibodies disappeared, normal thyroid function returned.[42] Hashimoto's thyroiditis is

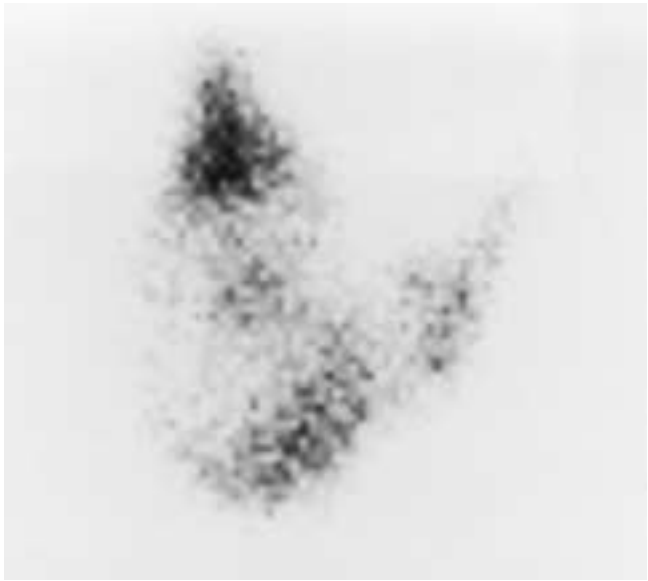

FIGURE 40-15 Toxic multinodular goiter. Technetium-99m pertechnetate scans show enlargement of the thyroid gland with regions of increased and decreased uptake.

VIEW IMAGE

Copyright © 2003, Mosby, Inc. All rights reserved.

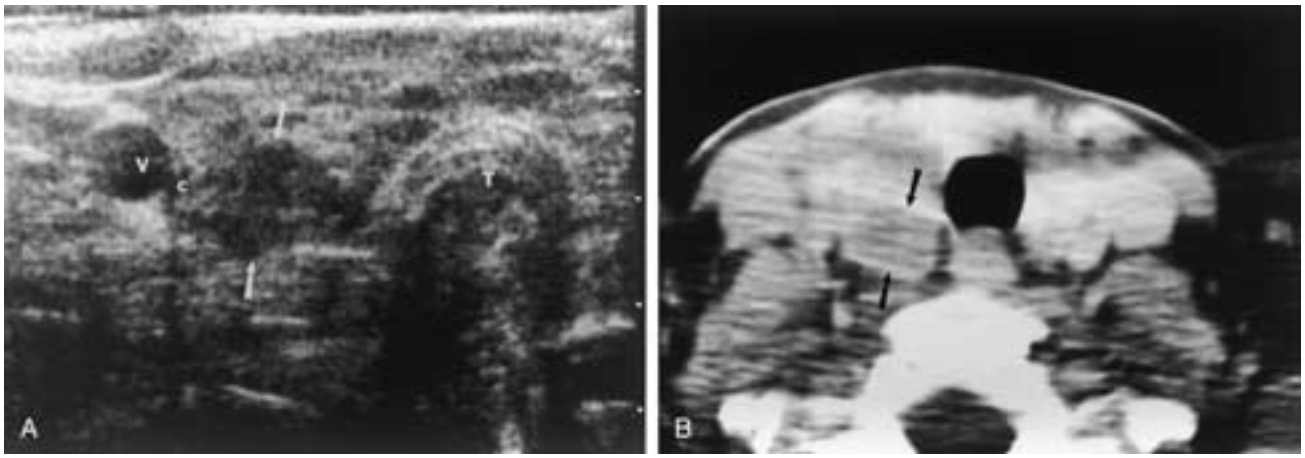

VIEW IMAGE

FIGURE 40-16 Hashimoto's thyroiditis. **A**, Transverse ultrasound image showing heterogeneity in the echotexture of the right lobe of the thyroid gland with a more focal region of decreased echogenicity posteriorly (*arrows*). *V*, Jugular vein; *C*, carotid; *T*, trachea. **B**, Corresponding enhanced axial CT scan shows a focal region of hypodensity (*arrows*) corresponding to the abnormality seen on ultrasound.

associated with other autoimmune disorders including lupus, Graves' disease, and pernicious anemia.

Hashimoto's thyroiditis occurs predominantly in women, most commonly presenting in the fourth and fifth decades of life. It may also present in children, in whom it is the most common thyroiditis.[43] The clinical presentation is frequently that of hypothyroidism.[44] Antibody titers are markedly elevated during the acute phase. In the acute phase of glandular destruction and hormone release, symptoms of hyperthyroidism may be evident. However, ultimately, hypothyroidism usually prevails.

The diagnosis of thyroiditis in general is based on the clinical presentation, and laboratory analysis of thyroid function and imaging is not a critical component of the initial workup of these patients. Although the radiologic findings are nonspecific, imaging can be useful, especially in patient follow-up and monitoring of disease.

On scintigraphy, there is no typical pattern in Hashimoto's thyroiditis. Uptake of radioiodine or Tc-99m pertechnetate is most commonly heterogeneous and patchy, and may be uniformly increased or mildly to severely decreased.[41, 45] In children, a homogeneous distribution of tracer is more common.[43]

Ultrasonography demonstrates a variety of patterns. The thyroid may be normal or enlarged in size and is diffusely abnormal, with heterogeneous echogenicity (Fig. 40-16). There may be numerous poorly defined, hypoechoic regions separated by fibrous strands.[19] Large nodules within the gland raise the possibility of superimposed non-Hodgkin's lymphoma. In end-stage disease, the thyroid gland may be atrophied and fibrotic, resulting in a heterogeneous echotexture.

On CT, there is an inhomogeneous distribution of iodine. With MR imaging, T2-weighted images may show areas of increased signal intensity. Linear, septated, low-intensity bands thought to represent fibrosis have been described.[16] Following contrast administration, there may be regions that enhance more than the remainder of the gland (Fig. 40-17).

Ultrasound may be used to follow patients with Hashimoto's thyroiditis to detect occult malignancy because there is a well-known increase in the incidence of non-Hodgkin's lymphoma in this setting.[46–49] Thyroid lymphoma may produce solitary or multiple focal hypoechoic lesions or diffuse disease that may be difficult to distinguish from Hashimoto's thyroiditis.[46, 47] The presence of cervical lymphadenopathy raises the suspicion of lymphoma. Primary thyroid carcinoma is unusual but has been reported.[50]

Silent, Painless Thyroiditis and Postpartum Thyroiditis

Silent, painless thyroiditis and postpartum thyroiditis are two different types of subacute lymphocytic thyroiditis, which are usually self-limited. When this inflammatory process occurs in the absence of pregnancy, it is termed *painless thyroiditis*. Low-titer antithyroid antibodies may be present, and the disorders are thought to be autoimmune.

During the early phase of lymphocytic infiltration, follicular disruption with hormone release usually causes patients to present with thyrotoxicosis. As the disease progresses, patients may be hypothyroid transiently before returning to a euthyroid state.[51] Patients may or may not have glandular

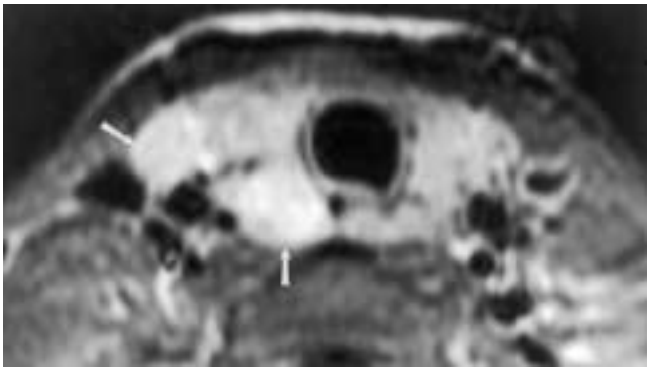

FIGURE 40-17 Hashimoto's thyroiditis. Enhanced axial T1-weighted MR image shows two nodules (*arrows*) in the right lobe of the thyroid gland that enhance more than the remainder of the gland.

VIEW IMAGE

Copyright © 2003, Mosby, Inc. All rights reserved.

enlargement. Radioactive iodine uptake is low, and the pattern on scintigraphy varies from no tracer uptake to diffuse or heterogeneous uptake.[34] Nuclear scans may return to normal in conjunction with resolution of the process.

Postpartum thyroiditis typically occurs 4 to 6 weeks following delivery. It occurs in up to 5% of postpartum women and may recur with subsequent pregnancy.[52] As with silent thyroiditis, women may present with goiter, thyrotoxicosis, and antithyroid antibodies. The process usually resolves after transient hypothyroidism; however, some patients progress to chronic lymphocytic thyroiditis.

De Quervain's Thyroiditis (Subacute Granulomatous Thyroiditis)

De Quervain's thyroiditis is a self-limited inflammatory process that usually occurs following a viral upper respiratory tract infection.[2, 22] The viral infections that have been associated with subacute thyroiditis include coxsackievirus and the mumps.[53] The peak incidence is in the second to fifth decades of life, with an occurrence three times more frequent in women. Early in the inflammatory process, follicles may be replaced with neutrophils forming microabscesses. Later, macrophages and multinucleated giant cells surround the damaged follicles, stimulating a granulomatous process.[2] Viral inclusions have not been found in the inflamed gland. With healing, there is regeneration of the follicles. The clinical presentation may include painful enlargement of the thyroid gland, fever, and thyrotoxicosis with low radioactive iodine uptake. Scintigraphy shows a variable pattern that usually reverts to normal as the patient returns to a euthyroid state.[6] On non-contrast CT, the gland is slightly enlarged and has a lower than normal attenuation.

Acute Suppurative Thyroiditis

Acute suppurative thyroiditis is uncommon and typically occurs due to seeding of the thyroid gland by bacterial, and occasionally fungal, organisms in immunocompromised or debilitated patients.[22] It may be associated with a fourth branchial cleft abnormality, and one of the roles of imaging is to exclude a fistula (from the pyriform sinus apex) as an etiology of the thyroiditis.[54] On cross-sectional imaging, the affected portion of the gland (lobe[s] and/or isthmus) will be enlarged and heterogeneous in CT density and MR signal intensity. With disease progression, focal abscesses may develop and there may be obliteration of the adjacent soft tissues in the neck resulting from associated myositis and cellulitis.[55]

Riedel's Thyroiditis (Struma)

Riedel's thyroiditis (struma) is a rare form of chronic thyroiditis characterized by a fibrosing reaction similar to that seen in retroperitoneal fibrosis, which destroys the thyroid and extends into the adjacent soft tissues of the neck. Within the fibrosing tissue is a lymphocytic and plasma cell infiltration and a vasculitis (phlebitis).[56] As a result, stridor, dysphagia, and vocal cord paralysis may result from recurrent laryngeal nerve involvement. In fact, Reidel's thyroiditis is one of the few nonmalignant thyroid causes of recurrent laryngeal nerve paralysis. The cause of Reidel's thyroiditis is unknown. It is more common in women and usually occurs in the fourth to seventh decades of life. On palpation, the thyroid is frequently firm, which may be confused with a malignancy.[57] One-third of patients will develop hypothyroidism. On ultrasound the thyroid may be hypoechoic, and on CT the involved thyroid may be hypodense compared to normal thyroid (Fig. 40-18).[17, 58] The characteristic MR appearance includes decreased signal intensity on T1-weighted and T2-weighted images believed to correspond to fibrosis, as well as infiltration of adjacent soft tissues in the neck.[57] Riedel's thyroiditis may be associated with mediastinal or retroperitoneal fibrosis as well as sclerosing cholangitis.

Thyroid Goiter

As mentioned, the term *goiter* refers to any clinical enlargement of the thyroid gland. A goiter develops because as the thyroid gland compensates for inadequate thyroid hormone output, the follicular epithelium undergoes compensatory hypertrophy to achieve a euthyroid state. As a result, either hypothyroidism or hyperthyroidism may develop. Although initially the goitrous enlargement is diffuse, with time it usually becomes nodular. If the impediment to thyroid hormone output abates, the thyroid gland may revert to normal during the diffuse state.

Diffuse nontoxic goiter is a diffuse nonnodular enlargement of the thyroid associated with a euthyroid state. There are two stages in its development. The first stage is hyperplasia (follicular cell growth) characterized by diffuse glandular enlargement and hyperemia. The second stage is colloid involution, which occurs when a euthyroid state is maintained. Endemic goiters are prevalent in iodine-deficient areas. In simple sporadic goiter, there is a female predominance and a peak incidence at puberty.[2] With time, most simple goiters progress to multinodular goiters that may remain nontoxic or may induce thyrotoxicosis.

Multinodular goiter is characterized by nodularity, focal hemorrhage, focal calcifications, cyst formation, and scarring. Glandular enlargement may be asymmetric, involving

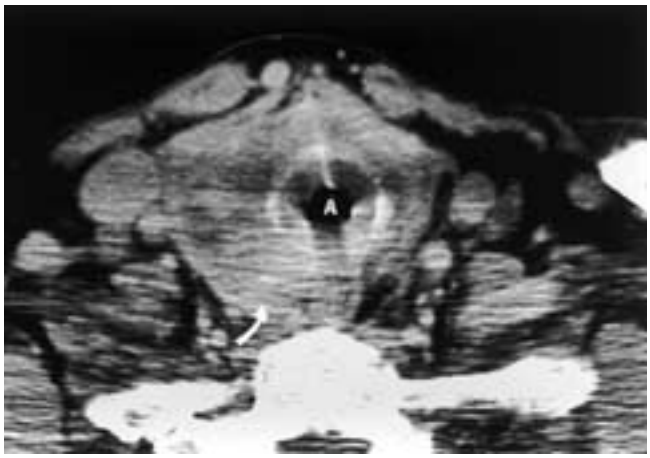

FIGURE 40-18 Riedel's thyroiditis (struma). An axial CT scan shows slight enlargement of the thyroid gland with multiple areas of poorly defined hypodensity. Note the associated narrowing of the subglottic airway (*A*), as well as obliteration of the fat in the right tracheoesophageal groove (*arrow*).

VIEW IMAGE

Copyright © 2003, Mosby, Inc. All rights reserved.

VIEW IMAGE

FIGURE 40-19 Papillary carcinoma developing within a goitrous gland. Axial T2-weighted MR image shows multiple demarcated solid and cystic nodules/masses diffusely within the thyroid gland. The large predominately solid nodule replacing the left gland (*arrows*) and the dominant nodule in the right lobe (*curved arrows*) represented papillary carcinoma at pathology.

one lobe more than the other and/or involving the isthmus. Thyroid goiters may extend substernally and into the anterior mediastinum.

Multiple patterns may be identified with nuclear scintigraphy (Fig. 40-15). Radioactive iodine or Tc-99m pertechnetate may accumulate in multiple foci throughout the gland or, less typically, in only a few nodules. Some nodules may demonstrate autonomous function. In patients with thyrotoxicosis, therapeutic doses of I-131 may be required to reduce thyroid function. Although it was previously thought that a solitary cold nodule in a multinodular goiter was less likely to be malignant than a solitary cold nodule in a normal gland, recent studies have demonstrated similar rates of malignancy.[58–60] A dominant or enlarging mass within a goitrous thyroid should be biopsied (Fig. 40-19).[61]

On ultrasonography, a simple goiter demonstrates diffuse glandular enlargement with uniform or irregular echogenicity that may be increased or decreased. A multinodular goiter is often irregular, showing diffuse inhomogeneous echogenicity or multiple focal hypoechoic nodules. On CT evaluation of multinodular goiter, the gland is asymmetric, with multiple low-density areas reflecting regions of hemorrhage, cyst formation, or necrosis (Fig. 40-20). More focal regions of hyperdensity are common, reflecting calcifications present in over one half of patients, hemorrhage, or colloid (Fig. 40-21). On MR imaging, multinodular goiter may show a wide spectrum of appearances.[62] On T1-weighted images, multiple foci of high signal intensity may represent cysts containing colloid or hemorrhage (methemoglobin). On T2-weighted images, diffuse heterogeneity may be present,[62] and nodules as small as 3 to 5 mm can be visualized.[16] Alternatively, multiple large, heterogeneous nodules may be present. Enhancement is usually inhomogeneous. Unlike CT, calcifications may be difficult to detect and, when visualized, may appear as low-intensity foci on T1- and T2-weighted sequences.

CT and MR imaging are useful in evaluating secondary manifestations of goiter including compression and displacement of the trachea, esophagus, and adjacent vessels (Fig. 40-4). Importantly, substernal and mediastinal extension is readily detected (Figs. 40-4 and 40-21). In contrast, nuclear scintigraphy and ultrasound may fail to

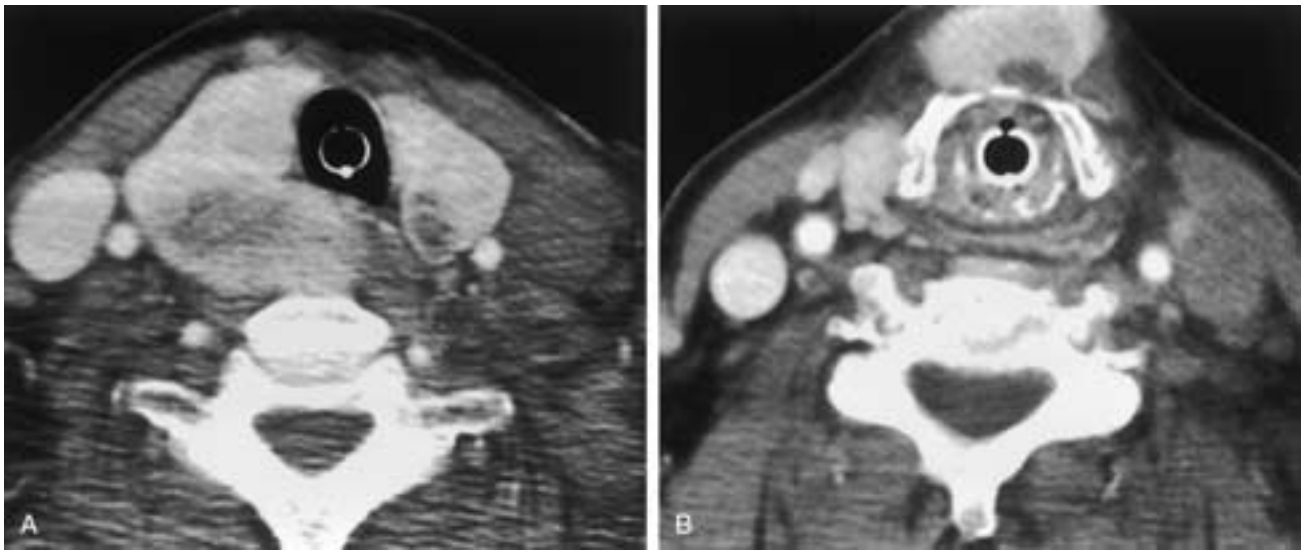

VIEW IMAGE

FIGURE 40-20 Multinodular goiter. **A**, Enhanced axial CT image shows asymmetry in the thyroid gland. Both lobes are enlarged (the right greater than the left), with multiple focal regions of low density consistent with goiter. **B**, Enhanced axial CT image superior to **A** shows nodular enlargement with a focal area of hypoattenuation within the isthmus of the gland. The patient has an orotracheal tube in place.

Copyright © 2003, Mosby, Inc. All rights reserved.

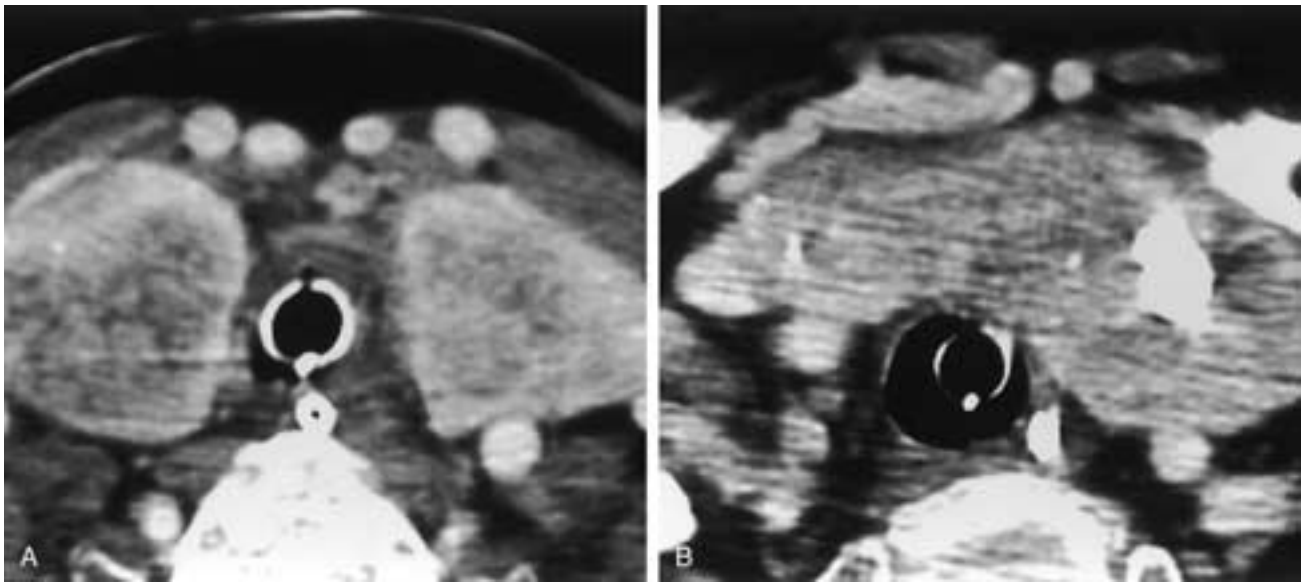

VIEW IMAGE

FIGURE 40-21 Multinodular goiter with substernal extension. **A**, Enhanced axial CT scan reveals extensive enlargement of the thyroid gland with diffuse heterogeneous hypodensity. The patient has an orotracheal tube in place. **B**, There was substernal extension of the thyroid goiter. Multiple calcifications are also noted.

show continuity between a cervical and a mediastinal goiter. When symptoms related to compression of the aerodigestive tract or vessels occur in elderly patients, nonsurgical candidates, or those refusing surgery, therapy with I-131 may be effective in reducing thyroid volume.[63]

Specifically on CT and MR reports, the radiologist must mention any shift in the axis of the trachea, the location of any tracheal narrowing, the degree of this narrowing, and the length of the stenotic segment. The location of the tracheal narrowing should be given with reference to the bottom of the cricoid cartilage, as this is an easily recognizable endoscopic landmark. The length of the segment in centimeters should then be mentioned. Finally, the percentage of the tracheal cross-sectional area reduction should be estimated. If the patient has normal pulmonary function, a 50% reduction in tracheal cross-sectional area usually is associated with dyspnea at rest. In addition, the greatest dimension of the enlarged thyroid gland and the most cranial and caudal levels of the gland should be noted. Thus, a typical report might mention that ''there is a large multinodular goiter of 9 cm in greatest dimension. The most cranial level of the gland is at the level of the true vocal cords, and the most caudal level is 1 cm below the level of the top of the manubrium. The tracheal axis is shifted to the right, and starting 2 cm below the level of the cricoid cartilage and extending over a 3 cm length of trachea, there is an approximately 30% narrowing of the cross-sectional tracheal area.'' Such a report provides all of the necessary information to the clinicians in order for them to make an appropriate treatment decision. The extension of a goiter outside of the normal thyroid bed occurs into the substernal area in 5.7% –20% of the cases. Extension into the posterior mediastinum occurs in 9.8%–12% of cases, and this always occurs in conjunction with extension into the anterior mediastinum. There are also (7.4%) of goiters that extend up behind or along the side of the pharynx.

Nodular Thyroid Disease

Palpable nodules in the thyroid gland are common, occurring in approximately 4% to 7% of the population, or an estimated 10 to 18 million people in the United States.[64] Furthermore, on CT and MR imaging studies of the neck performed for other reasons, as many as 14.5% of patients may be found to have incidental thyroid nodules.[65] Most represent follicular nodules that develop in adenomatous goiters following cycles of hyperplasia and colloid involution. However, since any nodule could represent a thyroid carcinoma, the challenge lies in identifying those lesions that are malignant in the most cost-effective, noninvasive manner.

It is difficult to distinguish benign from malignant nodules. Findings on ultrasound, CT, and MR imaging are nonspecific. A sonolucent halo around a thyroid nodule or a solid, hyperechoic lesion favors a benign process (Fig. 40-22).[18] The presence of calcification is nonspecific, seen in 10% to 15% of all benign and malignant lesions.[18] Similarly, malignant and benign lesions may be cystic, solid, or mixed.[18] Clinical factors that increase the likelihood of a nodule's representing a carcinoma include age (less than 20 or more than 60 years), male gender, low-dose irradiation during childhood for benign conditions, a family history of thyroid carcinoma or multiple endocrine neoplasia, ipsilateral lymph nodes, and longstanding goiter.[6, 66] However, most thyroid nodules occur sporadically and are not associated with these conditions.

Radionuclide scintigraphy plays an important role in distinguishing cold nodules (those that do not demonstrate radioactive iodine uptake relative to the normal gland) from hot or hyperfunctioning nodules (those that demonstrate increased uptake compared to the surrounding thyroid). Cold nodules have a higher incidence of malignancy (Fig. 40-23). The risk of cancer in cold nodules is approximately 20%, compared to less than 5% in hot nodules.[6, 67] The dy-

Copyright © 2003, Mosby, Inc. All rights reserved.

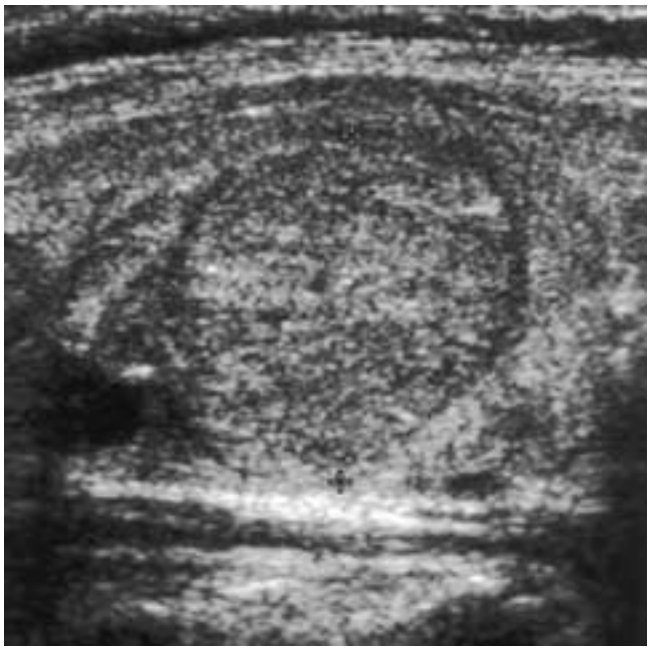

VIEW IMAGE

FIGURE 40-22 Ultrasonogrpahy of the thyroid gland in a patient with a palpable nodule. Note the homogeneous, echogenic nodule with a ''sonolucent halo'' suggestive of a benign thyroid lesion. At pathology this was shown to be a follicular adenoma. (Courtesy of Dr. Jill Langer, Department of Radiology, Ultrasound Division, University of Pennsylvania Medical Center.)

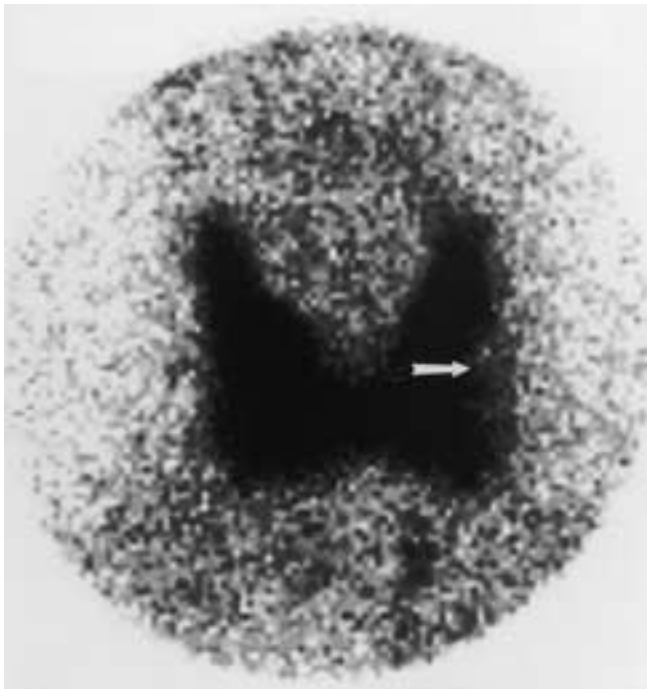

VIEW IMAGE

FIGURE 40-23 A 39-year-old male with a palpable thyroid nodule in the left thyroid gland. Nuclear scintigraphy shows a cold nodule (*arrow*) in the lateral aspect of the left lobe of the thyroid. Subsequent biopsy revealed follicular carcinoma. (Courtesy of Dr. Joseph Sam, Department of Radiology, Nuclear Medicine Division, University of Pennsylvania Medical Center.)

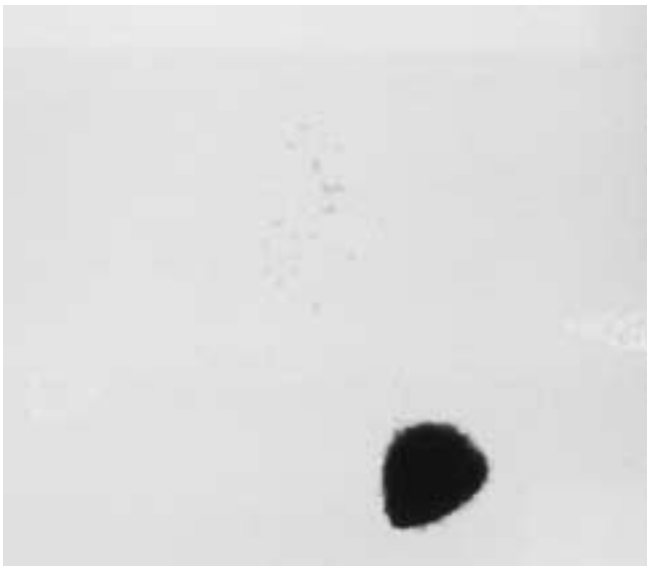

VIEW IMAGE

FIGURE 40-24 A 60-year-old woman presented with hyperthyroidism. The 24 hour uptake was 46% (upper limit of normal is 30%), and scintigraphy showed a hot nodule with suppression of the remainder of the gland consistent with an autonomous nodule. (Courtesy of Dr. Joseph Sam, Department of Radiology, Ultrasound Division, University of Pennsylvania Medical Center.)

namic phase in Tc-99m pertechnetate thyroid imaging may be useful in evaluating cold nodules, with studies suggesting that malignant nodules have a perfusion equal to or greater than that of the surrounding normal thyroid gland.[68]

Functioning or hot nodules in over 90% of cases reflect benign conditions, most commonly adenomas or hyperplasia.[6] If the adjacent normal thyroid tissue is suppressed on scintigraphy, and if, in turn, the nodule cannot be suppressed with exogenous thyroid hormone, it is considered to have autonomous function (Fig. 40-24). Because the incidence of carcinoma in hot nodules is low, these lesions are frequently managed conservatively with close follow-up.

While the majority of cold nodules are benign (adenomas, cysts, inflammation), because of their higher incidence of malignancy, they usually require biopsy or surgical removal.[7] Fine needle aspiration with palpation, CT or ultrasound guidance that ensures positioning of the needle within the lesion has gained wide acceptance as an accurate diagnostic method for evaluating thyroid nodules.[18, 69, 70] Specimens may be obtained with 22- to 25-gauge needles. Typically, on average, three separate passes are made to ensure the most adequate specimen possible. Interpretation requires a skilled cytopathologist. Benign nodules may be followed, and malignant or suspicious nodules are usually surgically resected. In instances where fine needle aspiration is nondiagnostic, repeat aspiration or surgical excision may be necessary.[70]

NEOPLASMS OF THE THYROID GLAND

Adenomas

Thyroid adenomas are true benign neoplasms distinctly separate from the adjacent thyroid tissue and encased by a

Copyright © 2003, Mosby, Inc. All rights reserved.

fibrous capsule. They are usually solitary and nonfunctioning, most commonly detected in young and middle-aged adults. Autonomously functioning adenomas are not usually associated with hyperthyroidism.[71] Toxicity is most commonly seen with large lesions and advanced age. Follicular adenomas slowly increase in size, usually not exceeding 4 cm.[2] Sudden enlargement of a follicular adenoma is usually related to spontaneous hemorrhage within the lesion.[72] Spontaneous degeneration of an adenoma may occur, and in fact, most thyroid cysts represent degeneration of adenomas. The presence of carcinoma within an adenoma is rare.[72] Hurthle cell adenomas are rare neoplasms composed of granular cells and pink-staining cytoplasm. Unlike follicular adenomas, these are not well circumscribed, and some believe they are malignant.

If an adenoma is autonomous (independent of TSH), ablation with I-131 may be performed, as the short-acting beta radiation will deposit preferentially in the nodule. Alternatively, the nodule may be surgically removed. In either case, the risk of postprocedural hypothyroidism is small. The previously suppressed normal thyroid tissue resumes normal function following treatment.

Recent reports describe successful treatment of autonomous thyroid and parathyroid adenomas with 95% ethanol injection. Results vary but generally show resolution of the hyperthyroid state without development of hypothyroidism.[73–78] A potential complication is inadvertent injection of ethanol into the recurrent laryngeal nerve at the level of the tracheoesophageal groove, which may result in vocal cord paralysis.[79]

Malignant Neoplasms

The incidence of thyroid cancer in men and women increased up to 1975. This increase was believed to reflect the use of low-dose radiation to treat the head and neck, particularly in children for benign diseases such as thymic enlargement and adenoidal hypertrophy.[80] There is a linear dose-response relationship between 100 and 2000 rads.[6, 81] Approximately 15% to 30% of patients who received radiation in this dose range will develop a thyroid nodule, and 6% to 8% will develop thyroid cancer. Long-term follow-up is necessary, as the latent period for the development of cancer may be as long as 30 years. Early detection is essential since carcinoma in this population is more aggressive and may require extensive surgical management to achieve a cure rate equivalent to that of nonirradiated patients.[66] Thyroid carcinoma following high-dose irradiation (greater than 2000 rads) is rare, likely because irradiation at these doses destroys thyroid tissue.[6] Individuals at increased risk (low-dose radiation exposure, genetic predisposition) of developing thyroid cancer may be screened and followed by obtaining serum calcitonin levels, as calcitonin serves as a sensitive marker for tumor development.

Approximately 12,000 new cases of thyroid carcinoma are diagnosed in the United States each year, and the annual death rate is approximately 1000.[82] Of interest, the prevalence of incidental thyroid carcinomas identified at autopsy is 3.9%[83] and at surgery it is 10.5%.[84] Differentiated thyroid carcinomas including papillary and follicular subtypes are most common and have a favorable prognosis.

Thyroid carcinoma arises from both follicular and parafollicular C cells. Malignant potential and behavior ranges from low-grade (papillary carcinoma) to aggressive (anaplastic carcinoma) and is reflected by mortality rates: papillary carcinoma 8% to 11%, follicular carcinoma 24% to 33%, medullary carcinoma 50%, and anaplastic carcinoma 75% to 90%.[66] The prognosis is dependent upon the biological behavior, the tumor size, and the tendency for hematogenous or lymphatic metastases. The major histologic classification of thyroid carcinoma includes papillary, follicular, medullary, and anaplastic types. The majority of carcinomas (60% to 80%) are papillary, while follicular, medullary, and anaplastic types each account for approximately 5% to 20% of thyroid cancers.[6, 85]

The major role of scintigraphy in assessing a dominant, palpable thyroid mass is to determine whether the lesion is hot or cold (Figs. 40-23 and 40-24). The risk of cancer in a cold nodule is four times that of a hot nodule.[6, 67] Ultrasonography, because of its availability, is frequently the first imaging modality used to assess a thyroid mass. It is useful in distinguishing solid from cystic lesions. Ultrasound also plays a significant role in the follow-up of patients treated for papillary carcinoma. Its main utility in this regard is in identifying cervical lymph nodes suspicious for regional metastases that can be biopsied with ultrasound guidance (Fig. 40-22). It should be remembered that the main role of cross-sectional imaging (ultrasound, CT, and MR) is not in the characterization of an intrathyroidal lesion, as there are no imaging findings that are histologically specific. The role of the radiologist is to assess the findings related to a thyroid mass, including invasion through the thyroid capsule and infiltration of adjacent tissues and structures in the neck, and to identify the presence of cervical lymph node metastases.

Papillary Carcinoma

Papillary carcinoma is a low-grade malignancy occurring most commonly in female adolescents and young adults. It comprises up to 80% to 90% of all thyroid cancers. However, despite being the most common thyroid carcinoma, it constitutes only about 1% of all malignancies diagnosed in the United States. Histologically, papillary carcinoma may have a spectrum of findings and may be purely papillary, mixed papillary and follicular, or completely follicular.[86–88] The mixed papillary subtype behaves like papillary carcinoma.[86] The completely follicular variant is also included under papillary carcinomas because, both biologically and clinically, it behaves like these tumors.[23, 89] Frequently, papillary carcinoma is multifocal and microscopic in the thyroid gland. This condition is believed to represent intraglandular lymphatic spread rather than multiple synchronous tumors. However, other patterns of papillary cancer are also common, including occult cancers (less than 1.5 cm), intrathyroidal encapsulated, and extrathyroidal cancers.[90, 91] In goiter belt areas of the world, not only is there a prevalence of goiter, but there is also a higher than average rate of anaplastic carcinoma. In the regions of the world that have introduced iodine into

Copyright © 2003, Mosby, Inc. All rights reserved.

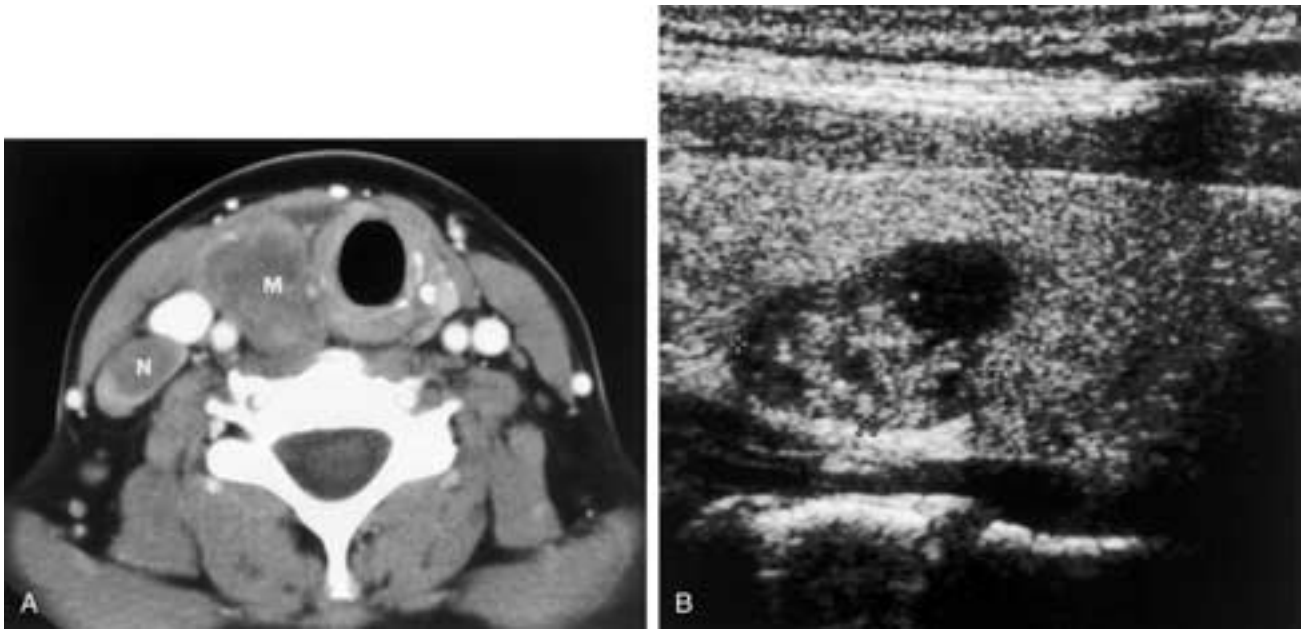

VIEW IMAGE

FIGURE 40-25 Papillary thyroid carcinoma in two different patients. **A**, Enhanced axial CT scan shows a dominant hypodense mass (*M*) replacing the right lobe of the thyroid gland. Also note the pathologic ipsilateral cervical lymph node (*N*). **B**, A sagittal sonogram of the right lobe of the thyroid shows a dominant nodule with heterogeneous echogenicity. There are both cystic and frond-like solid components. (Courtesy of Dr. Jill Langer, Department of Radiology, Ultrasound Division, University of Pennsylvania Medical Center.)

the diet to decrease the incidence of goiter, there has also been a decrease in the frequency of anaplastic thyroid carcinoma. However, an increase in the incidence of papillary carcinomas in these same regions has been noted.

At gross pathology these tumors are firm, and they may have calcium, hemorrhage, necrosis, and/or cysts. Histologically, papillary cancer is characterized by the presence of papillae (epithelial cells encasing a fibrovascular core) and clear nuclei.[87, 88] Psammoma bodies (microscopic calcified remnants of papillae) are present in over one third of papillary cancers.

Uncommon histologic subtypes of papillary cancer have been noted to behave more aggressively, including tall cell and columnar cell variants.[92] The tall cell variant is composed of oxyphilic (pink) cells.[92] At presentation these malignancies are frequently extrathyroidal, with vascular invasion, and they have a poorer prognosis than other papillary carcinomas.

The imaging appearance of papillary carcinoma is variable and may include a dominant nodule (Fig. 40-25), multifocal nodules (Fig. 40-26), diffuse infiltration of the gland that is manifest as heterogeneous hypodensity, or a normal-appearing gland on CT (Fig. 40-27). Thus, although not commonly reported, infiltrative papillary carcinoma may not be detected in the thyroid gland on imaging (Fig. 40-28). Papillary carcinoma has the highest incidence of the thyroid malignancies for cervical lymph node spread, seen in up to 50% of cases. Metastatic lymph nodes are not uncommonly normal in size (Fig. 40-27) and may be calcified (Fig. 40-29), cystic, hemorrhagic, or may contain colloid.[93] Cystic nodal metastases are characterized by a thin or imperceptible wall (Fig. 40-30), and they can be mistaken for benign cysts. Cystic nodes are different from the necrotic nodes frequently seen with metastatic squamous cell carcinoma that have central low density but retain a thick rind of residual lymphatic tissue. Hemorrhagic or colloid-containing nodes may be hyperintense on unenhanced T1-weighted MR images (Fig. 40-31). Although in the vast majority of cases regional nodal metastases from thyroid cancer occur in the anterior and posterior cervical lymph chains, occasionally (2%) metastases occur in retropharyngeal nodes (Fig. 40-32). Any lymph node seen in a patient with papillary carcinoma should raise the suspicion of metastatic disease because of the high rate of lymphatic spread. This is

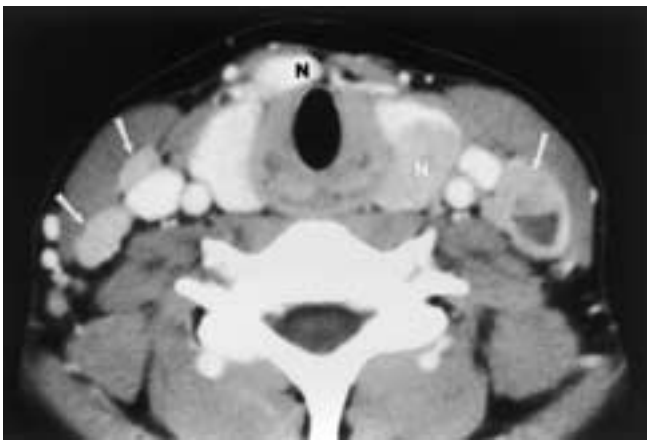

FIGURE 40-26 Papillary carcinoma presenting with multiple nodules. Enhanced axial CT scan shows a focal nodule (*N*) in the left thyroid lobe, as well as a focal nodule in the isthmus on the right (*N*). Both were found to be papillary carcinoma at histologic evaluation. Also note the bilateral cervical lymph node metastases (*arrows*).

VIEW IMAGE

Copyright © 2003, Mosby, Inc. All rights reserved.

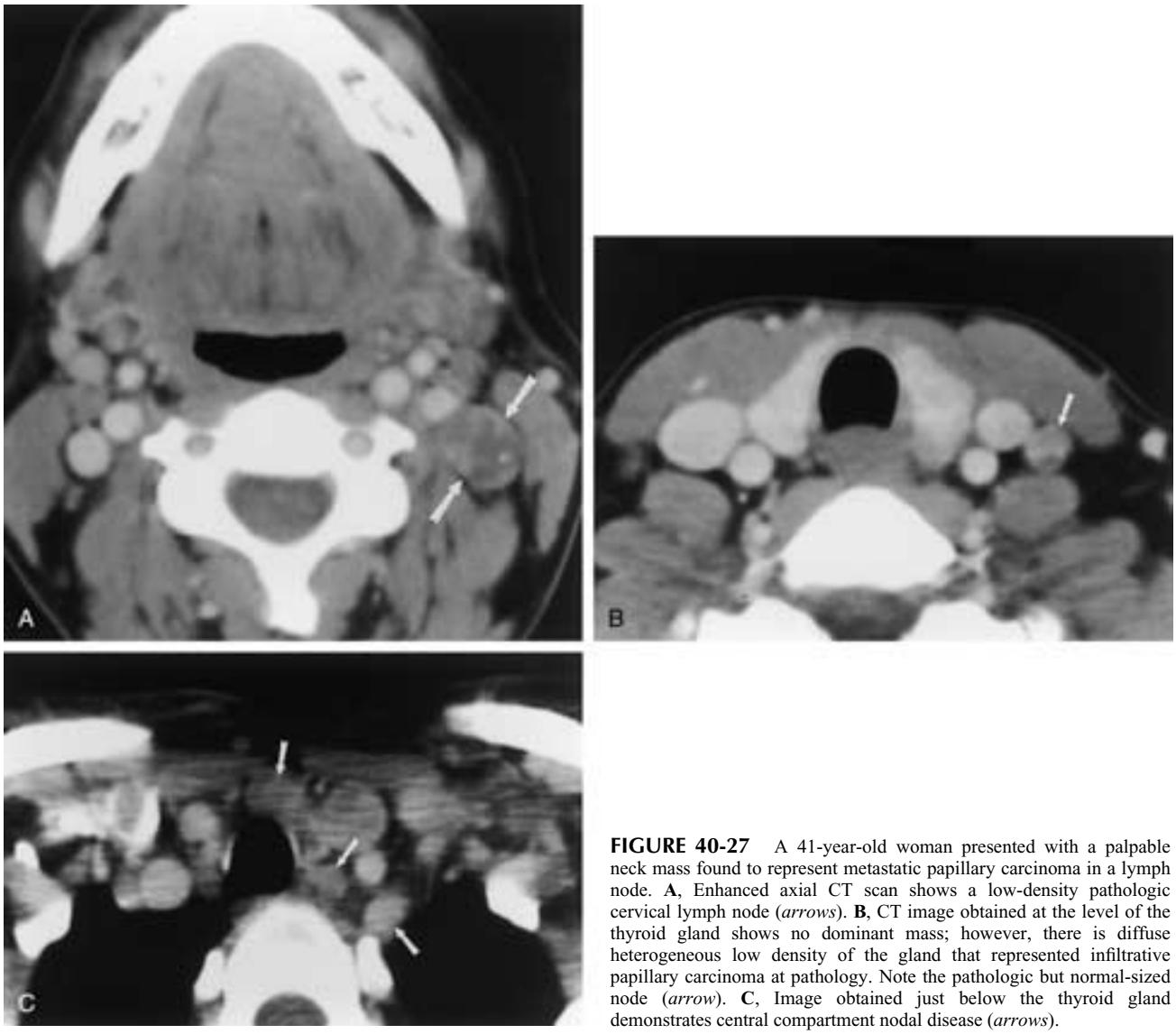

FIGURE 40-27 A 41-year-old woman presented with a palpable neck mass found to represent metastatic papillary carcinoma in a lymph node. **A**, Enhanced axial CT scan shows a low-density pathologic cervical lymph node (*arrows*). **B**, CT image obtained at the level of the thyroid gland shows no dominant mass; however, there is diffuse heterogeneous low density of the gland that represented infiltrative papillary carcinoma at pathology. Note the pathologic but normal-sized node (*arrow*). **C**, Image obtained just below the thyroid gland demonstrates central compartment nodal disease (*arrows*).

VIEW IMAGE

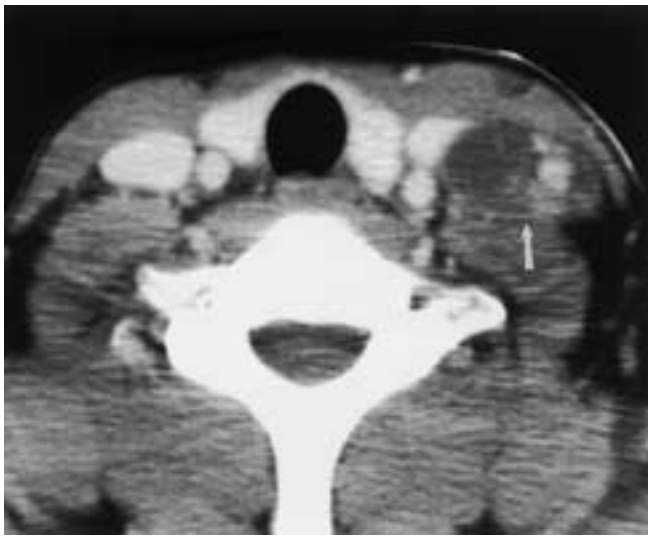

FIGURE 40-28 A 25-year-old woman who presented with a cervical nodal metastasis (*arrow*). In spite of the fact that no lesion could be detected in the thyroid gland, diffuse papillary carcinoma was found at histologic evaluation.

VIEW IMAGE

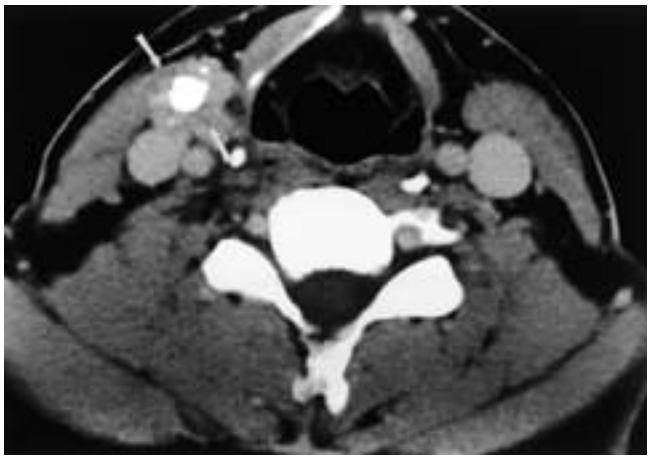

FIGURE 40-29 Metastatic papillary carcinoma. Enhanced axial CT image shows a calcified right cervical nodal metastasis (*arrows*).

VIEW IMAGE

Copyright © 2003, Mosby, Inc. All rights reserved.

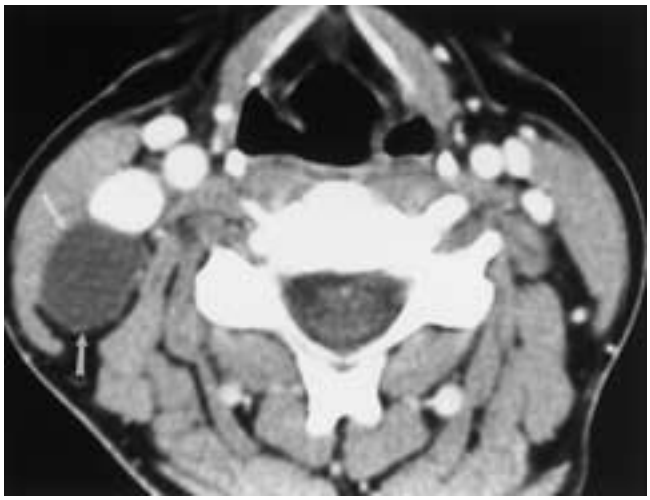

FIGURE 40-30 Metastatic papillary carcinoma. Enhanced axial CT image shows a cystic lymph node (*arrows*).

especially true if the node enhances, as these tumors are highly vascular.

Hematogenous spread to the lungs, bones (Fig. 40-33), and central nervous system may occur; however, this is less common (approximately 5%), especially in the absence of nodal disease. Since papillary carcinomas concentrate radioiodine, scanning with I-131 following thyroidectomy may be valuable in identifying recurrent/residual thyroid disease in the operative bed of the neck as well as in detecting distant metastases (Fig. 40-34). Subsequently, treatment with I-131 may be performed (Table 40-3). The prognosis for papillary thyroid carcinoma is excellent, with a 20-year survival rate of over 90%.[87, 88, 90, 91] The most important prognostic factors appear to be (1) age, as patients older than 50 years have a poorer prognosis than younger patients; (2) tumor size; (3) extrathyroidal extension (violation of the thyroid capsule); and (4) histologic subtype. In males, the age at presentation and the absence of gross nodal metastasis are predictors of survival. In females, in addition, tumor size and the number of structures adherent to the gland are predictors.

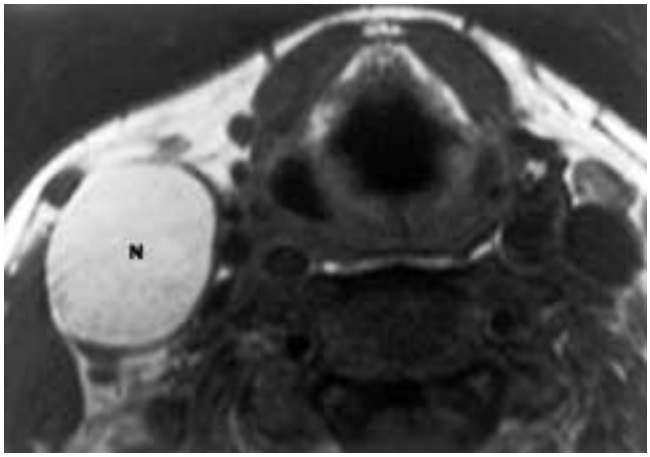

FIGURE 40-31 Colloid-containing metastatic cervical lymph node. Unenhanced axial T1-weighted MR image shows a hyperintense nodal mass (*N*).

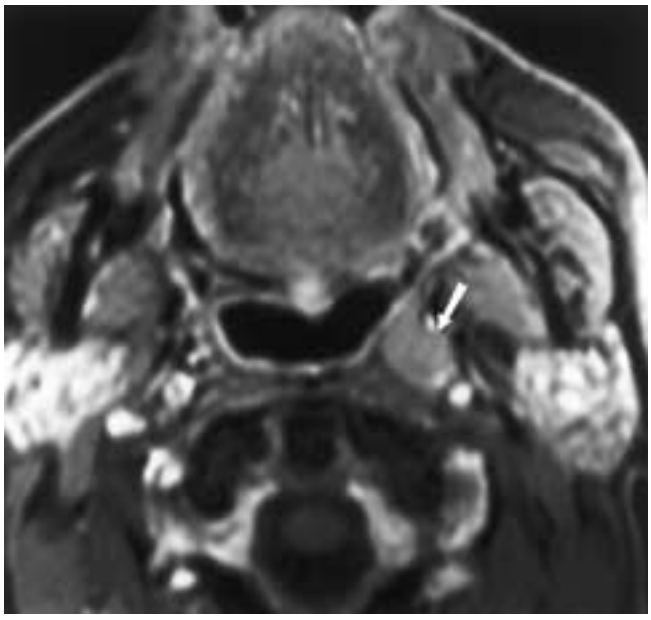

FIGURE 40-32 Metastatic papillary carcinoma in a retropharyngeal node. Enhanced fat-suppressed axial T1-weighted MR image shows a metastatic retropharyngeal lymph node (*arrow*).

Follicular Carcinoma

True follicular carcinomas of the thyroid gland constitute only 5% of all thyroid cancers. Follicular carcinomas are well-differentiated, relatively low-grade malignancies that are reportedly more common in the setting of iodine deficiency. They are slightly more aggressive than papillary carcinomas. On gross evaluation, they are either encapsulated or invasive. Pathologically, they are characterized by capsular and vascular invasion and are usually solitary lesions. Distant metastases to the lung and bone related to hematogenous seeding are more common than lymph node spread; the latter is seen in less than 8% of cases.[94] The 5-year survival rate for encapsulated variants is approximately 90%; however, invasive variants have a poorer prognosis. Like papillary carcinoma, follicular cancers concentrate iodine, and I-131 imaging may be useful in the follow-up of these patients.

Hurthle Cell Tumors

Hurthle cells are derived from follicular epithelium.[95] A Hurthle cell neoplasm must meet specific criteria including that of an isolated thyroid mass composed predominantly of Hurthle cells in the absence of inflammatory cells.[95, 96] These tumors are diagnosed according to the criterion of malignancy used for follicular neoplasms of the thyroid gland. Regional nodal metastases in addition to hematogenous dissemination may occur.

Medullary Carcinoma

Medullary carcinoma arises from parafollicular C cells that are believed to be derived from neural crest tissue in the ultimobranchial bodies. It is relatively uncommon and has a

Copyright © 2003, Mosby, Inc. All rights reserved.

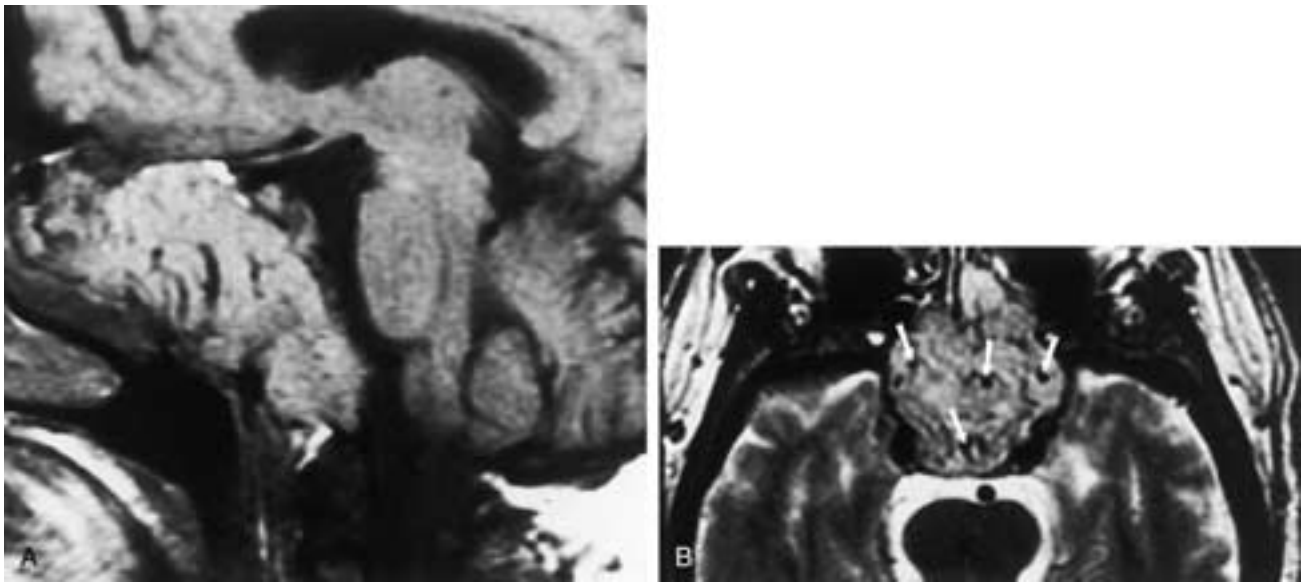

VIEW IMAGE

FIGURE 40-33 Metastatic papillary thyroid carcinoma. **A**, Unenhanced sagittal T1-weighted MR image shows a hypervascular (note the flow voids) metastasis to the clivus. **B**, Axial fast spin-echo T2-weighted MR image shows the clival mass with prominent flow voids (*arrows*).

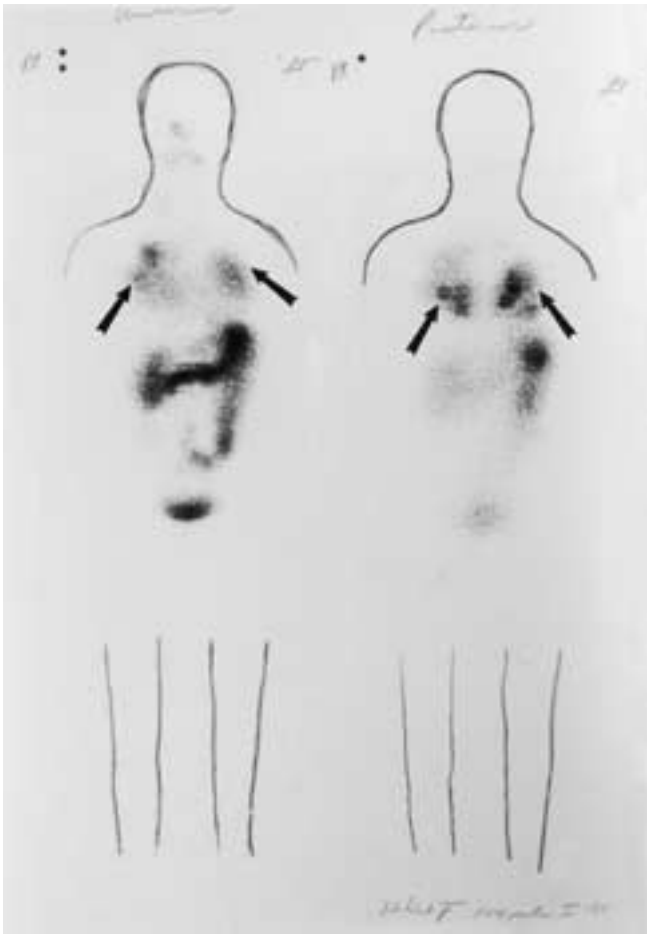

VIEW IMAGE

FIGURE 40-34 I-131 scintigraphy following thyroidectomy for papillary carcinoma. Whole body images obtained 72 hours after the administration of I-131 shows radiotracer uptake in diffuse lung metastases (*arrows*).

higher mortality rate than well-differentiated papillary and follicular malignancies. Medullary carcinomas are usually solitary lesions. They may invade locally (Fig. 40-35), may spread to regional cervical lymph nodes,[97] and may result in hematogenous seeding with distant metastases most commonly to the lungs, bones, and liver. Because of their origin from parafollicular C cells that secrete calcitonin (up to 90% of medullary carcinomas secrete calcitonin), calcitonin provides a specific hormonal marker for following these patients.[48, 98]

Medullary carcinoma occurs sporadically, but may also be inherited as an autosomal dominant trait (approximately 15% of cases are familial) and comprises a component of the multiple endocrine neoplasia (MEN) syndromes, types IIA and IIB, which include medullary thyroid carcinoma and adrenal pheochromocytomas.[99, 100] Hyperparathyroidism is common in MEN type IIA (Sipple's syndrome) due to hyperplasia of the parathyroid glands.[99, 100]

Medullary carcinomas may be encapsulated or infiltrative on gross pathology.[99, 100] Well-described patterns of medullary carcinoma include amyloid-containing, classic, trabecular, and epithelial types.[100] There is a broad spectrum of histologic and biochemical subtypes. The prognosis for medullary thyroid cancer is variable. Patients with thyroid cancer in the setting of MEN type IIB tend to have very aggressive, often fatal tumors that frequently occur at a young age, while those in association with MEN type IIA have favorable outcomes.[101] Sporadic tumors may behave in an indolent manner or may be aggressive.[101] Serum levels of calcitonin and carcinoembryonic antigen, as well as immunostaining of resected tumor, may help predict the tumor's behavior.[102]

Unlike papillary and follicular subtypes, medullary carcinoma does not concentrate radioiodine. However, radionuclides specific for neuroendocrine tissue such as I-131 meta-iodobenzylguanidine (MIBG) and the somato-

Copyright © 2003, Mosby, Inc. All rights reserved.

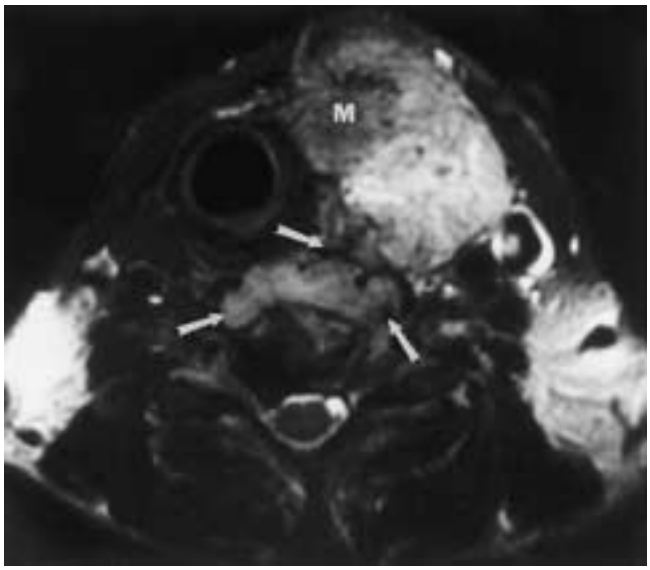

VIEW IMAGE

FIGURE 40-35 Medullary thyroid carcinoma with direct extension into the vertebral compartment. Axial T2-weighted MR image shows a large, heterogeneous mass (*M*) in the left lobe of the thyroid gland. There is direct invasion of the longus colli muscle complex and the spine (*arrows*).

statin analog I-111 pentetreotide have been used with some success to evaluate primary as well as metastatic medullary thyroid carcinoma.[103–106] These neoplasms may also take up gallium or thallium.

Anaplastic Carcinoma

Anaplastic carcinoma usually presents in elderly women (over the age of 60 years), and is highly aggressive and rapidly fatal. Life expectancy is measured in months. Approximately 10% of all thyroid malignancies are anaplastic. They commonly occur in patients with long-standing goiter. Anaplastic carcinoma actually comprises a group of high-grade thyroid neoplasms that are characterized by undifferentiated histology and a highly aggressive course. Other terms include *undifferentiated*, *dedifferentiated*, and *sarcomatoid carcinoma*. These cancers grow rapidly, and typically compress and invade the aerodigestive tract and vessels (Fig. 40-36). Lymphatic metastases occur in the majority of patients and are necrotic in approximately one half of cases (Fig. 40-36).[48, 107] These neoplasms do not concentrate radioiodine. On ultrasound they are frequently hypoechoic (Fig. 40-37).[17, 18, 97] On CT, punctate calcifications and necrosis are frequently present.[107]

Primary Lymphoma

Primary lymphoma of the thyroid gland is uncommon, representing less than 5% of all lymphomas arising in extranodal sites and approximately 1% to 3% of all thyroid malignancies. It usually presents in elderly women with a long history of goiter. In addition, patients with Hashimoto's thyroiditis have an increased incidence of developing lymphoma of the thyroid, usually the non-Hodgkin's type.[46, 47] The thyroid gland may also be involved secondarily by lymphoma.

Imaging, including MR imaging, cannot reliably distinguish lymphoma from thyroiditis in patients with Hashimoto's thyroiditis.[1, 108] Patients usually present with a rapidly enlarging thyroid mass and symptoms of obstruction related to compression of the aerodigestive tract.[1, 46] Thyroid lymphoma may present as multiple nodules, but more commonly (80%) it presents as a solitary mass.[1, 46] Usually it is hypoechoic on ultrasound[17, 18] and hypodense on CT.[46] While lymphoma is typically cold on iodine and technetium nuclear scintigraphy, it may show increased uptake on gallium scans. Necrosis and calcification are uncommon.[46] On MR imaging, lymphoma is usually hyperintense on T2-weighted images and isointense to normal thyroid on T1-weighted images.[1, 108]

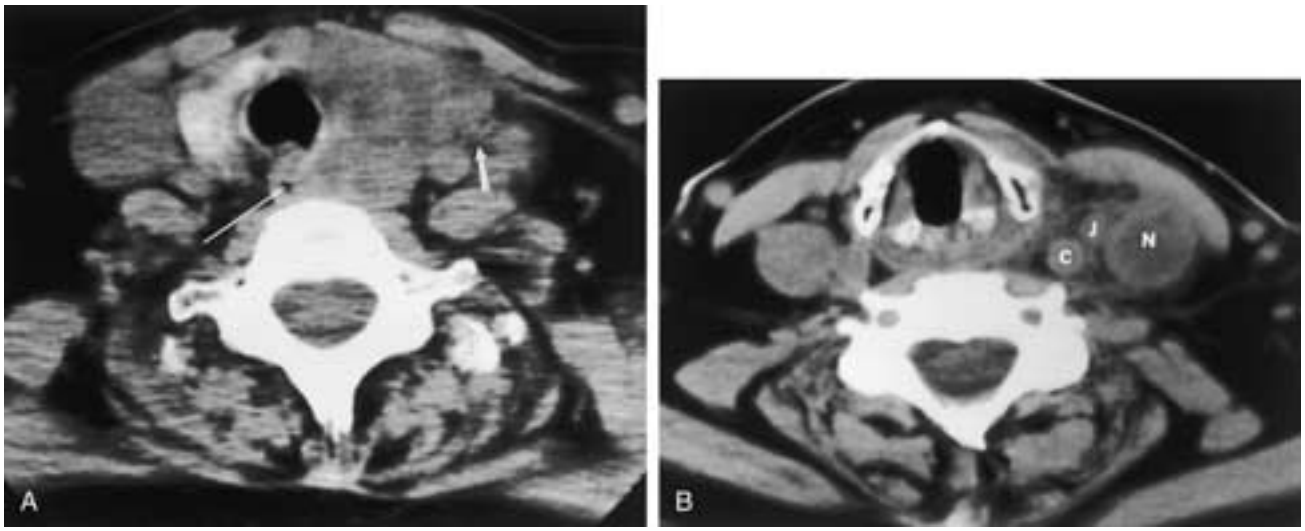

VIEW IMAGE

FIGURE 40-36 Anaplastic thyroid carcinoma. **A**, Unenhanced axial CT scan shows an infiltrative mass in the left lobe of the thyroid gland Extension outside the thyroid capsule is suggested by soft-tissue stranding in the adjacent neck fat (*arrow*). There is also obliteration of the fat plane between the thyroid and the esophagus (*long arrow*, esophageal lumen). **B,** Inferior image shows a necrotic metastatic lymph node (*N*). *C*, Carotid; *J*, jugular vein.

Copyright © 2003, Mosby, Inc. All rights reserved.

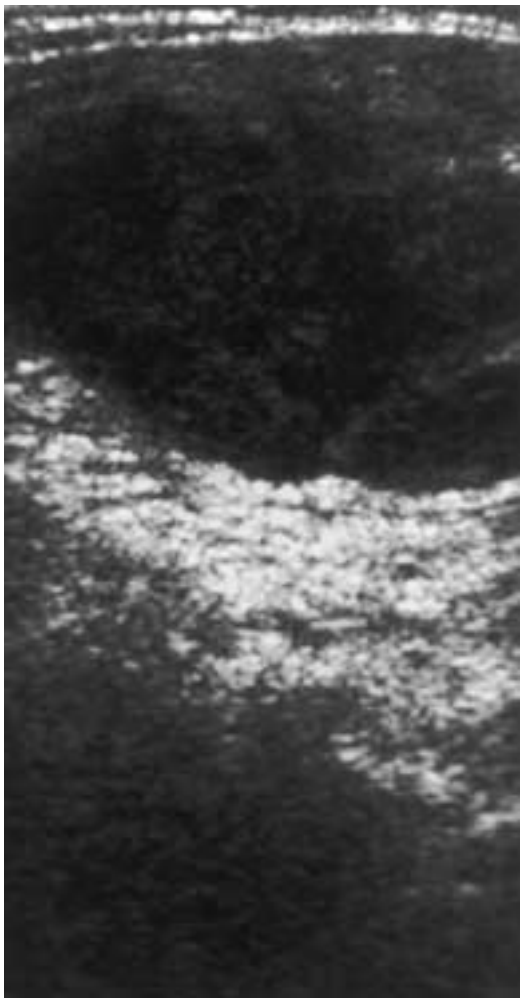

VIEW IMAGE

FIGURE 40-37 Anaplastic carcinoma. Sagittal sonographic image shows a large, hypoechoic mass in the thyroid gland.

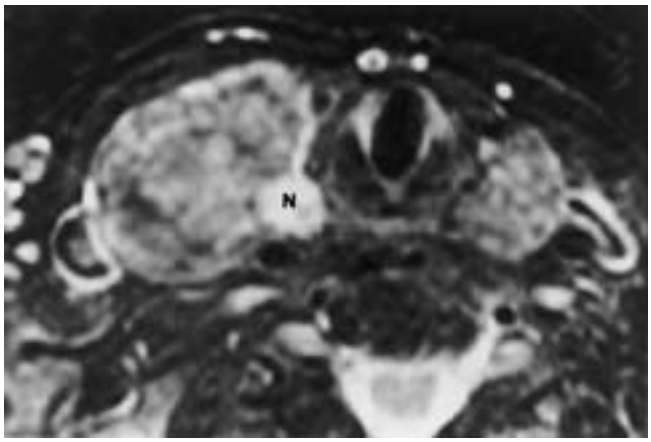

VIEW IMAGE

FIGURE 40-38 Mucoepidermoid carcinoma of the thyroid gland in a 76-year-old woman with a long-standing history of goiter. Axial fat-suppressed T2-weighted image shows diffuse goiter. A 1 cm hyperintense nodule (*N*) was biopsied and sdshown to be mucoepidermoid carcinoma.

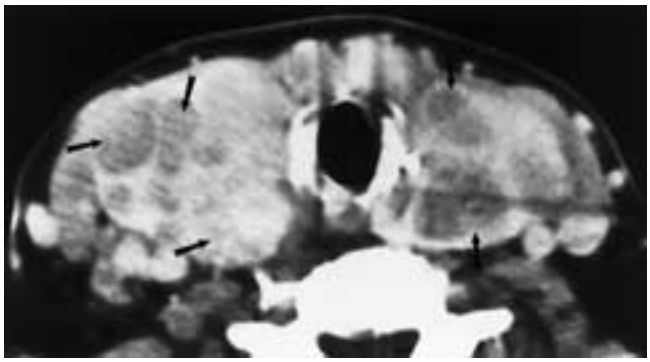

FIGURE 40-39 Metastatic renal cell carcinoma to the thyroid gland. Enhanced axial CT scan shows diffuse enlargement of the thyroid gland with multiple hypodense nodules (*arrows*) consistent with metastatic renal cell carcinoma confirmed pathologically.

VIEW IMAGE

Rare Malignancies

Primary squamous cell carcinoma of the thyroid gland is rare and may result from squamous metaplasia of epithelial cells. Similarly, rare sporadic cases of mucoepidermoid carcinoma may occur (Fig. 40-38). These are typically seen in patients with a long history of goiter and have a poor prognosis. There are no diagnostic imaging findings to distinguish these from other neoplasms. Primary sarcomas of the thyroid gland are extremely rare, can be radiation induced, and have a poor prognosis. Such lesions include liposarcomas, fibrosarcomas, leiomyosarcomas, chondrosarcomas, osteosarcomas, and angiosarcomas.

Teratomas in infants, and rarely in adults, may involve the thyroid gland. Thymus-related lesions may also rarely occur. About 1.5% of thyroid glands contain thymic tissue, and intrathyroidal thymomas can occur. Similarly, spindle and epithelial thymus-like tumors (SETTLE) and carcinoma with thymus-like features (CASTLE) have been reported. Even a very rare intrathyroidal paraganglioma has been reported.

Metastatic Disease

Metastatic disease to the thyroid gland is uncommon. Lung and breast carcinomas are the most common causes of thyroid metastases found at autopsy, while renal carcinoma is the most common metastasis detected clinically.[109] Metastatic melanoma and colon carcinoma metastatic to the thyroid gland have also been reported.[110] Multiple thyroid masses are usually present in the setting of metastatic disease (Fig. 40-39). When atypical histology of a resected thyroid mass is detected, metastatic disease should be considered. Testing to establish the presence of thyroglobulin and/or calcitonin supporting the belief that the neoplasm is thyroidal in origin may be extremely useful, and the absence of these markers favors metastatic disease.

REFERENCES

1. Shibata T, Noma S, Nakano Y, et al. Primary thyroid lymphoma: MR appearance. J Comput Assist Tomogr 1991;15(4):629–633.
2. De Lellis RA. The endocrine system. In Cotram R, Kumar V, Robbins SL, eds. Robbins Pathologic Basis of Disease, 4th ed. Philadelphia: WB Saunders, 1989:1214–1242.

Copyright © 2003, Mosby, Inc. All rights reserved.

3. Plummer HS. The clinical and pathologic relationship of simple and exophthalmic goiter. Am J Med Sci 1913;146:790–803.
4. Villadolid MC, Yokoyama N, Izumi M, et al. Untreated Graves' disease patients without clinical ophthalmopathy demonstrate a high frequency of extraocular muscle (EOM) enlargement by magnetic resonance. J Clin Endocrinol Metab 1995;80(9):2830–2833.
5. Takashima S, Nomura N, Tanaka H, et al. Congenital hypothyroidism: assessment with ultrasound. AJNR 1995;16:1117–1123.
6. Price DC. Radioisotopic evaluation of the thyroid and parathyroids. Radiol Clin North Am 1993;31:991–1015.
7. Sandler MP, Patton JA, Ossoff RH. Recent advances in thyroid imaging. Otolaryngol Clin North Am 1990;23:251–270.
8. Nygaard B, Nygaard T, Jensen LI, et al. Iohexol: effects on uptake of radioactive iodine in the thyroid and on thyroid function. Acad Radiol 1998;5:409–414.
9. Laurie AJ, Lyons SG, Lassen EC. Contrast material iodides: potential effects on radioactive thyroid uptake. J Nucl Med 1992; 33:237–238.
10. Sternthall E, Lipworth L, Stanley B, Abreau C, Fang SL, Braverman LE. Suppression of thyroid radioiodine uptake by various doses of stable iodide. N Engl J Med 1980;303:1083–1088.
11. Lauberg P, Boye N. Inhibitory effect of various radiographic contrast agents on secretion of thyroxine by the dog thyroid and on peripheral and thyroidal deiodination of thyroxine to triiodothyronine. J Endocrinol 1987;112:387–390.
12. Feine U, Lietzenmayer R, Hanke J, Wohrle H. Fluorine-18-FDG and iodine-131 uptake in thyroid cancer. J Nucl Med 1996;37:1468–1472.
13. Dietlein M, Scheidhauer K, Voth E, Theissen P, Schicha H. Fluorine-18 fluorodeoxyglucose positron emission tomography and iodine-131 whole body scintigraphy in the follow-up of differentiated thyroid cancer. Eur J Nucl Med 1997;24:1342–1348.
14. Wang W, Larson SM, Fazzari M, et al. Prognostic value of [^{18}F] fluorodeoxyglucose positron emission tomographic scanning in patients with thyroid cancer. J Clin Endocrinol Metab 2000;85:1107–1113.
15. Gotway MB, Higgins CB. MR imaging of the thyroid and parathyroid glands. Magn Reson Imaging 2000;8(1):163–182.
16. Gefter W, Spritzer CE, LiVolsi VA, et al. Thyroid imaging with high-field strength surface-coil MR. Radiology 1987;164: 483–490.
17. Gooding GA. Sonography of the thyroid and parathyroid. Radiol Clin North Am 1993;31(5):967–989.
18. Solbiati L, Volterrani L, Rizzatto G, et al. The thyroid gland with low uptake lesions: evaluation by ultrasound. Radiology 1985;155: 187–191.
19. Hopkins CR, Reading CC. Thyroid and parathyroid imaging. Semin US, CT, MRI 1995;16(4):279–295.
20. Quinn SF, Nelson HA, Demlow TA. Thyroid biopsies: fine-needle aspiration biopsy versus spring-activated core biopsy needle in 102 patients. J Vasc Intervent Radiol 1994;5(4):619–623.
21. Sanchez RB, van Sonnenberg E, D'Agostino HB, et al. Ultrasound guided biopsy of nonpalpable and difficult to palpate thyroid masses. J Am College Surgeons 1994;178(1):33–37.
22. LiVolsi VA. The thyroid and parathyroid. In: Sternberg SS, ed. Diagnostic Surgical Pathology, 2nd ed. New York: Raven Press, 1994;523–560.
23. Pintar JE, Toran-Allerand CD. Normal development of the hypothalamic-pituitary-thyroid axis. In: Braverman LE, Utiger RD, eds. Werner and Ingbar's, The Thyroid, 6th ed. Philadelphia: JB Lippincott, 1991;7–21.
24. Hammond RJ, Meakin K, Davies JE. Case report: lateral thyroid ectopia—CT and MRI findings. Br J Radiol 1996;69:1178–1180.
25. Morgan NJ, Emberton P, Barton RP. The importance of thyroid scanning in neck lumps— a case report of ectopic tissue in the right submandibular region. J Laryngol Otol 1995;109(7):674–676.
26. Guneri A, Ceryan K, Igci E, et al. Lingual thyroid: the diagnostic value of magnetic resonance imaging. J Laryngol Otol 1991;105(6): 493–495.
27. Montgomery ML. Lingual thyroid: comprehensive review. West J Surg 1985;43:661–671.
28. Neinas FW, Gorman CA, Devine KD, et al. Lingual thyroid. Clinical characteristics of 15 cases. Ann Intern Med 1973;79:205–210.
29. Kantelip B, Lusson JR, DeRiberolles C, et al. Intracardiac ectopic thyroid. Hum Pathol 1986;17:1293–1296.
30. Fujioka S, Takatsu Y, Tankawa H, Yamanaka K, Ando F. Intracardiac ectopic thyroid mass. Chest 1996;110:1366–1368.
31. Brandwein M, Som P, Urken M. Benign intratracheal thyroid. Arch Otolaryngol Head Neck Surg 1998;124:1266–1269.
32. Dominguez-Malagon H, Guerrero-Medrano J, Suster S. Ectopic poorly differentiated (insular) carcinoma of the thyroid. Report of a case presenting as an anterior mediastinal mass. Am J Clin Pathol 1995;104(4):408–412.
33. Takashima S, Nomura N, Tanaka H, et al. Congenital hypothyroidism: assessment with ultrasound. AJNR 1995;16(5):1117–1123.
34. Shibutani Y, Inoue D, Koshiyama H. Thyroid hemiagenesis with subacute thyroiditis. Thyroid 1995;5(2):133–135.
35. Pollice L, Caneso G. Struma cordis. Arch Pathol Lab Med 1986;110:452–453.
36. Hays LL, Marlow SF Jr. Papillary carcinoma arising in a thyroglossal duct cyst. Laryngoscope 1968;78:2189–2193.
37. Ralls PW, Matsumoto N, Fukui K, et al. Color flow Doppler sonography in Graves' disease: thyroid inferno. AJR 1988;150: 780–784.
38. Castagnone D, Rivolta R, Rescalli S, et al. Color Doppler sonography in Graves' disease: value in assessing activity of disease and predicting outcome. AJR 1996;166(1):203–207.
39. Kaneko T, Matsumoto N, Fukui K, et al. Clinical evaluation of thyroid: CT values in various thyroid conditions. J Comput Assist Tomogr 1979;3:1–4.
40. Volpe R. The pathology of thyroiditis. Hum Pathol 1978;9:429–438.
41. Wang PW, Chen HY, Li CH, et al. Tc-99m pertechnetate trapping and thyroid function in Hashimoto's thyroiditis. Clin Nucl Med 1994;19(3):177–180.
42. Takasu N, Yamada T, Takasu M, et al. Disappearance of thyrotropin-blocking antibodies and spontaneous recovery from hypothyroidism in autoimmune thyroiditis. N Engl J Med 1992;326: 513–518.
43. Alos N, Huot C, Lambert R, et al. Thyroid scintigraphy in children and adolescents with Hashimoto's disease. J Pediatr 1995;127(6): 951–953.
44. Doniach D, Bottazzo GF, Russell RCG. Goitrous autoimmune thyroiditis (Hashimoto's disease). Clin Endocrinol Metab 1979;8: 63–80.
45. Intenzo CM, Park H, Kim SM, et al. Clinical, laboratory, and scintigraphic manifestations of subacute and chronic thyroiditis. Clin Nucl Med 1993;18:302–306.
46. Takashima S, Ikezoe J, Morimoto S, et al. Primary thyroid lymphoma: evaluation with CT. Radiology 1988;168:765–768.
47. Ott RA, Calandra DB, McCall A, et al. The incidence of thyroid carcinoma in patients with Hashimoto's thyroiditis and solitary cold nodules. Surgery 1985;98:1202–1206.
48. Compagno J, Oertel JE. Malignant lymphoma and other lymphoproliferative disorders of the thyroid gland: clinicopathologic study of 245 cases. Am J Clin Pathol 1980;74:1–11.
49. Clark OH, Greenspan FS, Dunphy JE. Hashimoto's thyroiditis and thyroid cancer: indications for operations. Am J Surg 1980;140:65–71.
50. Nordmeyer JP, Shafeh TA, Heckmann C. Thyroid sonography in autoimmune thyroiditis: a prospective study on 123 patients. Acta Endocrinol 1990;122:391–395.
51. Mizukami Y, Michigishi T, Hashimoto T, et al. Silent thyroiditis: a histologic and immunohistochemical study. Hum Pathol 1988;19: 423–431.
52. Hamburger JI. The various presentations of thyroiditis: diagnostic considerations. Ann Intern Med 1986;104:219–224.
53. Hay ID. Thyroiditis: a clinical update. Mayo Clin Proc 1985;60: 836–843.
54. Hatabu H, Kasagi K, Yamamoto K, et al. Acute suppurative thyroiditis associated with pyriform sinus fistula: sonographic findings. AJR 1990;155:845–847.
55. Kawanaka M, Sugimoto Y, Suehiro M, et al. Thyroid imaging in a typical case of acute suppurative thyroiditis with abscess formation due to infection from a persistent thyroglossal duct. Ann Nucl Med 1994;8(2):159–162.
56. Malotte M, Chonkich GD, Zuppan CW. Riedel's thyroiditis. Arch Otolaryngol Head Neck Surg 1991;117:214–217.
57. Fontan JP, Carballido FC, Felipe FP, et al. Case report: Riedel thyroiditis: US, CT, and MR evaluation. J Comput Assist Tomogr 1993;17:324–325.

Copyright © 2003, Mosby, Inc. All rights reserved.

58. Belfiore A, LaRose GL, LaPorta GA, et al. Cancer risks in patients with cold thyroid nodules: relevance of iodine intake, sex, age, and multinodularity. Am J Med 1992;93:363–369.
59. Cerise EJ, Spears R, Ochsner A. Carcinoma of the thyroid and nontoxic nodular goiter. Surgery 1952;31:552–561.
60. McCall A, Jarosz H, Lawrence AM, et al. The incidence of thyroid carcinoma in solitary cold nodules and in multinodular goiters. Surgery 1986;100:1128–1132.
61. Shulkin BL, Shapiro B. The role of imaging tests in the diagnosis of thyroid carcinoma. Endocrinol Metab Clin North Am 1990;19(3): 523–543.
62. Noma S, Kanaoka M, Minami S, et al. Thyroid masses: MR imaging and pathologic correlation. Radiology 1988;168:759–764.
63. Huysmans DA, Hermus AR, Corstens FH, et al. Large, compressive goiters treated with radioiodine. Ann Intern Med 1994;121(10): 757–762.
64. Dworkin HJ, Meier DA, Kaplan M. Advances in the management of patients with thyroid disease. Semin Nucl Med 1995;25: 205–220.
65. Huang T, Loevner LA, Yousem DM. Management of incidental thyroid lesions detected on CT and MR imaging of the neck performed for other purposes. Presented at the 30th Annual Scientific Conference, American Society of Head and Neck Radiology, Los Angeles, April 24–28, 1996.
66. Harvey HK. Diagnosis and management of the thyroid nodule: an overview. Otolaryngol Clin North Am 1990;23:303–337.
67. Shamma FN, Abrahams JJ. Imaging in endocrine disorders. J Reprod Med 1992;37:39–45.
68. Klieger PS, Wilson GA, Greenspan BS. The usefulness of the dynamic phase in pertechnetate thyroid imaging for solitary hypofunctioning nodules. Clin Nucl Med 1992;17(8):617–622.
69. Gharib H, Goellner JR, Johnson DA. FNA cytology of the thyroid: a 12 year experience with 11,000 biopsies. Clin Lab Med 1995;13: 699–710.
70. Gharib H, Goellner JR. Fine needle aspiration of the thyroid: an appraisal. Ann Intern Med 1993;11:282–289.
71. Hamberger JI. Evolution of toxicity in solitary nontoxic autonomously functioning thyroid nodules. Clin Endocrinol Metab 1980;50:1089–1093.
72. Ross DS. Evaluation of the thyroid nodule. J Nucl Med 1991;32:2181–2192.
73. Livraghi T, Paracchi A, Ferrari, et al. Treatment of autonomous thyroid nodules with percutaneous ethanol injection: preliminary results. Radiology 1990;175:827–829.
74. Monzani F, Goletti O, Caraccio N, et al. Percutaneous ethanol injection treatment of autonomous thyroid adenoma: hormonal and clinical evaluation. Clin Endocrinol 1992;36:491–497.
75. Mazzeo S, Toni MG, DeGaudio C, et al. Percutaneous injection of ethanol to treat autonomous thyroid nodules. AJR 1993;161: 871–876.
76. Papini E, Panunzi C, Pacella CM, et al. Percutaneous ultrasound-guided ethanol injection: a new treatment of toxic autonomously functioning thyroid nodules. J Clin Endocrinol Metab 1993;76:411–416.
77. Livraghi T, Paracchi A, Ferrari C, et al. Treatment of autonomous thyroid nodules with percutaneous ethanol injection: 4-year experience. Radiology 1994;190:529–533.
78. Ozdemir H, Ilgit ET, Yucel C, et al. Treatment of autonomous thyroid nodules: safety and efficacy of sonographically guided percutaneous injection of ethanol. AJR 1994;163:929–932.
79. Solbiati L, Pra LD, Ierace T, et al. High-resolution sonography of the recurrent laryngeal nerve: anatomic and pathologic considerations. AJR 1985;145:989–993.
80. Duffy BJ Jr, Fitzgerald PJ. Cancer of the thyroid in children: a report of 28 cases. J Clin Endocrinol Metab 1950;10:1296–1311.
81. Favus MJ, Schneider AB, Stachura ME, et al. Thyroid cancer occurring as a late consequence of head-and-neck irradiation: evaluation of 1,056 patients. N Engl J Med 1976;294:1019–1025.
82. Mazzaferri EL. Management of a solitary thyroid nodule. N Engl J Med 1993;328:553–559.
83. Mazzaferri EL, de los Santos ET, Rofagha-Keyhani S. Solitary thyroid nodules: diagnosis and management. Med Clin North Am 1988;72:1177–1211.
84. Pelizzo MR, Piotto A, Rubello D, et al. High prevalence of occult papillary thyroid carcinoma in a surgical series for benign thyroid disease. Tumori 1990;76:255–257.
85. Sutton RT, Reading CC, Charboneau JW, et al. US-guided biopsy of neck masses in postoperative management of patients with thyroid cancer. Radiology 1988;168:769–772.
86. Chen KTK, Rosai J. Follicular variant of thyroid papillary carcinoma. A clinicopathologic study of 6 cases. Am J Surg Pathol 1977;1:123–130.
87. Rosai J, Zampi G, Carcangiu ML. Papillary carcinoma of the thyroid. A discussion of its several morphologic expressions, with particular emphasis on the follicular variant. Am J Surg Pathol 1983;7: 809–817.
88. Carcangiu ML, Zampi G, Pupi A, Castagnoli A, Rosai J. Papillary carcinoma of the thyroid. A clinicopathologic study of 244 cases treated at the University of Florence, Italy. Cancer 1985;55: 805–828.
89. Chen KTK, Rosai J. Follicular variant of thyroid papillary carcinoma: a clinicopathologic study of six cases. Am J Surg Pathol 1977;1:123–130.
90. Vickery AL. Thyroid papillary carcinoma. Pathological and philosophical controversies. Am J Surg Pathol 1983;7:797–807.
91. Hay ID. Papillary thyroid carcinoma. Endocrinol Metab Clin North Am 1990;19:545–576.
92. Hawk WA, Hazard JB. The many appearances of papillary carcinoma of the thyroid. Cleve Clin Q 1976;43:207–216.
93. Som PM, Brandwein M, Lidov M, et al. The varied appearance of papillary carcinoma cervical nodal disease: CT and MR findings. AJNR 1994;15:1129–1138.
94. Franssila KO, Ackerman LV, Brown CL, Hedinger CE. Follicular carcinoma. Semin Diagn Pathol 1985;2:101–102.
95. Roediger WEW. The oxyphil and C cells of the human thyroid gland. Cancer 1975;36:1758–1770.
96. Bondeson L, Bondeson AG, Ljungberg O, Tibblin S. Oxyphil tumors of the thyroid. Follow-up of 42 surgical cases. Ann Surg 1981;194:677–680.
97. Gorman B, Charboneau JW, James EM, et al. Medullary thyroid carcinoma: role of high-resolution US. Radiology 1987;162:147–150.
98. Melvin KEW, Miller HH, Tashjian AH. Early diagnosis of medullary carcinoma of the thyroid by means of calcitonin assay. N Engl J Med 1971;285:1115–1120.
99. Steiner AL, Goodman AD, Powers SR. Study of a kindred with pheochromocytoma, medullary thyroid carcinoma, hyperparathyroidism, and Cushing's disease: multiple endocrine neoplasia type 2. Medicine 1968;47:371–409.
100. Wolfe HJ, DeLellis RA. Familial medullary thyroid carcinomaand C-cell hyperplasia. Clin Endocrinol Metab 1981;10:351–365.
101. Kakudo K, Carney JA, Sizemore GW. Medullary carcinoma of thyroid: biologic behavior of the sporadic and familial neoplasm. Cancer 1985;55:2818–2821.
102. Busnardo B, Girelli ME, Simioni N, Nacamuilli D, Busetto E. Non-parallel patterns of calcitonin and carcinoembryonic antigen levels in the follow-up of medullary thyroid carcinoma. Cancer 1984;53:278–285.
103. Dorr U, Wurstlin S, Frank-Raue K, et al. Somatostatin receptor scintigraphy and magnetic resonance imaging in recurrent medullary thyroid carcinoma: a comparative study. Horm Metab Res Suppl 1993;27:48–55.
104. Lebouthillier G, Morais J, Picard M, et al. Tc-99m sestamibi and other agents in the detection of metastatic medullary carcinoma of the thyroid. Clin Nucl Med 1993;18(8):657–661.
105. Krenning EP, Kwekkeboom DJ, Bakker WH, et al. Somatostatin receptor scintigraphy with [111-In-DTPA-D-phe]- and [I-123-tyr]-octreotide: the Rotterdam experience with more than 1,000 patients. Eur J Nucl Med 1993;20:716–731.
106. Dorr U, Sautter-Bihl ML, Heiner B. The contribution of somatostatin receptor scintigraphy to the diagnosis of recurrent medullary carcinoma of the thyroid. Semin Oncol 1994;21:42–45.
107. Takashima S, Morimoto S, Ikezoe J, et al. CT evaluation of anaplastic thyroid carcinoma. AJR 1990;154:1079–1085.
108. Ohnishi T, Noguchi S, Murakami N, et al. MR imaging in patients with primary thyroid lymphoma. Am J Neuroradiol 1992;13(4): 1196–1198.
109. Haugen BR, Nawaz S, Cohn A, et al. Secondary malignancy of the thyroid gland: a case report and review of the literature. Thyroid 1994;4(3):297–300.
110. Czech JM, Lichtor TR, Carney JA, van Heerden JA. Neoplasms metastatic to the thyroid gland. Surg Gynecol Obstet 1982;155: 503–505.

Copyright © 2003, Mosby, Inc. All rights reserved.

SECTION TWO

THE PARATHYROID GLANDS

Primary hyperparathyroidism resulting in hypercalcemia is the most common presentation of parathyroid pathology and is usually related to a parathyroid adenoma, although less commonly it may be secondary to gland hyperplasia. Imaging of the parathyroid glands primarily focuses on the detection of adenomas in patients with primary hyperparathyroidism. A second focus is the detection of an unrecognized adenoma in a patient with persistent or recurrent hypercalcemia after prior surgery for hyperparathyroidism. The role of imaging (as well as which modality to use) for preoperative localization of the parathyroid glands continues to be a controversial issue, with practices differing from institution to institution.

The anatomy, physiology, and pathology of the parathyroid glands will be reviewed. The diagnostic utility of radiologic imaging including ultrasonography, CT, MR imaging, and nuclear scintigraphy will be discussed, particularly as it pertains to the evaluation of primary hyperparathyroidism.

ANATOMY OF THE PARATHYROID GLANDS

The parathyroid glands arise from the third and fourth branchial pouches. The upper or superior parathyroid glands arise from the fourth branchial pouch along with the lateral anlages of the thyroid gland. Because the superior parathyroid glands are closely related to the thyroid gland and have minimal descent, their positions are relatively constant along the dorsal aspect of the upper thyroid. Less than 2% of the superior parathyroid glands are ectopic in location. The lower or inferior parathyroid glands and thymus are derived from the third branchial pouch, and in contrast to the upper glands, the lower parathyroid glands descend a variable distance with the thymic anlage. As a result, the position of the inferior parathyroid glands, is more variable than that of the superior parathyroid glands, and the inferior glands may descend into the anterior mediastinum as far as the pericardium. On either side of the neck, a branch of the superior thyroidal artery usually supplies the upper parathyroid gland, while the inferior thyroidal artery supplies the lower parathyroid gland. Drainage from the glands is usually to the thyroidal veins. The cervical sympathetic plexus innervates the parathyroid glands.

The number of parathyroid glands ranges from 1 to 12, although most individuals (over 80%) have 4.[1] The most common anatomic location of the upper parathyroid glands is posterior to the middle one third of the thyroid gland (75% of the time). The majority of the remainder of the upper parathyroids are located behind the upper or lower one third of the thyroid, with approximately 7% found below the inferior thyroidal artery.[1] The upper glands may also be located behind the pharynx or esophagus.[2] The most common anatomic location of the lower parathyroid glands is lateral to the lower pole of the thyroid gland (50% of the time). The next most common location encompasses an area 1 cm below the lower thyroid pole (15%). The position of the remaining one third is variable along the thyrothymic tract, extending anywhere from the angle of the mandible to the lower anterior mediastinum. Intrathyroidal parathyroid glands are uncommon, occurring in 2% of cases. It is not possible with current imaging techniques to distinguish an intrathyroidal parathyroid adenoma from a primary thyroid lesion.[3–5]

The variability in number and location of the parathyroid glands can create problems for the surgeon exploring the neck for diseased glands in patients with primary hyperthyroidism. In addition, in patients having neck surgery for other reasons such as thyroid disease, the parathyroid gland(s) may accidentally be injured or removed.

ENDOCRINOLOGY OF THE PARATHYROID GLANDS

The normal parathyroid glands are each less than 9 mm in maximal dimension, and are composed of chief cells and oxyphil cells embedded within a fibrous capsule and intermixed with adipose tissue.[6] The role of the oxyphil cells is unknown. They appear at around puberty and increase with age. Chief cells secrete parathormone (PTH), which regulates the concentration of calcium in interstitial fluids. Serum calcium levels in turn regulate the secretion of PTH. Parathormone acts predominantly in three regions: (1) the skeleton to mobilize calcium into the plasma, (2) the kidneys to reduce calcium excretion, and (3) the gastrointestinal tract to increase calcium absorption.[7] Parathormone enhances the synthesis of 1,25-$(OH)D_3$ (vitamin D), which promotes the absorption of calcium by the intestines. In patients with elevated serum calcium concentrations, PTH should be suppressed. When a normal PTH level is encountered in the setting of hypercalcemia, it is referred to as hyperparathyroidism. In primary hyperparathyroidism, hypercalcemia is the result of excessive secretion of PTH from one or more of the parathyroid glands.

CLINICAL MANIFESTATIONS OF PARATHYROID DISEASE

Hyperparathyroidism

Primary hyperparathyroidism is common, more common in women, occurring in approximately 1 in 700 adults.[8] In most cases, patients are asymptomatic and the condition is detected by routine screening blood tests for serum calcium that individuals frequently have as part of their yearly checkup. It occurs secondary to hypersecretion of PTH, resulting in hypercalcemia. The causes of primary hyperparathyroidism include a single 1 to 3 cm parathyroid adenoma (75% to 85% of cases), parathyroid hyperplasia (10% to 15%), multiple parathyroid adenomas (2% to 3%), and, rarely, parathyroid carcinomas (less than 1%).[3, 9–11] Solitary adenomas vary widely in size, being very small (less than 1 cm) as well as very large (several centimeters).

Copyright © 2003, Mosby, Inc. All rights reserved.

VIEW IMAGE

FIGURE 40-40 Patient with recurrent primary hyperparathyroidism. **A**, Enhanced axial CT scan shows a hypodense mass (*arrows*) just posterior to the inferior pole of the left lobe of the thyroid gland. At surgery this was found to be a parathyroid adenoma separate from the thyroid. A clip in the right tracheoesophageal groove is from prior neck exploration. **B**, Bone scan showing markedly increased uptake in the calvarium and nonvisualization of the kidneys that has been described in association with hyperparathyroidism. **C**, Lateral plain film radiograph demonstrating the classic ''salt and pepper'' skull.

Hyperplasia typically involves multiple parathyroid glands. The classic clinical features of hypercalcemia include bone pain related to osseous demineralization, abdominal pain secondary to renal calculi, and occasional psychiatric disturbances (Fig. 40-40). Hypercalcemia left untreated can also result in pancreatitis, peptic ulcer disease, and musculoskeletal dysfunction.

The treatment of primary hyperparathyroidism is surgical excision of the abnormal parathyroid gland(s). Surgeons continue to debate over the ideal operative approach to cure primary hyperparathyroidism while limiting morbidity and controlling costs. Most surgeons still perform bilateral neck explorations since very small lesions or hyperplasia may be overlooked with current imaging techniques. Although the need for preoperative imaging localization remains a topic of debate, many surgeons report fewer complications and shorter operating times when abnormal parathyroid glands are identified prior to surgery.[3, 12–14] Importantly, preoperative imaging in many cases has allowed the surgeon to treat hyperparathyroidism successfully with only a unilateral neck exploration.[14, 15]

Nonetheless, there are clearly certain situations in which all would agree that imaging plays a very useful role. This includes high-risk surgery patients where imaging may permit the surgeon to resect the abnormal gland with only a unilateral neck exploration. Alternatively, percutaneous injection of absolute ethanol to ablate adenomas may be performed under ultrasound guidance in patients who are poor surgical candidates due to underlying medical illness.[16, 17] The success of treatment is monitored with serum calcium levels, which are followed until levels approach near-normal values. Also, when hyperparathyroidism recurs following surgery, imaging is indicated, as ectopic glands are prevalent in this group of patients.

Copyright © 2003, Mosby, Inc. All rights reserved.

There are also secondary and tertiary forms of hyperparathyroidism. Secondary hyperparathyroidism occurs in patients with long-standing renal failure leading to changes in calcium metabolism, which in turn results in enlargement of the parathyroid glands. In tertiary hyperparathyroidism, hypercalcemia occurs as a sequela of secondary hyperparathyroidism due to the autonomous secretion of PTH from chronically overstimulated parathyroid glands.

Hypoparathyroidism

Hypoparathyroidism is mainly a functional clinical disorder characterized by hypocalcemia and hyperphosphatemia secondary to a deficiency of PTH. The clinical manifestation may be subtle and include facial contractions brought on by tapping the facial nerve (Chvostek's sign), or carpal contractions initiated by applying a blood pressure cuff (Trousseau's sign). Hypoparathyroidism may be acute and transient, usually following parathyroid or thyroid surgery. Chronic hypoparathyroidism may be iatrogenic (surgery), developmental (agenesis is rare), autoimmune, infiltrative (secondary to cancers, amyloid, etc.), or part of a group of disorders called pseudohypoparathyroidism in which there is a resistance in the kidneys and skeleton to the physiologic effects of PTH. There is a group of patients that exhibit the characteristic phenotypical appearance of pseudohypoparathyroidism (short, round facies, brachydactyly), but lack the unresponsiveness to PTH (normal calcium and phosphate levels). These patients are said to have pseudopseudohypoparathyroidism.

IMAGING OF PATHOLOGY OF THE PARATHYROID GLANDS

Parathyroid Adenoma

Indications for preoperative localization of parathyroid adenomas remain a topic of debate. In addition, the choice of the appropriate imaging modality is also debated in the literature. When imaging is utilized, the modality options include ultrasonography, CT, MR imaging, and nuclear scintigraphy. Conventional catheter and digital subtraction angiography, as well as selective parathyroid venography with sampling and measurement of PTH levels, are highly accurate in detecting parathyroid adenomas; however, their major drawback is that they are relatively invasive and expensive.

At many institutions with experienced parathyroid surgeons, preoperative localization of the glands with imaging is not performed, as some studies suggest that the morbidity, mortality, and operative time are not greatly affected by preoperative localization.[18–20] In addition, some investigators argue that the cost of imaging outweighs its benefit.[18, 21] However, more recently, many surgeons have reported that imaging has resulted in reduced operative time, reduced morbidity, and lower costs.[14, 22] Specifically, when the cost of preoperative imaging was compared to that of increased operative time, imaging was found to be cheaper.[14]

The surgical technique includes exploration of the perithyroidal region bilaterally, with particular emphasis on the inferior poles of the thyroid glands, as this is where most parathyroid adenomas occur. In the hands of skilled surgeons, this procedure may be performed with a success rate of over 90%.[3, 18, 23–26] When a parathyroid adenoma is not identified in the perithyroidal location, the surgeon may explore the anterior mediastinum, the deep cervical space, and the carotid sheath regions. Successful surgery in these cases is lower (less than 70%), and the surgical complication rate is higher.[23]

Arguments for performing preoperative imaging to localize the parathyroid glands include (1) the need for only unilateral perithyroidal neck exploration when an adenoma is detected[14]; (2) the identification of ectopic adenomas[27]; (3) the detection of other head and neck masses (such as thyroid lesions); and (4) a reduction in operating room time.[13, 25, 28–30] In addition, the operative success rate improves from 90% to close to 100% when preoperative imaging is performed.[14, 31]

Ultrasonography

Ultrasonography of the parathyroid glands is typically performed with a high-resolution linear array transducer (7.5 to 10 MHz) and an experienced sonographer. The patient is imaged in the supine position with the neck mildly hyperextended. Examination includes evaluation of the perithyroidal areas and the region of the carotid sheaths extending from the angle of the mandible superiorly to the sternal notch inferiorly. The typical appearance of a parathyroid adenoma is that of a homogeneous, well demarcated mass with an echogenicity less than that of the thyroid gland (Fig. 40-41).[24, 32] Adenomas are encapsulated and are typically solid; however, they may have cystic and/or hemorrhagic components resulting in regions of decreased and increased echogenicity, respectively. In addition, adenomas may undergo cystic degeneration. Color Doppler may on occasion provide additional information that may help to distinguish thyroid from parathyroid lesions. Specifically, thyroid lesions tend to have some vascularity, whereas small parathyroid lesions more often lack Doppler signal. On occasion, larger parathyroid lesions may be vascular.[33]

For adenomas located in the perithyroidal region, ultrasonography is an excellent modality. Limitations of ultrasonography predominantly center on the fact that it is less accurate than other imaging modalities in identifying ectopic parathyroid adenomas, and evaluation of the anterior mediastinum is limited secondary to acoustic impedance by air and bone. In addition, scanning artifact may obscure adenomas close to air-filled structures such as the trachea or esophagus.

Ultrasonography identifies adenomas in 95% of glands weighing more than 1 g (individual normal parathyroid glands weigh 35 to 55 mg each).[1, 24] Investigators report sensitivity of 50% to 70%, and specificity of 90% to 95% for adenomas in hyperplastic glands.[9, 10, 14, 24, 32, 34, 35]

Cross-Sectional Imaging

Cross-sectional imaging (CT and MR imaging) provides evaluation of the neck from the skull base through the anterior mediastinum, allowing detection of ectopic parathyroid adenomas (Fig. 40-42). CT images should include contiguous thin (3 mm) sections. Intravenous contrast must be used in CT both to distinguish blood vessels from adenomas and because up to 25% of parathyroid adenomas

Copyright © 2003, Mosby, Inc. All rights reserved.

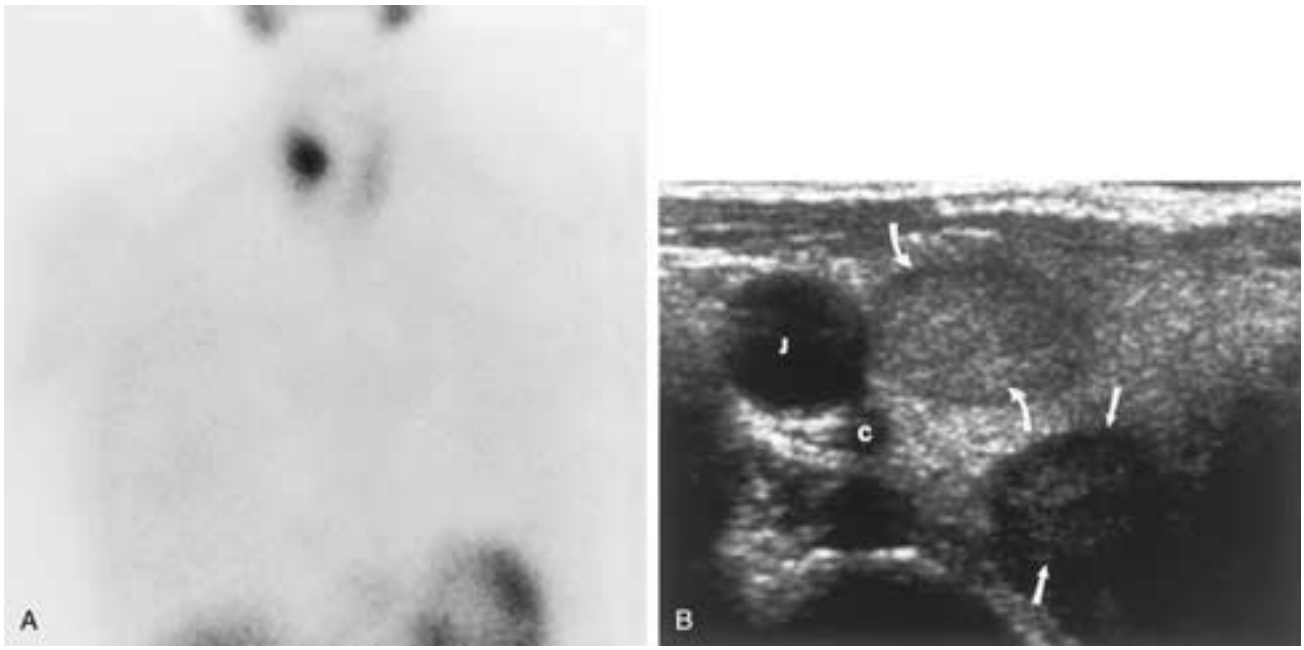

VIEW IMAGE

FIGURE 40-41 A pitfall in Tc-99m sestamibi scintigraphy is that thyroid lesions may concentrate sestamibi similarly to parathyroid adenomas. **A**, Sestamibi scan shows increased activity in the right lobe of the thyroid gland. **B**, Transverse ultrasound image reveals a well-demarcated mass in the thyroid (*curved white arrows*) that at surgery was found to be a thyroid adenoma, as well as a rounded mass hypoechoic to and posterior to the thyroid that was a parathyroid adenoma (*straight arrows*). *J*, Jugular vein; *C,* carotid artery.

enhance.[32] Limitations of CT in detecting adenomas include scanning artifacts related to swallowing and breathing. Lymph nodes, tortuous vessels, and the esophagus may also be mistaken for adenomas. As mentioned earlier, a drawback to using CT is the uptake of contrast by the thyroid gland, necessitating a wait of 6 to 8 weeks before nuclear scintigraphy with iodinated agents may be accurately performed.[36] In general, investigators have found that both the sensitivity and specificity of high-resolution CT are improved over those of ultrasound, being approximately 70% and 90%, respectively.[32, 37]

MR imaging, like CT, allows excellent evaluation of the mediastinum. This method offers superior soft-tissue discrimination and is more sensitive than CT for identifying parathyroid adenomas. MR imaging should be performed on a high field strength system. Accuracy may be improved and artifacts related to heart motion reduced by using cardiac gating. The imaging sequences utilized should include axial T1- and T2-weighted 4 to 5 mm thick images extending from the skull base through the mediastinum.[38] The administration of intravenous contrast material (gadolinium) can increase lesion conspicuity.

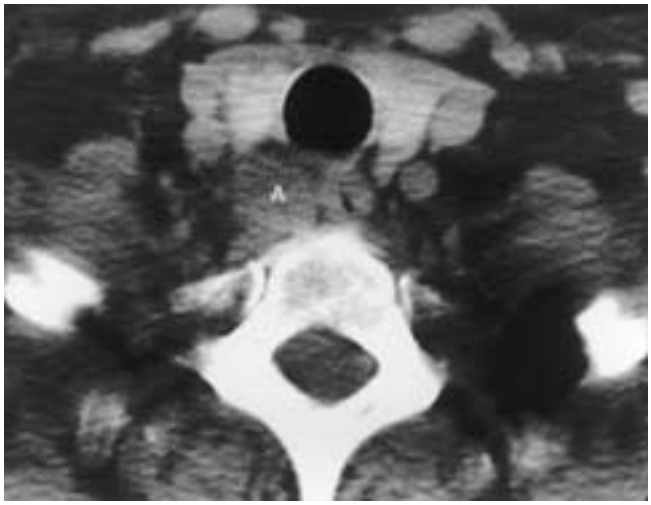

VIEW IMAGE

FIGURE 40-42 Parathyroid adenoma in the right perithyroidal region. Axial CT image shows the adenoma (*A*) that was detected in the evaluation of this patient with hypercalcemia.

The appearance of adenomas on MR imaging is variable.[39] Usually, adenomas are iso- to hypointense compared to the thyroid gland on T1-weighted images, and they are usually hyperintense on T2-weighted images. They may enhance avidly following intravenous gadolinium administration (Fig. 40-43). Some lesions with dense cellularity may be iso- to hyperintense compared to muscle on T1-weighted images and isointense on T2-weighted images (Fig. 40-44). It is uncommon for an adenoma to be hypointense on T2-weighted images. Pitfalls in detection of parathyroid adenomas on MR imaging include misinterpretation of enlarged cervical lymph nodes for adenomas,[38] large cervical ganglia, and a multiplicity of ectopic sites.[39] Distinction between abnormal gland and vessel is less of a problem with MR imaging due to its ability to readily identify vascular structures (flow voids). MR imaging has a reported accuracy of over 90%.[40]

Nuclear Scintigraphy

Nuclear scintigraphy to identify parathyroid adenomas may be performed with several radionuclides including thallium-201 (Tl-201)/Tc-99m pertechnetate subtraction scanning, Tc-99m sestamibi subtraction imaging with I-123 (Fig. 40-45) or Tc-99m pertechnetate, or Tc-99m sestamibi

Copyright © 2003, Mosby, Inc. All rights reserved.

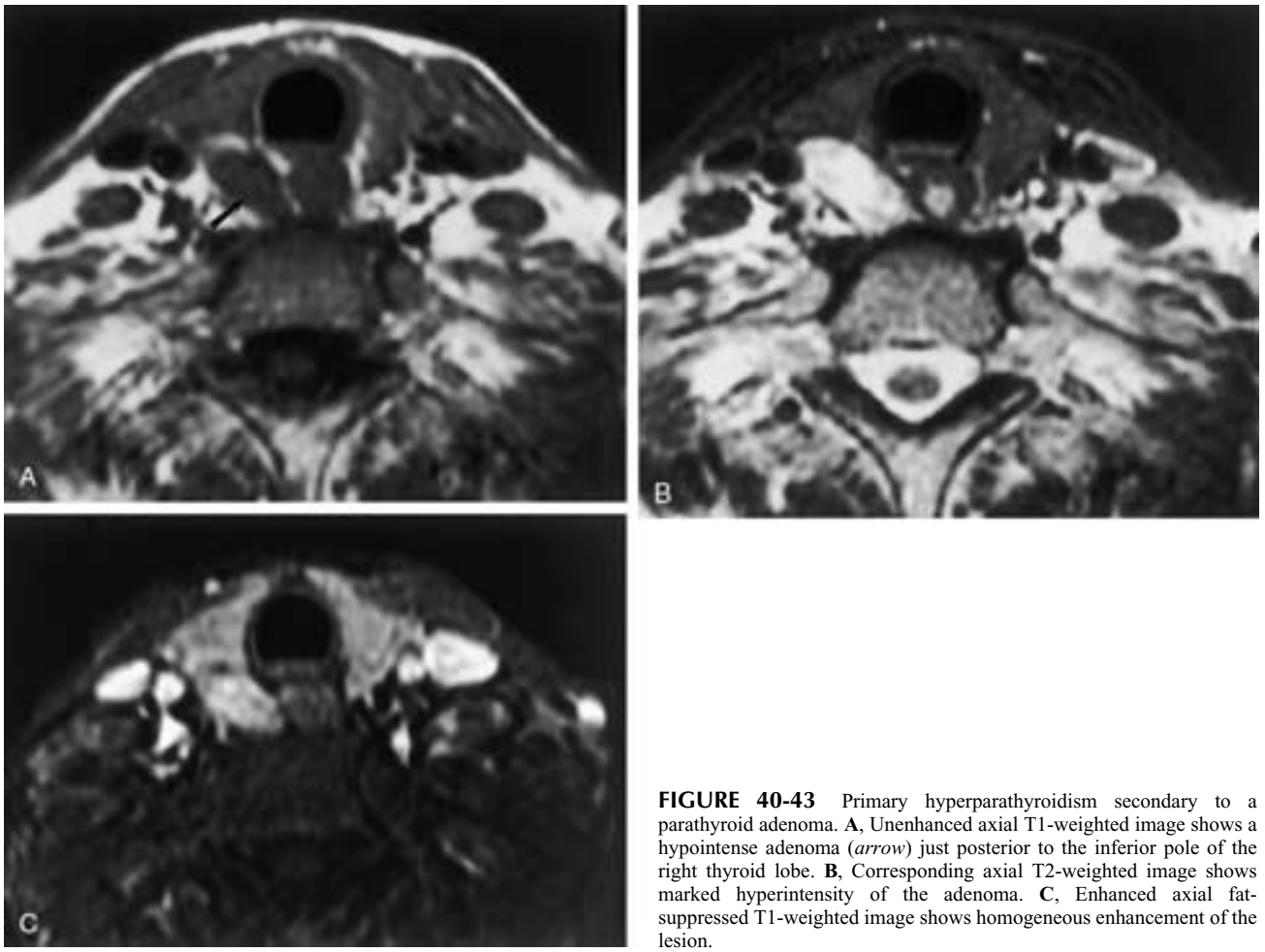

FIGURE 40-43 Primary hyperparathyroidism secondary to a parathyroid adenoma. **A**, Unenhanced axial T1-weighted image shows a hypointense adenoma (*arrow*) just posterior to the inferior pole of the right thyroid lobe. **B**, Corresponding axial T2-weighted image shows marked hyperintensity of the adenoma. **C**, Enhanced axial fat-suppressed T1-weighted image shows homogeneous enhancement of the lesion.

VIEW IMAGE

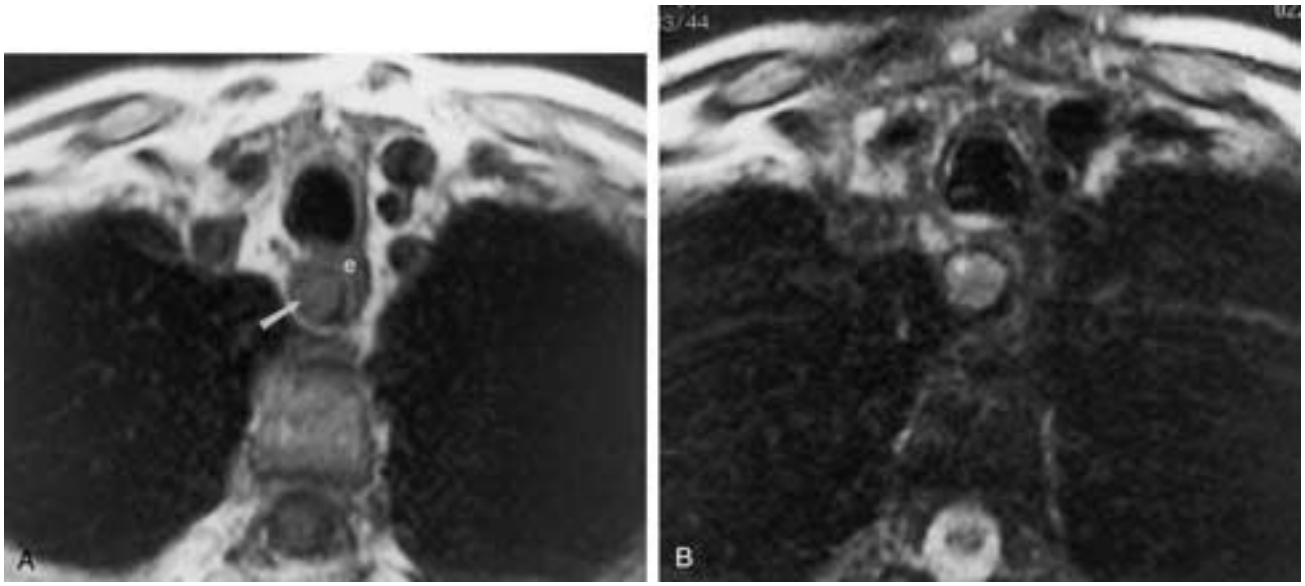

VIEW IMAGE

FIGURE 40-44 Ectopic parathyroid adenoma in the paraesophageal/tracheoesophageal tract. **A**, Unenhanced axial T1-weighted image shows a mass (*arrow*) impinging on the esophagus (*e*). **B**, Corresponding axial T2-weighted image shows an isointense adenoma. At histologic evaluation following surgical resection, the adenoma was highly cellular.

Copyright © 2003, Mosby, Inc. All rights reserved.

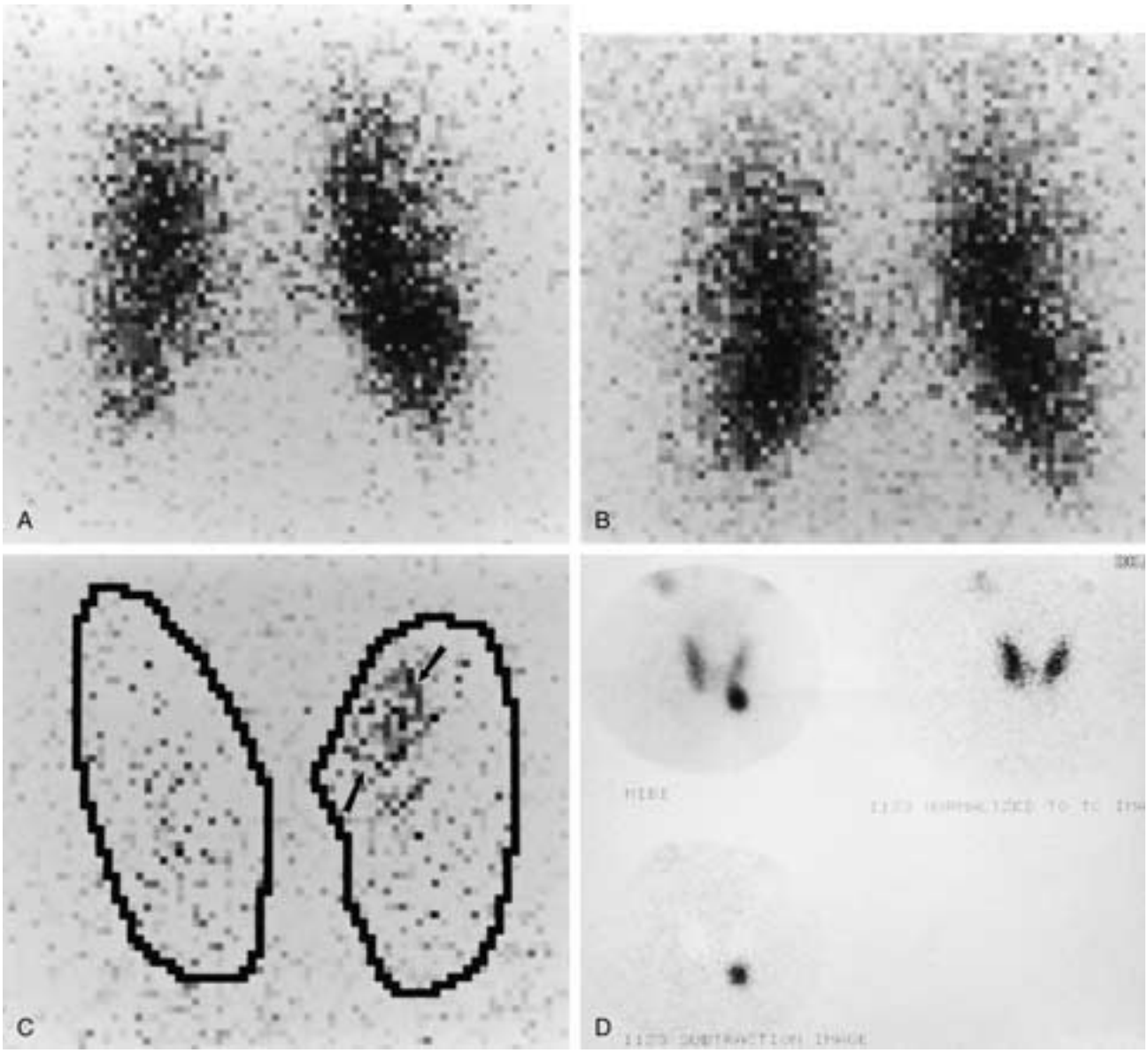

VIEW IMAGE

FIGURE 40-45 Parathyroid adenomas detected in two different patients by Tl-201/Tc-99m pertechnetate subtraction imaging (**A** to **C**) and by Tc-99m sestamibi subtraction imaging with I-123 (**D**). **A**, Tc-99m pertechnetate concentrated within the thyroid gland. **B**, Tl-201 concentrated within thyroid and parathyroid glands. **C**, Computer techniques allow technetium concentrated in the thyroid gland to be subtracted from thallium that accumulates within both thyroid and parathyroid tissue. After thyroid subtraction, a parathyroid adenoma is noted as a focus of increased thallium uptake (*arrows*). **D**, Tc-99m sestamibi subtraction imaging with I-123 shows an adenoma below the inferior pole of the left lobe of the thyroid gland. (Courtesy of Dr. Joseph Sam, Department of Radiology, Nuclear Medicine Division, University of Pennsylvania Medical Center.)

alone.[41–44] Because no radionuclides are taken up by the parathyroid glands alone, subtraction techniques allow radionuclides that are concentrated in the thyroid gland (technetium and iodine) to be subtracted from those that accumulate within both thyroid and parathyroid tissue (thallium and sestamibi). Tl-201 is a potassium analog that is taken up by the thyroid as well as concentrated in parathyroid adenomas due to changes in potassium turnover. As a sole imaging agent, it cannot distinguish a parathyroid adenoma from the thyroid gland. Thallium emits low-energy photons and washes out of adenomas rapidly. Technetium has higher-energy photons that better penetrate the anterior neck and mediastinum. Tc-99m is trapped in the thyroid gland but not in parathyroid tissue. When Tl-201 and Tc-99m pertechnetate images are coregistered, computer-based subtraction techniques can remove the thyroid component, permitting identification of abnormal parathyroid tissue.

Typically, 2 to 5 mCi of each radiotracer is administered intravenously, and either sequential or dual isotope imaging is performed. The mediastinum should be included in the field of view to assess for the possibility of ectopic adenomas. After thyroid subtraction, a perithyroidal parathyroid adenoma appears as a focus of increased thallium uptake (Fig. 40-45). The major limitation of this examina-

Copyright © 2003, Mosby, Inc. All rights reserved.

tion is motion artifact that may degrade the images, making superimposition of the images and subtraction unreliable and interpretation difficult.

The reported sensitivity and diagnostic accuracy of Tl-201/Tc-99m subtraction scintigraphy vary, but each is approximately 80% to 85%.[14, 45] False-positive examinations may result secondary to inflammatory conditions, lymphoma, and thyroid nodules. Lesion size is an important factor in determining the sensitivity of subtraction scintigraphy. Specifically, lesions less than 0.5 g are rarely visualized (the combined weight of all parathyroid glands in normal patients is usually less than 200 mg).[1] The histologic content of the adenoma also influences sensitivity, with greater accuracy seen in lesions having a high concentration of mitochondria.[46]

Tc-99m sestamibi scintigraphy was introduced in the late 1980s.[47] Tc-99m sestamibi is a positively charged, lipid-soluble myocardial perfusion tracer. The mechanism for sestamibi uptake is not completely understood, but it could correspond to cellular components (chief and oxyphil cells), mitochondrial density in oxyphil cells, blood flow within adenomas, and/or potassium turnover.[48, 49] However, it has been suggested that the number of oxyphil cells does not clearly affect the results of sestamibi imaging since it is small in most hyperfunctioning glands.[48] Electron microscopy has shown increased mitochondrial density in oxyphilic cells.[49] Uptake is also dependent on gland size as well as on their functional state.[48, 49] The intracellular distribution is determined by the negative transmembrane potential of cellular and mitochondrial membranes. Therefore, cells with high mitochondrial content are believed to retain more of the positively charged tracer.

Tc-99m sestamibi scintigraphy offers several advantages over subtraction imaging including dual-phase acquisition, handling of a single radiotracer, and the capability for single photon emission computed tomography (SPECT). Dual-phase Tc-99m sestamibi used alone takes advantage of the rapid washout of the tracer from the thyroid gland, while there is avid retention in parathyroid lesions. Delayed images are frequently all that are necessary for good localization. Immediately following injection (5 to 30 minutes) of 20 mCi of radiotracer, images are obtained of the neck and chest. Delayed images are obtained in the same sites approximately 1½ to 4 hours following radiotracer injection.[41, 50, 51] The addition of pinhole imaging in the delayed phase may further increase the detection of adenomas.[52] In difficult cases where Tc-99m sestamibi subtraction imaging with I-123 is being utilized, 200 to 300 mCi of I-123 is given orally and a pinhole image of the thyroid is obtained at 60 to 90 minutes. Subsequently, 20 mCi of Tc-99m sestamibi is injected, and immediate as well as 2 hour delayed images of the neck and chest are acquired. Parathyroid adenomas are identified as foci of increased radiotracer uptake. SPECT can be combined with Tc-99m sestamibi scintigraphy for more accurate adenoma localization. When SPECT is combined with sestamibi scintigraphy, early (10 to 30 minutes) and delayed (2 to 4 hours) images after injection are frequently acquired. Some studies suggest that for Tc-99m sestamibi SPECT, early images are more accurate in the detection and localization of adenomas.[53]

The accuracy of Tc-99m sestamibi is higher than that of Tl-201/Tc-99m pertechnetate subtraction scintigraphy, with the accuracy of sestamibi ranging from 80% to 100% and with a consistently high specificity.[14, 15, 35, 51, 54–59] The most recent data on sestamibi suggest that it surpasses all other imaging modalities, including ultrasound and CT, in both sensitivity and accuracy.[14, 15, 35, 51, 54–59] A few studies have been performed to compare the accuracy of sestamibi parathyroid scintigraphy with that of MR imaging. Most, but not all studies, suggest that sestamibi is slightly more accurate.[59–62]

In most studies assessing the accuracy of imaging in detecting parathyroid lesions, one or two imaging modalities were evaluated, and were compared and contrasted with each other. However, a handful of studies assessed the value of combining functional imaging (nuclear scintigraphy) with anatomic imaging (cross-sectional imaging). One study suggested that the greater specificity and anatomic coverage of sestamibi scintigraphy coupled with the greater anatomic detail provided by MR imaging may justify the use of both techniques in high-risk surgical patients or patients undergoing repeat surgery.[62] In a recent study that looked at the utility of scintigraphy combined with cross-sectional imaging (CT, ultrasound, MR imaging), the combination of scintigraphy and ultrasound had grater sensitivity, specificity, and accuracy than any imaging modality alone or than scintigraphy in combination with CT or MR imaging in the preoperative assessment of parathyroid disease.[5] In summary, sestamibi is a highly sensitive and accurate imaging tool for the preoperative localization of parathyroid disease. The addition of cross-sectional imaging in certain cases to provide anatomic detail is helpful, especially in patients with ectopic tissue or in patients who are high surgical risks where operative precision and short surgical times are paramount (Figs. 40-44 and 40-46).

Potential pitfalls in Tc-99m sestamibi scintigraphy include the occasional adenoma with rapid washout attributed to low mitochondrial content,[63] poor conspicuity of lesions near the heart,[15] and the occasional thyroid lesion or Hurthle cell tumor that may retain Tc-99m sestamibi.[38, 64] In addition, small lesions, especially those under 100 to 200 mg, may go undetected.[38, 49, 65] The high incidence of concomitant thyroid lesions (40% to 50%) in patients with parathyroid adenomas may lead to false-positive scintigraphy results because thyroid lesions may concentrate sestamibi to the same degree as parathyroid adenomas (Fig. 40-41).[4, 24, 38, 57, 58, 66] In addition, sestamibi uptake in thyroid cancers, as well as in nodal and distant metastases, can occur,[67, 68] and sestamibi retention in reactive lymph node hyperplasia has been reported.[69]

Reoperation for Hyperparathyroidism

In patients with recurrent hyperparathyroidism following surgery, reoperation reveals abnormal parathyroid glands in the perithyroidal region in 30% to 75% of cases (Fig. 40-40), likely corresponding to parathyroid disease overlooked during the initial surgery.[4, 20, 23] Parathyroid adenomas may also be detected in the anterior mediastinum in 30% of cases (Fig. 40-46), and they may be intrathyroidal in less than 10% of cases. The remainder of adenomas at reoperation are located in the deep cervical region.[4, 20, 70]

A consensus in the literature is that imaging prior to

Copyright © 2003, Mosby, Inc. All rights reserved.

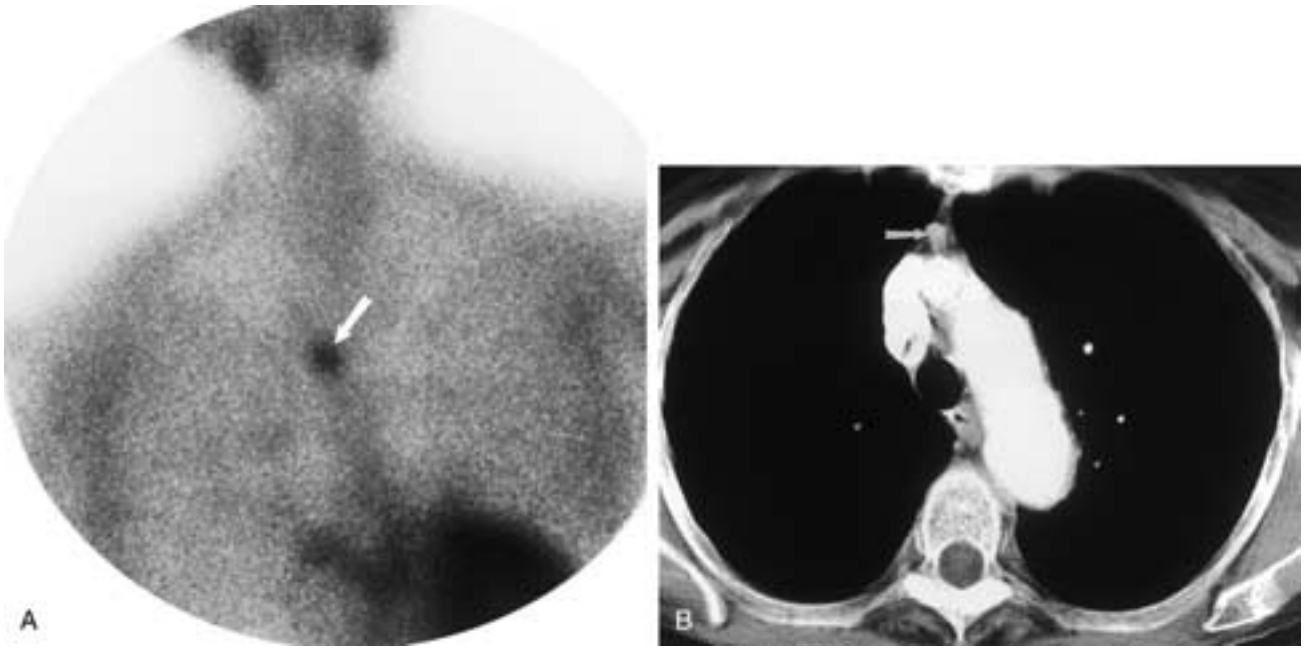

VIEW IMAGE

FIGURE 40-46 Ectopic parathyroid adenoma. **A**, Delayed image from a sestamibi scan shows increased uptake in a surgically proven ectopic parathyroid adenoma in the superior mediastinum (*arrow*). **B**, Enhanced chest CT scan shows the corresponding adenoma in the anterior mediastinum (*arrow*).

reoperation is useful despite the cost.[11, 71] When preoperative imaging is performed, the success rate of surgery is approximately 80% to 90% compared to 65% when imaging is not performed prior to reoperation.[11] In reoperations, the sensitivity of ultrasonography, CT, MR imaging, and scintigraphy is quite variable.[4, 11, 32, 72–74]

One of the major differences in imaging the patient who has failed prior surgery for detection of a parathyroid adenoma is that scar tissue in the operative bed in the perithyroidal region makes image interpretation as well as anatomic detection at surgery more difficult. As with cross-sectional imaging at initial surgery, lymphadenopathy may be mistaken for an adenoma. Because the incidence of false-positive examinations caused by lymphadenopathy is lowest with nuclear imaging,[4] sestamibi scintigraphy as a single study is probably the most accurate and cost-effective means to detect parathyroid adenomas. However, because of the increased surgical risk in cases of reoperation including vocal cord paralysis,[20] as well as the distortion of anatomic landmarks due to prior surgery, many surgeons believe that a functional scintigraphic study combined with an anatomic cross-sectional examination (MR imaging is less likely than CT and ultrasound to mistake a lymph node for an adenoma)[4] is warranted, as it provides the most accurate means of detecting parathyroid tissue despite the fact that it is not the most cost-effective approach. In general, MR imaging in combination with sestamibi scintigraphy allows accurate detection of parathyroid tissue.[62, 74, 75]

I-123 or Tc-99m pertechnetate and Tc-99m sestamibi subtraction images may increase the sensitivity of ectopic parathyroid adenoma detection in cases of failed initial neck explorations.[76] Finally, the sensitivity of sestamibi imaging in patients who require repeat surgery may be increased if the interval between initial surgery and imaging is extended to at least 2 weeks.[77] This is done to avoid trapping of the radiotracer in the thyroid gland that may occur as a result of postoperative inflammation.

Parathyroid Hyperplasia

Chief-cell parathyroid hyperplasia accounts for hyperparathyroidism in up to 15% of patients and may be associated with familial hyperparathyroidism or MEN syndromes.[78, 79] MEN is a spectrum of hereditary (autosomal dominant) conditions characterized by two or more hyperfunctioning endocrine tumors. MEN type I is associated with primary hyperparathyroidism, pancreatic islet cell tumors, and anterior pituitary neoplasms.[80–82] Primary hyperparathyroidism, which is usually multiglandular, is the most common clinical presentation. MEN type IIA is characterized by pheochromocytoma, medullary thyroid cancer, and hyperparathyroidism.[80–83] The hyperparathyroidism of MEN type IIA is also multiglandular but is less severe than that of MEN type I.

Chief-cell hyperplasia accounts for the majority of cases of parathyroid hyperplasia, although uncommonly, clear-cell hyperplasia may occur. Clear cells are chief cells with an abundant amount of cytoplasmic glycogen.[1] Histologically, there are numerous chief cells, occasional oxyphil cells, and sparse adipose tissue. Usually all of the parathyroid glands are enlarged, although usually not to significant degrees.[26, 84] Infrequently, one gland is disproportionately enlarged, and as a result may be mistaken intraoperatively for an adenoma.

Treatment of primary parathyroid hyperplasia is removal of most if not all parathyroid tissue, with or without autotransplantation to the forearm.[30, 78] Parathyroid hyperplasia is difficult to evaluate with any imaging

Copyright © 2003, Mosby, Inc. All rights reserved.

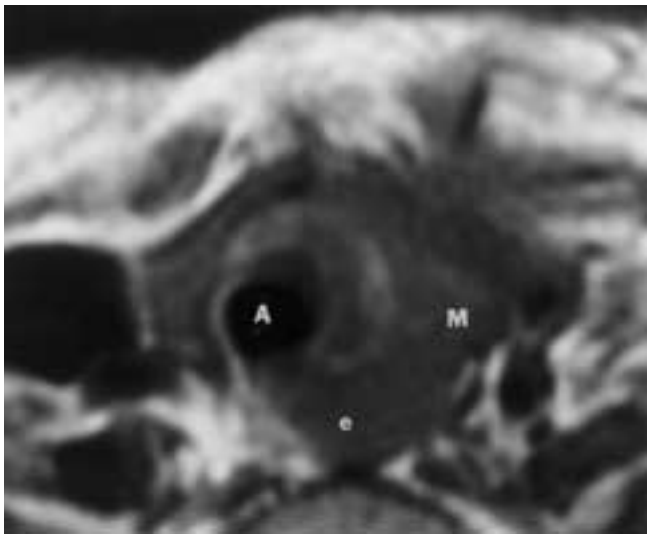

VIEW IMAGE

FIGURE 40-47 Parathyroid carcinoma invading the airway. Unenhanced axial T1-weighted MR image shows a poorly defined soft-tissue mass (*M*) just below the inferior pole of the left lobe of the thyroid gland. The fat plane between this mass and the esophagus (*e*) is obliterated, and there is extension into the left lateral wall of the adjacent airway (*A*).

modality due to the small size of the hyperplastic glands. Because there can be marked heterogeneity in gland size in parathyroid hyperplasia, imaging may detect the dominant gland but fail to identify the other hyperplastic glands.[26] Furthermore, when there is a discrepancy in the size of the glands, the surgeon may conclude that a single parathyroid adenoma is responsible for the hyperparathyroidism. The reported sensitivity for the detection of parathyroid hyperplasia is low, ranging from approximately 30% to 70% with cross-sectional imaging techniques.[9–11, 26, 32] More recently Tc99m sestamibi imaging has detected pararthyroid hyperplasia in 50% to 75% of cases.[10, 11, 15, 26, 38, 57, 65, 85]

Parathyroid Carcinoma

Parathyroid carcinoma is an unusual cause of hyperparathyroidism, accounting for less than 2% of all cases. However, hyperparathyroidism accounts for the clinical presentation of approximately 85% of all parathyroid carcinomas.[1] Patients usually have the typical symptoms associated with hypercalcemia. In addition, because these tumors are frequently large, many patients may have a palpable neck mass at presentation. Grossly, parathyroid carcinomas tend to be large (over 10 g), and histologically are noted to have tumor cells with mitotic figures admixed with fibrous tissue, as well as capsular and vascular invasion.[86]

Parathyroid carcinomas have no characteristic imaging features and may not be distinguishable from adenomas or other soft-tissue masses. Regional cervical and mediastinal lymph node metastases may occur in up to one third of

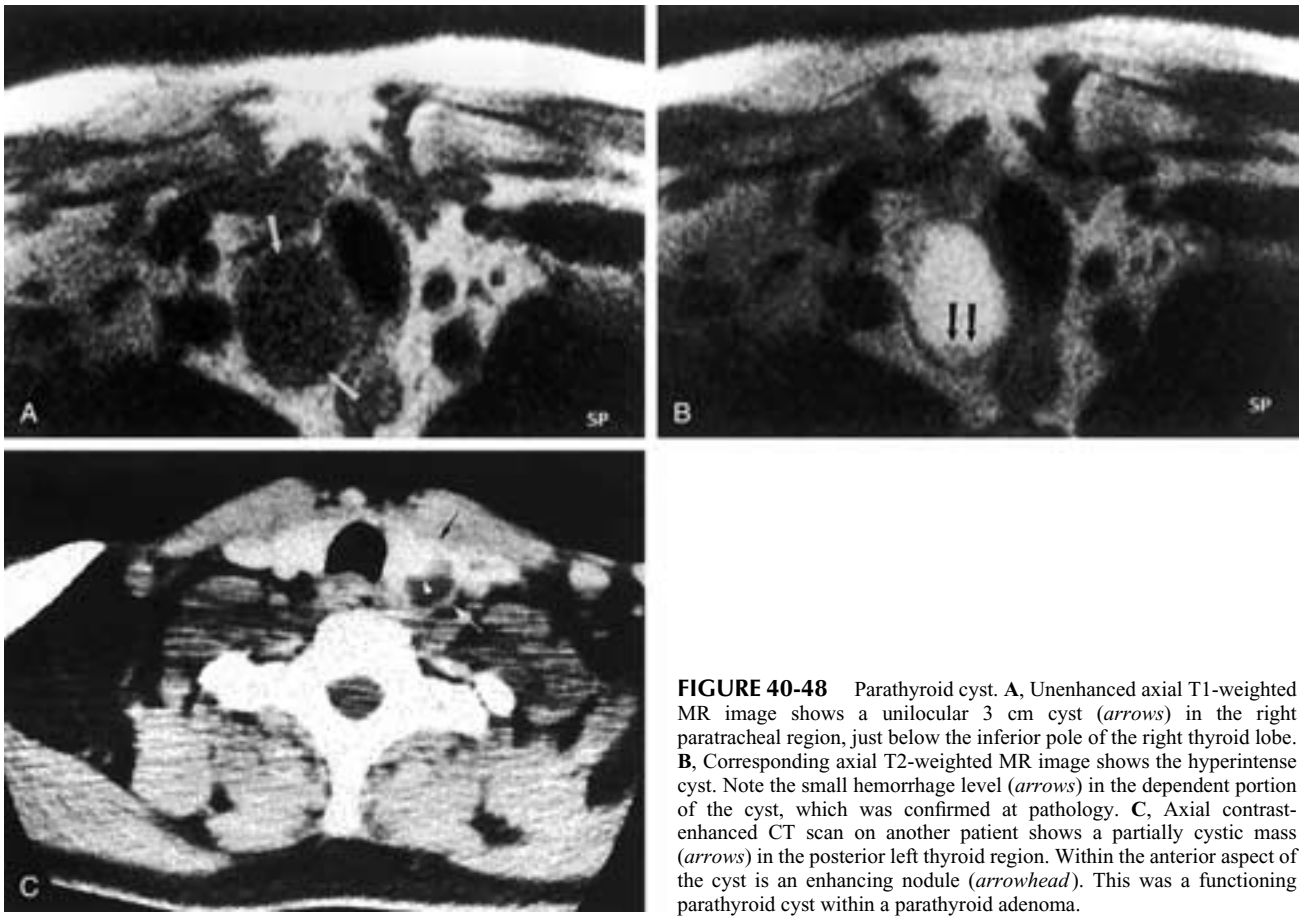

VIEW IMAGE

FIGURE 40-48 Parathyroid cyst. **A**, Unenhanced axial T1-weighted MR image shows a unilocular 3 cm cyst (*arrows*) in the right paratracheal region, just below the inferior pole of the right thyroid lobe. **B**, Corresponding axial T2-weighted MR image shows the hyperintense cyst. Note the small hemorrhage level (*arrows*) in the dependent portion of the cyst, which was confirmed at pathology. **C**, Axial contrast-enhanced CT scan on another patient shows a partially cystic mass (*arrows*) in the posterior left thyroid region. Within the anterior aspect of the cyst is an enhancing nodule (*arrowhead*). This was a functioning parathyroid cyst within a parathyroid adenoma.

Copyright © 2003, Mosby, Inc. All rights reserved.

patients and distant metastases (liver, lung, bone) in approximately 25% of patients. Parathyroid carcinomas may also invade adjacent tissues including surrounding fat, the cervical musculature, the aerodigestive tract, nerves, or the thyroid gland (Fig. 40-47).[87, 88] Only invasion of adjacent tissues, or lymph node or distant metastases, may distinguish a parathyroid carcinoma from an adenoma in the setting of hyperparathyroidism. Some parathyroid carcinomas may take up Tc-99m sestamibi.[89]

Parathyroid Cyst

Parathyroid cysts, like adenomas, most commonly arise in the inferior parathyroid glands (65% of cases), and 95% of these cysts occur below the level of the inferior thyroid border. They are rare in children, more common in women, and typically present in the fourth to fifth decades of life.[1, 90] They are usually large (1 to 4 cm).

Parathyroid cysts represent only 0.6% of all thyroid and parathyroid lesions. Nonfunctioning cysts account for the majority of cases and present at a mean age of 43.3 years. Functioning cysts account for 11.5% to 30% of the cases, are more common in men, and occur at a mean age of 51.9 years.

The origin of parathyroid cysts is unclear. They may arise from pharyngeal pouch remnants or they may be acquired. Proposed acquired etiologies include degeneration of parathyroid adenomas into cysts and enlargement or coalescence of parathyroid microcysts.

Similar to their appearance at gross pathology, on imaging they are usually large and unilocular and have variable MR imaging and CT characteristics, depending on their protein content (Fig. 40-48).[90] They may be difficult to distinguish from cystic or necrotic lymph nodes or from cysts derived from other sources such as solitary thyroid cysts and cervical thymic cysts.

REFERENCES

1. Livolsi V. The thyroid and parathyroid. In: Sternberg SS, ed. Diagnostic Surgical Pathology, ed 2. New York: Raven Press, 1994;523–560.
2. Akerstrom G, Malmaeus J, Bergstrom S. Surgical anatomy of human parathyroid glands. Surgery 1984;95:14–21.
3. Thompson CT. Localization studies in patients with hyperparathyroidism. Br J Surg 1988;75:97–98.
4. Miller DL, Doppman JL, Shawker TH, et al. Localization of parathyroid adenomas in patients who have undergone surgery. Part I. Noninvasive imaging methods. Radiology 1987;162:133–137.
5. De Feo ML, Colagrande S, Biagini C, Tonarelli A, Bisi G, Vaggelli L, Borrelli D, Cicchi P, Tonelli F, Amorosi A, Serio M, Brandi ML. Parathyroid glands: combination of 99m Tc MIBI scintigraphy and US for demonstration of parathyroid glands and nodules. Radiology 2000;214:393–402.
6. Akerstrom G, Grimelius L, Johansson H, Pertoft H, Lundquist H. Estimation of parathyroid parenchymal cell mass by density gradients. Am J Pathol 1980;99:685–694.
7. Rosenblatt M, Kronenberg HM. Pots JT. Parathyroid horomone. Physiology, chemistry, biosynthesis, secretion, metabolism and mode of action. In: DeGroot LJ, ed. Endocrinology, Vol. 2. Philadelphia: WB Saunders, 1989;848–891.
8. Clark OH, Duh QY. Primary hyperparathyroidism, a surgical perspective. Endocrinol Metab Clin North Am 1989;268:943–953.
9. Gooding GAW, Okerlund MD, Stark DD, et al. Parathyroid imaging: comparison of double-tracer (Tl-201, Tc-99m) scintigraphy and high-resolution ultrasound. Radiology 1986;161:57–64.
10. Gooding GAW. Sonography of the thyroid and parathyroid. Radiol Clin North Am 1993;31:967–989.
11. Price DC. Radioisotopic evaluation of the thyroid and the parathyroids. Radiol Clin North Am 1993;31:991–1015.
12. Lundgren EC, Gillott AR, Wiseman JS, et al. The role of preoperative localization in primary hyperparathyriodism. Ann Surg 1995;61:393–396.
13. Russell CF, Laird JD, Ferguson WR. Scan-directed unilateral cervical exploration for parathyroid adenoma: a legitimate approach? World J Surg 1990;14:406–409.
14. Song AU, Phillips TE, Edmond CV, Moore DW, Clark SK. Success of preoperative imaging and unilateral neck exploration for primary hyperparathyroidism. Otolaryngol Head Neck Surg 1999;121:393–397.
15. Pattoou F, Torres G, Mondragon-Sanchez A, et al. Correlation of parathyroid scanning and anatomy in 261 unselected patients with sporadic primary hyperparathyroidism. Surgery 1999;126:1123–1131.
16. Solbiati L, Giangrande A, De Pra L, et al. Percutaneous ethanol injection of parathyroid tumors and ultrasound guidance: treatment for secondary hyperparathyroidism. Radiology 1985;155:607–610.
17. Verges B, Cercueil JP, Pfitzenmyer P, et al. Percutaneous ethanol injection of parathyroid adenomas in primary hyperparathyroidism. Lancet 1991;337:1421–1422.
18. Roe SM, Burns RP, Graham LD, et al. Cost-effectiveness of preoperative localization studies in primary hyperparathyroid disease. Ann Surg 1994;219(5):582–586.
19. Carlson GK, Farndon JR, Clayton B, et al. Thallium isotope scintigraphy and ultrasonography: comparative studies of localization techniques in primary hyperthyroidism. Br J Surg 1990;77(3):327–329.
20. Miller DL. Preoperative localization and international treatment of parathyroid tumors: When and how? World J Surg 1991;15:706–715.
21. Uden P, Aspelin P, Berglund J, et al. Preoperative localization in unilateral parathyroid surgery. A cost-benefit study on ultrasound, computed tomography and scintigraphy. Acta Chir Scand 1990;150:29–35.
22. Okada Y, Mizutani Y, Takeuchi H, Shigeno C, Konishi J, Yoshida O. Preoperative imaging for parathyroid localization in primary hyperparathyroidism. Int J Urol 1997;4:338–342.
23. Edis AJ, Sheedy PF, Beahrs OH, et al. Results of reoperation for hyperthyroidism, with evaluation of preoperative localization studies. Surgery 1978;84:384–391.
24. Reading CC, Charboneau JW, James EM, et al. High-resolution parathyroid sonography. Am J Roentgenol 1982;139:539–546.
25. Satava RM, Beahrs OH, Scholz DA. Success rate of cervical exploration for hyperparathyroidism. Arch Surg 1975;110:625–627.
26. Berger AC, Libutti SK, Barlett DL, et al. Heterogeneous gland size in sporadic multiple gland parathyroid hyperplasia. J Am Coll Surg 1999;188:382–389.
27. Ishibashi M, Uchida M, Nishida H, Hiromatsu Y, Kohno K, Okuda S, Hayabuchi N. Pre-surgical localization of ectopic parathyroid glands using three-dimensional CT imaging, 99Tcm sestamibi, and 99Tcm tetrofosmin imaging. Br J Radiol 1999;72(855):296–300.
28. Mattar AG, Wright ES, Chittal SM, et al. Impact on surgery of preoperative localization of parathyroid lesions with dual radionuclide subtraction scanning. Can J Surg 1986;29:57–59.
29. Tibblin S, Bondeson AG, Ljungberg O. Unilateral parathyroidectomy in hyperparathyroidism due to single adenoma. Ann Surg 1982;195:245–252.
30. Wells SA, Farndon JR, Dale JK, Leight GS, Dilley WG. Long term evaluation of patients with primary parathyroid hyperplasia managed by total parathyroidectomy and heterotopic autotransplantation. Ann Surg 1980;192:451–458.
31. Casas AT, Burke GJ, Mansberger AR Jr, et al. Impact of technetium-99m sestamibi localization on operative time and success of operations for primary hyperparathyroidism. Am Surg 1994;60(1):12–16.
32. Stark DD, Gooding GAW, Moss AA. Parathyroid imaging: comparison of high-resolution CT and high-resolution sonography. Am J Roentgenol 1983;141:633–638.
33. Gooding GAW, Clark OH. Use of color Doppler imaging in the distinction between thyroid and parathyroid lesions. Am J Surg 1992;164:51–56.

Copyright © 2003, Mosby, Inc. All rights reserved.

34. Kneeland JB, Kruback AJ, Lawson TL, et al. Enlarged parathyroid glands: high-resolution local coil MR imaging. Radiology 1987;162: 143–146.
35. Torregrosa JV, Palomar MR, Pons F, et al. Has double-phase MIBI scintigraphy usefulness in the diagnosis of hyperparathyroidism? Nephrol Dial Transplant 1998;13(3):37–40.
36. Laurie AJ, Lyon SG, Lassen EC. Contrast material iodides: potential effects on radioactive iodine thyroid uptake. J Nucl Med 1992;33:237–238.
37. Sommer B, Welter HF, Spelsberg F, et al. Computed tomography for localizing enlarged parathyroid glands in primary hyperparathyroidism. J Comput Assist Tomogr 1982;6:521–526.
38. McDermott VG, Mendez Fernandez RJ, Meakem TJ III, Stolpen AH, Spritzer CE, Gefter WB. Preoperative MR imaging in hyperparathyroidism: results and factors affecting parathyroid detection. AJR 1996;166:705–710.
39. Higgins CB. Role of magnetic resonance imaging in hyperparathyroidism. Radiol Clin North Am 1993;31:1017–1028.
40. Spritzer CE, Gefter WB, Hamilton R, et al. Abnormal parathyroid glands: high resolution MR imaging. Radiology 1987;162: 487–491.
41. Nguyen BD. Parathyroid imaging with Tc-99m sestamibi planar and SPECT scintigraphy. RadioGraphics 1999;19:601–614.
42. Vallejos V, Martin-Comin J, Gonzalez MT. The usefulness of Tc-99m tetrofosmin scintigraphy in the diagnosis and localization of hyperfunctioning parathyroid glands. Clin Nucl Med 1999;24: 959–964.
43. Hindie E, Urena, P, Jeanguillaume C, et al. Preoperative imaging of parathyroid glands with technetium-99m labeled sestamibi and iodine-123 subtraction scanning in secondary hyperparathroidism. Lancet 1999;353:2200–2204.
44. Hiromatsu Y, Ishibashi M, Nishida H, Okuda S, Miyake I. Technetium-99m tetrofosmin parathyroid imaging in patients with primary hyperparathyroidism. Intern Med 2000;39:101–106.
45. Hauty M, Swartz K, McKlung M, et al. Technetium-thallium scintiscanning for localization of parathyroid adenomas and hyperplasia, a reappraisal. Am J Surg 1987;153:479–486.
46. Sandrock D, Merino MJ, Norton JA, et al. Ultrastructural histology correlates with results of thallium-201/technetium-99m parathyroid subtraction scintigraphy. J Nucl Med 1993;34:24–29.
47. Coakley AJ, Kettle AG, Wells CP, et al. Technetium-99m-sestamibi—a new agent for parathyroid imaging. Nucl Med Commun 1989;10:791–794.
48. Takebayashi S, Hidai H, Chiba T, Takagi Y, Nagatini Y, Matsubara S. Hyperfunctional parathyroid glands with ^{99m}Tc-MIBI scan: semiquantitative analysis correlated with histologic findings. J Nucl Med 1999;40:1792–1797.
49. Arbab AS, Koizumi K, Hemmi A, Toyama K, Arai T, Yoshitomi T, Araki T. Tc-99m-MIBI scintigraphy for detecting parathyroid adenoma and hyperplasia. Ann Nucl Med 1997;11:45–49.
50. Mitchell BK, Kinder BK, Cornelius E, et al. Primary hyperparathyroidism: preoperative localization using technetium-sestamibi scanning. J Clin Endocrinol Metab 1995;80(1):7–10.
51. Taillefer R, Boucher Y, Potvin C, et al. Detection and localization of parathyroid adenomas in patients with hyperparathyroidism using a single radionuclide imaging procedure with Technetium-99m-sestamibi (double phase study). J Nucl Med 1992;33:1801–1807.
52. Kipper MS, LaBarbera JJ, Krohn LD, Marcou LM. Localization of a parathyroid adenoma by the addition of pinhole imaging to Tc-99m sestamibi dual-phase scintigraphy. Clin Nucl Med 1997;22: 73–75.
53. Perez-Monte JE, Brown ML, Shah AN, Ranger NT, Watson CG, Carty SE, Clarke MR. Parathyroid adenomas: accurate detection and localization with Tc-99m sestamibi SPECT. Radiology 1996;201: 85–91.
54. Basso LV, Keeling C, Goris ML. Parathyroid imaging: use of dual isotope scintigraphy for the localization of adenomas before surgery. Clin Nucl Med 1992;17(5):380–383.
55. Hindie E, Melliere D, Simon D, et al. Primary hyperparathyroidism: is technetium 99m-sestamibi/iodine-123 subtraction scanning the best procedure to locate enlarged glands before surgery? J Clin Endocrinol Metab 1995;80(1):302–307.
56. Khan A, Samtani S, Varma VM, et al. Preoperative parathyroid localization: prospective evaluation of technetium-99m sestamibi. Otolaryngol Head Neck Surg 1994;111(4):467–472.
57. O'Doherty MJ, Kettle AG, Wells P, et al. Parathyroid imaging with technetium–99m-sestamibi: preoperative localization and tissue uptake studies. J Nucl Med 1992;33:313–318.
58. Oates E. Improved parathyroid scintigraphy with Tc-99m MIBI, a superior radiotracer. Appl Radiol 1994;37–42.
59. Ishibashi M, Nishida H, Hiromatsu Y, Kojima K, Tabuchi E, Hayabuchi N. Comparison of technetium-99m-MIBI, technetium-99m-tetrofosmin, ultrasound and MRI for localization of abnormal parathyroid glands. J Nucl Med 1998;39:320–324.
60. McBiles M, Lambert AT, Cote MG, Kim SY. Sestamibi parathyroid scintigraphy. Semin Nucl Med 1995;25:221–234.
61. Nunerow LM, Morita ET, Clark OH, Higgins CB. Persistent/recurrent hyperparathyroidism: a comparison of sestamibi scintigraphy, MRI, and ultrasonography. J Magn Reson Imaging 1995;5: 702–708.
62. Lee VS, Spritzer CE, Coleman RE, Wilkinson RH, Coogan AC, Leight GS. The complementary roles of fast spin-echo MR imaging and double-phase 99mTc-sestamibi scintigraphy for localization of hyperfunctioning parathyroid glands. AJR 1996;167:1555–1562.
63. Benard F, Lefebvre B, Beuvon F, et al. Rapid washout of technetium-99m-MIBI from a large parathyroid adenoma. J Nucl Med 1995;36:241–243.
64. Vattimo A, Bertelli P, Cintorino N, et al. Identification of Hurthle cell tumor by single-injection, double-phase scintigraphy with technetium-99m-sestamibi. J Nucl Med 1995;36:778–782.
65. Blocket D, Martin P, Schoutens A, Verhas M, Hooghe L, Kinnaert P. Presurgical localization of abnormal parathyroid glands using a single injection of technetium-99m methoxyisobutylisonitrile: comparison of different techniques including factor analysis of dynamic structures. Eur J Nucl Med 1997;24:46–51.
66. Funari M, Campos Z, Gooding GA, et al. MRI and ultrasound detection of asymptomatic thyroid nodules in hyperparathyroidism. J Comput Tomogr 1992;16:615–619.
67. Szybinski Z, Huszno B, Golkowski F, et al. Technetium 99m-methoxyisobutylisonitrile in early diagnosis of thyroid cancer. Endokrynologia Polska 1993;44:427–433.
68. Yen TC, Lin HD, Lee CH, et al. The role of technetium-99m sestamibi whole-body scans in diagnosing metastatic Hurthle cell carcinoma of the thyroid gland after total thyroidectomy: a comparison with iodine-131 and thallium-201 whole-body scans. Eur J Nucl Med 1994;21:980–983.
69. Leslie WD, Riese KT, Mohamed C. Sestamibi retention in reactive lymph node hyperplasia, a cause of false-positive parathyroid localization. Clin Nucl Med 2000;25:216–217.
70. Rodriquez JM, Tezelman S, Siperstein AE, et al. Localization procedures in patients with persistent or recurrent hyperparathyroidism. Arch Surg 1994;129(8):870–875.
71. Serchuk LS, Tomas MB, Patel M, Palestro CJ. SPECT and subtraction imaging in an ectopic parathyroid adenoma. Clin Nucl Med 1997;22:459–462.
72. Hamilton R, Greenburg BM, Gefter W, et al.: Successful localization of parathyroid adenomas by magnetic resonance imaging. Am J Surg 1988;155:370–373.
73. Peck WW, Higgins CB, Fisher MR, et al. Hyperparathyroidism: comparison of MR imaging with radionuclide scanning. Radiology 1987;163:415–420.
74. Kang YS, Rosen K, Clark OH, et al. Localization of abnormal parathyroid glands of the mediastinum with MR imaging. Radiology 1993;189(1):137–141.
75. Weber CJ, Vansant J, Alazraki N, et al. Value of technetium-99m-sestamibi iodine-123 imaging in reoperative parathyroid surgery. Surgery 1993;114(6):1011–1018.
76. Chen CC, Skarulis MC, Fraker DL, Alexander HR, Marx SJ, Spiegel AM. Technetium-99m-sestamibi imaging before reoperation for primary hyperparathyroidism. J Nucl Med 1995;36:2186–2195.
77. Gordon BM, Gordon L, Hoang K, Spicer KM. Parathyroid imaging with 99m Tc-sestamibi. AJR 1996;167:1563–1568.
78. Wang CA, Castleman B, Cope O. Surgical management of hyperparathyroidism due to primary hyperplasia. A clinical and pathologic study of 104 cases. Ann Surg 1981;193:26–29.
79. Marx JS, Spiegel AM, Brown EM, Aurbach GD. Familial studies in patients with primary parathyroid hyperplasia. Am J Med 1977;62: 698–706.
80. Fitzpatrick LA. Hypercalcemia in the multiple endocrine neoplasia syndromes. Endocrinol Metab Clin North Am 1989;18:741–752.

Copyright © 2003, Mosby, Inc. All rights reserved.

81. Skogseid B, Rastad J, Oberg K. Multiple endocrine neoplasia type I. Endocrinol Metab Clin North Am 1994;23:1–17.
82. Herfarth KK, Wells SA. Parathyroid glands and the multiple endocrine neoplasia syndromes and familial hypocalciuric hypercalcemia. Semin Surg Oncol 1997;13:114–124.
83. Steiner AL, Goodman AD, Powers SR. Study of a kindred with pheochromocytoma, medullary thyroid carcinoma, hyperparathyroidism, and Cushing's disease: multiple endocrine neoplasia type 2. Medicine 1968;47:371–409.
84. Castleman B, Schantz A, Roth SI. Parathyroid hyperplasia in primary hyperparathyroidism. Cancer 1976;38:1668–1675.
85. Lee VS, Wilkinson RH, Leight GS, Coogan AC, Coleman RE. Hyperparathyroidism in high-risk surgical patients: evaluation with double-phase technetium-99m sestamibi imaging. Radiology 1995; 197:627–633.
86. Schantz A, Castleman B. Parathyroid carcinoma: a study of 70 cases. Cancer 1973;31:600–605.
87. Edmonson GR, Charboneau JW, James EM, et al. Parathyroid carcinoma: high-frequency sonographic features. Radiology 1986;161: 65–67.
88. van Heerden JA, Weiland LH, ReMine WH, et al. Cancer of the parathyroid gland. Arch Surg 1979;114:475–479.
89. Kitapci MT, Tastekin G, Turgut M, et al. Preoperative localization of parathyroid carcinoma using Tc-99m MIBI. Clin Nucl Med 1993;18(3):217–219.
90. Ginsberg J, Young JEM, Walfish PG. Parathyroid cysts. JAMA 1978;240:1506–1507.

Copyright © 2003, Mosby, Inc. All rights reserved.

Copyright © 2003, Mosby, Inc. All rights reserved.

41

Skin and Soft-Tissue Lesions

Bradley N. Delman, Jane L. Weissman, and Peter M. Som

INTRODUCTION
SKIN AND SUBCUTANEOUS LESIONS
- Scar
- Hypertrophic Scar
- Keloid
- Epidermoid Cyst (Sebaceous Cyst)
- Pilomatrixoma
- Basal Cell Carcinoma
- Squamous Cell Carcinoma of the Skin
- Melanoma
- Merkel Cell Tumor
- Skin Metastasis
- Subcutaneous Fat Necrosis of the Newborn
- Sclerema Neonatorum
- Plexiform Neurofibroma and Skin Neurofibromas
- Silicon Augmentation
- Alloderm Augmentation
- Foreign Bodies

FAT-CONTAINING LESIONS
- Ordinary Lipoma
- Infiltrative (Intramuscular) Lipoma
- Madelung's Disease
- Liposarcoma

INTERSTITIAL LESIONS
- Fibrosarcoma
  - Benign Fibrous Lesions (Fibromatoses)
  - Desmoid Tumor
  - Congenital Fibromatosis (Generalized and Localized)
  - Nodular Fasciitis (Pseudotumor of the Skin)
- Proliferative Fasciitis
- Necrotizing Fasciitis

MUSCLE-RELATED LESIONS
- Levator Claviculae Muscle
- Denervation Atrophy
- Muscle Hypertrophy
- Fibromatosis Colli (Sternomastoid or Sternocleidomastoid Tumor)
- Muscular Torticollis
- Myositis
- Myositis Ossificans
- Muscular Dystrophies
- Myotonic Dystrophy
- Rhabdomyosarcoma
- Metastasis to Muscle

THE STYLOHYOID SYNDROMES
- Eagle's Syndrome
- Styloid Carotodynia
- Hyoid Fasciitis

BLOOD VESSELS AND VASCULAR VARIATIONS
- Veins
  - Asymmetry of the Internal Jugular Veins
  - Multiple Jugular Veins
  - Phlebectasia
  - Thrombosis
  - Pseudocollateral and Collateral Veins
  - Condylar Vein
- Arteries
  - Medial Deviation of the Carotid Artery
  - Aberrant Retroesophageal Right Subclavian Artery
  - Thrombosis and Dissection
  - Aneurysm
- Hemangioma
- Hemangiopericytoma

PERIPHERAL NERVE SHEATH TUMORS
PHARYNGOESOPHAGEAL LESIONS
- Zenker's Diverticulum
- Dilated/Obstructed Cervical Esophagus

Copyright © 2003, Mosby, Inc. All rights reserved.

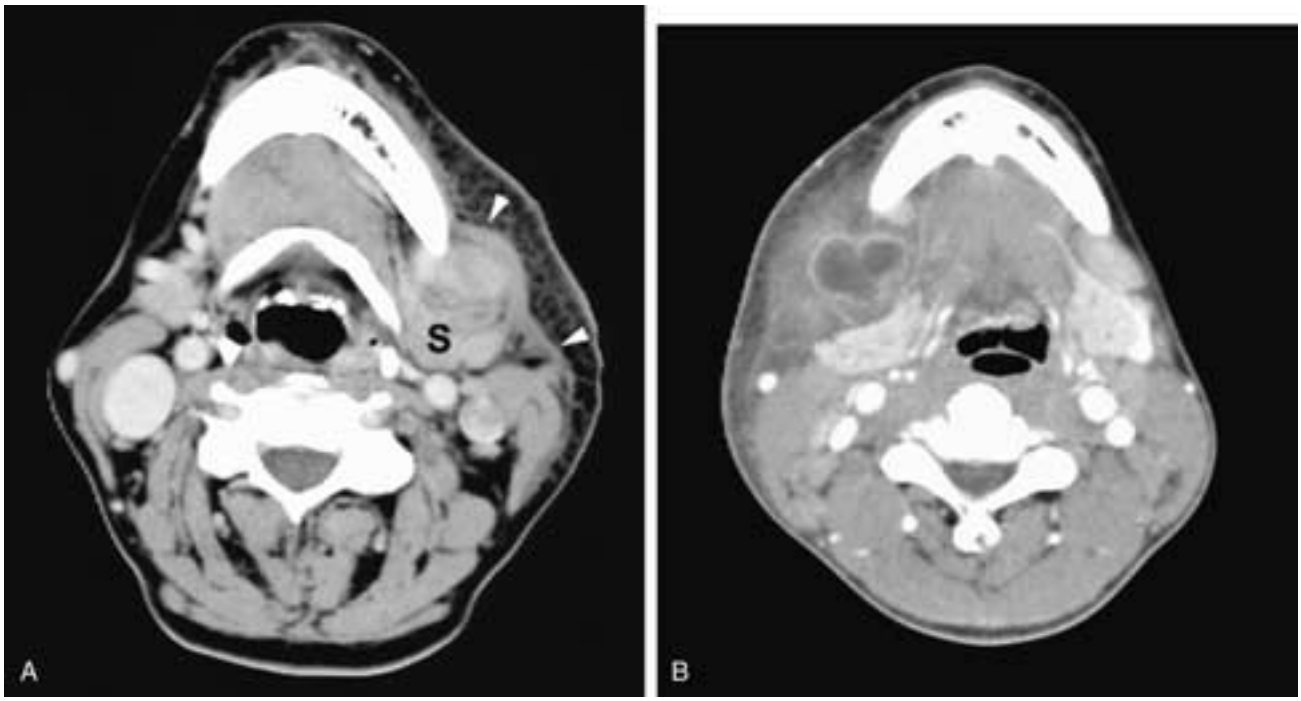

VIEW IMAGE

FIGURE 41-1 Axial contrast-enhanced CT scan (**A**) shows mild thickening of the skin in the left neck, marked thickening of the subcutaneous fat with prominence of dilated lymphatic and vascular capillaries and venules, and thickening of the platysma (*arrowheads*), all secondary to an acute left submandibular sialadenitis (*S*). Axial contrast-enhanced CT scan (**B**) on another patient shows the changes of cellulitis in the right submandibular triangle. In addition, there is an abscess with an enhancing rim. The abscess displaces the submandibular gland posteriorly.

INTRODUCTION

There are a variety of skin and soft-tissue lesions in the head and neck with manifestations that can be seen on CT and MR imaging. Although overall there are a large number of such lesions, this chapter will address only some of the more common ones and discuss pertinent differential diagnoses.

SKIN AND SUBCUTANEOUS LESIONS

The skin (integument, cutis) is largely ignored on CT and MR imaging. In this section, the skin (epidermis, dermis, and the skin appendages including the pilosebaceous units [hair, sebaceous and apocrine glands, and associated smooth muscle fascicles]) and the immediate subcutaneous tissues are considered.

Diffuse thickening of the skin is most commonly seen in edematous and inflammatory conditions. However, diffuse skin thickening can also be seen after irradiation or, rarely, with tumor infiltration. Almost always, there is associated thickening of the subcutaneous fat and injection of this fat with a rete-type pattern of soft tissue representing dilated lymphatic and vascular capillaries and venules. In addition, after trauma there can be subcutaneous hemorrhage and hematoma (Figs. 41-1 to 41-3). When clinical and imaging distinction between these entities is difficult, serial imaging may offer increased specificity: hematomas tend to show evolution and resolution; there is relative stability or improvement with radiation changes; and tumors may progress to variable degrees, depending on their histology and aggressiveness. Phlegmon, a collection of watery fluid within the interstitial tissues and spaces of the neck, is usually associated with an acute suppurative inflammation.

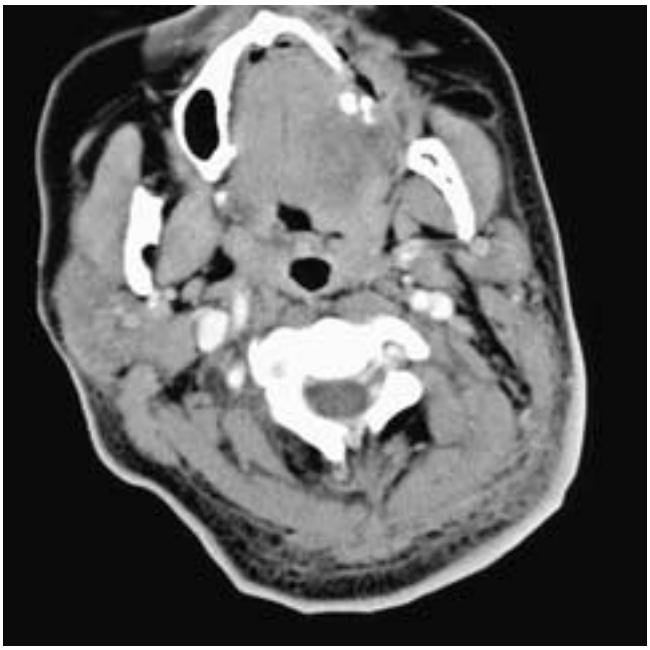

FIGURE 41-2 Axial contrast-enhanced CT scan shows marked thickening of the skin and subcutaneous tissues of the left posterior neck, all secondary to a cellulitis from a skin infection.

VIEW IMAGE

Copyright © 2003, Mosby, Inc. All rights reserved.

Cellulitis can be seen with simple phlegmon or abscess, with an abscess distinguished from phlegmon by the presence of an enhancing rim (Fig. 41-1B). Further examples of these changes can be seen throughout other sections in this book.

Scar

Scar formation occurs whenever there has been an ulceration or laceration of the skin. The type of scar often reflects the pattern of healing; thus, a scar may be flat, hypertrophic, or atrophic. It may also be firm or, as a result of collagen proliferation, hard. The skin appendages and skin lines are usually lost within the scar bed. On imaging, scars may vary significantly in appearance. The routine flat scar may not be clearly seen, so the only clue to the surgical line may be an infolding of the skin. Conversely, there may be an obvious skin thickening, often in conjunction with subcutaneous scar extending almost as deeply as the muscle line (Fig. 41-4).

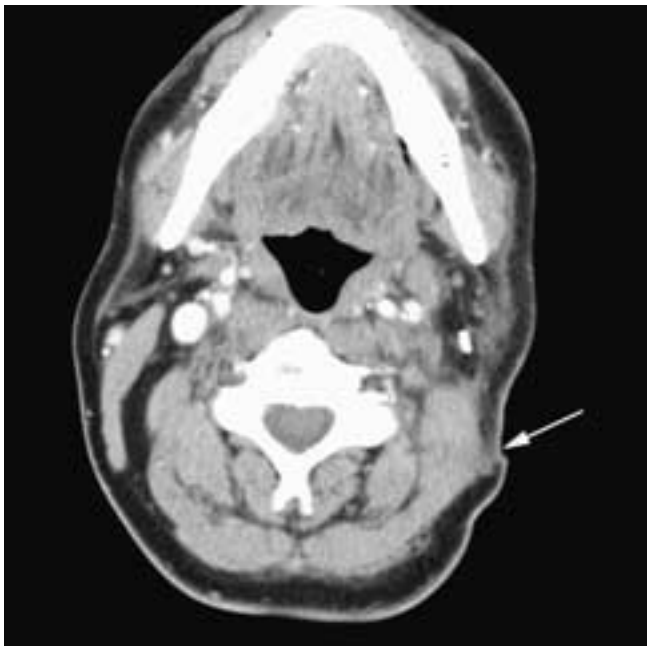

FIGURE 41-4 Axial contrast-enhanced CT scan on a patient who had a left radical neck dissection. A surgical clip is seen in the left neck. Note the thin scar line (*arrow*) and the relatively small amount of fibrosis within the subcutaneous tissues. Minimal edematous change is seen in the adjacent subcutaneous tissues.

VIEW IMAGE

Hypertrophic Scar

A hypertrophic scar usually develops when wound margins are placed under tension. The clinical features distinguishing hypertrophic scars from keloids include the observation that hypertrophic scars remain confined to the original scar line, and with time they tend to flatten out or regress spontaneously. Histologically, they lack hyalinized collagen bundles, and they contain little or no mucinous ground substance. Fibroblasts and foreign body granulomas are also common. Like keloids, these lesions have a higher water content than normal scar and skin, although the water content tends to diminish as the scars age.[1] While distinction from keloids may prove difficult by CT, studies on resected tissue have shown that the T1-weighted signal intensity of hypertrophic scar tends to reach normal levels within 1 to 2 years, unlike keloid, in which the T1-weighted signal intensity may take 10 years to normalize.[1] Treatment of hypertrophic scars is similar to that of keloids, but only about 10% of hypertrophic scars recur.[2]

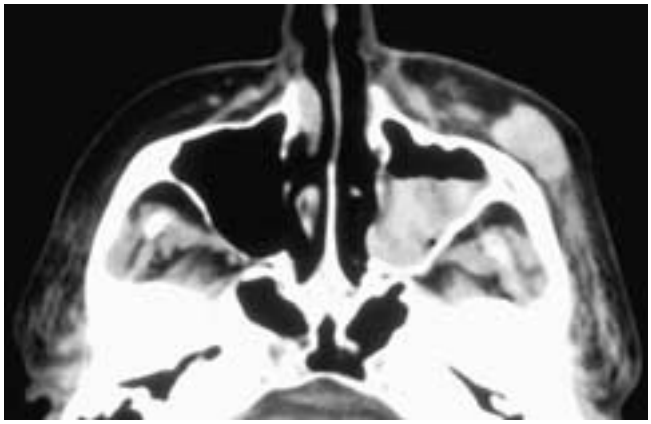

FIGURE 41-3 Axial CT scan shows a soft-tissue density in the subcutaneous tissues of the left facial area representing hematoma. There are also edematous changes in the adjacent soft tissues due to edema. There is dense fluid in the left maxillary sinus. This patient fell and developed a hematoma and edema in the left face with hemorrhage in the left antrum.

VIEW IMAGE

Keloid

Keloids are benign overgrowths of dermal scar tissue that usually develop after local trauma, although sometimes there has been no identifiable insult. They are more common in dark-skinned individuals and in people with blood group A, and a family history may be present. Their growth may be accelerated by pregnancy and puberty. Keloids are slightly more common in women, and most arise in people between 10 and 30 years of age, probably due to the higher incidence of trauma and acne in this age group.[2]

About 70% of postsurgical keloids develop within 6 months of surgery, but up to 17% may appear one year or more after surgery. Most keloids are significant only because of their cosmetic nature, although some may be associated with pruritis, pain, and/or paresthesias. Despite the fact that their borders are usually well demarcated, they tend to be irregular in outline. Keloids usually grow outward from the original scar line and extend into adjacent tissues. On imaging, they are bulky soft-tissue masses that project away from the skin line (Fig. 41-5). There may be subcutaneous infiltration, often related to prior surgery rather than directly to the keloid. Histologically, keloids are composed of thick, glassy, eosinophilic or hyalinized bundles of collagen, often associated with abundant mucinous ground substance. The bulky overgrowth of tissue may reflect an attempt to duplicate the tensile strength of normal skin within this disordered collagen-containing scar tissue. Treatment of

Copyright © 2003, Mosby, Inc. All rights reserved.

keloids includes excision, irradiation, and injection with corticosteroids, although up to 63% may recur after treatment.[2]

Epidermoid Cyst (Sebaceous Cyst)

The epidermoid cyst—the commonly used term *sebaceous cyst* is a misnomer—is the result of the proliferation of surface epidermoid cells within the dermis. The lining of many nontraumatic cysts is believed to be derived from the follicular infundibulum, as these cysts commonly develop from the occlusion of pilosebaceous follicles. Less common causes include the implantation of epidermal cells into the dermis secondary to a penetrating injury and the trapping of epidermal cells along the lines of embryonal fusion planes. These cysts are rare in children but common in adults, and patients with basal cell nevoid syndrome may have numerous lesions. On imaging, these cysts are ovoid in shape, with a noninfiltrating rim. The superficial margin of the cyst usually touches the deep skin line, and the cyst is filled with mucoid attenuation material and scattered dystrophic calcifications (Fig. 41-6).

These cysts are usually slowly growing, painless masses that elevate the skin and often have a central punctum that represents the plugged orifice of the pilosebaceous follicle. The cysts are filled with cheesy, keratinous yellow-white material. They may become infected; uncommonly, they may rupture, causing a foreign body reaction.[3]

The differential diagnosis includes pilar cyst of the scalp and face and steatocyst simplex.[4] Steatocysts are often confused with epidermoid cysts, although steatocysts can be distinguished by the yellow, oily fluid that they contain.

Pilomatrixoma

Pilomatrixoma, or calcifying epithelioma of Malherbe, is an uncommon benign neoplasm of hair follicle origin. These neoplasms favor the hair-bearing areas, and approximately half of the reported tumors have been in the head and neck region. The majority of cases have been reported in patients in their first two decades of life; however, there is a second peak of occurrence in older patients. Overall, there is a female predominance.

Histopathologically, there are hair matrix–like basaloid cells and shadow or ghost cells, which have a central unstained area that represents a shadow of a lost nucleus. Intracellular and stromal calcification is reported in about 70% of cases, and tumors with large areas or nests of shadow cells proportionally have increased calcium deposition. It has been suggested that osteopontin, a protein marker associated with bone production, may be produced by macrophages and play a role in the deposition of calcium phosphate in the shadow cell nests.

The typical patient presents with an asymptomatic, superficial, solitary, firm mass that is located either within the dermis or in the subcutaneous fat, with tethering to the dermis. The overlying skin often has a reddish-blue discoloration. Even though these tumors usually grow slowly (months to years), excision is usually recommended to avoid a foreign body reaction, associated inflammation, and resulting scar formation. Complete surgical excision is

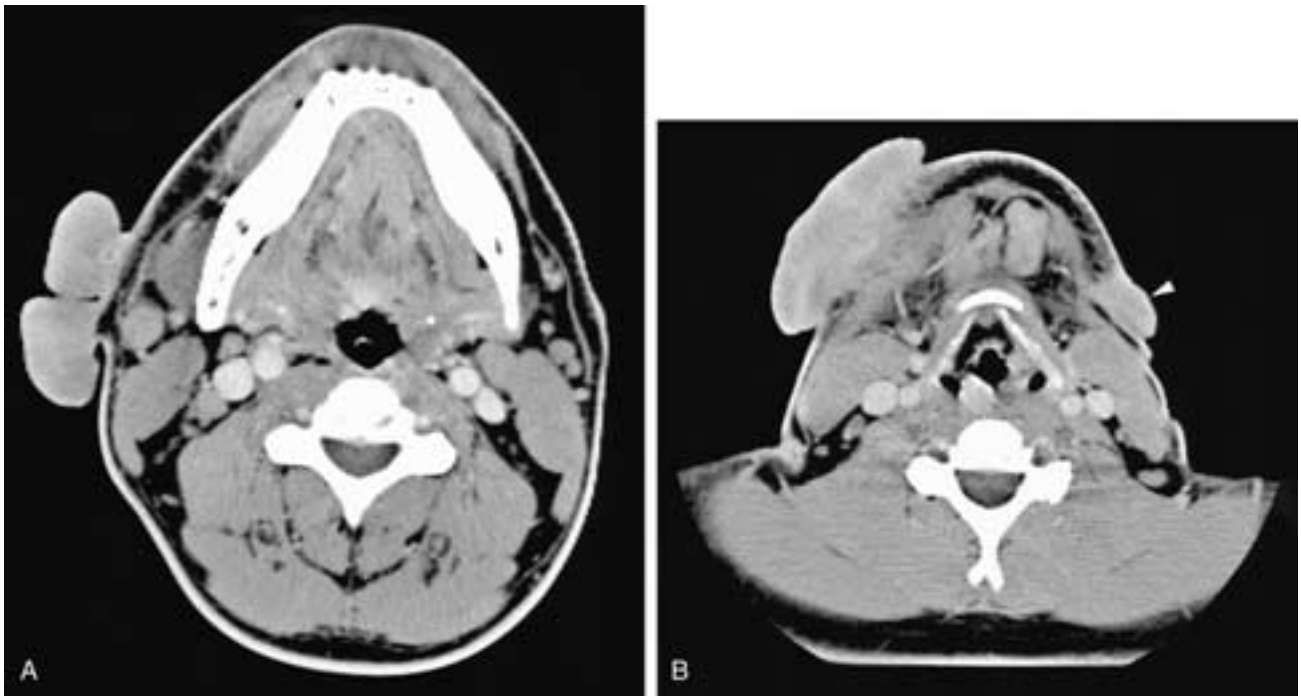

VIEW IMAGE

FIGURE 41-5 Axial contrast-enhanced cranial (**A**) and caudal (**B**) CT scans show a huge keloid in the right neck. Although there is some subcutaneous extension along the scar line, the vast majority of the mass is superficial to the skin. A second smaller keloid is present in the left neck (*arrowhead* in **B**). Incidentally noted is level I reactive adenopathy.

Copyright © 2003, Mosby, Inc. All rights reserved.

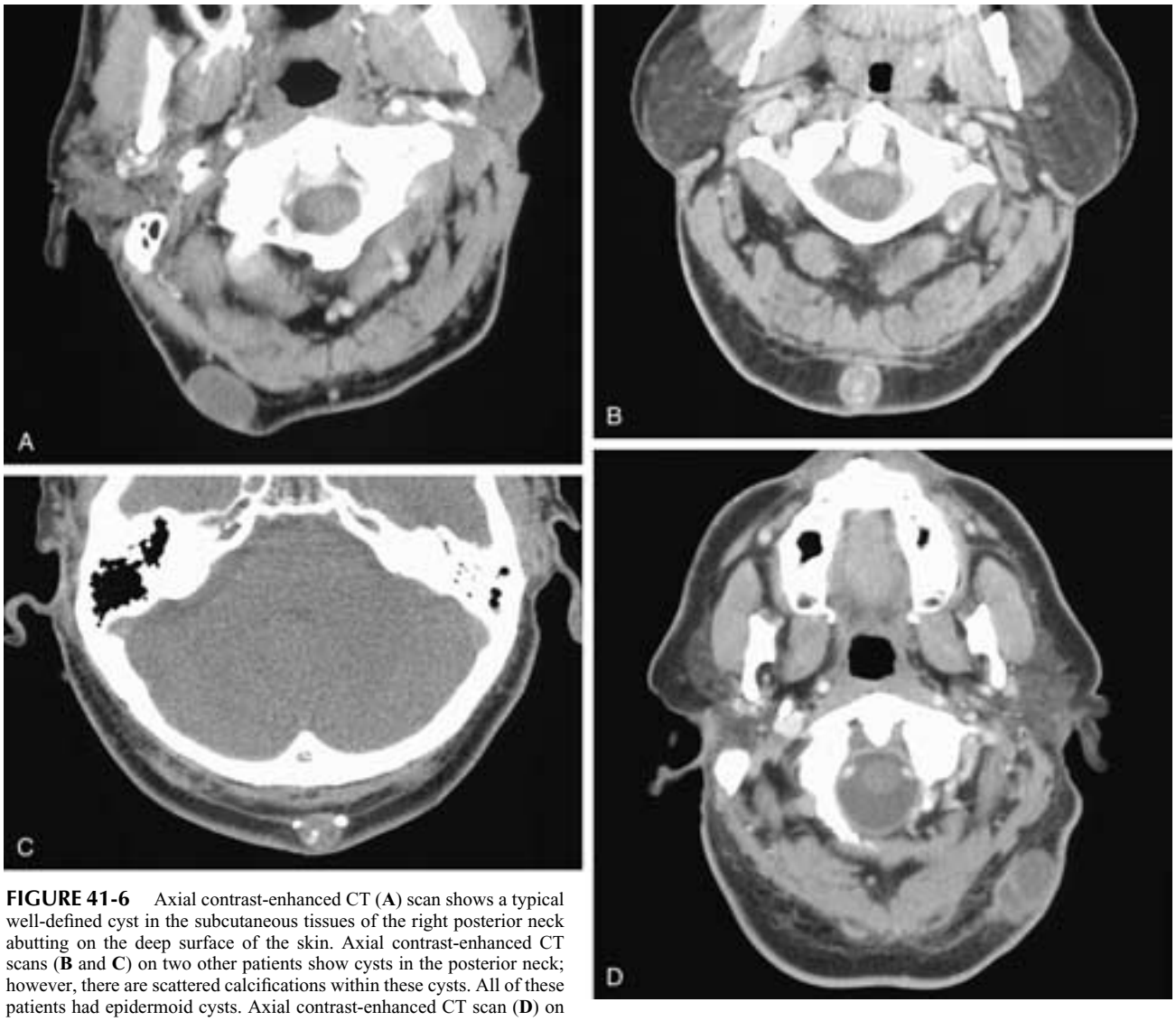

VIEW IMAGE

FIGURE 41-6 Axial contrast-enhanced CT (**A**) scan shows a typical well-defined cyst in the subcutaneous tissues of the right posterior neck abutting on the deep surface of the skin. Axial contrast-enhanced CT scans (**B** and **C**) on two other patients show cysts in the posterior neck; however, there are scattered calcifications within these cysts. All of these patients had epidermoid cysts. Axial contrast-enhanced CT scan (**D**) on another patient shows an infected cyst in the left neck. Note the enhanced, thickened posterior border of the cyst. Clinically, pus from this sebaceous cyst was evident.

curative. Multiple tumors account for 2% to 3.5% of reported cases, and there have been reported rare associations with myotonic muscular dystrophy, Gardner's syndrome, sarcoidosis, and skull dysostosis. A rare familial occurrence not associated with other syndromes has also been reported.[5]

On CT, the lesion appears as a noninfiltrating mass in the subcutaneous fat with varying degrees of focal calcification. There is no significant enhancement with iodinated contrast. The tumor margin cannot be separated from the epidermis; hence, the mass appears contiguous with the overlying skin. There is no extension into the underlying musculature (Fig. 41-7). Pilomatrixomas have a variable appearance on MR imaging, ranging from intermediate to slightly hyperintense on T1-weighted images and slightly hypointense to slightly hyperintense on T2-weighted images. One report suggests that bands of increased T2-weighted signal intensity seen extending from the periphery of the lesion to its center may represent basaloid sheets identified histologically.[6] No gadolinium enhancement has been described. On ultrasound, this well-defined lesion is typically hyperechoic centrally, with a thin hypoechoic rim; distal shadowing from calcifications is common.[7]

The differential diagnosis includes sebaceous cyst, foreign body reaction, ossifying hematoma, giant cell tumor, chondroma, dermoid cyst, degenerating fibroxanthoma, metastatic bone formation, and osteoma cutis. The very rare malignant counterpart of the pilomatrixoma is the pilomatrix carcinoma, which is characterized by vascular and muscle invasion as well as local recurrence following resection. Distant metastases are uncommon but have been reported. The differential diagnosis of this malignancy includes basal cell carcinoma with matrical differentiation, matricoma, and metastasis.[5] Proliferating trichilemmal tumors, which may appear similar to invasive pilomatrixomas, are instead likely to arise from trichilemmal cysts that have been exposed to trauma or inflammation.[4]

Copyright © 2003, Mosby, Inc. All rights reserved.

Basal Cell Carcinoma

Basal cell carcinoma is the most common type of skin carcinoma. It is more common in males and rarely occurs in dark-skinned people or Asians. The increased incidence in individuals with light hair, light skin, inability to tan, and prolonged sun exposure has long implicated actinic damage in the pathway of basal cell carcinoma development. In addition, patients who have basal cell carcinoma are three times more likely than the normal population to develop another UV–related malignancy, melanoma.[8] Basal cell carcinomas tend to occur in the central midface. Prognostically, these tumors tend to be more aggressive than basal cell tumors at other head and neck sites.[2]

After tumor site, histologic type is the most important factor in determining the prognosis. Overall, basal cell carcinomas rarely metastasize (0.1%), but tumors with squamous differentiation and/or an adenoid pattern occurring about the orbits have the highest incidence of metastasis. Perineural, lymphatic, and vascular-type metastasis can occur, and once metastasis has developed, the average survival is only 1 to 2 years. Histologic analysis shows that basal cell carcinomas grow into the dermis as cords, strands, and sheets of small basaloid cells; centrilobular necrosis is not uncommon.[9] Surgery is the treatment of choice.[2]

On imaging, basal cell carcinomas have a variable appearance, depending on the size of the tumor at the time of imaging. When small, they are soft-tissue masses in the skin line, usually with deep extension into the subcutaneous tissues (Fig. 41-8). When large, they appear as deeply infiltrating soft-tissue masses. Basal cell and squamous cell carcinomas can be difficult to distinguish by imaging, although secondary findings such as adenopathy favor the latter.

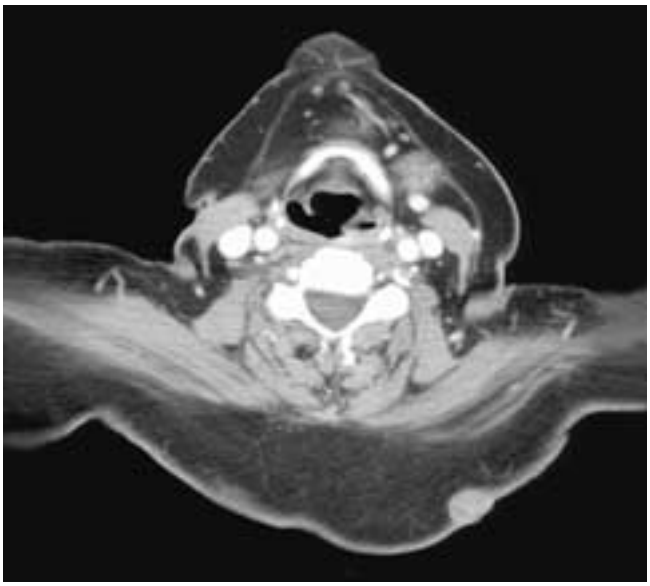

FIGURE 41-8 Axial contrast-enhanced CT scan shows a mass in the skin line of the left posterior neck. The deep margin is unsharp in some areas. This patient had a basal cell carcinoma.

VIEW IMAGE

Basal cell nevoid syndrome (Gorlin syndrome, Gorlin-Goltz syndrome) is an autosomal dominant disorder in which patients develop multiple basal cell carcinomas (especially at a young age), odontogenic keratocysts, palmar and plantar pitting, falx and dural calcifications, and skeletal malformations. Associations with many other benign and malignant tumors have also been reported. Other conditions in which relatively young patients develop basal cell carcinomas include xeroderma pigmentosum and nevus sebaceus.

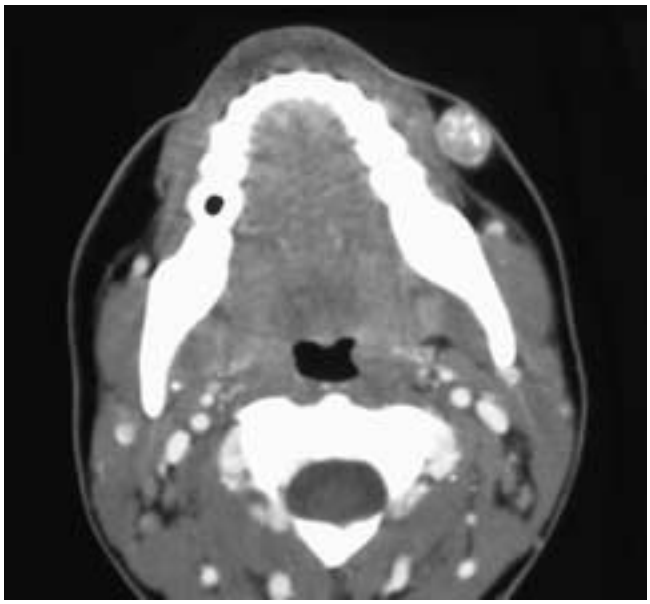

FIGURE 41-7 Axial contrast-enhanced CT scan shows a well-defined cystic-appearing mass with scattered calcifications in the subcutaneous soft tissues of the face. There is a broad margin of the mass abutting the deep aspect of the skin. This patient had a pilomatrixoma. Note the imaging similarity to a epidermoid cyst (Fig. 41-6).

VIEW IMAGE

Squamous Cell Carcinoma of the Skin

Squamous cell carcinoma of the skin commonly occurs in the head and neck. These tumors can arise de novo or in preexisting lesions such as actinic keratosis or squamous cell carcinoma in situ (Bowen's disease). There is a high incidence of squamous cell carcinomas in patients with hereditary skin diseases such as oculocutaneous albinism or xeroderma pigmentosum.[2] Men are more commonly affected than women (2:1), and most tumors arise in the sixth and seventh decades of life. Histologically, these are neoplasms of keratinocytes in the surface epidermis or in the epithelium of adnexal structures. Tumor typically penetrates the reticular dermis. The incidence of metastasis varies from 5% to 30%. Most researchers believe that the prognosis is not related to the histologic grade; however, the depth of invasion and the amount of surface area between the tumor and stroma may be related to the incidence of metastasis. Once squamous cell carcinoma of the skin has metastasized, the prognosis is poor, with 57.3% of patients dead of their disease within 5 years.[2]

Copyright © 2003, Mosby, Inc. All rights reserved.

Melanoma

Melanoma is a highly malignant tumor of melanocytes derived from the neural crest. The primary factor associated with the development of melanoma is excessive exposure to UV radiation, so patients with benign (melanocytic) nevi, freckles, dysplastic nevi, and a history of three or more severe sunburns are all at increased risk. Lymphoscintigraphy has proven useful in defining drainage pathways and suggesting which nodes are most likely to harbor metastatic deposits. Approximately one fourth of supraclavicular cutaneous melanomas arise on the neck; the second most common site is behind the scalp (36%); less frequent sites include the face (22%) and ear (14%).[10]

Numerous studies indicate that females have a better prognosis than males, possibly due to earlier detection and treatment. A possible increase in melanoma progression due to pregnancy and female hormone replacement therapy has recently been disproven.[11] Factors associated with improved survival include age less than 60 years and thinner lesions with less invasion.[12] The 10-year survival rate has been reported as high as 70% in males and almost 90% in females, although most studies report an overall 5-year survival rate of about 70%.[12, 13] Approximately 15% of patients die from their melanoma, and only 5% of patients with metastatic melanoma remain recurrence free for the remainder of their lives.[14] Mucosal melanomas are also associated with significant morbidity; these are discussed in Chapter 6.

Merkel Cell Tumor

Merkel cell tumor (trabecular carcinoma, cutaneous small cell undifferentiated carcinoma, primary neuroendocrine carcinoma) is an undifferentiated tumor of the skin, which in the elderly may clinically mimic a basal cell carcinoma. The typical patient is Caucasian and above 50 years of age.[15] As in melanoma, a neural crest origin is suspected. Approximately 25% of patients also develop squamous cell carcinoma in the same region, either separately or interspersed within the Merkel tumor itself.[9] Overall, the incidence correlates with sun exposure, and the head and neck region may account for two thirds of all cases, although the extremities and buttocks are also frequent sites (Fig. 41-9).[16] Patients with B-cell malignancies who have undergone organ transplantation are also at increased risk.[15] The Merkel cell tumor is usually identified as a slow growing nodule. The vast majority of patients present with localized skin lesions and no nodal disease. However, these are aggressive tumors and should be treated by wide surgical excision. Median survival is 29 months, with evidence that radiotherapy improves absolute 5-year survival (38% vs. 27%).[16, 17] Local recurrence occurs in about a third of patients, while nodal metastases are seen in 50% and visceral metastases in 15%.[2]

Skin Metastasis

Metastasis to the skin has been reported from a number of primary head and neck tumors, as well as from most of the common primary neoplasms arising below the clavicles.[18–27] In all cases, such metastases carry an associated dire prognosis. On imaging, the skin line soft-tissue mass is similar in appearance to a basal cell or squamous cell carcinoma (Fig. 41-10). Tumor implantation has also been reported about the tracts of drains placed during resection of numerous malignancies.

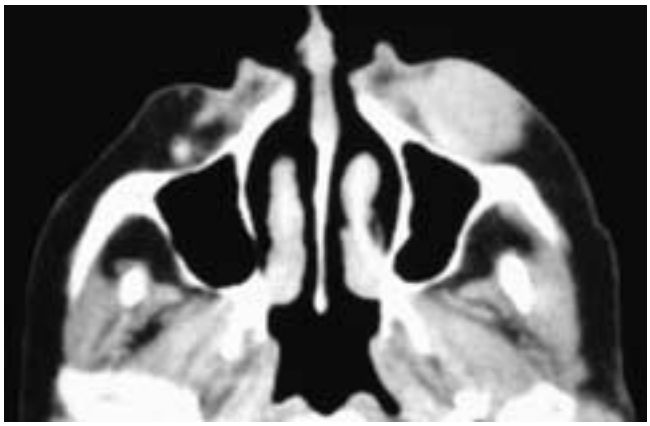

FIGURE 41-9 Axial CT scan shows a soft-tissue mass in the subcutaneous tissues of the left face. Portions of the contour of the lesion are unsharp, suggesting focal infiltration. This patient had a Merkel cell tumor.

VIEW IMAGE

Subcutaneous Fat Necrosis of the Newborn

Subcutaneous fat necrosis of the newborn (SCFN) is a condition affecting full or postterm infants, starting days to weeks after a complicated perinatal period. It is characterized by the appearance of one or more well-defined,

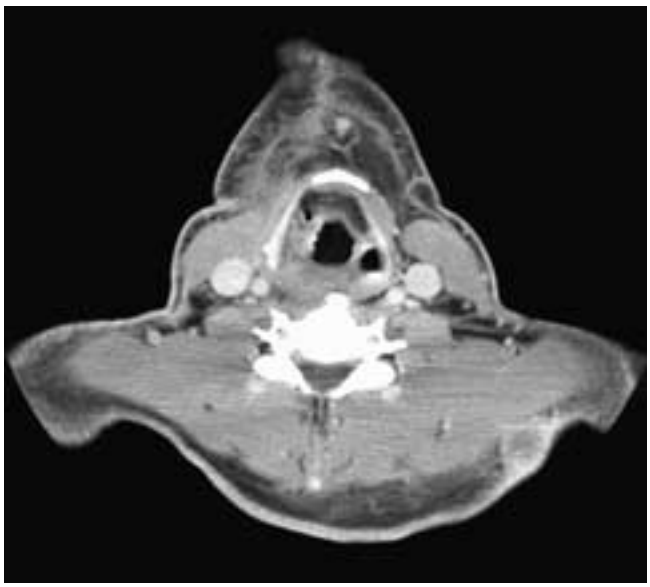

FIGURE 41-10 Axial contrast-enhanced CT scan shows a mass in the skin and subcutaneous tissues of the left posterior neck. The margins of the lesion are unsharp. This was a rare skin metastasis from a pharyngeal squamous cell carcinoma. Note the postoperative changes in the right anterior neck from the primary tumor resection.

VIEW IMAGE

Copyright © 2003, Mosby, Inc. All rights reserved.

nonsuppurative, erythematous or violaceous, mobile subcutaneous masses, often with taut overlying skin. There is usually a history of obstetric manipulation, perinatal asphyxia, meconium aspiration, or maternal disease. The typical lesions develop on the shoulders, back, buttocks, thighs, and cheeks. It has been postulated that these lesions result from localized tissue hypoxia and mechanical pressure, which further compromises the local circulation. It has also been suggested that thrombocytosis may play a role in the pathogenesis of adipose tissue necrosis by reducing blood perfusion, leading to relative hypoxia and hypothermia. The nodules of SCFN may enlarge for several weeks to months but then usually involute. Rare local complications include epidermal atrophy, ulceration, scarring, or infection.[28]

Pathologically, SCFN is characterized by clusters of adipocytes, histiocytes, fibroblasts, scant lymphocytes, and numerous foreign body giant cells. Granulomatous fat necrosis and calcifications are seen. Hypercalcemia is the most serious complication associated with SCFN; it is believed to be caused by an excess production of 1,25-dihydroxyvitamin D by the granulomatous macrophages. Because hypercalcemia may occur anytime from 1 to 6 months after the skin lesions first develop, these neonates should have calcium levels monitored for at least 6 months. The radiologist should monitor for possible renal complications of hypercalcemia, and renal ultrasonography is recommended to exclude nephrocalcinosis and nephrolithiasis. Other clinical associations with hypercalcemia include hypotonia, vomiting, anorexia, irritability, and failure to thrive.[29]

On CT, the lesions of SCFN appear localized to the subcutaneous tissues immediately deep to the skin. The nodules may have minimally infiltrative margins and areas of central low density only slightly higher in attenuation than that of fat. The nodules may partially obliterate the fat planes over the superficial margin of an adjacent deep muscle; however, the muscle itself and the deeper fat planes about the muscle are normal. There also may be a diffuse subcutaneous fullness with increased attenuation in the fat, without a discrete mass (Fig. 41-11).

Linear or sheet-like areas of diminished signal are typically seen on both T1-weighted and T2-weighted images, although increased signal intensity may also be noted on T2-weighted images. Findings are even more conspicuous on fat-suppressed, inversion recovery sequences, where involved areas appear bright.[29]

If the clinical situation warrants, fine needle aspiration of the subcutaneous lesions may be useful to confirm the diagnosis. The finding highly suggestive of SCFN is negatively stained, needle-shaped crystals within histiocytes and multinucleated giant cells. The main reason to establish the diagnosis of this self-limiting entity is to differentiate it from other lesions that may require surgery. The principal clinical differential diagnosis includes other histologically distinct soft-tissue lesions of infancy such as rhabdomyosarcoma, the spectrum of fibrous lesions, hemangioma, neurofibroma, and sclerema neonatorum.[28]

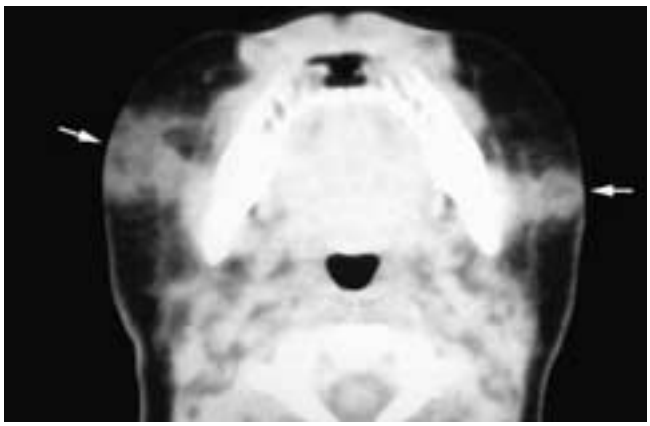

VIEW IMAGE

FIGURE 41-11 Axial CT scan shows a partially infiltrative-appearing subcutaneous soft-tissue mass (*arrows*) in each side of the face. This newborn had subcutaneous fat necrosis.

Sclerema Neonatorum

Sclerema neonatorum is a rare disease of the newborn that is characterized by a diffuse hardening of the subcutaneous adipose tissues. As such, it is distinct from the localized lesions of SCFN. Sclerema appears within the first postnatal week in neonates who are severely ill with pneumonia, peritonitis, or other infectious or congenital diseases. Premature infants are particularly susceptible, and the prognosis is grave. Sclerema may represent a disorder of lipolysis.[30] Histologic analysis has demonstrated subcutaneous fibrosis in all patients, with most having chronic dermal inflammation, epidermal thinning, and hypercollagenization of the dermis.[31]

Plexiform Neurofibroma and Skin Neurofibromas

The presence of a plexiform neurofibroma is sufficient to warrant the diagnosis of von Recklinghausen's disease even in the absence of other associated stigmata. A plexiform lesion can be seen as a fusiform or nodular mass, or as a tortuous enlargement of nerves that has been described as a ''giant nerve'' or ''bag of worms.'' In the head and neck, these lesions are often seen in the subcutaneous tissues (Fig. 41-12). The degree and pattern of calcification vary.

Another manifestation of neurofibromatosis is the presence of multiple neurofibromas on the skin, in addition to neurofibromas within the neck and facial region (Fig. 41-13). A discussion of both neurofibromas and schwannomas also appears in Chapter 6.

Silicon Augmentation

Silicon and silicon products have long been used as tissue expanders and for cosmetic surgery.[32] Historically, silicon had been injected subcutaneously to fill skin contours. Unfortunately, free silicon often invokes a granulomatous and fibrotic reaction that ultimately causes further deformity

Copyright © 2003, Mosby, Inc. All rights reserved.

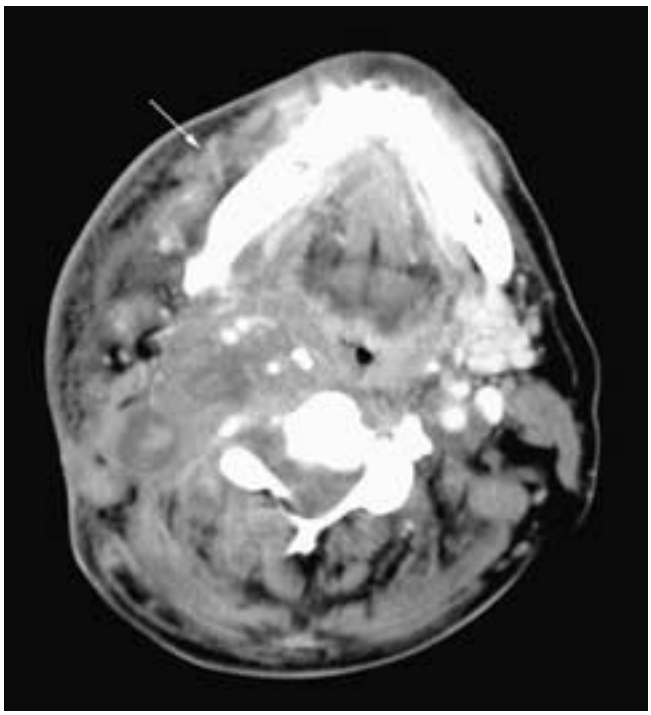

FIGURE 41-12 Axial contrast-enhanced CT scan shows multiple masses primarily in the right neck of this patient with neurofibromatosis. Some of the masses are partially cystic. In addition, in the subcutaneous right face there is a nodular, poorly defined soft-tissue mass with a few scattered calcifications (*arrow*) representing a plexiform neurofibroma.

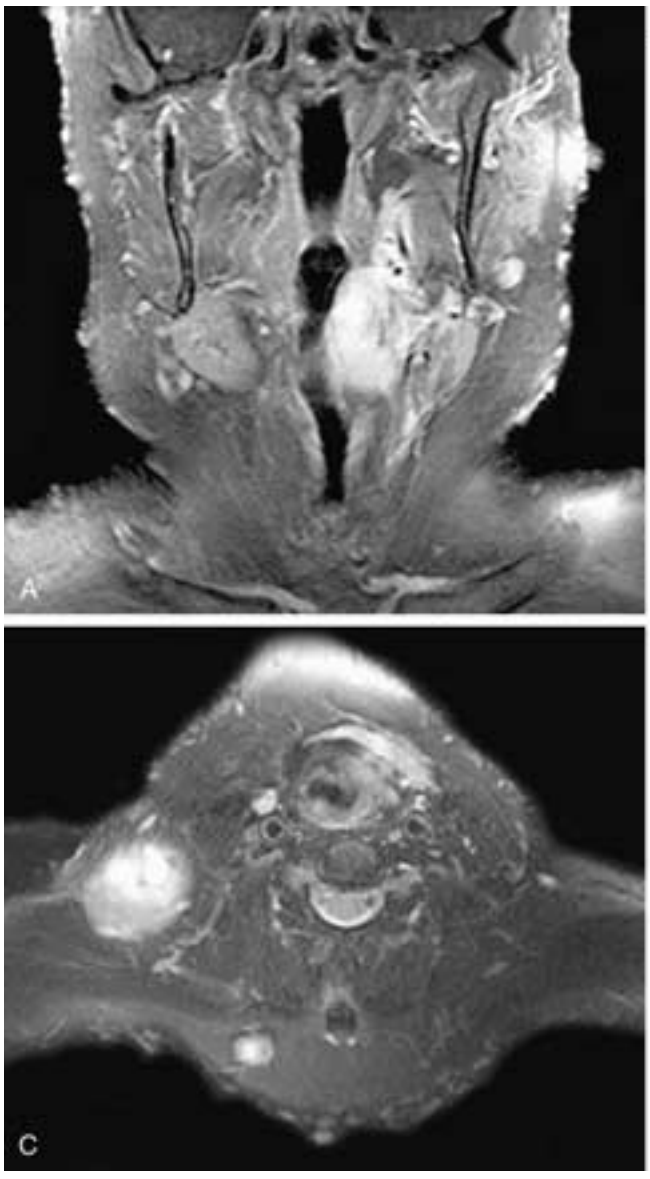

FIGURE 41-13 Coronal T1-weighted, fat-suppressed, contrast-enhanced MR image (**A**) shows an enhancing left hypopharyngeal neurofibroma and multiple small, enhancing skin neurofibromas. Axial T2-weighted MR image (**B**) shows the same hypopharyngeal neurofibroma and the innumerable skin neurofibromas. Axial T1-weighted, fat-suppressed, contrast-enhanced MR image (**C**) on another patient shows neurofibromas in the right supraclavicular fossa, the right back soft tissues, and the anterior left neck. In addition, there are multiple skin neurofibromas.

Copyright © 2003, Mosby, Inc. All rights reserved.

FIGURE 41-14 Axial contrast-enhanced cranial (**A**) and caudal (**B**) CT scans show areas of both increased density and intermediate density in the swollen subcutaneous soft tissues of both sides of the face. This patient had had silicon (increased density) injected in his cheeks several years earlier and then formed a foreign body reaction (intermediate density) to the silicon. Axial CT scan (**C**) shows a silicon insert (*arrow*) overlying the right zygoma. This is a fairly typical appearance of recent facial augmentation procedures.

VIEW IMAGE

of the overlying skin. On imaging, one sees thickening of the overlying skin, soft-tissue nodularity within the subcutaneous tissues, and scattered radiodensities (silicon) within this process (Fig. 41-14). If the fibrotic and granulomatous reactions are severe enough, there is considerable deformity of the skin contour. Silicon products are less frequently implanted today, and when used, they are encased in containers that cause little reaction in the adjacent soft tissues.

Alloderm Augmentation

Numerous materials, both autologous and nonautologous, have been used for augmentation of soft-tissue defects in the facial region. There is no ideal material for soft-tissue augmentation, as each material has its limitations. AlloDerm dermal graft (LifeCell Corporation, Branchburg, NJ) combines the benefits of autografts and allografts. There is a very low incidence of complications such as rejection, mobilization, absorption, dislocation, or extrusion. In addition, the use of Alloderm minimizes two surgical problems: donor site morbidity and lack of adequate tissue for reconstruction. Alloderm has been shown to be useful in facial plastic procedures and the repair of burn injuries.[33–42] On CT, Alloderm is of a fairly high attenuation, being greater than that of muscle but less than that of bone (Fig. 41-15). On MR imaging, if seen, it usually has a low-intermediate signal intensity on all sequences.

Foreign Bodies

In addition to surgically placed materials, foreign bodies may be identified following perforation or laceration. Overall, perforations are uncommon, and their major manifestations arise deep to the skin and subcutaneous tissues. Most foreign bodies in the neck are ingested and, after perforating the mucosa, migrate outside the pharynx or cervical esophagus. Oral cavity or oropharynx perforations (especially those involving the tonsillar pillars) are not uncommon in young children, who tend to walk, run, and fall with objects in their mouths; care must also be taken to exclude carotid injury. Finally, penetrating injuries from bullets, wires, knives, and other objects can result in retained foreign bodies. Focal lucency within soft tissues immediately following penetrating trauma often represents gas; however, hypodense foreign bodies made of plastic, glass, or wood can appear similar. While the density of many of these bodies may not change over time, that of rehydrated wood may gradually approach soft-tissue density. Gas may also be generated by certain bacteria in infected wounds. If not removed, foreign objects can cause abscess or pseudoaneurysm formation, or the foreign body can migrate into the chest, spine, or even intracranially.[43–56]

In recent decades, the dietary preferences of many people have changed to favor more fish and fowl and less meat. The bones of chickens, quails, and so on are fairly large and well ossified, making identification on either plain films or CT

Copyright © 2003, Mosby, Inc. All rights reserved.

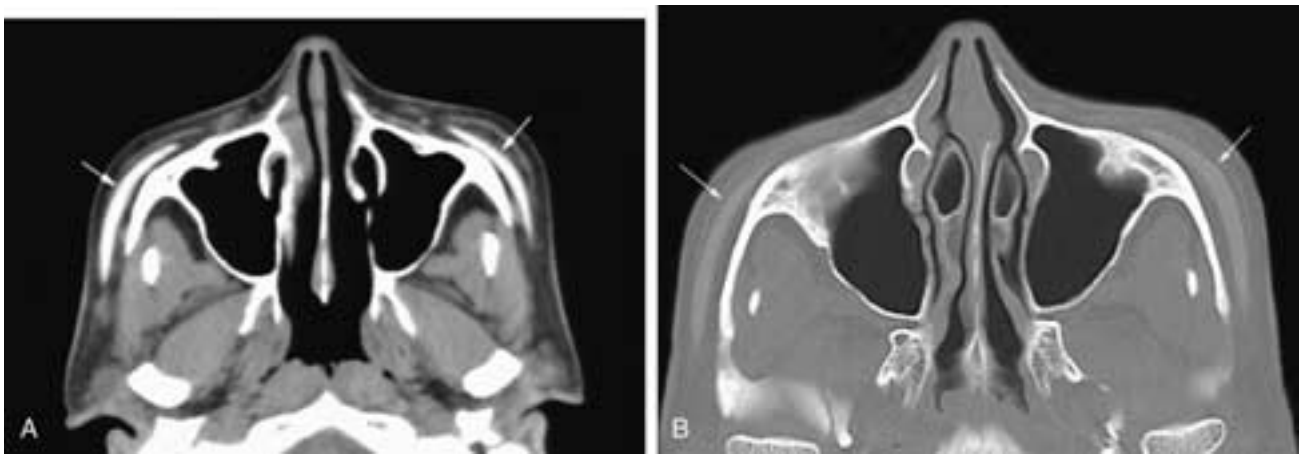

VIEW IMAGE

FIGURE 41-15 Axial CT scans at narrow (**A**) and wide (**B**) window settings on a patient who has had alloplast sheet (*arrows*) augmentations in her cheeks.

routine. However, special mention of the radiology of fish bones is warranted. Several studies have shown that CT examination identifies almost all types of fish bones, whereas plain films often fail to identify some varieties. Factors that affect the imaging identification of fish bones include the radiodensity of the fish bone, the orientation of the bone in relation to the imaging plane, and the location of the bone (e.g., tonsil, hypopharynx, cricopharyngeus, esophagus). Although there is some variation among reports, in general the bones of herring, salmon, mackerel, trout, blue fish, red fish, and pike are not well seen on plain films.[57–60] Thus, if one suspects that one of these varieties of bones has perforated, CT may provide greater sensitivity than plain film alone.

The bones of striped bass, sea bass, codfish, flounder, fluke, gray sole, haddock, halibut, porgie, red snapper, smelt, monk fish, plaice, gurnard, and white perch are all usually well seen on plain films and CT. Often on CT, the location of the fish bone is also identified by local enhancement due to an inflammatory reaction and small collections of air from the adjacent pharynx (Fig. 41-16).

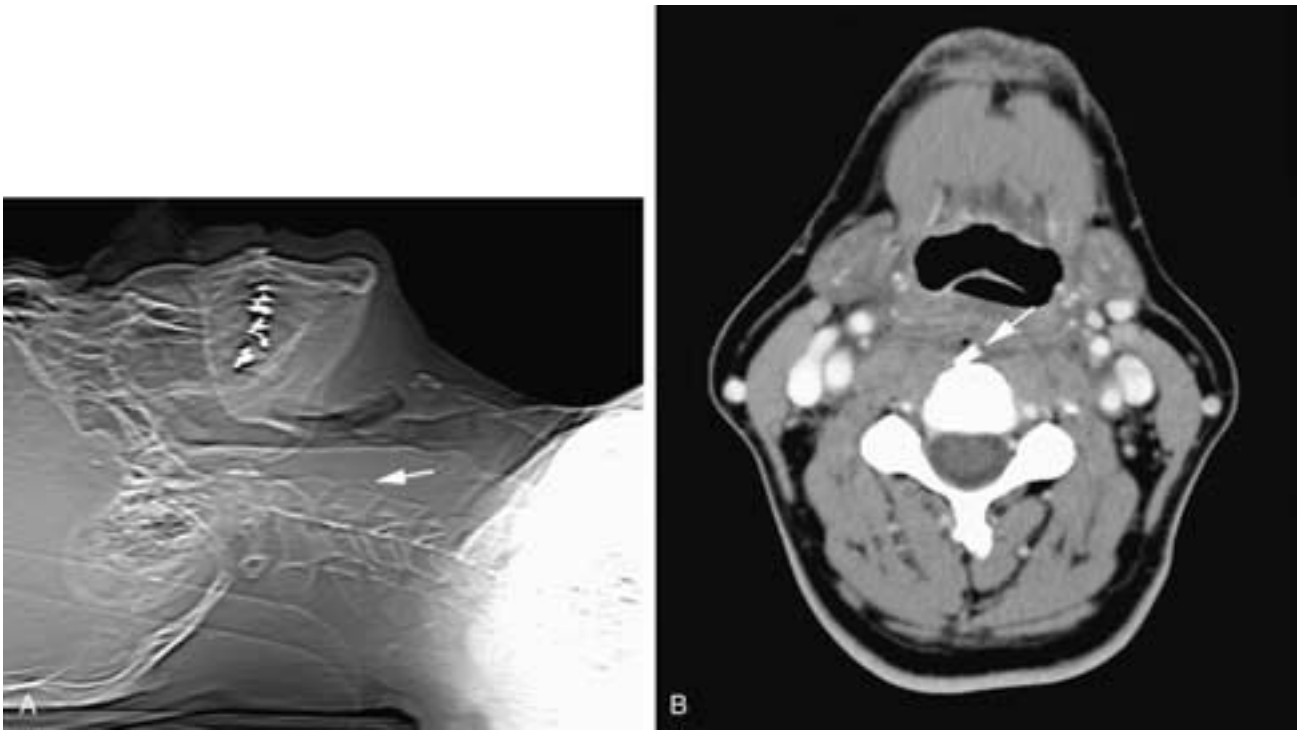

VIEW IMAGE

FIGURE 41-16 Lateral scout film (**A**) and axial contrast-enhanced CT scan (**B**). In **A**, there is marked thickening of the prevertebral soft tissues and flattening of the mucosal surface. A radiodense foreign body (*arrow*) is seen anterior to the C3 vertebral body. In **B**, the foreign body is well seen (*arrow*) with adjacent air and a water density phlegmon in the retropharyngeal space. In this patient, the foreign body was a flounder fish bone.

Copyright © 2003, Mosby, Inc. All rights reserved.

FAT-CONTAINING LESIONS

Ordinary Lipoma

Fatty or adipose tissue comprises 15% to 25% of the human body, although in obese individuals fat may represent over 40% of body weight.[61] Ordinary lipomas have been described in virtually every tissue of the body. In general, they are more common in females over the age of 40 years; however, in the head and neck, they may occur more frequently in males. The most common supraclavicular location is the posterior neck, with the anterior or lateral neck and the supraclavicular fossa also being frequent sites. Multiple lipomas may be seen in Gardner's syndrome, multiple endocrine neoplasia, neurofibromatosis, or, rarely, in familial lipomatosis, although lipomas are so prevalent that the vast majority are sporadic.[9] Once fat is within a lipoma, it cannot be utilized by the body, even in cases of profound starvation. Thus, when one gains weight a lipoma may enlarge, but when one loses weight the lipoma will not shrink.

Although there are various histologic types of lipoma (myxoid lipoma, angiolipoma, pleomorphic lipoma, spindle cell lipoma, and myelolipoma), on imaging they generally have smooth, noninfiltrative borders and contain almost exclusively fat (Fig. 41-17). Thus, on CT they have a low attenuation, while on MR imaging they have high signal on T1-weighted imaging and intermediate to high signal on fast spin-echo (FSE) T2-weighted imaging. Approximately 8% of ordinary lipomas contain less than 95% fat, in which case distinction from atypical lipomatous tumors may not be possible.[62] Rarely, hemorrhage can occur within an ordinary lipoma. In such cases, imaging shows a well-delineated mass with areas of high attenuation on CT and high signal on both T1-weighted and T2-weighted sequences.

Ultrasound characterizes lipomas as well-defined, compressible, elliptical masses with long axes parallel to the skin. Most are hyperechoic; however, one quarter are isoechoic or hypoechoic relative to muscle. Numerous echogenic lines are seen within the lipomas oriented parallel to the skin surface.[63] Detection of distal shadowing or distal augmentation suggests a different diagnosis.

Infiltrative (Intramuscular) Lipoma

Intramuscular lipomas are uncommon, benign unencapsulated tumors, also referred to as infiltrating lipomas because of their infiltrative growth pattern. Histologically, monovacuolar fat tissue is seen between muscle fibers and, in extreme cases, the muscle may be totally replaced by fatty tissue. Careful pathologic examination is necessary to avoid the mistaken diagnosis of a well-differentiated liposarcoma. Complete resection is often difficult, and the postoperative recurrence rate is 3% to 62%. In fact, incomplete resection is favored because development of muscle dysfunction due to fatty infiltration is gradual, and the patient tends to compensate well through recruitment of other muscles. By comparison, the rapid loss of function secondary to the surgical removal of a muscle is, in general, poorly tolerated.

On CT, the fatty mass is typically centered within the normal areas of adipose tissue within the neck. The MR findings of intramuscular lipoma can vary from those of a homogeneous ordinary lipoma to a large, inhomogeneous lesion with an infiltrative margin. The presence of infiltrative margins and intermingled muscle fibers in an intramuscular lipoma indicates a benign lesion rather than a malignancy, and such ingrowth of fatty tissue among the muscle fibers may be seen in up to one third of cases (Fig. 41-18).[64] In addition, uninodularity of the mass is helpful in differentiating intramuscular lipoma from the usually multinodular well-differentiated liposarcoma.[65–70]

Madelung's Disease

Multiple symmetric lipomatosis, described in Germany by Madelung in 1888 and in France by Launois and Bensaude in 1898, is a rare disease of unknown etiology. It is characterized by the presence of compartmentalized, but unencapsulated, fatty deposits in the neck and upper body. These deposits usually grow slowly, and their initial consequence is purely cosmetic. Rarely, however, they can lead to compression of the larynx, trachea, and cervical esophagus.

This disease usually affects middle-aged males of Mediterranean descent with a history of alcohol abuse. Although most cases have been sporadic, some investigators believe this disorder may be hereditary, and it is thought that this pathology originates from an alteration in lipid metabolism. Surgical removal of the fatty masses is the treatment of choice; however, recurrences are common.[71] The fatty deposits can be present virtually anywhere in the neck, but they are predominantly seen in the posterior neck deep to the trapezius and sternocleidomastoid muscles, in the supraclavicular fossa, and between the paraspinal muscles. Less often, the excess fat is seen in the anterior neck, superior mediastinum, pretracheal and prevertebral spaces, and over the cheeks.[72] On imaging, the compartmentalized appearance of the fat (Fig. 41-19) distinguishes the findings from obesity, in which there is a generalized increase in fat within the subcutaneous tissues (Fig. 41-20). The masses typically show no calcification or ossification, and there is no invasion of adjacent vascular structures.[72]

Liposarcoma

Liposarcomas represent 15% to 18% of all soft-tissue malignant tumors. They typically develop in the fourth through sixth decades and are more common in males. Liposarcomas are found mainly in the deep soft tissues, unlike lipomas, which usually arise superficially. With few exceptions, liposarcomas are believed to develop de novo and not from ordinary lipomas. About 3% occur in the head and neck, with most occurring in the neck and cheek.[61] The treatment of choice is wide surgical resection. Of the 25% to 46% of liposarcomas that recur, most are of the round cell or pleomorphic varieties.

On CT, liposarcomas can appear as ordinary lipomas or they can have variable scattered soft-tissue density (Fig. 41-21). In the more extreme cases, little fat is seen

Copyright © 2003, Mosby, Inc. All rights reserved.

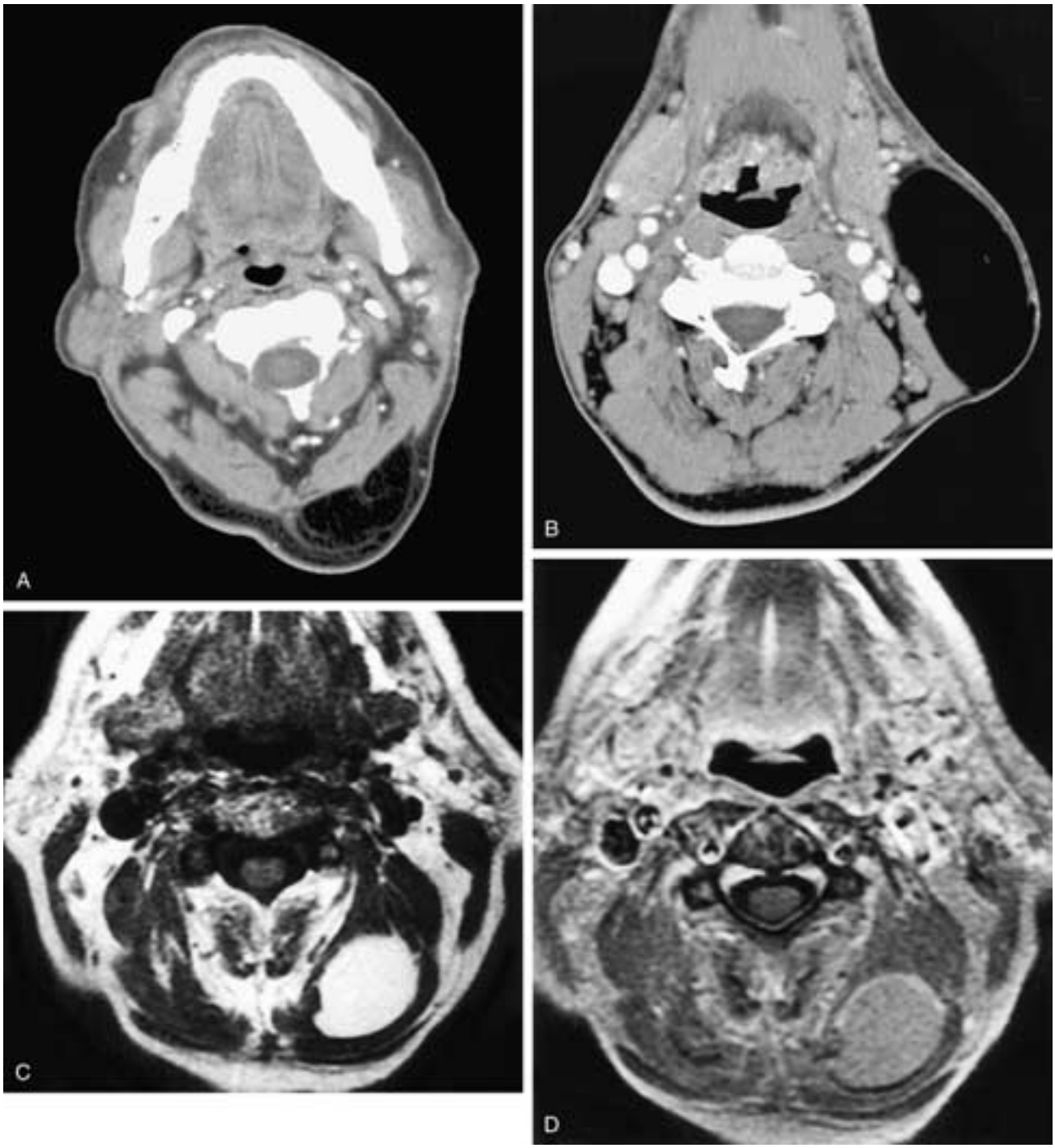

VIEW IMAGE

FIGURE 41-17 **A**, Axial contrast-enhanced CT scan shows a well-delineated fatty mass in the subcutaneous tissues of the back of the neck. **B**, Axial contrast-enhanced CT scan shows a well-delineated fatty mass in the subcutaneous tissues of the left neck. Despite the size of the mass, there are smooth, noninfiltrating borders. Axial T1-weighted image (**C**) shows a well-circumscribed high signal intensity mass situated between the left paraspinal muscles. The lesion is isointense to normal fat. **D**, Axial T1-weighted, fat-suppressed, contrast-enhanced MR image shows that the mass suppresses like normal fat. All of these patients had ordinary lipomas.

(Fig. 41-22). Well-differentiated liposarcomas can have a variety of MR imaging appearances. Typically, they have features suggestive of a benign lipoma (a well-defined mass with high T1-weighted and low-intermediate T2-weighted spin-echo [SE] signal intensities, with little or no contrast enhancement). In less well differentiated liposarcomas (myxoid, pleomorphic, and round cell), the majority of the tumor typically has a low T1-weighted signal intensity, and only scattered fatty islands and septa may be seen. T2-weighted images usually show most of the mass to be of intermediate to high signal intensity, with fatty islands of relatively low to intermediate signal intensity.[73] Much

Copyright © 2003, Mosby, Inc. All rights reserved.

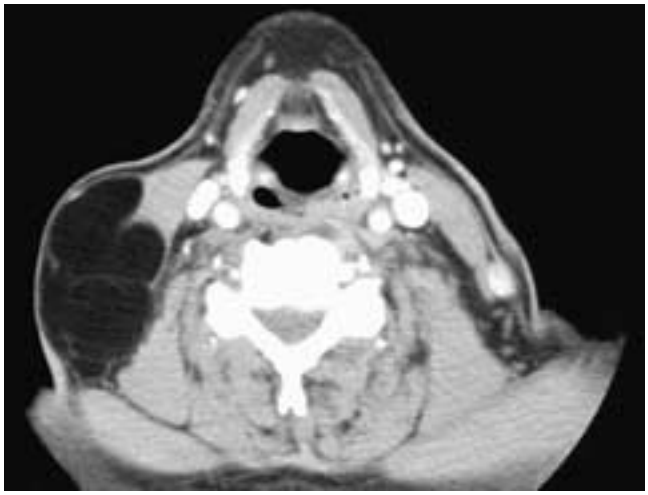

FIGURE 41-18 Axial contrast-enhanced CT scan shows a fat attenuation mass in the right neck. The mass invades the right sternocleidomastoid muscle. This patient had an infiltrating lipoma.

VIEW IMAGE

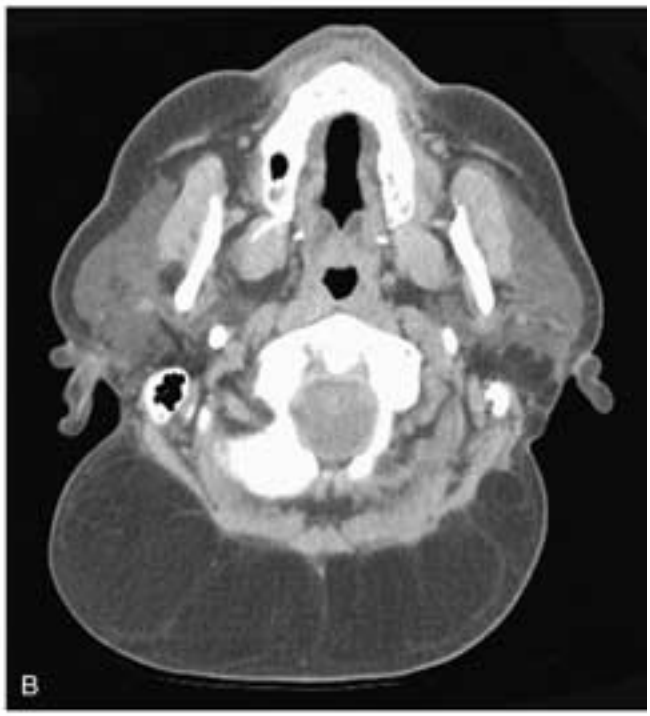

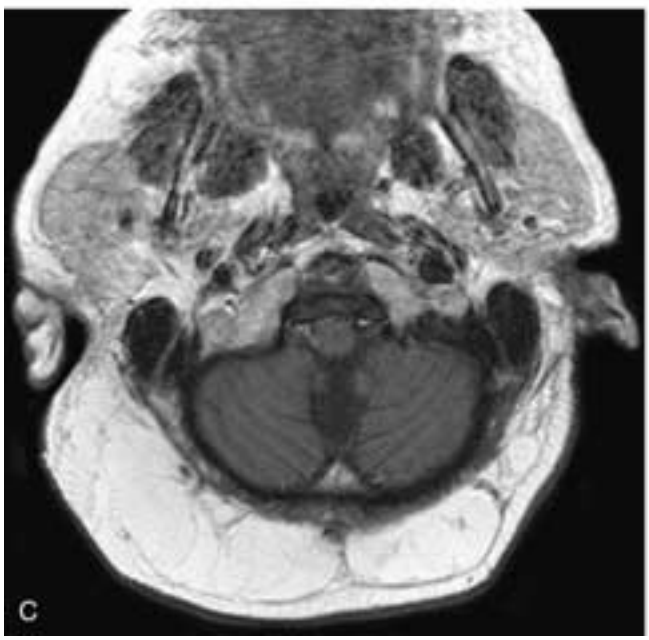

FIGURE 41-19 Axial CT scans (**A** and **B**) show multiple discrete fatty masses in the subcutaneous tissues of the back. Axial T1-weighted MR image (**C**) shows the well-delineated fatty collections in the posterior neck. This patient had Madelung's disease.

VIEW IMAGE

Copyright © 2003, Mosby, Inc. All rights reserved.

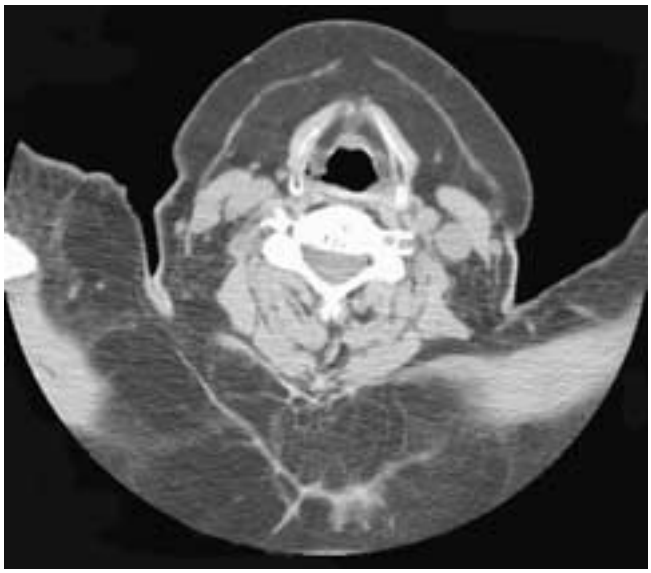

FIGURE 41-20 Axial CT scan shows extensive fat in the subcutaneous soft tissues of an obese patient. There are no discrete, well-defined collections of fat, as seen in Madelung's disease.

coarser stromal enhancement is seen in the less differentiated tumors.

INTERSTITIAL LESIONS

Fibrosarcoma

Although fibrosarcoma was once described as being among the most common sarcomas, the improved characterization of previously misdesignated fibromatoses has led to a lower reported incidence of fibrosarcoma. As a result, fibrosarcoma now lags well behind malignant fibrous histiocytoma in frequency.[74] Although it can be seen at any age, fibrosarcoma is most common in the fifth through eighth decades; a smaller peak is seen in the neonatal period and in infancy. There is an increased incidence in males and in sites of previous burn or radiation, but other radiation-induced sarcomas, such as malignant fibrous histiocytoma, are more common.

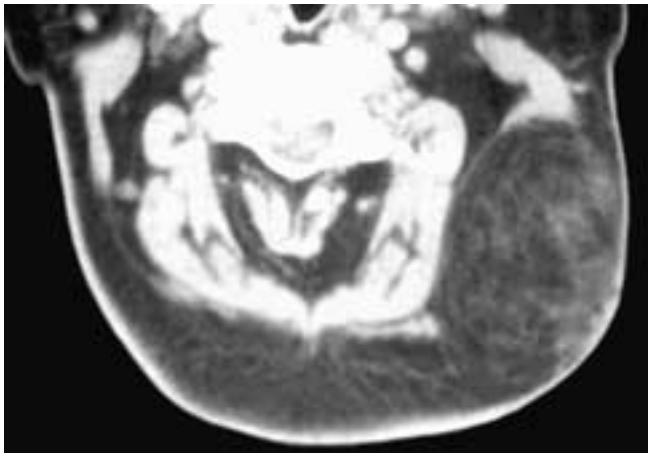

FIGURE 41-21 Axial contrast-enhanced CT scan shows a nonhomogeneous but primarily fatty mass in the posterior left neck. Portions of the lesion contour are well defined; others are poorly seen. This patient had a liposarcoma.

FIGURE 41-22 Axial contrast-enhanced CT scan on a patient who had had prior surgery on the pharynx and left neck for a liposarcoma. There was a sudden enlargement of the left neck, and this CT scan shows a well-defined, slightly enhancing, nonhomogeneous mass. At surgery, this was found to be a recurrent liposarcoma that had hemorrhaged.

Fibrosarcoma typically presents as a painless, slowly growing mass. It can arise superficially, from deep subcutaneous tissue, or deep within the soft tissues of the neck. Superficial tumors tend to be detected at a smaller size than deeper tumors.[74] The histologic appearance varies, with lower-grade tumors seen as solid and higher-grade lesions demonstrating necrosis and hemorrhage. Distinction of lower-grade lesions from aggressive fibromatosis can be difficult, but only fibrosarcoma will metastasize. The apparently worse prognosis of fibrosarcoma in the head and neck compared with extremity lesions may relate to the inability to obtain adequate tumor margins rather than differing biologic activity.

On imaging, the findings of fibrosarcoma are nonspecific. Low-grade lesions are homogeneous on CT and hypointense on T1-weighted and T2-weighted images. Mild to moderate enhancement is seen on MR imaging but not on CT.[75] Distinction from other aggressive fibromatoses can prove difficult, as they can appear quite similar. However, the presence of necrosis strongly favors the diagnosis of a higher-grade fibrosarcoma. Imaging, particularly MR imaging, has played a major role in defining the extent of these tumors. This is important for proper surgical planning or, if indicated, for planning of proper radiation fields.[75]

Copyright © 2003, Mosby, Inc. All rights reserved.

Benign Fibrous Lesions (Fibromatoses)

The fibromatoses are a heterogeneous group of histologically benign fibroproliferative disorders that share characteristics with both reparative processes and neoplasias. They may be localized or diffuse, symmetric or asymmetric, regress spontaneously or resist treatment and recur. Fibromatoses are often recognized in childhood, but they can occur at any age. Although most follow a benign course, compromise of vital structures may occur.[61] As a group, they do not metastasize.[76]

The etiology of these fibromatoses is unknown, and the classification of these lesions is mainly based on their clinical findings. Although a number of lesions are classified as fibromatoses, this section will only deal with desmoid fibromatosis, congenital fibromatosis, nodular fasciitis and proliferative fasciitis.

Desmoid Tumor

The term *fibromatosis* without any further qualifiers is generally taken to indicate desmoid fibromatosis, which is an infiltrative process not limited to the fascia. Rather, it arises from musculoaponeurotic structures and invades the contiguous tissues. Some pathologists consider them well-differentiated fibrosarcomas, particularly when scattered mitotic figures are identified. Unlike abdominal wall desmoids, which are more common in women, there is no clear gender predilection in head and neck desmoids. They are seen in all age groups, although there is a higher incidence in the first few decades of life.[74] Patients with Gardner's syndrome are at increased risk for developing desmoids.

These lesions are typically firm or hard and usually painless, although occasionally they are tender. Most neck desmoids are found in the upper neck; however, those seen more inferiorly may be more difficult to manage, as they can involve the great vessels, trachea, and brachial plexus. They are locally invasive but do not metastasize (Fig. 41-23).[61, 74] Surgery is the treatment of choice, and while lesions often extend 2 to 3 cm beyond their apparent boundaries, some cases with positive surgical margins may not recur. Irradiation and chemotherapy are reserved for recalcitrant cases.

Congenital Fibromatosis (Generalized and Localized)

Congenital generalized fibromatosis (infantile myofibromatosis) is a rare disease that starts in utero; however, additional lesions may continue to develop after birth. It presents as multiple superficial tumors of the skin and subcutaneous tissues. However, deep lesions involving the heart, lungs, skeletal muscles, viscera, and/or bones also occur, and many patients succumb to the disease. If the infant survives the first few months of life, the tumors often regress spontaneously over the next 6 to 18 months.[61] Somewhat paradoxically, fibrous-rich tissues such as tendons and fascia are rarely affected.

Congenital localized fibromatosis, which may be more common than the generalized form, presents at or just after birth and is localized to just one body area. Typically, the tumors arise in the subcutaneous tissues, skeletal muscle, or bone, and most nonvisceral lesions spontaneously regress. Recurrence following resection of solitary lesions is uncommon.

Histologically, the mesenchymal cells appear more immature than those seen in desmoid tumors, and there is occasional necrosis with calcification that is not seen in other fibromatoses.[74] On CT, the fibromatoses usually are infiltrating lesions that have an attenuation equal to or higher than that of muscle and that enhance significantly after contrast administration. On MR images, these lesions usually are heterogeneous and may be either of intermediate or low signal intensity on T2-weighted images. The signal on T1-weighted images is low to intermediate, and there is strong enhancement after contrast administration.[77, 78]

Nodular Fasciitis (Pseudotumor of the Skin)

Nodular fasciitis is a benign, nonneoplastic, self-limited fibroproliferative disorder. Its importance lies in its occasional pathologic confusion with a sarcoma. The head and neck region is the second most common site, lagging behind the upper extremities, where almost half of the lesions are found. Most often, this entity presents in the superficial fascia as a subcutaneous movable nodule that may be tender or painful. However, it also can arise from the deep fascia and may present as an intramuscular mass. Nearly half of the lesions grow rapidly over a few weeks and then slowly decrease in size over the next weeks to months. About 30% of the lesions show no change in size after presentation. Trauma or infection may increase the risk of developing nodular fasciitis, which is believed to represent a reactive or inflammatory process of the myofibroblasts that are normally concerned with skin repair.[79] Local excision is the treatment of choice, and a local recurrence (7% of cases) need not be resected if the diagnosis is established.

On CT, subcutaneous lesions are well defined by the adjacent fat, but intramuscular lesions may be poorly defined, usually with an attenuation slightly less than that of skeletal muscle. The lesions are well seen by MR imaging; intramuscular lesions are hyperintense to skeletal muscle on T1-weighted and hyperintense to fat on T2-weighted SE images. Subcutaneous lesions may be hypointense to skeletal muscle on all SE pulse sequences or hyperintense on T2-weighted images. Fairly pronounced enhancement occurs after contrast administration (Fig. 41-24). Because there are no unique imaging findings, nodular fasciitis must be included in the preoperative differential diagnosis of small soft-tissue masses.[80, 81] Among other lesions to be considered in this differential diagnosis are neurofibroma, schwannoma, fibrous histiocytoma, fibromatosis, fibrosarcoma, myxoid liposarcoma, and myxofibrosarcoma.

Proliferative Fasciitis

Though used by many researchers as a synonym for nodular fasciitis, the term *proliferative fasciitis* should be reserved for a peculiar subcutaneous and facial lesion that may represent the cutaneous counterpart of proliferative myositis. Proliferative fasciitis clinically is similar to nodular fasciitis except that it occurs in older patients and is less nodular and less defined, growing in the superficial fascia. Lesions may be painful, but the clinical course is benign and recurrences are rare.[61]

Copyright © 2003, Mosby, Inc. All rights reserved.

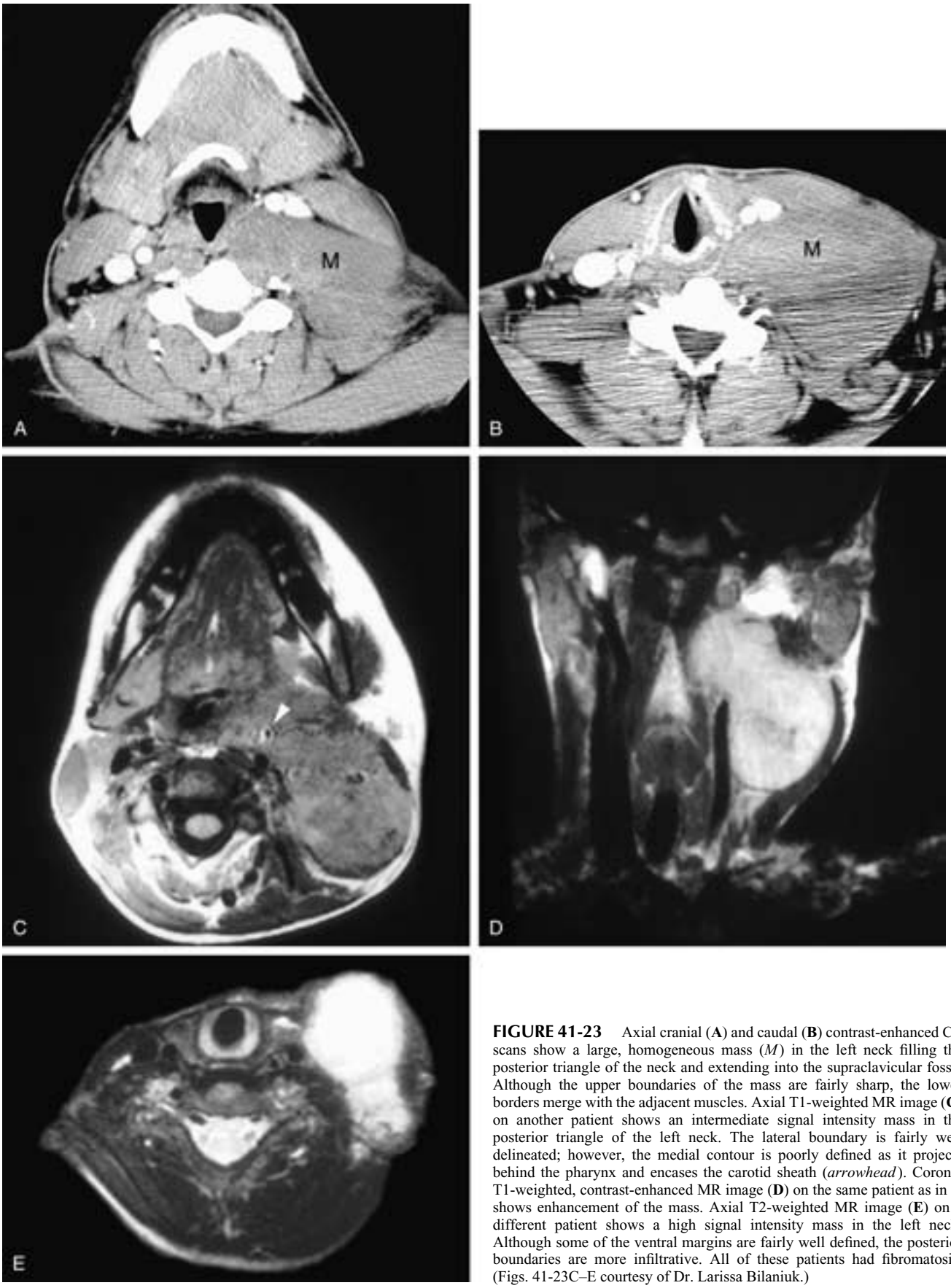

FIGURE 41-23 Axial cranial (**A**) and caudal (**B**) contrast-enhanced CT scans show a large, homogeneous mass (*M*) in the left neck filling the posterior triangle of the neck and extending into the supraclavicular fossa. Although the upper boundaries of the mass are fairly sharp, the lower borders merge with the adjacent muscles. Axial T1-weighted MR image (**C**) on another patient shows an intermediate signal intensity mass in the posterior triangle of the left neck. The lateral boundary is fairly well delineated; however, the medial contour is poorly defined as it projects behind the pharynx and encases the carotid sheath (*arrowhead*). Coronal T1-weighted, contrast-enhanced MR image (**D**) on the same patient as in **C** shows enhancement of the mass. Axial T2-weighted MR image (**E**) on a different patient shows a high signal intensity mass in the left neck. Although some of the ventral margins are fairly well defined, the posterior boundaries are more infiltrative. All of these patients had fibromatosis. (Figs. 41-23C–E courtesy of Dr. Larissa Bilaniuk.)

VIEW IMAGE

Copyright © 2003, Mosby, Inc. All rights reserved.

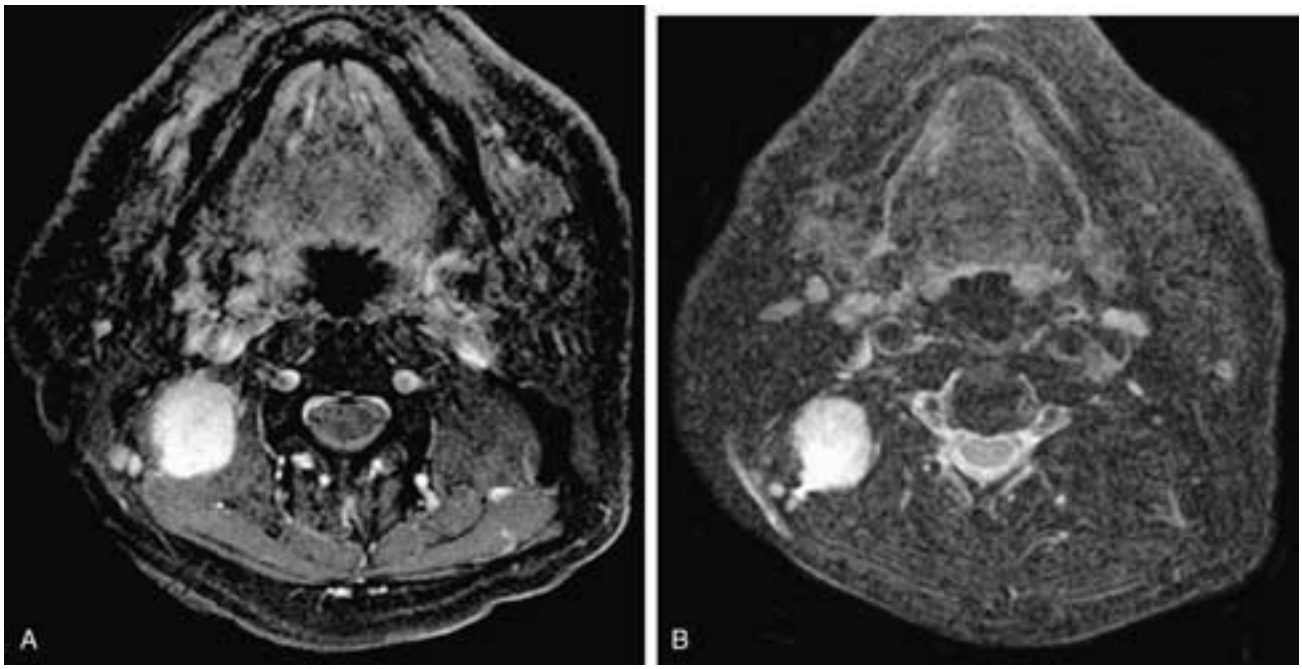

VIEW IMAGE

FIGURE 41-24 Axial T2-weighted MR image (**A**) shows a hyperintense nodule in the right paraspinal muscles. Axial T1-weighted, fat-suppressed, contrast-enhanced MR image (**B**) shows an intensely enhancing nodule. The appearance is not specific, as a primary muscle tumor or metastasis could have a similar appearance. This patient had nodular fasciitis.

Necrotizing Fasciitis

Necrotizing fasciitis is a potentially fatal bacterial infection that spreads within fascial planes. Although it is rare in the neck, possibly due to its relatively rich vascularity, this entity is included because of the potentially devastating sequelae of a delayed diagnosis.[82] Although it was once attributed primarily to extension of dental or pharyngotonsillar infections, numerous case reports have recently implicated sinus infections, epiglottitis, insect bites, radiotherapy, and trauma.[83–86] Inadequately treated infections can lead to mediastinal extension, considerable necrosis of the surrounding soft tissues and skin, and systemic toxicity.

Relatively constant CT findings in surgically proven necrotizing fasciitis include diffuse thickening and infiltration of the skin and subcutaneous tissue (cellulitis), enhancement and/or thickening of cervical fascia (fasciitis) and dominant muscles (myositis), and compartmental fluid collections.[87] Variable findings include soft-tissue gas, mediastinitis, and effusions. Subsequent CT imaging can demonstrate clinically unsuspected progression of disease, allowing for debridement sooner than would otherwise be considered.[87] MR imaging is sensitive for both cellulitis and fasciitis. In cellulitis without fasciitis, there may be enhancement of subcutaneous tissues or superficial fascia, as well as subcutaneous thickening and fluid collections. When fasciitis is present, however, there is thickening, enhancement, or increased T2-weighted signal intensity within the deep fascia, and deep fluid collections are not uncommonly seen. This fluid represents necrosis or abscess formation, the distinction of which can be difficult, as both are seen as areas lacking enhancement.[88]

MUSCLE-RELATED LESIONS

Levator Claviculae Muscle

The levator claviculae is a normal muscle found in 2% to 3% of the population. The muscle arises from the anterior tubercles of the transverse processes of the upper cervical vertebrae, runs down the neck medial to the sternocleidomastoid muscle, and inserts onto the middle third or lateral half of the clavicle (Fig. 41-25). It may be unilateral or bilateral. The imaging importance of this muscle lies in its recognition as a normal structure rather than as an enlarged lymph node, an unenhanced blood vessel, or some other mass.[89, 90]

Denervation Atrophy

Denervation of a muscle leads to predictable changes that end in a small, atrophic muscle, much of which is replaced by fat. Acute and subacute denervation results in a neurogenic edema that actually causes some muscle enlargement and high T2-weighted signal intensity on MR imaging.[91, 92] Chronic denervation is best seen on T1-weighted images, manifest as a loss of muscle bulk with diffuse areas of increased signal intensity within the muscle corresponding to fatty replacement. On CT, a similar pattern of fatty changes is seen, but it is slightly less well defined than on MR images. The rate of progression varies widely, with some investigators showing acute/subacute edematous findings persisting for up to 48 months after denervation in some patients and chronic fatty changes developing as early as 2 months in others.[92] On both CT and MR imaging,

Copyright © 2003, Mosby, Inc. All rights reserved.

end-stage fat replacement often results in fatty tissue without any identifiable muscle fibers (Fig. 41-26).

Muscle Hypertrophy

Muscle hypertrophy can develop as a result of exercise, in association with myotonic disorders (increased spontaneous activity), or idiopathically (some cases of masticator muscle hypertrophy). In true muscle hypertrophy, the muscle is enlarged but otherwise normal on all imaging. There also can be a pseudohypertrophy of muscle due to infiltration of the muscle by muscular dystrophies, amyloidosis, sarcoidosis, thyroid disease, and parasitic infestations. Lastly, a myositis can enlarge a muscle. On CT, the enlarged hypertrophic muscle may appear normal in density, but abnormal MR signal intensity is seen in most muscles that are enlarged due to pseudohypertrophy or a myositis.

A fairly common example of exercise muscle hypertrophy in the head and neck occurs with masticator muscle hypertrophy and in patients after a radical neck dissection (Fig. 41-27). After surgery, there is shoulder drop following denervation of the trapezius muscle; most patients, therefore, recruit the ipsilateral levator scapulae muscle to elevate the scapula. The resulting hypertrophy of the levator can been seen as a ''pseudomass'' on imaging, often misinterpreted as a tumor recurrence. Similarly, patients who lift weights often develop hypertrophy of the lower neck, upper back, and shoulder muscles, although these changes tend to be symmetric bilaterally.

Fibromatosis Colli (Sternomastoid or Sternocleidomastoid Tumor)

Torticollis may be either congenital or acquired. The cause may be muscular, neurogenic, infectious, neoplastic, posttraumatic, or even psychogenic. When torticollis is caused by a fibrocollagenous infiltration of the sternocleidomastoid muscle with a palpable mass in the newborn, the disease is called fibromatosis colli or sternocleidomastoid tumor. This must be distinguished from muscular torticollis, which is a tightening of the muscle without a palpable mass. However, between 15% and 20% of patients with fibromatosis colli progress to muscular torticollis despite therapy.[61] The right neck is affected in 75% of cases, and rarely, fibromatosis colli may be bilateral. About 70% of the cases present between birth and 2 months of age. Most cases spontaneously regress without resulting deformity, and conservative therapy is the treatment of choice. Although multiple explanations of the exact etiology have been offered, the cause remains unknown.[93, 94]

Sternocleidomastoid tumor presents as a benign, firm, fibrous swelling predominantly involving the middle or inferior third of the sternocleidomastoid muscle (Fig. 41-28). This pseudotumor affects 0.4% of infants in their first few weeks of life, with the vast majority showing complete regression over the ensuing few months. On ultrasound, fibromatosis usually appears as a hyperechoic mass or as diffuse enlargement of the sternocleidomastoid muscle of mixed echogenicity; other patterns are identified but are less common. The adjacent soft tissues should remain normal.[95] Although the signal characteristics relative to normal muscle may vary, signal intensity in fibromatosis is slightly increased on T2-weighted images and more significantly increased on gradient-recalled T1-weighted images; the SE T1-weighted signal intensity is essentially normal.[96]

Muscular Torticollis

Pathologically, muscular torticollis shows a limited collagenous and/or fibroblastic proliferation that does not cause a mass. It thus might be considered within the spectrum of fibromatosis colli, although 73% of cases of muscular torticollis present after 1 year of age. If it presents prior to 6 months of age, passive stretching may prove beneficial. After that age, a tenotomy may have to be performed.[61]

Congenital muscular torticollis, or idiopathic spasmodic torticollis, may be of unknown etiology, or may be related to

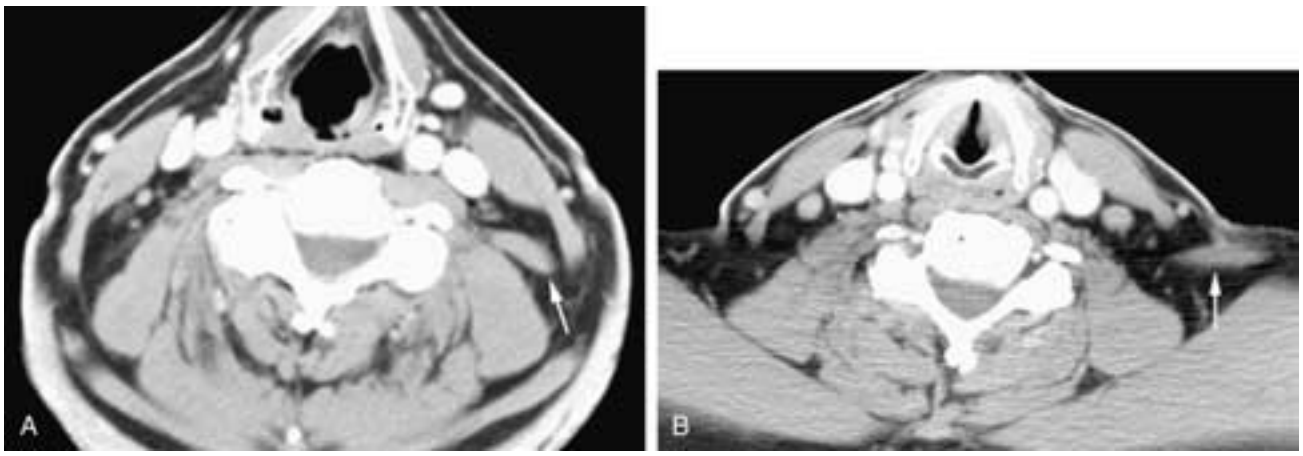

VIEW IMAGE

FIGURE 41-25 Axial cranial (**A**) and caudal (**B**) contrast-enhanced CT scans through the neck show a left-sided levator claviculae muscle (*arrows*). The levator lies deep to the sternocleidomastoid muscle in the midneck and lateral to it in the lower neck. (Courtesy of Dr. David Rubinstein.)

Copyright © 2003, Mosby, Inc. All rights reserved.

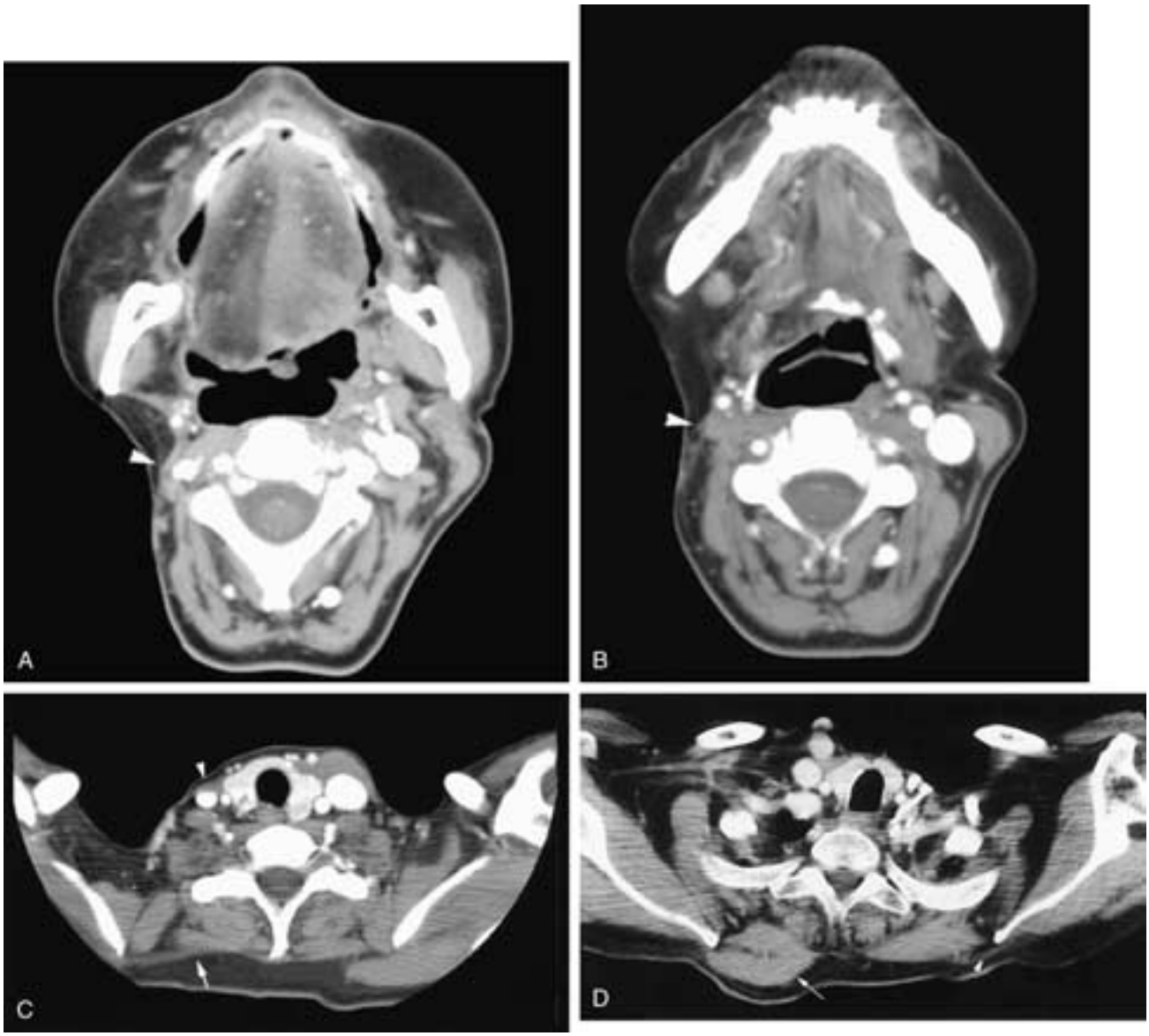

VIEW IMAGE

FIGURE 41-26 Serial axial contrast-enhanced CT scans from cranial (**A**) to caudal (**D**) on a patient who has had skull base surgery with damage to his right cranial nerves V, VII, and IX to XII. In **A**, there is marked atrophy of the right sternocleidomastoid muscle (*arrowhead*) and fatty replacement of the right-sided tongue muscles. As a result, the right base of the tongue prolapses back farther than the left side, possibly suggesting the presence of a mass on the right. The right internal pterygoid and masseter muscles are also smaller than their left-sided counterparts. In **B**, there is atrophy of the right sternocleidomastoid (*arrowhead*) and trapezius muscles. There also is atrophy of the muscles in the right side of the floor of the mouth. In **C**, the marked atrophy of the right sternocleidomastoid (*arrowhead*) and trapezius (*arrow*) muscles is clearly evident. In **D**, an axial contrast-enhanced CT scan through the lower neck of a different patient who has had a left radical neck dissection shows denervation atrophy of the left trapezius muscle (*arrowhead*). The right trapezius is normal, but its bulk could be mistaken for a mass (*arrow*).

trauma or found in conjunction with a variety of intracranial, atlantoaxial, and spinal pathology.[94, 97–125] Because of the association of congenital muscular torticollis with other intrauterine positioning disorders, it has been postulated that head positioning in utero may selectively injure the sternocleidomastoid muscle, leading to development of a compartment-type syndrome.[117] Singer et al. studied torticollis patients with CT and MR imaging and found signs suggestive of fibrosis within the sternocleidomastoid, which was confirmed at surgery.[113] Although congenital muscular torticollis is usually discovered in infancy or childhood, it may also present in adolescence or young adulthood. It should be considered in the differential diagnosis of nondystonic causes of abnormal head posture.

In a series of pediatric patients who presented with acute torticollis, including some without a history of trauma, almost two thirds (13/21) had atlantoaxial rotatory subluxation (AARS) on CT.[126] It has been suggested that torticollis related to AARS may not adequately resolve until this subluxation is addressed, either with fluoroscopically guided reduction or by fusion.[127] These reports underscore the importance of the cervical spine CT examinations in

Copyright © 2003, Mosby, Inc. All rights reserved.

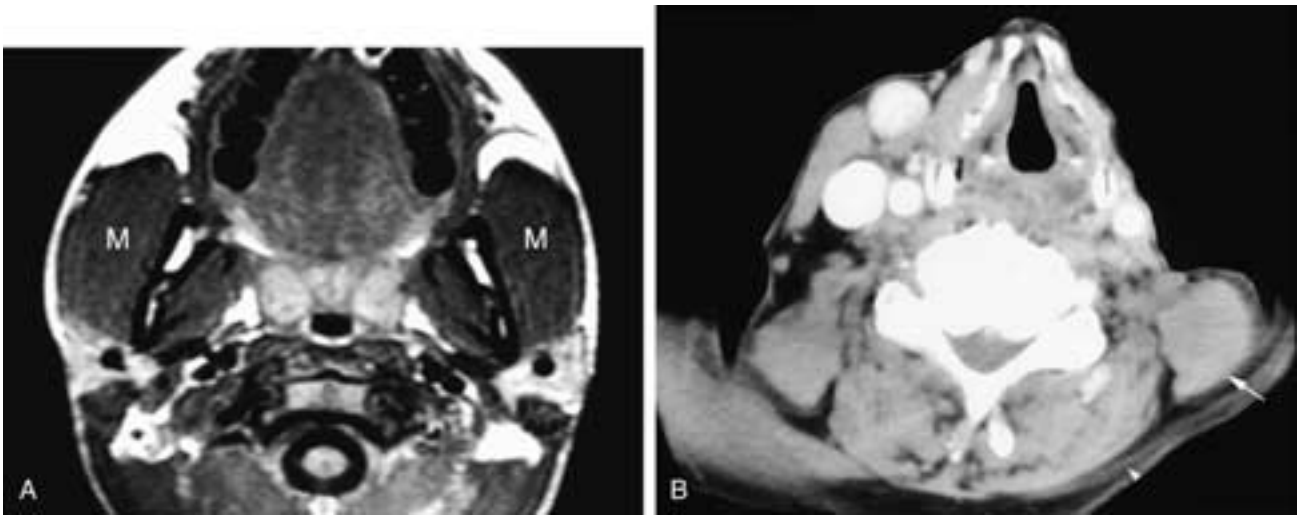

VIEW IMAGE

FIGURE 41-27 Axial T1-weighted MR image (**A**) shows bilateral enlargement of the masseter muscles (*M*) in this patient with masseteric hypertrophy. In **B**, an axial contrast-enhanced CT scan on a patient who has had a left radical neck dissection shows atrophy of the left trapezius muscle (*arrowhead*). There is early hypertrophic enlargement of the left levator scapulae muscle (*arrow*).

evaluating the cause of acute torticollis that does not resolve spontaneously.

In 1969, Snyder described paroxysmal torticollis, which developed in patients between ages 2 and 8 months. The spells of head tilting lasted for a few hours to three days and were occasionally accompanied by pallor, vomiting, and agitation at the beginning of the spells. In most children, the spells stopped spontaneously by age 5 years.[128] This disease may have a familial occurrence, and 12% of patients with benign paroxysmal vertigo of childhood previously had paroxysmal torticollis of infancy.[129]

The evaluation of torticollis is often performed by ultrasound, which shows a diffuse enlargement of the sternocleidomastoid muscle. The abnormality may be either isoechoic or hypoechoic, depending on the age of the lesion. Although the enlarged muscle may be mistaken for a mass, it always moves with the muscle on real-time sonography.[130] Because ultrasound is always abnormal in patients with

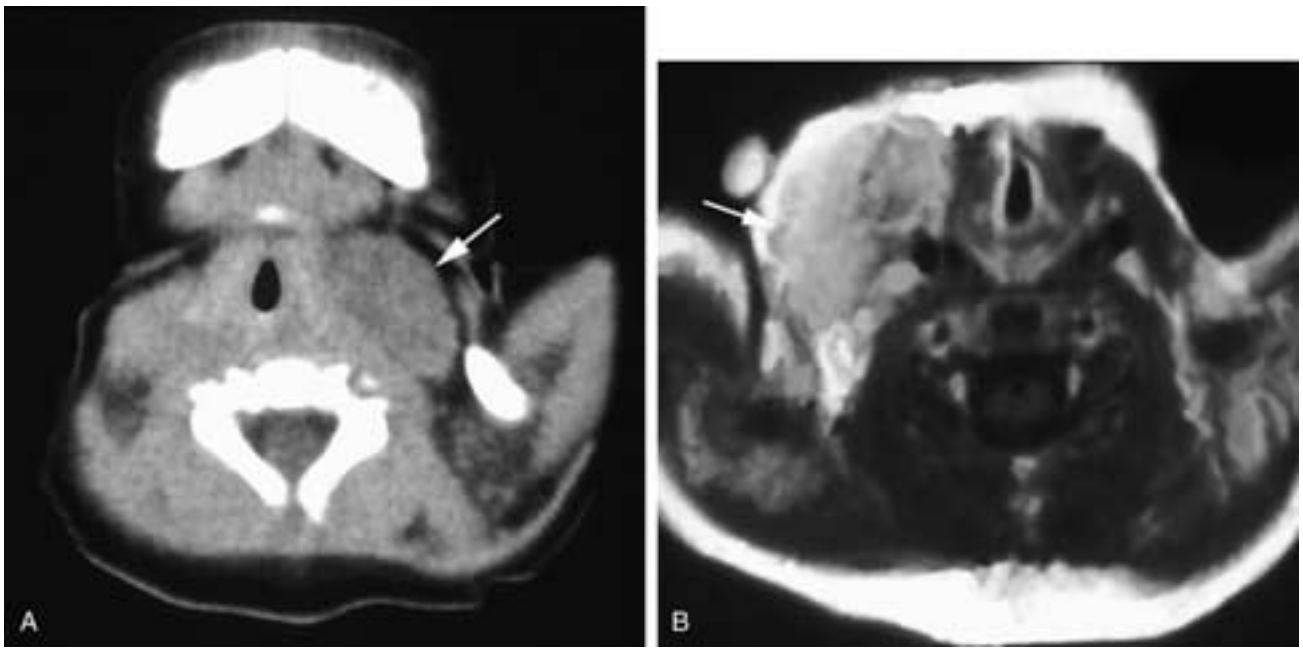

VIEW IMAGE

FIGURE 41-28 Axial CT scan (**A**) shows an enlarged left sternocleidomastoid muscle of slightly lower attenuation than that of normal muscle in this infant. Axial T1-weighted, contrast-enhanced MR image (**B**) on another patient shows enhancement of a grossly enlarged right sternocleidomastoid muscle (*arrow*). Both of these patients had fibromatosis colli. (Courtesy of Dr. Larissa Bilaniuk.)

Copyright © 2003, Mosby, Inc. All rights reserved.

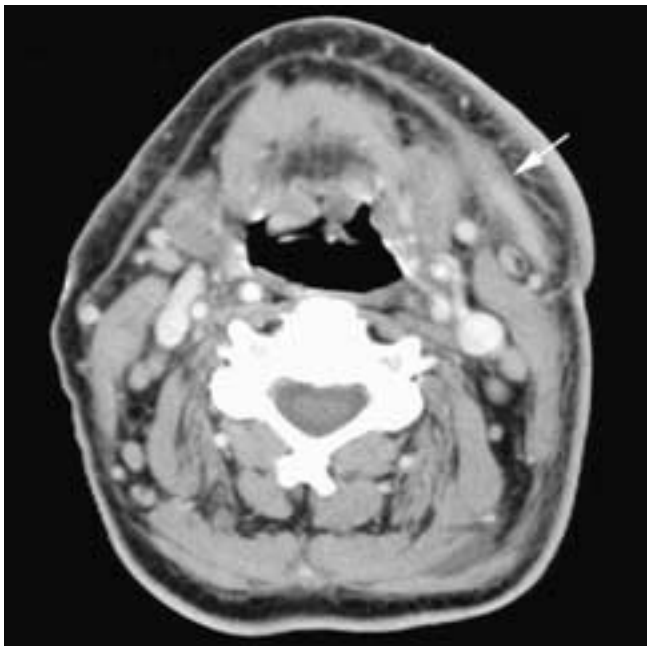

VIEW IMAGE

FIGURE 41-29 Axial contrast-enhanced CT scan shows cellulitis in the left neck. There is thickening of the skin, widening of the subcutaneous fat with increased attenuation, and thickening of the platysma (*arrow*) as a result of an inflammatory myositis.

fibromatosis colli, this study should be included in the evaluation of infants with this suspected condition.[131]

On CT, the enlarged sternocleidomastoid muscle is isodense to normal muscle and either homogeneous or slightly inhomogeneous. On MR images, the muscle can be either isointense or of a lower signal intensity than normal muscle, either homogeneous or slightly nonhomogeneous, and the caudal portion of the muscle is usually more affected than the cranial margin. It is important to exclude other neck masses such as branchial cleft cysts, cystic lymphangiomas, and malignancies such as rhabdomyosarcoma and neuroblastoma.[130]

Myositis

Skeletal muscle may be inflamed secondary to an adjacent cellulitis and/or abscess. In such instances, technically the term *myositis* can be applied. The muscle typically is swollen and enhances on both CT and MR images (Figs. 41-29 and 41-30). On MR imaging, the muscle has higher than normal T2-weighted signal intensity, and there is evidence of inflammation in adjacent structures.

The term *proliferative myositis* describes a rapidly growing pseudosarcomatous lesion of skeletal muscle. In the head and neck, it usually affects the sternocleidomastoid muscle. It tends to occur in older patients, and it is not seen

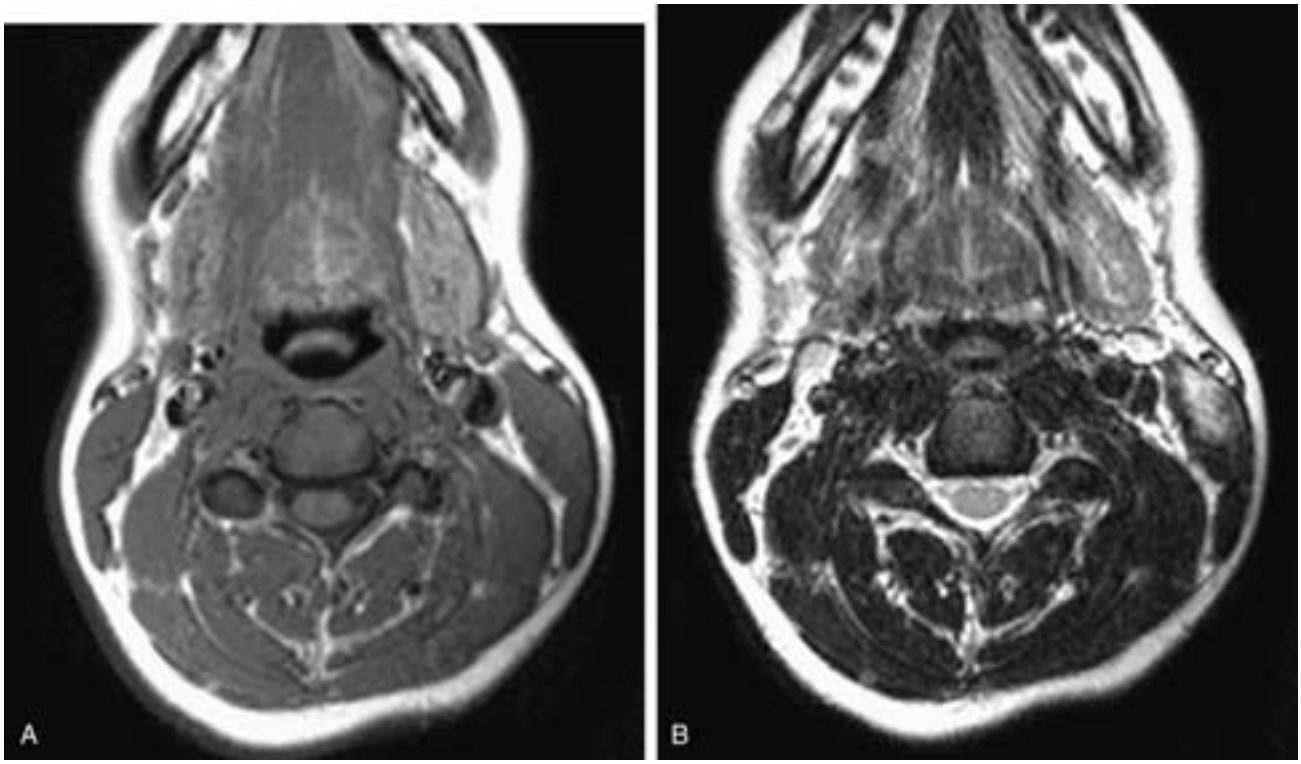

VIEW IMAGE

FIGURE 41-30 Axial T1-weighted (**A**) and T2-weighted (**B**) MR images show minimal thickening of the anterior left sternocleidomastoid muscle and an area of high T2-weighted signal intensity. This patient had a left submandibular gland acute sialadenitis with a cellulitis. He was treated with antibiotics, and although the other signs of infection subsided, he had persistent muscle pain in his sternocleidomastoid muscle. This was an inflammatory myositis.

Copyright © 2003, Mosby, Inc. All rights reserved.

in children. Rarely, foci of osteoid or bone may be present, and simple excision is curative.[61]

Focal myositis is a benign, inflammatory pseudotumor of skeletal muscle. It grows rapidly and involves a single muscle. Both children and adults are affected. It is rare in the head and neck but has been reported in the sternocleidomastoid muscle, the submental region, and the buccal region. Surgery is curative.

Myositis Ossificans

Myositis ossificans occurs in two forms. The more common variant is myositis ossificans circumscripta (MOC), which usually is a localized process that occurs outside the head and neck region. The rarer and more diffuse form of the disease is myositis ossificans progressiva. MOC is an uncommon disease that has been reported to occur in patients after trauma, burns, and infections and in patients with no known underlying pathology. Although the etiology remains unknown, most investigators believe that MOC represents a localized nonneoplastic, reactive process that results in the proliferation of undifferentiated mesenchymal tissue that then infiltrates into the surrounding soft tissues. Suggested etiologies include ossification of a hematoma, tearing of periosteum allowing subperiosteal cells to invade the muscle, and metaplasia of muscle and connective tissue. Although MOC can involve any skeletal muscle, it is uncommon within the head and neck; it has been reported in the masseter, medial pterygoid, temporalis, buccinator, geniohyoid, genioglossus, sternocleidomastoid, and paraspinal muscles. Although MOC occurs in both males and females, the most commonly affected group is young, athletic males. In cases where there is a definite history of trauma, the time period between injury and clinical detection of MOC ranges from 3 weeks to 20 years. From the time of documented trauma, radiographic evidence of calcification in MOC can be seen as early as 2 to 4 weeks and mature bone as soon as 4 to 5 months.[132]

On CT, mature MOC shows a peripheral shell of calcification and/or ossification in a focal mass. However, very early calcification may be misinterpreted as enhancement, especially if the protocol for CT imaging of the neck does not include both pre- and postcontrast studies. Early imaging may also suggest a neoplastic mass and adjacent inflammation. The appearance is consistent with the early histologic description of central fibroblast proliferation and myofibroblasts with associated edema (Fig. 41-31),[133, 134] which may hinder histopathologic distinction of MOC from malignancy. Therefore, the possibility of MOC should be communicated to the pathologist if a biopsy is performed.

Three phases of evolution of MOC have been described: a pseudoinflammatory phase, a pseudotumoral phase, and a chronic phase. Imaging findings depend on the phase of the disease. On T2-weighted SE images, early lesions typically show a nonhomogeneous soft-tissue mass with extensive surrounding edema. Postgadolinium images often show marked enhancement of the mass. Mature lesions are typically better defined, without associated edema. MR imaging, however, is not definitive in its ability to exclude malignancy.

MR imaging of mature lesions has shown well-defined, inhomogeneous masses with signal intensity close to that of fat on both T1-weighted and T2-weighted images, hypointense rims, and no surrounding edema (Fig. 41-32). On MR imaging, the differential diagnosis includes an early abscess, necrotic adenopathy, and neoplasm. The imaging appearance of pyomyositis and polymyositis can also mimic that of early MOC lesions on both CT and MR imaging. If fine needle aspiration is utilized to arrive at a diagnosis of MOC, a sample of the periphery of the lesion must be obtained.[132]

Muscular Dystrophies

The muscular dystrophies are a group of primary muscle disorders that are hereditary in nature. The underlying biochemical defects are not well described. Of the dystrophies, the primary one that affects the neck muscles is fascioscapulohumeral (FSH) dystrophy. Outliers dystrophy, which lies on a spectrum somewhere between Duchenne's and Becker's muscular dystrophies, affects the flexor muscles of the neck so that the supine patient cannot lift the head against gravity. Walking is also affected after the age of 12 years. Other dystrophies, such as Emery-Dreifuss muscular dystrophy and scapuloperoneal dystrophy, affect the shoulder muscles and may uncommonly involve muscle changes seen on neck imaging studies. There also are isolated dystrophies that seem to affect a single group of muscles, such as the extensor back muscles.

FSH dystrophy is inherited as an autosomal dominant trait. Its prevalence is about 1 per 100,000 population. The cause remains unknown. Variable facial weakness is usually first noted in the second decade of life. Shoulder weakness especially affects the scapular fixators. Leg weakness also may occur. A more severe form of the disease occurs in infancy. Treatment is supportive.[135]

On CT, there is almost total fatty replacement of the affected muscles (Figs. 41-33 and 41-34). On MR imaging, the muscle has signal intensities close to those of fat, and the normal low muscle signal intensity is absent.

Myotonic Dystrophy

Myotonic dystrophy is one of the most common dystrophies, with an incidence of 2.5 to 5 per 100,000 population. It is estimated that between 1/20,000 and 1/7500 people carry the gene mutation for the disease. The syndrome is inherited as an autosomal dominant trait with variable transmission. The abnormality has been mapped as a CTG trinucleotide repeat sequence on the q13.3 band of chromosome 19, and when the disease is inherited from the mother, it tends to be more severe. Paternal transmission is rare.[136, 137]

Typically, the disease presents in the second to fourth decades of life; however, children can also be affected. Commonly, the small muscles of the hands and the extensor muscles of the forearms are the first to atrophy. However, in some patients, ptosis and facial muscle atrophy are the initial findings. Usually affected are the masseter and sternocleidomastoid muscles, leading to a deformed mandible and a ''swan neck.'' The association of frontal baldness and a

Copyright © 2003, Mosby, Inc. All rights reserved.

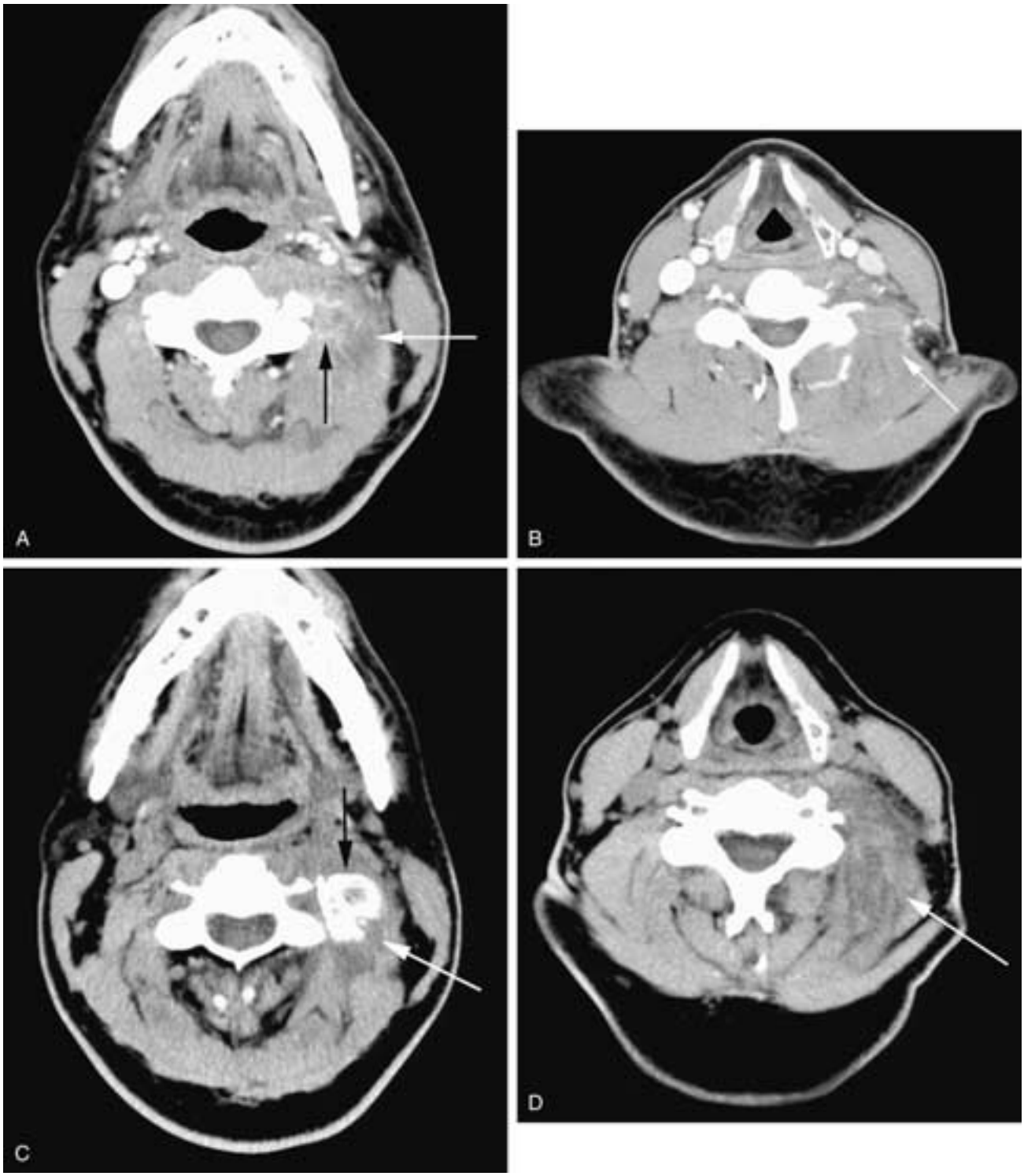

VIEW IMAGE

FIGURE 41-31 Axial contrast-enhanced CT scans (**A** and **B**) of the neck obtained 1 week after a 38-year-old male complained of neck pain. In **A**, there is a vague area of low attenuation and fullness in the left paraspinal muscles (*white arrow*), and there is a faint curvilinear density (*black arrow*) that could be interpreted as enhancement within the mass. A more caudal scan (**B**) shows a vague low attenuation and fullness in the left paraspinal muscles (*arrow*). Unenhanced CT scans (**C** and **D**) obtained 1 month after onset show that in **C** there is now a well-defined calcified/ossified density (*black arrow*) within the enlarged, otherwise low-attenuation (*white arrow*) left paraspinal muscles. This radiodensity corresponds to the area that may have been attributed to enhancement on the prior study (**A**). In **D**, there is enlargement and low attenuation in the left paraspinal muscles (*arrow*).

Copyright © 2003, Mosby, Inc. All rights reserved.

wrinkled forehead give the patient a distinctive appearance. Virtually all muscles can be affected, and most patients are confined to either a wheelchair or bed by the age of 15 to 20 years. Myotonia may precede muscle weakness (Fig. 41-35). Opacity of the lenses is common.

Also associated is a generalized hyperostosis affecting the skull and skull base. CT findings include thickened bone within the calvarium, mastoid portion of the temporal bone, petrous pyramid, anterior clinoid process, dorsum sellae, and clivus. Involvement of the glenoid fossa may lead to dislocation of the temporomandibular joint. Lytic and nonexpansile, sclerotic changes have also been seen in the temporal bone.[138, 139] Patients may also have huge frontal sinuses and a small sella turcica. Less common findings include craniokyphosis, a small nasal angle, narrowing of the internal auditory canals, hypotelorism, and enlargement of the mandible. Changes may be unilateral or bilateral. For the most part, the areas of expanded bone have a grossly normal cortical and trabecular pattern. The cause of these bony findings is still unknown.[140, 141]

Rhabdomyosarcoma

Rhabdomyosarcoma (RMS), the malignant tumor of striated muscle, accounts for 8% to 19% of all soft-tissue sarcomas, and 35% to 45% of such sarcomas occur in the head and neck. Almost all tumors (98% to 99%) containing skeletal muscle are RMS, with the small remainder representing rhabdomyomas.[74] RMS is primarily a tumor of children and young adults, with most cases arising in patients under 12 years and 43% seen in patients less than 5 years of age. It is the most common sarcoma in children and the seventh most common malignancy in children overall after leukemia, central nervous system tumors, lymphoma, neuroblastoma, Wilms' tumor, and bone cancer.[61] Varieties include embryonal, alveolar, pleomorphic, botryoid, and mixed types. Most pathologists consider mixed RMS to be composed of two or more of these histologic types.[75]

More than half of RMS are of the embryonal variety, and of those, 70% to 90% arise in the head and neck or genitourinary tract. Most are seen in patients less than 10 years of age; however, nearly one quarter of cases are seen after the second decade. Regional nodal metastasis occurs in 10% to 38% of cases.[61]

Alveolar RMS is the second most common variety, representing approximately one fifth of all cases of RMS. It occurs mainly in patients 15 to 25 years of age and primarily affects the extremities and trunk. Only 18% of cases occur in the head and neck. Nodal metastases are most common in this variety, with regional lymph node involvement seen in 33% of cases and regional or distant nodal disease in 75% to 85%.[61, 75]

Botryoid RMS differs from embryonal RMS only in its gross appearance. About 75% of these tumors arise in the vagina, prostate, or bladder. The remaining tumors arise in the head and neck or bile ducts. Most patients are between 2 and 5 years of age.

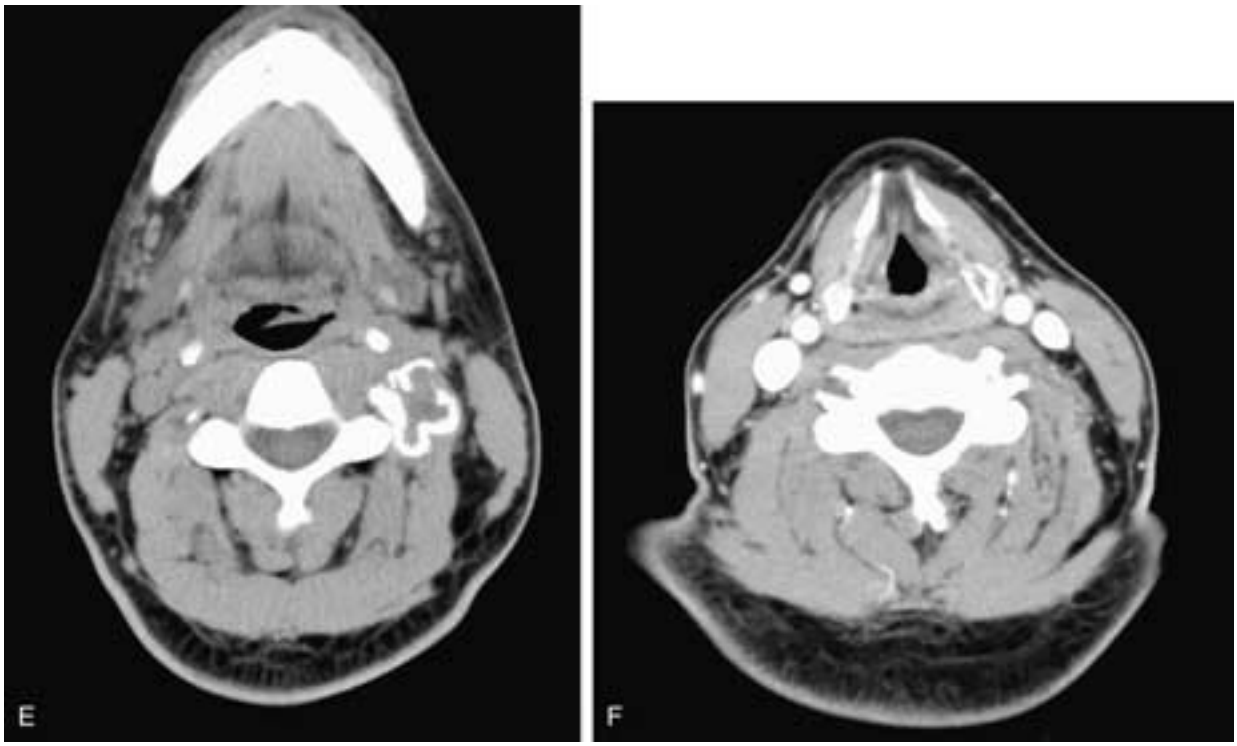

VIEW IMAGE

FIGURE 41-31 *Continued.* CT scans (**E** and **F**) obtained 4 months after onset show that in **E** the calcified/ossified density remains on this unenhanced image; however, the low attenuation and swelling of the left paraspinal muscles are no longer seen. Following contrast administration (**F**), there is now a symmetric and normal appearance of the paraspinal muscles. These findings illustrate the progression of myositis ossificans.

Copyright © 2003, Mosby, Inc. All rights reserved.

Pleomorphic RMS is seen primarily in patients 40 to 60 years of age, with only 6% discovered in patients less than 15 years of age. Most cases arise in the extremities, and only 7% affect the head and neck. Metastasis is primarily vascular, and only 9% of patients have regional nodal metastasis.[61] Survival is poorest with this variety of RMS.[75]

Clinically, RMS is usually a solitary, rapidly enlarging, firm mass that involves a striated muscle. Since the introduction of radiation and chemotherapy in RMS treatment, there has been significant improvement in long-term survival (now 85% or better).[74] The prognosis correlates more closely with extent of tumor involvement than with tumor type. By location, tumor in the orbit tends to be more localized and has a lower incidence of lymph node metastasis than other supraclavicular tumors; accordingly, orbital RMS has a significantly higher 5-year survival than RMS at other head and neck sites (89% vs. 55%).[74]

On imaging, RMS is seen as a densely cellular infiltrating

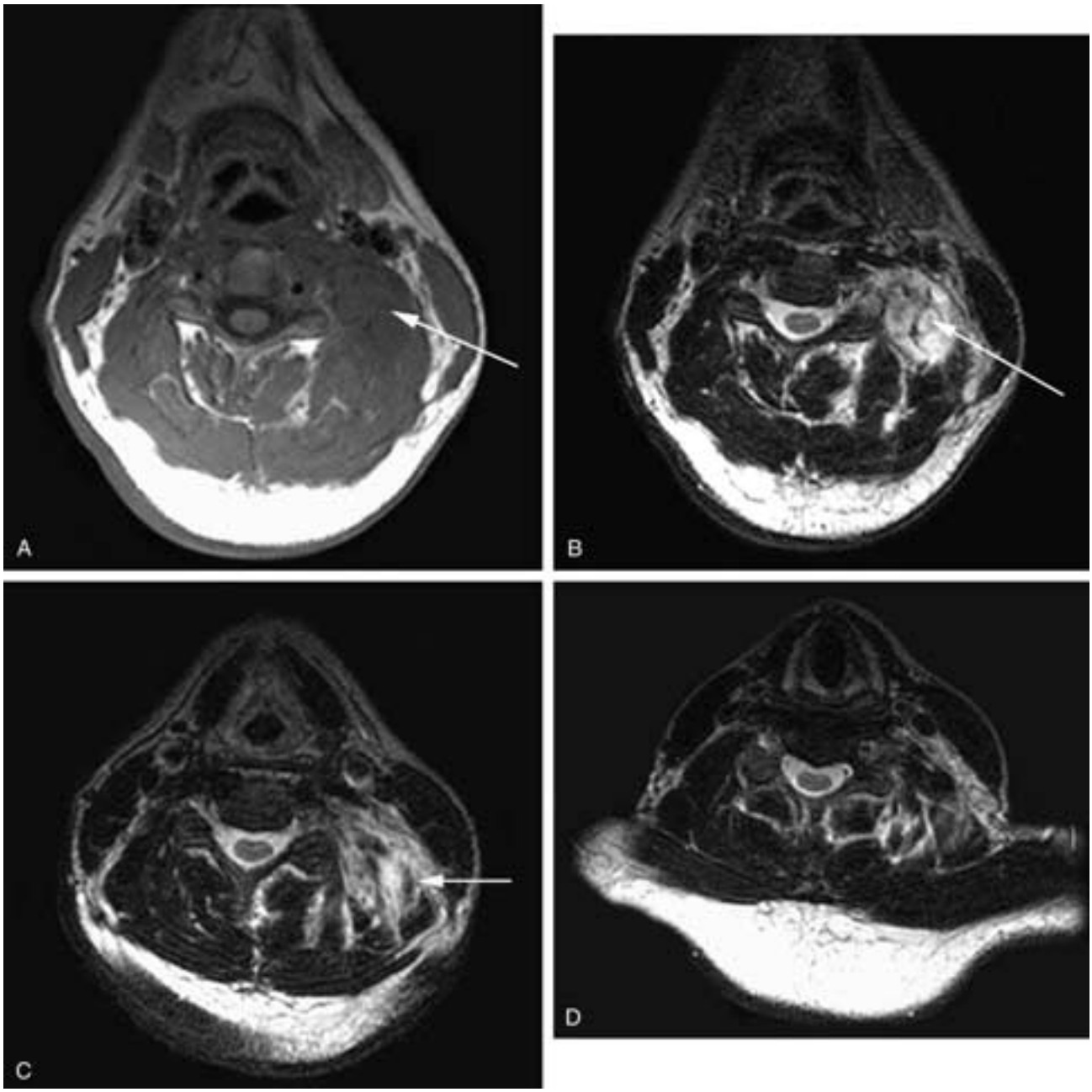

VIEW IMAGE

FIGURE 41-32 Same patient as in Figure 41-30. MR images obtained 1 week after onset of neck pain. In **A**, a T1-weighted MR image, there is a poorly defined soft-tissue mass (*arrow*), while in **B**, a T2-weighted MR image, the mass (*arrow*) has signal voids that could be interpreted as either vascular or fibrous in origin. There is also edematous-type high signal intensity in the immediate region. In **C**, a T2-weighted MR image more caudal in the neck, there is fullness and high signal intensity in the muscles and adjacent soft tissues (*arrow*). In **D**, a T2-weighted MR image obtained 1 month after onset, the mass and edema in the paraspinal muscles have decreased. This patient had myositis ossificans.

Copyright © 2003, Mosby, Inc. All rights reserved.

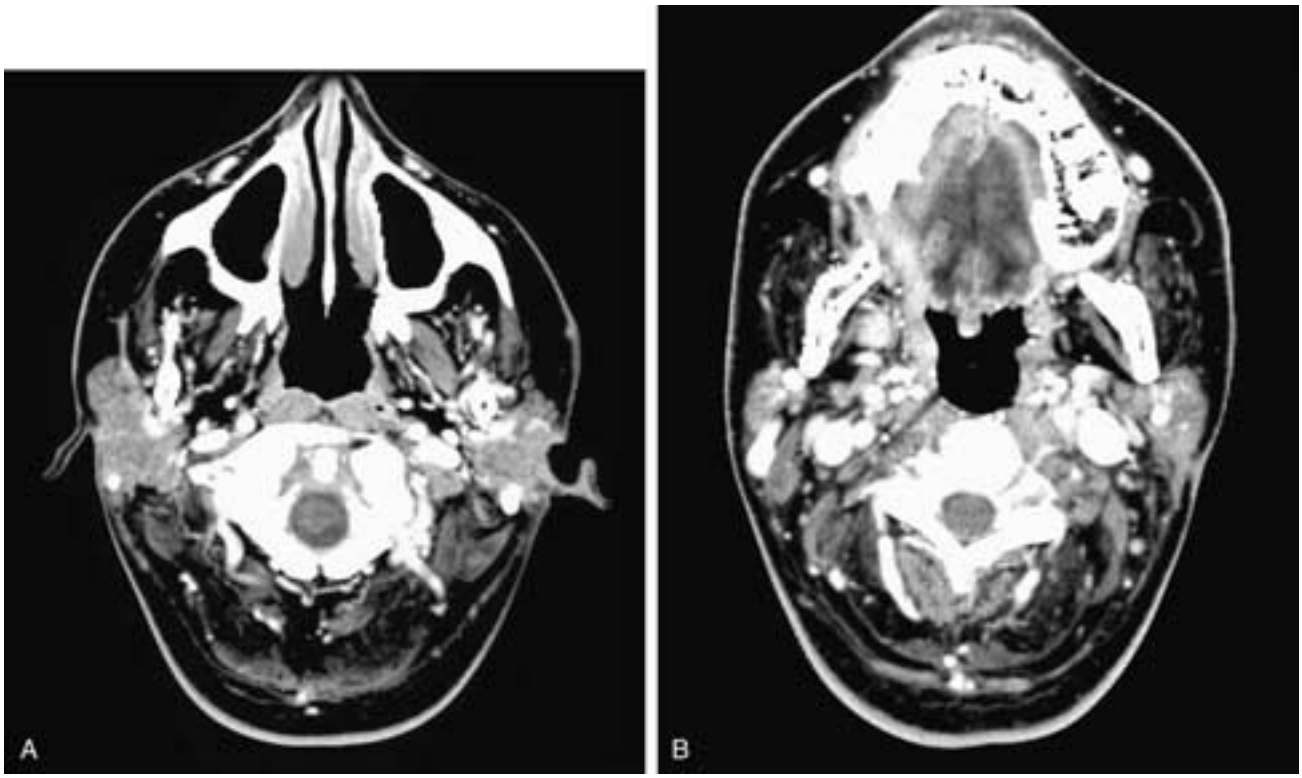

VIEW IMAGE

FIGURE 41-33 Axial cranial (**A**) and caudal (**B**) contrast-enhanced CT scans show fatty atrophy of virtually all of the muscles in the upper back and the floor of the posterior triangle. This patient had fascioscapulohumeral dystrophy.

neoplasm (Fig. 41-36). Skeletal muscle is always seen as the site of origin. On both CT and MR imaging, masses are typically homogeneous, with destruction of adjacent bone. Necrosis can be seen, but intratumoral hemorrhage is uncommon and calcification is typically absent. Tumor is isointense to muscle on T1-weighted images and hyperintense on T2-weighted images.[142] Just over half of the cases enhance homogeneously, and the degree of enhancement is similar to that of normal skeletal muscle. In most cases, tumor margins are poorly defined.

Metastasis to Muscle

Hematogenous metastasis to muscle is rare. The relatively low incidence may be related to muscle enzyme inhibitors, the acidic environment of muscle, or the vessel-squeezing effect of muscular contractions.[143] Most frequently, the metastases come from primary tumors in the lung, colon, pancreas, breast, or kidney. Although pain, tenderness, and a mass are usually present, some such metastases may be clinically silent (Fig. 41-37).

THE STYLOHYOID SYNDROMES

Three dominant syndromes are related to the stylohyoid structures: Eagle's syndrome, styloid carotodynia, and hyoid fasciitis.

Eagle's Syndrome

In 1937, Eagle described the elongated styloid process syndrome, which consists of pharyngeal pain, referred otalgia, and a foreign body sensation in the throat occurring after tonsillectomy. It is believed that this syndrome develops because of fibrosis between the tonsillar fossa and an elongated styloid process; hence, the symptoms are greatest during deglutition, phonation, and deep inspiration, when maximal pharyngeal movement occurs. Since the time of its discovery, the term *Eagle's syndrome* has come to be applied to any patient who has these symptoms and an abnormally elongated styloid process. The normal styloid process may be as long as 2.5 cm. Thus, Eagle's syndrome may be present whenever a longer styloid process is seen on imaging in a patient, whether or not there has been prior tonsillectomy (Fig. 41-38). Complicating the picture even more is that some patients also have ossified stylohyoid ligament(s), which can themselves fracture and become symptomatic.[144] The treatment, if any, is surgical removal of the elongated styloid process(es).[145–152] Because there are many asymptomatic patients who have elongated styloid processes and/or ossified stylohyoid ligaments, some clinicians question the validity of Eagle's syndrome. Nonetheless, in the symptomatic patient, shortening of the styloid process usually relieves the complaint. The presence of an elongated styloid process also makes this structure more prone to injury during flexion-type trauma. The symptoms related to Eagle's syndrome can also be confused with those

Copyright © 2003, Mosby, Inc. All rights reserved.

attributed to a wide variety of facial neuralgias as well as oral, dental, and temporomandibular diseases.

Styloid Carotodynia

A related syndrome is styloid carotodynia, caused by a normal or elongated styloid process whose tip is deviated so that it causes pressure on either the internal or external carotid arteries. This pressure causes stimulation of the pain-sensitive receptors found in the adventitia of these vessels and results in pain along the vascular distribution of the affected vessel. When the internal carotid artery is affected, pain occurs in the parietal and ophthalmic regions and there is little or no pain below the level of the orbits. When the external carotid artery is involved, the pain is in the ipsilateral face below the level of the orbit. Again, surgery is curative.

Hyoid Fasciitis

The least common of these syndromes is hyoid fasciitis, which is usually found in patients who have not had previous neck surgery. Pain and discomfort in the throat are exacerbated when the patient's head is turned to the affected side. The head turning stretches the muscles between the hyoid bone and the styloid process. Palpation of the neck elicits tenderness over the region of the hyoid bone. It is believed that this hyoid syndrome may be due to tendinitis/fasciitis of the muscular attachments (and of the attachment of the stylohyoid ligament) to the hyoid bone. Some researchers have proposed that certain patients with similar

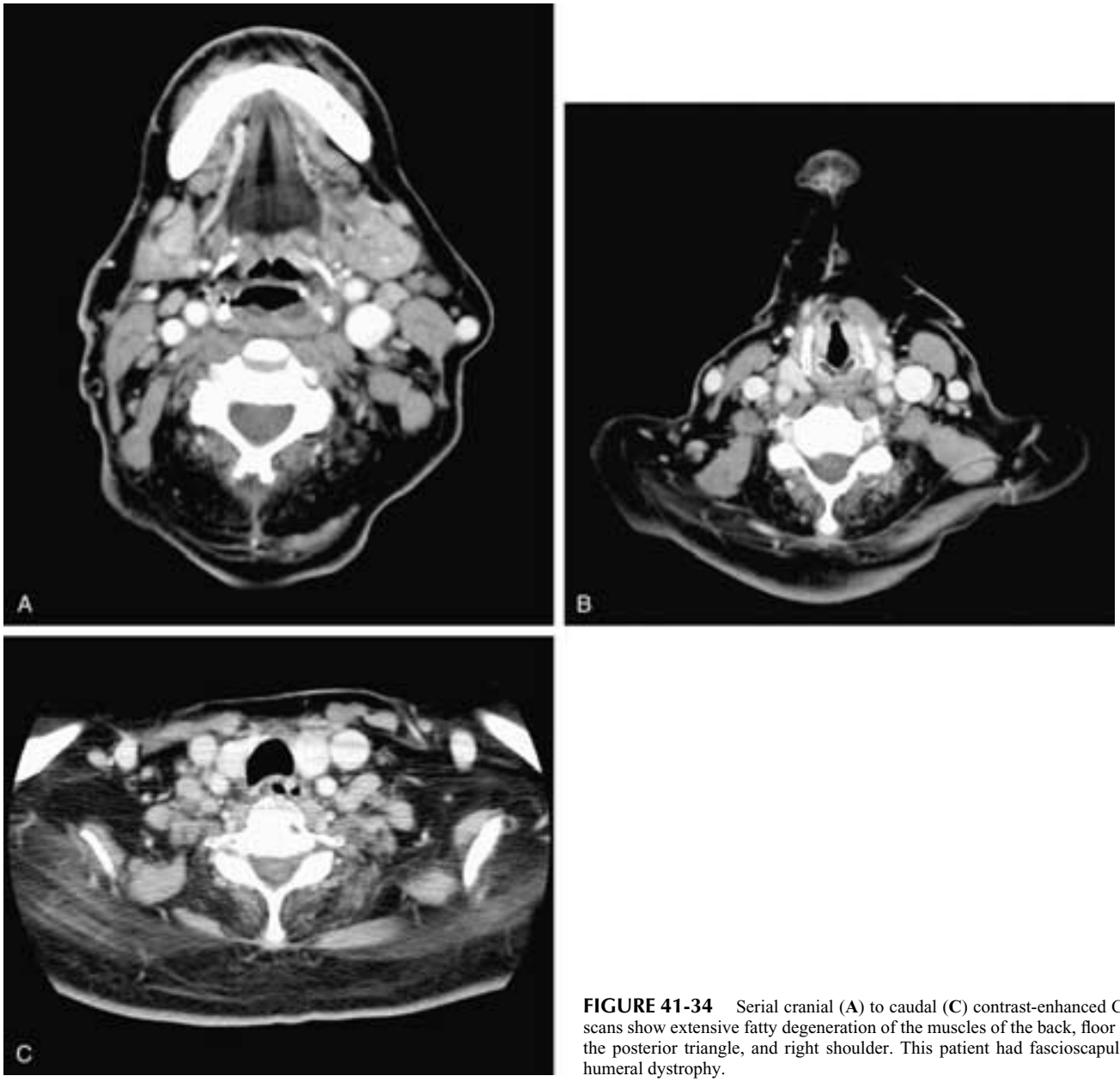

FIGURE 41-34 Serial cranial (**A**) to caudal (**C**) contrast-enhanced CT scans show extensive fatty degeneration of the muscles of the back, floor of the posterior triangle, and right shoulder. This patient had fascioscapulohumeral dystrophy.

VIEW IMAGE

Copyright © 2003, Mosby, Inc. All rights reserved.

FIGURE 41-35 Serial cranial (**A**) to caudal (**C**) contrast-enhanced CT scans show fatty degeneration of the sternocleidomastoid and trapezius muscles and, to a lesser degree, the muscles of the floor of the posterior triangle. There is also dilatation of the cervical esophagus, and the patient has a tracheotomy tube. This patient had myotonic dystrophy.

VIEW IMAGE

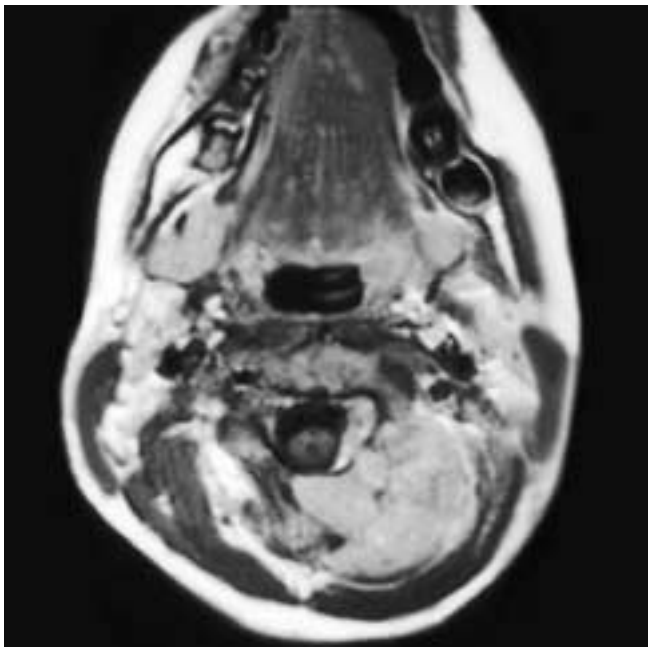

VIEW IMAGE

FIGURE 41-36 Axial T1-weighted, contrast-enhanced MR image shows an enhancing, poorly defined mass arising in the paraspinal muscles of the left neck. There is invasion of the left side of the vertebra. This patient had a rhabdomyosarcoma. (Courtesy of Dr. Larissa Bilaniuk.)

Copyright © 2003, Mosby, Inc. All rights reserved.

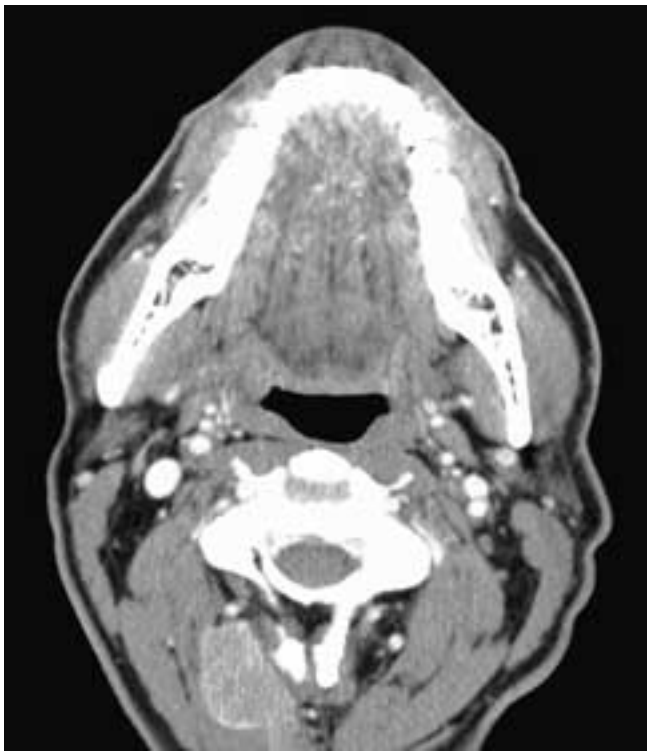

VIEW IMAGE

FIGURE 41-37 Axial contrast-enhanced CT scan shows an enhancing mass in the right paraspinal muscles. This is a nonspecific imaging appearance. This patient had metastasis to the muscles from a primary lung carcinoma.

symptoms may instead have a tenosynovitis of the intermediate tendon of the digastric muscle.[153] Treatment of hyoid fasciitis consists of local heat applied to the area and/or injection of an anesthetic combined with corticosteroids along the affected greater horn(s). If these measures fail, relief may be difficult to achieve, as surgery is not considered a good option.[154, 155]

BLOOD VESSELS AND VASCULAR VARIATIONS

Veins

There are usually at least three jugular veins on each side of the neck. They are named by their position relative to the sternocleidomastoid muscle. Thus, there are the anterior jugular, external jugular, and internal jugular veins. Of these, the internal jugular veins usually have the greatest venous flow and thus are the largest vessels.

Asymmetry of the Internal Jugular Veins

The internal jugular veins are almost always asymmetric, with the right one being larger in nearly 80% of people. In the upper neck, the crowding of structures often prevents passive venous distention, and the asymmetry in the internal jugular veins appears minimal. However, more inferiorly the asymmetry is most notable, as the larger spaces of the neck allow more passive distention of the veins. The asymmetry is usually more evident on CT or MR imaging than it is clinically. The disparity in the size of the veins can be so great as to cause the larger vein to be mistaken for a vascular mass. Tracing the course of the vein clarifies such a case. After a radical neck dissection, the shunting of venous blood to the contralateral internal jugular vein can also cause massive enlargement of the vein (Fig. 41-39); this is a normal postoperative finding.

Multiple Jugular Veins

Occasionally, one or both of the internal jugular veins may be multiple. In such cases, the more dorsal of the veins is usually the smaller and may not enhance as well as the larger ipsilateral vein on contrast-enhanced images. In these instances, on axial images the poorly enhanced vein may be mistaken for adenopathy. However, tracing the course of the vein will again clarify the situation.

The external jugular veins are even more variable than the internal jugular veins, and they may also be single or multiple. Rarely, they can be larger than the ipsilateral internal jugular vein. Similarly, the anterior jugular veins are usually asymmetric from side to side. These veins most often are seen along the anterior and medial margins of the sternocleidomastoid muscle. There is usually a small vein just above the level of the manubrium that provides communication between the two anterior jugular veins. Occasionally, this small vein may be severed during a tracheotomy, causing a bloodied operative field. This small vessel is rarely seen on CT or MR imaging.

Phlebectasia

Phlebectasia is an uncommon condition of the venous system, possibly of a congenital etiology. Clinically, phlebectasia usually presents as a neck mass that enlarges when the patient performs a Valsalva maneuver, talks, or lies down. This normally asymptomatic mass decreases in size at rest or when the patient sits upright. When the internal jugular vein is affected, it presents as a cervical swelling that can mimic the signs of either a pharyngocele or a laryngocele. Because of its rarity, phlebectasia is frequently misdiagnosed.

In the neck, phlebectasia most often affects the internal jugular vein in both children and adults. However, almost any of the cervicofacial veins, such as the anterior jugular vein or the anterior facial vein, may also be affected. Usually no treatment is necessary for this benign condition, although some authors have recommended surgical excision in selected asymptomatic patients for cosmetic and psychological purposes. Venography, anteriography, color Doppler sonography, and CT have previously been used to diagnose this unusual condition.[156–164]

Thrombosis

Thrombosis of the jugular veins can occur secondary to placement of a central line, placement of a porta-cath, infection, surgery, neoplasm, and intravenous drug abuse.[165, 166] On CT, a thrombosed jugular vein is usually enlarged, and on contrast-enhanced images, an older clot is of lower attenuation than the normal vessel; enhancement of the vasa vasorum causes the vessel wall to be well seen. On dynamic contrast-enhanced CT, a thrombus is usually less dense than opacified blood. An acute clot may appear as dense as contrast-enhanced blood. In such a case, the clot is

Copyright © 2003, Mosby, Inc. All rights reserved.

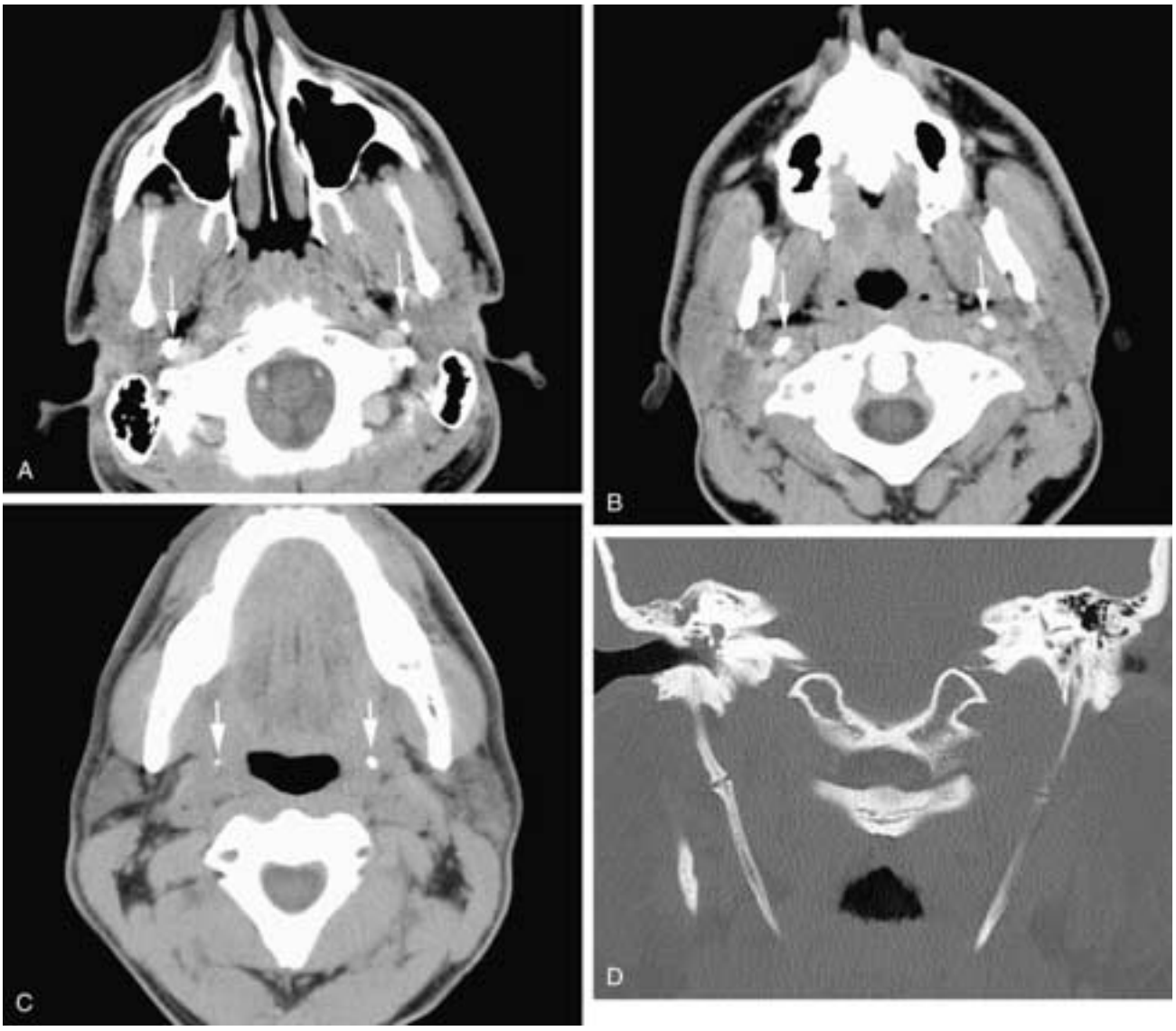

VIEW IMAGE

FIGURE 41-38 Serial cranial (**A**) to caudal (**C**) contrast-enhanced CT scans show elongation of the styloid process bilaterally (*arrows*). The normal styloid process is less than 2.5 cm. These styloid processes were 3.5 cm. This patient, who complained of pain on swallowing, had Eagle's syndrome. Coronal CT scan (**D**) on another patient with Eagle's syndrome shows bilaterally elongated styloid processes and ossification of the stylohyoid ligaments, virtually extending down to the hyoid bone.

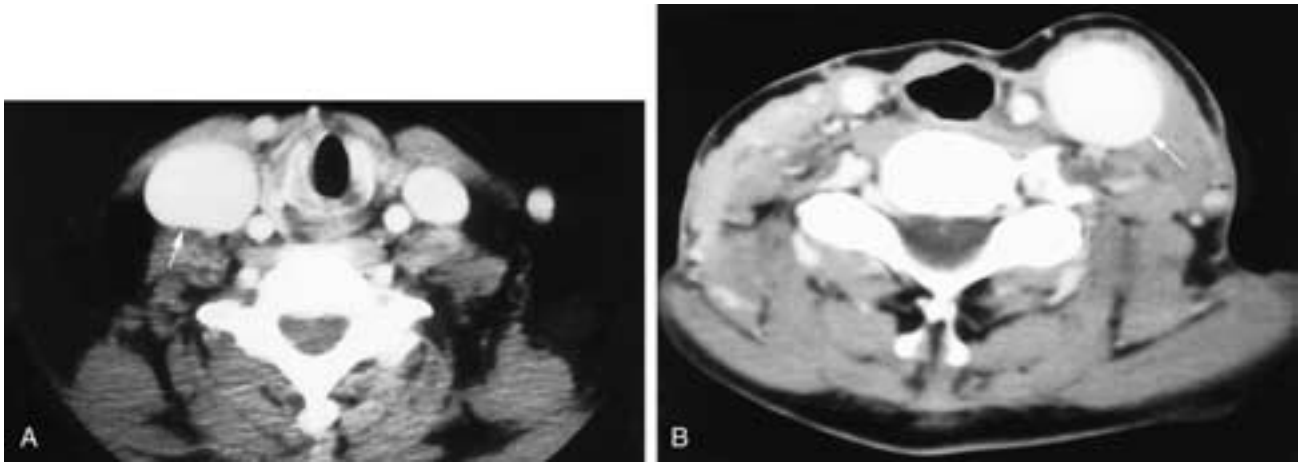

VIEW IMAGE

FIGURE 41-39 Axial contrast-enhanced CT scan (**A**) shows a large but normal right internal jugular vein (*arrow*). In about 80% of patients, the right internal jugular vein is dominant. Axial contrast-enhanced CT scan (**B**) of a patient who has had a right radical neck dissection. The right internal jugular vein was resected, and the left internal jugular vein (*arrow*) has become enlarged.

Copyright © 2003, Mosby, Inc. All rights reserved.

better seen on either noncontrast images or delayed, contrast-enhanced scans as the vascular density decreases (Fig. 41-40). If inflammation is present, there will be a fasciitis around the vein, with edema of the surrounding fat planes. On MR imaging, jugular venous thrombosis may be more difficult to detect because slow or turbulent flow may mimic a clot.

Lemierre's syndrome is the association of an acute pharyngotonsillitis (which is an anaerobic oropharyngitis), septic thrombophlebitis of the ipsilateral internal jugular vein, and septicemia with septic emboli, most often to the lungs and large joints.[167] There usually is an associated regional reactive lymphadenitis (see Chapter 38).

Pseudocollateral and Collateral Veins

Due to the current rapid CT scan times and the rapid injection of contrast with power injectors, contrast enhancement of collateral veins in the muscles of the neck and back may become quite conspicuous (Fig. 41-41). Such opacification occurs even when the internal jugular vein is patent and well opacified. In such cases, visualization of these veins does not necessarily imply thrombosis of the great veins in the lower neck or superior mediastinum. However, when asymmetric posterior muscular collaterals are seen, it is usually prudent to check the lower neck and superior mediastinal veins on that side for the possibility of thrombosis.

Condylar Vein

The vein of the condylar canal is a normal emissary vein that exits the skull base through the posterior condylar canal.[168] The condylar vein may be present on one side or both sides, or it may be absent bilaterally. When bilateral, the two veins may be quite asymmetric in size. The importance of familiarity with the condylar vein lies in not mistaking it for lymphadenopathy or a mass (Fig. 41-42).

Arteries

Medial Deviation of the Internal Carotid Artery

The internal carotid arteries are more consistently symmetric than the jugular veins. Thrombosis and dissection of the internal carotid artery are discussed further in Chapter 40 and postoperative thrombosis of the internal carotid artery is shown in Chapter 45. The medial positioning of the internal carotid artery(s) and, less frequently, of the carotid bulb may cause a bulge in the posterior pharyngeal wall; this is shown in Chapter 40 and in Figure 41-43. Recognition of this normal variant, and its inclusion in the written interpretation, will help to prevent potentially catastrophic biopsy of the associated pharyngeal wall fullness.

An aneurysmal dilatation of an artery may also cause an altered course of the vessel that may mimic a mass in the neck. This is especially so in the lower neck (Fig. 41-44).

Aberrant Retroesophageal Right Subclavian Artery

Although an aberrant retroesophageal right subclavian artery may be an incidental observation on CT or MR studies, it occasionally may cause symptoms of dysphagia (dysphagia lusoria). A barium swallow shows the artery's impression on the right posterolateral wall of the esophagus, and the vessel can be seen on CT and MR studies (Fig. 41-45). An

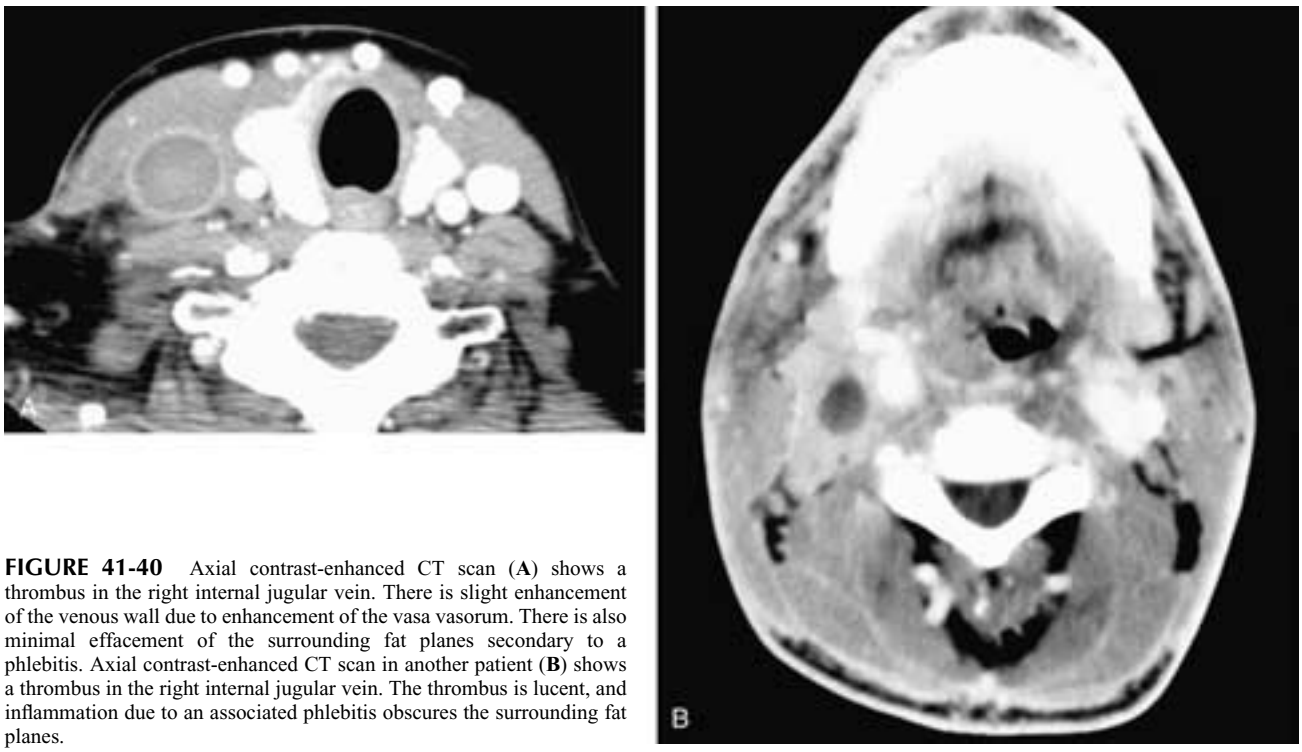

VIEW IMAGE

FIGURE 41-40 Axial contrast-enhanced CT scan (**A**) shows a thrombus in the right internal jugular vein. There is slight enhancement of the venous wall due to enhancement of the vasa vasorum. There is also minimal effacement of the surrounding fat planes secondary to a phlebitis. Axial contrast-enhanced CT scan in another patient (**B**) shows a thrombus in the right internal jugular vein. The thrombus is lucent, and inflammation due to an associated phlebitis obscures the surrounding fat planes.

Copyright © 2003, Mosby, Inc. All rights reserved.

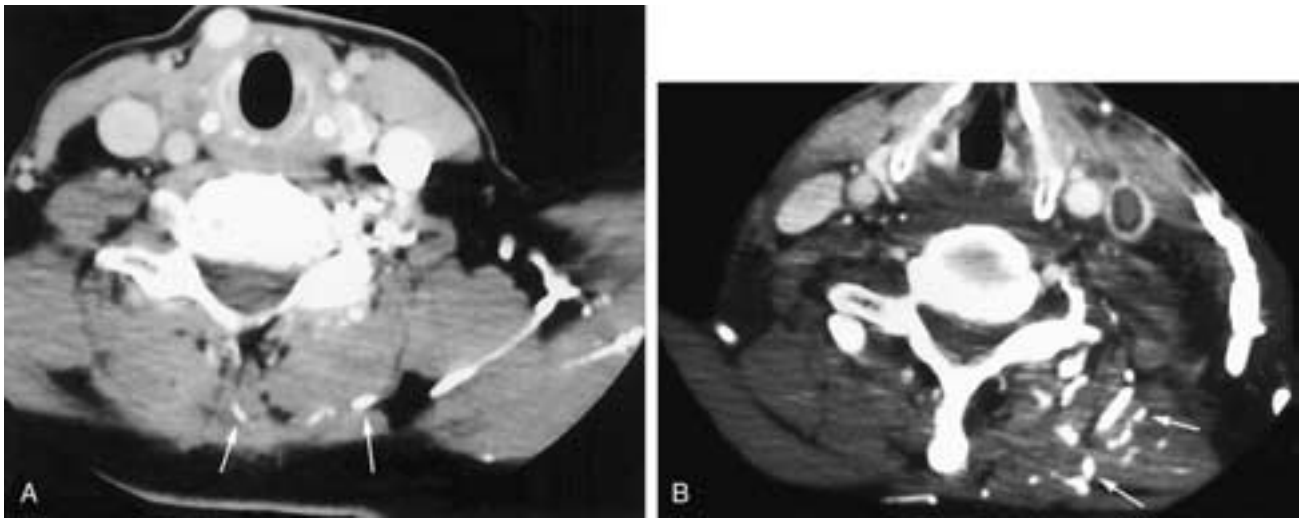

VIEW IMAGE

FIGURE 41-41 Axial contrast-enhanced CT scan (**A**) on a normal patient shows intense enhancement of the muscular vessels of the posterior neck (*arrows*). Although this could be seen in a patient with venous obstruction, there was no such obstruction and these were not collateral vessels. The contrast was administered by rapid injection, and the patient was scanned during contrast administration (1 second per scan). The vessels are probably veins opacified by reflux from the internal jugular vein (note the asymmetry of jugular opacity). Axial contrast-enhanced CT scan (**B**) shows a lucent thrombus in the left internal jugular vein and enhancement of the vein wall due to contrast in the vasa vasorum. There are also numerous large collateral venous channels (*arrows*) in the lateral and posterior left neck.

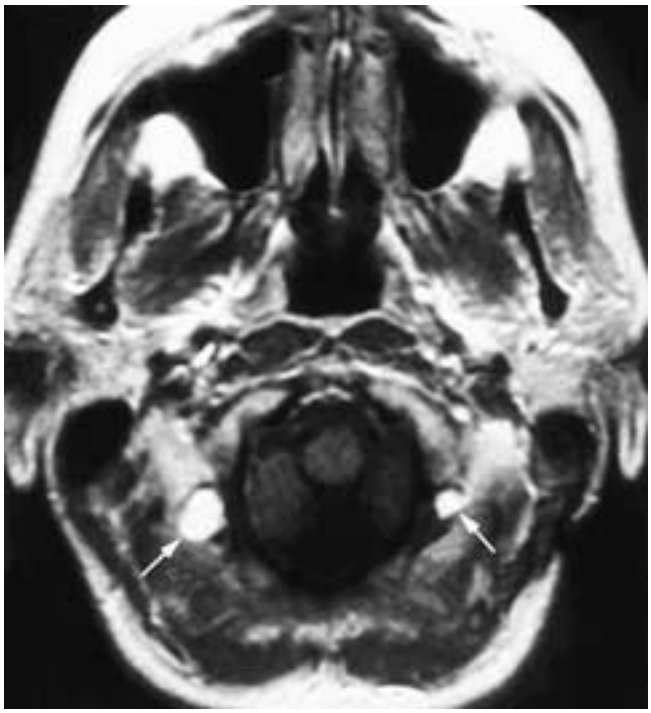

VIEW IMAGE

FIGURE 41-42 Axial T1-weighted image through the level of the foramen magnum shows a condylar vein with high signal intensity on each side of the neck (*arrows*). Asymmetry of the condylar veins is normal, and the high signal intensity reflects slow or turbulent venous flow. The importance of the condylar veins lies in their not being mistaken for abnormal lymph nodes.

aberrant right subclavian artery is associated with nonrecurrence of the recurrent laryngeal nerve.

Thrombosis and Dissection

Dissections of the great arteries in the neck can be spontaneous or related to blunt or penetrating trauma, strangulation, manipulation, angioplasty, infection, or intrinsic disorders of the vessels such as collagen-vascular disease.[169–171] Approximately one fourth of patients with internal carotid artery dissection will develop an associated pseudoaneurysm.[172] In a series of dissections related to manipulation, vertebral artery involvement was four times as frequent as carotid artery involvement; all vertebral lesions were seen around the atlantoaxial region, and 38% were bilateral.[170]

Imaging findings depend on the patient's age at the time of dissection and degree of resolution. On CT, fusiform narrowing of the arterial contrast column is more reliably demonstrated than actual subintimal hemorrhage. The classic MR appearance is that of a variably sized central flow void with a hyperintense rim or crescent on axial T1-weighted images, although this hyperintensity may not be seen in chronic cases (Fig. 41-46); conspicuity is augmented by fat saturation. MR angiography may falsely represent the degree of vascular compromise due to changes in flow rate through the dissection; the addition of contrast may help to better define the residual lumen.

Aneurysm

Aneurysms of the cervical internal carotid artery are rare lesions that typically present as pulsatile cervical masses. A series of 38 cases demonstrated relatively common associa-

Copyright © 2003, Mosby, Inc. All rights reserved.

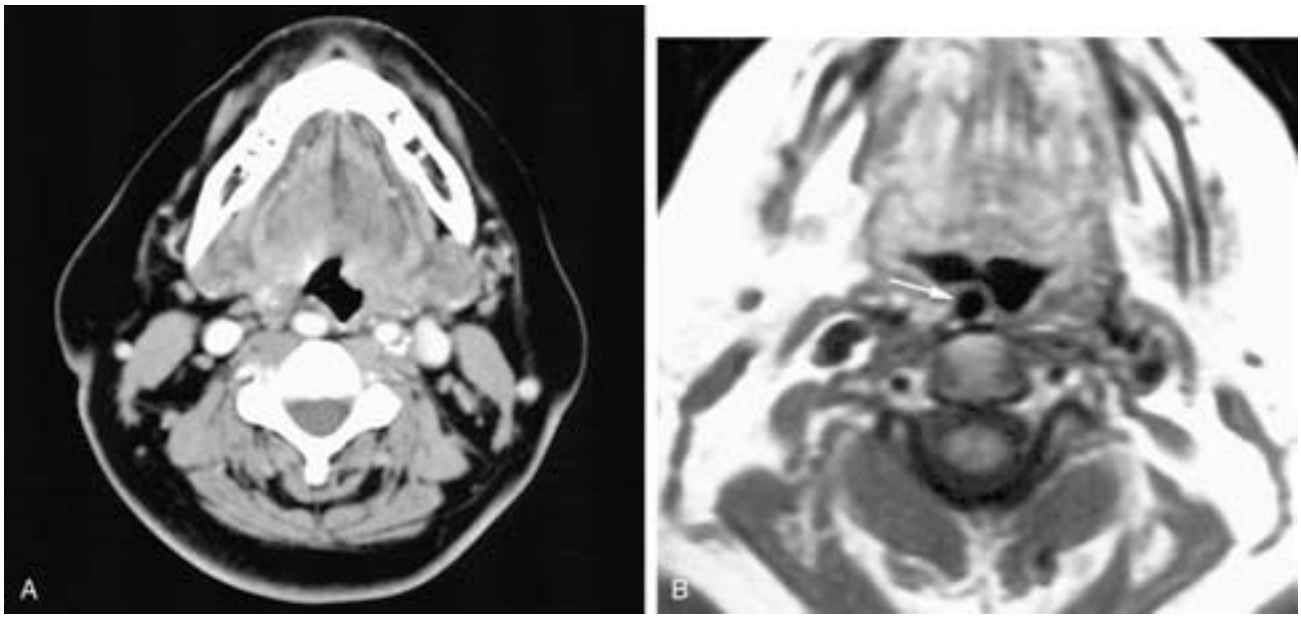

VIEW IMAGE

FIGURE 41-43 Axial contrast-enhanced CT scan (**A**) shows a normal variant, a medially displaced right carotid bulb indenting the posterior wall of the hypopharynx. The left carotid bulb, which has calcific atherosclerotic changes, is seen more laterally relative to the pharynx on the opposite side. Axial T1-weighted MR image of another patient (**B**) shows an almost midline-deviated right internal carotid artery (*arrow*). (Courtesy of Dr. David W. Johnson.)

tions with atherosclerosis, fibromuscular disease, dissection, and trauma.[173] These aneurysms tend to arise in the distal third of the cervical internal carotid artery, and pseudoaneurysms are more common than true aneurysms.[174] On imaging, there is intense enhancement. Since there may be significant flow-related signal loss within the aneurysm itself on MR imaging, the lumen may be better appreciated on contrast-enhanced CT (Fig. 41-44).

Hemangioma

Cutaneous hemangiomas are the most common tumors of infancy and childhood; pathologically, they are classified as infantile, capillary, or cellular. These tumors have a characteristic clinical course that consists of rapid postnatal growth (proliferating phase), slow, spontaneous regression (involuting phase), and finally, restoration of either normal or altered skin (involuted phase).[175] Pathologically similar lesions occur in adults, although these lesions do not spontaneously involute. Despite the difference in clinical behavior, most pathologists still tend to refer to all of these lesions as hemangiomas. However, there is an alternative clinical/pathologic classification that restricts the term *hemangioma* to the typical lesion described above, with onset in the infant or child. The pathologically similar lesion that has its onset in adults is referred to as a vascular malformation.[175] In addition, a variety of other vascular malformations occur in adults, which are classified by the dominant vessel (i.e., venous, arteriovenous, or arterial). The imaging of hemangiomas is described in various chapters in this book.

Hemangiopericytoma

Hemangiopericytomas are unusual tumors of vascular origin that usually present as painless masses. Approximately one in six tumors arise in the head and neck region, less frequently than those seen in the trunk, pelvis/retroperitoneum, and extremities. Males and females are affected equally, and the peak incidence is near the mid-fourth decade, although there is a wide age range at presentation (first through seventh decades).[176] The small percentage of these tumors seen in the neonatal period tend to be more benign, with some maturing to hemangiomas.[177]

Benign hemangiopericytomas are characterized histologically by branched vessels lined with normal epithelial cells and surrounded by a connective tissue matrix. Features of malignant transformation include increased mitoses, irregular or unusual vascular spaces, and proliferation of connective tissue; necrosis and hemorrhage do not appear to be common. Up to half of even benign-appearing tumors may recur, and wide local excision is recommended. Patients should be monitored carefully for delayed recurrences, which may be seen a decade or more after initial tumor excision.[176]

The majority of tumors arise in extramucosal sites.[178] The location of the tumor adds prognostic value, since soft-tissue tumors are more likely than mucosal tumors to recur locally and metastasize.[176] The utility of radiation therapy has been questioned, and its use may be limited to tumors with positive margins, high-grade tumors, and recurrences.[178] The tumor may be embolized preoperatively to minimize blood loss, although many surgeons first use

Copyright © 2003, Mosby, Inc. All rights reserved.

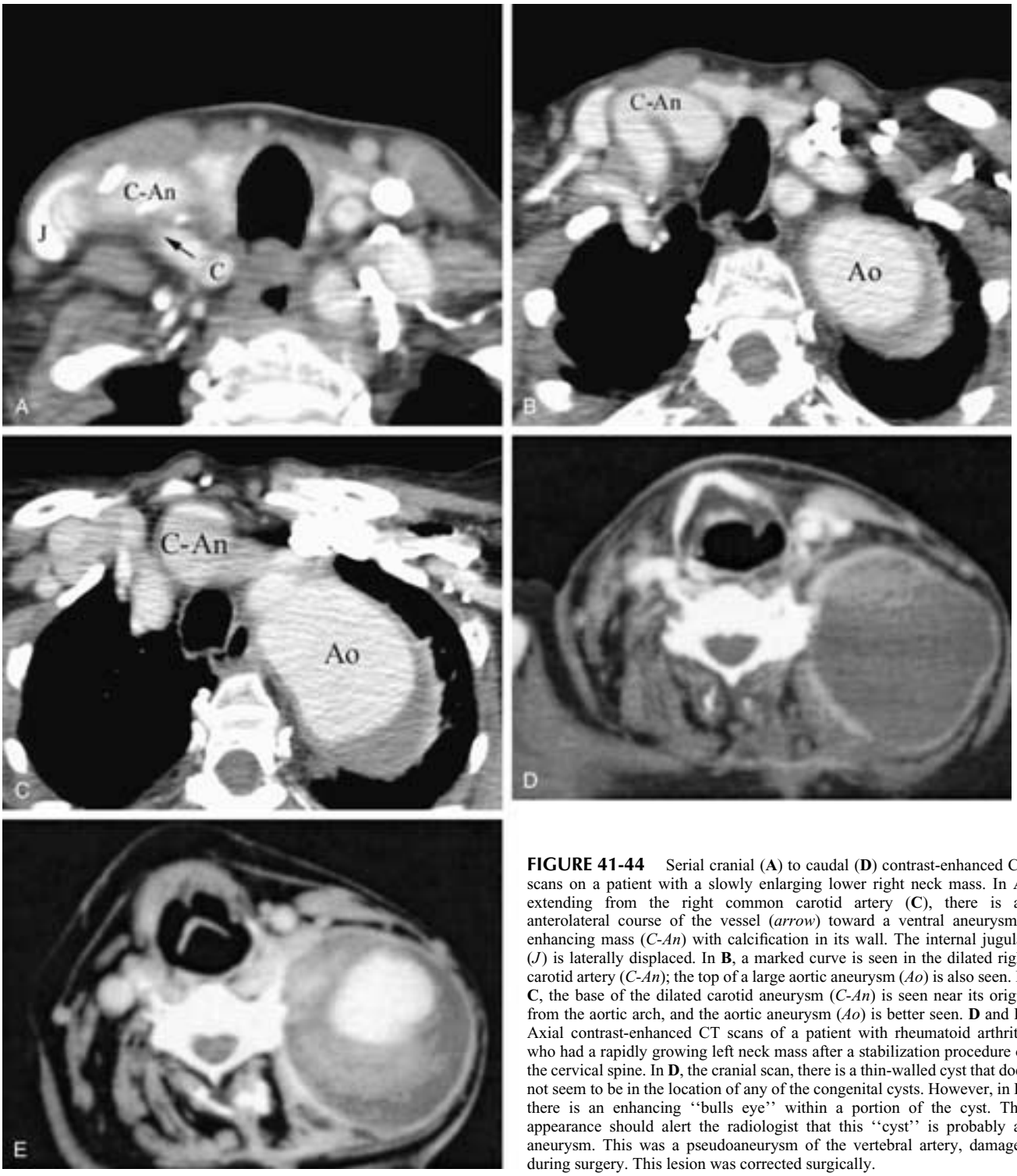

FIGURE 41-44 Serial cranial (**A**) to caudal (**D**) contrast-enhanced CT scans on a patient with a slowly enlarging lower right neck mass. In **A**, extending from the right common carotid artery (**C**), there is an anterolateral course of the vessel (*arrow*) toward a ventral aneurysmal enhancing mass (*C-An*) with calcification in its wall. The internal jugular (*J*) is laterally displaced. In **B**, a marked curve is seen in the dilated right carotid artery (*C-An*); the top of a large aortic aneurysm (*Ao*) is also seen. In **C**, the base of the dilated carotid aneurysm (*C-An*) is seen near its origin from the aortic arch, and the aortic aneurysm (*Ao*) is better seen. **D** and **E**, Axial contrast-enhanced CT scans of a patient with rheumatoid arthritis who had a rapidly growing left neck mass after a stabilization procedure of the cervical spine. In **D**, the cranial scan, there is a thin-walled cyst that does not seem to be in the location of any of the congenital cysts. However, in **E**, there is an enhancing ''bulls eye'' within a portion of the cyst. This appearance should alert the radiologist that this ''cyst'' is probably an aneurysm. This was a pseudoaneurysm of the vertebral artery, damaged during surgery. This lesion was corrected surgically.

VIEW IMAGE

Copyright © 2003, Mosby, Inc. All rights reserved.

embolization with recurrences, when adequate surgical margins may be difficult to obtain.

On imaging, hemangiopericytomas are usually well circumscribed. They have intermediate T1-weighted and increased T2-weighted signal intensities. The tumors enhance well on both CT and MR imaging, and flow voids are commonly seen on MR (Fig. 41-47). Calcification is an unusual feature. Prominent vascularity and tumor blush are seen on angiography. Sonographically, these tumors are well circumscribed and hypoechoic, with half showing sound through-transmission. To date, there are no reliable criteria to exclude malignancy; thus, all hemangiopericytomas should be considered potentially malignant.

PERIPHERAL NERVE SHEATH TUMORS

Peripheral nerve sheath tumors may be either benign or malignant. The benign lesions are either schwannomas or neurofibromas, and the neurofibromas may be solitary, multiple, or plexiform. The latter two varieties are usually associated with von Recklinghausen's disease. Malignant schwannoma, or malignant peripheral nerve sheath tumors, may occur spontaneously or arise from a neurofibroma or plexiform neurofibroma. Malignant transformation of a schwannoma is very rare.[179]

Schwannomas may arise from any nerve that contains Schwann cells and, with the exception of cranial nerves I and II, can occur in any cranial nerve, autonomic nerve, or peripheral nerve. The imaging of these lesions is discussed in various chapters throughout the book.

PHARYNGOESOPHAGEAL LESIONS

Zenker's Diverticulum

A Zenker's diverticulum is an outpouching lined by mucosa that extends through Killian's dehiscence, which

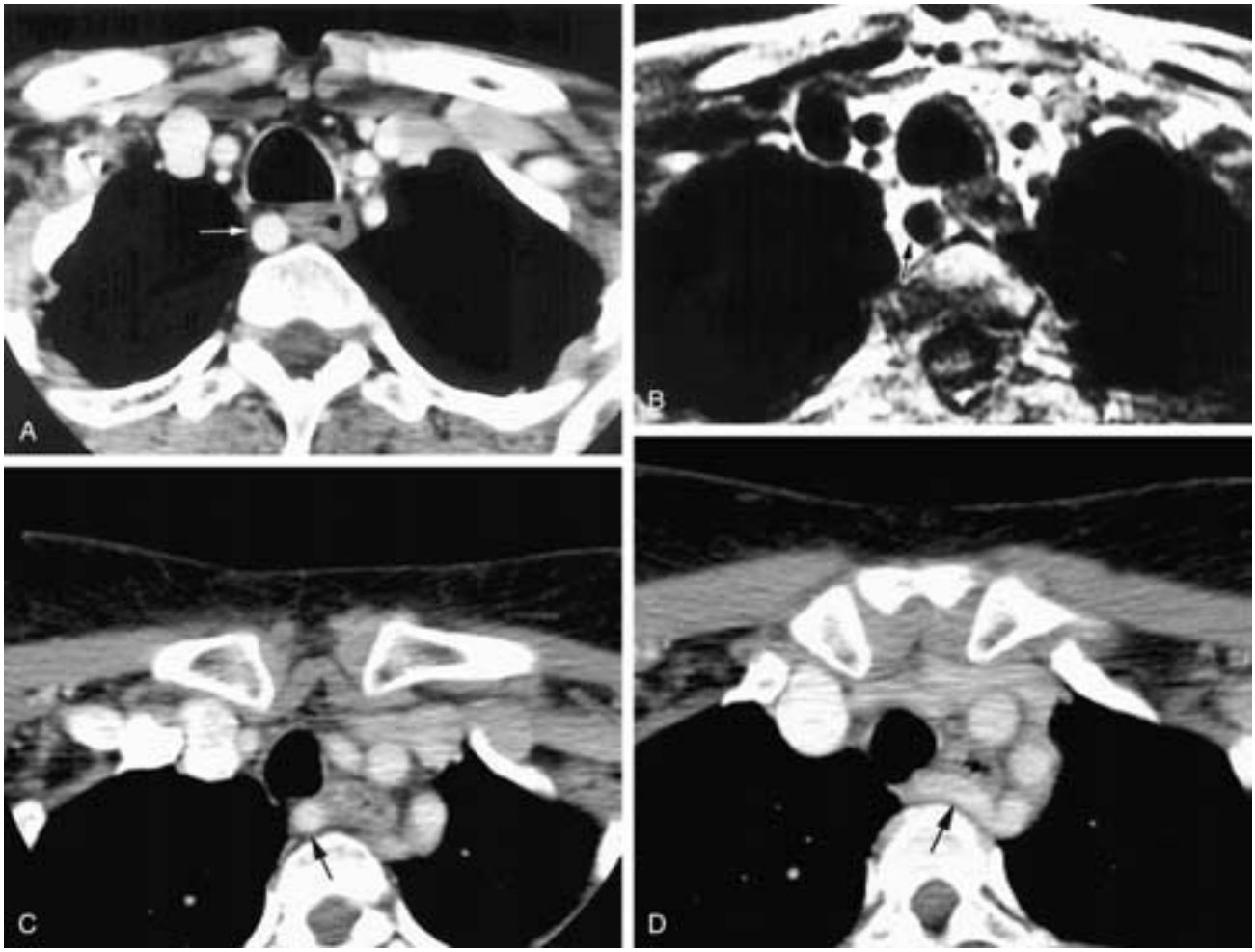

VIEW IMAGE

FIGURE 41-45 Axial contrast-enhanced CT scan (**A**) through the lower neck shows an aberrant right subclavian artery (*arrow*) adjacent to the cervical esophagus. A corresponding axial T1-weighted MR image (**B**) shows the aberrant artery (*arrow*). Cranial (**C**) and caudal (**D**) contrast-enhanced CT scans on another patient show an aberrant right subclavian artery (*arrows*) extending behind the cervical esophagus.

Copyright © 2003, Mosby, Inc. All rights reserved.

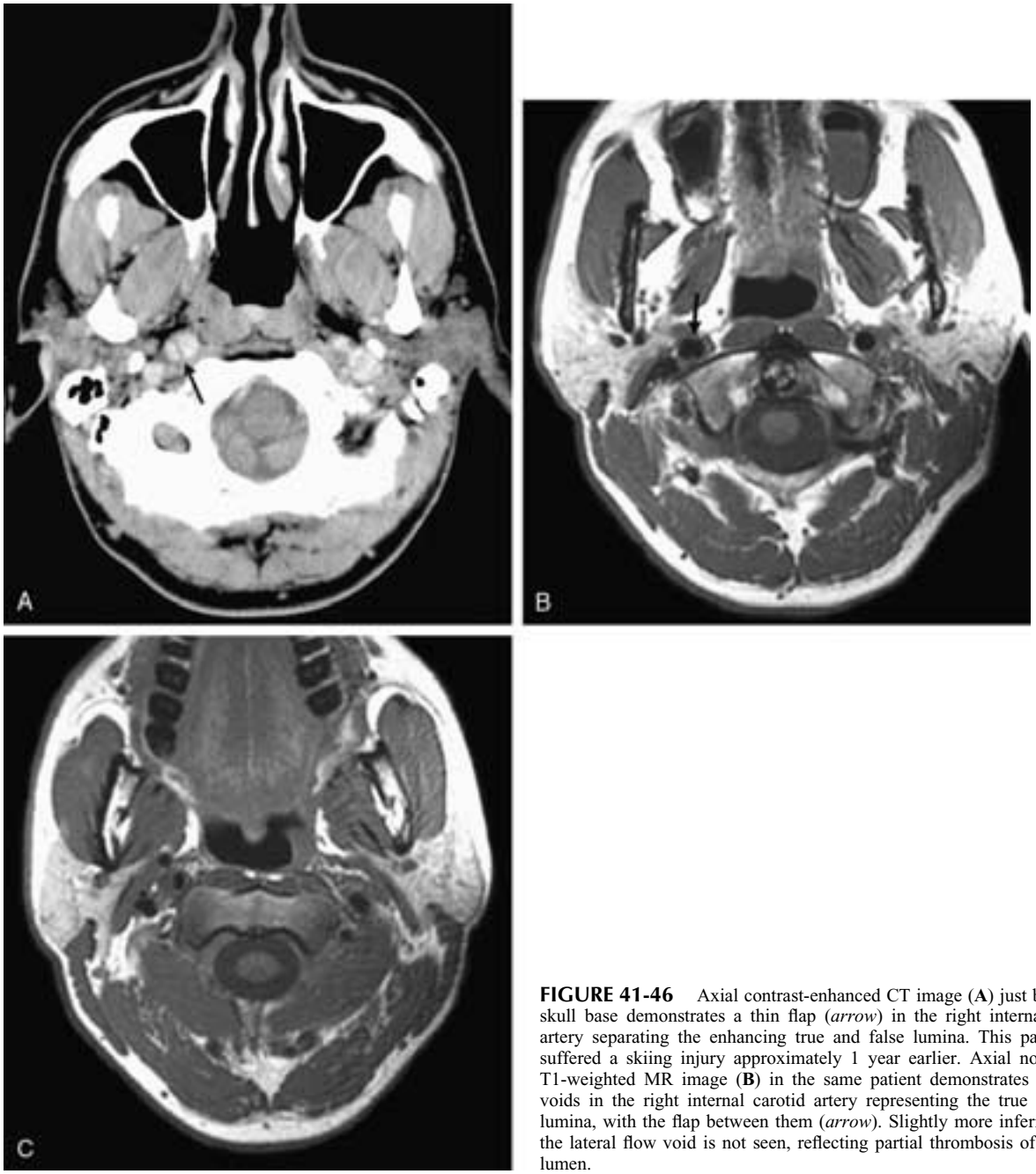

FIGURE 41-46 Axial contrast-enhanced CT image (**A**) just below the skull base demonstrates a thin flap (*arrow*) in the right internal carotid artery separating the enhancing true and false lumina. This patient had suffered a skiing injury approximately 1 year earlier. Axial noncontrast T1-weighted MR image (**B**) in the same patient demonstrates two flow voids in the right internal carotid artery representing the true and false lumina, with the flap between them (*arrow*). Slightly more inferiorly (**C**), the lateral flow void is not seen, reflecting partial thrombosis of the false lumen.

VIEW IMAGE

Copyright © 2003, Mosby, Inc. All rights reserved.

is above the cricopharyngeus muscle and below the caudal oblique fibers of the inferior pharyngeal constrictor. The diverticulum typically projects posterolaterally from the lumen, and dyssynergy of the cricopharyngeus muscle may play a role in its formation. The diagnosis is readily made on a barium swallow and, rarely, a large Zenker's diverticulum may be apparent on a CT scan (Fig. 41-48).

Dilated/Obstructed Cervical Esophagus

On rare occasions, a dilated cervical esophagus can present as a low neck mass, often clinically mimicking a thyroid mass (Fig. 41-49). Patients may not offer a history relating to esophageal dysfunction, or they may complain of weight loss, heartburn, or a sensation of fullness. Causes of a dilated cervical esophagus include achalasia, esophageal tumor, strictures, and, in the older patient, presbyesophagus.[180–185]

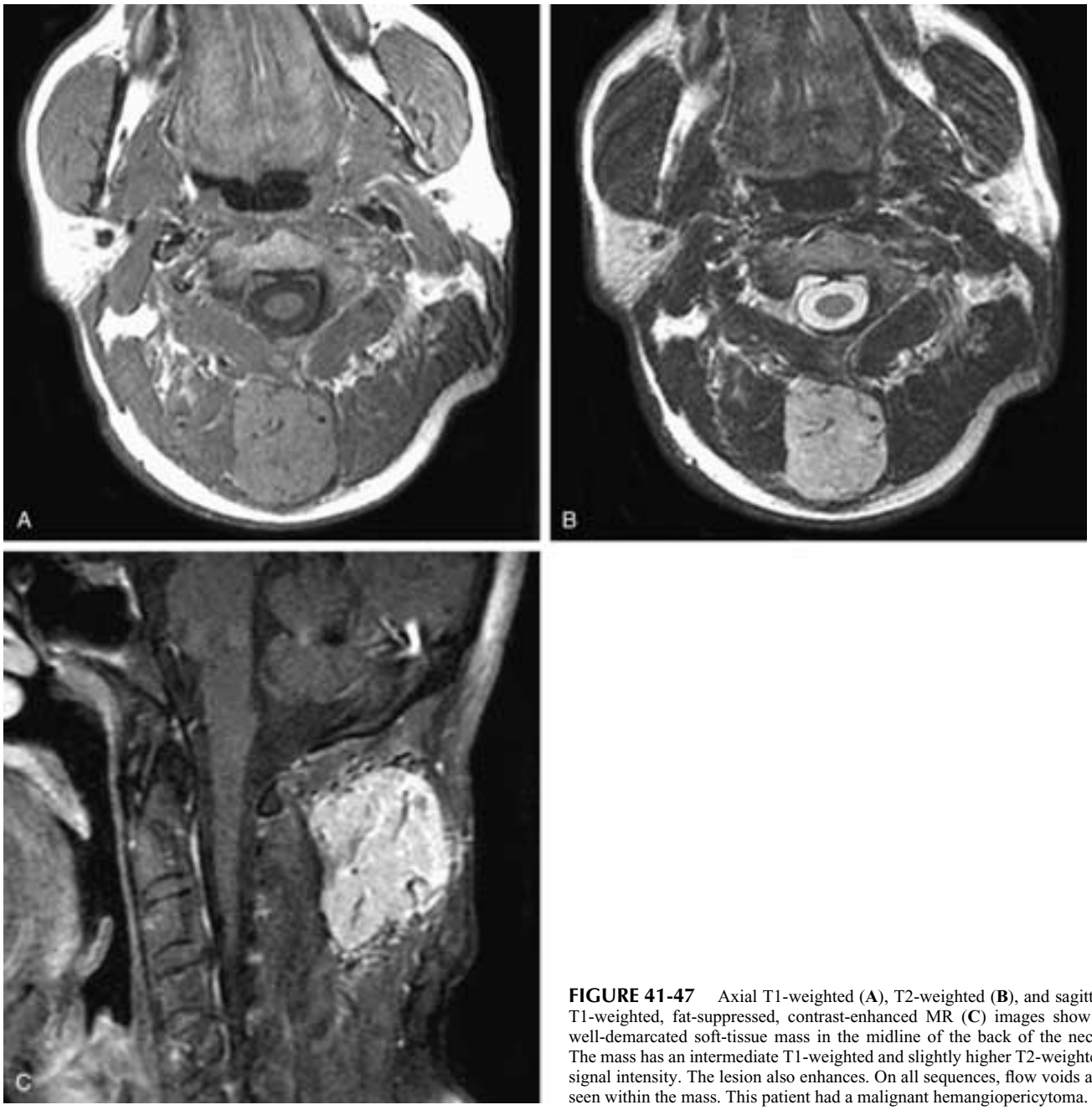

FIGURE 41-47 Axial T1-weighted (**A**), T2-weighted (**B**), and sagittal T1-weighted, fat-suppressed, contrast-enhanced MR (**C**) images show a well-demarcated soft-tissue mass in the midline of the back of the neck. The mass has an intermediate T1-weighted and slightly higher T2-weighted signal intensity. The lesion also enhances. On all sequences, flow voids are seen within the mass. This patient had a malignant hemangiopericytoma.

VIEW IMAGE

Copyright © 2003, Mosby, Inc. All rights reserved.

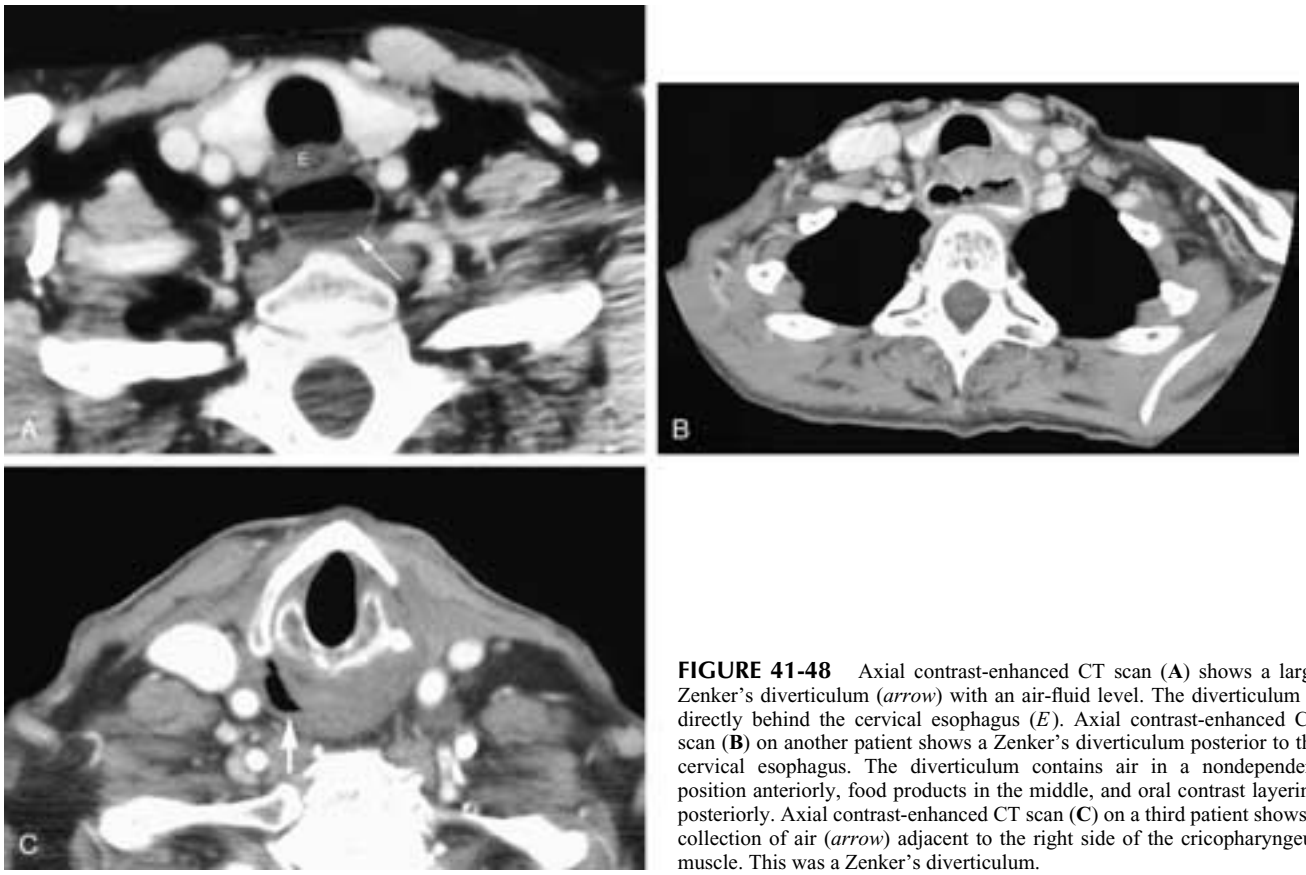

FIGURE 41-48 Axial contrast-enhanced CT scan (**A**) shows a large Zenker's diverticulum (*arrow*) with an air-fluid level. The diverticulum is directly behind the cervical esophagus (*E*). Axial contrast-enhanced CT scan (**B**) on another patient shows a Zenker's diverticulum posterior to the cervical esophagus. The diverticulum contains air in a nondependent position anteriorly, food products in the middle, and oral contrast layering posteriorly. Axial contrast-enhanced CT scan (**C**) on a third patient shows a collection of air (*arrow*) adjacent to the right side of the cricopharyngeus muscle. This was a Zenker's diverticulum.

VIEW IMAGE

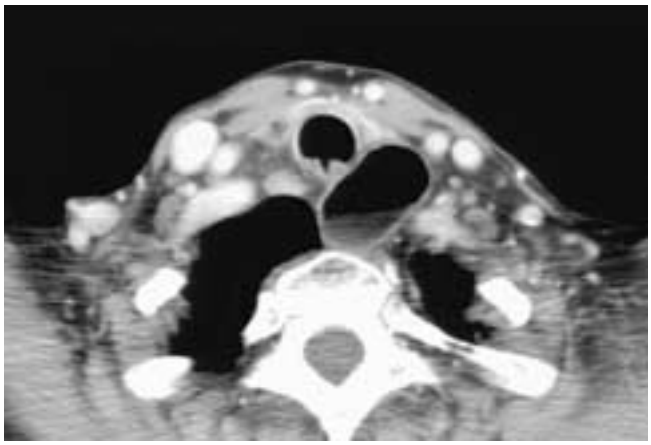

VIEW IMAGE

FIGURE 41-49 Axial contrast-enhanced CT scan shows a markedly dilated cervical esophagus with a fluid level within its lumen. The patient presented with a low left neck mass clinically thought to be in the thyroid gland. This patient had achalasia.

Copyright © 2003, Mosby, Inc. All rights reserved.

REFERENCES

1. Babu M, Bai RP, Suguna L, et al. Differentiation of keloid and hypertrophic scar; correlation of the water proton relaxation times with the duration of the scar. Physiol Chem Phys Med NMR 1993;25:113–120.
2. Silverman A, Nieland M. Pathology of selected skin lesions of the head and neck. In: Barnes L, ed. Surgical Pathology of the Head and Neck. Vol 2. New York: Marcel Dekker, 1985;1565–1633.
3. Ho V, McLean D. Benign epithelial tumors. In: Fitzpatrick T, Eisen A, Wolff K, et al., eds. Dermatology in General Medicine. Vol 1. New York: McGraw Hill, 1993;855–872.
4. Kim H-J, Kim T, Lee K-H, et al. Proliferating trichilemmal tumors: CT and MR imaging findings in two cases, one with malignant transformation. AJNR 2001;22:180–183.
5. Som PM, Shugar JM, Silvers AR. CT of pilomatrixoma in the cheek. AJNR 1998;19:1219–1220.
6. Hoffmann V, Roeren T, Moller P, Heuschen G. MR imaging of a pilomatrixoma. Pediatr Radiol 1998;28:272.
7. Hughes J, Lam A, Rogers M. Use of ultrasonography in the diagnosis of childhood pilomatrixoma. Pediatr Dermatol 1999;16: 341–344.
8. Bower C, Lear J, Bygrave S, et al. Basal cell carcinoma and risk of subsequent malignancies: A cancer registry-based study in southwest England. J Am Acad Dermatol 2000;42:988–991.
9. Wick M. Cutaneous tumors and pseudotumors of the head and neck. In: Gnepp D, ed. Diagnostic Surgical Pathology of the Head and Neck. Philadelphia: WB Saunders, 2001;777–856.
10. Carlson G, Murray D, Greenlee R, et al. Management of malignant melanoma of the head and neck using dynamic lymphoscintigraphy and gamma probe–guided sentinel lymph node biopsy. Arch Otolaryngol Head Neck Surg 2000;126: 433–437.
11. Grin C, Driscoll M, Grant-Kels J. The relationship of pregnancy, hormones, and melanoma. Semin Cutan Med Surg 1998;17: 167–171.
12. Balzi D, Carli P, Giannotti B, Buiatti E. Skin melanoma in Italy: a population-based study on survival and prognostic factors. Eur J Cancer 1998;34:699–704.
13. Gillgren P, Mansson-Brahme E, Frisell J, et al. A prospective population-based study of cutaneous malignant melanoma of the head and neck. Laryngoscope 2000;110:1498–1504.
14. Brown T, Nelson B. Malignant melanoma: a clinical review. Cutis 1999;63:275–278, 281–284.
15. Miller R, Rabkin C. Merkel cell carcinoma and melanoma: etiological similarities and differences. Cancer Epidemiol Biomarkers Prev 1999;8:153–158.
16. Nathu R, Mendenhall W, Parsons J. Merkel cell carcinoma of the skin. Radiat Oncol Investig 1998;6:233–239.
17. Tai P, Yu E, Winquist E, et al. Chemotherapy in neuroendocrine/Merkel cell carcinoma of the skin: case series and review of 204 cases. J Clin Oncol 2000;18:2493–2499.
18. Arce FP, Pinto J, Portero I, et al. Cutaneous metastases as initial manifestation of dedifferentiated chondrosarcoma of bone. An autopsy case with review of the literature [in process citation]. J Cutan Pathol 2000;27:262–267.
19. Bellezza G, Sidoni A, Bucciarelli E. Primary mucinous carcinoma of the skin. Am J Dermatopathol 2000;22:166–170.
20. Dorairajan LN, Hemal AK, Aron M, et al. Cutaneous metastases in renal cell carcinoma. Urol Int 2000;63:164–167.
21. Florez A, Roson E, Sanchez-Aguilar D, et al. Solitary cutaneous metastasis on the buttock: a disclosing sign of pancreatic adenocarcinoma. Clin Exp Dermatol 2000;25:201–203.
22. Guillou L, Gebhard S, Salmeron M, Coindre JM. Metastasizing fibrous histiocytoma of the skin: a clinicopathologic and immunohistochemical analysis of three cases [in process citation]. Mod Pathol 2000;13:654–660.
23. Ismail W, Pain S, al-Okati D, al Sewan M. Giant pilomatricoma simulating carcinoma of the male breast. Int J Clin Pract 2000;54:55–56.
24. Romero Hernandez R, Castillo Gonzalez A, Blanco Benavides R. [Cutaneous metastasis of gastric cancer]. Rev Gastroenterol Mex 1999;64:190.
25. Tankere F, Camproux A, Barry B, et al. [Prognostic influence of cutaneous involvement in malignant tumors of the oral cavity]. Ann Otolaryngol Chir Cervicofac 2000;117:85–90.
26. Zirwas MJ, Hunt S, Logan TF, et al. A painful cutaneous nodule as the presentation of metastatic transitional cell carcinoma of the renal pelvis. J Am Acad Dermatol 2000;42:867–868.
27. Miyamoto T, Ikehara A, Araki M, et al. Cutaneous metastatic carcinoma of the penis: suspected metastasis implantation from a bladder tumor. J Urol 2000;163:1519.
28. Norton K, Som P, Shugar J, et al. Subcutaneous fat necrosis of the newborn: CT findings in two cases. Am J Neuroradiol 1997;18:547–550.
29. Anderson D, Narla L, Dunn N. Subcutaneous fat necrosis of the newborn. Pediatr Radiol 1999;29:794–796.
30. Jardine D, Atherton D, Trompeter R. Sclerema neonatorum and subcutaneous fat necrosis of the newborn in the same infant. Eur J Pediatr 1990;150:125–126.
31. Dasgupta A, Ghosh R, Pal R, Mukherjee N. Sclerema neonatorum: histopathologic study. Indian J Pathol Microbiol 1993;36:45–47.
32. Fuleihan N, Webster R, Smith R. Facial implants. In: Cummings C, Fredrickson J, Harker L, et al., eds. Otolaryngology: Head and Neck Surgery. Vol 1. St. Louis: Mosby Year Book, 1993;612–624.
33. Sclafani AP, Romo T 3rd, Jacono AA, et al. Evaluation of acellular dermal graft in sheet (AlloDerm) and injectable (micronized AlloDerm) forms for soft tissue augmentation. Clinical observations and histological analysis. Arch Facial Plast Surg 2000;2:130–136.
34. Dubin MG, Feldman M, Ibrahim HZ, et al. Allograft dermal implant (AlloDerm) in a previously irradiated field. Laryngoscope 2000;110: 934–937.
35. Crook K. The use of AlloDerm and allograft to augment a mandibular arch for implant development. N M Dent J 1999;50:22–24.
36. Tark KC, Chung S, Shin KS, Park BY. Skin flap prefabrication using acellular dermal matrix and cultured keratinocytes in a porcine model. Ann Plast Surg 2000;44:392–397.
37. Ibrahim HZ, Kwiatkowski TJ, Montone KT, et al. Effects of external beam radiation on the allograft dermal implant. Otolaryngol Head Neck Surg 2000;122:189–194.
38. Castor SA, To WC, Papay FA. Lip augmentation with AlloDerm acellular allogenic dermal graft and fat autograft: a comparison with autologous fat injection alone. Aesthetic Plast Surg 1999;23: 218–223.
39. Achauer BM, VanderKam VM, Celikoz B, Jacobson DG. Augmentation of facial soft-tissue defects with AlloDerm dermal graft. Ann Plast Surg 1998;41:503–507.
40. Kridel RW, Foda H, Lunde KC. Septal perforation repair with acellular human dermal allograft. Arch Otolaryngol Head Neck Surg 1998;124:73–78.
41. Maas CS, Papel ID, Greene D, Stoker DA. Complications of injectable synthetic polymers in facial augmentation. Dermatol Surg 1997;23:871–877.
42. Wainwright DJ. Use of an acellular allograft dermal matrix (AlloDerm) in the management of full-thickness burns. Burns 1995;21:243–248.
43. Pinto FR, Durazzo MD, Cordeiro AC, Ferraz AR. [Cervical perforating foreign body: case report]. Rev Assoc Med Bras 2000;46: 77–80.
44. Nusbaum AO, Som PM, Rothschild MA, Shugar JM. Recurrence of a deep neck infection: a clinical indication of an underlying congenital lesion. Arch Otolaryngol Head Neck Surg 1999;125: 1379–1382.
45. Morales-Angulo C, Rodriguez Iglesias J, Mazon Gutierrez A, et al. [Diagnosis and treatment of cervical esophageal perforation in adults]. Acta Otorrinolaringol Esp 1999;50:142–146.
46. Tekavcic I, Smrkolj VA. The path of a wounding missile along the spinal canal: a case report. Spine 1996;21:639–641.
47. Wolf M, Faibel M, Leventon G, et al. Penetrating cervical injury caused by a needlefish. Ann Otol Rhinol Laryngol 1995;104:248–250.
48. Fraser AB, Sen C, Casden AM, et al. Cervical transdural intramedullary migration of a sublaminar wire. A complication of cervical fixation. Spine 1994;19:456–459.
49. Boyer JC, Helenon O, Coste A, et al. [Contribution of x-ray computed tomography in the diagnosis of cervical suppuration]. Ann Otolaryngol Chir Cervicofac 1994;111:59–68.

Copyright © 2003, Mosby, Inc. All rights reserved.

50. Braverman I, Gomori JM, Polv O, Saah D. The role of CT imaging in the evaluation of cervical esophageal foreign bodies. J Otolaryngol 1993;22:311–314.
51. Young WF Jr, Katz MR, Rosenwasser RH. Spontaneous migration of an intracranial bullet into the cervical canal. South Med J 1993;86:557–559.
52. Bendet E, Horowitz Z, Heyman Z, et al. Migration of fishbone following penetration of the cervical esophagus presenting as a thyroid mass. Auris Nasus Larynx 1992;19:193–197.
53. Murata K, Nishio A, Nishikawa M, et al. Subarachnoid hemorrhage and spinal root injury caused by acupuncture needle—case report. Neurol Med Chir (Tokyo) 1990;30:956–959.
54. Marsot-Dupuch K, Janklewicz P, Chabolle F, et al. Use of X-ray computed tomography in cervical infections. J Radiol 1988;69:175–186.
55. Scaglione M, Pinto F, Grassi R, et al. Migration of a foreign body from the pharynx to the soft tissues of the neck: delayed presentation with Horner's syndrome. AJR 1999;172:1131–1132.
56. Mathew JM, Rajshekhar V, Chandy MJ. MRI features of neurosurgical gossypiboma: report of two cases. Neuroradiology 1996;38:468–469.
57. Watanabe K, Kikuchi T, Katori Y, et al. The usefulness of computed tomography in the diagnosis of impacted fish bones in the oesophagus. J Laryngol Otol 1998;112:360–364.
58. Palme CE, Lowinger D, Petersen AJ. Fish bones at the cricopharyngeus: a comparison of plain-film radiology and computed tomography. Laryngoscope 1999;109:1955–1958.
59. Lue AJ, Fang WD, Manolidis S. Use of plain radiography and computed tomography to identify fish bone foreign bodies. Otolaryngol Head Neck Surg 2000;123:435–438.
60. Braverman I, Rosenmann E. Value of radiography in the management of possible fishbone ingestion. Ann Otol Rhinol Laryngol 1995;104:501.
61. Barnes L, Verbin R, Gnepp D. Diseases of the nose, paranasal sinuses and nasopharynx. In: Barnes L, ed. Surgical Pathology of the Head and Neck. Vol 1. New York: Marcel Dekker, 1985;725–880.
62. Einarsdottir H, Soderlund V, Larson O, et al. MR imaging of lipoma and liposarcoma. Acta Radiol 1999;40:64–68.
63. Ahuja A, King A, Kew J, et al. Head and neck lipomas: sonographic appearance. Am J Neuroradiol 1998;19:505–508.
64. Matsumoto K, Hukuda S, Ishizawa M, et al. MRI findings in intramuscular lipomas. Skeletal Radiol 1999;28:145–152.
65. Mattel SF, Persky MS. Infiltrating lipoma of the sternocleidomastoid muscle. Laryngoscope 1983;93:205–207.
66. Jagadha V, Ramaswamy G. Benign infiltrative lipomatous lesions [letter]. NY State J Med 1984;84:591–592.
67. Silanteva NK, Sviridova TV, Grishin GN. [A case of infiltrative lipoma of retroperitoneal space]. Vestn Rentgenol Radiol 1994:58.
68. Stubbs WP, Voges AK, Shiroma JT, Wolf J. What is your diagnosis? Infiltrative lipoma with chronic salivary duct obstruction. J Am Vet Med Assoc 1996;209:55–56.
69. Schellong H, Falcone A, Gunther M, Schmidt H. [Infiltrating intramuscular lipoma (see comments)]. Chirurgie 1997;68:279–282.
70. Matsumoto K, Hukuda S, Ishizawa M, et al. MRI findings in intramuscular lipomas. Skeletal Radiol 1999;28:145–152.
71. Mevio E, Calabro P, Redaelli GA, et al. [Benign symmetric lipomatosis: Madelung's disease]. Acta Otorhinolaryngol Ital 1997; 17:64–67.
72. Ahuja AT, King AD, Chan ES, et al. Madelung disease: distribution of cervical fat and preoperative findings at sonography, MR, and CT. AJNR 1998;19:707–710.
73. Uhl M, Roeren T, Schneider B, Kauffmann GW. [Magnetic resonance tomography of liposarcoma]. Rofo Fortschr Geb Rontgenstr Neuen Bildgeb Verfahr 1996;165:144–147.
74. El-Mofty S, Kyriakos M. Soft tissue and bone lesions. In: Gnepp D, ed. Diagnostic Surgical Pathology of the Head and Neck. Philadelphia: WB Saunders, 2001;505–604.
75. Patel SC, Silbergleit R, Talati SJ. Sarcomas of the head and neck. Top Magn Reson Imaging 1999;10:362–375.
76. Baerg J, Murphy J, Magee J. Fibromatoses: clinical and pathological features suggestive of recurrence. J Pediatr Surg 1999;34:1112–1114.
77. Flacke S, Pauleit D, Keller E, et al. Infantile fibromatosis of the neck with intracranial involvement: MR and CT findings. AJNR 1999;20:923–925.
78. Garant M, Remy H, Just N. Aggressive fibromatosis of the neck: MR findings. AJNR 1997;18:1429–1431.
79. Krasovec M, Burg G. Nodular fasciitis (pseudotumor of skin). Dermatology 1999;198:431–433.
80. Meyer CA, Kransdorf MJ, Jelinek JS, Moser RP Jr. MR and CT appearance of nodular fasciitis. J Comput Assist Tomogr 1991;15: 276–279.
81. Jelinek J, Kransdorf MJ. MR imaging of soft-tissue masses. Mass-like lesions that simulate neoplasms. Magn Reson Imaging Clin North Am 1995;3:727–741.
82. Sepulveda A, Sastre N. Necrotizing fasciitis of the face and neck. Plast Reconst Surg 1998;102:814–817.
83. Djupesland P. Necrotizing fasciitis of the head and neck: report of three cases and review of the literature. Acta Otolaryngol Suppl 2000;543:186–189.
84. Raboso E, Llavero M, Rosell A, Martinez-Vidal A. Craniofacial necrotizing fasciitis secondary to sinusitis. J Laryngol Otol 1998;112: 371–372.
85. Nguyen R, Leclerc J. Cervical necrotizing fasciitis as a complication of acute epiglottitis. J Otolaryngol 1997;26:129–131.
86. Aimoni C, Cilione A, Grandi E, et al. Cervical necrotizing fasciitis. Eur Arch Otorhinolaryngol 1999;256:510–513.
87. Becker M, Zbaren P, Hermans R, et al. Necrotizing fasciitis of the head and neck: role of CT in diagnosis and management. Radiology 1997;202:471–476.
88. Schmid M, Kossmann T, Duewell S. Differentiation of necrotizing fasciitis and cellulitis using MR imaging. Am J Roentgenol 1998;170:615–620.
89. Ginsberg L, Eicher S. Levator claviculae muscle presenting as a neck mass: CT imaging. J Comput Assist Tomogr 1999;23:538–539.
90. Rubenstein D, Escott E, Hendrick L. The prevalence and CT appearance of the levator claviculae muscle: a normal variant not to be mistaken for an abnormality. Am J Neuroradiol 1999;20:583–586.
91. Bredella MA, Tirman PF, Fritz RC, et al. Denervation syndromes of the shoulder girdle: MR imaging with electrophysiologic correlation. Skeletal Radiol 1999;28:567–572.
92. King A, Ahuja A, Leung S, et al. MR features of the denervated tongue in radiation induced neuropathy. Br J Radiol 1999;72:349–353.
93. Porter SB, Blount BW. Pseudotumor of infancy and congenital muscular torticollis. Am Fam Physician 1995;52:1731–1736.
94. Tavill MA, Wetmore RF. A case of familial sternocleidomastoid tumor of infancy. Int J Pediatr Otorhinolaryngol 1996;38:163–168.
95. Bedi D, John S, Swischuk L. Fibromatosis colli of infancy: variability of sonographic appearance. J Clin Ultrasound 1998;26:345–348.
96. Ablin D, Jain K, Howell L, West D. Ultrasound and MR imaging of fibromatosis colli (sternomastoid tumor of infancy). Pediatr Radiol 1998;28:230–233.
97. Burstein FD, Cohen SR. Endoscopic surgical treatment for congenital muscular torticollis. Plast Reconstr Surg 1998;101:20–24; discussion 25–26.
98. Haasbeek JF, Lessard JA. Isolated atlantoaxial rotatory fixation in a child with seronegative spondyloarthropathy presenting with torticollis. J Rheumatol 1998;25:169–172.
99. Svetel M, Sternic N, Filipovic S, Kostic V. Spasmodic torticollis associated with multiple sclerosis: report of two cases. Mov Disord 1997;12:1092–1094.
100. Krauss JK, Seeger W, Jankovic J. Cervical dystonia associated with tumors of the posterior fossa. Mov Disord 1997;12:443–447.
101. Entel RJ, Carolan FJ. Congenital muscular torticollis: magnetic resonance imaging and ultrasound diagnosis. J Neuroimaging 1997;7: 128–130.
102. Ackerman J, Chau V, Gilbert-Barness E. Pathological case of the month. Congenital muscular torticollis. Arch Pediatr Adolesc Med 1996;150:1101–1102.
103. Gupta AK, Roy DR, Conlan ES, Crawford AH. Torticollis secondary to posterior fossa tumors. J Pediatr Orthop 1996;16:505–507.
104. Brans J, Aramideh M, Bosch A, Speelman H. Late presentation of congenital muscular torticollis: a non-dystonic cause of torticollis. J Neurol 1996;243:354–356.
105. Maheshwaran S, Sgouros S, Jeyapalan K, et al. Imaging of childhood torticollis due to atlanto-axial rotatory fixation. Childs Nerv Syst 1995;11:667–671.
106. Milanov I, Georgiev D. Spasmodic torticollis and tremor due to multiple sclerosis: a case report. Funct Neurol 1995;10:281–285.

Copyright © 2003, Mosby, Inc. All rights reserved.

107. Hayashi S, Ito K, Kogure T, et al. Clinical evaluation of congenital muscular torticollis by using MR imaging. Nippon Igaku Hoshasen Gakkai Zasshi 1995;55:957–960.
108. Cammarota A, Gershanik OS, Garcia S, Lera G. Cervical dystonia due to spinal cord ependymoma: involvement of cervical cord segments in the pathogenesis of dystonia. Mov Disord 1995;10:500–503.
109. Kikuchi K, Kowada M, Kojima H. Hypoplasia of the internal carotid artery associated with spasmodic torticollis: the possible role of altered vertebrobasilar haemodynamics. Neuroradiology 1995;37: 362–364.
110. Youkilis RA, Koch B, Myer CM 3rd. Ultrasonographic imaging of sternocleidomastoid tumor of infancy. Ann Otol Rhinol Laryngol 1995;104:323–325.
111. Eysel P, Rompe JD. Osteoid osteoma of the axis. Eur Spine J 1994;3:231–232.
112. Bussieres A, Cassidy JD, Dzus A. Spinal cord astrocytoma presenting as torticollis and scoliosis. J Manipulative Physiol Ther 1994;17:113–118.
113. Singer C, Green BA, Bruce JH, et al. Late presentation of congenital muscular torticollis: use of MR imaging and CT scan in diagnosis. Mov Disord 1994;9:100–103.
114. Hladky JP, Lejeune JP, Singer B, et al. Osteoblastoma of the odontoid process. Pediatr Neurosurg 1994;21:260–262.
115. Cataltepe SU, Barron TF. Benign paroxysmal torticollis presenting as ''seizures'' in infancy. Clin Pediatr (Phila) 1993;32:564–565.
116. Yasutomo K, Hashimoto T, Miyazaki M, Kuroda Y. Recurrent torticollis as a presentation of moyamoya disease [letter]. J Child Neurol 1993;8:187–188.
117. Davids JR, Wenger DR, Mubarak SJ. Congenital muscular torticollis: sequela of intrauterine or perinatal compartment syndrome. J Pediatr Orthop 1993;13:141–147.
118. Hanko J, Hindfelt B, Matilainen T, Sjoberg S. CT-scanning and magnetic resonance imaging in idiopathic spasmodic torticollis. Acta Neurol Scand 1992;86:267–270.
119. Yasutomo K, Hashimoto T, Miyazaki M, et al. [Moyamoya disease manifested by recurrent torticollis]. No To Hattatsu 1992;24: 391–393.
120. Krauss JK, Mohadjer M, Braus DF, et al. Dystonia following head trauma: a report of nine patients and review of the literature. Mov Disord 1992;7:263–272.
121. Bredenkamp JK, Maceri DR. Inflammatory torticollis in children. Arch Otolaryngol Head Neck Surg 1990;116:310–313.
122. Isaac K, Cohen JA. Post-traumatic torticollis. Neurology 1989;39: 1642–1643.
123. Whyte AM, Lufkin RB, Bredenkamp J, Hoover L. Sternocleidomastoid fibrosis in congenital muscular torticollis: MR appearance. J Comput Assist Tomogr 1989;13:163–164.
124. Plant GT, Kermode AG, du Boulay EP, McDonald WI. Spasmodic torticollis due to a midbrain lesion in a case of multiple sclerosis. Mov Disord 1989;4:359–362.
125. Besson JA, Ebmeier KP, Gemmell HG, et al. Brain imaging and treatment response in spasmodic torticollis. Br J Psychiatry 1988;153:399–402.
126. Nicholson P, Higgins T, Forgarty E, et al. Three-dimensional spiral CT scanning in children with acute torticollis. Int Orthop 1999;23:47–50.
127. Schwarz N. The fate of missed atlanto-axial rotatory subluxation. Arch Orthop Trauma Surg 1998;117:288–289.
128. Snyder CH. Paroxysmal torticollis in infancy. A possible form of labyrinthitis. Am J Dis Child 1969;117:458–460.
129. Dunn DW, Snyder CH. Benign paroxysmal vertigo of childhood. Am J Dis Child 1976;130:1099–1100.
130. Crawford A, Harnsberger H, Johnson L, et al. Fibromatosis colli of infancy. AJR 1988;151:1183–1184.
131. Maddalozzo J, Goldenberg JD. Pseudotumor of infancy—the role of ultrasonography. Ear Nose Throat J 1996;75:248–254.
132. Mann SS, Som PM, Gumprecht JP. The difficulties of diagnosing myositis ossificans circumscripta in the paraspinal muscles of a human immunodeficiency virus–positive man: magnetic resonance imaging and temporal computed tomographic findings. Arch Otolaryngol Head Neck Surg 2000;126:785–788.
133. Kransdorf MJ, Meis JM, Jelinek JS. Myositis ossificans: MR appearance with radiologic-pathologic correlation. AJR 1991;157: 1243–1248.
134. Steiner M, Gould AR, Kushner GM, et al. Myositis ossificans traumatica of the masseter muscle: review of the literature and report of two additional cases. Oral Surg Oral Med Oral Pathol Oral Radiol Endod 1997;84:703–707.
135. Brooke M. Disorders of skeletal muscle. In: Bradley W, Daroff R, Fenichel G, Marsden C, eds. Neurology in Clinical Practice. Vol 2. Boston: Butterworth-Heinemann, 1991;1843–1886.
136. Wilson A, Mackay L, Ord R. Recurrent dislocation of the mandible in a patient with myotonic dystrophy. J Oral Maxillofac Surg 1989;47:1329–1332.
137. Vanier T. Dystrophia myotonica in chilhood. Br Med J 1960;2:1284–1288.
138. Kawamura T. Computed tomographic findings of brain and skull in myotonic dystrophy, [letter]. J Oral Maxillofac Surg 1987;50: 1723.
139. Cornacchia L, Marina R, Ballanini V, Sozzi G. Computed tomographic findings of brain and skull in myotonic dystrophy [letter]. J Oral Maxillofac Surg 1988;51:1463–1464.
140. Saitoh H. [CT findings of muscular dystrophy: limb girdle type (LG), myotonic type (MYD) and Duchenne type (DMD)]. Nippon Igaku Hoshasen Gakkai Zasshi 1991;51:790–798.
141. Som P, Rothschild M, Silvers A, Norton K. A painless retroauricular mass in a patient with myotonic dystrophy: computed tomographic documentation of the bone changes that occur in the skull base. J Skull Base Surg 1998;7:223–225.
142. Lee J, Lee M, Lee B, et al. Rhabdomyosarcoma of the head and neck in adults: MR and CT findings. Am J Neuroradiol 1996;17:1923–1928.
143. Resnick D, Niwayama G. Skeletal metastases. In: Resnick D, ed. Diagnosis of Bone and Joint Disorders. Vol 6. 3rd ed. Philadelphia: WB Saunders, 1995;4039–4064.
144. Blomgren K, Qvarnberg Y, Valtonen H. Spontaneous fracture of an ossified stylohyoid ligament. J Laryngol Otol 1999;113:854–855.
145. Miller DB. Eagle's syndrome and the trauma patient. Significance of an elongated styloid process and/or ossified stylohyoid ligament [in process citation]. Funct Orthod 1997;14:30.
146. Yetiser S, Gerek M, Ozkaptan Y. Elongated styloid process: diagnostic problems related to symptomatology. Cranio 1997;15: 236–241.
147. DuPont JS Jr. Panoramic imaging of the stylohyoid complex in patients with suspected Ernest or Eagle's syndrome. Cranio 1998;16: 60–63.
148. Lugmayr H, Krennmair G, Lenglinger F. [Ossification of the stylohyoid chain in computerized tomography—Eagle syndrome]. Aktuelle Radiol 1997;7:331–332.
149. Miyar V, Morais D, Santos J. [Surgery of the elongated styloid syndrome]. An Otorrinolaringol Ibero Am 1997;24:303–309.
150. Aral IL, Karaca I, Gungor N. Eagle's syndrome masquerading as pain of dental origin. Case report. Aust Dent J 1997;42:18–19.
151. de Souza EA, Hotta TH, Bataglion C. Association of a temporomandibular disorder and Eagle's syndrome: case report. Braz Dent J 1996;7:53–58.
152. Baugh RF, Stocks RM. Eagle's syndrome: a reappraisal. Ear Nose Throat J 1993;72:341–344.
153. Robinson P, Davis J, Fraser J. The hyoid syndrome: a pain in the neck. J Laryngol Otol 1994;108:855–858.
154. Mandel S. Facial pain. ''Why does my face hurt, doctor?'' Postgrad Med 1990;87:77–80.
155. Lim RY. Carotodynia exposed: hyoid bone syndrome. South Med J 1987;80:444–446.
156. Kwok KL, Lam HS, Ng DK. Unilateral right-sided internal jugular phlebectasia in asthmatic children [in process citation]. J Paediatr Child Health 2000;36:517–519.
157. Fan XD, Qiu WL, Tang YS. Internal jugular vein phlebectasia: case report. J Oral Maxillofac Surg 2000;58:897–899.
158. Uzun C, Taskinalp O, Koten M, et al. Phlebectasia of left anterior jugular vein. J Laryngol Otol 1999;113:858–860.
159. Aleman Lopez O, Polo Tomas I, Sancho Mestre M, et al. [Neck phlebectasia]. An Otorrinolaringol Ibero Am 1999;26:539–548.
160. Sander S, Elicevik M, Unal M, Vural O. Jugular phlebectasia in children: is it rare or ignored? J Pediatr Surg 1999;34:1829–1832.
161. Lubianca-Neto JF, Mauri M, Prati C. Internal jugular phlebectasia in children. Am J Otolaryngol 1999;20:415–418.
162. Indudharan R, Quah BS, Shuaib IL. Internal jugular phlebectasia—an unusual cause of neck swelling. Ann Trop Paediatr 1999;19:105–108.

Copyright © 2003, Mosby, Inc. All rights reserved.

163. Gurpinar A, Kiristioglu I, Dogruyol H. Jugular phlebectasia. Eur J Pediatr Surg 1999;9:182–183.
164. Som PM, Shugar JM, Sacher M, Lanzieri CF. Internal jugular vein phlebectasia and duplication: CT features. J Comput Assist Tomogr 1985;9:390–392.
165. Braun I, Hoffman J, Malko J, et al. Jugular venous thrombosis: MR imaging. Radiology 1985;157:357–360.
166. Fishman E, Pakter R, Gayler B, et al. Jugular vein thrombosis: diagnosis by computed tomography. J Comput Assist Tomogr 1987;8:963–968.
167. Sceaton N, Ravenel J, Lehner P, et al. Lemierre syndrome: forgotten but not extinct—report of four cases. Radiology 1999;213:369–374.
168. Weissman J. Condylar canal vein: unfamiliar normal structure as seen at CT and MR imaging. Radiology 1994;190:81–84.
169. Malek A, Higashida R, Halbach V, et al. Patient presentation, angiographic features, and treatment of strangulation-induced bilateral dissection of the cervical internal carotid artery. Report of three cases. J Neurosurg 2000;92:481–487.
170. Hufnagel A, Hammers A, Schonle P, et al. Stroke following chiropractic manipulation of the cervical spine. J Neurol 1999;246: 683–688.
171. Grau A, Brandt T, Forsting M, et al. Infection-associated cervical artery dissection. Three cases. Stroke 1997;28:453–455.
172. Guillon B, Brunereau L, Biousse V, et al. Long-term follow-up of aneurysms developed during extracranial internal carotid artery dissection. Neurology 1999;53:117–122.
173. Moreau P, Albat B, Thevenet A. Surgical treatment of extracranial internal carotid artery aneurysm. Ann Vasc Surg 1994;8:409–416.
174. McCollum C, Wheeler W, Noon G, DeBakey M. Aneurysms of the extracranial carotid artery. Twenty-one years' experience. Am J Surg Pathol 1979;137:196–200.
175. Enjolras O, Mulliken J. Vascular tumors and vascular malformations. In: James W, Cockerell C, Dzubow L, et al., eds. Advances in Dermatology. Vol 13. St. Louis: CV Mosby, 1997;375–423.
176. Billings K, Fu Y, Calcaterra T, Sercarz J. Hemangiopericytoma of the head and neck. Am J Otolaryngol 2000;21:238–243.
177. Rodriguez-Galindo C, Ramsey K, Jenkins J, et al. Hemangiopericytoma in children and infants. Cancer 2000;88:198–204.
178. Carew J, Singh B, Kraus D. Hemangiopericytoma of the head and neck. Laryngoscope 1999;109:1409–1411.
179. Kapadia S. Tumors of the nervous system. In: Barnes L, ed. Surgical Pathology of the Head and Neck. Vol 2. 2nd ed. New York: Marcel Dekker, 2000;787–888.
180. Andreev AL, Gallinger Iu I. [Endoscopic interventions in cicatricial strictures of esophageal anastomoses]. Khirurgiia (Mosk) 1992:8–13.
181. Stone MM, Fonkalsrud EW, Mahour GH, et al. Esophageal replacement with colon interposition in children. Ann Surg 1986;203: 346–351.
182. Uetake T, Fujino MA. [Aging-related physical and life style changes in the patients with reflux esophagitis] [in process citation]. Nippon Rinsho 2000;58:1892–1896.
183. Ren J, Shaker R, Kusano M, et al. Effect of aging on the secondary esophageal peristalsis: presbyesophagus revisited. Am J Physiol 1995;268(6 pt. 1):G772–779.
184. Michelsohn NH. [Presbyesophagus—the maturity of a concept (editorial)]. Arq Gastroenterol 1995;32:1–2.
185. Rosenzweig S, Traube M. The diagnosis and misdiagnosis of achalasia. A study of 25 consecutive patients. J Clin Gastroenterol 1989;11:147–153.

Copyright © 2003, Mosby, Inc. All rights reserved.

42

Brachial Plexus

Deborah L. Reede and Roy A. Holliday

INTRODUCTION
BRACHIAL PLEXUS
Normal Anatomy
Imaging Strategies
Clinical Findings
BRACHIAL PLEXOPATHIES
VAGUS NERVE
PHRENIC NERVE

INTRODUCTION

The thoracic inlet or root of the neck is a narrow space that serves as the junction between the neck and the thorax.[10, 18, 26, 29, 36] This space is widest in the transverse plane. Its boundaries are the manubrium anteriorly, the first thoracic vertebra posteriorly, and on either side, the first rib laterally. This area is delineated further by Sibson's fascia, which extends on either side of the neck from the transverse process of the seventh cervical vertebra posteriorly to the medial border of the first rib. Since the first rib slants caudally as it extends anteriorly, this fascia's posterior attachment to the rib is more cranial than its anterior aspect. Thus, the plane of the thoracic inlet is tilted downward anteriorly and laterally on either side, being highest medially and posteriorly. Because of this orientation, when viewed in the sagittal plane, the lung apices are seen posteriorly and the structures at the base of the neck are located anteriorly. On axial images the apices of the lungs are located in the posterior lateral aspect of the thoracic inlet, and the major visceral structures, which pass between the neck and the thoracic inlet, are located anteriorly between the lungs. The major structures found in the thoracic inlet are listed in Table 42-1.

The anterior scalene muscle is the key reference point used to locate the major neural and vascular structures in the region. This muscle originates from the anterior tubercles of the fourth through sixth cervical vertebrae and extends downward and laterally to insert on the superior aspect of the first rib on the scalene tubercle and ridge.

The subclavian vein is located anterior to the anterior scalene muscle. The anterior scalene muscle divides the subclavian artery into three anatomic portions. The first portion is found medial to the anterior scalene muscle as the artery crosses the apex of the lung superficial to the subpleural membrane. The second portion of the artery is directly posterior to the anterior scalene muscle, and the third portion is lateral to this muscle. The ansa subclavia (a connection between the middle and inferior (or stellate) sympathetic ganglia looping around the subclavian artery), phrenic nerve, and vagus nerve cross the thoracic inlet anterior to the first portion of the subclavian artery (Fig. 42-1). As they cross the inlet, the phrenic nerve is located laterally and the vagus nerve medially; between these nerves is the ansa subclavia. Components of the brachial plexus are found directly posterior or superior to all three portions of the subclavian artery. Also located posterior to the subclavian artery are some of the components of the cervical sympathetic chain.[5, 24, 30, 32, 47]

An understanding of this region is imperative for those who interpret cross-sectional images of the neck and chest, and knowledge of the location of the neural structures that traverse this region is important when looking for lesions that produce palsies of these nerves and when predicting what nerves will be affected by a mass in this region of the neck.

BRACHIAL PLEXUS

Normal Anatomy

The brachial plexus provides sensory and motor innervation to the upper extremity. It is formed by the ventral rami of C5-T1 with occasional contributions from C4 and T2. These roots join to form trunks, divisions, cords, and subsequently peripheral nerves (Fig. 42-2). Although the anatomic communication among these structures is complex, the components of the brachial plexus have a constant relationship to structures that are readily identified on both CT and MR imaging. The direct visualization of these nerves is accomplished more often with MR imaging than

Copyright © 2003, Mosby, Inc. All rights reserved.

Table 42-1
STRUCTURES FOUND IN THE THORACIC INLET

Neural structures
Vagus nerve (located in the carotid sheath)
Recurrent laryngeal nerve
Sympathetic chain
Phrenic nerve
Brachial plexus
Vascular structures
Subclavian artery and vein
Brachiocephalic artery and vein
Common carotid arteries and internal jugular veins (located in the carotid sheath)
Lymphatics
Thoracic and right lymphatic ducts
Trachea
Esophagus

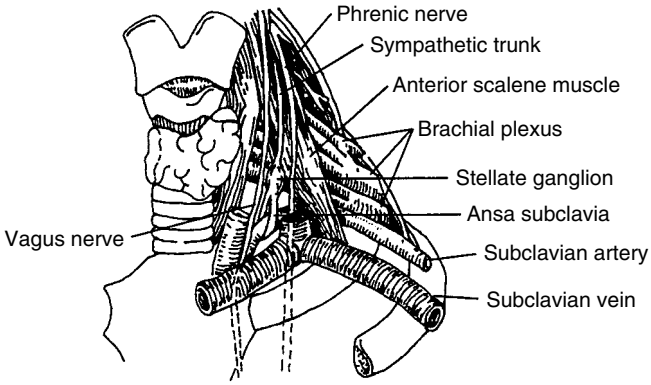

FIGURE 42-1 Thoracic inlet. Neural and vascular structures are shown. Note the relationship of these structures to the anterior scalene muscle.

VIEW IMAGE

with CT. Since these nerves are not routinely identified on conventional studies with either of these imaging modalities, one needs to be familiar with the location of the components of the brachial plexus and knowledgeable about specific imaging studies if cross-sectional imaging is to be used to evaluate patients with brachial plexopathies.

Due to the lordotic curvature of the spine, the more superior nerve roots are located anterior to the inferior nerve roots, and the cervical nerve roots in the upper neck are located posteromedially, adjacent to the neural foramina. The superior nerve roots run inferiorly, laterally, and anteriorly to pass between the anterior and middle scalene muscles (Fig. 42-3). Nerve roots C5 and C6 unite adjacent to the lateral border of the anterior scalene muscle to form the upper trunk of the brachial plexus, whereas the C7 nerve root travels by itself as the middle trunk. In the lower neck, the C8 and T1 nerves join behind the anterior scalene muscle to form the lower trunk (Fig. 42-4). Each trunk has an anterior and a posterior division. The divisions of the

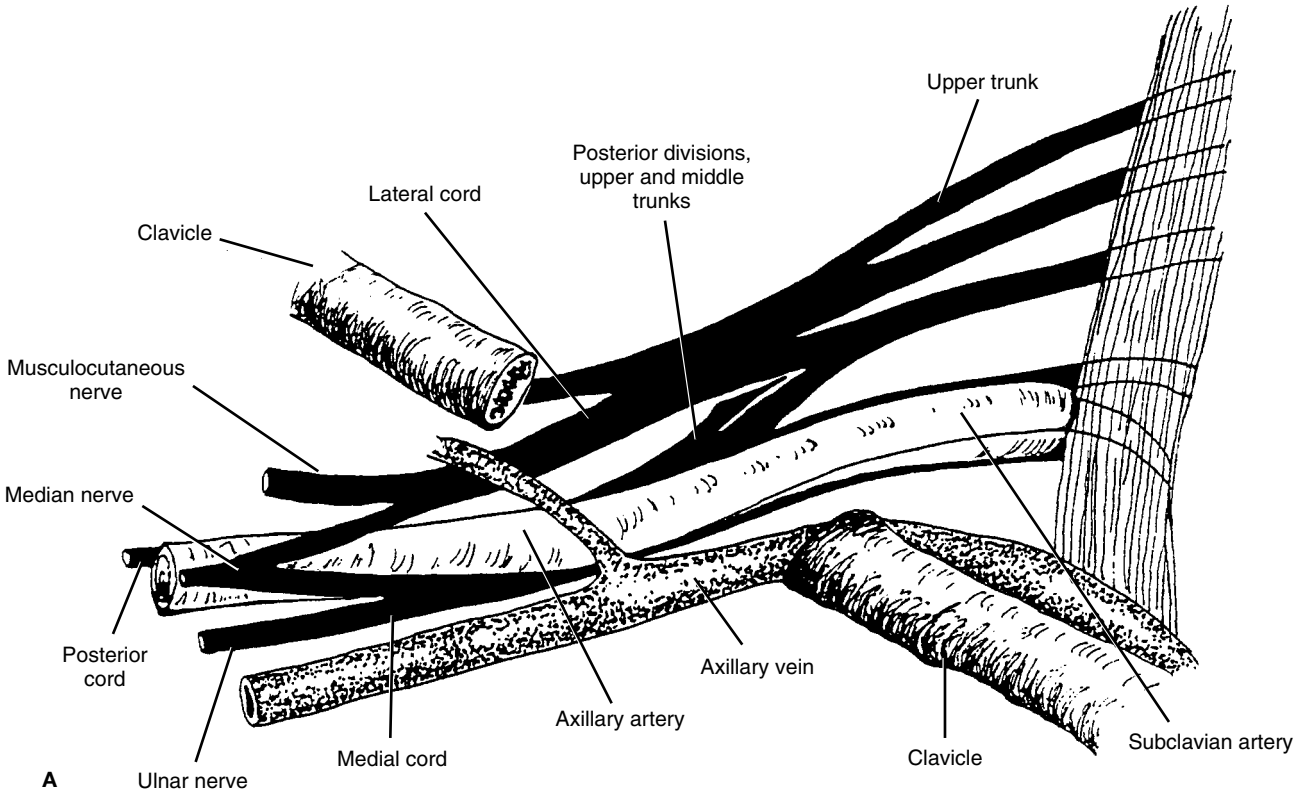

VIEW IMAGE

FIGURE 42-2 Brachial plexus. Diagram **A** shows the brachial plexus and its relationship to the anterior scalene muscle clavicle, subclavian artery, and axillary artery.

Illustration continued on following page

Copyright © 2003, Mosby, Inc. All rights reserved.

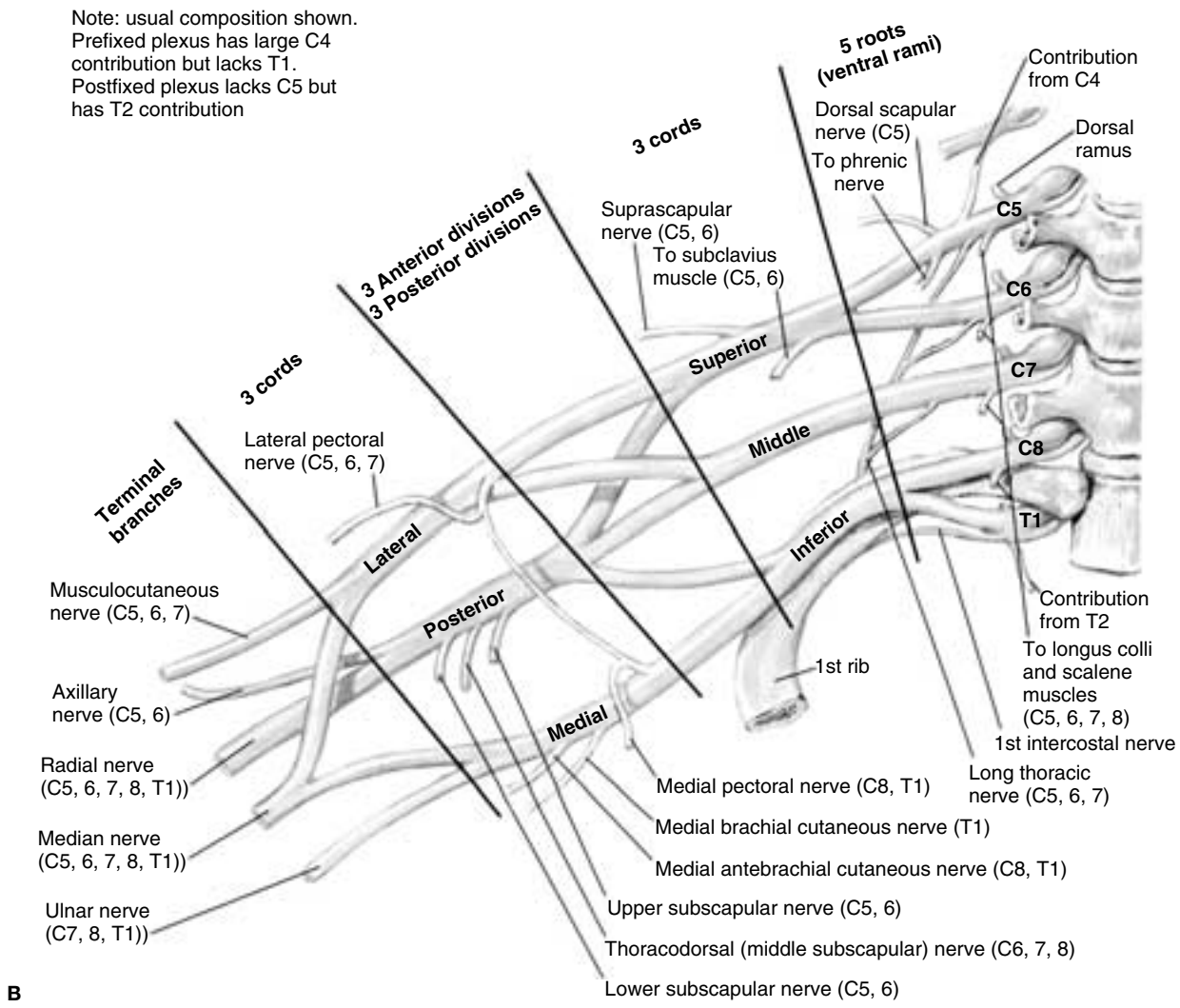

FIGURE 42-2 *Continued.* Diagram **B** shows the plexus, its segments, and the named nerve branches. Note: The usual composition is shown. The term ''prefixed'' applies if the plexus has a large C4 contribution but lacks T1. The ''postfixed'' plexus lacks C5 but has a T2 contribution. (Modified from Netter FH. Atlas of Human Anatomy. Summit, NJ: Ciba-Geigy Corporation, 1995; plate 405.)

VIEW IMAGE

FIGURE 42-3 Brachial plexus roots. Axial CT scan (**A**) and axial MR image (**B**) obtained at the level of the thyroid gland show cervical nerve roots (*arrow*) passing between the anterior (*A*) and middle (*M*) scalene muscles.

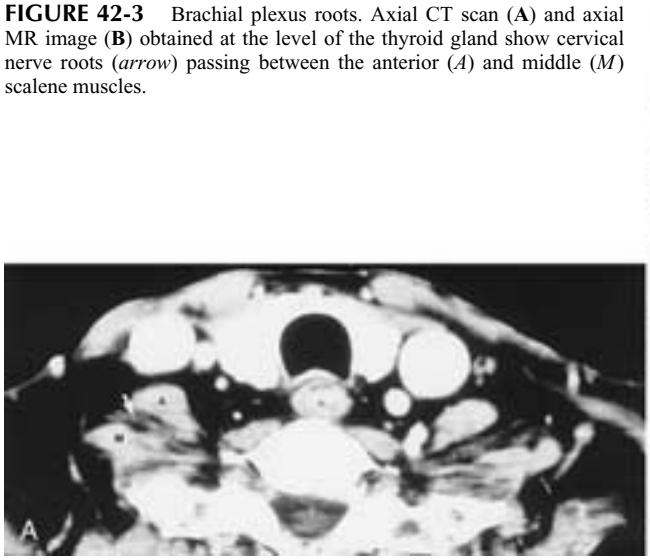

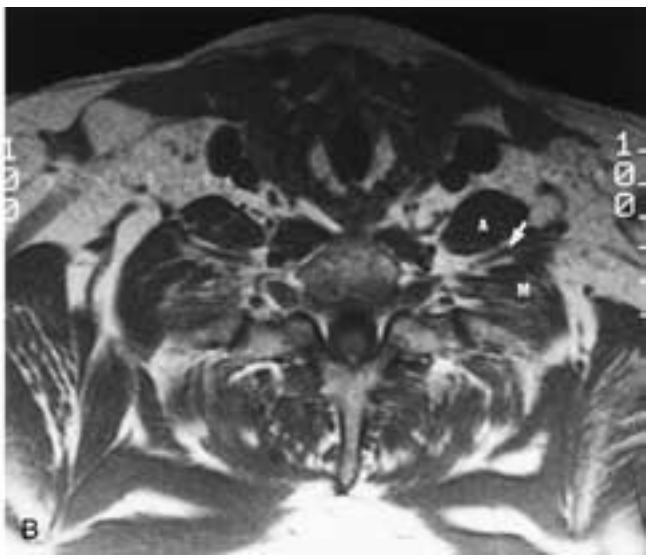

Copyright © 2003, Mosby, Inc. All rights reserved.

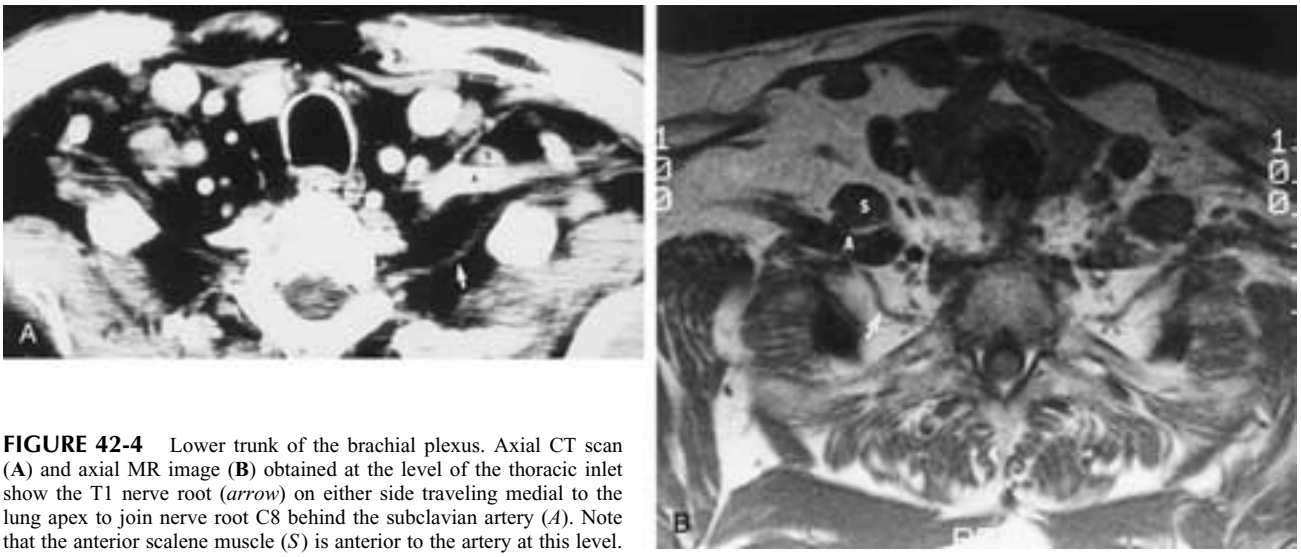

VIEW IMAGE

FIGURE 42-4 Lower trunk of the brachial plexus. Axial CT scan (**A**) and axial MR image (**B**) obtained at the level of the thoracic inlet show the T1 nerve root (*arrow*) on either side traveling medial to the lung apex to join nerve root C8 behind the subclavian artery (*A*). Note that the anterior scalene muscle (*S*) is anterior to the artery at this level.

superior and middle trunks form at or after the nerves pass lateral to the anterior scalene muscle. The divisions of the lower trunk are formed at or after the nerves cross the first rib (behind the clavicle or in the axilla). These components of the brachial plexus are found slightly above (superior and middle trunks) and directly posterior (inferior trunk) to the subclavian artery (Fig. 42-5).

Three cords are formed from the divisions:

1. The lateral cord is formed by the anterior divisions of the upper and middle trunks, which unite in the lower neck (i.e., the anterior divisions of nerves C5, C6, and C7).
2. The median cord is derived from the anterior division of the lower trunk in the lower neck (i.e., nerves C8 and T1).
3. The posterior cord is formed by the posterior divisions of all three trunks in the axilla (it has components of all of the nerves that form the brachial plexus).

These three cords enter the axilla by traveling between the clavicle and the first rib. Here they are found in the axillary sheath (a continuation of Sibson's fascia, a part of the deep layer of the deep cervical fascia) adjacent to the axillary artery and vein. After traveling a short distance in the axilla, the cords form peripheral nerves, lateral to the lateral margin of the pectoralis minor muscle. These nerves surround the axillary artery (Fig. 42-6). The peripheral nerves that originate from the cords of the brachial plexus are listed in Table 42-2.

Like the subclavian artery, the axillary artery is divided into three parts by a muscle. In this instance, it is the pectoralis muscle that crosses the axillary artery and divides it into three parts: the first part is medial, the second part is behind, and the third part is lateral to this muscle. The anatomic relationships of the nerves to the various parts of the axillary artery are listed in Table 42-3.[5, 24, 30, 32, 47]

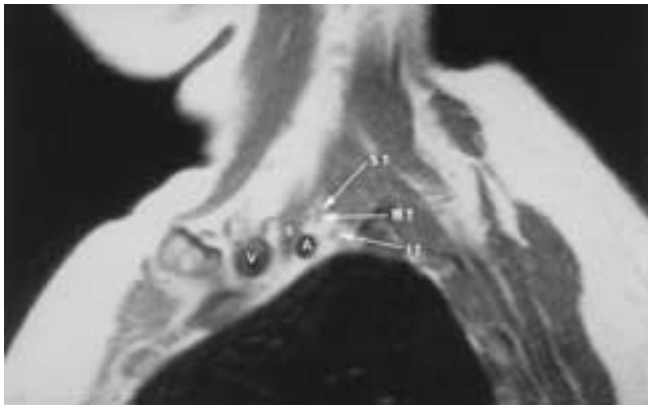

VIEW IMAGE

FIGURE 42-5 Sagittal MR T1-weighted image shows the trunks of the brachial plexus. The superior trunk (*ST*) and middle trunk (*MT*) are posterior superior and the inferior trunk (*IT*) is directly posterior to the subclavian artery (*A*). The subclavian vein (*V*) is anterior to the anterior scalene muscle (*S*).

Imaging Strategies

Although a number of imaging modalities, including plain films of the cervical spine and shoulder girdle, CT, MR imaging, and myelograms, can be used to evaluate patients with brachial plexopathies,[3, 9, 18, 38, 46] MR imaging has become the initial imaging modality of choice because its multiplanar capability allows for easier mapping of the course of the brachial plexus and reliable differentiation of vascular from nonvascular structures without the use of iodinated contrast. However, the initial imaging modality used should be determined by the clinical setting.

Optimal MR imaging of the brachial plexus is best accomplished by the use of phased array-surface coils.[23] Diagnostic-quality images, however, may also be obtained with a body-coil on 1.0 or 1.5 Tesla magnets (Fig. 42-7). One imaging protocol is a coronal localizer scout; sagittal T1-weighted images from the spinal canal to the lateral aspect of the clavicle on the affected side; axial T1-weighted images from the C4 vertebra to the carina, perpendicular to the long axis of the trachea (the field of view [FOV] should include the neck and thorax); oblique coronal T1-weighted images along the course of the distal subclavian and proximal axillary arteries (Fig. 42-8); and a T2-weighted

Copyright © 2003, Mosby, Inc. All rights reserved.

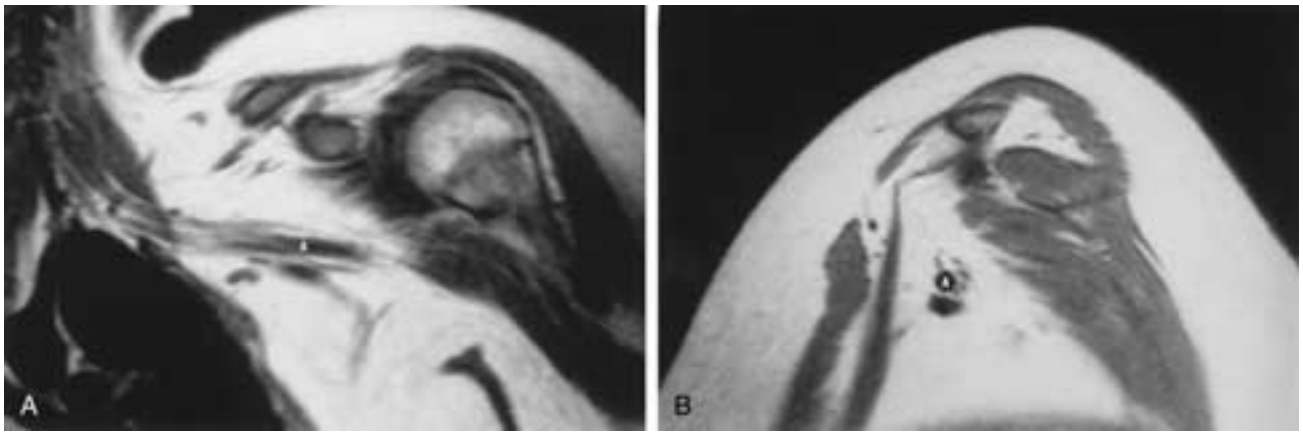

VIEW IMAGE

FIGURE 42-6 Brachial plexus, supraclavicular and axillary regions. Coronal MR image (**A**) shows the components of the brachial plexus in the supraclavicular region and axilla. The nerves surround the axillary artery (*A*). Sagittal MR image (**B**) obtained through the axilla demonstrates the peripheral nerves formed by the brachial plexus surrounding the axillary artery (*A*).

sequence usually in the axial plane. Factors such as slice thickness, slice gap, FOV, and number of acquisitions will vary with the equipment used. Ideally, slice thickness should be no greater than 5 mm, and higher-resolution matrices are recommended.

Rapid spin-echo (SE) or half-Fourier acquisition single shot turbo spin-echo (HASTE) images may be used to decrease scanning time. The effectiveness of routine contrast-enhanced MR imaging of the brachial plexus has yet to be proven. The administration of intravenous contrast may accentuate vascular artifacts and usually requires fat-saturation techniques to best identify subtle nerve enhancement.

An alternate protocol uses a torso coil. This protocol is designed to image in all three planes, and to utilize the ability to compare the involved side with the contralateral side to help define the normal anatomy in each patient and to aid in detection of subtle changes. Imaging starts with a T1-weighted SE coronal localizing sequence (5 mm thickness × 2.5 mm interslice gap, 48 cm FOV). From this localizer are planned the axial T1-weighted, SE and axial T2-weighted fast spin-echo (FSE) sequences with an adequate field to cover both plexi simultaneously (5 × 2.0 mm, 38 cm FOV). Detailed pre- and postgadolinium T1-weighted SE sequences of each plexus are then performed using a smaller FOV (24 cm) in the coronal oblique (4 × 1 mm) and sagittal oblique (5 × 3.0 mm) planes, oriented parallel and perpendicular to the nerves, respectively. Saturation bands are used to minimize artifacts from cardiac pulsation, and fat saturation is used on the postgadolinium sequences to increase lesion conspicuity.

The use of CT for the evaluation of the brachial plexus is largely reserved for patients who cannot undergo diagnostic MR imaging or in whom a biopsy of a mass using CT imaging guidance is contemplated.[11] Contrast should be administered via the asymptomatic arm to avoid obscuring subtle disease adjacent to the axillary or subclavicular veins.

Table 42-2
PERIPHERAL NERVES THAT ORIGINATE FROM THE CORDS OF THE BRACHIAL PLEXUS

Branches from the lateral cord
Lateral pectoral nerve
Musculocutaneous nerve
Lateral head of the median nerve*
Branches from the median cord
Medial pectoral nerve
Medial cutaneous nerve of the upper arm
Medial cutaneous nerve of the forearm
Medial root of the median nerve*
Ulnar nerve*
Branches from the posterior cord
Upper subscapular nerve
Thoracodorsal nerve
Lower subscapular nerve
Axillary nerve*
Radial nerve*

* Terminal branches.

Table 42-3
RELATIONSHIP OF NERVES TO THE AXILLARY ARTERY

First part of the axillary artery
Posteriorly: medial cord of the brachial plexus
Laterally: lateral and posterior cords of the brachial plexus
Second part of the axillary artery
Posteriorly: posterior cord of the brachial plexus
Laterally: lateral cord of the brachial plexus
Medially: medial cord of the brachial plexus
Third part of the axillary artery
Anteriorly: medial root of the median nerve
Posteriorly: radial and axillary nerves
Laterally: lateral root and trunk of the median nerve and for a short distance the musculocutaneous nerve
Medially: median cutaneous nerve of the upper arm and forearm, ulnar nerve

Copyright © 2003, Mosby, Inc. All rights reserved.

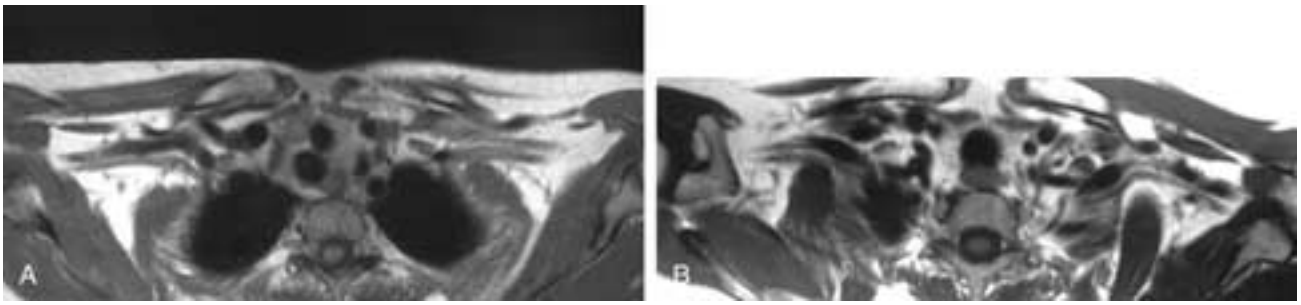

VIEW IMAGE

FIGURE 42-7 Body coil. Axial T1-weighted MR images at comparable levels using a body coil (**A**) and a phased array coil (**B**). Both images are of diagnostic quality. Image **B** was obtained in two thirds of the time required for image **A**. Note the detail in the axilla.

The development of nonincremental (helical, spiral) CT scanners and the newer multidetector CT scanners have greatly improved the CT evaluation of the brachial plexus. A screening examination should be performed with images obtained from the superior aspect of the C4 vertebra to the level of the carina. Placing the arms away from the lateral chest wall facilitates the identification of structures in the axilla and the proximal arm.

A survey examination consisting of images with 5 mm collimation and 4 mm spacing may be obtained using a pitch from 1.2 to 1.4 to 1, depending upon the patient's size. Image data may be targeted retrospectively or manipulated at a workstation for analysis in the sagittal, coronal, and oblique-coronal projections. If such CT scanners are not available, the examination should be performed in two distinct acquisitions, cervical and thoracic, by using appropriate FOVs for each segment.

The sonographic features of the normal brachial plexus have been described. A linear transducer of at least 7.5 MHz is recommended to perform these examinations. The nerve roots are identified by imaging the lower neck in an oblique coronal plane. The trunks can be identified in the supraclavicular fossa when the transducer is positioned at a right angle to the subclavian artery. The cords are identified by scanning in a plane parallel to the axillary artery inferior to the clavicle.[41]

Sonography can be used as a guide in catheter placement for brachial plexus anesthesia.[50] However, the role of sonography in the evaluation of patients with brachial plexopathy has yet to be determined.

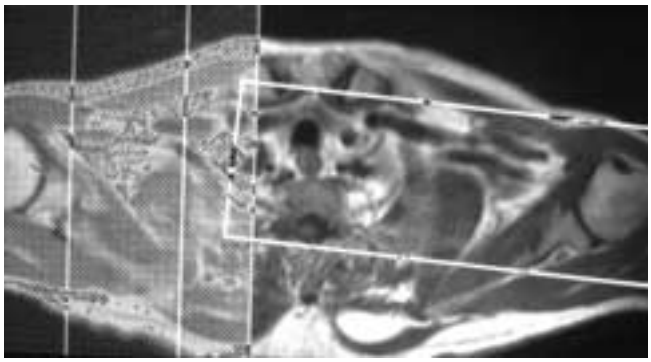

VIEW IMAGE

FIGURE 42-8 Axial scout localizer used to obtain an oblique coronal T1-weighted MR image. Note that these images are obtained parallel to the course of the subclavian and axillary arteries.

Clinical Findings

Brachial plexopathies develop when lesions occur anywhere along the course of the brachial plexus or, in some cases, adjacent to the brachial plexus. Patients with brachial plexopathies may present with pain and with sensory and motor deficits in the upper extremities. Pain, if present, may increase with neck traction, shoulder movement, or deep inspiration. Palpation or percussion in the supraclavicular fossa often elicits tenderness. Occasionally, a mass is palpated in the lower neck or axilla.

Long-term complications of brachial plexopathies include muscle wasting, arm edema, joint contractures, osteoporosis, and degenerative joint disease.[34] Localization of the precise site of involvement based on physical examination may be difficult since several sites of involvement may produce similar signs and symptoms.

Since the nerves that form the brachial plexus cover a wide territory from their point of origin in the spine to the muscles they innervate, an attempt should be made to localize the site of the abnormality (central or peripheral) prior to performing an imaging study. Such information can direct the imaging to a cervical spine examination instead of a brachial plexus study. Electromyography (EMG) may aid in distinguishing a lesion involving the nerve roots (central lesion) from one affecting the brachial plexus. EMG abnormalities in the paraspinal muscles indicate that a lesion is proximal to the plexus trunks, suggesting that there is a central lesion in the epidural space or neural foramen. EMG abnormalities in the peripheral muscles will define which peripheral nerve territories are involved.[37]

Neurologic evaluation of a patient with brachial plexopathy should include a search for other nerve dysfunction, as this may help localize the site of the abnormality. For example, the presence of Horner's syndrome points to involvement of the lower trunk. This is usually secondary to a mass in the lung apex, and chest radiography should be performed in these patients prior to cross-sectional imaging of the brachial plexus. Similarly, the combination of brachial plexopathy and phrenic nerve dysfunction should prompt careful analysis of the upper trunk of the plexus.

A patient questionnaire is useful in obtaining the basic

Copyright © 2003, Mosby, Inc. All rights reserved.

information needed to tailor the cross-sectional examination and to analyze the sectional images. Questions to be asked include:

1. Are symptoms unilateral or bilateral? The presence of bilateral brachial plexopathies is usually associated with a lesion in the epidural space or neural foramina, and these patients should be evaluated initially with a dedicated imaging study of the cervical spine.
2. Is there a history of trauma? These patients often require dedicated sectional imaging studies of the cervical spine to supplement the evaluation of the peripheral components of the plexus.
3. Is there an associated mass in the neck, supraclavicular fossa, or axilla? Characterization of a palpable mass may require the use of double-echo—T2-weighted rather than SE—T2-weighted sequences and the administration of intravenous contrast.
4. Are the symptoms produced by a particular arm position? Hand pain with arm elevation is a common finding with thoracic outlet syndrome secondary to a cervical rib, and identification of a cervical rib on a frontal radiograph should prompt further evaluation of the subclavian and axillary arteries rather than the soft-tissue components of the brachial plexus.
5. Does the patient have a prior history of carcinoma? Studies of patients with a history of malignancy require a careful search for abnormal signal within the trabecular bone of the cervical spine, clavicle, scapula, and shoulder as well as the soft tissues adjacent to the nerves. This is especially important if pain is the only presenting symptom.
6. Is there a history of surgery or radiation therapy to the affected axilla, neck, or supraclavicular fossa? Images of the affected side in these patients are often confusing, and oblique coronal and sagittal imaging of the opposite brachial plexus is often useful for comparison and identification of subtle changes.

BRACHIAL PLEXOPATHIES

Brachial plexopathies have a number of causes, which can be categorized as being either traumatic or nontraumatic. Trauma accounts for approximately 50% of the cases. The traumatic and nontraumatic causes of brachial plexopathy are listed in Tables 42-4 and 42-5, respectively. Posttraumatic injuries, with or without fractures, can cause compression, stretching, or tearing of the nerve roots. In these cases, the upper trunk is most frequently involved and the middle trunk is traumatized infrequently.

The primary concern in patients who have suffered a traumatic injury and who have a brachial plexopathy is whether there is a fracture (cervical spine or clavicle) or an avulsed nerve root, but it should be noted that soft-tissue swelling and/or hematomas in the region of the brachial plexus can produce the same symptoms (Fig. 42-9). If a fracture is suspected, a plain film examination of the area in question should be the initial radiographic study.

Table 42-4
TRAUMATIC CAUSES OF BRACHIAL PLEXOPATHY

Fractures of the cervical spine or clavicle
Nerve root avulsion with or without an associated pseudomeningocele
Soft-tissue edema
Hematoma

Table 42-5
NONTRAUMATIC CAUSES OF BRACHIAL PLEXOPATHY

Primary neural tumors such as meningiomas and schwannomas
Metastatic disease
Pancoast tumor
Postirradiation injury
Radiculopathy secondary to disk disease
Bony abnormalities such as cervical ribs

Cross-sectional imaging is usually not performed until at least 4 to 6 weeks after a suspected traumatic brachial plexus injury, and the primary goal of the study is to differentiate intraforaminal from extraforaminal causes. Intraforaminal (also know as preganglionic) injuries of the brachial plexus are characterized by a range of abnormalities including traumatic pseudomeningoceles, nerve root avulsions, and, less commonly, spinal cord contusion. The most common of these abnormalities are the traumatic pseudomeningoceles, which are bulges of the arachnoid membrane through a dural tear.[17] Although pseudomeningoceles are commonly associated with a nerve root avulsion, approximately 20% of nerve root avulsions are not associated with pseudomeningoceles.[22]

Extraforaminal (also known as postganglionic) injuries account for as much as one quarter of all cases of traumatic brachial plexopathies. Extraforaminal injuries, which carry a better prognosis than intraforaminal injuries, can be divided into two groups: lesions immediately deep or inferior to the clavicle and lesions distal to the plexus, commonly

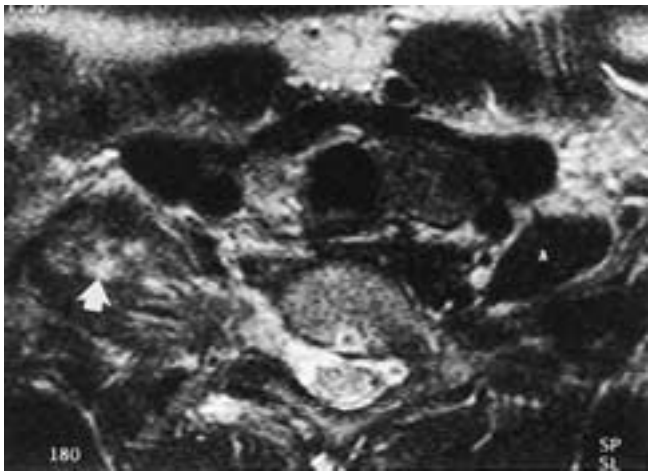

FIGURE 42-9 Soft-tissue injury of the anterior and middle scalene muscles. Axial T1-weighted MR image shows increased signal in the region of the right anterior scalene muscles (*arrow*). The normal anterior (*A*) scalene muscle is seen on the left. This patient had a normal CT scan and myelogram.

VIEW IMAGE

Copyright © 2003, Mosby, Inc. All rights reserved.

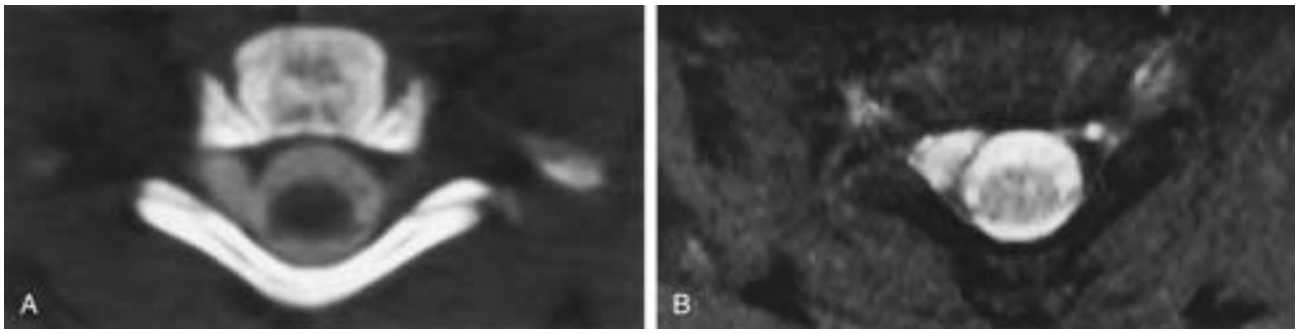

VIEW IMAGE

FIGURE 42-10 Pseudomeningocele. Axial CT myelogram (**A**) and T2-weighted MR image (**B**) demonstrate a CSF collection lateral to the thecal sac on the right extending into the neural foramen.

involving the terminal branches such as the suprascapular, axillary, or musculocutaneous nerves.[1]

High-resolution CT myelography has been traditionally advocated as the standard of reference for the detection of nerve root avulsion.[46] However, three-dimensional MR imaging has been suggested as a screening examination of the cervical spine.[17] On MR imaging, the absence of the low signal intensity nerve root in the fat of the neural foramen on the T1-weighted images is consistent with a nerve root avulsion, and this is best appreciated on parasagittal images. Increased T2-weighted signal intensity has also been observed in traumatized nerves,[27, 42, 48] and although the cause of the high signal intensity is uncertain, it is believed to be the result of neural edema.[37] Small pseudomeningoceles appear as an extra-arachnoid CSF intensity mass extending outside the spinal canal, and axial and coronal scans offer the best visualization of such lesions (Fig. 42-10). Increased signal intensity in the posterior cervical paraspinal muscles on T2-weighted or T2*-weighted images has also been reported as a reliable indicator of nerve root avulsion; however, the absence of such increased signal on MR studies does not imply nerve root integrity.[44] Because neither CT myelography nor MR imaging has 100% sensitivity or specificity for depicting nerve root avulsion, intraoperative neurophysiologic testing is an essential component of surgical attempts to repair the plexus.[13]

MR imaging is useful for the detection of extraforaminal lesions that are amenable to neurolysis or nerve grafting. Posttraumatic neuromas are identified on T1-weighted images as irregular areas of plexus thickening, largely isointense to skeletal muscle (Figs. 42-11 and 42-12). Neuromas have a marked increase in signal intensity on T2-weighted or short time inversion recovery (STIR) images. STIR images are also useful in identifying injury in cases in which a neuroma cannot be identified. Edema or other inflammatory responses in the tissues adjacent to the plexus appear as areas of abnormally increased signal intensity.[35]

Obstetric brachial plexus palsy occurs as the result of extreme lateral traction on the head during the last phase of delivery, with resulting stretching of the brachial plexus. The traction is exerted via the shoulder in delivering the head in a breech delivery and via the head in delivering the shoulder in a cephalic delivery. The upper roots are most vulnerable, although total paralysis can occur. *Erb's palsy*, a term erroneously thought synonymous with *obstetric brachial plexus palsy*, is but one type of brachial plexus injury characteristically involving the fifth and sixth cervical roots. In this palsy, there is weakness of shoulder abduction, external rotation, flexion and supination of the elbow, and extension of the wrist and fingers. This results in the characteristic ''waiter's tip'' posture. As with adult traumatic plexopathy, there is no role for sectional imaging in the acute phase of the injury, and many infants recover with no or minor residual functional impairment.[7]

At a number of institutions MR imaging has replaced CT myelography, which requires a lumbar puncture, iodinated contrast material, ionizing radiation, and general anesthesia for the evaluation of persistent obstetric brachial plexopathy. A combination of high-resolution MR imaging and intraoperative neurophysiologic testing is adequate for the evaluation and surgical planning of obstetric plexopathy.

A suggested imaging protocol usually requires sedation of the infant. The examination is performed on a 1.5 Tesla MR scanner with the infant in the head coil. For evaluation of potential intraforaminal abnormalities, thin-slice (2 to 3 mm) rapid SE T2-weighted imaging is used, rather than the axial T2*-weighted imaging used in adult cervical spine imaging. The evaluation for potential extraforaminal lesions consists of axial STIR and oblique coronal high-resolution T2-weighted images. T1-weighted images are obtained only when the high-resolution T2-weighted images provide insufficient anatomic detail. Since posterior glenohumeral

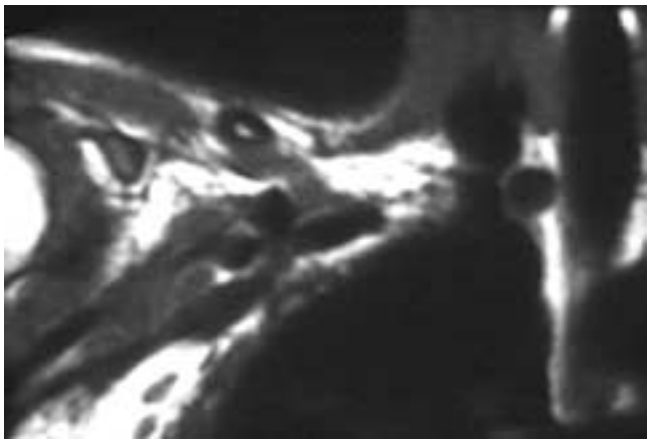

FIGURE 42-11 Status after a traction injury of the right shoulder. T1-weighted coronal image shows nodularity and thickening of the brachial plexus consistent with ganglion formation.

VIEW IMAGE

Copyright © 2003, Mosby, Inc. All rights reserved.

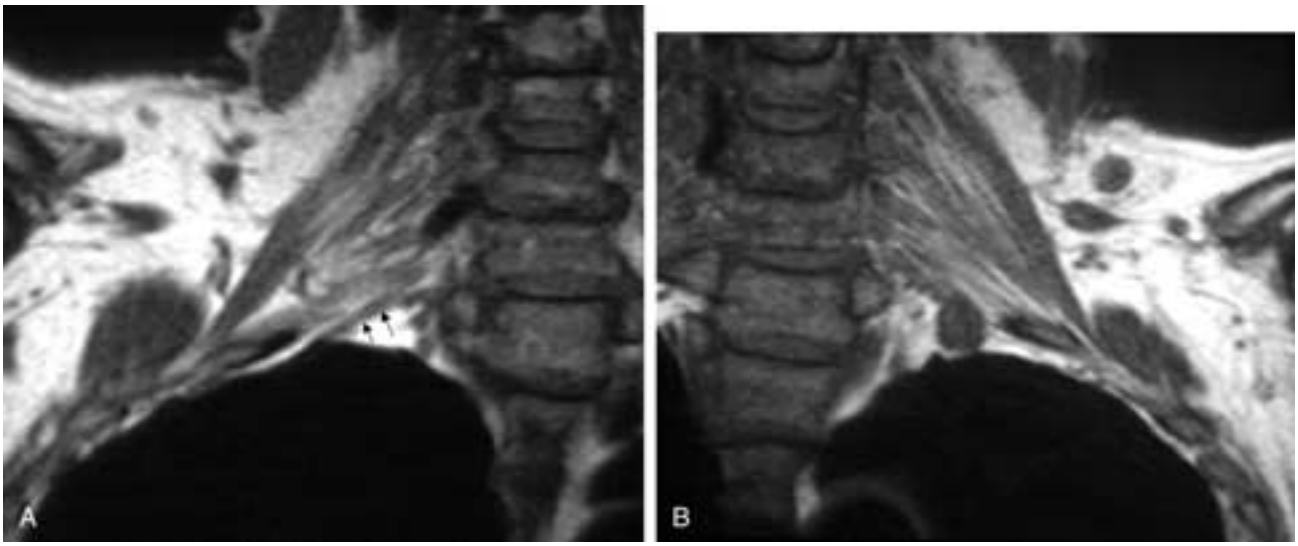

VIEW IMAGE

FIGURE 42-12 Status after a stab wound to the root of the neck with increasing arm pain. T1-weighted MR coronal image (**A**) shows a normal inferior trunk of the right brachial plexus (*arrows*). Image **B** demonstrates a well-circumscribed intermediate signal intensity lesion inseparable from the inferior trunk of the brachial plexus on the left. This is consistent with a posttraumatic neuroma.

dislocations are common in obstetric trauma, axial and oblique coronal images are obtained by using an FOV large enough to include the shoulder.

The MR evaluation of patients with posttraumatic brachial plexopathy should focus on certain specific findings. Analysis of the central spinal axis should focus more on the integrity of the nerve roots than on the identification of pseudomeningoceles. Matted or lobulated nerve roots should prompt an analysis of the spinal cord for evidence of posttraumatic changes. Extraforaminal abnormalities, particularly suspected posttraumatic neuromas, should be localized with respect to both the clavicle and the acromion process of the scapula to facilitate identification at surgery. This will aid in making decisions regarding the surgical approach. Lesions located above the clavicle (involving the roots and trunks) can usually be treated via a supraclavicular approach. The divisions of the brachial plexus are retroclavicular in location, and the cords are infraclavicular.

The analysis of sectional imaging studies in cases of nontraumatic brachial plexopathy should be a two-step process. First, one should identify any mass lesion(s) involving the plexus. The most common masses compromising the plexus are metastatic tumors, neural tumors, and extrathoracic extension of primary lung neoplasms (Pancoast tumors). Second, an analysis of the contour and signal characteristics of plexus components should be performed. Inflammatory processes such as radiation-induced brachial plexopathy, infectious brachial neuritis, or postsurgery-related brachial neuritis commonly present as abnormalities of plexus contour and signal intensity (Fig. 42-13).

Common conditions such as cervical disk disease should

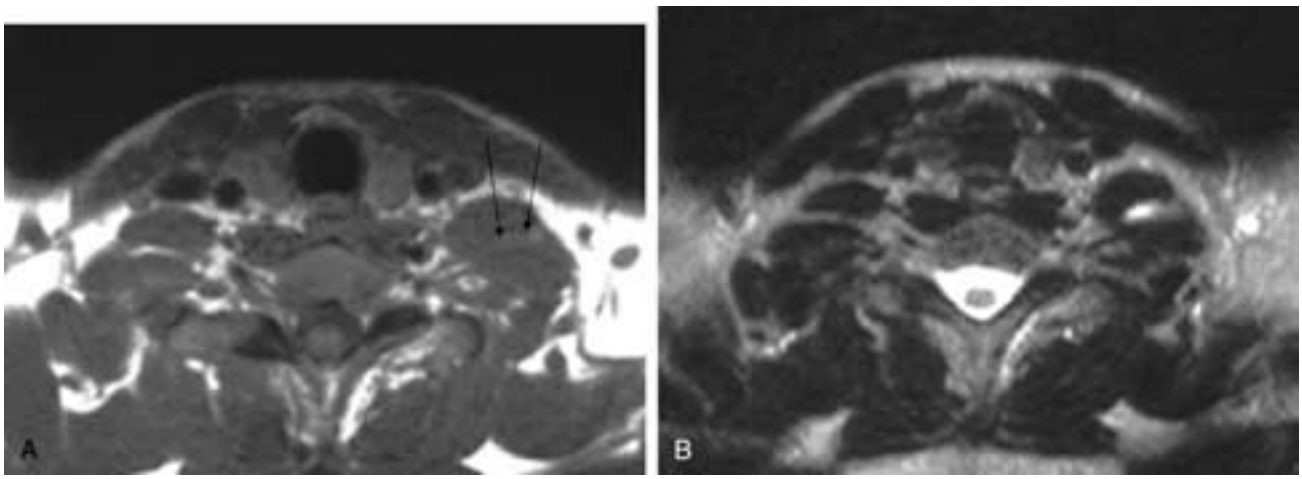

VIEW IMAGE

FIGURE 42-13 Neuritis. This is a patient after a scalene nerve block. Axial T1-weighted MR image (**A**) shows loss of fat between the left anterior and middle scalene muscle (*arrows*). Axial T2-weighted MR image (**B**) shows an area of increased signal in the same region. This is consistent with a neuritis.

Copyright © 2003, Mosby, Inc. All rights reserved.

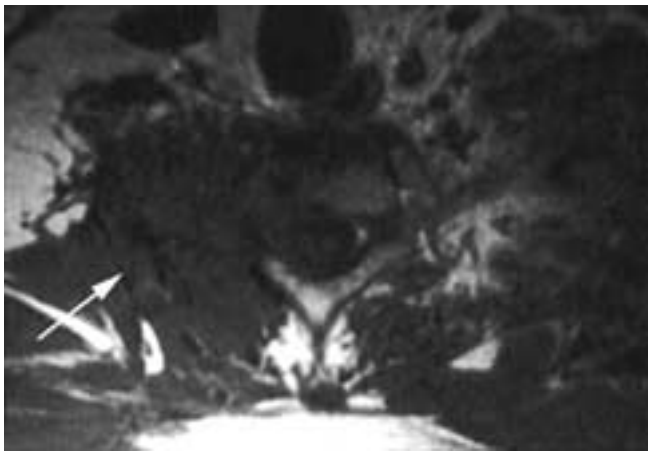

VIEW IMAGE

FIGURE 42-14 Metastatic lung carcinoma. T1-weighted MR axial image demonstrates a large soft-tissue mass (*arrow*) that engulfs the right scalene muscles.

be ruled out before undertaking expensive and extensive radiologic evaluations. From 80% to 90% of cervical radiculopathy secondary to disk disease occurs at the C5-C6 (C6 root) and C6-C7 (C7 root) levels, and the clinical symptoms produced by disk and degenerative disease at these levels may mimic those seen in other causes of brachial plexopathy. These patients often present with pain, numbness, and sensory deficit in the upper extremity, and the upper extremity reflexes may be absent or decreased (biceps, triceps, and radioperiosteal [brachioradial] jerks). Coughing, sneezing, or lateral head movement often exacerbates the pain and causes it to radiate into the ipsilateral upper extremity, and the ipsilateral paraspinal muscles are often tender when palpated.[20, 43]

With nontraumatic cases, an attempt should be made to determine if the plexopathy is idiopathic, since this is a benign, self-limiting condition that usually resolves within 3 years. However, the most common cause of nontraumatic brachial plexopathy is metastatic disease, and a mass should be suspected as the cause of a brachial plexopathy if Horner's syndrome, lower plexus symptoms, and/or a history of a neoplasm are present.

Metastatic disease involving the plexus is usually secondary to extracapsular tumor extension of nodal metastases in the axilla, supraclavicular fossa, or scalene nodes (Figs. 42-14 and 42-15). A wide variety of carcinomas, including breast, lung, gastrointestinal, thyroid, and head and neck carcinomas may metastasize to these nodes.[34] The signal characteristics of metastatic nodes are typically nonspecific, appearing isointense or mildly hyperintense to skeletal muscle on T1-weighted images and moderately hyperintense to skeletal muscle on T2-weighted images (see Chapter 36).[25] Extracapsular extension of nodal metastases is often manifested as nodes with spiculated or indistinct margins, and this extracapsular disease is visible more often on CT than on MR studies.

Primary neural tumors involving the brachial plexus are rare and consist of neurofibromas, schwannomas, and malignant peripheral nerve sheath tumors (malignant schwannomas).[12, 31, 40] Benign lesions are more common, and neurofibromas are more common than schwannomas. In two studies, only 14% of the neural tumors in this region were malignant.[13, 31] The majority of neurofibromas affecting the brachial plexus are sporadic; only one third occur in association with neurofibromatosis type I.

The imaging characteristic of neural tumors on CT and MR imaging have been well described in the literature, and it has been shown that it is impossible to distinguish a neurofibroma from a schwannoma based on imaging characteristics.[34] The internal architecture and degree of contrast enhancement are subject to a wide range of variation on both CT and MR imaging. Regardless of their internal appearance, all benign tumors appear smoothly marginated and well encapsulated on sectional imaging studies.

Patients with known neoplasms who have had previous radiation therapy may develop brachial plexopathies, which are secondary to either recurrent disease or radiation fibrosis. A study of 100 such cases showed that the clinical findings in these two entities were different. Radiation fibrosis is unlikely to occur with doses of less than 60 Gy. If neurologic symptoms occur in less than a year after a dose of 60 Gy or more, radiation damage is the most likely diagnosis. If the symptoms occur after a year, the plexopathy may be secondary to tumor recurrence or radiation damage.

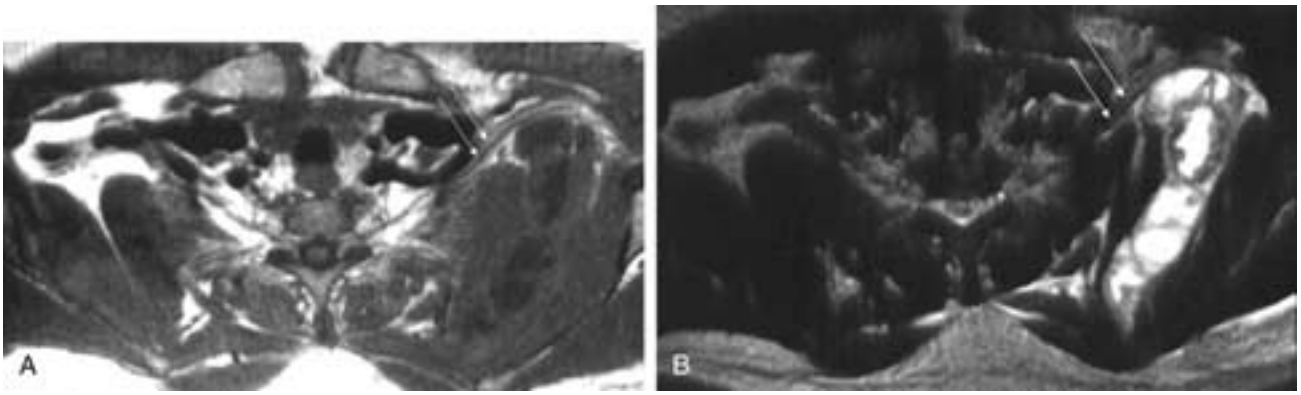

VIEW IMAGE

FIGURE 42-15 Metastatic melanoma—nodal disease. This patient complained of right arm discomfort. No physical evidence of brachial plexopathy was noted on physical examination. Axial T1-weighted (**A**) and T2-weighted (**B**) MR images show large, bulky, centrally cystic masses stretching the brachial plexus (*arrows*). No extracapsular disease was noted.

Copyright © 2003, Mosby, Inc. All rights reserved.

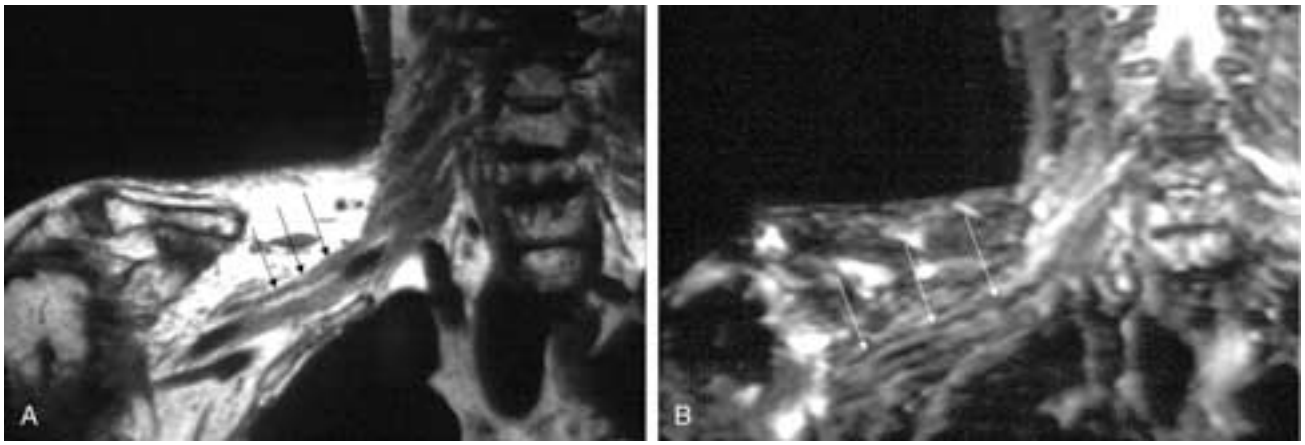

VIEW IMAGE

FIGURE 42-16 Radiation fibrosis. Status postradiation therapy for breast cancer. T1-weighted (**A**) and T2-weighted fat-suppressed (**B**) coronal MR images demonstrate a sharply marginated area of thickening adjacent to the brachial plexus (*arrows*). This area is isointense to muscle on both sequences.

Pain and weakness in the distribution of the lower plexus and Horner's syndrome suggest metastatic disease. Patients with postradiation plexopathy usually have painless weakness of the shoulder abductors and arm flexors as well as lymphedema.[28]

MR imaging can be used to distinguish between radiation fibrosis and recurrent disease. Radiation fibrosis has a signal intensity similar to that of muscle on T1-weighted and T2-weighted sequences;[19] that is, fibrous tissue has a long T1-weighted and a short T2-weighted relaxation time.[15] Although tumor and fibrosis may have a similar appearance on T1-weighted sequences, their signal intensities are different on T2-weighted sequences, with tumor being hyperintense to muscle and radiation fibrosis being isointense to muscle (Fig. 42-16). It should be noted that hemorrhage and infection may produce high signal intensity T2-weighted images and thus may simulate tumor recurrence. Immature radiation fibrosis may mimic recurrent disease. In some cases, correlation of sectional imaging with function imaging studies or tumor antibody titers may be required to obviate biopsy.

Brachial neuritis, whether infectious, postradiation, or idiopathic, is often a self-limited condition. Sectional imaging in these patients is usually deferred until 2 to 3 months after the onset of symptoms. In cases of brachial neuritis, the plexus components appear diffusely thickened on T1-weighted images, often without the indistinct contour seen in cases of radiation fibrosis. The components also may have abnormally increased signal intensity on T2-weighted or contrast-enhanced T1-weighted images.[33]

In 1932 Henry Pancoast described a clinical syndrome associated with tumors in the lung apex. This syndrome (Pancoast's syndrome) consists of a constellation of signs and symptoms that include shoulder and arm pain in the distribution of the C8, T1, and T2 nerve roots, Horner's syndrome, and atrophy of the hand muscles. Horner's syndrome is the clinical triad of ipsilateral ptosis, miosis, and anhydrosis. This syndrome, when seen in conjunction with a tumor in the lung apex, is caused by invasion of the prevertebral sympathetic chain or the inferior or stellate ganglion.[2, 4, 13, 14, 16] The inferior cervical and first thoracic sympathetic ganglia are fused in 80% of patients, and when this occurs, the resultant ganglion is called the stellate ganglion.

Most cases of Pancoast's syndrome are caused by a non-small cell bronchogenic carcinoma; squamous cell carcinoma is the most common, followed by adenocarcinoma and large cell carcinoma. Other etiologies of this syndrome include lymphoma, plasmacytoma, and infection.[2]

Pancoast tumors at the time of presentation are usually T3 lesions because of their involvement of the chest wall. These tumors are classified as T4 lesions when there is involvement of the brachial plexus, mediastinal structures or vertebrae. Staging for lymph node involvement and distant metastasis is the same as that used for non-small cell carcinoma in other locations in the lung. The presence of lymph node involvement or distant metastases usually eliminates surgery as a treatment option.

A Pancoast tumor should be ruled out whenever unilateral apical pleura thickening or asymmetric thickening greater than 5 mm is noted on a chest radiograph.[16] CT or MR imaging can be used to evaluate patients with these findings, as both imaging modalities can detect the presence and extent of tumor. However, MR imaging is presently superior for the detection of brachial plexus and chest wall involvement (Figs. 42-17 and 42-18), although with the use of spiral and multidetector machines, CT with multiplanar reformatted images may become comparable to MR imaging.

Although either CT or MR imaging can be used to evaluate patients in the nontraumatic category of brachial plexopathy,[1, 5, 7, 14, 23] MR imaging is the imaging modality of choice because of its ability to visualize nerves and blood vessels directly, its relative lack of artifact, and its multiplanar imaging capabilities. One of the major disadvantages of CT in the evaluation of the lower neck is that only direct axial images can be obtained routinely. Additionally, beam-hardening artifacts are encountered at the level of the thoracic inlet, and contrast administration is required to visualize blood vessels. But, regardless of which of these imaging modalities is used, knowledge of the location of the components of the brachial plexus is

Copyright © 2003, Mosby, Inc. All rights reserved.

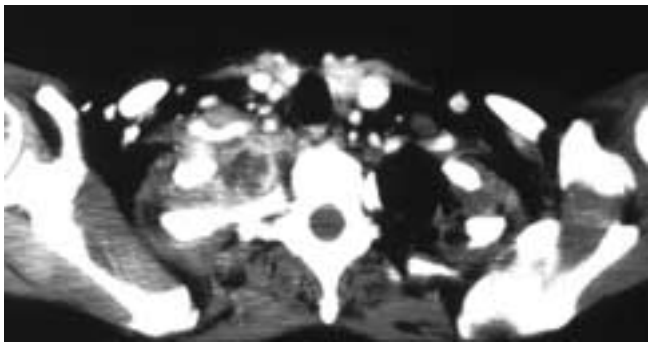

VIEW IMAGE

FIGURE 42-17 Pancoast tumor. Contrast-enhanced CT scan shows a necrotic mass with heterogeneous enhancement in the right lung apex. This mass involves the right chest wall between the first and second thoracic vertebrae and extends to the posterior branches of the subclavian artery. The inferior trunk of the brachial plexus is located posterior to the subclavian artery.

necessary to diagnose a mass or an anatomic alteration that is likely to be the cause of a brachial plexopathy. To achieve this goal, the following discussion covers examples of lesions along the course of the brachial plexus as seen on both CT and MR imaging.

The most common causes of disease in the region of the nerve roots are neural tumors (whose point of origin in the neural foramen or spinal canal can often be identified), posttraumatic injuries, and metastatic disease. Since the nerve roots pass between the anterior and middle scalene muscles, they may also be affected by lesions in this region (Figs. 42-19 and 42-20). Although axial CT and MR imaging are ideal for the evaluation of this region, coronal and sagittal images may also be advantageous, with sagittal images being particularly useful when assessing an absent nerve root (avulsion) in the neural foramen.

Lesions involving the trunks and divisions of the brachial plexus occur in the posterior triangle of the neck lateral to the anterior scalene muscle, and in the supraclavicular and retroclavicular regions. Metastatic disease and Pancoast tumors are primarily encountered in this region. Occasionally, neural tumors are seen in the supraclavicular region and near the apex of the lung. These tumors tend to be well circumscribed and have a sharp interface with adjacent structures (Fig. 42-21). By comparison, metastatic disease and primary neoplasms tend to have irregular infiltrating borders (Figs. 42-22 to 42-24). Lesions in the supraclavicular region and thoracic inlet may produce Horner's syndrome, either by direct invasion of the sympathetic chain, which is located anterior to the prevertebral muscles (Fig. 42-25), or by involving the ansa subclavia as it loops around the first portion of the subclavian artery.

The cords and proximal portions of the peripheral nerves formed by the brachial plexus are located in the axilla, where they are found adjacent to the axillary artery. Thus, a lesion that abuts the axillary artery anywhere in the axilla may produce brachial plexus symptoms (Fig. 42-26). Metastatic disease is commonly encountered in this region (Fig. 42-27). Primary neural tumors (Fig. 42-28) and soft-tissue tumors, as well as trauma, may affect the brachial plexus in this area.

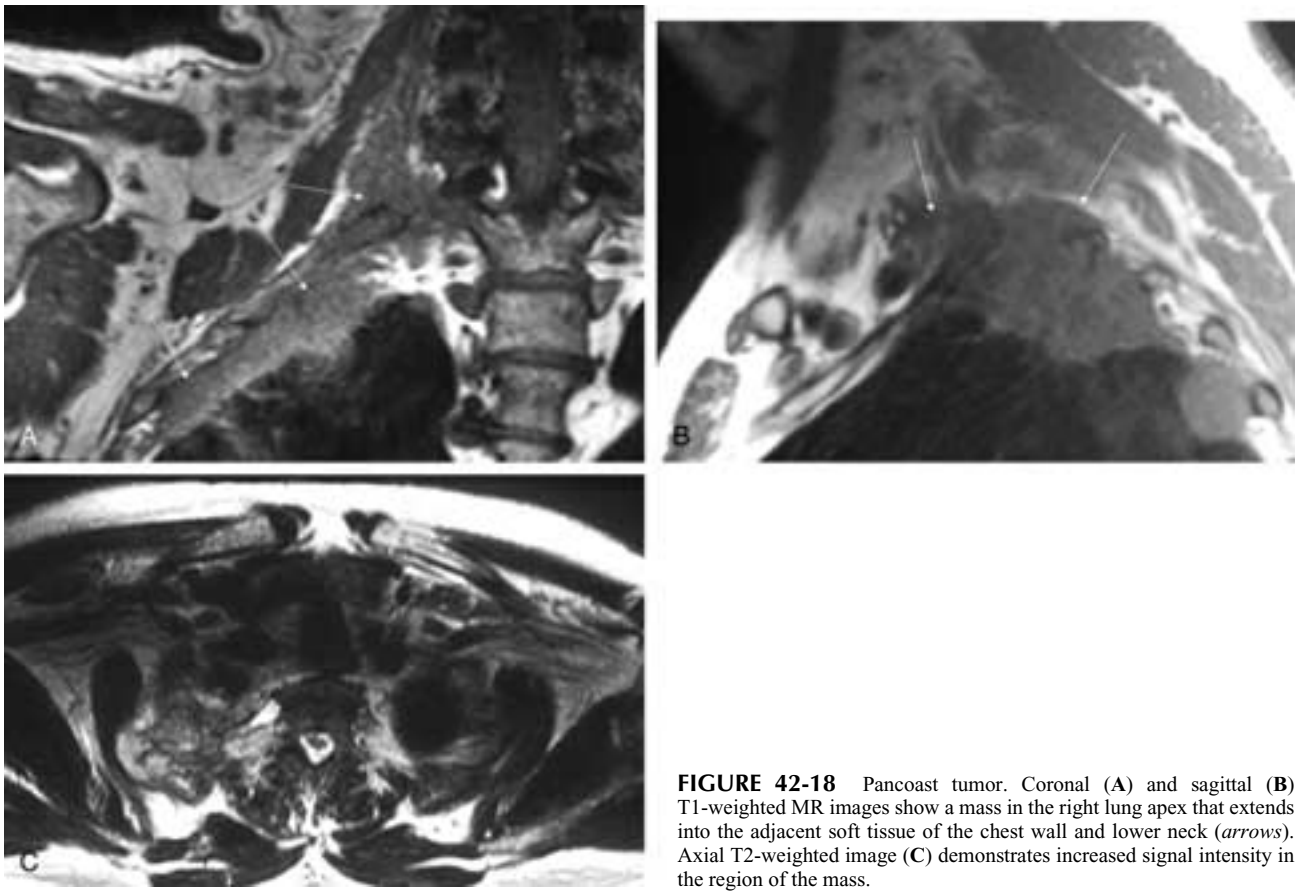

FIGURE 42-18 Pancoast tumor. Coronal (**A**) and sagittal (**B**) T1-weighted MR images show a mass in the right lung apex that extends into the adjacent soft tissue of the chest wall and lower neck (*arrows*). Axial T2-weighted image (**C**) demonstrates increased signal intensity in the region of the mass.

VIEW IMAGE

Copyright © 2003, Mosby, Inc. All rights reserved.

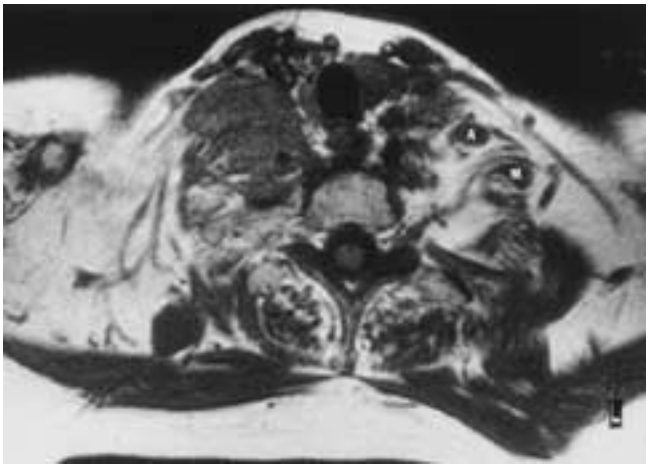

VIEW IMAGE

FIGURE 42-19 Metastatic breast carcinoma. Axial T1-weighted MR image shows an intermediate signal intensity lesion surrounding the right anterior and middle scalene muscles. Normal anterior (*A*) and middle (*M*) scalene muscles are seen on the left.

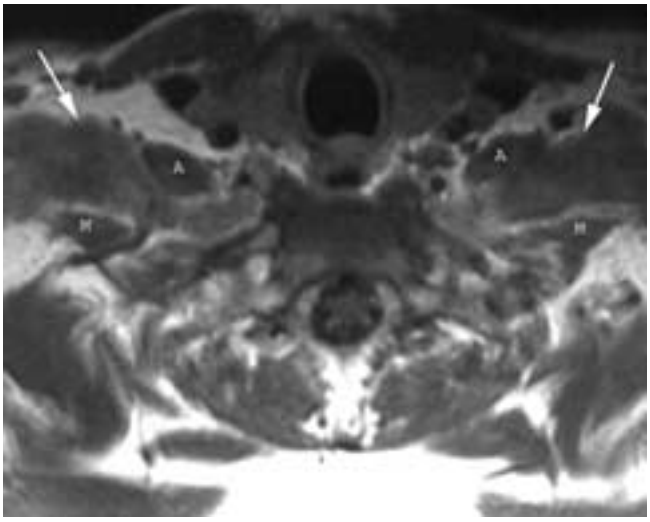

FIGURE 42-20 Neurofibromatosis. Axial T1-weighted MR image shows bilateral circumscribed intermediate signal intensity lesions (*arrows*) between the anterior (*A*) and middle (*M*) scalene muscles.

VIEW IMAGE

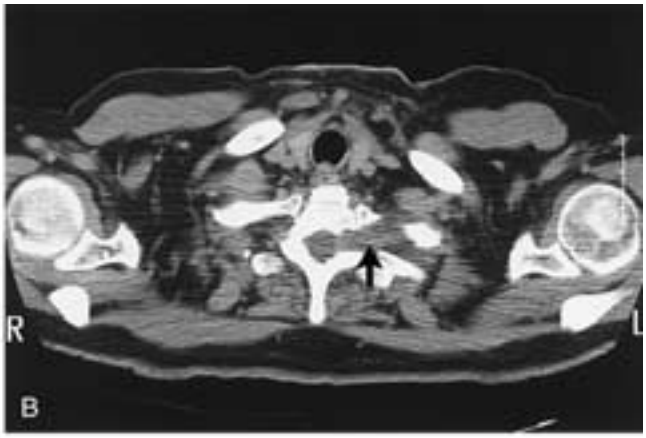

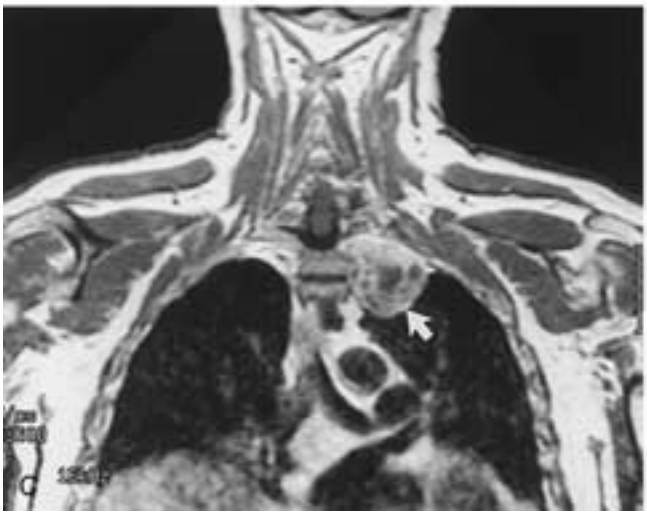

FIGURE 42-21 Neural tumor. Axial CT images obtained through the lung apex (**A**) and lower neck (**B**) show a well-circumscribed lesion in the left lung apex that extends into the neural foramen (*arrow*) in the lower neck. Coronal postgadolinium T1-weighted MR image (**C**) shows heterogeneous enhancement in the lesion (*arrow*). Note the smooth interface between the lesion and the lung.

VIEW IMAGE

Copyright © 2003, Mosby, Inc. All rights reserved.

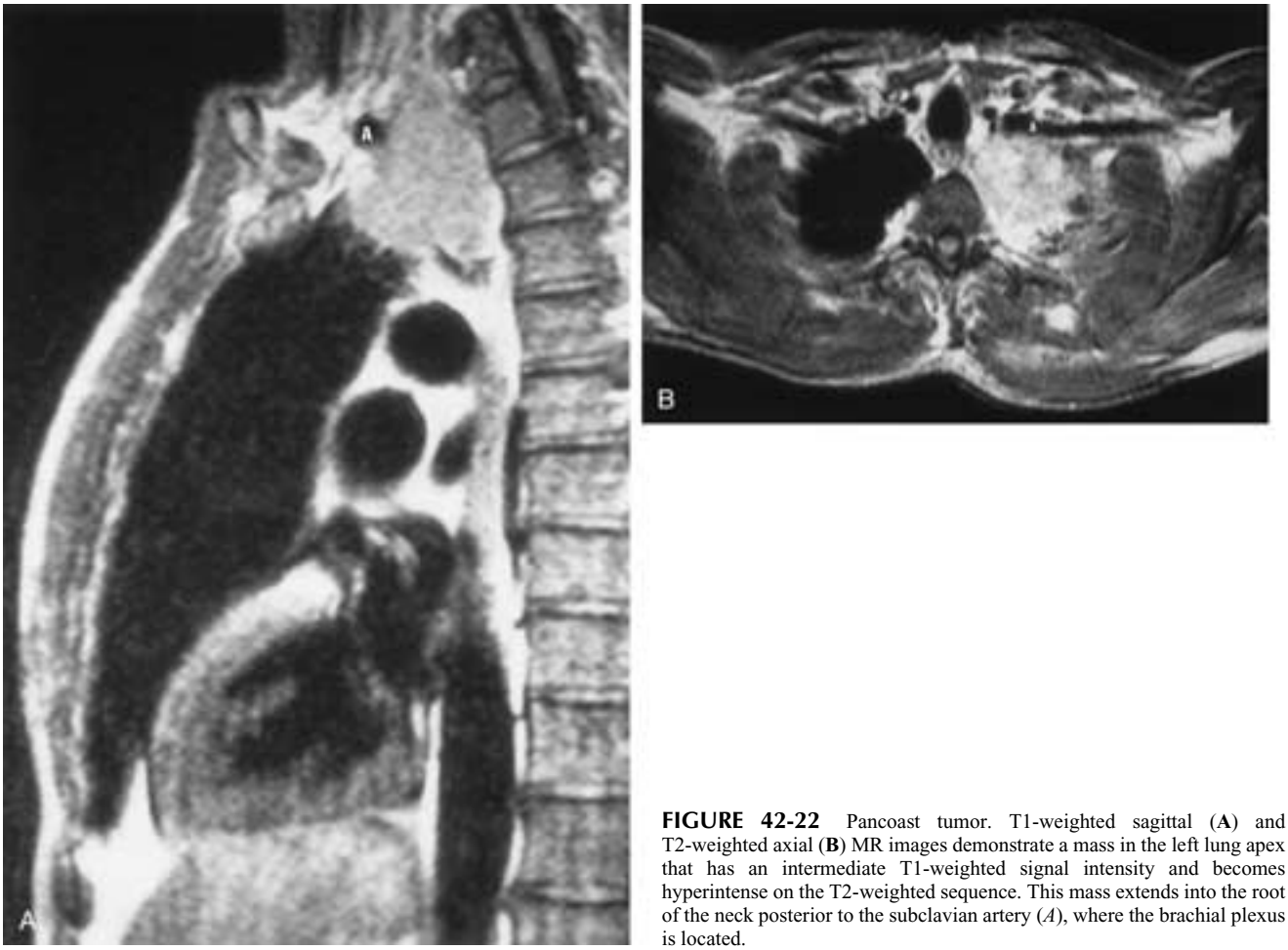

FIGURE 42-22 Pancoast tumor. T1-weighted sagittal (**A**) and T2-weighted axial (**B**) MR images demonstrate a mass in the left lung apex that has an intermediate T1-weighted signal intensity and becomes hyperintense on the T2-weighted sequence. This mass extends into the root of the neck posterior to the subclavian artery (*A*), where the brachial plexus is located.

VIEW IMAGE

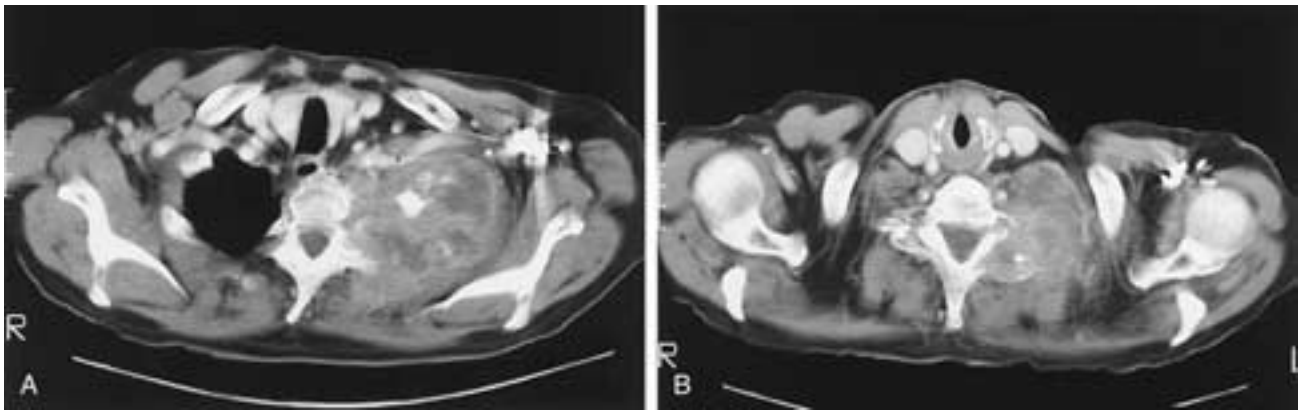

VIEW IMAGE

FIGURE 42-23 Pancoast tumor. Axial CT scan through the lung apex (**A**) and lower neck (**B**) shows a mass that extends to the posterior border of the subclavian artery (*A*) at the level of the thoracic inlet. This lesion encases the scalene muscles in the neck.

Copyright © 2003, Mosby, Inc. All rights reserved.

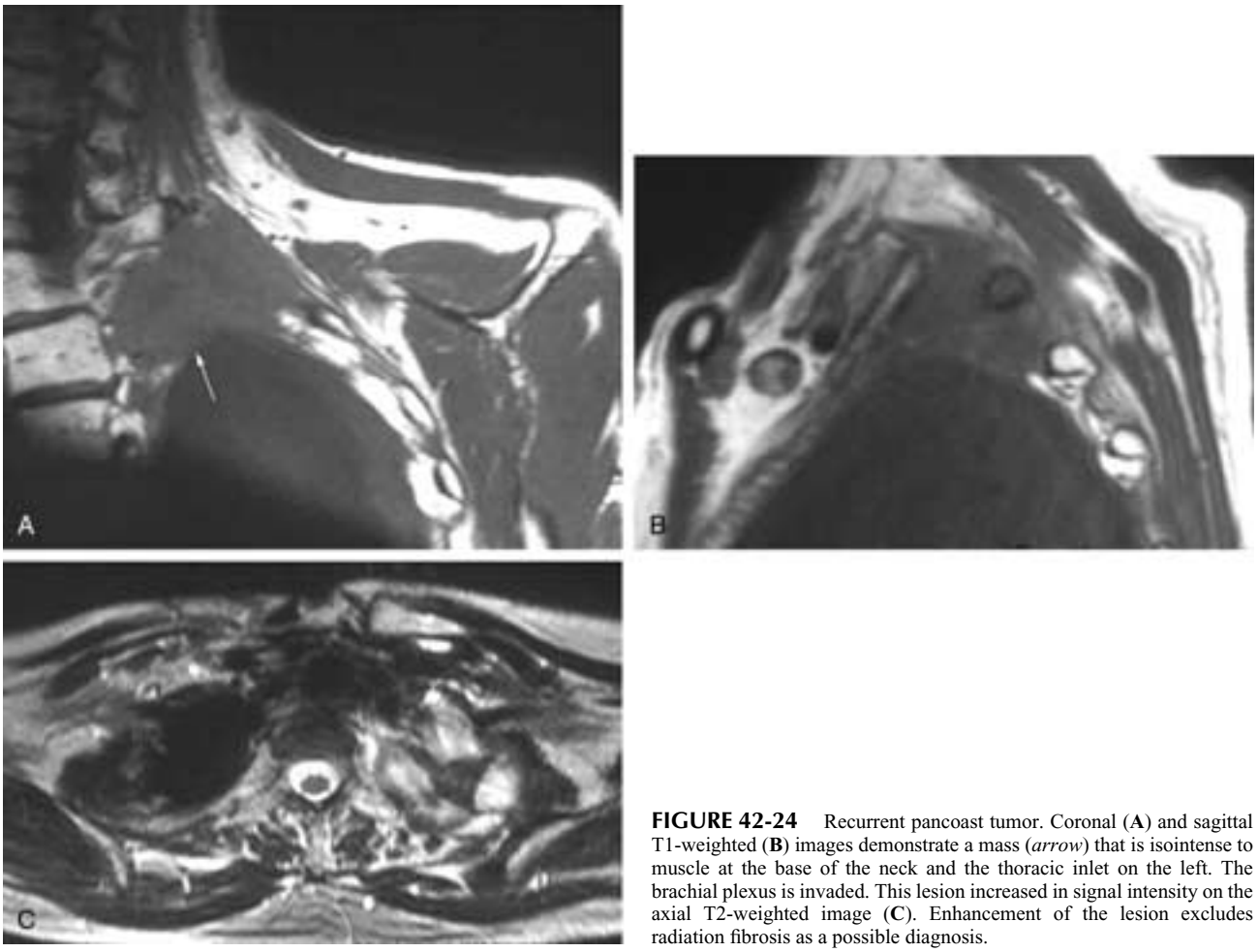

FIGURE 42-24 Recurrent pancoast tumor. Coronal (**A**) and sagittal T1-weighted (**B**) images demonstrate a mass (*arrow*) that is isointense to muscle at the base of the neck and the thoracic inlet on the left. The brachial plexus is invaded. This lesion increased in signal intensity on the axial T2-weighted image (**C**). Enhancement of the lesion excludes radiation fibrosis as a possible diagnosis.

VIEW IMAGE

The bones of the cervical spine, shoulder, and thoracic inlet should be evaluated in patients with brachial plexopathy. Alterations in the bony anatomy in the lower neck and thoracic inlet, such as cervical ribs or lesions of the first rib and clavicle, may impinge on the nerves, and this may lead to the development of brachial plexus symptoms. Alternatively, primary bone lesions of the shoulder may produce symptoms that mimic those seen in brachial plexopathies (Figs. 42-29 and 42-30).

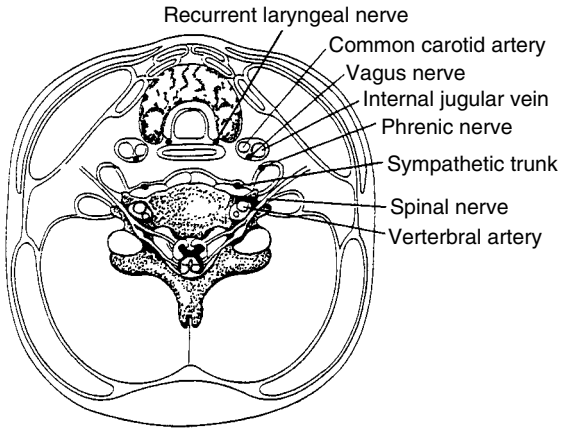

FIGURE 42-25 Cross-sectional diagram showing the location of the major nerves in the neck.

VIEW IMAGE

Cervical ribs are seen in approximately 1% of the population, are symptomatic in only 10%, are unilateral in 50% to 80%, and are twice as common in females as in males.[24] These ribs vary in length and may be connected to the first rib by a fibrous band.

Cervical ribs may affect the nerves of the brachial plexus in one of two ways. First, the cervical rib may narrow the space between the posterior aspect of the first rib and the anterior scalene muscle through which the nerves and subclavian artery must pass en route to the axilla. Second, the cervical rib may be situated such that a portion of the brachial plexus must pass over it in order to enter the axilla. In the latter situation, the lower plexus trunk rests against the top of the cervical rib.[24] If the lower trunk is stretched as it crosses the cervical rib, or if the fibrous band that attaches the cervical rib to the first rib abuts the trunk, symptoms may develop. This is called the cervical rib syndrome, and it is seen primarily in females. Sensory symptoms, either pain or paresthesias, usually antedate motor involvement and occur along the ulnar border of the forearm and hand. Muscle weakness and wasting are seen primarily in the thenar eminence. In long-standing cases, there is generalized wasting of the small hand muscles.[37]

Copyright © 2003, Mosby, Inc. All rights reserved.

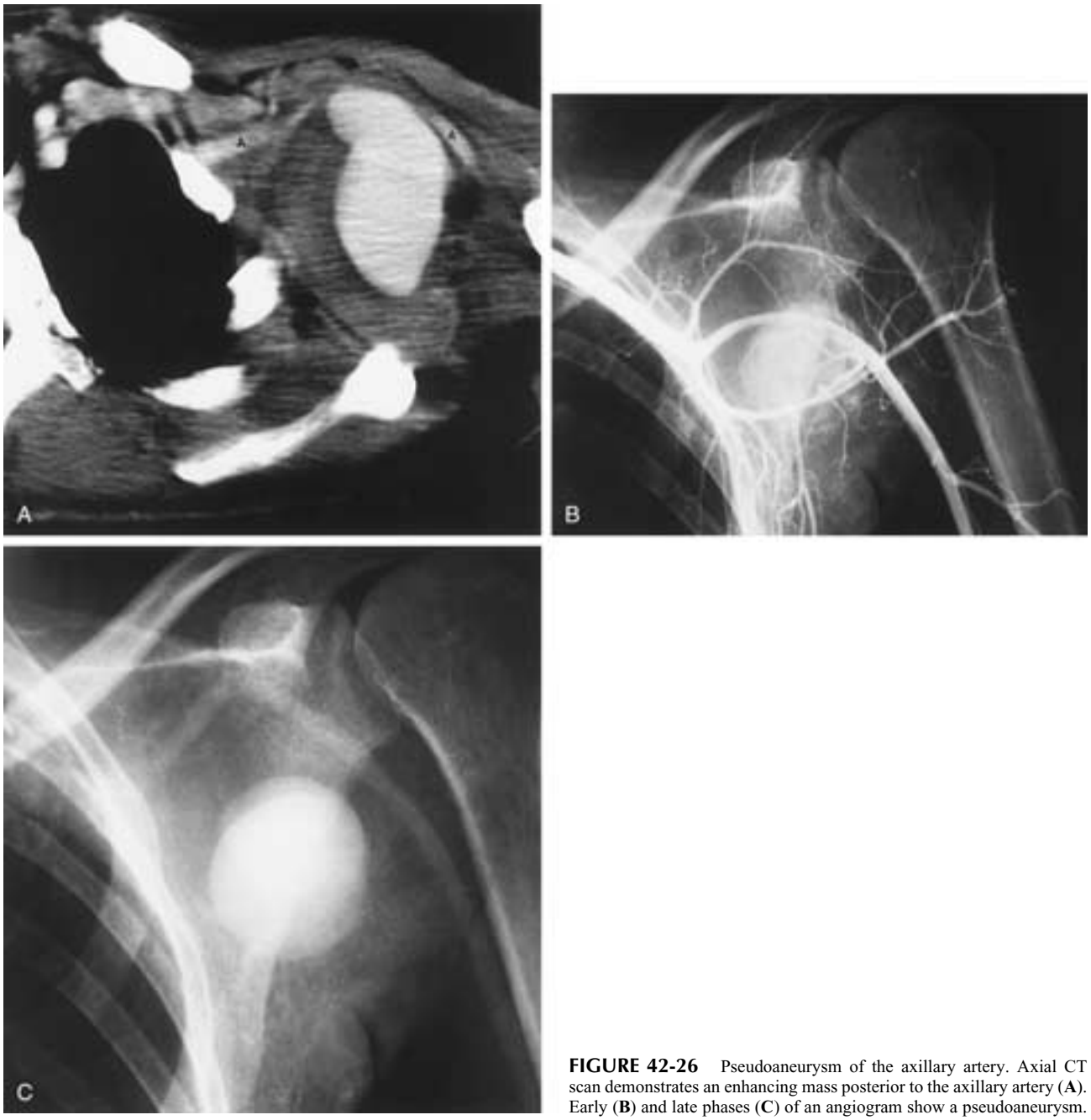

FIGURE 42-26 Pseudoaneurysm of the axillary artery. Axial CT scan demonstrates an enhancing mass posterior to the axillary artery (**A**). Early (**B**) and late phases (**C**) of an angiogram show a pseudoaneurysm.

VIEW IMAGE

VAGUS NERVE

The vagus nerve has the longest course of all the cranial nerves, and portions of this nerve can be found extending from the brainstem to the abdomen. This nerve originates from four nuclei in the medulla. Nerve fibers from three of these nuclei—the dorsal vagal nucleus, the nucleus solitarius, and the spinal nucleus of the trigeminal nerve—emerge as rootlets from the medulla, below the glossopharyngeal nerve in the retro-olivary sulcus between the olive and the inferior cerebellar peduncle. These rootlets converge in the basal cistern to form a single nerve that exits from the skull through the jugular foramen. There are two sensory ganglia of the vagus nerve. The superior (jugular) ganglion is situated within the jugular fossa, and the inferior (nodose) ganglion is situated just caudal to the jugular foramen. Fibers from the nucleus ambiguus that travel with the spinal accessory nerve for a short distance join the vagus nerve after the nerve passes below the inferior ganglion.

In the neck, the vagus nerve is located in the posterior aspect of the carotid sheath between the carotid artery (medially) and the internal jugular vein (laterally) (Fig. 42-25). There are three major branches of the vagus nerve in the neck; the pharyngeal branch, the superior laryngeal nerve, and the recurrent laryngeal nerve.

The pharyngeal branch is formed on the superior aspect of the inferior ganglion of the vagus nerve and consists primarily of fibers from the spinal accessory nerve. It travels

Copyright © 2003, Mosby, Inc. All rights reserved.

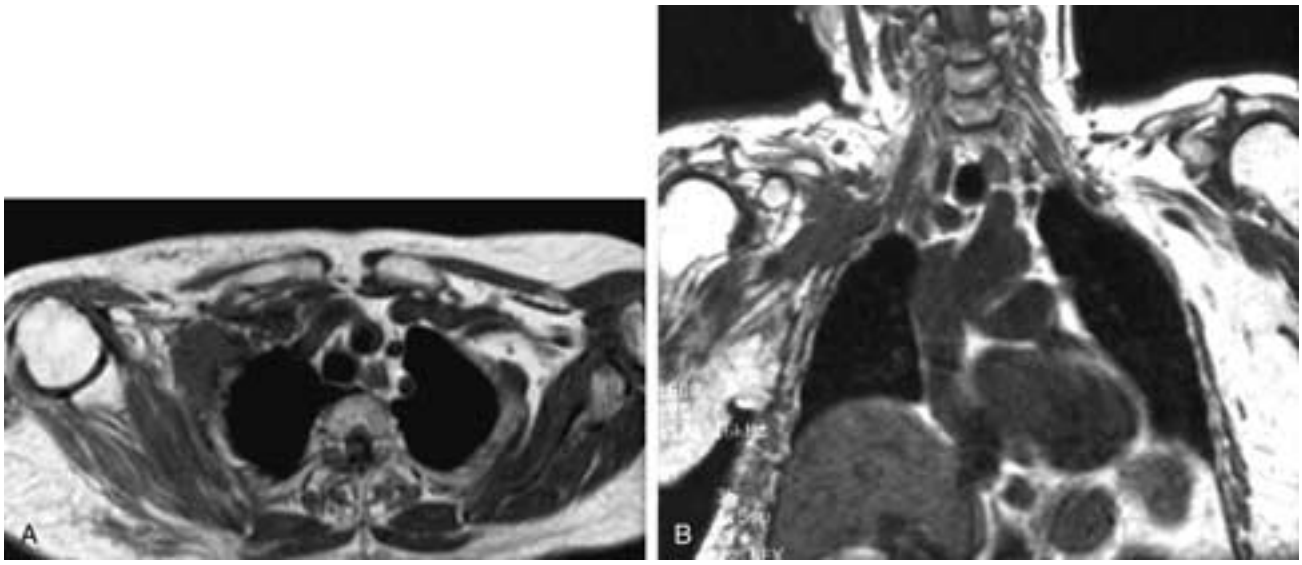

VIEW IMAGE

FIGURE 42-27 Metastatic breast carcinoma. Axial (**A**) and coronal (**B**) T1-weighted MR images show a mass in the right axilla that surrounds the axillary artery. Note the increased signal in the muscles of the right shoulder girdle. This is consistent with denervation atrophy.

between the internal and external carotid arteries to the superior border of the middle constrictor muscle. There it divides into numerous branches that join branches of the sympathetic trunk, glossopharyngeal nerves, and external laryngeal nerves to form the pharyngeal plexus. This plexus is the principal motor supply to the muscles of the pharynx and the levator veli palatini muscles.

The superior laryngeal nerve originates from the inferior ganglion of the vagus nerve, caudal to the pharyngeal branch. It also receives branches from the superior cervical ganglion of the sympathetic trunk. It descends adjacent to the pharynx, and at the level of the hyoid bone divides into the external (motor) and internal (sensory) laryngeal nerves. The external laryngeal nerve (branch) of the superior laryngeal nerve sends motor fibers to the inferior constrictor and cricothyroid muscles. It also has branches that join the pharyngeal plexus and the superior cardiac nerves. The internal laryngeal nerve (branch) of the superior laryngeal nerve enters the larynx via the thyrohyoid membrane and gives the sensory supply to the mucous membranes of the hypopharynx and larynx.

The points of origin of the left and right recurrent laryngeal nerves differ. On the right side, the recurrent laryngeal nerve arises from the vagus nerve below the level

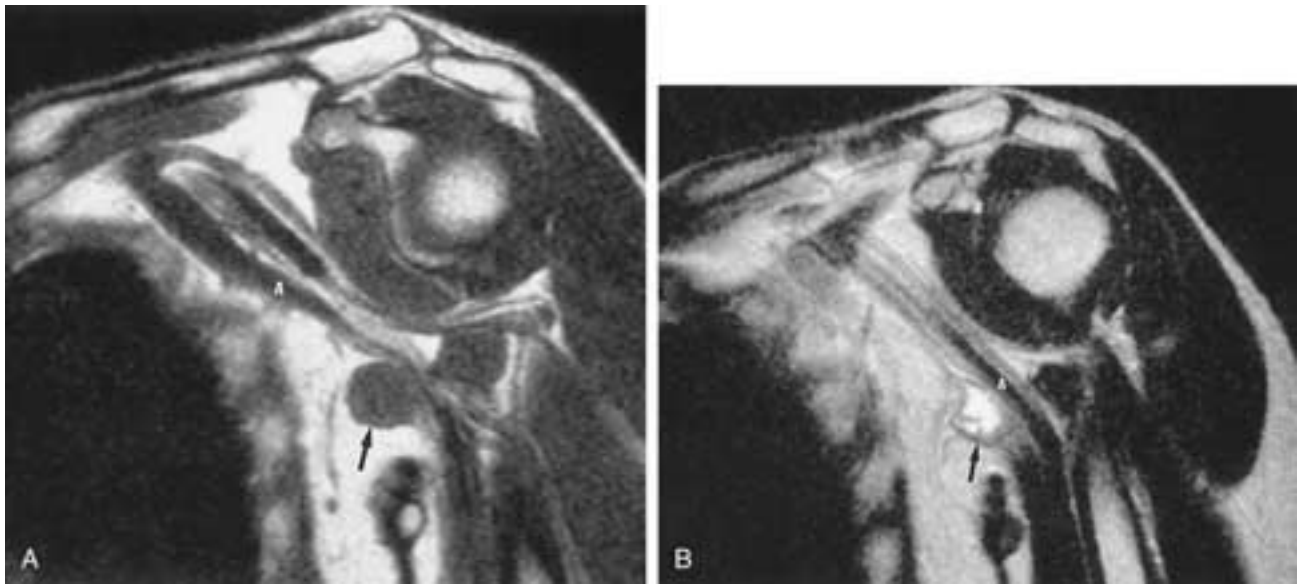

VIEW IMAGE

FIGURE 42-28 Neural tumor. Coronal T1-weighted (**A**) and T2-weighted (**B**) MR images through the region of the axilla show a mass (*arrow* in **B**) arising from one of the nerves medial to the axillary artery (*A*). This mass has an intermediate signal on T1-weighted images and becomes hyperintense on T2-weighted sequences.

Copyright © 2003, Mosby, Inc. All rights reserved.

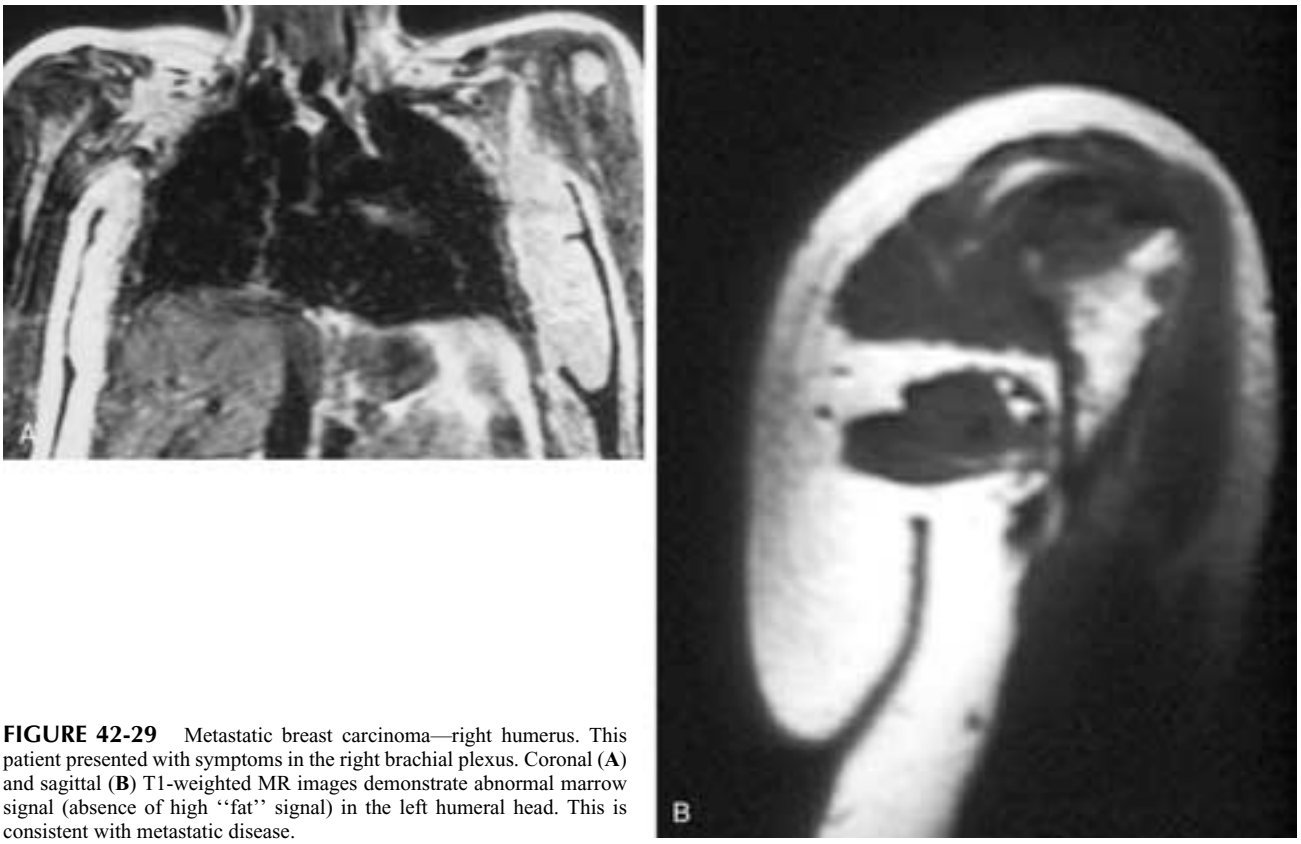

VIEW IMAGE

FIGURE 42-29 Metastatic breast carcinoma—right humerus. This patient presented with symptoms in the right brachial plexus. Coronal (**A**) and sagittal (**B**) T1-weighted MR images demonstrate abnormal marrow signal (absence of high ''fat'' signal) in the left humeral head. This is consistent with metastatic disease.

of the subclavian artery at the level of the thoracic inlet. The right recurrent laryngeal nerve loops under the artery to lie on its posterior surface, and then travels superiorly in the tracheoesophageal sulcus (Fig. 42-31) en route to the larynx, where it enters the larynx above the cricothyroid articulation. On the left side, the recurrent laryngeal nerve arises from the vagus nerve in the mediastinum after the nerve crosses the aortic arch anterolaterally. The left recurrent laryngeal nerve then loops under the aortic arch, traveling between the aorta and the left pulmonary artery in the aortic pulmonic window, extends posteriorly to reach the tracheoesophageal sulcus, and then ascends in this sulcus to enter the larynx above the cricothyroid joint. Because the left recurrent laryngeal nerve has an intrathoracic course, it is susceptible to damage from mediastinal pathology as well as from disease in the neck.[8, 24, 30, 32, 47]

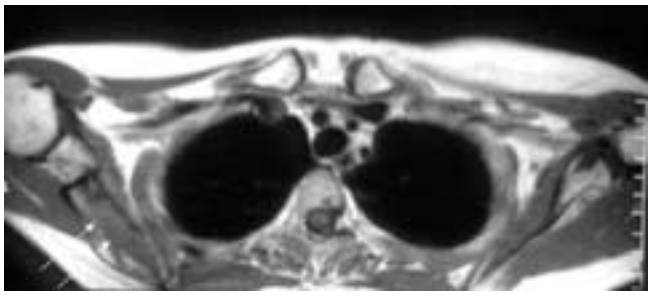

VIEW IMAGE

FIGURE 42-30 Metastatic breast carcinoma—right scapula. T1-weighted axilla MR image shows a decrease in the marrow signal (*arrows*) in the right scapula.

The list of causes of recurrent laryngeal palsy is lengthy and includes broad categories of disease such as inflammatory neuropathies, neoplasms of the neck and chest, trauma, cardiovascular disease (aortic aneurysm and left atrial enlargement), Parkinson's disease, and idiopathic disorders. The nerve paralysis may be acute or chronic; in either case, the patient will have hoarseness and vocal cord paralysis.

An acute unilateral recurrent laryngeal nerve paralysis is often idiopathic, secondary to a toxic or infectious condition or the result of trauma. Most of these patients recover complete vocal cord function, especially when the cause is inflammatory or idiopathic, in which over 80% of the patients recover spontaneously within 6 months of the onset of paralysis. However, recovery is unlikely if function has not returned within 9 months.

A chronic unilateral nerve palsy is usually secondary to a neoplasm most commonly in the thyroid gland or the adjacent extralaryngeal tissues.

The radiologist is often asked to evaluate patients with vocal cord paralysis. Since lesions anywhere along the course of the vagus nerve can produce vocal cord paralysis, it is important to try to identify the level of the abnormality prior to proceeding with an imaging evaluation. A paralyzed cord may be in an intermediate (almost completely abducted) or a paramedian (off midline) position. Lesions above the jugular foramen may result in paralysis of the vocal cord in either the intermediate or paramedian position. Supratentorial and brainstem lesions may produce bilateral cord paralysis, and hemiparesis may be seen in association with supratentorial lesions. Infarcts in the posterior inferior cerebellar artery territory are often the cause of Wallen-

Copyright © 2003, Mosby, Inc. All rights reserved.

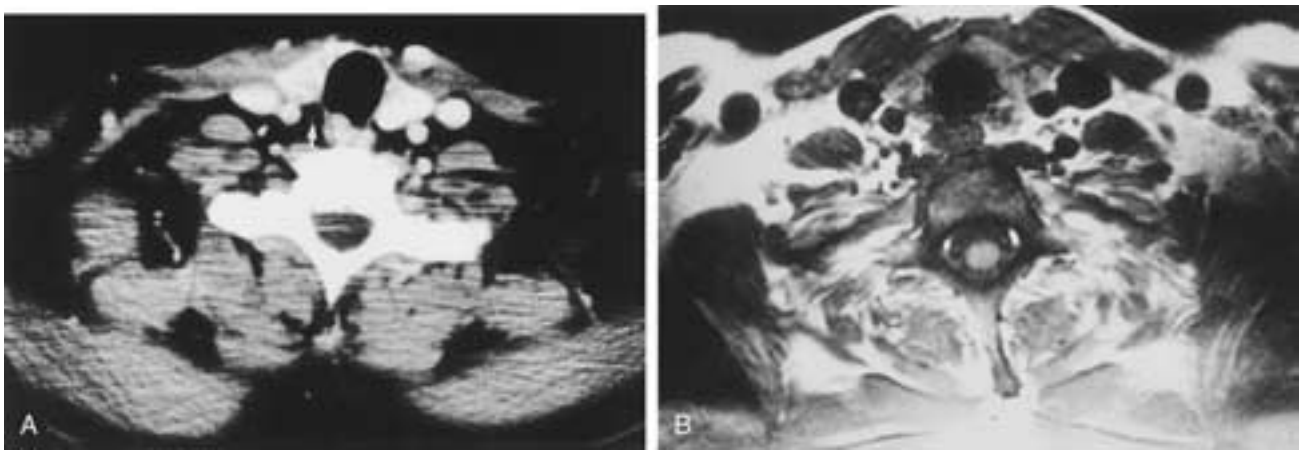

VIEW IMAGE

FIGURE 42-31 Recurrent laryngeal nerve—tracheoesophageal sulcus. Axial CT scan (**A**) and T1-weighted MR image (**B**) show the right recurrent laryngeal nerve in the tracheoesophageal sulcus (*arrow*).

berg's syndrome (lateral medullary plate syndrome). Patients with this syndrome present with ipsilateral loss of facial sensation, contralateral loss of pain and temperature sensation over the body, ipsilateral Horner's syndrome, vertigo, hiccups, dysphagia, and ipsilateral ataxia of limbs. Involvement of the nerve in the jugular foramen above the recurrent laryngeal nerve tends to produce a paralyzed cord in the intermediate position, whereas lesions of the recurrent laryngeal nerve tend to result in cord paralysis in the paramedian position. If a lesion is situated between the pharyngeal branch and the superior laryngeal nerve, the cord usually is in the paramedian position and there is loss of sensation in the hypopharynx and pharynx.[5, 20, 21, 49]

If the lesion causing the vocal cord paralysis is cranial to the origin of the recurrent laryngeal nerve, there usually is paralysis of the ipsilateral pharyngeal constictor muscles, and the ipsilateral pharyngeal wall may be seen to be thinned and dilated compared to the normal contralateral side.

Thus, the position of the vocal cord, as well as the presence of other cranial nerve palsies and neurologic findings, may assist in identifying the level of the lesion. By dividing the vagal neuropathies into proximal and distal categories based on clinical findings, it is possible to determine the region to be scanned and the preferred imaging modality to use. The neurologic manifestations commonly encountered with lesions at various levels along the course of the vagus nerve are summarized in Table 42-6 and Figure 42-32.

Lesions involving the proximal portion of the vagus nerve usually are accompanied by neuropathies of one or more associated cranial nerves (IX, XI, XII), since these nerves travel in close proximity to the vagus nerve both at their point of origin in the brainstem and below the skull base.[39] MR imaging is the imaging modality of choice in these patients. The scans should be obtained through the levels of the brainstem and oropharynx. T1-weighted

Table 42-6
VOCAL CORD PARALYSIS CAUSED BY LESIONS AT VARIOUS LEVELS

	Level of Pathology	Vocal Cord Position	Cranial Nerve Deficit	Associated Findings
I.	Supratentorial	Variable Typically bilateral	None	Hemiparesis, etc.
II.	Brainstem	Variable Sometimes bilateral	Multiple	Wallenberg, etc.
III.	Cisternal	Variable	IX, X, XI, XII	Sometimes paralysis of soft palate
IV.	Skull base/jugular bulb	Usually Intermediate	IX, X, XI	Paralysis of soft palate
	Proximal to pharyngeal branch	Usually Intermediate	X, sometimes IX, and/or XI	Paralysis of soft palate
V.	Proximal to superior laryngeal nerve	Usually Intermediate	X	No paralysis of soft palate
VI.	Distal to superior laryngeal nerve	Usually Paramedian	X	No paralysis of soft palate
VII.	Recurrent laryngeal nerve	Usually Paramedian	Other vagal functions intact	No paralysis of soft palate

From RSNA Exhibit, 1994: ''A Segmental Anatomical Approach to Abnormalities of Vocal Cord Movement.'' Noble ER, Laine FJ, Smoker WRK.

Copyright © 2003, Mosby, Inc. All rights reserved.

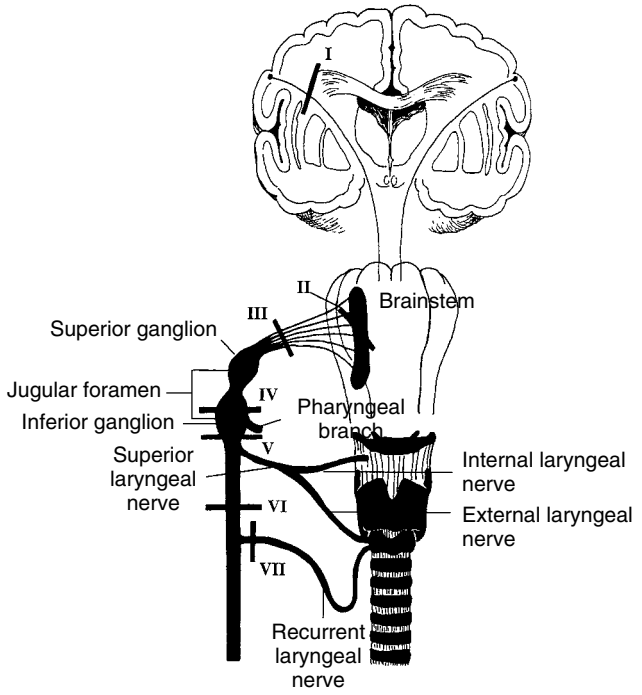

FIGURE 42-32 Diagram of the site of lesions along the course of the vagus nerve (see corresponding Table 42-6).

images are most helpful in the extracranial region, whereas T2-weighted images are more diagnostic in the brainstem.[21, 42]

If a patient presents with an isolated recurrent laryngeal nerve palsy (distal vagal neuropathy), CT is the preferred imaging modality and the scans should be obtained with intravenous contrast. With today's rapid acquisition CT studies, the scan plane should be aligned with the true vocal cords as seen on a lateral scout film, and the entire neck down to the carina should be scanned. Such a protocol includes the entire distal course of both recurrent laryngeal nerves. In the neck, a lesion in the tracheoesophageal sulcus (Figs. 42-33 and 42-34) or carotid sheath (Fig. 42-22) may produce a recurrent laryngeal palsy, and both recurrent laryngeal nerves can be involved by lesions at the level of the thoracic inlet. As mentioned, because the left recurrent laryngeal nerve has a longer intrathoracic course, it is

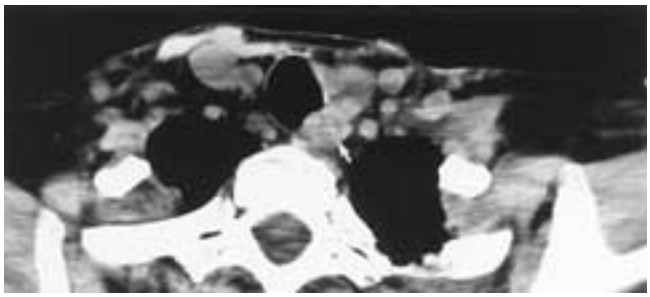

FIGURE 42-33 Metastatic squamous cell carcinoma. Axial CT scan shows an enlarged metastatic node in the left tracheoesophageal sulcus (*arrow*).

commonly involved by mediastinal pathology (Figs. 42-35 to 42-37).

PHRENIC NERVE

The phrenic nerve is formed primarily from the C4 nerve root, with minor contributions from C3 and C5. It is formed adjacent to the superior lateral border of the anterior scalene muscle and travels across this muscle beneath the deep layer of the deep cervical fascia that envelopes the muscle. This nerve has a vertical course that crosses the muscle from superolaterally to inferomedially. Inferiorly, the nerve passes medial to the muscle (Fig. 42-38) and thus comes to lie on the anterior surface of the first portion of the subclavian artery.

Both phrenic nerves in the mediastinum are in contact with the mediastinal pleura laterally. However, the length, vertical orientation, and medial relationships of these two nerves differ.

The right phrenic nerve is shorter and more vertically oriented that the left. Medially throughout its course, this nerve borders venous structures (right brachiocephalic vein, superior vena cava, right atrium, and inferior vena cava). This nerve crosses the diaphragm either through the inferior vena cava orifice or lateral to it.

The left phrenic nerve is found between the left common carotid and subclavian arteries in the superior mediastinum. It then passes medially and anteriorly, superficial to the left vagus nerve above the level of the aortic arch. It crosses the

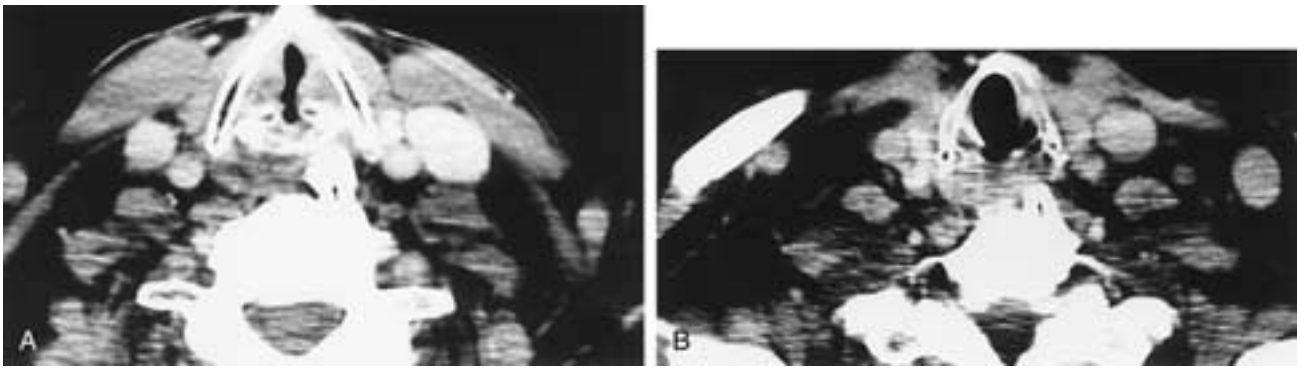

FIGURE 42-34 Vocal cord paralysis—enlarged cervical osteophyte. Axial CT scan at the level of the true vocal cord (**A**) and below (**B**) identifies osteophytes (*arrows*) extending into the left tracheoesophageal sulcus.

Copyright © 2003, Mosby, Inc. All rights reserved.

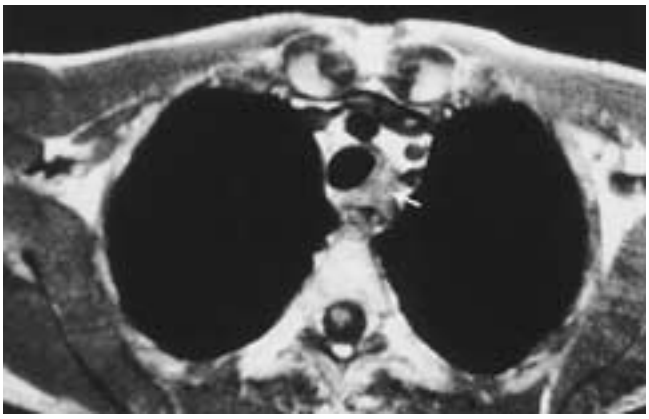

VIEW IMAGE

FIGURE 42-35 Esophageal carcinoma. T1-weighted MR image shows a circumferential lesion of the esophagus that extends into the left tracheoesophageal sulcus (*arrow*).

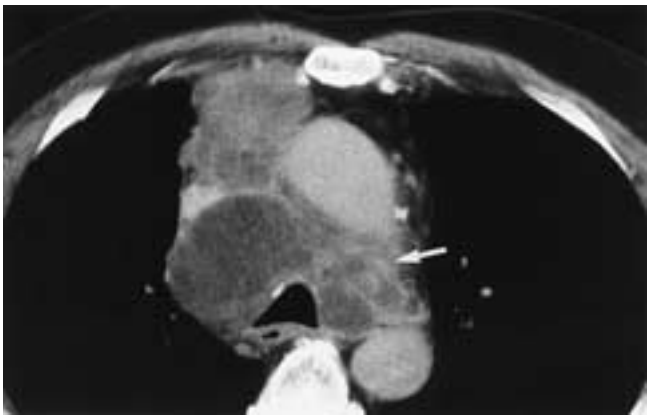

VIEW IMAGE

FIGURE 42-36 Small cell carcinoma with mediastinal nodes. Axial CT scan demonstrates enlarged anterior mediastinal, pretracheal retrovascular, and AP window nodes. The nodes in the AP window (*arrow*) are responsible for the patient's vocal cord paralysis.

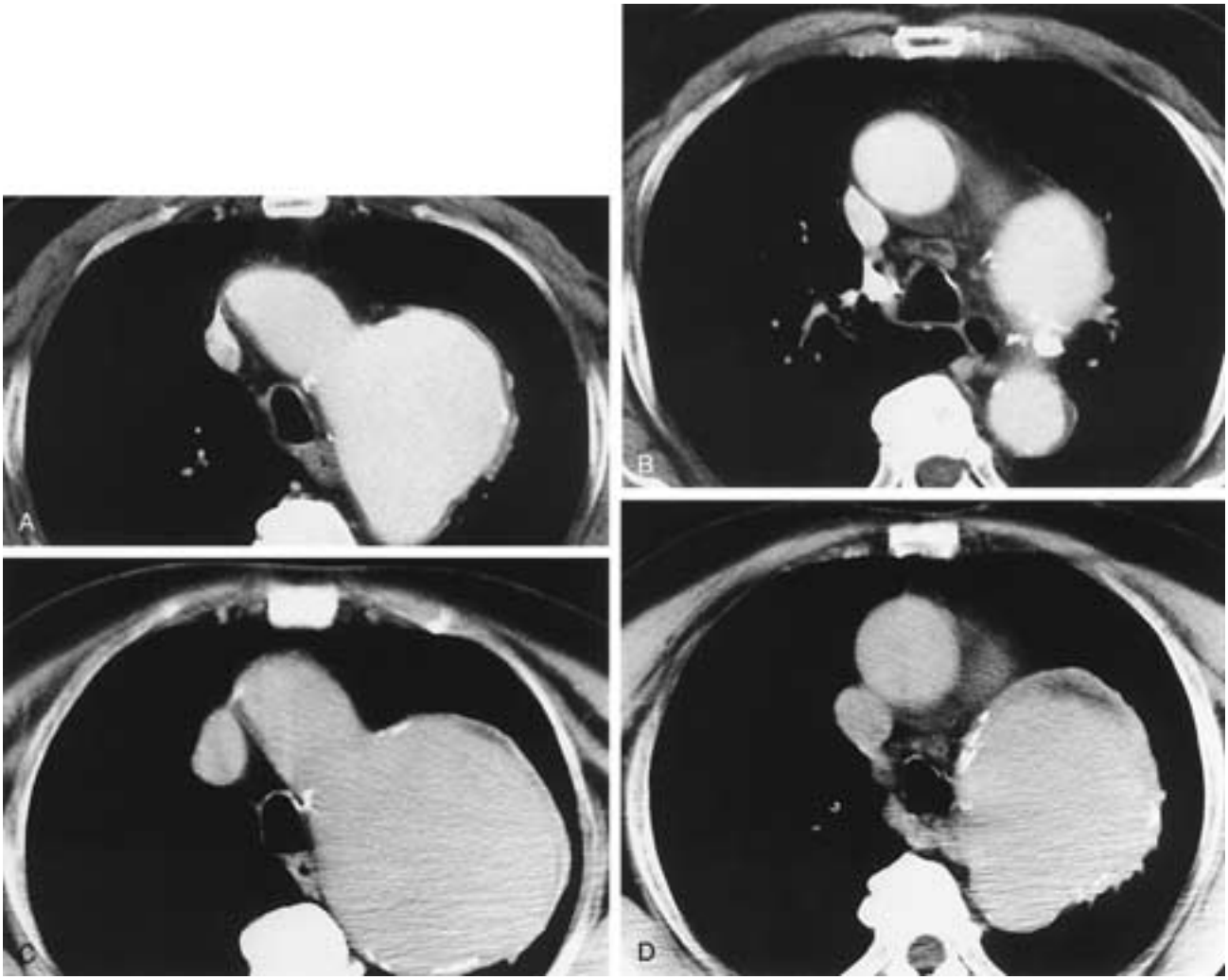

VIEW IMAGE

FIGURE 42-37 Aortic aneurysm. Axial CT scans in June 1993 (**A** and **B**) and March 1995 (**C** and **D**) show an aneurysm of the aorta. The aneurysm extends into the AP window. The enlargement of the aneurysm resulted in a left vocal cord paralysis. There was normal cord mobility in June 1993.

Copyright © 2003, Mosby, Inc. All rights reserved.

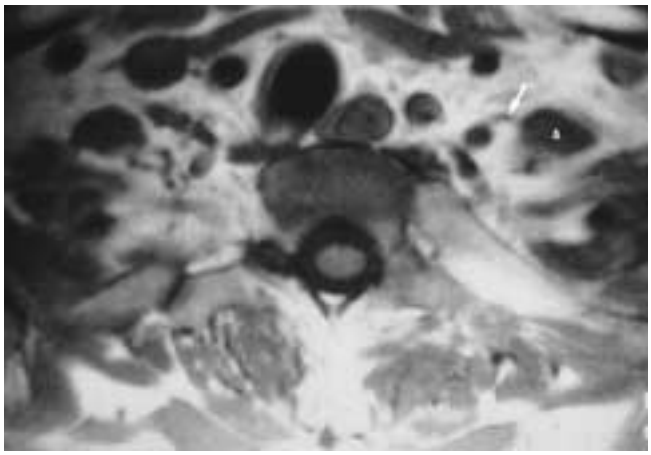

VIEW IMAGE

FIGURE 42-38 Phrenic nerve. Axial T1-weighted MR image demonstrates the phrenic nerve (*arrow*) medial to the anterior scalene muscle (*A*).

aortic arch superficial to the superior intercostal vein and then passes laterally over the pericardium and left ventricle. This nerve passes through the muscular portion of the diaphragm anterior to the central tendon adjacent to the left side of the heart.

The phrenic nerve is usually the sole motor supply to the diaphragm. Occasionally, there may be an accessory phrenic nerve that is derived from C4, C6, or the ansa subclavia. Paralysis and atrophy of the diaphragm are manifestations of phrenic nerve palsy. This diagnosis can be made when diaphragmatic motion is absent on inspiratory and expiratory plain films or when paradoxical motion of the diaphragms is observed on fluoroscopy. However, it should be remembered that if the patient has an accessory phrenic nerve, the diaphragm may not be completely paralyzed.

Phrenic nerve palsy has a number of causes including viral neuritis, a mass pressing on the nerve, trauma, and iatrogenic causes (surgery). Radiographically, the goal is to identify a mass along the course of the nerve. Thus, a mass

FIGURE 42-40 Metastatic breast carcinoma. Axial CT scan through the superior mediastinum shows a mass anterior and lateral to the left carotid artery (*C*). This involves the phrenic nerve. Also noted is a node (*arrow*) in the left tracheoesophageal sulcus. This accounts for the patient's left vocal cord paralysis.

VIEW IMAGE

that abuts the anterior border of the anterior scalene muscle in the neck (Fig. 42-39) or the anterior border of the subclavian artery at the thoracic inlet, or that lies in the mediastinum lateral to the vascular structures, can produce a phrenic nerve palsy (Fig. 42-40).

REFERENCES

1. Alnot JY. Traumatic brachial plexus lesions in the adult: indications and results. Hand Clin North 1995;11:623–632.
2. Arcasov SM, Jett JR. Superior pulmonary sulcus tumors and pancoast's syndrome. N Engl J Med 1997;337:1370–1376.
3. Armington WG, Harnsberger HR, Osborn AG, Seay AR. Radiographic evaluation of brachial plexopathy. Am J Neuroradiol 1987;8:361–367.
4. Attar S, Krasna MJ, Sonett JR et al. Superior sulcus (Pancoast) tumor: experience with 105 patients. Ann Thorac Surg 1998;66:193–198.
5. Becker W, Naumann HH, Pfaltz CR. Ear, Nose, and Throat Diseases. New York: Thieme, 1989;386–432.
6. Berkovitz BKB, Moxham BJ. A Textbook of Head and Neck Anatomy. London: Yearbook Medical/Wolfe, 1988.
7. Clarke HM, Curtis CG. An approach to obstetrical brachial plexus injuries. Hand Clin North Am 1995;11:563–582.
8. Carpenter MB, Sutin J. Human Neuroanatomy, 8th ed. Baltimore: Williams & Wilkins, 1983;342–350.
9. Castagno AA, Shuman WP. MR imaging in clinically suspected brachial plexus tumor. Am J Roentgenol 1987;149:1219–1222.

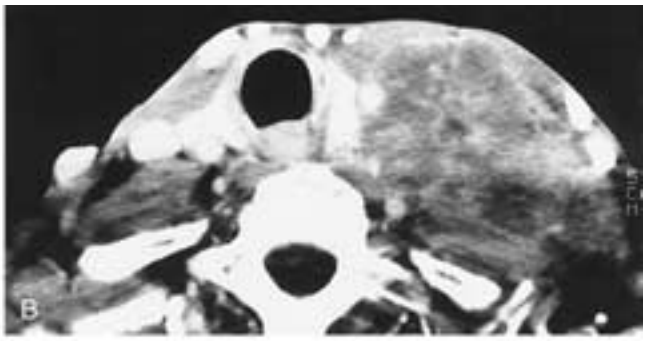

FIGURE 42-39 Lung carcinoma. CT scout scan (**A**) shows elevation of the left hemidiaphragm. Axial CT scan (**B**) demonstrates a large, inhomogeneous mass in the left side of the neck. This mass is encasing the scalene muscles, resulting in phrenic nerve palsy and brachial plexopathy.

VIEW IMAGE

Copyright © 2003, Mosby, Inc. All rights reserved.

10. Chiles C, Davis KW, Williams DW. Navigating the thoracic inlet. RadioGraphics 1999;19:1161–1176.
11. Cole JW, Quint DJ, McGillicuddy JE et al. CT-guided brachial plexus biopsy. AJNR 1997;18:1420–1422.
12. Dart LHJ, MacCarty CS, Love JG, et al. Neoplasms of the brachial plexus. Minn Med 1970;53:959–964.
13. Deletis V, Morota N, Abott IR. Electrodiagnosis in the management of brachial plexus surgery. Hand Clin North Am 1995;11:555–562.
14. Detterbeck FC. Pancoast (superior sulcus) tumors. Ann Thorac Surg 1997;63:1810–1818.
15. Farmer DW, Moore E, Amparo E, Webb WR, et al. Calcific fibrosing mediastinitis: demonstration of pulmonary vascular obstruction by magnetic resonance imaging. Am J Roentgenol 1984;143:1189–1191.
16. Fraser RS, Pare JAP, Fraser RC, Pare PD. Synopsis of Diseases of the Chest. Philadelphia: WB Saunders, 1994.
17. Gasparotti R, Ferraresi S, Pinelli L, et al. Three-dimensional MR myelography of traumatic injuries of the brachial plexus. AJNR 1997;18:1733–1742.
18. Gebarski KS, Glazer GM, Gebarski SS. Brachial plexus: anatomic, radiologic and pathologic correlation using computed tomography. J Comput Assist Tomogr 1982;6:1058–1063.
19. Glazer HS, Lee JKT, Levitt RG et al. Radiation fibrosis: differentiation from recurrent tumor by MR imaging. Radiology 1985;156:721–726.
20. Guberman, A. An Introduction to Clinical Neurology: Pathophysiology, Diagnosis and Treatment. Boston: Little, Brown, 1994.
21. Harnsberger HR. The lower cranial nerves. In: Harnsberger HR, ed. Head and Neck Imaging. Chicago: Mosby-Yearbook, 1990;420–450.
22. Hashimoto T, Mitomo M, Hirabuki N, et al. Nerve root avulsion of birth palsy: comparison of myelography with CT myelography and somatosensory evoked potential. Radiology 1991;178:841–845.
23. Hayes CE, Tsuruda JS, Mathis CM et al. Brachial plexus: MR imaging with a dedicated phased array of surface coils. Radiology 1997;203: 286–289.
24. Hollinshead WH. Anatomy for Surgeons, Vol 1. The Head and Neck. New York: Harper & Row, 1968.
25. Iyer RB, Fenstermacher MJ, Libshitz HI. MR imaging of the treated brachial plexus. AJR 1996;167:225–229.
26. Kellman GM, Kellman JB, Middleton WD et al. MR imaging of the supraclavicular region: normal anatomy. AJR 1987;148:77–82.
27. Kneeland JB, Kellman GM, Middleton WD et al. Diagnosis of disease of the supraclavicular region by use of MR imaging. AJR 1987;148:1149–1151.
28. Kori WH, Foley KM, Posner JB. Brachial plexus lesions in patients with cancer: 100 cases. Neurology 1981;31:45–50.
29. Kurihara Y, Yakushiji YK, Matsumoto J et al. The ribs: anatomic and radiologic considerations. RadioGraphics 1999;19:105–119.
30. Last RJ. Anatomy: Regional and Applied, 6th ed. New York: Churchill Livingstone, 1978.
31. Lusk MD, Kline DG, Garcia CA. Tumors of the brachial plexus. Neurosurgery 1987;21:439–453.
32. Montgomery RL. Head and Neck Atlas with Clinical Correlations. New York: McGraw-Hill, 1981.
33. Mountain CF. Revisions in the international system for staging lung cancer. Chest 1997;111:1710–1717.
34. Mukherji SK, Castillo M, Wagle AG. The brachial plexus. Semin US CT MR 1996;17:519–538.
35. Panasci DJ, Holliday RA, Shpizner B. Advanced imaging techniques of the brachial plexus. Hand Clin North Am 1995;11:545–554.
36. Obuchowski AM, Ortiz AO. MR imaging of the thoracic inlet. MRI Clin North Am 2000;8:183–203.
37. Perkin GD, Rose FC, Blackwood W, Shawdon HH. Atlas of Clinical Neurology. Philadelphia: JB Lippincott, 1986.
38. Rapaport S, Blair DN, McCarthy SM et al. Brachial plexus: correlation of MR imaging with CT and pathologic findings. Radiology 1988;167:161–165.
39. Remley KB, Latchaw RE. Imaging of cranial nerves IX, X and XI: functional anatomy and pathology. Neuroimag Clin North Am 1993;3:171–191.
40. Sell PJ, Semple JC. Primary nerve tumours of the brachial plexus. Br J Surg 1987;74:73–74.
41. Sheppard DG, Iyler RB, Fenstermacher MJ. Brachial plexus: demonstration at US. Radiology 1998;208:402–406.
42. Sherrier RH, Sostman HD. Magnetic resonance imaging of the brachial plexus. J Thorac Imag 1993;8:27–33.
43. Swanson PD. Signs and symptoms in neurology. JB Lippincott, 1984.
44. Uetani M, Hayashi K, Hashmi R et al. Traction injuries of the brachial plexus: signal intensity changes of the posterior cervical paraspinal muscles on MRI. J Comput Assist Tomogr 1997;21:790–795.
45. Van Es HW. MRI of the brachial plexus. Eur Radiol 2001;11:325–336.
46. Walker AT, Chaloupka JC, de Lothiniere ACJ et al. Detection of nerve root avulsion of CT myelography in patients with birth palsy and brachial plexus injury after trauma. AJR 1996;167:1283–1287.
47. Warwick R, Williams PL, eds. Gray's Anatomy, 35th British ed. Philadelphia: WB Saunders, 1973.
48. Webb WR, Sostman HD. MR imaging of thoracic disease: Clinical uses. Radiology 1992;182:621–630.
49. Wilson-Pauwels L, Akesson EI, Stewart PA. Cranial Nerves. Toronto: BC Decker, 1988;126–133.
50. Yang WT, Chui PT, Metreweli C. Anatomy of the normal brachial plexus revealed by sonography and the role of sonographic guidance in anesthesia of the brachial plexus. AJR 1998;171:1631–1636.

Copyright © 2003, Mosby, Inc. All rights reserved.

43

The Posttreatment Neck: Clinical and Imaging Considerations

Peter M. Som, William Lawson, and Mark L. Urken

INTRODUCTION
TYPES OF NECK DISSECTION
RADICAL NECK DISSECTION (I, II, III, IV, V)
MODIFIED NECK DISSECTION (I, II, III, IV, V) WITH PRESERVATION OF ONE OR MORE STRUCTURES—THE IPSILATERAL INTERNAL JUGULAR VEIN, SPINAL ACCESSORY NERVE, STERNOCLEIDOMASTOID MUSCLE, AND SUBMANDIBULAR GLAND
SELECTIVE NECK DISSECTION
Supraomohyoid Type of Selective Neck Dissection (I, II, III)
Lateral Type of Selective Neck Dissection (II, III, IV)
Posterolateral Type of Selective Neck Dissection (II, III, IV, V)
Anterior Compartment Type of Selective Neck Dissection (VI, VII)
Extended Radical Neck Dissection (Additional Structures Removed)
RETROPHARYNGEAL NODAL DISEASE
SURGERY: WITH AND WITHOUT RECONSTRUCTION
RADIATION THERAPY
ROUTINE POSTOPERATIVE AND POSTRADIATION IMAGING CHANGES
BASELINE SURVEILLANCE IMAGING
SURVEILLANCE PROTOCOL
IMAGING SUSPICION OF A RECURRENCE
BIOPSY OF SUSPECTED RECURRENCE SEEN ON IMAGING
THE IMAGING DETECTION OF VASCULAR COMPLICATIONS
THE IMAGING DETECTION OF OSSEOUS COMPLICATIONS
POST–NECK DISSECTION CHYLOUS FISTULA
POSTTRAUMATIC NEUROMA
DERMAL METASTASIS
NEWER TECHNIQUES

INTRODUCTION

Any discussion of the posttreatment neck, especially the postoperative neck, should be based on an understanding of the current treatment philosophies regarding neck metastases, as the management of cervical nodal disease is a critical part of the overall treatment of patients with head and neck squamous cell carcinoma. Since the early 1900s, surgery has been the primary treatment modality, and the operation of choice has been the radical neck dissection (RND).[1] However, in the past two decades, a number of surgical options other than the RND have been devised. In addition, radiation therapy with or without chemotherapy has become a major component of treatment.

The development of any rational approach to the treatment of cervical nodal metastases requires an understanding of the frequency, pattern of distribution, and prognostic implications of such nodal disease for the various head and neck primary tumors. Further discussion on this topic is presented in Chapter 36.

The early work on the incidence of cervical nodal metastasis was based almost exclusively on physical examination.[2] More recently, data from those studies have been modified by statistics that include palpation, clinical assessment, and histologic evaluation of surgical specimens.[3, 4] The results of these studies have shown a wide range of nodal involvement, depending on the primary site of the tumor. Carcinomas arising in the nasopharynx, palatine tonsil, hypopharynx, and base of the tongue have nodal metastases in 70% to 90% of cases, whereas

Copyright © 2003, Mosby, Inc. All rights reserved.

carcinomas of the oral cavity have nodal metastases in only 2% to 25% of the cases.[1]

With regard to the pattern of nodal metastases in the neck from specific primary tumor sites, it has been well documented that carcinomas of the oral cavity tend to spread to nodes in levels IA, IB, II, and III, while carcinomas of the oropharynx, hypopharynx, and supraglottic larynx tend to metastasize to nodes in levels II, III, and IV (see Chapter 36). The clinically silent but imaging-identified retropharyngeal nodes tend to harbor metastases from primaries in the hypopharynx, lateral and posterior oropharynx, tonsillar fossa, and soft palate. The visceral nodes (levels VI and VII) tend to be involved in primary carcinomas of the subglottic larynx, cervical esophagus, cervical trachea, and thyroid.[1] These patterns of spread have been utilized to develop rational surgical alternatives to the standard RND, with the selection of a modified or selective neck dissection strongly influenced by the location of the primary tumor.

The treatment of one particular group of patients with head and neck carcinomas remains controversial and illustrates the problems that persist in creating treatment decision algorithms. This specific group includes patients who present with a primary carcinoma and no clinical or imaging evidence of nodal disease (N0). Specifically, the problem of the N0 neck focuses on how to select those patients who require surgery, since when one considers all head and neck primary sites, only about 15% of N0 necks will eventually develop clinical nodal metastasis.[5, 6]

The recent literature contains guidelines, based on the above-cited studies, to approach the treatment of the N0 neck patient. That is, an elective or prophylactic neck dissection is not generally considered necessary for a patient with an N0 neck who has a T1 tumor with a risk of occult metastasis of less than 20% (i.e, true vocal cord, suprahyoid epiglottis).[7] However, the treatment of the patient with an N0 neck and a T1 carcinoma at a site that has a high probability of metastatic neck disease (i.e., pharynx, tonsil, tongue, and supraglottic larynx) is a clinically relevant issue because the possibility that metastatic nodal disease will develop in one or both sides of the neck is greater than 20%.[5, 8]

Once a decision has been made to treat a neck, the surgeon must select the type of neck dissection most appropriate for that patient. Except in cases of advanced nodal disease, most surgeons no longer believe that a standard RND is necessary, especially in patients with N0 and N1 staged necks.[6] However, most surgeons believe that some form of initial neck treatment is necessary, as there is evidence that failure to primarily treat such a neck results in a lower survival rate.[9]

Radiotherapy (RT) is another treatment option in these patients. Supporters of elective regional neck RT believe that irradiation is at least as effective as neck dissection, with a similar or lesser morbidity. They contend that elective neck irradiation can sterilize an N0 neck with subclinical disease.[9, 10] However, others suggest that substantive scientific evidence is limited, being for the most part indirect, inferential, and not well supported by direct comparison with surgery in formal clinical trials.[10] Nevertheless, RT is a recognized treatment option in these patients, and it can be utilized primarily or postoperatively, especially if extracapsular nodal spread has been found. Alternatively, it may be held in reserve for treatment of a late recurrence.

Chemotherapy also has a role in the treatment of head and neck cancer, either as part of an organ-sparing protocol, along with definitive or preoperative RT, or as part of a palliative or salvage treatment. A clinical observation now well established in the literature is that a rapid tumor response to chemoradiation is not predictive of improved survival, and ongoing treatment strategies should not be altered on the basis of initial tumor regression.[11, 12] Similarly, the inability to identify tumor on imaging studies, or the lack of interval change on serial imaging obtained during chemotherapy, should not be interpreted as indicating the absence of tumor. In most cases of head and neck cancer, the carcinoma will recur after the cessation of chemotherapy.

TYPES OF NECK DISSECTION

When considering the surgical treatment of neck disease, in addition to the traditional or full RND, there are five other recognized, more limited types of neck dissection: (1) the modified neck dissection, (2) the supraomohyoid type of selective neck dissection, (3) the lateral type of selective neck dissection, (4) the posterolateral type of selective neck dissection, and (5) the anterior compartment type of selective neck dissection.[6] There is also the option to perform a more extensive operation than the standard RND, the extended radical neck dissection. The nodal levels referred to are defined by the standard nomenclature used either in the 1997 version of the American Joint Committee on Cancer or the imaging-based nodal classification of 1999 (Fig. 43-1).[13, 14]

However, there are some procedures that do not precisely fit into such a classification system because a specific nodal level was or was not resected. It has been suggested that the procedure be described by a listing of the specific nodal levels resected. In this system, the nonnodal structures resected in modified neck dissection should also be identified. It is hoped that this strategy will eliminate any confusion, and it will be used in the discussion following.

Although a number of other surgical classifications are suggested in the literature, the nomenclature most widely used to describe the various types of neck dissections is the one developed by the Committee for Head and Neck Surgery and Oncology of the American Academy of Otolaryngology/Head and Neck Surgery.[6, 15–17] It is based on the concept that the RND is the standard or basic procedure for treating cervical lymphadenopathy in the cancer patient.[6] The RND removes en bloc all of the ipsilateral nodes extending from the mandible to the clavicle, the sternocleidomastoid muscle, internal jugular vein, and spinal accessory nerve. Compared to the RND, if the surgery preserves one or more nonlymphatic structures, the procedure is called a modified neck dissection (MND). When the procedure involves preservation of one or more lymph node levels (primarily relating to levels I to V), the

Copyright © 2003, Mosby, Inc. All rights reserved.

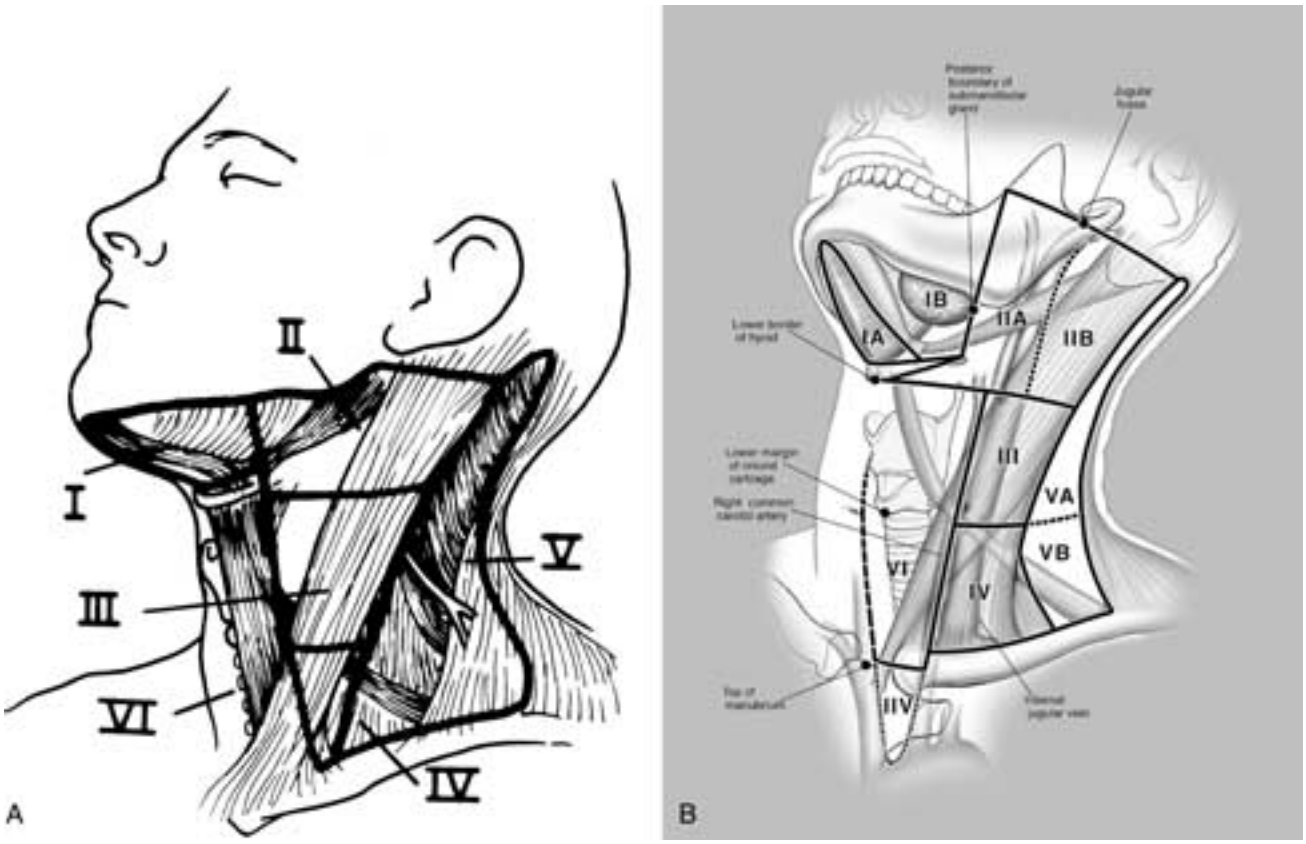

VIEW IMAGE

FIGURE 43-1 **A**, Drawing of the left side of the neck with the skin and superficial faciae removed. The clinical level staging system is used. The bold lines outline the limits of a radical lymph node dissection, and the roman numerals refer to the nodal levels. Note the locations of the spinal accessory nerve and the inferior belly of the omohyoid muscle in the posterior triangle of the neck. (Modified from Robbins KT, Medina JE, Wolfe GT. Standardizing neck dissection terminology. Official report of the Academy's Committee for Head and Neck Surgery and Oncology [see comments]. Arch Otolaryngol Head Neck Surg 1991;117:601–605.) **B**, Drawing of the left side of the neck viewed from anteriorly and obliquely. The pertinent anatomy used to define the imaging-based nodal classification is illustrated. The bold lines outline the nodal level boundaries, and the roman numerals refer to the nodal levels.

surgery is referred to as a selective neck dissection (SND). Finally, when the procedure involves the removal of lymph node groups or nonlymphatic structures in addition to those encompassed by an RND, the procedure is referred to as an extended radical neck dissection (ERND).

Although there is some variation among surgeons as to when each type of operation is performed, there is a generally accepted approach to which most surgeons adhere. If there is extensive neck disease, with or without extracapsular nodal extension, the RND is the operation of choice. When there is extracapsular nodal tumor, most surgeons will give postoperative RT to the neck. The MND is considered when there is limited neck disease in an N1 or N2 neck, without extracapsular tumor spread. That is, the nodal disease is anatomically localized to areas that allow some nonnodal structures to be spared. If a MND is considered preoperatively and extracapsular nodal spread is found at surgery, most surgeons will perform a RND. The SND is performed on N0 necks. If nodal metastasis is found at surgery, most surgeons will perform a more comprehensive procedure such as a MND or, if extracapsular tumor is present, a RND.

RADICAL NECK DISSECTION (I, II, III, IV, V)

Using the level classifications described in Chapter 36, and in particular the imaging-based classification (Fig. 43-2), the classic RND removes en bloc all of the ipsilateral nodes extending from the mandible to the clavicle[14] (Fig. 43-1B). The resection extends anteriorly from the lateral border of the sternohyoid muscle, hyoid bone, and contralateral medial border of the anterior belly of the digastric muscle to the anterior border of the trapezius muscle posteriorly. The specimen thus includes all of the level I to V nodes, the ipsilateral submandibular gland, spinal accessory nerve, internal jugular vein, and sternocleidomastoid muscle. Occasionally included in the resection are the ipsilateral sternohyoid and sternothyroid muscles, one or both of the muscle bellies of the ispsilateral digastric muscle, and the ipsilateral thyroid lobe. This procedure does not include removal of the postauricular and suboccipital nodes, the periparotid nodes (except for a few nodes in the tail of the parotid gland), the perifacial and buccinator nodes, the retropharyngeal nodes, and the level VI and VII nodes. As a result of the surgery, the denervated trapezius atrophies, and

Copyright © 2003, Mosby, Inc. All rights reserved.

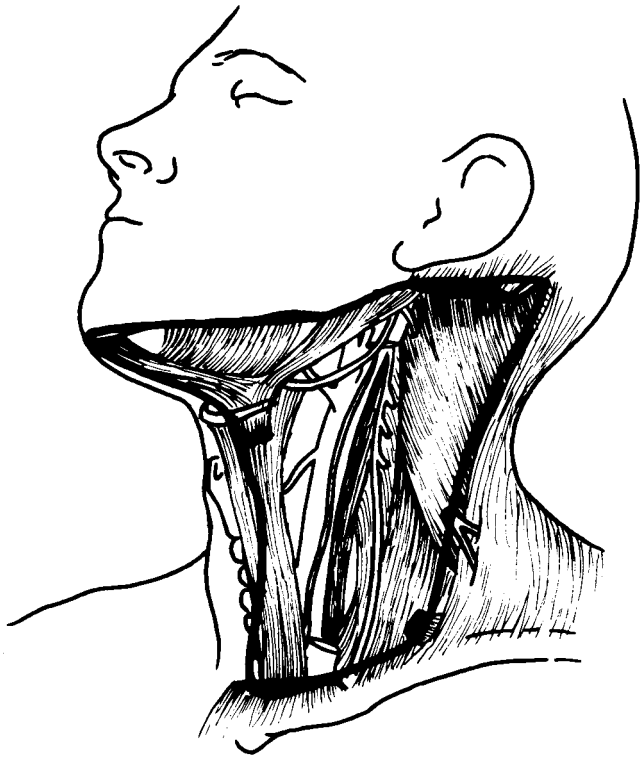

VIEW IMAGE

FIGURE 43-2 Diagram of radical neck dissection. The skin and superficial fasciae have been removed, and the bold lines define the surgical boundaries that contain the nodal levels removed. Removed are the sternocleidomastoid muscle, the internal jugular vein, and the spinal accessory nerve. The lymph nodes removed include those in levels I, II, III, IV, and V.

the patient develops the shoulder syndrome, which is characterized by progressive shoulder drop, shoulder pain, scapula prominence and deformity of the shoulder girdle, and limitation of shoulder abduction. Usually there is compensatory hypertrophy of the ipsilateral levator scapulae muscle. The RND is utilized in patients with extensive nodal metastases, with or without extranodal tumor extension that involves the spinal accessory nerve and/or the internal jugular vein.[6, 17]

MODIFIED NECK DISSECTION (I, II, III, IV, V) WITH PRESERVATION OF ONE OR MORE STRUCTURES—THE IPSILATERAL INTERNAL JUGULAR VEIN, SPINAL ACCESSORY NERVE, STERNOCLEIDOMASTOID MUSCLE, AND SUBMANDIBULAR GLAND

The MND removes all of the lymph nodes routinely removed in a RND but preserves one or more of the following structures: the ipsilateral internal jugular vein (IJV), the spinal accessory nerve (SAN), the sternocleidomastoid muscle (SCM), and the submandibular gland (SMG) (Fig. 43-3). When describing the operation, the particular structures preserved should be specifically mentioned. For example, a MND that preserves the SAN should be described as a ''MND with preservation of SAN.''

The greatest decrease in morbidity when compared to the RND comes from the preservation of the SAN. The decrease in morbidity from preserving the IJV and the SCM muscle is small unless bilateral neck dissections are required. Occasionally, resection of a dominant right IJV may result in massive head and neck edema equal to that found with bilateral vein ligation. If bilateral neck dissections are deemed necessary, by utilizing a modified neck operation with preservation of the IJV, there is less severe facial and neck swelling and little if any increase in intracranial pressure compared to what is seen with bilateral radical neck dissections.[6, 17]

The terms *functional neck dissection* and *conservation neck dissection* also previously appeared in the literature to describe the physiologic benefits of this procedure. However, at present, the term *modified neck dissection* is the one used by most clinicians.[6, 17, 18] The MND is an en bloc removal of level I to V nodes. The dissection extends from the inferior border of the mandible to the clavicle. It extends medially from the lateral border of the strap muscles to the anterior border of the trapezius muscle laterally. However, as already described, there is preservation of the ipsilateral IJV, SAN, SMG, and SCM, either singly or in some combination.

The major indication for performing a MND is to remove probable or grossly visible nodal disease that is not directly infiltrating the nonlymphatic structures mentioned.[6, 17]

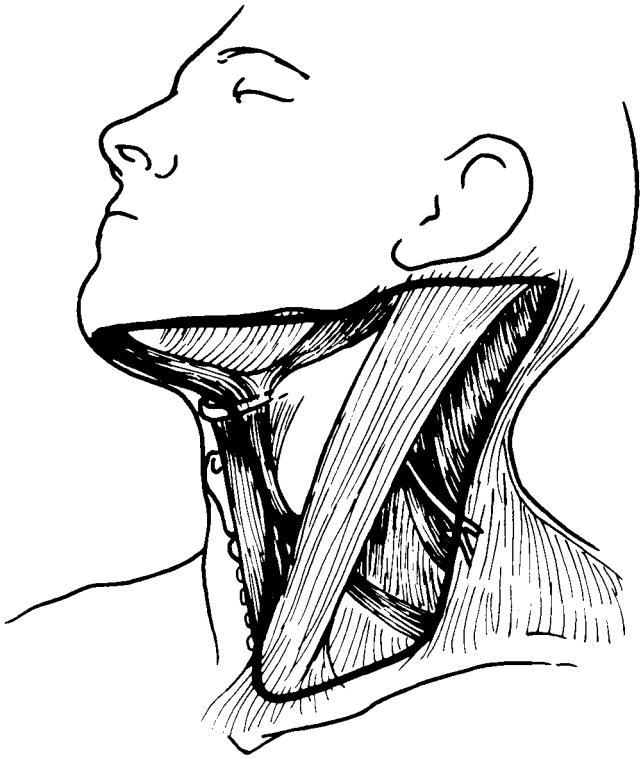

FIGURE 43-3 Diagram of a modified neck dissection. The skin and superficial fasciae have been removed, and the bold lines define the surgical boundaries that contain the nodal levels removed. The dissection preserves one or more of the following structures: the ipsilateral IJV, the SAN, the SCM, and the SMG. The lymph nodes removed include those in levels I, II, III, IV, and V.

VIEW IMAGE

Copyright © 2003, Mosby, Inc. All rights reserved.

SELECTIVE NECK DISSECTION

The various types of selective neck dissections are performed on patients at risk for early nodal metastases. These procedures are based on the concept of prophylactically removing those lymph node levels at greatest risk for spread in patients with N0 neck disease. They consist of en bloc removal of one or more of the nodal levels, depending on the location of the primary tumor and its known pattern of nodal metastasis. As previously mentioned, several studies have demonstrated that tumors in the oral cavity most frequently metastasize to level I, II, and III nodes. Tumors involving the oropharynx, hypopharynx, and supraglottic larynx most commonly metastasize to level II, III, and IV nodes. It has been found that whenever metastatic nodes were found in other areas of the neck with these primary tumors, there were always positive nodes in the stated regions most at risk.[2, 4, 19–21]

Recently, it has been suggested that the name of the type of SND be followed by the nodal levels removed. This approach clearly identifies the procedure performed.

Supraomohyoid Type of Selective Neck Dissection (I, II, III)

The supraomohyoid SND consists of en bloc removal of the lymph nodes in levels I, II, and III (Fig. 43-4). If the nodes in level IV are also removed, the procedure is referred to as an extended supraomohyoid SND. This procedure is indicated for patients with oral cavity cancers and N0 necks. These cancers are associated with at least a 20% risk of nodal metastasis. Neck dissection for floor of mouth cancers should remove nodes in levels I, II, and III; however, with carcinoma of the tongue, level IV nodes should also be included.

If there is palpable nodal disease (N+) in a patient with an oral cavity cancer, level IV and V nodes should also be removed. The exception to this rule is when intraoperative assessment reveals disease confined to levels I and II. In this situation, level I to IV nodes should be removed.

Surgical treatment of the contralateral neck is indicated in patients with cancers in the floor of the mouth, in the ventral surface of the tongue, and/or with midline tongue involvement in whom postoperative RT is not planned. In patients with oral cavity cancer, surgery on the contralateral neck is recommended if the patient has an N2C neck at presentation.[6] Whenever level I nodes are removed in these procedures, the ipsilateral SMG is also removed to control tumor spread.

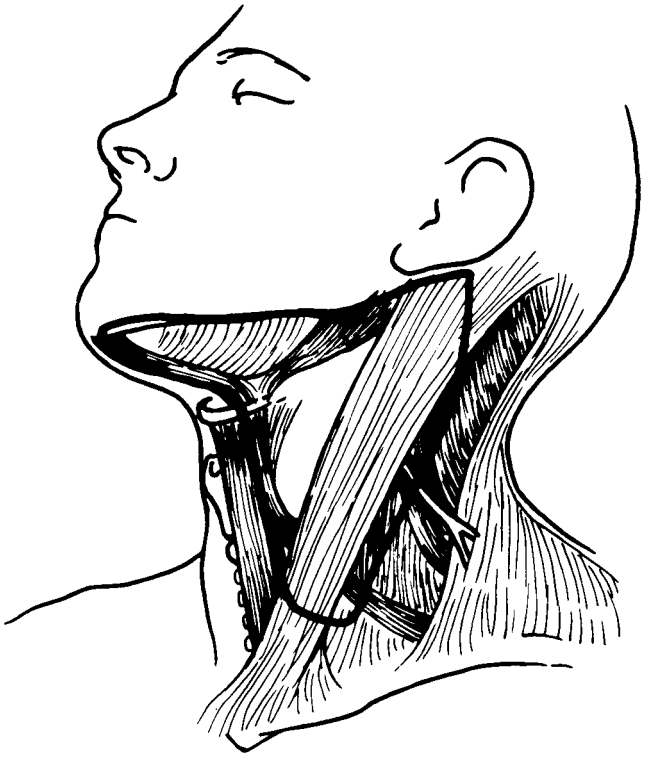

VIEW IMAGE

FIGURE 43-4 Diagram of a supraomohyoid neck dissection. The skin and superficial fasciae have been removed, and the bold lines define the surgical boundaries that contain the nodal levels removed. The lymph nodes removed include those in levels I, II, and III. The dissection extends to the posterior border of the SCM, which is preserved, as are the IJV and the SAN.

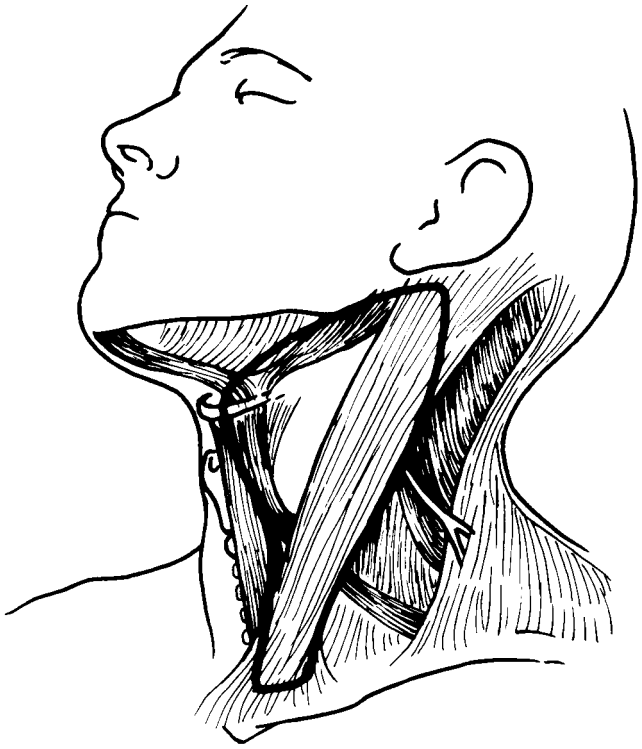

VIEW IMAGE

FIGURE 43-5 Diagram of a lateral-type neck dissection. The skin and superficial fasciae have been removed, and the bold lines define the surgical boundaries that contain the nodal levels removed. The lymph nodes removed include those in levels II, III, and IV.

Lateral Type of Selective Neck Dissection (II, III, IV)

The lateral SND consists of en bloc removal of the nodes in levels II, III, and IV (Fig. 43-5). This procedure is

Copyright © 2003, Mosby, Inc. All rights reserved.

recommended in patients with cancers arising in the oropharynx, hypopharynx, and supraglottic larynx. Because these cancers involve the midline visceral structures that have bilateral lymphatic drainage, this type of neck dissection is usually performed bilaterally.[6] With very extensive level II, III, and IV nodal disease, level V should also be resected.

Posterolateral Type of Selective Neck Dissection (II, III, IV, V)

The posterolateral SND removes the nodes in levels II, III, IV, and V and the suboccipital and postauricular nodes. The perifacial (buccinator) and external jugular nodes may also be resected (Fig. 43-6). This procedure is used in the treatment of cutaneous malignancies and soft-tissue sarcomas arising in the posterior scalp, nuchal ridge, occiput, or posterior neck. The dissection is designed to remove the lymph node bearing fibrofatty tissue in the posterior and lateral compartments of the neck. Included in the dissection should be the intervening subdermal fat and underlying fascia between the nodal groups and the primary tumor. This latter dissection is designed to eliminate the nests of tumor cells that are characteristically associated with cutaneous malignancies.[6]

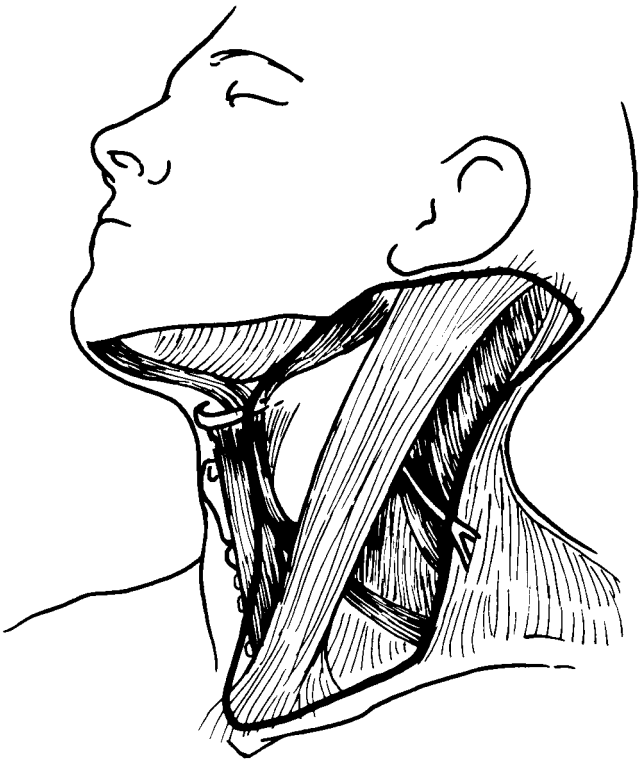

VIEW IMAGE

FIGURE 43-6 Diagram of a posterolateral neck dissection. The skin and superficial fasciae have been removed, and the bold lines define the surgical boundaries that contain the nodal levels removed. The lymph nodes removed include those in levels II, III, IV, and V. The suboccipital and retroauricular nodes are also removed.

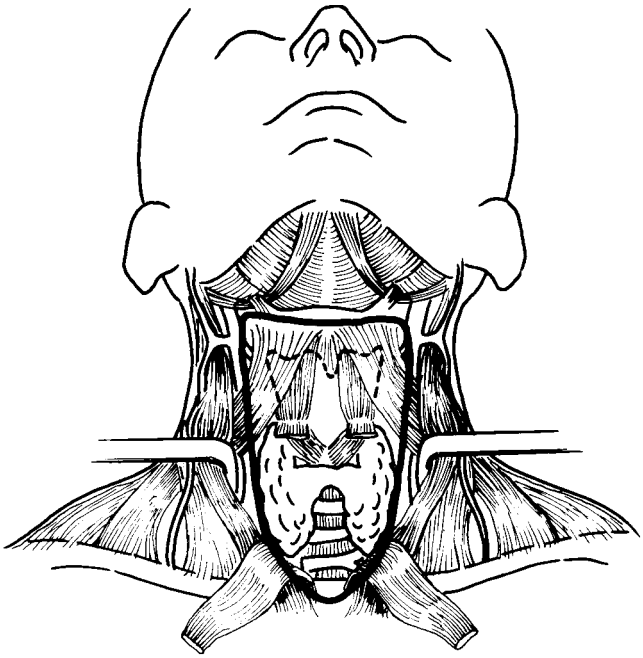

FIGURE 43-7 Diagram of an anterior compartment lateral-type neck dissection. The skin and superficial fasciae have been removed, and the bold lines define the surgical boundaries that contain the nodal levels removed. The strap muscles are severed. The lymph nodes removed are the level VI nodes and occasionally level VII nodes.

VIEW IMAGE

Anterior Compartment Type of Selective Neck Dissection (VI, VII)

The anterior compartment SND consists of en bloc removal of the nodes in level VI (Fig. 43-7). The procedure is indicated primarily for cancers arising in the thyroid gland, hypopharynx, cervical trachea, and cervical esophagus, as well as for those laryngeal cancers with subglottic disease. The dissection consists of en bloc removal of the cervical portions of the perithyroidal, pretracheal, and paratracheal nodes. In addition, the Delphian (precricoid node[s]) and the nodes along the course of the recurrent laryngeal nerves are resected. The boundaries of the dissection are the carotid sheaths laterally, the hyoid bone superiorly, and the suprasternal notch inferiorly. If there is known nodal disease at the level of the suprasternal notch, level VII nodes should also be resected. If the contralateral neck is N0 in patients with unilateral laryngeal and/or hypopharyngeal cancers, the dissection may be limited to the ipsilateral side. This reduces damage to the vascular supply to the parathyroid glands and eliminates the need to reimplant them.[6]

Extended Radical Neck Dissection (Additional Structures Removed)

The ERND refers to the removal of one or more additional lymph node groups or nonlymphatic structures, or both, not normally encompassed by an RND. Such nodal groups include the retropharyngeal, superior mediastinal (VII), perifacial (buccinator), and paratracheal (VI). Nonlymphatic structures include the carotid artery, hypoglossal

Copyright © 2003, Mosby, Inc. All rights reserved.

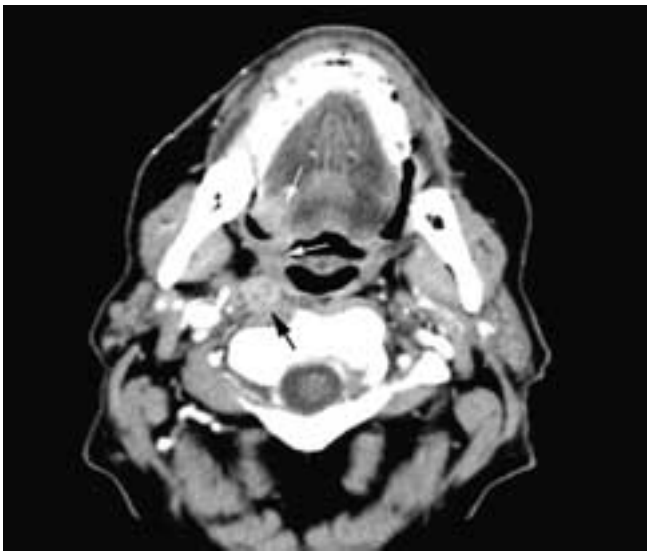

VIEW IMAGE

FIGURE 43-8 Axial contrast-enhanced CT scan shows a squamous cell carcinoma thickening the right oropharyngeal wall with extension to the right base of the tongue (*white arrows*). There is a nonhomogeneous right retropharyngeal node (*black arrow*).

nerve (XII), vagus nerve (X), and paraspinal muscles. The additional lymphatic and nonlymphatic structures resected should be identified when describing the procedure.

RETROPHARYNGEAL NODAL DISEASE

Special mention should be made of the presence of retropharyngeal nodes in patients with pharyngeal wall cancers (Fig. 43-8). As many as 44% of patients with pharyngeal carcinomas have been found to have retropharyngeal nodes, and if surgery is to be performed, the dissection must be extended to include these nodes.[22] The retropharyngeal nodes are also at risk in patients with base of tongue, tonsil, soft palate, and retromolar trigone cancers when the tumor extends to involve the lateral and/or posterior oropharyngeal walls. The pretreatment imaging identification of such nodes lying medial to the internal carotid arteries near the skull base clearly signals the need for such a modification of the dissection boundaries. Alternatively, if RT is the treatment of choice, the routine fields must be modified to dose these nodes properly.

SURGERY: WITH AND WITHOUT RECONSTRUCTION

The surgical approaches directed to both the primary tumor site and any cervical nodal metastases can be divided into two general groups: those operations that simply remove the known disease, without a need for reconstruction, and those operations that resect the disease but require a reconstructive procedure to repair or close the defect and provide function and/or comesis.[18] With regard to the reconstructive techniques, it is only within the past two decades that great advances have occurred, which restore the patient to a more normal appearance, a better functional status, and ultimately a better quality of life.

Management of a surgical defect varies from healing by secondary intention to the complex transfer of tissue to the head and neck using microvascular techniques. When the surgical defect requires tissue transfer to provide proper closure, there are two major types of flaps available for use: pedicled and free flaps, both based on the blood supply to the skin coming from tiny perforating vessels on the surface of the underlying muscle that is nourished by a named artery and vein. The en bloc transfer of the needed skin and its underlying muscle, with intact perfusion of its vascular supply, ensures the viability of the transposed tissues. The myocutaneous flap consists of the rotation of regional skin and underlying muscle on the preserved vascular pedicle of the muscle. The free flap consists of skin, subcutaneous tissue, muscle, and even bone, as required for reconstruction, to be transferred from a distant site to the surgical field, with the blood supply to the flap being reestablished by microvascular anastomosis to local blood vessels.

When myocutaneous flaps are utilized in these reconstructions, the muscle used can be from the head and neck (i.e., temporalis, sternocleidomastoid, and levator scapulae) or from the chest wall or upper back (i.e., pectoralis major, trapezius, latissimus dorsi). The primary nutrient vessels to the involved muscle are preserved, and on imaging, the vascular attachment of the flap can usually be seen at the lower margin of the flap. In contrast, with the free flaps on imaging, no vascular pedicle is identified.[23, 24]

In general, myocutaneous flaps are utilized to reconstruct surgical soft-tissue defects. When bone needs to be replaced, a composite-free osteomyocutaneous flap is utilized. This usually occurs with reconstruction of the mandible and hard palate, and the flap sites harvested are most often from the pelvis, scapula, or fibula. Examples of postoperative CT and MR scans are shown in Figures 43-9 to 43-18.

RADIATION THERAPY

The decision as to the optimal treatment of cervical metastatic nodal disease depends on a number of factors including the extent and location of the primary tumor, the nodal levels involved, and the presence of extranodal disease in the neck. In addition, the medical condition and age of the patient play important roles in the final selection of treatment.[25] As previously mentioned, it was not until the past two decades that treatment options other than RND were considered as suitable alternatives. However, presently RT, with or without chemotherapy, is not only useful adjunctive therapy but has become an effective primary treatment approach.[25] Another consideration in the algorithm for the management of cervical nodes is that early-stage tumors can be treated comparably by surgery or RT, and the decision as to which modality to use for the treatment of the primary tumor and the neck is often determined by the fact that most centers favor utilization of a single treatment modality.

Evidence now supports the prophylactic treatment of an N0 neck, not only to decrease the clinical development of neck disease, but also to decrease the incidence of distant

Copyright © 2003, Mosby, Inc. All rights reserved.

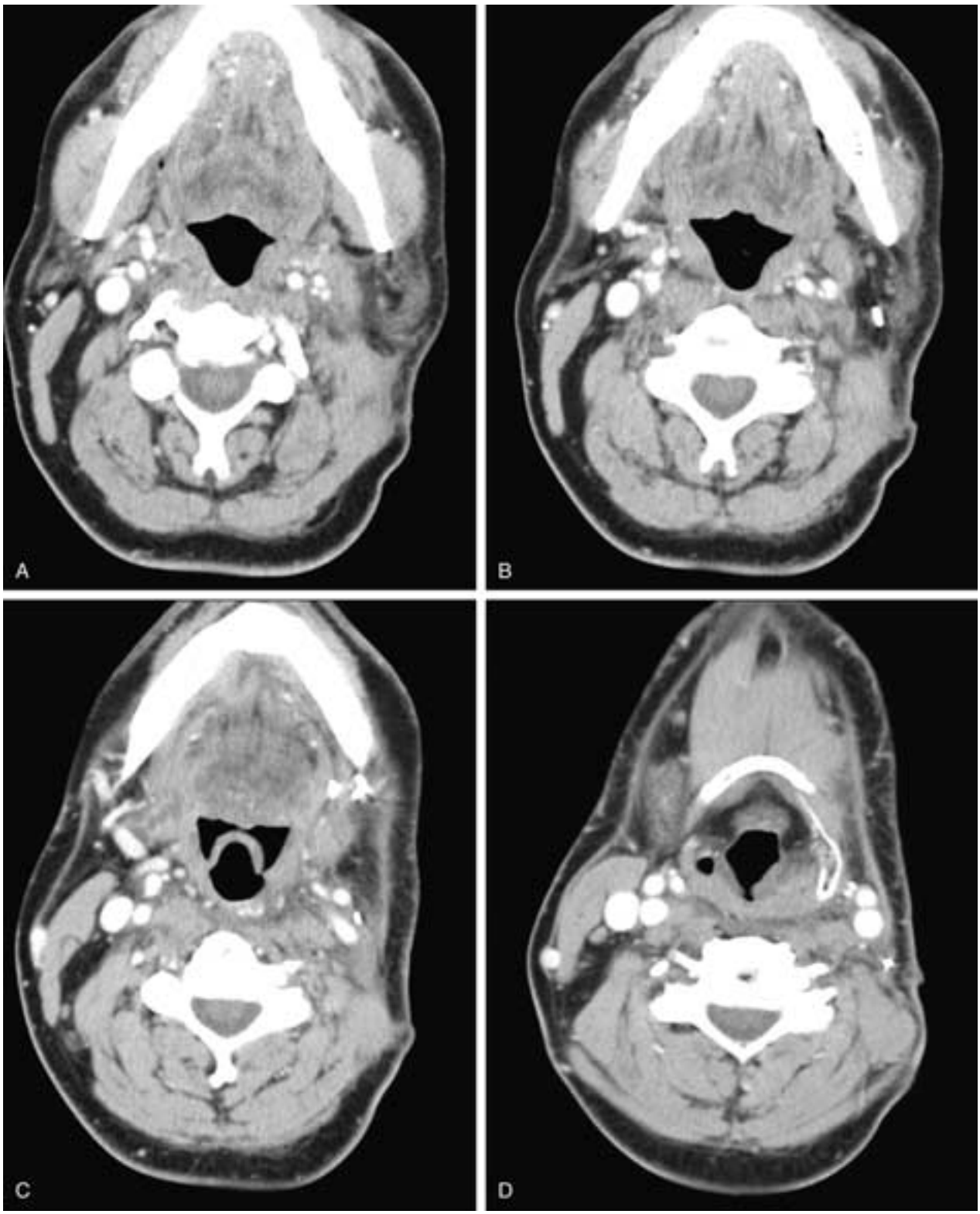

FIGURE 43-9 Serial axial contrast-enhanced CT scans from cranial (**A**) to caudal (**F**) on a patient who has had a left radical neck dissection. In this patient, the IJV, SAN, and SCM were resected. Note the typical shoulder drop and the beginning hypertrophy of the levator scapulae muscle (*arrow*) in **F**.

VIEW IMAGE

Copyright © 2003, Mosby, Inc. All rights reserved.

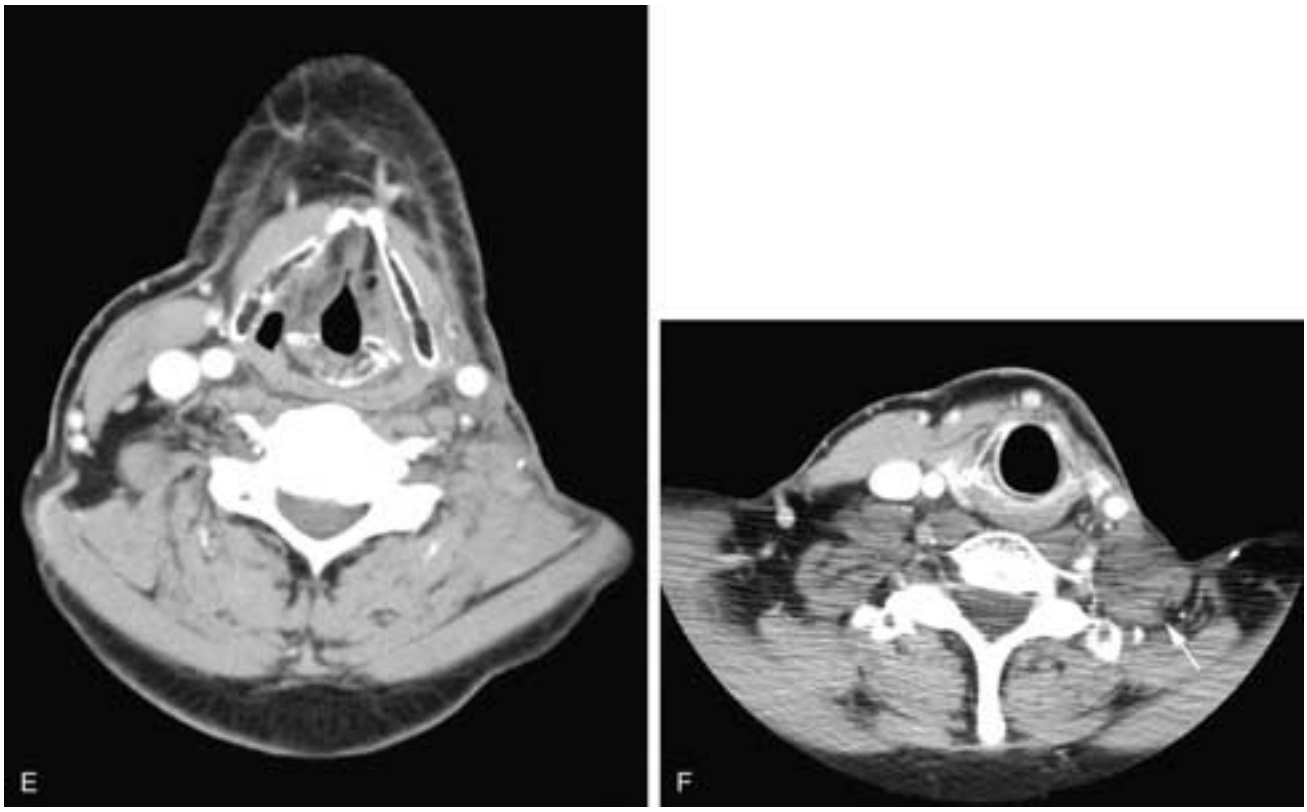

FIGURE 43-9 *Continued*

VIEW IMAGE

metastases by controlling neck disease.[25] However, the likelihood of regional neck control also depends on control of the primary site, as reseeding of the neck may occur from an uncontrolled primary tumor.[26]

The effectiveness of RT for palpable nodal disease depends on a number of factors including nodal size, nodal fixation, and the number of nodes present. Small (less than 3 cm), solitary, mobile nodes respond best to RT. Compared to surgery, control of regional neck disease with RT for multiple large, fixed nodes is poor. Improved regional control rates have been noted with RT when the treatments are delivered without interruption, that is, continuous-course rather than split-course treatments. Interruption of treatments generally results from intolerance of the RT.[25] Such problems are often related to the dose delivered, which is determined by nodal size. Doses of 65 Gy are adequate to control nodal disease when the nodes are less than 1 cm. However, 70 Gy is suggested to control nodes of 1 to 2 cm, and 75 Gy is necessary for nodes of 2 to 3 cm. In addition, since adequate coverage of the neck is necessary for nodal control, larger fields require larger doses, and this results in decreased patient tolerance.

Trials of prophylactic RT performed 20 to 30 years ago revealed that doses of 20 Gy decreased neck recurrence rates compared to the decreases achieved with RND without RT. In 1987, the Radiation Therapy Oncology Group Trial 73-03 demonstrated that postoperative RT improved regional control and possibly survival compared to preoperative RT. Postoperative RT also allowed for better pathologic analysis of the surgical specimen, and most surgeons preferred to operate in a nonirradiated field.[25, 27] Nevertheless, preoperative RT remains an important treatment option. Although a good clinical response to RT suggests a favorable regional control rate, some poor clinical responders may achieve long-term regional control. Furthermore, high-dose, hyperfractionated preoperative RT may further improve regional control, especially in patients with advanced neck disease.[25, 28]

Postoperative RT appears to be necessary when macroscopic extranodal tumor extension and perineural invasion are present. Other indications include the finding of multiple involved nodes and large nodal size at surgery.

Data from the Memorial Sloan-Kettering Cancer Center and the Veterans Administration Cooperative Study on organ preservation using cisplatin-based chemotherapy followed by RT suggest that patients with clinically palpable nodal disease who have a complete clinical response after induction chemotherapy will achieve excellent regional control of their neck disease after high-dose RT, rendering RND unnecessary.[25, 29, 30] Neoadjuvant therapy is designed as an organ preservation treatment alternative to surgery for selected patients who have advanced laryngeal and hypopharyngeal carcinomas. Initially, these patients were first treated with chemotherapy, with the responders then given RT in a curative attempt. Presently, these patients are given concomitant chemotherapy and RT. In those cases that are good responders, either no surgery or limited neck dissection is necessary.

Improved control of advanced regional neck disease may also be achieved by the use of brachytherapy, which is the

Copyright © 2003, Mosby, Inc. All rights reserved.

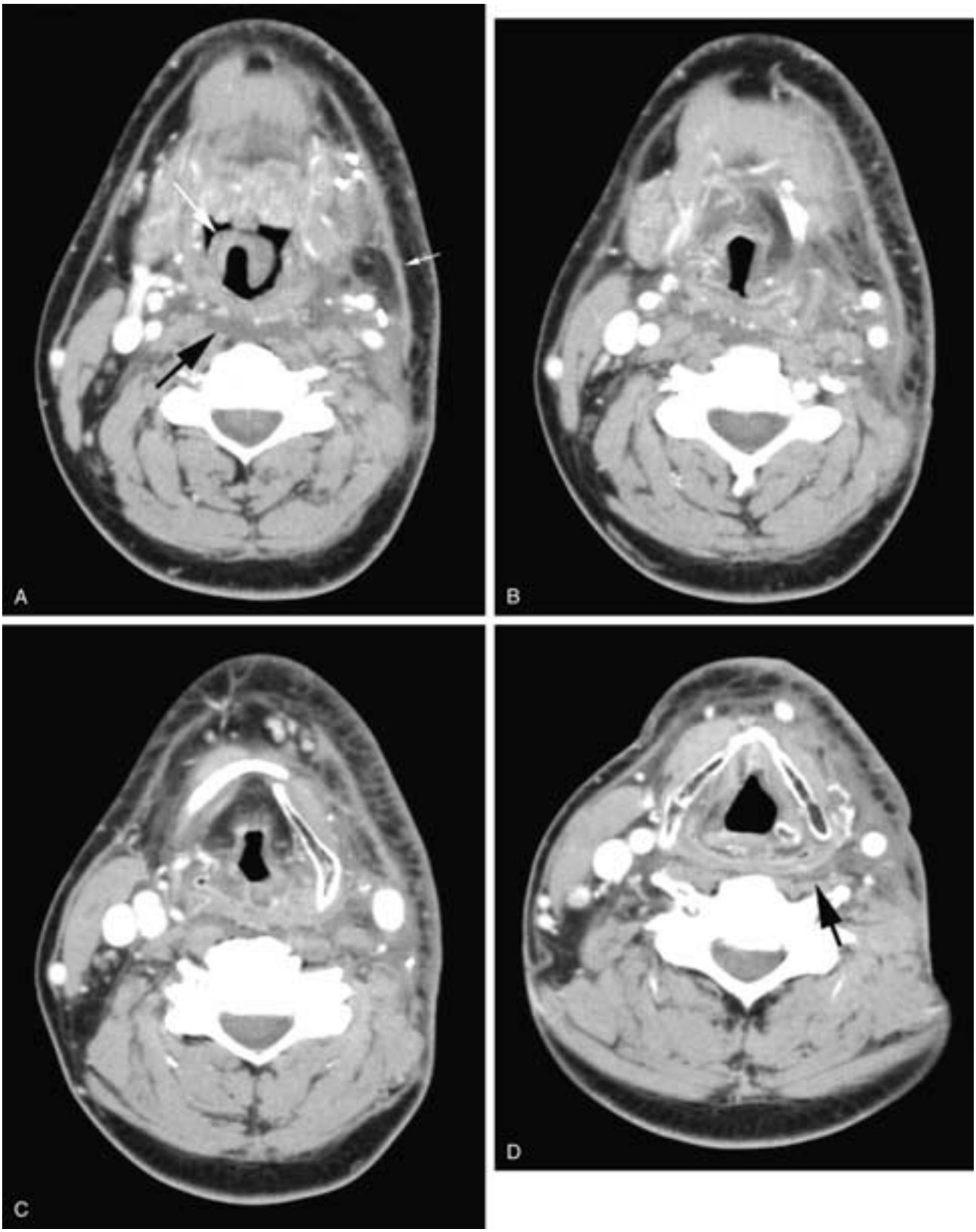

VIEW IMAGE

FIGURE 43-10 Serial axial contrast-enhanced CT scans from cranial (**A**) to caudal (**F**) on a patient who has had a left radical neck dissection and RT. Note the thickening of the epiglottis and supraglottic mucosal surfaces (*large arrows*) and the thickening of the platysma (*small arrows*). There is also thickening of the overlying left subcutaneous tissues and skin, and a rete pattern of obstructed venules and lymphatics is seen within the subcutaneous fat. The glottic and subglottic larynges are normal. This is the typical appearance of postradiation changes in the neck and larynx. Also, note in all images (*black arrows* in **A** and **D**) the zone of edema and fluid in the retropharyngeal space. This is a common postradiation imaging finding.

Copyright © 2003, Mosby, Inc. All rights reserved.

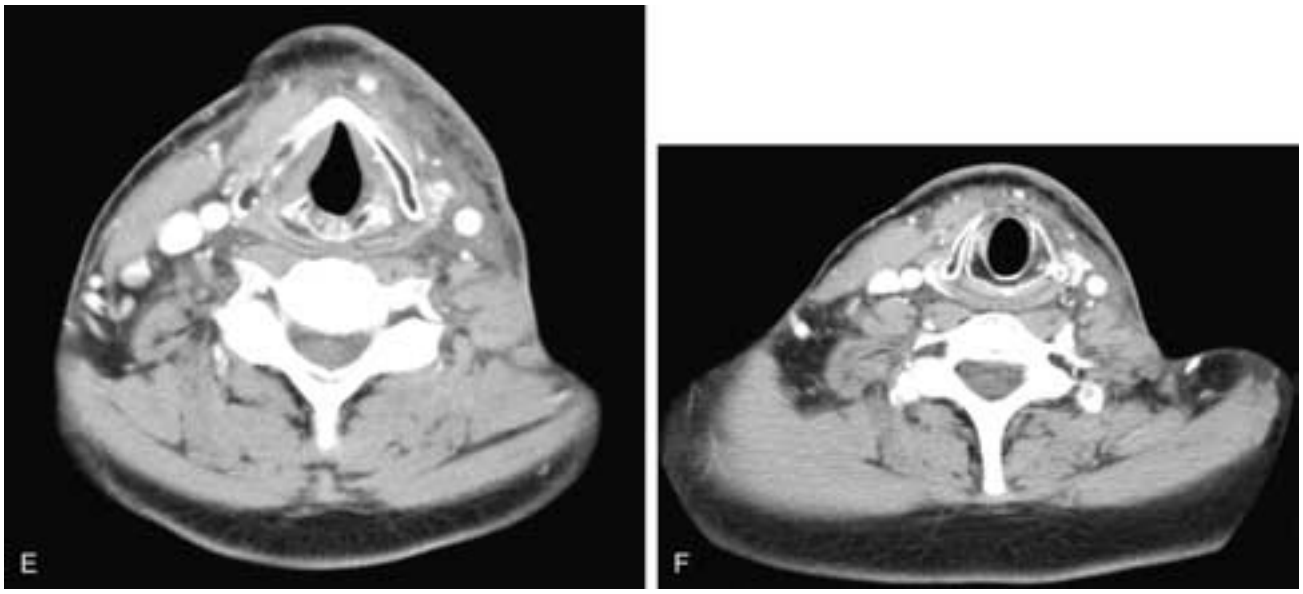

FIGURE 43-10 *Continued*

VIEW IMAGE

intraoperative implantation of iodine-125 sutures, pins, catheters, or other radioactive substances after surgical excision of the disease. Both improved regional control and improved survival have been reported.[25, 31, 32]

ROUTINE POSTOPERATIVE AND POSTRADIATION IMAGING CHANGES

Any trauma to the neck, whether external beam irradiation, needle biopsy, or surgical manipulation, results in edema and hemorrhage of the local soft tissues secondary to either obstruction or rupture of vascular and lymphatic capillaries. With minimal trauma (i.e., needle biopsy), these changes are usually not identified on CT and MR images or are seen for less than 2 to 3 weeks as a localized inflammatory-type response. However, after surgery and RT, these soft-tissue changes are more extensive and may persist for months or years. In the immediate postoperative period, the imaging findings are further complicated by the possible presence of cellulitis, hemorrhage, and lymph or suppurative collections, with or without an enhancing rim. By 4 to 6 weeks after surgery, there is generally a noticeable decrease in these imaging findings as the neck starts to return to a near-normal posttreatment appearance. It is not known why in some patients these imaging posttreatment changes rapidly disappear, while other patients retain them for months or years. When postoperative RT is utilized, these findings persist much longer than if only surgery was performed.

On CT, the findings, primarily within the subcutaneous fat, consist of a rete-like (reticular) pattern of interconnecting thin strands that primarily represent obstructed venules and lymphatic capillaries. In addition, the attenuation of fat (primarily subcutaneous fat) is increased as interstitial fluid permeates these regions and the subcutaneous fat layer is thickened. On MR imaging, only the rete pattern and swelling of the fat are seen, as the fat otherwise appears normal in signal intensity.

With treatment and time, these changes start to resolve, in most cases by the end of the first postoperative month. However, in the immediate post-RT period or even during RT treatments, the soft-tissue swelling and rete pattern may not be well appreciated, often requiring about a month or more after cessation of treatments to be fully manifest on imaging. In addition to the soft-tissue swelling, the most notable imaging changes after neck RT are a mild diffuse swelling of the hypopharyngeal mucosa and supraglottic mucosal laryngeal surfaces and a thin zone of water attenuation (edema and phlegmon) in the retropharyngeal space behind the hypopharynx and lower oropharynx (Figs. 43-10, 43-17, and 43-18).[33–38]

After an SND, it may be difficult to determine that surgery was performed. Often the best imaging hint is a reduced fat volume in the fat deep to the SCM and, if appropriate, in the submandibular triangle of the neck. This reduced fat volume may make identification of nodal disease more difficult, and care should be taken to examine such necks very thoroughly.

The incision line can usually be identified on axial imaging studies because of an infolding of the skin line and often a localized area of subjacent scar tissue. Based purely on the imaging, a local recurrence could have the same appearance; however, as it is so close to the skin, clinical assessment usually confirms its benign etiology. By comparison, transverse skin incisions are most often not identified on axial images, especially in patients who have had thyroid surgery. In these cases, identification of the prior surgery is made by noting the absence of one or both lobes of the thyroid gland and the resulting medial location of the common carotid artery (and possibly the IJV) just lateral to the trachea (Fig. 43-13).

After a MND or a RND, there is flattening of the ipsilateral neck contour, nonvisualization of the ipsilateral nodes, and absence of some or all of the ipsilateral SCM,

Copyright © 2003, Mosby, Inc. All rights reserved.

SAN, SMG, and IJV. Identification of such surgery should not present a problem to the imager.

BASELINE SURVEILLANCE IMAGING

While it might seem desirable to delay a postoperative baseline scan as long as possible to allow the most complete resolution of these posttreatment findings, if one waits too long, there is a greater chance that a tumor recurrence may be present and misidentified as part of the normal posttreatment appearance of the patient. The time at which tumor recurrence develops is variable and depends upon such factors as host resistance, the presence of tumor-free margins at the time of surgery, and the biologic aggressiveness of the tumor. However, with tumor-free margins, it is rare for tumor to recur within 4 to 6 weeks after surgery.

Considering all of these factors, it is suggested that the baseline scan be obtained 4 to 6 weeks after surgery, as most of the postoperative changes have resolved, the new

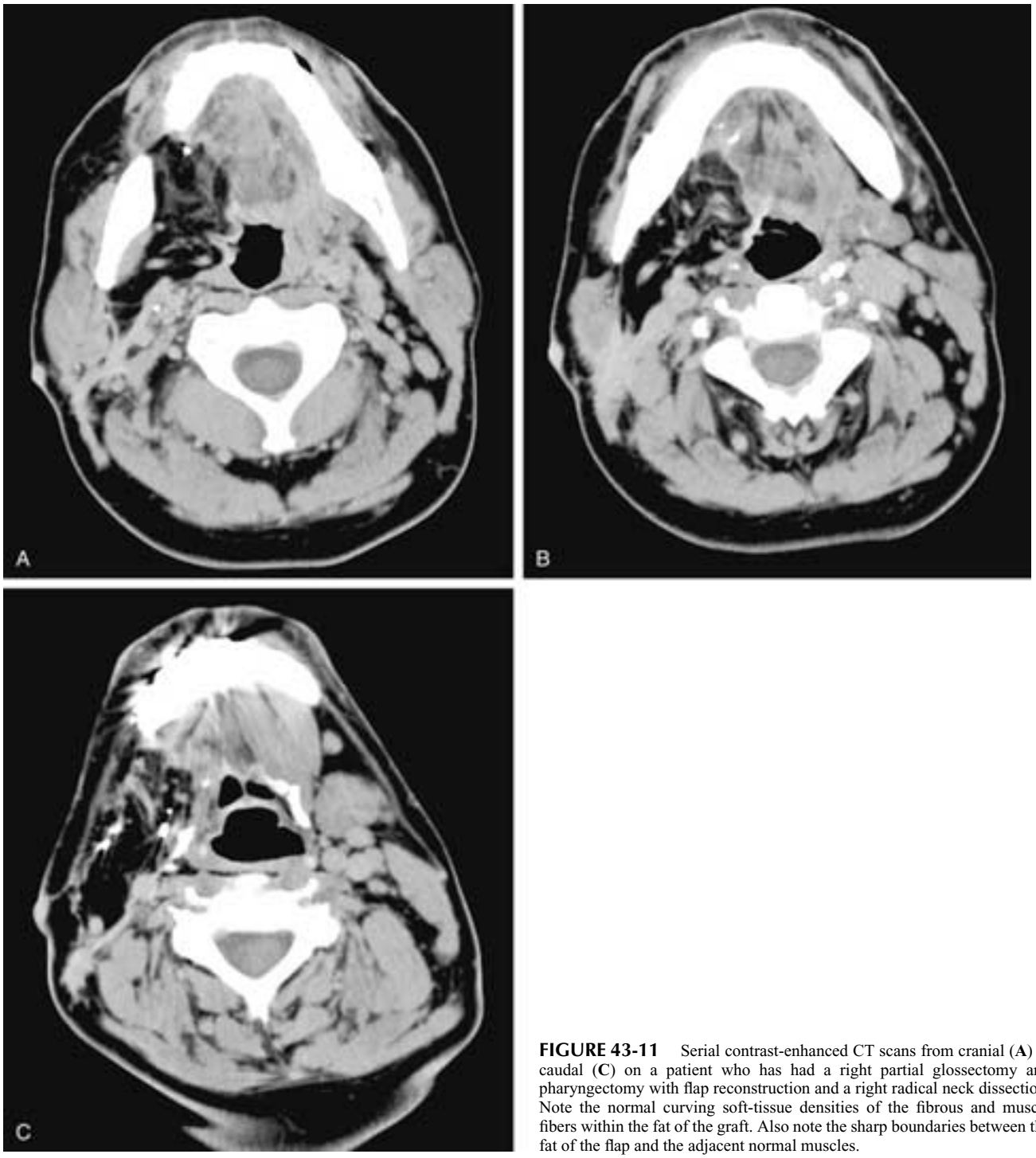

FIGURE 43-11 Serial contrast-enhanced CT scans from cranial (**A**) to caudal (**C**) on a patient who has had a right partial glossectomy and pharyngectomy with flap reconstruction and a right radical neck dissection. Note the normal curving soft-tissue densities of the fibrous and muscle fibers within the fat of the graft. Also note the sharp boundaries between the fat of the flap and the adjacent normal muscles.

VIEW IMAGE

Copyright © 2003, Mosby, Inc. All rights reserved.

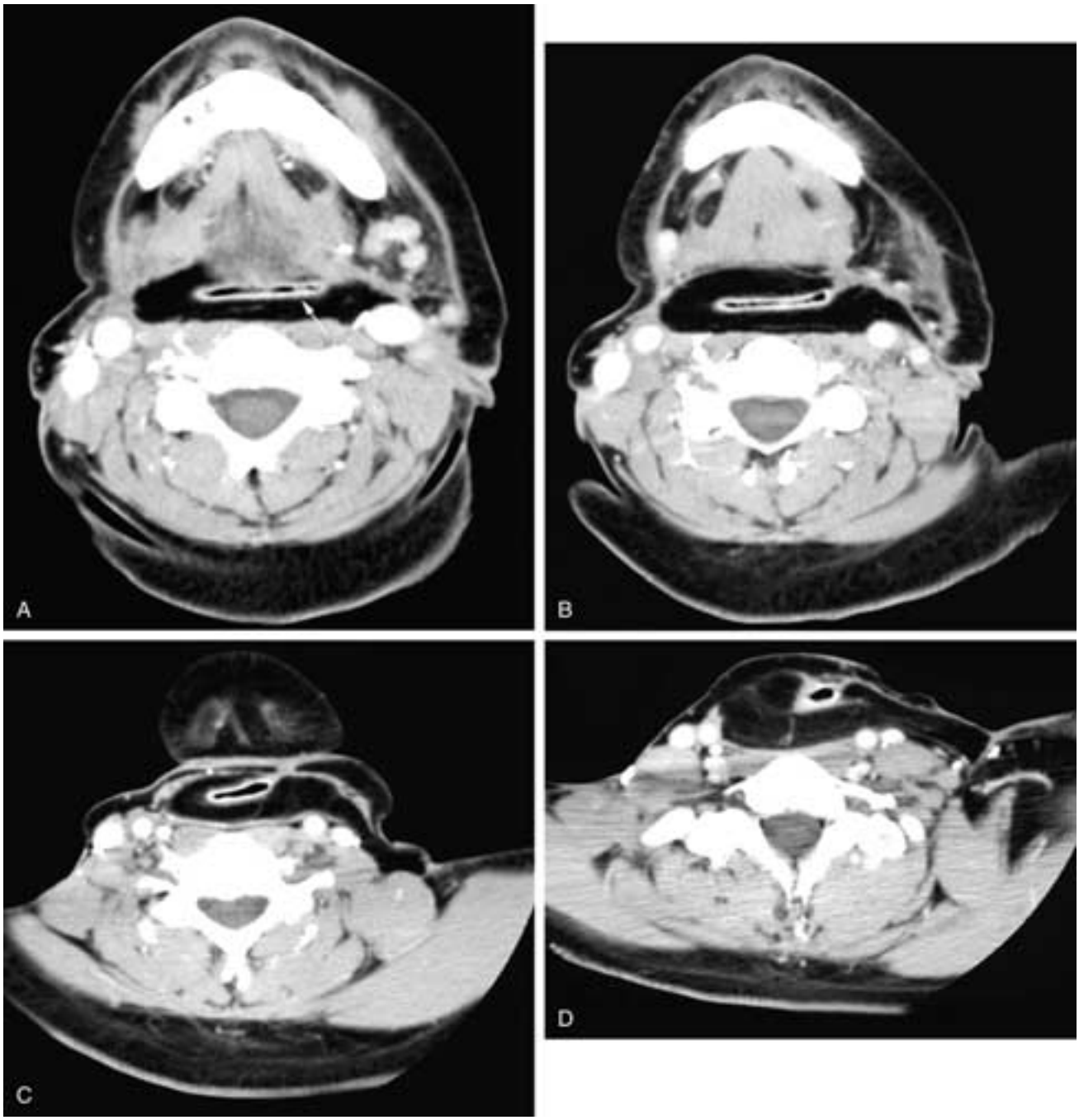

VIEW IMAGE

FIGURE 43-12 Serial contrast-enhanced CT scans from cranial (**A**) to caudal (**D**) on a patient who has had a pharyngectomy and laryngectomy and bilateral radical neck dissections. Note the normal thin, uniform mucosal surface of the flap creating the surface of the neopharynx. Also note the normal circular/ovoid configuration of the fat of the flap as it forms the neopharynx and the sharp margin between the fat and the adjacent soft tissues of the neck. More caudally, note how the flap extends into the more superficial soft tissues of the neck and how, on the left side, the flap covers and protects the carotid artery.

anatomy is present, and it is unlikely that a tumor recurrence is grossly present.[23, 24] Similarly, if only RT is given, the 4- to 6-week posttreatment interval is also optimal to obtain a baseline imaging study.

When subsequent surveillance imaging studies are obtained and compared to the baseline examination, any soft-tissue fullness on the baseline study that has become progressively smaller is presumed to be related to post-treatment healing. Conversely, if a mass has enlarged, it must be considered recurrent disease until proven otherwise.[6, 17, 23, 24, 39–42]

An exception to this surveillance protocol is the patient receiving concurrent chemotherapy. Lack of growth and maintenance of configuration has been seen in these patients on serial scans for up to 18 months; however, at the completion of chemotherapy, tumor growth can occur.

Copyright © 2003, Mosby, Inc. All rights reserved.

Consequently, in patients receiving chemotherapy, the absence of change on serial surveillance scans does not necessarily indicate the absence of tumor. In general, chemotherapy protocols tend to be effective for longer periods of time with sarcomas than with carcinomas.

In some patients, the posttreatment soft-tissue changes may persist indefinitely, and without the ability to compare surveillance scans to a prior imaging study, the interpretation of the surveillance scans is difficult. The persistence of areas of thickening may be related to the development of what can best be described as vascularized scar. This tissue is not a true granulation tissue but rather a vascularized fibrotic tissue that enhances with contrast in a manner similar to cellular tumor. In addition, vascularized scar tissue has CT attenuation and MR signal intensities similar to those of recurrent tumor. On serial scans, the vascularized scar tends to either remain stable in size and configuration or to slowly decrease in size. This may be the only way, short of biopsy, to distinguish between such vascularized scar and recurrent tumor.[6, 17, 23, 24, 39–42] Examples of tumor recurrences and vascularized scar tissue are shown in Figures 43-19 to 43-34.

SURVEILLANCE PROTOCOL

Most tumor recurrences occur within 2 years after initial treatment, and most cancer deaths occur within 3 years of the initial diagnosis.[10, 24, 39] Thus, the patient is at greatest risk within the first 2 to 3 years after diagnosis and initial treatment. Consequently, surveillance imaging should be performed more often during this period. Most patients receive routine surveillance studies at 6-month intervals for the first year. However, those patients who have tumors with an aggressive histology or clinical course should probably receive scans at 4-month intervals for at least the first year. Yearly imaging examinations are then scheduled for at least 2 more years, although many patients continue with yearly scans indefinitely, as the presence of one upper aerodigestive malignancy raises the probability that a second tumor will develop.

Surveillance imaging should always be accompanied by a clinical examination. This recommended surveillance schedule presumes that the patient has no clinical evidence of a new mass, neurologic deficits, pain, or vascular compromise. The development of any of these signs and symptoms necessitates an immediate clinical examination and an imaging study. By following this policy, the radiologist and clinician are best able to identify early recurrent disease so that a further attempt at cure can still be made. While a cure is achieved in only a few of these patients, the literature supports the concept that early recognition and treatment of recurrent disease allows better palliation, often with a relatively good quality of life.

When an isolated recurrence occurs in a previously

FIGURE 43-13 Serial CT contrast-enhanced scans from cranial (**A**) to caudal (**B**) on a patient who has had a total laryngectomy and a partial pharyngectomy. Note the smooth outer contour (*arrows*) of the neopharynx that can be created either from a rotated flap or, as in this patient, with a portion of intestine. In **B**, also note that the left thyroid lobe has been resected and the right thyroid lobe reimplanted anterior to the normal thyroid bed. This allows the carotid arteries to move medially into the thyroid bed. Axial contrast-enhanced CT scan (**C**) on a patient who has had a total thyroidectomy and a right neck dissection. Note the absence of the thyroid gland and the medial location of the carotid arteries as they move into the thyroid bed.

VIEW IMAGE

Copyright © 2003, Mosby, Inc. All rights reserved.

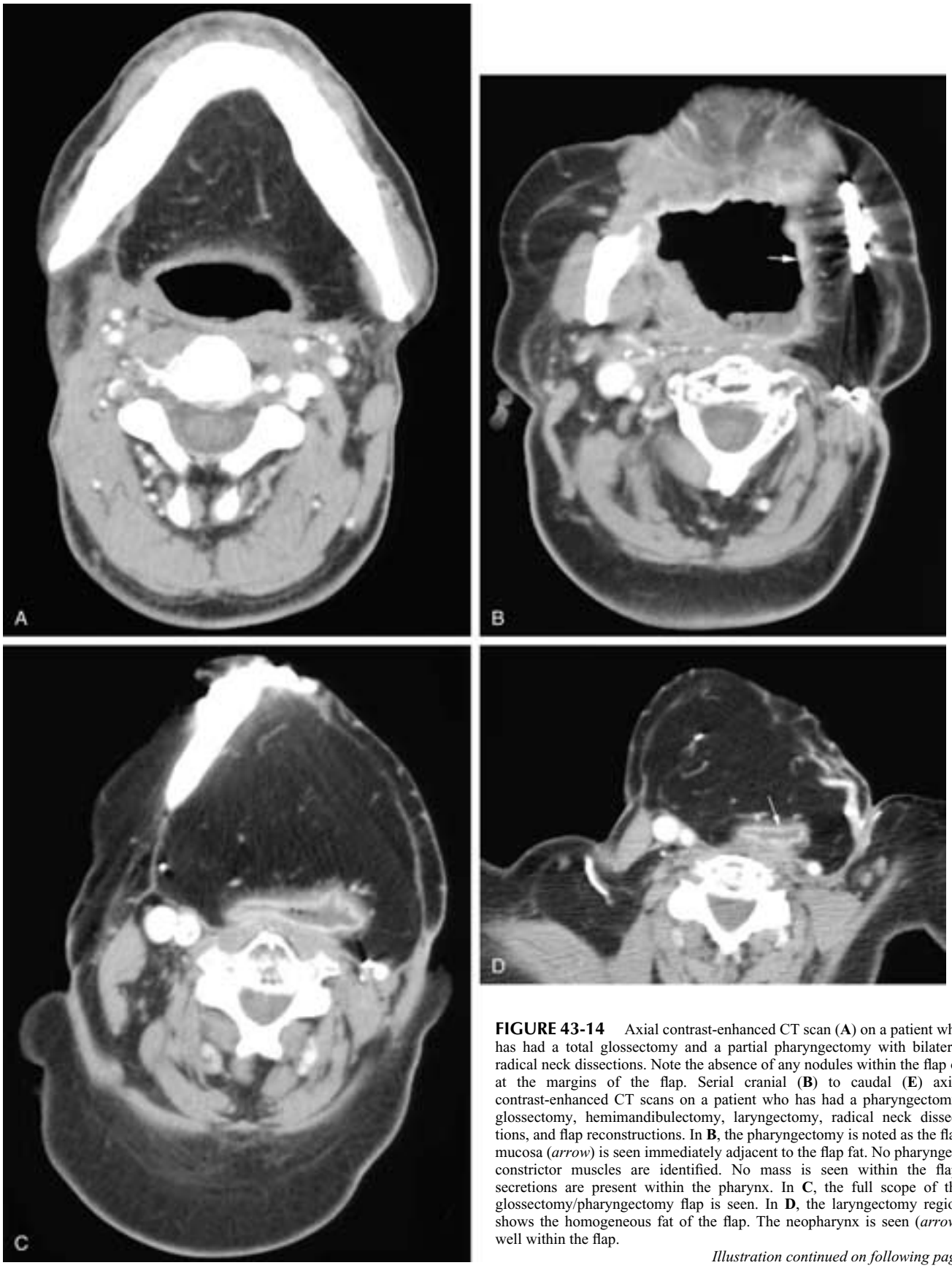

FIGURE 43-14 Axial contrast-enhanced CT scan (**A**) on a patient who has had a total glossectomy and a partial pharyngectomy with bilateral radical neck dissections. Note the absence of any nodules within the flap or at the margins of the flap. Serial cranial (**B**) to caudal (**E**) axial contrast-enhanced CT scans on a patient who has had a pharyngectomy, glossectomy, hemimandibulectomy, laryngectomy, radical neck dissections, and flap reconstructions. In **B**, the pharyngectomy is noted as the flap mucosa (*arrow*) is seen immediately adjacent to the flap fat. No pharyngeal constrictor muscles are identified. No mass is seen within the flap; secretions are present within the pharynx. In **C**, the full scope of the glossectomy/pharyngectomy flap is seen. In **D**, the laryngectomy region shows the homogeneous fat of the flap. The neopharynx is seen (*arrow*) well within the flap.

Illustration continued on following page

VIEW IMAGE

Copyright © 2003, Mosby, Inc. All rights reserved.

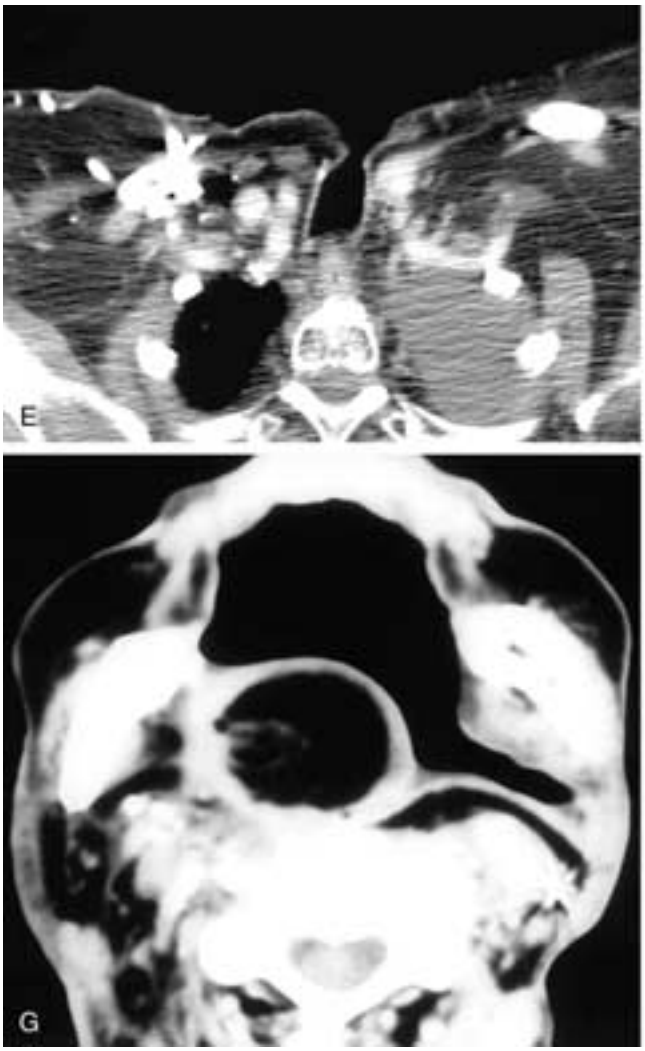

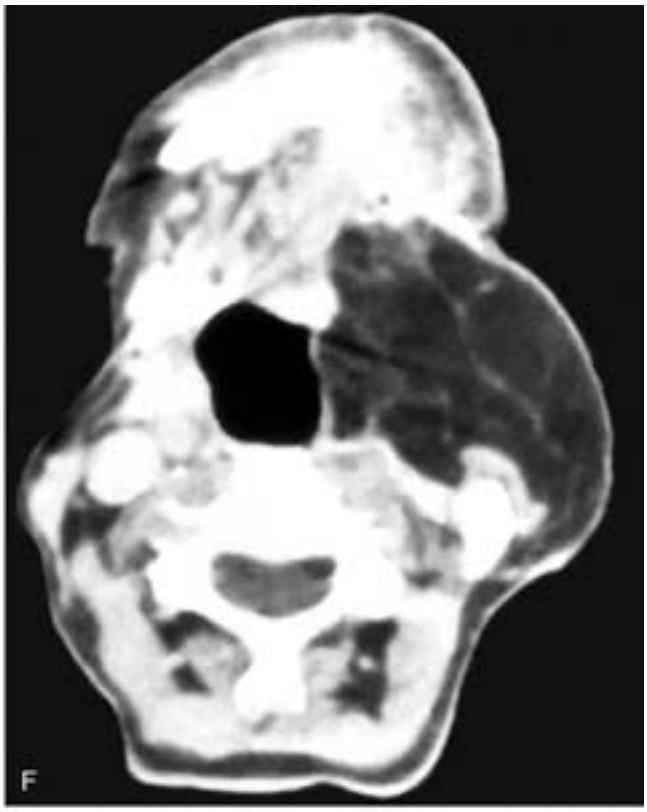

FIGURE 43-14 *Continued.* In **E** through the lower neck, note the smooth, thin contours of the tracheostomy site. There is also incidental scarring of the left pleura. Axial contrast-enhanced CT scan (**F**) on a patient who has had a left partial pharyngectomy and a radical neck dissection with a myocutaneous flap reconstruction. Note the fatty appearance of the flap and the smooth contours of the margins of the flap. The flap also helps protect the carotid artery. Axial contrast-enhanced CT scan (**G**) on a patient who has had a pharyngectomy and a left radical neck dissection. Note the swirling minimal soft-tissue density within the bulk of the rotated flap and the smooth margins of the operative site. No soft-tissue nodularity is present.

VIEW IMAGE

treated neck in a patient with squamous cell carcinoma, factors that are associated with a less favorable outcome after aggressive salvage therapy include other serious medical problems, the patient's refusal of further treatment, development of the recurrence in the contralateral neck, development of the recurrence in the neck after a neck dissection, and a recurrence that measures >3 cm and/or is fixed.[43]

IMAGING SUSPICION OF A RECURRENCE

There are two tenets for the imaging identification of early tumor recurrence. First, if a flap was not used for reconstruction, then surgery removes tissue, and, except for edema, there should not be extra postoperative bulk or a mass in the operative site. If such fullness is seen, an explanation of the etiology of this tissue must be sought, as recurrent tumor must be considered the principal cause. Second, the most likely location for a tumor to recur is either in the operative bed or at the margin of the surgical site. With this in mind, attention must be paid to assessing regional muscle, fibrous, and vascularized soft tissue (Figs. 43-19 to 43-34).

Normal muscle tends to have a fairly linear or curvilinear configuration, with smooth contours. However, after surgery, muscle rotated within a flap may appear on end in an area where no such muscle is normally expected and may mimic a tumor mass. Apart from comparing attenuation values or signal intensities to those of adjacent normal muscle, the only way to distinguish such muscle from tumor may be the careful sequential tracing of the muscle path throughout the operative field. Most muscles manipulated during surgery tend to have mild enhancement, again potentially mimicking a tumor. Muscle within a flap also tends to be curvilinear in shape, as it is often wrapped or twisted around within the flap tissue to fill the operative defect. Localized bulges within a muscle are not normal and may represent hemorrhage or tumor.

The presence of any focal ''ovoid'' mass not identified on a previous surveillance scan in a postoperative neck must be suspicious for recurrence. This is especially true if the mass has infiltrative or spiculated margins. A useful sign on CT is the observation that tumor has an attenuation similar to that of muscle. Thus, if a suspected mass has an attenuation less

Copyright © 2003, Mosby, Inc. All rights reserved.

than that of muscle, it is unlikely to be carcinoma and often is related to edema.

The identification of a mass deep to a flap may be the first evidence of a recurrence. Due to the bulk of the flap, the often ''woody'' feel of the skin and subcutaneous tissues after irradiation, and the deep location of the disease, this region is usually inaccessible to clinical evaluation.

As stated, the major diagnostic imaging problem lies in differentiating a recurrent tumor mass from dense scar and vascularized scar, both of which may have infiltrative margins and can be indistinguishable from tumor on both CT and MR imaging. The progressive decrease in T2-weighted signal intensity of a soft tissue area as seen on serial surveillance MR scans, strongly suggests the presence of dense scar. If the patient has recent pain or discomfort in the region, tumor recurrence is the most likely diagnosis, provided that there is no other evidence of local infection. Thus, such local pain would negate waiting up to 6 months

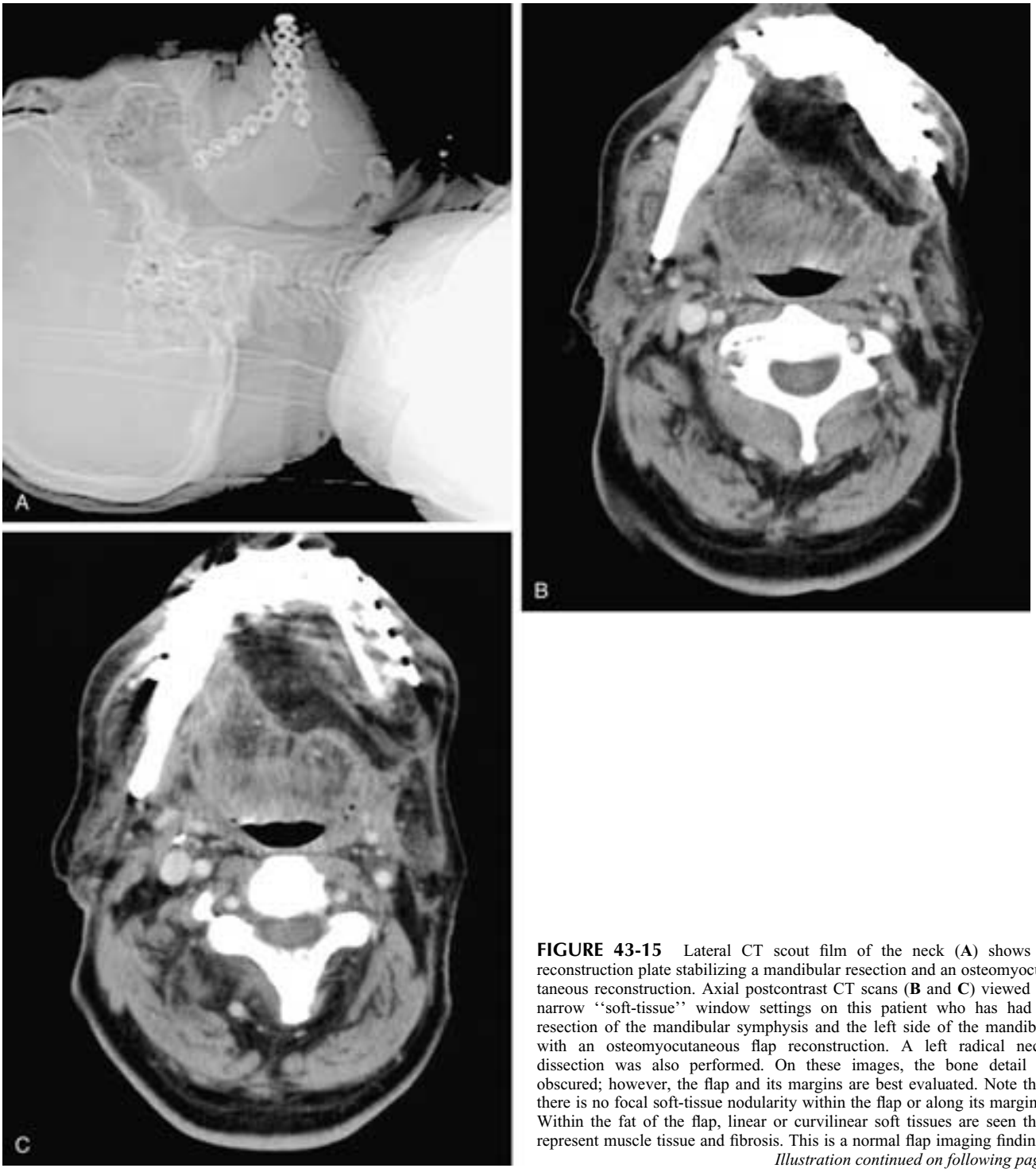

FIGURE 43-15 Lateral CT scout film of the neck (**A**) shows a reconstruction plate stabilizing a mandibular resection and an osteomyocutaneous reconstruction. Axial postcontrast CT scans (**B** and **C**) viewed at narrow ''soft-tissue'' window settings on this patient who has had a resection of the mandibular symphysis and the left side of the mandible with an osteomyocutaneous flap reconstruction. A left radical neck dissection was also performed. On these images, the bone detail is obscured; however, the flap and its margins are best evaluated. Note that there is no focal soft-tissue nodularity within the flap or along its margins. Within the fat of the flap, linear or curvilinear soft tissues are seen that represent muscle tissue and fibrosis. This is a normal flap imaging finding.

Illustration continued on following page

VIEW IMAGE

Copyright © 2003, Mosby, Inc. All rights reserved.

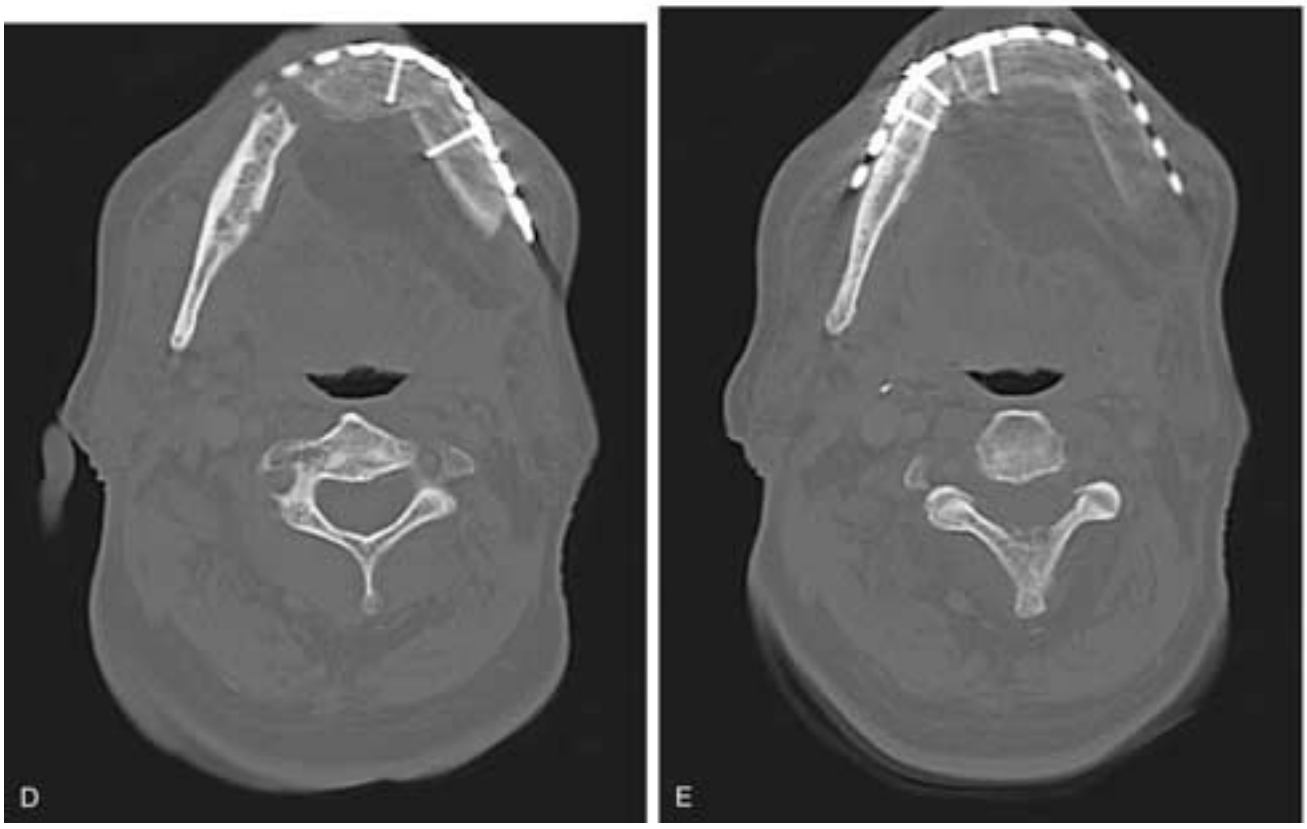

VIEW IMAGE

FIGURE 43-15 *Continued.* In **D** and **E**, the same images as **C** and **D** are shown at wide ''bone'' window settings. Note that the anterior edge of the native right mandible is sharp, with no evidence of erosion. The small low-attenuation areas with dense margins seen in the aspect of the right mandible were related to fixation screws. Also note that two transplanted bones have no evidence of erosion. This is a normal imaging appearance for this operative procedure.

to see if the mass identified on a particular study has grown and a CT-guided fine needle aspiration biopsy should be performed as soon as possible.[44] Alternative suggestions have been to utilize PET, thallium-201, and MR spectroscopy (see Chapter 45).

With specific regard to metastatic lymph nodes in patients with head and neck carcinomas who undergo concurrent chemotherapy and RT, it has been suggested that when there is a nodal volume reduction of greater than 90%, the metastatic node has been sterilized.[45] This may affect the need for further neck dissections in such patients.

BIOPSY OF SUSPECTED RECURRENCE SEEN ON IMAGING

Once a potential recurrence is seen on a surveillance scan, a CT or ultrasound-guided fine needle aspiration biopsy needs to be performed as soon as possible. Although a 22-gauge needle is often recommended, a 25-gauge spinal needle is easier to steer for accurate placement in deeply situated masses. A cytopathologist should be present at the biopsy to assess the adequacy of the specimen obtained utilizing an air-dried quick stain technique. A maximum of five passes may be required until an adequate specimen is obtained. The samples are subsequently evaluated with Papanicolaou-stained slides and cell block analysis. There are few complications with this procedure.[46–53]

THE IMAGING DETECTION OF VASCULAR COMPLICATIONS

Thombosis of the IJV or the carotid artery may occur from ligation or other intraoperative manipulation.[54] It is not rare on surveillance imaging to identify thrombosis of these vessels, especially the carotid artery (Fig. 43-35A). Usually this is a clinically silent event. Arterial stents from unrelated prior surgery can also occasionally be seen on surveillance imaging (Fig. 43-35B). On CT and MR imaging, arteritis may be seen as thickening and enhancement of the arterial wall. In documenting this potentially serious side effect of neck irradiation, an increased frequency of carotid artery wall thickening has been identified utilizing ultrasound in young patients with Hodgkin's disease treated by RT.[55] RT-related arteritis can also lead to complications during endarterectomy and other vascular surgery, and irradiated patients also can develop radiation-accelerated atherosclerosis (Fig. 43-36).[56–59]

With specific reference to the IJV, examination with color Doppler ultrasound has found that the vein remained patent in 88% of patients after an MND, in 57% of patients

Copyright © 2003, Mosby, Inc. All rights reserved.

treated with RT alone, and in only 18% of patients receiving MND and RT.[1] Examination of the IJV in patients after MND and SND showed that in 26.4% of these patients there was evidence of thrombosis within the first postoperative week. However, on long-term follow-up, the incidence of thrombosis was only 5.8%, suggesting that some veins recanalize.[60]

THE IMAGING DETECTION OF OSSEOUS COMPLICATIONS

When a primary tumor involves the mandible, some type of bone resection is performed. This may vary from a marginal resection to a segmental or total mandibulectomy. Currently, the trend is to perform a primary repair of the osseous defect at the time of resection by using a free-composite flap containing bone (osteomyocutaneous flap). Consequently, postoperative imaging visualizes both native mandible and transplanted bone, the latter usually harvested from the scapula, pelvis, or fibula. Many of these patients are irradiated postoperatively, and mandibular radionecrosis develops in 2% to 3% of the patients. Distinction between radionecrosis and recurrent tumor may be impossible on CT and MR imaging studies. The imaged bone can have areas of sclerosis, rarefaction, and sequestration, all of which can be seen with both radionecrosis and tumor (Fig. 43-37). It is therefore essential to examine carefully the bony margins of

Text continued on page 2262

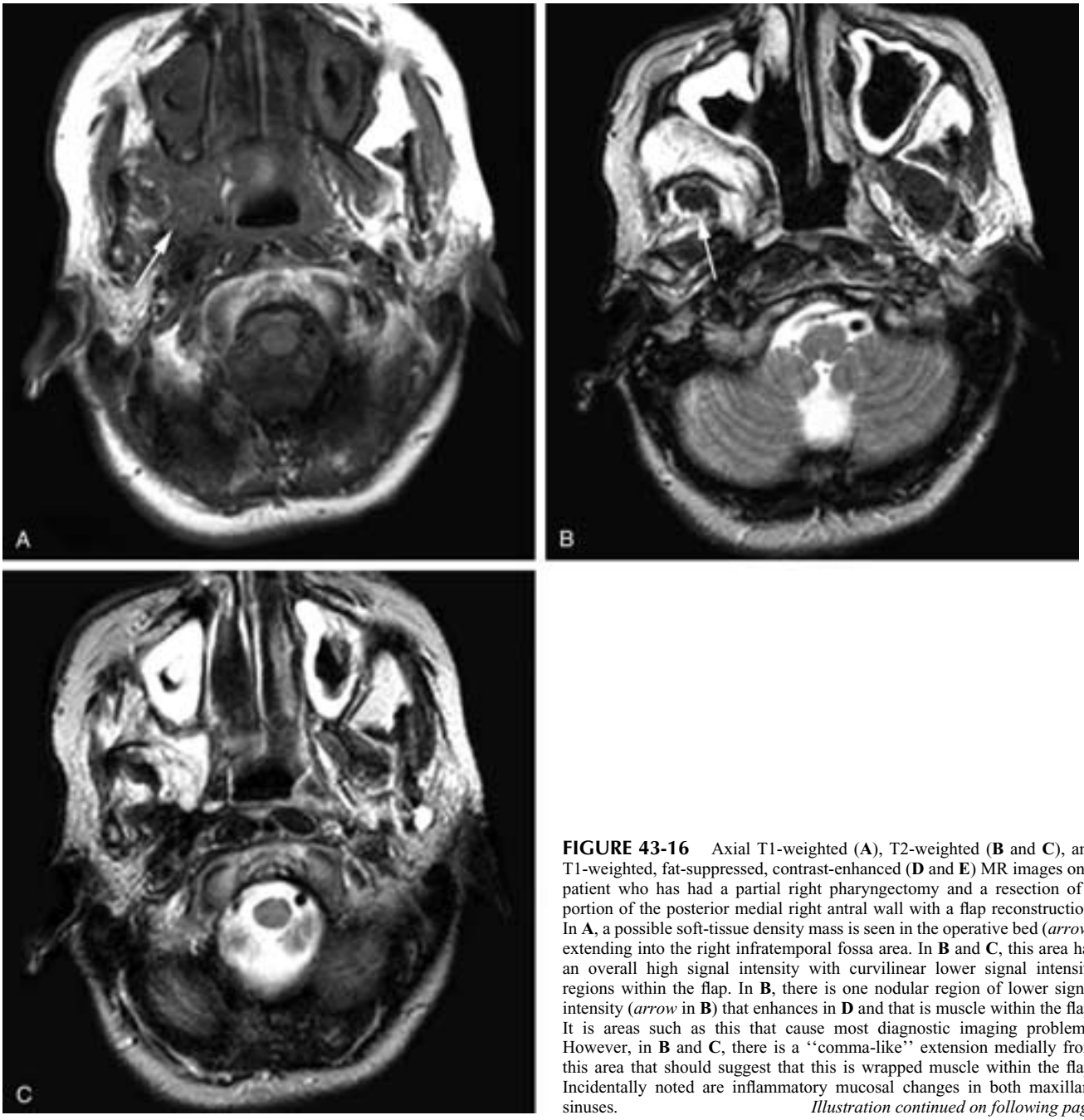

FIGURE 43-16 Axial T1-weighted (**A**), T2-weighted (**B** and **C**), and T1-weighted, fat-suppressed, contrast-enhanced (**D** and **E**) MR images on a patient who has had a partial right pharyngectomy and a resection of a portion of the posterior medial right antral wall with a flap reconstruction. In **A**, a possible soft-tissue density mass is seen in the operative bed (*arrow*) extending into the right infratemporal fossa area. In **B** and **C**, this area has an overall high signal intensity with curvilinear lower signal intensity regions within the flap. In **B**, there is one nodular region of lower signal intensity (*arrow* in **B**) that enhances in **D** and that is muscle within the flap. It is areas such as this that cause most diagnostic imaging problems. However, in **B** and **C**, there is a ''comma-like'' extension medially from this area that should suggest that this is wrapped muscle within the flap. Incidentally noted are inflammatory mucosal changes in both maxillary sinuses.

Illustration continued on following page

VIEW IMAGE

Copyright © 2003, Mosby, Inc. All rights reserved.

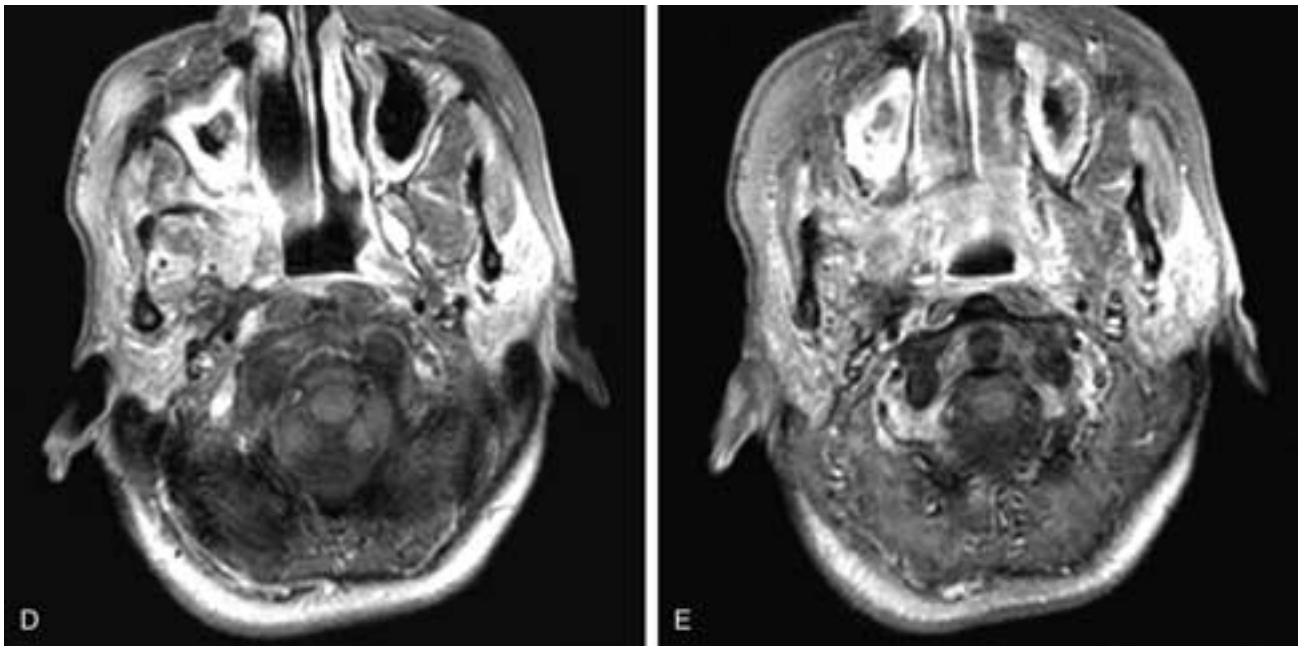

VIEW IMAGE

FIGURE 43-16 *Continued.* In **D** and **E**, areas of muscle and inflammation enhance, often further confusing the MR diagnosis. Often, it is only by fine needle aspiration–guided biopsy or by comparison to other studies that an early recurrence in such areas can be eliminated from diagnostic consideration.

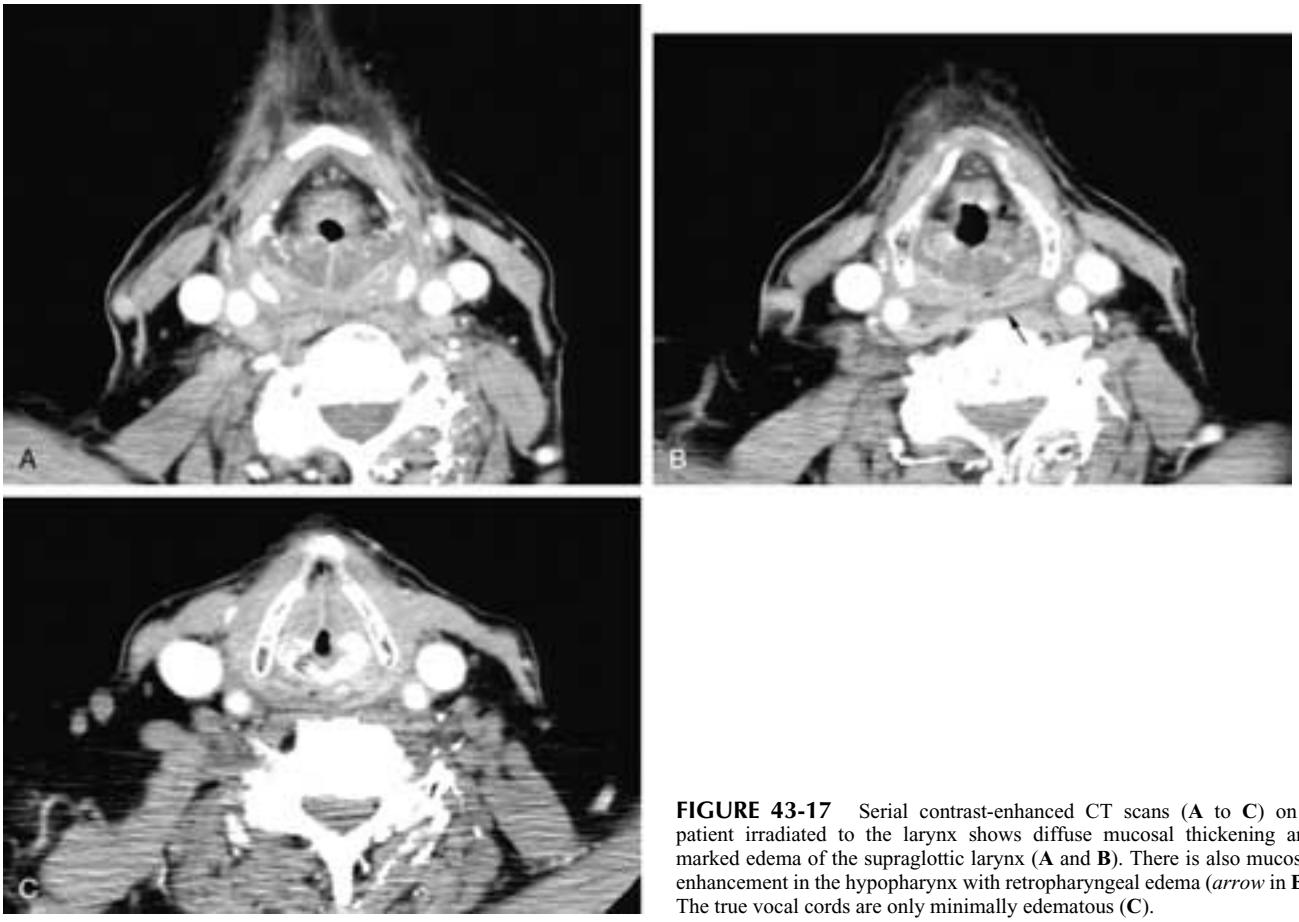

FIGURE 43-17 Serial contrast-enhanced CT scans (**A** to **C**) on a patient irradiated to the larynx shows diffuse mucosal thickening and marked edema of the supraglottic larynx (**A** and **B**). There is also mucosal enhancement in the hypopharynx with retropharyngeal edema (*arrow* in **B**). The true vocal cords are only minimally edematous (**C**).

VIEW IMAGE

Copyright © 2003, Mosby, Inc. All rights reserved.

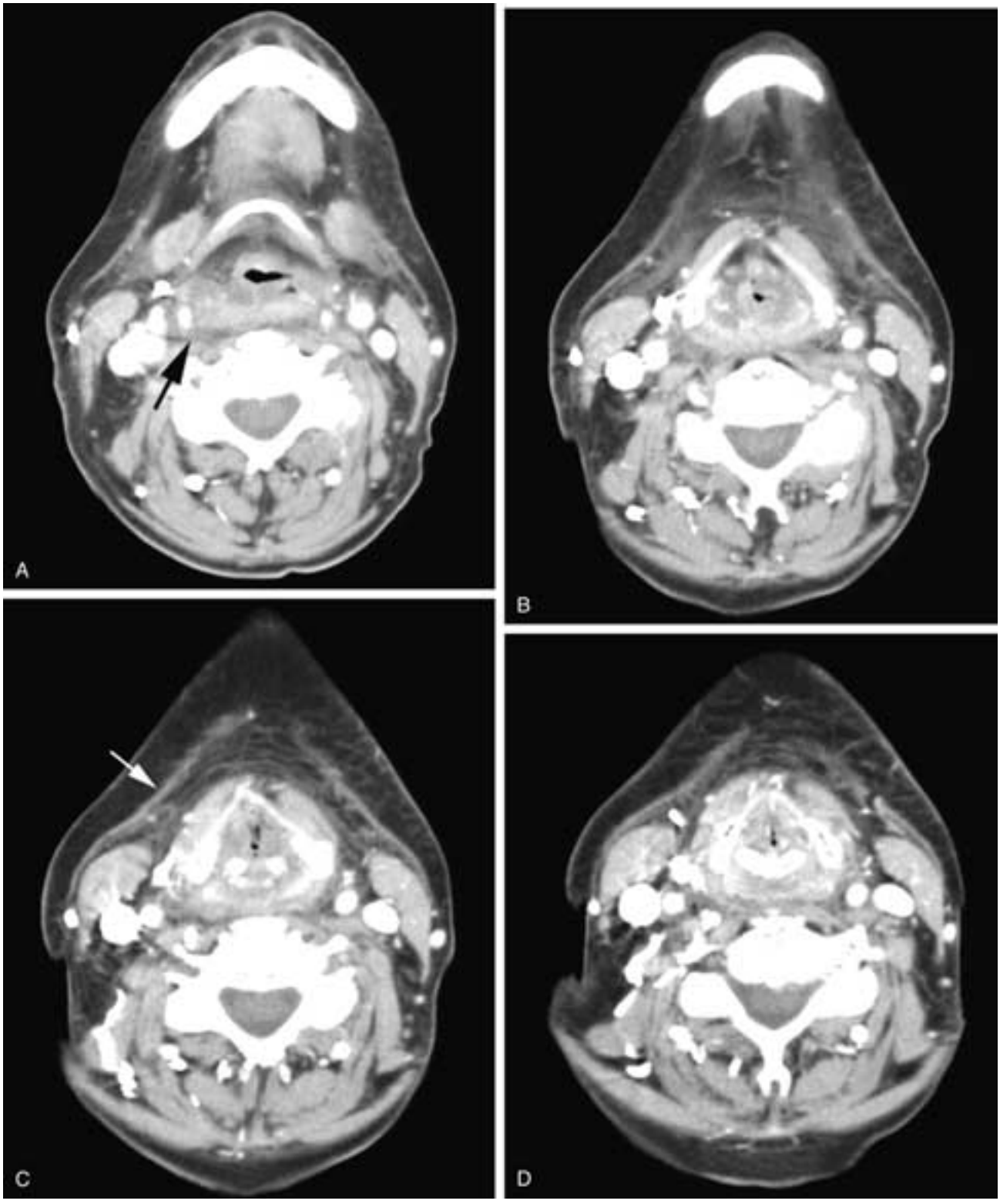

FIGURE 43-18 Serial axial contrast-enhanced CT scan from cranial (**A**) to caudal (**D**) in a patient who received RT to the neck. There is marked thickening of the mucosal surfaces, not only in the supraglottic larynx (**A** and **B**) but also in the glottic (**C**) and subglottic (**D**) larynx. This is a more pronounced reaction than normal (see Fig. 43-10). Note that the attenuation of the supraglottic laryngeal soft tissues is less than that of muscle, suggesting that it represents edema. Also note the retropharyngeal edema (arrow in **A**) usually seen in irradiated patients (see Fig. 43-10). In addition, there are edematous, inflammatory-type changes in the superficial subcutaneous fat with thickening of the platysma (*arrow* in **C**). Despite the apparent airway narrowing on imaging, many of these patients have no dyspnea.

VIEW IMAGE

Copyright © 2003, Mosby, Inc. All rights reserved.

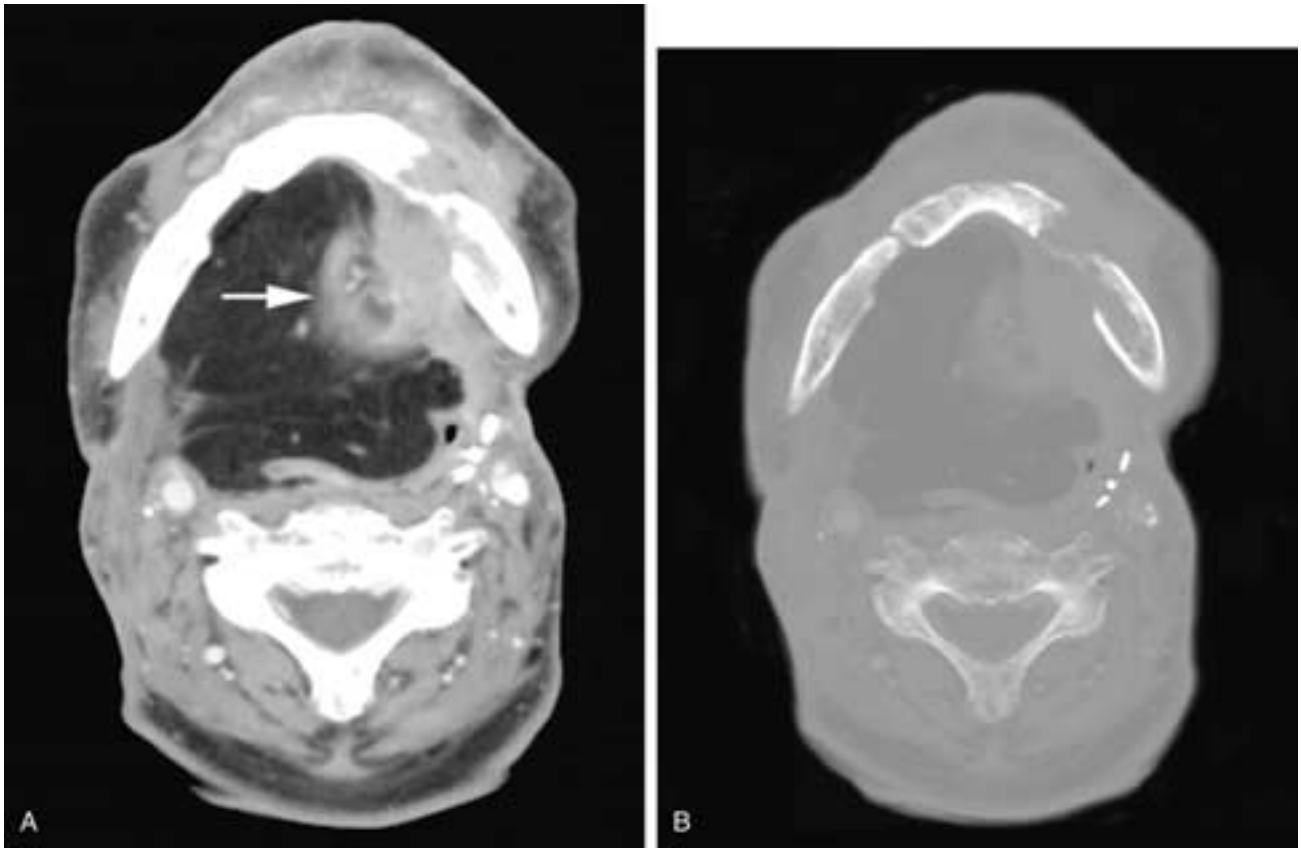

VIEW IMAGE

FIGURE 43-19 Axial contrast-enhanced CT scan on a patient who has had a total glossectomy and partial mandibulectomy with osteomyocutaneous flap reconstruction and bilateral neck dissections. In **A**, note the soft-tissue nodular recurrence (*arrow*) within the left side of the flap and the infiltrating extension into the mandible. In **B**, the destruction of both the native left mandible and the back of the left side of the transplanted bone is better seen.

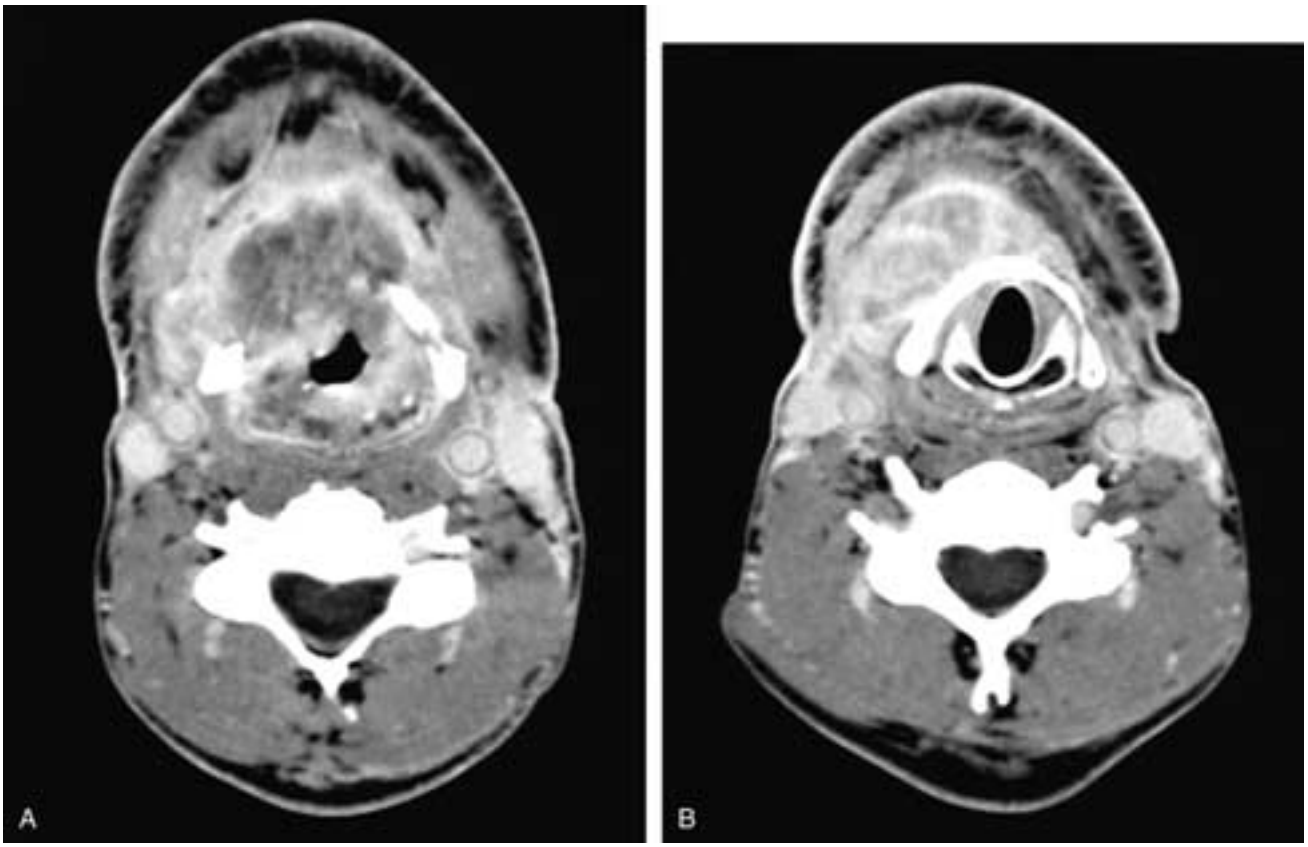

VIEW IMAGE

FIGURE 43-20 Axial contrast-enhanced CT scans from cranial (**A**) to caudal (**B**) in a patient who has had a supraglottic laryngectomy and bilateral modified neck dissections (IJVs are present). There is an extensive recurrence of squamous cell carcinoma throughout the operative bed extending from the pharynx into the base of the tongue and the floor of the mouth. The tumor then extends caudally (**B**) into the strap muscles and anterior neck.

Copyright © 2003, Mosby, Inc. All rights reserved.

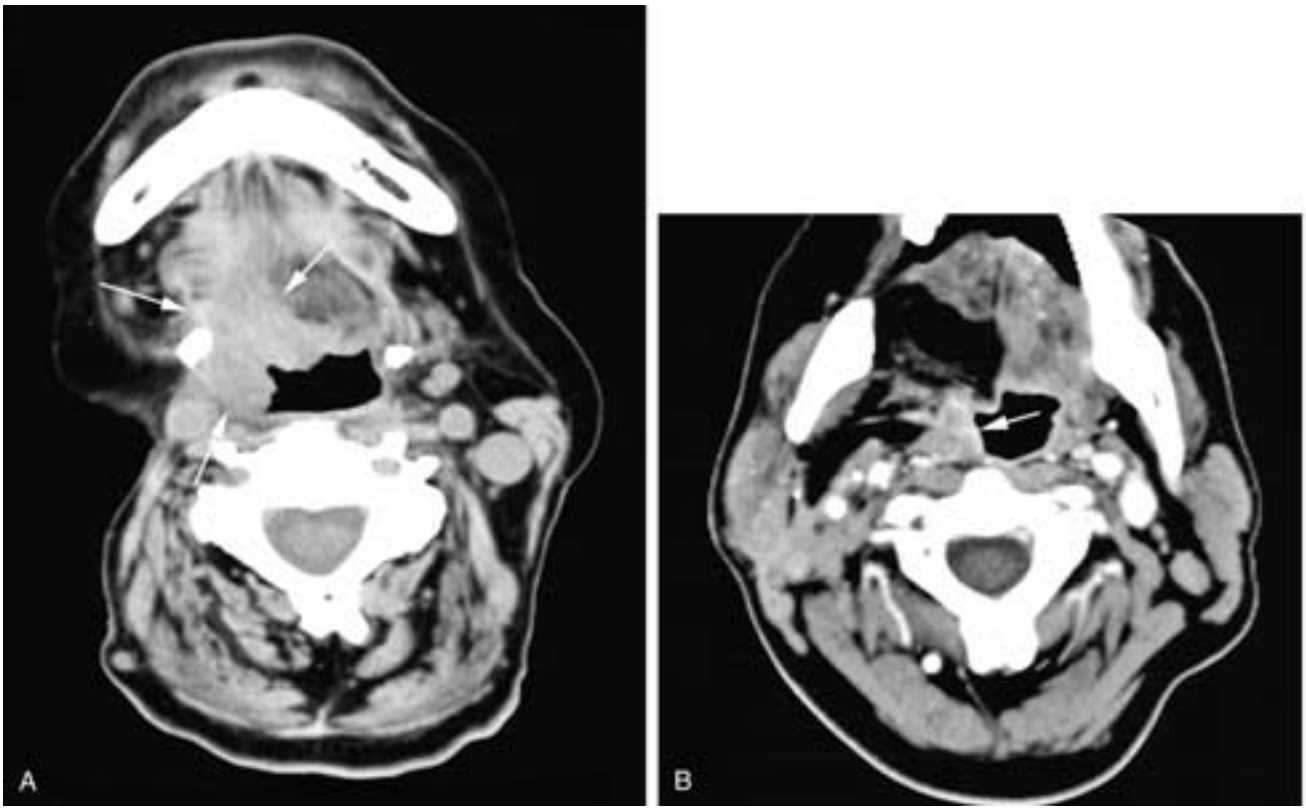

VIEW IMAGE

FIGURE 43-21 Axial CT contrast-enhanced scan (**A**) on a patient who has had a partial right glossectomy and a right neck dissection. There is a large recurrence of squamous cell carcinoma within the operative bed (*arrows*). Axial contrast-enhanced CT scan (**B**) on a different patient who has had a right partial glossectomy and pharyngectomy with flap reconstruction. Along the upper posterior operative margin is a soft-tissue nodule (*arrow*) that was a recurrence of squamous cell carcinoma.

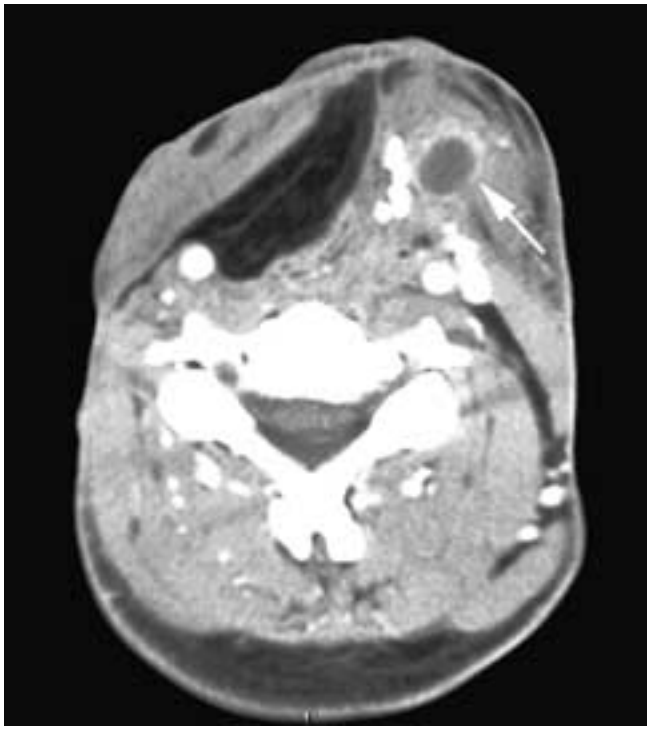

VIEW IMAGE

FIGURE 43-22 Axial contrast-enhanced CT scan on a patient who has had a total laryngectomy and a right neck dissection with flap reconstruction, and who received RT. Deep to the overlying soft tissues there is a necrotic area (*arrow*) of recurrent squamous cell carcinoma. This was not identified clinically, in part, because of the ''woody'' nature of the more superficial irradiated soft tissues.

Copyright © 2003, Mosby, Inc. All rights reserved.

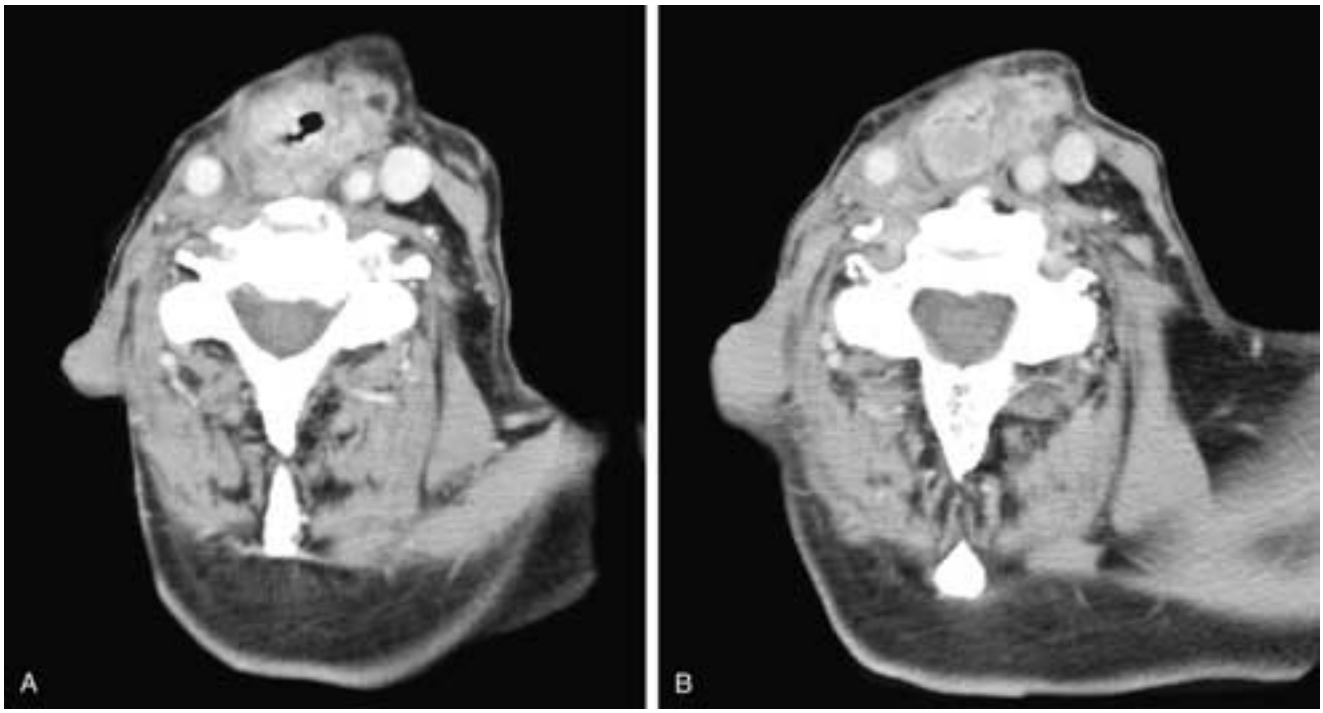

VIEW IMAGE

FIGURE 43-23 Axial contrast-enhanced CT scans from cranial (**A**) to caudal (**B**) in a patient who has had a total laryngectomy and a right neck dissection. In **A**, there is tumor nodularity both within the lumen and around the neopharynx (compare to Figs. 43-12 and 43-13). In **B**, the squamous cell carcinoma recurrence has infiltrated the entire operative bed.

both the remaining native and transplanted bone in the operative field. In addition, at the site of these changes there may be ulceration, necrosis, and inflammation of the soft tissues. Often it is only by biopsy or local resection that the distinction between tumor and infection can finally be established.[61–63]

POST–NECK DISSECTION CHYLOUS FISTULA

A postoperative chylous fistula occurs in about 1% to 2% of neck dissection patients. Most of these fistulas occur when level IV nodes are dissected and there is the potential for injury to the thoracic duct. With CT and MR imaging, there is the appearance of a cystic mass with the characteristics of water. The cyst is almost always located in the lower left neck near the carotid sheath and the region of the thoracic duct (Fig. 43-38).

POSTTRAUMATIC NEUROMA

The development of a traumatic neuroma after neck surgery is an uncommon event. These lesions are not true neoplasms but rather reparative-type pseudotumors. When a peripheral nerve is disrupted at surgery, the distal end undergoes Wallerian degeneration while the proximal end initiates a proliferative reparative-type response. If there is only a small gap between the nerve ends, healing occurs. However, if there is a large gap, or if the gap is filled with scar, blood, or inflammatory or granulation-type tissue, the nerve ends cannot meet and a haphazard growth of the axons occurs, creating the traumatic neuroma. Most of these tumors are less than 2 cm in diameter, and they tend to occur along the dorsal margin of the incision line and involve cutaneous nerves from the cervical plexus.[64–73] Typically, there is localized pain or discomfort, with a ''trigger'' point often present. Fine needle aspiration biopsy of these superficial lesions is difficult because of their painful nature. These lesions can be observed for years; however, if the patient is very symptomatic, surgical excision is recommended.

Imaging reveals a mass with a relatively low attenuation central region; however, without clinical correlation, CT cannot confidently differentiate it from a localized implant-type recurrence or scarring (Fig. 43-39).

DERMAL METASTASIS

Metastasis to the skin from head and neck mucosal carcinomas is rare, developing in about 1% of cases. The median time to occurrence is 6 months, and 90% of the patients die of their disease within a median period of 3 months following diagnosis.[74] The development of skin metastasis is most closely related to the presence of two or more cervical metastases and/or the presence of extracapsular nodal spread in the cervical metastases. Similar risk factors have been identified for the development of distant metastases to other sites. Such metastases occur with greater frequency in immunocompromised patients, such as those

Text continued on page 2270

Copyright © 2003, Mosby, Inc. All rights reserved.

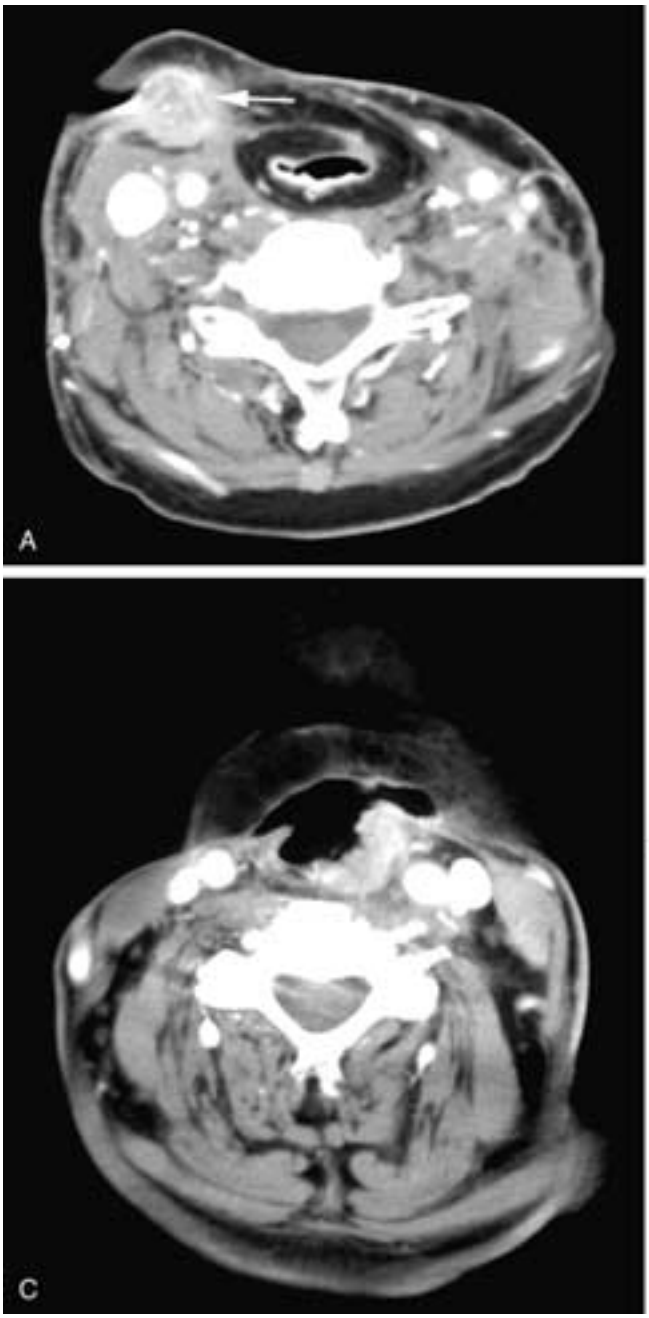

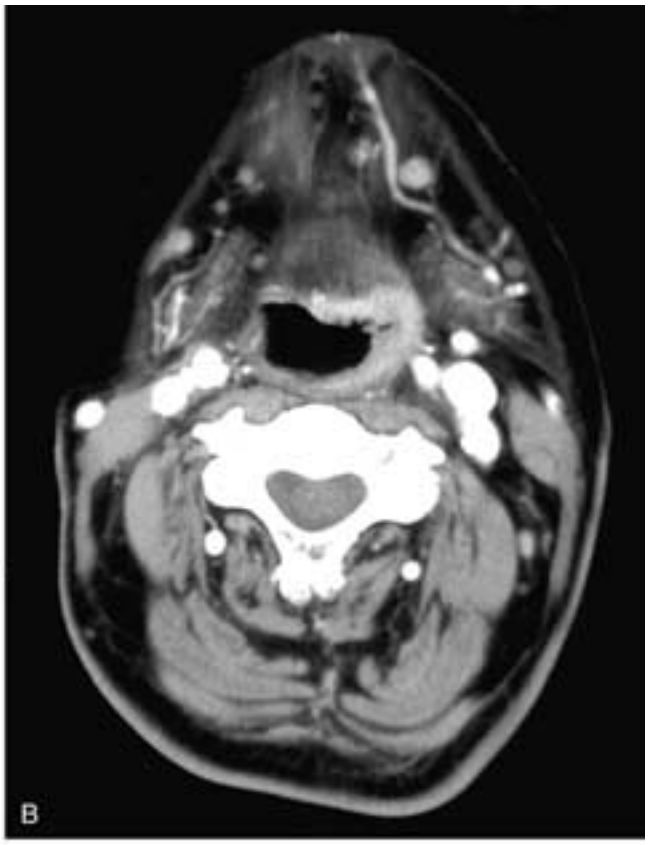

FIGURE 43-24 Axial contrast-enhanced CT scan (**A**) on a patient who has had a total laryngectomy and a left neck dissection. There is an enhancing nodule (*arrow*) of recurrent squamous cell carcinoma along the right margin of the flap. Axial contrast-enhanced CT scans (**B** and **C**) on a different patient who has had a total laryngectomy and partial pharyngectomy shows an enhancing tumor recurrence along the upper left posterior operative margin. This is a common site for recurrent squamous cell carcinoma.

VIEW IMAGE

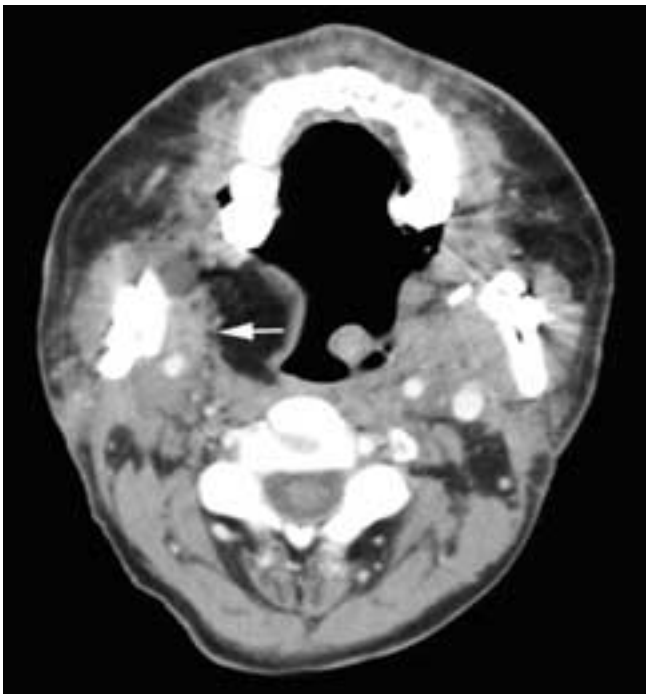

VIEW IMAGE

FIGURE 43-25 Axial contrast-enhanced CT scans on a patient who has had a partial mandibulectomy, a partial right pharyngectomy, and bilateral neck dissections. There is a soft-tissue mass deep to the operative site of the right mandibular ramus (*arrow*). Fine needle aspiration revealed vascularized scar rather than tumor recurrence.

Copyright © 2003, Mosby, Inc. All rights reserved.

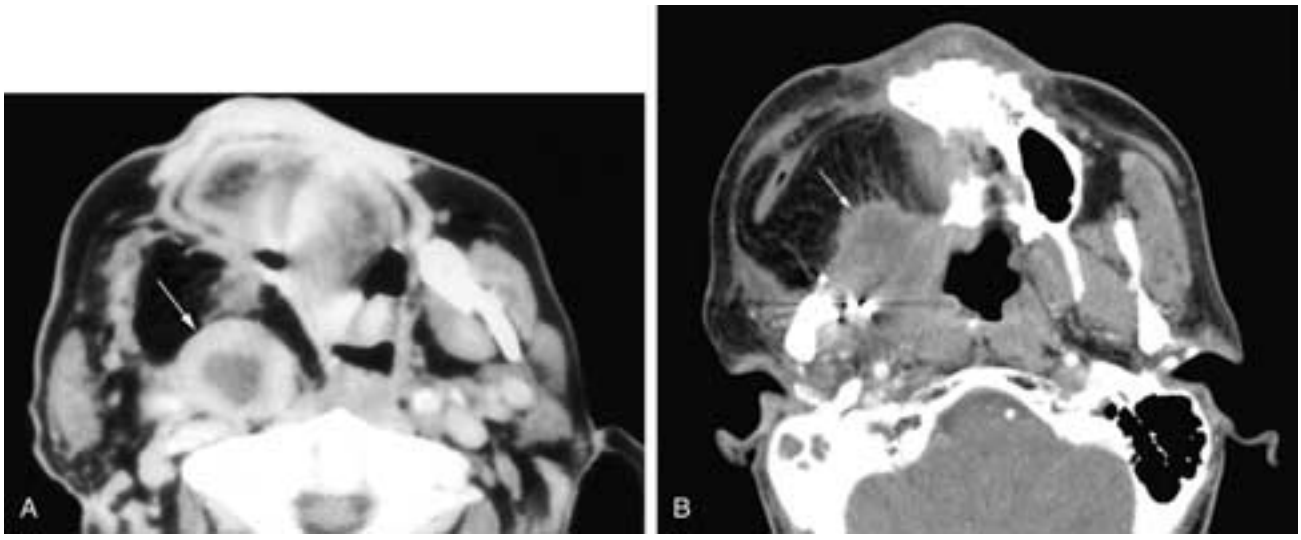

VIEW IMAGE

FIGURE 43-26 Axial contrast-enhanced CT scan (**A**) on a patient who has had a right mandibulectomy and right pharyngectomy with a right neck dissection. There is a nodule of recurrent squamous cell carcinoma within the flap (*arrow*). This was not identified clinically due to its deep location within the flap. Contrast-enhanced CT scan (**B**) on a patient with a mass similar to that in **A**. There is a clinically undetected recurrence (*arrow*) deep within the flap.

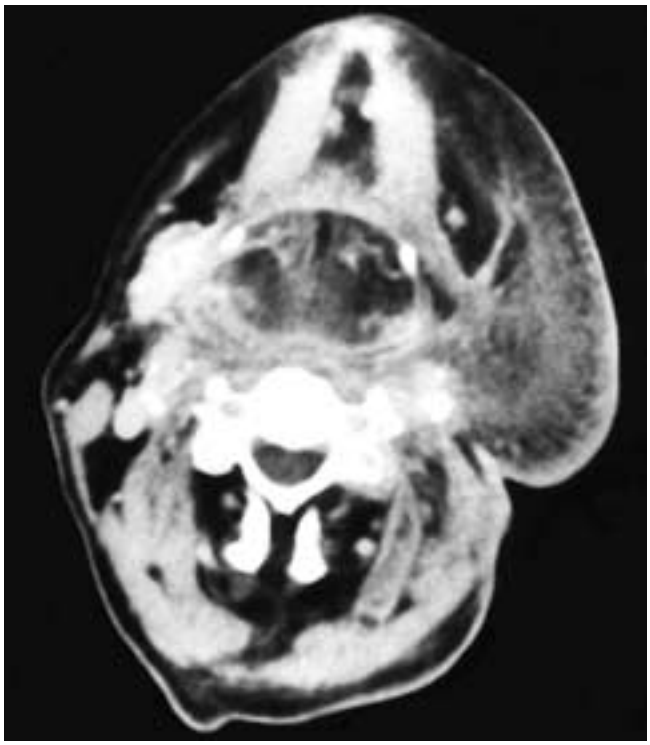

VIEW IMAGE

FIGURE 43-27 Axial contrast-enhanced CT scan on a patient who has had a left radical neck dissection with a flap reconstruction. There is thickening and injection of the flap suggestive of infection, but the patient had no pain. This was early squamous cell carcinoma infiltrating the flap. Without clinical correlation, the imaging diagnosis cannot be refined in many of these posttreatment patients.

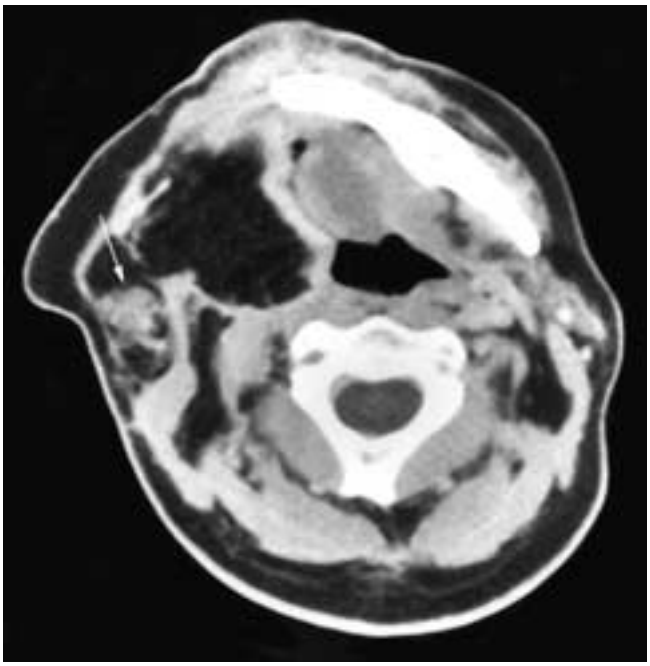

FIGURE 43-28 Axial contrast-enhanced CT scan on a patient who has had right mandibulectomy and a right neck dissection with a myocutaneous flap reconstruction. Within the flap, there is a nodule (*arrow*) of recurrent squamous cell carcinoma that was not clinically evident.

VIEW IMAGE

Copyright © 2003, Mosby, Inc. All rights reserved.

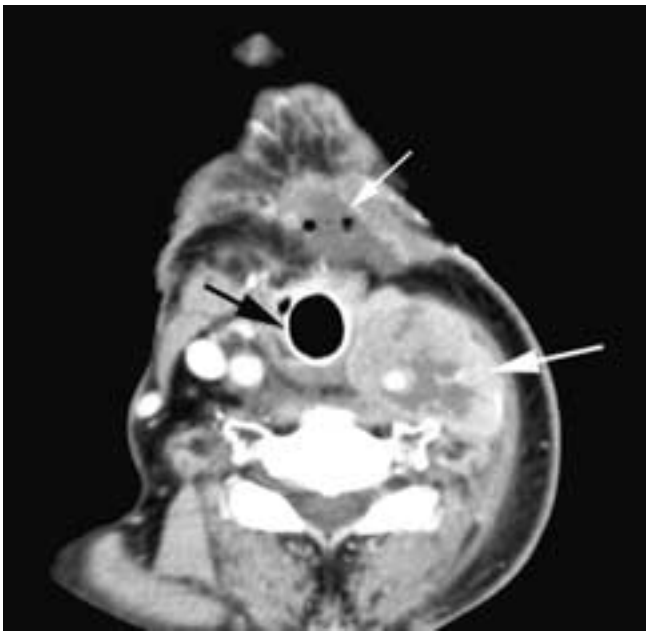

VIEW IMAGE

FIGURE 43-29 Axial contrast-enhanced CT scan on a patient who has had a total laryngectomy and a left neck dissection with flap reconstruction. There was a clinically evident area of drainage in the anterior neck (*small arrow*) that was a recurrence of squamous cell carcinoma along the anterior operative margin. The second site of tumor recurrence deep within the flap (*large arrow*) was not clinically identified. The carotid artery is completely surrounded, almost ensuring tumor invasion of this vessel. The patient had an esophageal diversion tube (*black arrow*) in place.

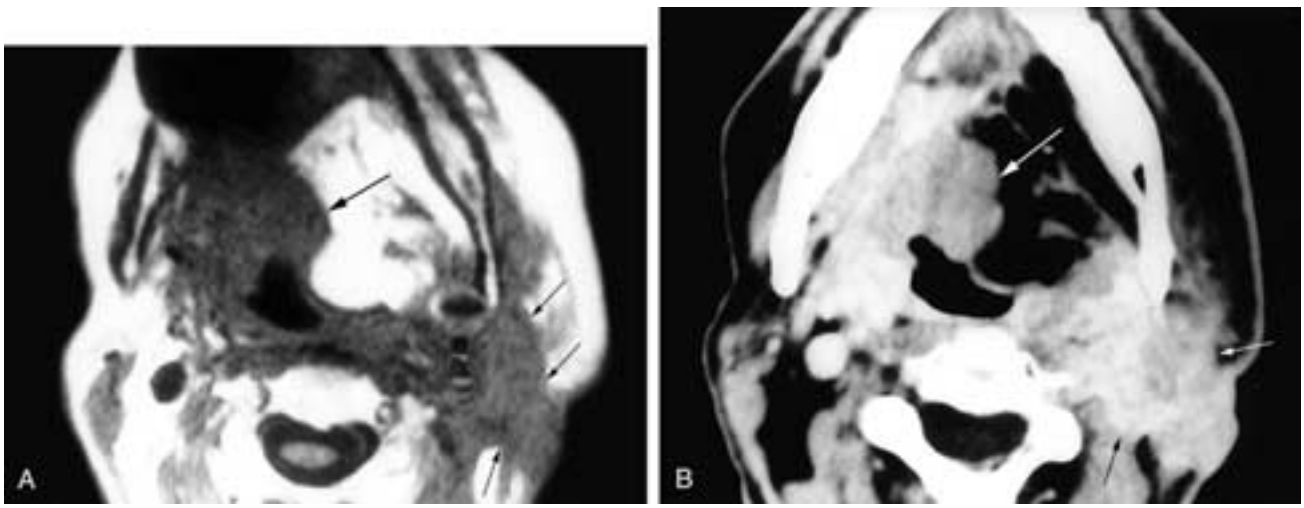

VIEW IMAGE

FIGURE 43-30 Axial T1-weighted MR image (**A**) and an axial contrast-enhanced CT scan (**B**) on a patient who has had a near-total glossectomy with flap reconstruction and a left neck dissection. There is a soft-tissue nodule (*large arrows*) within the operative tongue site indenting the fat of the flap. There is a second area of soft-tissue nodularity (*small arrows*) extending from the skin line toward the carotid artery. On biopsy the tongue mass was vascularized scar, while the lateral neck mass was recurrent squamous cell carcinoma.

Copyright © 2003, Mosby, Inc. All rights reserved.

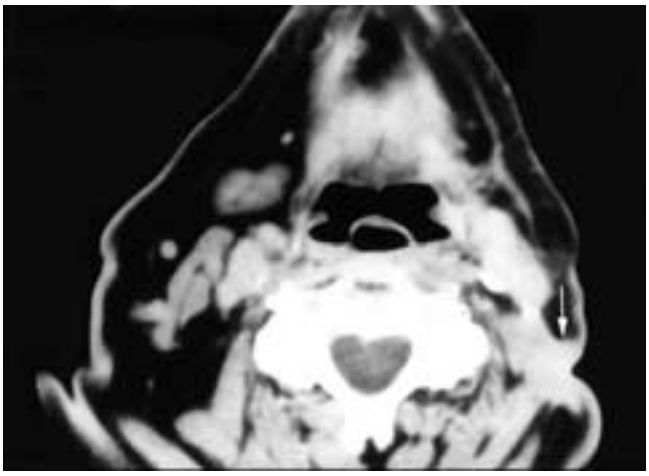

FIGURE 43-31 Axial contrast-enhanced CT scan on a patient who has had a left radical neck dissection. A soft-tissue fullness is present at the scar line (*arrow*). Although a recurrence was not clinically suspected, fine needle aspiration revealed a recurrence of squamous cell carcinoma.

VIEW IMAGE

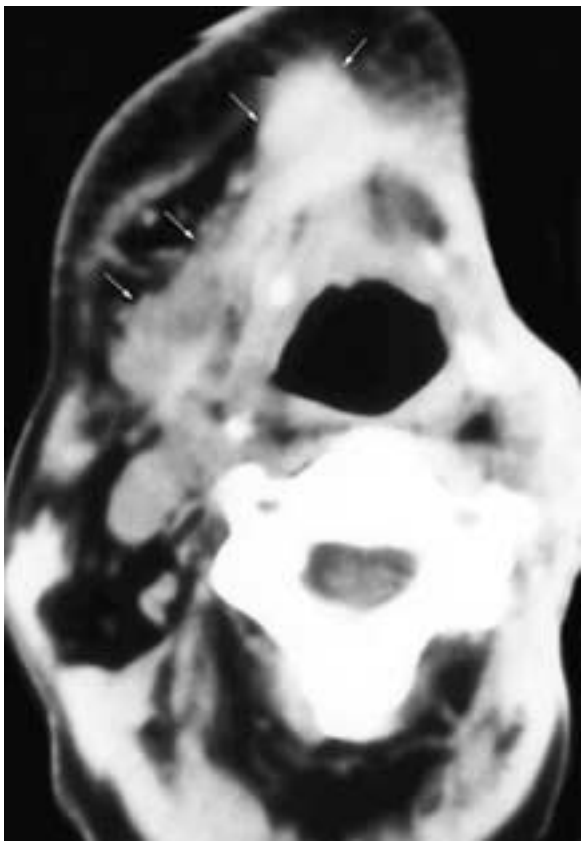

VIEW IMAGE

FIGURE 43-32 Axial CT scan on a patient who had a left radical neck dissection, a right modified neck dissection, and flap reconstruction of the floor of the mouth. A zone of soft tissue (*arrows*) is present within the flap, extending obliquely in the right floor of the mouth and ending in a nodule anteriorly. This was followed on serial CT scans without change for 13 months; however, because of clinical concern, a biopsy was performed that revealed this to be a vascularized scar and not tumor recurrence.

Copyright © 2003, Mosby, Inc. All rights reserved.

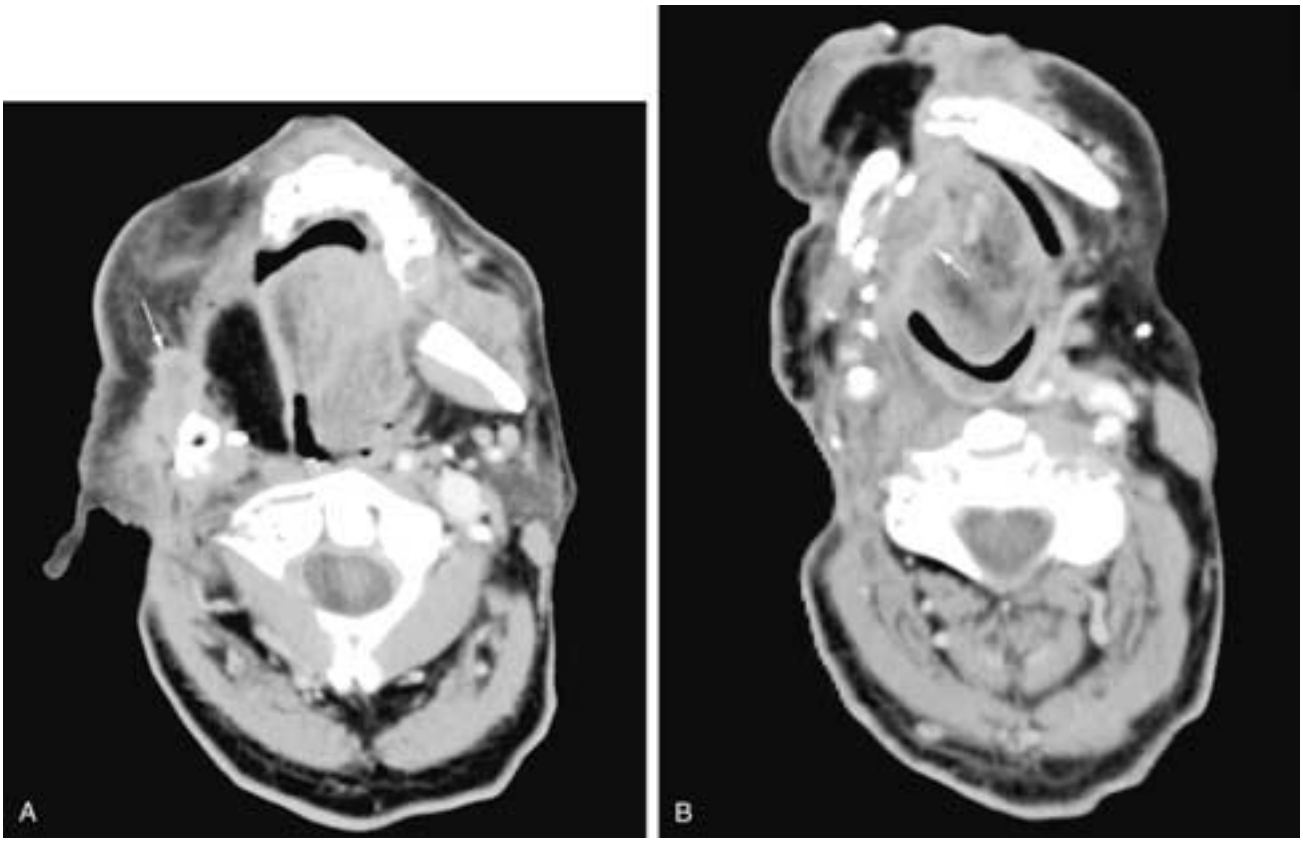

VIEW IMAGE

FIGURE 43-33 Axial contrast-enhanced CT scans from cranial (**A**) to caudal (**B**) on a patient who has had a right mandibulectomy with a flap reconstruction. This was a routine surveillance scan; the patient had no major symptoms. In **A**, there is a necrotic region within the flap (*arrow*) along the anterior aspect of the transplanted bone. In **B**, there is a necrotic area along the right anterior flap margin (*arrow*). This mass invaded the lower anterior tongue. Both areas were recurrent squamous cell carcinoma.

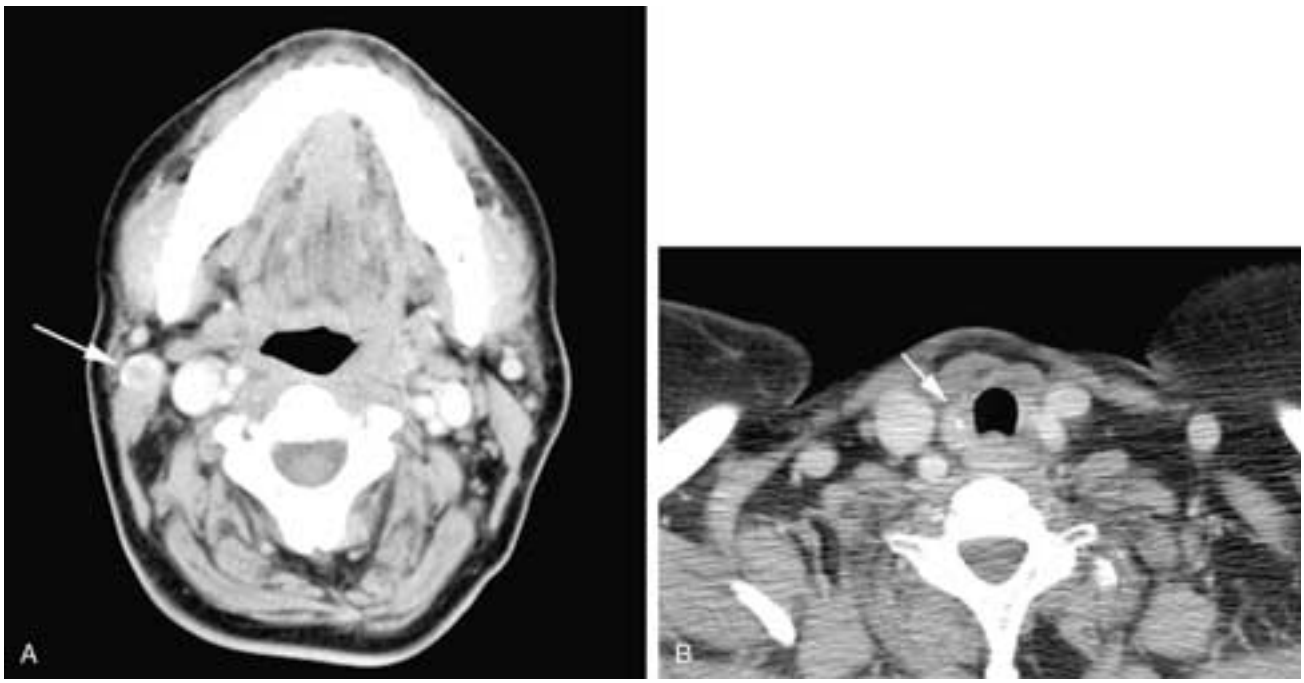

VIEW IMAGE

FIGURE 43-34 Axial contrast-enhanced CT scans from cranial (**A**) to caudal (**B**) on a patient who has had a total thyroidectomy. In **A**, there is an enhancing lymph node (*arrow*) in the right level II region. In **B**, within the right thyroid bed there is a soft-tissue mass (*arrow*) with a calcification. The node was metastatic, and the mass was a local recurrence of papillary thyroid carcinoma.

Copyright © 2003, Mosby, Inc. All rights reserved.

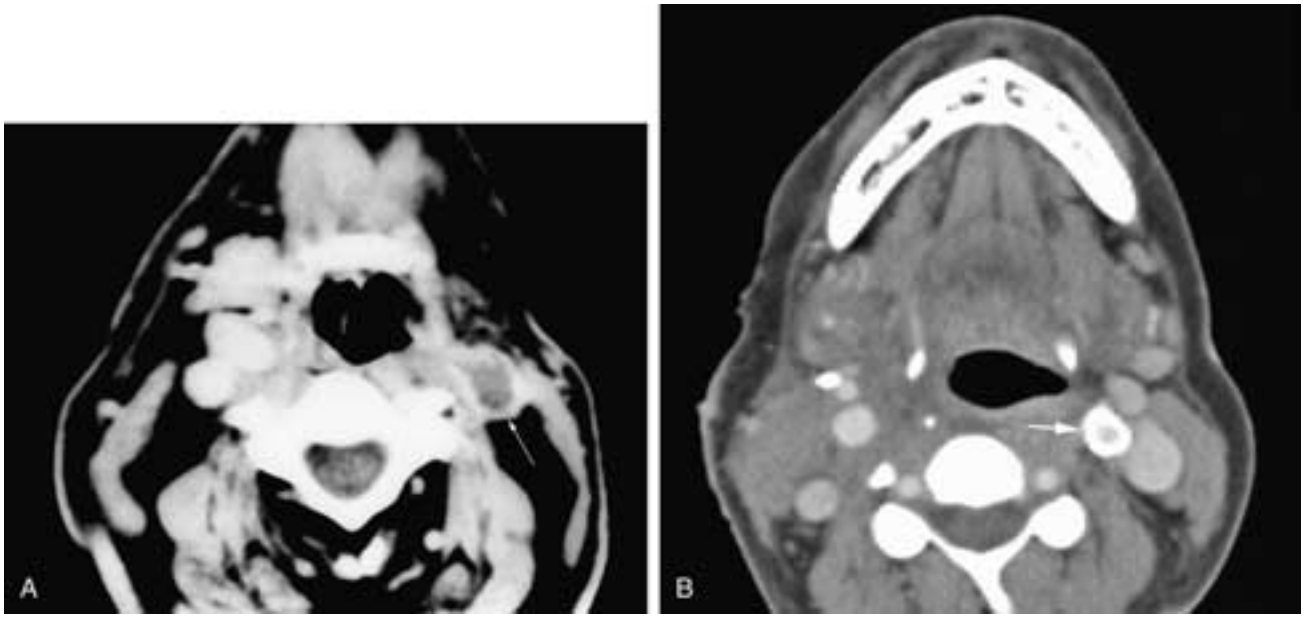

VIEW IMAGE

FIGURE 43-35 Axial contrast-enhanced CT scan (**A**) on a patient who has had a left modified neck dissection. The IJV has been resected, but the SCM is present. There is clinically silent thrombosis of the left carotid artery (*arrow*). Axial CT scan (**B**) on another patient who has had a prior left carotid stent placed (*arrow*). The soft-tissue fullness in the right neck deep to the SCM is related to a recent right-sided endarterectomy.

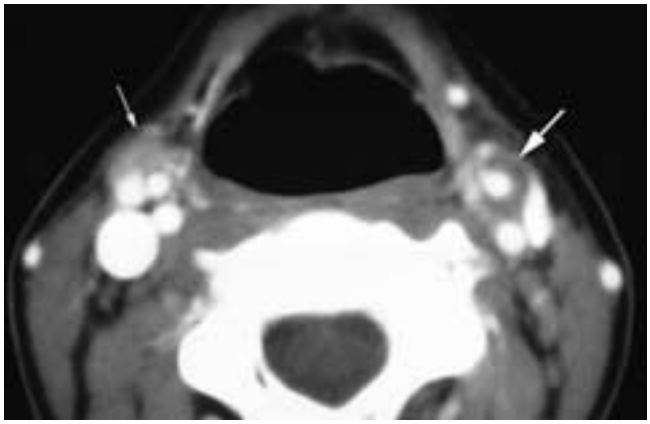

FIGURE 43-36 Axial contrast-enhanced CT scan on a patient who has had RT shows a zone of nonenhancing soft tissue (*large arrow*) around the left carotid artery. This was radiation-related arteritis. A level III node is present in the right neck (*small arrow*).

VIEW IMAGE

Copyright © 2003, Mosby, Inc. All rights reserved.

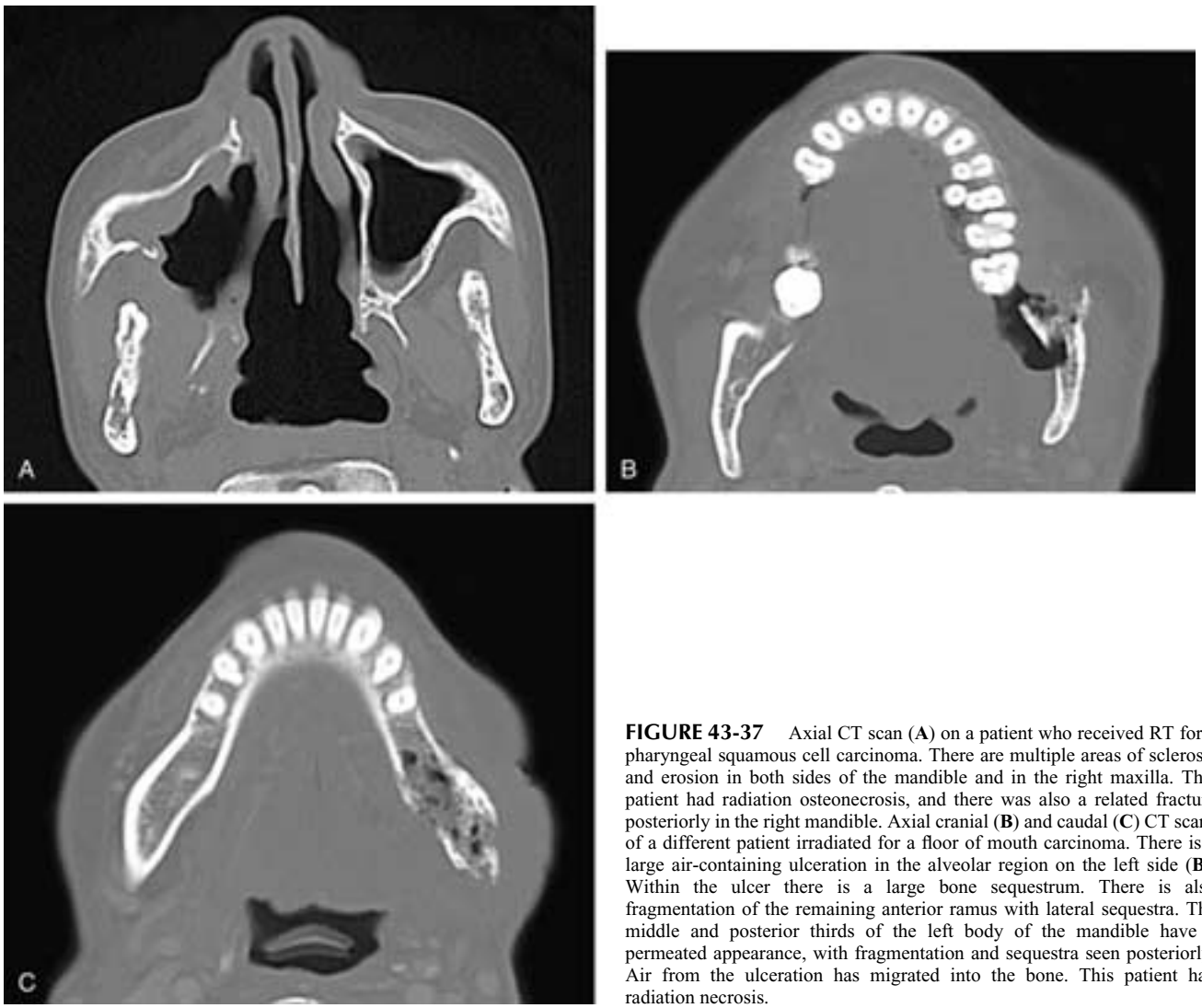

VIEW IMAGE

FIGURE 43-37 Axial CT scan (**A**) on a patient who received RT for a pharyngeal squamous cell carcinoma. There are multiple areas of sclerosis and erosion in both sides of the mandible and in the right maxilla. This patient had radiation osteonecrosis, and there was also a related fracture posteriorly in the right mandible. Axial cranial (**B**) and caudal (**C**) CT scans of a different patient irradiated for a floor of mouth carcinoma. There is a large air-containing ulceration in the alveolar region on the left side (**B**). Within the ulcer there is a large bone sequestrum. There is also fragmentation of the remaining anterior ramus with lateral sequestra. The middle and posterior thirds of the left body of the mandible have a permeated appearance, with fragmentation and sequestra seen posteriorly. Air from the ulceration has migrated into the bone. This patient had radiation necrosis.

VIEW IMAGE

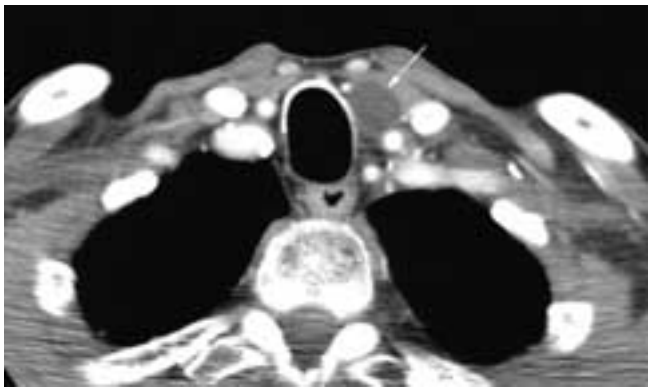

FIGURE 43-38 Axial contrast-enhanced CT scan on a patient who had an open biopsy procedure in the lower left neck. After surgery, a mass developed in the region. A smooth-walled cyst (*arrow*) is present just anterior and medial to the carotid artery. This patient had a thoracic duct cyst.

Copyright © 2003, Mosby, Inc. All rights reserved.

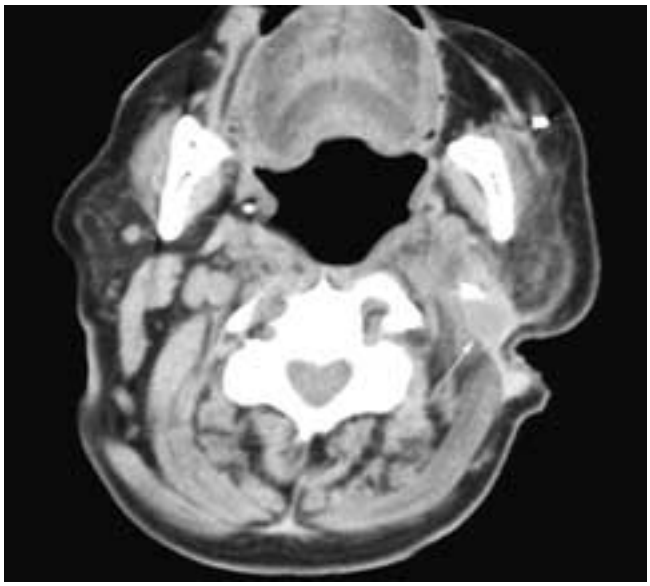

VIEW IMAGE

FIGURE 43-39 Axial contrast-enhanced CT scan on a patient who has had a left neck dissection shows a slightly low attenuation nodule (*arrow*) along the scar line. This was a postoperative traumatic neuroma.

with HIV infection or chronic lymphocytic leukemia, or in cardiac transplant patients.[74–78] In HIV patients, rarely such dermal metastasis may occur in very aggressively behaving carcinomas prior to the identification of cervical nodal metastasis (Fig. 43-40).

NEWER TECHNIQUES

A discussion of the use of PET, thallium-201, and MR spectroscopy to better differentiate tumor from a nontumorous mass appears in Chapter 45. In the future, these techniques may offer the next echelon of diagnostic testing, beyond or in combination with routine CT and MR imaging.[18, 79–97]

VIEW IMAGE

FIGURE 43-40 Axial CT contrast-enhanced scan on a patient who had a right hypopharyngeal carcinoma (*small arrow*) and was HIV positive. He was undergoing RT when a subcutaneous tumor nodule appeared in his back (*large arrow*). This is a rare occurrence.

REFERENCES

1. Medina J, Houck JJ, O'Malley B. Management of cervical lymph nodes in squamous cell carcinoma of the head and neck. In: Harrison L, Sessions R, Hong W, eds. Head and Neck Cancer: A Multidisciplinary Approach. Philadelphia: JB Lippincott-Raven, 1999;353–389.
2. Lindberg R. Distribution of cervical lymph node metastases from squamous cell carcinoma of the upper respiratory and digestive tracts. Cancer 1972;29:1446–1449.
3. Byers R, Wolf P, Ballantyne A. Rationale for elective modified neck dissection. Head Neck Surg 1988;10:160–167.
4. Shah JP. Patterns of cervical lymph node metastasis from squamous carcinomas of the upper aerodigestive tract. Am J Surg 1990;160: 405–409.
5. Stell P. Total laryngectomy. New York: Theime Medical, 1991. CE S, ed. Laryngeal Cancer; 212–214.
6. Robbins K. Classification of neck dissection: current concepts and future considerations. Otolaryngol Clin North Am 1998;31: 639–655.
7. Kowalski L, Medina J. Nodal metastases: predicative factors. Otolaryngol Clin North Am 1998;31:621–637.
8. Ogura J, Biller H, Weth R. Elective neck dissection for pharyngeal and laryngeal cancers. Ann Otolaryngol 1971;80:646–651.
9. Bocca E, Pignataro O, Oldini C, Cappa C. Functional neck dissection: an evaluation and review of 843 cases. Laryngoscope 1984;94: 942–945.
10. Cummings B. Radiation therapy and the treatment of the cervical lymph nodes. In: Cummings C, Fredrickson J, Harker L, et al, eds. Otolaryngology: Head and Neck Surgery. Vol 2. 2nd ed. St. Louis: Mosby Year Book, 1993;1626–1648.
11. Denys D, Kumar P, Wong FS, et al. The predictive value of tumor regression rates during chemoradiation therapy in patients with advanced head and neck squamous cell carcinoma. Am J Surg 1997;174:561–564.
12. Gasparini G, Bevilacqua P, Bonoldi E, et al. Predictive and prognostic markers in a series of patients with head and neck squamous cell invasive carcinoma treated with concurrent chemoradiation therapy. Clin Cancer Res 1995;1:1375–1383.
13. Fleming I, Cooper J, Henson D, et al. American Joint Committee on Cancer Staging Manual. 5th ed. Philadelphia: Lippincott-Raven, 1997.
14. Som P, Curtin H, Mancuso A. An imaging-based classification for the cervical nodes designed as an adjunct to recent clinically based nodal classifications. Arch Otolaryngol Head Neck Surg 1999;125: 388–396.
15. Medina J, Byers R. Supraomohyoid neck dissection: rationale, indications and surgical technique. Head Neck Surg 1989;11: 111–122.
16. Spiro RH, Strong EW, Shah JP. Classification of neck dissection: variations on a new theme. Am J Surg 1994;168:415–418.
17. Robbins KT, Medina JE, Wolfe GT, et al. Standardizing neck dissection terminology. Official report of the Academy's Committee for Head and Neck Surgery and Oncology [see comments]. Arch Otolaryngol Head Neck Surg 1991;117:601–605.
18. Petroff M, Fee WJ. Neck dissection: comparison of available options. In: Cummings C, Fredrickson J, Harker L, et al, eds. Otolaryngology: Head and Neck Surgery. Vol 2. St. Louis: CV Mosby, 1986;1693–1698.
19. Rouviere H. Lymphatic System of the Head and Neck. Ann Arbor, Mich: Edwards Brothers, 1938;5–28.
20. Fisch U, Sigel M. Cervical lymphatic system as visualized by lymphography. Ann Otol Rhinol Laryngol 1964;73:869–882.
21. Skolnik E, King F, Friedman M, et al. The posterolateral triangle in radical neck surgery. Arch Otolaryngol Head Neck Surg 1976; 102:1.
22. Clayman G, Weber R, O'Malley B. Cancer of the hypopharynx and cervical esophagus. In: Harrison L, Sessions R, Hong W, eds. Head and Neck Cancer: A Multidisciplinary Approach. Philadelphia: Lippincott-Raven, 1999;529–554.
23. Som P, Biller H. Computed tomography of the neck in the postoperative patient: radical neck dissection and myocutaneous flap. Radiology 1983;148:157–160.
24. Som PM, Urken ML, Biller H, Lidov M. Imaging the postoperative neck. Radiology 1993;187:593–603.

Copyright © 2003, Mosby, Inc. All rights reserved.

25. Zelefsky M. Nonsurgical and combined therapy for squamous cell cancer of the neck. In: Harrison L, Sessions R, Hong W, eds. Head and Neck Cancer: A Multidisciplinary Approach. Philadelphia: Lippincott-Raven, 1999;379–389.
26. Chow J, Levin B, Krivit J, et al. Radiotherapy or surgery for subclinical cervical node metastases. Arch Otolaryngol Head Neck Surg 1989;115:981–984.
27. Kramer S, Gelber RD, Snow JB, et al. Combined radiation therapy and surgery in the management of advanced head and neck cancer: final report of study 73-03 of the Radiation Therapy Oncology Group. Head Neck Surg 1987;10:19–30.
28. Parsons JT, Mendenhall WM, Cassisi NJ, et al. Neck dissection after twice-a-day radiotherapy: morbidity and recurrence rates. Head Neck 1989;11:400–404.
29. Wolf GT, Fisher SG. Effectiveness of salvage neck dissection for advanced regional metastases when induction chemotherapy and radiation are used for organ preservation. Laryngoscope 1992;102: 934–939.
30. Armstrong J, Pfister D, Strong E, et al. The management of the clinically positive neck as part of a larynx preservation approach. Int J Radiat Oncol Biol Phys 1993;26:759–765.
31. Matsuura K, Hirokawa Y, Fujita M, et al. Treatment results of stage I and II oral tongue cancer with interstitial brachytherapy: maximum tumor thickness is prognostic of nodal metastasis. Int J Radiat Oncol Biol Phys 1998;40:535–539.
32. Krull A, Friedrich RE, Schwarz R, et al. Interstitial high dose rate brachytherapy in locally progressive or recurrent head and neck cancer [in process citation]. Anticancer Res 1999;19:2695–2697.
33. Dietz A, Rudat V, Nollert J, et al. [Chronic laryngeal edema as a late reaction to radiochemotherapy (see comments)]. Hno 1998;46: 731–738.
34. Bousson V, Marsot-Dupuch K, Lashiver X, Tubiana JM. [Post-radiation necrosis of the cricoid cartilage: an uncommon case]. J Radiol 1995;76:517–520.
35. Amdur RJ, Conine FE, Harris RD, Leopold KA. Arytenoid sparing during irradiation of early stage vocal cord cancer. Int J Radiat Oncol Biol Phys 1995;32:801–808.
36. Zompatori M, Rimondi MR. [Diffuse ground-glass opacity of the lung. A guide to interpreting the high-resolution computed tomographic (HRCT) picture]. Radiol Med (Torino) 1994;88:576–581.
37. Mukherji SK, Mancuso AA, Kotzur IM, et al. Radiologic appearance of the irradiated larynx. Part I. Expected changes. Radiology 1994;193:141–148.
38. Motozaki T, Ban S, Yamamoto T, Hamasaki M. [Peritumoral hemorrhage after radiosurgery for metastatic brain tumor: a case report]. No Shinkei Geka 1994;22:789–793.
39. Hudgins PA, Burson JG, Gussack GS, Grist WJ. CT and MR appearance of recurrent malignant head and neck neoplasms after resection and flap reconstruction. AJNR 1994;15:1689–1694.
40. Ohgi K, Kohno A, Itabashi K, et al. Head and neck reconstruction with pectoralis major myocutaneous flap: CT evaluation. J Comput Assist Tomogr 1990;14:286–290.
41. Glazer H, Niemeyer J, Balfe D, et al. Neck Neoplasms: MR imaging, part II. Posttreatment evaluation. Radiology 1986;160: 349–354.
42. Gussack G, Hudgins P. Imaging modalities in recurrent head and neck tumors. Laryngoscope 1991;101:119–124.
43. Krol B, Righi P, Weisberger E, et al. Isolated cervical recurrence of squamous cell carcinoma in the previously treated neck. Am J Otolaryngol 2000;21:360–365.
44. Som P, Silvers A, Urken M. Surveillance CT and the prompt use of CT guided fine needle aspiration in the post-operative head and neck cancer patient. Am J Roentgenol 1999;173:1505–1508.
45. Labadie RF, Yarbrough WG, Weissler MC, et al. Nodal volume reduction after concurrent chemo- and radiotherapy: correlation between initial CT and histopathologic findings. AJNR 2000;21: 310–314.
46. Abemayor E, Ljung B, Ward P, et al. CT-directed fine needle aspiration biopsies of masses in the head and neck. Laryngoscope 1985;95:1382–1386.
47. Atula TS, Varpula MJ, Kurki TJ, et al. Assessment of cervical lymph node status in head and neck cancer patients: palpation, computed tomography and low field magnetic resonance imaging compared with ultrasound-guided fine-needle aspiration cytology. Eur J Radiol 1997;25:152–161.
48. Berg H, Jacobs J, Kaufman D, Reede DL. Correlation of fine needle aspiration biopsy and CT scanning of parotid masses. Laryngoscope 1986;96:1357–1362.
49. Citardi M, Abrahams J, Flynn S, Sasaki C. Efficacy of transcutaneous computed tomography guided fine needle aspiration biopsy in patients with laryngeal squamous cell carcinoma, probable failed radiation therapy, and negative transmucosal biopsies. Laryngoscope 1996;106: 1244–1247.
50. Gatenby R, Mulhern CJ, Richter M, Moldofsky P. CT-guided biopsy for the detection and staging of tumors of the head and neck. AJNR 1984;5:287–290.
51. Duckwiler G, Lufkin R, Teresi L, et al. Head and neck lesions: MR-guided aspiration biopsy. Radiology 1989;170:519–522.
52. Ljung B, Larsson S, Hanafee W. Computed tomography guided aspiration cytologic examination in head and neck lesions. Arch Otolaryngol 1984;110:604–607.
53. Robbins K, van Sonnenberg E, Casola G, Varney R. Image guided needle biopsy of inaccessible head and neck lesions. Arch Otolaryngol 1990;116:957–961.
54. Riediger D, Ehrenfeld M. [Pathogenesis and clinical manifestation of the styloid syndrome]. Dtsch Zahnarztl Z 1989;44:968–970.
55. King L, Hasnain S, Webb J, et al. Asymptomatic carotid arterial disease in young patients following neck radiation therapy for Hodgkin lymphoma. Radiology 1999;213:167–172.
56. Foreman NK, Laitt RD, Chambers EJ, et al. Intracranial large vessel vasculopathy and anaplastic meningioma 19 years after cranial irradiation for acute lymphoblastic leukaemia. Med Pediatr Oncol 1995;24:265–268.
57. Rockman CB, Riles TS, Fisher FS, et al. The surgical management of carotid artery stenosis in patients with previous neck irradiation. Am J Surg 1996;172:191–195.
58. Chuang VP. Radiation-induced arteritis. Semin Roentgenol 1994;29: 64–69.
59. Hemar P, Kennel P, Piller P, et al. [Lingual necrosis after neck irradiation]. Ann Otolaryngol Chir Cervicofac 1993;110: 351–354.
60. Quraishi H, Wax M, Granke K, Rodman S. Internal jugular vein thrombosis after functional and selective neck dissection. Arch Orolaryngol Head Neck Surg 1997;123:969–973.
61. Bras J, de Jonge HK, van Merkesteyn JP. Osteoradionecrosis of the mandible: pathogenesis. Am J Otolaryngol 1990;11:244–250.
62. Schratter-Sehn AU, Handl-Zeller L, Strassl H, et al. [Incidence of osteoradionecrosis after combined radiotherapy-chemotherapy of head and neck tumors]. Strahlenther Onkol 1991;167:165–168.
63. Artazkoz del Toro JJ, Dalmau Galofre J, Faubel Serra M, et al. [Mandibular osteoradionecrosis caused by radiotherapy of lip cancer. Differential diagnosis with tumor recurrence]. An Otorrinolaringol Ibero Am 1992;19:283–290.
64. Lee EJ, Calcaterra TC, Zuckerbraun L. Traumatic neuromas of the head and neck. Ear Nose Throat J 1998;77:670–674, 676.
65. Kus H, Araszkiewicz H, Wlodarska-Araszkiewicz A, et al. [Multiple post-traumatic neuromas of the cervical plexus with atypical symptoms]. Neurol Neurochir Pol 1983;17:597–599.
66. Sung JH, Mastri AR. Aberrant peripheral nerves and microneuromas in otherwise normal medullas. J Neuropathol Exp Neurol 1983;42: 522–528.
67. Iida S, Shirasuna K, Kogo M, Matsuya T. Amputation neuroma following radical neck dissection—report of 3 cases. J Osaka Univ Dent School 1995;35:1–4.
68. de Chalain T, Nahai F. Amputation neuromas of the great auricular nerve after rhytidectomy. Ann Plast Surg 1995;35:297–299.
69. Toriumi DM, Sykes J, Wolff A. Pathologic quiz case 1. Amputation neuroma of the great auricular nerve. Arch Otolaryngol Head Neck Surg 1987;113:888–890.
70. Rauchfuss A, Caselitz J. [Scar neuroma following tumor operations of the head and neck. Immunohistologic studies, differential diagnosis, therapy]. Hno 1987;35:84–87.
71. Hobsley M. Amputation neuroma of the great auricular nerve after parotidectomy. Br J Surg 1972;59:735–736.
72. Barnes L, Peel R. Tumors of the nervous system. In: Barnes L, ed. Surgical Pathology of the Head and Neck. Vol 1. New York: Marcel Dekker, 1985;659–724.
73. Huang L, Weissman J, Fan C-Y. Traumatic neuroma after neck dissection: CT characteristics in four cases. AJNR 2000;21:1676–1680.

Copyright © 2003, Mosby, Inc. All rights reserved.

74. Pitman KT, Johnson JT. Skin metastases from head and neck squamous cell carcinoma: incidence and impact. Head Neck 1999;21: 560–565.
75. Cole RD, McGuirt WF. Prognostic significance of skin involvement from mucosal tumors of the head and neck. Arch Otolaryngol Head Neck Surg 1995;121:1246–1248.
76. Hartley BE, Searle AE, Breach NM, et al. Aggressive cutaneous squamous cell carcinoma of the head and neck in patients with chronic lymphocytic leukaemia. J Laryngol Otol 1996;110:694–695.
77. Veness MJ, Quinn DI, Ong CS, et al. Aggressive cutaneous malignancies following cardiothoracic transplantation: the Australian experience. Cancer 1999;85:1758–1764.
78. Kmucha ST, Troxel JM. Dermal metastases in epidermoid carcinoma of the head and neck. Arch Otolaryngol Head Neck Surg 1993;119:326–330.
79. Olmos RV, Balm A, Hilgers F, et al. Thallium-201 SPECT in the diagnosis of head and neck cancer. J Nucl Med 1997;38:873–879.
80. Mukherji SK, Gapany M, Phillips D, et al. Thallium-201 single-photon emission CT versus CT for the detection of recurrent squamous cell carcinoma of the head and neck [in process citation]. AJNR 1999;20:1215–1220.
81. Nakada K, Katoh C, Morita K, et al. Relationship among 201T1 uptake, nuclear DNA content and clinical behavior in metastatic thyroid carcinoma. J Nucl Med 1999;40:963–967.
82. Yigitbasi OG, Tutus A, Bozdemir K, et al. 201Tl imaging for differentiating between malignant and benign neck masses. Nucl Med Commun 1998;19:555–560.
83. Ortega F, Maldonado A, Maranes P, et al. [PET-FDG in thyroid cancer with high thyroglobulin levels and negative 131-I scan. A case report]. Rev Esp Med Nucl 1999;18:50–54.
84. James C, Starks M, MacGillivray DC, White J. The use of imaging studies in the diagnosis and management of thyroid cancer and hyperparathyroidism. Surg Oncol Clin North Am 1999;8:145–169.
85. Takei H, Iino Y, Endo K, et al. The efficacy of technetium-99m-MIBI scan and intraoperative methylene blue staining for the localization of abnormal parathyroid glands. Surg Today 1999;29:307–312.
86. Laubenbacker C, Saumweber D, Wagner-Manslau C, et al. Comparison of fluorine-18-fluorodeoxyglucose PET, MRI and endoscopy for staging head and neck squamous carcinomas. J Nucl Med 1995;36: 1747–1757.
87. Maublant J, Vuillez JP, Talbot JN, et al. Positron emission tomography (PET) and (F-18)-fluorodeoxyglucose (FDG) in cancerology. Bull Cancer 1998;85:935–950.
88. Stokkel MP, ten Broek FW, van Rijk PP. The role of FDG PET in the clinical management of head and neck cancer. Oral Oncol 1998;34:466–471.
89. Wong WL, Saunders M. Role of PET FDG in the management of head and neck squamous cell cancer. Clin Oncol 1998;10:361–366.
90. Sakamoto H, Nakai Y, Ohashi Y, et al. Monitoring of response to radiotherapy with fluorine-18 deoxyglucose PET of head and neck squamous cell carcinomas. Acta Otolaryngol Suppl 1998;538: 254–260.
91. Mattei R, Rubello D, Ferlin G, Bagatella F. Positron emission tomography (PET) with 18-fluorodeoxyglucose (FDG) in the diagnosis and preoperative staging of head and neck tumors: a prospective study. Acta Otorhinolaryngol Ital 1998;18:387–391.
92. Jadvar H, McDougall IR, Segall GM. Evaluation of suspected recurrent papillary thyroid carcinoma with [18F]fluorodeoxyglucose positron emission tomography. Nucl Med Commun 1998;19:547–554.
93. Jiang GL, Ang KK, Peters LJ, et al. Maxillary sinus carcinomas: natural history and results of postoperative radiotherapy. Radiother Oncol 1991;21:193–200.
94. Borisov AV, Petrenko VM. The development of the thoracic duct lymphangions in the prenatal period of human ontogeny. Ontogenez 1992;23:254–259.
95. Petrenko VM. The formation of definitive variants in the organization of the rudimentary portion of the thoracic duct in the prenatal period of human ontogeny. Morfologiia 1993;104:66–74.
96. Valvassori GE, Guzman M. Magnetic resonance imaging of the posterior cranial fossa. Ann Otol Rhinol Laryngol 1988;97:594–598.
97. Blizzard R, Chandler R, Landing BH, et al. Maternal autoimmunization to thyroid as a probable cause of athyrotic cretinism. N Engl J Med 1960;263:327–336.

Copyright © 2003, Mosby, Inc. All rights reserved.

44

Genetics of Tumor Development and Metastasis

Edward M. Johnson

INTRODUCTION
- Basic Mechanisms of Entering and Exiting the Cell Division Cycle
- Gene Alterations Define Neoplasia
- Characteristics Common to All Neoplasia Conferred by a Variety of Genetic Alterations

DOMINANTLY ACTING ONCOGENES
- Viral Oncogenes
  - Detection of Oncogenes in Human Tumors
- Oncogenes Are Activated in Cells in a Variety of Ways
  - Insertional Mutagenesis
  - Mutational Alteration of Gene Transcription
  - Mutational Alteration of the Protein Coding Sequence
  - Chromosome Translocation to Generate an Aberrant Fusion Protein
  - Selective Gene Amplification
- Growth Factors and Growth Factor Receptors as Oncogenes
  - Autocrine and Paracrine Loops
- Oncogenes in Intracellular Signal Transduction Pathways
- *Ras* Gene Activation in Multiple Neoplasms
- The c-*myc* Oncogene in Burkitt's Lymphoma
- Translocations That Create Oncogenic Fusion Proteins
  - The Philadelphia Chromosome
  - Translocations Involving Transcription Factors

TUMOR SUPPRESSOR GENES
- Familial Cancer Syndromes
  - Retinoblastoma and *RB*
  - Li-Fraumeni Syndrome and *p53*
- Guardians and Gatekeepers
- The Retinoblastoma Protein, Rb, and Cell Cycle Control
- The p53 Protein and DNA Damage
- Genome Instability Syndromes
  - Hereditary Nonpolyposis Colon Cancer
  - Bloom and Werner Syndromes
- A Variety of Tumor Suppressor Genes Regulating Protective Mechanisms
  - The Gene Mutated in Ataxia-Telangiectasia, *ATM*
  - *ARF* and *p16*: Unusual Overlapping Tumor Suppressor Genes
  - *BRCA1* and *BRCA2* in Breast and Ovarian Cancer
  - *NF-1* and Von Recklinghausen's Neurofibromatosis
  - *PTEN*: A Tumor Suppressor Gene Encoding a Phosphatase
  - *WT-1* and *WT-2* and Wilms' Tumor

CIRCUMVENTING APOPTOSIS

TELOMERASE AND ONCOGENIC TRANSFORMATION

INTERACTION OF TUMOR SUPPRESSOR GENE PRODUCTS WITH PROTEINS ENCODED BY ONCOGENIC DNA VIRUSES
- Human Papilloma Viruses and Cervical Cancer
- Are SV40 or Other Papovaviruses Involved in Human Cancer?
- Hepatitis Virus Types B and C and Hepatocellular Carcinoma

NEOPLASIA IN AIDS
- Kaposi's Sarcoma and HHV8
- Primary Central Nervous System Lymphoma and Epstein-Barr Virus

GENES INVOLVED IN MULTIPLE STEPS OF METASTASIS

TUMOR ANGIOGENESIS
- Tumor Size Restricted by Blood Supply
- Activation in Tumors of Genes Encoding Angiogenic Growth Factors
- Imaging of Tumor Angiogenesis

FUTURE OF CANCER TREATMENTS

Copyright © 2003, Mosby, Inc. All rights reserved.

INTRODUCTION

Basic Mechanisms of Entering and Exiting the Cell Division Cycle

Knowledge of the genetics of tumor development and metastasis may not be essential to the interpretation of all radiology studies. However, many of these imaging examinations are performed on patients who have malignancies, and the informed radiologist should understand the way in which these tumors develop. In addition, genetics-based imaging, a field now in its infancy, should become considerably more important in the near future. This chapter will review the current concepts of the genetics of tumors and metastasis. An understanding of this chapter requires a certain amount of knowledge regarding the basic biology of the cell cycle. While a thorough review of the cell cycle is beyond the scope of this chapter, a brief review is provided in the following paragraph that should facilitate absorption of concepts and terminology in the remainder of the chapter. In addition, a brief glossary appears at the end of this chapter.

Tumors generally arise through clonal expansion beginning with a single cell that has become aberrant, that is, transformed into a neoplastic state. It is important to note, however, that neoplasia does not just represent uncontrolled cell proliferation but may also represent failure of a cell to differentiate properly and, for that matter, failure to die under appropriate circumstances. Thus, many of the alterations that lead to transformation involve pathways controlling the cell division cycle and its relations to differentiation and to programmed cell death, termed *apoptosis*. The cell cycle is commonly described in terms of the phases G1, S, G2, and M. Gap1, or G1, is the gap between mitosis, M, and DNA synthesis, S. During G1, genes are activated and proteins synthesized to prepare the cell for DNA replication. S-phase is the period during which all of the DNA of a cell is replicated once and only once. Gap2, or G2, is the gap between DNA synthesis and mitosis. During G2, genes are activated and proteins synthesized to prepare the cell for mitosis, M, or cell division, at which time the duplicated DNA is distributed equally to each of the two daughter cells. Cells that are proliferating repeat these phases in that order. The cell cycle includes several checkpoints, which are referred to throughout this chapter. At these points, in response to aberrant progression a cell may exit the cycle. For example, G1 includes a ''start'' point at approximately midphase. Once a cell has traversed the start point, it is committed to undergo DNA replication. In response to signals indicating DNA damage, however, a cell may not traverse the start point. Such cells cease to proliferate, and most such cells undergo apoptosis. The start checkpoint is thus an important point at which cells with mutated DNA may be prevented from becoming cancerous. As discussed later in this chapter, several protein products of tumor suppressor genes participate in pathways impinging on start and other checkpoints. Another way for cells to exit the cell cycle is to enter the state known as G0, G-zero. The G0 state is frequently called quiescent since cells in it are not proliferating. In G0, however, cells may be active in various synthetic processes. Most differentiated cells in the body are in G0. Cells may leave the division cycle at start to enter G0. Conversely, cells in G0 may, in response to proliferative signals, reenter the cell cycle, and such reentry occurs at the start point in mid-G1. The proliferative capacity of a normal cell is not infinite. It is generally accepted that nontransformed cells of most tissues can divide 50 to 60 times before undergoing senescence. Senescence is a state in which cells live and may continue to grow, although they have lost their ability to proliferate. Neoplastic cells evade senescence and thus become immortal. Senescence is not considered in detail in this chapter, although it is presented in relation to the concept of renewal of telomeres, which are the ends of the linear DNA of chromosomes. As discussed, telomere renewal is important in the establishment of immortality in tumor cells. Understanding the relationship between controls over the cell cycle and its exit points sets the stage for an understanding of the genetic changes that lead to neoplasia.

Frequently, a given gene has the same abbreviation as the protein it encodes. In this chapter, in order to facilitate a distinction, gene names are italicized, while the names of corresponding proteins are not.

Gene Alterations Define Neoplasia

The revolution in molecular biology that accompanied the onset of gene cloning has now allowed the enumeration of certain genetic principles that are common to all cancers. These principles can be generalized as follows: (1) All cancers are caused by successive mutations in multiple genes that allow a cell to evade or override controls over a variety of processes that govern normal cell proliferation, adhesion, and mortality. (2) While certain of these mutations can be inherited, leading to a predisposition to cancer, the bulk of the mutations are acquired through action of environmental factors, including products of normal metabolism. (3) While gene mutations affecting a small, well-defined set of regulatory gene categories are necessary for and sufficient to induce neoplasia, mutations in many other genes affect tumor growth, metastasis, and the response to therapy.

Historically, our knowledge of the dominantly acting oncogenes came first because many of these genes were discovered as the transforming genes of acutely transforming retroviruses. A notable example is the *src* gene, the transforming gene of Rous sarcoma virus, which causes tumors in chickens. The Rous virus was discovered in 1911. However, the actual identification of the *src* gene did not occur until the elucidation of the genetic roles of DNA and RNA, as well as the understanding of the structure and replication of retroviruses in the 1950s and 1960s. With the discovery of the enzyme reverse transcriptase, the stage was set for rapid advances in the understanding of tumor genetics. Advances were also greatly facilitated by the discovery of restriction endonucleases, which allowed the development of the technology of molecular cloning in the mid-1970s.

As mentioned, traditionally the genes mutated in oncogenesis were categorized as either dominantly acting oncogenes or tumor suppressor genes. However, this neat

Copyright © 2003, Mosby, Inc. All rights reserved.

categorization has recently been blurred by discoveries of the multifunctionality of many proteins, so that genes encoding certain proteins can take on aspects of either oncogenes or tumor suppressor genes. In addition, there are genes that cause instability, and while these genes do not contribute to the maintenance of a malignant phenotype, they lead to other gene changes that do. That is, our view of oncogenes and tumor suppressor genes has evolved from a perception of them as separate categories to one that views them as a continuum, with stages between the extreme positions of recessive loss of function and dominant gain of function. It is now understood that certain genes, when mutated, may gain a function that contributes to cancer while losing other functions that may protect against cancer. In addition, certain mutations of tumor suppressor genes can confer a dominant negative phenotype on the encoded protein. Such a mutation would thus resemble a gain-of-function mutation characteristic of a dominantly acting oncogene. The *p53* gene is a notable example of this, having originally been considered a dominantly acting oncogene but later, with enhanced understanding of the types of mutations that can affect the gene, having been categorized as a tumor suppressor gene.

It is now generally recognized that combinations of genes must be sequentially altered to allow the progression toward cancer.[1] All cancers have alterations in oncogenes that confer advantages on specific cells to evade normal proliferative controls in order to form expanding clonal populations of cells. In addition, all cancers must have alterations in tumor suppressor genes to inactivate the ability of the products of these genes to confer a protective effect against evasion of growth controls. Our present knowledge is beginning to allow a generalization of the overall complex functions in which the products of these oncogenes and tumor suppressor genes are involved. The sequential involvement of an array of genes raises the question of how many mutational steps it takes to cause any given cancer. Initially, much of the work in this area came from in vitro studies on cultured cells. Many of the early oncogenes were identified as such by their ability to transform these cells to form tumors in immunologically compromised mice (see the section on Detection of Oncogenes in Human Tumors).

Do these in vitro studies indicate that only one or two genetic changes accompany the progreion to cancer in humans? Not necessarily, as studies of tumorigenesis in transgenic mice have indicated the necessity for multiple rate-limiting steps. Renan[2] considered the age-dependant diagnosis of many cancers in humans and suggested that four to seven stochastic, rate-limiting genetic alterations are involved. Studies of colon cancer by Vogelstein and colleagues[1] indicated that genetic changes accompany a series of premalignant states that ultimately culminate in metastatic cancer. In addition, further genetic changes are known to alter the ability of a tumor to respond to treatment. The ultimate summary of the studies on cell transformation, animal models, and statistical analyses of human tumors is that the development of a tumor proceeds through a series of genetic changes, each of which confers an advantage on a population of cells that allows that population to receive each successive genetic alteration more readily.

Characteristics Common to All Neoplasia Conferred by a Variety of Genetic Alterations

It is clear that various neoplasias can be caused by acquired mutations in multitudes of different cellular genes. The accumulation of data regarding the genes affected now allows investigators to discern patterns in the phenotypic characteristics that result from these changes, and it is evident that there is a set of acquired characteristics that are common to the development of most, if not all, cancers. In a review of the hallmarks of cancer, Hanahan and Weinberg[3] have enumerated six essential physiologic characteristics that are, taken together, sufficient to dictate malignant growth. These characteristics, which result from the wide variety of gene alterations, are self-sufficiency in growth signals, insensitivity to growth-inhibitory signals, evasion of programmed cell death (apoptosis), replicative immortality, sustained angiogenesis, and the capacity for tissue invasion and metastasis. These characteristics are summarized in Figure 44-1. The following discussion of oncogenes and tumor suppressor genes will demonstrate that most changes in dominantly acting oncogenes serve to confer on cells a self-sufficiency in growth signaling. Many such changes lead to growth signaling pathways that are constitutive and no longer reliant on induction by an extracellular signal. Most tumor suppressor gene products participate in pathways that are growth inhibitory or that lead cells with damaged DNA toward apoptosis. Acquisition of replicative immortality requires changes that allow a cell to regenerate chromosome telomeric repeats, tandemly repeated nucleotide sequences at the ends of chromosomes that ordinarily become progressively shorter with each round of DNA replication. Not all neoplasias require angiogenesis, and not

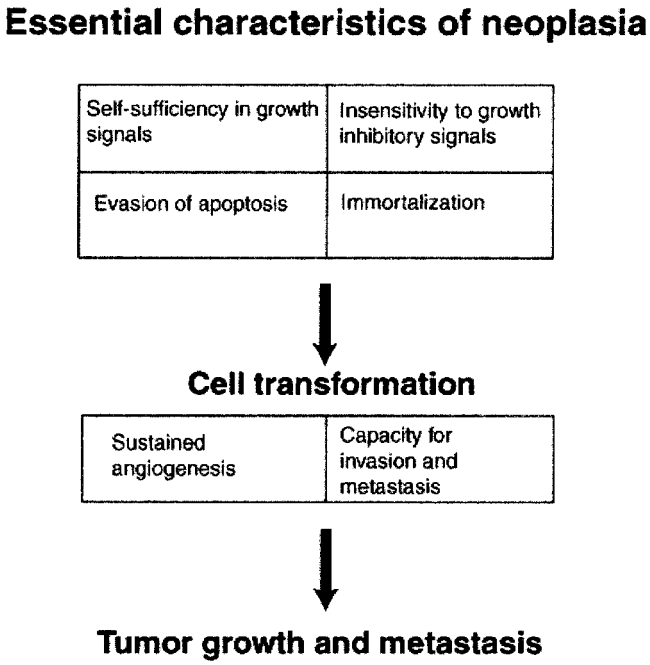

FIGURE 44-1 Six characteristics sufficient to dictate malignant growth. The characteristics of cells (large rectangle) and tumors (small rectangle) that can confer malignant tumor formation are described in detail by Hanahan and Weinberg.[3]

VIEW IMAGE

Copyright © 2003, Mosby, Inc. All rights reserved.

all are invasive or metastatic. Cells of virtually all neoplasias that produce a tumor mass, however, can undergo genetic alterations that bestow these characteristics on them. Such alterations may allow cells to produce factors that promote new blood vessel growth, or they may inactivate cadherins or integrins to allow cells to escape their usual sites of tethering. Clearly, not all of the genes altered in the progression to cancer fall neatly into the categories of dominantly acting oncogenes or tumor suppressor genes. Nonetheless, a discussion of these two broad classes of genes is informative in terms of understanding the mechanisms by which cancer cells acquire abnormal mechanisms of proliferation.

DOMINANTLY ACTING ONCOGENES

An oncogene is a cellular gene, the expression of which contributes in a dominant fashion to the development of cancer. Oncogenes of tumors arise through somatic mutation of normal cellular genes. Such genes perform various functions that contribute to the normal phenotype of cells. However, when they are mutated, they gain a function that confers on them the ability to avoid or to subvert a normal growth pattern. The functions of many of these normal genes, frequently referred to as proto-oncogenes, are not known. Most oncogenes have been discovered by their transforming characteristics and have thus been most thoroughly studied in their mutated, oncogenic forms. The oncogenes discussed here, as distinct from the tumor suppressor genes (which require both alleles to be mutated), require only one allele to be mutated to produce their oncogenic effects.

Viral Oncogenes

Many cellular oncogenes were first discovered by their homology to the transforming genes of various acutely transforming retroviruses. For example, the *myc* oncogene is the transforming gene of MC29 myelocytomatosis virus, which infects chickens. The *ErbB* oncogene is the transforming gene of Avian erythroblastosis virus, which also infects chickens. The *ras* oncogene is the transforming gene of rat sarcoma virus, and a similar viral oncogene is found in the Harvey murine sarcoma virus that infects mice. When hybridized to the DNA of host cells, the viral genomes were found to contain sequences that were also present in the genome of the host cell. It is now clear that the acutely transforming retroviruses gained their transforming genes through the transduction of genes normally present in uninfected host cells. Retroviruses that contain such an oncogene are capable of transforming cells in animal tissues with very high efficiency.

Not all retroviruses are oncogenic, and many oncogenic retroviruses do not contain transforming genes. All the genes just described, and many others mentioned in Table 44-1, are very homologous to their human counterparts. It is, in fact, rare for any human cancer to be associated with retroviral infection. The only human cancer directly caused by a retrovirus is human T-cell leukemia, the etiologic agent of which is the virus HTLV-1.

Detection of Oncogenes in Human Tumors

The characteristic that facilitated the early discovery of oncogenes versus tumor suppressor genes is the ability of the former to transform cells in tissue culture on DNA transfection. The ability to clone genomic libraries of DNA from tumor cells, to transfect noncancerous human cells in tissue culture, and to rescue the resulting transforming genes has been a standard means of detecting oncogenes for many years. In most early experiments, the mouse NIH3T3 cell line was a standard tool for such transformation studies. These cells are an immortalized mouse line. When transformed with DNA including an oncogene, they grow as anchorage-independent foci in soft agar, and plasmid rescue techniques can then be used to reextract and clone the transforming genes of such foci.

The immortalized NIH3T3 cells may already possess one or more altered genes contributing to a transformed phenotype. This type of assay obviously detects dominantly acting oncogenes and thus excludes genes in which the transforming mutation produces a loss of function. An early experiment of Robert Weinberg and coworkers showed that c-*myc* and H-*ras* can cooperate in transforming nonimmortalized mouse cells.[3] In this experiment, NIH3T3 cells were transformed by the transfection of H-*ras* alone. The nonimmortalized fibroblasts were, however, not transformed by H-*ras* alone. Nor did transfection with c-*myc* alone induce transformation. However, when the nonimmortalized fibroblasts were transfected with c-*myc*, they became immortalized and were subsequently transformed by transfection with H-*ras*. This experiment illustrates the concept that alteration of one oncogene may confer an advantage on a cell that facilitates transformation by a successive oncogene.

Human cells have been notoriously more difficult to transform with combinations of oncogenes than have mouse cells. Recently, however, transformation of nonimmortalized human cells has been achieved with combinations of oncogenes and tumor suppressor genes in further experiments by Weinberg and coworkers.[4] These experiments reinforce the point that dominantly acting oncogenes are critical, but not sufficient, components in the sequential progression of gene changes that lead to cancer.

Oncogenes Are Activated in Cells in a Variety of Ways

Oncogenes are activated in cancer cells in a variety of ways, all of which represent different forms of mutagenesis. In each case, the DNA sequence of a proto-oncogene or its transcriptional regulatory region is altered, but the means of alteration may be responsible for different effects on the activity of the protein ultimately expressed.

Insertional Mutagenesis

One means of oncogene activation is genomic insertion of a retroviral promoter, which can then activate the transcription of a particular downstream proto-oncogene while not necessarily altering the protein product of that gene. This mechanism of mutagenesis was first discovered with respect to the avian c-*myc* gene, the transcription of

Copyright © 2003, Mosby, Inc. All rights reserved.

Table 44-1
INHERITED NEOPLASTIC SYNDROMES WITH KNOWN ASSOCIATED GENES

Disease	Chromosome Alteration	Chromosome Instability or Tumor Suppressor Gene	Associated Neoplasia
Ataxia telangiectasia	11q23	*ATM*	Non-Hodgkins lymphoma, stomach carcinoma, breast carcinoma
Beckwith-Wiedemann syndrome	11p15	*WT2*	Wilms tumor, adrenal cortical carcinoma, hepatoblastoma, rhabdomyosarcoma
Bloom syndrome	15q26	*BLM*	Leukemias, gastrointestinal cancers
Breast cancers	11q23 17q21 13q12	*ATM* *BRCA1* *BRCA2*	Breast carcinoma
Familial adenopolyposis coli (FAP)	5q21	*APC*	Colorectal adenocarcinoma
Hereditary non-polyposis colon cancer (HNPCC)	2p16 3p21	*MSH2* *MLH1*	Colorectal adenocarcinoma
Fanconi anemia group C	9q22	*FACC*	Leukemias, squamous cell carcinoma
Li-Fraumeni syndrome	17p13	*p53*	Breast, colon, lung carcinomas, bone, various sarcomas, brain tumors
Multiple endocrine neoplasia type 1	11q13	*MEN1*	Pancreatic, pituitary, parathyroid, duodenal tumors
Multiple tumor syndrome	9q21	*p16(1NK4)-ARF*	Melanoma, AML, bladder cancer, gliomas, mesothelioma
Neurofibromatosis type 1 (Von Recklinghausen's neurofibromatosis)	17q11	*NF1*	Schwannoma, pheochromocytoma, astrocytoma
Neurofibromatosis type 2	22q12	*NF2*	Schwannoma, meningioma
Retinoblastoma	13q14	*RB*	Retinoblastoma, osteosarcoma, breast carcinoma, lung carcinoma
Von Hippel-Lindau syndrome	3p25	*VHL*	Cerebellar hemangioblastoma, retinal angioma, renal cell carcinoma
Werner syndrome	8p11	*WRN*	Sarcomas
Wilms tumor	11p13	*WT1*	Nephroblastoma
Xeroderma pigmentosum group A	9q22	*XPA*	Skin cancers

which was observed to be activated from an inserted avian leukosis virus retroviral LTR promoter.

Another related but distinct mechanism of activation is genomic integration of an acutely transforming retrovirus. In this case, the virus carries its own activated oncogene with it, under the control of its LTR promoter. This is the mechanism of oncogenic transformation effected by acutely transforming retroviruses in animals. In yet another insertional mechanism, a retrovirus that does not necessarily contain a transforming gene may insert in a coding region or a regulatory region of a particular gene, disrupting production of the product of that gene.

Mutational Alteration of Gene Transcription

A proto-oncogene can become an oncogene through changes in its transcriptional regulation that cause it to be ectopically expressed. That is, the sequence within a gene regulatory region may be disrupted, causing the gene to be activated in the wrong place or at the wrong time. This type of activation frequently accompanies chromosome rearrangements, as exemplified by the c-*myc* gene in some cases of Burkitt's lymphoma, in which the transcription of the gene is activated, whereas the protein product of the gene remains unaffected. In many cases of Burkitt's lymphoma the c-*myc* gene undergoes a well-characterized translocation from its position on chromosome 8 to a position on chromosome 14, where it is subject to transcriptional activation by powerful immunoglobulin gene enhancers. In that mechanism, an ectopic expression of the gene is induced while the actual protein product of the gene remains normal.

Mutational Alteration of the Protein Coding Sequence

One mechanism of oncogene activation is mutation to alter the protein product of a particular proto-oncogene. For example, point mutations in the *ras* gene at codon 12 are known to result in an increased affinity of the *ras* protein for GTP, leading to activation of growth signal transduction pathways. Mutation to alter either gene regulation or protein structure may be induced by ionizing radiation as well as by the formation of DNA adducts resulting from exposure to chemical carcinogens. It has been noted that the vast majority of cancers are caused by exposure to chemical carcinogens. While these carcinogens certainly include many synthetically produced or released chemicals, they may also include chemicals generated by activities such as ingesting and metabolizing food. For example, oxygen free radicals generated as a normal metabolic by-product are believed to be responsible for most accumulating, inevitable DNA damage.

Chromosome Translocation to Generate an Aberrant Fusion Protein

Chromosome translocation frequently puts the product of one gene in a position to form an aberrant fusion protein

Copyright © 2003, Mosby, Inc. All rights reserved.

with the product of another gene. A thoroughly studied example of this mechanism is the chromosome 9:22 translocation that results in formation of a BCR-Abl fusion protein in chronic myelogenous leukemia (CML). In that case, the tyrosine kinase activity of Abl is altered, subject to characteristics of its BCR fusion. This mechanism is frequently associated with alteration in the characteristics of a variety of transcription factors, each of which may alter the course of cell differentiation, leading to cancer.

Selective Gene Amplification

One frequent mechanism of oncogene activation is selective gene amplification. In this mechanism, a chromosome region including, but not limited to, the relevant oncogene is multiply replicated relative to the genomic DNA. It is not fully understood how one segment of a chromosome is replicated relative to its flanking DNA sequences, but many investigators believe the process involves generation of a large extrachromosomal circular segment of DNA, through an aberrant recombination event, which can replicate autonomously. In cultured cells at an early passage following an amplification event, many small extrachromosomal segments containing the amplified region can be seen in metaphase spreads, and these appear almost as tiny chromosomes. These amplification products are termed *double minutes*. At a later stage following amplification, the amplified region can be visualized as a chromosomally integrated, homogeneously staining region (HSR). It is not known whether the HSR represents reintegration of extrachromosomally amplified material. Amplification has the effect of increasing the protein product of any active gene in the amplified region. It is known that in certain cases amplification arises in response to selective pressure. For example, in cancer cells treated with methotrexate or aminopterin, the dihydrofolate reductase gene, *DHFR*, may be amplified. This has the effect of reducing the effect of the chemotherapy and thus represents a survival mechanism for cancer cells. Examples of amplified oncogenes include the *myc* gene family members c-*myc*, l-*myc* and n-*myc*, each of which has been found to be amplified in small cell lung carcinoma. If one member of this family is amplified, other members of the family generally are not, leading to the notion of redundant intracellular function for the protein products of those genes. The *myc* gene family members are also amplified in several other cancers. c-*myc* is amplified in colon and breast carcinomas. n-*myc* is amplified in neuroblastoma and is associated with a poor prognosis.[5] Another example of selective amplification is the *ErbB-2* gene in breast cancer. As in the case of c-*myc* and breast cancer, amplification of *ErbB-2* is seen to occur at a late stage in cancer development and is associated with a poor prognosis.

Growth Factors and Growth Factor Receptors as Oncogenes

Most oncogenes are altered forms of genes that serve a normal function in pathways that convey a signal from outside of the cell to the cell nucleus in order to stimulate proliferation. The sequences of several oncogenes resemble those of extracellular growth factors, and the sequences of several more resemble those of growth factor receptors. For example, the sequence of the N-terminal 109 amino acids of the β-chain of platelet-derived growth factor (PDGF) is nearly identical to that of the protein $p28^{sis}$, the product of the transforming gene, *v-Sis* of the simian sarcoma virus. On the other hand, the *v-Erb-B* protein has sequence homology to the transmembrane and cytoplasmic domains of the epidermal growth factor (EGF) receptor. The cytoplasmic domain of the EGF receptor was revealed to possess tyrosine kinase activity, and it was subsequently shown that binding of the receptor to its ligand results in autophosphorylation of tyrosine residues in the cytoplasmic domain. This phosphorylation of tyrosine residues is a recurring theme among signal transduction proteins that can become oncogenes. The first tyrosine kinase to be discovered, in fact, was the *Src* protein of Rous sarcoma virus. Src is not itself a growth factor receptor, but rather a protein active near the cell membrane in signal transduction. It is now known that there are multiple growth factor receptors that utilize autophosphorylation of tyrosine residues to mediate signal transduction. These receptors are termed *receptor tyrosine kinases* (RTKs).

The RTKs are transmembrane proteins that contain an extracellular ligand-binding domain, a transmembrane domain, and cytoplasmic tyrosine kinase and carboxy-tail domains. The RTKs are capable of some fluidity within the cell membrane. It is believed that in response to ligand binding the receptors form dimers or higher oligomers, triggering autophosphorylation of the intracellular cytoplasmic domains. The tyrosine kinase activity of the receptors is essential for initiating an intracellular signal cascade mechanism.

Oncogene members of the RTK family can be activated by a variety of genetic alterations. Several such alterations involve the extracellular ligand-binding region of receptors, in which case they may create a receptor molecule that is constitutively active even in the absence of ligand. As mentioned, the *v-Erb-B* oncogene is a truncated form of the EGF receptor, lacking the ligand-binding domain. The *v-Ros* oncogene also has a large deletion of the ligand-binding domain. In other RTK oncogenes, however, mutations in either the transmembrane or tyrosine kinase domains have been observed to enhance the transforming potential. As noted, the *Erb-B2* gene is amplified in certain cases of breast cancer. This has the effect of increasing the number of cell surface receptors, thereby enhancing the response of the breast cell to the relevant growth factor ligand.

Autocrine and Paracrine Loops

The interplay between growth factors and receptors can create situations highly conducive to tumor growth.[6] One example of this is the autocrine loop, which can arise when a cell produces a growth factor to which its own receptors respond. If, for example, a cell has an activated *Sis* oncogene and PDGF receptors on its cell surface, then it will overproduce a growth factor to which its own receptors respond by signaling for increased proliferation. A similar loop can exist if a cell overproduces a growth factor receptor that responds to a factor that is also produced by the cell. That may be the case in cells that possess an amplified *Erb-B2* gene. It is now recognized that paracrine loops may

Copyright © 2003, Mosby, Inc. All rights reserved.

be very important in the development of certain solid tumors. A paracrine loop can exist when two different cell types within a tissue each respond to a growth factor produced by the other. It is important to note that only one of the two cell types may have an activated oncogene and that thus only one of the types may constitute the tumor. This type of paracrine loop highlights the fact that normal cells are a component of many tumors and that the presence of such cells may be an important factor in tumor development.

Oncogenes in Intracellular Signal Transduction Pathways

The binding of a growth factor to its cell surface receptor triggers an intracellular response that culminates in a signal molecule entering the cell nucleus and activating gene transcription and/or DNA replication. This process of conveying a signal from the cell surface to the nucleus is called signal transduction. Several different pathways of signal transduction have now been identified, and they all have one feature in common: they rely on cascades of protein phosphorylation reactions involving protein kinases located at different positions in the cell. One such pathway, the Ras-MAP kinase pathway, is illustrated in Figure 44-2. This pathway is notable because several components of it are genetically altered in a variety of neoplasms. One component, Ras, is so frequently altered that it will be considered in detail in the next section. In this pathway, Grb-2 and Shc are adaptor proteins that recognize and bind to phosphorylated tyrosine residues in the intracellular domains of an activated RTK. Sos (son of sevenless) is a protein that is recruited to the inner surface of the cell membrane by its association with Grb-2. Sos is, in turn, a guanine-nucleotide exchange factor that activates Ras. Sos promotes the release of GDP by Ras and the subsequent binding of GPT, which configures Ras for active signal transduction. Several proteins can affect the Ras-GTP interaction. One such set of proteins are called GAP proteins or GTPase-activating proteins. These proteins play an inhibitory role in Ras activation by promoting GTP breakdown. One important GAP protein is neurofibromin, encoded by the neurofibromatosis tumor suppressor gene, *NF-1*. Activated Ras binds to and activates the serine-threonine protein kinase, Raf. The details of this activation are not completely known, but the activation appears to require participation of additional cellular proteins. A truncated form of Raf has been identified as a retroviral oncogene in animals. Raf phosphorylates and activates mitogen/extracellular signal-activated kinase (MEK), which, in turn, phosphorylates and activates mitogen-activated protein kinase (MAPK). Members of the MAPK family phosphorylate and activate transcription factors, exemplified in Figure 44-2 by Fos and Jun, which act in the cell nucleus to activate transcription. In this

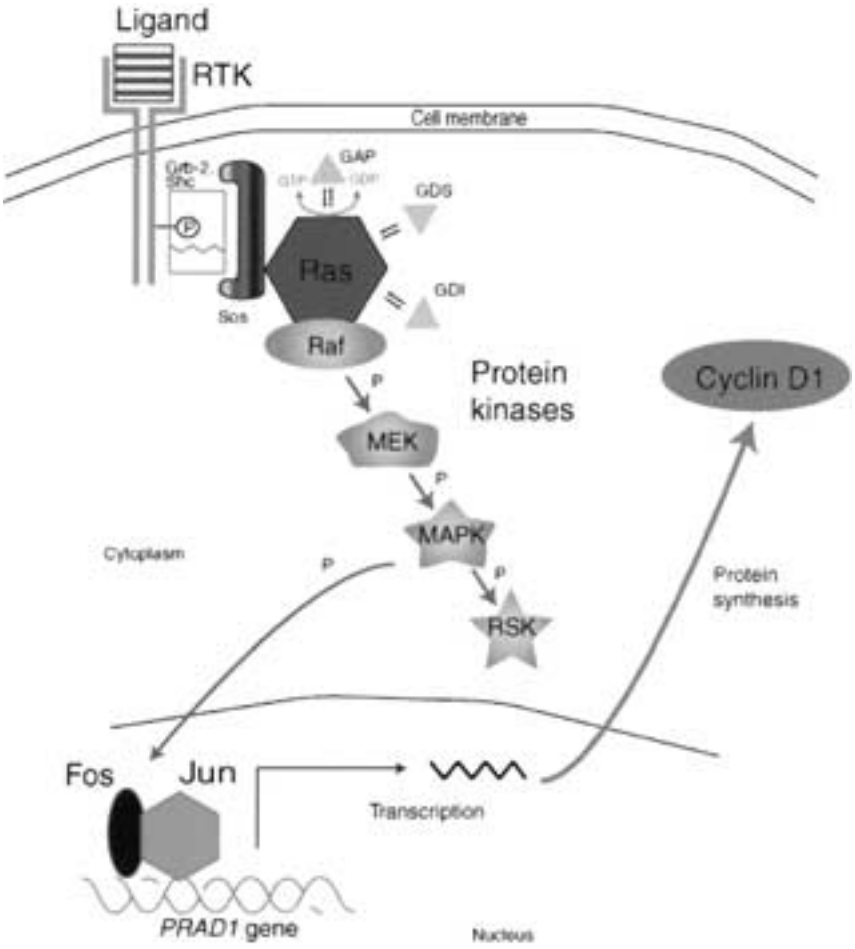

VIEW IMAGE

FIGURE 44-2 The Ras-Map kinase pathway for intracellular growth factor signal transduction. The figure depicts signal transduction initiated by binding of a generalized growth factor to a dimerized receptor tyrosine kinase (RTK) at the cell plasma membrane. Ras is recruited to the inner surface of the membrane by the proteins shown in response to internal phosphorylation of tyrosine in the RTK. In its active GTP-bound form, Ras interacts with and activates the protein kinase Raf, initiating a cascade of protein phosphorylation events denoted by *P*. A GTPase-activating protein, GAP, interconverts active and inactive Ras forms. Mitogen-activated kinase (MAPK) can phosphorylate several transcription factors that enter the nucleus, as exemplified here by Fos and Jun, which together activate transcription of several genes, including the *PRAD1* gene, which encodes the protein cyclin D1. The protein kinase RSK is involved in translational aspects of protein synthesis. Mutation of genes encoding several proteins in this pathway can lead to self-sufficiency of growth signaling independence of the extracellular factor. (See Color Plate 1)

Copyright © 2003, Mosby, Inc. All rights reserved.

figure the gene *PRAD-1* is shown being activated. *PRAD-1*, itself oncogenically mutated in some cancers, encodes the protein cyclin D1, which plays a role in traversing the G1-S boundary in the cell cycle. Other transcription factors besides Fos and Jun may also be phosphorylated by MAPK. While activated Fos and Jun are capable of oncogenic transformation of cells in culture, they have not yet been linked to any human tumor. The activated protein kinase RSK phosphorylates certain substrates that facilitate protein translation. It is notable that this particular signal transduction pathway involves both tyrosine protein kinases (RTK) and serine-threonine protein kinases (MEK, MAPK, and RSK). Several other similar pathways are at various stages of elucidation, and certain of these may also be activated by Ras.

Two signaling pathways that are independent of Ras and that are known to be involved in certain cancers have recently been characterized to some degree. These are the Wnt pathway and the Hedgehog/Patched pathway. The Wnt proteins are members of a large family of ligands that mediate signaling related to tissue development. Wnt binds to the receptor Frizzled, triggering a cascade that culminates in translocation of the protein β-Catenin to the cell nucleus. β-Catenin had previously been identified as a protein involved in forming links between the intracellular domains of cadherins and the cytoskeleton, and its activity in the nucleus was thus surprising. In the nucleus, β-catenin interacts with the TCF/LEF transcription factor to activate genes involved in cell growth. The *Wnt* oncogene in mice is activated by integration of mouse mammary tumor virus, but human *Wnt* has not yet been linked to any tumor. The β-catenin gene, however, is mutated in several neoplasms including colon carcinoma and melanomas. The Hedgehog/Patched pathway is also involved in tissue development. Its arcane nomenclature stems from the fact that the pathway was largely worked out in *Drosophila*, where gene mutations can frequently have dramatic phenotypes. In *Drosophila* the Wnt and Hedgehog/Patched pathways frequently oppose each other in the development of polarized tissue structures. The secreted ligand Hedgehog binds to the receptor Smoothened, which has multiple transmembrane domains, triggering a cascade leading to cell growth. Smoothened activity is normally inhibited by another protein, Patched, and binding of Hedgehog relieves that inhibition. Mutations in the human homolog of Patched are detected in the hereditary nevoid basal cell carcinoma.

Ras Gene Activation in Multiple Neoplasms

The *Ras* genes are paradigmatic examples of genes that undergo dominant gain of function related to oncogenic transformation as a result of mutation of one allele. Members of the *Ras* gene family are mutated in approximately 30% of all human tumors and are thus the most frequently encountered oncogenes. In addition to their frequent mutation in lung and colon cancer, *Ras* mutations are detected in more than 90% of cases of pancreatic cancer. Among the known members of the *Ras* gene family are H-*ras* and K-*ras*, both of which are homologous to genes originally discovered as retroviral transforming genes. H-*ras* encodes a 21 kDa protein that, as described in the last section, is a GTP-binding signal transduction protein. Binding of GTP to Ras induces a conformational change in the protein that activates it for signal transduction to downstream proteins. Ras also hydrolyzes GTP to GDP, and bound GDP is inhibitory to activation. Most mutations in Ras genes are point mutations in codons that inhibit the ability of Ras to hydrolyze GTP. Codons 12 and 61 are the ones most frequently mutated. Little is known about differences in the functions of various Ras family members, but they appear to play important roles in different cell types. H-*ras* is most frequently mutated in colon cancer, and K-*ras* is most frequently mutated in pancreatic cancer. N-*ras* has been detected in neuroblastoma. Intriguingly, certain tumors have no *Ras* mutations. For example, no primary neuronal tumors have been found with *Ras* mutations. In many of these tumors, however, inactivating mutations are detected in the *NF-1* protein, neurofibromin, which is inhibitory to Ras activation. Therefore, activated *Ras* may be an important factor in development of these tumors as well.

The c-*myc* Oncogene in Burkitt's Lymphoma

The c-*myc* gene is located near the telomeres of the long arms of chromosome 8, at band 8q24. It consists of three exons that encode a protein that serves, among other possible functions, as a transcription factor. The Myc protein, together with a partner protein, Max, activates several genes involved in stimulating cell proliferation. Myc also plays a role in immortalization of cells, that is, allowing the cells to escape senescence after several rounds of cell division. Mutations in c-*myc* in the B-cell tumor, Burkitt's lymphoma, involve chromosome translocations. As opposed to mutations in *Ras* genes, mutations in c-*myc* frequently do not alter the protein structure at all. In approximately 75% of cases of Burkitt's lymphoma, the c-*myc* gene is translocated to the long arm of chromosome 14, to band 14q32. In these cases the c-*myc* gene is placed in the transcriptional control region of the immunoglobulin heavy chain (C_μ) gene. In 25% of cases a portion of either chromosome 2 or 22 is translocated to chromosome 8, and in these cases c-*myc* is placed in the transcriptional control region of immunoglobulin light chain loci. In other words, in virtually every case of Burkitt's lymphoma, the c-*myc* gene, which is normally minimally active in B cells, is placed under the control of a control region promoting high transcriptional activity, that is, the control region of a gene making antibodies for the B cells. Thus, activation of the c-*myc* gene usually involves increased production of the Myc protein rather than a change in the structure of the encoded protein. In Africa, Burkitt's lymphoma occurs in a geographic belt that coincides with a belt of Epstein-Barr virus (EBV) infection, and most cases of Burkitt's lymphoma involve B cells infected with that virus. For a long time it was suspected that EBV was a causative agent of Burkitt's lymphoma. In the United States, however, most cases of Burkitt's lymphoma do not involve EBV infection, although all cases show translocations involving c-*myc*. It is now believed that EBV helps to promote the development of Burkitt's lymphoma by promoting clonal expansion of populations of B cells. This may provide a favorable environment for expansion of a clone containing, or about to contain, a critical chromosome 8 translocation.

Copyright © 2003, Mosby, Inc. All rights reserved.

Translocations That Create Oncogenic Fusion Proteins

The Philadelphia Chromosome

In more than 90% of cases of chronic myelogenous leukemia (CML), cytogenetics reveals the presence of a small, readily identifiable chromosome known as the Philadelphia chromosome. This chromosome is also present in approximately 20% of cases of acute lymphocytic leukemia (ALL) and 5% of acute myelogenous leukemia (AML). This aberrant chromosome is now known to be the result of a translocation between chromosomes 9 and 22. In this translocation, the C-terminal portion of the coding region of the c-*abl* gene, located near the telomeres of chromosome 9, is translocated to a region of chromosome 22 called the breakpoint cluster region (bcr). This translocation is an example of a phenomenon now known to be very widespread in neoplasia, that is, the generation of an oncogenic fusion protein. The N terminus of this new chaemeric protein is a portion of a protein of unknown function called bcr, and the C terminus is that portion of c-*abl* containing tyrosine kinase activity. In most cases of CML a bcr-abl fusion protein of 210 kDa is generated, while in most cases of ALL the fusion protein is 190 kDa. In both cases, the bcr-abl fusion protein has enhanced tyrosine kinase activity compared to that of intact Abl. The normal cellular functions of Abl are not completely known, but as tyrosine kinases are important in intracellular signaling, it is presumed that enhanced kinase activity would lead to enhanced downstream signaling effects.

Translocations Involving Transcription Factors

Recently, several chromosome translocations that create oncogenic fusion proteins in various leukemias have been characterized. Intriguingly, many of these involve transcription factors. In pre-B-cell lymphoblastic leukemia a t(1:19) translocation creates the E2A-PBX1 fusion protein, in which the transcriptional activation domain from E2A is fused to the DNA-binding homeodomain of PBX1. This allows E2A to strongly activate transcription from promoter regions containing the PBX1 binding site. In a very similar situation, the gene encoding another homeoprotein, hrx, is disrupted by translocations at 11q23 occurring in myeloid and lymphoid leukemias. In these cases, hrx may be fused with a wide variety of other proteins. It is believed that most of the fusion partners of hrx possess dimerization domains that can enhance DNA-binding effects of the hrx portion of the protein.

TUMOR SUPPRESSOR GENES

A tumor suppressor gene is defined as a gene in which both alleles must be inactivated in order for cancer to develop. Although tumor suppressor genes are frequently called recessive oncogenes, a *predisposition* to cancer is inherited as a dominant phenotype. The proteins encoded by tumor suppressor genes generally function to confer a protective effect against cancer. Mutations thus cause a loss of function. This is in distinct contrast to dominantly acting oncogenes, which encode proteins that gain a function, usually not related to the original function of the protein, that leads to cancer.

Familial Cancer Syndromes

Mutations in tumor suppressor genes are responsible for inherited cancer syndromes. This phenomenon is explained by the *two-hit* hypothesis of Knudsen.[7] In that scenario, a mutation in one allele of a tumor suppressor gene is inherited through the germ line. This does not cause cancer, but since every cell of the inheriting individual carries one mutated allele, it becomes statistically more likely that a second mutation will be acquired in the remaining allele. Most, but not all, familial cancer syndromes involve several kinds of cancer. It remains to be explained why different tumor suppressor genes predispose to specific kinds of cancers.

Retinoblastoma and RB

Retinoblastoma is the most common malignant intraocular tumor of childhood. While it is rare, it accounts for nearly 1% of all childhood neoplasms. The disease is believed to originate in developing cells of the cone lineage. Retinoblastoma occurs in either a hereditary form or a sporadic form. In the hereditary form, aberrations can be detected in chromosome band 13q14 in every somatic cell of the body, indicating germ line transmission of a defective allele. In the tumor cells, both alleles of the target gene at this band, termed the *RB* gene, are defective. In the sporadic form of retinoblastoma, somatic cells do not reveal *RB* aberrations, but again, the tumor cells possess two defective *RB* alleles. The differences between the hereditary and sporadic forms of retinoblastoma are satisfactorily accounted for by the two-hit hypothesis put forth by Knudsen and summarized in Figure 44-3.

Approximately 40% of all retinoblastoma cases are hereditary, and in these cases the disease is usually bilateral, that is, affecting both eyes of an individual. In the hereditary form, the affected individual does not inherit the tumor but rather a predisposition to acquiring the tumor. That predisposition is transmitted in the form of one defective *RB* allele. That inherited defect is the first hit in the two-hit progression. Evidently, the possession of one normal *RB* allele provides sufficient protein to retain its tumor suppressive activities. Hit two is an environmentally acquired defect in the remaining *RB* allele, and this occurs in cells giving rise to the tumor. It remains mysterious why cells in the retina preferentially acquire hit two since, after all, every cell of the body possesses hit one. It is quite conceivable that cells of the retina respond to light radiation in ways that, as an unintended by-product, facilitate mutagenesis. This is consistent with the observation that many hereditary retinoblastomas are bilateral, that is, that the statistical probability of acquiring hit two in a retinal cell is so high that the event can occur twice in the same individual. In the sporadic form of retinoblastoma, hits one and two are both acquired. The sporadic forms may involve bilateral tumors, but most frequently they are unilateral. Of course, the probability of acquiring two hits in the *RB* gene is much lower than that of acquiring one hit. This accounts for the fact that the incidence of sporadic retinoblastoma is very low, affecting about 1 in 30,000 people.

Copyright © 2003, Mosby, Inc. All rights reserved.

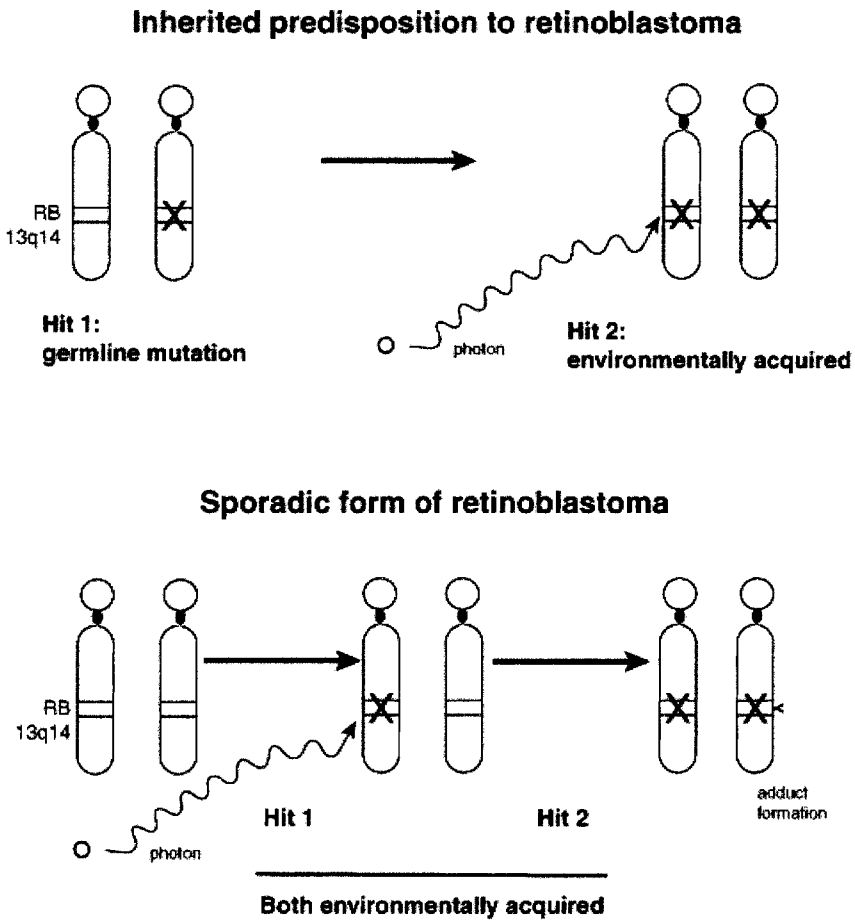

FIGURE 44-3 The two-hit hypothesis of tumor suppressor gene inactivation. This hypothesis was first promulgated by Alfred Knudsen[7] to explain the inheritance of a predisposition to neoplasia in familial neoplastic syndromes. It is exemplified here by inactivation of the *RB* gene on chromosome 13 in retinoblastoma. The essence of this hypothesis is that some people inherit an inactivating mutation of one allele of a tumor suppressor gene. Note that they thus dominantly inherit a predisposition to neoplasia, not the neoplasia itself. The predisposition is due to the fact that only one additional environmental hit is required for transformation.

VIEW IMAGE

Defects in *RB* are not exclusively associated with retinoblastoma. Retinoblastoma is a familial cancer syndrome potentially involving multiple tumors, and people who have had ocular tumors removed remain at risk for additional tumors, most notably osteosarcoma and mammary carcinoma. In addition, defects in the *RB* gene have been detected in a wide variety of cancers not associated with retinoblastoma. Defects in the structure or expression of the Rb protein have been found in a high percentage of both small-cell and non-small-cell lung carcinomas. Such defects have also been found in approximately 22% of all mammary carcinomas.

Li-Fraumeni Syndrome and p53

Li-Fraumeni syndrome is an inherited predisposition to develop a wide variety of cancers.[8] Comparable to the relationship described above between retinoblastoma and a mutated *RB* gene, the predisposition to cancer in Li-Fraumeni syndrome results from inheritance of a single mutated *p53* gene at chromosome band 17p13. Cancers in different organs thus develop via acquired mutations in the remaining *p53* allele, consistent with the two-hit hypothesis of Knudsen. Of all known tumor suppressor genes, *p53* is implicated in the widest variety of neoplasms, including high percentages of the three most common cancers: those of the lung, colon, and breast. The p53 protein is mutated or absent in a majority of cases of small-cell lung carcinoma. Similarly, p53 is inactivated in approximately 75% of cases of colorectal carcinoma. p53 has also been implicated in hepatocellular carcinoma, glial cell tumors of the brain, certain cases of malignant mesothelioma, and many additional neoplasms.

The gene encoding p53 was actually discovered prior to that encoding Rb, but it was not initially recognized as a tumor suppressor gene. In part this was due to the fact that certain mutations of p53 confer upon it a dominant-negative activity. That is, structural alterations can confer upon the mutated p53 protein the ability to interfere with activity of the protein encoded by the remaining normal allele. In that situation, mutation of p53 more closely resembles that of a dominantly acting oncogene than that of a tumor suppressor gene. The p53 protein is a transcription factor involved in pathways of response to DNA damage. As such, it either protects a cell against oncogenic transformation or ensures that a cell with excessive DNA damage undergoes programmed cell death. As will be described subsequently, several oncogenic DNA viruses encode proteins that bind to and inactivate p53 and/or Rb. They presumably do so by mimicking the protein-binding capacities of normal cellular proteins. Figure 44-4 summarizes the relationship between inactivation of p53 by mutations and by interaction with viral proteins, both of which target regions in the p53 DNA-binding domains.

Li-Fraumeni syndrome was recognized as a familial cancer syndrome only in the mid-1980s.[8] The reason for this slow recognition is simply that the wide variety of cancers

Copyright © 2003, Mosby, Inc. All rights reserved.

for which a predisposition is inherited obscures the familial relationship. For example, breast cancer in one family member may not be perceived as related to, say, brain tumor in a cousin. The functional activities of tumor suppressor gene products, including p53, are being intensively studied, and results are yielding important information regarding potential courses of therapy. Using Rb and p53 as examples, these activities are discussed in some detail below.

Guardians and Gatekeepers

The protein products of tumor suppressor genes have commonly been characterized in terms of their classification as either *guardians* or *gatekeepers*. These two broad categories reflect the protective roles of many tumor suppressor gene products. The underlying concept is that guardians prevent the accumulation of DNA damage that would lead to oncogenic transformation, whereas gatekeepers prevent cells that have accumulated such damage from passing through critical cell cycle checkpoints. While useful in considering protein functions, our now detailed knowledge of cell cycle regulatory pathways renders this classification a bit simplistic. The multiple functions of certain tumor suppressor gene products can blur the distinction between these classes. For example, the p53 protein could be considered either a guardian or a gatekeeper. It is a transcription factor, the activity of which is enhanced by DNA damage. The p53 protein activates a variety of cellular processes leading to DNA repair or, in the case of extensive DNA damage, leading to exit of the cell cycle through apoptosis. Thus, p53 guards against a highly mutated cell progressing to cancer. On the other hand, one gene induced by p53 is that encoding the CDK inhibitor, p21. Since p21 inhibits phosphorylation of the retinoblastoma protein, Rb, it can prevent the G1-S transition. Thus, transcriptional activating activity of p53 could also qualify it as a gatekeeper. Rb could be considered a gatekeeper since in its hypophosphorylated form it binds several regulatory proteins and prevents them from mediating the entry into S-phase. In G1 of the cell cycle, or in response to several growth signals, Rb becomes hyperphosphorylated, upon which it releases regulatory proteins that promote entry to S-phase. The phosphorylation of Rb is sensitive to signals stemming from DNA damage. Thus, Rb controls passage through an important checkpoint for cell proliferation. On the other hand, since several proteins regulating Rb phosphorylation are sensitive to DNA damage, this pathway could be perceived as guarding against accumulation of such damage. Figure 44-5 summarizes certain interactive aspects of Rb- and p53-related pathways of cell cycle control.

The Retinoblastoma Protein, Rb, and Cell Cycle Control

RB is the first gene to be characterized as a tumor suppressor gene. It had been known for decades that childhood retinoblastoma is associated with aberrations at chromosome band 13q14. In the mid-1980s the gene was

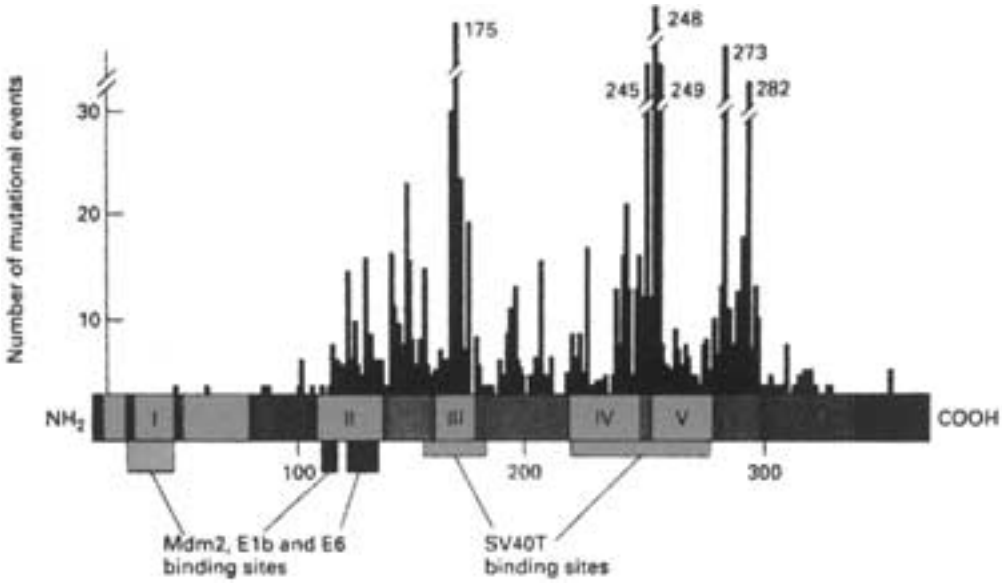

FIGURE 44-4 Distribution of mutations in the *p53* tumor suppressor gene in various tumors. The p53 protein is schematized, and amino acids are enumerated on the x-axis.[19] On the y-axis, numbers of mutations at each amino acid position are presented as recorded in a variety of tumors. The majority of mutations occur in the central DNA-binding domains of p53. Note that regions in these domains are also targeted for binding by viral proteins that inactivate p53. E1b is an adenoviral protein, E6 is a papilloma viral protein, and the SV40 large T antigen is a simian virus 40 protein. The site specificity of the mutations is due in part to the environmental agents that caused them. For example, certain sites are preferentially mutated by aflatoxin B1 in hepatocellular carcinoma, and other sites are preferentially observed in lung adenocarcinoma, presumably mutated by benzo-a-pyrene or other agents in cigarette smoke. (From Denissenko MF, Pao A, Tang M, Pfeifer GE. Preferential formation of benzo [a]pyrene adducts at lung cancer mutational hotspots in P53. Science 1996;274:430. Copyright 1996 American Association for the Advancement of Science.) (See Color Plate 2)

VIEW IMAGE

Copyright © 2003, Mosby, Inc. All rights reserved.

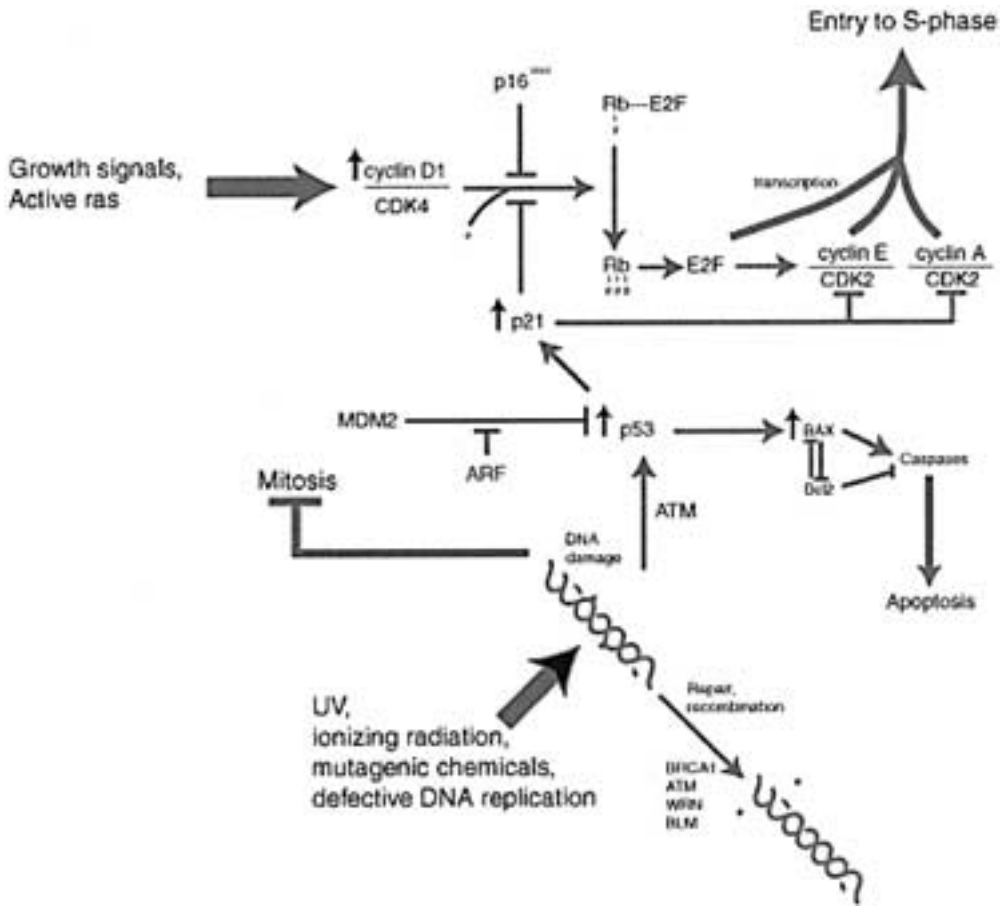

VIEW IMAGE

FIGURE 44-5 Involvement of several tumor suppressor gene products in pathways leading to cessation of cell growth or to apoptosis in response to DNA damage. Processes leading to activated cell proliferation, that is, entry to S-phase of the cell cycle, are indicated in green. Processes inhibiting cell proliferation are indicated in red. In response to DNA damage, such as that caused by ionizing radiation, for example, the ATM protein kinase phosphorylates and activates p53. The p53 protein, in turn, through effects on gene transcription, activates pathways leading to either apoptosis or cessation of cell growth. Transcription of the *p21* gene is activated by p53. The p21 protein is an inhibitor of both CDK2, necessary for initiation of DNA replication, and CDK4, which catalyzes phosphorylation of Rb. Hyperphosphorylation of Rb is necessary to trigger events leading to the G1-S transition. Two different products of another tumor suppressor gene, *p16/ARF*, play important roles in inhibiting cell proliferation. ARF binds to MDM2 and prevents it from targeting p53 for proteolytic destruction. The p16 protein specifically inhibits CDK4 kinase activity, preventing phosphorylation of Rb. Several proteins are indicated in magenta. It is believed that at least one of the four genes encoding these proteins, *ARF/p16*, *cyclin D1*, *p53*, and *Rb*, is mutated in every neoplasia. (See Color Plate 3)

identified and sequenced by W.-H. Lee and colleagues, revealing its product to be a protein of approximately 110 kDa.[9, 10] The phosphorylation of Rb is cell cycle dependent. In mid-G1, phosphorylation is begun by the cyclin D1/CDK4 protein kinase. Rb is then further phosphorylated by other D cyclins and CDKs and by cyclin E/CDK2. Rb, when hyperphosphorylated, releases a transcription factor, E2F1, which activates several genes necessary for entry into S-phase. Another important function of Rb is to repress transcription by binding to transcription factors, such as E2F1, when they are bound to gene promoters. To do this, Rb attracts the enzyme histone deacetylase, which configures chromatin to be inactive. Rb phosphorylation is inhibited by the protein p21, and the p21 gene is in turn upregulated by p53. Thus, there is an intimate link between the pathways regulated by Rb and p53. The product of another tumor suppressor gene, $p16^{INK4}$, also inhibits Rb phosphorylation. Both p21 and p16 block phosphorylation by the protein kinase CDK4, which is regulated by cyclin D1. Cyclin D1, in turn, is upregulated by the Ras-MAP kinase pathway, thereby promoting passage through the G1 start point of the cell cycle. It is believed that at least one of the following four genes is disrupted in virtually every form of cancer: *RB*, *p53*, $p16^{INK4}$, or *PRAD1* (the last encodes cyclin D1).

The p53 Protein and DNA Damage

The *p53* gene is the tumor suppressor gene most frequently mutated in cancer. The activity of the p53 protein is modulated by DNA damage. Association of p53 with another protein, MDM2, targets p53 for destruction. However, p53 is stabilized by phosphorylation catalyzed by

Copyright © 2003, Mosby, Inc. All rights reserved.

the protein kinase ATM. ATM may be a signal-transducing link between DNA repair enzymes, activated by DNA damage, and pathways activated by p53.[11] The *ATM* gene is itself a tumor suppressor gene mutated in many cases of breast cancer. Another protein, ARF, also stabilizes p53, in this case by inhibiting the action of MDM2. ARF is a gene product encoded by an alternate frame of the *p16* locus, and thus *ARF* is also a tumor suppressor gene. The protective functions of both p16 and ARF may be lost by a single mutation in the *p16/ARF* locus. The p53 protein, as a transcription factor, upregulates the gene encoding p21, which is an inhibitor of both CDK2 and CDK4 kinases. Thus, in response to DNA damage, pathways inhibiting cell cycle progression are activated by p53. The p53 protein also upregulates the gene for BAX, a protein activating caspase pathways leading to apoptosis.

Another aspect of p53 activity may serve to facilitate DNA repair. The p21 protein, upregulated by p53, performs an additional function separate from its ability to inhibit CDK kinases. p21 also binds to the protein PCNA and modulates its activity. PCNA is a processivity factor for DNA polymerase, and it may function in DNA recombination/repair pathways. The activities of the p53 protein are thus ordered in two somewhat disparate directions. Some functions are directed toward DNA repair, a process that facilitates cell survival. Other functions of p53 are directed toward eliminating cells with excessive DNA damage through apoptosis. The regulatory mechanisms through which p53 activities are directed to either DNA repair or apoptosis have yet to be fully elucidated.

Genome Instability Syndromes

Hereditary Nonpolyposis Colon Cancer

One class of tumor suppressor genes does not fit neatly into either the guardian or gatekeeper category. Several genes in this class encode proteins, the loss of function of which through mutation leads to genome instability. Frequently, these proteins are involved in DNA repair. For example, the *MSH2* and *MLH1* genes, mutated in hereditary nonpolyposis colon cancer, carry out steps in DNA mismatch repair. This disease is an inherited predisposition to colon adenocarcinoma that is not associated with familial polyposis. When both alleles of these genes are inactivated, the rate of mutation in an affected cell can increase up to 1000-fold. Thus, generations of affected cells accumulate mutations, ultimately culminating in oncogenic transformation. Any mutated gene that results in such genome instability is said to confer a mutator phenotype. Such genes constitute an unusual class of tumor suppressor genes since two mutated alleles can be inherited. In that case, the predisposition to cancer can be inherited in a recessive fashion.

Bloom and Werner Syndromes

Two genome instability syndromes, Bloom syndrome and Werner syndrome, are highly interesting because the mutated genes encode DNA helicases of the recQ family. The two genes are termed *BLM* and *WRN*, respectively. Bloom syndrome is associated with multiple leukemias and gastrointestinal cancers, and Werner syndrome is associated with multiple sarcomas. The enzymatic nature of the BLM and WRN helicases is to unwind DNA in a processive, ATP-dependent manner. While the exact functions of these two proteins are not known, such unwinding is an important aspect of DNA replication, recombination, and repair. Disruption of the *WRN* gene also leads to many changes characteristic of premature aging, including wrinkling, cardiovascular changes, cataracts, and others. Such changes due to inactivation of a single gene highlight the relevance of accumulating DNA damage to the aging process.

A Variety of Tumor Suppressor Genes Regulating Protective Mechanisms

Presently, *RB* and *p53* are the two most thoroughly characterized tumor suppressor genes and two of the most commonly mutated genes in all neoplasms. In fact, mutations or deletions in *p53* are currently the genetic aberrations most widely detected in cancer. In addition, as discussed with regard to viral causes of cancer, inactivation of the products of these two genes is sufficient to allow DNA tumor viruses' oncogenic potential. Nonetheless, the list of known tumor suppressor genes is expanding rapidly, and we are just beginning to appreciate the extent to which certain other such genes may be involved in neoplastic transformation. These genes encode proteins involved in highly diverse cell activities. In general, these processes confer a protective effect against neoplastic transformation, either by protecting the genome from damage or by ensuring that a cell with potential oncogenic damage does not continue to grow. The following discussion and the list in Table 44-1 are not compendia of known tumor suppressor genes, since that number is growing constantly, but rather a discussion of selected genes the functions of which are enhancing our understanding of tumor suppressive pathways. While the familial syndromes associated with defects in these genes include various cancers, in many cases they are not limited to cancer.

The Gene Mutated in Ataxia-Telangiectasia, ATM

The gene mutated in the genetic disorder ataxia-telangiectasia (AT), is critical in providing a protective effect against ionizing radiation. AT is characterized by cerebellar ataxia, enhanced sensitivity to ionizing radiation, immunodeficiency, and the evasion of cell cycle checkpoints leading to a predisposition to cancer. The gene *ATM*, for AT mutated, has been identified as a major tumor suppressor gene for breast cancer. The ATM protein is a protein kinase with multiple substrates within the cell. Cells cultured from individuals with AT are defective in the G1/S cell cycle checkpoint activated by radiation damage. This defect has been shown to be a consequence of a defective p53 response pathway. In this pathway, cells with extensive DNA damage are directed toward leaving the cell cycle and undergoing apoptosis. ATM phosphorylates p53 on serine residue 15, and this phosphorylation contributes to the activation of p53 and to its stabilization by countering the ability of protein MDM2 to target p53 for degradation. ATM phosphorylation of other cellular substrates is also undoubtedly important since the AT cells display a highly complex phenotype.

Copyright © 2003, Mosby, Inc. All rights reserved.

Transfection of AT cells to overexpress ATM restores the normal phosphorylation of p53 in response to ionizing radiation. Clearly, tumors with defects in the *ATM* or *p53* genes will show a reduced ability to respond positively to the therapeutic effects of radiation.

ARF *and* p16: *Unusual Overlapping Tumor Suppressor Genes*

The *INK4a-ARF* locus, at chromosome band 9q21, encodes two proteins, mRNAs, which are transcribed in the same direction from a single promoter. The two proteins, however, are completely distinct since they are generated from alternate reading frames, depending upon mRNA splicing. The proteins, p16(INK4) and p19(ARF), each display growth inhibitory properties, the first by influencing Rb checkpoint control and the second by influencing p53-mediated growth arrest. P16(INK4a) is an inhibitor of CDK4 and can prevent cyclin D1/CDK4 from phosphorylating Rb and thus from mediating the G1/S transition. The *INK4a* gene has been identified as a tumor suppressor gene in many cancers including melanomas. Mutations in the *INK4a* gene are capable of simultaneously inactivating ARF. ARF binds directly to both p53 and MDM2 and stabilizes p53 with regard to degradation. ARF can bind to p53-DNA complexes and can enhance induction of the CDK inhibitor, p21(CIP1). p21 inhibits both CDK4 and CDK2 and thus contributes to inhibition of cell proliferation. The overall effect of inactivation of the *INK4a-ARF* locus is to help the cell evade arrest at the G1/S checkpoint, and subsequent apoptosis, in response to DNA damage, including that arising from ionizing radiation.

BRCA1 *and* BRCA2 *in Breast and Ovarian Cancer*

These genes are notable because they are responsible for a high percentage of cancers specific for women. The two protein products, which are not homologous, frequently colocalize together, and they may function together. BRCA1 is probably a multifunctional protein. Evidence suggests that it can act as a transcription factor and that it is involved in upregulating the *p21* gene, thus paralleling p53. Alternatively, BRCA1 and BRCA2 may function in DNA recombinational repair. BRCA1 and BRCA2 both colocalize with Rad51 on the presynapsing regions of synapsing chromosomes in female meiosis.[12] Rad 51 is a human homolog of the bacterial RecA protein, which mediates strand invasion in recombination. BRCA1 may also affect ubiquitin ligation, a process involved in protein degredation, with resulting effects on chromatin structure. *BRCA1* and *BRCA2* are classic tumor suppressor genes in that the predisposition to cancer through mutation is inherited in a dominant fashion. Genetic inactivation of both *BRCA1* alleles in mice causes embryonic mortality. Figure 44-6 is a fluorescence photomicrograph demonstrating BRCA1 located in both basal (b) and luminal (l) epithelial cells of a breast tissue explant. High levels of BRCA1 are found in mitotic cells (*arrows*), as might be consistent with a role in recombination/repair. Yellow shows colocalization with vimentin, a basal cell marker, at the upper left and, with cytokeratin 19, a luminal cell marker, at the lower right. Staining for each of the latter two proteins is green.

NF-1 *and Von Recklinghausen's Neurofibromatosis*

The *NF-1* gene, located at chromosome band 17q11, encodes a protein, neurofibromin, which is an important GTPase-activating protein (GAP) inhibiting the activity of Ras proteins. Inactivation of this gene can thus lead to enhanced Ras pathway signaling in affected cells. Mutation in the *NF-1* gene leads to an inherited predisposition to Von Recklinghausen's neurofibromatosis, characterized by multiple nodules of peripheral nerve cell growth.

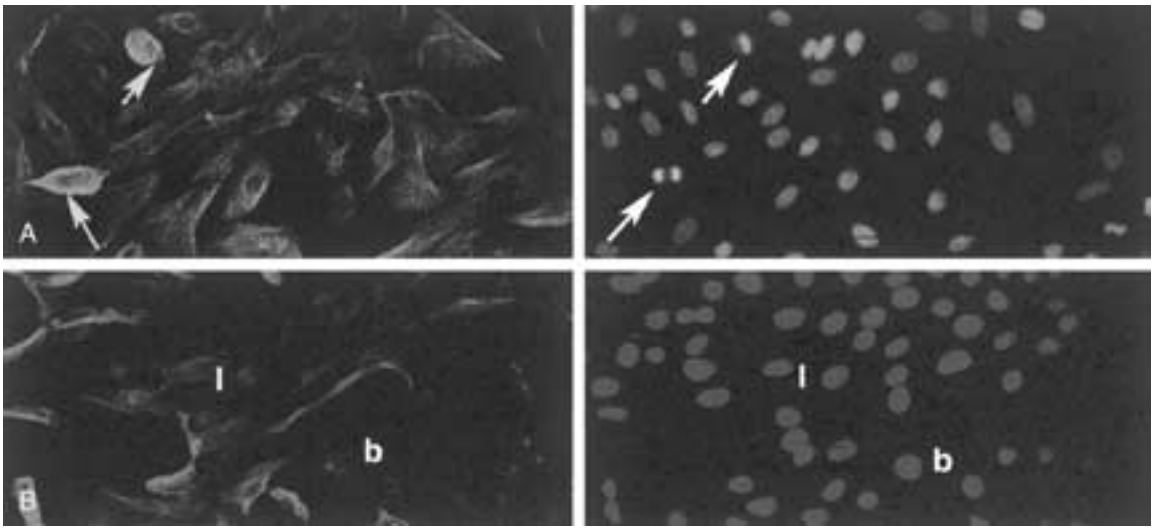

FIGURE 44-6 Presence of the breast cancer tumor suppressor gene product BRCA1 in both basal and luminal epithelial cells of the breast. BRCA1 is detected in the nuclei of both basal and luminal cell types when using double immunofluorescence labeling. *Left panel*: **A**, Edge of the basal outgrowth costained with MAbs to BRCA1 (red) and vimentin (green). **B**, Edge of luminal outgrowth costained with MAbs to BRCA1 (red) and cytokeratin 19 (green). *Right panel*: **A** and **B**, DAPI counterstain of the same fields of cells. Note: photo mask was left in the light path to help orient fields and is visible in some of the photographs. *b*, Basal; *l*, luminal. Arrows are identified in text. (Daniel DC. Dual immunofluorescence labeling with cell-specific markers localizes BRCA1 in both basal and luminal epithelial cells in primary outgrowth from noncancerous mammary ductal and alveolar preparations. Cell Tissue Res (1999) 298:481.) (See Color Plate 4)

VIEW IMAGE

Copyright © 2003, Mosby, Inc. All rights reserved.

PTEN: *A Tumor Suppressor Gene Encoding a Phosphatase*

The chromosome band region 10q23 is frequently altered in several neoplasms, including melanomas, endometrial carcinoma, and prostate tumors. A tumor suppressor gene in this region has recently been identified as a phosphatase that can dephosphorylate the intracellular second messengers phosphatidylinositol 3,4,5-trisphosphate and phosphatidylinositol 3,4-bisphosphate. These lipid phosphate molecules are phosphorylated in the phosphoinositol 3-kinase (PI-3 kinase) pathway, a growth signaling pathway distinct from the Ras-MAP kinase pathway, and their dephosphorylation exerts a growth inhibitory effect. Thus far, *PTEN* is the only phosphatase identified as a tumor suppressor.

WT-1 *and* WT-2 *and Wilms' Tumor*

Two genes on chromosome 11 are linked to an inherited predisposition to Wilms' tumor of the kidney. The *WT-1* gene, located at band 11p13, is a transcription factor containing a zinc finger, a chelated zinc amino acid motif that is usually involved in DNA binding. *WT-1* binds to a GC-rich DNA element and can act as either a transcriptional activator or a repressor, depending on its interaction with other factors. *WT-1* is expressed in developing kidney, testis, and ovary. Genitourinary tissues are thought to be sites of origin of Wilms' tumor. Less is known about the function of the *WT-2* gene, located at band 11p15.5, but inactivation of this gene is linked to Beckwith-Wiedemann syndrome, a familial neoplastic syndrome that includes kidney, adrenocortical, and liver tumors.

CIRCUMVENTING APOPTOSIS

It is clear that many of the genetic changes leading to cancer are involved in the circumvention of normal pathways leading to apoptosis. Apoptosis is programmed cell death. It is a process frequently accompanying normal tissue differentiation, in which case it is genetically controlled. Figure 44-7 shows apoptosis, darkly stained via an assay for DNA fragmentation, at a highly specific stage of mouse testicular development. Apoptosis is also invoked in the cellular response to DNA damage, and in this case it is an important protector from the development of neoplasia. Several reports have documented pathways of the apoptotic response of cells to ionizing radiation. In response to DNA damage, p53 upregulates the p21 CDK inhibitor and upregulates BAX, which through a convoluted pathway ultimately triggers a cascade of caspases, which are involved in proteolytic activity. Upregulation of p21 by p53 also blocks the cell cycle at the G1/S boundary. This is because p21 inhibits the CDK4- and CDK2-catalyzed phosphorylation of Rb and replicative enzymes responsible for entry into S-phase. Certain elements of the pathways of apoptosis relevant to ionizing radiation are depicted in Figure 44-4. The effects of p53 on DNA replication may also involve CDK2 inhibition at the onset of S-phase. CDK2 has been implicated in phosphorylation of MCM4, a protein that is part of a putative DNA helicase complex, consisting of MCMs 4, 6, and 7, that is required for initiation of DNA replication. MCM intranuclear levels are highly cell-cycle regulated, and reports indicate that MCM protein levels are

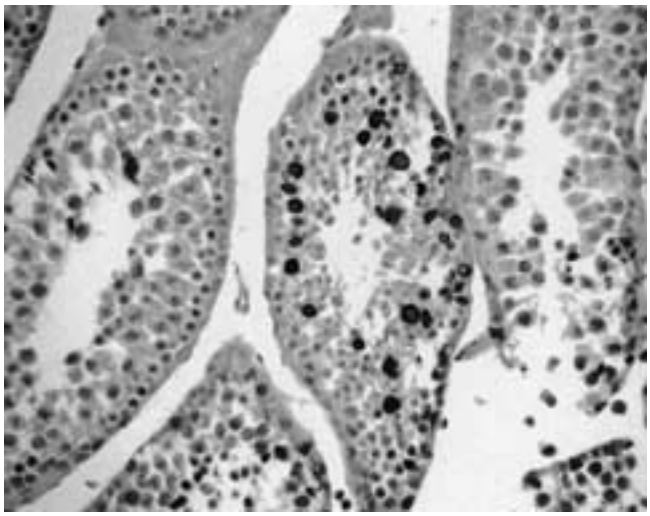

FIGURE 44-7 Apoptosis is highly stage-specific in normal spermatogenesis in the mouse. Shown is a section from normal mouse testis approximately 20 days after birth. Staining for apoptosis, or programmed cell death, is done by the TUNEL assay, which detects DNA fragmentation. This is early in spermatogenesis, but cells develop toward the center of the seminiferous tubule. Note that darkly stained apoptotic cells are visualized in a specific layer in development. Note also how apoptosis, which affects specific cells in a defined region, differs from necrosis, a nonprogrammed form of cell death that usually affects multiple contiguous cells in a focus. (See Color Plate 5)

VIEW IMAGE

preferentially elevated in oncogenically transformed cells. An example of selectively elevated MCM7 in ovarian cancer can be seen in Figure 44-8. In this case, the slower-growing cells of ovarian cysts are not stained, whereas the more aggressive malignant cells are.

It should be clear from the presented pathways that many of the tumor suppressor genes commonly altered in

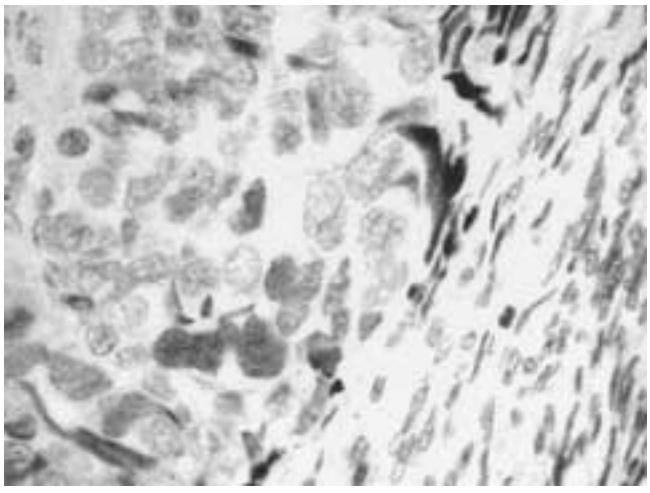

FIGURE 44-8 DNA replication protein MCM7 as a marker for ovarian cancer. Many recently developed tumor cell markers are proteins involved in DNA replication. MCM7 is part of an MCM 4, 6, 7 DNA complex essential for initiation of DNA replication. Its levels are cell-cycle regulated. Staining, visualized as red-brown, was with anti-MCM7 antibody and secondary antibody coupled to horseradish peroxidase. Note the high percentage of large tumor cells with mottled nuclear staining as opposed to the lack of staining of adjacent normal ovarian tissue on the right. (See Color Plate 6)

VIEW IMAGE

Copyright © 2003, Mosby, Inc. All rights reserved.

neoplasia are participants in apoptotic mechanisms. The importance of such alteration to treatment is becoming ever more clear. For example, if a tumor possesses inactive p53, one should carefully evaluate any treatment strategy that involves radiation or chemotherapeutic agents that damage DNA. If apoptosis were absent from tumor cells, such treatments would not be effective. Visually, apoptosis is characterized by chromatin aggregation around the inside of the nuclear membrane, nuclear fragmentation, and ultimately cell fragmentation. It is a process completely distinct from necrosis, another visually identifiable presentation of cell death. Necrosis involves general degrading of cell features, and it is not programmed. Necrosis usually involves all cells immediate to a traumatic focus, whereas apoptosis involves selected cells within a tissue area.

TELOMERASE AND ONCOGENIC TRANSFORMATION

It had been notably difficult to transform primary human cells to oncogenicity by transfecting them with activated oncogenes. As described in this chapter, such transformation could be achieved with mouse cells. Human cells, however, do not respond the same way. Recently, an important experiment was performed by R.A. Weinberg and colleagues.[4] They were able to transform primary human cells in culture by adding to them genes encoding SV40 large T antigen, which binds Rb and p53 and inhibits their activities; activated Ras, which provides a continuously active growth signal transduction pathway; and the catalytic subunit of human telomerase. Telomerase was the key to the success of this experiment.[13] The ends of chromosomes, termed *telomeres*, consist of long repeats of the sequence (in humans) of CCCTAA and TTAGGG. It is now known that the lengths of these repeats in mouse cells are considerably different from those in human cells, and thus the mechanisms for their maintenance may also differ. Continuously growing cells require telomerase for the following reason. The DNA of mammalian chromosomes is linear, and the telomeres can thus not replicate fully through normal DNA synthesis in each replication cycle because there is no position for a primer for the last Okazaki fragment to elongate the 3′ end. Multiple rounds of replication would therefore literally erode the ends of chromosomes. Telomerase can ameliorate this problem by supplying a template in the form of an RNA sequence bound to the protein.[13] Telomerase, denoted hTERT, essentially acts as a reverse transcriptase, using its RNA moiety as a template to synthesize blocks of DNA to elongate repeats at the 3′ overhang of one strand of the DNA end. In cells not oncogenically transformed, telomerase activity is absent or nearly so. Such cells can divide only a finite number of times before undergoing senescence. Telomere maintenance is required for indefinite proliferation. Thus, the acquisition of telomerase activity is a step in cell immortalization, which is itself a step in oncogenic transformation. Research indicates that there exist other, nontelomerase-dependent mechanisms for telomere maintenance. Telomerase, however, appears to be preferentially utilized in neoplasia since its levels are elevated in a high percentage of all tumor cells.

INTERACTION OF TUMOR SUPPRESSOR GENE PRODUCTS WITH PROTEINS ENCODED BY ONCOGENIC DNA VIRUSES

The importance of the Rb-p53 linked pathways for protection against cancer is highlighted by the action of certain DNA tumor viruses. Large T antigen of SV40 binds to both Rb and p53, inhibiting their actions. The E7 protein of human papilloma virus, linked to cervical cancer, binds to Rb, whereas the E6 protein binds to p53. Similarly, the E1A protein of adenovirus binds to Rb, whereas the E1B protein binds to p53. Thus, all of these DNA viruses, each capable of oncogenic transformation of cells, at least in culture, subvert the cells' protective mechanisms by similar means. Not all of these viruses have been firmly linked to cancer in humans. Nonetheless, there are firm links for certain viruses and ample reason to continue to monitor the potential links for others.

Human Papilloma Viruses and Cervical Cancer

Human papilloma virus (HPV) is a large circular DNA virus implicated in the formation of many types of benign warts. There are more than 50 known strains of HPV, most of which are capable of causing genital warts in women that are sexually transmitted. A small percentage of these strains have been firmly linked to the development of cervical carcinoma. Strain types 16 and 18 account for most cases in which cancer has developed from HPV-induced warts.[14] Recent epidemiologic studies have indicated that sequences representing these strains can be detected in as many as 33% of college women. Clearly, HPV is a major sexually transmitted disease. It is also clear, however, that a far smaller percentage of college women develop cervical cancer, underscoring the belief that, in addition to inactivation of tumor suppressor gene products, other genetic changes are also instrumental in the progression to cancer. All strains of HPV produce the E6 and E7 proteins, which bind to p53 and Rb, respectively. Why then do only a few strains cause cancer? The transforming proteins of HPV strains 16 and 18 have a higher affinity for their respective tumor suppressor gene products than do the proteins of their counterparts linked to benign warts. It is believed that binding of the viral proteins to the tumor suppressor gene products targets the latter for degradation within cells, a process that is thus more efficient in cells infected by types 16 and 18. It is interesting that Rb and p53 are thus far the only tumor suppressor gene products known to be inactivated by DNA transforming viruses. Thus, simultaneous inactivation of these two proteins may be capable of the subversion of cellular protective pathways sufficient to allow oncogenic transformation.

Are SV40 or Other Papovaviruses Involved in Human Cancer?

Simian virus 40 (SV40) is a circular DNA virus that is known to cause kidney tumors in monkeys and is capable of

Copyright © 2003, Mosby, Inc. All rights reserved.

oncogenic transformation of cultured human cells. As discussed above, the transforming protein of SV40 is the large T antigen, which interacts with both Rb and p53. Whether SV40 is capable of causing tumors in humans is a very important question since as many as 30 million Americans may have been injected with live SV40 virus in the 1950s. That situation came about because the first preparations of the Salk polio vaccine were made from monkey cells that, unknown at the time, harbored SV40 infection. A large-scale study concluded in 1998 that there was no correlation between the presence of SV40 DNA sequences in serum and several types of cancer.[15] These data were less conclusive for certain relatively rare forms of cancer, for which only a few subjects were analyzed. Nonetheless, the data clearly show that SV40, taken alone as a risk factor, is not a major cause of cancer in humans and that a perceived rise in the rates of certain forms of cancer since the 1950s cannot be attributed solely to SV40. Ongoing studies will determine whether SV40 may be significant when considered together with other known risk factors.

Two papovaviruses related to SV40 are known to infect humans, and both of these produce T antigen closely related to that of SV40. Sequences of the polyoma virus BK (BKV) have been detected in kidney and urine but are not known to cause any disease. Sequences of the polyoma virus JC (JCV) have been detected in nearly 93% of people over the age of 17, and JCV is known to be associated with a human disease. JCV is the etiologic agent of progressive multifocal leukoencephalopathy (PML). PML was formerly very rare, affecting primarily immunocompromised individuals, but with the onset of the AIDS epidemic, PML has been diagnosed in nearly 4% of people with AIDS, in whom it has nearly always been fatal. Antiretroviral therapy has recently reduced the mortality due to PML. In the disease, JCV infection of oligodendroglial cells in the central nervous system leads to progressive demyelination and loss of neuronal function. Recent results indicate that the presence of HIV in the brain may play a major role in activating JCV infection. JCV has recently been linked to certain brain tumors in individuals who do not have AIDS, as JCV sequences were detected in tumor tissues of medulloblastomas and pituitary tumors but not in adjacent normal tissue. This detection does not establish causality, but if the connection remains firm, it may point to new routes of therapy for these usually intractable cancers.

Hepatitis Virus Types B and C and Hepatocellular Carcinoma

Infection with either hepatitis B or C virus confers an increased risk of hepatocellular carcinoma. Hepatitis C, however, is more strongly linked since nearly 20% of people with chronic hepatitis C infection develop cancer within 10 years. Thus far, no transforming protein of any hepatitis virus has been shown to interact with and inactivate a tumor suppressor gene product as, say, the E6 and E7 proteins of papilloma viruses do. With hepatitis C, the development of liver carcinoma is believed to be due to the nature of the chronic infection. At a low level, the virus is constantly damaging liver tissue that is constantly being regenerated. This regeneration involves proliferative expansion of selected cells, and it would provide a favorable environment for expansion of clones of cells with oncogenic mutations. It takes many years for most individuals with chronic hepatitis C to develop hepatocellular carcinoma. Thus, it is likely that the expansion of cells due to regeneration predisposes cells to acquire additional genetic alterations.

NEOPLASIA IN AIDS

There are certain malignancies that were formerly rarely encountered but, with the onset of AIDS, are now so strongly associated with that disease that they are virtually signatures of it. In general, cancer in AIDS involves difficult treatment decisions, primarily because the usual chemotherapeutic or radiologic options, frequently immunosuppressive, may not be suitable. In addition, patients may be under treatment for HIV infection, which may comprise highly aggressive antiretroviral therapy (HAART), which includes a combination of inhibitors of viral proteases and replicative enzymes. Treatment of neoplasia in AIDS may require consideration not only of the viral nature of AIDS, but also of certain of the cancers characteristic of it.

Kaposi's Sarcoma and HHV8

Kaposi's sarcoma (KS), a malignant neoplasm of endothelial cell origin, is the most common neoplasm preferentially associated with AIDS. Prior to the AIDS epidemic, it was considered a sporadic disease affecting primarily European Jewish males, usually after the seventh decade of life. With the advent of AIDS, however, KS has become virtually epidemic, especially among HIV-infected homosexual males. It is now recognized that there are different variants of KS and that HIV infection may play a direct role in the prevalence of KS in AIDS. In the classic sporadic form of KS, lesions occur as purple to brown nodules largely confined to the skin in the lower extremities. KS has been found in highly immunosuppressed individuals other than those with AIDS—for example, in organ transplant patients; in these cases, nodules are not localized to skin or to the lower extremities. KS nodules in AIDS patients are extremely widespread and may occur in viscera including the GI tract and lungs. Mucosal lesions are also common in AIDS, as seen in Figure 44-9, and nodules are frequently seen in the nasopharyngeal mucosa. The incidence of KS in HIV-1-infected individuals is more than 100-fold higher than in people with other types of acquired immunosuppression.

Human herpesvirus 8 (HHV8) has now been linked to the development of KS, but the etiologic nature of this link remains to be fully explained. Less than 20% of the general population is seropositive for HHV8, and infection by this agent is essentially latent, involving endothelial cells, B lymphocytes, and certain epithelial cells. HIV-1, in contrast, infects classes of T lymphocytes, macrophages, and certain glial cells of the CNS. Recent research suggests that there is potential for a reciprocal interaction between these two viruses. HIV-1-induced cytokines can have a direct stimula-

Copyright © 2003, Mosby, Inc. All rights reserved.

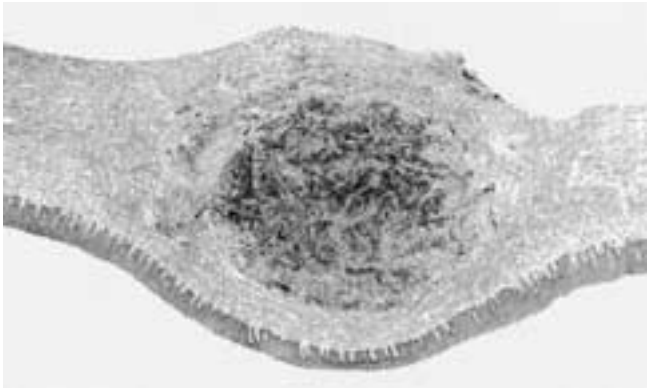

VIEW IMAGE

FIGURE 44-9 Nasopharyngeal lesion of KS, linked to HHV8, in an individual with AIDS. (Micrograph courtesy of Dr. H. Lummerman, Department of Pathology, Mount Sinai School of Medicine.)

tory effect on endothelial cell growth. In addition, the Tat protein encoded by HIV-1, a potent transcriptional regulator, is secreted by infected cells and has been demonstrated to be incorporated by neighboring cells in functional form. Tat directly activates growth factor receptors in endothelial cells. Tat can also interact with HHV8-encoded proteins to reciprocally and synergistically activate the gene expression of both viruses. In a majority of cases, KS regresses partially or completely in response to HAART. Such regression does not allow a distinction between immunosuppression versus a role for HIV in the mechanism of KS origin since HAART both increases $CD4^+$ T-cell counts and decreases the HIV viral load.

Primary Central Nervous System Lymphoma and Epstein-Barr Virus

Non-Hodgkin's lymphomas are the second most common neoplasm encountered in AIDS. They are found in AIDS patients more than 100-fold more frequently than in the general population. Of these lymphomas, primary central nervous system lymphoma (PCNSL) is preferentially associated with AIDS, affecting more than 3% of HIV-infected individuals. PCNSL is essentially a signature of AIDS, as it occurs in AIDS patients more than 3000-fold more frequently than in the general population. PCNSL is also seen in immunosuppressed transplant patients, occurring nearly 35-fold more frequently than in the general population. In North America, PCNSL cases are generally $CD20^+$, parenchymal B-cell lymphomas. Brain masses are most easily diagnosed by enhanced-contrast CT, MR imaging, and brain biopsy. Recent advances in CT imaging, particularly the use of single photon emission computed tomography using thallium 201, have reduced the necessity for brain biopsy. Intriguingly, PCNSL is associated with activation of a circular DNA virus, as is KS. Recent studies indicate that virtually all PCNSL tumors are positive for the genome of EBV, a herpes-like virus. EBV, latent in most people, can be activated in B cells, where it most notably causes mononucleosis. Infection of B cells in PCNSL is apparently latent. PCNSL lesions typically consist of masses of immunoblastic or plasmacytic B cells in a perivascular cuffing pattern, as seen in Figure 44-10. Histologic examination frequently shows the aggressive large cell subtype, as seen in Figure 44-10, in which staining employs an anti-EBV protein antibody. The histology in PCNSL is very different from that in Burkitt's lymphoma, in which a smaller, non-cleaved B-cell subtype is more common. In keeping with this observation, and with an EBV etiology, PCNSL does not involve translocations of the c-*myc* gene, as does Burkitt's lymphoma. The incidence of PCNSL decreased after the introduction of HAART. This may be due to restored immunocompetence preventing the onset of the disease. It may also, however, be due to a decreased HIV viral load in the brain.

GENES INVOLVED IN MULTIPLE STEPS OF METASTASIS

The ability to spread to distant sites in the body greatly enhances the lethality of most solid tumors. For such metastases to be successful, a cancer cell must detach from its original tumor location, invade a blood or lymphatic vessel, travel to a distant and compatible site in the body, exit the blood or lymphatic system, in many cases reattach to adjacent cells and/or to the extracellular matrix, and, finally, begin clonal proliferation.[16] Much recent work has been devoted to identifying the genes involved in each of these steps in metastasis. Cells that are not oncogenically transformed do not ordinarily form colonies when they are not attached to the extracellular matrix. Several dominantly acting oncogenes can confer the property of anchorage-

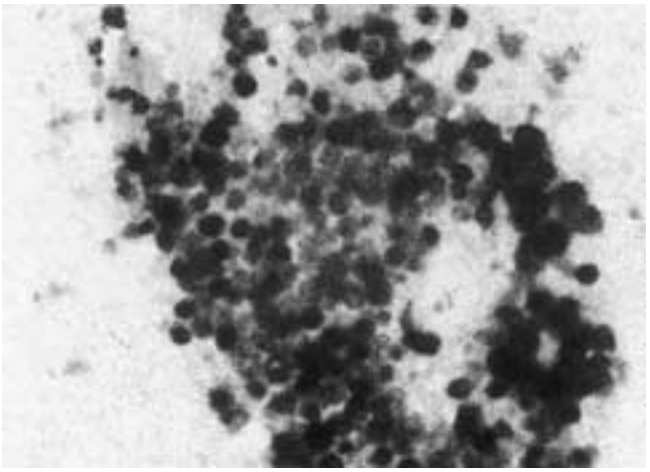

VIEW IMAGE

FIGURE 44-10 Large cell lymphoma of the brain staining positive for EBV. This brain tissue section was hybridized in situ to a digoxygenin-labeled probe for EBV EBER1 mRNA. Staining was with antidigoxygenin antibody coupled to alkaline phosphatase. Note the blood vessel at the center surrounded by positively staining tumor cells. More than 95% of such lymphomas, frequently occurring in AIDS, are positive for EBV. (Micrograph courtesy of Dr. S. Morgello of the Manhattan HIV Brain Bank, Mount Sinai School of Medicine.)

Copyright © 2003, Mosby, Inc. All rights reserved.

independent growth on cells. For example, activating mutations in members of the *ras* gene family confer a variety of morphologic and cell-cycle regulatory changes that result in anchorage-independent growth. Several proteases are important for the processes of detachment from the matrix and from adjacent cells. The protease plasmin is involved in release from the basement membrane, and it is activated by a protease called plasminogen activator. Overexpression of plasminogen activator in cells enhances their metastatic potential. Integrins are cell surface receptors that mediate interactions between cells and between cells and the extracellular matrix. Integrins are frequently upregulated in cells with high metastatic potential. Similarly, the expression of proteins of the immunoglobulin superfamily, such as ICAM1, correlates positively with high metastatic potential. In contrast, expression of cadherins and catenins is frequently downregulated in metastatic cells. Cadherins are cell-cell adhesion molecules that are calcium-dependent transmembrane glycoproteins, and catenins form links between the intracellular domains of cadherins and the cytoskeleton.

TUMOR ANGIOGENESIS

Tumor Size Restricted by Blood Supply

All solid tumors must recruit a blood supply to promote expansion. Stimulation of the growth of new capillaries from existing blood vessels is termed *angiogenesis*. Folkman and Beckner first hypothesized that virtually all solid tumors are restricted in size to approximately 2 mm in diameter prior to the onset of angiogenesis.[17] It is now recognized that most such tumors arise in the absence of angiogenesis and exist as lesions in situ, after which a small percentage acquire an angiogenic phenotype. The vast majority of in situ carcinomas remain as microscopic lesions throughout the individual's life. The remaining small percentage progress to engendering new blood vessels. This angiogenic switch is critical at both ends of the metastatic cascade, described in the previous section. Newly developed tumor blood vessel endothelium is generally hyperpermeable relative to that of nontumor tissue. Thus, a high percentage of cells from a primary tumor are capable of entering the blood supply, thus initiating metastasis. Once metastatic cells colonize a new site, the resulting tumor is restricted in size until the angiogenic switch triggers the growth of new blood vessels. There are essentially four ways in which the angiogenic switch may be activated. The most common mechanism is that an avascular carcinoma can stimulate neovascularization in an adjacent vascular bed. Secondly, endothelial precursor cells in the blood can colonize an avascular tumor. Thirdly, cells in a tumor can induce fibroblasts or myeloid cells adjacent to or within the tumor to produce angiogenic factors. Finally, preexisting blood vessels can provide axes of growth for a developing tumor. Each of these cellular angiogenic mechanisms may involve the participation of multiple gene products. At this point, more than 20 genes encoding factors capable of modulating angiogenesis, either positively or negatively, have been identified.

Activation in Tumors of Genes Encoding Angiogenic Growth Factors

In response to hypoxia, cells in a tumor are known to induce genes encoding a host of angiogenic peptide growth factors. Well-characterized factors at this time include vascular endothelial growth factor (VEGF), platelet-derived endothelial cell growth factor (PD-ECGF), and acidic and basic fibroblast growth factors (aFGF, bFGF). To stimulate neovascularization, the tumor must produce sufficient angiogenic growth factors to overcome the action of the body's naturally produced angiogenesis inhibitors, such as angiostatin. The angiogenic growth factors diffuse toward existing blood vessels, at which point they initiate a cascade of molecular events, as exemplified here by VEGF. VEGF binds at the endothelial cell surface to any of a number of cognate VEGF receptor molecules, which are similar to the transmembrane receptors previously described for various growth factors. This binding triggers receptor dimerization and activation of intracellular signal transduction pathways, including tyrosine phosphorylation and the MAP kinase pathway, leading to increased cell proliferation. This proliferation results in the creation of a new mother vessel, which is hyperpermeable. The mother vessels are transient and rapidly differentiate into new arteries and veins. This differentiation requires participation of an intriguing class of transmembrane ligands and receptors, the ephrins and Ephs. The interaction at the endothelial cell surface between ephrin-B2 and Eph-B4 has been implicated in the patterned development of arterial-venous boundaries.

Imaging of Tumor Angiogenesis

Angiogenesis is of particular relevance with regard to imaging solid tumors since many existing imaging methods are dependent on visualization of the vascular system.[17, 18] Furthermore, size is a critical factor in imaging a tumor; angiogenic tumors are frequently of detectable size, whereas nonangiogenic tumors are not. A variety of therapeutic strategies aimed at inhibiting tumor angiogenesis are presently being developed, and the use of imaging to monitor such therapy will become an increasingly important consideration. All major existing imaging technologies have been useful in capturing parameters related to tumor vascularity. CT, ultrasound, and positron emission tomography (PET), employed with contrast-enhancing agents or radioactive tracers, are capable of documenting blood volume, blood flow, and mean transit time. MR imaging and PET have been particularly useful in defining the permeability of the tumor vascular system.

Recently, certain novel imaging strategies have been developed to specifically target angiogenic endothelial cells. Angiogenic endothelial cells express cell surface integrin molecules possessing an Arg-Gly-Asp (RGD) motif. Monoclonal antibodies have been prepared that target these integrins and that are linked to paramagnetic liposomes in order to essentially create an imaging system directed at the cell surface of developing endothelial cells. These liposomes may also carry a cargo in the form of an antiangiogenic factor or a cytotoxic agent.

Copyright © 2003, Mosby, Inc. All rights reserved.

FUTURE OF CANCER TREATMENT

Although the knowledge of tumor genetics is vast, it is approaching a turning point with regard to clinically useful application. With the sequence of the human genome completely elucidated, investigators will soon have a working knowledge, if not a functional understanding, of all of the genes altered in neoplasia. Thus, work will shift from the basic task of identifying the genes involved in neoplasia to the perhaps more difficult task of applying this knowledge to treat neoplasia. The nature of experimental investigation will thus shift from its present focus on genomics toward a focus on understanding the interactions of proteins encoded by genes involved in neoplasia and to an understanding of the pathways in which these proteins function. The treatment of cancer will then progress with the use of ever more specific inhibitors of protein-protein interactions and enzyme activities.

REFERENCES

1. Vogelstein B, Kinzler KW. The multistep nature of cancer. Trends Genet 1993;9:138–141.
2. Renan MJ. How many mutations are required for tumorigenesis? Implications from human cancer data. Mol Carcinog 1993;7: 139–146.
3. Hanahan D, Weinberg RA. The hallmarks of cancer. Cell 2000;100: 57–70.
4. Hahn WC, Counter CM, Lundberg AS, Beijersbergen RL, Brooks MW, Weinberg RA. Creation of human tumour cells with defined genetic elements. Nature 1999;400:464–468.
5. Brodeur GM, Seeger RC, Schwab M, Varmus HE, Bishop JM. Amplification of N-myc in untreated human neuroblastomas correlates with advanced disease stage. Science 1984;224:1121–1124.
6. Aaronson SA. Influences of growth factors and their signaling pathways in malignancy. Harvey Lect 1991;87:17–34.
7. Knudson AG. Antioncogenes and human cancer. Proc Natl Acad Sci USA 1993;90:10914–10921.
8. Li FP, Fraumeni JF Jr, Mulvihill JJ, et al. A cancer family syndrome in twenty-four kindreds. Cancer Res 1988;48:5358–5362.
9. Zheng L, Lee WH. The retinoblastoma gene: a prototypic and multifunctional tumor suppressor. Exp Cell Res 2001;264:2–18.
10. Lee WH, Bookstein R, Hong F, Young LJ, Shew JY, Lee EY. Human retinoblastoma susceptibility gene: cloning, identification, and sequence. Science 1987;235:1394–1399.
11. Morgan SE, Kastan MB. p53 and ATM: cell cycle, cell death, and cancer. Adv Cancer Res 1997;71:1–25.
12. Scully R, Chen J, Plug A, et al. Association of *BRCA1* with Rad51 in mitotic and meiotic cells. Cell 1997;88:265–275.
13. Blackburn EH. Telomere states and cell fates. Nature 2000;408:53–56.
14. Werness BA, Levine AJ, Howley PM. Association of human papillomavirus types 16 and 18 E6 proteins with p53. Science 1990;248:76–79.
15. Strickler HD, Rosenberg PS, Devesa SS, Hertel J, Fraumeni JF Jr, Goedert JJ. Contamination of poliovirus vaccines with simian virus 40 (1955-1963) and subsequent cancer rates. JAMA 1998;279:292–295.
16. Ruoslahti E. How cancer spreads. Sci Am 1996;275:72–77.
17. Folkman J, Beckner K. Angiogenesis imaging. Acad Radiol 2000;7:783–785.
18. Li WW. Tumor angiogenesis: molecular pathology, therapeutic targeting, and imaging. Acad Radiol 2000;7:800–811.

GLOSSARY

Allele one of two gene copies, each of which is inherited from one or both parents of the individual. These alleles may or may not be identical.

Apoptosis programmed cell death. Apoptosis occurs normally during tissue development. It also occurs in response to signals indicating cell or DNA damage and thus represents an important mechanism for preventing neoplasia.

CDK acronym for cyclin-dependent kinase. A class of protein kinases dependent for their activity on association with another protein, called a cyclin, the presence of which is specific for a certain phase or phases of the cell division cycle. Each CDK interacts with specific cyclins.

Checkpoint when used in relation to the cell division cycle, a time point at which a cell may, in response to certain signals, particularly for cell or DNA damage, exit the cycle.

Cyclins a class of proteins that interact with CDK protein kinases to stimulate their activity. Cyclins are degraded at a specific point in the cell cycle and synthesized at another point. They are thus available to activate a particular CDK in a cell cycle–dependent manner. Each cyclin activates specific CDKs.

Dimer a compound produced by the combination of two like molecules, without loss of atoms.

Helicase an enzyme that unwinds DNA or RNA in an energy (i.e., ATP)-dependent, processive fashion. Processive means that the enzyme can proceed to unwind the polynucleotide duplex for a significant distance.

Ligand an entity that interacts with a receptor to modulate the signaling pathway stemming from that receptor.

LTR an acronym for long terminal repeat, a repeated sequence at the ends of a linear retroviral RNA molecule. The LTR contains a promoter for regulating transcription of the viral RNA molecule once integrated into the DNA of the host genome.

Oncogene a cellular gene, the expression of which contributes in a dominant fashion to the development of cancer. Oncogenes of tumors arise through somatic mutation of normal cellular genes, termed *proto-oncogenes*. The mutated gene may thus gain a function unrelated to the function of the original proto-oncogene.

Promoter a DNA sequence, generally upstream of a gene, that contains elements binding proteins that regulate expression of the gene.

Protein kinase an enzyme that catalyzes the transfer of a phosphate group from ATP to an amino acid in another protein, termed its *substrate*. Each protein kinase has specific protein substrates.

Protein phosphatase an enzyme that catalyzes the removal of a phosphate group from another protein that has been phosphorylated by a protein kinase.

Proto-oncogene a normal cellular gene that, when mutated, becomes an oncogene. The product of a proto-oncogene may serve a cellular function unrelated to growth control or cancer. Mutation of only one allele creates a protein with newly acquired oncogenic properties.

Retrovirus an RNA virus that must be reverse-transcribed to make DNA, which then integrates into the host genome.

Telomere either end of the continuous DNA strand that comprises a chromatid of each chromosome. Each human telomere consists of multiple repeats of the sequence TTAGGG. These repeats must be replicated in a special manner to maintain telomere length over multiple cell divisions.

Copyright © 2003, Mosby, Inc. All rights reserved.

Transduction the process, requiring DNA recombination, by which a virus infecting a cell incorporates all or part of a cellular gene, thus becoming a part of the virus and conferring on it new viral properties.

Translocation an event, requiring DNA recombination, in which DNA of part of one chromosome is transferred to another chromosome. This may involve an exchange of DNA sequences between chromosomes. If the translocation DNA breakpoints lie in two different genes, the event can generate a fusion gene encoding a protein with the N terminus of one of the two original genes and the C terminus of the other. Several oncogenes have been generated by translocation.

Tumor suppressor gene a gene of which both alleles must be inactivated in order for cancer to develop. Although tumor suppressor genes are frequently called recessive oncogenes, a *predisposition* to cancer is inherited as a dominant phenotype. To lead to neoplasia in a familial cancer syndrome, one inactivated allele of a tumor suppressor gene is inherited at birth and the other allele is subsequently inactivated environmentally.

Copyright © 2003, Mosby, Inc. All rights reserved.

45

New Imaging Techniques

Suresh K. Mukherji, Nancy J. Fischbein, and J. A. Castelijns

INTRODUCTION
POSITRON EMISSION TOMOGRAPHY
- Introduction
- Technical Aspects
  - Positron Emission
  - Radiopharmaceuticals
    - *^{18}F-Fluorodeoxyglucose*
    - *^{11}C-Labeled Amino Acids*
    - *^{11}C-Labeled Thymidine*
  - Scanner/Detectors
  - Image Generation
  - Quantification/Standardized Uptake Value
  - Image Registration
  - Imaging FDG Metabolism Without a Dedicated PET Scanner
- Clinical Applications
  - Normal Appearance in the Head and Neck
  - Postirradiated Appearance
  - Head and Neck Cancer
    - *Unknown Primary/Second Primary*
    - *Nodal Staging*
    - *Residual/Recurrent Disease*
    - *Response to Therapy*
    - *Evaluation of Metastases*
  - Non-SCC Malignancy
    - *Thyroid Cancer*
    - *Lymphoma*
- Pitfalls
  - False Positives
  - False Negatives
- Conclusion

THALLIUM-201 SINGLE PHOTON EMISSION TOMOGRAPHY
- Introduction
- Mechanism
- Limitations
- Clinical Applications

PROTON MAGNETIC RESONANCE SPECTROSCOPY
- Introduction
- Metabolites
- Clinical Applications
  - Differentiation of Recurrent Tumor from Posttreatment Changes
  - Prospective Treatment Monitoring
- Limitations and Imaging Strategies
- Conclusion

ULTRASMALL SUPERPARAMAGNETIC IRON OXIDE MR CONTRAST AGENTS
- Introduction
- Mechanism
- Technique
- Clinical Applications
  - Detection of Nodal Metastases
  - Primary Site Evaluation

RADIOIMMUNOSCINTIGRAPHY IN HEAD AND NECK CANCER
- Introduction
- Technique
- Early Results
- Future Trends

CONCLUSIONS

Copyright © 2003, Mosby, Inc. All rights reserved.

INTRODUCTION

The past 15 years have witnessed dramatic changes in the imaging of a variety of head and neck disorders. Although initially the emphasis of imaging was on morphologic analysis, the areas of most active recent investigation have involved metabolic and functional imaging techniques. The primary goal of head and neck imaging has always been to provide anatomic information that accurately maps a lesion, especially in areas where the clinician cannot directly use palpation. However, the early results of the new metabolic imaging techniques suggest that they may be more useful than cross-sectional anatomic imaging in improving the radiologist's ability to accurately identify recurrent tumor, monitor treatment, and identify cervical metastases. This chapter will review the most promising of these metabolic techniques and discuss their potential clinical applications.

POSITRON EMISSION TOMOGRAPHY

Introduction

Unlike computed tomography (CT) and magnetic resonance (MR) imaging, which depict structural anatomy, positron emission tomography (PET) is a functional imaging technique that depicts tissue metabolic activity. As most tumors show increased glycolytic activity compared with nonneoplastic tissues, ^{18}F-labeled fluorodeoxyglucose, a glucose analogue, has proven to be a very useful marker of tumor activity in many parts of the body, including the head and neck. In this chapter, the basic physics and technical aspects of PET will be reviewed, as will the radiopharmaceuticals that have been applied most commonly in the head and neck. The performance of PET in the evaluation of the patient with head and neck cancer will then be discussed.

Technical Aspects

Positron Emission

PET imaging relies on the use of radioisotopes that are unstable, because their nuclei contain an excess of protons, and that decay with emission of positively charged particles (positrons). These radioisotopes are cyclotron produced and short-lived. The emitted positrons travel only a short distance (1 to 2 mm) in tissue before combining with a negatively charged electron. This collision results in mutual annihilation, with conversion of mass to energy and the emission of two 511-keV photons directed approximately 180° to one another. These photons are more penetrating than positrons and exit the body easily, so that they can then be detected with a scanner.

These events (annihilation and photon emission) establish the fundamental physical limitations on the resolution of PET imaging. First, the annihilation event does not occur at the site of the decaying radionuclide, but rather at a distance that is determined by both the density of the subject matter and the energy of the emitted positron. Second, the two annihilation photons are not emitted in perfect collinearity, this divergence being dictated by the rules of conservation of momentum.[1] The combination of these two factors leads to a degree of unsharpness that is on the order of 2 to 3 mm.

Radiopharmaceuticals

The metabolism of cancer cells is altered compared to that of normal cells of the same tissue origin. In cancer cells, both glucose metabolism and the rate of protein synthesis are increased. In addition, in order to meet the needs of actively proliferating cells, there is an increased need for fatty acids and nucleic acids. Short-lived positron emitters such as ^{18}F and ^{11}C can be used to label a wide range of biologic substrates without altering their character, and these substrates can be used to study a variety of physiologic processes. A range of physiologic tracers has been developed for PET imaging, the most widely used of which is 2-[^{18}F]fluoro-2-deoxy-D-glucose (FDG).

^{18}F-Fluorodeoxyglucose

FDG is a glucose analogue with a fluorine-for-hydroxyl substitution on a D-glucose substrate. It is the most commonly used radiopharmaceutical in PET imaging. ^{18}F is cyclotron-produced and has a half-life of 110 minutes, making its use feasible for sites that do not have an on-site cyclotron. A typical dose of FDG in the adult patient is on the order of 370 MBq (10 mCi). FDG is taken up by glucose transporters and phosphorylated by hexokinase to FDG-6-phosphate, but further metabolism is then blocked by the presence of the extra hydroxyl moiety. FDG-6-phosphate therefore accumulates in the cell and provides a marker for glucose uptake and utilization. Because FDG and serum glucose compete for uptake, patients should fast for at least 4 hours prior to an FDG PET study. As neoplastic cells characteristically have high rates of glycolysis even in the presence of oxygen, contrast between tumors and normal tissue is high.[2] Uptake of glucose and FDG into malignant cells is facilitated by increased expression of glucose transporter molecules at the cell surface, and activity of hexokinase has also been shown to be significantly higher in malignant cells.[3, 4] Tumor concentration of FDG generally reaches a peak at 30 minutes, remains relatively constant for up to 60 minutes, and then slowly declines.[4] It must be recognized that nonneoplastic but rapidly metabolizing cells such as macrophages may also accumulate FDG[5]; therefore, accumulation of FDG is not specific for neoplastic cells.

^{11}C-Labeled Amino Acids

Another family of radiopharmaceuticals that has been investigated for oncologic imaging is the ^{11}C-labeled amino acids, notably ^{11}C-methionine and ^{11}C-tyrosine. As the half-life of ^{11}C is only 20 minutes, this label can only be used with an on-site cyclotron. Methionine is an essential amino acid needed for protein synthesis, polyamine synthesis, transmethylation reactions, and the transsulfuration pathway.[6] ^{11}C-tyrosine also is an essential amino acid required for protein synthesis.[7] Malignant transformation accelerates these syntheses and reactions, making labeled amino acids potentially useful markers of tumor activity.

^{11}C-Labeled Thymidine

^{11}C-labeled thymidine PET has been suggested as a way to assess tumor proliferation in vivo.[8] Determination of the proliferative capacity of tumors is increasingly used in

Copyright © 2003, Mosby, Inc. All rights reserved.

clinical trials of head and neck tumors to select patients for particular therapies. Thymidine is one of the building blocks of DNA, and in vivo measurement of its incorporation into DNA offers a potential means to quantify proliferative activity.

Scanner/Detectors

The distribution of positron-emitting radionuclides in vivo cannot be imaged directly because of the positron's short range in matter. PET imaging therefore relies, as previously described, on the detection of photons traveling at 180° to each other, which represent the footprints of annihilation reactions. The system is set up so that an event is registered only when two oppositely located detectors record the arrival of a photon within some finite resolving time, establishing a ''coincidence'' event. An image consists of true coincidences as well as signals resulting from random false coincidences, which are a major contributor to system noise and which tend to degrade the image. The detectors used in PET consist of a scintillator (typically bismuth-germanate, or BGO), photomultiplier tubes, and an amplifier. A mechanical gantry holds the detector system and shielding, as well as septa that are used between detectors for interplane shielding in multiple ring detector systems.[9]

The most common design for a PET scanner makes use of multiple rings of detectors that produce multiple slices simultaneously. Some scanners can be operated in either a high-resolution mode or a high-sensitivity mode.[10] In the high-sensitivity mode, direct slices include coincidence events recorded not only from directly opposing crystals, but also from the two crossing planes of neighboring crystals. In the high-resolution mode, the direct slices include only events from directly opposing crystals. Similarly, for cross-planes, coincidence paths are accepted in four crossing planes for the high-sensitivity mode, but only from the two nearest cross-planes in the high-resolution mode. In the high-resolution mode, a PET gantry with n rings of detectors provides $2n$-1 slices through utilization of cross-coincidences between two adjacent rings.

Three types of resolution of a PET scanner are typically defined: radial, tangential, and axial. Radial resolution, also called in-slice resolution, is best at the center of the field of view and poorest at the periphery. Tangential resolution is measured in-plane, but tangential to a radial line, and is also best in the center of the field. Axial resolution is measured along the long axis and depends upon detector size, interdetector spacing in the axial direction, and type of collimation.

Image Generation

The data acquired in PET are a function of at least two variables: the distribution of the source of annihilation photons included in the field of view and the modulation of the above by the attenuation of photons that occurs between their source and the detectors.[1] An attenuation correction must be made for each data point recorded. An attenuation correction factor can be applied to each scan projection or, more commonly, transmission attenuation can be measured with an external source and this correction can be applied to the data. Correction is usually made by acquiring ''transmission'' images that measure the attenuation of 500 keV radiation in the subject (usually from a rotating ^{68}Ge source), and this information is used to correct the emission data before reconstruction.

Transverse tomographic images are reconstructed from a series of measurements taken from different angles around the object to be imaged. The two main reconstruction methods by which activity distribution is estimated from the coincidence measurements of annihilation events are filtered backprojection and statistical model-based iterative reconstruction. Reconstruction algorithms are necessary since the position of an annihilation event can be placed along a straight line joining two detectors, but no information is available as to the location of the event along that line. In filtered backprojection, a choice of reconstruction filter offers a trade-off between resolution and noise in the reconstructed images.[11] Filtered backprojection also suffers from ''spray'' or ''starburst'' artifact (Fig. 45-1). The ability of iterative reconstruction algorithms to take account of the statistical nature of the acquired data by incorporating models such as resolution, attenuation, and scatter during the reconstruction process can, in general, improve the quality of the reconstructed image compared to that of filtered backprojection.[12] Iterative reconstruction also allows whole-body attenuation-corrected images to be obtained in a reasonable length of time.[13] In the future, with improved temporal resolution and computing power, the difference in arrival time of two photons will allow the exact location of the originating event to be deduced (so-called time-of-flight PET), and events will be directly located along a line between two detectors rather than being placed using an algorithm. At present, images are generally displayed and interpreted directly on a computer console, which allows simultaneous viewing of axial, sagittal, and coronal planes, as well as the ability to rotate images.

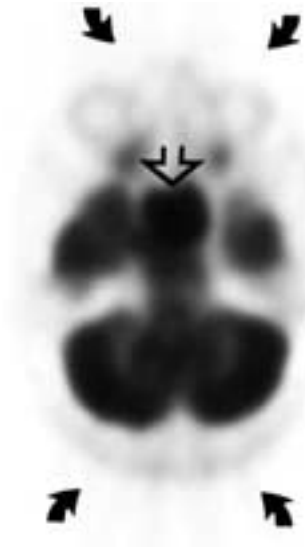

FIGURE 45-1 An FDG PET examination performed on a patient with nasopharyngeal carcinoma and reconstructed with filtered backprojection demonstrates a focus of intense activity in the nasopharynx (*open arrow*). Note that spray artifact is prominent around the periphery of the image (*arrows*).

VIEW IMAGE

Copyright © 2003, Mosby, Inc. All rights reserved.

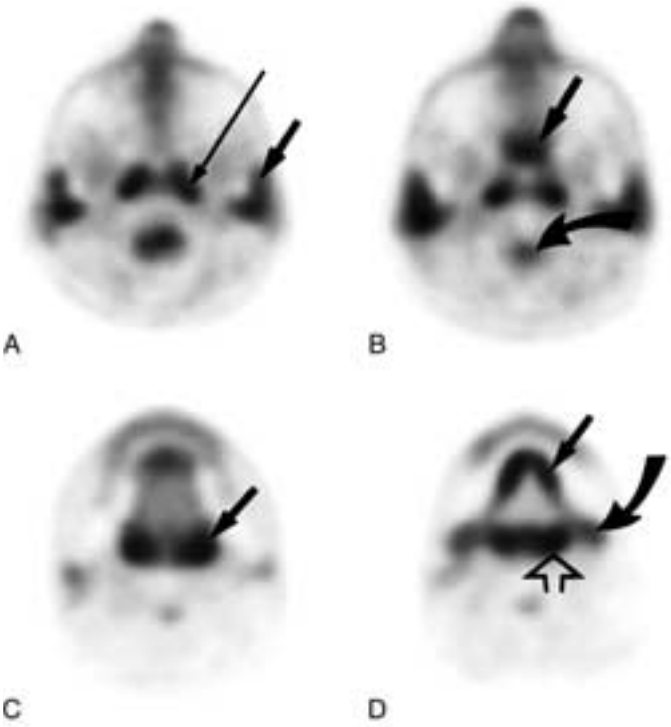

VIEW IMAGE

FIGURE 45-2 Multiple FDG PET images show the normal distribution of tracer accumulation in the head and upper neck. Normal activity is demonstrated in the (**A**) nasopharynx (*thin arrow*) and parotid glands (*thick arrow*), (**B**) soft palate (*straight arrow*), (**C**) palatine tonsils (*arrow*), and (**D**) submandibular glands (*curved arrow*), sublingual glands (*straight arrow*), and lingual tonsils (*open arrow*). Note that the maxillary sinuses, maxilla, and mandible are photopenic. Faint activity is seen in the spinal cord on all images (*curved arrow* in **B**).

Quantification/Standardized Uptake Value

Attenuation correction allows results to be quantified. Quantified results are generally presented as the standardized uptake value (SUV), which is the amount of radiotracer in a region (as measured by a PET scanner) normalized by the injected dose and the patient's body mass. The general equation is:

$$\text{SUV} = \frac{\text{injected dose (nCi)/body weight (g)}}{\text{tissue concentration (nCi/g)}}$$

SUVs are widely reported but are subject to multiple sources of variability, which are often not accounted for in reported studies.[14] Among these sources of variability are (1) patient's body composition and habitus, which are not accounted for by weight; (2) lack of standardization of the uptake period, the time from tracer injection to PET scanning; (3) actual plasma glucose level at the time of scanning; (4) recovery coefficients and partial volume effects; and (5) region of interest effects. Attempts have been made to reduce the variability of the SUV using other constants such as K_i, the net influx constant, but these can be problematic as well.[15] Recently, SUVs based on lean body mass (SUV_{lbm}) and body surface area (SUV_{bsa}) have been investigated as weight-independent indices of FDG uptake, with SUV_{lbm} appearing to be more appropriate for quantifying FDG uptake in order to avoid overestimation of glucose utilization in obese patients.[16] For clinical purposes, a visual analysis of the images is usually sufficient,[17] but quantification may be useful in particular clinical circumstances (e.g., predicting the response to chemoradiotherapy) and certainly in more basic research.[18]

Image Registration

Although highly sensitive, PET does not provide the same definition of anatomic detail that is provided by CT or MR imaging and therefore does not necessarily allow precise localization of pathology or determination of exactly what structures are involved by a pathologic process. Computerized coregistration of PET and CT/MR images helps circumvent this limitation and provides additional clinically relevant information.[19] One method of registration makes use of an iterative surface-fit algorithm that performs the scaling, translation, and rotation of one of the surfaces and obtains the best fit of the two surfaces under comparison after manual alignment.[20] Anatomic landmarks such as the nasal profile or curvature of the brain may be used to guide the registration, or external markers may be placed. The development of combined CT/PET scanners should reduce the difficulty of anatomic correlation (Fig. 45-2).[21]

Imaging FDG Metabolism Without a Dedicated PET Scanner

Positron emission events are imaged most efficiently and with highest resolution using a dedicated PET scanner with full-ring bismuth germanate crystal block detectors. However, as these scanners are of limited availability, interest has focused on the ability of conventional or modified gamma cameras to image positron emission events. Conventional multiheaded single photon emission computed tomography (SPECT) cameras are in widespread use, but attempts to image FDG using these cameras fitted with high-energy collimators have proved to be of limited value due to low spatial resolution and low sensitivity.[22, 23] This poor performance is a consequence of limited efficiency for the detection of 511-keV photons using a camera optimized for detection of 140-keV photons, as well as constraints imposed on system spatial resolution as a result of physical collimation of high-energy photons. Results are improved by operating a modified gamma camera fitted with thicker (1.6 cm versus the usual 0.95 cm) NaI crystals in

Copyright © 2003, Mosby, Inc. All rights reserved.

coincidence mode. In this situation, there are limitations due to the count rate, as well as a substantial contribution of accidental coincidences.[22] Several recent studies, however, have demonstrated that a dual-head camera with PET capability is sensitive in the detection of primary head and neck cancers and accurate in the preoperative assessment of lymph node metastases and detection of local recurrences.[24–26]

Clinical Applications

The literature on the role of PET in head and neck oncology is rapidly expanding. The vast majority of these studies are FDG-based, and these will be the focus of this chapter.

Normal Appearance in the Head and Neck

Before interpreting the abnormal, it is important to have a firm understanding of the normal distribution of FDG in the body and, in particular, in the head and neck region. On a whole body scan, the most intense activity is in the brain, followed by the myocardium, renal collecting systems, and bladder. There is moderate activity in the liver, spleen, and bone marrow and variable activity in the bowel, breast (reflecting the amount of proliferative glandular breast tissue), and muscle.[27] In the head and neck, there is marked accumulation of FDG in the floor of the mouth, generally attributed to the sublingual glands, and in the lymphoid tissue of Waldeyer's ring. Moderate activity is present in the parotid and submandibular glands, as well as in the extraocular muscles. Mild activity is also present in the nasal turbinates (Fig. 45-3). The thyroid gland may demonstrate striking FDG uptake, especially if it is goitrous. Striated muscle uptake is usually mild unless the patient is talking or has recently exerted the neck or shoulder muscles. Bones and fat are photopenic.[28]

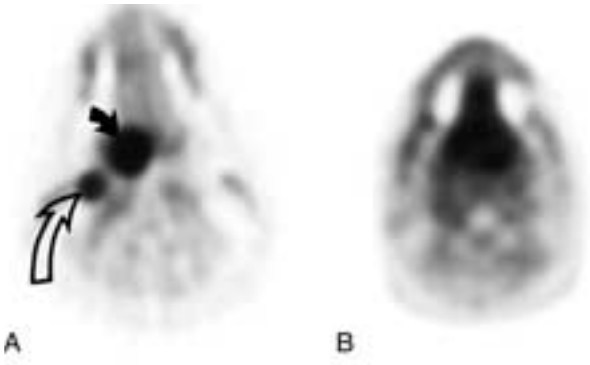

VIEW IMAGE

FIGURE 45-3 A 73-year-old man with SCC of the base of the tongue underwent staging evaluation with FDG PET. **A**, An initial pretreatment scan shows intense tracer accumulation in the base of the tongue (*solid arrow*) and in a metastatic right upper jugular lymph node (*open arrow*). This older scan, reconstructed using filtered backprojection, also shows mild spray artifact. **B**, A follow-up scan obtained 6 months after completion of radiation therapy demonstrates resolution of focal uptake at the base of the tongue and the cervical lymph node, but there is a mild generalized increase in soft-tissue uptake, as is typically seen following radiation therapy. Note the absence of spray artifact on this image reconstructed using an iterative method.

VIEW IMAGE

FIGURE 45-4 An FDG PET scan was performed in a patient with a small (5-mm), superficial, moderately well differentiated SCC of the left posterior buccal mucosa and retromolar trigone. The primary lesion is seen (*arrow*).

Postirradiated Appearance

Radiation therapy causes little or no change in normal uptake patterns of FDG in the head and neck except for a mild generalized increase in soft-tissue uptake (Fig. 45-4). In a series of 11 patients with squamous cell carcinoma (SCC) of the head and neck studied before, during, and after a 6-week course of radiation therapy, Rege et al. found that the average metabolic ratio in the tonsils, nasal turbinates, soft palate, and gingiva did not change significantly with treatment, while FDG uptake decreased dramatically in SCC.[29] The salivary glands also maintained normal FDG uptake, though their function was decreased following radiation therapy.

Head and Neck Cancer

FDG PET has a number of proven and potential roles in the assessment of patients with head and neck cancer, the majority of whom have SCC. FDG PET has been used to look for unknown primary lesions and second primaries, to stage disease prior to therapy, to detect residual and/or recurrent disease after therapy, to assess the response to therapy, and to detect distant metastases. The performance of FDG PET in each of these areas will now be reviewed.

Unknown Primary/ Second Primary

FDG PET detects more than 95% of SCCs with a volume of 1 cc (Fig. 45-5), with uptake seemingly unrelated to the histologic grade of the tumor.[30–32] Small superficial lesions may go undetected by FDG PET but can often be seen endoscopically.[33] About 5% of patients with SCC present solely with evidence of cervical nodal metastases and no identifiable primary lesion on head and neck examination. Anatomic imaging with CT/MR and endoscopy with random biopsy of likely primary sites (nasopharynx, tonsil, base of the tongue, pyriform sinus) will identify primary sites in 10% to 20% of these patients.[34] If no primary tumor site is found on CT/MR imaging, or on endoscopy with biopsy, then there are three basic therapeutic approaches: (1) a patient may undergo neck dissection followed by watchful waiting (controversial); or (2) neck dissection followed by radiation therapy to one or both sides of the neck and all possible primary tumor sites, including the nasopharynx; or (3) radiation therapy to all likely primary sites and the neck, followed by consideration of a neck dissection. The

Copyright © 2003, Mosby, Inc. All rights reserved.

FIGURE 45-5 A 44-year-old man presented with a right neck mass, and SCC was diagnosed on fine needle aspiration. The clinical examination was unremarkable, as was routine imaging. **A**, An FDG PET scan shows a focus of markedly increased FDG uptake in the area of the right tonsil (*arrow*). Asymmetric activity in the floor of the mouth is of uncertain significance. **B**, The contrast-enhanced CT image at this level shows no appreciable tonsillar asymmetry. Multiple biopsies of the right tonsil yielded a diagnosis of SCC, and the patient underwent radiation therapy.

identification of a primary site allows for more focused treatment that reduces morbidity and is therefore of considerable benefit to the patient. Such focused treatment is also associated with a better 5-year survival.

The reported success of FDG PET in identifying unknown primary lesions in patients presenting with metastatic cervical adenopathy is variable but promising. A number of series that have assessed 4 to 18 patients have reported successful location of unknown primary lesions in 20% to 50% of cases, with most of these lesions not seen on conventional anatomic imaging (Fig. 45-6).[31, 35–39] It should be noted that one of these series made use of FDG SPECT rather than FDG PET, with good success.[36] In one series, a 4-mm lesion was missed with PET and found endoscopically, and in another series a nasopharyngeal primary was identified at postradiation therapy follow-up PET.[35, 38] There was also a 20% to 30% rate of presumed false-positive diagnoses, assuming that biopsy is the gold standard.[36, 37] This latter assumption is not necessarily valid, as biopsy is operator dependent and may miss small or deep submucosal deposits. Of interest, in each series there were a number of patients in whom no primary site was ever identified by PET, endoscopic biopsy, or clinical follow-up. It is assumed that (1) some small primary tumors might have been eliminated by the body's own immune surveillance system, or (2) that these tumors might have been cured by radiation therapy (assuming that this is the treatment approach taken), or (3) that a prior now-forgotten SCC of the skin may be the actual primary site. The fact that a number of primary lesions are never identified by any method makes it difficult to calculate values for sensitivity and specificity.

One recent study reported a much poorer performance for FDG PET in the search for an unknown primary, with a primary site correctly identified in only 1/13 patients and apparent false-positive results in 6/13 patients.[40] Suggested reasons for the discrepancy between this and other studies include relatively poor resolution of the PET system being used (though SPECT has even lower resolution), the small size of two of the primary lesions identified by endoscopy and biopsy, and the possibility that biopsy sampling errors

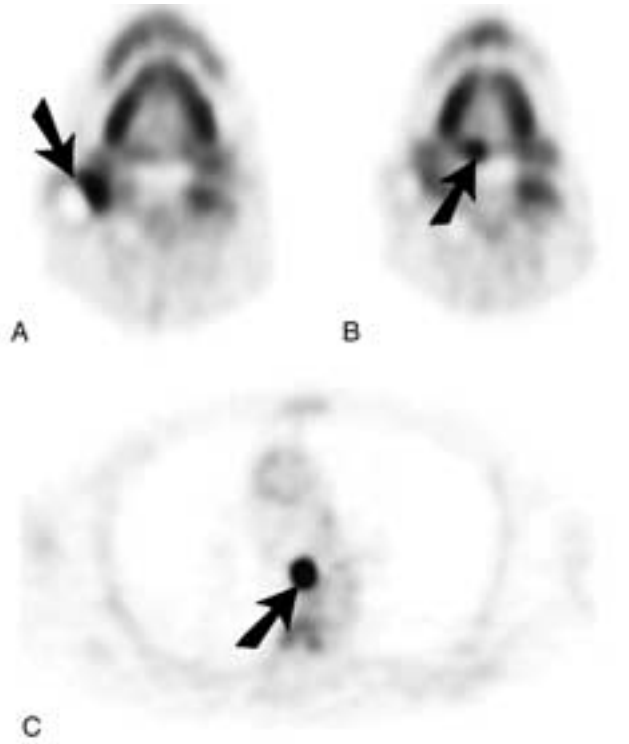

FIGURE 45-6 A 59-year-old man presented with a right neck mass, and fine needle aspiration was consistent with SCC. No primary lesion was noted on careful mucosal examination. A CT scan showed a mixed cystic and solid nodal mass, but no primary lesion was detected. An FDG PET scan was obtained to look for occult primary lesions and to focus the endoscopic examination. **A**, The right neck mass shows focal accumulation of FDG adjacent to a photopenic area, consistent with the known partially necrotic nodal mass (*arrow*). **B**, A slightly more inferior image shows focal activity at the right base of the tongue (*arrow*). No palpable abnormality was present at this location. **C**, An image through the chest shows intense focal activity in the region of the esophagus (*arrow*). Endoscopic biopsies of both sites subsequently showed SCC, with the nodal metastasis presumed to be related to the primary lesion at the base of the tongue. The patient received radiation treatment to both primary sites and the neck. (From Fischbein N, Anzai Y, Mukherji SK. Application of new imaging techniques for the evaluation of squamous cell carcinoma of the head and neck. Semin US CT MRI 1999;20:187–212.)

Copyright © 2003, Mosby, Inc. All rights reserved.

VIEW IMAGE

FIGURE 45-7 A 58-year-old woman presented with dysphagia and was found on examination to have extensive involvement of the epiglottis by SCC. MR showed no clearly pathologic adenopathy, but FDG PET demonstrated suspicious areas of tracer uptake bilaterally (*arrows*). The patient underwent total laryngectomy, partial glossectomy, and bilateral modified radical neck dissections. Pathologically, both nodes contained small foci of tumor on the order of 3 to 4 mm in diameter.

could lead to apparent false-positive FDG PET results. In the search for an unknown primary, it is always preferable that imaging studies (CT, MR, FDG PET) be done before endoscopy and biopsy; otherwise, sites of recent tissue sampling may be mistaken for tumor on postbiopsy images. Furthermore, the imaging evaluation may help to focus the endoscopic evaluation on the area most likely to yield positive material. If a larger volume of sample can be obtained from suspicious areas, the diagnostic yield may be increased over that of more limited, speculative biopsies.

The issue of second primary lesions is also relevant for patients with head and neck cancer, as these patients, many of whom use tobacco and alcohol, are at risk for synchronous or metachronous lesions of the head and neck, lung, or esophagus. The risk of second primary lesions in patients with head and neck cancer has been estimated at 4% per year, with second primary sites being predominantly located in the oral cavity, pharynx or larynx (40%), lungs (31%), and esophagus (9%).[41] The issue of whether to include the chest is relevant for sites for which whole-body scans are not routinely done. The added value of including the chest and abdomen has been debated, particularly given FDG PET's sensitivity to inflammatory as well as neoplastic conditions, leading to more imaging tests to sort out false-positive results.[42] Stokkel et al., however, studied 68 patients with head and neck cancer using dual-head FDG PET of the head, neck, and chest.[24] In 12 patients (18%), a second simultaneous primary malignant tumor was found, only five of which were detected by clinical or routine radiologic examination. Our own experience suggests that inclusion of the chest and abdomen is useful in the evaluation of patients with head and neck cancer (Fig. 45-7).

Nodal Staging

The staging of the neck is an essential task for the head and neck surgeon, radiation therapist, and oncologist. As most primary tumor sites in the head and neck have a relatively high incidence of nodal metastases, the neck must always be evaluated when a therapeutic plan is developed. Staging is generally done by a combination of clinical palpation and anatomic imaging. Clinical palpation is limited by the patient's body habitus, inaccessibility of certain nodal groups to palpation (e.g., retropharyngeal nodes), and tissue changes induced by prior therapy.

CT and MR imaging allow assessment of areas that cannot be palpated, and they can demonstrate areas of focal necrosis that confirm metastatic nodal disease (see Chapter 36). However, both techniques are limited by the fact that normal-sized, nonnecrotic nodes may harbor foci of tumor, while enlarged nodes may be reactive rather than neoplastic. Size criteria for determination of nodal metastases have been extensively reviewed in the literature and are also discussed in Chapter 36.[43] The performance of CT and MR for detecting metastatic foci in nonnecrotic nodes varies with the size criteria selected for assessing a node as abnormal. If a node equal to or greater than 5 mm is considered abnormal using CT and MR imaging, there is a sensitivity of 92% to 98% but a specificity of only 13% to 20%. When a 10-mm node is considered abnormal, the sensitivity is reduced to 81% to 88% and the specificity increases to 39% to 48%.[43] FDG PET affords another opportunity to detect metastatic nodes based on abnormal accumulation of FDG by foci of tumor.

The sensitivity of FDG PET for the detection of cervical nodal metastases in head and neck cancer ranges from 50% to 100% in various series[44–51] (Table 45-1). FDG PET can detect tumor-involved lymph nodes as small as 4 mm (Fig. 45-8), though below this level, lesions can certainly be missed. As histopathologic studies have shown that more than 40% of all lymph node metastases may be localized in lymph nodes smaller than 1 cm, a number of metastatic foci will certainly go undetected by any imaging method.[52] The specificity of FDG PET in detecting cervical nodal metastases ranges from 80% to 100%, with false positives due to reactive rather than neoplastic nodes. A recent study that prospectively compared FDG PET with conventional imaging modalities (CT, MR, ultrasound) in lymph node staging of head and neck cancer found that FDG PET had a sensitivity and specificity of 90% and 94% respectively, compared to 82% and 85% for CT, 80% and 79% for MR, and 72% and

Table 45-1
SUMMARY OF FDG-PET RESULTS FOR NODAL STAGING

Reference	Sensitivity	Specificity
Adams et al. (44)	90	94
Bailet et al. (45)	71	98
Benchaou (46)	72	99
Braams (47)	91	88
Jabour (28)	74	NA
Laubenbacher (48)	90	96
McGuirt (49)	83	82
Myers (50)	78	100
Myers (51)	100	100*
Paulus (33)	50	100
Stokkel (25)	100	90**
Wong (32)	67	100

* 11 clinically N_0 patients with 19 neck dissections
**Calculated per neck side using a dual-head coincidence camera
(Modified from Fischbein N, Anzai Y, Mukherji SK. Application of new imaging techniques for the evaluation of squamous cell carcinoma of the head and neck. Seminars US CT MRI 1999; 20:187–212.)

Copyright © 2003, Mosby, Inc. All rights reserved.

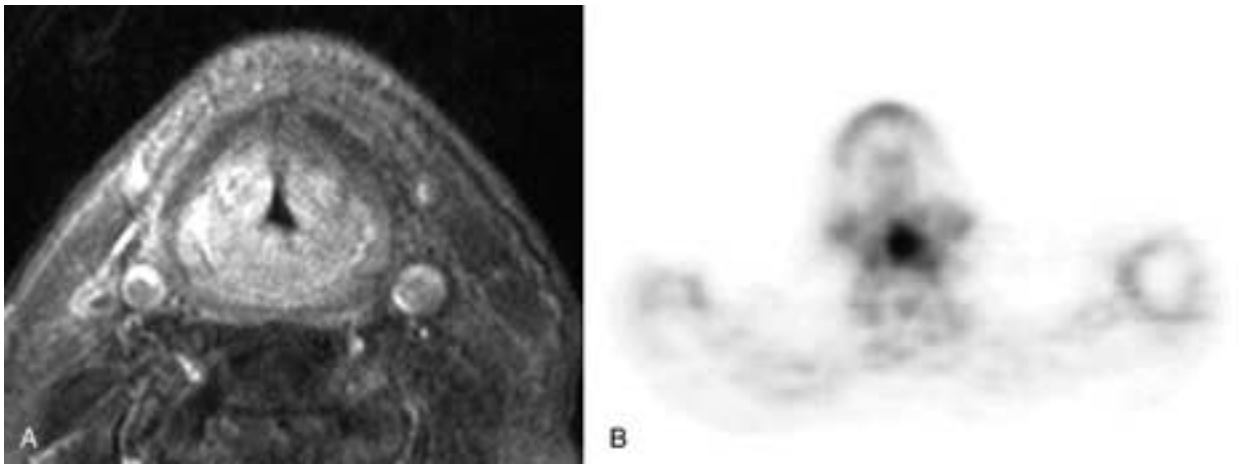

VIEW IMAGE

FIGURE 45-8 A 63-year-old man underwent radiation therapy for SCC of the larynx. Six months following completion of therapy, he had persistent severe pain and occasional hemoptysis. Endoscopic examination demonstrated marked diffuse mucosal edema and erythema. **A**, An axial T1-weighted, postgadolinium, fat-saturated MR image demonstrates marked laryngeal edema and moderate enhancement without a focal abnormality. **B**, The FDG PET scan demonstrates a focus of intense activity in the larynx and no evidence of pathologic nodes. Mild diffuse soft-tissue activity is due to prior radiation therapy. Because of persistent symptoms and the suspicious PET scan, a laryngectomy was performed. SCC was demonstrated at pathologic examination.

70% for ultrasound.[44] In this study, regional lymph nodes were considered pathologic on conventional imaging if they were more than 12 mm in diameter or if there were other signs of malignancy such as central necrosis.

A particular setting in which FDG PET has been evaluated is in the management of the so-called N0 neck. The N0 neck shows no evidence of pathologic lymphadenopathy by clinical or conventional radiographic evaluation. However, N0 patients may harbor subclinical metastatic foci in as many as 20% to 30% of cases, and therefore the neck is often treated surgically or with radiation therapy in order to eradicate subclinical disease.[53] If a negative PET could be considered reassuring enough that a ''watchful waiting'' approach could be safely adopted, then the neck could be spared treatment in the N0 patient. Myers and Wax looked at 11 N0 patients with SCC of the oral cavity who underwent 19 neck dissections and found that FDG PET had 100% sensitivity and specificity for the presence or absence of disease in the neck.[51] Given that FDG PET is relatively insensitive to metastatic foci smaller than 3 to 4 mm, these numbers will likely fall as more patients are studied. However, it is probable that FDG PET will come to play an important role in the selection of therapeutic approach in the cancer patient with an N0 neck. The ability of PET to detect smaller foci of disease than either CT or MR imaging increases the likelihood that an apparently N0 neck is, in fact, truly N0. This information may make a watchful waiting approach more acceptable to both patient and physician.

Residual/Recurrent Disease

Following surgery and/or radiation therapy, it can be difficult to detect residual or recurrent tumor clinically, though findings such as the presence of a mass, increasing pain, or soft-tissue necrosis may suggest a recurrence. Disease may also be difficult to detect on posttherapeutic CT and MR imaging studies due to edema, scarring, and flap reconstruction.[54, 55] However, earlier detection of persistent or recurrent tumor may allow institution of more timely and more effective salvage therapy. Biopsy of suspicious areas can be performed, but biopsy of an irradiated area may precipitate tissue necrosis.[56] This is a particular problem in the larynx, where chondronecrosis may necessitate laryngectomy. Biopsy is also not a perfect gold standard, as failure to biopsy deeply enough or in the correct location may cause a focus of tumor located in desmoplastic, poorly vascularized tissue to be missed. FDG PET can be very effective in this setting, as it is not limited by anatomic distortion, as are CT and MR imaging, and the PET result may be useful to guide fine needle biopsy.[57, 58]

The performance of FDG PET in the detection of residual/recurrent disease following primary therapy has been assessed by multiple groups[57, 58] (Table 45-2). Sensitivity for detection of disease generally ranges from 80% to 100%, while specificity ranges from 43% to 100%. The high sensitivity suggests that disease is unlikely to be missed if present (Fig. 45-9), though false positives are a significant issue necessitating close clinical and imaging correlation. A negative result is generally highly reassuring, as the negative predictive value of FDG PET has been shown to be high.[26, 59] At present, most FDG PET scans that are performed in patients at risk for recurrent disease are performed because of clinical suspicion of disease. The role of FDG PET in routine surveillance of the posttherapy head and neck cancer patient has not yet been determined, though it has been suggested as a natural (and cost-effective) extension of the above results.[57] Stokkel et al. suggest that in patients suspected of having recurrent laryngeal or hypopharyngeal cancer in whom FDG PET is negative, endoscopy may be omitted for at least 6 months and possibly up to a year, resulting in a considerable cost saving.[26] At present, several institutions are beginning to move in this direction, with patients undergoing regular clinical follow-up, baseline posttherapy (surgery and/or irradiation) imaging, and serial

Copyright © 2003, Mosby, Inc. All rights reserved.

FDG PET. Additional anatomic imaging is performed if the findings on FDG PET require correlation.

Response to Therapy

In those cases where radiation therapy, alone or in combination with chemotherapy, is used as the initial therapy for SCC of the head and neck, PET may be useful to monitor the response to therapy and potentially to predict which patients will have a durable response. This should be particularly useful in the context of organ preservation protocols, where the concern about missing the window of opportunity for surgical salvage is always present.

Greven et al. evaluated a group of patients both before and after radiation therapy.[63] FDG PET scans obtained 1 month after high-dose radiation therapy showed decreased uptake in all tumors identified on the pretherapy scans. There was persistent disease in 3/16 patients who had normal posttherapy scans, while 6/6 patients with decreased but persistent uptake all had persistent disease. Thus, on FDG PET scans obtained 1 month following high-dose radiation therapy, a negative scan was not an accurate indicator of disease status, though a positive scan suggests that persistent disease is likely. By 4 months posttherapy, negative scans became more reliable. However, some surgeons fear that by this time, the surgical window of opportunity may have been missed. Similar early post–radiation therapy findings were reported by Lindholm et al. using ^{11}C-methionine, with high uptake on the scan suggesting persistent disease.[64]

Haberkorn et al. performed FDG PET studies both before and after chemotherapy in 11 patients and found that the change in FDG uptake was highly correlated with tumor regression.[65] In addition, primary lesions and multiple metastatic lymph nodes in the same patient often had different baseline metabolism and different changes following therapy, a potentially interesting commentary on tumor heterogeneity even in the same patient and consistent with the known clinical finding that nodes respond less well than primary sites to radiation therapy. Reisser et al. studied 12 patients with metastatic SCC before and after the first chemotherapeutic cycle.[66] They found that one patient with a lymph node that had increasing metabolism, and three patients who had no significant metabolic changes after therapy, were clinically unresponsive and showed progressive tumor growth. However, in some patients with an excellent initial response, survival was poor. Therefore, although nonresponders certainly may be directed early to other therapies, the predictive value of an initial improvement is uncertain.

Kitagawa et al. studied the effects of combined chemotherapy and radiation therapy in 15 patients with SCC of the head and neck and found that pretreatment FDG PET is

Table 45-2
FDG-PET IN THE DETECTION OF RESIDUAL/RECURRENT SCC OF THE HEAD AND NECK

Authors (reference#)	# Pt.	#Scans	Sensitivity	Specificity	Scan Indications	Comments
Anzai et al. (57)	11	11	0.86	1.00	Clinical suspicion of recurrence	A case of melanoma is excluded
Bailet et al. (45)	10	NS	1.00	NA	Protocol: scans at 2-4 month intervals	Followed until positive scan, then biopsied
Farber et al. (58)	28	28	0.86	0.93	Clinical suspicion, but no obvious mass or lesion to bx	Scanner consists of six large NaI detectors
Fischbein et al. (59)	35	36	1.00 (P) 0.93 (N)	0.64 (P) 0.77 (N)	Suspicious or equivocal f/u clinical or imaging exam	Over half the patients had no clinical evidence of recurrence
Greven et al. (60)	11	11	1.00 (P)	0.83 (P)	Suspected persistent or recurrent disease	Only one case specifically commented on nodes
Hanasono (39)	34	34	1.00 (P) 1.00 (N)	0.85 (P) 0.89 (N)	Clinical details NA	Scanned 3 months to 4 years post primary therapy
Keyes et al. (42)	31	NS	0.80	0.81	Symptoms of recurrence	Institutional experience reviewed, specifics NA
Lapela et al. (61)	15	17	0.94	0.43	Clinical suspicion of recurrence	Both ‘‘suspicious’’ and ‘‘clearly positive’’ cases included
			0.88	0.86		Only ‘‘clearly positive’’ cases included
Manolidis et al. (62)	15	15	0.92 (P) 0.75 (N)	1.0 (P) 1.0 (N)	Clinically suspicious, difficult to diagnose	Fourteen patients with non-SCC were also studied
Paulus et al. (33)	13	13	0.71 (P) 0.75 (N)	1.00 (P) 0.80 (N)	Recurrent cancer vs post-radiation soft tissue changes	FDG PET modified clinical management in 4/13
Rege et al. (31)	14	18	1.00 (P)	0.64 (P)	Clinical suspicion of recurrence	1 patient lost to f/u
			1.00 (N)	0.94 (N)		Length of f/u for nodal disease not noted
Stokkel et al. (26)	48	48	1.00	0.71	Clinical suspicion of recurrence	Scans performed with a dual-head PET camera

Note: information about primary site and nodal recurrence is presented separately when possible
Legend: P = primary site; N=nodal disease; NA = not available; NS = not specified; f/u = follow-up; bx = biopsy
(Modified from Fischbein N, Anzai Y, Mukherji SK. Application of new imaging techniques for the evaluation of squamous cell carcinoma of the head and neck. Seminars US CT MRI 1999; 20:187-212.)

Copyright © 2003, Mosby, Inc. All rights reserved.

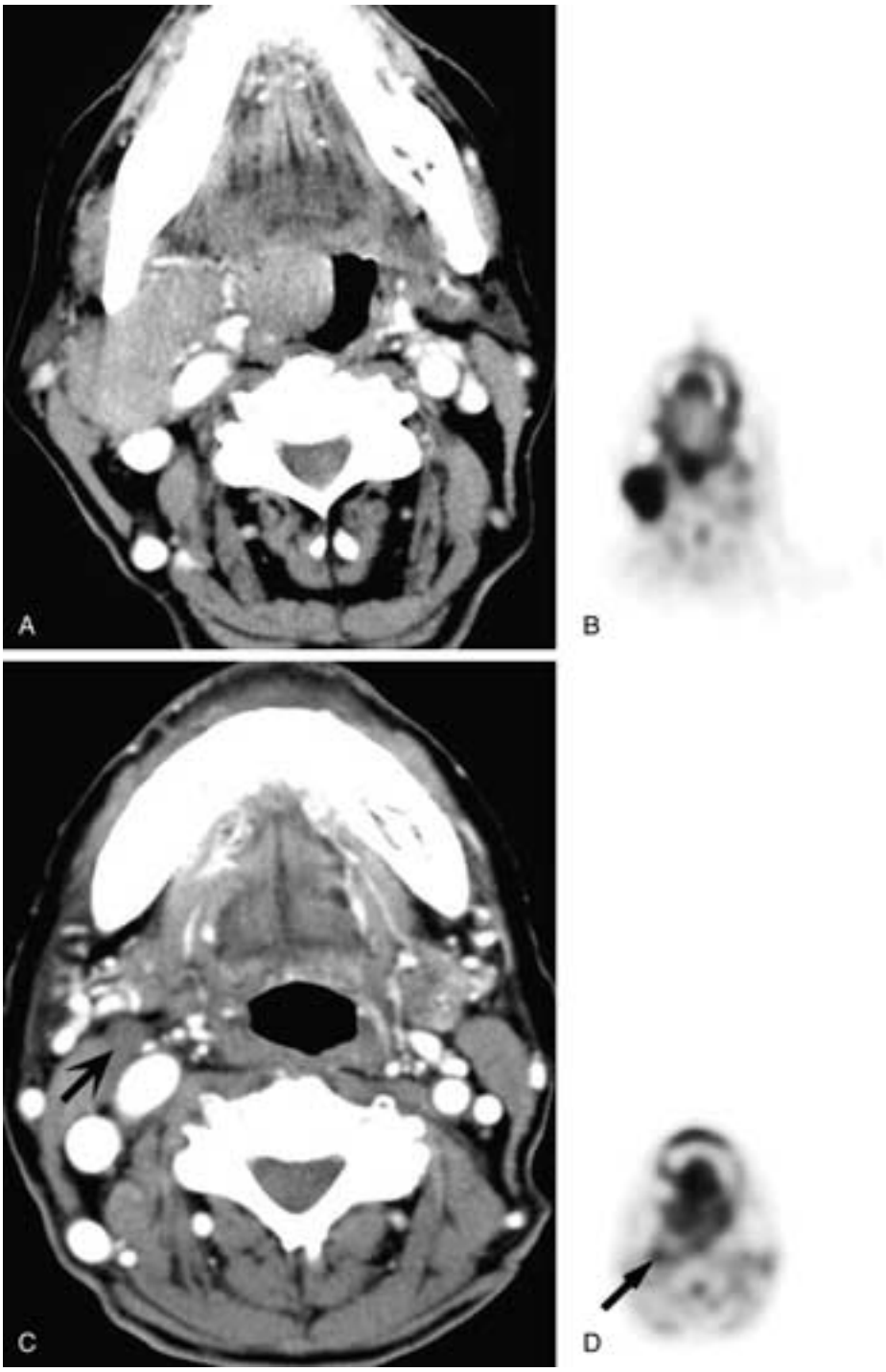

VIEW IMAGE

FIGURE 45-9 A 65-year-old woman presented with a neck mass that was positive for SCC on fine needle aspiration. Head and neck examination demonstrated a mass in the right tonsillar fossa extending toward the right base of the tongue. **A**, Contrast-enhanced CT scan shows an exophytic mass emanating from the right tonsillar fossa as well as a large nodal mass. **B**, An FDG PET scan demonstrates intense uptake in the right tonsil and the right neck mass. The patient was treated with combined radiation therapy and chemotherapy, which she tolerated well. The neck mass resolved clinically, and the tonsillar fossa appeared unremarkable. **C**, A follow-up CT scan obtained with slightly different angulation shows a normal-appearing right tonsillar fossa but persistent soft tissue in the location of the conglomerate nodal mass (*arrow*). **D**, A follow-up FDG PET scan was obtained that showed minimal asymmetry of the tonsils and a small, questionable focus of activity (*arrow*) at approximately the site of the markedly decreased nodal mass. A neck dissection was performed that showed a focus of tumor only at the level that was suspicous on FDG PET, and the patient has remained well at follow-up.

useful in predicting the response to treatment, while posttreatment FDG PET can evaluate residual viable cells.[18] Lowe et al. studied 28 patients with stage III/IV head and neck cancer who were participating in organ preservation protocols.[67] FDG PET was performed before and 1 to 2 weeks after chemotherapy. The sensitivity and specificity of PET for residual cancer after therapy were 90% and 83%, respectively. This group believes that, in general, biopsy of most lesions after therapy will provide the lowest-cost approach to therapy evaluation as long as the lesion is visible and accessible. They recommend that PET be done when biopsy access is difficult (e.g., some paranasal sinus tumors), when posttherapeutic biopsy results are questionable for some reason, or when the tumor site has a normal, reepithelialized appearance after therapy (Fig. 45-10).

^{11}C-methionine PET (MET PET) has also been applied to evaluate the early response to radiotherapy in head and neck cancer.[68] MET uptake in tumor decreased significantly during the first 2 to 3 weeks of radiotherapy, but the rate of decrease in tracer uptake was comparable in relapsing

Copyright © 2003, Mosby, Inc. All rights reserved.

patients and those who remained locally controlled, thereby limiting the use of MET PET for prediction of the response to radiotherapy.

Evaluation of Metastases

Patients with recurrent or advanced-stage head and neck cancer are at particularly high risk of distant metastases, usually to lung and liver, but also potentially to bone and other sites. The exclusion of distant metastatic disease is important in staging and prognostication. It is also important when a major surgical procedure is contemplated, since the presence of distant metastases is a contraindication to aggressive surgical and radiotherapeutic procedures aimed at cure rather than palliation (Fig. 45-11). Patients have typically been staged with chest x-ray and liver function tests, though many clinicians selectively use CT scans of the chest and abdomen for staging. Whether the whole body is imaged during a PET scan or whether the examination is limited to the head and neck varies among institutions. Keyes et al. reported having modified their scanning protocol to include the lungs, but in only one case did PET show a significant lesion not found by routine evaluation; as a result, this approach was abandoned.[42] Manolidis et al. examined the detection of occult metastatic disease in 29 patients.[62] Ten metastases were confirmed histopathologically, and the PET scan was positive in 9/10 instances. One false positive and one false negative occurred, making the sensitivity in detecting distant metastases 90%, the specificity 94%, the positive predictive value 90%, and the negative predictive value 94% in this small cohort. With improvements in scanner technology and reconstruction methods, it is likely that whole-body screening for distant disease will become a useful adjunct when evaluating patients with head and neck cancers by PET.

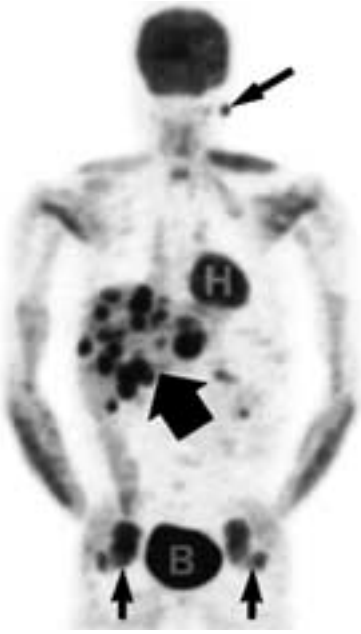

VIEW IMAGE

FIGURE 45-10 A 36-year-old HIV-positive man with a history of Merkel cell carcinoma of the parotid region, was referred with locally recurrent disease for consideration of definitive therapy. A staging chest x-ray and liver function tests were normal. A whole-body FDG PET scan demonstrates focal activity in the left parotid region (*long, thin arrow*), as well as multiple foci of intense tracer accumulation in the liver (*thick arrow*). Abdominal CT scan and fine needle aspiration confirmed metastatic Merkel cell carcinoma, and the patient was treated with palliative chemotherapy. The whole-body scan shows normal activity in the heart (*H*) and bladder (*B*), as well as activity in the hands bilaterally (*short, thin arrows*) and forearm muscles related to finger clenching.

Non-SCC Malignancy

Most, but not all, of the above-referenced articles contain a mix of histologies under the rubric of ''head and neck cancer,'' including adenoid cystic carcinoma, mucoepidermoid carcinoma, mucosal melanoma, and basal cell carcinoma in addition to the dominant SCC. The numbers of these other malignancies are generally small, and it is not possible to extract separate conclusions about them. However, the general experience seems to reflect similar performance by FDG PET for these malignancies compared to SCC.

Salivary tumors have been looked at specifically to see if FDG PET could correctly differentiate benign from malignant disease.[69] Subjective PET findings correctly differentiated malignant from benign disease in 69% of cases, with 100% of malignant lesions but only 42% of benign lesions correctly classified. PET findings were false positive for malignancy in 30% of cases, and SUV analysis and ratios failed to distinguish benign from malignant disease. These authors concluded that FDG PET was not useful in distinguishing malignant from benign salivary gland tumors. FDG PET has also been shown to be useful in evaluating metastases from mucosal and nonmucosal melanoma.[70] Thyroid cancer and lymphoma have also been looked at more specifically, and these will be discussed next.

Thyroid Cancer

In the determination of management and further therapeutic options in the patient with differentiated thyroid cancer who has already undergone thyroidectomy and radioactive iodine ablative therapy, whole body ^{131}I scintigraphy (WBS) is the most important functional imaging technique. In many patients, however, thyroid cancer tissue does not concentrate ^{131}I and therefore cannot be localized by this method. The loss of ^{131}I concentrating ability results in false-negative WBS in approximately 20% of cases of metastatic thyroid cancer.[71] There is considerable evidence that FDG PET is useful in planning the treatment and follow-up of thyroid cancer patients with negative WBS (Fig. 45-12).[71–77] In patients with either papillary/follicular or medullary thyroid cancer suspected of having locally recurrent or metastatic cancer on the basis of elevated or rising blood markers, FDG PET has demonstrated the ability to identify residual or recurrent disease when conventional imaging with WBS fails to demonstrate disease. Grunwald et al. found that FDG PET had greater than 80% sensitivity for suspected recurrence and/or metastases in the setting of negative WBS, while Chung et al. found that FDG PET was 94% sensitive and 95% specific for localization of metastatic sites in 33 patients with negative ^{131}I scans.[72, 74] FDG PET may not, however, be sensitive enough to detect minimal disease in cervical lymph nodes or to reliably demonstrate pulmonary metastases smaller than 1 cm.[71, 75] As a general management issue, if the thyroglobulin level (or calcitonin level with medullary carcinoma of the thyroid) is elevated

Copyright © 2003, Mosby, Inc. All rights reserved.

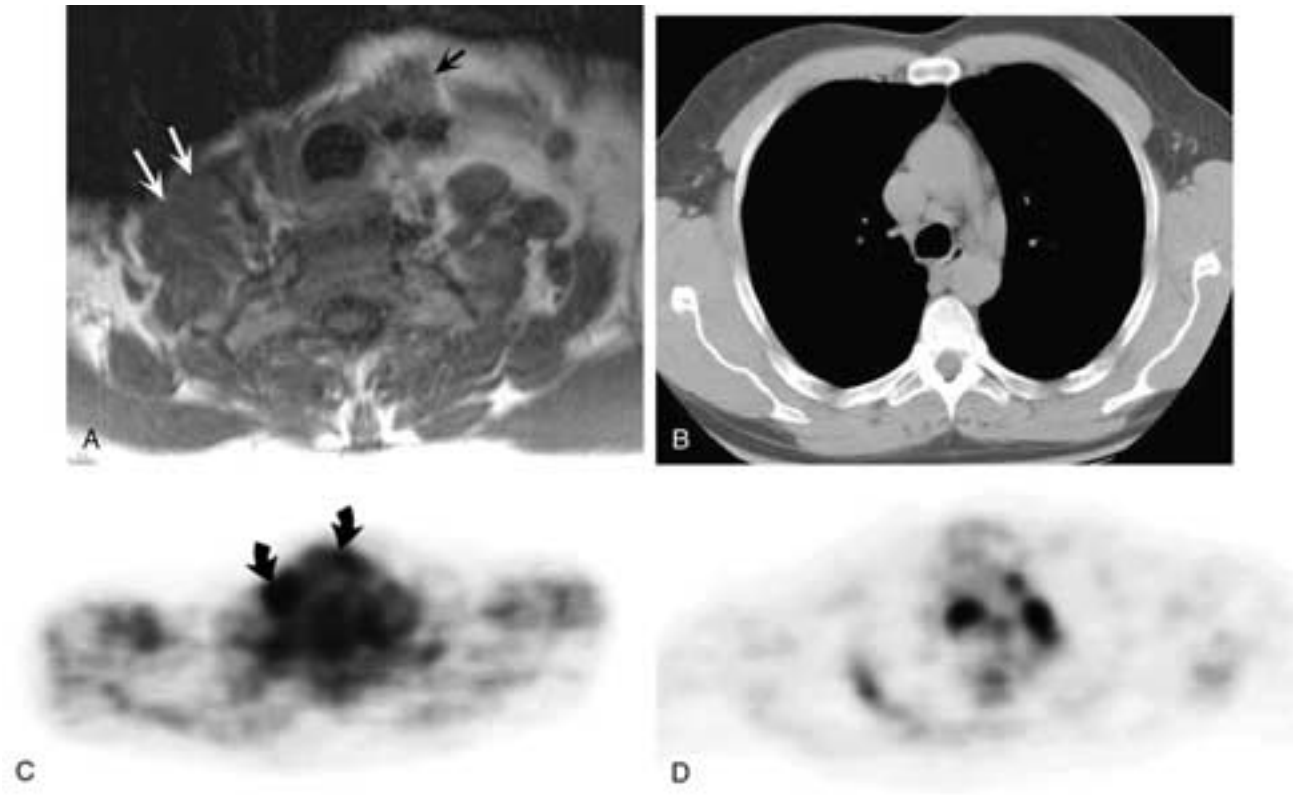

VIEW IMAGE

FIGURE 45-11 A 49-year-old man underwent total thyroidectomy and right neck dissection for poorly differentiated papillary carcinoma of the thyroid. He was subsequently treated with radioiodine, and follow-up whole body ^{131}I scans were negative. The patient was reimaged because of rising thyroglobulin levels and concern for recurrent disease. **A**, An axial T1-weighted image from an MR scan of the neck demonstrates soft tissue in the right anterior low neck (*white arrows*), but it is unclear if this is scarring and fibrosis related to prior neck dissection or residual or recurrent tumor. Focal soft tissue in the left anterior neck (*black arrow*) may similarly represent either treatment effects or tumor. **B**, An axial image from a noncontrast CT scan of the chest demonstrates pretracheal and anteroposterior window lymph nodes, none of which are clearly pathologic. **C**, An FDG PET image through the low neck confirms focal tracer accumulation in both sites in the neck that were suspicious on MR imaging (*arrows*). **D**, Multiple mediastinal nodes also accumulate tracer. Further neck surgery and mediastinoscopy confirmed the presence of thyroid cancer at these sites.

and a WBS is negative, FDG PET can be used to detect metastases and as a complement to anatomic imaging. If intervention such as dissection of iodine-negative lymph node metastases is contemplated, then a spiral CT scan of the lungs is probably useful to assess for pulmonary metastases.[75]

Lymphoma

Early results using FDG PET to assess malignant lymphoma of the head and neck suggested that the degree of FDG uptake correlated well with proliferative activity and that FDG PET was useful in prognostication.[78, 79] Walsh et al. evaluated four patients with non-Hodgkin's lymphoma of the head and neck and found that FDG PET enabled the extent of disease to be seen.[80] FDG PET has taken on a major role in the staging of lymphoma and has been suggested as a replacement for CT scanning and bone scintigraphy.[81, 82] A residual mass after treatment of lymphoma is a clinical challenge, because it may represent vital tumor as well as tissue fibrosis. Metabolic imaging by FDG PET offers the advantage of functional tissue characterization that is largely independent of morphologic criteria.[83, 84]

One caution, however, involves the role of whole-body FDG PET in the staging of extranodal B-cell lymphoma of the mucosa-associated lymphoid tissue (MALT) type, an increasingly recognized subtype of lymphoma affecting the head and neck (primarily the salivary and lacrimal glands). These generally low-grade malignancies do not show up well on FDG PET, leading to numerous false-negative results and poor correlation with staging by clinical and conventional anatomic imaging methods.[85]

Pitfalls

Like any test, FDG PET is subject to a number of limitations and also to certain pitfalls. In order to interpret FDG PET images accurately, one must be aware of the normal physiologic distribution of tracer, the spectrum of normal variations in uptake, and benign causes of FDG uptake that may be confused with malignancy.[27] Furthermore, one must be aware of the circumstances under which disease may be occult or very subtle on FDG PET. Knowledge of prior therapy is also important, as prior

Copyright © 2003, Mosby, Inc. All rights reserved.

surgery can result in significant tissue asymmetry that may make the normal side appear diseased in comparison with low activity on the side of prior surgery. Some of these factors have been commented on earlier but will be reviewed below, as they pertain specifically to the head and neck.

False Positives

Since FDG is taken up nonspecifically by glycolytically active cells, it accumulates in areas of inflammation as well as in tumors. In inflammation, its uptake is by macrophages and other inflammatory cells.[5, 86–88] It is possible that dynamic methods may be useful to distinguish granulation tissue from tumor tissue, but this is generally not clinically feasible using current methods.[89] Reactive or inflamed lymph nodes are a common cause of false-positive readings in the head and neck, limiting the specificity of FDG PET for detecting lymph node metastases. Ongoing inflammation at the site of a previously treated tumor may also account for false-positive readings and makes it difficult to determine whether a patient harbors residual or recurrent disease.[90] Muscular activity can also be confusing, and patients generally should lie quietly and refrain from speaking in order to avoid uptake in the cricopharyngeal area. In some cases, a muscle relaxant may be necessary to avoid muscular uptake artifacts.[33] Other potential sources of false-positive findings in the head and neck include healing bone and paranasal sinus inflammatory disease. Foreign body granuloma has also been reported to cause a false-positive result.[33]

False Negatives

A significant limitation of FDG PET scanning is its insensitivity to very small tumor deposits, on the order of 3 to 4 mm or less. Because of this, micrometastases are not reliably detected with FDG PET, and cervical nodal disease in patients with head and neck cancer may not be detected. Thus, in the N0 neck, how reliable a negative FDG PET scan of the neck is when planning a watchful waiting approach, rather than surgery or radiation therapy, remains an unanswered question. A purely cystic node with only a very thin rim of viable neoplastic tissue may also be overlooked on an FDG PET scan but would likely be detected by clinical palpation or conventional anatomic imaging. Finally, a false-negative scan may occur if FDG PET imaging is performed too soon after radiation therapy.[60]

Conclusion

FDG PET has become a powerful tool in oncologic imaging. In the field of head and neck cancer, it has proven to be useful in locating unknown primary and second primary lesions, staging nodal disease, detecting residual or recurrent disease following surgery and/or radiation therapy,

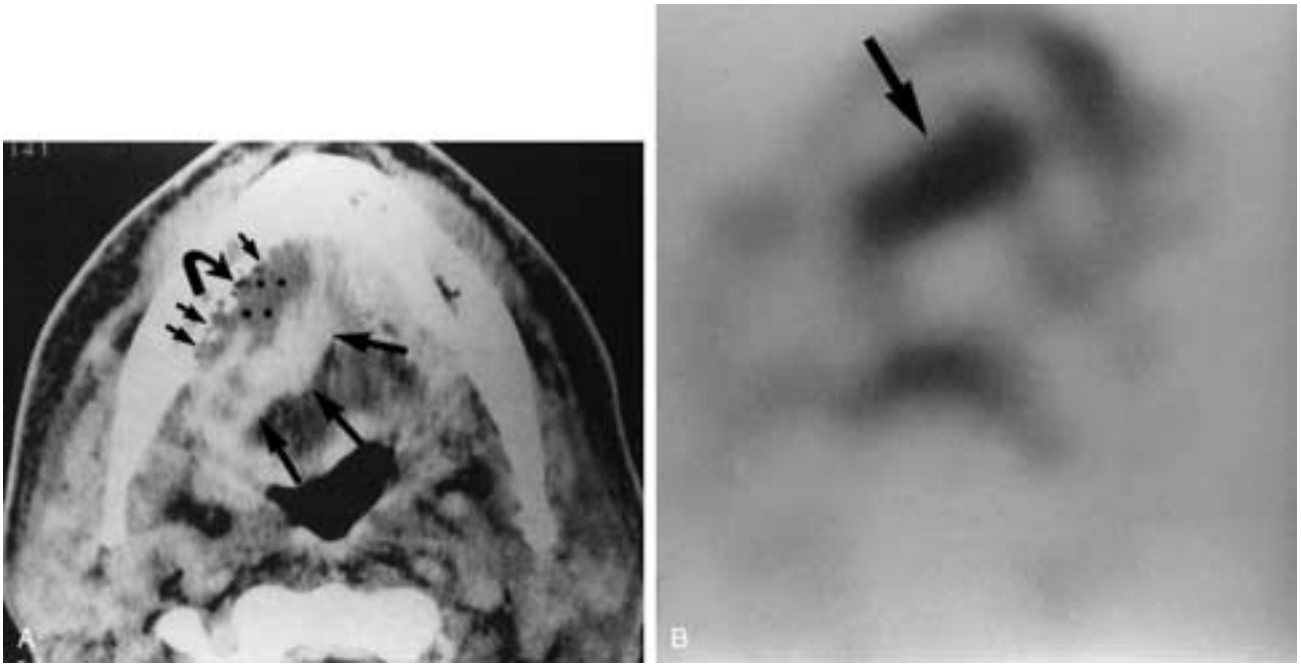

VIEW IMAGE

FIGURE 45-12 Correct identification of recurrent SCC by Tl-201 SPECT. **A**, Axial contrast-enhanced CT scan performed in a patient with a floor of mouth carcinoma 6 months after completion of combination radiation therapy and chemotherapy. The study shows a heterogeneously enhancing mass that has soft tissue (*large, straight arrows*) and low-attenuation components (*). Note the erosion along the lingual cortex of the mandible (*small, straight arrows*) and the presence of gas (*curved arrow*). These findings were suspicious for recurrent tumor. **B**, Axial Tl-201 SPECT image obtained at the floor of the mouth in the same patient illustrated in **A**. This study shows abnormal radiotracer uptake (*arrow*) in the region of the abnormality shown in **A**. Biopsy of this area revealed SCC. (From Mukherji SK, Gapany M, Phillips D, Neelon B, et al. Thallium-201 single-photon emission CT versus CT for the detection of recurrent squamous cell carconima of the head and neck. AJNR 1999;20:1215–1220.)

Copyright © 2003, Mosby, Inc. All rights reserved.

monitoring the response to organ preservation therapy, and detecting distant metastases. FDG PET may prove to be a cost-effective cancer surveillance tool in patients with a prior diagnosis of head and neck cancer. It also has a significant role in evaluation and treatment planning in patients with thyroid cancer and negative ^{131}I WBS. Both false-positive and false-negative scans do, of course, occur, and knowledge of these issues is important in the accurate interpretation of FDG PET scans.

THALLIUM-201 SINGLE PHOTON EMISSION TOMOGRAPHY

Introduction

Another technique in which initial investigations have been promising in the area of head and neck oncology is thallium-201 single photon emission tomography (Tl-201 SPECT). Initial investigations have shown that Tl-201 SPECT may be beneficial in attempting to differentiate recurrent tumor from posttreatment changes, and may be useful for both predicting and assessing the response of patients treated with nonsurgical organ preservation therapy.[90–97]

Mechanism

The primary mechanism of thallium entry into the cell is believed to be coupled to the sodium/potassium ATPase pump located in the cell membrane.[98] This system actively transports potassium into the cell in exchange for sodium, thereby creating a high intracellular potassium concentration. Thallium-201 is believed to act similarly to potassium and competes with potassium for intracellular transport across the cell membrane via the sodium/potassium ATPase system (potassium analogue).[98–101] The reason for the elevated thallium-201 uptake in tumor has not been entirely elucidated but is likely due to the increased cellular proliferation of neoplastic cells compared to adjacent normal tissue.[98, 102, 103]

Limitations

The primary disadvantage of thallium-201 imaging of the upper aerodigestive tract is the background uptake of thallium-201 by salivary and thyroid glands, as thallium-201 is normally taken up by the parotid, submandibular, and thyroid glands.[104] The uptake within the parotid and salivary glands can be especially problematic since the saliva will also have increased activity. Pooling of the saliva in the floor of the mouth may prevent accurate evaluation of lesions involving the oral cavity and may reduce the conspicuity of tumors in this area. This activity may be reduced by placing gauze in the patient's mouth and drying the oral mucosa. Another alternative in patients who have no medical contraindication to the administration of atropine is to use this drug to reduce salivary function prior to imaging.

Clinical Applications

Several studies have demonstrated that SCC is thallium avid, and previous investigators have suggested that thallium-201 may be able to detect lesions larger than 1 cc.[104] As a result, it has been suggested that thallium-201 may be useful in the evaluation of patients with unknown primary tumors in a manner similar to FDG PET scanning. Isolated cases of the successful use of thallium-201 for localizing unknown primary tumors have been reported.[97] However, larger series that have prospectively evaluated the role of thallium-201 in identifying unknown primary tumors have not yet been performed.

Initial results have shown that thallium-201 SPECT may be helpful in attempting to differentiate recurrent tumor from posttreatment changes and may be more accurate than CT or MR imaging for making this important distinction (Figs. 45-13 and 45-14). Valdes-Olmes et al. reported a higher diagnostic accuracy for thallium-201 SPECT (sensitivity = 93%, specificity = 78%) than for CT/MR imaging (sensitivity = 76%, specificity = 30%).[97] Mukherji et al. reported higher specificity for thallium-201 SPECT (sensitivity = 88%, specificity = 94%) than for CT (sensitivity = 100%, specificity = 24%) when attempting to identify recurrent tumor.[91]

Leitha et al. reported a sensitivity and a specificity of 95.3% and 78.4%, respectively, for the ability of technetium-99m-MIBI (hexakis-2-methoxyisobutyl isonitrile) SPECT to differentiate recurrent head and neck SCC from posttreatment changes.[105] If these results are substantiated, PET FDG, thallium-201, and technetium-99m-MIBI imaging all compare favorably for detecting tumors in patients with head and neck SCC.

There may be potential advantages to using thallium-201 SPECT rather than FDG PET, especially when imaging nasopharyngeal carcinoma and other skull base tumors. Unlike FDG, the background uptake of thallium-201 by normal brain is low. As a result, the conspicuity of nasopharyngeal and skull base tumors may be reduced on PET-FDG, as these tumors are directly adjacent to the normal high brain FDG activity. However, because of the low background activity in the normal brain, these tumors tend to be well delineated on thallium-201 imaging.[91]

Initial reports have suggested that thallium-201 SPECT may be useful in predicting the response to definitive radiation therapy and for assessing the response within 6 weeks after the completion of nonsurgical organ preservation therapy. Nagamachi et al. demonstrated that quantitative measurements of thallium-201 uptake may be useful in predicting the response of SCC of the upper aerodigestive tract to radiotherapy alone.[94] Mukherji et al. suggested that Tl-201 SPECT may be a reliable technique for assessing the response to treatment performed within 6 weeks after the completion of combined chemotherapy and radiation therapy (Figs. 45-15 and 45-16).[92] As previously mentioned, due to a high false-negative rate, FDG PET has been shown to be unreliable in predicting the treatment response when performed within 1 to 2 months after completion of radiation therapy.[63] Thus, initial results suggest that thallium-201 may be able to predict radioresponsiveness and assess the success of treatment earlier than can FDG-PET or cross-sectional

Copyright © 2003, Mosby, Inc. All rights reserved.

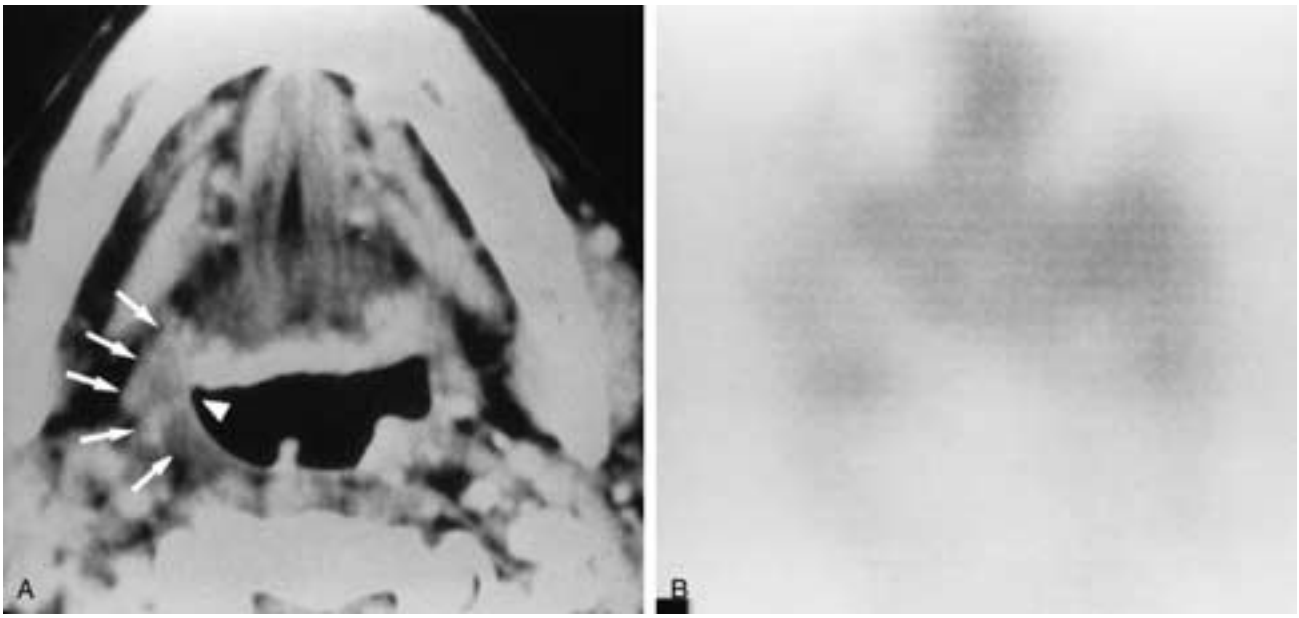

VIEW IMAGE

FIGURE 45-13 Correct exclusion of recurrent SCC by Tl-201 SPECT. **A**, Contrast-enhanced CT image in a patient with a right tonsil carcinoma previously treated with surgery and radiation therapy 14 months prior to this study. The patient presented with a right-sided nodal recurrence. This patient was a candidate for salvage surgery if no recurrent tumor was present at the primary site. Pretreatment studies were unavailable for comparison. CT shows an asymmetric soft-tissue mass involving the right tonsil (*arrows*). This is associated with asymmetry of the right glossotonsillar sulcus (*arrowhead*). Compare this to the appearance of the normal contralateral side. **B**, Axial Tl-201 SPECT image through the low oropharynx obtained in the patient in **A** shows no abnormal radiotracer uptake in the right tonsil. This patient has been followed for over 2 years after completion of treatment and has no evidence of recurrent tumor at the primary site. (From radiotracer uptake (*arrow*) in the region of the abnormality shown in **A**. Biopsy of this area revealed SCC. (From Mukherji SK, Gapany M, Phillips D, Neelon B, et al. Thallium-201 single-photon emission CT versus CT for the detection of recurrent squamous cell carconima of the head and neck. AJNR 1999;1213–1220.)

imaging. However, further studies are needed to confirm these early results.

PROTON MAGNETIC RESONANCE SPECTROSCOPY

Introduction

Recent in vitro and in vivo investigations have suggested that proton magnetic resonance spectroscopy (^{1}H-MRS) may be helpful in providing metabolic information about abnormalities in the extracranial head and neck. Several studies have found that assessment of the relative levels of choline (Cho) and creatine (Cr) can provide information that may help differentiate SCC from nonneoplastic tissue and may provide information that helps assess the response to nonsurgical organ preservation treatment protocols.[106–110] Elevation of the Cho/Cr ratio appears to be a consistent finding for SCC and has been demonstrated in cell cultures and from tissue samples from both the primary tumor site and metastatic lymph nodes (Figs. 45-17 to 45-19).[107] These in vitro findings have also been demonstrated in vivo. ^{1}H-MRS analysis of SCC performed at 1.5T has demonstrated significant elevation of the Cho/Cr ratio in patients with tumors compared with normal tongue muscle (Figs. 45-20 and 45-21). A complete review of ^{1}H-MRS is outside the scope of this discussion. The purpose of this section is to summarize the recent investigations that have been performed to evaluate ^{1}H-MRS in SCC and to comment on the potential clinical role of MRS in the extracranial head and neck.

Metabolites

The majority of ^{1}H-MRS tissue characterization in the upper aerodigestive tract has focused on two metabolites, Cho and Cr. Cho is a nutrient that is present in most foods, is absorbed from the diet, and serves as a precursor of two important molecules: acetylcholine and phosphatidylcholine.[111] Cho is also believed to be an important constituent in the phospholipid metabolism of all cell membranes.[112] The Cho molecule is transported intracellularly by a low-affinity system with its mechanism coupled to the synthesis of phosphatidylcholine.[113] Once intracellular, Cho is initially phosphorylated by Cho phosphotransferase to form phosphocholine. This latter molecule is the precursor of phosphatidylcholine, which is formed by the Kennedy pathway.[114] The *N*-methyl [$^{\pm}$N$(CH_3)_3$] group of Cho and Cho-based metabolites is detected spectroscopically at 3.2 ppm.[115] The total Cho resonance peak is believed to be composed of Cho, phosphocholine, phosphatidylcholine, and glycerophosphocholine. Elevation of this peak is not specific for SCC and has been demonstrated in several tumors. Increased levels of Cho are thought to be related to

Copyright © 2003, Mosby, Inc. All rights reserved.

increased cellular membrane phospholipid biosynthesis and are, therefore, believed to be an active marker for cellular proliferation.[116–121]

Cr is thought to play a role in the maintenance of energy metabolism. Phosphocreatine acts as a store for high-energy phosphates in the cytosol of muscles and neurons and is also believed to buffer cellular adenosine triphosphate and adenosine diphosphate.[111, 112] It may be obtained from the diet or synthesized de novo within the liver, kidneys, and pancreas by precursor molecules, which include arginine, glycine, and S-adenosylmethionine.[111, 121] Cr is converted to phosphocreatine by the enzyme creatine kinase. Because phosphocreatine is a high-energy phosphate compound, it has been suggested that it may help sustain the level of adenosine triphosphate in energy-demanding tissues such as actively proliferating tumors. Spectroscopically, the Cr

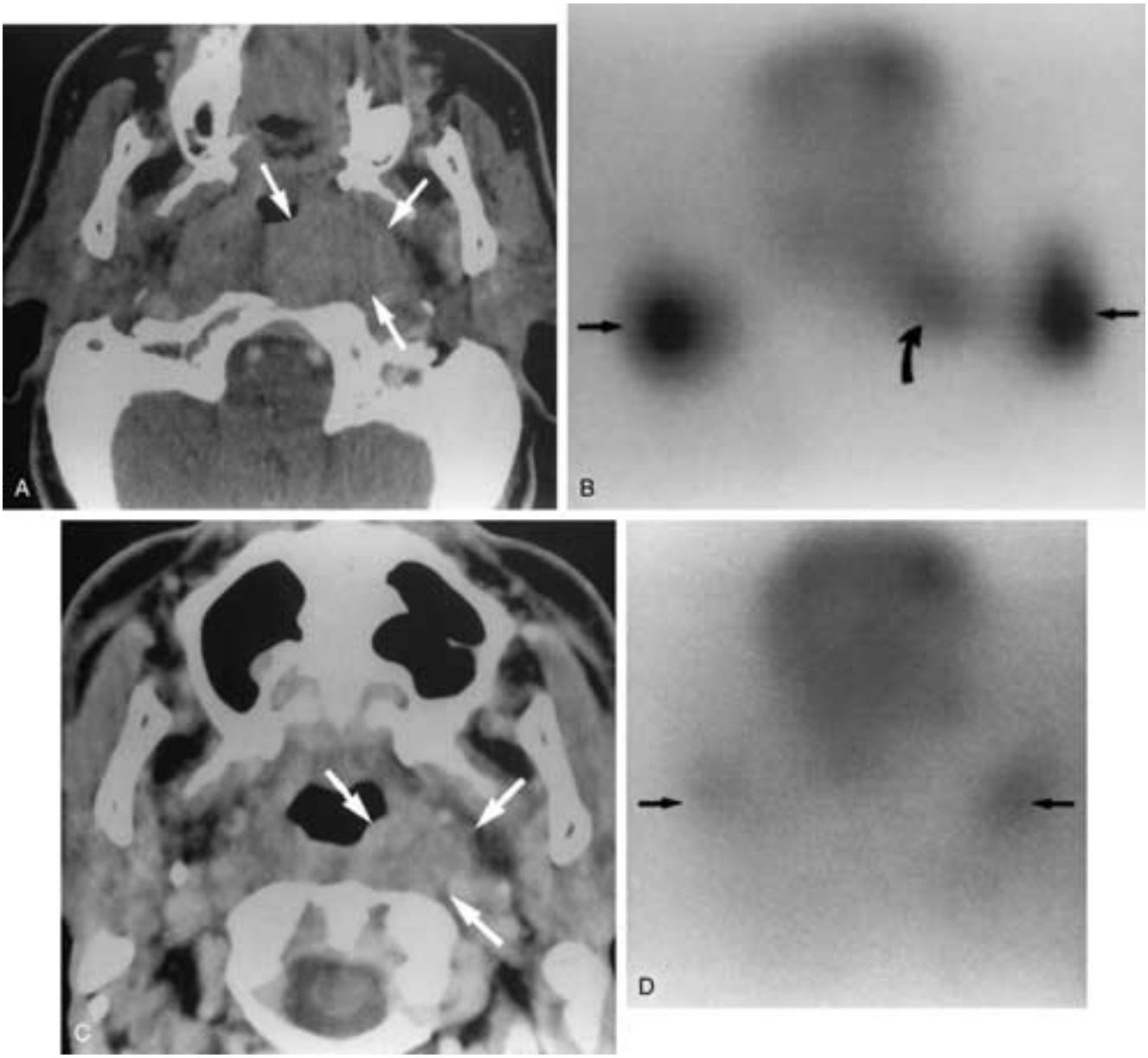

VIEW IMAGE

FIGURE 45-14 Successful local control following nonsurgical organ preservation therapy. **A**, Axial pretreatment contrast-enhanced CT image demonstrates an SCC involving the left side of the nasopharynx (*arrows*). **B**, Axial image from a pretreatment thallium-201 SPECT scan obtained at approximately the same level as **A** shows an area of abnormal radiotracer uptake corresponding to the abnormality seen on CT (*curved arrow*). Normal parotid gland uptake (*small arrows*). **C**, CT scan performed 6 weeks after completion of treatment demonstrates a persistent mass in the region of the primary site (*arrows*). **D**, Posttreatment thallium study obtained at approximately the same level as **C** shows no abnormal radiotracer uptake 6 weeks after completion of therapy. This patient had no evidence of recurrent disease at the primary site 2 years after completion of treatment. Note the reduction in parotid gland uptake following treatment (*arrows*). (From Mukherji SK, Gapany M, Neelon B, et al. Evaluation of ^{201}T1 SPECT for predicting early treatment response in patients with squamous cell carcinoma of the extracranial hand and neck treated with nonsurgical organ preservation therapy: Initial results. J Comput Assist Tomogr 2000;24:146–151.)

Copyright © 2003, Mosby, Inc. All rights reserved.

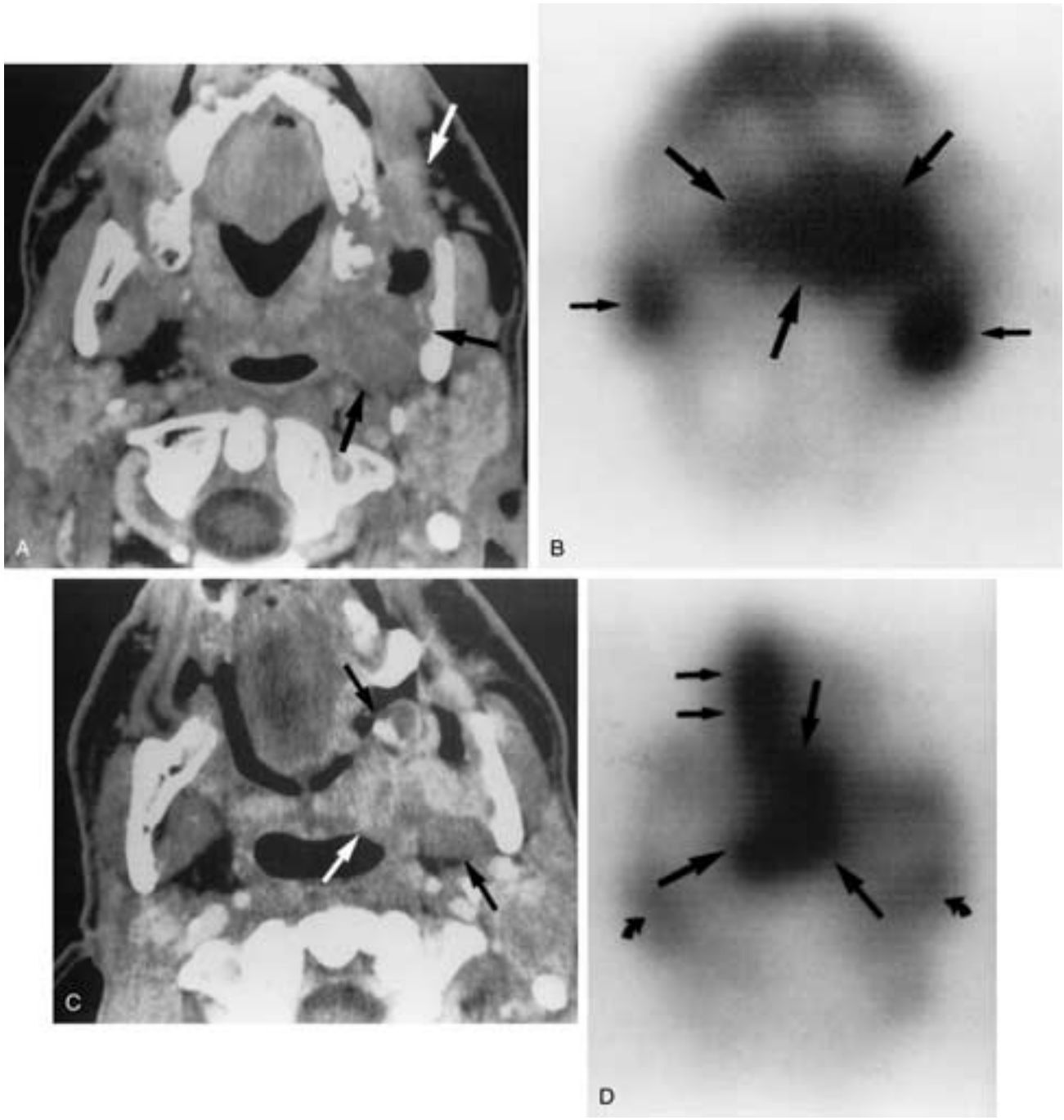

VIEW IMAGE

FIGURE 45-15 Local failure following nonsurgical organ preservation therapy. **A**, Axial pretreatment contrast-enhanced CT image demonstrates an SCC involving the left tonsil that extends deeply to involve the masticator space (*arrows*). **B**, Axial image from a pretreatment thallium-201 SPECT study obtained at approximately the same level as **A** shows an area of abnormal radiotracer uptake corresponding to the abnormality seen on CT (*large arrows*). Normal parotid gland uptake (*small arrows*). **C**, CT scan performed 6 weeks after completion of treatment demonstrates a persistent mass in the region of the primary site (*arrows*). **D**, Posttreatment thallium study obtained at approximately the same level as **C** shows persistent abnormal radiotracer uptake 6 weeks after completion of therapy (*large arrows*). This patient had biopsy-proven persistent disease at the primary site 6 weeks after completion of therapy. Note the reduction in parotid gland uptake following treatment (*curved arrows*). Probable nasal mucosa uptake (*small arrows*). (From Mukherji SK, Gapany M, Neelon B, et al. Evaluation of ^{201}T1 SPECT for predicting early treatment response in patients with squamous cell carcinoma of the extracranial hand and neck treated with nonsurgical organ preservation therapy: Initial results. J Comput Assist Tomogr 2000;24:146–151.)

Copyright © 2003, Mosby, Inc. All rights reserved.

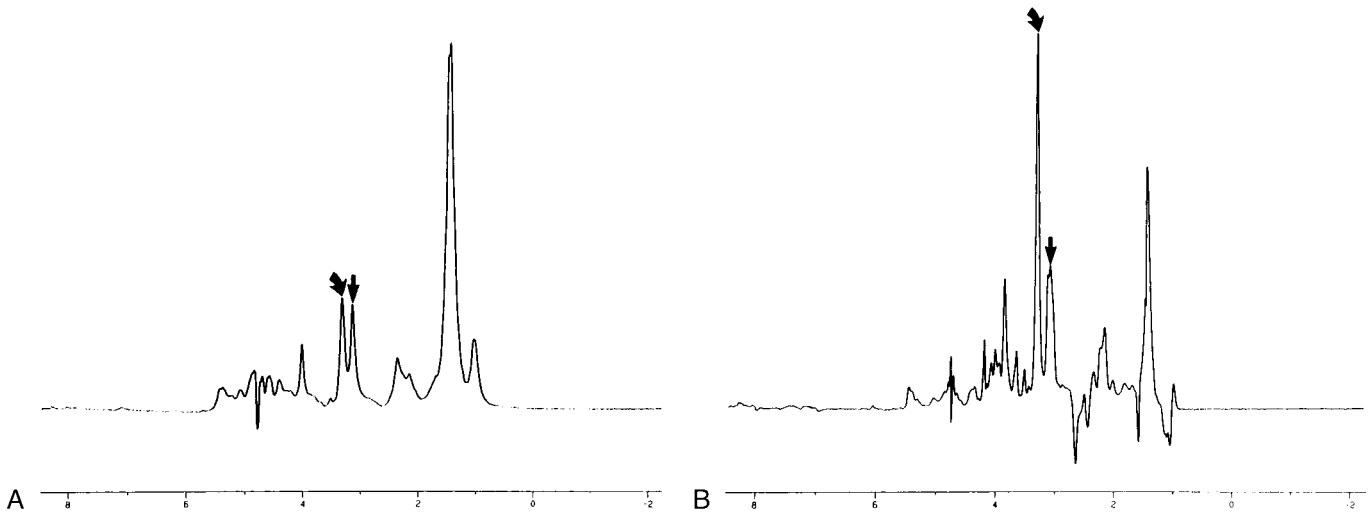

VIEW IMAGE

FIGURE 45-16 In vitro ^{1}H MRS (TR = 2000 msec, TE = 136 msec). **A**, ^{1}H MRS of a normal tissue sample obtained from strap muscle shows similar areas of the Cho (*curved arrow*) and Cr (*straight arrow*) resonances. The Cho/Cr ratio is 1.06. **B**, ^{1}H MRS of an epiglottic SCC tissue sample obtained from the same patient in **A** shows elevation of the Cho resonance (*curved arrow*) with respect to the Cr resonance (*straight arrow*). The Cho/Cr ratio is 1.92. (From Mukherji SK, Schiro S, Castillo M, et al. Proton MR spectroscopy of squamous cell carcinoma of the extracranial head and neck: in vitro and in vivo studies. AJNR 1997;18:1057–1072.)

resonance is observed at 3.02 ppm, and it is believed to be comprised of both phosphocreatine and Cr.[121]

Clinical Applications

The importance of identifying and isolating consistent and reproducible ^{1}H-MRS metabolic markers for malignancies of the upper aerodigestive tract rests not so much in the ability of ^{1}H-MRS to initially diagnose tumor, but in its ability to identify early recurrent tumor and to monitor tumor response during therapy.[106, 109, 122–124] Because both surgery and radiotherapy result in scarring and soft-tissue edema, physical examination and CT/MR imaging often are inadequate in detecting early tumor recurrence after treatment.

Radiation therapy causes significant erythema and induration within the treated area, and this inflammatory response may be exacerbated with the addition of concomitant chemotherapy.[125] In most sites, this inflammatory response progresses to end-stage fibrosis (scar) within 3 to 4

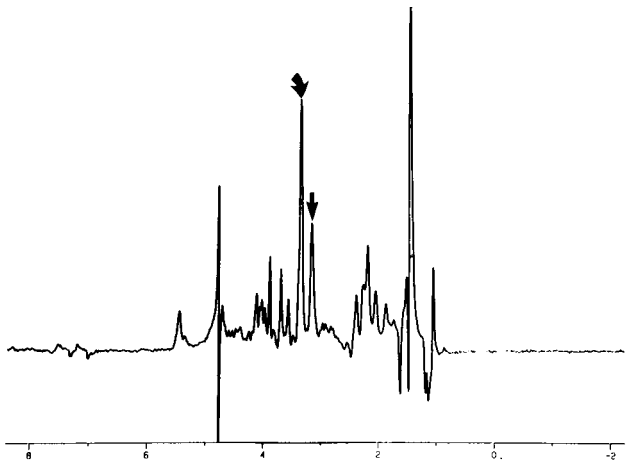

VIEW IMAGE

FIGURE 45-17 In vitro 1D ^{1}H MRS of metastatic cervical lymph node (TR = 2000 msec, TE = 136 msec). One-dimensional ^{1}H MRS demonstrates elevation of Cho/Cr ratio that measures 1.98 (Cho, *curved arrow*; Cr, *straight arrow*). (From Mukherji SK, Schiro S, Castillo M, et al. Proton MR spectroscopy of squamous cell carcinoma of the extracranial head and neck: in vitro and in vivo studies. AJNR 1997;18:1057–1072.)

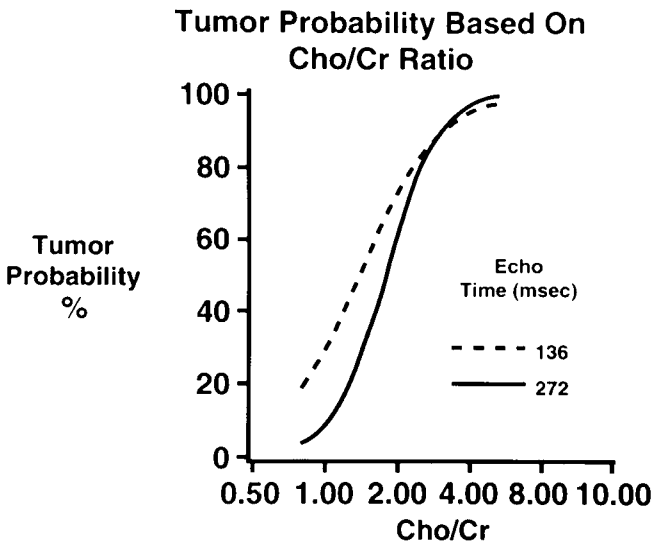

VIEW IMAGE

FIGURE 45-18 Plot of the tumor probabilities based on the Cho/Cr ratio. The curves have an S-shaped configuration (ogive) and support the contention that the Cho/Cr ratio is an important metabolic marker that differentiates tumor and normal tissue. The greater slope of the 272 curve compared to the 136 curve between the 20th and 80th percentiles suggests that a longer TE may provide better discrimination between tumor and normal tissue. (From Mukherji SK, Schiro S, Castillo M, et al. Proton MR spectroscopy of squamous cell carcinoma of the extracranial head and neck: in vitro and in vivo studies. AJNR 1997;18:1057–1072.)

Copyright © 2003, Mosby, Inc. All rights reserved.

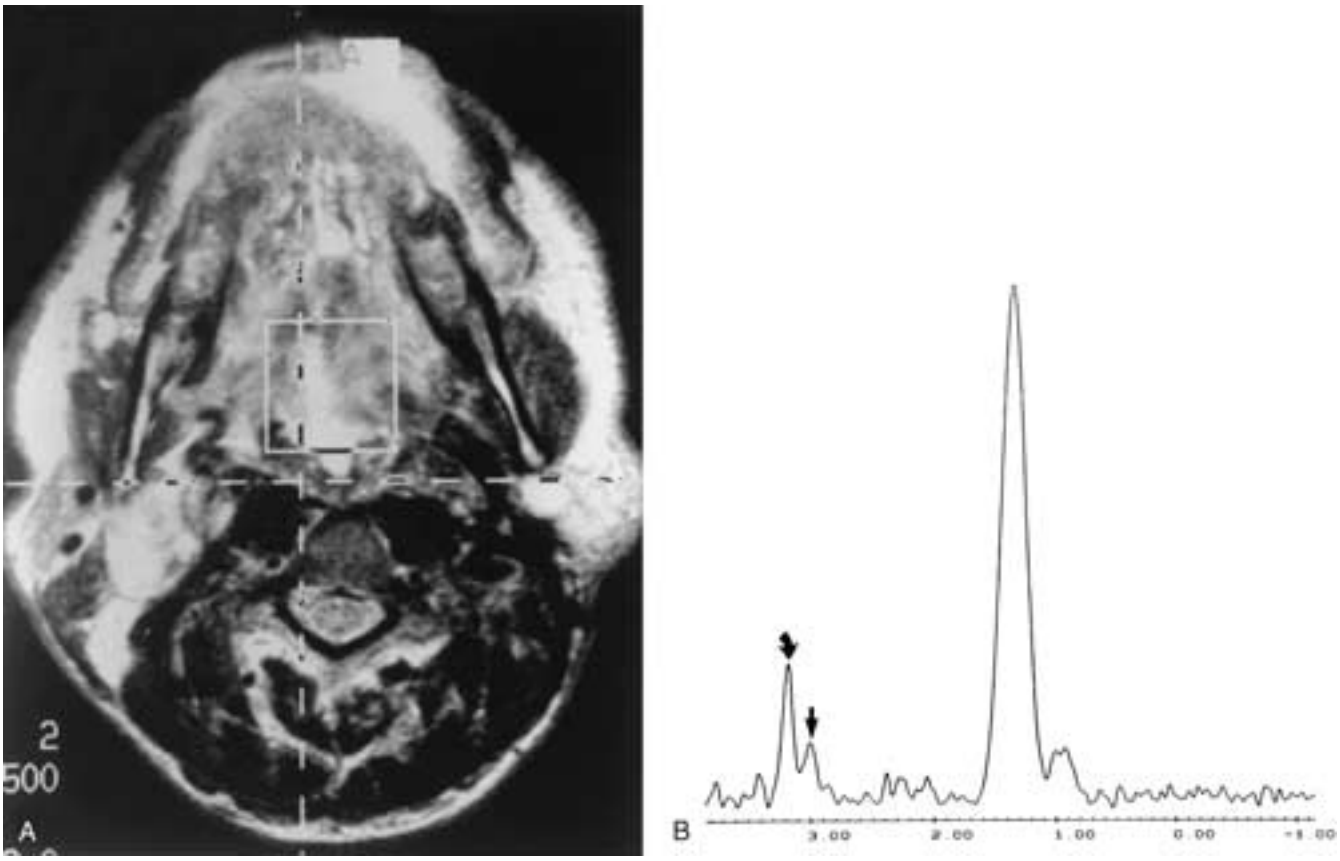

VIEW IMAGE

FIGURE 45-19 In vivo (1.5T) ^{1}H MRS of SCCA arising from the tongue base (TR = 2000 msec, TE = 136 msec). **A**, Axial T2-weighted image shows the location of voxel for **B**. **B**, In vivo ^{1}H MRS demonstrates elevation of the Cho peak (*curved arrow*) compared to the Cr peak (*straight arrow*). The Cho/Cr ratio was 3.33. (From Mukherji SK, Schiro S, Castillo M, et al. Proton MR spectroscopy of squamous cell carcinoma of the extracranial head and neck: in vitro and in vivo studies. AJNR 1997;18:1057–1072.)

months after the completion of radiation therapy.[54, 126, 127] These treatment-associated changes often prevent thorough endoscopic evaluation and reduce the ability to accurately detect persistent tumor that is unresponsive to therapy. This task is made even more difficult since persistent tumors are often situated deep to the mucosal surfaces and are not often directly visualized on physical examination. Although CT and MR imaging can be used to complement the clinical examination following treatment, their role is somewhat limited due to their inability to confidently differentiate posttreatment changes from early tumor recurrence.[125] In addition, the expected posttreatment imaging findings differ somewhat with the type of treatment given and with the location and extent of the primary tumor.[54, 126, 127]

Differentiation of Recurrent Tumor from Posttreatment Changes

Early results suggest that the ^{1}H-MRS may be used to differentiate recurrent tumor from posttreatment changes in patients with a malignancy of the upper aerodigestive tract who have undergone previous treatment.[106] Elevation of the Cho/Cr ratio in an indeterminate mass seen on CT or MR imaging is suggestive of recurrent tumor, whereas a ratio close to 1 is suggestive of posttreatment changes.[106] Despite the encouraging early ^{1}H-MRS results, it is unlikely that microscopic foci of tumor can be completely excluded by ^{1}H-MRS alone, regardless of field strength. Thus, indeterminate masses without the characteristic spectral tumor markers still warrant close clinical and radiographic follow-up, regardless of the MRS findings.

Prospective Treatment Monitoring

One of the most promising clinical applications for ^{1}H-MRS is the noninvasive treatment monitoring of patients with SCC of the upper aerodigestive tract who are treated nonsurgically. The accurate assessment of the primary tumor's response to radiation therapy and/or chemotherapy is extremely important, as early identification of an unresponsive malignancy may indicate the need for either additional therapy or surgical (salvage) resection. Previous studies have shown that cross-sectional imaging may be helpful in predicting tumor response by demonstrating a reduction in tumor size. However, these serial studies are most accurate when performed at least 3 to 4 months after completion of nonsurgical organ preservation treatment. By comparison, ^{1}H-MRS has the potential to be a much earlier indicator of tumor response, not by measuring volumetric changes but by measuring the internal chemistry of the treated tumor cells. The noninvasive nature of ^{1}H-MRS allows frequent interval studies to be performed both during and following treatment, and the utility of ^{1}H-MRS in prospective treatment monitoring for SCC is currently being investigated.

Copyright © 2003, Mosby, Inc. All rights reserved.

Preliminary investigations have shown that progressive reduction in Cho concentrations during treatment is indicative of a tumor response.[106, 128] In fact, some investigators have suggested that alterations in ^{1}H-MRS may be able to predict the response prior to changes in tumor volume.[106, 128, 129] Thus, persistent elevation of the Cho/Cr ratio suggests a nonresponsive tumor, while resolution of the Cho peak is indicative of a tumor response (Fig. 45-22). No information is available regarding the specific time interval following the initiation of treatment when one would expect to see resolution of spectral markers in tumors that are being successfully treated. Large-scale prospective studies are warranted to determine if ^{1}H-MRS can be a reliable technique for assessing the response during treatment monitoring.

Limitations and Imaging Strategies

The upper aerodigestive tract is an inherently difficult area to perform MRS. To obtain highly resolved spectra, a very homogeneous magnetic field is required in the area to be examined (i.e., ≤0.1 ppm deviation in the magnetic field). Numerous structural interfaces exist in this region that result in large magnetic field inhomogeneities. In many cases, these large field inhomogeneities cannot be corrected by the use of magnetic field shim. Susceptibility artifact from the paranasal sinuses and pharyngeal airway often prohibits analysis of low-volume tumors located adjacent to these structures. Susceptibility artifact from bone prevents spectral analysis of small to moderate-sized tumors that directly abut the skull base or mandible. Pulsations from the carotid artery result in rhythmic field inhomogeneities and may prevent spectral analysis of lesions that involve the poststyloid parapharyngeal space.[106]

Motion artifact is much more problematic in the upper aerodigestive tract than in the brain or extremities. Normal respiration usually does not interfere with analysis of primary parapharyngeal, nasopharyngeal, tonsillar, or masticator space masses. However, masses that arise in the upper airway often partially obstruct the airway and cause dyspnea. In addition, patients with upper airway tumors often have difficulty handling their secretions. This usually results in an exaggerated swallow and motion artifact. The result of these problems is increased motion that may prevent adequate shimming prior to spectral analysis. Thus, the role of ^{1}H-MRS for evaluating advanced laryngeal or hypopharyngeal carcinomas is very limited, especially if the patient is tracheostomy dependent.[106]

Fat contamination of the proton spectra is another major problem when performing one-dimensional ^{1}H-MRS in the extracranial head and neck. The fat planes surrounding the

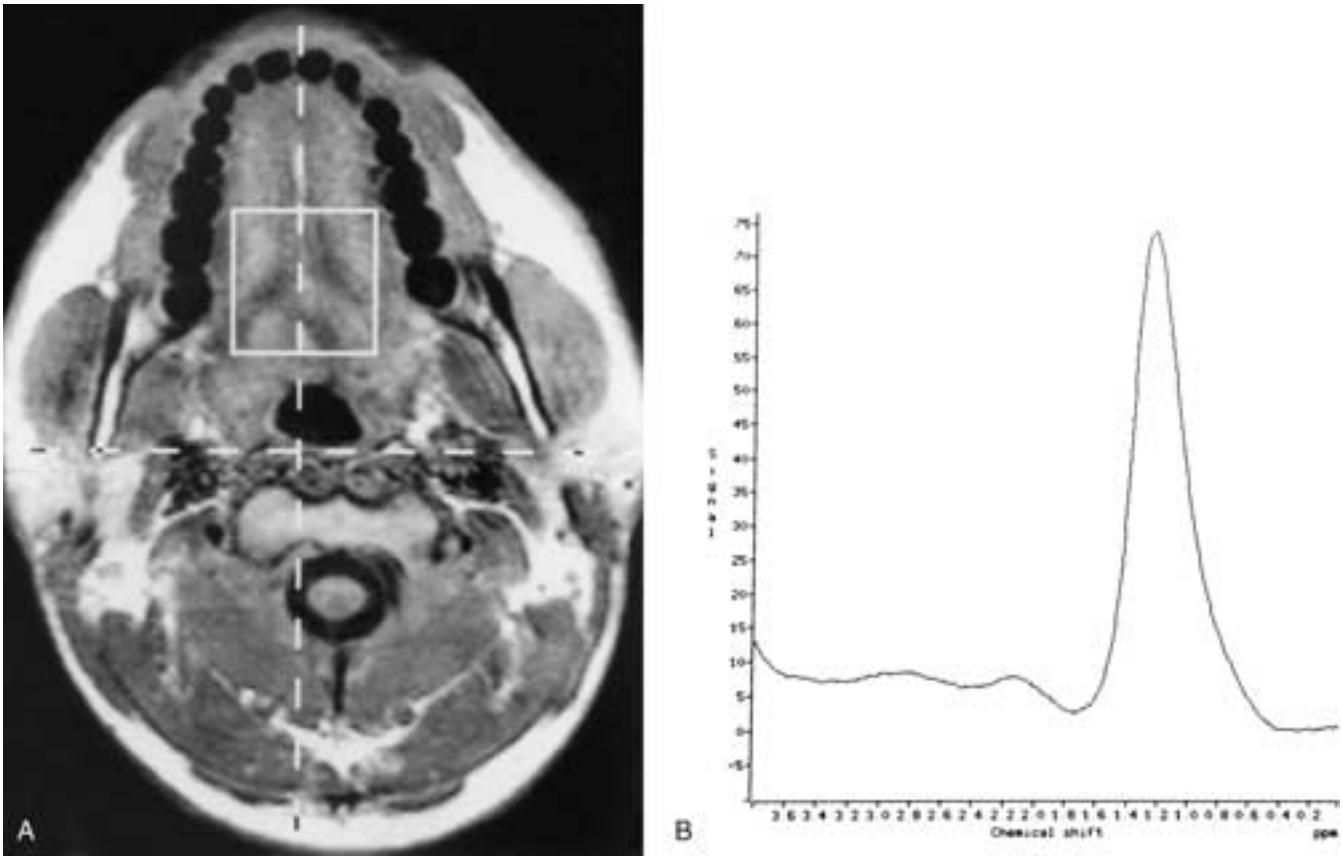

VIEW IMAGE

FIGURE 45-20 In vivo (1.5T) ^{1}H MRS of the normal tongue base (TR = 2000 msec; TE = 136 msec). **A**, Axial T2-weighted image illustrates the location of voxel for **B**. **B**, In vivo ^{1}H MRS demonstrates no detectable levels of Cho or Cr. (From Mukherji SK, Schiro S, Castillo M, et al. Proton MR spectroscopy of squamous cell carcinoma of the extracranial head and neck: in vitro and in vivo studies. AJNR 1997;18:1057–1072.)

Copyright © 2003, Mosby, Inc. All rights reserved.

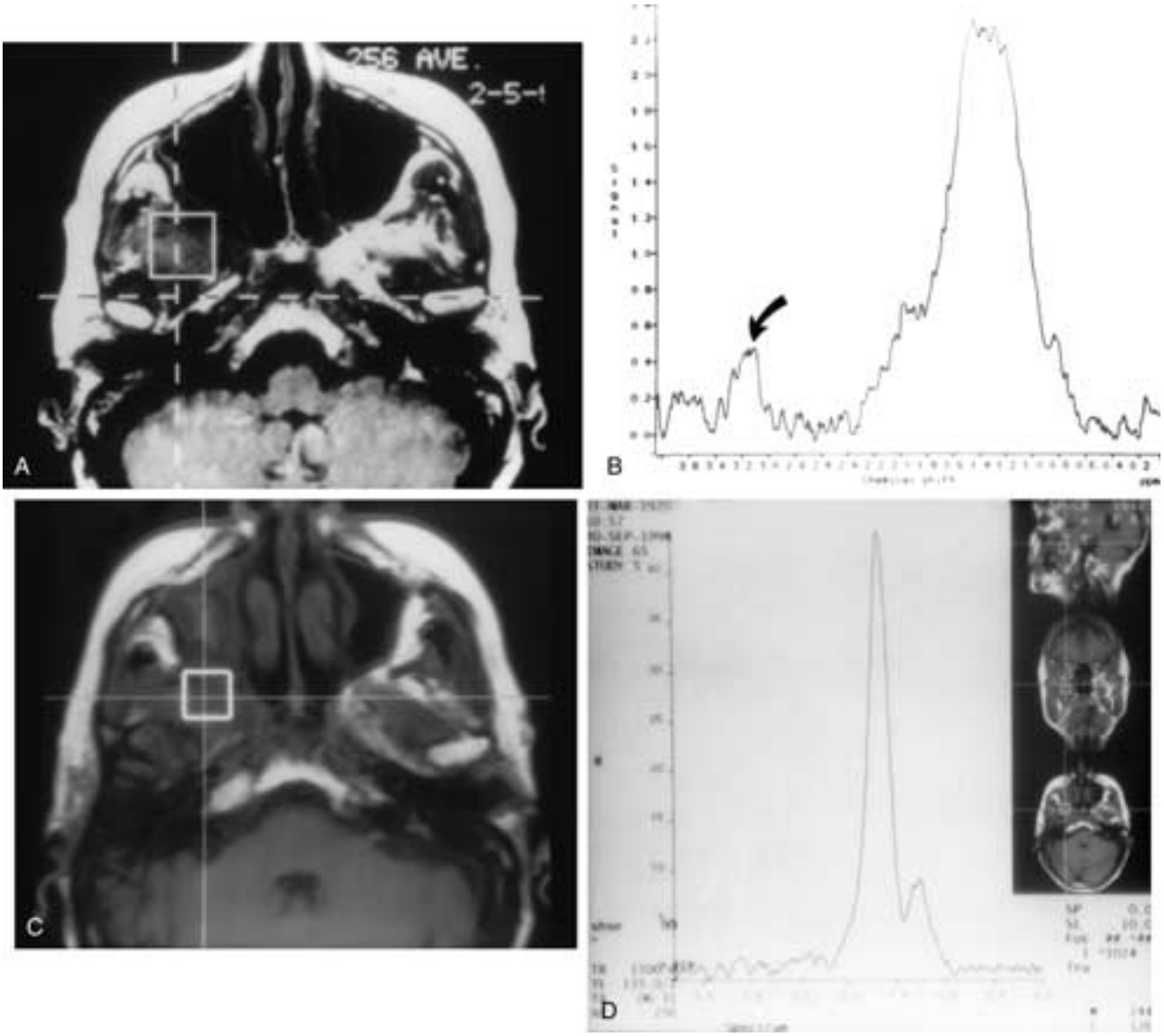

VIEW IMAGE

FIGURE 45-21 In vivo (1.5T) ^{1}H MRS prospective treatment monitoring of adenoid cystic carcinoma following treatment with neutron beam therapy. **A**, Axial T1-weighted image shows the location of a voxel in a patient with adenoid cystic carcinoma of the pterygopalatine fossa. **B**, In vivo ^{1}H MRS demonstrates elevation of the Cho peak (*curved arrow*). **C**, Axial T1-weighted scan performed 6 weeks after completion of neutron beam therapy illustrates the location of the voxel for **C**. **D**, In vivo ^{1}H MRS demonstrates a reduction in the Cho peak compared to the pretreatment spectra. This patient has no evidence of recurrent disease 2 years after completion of treatment.

various muscle groups are very helpful in identifying deep extension of tumor on CT or noncontrast T1-weighted MR imaging. However, these fat planes can result in contamination of proton spectra by a dominant lipid peak that prevents identification of the Cho or Cr peak.[106] When evaluating lesions that abut fat, every attempt should be made to center the voxel directly over the lesion. In these cases, it is especially important to minimize voxel size without excessively increasing acquisition time. However, despite proper placement of the voxel over a tumor, the intrinsically high fat content of the tissue may often result in sufficient fat contamination to obliterate the Cho and Cr resonances and render ^{1}H-MRS useless.[106]

Today, ^{1}H-MRS may be routinely performed on patients with nonobstructing head and neck tumors. However, because voxel size and acquisition time are competing factors, the study parameters have to be individualized, depending on the patient's clinical status and the location of the lesion in question. Thus, a smaller voxel size with a longer acquisition time could be used in a cooperative patient with a nonobstructive mass such as a masticator space lesion. However, a larger voxel size, which allows a reduction in acquisition time, may be a better strategy in a patient with a mass that extends into the airway, with resulting mild to moderate dyspnea. In the future, the best MRS results will likely be obtained by using dedicated spectroscopy coils developed solely for use in the extracranial head and neck.

Copyright © 2003, Mosby, Inc. All rights reserved.

Conclusion

Elevation of the Cho/Cr ratio has been demonstrated both in vivo and in vitro in SCC of the upper aerodigestive tract. This finding is not specific to SCC of the head and neck. It has been identified in a variety of malignant neoplasms including various brain tumors, gynecologic tumors, and lymphomas.[122–124] These findings suggest that the Cho/Cr ratio is a ubiquitous ^{1}H-MRS tumor marker that may be used to identify the presence of a variety of tumors.

ULTRASMALL SUPERPARAMAGNETIC IRON OXIDE MR CONTRAST AGENTS

Introduction

An area of active investigation is the role of new intravenous contrast agents for evaluation of metastatic disease. Over the past 15 years, superparamagnetic iron oxide compounds have been investigated primarily to detect the presence of liver metastases. However, there has been growing interest in investigating the ability of dextran-coated ultrasmall superparamagnetic iron oxide (USPIO) to detect metastatic nodal disease. This section will review the current information regarding the ability of USPIO to detect nodal metastases and evaluate primary tumors.

Mechanism

AMI 227, Combidex TM (Advanced Magnetics, Inc., Cambridge, MA), is a dextran-coated monocrystalline superparamagnetic iron oxide particle with an average particle size of 18 nm.[109, 130–132] Two major factors determine the physiologic distribution of these particles: their size and their surface properties. Iron particles with a diameter between 80 and 100 nm are trapped in liver and spleen, but not in lymph nodes and bone marrow.[133, 134] However, ultrasmall iron particles, which are less than 20 nm in diameter, can traverse the capillary walls, enter the interstitial spaces, and eventually appear in the lymphatics. These particles are then phagocytized by macrophages within lymph nodes.[130, 135, 136]

Thus, in a normally functioning lymph node, USPIO are trapped due to the normal phagocytic ability of the node. If tumor replaces portions of the node, such phagocytosis of the USPIO will not occur. Superparamagnetic iron oxide particles cause local MR field effects. Therefore, because of the functional nodal alterations caused by tumor, USPIO allows differentiation of a metastatic node from a normal or reactive node. This assessment is based on alterations of nodal signal intensities rather than on nodal morphology (size, shape, or architecture). Compared to its noncontrast signal intensities, a normally functioning node after the administration of USPIO demonstrates markedly reduced T1-weighted and T2-weighted signal intensities due to both T2 relaxation and magnetic susceptibility effects that result from the uptake of the iron particles (Fig. 45-23). By contrast, a metastatic node does not have a signal intensity loss on postcontrast images because the node's macrophages have been replaced and so fail to capture the iron particles (Fig. 45-24). Because USPIO is administered intravenously, this technique has the potential to evaluate all of the lymph nodes throughout the body. This is a significant advantage over traditional lymphography and sentinel node imaging, since these techniques only image lymph nodes in the primary drainage pathway of the injection site.

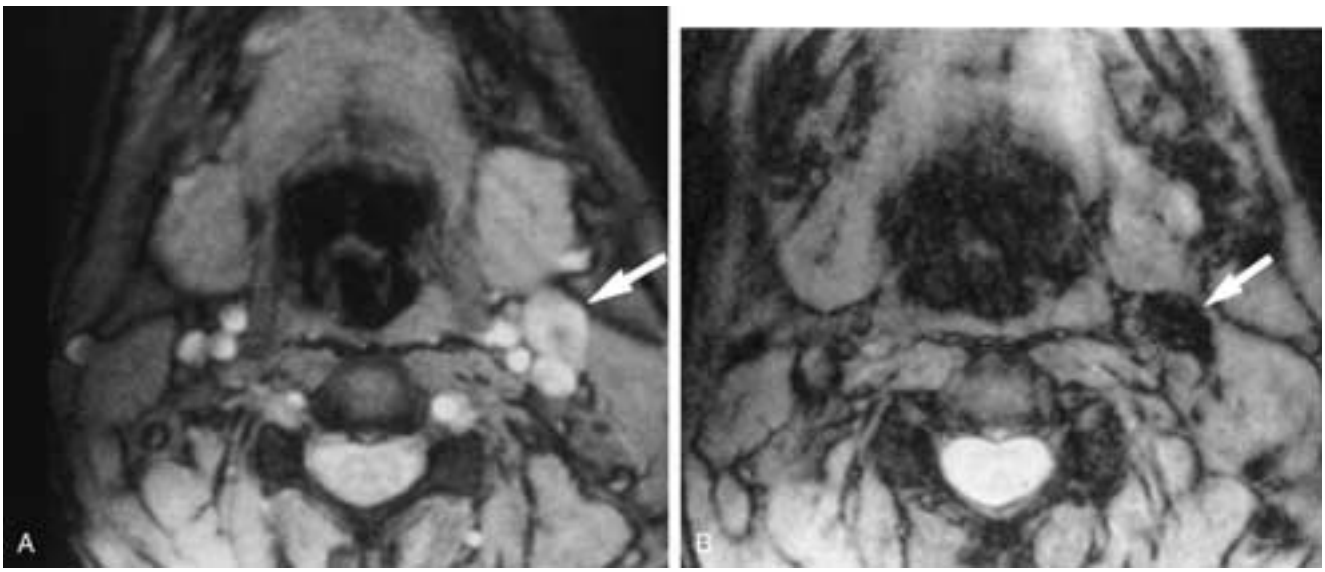

VIEW IMAGE

FIGURE 45-22 Appearance of a nonmetastatic cervical lymph node using USPIO. **A**, Axial gradient-echo image (500/20/flip angle = 20°) demonstrates a 1.8-mm group II lymph node in a patient with a left tonsillar carcinoma. Note the increased signal within the lymph node (*arrow*). **B**, After administration of USPIO, there is complete loss of signal within the lymph node (*arrow*). These findings were believed to be negative for metastases. No metastases were found at pathology. (Courtesy of Dr. Ken Maravilla, University of Washington.)

Copyright © 2003, Mosby, Inc. All rights reserved.

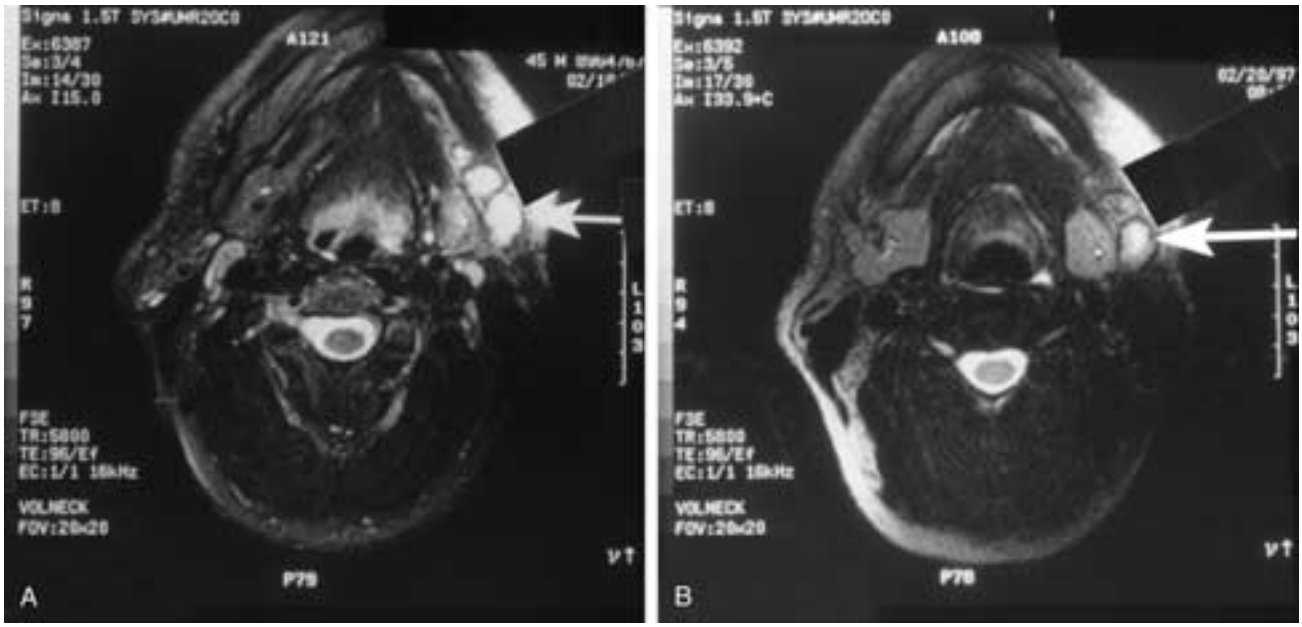

VIEW IMAGE

FIGURE 45-23 Appearance of a metastatic cervical lymph node using USPIO. **A**, Axial gradient-echo image (500/20/flip angle = 20°) in a patient with a left maxillary sinus carcinoma shows a high signal group I lymph node (*arrow*). **B**, Following administration of USPIO, there is loss of signal along the periphery but persistent increased signal within the center of the node (*arrow*). These findings were suspicious for metastases. On pathologic examination, metastases were found within the lymph node. (Courtesy of Dr. Ken Maravilla, University of Washington.)

Technique

The current recommendation is to perform MR imaging from the skull base to the thoracic inlet before and after the intravenous administration of USPIO. Currently, the most commonly used MR parameters used to evaluate the distribution of USPIO are a (TR) of 500 msec, a (TE) of 20 msec, and a flip angle of 20°. The optimum time for postcontrast imaging appears to be between 24 and 36 hours after intravenous USPIO administration.[137] It is possible that future recommendations may allow the preadministration study to be omitted. This is currently under investigation.

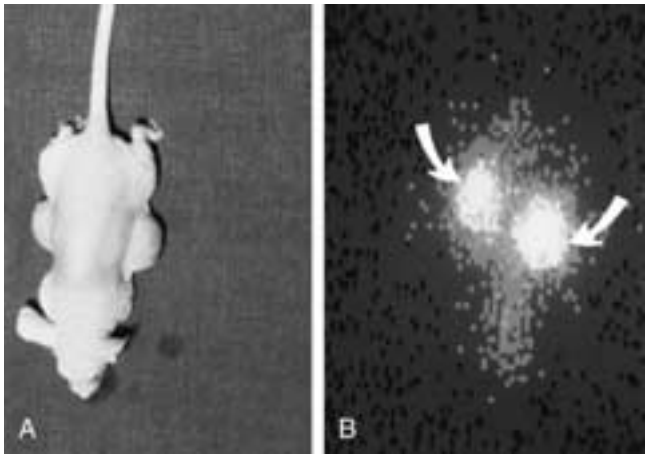

VIEW IMAGE

FIGURE 45-24 Whole-body scintigraphic image of an athymic mouse bearing two subcutaneous head and neck squamous cell carcinoma xenografts (**A**). The scintigraphic image (**B**) was taken 3 days after injection of 10 mCi of I-131-labeled anti–SCC of the head and neck MAb. Note the focal radiotracer uptake in the area corresponding to the location of the xenografts (*arrows* in **B**).

Clinical Applications

Detection of Nodal Metastases

Identification and staging of nodal metastases is one of the most important prognostic procedures for patients with SCC of the upper aerodigestive tract, and both treatment and outcome are directly affected by information regarding the presence of nodal metastases. The diagnostic accuracy of the physical examination in detecting nodal metastasis is unsatisfactory, and the ability of cross-sectional imaging to detect metastatic disease is discussed in Chapter 36.

Several studies have been performed to evaluate the diagnostic accuracy of USPIO in detecting metastatic lymph nodes. The initial multicenter phase II trial of USPIO demonstrated a sensitivity of 84% and a specificity of 95% in detecting metastatic lymph nodes.[132] The recently completed phase III multicenter European and U.S. studies confirmed the results of the phase II studies. These trials reported similar diagnostic accuracy in detecting metastatic disease on postcontrast studies. The sensitivity and specificity of the U.S. and European trials in detecting metastases in individual lymph nodes was as follows: 96% and 87% (U.S.), 95% and 86% (European).[138, 139] If a lymph node loses virtually all of its signal intensity on the postcontrast MR imaging study, it is very likely that the node contains metastatic disease. Conversely, if there is no drop in signal intensity, the node is likely reactive. However, a problem arises when only part of the node loses signal intensity. At present, it has been suggested that if half of the node loses

Copyright © 2003, Mosby, Inc. All rights reserved.

signal intensity on the postcontrast study, there is about an 80% likelihood that the node contains tumor.[138-140, 147] These results suggest that USPIO MR contrast agents may become important adjuncts in evaluating metastatic nodal disease for SCC of the upper aerodigestive tract.

Primary Site Evaluation

Investigations are now underway to determine the ability of USPIO to evaluate the primary tumor site. Following administration of USPIO, the pituitary gland, cavernous sinuses, nasal turbinates (concha), and pharyngeal mucosa all show increased T1-weighted signal intensity. These structures appear slightly dark on T2-weighted images due to the T2 shortening effect of iron oxide particles. Early results suggest that the T2-weighted signal intensity of a primary tumor in the head and neck does not substantially change from that of precontrast T2-weighted imaging. Since the normal pharyngeal mucosa and nasal turbinates lose T2-weighted signal intensity following USPIO administration, it is possible that administration of USPIO may improve the conspicuity and margins of SCC of the upper aerodigestive tract.[138] However, further investigations are necessary to determine the utility of USPIO for evaluation of the primary site.

RADIOIMMUNOSCINTIGRAPHY IN HEAD AND NECK CANCER

Introduction

Monoclonal antibodies (MAbs) directed against tumor-specific and tumor-associated antigens can be used for selective tumor targeting. This imaging technique is called radioimmunoscintigraphy (RIS). MAbs can be produced to bind to specific targets and can be labeled with radionuclides that emit gamma rays. Thus, specific tumors can be visualized using gamma cameras. Because RIS identifies biologic antigenic targets on the tumor cell, this technique differs fundamentally from anatomic imaging modalities. The potential of RIS depends on the tumor antigen, the MAb, the radionuclide, the tumor, and the imaging technique.

The hybridoma technology introduced in 1975 by Köhler and Milstein made it possible to develop MAbs directed against specific cellular antigens[141] The ideal antigenic target for RIS is one that is expressed on the cell surface by all tumors that are to be studied. Unfortunately, such tumor-specific antigens have only been found in experimentally induced tumors and not in so-called spontaneous tumors. Most identified antigens in human tumors are tumor-associated antigens, which are present on both tumor and normal tissues. Expression of a target antigen in normal tissue is acceptable for RIS when this normal tissue is poorly accessible to MAb or when it is localized at a site outside the anatomic region of interest.

The uptake of a MAb in a tumor depends on the antigen recognized by the MAb, as well as on the molecular size of the MAb. An intact MAb is a large immunoglobulin molecule with a molecular weight of 150 kDa. Such large molecules have a limited ability to penetrate a tumor and the residence time of such an intact MAb in blood is long, resulting in low tumor/nontumor uptake ratios. For RIS, the use of smaller MAb fragments such as $F(ab')_2$ (mol. wt. ≈ 100 kDa), Fab (mol. wt. ≈ 50 kDa), and Fv (mol. wt. ≈ 25 kDa) can be advantageous. Such smaller fragments have better penetration than whole immunoglobulin and therefore have the potential for more rapid tumor targeting, a high tumor/nontumor ratio, and earlier scan times after injection (Fig. 45-25). The radionuclides most commonly used in RIS are ^{131}I (half-life: 8 days), ^{123}I (half-life: 13 hours), ^{111}In (half-life: 68 hours), and ^{99m}Tc (half-life: 6 hours).

Efforts to develop RIS for the detection of primary tumors and lymph node metastases in patients with SCC of the head and neck are currently underway. These investigations have led to the following initial conclusions: ^{131}I and ^{123}I labels are not favorable, because the detachment of ^{131}I from MAbs (dehalogenation) will result in activity uptake in the thyroid, which may disturb imaging of SCC of the head and neck in this region. Similar considerations can be made for detached ^{111}In, which can accumulate in lymphocytes present in the lymph nodes and liver. In addition, the high cost (^{111}In, ^{123}I), patient radiation exposure (^{111}In), limited availability (^{123}I), long half-life (^{131}I), and poor imaging qualities (^{131}I) are other drawbacks to these radionuclides. ^{99m}Tc appears to have the most favorable characteristics for RIS in the upper aerodigestive tract. These favorable characteristics include minimal radiation delivery to the patient (short half-life time and low gamma energy), favorable characteristic for gamma camera imaging (high

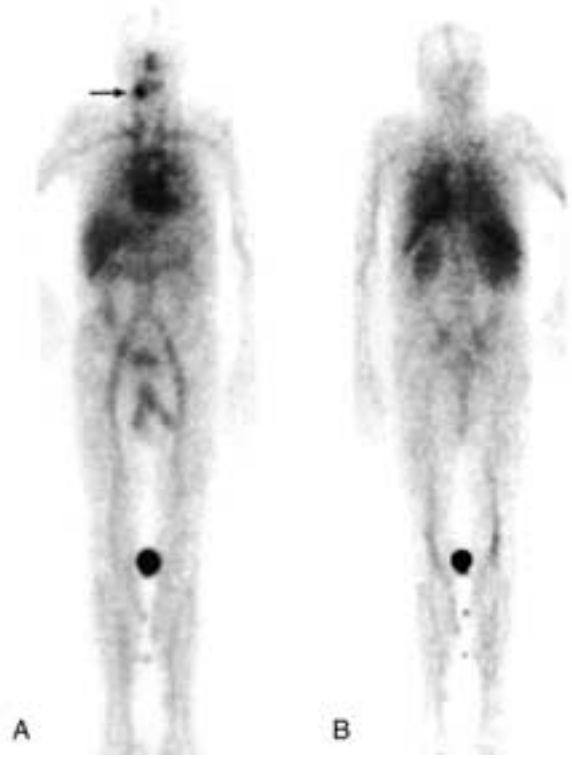

FIGURE 45-25 Anterior (**A**) and posterior (**B**) whole-body scans were performed in a patient with a right inferior alveolar ridge carcinoma 16 hours after injection of Tc-99m-labeled U36 IgG. Note the focal uptake at the site of the tumor (*arrow*) best seen on the anterior view (**A**).

VIEW IMAGE

Copyright © 2003, Mosby, Inc. All rights reserved.

photon abundance), low cost, and wide availability. Recent developments have also simplified the labeling methods for ^{99m}Tc.

Technique

The first images are usually acquired within a few minutes after injection of the radioimmunoconjugate. These early images serve as a baseline reference for subsequent images. For most intact MAbs or fragments labeled with ^{99m}Tc, the time for optimal imaging is 4 to 24 hours after injection. The later images are whole-body images and images of the head and neck region. SPECT images are often acquired in addition. Axial, coronal, and sagittal sections can be used to separate activity in the tumor from uptake in normal tissues including the blood vessels.

Early Results

It is only during the past decade that MAbs have become available with a high specificity for SCC of the head and neck and a restricted reaction pattern on normal tissues. Among the best-characterized MAbs are MAb E48 and U36, which both react with SCC of the head and neck as well as with normal squamous epithelium. These MAbs were administered to 49 patients with SCC of the head and neck who were at risk for having neck node metastases and who were scheduled to undergo neck dissection(s).[141–143] Patients received 1 to 50 mg E48 $F(ab')_2$ fragment (15 patients), E48 intact IgG (24 patients), or U36 intact IgG (10 patients) labeled with approximately 740 MBq ^{99m}Tc by intravenous injection. All 44 primary tumors in 49 patients were visualized by RIS. Thirty-two patients underwent unilateral neck dissection, and 17 patients had bilateral neck dissection. A total of 318 nodal levels were histopathologically evaluated. Fifty-one of the 66 operated sides contained metastases in a total of 77 levels. RIS detected lymph node metastases in 42 of the 77 levels (sensitivity, 55%) and in 35 of 51 sides (sensitivity, 69%). For CT and MR imaging, these figures were 60% for nodal level and 84% for neck side. Interpretation of RIS was correct in 276 of 316 levels (accuracy, 87%) and in 47 of 65 sides (accuracy, 72%). The accuracy of CT and MR imaging was, per level, 86% and 88%, respectively, and per side, 82% and 77%, respectively. The paraffin sections of the metastatic lymph nodes not detected by RIS were reexamined histopathologically.[141–143] The missed lymph nodes all were less than 2 cm in diameter and contained small tumor deposits (micrometastases) or metastases with large proportions of necrosis, keratin, or fibrin deposits. Furthermore, these examinations showed that the smallest tumor-involved lymph nodes detected by RIS had diameters of 5 mm and 9 mm in the axial plane, with a tumor burden of 50%.

In their present form, these initial studies suggest that RIS is not yet a preferred method for evaluating cervical nodal metastases. However, the immunohistochemical analyses performed during the initial RIS studies revealed that MAbs E48 and U36 had targeted all tumor-involved lymph nodes, as well as deposits that had not been visualized by RIS. Thus, MAbs were identifying lymph node metastases despite not being visualized on gamma camera imaging.

Future Trends

Investigations are now underway to improve the accuracy of RIS imaging. Ongoing investigations are aimed at reducing the time that MAbs reside in the blood pool. One concept is to use pretargeting strategies that provide rapid clearance from the bloodstream and result in high tumor/nontumor MAb ratios. Another area of active investigation is the integration of MAbs into PET technology. For this purpose, MAbs must be labeled with positron-emitting radionuclides, among which ^{124}I and ^{89}Zr are particularly suitable. Studies in tumor-bearing mice have shown that ^{89}Zr-labeled MAbs can easily be visualized with a PET camera, allowing detection of tumors as small as 50 mg.[144] On the basis of these preliminary studies, it can be anticipated that antibody-PET may eventually emerge as superior to conventional antibody-SPECT in sensitivity, resolution, and quantification.

CONCLUSIONS

The integration of new metabolic imaging techniques has led to dramatic changes in the evaluation of a variety of head and neck disorders. Because of the rapid pace of developments in the areas of metabolic and functional imaging, it is likely that currently unsuspected and unknown future applications will fall within the purview of radiologists.[145] It is imperative that our specialty continue to pursue new investigations that were once believed to be outside the realm of imaging.[146]

ACKNOWLEDGMENT

The authors appreciate the assistance of Gary Caputo, M.D., in reviewing the PET section of this chapter; the assistance of Carole Schreck, R.T., C.N.M.T., in figure preparation; and the clinical comments of Michael J. Kaplan, M.D.

REFERENCES

1. Ter-Pogossian MM. Positron emission tomography instrumentation. In Reivich M, Alalavi A, eds. Positron Emission Tomography. New York: Alan R. Liss, 1985;43–61.
2. Warburg O. On the origin of cancer cells. Science 1956;123: 309–314.
3. Reisser C, Eichhorn K, Herold-Mende C, et al. Expression of facilitative glucose transport proteins during development of squamous cell carcinomas of the head and neck. Int J Cancer 1999;80:194–198.
4. Som P, Atkins HL, Bandoypadhyay D, et al. A fluorinated glucose analog, 2-fluoro-2-deoxy-D-glucose (F-18): nontoxic tracer for rapid tumor detection. J Nucl Med 1980;21:670–675.
5. Kubota R, Yamada S, Kubota K, et al. Intratumoral distribution of fluorine-18-fluorodeoxyglucose in vivo: high accumulation in macrophages and granulation tissues studied by microautoradiography. J Nucl Med 1992;33:1972–1980.

Copyright © 2003, Mosby, Inc. All rights reserved.

6. Leskinen-Kallio S, Lindholm P, Lapela M, et al. Imaging of head and neck tumors with positron emission tomography and methionine. Int J Radiat Oncol Biol Phys 1994;30:1195–1199.
7. Braams JW, Pruim J, Nikkels PGJ, et al. Nodal spread of squamous cell carcinoma of the oral cavity detected with PET-tyrosine, MRI, and CT. J Nucl Med 1996;37:897–901.
8. Van Eijkeren ME, Thierens H, Seuntjens J, et al. Kinetics of [methyl-^{11}C] thymidine in patients with squamous cell carcinoma of the head and neck. Acta Oncol 1996;35:737–741.
9. Ahluwalia BD. Positron emission tomography imaging systems and applications. In Ahluwalia BD, ed. Tomographic Methods in Nuclear Medicine: Physical Principles, Instruments, and Clinical Applications. Boca Raton, Fla: CRC Press, 1989;105–122.
10. DeGrado TR, Turkington TG, Williams JJ, et al. Performance characteristics of a whole-body PET scanner. J Nucl Med 1994; 35:1398–1406.
11. Knesaurek K, Machac J, Vallabhajousula S, Buchsbaum MS. A new iterative reconstruction technique for attenuation correction in high-resolution positron emission tomography. Eur J Nucl Med 1996;23:656–661.
12. Wang CX, Snyder WE, Bilbro G, Santago P. Performance evaluation of filtered backprojection reconstruction and iterative reconstruction methods for PET images. Comput Biol Med 1998;28:13–25.
13. Lonneux M, Borbath I, Bol A, et al. Attenuation correction in whole-body FDG oncological studies: the role of statistical reconstruction. Eur J Nucl Med 1999;26:591–598.
14. Keyes JW Jr. SUV: standard uptake or silly useless value? J Nucl Med 1995;36:1836–1839.
15. Sadato N, Tsuchida T, Nakamura S, et al. Non-invasive estimation of the net influx constant using the standardized uptake value for quantification of FDG uptake in tumours. Eur J Nucl Med 1998;25: 559–564.
16. Sugawara Y, Zasadny KR, Neuhoff AW, Wahl RL. Reevaluation of the standardized uptake value for FDG: variations with body weight and methods for correction. Radiology 1999;213:521–525.
17. Leskinen S, Lapela M, Lindholm P, Minn H. Metabolic imaging by positron emission tomography in oncology. Ann Med 1997;29: 271–274.
18. Kitagawa Y, Sadato N, Azuma H, et al. FDG PET to evaluate combined intra-arterial chemotherapy and radiotherapy of head and neck neoplasms. J Nucl Med 1999;40:1132–1137.
19. Wong WL, Hussain K, Chevretton E, et al. Validation and clinical application of computer-combined computed tomography and positron emission tomography with 2-[18F]fluoro-2-deoxy-D-glucose head and neck images. Am J Surg 1996;172:628–632.
20. Sercarz JA, Bailet JW, Abemayor E, et al. Computer coregistration of positron emission tomography and magnetic resonance images in head and neck cancer. Am J Otolaryngol 1998;19:130–135.
21. Kinahan PE, Townsend DW, Beyer T, Sashin D. Attenuation correction for a combined 3D PET/CT scanner. Med Phys 1998;25:2046–2053.
22. Shreve PD, Steventon RS, Deters EC, et al. Oncologic diagnosis with 2-[fluorine-18]fluoro-2-deoxy-D-glucose imaging: dual-head coincidence gamma camera versus positron emission tomographic scanner. Radiology 1998;207:431–437.
23. Macfarlane DJ, Cotton L, Ackermann RJ, et al. Triple-head SPECT with 2-[fluorine-18]fluoro-2-deoxy-D-glucose (FDG): initial evaluation in oncology and comparison with FDG PET. Radiology 1995;194:425–429.
24. Stokkel MP, Moons KG, ten Broek FW, et al. 18F-fluorodeoxyglucose dual-head positron emission tomography as a procedure for detecting simultaneous primary tumors in cases of head and neck cancer. Cancer 1999;86:2370–2377.
25. Stokkel MPM, ten Broek FW, van Rijk PP. Preoperative assessment of cervical lymph nodes in head and neck cancer with fluorine-18 fluorodeoxyglucose using a dual-head coincidence camera: a pilot study. Eur J Nucl Med 1999;26:499–503.
26. Stokkel MPM, Terhaard CHJ, Hordijk GJ, van Rijk PP. The detection of local recurrent head and neck cancer with fluorine-18 fluorodeoxyglucose dual-head positron emission tomography. Eur J Nucl Med 1999;26:767–773.
27. Shreve PD, Anzai Y, Wahl RL. Pitfalls in oncologic diagnosis with FDG PET imaging: physiologic and benign variants. Radiographics 1999;19:61–77.
28. Jabour BA, Choi Y, Hoh CK, et al. Extracranial head and neck: PET imaging with 2-[F-18] fluoro-2-deoxy-D-glucose and MR imaging correlation. Radiology 1993;186:27–35.
29. Rege SD, Chaiken L, Hoh CK, et al. Change induced by radiation therapy in FDG uptake in normal and malignant structures of the head and neck: quantitation with PET. Radiology 1993;189:807–812.
30. Bailet JW, Abemayor E, Jabour BA, et al. Positron emission tomography: a new, precise imaging modality for detection of primary head and neck tumors and assessment of cervical adenopathy. Laryngoscope 1992;102:281–288.
31. Rege S, Maass A, Chaiken L, et al. Use of positron emission tomography with fluorodeoxyglucose in patients with extracranial head and neck cancer. Cancer 1994;73:3047–3058.
32. Wong WL, Chevretton EB, McGurk M, et al. A prospective study of PET-FDG imaging for the assessment of head and neck squamous cell carcinoma. Clin Otolaryngol 1997;22:209–214.
33. Paulus P, Sambon A, Vivegnis D, et al. 18FDG PET for the assessment of primary head and neck tumors: clinical, computed tomography, and histopathological correlation in 38 patients. Laryngoscope 1998;108:1578–1583.
34. Muraki AS, Mancuso AA, Harnsberger HR. Metastatic cervical adenopathy from tumors of unknown origin: the role of CT. Radiology 1984;152:749–753.
35. Braams JW, Pruim J, Kole AC, et al. Detection of unknown primary head and neck tumors by positron emission tomography. Int J Oral Maxillofac Surg 1997;26:112–115.
36. Mukherji SK, Drane WE, Mancuso AA, et al. Occult primary tumors of the head and neck: detection with 2-[F-18] fluoro-2-deoxy-D-glucose SPECT. Radiology 1996;199:761–766.
37. AAssar OS, Fischbein NJ, Caputo GR, et al. Metastatic head and neck cancer: role and usefulness of FDG PET in localizing occult primary tumors. Radiology, 1999;210:177–181.
38. Safa AA, Tran LM, Rege S, et al. The role of positron emission tomography in occult primary head and neck cancers. Cancer J Sci Am 1999;5:214–218.
39. Hanasono MM, Kunda LD, Segall GM, et al. Uses and limitations of FDG positron emission tomography in patients with head and neck cancer. Laryngoscope 1999;109:880–885.
40. Greven KM, Keyes JW Jr, Williams DW III, et al. Occult primary tumors of the head and neck: lack of benefit from positron emission tomography imaging with 2-[F-18]fluoro-2-deoxy-D-glucose. Cancer 1999;86:114–118.
41. Leon X, Quer M, Diez S, et al. Second neoplasm in patients with head and neck cancer. Head Neck 1999;21:204–210.
42. Keyes JW Jr, Watson NE Jr, Williams DW III, et al. FDG PET in head and neck cancer. AJR 1997;169:1663–1669.
43. Curtin HD, Ishwaran H, Mancuso AA, et al. Comparison of CT and MR imaging in staging of neck metastases. Radiology 1998;207: 123–130.
44. Adams S, Baum RP, Stuckensen T, et al. Prospective comparison of 18F-FDG PET with conventional imaging modalities (CT, MR, US) in lymph node staging of head and neck cancer. Eur J Nucl Med 1998;25:1255–1260.
45. Bailet JW, Sercarz JA, Abemayor E, et al. The use of positron emission tomography for early detection of recurrent head and neck carcinoma in postradiotherapy patients. Laryngoscope 1995;105: 135–139.
46. Benchaou M, Lehmann W, Slosman DO, et al. The role of FDG-PET in the preoperative assessment of N-staging in head and neck cancer. Acta Otolaryngol 1996;116:332–335.
47. Braams JW, Pruim J, Freling NJM, et al. Detection of lymph node metastases of squamous cell cancer of the head and neck with FDG-PET and MRI. J Nucl Med 1995;36:211–216.
48. Laubenbacher C, Saumweber D, Wagner-Manslau C, et al. Comparison of fluorine-18-fluorodeoxyglucose PET, MRI and endoscopy for staging head and neck squamous cell carcinomas. J Nucl Med 1995;36:1747–1757.
49. McGuirt WF, Williams DW III, Keyes JW Jr, et al. A comparative diagnostic study of head and neck nodal metastases using positron emission tomography. Laryngoscope 1995;105:373–375.
50. Myers LL, Wax MK, Nabi H, et al. Positron emission tomography in the evaluation of the N0 neck. Laryngoscope 1998;108:232–236.
51. Myers LL, Wax MK. Positron emission tomography in the evaluation of the negative neck in patients with oral cavity cancer. J Otolaryngol 1998;27:342–347.

Copyright © 2003, Mosby, Inc. All rights reserved.

52. Eichhorn T, Schroeder HG, Glanz H, Schwerk WB. Histologically controlled comparison of palpation and sonography in the diagnosis of cervical lymph node metastases. Laryngol Rhinol Otol 1987;66: 266–274.
53. McGuirt WF Jr, Johnson JT, Myers EN, et al. Floor of mouth carcinoma. The management of the clinically negative neck. Arch Otolaryngol Head Neck Surg 1995;121:278–282.
54. Mukherji SK, Mancuso AA, Kotzur IM, et al. Radiologic appearance of the irradiated larynx. Part I: expected changes. Radiology 1994;193:141–148.
55. Hudgins PA, Burson JG, Gussack GS, Grist WJ. CT and MR appearance of recurrent malignant head and neck neoplasms after resection and flap reconstruction. AJNR 1994;15:1689–1694.
56. Fu KK, Woodhouse RJ, Quivey JM, et al. The significance of laryngeal edema following radiotherapy of carcinoma of the vocal cord. Cancer 1982;49:655–658.
57. Anzai Y, Carroll WR, Quint DJ, et al. Recurrence of head and neck cancer after surgery or irradiation: prospective comparison of 2-deoxy-2- [F-18] fluoro-D-glucose PET and MR imaging diagnoses. Radiology 1996;200:135–141.
58. Farber LA, Benard F, Machtay M, et al. Detection of recurrent head and neck squamous cell carcinoma after radiation therapy with 2-18F-fluoro-2-deoxy-D-glucose positron emission tomography. Laryngoscope 1999;109:970–975.
59. Fischbein NJ, AAssar OS, Caputo GR, et al. Clinical utility of positron emission tomography with 18F-fluorodeoxyglucose in detecting residual/recurrent squamous cell carcinoma of the head and neck. AJNR 1998;19:1189–1196.
60. Greven KM, Williams DW III, Keyes JW Jr, et al. Distinguishing tumor recurrence from irradiation sequelae with positron emission tomography in patients treated for larynx cancer. Int J Radiat Oncol Biol Phys 1994;29:841–845.
61. Lapela M, Grenman R, Kurki T, et al. Head and neck cancer: detection of recurrence with PET and 2-[F-18] fluoro-2-deoxy-D-glucose. Radiology 1995;197:205–211.
62. Manolidis S, Donald PJ, Valk P, Pounds TR. The use of positron emission tomography scanning in occult and recurrent head and neck cancer. Acta Otolaryngol (Stockh) 1998;Suppl 534:1–11.
63. Greven KM, Williams DW III, Keyes JW Jr, et al. Positron emission tomography of patients with head and neck carcinoma before and after high dose irradiation. Cancer 1994;74:1355–1359.
64. Lindholm P, Leskinen-Kallio S, Grenman R, et al. Evaluation of response to radiotherapy in head and neck cancer by positron emission tomography and [11C]methionine. Int J Radiat Oncol Biol Phys 1995;32:787–794.
65. Haberkorn U, Strauss LG, Dimitrakopoulou A, et al. Fluorodeoxyglucose imaging of advanced head and neck cancer after chemotherapy. J Nucl Med 1993;34:12–17.
66. Reisser C, Haberkorn U, Strauss A, et al. Chemotherapeutic management of head and neck malignancies with positron emission tomography. Arch Otolaryngol Head Neck Surg 1995;121:272–276.
67. Lowe VJ, Dunphy FR, Varvares M, et al. Evaluation of chemotherapy response in patients with advanced head and neck cancer using [F-18] fluorodeoxyglucose positron emission tomography. Head Neck 1997;19:666–674.
68. Nuutinen J, Jyrkkio S, Lehikoinen P, et al. Evaluation of early response to radiotherapy in head and neck cancer measured with [11C]methionine-positron emission tomography. Radiother Oncol 1999;52:225–232.
69. Keyes JW Jr, Harkness BA, Greven KM, et al. Salivary gland tumors: pretherapy evaluation with PET. Radiology 1994;192:99–102.
70. Holder WD Jr, White RL Jr, Zuger JH, et al. Effectiveness of positron emission tomography for the detection of melanoma metastases. Ann Surg 1998;227:764–769.
71. Wang W, Macapinlac H, Larson SM, et al. [18F]-2-fluoro-2-deoxy-D-glucose positron emission tomography localizes residual thyroid cancer in patients with negative diagnostic (131)I whole body scans and elevated serum thyroglobulin levels. J Clin Endocrinol Metab 1999;84:2291–2302.
72. Grunwald F, Briele B, Biersack HJ. Non-131I scintigraphy in the treatment and follow-up of thyroid cancer. Single-photon-emitters or FDG-PET? Q J Nucl Med 1999;43:195–206.
73. Conti PS, Durski JM, Bacqai F, et al. Imaging of locally recurrent and metastatic thyroid cancer with positron emission tomography. Thyroid 1999;9:797–804.
74. Chung JK, So Y, Lee JS, et al. Value of FDG PET in papillary thyroid carcinoma with negative 131I whole-body scan. J Nucl Med 1999;40:986–992.
75. Dietlein M, Scheidhauer K, Voth E, et al. Fluorine-18 fluorodeoxyglucose positron emission tomography and iodine-131 whole-body scintigraphy in the follow-up of differentiated thyroid cancer. Eur J Nucl Med 1997;24:1342–1348.
76. Feine U, Lietzenmayer R, Hanke JP, et al. Fluorine-18-FDG and iodine-131-iodide uptake in thyroid cancer. J Nucl Med 1996;37: 1468–1472.
77. Grunwald F, Schomburg A, Bender H, et al. Fluorine-18 fluorodeoxyglucose positron emission tomography in the follow-up of differentiated thyroid cancer. Eur J Nucl Med 1996;23:312–319.
78. Okada J, Oonishi H, Yoshikawa K, et al. FDG-PET for predicting the prognosis of malignant lymphoma. Ann Nucl Med 1994;8:187–191.
79. Okada J, Yoshikawa K, Itami M, et al. Positron emission tomography using fluorine-18-fluorodeoxyglucose in malignant lymphoma: a comparison with proliferative activity. J Nucl Med 1992;33:325–329.
80. Walsh RM, Wong WL, Chevretton EB, Beaney RP. The use of PET-18FDG imaging in the clinical evaluation of head and neck lymphoma. Clin Oncol 1996;8:51–54.
81. Moog F, Kotzerke J, Reske SN. FDG PET can replace bone scintigraphy in primary staging of malignant lymphoma. J Nucl Med 1999;40:1407–1413.
82. Wiedmann E, Baican B, Hertel A, et al. Positron emission tomography (PET) for staging and evaluation of response to treatment in patients with Hodgkin's disease. Leuk Lymphom 1999;34:545–551.
83. Jerusalem G, Beguin Y, Fassotte MF, et al. Whole-body positron emission tomography using 18F-fluorodeoxyglucose for posttreatment evaluation in Hodgkin's disease and non-Hodgkin's lymphoma has higher diagnostic and prognostic value than classical computed tomography scan imaging. Blood 1999;94:429–433.
84. Zinzani PL, Magagnoli M, Chierichetti F, et al. The role of positron emission tomography (PET) in the management of lymphoma patients. Ann Oncol 1999;10:1181–1184.
85. Hoffmann M, Kletter K, Diemling M, et al. Positron emission tomography with fluorine-18-2-fluoro-2-deoxy-D-glucose (F18-FDG) does not visualize extranodal B-cell lymphoma of the mucosa-associated lymphoid tissue (MALT)-type. Ann Oncol 1999;10:1185–1189.
86. Hautzel H, Muller-Gartner HW. Early changes in fluorine-18-FDG uptake during radiotherapy. J Nucl Med 1997;38:1384–1386.
87. Yamada S, Kubota K, Kubota R, et al. High accumulation of fluorine-18-fluorodeoxyglucose in turpentine-induced inflammatory tissue. J Nucl Med 1995;36:1301–1306.
88. Palmer WE, Rosenthal DI, Schoenberg OI, et al. Quantification of inflammation in the wrist with gadolinium-enhanced MR imaging and PET with 2-[F-18]-fluoro-2-deoxy-D-glucose. Radiology 1995; 196:647–655.
89. Kubota R, Kubota K, Yamada S, et al. Microautoradiographic study for the differentiation of intratumoral macrophages, granulation tissues and cancer cells by the dynamics of fluorine-18-fluorodeoxyglucose uptake. J Nucl Med 1994;35:104–112.
90. Strauss LG. Fluroine-18 deoxyglucose and false-positive results: a major problem in the diagnostics of oncological patients. Eur J Nucl Med 1996;23:1409–1415.
91. Mukherji SK, Gapany M, Phillips D, et al. Squamous cell carcinoma of the upper aerodigestive tract: the ability of thallium-201 SPECT to detect recurrent tumor. Am J Neuroradiol 1999;20:1215–1220.
92. Mukherji SK, Gapany M, Neelon B, McCartney W. Evaluation of thallium-201 single photon emission computed tomography for predicting early treatment response in patients with squamous cell carcinoma of the extracranial head and neck treated with non-surgical organ preservation therapy: initial results. J Comput Assist Tomogr 2000;24:146–151.
93. Gapany M, Grund FM. Thallium-201 imaging for upper aerodigestive tract cancer. In: Mukherji SK, Castelijns JA, eds. Modern Head and Neck Imaging. Heidelberg: Springer-Verlag, 1998; 107–110.
94. Nagamachi S, Hoshi H, Jinnouchi S, et al. Tl-201 SPECT for evaluating head and neck cancer. Ann Nucl Med 1996;10: 105–111.

Copyright © 2003, Mosby, Inc. All rights reserved.

95. Nagamachi S, Jinnouchi S, Flores LG, et al. The use of Tl-201 SPECT to predict the response to radiotherapy in patients with head and neck cancer. Nuc Med Commun 1996;17:935–942.
96. Gregor T, Valdes-Olmes RA, Koops W, et al. Preliminary experience with thallous chloride Tl 201-labeled single photon emission computed tomography scanning in head and neck cancer. Arch Otolaryngol Head Neck Surg 1996;122:509–514.
97. Valdes-Olmos RA, Balm AJM, Hilgers FJM, et al. Tl-201 SPECT in the diagnosis of head and neck cancer. J Nucl Med 1997;38:873–879.
98. Waxman AD. Thallium-201 in nuclear oncology. In: Freeman LM, ed. Nuclear Medicine. Annual 1991. New York: Raven Press, 1991; 193–207.
99. Gehring PJ, Hammand PB. The interrelationship between thallium and potassium in animals. J Pharmacol Exp Ther 1967;155:187–201.
100. Lebowitz E, Greene MW, Greene R, et al. Thallium-201 for medical use I. J Nucl Med 1975;16:151–155.
101. Bradley-Moore PR, Lebowitz E, Greene MW, et al. Thallium-201 for medical use II. biological behavior. J Nucl Med 1975;16: 156–160.
102. Elgazzar AH, Fernandez-Ulloa M, Silberstein EB. Tl-201 as a tumour-localizing agent: current status and future considerations. Nucl Med Commun 1993;14:96–103.
103. Ozcan Z, Burak Z, Ozcan C, et al. Is Tl-201 a reliable agent in tumour imaging. Nucl Med Commun 1996;17:805–809.
104. Mukherji SK, Drane WE, Tart RP, et al. Comparison of thallium-201 and F-18 FDG SPECT uptake in squamous cell carcinoma of the head and neck. AJNR 1994;15:1837–1842.
105. Leitha T, Glaser C, Pruckmeyer M, et al. Technetium-99m-MIBI in primary and recurrent head and neck tumors: contribution of bone SPECT image fusion. J Nucl Med 1998;39:1136–1171.
106. Mukherji SK, Kwock L, Schiro S. Magnetic resonance spectroscopy of the extracranial head and neck. In: Mukherji SK, ed. Clinical Applications of Magnetic Resonance Spectroscopy. New York: Wiley, 1998.
107. Mukherji SK, Schiro S, Castillo M, et al. MR proton spectroscopy of squamous cell carcinoma of extracranial head and neck: in vitro and in vivo studies. AJNR 1997;18:1057–1072.
108. Mukherji SK, Schiro S, Castillo M. Proton MR spectroscopy of squamous cell carcinoma of the upper aerodigestive tract: in vitro characteristics. AJNR 1996;17:1485–1490.
109. Fischbein N, Anzai Y, Mukherji SK. Application of new imaging techniques for the evaluation of squamous cell carcinoma of the head and neck. Semin Comput Tomogr Ultrasound Magn Reson Imag 1999;20:187–212.
110. Star-Lack JM, Adalsteinsson E, Adam MF, et al. In vivo ^{1}H MR spectroscopy of human head and neck lymph node metastases and comparison with oxygen tension measurements. AJNR 2000;21: 183–193.
111. Miller BL. A review of chemical issues in 1-H NMR spectroscopy: n-acetyl-L-aspartate, creatine and choline. NMR Biomed 1991;4: 47–52.
112. Kinoshita Y, Kajiwara H, Yokata A, Koga Y. Proton magnetic resonance spectroscopy of brain tumors: an in vitro study. Neurosurgery 1994;35:606–614.
113. Thompson GA. Phospholipid metabolism in animal tissues. In: Ansell GB, Jawthorne JN, Dawson RMC, eds. Form and Function of Phospholipids. Amsterdam: Elsevier, 1973;67–96.
114. Wurtman JJ. Sources of choline and lecithin in the diet. Nutri Brain 1979;5:73–81.
115. Mountford CE, Wright LC, Holmes KT, et al. High resolution nuclear magnetic analysis of metastatic cancer cells. Science 1984;226:1415.
116. Lean CL, MacKinnon WB, Delikatny J, et al. Cell-surface fucosylation and magnetic resonance spectroscopy characterization of human malignant colorectal cells. Biochemistry 1992;31:11092–11105.
117. Ruiz-Cabello J, Cohen JS. Phospholipid metabolites as indicators of cancer cell function. NMR Biomed 1992;5:226–233.
118. Negendak WG, Brown TR, Evelhoch JL, et al. Proceedings of a National Cancer Institute Workshop: MR spectroscopy and tumor cell biology. Radiology 1992;185:875–883.
119. Mountford CE, Lean CL, Hancock R, et al. Magnetic resonance spectroscopy detects cancer in draining lymph nodes. Invasion Metastasis 1993;13:57–59.
120. Kuesel AC, Graschew G, Hull WE, et al. ^{31}P NMR studies of cultured human tumor cells: influences of pH on phospholipid metabolite levels and the detection of CDP-choline. NMR Biomed 1990;3:78–89.
121. De Cestaines JD, Larsen VA, Podo F, et al. In vivo P–31 MRS of experimental tumors. NMR Biomed 1993;6:345–365.
122. Ross BD. The biochemistry of living tissues: examination by MRS. NMR Biomed 1992;5:215–219.
123. Gill SG, Thomas DGT, Van Bruggen NV, et al. Proton MR spectroscopy of intracranial tumours: in vivo and in vitro studies. J Comput Assist Tomogr 1990;14:497–504.
124. Delikatny EJ, Russell P, Hunter JC, et al. Proton MR and human cervical neoplasia: ex vivo spectroscopy allows distinction of invasive carcinoma of the cervix from carcinoma in situ and other preinvasive lesions. Radiology 1993;188:791–796.
125. Negendank W, Sauter R, Brown TR, et al. Proton magnetic spectroscopy in patients with glial tumors: a multicenter study. J Neurosurg 1996;84:449–458.
126. Mancuso AA, Mukherji SK, Mendenhall WE, et al. Value of pretreatment CT as a predictor of outcome in supraglottic cancer treated with radiation therapy alone. J Clin Oncol 1999;17: 631–636.
127. Mukherji SK, Mancuso AA, Kotzur IM, et al. Radiographic appearance of the irradiated larynx: part II: primary site response. Radiology 1994;193:149–154.
128. Manara M. Histological changes of the human larynx irradiated with various technical therapeutic methods. Arch Ital Otolaryngol 1966;79:596–635.
129. Bizzi A, Movsas B, Tedeschi G, et al. Response of non-Hodgkin lymphoma to radiation therapy: early and long term assessment with H-1 MR spectroscopic imaging. Radiology 1995;194:271–276.
130. Van Zijl PCM, Moonen CTW, Gillen J, et al. Proton magnetic resonance spectroscopy of small regions (1 mL) localized inside superficial human tumors. A clinical feasibility study. NMR Biomed 1990;3:227–232.
131. Mancuso AA, Harnsberger HR, Muraki AS, Stevens MH. Computed tomography of cervical and retropharyngeal lymph nodes: normal anatomy, variants of normal, and applications in staging of head and neck cancer. Part II. Pathology. Radiology 1983;148: 715–723.
132. Som PM. Detection of metastasis in cervical lymph nodes: CT and MR criteria and differential diagnosis. AJR 1992;158: 961–969.
133. Van den Brekel MWM, Stel HV, Castelijins JA, et al. Cervical lymph node metastases: assessing of radiological criteria. Radiology 1990;177: 379–384.
134. Frank H, Weissleder R, Brady TJ. Enhancement of MR angiography with iron oxide: preliminary studies in whole-blood phantom and in animals. AJR 1994;162(1):209–213.
135. Mayo-Smith WW, Saini S, Slater G, et al. MR contrast material for vascular enhancement: value of superparamagnetic iron oxide. AJR 1996;166:73–77.
136. Anzai Y, Prince MR, Chenevert TL, et al. MR angiography with an ultrasmall superparamagnetic iron oxide blood pool agent. J Magnetic Reson Imag 1997;7:209–214.
137. Mancuso AA, Maceri D, Rice D, et al. CT of cervical lymph node cancer. AJR 1981;136:381–385.
138. Hudgins P, Anzai Y, Morris M. Dextran-coated superparamagnetic iron oxide MR contrast agent (Combidex™) for imaging cervical lymph nodes: optimal dose, time of imaging, and pulse sequence (abstract). ASHNR 1996;149.
139. Anzai Y, Prince MR. Iron oxide–enhanced MR lymphography: the evaluation of cervical lymph node metastases in head and neck cancer. J Magn Reson Imag 1997;7:75–81.
140. Sigal RC, Vogl TJ, Casselman JW, et al. Comparison of SINERAM registered MR to plain MR in the diagnosis of lymph node metastases from head and neck cancer (abstract). RSNA 2000.
141. Köhler G, Milstein C. Continuous cultures of fused cells secreting antibody of predefined specificity. Nature 1975;256: 495–497.
142. De Bree R, Roos JC, Quak JJ, et al. Clinical imaging of head and neck cancer with ^{99m}Tc-labeled monoclonal antibody E48 IgG or F(ab′)$_2$. J Nucl Med 1994;35:775–783.

Copyright © 2003, Mosby, Inc. All rights reserved.

143. De Bree R, Roos JJ, Quak JJ, et al. Radioimmunoscintigraphy with ^{99m}Tc-labeled monoclonal antibody U36 and its biodistribution in patients with head and neck cancer. Clin Cancer Res 1995;1:591–598.
144. De Bree R, Roos JC, Quak JJ, et al. Selection of monoclonal antibody E48 IgG or U36 for adjuvant therapy in head and neck cancer patients. Br J Cancer 1997;75:1049–1060.
145. Meijs WE, Haisma HJ, Klok RP, et al. Zirconium 88/89 labeled monoclonal antibodies: distribution in tumor-bearing nude mice. J Nucl Med 1997;38:112–118.
146. Mukherji SK. Head and neck imaging: the next ten years. Radiology 1998;209:8–14.
147. Mack MG, Balzer JO, Straub R, Eichler K, et al. Superparamagnetic iron oxide–enhanced MR imaging of head and neck lymph nodes. Radiology 2002;222:239–244.

Copyright © 2003, Mosby, Inc. All rights reserved.

Index

Note: Page numbers followed by f indicate figures; those followed by t indicate tables.

A

AAO-HNS nodal classification system, 1872, 1874t–1875t
ABCs. *See* Aneurysmal bone cysts (ABCs).
Abducens nerve, 542
  branchial arches and, 1759
Aberrant fusion proteins, chromosome translocation to generate, oncogene activation by, 2277–2278
Abscesses
  Bezold, 1178f
  cerebellar, 1179f
  cerebral, nasal dermal sinus resection for, 34–35
  epidural
    in sinusitis, 582f
    with mastoiditis, 1182, 1182f
  epiglottic, 1569f
  in submandibular gland space, 1821f
  in toxoplasmosis, 778f
  intracranial, 250
  laryngeal, 1672f
  of masticator space, 1822f, 1990f
  of oral cavity, 1400, 1401f–1403f, 1402
  of pinna, 2108f
  of sphenoid sinuses, 582f
  orbital, 575, 578f
  parotid, 2027, 2027f, 2028f, 2042f, 2047f
  peritonsillar, 1504–1505, 1506f, 1565f, 1566f
  postoperative, following craniofacial resection, 435f
  retropharyngeal, 1565f, 1817f, 1820f
  septal, 380
  subperiosteal, 580f–582f, 580–581
ACCs. *See* Acinic cell carcinomas (ACCs); Adenoid cystic carcinomas (ACCs; AdCCs).
Achalasia, 2211f
Achondroplasia, 1110t, 1165f
  of skull base, 857
Acinic cell carcinomas (ACCs), 2096
Acoustic nerve, hamartomas of, 1303, 1311f
Acoustic schwannomas, 1276–1285
  bilateral, 1277–1278, 1278f
  clinical evaluation with, 1278–1279, 1279f
  imaging appearance of, 1280–1285
    on computed tomography, 1280, 1281f, 1282f, 1283
    on magnetic resonance imaging, 1280f–1284f, 1283–1284
    secondary changes and, 1284–1285, 1285f
    size, location, and configuration and, 1280, 1280f–1283f
  incidence and terms for, 1276–1277, 1277t
  intracanalicular, 1303
  pathology of, 1277
  treatment of, 1279–1280
Acquired immunodeficiency syndrome (AIDS). *See also* Human immunodeficiency virus (HIV) infections.
  coccidioidomycosis in, 1896
  neoplasia in, 2289–2290
  pharynx and, 1509, 1510f, 1511f, 1511–1512
  sinusitis in, 255
Acrocephalosyndactyly. *See* Apert's syndrome; Craniofacial dysostosis; Pfeiffer syndrome; Saethre-Chotzen syndrome.
Acromegaly, sinus enlargement in, 250f
Actinomycosis
  salivary glands and, 2037–2038
  sinonasal, 232–234
AdCCs. *See* Adenoid cystic carcinomas (ACCs; AdCCs).
Adductor paralysis, 1682, 1683f
Adelaide craniosynostosis. *See* Muenke syndrome.
Adenitis
  lacrimal, orbital pseudotumors and, 587, 590f
  retropharyngeal, 1505f
Adenoameloblastomas, 952–953, 957f
Adenocarcinomas
  basal cell, of salivary glands, 2084–2086, 2085f
  buccal, 1994f
  laryngeal, 1645
  low-grade, of salivary glands, 2096–2097, 2097f
  metastatic, lymph nodes in, 1927f, 1928f
  not otherwise specified, of salivary glands, 2104–2105, 2105f, 2106f
  ocular, 513
  of hard palate, 1444f
  of lacrimal gland, 644f
  of oral cavity, 1440, 1444f
  of parotid gland, with perineural tumor spread, 879f
  recurrent, following craniofacial resection, 435f
  sinonasal, 272, 274, 276–277, 282f
    intestinal-type, 274, 276–277
Adenoid(s)
  hypertrophic, 1509, 1510f, 1578, 1578f, 1579f
  retention cysts of, 1579f
Adenoid cystic carcinomas (ACCs; AdCCs)
  of facial nerve, 1327f
  of lacrimal gland, 645f
  of oral cavity, 1433, 1438, 1440f–1442f
  of parapharyngeal space, 1972, 1977f

Adenoid cystic carcinomas (ACCs; AdCCs) *(Continued)*
of salivary glands, 277–280, 279f, 1964f, 2090–2091, 2093f–2095f, 2093t, 2093–2096
of tongue base, 1496f
on proto magnetic resonance spectroscopy, 2314f
palatal, 851f–852f
of hard palate, with perineural tumor spread, 872f
with perineural tumor spread, 874f
perineural tumor spread of, 809f
sinonasal, 282f–284f
tracheal, 1718–1719, 1721f
Adenoidal tonsillar tissue, 1797f
Adenomas
basal cell, of salivary glands, 2084–2086, 2085f
benign, of lacrimal gland, 644f
canalicular, of salivary glands, 2086
follicular, of thyroid, 2150f
monomorphic, 1385
ocular, 513
parathyroid, 1839f, 2162–2166
on cross-sectional imaging, 2162–2163, 2163f, 2164f
on nuclear scintigraphy, 2163, 2165f, 2165–2166, 2167f
on ultrasonography, 2162, 2163f
pituitary. *See* Pituitary adenomas.
pleomorphic
of oral cavity, 1408, 1410, 1412f
of salivary glands, 280, 280f–284f, 1943, 1943f
sebaceous, of salivary gland origin, 2099
thyroid, 2150–2151
Adenomatoid hyperplasia, of mucous salivary glands, 2052
Adenomatoid odontogenic tumors, 952–953, 957f
Adenomatous tumors, of middle ear, 1342, 1346f
Adenopathy
generalized, persistent, in HIV infections, 1889
malignant, submental, 1395, 1398f
mycobacterial infections and, 1567, 1567f
Adenosis, sclerosing, of salivary glands, 2103–2104, 2104f
Adenosquamous carcinomas (ASCs), of salivary glands, 2098
Adenotonsillitis
bacterial, 1562–1564, 1564f–1567f, 1566
streptococcal, 1564f
viral, 1562
AFD Nager. *See* Nager acrofacial dysostosis syndrome (AFD Nager).
AFLNH. *See* Angiofollicular lymph node hyperplasia (AFLNH).
Agger nasi, 509
cells of, 97, 134f, 153–154
on computed tomography, 154f
Aging, oropharyngeal swallowing and, 1734–1735
AIDS. *See* Acquired immunodeficiency syndrome (AIDS).
AIDS-related cysts, of salivary glands, 2060–2063
Aileron, 1822
Air
humidification of, as nasal function, 93
in nasopharynx and oropharynx, on plain films, 121
in retropharyngeal space, 1820f
warming of, as nasal function, 93
Air cells
apical, giant, 1147
of temporal bone, 1061
Air-fluid levels, 196–198, 197f–199f, 200
on computed tomography, 197f–199f
on plain films, 197f–199f
Airway disorders, pediatric, 1525–1588
clinical evaluation in, 1525–1526
of obstructive sleep apnea, 1525–1526
of stridor, 1525
congenital, 1538–1561
craniofacial malformations, 1543–1544, 1544f, 1545f
laryngeal obstruction and, 1551–1553
nasal obstruction and, 1538–1543
oropharyngeal obstruction and, 1544, 1546–1550
subglottic obstruction and, 1553–1554
tracheal obstruction and, 1554–1556
vascular, 1556–1561
compression due to, 1555–1556, 1557f, 1558f
foreign bodies, 1575–1577, 1577f
infectious and inflammatory, 1562–1570
radiographic techniques for, 1526–1528
computed tomography, 1528
fluoroscopy, 1527–1528
magnetic resonance imaging, 1528
plain films, 1526f, 1526–1527, 1527f
traumatic, 1570–1578
tumors and tumor-like conditions
benign, 1578–1583
malignant, 1583–1588
AJCC. *See* American Joint Commission on Cancer (AJCC).
Alagille syndrome, 1110t, 1127
Alar cartilages, 10
Alar lobule, 88, 88f, 89
Alar rim, 88
Alar-facial junction, 88
Albers-Schonberg disease, of temporal bone, 1263–1264, 1264f–1266f
differential diagnosis of, 1263–1264
Albright's syndrome, 331
ALHE. *See* Angiolymphoid hyperplasia with eosinophilia (ALHE).
Allergic polyps, sinusitis and, 203
Allergic sinusitis, 200–201
radiographic appearance of, 169
Alloderm augmentation, skin lesions due to, 2182, 2183f
Alloplasts, for orbital fractures, 397
Alveolar artery
anterosuperior and posterosuperior, 102
inferior, 1797f
Alveolar nerve, superior, 102
posterior, canal for, 116, 116f
Alveolar process, 896f, 897, 899, 899f, 900f, 902f, 903
Alveolar recesses, 102
of maxillary sinus, 115, 116f
Alveolar ridge carcinoma, ultrasmall superparamagnetic iron oxide imaging of, 2317f
Alx3/Alx4 mutation, median cleft face syndrome and, 27
Ameloblastic carcinomas, 356
Ameloblastic fibroodontomas, 951–952, 957f
Ameloblastomas, 354–356, 358f, 359f, 946–948, 947f–954f
of jaw, 971
of oral cavity, 1422, 1425f
on computed tomography, 354, 358f, 948f, 951f, 953f
on magnetic resonance imaging, 354–355, 359f, 948f, 949f, 952f, 953f
on plain films, 947f, 948f, 951f, 953f, 954f
unicystic, 356
Amelogenesis imperfecta, 989, 990f
American Joint Commission on Cancer (AJCC), nodal classification system of, 1870, 1871f, 1871t, 1874t–1876t
refinement of, 1880, 1882t
Amniotic band syndrome, 30
Amniotoceles, 714, 715f
Amyloid, laryngeal, 1682, 1683f, 1684f
pediatric, 1582
Amyloid tumors, of lacrimal gland, 646
Amyloidosis
lymph nodes in, 1927f
orbital, 603, 603f, 604f
trachea and, 1711, 1713f–1714f
Anaplastic carcinomas
laryngeal, 1645
of jugular foramen, 1324f
thyroid, 2156, 2156f, 2157f
Aneurysm(s)
berry
carotid, tinnitus due to, 1365f

Aneurysm(s) *(Continued)*
of anterior internal carotid artery, 1294–1295, 1302f
false, carotid, 1366f
giant
of anterior internal carotid artery, 1295, 1302f
of parapharyngeal space, 1987f
intracavernous, 760f, 761f
intracranial, 252f, 757–760
clinical findings with, 758–759
on computed tomography, 759, 760f, 761f
on magnetic resonance imaging, 759–760, 760f–763f
pathologic findings with, 759
mycotic, 582, 583f
of carotid artery, 1349
false, 1366f
internal, 1981–1982, 1983f–1984f, 2205–2206
giant, 1295, 1302f
tinnitus due to, 1365f
of petrous apex, 846f
of skull base, 840, 842, 843f–846f, 844
on computed tomography, 843f
on magnetic resonance angiography, 846f
on magnetic resonance imaging, 843f–846f
thrombosed, 763f
Aneurysmal bone cysts (ABCs)
fibrous dysplasia versus, 1256
of jaw, 943–944, 946f
of skull base, 833
orbital, 574, 578f
sinonasal, 336–338, 341f, 342f
on computed tomography, 342f
on magnetic resonance imaging, 342f
Aneurysms, giant
of anterior internal carotid artery, 1295, 1302f
of parapharyngeal space, 1987f
Angiitis, hypersensitivity, orbital, 603
Angiocentric T-cell lymphomas, sinonasal, 301–302
Angiofibromas
nasopharyngeal, juvenile, 1579–1580, 1580f
of skull base, juvenile, 827, 829, 829f, 830f
sinonasal, 308–310, 310f–312f
on angiography, 310, 312f
on computed tomography, 310, 310f, 311f
on magnetic resonance imaging, 310, 312f
on plain films, 310, 310f
Angiofollicular lymph node hyperplasia (AFLNH), 1902–1903
Angiogenesis, in tumors, 2291
imaging of, 2291
Angiography. *See specific regions and conditions.*
Angioimmunoblastic lymphadenopathy, 1903
Angiolymphoid hyperplasia with eosinophilia (ALHE), of parapharyngeal space, 1979
Angiomas, retinal
in von Hippel-Lindau disease, 499–500
phakoma of, 509
Angiomatosis, bacillary, lymphadenitis in, 1892
Angiomatosis retinae, 509
Angiomatous polyps, sinonasal, 310–311, 313f
on computed tomography, 313, 313f
Angioneurotic edema, hereditary, 1570
Angiosarcomas
cutaneous, 312
sinonasal, 312–314
Angular vein, 127
Ankylosis, bony, of temporomandibular joint, following temporary Silastic implant, 1032f
Anophthalmia, 461
Anophthalmic socket, 521, 522f, 523f
Anosmia, 94, 95f, 251–252, 255f
Anterior chamber, embryology of, 532f
Anterior commissure, 1596
Anterior tonsillar pillar (ATP), malignancies of, 1485, 1486f, 1486t
Antoni patterns, 628
Antrochoanal polyps, pediatric, 1581f, 1582
Antrum
hypoplastic, 114
roof of, 116, 116f
wall of, 115, 115f
Aortic aneurysms, vocal cord paralysis due to, 2236f
Aortic arch, 1702, 1803f
double, 1557f, 1558f
embryology of, 1769
Apert's syndrome, 71, 77, 78f, 79, 1110t
ocular motility disorders in, 651
orbit in, 559, 563f
Apoptosis, 2274
circumventing, 2287f, 2287–2288
Appendage cysts, orbital, 569–570
Aqueduct, apex of, reconstruction of computed tomography images of, 1105f
Aqueous chamber, embryology of, 449
Arachnoid, of optic nerve, 541
Arachnoid cysts, 569, 571f, 1282f
of cerebellopontine angle, 1290, 1295f, 1296f
Arachnoid granulations
of skull base, 859, 859f
of sphenoid bone, 792, 800f
with otitis media, 1182, 1183f
Arcuate eminence, on magnetic resonance imaging, 1100f
ARF protein, 2286
Arnold's nerve, 1065, 1786
Arterial malformations, of oral cavity, 1388–1389, 1391f, 1392f
Arteriohepatic dysplasia, 1110t, 1127
Arteriovenous fistulas (AVFs)
direct, tinnitus due to, 1369–1370, 1370f
dural, tinnitus due to, 1368f, 1368–1369, 1369f
of cerebellopontine angle, 1298, 1305f
Arteriovenous malformations (AVMs)
of cerebellopontine angle, 1298, 1305f
of neck, 1856, 1858f
orbital, 620
Arteritis
lymph node necrosis with, 1919f
radiation-related, 2268f
Arthritides. *See also specific conditions.*
of temporomandibular joint, 1036–1037, 1041f, 1042f
Arthrography. *See specific regions.*
Artifacts, on computed tomography, 123
Aryepiglottic fold, 1800f
Arytenoid cartilages, 1598, 1598f, 1801f
embryology of, 1768
radiation effects on, on videofluoroscopic swallowing study, 1737f
Arytenoid dislocation, 1664, 1666, 1676f
Arytenoid prominence, 1596f
ASCs. *See* Adenosquamous carcinomas (ASCs).
Aspergillosis
nasolacrimal obstruction in, 687
on computed tomography, 241f
on magnetic resonance imaging, 226f, 227f
orbital cellulitis and, 583–584, 585f
sinusitis in, 201–202
sphenoid sinus obstruction in, 809, 810f, 811f
Aspiration, in videofluoroscopic swallowing study, 1749, 1749f, 1750f
Aspirin triad syndrome, sinusitis in, 255
Astrocytomas
anaplastic, intracranial, 775f
intracranial, 772, 775, 775f
pilocytic, intracranial, 776f
retinal, 496, 496f, 497f
Asymmetric head, 67, 68f, 69
Ataxia-telangiectasia
gene mutated in, 2285–2286
sinusitis in, 256
Atherosclerosis, tinnitus due to, 1363
ATM protein, 2285–2286
ATP. *See* Anterior tonsillar pillar (ATP).
Atrium, nasal, 92f, 98
Atypical lymphoid hyperplasia, 1897
Auditory ossicles, 1238f. *See also specific bones.*
abnormalities of, with outer ear anomalies, 1114
anatomy of, 1069

Auditory ossicles *(Continued)*
congenital anomalies of, 1116–1118, 1117f–1120f, 1166f, 1167f
dislocation and fracture of, with temporal bone fractures, 1236–1239, 1238f–1241f
erosion of, 1196, 1197f, 1198f
fixation of, 1196, 1199, 1199f
malformation of, in hemifacial microsomia, 60–61
of middle ear, 1061
resorption of, following chronic otitis media, 1195, 1197f
Auricle. *See* Pinna.
Auricular artery, posterior, 127, 130f
Auricular hillocks, 8–9
Auricular nerves, 127, 128f, 881f, 1788
Auricular vein, posterior, 127
Auriculares muscles, 91t
Auriculotemporal nerve, 870, 875f, 1784
perineural tumor spread involving, 868, 874f
Autoimmune diseases
of inner ear, 1210
of salivary glands, 2043–2046, 2044f–2049f, 2048–2050
optic neuritis, 629
thyroid, 2143–2147
Automastoidectomy, 1195, 1196f
Autonomic ganglia, of face and neck, 1790
Autonomic nervous system, nasal resistance, humidification, and temperature regulation by, 93, 96
Avascular necrosis, in mandibular condyle, 1018, 1025f, 1026f
AVFs. *See* Arteriovenous fistulas (AVFs).
AVMs. *See* Arteriovenous malformations (AVMs).
Ax head, 66, 68f
Axial view, for paranasal sinus computed tomography, 123
Axillary artery, 1803f
brachial plexus related to, 2219, 2220t
pseudoaneurysm of, 2231f
Azygous vein, 1702

B

BA. *See* Bacillary angiomatosis (BA).
Bacillary angiomatosis (BA), lymphadenitis in, 1892
Bacterial tracheitis, 1569–1570, 1570f
Baere-Stevenson cutis gyrata syndrome, 79
Balloon dacryocystoplasty, 720, 721f–723f, 722–725
Barium swallow
modified. *See* Videofluoroscopic swallowing study (VFSS).
videofluoroscopic swallowing study compared with, 1729
Barotrauma, air-fluid levels due to, 197–198
Barry Perkins Young syndrome, with sinusitis, 253
Bartholin's duct, on sialography, 2017
Basal cell(s), olfactory, 94
Basal cell adenocarcinomas (BCACs), of salivary glands, 2084–2086, 2085f
Basal cell adenomas (BCAs), of salivary glands, 2084–2086, 2085f
Basal cell carcinomas (BCCs)
metastatic to sinonasal cavities, 362
of external ear, 1214
of skin, 2178, 2178f
Basal cell nevus syndrome, 938, 944f
Basal cephaloceles, 49, 51–52
Basal lamellae
of ethmoid sinus, 97, 98
on computed tomography, 154f
Basaloid squamous carcinomas, of salivary glands, 2098
Base view, for paranasal sinus plain films
modified, 104, 106f
of associated structures, 115f, 120–122, 121f
of frontal sinuses, 3f, 109, 109f
of maxillary sinuses, 109f, 114, 115, 115f, 118
of sphenoid sinuses, 115f, 119
Basicranium. *See* Skull base.
Basilar artery, 1796f
Basilar invagination, 857
platybasia versus, 853–854
Basilar membrane, 1099f
Basioccipital center, 10, 30f
Basioocciput. *See* Skull base.
Basisphenoidal center, 10, 30f
BCACs. *See* Basal cell adenocarcinomas (BCACs).
BCAs. *See* Basal cell adenomas (BCAs).
BCCs. *See* Basal cell carcinomas (BCCs).
B-cell lymphomas, orbital, 601
BCL3 gene product, cleft lip/palate and, 19
Bell stage, of tooth development, 891
Bell's palsy, 1224, 1225f
Benign lymphoepithelial lesions (BLELs), of salivary glands, 2099–2100, 2101
Benign masseteric hypertrophy (BMH), 1458, 1458f
Benign mixed tumors. *See* Pleomorphic adenomas.
Berry aneurysms, of carotid artery
anterior internal, 1294–1295, 1302f
tinnitus due to, 1365f
Bertin, bones of, 787
Bezold abscesses, 1178f
BFM. *See* Bifacial microsomia (BFM).
Bifacial microsomia (BFM), 58
Bilaminar zone, of temporomandibular joint, 996
Bill's bar, 1064
Bipolar neurons, olfactory, 93–94
Birbeck granules, 603
Bitewing radiographs, 915, 915f
Bladder carcinomas, temporal bone metastases from, 1309f
Blastomycosis
North American, paranasal, 239, 241
South American, paranasal, 241
BLELs. *See* Benign lymphoepithelial lesions (BLELs).
Bloom syndrome, 2285
Blue-rubber bleb nevus syndrome, 1561
BMH. *See* Benign masseteric hypertrophy (BMH).
Boder-Sedgwick syndrome
gene mutated in, 2285–2286
sinusitis in, 256
Bone(s). *See also specific bones.*
malignant transformations of, with fibrous dysplasia, 332
sclerotic, sinonasal tumors and, 265–266
sinonasal tumors and, 264–266, 266t
Bone cavity cysts, static, of jaw, 944–945, 946f, 947f
Bone cysts
aneurysmal. *See* Aneurysmal bone cysts (ABCs).
benign, of masticator space, 1995f
solitary (hemorrhagic; simple)
of jaw, 942–943, 945f
of temporomandibular joint, 1036, 1040f
Bone grafts, for cricoid cartilage repair, 1693, 1695
Bone marrow, of mandibular condyle, abnormalities of, 1018, 1024f–1026f
Bones of Bertin, 787
Bony labyrinth
anatomy of, 1071, 1072f, 1073
embryology and developmental anatomy of, 1060
otosclerosis of. *See* Otosclerosis.
Borrelia burgdorferi. See Lyme disease.
BORS. *See* Branchio-oto-renal syndrome (BORS).
Bourneville's disease, choroidal hemangiomas in, 508
Brachial neuritis, 2224f, 2226
Brachial plexopathies, 2221, 2222f–2233f, 2222t, 2222–2227, 2230
clinical findings in, 2221–2222
lung carcinoma causing, 2237f
obstetric, 2223
on computed tomography, 2223f, 2227f–2229f, 2231f
on magnetic resonance imaging, 2222f–2230f, 2232f, 2233f
Brachial plexus, 1802f, 2216–2230
anatomy of, 2216–2217, 2217f–2220f, 2219, 2220
imaging strategies for, 2219–2221, 2221f
metastatic disease of, 2225, 2225f, 2228f, 2232f
schwannoma of, 1811f

Brachiocephalic artery, 1702, 1803f
Brachycephaly, 66–67, 68f
Brain
  atrophy of, 1123f
  holoprosencephaly and, 53–58, 54f, 55t, 56–57
  metastatic disease of, 772, 774f
  tumors of, 1300–1302, 1305f–1308f. *See also specific tumors.*
Brain survey, routine, 1098
Brain tissue
  herniation through cranial defects. *See* Cephaloceles.
  heterotopic
    nasal, 37, 39–42, 40f–43f
      extranasal, 39–40, 41
      histology of, 41–42
      intranasal, 40f, 40–41
      mixed, 41, 41f
    nonnasal, 42–43
Brainstem
  on magnetic resonance imaging, 1104f
  tumors of, 1300, 1305f
Branchial anomalies, 1828–1838
  of first branchial cleft, 1829–1830, 1830f, 1831f
  of fourth branchial cleft, 1831, 1836–1838, 1839f
    parathyroid, 1837–1838, 1839f
  of second branchial cleft, 1831–1832, 1832f–1836f
  of third branchial cleft, 1831, 1832–1833, 1836, 1836f, 1837f
Branchial apparatus, 1758
  embryology of, 1759–1770, 1761f, 1762f
    branchial arches and, 1768–1770, 1769f, 1770t
    parathyroid glands and, 1762
    pharynx, larynx, and trachea and, 1765, 1766f, 1767f, 1767–1768
    pouch derivatives and, 1760, 1762f
    thymus and, 1760, 1762
    tongue and thyroid gland and, 1762–1765, 1763f–1766f
Branchial arch syndrome, of first and second arches, 58–66
  bony orbit in, 562
  branchio-oto-renal, 63
  hemifacial microsomia, 58f, 58–63
  mandibulofacial dysostosis, 63, 64f
  maxillary sinus hypoplasia in, 101
  Nager acrofacial dysostosis, 65
  pathogenesis of, 58
  Pierre Robin sequence, 65f, 65–66
Branchial arches
  cartilages of, 1768–1769
  derivatives of, 1770t
  embryology of, 1768–1770, 1769f, 1770t
  numbering of, 1760
  terminology for, 1758
Branchial cleft, second, cyst of, 1410f
Branchial cysts, 1829. *See also* Branchial anomalies; Lymphoepithelial cysts.
  in parapharyngeal space, 1976, 1979, 1979f–1980f
  of first branchial cleft, 2053f
  of salivary glands, 2053f, 2054f, 2054–2055
  of second branchial cleft, 1808f
  on ultrasound, 1948, 1949f
Branchial fistulas, 1829
Branchial groove, 1061
Branchial pouches, 1760, 1761f
Branchial sinuses, 1829
Branchio-oto-renal syndrome (BORS), 63, 1110t, 1166f
  semicircular canals in, 1126f
BRCA1/BRCA2 genes, 2286, 2286f
Breast carcinomas
  BRCA1/BRCA2 genes in, 2286, 2286f
  metastatic to brachial plexus, 2228f, 2232f
  metastatic to brain, 772, 774f
  metastatic to carotid sheath, 1456
  metastatic to humerus, 2233f
  metastatic to masticator space, 1996f
  metastatic to neck, 1809f, 1810f
  metastatic to orbit, 646f
  metastatic to salivary glands from, 2109f, 2110f
  metastatic to tracheoesophageal sulcus, 2237f
  metastatic to visual pathway, 772, 774f, 775, 777, 777f
Breschet's canals, 100
Broad head, 66–67, 68f
Bronchogenic cysts, cervical, 1860
Bronchoscopy, virtual, 1703–1704, 1704f, 1705f
Brown tumor of hyperparathyroidism, 334, 341f
  in skull base, 832–833
Brown's superior oblique tendon sheath, 648, 649f, 650f
Bruch's membrane, 455, 456f
Buccal bifurcation cysts, 941
Buccal fat, 1798f, 1989
Buccal mucosa, squamous cell carcinoma of, on positron-emission tomography, 2298f
Buccal nerve, 1784
Buccinator lymph nodes, drainage of, 1881t
Buccinator muscle, 91t, 127, 128f, 897, 899f, 1379t, 1793t, 1798f
Buccomasseteric region, normal anatomy of, 1384–1386, 1385f, 1386f
Buckley's syndrome, with sinusitis, 253–254
Bulbar fascia. *See* Tenon's capsule.
Bulla ethmoidectomy, 170
Bullae, frontal, 99
Bullae ethmoidalis, 92f, 97, 98, 140f
Buphthalmos, 462
Burkitt's lymphoma, *c-myc* oncogene in, 2280
Burns
  laryngeal, 1667, 1677f
  pharyngeal, 1513

C

CADs. *See* Congenital aural dysplasias (CADs).
Calcification(s)
  in inverted papillomas, 268, 270f
  intraocular, 475, 477, 479t
  of lymph nodes, 1920, 1926t, 1927f–1928f
  of tympanic membrane, 1199, 1199f, 1200f
  on videofluoroscopic swallowing study, 1738
  sinonasal, 251, 253f, 254f
Calcifying odontogenic cysts, 352, 938, 944f
Calcium pyrophosphate arthropathy, of temporomandibular joint, 1035, 1038f, 1039f
Caldwell view, for paranasal sinus plain films
  modified, 103, 104f
  of associated structures, 120
  of ethmoid sinuses, 112f, 112–113, 113f
  of frontal sinuses, 109, 110f, 111, 111f
  of maxillary sinuses, 114, 117
  of sphenoid sinuses, 118, 119f
Calvarium, development of, 66, 67f
Cambium, periorbital, 537
Camurati-Engelmann-Ribbing syndrome, 858f
  of temporal bone, 1264, 1265–1266, 1267f, 1268f
    differential diagnosis of, 1266
  Paget's disease versus, 858f
Canalicular adenomas, of salivary glands, 2086
Canaliculi
  mastoid, pseudofracture of, 1237f
  nasolacrimal
    anatomy of, 672–674, 673f
    duplication of, 716
    obstruction of, 721f–722f
    stenosis of, 687f, 691f–692f
  tympanic, pseudofracture of, 1238f
Canaliculitis, chronic, 688, 690
Cancer treatment. *See also specific treatments and cancers.*
  future of, 2292
Candida sinusitis, 202–203
Canine tooth, 139f
Canoe head, 66, 68f
Canthal cysts, 685f
Canthocystostomy, 671–672

Canthus, inner, mass lesions of, 702, 704f–705f, 704–705, 711t, 717f–718f
Capillary hemangiomas
of neck, 1854, 1856
of salivary glands, 2107
orbital, 613–614, 617f, 618f
Capillary lymphangiomas, 1851, 1855f
Capillary malformations, of oral cavity, 1388
Capsulopalpebral fascia, 540
Carcinoid tumors, tracheal, 1723
Carcinoma(s). *See also specific types of carcinoma.*
esophageal, 2236f
lymphoepithelial, 2100, 2101
metastatic nodes and, clinical significance of, 1869, 1869t, 1870t
metastatic to salivary glands, 2105–2107, 2108f–2110f
of jaw, 971–972, 972f
of skull base, 836, 841f
parathyroid, 2168f, 2168–2169
pharyngeal, 1819f
sinonasal, 262
tonsillar, 1916f, 1994f
Carcinoma ex pleomorphic adenoma, of salivary glands, 2071, 2074–2075, 2076f
Carcinoma-ex-inverted papilloma, 267
Cardinal veins, embryology of, 1772, 1772f
Carotid arteries, 788
aberrant, tinnitus due to, 1364, 1364f
aneurysms of, petrous, 1349
tinnitus due to, 1364
common, 130f, 1800f, 1801f, 1802f, 1803f
deviation of, 1685, 1687f
dissection of, tinnitus due to, 1363–1364, 1365f
embryology of, 1771
external, 101, 127, 130f, 1798f, 1799f
internal, 101, 127, 130f, 798–799, 1797f, 1798f, 1799f
aberrant course of, 1140, 1142, 1159f
agenesis of, 1142–1144, 1160f
aneurysms of, 757–760, 842, 1965f, 1981–1982, 1983f–1984f, 2205–2206
clinical findings with, 758–759
on computed tomography, 759, 760f, 761f
on magnetic resonance imaging, 759–760, 760f–763f
pathologic findings with, 759
anterior
berry aneurysms of, 1294–1295, 1302f
giant aneurysms of, 1295, 1302f
infarct of, 1302, 1308f
vascular loop of, 1294
congenital absence of, 1160f
Carotid arteries *(Continued)*
medial deviation of, 2204, 2206f, 2207f
normal anatomy of, 1156f
partial absence of, 1140, 1142, 1156f
stenosis of, 1141f, 1142f
thrombosis of, 2205, 2209f
tumor invasion of, 1917, 1919
laterally displaced, tinnitus due to, 1366
on magnetic resonance imaging, 1099f, 1106f
thrombosis of, 2268f
tortuous, 1513, 1687f, 1983, 1985, 1985f
variants of, 784, 805f
with skull base trauma, 852, 855f
Carotid bifurcation, 1800f
Carotid body
paraganglioma of, 1950
tumors of, 1969, 1975f
Carotid canal, 135f, 143f
CT surface reconstruction of, 1097f
Carotid sheath, 1814, 1815f
breast carcinoma metastatic to, 1456
cavity within, 1816, 1825t, 1826t
Carotid triangle, masses in, differential diagnosis of, 1794, 1794t
Carotid triangles, 1778, 1779f
Cartilage(s). *See specific cartilages.*
Cartilaginous grafts, for cricoid cartilage repair, 1693, 1694f, 1695
Cartilaginous tumors, tracheal, 1722
Castleman's disease, 600, 1900f
Cat-scratch disease (CSD), lymphadenitis in, 1891–1892
Caustic ingestions, in children, 1574
Cavernous fistulas, carotid, orbits and, 620, 624f, 625f
Cavernous hemangiomas
of neck, 1856, 1857f
on ultrasound, 1950f, 1950–1951
of salivary glands, 2107
orbital, 615–616, 619f–621f
Cavernous lymphangiomas, 1850, 1855f
Cavernous malformations, cerebral, 1561
Cavernous sinus, 127, 802f
fungal infections of, 807, 810f, 811f
squamous cell carcinoma of, with perineural tumor spread, 884f
thrombosis of, 807, 811f
Cavernous sinus thrombosis (CST)
bilateral, 583f
orbital, 581–582
right, 583f
CCFs. *See* Central cementifying fibromas (CCFs).
Cebocephaly, in holoprosencephaly, 55, 56f
Cell division cycle, mechanisms of entering and exiting, 2274
Cellulitis
localized, of superficial cervical fascia, 1807f
necrotizing, streptococcal, 1567f
of masticator space, 1989–1990, 1990f
of salivary glands, 2027f, 2029f, 2033f, 2034f, 2036f, 2108f
of skin, 2174f
of submandibular gland, 2194f
orbital, sinusitis with, 706f
retropharyngeal, 1567f
with lacrimal sac mucoceles, 688f
Cemental caries, 918
Cemental dysplasia
florid, 955, 960f, 961f
periapical, 954–955, 958f, 959f
Cementoblastomas, 357, 359f
benign, 955–956
gigantiform, 357
Cementomas, multiple, familial, 357
Cemento-osseous dysplasia, 357
florid, 955, 960f, 961f
sinonasal, 332–333
Cemento-ossifying fibromas, 330, 331f, 332f, 1420
active, pseudomonatous, juvenile, 574, 578f
central, 1420, 1421f
fibrous dysplasia versus, 1255
of jaw, 968, 969f
sinonasal, 330–331, 331f, 332f
on computed tomography, 330, 331f, 332f
Central cementifying fibromas (CCFs), 1420, 1421f
Cephaloceles, 31, 31f, 37, 43–52, 165, 166f
basal, 49, 51–52
ethmoidal, anterior and posterior, 52
sphenoethmoidal, 51
sphenomaxillary, 51
sphenoorbital, 51
sphenopharyngeal, 51
transethmoidal, 51
transsphenoidal, 51
frontoethmoidal, etiologies of, 49
of skull base, 803–804, 804f–808f
on computed tomography, 805f, 806f, 808f
on magnetic resonance imaging, 804f, 805f, 808f
on plain films, 805f, 807f
orbital, 569
sincipital, 43–49, 45f, 46f, 46t
frontoethmoidal, 44–45, 46t, 47–49
concurrent malformations with, 47, 49
frontonasal subtype of, 44–45, 47, 47f–49f
nasoethmoidal subtype of, 47
nasoorbital subtype of, 47, 50f–52f
interfrontal, 44
types of, 804, 804f–806f

Cephalo-oculocutaneous telangiectasia syndrome
gene mutated in, 2285–2286
sinusitis in, 256
Cerebellar abscesses, 1179f
Cerebellar artery, inferior, anterior, 1074
Cerebellopontine angle (CPA)
3D reconstruction of magnetic resonance imaging of, 1104f
tumors of, 1285–1306
epidermoid and other cysts, 1288, 1290–1291, 1292f–1297f
intraaxial, 1300–1302, 1305f–1308f
intracanalicular, 1303, 1306, 1309, 1309f–1312f
meningiomas and simulants, 1286–1288, 1287f–1291f
nonacoustic posterior fossa schwannomas, 1291–1293, 1297f–1300f
of petrous bone, 1298
paragangliomas, 1298, 1300
statistics and categorization of, 1285–1286, 1286t
vascular, 1293–1295, 1298, 1300f–1305f
Cerebellopontine angle cistern, 1099f, 1100f
Cerebellum, 1101f, 1102f, 1103f
tumors of, 1300–1301
Cerebral abscesses, nasal dermal sinus resection for, 34–35
Cerebral arteries, 1100f, 1106f
Cerebral arteriovenous malformations, tinnitus due to, 1367–1368
Cerebral infarction, 760–768
clinical findings with, 761, 763f, 764f
on computed tomography, 763, 764f, 765f, 766, 768f
on magnetic resonance imaging, 763f–768f, 766, 768
pathologic findings with, 761–763
Cerebral neoplasms, 770–777. *See also specific neoplasms.*
clinical findings with, 771–772
on computed tomography, 772, 774f
on magnetic resonance imaging, 772, 773f–778f, 775, 777
pathologic findings with, 772, 773f, 774f
Cerebritis, in sinusitis, 582f
Cerebrospinal fluid (CSF), sphenoid bone abnormalities and, 807
Cerebrospinal fluid fistulas
after skull base surgery, 859–860
with functional endoscopic sinus surgery, 176
Cerebrospinal fluid leaks
skull base and, 858–860, 859f
with functional endoscopic sinus surgery, 177–178, 178f, 179f
on computed tomography, 178
Cerebrospinal fluid leaks *(Continued)*
on CT cisternography, 177, 178, 178f, 179f
on MR cisternography, 177
on radionuclide studies, 177–178
with skull base trauma, 852, 855f
with temporal bone trauma, 1239, 1241, 1241f
Cerebrospinal fluid rhinorrhea
air-fluid levels and, 198, 200
with functional endoscopic sinus surgery, 177
Ceruminomas, 1341
Ceruminous glands, rumors of, 1214–1215
Cervical cancer, human papilloma viruses and, 2288
Cervical cutaneous nerve, 127, 129f
Cervical dorsal rami, 129f
Cervical esophagus, 1802f
Cervical ganglia, of sympathetic nervous system, 1789
Cervical lymph nodes, drainage of, 1881t
Cervical nerves, 127
Cervical plexus, 881f, 1786, 1788, 1788f
superficial, 127
Cervical ribs, 2230
Cervical spine, on videofluoroscopic swallowing study, 1737f, 1737–1738
Cervical veins, deep, 127
Cervicooculoacoustic syndrome, 1113t
Chalazion, 569
Chalk bones, 1263
Chamberlin's line, 853
CHARGE association, 1110t, 1166f, 1538
semicircular duct aplasia in, 1124, 1127, 1128f
CHD. *See* Conductive hearing deficit (CHD).
Cheeks
movements of, during oropharyngeal swallowing, 1739
muscles of, 127, 128f
soft-tissue swelling of, on plain films, 118
Chemotherapy, nasolacrimal system and, 691–692
Cherubism, 333
Chicken pox, lymphadenitis in, 1888
Chievitz, organ of, 1775
Chloral hydrate, for magnetic resonance imaging imaging of eye, 451
Choanal atresia, 1538f, 1538–1540, 1539f
Chocolate cysts, orbital, 569
Cholesteatomas, 244, 245f, 246, 246f, 1165f. *See also* Cholesterol granulomas (cysts); Epidermoid cysts.
antral, keratocysts versus, 244, 246
bone erosion with, 1190–1191, 1191f–1196f, 1191t, 1195
congenital, 1184, 1186
of middle ear, 1167f
Cholesteatomas *(Continued)*
external auditory canal atresia with, 1115f, 1116f
following chronic otitis media, 1184, 1186f–1196f, 1186–1187, 1190–1191, 1195
in Prussak's space, 1186–1187, 1187f–1189f
mucoceles versus, 244, 245f
of external auditory canal, 1340, 1342f
of external ear, 1215, 1215f
of facial recess, 1189f
of middle ear, 1120, 1122f
of pars tensa, 1186, 1189f
of petrous apex, 1203–1205, 1204f, 1205f
of salivary glands, 2055
of supratubal recess, 1190, 1190f
primary, of cerebellopontine angle, 1288, 1290–1291, 1292f–1297f
Cholesterol, deficiency of, holoprosencephaly and, 55
Cholesterol granulomas (cysts)
of petrous apex, 1203, 1204f, 1347–1349, 1348f
of temporal bone, 1339, 1340f
orbital, 568t, 572, 573–574, 575f, 577f
Chondrification centers, 786
Chondroblastomas, fibrous dysplasia versus, 1255
Chondrodysplasia fetalis, 1110t, 1165f
of skull base, 857
Chondromas
of jaw, 959
of oral cavity, 1423
of parapharyngeal space, 1986f
sinonasal, 329
Chondromatosis, synovial
of jaw, 959, 961
of temporomandibular joint, 2121
Chondromyxoid fibromas, of skull base, 820, 821, 822f
Chondronecrosis, following radiation therapy, 1694f
Chondrosarcomas (CSs)
fibrous dysplasia versus, 1256
laryngeal, 1645, 1647, 1652f–1655f
mandibular, 1445f
mesenchymal
orbital, 640, 642t
sinonasal, 345
of jugular foramen, 1322, 1325f
of oral cavity, 1440, 1445f
of parapharyngeal space, 1986f
of petrous apex, 1325f, 1349–1350
of skull base, 816–817, 818f–821f, 1325f
chordomas versus, 817–820
myxoid, 817–819
of temporal bone, in petroclival synchondrosis, 1259f
of temporomandibular joint, 1036

Chondrosarcomas (CSs) *(Continued)*
sinonasal, 340, 341–342, 345f
on computed tomography, 346f, 348f
on magnetic resonance imaging, 345f–349f
tracheal, 1720
Chordomas
of skull base, 812f–817f, 812–816
chondroid, 813, 813f, 817
chondrosarcomas versus, 817–820
dedifferentiated, 813
on computed tomography, 814, 814f, 815f
on magnetic resonance imaging, 814f–817f, 814–815
sinonasal, 298–299, 299f–300f
on computed tomography, 300f
on magnetic resonance imaging, 299f
Choriocapillaris, 455–456
Choristomas, 1397–1398, 1400f
complex, 564
conjunctival, 563–564, 568t
in hemifacial microsomia, 61, 63f
of facial nerve, 1337, 1338f
of neck, 1859
orbital, 563
sinonasal, 299–301
Choroid, 455
calcification of, 479t
embryology of, 450, 532f
function of, 456
hemangiomas of, 500, 508–509
clinical features of, 509
diagnostic imaging in, 509, 510f, 511f
hemorrhage of, 509, 512f
osteoma of, 498–499
clinical diagnosis of, 498–499
differential diagnosis of, 499
imaging diagnosis of, 499, 499f
Choroid fissure, 444f
Choroid plexus
carcinoma of, 741f
papillomas of, 1301, 1306f, 1307f
Choroidal cysts, 509
Choroidal detachment, 470–472, 471f–475f, 509
hemorrhagic, 471, 471f
on computed tomography, 471f, 472f, 474f
on magnetic resonance imaging, 471–472, 472f–475f
Choroidal effusion, on magnetic resonance imaging, 475f
Choroidal stroma, 456
Chromosome 18 deletion, 1110t
Chromosome translocation, to generate aberrant fusion proteins, oncogene activation by, 2277–2278
Churg-Strauss syndrome, with sinusitis, 254–255
Cilia, nasal, 93
Ciliary arteries, 543
Ciliary body, 455
anatomy of, 456–457
calcification of, 479t
embryology of, 448–449, 450f
mesoectodermal leiomyomas of, 513
Ciliary dyskinesia syndrome, primary, with sinusitis, 252–253
Ciliary ganglion, 1790
Cine-swallow study. *See* Videofluoroscopic swallowing study (VFSS).
Cisternography, radionuclide, 860
^{11}C-labeled amino acids, in positron-emission tomography, 2295
^{11}C-labeled thymidine, in positron-emission tomography, 2295–2296
Clavicle, 1801f, 1802f
head of, 1803f
Clear cell tumors
carcinomas, of salivary glands, 2087–2088
primary, 2087
Cleft lip. *See also* Cleft lip/palate; Facial clefts.
bilateral, 19, 20t
complete, 21–22, 22f
median, 23–29, 24f–26f
concurrent malformations with, 29
inferior, 23, 24, 24f, 25f, 26–27, 27t
molecular genetics of, 27, 29
of lower lip, with cleft mandible, 29–30
superior, 23–24, 26f, 27, 28f, 29t
true, 16, 16f
upper, 26–27, 27f
unilateral, 19, 20t
complete, 20–21, 21f
incomplete, 21
Cleft lip/palate, 1543–1544, 1544f
common, 18–23, 20t
bilateral, 17f
clinical features of, 20
concurrent malformations with, 23
deformities in parents of children with, 23
genetics of, 19–20
maxillary deformities with, 23
nasal deformities with, 23
of lip, 20–21, 21f, 22f, 23
pathogenesis of, 19
unilateral, 17f, 19, 20t
variation among populations, 18–19, 20t
hypertelorism and, 16, 16f
Cleft neck, with cleft lower lip and mandible, 30
Cleft nose, 23
Cleft palate. *See also* Cleft lip/palate; Facial clefts.
bilateral, 19, 20t
hypotelorism and, 16, 16f
nasopharyngeal lesions with, 42
Cleft palate *(Continued)*
nonsyndromic, genetics of, 19–20
point prevalence of, 19, 20t
unilateral, 19, 20t
Cleidocranial dysostosis, 1110t
Clinoid process
anterior, 133f, 142f, 144f
CT surface reconstruction of, 1096f
posterior, groove for, CT surface reconstruction of, 1097f
Clivus, 135f, 1797f
Cloison sagittale fascia, 1822
Cloverleaf skull, 68f, 69
CMV. *See* Cytomegalovirus (CMV) infections.
c-myc, 2280
detection in human tumors, 2276
Coats' disease, 468f, 492–493
clinical presentation and diagnosis of, 493
diagnostic imaging in, 493, 494f–495f
Cocaine, crack
laryngeal burns due to, 1677f
pharyngeal burns due to, 1513
Coccidioidomycosis
lymphadenitis in, 1895–1896, 1896f
sinusitis and, 203
Cochlea
anatomy of, 1073, 1073f
aplasia of, 1209f
common cavity for vestibule and, 1129, 1133f, 1134f
congenital anomalies of, 1127, 1129–1130, 1131f–1138f, 1132
aplasia, 1129–1130
dysplasia, 1123f
hyperplasia, 1126f
hypoplasia, 1130, 1166f
CT surface reconstruction of, 1098f
''dwarf,'' 1134, 1152f
on magnetic resonance imaging, 1099f, 1100f, 1101f, 1102f, 1104f
scalar asymmetry within, 1132, 1134, 1155f
3D reconstruction of magnetic resonance imaging of, 1104f
Cochlear aqueduct, 1060
on magnetic resonance imaging, 1100f
pseudofracture of, 1236f
Cochlear duct, anatomy of, 1073–1074
Cochlear fossette, stenotic, 1168f
Cochlear implantation, temporal bone following, 1222, 1223f, 1224
Cochlear nerve, on magnetic resonance imaging, 1099f, 1101f
Cochlear neuritis, focal, 1311f
Cochlear otosclerosis, 1249–1250, 1251f–1253f, 1252–1253, 1263f
Cockayne's syndrome, 1123f
Cogan's syndrome, inner ear in, 1210
Collateral veins, 2204, 2205f
Collet-Sicard's syndrome, 1312

Colobomas, 463–464, 464f
diagnostic imaging of, 464, 465f
in hemifacial microsomia, 61, 63f
Colobomatous cysts, 464, 465f, 465t
Colobomatous orbital cysts, 568, 570f
Columella, 88, 88f, 89, 138f
Commissure, anterior, 1801f
Common cold, 193–194
Common crus
on magnetic resonance imaging, 1102f
reconstruction of computed tomography images of, 1105f
Communicating artery, on magnetic resonance imaging, 1106f
Compressor naris muscle, 90, 90f
Computed tomography (CT). *See also specific regions and conditions.*
axial view for, 123
coronal view for, 123
dental CT reformatting programs and. *See* Dental CT reformatting programs.
for postoperative imaging, of sinonasal cavities, 403
magnetic resonance imaging compared with, in sinonasal disease, 109
of paranasal sinuses, window setting for, 212, 213f
radiation dose with, 108
spiral, 123
with dacryocystography, 710–711, 713–716
in pediatric patients, 714–716, 715f
Concha bullosa, 136f, 140f, 157–158, 162f
mucocele of, 240f
Conchae, nasal. *See* Nasal turbinates.
Conductive hearing deficit (CHD), with ossicular disorders, 1195–1196, 1197f–1199f, 1199
Condylar vein, 2204, 2205f
Congenital aural dysplasias (CADs), 1114
Conjunctival inclusion cysts, 570
Constrictor muscles, pharyngeal, 1466
Conus elasticus, 1599, 1599f
Cookie swallow. *See* Videofluoroscopic swallowing study (VFSS).
Cornea
anatomy of, 455
calcification of, 479t
embryology of, 450–451, 532f
Corniculate cartilages, 1596, 1598
Coronal suture synostosis, 557–558, 558f
Coronal synostosis, 810f
unilateral, premature, 69, 70f
Coronal view, for paranasal sinus computed tomography, 123
Coronoid hyperplasia, of temporomandibular joint, 1038, 1044f
Coronoid process, 896f, 897, 898, 899, 900f, 1796f
of mandible, 1797f
tip, 1796f
Corrugator supercilii muscle, 91t, 126, 128f
Cortical dense white line, surrounding frontal sinuses, 133f
Costochondral joints, for temporomandibular joint, 1028, 1032, 1033f, 1034f
CPA. *See* Cerebellopontine angle (CPA).
Cranial fossae
anterior, 133f, 143f
medial, CT surface reconstruction of, 1097f
middle, 143f
meningocele of, 1164f–1165f
superior bony margin of, on plain films, 118, 118f
on plain films, 119, 120, 121f
penetration of, with functional endoscopic sinus surgery, 176
Cranial meningoceles, 43
Cranial nerve(s). *See also specific nerves.*
anatomy of, 1782, 1784–1786, 1785f, 1787f
ganglia of, embryology of, 1760
perineural tumor spread involving. *See* Perineural tumor spread (PNS).
Cranial nerve palsy, with internal carotid artery dissection, 1982
Craniodiaphysial dysplasia, of temporal bone, 1267
Craniofacial dysostosis, 69, 71f–72f, 71–79, 76f, 77f, 1111t
bony orbit in, 558
cranial suture morphogenesis related to, 74, 75f
eponymous, 75–79, 76f–78f
molecular genetics of, 71–74, 72t, 73f
ocular motility disorders in, 651
orbit in, 559, 562f, 564f
Craniofacial malformations
causes of, 4, 5f
congenital, 1543–1544, 1544f, 1545f
Craniofacial microsomia. *See* Branchial arch syndrome, of first and second arches.
Craniofacial resection, 425, 429, 430f–437f, 435
on computed tomography, 429, 430f–432f, 435f–437f
on magnetic resonance imaging, 429, 432f–434f
Craniometaphyseal dysplasia, 1110t
of temporal bone, 1267, 1268, 1270f, 1271f
Craniopharyngiomas, 751–752
clinical findings in, 751
of skull base, 824–826, 828f
on computed tomography, 752f, 751-752
on magnetic resonance imaging, 752, 753f
pathologic findings in, 751
sinonasal, 297–298
Craniosynostoses, 66–79, 67f
ocular motility disorders in, 651
orbits in, 561f
primary
nonsyndromic, 69, 70f
relative frequencies of, 66, 66t
skull shape in, 66–69, 68f
syndromic, 69, 71f–72f, 71–79
cranial suture morphogenesis related to, 74, 75f
eponymous, 75–79, 76f–78f
molecular genetics of, 71–74, 72t, 73f
Cranium. *See* Skull *entries.*
Cribriform plate, 30, 89–90, 140f, 145f
on plain films, 120, 121f
ossification of, 11, 12f
Cricoarytenoid muscles, 1599f, 1600f, 1601
Cricoid cartilage, 1596–1597, 1597f, 1598, 1801f, 1802f
arch of, 1802f
bone grafts for repair of, 1693, 1694f, 1695
embryology of, 1767–1768
lamina of, 1801f
Cricoid fractures, 1663–1664, 1674f, 1675f
Cricoid ring, 1598f
Cricopharyngeus muscle, 1466, 1801f, 1802f
during oropharyngeal swallowing, 1745f, 1745–1746
Cricothyroid dislocation, 1666, 1676f
Cricothyroid joint, 1802f
Cricothyroid membrane, 1802f
Cricothyroid muscle, 1801f, 1802f
Crista galli, 10f, 11f, 30, 133f, 140f, 145f
aerated, 165
anatomic relationships at birth, 30f
distortion of, with nasal dermoid cysts, 36–37
ossification of, 11, 12f
‘‘Cristal cross,’’ 13
Croup, 1568–1569, 1569f, 1654–1656, 1669f
trachea and, 1710
with sinusitis, 255
Crouzon’s disease. *See* Craniofacial dysostosis.
Crura
lateral, 88f, 89
medial, 88f, 89, 89f
Cryptococcosis
lymphadenitis in, 1894–1895, 1895f
sinusitis and, 203
Cryptophthalmos, 463
CSD. *See* Cat-scratch disease (CSD).
CSF. *See* Cerebrospinal fluid (CSF).
CSs. *See* Chondrosarcomas (CSs).
CST. *See* Cavernous sinus thrombosis (CST).

CT. *See* Computed tomography (CT); *specific regions and conditions.*
Cuneiform cartilages, 1596, 1599
Cutaneous hemangioma-vascular complex syndrome, 1854
Cutaneous lesions, 2174f, 2174–2183, 2175f
Cutaneous nerve of neck, transverse, 129f
Cyclic vomiting syndrome, sinusitis in, 256
Cyclopia, in holoprosencephaly, 55, 56f
Cylindric cell papillomas. *See* Schneiderian papillomas.
Cyst(s)
  AIDS-related, of salivary glands, 2060–2063
  arachnoid, 569, 571f, 1282f
    of cerebellopontine angle, 1290, 1295f, 1296f
  attenuation, mucoid, of salivary glands, 2061f
  bone. *See* Aneurysmal bone cysts (ABCs); Bone cysts.
  branchial. *See* Branchial anomalies; Branchial cysts; Lymphoepithelial cysts.
  bronchogenic, cervical, 1860
  canthal, 685f
  cholesterol
    of petrous apex, 1203, 1204f, 1347–1349, 1348f
    of temporal bone, 1339, 1340f
    orbital, 568t, 572, 573–574, 575f, 577f
  choroidal, 509
  colobomatous, 464, 465f, 465t
  dentigerous, of oral cavity, 1422, 1425f
  dermoid. *See* Dermoid cysts.
  developmental
    odontogenic, 353–354, 357f, 358f
    orbital, 563–566, 565t, 566f, 566t, 567f
  ductal, of salivary glands, 2059, 2060f–2062f
  endonasal, 53, 54f
  epidermoid. *See* Epidermoid cysts.
  foregut, pediatric, 1547–1548, 1549f
  hemorrhagic, of salivary glands, 2060f
  incisive canal (nasopalatine duct), of oral cavity, 1422–1423, 1426f
  incisive foramen, of oral cavity, 1426f
  inclusion
    conjunctival, 570
    epidermoid. *See* Cholesteatomas.
  laryngeal, congenital, 1552
  lingual, 1397–1398, 1400f
    pediatric, 1546–1548, 1547f–1549f
  lymphoepithelial, of salivary glands, 2053–2054, 2056f–2059f
  Merkel's, of salivary glands, 2057
Cyst(s) *(Continued)*
  mucosal
    gastrointestinal, 1397–1398, 1400f
    laryngeal, 1651–1652, 1661f
  mucus, of tongue, 1397–1398, 1400f
  of jaw
    aneurysmal bone cysts, 943–944, 946f
    definition and classification of, 931, 933
    incisive canal, 941–942, 945f
    medullary pseudocyst, 945
    odontogenic. *See* Odontogenic cysts.
    solitary (hemorrhagic; simple), 942–943, 945f
    Stafne, 944–945, 946f, 947f
  of lacrimal gland, 646f
  of lacrimal sac, 679, 680f
  of parotid gland, 2049f
  of salivary glands, 2052–2066
    acquired, 2059–2066
    congenital, 2053f–2055f, 2053–2057
  optic nerve sheath, 569, 571f, 1282f, 1290, 1295f, 1296f
  orbital. *See* Orbital cysts.
  parathyroid, 1837–1838, 1839f, 2168f, 2169
  polycystic disease of salivary glands and, 2055, 2057
  primordial, of oral cavity, 1422
  radicular, of oral cavity, 1422
  Rathke's pouch, 826, 828f
  retention. *See* Retention cysts.
  saccular, 1652, 1662f, 1665f–1668f
    congenital, 1552
    external, 1652
  sebaceous, of salivary glands, 2121, 2124f
  sialocysts, 2059–2060, 2062f
  subglottic, pediatric, 1576f
  synovial, of temporomandibular joint, 1036, 1039f
  thyroid, 1837, 1838f, 1839f
  tracheoesophageal, 1860
  vallecular, 1661, 1844f
Cystadenoma lymphomatosum, papillary, 1943f, 1943–1944, 1944f, 1962, 2076–2077, 2079–2080, 2080f–2082f, 2082
Cystic eye, congenital, 568, 570f
Cystic fibrosis
  nasal obstruction in, 1581f
  nasal polyps in, 201
  sinusitis and, 204
Cystic hygromas, 1849–1850, 1850f–1854f
  of parapharyngeal space, 1978, 1981f
  of salivary glands, 2108–2109, 2111f, 2112f
  on computed tomography, 1849–1850, 1850f–1852f
Cystic hygromas *(Continued)*
  on magnetic resonance imaging, 1850, 1853f, 1854f
  on ultrasound, 1949
Cysticercosis
  of cerebellopontine angle, 1290–1291, 1296f
  orbital, 568t, 577, 579f
Cytomegalovirus (CMV) infections
  labyrinthitis due to, 1206
  lymphadenitis in, 1887, 1887f
Cytoplasmic domain of fibroblast growth factor receptors, 72

D

Dacryoadenitis, 641–643, 643f
  in sarcoidosis, 595f
Dacryoceles, 568t, 571–572, 572f
Dacryocutaneous fistula, 683f
Dacryocystitis, 688f
  chronic, 706f
  on computed tomography, 701, 704f–710f, 707f–708f
  with functional endoscopic sinus surgery, 179
Dacryocystoceles, 52–53, 53f, 54f, 714, 715f
Dacryocystography (DCG), 179
  computed tomography with, 710–711, 713–716
    in pediatric patients, 714–716, 715f
  contrast, 656f–672f, 656–660
    contrast materials for, 656–657
    equipment for, 656
    injection techniques for, 657–660
    radiographic techniques for, 657
  digital subtraction, 657, 660–663
  distention, 657
  in nasolacrimal obstruction, 676–677, 677f–682f
  indications for, 671
  kinetic, 657
  magnetic resonance, 716, 717f–718f, 718–720
  normal anatomy on, 672–674, 673f, 674t
  subtraction, 657
  tomographic, 657
Dacryocystoplasty (DCP), 720, 721f–723f, 722–725
  balloon, 720, 721f–723f, 722–725
  endoscopic, 672
  stent placement with, 725–727
Dacryocystorhinostomy (DCR), 671, 672
  anatomy and, on computed tomography, 697, 699
  dacryocystography following, 671f
  endonasal, 672
  postsurgical considerations with, 690–691, 691f–692f
Dacryolithiasis, 679–682, 684, 684f–690f, 687–688

Dacryoscintigraphy, 692–696, 693f, 694f
  in complete obstruction, 696
  in incomplete obstruction, 696
  normal examination with, 693–696, 695f
  sensitivity of, 696
  technique for, 692–693
Danger space, of neck, 1816, 1825t, 1826t
Darling's disease
  lymphadenitis in, 1895, 1895f
  sinusitis and, 203
  tracheal, 1710–1711
DCG. *See* Dacryocystography (DCG).
DCP. *See* Dacryocystoplasty (DCP).
DCR. *See* Dacryocystorhinostomy (DCR).
Deep cervical fascia, of neck, 1806–1814
  deep layer of, 1809–1811, 1810f, 1811f
  middle layer of, 1811–1812, 1813f, 1814, 1814f
    in infrahyoid neck, 1811–1812
    in suprahyoid neck, 1812, 1813f, 1814, 1814f
  superficial layer of, 1806–1809, 1808f, 1809f
Deep layer of deep cervical fascia (DLDCF), 1809–1811, 1810f, 1811f
Defense, as nasal function, 93
Dejerine-Sottas disease, 1303, 1312f
Delayed swallow, 1747, 1747f
Delivery, brachial plexopathy due to, 2223
Deltoid muscle, 1802f, 1803f
Demyelinating disease. *See* Multiple sclerosis.
DeMyer classification, of median cleft face syndrome, 27, 29t
Denervation atrophy, 2190–2191, 2192f
  of brachial plexus, 2232f
  of masticator muscles, 1991, 1992f
  of oral cavity, 1448, 1450f, 1451, 1451t
Dens in dente, 988, 988f
Dens invaginatus, 988, 988f
Dental anomalies, 987–990
Dental caries, on intraoral radiographs, 915f, 916–918, 917f, 918f
Dental CT reformatting programs, 907–918, 908f, 909f–910f
  image and measurement interpretation and, 908–910
  intraoral radiography and, 914–916
    bitewing, 915, 915f
    dental caries on, 916–918, 917f, 918f
    occlusal, 915–916
    periapical, 915, 915f
    periodontal disease on, 916, 916f, 917f
  mandibular canal identification and, 910–912, 912f, 913f
  panoramic radiography and, 913–914, 914f, 915f
  report and, 912–913, 914f
  running, 908, 911f–912f
  scan parameters for, 907–908
Dental implants, 919–924
  abutment for, 919–920, 920f, 921f
  blade form of, 919, 920f
  prosthesis and, 920, 921f
  radiology for, 924, 924f
    dental CT reformatting programs and. *See* Dental CT reformatting programs.
  root form of, 919, 920f, 921f
  subperiosteal form of, 919, 921f
  surgical procedure for, 920–924
    for abutment connection, 921
    for fixture placement, 920–921, 922f–923f
    prosthodontic, 924
Dental lamina, 891
DentaScan. *See* Dental CT reformatting programs.
Dentigerous cysts, 345–347, 352f–355f, 934, 934f–936f
  of oral cavity, 1422, 1425f
  on computed tomography, 352f, 354f, 355f
  on magnetic resonance imaging, 228f, 346–347, 353f, 354f
  orbital, 569
Dentin
  dysplasia of, 990
  opalescent, hereditary, 990
Dentinogenesis imperfecta (DI), 989–990, 990f
Depressor anguli oris muscle, 90t, 1798f, 1799f
Depressor labii inferioris muscle, 90t, 127, 128f, 1799f
Depressor septi muscle, 89, 90f, 90t
DeQuervain's thyroiditis, 2147
Dermatofibromas. *See* Fibrous histiocytomas, benign.
Dermatome, 1758
Dermatopathic lymphadenopathy (DPL), 1902
Dermoid cysts
  limbal, solid, 563
  nasal, 32–37, 35f, 36f
    depth of extension of, 34, 39f
    foraminal enlargement and cristal distortion with, 36–37
    intracranial extension of, 34, 36, 37f, 38f
    nasal obstruction due to, 1543
  nasolacrimal, 702, 704, 705f
  of neck, 1858–1859, 1860f
  of oral cavity, 1389–1392, 1394, 1394f–1396f, 1859
  of skull, 31–32, 32f
  on ultrasound, 1948–1949
  orbital, 563, 567f, 568t
  pediatric, 1546, 1549f
Dermolipomas, orbital, 563–564, 566f, 568t
Desmocranium, 786
Desmoid tumors, 2188, 2189f
  of oral cavity, 1413f
  sinonasal, 318
Desmoplastic fibromas, in parapharyngeal space, 1975–1976
Detectors, for positron-emission tomography, 2296
Developmental cysts
  odontogenic, 353–354, 357f, 358f
  orbital, 563–566, 565t, 566f, 566t, 567f
dHAND transcription factor, cleft lip/palate and, 19
DI. *See* Dentinogenesis imperfecta (DI).
Diaphyseal dysplasia, progressive, 858f
Dictyomas, 513, 513f
Digastric fossae, 896f, 897, 899, 899f
Digastric groove, 1798f
Digastric muscle, 1379t, 1383
  anomalies of, 1387, 1387f
  anterior belly of, 1791t, 1799f, 1800f
  posterior belly of, 1791t, 1798f, 1799f
DiGeorge syndrome, 1111t
Diiodotyrosine (DIT), 2136
Dilator naris muscle, 90, 90f, 92
Diphenhydramine (Benadryl), for magnetic resonance imaging imaging of eye, 451
Diploic space, on plain films, 111
Disappearing bone disease, 837–838, 841f
Dishface deformity, 382
Distodents, 987
Distomolars, 987
DIT. *See* Diiodotyrosine (DIT).
Diverticula
  pharyngeal, 1682–1683, 1684f, 1685f
  tracheal, 1707, 1707f
  Zenker's, 1513, 1514f, 1683–1684, 1685f, 1686f, 2208, 2210, 2211f
    swallowing and, 1746, 1746f
DLDCF. *See* Deep layer of deep cervical fascia (DLDCF).
DNA damage, *p53* gene and, 2284–2285
Docetaxel, nasolacrimal system and, 691–692
Dolichocephaly, 66, 68f
Dorsal rami, 1786
Dorsum sellae, 133f, 788
Double elevator palsy, 648, 650f
Double minutes, 2278
Down syndrome. *See* Trisomy 21.
Downey cells, in infectious mononucleosis, 1885, 1886f
DPL. *See* Dermatopathic lymphadenopathy (DPL).
Draft-type drill out, 188
Drainage shunts, ocular, postsurgical changes with, 521, 522f
Drusen, of optic nerve head, 498, 498f
Ductal cysts, of salivary glands, 2059, 2060f–2062f
Dura, of optic nerve, 541

Dural ectasia, 569, 571f, 1282f, 1290, 1295f, 1296f
Dural sinus thrombosis, with otitis media and mastoiditis, 1176, 1178–1179, 1179f–1181f
Duration of stage transition, 1747, 1747f
Dye tests, of nasolacrimal drainage system, 669–670
Dyke-Davidoff-Masson syndrome, 99
Dynamic swallow study. *See* Videofluoroscopic swallowing study (VFSS).
Dyskinetic cilia syndrome, with sinusitis, 252–253
Dysosteosclerosis, of temporal bone, 1267–1268
Dysphagia, 1513, 1515f

E

EAC. *See* External auditory canal (EAC).
Eagle's syndrome, 2199–2200, 2203f
Ear(s)
  congenital syndromes involving, 1151, 1161, 1165f–1169f
  inner. *See* Inner ear.
  middle. *See* Middle ear.
  outer (external). *See* External auditory canal (EAC); Outer ear.
  sound amplification by, 1075
Ear pits-deafness syndrome, 63
Ear tubercles, 7f
EBV. *See* Epstein-Barr virus (EBV) infections.
Ectoderm, 5
Ectodermal dysplasia, 987, 988f
Ectopic pituitary, 301
Ectopic thyroid. *See* Thyroid gland, ectopic.
Eczema-thrombocytopenia syndrome. *See* Wiskott-Aldrich syndrome.
Edema, preseptal, bacterial preseptal cellulitis and, 579–580
Edwards syndrome. *See* Trisomy 18.
Effective dose equivalent, with computed tomography, 152, 152t
EGs. *See* Eosinophilic granulomas (EGs).
ELSTs. *See* Endolymphatic sac tumors (ELSTs).
Embryo, definition of, 1758
Embryogenesis. *See also specific regions.*
  definition of, 1758
Embryonic germ disk, in skull development, 786
EMECs. *See* Epithelial-myoepithelial carcinomas (EMECs).
Emissary veins, large, tinnitus due to, 1371
Emphysema, subcutaneous, spontaneous, pediatric, 1575f
EMPs. *See* Extramedullary plasmacytomas (EMPs).
Emx1 and *Emx2* genes, holoprosencephaly and, 55
Enamel, on computed tomography, 894
Enamel formation, 891
Enamel pearls, 988, 989f
Encephalitis, following functional endoscopic sinus surgery, 171f
Encephaloceles
  anomalies associated with, 17, 17t
  basal, 804, 804f–806f
  nasal obstruction due to, 1543
  orbital, 839f
  with cholesteatomas, 1195f
  with median cleft upper lip, 26–27, 27f
END1, cleft lip/palate and, 19
Endodontal disease, 925–926
Endolymphatic duct
  anatomy of, 1074
  large, 1139, 1154f, 1155f
  on magnetic resonance imaging, 1099f
Endolymphatic labyrinth, embryology and developmental anatomy of, 1058–1059, 1060f
Endolymphatic sac
  anatomy of, 1074
  large, 1139, 1154f, 1155f
  on magnetic resonance imaging, 1099f, 1102f
  reconstruction of computed tomography images of, 1105f
Endolymphatic sac tumors (ELSTs), of petrous apex, 1350–1351
Endometrial carcinomas, metastatic to sinonasal cavities, 362
Endonasal cysts, 53, 54f
Endophthalmitis. *See* Toxocariasis, ocular.
Endophytic papillomas. *See* Inverted papillomas.
Endoscopes, intracranial extension of, following functional endoscopic sinus surgery, 171f
Endoscopy, of nasolacrimal drainage system, 727–728, 728f
Endosteal hyperostosis, of temporal bone, 1267, 1269f
  fibrous dysplasia versus, 1255
endothelin-1 gene, cleft lip/palate and, 19
Engelmann's disease, 858f
Enterocystomas, of neck, 1859
Enterogenous cysts, orbital, 568t, 569
Eosinophilia, in allergic sinusitis, 201
Eosinophilic granulomas
  of middle ear, 1346f
  of oral cavity, 1424f
Eosinophilic granulomas (EGs), 603
  in skull base, 834
  of jaw, 964–965, 965f
  of temporomandibular joint, 1036, 1040f
Ependymomas, 1301, 1306f
  of cerebellopontine angle, 1306f
Epicardial ridge, 1770t
Epicranius muscle, 91t, 126, 128f
Epidermoid cysts. *See also* Cholesteatomas; Cholesterol granulomas (cysts).
  acquired, of temporal bone, 1337f
  congenital, of petrous apex, 1336f
  cutaneous, 2176, 2177f
  intracranial, 772, 773f
  nasal, 31, 31f, 33, 34, 36f
  of cerebellopontine angle, 1288, 1290–1291, 1292f–1297f
  of facial nerve, 1335, 1337, 1337f
  of petrous apex, 1349
  of skull base, 1336f
  orbital, 563, 567f, 568t
Epidermolysis bullosa, 987
Epidural abscesses
  in sinusitis, 582f
  with mastoiditis, 1182, 1182f
Epiglottic abscesses, 1569f
Epiglottis, 1596f, 1598, 1602, 1800f
  anomalies of, 1553
  movements of, during oropharyngeal swallowing, 1741–1743, 1742f
  on videofluoroscopic swallowing study, 1736
  radiation effects on, on videofluoroscopic swallowing study, 1737f
  squamous cell carcinoma of, on positron-emission tomography, 2300f
Epiglottitis, 1670f, 6275f
  emphysematous, 1670f
  pediatric, 1568, 1568f, 1569f
Epignathus teratomas, 42–43
Epipericardial ridge, 1760
Epiphora, 684f, 704f–705f, 728–729
  dacryocystography in, 671
  surgical procedures for, 671–672
  with functional endoscopic sinus surgery, 179
Episcleritis, 474
Epithelial cysts, orbital, 569–570
Epithelial-myoepithelial carcinomas (EMECs), of salivary glands, 280, 2087, 2088f
Epithelioid hemangioendotheliomas, of oral cavity, 1424
Epitympanic recess, anatomy of, 1068–1069
Epstein-Barr virus (EBV) infections
  lymphadenitis in, 1885f, 1885–1887, 1886f
  primary central nervous system lymphoma and, 2290, 2290f
  with adenotonsillitis, 1562, 1563f
Epulides, 43
Erb's palsy, 2223
Erdheim-Chester disease, 607, 609, 610f
Erosions, of temporomandibular joint, following temporary Silastic implant, 1032f
''Eskimo tumor,'' 2100–2101

Esophageal atresia, tracheoesophageal fistula with, 1707–1708, 1708f–1710f
Esophageal stage of swallowing, 1734
Esophagitis, moniliasis, 1671f
Esophagus, 1803f
  carcinoma of, 2236f
  cervical, 1802f
    dilated/obstructed, 2210, 2211f, 2212
  lymph node drainage of, 1881t
  movements of, during oropharyngeal swallowing, 1746
  perforation of, by foreign body, 1577f
  Zenker's diverticulum of, 2208, 2210, 2211f
Espundia, 242
ESs. *See* Ewing's sarcomas (ESs).
Esthesioneuroblastomas, 811f
ET. *See* Eustachian tube (ET).
Ethmocephaly, in holoprosencephaly, 55, 56f
Ethmoid bone, 11f, 13, 30, 97, 102
  development of, 10, 10f
  on computed tomography and magnetic resonance imaging, 125
  on plain films, 112, 112f
  perpendicular plate of, 89, 89f, 139f, 142f
Ethmoid bulla, 92f, 97, 98, 140f
  anatomy of, 155, 157f
  variations of, 163
Ethmoid cells
  posterior, 97, 163
    pneumatization of, with functional endoscopic sinus surgery, 176
  supraorbital, on plain films, 113, 113f
Ethmoid foramina, 98
Ethmoid roof, asymmetry in height of, 165
Ethmoid sinus(es), 97–99, 133f, 134f, 135f, 136f, 140f, 144f, 145f
  air-fluid levels in, 198, 199f
  basal lamellae of, 97
  development of, 97
  drainage patterns of, 97
  hypoplasia of, with functional endoscopic sinus surgery, 182–183
  mucocele of, 710f
  mucosal thickening in, 209, 211f
  ostia of, 92f, 97
  plain film anatomy of, 112f, 112–113, 113f
  posterior
    anatomic relationship to sphenoid sinuses, 156, 160f
    anatomy of, 156
  roof of, 98
    following functional endoscopic sinus surgery, 172
  septum separating frontal sinuses from, 139f
  tumors of, 262
Ethmoid veins, 95
Ethmoidal arteries, 95, 95f, 99
  injury of, with functional endoscopic sinus surgery, 181–182, 182f
Ethmoidal basal cephaloceles, anterior and posterior, 52
Ethmoidal bulla, on computed tomography, 154f
Ethmoidal canals
  anterior, 133f, 134f, 140f
  on computed tomography and magnetic resonance imaging, 125
  on plain films, 112–113, 113f
  posterior, 134f, 140f
Ethmoidal infundibulum, 99
Ethmoidal nerve, 96, 99, 101
Ethmoidal veins, 99
Ethmoidectomy, 409–412, 414f
  bulla, 170
  external, 409
  internal, 409
  posterior, 170
  postoperative findings with, 188–189, 189f
  transantral, 409–412, 414f–418f
    on computed tomography, 415f–418f
    on magnetic resonance imaging, 418f
    on plain films, 414f
Ethmoidomaxillary plate, on plain films, 113, 113f
Eumycotic mycetomas, of parapharyngeal space, 1979–1980
Eustachian tube (ET), 1796f, 1797f
  anatomy of, 1068
  function of, 1174t, 1174–1175
  occlusion of, in chronic otitis media, 1183
  opening of, 92f, 1797f
Ewing's sarcomas (ESs)
  of jaw, 975
  of skull base, 835
  sinonasal, 290, 292
Exophthalmos, 556
  pulsatile, with skull base fracture, 855f
Exorbitism, 556
Exostoses
  of external auditory canal, 1214f, 1215, 1215f, 1340, 1343f, 1344f
  of jaw, 958–959, 961f–963f
  of oral cavity, 1417–1418, 1418f, 1419f
  osteocartilaginous, of oral cavity, 1423
  osteomas and, 321–322, 326f, 327f
External auditory canal (EAC), 1796f
  anatomy of, 1066
  cartilage of, 1796f
  congenital anomalies of, 1113, 1114, 1114f–1116f
  CT surface reconstruction of, 1097f
  exostoses of, 1343f
  lymph node drainage of, 1881t
  on CT surface reconstruction, 1096f
  on magnetic resonance imaging, 1103f
External auditory canal (EAC) *(Continued)*
  on surface magnetic resonance imaging, 1096f
  squamous cell carcinoma of, 1324f, 1339f
  tumors of, 1339–1342
    benign, 1339–1340, 1342f–1345f
    malignant, 1340–1342, 1345f, 1346f
External carotid artery, 1797f
External ear. *See* Outer ear; Pinna.
Extracellular domain of fibroblast growth factor receptors, 71, 72
Extraforaminal injuries, brachial plexopathies and, 2222–2223, 2223f
Extramedullary plasmacytomas (EMPs), sinonasal, 304–305, 306f, 307f
  on computed tomography, 306f
  on magnetic resonance imaging, 307f
Extraocular muscles
  anatomy of, 539–540
    on computed tomography, 546, 546f
    on magnetic resonance imaging, 546, 547f–552f
  avulsions of, 518
  blood supply to, 540
  embryology of, 531, 1759f
  enlarged, causes of, 553
  ocular motility disorders and. *See* Ocular motility disorders.
  seventh, 539–540
Eye(s), 441–521. *See also* Ocular *entries;* Ophthalmic *entries; specific conditions; specific parts of eye.*
  computed tomography of, 452
  congenital anomalies of, 461–464
  detachments of, 466–477
  embryology of, 442, 443f–447f, 444–451
  in hemifacial microsomia, 61, 63f
  in holoprosencephaly, 55, 56f
  inflammatory disorders of, 472–477, 476f
  magnetic resonance imaging of, 450f, 451–452, 459, 460
    artifacts and, 452, 453f
    with foreign bodies, 452
  normal imaging of, 459–460, 460f
  potential spaces of, 459, 459f
  traumatic injury of, 514–521, 515f
  vascular system of, embryology of, 451
Eyeball. *See* Globe.
Eyelid(s)
  embryology of, 531, 532f
  lower, retractors for, 540
  movements of, 540
  orbits and, 537–538

F

Face. *See also specific facial regions and structures.*
  arteries of, 127, 130f

Face *(Continued)*
embryology of, 5, 7f, 7–9, 8f, 1522, 1522f
lymph node drainage of, 1881t
molecular signaling in, 9
craniofacial malformations and, 4–5
muscles of, 90t–91t
nerve supply of, 127, 129f
veins of, 127, 130f, 131
Facet, of nose, 89
Facial artery, 102, 127, 130f, 1797f, 1798f, 1799f
transverse, 127, 130f
Facial asymmetry, in hemifacial microsomia, 59, 60f–61f
Facial buttresses, 375
Facial clefts, 15–30. *See also* Cleft lip; Cleft lip/palate; Cleft nose; Cleft palate.
median, 23–29, 24f–26f, 26f, 27, 28f, 29t
oblique, 18, 18f
relative incidence of, 18, 19t
transverse, 18, 18f, 29, 59, 62f
Facial diplegia, congenital, 111t, 1147f
Facial duplications, 1544, 1545f
Facial fractures, 374–401
buttresses for, 375
clinical diagnosis and treatment of, 376f, 477
compound, 376
lack of, with minor trauma, 377f, 377–378
Le Fort I, 381, 385f
on computed tomography, 385f
on tomography, 385f
Le Fort II, 382, 386f
on computed tomography, 386f
Le Fort III, 382, 384, 386f, 387f
on computed tomography, 387f
maxillary, 381, 383f–385f
alveolar, 381
on computed tomography, 384f, 385f
on tomography, 383f
nasal, 378f–381f, 378–381
lateral blows causing, 378–379, 379f–380f
septal abscesses with, 380
nasoorbital, 381, 382f, 383f
of frontal sinus, 397f–402f, 397–399
on computed tomography, 398, 398f–401f
on magnetic resonance imaging, 401f
on plain films, 24, 397f, 398f
of orbital wall, 386, 389, 391f–396f, 391–394
alloplasts for, 397
on computed tomography, 392f, 393f, 394, 395f, 396f
on magnetic resonance imaging, 394f
on plain films, 392f, 394f, 395f
of sphenoid sinus, 399
on computed tomography, 377
Facial fractures *(Continued)*
on magnetic resonance imaging, 377
palatal, sagittal, 381
pediatric, 399, 401
skull base imaging with, 377
trimalar (zygomatic), 385, 387t, 387–388, 388f–390f
on computed tomography, 389f, 390f
on plain films, 388f
Wassmund IV, 384, 386f
zygomatic arch, 388, 390f, 391f
zygomaticomandibular, 388
zygomaticomaxillary, 388
Facial hiatus, 880f
perineural tumor spread involving, 873, 880f
Facial lymph nodes
deep, drainage of, 1881t
drainage of, 1881t
Facial muscles, 126
Facial nerve, 96, 1451, 1455f
adenoid cystic carcinoma of, 1327f
anatomy of, 1784, 1785f, 2008, 2009f
branchial arches and, 1759
CT surface reconstruction of, 1098f
dehiscent, 1120f
denervation of, 1455f
duplication of, 1136–1137, 1150f, 1151f
dysfunction of. *See also* Facial palsy.
with temporal bone trauma, 1242–1243
hypoplastic or aplastic, 1136f, 1146f, 1147f
in congenital aural dysplasia, 1116
on computed tomography, 1094f, 1095f
on magnetic resonance imaging, 1099f, 1100f, 1101f, 1102f, 1103f, 1104f
perineural tumor spread involving, 871, 873, 879f
route of, 1070–1071
anomalous, 1121f, 1137–1138, 1148f, 1152f, 1153f
with ossicular chain anomalies, 1117–1118, 1120f, 1121f
schwannomas of, 1292, 1298f, 1299f, 1303
tumors of, 1322, 1326–1339
choristomas, 1337, 1338f
epidermoid cysts, 1335, 1337, 1337f
manifestations and lesion localization with, 1326–1328, 1327f, 1328f
papillary cystadenomatous tumor, 1337, 1338f, 1339
schwannomas, 1328–1330, 1330f–1336f, 1334
on computed tomography, 1330f–1336f
on magnetic resonance imaging, 1330f–1333f, 1335f, 1336f
vascular, benign, 1334
Facial nerve canal
erosion of, with cholesteatomas, 1191, 1193f–1194f
labyrinthine segment of, widened, 1148, 1164f–1165f
Facial palsy
idiopathic, 1224, 1225f
in necrotizing otitis externa, 1212–1213
with otitis media, 1176
Facial recess, 1067, 1067f
cholesteatomas of, 1189f
Facial skeleton, 10f–13f, 10–11, 13–14
Facial trauma. *See also* Facial fractures.
pediatric, 1570–1571, 1571f
Facial vein, 127, 130f, 1796f
anterior, 95, 127
common, 127
posterior, 127
Facioscapulohumeral (FSH) dystrophy, 2195, 2199f, 2200f
Falx, 30
Familial cancer syndromes, 2281–2283
Li-Fraumeni, 2282–2283, 2283f
retinoblastoma, 2281–2282, 2282f
(P)FAPA syndrome, sinusitis in, 256
Farcy, 242
Fascia, of neck. *See* Neck, fascia of.
Fascia bulbi. *See* Tenon's capsule.
Fascial sheath. *See* Tenon's capsule.
Fasciitis
necrotizing
of skin and soft tissue, 2190
with sinusitis, 196
nodular
in parapharyngeal space, 1976
of salivary glands, 2117
of skin and soft tissue, 2188, 2190f
orbital, 632, 635f
proliferative, 2188
Fat
buccal, 1989
subcutaneous fat necrosis of newborn and, 2179–2180, 2180f
Fat-containing lesions, 2184–2187. *See also* Lipomas; Liposarcomas.
FD. *See* Fibrous dysplasia (FD).
FDG. *See* ^{18}F-Fluorodeoxyglucose (FDG).
Fenestral otosclerosis, 1246–1249, 1247f–1250f
FESS. *See* Functional endoscopic sinus surgery (FESS).
Fetal age, embryology of various systems related to, 1776t
Fetal period, definition of, 1758
^{18}F-Fluorodeoxyglucose (FDG), 2295
metabolism of, imaging without dedicated PET scanner, 2297–2298
FGFRs. *See* Fibroblast growth factor receptors (FGFRs).

Fibroblast growth factor(s) (FGFs)
craniosynostosis and, 74, 75f
FGF7, palatal development and, 9
FGF8, holoprosencephaly and, 9, 55
Fibroblast growth factor receptors (FGFRs)
craniofacial dysostoses and, 71–73, 72t, 73f
structure of, 71–72, 73f
Fibroblastomas, peripheral. *See* Schwannomas.
Fibromas
cemento-ossifying. *See* Cemento-ossifying fibromas.
chondromyxoid, of skull base, 820, 821, 822f
desmoplastic, in parapharyngeal space, 1975–1976
of jaw, 968, 969f
orbital, 634f, 104104
Fibromatoses, 2188, 2189f
congenital, 2188
infantile, 1410–1412, 1413f, 1414f, 1415
of oral cavity, aggressive, 1410–1412, 1413f, 1414f, 1415
pharyngeal, 1500–1501, 1501f
sinonasal, 318
Fibromatosis colli, 2191, 2193f
on ultrasound, 1951, 1951f
Fibromuscular dysplasia (FMD), tinnitus due to, 1363, 1364f, 1365f
Fibromyxomas, sinonasal, 321
on computed tomography, 321f
on magnetic resonance imaging, 322f
Fibroodontomas, ameloblastic, 951–952, 957f
Fibroosseous lesions, of oral cavity, 1418–1422
Fibrosarcomas, 2187–2188
of jaw, 974–975
of masticator space, 1996f
orbital, 634f, 104104
sinonasal, 318–319, 320f
on computed tomography, 319, 320f
Fibrosis, of subcutaneous tissues, 2175f
Fibrous dysplasia (FD)
hereditary, 333
in temporal bone, 1253–1256, 1255f–1258f
differential diagnosis, 1254–1256, 1259f
of airway, pediatric, 1581f, 1582
of external auditory canal, 1340, 1345f
of jaw, 965–966, 966f–968f, 968
of mastoid, 1345f
of oral cavity, 1418–1419, 1420f
of skull base, 854–856, 855f–857f
of temporal bone, Paget's disease versus, 1257
Fibrous dysplasia (FD) *(Continued)*
sinonasal, 331–332, 332f–340f
on computed tomography, 333f–335f, 338f
on magnetic resonance imaging, 336f, 337f, 339f
on plain films, 332f
Fibrous histiocytomas
benign, sinonasal, 319–320, 320f
malignant, sinonasal, 319–320, 320f
of salivary glands, 2117, 2121f
Fibrous tissue lesions, of salivary glands, 2116–2118, 2121f
Fibrous tumors. *See also specific tumors.*
in parapharyngeal space, 1975–1976
solitary, sinonasal, 321
Filters, ocular, postsurgical changes with, 521
Fine-needle aspiration (FNA)
of salivary glands, 2026
ultrasound-guided
of neck, 1936, 1936f
of thyroid, 1941
First and second branchial syndrome. *See* Branchial arch syndrome, of first and second arches.
Fissula antefenestram, 1147
Fissural odontogenic cysts, 352–353, 357f
Flat torus, 15
Florid cemental dysplasia, 955, 960f, 961f
Fluid perilymphatic, 1074–1075
FMD. *See* Fibromuscular dysplasia (FMD).
FNA. *See* Fine-needle aspiration (FNA).
Follicular adenomas, of thyroid, 2150f
Follicular carcinomas
of thyroid, 2150f
thyroid, 2154
Follicular cysts, 345–347, 352f–355f, 934, 934f–936f
on computed tomography, 352f, 354f, 355f
on magnetic resonance imaging, 346–347, 353f, 354f
Fonticulus frontonasalis, 30
Foramen cecum
anatomic relationships at birth, 30f
enlarged, with nasal dermoid cysts, 36–37
Foramen lacerum, 144f
CT surface reconstruction of, 1096f, 1097f
Foramen magnum, CT surface reconstruction of, 1096f
Foramen of Vesalius, 806
Foramen ovale, 143f, 797
anatomy of, 790, 791, 794f
CT surface reconstruction of, 1096f, 1097f
perineural tumor spread involving, 870, 875f–878f
Foramen rotundum/canal, 142f, 143f, 788, 790–791, 802f
CT surface reconstruction of, 1096f
on computed tomography and magnetic resonance imaging, 125
on plain films, 116, 116f, 117
Foramen spinosum, CT surface reconstruction of, 1096f, 1097f
Forebrain, embryological development of, 5f, 6f
Foregut cysts, pediatric, 1547–1548, 1549f
Forehead, 126
squamous cell carcinoma in, with perineural tumor spread, 882f
Foreign bodies
aspirated, in children, 1575–1577, 1577f
esophageal, 1577f
in salivary glands, 2042
in sinonasal cavities, 251, 253f, 254f
ingested, in children, 1575
intraocular, 515f, 515–517
magnetic resonance imaging of, 452
laryngeal, 1667
of skin and subcutaneous tissue, 2182–2183, 2183f
Fossa of Rosenmuller, 1797f
Fovea, embryology of, 447
Fovea ethmoidalis, 98, 140f
asymmetry of, 13–14
on plain films, 120, 121f
Fracture line, infections of, with facial fractures, 376
Fractures. *See specific sites.*
Framboesia tropica, syphilis versus, 236
Franceschetti-Zwalen-Klein syndrome, 58, 63, 64f
Frey's syndrome, salivary, 2121
Frontal bone, 100, 133f, 134f
anatomic relationships at birth, 30f
fovea ethmoidalis of, 140f
on computed tomography and magnetic resonance imaging, 125
on plain films, 110, 121
Frontal bullae, 99
Frontal cells, 154–156, 156f–160f, 157t
Frontal nerve, perineural tumor spread involving, 867, 868f
Frontal notch, on computed tomography and magnetic resonance imaging, 125
Frontal prominence, 7f
Frontal recess, 92f, 153, 155f, 156f
anatomy of, 153, 154
following functional endoscopic sinus surgery, 170, 172
Frontal sinus(es), 92f, 99–100, 133f, 139f, 144f, 145f
air-fluid levels in, 198, 198f, 199f
aplastic, on plain films, 109, 110f, 111
carcinoma of, 271
development of, 99, 111

Frontal sinus(es) *(Continued)*
fractures of, 397f–402f, 397–399
on computed tomography, 398, 398f–401f
on magnetic resonance imaging, 401f
on plain films, 24, 397f, 398f
hypoplastic, on plain films, 109–110, 110f, 222
obstruction of, after functional endoscopic sinus surgery, 188, 189f
on computed tomography, 153, 154f, 155f
ostia of, 99
plain film anatomy of, 109f–111f, 109–112
septa in, 100, 133f
displacement of, on plain films, 109, 110f
on plain films, 111
separating ethmoid sinuses from frontal sinuses, 139f
tumors of, 262
Frontal sinus surgery, 404–409
Killian procedure, 405–406, 407f
Lynch procedure, 405, 406f, 407f
on computed tomography, 406f
on magnetic resonance imaging, 407f
osteoplastic flap procedure, 406, 408f–414f, 408–409
on computed tomography, 410f–413f
on magnetic resonance imaging, 413f, 414f
on plain films, 408f
on tomography, 409f
Riedel procedure, 406, 407f
trephination, 404–405, 405f
Frontal vein, 127
Frontoethmoidal cephaloceles, 44–45, 46t, 47–49
concurrent malformations with, 47, 49
etiologies of, 49
frontonasal subtype of, 44–45, 47, 47f–49f
nasoethmoidal subtype of, 47
nasoorbital subtype of, 47, 50f–52f
Frontometaphyseal dysplasia, 1111t, 1270f
Frontonasal dysplasia, 23–24, 26f, 27, 28f, 29t
Frontonasal frontoethmoidal cephaloceles, 44–45, 47, 47f–49f
Frontonasal prominence, 7–8
Frontonasal suture, 30
anatomic relationships at birth, 30f
Frontoorbital dysplasia, 1542f
Frontotemporal dermoids, 31–32
Fronto-zygomatic suture, 140f
FSH. *See* Facioscapulohumeral (FSH) dystrophy.
Functional endoscopic sinus surgery (FESS), 175–190
intracranial complications of, 171f
introduction of, 150
Functional endoscopic sinus surgery (FESS) *(Continued)*
outcomes with, 184–185, 185t
postoperative complications of, 175–184
computed tomography evaluation of, 183–184
hemorrhage and vascular injury as, 176, 176f
major and minor, 175
orbital, 179, 181–184, 182f, 183f
skull base injury as, 176–179, 177f–181f
postoperative findings with, on computed tomography, 186t, 186–188, 187f–190f, 190
procedure for, 185–186
radiographic evaluation following, 170–172
expected findings on, 170, 171f, 172
theoretical basis of, 184
treatment options for, 184, 184f
types of, 170
Functional nasolacrimal duct obstruction (FNLDO), 696
Fungal infections
of cavernous sinus, 807, 810f, 811f
orbital cellulitis secondary to, 582–584, 584f, 585f
Fungal sinusitis, 201–203
in hyphal diseases, 201–202
yeasts and, 202–203
Fungiform papillomas, sinonasal, 267

G

Ganglion. *See also specific ganglia.*
with brachial plexopathy, 2223f
Ganglioneuroblastomas, sinonasal, 285
Gardner's syndrome, 959, 963f
on computed tomography, 325f
Gastrointestinal mucosal cysts, 1397–1398, 1400f
Gatekeepers, 2283, 2284f
GCCs. *See* Giant cell granulomas (GCGs).
GCPS. *See* Greig cephalopolysyndactyly (GCPS).
GCTs. *See* Giant cell tumors (GCTs).
Gene(s)
encoding angiogenic growth factors, activation of, 2291
involved in multiple steps of metastasis, 2290–2291
Gene alterations, defining neoplasia, 2274–2275
Gene amplification, selective, oncogene activation by, 2278
Gene transcription, mutational alteration of, oncogene activation by, 2277
Genial tubercle, 896, 896f, 899, 901f
Geniculate ganglion, 96
on computed tomography, 1094f, 1095f
Geniculate ganglion area, on magnetic resonance imaging, 1104f
Geniculate intertemporal vascular tumor, 1334f
Genioglossus muscle, 1378, 1379t, 1380, 1791t, 1798f, 1799f
Geniohyoid muscle, 896, 899f, 901f, 1379t, 1383, 1791t, 1799f
Genital herpes, 1888
Genome instability syndromes, 2285
German measles, lymphadenitis in, 1889
Ghost cell tumors, malignant, of jaw, 971–972
Giant aneurysms
of anterior internal carotid artery, 1295, 1302f
of parapharyngeal space, 1987f
Giant cell granulomas (GCGs), sinonasal, 335–336, 341f
Giant cell tumors (GCTs)
of jaw, 961–962, 964f, 965f
of oral cavity, 1421–1422, 1422f–1424f, 1423f, 1424f
of skull base, 832–833, 839f
of temporal bone, 1324f, 1339, 1340f
sinonasal, 333–335, 341f
Gigantiform cementoblastomas, 357
Gingiva
embryologic development of, 9
epulis of, 43
Gingivobuccal region
mucosa of, squamous cell carcinoma of, 1431, 1435f, 1436f
normal anatomy of, 1384
GL13 transcription factor, craniofacial dysostoses and, 73–74
Glanders, 242
Glenoid fossa, 1797f
Glioblastoma multiforme
intracranial, 772, 774f, 775
pontine, 1305f
Gliomas
nasal, 31, 31f, 32f, 37, 39–42, 40f–43f, 299, 300f, 301
extranasal, 39–40, 41
histology of, 41–42
intranasal, 40f, 40–41
mixed, 41, 41f
on computed tomography, 300f
optic, 742–744
clinical features of, 742–743
on computed tomography, 744, 744f
on magnetic resonance imaging, 743f, 744, 745f, 746f
pathologic findings with, 743f, 743–744
Glioneuromas, ocular, 497
Gliosis, retinal, 499
Globe
anatomy of, 452–453, 549, 551
crenated appearance of, 517, 517f, 518f
enlargement of, 461–463, 463f
movements of, 540

Globe *(Continued)*
postsurgical changes in, 518, 520f–522f, 520–521
traumatic injury of, 517f–519f, 517–518
on computed tomography, 517f, 518f, 519f
on magnetic resonance imaging, 519f
underdevelopment of, 461, 462f, 463f, 463t
Globulomaxillary cysts, 353, 357f, 942, 945f
Glomangiomas, multiple, familial, 1561
Glomus jugulare tumors, 1313f, 1314f, 1316f–1319f, 1972f
Glomus tympanicum tumors, 1312f, 1313, 1313f
Glomus vagale tumors, 1970f, 1971f, 1973f, 1974f
Glossectomy, 1736f
near-total, postsurgical imaging and, 2265f
partial, postsurgical imaging and, 2250f, 2261f
swallowing and, 1740, 1740f
total, postsurgical imaging and, 2253f, 2260f, 2261f
Glossoceles, 1397–1398, 1400f
Glossoepiglottic fold, median, 1800f
Glossopharyngeal nerve
anatomy of, 1784–1785, 1785f
branchial arches and, 1759, 1763
Glossoptosis, congenital, 1548–1549
Glottic airway, 1801f
Glottis, 1602
movements of, during oropharyngeal swallowing, 1744–1745
squamous cell carcinoma of, evaluation for, 1635–1640, 1640f–1647f
on computed tomography, 1641f, 1642f, 1646f
on magnetic resonance imaging, 1643f–1645f, 1647f
Gnathogingival segment, 8
Godwin's tumor, 2043, 2044f
Goiter, 1399f, 1817f, 1818f, 1846f, 1939, 2147–2149, 2148f, 2149f
diffuse, 2157f
intratracheal, 1724f, 1725
multinodular, 1687f, 2138f, 2147–2148, 2149f
on ultrasound, 1939, 1939f, 1940f
toxic, 2145f
Goldenhar's syndrome, 58f, 58–63, 564, 1111t
ears in, 60, 60f, 61
eyes in, 61, 63f
mouth in, 59
plagiocephaly in, 63
Goltz's syndrome, 570f
Gorham's disease, 837–838, 841f
Gorlin-Goltz syndrome, 350, 352, 938, 944f
Gorlin-Hunt syndrome, 1111t, 1270f
Gorlin's syndrome, 350, 352, 938, 944f
Gortex, for guided tissue regeneration, 928
Gradenigo's syndrome, 1200
Graft-versus-host disease (GVHD), acute, after bone marrow transplantation, sinus imaging in, 196
Granular cell tumors
laryngeal, 1651
pharyngeal, 1497–1498, 1500
imaging features of, 1500, 1500f
sinonasal, 295–297, 297f
on computed tomography, 297f
Granulation tissue
following chronic otitis media, 1184, 1186f
ossicular, noncholesteatomatous, 1197f
tracheal, pediatric, 1576f
with cholesteatomas, 1196f
Granulocytic sarcomas, sinonasal, 302–303
Granulomas
cholesterol (histiocytic; lipid)
of petrous apex, 1203, 1204f, 1347–1349, 1348f
of temporal bone, 1339, 1340f
orbital, 568t, 572, 573–574, 575f, 577f
eosinophilic, 603
of oral cavity, 1424f
following tracheostomy, 1716
giant cell, sinonasal, 335–336, 341f
laryngeal, 1679f
mediastinal, 1711
midline, lethal, 242
sinonasal
beryllium as cause of, 243
chromate salts as cause of, 243, 243f
tracheal, pediatric, 1576f
Granulomatosis
Langerhan's cell, sinonasal, 305–308
larval, ocular, 475, 479f
lymphomatoid, 611f
Granulomatous diseases
pediatric infections, 1566–1567, 1567f
sinonasal
cocaine as cause of, 243f
on computed tomography, 243, 243f–245f
on magnetic resonance imaging, 243–244
tracheal, 1711
Granulomatous thyroiditis, subacute, 2147
Graves' disease, 591–595, 1940, 1940f, 2135, 2135f, 2143–2145, 2145f
diagnosis of, 592
diagnostic imaging in, 592–593, 593f, 594f, 595
pathology of, 591–592
Gray (Gy), 151
Great vessels, embryology of, 1524, 1524f
Greig cephalopolysyndactyly (GCPS), 73
Growth factor(s)
angiogenic, genes encoding, activation in tumors, 2291
as oncogenes, 2278–2279
autocrine and paracrine loops and, 2278–2279
fibroblast
craniosynostosis and, 74, 75f
FGF7, palatal development and, 9
FGF8, holoprosencephaly and, 9, 55
Growth factor receptors
as oncogenes, 2278–2279
autocrine and paracrine loops and, 2278–2279
fibroblast
craniofacial dysostoses and, 71–73, 72t, 73f
structure of, 71–72, 73f
Guardians, 2283, 2284f
Guérin's fractures, 381, 385f
on computed tomography, 385f
on tomography, 385f
Guided tissue regeneration, for dental implants, 928
Gumma, syphilitic, 236
Gusher ear, 1140f
GVHD. *See* Graft-versus-host disease (GVHD).
Gy. *See* Gray (Gy).

H

Haller cells, 97, 161–162, 164f
Hamartomas
hypothalamic, 1582
neuroglial, 1582, 1582f
of acoustic nerve, 1303, 1311f
of retinal pigment epithelium and retina, 497
sinonasal, 360–361
tracheal, 1722–1723
Hamulus, of medial pterygoid plate, 1798f
Hand-Schuller-Christian (HSC)
disease, 603
in skull base, 834
of jaw, 963–964
Hard palate, 90, 138f, 902f, 903
adenocarcinoma of, 1444f
adenoid cystic carcinoma of, with perineural tumor spread, 872f
anatomic relationships at birth, 30f
midline suture between left and right halves of, 138f
on computed tomography and magnetic resonance imaging, 124
on plain films, 115f, 120
squamous cell carcinoma of, 1431–1432, 1436f
torus palatinus on, 14f, 14–15
Hashimoto's thyroiditis, 1940, 1941f, 2145–2146, 2146f
HCC. *See* Hepatocellular carcinoma (HCC).

HD. *See* Hodgkin's disease (HD).
Head and neck. *See also* Neck; *specific regions and structures.*
development of, terminology for, 1758
embryology of
early, 1758–1759
mesodermal layers, somitomeres, and somites and, 1758–1759, 1759f
of aortic arches, 1771, 1771f
of branchial apparatus. *See* Branchial apparatus, embryology of.
of lymphatic system, 1772–1773, 1773f, 1774f
of salivary glands, 1773, 1775, 1775f, 1776t
of veins, 1772, 1772f
Headache, in sinusitis, 194–195
Hearing loss
conductive, with ossicular disorders, 1195–1196, 1197f–1199f, 1199
following ossiculoplasty, 1220
sensorineural
internal auditory canal anomalies associated with, 1136
vestibular aqueduct and, 1138–1140, 1154f, 1155f
with temporal bone trauma, 1242, 1243f
Heerfordt's syndrome, 600
Helix, of ear, on surface magnetic resonance imaging, 1096f
Hemangioblastomas, of optic nerve, 628, 629f
Hemangioendotheliomas
benign
of neck, 1854, 1856
of salivary glands, 2107
orbital, 613–614, 617f, 618f
epithelioid, of oral cavity, 1424
tracheal, 1721
Hemangiolymphangiomas, of salivary glands, 2112f
Hemangiomas
capillary
of neck, 1854, 1856
of salivary glands, 2107
orbital, 613–614, 617f, 618f
cavernous
of neck, 1856, 1857f
on ultrasound, 1950f, 1950–1951
of salivary glands, 2107
orbital, 615–616, 619f–621f
choroidal, 500, 508–509
clinical features of, 509
diagnostic imaging in, 509, 510f, 511f
congenital, of neck, 1852–1854, 1856f
cutaneous, 2206
laryngeal, 1648–1649, 1658f, 1659f
of airway, pediatric, 1556–1558, 1559f
of cerebellopontine angle, 1298
of internal auditory canal, 1304f
of jaw, 969–970, 970f
Hemangiomas *(Continued)*
of neck, 1808f, 1852–1854, 1856f
of salivary glands, 2107, 2110f, 2111f
of skull base, 835
pharyngeal, 1501, 1502f
sclerosing, orbital, 616, 621f, 639f
sinonasal
on computed tomography, 312, 313f, 314f
on magnetic resonance imaging, 312, 314f
sinonasal, 311–312, 313f, 314f
subglottic, 1672
tracheal, 1721
Hemangiopericytomas (HPCs), 2206, 2208, 2210f
orbital, 621, 623, 626f, 627f
sinonasal, 314–315, 315f
on computed tomography, 315, 315f
Hematic cysts
of petrous apex, 1203, 1204f, 1347–1349, 1348f
of temporal bone, 1339, 1340f
orbital, 568t, 572, 573–574, 575f, 577f
Hematogenous metastasis, to skull base, 848, 853f
Hematomas
laryngeal, 1672f
of subcutaneous tissues, 2175f
of temporal lobe, 739f
orbital, with functional endoscopic sinus surgery, 181
pharyngeal, 1512f
subperiosteal
diagnostic imaging of, 572, 573f, 574f, 576f
orbital, 572–574
Hematotympanum, diffuse, 1235f
Hemianopsia
bitemporal, 758f, 762f
homonymous, 767f, 770f
Hemifacial microsomia (HFM), 58f, 58–63, 562, 1038, 1045f, 1046f, 1111t, 1167f
central nervous system in, 63
ears in, 60f, 60–61
eyes in, 61, 63f
face in, 59, 60f–61f
mouth in, 59, 62f
plagiocephaly in, 63
Hemiglossectomy, swallowing and, 1740f, 1741
Hemilaryngectomy
frontolateral, vertical
contraindications to, 1640
evaluation for, 1635
vertical, postsurgical appearance and, 1687–1688, 1691f
Hemorrhage
air-fluid levels and, 198
choroidal, 509, 512f
into eye, 517
Hemorrhage *(Continued)*
intralabyrinthine, 1243f
with functional endoscopic sinus surgery, 176, 176f
Hemorrhagic bone cysts
of jaw, 942–943, 945f
of temporomandibular joint, 1036, 1040f
Hepatitis viruses B/C, hepatocellular carcinoma and, 2289
Hepatocellular carcinoma (HCC), hepatitis viruses B/C and, 2289
Hereditary nonpolyposis colon cancer, 2285
Heredopathia atactica polyneuritiformis, 1112t
Herpes pharyngitis, 1510f
Herpes simplex virus (HSV) infections, lymphadenitis in, 1887–1888
Herpes zoster infections
herpes zoster oticus, 1207, 1207f
lymphadenitis in, 1886f
Herpetic whitlow, 1888
Heterotopic tissue
brain
nasal, 37, 39–42, 40f–43f
extranasal, 39–40, 41
histology of, 41–42
intranasal, 40f, 40–41
mixed, 41, 41f
nonnasal, 42–43
in parapharyngeal space, 1975
tongue, 1397–1398, 1400f
HEV. *See* High endothelial venules (HEV).
HFM. *See* Hemifacial microsomia (HFM).
HHV8. *See* Human herpesvirus 8 (HHV8).
Hiatus, superior, 97
Hiatus semilunaris, 92f, 98, 102, 144f
anatomy of, 155, 157f
HIE syndrome, with sinusitis, 253–254
High endothelial venules (HEV), 1867–1868
Histiocytic disorders. *See also specific disorders.*
proliferative, 1905–1908, 1908f
Histiocytic granulomas
of petrous apex, 1203, 1204f, 1347–1349, 1348f
of temporal bone, 1339, 1340f
orbital, 568t, 572, 573–574, 575f, 577f
Histiocytomas
fibrous
benign, 320
malignant, sinonasal, 319–320, 320f
of salivary glands, 2117, 2121f
orbital, 631–632, 632f–634f
malignant
orbital metastasis from, 647f
sinonasal, 319–320, 320f
Histiocytosis, sinus, with massive lymphadenopathy, 1899, 1899f

Histiocytosis X. *See* Langerhan's cell granulomatosis (LCG).
Histoplasmosis
lymphadenitis in, 1895, 1895f
sinusitis and, 203
tracheal, 1710–1711
HIV. *See* Human immunodeficiency virus (HIV) infections.
^{H}-MRS. *See* Proton magnetic resonance spectroscopy (^{1}H-MRS).
Hodgkin's disease (HD), pediatric, 1583
Holoprosencephaly, 53–58, 54f, 55t
alobar form of, 54f, 55, 57–58
brain malformations in, 56–57
correlations between facies and, 57f, 57–58
facies in, 55, 56f
hypertelorism and, 16, 16f
hypotelorism and, 16, 16f
lobar form of, 57–58
molecular signaling and, 9
semilobar form of, 56–58, 57f
Horizontal beam 5° off-lateral view, for paranasal sinus plain films, 103, 103f
Hormones, of thyroid, 2136–2137
Hox genes, terminology for, 1758
HPCs. *See* Hemangiopericytomas (HPCs).
HPV. *See* Human papilloma viruses (HPVs).
H-*ras,* detection in human tumors, 2276
HSC. *See* Hand-Schuller-Christian (HSC) disease.
HSV. *See* Herpes simplex virus (HSV) infections.
Human herpesvirus 8 (HHV8), Kaposi's sarcoma and, 2289–2290, 2290f
Human immunodeficiency virus (HIV) infections. *See also* Acquired immunodeficiency syndrome (AIDS).
lymphadenitis in, 1889
oral cavity and, 1405
sinusitis in, 204
Human papilloma viruses (HPVs), cervical cancer and, 2288
Humerus, metastatic disease of, 2233f
Humidification of air, as nasal function, 93
Hurthle cell tumors, 2154
Hyaloid detachment, posterior, 457f, 466, 466f
Hyaloid vessels, 444f, 445f
Hybrid carcinomas, of salivary glands, 2102
Hydatid cysts, orbital, 568t, 575, 577
Hydrocephalus, 1282f
otitic, 1182–1183
Hygroma, perioptic, 569, 571f, 1282f, 1290, 1295f, 1296f
Hyoepiglottic ligament, 1602, 1800f
Hyoepiglottis, 1599
Hyoglossus muscle, 1379t, 1380, 1791t, 1798f, 1799f
Hyoid arch, 7f
Hyoid bone, 1599
anatomy of, 1778
body of, 1800f
fibrous junction in, 1800f
following Sistrunk procedure, 1847, 1848f
greater cornu of, 1800f
movements of, during oropharyngeal swallowing, 1743
Hyoid fasciitis, 2200, 2202
Hyomandibular crest, 7f
Hyperimmunoglobulinemia E syndrome (hyper IgE syndreome), with sinusitis, 253–254
Hyperlipidemia, salivary glands and, 2050
Hypernephromas, metastatic, 1924f
to parapharyngeal space, 1976f
to sinonasal cavities, 365f
Hyperostosis, 1323f
endosteal, of temporal bone, fibrous dysplasia versus, 1255
Hyperparathyroidism
brown tumor of, 334, 341f, 832–833
clinical manifestations of, 2160–2162, 2161f
fibrous dysplasia versus, 1255
Paget's disease versus, 1257–1258
primary, ultrasound in, 1942
reoperation for, 2166–2167
skull base and, 858
temporal bone in, 1271, 1271f
Hyperphosphatasia, hereditary
of temporal bone, 1268, 1270
Paget's disease versus, 1258
Hypersensitivity angiitis, orbital, 603
Hypersinuses, 247, 247f
Hypertelorism
cleft lip/palate and, 16, 16f
holoprosencephaly and, 16, 16f
in median cleft face syndrome, 27
orbital, 554, 556
Hypertension, intracranial
otitic, 1182–1183
tinnitus due to, 1370–1371
Hypertrophic scars, 2175, 2175f
Hypodontia, 987, 988f
Hypoglossal canal
CT surface reconstruction of, 1096f, 1097f
meningioma of, 1457f
Hypoglossal nerve, 1451, 1455f–1457f, 1456
anatomy of, 1785f, 1786, 1787, 1787f
branchial arches and, 1759
denervation of, 1455f, 1456f, 1457f
Hypoparathyroidism, clinical manifestations of, 2162
Hypopharyngeal carcinomas, 1489–1490, 1490t, 1491f–1494f, 1493, 1493t, 2270f
Hypopharynx, 1800f
anatomy of, 1471f–1474f, 1471–1473
pediatric, anatomy of, 1530
Hypopharynx *(Continued)*
radiation effects on, on videofluoroscopic swallowing study, 1737f
Hypophysectomy, transsphenoidal, 421–422
Hypotelorism
cleft lip and, 16, 16f
cleft palate and, 16, 16f
in holoprosencephaly, 55, 56f
orbital, 556
Hypothalamic hamartomas, 1582
Hypothyroidism
clinical manifestations of, 2138
congenital, 1583, 1583f, 1840f
Hyrtl's fissure, 1147

I

IBVTs. *See* Intratemporal benign vascular tumors (IBVTs).
Iligodendromas, intracranial, 772, 774f
IM. *See* Infectious mononucleosis (IM).
Image generation, for positron-emission tomography, 2296, 2296f
Imaging-based nodal classification system, 1872, 1872t, 1873f, 1874t–1876t, 1875–1880
levels in, 1876–1878, 1877f–1880f, 1880, 1881t
scanning technique for, 1875
use of, 1875–1876
IMFTs. *See* Inflammatory myofibroblastic tumors (IMFTs).
Immotile cilia syndrome, with sinusitis, 252–253
Immunoblastic lymphomas, nasopharyngeal, 1509, 1510f
Implantation cysts, epithelial, orbital, 568t, 571, 571f
Incisive canal, 138f, 140f, 145f
Incisive canal cysts, 941–942, 945f
of oral cavity, 1422–1423, 1426f
Incisive foramen, 138f, 139f, 140f, 902f, 903
on computed tomography and magnetic resonance imaging, 124
Incisive foramen cysts, of oral cavity, 1426f
Incisors
central, 139f
embryologic development of, 9
lateral, 139f
Inclusion cysts
conjunctival, 570
epidermoid. *See* Cholesteatomas.
posttraumatic, 710f
Incontinentia pigmenti, ocular, 497
Incudal fossa, 1067
Incudomalleal joint, on computed tomography, 1095f
Incus, long process of, on computed tomography, 1095f
Incus necrosis, 1220–1221, 1223f

Infancy, melanotic neuroectodermal tumor of, 290
Infant(s)
  retinopathy of prematurity and, 491–492
    diagnostic imaging in, 492, 492f
    ophthalmoscopy in, 491–492
  sclerema neonatorum of, 2180
  sedation of, for magnetic resonance imaging of eye, 451
  subcutaneous fat necrosis of, 2179–2180, 2180f
  ultrasound for, 1950f, 1950–1951, 1951f
Infantile fibromatosis, 1410–1412, 1413f, 1414f, 1415
Infections. *SEe also specific infections.*
  of neck, on ultrasound, 1949
  of parapharyngeal space, 1959–1960, 1961f
  of salivary glands, 2026–2039
    acute, 2026–2029
      bacterial, 2027f–2028f, 2027–2028
      viral, 2028–2029
    chronic, 2029–2039
      bacterial, 2031–2036, 2037–2039
      protozoan, 2036–2037
  sphenoethmoid, 418f
  tracheal, 1710
Infectious mononucleosis (IM)
  lymphadenitis in, 1885f, 1885–1887, 1886f
  with adenotonsillitis, 1562, 1563f
Inferior orbitomeatal (IOM) line, on computed tomography, 123
Infertility, male, with sinusitis, 253
Inflammatory conditions. *See also specific conditions.*
  of masticator space, 1989–1991, 1990f, 1991f
  of skull base, 807, 809, 810f, 811f
  orbital, 577–603, 579f
  preseptal versus orbital, 706f–708f
Inflammatory cysts, orbital, 575, 578f
Inflammatory myofibroblastic tumors (IMFTs), 250, 1908–1909
  sinonasal, 320–321
Infraglottic region, squamous cell carcinoma of, evaluation for, 1635–1640, 1640f–1647f
  on computed tomography, 1641f, 1642f, 1646f
  on magnetic resonance imaging, 1643f–1645f, 1647f
Infrahyoid muscles, 1780, 1781f
Infrahyoid region, 1602
Infraorbital artery, 102
Infraorbital canal, 135f, 136f, 137f, 140f, 141f, 143f
  on computed tomography and magnetic resonance imaging, 125
Infraorbital ethmoid cells, 97, 161–162, 164f
Infraorbital fissure, on plain films, 117, 117f
Infraorbital foramen, 102, 137f, 143f
  on computed tomography and magnetic resonance imaging, 125
Infraorbital lymph nodes, drainage of, 1881t
Infraorbital nerve, 102
  perineural tumor spread involving, 868, 869f, 870f
Infratemporal fossa, 1796f
Infundibulotomy, in functional endoscopic sinus surgery, 186
Infundibulum, 102, 140f
  anatomy of, 153, 154, 155, 157f
Inner ear
  congenital anomalies of, 1119–1140
    imaging techniques for, 1119–1122, 1123f
    membranous and bony labyrinthine, 1122, 1124, 1127–1132
  embryology and developmental anatomy of, 1058–1060
    of bony labyrinth, 1060
    of endolymphatic labyrinth, 1058–1059, 1060f
    of perilymphatic labyrinth, 1059–1060
  in hemifacial microsomia, 61
  inflammatory disorders of, 1205t, 1205–3433–1212
Innominate artery, 1702
Innominate vein, 1702
Insertional mutagenesis, oncogene activation by, 2276–2277
Interclinoid ligament, 133f
Intercostal muscle, 1803f
Intercostal vein, 1803f
Interfrontal cephaloceles, 44
Intermaxillary segment
  absence of, in holoprosencephaly, 55, 56f
  hypoplastic, in holoprosencephaly, 55, 56f
Internal auditory canal (meatus)
  congenital anomalies of, 1113, 1134, 1136, 1141f, 1142f
  CT surface reconstruction of, 1096f, 1097f
  double, 1149f
  hypoplastic, 1151f
  inflammation of, chronic, 1311f
  on computed tomography, 1095f
  on magnetic resonance imaging, 1099f, 1100f, 1101f, 1104f
  stenotic, 1123f
  3D reconstruction of magnetic resonance imaging of, 1104f
Interstitial lesions, 2187–2190
Intestinal-type adenocarcinomas (ITACs), sinonasal, 274, 276–277
Intraaxial tumors, 1300–1302, 1305f–1308f
Intracanalicular lesions, 1303, 1306, 1309, 1309f–1312f
Intracellular cytoplasmic domain of fibroblast growth factor receptors, 71–72
Intracranial abscesses, 250
Intracranial aneurysms, 252f
Intracranial hypertension
  otitic, 1182–1183
  tinnitus due to, 1370–1371
Intralingual cysts, of foregut origin, 1400f
Intraocular foreign bodies (IOFBs), 515f, 515–517
Intraocular lens (IOL), implantation of, postsurgical changes with, 520–521
Intraoral radiography, 914–916
  bitewing, 915, 915f
  dental caries on, 915f, 916–918, 917f, 918f
  occlusal, 915–916
  periapical, 915, 915f
  periodontal disease on, 915f, 916, 916f, 917f
Intraosseous carcinomas, primary, of jaw, 971
Intraosseous wiring, for facial fractures, 376, 376f
Intraparotid lymphadenopathy, 2114
Intratemporal benign vascular tumors (IBVTs), 1334
Intubation
  tracheal injuries due to, 1715–1717, 1716f–1718f
  trauma due to, in children, 1574–1575, 1576f
Inverted papillomas
  on computed tomography, 424f
  sinonasal, 267, 267f–270f
    calcifications within, 268, 270f
    on magnetic resonance imaging, 263f
‘‘Iodine mumps,’’ 2039
IOFBs. *See* Intraocular foreign bodies (IOFBs).
IOL. *See* Intraocular lens (IOL).
IOM. *See* Inferior orbitomeatal (IOM) line.
Iris, 455
  anatomy of, 457
  embryology of, 449, 532f
Irrigation, of nasolacrimal drainage system, 669
ITACs. *See* Intestinal-type adenocarcinomas (ITACs).

J

Jackson-Weiss syndrome, 69
Jacobson’s nerve, 1065

Jaw(s), 930–991. *See also* Dental *entries;* Mandibles; Maxillae; Teeth.
benign tumors and tumorlike conditions of
cemental lesions of, 954–956
nonodontogenic, 957–962
odontogenic, 946–954
cysts of, 931, 933–945
diagnostic imaging of, 982f, 982–985, 983f
for mixed radiolucent-radiopaque lesions, 983, 985t
for radiolucent lesions, 983, 984t
for radiopaque lesions, 984, 986t
magnetic resonance imaging as, 984–985, 986f
embryological development of, 5, 7f, 7–9, 8f
embryology of, 889–890, 890f–891f
fibroosseous lesions of, 965–969
Langerhans' cell histiocytosis of, 962–965
eosinophilic granuloma, 964–965, 965f
Hand-Schuller-Christian disease, 963–964
Letterer-Siwe disease, 962–963
malignant tumors of, 971–977
neurogenic tumors of, 970–971
vascular lesions of, 969–970
WHO classification of lesions of, 931, 932t
JD. *See* Jugular diverticulum (JD).
JNA. *See* Juvenile nasopharyngeal angiofibroma (JNA).
Job's syndrome, with sinusitis, 253–254
Joint effusions, of temporomandibular joint, 1018, 1021f–1023f
Jones 1 test, 669
Jones 2 test, 670
Jugular artery, internal, 1797f
Jugular bulb
agenesis of, 1145
large or exposed, tinnitus due to, 1371
protruding/dehiscent, 1144, 1160f–1162f
stenosis of, 1145, 1163f
Jugular canal, CT surface reconstruction of, 1097f
Jugular diverticulum (JD), 1144–1145, 1162f
Jugular foramen
CT surface reconstruction of, 1096f
schwannomas of, 1292–1293, 1300f
tumors of, 1306–1307, 1312, 1319f, 1320–1322, 1321t, 1333f
Jugular fossa, 1797f
CT surface reconstruction of, 1097f
on magnetic resonance imaging, 1100f, 1102f
reconstruction of computed tomography images of, 1105f
Jugular lymphatic obstruction sequence, 1849
Jugular tubercle, CT surface reconstruction of, 1096f, 1097f
Jugular veins
anterior, 1800f, 1801f, 1802f, 1803f
external, 127, 130f, 1799f, 1800f, 1801f, 1802f
internal, 130f, 1797f, 1798f, 1799f, 1800f, 1801f, 1802f, 1803f
asymmetry of, 2202, 2203f
phlebectasia of, 1856, 1858
thrombosed, 1982f
multiple, 2202
on magnetic resonance imaging, 1106f
Juvenile angiofibromas, of skull base, 827, 829, 829f, 830f
Juvenile nasopharyngeal angiofibroma (JNA), 1579–1580, 1580f
Juvenile pseudomonatous active ossifying fibromas, 574, 578f
Juvenile xanthogranuloma (JXG), orbital, 606–607
clinical features of, 607
diagnostic imaging in, 607, 608f, 609f
histopathologic features of, 607, 607f
JXG. *See* Juvenile xanthogranuloma (JXG).

K

Kallman's syndrome, 252, 255f
Kaposi's sarcoma (KS), 1909
human herpesvirus 8 and, 2289–2290, 2290f
laryngeal, 1655f
pharyngeal, 1509, 1511, 1511f
sinonasal, 315
Kartagener's syndrome, with sinusitis, 252
Kawasaki's syndrome, lymphadenopathy associated with, 1903
Keel-shaped deformity, 66, 68f
Keloids, 2175–2176, 2176f
Keratitis, necrotizing, 476f
Keratocysts
antral cholesteatomas versus, 244, 246
odontogenic, 347, 350, 352
of oral cavity, 1422, 1425f
Keratosis obturans (KO), 1215–1216, 1216f, 1339, 1342f
Kiesselbach's area, 95
Kiesselbach's plexus, 95, 95f, 96t
Kikuchi-Fujimoto disease, lymphadenopathy associated with, 1899
Killian procedure, 405–406, 407f
Kimura's disease
lymphadenopathy associated with, 1897–1898, 1901f
of lacrimal gland, 646, 647f
of salivary glands, 2121–2123, 2123f, 2124f
Klebsiella rhinoscleromatis infections, paranasal, 236, 239
Kleeblattschädel, 68f, 69
Klippel-Feil syndrome, 1111t, 1133f, 1168f
KO. *See* Keratosis obturans (KO).
Krause, valves of, 699
Krönlein procedure, 420, 420f, 421f
KS. *See* Kaposi's sarcoma (KS).
Kussmaul's disease, of salivary glands, 2042
Küttner tumors, 2040

L

Labial artery, superior, 95, 95f
Labiogingival groove, 9
Labyrinth
aplasia of, 1129
bony
anatomy of, 1071, 1072f, 1073
embryology and developmental anatomy of, 1060
otosclerosis of. *See* Otosclerosis.
endolymphatic, embryology and developmental anatomy of, 1058–1059, 1060f
hemorrhage in, 1243f
perilymphatic (periotic), embryology and developmental anatomy of, 1059–1060
Labyrinthine fistulas, with cholesteatomas, 1191, 1192f–1194f
Labyrinthitis, 1183, 1205t, 1205–1208
bacterial, 1205–1206, 1206f
posttraumatic, 1206
sclerosing, 1207–1208, 1208f, 1209f
viral, 1206–1207
Labyrinthitis ossificans, 1128f, 1207–1208, 1208f, 1209f
Lacrimal adenitis, orbital pseudotumors and, 587, 590f
Lacrimal apparatus, anatomy of, 543–544
Lacrimal artery, 543
Lacrimal bone, 98–99, 99, 134f, 135f
anatomy of, 699
development of, 10
on computed tomography and magnetic resonance imaging, 125
Lacrimal ducts, embryology of, 1522
Lacrimal gland
anatomy of, 547
embryology of, 531, 533
lesions of
diagnostic imaging in, 643–646, 644f–646f
tumors, 641–646, 643f–645f
lymphoma of, 590f
sarcoidosis of, 597, 599f
Lacrimal gland cysts, 571, 571f, 572f
Lacrimal gland fossa, on computed tomography and magnetic resonance imaging, 126

Lacrimal groove, on computed tomography and magnetic resonance imaging, 126
Lacrimal nerve, perineural tumor spread involving, 867
Lacrimal pump, 695, 695f
Lacrimal puncta, congenital atresia of, 714–716, 715f
Lacrimal sac, 135f
  air in, on computed tomography, 697, 699f
  anatomy of, 673f, 673–674, 699
  cysts of, 679, 680f
  diverticula of, on computed tomography, 701
  embryology of, 533
  mucoceles of, 571–572, 572f, 688f
  normal dimensions of, 674, 674t
  tumors of, 705–708, 711t
Lacrimal sac fossa, 139f, 140f
  anatomy of, on computed tomography, 697
Lacrimation, excessive, 674–675
Lamina papyracea, 98, 133f, 134f, 135f, 140f
  anterior, injury of, with functional endoscopic sinus surgery, 182, 182f
  dehiscent, 134f
  following functional endoscopic sinus surgery, 172
  medial deviation or dehiscence of, 163, 165, 165f
  on computed tomography and magnetic resonance imaging, 125–126
  on plain films, 112, 112f
Langerhans' cell granulomatosis (LCG), sinonasal, 305–308
Langerhans' cell histiocytosis (LCH)
  of jaw, 962–965
    eosinophilic granuloma, 964–965, 965f
    Hand-Schuller-Christian disease, 963–964
    Letterer-Siwe disease, 962–963
  of mastoid, 1343, 1345, 1346f
  of skull base, 833–835, 840f
  orbital, 603–606
    clinical features of, 604–605
    diagnostic imaging in, 605f, 605–606, 606f
    histopathologic features of, 605, 605f
    historical background of, 604
    immunohistochemistry of, 605, 605f
Langer's cleavage lines, 126
Large endolymphatic duct and sac (LEDs), 1139, 1154f, 1155f
Larmor frequency, 206
Laryngeal artery, 1602
Laryngeal carcinomas, pediatric, 1587–1588
Laryngeal cartilages
  benign changes of, 1684, 1686f, 1687f
  embryology of, 1767f, 1767–1768
  in squamous cell carcinoma, 1617–1619, 1618f–1620f, 1621, 1622f–1625f
    on computed tomography, 1617, 1618f, 1619f, 1622f
    on magnetic resonance imaging, 1617–1619, 1620f, 1621, 1622f–1625f
Laryngeal clefts, 1553, 1553f
Laryngeal cysts, congenital, 1552
Laryngeal muscles, 1600f, 1601
Laryngeal nerve
  recurrent, 1701, 1702
    thyroid carcinoma invading, 1681f
    vocal cord paralysis and, 1678, 1680f–1682f
  superior, 1601–1602
    vocal cord paralysis and, 1676
Laryngeal obstruction, congenital, 1551–1553
Laryngeal ventricle, 1601
  saccule of, 1652, 1661f
Laryngeal vestibule, 1596, 1801f
Laryngeal webs, 1553
Laryngectomy
  near-total, of Pearson et al., postsurgical appearance and, 1688–1689
  on videofluoroscopic swallowing study, 1738, 1738f
  partial, 2251f
    supracricoid, postsurgical appearance and, 1688, 1692f
  supraglottic, 1626
    contraindications to, 1621
    postsurgical appearance and, 1686–1687, 1689f, 1690f
    postsurgical imaging and, 2260f
  swallowing and, 1742f, 1742–1743
  total
    postsurgical appearance and, 1685–1686, 1688f
    postsurgical imaging and, 2262f, 2263f, 2265f
Laryngoceles, 1652, 1662f, 1665f–1668f
  congenital, 1552
  external, 1652
Laryngomalacia, 1670
  congenital, 1551
Laryngopyoceles, 1652, 1668f
Laryngotracheal clefts, 1672
Laryngotracheal separation, 1664, 1675f
Laryngotracheobronchial papillomatosis, 1722, 1724f
Laryngotracheobronchitis (LTB), 1568–1569, 1569f, 1654–1656, 1669f
  trachea and, 1710
  with sinusitis, 255
Larynx, 1595–1695
  abscess of, 1672f
  adenocarcinoma of, 1645
  amyloid of, 1682, 1683f, 1684f
  anaplastic carcinoma of, 1645
  anatomy of, 1596f–1600f, 1596–1602
    of innervation and blood supply, 1601–1602
    of lymphatic drainage, 1602
    of regions, 1602
    of spaces, 1601, 1602f
  atresia of, 1553, 1670, 1672, 1678f
  benign tumors of, 1647–1649, 1651, 1656f–1660f
    on computed tomography, 1656f, 1658f, 1659f
    on magnetic resonance imaging, 1659f, 1660f
    on plain films, 1657f, 1658f
  caustic ingestions and, in children, 1574
  chondrosarcoma of, 1645, 1647, 1652f–1655f
  congenital lesions of, 1669–1670, 1672
  crack cocaine burns of, 1677f
  embryology of, 1523, 1523f, 1524f, 1669–1670, 1759f, 1765, 1766f, 1767f, 1767–1768
  following radiation therapy, 1689, 1692f–1694f, 1693
  functions of, 1596
  granular cell tumor of, 1651
  granulomas of, 1679f
  hemangiomas of, 1648–1649, 1658f
  hematomas of, 1672f
  imaging of, 1603–1613
    angiography for, 1613
    barium swallow for, 1606, 1607f, 1608f
    computed tomography for, 1606–1608, 1609f–1612f
    contrast examinations for, 1605–1606
    fluoroscopy for, 1605
    magnetic resonance imaging for, 1608–1609, 1612f–1615f, 1613
    plain films for, 1604f, 1604–1605, 1605f
    respiratory maneuvers for, 1603, 1603f, 1604f
    scintigraphy for, 1613
    tomography for, 1605
    ultrasonography for, 1613
  Kaposi's sarcoma of, 1655f
  lipoma of, 1648, 1658f
  lymph node drainage of, 1881t
  metastatic disease of, 1647
  movements of, during oropharyngeal swallowing, 1743
  mucosal cysts of, 1651–1652, 1661f
  oncocytic tumors of, 2084
  papilloma of, 1648, 1657f
  papillomatosis of, pediatric, 1580f
  paragangliomas of, 1649, 1651, 1659f

Larynx *(Continued)*
pediatric, anatomy of, 1530–1531, 1533, 1534f–1537f
relapsing polychondritis of, 1657, 1659
rheumatoid disease of, 1656–1657, 1659
rhinoscleroma of, 1656, 1671f
sarcoid of, 1656
sarcomas of, 1645
schwannomas of, 1651, 1660f
soft-tissue infection of neck extension to, 1656, 1672f
spindle cell carcinoma of, 1645
squamous cell carcinoma of, 1615–1621, 1621, 1626f, 1648f
barium swallow examination in, 1621
cartilage involvement in, 1617–1619, 1618f–1620f, 1621, 1622f–1625f
chest radiography in, 1621
nodal metastasis of, 1621
on positron-emission tomography, 2301f
site-specific evaluation for, 1621–1644
glottic and infraglottic, 1635–1640, 1640f–1647f
pharyngeal, 1640–1642, 1644, 1649f–1651f
supraglottic, 1621–1622, 1626, 1626f–1639f, 1629–1631, 1634–1635
ventricular, 1640, 1648f
staging of, 1615, 1616
voice conservation therapy for, 1615, 1617
workup for, 1621, 1626f
stenosis of, 1672, 1674, 1676, 1679f
subglottic stenosis and, 1670, 1677f
subglottic webs and, 1670
thermal trauma to, in children, 1574, 1575f
thyroglossal duct cysts of, 1652, 1654, 1669f
traumatic injury of, 1661, 1663–1664, 1666–1667, 1672f–1677f
arytenoid dislocation, 1664, 1666, 1676f
burns, 1667, 1677f
cricoid fractures, 1663–1664, 1674f, 1675f
cricothyroid dislocation, 1666, 1676f
foreign bodies and, 1667
laryngotracheal separation, 1664, 1675f
on computed tomography, 1672f–1676f
on magnetic resonance imaging, 1674f, 1677f
pediatric, 1571–1574, 1573f, 1574f
thyroid cartilage fractures, 1663, 1673f, 1674f
tuberculosis of, 1656, 1670f
verrucous carcinoma of, 1645
Lateral view, for paranasal sinus plain films
of associated structures, 120, 121, 121f, 122
of ethmoid sinuses, 112, 113
of frontal sinuses, 103f, 109, 109f, 111f, 111–112
of maxillary sinuses, 114, 114f–116f, 115, 116
of sphenoid sinuses, 114f, 119
Lathrop procedure, intranasal, modified, 188
Lattice, in magnetic resonance, 206
LCG. *See* Langerhans' cell granulomatosis (LCG).
LCH. *See* Langerhans' cell histiocytosis (LCH).
Le Fort I fractures, 381, 385f
on computed tomography, 385f
on tomography, 385f
Le Fort II fractures, 382, 386f
on computed tomography, 386f
Le Fort III fractures, 382, 384, 386f, 387f
on computed tomography, 387f
LECs. *See* Lymphoepithelial carcinomas (LECs).
LEDs. *See* Large endolymphatic duct and sac (LEDs).
Leiomyomas
ocular, 512–513, 532f
sinonasal, 315–316, 315–317, 316f, 317
Leishmaniasis, 242
Lemierre's syndrome, lymphadenitis in, 1891, 1891f
Lens, 445f
anatomy of, 460–461, 461f
calcification of, 479t
dislocation of, 517–518, 519f
embryology of, 447–448, 448f, 449f
suspensory ligaments of, embryology of, 449
vascular capsule of, 448
Lens capsule, perforation of, 518, 519f
Lens fibers, embryology of, 532f
Lens pit, 443f
Lens placode, 443f
Lens vesicle, 444f
Leprosy, 241–242, 242f
lymphadenitis in, 1894
Letterer-Siwe disease, 603
in skull base, 834–835
of jaw, 962–963
Leukemia, 1904–1905, 1905f
ocular, 512
of jaw, 977, 977f
orbital, 612, 615f–617f
Leukokoria, 477, 480t
Levator anguli oris muscle, 90t, 127, 128f, 1797f, 1798f
Levator claviculae muscle, lesions of, 2190, 2191f
Levator labii superioris alaeque nasi muscle, 89, 90, 127, 128f
Levator labii superioris muscle, 90, 90f, 127, 128f, 1796f
Levator muscle, extraocular, 539–540
Levator palpebrae superioris muscle, 91t, 128f
Levator scapulae muscle, 1793t, 1799f, 1800f, 1801f, 1802f
Levator veli palatini muscle, 1466, 1792t, 1796f, 1797f, 1798f
Liesgang's rings, 360
Li-Fraumeni syndrome, 2282–2283, 2283f
Ligamentum nuchae, 1799f
Ligands, craniofacial malformations and, 4
Limen vestibuli, 90, 92f
Linea innominata, on plain films, 117–118, 118f
Lingual artery, 1798f, 1799f
aneurysms of, 1396, 1400f
Lingual cysts, 1397–1398, 1400f
pediatric, 1546–1548, 1547f–1549f
Lingual nerve, 1784
Lingual thyroid, 1395, 1399f
Lip(s), 1798f
cleft. *See* Cleft lip; Cleft lip/palate; Facial clefts.
embryologic development of, 9
movements of, during oropharyngeal swallowing, 1739
muscles of, 89, 90, 90f, 91t, 127, 128f
normal anatomy of, 1384
squamous cell carcinoma of, 1428
with perineural tumor spread, 875f, 876f
upper, on plain films, 118, 118f
Lipid granulomas
of petrous apex, 1203, 1204f, 1347–1349, 1348f
of temporal bone, 1339, 1340f
orbital, 568t, 572, 573–574, 575f, 577f
Lipodermoids, orbital, 563–564, 566f, 568t
Lipomas, 2184, 2185f
infiltrative, 2184, 2186f
intracanalicular, 1303
laryngeal, 1648, 1658f
of cerebellopontine angle, 1291, 1297f
of neck, on ultrasound, 1949–1950
of oral cavity, 1415–1416, 1416f
of parapharyngeal space, 1979, 1982f
of salivary glands, 2114–2115, 2119f
pharyngeal, 1501–1502
sinonasal, 317
Liposarcomas, 2184–2185, 2187, 2187f
of oral cavity, 1438, 1444f
of parapharyngeal space, 1972, 1978f
sinonasal, 317–318
Little's area, 95
LMs. *See* Lymphatic malformations (LMs).
Lobular torus, 15

Lobule, of ear, on surface magnetic resonance imaging, 1096f
Locking, of temporomandibular joint, 1020–1021, 1028f
Lofgren's syndrome, 596–597
Longissimus capitis muscle, 1798f, 1799f, 1800f
Longissimus cervicis muscle, 1801f
Longitudinal constrictor muscles, of oral cavity, 1379t
Longus capitis muscle, 1792t, 1796f, 1797f, 1798f, 1799f, 1800f, 1801f
Longus colli muscle, 1792t, 1798f, 1799f, 1800f, 1801f, 1802f
Louis-Bar's syndrome
  choroidal hemangiomas in, 508
  gene mutated in, 2285–2286
  sinusitis in, 256
Low-grade papillary adenocarcinoma of salivary origin, of salivary glands, 2096–2097, 2097f
LTB. *See* Laryngotracheobronchitis (LTB).
Ludwig's angina, 1403–1405, 1407f
Lund staging system for rhinosinusitis, 185, 185t
Lung(s), 1802f
  embryology of, 1765, 1766f
Lung apex, 1802f
Lung carcinomas
  brachial plexopathy due to, 2237f
  metastatic to brachial plexus, 2225f
  metastatic to muscle, 2202f
  metastatic to occipital lobe, 740f
  metastatic to salivary glands, 2109f
  metastatic to sinonasal cavities, 364f, 365f
Lupus erythematosus, orbital, 603
Lupus vulgaris (LV), lymphadenitis in, 1893
LV. *See* Lupus vulgaris (LV).
Lyme disease, 750–751
  clinical findings in, 751
  lymphadenitis in, 1892
  middle ear and, 1209–1210
  on computed tomography, 751
  on magnetic resonance imaging, 751, 751f
  pathologic findings in, 751
Lymph, 1866
  peripheral, 1866
Lymph flow, 1866
Lymph nodes, 1865–1929. *See also specific sites.*
  biopsy of, nondiagnostic, 1883
  cervical
    imaging of, limitations in, 1883, 1884f
    ultrasound of, 1938–1939, 1939f
  classification of, 1870–1880
    AAO-HNS system for, 1872, 1874t–1875t
Lymph nodes *(Continued)*
    AJCC system for, 1870, 1871f, 1871t, 1874t–1876t
      refinement of, 1880, 1882t
    imaging-based, 1872, 1872t, 1873f, 1874t–1876t, 1875–1880
      levels in, 1876–1878, 1877f–1880f, 1880, 1881t
      scanning technique for, 1875
      use of, 1875–1876
    Rouvière system for, 1873, 1875, 1876t
  clinicopathologic correlation and, 1883–1884, 1884f
  drainage areas of, 1881t
  imaging of
    arterial tumor invasion and, 1917, 1919
    extranodal tumor extension and, 1916, 1919t, 1920t
    newer approaches for, 1922, 1924, 1926–1927, 1929, 1929f
    nodal calcifications and, 1920, 1926t, 1927f–1928f
    node enhancement for, 1920, 1925f–1926f, 1926t
    of metastatic nodes, 1910–1916
      central necrosis and, 1912f–1918f, 1912–1913, 1915
      size criteria for, 1910–1912, 1911f, 1912t
      subcapsular nodal tumor and, 1915–1916, 1918f
    of ''normal'' reactive nodes, 1910, 1911f
    of retropharyngeal abscessed nodes, 1922, 1928f
    with metastatic thyroid carcinoma, 1920, 1921f–1925f
  in parapharyngeal space, 1974–1975, 1978f
  inclusions in, 1903–1904, 1904f
  lymph and lymphatic flow and, 1866
  metastatic, 1909–1910, 1910f, 1910t
    clinical significance of, 1869, 1869t, 1870t
    imaging of, clinical impact of, 1869–1870
    in squamous cell carcinoma, 1906f
    metastatic pathways and, 1868–1869
    pathology of, 1882–1883
    primary tumor site and, 1883
    ultrasmall superparamagnetic iron oxide imaging of, 2316f, 2316–2317
    with anaplastic thyroid carcinoma, 2156f
    with papillary thyroid carcinoma, 2154f
  normal, ultrasmall superparamagnetic iron oxide imaging of, 2315f
Lymph nodes *(Continued)*
  proliferative histiocytic disorders and, 1905–1908, 1908f. *See also* Langerhans' cell histiocytosis (LCH).
  sentinel, detection of, 1947, 1947f
  spindle cell neoplasms of, 1908–1909, 1909t
  staging of, 1880, 1882, 1882t
    for nasopharyngeal carcinoma, 1882, 1882t
    for thyroid carcinoma, 1882, 1882t
  structure and function of, 1867f, 1867–1868
  vascular neoplasms of, 1909
Lymphadenitis
  nonneoplastic, ultrasound in, 1944f, 1944–1945, 1945f
  streptococcal, 1564f
Lymphadenocarcinomas, sebaceous, of salivary gland origin, 2099
Lymphadenomas, sebaceous, of salivary gland origin, 2099
Lymphadenopathy
  bacterial infections and, 1562–1564, 1564f–1567f, 1566
  bacterial lymphadenitides and, 1889–1894, 1890f, 1891f
  foreign body, 1903
  fungal lymphadenitides and, 1894–1896
  intraparotid, 2114
  metastatic, ultrasound in, 1945–1947, 1946f, 1946t, 1947f, 1947t
  reactive lymphadenopathies and, 1897
  toxoplasmosis and, 1896–1897
  tuberculous, ultrasound in, 1945f
  tumor-reactive, 1903
  vascular, 1903
  viral infections and, 1562, 1563f
  viral lymphadenitides and, 1885f–1886f, 1885–1889
  with clinical syndromes, 1897–1903, 1898f–1901f
Lymphangiomas
  capillary, 1851, 1855f
  cavernous, 1850, 1855f
  in parapharyngeal space, 1823f
  of neck, 1847–1852
    capillary, 1851, 1855f
    cavernous, 1850, 1855f
    classification of, 1848–1849
    cystic, 1849–1850, 1850f–1854f
      on computed tomography, 1849–1850, 1850f–1852f
      on magnetic resonance imaging, 1850, 1853f, 1854f
    pathogenesis of, 1848
  of oral cavity, 1389, 1392f, 1393f
  of salivary glands, 2107–2109, 2111f, 2112f
  orbital, 569, 616–617, 621f, 622f
Lymphatic malformations (LMs), 1558, 1560f, 1560–1561

Lymphatic system, 1866
Lymphetheliomas, 1479
Lymphoepithelial carcinomas (LECs), 2100, 2101
of salivary glands, 2099–2101
Lymphoepithelial cysts. *See also* Branchial cysts.
of salivary glands, 2053–2054, 2056f–2059f
Lymphoepithelial lesions
benign. *See also specific lesions.*
of salivary glands, 2043, 2044f, 2099–2100, 2101
malignant, of salivary glands, 2100
Lymphoepitheliomas, pharyngeal, 1480f
Lymphoid hyperplasia
reactive, 590f
uveal, 473
Lymphomas, 1904, 1904f–1907f
B-cell, orbital, 601
immunoblastic, nasopharyngeal, 1509, 1510f
intracanalicular, 1303, 1310f
large cell, 1904f–1907f
lymph nodes in, 1911f
malignant, ultrasound in, 1945, 1946f
metastatic to temporomandibular joint, 1041f
nasolacrimal, dacryocystography in, 678f–679f
ocular, 511–512, 512f
of central nervous system, primary, Epstein-Barr virus and, 2290, 2290f
of cerebellopontine angle, 1302, 1307f
of jaw, 975–976, 976f
of lacrimal gland, 590f, 643, 643f
of nasolacrimal sac, 662f
of oral cavity, 1433
of salivary glands, 2109, 2112–2113, 2113f–2118f, 2113t
of skull base, 835
on positron-emission tomography, 2305
orbital, 600, 610–612, 698f
diagnostic imaging in, 611f–614f, 611–612
pediatric, 1583–1584, 1584f, 1585f
pharyngeal, 1493–1494, 1511f
imaging findings in, 1494, 1495f, 1496f
REAL classification and Working Formation of, 1907t
sinonasal, 301t–303t, 301–302, 304f–306f
on computed tomography, 302, 304f, 305f
on magnetic resonance imaging, 302, 304f, 306f
T-cell
angiocentric, sinonasal, 301–302
orbital, 601
thyroid, 2156
Lymphomatoid granulomatosis, 611f
Lymphoplasmacytic tumor. *See* Myelomas, multiple.
Lymphoproliferative disorders, 1904f–1907f, 1904–1905, 1907t.
See also Leukemia; Lymphomas.
posttransplantation, 1903
Lynch procedure, 405, 406f, 407f
on computed tomography, 406f
on magnetic resonance imaging, 407f

M

Macrodacryocystography, 657
digital subtraction, 660–663
Macrodontia, 987, 988f
Macroglossia, congenital, 1549, 1549f
Macrophthalmia, 461–463, 463f
Macular area, embryology of, 446–447
Macular degeneration, senile, 514, 514f
Madelung's disease, 2184, 2186f, 2187f
Maffucci's syndrome, 821, 823f
in petroclival synchondrosis, 1259f
Magnetic resonance, of protein solutions, 206f–210f, 206–208
Magnetic resonance dacryocystography (MR-DCG), 716, 717f–718f, 718–720
Magnetic resonance imaging (MRI). *See also specific regions and conditions.*
artifacts in, 452, 453f
computed tomography compared with, in sinonasal disease, 109
for postoperative imaging, of sinonasal cavities, 403
short tau inversion recovery, 545
T1-weighted fat-suppression technique for, 545
ultrasmall superparamagnetic iron oxide contrast agents for, 2315–2317
clinical applications for, 2316–2317
notal metastasis detection, 2316–2317
primary site evaluation, 2317
mechanism of, 2315, 2316f
technique for, 2316
Magnetic resonance spectroscopy (MRS). *See also* Proton magnetic resonance spectroscopy (^{1}H-MRS); *specific regions and conditions.*
of salivary glands, 2024
of temporomandibular joint, 1050
Maier, sinus of, 673
Malignant fibrous histiocytomas (MFHs), sinonasal, 319–320, 320f
inflammatory, 320
Malignant lymphoepithelial lesions (MLELs), of salivary glands, 2100
Malignant melanomas
orbital, 639f
sinonasal, 289f–291f, 289–290
on computed tomography, 289f, 290f
on magnetic resonance imaging, 289f, 290f
Malignant melanomas *(Continued)*
uveal, 500–506
clinical diagnosis of, 500
diagnostic imaging in, 500–501, 501f–505f, 503–505
differential diagnosis of, 505–506, 506f, 506t
on computed tomography, 500f
on magnetic resonance imaging, 501f–506f
Malignant peripheral nerve sheath tumors (MPNSTs), 294
of mandibular nerve, 1448f
sinonasal, 294, 296f
Malleus
handle of, on computed tomography, 1095f
head of, on computed tomography, 1095f
Mandibles, 895–899, 898f–901f, 902
asymmetry of, 1038, 1047f–1049f, 1049
body of, 896f, 897
buccal surface of, 897
on computed tomography, 899
chondrosarcoma of, 1445f
cleft, cleft lower lip with, 29–30
condyle of, 1797f
bifid, 1038, 1045f
marrow abnormalities of, 1018, 1024f–1026f
on CT surface reconstruction, 1096f
osteochondroma of, 1037f
coronoid process of, 137f, 1796f, 1797f
on plain films, 118–119, 119f
CT surface reconstruction of, 1097f
embryologic development of, 7f
extravasation mucocele of, 1411f
genial processes of, 1799f
head of, 135f, 1796f, 1797f
lesions of, 2119, 2121f–2123f
lingual surface of, 895–897, 901f
on computed tomography, 898–899
osteogenic sarcoma of, 1445f
osteomyelitis of, 1401f
osteosarcoma of, 1995f
prostate carcinoma metastatic to, 1447f
reconstruction of, 1735f
rectal carcinoma metastatic to, 1448f
superior surface of, 897–898
on computed tomography, 899
Mandibular arch, 7f
Mandibular body space, 1816, 1825t, 1826t
Mandibular canal, identification of, with dental CT reformatting programs, 910–912, 912f, 913f
Mandibular hypoplasia, in hemifacial microsomia, 59, 60f–61f
Mandibular nerve, 129f, 1782, 1784
perineural tumor spread involving, 870, 877f
Mandibular node, 1797f

Mandibular notch, 138f, 896f, 897, 1797f
Mandibular prominences, 7f, 8
Mandibular ramus, 1797f
Mandibular resection, postsurgical imaging and, 2255f–2256f
Mandibulectomy
  partial, postsurgical imaging and, 2260f, 2263f
  postsurgical imaging and, 2264f, 2267f
Mandibulofacial dysostosis (MFD), 58, 63, 64f, 101, 565f
  bony orbit in, 562, 565f
  orbit in, 562, 562f
Manubrium, 1803f
Marble bone disease, of temporal bone, 1263–1264, 1264f–1266f
  differential diagnosis of, 1263–1264
Masseter muscle, 128f, 897, 899f, 1379t, 1793t, 1796f, 1797f, 1798f
  myositis of, 1403f
Masseteric hypertrophy, 2118, 2121f
  benign, 1458, 1458f
Masticator muscles
  anatomy of, 1988
  denervation atrophy of, 1991, 1992f
  hypertrophy of, 1991, 1993, 1993f
  in hemifacial microsomia, 59
Masticator space, 1819–1820, 1822f, 1826t, 1987–1996
  abscess in, 1822f
  anatomy of, 1987–1988, 1988f, 1988t
    of muscles, 1988
  benign bone cyst of, 1995f
  breast cancer metastatic to, 1996f
  buccal fat in, 1989
  denervation atrophy of, 1991, 1992f
  fibrosarcoma of, 1996f
  infections of, 1989–1991, 1990f, 1991f
  inflammatory diseases of, 1989–1991, 1990f, 1991f
  masses in, 1993, 1994f–1999f, 1995–1996
    clinical presentation of, 1988–1989
  metastatic meningioma of, 1995f
  radiation necrosis of, 1995f
  rhabdomyosarcoma of, 1809f
  sarcoma of, undifferentiated, 1996f
Mastoid
  fibrous dysplasia of, 1345f
  Langerhans' cell histiocytosis of, 1343, 1345, 1346f
  on magnetic resonance imaging, 1099f, 1103f
  tip of, CT surface reconstruction of, 1097f
  tumors of, 1343, 1345, 1347f
  undifferentiated carcinomas of, 1347f
Mastoid air cells, reconstruction of computed tomography images of, 1105f
Mastoid lymph nodes, drainage of, 1881t
Mastoid process, 1798f
  formation of, 1062
Mastoidectomy
  cavity from, cholesterol granuloma in, 1203, 1204f
  temporal bone following, 1216t, 1216–1218, 1217f, 1218f
Mastoiditis
  acute, 1175, 1176f
  coalescent, 1176, 1177f–1179f
  dural sinus thrombosis associated with, 1176, 1178–1179, 1179f–1181f
  meningitis with, 1182, 1182f
  tuberculous, 1179f, 1199
  venous infarction associated with, 1179, 1182
  with epidural abscess, 1182, 1182f
Maxillae
  alveolus of, 1797f
  ascending process of, 98
  deformity of, in cleft lip/palate, 23
  development of, 10, 10f
  frontal process of, 134f, 135f, 137f, 139f
    on computed tomography and magnetic resonance imaging, 124
  nasal crest of, 89f
  on plain films, 115f, 121, 121f
  osteitis of, 710f
  osteogenic sarcoma of, 1446f
  palatine process of, 90, 138f, 141f
    on computed tomography and magnetic resonance imaging, 124
Maxillary alveolus, 139f, 141f
Maxillary artery, 102
  sphenopalatine branch of, 101
Maxillary exostoses, 141f
  multiple, 959
Maxillary fractures, 381, 383f–385f
  alveolar, 381
  on computed tomography, 384f, 385f
  on tomography, 383f
Maxillary hiatus, 102
Maxillary lymph nodes, drainage of, 1881t
Maxillary nerve, 129f, 1782
Maxillary process, 7f
Maxillary prominences, 7f, 8
Maxillary sinus(es), 101–102, 135f, 143f, 144f, 1796f, 1797f
  air-fluid levels in, 196–198, 197f, 198f
  alveolar recess of, 138f
  carcinoma of, 270f, 270–271
  CT surface reconstruction of, 1097f
  development of, 101
  hypoplasia of, 209
    with functional endoscopic sinus surgery, 183, 183f
  hypoplastic, 101
    on plain films, 113–114, 114f
  infection of, from dental disease, 926, 927f
  malignancy of, surgery for, 422–423
  on computed tomography, 154f
Maxillary sinus(es) *(Continued)*
  ostia of, 92f, 102
  palatal recesses of, 141f
  plain film anatomy of, 113–119, 114f–119f
  pneumatization of, asymmetric, 1424, 1427f
  retention cysts in, 2011f
  sarcomas of, 857f
  sclerosis in, 211, 211f
  septum of, 143f
  tumors of, 262
  walls of
    on computed tomography and magnetic resonance imaging, 126
    on plain films, 114
Maxillary sinus surgery, 412, 414–415, 418–420
  Caldwell-Luc procedure, 412, 414–415, 418f–421f, 420
    on computed tomography, 419f, 420f
Maxillary teeth roots, 139f
Maxillary tuberosity, 1798f
Maxillary vein, 101, 102, 127
  internal, 127
Maxillectomy
  medial, 422, 422f
  total, 422f–427f, 423
    on computed tomography, 423f–426f
    on magnetic resonance imaging, 427f
McCune-Albright syndrome, 1581f
McGregor's line, 853
Measles
  labyrinthitis due to, 1207
  lymphadenitis in, 1888–1889
Measles encephalitis, 1207
Meatal antrostomy
  inferior, 102
  middle, postoperative findings with, 187, 188f
Meatus
  inferior, 137f, 140f, 144f
  middle, 136f, 140f, 144f
    anatomy of, 153, 154
  of nasal conchae, 91
Meckel's cartilage, 889, 1768
Meckel's cave, 796f, 797, 797f, 798
  squamous cell carcinoma of, with perineural tumor spread, 884f
MECs. *See* Mucoepidermoid carcinomas (MECs).
Median cleft face syndrome, 23–24, 26f, 27, 28f, 29t
Median lingual cysts, 1397–1398, 1400f
Mediastinal granulomas, 1711
Medullary carcinoma, thyroid, 2154–2156, 2156f
Medullary pseudocysts, mandibular, 945
Medulloepitheliomas, 513, 513f
Megalophthalmos, 462
Melanocytomas, 506–507, 507f

Melanomas, 2179
desmoplastic, facial, with perineural tumor spread, 870f
internal auditory canal metastases from, 1309f
intracanalicular, 1303
malignant. *See* Malignant melanomas.
metastatic to sinonasal cavities, 364f
nasolacrimal, 705f
of Tenon's capsule, 453, 454f
sinonasal, on magnetic resonance imaging, 266f
uveal, 469f
Melanotic neuroectodermal tumor of infancy, 290
Melnick-Fraser syndrome, 63, 1110t, 1166f
semicircular canals in, 1126f
Membranous septum, 89
Meningeal sheaths, of optic nerve, 541
Meningiomas
intracranial, 775, 776f
metastatic
of masticator space, 1995f
to salivary glands, 2109f
of cerebellopontine angle, 1286–1288, 1287f–1291f
of hypoglossal canal, 1457f
of parapharyngeal space, 1987f
of skull base, 821–824, 824f–827f
of temporal bone, 1321–1322, 1323f
Paget's disease versus, 1259
of trigeminal nerve, 1453f
perioptic, 738f, 744, 746
clinical findings with, 744
on computed tomography, 746
on magnetic resonance imaging, 746, 747f, 748f
pathologic findings with, 744, 746f
sinonasal, 297
on magnetic resonance imaging, 297f, 298f
sphenoid, 247
suprasellar, 772f
Meningitis
in sinusitis, 582f
petrous bone malformations associated with, 1145–1148, 1150–1151, 1163f
perilabyrinthine fistulas, 1146–1148, 1163f–1165f
translabyrinthine fistulas, 1148, 1150–1151, 1163f
pneumococcal, 750f
tuberculous, 750f
with mastoiditis, 1182, 1182f
Meningoceles
apical, 1148
cranial, 43
nasal obstruction due to, 1543
of optic nerve, 571f
Meningoceles *(Continued)*
of petrous apex, 1351–1352
of skull base/middle cranial fossa, 1164f–1165f
optic nerve sheath, 569, 571f
Meningoencephaloceles, 43
with functional endoscopic sinus surgery, on magnetic resonance imaging, 179, 181f
with temporal bone trauma, 1241f
Mental foramen, 899, 900f
Mental protuberance, 897, 899f
Mentalis muscle, 91t, 127, 128f, 1799f
Menti muscle, transverse, 127
Merkel cell carcinomas
of salivary glands, 2121, 2125f
on positron-emission tomography, 2304f
Merkel cell tumors, of skin and subcutaneous tissues, 2179, 2179f
Merkel's cysts, of salivary glands, 2057
MESA. *See* Myoepithelial sialoadenitis (MESA).
Mesenchymal chondrosarcomas, sinonasal, 345
Mesiodens, 987
Mesoderm
paraxial, 5
prechordal, 5
Mesoethmoidal center, 10, 30f
Metabolic disorders, dental manifestations of, 990–991
Metaphyseal dysplasia, of temporal bone, 1267, 1268
Metastasis
from sinonasal carcinomas, 263
genes involved in multiple steps of, 2290–2291
perineural spread and. *See* Perineural tumor spread (PNS).
Metastatic disease. *See also* Lymph nodes, metastatic.
adenocarcinoma, 1927f, 1928f
cutaneous, 2179, 2179f
intracanalicular, 1303, 1309f
intracranial, 772, 774f
laryngeal, 1647
squamous cell carcinoma and, 1621
leptomeningeal, loculated, 1290f
lymphadenopathy in, ultrasound in, 1945–1947, 1946f, 1946t, 1947f, 1947t
meningeal, from prostate cancer, 1290f
multiple lesions in, 364
of brachial plexus, 2225, 2225f, 2228f, 2232f
of carotid sheath, from breast carcinoma, 1456
of humerus, 2233f
of jaw, 972–973, 973f
of masticator space, 1996f
Metastatic disease *(Continued)*
of muscle, 2199, 2202f
of neck, 1809f, 1810f
of occipital lobe, 740f
of oral cavity, 1440, 1446f, 1448f
from prostate carcinoma, 1447f
from rectal carcinoma, 1448f
of salivary glands, 2105–2107, 2108f–2110f, 2109f, 2110f
of scapula, 2233f
of skull base, 844, 846–848
direct encroachment and, 844, 846–847, 847f, 848f
hematogenous spread and, 848, 853f
perineural tumor spread and, 847–848, 849f–853f
of temporal bone
fibrous dysplasia versus, 1256
Paget's disease versus, 1259
of temporomandibular joint, 1036, 1041f, 2123f
of thyroid, 2157, 2157f
of tracheoesophageal sulcus, 2235f, 2237f
of visual pathway, 772, 774f, 775, 777, 777f
orbital, 646f
calcification in, differential diagnosis of, 553
papillary thyroid carcinoma, 1925f
pathology, 1882–1883
squamous cell carcinoma, 1910f
lymph nodes in, 1913f, 1914f, 1917f–1919f
thyroid, 2153f–2157f
to sinonasal cavities, 361–362, 363f–367f, 364
tracheal, 1721f
uveal, 507, 508f
Metopic synostosis, premature, 69, 70f
MFD. *See* Mandibulofacial dysostosis (MFD).
MFHs. *See* Malignant fibrous histiocytomas (MFHs).
Michel's deformity, 1129
Micrognathia, 1549–1550, 1550f
Microphthalmia, 461, 462f, 463f, 463t, 558f
on computed tomography, 461, 463f
on magnetic resonance imaging, 461, 462f
Microplates, for facial fractures, 375–376, 376f
Microsomia
craniofacial. *See* Branchial arch syndrome, of first and second arches.
hemifacial, 562
Microtia, in hemifacial microsomia, 60, 60f
Microvillar cells, olfactory, 94
Midazolam (Versed), for magnetic resonance imaging imaging of eye, 451

Middle ear
anatomy of, 1066–1070
of auditory ossicles, 1069
of carotid (anterior) wall, 1067–1068
of epitympanic recess, 1068–1069
of eustachian tube, 1068
of floor (jugular wall), 1067
of lateral (membranous) wall, 1068
of ligaments, 1069
of mastoid (posterior) wall, 1067, 1067f
of medial (labyrinthine) wall, 1068
of muscles, 1069
of nerves and vessels, 1070
of roof (tegmental wall), 1066–1067
congenital anomalies of, 1116–1118, 1117f–1122f
embryology and developmental anatomy of, 1061
eosinophilic granulomas of, 1346f
in hemifacial microsomia, 60–61
pneumatization of, reduction in congenital aural dysplasias, 1114
squamous cell carcinoma of, 1324f
tumors of, 1342–1343
benign, 1342–1343, 1346f
malignant, 1343
Middle ear effusions, in chronic otitis media, 1184, 1185f
Middle layer of deep cervical fascia (MLDCF), 1811–1812, 1813f, 1814, 1814f
in infrahyoid neck, 1811–1812
in suprahyoid neck, 1812, 1813f, 1814, 1814f
Midfacial hypoplasia, with common cleft lip/palate, 23
Midline dermoids, of skull, 31
Midline low-density plane, 1378, 1381f, 1382f
Mikulicz's syndrome, 2043
Miniplates, for facial fractures, 376, 376f
Minor salivary gland tumors (MSGTs), 1494, 1496f–1498f, 1497
imaging features of, 1497, 1499f
Mixed cell tumors, benign. *See also* Pleomorphic adenomas.
tracheal, 1723
MLDCF. *See* Middle layer of deep cervical fascia (MLDCF).
MLELs. *See* Malignant lymphoepithelial lesions (MLELs).
MMs. *See* Multiple myelomas (MMs).
Modified barium swallow. *See* Videofluoroscopic swallowing study (VFSS).
Modiolus
deficient, 1138f, 1155f, 1168f
on magnetic resonance imaging, 1099f
Moebius syndrome, 1111t, 1147f
Mohr syndrome, 16, 16f
Molars, 139f
Molecular signaling
in face, 9
craniofacial malformations and, 4–5
palatal development and, 9
Molecular theory of olfaction, 94
Mondini's dysplasia, 1130, 1134f–1136f
Moniliasis, esophagitis and pharyngitis due to, in AIDS, 1671f
Monoiodotyrosine (MIT), 2136
Monomorphic adenomas, 1385
Morning glory anomaly, 464, 464f
Mounier-Kuhn syndrome, 1713–1714, 1715f
Mouth. *See* Oral cavity; *specific oral structures.*
MPNSTs. *See* Malignant peripheral nerve sheath tumors (MPNSTs).
MR-DCG. *See* Magnetic resonance dacryocystography (MR-DCG).
MRI. *See* Magnetic resonance imaging (MRI); *specific regions and conditions.*
MRS. *See* Magnetic resonance spectroscopy (MRS); Proton magnetic resonance spectroscopy (^{1}H-MRS); *specific regions and conditions.*
MSGTs. *See* Minor salivary gland tumors (MSGTs).
MSX1 gene, cleft lip/palate and, 19
MSX1 gene product, cleft lip/palate and, 19
MSX2 transcription factor, craniofacial dysostoses and, 73f, 74
Mucoceles, 204–205, 221–222, 224, 228–230, 229f–239f, 809, 1405–1406, 1408, 1408f–1411f, 2063, 2064f, 2065f, 2065–2066
antral, 224, 228, 230f
cholesteatomas versus, 244, 245f
ethmoid, 224, 710f
supraorbital, 578
extravasation, mandibular, 1411f
frontoethmoidal, following functional endoscopic sinus surgery, 188, 189f
infected, 229, 236f
lacrimal sac, 571–572, 572f
laryngeal, 1652, 1662f, 1665f–1668f
congenital, 1552
external, 1652
nasolacrimal, 702, 706f, 714, 715f
of lacrimal sac, 688f
of petrous apex, 1349, 1350f
of salivary glands, 2060f, 2061f
of skull base, 838, 840, 842f, 843f
on computed tomography, 223f, 228–229, 231f–237f, 429f
on magnetic resonance imaging, 229–230, 237f–240f
on plain films, 229f, 230f
on tomography, 230f
on ultrasound, 1948, 1949f
physiological functions of frontal sinuses, on plain films, 111
Mucoceles *(Continued)*
polypoid, 224
retention cysts versus, 203, 205
sphenoid, 228
Mucociliary clearance, 153
Mucoepidermoid carcinomas (MECs)
of jaw, 972, 973f
of oral cavity, 1438, 1442f, 1443f
of salivary glands, 280, 281f, 282f, 2088–2090, 2089f–2093f, 2089t
thyroid, 2136, 2157f
tracheal, 1705f, 1719–1720
Mucoid attenuation cysts, of salivary glands, 2061f
Mucoperiosteal white lines, on plain films, 111
Mucoperiosteum, 96
Mucopyoceles, 229, 230, 236f
air-fluid levels and, 198, 199f
Mucormycosis
orbital cellulitis and, 583, 584f
rhinocerebral, sinusitis and, 202
Mucosa
after functional endoscopic sinus surgery, 186
in bacterial sinusitis, acute, 194, 194f
injury to, air-fluid levels due to, 197, 197f, 198f
normal, imaging of, 205–206
of nasal fossae, 93
of nasal septum, 96
of paranasal sinuses, 93, 96
olfactory, 93–94
polypoid, hypertrophic, 200
Mucositis, radiation-induced, 1515f
Mucpolysaccharidoses, skull base and, 858
Mucus cysts, of tongue, 1397–1398, 1400f
Muenke syndrome, 79
Müller's muscle, 539
Multifidus muscle, 1801f
Multilocular cystic disease of jaw, familial, 333
Multiple myelomas (MMs)
of jaw, 976–977, 977f
orbital, 612, 615f
sinonasal, 303–304
Multiple sclerosis, 768–770
brain lesions in, 1302, 1307f
clinical findings in, 768–769
on computed tomography, 769, 770f
on magnetic resonance imaging, 769–770, 770f, 771f
optic nerve enlargement in, 742f
pathologic findings in, 769
Multiple tori, 14
Mumps
iodine, 2039
labyrinthitis due to, 1207
parotitis due to, 2028–2029
Muscle(s). *See also specific muscles.*
facial, 126
lesions of, 2190–2199

Muscle(s) *(Continued)*
denervation atrophy, 2190–2191, 2192f
fibromatosis colli, 2191, 2193f
hypertrophic, 2191, 2193f
metastatic, 2199, 2202f
muscular dystrophies, 2195, 2199f, 2200f
muscular torticollis, 2191–2194
myositis, 2194f, 2194–2195
myositis ossificans, 2195, 2196f–2198f
myotonic dystrophy, 2195, 2197, 2201f
of levator claviculae muscle, 2190, 2191f
rhabdomyosarcoma, 2197–2199, 2201f
metastatic disease of, 2202f
nasal, 89, 90f, 90t–91t
of cheek, 127, 128f
of forehead, 126
of lips, 127, 128f
of mastication
atrophy of, 1038, 1046
in hemifacial microsomia, 59
of scalp, 126
sarcomas of, sinonasal, 315–317
Muscle atrophy, denervation, 2190–2191, 2192f
of brachial plexus, 2232f
of masticator muscles, 1991, 1992f
of oral cavity, 1448, 1450f, 1451, 1451t
Muscleongus colli, tendinitis of, 1505, 1507, 1507f–1508f
Muscular dystrophies, 2195, 2199f, 2200f
Muscular torticollis, 2191–2194
Muscular triangles, of neck, 1780, 1780f
masses in, differential diagnosis of, 1794–1795, 1795t
Musculus uvulae, 1792t
Mutagenesis, insertional, oncogene activation by, 2276–2277
Mycetomas, 218
sinusitis and, 202
Mycobacterial infections. *See also specific infections.*
atypical, lymphadenitis in, 1893–1894
lymphadenitis in, 1893, 1893f
nontuberculous, adenopathy and, 1567, 1567f
of salivary glands, 2028f, 2031–2032
Mycobacterium leprae infections, 241–242, 242f
lymphadenitis in, 1894
Mycobacterium tuberculosis infections, lymphadenitis in, 1893
Mycotic infections. *See also specific infections.*
of temporal bone, 1199
Myeloma, multiple, orbital, 612, 615f
Myelomas, 1429f
multiple
of jaw, 976–977, 977f
orbital, 612, 615f
sinonasal, 303–304
solitary, of petrous apex, 1351f
Mylohyoid line, 899, 900f
Mylohyoid muscle, 896, 899f, 1379t, 1383, 1791t, 1799f, 1800f
Mylohyoid nerve, 896, 896f
Myoblast(s), 1758
Myoblastomas, granular cell, of oral cavity, 1416–1417
Myocytes, 1758
Myoepithelial carcinomas, of salivary glands, 2086–2087
Myoepithelial sialoadenitis (MESA), 2100
Myoepitheliomas, of salivary glands, 2086–2087
Myofibroblastic tumors, inflammatory, 250
sinonasal, 320–321
Myositis, 2194f, 2194–2195
cystic, orbital, 574–575
of extraocular muscles, 648, 651
orbital, orbital pseudotumors and, 586–587, 587f–590f
proliferative, 2194f, 2194–2195
Myositis ossificans, 2195, 2196f–2198f
Myospherulosis, sinusitis and, 203
Myotome, 1758
Myotonic dystrophy, 2195, 2197, 2201f
Myotubes, 1758
Myringostapediopexy, 1184f
Myringotomy tubes, 1185f
Myxedema, 2138
Myxomas
odontogenic, 953–954, 957f, 958f
sinonasal, 321
on computed tomography, 321f, 323f
on magnetic resonance imaging, 323f

N

NA. *See* Nasopharyngeal atresia (NA).
Nager acrofacial dysostosis syndrome (AFD Nager), 65
Nares, 89, 138f
Nasal alae, 89, 1796f
on plain films, 118, 118f
Nasal atrium, on computed tomography and magnetic resonance imaging, 125
Nasal bone, 88, 124, 135f, 139f, 145f
anatomic relationships at birth, 30f
development of, 10
on plain films, 122
Nasal bone axial view, for paranasal sinus plain films, 106, 108f
Nasal bone lateral view, for paranasal sinus plain films, 105, 107f
Nasal capsule, anatomic relationships at birth, 30f
Nasal cartilaginous pyramid, 88, 88f
Nasal cavities. *See* Nasal fossae.
Nasal choanae, 10
Nasal conchae. *See* Nasal turbinates.
Nasal cycle, 93
magnetic resonance imaging and, 152, 152f
normal, on magnetic resonance imaging, 214f
Nasal dermal sinuses, 31, 31f, 32, 33f, 33t, 34f
depth of extension of, 34, 39f
infected, 34f
resection of, 34–35
Nasal dermoid cysts, 32–37, 35f, 36f
depth of extension of, 34, 39f
foraminal enlargement and cristal distortion with, 36–37
intracranial extension of, 34, 36, 37f, 38f
Nasal dorsum, 88, 88f
Nasal epidermoid cysts, 31, 31f, 33, 34, 36f
Nasal fins, 8
Nasal fossae, 89–90, 92f, 136f
air space of, 140f
anatomy of, 88–90, 89f, 90t–91t, 92f, 1528–1529, 1529f
base of, 138f
embryologic development of, 9–10
embryology of, 1522–1523
lymph node drainage of, 1881t
mucosa of, 93
sarcomas of, 857f
stenosis in, 1542
vascular supply of, 95f, 95–96, 96t
Nasal fractures, 378f–381f, 378–381
lateral blows causing, 378–379, 379f–380f
on plain films, 122
septal abscesses with, 380
Nasal gliomas, 31, 31f, 32f, 37, 39–42, 40f–43f, 299, 300f, 301
extranasal, 39–40, 41
histology of, 41–42
intranasal, 40f, 40–41
mixed, 41, 41f
on computed tomography, 300f
Nasal muscles, 89, 90f, 90t–91t
Nasal nerve, posterior, superior, 898f, 903
Nasal obstruction
congenital, 1538–1543
neonatal, by dacryocystoceles, 52
paradoxical, 93
Nasal pits, 7f, 8
Nasal placodes, 7f, 8
Nasal polyps
antrochoanal, 204
chronic sinusitis and, 200
allergic, 201
in cystic fibrosis, 201
on computed tomography, 291f
sinusitis and, 203–204
Nasal resistance, 92–93

Nasal septum, 30, 89, 89f, 90, 134f, 139f, 145f, 1796f, 1797f. *See also* Septal cartilage.
abscesses of, 244f, 380
after septoplasty, 184f, 186
air cells in, posterior, 165, 167f
base of, 138f
bony, on plain films, 120
deviation of, 159, 163f
hematomas of
infected, 380
pediatric, 1571f
mucosa of, 96
on computed tomography and magnetic resonance imaging, 125
Nasal sidewalls, 88, 88f
Nasal sinus polyps, antrochoanal, 215–216, 218f–219f
Nasal spine, anterior, 138f, 1796f
on plain films, 120
Nasal surgery, 403, 404f, 405f
Nasal tip, 88, 88f
Nasal turbinates, 90–91, 92f, 98
black necrosis of, 583
concha bullosa of, 136f, 140f
inferior, 102, 135f, 137f, 140f, 141f, 144f, 145f, 1797f
on computed tomography, 154f
middle, 135f, 136f, 140f, 141f, 144f, 145f
after functional endoscopic sinus surgery, 186–187
anatomy of, 155, 157f, 158f
basal lamella of, 97, 145f
displacement of, 158, 163f
on computed tomography, 154f
pneumatization of. *See* Concha bullosa.
variations of, 156–158, 162f, 163f
on plain films, 114
overhangs of, 98
superior, 100, 141f
on computed tomography, 154f
Nasal valve, 88
Nasal valve angle, 88–89
Nasal veins, 99
Nasal vestibule, 1796f
Nasalis muscle, 128f
Nasion, 88, 88f
Nasoalveolar cysts, 353–354, 358f
Nasocardiac reflex, 94–95
Nasociliary nerve, 96
Nasoethmoid surgery, extensive, 423, 425, 428f, 429f
Nasoethmoidal frontoethmoidal cephaloceles, 47
Nasofrontal duct, 99, 144f
Nasofrontal suture, 139f
Nasogastric tubes
during videofluoroscopic swallowing study, 1736, 1736f
Nasogastric tubes *(Continued)*
placement of, air-fluid levels due to, 196–197
Nasoglabellar dermoids, 32
Nasolabial cysts, 353–354
Nasolacrimal canal, 140f
anatomy of, 699–701
Nasolacrimal drainage system (NLDS), 655–729
air in, 697, 699f
anatomy of, on dacryocystography, 672–674, 673f, 674t
calculi in, 679–682, 684, 684f–690f, 687–688
canaliculitis of, chronic, 688, 690
clinical tests for, 664, 669–671
dye tests, 669–670
irrigation, 669
probing, 663
Schirmer's test, 670
Valsalva DCR bubble test, 670–671
computed tomography of, 697–710
anatomy on, 697, 698f, 699f, 699–701, 700t, 702t, 703t
dacryocystography with, 710–711, 713–716
in pediatric patients, 714–716, 715f
pathology on, 701–702, 704f–710f, 704–710, 711t
dacryocystography and. *See* Dacryocystography (DCG).
dacryoscintigraphy and, 692–696, 693f, 694f
in complete obstruction, 696
in incomplete obstruction, 696
normal examination with, 693–696, 695f
sensitivity of, 696
technique for, 692–693
diverticula of, 677–679
endoscopy of, 727–728, 728f
filling defects of, 664f–668f
fistulae of, 677, 683f
lacrimal sac cysts of, 679
obstruction of, 667f, 669f, 675–677, 677f–682f
acquired, primary, 681, 700
obstruction-stenosis of, 709f
posttreatment considerations and, 690–692
postchemotherapy, 691–692
postirradiation, 691
postsurgical, 690–691, 691f–692f
stenosis-obstruction of, 660f–663f
traumatic injury of, 712f
Nasolacrimal duct(s), 98, 135f, 136f, 144f
air in, on computed tomography, 697, 699f
embryology of, 533
normal dimensions of, 674, 674t
Nasolacrimal duct(s) *(Continued)*
obstruction of
functional, 696
primary acquired, 681, 700
secondary, 700, 700t
on computed tomography and magnetic resonance imaging, 126
opening of, 92f
into middle meatus, 137f
Nasolacrimal duct cysts, pediatric, 1539f, 1540, 1540f, 1541f
Nasolacrimal duct sacs, distended, 52–53, 53f, 54f
Nasolacrimal grooves, 8
Nasolacrimal sac, lymphoma of, 662f
Nasolateral process, 7f, 8
Nasomaxillary dysplasia, 1542f
Nasomaxillary sutures, on plain films, 122
Nasomedial process, 7f, 8
Nasooptic furrow, 7f
Nasoorbital fractures, 381, 382f, 383f
Nasoorbital frontoethmoidal cephaloceles, 47, 50f–52f
Nasopalatine artery, 95f
Nasopalatine cysts, 353, 357f, 358f
Nasopalatine duct cysts, 941–942, 945f
of oral cavity, 1422–1423, 1426f
Nasopalatine nerve, 96
on computed tomography and magnetic resonance imaging, 125
Nasopharygneal carcinoma, on positron-emission tomography, 2296f
Nasopharyngeal angiofibroma, juvenile, 1579–1580, 1580f
Nasopharyngeal atresia (NA), 1542–1543, 1543f
Nasopharyngeal carcinomas, 1185f, 1478t, 1478–1482
imaging features of, 1479, 1479f–1485f, 1479t, 1482
jugular foramen extension of, 1322, 1326f
metastatic to skull base, direct encroachment and, 844, 846–847, 847f
nodal staging of, 1882, 1882t
of petrous apex, 1351
pediatric, 1587
with perineural tumor spread, 873f, 877f
Nasopharyngeal regurgitation, 1741, 1742f
Nasopharyngeal stenosis, pediatric, 1577–1578
Nasopharynx, 145f, 1796f, 1797f
anatomy of, 1466–1468, 1467f–1470f, 1470
brain heterotopias of, 42
pediatric, anatomy of, 1529, 1529f–1531f
soft tissues of, on plain films, 121
Nasopulmonary reflex, 94–95
NBS. *See* Nijmegen paragraph signbreakage syndrome (NBS).

Neck
carotid sheath of, 1814, 1815f
choristomas of, 1859
cleft, with cleft lower lip and mandible, 30
congenital lesions of, 1828–1860
branchial, 1828–1838
of first branchial cleft, 1829–1830, 1830f, 1831f
of fourth branchial cleft, 1831, 1836–1838, 1839f
of second branchial cleft, 1831–1832, 1832f–1836f
of third branchial cleft, 1831, 1832–1833, 1836, 1836f, 1837f
ectopic thyroid. *See* Thyroid gland, ectopic.
lymphatic, 1847–1852
capillary lymphangioma, 1851, 1855f
cavernous lymphangioma, 1850, 1855f
classification of, 1848–1849
cystic hygroma, 1849–1850, 1850f–1854f
pathogenesis of, 1848
vasculolymphatic, 1852
rare, 1859–1860
teratomas, 1858–1859
thyroglossal duct. *See* Thyroglossal duct cysts (TGDCs).
thyroid, 1838–1840
vascular, 1852–1858
arterial, 1856, 1858, 1858f
capillary malformations, 1854, 1856
hemangiomas, 1852–1854, 1856f
vascular malformations, 1854
venous, 1856, 1857f
differential diagnosis of lesions of, 1790, 1794t, 1794–1795, 1795t
enterocystomas of, 1859
fascia of, 1805–1814
cervical, deep, 1806–1814
deep layer of, 1809–1811, 1810f, 1811f
middle layer of, 1811–1812, 1813f, 1814, 1814f
superficial layer of, 1806–1809, 1808f, 1809f
Sibson's, 1811
superficial, 1806, 1807f
fascial spaces of, 1805–1806, 1815–1824, 1825t–1826t
danger, 1816, 1825t, 1826t
masticator, 1819–1820, 1822f, 1826t
abscess in, 1822f
rhabdomyosarcoma of, 1809f
of carotid sheath, 1816, 1825t, 1826t
of mandibular body, 1816, 1825t, 1826t
Neck *(Continued)*
of parotid gland, 1818, 1825t, 1826t
of visceral compartment, 1815
parapharyngeal, 1820, 1822–1824, 1823f, 1826t
''paravertebral,'' 1824, 1826t
peritonsillar, 1824, 1826t
''posterior triangle,'' 1824, 1824f, 1825f, 1826t
pretracheal, 1811, 1815, 1825t, 1826t
prevertebral, 1816, 1825t, 1826t
schwannoma in, 1811f
retropharyngeal, 1817f, 1825t, 1826t
abscess in, 1817f, 1820f
air in, 1820f
retrovisceral, 1815–1816, 1817f–1820f, 1825t, 1826t
sublingual, 1825t, 1826t
submandibular, 1816, 1818–1819, 1821f, 1825t, 1826t
abscess in, 1821f
submaxillary, 1825t
muscles of, 1791t–1793t
normal anatomy of, postnatal, 1775, 1777f–1784f, 1777–1778, 1780–1782
posttreatment, 2239–2270. *See also* Neck dissection.
baseline surveillance imaging and, 2250–2251, 2260f–2267f
biopsy of suspected recurrence seen on imaging and, 2256
chylous fistula and, 2262, 2269f
dermal metastasis and, 2262, 2270, 2270f
imaging suspicion of recurrence and, 2254–2256
neuroma development and, 2262, 2270f
osseous complications and, imaging detection of, 2257, 2262, 2269f
routine postoperative and postradiation imaging changes and, 2249–2250
surveillance protocol and, 2252, 2254
vascular complications and, imaging detection of, 2256–2257, 2268f
radiation therapy of, 2245, 2247, 2249
retropharyngeal nodal disease of, 2245, 2245f
schwannoma of, 1815f
soft-tissue infection of, laryngeal extension of, 1656, 1672f
surgical treatment of. *See also* Neck dissection.
with and without reconstruction, 2245, 2246f–2259f
triangles of, 1775, 1777f–1784f, 1777–1778, 1780–1782, 1824, 1824f, 1825f, 1826t
differential diagnosis based on, 1794t, 1794–1795, 1795t
ultrasound of, 1935–1951
Neck *(Continued)*
examination technique for, 1935–1936, 1936f
fine-needle aspiration cytology guided by, 1936, 1936f
in infants and young children, 1950f, 1950–1951, 1951f
in pathological conditions, 1939–1950
cystic lesions, 1948f, 1948–1949, 1949f
infectious disease, 1949
lipomas, 1949–1950
malignant lymphomas, 1945
metastatic lymphadenopathy, 1945–1947, 1946f, 1946t, 1947f, 1947t
neurogenic tumors, 1950, 1950f
nonneoplastic lymphadenopathy, 1944f, 1944–1945, 1945f
of parathyroid, 1942
of salivary glands, 1943–1944
of thyroid, 1939–1942
of normal neck, 1936–1939
cervical lymph nodes and, 1938–1939, 1939f
parathyroid gland and, 1938
salivary glands and, 1938, 1938f
thyroid gland and, 1937, 1937f
Neck dissection
imaging changes following, 2251f–2254f
modified
postsurgical imaging and, 2260f, 2268f
with preservation of one or more structures, 2242, 2242f
postsurgical imaging and, 2261f, 2262f, 2263f, 2265f
radical, 2241–2242, 2242f, 2246f–2249f
postsurgical appearance and, 1685
postsurgical imaging and, 2264f, 2266f
selective, 2243–2245
anterior compartment type, 2244, 2244f
extended radical, 2244–2245
lateral type, 2243f, 2243–2244
posterolateral type, 2244, 2244f
supraomohyoid type, 2243, 2243f
types of, 2240–2241, 2241f
Necrobiotic xanthogranuloma, orbital, 610
Necrosis
of lymph nodes, 1912f–1919f, 1912–1913, 1915
radiation, 2269f
of masticator space, 1995f
Necrotizing cellulitis, streptococcal, 1567f

Necrotizing fasciitis
of skin and soft tissue, 2190
with sinusitis, 196
Necrotizing otitis, 807, 809
Necrotizing sialometaplasia, 2052
Nelson's syndrome, 301
Neoplasia. *See also specific neoplasias and sites.*
characteristics common to, 2275f, 2275–2276
gene alterations defining, 2274–2275
in AIDS, 2289–2290
Neoplastic syndromes, inherited, with know associated genes, 2277t
Neovascular membranes, subretinal, 499
Nerve sheath tumors. *See* Schwannomas.
Neural crest cells, 5
cranial, differentiation of, 74
migration of, 7
branchial arch syndromes and, 58
Neural fold, 443f
Neural foramina, asymmetric enhancement of, 883, 884f
Neural groove, 443f
Neural tube, 443f
Neurilemomas. *See* Schwannomas.
Neurinomas. *See* Schwannomas.
Neuroblastomas
olfactory
on computed tomography, 285, 286f
on magnetic resonance imaging, 285, 286f–288f
pediatric, 1587
Neuroectodermal tumors, melanotic of infancy, 290
oropharyngeal, 42
Neuroendocrine carcinomas
primary. *See* Merkel cell tumors.
sinonasal, 285, 287–289
Neurofibromas
airway obstruction due to, in children, 1582, 1583f
cutaneous, 2208
of brachial plexus, 2228f
of cranial nerves, 832, 836f–839f
of oral cavity, 1416
of parapharyngeal space, 1967f
of salivary glands, 2115, 2120f
of skin, 2180, 2181f
orbital, 624–625, 627f–629f, 628
on computed tomography, 625, 625f, 627f
on magnetic resonance imaging, 625, 625f, 628f
pharyngeal, 1501, 1501f
plexiform, 624–625, 832, 837f–839f, 2180, 2181f
orbital, 839f
sinonasal, 294, 296f
on computed tomography, 294
Neurofibromas *(Continued)*
on magnetic resonance imaging, 294, 296f
Neurofibromatosis
fibrous dysplasia versus, 1255
orbit in, 564, 564f
sphenoid bone in, 806f, 807f
type 1, optic nerve gliomas in, 743f–744f
Neurogenic tumors. *See also specific tumors.*
of jaw, 970–971
of neck, on ultrasound, 1950, 1950f
of parapharyngeal space, 1965–1966, 1967f–1969f
of salivary glands, 2115–2116, 2120f
of skull base, 831f–839f, 831–832
on computed tomography, 835f
on magnetic resonance imaging, 831f, 833f, 834f, 836f–839f
Neuroglial hamartomas, 1582, 1582f
Neuroglial heterotopia, 1543
Neuromas
acoustic. *See* Acoustic schwannomas.
brachial plexopathy and, 2224f
postoperative, 2270f
traumatic, sinonasal, 294
Neurosarcoidosis, 600
Neurovascular bundle, of tooth, 894
Nevoid basal cell carcinoma syndrome, 350, 352, 938, 944f
Nevus, uveal, 508
Nevus flammeus, of neck, 1854, 1856
''New World'' sore, 242
NF-1 gene, 2286
NHL. *See* Non-Hodgkin lymphoma (NHL).
Nijmegen paragraph signbreakage syndrome (NBS), with sinusitis, 255
NLDS. *See* Nasolacrimal drainage system (NLDS).
Nodular fasciitis
in parapharyngeal space, 1976
of salivary glands, 2117
of skin and soft tissue, 2188, 2190f
orbital, 632, 635f
Nodular torus, 15
Nodules, thyroid, 1940–1941, 1941f, 2149–2150, 2150f
Non-Hodgkin lymphoma (NHL)
pediatric, 1583–1584, 1584f, 1585f
pharyngeal, 1493–1494
Norrie's disease, 489
diagnostic imaging in, 489, 490f
North American blastomycosis, paranasal, 239, 241
Nose, 139f. *See also* Nasal *entries.*
anatomy of, 88f–90f, 88–91, 90t–91t, 92f
cleft, 23
Nose *(Continued)*
congenital absence of, 1542
lateral wall of, 90–91, 92f
physiology of, 91–95, 95t
vasculature of, 95f, 95–96, 96t
resistance, humidification, and temperature regulation by, 93
Nostrils, 89, 138f
Notochord, 443f, 786, 787f
Nuclear scintigraphy. *See specific regions and conditions.*

O

OAV. *See* Oculoauriculovertebral (OAV) complex.
Oblique view, for paranasal sinus plain films, 104–105, 107f
Obliquus capitis inferior muscle, 1798f, 1799f
Obstructive sleep apnea, clinical evaluation of, 1525–1526
Occipital artery, 127, 130f, 1798f, 1799f
Occipital bone, anatomy of, 792, 801f
Occipital condyle, CT surface reconstruction of, 1097f
Occipital infarct, 740f
Occipital lobe, metastatic disease of, 740f
Occipital lymph nodes, drainage of, 1881t
Occipital nerve
greater, 129f
lesser, 127, 129f, 1788
Occipital protuberance, internal, 1796f
Occipital triangles, of neck, 1781–1782, 1783f
Occipital vein, 127
Occipital vessels, 1797f
Occipitofrontal muscle, 126
Occipitomastoid sutures, pseudofracture of, 1236f
Occiput, perisutural sclerosis of, lambdoidal, on plain films, 111, 111f
Occlusal radiographs, 915–916
Ocular adenocarcinomas, 513
Ocular adenomas, 513
Ocular hypotony, 471
Ocular leukemia, 512
Ocular motility disorders, 647–651
congenital anomalies causing, 651
in Brown's superior oblique tendon sheath syndrome, 648, 649f, 650f
in double elevator palsy, 648, 650f
in myositis, 648, 651
noncomitant strabismus without associated malformations, 651
traumatic injuries causing, 651
Oculoauriculovertebral (OAV) complex, 58f, 58–63
central nervous system in, 63
mouth in, 59

Oculoauriculovertebral dysplasia, 58f, 58–63, 564, 1111t
ears in, 60, 60f, 61
eyes in, 61, 63f
mouth in, 59
plagiocephaly in, 63
Oculoauroculovertebral dysplasia. *See* Branchial arch syndrome, of first and second arches.
Oculodentodigital syndrome, of temporal bone, 1267
Oculo-dento-osseous dysplasia, of temporal bone, 1267
Oculomotor nerve, 542
branchial arches and, 1759
Oculomotor nerve palsy, 593f
Odontoblasts, 891
Odontogenesis, 890–892, 892f–894f, 894t
Odontogenic carcinomas, 971
Odontogenic cysts, 345–347, 350, 352–354, 931, 933–941
buccal bifurcation, 941
calcifying, 352, 938, 944f
developmental, 353–354, 357f, 358f
epithelium in, carcinomatous transformation of, 971
fissural, 352–353, 357f
follicular (dentigerous), 345–347, 352f–355f, 934, 934f–936f
on computed tomography, 352f, 354f, 355f
on magnetic resonance imaging, 346–347, 353f, 354f
globulomaxillary, 353, 357f
in maxillary sinus, 230, 240f
keratocysts, 347, 350, 352, 936–938, 937f–943f
nasolabial (nasoalveolar), 353–354
nasopalatine, 353, 357f, 358f
paradental, 940, 941
periapical (radicular), 933f, 933–934, 934f
periodontal, 347, 355f, 356f
lateral, 940
residual, 931
Odontogenic ghost cell tumor, 350, 352, 938, 944f, 971–972
Odontogenic keratocysts (OKCs), 347, 350, 352, 936–938, 937f–943f
of oral cavity, 1422, 1425f
Odontogenic tumors, 354–360. *See also specific tumors.*
adenomatoid, 952–953, 957f
ameloblastoma, 354–356, 358f, 359f
in magnetic resonance imaging, 354–355, 359f
on computed tomography, 354, 358f
cementoblastoma, 357, 359f
epithelial, calcifying, 359–360, 362f, 949, 954f
myxomas, 953–954, 957f, 958f
Odontogenic tumors *(Continued)*
odontoma, 358–359, 360f, 361f
of oral cavity, benign, 1422, 1425f
Odontomas, 358–359, 360f, 361f, 949–954
adenomatoid odontogenic tumors, 952–953, 957f
ameloblastic fibroodontomas, 951–952, 957f
complex, 950, 955f
compound, 950–951, 956f
odontogenic myxomas, 953–954, 957f, 958f
of oral cavity, 1387, 1388f
OFC (orofacial clefing). *See* Cleft lip; Cleft lip/palate; Cleft nose; Cleft palate; Facial clefts.
OFC1-3 genes, cleft lip/palate and, 19
OFs (ossifying fibormas). *See* Cemento-ossifying fibromas.
Ohngren's line, 270, 270f, 271
OKCs. *See* Odontogenic keratocysts (OKCs).
''Old World'' sore, 242
Olfaction
abnormalities of, 94, 95t
as nasal function, 93–94, 95t
theories of, 94
Olfactory bulb, 94
Olfactory carcinomas, sinonasal, 288, 288f
Olfactory epithelium, 93
Olfactory groove, 133f, 140f
Olfactory mucosa, 93–94
cell types in, 93–94
Olfactory neuroblastomas (ONBs), 285, 286f–288f
Olfactory receptor cells, 94
Olfactory recess, 92f, 134f, 140f
on computed tomography and magnetic resonance imaging, 125
Oligodendromas, of soft palate and nasopharynx, 42
Omohyoid muscle, 1792t, 1802f
OMU. *See* Osteomeatal unit (OMU).
ONBs. *See* Olfactory neuroblastomas (ONBs).
Oncocytic tumors, of salivary glands, 2082–2084
Oncogenes, 2276–2281
activation in cells, 2276–2278
by chromosome translocation to generate aberrant fusion proteins, 2277–2278
by insertional mutagenesis, 2276–2277
by mutational alteration of gene transcription, 2277
by mutational alteration of protein coding sequence, 2277
by selective gene amplification, 2278
c-myc, 2280
detection in human tumors, 2276
Oncogenes *(Continued)*
growth factors and growth factor receptors as, 2278–2279
autocrine and paracrine loops and, 2278–2279
in intracellular signal transduction pathways, 2279f, 2279–2280
Ras gene activation and, 2280
transformation of, 2288
translocations creating oncogenic fusion proteins and, 2281
viral, 2276, 2277t
Onodi cells, 97, 163
pneumatization of, with functional endoscopic sinus surgery, 176
Ophthalmic artery, 543
aneurysm of, 760f–762f
posterior ethmoidal branch of, 101
Ophthalmic nerve, 129f, 1782
Ophthalmic vein, 127, 543
superior, 100
thrombosis of, 582f
Ophthalmopathy, thyroid, 421f
clinical manifestations of, 2137f, 2137–2138
Ophthalmoplegia, external, painful, orbital pseudotumors and, 587–588, 591
Optic canal, 133f, 142f, 144f
on computed tomography and magnetic resonance imaging, 125
with skull base trauma, 850, 852, 854f
Optic cup, embryology of, 443f, 444f, 446, 447
Optic disc, embryology of, 447
Optic fissure, embryology of, 443f, 445f
Optic gliomas, 742–744
clinical features of, 742–743
on computed tomography, 744, 744f
on magnetic resonance imaging, 743f, 744, 745f, 746f
pathologic findings with, 743f, 743–744
Optic groove, embryology of, 443f
Optic nerve, 101
anatomy of, 549, 737
calcification of, 479t
embryology of, 101, 445f, 446
injury of, with functional endoscopic sinus surgery, 183
enlargement of, in multiple sclerosis, 742f
head of
drusen of, 498, 498f
inflammation of, 497–498
sarcoidosis of, 595, 596f, 597, 598f, 600–601
Optic nerve sheath
ectasia of, 571f
enlargement of, 628, 629f
Optic nerve sheath meningoceles (cysts), 569, 571f, 1282f, 1290, 1295f, 1296f

Optic neuritis, 628–630, 630f, 631f
autoimmune, 629
on computed tomography, 630, 630f
on magnetic resonance imaging, 630, 630f, 631f
postradiation, 630f
with sphenoid sinusitis, 196, 196f
Optic stalk, 444f, 445f
Optic tract, 737
Optic vesicle, 7f
Oral cavity, 1377–1459, 1379t–1380t
abscesses of, 1400, 1401f–1403f, 1402
adenocarcinoma of, 1440, 1444f
adenoid cystic carcinoma of, 1433, 1438, 1440f–1442f
chondrosarcoma of, 1440, 1445f
congenital anomalies of, 1386–1387
denervation muscle atrophy and, 1448, 1450f, 1451, 1451t
dermoid cysts of, 1389–1392, 1394, 1394f–1396f, 1859
desmoid tumors of, 1413f
embryologic development of, 7f
exostoses of, 1417–1418, 1418f, 1419f
facial nerve and, 1451, 1455f
fibromatosis of, aggressive, 1410–1412, 1413f, 1414f, 1415
fibroosseous lesions of, 1418–1422
hemangiomas of, 1387, 1388f
HIV involvement of, 1405
hypoglossal nerve and, 1451, 1455f–1457f, 1456
in hemifacial microsomia, 59, 62f
infections and inflammatory lesions of, 1398, 1400–1408
lingual artery aneurysms and, 1396, 1400f
lingual thyroid and, 1395, 1399f
lipomas of, 1415–1416, 1416f
liposarcoma of, 1438, 1444f
Ludwig's angina and, 1403–1405, 1407f
lymph node drainage of, 1881t
lymphoma of, 1433
mandibular division of trigeminal nerve and, 1451, 1451f–1454f
masseteric hypertrophy and, benign, 1458, 1458f
metastatic disease of, 1440, 1446f, 1448f
mucoepidermoid carcinoma of, 1438, 1442f, 1443f
muscles of, 1791t–1793t
nerve sheath tumors of, 1416–1417
normal anatomy of, 1378, 1380–1386
of buccomasseteric region, 1384–1386, 1385f, 1386f
of floor of mouth, 1380, 1383–1384
of gingivobuccal region, 1384
Oral cavity *(Continued)*
of lips, 1384
of submandibular space, 1384
of tongue, 1378, 1380, 1381f, 1382f
extrinsic muscles and, 1378, 1380
intrinsic muscles and, 1378, 1382f
motor autonomic nervous system sensory innervation and, 1380
odontogenic lesions of, benign, 1422, 1425f
oncocytic tumors of, 2084
osteosarcoma of, 1440, 1445f
pleomorphic adenomas of, 1408, 1410, 1412f
ranulas of, 1405–1406, 1408, 1408f–1411f
rhabdomyomas of, 1415, 1415f
rhabdomyosarcoma of, 1438, 1440
schwannomas of, 1440, 1448f
sialoliths and, 1402–1403, 1404f–1406f
squamous cell carcinoma of, 1427t, 1427–1433, 1428f–1439f
with perineural tumor spread, 883f
stylohyoid ligament ossification and, 1440, 1449f
thyroglossal duct cysts, 1394–1395, 1397f, 1398f
tumors of
benign, 1408, 1410–1424
malignant, 1425, 1427t, 1427–1440
vascular malformations of, 1388–1398
arterial, 1388–1389, 1391f, 1392f
capillary, 1388
lymphatic, 1389, 1392f, 1393f
venous, 1388, 1389f, 1390f
Oral preparatory stage of swallowing, 1732
Oral transport stage of swallowing, 1732, 1733f
Orbicularis oculi muscle, 91t, 126, 128f, 1796f
anatomy of, 538–539
Orbicularis oris muscle, 91t, 127, 128f, 1797f, 1798f
Orbit(s), 126, 133f, 529–651
abscesses of, 575, 578f
anatomic abnormalities of, 556–558, 557f, 558f
anatomy of
on computed tomography, 545–546, 546f
on magnetic resonance imaging, 546, 547f–552f
apex of, anatomy of, 535f, 535–537, 536f
autonomic nerves of, 542
bacterial sinusitis spread to, 195, 195f
Orbit(s) *(Continued)*
bony
abnormalities of, 558
anatomy of, 533f, 533–535, 534f
defects of, 561–562
floor of, anatomy of, 533f, 534f, 534–535
in craniofacial dysostosis, 558
in craniofacial microsomia, 562
in mandibulofacial dysostosis, 562, 565f
lateral wall of, anatomy of, 533f, 534f, 535
medial wall of, anatomy of, 533f, 533–534, 534f
roof, anatomy of, 533, 533f, 534f
bony interorbital distance and, 551, 553–554, 555f, 555t, 556f
calcification of
dystrophic, differential diagnosis of, 554
metastatic, differential diagnosis of, 553
compartments of, 546–547
congenital abnormalities of, 556, 568, 569f, 570f
developmental abnormalities of, 556–558, 557f, 558f
diagnostic imaging of, 566, 568t
embryology of, 531–533
extraocular muscles and, 531
eyelids and, 531, 532f
lacrimal gland and, 531, 533
lacrimal sac and, 533
nasolacrimal duct and, 533
encephaloceles of, 839f
exophthalmos and, 556
exorbitism and, 556
extraconal peripheral lesions of, 553
fascia of, anatomy of, 537, 538f
fatty reticulum of, anatomy of, 539
fibrous tissue tumors of, 630–632
floor of, on plain films, 116, 116f
granulomatous disorders of, 601, 602f, 606–609, 610
hypertelorism of, 554, 556
hypotelorism of, 556
in Apert's disease, 559, 563f
in Crouzon's disease, 559, 562f, 564f
in mandibulofacial dysostosis, 562
in neurofibromatosis, 564, 564f
in plagiocephaly, 559, 560f, 561f
in Saethre-Chotzen syndrome, 559, 561
in sinusitis, 169–170
inflammatory diseases of, 577–603, 579f. *See also specific conditions.*
anterior, orbital pseudotumors and, 586, 586f
apical, orbital pseudotumors and, 587, 591f

Orbit(s) *(Continued)*
preseptal inflammatory lesions versus, 706f–708f
injury of, with functional endoscopic sinus surgery, 181–183, 182f, 183f
intraconal lesions of, 552
Langerhans' cell histiocytosis and, 603–606
clinical features of, 604–605
diagnostic imaging in, 605f, 605–606, 606f
histopathologic features of, 605, 605f
historical background of, 604
immunohistochemistry of, 605, 605f
leukemia of, 612, 615f–617f
lymph node drainage of, 1881t
lymphomas of, 600, 610–612, 698f
diagnostic imaging in, 611f–614f, 611–612
lymphoplasmacytic tumor of, 612, 615f
magnetic resonance imaging of, techniques for, 545
margins of, on computed tomography and magnetic resonance imaging, 125–126
motor innervation of, 542
neural anatomy of, 548
neural lesions of, 623–625, 628
neurofibromas of, plexiform, 839f
peripheral nerves of, 541
proptosis and, 556
pseudorheumatoid nodules and, 609–610, 610f
pseudotumors of, 600, 704f, 705
simulating rhabdomyosarcomas, 638, 639f
roof, 133f
on plain films, 120, 121f
sensory innervation of, 541
subperiosteal lesions of, 553
techniques for, computed tomography of, 544–545
telecanthus of, 556
tumors of, secondary, 646–647, 647f
vascular anatomy of, 543, 547–548
vascular conditions of, 612–623
Orbital cellulitis
bacterial
classification of, 579, 579t
postseptal, 580, 581f
preseptal, preseptal edema and, 579–580
on computed tomography, 195f
sinusitis and, 579, 706f
with fungal infections, 582–584, 584f, 585f
Orbital cysts
appendage, 569–570
bone, aneurysmal, 574, 578f
chocolate, 569
colobomatous, 568, 570f
dacryoceles, 568t, 571–572, 572f
dentigerous, 569
developmental, 563–566, 565t, 566f, 566t, 567f
diagnostic imaging of, 567, 568t
enterogenous, 568t, 569
epithelial, 569–570
hematic, 568t, 572, 575f
hydatid, 568t, 575, 577
implantation, epithelial, 568t, 571, 571f
in congenital cystic eye, 568, 570f
in cystic myositis, 574–575
in cysticercosis, 568t, 577, 579f
inflammatory, 575, 578f
lacrimal gland, 571, 571f, 572f
lymphangioma, 569
optic nerve sheath meningocele, 569, 571f, 1282f, 1290, 1295f, 1296f
varix, 569
Orbital dermoids, 32
Orbital fissures
inferior, 135f, 141f, 142f, 143f, 144f
anatomy of, 536, 536f, 537f
on computed tomography and magnetic resonance imaging, 125
superior, 133f, 134f, 142f, 143f, 144f
anatomy of, 535f, 536
CT surface reconstruction of, 1096f
on plain films, 117, 117f
Orbital fractures, blow-out and blow-in, 386, 389, 391f–396f, 391–394
alloplasts for, 397
extraocular muscle injury with, 651
nasolacrimal injury with, 712f
on computed tomography, 392f, 393f, 394, 395f, 396f
on magnetic resonance imaging, 394f
on plain films, 392f, 394f, 395f
Orbital implants, 521, 522f, 523f
Orbital myositis, orbital pseudotumors and, 586–587, 587f–590f
Orbital pseudotumor, 611f
Orbital rim, superomedial, flattening of, 111
Orbital septum, anatomy of, 537–538
Orbital tendon, superior, 539
Orbitopathy, thyroid, 591–595
diagnosis of, 592
diagnostic imaging in, 592–593, 593f, 594f, 595
pathology of, 591–592
Organ of Chievitz, 1775
Organ transplantation
lymphoproliferative disorders following, 1903
posttransplant lymphoproliferative disorder and, 1584, 1585f
Organogenesis, definition of, 1758
Oriental sore, 242
Orofacial clefting (OFC). *See* Cleft lip; Cleft lip/palate; Cleft nose; Cleft palate; Facial clefts.
Orofacial digital syndrome
type I, 16f
type II. *See* Mohr syndrome.
Oronasal membrane, 9–10
Oropharyngeal carcinomas, 1485t, 1485–1489
lymph nodes in, 1912f
Oropharyngeal membrane, 7f
Oropharyngeal motility swallowing study. *See* Videofluoroscopic swallowing study (VFSS).
Oropharyngeal obstruction, congenital, 1544, 1546–1550
Oropharyngeal stenosis, radiation-induced, 1570, 1570f
Oropharyngeal swallowing. *See* Swallowing; Videofluoroscopic swallowing study (VFSS).
Oropharynx
anatomy of, 1470f, 1470–1471, 1471f
on plain films, 121
pediatric, anatomy of, 1529–1530, 1532f, 1533f
teratomas of, 42–43
traumatic injury of, pediatric, 1571, 1571f, 1572f
ORPs. *See* Ossicular reconstruction prostheses (ORPs).
Orthopantomographic radiography, 913–914, 914f, 915f
Osler Weber Rendu syndrome, air-fluid levels and, 198
OSs. *See* Osteogenic sarcomas (OSs).
Ossicular reconstruction, temporal bone following, 1218–1222, 1219f–1223f
Ossicular reconstruction prostheses (ORPs), 1219f–1221f, 1219–1220
Ossiculoplasty, temporal bone following, 1218–1222, 1219f–1223f
Ossification
of laryngeal cartilages, 1598
of skull base, alterations of, 804–805
Ossification centers, embryology of, 786, 787f, 787–788
Ossifying fibromas (OFs). *See* Cemento-ossifying fibromas.
Osteitis
maxillary, 710f
of luetic otosyphilis, 1209, 1209f
postirradiation, in sinusitis, 212, 213f
Osteitis condensans, 901f, 926
Osteitis deformans. *See* Paget's disease.

Osteoarthritis, of temporomandibular joint, 1018, 1023f, 1024f
Osteoblastic skeletogenic differentiation, 74
Osteoblastomas, sinonasal, 329–330, 330f
Osteocartilaginous exostoses, of oral cavity, 1423
Osteochondritis dissecans, of temporomandibular joint, 1019, 1026f, 1027f
Osteochondromas
  of jaw, 959
  of mandibular condyle, 1037f
  of oral cavity, 1423
  of temporomandibular joint, 1034, 1037f
Osteoclastomas
  of jaw, 961–962, 964f, 965f
  of oral cavity, 1421–1422, 1422f–1424f, 1423f, 1424f
  of skull base, 832–833, 839f
  of temporal bone, 1324f, 1339, 1340f
  sinonasal, 333–335, 341f
Osteogenesis imperfecta, 1111t
  of skull base, 857–858
  of temporal bone, Paget's disease versus, 1258
Osteogenic sarcomas (OSs)
  mandibular, 1445f
  maxillary, 1446f
  of jaw, 973–974, 974f, 975f
  sinonasal, 339–341, 345f, 349f
    on computed tomography, 350f–352f
    on magnetic resonance imaging, 351f
Osteoid osteomas
  giant, sinonasal, 329–330, 330f
  sinonasal, 329
Osteolysis, massive, 837–838, 841f
Osteomas, 1214, 1215f
  choroidal, 498–499
    clinical diagnosis of, 498–499
    differential diagnosis of, 499
    imaging diagnosis of, 499, 499f
  exostosis and, 321–322, 326f, 327f
  intracanalicular, 1303, 1310f
  of external auditory canal, 1340, 1345f
  of internal auditory canal, 1310f
  of jaw, 959, 963f
  of oral cavity, 1421, 1421f
  osteoid
    giant, sinonasal, 329–330, 330f
    sinonasal, 329
  sinonasal, 321–323, 324f–329f, 327–328
    on computed tomography, 324f–327f
    on magnetic resonance imaging, 324f
Osteomastoiditis, tuberculous, 1179f
Osteomeatal unit (OMU)
  computed tomography of, 150
  following functional endoscopic sinus surgery, 171f, 172
  normal anatomy of, 153f–156f, 153–154
  on computed tomography, 123
  opacification of, 169
Osteomyelitis
  in necrotizing otitis externa, 1213
  in sinusitis, 212, 212f
  of mandible, 977–980, 1401f
  of oral cavity, 1403f
  of skull base, 1326
  sclerosing, of mandible, 978, 980f, 981f
  suppurative, of mandible, 978, 979f
  tuberculous, of mandible, 978, 980f
  with facial fractures, 376
  with periostitis, of mandible, 978, 980f
  with sinusitis, 251
Osteomyocutaneous reconstruction, postsurgical imaging and, 2255f–2256f
Osteonecrosis, radiation, 2269f
Osteoneogenesis, in chronic otitis media, 1184
Osteopathia striata, of temporal bone, 1271
Osteopetrosis, 1112t
  of temporal bone, 1263–1264, 1264f–1266f
    differential diagnosis of, 1263–1264
Osteophytes, of spine, 1684, 1686f
  on videofluoroscopic swallowing study, 1737, 1737f
Osteoplastic flap procedure, 406, 408f–414f, 408–409
  on computed tomography, 410f–413f
  on magnetic resonance imaging, 413f, 414f
  on plain films, 408f
  on tomography, 409f
Osteoporosis circumscripta, 1259f
Osteoradionecrosis, 1214, 1214f
  of jaw, 980, 981f
Osteosarcomas
  of mandible, 1995f
  of oral cavity, 1440, 1445f
Otic capsule, ossification of, 1058, 1060
Otic ganglion, 1790
Otitic hydrocephalus, 1182–1183
Otitis externa, 1212
  differential diagnosis of, 1214
  necrotizing (malignant), 1212f, 1212–1214, 1213f
Otitis media, 1175f, 1175–1176
  arachnoid granulations associated with, 1182, 1183f
  chronic
    sequelae of, 1184, 1186–1189
    with effusion, 1183f–1185f, 1183–1184
  dural sinus thrombosis associated with, 1176, 1178–1179, 1179f–1181f
Otitis media *(Continued)*
  facial nerve palsy associated with, 1176
  tuberculous, 1199
  venous infarction associated with, 1179, 1182
Otocysts, 1058
Otomandibular dysostosis. *See* Branchial arch syndrome, of first and second arches.
Otosclerosis, 1245–1253, 1246f, 1247f
  cochlear (retrofenestral), 1249–1250, 1251f–1253f, 1252–1253, 1263f
  differential diagnosis of, 1253, 1254f
  fenestral, 1246–1249, 1247f–1250f
  rubeola and, 1207
  tinnitus due to, 1367
Otosclerotic plaques, continued growth of, 1221
Otospongiosis, tinnitus due to, 1367
Otosyphilis, 1208–1209, 1209f
Otx1 and *Otx2* genes, holoprosencephaly and, 54–55
Outer ear
  congenital anomalies of, 1113–1116, 1114f–1116f
    middle ear abnormalities associated with, 1114
    ossicular abnormalities associated with, 1114
    surgical considerations with, 1116
  embryologic development of, 7f, 8–9
  embryology and developmental anatomy of, 1061
  in hemifacial microsomia, 60, 60f
  inflammatory disease of, 1212–1216
  pinna of, 1796f
    abscess of, 2108f
    development of, 1061
    lymph node drainage of, 1881t
    on plain films, 122
    on surface magnetic resonance imaging, 1096f
Oval window
  atresia of, 1118, 1121f
  congenital absence of, 1118, 1121f
  in congenital aural dysplasia, 1116
  in otosclerosis, 1246–1249, 1247f–1250f
  stenosis of, 1167f
Ovarian cancer, *BRCA1/BRCA2* genes in, 2286
Overhangs, of turbinates
  inferior, 98
  superior, 98
Oxycephaly, 67
p53 gene
  DNA damage and, 2284–2285
  Li-Fraumeni syndrome and, 2282–2283, 2283f

P

p16 protein, 2286
Pachymeningitis, hypertrophic, idiopathic, 1291f
Paget's disease
  juvenile
    of temporal bone, 1268, 1270
    Paget's disease versus, 1258
  of jaw, 968–969
  of skull base, 857, 857f
  of temporal bone, 1256–1259, 1259f–1262f
    differential diagnosis of, 1257–1259
    fibrous dysplasia versus, 1255
  sinonasal, 338–339, 343f, 344f
    on computed tomography, 338–339, 343f
    on magnetic resonance imaging, 339, 344f
  tinnitus due to, 1367
Pain, in sinusitis, 194–195
Palatal fractures, sagittal, 381
Palatal shelves, 9
Palate
  adenoid cystic carcinoma of, 851f–852f
    with perineural tumor spread, 874f
  cleft. *See* Cleft lip/palate; Cleft palate; Facial clefts.
  embryogenesis of, 8, 8f, 9
  embryology of, 1522, 1523f
  floating, 381, 385f
  fusion of, 10
    factors influencing, 9
  hard. *See* Hard palate.
  primary, 8, 8f, 9
  soft. *See* Soft palate.
Palatine artery, greater, 95, 95f, 102
Palatine bone, 90
  development of, 10
  horizontal plate of, 138f
  on computed tomography and magnetic resonance imaging, 124
Palatine canal
  greater, 137f, 138f, 142f, 144f
  lesser, 137f, 138f
Palatine foramina, on computed tomography and magnetic resonance imaging, 124
Palatine grooves, on computed tomography and magnetic resonance imaging, 124
Palatine nerve, 794, 801, 802f, 902f, 903
  anterior, 102
  perineural tumor spread involving, 868, 871f, 872f
Palatine process, 8f, 9
  of maxillae, 90
Palatine recess, 102
Palatine spine, on computed tomography and magnetic resonance imaging, 124
Palatine suture, maxillary, 138f
Palatine tonsils, 1799f
  on plain films, 121f, 121–122
Palatoglossus muscle, 1380, 1792t, 1798f, 1799f
Palatopharyngeus muscle, 1792t
Palatopharyngeus sphincter muscle, 1466
Pallister-Hall syndrome (PHS), 73
Palpebral veins
  inferior, 127
  superior, 127
Pancoast tumors, 2226, 2227f, 2229f, 2230f
Pancoast's syndrome, 2226
PANDO. *See* Primary acquired nasolacrimal duct obstruction (PANDO).
Panorex films, 913–914, 914f, 915f
PAP-A. *See* Postaxial polydactyly A (PAP-A).
Papillary carcinomas
  of oral cavity, 1398f
  thyroid, 1846f, 1847f, 1921f–1924f, 2140f, 2148f, 2151–2152, 2152f–2155f, 2154
    metastatic, 1904f, 1925f, 1976f
    on positron-emission tomography, 2305f
    recurrence of, 2267f
Papillary cystadenoma lymphomatosum, 1943f, 1943–1944, 1944f, 1962, 2076–2077, 2079–2080, 2080f–2082f, 2082
Papillary cystadenomatous tumor, of facial nerve, 1337, 1338f, 1339
Papilledema, 473, 476f
Papillitis, 497–498
Papillomas
  choroid plexus, 1301, 1306f, 1307f
    of cerebellopontine angle, 1306f
  fungiform, sinonasal, 267
  inverted (endophytic)
    on computed tomography, 424f
    sinonasal, 267, 267f–270f
      calcifications within, 268, 270f
      on magnetic resonance imaging, 263f
  laryngeal, 1648, 1657f
  of parapharyngeal space, 1972
  Schneiderian (cylindric cell), oncocytic, sinonasal, 267, 268f
  sinonasal, 267f–270f, 267–268
    carcinoma associated with, 267
    inverted (endophytic), 267, 267f–270f
      calcifications within, 268, 270f
      on magnetic resonance imaging, 263f
    on computed tomography, 268f–270f
    on magnetic resonance imaging, 269f
Papillomas *(Continued)*
  squamous
    nasolacrimal, 681f–682f
    tracheal, 1721–1722, 1723f, 1724f
Papillomatosis
  laryngeal, pediatric, 1580f
  respiratory, recurrent, 1578–1579, 1580f
Paradental cysts, 347, 940, 941
Paradoxical nasal obstruction, 93
Paragangliomas
  laryngeal, 1649, 1651, 1659f
  of carotid body, 1950
  of cerebellopontine angle, 1298, 1300
  of parapharyngeal space, 1966–1967, 1969–1972, 1970f–1976f
    on computed tomography, 1970f, 1974f, 1975f
    on magnetic resonance imaging, 1970f–1976f
    on plain films, 1971f, 1974f, 1975f
  of temporal bone, 1306, 1309, 1311–1322
    angiographic features of, 1314–1315
    clinical features of, 1312f–1319f, 1312–1313
    differential diagnosis of, 1317, 1319–1322
    growth patterns and computed tomography findings with, 1313–1314, 1319f
    incidence, origin, and terms for, 1306, 1309, 1311, 1312f
    magnetic resonance imaging appearance of, 1315–1316
    on radionuclide scintigraphy, 1316
    retrotympanic (intratympanic), 1321
    treatment and surgical classification of, 1316–1317, 1320t
  sinonasal, 283, 284f, 285
  tinnitus due to, 1367
Paraglottic space, 1601
Paramolars, 987
Paranasal polyps, 214f–228f, 214–218, 221
  on computed tomography, 214–215, 215f, 216, 216f–223f, 217, 225f–228f
  on magnetic resonance imaging, 216f–219f, 216–217, 218, 221, 222f–228f
  on plain films, 214f, 215, 215f
  sinusitis and, 203–204
Paranasal sinuses. *See also specific sinuses.*
  aerated
    enlarged, 246–248, 247f–250f
    small or absent, 248–249

Paranasal sinuses *(Continued)*
anatomy of, 96–102
of ethmoid sinus, 97–99
of frontal sinus, 99–100
of maxillary sinus, 101–102
of sphenoid sinus, 100–101
on plain films, 109–122
associated structures surrounding, plain film anatomy of, 120–122, 121f
computed tomography of, 106, 108–109, 122f, 122–124, 150–152
anatomy on, 124–126
artifacts in, 123
axial, 123
contrast, 123
coronal, 123
examination protocol for, 151, 151f
image display and, 152, 152t
narrow and wide window settings for, 122f, 122–124
radiation exposure with, 151t, 151–152
spiral, 123
functions of, 96–97
interpretation of imaging studies of, 153
magnetic resonance imaging of, 108, 123–124, 152
anatomy on, 124–126
contrast-enhanced, 124
mucociliary clearance and, 153
mucosa of, 93, 96
normal anatomy of, 153–156, 154f–156f
mucociliary clearance and, 153
of frontal cells, 154–156, 156f–160f, 157t
obstruction of, 228, 231f
plain films of, 102–106, 108, 150
anatomy on, 109–122
clinical use of, 102–103
views used for, 102–106
preoperative imaging of, need for, 251, 252f
systematic radiographic evaluation of, 165, 167–168
Parapharyngeal space, 1797f, 1798f, 1820, 1822–1824, 1823f, 1826t, 1954–1987
adenoid cystic carcinomas of, 1972, 1977f
anatomy of, 1957–1958, 1958f
angiolymphoid hyperplasia of, 1979
branchial cysts in, 1976, 1979, 1979f–1980f
branchial cysts of, 1976, 1978, 1979f–1980f
clinical assessment of, 1954, 1955f, 1956f
computed tomography assessment of, 1955–1956, 1957f
cystic hygromas of, 1978, 1981f
Parapharyngeal space *(Continued)*
desmoplastic fibromas in, 1975–1976
disorders arising in, 1959–1986
disorders arising in skull base and, 1986, 1986f
disorders arising intracranially and, 1986–1987, 1987f
eumycotic mycetomas of, 1979–1980
fibrous tumors in, 1975–1976
giant aneurysm of, 1987f
heterotopic tissue in, 1975
infections in, 1959–1960, 1961f
magnetic resonance imaging assessment for, 1956–1957
meningioma of, 1987f
nodular fasciitis in, 1976
nodular fasciitis of, 1976
papillomas of, 1972
rhabdomyosarcomas of, 1972, 1977f
teratoma of, 1975
traumatic injuries of, 1986
tumors of, 1960–1972
clinical presentations of, 1958–1959, 1959t, 1960t
fibrous, 1975–1976
lipomas, 1979, 1982f
liposarcoma, 1972, 1978f
lymphomas, 1974
neurofibromas, 1979
neurogenic, 1965–1966, 1967f–1969f
of lymph nodes, 1974–1975, 1978f
of salivary glands. *See* Salivary glands, tumors of.
paragangliomas, 1966–1967, 1969–1972, 1970f–1976f
squamous cell carcinoma, 1972, 1977f, 1978f
teratomas, 1975
vascular disorders of, 1980–1983, 1982f–1985f, 1985
Parasympathetic ganglia, of face and neck, 1790
Parathormone (PTH), 2160
Parathyroid cysts, 1837–1838, 1839f
Parathyroid glands, 2160–2169
adenoma of, 2162–2166
on cross-sectional imaging, 2162–2163, 2163f, 2164f
on nuclear scintigraphy, 2163, 2165f, 2165–2166, 2167f
on ultrasonography, 2162, 2163f
adenomas of, 1839f
anatomy of, 2160
carcinoma of, 2168f, 2168–2169
cysts of, 2168f, 2169
endocrinology of, 2160
hyperparathyroidism and
clinical manifestations of, 2160–2162, 2161f
reoperation for, 2166–2167
hyperplastic, 2167–2168
Parathyroid glands *(Continued)*
hypoparathyroidism and, clinical manifestations of, 2162
lymph node drainage of, 1881t
ultrasound of
in primary hyperparathyroidism, 1942
indications for, 1942, 1942f
of normal parathyroid, 1938
‘‘Paravertebral’’ space, 1824, 1826t
Paraxial mesoderm, 5
Parietal dermoids, 31
Parietal emissary vein, 127, 131
Parietal vein, 127
Parosmia, 94
Parotid gland(s), 1797f, 1798f, 1799f
abscess of, 2027, 2027f, 2028f, 2042f, 2047f
adenocarcinoma of, with perineural tumor spread, 879f
anatomy of, 2007f–2009f, 2007–2010
benign tumor of, 803f
computed tomography of, 2018–2019, 2020f
congenital absence of, 2011f
cysts of, 2049f
deep portion of, 1798f
embryology of, 1773, 1775, 1775f
magnetic resonance imaging of, 2020–2021, 2021f
normal, ultrasound of, 1938, 1938f
on magnetic resonance imaging, 1103f
sialography of, 2015–2016, 2016f
squamous cell carcinoma of, with perineural tumor spread, 882f
tumors of, 1962, 1962f, 1963f
Parotid gland space, 1818, 1825t, 1826t
Parotid lymph nodes, drainage of, 1881t
Parotid region, squamous cell carcinoma in, with perineural tumor spread, 881f
Parotid tissue, accessory, 1386–1387, 1387f
Parotitis, 2108f
mumps, 2028–2029
suppurative, 2027, 2027f, 2028f
Pars flaccida retraction pockets, 1187f, 1188f
Pars tensa, cholesteatomas arising from, 1186, 1189f
PAS. *See* Pyriform aperture stenosis (PAS).
Patau syndrome. *See* Trisomy 13-15.
PATCHED gene, holoprosencephaly and, 54
Paterson-Brown syndrome, 1493
Pearly tumors, of cerebellopontine angle, 1288, 1290–1291, 1292f–1297f
Pectoralis major muscle, 1803f
Pectoralis minor muscle, 1803f
Pediatric patients. *See also* Infant(s).
dacryocystography in, with computed tomography, 714–716, 715f
facial fractures in, 399, 401

Pediatric patients *(Continued)*
rhabdomyosarcomas in, orbital, 635–636
sedation of, for magnetic resonance imaging imaging of eye, 451
sinusitis in, 204
teeth of, 893–894
ultrasound for, 1950f, 1950–1951, 1951f
Pendred's syndrome, 1112t, 1155f
Periapical cemental dysplasia, 954–955, 958f, 959f
Periapical cysts, 933f, 933–934, 934f
Periapical radiographs, 915, 915f
Periarteritis nodosa
inner ear in, 1210
orbital, 601, 603
Perichondritis, following radiation therapy, 1693, 1694f
Perilabyrinthine fistulas, 1146–1148, 1163f–1165f
Perilymph fistula, 1211f, 1211–1212
Perilymphatic fistula, with temporal bone trauma, 1241–1242, 1242f
Perilymphatic hydrops, 1148
Perilymphatic (periotic) labyrinth, embryology and developmental anatomy of, 1059–1060
Perilymphatic spaces, 1060
anatomy of, 1074–1075
Perineural tumor spread (PNS), 809f, 865–885
along mandibular division of trigeminal nerve, 868, 870–871, 875f–878f
along facial nerve, 871, 873, 879f
along maxillary division of trigeminal nerve, 868, 869f–874f
along ophthalmic division of trigeminal nerve, 867, 867f, 868f
along spinal nerves, 873, 876, 881f
antegrade, 872f, 873f, 883
clinical settings associated with, 866–867
imaging of, 876–877, 880, 883
asymmetrical foraminal enhancement and, 883, 884f
diagnostic, 880, 882f, 883
on computed tomography, 880, 882f
on magnetic resonance imaging, 880, 882f
pitfalls in, 883
posttreatment, 883–884
secondary imaging findings and, 883, 883f
technical considerations with, 877, 880, 883
invasion versus spread and, 865–866
mimics of, 884f, 884–885
primary sites associated with, 866
questionable, 883
signs and symptoms associated with, 866
Perineural tumor spread (PNS) *(Continued)*
to skull base, 847–848, 849f–853f
on computed tomography, 853f
on magnetic resonance imaging, 849f–852f
trigeminal nerve interconnections with other cranial nerves and, 873, 879f, 880f
tumor histologies associated with, 866
Perineuritis, orbital pseudotumors and, 587
Periodontal cysts, 347, 355f, 356f
lateral, 940
Periodontal disease, 925, 925f, 926f
on intraoral radiographs, 915f, 916, 916f, 917f
Periodontal space, 895
Perioptic hygroma, 569, 571f, 1282f, 1290, 1295f, 1296f
Perioptic meningiomas, 744, 746
clinical findings with, 744
on computed tomography, 746
on magnetic resonance imaging, 746, 747f, 748f
pathologic findings with, 744, 746f
Periorbita, anatomy of, 537, 538f
Periosteal bone, 1060
Periosteal reaction, with osteogenic sarcomas, 342, 349f
Peripheral nerve sheath tumors, 2208. *See also* Granular cell tumors; Neurofibromas; Neuromas; Schwannomas.
malignant, 294
of parapharyngeal space, 1966
Peripheral nerves(s), orbital, 541
Peripheral nervous system (PNS), 1782, 1784–1790. *See also* Cranial nerve(s); *specific nerves.*
autonomic ganglia of face and neck and, 1790
spinal nerves and, 1786–1788, 1788f, 1789f
sympathetic system and, 1788–1790
Periscleritis, orbital pseudotumors and, 587
Peritonsillar abscesses, 1504–1505, 1506f, 1565f, 1566f
Peritonsillar space, 1824, 1826t
Persistent generalized adenopathy (PGA), in HIV infections, 1889
Persistent hyperplastic vitreous (PHPV), 484, 487–489
clinical diagnosis of, 487–488, 488f
on magnetic resonance imaging, 488–489, 489f
Persistent stapedial artery (PSA), 1142, 1156f–1158f
tinnitus due to, 1366, 1367f
PET. *See* Positron emission tomography (PET); *specific regions and conditions.*
Petroclival synchondrosis
chondrosarcomas in, 1259f
Mafucci's syndrome arising in, 1259f
Petromastoid canal, 1148
pseudofracture of, 1237f
Petrosal nerve
deep, 96
superficial, greater, 96
on computed tomography, 1094f
perineural tumor spread involving, 873, 879f, 880f
Petrosal sinus, groove for, CT surface reconstruction of, 1096f, 1097f
Petrotympanic fissure, 1065
Petrous apex, 135f, 1200–1205
acute petrositis and, 1200–1201, 1201f–1203f, 1203
aeration abnormalities of, 1200
aneurysm of, 846f
carotid artery aneurysms of, 1349
cholesteatomas of, 1203–1205, 1204f, 1205f
cholesterol granuloma of, 1203, 1204f, 1347–1349, 1348f
chondrosarcomas of, 1325f, 1349–1350, 1351f
congenital, 1336f
CT surface reconstruction of, 1097f
effusion and, 1200, 1201f, 1203
endolymphatic sac tumors of, 1350–1351
epidermoid cysts of, 1349
lesions of, 1345, 1347–1352, 1348t
meningoceles of, 1351–1352
mucoceles of, 1349, 1350f
nasopharyngeal carcinoma in, 1351
on magnetic resonance imaging, 1099f, 1100f
xanthomas in, 1351–1352
Petrous bone
facial nerve course in, 1071
malformations of, associated with meningitis, 1145–1148, 1150–1151, 1163f
perilabyrinthine fistulas, 1146–1148, 1163f–1165f
translabyrinthine fistulas, 1148, 1150–1151, 1163f
tumors of, 1298
Pfeiffer syndrome, 69, 79
PFTs. *See* Plexiform fibrohistiocytic tumors (PFTs).
PGA. *See* Persistent generalized adenopathy (PGA).
Phantom bone disease, 837–838, 841f
Phantosmia, 94
Pharyngeal arches, 1758
Pharyngeal artery, 1798f
ascending, 1798f
Pharyngeal constrictor muscles, 1601, 1792t, 1798f, 1800f
swallowing and, 1743

Pharyngeal contraction wave, 1743
Pharyngeal delay, 1747, 1747f
Pharyngeal pouch, 1061
Pharyngeal reconstruction, postsurgical appearance and, 1689
Pharyngeal stage of swallowing, 1732, 1734
Pharyngectomy
  partial, postsurgical imaging and, 2252f–2254f, 2257f–2258f, 2261f, 2263f
  postsurgical imaging and, 2250f, 2251f, 2261f, 2264f
Pharyngitis
  bacterial, lymphadenitis in, 1890f
  herpes, 1510f
  moniliasis, 1671f
  reactive lymph nodes in, 1911f
  streptococcal, 1564f
Pharyngobasilar fascia, 1797f
Pharyngoceles, 1513, 1513f, 1514f, 1744f
Pharyngoepiglottic fold, 1800f
Pharyngoesophageal lesions, 2208, 2210–2212
Pharyngoesophageal segment, movements of, during oropharyngeal swallowing, 1745–1746, 1746f
Pharynx, 1465–1518. *See also* Hypopharyngeal *entries;* Nasopharyngeal *entries;* Oropharyngeal *entries.*
  adenoidal hypertrophies and, 1509, 1510f
  AIDS and, 1509, 1510f, 1511f, 1511–1512
  anatomy of, 1465–1466
    of hypopharynx, 1471f–1474f, 1471–1473
    of nasopharynx, 1466–1468, 1467f–1470f, 1470
    of oropharynx, 1470f, 1470–1471, 1471f
  carcinoma of, 1819f
  carotid artery tortuosity and, 1513
  crack cocaine burns of, 1513
  diverticula of, 1682–1683, 1684f, 1685f
  dysphagia and, 1513, 1515f
  embryology of, 1466, 1523, 1765, 1766f
  fibromatoses of, 1500–1501, 1501f
  granular cell tumors of, 1497–1498, 1500
    imaging features of, 1500, 1500f
  hemangiomas of, 1501, 1502f
  hypopharyngeal carcinomas and, 1489–1490, 1490t, 1491f–1494f, 1493, 1493t
  imaging techniques for, 1473, 1475–1476
    barium studies, 1473, 1475, 1475f
    computed tomography, 1475–1476
Pharynx *(Continued)*
    magnetic resonance imaging, 1476
    tissue differentiation and, 1476, 1477f, 1478f
  laceration of, 1672f
  lipomas of, 1501–1502
  lymph node drainage of, 1881t
  lymphomas of, 1493–1494
    imaging findings in, 1494, 1495f, 1496f
  muscles of, 1791t–1793t
  neurofibromas of, 1501, 1501f
  pharyngoceles and, 1513, 1513f, 1514f
  posttreatment, 1513, 1515–1518
    following radiation therapy, 1513, 1515f, 1515–1517, 1516f
    following surgery, 1517f, 1517–1518
  retropharyngeal infections of, 1503–1504
    imaging features of, 1504, 1504f, 1505f
  rhabdomyomas of, 1500, 1500f
  rhabdomyosarcomas of, 1497
  salivary gland retention cysts and, 1513
  salivary gland tumors and, 1494, 1496f–1498f, 1497
    imaging features of, 1497, 1499f
  schwannomas of, 1501, 1502f
  squamous cell carcinoma of, evaluation for, 1640–1642, 1644, 1649f–1651f
  tendinitis of longus colli and, 1505, 1507, 1507f–1508f
  Tornwaldt's cysts and, 1507–1508
    imaging features of, 1507–1508, 1508f, 1509f
  trauma to, 1512, 1512f, 1513f
  unknown primary tumors of, 1502–1503
    imaging findings with, 1502–1503, 1503f
  wall of, movements of, during oropharyngeal swallowing, 1743–1744, 1744f
Pheochromocytomas, metastatic to sinonasal cavities, 367f
Philadelphia chromosome, 2281
Phlebectasia, 2202
  of internal jugular vein, 1856, 1858
Phleboliths, 1561f
  of oral cavity, 1390f
Phlegmon, subperiosteal, 580–581, 582f, 583f
PHPV. *See* Persistent hyperplastic vitreous (PHPV).
Phrenic nerve, 1788, 1789f, 2235, 2237, 2237f
PHS. *See* Pallister-Hall syndrome (PHS).
Phthisis bulbi, 461, 463f
Phycomycosis, sinusitis and, 202
Pia, of optic nerve, 541
Pierre Robin syndrome, 65f, 65–66, 1112t
Pigmented villonodular synovitis, of temporomandibular joint, 1033–1034, 1036f
Pilomatrixomas, 570, 2176–2177, 2178f
Pindborg tumors, 359–360, 362f, 949, 954f
Pinna, 1796f
  abscess of, 2108f
  development of, 1061
  lymph node drainage of, 1881t
  on plain films, 122
  on surface magnetic resonance imaging, 1096f
PIP. *See* Posterior tonsillar pillar (PTP).
Pit and fissure caries, 917, 917f
Pituitary adenomas, 349f, 754–757
  clinical findings with, 754
  metastatic to sinonasal cavities, 367f
  of skull base, 829–831, 830f, 831f
  on computed tomography, 755, 755f–757f
  on magnetic resonance imaging, 739f, 755–757, 757f–759f
  pathologic findings with, 754–755
Pituitary apoplexy, 757f
Pituitary gland
  ectopic, 301
  herniation of, 805f
  masses in. *See also specific masses.*
    enlarging, 301
    on plain films, 119
Plagiocephaly, 67, 68f, 69
  orbit in, 559, 560f, 561f
Plain films. *See specific regions and conditions.*
Planum sphenoidale, 142f, 145f
  on plain films, 120, 121f
Plasma cell tumor. *See* Myelomas, multiple.
Plasmacytomas
  extramedullary, sinonasal, 304–305, 306f, 307f
    on computed tomography, 306f
    on magnetic resonance imaging, 307f
  of salivary glands, 2110f
  of skull base, 835–836
Plastics, intraocular, 516
Platybasia, basilar invagination versus, 853–854
Platysma muscle, 91t, 127, 128f, 1791t, 1799f, 1800f
Pleomorphic adenomas
  of oral cavity, 1408, 1410, 1412f
  of salivary glands, 280, 280f–284f, 1943, 1943f, 1962–1963, 1963f–1965f, 2067–2071, 2069f–2079f, 2069t, 2074–2076
  of tongue base, 1497f
Plexiform fibrohistiocytic tumors (PFTs), of salivary glands, 2117–2118
PLGAs. *See* Polymorphous low-grade adenocarcinomas (PLGAs).

Plummer-Vinson syndrome, 1493
PNETs. *See* Primitive neuroectodermal tumors (PNETs).
Pneumatic cells, of temporal bone, 1061
Pneumatization
of middle ear cavity, reduction in congenital aural dysplasias, 1114
of tympanum, 1061
Pneumatoceles, 247, 248f, 249f, 630
of salivary glands, 2060, 2063f
on computed tomography, 701
Pneumocephalus, with functional endoscopic sinus surgery, 176, 177f
Pneumococcal meningitis, 750f
Pneumocystosis, lymphadenitis in, 1896
Pneumonectomy, postpneumonectomy syndrome and, 1704f
Pneumoparotitis, 2063f
Pneumosinus dilatans, 630–631, 631f, 823, 824f, 825f
Pneumosinus disease, 247, 247f
PNS. *See* Perineural tumor spread (PNS); Peripheral nervous system (PNS).
Pollinosis, seasonal, 200
Polyarteritis nodosa
inner ear in, 1210
orbital, 601, 603
Polychondritis, relapsing, trachea in, 1711
Polycystic disease, of salivary glands, 2055, 2057
Polymorphous low-grade adenocarcinomas (PLGAs), of salivary glands, 2096–2097, 2097f
Polyp(s)
antrochoanal, pediatric, 1581f, 1582
nasal
antrochoanal, 204
chronic sinusitis and, 200
allergic, 201
in cystic fibrosis, 201
on computed tomography, 291f
sinusitis and, 203–204
of vocal cords, 1648, 1656f
paranasal. *See* Paranasal polyps.
Polyposis, sinonasal, recurrent, following functional endoscopic sinus surgery, 188, 190f
Pons, on magnetic resonance imaging, 1100f
Porous acousticus internis, on magnetic resonance imaging, 1099f
Port-wine stains, of neck, 1854, 1856
Positron emission tomography (PET), 2295–2307. *See also specific regions and conditions.*
clinical applications of, 2298–2305
head and neck cancer, 2298–2304
evaluation of metastases and, 2304, 2305f
nodal staging and, 2300t, 2300–2301, 2301f
Positron emission tomography (PET) *(Continued)*
response therapy therapy and, 2302–2304, 2304f
with residual/recurrent disease, 2301–2302, 2302t, 2303f
with unknown primary/second primary, 2298–2300, 2299f, 2300f
non-squamous cell carcinoma
malignancy, 2304–2305
lymphoma, 2305
thyroid, 2304–2305, 2306f
normal appearance in head and neck and, 2298, 2298f
postirradiated appearance and, 2298, 2298f
of salivary glands, 2026
pitfalls of, 2305–2306
technical aspects of, 2295–2298
image generation, 2296, 2296f
image registration, 2297, 2297f
imaging FDG metabolism without dedicated PET scanner, 2297–2298
positron emission, 2295
quantification/standardized uptake value, 2297
radiopharmaceuticals, 2295–2296
scanner/detectors, 2296
Postaxial polydactyly A (PAP-A), 73–74
Postcricoid region, 1602
Postcricoid tumors, 1490, 1493, 1493f, 1494f
Posterior fossa, schwannomas of, nonacoustic, 1291–1293, 1297f–1300f
Posterior tonsillar pillar (PTP), malignancies of, 1485–1486
Posterior triangle, of neck, 1781, 1781f, 1782f, 1824, 1824f, 1825f, 1826t
masses in, differential diagnosis of, 1795, 1795t
Postoperative imaging, of sinonasal cavities, 402–403
Postpartum thyroiditis, 2146, 2147
Postpneumonectomy syndrome, 1704f
Posttransplant lymphoproliferative disorders (PTLDs), 1584, 1585f, 1903
Pouches, of branchial apparatus, 1760, 1762f
PPF. *See* Pterygopalatine fossa (PPF).
Preauricular lymph nodes, drainage of, 1881t
Precardinal veins, embryology of, 1772, 1772f
Prechordal mesoderm, 5
Pre-epiglottic space, 1601, 1801f
Premature metopic synostosis, 69, 70f
Premature sagittal synostosis, 69
Premature unilateral coronal synostosis, 69, 70f
Premaxillary bone, 9
development of, 10
Premolars
first, 139f
second, 139f
Prenasal space, 30, 30f
Preseptal inflammatory lesions, orbital inflammatory lesions versus, 706f–708f
Presphenoidal center, 10, 30f
Prestyloid space, 1823
Pretracheal space, 1811, 1815, 1825t, 1826t
Prevertebral space, 1816, 1825t, 1826t
schwannoma in, 1811f
Prevertebral tendinitis, calcific, acute, 1505, 1507, 1507f–1508f
Primary acquired nasolacrimal duct obstruction (PANDO), 681, 700
Primary ciliary dyskinesia syndrome, with sinusitis, 252–253
Primitive neuroectodermal tumors (PNETs)
of cerebellopontine angle, 1302, 1308f
of salivary glands, 2115–2116
sinonasal, 290, 292, 292f
on computed tomography, 292f
Primordial cysts, of oral cavity, 1422
Probing, of nasolacrimal drainage system, 663
Proboscis, in holoprosencephaly, 55
Procerus muscle, 90, 90f, 128f
Progonomas, melanotic, 42
Progressive diaphyseal dysplasia, 858f
of temporal bone, 1264, 1265–1266, 1267f, 1268f
differential diagnosis of, 1266
Paget's disease versus, 1258
Prolabium, 8
Proliferative fasciitis, 2188
Proptosis, 556
with rhabdomyosarcomas, in children, 635–636
Prostate carcinomas
meningeal metastases from, 1290f
metastatic to mandible, 1447f
metastatic to sinonasal cavities, 362, 364, 366f, 367f
Prostheses, ossicular reconstruction, 1219f–1221f, 1219–1220
Protein coding sequence, mutational alteration of, oncogene activation by, 2277
Protein solutions, magnetic resonance of, 206f–210f, 206–208
Proton magnetic resonance spectroscopy (^{1}H-MRS), limitations and imaging strategies for, 2313–2314, 2308–2309, 2311f–2314f, 2311–2315
clinical applications of, 2311–2313
differentiation of recurrent tumor form posttreatment changes, 2312

Proton magnetic resonance spectroscopy (^{1}H-MRS), limitations and imaging strategies for *(Continued)*
prospective treatment monitoring, 2312–2313, 2315f
limitations and imaging strategies for, 2313–2314
metabolites and, 2308–2309, 2311
Prussak's space, 1186, 1186f
cholesteatomas in, 1186–1187, 1187f–1189f
Prx1-2 genes, cleft lower lip and mandible and, 30
PSA. *See* Persistent stapedial artery (PSA).
Pseudallescheria boydii, sinusitis and, 202
Pseudoaneurysms
of axillary artery, 2231f
of vertebral artery, 2207f
Pseudocholesteatomas, 244
Pseudocollateral veins, 2204
Pseudocysts, medullary, mandibular, 945
Pseudodacryocystitis, with sinusitis, 195f, 196
Pseudoepiglottitis, 1688f
Pseudogliomas, ocular, 496
Pseudogout, of temporomandibular joint, 1035, 1038f, 1039f
Pseudomeningoceles, 2223f
with functional endoscopic sinus surgery, on magnetic resonance imaging, 179, 180f
Pseudomonas aeruginosa, necrotizing otitis externa and, 1212f, 1212–1214, 1213f
Pseudomonas mallei infections, 242
Pseudomonatous active ossifying fibromas, juvenile, 574, 578f
Pseudorheumatoid nodules, orbital, 609–610, 610f
Pseudotumors
antral, 250, 250f, 251f
inflammatory, 250
of lacrimal gland, 643, 643f
of skin, 2188, 2190f
of Tenon's capsule, 453, 454f
orbital, 584–591, 600, 611f, 704f, 705
anterior orbital inflammation and, 586, 586f
apical orbital inflammation and, 587, 591f
diffuse, 586, 586f, 587f
histopathology of, 584–586
lacrimal adenitis and, 587, 590f
orbital myositis and, 586–587, 587f–590f
painful external ophthalmoplegia and, 587–588, 591
perineuritis and, 587
periscleritis and, 587
simulating rhabdomyosarcomas, 638, 639f
tonsillar, 1495f
PTEN gene, 2287
Pterygoid canal, 142f, 143f, 144f.
See Vidian canal.
anatomy of, 790, 791, 794f
on computed tomography and magnetic resonance imaging, 125, 126
Pterygoid fossa, 137f
on plain films, 120, 121
Pterygoid muscles, 897, 899f, 1380t, 1793t, 1796f, 1797f, 1798f
Pterygoid plates, 137f, 142f, 143f, 144f, 1796f, 1797f
hamulus of, 138f, 142f, 144f, 1798f
on computed tomography and magnetic resonance imaging, 125
on plain films, 114, 114f, 120–121
Pterygoid plexus, 101, 102, 127, 1796f, 1797f
Pterygoid process, 100
CT surface reconstruction of, 1097f
of sphenoid, 793, 801f
fractures and, 850
on plain films, 119, 120f
Pterygomandibular space, 1798f
Pterygopalatine canal, on computed tomography and magnetic resonance imaging, 124
Pterygopalatine fossa (PPF), 96, 135f, 136f, 137f, 142f, 143f, 144f, 793, 795f, 797, 902f, 903, 904f
anatomy of, 536f, 536–537, 1782
enlargement of, 1485f
on computed tomography and magnetic resonance imaging, 124–125
on plain films, 114, 114f
Pterygopalatine ganglion, 96, 1790
Pterygopalatine nerve, 898f, 903
PTH. *See* Parathormone (PTH).
PTLDs. *See* Posttransplant lymphoproliferative disorders (PTLDs).
Pulp stones, 988, 989f
Pulsatile masses, intratympanic, 1319–1320, 1321t
Pupil(s), atresia of, congenital, 448
Pyknodysostosis, Paget's disease versus, 1258–1259
Pyle's disease, 1110t
of temporal bone, 1267, 1268, 1270f, 1271f
Pyriform, 1596f
Pyriform aperture, 88
Pyriform aperture stenosis (PAS), 1539f, 1540–1542, 1541f
Pyriform cartilage, 1596
Pyriform sinus, 1601, 1602f, 1800f, 1801f
fistula of, 1566f
squamous cell carcinoma of, 1640, 1649f, 1650f
tumors of, 1490, 1491f–1493f

Q

Quadrangular cartilage, 89
Quadrangular membrane, 1599, 1599f

R

Rad, 151
Radiation, exposure, with computed tomography, of paranasal sinuses, 151
Radiation dose, with computed tomography, 108
Radiation dose equivalent, 151, 151t
Radiation necrosis, 2269f
of masticator space, 1995f
Radiation therapy
arteritis related to, 2268f
for laryngeal squamous cell carcinoma, 1624
laryngeal changes following, 1689, 1692f–1694f, 1693
of lacrimal system, 691
of neck, 2245, 2247, 2249
imaging changes following, 2249–2250
oropharyngeal stenosis induced by, 1570, 1570f
pharynx following, 1513, 1515f, 1515–1517, 1516f
sialoadenitis following, 2052
swallowing and, 1741
Radiation-absorbed dose, with computed tomography, 151
Radicular cysts, 933f, 933–934, 934f
of oral cavity, 1422
Radioimmunoscintigraphy, 2317f, 2317–2318
Radionuclide imaging.
See Dacryoscintigraphy; *specific regions and conditions.*
Radiopharmaceuticals, for positron-emission tomography, 2295–2296
Ramsay-Hunt syndrome, 1207, 1207f
Ranulas. *See* Mucoceles.
RARA. *See* Retinoic acid receptor alpha (RARA) gene product.
Ras gene activation, 2280
Rathke's cleft cyst, 752, 754
clinical findings in, 752
on computed tomography, 752, 754
on magnetic resonance imaging, 754, 754f, 755f
pathologic findings with, 752
Rathke's pouch, 786
Rathke's pouch cysts, 826, 828f
RB gene, 2281–2282, 2282f, 2283–2284
Rbs. *See* Retinoblastomas (Rbs).
RCC. *See* Renal cell carcinoma (RCC).
REAL. *See* Revised European and American Lymphoma classification (REAL).
REAL classification, 1907t

Receptor tyrosine kinases (RTKs), 2278
Recirculation syndrome, after functional endoscopic sinus surgery, 187, 188f
Rectal carcinoma, metastatic to mandible, 1448f
Rectus capitis muscle, 1793t, 1798f
Rectus muscle, injury to, with functional endoscopic sinus surgery, 181, 182f
Recurrent respiratory papillomatosis (RRP), 1578–1579, 1580f
Refsum syndrome, 1112t
Regurgitation, nasopharyngeal, 1741, 1742f
Reichert's cartilage, 1768
Relapsing polychondritis
  inner ear in, 1210
  laryngeal, 1657, 1659
  trachea in, 1711
Relaxation times
  T1, 206, 206f–210f, 207–208
  T2, 206–208, 207f–210f
Rem, 151
Renal cell carcinoma (RCC)
  metastatic to sinonasal cavities, 361–362, 363f
  metastatic to thyroid, 2157f
Residual cysts, 931
Respiration, nasal role in, 91–93
Respiratory papillomatosis, recurrent, 1578–1579, 1580f
Respiratory system embryology, 1765, 1766f, 1767f, 1767–1768
Resurfacing, with perineural tumor spread, 876f, 882f, 883
Retention cysts, 214f–228f, 214–218, 221, 1844f
  adenoidal, 1579f
  in maxillary sinus, 2011f
  mucoceles versus, 205
  mucous. *See also* Mucoceles.
    mucoceles versus, 203
    sinusitis and, 203
  of salivary glands, 1513, 2061f, 2062f
  of tongue, 1397–1398, 1400f
  on computed tomography, 214–215, 215f, 216, 216f–223f, 217, 225f–228f, 424f
  on magnetic resonance imaging, 216f–219f, 216–217, 218, 221, 222f–228f
  on plain films, 214f, 215, 215f
  serous, 203
  tonsillar, 1478f
Retina, 453
  anatomy of, 457–458
  calcification of, 479t
  embryology of, 532f
  ganglion cells of, embryology of, 447
  hamartoma of, 497
  myelinated nerve fibers in, 499
Retinal angiomatosis, von Hippel-Lindau, 499–500
Retinal detachment, 466–470, 467f–471f, 499
  on computed tomography, 467f, 468f, 470f, 471f
  on magnetic resonance imaging, 467f–470f
  postradiation, 504f
  uveal melanomas and, 514
Retinal dysplasia, 489–521. *See also specific conditions.*
Retinal gliosis, 499
Retinal pigment epithelium, hamartoma of, 497
Retinoblastomas (Rbs), 468f, 477–478, 480t, 480–484, 502, 2281–2282, 2282f
  clinical diagnosis of, 481, 482f
  diagnostic imaging of, 481, 483, 483t, 484f
  lesions simulating, 483–484
  of Tenon's capsule, 453, 454f
  on magnetic resonance imaging, 483, 485f–487f
  tetralateral, 481
  trilateral, 481
Retinoic acid, signaling by
  branchial arch syndromes and, 58
  in face, 9
Retinoic acid receptor alpha (RARA) gene product, cleft lip/palate and, 19
Retinopathy of prematurity, 491–492
  diagnostic imaging in, 492, 492f
  ophthalmoscopy in, 491–492
Retinoschisis, X-linked, 499
Retractors, extraocular, 539
Retroauricular lymph nodes, drainage of, 1881t
Retrobulbar recess cell, anatomy of, 155–156, 158f
Retrobulbar visual pathway, 735–736, 736f
Retrochiasmatic visual pathway, embryology of, 736–737
Retrofenestral otosclerosis, 1249–1250, 1251f–1253f, 1252–1253, 1263f
Retrognathia, 1549–1550, 1550f, 1551f
Retromandibular vein, 127, 1797f, 1798f, 1799f
Retromolar fossa, 896f, 898, 899, 900f
Retromolar triangle, 896f, 897, 899, 900f
Retromolar trigone, 1384, 1798f
  squamous cell carcinoma of, 1432–1433, 1437f–1439f
Retropharyngeal abscesses, 1565f
Retropharyngeal cellulitis, 1567f
Retropharyngeal lymph nodes, drainage of, 1881t
Retropharyngeal nodes, 1797f
  with pharyngeal wall cancers, 2245, 2245f
Retropharyngeal space, 1800f, 1817f, 1825t, 1826t
  abscess in, 1817f, 1820f
  air in, 1820f
  infections of, 1503–1504
    imaging features of, 1504, 1504f, 1505f
Retrovisceral space, 1815–1816, 1817f–1820f, 1825t, 1826t
Revised European and American Lymphoma classification (REAL), 301, 301t
Rhabdoid tumors, malignant, pediatric, 1587, 1588f
Rhabdomyomas
  of oral cavity, 1415, 1415f
  pharyngeal, 1500, 1500f
  sinonasal, 317
Rhabdomyosarcomas (RMSs), 2197–2199, 2201f
  following craniofacial resection, 437f
  of masticator space, 1809f
  of oral cavity, 1438, 1440
  of parapharyngeal space, 1972, 1977f
  orbital, 632–633, 635–640
    diagnostic imaging in, 636, 636f–641f, 638–640
    on computed tomography, 636, 636f, 637f, 638, 640f
    on magnetic resonance imaging, 636, 637, 637f, 638, 641f
  pediatric, 1586f, 1586–1587, 1587f
  pharyngeal, 1497
    imaging features of, 1497, 1499f
  sinonasal, 317, 317f–319f
    on computed tomography, 317, 317f, 319f
    on magnetic resonance imaging, 317, 318f
Rhese view, for paranasal sinus plain films, 104–105, 107f
  of ethmoid sinuses, 112
  of frontal sinuses, 109, 111
Rheumatoid arthritis
  inner ear in, 1210
  of temporomandibular joint, 1041f, 1042f
Rheumatoid disease, laryngeal, 1656–1657, 1659
Rhinectomy, 405f
Rhinion, 88
Rhinitis, vasomotor, 201
Rhinoentomophthoromycosis, granulomatous, sinusitis and, 202
Rhinoliths, 253f, 254f
Rhinoscleroma, 236, 239
  laryngeal, 1656, 1671f
Rhinosporidiosis, 242
Rhinotomy, lateral, 423, 425, 428f, 429f
Rhizotomy injections, 860, 860f
  skull base and, 860, 860f
Rhomboid minor muscle, 1801f

Rib(s), first, 1802f, 1803f
Riedel procedure, 406, 407f
Riedel's thyroiditis, 2147
Ring-string complex, 1556
Risorius muscle, 90t, 127, 128f, 1797f, 1798f
RMSs. *See* Rhabdomyosarcomas (RMSs).
Root caries, 918
Rosai-Dorfman disease, 308
Rosenmüller, fossa of, 1797f
Rosenmüller valve, 673
Round window
  anatomy of, 1074
  in congenital aural dysplasia, 1116
Rouvière nodal classification system, 1873, 1875, 1876t
RRP. *See* Recurrent respiratory papillomatosis (RRP).
RTKs. *See* Receptor tyrosine kinases (RTKs).
Rubella
  labyrinthitis due to, 1206
  lymphadenitis in, 1889
Rubeola
  labyrinthitis due to, 1207
  lymphadenitis in, 1888–1889

S

Saber-sheath trachea, 1712
Saccular cysts, 1652, 1662f, 1665f–1668f
  congenital, 1552
  external, 1652
Saccule, 1058, 1060f, 1074
Saethre-Chotzen syndrome, 79
  orbit in, 559, 561
Sagittal sinus, superior, 127
Sagittal synostosis, premature, 69
Saliva
  formation of, 2012, 2012f
  functions of, 2012
Salivary duct carcinomas (SDCs), 2097–2098, 2098f
Salivary gland(s), 2005–2126. *See also specific glands.*
  actinomycosis and, 2037–2038
  AIDS-related cysts of, 2060–2063
  anatomy of, 2007–2011
    of minor salivary glands, 2011
    of parotid gland, 2007f–2009f, 2007–2010
    of sublingual gland, 2010–2011
    of submandibular gland, 2010, 2010f
  autoimmune diseases of, 2043–2046, 2044f–2049f, 2048–2050
  branchial cleft cysts of, 2053f, 2054f, 2054–2055
  cat-scratch disease and, 2034–2036
  cellulitis of, 2027f, 2029f, 2108f
  congenital sialectasis and, 2057
  cysts of, 2052–2066
    acquired, 2059–2066
    congenital, 2053f–2055f, 2053–2057
Salivary gland(s) *(Continued)*
  developmental anomalies of, 2011f, 2011–2012
  disease patterns in, 2123, 2125–2126
  ductal cysts of, 2059, 2060f–2062f
  ductal foreign bodies in, 2042
  embryology of, 1773, 1775, 1775f, 1776t
  epidermoid inclusion cysts of, 2055
  fibrous histiocytomas of, 2117, 2121f
  hemorrhagic cysts of, 2060f
  hyperlipidemia and, 2050
  imaging of, 2012–2026
    angiography for, 2025
    catheter dilation and endoscopy for, 2026
    fine-needle aspiration and, 2026
    overall approach for, 2012–2013
    plain films for, 2013, 2013f, 2014f
    positron-emission tomography for, 2026
    radionuclide, 2025
    sectional imaging for, 2017–2024
      computed tomography, 2018–2019, 2020f, 2023–2024
      CT sialography, 2024, 2025f
      general considerations with, 2017–2018, 2019f
      magnetic resonance imaging, 2020–2021, 2021f–2023f, 2024
      MR sialography, 2021–2023, 2023f
      MR spectroscopy, 2024
    sialography for, 2013–2017, 2015f
      computed tomography, 2024, 2025f
      magnetic resonance imaging, 2021–2023, 2023f
      parotid gland study using, 2015–2016, 2016f
      submandibular gland study using, 2016–2017, 2017f
    ultrasound for, 2024–2025
  infections of, 2026–2039
    acute, 2026–2029
      bacterial, 2027f–2028f, 2027–2028
      viral, 2028–2029
    chronic, 2029–2039
      bacterial, 2031–2036, 2037–2039
      protozoan, 2036–2037
  Kussmaul's disease of, 2042
  lymph node drainage of, 1881t
  lymphoepithelial cysts of, 2053–2054, 2056f–2059f
  Merkel's cysts of, 2057
  metastatic disease of, 2108f, 2109f, 2110f
  minor
    anatomy of, 2011
    oncocytic tumors of, 2084
    tumors of, 1494, 1496f–1498f, 1497
      imaging features of, 1497, 1499f
  mucoid attenuation cysts of, 2061f
Salivary gland(s) *(Continued)*
  mucous, adenomatoid hyperplasia of, 2052
  necrotizing sialometaplasia of, 2052
  neurofibromas of, 2115, 2120f
  nodular fasciitis of, 2117
  physiology of, 2012, 2012f
  plasmacytoma of, 2110f
  plexiform fibrohistiocytic tumors of, 2117–2118
  pneumoceles of, 2060, 2063f
  polycystic disease of, 2055, 2057
  primitive neuroectodermal tumors of, 2115–2116
  ranulas of, 2063, 2064f, 2065f, 2065–2066
  retention cysts of, 1513, 2061f, 2062f
  sarcoidosis and, 2038–2039, 2039f, 2055f
  schwannomas of, 2120f
  sebaceous cysts of, 2124f
  sialoadenitis and
    chronic recurrent, 2040f–2042f, 2040–2041
    postirradiation, 2052
  sialocysts of, 2059–2060, 2062f
  sialosis and, 2050, 2051f
  stones in, 1402–1403, 1404f–1406f, 1943, 2033f–2038f, 2039–2040, 2040f
    on plain films, 2013, 2013f, 2014f
  syphilis and, 2032, 2034
  toxoplasmosis and, 2036–2037
  traumatic injury of, 2042–2043
  tuberculosis and, 2028f, 2031
  tumors and tumor-like conditions of, 277–280, 1962f–1966f, 1962–1963, 2066–2123, 2067t, 2068t
    acinic cell carcinoma, 1944, 1944f
    adenoid cystic carcinoma, 277–280, 279f
    epithelial, 2067–2107
      acinic cell carcinoma, 2096
      adenocarcinoma not otherwise specified, 2104–2105, 2105f, 2106f
      adenoid cystic carcinoma, 2090–2091, 2093f–2095f, 2093t, 2093–2096
      adenosquamous carcinoma, 2098
      basal cell adenoma and basal cell adenocarcinoma, 2084–2086, 2085f
      basaloid squamous carcinoma, 2098
      canalicular adenoma, 2086
      carcinoma ex pleomorphic adenoma, 2071, 2074–2075, 2076f
      carcinoma metastatic to salivary glands, 2105–2107, 2108f–2110f
      clear cell carcinoma, 2087–2088

Salivary gland(s) *(Continued)*
epithelial-myoepithelial carcinoma, 2087, 2088f
hybrid carcinoma, 2102
low-grade adenocarcinomas, 2096–2097, 2097f
lymphoepithelial carcinoma, 2099–2101
mucoepidermoid carcinoma, 2088–2090, 2089f–2093f, 2089t
myoepithelioma and myoepithelial carcinoma, 2086–2087
oncocytic, 2082–2084
pleomorphic adenoma, 2067–2071, 2069f–2079f, 2069t, 2074–2076
primary squamous cell carcinoma, 2099, 2100f
salivary duct carcinoma, 2097–2098, 2098f
sclerosing adenosis, 2103–2104, 2104f
sebaceous neoplasms of salivary gland origin, 2098–2099
sialoblastoma, 2102–2103, 2103f
undifferentiated carcinoma, 2101–2102
Warthin's tumor, 1943f, 1943–1944, 1944f, 1962, 2076–2077, 2079–2080, 2080f–2082f, 2082
epithelial-myoepithelial carcinoma, 280
Frey's syndrome, 2121
Kimura's disease, 2121–2123, 2123f, 2124f
malignant, 1944, 1944f
masseteric hypertrophy, 2118, 2121f
Merkel cell carcinoma, 2121, 2125f
mucoepidermoid carcinoma, 280, 281f, 282f
nonepithelial, 2107–2118
fibrous tissue lesions, 2116–2118, 2121f
hemangioma, 2107, 2110f, 2111f
intraparotid lymphadenopathy, 2114
lipoma, 2114–2115, 2119f
lymphangioma, 2107–2109, 2111f, 2112f
lymphoma, 2109, 2112–2113, 2113f–2118f, 2113t
neurogenic, 2115–2116, 2120f
pleomorphic adenoma, 280, 280f–284f, 1943, 1943f
sebaceous cysts, 2121, 2124f
staging of, 2066, 2067t
temporomandibular joint and mandibular lesions, 2119, 2121f–2123f
ultrasound of, 1943–1944
in sialolithiasis, 1943
of normal glands, 1938, 1938f
Salivary gland(s) *(Continued)*
with tumors and tumor-like conditions, 1943–1944
Salivary gland ducts, calculi of, 1404f–1406f
Salpingopharyngeus muscle, 1466, 1792t
SAM. *See* Spindled atypical mycobacteriosis (SAM).
Sarcoid, laryngeal, 1656
Sarcoidosis
dacryoadenitis due to, 642, 643f
granulomas in, 245f
lymphadenopathy associated with, 1898f, 1899, 1901–1902, 1902f
of lacrimal gland, 597, 599f
of optic nerve, 595, 596f, 597, 598f, 600–601
ophthalmic involvement in, 746–750
clinical findings with, 747
on computed tomography, 748
on magnetic resonance imaging, 748, 749f, 750, 750f
pathologic findings with, 747–748
orbital, 587, 591f, 593f, 595f, 595–601, 596f
clinical features of, 596–597, 597f–599f, 599–600
pathologic and immunologic features of, 595–596
salivary glands and, 2038f, 2038–2039, 2055f
sinonasal, 242–243
trachea and, 1711, 1712f
Sarcomas
Ewing's
of jaw, 975
of skull base, 835
sinonasal, 290, 292
granulocytic, sinonasal, 302–303
Kaposi's, 1909
human herpesvirus 8 and, 2289–2290, 2290f
laryngeal, 1655f
pharyngeal, 1509, 1511, 1511f
sinonasal, 315
laryngeal, 1645
metastatic to sinonasal cavities, 366f
ocular, 468f
of maxillary sinus, 857f
of nasal cavity, 857f
osteogenic. *See* Osteogenic sarcomas (OSs).
synovial
metastatic to temporomandibular joint, 2123f
of temporomandibular joint, 1036
undifferentiated, of masticator space, 1996f
Scala tympani, on magnetic resonance imaging, 1099f
Scala vestibuli, on magnetic resonance imaging, 1099f
Scalene muscle, 1793t
anterior, 1799f, 1800f, 1801f, 1802f
brachial plexus and, 2216, 2217, 2219f
middle, 1800f, 1801f, 1802f
posterior, 1800f, 1801f, 1802f
Scalp, 126
arteries of, 127, 130f
lymph node drainage of, 1881t
veins of, 127, 130f, 131
Scanners, for positron-emission tomography, 2296
Scaphocephaly, 66, 68f
Scapula, 1802f
metastatic disease of, 2233f
Scar(s), 2175, 2175f
SCCs. *See* Squamous cell carcinomas (SCCs).
SCF. *See* Superficial cervical fascia (SCF).
SCFN. *See* Subcutaneous fat necrosis of the newborn (SCFN).
Schirmer's test, 670
Schneiderian papillomas, oncocytic, sinonasal, 267, 268f
Schwann cells, 292
Schwannomas
acoustic. *See* Acoustic schwannomas.
cutaneous, 2208
facial, 1292, 1298f, 1299f
hypoglossal, 1321, 1322f
in prevertebral space, 1811f
laryngeal, 1651, 1660f
malignant. *See* Malignant peripheral nerve sheath tumors (MPNSTs).
ocular, primary, 512
of branchial plexus, 1811f
of cavernous sinus/Meckel's cave, with perineural tumor spread, 884f
of facial nerve, 1303, 1328–1330, 1330f–1336f, 1334
on computed tomography, 1330f–1336f
on magnetic resonance imaging, 1330f–1333f, 1335f, 1336f
of jaw, 970
of jugular foramen, 1292–1293, 1300f, 1320–1321
of Meckel's cave, 831f
of neck, 1815f
of oral cavity, 1416–1417, 1417f, 1440, 1448f
of parapharyngeal space, 1965–1966, 1968f–1969f
of salivary glands, 2120f
of trigeminal nerve, 1452f
orbital, 623–624, 625, 627, 628f, 629f
pharyngeal, 1501, 1502f
posterior fossa, nonacoustic, 1291–1293, 1297f–1300f
sinonasal, 292, 293f–295f
on computed tomography, 265f, 292f–295f

Schwannomas *(Continued)*
on magnetic resonance imaging, 292f, 294f, 295f
trigeminal, 831f–835f, 831–832, 1291–1292, 1297f, 1298f
vagal, 1292, 1299f
vestibular, 1277
Schwarz-Lèlek syndrome, 1267
Scintigraphy. *See* Dacryoscintigraphy; *specific regions and conditions.*
Sclera, 452–453
anatomy of, 453–455
calcification of, 479t
embryology of, 450, 532f
Scleral buckle/banding, postsurgical changes with, 520, 520f–521f
Sclerema neonatorum, 2180
Scleritis, 474, 476f, 477f
Sclerosing adenosis, of salivary glands, 2103–2104, 2104f
Sclerosing hemangiomas, orbital, 616, 621f
Sclerosis, in sinusitis, 211f, 211–212, 212f
Sclerostenosis
fibrous dysplasia versus, 1255
of temporal bone, 1267
Sclerotherapy, ultrasound-guided, of thyroid cysts, 1941–1942
Sclerotome, 1758
SCPL. *See* Supracricoid partial laryngectomy (SCPL).
Screws, for facial fractures, 376, 376f
Scutum, erosion of, with cholesteatomas, 1190–1191
SDCs. *See* Salivary duct carcinomas (SDCs).
Seasonal pollinosis, 200
Sebaceous cysts, of salivary glands, 2121, 2124f
Sebaceous neoplasms
carcinomas, of salivary gland origin, 2099
of salivary gland origin, 2098–2099
Sedano classification, of median cleft face syndrome, 27, 29t
Sedano facies, 26f
Sella turcica, 133f, 145f
floor of, 134f
lamina dura of, 145f
Semicircular canals
anatomy of, 1071, 1072f, 1073
congenital anomalies of, 1122, 1124, 1124f–1130f, 1127
CT surface reconstruction of, 1098f
on magnetic resonance imaging, 1099f, 1100f, 1102f, 1103f, 1104f
3D reconstruction of magnetic resonance imaging of, 1104f
Semicircular ducts, 1074
Semilunar ganglion, 796f, 797, 797f, 798
squamous cell carcinoma of, with perineural tumor spread, 884f
Semispinalis capitis muscle, 1797f, 1798f, 1799f, 1800f, 1801f
Semispinalis cervicis muscle, 1799f, 1800f
Semisplenius muscle, 1797f, 1798f
Sensorineural hearing loss (SNHL)
internal auditory canal anomalies associated with, 1136
vestibular aqueduct and, 1138–1140, 1154f, 1155f
Sentinel lymph nodes, detection of, 1947, 1947f
Septal arteries, posterior, 95
Septal cartilage, 11, 11f. *See also* Nasal septum.
age-related changes in, 11, 13
development of, 10, 10f
on plain films, 120
Septal tissue, of optic nerve, 540
Septoplasty, in functional endoscopic sinus surgery, 186
Septum(a). *See* Nasal septum; Septal cartilage; *specific sinuses.*
Seromucinous glands, oncocytic tumors of, 2084
Serratus muscle, anterior, 1802f, 1803f
Sertoli-cell-only syndrome, with sinusitis, 253
Sesamoid cartilages, 89
SFTs. *See* Solitary fibrous tumors (SFTs).
Shingles, lymphadenitis in, 1888
Shoulder, traction injury of, 2223f
Shunts, ocular, postsurgical changes with, 521, 522f
Sialadenitis, 2030f, 2031f, 2033f–2038f, 2042f, 2047f, 2055f, 2064f, 2174f, 2194f
acute, suppurative, 2027–2028, 2029f
chronic recurrent, 2040f–2042f, 2040–2041
myoepithelial, 2100
postirradiation, 2052
Sialectasis, congenital, 2057
Sialendoscopy, 2026
Sialoblastomas, 2102–2103, 2103f
Sialoceles, 2062f
Sialocysts, 2059–2060, 2062f
Sialodochitis, 2027, 2030f, 2033f–2035f, 2041f, 2042f, 2047f
Sialography, 2013–2017, 2015f. *See also* Salivary gland(s).
Sialolith(s), 1402–1403, 1404f–1406f
on plain films, 2013, 2013f, 2014f
Sialolithiasis, 1943, 2033f–2038f, 2039–2040, 2040f
Sialometaplasia, necrotizing, 2052
Sialosis, 2050, 2051f
Sibson's fascia, 1811
Sicca syndrome, 2043
Siderosis, superficial, 1303f
Sievert (SV), 151
Sigmoid sinus
groove for, CT surface reconstruction of, 1096f, 1097f
on magnetic resonance imaging, 1106f
reconstruction of computed tomography images of, 1105f
Sigmoid sinus plate, with cholesteatomas, 1191
Signal transduction pathways, oncogenes in, 2279f, 2279–2280
Silent sinus syndrome, sinusitis in, 256
Silicon augmentation, skin lesions due to, 2180, 2182, 2182f
Simian virus 40, in human cancer, 2288–2289
Simple bone cysts
of jaw, 942–943, 945f
of temporomandibular joint, 1036, 1040f
Sincipital cephaloceles, 43–49, 45f, 46f, 46t
frontoethmoidal, 44–45, 46t, 47–49
concurrent malformations with, 47, 49
frontonasal subtype of, 44–45, 47, 47f–49f
nasoethmoidal subtype of, 47
nasoorbital subtype of, 47, 50f–52f
interfrontal, 44
Single-photon emission computed tomography (SPECT), thallium-201, 2307–2308, 2308f–2311f
Singular canal, pseudofracture of, 1237f
Sinoliths, 254f
Sinonasal cavity, oncocytic tumors of, 2084
Sinonasal infections, on plain films, 111
Sinonasal lymphomas (SNLs), 301t–303t, 301–302, 304f–306f
on computed tomography, 302, 304f, 305f
on magnetic resonance imaging, 302, 304f, 306f
Sinonasal neuroendocrine carcinomas (SNECs), 285, 287–289
Sinonasal tumors, 261–364. *See also specific tumors.*
bone involvement with, 264–265
calcification of, 266–267
detection of, 264
sclerotic bone and, 265–266
symptoms of, 262
tumor mapping and staging of, magnetic resonance imaging for, 262–263, 263f
types of, 262
Sinonasal undifferentiated carcinomas (SNUCs), 285, 287–289
Sinopulmonary infectious syndrome
gene mutated in, 2285–2286
sinusitis in, 256
Sinus antrostomy, 170

Sinus histiocytosis, with massive lymphadenopathy, 1899, 1899f
Sinus lateralis. *See* Retrobulbar recess cell.
Sinus of Maier, 673
Sinus ostia, 33. *See also specific sinuses.*
Sinus tympani, 1067, 1067f
  erosion of, with cholesteatomas, 1193f
Sinusitis
  acute, 193–196, 194f–196f
    bacterial, 194, 196
      orbital spread of, 195, 195f
    headache with, 194–195
    lacrimal system in, 195f, 196
    mucosal inflammation in, 194, 194f
    on computed tomography, 194f–196f, 213f
    periodontal disease and, 196
    radiographic appearance of, 168–169
  air-fluid levels due to, 196–198, 197f–199f, 200
  allergic, radiographic appearance of, 169
  antral, on magnetic resonance imaging, 433f
  benign
    on computed tomography, 212, 212f, 213f
    on magnetic resonance imaging, 212, 214f
    on plain films, 208–209, 210f, 211, 211f
  cerebritis in, 582f
  chronic, 200f, 200–203
    allergic, 200–201
    fungal, 201–203
    on computed tomography, 200, 200f
    on magnetic resonance imaging, 209f, 214f
    patterns of, 169, 169f
    radiographic appearance of, 169, 169f
    vasomotor rhinitis and, 201
  complications of, 249–251, 250f, 251f
  correlation of imaging and clinical findings in, 205
  epidural abscess in, 582f
  functional endoscopic sinus surgery of. *See* Functional endoscopic sinus surgery (FESS).
  fungal, 201–203, 231–232, 241f
    in hyphal diseases, 201–202
    radiographic appearance of, 169
    yeasts and, 202–203
  historical background of, 149–150
  in pediatric patients, 204
  Lund staging system for, 185, 185t
  maxillary, on magnetic resonance imaging, 434f
  meningitis in, 582f
  on computed tomography, 417f
  orbital cellulitis and, 579
  orbital complications of, radiographic appearance of, 169–170
Sinusitis *(Continued)*
  recurrent, after functional endoscopic sinus surgery, 186, 187, 187f, 188, 189f
  sphenoid, 807, 810f
    skull base osteomyelitis secondary to, 1213f
  with orbital cellulitis, 706f
  with visual loss, 777f
Sinusitis infertility syndrome, with sinusitis, 253
Sinusotomy, sphenoid, 421, 422f
Sistrunk procedure, imaging following, 1847, 1848f
SIX3 transcription factor, holoprosencephaly and, 54
Sjögren's syndrome (SS)
  ocular, 601
  salivary glands and, 2043–2046, 2044f–2047f, 2048–2050
Skew head, 67, 68f, 69
Skin and subcutaneous lesions, 2174f, 2174–2183, 2175f. *See also specific lesions.*
  alloderm augmentation and, 2182, 2183f
  basal cell carcinoma, 2178, 2178f
  epidermoid cysts, 2176, 2177f
  foreign bodies and, 2182–2183, 2183f
  keloids, 2175–2176, 2176f
  metastatic, 2179, 2179f
  neurofibromas, 2180, 2181f
  pilomatrixomas, 2176–2177, 2178f
  pseudotumor, 2188, 2190f
  scars, 2175, 2175f
  sclerema neonatorum, 2180
  silicon augmentation and, 2180, 2182, 2182f
  squamous cell carcinoma, 2178
Skin tags, in hemifacial microsomia, 59
Skip lesions, with perineural tumor spread, 876f, 882f, 883
Skull
  dermoids of, 31–32, 32f
  shape of, in craniosynostoses, 66–69, 68f
  sutures of, 66, 67f, 74
Skull base, 785–860, 1797f
  anatomy of, 788, 789f, 790–799
    of bone, 788, 790f–801f, 791–792
    of bordering soft tissues, 792–794, 797–799
      extracranial, 792–794, 797, 801f, 802f
      intracranial, 797–799, 802f
  aneurysms of, 840, 842, 843f–846f, 844
    on computed tomography, 843f
    on magnetic resonance angiography, 846f
    on magnetic resonance imaging, 843f–846f
  basilar invagination of, platybasia versus, 853–854
Skull base *(Continued)*
  cephaloceles of, 803–804, 804f–808f
    on computed tomography, 805f, 806f, 808f
    on magnetic resonance imaging, 804f, 805f, 808f
    on plain films, 805f, 807f
  cerebrospinal fluid leaks and, 858–860, 859f
  chondrosarcomas of, 1325f
  developmental anomalies of, caused by extrinsic factors, 806–807, 810f
  dysplasias of, 852–853
    fibrous, 854–856, 855f–857f
    of bone, 857, 858f
  embryology of, 786–788, 787f
  epidermoid cyst of, 1336f
  erosion of, nasopharyngeal carcinoma and, 1482f, 1483f
  hyperparathyroidism and, 858
  hypoplasia of, 1165f
  inflammation and obstruction of, 807, 809, 810f, 811f
  meningocele of, 1164f–1165f
  metastatic disease of, 844, 846–848
    direct encroachment and, 844, 846–847, 847f, 848f
    hematogenous spread and, 848, 853f
    perineural tumor spread and, 847–848, 849f–853f
  mucoceles of, 838, 840, 842f, 843f
  mucpolysaccharidoses and, 858
  on computed tomography, 799
  on magnetic resonance imaging, 799, 801, 803, 803f
  on plain films, 799
  ossification alterations of, 804–805
  ossification centers of, 10–11, 11f
  osteogenesis imperfecta of, 857–858
  osteomyelitis of, 1326
    secondary to sphenoid sinusitis, 1213f
  Paget's disease of, 857, 857f
  parapharyngeal space disease and tumors arising in, 1986, 1986f
  platybasia of, basilar invagination versus, 853–854
  rhizotomy injections and, 860, 860f
  traumatic injuries of, 848–850, 852, 854f, 855f
  tumors and tumor-like conditions of, 809, 811–844, 812f
    aneurysmal bone cysts, 833
    carcinomas, 836, 841f
    chondromyxoid fibromas, 820, 821, 822f
    chondrosarcomas, 816–817, 818f–821f
      chordomas versus, 817–820
    chordomas, 812f–817f, 812–816
      chondrosarcomas versus, 817–820
    craniopharyngiomas, 824–826, 828f
    Gorham's disease, 837–838, 841f

Skull base *(Continued)*
juvenile angiofibromas, 827, 829, 829f, 830f
Langerhans' cell histiocytosis, 833–835, 840f
lymphoma, 835
meningiomas, 821–824, 824f–827f
neurogenic, 831f–839f, 831–832
on computed tomography, 835f
on magnetic resonance imaging, 831f, 833f, 834f, 836f–839f
pituitary adenomas, 829–831, 830f, 831f
plasmacytoma of, 835–836
Rathke's pouch cysts, 826, 828f
vascular, 836
vascular variants of, 805–806, 809f
SLDCF. *See* Superficial layer of deep cervical fascia (SLDCF).
Small cell carcinoma, vocal cord paralysis due to, 2236f
SMAS. *See* Superficial musculoaponeurotic system (SMAS).
Smell sense
abnormalities of, 94, 95t
as nasal function, 93–94, 95t
theories of, 94
Smoking, maternal, cleft lip/palate and, common, 19
Smooth surface caries, 917, 918f
SNECs. *See* Sinonasal neuroendocrine carcinomas (SNECs).
SNHL. *See* Sensorineural hearing loss (SNHL).
SNLs. *See* Sinonasal lymphomas (SNLs).
SNUCs. *See* Sinonasal undifferentiated carcinomas (SNUCs).
Soft palate, 1798f
clefting of, nasopharyngeal lesions with, 42
malignancies of, 1486–1487, 1488f, 1489f
squamous cell carcinoma, with perineural tumor spread, 871f
movements of, during oropharyngeal swallowing, 1741, 1742f
on videofluoroscopic swallowing study, 1736
Soft tissues, bordering skull base, 792–794, 797–799
extracranial, 792–794, 797, 800f, 802f
intracranial, 797–799, 802f
Soft-tissue sarcomas (STSs), malignant, sinonasal, 315–317
Solitary bone cysts
of jaw, 942–943, 945f
of temporomandibular joint, 1036, 1040f
Solitary fibrous tumors (SFTs), sinonasal, 321
Somites, 1758, 1759, 1759f
Somitomeres, 1758, 1759, 1759f
Sonic hedgehog, holoprosencephaly and, 9
Sonic hedgehog
median cleft face syndrome and, 27
upstream regulators of, 30
Sonic Hedgehog gene, holoprosencephaly and, 54, 55
South American blastomycosis, paranasal, 241
SPECT. *See* Single-photon emission computed tomography (SPECT).
Sphenoethmoid recess, anatomy of, 153, 155
Sphenoethmoidal basal cephaloceles, 51
Sphenoethmoidal cephaloceles, 804, 804f
Sphenoethmoidal recess, 92f, 100, 144f, 145f
anatomy of, 156, 159f
Sphenoid bone, 133f, 136f, 143f, 144f
anatomy of, 788, 790f–800f, 790–792
cerebrospinal fluid and, 807
embryology of, 786–787
greater wing of, 142f
on plain films, 115f, 120
lesser wing of, 142f
limbus of, 133f
neurofibromatosis and, 806f, 807f
pterygoid process of, 137f, 142f
rostrum of, 136f, 142f, 145f
Sphenoid sinus(es), 98, 100–101, 134f, 135f, 136f, 144f
abscess of, 582f
air cell development and, 792
air-fluid levels in, 198, 199f, 200
anatomy of, 156, 159f
carcinoma of, 271
development of, 100
following functional endoscopic sinus surgery, 172
fractures of, 399
lateral recess of, 135f, 136f, 143f
mucosal thickening in, 209
obstruction of, 809, 810f, 811f
on computed tomography, 154f
ostia of, 100, 145f
plain film anatomy of, 119, 119f, 120f
pneumatization of, extensive, 163, 165f
posterior, anatomic relationship to ethmoid sinuses, 156, 160f
pterygoid recess of, 135f
sclerosis in, 211–212, 212f
septa in, 100–101, 135f
on computed tomography and magnetic resonance imaging, 126
septations in, 792
tumors of, 262
Sphenoid sinus surgery, 420–422, 422f
on computed tomography, 422f
transnasal approach for, 420–421
Sphenoidal conchae, 100
Sphenoidectomy, 170
Sphenomaxillary basal cephaloceles, 51
Sphenomaxillary encephaloceles, 804, 808f
Sphenooccipital synchondrosis, 792, 800f
Sphenoorbital basal cephaloceles, 51
Sphenopalatine artery, 95, 95f, 99, 102
on computed tomography and magnetic resonance imaging, 125
Sphenopalatine foramen
on computed tomography and magnetic resonance imaging, 125
perineural tumor spread involving, 868, 873f
Sphenopalatine ganglion, 96, 101
greater palatine branch of, 96
Sphenopalatine nerve, posterolateral nasal branches of, 99
Sphenopalatine vein, 95
Sphenopharyngeal basal cephaloceles, 51
Sphenopharyngeal encephaloceles, 804
Sphenopharyngeal ligament, 1822
Sphenotemporal suture, 133f
Sphenozygomatic suture, 133f
Spinal accessory lymph nodes, drainage of, 1881t
Spinal accessory nerve
anatomy of, 1785f, 1786
branchial arches and, 1759, 1769
Spinal nerves
anatomy of, 1786–1788, 1788f, 1789f
perineural tumor spread involving, 873, 876, 881f
Spindle cell neoplasms
carcinomas, laryngeal, 1645
of lymph nodes, 1908–1909, 1909t
Spindle torus, 15
Spindled atypical mycobacteriosis (SAM), 1909
Spine
cervical, on videofluoroscopic swallowing study, 1737f, 1737–1738
osteophytes of, 1684, 1686f
on videofluoroscopic swallowing study, 1737, 1737f
Spiral lamina, on magnetic resonance imaging, 1099f
Spiral of Tillaux, 539
Splenius capitis muscle, 1793t, 1797f, 1799f, 1801f
Squamous cell carcinomas (SCCs)
basaloid, sinonasal, 272, 279f
in parotid region, with perineural tumor spread, 881f
infraorbital, with perineural tumor spread, 869f
laryngeal. *See* Larynx, squamous cell carcinoma of.
lymph nodes in, 1913f, 1926f, 1927f
metastatic, 1910f
lymph nodes in, 1913f, 1914f, 1917f–1919f
metastatic nodes and, 1906f
metastatic to salivary glands, 2108f

Squamous cell carcinomas (SCCs) *(Continued)*
metastatic to sinonasal cavities, 362
metastatic to skin, 2179f
metastatic to tracheoesophageal sulcus, 2235f
nasoethmoid, 717f–718f
nasopharyngeal, 1478–1479, 1481f
of buccal mucosa, on positron-emission tomography, 2298f
of epiglottis, on positron-emission tomography, 2300f
of external auditory canal, 1324f, 1339f
of external ear, 1214
of forehead, with perineural tumor spread, 882f
of jaw, 972f
of lip, 1428
with perineural tumor spread, 875f, 876f
of middle ear, 1324f
of oral cavity, 1427t, 1427–1433, 1428f–1439f
of floor of mouth, 1428f–1430f, 1428–1430
of gingiva/buccal mucosa, 1431, 1435f, 1436f
of hard palate, 1431–1432, 1436f
of lip, 1428
of retromolar trigone, 1432–1433, 1437f–1439f
of tongue, 1430–1431, 1431f–1434f
of parapharyngeal space, 1972, 1977f, 1978f
of parotid gland, with perineural tumor spread, 882f
of retromolar trigone, with perineural tumor spread, 878f
of salivary glands, primary, 2099, 2100f
of skin, 2178
of soft palate, with perineural tumor spread, 871f
of tongue, 1503f
of tongue base, 1490f
on positron-emission tomography, 2298f
on proton magnetic resonance spectroscopy, 2312f
on single photon emission computed tomography, 2306f
oral, with perineural tumor spread, 883f
preauricular, with perineural tumor spread, 877f
recurrence of, 2261f–2266f
retropharyngeal nodes with, 2245, 2245f
sinonasal, 264, 268, 270f–279f, 270–272
histology of, 268, 270f
on computed tomography, 264f, 272, 272f, 273f, 278f, 279f
on magnetic resonance imaging, 263f, 265f, 272, 273f–278f
Squamous cell carcinomas (SCCs) *(Continued)*
on plain films, 264f, 271f, 271–272
sphenoethmoid, 418f
thyroid, 2157, 2157f
tracheal, 1704f, 1718, 1720f, 1721f
Squamous cell papillomas, tracheal, 1721–1722, 1723f, 1724f
SS. *See* Sjögren's syndrome (SS).
Stafne cysts, 944–945, 946f, 947f
Stage transition duration, 1747, 1747f
Stapedial artery
embryology of, 1771
persistent, 1142, 1156f–1158f
tinnitus due to, 1366, 1367f
Stapes, otosclerosis of. *See* Otosclerosis.
Stapes gusher, 1148
Staphylomas, 463, 470f
Static bone cavity cysts, of jaw, 944–945, 946f, 947f
Stellate ganglion, 1789–1790
Stensen's duct, 1798f, 2008, 2009
stricture of, 2062f
Stents
following dacryocystoplasty, 725–727
for cricoid cartilage repair, 1693, 1695
for tracheal stenosis, following intubation, 1717, 1718f
Sternoclavicular joint, 1803f
Sternocleidomastoid muscle, 128f, 1791t, 1798f, 1799f, 1800f, 1801f, 1802f, 1803f
anatomy of, 1777–1778
Sternocleidomastoid tumor, 1951, 1951f, 2191, 2193f
Sternohyoid muscle, 1792t, 1800f, 1801f, 1802f
Sternomastoid tumor, 1951, 1951f, 2191, 2193f
Sternothyroid muscle, 1792t, 1802f
Stomodeum, 5
primordia surrounding, 7f, 7–8
Strabismus, 647–648
noncomitant, without associated malformations, 651
Stridor, clinical evaluation of, 1525
Stroke, ischemic, sinusitis related to, 196
Struma, 2147
STSs. *See* Soft-tissue sarcomas (STSs).
Sturge-Weber disease, choroidal hemangiomas in, 508
Styloglossus muscle, 1379t, 1380, 1792t, 1798f
Stylohyoid ligament ossification, 1440, 1449f
Stylohyoid muscle, 1791t, 1798f
Stylohyoid syndromes, 2199–2200, 2202
Styloid carotid compression, tinnitus due to, 1364
Styloid carotodynia, 2200
Styloid process, 1065, 1066, 1797f, 1798f
Stylomastoid foramen
CT surface reconstruction of, 1097f
on magnetic resonance imaging, 1103f
Stylopharyngeus muscle, 1466, 1792t
Subcapsular nodal tumors, 1915–1916, 1918f
Subclavian arteries, 1802f, 1803f
embryology of, 1771
left, aberrant, 1558f
retroesophageal, right, aberrant, 2204–2205, 2208f
Subclavian triangles, of neck, 1782, 1784f
Subclavian vein, 130f, 1803f, 2216
Subclavius muscle, 1802f, 1803f
Subcutaneous fat necrosis of the newborn (SCFN), 2179–2180, 2180f
Subcutaneous lesions, 2174f, 2174–2183, 2175f
Subdural hematomas, following functional endoscopic sinus surgery, 171f
Subglottic airway, 1801f
bottom, 1802f
Subglottic cysts, pediatric, 1576f
Subglottic hemangiomas, 1672
Subglottic obstruction, congenital, 1553–1554
Subglottic stenosis, 1670, 1677f
congenital, 1553–1554, 1705–1706
Subglottic webs, 1670
Subglottis, 1602
Sublingual fossa, 896, 896f, 899, 900f
Sublingual glands, 896, 899f
anatomy of, 2010–2011
computed tomography of, 2021
magnetic resonance imaging of, 2021, 2022f–2023f
Sublingual space, 896, 899f, 1383f, 1383–1384, 1825t, 1826t
Submandibular fossa, 896, 896f, 899, 900f
Submandibular ganglion, 1790
Submandibular gland space, 1816, 1818, 1825t, 1826t
abscess in, 1821f
Submandibular glands, 1799f, 1800f
anatomy of, 2010, 2010f
computed tomography of, 2021
magnetic resonance imaging of, 2021, 2022f–2023f
normal, ultrasound of, 1938, 1938f
sialography of, 2016–2017, 2017f
Submandibular lymph nodes, drainage of, 1881t
Submandibular space, 1816, 1818–1819, 1821f, 1825t, 1826t
normal anatomy of, 1384
Submandibular triangles, 1778, 1779f
abscess in, 1821f
masses in, differential diagnosis of, 1794, 1794t
Submaxillary space, 1825t
Submental lymph nodes, drainage of, 1881t

Submental space, 1384
Submental triangle, 1778, 1778f
  masses in, differential diagnosis of, 1794, 1794t
Submentovertical (submentovertex) view, for paranasal sinus plain films, 104, 106f
  of associated structures, 115f, 120–122, 121f
  of frontal sinuses, 3f, 109, 109f
  of maxillary sinuses, 109f, 118
  of sphenoid sinuses, 115f, 119
Subparotid lymph nodes, drainage of, 1881t
Subretinal effusion, hemorrhagic, 505f
Superficial cervical fascia (SCF), 1806, 1807f
Superficial fascia, of neck, 1806, 1807f
Superficial layer of deep cervical fascia (SLDCF), 1806–1809, 1808f, 1809f
Superficial musculoaponeurotic system (SMAS), 126
Superior thyroid cartilage notch, 1800f, 1801f
Supernumerary teeth, 987, 987f
Suppurative thyroiditis, acute, 2147
Supraalar facets, 88
Suprachoroidea, 456
Supraclavicular fossa, 1801f
Supraclavicular nerve, 127, 129f, 1788
Supracricoid partial laryngectomy (SCPL), postsurgical appearance and, 1688, 1692f
Supraglottis, 1602
  squamous cell carcinoma of, evaluation for, 1621–1622, 1626, 1626f–1639f, 1629–1631, 1634–1635
    on computed tomography, 1627f–1632f, 1635f, 1638f, 1639f
    on magnetic resonance imaging, 1622, 1626, 1633f, 1634f, 1636f–1638f
Supraglottitis, 1656
  pediatric, 1568, 1568f, 1569f
Suprahyoid region, 1602
Supramandibular lymph nodes, drainage of, 1881t
Supraorbital artery, 100, 127, 130f
Supraorbital canal, 139f, 143f
Supraorbital groove, 133f, 139f
Supraorbital margin, on CT surface reconstruction, 1096f
Supraorbital notch (foramen), on computed tomography and magnetic resonance imaging, 125
Supraorbital vein, 127
Suprasternal notch region, 1803f
Supratrochlear artery, 100, 127, 130f
Supratubal recess, cholesteatomas of, 1190, 1190f
Surgery. *See also specific procedures, sites, and conditions.*
  laryngeal changes following, 1685–1689, 1688f–1692f
  of neck, postsurgical changes and. *See* Neck, posttreatment; Neck dissection.
  pharynx following, 1517f, 1517–1518
Surveillance imaging
  baseline, 2250–2252, 2260f–2267f
  protocol for, 2252, 2254
Sutures, cranial, 66, 67f, 74
SV. *See* Sievert (SV).
Swallowing
  aging and, 1734–1735
  normal, 1731–1734
    esophageal stage of, 1734
    oral preparatory stage of, 1732
    oral transport stage of, 1732, 1733f
    pharyngeal stage of, 1732, 1734
  videofluoroscopic examination of. *See* Videofluoroscopic swallowing study (VFSS).
Sympathetic nervous system, 1788–1790
Sympathetic trunk, 1799f
Synchondroses, 787
  sphenooccipital, 792, 800f
Syndrome of amniotic bands, 18, 19f, 30
Synophrys, in holoprosencephaly, 56f
Synovial cell sarcomas, of temporomandibular joint, 1036
Synovial chondromatosis
  of jaw, 959, 961
  of temporomandibular joint, 1032–1033, 1035f, 2121
Synovial cysts, of temporomandibular joint, 1036, 1039f
Synovial sarcomas
  metastatic to temporomandibular joint, 2123f
  pediatric, 1588, 1588f
Synovitis, villonodular
  of temporomandibular joint, 2122f
  pigmented, of temporomandibular joint, 1033–1034, 1036f
Syphilis
  congenital, 236, 1208–1209
  differential diagnosis of, 236
  lymphadenitis in, 1892
  of inner ear, 1208–1209, 1209f
  phases of, 235–236
  salivary glands and, 2032, 2034
  sinonasal, 235–236
Systemic conditions, dental manifestations of, 991
Systemic lupus erythematosus, inner ear in, 1210

T

T_3. *See* Triiodothyronine (T_3).
T_4. *See* Thyroxine (T_4).
T1 relaxation time, 206, 206f–210f, 207–208
T2 relaxation time, 206–208, 207f–210f
TAM. *See* Thyroarytenoid muscle (TAM).
Target sign, with neurofibromas, in children, 1582
Taurodontia, 990, 990f
TB. *See* Tuberculosis (TB).
T-cell lymphomas
  angiocentric, sinonasal, 301–302
  orbital, 601
TCS gene, mandibulofacial dysostosis and, 63
Teacher Collins syndrome. *See* Mandibulofacial dysostosis (MFD).
Teeth, 139f. *See also* Dental *entries.*
  absence of, 987, 988f
  amelogenesis imperfecta and, 989, 990f
  anatomy of, 892–895, 895f–897f
  atrophy and augmentation procedures and, 926, 928, 928f
  dens in dente and, 988, 988f
  dental CT reformatting programs and. *See* Dental CT reformatting programs.
  dentin dysplasias and, 990
  dentinogenesis imperfecta and, 989–990, 990f
  embryology of, 890–892, 892f–894f, 894t
  enamel pearls and, 988, 989f
  endodontal disease of, 925–926
  in hemifacial microsomia, 59
  in metabolic diseases, 990–991
  in nasolacrimal fossa, 709f
  in systemic diseases, 991
  maxillary, roots of, 139f
  maxillary sinus, intrasinus, 254f
  maxillary sinus infection from disease of, 926, 927f
  osteitis condensans and, 926
  periodontal disease and, 925, 925f, 926f
  pulp stones and, 988, 989f
  size of, 987, 988f
  supereruption of, 914f
  supernumerary, 987, 987f
  surfaces of, 894–895
  taurodontia and, 990, 990f
  with pediatric facial fractures, 399, 401
TEF. *See* Tracheoesophageal fistula (TEF).
Teflon, for vocal cord paralysis, 1695, 1696f, 1697f
Tegmen tympani
  dehiscence of, 1146–1147
  with cholesteatomas, 1191, 1193f–1195f
Telecanthus, 556
Telomerase, 2288
Temporal arteries, superficial, 127, 130f, 1796f, 1797f
Temporal bone, 1057–1089, 1093–1107. *See also* Inner ear; Middle ear; Outer ear; Petrous apex.

Temporal bone *(Continued)*
computed tomography of, 1093–1095, 1094f–1098f
congenital anomalies of, 1109–1161, 1110t–1113t
involving ear, 1151, 1161, 1165f–1169f
of inner ear, 1119–1140
imaging techniques for, 1119–1122, 1123f
membranous and bony labyrinthine, 1122, 1124, 1127–1132
of middle ear, 1116–1118, 1117f–1122f
of outer ear, 1113–1116, 1114f–1116f
petrous, associated with meningitis, 1145–1148, 1150–1151, 1163f
vascular, 1140, 1142–1145
of internal carotid and stapedial arteries, 1140, 1142–1144
of jugular vein, 1144–1145
development of, 1109
embryology and developmental anatomy of, 1058–1062, 1059f
of inner ear, 1058–1060, 1060f
of mastoid process formation, 1062
of neonatal temporal bone, 1061–1062, 1062f
of outer and middle ear, 1061
of pneumatic cells, 1061
fibrous dysplasia in, 1253–1256, 1255f–1258f
differential diagnosis, 1254–1256, 1259f
fractures of, 1230–1233
complications of, 1239, 1241–1243
dislocation and, 1234f
longitudinal, 1230–1233, 1232f–1234f
mixed, complicated, 1233f
ossicular dislocation and fracture with, 1236–1239, 1238f–1241f
transverse, 1233, 1234f–1236f
infections of, 1173–1174. *See also specific infections and locations.*
magnetic resonance imaging of, 1093, 1095, 1097–1099, 1099f–1106f, 1103
gradient echo, 1097
high-resolution T-1 weighted, 1103
high-resolution T-2 weighted, 1098–1099, 1103
imaging protocols for, 1097–1098, 1106t
routine brain survey and, 1098
mastoid portion of, on CT surface reconstruction, 1096f
metastatic disease of, fibrous dysplasia versus, 1256
neonatal, development of, 1061–1062, 1062f
Temporal bone *(Continued)*
normal anatomy of, 1062–1075, 1063f
of external auditory canal, 1066
of facial nerve route, 1070–1071
of inner ear, 1071–1074
of mastoid portion, 1064
of middle ear, 1066–1070
of perilymphatic spaces and fluid systems, 1074–1075
of petrous portion, 1064–1065
of squamous portion, 1062–1064
of styloid process, 1066
of tympanic portion, 1065
on computed tomography, 1119, 1120–1121
on magnetic resonance imaging, 1119–1120, 1122, 1123f
postoperative, 1216–1222
following cochlear implantation, 1222, 1223f, 1224
following mastoidectomy, 1216t, 1216–1218, 1217f, 1218f
following ossiculoplasty and ossicular reconstruction, 1218–1222, 1219f–1223f
pseudofractures of, 1233–1236, 1236f–1238f
tinnitus and. *See* Tinnitus.
tumors of, 1275–1352. *See also specific tumors.*
cerebellopontine angle. *See* Cerebellopontine angle (CPA), tumors of.
clinical overview of, 1276
imaging overview of, 1276
involving facial nerve. *See* Facial nerve, temporal bone tumors involving.
of external auditory canal, 1339–1342
of internal auditory canal and cerebellopontine angle, differential diagnosis of, 1285–1306
of mastoid, 1343, 1345, 1347f
of middle ear, 1342–1343
of petrous apex. *See* Petrous apex, tumors of.
tympanic portion of, on CT surface reconstruction, 1096f
Temporal crest, 896f, 898
Temporal fossa, inferior, 143f
Temporal horn, on magnetic resonance imaging, 1101f
Temporal lobes
hematomas of, 739f
on magnetic resonance imaging, 1100f, 1102f
Temporal spatial theory of olfaction, 94
Temporal vein
middle, 127
superficial, 127, 130f
Temporalis muscle, 897, 899f, 1380t, 1793t, 1796f, 1797f
Temporomandibular joint (TMJ), 995–1050
accuracy of imaging of, 1021–1022, 1029f, 1029t
anatomy of, 996f, 996–997
arthritides of, 1036–1037, 1041f, 1042f
arthrography of, 1002–1006
abnormal findings on, 1006, 1006f, 1007f
complications following, 1006
development of, 1002
double-contrast technique for, 1005
indications and contraindications to, 1003
normal findings on, 1005f, 1005–1006
radiologic equipment and procedure for, 1003
single- and double-contrast, 1002–1003, 1004f
single-contrast technique for, 1004–1005, 1005f
computed tomography of, 1006–1009, 1008f–1010f
findings on, 1009, 1012f
magnetic resonance imaging compared with, 1009, 1013
technique for, 1007–1009, 1011f
congenital anomalies of, 1038
coronoid hyperplasia of, 1038, 1044f
disc perforation and, 999
disc position and, terminology for describing, 998
function of, 997, 997f
imaging of, 1000–1032
internal derangement of
classification of, 1001
related to displacement of disc, 997–1000, 998f, 999f
clinical aspects of, 1000, 1001
disc deformity and, 999, 999f
joint effusion and, 1018, 1021f–1023f
last-stage changes following, 999–1000, 1000f
lock and, 1020–1021, 1028f
marrow abnormalities of mandibular condyle and, 1018, 1024f–1026f
osteoarthritis and, 1014f, 1018, 1023f
osteochondritis dissecans and, 1019, 1026f, 1027f
stuck disc and, 1019–1020, 1027f, 1028f
with reduction, 998–999
without reduction, 999
treatment of
alloplastic implants for, 1025–1026, 1031f–1033f
costochondral grafts for, 1028, 1032, 1033f, 1034f

Temporomandibular joint (TMJ) *(Continued)*
imaging after, 1022
imaging techniques after, 1024–1025, 1030f, 1031f
modalities for, 1024
total joint replacement as, 1028, 1033f
lesions of, 2119, 2121f–2123f
magnetic resonance imaging of, 1009–1017, 1012f
computed tomography compared with, 1009
contraindications to, 1013
disc deformity on, 1016–1017, 1020f
disc displacement on, 1012–1014, 1016, 1016f–1020f
dynamic, 1046, 1049
field strength and, 1009, 1013f
metallic artifacts in, 1032, 1034f
normal findings on, 1011–1012, 1015f
surface coil and scanning technique for, 1009–1011, 1014f, 1014t
thin-section, 1046, 1050f
magnetic resonance spectroscopy of, 1050
muscular atrophy and, 1038, 1046
on magnetic resonance imaging, 1102f
plain films of, transcranial and transmaxillary projections for, 1000–1001, 1002f
radionuclide imaging of, 1046, 1049f
synovial chondromatosis of, 2121
synovial sarcoma metastatic to, 2123f
tomography of, 1001–1002, 1002f
traumatic injuries of, acute, 1037, 1042f–1044f
tumors and tumor-like conditions of, 1032–1036
villonodular synovitis of, 2122f
Temporoparietalis muscle, 91t, 128f
Tendinitis, of longus colli, 1505, 1507, 1507f–1508f
Tendon of Lockwood, common, 539
Tenon's capsule, anatomy of, 453, 454f, 539
Tenon's space, anatomy of, 539
Tensor veli palatini muscle, 1466, 1792t, 1796f, 1797f
Tentorium, on magnetic resonance imaging, 1100f, 1102f
Teratogens
cleft lip/palate and, common, 19
holoprosencephaly and, 55
Teratomas
epignathus, 42–43
fetal, 1582f
of neck, 1858–1859
of parapharyngeal space, 1975
orbital, 565–566
pediatric, 1582
Teratomas *(Continued)*
sinonasal, 361
thyroid, 2157
TGB-ß3 gene, cleft palate and, 20
TGDCs. *See* Thyroglossal duct cysts (TGDCs).
TGF-alpha gene product, cleft lip/palate and, 19
TGIF. *See* Transforming growth-interacting factor (TGIF).
Thalassemia, sinonasal, 308, 308f, 309f
on computed tomography, 308f
on magnetic resonance imaging, 309f
Thalassemia major, 101
Thalidomide embryopathy, 1112t
Thermal trauma, laryngeal, in children, 1574, 1575f
Thoracic duct cysts, 2269f
Thoracic inlet, 2216
Thrombosis, 2202, 2204, 2204f
arterial, 2205, 2209f
of carotid artery, 2268f
of cavernous sinus, 807, 811f
Thrombus, with aneurysms, on magnetic resonance imaging, 844
Thymic cysts, 1836, 1838f
Thymus, embryology of, 1760, 1762
Thyroarytenoid muscle (TAM), 1598f, 1599f, 1600f, 1601
squamous cell carcinoma and, 1629, 1634f
Thyroepiglottic ligament, 1599
Thyroglossal duct cysts (TGDCs), 800f, 1840f–1844f, 1840–1842, 2142f–2144f, 2142–2143
in infrahyoid neck, 1841, 1843f, 1844f
in suprahyoid neck, 1840–1841, 1841f, 1842f
laryngeal, 1652, 1654, 1669f
neoplasms arising within, 1847, 1847f
of oral cavity, 1394–1395, 1397f, 1398f
on computed tomography, 1841f–1844f, 1841–1842
on magnetic resonance imaging, 1842, 1844f
on ultrasound, 1948, 1948f, 1949f
pediatric, 1544, 1546f
Thyroglottic ligament, 1599–1600
Thyrohyoid muscle, 1792t, 1800f, 1801f
Thyroid carcinomas, 1719f
anaplastic, 1819f, 2156, 2156f, 2157f
follicular, 2150f, 2154
medullary, 2154–2156, 2156f
metastatic, lymph nodes in, 1920, 1921f–1925f
metastatic to sinonasal cavities, 362
mucoepidermoid, 2136, 2157f
nodal staging of, 1882, 1882t
on positron-emission tomography, 2304–2305, 2306f
Thyroid carcinomas *(Continued)*
papillary, 1846f, 1847f, 1921f–1924f, 2140f, 2148f, 2151–2152, 2152f–2155f, 2154
metastatic, 1904f, 1925f
metastatic to parapharyngeal space, 1976f
on positron-emission tomography, 2305f
recurrence of, 2267f
pediatric, 1544, 1546f, 1587
recurrent laryngeal nerve invaded by, 1681f
squamous cell carcinoma, 2157, 2157f
Thyroid cartilage, 1597f, 1597–1598, 1598f, 1800f, 1801f
bottom of, 1801f
embryology of, 1767
fractures of, 1663, 1673f, 1674f
inferior cornu of, 1801f
ossified, 1801f
Thyroid gland, 1802f, 1803f, 2134–2157. *See also* Thyroid carcinomas.
adenomas of, 2150–2151
anatomy of, 1780–1781, 2135f, 2135–2136
asymmetrical, 1687f
autoimmune disease of, 2143–2147
clinical manifestations of disease of, 2137f, 2137t, 2137–2138, 2138f
congenital anomalies of, 1838–1840, 2141–2143, 2142f–2144f
cysts of, 1837, 1838f, 1839f
ectopic, 2142
arising from lateral anlage, 1846–1847
arising from median anlage, 1842, 1845f, 1845–1846, 1846f
neoplasms arising within, 1847
pediatric, 1544, 1546, 1546f, 1547f
tracheal, 1723, 1724f, 1725
embryology of, 1762–1765, 1763f–1766f
endocrinology of, 2136–2137, 2137t
enlarged, 1939–1940. *See also* Goiter.
follicular adenoma of, 2150f
goiter and, 2147–2149, 2148f, 2149f
imaging of, 2138–2141
cross-sectional, 2139–2141, 2140f
nuclear scintigraphy for, 2138–2139, 2139t, 2140f
ultrasonography for, 2141, 2141f
ultrasound for
in diffuse thyroid disease, 1939f–1941f, 1939–1940
in focal thyroid disease, 1940–1941, 1941f
of normal thyroid, 1937, 1937f
percutaneous aspiration guided by, 1941
sclerotherapy of cysts guided by, 1941–1942

Thyroid gland *(Continued)*
tumor recurrence after thyroidectomy and, 1941, 1942f
lingual, 1395, 1399f
lymph node drainage of, 1881t
lymphoma of, 2156
malignant neoplasms of, 2151–2157
metastatic disease of, 2153f–2157f, 2157, 2157f
teratoma of, 2157
top of, 1801f
Thyroid nodules, 2149–2150, 2150f
Thyroid ophthalmopathy, 421f
Thyroid orbitopathy, 591–595
diagnosis of, 592
diagnostic imaging in, 592–593, 593f, 594f, 595
pathology of, 591–592
Thyroid peroxidase, 2136
Thyroidectomy, total, postsurgical imaging and, 2252f, 2267f
Thyroiditis, 2143, 2145f
DeQuervain's (subacute granulomatous), 2147
Hashimoto's, 2145–2146, 2146f
postpartum, 2146, 2147
Riedel's, 2147
silent, painless, 2146–2147
suppurative, acute, 2147
Thyrotoxicosis, clinical manifestations of, 2137, 2137t
Thyroxine (T_4), 2136, 2137
Tinnitus, 1362–1372
arterial causes of, 1363–1367
aberrant carotid artery, 1364, 1364f
atherosclerosis, 1363
carotid or vertebral artery dissection, 1363–1364, 1365f
fibromuscular dysplasia, 1363, 1364f, 1365f
laterally displaced carotid artery, 1366
persistent stapedial artery, 1366, 1367f
petrous carotid aneurysm, 1364
styloid carotid compression, 1364
arteriovenous causes of, 1367–1370
cerebral malformations, 1367–1368
direct arteriovenous fistula, 1369–1370, 1370f
dural arteriovenous fistula, 1368f, 1368–1369, 1369f
Otosclerosis, 1367
otospongiosis, 1367
Paget's disease, 1367
paraganglioma, 1367
vascular head and neck tumors, 1367
radiologic investigation of, 1371–1372
venous causes of, 1370–1371
idiopathic, 1371
in intracranial hypertension, 1370–1371
Tinnitus *(Continued)*
in systemic conditions, 1370
large emissary veins, 1371
large or exposed jugular bulb, 1371
transverse sinus stenosis, 1371
Tissue patterning, molecular signaling in, 9
TMJ. *See* Temporomandibular joint (TMJ).
TNM classification, for laryngeal squamous cell carcinoma, 1615, 1616
Toes, great, reduplicated, in Mohr syndrome, 16f
Tolosa-Hunt syndrome, 587–588, 591
Tongue, 1798f
base of, 1798f
adenoid cystic carcinoma of, 1496f
on proton magnetic resonance spectroscopy, 2313f
on videofluoroscopic swallowing study, 1736–1737, 1737f
pleomorphic adenomas of, 1497f
resection of, swallowing and, 1740–1741
squamous cell carcinoma of, on positron-emission tomography, 2298f
tumors of, 1487, 1489, 1489f, 1490f
bifid, with cleft lower lip and mandible, 29
bound, with cleft lower lip and mandible, 29–30
congenital absence of, 1386
embryology of, 1759f, 1762–1765, 1763f–1766f
glossoptosis of, congenital, 1548–1549
hemangiomas of, congenital, 1559f
heterotopic tissues of, 1397–1398, 1400f
lymph node drainage of, 1881t
macroglossia and, 1459, 1459t
macroglossia of, congenital, 1549, 1549f
median raphe, 1798f
movements of, during oropharyngeal swallowing, 1739f, 1739–1741, 1740f
muscles of, 1791t
normal anatomy of, 1378, 1380, 1381f, 1382f
extrinsic muscles and, 1378, 1380
intrinsic muscles and, 1378, 1382f
motor autonomic nervous system sensory innervation and, 1380
on plain films, 121
on videofluoroscopic swallowing study, 1736, 1736f
squamous cell carcinoma of, 1430–1431, 1431f–1434f, 1503f
transverse muscles of, 1798f
shadow of, 1799f
vascular malformations of, 1502f
Tonsil(s)
carcinoma of, 1516f, 1916f, 1994f
embryology of, 1773
hypertrophy of, 1578
lingual, hypertrophy of, 1532f
palatine
hypertrophy of, 1532f
lymph node drainage of, 1881t
on plain films, 121f, 121–122
retention cysts of, 1478f
Tonsillar fossa
hematoma in, 1512f
malignancies of, 1486, 1487f, 1488f
Tonsillar pillar
anterior, malignancies of, 1485, 1486f, 1486t
posterior, malignancies of, 1485–1486
Tonsillitis
bacterial, 1562–1564, 1564f–1567f, 1566
streptococcal, 1564f
viral, 1562
Tonus tubarius, 1796f
Tooth. *See* Teeth.
Tori. *See also specific tori.*
multiple, 14
Tornwaldt's cysts, 1507–1508
imaging features of, 1507–1508, 1508f, 1509f
Torticollis, muscular, 2191–2194
Torus mandibularis, 14, 15, 15f, 958, 961f, 962f
Torus maxillaris, 14
Torus palatinus, 14f, 14–15, 138f, 141f, 958, 962f, 963f, 1418f, 1419f
Torus tubarius, 144f
Toti's operation, 672
Tower head, 67
Towne view, for paranasal sinus plain films, of maxillary sinuses, 117, 117f, 118
Toxic shock syndrome (TSS), sinusitis in, 256
Toxocariasis, ocular, 475, 479f, 495–496
diagnostic imaging in, 496, 496f
Toxoplasmosis
abscesses in, 778f
lymphadenitis in, 1896–1897
salivary glands and, 2036–2037
Trabecular carcinomas. *See* Merkel cell tumors.
Trachea, 1700–1725, 1802f, 1803f
adenoid cystic carcinoma of, 1718–1719, 1721f
amyloidosis and, 1711, 1713f–1714f
anatomy of
gross, 1701
of innervation and blood supply, 1701–1702
of lymphatic drainage, 1702
of surrounding structures, 1702
pediatric, 1533, 1535

Trachea *(Continued)*
benign mixed cell tumors of, 1723
carcinoid tumors of, 1723
cartilaginous tumors of, 1722
chondrosarcoma of, 1720
congenital abnormalities of, 1704–1709
croup and, 1710
diffuse disorders of, 1709–1714
embryology of, 1523–1524, 1768
granulation tissue in, in children, 1576f
granulomatous disease of, 1711
in children, 1576f
hamartomas of, 1722–1723
hemangioendotheliomas of, 1721
hemangiomas of, 1721
histoplasmosis and, 1710–1711
mucoepidermoid carcinoma of, 1705f, 1719–1720
radiographic evaluation of, 1702–1704
computed tomography for, 1702–1703, 1703f
magnetic resonance imaging for, 1703
plain films for, 1702, 1703f
virtual bronchoscopy for, 1703–1704, 1704f, 1705f
relapsing polychondritis and, 1711
saber-sheath, 1712
sarcoidosis and, 1711, 1712f
squamous cell carcinoma of, 1704f, 1718, 1720f, 1721f
squamous cell papillomas of, 1721–1722, 1723f, 1724f
tracheopathia osteochondroplastica and, 1712, 1715f
traumatic injuries of, 1714–1717
pediatric, 1574, 1575f
tuberculosis and, 1710
tumor-like conditions of, 1723, 1724f, 1725
tumors of, 1717–1723
benign, 1720–1723, 1722f
malignant, 1718–1720, 1719f
Tracheal bronchus, 1706–1707, 1707f
Tracheal cartilages, 1701
Tracheal diverticula, 1707, 1707f
Tracheal obstruction, congenital, 1554–1556
Tracheal stenosis, 1717f
congenital, 1705–1706
intrinsic, 1554–1555, 1555f
Tracheitis, bacterial, 1569–1570, 1570f
Tracheobronchomegaly, 1713–1714, 1715f
Tracheoceles, 1707, 1707f
Tracheoesophageal cysts, 1860
Tracheoesophageal fistula (TEF), 1707–1708, 1708f–1710f
following intubation, 1717
with esophageal atresia, 1707–1708, 1708f–1710f
Tracheoesophageal sulcus
carcinoma of, 2235f
metastatic disease of, 2235f, 2237f
Tracheomalacia, 1554, 1554f, 1704–1705, 1706f
Tracheomegaly, secondary, 1714, 1714f
Tracheopathia osteochondroplastica, 1712, 1715f
Tracheostomy, injuries due to, 1715, 1716, 1717, 1717f
Tracheostomy tubes, 1695, 1695f
on videofluoroscopic swallowing study, 1738–1739
Transethmoidal basal cephaloceles, 51
Transethmoidal encephaloceles, 804
Transforming growth-interacting factor (TGIF), holoprosencephaly and, 54
Transitional cell carcinomas, nasolacrimal, dacryocystography in, 677f–678f
Translabyrinthine fistulas, 1148, 1150–1151, 1163f
Translocations, creating oncogenic fusion proteins, 2281
Transmembrane domain of fibroblast growth factor receptors, 71
Transsphenoidal basal cephaloceles, 51
Transsphenoidal cephaloceles, 804, 805f
Transverse muscles, of oral cavity, 1379t
Transverse sinus stenosis, tinnitus due to, 1371
Trapezius muscle, 128f, 1793t, 1798f, 1799f, 1800f, 1801f
Trapezius tendon, 1798f
Traumatic bone cysts, of jaw, 942–943, 945f
Treacher-Collins syndrome, 58, 63, 64f, 101, 565f, 1112t, 1169f
bony orbit in, 562, 565f
orbit in, 562, 562f
Treacle protein, mandibulofacial dysostosis and, 63
Tremors, lingual, swallowing and, 1741
Trephination, of frontal sinus, 404–405, 405f
Treponema pallidum infections. *See* Syphilis.
Treponema pertenue infections, paranasal, 236
Triangularis muscle, transverse menti part of, 90t
Trigeminal artery
persistent, 809f
variants of, 784, 805f
Trigeminal nerve, 102, 127
anatomy of, 1782, 1785f
branchial arches and, 1759, 1763
branching of, 801f
interconnections with other cranial nerves, 873, 879f, 880f
mandibular division of, 1451, 1451f–1454f
Trigeminal nerve *(Continued)*
perineural tumor spread involving, 868, 870–871, 875f–878f
maxillary division of, 96, 99, 101
olfaction and, 94
perineural tumor spread involving, 868, 869f–874f
meningioma of, 1453f
motor dysfunction of, in chronic otitis media, 1184
on magnetic resonance imaging, 1100f
ophthalmic division of, 96, 99, 101
perineural tumor spread involving, 867, 867f, 868f
schwannoma of, 1291–1292, 1297f, 1298f, 1452f
Trigonocephaly, 66, 68f, 70f
Triiodothyronine (T_3), 2136, 2137
Trimalar fractures, 385, 387t, 387–388, 388f–390f
on computed tomography, 389f, 390f
on plain films, 388f
Trismus, 1437f, 1439f
Trisomy 13, holoprosencephaly with, 54
Trisomy 13-15, 1112t
Trisomy 18, 1112t
holoprosencephaly with, 54
Trisomy 21, 1113t
Triticeal cartilage, 1599
Trochlear nerve, 542
branchial arches and, 1759
TSS. *See* Toxic shock syndrome (TSS).
Tuberculosis (TB)
laryngeal, 1656, 1670f
lymph nodes in, 1928f
lymphadenitis in, 1890f, 1891f, 1893
mastoiditis due to, 1199
of salivary glands, 2028f, 2031
orbital, 609f
otitis media due to, 1199
sinonasal, 234–235
tracheal, 1710
Tuberculous lymphadenopathy, ultrasound in, 1945f
Tuberculous meningitis, 750f
Tuberculous osteomastoiditis, 1179f
Tuberculum sellae, 133f
Tuberosity recesses, 102
Tullio's phenomenon, 1127, 1129f, 1209
Tumor angiogenesis, 2291
imaging of, 2291
Tumor extension, extranodal, 1916, 1919f, 1920t
Tumor suppressor genes, 2281–2287
familial cancer syndromes and, 2281–2283
Li-Fraumeni, 2282–2283, 2283f
retinoblastoma, 2281–2282, 2282f
genome instability syndromes and, 2285
guardians and gatekeepers and, 2283, 2284f

Tumor suppressor genes *(Continued)*
interaction with proteins encoded by oncogenic DNA viruses, 2288
p53 gene and DNA damage and, 2284–2285
regulating protective mechanisms, 2285–2287
retinoblastoma protein, Rb, and cell cycle control and, 2283–2284
Tumor-reactive lymphadenopathy, 1903
Turbinates. *See* Nasal turbinates.
Turbinectomy, middle, postoperative findings with, 187, 187f
Turricephaly, 67
TWIST transcription factor, craniofacial dysostoses and, 73f, 74
Two-hit hypothesis of Knudsen, 2281
Tympanic cavity, parts of, 1066
Tympanic membrane
anatomy of, 1066
calcification of, 1199, 1199f, 1200f
Tympanoplasty, 1221–1222
Tympanosclerosis, 1199, 1199f, 1200f
Tympanostomy tubes, 1184, 1185f, 1219f
Tympanum, pneumatization of, 1061

U

Ultrasmall superparamagnetic iron oxide (USPIO) MR contrast agents, 2315–2317
clinical applications for, 2316–2317
notal metastasis detection, 2316–2317
primary site evaluation, 2317
mechanism of, 2315, 2316f
technique for, 2316
Ultrasound. *See specific regions.*
of neck. *See* Neck, ultrasound of.
Uncibullous groove, 101
Uncinate bulla, 161, 164f
Uncinate process, 92f, 97, 98, 101, 102, 140f, 144f
anatomy of, 155, 157f
attachment of, 160–161, 164f
deviation of, 160, 163f
pneumatization of, 161, 164f
Uncinatectomy, 170
Uncinectomy, postoperative findings with, 187
Undifferentiated carcinomas
large cell, of salivary glands, 2101–2102
of mastoid, 1347f
of salivary glands, 2101–2102
sinonasal, 285, 287–289
small cell
cutaneous. *See* Merkel cell tumors.
of salivary glands, 2101
Usher's syndrome, 1113t
USPIO. *See* Ultrasmall superparamagnetic iron oxide (USPIO) MR contrast agents.
Utricle, 1074
Utriculosaccular anomalies, 1121f, 1127, 1130f
Uvea, 453
anatomy of, 455f, 455–456
hemangiomas of, 509
lymphoid hyperplasia of, 473
lymphomas of, 511–512, 512f
melanomas of, 469f
malignant, 500–506
clinical diagnosis of, 500
diagnostic imaging in, 500–501, 501f–505f, 503–505
differential diagnosis of, 505–506, 506f, 506t
on computed tomography, 500f
on magnetic resonance imaging, 501f–506f
retinal detachment and, 514
metastatic disease of, 507, 508f
Uveal nevus, 508
Uveitis, 475, 478f
anterior, in sarcoidosis, 747
in sarcoiditis, 597, 597f
Uveoparotid fever, 600
Uvula, 1798f
on plain films, 121

V

Vaccinia, lymphadenitis in, 1888
Vagus nerve, 96, 1601, 1702, 2231–2235, 2234f–2236f, 2234t
anatomy of, 1785f, 1785–1786
branchial arches and, 1759, 1769
on magnetic resonance imaging, 1100f
pharyngeal branch of, 2231–2232
schwannomas of, 1292, 1299f
Vallecula, 1800f
Vallecular cyst, 1661, 1844f
Valsalva DCR bubble test, 670–671
Valves of Krause, 699
Van Buchem's disease. *See* Endosteal hyperostosis.
van der Hoeve's syndrome. *See* Osteogenesis imperfecta.
Vanishing bone disease, 837–838, 841f
Varicella zoster virus (VZV) infections
labyrinthitis due to, 1207, 1207f
lymphadenitis in, 1888
Varix, orbital, 569, 617, 619–620, 621f, 624f
Vascular disorders. *See also specific disorders.*
congenital, 1556–1561
neoplastic
of lymph nodes, 1909
of skull base, 836
tinnitus due to, 1367
of oral cavity, 1387, 1387f
Vascular loop, 1294, 1302f
Vascular lymphadenopathies, 1903
Vascular malformations
of jaw, 970
of oral cavity, 1388–1398
arterial, 1388–1389, 1391f, 1392f
capillary, 1388
lymphatic, 1389, 1392f, 1393f
venous, 1388, 1389f, 1390f
of tongue, 1502f
tracheal, 1708–1709, 1710f
Vascular rings
pediatric, 1557f
tracheal, 1709, 1710f
Vascular slings, 1709
Vascularized polyps, sinusitis and, 203–204
Vasculolymphatic malformations, of neck, 1852
Vasomotor rhinitis, 201
VATER association, 1113t
OAV complex and, 58
VB. *See* Virtual bronchoscopy (VB).
VCN. *See* Vestibulocochlear nerve (VCN).
VCP. *See* Vocal cord paralysis (VCP).
VDB. *See* Vertebrobasilar dolichoectasia (VDB).
Venous infarction, with otitis media and mastoiditis, 1179, 1182
Venous malformations
congenital, 1561, 1561f, 1562f
of oral cavity, 1388, 1389f, 1390f
Ventricular dilatation, 413f
Ventricular ligament, 1599
Vermian tumors, 1300–1301
Vernet's syndrome, 1312
Verrucous carcinomas, laryngeal, 1645
Vertebral arteries, 1798f, 1800f, 1801f
dissection of, tinnitus due to, 1363–1364
on magnetic resonance imaging, 1100f
pseudoaneurysms of, 2207f
Vertebral veins, 127
Vertebrobasilar dolichoectasia (VDB), 1293–1294, 1300f, 1301f
vertical/oblique muscles, of oral cavity, 1379t
Vesalius, foramen of, 806
Vestibular aqueduct
pseudofracture of, 1237f
reconstruction of computed tomography images of, 1105f
sensorineural hearing loss and, 1138–1140, 1154f, 1155f
Vestibular folds, 1596
Vestibular nerve, on magnetic resonance imaging, 1099f, 1100f, 1101f
Vestibular schwannomas, 1277
Vestibular sense organs, anatomy of, 1074
Vestibule
common cavity for cochlea and, 1129, 1133f, 1134f
congenital anomalies of, 1121f, 1127, 1130f
enlarged, 1124f, 1125f
of bony labyrinth
anatomy of, 1071, 1072f

Vestibule *(Continued)*
on magnetic resonance imaging, 1099f
of nose, 90
on magnetic resonance imaging, 1102f, 1104f
3D reconstruction of magnetic resonance imaging of, 1104f
Vestibulocochlear nerve (VCN)
congenital anomalies of, 1136, 1142f–1145f
on magnetic resonance imaging, 1100f
VFSS. *See* Videofluoroscopic swallowing study (VFSS).
Videofluoroscopic swallowing study (VFSS), 1727–1731, 1728t
barium swallow compared with, 1729
clinical examination and, 1729
findings on, 1735t, 1735–1751
biomechanical movements, 1739–1746
glottic closure and, 1744–1745
of cricopharyngeus/pharyngoesophageal segment, 1745f, 1745–1746, 1746f, 1747t
of epiglottis, 1741–1743, 1742f
of esophagus, 1746
of hyoid, 1743
of larynx, 1743
of lips and cheeks, 1739
of pharyngeal wall, 1743–1744, 1744f
of soft palate, 1741, 1742f
of tongue, 1739f, 1739–1741, 1740f
laryngeal penetration and transglottic aspiration and, 1748f, 1748–1749, 1749f, 1749t
normal and abnormal anatomy, 1735f–1738f, 1735–1739
oral and pharyngeal transit duration and, 1748
temporal coordination of biomechanical events in relation to bolus flow and, 1746–1747
therapeutic strategy evaluation and, 1749–1751, 1750f, 1751t
timeliness of pharyngeal swallow and, 1747f, 1747–1748
indications for, 1729
multidisciplinary nature of, 1728–1729
normal, overview of, 1751–1752
procedure for, 1730t, 1730–1731
contrast agents and, 1730–1731
positioning and, 1730, 1730f
recording and, 1731
reporting of findings and, 1731
Vidian canal, 142f, 143f, 144f
anatomy of, 790, 791, 794f
on computed tomography and magnetic resonance imaging, 125, 126
Vidian nerve, 96
perineural tumor spread involving, 868, 874f
Villonodular synovitis
of temporomandibular joint, 2122f
pigmented, of temporomandibular joint, 1033–1034, 1036f
Viral oncogenes, 2276, 2277t
Virtual bronchoscopy (VB), 1703–1704, 1704f, 1705f
Visceral compartment, of neck, 1815
Visceral fascia, 1812
Visual fields, 737
Visual pathways
anatomy of, 737, 738f–740f
on computed tomography, 741–742
on magnetic resonance imaging, 742
imaging techniques for, 738–739, 741, 741f, 742f
pathologic conditions affecting. *See specific conditions.*
retrobulbar, 735–736, 736f
retrochiasmatic, embryology of, 736–737
Vitreous
anatomy of, 458–459
embryology of, 449–450
opacities in, 499
Vitreous body, embryology of, 532f
Vocal cord(s)
contusion of, 1574f
false, 1596, 1596f
nodules of, 1648, 1656f
true, 1596, 1596f, 1801f
Vocal cord paralysis (VCP), 1676, 1678, 1682, 2233–2235, 2235f–2237f
adductor, 1682, 1683f
congenital, 1551–1552
level of pathology and, 2234t, 2234–2235, 2235t
pediatric, 1573f
recurrent laryngeal nerve deficit and, 1678, 1680f–1682f
superior laryngeal nerve deficit and, 1676
Teflon injections for, 1695, 1696f, 1697f
Vocal fold(s), adduction of, on videofluoroscopic swallowing study, 1738
Vocal fold paralysis, on videofluoroscopic swallowing study, 1738
Vocal ligaments, 1598f, 1599
Voice conservation therapy, for laryngeal squamous cell carcinoma, 1615, 1617
Voice valves, 1695, 1695f
Vomer, 11f, 12f, 13, 89, 89f, 140f, 142f, 1796f
anatomic relationships at birth, 30f
development of, 10, 10f
Vomerine groove, 10–11, 11f
Vomeronasal cartilage, 89f
Von Hippel-Lindau disease, 509
choroidal hemangiomas in, 508
Von Hippel-Lindau retinal angiomatosis, 499–500
Von Recklinghausen's disease, 624, 2286. *See also* Neurofibromas.
von Willebrand's disease, air-fluid levels and, 198
Voorhoeve syndrome. *See* Osteopathia striata.
Vorticose veins, 543
VZV. *See* Varicella zoster virus (VZV) infections.

W

Waardenburg syndrome, 1113t, 1127
Waldeyer's ring, 7
Warburg's syndrome, 467f, 490–491
clinical diagnosis of, 491
diagnostic imaging in, 491, 491f
Warming of air, as nasal function, 93
Warthin's tumors, 1943f, 1943–1944, 1944f, 1962, 2076–2077, 2079–2080, 2080f–2082f, 2082
Wassmund IV fractures, 384, 386f
Waters view, for paranasal sinus plain films
modified, 103–104, 105f
of ethmoid sinuses, 112, 112f, 113
of frontal sinuses, 109, 111
of maxillary sinuses, 113–114, 114f, 115, 116, 116f, 117, 118, 118f
of sphenoid sinuses, 119, 120f
Wegener's granulomatosis
inner ear in, 1210
orbital, 592f, 601, 602f
pediatric, 1570
sinonasal, 242, 244f
Werner syndrome, 2285
Wharton's duct
on sialography, 2016, 2017
structure of opening of, 2064f
Whitnall's ligament, 539
Wildervanck syndrome, 1113t
Wilms' tumor, 2287
Wiskott-Aldrich syndrome, sinusitis in, 256
Wiskott-Aldrich-Huntley syndrome. *See* Wiskott-Aldrich syndrome.
Wooden foreign bodies, intraorbital, 517
Working Formulation, 1907t
Worth's syndrome, of temporal bone, 1267
WT-1/WT-2 genes, 2287

X

Xanthogranulomas
juvenile, ocular, 497, 497f
necrobiotic, orbital, 610
Xanthomas
of petrous apex, 1351–1352
of petrous bone, of temporal bone, 1339, 1341f
Xanthomatosis. *See* Cholesterol granulomas (cysts).

X-linked progressive mixed hearing loss, 1111t, 1132, 1139f–1141f

Y

Yaws, syphilis versus, 236
Yellow nail syndrome, sinusitis in, 256
Yellow nails-bronchiectasis-lymphedema syndrome. *See* Yellow nail syndrome.
Young's syndrome, with sinusitis, 253

Z

Zenker's diverticulum, 1513, 1514f, 1683–1684, 1685f, 1686f, 2208, 2210, 2211f
  swallowing and, 1746, 1746f
ZIC2 gene, holoprosencephaly and, 54
Zygoma, on plain films, 109f, 115f, 118, 118f, 121, 121f
Zygomatic arch, 135f, 142f, 1796f, 1797f
  fractures of, 388, 390f, 391f
  on plain films, 109f, 118, 118f
Zygomatic bone, 140f
  fractures of, 385, 387t, 387–388, 388f–390f
    on computed tomography, 389f, 390f
    on plain films, 388f
  on CT surface reconstruction, 1096f
Zygomatic nerve, 1782
  perineural tumor spread involving, 868, 870f
Zygomatic process
  on CT surface reconstruction, 1096f
  on plain films, 114
Zygomatic recess, 102
  walls of, on plain films, 114, 114f, 115f
Zygomaticofacial nerve, 1782
Zygomaticomandibular fractures, 388
Zygomaticomaxillary fractures, 388
Zygomaticotemporal canal, 140f
Zygomaticotemporal nerve, 1782
Zygomaticotemporal suture, on plain films, 118
Zygomaticus major muscle, 90t, 127, 128f
Zygomaticus minor muscle, 90t, 127, 128f
Zygomaticus muscle, 1797f
Zygomycosis, sinusitis and, 202